ECCOMAS
European Community on
Computational Methods in
Applied Sciences

ECCOMAS
Thematic Conference

COMPDYN 2011

3rd International Conference on
Computational Methods in Structural Dynamics and Earthquake Engineering

PROCEEDINGS

An IACM Special Interest Conference

M. Papadrakakis, M. Fragiadakis and V. Plevris (Eds)

Computational Methods in Structural Dynamics and Earthquake Engineering

Proceedings of the 3rd International Conference on Computational
Methods in Structural Dynamics and Earthquake Engineering
Held in Corfu, Greece
25-28 May 2011

Edited by:

M. Papadrakakis
National Technical University of Athens, Greece

M. Fragiadakis
National Technical University of Athens, Greece

V. Plevris
School of Pedagogical and Technological Education, Greece

A publication of:

Institute of Structural Analysis and Antiseismic Research
School of Civil Engineering
National Technical University of Athens (NTUA)

Computational Methods in Structural Dynamics and Earthquake Engineering
M. Papadrakakis, M. Fragiadakis, V. Plevris (Eds.)

First Edition, February 2012

©The authors

ISBN : **978-960-99994-1-0**

PREFACE

This volume contains the full-length papers presented in the 3rd International Conference on Computational Methods in Structural Dynamics and Earthquake Engineering (COMPDYN 2011) that was held on May 25-28, 2011 on the Corfu island, Greece.

COMPDYN 2011 is one of the thematic Conferences of the European Community on Computational Methods in Applied Sciences (ECCOMAS) and a Special Interest Conference of the International Association for Computational Mechanics (IACM). COMPDYN 2011 has been also promoted by the European Committee on Computational Solid and Structural Mechanics (ECCSM) of ECCOMAS. The purpose of the Conference was to bring together the scientific communities of Computational Mechanics, Structural Dynamics and Earthquake Engineering in an effort to facilitate the exchange of ideas in topics of mutual interests and to serve as a platform for establishing links between research groups with complementary activities.

The editors of this volume would like to thank all authors for their contributions. Special thanks go to the colleagues who contributed to the organization of the Minisymposia and to the reviewers who, with their work, contributed to the scientific quality of this e-book.

M. Papadrakakis
National Technical University of Athens, Greece

M. Fragiadakis
National Technical University of Athens, Greece

V. Plevris
School of Pedagogical and Technological Education, Greece

ACKNOWLEDGEMENTS

The conference organizers acknowledge the support towards the organization of the Computational Methods in Structural Dynamics and Earthquake Engineering to the following organizations:

- European Community on Computational Methods in Applied Sciences, ECCOMAS
- International Association for Computational Mechanics (IACM)
- School of Civil Engineering, National University of Athens
- Greek Association for Computational Mechanics (GRACM)
- European Association for Earthquake Engineering (EAEE)
- John Argyris Foundation
- Attiko Metro S.A., Greece
- Information Technologies & Digital Engineering, Ioannina, Greece
- TWT Science &Innovation, Stuttgart, Germany
- STRUDL Europe
- Earthquake Planning and Protection Organization (OASP), Greece

Plenary Speakers and Invited Session Organizers

We would also like to thank the Plenary and Semi-Plenary Speakers and the Minisymposia Organizers for their help in the setting up of a high standard Scientific Programme.

Plenary Speakers : A. Elnashai, C. Felippa, Th. Hughes, A. Shabana

Semi-Plenary Speakers: O. Allix, T. Burczynski, A. Combescure, F. Filippou, G. Hulbert, J. Ingham, R. Ohayon, K. C. Park, P. Steinmann, K. Tamma, W. A. Wall, Sh. Yoshimura

MS Organizers: Guglielmo S. Aglietti, Antonio Arede, Domenico Asprone, Ivan Au, Ferdinando Auricchio, Alessandro Baratta, Michele Barbato , Rui Carneiro Barros, Svetlana M. Bauer, Michael Beer, Rui Calcada, Adriano Calvi, Alain Combescure, Gian Paolo Cimellaro, Joel P. Conte, Panos Dakoulas, Raimundo Delgado, Pedro Delgado, John Dolbow, Anders Eriksson, Dan Givoli, Isaac Harari, Muneo Hori, Hector Jensen, Boris Jeremic, Andreas Kappos, Spyros Karamanos, Nikos D. Lagaros, Adrian Lew, Dimitrios Lignos, David Littlefield, Giuseppe Carlo Marano, Mikayel Melkumyan, Andrei Metrikine, Chara Ch. Mitropoulou, Michalis Fragiadakis, Makoto Ohsaki, Stavroula Pantazopoulou, Manolis Papadrakakis, Costas Papadimitriou, Vagelis Plevris, Alessandro Reali, Guido De Roeck, Evangelos Sapountzakis, Gerhart Schueller, Geza Seriani, Anastasios Sextos, Stefano Sibilla, Andrei L. Smirnov, Lena Smyrou, Christian Soize, Sergey V. Sorokin, Aram Soroushian, Costas Spyrakos, George Stefanou, Mahdi Taiebat, Yiannis Tsompanakis, Dimitrios Vamvatsikos, Ioannis Vayas, Shinobu Yoshimura, Farzin Zareian

SUMMARY

Minisymposia

CONTENTS

MS 01 Accuracy and Computational Efficiency in Seismic Structural Analysis

MS 02 Advances in Computational Mechanics for Security Applications

MS 03 Advances in Computational Structural Vibrations

MS 04 Advances in Numerical Methods for Linear and Nonlinear Dynamics

MS 06 Balloon Mechanics in Biology and Medicine

MS 07 Computational Methods for Interface Problems

MS 08 Control of Vibrations in Civil Engineering by Passive Active and Semi-Active Devices

MS 09 Dynamic Effects On High-Speed Railway Tracks

MS 10 Dynamic Soil-Structure Interaction

MS 11 Fuzzy Methods in Computational Dynamics

MS 12 Identification Methods in Structural Dynamics

MS 13 Innovative Algorithms for Transient Computations

MS 14 Innovative vs. Conventional Retrofitting of Existing Buildings

MS 15 Linear Wave Propagation in Advanced Elastic Wave Guides

MS 16 Meshless Methods

MS 17 Optimization Methods and Applications in Structural Dynamics and Earthquake Engineering

MS 18 Performance - Based Engineering

MS 19 Progress and Challenges in Spacecraft Structural Dynamics

MS 20 Recent Developments in Assessment and Design of Masonry Structures

MS 21 Reliability of Structural and Mechanical Systems for Uncertain Operating Conditions

MS 22 Resilience Assessment of Communities and Infrastructures

MS 23 Seismic Analysis and Design of Industrial Facilities and Pipelines

MS 24 Seismic Assessment of Heritage Structures and Monuments Through Simulation

MS 25 Seismic Performance Evaluation Under Uncertainty

MS 26 Seismic Safety Assessment of Structures

MS 27 Steel Structures Under Dynamic and Seismic Loading

MS 29 The Stochastic Finite Element Method: Applications To Structural Dynamics

MS 30 The Synchronization Phenomenon in Modern Structural Dynamics: Wind, Flow, Ice and Pedestrian - Induced Vibrations of Structures

MS 31 Uncertainty and Reliability in Computational Structural Dynamics

MS 32 Waves and Computation

MS 33 High-Performance Computing for Structural Mechanics and Earthquake Engineering

MS 34 Information & Communication Technologies in Earthquake Engineering and Structural Dynamics

MS 35 Practical Analytical Methods in Estimation of Engineering Demands of Structural Systems Subjected To Natural and Man-Made Hazards

MS 05 Analysis Methods for the Seismic Design and Assessment of Bridges

Plenary Lecture

RS 01 Numerical Simulation for Structural Dynamics

RS 02 RC Structures

RS 05 FEM: Modelling and Simulation

RS 07 Masonry Structures

RS 08 Soil-Structure Interaction

RS 10 Active - Passive Control

RS 12 Computational Methods in Geotechnical Earthquake Engineering

RS 15 Design Methods Under Dynamic and Seismic Action

RS 18 Repair and Retrofit of Structures

RS 19 Solution Algorithms and Reduced Order Methods

RS 20 Steel Structures

Semi - Plenary Lectures

COMPDYN 2011
III ECCOMAS Thematic Conference on
Computational Methods in Structural Dynamics and Earthquake Engineering
M. Papadrakakis, M. Fragiadakis, V. Plevris (eds.)
Corfu, Greece, 25–28 May 2011

AN EFFICIENT QUADRATURE BEAM MODEL TO SIMULATE INELASTIC SEISMIC BEHAVIOR OF STEEL FRAMES

R. He[1], R. Zhang[1], and H. Zhong[1]

[1] Department of Civil Engineering, Tsinghua University
Beijing 100084, China
e-mail: ruihe@tsinghua.edu.cn

Keywords: Distributed Plasticity, Consistent Mass Matrix, Seismic Time History Analysis, Quadrature Beam Model, Force-based Beam Model.

Abstract. *Developing nonlinear structural models with high accuracy and affordable computing cost is a challenging issue and one of the pressing needs in earthquake engineering. The paper presents a quadrature beam model for distributed plasticity seismic analysis of steel frames. It is based on the newly developed weak-form quadrature element method, in which the variation principle and the differential quadrature analog are combined. One quadrature beam element can simulate a beam-column member with varying cross-section and non-uniformly distributed loads. The formulations of tangent stiffness matrix and consistent mass matrix are derived. The section constitutive relation of a beam-column member is directly derived using fiber model and material properties. Inelastic time history analysis of the LA 3-story moment-resisting steel frame is conducted to demonstrate the accuracy and efficiency of the quadrature beam model. For verification and comparison, the frame is also analyzed using ANSYS with its BEAM188 element and OpenSEES with the force-based beam element. It is shown that: a) by increasing the number of integration points in one element, results of the quadrature beam model are in excellent agreement with those computed by the displacement-based model in ANSYS; b) degrees of the freedom and the CPU time consumption of the quadrature beam model are much lower than those of the displacement-based model; c) the convergence rate of the quadrature beam model is comparable to that of the force-based model, and the time consumption of the quadrature beam model is slightly higher. In contrast to the only available lumped mass matrix of the force-based model, it is easy to acquire consistent mass matrix in the quadrature beam model for inelastic dynamic analysis, highlighting its great potentials in seismic analysis of frames.*

1 INTRODUCTION

Developing nonlinear structural models with high accuracy and affordable computing cost is a challenging issue and one of the pressing needs in earthquake engineering [1]. For inelastic seismic analysis of frame structures, the lumped plasticity model [2] enjoys simplicity and computational efficiency but it cannot simulate the spread of plasticity and its empirical designation of hinge positions and spring properties sometimes leads to unreliable results. The distributed plasticity model is usually regarded to be more accurate.

One way to construct a distributed plasticity model is using displacement-based (DB) finite beam elements. Elements based on cubic [3] and quartic [4] shape functions were previously studied. These elements with only a few internal nodes are insufficient to carry out seismic analysis of frames with one element per member. When using a higher-order nodal element, the whole set of shape functions has to be reformulated when increasing the order and the simple choice of nodal points may yield ill-condition stiffness matrices [5]. The research work extending the p-version element to inelastic analysis of frames has been rather sparse yet.

Another way is using a force-based (FB) beam element, which adopts exact interpolation functions for internal forces and avoids discretization errors accordingly [6-8]. It realizes simulation of a nonlinear frame member with one beam element, leading to lower DOFs. The FB element prevails in earthquake engineering platform OpenSEES [6] for seismic analysis of frames. However, implementation of FB elements in a finite element program suffers some inconvenient procedures when dealing with non-uniformly distributed loads, state determination [7-8], geometrical nonlinearity [9] and consistent mass matrices [10], etc.

In this paper, a new distributed plasticity model, named as quadrature beam (QB) model, is presented for seismic analysis of structures. It is based on the newly developed weak-form quadrature element method, in which the variation principle and the differential quadrature analog are combined. The weak-form quadrature element method has been validated to be accurate and efficient in elastic problems of varying cross sections [11-12]. In this paper, a distributed plasticity QB beam model is formulated. Its consistent mass matrix is given for dynamic analysis. Inelastic time history analysis of the LA 3-story steel frame [13] is conducted as an example. The accuracy, convergence and CPU time consumption of the QB model are evaluated, and compared with those of the DB and FB models. Results indicate that the quadrature beam model is accurate and efficient.

2 DIFFERENTIAL QUADRATURE ANALOGS

The essence of the conventional differential quadrature analog is that the derivative of a function at a grid point is expressed by weighted linear summation of function values at all grid points in the domain of problem [14]. For instance, the first order derivative of a function f with respect to a variable ξ at a grid point $\xi = \xi_i$ is approximated by

$$\left.\frac{\mathrm{d}f}{\mathrm{d}\xi}\right|_{\xi=\xi_i} = \sum_{j=1}^{M} C_{ij}^{(1)} f(\xi_j),\ i = 1, 2, \cdots, M \tag{1}$$

where $C_{ij}^{(1)}$ are the weighting coefficients for first order derivatives, which are only dependent upon the number of grid points M and their explicit expressions are given by [12]

$$C_{ij}^{(1)} = \begin{cases} \dfrac{g'(\xi_i)}{(\xi_i - \xi_j)g'(\xi_j)}, & i \neq j; \\ -\sum\limits_{k=1,k\neq i}^{M} C_{ik}^{(1)}, & i = j; \end{cases} \qquad g(\xi) = \prod_{j=1}^{M} (\xi - \xi_j) \tag{2}$$

For Bernoulli-Euler beam analysis, the C1 continuity at ends of the element requires generalized differential quadrature analogs where the first order derivative of the function at each end is included in approximation. Thus, the *n*th order derivatives is approximated by

$$\left.\frac{\mathrm{d}^n f}{\mathrm{d}\xi^n}\right|_{\xi=\xi_i} = G_{i1}^{(n)} \left.\frac{\mathrm{d}f}{\mathrm{d}\xi}\right|_{\xi=\xi_1} + \sum_{j=1}^{M} G_{i(j+1)}^{(n)} f(\xi_j) + G_{i(M+2)}^{(n)} \left.\frac{\mathrm{d}f}{\mathrm{d}\xi}\right|_{\xi=\xi_\mathrm{M}} \tag{3}$$

where $G_{ij}^{(n)}$ are the weighting coefficients which can be determined by Hermitian interpolation functions, i.e.

$$G_{i1}^{(n)} = h_{11}^{(n)}(\xi_i), \quad G_{i(M+2)}^{(n)} = h_{M1}^{(n)}(\xi_i), \quad G_{i(j+1)}^{(n)} = h_{j0}^{(n)}(\xi_i), \quad j = 1, 2, \cdots, M \tag{4}$$

where Hermitian interpolation functions are given by

$$\begin{aligned} h_{11}(\xi) &= \frac{(\xi - \xi_1)(\xi - \xi_M)}{\xi_1 - \xi_M} l_1(\xi), \\ h_{M1}(\xi) &= \frac{(\xi - \xi_1)(\xi - \xi_M)}{\xi_1 - \xi_M} l_M(\xi), \\ h_{10}(\xi) &= \frac{\xi - \xi_M}{\xi_1 - \xi_M}[1 - (\xi - \xi_1)(l_1'(\xi_1) + \frac{1}{\xi_1 - \xi_M})] l_1(\xi), \\ h_{M0}(\xi) &= \frac{\xi - \xi_1}{\xi_M - \xi_1}[1 - (\xi - \xi_M)(l_M'(\xi_M) + \frac{1}{\xi_M - \xi_1})] l_M(\xi), \\ h_{j0}(\xi) &= \frac{(\xi - \xi_1)(\xi - \xi_M)}{(\xi_j - \xi_1)(\xi_j - \xi_M)} l_j(\xi), \quad j = 2, 3, \cdots, M-1 \end{aligned} \tag{5}$$

with

$$l_j(\xi) = \frac{g(\xi)}{(\xi - \xi_j)g'(\xi_j)} \tag{6}$$

Differential quadrature analogs are characterized by that only the function values and derivatives at grid points are concerned, so approximation of derivatives is direct and efficient.

3 FORMULATION OF THE QUADRATURE BEAM MODEL

3.1 Model and assumptions

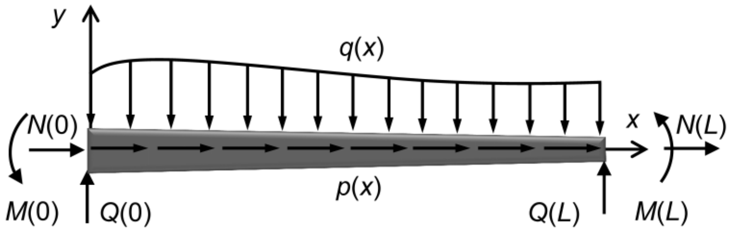

Figure 1: A planar beam model with varying cross-section

A planar beam model with varying cross section is shown in Figure 1. The Bernoulli-Euler beam theory and the hypothesis of plane section hold true. Small deflections and moderate rotation are assumed. The transverse shear deformations are not considered here. In Figure 1, (x, y) is the local coordinate system attached to the beam where x is in the axial direction. L is the beam length. N and Q are axial and shear forces at beam ends, and M is concentrated moments. p and q are non-uniform distributed loads in the x and y directions, respectively. u and v are the translational displacement components along x and y directions, respectively.

For a Bernoulli-Euler beam, the deformations at a certain section x are usually represented by the axial strain at the reference axis ε_x and curvatures κ. And the corresponding section forces are the axial load N and the bending moment M. Generally the section deformation is given in terms of the displacements as

$$\boldsymbol{\varepsilon}(x)=\begin{Bmatrix}\varepsilon_x\\ \kappa\end{Bmatrix}=\begin{Bmatrix}\dfrac{\mathrm{d}u}{\mathrm{d}x}\\ \dfrac{\mathrm{d}^2v}{\mathrm{d}x^2}\end{Bmatrix} \tag{7}$$

For nonlinear problems, an incremental section constitutive relation is usually written, i.e.

$$\delta\mathbf{R}(x)=\mathbf{k}(x)\delta\boldsymbol{\varepsilon}(x) \tag{8}$$

where $\mathbf{R}(x) = [N \;\; M]^{\mathrm{T}}$ is the vector of internal forces at section x. $\mathbf{k}(x)$ is the section stiffness matrix given by

$$\mathbf{k}(x)=\begin{bmatrix}k_{11} & k_{12}\\ k_{21} & k_{22}\end{bmatrix} \tag{9}$$

Once the section deformation $\boldsymbol{\varepsilon}(x)$ is known, the internal forces $\mathbf{R}(x)$ and section stiffness matrix $\mathbf{k}(x)$ can be obtained using either fiber section models or load-deformation relations of sections. Details of inelastic section models can be found in [4] and [8]. Different models at sections in one member can be used to deal with problems of varying cross sections and even varying material properties.

3.2 Variation principles and static equilibrium equations

Inducing a dimensionless coordinate $\xi = 2x/L-1$, the governing equations of the above problem are established from virtual work principle, i.e.

$$\delta U_{\text{int}}^{(\text{e})} + \delta U_{\text{ext}}^{(\text{e})} = 0 \tag{10}$$

where the internal virtual work and the external virtual work are given by

$$\begin{aligned} \delta U_{\text{int}}^{(\text{e})} &= S\int_{-1}^{1} \delta\bar{\boldsymbol{\varepsilon}}^{\text{T}}\mathbf{R}\,\mathrm{d}\xi \\ \delta U_{\text{ext}}^{(\text{e})} &= -S\int_{-1}^{1}\left(p\delta u + q\delta v\right)\mathrm{d}\xi - \left.(N\delta u + Q\delta v + \frac{M}{S}\frac{\mathrm{d}v}{\mathrm{d}\xi})\right|_{\xi=-1} - \left.(N\delta u + Q\delta v + \frac{M}{S}\frac{\mathrm{d}v}{\mathrm{d}\xi})\right|_{\xi=+1} \end{aligned} \tag{11}$$

and $S = L/2$. Lobatto integration rule with M sampling points (see Fig. 2) is used to evaluate the integrals, resulting in

$$S\sum_{i=1}^{M} W_i \delta\bar{\boldsymbol{\varepsilon}}_i^{\text{T}}\mathbf{R}_i = \delta\mathbf{d}^{(\text{e})\text{T}}\mathbf{F}^{(\text{e})} \tag{12}$$

where $\boldsymbol{\varepsilon}_i = \boldsymbol{\varepsilon}(\xi_i)$, $\mathbf{R}_i = \mathbf{R}(\xi_i)$, ξ_i and W_i are the Lobatto sampling points and weighting coefficients [15]. The element nodal displacement vector in Eq. (12) is written as

$$\mathbf{d}^{(\text{e})} = \begin{bmatrix} \mathbf{d}_1^{\text{T}} & \mathbf{d}_M^{\text{T}} & \mathbf{d}_2^{\text{T}} & \cdots & \mathbf{d}_{M-1}^{\text{T}} \end{bmatrix}^{\text{T}} \tag{13}$$

where

$$\mathbf{d}_i^{\text{T}} = \begin{cases} \begin{bmatrix} u_i & v_i & \left(\dfrac{\mathrm{d}v}{\mathrm{d}\xi}\right)_i \end{bmatrix}, & i = 1, M; \\ \begin{bmatrix} u_i & v_i \end{bmatrix}, & i = 2, \ldots, M\text{-}1. \end{cases} \tag{14}$$

Correspondingly, the element nodal force vector in Eq. (12) is expressed by

$$\mathbf{F}^{(\text{e})} = \begin{bmatrix} \mathbf{F}_1^{\text{T}} & \mathbf{F}_M^{\text{T}} & \mathbf{F}_2^{\text{T}} & \cdots & \mathbf{F}_{M-1}^{\text{T}} \end{bmatrix}^{\text{T}} \tag{15}$$

where

$$\mathbf{F}_i^{T} = \begin{cases} \begin{bmatrix} N(\xi_i) + SW_i p(\xi_i) & Q(\xi_i) + SW_i q(\xi_i) & M(\xi_i)/S \end{bmatrix}, & i = 1, M; \\ \begin{bmatrix} SW_i p(\xi_i) & SW_i q(\xi_i) \end{bmatrix}, & i = 2, \ldots, M. \end{cases} \tag{16}$$

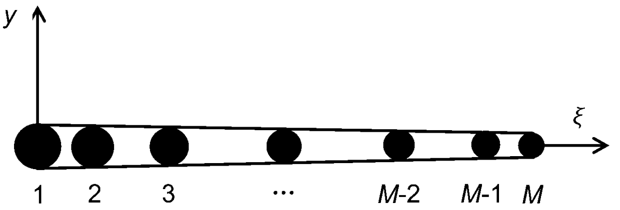

Figure 2: Lobatto points of a QB element

Based on differential quadrature analogs, the derivatives in section deformation vectors at the Lobatto points $\boldsymbol{\varepsilon}_i$ are directly approximated using the nodal displacement vector $\mathbf{d}^{(\text{e})}$. The section deformation vector at Lobatto points i is expressed in terms of ξ coordinate as

$$\boldsymbol{\varepsilon}_i = \mathbf{D}\boldsymbol{\varepsilon}_{0i} \tag{17}$$

where $\mathbf{D} = \mathrm{diag}\left[1/S \quad 1/S^2 \quad 1/S^2\right]$ and

$$\begin{aligned}
&\boldsymbol{\varepsilon}_{0i} = \left[\left(\frac{\mathrm{d}u}{\mathrm{d}\xi}\right)_i \quad \left(\frac{\mathrm{d}^2 v}{\mathrm{d}\xi^2}\right)_i\right]^{\mathrm{T}} = \mathbf{B}_{0i}\mathbf{d}^{(\mathrm{e})}, \quad (i = 1, \cdots, M);\\
&\mathbf{B}_{0i} = \left[\mathbf{B}_{0i,2} \quad \tilde{\mathbf{B}}_{0i,1} \quad \mathbf{B}_{0i,M+1} \quad \tilde{\mathbf{B}}_{0i,M+2} \quad \mathbf{B}_{0i,3} \quad \cdots \quad \mathbf{B}_{0i,M}\right]\\
&\mathbf{B}_{0i,j} = \begin{bmatrix} C^{(1)}_{i(j-1)} & 0 \\ 0 & G^{(2)}_{ij} \end{bmatrix}, \tilde{\mathbf{B}}_{0i,j} = \begin{bmatrix} 0 & 0 \\ 0 & G^{(2)}_{ij} \end{bmatrix}
\end{aligned} \tag{18}$$

After substitution of the section deformation approximation in Eqs. (17-18) into Eq. (12), the incremental-form equilibrium equations are obtained as

$$\delta\mathbf{F}^{(\mathrm{e})} = \mathbf{K}^{(\mathrm{e})}\delta\mathbf{d}^{(e)} \tag{19}$$

where the element tangent stiffness matrix is given by

$$\mathbf{K}^{(\mathrm{e})} = S\sum_{i=1}^{M} W_i \mathbf{B}_{0i}^{\mathrm{T}}\mathbf{D}\mathbf{k}_i\mathbf{D}\mathbf{B}_{0i}, \tag{20}$$

3.3 Consistent mass matrix

The kinematic energy of the beam element is given by

$$\begin{aligned}
T^{(\mathrm{e})} &= \frac{1}{2}\int_0^L \rho\mathrm{A}(x)\left(\dot{u}^2 + \dot{v}^2\right)\mathrm{d}x + \frac{1}{2}\int_0^L \rho\mathrm{I}(x)\left(\frac{\partial\dot{v}}{\partial x}\right)^2 \mathrm{d}x\\
&= \frac{S}{2}\sum_{i=1}^{M} W_i\rho\mathrm{A}_i\left(\dot{u}_i^{\,2} + \dot{v}_i^{\,2}\right) + \frac{1}{2S}\sum_{i=1}^{M} W_i\rho\mathrm{I}_i\left(\frac{\partial\dot{v}}{\partial\xi}\Big|_{\xi=\xi_i}\right)^2
\end{aligned} \tag{21}$$

where $\rho\mathrm{A}(x) = \iint \rho(y,z)\,\mathrm{d}y\mathrm{d}z$ and $\rho\mathrm{I}(x) = \iint \rho(y,z)\,y^2\mathrm{d}y\mathrm{d}z$, respectively. The derivatives in the integral are also approximated using differential quadrature analogs. Therefore, the kinematic energy can be written as

$$T^{(\mathrm{e})} = \frac{1}{2}\dot{\mathbf{d}}^{(\mathrm{e})\mathrm{T}}\mathbf{M}^{(\mathrm{e})}\dot{\mathbf{d}}^{(\mathrm{e})} = \frac{1}{2}\dot{\mathbf{d}}^{(\mathrm{e})\mathrm{T}}\left(\mathbf{M}_0^{(\mathrm{e})} + \mathbf{M}_{\mathrm{R}}^{(\mathrm{e})}\right)\dot{\mathbf{d}}^{(\mathrm{e})} \tag{22}$$

$\mathbf{M}_0^{(\mathrm{e})}$ is the translational component of mass matrix and $\mathbf{M}_{\mathrm{R}}^{(\mathrm{e})}$ is the rotational component of mass matrix, given by

$$\mathbf{M}_0^{(\mathrm{e})} = S\left[\begin{array}{ccc|ccc} W_1\rho \mathrm{A}_1\mathbf{I} & & & & & \\ & \mathbf{0} & & & \mathbf{0} & \\ & & W_M\rho \mathrm{A}_M\mathbf{I} & & & \\ & & \mathbf{0} & & & \\ \hline & & & W_2\rho \mathrm{A}_2\mathbf{I} & & \\ & \mathbf{0} & & & \ddots & \\ & & & & & W_{M\text{-}1}\rho \mathrm{A}_{M\text{-}1}\mathbf{I} \end{array}\right] \tag{23}$$

$$\mathbf{M}_{\mathrm{R}}^{(\mathrm{e})} = \frac{1}{S}\sum_{i=1}^{M} w_i \rho \mathrm{I}_i \mathbf{B}_{\mathrm{G}i}^{\mathrm{T}}\mathbf{B}_{\mathrm{G}i}$$

in which $\mathbf{I}$ is a 2×2 unity matrix, and $\mathbf{B}_{\mathrm{G}i}$ is a vector given by

$$\begin{aligned} \mathbf{B}_{\mathrm{G}i} &= \begin{bmatrix} \mathbf{b}_{\mathrm{G}i,2} & \mathbf{b}_{\mathrm{G}i,1} & \mathbf{b}_{\mathrm{G}i,M+1} & \mathbf{b}_{\mathrm{G}i,M+2} & \mathbf{b}_{\mathrm{G}i,3} & \cdots & \mathbf{b}_{\mathrm{G}i,M} \end{bmatrix} \\ \mathbf{b}_{\mathrm{G}i,j} &= \begin{bmatrix} 0 & G_{ij}^{(1)} \end{bmatrix} \end{aligned} \tag{24}$$

Since the numerical integration scheme and differential quadrature analog in the mass matrix formulation are consistent with those in stiffness matrix, the mass matrix in this section is still called “consistent mass matrix”.

4 ANALYSIS OF LA 3-STORY MOMENT-RESISTING FRAME

Time history analysis of a 3-story moment-resisting steel frame (Figure 3) is presented to verify the QB model. The frame is in the North-South (NS) direction, as a piece of the Los Angeles 3-story model building in the SAC steel project [13]. The material is bilinear kinematic hardening, with the elastic modulus 210, 000MPa, and the hardening modulus 6,300MPa. The yielding stress of the steel is 248MPa for all beams, and 345MPa for all columns. The distributed load on the first and second story beams is 13.90KN/m, while on the third story beams 4.57KN/m. The additional floor mass on the first and second story beams is 1,372Kg/m, while on the third story beams 915Kg/m. The mass of walls is added on the columns, which on the side columns is 1,098Kg/m and on the inner columns is 1,555Kg/m.

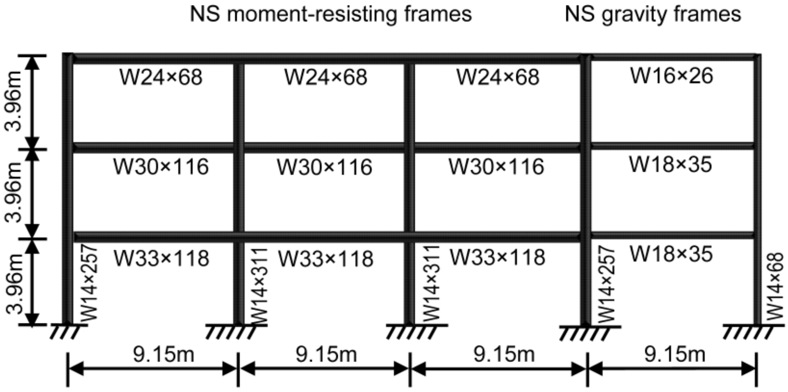

Figure 3: Elevation and member sizes of the LA 3-story Frame.

An acceleration time history of the TAFT earthquake is chosen (Figure 4) and scaled to generate ground motions with the Peak Ground Accelerations (PGAs) 0.10, 0.20, 0.30, 0.40, 0.45, 0.50 and 0.55g respectively. Time interval of the ground motions is 0.005s. Dynamic analysis of the frame is undertaken using the QB model with consistent mass matrix, coded in Fortran. To reduce the computational cost, a Guyan condensation procedure is included to condense the internal DOFs of each QB element. The characteristics of convergence and computational efficiency are studied. Dynamic analysis using the BEAM188 element with consistent mass matrix is conducted in ASNYS [16] for verification. Meantime, comparison is made with the FB beam model in OpenSEES (v2.2.0), in which only lumped mass matrix is available for inelastic dynamic analysis of frames. All computations were performed on a laptop computer with a 5-core processor @2.65GHz and 4.00G memory. The convergence criterion of Newton-Raphson iteration process is set as that the Euclid norm of residual forces is controlled to be less than 10^{-6}.

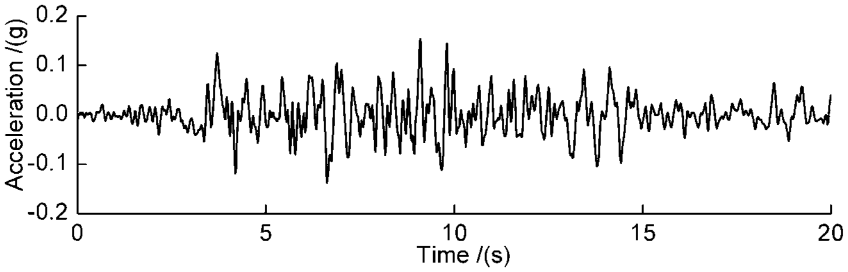

Figure 4: An acceleration time history of the TAFT earthquake.

Figures 5 and 6 show the displacement responses and acceleration responses at the roof for the three models. In QB and FB models, the number of integration points in one element is chosen as M = 10. In ANSYS, 10 four-node BEAM188 elements are used to simulate one frame member, and shear deformation is adjusted to be negligible. The QB results agree with ANSYS results, and are slightly different from the FB results in OpenSEES.

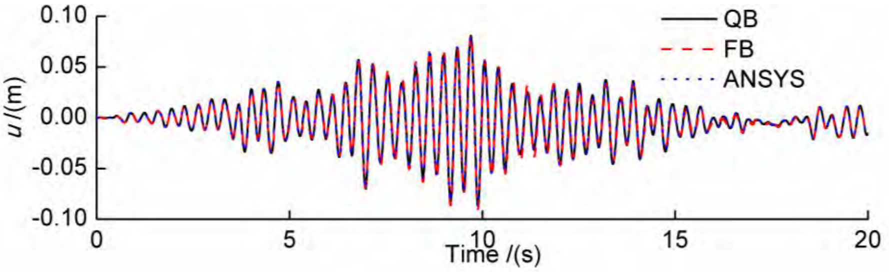

Figure 5: Time histories of the roof displacement responses for the three models, PGA=0.50g.

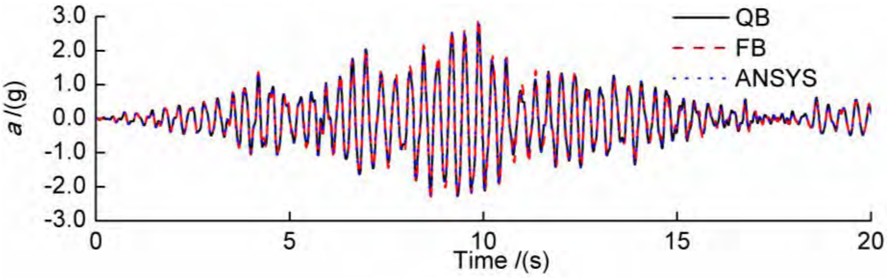

Figure 6: Time histories of the roof acceleration responses for the three models, PGA=0.50g.

The peak values of the responses are illustrated in Figures 7 and 8. Referring to the ANSYS results, the QB model is accurate in the inelastic dynamic analysis. The FB results have relative errors about 5% to 10%. It is believed that the lumped mass matrix of the FB model reduces the accuracy.

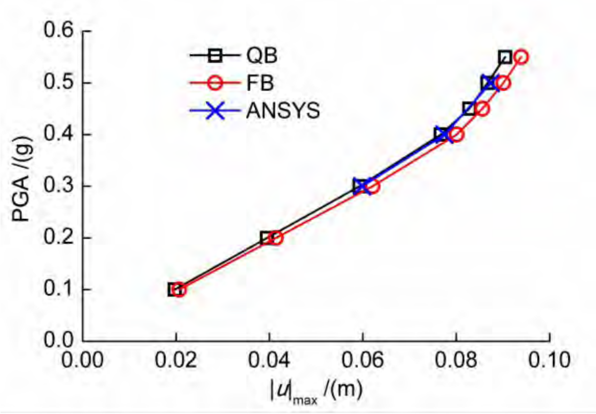

Figure 7: Peak values of the roof displacement responses for different PGAs.

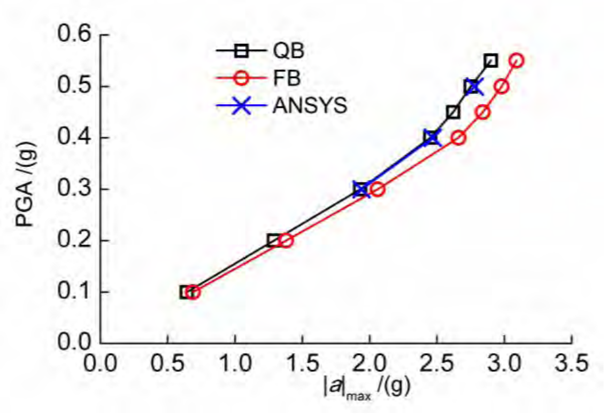

Figure 8: Peak values of the roof acceleration responses for different PGAs.

Figure 9 gives the convergence of the peak response $|u|_{\max}$ of the QB and FB models under PGA=0.50g for different number of integration points *M*. In OpenSEES, *M* is restricted to be not greater than 10. Results of both models can converge by increasing *M*, and their convergence rates are similar.

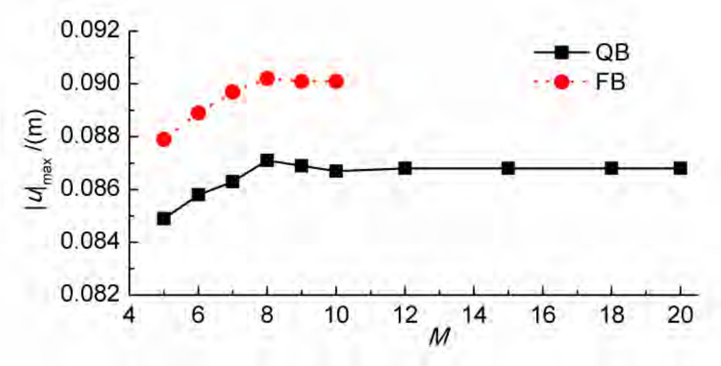

Figure 9: Peak values of the roof displacement responses for different *M*, PGA = 0.50g.

The CPU time consumptions of the three models are listed in the Tables 1 and 2. The commercial code ANSYS is versatile and accurate, but its computational cost is much greater for seismic analysis of an entire structure. The computational cost of the QB model is close to that of the FB model in OpenSEES. When increasing the number of integration points *M*, the CPU time consumption of the QB model increases almost linearly. The quadrature beam model is efficient and suitable for seismic analysis of frames.

PGA /(g)	t_{QB} /(s)	$t_{OpenSEES}$ /(s)	t_{ANSYS} /(h)
0.10	40.0	33.5	—
0.20	40.1	33.6	—
0.30	40.3	33.2	12.5
0.40	47.9	33.8	13.0

0.45	49.4	34.8	—
0.50	54.2	35.5	13.5
0.55	59.8	36.0	—

Table 1: CPU time consumptions for different PGAs.

M	t_{QB} /(s)	t_{OpenSEES} /(s)
5	25.1	18.2
6	31.8	21.5
7	35.5	24.5
8	41.4	27.2
9	48.9	30.8
10	54.2	35.5
15	83.5	—
20	120.5	—

Table 2: CPU time consumptions for different *M*.

5 CONCLUSIONS

- A distributed-plasticity quadrature beam (QB) model with consistent mass matrix is formulated in this paper. For inelastic dynamic seismic analysis of frames, one member is simulated by one QB element.
- The accuracy and the convergence of the QB model are verified. Results of the QB model are in excellent agreement with those of the DB model in ANSYS, but the CPU time consumption is much lower. The convergence rates of the QB and the FB models are comparable, and the time consumption of the QB model is slightly higher. In contrast to the only available lumped mass matrix of the FB model, however, the consistent mass matrix of the QB model makes it advantageous for inelastic dynamic analysis.
- The quadrature beam model is accurate and efficient, highlighting its great potentials in seismic analysis of frames.

ACKNOWLEDGEMENT

This present work was undertaken under the support of the National Natural Science Foundation of China (No. 50778104) and China Postdoctoral Science Foundation (No. 20100480320).

REFERENCES

[1] M. Ohsaki, T. Miyamura and M. Kohiyama *et al*, High-precision finite element analysis of elasto-plastic dynamic responses of super-high-rise steel frames. *Earthquake Engineering & Structural Dynamics*, **38**(5), 635-654, 2009.

[2] D.W. White, Plastic hinge methods for advanced analysis of steel frames. *Journal of Construction Steel Research*, **24**(2), 121–52, 1993.

[3] A. R. Mari, A. C. Scordelis, Nonlinear geometric, material and time dependent analysis of three-dimensional reinforced and prestressed concrete frames. *Report UCB/SESM-84/12*, U. C. Berkeley, 1984.

[4] B. A. Izzuddin, A. Siyam, Smith D L, An efficient beam-column formulation for 3D reinforced concrete frames. *Computers & Structures*, **80**, 659-676, 2002.

[5] P. Šolín, K. Segeth, I. Doležel, *Higher-order finite element methods*. Chapman & Hall/CRC, USA, 2003.

[6] S. Mazzoni, F. McKenna, M. H. Scott, G. L. Fenves, *OPENSEES user's manual*. PEER, U. C. Berkeley, 2007.

[7] V. Ciampi, L. Carlesimo, A nonlinear beam element for seismic analysis of structures. *8th European Conference on Earthquake Engineering*, Laboratorio Nacional de Engenharia Civil, Lisbon, 1986.

[8] E. Spacone, F. C. Filippou, F. F. Taucer, Fibre beam-column model for non-linear analysis of R/C frames: part I. Formulation. *Earthquake Engineering & Structural Dynamics*, **25**(7), 711–725, 1996.

[9] A. Neuenhofer, F. C. Filippou, Geometrically nonlinear force-based frame finite element. *Journal of Structural Engineering ASCE*, **124**(6), 704-711, 1998.

[10] C. Molins, P. Roca, A. H. Barbat, Force-based linear dynamic analysis of complex structures with curved-3d beams. *Earthquake Engineering and Structural Dynamics*, **27**, 731-747, 1998.

[11] H. Zhong, M. Gao, Quadrature element analysis of planar frameworks. *Archive of Applied Mechanics*, **80**, 1391-1405, 2010.

[12] H. Zhong, Y. Wang, Weak form quadrature element analysis of Bickford beams. *European Journal of Mechanics A/Solids*, **29** (5), 851-858, 2010.

[13] FEMA-355C. *State of the art report on systems performance of steel moment frames subjected to earthquake ground shaking*. Federal Emergency Management Agency, 2000.

[14] R. E. Bellman, J. Casti, Differential quadrature and long term integration. *Journal of Mathematical Analysis and Applications*, **34**, 235-238, 1971.

[15] P. I. Davis, P. Rabinowitz, *Methods of Numerical Integration (2nd edition)*. Academic Press, Orlando, 1984.

[16] *ANSYS User's Manual, Version 8.0,* Swanson Analysis Systems Inc. (SASI), Houston, PA, 2004.

COMPDYN 2011
3rd ECCOMAS Thematic Conference on
Computational Methods in Structural Dynamics and Earthquake Engineering
M. Papadrakakis, M. Fragiadakis, V. Plevris (eds.)
Corfu, Greece, 25–28 May 2011

ON THE PERFORMANCE OF A TECHNIQUE FOR MORE EFFICIENT TIME INTEGRATION WHEN APPLIED TO BRIDGE STRUCTURES SEISMIC ANALYSIS

A. Soroushian[1], M. Hosseini[2], and A. Vasseghi[3]

[1] Structural Engineering Research Center,
IIEES, Farmaniyeh, North Dibaji, No. 21, Tehran 19395, Iran,
e-mail: a.soroushian@iiees.ac.ir

[2] Structural Engineering Research Center,
IIEES, Farmaniyeh, North Dibaji, No. 21, Tehran 19395, Iran,
e-mail: hosseini@iiees.ac.ir

[3] Structural Engineering Research Center,
IIEES, Farmaniyeh, North Dibaji, No. 21, Tehran 19395, Iran,
e-mail: vasseghi@iiees.ac.ir

Keywords: Seismic analysis, Bridge, Time integration, Accuracy, Computational cost; Convergence.

Abstract. *The true behavior of structural systems is dynamic, that in many cases can not be simplified to static. The most versatile tool for structural dynamic analyses, is time integration, and, hence, under special attention in the seismic analyses of structural systems, becoming more complicated everyday. Nevertheless, the responses of time integration are inexact and generally being obtained after considerable computational cost. Considering these, besides the digitized nature of ground strong motion records, a technique for considerably reducing the computational cost with small loss of accuracy is recently proposed. With attention to the notion of convergence and its role in numerical analyses, the technique replaces seismic records, with records, digitized at larger steps. The good performance of the technique is displayed in implementation in simple and complicated structural systems analyses. In continuation of the studies, the objective, in this paper, is to examine whether we can successfully implement the technique in time integration of bridges structural systems. The technique is briefly reviewed, and after introdcung a bridge structural system, designed according to the Iranian practice, the finite element model of the system is time integrated, once ordinarily, and then again, after implementing the technique. The numerical results evidence the good performance of the technique, and the essentiality of further inverstigations.*

1 INTRODUCTION

The true behavior of structural systems is dynamic, that, when subjected to severe seismic excitations, cannot be simplified to static. In order to study the dynamic behaviors, the broadly accepted approach is to discretize the structural and mathematical models in space and arriving at the semi-discretied model below:

$$
\begin{gathered}
\mathbf{M}\,\ddot{\mathbf{u}} + \mathbf{f}_{\text{int}} = \mathbf{f}(t) \\
\text{Initial Conditions : } \left| \begin{array}{l} \mathbf{u}(t=0) = \mathbf{u}_0 \\ \dot{\mathbf{u}}(t=0) = \dot{\mathbf{u}}_0 \\ \mathbf{f}_{\text{int}}(t=0) = \mathbf{f}_{\text{int}_0} \end{array} \right. \\
\text{Additional Constraints : } \mathbf{Q} \\
0 \le t < t_{end}
\end{gathered}
\tag{1}
$$

analyze equations (1) with an appropriate method [1-4]. In equations (1), t and t_{end} imply the time and the duration of the dynamic behavior, $\mathbf{M}$ is the mass matrix, $\mathbf{f}_{\text{int}}$ and $\mathbf{f}(t)$ stand for the vectors of internal force and excitation, $\mathbf{u}$, $\dot{\mathbf{u}}$, and $\ddot{\mathbf{u}}$ denote the unknown vectors of displacement, velocity, and acceleration, $\mathbf{u}_0$, $\dot{\mathbf{u}}_0$, and $\mathbf{f}_{\text{int}_0}$, representing the vectors of displacements, velocities, and internal forces at $t = 0$, together, define the initial status of the model (regarding the essentiality of considering $\mathbf{f}_{\text{int}_0}$ in equations (1), also, see [4]), and $\mathbf{Q}$ indicates some restricting conditions, e.g. additional constraints in problems involved in impact or elastic-plastic behavior [5,6]. The most versatile method to analyze equations (1) is direct time integration [7,8]. However, especially, for nonlinear multi-degree-of-freedom problems, the formulations of time integration methods are inexact and hence the obtained responses are approximations [9,10]. This inexactness, when considered together with the step-by-step nature of time integration methods, summarized in marching throughout the integration interval, computing the responses at distinct time stations from the responses at previous stations, consecutively, (see Figure 1), implies the importance of integration step sizes, in time integration analyses (specially, regarding the accuracy and computational cost of the analysis). Considering Δt, as a positive definite parameter, scaling (linearly controlling) the size of integration steps, throughout t $0 \le t < t_{end}$ [11], one of the broadly accepted comments, for the selection of Δt, is as noted below [11-13]:

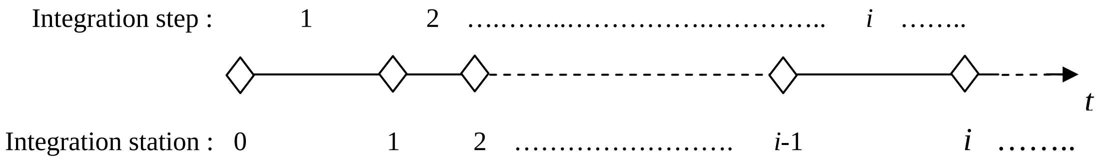

Figure 1: Typical arrangement of time steps and time stations in time integration analyses.

$$
\Delta t = \text{Min}\left(h_s, \frac{T}{10}, {}_f\Delta t \right) \tag{2}
$$

In equation (2), T is the smallest dominant period in the response, in general, approximated with the smallest natural period of the system at $t = 0$, likely effectual in the response, h_s is the largest value of the integration step, providing numerically stable responses ($h_s = \infty$ for unconditionally stable methods), and ${}_f\Delta t$ is the digitization step size for excitations available as digitized records (for other excitations ${}_f\Delta t = \infty$). When, ${}_f\Delta t$ dominates equation (2), i.e.

$$\Delta t = {}_f\Delta t < \mathrm{Min}\left(h_s , \frac{T}{10} \right) \tag{3}$$

Δt is to be set smaller than required for accuracy (see the inequality in equation (3), merely because of the size of digitization steps, ${}_f\Delta t$. This leads to additional computational cost. With the aim of decreasing this computational cost, a technique is recently proposed [11].

The technique changes ${}_f\Delta t$ to the larger value ${}_f\Delta t'$,

$${}_f\Delta t' = n\ {}_f\Delta t \cong \mathrm{Min}\left(h_s , \frac{T}{10} \right) \quad , \quad n = 1, 2, 3 \ldots \tag{4}$$

($n = 1$ implies the limiting case, when the inequality in equation (3) is being replaced with equality), and replaces the excitation with a new excitation, digitized at steps equal to ${}_f\Delta t'$, such that in time integration analysis of the system subjected to the new excitation,

$$\Delta t = {}_f\Delta t' \cong \mathrm{Min}\left(h_s , \frac{T}{10} \right) \tag{5}$$

and meanwhile the replacement of the excitation preserves responses convergence and the rate of convergence. (Convergence is the most important essentiality for all approximate analyses [14,15].) The technique is already successfully implemented in the analysis of some simple structural systems [11], i.e. a tall building [16], a fuel storage tank [17], and a silo [18], and also subjected to further theoretical investigation [19]. In continuation of the carried out investigations, this paper presents a study on the performance of the technique, when applied to the analysis of a traditionally designed bridge against a ground strong motion.

A brief review of the recent technique is presented in Section 2, after which, a bridge structural system is introduced and examined for the performance of the technique in Section 3, and finally, with a set of conclusions and guidelines for future research, the paper is ended in Section 4.

2 THE RECENT TECHNIQUE IN BRIEF

In order to replace the digitized excitation with a new excitation digitized at larger steps, such that the responses rate of convergence (generally two) [9,10,20] is preserved, a theory is set [11,21,22] and formulated in view of four assumptions. In brief, provided the assumptions below (implied in Figure 2):

1- The excitation steps, ${}_f\Delta t_i\ i = 1,2,\ldots$, are equally sized,

$$\forall\, i, j \quad {}_f\Delta t_i = {}_f\Delta t_j = {}_f\Delta t > 0 \tag{6}$$

2- The integration steps, $\Delta t_i\ i = 1,2,\ldots$, are equally sized,

$$\forall\, i, j \quad \Delta t_i = \Delta t_j = \Delta t > 0 \tag{7}$$

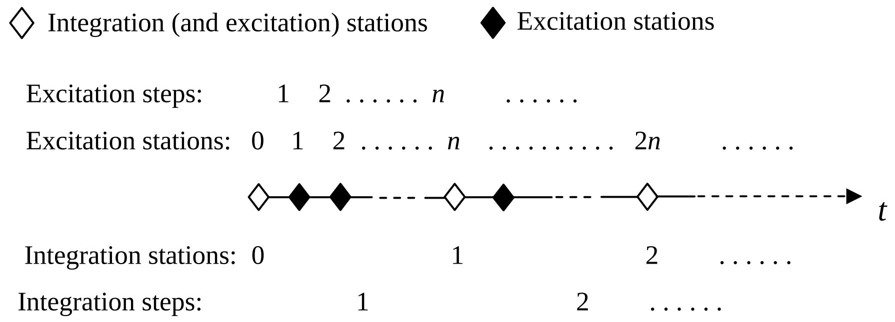

Figure 2: Typical distribution of excitation and integration stations in the recent technique [11].

3- The excitation steps are embedded by the integration steps (the first time station, i.e. t_0, is a station for both excitation and integration),

$$\exists \quad n \in Z^{+} \qquad \frac{\Delta t}{{}_f\Delta t} = n < \infty \tag{8}$$

4- The $\mathbf{f}(t)$ in equations (1) is a digitized representation of an actual excitation, $\mathbf{g}(t)$, smooth [23] with respect to time, i.e.,

$$\begin{aligned}
&\mathbf{f}(t) = \mathbf{g}(t)\delta(t-\alpha_i) \\
&\mathbf{g}(t): \text{ smooth with respect to time} \\
&\alpha_i = i\,{}_f\Delta t \ \ , \ \ i = 0,1,2,\ldots \\
&\delta(t-\alpha_i) = \begin{cases} 1 & t = \alpha_i \\ 0 & t \neq \alpha_i \end{cases}
\end{aligned} \tag{9}$$

(and hence, the temporal derivatives of $\mathbf{f}(t)$, though rarely known, exist).

we can replace the excitation in equations (1), **f**, with the new excitation, $\tilde{\mathbf{f}}$, digitized at steps equal to $n\,{}_f\Delta t$, according to:

$$\begin{aligned}
t_i = 0: &\qquad \tilde{\mathbf{f}}_i = \mathbf{f}(t_i), \\
0 < t_i < t_{end}: &\qquad \tilde{\mathbf{f}}_i = \frac{1}{2}\mathbf{f}(t_i) + \frac{1}{4n'}\sum_{k=1}^{n'}\left[\mathbf{f}\left(t_{i+k/n}\right) + \mathbf{f}\left(t_{i-k/n}\right)\right], \\
t_i = t_{end}: &\qquad \tilde{\mathbf{f}}_i = \mathbf{f}(t_i),
\end{aligned} \tag{10}$$

where,

$$\begin{aligned}
t = \Delta t \ : &\qquad n' = n-1 \\
\Delta t < t < t_{end} - \Delta t \ : &\qquad n' = \begin{cases} \dfrac{n}{2} & n = 2j \quad j \in Z^{+} \\ \dfrac{n-1}{2} & n = 2j+1 \quad j \in Z^{+} \end{cases} \\
t = \Delta t \ : &\qquad n' = n-1
\end{aligned} \tag{11}$$

and Δt and n ($n \in Z^{+}$) are the largest values satisfying

$$\Delta t = n_f \Delta t \le \mathrm{Min}\left(h_s , \frac{T}{10} \right) \le t_{end} \qquad (12)$$

with generally small loss of accuracy in time integration. Since, the new excitation, $\tilde{\mathbf{f}}$, is digitized at steps equal to $n_f \Delta t$, when considered instead of the original excitation, can lead to a reduction in computational cost (including the time spent and memory essential for the analysis), A_C , about and not more than

$$A_C = 100\left(\frac{n-1}{n} \right)\% \qquad (13)$$

3 NUMERICAL STUDY

Consider the structural system introduced in Figure 3. The structure is a three span precast concrete girder bridge with equal spans of 30 meters. The superstructure is 12 meters wide and carries two traffic lanes. The superstructure consists of a 25 centimeters thick concrete slab and five reinforced concrete girders. The girders are connected by transverse diaphragm and at each end simply supported on 400×400 millimeters steel reinforced elastomeric bearings. Each bearing consists of two exterior layers with 6 millimeters thickness, four interior layers with 12 millimeters thickness, and five 2 millimeters steel reinforcement. The stiffness properties of the bearings are as noted below:

$$\begin{aligned} &\text{Vertical Stiffness}: \quad 3227000 \quad KN/m \\ &\text{Shear Stiffness}: \quad 5220 \quad KN/m \\ &\text{Rotational Stiffness}: \quad 1420 \quad KNm/Rad \\ &\text{Torsional Stiffness}: \quad 118 \quad KNm/Rad \end{aligned} \qquad (14)$$

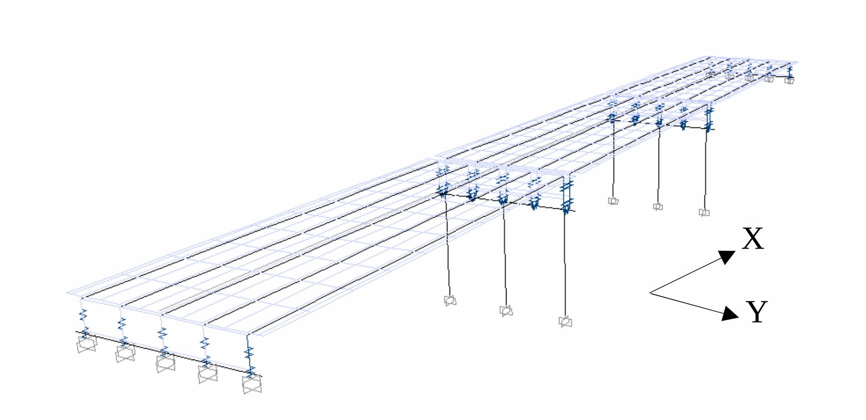

Figure 3: The bridge structural model considered in the numerical study in this paper.

The substructure consists of two closed end seat type abutments and two interior bents. Each bent consists of three concrete columns, each with 7.75 meters height and 1.2 meters diameter. The abutments are assumed to be rigid. The finite elements model, in Figure 3, is consisted of frame elements for the girders and shell elements for the superstructure slab. The shell elements are vertically offset to locate them at their actual position, and the columns are modeled using frame elements, and are assumed fixed at pile cap interface. The elastomeric bearings are modeled by spring elements with appropriate stiffness properties for all six degrees of freedoms (see equations (14)). The model is subjected to the excitation in Figure 4, once ap

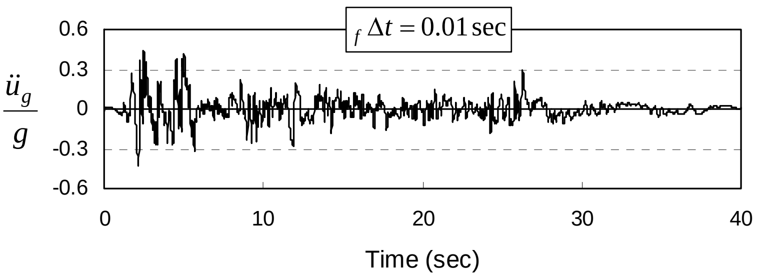

Figure 4: The digitized ground strong motion applied to the structural model in Figure 3 once in the *x* and then in the *y* direction.

plied in the *x* direction and then again in the *y* direction (see Figure 1, where, $\ddot{u}_g$ and g respectively stand for the ground acceleration and the constant of gravity, i.e. $9.81\ m/\mathrm{sec}^2$). The excitation step size, ${}_f\Delta t$, equals $0.01\,\mathrm{sec}$. The geometry and structural design of the bridge model is according to the practice, conventional in Iran [24-26].

In view of the approximate response partially reported in Figure 5, a good selection for T is as noted below:

$$T \cong 0.25 \tag{15}$$

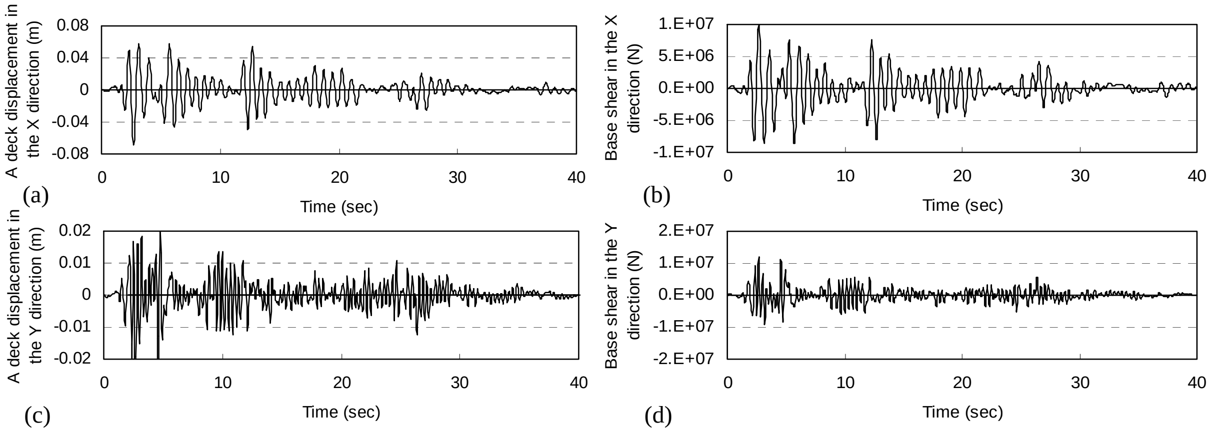

(a) (b) (c) (d)

Figure 5: The approximate responses when applying the excitation to the structural model in Figure 3: (a) *x* direction, a deck displacement, (b) *x* direction, base shear, (c) *y* direction, a deck displacement, (d) *y* direction, base shear.

and hence, with attention to equations (4) and (12),

$$n = 2 \tag{16}$$

is an appropriate selection for the n in equations (11) and (12). Nevertheless, for a broader study, the cases:

$$n = 2, 4, 8, 20 \tag{17}$$

are also considered in time integration analyses with the Newmark average acceleration method [27]. The accuracies are compared in Figures 6 and 7. Considering the time spent and CPU memory essential for the computation, the computational costs are reported in Table 1, and, for the sake of completion, the original and new excitation records are reported in Figure 8. Figures 6 and 7 and Table 1 clearly display the good performance of the recent technique and imply that the technique has a good chance to reduce the computational costs in analyses of bridges seismic behaviors by time integration.

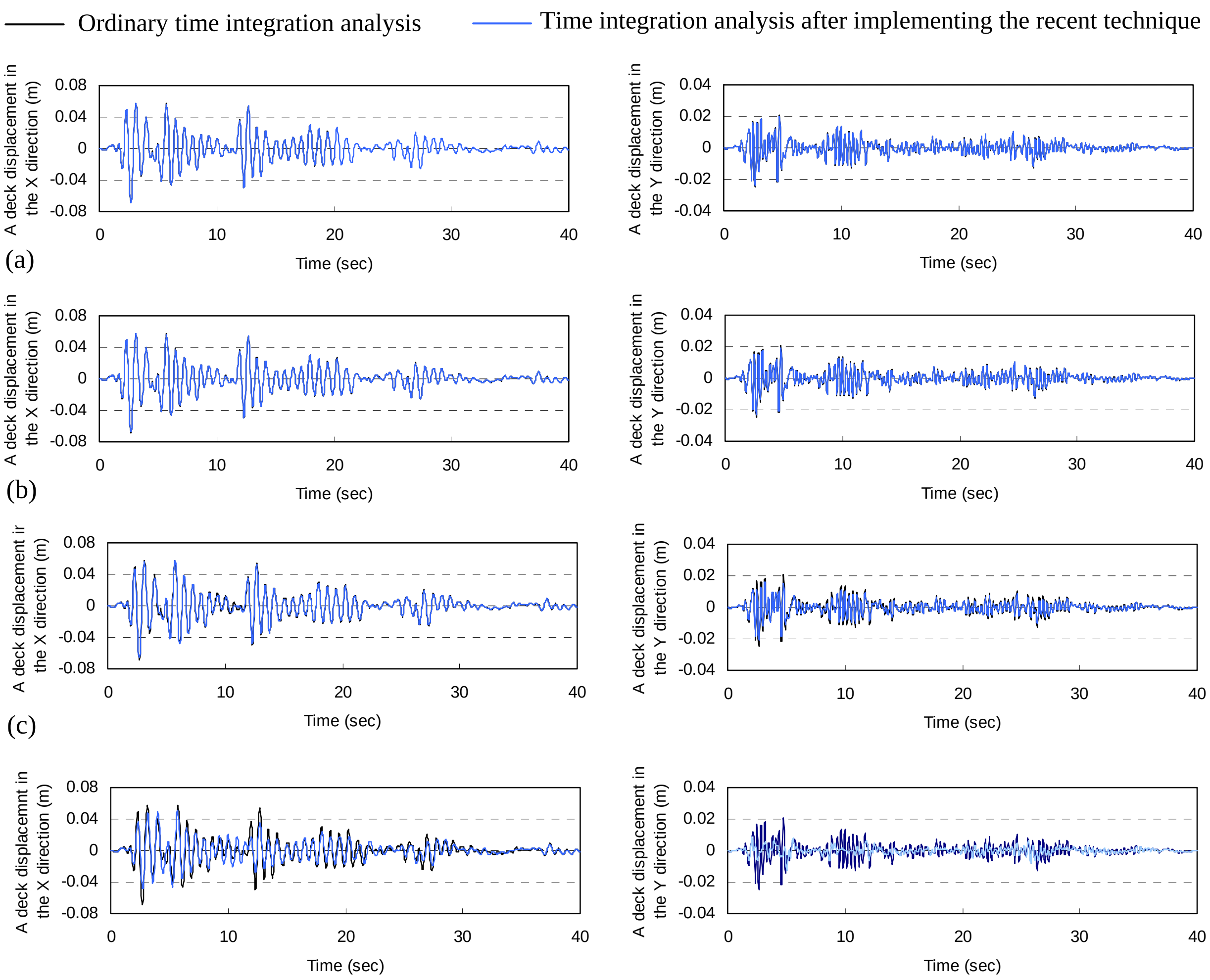

Figure 6: The performance of the recent technique when implemented in direct time integration analysis of the structural system introduced in Figures 3 and 4 and equations (14), by the average acceleration Newmark method [27], for a deck displacement: (a) $n = 2$, (b) $n = 4$, (c) $n = 8$, (d) $n = 20$.

The bridge structural system and excitation, considered in the numerical study, presented above, are common in Iran. Nevertheless, since, in view of the explanations in Section 2 and specifically equations (10)-(13), the performance of the technique might be different for different values of *n*, and *n* depends on both the structural system and the excitation, further study regarding the sensitivities is essential. Meanwhile, from the point of view of the analysis method, specifically, when considering behaviors against severe earthquakes, it is essential to study the performance of the technique, in presence of nonlinearities, considering a variety of integration methods, and different iterative nonlinearity solution methods.

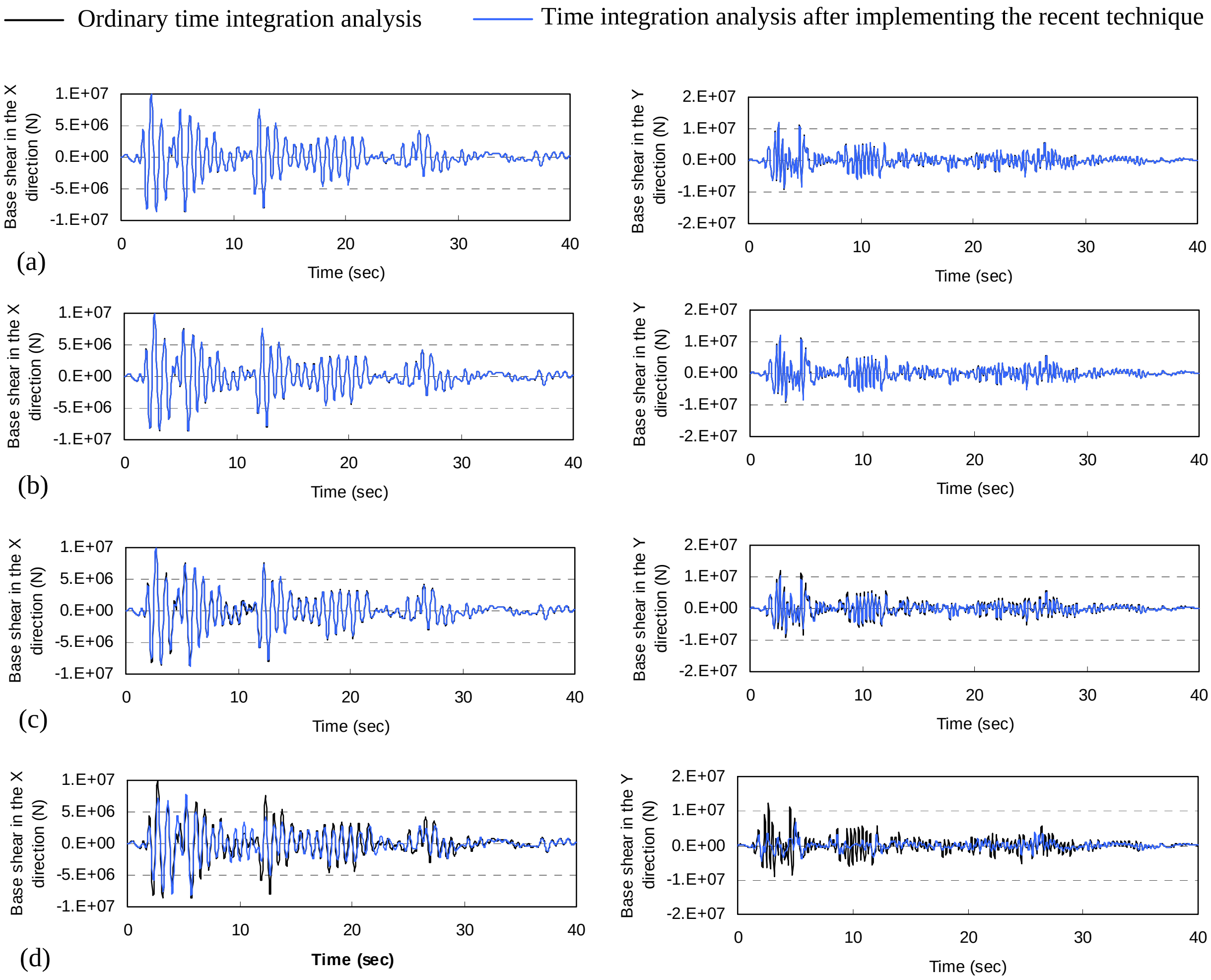

Figure 7: The performance of the recent technique when implemented in direct time integration analysis of the structural system introduced in Figures 3 and 4 and equations (14), by the average acceleration Newmark method [27], for base shear: (a) $n = 2$, (b) $n = 4$, (c) $n = 8$, (d) $n = 20$.

Ordinary	$n = 2$	$n = 4$	$n = 8$	$n = 20$
100	50	25	12.5	5

Table 1: An approximate study on the computational costs, $100 - A_C$, when implementing the recent technique [11], compared to the ordinary analysis, with computational cost 100.

4 CONCLUSIONS

The performance of a new technique proposed for reducing the computational cost of seismic analysis by time integration is examined considering a bridge structural system common in Iranian practice. The numerical results display that, for the bridge structural system studied here, considerable reduction of computational cost is attained and the loss of accuracy is even less than expected. Further study in this regard, considering different bridge structural systems, different ground strong motions, different integration methods, and different nonlinearity solution methods is suggested for further research.

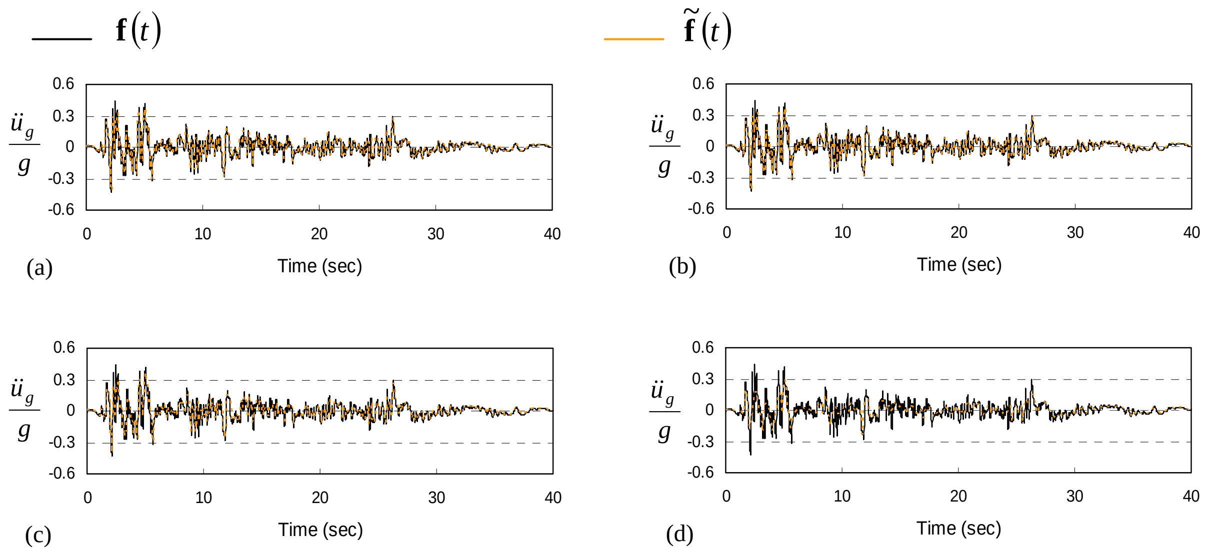

Figure 8: The excitations, $\tilde{\mathbf{f}}(t)$, when implementing the recent technique in the numerical study considering: (a) $n=2$, (b) $n=4$, (c) $n=8$, (d) $n=20$.

REFERENCES

[1] J. Henrych, *Finite Models and Methods of Dynamics in Structures*. Elsevier, 1990.

[2] J. Argyris, J.P. Mlejnek, *Dynamics of structures*. Elsevier, 1991.

[3] T. Belytschko, W.K. Liu, B. Moran, *Non-linear Finite Elements for Continua and Structures*. John Wiley & Sons, 2000.

[4] A. Soroushian, *New methods to maintain responses' convergence and control responses' errors in the analysis of nonlinear dynamic models of structural systems, Ph.D. Thesis*. University of Tehran, 2003 (in Persian).

[5] P. Wriggers, *Computational contact mechanics*. John Wiley & Sons, 2002.

[6] T.J.R. Hughes, K.S. Pister, R.L. Taylor, Explicit–explicit finite elements in nonlinear transient analysis. *Computer Methods in Applied Mechanics and Engineering*, **17/18**:159–182, 1979.

[7] A.K. Chopra, *Dynamics of Structures: Theory and Application to Earthquake Engineering, 1st Edition*. Prentice-Hall, 1995.

[8] J. Chung, G.M. Hulbert, A family of single-step Houbolt time integration algorithms for structural dynamics. *Computer methods in applied mechanics and engineering*, **118**: 1-11, 1994.

[9] T. Belytschko, T.J.R. Hughes, *Computational methods for transient analysis*. Elsevier, 1983.

[10] W.L. Wood, *Practical time stepping schemes*. Oxford, 1990.

[11] A. Soroushian, A technique for time integration analysis with steps larger than the excitation steps. *Communications in Numerical Methods in Engineering*, **24**: 2087-2111, 2008.

[12] K.J. Bathe, *Finite element procedures, 2nd Edition*. Prentice-Hall, 1996.

[13] R.W. Clough, J. Penzien, *Dynamics of structures, 2nd Edition*. McGraw-Hill, 1993.

[14] P. Henrici, *Discrete variable methods in ordinary differential equations*. Prentice-Hall, 1962.

[15] J.C. Strikwerda, *Finite difference schemes and partial differential equations*. Wadsworth & Books/Cole, 1989.

[16] A. Soroushian, A. Aziminejad, More efficient seismic analysis of tall buildings by implementing a recently proposed technique. A. Tasnimi ed., *6th International Conference on Seismology and Earthquake Engineering (SEE6)*, Tehran, Iran, May 16-18, 2011.

[17] A. Soroushian, A. Saaed, M. Arghavani, M.Rajabi, M.M. Sharifpour, Less computational costs in the analysis of reservoirs seismic behaviors by time integration. B. Marvalova ed., *10th Biennial International Conference on Vibration Problems*, Technical University of Liberec, Prague, Czech Republic, September 5-8, 2011.

[18] F. Nateghi, M. Yakhchalian, On less computational costs for the analysis of silos seismic behaviors by time integration. M. Papadrakakis, M. Fragiadakis, V. Plevris eds. *3rd ECCOMAS Thematic Conference on Computational Methods in Structural Dynamics and Earthquake Engineering*, Corfu, Greece, May 25-28, 2011.

[19] A. Soroushian, A comparison between two methods for disregarding excitation steps in seismic analyses. A. Tasnimi ed., *6th International Conference on Seismology and Earthquake Engineering (SEE6)*, Tehran, Iran, May 16-18, 2011.

[20] T.J.R. Hughes, *The finite element method: linear static and dynamic finite element analysis*. Prentice-Hall, 1987.

[21] S.N. Penry, W.L.Wood, Comparison of some single-step methods for the numerical solution of the structural dynamic equation. *International Journal of Numerical Methods in Engineering*, **21**: 1941-1955, 1985.

[22] X. Zhou, K.K. Tamma, Design, analysis, and synthesis of generalized single step single solve and optimal algorithms for structural dynamics. *International Journal of Numerical Methods in Engineering*, **59**: 597-668, 2004.

[23] J.W. Brown, R. Churchill, *Fourier series and boundary value problems*. McGraw-Hill, 1993.

[24] Bureau of Technical Execution System, *The Iranian code of practice for the analysis and design of concrete bridges*, Office of Deputy for Strategic Supervision, 2008.

[25] The American Association of State Highway and Transportation Officials, *Standard specification for highway bridges*, AASHTO, 2001.

[26] W.F. Chen, L. Duna, *Bridge engineering: seismic design*. CRC, 2003.

[27] N.M. Newmark, A method of computation for structural dynamics. *Journal of Engineering Mechanics, ASCE,* **85**: 67-94, 1959.

COMPDYN 2011
ECCOMAS Thematic Conference on
Computational Methods in Structural Dynamics and Earthquake Engineering
M. Papadrakakis, M. Fragiadakis, V. Plevris (eds.)
Corfu, Greece, 25-28 May 2011

CO-ROTATIONAL DYNAMIC FORMULATION FOR 2D BEAMS

Thanh-Nam Le[1,2], **Jean-Marc Battini**[2], **Mohammed Hjiaj**[1]

[1]Structural Engineering Research Group /LGCGM , INSA de Rennes, 20 Avenue des Buttes de Coësmes, 35708 Rennes Cedex 7, France
e-mail: Thanh-Nam.Le@insa-rennes.fr, mohammed.hjiaj@insa-rennes.fr

[2]Department of Civil and Architectural Engineering, KTH, Royal Institute of Technology, SE-10044 Stockholm, Sweden
email: Jean-Marc.Battini@byv.kth.se

Keywords: Corotational method, Nonlinear dynamic analysis, 2D beam element.

Abstract. *The corotational method is an attractive approach to derive non-linear finite beam elements. In a number of papers, this method was employed to investigate the non-linear dynamic analysis of 2D beams. However, most of the approaches found in the literature adopted either a lumped mass matrix or linear local interpolations to derive the inertia terms (which gives the classical linear and constant Timoshenko mass matrix), although local cubic interpolations were used to derive the elastic force vector and the tangent stiffness matrix. In this paper, a new corotational formulation for dynamic nonlinear analysis is presented. Cubic interpolations are used to derive both the inertia and elastic terms. Numerical examples show that the proposed approach is more efficient than using lumped or Timoshenko mass matrices.*

1 Introduction

The corotational approach is an attractive method to derive efficient nonlinear finite beam elements [1, 2, 3, 4, 5, 6, 7, 8, 9, 10, 11]. The main idea of the method can be summarized as follow: the motion of the beam element is decomposed into rigid body and pure deformational parts. A local coordinates system, which moves and rotates with the element's overall rigid body motion, is defined. The deformational part is measured in this local system.

Many different assumptions to represent the local deformations, giving different possibilities for the local element formulation, can be found in the literature. If linear interpolations are used for the local formulation, inertia corotational terms are easily derived and the classical linear and constant Timoshenko mass matrix is obtained. However, this assumption has the drawback that the local vertical displacements are zero along the element, which is not accurate, especially for flexible beams. If cubic interpolations are used for the local formulation, then the derivation of the inertia terms becomes very complicated. To avoid this complexity, Crisfield and al.[2] used the constant Timoshenko mass matrix, although they used local cubic interpolations to derive the elastic force vector and tangent stiffness matrix. The same approach was adopted in [6]. In [7, 8, 9], the authors used a constant lumped mass matrix without any attempt to check its accuracy. In [10], Behdinan and al. proposed a corotational dynamic formulation. However, the cubic shape functions were used to describe the global displacements, which is not consistent with the idea of the corotational method.

In this paper, a new corotational formulation is presented where cubic shape functions are adopted. In order to consider the bending shear deformations, the cubic shape functions of the Interpolation Interdependent Element (IIE) [12] are used to derive the local elastic force vector and local tangent stiffness matrix. It is shown that with some simplifications, the inertia terms can be derived. The new formulation provide accurate results with a minimum number of elements.

The paper is organized as follows: in Section 2 and 3 the corotational kinematic of a 2D beam element and the derivation of the elastic force vector and tangent stiffness matrix are presented. More details about that can be found in [13]. Section 4 and 5 are devoted to the derivation of the inertia terms. In Section 6, two examples are presented in order to assess the accuracy of the present dynamic formulation. Finally conclusions are given in Section 7.

2 Beam kinematics

The notations used are defined in Fig. 1. The coordinates for the nodes 1 and 2 in the global coordinate system (x,z) are (x_1, z_1) and (x_2, z_2). The vector of global displacements is defined by

$$\mathbf{q} = \begin{bmatrix} u_1 & w_1 & \theta_1 & u_2 & w_2 & \theta_2 \end{bmatrix}^{\mathrm{T}} \tag{1}$$

The vector of local displacements is defined by

$$\overline{\mathbf{q}} = \begin{bmatrix} \overline{u} & \overline{\theta}_1 & \overline{\theta}_2 \end{bmatrix}^{\mathrm{T}} \tag{2}$$

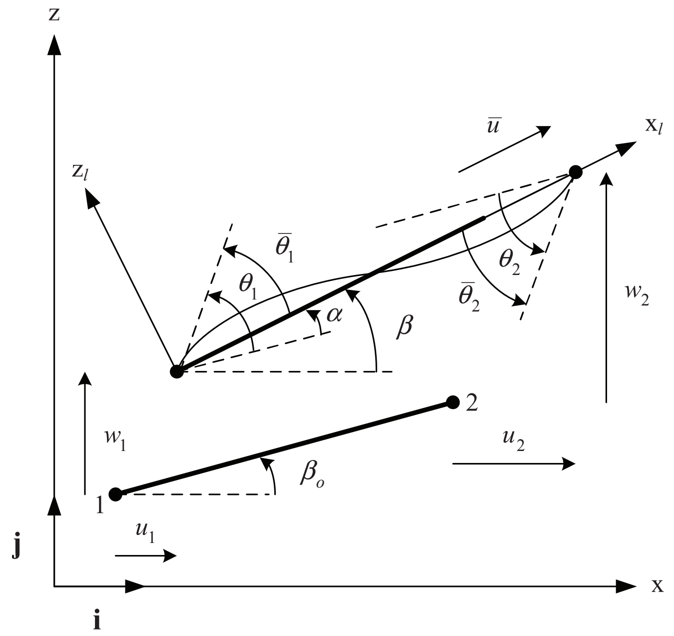

Figure 1: Beam kinematics 1.

The components of $\overline{\mathbf{q}}$ can be computed according to

$$\overline{u} = l_n - l_o \tag{3}$$

$$\overline{\theta}_1 = \theta_1 - \alpha = \theta_1 - \beta - \beta_o \tag{4}$$

$$\overline{\theta}_2 = \theta_2 - \alpha = \theta_2 - \beta - \beta_o \tag{5}$$

In (3), l_o and l_n denote the initial and current lengths of the element, respectively. The current angle of the local system with respect to the global system is denoted as β and is given by

$$c = \cos\beta = \frac{1}{l_n}(x_2 + u_2 - x_1 - u_1) \tag{6}$$

$$s = \sin\beta = \frac{1}{l_n}(z_2 + w_2 - z_1 - w_1) \tag{7}$$

The differentiation of equation (7) gives

$$\delta\beta = \frac{1}{l_n}\left[\begin{array}{cccccc} s & -c & 0 & -s & c & 0 \end{array}\right]\delta\mathbf{q} \tag{8}$$

The differentiation of equations (3) to (5) gives

$$\delta\overline{\mathbf{q}} = \mathbf{B}\,\delta\mathbf{q} \tag{9}$$

with

$$\mathbf{B} = \begin{bmatrix} \mathbf{b}_1 \\ \mathbf{b}_2 \\ \mathbf{b}_3 \end{bmatrix} = \begin{bmatrix} -c & -s & 0 & c & s & 0 \\ -s/l_n & c/l_n & 1 & s/l_n & -c/l_n & 0 \\ -s/l_n & c/l_n & 0 & s/l_n & -c/l_n & 1 \end{bmatrix} \tag{10}$$

3 Elastic force vector and tangent stiffness matrix

By equating the virtual work in the local and global systems, the relation between the local elastic force vector $\mathbf{f}_l$ and the global one $\mathbf{f}_g$ is obtained as

$$V = \delta\mathbf{q}^{\mathrm{T}}\,\mathbf{f}_g = \delta\overline{\mathbf{q}}^{\mathrm{T}}\,\mathbf{f}_l = \delta\mathbf{q}^{\mathrm{T}}\,\mathbf{B}^{\mathrm{T}}\,\mathbf{f}_l \tag{11}$$

The equation (11) must apply for any arbitrary $\delta\mathbf{q}$. Hence the global elastic force vector $\mathbf{f}_g$ is given by

$$\mathbf{f}_g = \mathbf{B}^{\mathrm{T}}\,\mathbf{f}_l \qquad \mathbf{f}_l = \begin{bmatrix} N & M_1 & M_2 \end{bmatrix}^{\mathrm{T}} \tag{12}$$

The global tangent stiffness matrix is defined by

$$\delta\mathbf{f}_g = \mathbf{K}_g\,\delta\mathbf{q} \tag{13}$$

By taking the differentiation of (12), it is obtained

$$\mathbf{K}_g = \mathbf{B}^{\mathrm{T}}\,\mathbf{K}_l\,\mathbf{B} + \frac{\mathbf{z}\,\mathbf{z}^{\mathrm{T}}}{l_n}N + \frac{1}{l_n^2}(\mathbf{r}\,\mathbf{z}^{\mathrm{T}} + \mathbf{z}\,\mathbf{r}^{\mathrm{T}})(M_1 + M_2) \tag{14}$$

where

$$\mathbf{r} = \begin{bmatrix} -c & -s & 0 & c & s & 0 \end{bmatrix}^{\mathrm{T}} \tag{15}$$

$$\mathbf{z} = \begin{bmatrix} s & -c & 0 & -s & c & 0 \end{bmatrix}^{\mathrm{T}} \tag{16}$$

The local elastic force vector $\mathbf{f}_l$ and local tangent stiffness matrix $\mathbf{K}_l$, which is defined by $\delta\mathbf{f}_l = \mathbf{K}_l\,\delta\overline{\mathbf{q}}$, depend on the definition of the local formulation. In this work, the shape functions of the IIE (Interdependent Interpolation Element) are used together with a shallow arch beam theory. The shallow arch longitudinal and shear strains are given by

$$\epsilon = \frac{1}{l_o}\int_{l_o}\left[\frac{\partial u}{\partial x} + \frac{1}{2}\left(\frac{\partial w}{\partial x}\right)^2\right]\mathrm{d}x - \frac{\partial^2 w}{\partial x^2}\,z \tag{17}$$

$$\gamma = \frac{\partial w}{\partial x} - \vartheta \tag{18}$$

Using IIE's shape functions taken from [12], the axial displacement u, the vertical displacement w and the local rotation ϑ are given by

$$u = \frac{x}{l_o}\,\overline{u} \tag{19}$$

$$w = \varphi_1\overline{\theta}_1 + \varphi_2\overline{\theta}_2 \tag{20}$$

$$\vartheta = \varphi_3\overline{\theta}_1 + \varphi_4\overline{\theta}_2 \tag{21}$$

where

$$\varphi_1 = \mu\, x \left[6\,\Omega \left(1 - \frac{x}{l_o} \right) + \left(1 - \frac{x}{l_o} \right)^2 \right] \tag{22}$$

$$\varphi_2 = \mu\, x \left[6\,\Omega \left(\frac{x}{l_o} - 1 \right) - \frac{x}{l_o} + \frac{x^2}{l_o^2} \right] \tag{23}$$

$$\varphi_3 = \mu\, \left(1 + 12\,\Omega - \frac{12\,\Omega\, x}{l_o} - \frac{4\,x}{l_o} + \frac{3\,x^2}{l_o^2} \right) \tag{24}$$

$$\varphi_4 = \mu \left(\frac{12\,\Omega\, x}{l_o} - \frac{2\,x}{l_o} + \frac{3\,x^2}{l_o^2} \right) \tag{25}$$

$$\Omega = \frac{E\, I}{G\, A\, K_s\, l_o} \tag{26}$$

$$\mu = \frac{1}{1 + 12\Omega} \tag{27}$$

$A,\ I$: Section's area and inertia moment

K_s : Shear correction coefficient.

For a rectangular cross-section, $K_s = \dfrac{5}{6}$

With $\Omega = 0$, the hermitian shape functions of the classical Bernoulli elements are obtained. The interest of IIE formulation is to keep the accuracy inherent to the cubic interpolation and with Ω to add the bending shear deformation.

4 Inertia force vector and mass matrix

The inertia force vector is calculated from the kinetic energy by using the Lagrange's equation of motion:

$$\mathbf{f}_K = \frac{\mathrm{d}}{\mathrm{d}t} \left[\frac{\partial K}{\partial \dot{\mathbf{q}}} \right] - \left[\frac{\partial K}{\partial \mathbf{q}} \right] \tag{28}$$

The kinetic energy K of an element is given as

$$K = \frac{1}{2} \rho \Big\{ \int_{l_o} A(\dot{u}_{\mathrm{G}}^2 + \dot{w}_{\mathrm{G}}^2) \mathrm{d}l + \int_{l_o} I\, \dot{\theta}^2 \mathrm{d}l \Big\} \tag{29}$$

where

ρ : Mass density

u_{G} , w_{G}: Global displacements of the centroid of the cross-section

θ : Global rotation of the cross-section

The global position of the centroid of the cross-section is given by (see Fig. 2)

$$\mathrm{OG} = (x_1 + u_1)\, \mathbf{i} + (z_1 + w_1)\, \mathbf{j} + \frac{l_n}{l_o} x\, \mathbf{a} + w\, \mathbf{b} \tag{30}$$

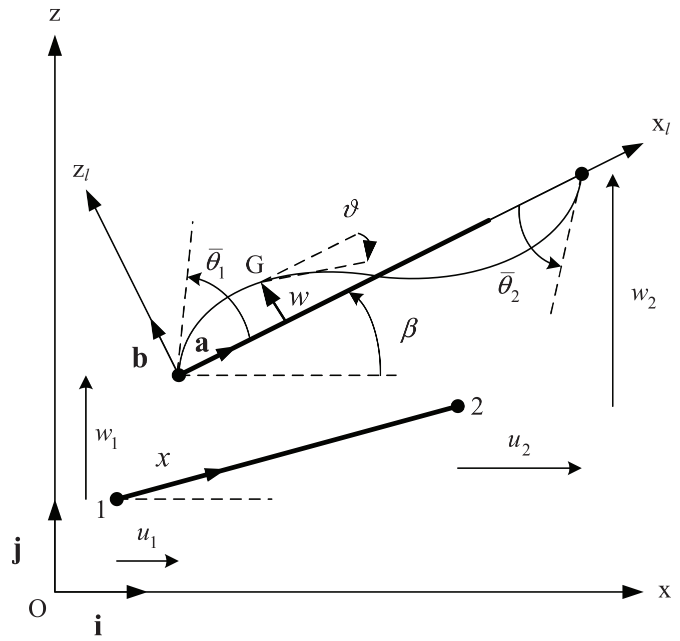

Figure 2: Beam kinematics 2.

with

$$\mathbf{a} = \cos\beta\,\mathbf{i} + \sin\beta\,\mathbf{j} \tag{31}$$

$$\mathbf{b} = -\sin\beta\,\mathbf{i} + \cos\beta\,\mathbf{j} \tag{32}$$

After some algebraic manipulations, the velocities components can be derived

$$\dot{u}_{\mathrm{G}} = \dot{u}_1 + \frac{x}{l_o}(\dot{u}_2 - \dot{u}_1) - \dot{w}\sin\beta - w\dot{\beta}\cos\beta \tag{33}$$

$$\dot{w}_{\mathrm{G}} = \dot{w}_1 + \frac{x}{l_o}(\dot{u}_2 - \dot{u}_1) + \dot{w}\cos\beta - w\dot{\beta}\sin\beta \tag{34}$$

The global rotation of the cross section is given by

$$\dot{\theta} = \dot{\vartheta} + \dot{\alpha} = \dot{\vartheta} + \dot{\beta} \tag{35}$$

For the dynamic formulation, Ω is taken to 0. It is worth mentioning that assumption simplify the computations. Furthermore, extensive numerical studies performed by the authors have shown that this simplification does not modify the numerical results. The exact expression of the kinetic energy K can be obtained by substituting (33),(34) and (35) into (29), and by using (8) to calculate $\dot{\beta}$. K can be written as

$$K = \frac{1}{2}\dot{\mathbf{q}}^{\mathrm{T}}\,\mathbf{M}\,\dot{\mathbf{q}} \tag{36}$$

The local mass matrix $\mathbf{M}_l$ is defined by

$$\mathbf{M} = \mathbf{T}^{\mathrm{T}}\,\mathbf{M}_l\,\mathbf{T} \tag{37}$$

where $\mathbf{T}$ is rotation matrix.
Consequently, one obtains

$$K = \frac{1}{2}\dot{\mathbf{q}}^{\mathrm{T}}\,\mathbf{T}^{\mathrm{T}}\,\mathbf{M}_l\,\mathbf{T}\,\dot{\mathbf{q}} \tag{38}$$

At this point, two simplifications are introduced in the expression of the local mass matrix: the local displacement w is assumed small and therefore the terms containing w^2 are neglected; due to the assumption of the small deformation, the approximation $l_n = l_o$ is taken. With these simplifications, the local mass matrix is only function of $\overline{\theta}_1$ and $\overline{\theta}_2$ and is given by

$$\mathbf{M}_l = \mathbf{M}_{l\,1} + \mathbf{M}_{l\,2} \tag{39}$$

where $\mathbf{M}_{l\,1}$ is the mass matrix for local axial and vertical displacements, defined as

$$\mathbf{M}_{l\,1} = \frac{\rho\,A\,l_o}{420}\begin{bmatrix} 140 & m_1 & 0 & 70 & -m_1 & 0 \\ m_1 & 156 & 22l_o & m_2 & 54 & -13l_o \\ 0 & 22l_o & 4l_o^2 & 0 & 13l_o & -3l_o^2 \\ 70 & m_2 & 0 & 140 & -m_2 & 0 \\ -m_1 & 54 & 13l_o & m_2 & 156 & -22l_o \\ 0 & -13l_o & -3l_o^2 & 0 & 22l_o & 4l_o^2 \end{bmatrix}$$

with

$$m_1 = (21\overline{\theta}_1 - 14\overline{\theta}_2)$$
$$m_2 = (14\overline{\theta}_1 - 21\overline{\theta}_2)$$

$\mathbf{M}_{l\,2}$ is the mass matrix for rotation, defined as

$$\mathbf{M}_{l\,2} = \frac{\rho\,I}{30\,l_o}\begin{bmatrix} 0 & 0 & 0 & 0 & 0 & 0 \\ 0 & 36 & 3l_o & 0 & -36 & 3l_o \\ 0 & 3l_o & 4l_o^2 & 0 & -3l_o & -l_o^2 \\ 0 & 0 & 0 & 0 & 0 & 0 \\ 0 & -36 & -3l_o & 0 & 36 & -3l_o \\ 0 & 3l_o & -l_o^2 & 0 & -3l_o & 4l_o^2 \end{bmatrix}$$

The differentiations of the kinetic energy can be computed as

$$\frac{\partial K}{\partial \dot{\mathbf{q}}} = \mathbf{M}\,\dot{\mathbf{q}} \tag{40}$$

$$\frac{\mathrm{d}}{\mathrm{d}t}\left[\frac{\partial K}{\partial \dot{\mathbf{q}}}\right] = \mathbf{M}\,\ddot{\mathbf{q}} + \dot{\mathbf{M}}\,\dot{\mathbf{q}} \tag{41}$$

$\mathbf{M}$ is function of $\beta, \overline{\theta}_1, \overline{\theta}_2$ which are dependent on the time:

$$\dot{\mathbf{M}} = \frac{\partial \mathbf{M}}{\partial \beta}\,\dot{\beta} + \frac{\partial \mathbf{M}}{\partial \overline{\theta}_1}\,\dot{\overline{\theta}}_1 + \frac{\partial \mathbf{M}}{\partial \overline{\theta}_2}\,\dot{\overline{\theta}}_2 \tag{42}$$

Using the notation $\dfrac{\partial \mathbf{M}}{\partial \beta} = \mathbf{M}_\beta$; $\dfrac{\partial \mathbf{M}}{\partial \overline{\theta}_1} = \mathbf{M}_{\overline{\theta}_1}$; $\dfrac{\partial \mathbf{M}}{\partial \overline{\theta}_2} = \mathbf{M}_{\overline{\theta}_2}$, the above equation can be rewritten in a more compact form

$$\dot{\mathbf{M}} = \mathbf{M}_\beta\Big(\frac{\mathbf{z}^{\mathrm{T}}}{l_n}\dot{\mathbf{q}}\Big) + \mathbf{M}_{\overline{\theta}_1}(\mathbf{b}_2^{\mathrm{T}}\dot{\mathbf{q}}) + \mathbf{M}_{\overline{\theta}_2}(\mathbf{b}_3^{\mathrm{T}}\dot{\mathbf{q}}) \tag{43}$$

The differentiation of K with respect to $\mathbf{q}$ is given by

$$\begin{aligned}\left[\frac{\partial K}{\partial \mathbf{q}}\right] &= \frac{\partial K}{\partial \beta}\frac{\partial \beta}{\partial \mathbf{q}} + \frac{\partial K}{\partial \bar{\theta}_1}\frac{\partial \bar{\theta}_1}{\partial \mathbf{q}} + \frac{\partial K}{\partial \bar{\theta}_2}\frac{\partial \bar{\theta}_2}{\partial \mathbf{q}} \\ &= \Big(\frac{1}{2}\dot{\mathbf{q}}^{\mathrm{T}}\mathbf{M}_{\beta}\dot{\mathbf{q}}\Big)\frac{\mathbf{z}}{l_n} + \Big(\frac{1}{2}\dot{\mathbf{q}}^{\mathrm{T}}\mathbf{M}_{\bar{\theta}_1}\dot{\mathbf{q}}\Big)\mathbf{b}_2 + \Big(\frac{1}{2}\dot{\mathbf{q}}^{\mathrm{T}}\mathbf{M}_{\bar{\theta}_2}\dot{\mathbf{q}}\Big)\mathbf{b}_3 \end{aligned} \tag{44}$$

Substituting (43), (44) into (28), one obtains the expression of $\mathbf{f}_K$ as

$$\begin{aligned}\mathbf{f}_K = \mathbf{M}\,\ddot{\mathbf{q}} &+ \Big\{\mathbf{M}_{\beta}\Big(\frac{\mathbf{z}^{\mathrm{T}}}{l_n}\dot{\mathbf{q}}\Big) + \mathbf{M}_{\bar{\theta}_1}(\mathbf{b}_2^{\mathrm{T}}\dot{\mathbf{q}}) + \mathbf{M}_{\bar{\theta}_2}(\mathbf{b}_3^{\mathrm{T}}\dot{\mathbf{q}})\Big\}\dot{\mathbf{q}} \\ &- \Big(\frac{1}{2}\dot{\mathbf{q}}^{\mathrm{T}}\mathbf{M}_{\beta}\dot{\mathbf{q}}\Big)\frac{\mathbf{z}}{l_n} - \Big(\frac{1}{2}\dot{\mathbf{q}}^{\mathrm{T}}\mathbf{M}_{\bar{\theta}_1}\dot{\mathbf{q}}\Big)\mathbf{b}_2 - \Big(\frac{1}{2}\dot{\mathbf{q}}^{\mathrm{T}}\mathbf{M}_{\bar{\theta}_2}\dot{\mathbf{q}}\Big)\mathbf{b}_3 \end{aligned} \tag{45}$$

The expression of $\mathbf{M}_{\beta}$ is given by

$$\mathbf{M}_{\beta} = \frac{\mathrm{d}\mathbf{T}}{\mathrm{d}\beta}^{\mathrm{T}}\,\mathbf{M}_l\,\mathbf{T} + \mathbf{T}^{\mathrm{T}}\,\mathbf{M}_l\,\frac{\mathrm{d}\mathbf{T}}{\mathrm{d}\beta} \tag{46}$$

where

$$\frac{\mathrm{d}\mathbf{T}}{\mathrm{d}\beta} = \begin{bmatrix} 0 & 1 & 0 & 0 & 0 & 0 \\ -1 & 0 & 0 & 0 & 0 & 0 \\ 0 & 0 & 0 & 0 & 0 & 0 \\ 0 & 0 & 0 & 0 & 1 & 0 \\ 0 & 0 & 0 & -1 & 0 & 0 \\ 0 & 0 & 0 & 0 & 0 & 0 \end{bmatrix}\mathbf{T} = \mathbf{I}_1\,\mathbf{T} \tag{47}$$

Hence,

$$\mathbf{M}_{\beta} = \mathbf{T}^{\mathrm{T}}(\mathbf{I}_1^{\mathrm{T}}\,\mathbf{M}_l + \mathbf{M}_l\,\mathbf{I}_1)\mathbf{T} = \mathbf{T}^{\mathrm{T}}\mathbf{M}_l^{\beta}\mathbf{T} \tag{48}$$

$\mathbf{M}_{\bar{\theta}_1}, \mathbf{M}_{\bar{\theta}_2}$ are calculated by

$$\mathbf{M}_{\bar{\theta}_1} = \mathbf{T}^{\mathrm{T}}\,\frac{\partial \mathbf{M}_l}{\partial \bar{\theta}_1}\,\mathbf{T} = \mathbf{T}^{\mathrm{T}}\mathbf{M}_{l,\bar{\theta}_1}\mathbf{T} \tag{49}$$

$$\mathbf{M}_{\bar{\theta}_2} = \mathbf{T}^{\mathrm{T}}\,\frac{\partial \mathbf{M}_l}{\partial \bar{\theta}_2}\,\mathbf{T} = \mathbf{T}^{\mathrm{T}}\mathbf{M}_{l,\bar{\theta}_2}\mathbf{T} \tag{50}$$

where

$$\mathbf{M}_{l,\bar{\theta}_1} = \frac{\rho A l_o}{60}\begin{bmatrix} 0 & 3 & 0 & 0 & -3 & 0 \\ 3 & 0 & 0 & 2 & 0 & 0 \\ 0 & 0 & 0 & 0 & 0 & 0 \\ 0 & 2 & 0 & 0 & -2 & 0 \\ -3 & 0 & 0 & -2 & 0 & 0 \\ 0 & 0 & 0 & 0 & 0 & 0 \end{bmatrix}$$

$$\mathbf{M}_{l,\bar{\theta}_2} = \frac{\rho A l_o}{60}\begin{bmatrix} 0 & -2 & 0 & 0 & 2 & 0 \\ -2 & 0 & 0 & -3 & 0 & 0 \\ 0 & 0 & 0 & 0 & 0 & 0 \\ 0 & -3 & 0 & 0 & 3 & 0 \\ 2 & 0 & 0 & 3 & 0 & 0 \\ 0 & 0 & 0 & 0 & 0 & 0 \end{bmatrix}$$

5 Non-linear equation of the motion

The non-linear equation of motion is

$$\mathbf{f}_K(\mathbf{q},\dot{\mathbf{q}},\ddot{\mathbf{q}}) + \mathbf{f}_g(\mathbf{q}) = \mathbf{p} \tag{51}$$

where

$\mathbf{f}_K$: Inertia force vector

$\mathbf{f}_g$: Elastic force vector

$\mathbf{p}$: Applied external loads

To solve (51), the differentiation of each terms must be calculated. The following notations are used

$$\mathbf{K}_g = \frac{\partial \mathbf{f}_g}{\partial \mathbf{q}} \tag{52}$$

$$\mathbf{M} = \frac{\partial \mathbf{f}_K}{\partial \ddot{\mathbf{q}}} \tag{53}$$

$$\mathbf{C}_K = \frac{\partial \mathbf{f}_K}{\partial \dot{\mathbf{q}}} \tag{54}$$

$$\mathbf{K}_K = \frac{\partial \mathbf{f}_K}{\partial \mathbf{q}} \tag{55}$$

The stiffness matrix $\mathbf{K}_g$ and the mass matrix $\mathbf{M}$ are defined in previous sections. Using (45), $\mathbf{C}_K$ can be computed as

$$\mathbf{C}_K = \dot{\mathbf{M}} + \mathbf{C}_1 - \mathbf{C}_1^{\mathrm{T}} \tag{56}$$

with

$$\mathbf{C}_1 = \mathbf{M}_\beta \left(\dot{\mathbf{q}}\,\frac{\mathbf{z}^{\mathrm{T}}}{l_n}\right) + \mathbf{M}_{\bar{\theta}_1}\left(\dot{\mathbf{q}}\,\mathbf{b}_2^{\mathrm{T}}\right) + \mathbf{M}_{\bar{\theta}_2}\left(\dot{\mathbf{q}}\,\mathbf{b}_3^{\mathrm{T}}\right) \tag{57}$$

The matrix $\mathbf{K}_K$ can be written as follow

$$\mathbf{K}_K = \mathbf{K}_1 + \mathbf{K}_2 - \mathbf{K}_3 \tag{58}$$

where

$$\mathbf{K}_1 = \mathbf{M}_\beta \ddot{\mathbf{q}}\frac{\mathbf{z}^{\mathrm{T}}}{l_n} + \mathbf{M}_{\bar{\theta}_1}\ddot{\mathbf{q}}\mathbf{b}_2^{\mathrm{T}} + \mathbf{M}_{\bar{\theta}_2}\ddot{\mathbf{q}}\mathbf{b}_3^{\mathrm{T}} \tag{59}$$

$$\begin{aligned}\mathbf{K}_2 = {} & \Big(\frac{\mathbf{z}^{\mathrm{T}}}{l_n}\dot{\mathbf{q}}\Big)\Big(\frac{\partial \mathbf{M}_\beta}{\partial \beta}\,\dot{\mathbf{q}}\frac{\mathbf{z}^{\mathrm{T}}}{l_n} + \frac{\partial \mathbf{M}_\beta}{\partial \bar{\theta}_1}\,\dot{\mathbf{q}}\mathbf{b}_2^{\mathrm{T}} + \frac{\partial \mathbf{M}_\beta}{\partial \bar{\theta}_2}\,\dot{\mathbf{q}}\mathbf{b}_3^{\mathrm{T}}\Big) + (\mathbf{b}_2^{\mathrm{T}}\dot{\mathbf{q}})\,\frac{\partial \mathbf{M}_{\bar{\theta}_1}}{\partial \beta}\,\dot{\mathbf{q}}\frac{\mathbf{z}^{\mathrm{T}}}{l_n} \\ & + (\mathbf{b}_3^{\mathrm{T}}\dot{\mathbf{q}})\,\frac{\partial \mathbf{M}_{\bar{\theta}_2}}{\partial \beta}\,\dot{\mathbf{q}}\frac{\mathbf{z}^{\mathrm{T}}}{l_n} - \Big(\mathbf{M}_\beta - \mathbf{M}_{\bar{\theta}_1} - \mathbf{M}_{\bar{\theta}_2}\Big)\dot{\mathbf{q}}\,\dot{\mathbf{q}}^{\mathrm{T}}\Big(\frac{\mathbf{r}\,\mathbf{z}^{\mathrm{T}} + \mathbf{r}\,\mathbf{z}^{\mathrm{T}}}{l_n^2}\Big)\end{aligned} \tag{60}$$

$$\begin{aligned}\mathbf{K}_3 = {} & \frac{1}{2}\Big[\Big(\dot{\mathbf{q}}^{\mathrm{T}}\,\frac{\partial \mathbf{M}_\beta}{\partial \beta}\,\dot{\mathbf{q}}\Big)\frac{\mathbf{z}\,\mathbf{z}^{\mathrm{T}}}{l_n^2} + \Big(\dot{\mathbf{q}}^{\mathrm{T}}\,\frac{\partial \mathbf{M}_\beta}{\partial \bar{\theta}_1}\,\dot{\mathbf{q}}\Big)\frac{\mathbf{z}}{l_n}\mathbf{b}_2^{\mathrm{T}} + \Big(\dot{\mathbf{q}}^{\mathrm{T}}\,\frac{\partial \mathbf{M}_\beta}{\partial \bar{\theta}_2}\,\dot{\mathbf{q}}\Big)\frac{\mathbf{z}}{l_n}\mathbf{b}_3^{\mathrm{T}} \\ & + \Big(\dot{\mathbf{q}}^{\mathrm{T}}\,\frac{\partial \mathbf{M}_\beta}{\partial \bar{\theta}_1}\,\dot{\mathbf{q}}\Big)\mathbf{b}_2\frac{\mathbf{z}^{\mathrm{T}}}{l_n} + \Big(\dot{\mathbf{q}}^{\mathrm{T}}\,\frac{\partial \mathbf{M}_\beta}{\partial \bar{\theta}_2}\,\dot{\mathbf{q}}\Big)\mathbf{b}_3\frac{\mathbf{z}^{\mathrm{T}}}{l_n} \\ & - \dot{\mathbf{q}}^{\mathrm{T}}\Big(\mathbf{M}_\beta - \mathbf{M}_{\bar{\theta}_1} - \mathbf{M}_{\bar{\theta}_2}\Big)\dot{\mathbf{q}}\Big(\frac{\mathbf{r}\,\mathbf{z}^{\mathrm{T}} + \mathbf{r}\,\mathbf{z}^{\mathrm{T}}}{l_n^2}\Big)\Big]\end{aligned} \tag{61}$$

The expressions of $\dfrac{\partial \mathbf{M}_\beta}{\partial \beta}$, $\dfrac{\partial \mathbf{M}_\beta}{\partial \bar{\theta}_1}$ and $\dfrac{\partial \mathbf{M}_\beta}{\partial \bar{\theta}_2}$ can be easily derived from (48), (49) and (50).

6 Numerical examples

Two numerical applications are presented in this section in order to assess the performance of the dynamic corotational formulation proposed in Sections 4 and 5. In particular, the accuracy of the new formulation is compared to the one of two formulations usually found in the literature, i.e. the lumped mass matrix and the Timoshenko mass matrix. These two constant mass matrices are given by

$$\mathbf{M}_{\text{Lumped}} = \frac{\rho\, A\, l_o}{2} \begin{bmatrix} 1 & 0 & 0 & 0 & 0 & 0 \\ 0 & 1 & 0 & 0 & 0 & 0 \\ 0 & 0 & l_o^2/12 & 0 & 0 & 0 \\ 0 & 0 & 0 & 1 & 0 & 0 \\ 0 & 0 & 0 & 0 & 1 & 0 \\ 0 & 0 & 0 & 0 & 0 & l_o^2/12 \end{bmatrix}$$

$$\mathbf{M}_{\text{Timoshenko}} = \rho\, l_o \begin{bmatrix} A/3 & 0 & 0 & A/6 & 0 & 0 \\ 0 & A/3 & 0 & 0 & A/6 & 0 \\ 0 & 0 & I\, l_o/3 & 0 & 0 & I\, l_o/3 \\ A/6 & 0 & 0 & A/3 & 0 & 0 \\ 0 & A/6 & 0 & 0 & A/3 & 0 \\ 0 & 0 & I\, l_o/3 & 0 & 0 & I\, l_o/3 \end{bmatrix}$$

For all dynamic formulations, the elastic force vector and tangent stiffness matrix have been derived using the IIE shape functions in order to account for shear deformability. For each example, the three dynamic formulations are compared with a reference solution. This solution is obtained with a large number of elements and is identical for the three considered dynamic formulations. The reference solution has also been checked with Abaqus (Total Lagrangian formulation) and the same results have been obtained.

To solve the equation of motion, the Alpha method, which is presented in [14], is employed, with $\alpha = -0.01$. This moderate value of α gives a small numerical damping, which limits the influence of higher frequencies on the response. Damping is not considered.

For the presentation of the results, the following colors are used in all figures:

— Reference solution — Lumped mass matrix
— Timoshenko mass matrix — New formulation

6.1 Shallow arch

Consider a shallow, circular, elastic arch (see Fig. 3) of span $L = 10m$ with clamped ends. The radius R of the arch is equal to 10m with $\phi = 30°$. The shallow arch has a uniform rectangular cross-section and is subjected to a sinusoidal concentrated vertical force $P = P_o \sin(wt)$ at mid-span. The amplitude of the load P_o is taken equal to -80 MN and its frequency w is 1000 rad/s. The arch has cross-sectional area $A = 0.087$ m^2, modulus of elasticity $E = 210GPa$, second moment of area $I = 3.562 \cdot 10^{-3}\text{m}^4$ and mass per unit volume $\rho = 7850\text{kg/m}^3$. The time step size is chosen to be $\Delta t = 5 \cdot 10^{-5}$ s. In Fig. 4, the mid-span vertical displacement $v(t)$ history is depicted for the 3 different dynamic formulations as well as the reference solution, which has been obtained with 48 elements. Only 6 elements have been used for the

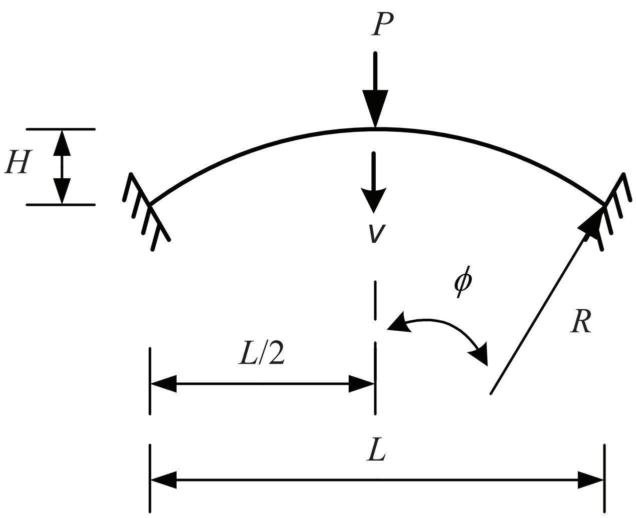

Figure 3: Shallow arch: geometrical data

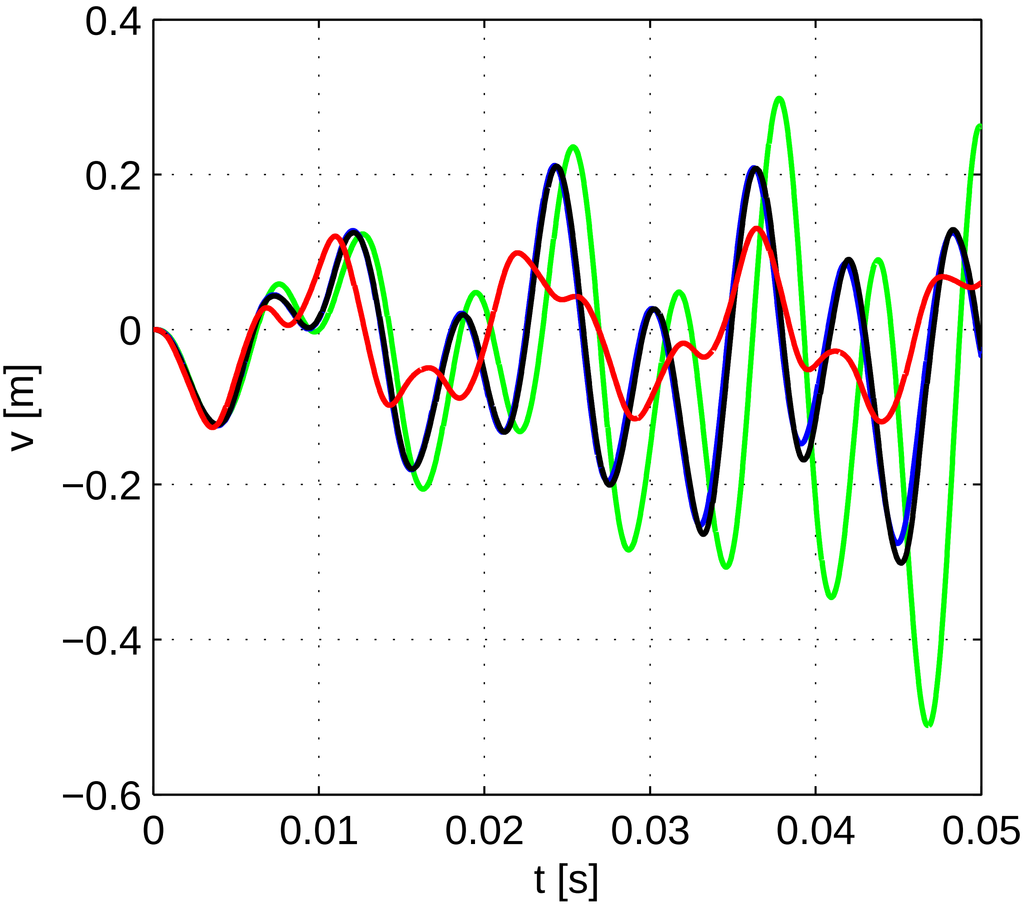

Figure 4: Shallow arc - Vertical displacement history

computations with the 3 formulations. It can be observed that the results obtained with the new approach are nearly identical to the reference solution. However, large discrepancies between the results obtained with the lumped and Timoshenko approaches and the reference solution can be observed. This indicates that the present formulation is able to capture the nonlinear dynamical behaviour of structures with minimal number of elements.

6.2 Lee's frame

A Lee's frame with uniform rectangular cross-section subjected to a suddenly applied constant load $P_o = 4.1$ MN is considered, (see Fig. 5). The frame and cross-section data (see Fig. 5) are : $L = 2.4\mathrm{m}$, $a = 0.2\mathrm{m}$ and $e = 0.3\mathrm{m}$. The members of the frame have modulus of elasticity $E = 210\mathrm{GPa}$ and mass per unit volume $\rho = 7850\mathrm{kg/m}^3$. The loading is defined as follows:

$$P = \begin{cases} 0 & \text{if } t \leq 0 \\ P_o & \text{if } t > 0 \end{cases}$$

The reference solution, obtained with 60 elements, and the results obtained with 10 elements

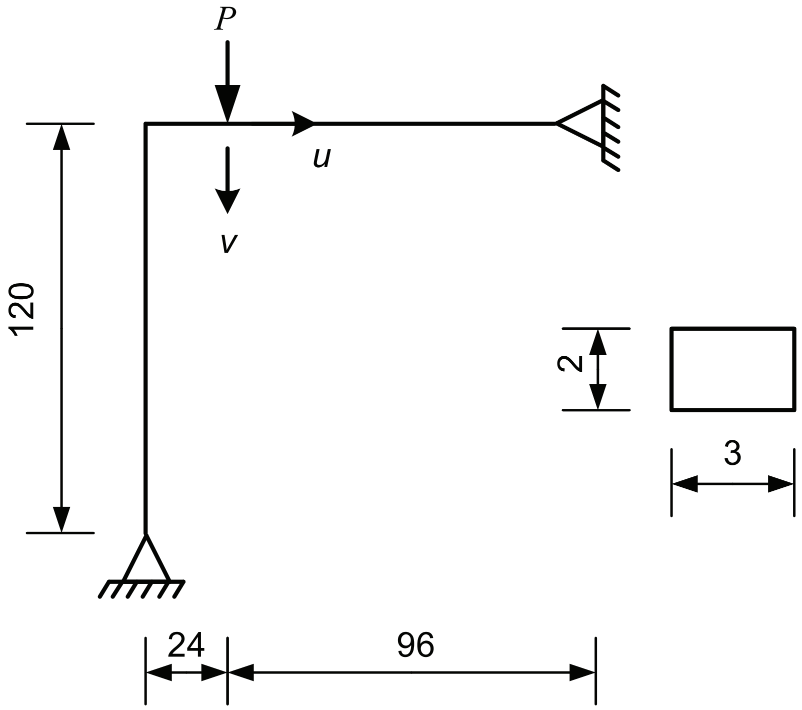

Figure 5: Lee's frame: geometrical data

are presented in Fig. 6. The time step size is $\Delta t = 2.5 \cdot 10^{-3}$ s. It can be noted that, with 10 elements, the results obtained with the new approach are in good agreement with the reference solution. However, the discrepancy between the results obtained with the lumped or Timoshenko approaches and the reference solution is not negligible.

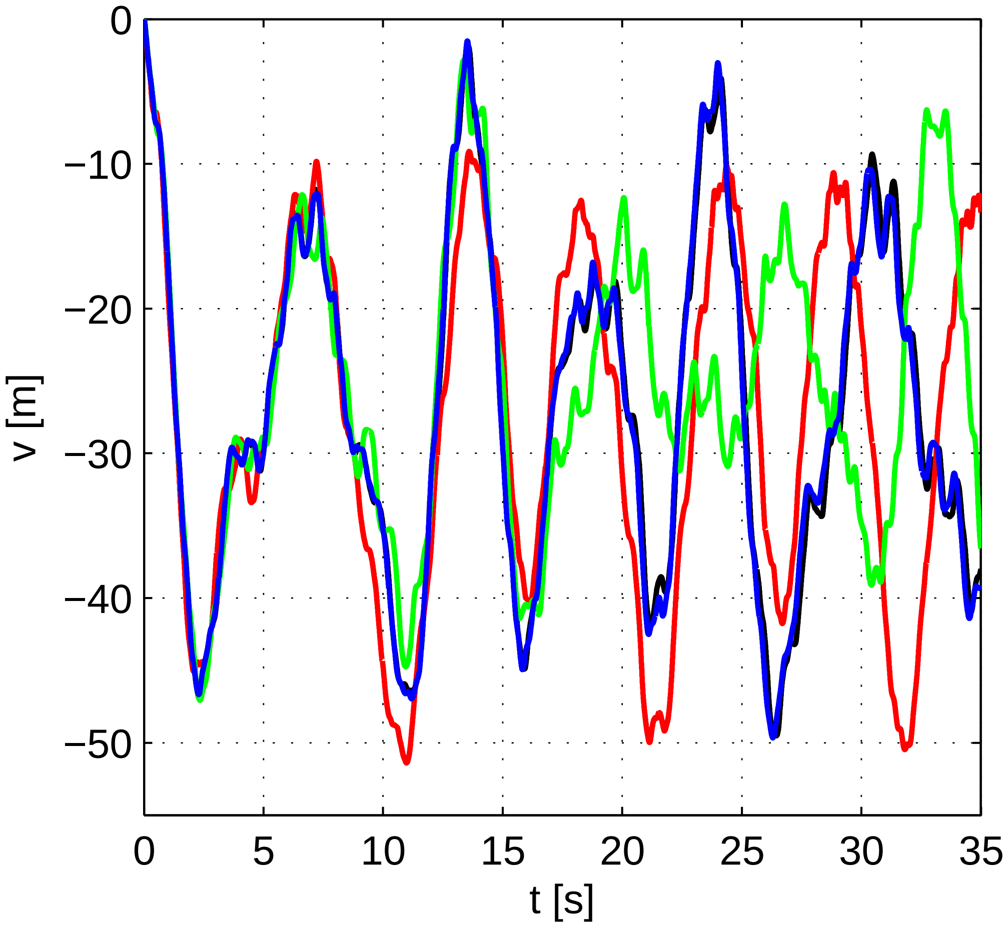

Figure 6: Lee's frame - Vertical displacement history

7 Conclusion

In this paper, a new dynamic formulation for corotational 2D beam has been presented. The new feature is that cubic interpolations are used to derive both inertia and elastic terms. The inertia terms are analytically derived by introducing some simplifications. Two numerical examples were implemented to compare this new formulation with linear Timoshenko and lumped mass matrices, which are often used in literature. The results show that the new formulation requires more computational time but allows to reduce significantly the number of elements. This advantage is due to a better representation of the local displacements in the inertia terms.

References

[1] M.A. Crisfield, J. Shi, *An energy conserving co-rotational procedure for non-linear dynamics with finite elements*, Nonlinear Dynamics, **9**, 37-52, 1994.

[2] M.A. Crisfield, U. Galvanetto, G. Jelenic, *Dynamics of 3-D co-rotational beams*, Computational Mechanics, **20**, 507-519, 1997.

[3] U. Galvanetto, M.A. Crisfield, *An energy conserving co-rotational procedure for dynamics of planar beam structures*, Int. J. Num. Methods. Engrg., **39**, 2265-2282, 1996.

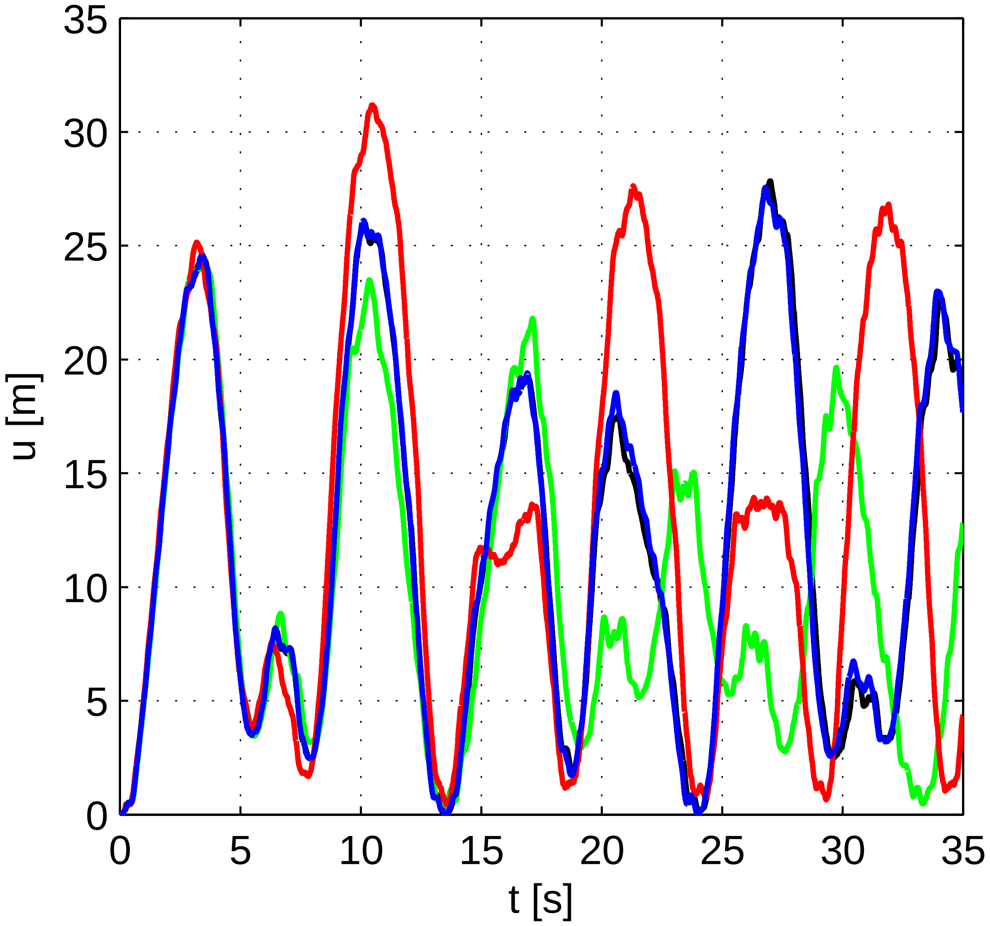

Figure 7: Lee's frame - Horizontal displacement

[4] K.M. Hsiao, R.T. Yang, *A co-rotational formulation for nonlinear dynamic analysis of curved Euler beam*, Compt.Struct. , **54**, No.6, 1091-1097, 1995.

[5] K.M. Hsiao, J.Y. Lin, W.Y. Lin, *A consisten co-rotational finite element formulation for geometrically nonlinear dynamic analysis of 3-D beams*, Comput. Methods Appl. Mech. Engrg., **169**, 1-18, 1999.

[6] M. Iura and S.N. Atluri, *Dynamic analysis of planar flexible beams with finite rotations by using inertial and rotating frames*, Comput. Struct., **55**, No.3, 453-462, 1995.

[7] C. Oran, A. Kassimali, *Large deformations of framed structures under static and dynamic loads*, Compt.Strut., **6**, 539-547, 1976.

[8] N. Masuda. T. Nishiwaki and M. Minaaawa, *Nonlinear dynamic analysis of frame structures*, Comput. Struct., **27**, No.1, 103-110, 1987.

[9] Q. Xue and J.L Meek, *Dynamic response and instability of frame structures*, Comput. Methods Appl. Mech. Engrg., **190**, 5233-5242, 2001.

[10] K. Behdinan, M.C Stylianou, B. Tabarrok, *Co-rotational dynamic analysis of flexible beams*, Comput. Methods Appl. Mech. Engrg., **154**, 151-161, 1998.

[11] H.A. Elkaranshawy and M.A. Dokainish, *Corotational finite element analysis of planar flexible multibody systems*, Comput. Struct., **54**, No.5, 881-890, 1995.

[12] J.N. Reddy, *On locking-free shear deformable beam finite elements*, Comput. Methods Appl. Mech. Engrg., **149**, 113-132, 1997.

[13] M.A. Crisfield, *Non-Linear Finite Element Analysis of Solids and Structures, Volume 1: Essentials*, 201-233. Wiley, Chischester, England, 1997.

[14] M.A. Crisfield, *Non-Linear Finite Element Analysis of Solids and Structures, Volume 2: Advanced Topics*, 455-456. Wiley, Chischester, England, 1997.

COMPDYN 2011
III ECCOMAS Thematic Conference on
Computational Methods in Structural Dynamics and Earthquake Engineering
M. Papadrakakis, M. Fragiadakis, V. Plevris (eds.)
Corfu, Greece, 25–28 May 2011

ON LESS COMPUTATIONAL COSTS FOR ANALYSIS OF SILOS SEISMIC BEHAVIOR BY TIME INTEGRATION

Fariborz. Nateghi[1], **Mansoor. Yakhchalian**[2]

[1] International Institute of Earthquake Engineering and Seismology
No. 21, West Arghavan, North Dibajee, Farmanieh, Tehran, 19395-3913, Iran

Nateghi@iiees.ac.ir

[2] International Institute of Earthquake Engineering and Seismology
No. 21, West Arghavan, North Dibajee, Farmanieh, Tehran, 19395-3913, Iran

M.yakhchalian@iiees.ac.ir

Keywords: Time Integration, Steel Silo, Computational Cost, Earthquake Excitation.

Abstract. *Time integration is the most versatile tool for analyzing semi-discretized equations of motion. Nevertheless, the associated computational costs are generally high and the computed responses are approximate. Integration step size is the main parameter affecting the computational cost and accuracy, in different ways; and hence, should be set equal to the largest value, acceptable from the point of view of accuracy. For practical cases, subjected to digitized excitations, an additional restriction, potentially increasing the computational costs, is the digitization size of the recorded excitations. Recently, a technique uses a convergence-based replacement of the digitized excitations with excitations digitized at larger steps, to arrive at time integration analyses in need of less computational cost. The good performance of the proposed technique regarding simple linear and nonlinear structural dynamic systems and shear frame structures has been displayed. Considering these, the importance of time history analysis in seismic analyses, the fact that the sizes and complicatedness of structural systems are in increase and the earthquakes are likely being recorded in smaller steps everyday, and meanwhile, the strategical role of silos in most of countries, the objective in this paper is to study the effectiveness of the new technique, when applied to analysis of silos seismic behaviors. After brief theoretical discussion, a steel silo designed based on existing codes, is once analyzed without implementing the technique, and then again, when implementing it, considering 80 percent of the mass of granular material inside silo as the effective mass. The numerical results clearly evidence the good performance of the technique.*

1 INTRODUCTION

Time integration is the most versatile tool to analyze the semi-discretized equation of motion, below:

$$\mathbf{M}\ddot{\mathbf{u}}(t)+\mathbf{f}_{\text{int}}(t)=\mathbf{f}(t) \tag{1}$$

$$\text{Initial conditions:}\ \left|\begin{array}{l}\mathbf{u}(t=0)=\mathbf{u}_0\\ \dot{\mathbf{u}}(t=0)=\dot{\mathbf{u}}_0\\ \mathbf{f}_{\text{int}}(t=0)=\mathbf{f}_{\text{int}_0}\end{array}\right.$$

$$\text{Additional constraints: } \mathbf{Q}$$

$$0\le t<t_{end}$$

In equations (1) t and t_{end} imply the time and duration of dynamic behavior; $\mathbf{M}$ is the mass matrix; $\mathbf{f}_{\text{int}}(t)$ and $\mathbf{f}(t)$ represent the vectors of internal force and excitation; $\mathbf{u}(t)$, $\dot{\mathbf{u}}(t)$ and $\ddot{\mathbf{u}}(t)$ are the unknown vectors of displacement, velocity, and acceleration, $\mathbf{u}_0$, $\dot{\mathbf{u}}_0$, and $\mathbf{f}_{\text{int}_0}$ define the initial status of the model, and $\mathbf{Q}$ represents some restricting conditions, e.g. additional constraints in problems involved in impact or elastic-plastic behavior. In spite of the versatility, time integration analyses suffer from considerable computational cost and computational errors [1], both mainly depending on integration step size, Δt . Time integration initiates with selection of time step size or a criterion for adaptive time stepping, then considering the initial conditions, the analysis is being continued with marching along the time axis and computing the responses for distinct time stations. Typical arrangement of time steps and time stations in time integration analyses is shown in Figure 1.

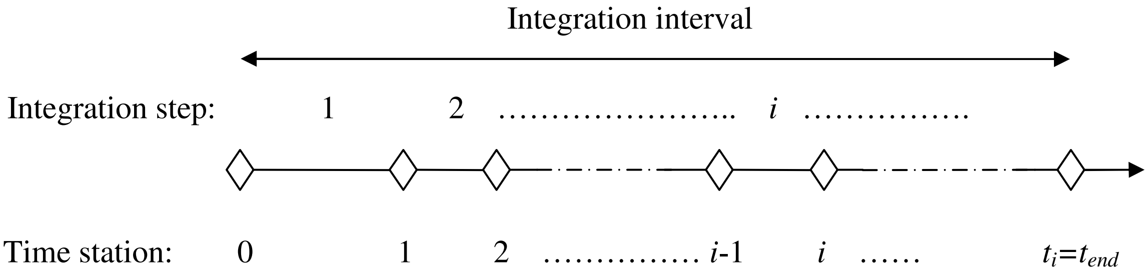

Figure 1. Typical arrangement of time steps and time stations in time integration analyses [2].

Due to the fact that smaller integration steps result in more precision and also more computational cost, it is mandatory to select time step sizes as small as acceptable from precision point of view. The existing proposed values for Δt in technical literature are presented below [3,4,5].

$$\Delta t = \text{Min}\left(h, \frac{T}{10}, {}_f\Delta t \right) \qquad \text{for linear systems}$$

$$\Delta t = \text{Min}\left(h, \frac{T}{100}, {}_f\Delta t \right) \qquad \text{for nonlinear systems} \tag{2}$$

In equations (2) h represents the requirements regarding response numerical stability and consistency, T is the dominating period of oscillations, not precisely known in advance, and ${}_f\Delta t$, representing an additional restriction for practical cases where the excitation $\mathbf{f}(t)$ is available as digitized record, implies the size by which the excitation is recorded. Reducing the effect of ${}_f\Delta t$ in equations (2) can decrease the computation cost considerably. Recently a technique is proposed [2], which replaces the digitized excitations with the step size equal to ${}_f\Delta t$ with excitations digitized at steps equal to $n\ {}_f\Delta t$, $n \in Z^+$, such that to preserve responses rate of convergence. The technique is implemented in simple linear and nonlinear systems analysis and also in a shear frame model analysis and led to considerable computational cost reduction with tolerable loss of accuracy [2,6]. In this paper the performance of this technique is investigated in the case of a steel silo.

2 THE RECENTLY PROPOSED TECHNIQUE [2]

In view of equations (2), considering the case when ${}_f\Delta t < \text{Min}(h, T/(10 \text{ or } 100))$ and taking into account the four assumptions mentioned below:

1- The excitation steps are equally sized, (see Figure 2)

$$\forall i, j \quad {}_f\Delta t_i = {}_f\Delta t_j = {}_f\Delta t > 0 \tag{3}$$

2- The integration steps are equally sized,

$$\forall i, j \quad \Delta t_i = \Delta t_j = \Delta t > 0 \tag{4}$$

3- The excitation steps are embedded by the integration steps (the first time station is a station for both excitation and integration),

$$\exists \quad n \in Z^+ \quad \frac{\Delta t}{{}_f\Delta t} = n < \infty \tag{5}$$

4- The $\mathbf{f}(t)$ in equations (1) is a digitized representation of an actual excitation $\mathbf{g}(t)$ which is smooth with respect to time,

$$\begin{gathered}\mathbf{f}(t)=\mathbf{g}(t)\delta(t-\alpha_i)\\ \mathbf{g}(t)\text{: smooth with respect to time}\\ \alpha_i = i_f\Delta t\ ,\ i=0,1,2,...\\ \delta(t-\alpha_i)=\begin{cases}1 & t=\alpha_i\\ 0 & t\neq\alpha_i\end{cases}\end{gathered}\tag{6}$$

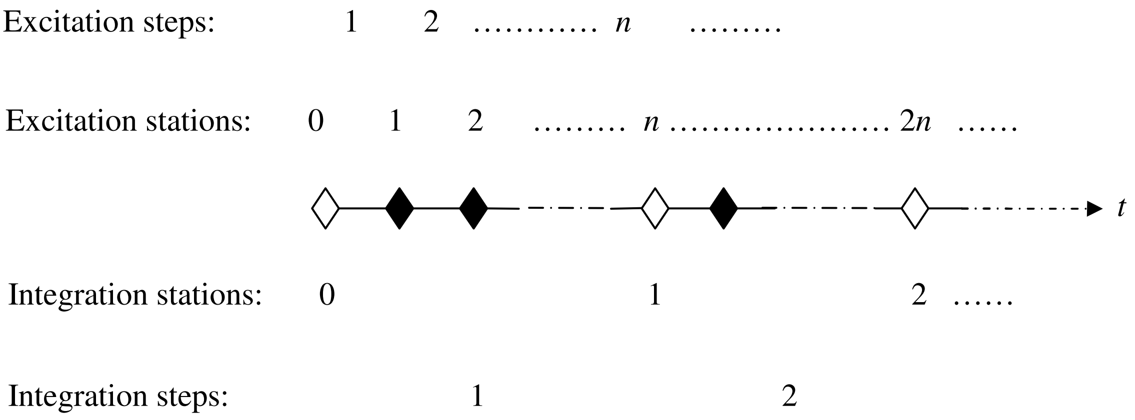

Figure 2. Typical distribution of excitation and integration stations in [2].

we can replace the original excitation with a new excitation defined by:

$$\begin{gathered}t_i=0:\quad \tilde{\mathbf{f}}_i=\mathbf{f}(t_i)\,,\\ 0<t_i<t_{end}:\ \tilde{\mathbf{f}}_i=\frac{1}{2}\mathbf{f}(t_i)+\frac{1}{4n'}\sum_{k=1}^{n'}[\mathbf{f}(t_{i+k/n})+\mathbf{f}(t_{i-k/n})],\\ t_i=t_{end}:\quad \tilde{\mathbf{f}}_i=\mathbf{f}(t_i)\,,\end{gathered}\tag{7}$$

where,

$$\begin{gathered}t=\Delta t\quad :\quad n'=n-1\\ \Delta t<t<t_{end}-\Delta t\quad :\quad n'=\begin{cases}\dfrac{n}{2} & n=2j\quad j\in Z^+\\ \dfrac{n-1}{2} & n=2j+1\quad j\in Z^+\end{cases}\\ t=\ t_{end}-\Delta t\quad :\quad n'=n-1\end{gathered}\tag{8}$$

and Δt and n ($n\in Z^+$) are the largest values satisfying

$$\Delta t = n_f \Delta t \leq \mathrm{Min}\left(h, \frac{T}{10}\right) \qquad \text{for linear systems}$$

$$\Delta t = n_f \Delta t \leq \mathrm{Min}\left(h, \frac{T}{100}\right) \qquad \text{for nonlinear systems} \tag{9}$$

$$\Delta t \leq t_{end}$$

and obtain responses from time integration with much less computational cost. Following the numerical examples already successfully examined in the literature [2,6], the technique is in the next section implemented in the analysis of a steel silo by time integration.

3 SEISMIC ANALYSIS OF A STEEL SILO

In this paper a steel silo subjected to an earthquake excitation is taken into account. The mass density of granular material inside silo is considered equal to 1500 kg/m^3. Dimensions of the silo model are presented in Table 1 [7]. ABAQUS finite element package [8] is used for finite element modeling. 4-noded shell element S4R is used for modeling the wall of silo. The modulus of elasticity of the wall of silo is considered equal to 2×10^5 MPa. For decreasing the computation time only half of silo is modeled and symmetric boundary conditions are used at the center of silo. Eurocode 8 Part 4 [9] has proposed that if more accurate evaluations are not undertaken, the global seismic response and the seismic action effects in the supporting structure may be calculated assuming that the particulate contents of the silo move together with the silo shell and modeling them with their effective mass, the contents of the silo may be taken to have an effective mass equal to 80 percent of their total mass, In common silo design in ACI 313 [10], 80 percent of granular material mass is proposed to be considered as effective mass for calculation of seismic loads. For modeling the silo, 80 percent of granular material mass is uniformly applied to the wall of the silo. The computed fundamental period, T, equals 0.2038 sec. The finite element mesh of the model is shown in Figure 3.

Silo height H (m)	Diameter D (m)	Silo wall thickness t (m)
20	10	0.03

Table 1. Dimensions of the silo model.

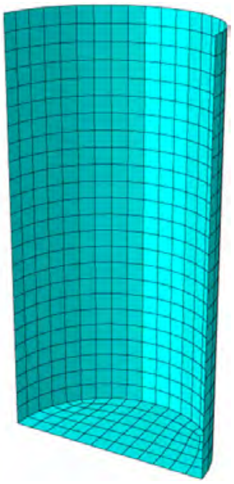

Figure 3. The finite element mesh of silo model (half of silo is considered).

The excitation which is a strong motion record, digitized at steps equal to ${}_f\Delta t = 0.005$ is shown in Figure 4. Generally in conventional time integration analyses using integration steps as small as ${}_f\Delta t$ is essential, but by using the technique described in Section 2, we can consider n =2,3,4 to perform time integration analyses by replacing the digitized excitation shown in Figure 4 with the step size of ${}_f\Delta t = 0.005$ with excitations digitized at steps equal to $n\ {}_f\Delta t = 0.01, 0.015, 0.02$ in consistence with equations (2), Hilber-Hughes-Taylor method [11] is implemented as the integration method, with a parameter, α, equal to -0.05. The base shear and top displacement histories of the silo structural system subjected to the original excitation and when considering the technique with n =2,3,4 are reported in Figures 5 and 6. As shown, the results obtained considering new excitations with n =2,3,4 have a good correlation with the results obtained from the conventional time integration by applying the earthquake excitation depicted in Figure 4 to the silo model. The computation time and the computation cost saved for each analysis are presented in Table 2. As shown in Table 2, the computation cost saved when integration steps are equal to $4_f\Delta t$ is 77.65 percent with a negligible loss of accuracy (see Figures 5-6). The obtained results clearly display that the recently proposed technique can be successful in time integration of silos structural system.

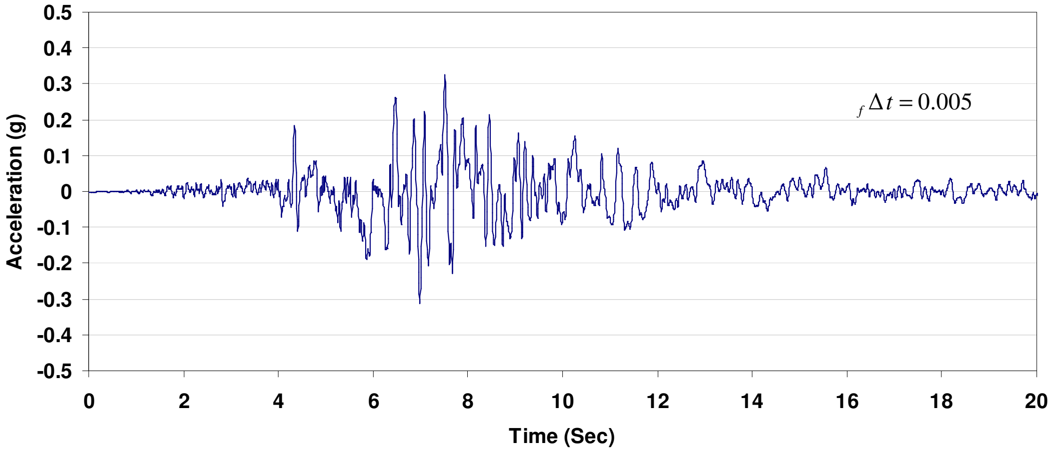

Figure 4. The earthquake excitation.

Type of analysis	Computation time (sec)	Computation cost saved (%)
Integration steps equal to ${}_f\Delta t$ (conventional)	1383	-------
Integration steps equal to $2_f\Delta t$	716	48.22
Integration steps equal to $3_f\Delta t$	468	66.16
Integration steps equal to $4_f\Delta t$	309	77.65

Table 2. Computational costs when implementing the technique with different values of *n*.

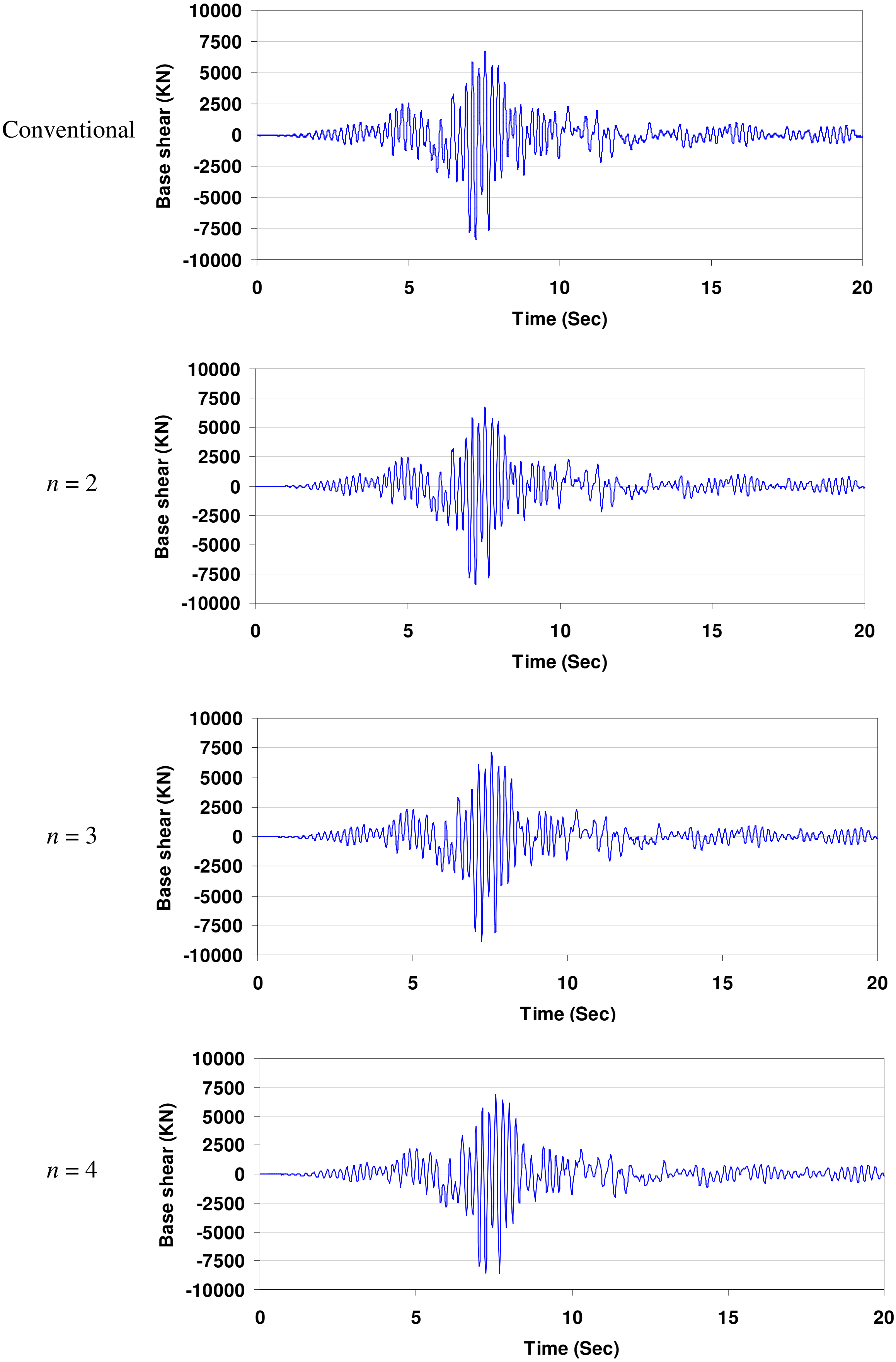

Figure 5. Comparison between base shear time histories for different values of *n*.

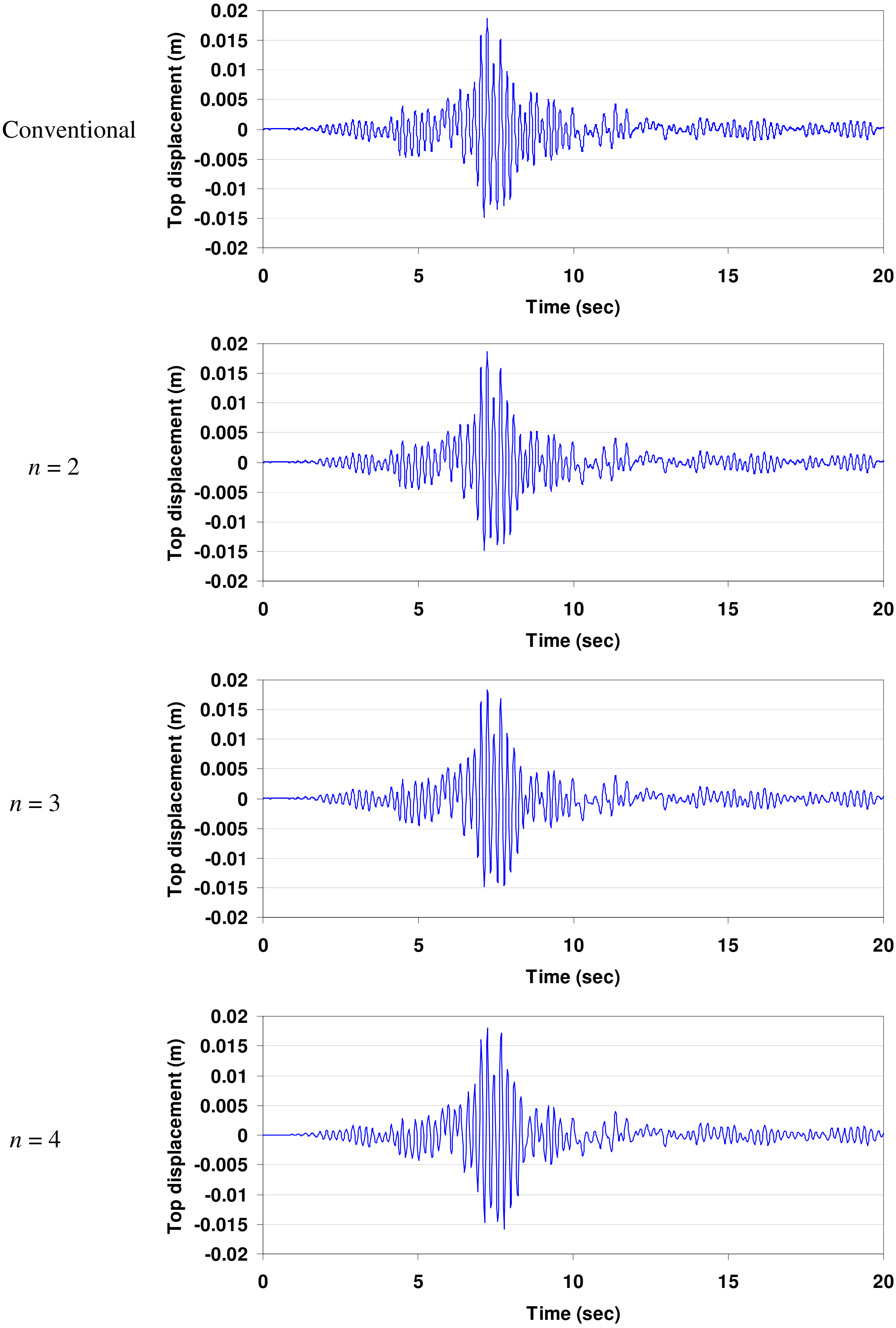

Figure 6. Comparison between top displacement time histories for different values of *n*.

4 CONCLUSIONS

In this paper, the performance of a new technique recently proposed for decreasing the computational cost of time integration analysis is investigated in the case of seismic analysis of a steel silo. The results show that using the new technique leads to significant computational cost reduction with negligible loss of accuracy. Further study in this regard, especially with different silos, different strong motion records and different integration methods is recommended.

ACKNOWLEDGMENTS

We happily acknowledge Dr Aram Soroushian for his useful guides and generating the digitized excitations for us.

REFERENCES

[1] A.K. Chopra, *Dynamics of structures: Theory and application to earthquake engineering*, Prientce-Hall, 1995.

[2] A. Soroushian, A technique for time integration with steps larger than the excitation steps. *Communications in Numerical Methods in Engineering*, **24**, 2087-2111, 2008.

[3] R.W. Clough, J. Penzien, *Dynamics of structures*, McGraw-Hill, 1993.

[4] K.J. Bathe, *Finite element procedures*, Prientce-Hall, 1996.

[5] J.F. McNamara, Solution schemes for problems of nonlinear structural dynamics. *Journal of Pressure vessels*, **96**, 147-155, 1974.

[6] A. Soroushian, On practical performance of a technique recently proposed for time integration analysis with less computational cost, *the 17th International congress on sound and vibration*, Cairo, Egypt, July 18-22, 2010.

[7] R. Wagner, S.Y. Noh, C. Butenweg and K. Meskouris, Seismic excited granular material silos, *In Proceedings of European conference on structural dynamics, EURODYN 2002*, Munich, Germany, September 2-5, 2002.

[8] Dassault Systèmes. ABAQUS user's manual, version 6.9. 2009.

[9] European Committee for Standardization. *Eurocode 8: Design of Structures for Earthquake Resistance, Part 4: Silos, Tanks and Pipelines*. 2006.

[10] American Concrete Institute. *ACI 313. Standard practice for design and construction of concrete silos and stacking tubes for storing granular materials*. 1997.

[11] H. M. Hilber, T. J. R. Hughes, R. L. Taylor, Collocation, dissipation and `overshoot' for time integration schemes in structural dynamics. *Earthquake Engineering and Structural Dynamics*, **6**, 99-117, 1978.

COMPDYN 2011
III ECCOMAS Thematic Conference on
Computational Methods in Structural Dynamics and Earthquake Engineering
M. Papadrakakis, M. Fragiadakis, V. Plevris (eds.)
Corfu, Greece, 25–28 May 2011

ERROR ESTIMATION AND IMPROVEMENT OF CONVERGENCE OF A TIME STEPPING ALGORITHM BASED ON A FINITE ELEMENT APPROACH IN TIME

Dirk Ostermann[1]

[1] Klosterhofstraße 28, 69469 Weinheim, Germany
www.dirk-ostermann.de
e-mail: kontakt@dirk-ostermann.de

Keywords: Finite Element Method, Betsch-Method, Time Stepping Algorithm, Convergence.

Abstract. *In seismic engineering either a modal analysis (based on the response spectra method) or a time history analysis may be performed. The response spectra method usually over-estimates the dynamic reactions of the structure. Therefore, the time history analysis is more appropriate if realistic results shall be obtained. In time history analysis the convergence of the times stepping algorithm that is used is of key importance.*

In the current paper an error estimation is performed for a time stepping algorithm based on a Finite Element approach in time (the so-called Betsch method, see [1] and [2]). The convergence rate of the time stepping algorithm is derived analytically and proofed numerically for different polynomial degrees of the shape functions. In order to increase the convergence rate a 3-step algorithm according to Tarnow [6] is implemented into the Betsch method. This allows high accurate results even when large time steps and only linear shape functions are used.

1 INTRODUCTION

The Finite Element Method is an approximation method. Hereby the accuracy of the results depends on the discretization (i.e. the number of elements used) and the quality of the elements (i.e. the polynomial degree of the shape functions). When the accuracy of the results is insufficient, the user has two methods to improve the accuracy: He can either increase the number of elements (h-method) or he can use elements with shape functions of higher polynomial degree (p-method).

The Finite Element method is not limited to a spacial discretization. It is also possible to derive a time stepping algorithm that is based on a Finite Element Approach in time, see [2]. Then the h-method means smaller time steps. The p-method is often not possible, because in most commercial Finite Element programs only very few time stepping algorithms are implemented and time stepping algorithms based on approaches of high polynomial degree are rarely available.

In the current contribution a third possibility to increase the accuracy of the solution is introduced: A 3-step algorithm according to Tarnow [6] is described. Hereby the step size is chosen in a way, that the errors of first and second order are eliminated and the method has the same order of convergence as if elements with quadratic shape functions were used.

2 ABREVIATIONS AND NOMENCLATURE

e	Error
h_n	Time step size
$\mathbf{p}$	Generalized momentum
$\mathbf{q}$	Generalized displacement
t	Time
$\mathbf{F}$	Force
H	Hamiltonian function of total energy
M_I	Shape function
$\mathbf{M}$	Mass matrix
α	Local coordinate $0 \le \alpha \le 1$

3 TIME STEPPING ALGORITHM

The time stepping algorithm that is presented in this section goes back to an idea of Betsch and is described in detail in [1] and [2]. In this section a brief summary of the Betsch method is given.

The basis for the time stepping algorithm is formed by Hamilton’s equations of motion:

$$\begin{aligned} \frac{\partial H}{\partial \mathbf{p}} - \dot{\mathbf{q}} &= \mathbf{0} \\ \frac{\partial H}{\partial \mathbf{q}} + \dot{\mathbf{p}} &= \mathbf{0} \end{aligned} \tag{1}$$

These equations can be transferred into the variational form either by multiplication with test functions and integration over the time domain or by formal variation of the Lagrangian function. Both methods lead to

$$\int_0^T \left(\frac{\partial H}{\partial \mathbf{p}} - \dot{\mathbf{q}}\right) \cdot \delta\mathbf{p} - \left(\frac{\partial H}{\partial \mathbf{q}} + \dot{\mathbf{p}}\right) \cdot \delta\mathbf{q} \quad dt = 0 \tag{2}$$

Now the time domain is subdivided into time steps of size $h_n = t_{n+1} - t_n$ and the abbreviation $\alpha = (t - t_n)/h_n$ is introduced. The local coordinate α is 0 at the beginning of each time step and 1 at the end of each time step. The generalized coordinate **q** and the momentum **p** are interpolated with the functions M_I of polynomial degree k, which are continuous at the element borders:

$$\begin{aligned} \mathbf{q}^h(\alpha) &= \sum_{I=1}^{k+1} M_I(\alpha)\, \mathbf{q}_I \\ \mathbf{p}^h(\alpha) &= \sum_{I=1}^{k+1} M_I(\alpha)\, \mathbf{p}_I \end{aligned} \tag{3}$$

The same is done for the virtual generalized coordinate $\delta\mathbf{q}$ and the virtual generalized momentum $\delta\mathbf{p}$. Hereby shape functions of polynomial degree (k-1) are used, which are discontinuous at the element borders:

$$\begin{aligned} \delta\mathbf{q}^h(\alpha) &= \sum_{I=1}^{k} \tilde{M}_I(\alpha)\, \delta\mathbf{q}_I \\ \delta\mathbf{p}^h(\alpha) &= \sum_{I=1}^{k} \tilde{M}_I(\alpha)\, \delta\mathbf{p}_I \end{aligned} \tag{4}$$

The time derivatives of **q** and **p** can be expressed by the derivatives of the shape functions M_I:

$$\begin{aligned} \dot{\mathbf{q}}(\alpha) &= \frac{1}{h_n} \sum_{I=1}^{k} \frac{dM_I(\alpha)}{d\alpha}\, \mathbf{q}_I = \sum_{I=1}^{k} \tilde{M}_I(\alpha) \cdot \tilde{\mathbf{q}}_I \\ \dot{\mathbf{p}}(\alpha) &= \frac{1}{h_n} \sum_{I=1}^{k} \frac{dM_I(\alpha)}{d\alpha}\, \mathbf{p}_I = \sum_{I=1}^{k} \tilde{M}_I(\alpha) \cdot \tilde{\mathbf{p}}_I \end{aligned} \tag{5}$$

As the polynomial degree decreases by derivation for the time derivatives of **q** and **p** the virtual functions $\tilde{M}$ of polynomial degree (k-1) can be used. Inserting this into the variational form of Hamilton's equations leads to

$$\begin{aligned}
&\sum_{I=1}^{k} \delta\mathbf{p}_I{}^T \left(\sum_{J=1}^{k} \int_0^1 \tilde{M}_J \tilde{M}_I d\alpha \; \tilde{\mathbf{q}}_J - h_n \sum_{J=1}^{k+1} \mathbf{M}^{-1} \int_0^1 M_J \tilde{M}_I d\alpha \; \mathbf{p}_J \right) = 0 \\
&\sum_{I=1}^{k} \delta\mathbf{q}_I{}^T \left(\sum_{J=1}^{k} \int_0^1 \tilde{M}_J \tilde{M}_I d\alpha \; \tilde{\mathbf{p}}_J + h_n \int_0^1 \left(\mathbf{F}_{\text{int}} - \mathbf{F}_{ext}\right) \tilde{M}_I \; d\alpha \right) = 0
\end{aligned} \tag{6}$$

For linear shape functions M_I one obtains a residual equation that can be solved for the unknown vector $\mathbf{q}_{n+1}$:

$$\mathbf{R} \;=\; \frac{2}{h_n}\mathbf{M} \; \left(\mathbf{q}_{n+1} - \mathbf{q}_n\right) \;-\; 2\mathbf{p}_n \;+\; h_n \int_0^1 \left(\mathbf{F}_{\text{int}} - \mathbf{F}_{ext}\right) d\alpha \;=\; \mathbf{0} \tag{7}$$

For quadratic shape functions M_I one obtains

$$\mathbf{R} = \begin{bmatrix} \dfrac{1}{h_n}\mathbf{M}\left(-\mathbf{q}_n + \mathbf{q}_{n+1}\right) - \; \mathbf{p}_n + \; h_n \displaystyle\int_0^1 (1-\alpha)\left(\mathbf{F}_{\text{int}} - \mathbf{F}_{ext}\right) d\alpha \\ \dfrac{1}{h_n}\mathbf{M}\left(5\mathbf{q}_n - 8\mathbf{q}_{n+\frac{1}{2}} + 3\mathbf{q}_{n+1}\right) + \; \mathbf{p}_n + \; h_n \displaystyle\int_0^1 \alpha\left(\mathbf{F}_{\text{int}} - \mathbf{F}_{ext}\right) d\alpha \end{bmatrix} = \mathbf{0} \tag{8}$$

And for cubic shape functions one obtains

$$\mathbf{R} = \begin{bmatrix} \dfrac{1}{h_n}\mathbf{M}\left(-\dfrac{5}{2}\mathbf{q}_n + \dfrac{3}{2}\mathbf{q}_{n+\frac{1}{3}} + \dfrac{3}{2}\mathbf{q}_{n+\frac{2}{3}} - \dfrac{1}{2}\mathbf{q}_{n+1} \right) & -\mathbf{p}_n & + h_n \displaystyle\int_0^1 \left(2\alpha^2 - 3\alpha + 1\right) \left(\mathbf{F}_{\text{int}} - \mathbf{F}_{ext}\right) d\alpha \\ \dfrac{1}{h_n}\mathbf{M}\left(3\mathbf{q}_n - 3\mathbf{q}_{n+\frac{1}{3}} - 3\mathbf{q}_{n+\frac{2}{3}} + 3\mathbf{q}_{n+1}\right) & & + h_n \displaystyle\int_0^1 \left(-4\alpha^2 + 4\alpha\right) \left(\mathbf{F}_{\text{int}} - \mathbf{F}_{ext}\right) d\alpha \\ \dfrac{1}{h_n}\mathbf{M}\left(-7\mathbf{q}_n + 15\mathbf{q}_{n+\frac{1}{3}} - 12\mathbf{q}_{n+\frac{2}{3}} + 4\mathbf{q}_{n+1}\right) & -\mathbf{p}_n & + h_n \displaystyle\int_0^1 \left(2\alpha^2 - \alpha\right) \left(\mathbf{F}_{\text{int}} - \mathbf{F}_{ext}\right) d\alpha \end{bmatrix} = \mathbf{0} \tag{9}$$

The procedure for shape functions of higher polynomial degree is described in [5].

4 THEORETICAL DERIVATION OF THE CONVERGENCY RATE

The Betsch algorithm described in section 3 can only be an approximation of an exact solution **q***(t). The exact solution **q***(t) can be developed into a Fourier series:

$$\begin{aligned}\mathbf{q}^{*}(t) &= \mathbf{q}^{*}(t_n) + \frac{\mathbf{q}^{*\prime}(t_n)}{1!}(t-t_n) + \frac{\mathbf{q}^{*\prime\prime}(t_0)}{2!}(t-t_n)^2 + \ldots \\ &= \sum_{i=0}^{\infty} \mathbf{a}_i (t-t_n)^i\end{aligned} \tag{10}$$

$$\text{with } \mathbf{a}_i = \frac{\mathbf{q}^{*(i)}(t_n)}{i!}$$

The solution $\mathbf{q}^h(t)$ is approximated by the shape functions M_I of polynomial degree k as described in section 3.

$$\mathbf{q}^h(t) = \sum_{I=1}^{k+1} M_I \; \mathbf{q}_I \tag{11}$$

When both expressions are compared it is found that the exact solution **q***(t) contains all terms with polynomial degree i ≥ 0. However, the approximation $\mathbf{q}^h(t)$ does only contain terms with polynomial degree 0 ≤ I ≤ k.

Therefore the difference between the exact solution **q***(t) and the approximation $\mathbf{q}^h(t)$ is of order $(t-t_n)^{k+1}$:

$$\left\| \mathbf{q}^{*}(t) - \mathbf{q}^{h}(t) \right\| \sim (t-t_0)^{k+1} \tag{12}$$

Hereby the term $(t-t_0)$ is limited by the time step size h_n.

The error e can also be written as a product of an (unknown) coefficient C and the time step size hn with exponent (k+1):

$$e = \left\| \mathbf{q}^{*}(t) - \mathbf{q}^{h}(t) \right\| = C \cdot h_n^{k+1} \tag{13}$$

Normally the error is displayed in a diagram with double-logarithmic axes. Then the equation describes a straight line with slope (k+1):

$$\log e = \log C + (k+1) \cdot \log h_n \tag{14}$$

However, when the error is evaluated only in the nodes (i.e. at the end of each time step and not within each time step), the slope of the convergence line is (2k) instead of (k+1). A detailed proof can be found in [4].

5 NUMERICAL DERIVATION OF THE CONVERGENCY RATE

The convergence rate can also be calculated numerically. Therefore the “accurate” solution is calculated with the algorithm explained in section 3 with a very small size of time steps. Then the error is negligibly small, so that this displacement-time process may be used as a reference solution **q***(t).

The diagram in Figure 1 shows the displacement-time process for the reference solution **q*** (continuous line) and for an approximation $\mathbf{q}^h$ with time step size h_n=0.5s (dashed line).

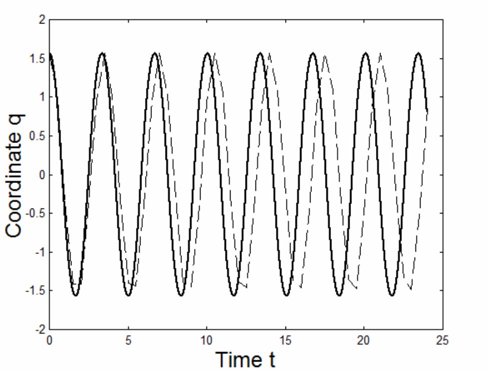

Figure 1: Displacement time process for reference solution **q*** (continuous line) and for the approximation $\mathbf{q}^h$ (dashed line)

During the first seconds both solutions are almost identical. But with the time both solutions are drifting apart. After about 24s the reference solution **q*** and the approximation $\mathbf{q}^h$ are out of phase.

The error can be calculated as the sum of the differences between the reference solution **q*** and the approximation $\mathbf{q}^h$ over the investigated time domain:

$$\| e \|_{L2} = \left(\sum_i \left(q_i^h - q_i^* \right)^2 \cdot \Delta t_i \right)^{\frac{1}{2}} \tag{15}$$

Hereby the time interval Δt can either be equal to the time step size h_n (when the error is evaluated only in the nodes, i.e. at the end of each time step) or the time interval Δt can be less than the time step size h_n (when the error is evaluated also within each time step).

The couple of time step size h_n and error e gives one particular point of the convergence line in Figure 2. When the displacement-time process is calculated with other time step sizes and the error is evaluated for each of these calculations more points of the convergence line are obtained and a trend of the convergence line can be found. This has already been proofed in [1].

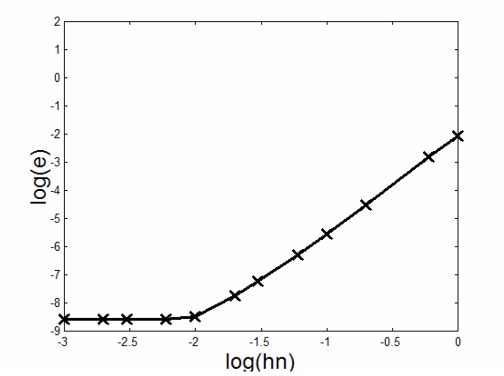

Figure 2: Convergence line

For very small time step sizes (in this particular case $h_n < 0.01s$) the convergence line tends to the horizontal. Here the accuracy of the computer is reached because the calculations are performed only with a fixed number of digits. A further reduction of the time step size does not result in a more accurate solution.

5.1 Linear Shape Functions

For linear shape functions one obtains the convergence lines displayed in Figure 3. The left diagram is obtained when the error is evaluated only in the nodes (i.e. at the end of each time step). The slope of the convergence line is (2k)=2.

The right diagram is obtained when the error is evaluated also within the time steps. Hereby the displacement within the time steps is approximated with the shape functions M_I. Then the slope of the convergence line is (k+1)=2. This has already been proofed in [1]. Both findings confirm the theoretical considerations from section 4.

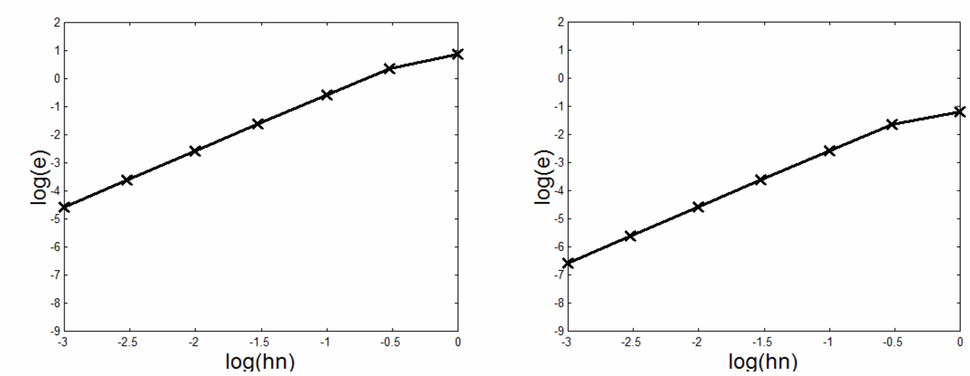

Figure 3: Convergence for linear shape functions
(left diagram: error evaluation only in the nodes, right diagram: error evaluation also between the nodes)

5.2 Quadratic Shape Functions

For quadratic shape functions one obtains the convergence lines displayed in Figure 4. Again, the left diagram shows the convergence line when the error is evaluated only in the nodes. This gives a slope of the convergence line of (2k)=4.

The right diagram shows the convergence line when the error is evaluated also between the nodes. In this case, the slope of the convergence line is (k+1)=3. The lower slope of the convergence line (3 instead of 4) is only due to a different definition of the error evaluation. Of course, the results in the nodes are of the same accuracy in both cases.

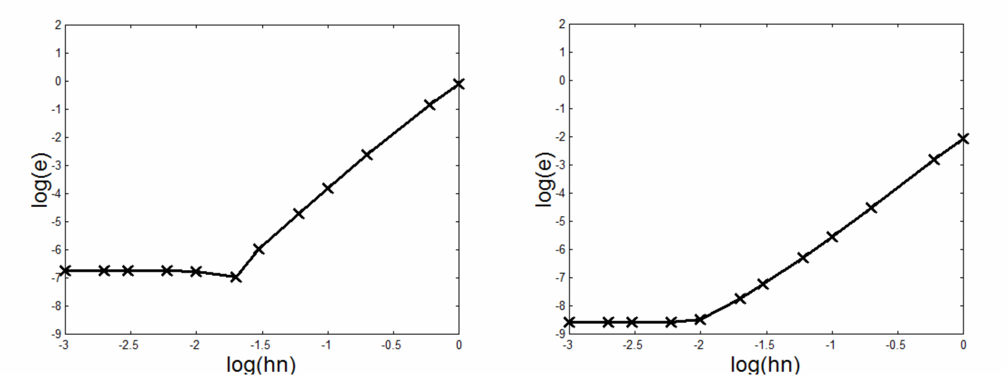

Figure 4: Convergence for quadratic shape functions
(left diagram: error evaluation only in the nodes, right diagram: error evaluation also between the nodes)

5.3 Cubic Shape Functions

The convergence lines for cubic shape functions are displayed in Figure 5. In the left diagram (evaluation of the error only in the nodes) the slope of the convergence line is (2k)=6 while the slope of the convergence line in the right diagram (evaluation of the error also between the nodes) is (k+1)=4.

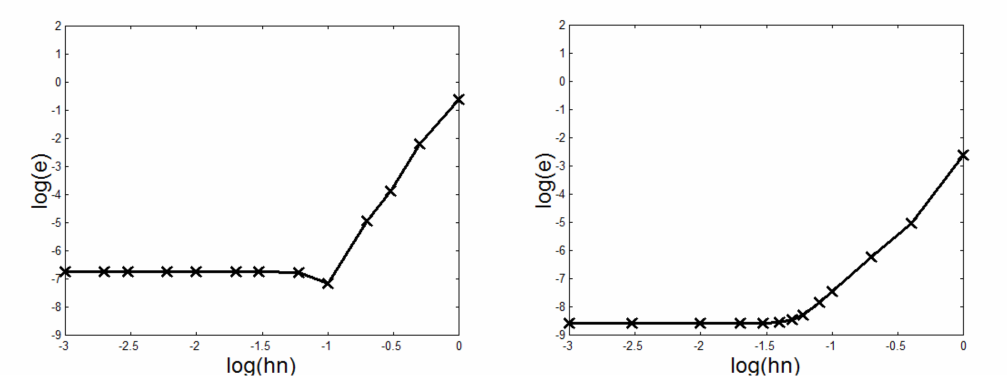

Figure 5: Convergence for cubic shape functions
(left diagram: error evaluation only in the nodes, right diagram: error evaluation also between the nodes)

6 3-STEP-METHOD FOR IMPROVEMENT OF THE CONVERGENCY RATE

As seen in the last section, it is high effort to obtain relatively accurate results. Either the time step size has to be reduced significantly (leading to high computational costs) or the polynomial degree of the shape functions has to be increased (often these high sophisticated algorithms are not available). Therefore a method would be desirable that gives high accurate results with relatively large time steps, although using linear shape functions. This goal can be reached by implementing the Tarnow method (see [6] and [7]) into the above described time stepping algorithm of Betsch. The procedure of the 3-step algorithm according to Tarnow is as follows:

- The values at time t_n are known from the previous time step. The values at time t_{n+1} shall be calculated. The Tarnow method does not calculate these values directly. Instead, the values at time $t_{n+\alpha}$ are calculated in a first step. The values are not accurate, they include an error of second order, third order and higher order because linear shape functions are used.
- In a second step, the values at time $t_{n+1-\alpha}$ are calculated based on the results at time $t_{n+\alpha}$. Again, the results include an error of second order, third order and higher order.
- In a third step, the values at time t_{n+1} are calculated based on the results at time $t_{n+1-\alpha}$. In this step the errors are again of second order, third order and higher order.

The parameter α can now be chosen in a way that the errors of second order and third order are compensated in the intermediate steps and only an error of forth and higher order remains. This is the case when the parameter α is chosen to 1.3512. A detailed proof of this method can be found in [6].

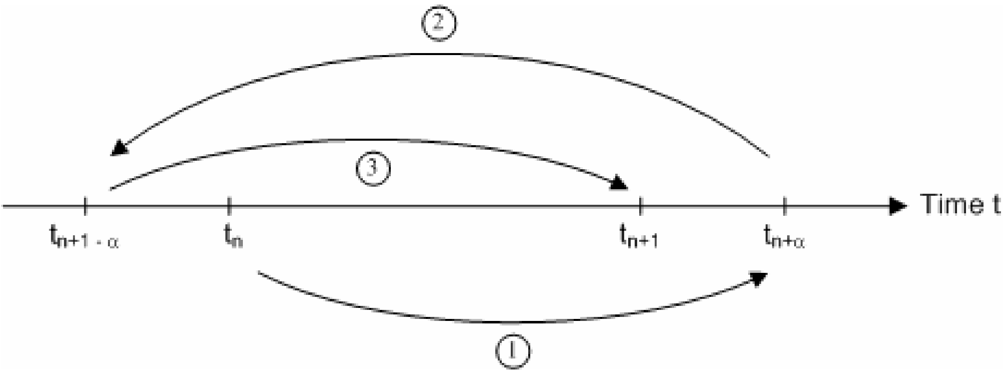

Figure 6: 3-step algorithm according to Tarnow

The above described Tarnow method has now been implemented into the time stepping algorithm of Betsch. Figure 7 shows the results when the Betsch algorithm is used with linear shape functions and the 3-step algorithm. The results are of 4th order accurate, therefore the slope of the convergence line is 4. So the same accuracy is reached as for a 1-step algorithm with quadratic shape functions.

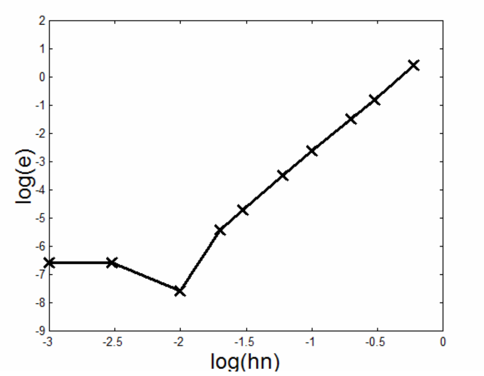

Figure 7: Convergence for linear shape functions with 3-step algorithm

7 SUMMARY

The convergence rate of the Betsch method depends on the polynomial degree of the shape functions. For linear shape functions a convergence rate of 2 was found. When the 3 step algorithm according to Tarnow is implemented into the Betsch method, the convergence rate is increased from 2 to 4. This allows high quality results, even when only linear shape functions and large time steps are used.

8 REFERENCES

[1] Betsch, P., Steinmann, P.: *Inherently Energy Conserving Time Finite Elements for Classical Mechanics*, Journal for Computational Physics, 160, 88-116, 2000

[2] Betsch, P.: *Computational Methods for Flexible Multibody Dynamics*, Habilitation Lehrstuhl für Technische Mechanik, Universität Kaiserslautern, UKL/LTM T02-02, 2002

[3] Henrici, P.: *Discrete Variable Methods in Ordinary Differential Equations*, Wiley, New York, 1962

[4] Hulme, B.L.: *One-Step Piecewise Polynomial Galerkin Methods for Initial Value Problems*, Mathematics of Computation, 26, 415-426, 1972

[5] Ostermann, D.: *Kontinuierliche und diskontinuierliche Galerkin-Methoden in der Elastodynamik und ihre Anwendung auf Probleme der Strukturmechanik*, Dissertation, TU Darmstadt, Shaker, 2005

[6] Tarnow, N.: *Energy and Momentum Conserving Algorithms for Hamiltonian Systems in the Nonlinear Dynamics of Solids*, Dissertation, Department of Mechanical Engineering, Standford University, 1993

[7] Tarnow, N., Simo, J.C.: *How to render second order accurate time-stepping algorithms fourth order accurate while retaining the stability and conservation properties*, Computational Methods in Applied Mechanical Engineering, 115, 233-252, 1994

[8] Wriggers, P.: *Nichtlineare Finite-Element-Methoden*, Springer, 2001

COMPDYN 2011
III ECCOMAS Thematic Conference on
Computational Methods in Structural Dynamics and Earthquake Engineering
M. Papadrakakis, M. Fragiadakis, V. Plevris (eds.)
Corfu, Greece, 26–28 May 2011

PHYSICALLY SIMPLIFIED MODEL OF MULTI-STORY BUILDINGS FOR THEIR QUICK DYNAMIC ANALYSIS

Mahmood Hosseini[1] **and Amir Ashtari Larki**[2]

[1] Associate Prof., International Institute of Earthquake Engineering and Seismology (IIEES)
No. 21 Arghavan, North Dibaji St., Farmanieh, Tehran, Iran
hosseini@iiees.ac.ir

[2] Ph. D. Candidate in Science & Research Branch of the Islamic Azad University (IAU),
Poonak, Ashrafi Esfahani Highway, Tehran, Iran
ashtari.amir@yahoo.com

Key words: Time History Analysis, Base shear, Base moment, Required calculation time

Abstract. *To increase the tendency of practicing engineers, engaged in the seismic design and evaluation of structural systems, to performing dynamic or Time History Analyses (THA) one way is reducing the volume of data, engaged in THA, and therefore, the volume of dynamic calculations. This would increase the computational efficiency in seismic structural analyses. One way for reducing the volume of input data and the corresponding output and information is the physical simplification of Multi-Degree-Of-Freedom (MDOF) systems, so that instead of working with* $n \times n$ *matrices, resulted from the n-Degree-Of-Freedom system, the engineer works with* $n_r \times n_r$ *matrices* ($n_r << n$)*, belonging to a physically simplified system which has* n_r *degrees of freedom. For multi-story shear beam type buildings finding the equivalent simplified system is not very difficult. In fact, it is possible to introduce for a multi-story building an equivalent building with the same overall height, but having fewer number of stories with the same story mass while the stories' heights are more so that their stiffness values are less and the proportion of stiffness and mass of the original building is kept in the simplified model. In this way the modal frequencies of the reduced model will be correspondingly equal to the first few modal frequencies of the original building. However, the amount of base shear force and base moment of the reduced model will be less than that of the original building, and will be related to them by some specific factors which are functions of the ratio of number of stories of the original building and the reduced model. Several examples of response time histories calculated for a series of multi-story buildings and their simplified reduced models, obtained by using the proposed method, show that by using the proposed simplification technique the volume of elaborations needed for THA of building systems are reduced drastically. The amount of reduction in the 'required calculation time', and also the achieved level of precision in response values both depend on the number of stories of the original building and the ratio of number of stories of the original building and the reduced model.*

1 INTRODUCTION

The tendency of practicing engineers, engaged in seismic design and evaluation of structural systems, to performing dynamic or Time History Analysis (THA) of structures is very little. The main reason behind this fact is the very large volume of elaborations and computational materials required in THA of structures. These include the several time steps in which the response values should be calculated on the one hand, which make the calculations very time consuming, and the input, and particularly output data required for evaluation, on the other hand, which requires a large storage volume in the computer for saving and handling the data. On this basis, if the volume of data, engaged in THA, is reduced by some way it would be very useful for increasing the computational efficiency in seismic structural analyses.

Since mid 80s some researchers have tried to present simple dynamic or pseudo-dynamic analysis methods for this purpose. Cruz and Chopra (1986) have presented some simplified procedures for earthquake analysis of buildings [1]. Lai and his colleagues (1992) have also proposed a simplified analysis method for evaluation of earthquake actions and their distribution on regular high-rise buildings [2]. They have considered shear type, shear-bending type and bending type regular high-rise buildings and have used the modal analysis through response spectrum procedure and lumped mass story models. Wilkinson and Thambiratnam (2001) have also proposed a simplified procedure for seismic analysis of asymmetric buildings [3]. Their method is based on modification of the shear beam model, and has been applied to treat the seismic analysis of asymmetric buildings, as well. Their three dimensional procedure accounts for torsional coupling and the bending rotations at beam–column junctions and it can be used with a personal computer to give fast and reasonably accurate results, which compare well with those from comprehensive finite element analysis. They have claimed that their procedure is useful for preliminary seismic analysis and design of buildings.

In 2005 Miranda has proposed a simplified building response analysis for rapid seismic performance evaluation of existing buildings [4]. His simplified seismic analysis tool uses a continuum model consisting of a flexural beam coupled with a shear beam. Expressing that the earthquake response of many buildings can be estimated by considering only the first two vibration modes in the response spectrum analysis (RSA) procedure, Miranda has presented a simplified response spectrum analysis (SRSA) procedure, which provides very similar estimates of design forces for many buildings. With the development of the SRSA, a hierarchy of four analysis procedures to determine the earthquake forces are available to the building designer: code-type procedure, SRSA, RSA, and RHA (response history analysis). Miranda claims that the criteria presented to evaluate the results from each procedure and to decide whether it is necessary to improve results by proceeding to the next procedure in the hierarchy use all the preceding computations and are, therefore, convenient

An alternative way for reducing the volume of input data and output and information is the physical simplification of Multi-Degree-Of-Freedom (MDOF) systems, so that instead of working with $n\times n$ matrices, resulted from the n-Degree-Of-Freedom system, the engineer works with $n_r\times n_r$ matrices ($n_r<<n$), belonging to a physically simplified system which has n_r degrees of freedom. Details of this method are presented in the next section of the paper for shear beam type buildings.

2 PHYSICAL SIMPLIFICATION OF SHEAR BUILDINGS

The main idea for this physical simplification is finding an appropriate reduced n_r-Degree-Of-Freedom system for the original n-Degree-Of-Freedom system in such a way that the modal frequencies of the simplified system are correspondingly equal to the first nr frequencies (the lower modes) of the original system. Obviously, this can be achieved by adjusting the amount of stiffness and mass in various parts of the simplified system. In this way the modal frequencies of the reduced model will be correspondingly equal to the first n_r modal frequencies of the original building. However, the amounts of base shear force and also base moment of the reduced model will be less than that of the original building, and related to them by some specific factors which are functions of n/n_r ratio and story mass and height in both original and simplified models of building.

For multi-story shear beam type buildings finding the equivalent simplified system is not very difficult. In fact, it is possible to introduce an n_r-story building with the same height and story mass as the original n-story building, in which the stiffness values of the stories have been decreased in a specific way to keep the existing proportionality of stiffness and mass of the original n-story building. For this purpose, it is enough to consider the stories with the same story mass m of the original building just in every other story level, or every other two, three, four story level, and so on, while keeping the rotation restraints imposed to columns at story levels.

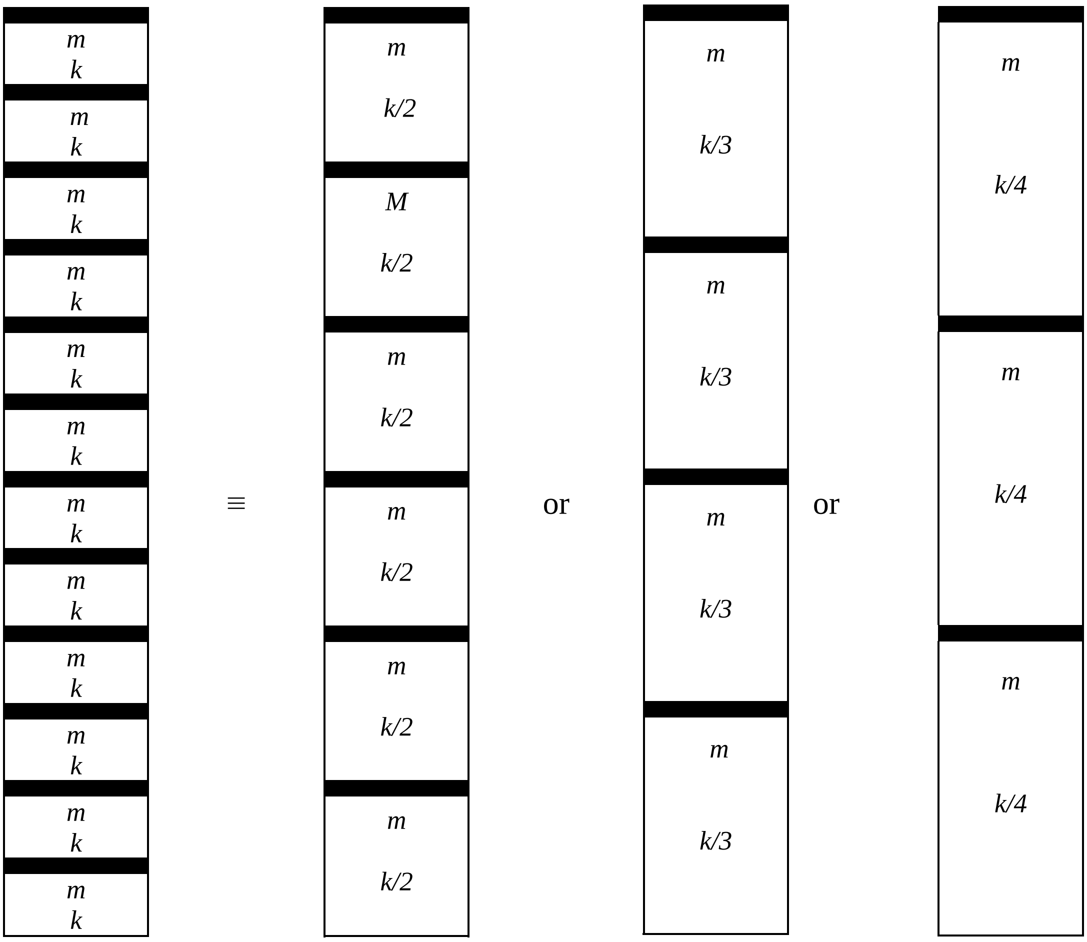

a) The original 12-story bldg b) Simplified 6-story bldg c) Simplified 4-story bldg d) Simplified 3-story bldg

Figure 1: Physical simplification of a 12-story building (a) with total mass of 12m to: b) a 6-story building with total mass of 6m, c) a 4-story building with total mass of 4m, and d) a 3-story building with total mass of 3m

In this way the stiffness of each column in the simplified model of the building, which the height of $2h$ (h being the story height), $3h$, $4h$ and so on, depending on the number of deleted stories, will be obtained based on the formula of springs in series, that is:

$$\frac{1}{k_{eq}} = \frac{1}{k_1} + \frac{1}{k_2} + \frac{1}{k_3} + \ \dots \qquad (1)$$

where k_{eq} is the stiffness of the equivalent column in the simplified model of the building, and k_1, k_2, k_3 and so on are the stiffness values of the successive columns in one vertical line. Considering the same stiffness value of k for the successive columns, Equation (1) leads to a value of $k/2$, $k/3$, $k/4$ and so on, corresponding to deletion of, respectively, every other one story, every other two, three, four stories, and so on, as shown in Figure 1.

As shown in Figure 1, the original building (a) has a total mass of $12m$, while in case (b) the simplified model has a mass of $6m$, which is as half of the original building, and proportionally the stiffness of stories is k/2. In cases (c) and (d) the total mass of the simplified model is, respectively, 1/3rd and 1/4th of the original building, and accordingly the stiffness of stories in these two cases is, respectively, 1/3rd and 1/4th of the original building as well.

Based on this logic, the modal frequencies of the reduced model of an n-story building will be correspondingly equal to the first n_r modal frequencies of the original building. However, the amounts of base shear force and base moment of the simplified model, subjected to any accelerogram of a horizontal component of an earthquake ground motion, will be obviously less than that of the original building, due to the lower mass of the simplified model. Paying attention to the ratios between the masses and story heights of the simplified model and the original building, in case of buildings with the same story masses and equal story heights, the modification factors for the base shear force and the base moment, by which the values obtained for the simplified model should be multiplied, to give the values of base force and base moment of the original building, are respectively:

$$Base\ Shear\ Modification\ Factor = \frac{n}{n_r} \qquad (2)$$

and

$$Base\ Moment\ Modification\ Factor = \frac{\sum_i^n H_i}{\sum_j^{n_r} H_j} \qquad (3)$$

where H_i and H_j are height of, respectively, the ith floor of the original building, and the jth floor of the simplified model above foundation level. For buildings with unequal story masses and heights the given modification factors will have some errors. However, the amount of error will not be remarkable for most of actual cases, as shown in the next section, in which some numerical examples are presented.

3 NUMERICAL EXAMPLES

Several examples of response time histories calculated for a series of multi-story buildings and their simplified (reduced) models, obtained by using the proposed method have been worked out, of which some are presented in this section of the paper to show the efficiency of the proposed simplification technique. These examples include a 10-story building simplified as a 3-story model, a 21-story building, simplified once as a 3-story and once again as a 5-story model, a 40-story building, simplified as a 10-story model, and finally a 60-story building, simplified as a 15-story model. The original buildings have been assumed to be regular in both plan and elevation to avoid the torsion effects. The buildings have been designed by considering the drift limitation of the seismic design code, and therefore, their fundamental period values are close to the code value. Results of the 40-story and 60-story buildings are shown in this section. These results include the time histories of roof displacement, roof acceleration, base shear, and base moment of the original and the simplified buildings. Table 1 shows the modal periods of the original 40-story building and the simplified 10-story model for their first ten modes.

Table 1: Modal periods (in seconds) of the original 40-story building and its simplified 10-story model

Mode No.	40-Story Original Building	10-Story Simplified Building	Accuracy (%)
1	3.06	2.91	95
2	2.81	2.78	99
3	2.49	2.41	97
4	1.01	1.09	92
5	0.93	1.05	88
6	0.83	0.93	89
7	0.57	0.63	91
8	0.55	0.61	88
9	0.50	0.54	91
10	0.41	0.43	95

As it is seen in Table 1 the modal periods of the simplified model match very well with those of the original building. This shows that the proposed simplification technique has a very good precision. For the THA the accelerograms of two well-know earthquakes of Kobe (1996 - FUK090_AT2 Component) and El Centro (1940 - Imperial Valley Station, I-ELC180_AT2 Component) have been used, which have different frequency contents. Figures 2 to 5 respectively show the time histories of roof displacement, roof acceleration, base shear, and base moment of the original and the simplified buildings for the case of 40-story building subjected to Kobe accelerogram.

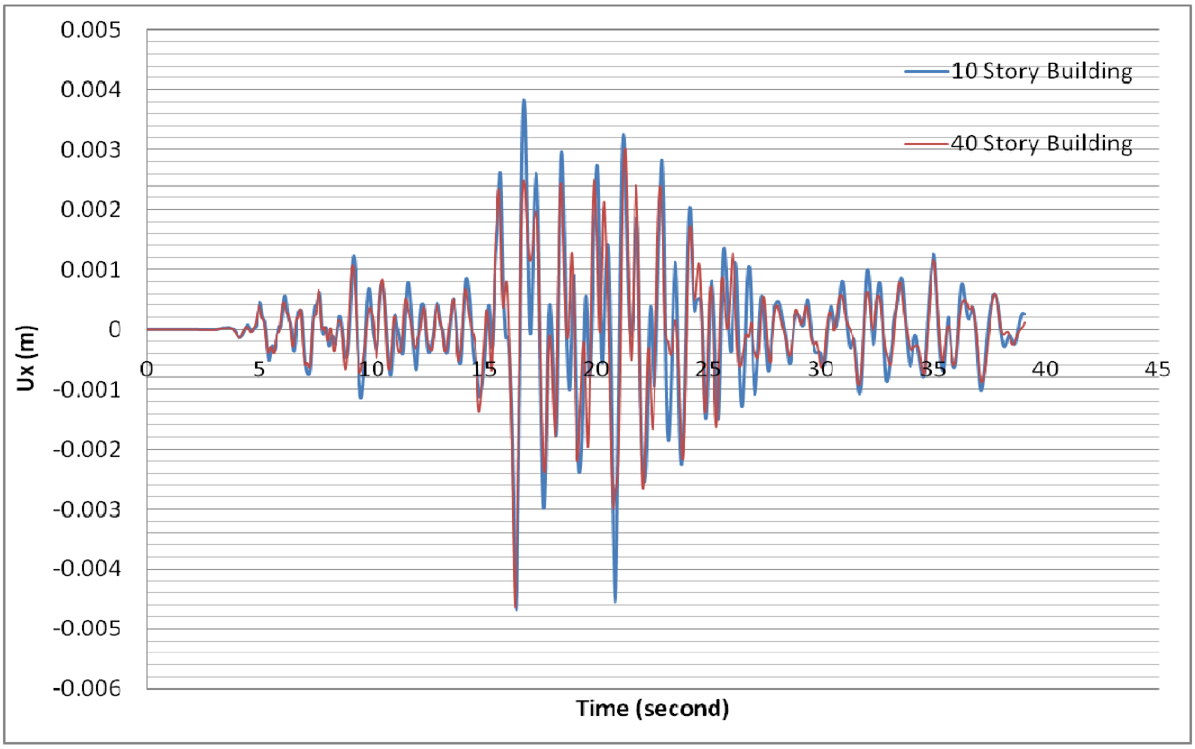

Figure 2: Roof displacement time histories of the original and simplified models for the case of 40-story building subjected to Kobe earthquake accelerogram

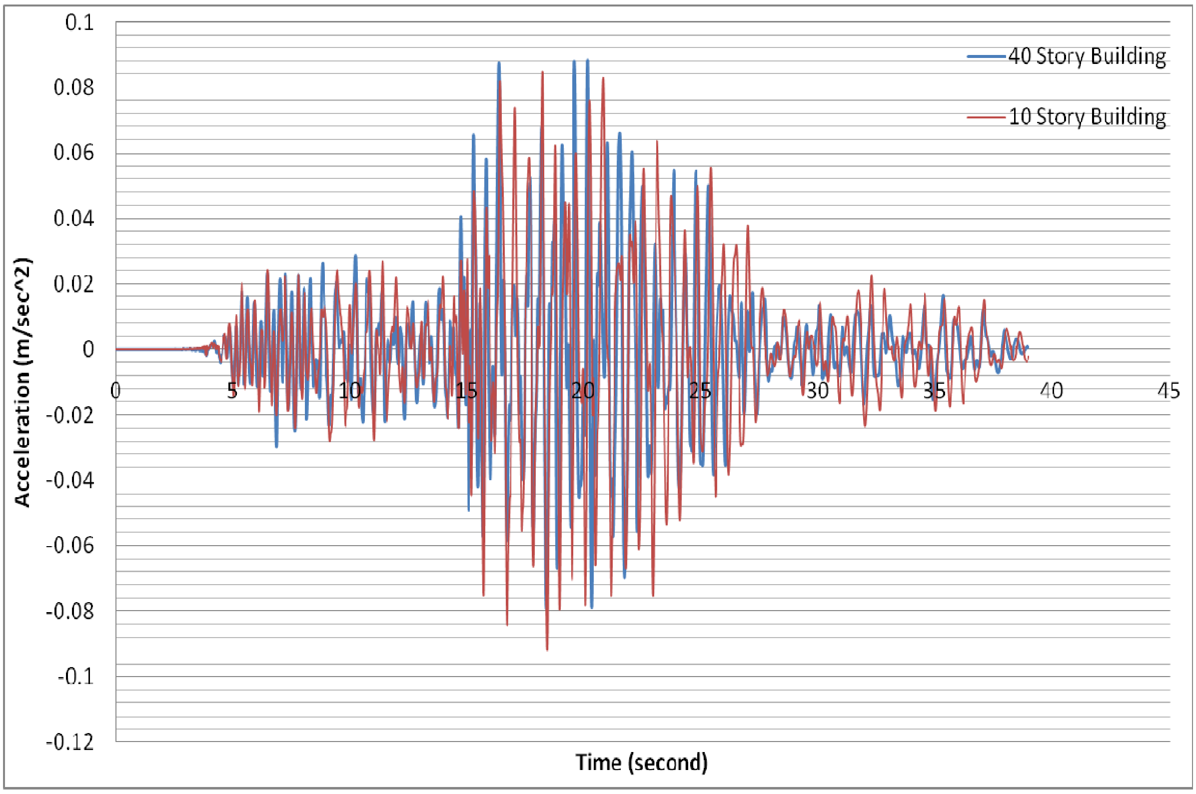

Figure 3: Roof acceleration time histories of the original and simplified models for the case of 40-story building subjected to Kobe earthquake accelerogram

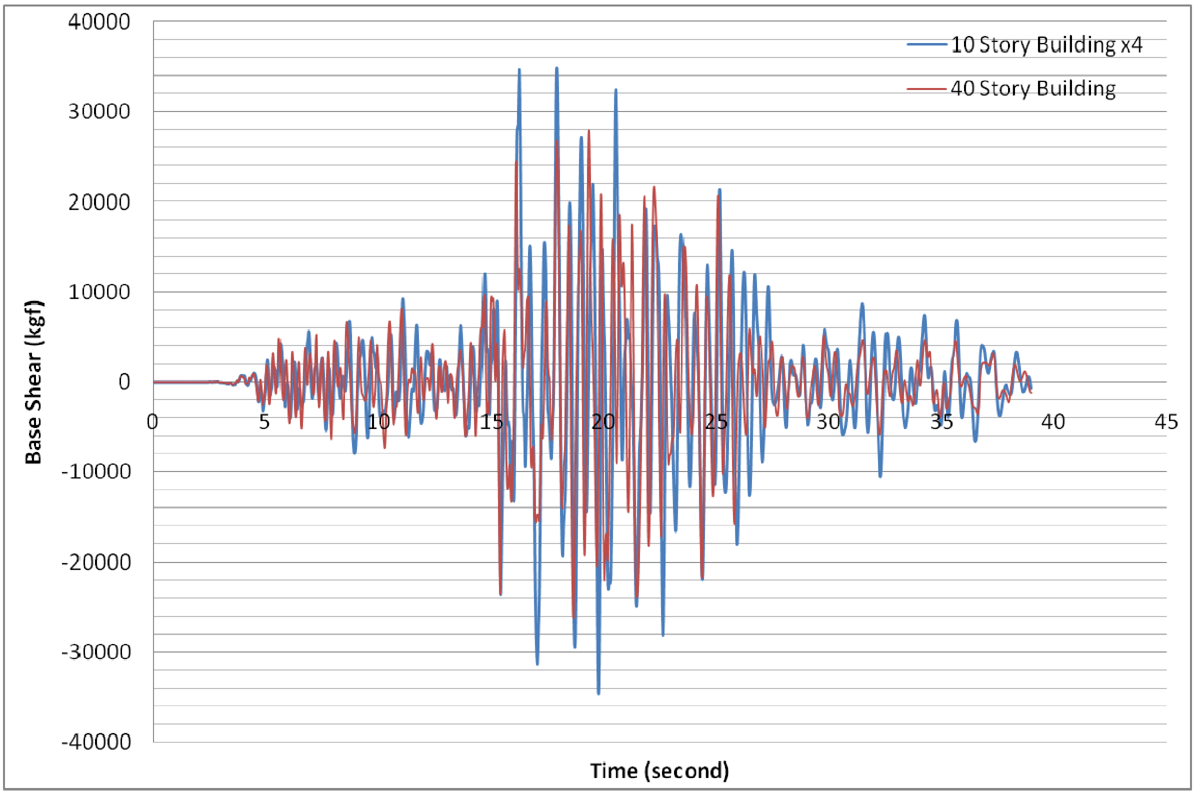

Figure 4: Base shear force time histories of the original and simplified models for the case of 40-story building subjected to Kobe earthquake accelerogram

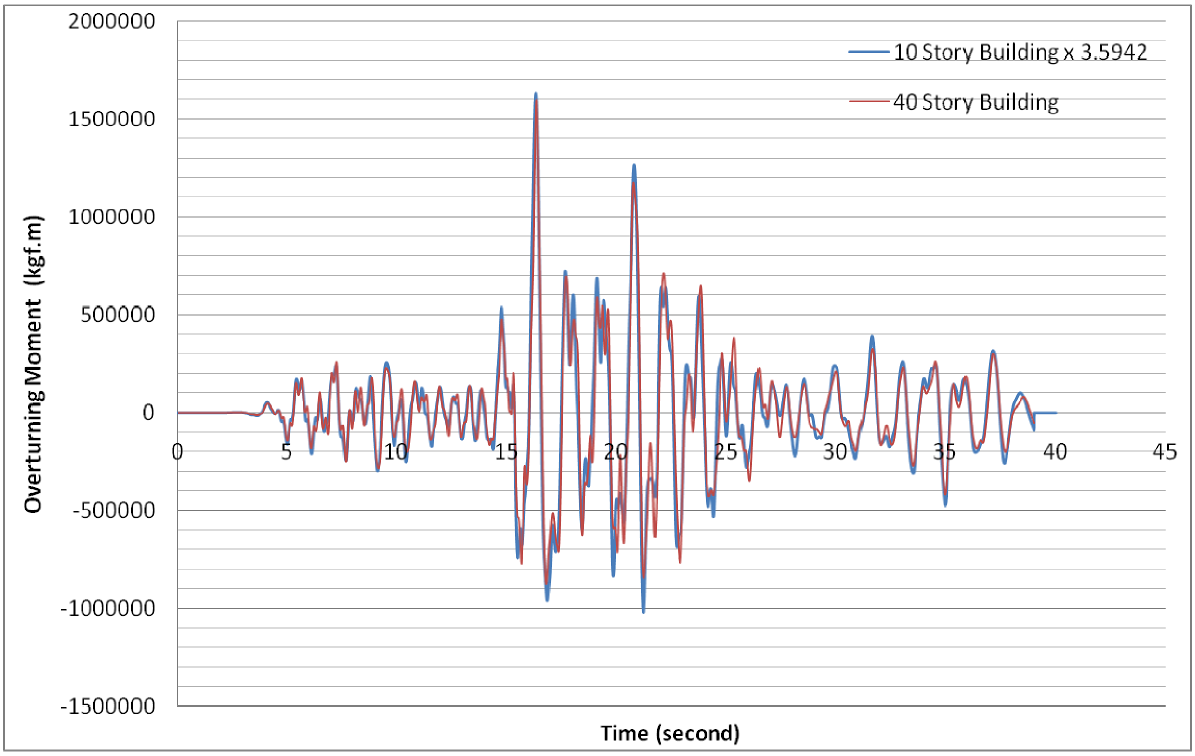

Figure 5: Base moment time histories of the original and simplified models for the case of 40-story building subjected to Kobe earthquake accelerogram

Figures 6 to 9 show the same four set of results of the 40-story building and its 10-story simplified model subjected to El Centro earthquake.

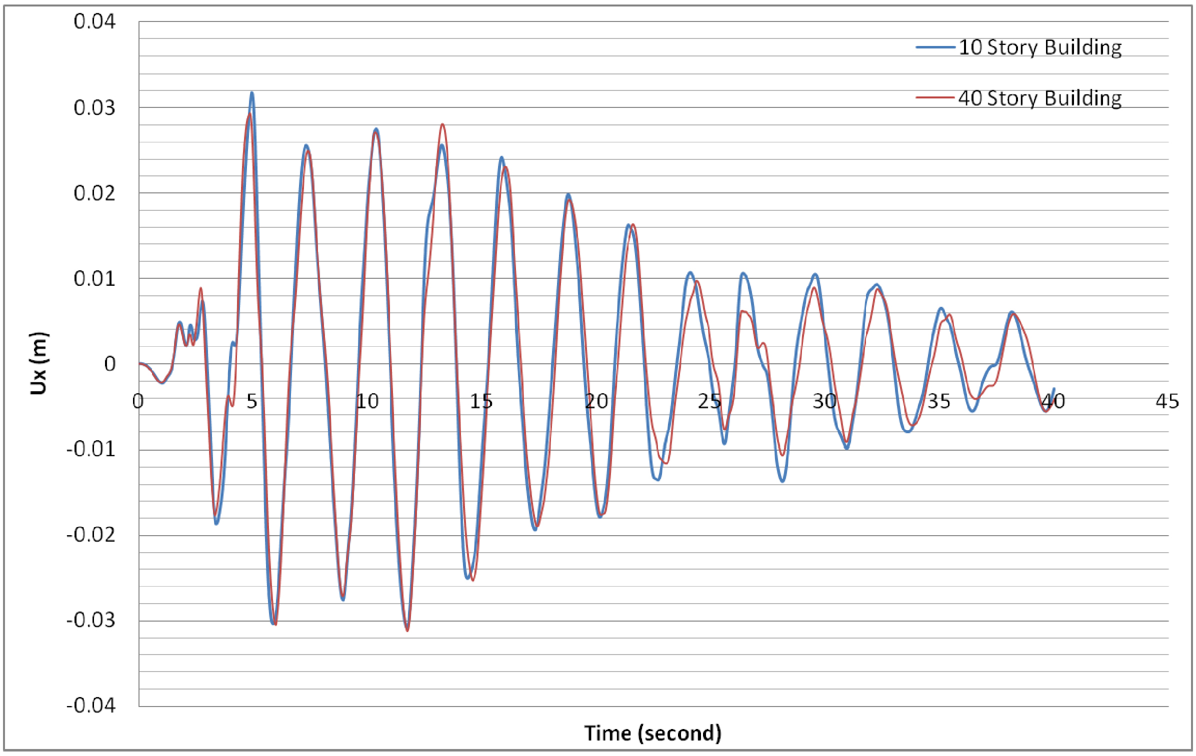

Figure 6: Roof displacement time histories of the original and simplified models for the case of 40-story building subjected to El Centro earthquake accelerogram

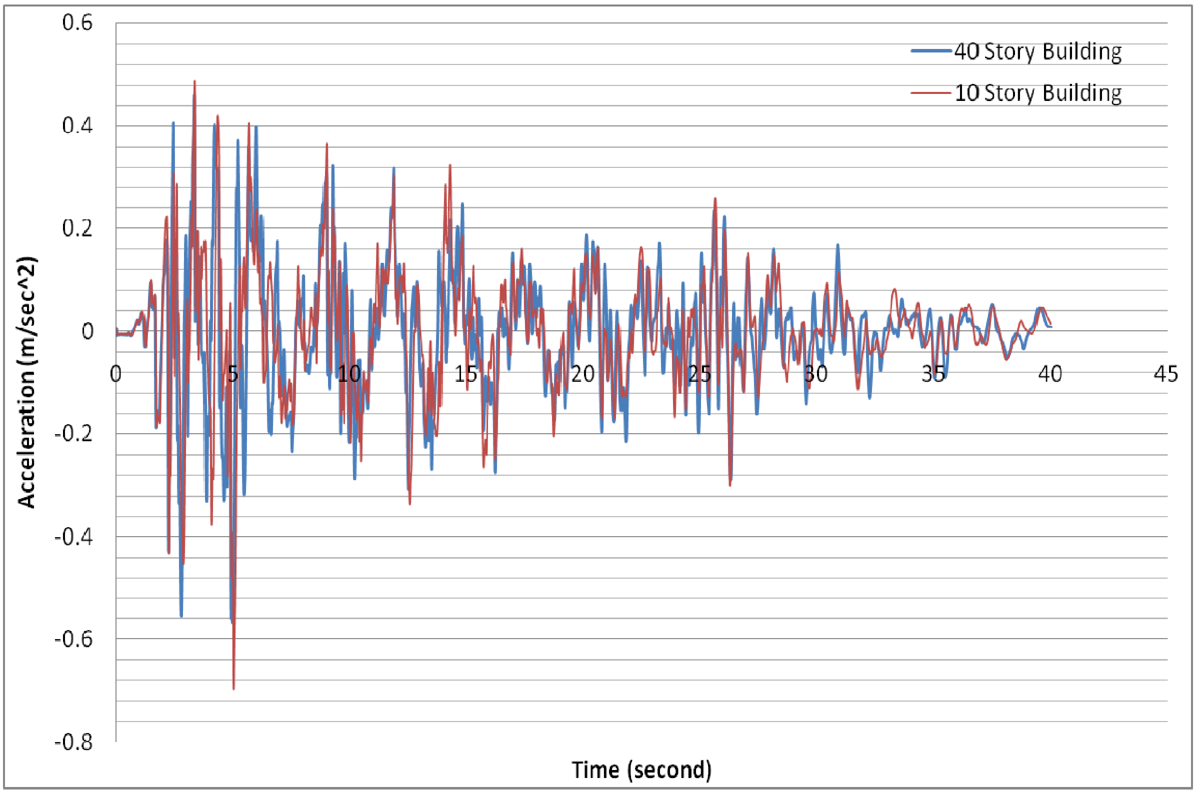

Figure 7: Roof acceleration time histories of the original and simplified models for the case of 40-story building subjected to El Centro earthquake accelerogram

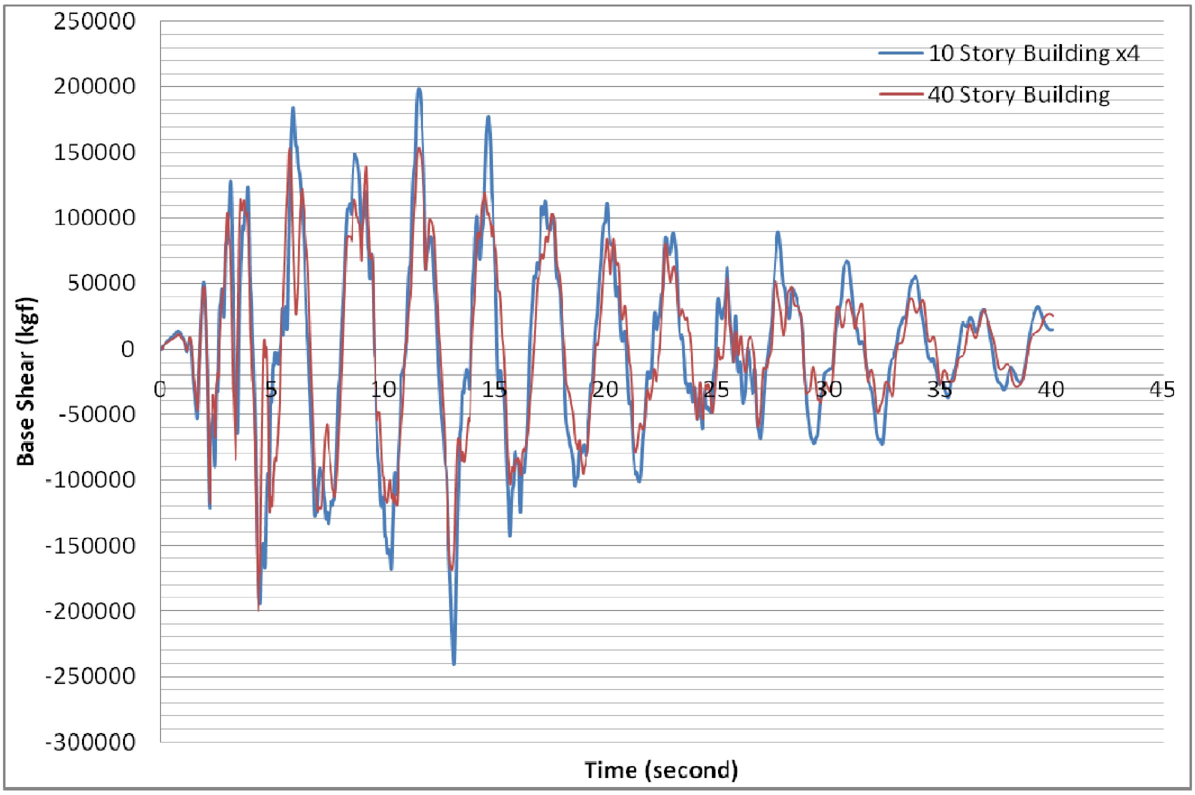

Figure 8: Base shear time histories of original and simplified models for the case of 40-story building subjected to El Centro earthquake accelerogram

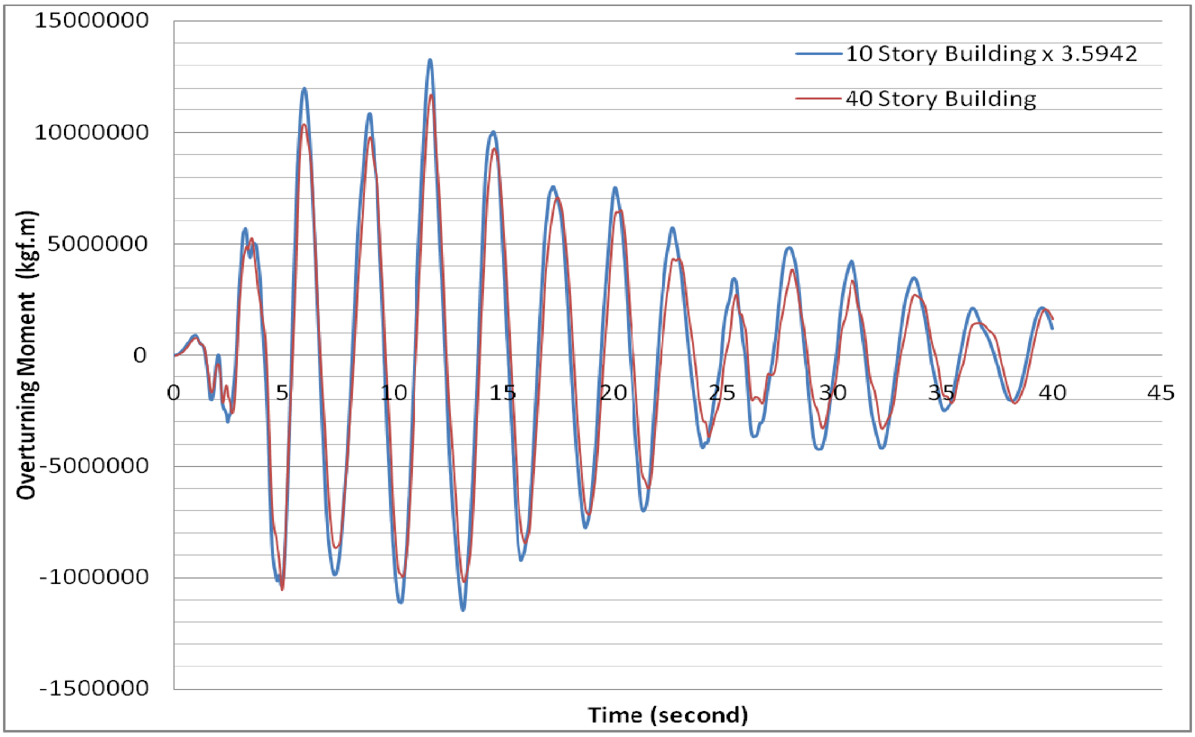

Figure 9: Base moment time histories of original and simplified models for the case of 40-story building subjected to El Centro earthquake accelerogram

Comparing Figure 2 with Figure 3 and also Figure 6 with Figure 7, it can be seen that the agreement between displacement time histories is better than that between acceleration time histories. The reason behind this fact is that the acceleration response is more sensitive than displacement response to high frequency excitations. Better agreement of results in case of El Centro earthquake than Kobe earthquake can be also due to the lower frequency content of El Centro earthquake. Table 2 compares the modal periods of the original 60-story building and its simplified 15-story model, which are again in good agreement .

Table 2: Modal periods (in seconds) of the original 60-story building and its simplified 15-story model

Mode No.	60-Story Original Building	15-Story Simplified Building	Accuracy (%)
1	4.30	4.17	97
2	3.98	3.95	99
3	3.22	2.78	86
4	1.42	1.47	97
5	1.33	1.40	94
6	1.12	1.11	98
7	0.81	0.83	97
8	0.77	0.80	95
9	0.66	0.65	98
10	0.56	0.55	100
11	0.53	0.54	99
12	0.46	0.45	96
13	0.41	0.40	96
14	0.40	0.39	98
15	0.35	0.33	94

Figures 10 to 13 show the four set of results of the 60-story building and its 15-story simplified model subjected to El Centro earthquake.

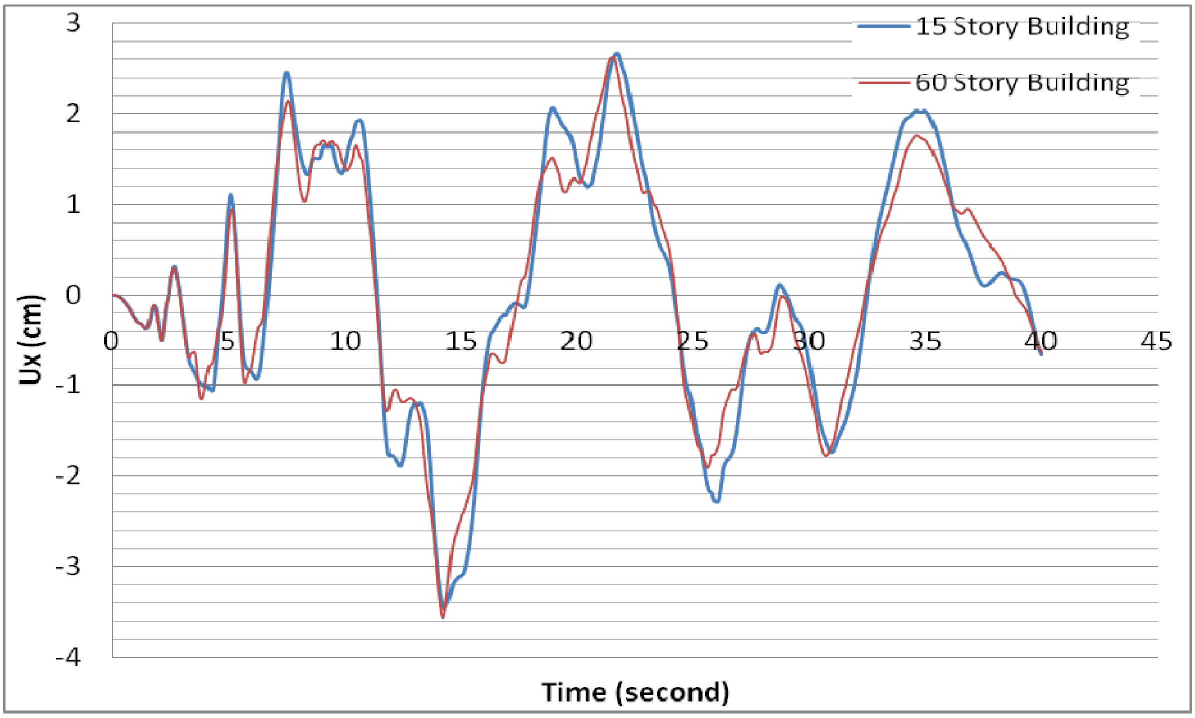

Figure 10: Roof displacement time histories of the original and simplified models for the case of 60-story building subjected to El Centro earthquake accelerogram

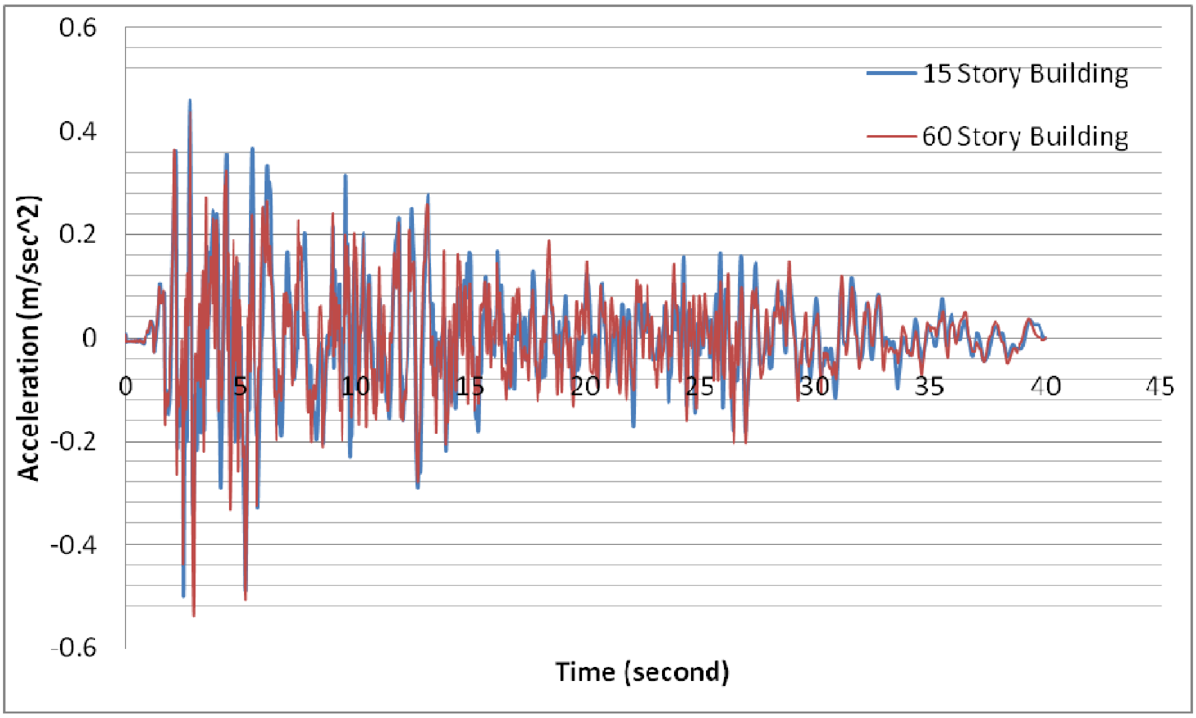

Figure 11: Roof acceleration time histories of the original and simplified models for the case of 60-story building subjected to El Centro earthquake accelerogram

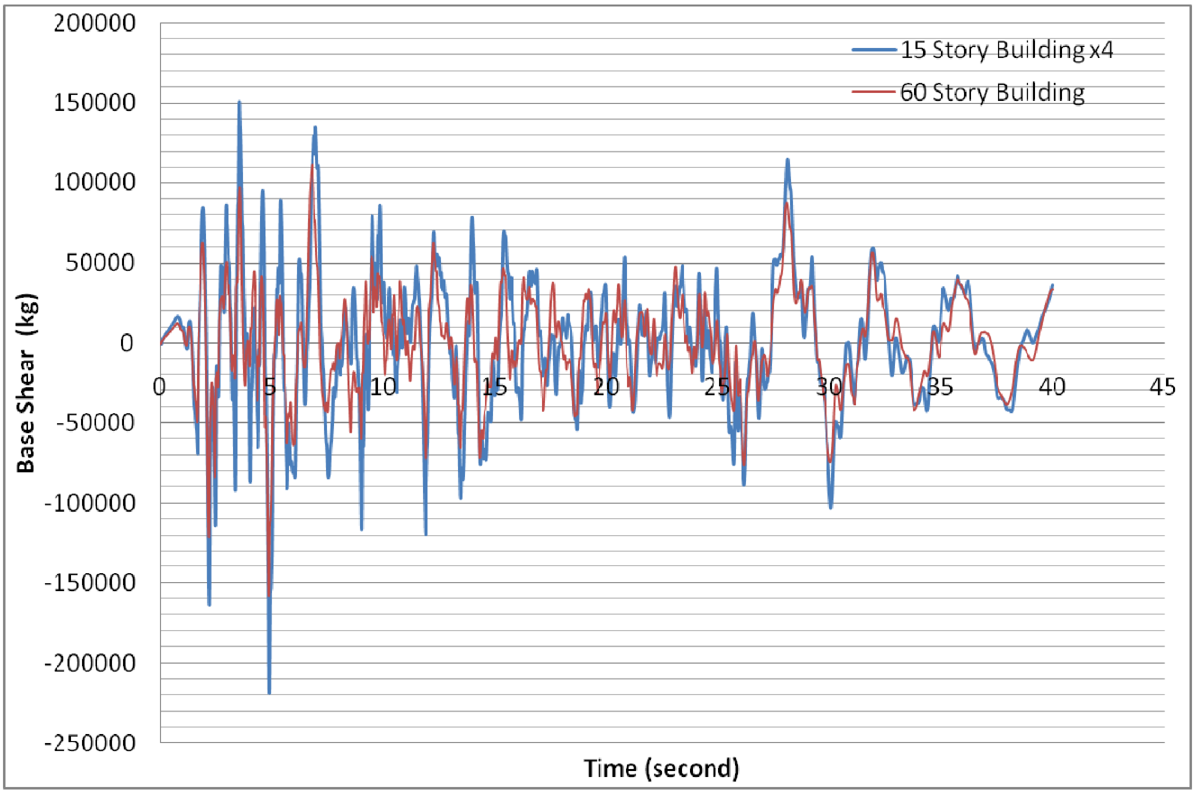

Figure 12: Base shear time histories of original and simplified models for the case of 60-story building subjected to El Centro earthquake accelerogram

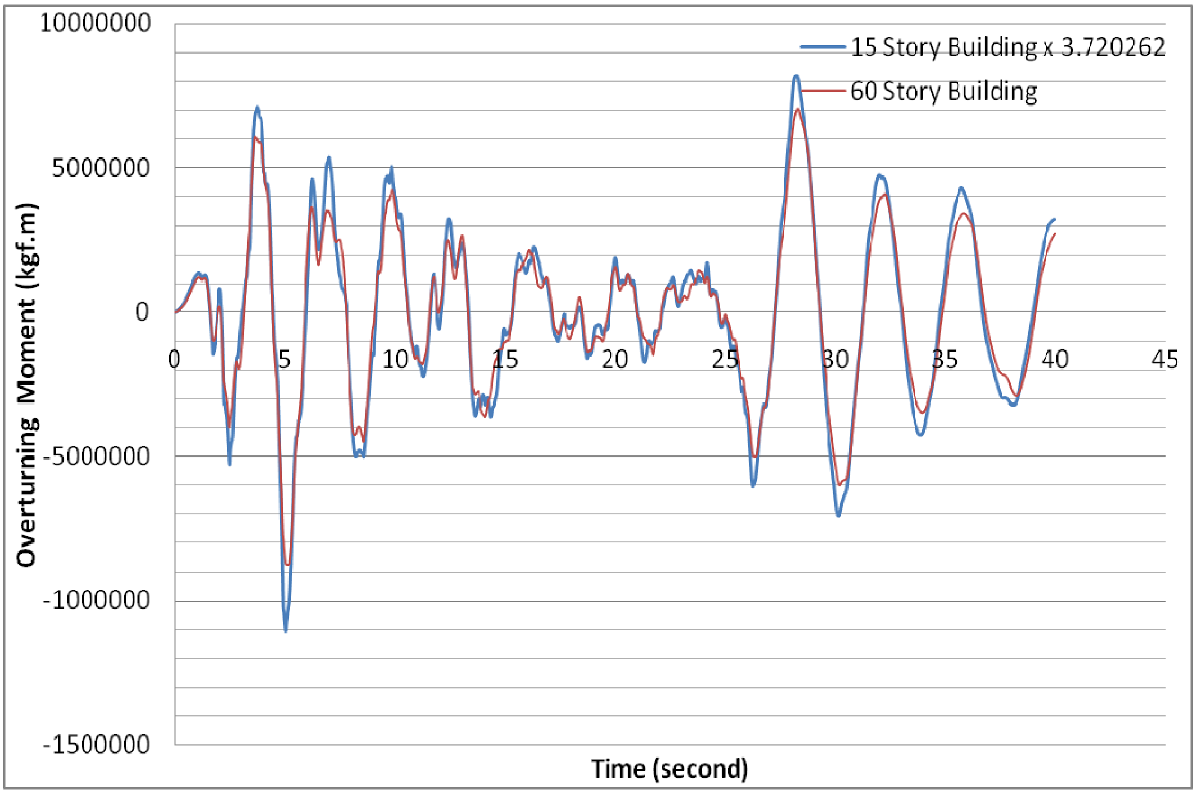

Figure 13: Base moment time histories of original and simplified models for the case of 60-story building subjected to El Centro earthquake accelerogram

Figures 10 to 13 show again that the proposed simplification technique leads to very satisfactory results, and therefore, it can be considered as a high efficiency method for THA of multi-story buildings.

4 CONCLUSIONS

Several examples of response time histories calculated for a series of multi-story buildings and their simplified reduced models, obtained by using the proposed method, show that:

- by using the proposed simplification technique the volume of elaborations needed for THA of building systems are reduced drastically.
- The amount of reduction in the ‘required calculation time’, and also the achieved level of precision in response values both depend on n and also the n/n_r ratio.
- By using a value of 4 or 5 for n/n_r ratio, the response values can be calculated with negligible error, while the required calculation time for THA is significantly reduced, particularly for buildings with larger number of stories.

REFERENCES

[1] Ernesto F. Cruz and Anil K. Chopra, Simplified Procedures for Earthquake Analysis of Buildings, *Journal of Structural Engineering*, ASCE, Vol. 112, No. 3, pp. 461-480, March 1986.

[2] Lai Ming, Li Yingmin, Xiao Mingkui, Hong Ju, Simplified Analysis for Earthquake Actions and Their Distribution on Regular High-rise Buildings, *Journal of Building Structures*, Vol. 3, 1992.

[3] Sean Wilkinson and David Thambiratnam, Simplified procedure for seismic analysis of asymmetric buildings, *Computers & Structures*, Volume 79, Issue 32, Pages 2833-2845, December 2001.

[4] Eduardo Miranda, Simplified Building Response Analysis for Rapid Seismic Performance Evaluation of Existing Buildings, *Proceedings of the International Symposium on Earthquake Engineering Commemorating Tenth Anniversary of the 1995 Kobe Earthquake* (ISEE Kobe 2005), Japan Association for Earthquake Engineering, 2005.

COMPDYN 2011
ECCOMAS Thematic Conference on
Computational Methods in Structural Dynamics and Earthquake Engineering
M. Papadrakakis, N.D. Lagaros, M. Fragiadakis (eds.)
Corfu, Greece, 26-28 May 2011

DYNAMICS OF MARINE STATIONARY PLATFORM UNDER ACTION OF HORIZONTAL SEISMIC LOADING

Vyacheslav A.Shekhovtsov[1], **Petr E.Tovstik**[2], **Tatiana M.Tovstik**[2]

[1]St. Petersburg State University of Architecture and Civil Engineering
St.Petersburg, Russia
e-mail: a.sheh-411@yandex.ru

[2]St.Petersburg State University
St.Petersburg, Russia
e-mail: peter.tovstik@mail.ru

Keywords: Earthquake, Oilindustrial Engineering, Marine Stationary Platform, Horizontal Seismic Loading, Beam Model, Tube-like Ferroconcrete Rod.

Abstract. *Dynamics of a marine stationary platform under action of the seismic loading is investigated. The structure consists of a tube-like ferroconcrete rod of variable cross-section. To describe the rod vibrations the beam-like model is used. The system of partial differential equation is reduced to the system with 6 degrees of freedom. Some numerical examples are studied. It is established that at design it is necessary to pay the main attention to the concrete strength when the extension deformations appear.*

INTRODUCTION

One of the possible structures of a marine stationary platform for the oilindustrial engineering is studied. The platform consists of a tube-like ferroconcrete rod with the upper operating floor. This structure may be used for the depth of see near 250 m. At the design of structure some external forces are to be taken into account. Among them there are the influence of a surface gravity waves, of a wind acting on the operating floor, of a water stream, and at last of an earthquake. For this structure the influence of surface waves is investigated in [1]. Here we study only the action of a horizontal seismic excitation and find the rod bending deformations. Peculiarity of this system is that its lowest natural frequency is much smaller than the typical frequency of the seismic excitation. That is why we seek the solution as a sum of 6 natural modes. For calculation we take not real, but model seismic impulse which alloys us to find the dependence of rod vibrations on its frequency. The main result of this investigation is that at design it is necessary to pay the main attention to the concrete strength when the extension deformations appear.

1 MATHEMATICAL MODEL OF PLATFORM

The structure consists of a tube-like ferroconcrete rod of variable cross-section. Below the rod is attached to the foundation which can move in the horizontal direction and rotate around the horizontal axis. The operating floor is attached above the rod. Vibrations in one plane ate studied. The attached mass of water and the resistant force of water proportional to the square of the cross-section velocity are taken into account. It is assumed that the water is stationary, influence of the surface waves and of the stream is ignored. The seismic load is horizontal, and the ground acceleration $a(t)$ is given as a function of time and in the limits of foundation it is not depend on the spatial co-ordinates. The mathematical model used here is described in [1], the difference is that instead the surface waves here the action of the seismic load is studied.

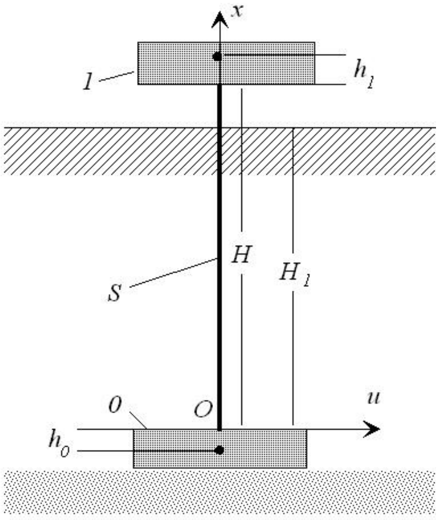

Figure 1: The structure diagram.

The foundation and the basic platform are supposed to be rigid bodies *0* and *1* (see Fig. 1), which are attached to the rod S. For the rod the beam model is accepted. Equation of the rod bending in the movable co-ordinate system is

$$\frac{\partial^2 M}{\partial x^2} + \frac{\partial}{\partial x}\left(P(x)\frac{\partial u}{\partial x}\right) + \rho(x)\frac{\partial^2 u}{\partial t^2} = f(u,x,t), \tag{1.1}$$

where

$$M = J(x)\left(\kappa\psi(\kappa,x) + \frac{\beta_0}{\omega}\frac{\partial\kappa}{\partial t}\right), \quad \kappa = \frac{\partial^2 u}{\partial x^2}, \quad f = -\rho(x)a(t) - f_v. \tag{1.2}$$

Here $u(x,t)$ is the horizontal deflection of the rod cross-section x, $0 \le x \le H$, H is the rod height, M is the bending moment, κ is the curvature, J is the rod bending stiffness in linear approximation, f is the external load her unit length. The moment M is given with the account of the nonlinear visco-elastic properties of the cross-section materials. The function ψ is describer in Section 2, in linear approximation $\psi = 1$. In (1.2) β_0 is the dimensionless resistant coefficient, ω is the typical frequency.

The water resistance force per unit length is denoted as f_v and it is equal to

$$f_v = C_v\gamma_w R(x)v|v|, \quad v = \frac{\partial u}{\partial t} + v_0, \quad v_0(t) = \int_0^t a(t)\,dt, \tag{1.3}$$

where C_v is the dimensionless coefficient, γ_w is the water density, $R(x)$ is the cross-section diameter.

In (1.1) $P(x)$ is the axial compressing force

$$P(x) = \left(m_1 + m_s - \int_0^x \rho_s(x)\,dx\right)g, \quad m_s = \int_0^H \rho_s(x)\,dx, \tag{1.4}$$

where m_1 and m_s are the masses of the body *1* and of the rod, $\rho_s(x)$ is the rod density per unit length, $g = 9.81\,(m\,c^{-2})$ is the gravity acceleration

$$\rho(x) = \rho_s(x) + \xi(x)\rho_w(x), \quad \rho_w(x) = \pi R^2(x)\gamma_w, \tag{1.5}$$

$\rho_w(x)$ is the density of the additional mass of water, and $\xi(x) = 1$ at $x < H_1$, $\xi(x) = 0$ at $x > H_1$, $H_1 < H$ is the depth of water.

The boundary conditions at the bottom $x = 0$ and at the upper end $x = H$ are the motion equations of the bodies *0* and *1*

$$\begin{aligned}
&m_0\left(\frac{d^2u_0}{dt^2} + a\right) = -\left.\frac{dM}{dx}\right|_{x=0} - P(0)\varphi(0) + F_0, \quad u_0 = u(0) - h_0\varphi(0),\\
&J_0\frac{d^2\varphi(0)}{dt^2} = M(0,t) - h_0\left.\frac{dM}{dx}\right|_{x=0} + L_0 + (h_0 - h_*)F_0,\\
&m_1\left(\frac{d^2u_1}{dt^2} + a\right) = \left.\frac{dM}{dx}\right|_{x=H} + P(H)\varphi(H), \quad u_1 = u(H) + h_1\varphi(H),\\
&J_1\frac{d^2\varphi(H)}{dt^2} = -M(H) + h_1\left.\frac{dM}{dx}\right|_{x=H}, \qquad \varphi = \frac{\partial u}{\partial x},
\end{aligned} \tag{1.6}$$

where m_0, m_1 are the bodies masses, J_0, J_1 are the central inertia moments, h_0, h_1 are the distances to the mass centers (see Fig. 1) of the bodies *0* and *1* respectively.

The non-linear force F_0 and moment L_0 of the ground and the foundation interaction are accepted as [2]

$$\begin{aligned}
&F_0 = -c_u u_* \phi_u(u_*) - \frac{\beta_u c_u}{\omega}\dot{u}_*, \quad u_* = u(0) - h_*\varphi(0), \\
&L_0 = -c_\varphi \varphi_0 \phi_\varphi(\varphi(0)) - \frac{\beta_\varphi c_\varphi}{\omega}\dot{\varphi}(0), \\
&\phi_u = \left(1 + \left|\frac{u}{u_{cr}}\right|^{m_u}\right)^{-1/m_u}, \qquad \phi_\varphi = \left(1 + \left|\frac{\varphi}{\varphi_{cr}}\right|^{m_\varphi}\right)^{-1/m_\varphi},
\end{aligned} \tag{1.7}$$

where h_* is the distance to the force horizontal center of the ground and the foundation interaction, parameters $c_u, c_\varphi, \beta_u, \beta_\varphi, m_u, m_\varphi, u_{cr}, \varphi_{cr}$ are to be given. In linear approximation $\phi_u = \phi_\varphi = 1$. The second summands in relations (1.7) take into account the visco-elastic ground properties.

2 THE BENDING ROD STIFFNESS

The rod is the three layered ferroconcrete tube with the variable cross-section (see Fig. 2). The outer layers $r_1 \le r \le r_2$ $r_3 \le r \le r_4 = R$ are steel, and the middle layer $r_2 \le r \le r_3$ is concrete.

$$r_k(x) = r_{k0} - bx, \; k = 1,2,3,4, \quad b = \frac{R_0 - R_1}{H}, \tag{2.1}$$

where r_{k0} are the layers radii at $x = 0$, R_0 and R_1 are the radii of lower and upper tube cross-sections.

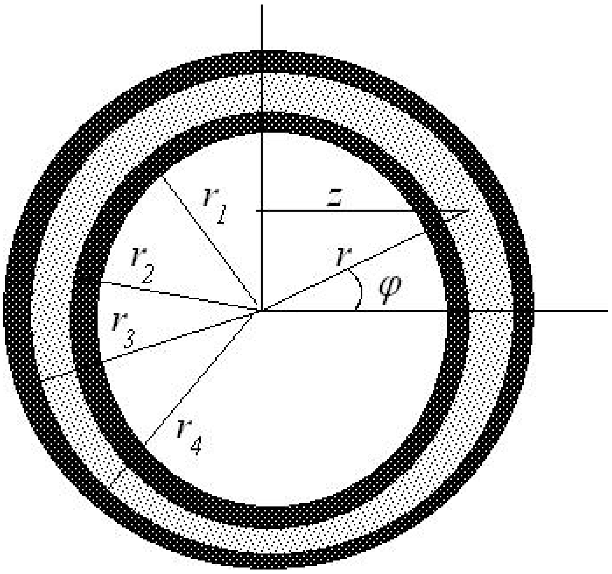

Figure 2: The three layered tube cross-section.

We accept the following dependences between stresses σ and strains ε (in the vertical direction neglecting the other stresses and strains):
for the steel

$$\sigma = E_s \begin{cases} -\varepsilon_s & at \quad \varepsilon < -\varepsilon_s, \\ \;\;\varepsilon & at \quad |\varepsilon| \le \varepsilon_s, \\ \;\;\varepsilon_s & at \quad \varepsilon > \varepsilon_s, \end{cases} \qquad \sigma_s = E_s \varepsilon_s \tag{2.2}$$

and for the concrete

$$\sigma = E_c \begin{cases} -\varepsilon_c & at \quad \varepsilon < -\varepsilon_c, \\ \varepsilon & at \quad -\varepsilon_c \le \varepsilon \le 0, \\ 0 & at \quad \varepsilon > 0, \end{cases} \qquad \sigma_c = E_c \varepsilon_c. \tag{2.3}$$

Here E_s E_c are the Young modules for steel and for concrete, ε_s is the yield limit of steel which is accepted identical at extension and at compression, ε_c is the flowing limit for concrete at compression. Relations (2.2) and (2.3) correspond to the Prandtl model, and relation (2.3) fixes the assumption that the concrete does not resist the extension. In the linear approximation the both materials are linearly elastic ones, and for the steel $\sigma = E_s\varepsilon$ and for the concrete $\sigma = E_c\varepsilon$.

The rod cross-section x is compressed by the axial force P and let the curvature $\kappa(x)$ is given. Our aim is to find the dependence between the bending moment M and the curvature κ. It is supposed that the hypothesis about the plane cross-sections if fulfilled. According to this hypothesis the deformation ε of the fibre lying at the distance z from the cross-section diameter is equal

$$\varepsilon(r, \varphi) = \varepsilon_0 + \kappa z, \quad z = r\cos\varphi. \tag{2.4}$$

In the linear approximation

$$\begin{aligned} P &= -K\varepsilon_0, \qquad K = \pi \left(E_s(r_2^2 - r_1^2) + E_c(r_3^2 - r_2^2) + E_s(r_4^2 - r_3^2)\right), \\ M &= J\kappa, \qquad J = \frac{\pi}{4}\left(E_s(r_2^4 - r_1^4) + E_c(r_3^4 - r_2^4) + E_s(r_4^4 - r_3^4)\right). \end{aligned} \tag{2.5}$$

Due to the compression $P > 0$ we get $\varepsilon_0 < 0$, therefore for the small enough curvature κ the linear relations (2.5) are valid. At

$$|\kappa| > \kappa_* = \min\left\{\frac{\varepsilon_0 + \varepsilon_s}{r_4}, \frac{\varepsilon_0 + \varepsilon_c}{r_3}, \frac{-\varepsilon_0}{r_3}\right\} \tag{2.6}$$

one or the both materials become as the nonlinear ones and the relations (2.5) are to be corrected.

$$P = \int \sigma(r, \varphi, \varepsilon_0)\, r\, dr\, d\varphi, \qquad M = \int \sigma(r, \varphi, \varepsilon_0)\, r^2 \cos\varphi\, dr\, d\varphi, \tag{2.7}$$

where the integration is fulfilled on the circular area occupied by materials, and the stress $\sigma(r, \varphi, \varepsilon_0)$ is calculated by the relation (2.2) or (2.3). If the curvature κ and the compressing force P are given then by the first relation (2.7) we find the deformation ε_0, and then by the second relation (2.7) we calculate the moment M. Therefore the function $\psi(\kappa) = M/(J\kappa)$ is build.

3 THE MODEL OF THE GROUND ACCELERATION AT THE EARTHQUAKE

For the analytical description of the acceleration $a(t)$ we use the relation

$$a(t) = At^2 e^{-\alpha t} \sin(\nu t + \theta). \tag{3.1}$$

It is necessary to put the following restriction on the function $a(t)$

$$\int_0^\infty a(t)dt = 0, \tag{3.2}$$

because in the opposite case the ground will move after the seismic impulse is finished. For the function (3.1) the relation (3.2) is fulfilled if

$$\alpha(3\nu^2 - \alpha^2)\sin\theta + \nu(\nu^2 - 3\alpha^2)cos\theta = 0. \tag{3.3}$$

In Fig. 3 the impulse with the parameters $A = 0.295$, $\alpha = 0.4$, $\nu = 10$ is shown (the value θ is to be found from the equation (3.3)).

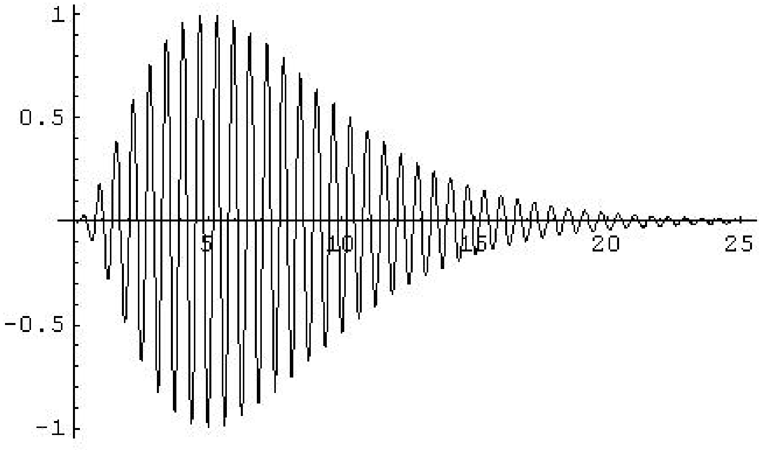

Figure 3: The seismic impulse.

4 THE APPROXIMATE SOLUTION OF THE EQUATION (1.1)

In Sections 1–3 the problem is formulated. We seek its solution satisfying to the initial condition $u(x, 0) = 0$ as a partial sum of the Fourier series of eigen functions $U_k(x)$ of the linear boundary value problem

$$u(x,t) = \sum_{k=1}^{K} U_k(x) q_k(t). \tag{4.1}$$

The boundary value problem for natural modes $U_k(x)$ and for the corresponding natural frequencies ω_k is to be obtained from equation (1.1) and boundary conditions (1.6) after replacements

$$\frac{\partial^2}{\partial t^2} = -\omega^2, \quad f = a = \beta_0 = \beta_u = \beta_\varphi = 0, \quad \psi = \phi_u = \phi_\varphi = 1. \tag{4.2}$$

For $\omega_k \neq \omega_n$ the natural modes satisfy to the orthogonality condition

$$\int_0^H \rho U_k U_n dx + m_0 U_{k0} U_{n0} + J_0 U_k'(0) U_n'(0) + m_1 U_{k1} U_{n1} + J_1 U_k'(H) U_n'(H) = 0, \tag{4.3}$$

Where by the trait the derivative with respect to x is denoted.

At $n = k$ the left side of the equality (4.3) gives the equivalent mass M_k corresponding to the k^{th} natural mode

$$M_k = \int_0^H \rho U_k^2 dx + m_0 U_{k0}^2 + J_0 (U_k'(0))^2 + m_1 U_{k1}^2 + J_1 (U_k'(H))^2. \tag{4.4}$$

To construct the equations for unknowns $q_k(t)$ in (4.1) we use the Bubnov–Galerkin method according which the work of active forces and of inertia forces on the displacement $U_k(x)$ is equal to zero. As a result we get

$$M_k \left(\ddot{q}_k + \beta_k \omega_k \dot{q}_k + \omega_k^2 q_k \right) + M_k^a a = Q_v + Q_s + Q_F, \quad k = 1, \dots, K. \tag{4.5}$$

whis

$$M_k^a = \int_0^H \rho U_k \, dx + m_0 U_{k0} + J_0 U_k'(0) + m_1 U_{k1} + J_1 U_k'(H). \tag{4.6}$$

By dots the derivatives with respect to time t are denoted. The summand $\beta_k\omega_k\dot{q}_k$ in (4.5) (β_k are the dimensionless resistant coefficients) takes into account the resistance of the k^{th} natural mode. Here we make the additional assumption that the decreases of various natural modes are not connected to each other. As Q_k^v, Q_k^s Q_k^F we denote the nonlinear generalized forces which are connected with the resistance of water, with the plastic properties of the rod, and with the interaction forces between the foundation and the ground respectively

$$\begin{aligned}
&Q_k^v = -\int_0^H C_v\gamma R(x)v|v|U_k(x)dx, \quad v = \int_0^t a(t)\,dt + \sum_{i=1}^K U_i(x)\dot{q}_i(t),\\
&Q_k^s = -\int_0^H J(x)(1-\psi(\kappa))U_k''(x)dx, \quad \kappa = \sum_{i=1}^K U_i''(x)\dot{q}_i(t),\\
&Q_k^F = c_u u_*(1-\phi_u(u_*))U_{k*} + c_\varphi u'(0)(1-\phi_\varphi(u'(0)))U_k'(0), \qquad (4.7)\\
&\qquad u_* = \sum_{i=1}^K (U_i(0) - h_*U_i'(0))q_i(t), \quad U_{k*} = U_k(0) - h_*U_k'(0),\\
&\qquad u'(0) = \sum_{i=1}^K U_i(0)q_i(t).
\end{aligned}$$

At $Q_v = Q_s = Q_F = 0$ the system (4.5) divides to K independent equations.

5 NUMERICAL RESULTS.

We fix the values of structure parameters and study the series of values of parameters of the seismic acceleration in (3.1).

We take the following parameters given in SI. The dimensions of structure and radii of the rod layers: $H_1 = 235$, $H = 250$, $r_{10} = 4.9$, $r_{20} = 4.95$, $r_{30} = 5.95$, $r_{40} = R_0 = 6$, $R_1 = 5$. The densities of water, steel, and concrete: $\gamma_w = 10^3$, $\gamma_s = 7.85\cdot 10^3$, $\gamma_c = 2.2\cdot 10^3$. The Young modules and the yield limits of steel and concrete: $E_s = 2.06\cdot 10^{11}$, $E_c = 0.131E_s$, $\varepsilon_s = 0.00134$, $\varepsilon_c = 1.16\varepsilon_s$. The mass parameters and the distances to the mass centers of bodies *0* and *1*: $m_s = 2.32\cdot 10^7$, $m_0 = 10^7$, $m_1 = 10^7$, $J_0 = 15m_0$, $J_1 = 10m_1$, $h_0 = 3$, $h_1 = 3$. The foundation parameters: $c_u = 10^7$, $c_\varphi = 10^{12}$, $u_{cr} = 10$, $\varphi_{cr} = 0.1$, $m_u = 2$, $m_\varphi = 2$. The visco-elastic resistant parameters: $\beta_k = 0.1,\ k = 1,2,3,4$. The resistant coefficient of motion in water $C_v = 2.2$.

We take $K = 6$. In Table 1 there are the first six natural frequencies ω_k, the corresponding periods, and the mass parameters $M_k,\ M_k^a$.

k	1	2	3	4	5	6
ω_k	0.256	0.688	3.117	8.158	15.89	26.39
T_k	24.56	9.15	2.02	0.77	0.40	0.24
$M_k\cdot 10^{-7}$	2.58	7.20	7.19	19.30	66.13	931.00
$M_k^a\cdot 10^{-7}$	1.32	−0.22	2.52	1.42	4.91	46.28
M_k^a/M_k	0.514	−0.031	0.351	0.074	0.071	0.050

Table 1: The natural frequencies and the mass parameters.

In the last line of Table 1 there is parameter M_k^a/M_k, which characterizes the level of the k^{th}

eigen mode excitation. We see that the modes with $k = 1$ and $k = 3$ are excited larger than the other ones.

We bound with the analysis of the seismic impulses of the form shown in Fig. 3 and change the maximal amplitude $A_{max} = \max_t |a(t)|$ and frequency ν. Then the parameters in (3.1) are $A = 0.295 A_{max},\ \alpha = 0.4$, and the parameter θ is to be found from (3.3).

We change the frequency ν of seismic impulse in the limits $0.5 \le \nu \le 30$ (1/c), and will increase A_{max} nd fix the value, for which the rod material turns in the nonlinear area according the condition (2.6). Calculations show (see also Table 2) that in all studied cases the condition when the concrete is extended is critical. Such deformations are inadmissibe from the point of view of the concrete strength.

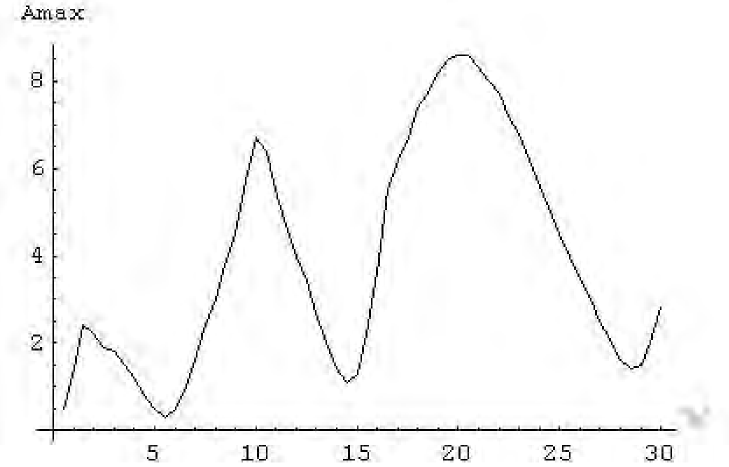

Figure 4: The boundary of the parameters ($\nu\,(1/c), A_{max}\,(m/c^2)$) area, below which the concrete is compressed only.

In Fig. 4 the boundary of parameters area in the plane (ν, A_{max}), upper which the concrete may be stretched. The more dangerous are impulses with the lower values of the frequency ν, which are not typical for the seismic ones. For seismic impulses the values $10 \le \nu \le 300$ [3]. Here the impulses with $\nu \le 30$ are studied because for $\nu > 30$ the used beam model is doubtful.

k	ν	A^{k0}_{max}	$u^{k0}(H_1)$	A^{ks}_{max}	$u^{ks}(H_1)$	A^{kc}_{max}	$u^{kc}(H_1)$
1	10	6.7	0.06	18.1	0.24	24.4	0.28
2	15	1.3	0.01	14.4	0.07	14.9	0.08
3	20	8.6	0.02	23.7	0.07	33.3	0.10

Table 2: The amplitudes of transition in the nonlinear area of the rod deformations.

In Table 2 three values of ν are studied, and the values ν_1 and ν_3 correspond to the points of the relative maximum of the curve $A_{max}(\nu)$ (Fig. 3), and ν_2 corresponds to the minimal point. As A^k_{max} and $u^k(H_1)$ the maximal amplitude of the seismic impulse (in m/c^2) and the maximal deflection of the upper body *1* (in m). Indexes $0,\ s,\ c$ correspond to appear extended deformations in concrete, to appear the yield of steel and to appear the yield of concrete at compression. It is clear that the values A^{ks}_{max} and A^{kc}_{max} are too large for seismic impulses. Therefore at design it is necessary to pay the main attention to the concrete strength.

6 CONCLUSIONS

In book [1] there is the investigation of the platform dynamics under action of surface gravity waves. In this problem the typical frequency of waves in some cases is close to the first natural frequency of structure. That is why it is possible in [1] to reduce the system to the single equation of the first order (with $K = 1$). At the seismic excitation the typical frequencies are much larger than the first natural frequency of structure. We take $K = 6$ but for $\nu > 30$ the exactness of the system (1.1) is not enough (see the values ω_k in Table 1) and it is desirable to use the more complex mathematical models of this structure.

Plans of the following investigation of this structure may consist in the complification of model by introducing the shear rod deformations. It is important in one side if we want to study the seismic excitations with the more high frequencies, and in the other side to take an attention that the concrete badly hold the shear stresses. Also it is necessary to study the vertical seismic excitation and the corresponding vertical vibrations of the rod. At last it is desirable to study the simultaneous action of the horizontal and the vertical seismic excitation and the interaction of the bending and the longitudinal rod vibrations.

Here we take the model seismic impulse. It seems that the real random seismic impulse with the same maximal amplitude leads to the smaller amplitude of the rod vibrations. Nevertheless it is desirable to study the structure reaction under action of the random seismic impulse with the given spectral density.

ACKNOWLEDGEMENTS

The work is supported by the Russian Foundation of Basic Researches, grant 10.01.00420 a.

REFERENCES

[1] V.A. Shekhovtsov. *Random nonlinear vibrations of the marine stationary platforms*. St. Petersburg. 2004. 246 p. (in Russian)

[2] Ju.M. Kolesnikov. *Investigation and design of piles. In.: Oilindustrial engineering*. Moscow. 1980. (in Russian)

[3] A.N. Birbraer. *Design of structures to seismic resistance*. St. Petersburg. ”Nauka”. 1998. 255 p. (in Russian)

COMPDYN 2011
III ECCOMAS Thematic Conference on
Computational Methods in Structural Dynamics and Earthquake Engineering
M. Papadrakakis, M. Fragiadakis, V. Plevris (eds.)
Corfu, Greece, 26–28 May 2011

SIMPLIFIED DYNAMIC ANALYSIS OF SLOSHING PHENOMENON IN TANKS WITH MULTIPLE BAFFLES SUBJECTED TO EARTHQUAKE

Mahmood Hosseini[1] and Pegah Farshadmanesh[2*]

[1] Structural Eng. Research Center, Int'l Institute of Earthquake Engineering and Seismology (IIEES)
No. 21 Arghavan, North Dibaji St., Farmanieh, Tehran 19537, Iran
hosseini@iiees.ac.ir

[2] Hydraulic Eng. Group, Civil Eng. Dept., Tehran South Branch of the Islamic Azad University (IAU)
Ahang Blvd, Tehran, Iran
(p.farshadmanesh@gmail.com)

Key words: Multiple vertical baffles**,** Time history analysis, Neural network, Required calculation time

Abstract. *Sloshing is a well-known phenomenon in liquid storage tanks subjected to base or body motions. In recent years the use of baffles for reducing the sloshing effects in tanks subjected to earthquake has been studied by some researchers. However, the use of multiple baffles has not been taken into consideration so much. On the other hand, although some of the existing computer programs are capable to model sloshing phenomenon by acceptable accuracy, the full dynamic analysis subjected to random excitations such as earthquake induced motions is very time consuming, particularly when there are vertical and horizontal baffles inside the tank, which postpone the convergence of response calculations. Therefore, a simplified method for evaluation of sloshing effects in baffled tanks is desired. In this paper a method is presented for this purpose based on conducting several dynamic analysis cases, by using a powerful Finite Element (FE) method for rectangular tanks with various dimensions, subjected to both harmonic and seismic excitations, and then using neural network to create simple relationships between the dominant frequency and amplitude of the base excitations and the maximum level of liquid in the tank during the sloshing and also the maximum dynamic pressure on the tank wall. At first, the FE numerical modeling has been verified by using some existing experimental data. Then, dynamic analyses have been conducted to obtain the required numerical results for teaching the neural network. In the next stage, the neural network model has been developed. Finally, the predicted results of the neural network have been compared with those obtained by some other cases of analyses as control values, to make sure on the accuracy of the neural network model. The proposed simplified neural network model can be used also for finding the proper number and features of baffles for minimizing the sloshing effect on the tank for a group of given earthquakes, or other cases of base excitations.*

1 INTRODUCTION

One of the most important phenomena in fluid storage tanks, either buried, semi-buried, aboveground or elevated, is the oscillation of fluid due to the movements of the tank body, because of its base motions during an earthquake. Past earthquakes have shown that this phenomenon can result in sever damages to water storage tanks. To prevent tanks against sloshing induced damages, the use of baffles have been suggested and studied by some researchers since mid 60s [1], however, just few studies have been conducted on using baffles for reducing the earthquake induced sloshing effects.

As one of the first works in this regard Shaaban and Nash (1977) studied on response of partially filled liquid-storage circular cylindrical tank with or without an interior cylindrical baffle under seismic actions using Finite Element (FE) technique [2]. They worked on an elastic cylindrical liquid storage tank attached to a rigid base slab. Their studied tank was either empty or filled to an arbitrary depth with an in-viscid, incompressible liquid. They presented a FE analysis for both tank and liquid, to investigate the free vibration of the coupled system permitting determination of natural frequencies and associated mode shapes. They employed Sanders shell theory to express the strain-displacements relationship in the derivation of the shell FE. They determined the response of the tank to artificial earthquake excitation, and performed similar investigations with the addition of an elastic cylindrical perforated baffle to control the system natural frequencies.

In 1999 Gedikli and Ergüven worked on the seismic analysis of a liquid storage cylindrical tank with a rigid baffle [3]. In that study the fluid was assumed to be incompressible and in-viscid, and its motion was assumed to be ir-rotational. They implemented method of superposition of modes to compute the seismic response, and used the boundary element method to evaluate the natural modes of liquid in the tank. In that study the linearized free surface conditions was taken into consideration.

Yasuki and his colleagues (2000) conducted a study on suppression of seismic sloshing in cylindrical tanks with baffle plates [4]. The purpose of that study was proposing the evaluation model of damping characteristics of cylindrical tank with ring baffle plates. They carried out shaking table tests, in which the location and geometry of the baffle plates were varied, with sinusoidal excitation. Their experimental results showed that the damping characteristic is dependent on the location and geometry of baffle plates. Their model for solid baffle plates was extended to be applicable to both solid and perforated baffle plates, and the validity of their evaluation model was confirmed with the experimental results.

Maleki and Ziyaeifar (2007) conducted a study on damping enhancement of seismic isolated cylindrical liquid storage tanks using baffles [5]. Mentioning that in moving liquid containers, baffles play an important role in damping the liquid motion, to study the effects of using baffles in seismically isolated tanks, in the first instance they have analyzed the velocity contours in a cylindrical tank to determine the most effective shape of baffle. Then they have determined the damping coefficients analytically for horizontal ring shape and vertical blade shape baffles. To estimate the sloshing height level and the damping ratio, Maleki and Ziyaeifar have developed a methodology, based on Tank Body Spectra, in which the higher sloshing amplitude and the relative fluid velocity with respect to baffles in base isolated tanks are taken into consideration. They have also developed a computer program to put all these together and investigate the effect of baffles for different tank dimensions under the effect of earthquakes. Their results show that the average damping ratio of sloshing mode due to ring baffle increases with a decrease in liquid height and highest damping may be achieved for height to radius ratios of 1.0 to 1.5. In addition, for reasonable ring baffle dimensions, an average reduction of 6% in base displacement of base isolated tanks and an average reduction of more than 30% in the sloshing height of base isolated and fixed base tanks may be achieved. To study the effect of baffles on the distribution of hydrodynamic and tank body forces with height, Maleki and Ziyaeifar have proposed a simple dynamic model. The results of analyses using this model indicate a constant reduction in sloshing forces and different reductions in moment and shear forces for different heights. This happens because contribution of the sloshing force to the total hydrodynamic force varies with height.

Wu (2010) has conducted a thorough study the nonlinear liquid sloshing in a 3D tank with baffles, in which the mechanism of liquid sloshing and the interaction between the fluid and internal structures have been investigated [6]. He has applied a developed 3D time-independent finite difference method to solve liquid sloshing in tanks with or without the influence of baffles under the ground motion of six-degrees of freedom. He has solved the 3D Navier-Stokes equations and has transformed to a tank-fixed coordinate system, and has considered the fully nonlinear kinematic and dynamic free surface boundary conditions for fluid sloshing in a rectangular tank with a square base. In that study the fluid was assumed incompressible. The complicated interaction in the vicinity of the fluid-structure interface was solved by implementing one dimensional ghost cell approach and the stretching grid technique near the fluid-structure boundaries were used to catch the detailed evolution of local flow field. A PC-cluster was established by linking several single computers to reduce the computational times due to the implementation of the 3D numerical model. The Message Passing Interface (MPI) parallel language and MPICH2 software were utilized to code the computer codes and to carry out the circumstance of parallel computation, respectively.

Wu has verified his developed numerical scheme by rigorous benchmark tests, and has also performed some further experimental investigations [6]. In that study for a tank without internal structures, the coupled motions of surge and sway were simulated with various excitation angles, excitation frequencies and water depths. The characteristics of sloshing waves were dissected in terms of the classification of sloshing wave types, sloshing amplitude, beating phenomenon, sloshing-induced forces and energy transfer of sloshing waves. Six types of sloshing waves, named single-directional, diagonal, square-like, swirling-like, swirling and irregular waves, were found and classified in Wu’s study and he found that the occurrence of these waves are tightly in connection with the excitation frequency of the tank. The effect of excitation angle on the characteristics of sloshing waves was explored and discussed, especially for swirling waves. In that study the spectral analyses of sloshing displacement of various sloshing waves were examined and a clear evidence of the correlation between sloshing wave patterns and resonant modes of sloshing waves were demonstrated. The mechanism of switching direction of swirling waves was also discussed by investigating the situation of circulatory flow, the instantaneous free surface, the gravitational effect and the instantaneous direction of external forcing.

Wu also considered a 2D tank with vertically tank bottom-mounted baffles and has discussed the influence of baffle height on the natural mode of the tank, the evolution of vortices and vortex shedding phenomenon, the relationship between the vortex shedding frequency and the excitation frequency of the tank, the vortex size generated in the vicinity of the baffle tip, and the interaction of vortices inside the tank [6]. Based on the results the baffle height shows a significant influence on the shift of the first natural frequency of the baffled tank and the liquid depth also plays an important part in determining this influence. In other words, the shift of the first natural mode due to various baffle heights varies with water depths. Wu has claimed that the design of two baffles separated by 0.2 times the tank breadth is an efficient tool to not only reduce the sloshing amplitude, but also switch the first natural frequency of the tank. The results also show that sloshing displacement is affected distinctly by different numbers of baffles mounted vertically on the tank bottom. The more baffles mounted onto the tank bottom, the smaller the sloshing displacement is presented in both the transient and steady-state periods. Wu has categorized the processes of the evolution of vortices near the baffle tip into four phases: the formation of separated shear layer and generation of vortices, the formation of a vertical jet and shedding of vortices, the interaction between shedding vortices and sloshing flow (the generation of snaky flow) and the interaction between snaky flow and sloshing waves. Results show that vortex shedding phenomenon due to stronger vertical jets occurs when the excitation frequency is close to the first natural mode of the baffled tank, and that is discussed and the size of vortex, generated near the baffle tip, is closely correlated with the baffle height. In that study two types of 3D tuned liquid dampers, a vertically tank bottom-mounted baffle and a vertical plate, were discussed for a tank under coupled surge-sway motions. Results show that the wave types of diagonal and single-directional waves switch to the swirling type due to the influence of the baffle. The phenomenon of square-like waves or irregular waves coexisting with swirling waves is found in the baffled tank under diagonal excitation. The shift of the first natural mode of the baffled tank due to various baffle heights is remarkable. The length of the plate can cause a significant influence on not only the variation of the natural frequencies but the type of the sloshing waves. The influence of the vertical plate on the irregular waves is insignificant and several peaks appear in the spectral analysis of the sloshing displacement for the irregular waves and the numbers of peaks are more than that of the baffled tank.

It is seen in the review of the literature that the analysis of baffled tanks in general is very complicated and time consuming, even with just one or two baffle(s). It is then clear that multiple baffles make the behavior of the liquid inside the tank more complicated, and accordingly makes the analysis much more difficult and time consuming. In this study a simplified method for evaluation of sloshing effects in rectangular tanks with multiple baffles is presented. The method is based on conducting several dynamic analysis cases, by using a powerful FE method for tanks with various dimensions, subjected to both harmonic and seismic excitations, and the use of neural network to create simple relationships between the dominant frequency and amplitude of the base excitations and the maximum level of liquid in the tank during the sloshing and also the maximum dynamic pressure on the tank wall. The details of the study are discussed in the following section of the paper.

2 FINITE ELEMENT MODELING AND ITS VERIFICATION

In order to verify the numerical modeling of the tanks by FE analysis at first the numerical FE model of a tank, previously tested at the Hydraulic Institute of Stuttgart University on shake table (Figure 1) by some other colleagues (Goudarzi et al. 2010) [7], were developed by the employed computer program.

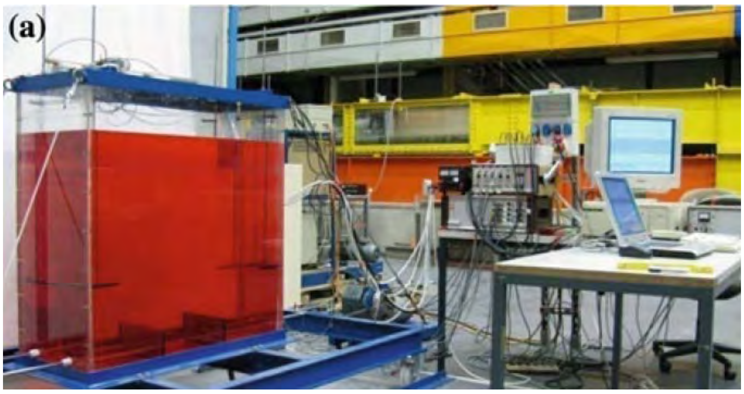

Figure 1: The scaled-down tank model on the shake-table [7]

The length, height, and width of the liquid volume inside the tank have been respectively 1.00, 0.64, and 0.40 meters. Figures 2 and 4 show experimental, analytical, and numerical results of sloshing in the considered scaled tank model all together, studied by Goudarzi and his colleagues subjected to sinusoidal base excitations $(u_b(t) = u_0 sin\omega t, u_0 = 5\ mm)$ in two cases of, respectively, resonant $(\omega = \omega_N)$ and with a lower frequency $(\omega < \omega_N)$, and Figures 3 and 5 show the results obtained by the FE model developed in this study.

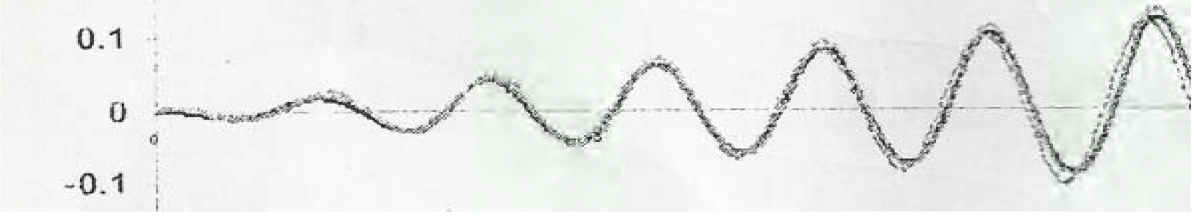

Figure 2: Experimental, analytical and numerical results of sloshing in the tank scaled model subjected to sinusoidal base excitations at resonance [7]

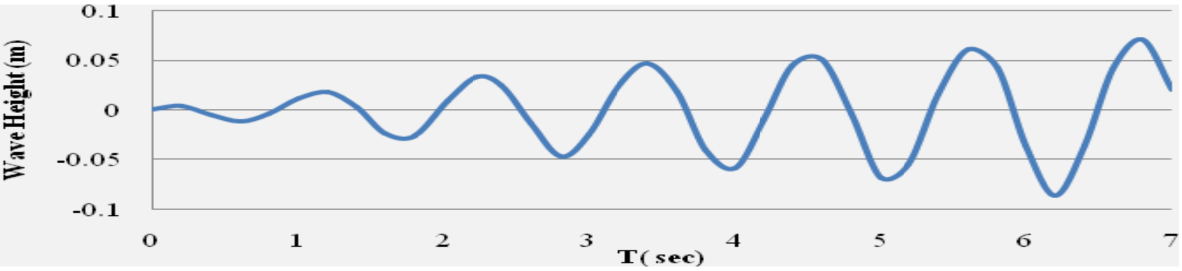

Figure 3: Numerical results obtained by FE analysis of sloshing in the tank scaled model whose experimental and analytical results for sinusoidal base excitations at resonance are shown in Figure 2

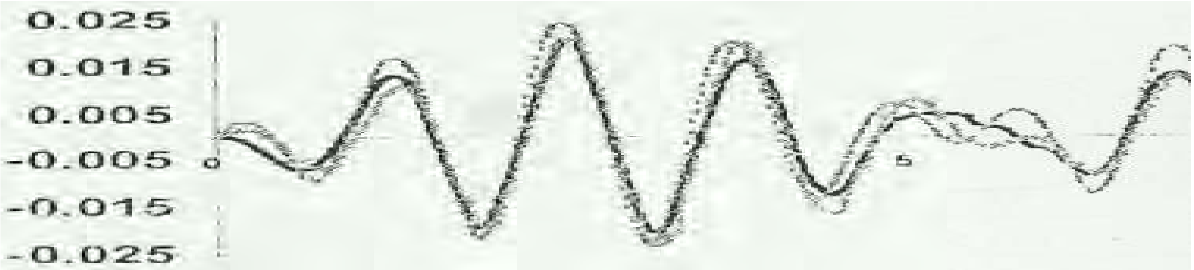

Figure 4: Experimental, analytical, and numerical results of sloshing in the tank scaled model subjected to sinusoidal base motion with $\omega < \omega_N$, [7]

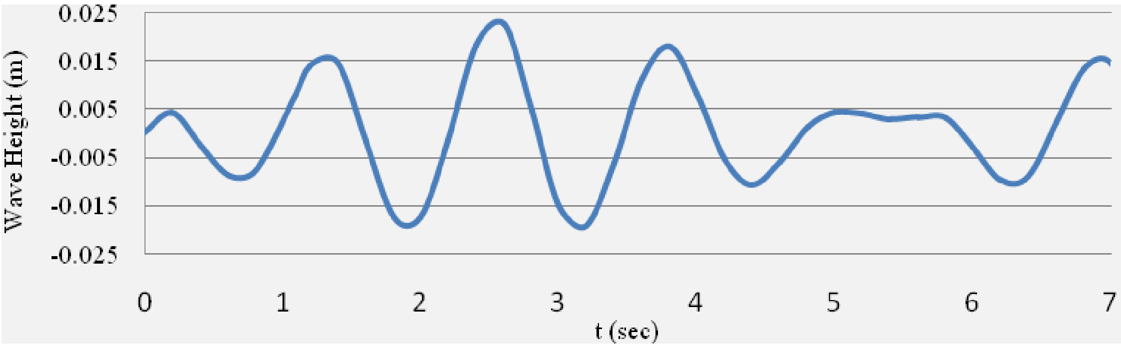

Figure 5: Numerical results obtained by FE analysis of sloshing in the tank scaled model whose experimental and analytical results for sinusoidal base excitations with $\omega < \omega_N$ are shown in Figure 4

Comparing Figure 3 with Figure 2 and also Figure 5 with Figure 4, the very good agreement between the numerical result obtained by the FE model, developed in this study, and the experimental and analytical results can be seen. Based on this verification, the employed FE modeling process could be used for more detailed analysis of sloshing in tanks as explained in next sections.

3 CONSIDERED TANKS FOR THE FINITE ELEMENT ANLYSES

In this study the typical double-compartment aboveground water tanks, used in water supply system in Iran, were used. The general geometric features of the tanks, considered for the study, are shown in Figure 6.

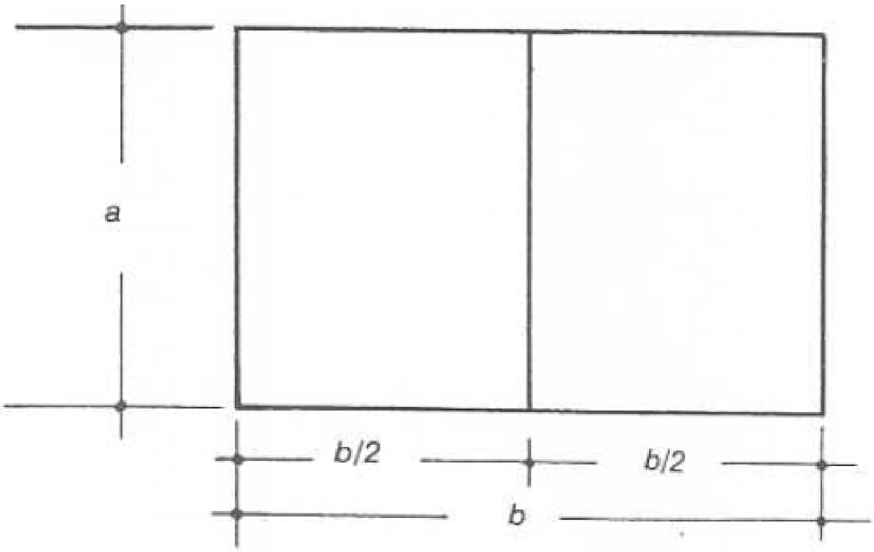

Figure 6: General geometric plan features of the double-containment tanks considered for the study

To have the minimum length of the tank’s wall (to minimize the amount of required construction materials) for a given tank’s area, in the case of double-compartment tanks shown in Figure 6, it can be shown easily that *b* should be around 1.5a. Also usually the water depth in the tank, *h*, is considered not to be less than 0.1 of the width, a, and not more than 6 meters. The common specifications of tanks with different water volumes or capacities, based on the above conditions, are as shown in Table 1.

Table 1: Common specifications of tanks with different water volumes, and their fundamental sloshing period

The tank water capacity (m^3)	Tank water height, *h*, in the tank (m)	a (m)	*b*=1.5a	*h*/a	*h/b*	*T* (sec)
125	3.0	5.270	7.905	0.758	0.569	2.619
250	3.0	7.453	11.180	0.536	0.402	3.197
500	3.0	10.540	15.811	0.379	0.284	4.029
1000	3.0	14.907	22.360	0.268	0.201	5.270
5000	4.0	28.867	43.301	0.184	0.138	8.408
10000	5.0	36.514	54.772	0.182	0.136	9.502
15000	5.5	42.640	63.960	0.171	0.128	10.523
20000	5.5	49.236	73.854	0.148	0.111	12.019
30000	6.0	57.735	86.602	0.138	0.103	13.434

The values of the first or fundamental sloshing modes of tanks in Table 1 have been calculated based on the following formula which gives the natural angular frequencies of sloshing modes in tanks [8]:

$$\omega_n^2 = \pi(2n-1)\left(\frac{g}{a}\right) tanh\,[(\pi(2n-1)\left(\frac{h}{a}\right)] \qquad (1)$$

where n is the sloshing mode number and g in the acceleration of gravity. Based on the above explanations, and considering the exponentially growth of the required computational time with number of elements in the FE analysis, on the one hand, and the time step size in the time history analysis, on the other, explained in the next section of the paper, in this study the following values were considered as the basic case of the tank for analyses:

a = 1.00 m
b = 1.50 m
h = 0.15 m

By using some appropriate scaling factors these dimensions can be used for tanks of real size, such as those given in Table 1. The scaling requirements are explained in the following section, along with the presentation of numerical results.

4 SCALING EFFECTS AND SLOSHING RESPONSE TO HORMONIC BASE EXCITATIONS

Regarding that in this study the effects of using multiple vertical baffles is the main concern; the base excitation and accordingly the induced sloshing have been assumed to occur in just one main direction of the tank length. On this basis, it was important to know if the tank's width, which is the dimension in direction perpendicular to the excitation direction, does have any effect on the analyses results. For this purpose various values were considered for the parameter b and by using a specific excitation the analysis was repeated, of which the results are shown in Figure 7.

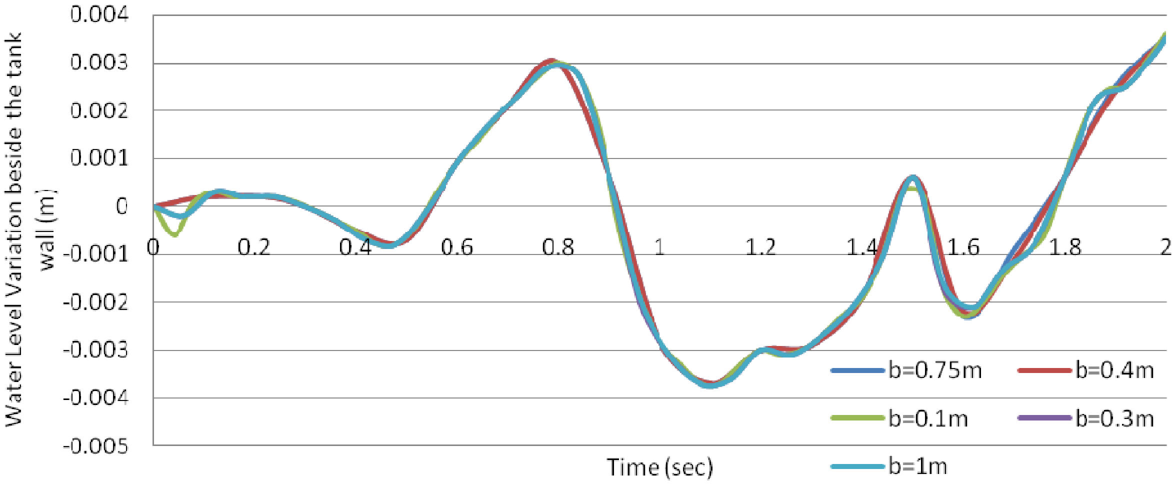

Figure 7: The effect of the tank's width on the water level variation when excitation is along the tank's length

Figure 7 indicate that, as long as the excitation is just in one main direction of the tank plan, the tank dimension perpendicular to the excitation direction does not have any major effect on the response values. On this basis, in all analyses cases, a constant value of 0.1 m (instead of 1.5 m) was used for the tank's width to reduce the required time for the analysis.

Another important factor, which affects the required time for the response analysis, is the size of the tank. In fact, the experience gained in this study showed that the required analysis time for a scaled-down model of a tank is several times less than that of the real tank. The main reason behind this fact is in the size of the time step, which should be used for a scaled-down tank. Actually, considering that based on Equation (1) the sloshing frequencies vary inversely with variation of the square root of the tank's length, shown in the equation by 'a', it can be easily seen that the sloshing period in a scaled model, T_m, is related to the sloshing period in the prototype tank, T_p, by:

$$\frac{T_m}{T_p} = \sqrt{\frac{L_m}{L_p}} \tag{2}$$

where L_m and L_p are respectively the length of the scaled model tank and that of the prototype tank. On this basis, it is clear that the sloshing period in a scaled-down model with the length of 1/36 (for example) of the real size tank will be 6 times shorter than the sloshing period in the prototype tank. This means that the size of the time step of the earthquake digitized record, considered for analyzing the scaled-down model, should be also scaled down by the same factor of 6 to keep the proportions of the excitation periods with respect to the sloshing period in the prototype tank. Accordingly, the duration of the record, used for the scaled-down model, will be 6 time shorter than the real record, although the number of time steps is the same as the original record. It is clear that using a much shorter time step in time history analysis leads to much higher convergence rate, which in turn, reduces the required analysis time to a great extent. On this basis, it was decided in this study to use a scaled-down model tank with the length of 1.0 meter, which is almost 1/36 of a tank with 10000 m3 capacity, as shown in Table 1. This capacity relates to a very common set of tank features, as shown in table 1, with 5.0 m water height, and plan dimensions of 36.5 m by 54.8 m. In the 1/36 scaled-down model with 1.00 meter length and of 0.15 meter water height, the periods of the first three modes can be calculated based on the corresponding natural frequencies given by Equation (1) in previous section. Their values are respectively 1.708, 0.693, and 0.511 seconds. The first set of dynamic response analyses of the modeled tank is related to the base harmonic excitation of the form of $u_b(t) = u_0 sin\omega t, u_0 = 5\,mm$ with the frequency of each of the first 3 sloshing modes. Figure 8 shows a sample of the water surface profile in the case of excitation with the 1st sloshing mode frequency, when various number of baffles are used.

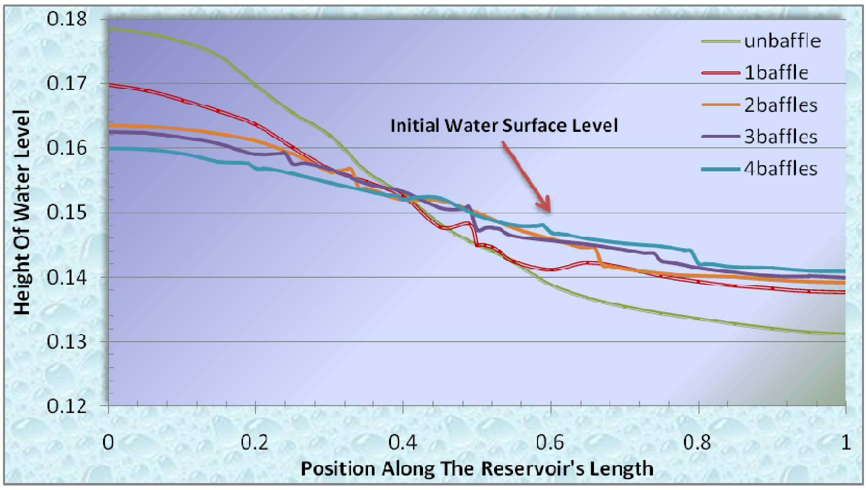

Figure 8: The water surface profile in the time instance of 5.1 seconds in the case of excitation with the 1st sloshing mode frequency when using no, 1, 2, 3, or 4 vertical baffle(s)

In case of using just one baffle it has been considered to be at the middle of the tank's length, and in cases of using 2, 3, or 4 baffles they have been considered equally spaced, so that the tank's length have been divided accordingly into 3, 4, or 5 parts of equal lengths. As in can be seen in Figure 8, there is an abrupt change of water surface elevation at the location of each baffle. Looking at Figure 8 it seems that using more baffles leads to more decrease of the water level rising, however, since Figure 8 is showing only one instant of the time history, to make sure the using more baffles has a decreasing effect on the water level rising at all points along the reservoir's length, the maximum water level beside either the tank's wall or the baffle(s) should be studied. For this purpose the water level variation beside the tank wall was studied first. Figures 9 to 11 show these variations in cases of harmonic excitation with the frequency of respectively the 1st, the 2nd, and the 3rd sloshing mode in the tank, when using no, 1, 2, 3, or 4 baffle(s).

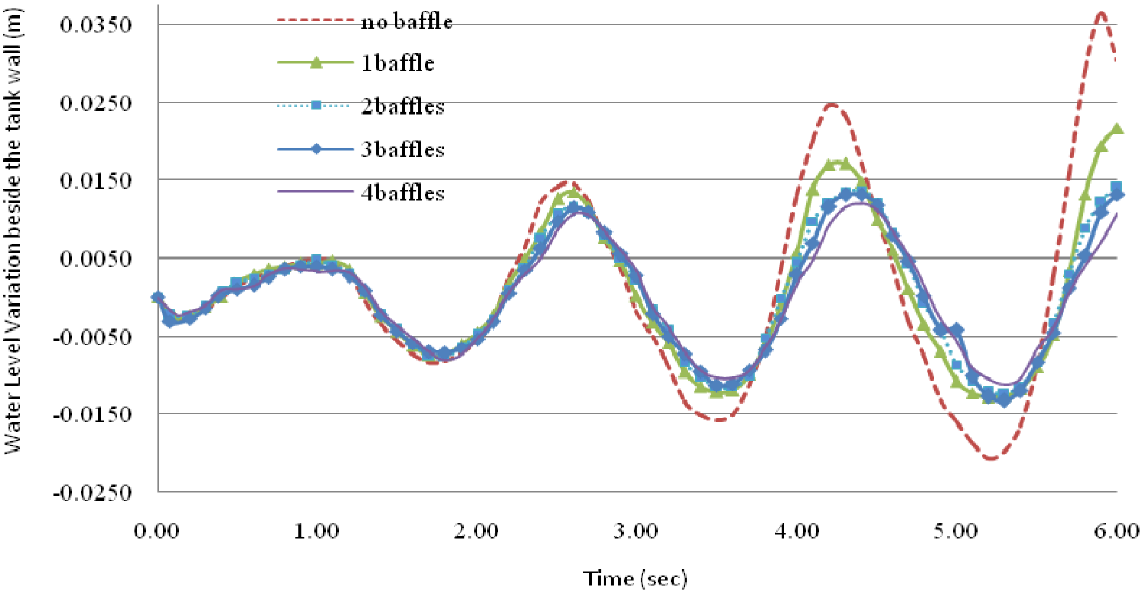

Figure 9: Water level variation beside the tank wall in the first sloshing mode with various number of baffles

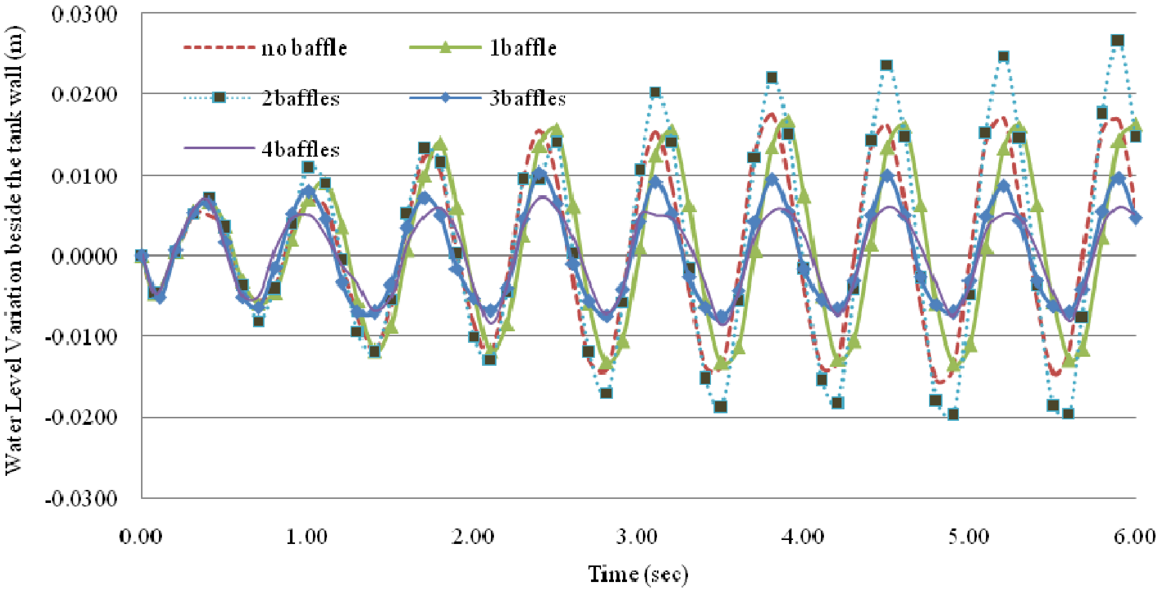

Figure 10: Water level variation beside the tank wall in the second sloshing mode with various number of baffles

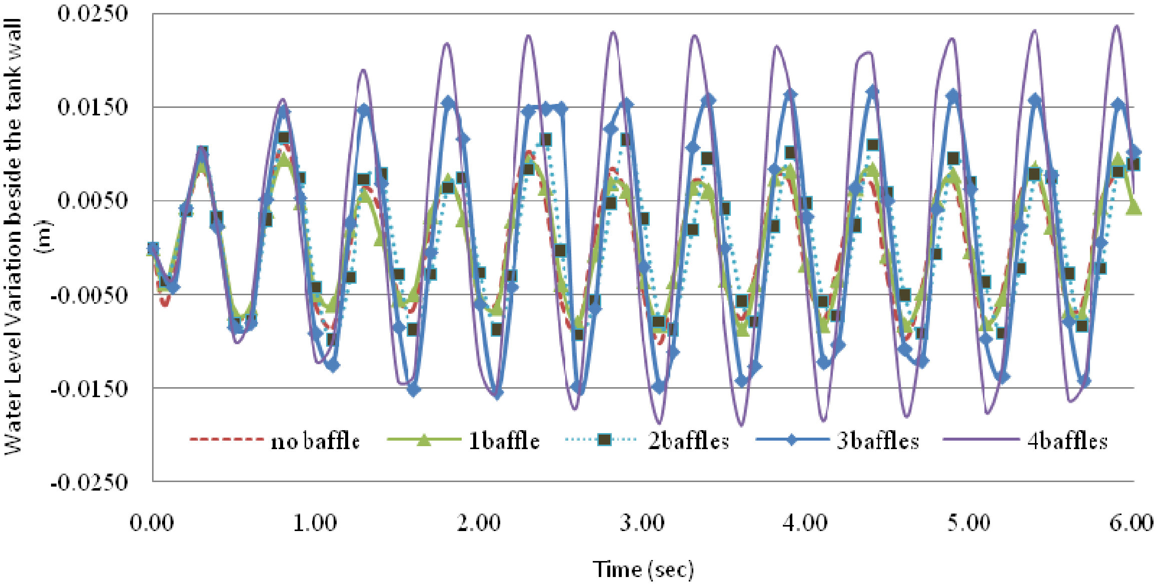

Figure 11: Water level variation beside the tank wall in the third sloshing mode with various number of baffles

It can be seen in Figure 9 that using more vertical baffles results in more reduction in the maximum water level variation, when the excitation frequency is equal to the frequency of the first sloshing mode. Figure 10 shows that when the excitation frequency is equal to that of the second sloshing mode, using two baffles leads to increase, rather than decrease, of the maximum water level variation comparing with the case of using no baffle, however, the maximum water level variation is less than its values in the case of excitation with the first sloshing mode frequency. Also, Figure 10 shows that when the excitation frequency is equal to that of the third sloshing mode, using more baffles again results in more increase in the maximum water level variation comparing with the case of using no baffle, however, the maximum water level variation is less than its value in the case of excitations with the first and second sloshing mode frequencies. Furthermore, comparing Figures 9, 10, and 11 it can be observed that the rate of increase in the maximum amplitude of water level variations, and reaching its steady state response increases with increasing the excitation frequency. This implies that the water body shows larger values of damping when it is subjected to higher frequency excitations. After realizing the effects of using multiple vertical baffles in sloshing response to harmonic excitations, by considering some appropriate earthquake records the sloshing response to seismic excitations, and the effect of using multiple vertical baffles in that case was studied, as explained in the next section of the paper.

5 SLOSHING RESPONSE TO SEISMIC EXCITATIONS AND THE EFFECT OF USING MULTIPLE VERTICAL BAFFLES

To investigate the effect of using multiple vertical baffles in the sloshing response in tanks, when subjected to seismic excitations, and establishing a reasonable relationship between the baffles' number and their features as well as the seismic excitation's characteristics as the input and the maximum water level variation as well as maximum hydrodynamic pressure on the tank wall, as the output, some earthquake records were considered based on their frequency content, and were applied with various scales. The earthquake records were selected by considering the sloshing frequencies of tanks with real size, which are generally low, for tanks with common sizes, which as shown in Table 1, have sloshing periods in range of 2.5 to 13.5 seconds. Among the available earthquakes, Chi-Chi (CHY024 component), Taiwan earthquake of 1999, San Fernando earthquake of 1971, and Northridge earthquake of 1994, were selected, whose spectral pseudo velocity curves are shown in Figure 12.

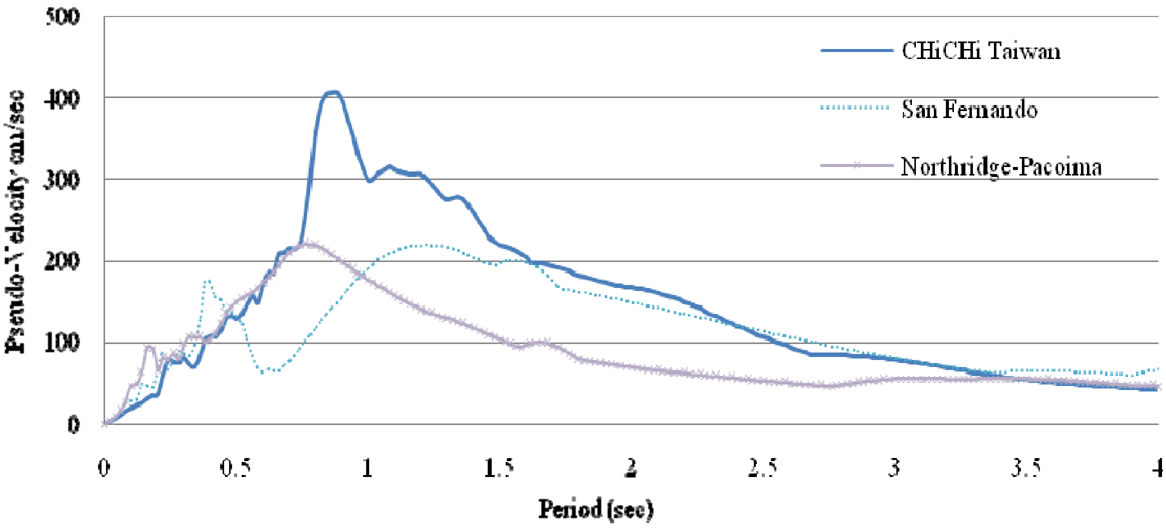

Figure 12: Pseudo-velocity response spectra of the three selected earthquakes for time history analyses

As it is seen in Figure 12, the selected earthquakes have relatively high energy in the range of long periods, and can excite well the sloshing modes in relatively large tanks with sloshing periods of larger than 2.5 seconds. All of these earthquakes have long period oscillations in their displacement history in the period range of 2.5 to 10 seconds. For example, the long period motions of Chi-Chi earthquake, as a sample, can be seen in Figure 13, which shows the displacement time history of this earthquake component.

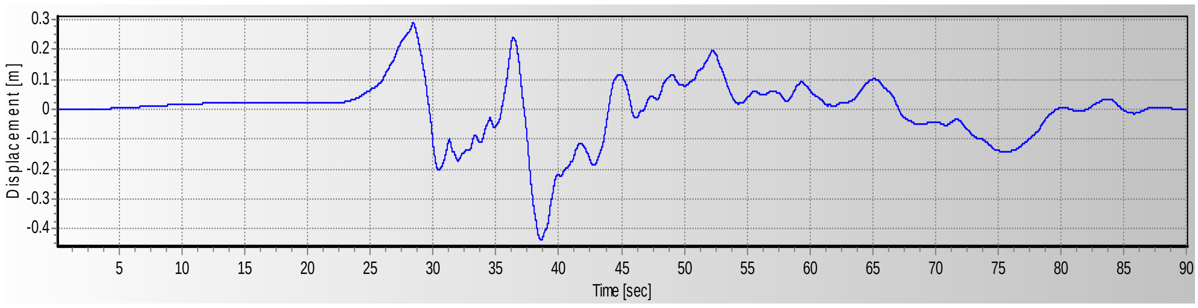

Figure 13: Displacement time history of Chi-Chi earthquake (CHY024 component)

The displacement histories of these earthquakes, when scaled-down by a factor of 1/6, as explained in the previous section, have displacement oscillations in the period range of around 0.5 to 1.5 seconds. To reduce the required analysis time, only the 6 seconds of the strong ground motion parts of the scaled records, containing about 4 to 12 major oscillations, were used in time history analyses. As mentioned before, the variation of water level beside either the tank wall or the baffle(s) is a good response value for studying the sloshing phenomenon and the effect of using baffles on it. Therefore, these variations, corresponding to the aforementioned earthquakes, are shown in Figures 14 to 16, which show respectively response to Northridge earthquake in cases of using no baffle comparing to the cases of using 1, 2, or 3 baffles, response to Chi-Chi earthquake in case of using no baffle comparing to the cases of using 2 or 3 baffles, and finally response to San Fernando earthquake in case of using no baffle comparing to the cases of 1 or 3 baffles.

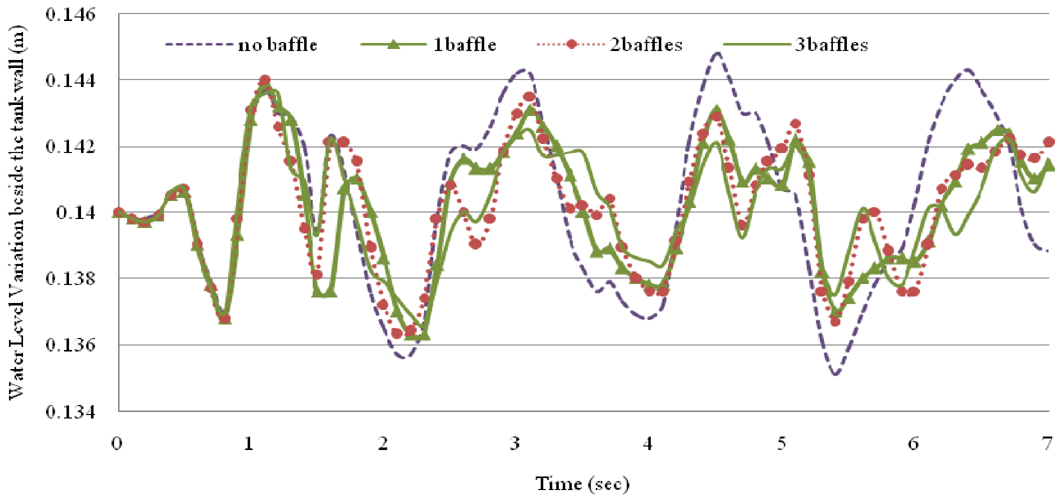

Figure 14: Water level variations beside the tank wall with different number of baffles, when subjected to the scaled Northridge record

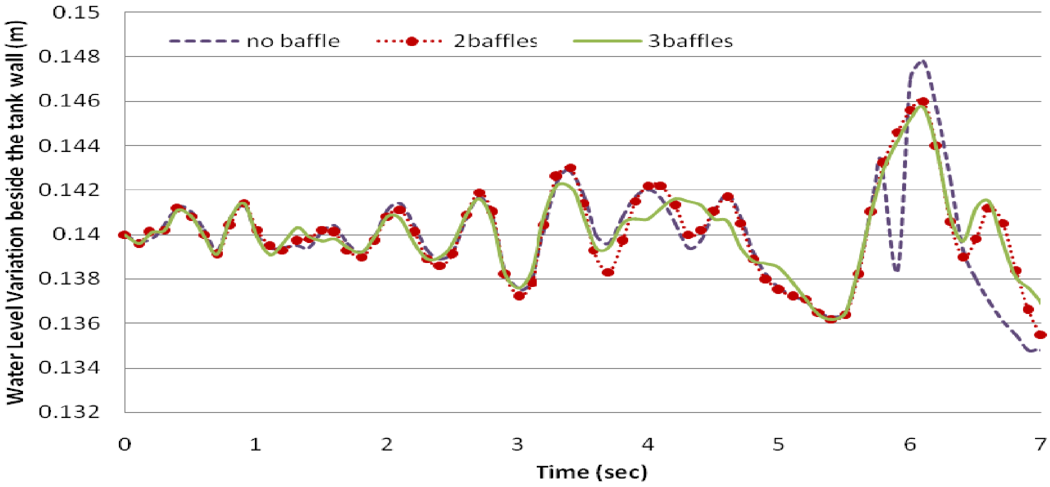

Figure 15: Water level variations beside the tank wall with different number of baffles, when subjected to the scaled Chi-Chi (Chy024) record

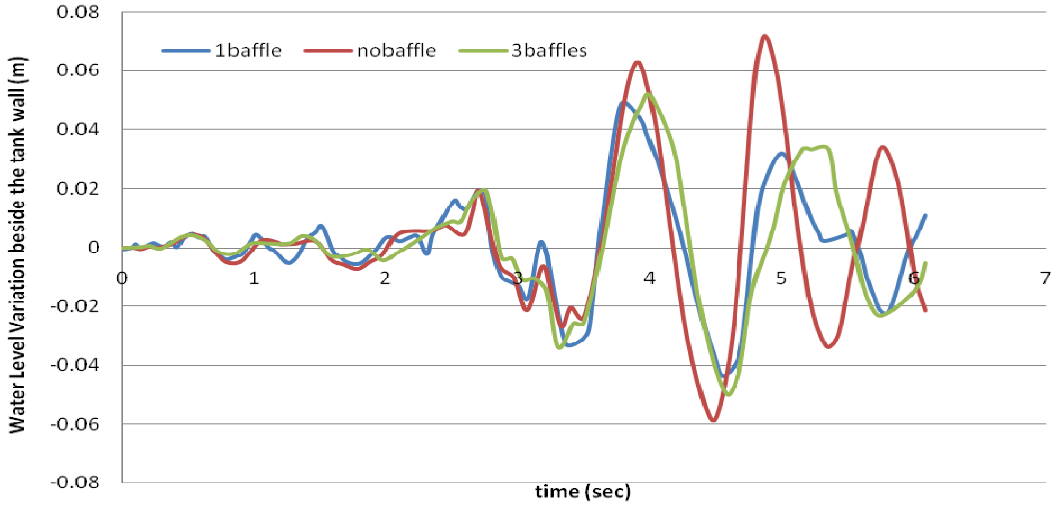

Figure 16: Water level variations beside the tank wall with different number of baffles, when subjected to the scaled San Fernando record

It is seen in Figures 14 to 16 that using baffles in general leads to decrease in the water level variations (the maximum water rising), and using more baffles results in more decrease in water level rising. However, similar analyses by using other earthquake records, such as Tabas, Iran (1987) and Kocaeli, Turkey (1999) showed that using more than 3, and in some cases 2, baffles does not change the results so much. Therefore, it can be recommended that 2 baffles are used in tanks of the sizes around the size of the studied tank.

6 NEURAL NETWORK AND ITS TRAINING FOR SLOSHING RESPONSE PREDICTION

To train a neural network for prediction of the sloshing response to earthquake excitations, the results of Kocaeli (1999), Tabas (1987), and Chi-Chi (Chy024 component -1999) earthquakes were used. The values of pseudo velocities corresponding to the 1st, 2nd, and 3rd sloshing modes in the tank, along with the number of baffles were used and the input data, and the ratio of water level increase to the water depth was used as the output data (Table 2).

Table 2: Input and output data used for training the considered neural network

	Name of Earthq.	X_1=Number of baffle(s)	X_2=Pseudo velocity	Water level increase (cm)	Y_1=Water level increase / Water depth
1	Kocaeli	0	0.3463	26	0.565217391
2			0.827	26	0.565217391
3			1.001	26	0.565217391
4		1	0.3463	26	0.565217391
5			0.827	26	0.565217391
6			1.001	26	0.565217391
7		2	0.3463	21	0.512195122
8			0.827	21	0.512195122
9			1.001	21	0.512195122
10		3	0.3463	21	0.512195122
11			0.827	21	0.512195122
12			1.001	21	0.512195122
13	Tabas	0	0.5658	7.5	0.272727273
14			0.8988	7.5	0.272727273
15			0.7549	7.5	0.272727273
16		1	0.5658	4.05	0.168399168
17			0.8988	4.05	0.168399168
18			0.7549	4.05	0.168399168
19		2	0.5658	3.6	0.152542373
20			0.8988	3.6	0.152542373
21			0.7549	3.6	0.152542373
22		3	0.5658	2.4	0.107142857
23			0.8988	2.4	0.107142857
24			0.7549	2.4	0.107142857
25	Chi-Chi (CHY024)	0	0.6337	60	0.75
26			0.7192	60	0.75
27			0.4451	60	0.75
28		1	0.6337	31.5	0.611650485
29			0.7192	31.5	0.611650485
30			0.4451	31.5	0.611650485
31		2	0.6337	36	0.642857143
32			0.7192	36	0.642857143
33			0.4451	36	0.642857143
34		3	0.6337	34.5	0.633027523
35			0.7192	34.5	0.633027523
36			0.4451	34.5	0.633027523

Based on the data given in Table 2, and by considering a neural network with one intermediate or hidden layer [8] (Figure 17), the network was trained. After training the neural network, to test its capability in response prediction, another earthquake (Chi-Chi, Chy101 component) was considered, whose displacement record is shown in Figure 17.

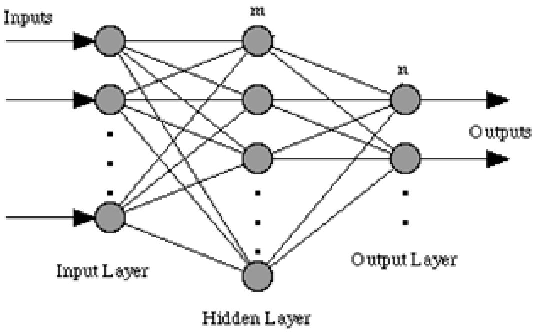

Figure 17: the neural network with one intermediate (hidden) layer [8]

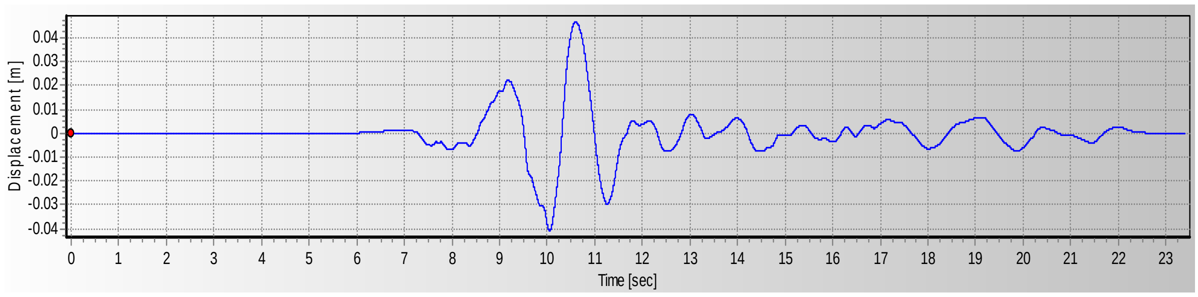

Figure 17: Displacement time history of Chi-Chi earthquake (CHY101 component)

The results, obtained by FE element analysis of the sloshing response of the tank, subjected to the test record are given in Table 3.

Table 3: Input and output data obtained from the test record for checking the trained neural network

	Name of Earthq.	X_1=Number of baffle(s)	X_2=Pseudo velocity	Water level increase (cm)	Y1=Water level increase / Water depth
1	Chi-Chi (CHY101)	0	0.5358	33*	0.622641509
2			0.4025	33	0.622641509
3			0.3115	33	0.622641509
4		1	0.5358	27	0.574468085
5			0.4025	27	0.574468085
6			0.3115	27	0.574468085
7		2	0.5358	18	0.473684211
8			0.4025	18	0.473684211
9			0.3115	18	0.473684211
10		3	0.5358	18	0.473684211
11			0.4025	18	0.473684211
12			0.3115	18	0.473684211

* Results are related to the tank with actual size.

Figure 18 shows the results obtained by the trained neural network in comparison with those obtained by the time history analysis of the numerical FE model.

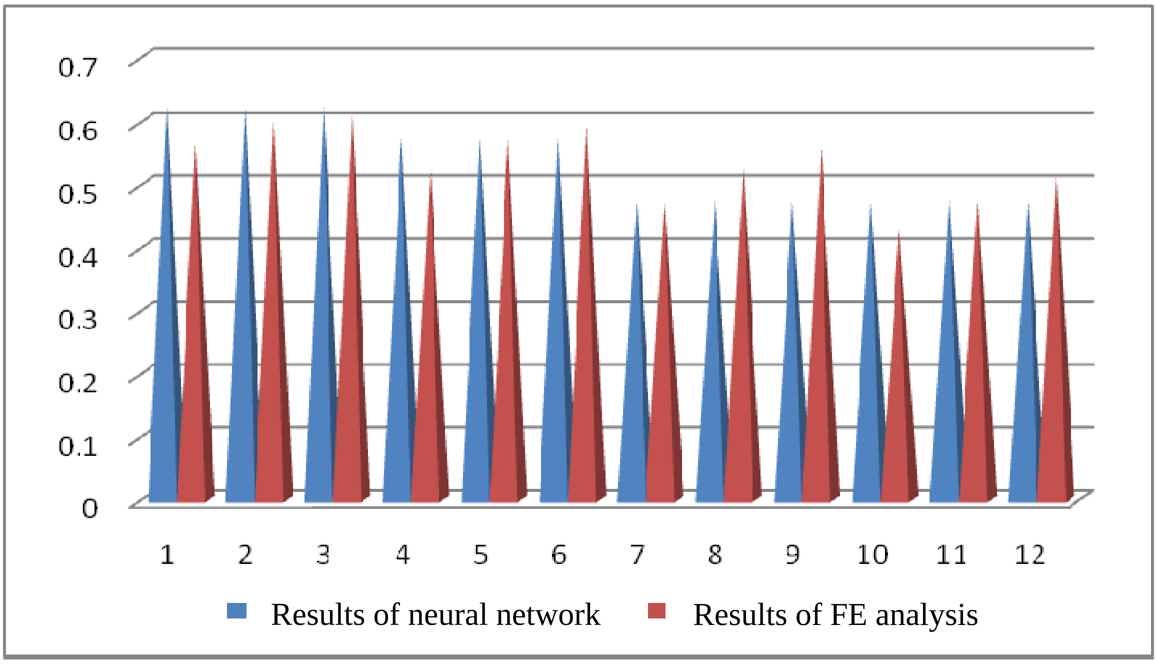

Figure 18: The results of the trained neural network in comparison with those of the FE analysis

It can be seen in Figure 18 that the trained neural network can predict the sloshing response with satisfactory precision.

7 CONCLUSIONS

Based on the numerical finite element analysis of the tanks in this study and the proposed neural network response prediction method, it can be concluded that:

- Using scaled down numerical models of tanks, which results in shorter time steps, and accordingly shorter durations, for time history analyses lead to significant reduction of the analysis required time.
- When the excitation is in one of the main directions of the rectangular tank, the width of tank can be chosen as small as 10 cm. This also will lead to reduction of the analysis required time.
- Using 2 to 4 vertical baffles, equally spaced along the rectangular tanks, can reduce the sloshing effect to a great extent.
- The proposed neural network can be used for predicting the sloshing response in tanks with satisfactory precision, and therefore, it is recommended that this approach is used for studying the sloshing problem in tanks instead of time history analysis, which is very time consuming.

REFERENCES

[1] H.N. Abramson, *The dynamic behavior of liquids in moving containers*, NASA SP-106, National Aeronautics and Space Administration, Washington DC, 1966.

[2] Samia H. Shaaban and William A Nash, Effect of a baffle on response of a liquid storage tank to seismic excitation, *Proceedings of Canadian Congress of Applied Mechanics*, Quebec, Canada: Universite Laval, p. 695-696, 1977.

[3] A. Gedikli and M. E. Ergüven, Seismic analysis of a liquid storage tank with a baffle, *Journal of Sound and Vibration*, Volume 223, Issue 1, Pages 141-155, Elsevier, 27 May 1999.

[4] Otori Yasuki, Masuko Yoshio, and Kurihara Chizuko, Suppression of Seismic Sloshing in Cylindrical Tanks with Baffle Plates (in Japanese), *Denryoku Chuo Kenkyujo Abiko Kenkyujo Hokoku* (Journal Name), No. U98076; Page 24p, 2000.

[5] Abbas Maleki and Mansour Ziyaeifar, Damping enhancement of seismic isolated cylindrical liquid storage tanks using baffles, *Engineering Structures*, Volume 29, Issue 12, Pages 3227-3240, Elsevier, December 2007.

[6] Chih-Hua Wu, Nonlinear liquid sloshing in a 3D tank with baffles, Ph.D. thesis submitted to Department of Marine Environment and Engineering, National Sun Yat-sen University (NSYSU), Taiwan, 2010.

[7] M.A. Goudarzi, S.R. Sabbagh-Yazdi and W. Marx, Investigation of sloshing damping in baffled rectangular tanks subjected to the dynamic excitation, *Bulletin of Earthquake Engineering*, 8:1055–1072, 2010.

[8] M.T. Hagan, H.B. Demuth, and, M.H. Beale, *Neural Network Design*, PWS Publishing, Boston, 1996.

COMPDYN 2011
3rd ECCOMAS Thematic Conference on
Computational Methods in Structural Dynamics and Earthquake Engineering
M. Papadrakakis, M. Fragiadakis, V. Plevris (eds.)
Corfu, Greece, 25–28 May 2011

ON THE ROLE OF COMPUTATIONAL METHODS IN EARTHQUAKE ENGINEERING

A. Soroushian[1], Abbas Ganji[2], Massomeh Hassanzadeh[3], Abdolreza Sarvghad Moghadam[4], Hamidreza Sarmadi[5]

[1] Structural Engineering Research Center,
IIEES, Farmaniyeh, North Dibaji, No. 21, Tehran 19395, Iran,
e-mail: a.soroushian@iiees.ac.ir

[2] Geotechnical Engineering Research Center,
IIEES, Farmaniyeh, North Dibaji, No. 21, Tehran 19395, Iran,
e-mail: a.ganji@iiees.ac.ir

[3] Structural Engineering Research Center,
IIEES, Farmaniyeh, North Dibaji, No. 21, Tehran 19395, Iran,
e-mail: m.hassanzadeh@iiees.ac.ir

[4] Structural Engineering Research Center,
IIEES, Farmaniyeh, North Dibaji, No. 21, Tehran 19395, Iran,
e-mail: moghadam@iiees.ac.ir

[5] Structural Engineering Research Center,
IIEES, Farmaniyeh, North Dibaji, No. 21, Tehran 19395, Iran,
e-mail: h.sarmadi@iiees.ac.ir

Keywords: Earthquake Engineering, Computational methods, Research Contribution, Search Engine, Scirus, Google Scholar.

Abstract. *In view of reasons like the size and complicatedness of current civil and structural engineering projects, and the lack of sufficient knowledge about exact, versatile, and robust analysis methods and solutions, the computational issues of structural and earthquake engineering are in considerable attention. Considering this and the limitations existing on the financial sources and facilities supporting research projects, proper allocation of facilities is of vital importance. Accordingly, in order to dedicate the sources and facilities in a more optimized and appropriate manner, budget the research funds in a better way, and clarify the main streams of research, it is meaningful to study the importance of computational issues in earthquake engineering. Consequently, the objective, in this paper, is to take a step forward towards better knowledge on the contribution of computational issues in earthquake engineering.*

1 INTRODUCTION

The size of civil and structural engineering projects and their complicatedness are in every day increase. By considering this and the stochastic nature of natural hazards, e.g. earthquakes, tsunamis, tornados, etc., the importance and essentiality of further study regarding better understanding of structures behaviors, for instance against earthquakes, can be simply explained. For arriving at further knowledge about the seismic behaviors of structural systems, implementing computational methods is inevitable. Meanwhile, limitations exist on facilities and financial sources supporting the research projects, specifically in earthquake engineering as a non-directly profitable branch of science and engineering. Consequently, an overview on the contribution and importance of the computational methods in earthquake engineering would be helpful. With such an insight, regarding the contributions of computational issues, the financial supports and facilities can be allocated in a better way, and more reasonable programming and budgeting on sources would be possible.

In this paper, the objective is to take a step in this direction. The contributions are compared based on the number of relevant literature, according to a unique search engine. In Section 2, two available search engines are compared, and the one, more appropriate, is set as the search engine, throughout the study. In Section 3, the phrases to be searched are set, the searches are done throughout the interval 1981-2010, the outcomes are reported, and a brief discussion is presented; and with a set of the conclusions the paper is ended, in Section 4.

2 SELECTION OF SEARCH ENGINE

The two search engines available for the authors of this paper were Google Scholar and Scirus, respectively available from:

a. http://scholar.google.com/schhp?h1=en&tab=ws
b. http://scirus.com

In an investigation on the reliability of the number of literature found by the two search engines, shortcomings were observed. The main points are as noted below:

1. The "with at least one of the words" box, hereafter addressed as Box A, in Google Scholar, seems not working properly. A simple example is reported in Table 1,

The phrase in the Box A	Number of Literature found
Apple	1,360,000
Tree	3,070,000
apple tree	2,780,000

Table 1: An example for the first problem existing in the Google Scholar search engine.

   where, apparently, different from what expected, the number in the forth row is less than the number in the third row.
2. Likewise, the first shortcoming, the "OR" search tip, in Google Scholar, seems not working properly; see Table 2.

The phrase in the Box "find articles with all of the words"	Number of Literature found
Apple	1,360,000
Tree	3,070,000
apple OR tree	2,780,000

Table 2: An example for the second problem existing in the Google Scholar search engine.

Besides, as correctly mentioned, in the Google Scholar report page, the number of literature found by Google Scholar is merely an approximation. However, the amount of this approximation is such that, when the numbers of literature found in two searches are considerably different, the logical combination of the searches might be meaningless.

Scirus does not suffer from the problems above, see Table 3 and 4 .

apple	2,819,569
tree	7,142,515
apple OR tree	9,601,404

Table 3: The results of the searches corresponding to Tables 1 and 2 in Scirus.

Scirus		Google Scholar	
Photosynthesis	461,368	photosynthesis	610,000
Cell	22,826,734	Cell	5,940,000
photosynthesis OR cell	23,056,129	photosynthesis OR cell	5,620,000
Photosynthesis AND cell	231,973	Photosynthesis AND cell	352,000

Table 4: A comparison between logical combinations in Scirus and Google Scholar, when the numbers of the two main searches are considerably different.

where, regarding Table 3, as expected, from mathematics [1],

$$\mathrm{Max}\left(2{,}819{,}569\,,7{,}142{,}515\right) \leq 9{,}601{,}404 \leq 2{,}819{,}569 + 7{,}142{,}515 \tag{1}$$

and, for meaningless computations, in view of Table 4,

$$\begin{aligned} &\text{Scirus}: \quad 22{,}826{,}734 + 461{,}368 - 231{,}973 = 23{,}056{,}129 \\ &\text{Google Scholar}: \quad 5{,}940{,}000 + 610{,}000 - 352{,}000 = 6{,}198{,}000 \neq 5{,}620{,}000 \end{aligned} \tag{2}$$

(Since, the settings in the search engines are kept as defaults, the differences between the corresponding numbers in Table 1-4 are not meaningful.)

In a further control on the Scirus search engine, the authors could not find some the contributions [2-4] of the first author. In an e-communication with the authorities in the Scirus search engine, the reason is the not collaboration of some publishers with Scirus [5].

In view of the objective of this study, since, some of the searches, in this study, may include logical operators, e.g. OR, and some may not, the shortcomings, of Google Scholar might be more effective on the consequences, while the shortcoming, of Scirus would likely scale the numerically obtained graphs. Considering these, Scirus is set as the search engine to be implemented in the investigations, in this paper.

3 FROM PHRASES SELECTION TO BRIEF DISCUSSION ON THE OUTCOMES OF THE SEARCHES

In order to check the contribution of numerical analyses in earthquake engineering research, first the number of articles found for a search on the phrase below:

"earthquake" OR "strong motion" OR "seismic" (3)

hereafter, addressed as X, is compared with the number of the articles for the search below:

(X AND "computational efficiency") OR (X and "computational cost") OR (X AND "approximate computation") (4)

The results of the two searches, in different years, are as depicted in Figure 1, respectively in black and orange. Though there may exist ambiguities regarding the selected phrases, the trends of changes in Figure 1, considered together with the large number of research areas in earthquake engineering, e.g. steel buildings, concrete dams, liquefaction, performance based design, masonry and historical buildings, etc. clearly reveals the proper and robust growth of research on the computational issues in earthquake engineering; see the almost constant distant between the two graphs in Figure 1. Then, in order to compare the importance of computational issues with that of the other subjects in earthquake engineering, the search is repeated for the phrase below:

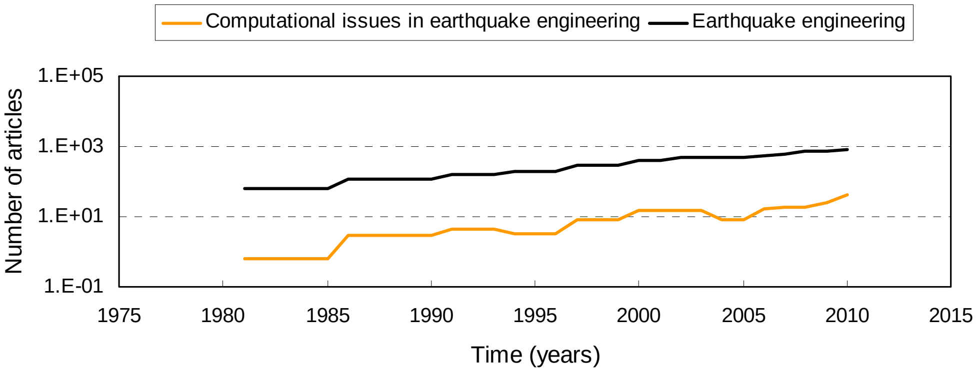

Figure 1: An approximate, based on number of articles, illustration for the contribution of computational issues in earthquake engineering research throughout 1981-2010.

(X AND "passive control") OR (X and "active control") (5)

considering, structural control as a typical important research issue in earthquake engineering. The results of the searches implied in equations (4) and (5) lead to Figure 2. Similar to Figure 1, the trend of the graphs in Figure 2 imply the considerable contribution of computational issues in earthquake engineering, from some other point of view. Extending the study to both article and non-article literature, leads to Figures 3 and 4 respectively corresponding to Figures 1 and 2, clearly revealing the considerable significance of computational issues, even compared to issues like structural control.

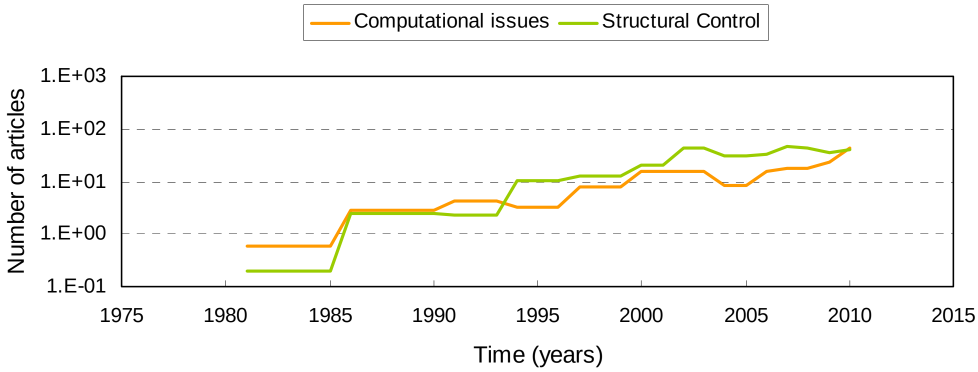

Figure 2: An approximate, based on number of articles, comparison between the contributions of computational issues and structural control in earthquake engineering research, throughout 1980-2010.

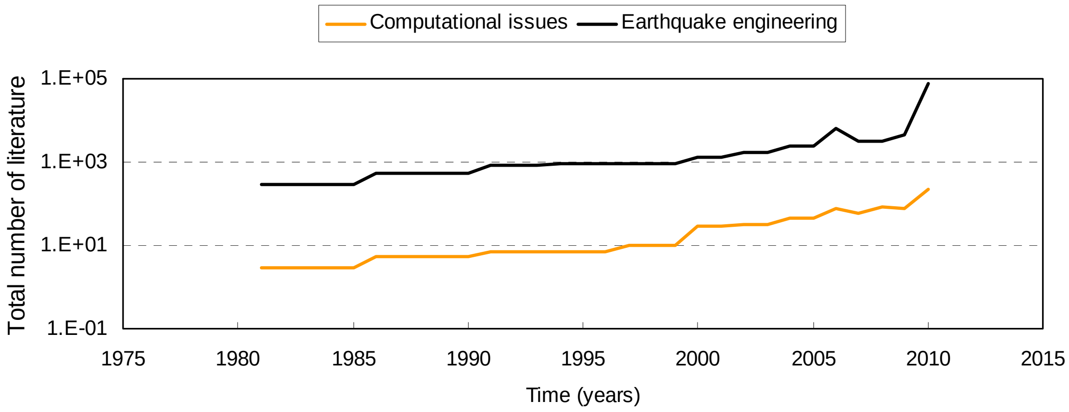

Figure 3: An extension of the study reported in Figure 1 to article and non-article literature.

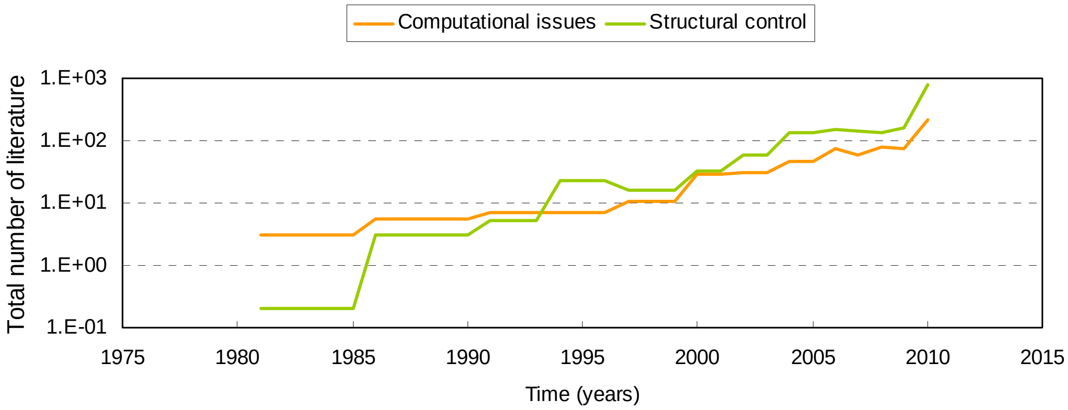

Figure 4: An extension of the study reported in Figure 2 to article and non-article literature.

The observations can be simply explained by paying attention to the fact that computational methods and experimental studies are two main alternatives in structural behavior study, with completely different level of price and financial needs, very important nowadays.

4 CONCLUSION

In this paper, the contribution of computational issues in earthquake engineering is studied, in view of the Scirus search engine, throughout 1981-2010. Scirus is selected as the search engine based on the reliability of the number of the literature found in the searches. After selecting the phrases to be searched, and carrying out the searches, the main observations are as noted below:

. Considering the number of issues and branches in earthquake engineering, computational issues are of considerable importance and contribution in earthquake engineering; see Figures 1 and 3.

. The contribution of computational issues in earthquake engineering is in gradual increase; see Figure 3.

. The contribution of computational issues in earthquake engineering is comparable with important issues like structural control; see Figures 2 and 4.

The main reasons of the observations are:
. the everyday increasing size and complicatedness of structural systems,
. the low price of structural behavior study by computational methods compared to experimental work, also related to
. the fact that computational, numerical, and approximate analyses, become cheaper everyday by the accelerated improvement of electronics and computer hardware engineering.

REFERENCES

[1] T.M. Apostol, *Calculus, Vol I.* John Wiley & Sons, 1967.

[2] A. Soroushian, P. Wriggers, J. Farjoodi, Asymptotic upper-bounds for the errors of Richardson Extrapolation with practical application in approximate computations. *International Journal for Numerical Methods in Engineering*, **80**: 565-595, 2009.

[3] A. Soroushian, J. Farjoodi, A unified starting procedure for the Houbolt method. *Communications in Numerical Methods in Engineering*, **24**: 1-13, 2008.

[4] A. Soroushian, J. Farjoodi, More reliable responses for time integration analyses. *Structural Engineering and Mechanics An International Journal*, **16**: 219-240, 2003.

[5] Email communication between the first author and the Scirus search engine, The reliability of figures, March 2011.

COMPDYN 2011
3rd ECCOMAS Thematic Conference on
Computational Methods in Structural Dynamics and Earthquake Engineering
M. Papadrakakis, M. Fragiadakis, V. Plevris (eds.)
Corfu, Greece, 25–28 May 2011

ON THE ESSENTIALITY OF FURTHER RESEARCH ON COMPUTATIONAL ISSUES OF EARTHQUAKE ENGINEERING IN DIFFERENT COUNTRIES

A. Soroushian[1], Abbas Ganji[2], Massomeh Hassanzadeh[3], Abdolreza Sarvghad Moghadam[4]

[1] Structural Engineering Research Center,
IIEES, Farmaniyeh, North Dibaji, No. 21, Tehran 19395, Iran,
e-mail: a.soroushian@iiees.ac.ir

[2] Geotechnical Engineering Research Center,
IIEES, Farmaniyeh, North Dibaji, No. 21, Tehran 19395, Iran,
e-mail: a.ganji@iiees.ac.ir

[3] Structural Engineering Research Center,
IIEES, Farmaniyeh, North Dibaji, No. 21, Tehran 19395, Iran,
e-mail: m.hassanzadeh@iiees.ac.ir

[4] Structural Engineering Research Center,
IIEES, Farmaniyeh, North Dibaji, No. 21, Tehran 19395, Iran,
e-mail: moghadam@iiees.ac.ir

Keywords: Earthquake Engineering, Computational Issues, Research, Countries, Seismic Hazard, Financial Potential.

Abstract. *Further research on different issues of earthquake engineering is a major tool in global seismic protection. Considering the different, including financial, supports needed for carrying out appropriate researches, the nature of earthquakes, and the fact that the disastrous effects are not limited to one country or even region, financing earthquake engineering researches, in an international manner, is reasonable. Nevertheless, for materializing the financing, it is essential, especially in the nowadays hard financial situation, after the financial crisis, few years ago, to make an idea about the sections of the research in further need of support. As a seemingly staring step in this regard, the objective in this paper is to compare the need of further seismic research in different countries. And, in view of the considerable role of computational issues in other areas of earthquake engineering and meanwhile the title of the COMPDYN 2011 conference, the main attention in this paper is on the computational issues of earthquake engineering and comparing the essentialities of further researches in several countries based on their seismic hazard, carried out researches, and financial capabilities. As a main conclusion, Italy is the country with least essentiality and Chile and Iran are the countries with most essentialities for further research on the computational issues of earthquake engineering.*

1 INTRODUCTION

Earthquake is a natural disaster causing the most losses both in the number of human beings death and also from a financial point of view (see also Fig.1), e.g. the financial (export, im port,…), ecological (radiation, air pollution . . .) . . . inter-connections between different countries and neighboring regions of the globe, the effects of an earthquake is not limited to the country, where the earthquake has occurred, or even, in cases, to the neighboring countries; for instance, consider the effects of the March 11 th, 2011 earthquake and Tsunami at Japan. Consequently, international financing on different issues of earthquake engineering research is meaningful; and hence, considering the nowadays hard financial situations (originating in the financial crisis, few years ago), and the fact that there are many earthquake engineering (including seismological) issues, special and local for each country (e.g. seismicity, some types of construction, some geotechnical problems), it is reasonable to investigates and compare the research needs in different countries, such that, to also dedicate the international and even national financial supports, in a better and when possible optimized manner.

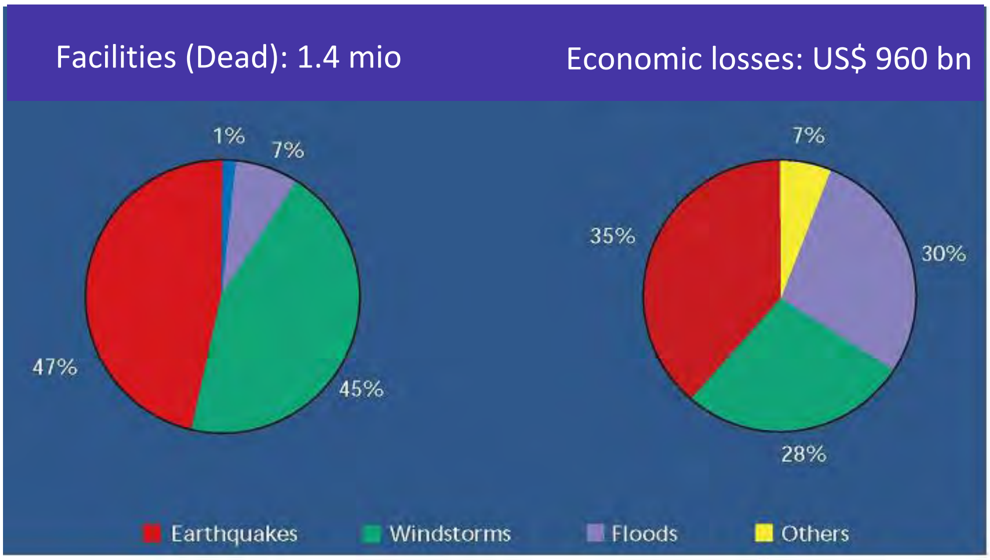

Figure1: A comparison between losses originated in natural disasters, from 1955-1999 [1].

The explanation above, the significant role of research on the computational issues of earthquake engineering on other issues and branches of earthquake engineering, and the title of the COMPDYN 2011 conference, together, lead to the essentiality of the objective of this paper implied in its title. The aim of this paper is to investigate the superiorities (between countries), for further research on computational issues of earthquake engineering. Based on the seismic risk, amount of researches carried out, and the financial potentials, the key idea is explained in Section 2, the comparisons are made in Section 3, the reasons of the observations are briefly explained and led to an extension of the observations in Section 4, some complementary discussion is stated in Section 5, and eventually, the paper is concluded in Section 6.

2 THEORY

2.1 Key idea

Considering the seismic hazards and financial potentials in different countries and regions, a reasonable expectation is more researches in countries, subjected to more seismic hazard and with more financial potentials. For a robust improvement (and also as seen in a separate study [2]), the expectation of more research, noted above, is not only regarding research on earthquake engineering, but also, is valid for the relevant computational issues. Hence, by following the procedure below:

1. Selection of some countries/regions, with considerable earthquake hazard and different financial potentials.
2. Studying the amount of researches on earthquake engineering and the computational issues, in each country/region.
3. Based on the selections and achievements in the two stages above, making an idea about the countries/regions with more essentiality of further research on earthquake engineering and the relevant computational issues.

we would be able to materialize the objective of this paper.

2.2 Some selections

2.2.1 Countries/regions

Since the outcomes of researches are in general being reflected in publications, indexed, with their titles, the name of authors/coauthors, affiliations, keywords, and titles of journals/scientific events, in this likely first study on the subject, it is much simpler to select and consider some countries from different parts of the globe, as representative of the regions they are located in. In this regard, Chile, Greece, Iran, Italy, Japan, Mexico, and USA are the seven countries under consideration in this paper.

2.2.2 How to determine the amount of researches

2.2.2.1 Approach

In order to evaluate the amount of researches, an appropriate approach (in view a slight assumption) is to study the number of relevant documents in the literature; also see [2]. For materializing this approach, a scientific search engine, reliable, regarding the number of documents, is to be selected. In view of the existing literature, www.scirus.com and its advanced version provides the capability of reliable searches [2, 3], and hence is herein set as the search engine.

2.2.2.2 Phrases to be implemented in the search

Consider the phrase X, defined below:

$$X: \quad \text{"earthquake" OR "strong motion" OR "seismic"} \tag{1}$$

and its combination with names of the countries, set in Section 2.2.1, as:

$$X_i: \quad X \text{ and } \textit{name of country} \quad , \quad i=1, 2, 3 \ldots 7 \tag{2}$$

where,

$$\begin{array}{l} i=1\text{: } \textit{name of country}= \text{"Chile"} \\ i=2\text{: } \textit{name of country}= \text{"Greece"} \\ i=3\text{: } \textit{name of country}= \text{"Iran"} \\ i=4\text{: } \textit{name of country}= \text{"Italy"} \\ i=5\text{: } \textit{name of country}= \text{"Japan"} \\ i=6\text{: } \textit{name of country}= \text{"Mexico"} \\ i=7\text{: } \textit{name of country}= \text{"USA"} \end{array} \tag{3}$$

and, obviously X_i implies the amount of the researches carried out on earthquake engineering in the *i* th country. In order to study the amount of researches on the computational issues of earthquake engineering, we can consider the phrase:

$$Y: \quad \text{"computational efficiency" OR "computational cost" OR "approximate computation"} \tag{4}$$

and define the search phrase below:

$$Y_i: \quad X_i \text{ AND } Y \quad , \qquad i=1, 2, 3 \ldots 7 \tag{5}$$

as the amount of the researches carried out on the computational issues of earthquake engineering.

2.2.2.3 Type of the documents and the scope of search

"Any information type" is selected as the type of literature document ("content sources") to be searched for, in www.scirus.com (advanced version), and the scope is set, by selecting the two alternatives "Earth and planetary sciences" and "Engineering, Energy and Technology" as the "subjects area" in the www.scirus.com.

2.2.2.4 Time interval

Lack of literature in a single year and/or abrupt changes of the existing literature in consecutive years may cause problems in arriving at reliable achievements and ideas. Hence, it is meaningful to carry out the searches throughout years. Considering this, the comparisons are based on the literature searches carried out in the interval 1981-2010 (see also [2]).

3 EVALUATIONS

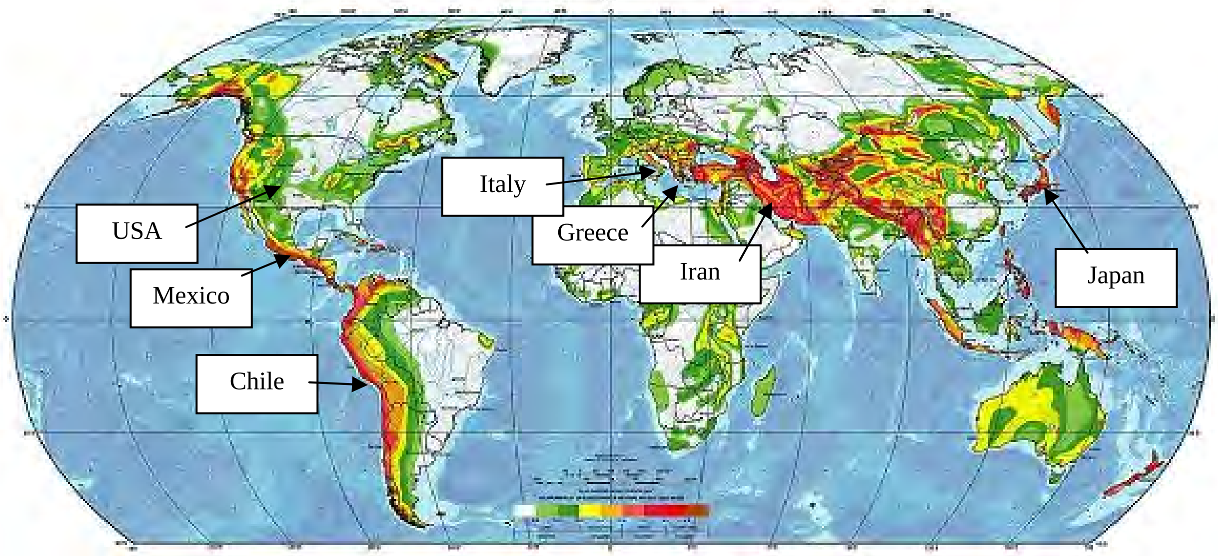

Figure 2: World seismic hazard map with the selected countries highlighted (taken form internet).

of the seven countries are roughly compared in Table 1, after some personal talks with some experts. The outcomes of the searches are compared in Fig. 3 and Table 2. In view of Fig. 3 and Tables 1 and 2, Chile and Iran are the countries with more essentiality of further research on earthquake engineering and the computational issues in earthquake engineering.

Chile (1)	Mexico, Greece, Japan (2, 5, 6)	Italy, Iran (3, 4)	USA (7)
More financial potential			

Table 1: A rough comparison between financial potentials of the seven countries, selected in Section 2.1.

Country	1	2	3	4	5	6	7
Percentage of the earthquake engineering research relevant to computational issues	38	61	38	72	56	44	73

Table 2: The earthquake engineering research dedicated/involved in computational issues, in different countries.

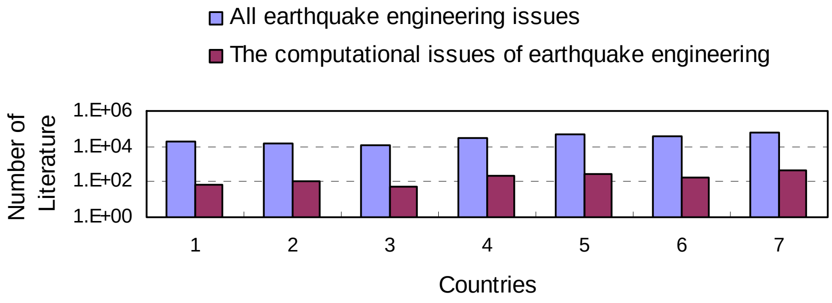

Figure 3: Number of literature on earthquake engineering and the relevant computational issues in countries.

Specifically, considering the financial conditions, notified in Table 1, Iran is the country, where, acceleration of research on the computational issues of earthquake engineering is not only essential but can have a much simpler explanation. On the other end of the spectrum, Italy is the country, where, the amount of research is comparatively good; still further research is surely recommended.

4 FROM EXPLANATION TO EXTENSION

Obviously at countries with high seismic hazard, more research is essential (especially, when the existing financial potentials are considerable). Nevertheless, when the countries are not well developed, the financial potentials are not being implemented in research projects, sufficiently, and in an appropriate manner; hence, further financings become essential. On the other hand, at developed countries, with moderate seismic hazard, and moderate financial potential, the developments of the countries lead to good managements of the financial potentials, towards the not considerable research needs (the seismic hazards are moderate), and hence, less essentiality of further research is being observed.

Researches on earthquake engineering and the relevant computational issues, in the past decades, were in very similar growth [2]. Meanwhile, many issues in earthquake engineering are being affected by the results of research on the computational issues. Considering these, the explanations in the previous paragraph sounds valid, for both earthquake engineering and the computational issues of earthquake engineering, not only for the countries taken under consideration here, but also, for arbitrary country/region in the world.

5 COMPLEMENTARY REMARKS

The approaches and achievements in the previous sections are rough. Ambiguities regarding number of countries, selection of countries and the relation between the need to further research, seismic hazard and financial potentials exist, all, implying the essentiality of more through study on the subject, briefly discussed in this paper.

6 CONCLUSION

Under some simplifying assumptions, the existing amount of research on computational issues of earthquake engineering is evaluated in view of the need to progress and research (seismic hazard) and financial potential. As a consequence,

1. Further research is essential in less developed regions/countries, subjected to high seismic hazard, e.g. Iran and Chile. Such a research can be simply explained when the financial potentials are considerable.
2. Regions/countries subjected to moderate seismic hazard, possessing moderate or good financial capabilities, specifically, when developed, e.g. Italy, are in the best conditions of research on earthquake engineering and the computational issues.
3. Countries/regions with high seismic hazard and moderate or good financial capabilities are also generally in a good condition regarding research on earthquake engineering and the computational issues of earthquake engineering.

Still, further research is recommended, in all conditions, with emphasis on the essentiality of further research in less developed countries under high seismic hazard.

ACKNOWLEDGEMENT

The authors sincerely appreciate the kind guidance of Dr. S. Esghi, regarding the first reference and especially Fig. 1.

REFERENCES

[1] H. Bachmann, *Seismic conceptual design of buildings – basic principles*. Swiss Federal Office for Water and Geology and Swiss Agency for Development and Cooperation, 2002.

[2] A. Soroushian, A. Ganji, M. Hassanzadeh, A.S. Moghadam, H. Sarmadi, On the role of computational methods in earthquake engineering. M. Papadrakakis, M. Fragiadakis, V. Plevris eds. *3rd ECCOMAS Thematic Conference on Computational Methods in Structural Dynamics and Earthquake Engineering,* Corfu, Greece, May 25-28, 2011.

[3] Email communication between the first author and the Scirus search engine, The reliability of figures, March 2011.

COMPDYN 2011
3rd ECCOMAS Thematic Conference on
Computational Methods in Structural Dynamics and Earthquake Engineering
M. Papadrakakis, M. Fragiadakis, V. Plevris (eds.)
Corfu, Greece, 25–28 May 2011

FASTER TIME INTEGRATION ANALYSIS FOR BUILDING STRUCTURS SUBJECTED TO 3-COMPONENET EARTHQUAKES

O. Bahar[1*] **and S. Ramezani**[2]

[1] Structural Engineering Research Center,
IIEES, Farmaniyeh, North Dibaji, No. 21, Tehran 19395, Iran,
e-mail: omidbahar@iiees.ac.ir

[2] Structural Engineering Research Center,
IIEES, Farmaniyeh, North Dibaji, No. 21, Tehran 19395, Iran,
e-mail: s.ramezani@iiees.ac.ir

Keywords: Linear dynamic analysis, Time history analysis, Building structure, 3-component earthquake, Computational cost, Accuracy.

Abstract. *Time integration is the most versatile tool to analyze and recognize dynamic behavior of structures. However, besides the versatility and simplicity, the resulting responses are accompanied by many approximations, while the computational efforts are considerable. The main parameter controlling the accuracy and computational cost is the integration step size, a positive definite parameter, uniformly controlling the size of integration steps throughout the integration interval. For an efficient time integration analysis it is conventional to implement integration step sizes as much as small enough to provide sufficient accuracy. An exceptional case is time integration of structural systems, subjected to digitized excitations, when the digitization step size is smaller than the size essential for sufficient accuracy. In such analyses, additional computational cost should be spent, merely to consider the digitized excitations. Recently, a technique to overcome the deficiency is proposed and successfully implemented in time integration analysis of different practical cases, e.g. simple linear and nonlinear examples, tall buildings, bridges, silos, reservoirs. However, in all examples the seismic excitations are considered as one-component records. The aim of this study is to examine the performance of the recently proposed technique in dynamic time history analysis of a building structure subjected to a three-component earthquake record.*

1 INTRODUCTION

In many cases, in order to evaluate real performance of civil engineering structures during extra loadings, in general, using the time integration analysis is inevitable. Nowadays, seismic evaluations and retrofitting design process need deep understanding of the real behavior especially seismic behavior of buildings and bridges during strong ground motions. In this regard, understanding of building performances against natural disaster are only achieved by considering their dynamic time history analysis. Such analyses need some special features like detailed modeling of the building, recognizing realistic loadings may happen in the future, and a comprehensive and consistent analysis method. Also, we know that considering unusual behavior of infrastructures during environmental loadings may not be simplified to static or even pseudo-static evaluations. On the other hand, performing a dynamic time history analysis in real world is accompanied by some errors causing the results to be inexact representing of the real behavior but only an approximate one. Difficulties emerge when we do not know values and sources of errors. Now, it is clearly recognized that in any numerical method, the magnitude of the selected time steps is strongly affect the accuracy and also stability of the step-by-step integration methods. Many analysis methods to ensure satisfying stability criteria need assigning small time steps. Hence, selection of the proper time increment, Δt, is an important problem. Among various effective parameters the two following factors should be carefully considered: (1) the period of the last effective mode of the structure, whcih should be considered in the analysis; (2) the digitization steps of the seismic excitations. If the nonlinear behavior of the system is included in the analysis, nature of the changes of the stiffness and damping matrices during the following steps may be an effective parameter influence on the selection of time step [1].

In general, it is known that sufficiently accurate results can be obtained if the time increment is selected to be no longer than one-tenth of the period of the last effective mode of the structure. However, using step-by-step time integration analyses with so small time step significantly increase the computational costs. Hence, if we can lengthen time steps such that it guarantees the accuracy and stability of the analysis, the size of time step is limited to the values by which, the excitation is recorded. Recently, a technique by Soroushian [2] is proposed for decreasing the computational cost in which, size of the time steps of a recorded earthquake ground motion is lengthen without changing other characteristics of the record. In 2010, Soroushian [3] used this method for considering linear and nonlinear behavior of a single degree of freedom excited by an earthquake record. In this paper, we aim to evaluate this method for a 3-componenet earthquake when applied to an 8-story 3-dimensional building using conventional time integration methods. A brief review of the recent technique is presented in the following section.

2 THE RECENT TECHNIQUE IN BRIEF

According to Soroushian [2], in order to replace the original excitation with a new digitized excitation with larger steps such that the responses rate of convergence is preserved four steps are designed as follows:

1- The excitation steps, ${}_f\Delta t_i \ i = 1,2,\ldots$, are equally sized,

2- The integration steps, $\Delta t_i \ i = 1,2,\ldots$, are equally sized,

3- The excitation steps are embedded by the integration steps (the first time station, i.e. t_0, is a station for both excitation and integration),

4- If we assumed that $\mathbf{f}(t)$ is a digitized representation of an actual excitation we can replace it with a new excitation, $\tilde{\mathbf{f}}$, digitized at steps equal to n times larger, according to:

$$\begin{aligned} t_i = 0: &\qquad \tilde{\mathbf{f}}_i = \mathbf{f}(t_i), \\ 0 < t_i < t_{end}: &\qquad \tilde{\mathbf{f}}_i = \frac{1}{2}\mathbf{f}(t_i) + \frac{1}{4n'}\sum_{k=1}^{n'}\left[\mathbf{f}(t_{i+k/n}) + \mathbf{f}(t_{i-k/n})\right], \\ t_i = t_{end}: &\qquad \tilde{\mathbf{f}}_i = \mathbf{f}(t_i), \end{aligned} \tag{1}$$

where,

$$\begin{aligned} t = \Delta t: &\qquad n' = n - 1 \\ \Delta t < t < t_{end} - \Delta t: &\qquad n' = \begin{cases} \dfrac{n}{2} & n = 2j \quad j \in Z^{+} \\ \dfrac{n-1}{2} & n = 2j + 1 \quad j \in Z^{+} \end{cases} \\ t = t_{end} - \Delta t: &\qquad n' = n - 1 \end{aligned} \tag{2}$$

and Δt and n $(n \in Z^{+})$ are the largest values such that accuracy of the results and stability of the method are satisfied with generally accepting a small loss of accuracy in time integration. Since, the new excitation, $\tilde{\mathbf{f}}$, is digitized at steps equal to $n_f \Delta t$, when considered instead of the original excitation, can lead to a reduction in computational cost including the time spent and memory, which is essential for the analysis.

3 STRONG GROUND MOTION

On Jun-20-1990, a destructive earthquake occurred in Gilan and Zanjan provinces. The strongest ground motions of this earthquake have been recorded at the Abbar station at a 10 km distant from earthquake fault. [4]. In this research, the three components of this earthquake, *i.e.* longitudinal, transversal, and vertical directions, which are digitized by a time step equal to 0.005 sec is used as the strong ground motion. Using the new proposed method [2] the three components of the Abbar earthquake records are digitized at steps 2, 3, 4, and 10 times larger than the steps in the original records, *i.e.* 0.01, 0.015, 0.02, 0.05 sec. Filtering or baseline correction are not applied on the new digitized records. The acceleration records derived from the longitudinal direction of the earthquake record for various time steps are separately shown in Figure 1. By visual comparing the new digitized records in Figure 1, it can be seen that configuration of the records are preserved except for the last one, *i.e.* time step 0.05 sec. The time history of the velocity and displacements derived from the acceleration digitized records by carrying out a numerical integration process, are shown in Figure 2. It is mentioned that the velocity and displacement of the digitized record with 0.05 sec. step size, show slight and major differences respectively with respect to the other related results. It emphasizes our previous visual conclusion.

In order to better understanding the changes occurred in the new digitized records their other characteristics of this direction are compared. The response spectra of the digitized records are considered in Figure 3. This figure shows the maximum acceleration response of a single degree of freedom system against the longitudinal direction of the digitized records. It is seen that large time steps, like 10 times larger, may lessen the power of the short periods of the main record. It is because if sampling rate of the new digitized record is assumed to be 0.05 sec, the Nyquist frequency is 10 Hz, the modes with periods shorter than 0.1 sec are not considered in the record, and they may produce conflict in the results. This may observe in the acceleration and velocity responses of systems. So, we expect that the results related to this record because unexciting high frequency modes of the building model in comparison to the other digitized records produce farther results with respect to the original record.

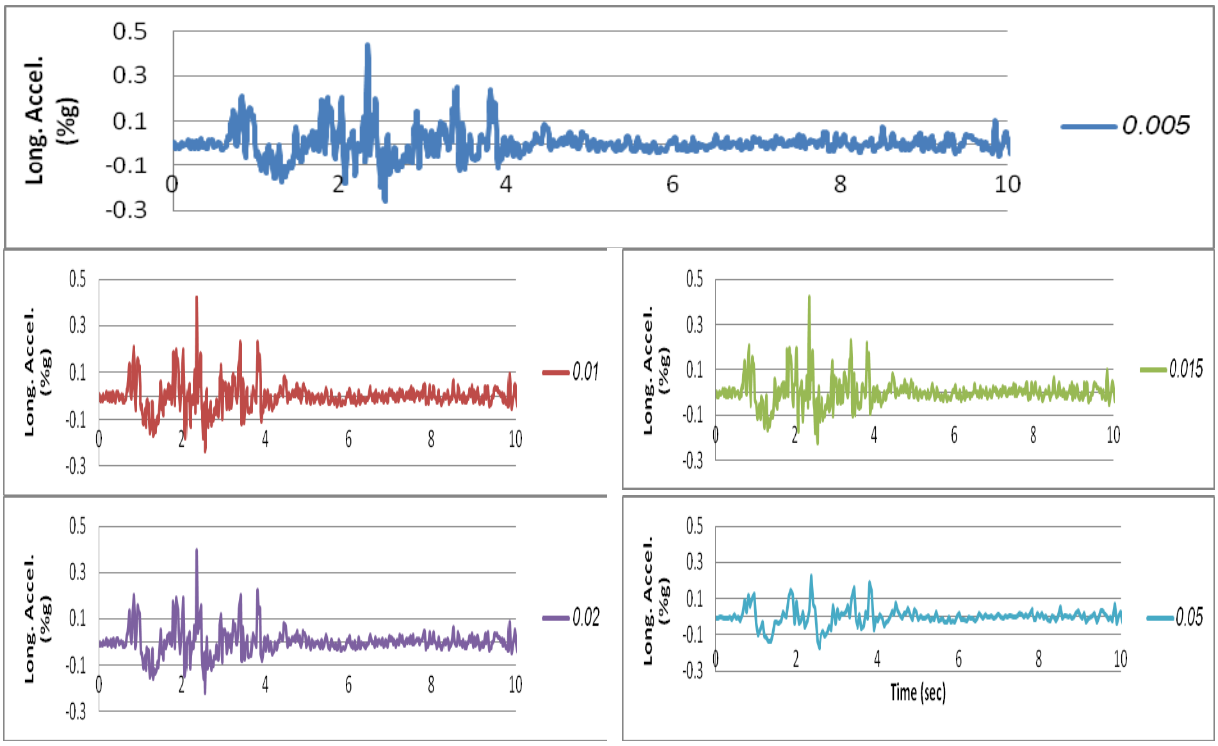

Figure 1: The digitized acceleration records of the longitudinal direction with various step sizes.

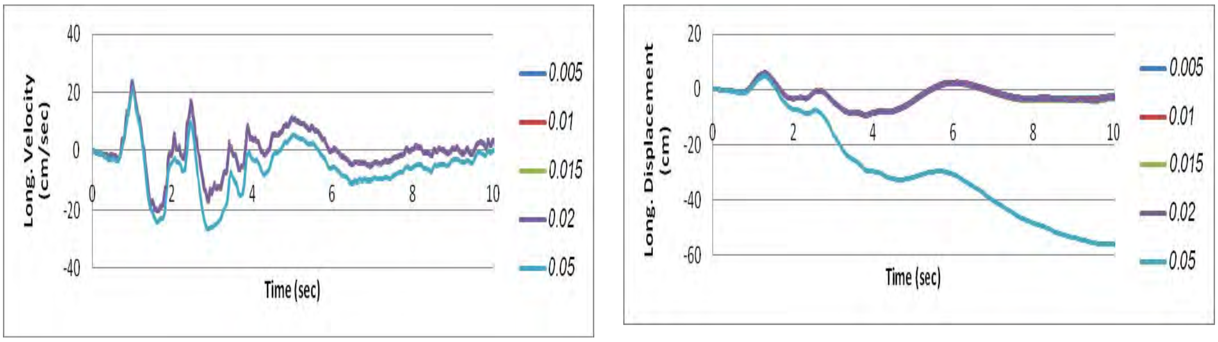

Figure 2: The digitized velocity (left) and displacement (right) records of the longitudinal direction with various step sizes.

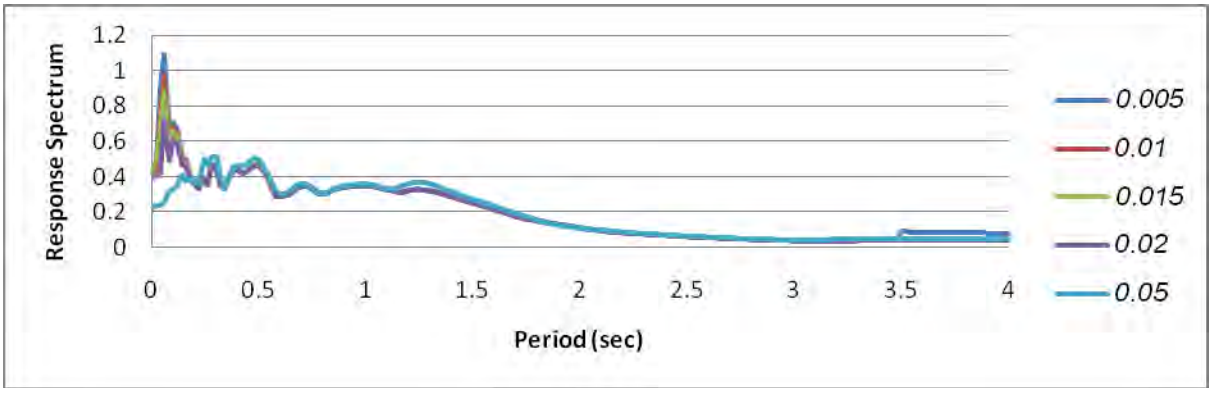

Figure 3: The response spectrum of the longitudinal direction of the digitized records with various step sizes.

Arias intensity drawn in Figure 4 (left side), is a ground motion parameter that captures the potential destructiveness of an earthquake as the integral of the square of the acceleration-time history. It correlates well with commonly used demand measures of structural performance, and several demands related to geotechnical appearances like liquefaction and seismic slope stability. Arias intensities in Figure 4, shows that we may suppose that the performance of the building against digitized records with various time steps are not so different. Energy flux drawn in Figure 4 (right side) is the total rate of energy transfer through a surface. The results show that the rate of transferring energy to the building due to the digitized record by time step equal to 0.05 sec is completely different from the other records. Hence, it may cause the response of the building to be more excited at the end of the mentioned record. It is emphasized that performance of the building due to the other digitized records will be very similar.

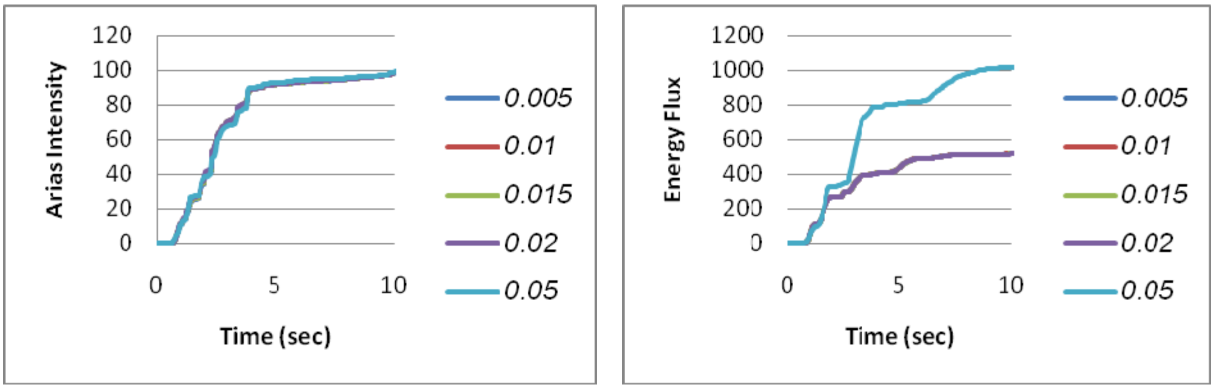

Figure 4: Arias intensity (left) and energy flux (right) related to the longitudinal direction of the digitized records with various step sizes.

The maximum acceleration, velocity, and displacement of the digitized records with various time steps presented in Table 1 are compared with the values of the original record. The results show that the main characteristics of the digitized records with time steps even 4 times larger than the original one are not seriously changed. It refers to the power of the new proposed method to re-digitized records by using larger time steps [2]. Hence, it is recognizable that the response of the building may not so change until time steps 4 times larger but it may completely different when using 10 times larger time step. Meanwhile, using combination of the three components of the earthquake records may slightly affect our guesses.

Table 1: The maximum ground acceleration, velocity, and displacement of the records digitized by various time step sizes.

Time step (Sec)	0.005			0.015			0.020			0.05		
Dir.	L	T	V	L	T	V	L	T	V	L	T	V
PGA (%g)	0.44	0.32	0.30	0.42	0.30	0.26	0.40	0.29	0.25	0.22	0.25	0.20
PGV (cm/sec)	23.67	40.06	30.54	23.35	39.70	30.34	23.11	39.34	30.09	26.56	37.69	39.10
PGD (cm)	9.22	131.13	107.74	9.63	129.00	107.13	9.65	127.97	105.50	57.35	135.08	203.72

4 NUMERICAL STUDY

In this section, seismic behavior of an 8-story 3-dimensional steel structure against different 3-component earthquake records digitized by assuming various time steps is presented.

The building is symmetric about X and Y directions, includes four special moment resisting frame in each direction, and eight equal height floors. It has three equal spans 5 meters length in each direction, and each floor height is assumed to be 3 meters. This building is designed according to the Iranian codes [5-7]. Using the linear dynamic time history analysis, seismic evaluation of the building against the 3-component original earthquake records and the digitized earthquake records with 2, 3, 4, and 10 times larger than the original step size are carried out. The acceleration and displacement responses of the top floor of the building in X-direction due to the different 3-componenet digitized earthquake records are shown in Figure 5. Although, one may observe some dispersion in the acceleration response of the top floor due to unconsidered higher modes, but the displacement response is very smooth and similar for different time steps such that the differences of maximum values in each cycle are not assessable. It is because the displacement responses are highly influenced by the excitation of the lower modes of the building.

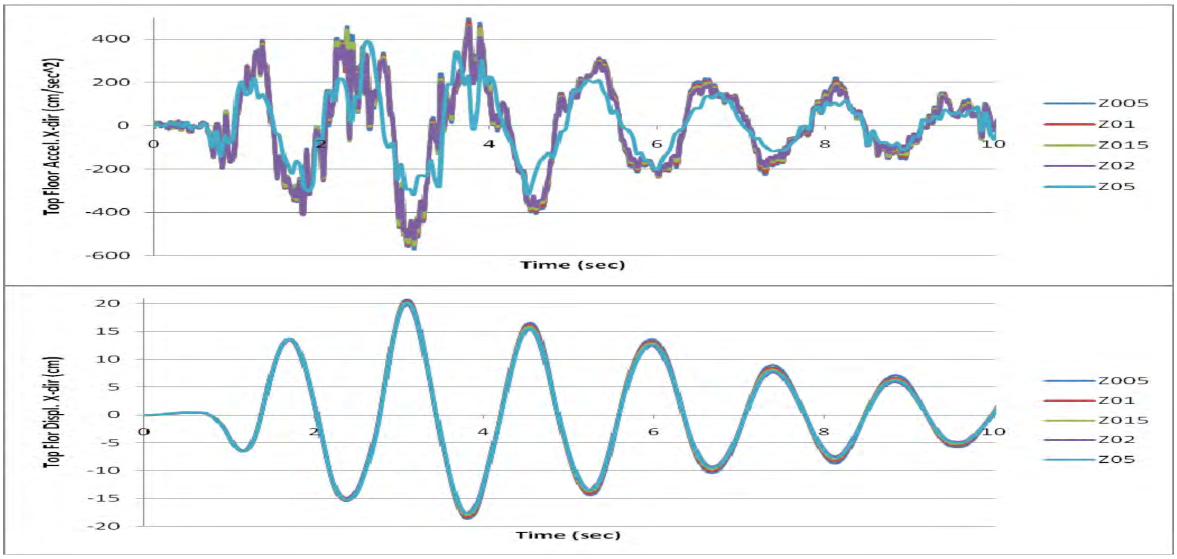

Figure 5. The acceleration (up) and displacement (below) responses of the top floor in X-direction during different 3-componenet digitized earthquake records.

The base shear responses of the building in X-direction due to the different 3-component digitized records are shown in Figure 6. It appears that they are almost identical. It is reasonable because the base shear variations to a great extent follow changes in the displacement responses. So, we may expect that almost all the results show good agreement with the responses of the building due to the original 3-component earthquake record.

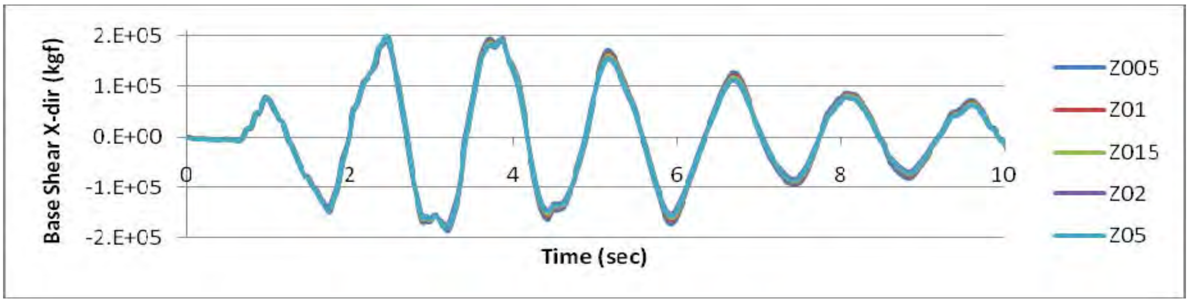

Figure 6. The base shear responses of the building structure in X-direction during different 3-componenet digitized earthquake records.

Figure 7 shows the maximum displacements of the even floors in positive (right) and negative (left) directions. The values are very similar even for step size 10 times larger. There is only a slight decrease in the responses due to 4 and 10 times larger time steps. But, its differences are not recognizable. Hence, it may conclude that except for the acceleration responses, even using 10 times larger time step may be acceptable and meet the designers' goals.

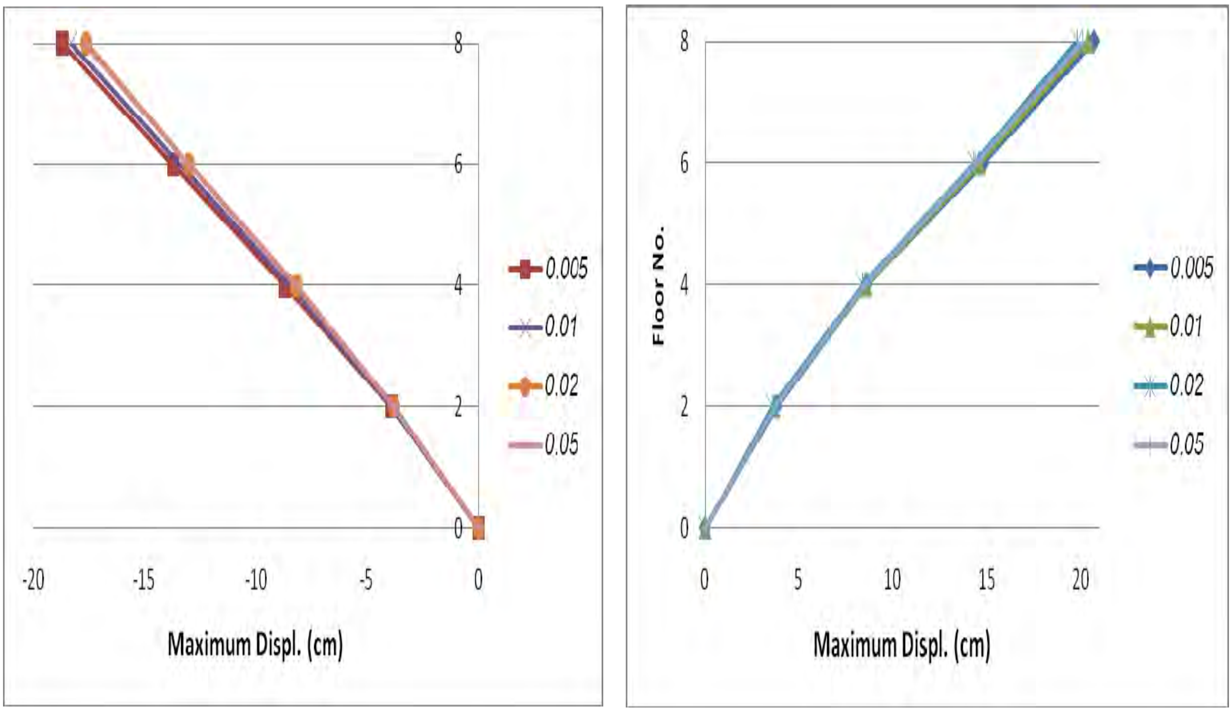

Figure 7. Maximum displacements of the even floors of the building structure in X-direction during different 3-componenet digitized earthquake records.

Now, we consider the error percentages of the acceleration and displacement responses of the top and the 1st floors due to the earthquake records digitized by various time steps. The results are tabulated in Table 2. It is clear that the values of the displacement responses for positive and negative side are very similar to the correct values. It is noticeable that the error related to the step size 4 times larger is greater than that of 10 times larger. However, considering the acceleration responses show that rapidly incorrect increasing the values of the acceleration responses may happen as the step size of the original earthquake record increases. It is because the higher modes are not considered in the analysis.

Table 2: The error percentages of the top and the 1st floors responses due to the earthquake records digitized by various time steps.

Error Value %		0.01	0.015	0.02	0.05
Top floor acceleration response	right side	-3.0	-7.0	-8.2	-11.8
	left side	-3.4	-3.6	-8.2	-6.6
1st floor acceleration response	right side	-4.0	-5.6	-20.2	-18.7
	left side	-4.4	-3.2	-9.0	-43.8
Top floor displacement response	right side	-1.4	-2.9	-4.4	-3.2
	left side	-1.9	-3.8	-5.8	-5.4
1st floor displacement response	right side	-1.4	-2.9	-4.5	-2.6
	left side	-1.1	-2.2	-3.6	-2.2

Finally, the overall time consuming for each analysis are compared in Table 3. Since, the building structure belongs to relative short height building, differences are not effective. Based on the results represented in Tables 2 and 3, it seems using step size 3 times larger presents the best corrected results and decreased time needed for analysis. But, if the acceleration response has not influence in our considering, it may use step size 10 times larger.

Table 3: The time consumes during linear dynamic time history analysis due to the earthquake records digitized by various time steps.

Time Step (sec)	0.005	0.01	0.015	0.02
Run Time	37' 33"	18' 40"	15' 20"	12' 14"

Discussion presented by considering the differences occurred in the inherent characteristics of the new digitized records does not necessarily result in predetermined performance of the building. Because, it is strongly related to the parameter of the considered building, characteristics of the original earthquake even including 1, 2, or 3 components in the analysis, and finally to the conditions and assumptions of the analysis. Some discrepancies may be related to the records before and after regeneration are not corrected by baseline procedure. This may slightly change the characteristics of the digitized earthquakes and influence the performance of the building. But overall, considering the results show that the new proposed method has effective influence on decreasing time consuming and memory used by preserving correctness of the building performance.

5 CONCLUSIONS

In this paper, a new proposed method to regenerating earthquakes by larger step sizes and its influence on seismic performance of a 3-dimensional 8-story special moment resisting frame steel structure is examined. Considered earthquake is the first 10 sec of the 3 components of the Abbar earthquake records. The results are not filtered or baseline corrected. Evaluation of the different parameters and characteristics of the records show that the proposed method using step size until 4 times of the original record almost not change the original features of the earthquake records. Considering responses of the building shows that using large time steps cannot significantly change the base shear and displacement responses of the building but may strongly affect the acceleration responses, which is excited by eliminating higher modes of the building. On the other hand, the new method can significantly reduce the computational cost and used memory.

These results are related to the linear dynamic time history analysis of a 3-dimensional steel structure due to more than one component earthquake records. However, these results may be changed if different parameters are included, like material and/or geometric nonlinearities, P-delta effect, using different numerical method with other convergence speed, structure with complex modes, closeness of the modal characteristics, and finally parameters of earthquake records especially include intense changes during short times.

ACKNOWLEDGEMENT

We are sincerely grateful to Dr. A. Soroushian for his help to generating new earthquake records using various time steps. Also, Mr. A. Mahmoodian Aghdam is greatly acknowledged for carrying out computer analyses regarding the main characteristics of generated earthquake records.

REFERENCES

[1] M. Paz, *Structural Dynamics, Theory and Computation, 3rd Edition*, Van Nostrand Reinhold, New York, 1991.

[2] A. Soroushian, A technique for time integration analysis with steps larger than the excitation steps. *Communications in Numerical Methods in Engineering*, **24**: 2087-2111, 2008.

[3] **A.** Soroushian, On the performance of a conventional accuracy controlling method applied to linear and nonlinear structural dynamics. *Proceedings of the 17th International Congress on Sound & Vibration*, ICSV 17, Cairo, July 2010.

[4] http://www.BHRC.ac.ir/

[5] *Iranian Code of Practice for Seismic Resistant Design of buildings.* Standard No. 2800, 3rd ed., Building and Housing Research Center, Tehran, Iran, 2005.

[6] *Iranian National Building Code, Part 6: Structural Loadings.* Ministry of Housing and Urban Development, Tehran, Iran, 2004.

[7] *Iranian National Building Code Part 10: Steel Structures.* Ministry of Housing and Urban Development, Tehran, Iran, 2006.

COMPDYN 2011
3rd ECCOMAS Thematic Conference on
Computational Methods in Structural Dynamics and Earthquake Engineering
M. Papadrakakis, M. Fragiadakis, V. Plevris (eds.)
Corfu, Greece, 25–28 May 2011

The Effect of Initial Geometric Imperfection on the Load Bearing Capacity of Double Layer Barrel Vault Space Structures

M.Mohabbi Yadollahi [1] , R.Gül[2] , R.Polat[3], B.Mohebbi Yadollahi[4],M.S.Gül[5]

Department of Civil Engineering

Atatürk University, 25240, Erzurum, Turkey

Mehrzad[1]@atauni.edu.tr

Department of Civil Engineering Atatürk University

{rgul[2], rizapolat[3],msgul[5]}@atauni.edu.tr

East Azarbaijan Regional Watercorp

East Azarbaijan Regional Watercorp,Tebriz,Iran

gozaltabriz[4]@yahoo.com

Keywords: Random Imperfection, Geometric Nonlinearity, Monte Carlo Method, Buckling Strength, Initial Geometric Imperfection, Reliability, Certainty, Imperfection Sensitivity

Abstract. *The existence of some geometrically imperfect members in space structures are almost inevitable, beside that there are some imperfections in botching the structures and the fact that they are effective in producing internal forces is undeniable. When a compressing member yields, in spite of that, continues bearing a lot of load, on the other hand the buckled compressive member goes to a critical situation and losses its stiffness and shed its load on the other members, causing a progressive collapse. Double layer barrel vaults which have statically highly indeterminate degree , may cause this phenomena because of unsuitable members .As the members initial curvature is the most popular geometric imperfection which is common in practical structures , in this thesis has chosen as an effective imperfection ,for research. We have tried to study this effect on the load bearing capacity of model structure. The selected model is a double layer barrel vault which is subjected to uniform concentrated load applied vertically downward to each node of the upper layer and members assumed to be pin-ended .The ratio of pure height of structure to pure opening mouth is 0.22 and the kind of layers decoration is a square on square. Two forms of analysis carried out; one for monotonous imperfections and the other for 30 cases of random imperfections which based on Monte Carlo Methods. After analysis, the ratio of maximum reduction to common case was about %41, also the suitable way of certain conclusion is presented with Monte Carlo Method.*

1 INTRODUCTION

Double layer reticulated structures are generally indeterminate from statically point of view. As occasionally there will not be any problem in stability and structure efficiency even with elimination of structure elements 15% to 25%, sometimes this preconception causes the engineers misleading about the estimation of structure safety factor [9] When one of the compressive element yields, truss stiffness decreases. After the buckling of compressive element, its force is shed among the other elements [3]. Consequently other bars are buckled and lead to progressive collapse phenomenon which imposes impact dynamic effect on the structure [2, 4]. While the development of double-layer reticulated shells on the architectural /executive ground, the buckling issue of such structures has not completely solved yet. Reticulated shells have the same specification with the reticulated and shell structures, so they will encounter with both structures problems and these problems will resonate and combine [7]. In a truss system, the structure elements are essentially under the axial forces and the element of the structures may be collapsed either under being yield of tension or buckling under compress. If one of the elements of the structure buckles the behavior of its element will conform the post critical characteristics [5, 12]. So in the case of determining behavior of tensional and compressive elements after reaching the critical load, the structure can be analyzed and continue the analysis until the overall collapse of the structure occur. On the other hand, having post critical characteristics the behavior of tensional and compressive element of the structure analysis will be possible between the ranges of the first local buckle to the total structure buckling. Usually when a tensional element reaches yield load, its load capacity increases somehow due to strain hardening [8], but when a compressive element buckles load capacity decreases with increasing axial shortening. I.e., the element cannot resist and consequently sheds its load into the other structure elements. The stiffness of post buckling compressive element has an effective influence on the total behavior of the element. It means that, if compressive element becomes unstable and abruptly shed its load to the other elements, its effect will be worse than when the load gradually sheds on the other elements [6]. Presentation of the compressive element behavior has an essential role in the buckling analysis. In the most buckling methods, first of all the load-displacement behavior of compressive element should be determined, and then the results can be used in the modeling of nonlinear compressive elements behavior. Hence, in order to determine the compressive element behavior, the behavior of post buckling element should be determined. There will be three collapse mechanisms for the structures as mentioned below: overall collapse, local collapse with dynamic snap through, local collapse without snap –through [2].

The essential factors in determining compressive buckling element and general structure behavior are the material and the geometric imperfections and there are several geometric varieties such as: nodal imperfections, increase or decrease in element length rather than desired length and element initial curve which is considered as an effective imperfection. In fact the imperfection effect of capacity rather than double layer barrel vault space structure is the main problem of this study. Fundamental theory of this study is based on the existing geometric imperfection which causes the decrease in load capacity and overall /local instability. In this study as double layer barrel vault load increases incrementally in top nodes of double layer grid, the load bearing capacity of the structure decreases. Also, distribution of existing imperfection has been done randomly. In the distribution of imperfect elements in the critical area Monte Carlo analysis standards [16] has been considered. Finally, in order to determine safety factor for structures load bearing capacity a new method is offered.

2 SPACE TRUSS FOR OBSERVATION AND ANALYTICAL METHOD

As the element of the space trusses are usually manufactured in factory, involving some nonstandard products about 1% of space trusses. In order to simplifying the study five types of imperfections for elements are use. Of course, practically due to the diversity of imperfection elements, the distribution will be continuum based on gamma distribution.

2.1 Modeling

The double-layer barrel vault truss includes the pin-ended connections. The dimension of the structure plan is 20*21.3 meters which is almost square on square. The distance between two layers is 1.63meter.also; the ratio of net height to net bay is 0.22. Double-layer grid is designed as all of the lower and upper elements have 2 meters length with a diagonal 2.4 meter length. In this model internal length of structure is 4.42 meters and net bay is 19.38 meters. (Figure 1)

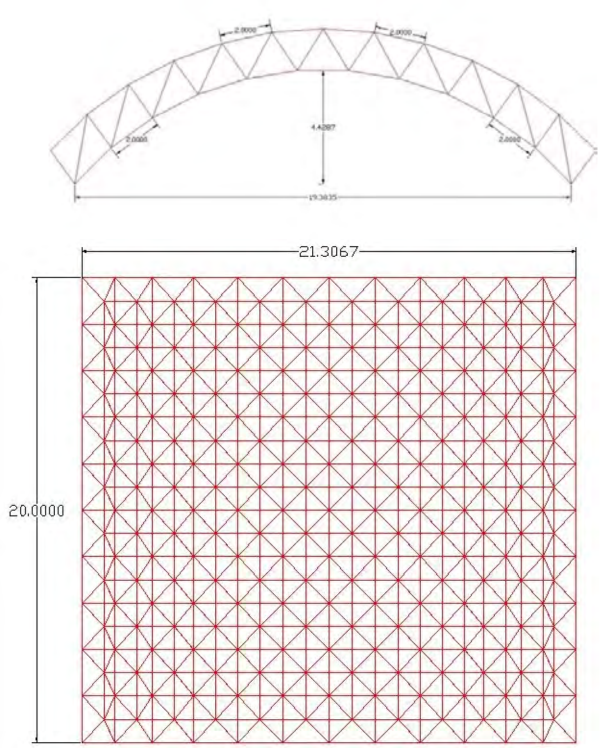

Figure1. Layout of studied space trusses

2.1.1 Material specifications

The material is steel and its yield stress is 360 Mpa and yang module is 210000 Mpa.

2.1.2 Elements specifications

Regarding to 1.5 ton/joint loading for all upper layer nodes and the structure linear analysis, all profiles are selected from steel tube with an external radius of 41.275mm and a wall thickness of 9.52 mm.

2.1.3 Imperfection specifications

The kind of used imperfection is geometrical imperfection with an initial deviation [5]. The maximum initial deviation of the member at mid-point from the chord line was taken to be ε.

2.1.4 Computer program specifications

In order to carry out nonlinear pre-buckling and post-buckling analysis, Lusas software including BM3 for compressive element modeling has been used. [1]

2.1.5 Loading specification:

The starting point of incremental loading is 100N and has been continued until structure collapse. (Figure2)

2.1.6 Supporting specifications:

All of the supports are pin-ended and positioned along with the lower layer edges. (Figure2)

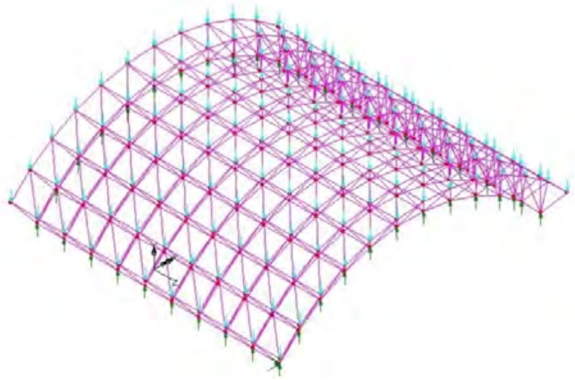

Figure2. Truss loading & linear edged support position

2.2 Determining the buckling behavior of compressive element in a finite element method

In order to do nonlinear analysis of the modeled structure, determining load-displacement relationship in pre-buckling and post buckling stage of structural members with consideration of its imperfection is essential [5]. Applying tubular profile in the space structures is typical. So as it already mentioned, using linear analysis, profile sections with the 41.275mm radius and with the wall thickness of 9.52mm in the 2.4 and 2 lengths have been selected.

2.2.1 The assumptions of analyses of compressive elements in the finite element method are:

-Complete elasto-plastic stress-strain relationship for material is considered and regardless of hardening effect, we assume symmetric relationship for stress-strain diagram. [4]

-We assume the element section prismatic and symmetric.

-We generalize each element to ten equal parts to achieve precious and reliable results.

-We use the Kirchhoff thin beam model to determine the behavior of the compressive elements regardless of the shear deforming effect.

-If the compressive elements become straight with homogenous material, pure compressive condition will be occurred. But there would not be any ideal compressive elements with the mentioned characteristics. Somehow some imperfections such as the following ones may create bending moment in the compressive elements and decrease the load bearing capacity.

-Initial element deviation, eccentric loading, diversity of local specifications, being inhomogeneous, residual stress in element section

-In this study merely the compressive element initial curvature as a geometric imperfection has been considered. It is assumed that, maximum initial deviation of the member at mid-point from the chord line was taken to be ε and it is symmetric as well. For imperfection (ε=0.0005L, ε=0.001L, ε=0.005L, ε=0.01L and ε=0.02L), the elements behavior have been determined.

-We assume that compressive elements do not have local instability. In order to determine compressive element load-displacement relationship; we can use a statically large deformation elasto-plastic nonlinear analysis and both material and geometric nonlinearity in analysis have been used [7]. (Figure3)

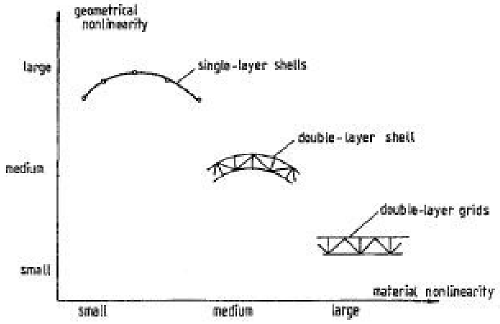

Figure3. Effects of nonlinearities

-Drawing an equilibrium nonlinear route until reaching the buckling load has been done by Newton-Raphson repetitive method as this method has been diverged due to being singular stiffness matrix adjacent to buckling critical point; consequently it would not be efficient. So, in order to draw balanced route adjacent with critical point, we have used arc length method.

-The quantity of compressive element critical load is calculated for member initial maximum imperfection and the obtained quantities will be reliable if the load is less than Euler buckling load. Otherwise, the initial buckling load will be considered.

2.2.2 Drawing stress-strain relationship based on the above assumptions

Members length has been analyzed with the imperfections (ε=0.0005L, ε=0.001L, ε=0.005L, ε=0.01L and ε=0.02L) and all behavior were compared [10, 11]. The slenderness of the elements is medium and stress-strain curvature has been calculated according to the force-displacement which their diagram have been illustrated below. Note that, sometimes the above diagrams have been illustrated based on 1000 case of incremental loading. Determining of these points to structure analysis for finite elements program may be time consuming. In this study nonlinear curves have been considered in calculation with 6 points. (Figure 4, 5)

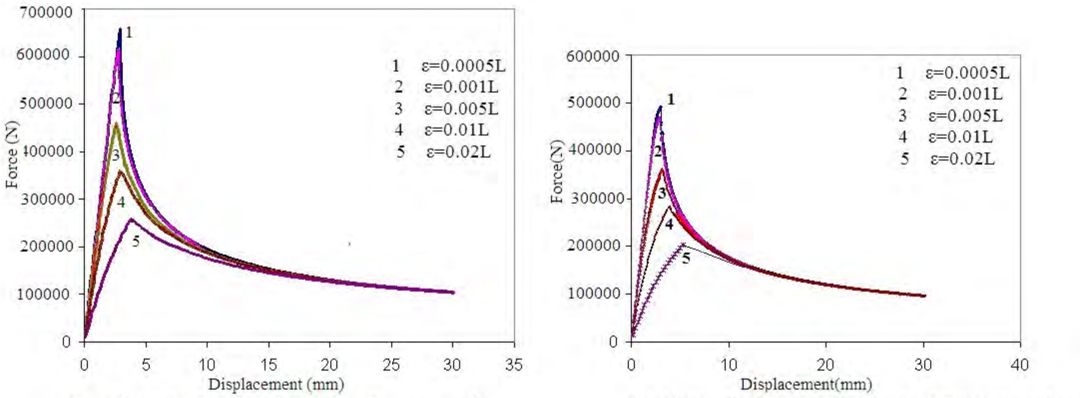

Axial force-displacement diagram for 2meters member

Axial force-displacement diagram for 2.4meters member

Figure4. Axial force-displacement diagram for 2and 2.4 members

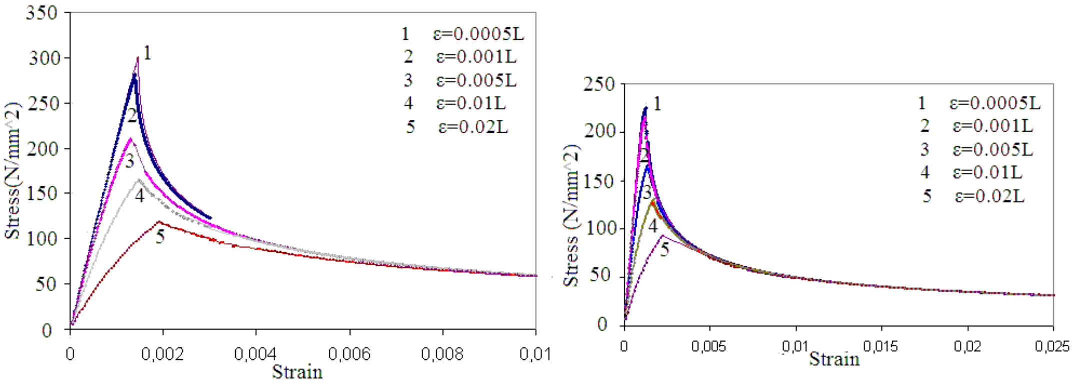

Stress-strain diagram for 2 meters member

Stress-strain diagram for 2.4 meters member

Figure5. Stress-strain diagram for 2and 2.4 members

According to the depicted diagrams, it is clear that the applicable elements behaviors are brittle. Hence, final strength of such elements has been decrease with increase in the imperfection as a result ductile behavior is formed.

2.3 Double layer barrel vault truss analysis

Analyze the barrel vault in two manners. Firstly under uniform imperfection for all elements and secondly under random imperfection about 30 cases

2.3.1 Analyzing under uniform imperfection for all elements

Study the truss under Quadra imperfections (ε=0.0005L, ε=0.001L, ε=0.005L, ε=0.01L).it is assumed that, all of the elements have the same imperfection and the result of the analysis have been drawn in a displacement-load diagrams. It is clear that, with increasing the imperfections quantity in a current mode, total structure strength is influenced effectively. (Figure 6)

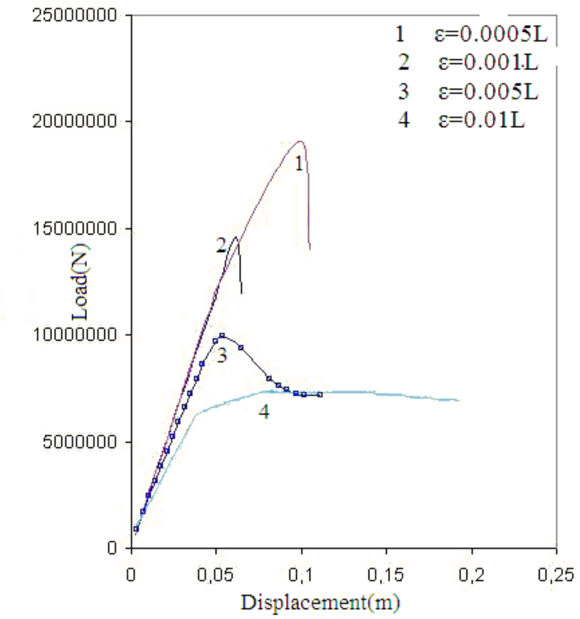

Figure6. Behavior of the truss under uniform geometrical imperfections

2.3.2 Analyzing truss under random imperfections distributions

Due to being time consuming of nonlinear analysis and likelihood of all possible imperfections, 30 analysis cases based on Monte Carlo standards have been used to estimate load capacity. For each analysis, consider a different distribution for imperfections consequently; use a program in visual basic to determine the random imperfections distributions. Note that, the purpose of complete status or comparative standards, is (ε=0.001L) total imperfections for all elements. Also as linear analysis result show that, lower layer and diagonal elements cannot reach the plastic stage so they would not be critical. Consequently critical area is selected in the critical area of truss upper layer. (Figure7)

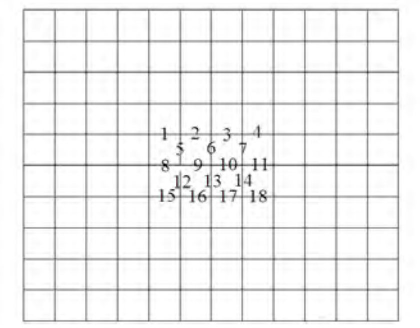

Figure7. The position of randomly distributed elements of the truss top layer in the critical area

2.3.2.1 The method of determining the quantity of each existing imperfection

The quantity of each existing imperfections resulting from gamma distribution has been selected [13] according to the following diagram. (Figure8)

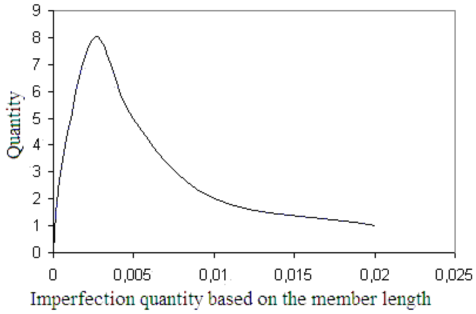

Figure8.Quantity-imperfection diagram via gamma distribution

2.3.2.2 Consideration of random analysis result

We compared the obtained results of random analysis to achieve the quantity of strength decline according to changes in imperfection elements locations. (Figure9)

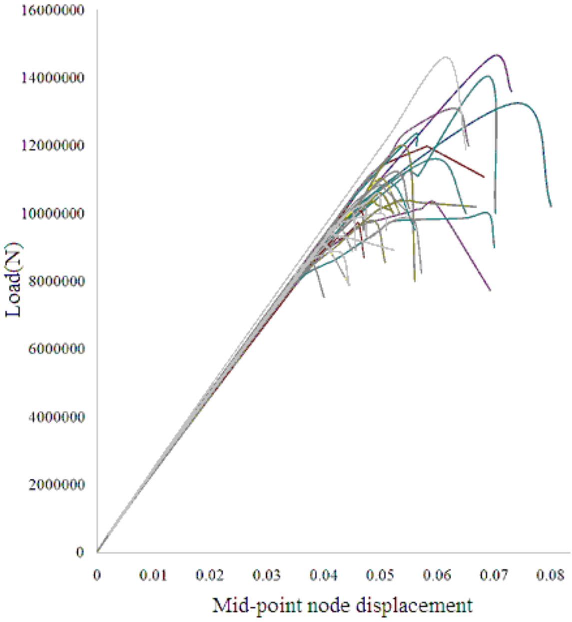

Figure9. Node mid-point Load-displacement behavior for 30 random and a perfect modes

2.3.2.3 The structure sensitivity

The structure sensitivity rather than imperfection distribution of truss in the critical area is completely evident. According to the analysis, the strength average of structure for different conditions is 10795004.07 N and strength decline diagram is drawn based on random analysis. (Figure10)

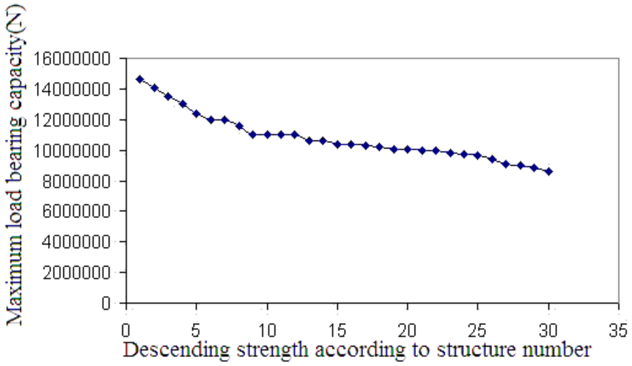

Figure10. Descending strength according to structure number

According to analysis based on Monte Carlo criteria and its accordance with normal distribution the diagrams are

1-frequency-strength related to quantity of resulted strength. (Figure11)

2-probability density function diagram

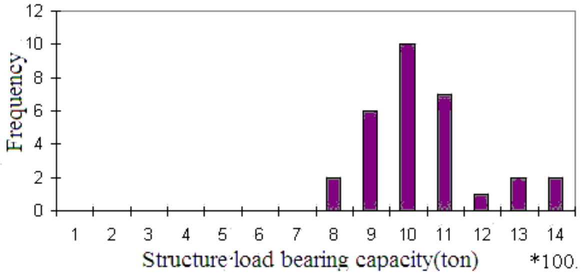

Figure11. Histograms of the structure load bearing capacity for 30 random analyses

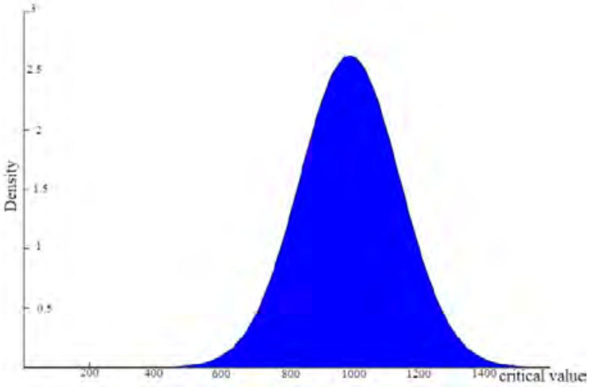

Figure12. Analysis density distribution function

As a result based on the illustrated diagrams and regarding to the possibility of desired occurrence, estimating of the structure strength would be possible. This method for determining safety factor has been mentioned in [14], [15] references.

3 SUMMERY AND CONCLUSION

According to the analysis, we conclude that:

-The applied imperfections in the critical area have not have a remarkable effect on the structure initial stiffness. Indeed, the most important effect of such measurements is decreasing the maximum load bearing capacity.

-The double layer barrel vault space structure is sensitive to geometric imperfections.

-For different modes of randomly imperfections distributions, in the worst mode the structure has shown 41% strength decline.

-In this study the only geometric imperfections is initial deviation contributed in the result. Furthermore, the other imperfections effect and the combination of the local instabilities have not been considered. Randomly distribution of the imperfections in the critical area based on Monte Carlo method, leads to finding a suitable method way to estimate the structure actual and practical strength.

-Based on the analysis of Monte Carlo method and drawing related curvature (including strength-possibility and frequency-strength), the possibility of desired strength occurrence is assessed.

4 RECOMMENDATIONS

The main logical method in such structures, having more accuracy in manufacturing and controlling the parts before assembly. So, if there are more member imperfections, they should not be used in the compressive critical area. In the double layer barrel vault space structure, the critical member located in upper layer and these members are much more sensitive to the geometric imperfection; so, more strengthening the members in the critical area of the truss leads to increasing the structure load bearing capacity and decline the structure sensitivity to the imperfection as well. In summary it is not possible to monitor the structure in all conditions so, it is recommended to apply fuzzy logic and artificial neural network in future studies.

5 ACKNOWLEDGEMENTS

The authors would like to thank Fatemeh Goharkhaneh Asli for her assistance in preparation the article.

6 REFERENCES

[1] M.R. Sheidaii, K. Abedi, A. Behravesh, An investigation into the Collapse behavior of double layer grid space structure. *Proceeding of the LUSAS User Conference,* LondonEngland, 200

[2] M.R.Sheidaii, G.A.R.Parke, K.Abedi, A.Behravesh, Dynamic snap-through buckling of truss-type structures, *International Journal of Space Structures*, Vol. **16**, No. 2, 2001.

[3] M.R.Sheidaii, G.A.R.Parke, K.Abedi, A.Behravesh ,An investigation into the collapsebehavior of double layer grid space trusses, *Iranian Journal of Science and Technology*, Vol. **27**, No B1, 7-20, 2003.

[4] K.Abedi, M.R.Sheidaii, Investigation of Double layer Grid Space Structure Resistance to Progressive Collapse. *Esteghlal*, Vol.**1**, 2007. (In Persian)

[5] K.Abedi , M.R.Sheidaii , Evaluation of Compression Member Buckling and Post-Buckling behavior Using finite element method, *first thin wall structures conference in iran,131-138*, Urmiye , Iran,2003. (In Persian)

[6] M.R. Sheidaii, K. Abedi, A. Behravesh, Collapse behavior of Double layer grid spacestructure. *Proceedings of the IASS symposium on Theory Design and Realization of Shell and Spatial Structure*, Nagoya, Japan, 2001

[7] V. Gioncu, Buckling of reticulated shells: state-of-art. *International journal of Spac Structure* Vol. **10** No.1, 1995 [8] A. Sheikh, Sensitivity of Space Trusses to Member Geometric Imperfections. *International Journal of Space Structure* Vol. **10**.No .2, 1995

[9] G.S .Ramaswamy**,** Analysis, design and construction of steel space frames**,** Thomas Telford, London, 2002.

[10] E-Smith. Murtha, Compression Member Models for Space Trusses: Review .*Journal of Space Structure* Vol.**120**, No. 8, 2399-2407, 1994

[11] S.Toma, W.chen, Inelastic Cyclic Analysis of Pin ended Tubes. *Journal Structure .Eng. ASCE,* Vol.**108**, No .10, 2279-2294, 1982

[12] V.Gioncu, Stability of Space Structures. *International Journal of Space Structure*, No. 1992Vol.**7**.

[13] A.Tegola, Ultimate Limit States of Space Reticular Structures with Random Behavior Elements. *International Journal of Space Structure,* Vol.**7** No.4, 1992.

[14] J.Stroud, T.Krishnamurthy, N.Sykes, I.Elishakoff: Effect of Bow -Type InitialImperfection on Reliability of Minimum-Weight Stiffened Structural Panels. *NASA Technical Paper 3263*, 1992.

[15] A. Wada, Z.Wang, Influences of Uncertainties on Behavior of a Double-Layer Space Truss. *International Journal of Space Structures,* Vol.**7** No.3, 1992.

[16] V. Papadopoulos, M. Papadrakakis, The effect of material thickness Variability on the buckling load of shells with random initial imperfections. *International Journal of Space Structures* ,**194**.1405-1426, 2005.

COMPDYN 2011
III ECCOMAS Thematic Conference on
Computational Methods in Structural Dynamics and Earthquake Engineering
M. Papadrakakis, M. Fragiadakis, V. Plevris (eds.)
Corfu, Greece, 25–28 May 2011

MULTISCALE RKPM FORMULATION FOR MODELING PENETRATION OF AN ULTRA HIGH-STRENGTH CONCRETE MATERIAL

M. J. Roth[1], J. S. Chen[2], T. R. Slawson[1], R. N. Boone[1], X. Ren[2], S. W. Chi[2], C. H. Lee[2], and P. C. Guan[2]

[1] U.S. Army Engineer Research and Development Center
3909 Halls Ferry Road, Vicksburg, MS, 39180
e-mail: {michael.j.roth, thomas.r.slawson, nicholas.boone}@usace.army.mil

[2] Department of Civil and Environmental Engineering
University of California, Los Angeles
P.O. Box 159310, Los Angeles, CA, 90095-1593
jschen@seas.ucla.edu, chishengwei@ucla.edu, rxd1981@gmail.com, ch.lee@ucla.edu,
paichen@ntou.edu.tw

Keywords: RKPM, multiscale, microcrack, damage model, ultra high-strength concrete, penetration

Abstract. *Impact and penetration events involve complex response phenomena such as damage and fragmentation, which present particular challenges to numerical methods like the finite element method. Further, the commonly used phenomenological damage law gives no direct consideration to the evolution of continuum-scale damage with respect to microcrack formation and growth within the substructure. In this work, we introduced the reproducing kernel particle method (RKPM) to impact and penetration problems, and a hierarchical multiscale modeling technique under the framework of RKPM is proposed. A multiscale damage model is developed based on homogenization of a cracked microscopic cell, which is termed the microcrack-informed damage model (MIDM). Bridging between scales is accomplished by a novel energy equivalence approach. Application of the MIDM to a specific ultra high-strength concrete material is discussed, and results from the analysis of a benchmark penetration problem are presented.*

1 INTRODUCTION

Impact and penetration events represent a class of complex physical problems that are of significant interest in both military and commercial applications. These can generally be considered as “strong dynamics” problems, which exhibit high strain rates (10^3-10^7 s^{-1} for ballistic events [1]), large velocity gradients, and fast-evolving strong and weak discontinuities that lead to extensive material and structural damage and fragmentation. The level of complexity is further enhanced when considered in the context of concrete structures due to concrete’s brittle response and highly heterogeneous microstructure. In particular, material fragmentation poses a significant challenge to structured-mesh-based methods such as the finite element method (FEM). Due to extensive material deformation and separation, techniques such as element erosion have been commonly implemented to circumvent instabilities resulting from excessive mesh distortion. However, erosion is not consistent with the physical event, and subsequently precludes accurate modeling of certain effects such as debris generation from the impact zone. Therefore new meshfree methods, which do not exhibit the structured-mesh dependency of FEM, can provide significantly enhanced capabilities for impact and penetration modeling.

Accurate mathematical description of material softening, degradation and failure processes plays a dominant role in the accuracy of penetration modeling. The typical phenomenological description of damage evolution at the continuum scale lacks a direct link to the underlying microstructure processes. Damage processes in brittle solids such as concrete are driven by the distribution of microcracks and their evolution, and thus the applicability of continuum damage models requires further enhancement. In this work, a multiscale approach is introduced to link the continuum damage evolution to substructure crack propagation based on an energy bridging approach. This multiscale model is developed under the framework of the meshfree reproducing kernel particle method to model concrete penetration. The resulting multiscale damage evolution model has been termed the microcrack-informed damage model (MIDM) [7]. An ultra high-strength concrete developed by the U.S. Army Engineer Research and Development Center (ERDC) was adopted as a material for use in the formulation development.

The purpose of this paper is to provide an overview of the RKPM formulation for penetration modeling and discuss the development of the microcrack-informed damage model. Organization of the paper is as follows. Section 2 provides an overview of RKPM utilizing a semi-Lagrangian formulation, and Section 3 discusses the microcrack-informed damage model formulation. Section 4 presents implementation of the MIDM into a concrete constitutive model developed for penetration, and a benchmark penetration problem is analyzed in Section 5. Concluding remarks are given in Section 6.

2 REPRODUCING KERNEL PARTICLE METHOD

The reproducing kernel particle method (RKPM) [2,3] is a meshfree method in which the approximation and domain discretization of a partial differential equation are accomplished by a set of nodes related through domains of influence, also known as support zones. The support zones are non-conforming, which alleviates many of the structured-mesh dependent problems associated with FEM. This minimization of mesh dependency provides a distinct advantage when applying RKPM to impact and penetration problems, where very large material deformation and/or separation are common. A typical RKPM discretization is shown in Figure 1a, where the non-conforming support zone of node **I** is highlighted. The corresponding shape function over the i^{th} node's compact support is shown in Figure 1b.

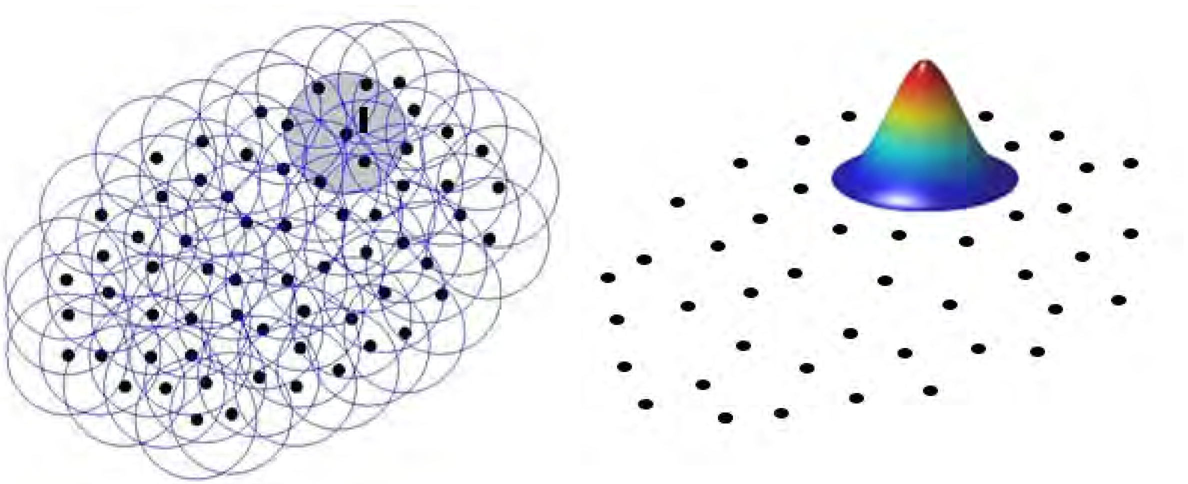

(a) **(b)**

Figure 1. a) Non-conforming, compact support of i^{th} node, b) RKPM shape function for i^{th} node

2.1 Semi-Lagrangian RKPM

In the following discussions, we use the general d-dimensional notation, where $x^{\alpha} = x_1^{\alpha_1} \cdots x_d^{\alpha_d}$ and $|\alpha| = \sum_{i=1}^{d} \alpha_i$. For the subject of interest, we consider the reproducing kernel (RK) approximation of degree p of a displacement field, $\boldsymbol{u}$, denoted by $\boldsymbol{u}^h$ as

$$\boldsymbol{u}^h(\boldsymbol{x}) = \sum_{I=1}^{n} C(\boldsymbol{x}; \boldsymbol{x} - \boldsymbol{x}_I) \Phi_a(\boldsymbol{x} - \boldsymbol{x}_I) \boldsymbol{d}_I \equiv \sum_{I=1}^{n} \Psi_I(\boldsymbol{x})\, \boldsymbol{d}_I \tag{1}$$

where $\Psi_I(\boldsymbol{x})$ is the RK shape function, $\Phi_a(\boldsymbol{x} - \boldsymbol{x}_I)$ is a scalar-valued kernel function with compact support (for example, the cubic B-spline function), $\boldsymbol{d}_I$ are the RK approximation coefficients for displacement, and $C(\boldsymbol{x}; \boldsymbol{x} - \boldsymbol{x}_I)$ is the correction function expressed as

$$C(\boldsymbol{x}; \boldsymbol{x} - \boldsymbol{x}_I) = \boldsymbol{H}^T(\boldsymbol{x} - \boldsymbol{x}_I)\, \boldsymbol{b}(\boldsymbol{x}) \tag{2}$$

where $\boldsymbol{H}^T(\boldsymbol{x} - \boldsymbol{x}_I) = \{(\boldsymbol{x} - \boldsymbol{x}_I)^{\alpha}\}_{|\alpha| \le p}$ is a vector of monomial basis functions of degree p, and $\boldsymbol{b}^T(\boldsymbol{x}) = \{b_{\alpha}(\boldsymbol{x})\}_{|\alpha| \le p}$ is a vector of unknown coefficients to be solved by using the reproducing conditions

$$\sum_{I=1}^{n} \Psi_I(\boldsymbol{x})\, \boldsymbol{x}_I^{\alpha} = \boldsymbol{x}^{\alpha} \quad \alpha \le p \tag{3}$$

Utilizing the reproducing condition of (3), $\boldsymbol{b}(\boldsymbol{x})$ may be solved by

$$\boldsymbol{b}(\boldsymbol{x}) = \boldsymbol{M}^{-1}(\boldsymbol{x}) \boldsymbol{H}(\boldsymbol{0}) \tag{4}$$

where $\boldsymbol{H}^T(\boldsymbol{0}) = [1, 0, 0 \ldots 0]$ and $\boldsymbol{M}(\boldsymbol{x})$ is a moment matrix defined as

$$\boldsymbol{M}(\boldsymbol{x}) = \sum_{I=1}^{n} \boldsymbol{H}(\boldsymbol{x} - \boldsymbol{x}_I) \boldsymbol{H}^T(\boldsymbol{x} - \boldsymbol{x}_I) \Phi_a(\boldsymbol{x} - \boldsymbol{x}_I) \tag{5}$$

Utilizing (2) and (4) in conjunction with (1), the complete RK approximation is given as

$$\boldsymbol{u}^h(\boldsymbol{x}) = \sum_{I=1}^{n} \boldsymbol{H}^T(\boldsymbol{0}) \boldsymbol{M}^{-1}(\boldsymbol{x}) \boldsymbol{H}(\boldsymbol{x} - \boldsymbol{x}_I) \Phi_a(\boldsymbol{x} - \boldsymbol{x}_I) \boldsymbol{d}_I \tag{6}$$

The RK approximation may be formulated in a Lagrangian [4] or semi-Lagrangian [5] form, based on update of the support zone for each node. In the Lagrangian formulation, the support of each node is defined in the initial configuration, as shown in Figure 2a. This determines a "list" of neighboring nodes contained within the i^{th} node's support zone. The definition of nodal support is not modified during the calculation, so that the same nodes remain in the *ith* node's support throughout. As a result, the support zones deform with the material, as shown in Figure 2b. However, the Lagrangian formulation and discretization of conservation laws breaks down when mapping between the initial and current configurations is no longer one-to-one. This occurs under conditions such as new free surface formation (i.e. material separation) or free-surface closure, which commonly exist in damage processes of geomaterials.

Similar to the Lagrangian formulation, in the semi-Lagrangian formulation the nodal support conditions are first defined in the initial configuration. However, in the semi-Lagrangian formulation the neighboring node list is incrementally updated based on the material deformation and readjustment of support size. As a result, in the semi-Lagrangian formulation nodes are allowed to move in and out of the i^{th} node's support. Consequently, the nodal support zones do not deform with the material, as shown in Figure 2c. This property is necessitated in impact and penetration problems due to material separation and moving contact surfaces [6].

According to [5], the semi-Lagrangian RK shape function is expressed as

$$\Psi_I^{SL}(\boldsymbol{x}) = \boldsymbol{H}^T\big(\boldsymbol{x}-\boldsymbol{x}(\boldsymbol{X}_I,t)\big)\boldsymbol{b}(\boldsymbol{x})\Phi_a(\boldsymbol{x}-\boldsymbol{x}(\boldsymbol{X}_I,t)) \tag{7}$$

where $\boldsymbol{x}-\boldsymbol{x}(\boldsymbol{X}_I,t)$ indicates distance measurements taken in the current configuration and $\Psi_I^{SL}(\boldsymbol{x})$ is used to denote the semi-Lagrangian shape function. Let the velocity approximation be expressed by the semi-Lagrangian RK shape function

$$\dot{\boldsymbol{u}}^h(\boldsymbol{x},t) = \boldsymbol{v}^h(\boldsymbol{x},t) = \textstyle\sum_{I=1}^{n}\Psi_I^{SL}(\boldsymbol{x})\,\boldsymbol{v}_I(t) \tag{8}$$

where $\dot{\boldsymbol{u}}^h$ is the time derivative of $\boldsymbol{u}^h$ and $\boldsymbol{v}_I(t)$ are the RK approximation coefficients for velocity. Taking the time derivative of (8) gives the approximation of acceleration as

$$\ddot{\boldsymbol{u}}^h(\boldsymbol{x},t) = \dot{\boldsymbol{v}}^h(\boldsymbol{x},t) = \textstyle\sum_{I=1}^{n}[\Psi_I^{SL}(\boldsymbol{x})\dot{\boldsymbol{v}}_I(t) + \Psi_I^*(\boldsymbol{x})\boldsymbol{v}_I(t)] \tag{9}$$

where

$$\Psi_I^*(\boldsymbol{x}) = C\big(\boldsymbol{x};\boldsymbol{x}-\boldsymbol{x}(\boldsymbol{X}_I,t)\big)\dot{\Phi}_a\big(\boldsymbol{x}-\boldsymbol{x}(\boldsymbol{X}_I,t)\big) \tag{10}$$

$$\dot{\Phi}_a\left(\frac{\|\boldsymbol{x}-\boldsymbol{x}(\boldsymbol{X}_I,t)\|}{a}\right) = \Phi_a'\left(\frac{\|\boldsymbol{x}-\boldsymbol{x}(\boldsymbol{X}_I,t)\|}{a}\right)\frac{\boldsymbol{n}\cdot(\boldsymbol{v}-\boldsymbol{v}_I)}{a} \tag{11}$$

In (10), $\dot{\Phi}_a(\cdot)$ is the time derivative of the kernel function which takes into account the nodal transport effect in the semi-Lagrangian formulation.

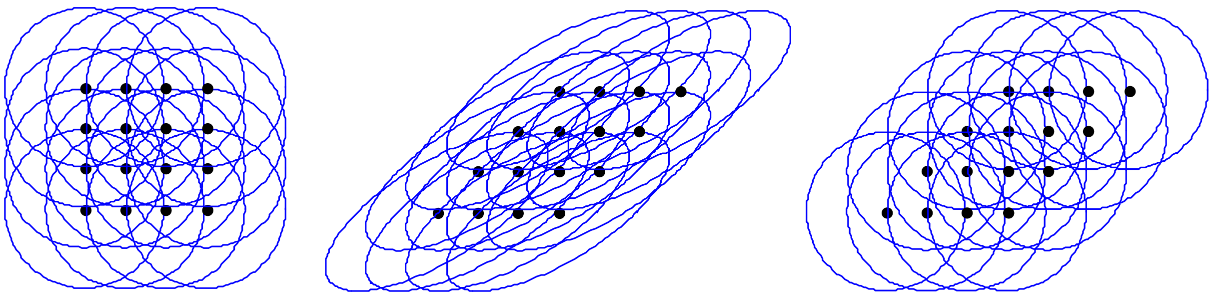

(a) **(b)** **(c)**

Figure 2. Nodal support definitions in a) initial configuration for Lagrangian or semi-Lagrangian formulation, b) Lagrangian formulation after deformation, c) semi-Lagrangian formulation after deformation

3 MICROCRACK-INFORMED DAMAGE MODEL

A microcrack informed damage model (MIDM) is proposed for describing the softening behavior of brittle solids, in which damage evolution is treated as a consequence of microcrack propagation [7]. The homogenized stress-strain relation in a cracked microscopic cell defines the degradation tensor, which can be obtained by the equivalence between averaged Helmholtz free energy (HFE) of the microscopic cell and HFE of the damaged continuum, $\bar{\Psi}$,as follows (with reference to Fig. 3).

$$\bar{\Psi} = \frac{1}{V_y}\left(\int_{\Omega_y} \Psi^{\varepsilon}\, d\Omega + \frac{1}{2}\oint_{\Gamma_c} \boldsymbol{u}^{\varepsilon} \cdot \boldsymbol{h}\, ds\right) \tag{12}$$

Here superscript "ε" is used for the fine scale variables, $\boldsymbol{u}^{\varepsilon}$ is the displacement field in the microscopic cell, $\boldsymbol{h}$ is the cohesive traction acting on the crack surface Γ_c, Ψ^{ε} is the HFE of the microscopic cell, and V_y is the volume of the microscopic cell with domain Ω_y . This energy equivalence relationship serves as an energy bridging vehicle between the damaged continuum and the cracked microstructure.

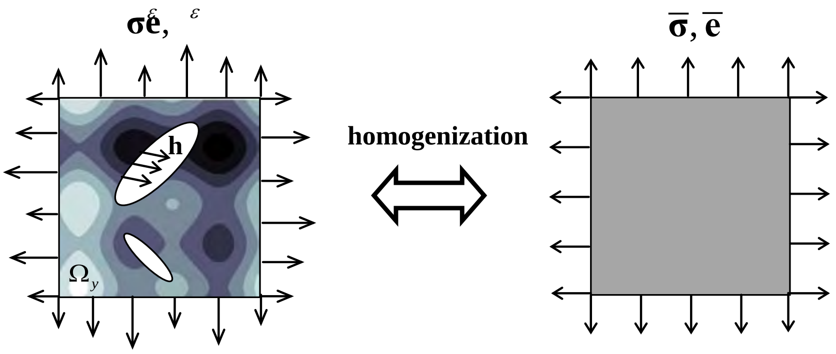

Figure 3. Homogenization of microscopic cell with fluctuating fields

By introducing bridging based on HFE, the damage tensor for the continuum can be obtained. Recall (12), and let $\bar{\Psi}$ computed from the microscopic cell be related to the damaged continuum by

$$\bar{\Psi} = \frac{1}{2}\bar{\boldsymbol{e}} : (\boldsymbol{I} - \boldsymbol{D}) : \bar{\boldsymbol{C}}_0 : \bar{\boldsymbol{e}} \tag{13}$$

where $\bar{\boldsymbol{e}}$, $\bar{\boldsymbol{C}}_0$, and $\mathbf{D}$ are the homogenized strain tensor, undamaged material response tensor, and the continuum damage tensor, respectively. The damage energy release rate is defined as

$$\boldsymbol{Y} = -\frac{\partial\bar{\Psi}}{\partial\boldsymbol{D}} = \frac{1}{2}\bar{\boldsymbol{e}} : \bar{\boldsymbol{C}}_0 : \bar{\boldsymbol{e}} \tag{14}$$

By taking the derivative of the HFE of the microscopic cell in (12) with respect to the damage energy release rate, $\mathbf{Y}$, we obtain the damage tensor

$$\boldsymbol{D} = \boldsymbol{I} - \frac{\partial\bar{\Psi}}{\partial\boldsymbol{Y}} \approx \boldsymbol{I} - \frac{\Delta\bar{\Psi}}{\Delta\boldsymbol{Y}} \tag{15}$$

Here a finite difference approach could be used in (15) to obtain the fourth-order damage tensor using $\Delta\bar{\Psi}$ and $\Delta\mathbf{Y}$. This general approach can be reduced to scalar or bi-scalar damage models as discussed in [7].

4 IMPLEMENTATION

The MIDM was implemented into the Advanced Fundamental Concrete (AFC) model, developed by the U.S. Army ERDC [8]. The AFC model is a 3-invariant plasticity model which incorporates damage evolution, strain rate effects, and a nonlinear pressure-volume relationship. In the original AFC model, a single-scalar damage variable was used for failure surface evolution as a function of volumetric and effective deviatoric plastic strains. As an enhancement, in this work the damage variable was decomposed into two terms, one to consider damage in compression and another to consider damage in tension. The compression damage term, d_c, was calculated using the original AFC damage evolution equation. The tensile damage term, d_t, was calculated from the MIDM.

For use during implementation of the MIDM, an ultra high-strength, fiber-reinforced concrete known as CorTuf [9] was considered. CorTuf is reinforced with approximately 30-mm long, randomly distributed steel fibers, the effects of which were considered in the microscopic cell analysis.

4.1 Microscopic cell analysis

To determine the microcrack-informed tensile damage evolution function, the microscopic cell analysis was based on Mode I crack propagation in a center-cracked cell. Crack propagation in the cell was modeled using a cohesive crack model with a modified cohesive law. The conventional cohesive crack law applies cohesive stresses over a fracture processing zone near the crack tip, which extends from the so-called mathematical crack tip to the physical tip. The cohesive law is then expressed as the relationship between cohesive stresses and crack opening displacement (COD), and the area under the resulting curve is equal to the fracture energy, G, of the material. The modified cohesive law was formulated to consider the effect of fiber bridging in CorTuf, such that cohesive stresses extend beyond the typical fracture processing zone. Based on a Griffith-type crack formation, the cohesive stress versus COD relationship was assumed to consist of a constant stress region which represents fiber bridging effects and a softening region which corresponds to a region of fiber failure. Fracture energy of the modified law was equivalent to experimentally determined values.

Solving the microscopic cell problem by RKPM, the average microscopic cell strain, stress, and HFE were determined. Utilizing the microscopic cell results in conjunction with the homogenization relationships in Section 3, the tensile damage parameter versus homogenized continuum strain relationship was determined, as shown in Figure 4. Here nonlinearity of the microcrack-informed tensile damage evolution function is noted.

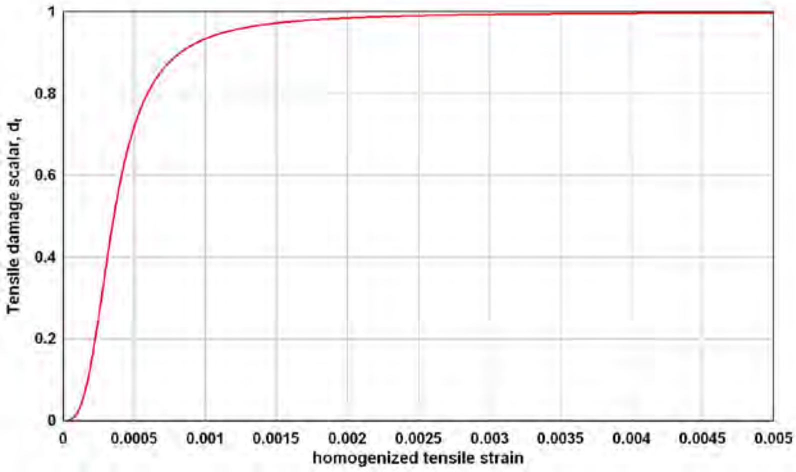

Figure 4. Microcrack-informed tensile damage evolution function for CorTuf concrete

Evolution of the AFC model yield surfaces with and without the microcrack-informed tensile damage function are shown in Figure 5. Sign convention is adopted such that $(+)I_1$ indicates compression and $(-)I_1$ indicates tension. From Figure 5a, it is seen that when a single scalar damage term is used, the tension and compression yield surfaces contract together with damage evolution. However, from Figure 5b it is observed that when the damage variables are separated, the tensile yield surface may evolve independently of the compression yield surface.

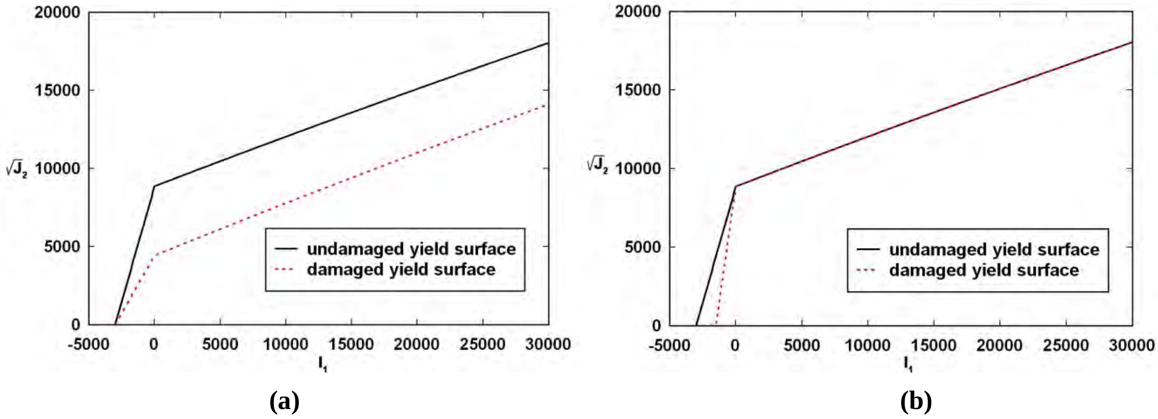

Figure 5. AFC model yield surface with a) compression damage only (d_c=0.5) b) separated tension and compression damage (d_c=0, d_t=0.5); (I_1=first stress invariant, J_2=second deviatoric stress invariant)

5 BENCHMARK PROBLEM

The multiscale RKPM formulation for penetration and impact was implemented into the *Nonlinear Meshfree Analysis Program* (*NMAP*) parallel code [10], which was used to analyze a series of benchmark penetration problems. The benchmark problems followed penetration experiments performed by ERDC in their small-caliber ballistic test facility [11]. The experiments were conducted by firing spherical projectiles (S2 tool steel) into thin-panel CorTuf targets where impact velocity, projectile size and panel thickness were varied to achieve a range of terminal ballistic conditions. Results from one of these experiments are presented here, where an 11-mm diameter projectile with a mass of 86 grains was fired into an approximately 25-mm-thick panel. Impact velocity of the projectile was 538 m/s. The projectile exited the panel's back face, but with insufficient velocity to reach the exit-face-velocity measuring devices.

For the *NMAP* model, the projectile and panel were discretized using 1,163 nodes and 190,000 nodes, respectively. This provided a nodal spacing of approximately 1 mm on the surface of the projectile and 1.4 mm in the impact region of the panel. The projectile was modeled using a J2 plasticity model with isotropic hardening, with material model parameters as given in Table 1. The CorTuf target was modeled using both the original AFC model and the MIDM-enhanced formulation.

parameter	value
Young's modulus, E	200 GPa
Poisson's ratio, ν	0.26
yield stress, σ_y	2400 MPa
hardening modulus, H	2500 MPa
density	7806 kg/m^3

Table 1. J2 plasticity model parameters for projectile

Snapshots from the penetration process are shown in Figure 6. Notable is the debris generated from the exit face. Because each "flying" node contains velocity and mass data, this can be directly translated to momentum and energy of debris generated from the impact event.

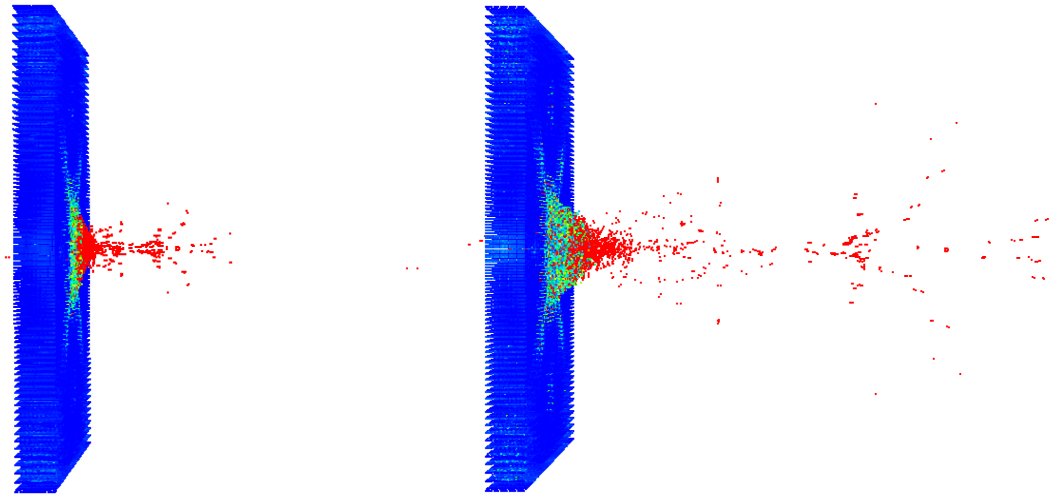

(a) (b)

Figure 6. Penetration process using MIDM-enhanced AFC formulation a) 300 µsec after impact, b) 1000 µsec after impact.

Exit velocity, velocity reduction, and mass loss of the projectile are compared in Table 2. As seen from the data, both sets of numerical results are in excellent agreement with the experimental data. The MIDM-enhanced formulation predicted a marginally higher exit velocity than the original AFC formulation, but both solutions were within approximately 0.3 percent of the experimental results. In terms of projectile mass loss, both models slightly under predicted the experimental result. This is due to the fact that damage was not included in the projectile material model. However, as with the exit velocities, the numerically predicted projectile mass loss is still in good agreement with the experimental results.

	impact velocity, m/s	exit velocity, m/s	velocity reduction, %	projectile mass loss, %
experiment	538	~0	~100	0.2
original AFC	538	1.2	99.8	0
MIDM-enhanced AFC	538	1.7	99.7	0

Table 2. Comparison of results

Experimental and numerical damage patterns on the panel faces are compared in Figure 7. Simulation data are shown for the MIDM-enhanced model, where edges of the experimentally measured craters are shown in black. As seen, the calculated zones of heavy damage generally matched the crater limits, with some additional damage extending beyond. Extension of panel damage beyond the crater limits is commonly observed in this type of penetration experiments, indicating generally good agreement between the experimental and numerical results. Notably, damage zones calculated without the multiscale enhancement were smaller, and did not appear to capture the panel damage as well.

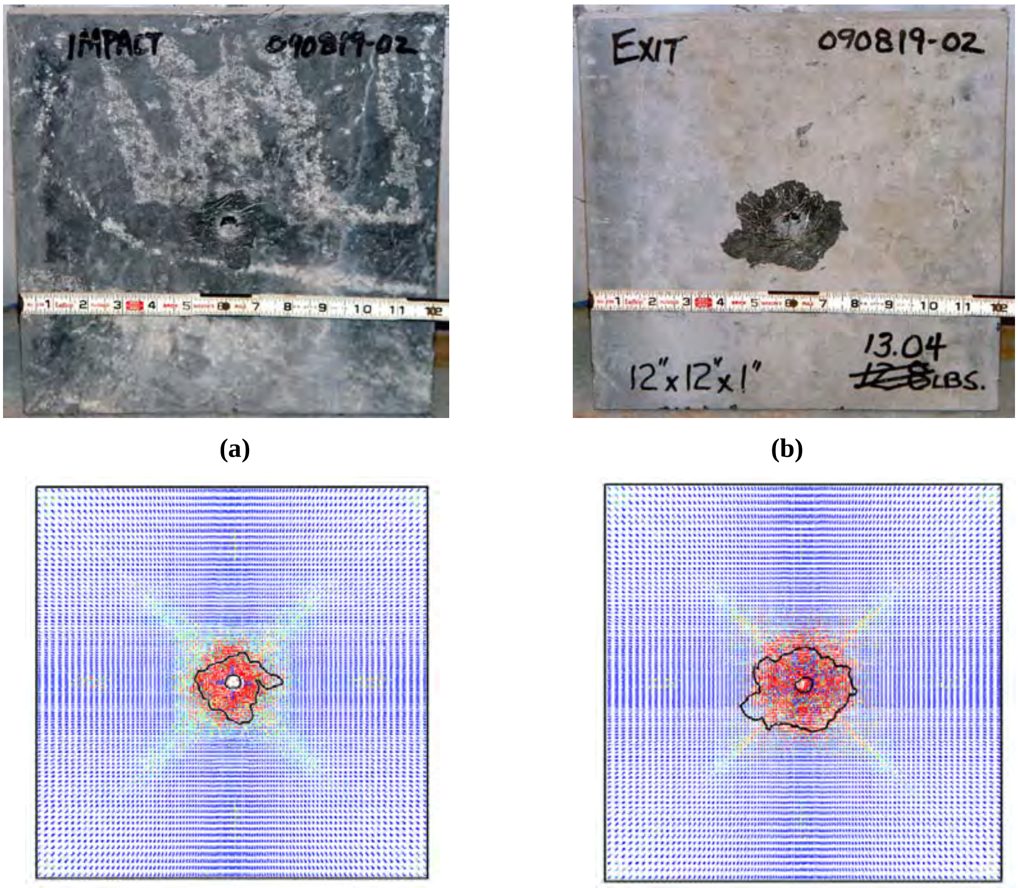

(a) (b)

(c) (d)

Figure 7. Comparison of experimental and numerical damage patterns (tensile damage parameter plotted). a) experimental impact face, b) experimental exit face, c) numerical impact face, d) numerical exit face.

6 CONCLUSIONS

In this research an RKPM formulation was developed for penetration modeling, which was successfully used to model the penetration of ultra high-strength concrete targets. From the benchmark problem, it was seen that due to the reduced mesh-dependency of RKPM, large-scale material failure and separation was captured without problem. This implies that the method not only has capability to accurately model terminal ballistic effects within the target, but can also accurately capture secondary effects such as behind-target debris – which is of great interest in certain applications.

A multiscale model for damage evolution in ultra high-strength concrete was also developed and implemented into the RKPM-based *NMAP* code. The basic approach was to utilize a microscale calculation to determine constitutive model parameters (in this case the damage evolution function) which otherwise would be phenomenologically determined. Therefore, in essence the microscopic cell analysis serves as a microscale numerical experiment, where microcrack propagation within the material can be modeled explicitly. Scale bridging is used to link the microscale cracking to continuum-scale damage evolution, and as a result damage evolution in the continuum is based on a more fundamental aspect of material response. A novel energy-bridging method was also developed for scale bridging, which provides a more computationally efficient link between the micro- and macroscales. Note that for the example given, the multiscale model was used to define tensile damage evolution, and therefore the microscopic cell analysis only considered Mode I crack propagation. However, more complex conditions within the microscopic cell could also be addressed under this multiscale modeling framework. This is a topic of ongoing research within the program.

From results of the benchmark problem, it was seen that both the original AFC model and the MIDM-enhanced model were in excellent agreement with the experimentally measured exit velocity. The MIDM-enhanced AFC model also provided a very good prediction of panel damage on both the impact and exit faces, while the original AFC model tended to predict smaller damage areas.

ACKNOWLEDGEMENT

Permission to publish was granted by Director, Geotechnical and Structures Laboratory. Simulations were partly performed on the Department of Defense Super Computing Resource Center high performance computers.

REFERENCES

[1] I. Rohr, H. Nahme, K. Thoma, Material characterization and constitutive modelling of ductile high strength steel for a wide range of strain rates, *International Journal of Impact Engineering*, **31**, 401-433, 2005.

[2] J.S. Chen, C. Pan, C.T. Wu, and W.K. Liu, Reproducing kernel particle methods for large deformation analysis of nonlinear structures, *Computer Methods in Applied Mechanics and Engineering*, **139**, 49-74, 1996.

[3] W.K. Liu, S. Jun, and Y.F. Zhang, Reproducing kernel particle methods, *International Journal for Numerical Methods in Fluids*, **20**, 1081-1106, 1995.

[4] J.S. Chen, C. Pan, C. Roque, and H.P. Wang, A Lagrangian reproducing kernel particle method for metal forming analysis, *Computational Mechanics*, **22**, 289-307, 1998.

[5] P. Guan, J.S. Chen, Y. Wu, H. Teng, J. Gaidos, Hofstetter, K, and M. Alsaleh, A semi-Lagrangian reproducing kernel formulation for modelling earth moving operations, *Mechanics of Materials*, **41**, 670-683, 2009.

[6] P.C. Guan, S.W. Chi, J.S. Chen, T.R. Slawson, and M.J. Roth, Semi-Lagrangian reproducing kernel particle method for fragment-impact problems, *International Journal of Impact Engineering*, submitted.

[7] X. Ren, J.S. Chen, J. Li, T.R. Slawson, M.J. Roth, Micro-cracks informed damage model for brittle solids, *International Journal for Solids and Structures*, accepted, 2011.

[8] Adley, M.D., Frank, A.O., Danielson, K.T., Akers, S.A., O'Daniel, J.L., The Advanced Fundamental Concrete (AFC) Model, *Technical Report ERDC/GSL TR-11-xx (in publication)*, U.S. Army Engineer Research and Development Center, Vicksburg, MS.

[9] Williams, E.M., Graham, S.S., Reed, P.A., and Rushing, T.S., Laboratory Characterization of Cor-Tuf Concrete With and Without Steel Fibers, *Technical Report ERDC/GSL TR-09-22*, U.S. Army Engineer Research and Development Center, Vicksburg, MS.

[10] Roth, M.J., Chen, J.S., Slawson, T.R., Chi, S.W., and Lee, C.H., User's Manual for Nonlinear Meshfree Analysis Program (NMAP), Version 1.0, *Technical Report ERDC/GSL TR-11-xx (in publication)*, U.S. Army Engineer Research and Development Center, Vicksburg, MS.

[11] Boone, R.N., Ballistic Impact and Perforation of Ultra-high Strength Concrete Panels, *M.S. thesis (in preparation)*, Mississippi State University.

COMPDYN 2011
III ECCOMAS Thematic Conference on
Computational Methods in Structural Dynamics and Earthquake Engineering
M. Papadrakakis, M. Fragiadakis, V. Plevris (eds.)
Corfu, Greece, 25–28 May 2011

ON THE CALIBRATION OF HIGH EXPLOSIVE THERMODYNAMIC EQUATIONS OF STATE FOR BROAD APPLICATION

Ernest L. Baker[1], Gregory Stunzenas[1], Leonard I. Stiel[2] and Dan Murphy[1]

[1] U.S. Army Armament Research, Development and Engineering Center
Picatinny Arsenal, NJ 07806 USA
ernest.l.baker@us.army.mil

[2]Brooklyn Polytechnic Institute of NYU
Six Metrotech Center, Brooklyn, NY 11201USA

Keywords: Explosives, Blast, Equation of State, Detonation, Security.

Abstract. *There is an increasing emphasis on the modeling of security related blast events that produce both fragmentation and blast loading. The Jones-Wilkins-Lee-Baker (JWLB) thermodynamic equation of state was originally developed to more accurately describe overdriven detonation, while maintaining an accurate description of high explosive products early expansion work output associated with metal pushing and fragmentation. The equation of state is more mathematically complex than the Jones-Wilkins-Lee equation of state, as it includes an increased number of parameters to describe the principle isentrope, as well as a Gruneisen parameter formulation that is a function of specific volume. Although the increased mathematical complexity over JWL was originally implemented in order to model both overdriven detonation and early volume expansion work output, it has been found that this increased mathematical complexity also allows the flexibility to parameterize higher volume work output associated with blast output. As increased numbers of parameters can mean increased calibration complexity and does not guarantee increased accuracy for practical problems of interest, calibration techniques have been developed to provide robust detonation products equation of state parameters that are applicable to the broad range of high explosive work output associated with overdriven detonation (wave shapers), early volume expansion (metal pushing) and late volume expansion (blast). This paper presents a method of parameter calibration: formal optimization using JAGUAR thermo-chemical predictions to cylinder test and high volume total work output associated with blast overpressure and impulse. The calibration procedure details are presented, along with equation of state parameter sets and ALE3D modeling comparisons. Although reasonable agreement to empirically based peak overpressures is achieved, the results indicate that an explosive products afterburning model is required to achieve further agreement with empirically based peak overpressures and impulse.*

1 INTRODUCTION

There is an increasing emphasis on the modeling of security related blast events that produce both fragmentation and blast loading. The combined loading of blast and fragments, caused by explosions, is known to often produce damage greater than the sum of the damage caused by the blast and fragment loading treated separately. This phenomenon is well known and is pointed out in literature and design manuals within the area of protective design [1]. However, due to a lack of more sophisticated modeling [2] and the complex nature of combined blast and fragment loading, the design manuals normally disregard the effect or treat it in a very simplified manner [1]. One missing aspect for combined blast and fragment loading modeling, is the development of detonation products equations of state that are accurate for a broad range of volume expansions. This is required in order to predict the fragmentation characteristics produced at early detonation products volume expansion, as well as to predict the total work output produced at very high detonation products volume expansions. The Jones-Wilkins-Lee-Baker (JWLB) thermodynamic equation of state was investigated in an effort to accurately predict both early volume expansion and highly expanded behavior associated with air blast. In this study, the explosives TNT and LX-14 were used for computational investigations.

2 JONES-WILKINS-LEE EQUATION OF STATE

The Jones-Wilkins-Lee-Baker (JWLB) thermodynamic equation of state was originally developed to more accurately describe overdriven detonation, while maintaining an accurate description of high explosive products early expansion work output associated with metal pushing and fragmentation [3]. The equation of state is more mathematically complex than the Jones-Wilkins-Lee equation of state, as it includes an increased number of parameters to describe the principle isentrope, as well as a Gruneisen parameter formulation that is a function of specific volume. The JWLB mathematical form is:

$$P = \sum_{n} A_i \left(1 - \frac{\omega}{R_i V^*}\right) e^{-R_i V^*} + \frac{\lambda E}{V^*} \tag{1}$$

$$\lambda = \sum_{i} (A_{\lambda i} V^* + B_{\lambda i}) e^{-R_{\lambda i} V^*} + \omega \tag{2}$$

where V* is the relative volume, E is the product of the initial density and specific internal energy and λ is the Gruneisen parameter. Although the increased mathematical complexity over JWL was originally implemented in order to model both overdriven detonation and early volume expansion work output, it has been found that this increased mathematical complexity also allows the flexibility to parameterize higher volume work output associated with blast output. As increased numbers of parameters can mean increased calibration complexity and does not guarantee increased accuracy for practical problems of interest, calibration techniques have been developed to provide robust detonation products equation of state parameters that are applicable to the broad range of high explosive work output associated with early volume expansion (metal pushing) and late volume expansion (blast).

3 JWLB EQUATION OF STATE CALIBRATION

For this study, the JWLB equation of state was parameterized for early volume expansion through the use of JAGUAR thermo-chemical equation of state calculations for detonation properties and associated cylinder test velocities. Formal optimization was used to parameterize JWLB for TNT and LX-14. The early volume detonation state and early volume expansion cylinder velocities were held constant, while the high volume work output associated with isentropic expansion was adjusted to increasingly higher values in order to approximate the energy output associated with explosive products afterburning.

3.1 Detonation and Cylinder Velocity Calculations

JAGUAR analytical procedures have been developed for the accurate calculation of detonation properties and cylinder test products expansion for H-C-N-O near ideal explosives. These routines use extended JCZ3 thermo-chemical equation of state procedures with EXP-6 potentials for H-C-N-O detonation products [4]. An analytic cylinder test model has long been used by ARDEC for explosive equation of state calibration and verification [5]. This analytic model has been shown to provide close agreement to high rate continuum modeling. The analytic model is based on adiabatic expansion along the principle isentrope from the Chapman-Jouguet state. Figure 1 presents a sketch of the analytic cylinder test model and ALE3D modeling of a cylinder test.

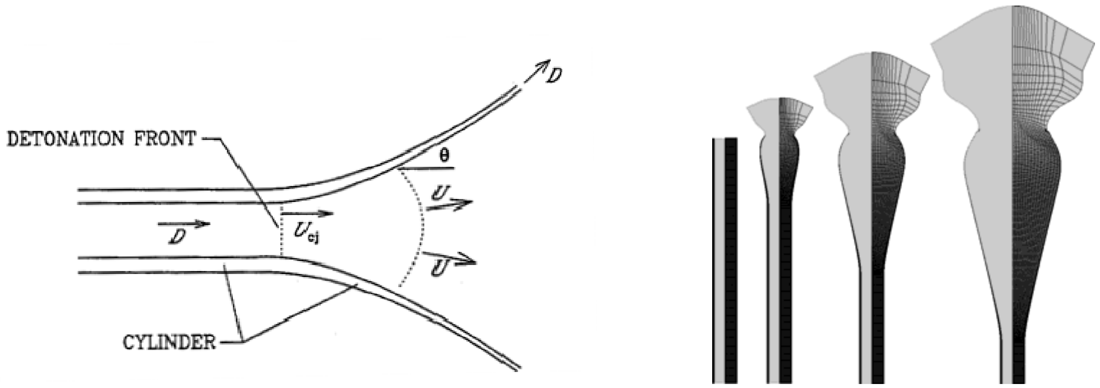

Figure 1. Analytic cylinder model (left) and ALE3D cylinder test modeling (right).

ALE3D high rate continuum modeling was compared to analytic cylinder test modeling using identical JWLB equations of state for TNT and LX-14. The JWLB equations of state were parameterized using JAGUAR thermo-chemical equation of state modeling [5]. Two different copper cylinder thicknesses, 1.2” OD, 1” ID 10” long and 1.3” OD, 1” ID 10” long, was modeled using the Johnson-Cook material model. Figure 2 presents the comparison of the analytic cylinder test model to the ALE3D modeling for TNT and LX-14 respectively.

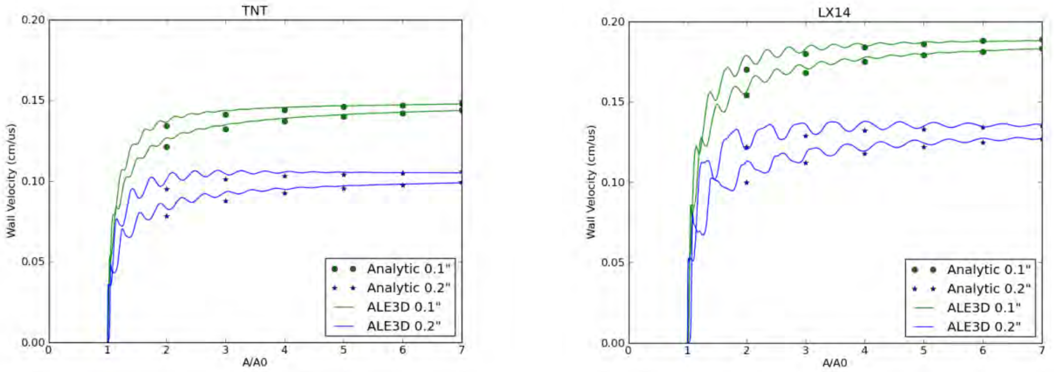

Figure 2. TNT (left) and LX-14 (right) analytic cylinder model results compared toALE3D calculations.

For each pair of curves, the higher curve represents the velocity history of the inside of the copper cylinder and the lower curve represents the velocity history of the outside of the cylinder. The analytic cylinder model slightly under predicts the velocities at 2 and 3 inside area expansions, but is in very close agreement by 6 and 7 inside area expansions. This is consistent with the fact that this analytic modeling approach neglects initial acceleration due to shock processes. Strong shock effects are typically observed in the 2 to 3 volume expansion region and are significantly damped out by 6 volume expansions, where very close agreement between the analytic model and ALE3D results are observed.

3.2 High Volume Products Expansion and Blast Calibration

For the modified total work output JWLB equations of state, the detonation state and early volume expansion cylinder velocities were held constant, while the high volume work output associated with isentropic expansion to ambient pressure was adjusted to increasingly higher values. This increased total work output was incorporated in order to approximate the energy output associated with explosive products afterburning, as both TNT and LX-14 are negatively oxygen balanced (TNT: -74%, LX-14: -29.5%). Table 1 presents the standard TNT JWL parameters. Table 2 presents the TNT and LX-14 JWLB parameters for the modified total work output study. Table 3 presents the analytically predicted cylinder velocities and associated predicted Gurney constants associated with each of the modified total work output JWLB parameter sets using a 1” ID and 1.2” OD copper cylinder. The presented cylinder velocities and Gurney energies demonstrate that although the modified work output JWLB parameter sets have increased total work output E0 values, the equation of states maintain the same predicted cylinder velocities and associated early volume expansion characteristics.

Explosive	TNT	LX-14
E0 (Mbar)	0.0662	0.101
Density (g/cc)	1.59	1.835
Mass (g)	2212.3101	2553.20065
Gamma+1	4.0919194	3.75486
A (Mbar)	7.967686	7.558595
B (Mbar)	0.146069	0.2268433
R1	5.5	4.44
R2	1.3	1.5
W	0.3	0.3
D (cm/microsecond)	0.698	0.883

Table 1: Standard JWL parameter sets.

3.3 Blast Calculations

ALE3D was used to model the explosive detonation and subsequent blast produced by using standard JWL equations of state and modified total work output JWLB equations of state. Air was modeled using the ideal gas equation of state with an adiabatic gamma of 1.4. A 13.85 cm diameter sphere of high explosive was detonated in the center of a high resolution mesh consisting of 5 million cells on a 200 cm cube. Tracer particles were placed at 9 positions evenly spaced from 2.5 foot (76.2 cm) to 6.5 foot (198.1 cm) from the charge center. Figure 3 presents pressure color plots from the computations at 30, 200 and 500 microseconds.

Explosive	TNT	TNT	TNT	LX-14	LX-14	LX-14
E0 (Mbar)	0.075	0.085	0.095	0.1025	0.1035	0.135
Density (g/cc)	1.63	1.63	1.63	1.82	1.82	1.82
Mass (g)	2267.96	2267.96	2267.96	2532.33	2532.33	2532.33
Gamma+1	3.91913	3.91913	3.91913	3.04639	3.04653	3.04653
A1	4.93334E+02	5.00011E+02	5.00000E+02	5.00013E+02	3.99193E+02	4.99687E+02
A2	1.37703E+02	9.60843E+00	9.36187E+00	9.76724E+00	5.00860E+01	9.43807E+00
A3	1.11378E+00	1.78766E+00	3.23146E+00	3.54600E+00	1.40988E+00	6.75520E+00
A4	1.13326E-02	-9.77879E-22	2.08801E+00	3.44010E-28	4.91307E-03	1.14440E-22
R1	3.52477E+01	1.40202E+01	1.58048E+01	1.30200E+01	2.85618E+01	1.51089E+01
R2	1.13814E+01	1.39896E+01	1.55723E+01	1.29893E+01	8.34812E+00	1.52031E+01
R3	2.71715E+00	3.27981E+00	4.04198E+00	3.44898E+00	2.46220E+00	4.25166E+00
R4	2.74025E-01	3.31329E-01	3.80382E-01	4.02688E-01	4.28122E-01	1.01185E+00
C0 (Mbar)	1.09815E-02	1.58447E-02	2.07079E-02	2.89610E-02	1.17947E-02	3.67933E-02
W	2.81079E-01	2.81079E-01	2.81079E-01	3.66767E-01	3.66767E+00	3.66767E-01
AL1	6.16074E+00	6.16074E+00	6.16074E+00	4.71547E+01	4.71547E+01	4.71547E+01
AL2	2.02825E+01	2.02825E+01	2.02825E+01	5.22117E+00	5.22117E+00	5.22117E+00
BL1	-2.81032E+00	-2.81032E+00	-2.81032E+00	3.22103E+00	3.22103E+00	3.22103E+00
BL2	7.44947E+00	7.44947E+00	7.44947E+00	-3.26476E+00	-3.26476E+00	-3.26476E+00
RL1	1.76848E+00	1.76848E+00	1.76848E+00	2.73809E+0	2.73809E+01	2.73809E+01
RL2	2.62612E+01	2.62612E+01	2.62612E+01	1.49825E+00	1.49825E+00	1.49825E+00
D (cm/μs)	6.81789E-01	6.81789E-01	6.81789E-01	8.63240E-01	8.63240E-01	8.63240E-01

Table 2: Increased total work output JWLB parameter sets.

Explosive	**E0 (Mbar)**	**Cylinder Volume Expansion (A/A0)**	**Analytic Inside Cylinder Velocity (cm/μs)**	**Analytic Outside Cylinder Velocity (cm/μs)**	**Gurney constant (cm/μs)**
TNT	0.075	2	0.130889091	0.137144785	0.202167448
		5	0.143051938	0.137144785	0.233973672
		7	0.145943951	0.141562639	0.241510681
TNT	0.085	2	0.125542523	0.113660859	0.193909295
		5	0.141877562	0.136018903	0.232052879
		7	0.146201877	0.141812823	0.241937503
TNT	0.095	2	0.119447602	0.108142778	0.18449526
		5	0.140724121	0.134913092	0.230166328
		7	0.146427035	0.142031221	0.242310098
LX-14	0.1025	2	0.160033448	0.144887476	0.236255505
		5	0.180708841	0.173246693	0.282498434
		7	0.185932388	0.180350604	0.294082168
LX-14	0.1035	2	0.170929044	0.154751885	0.252340547
		5	0.184720626	0.177092816	0.288769975
		7	0.186802397	0.181194494	0.295458227
LX-14	0.135	2	0.152699824	0.138247925	0.225428962
		5	0.178989614	0.171598459	0.279810801
		7	0.1856975	0.180122766	0.293710654

Table 3: Modified total work output JWLB predicted cylinder velocities for a 1” ID, 1.2:” OD copper tube.

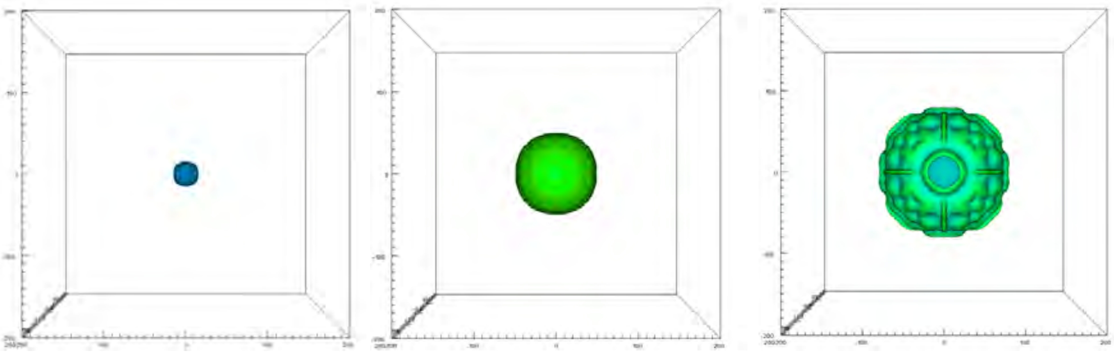

Figure 3. Pressure color plots from the TNT air blast computations at 30, 200 and 500 microseconds.

Figure 4 presents the TNT peak overpressure computational results as a function of distance. Figure 5 presents the TNT incident impulse air blast computational results as a function of distance. Figure 6 presents the LX-14 peak overpressure computational results as a function of distance. Figure 7 presents the LX-14 incident impulse air blast computational results as a function of distance. The results are compared to empirically based analytic calculations from CONWEP [6].

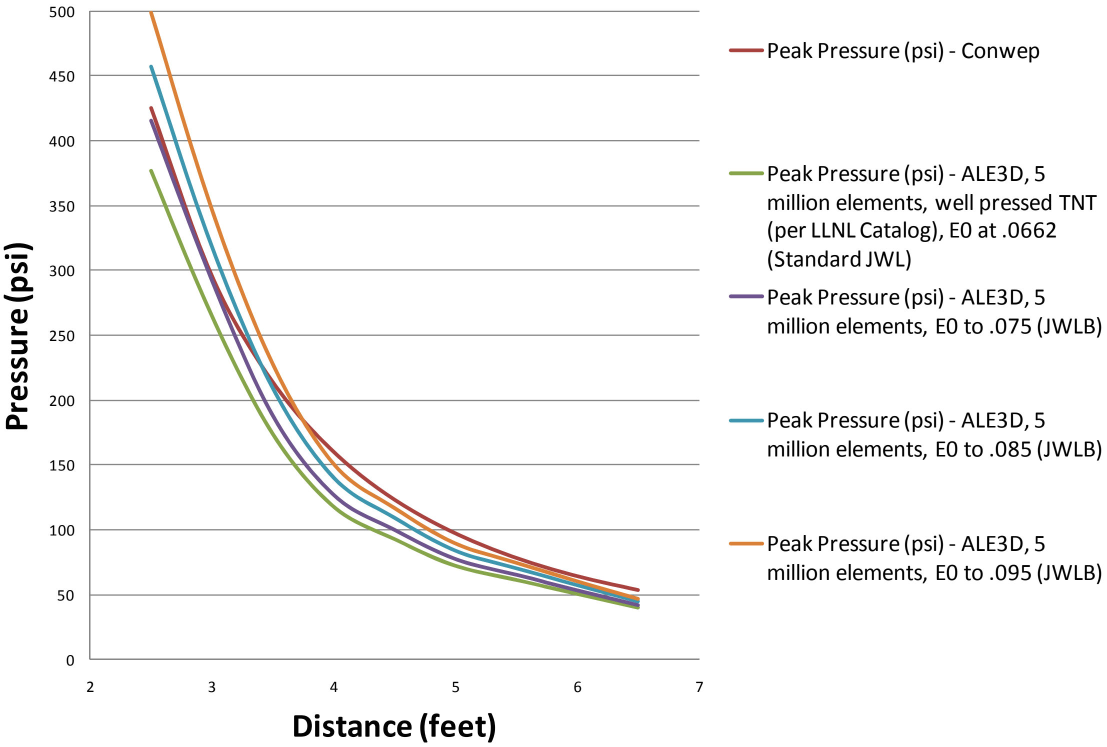

Figure 4. ALE3D TNT peak overpressure computational results as a function of distance.

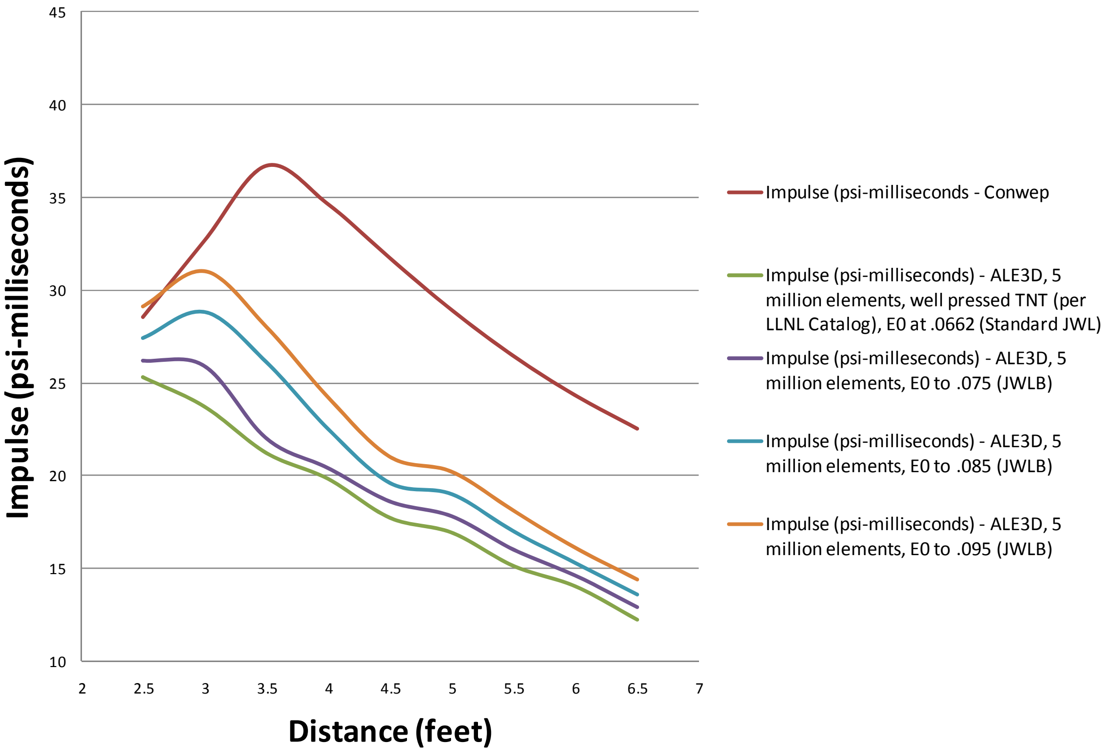

Figure 5. ALE3D TNT blast incident impulse computational results as a function of distance.

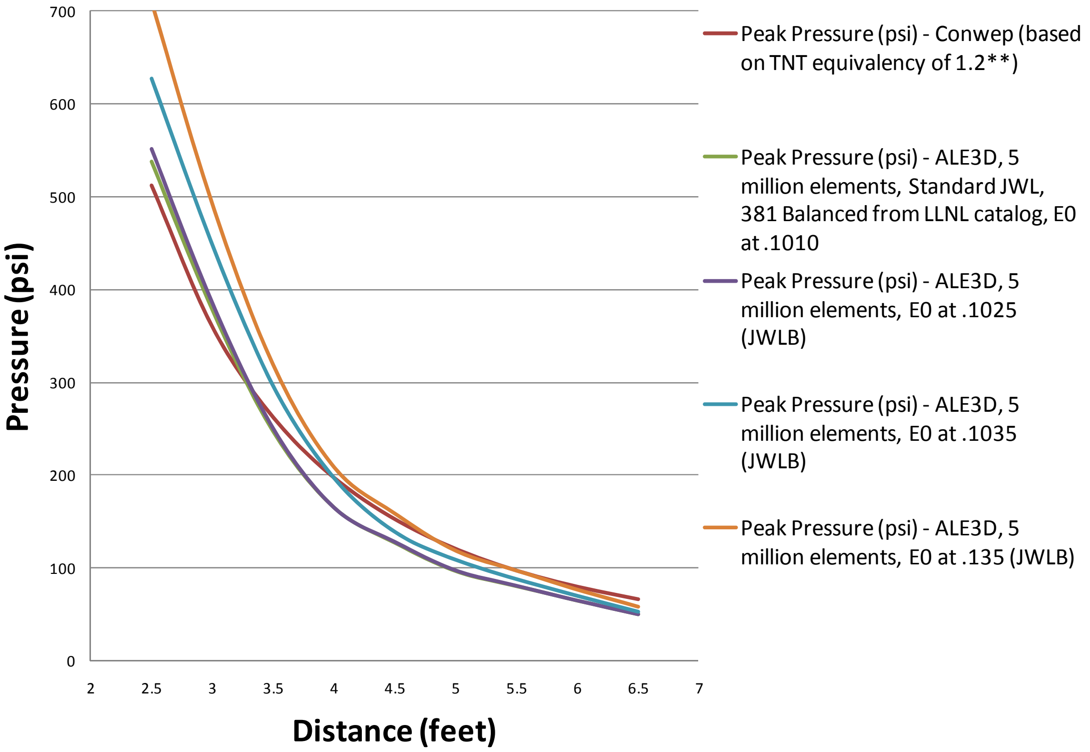

Figure 6. ALE3D LX-14 peak overpressure computational results as a function of distance.

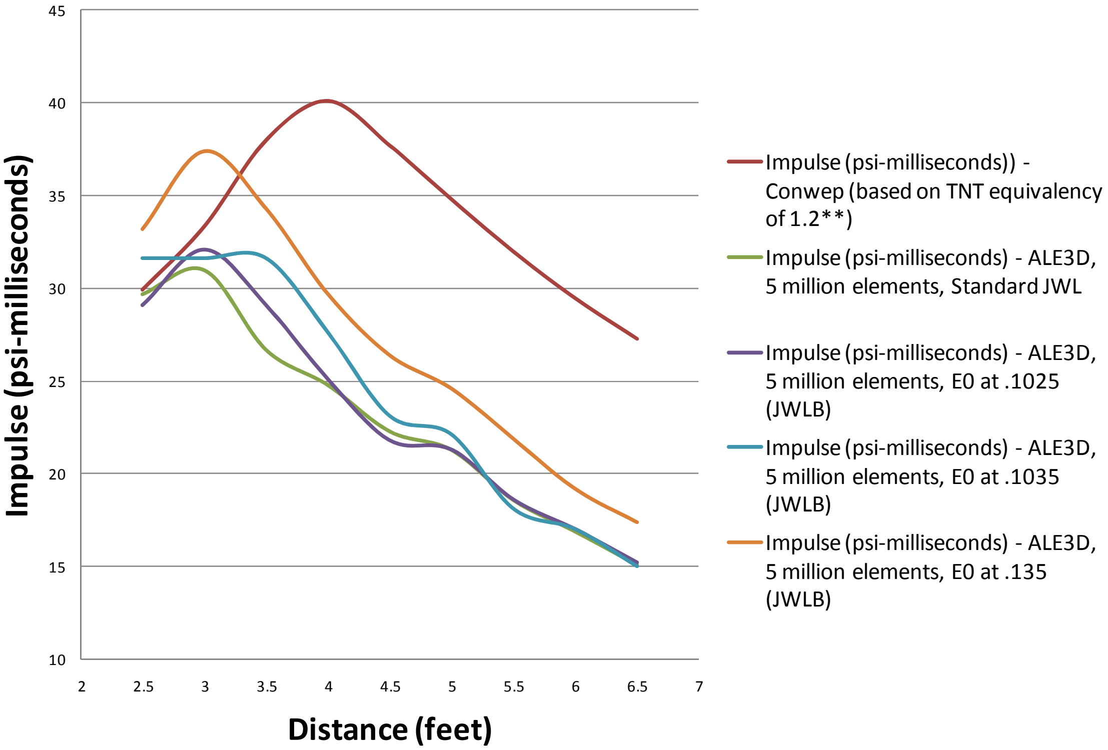

Figure 7. ALE3D LX-14 blast incident impulse computational results as a function of distance.

4 CONCLUSIONS

It is possible to produce increased total work output using the JWLB equation of state, while maintaining agreement accepted detonation characteristics and cylinder test data. This was done in an attempt to account for explosive detonation products afterburning with air, while avoiding the use of potentially inaccurate and computationally expensive air mixing, diffusion and combustion models. This modified equation of state approach seems reasonable, as it can be viewed as an analogous approach to the currently used empirical blast scaling. It is clear from the computational results, that agreement with empirical peak blast overpressures can be achieved and that the trend moving towards agreement incident blast impulse occurs as the total work output is increased. However, reasonable parameter sets become increasingly difficult to achieve as the total work output is increased. This is due to the difficulty in maintaining agreement with cylinder velocity values consistent with early detonation products expansion up to 7 times the initial unreacted explosive volume. Although reasonable agreement to the empirically based peak overpressures can be achieved, the results indicate that an explosive products afterburning model is required to achieve further agreement with empirically based peak overpressures and impulse. There is clear evidence of the effect of afterburning [7] with limited practical high rate continuum model development [8, 9] to date. One potential simplified approach is to use a partial equilibrium equation of state that was previously used successfully for the modeling of combined effects explosives aluminum reaction [10].

REFERENCES

[1] E.J. Conrath, Structural design for physical security– state of the practice. *American Society of Civil Engineers Task committee*, Reston, VA, USA, 1999 (p. 264).

[2] U. Nyström and K. Gylltoft, Numerical studies of the combined effects of blast and fragment loading, *International Journal of Impact Engineering*, Volume 36, Issue 8, August 2009, (p. 995-1005).

[3] E.L. Baker, An application of variable metric nonlinear optimization to the parameterization of an extended thermodynamic equation of state", *Proceedings of the Tenth International Detonation Symposium*, Edited by J. M. Short and D. G. Tasker, Boston, MA, pp. 394-400, July 1993.

[4] L.I. Stiel, and E.L. Baker, Detonation energies of explosives by optimized JCZ3 procedures, *Proceedings of the APS Topical Conference on Shock Compression of Condensed Matter*, New Hampton, MA, August 1997.

[5] E.L. Baker, and L.I. Stiel, Improved cylinder test agreement with JAGUAR optimized extended JCZ3 procedures", *Proceedings of the International Workshop on New Models and Numerical Codes for Shock Wave Processes in Condensed Media*, St. Catherines College, Oxford, UK, September 1997.

[6] D.W. Hyde, Microcomputer programs CONWEP and FUNPRO, applications of TM 5-855-1, *Instructions Report SL-88-1 (ADA195867)*, Structure Lab, Army Engineer Waterways Experiment Station, Vicksburg, MS, APR 1988.

[7] A.L. Kuhl, J. Forbes, J. Chandler, A.K. Oppenheim, R. Spektor, and R.E. Ferguson, Confined combustion of TNT explosion products in air, *8th International Colloquium on Dust Explosions*, Schaumburg, IL, USA, September 21-25, 1998.

[8] E. Salzano, A. Basco, and F. Cammarota, Confined after-burning of display pyrotechnics and explosives, *Combustion Colloquia 2009, 32nd Meeting on Combustion*, Universita Degli Studi di Napoli "Federico II", Napoli, Italy, 26-28 April 2009.

[9] L.D. Daily, Simulating afterburn with LLNL hydrocodes, *LLNL Technical Report UCRL-TR-206313*, Lawrence Livermore National Laboratory, Livermore, CA, USA, 31 August 2011.

[10] E.L. Baker, C. Capellos and L.I. Stiel, Generalized thermodynamic equation of state for reacting aluminized explosives, *Proceedings of the 13th International Detonation Symposium*, Norfolk, VA, USA, 23-28 July 2006.

COMPDYN 2011
III ECCOMAS Thematic Conference on
Computational Methods in Structural Dynamics and Earthquake Engineering
M. Papadrakakis, M. Fragiadakis, V. Plevris (eds.)
Corfu, Greece, 25–28 May 2011

DYNAMIC LOAD ALLOWANCE FOR REINFORCED CONCRETE BRIDGES

Jerry W. Wekezer[1*], Eduardo E. Taft[1]

[1]Florida A&M University – Florida State University College of Engineering
2525 Pottsdamer Street, Tallahassee, FL 32310-6046, USA
wekezer@eng.fsu.edu, et05@fsu.edu

Key words: Structural Dynamics, Dynamic Load Allowance, Reinforced Concrete Bridges

Abstract. *A dynamic load allowance (DLA) is a quantitative measure of dynamic effects exerted in addition to static loads by moving vehicles on highway bridges. The American Association of State Highway and Transportation Officials (AASHTO) recommends using 33% as a maximum value of DLA [1]. The paper presents results of extensive investigation of DLA, which was carried out for the Florida Department of Transportation (FDOT) for a broad class of prestressed reinforced concrete bridges. FDOT manages over 6400 such bridges and precise information about their performance, due to heavy (so called: permit) vehicles, is critical for its Maintenance Office. Two parallel tracks: experimental and analytical, were designed and implemented as integral parts of this research. Each track resulted in data which was used to calculate DLA. Comparison of these results showed a good correlation between experiments and analyses, and was used to verify and validate finite element (FE) models developed.*

All experimental tests were carried out on a selected, typical, prestressed, reinforced concrete bridge #500133 on US 90 in north eastern Florida. It was a newer bridge, built in 1999 with three simply supported spans and AASHTO type III girders. A selected span of the bridge was instrumented with: (a) two linear variable displacement transformers (LVDT), (b) 38 strain gauges and (c) 14 accelerometers installed at the top of the bridge deck. 35 static and dynamic tests were carried out with the speed of 48 km/hr and 80 km/hr. Three representative permit vehicles were used for the tests. Data acquisition from experimental testing allowed for calculation of DLA.

The second research track consisted of FE model development and computational analysis using LS-DYNA computer code. In addition to the bridge #500133, two other local, prestressed, reinforced concrete bridges were selected for analytical studies of DLA. Their superstructure consisted of AASHTO type II and IV prestressed reinforced concrete girders. The FE model of the bridge #500133 was validated and verified using experimental data. DLA factors were calculated for all bridges as functions of vehicle types and their velocities. They were determined based on maximum displacements and strains. Several factors were identified as triggering significant DLA. They included: surface imperfections (as joint abutments and bridge approach depression), loosely attached cargo producing so called hammering effect, and characteristics of the vehicle suspension. This paper presents the latest results of the project, for which some earlier data was reported in [2] through [4].

1. INTRODUCTION

The Florida Department of Transportation (FDOT) has set a mission to rehabilitate the state transportation system, including roads highways and highway bridges. This research project responds to the call from the FDOT to improve the transportation system and to meet the needs for providing safer transportation. The state will need a huge investment over the next years to improve the transportation system. To decrease the total investment needed, the FDOT needs to significantly improve the operation and make sure that the proper maintenance of highway bridges is performed. In order to achieve this, more knowledge about certain effects resulting from dynamic loading of bridges is imperative. The information not only will help the FDOT make decisions on heavy vehicle permitting but also to establish permissible weight limits for bridges.

Traditional methods used for analysis of dynamic live loads on bridges use simplifications. This results in dynamic loads tending to be very conservative if not ignored. Ignoring the dynamic nature of live loads is not very convenient, and may result in premature damage of the bridge structure or a decrease in the bridge lifespan.

Dynamic live loads are taken into account by using dynamic load allowances (DLA), which is a factor to scale up the magnitude of the static load. By using a DLA engineers usually ignore vibrations and other damaging effects induced by heavy vehicles into bridges.

Reinforced concrete bridges usually have a behavior that is hard to explain, and applying advanced structural analysis to this type of structure is not simple. With advances in computational power and methods in computational mechanics, newer methods to analyze complex structures like bridges are coming to light. This advances in computer technology and computational capabilities, followed by development of commercial finite element (FE) software have made 3-D dynamic analysis of bridge structures more effective.

Further development of FE software in material models, and different applications of constraint and damping allows the software to more accurately represent the actual behavior of the bridge structure. The vast variety of element and material types allow for a better representation of vehicle components like the suspension system, which is critical in the interaction between vehicle and bridge. All these advancements in FE model software provide a powerful tool for the assessment of complex structural and mechanical phenomena such as a wheel rolling on the pavement. Most important for this type of analysis is the dependence of moving live loads varying with time caused by dynamic interaction of masses for the vehicle and the bridge components.

Experimental testing of bridges in the field is expensive and can only provide a limited amount of data. This project seeks to conduct comprehensive research on transient analysis of the dynamic interaction between heavy vehicles and prestressed concrete bridges using computational mechanics. Such approach offers less expensive and more accurate ways to conduct this research on dynamic load allowance factors.

Verification and validation of numerical models is a process that builds the credibility of the model. It is usually done by comparing a numerical model of a phenomena to the data obtained from the actual physical tests. Validated FE models can provide accurate information about the behaviour of the structure which are expensive and difficult if only experiments are used. This paper focuses on the use of validated FE models for the assessment of DLA of reinforced concrete bridges.

Three heavy permit vehicles were selected for analysis and their FE models were developed. The vehicles were selected based on their span length, number of axles, weight distribution, and suspension characteristics. The vehicle FE models were verified and validated through experimental testing of the vehicles crossing over a speed bump.

Three reinforced concrete bridges were also selected from the northern part of Florida and their FE models were also developed. The selected bridges varied in span length, width, and girder type. The FE models of the bridges included road surface irregularities to assess the influence of the road surface imperfections on the bridge response. The FE models of the bridges were verified and validated through experimental tests conducted on one of the bridges.

The analyses performed in the project were based on explicit, dynamic, non-linear finite element computational mechanics using LS-DYNA computer code [8].

2. FE MODELS OF PERMIT VEHICLES

The FE models of the vehicles were simple but still reliable, with a good geometrical and physical representation of the actual trucks. The simplicity of the model reduced the necessary calculation time needed for numerical simulations and increased the performance and stability of the simulations.

Three vehicles were selected for analysis and FE models of them were developed. The vehicles selected were: a CH613 truck tractor with a single drop lowboy trailer, a Terex T-340 Crane, and a FDOT truck.

The FE models of the selected vehicles were developed using direct measurement and constant inspection of the vehicle, as blueprints or files with the data for the selected vehicles were not available. Extended efforts were made on the development of the vehicle's components which have a significant influence in the interaction with the road. Some of these components include: the vehicle's elastic tires, wheels, suspension system, single and tandem axles, and the chassis.

The first vehicle, the tractor-trailer, was selected because of its well designed suspension system, its length, and uniform weight distribution. The FE model of the tractor-trailer was developed using 2-D 3- and 4-node shell elements, and 3-D 6- and 8- node fully integrated solid elements for most of the vehicle component. The suspension system was modelled using 1-D discrete beam elements, with discrete spring and damper material models. Constitutive material models included elastic material for the truck frame, and fabric and rubber material for the wheels. Other components of the vehicle which were modelled as rigid parts include the driver cab, hood, and engine. The FE model of the tractor-trailer is summarized in Table 1 and is presented in Figure 1.

Specification		Specification	
Number of parts	204	Number of elements	26,194
Number of nodes	19,941	- solid elements	1128
Number of material models	38	- shell elements	24,790
		- beam elements	248
		- discrete elements	22
		- mass elements	6

Table 1: Summary of complete FE model of tractor-trailer [5].

Figure 1: An FE model of the tractor-trailer.

The second vehicle, the Terex crane, was selected because of its short length, and heavy load. The distribution of the heavy load over a short span created a compact setup which was very different from that of the tractor-trailer. The FE model of the Terex crane was developed using the same technique as for the tractor-trailer with the same material models with slight variation on the properties of steel. This FE model was the simplest one with most of its components being rigid. More detailed information about the development of the FE model of the Terex crane is available in [5]. The FE model of the Terex crane is summarized in Table 2 and is presented in Figure 2.

Specification		Specification	
Number of parts	153	Number of elements	20,837
Number of nodes	17,401	- solid elements	1,338
Number of material models	29	- shell elements	19,323
		- beam elements	142
		- discrete elements	28
		- mass elements	6

Table 2: Summary of complete FE model of Terex crane [5].

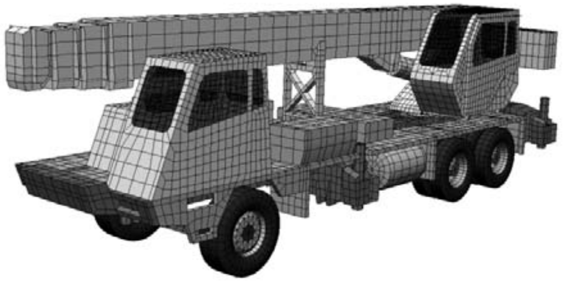

Figure 2: An FE model of the Terex crane.

The third vehicle, the FDOT truck, was chosen because of its purposedly designed stiff suspension. The FDOT truck was custom-built for the FDOT to conduct dynamic tests on bridge structures and so was designed with the worst possible suspension characteristics to test the worst case dynamic loadings. The truck consists of a very simple suspension system with two tandem axles which were easy to model.The FE model of the FDOT truck was developed using the same technique as the other two vehicles,with the same material models and element types. The FE model of the FDOT truck is summarized in Table 3 and is presented in Figure 3.

Specification		Specification	
Number of parts	181	Number of elements	18,569
Number of nodes	13,031	- solid elements	926
Number of material models	25	- shell elements	17,137
		- beam elements	440
		- discrete elements	58
		- mass elements	8

Table 3: Summary of complete FE model of FDOT truck [5].

Figure 3: An FE model of the FDOT truck.

3. VERIFICATION AND VALIDATION OF VEHICLE FE MODELS

Verification and validation of the vehicle’s FE model was obtained through comparison with data obtained from experimental testing on the actual vehicles. For the purpose of validation of the vehicle mass, each vehicle axle loads were measured using scales. Each axle of the FE models was then dropped into planar rigid walls for which LS-DYNA [8] allows an easy measurement of the load. The final measurements of the experiment and the virtual trucks are summarized in Table 4.

A test was designed and conducted in Broadmoor Estate in Tallahassee for validation of the suspension system of the vehicles. The vehicles were equipped with displacement gauges and accelerometers, and then driven over a speed bump at speeds varying from 8 to 32 km/h. Lower velocities were used to ensure the driver’s safety and preserve the testing equipment, which is a common practice found in the literature. The test measured the acceleration of a point in the frame and the change in distance between a point in the frame and the axle. The test was then replicated virtually with the vehicles driven over the same speed bump at the same speeds. To ensure the numerical analysis matched the actual test, the asphalt speed bump was modelled using the exact geometry of the bump which was obtained from an Optech’s Intelligent Laser Ranging and Imaging System (ILRIS) scanner. More detailed information about the development of the speed bump FE model is available in [5]. Experimental and virtual results of the tractor-trailer are compared in Figure 4.

Axle No.	Axle type	Axle load (kN)		Relative error (%)
		Measurements	FE model	
1	Front steer axle	42.184	42.291	0.25
2	Forward tandem drive axle	89.440	89.439	0.00
3	Rear tandem drive axle	94.957	95.008	0.05
4	First trailer axle	94.601	93.946	-0.69
5	Second trailer axle	98.517	97.908	-0.62
6	Third trailer axle	100.831	101.754	0.92
TOTAL		520.530	520.346	-0.04

Table 4: Axle loads for the tractor trailer in experiment and FE analysis [5].

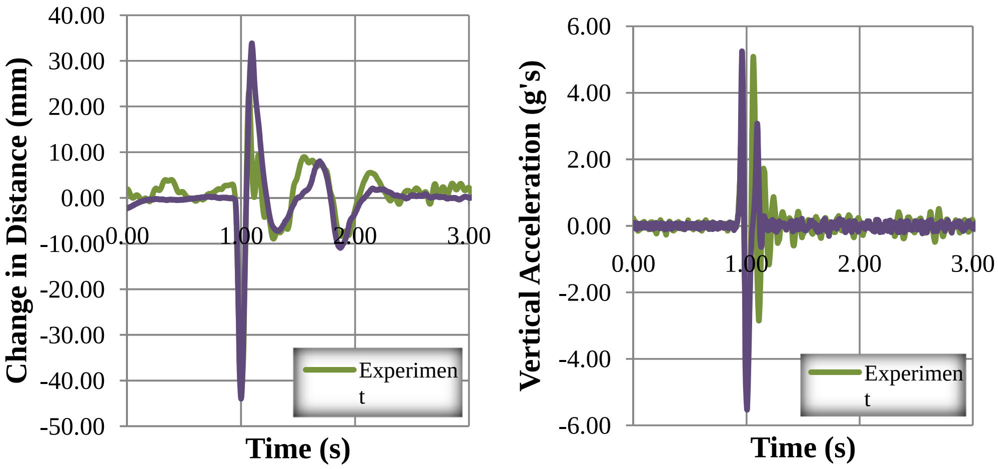

Figure 4: Time histories from experiment and FE analysis of the tractor trailer at 24 km/h.

The load measurements of the truck and its FE model were matched quantitatively; this was obtained by adding discrete mass points in the FE model and making changes in material densities.

The spring and damper coefficients for the FE models were initially obtained from the manufacturer's websites. The results of the test were matched with the numerical analysis quantitatively by modifying the spring stiffness until there was conformity between the two. The process was done carefully to keep the proper distribution of sprung and unsprung mass, as well as to maintain the proper length of the springs in its static configuration. This process was applied to all the FE models of the permit vehicles used in this study. The vehicles were then considered to be validated.

4. FE MODELS OF REINFORCED CONCRETE BRIDGES

FE modelling of 3-D bridges became more common over the past decade [3], [4], [5], [6]. The models are becoming more sophisticated due to the increased efficiency and capability of computer software.

Three highway bridges near Tallahassee were selected for analysis of DLA factors. These bridges were selected because they consisted of prestressed reinforced concrete girders according to the American Association of State Highway and Transportation Officials

(AASHTO) [1]. Data for one span of each of the three bridges selected for analysis is summarized in Table 5.

Bridge Name	Bridge No.	AASHTO Girder Type	Span Length (m)	Width (m)
No Name Creek	#540074	II	12.1	11.6
Chattahoochee	#500133	III	21.0	13.1
St. Mark's	#590056	IV	29.3	12.6

Table 5: Summary of selected bridges for analysis.

An FE model of one span of each bridge was developed. The bridge model included six different components such as: bearing pads, concrete girders, diaphragm, concrete deck, bridge barriers, and bridge approach surface. The components were modelled according to geometric data obtained from one of the bridge’s blueprints provided by the FDOT. The other two bridges were modelled using measurements obtained in situ.

Unreinforced neoprene bearing pads were used to support the FE model of the girders at each end. The bearing pads were modelled using 3-D 8-node fully integrated solid elements with a viscoelastic material model selected for analysis. The material properties of the neoprene pads were inspected and assessed in [7].

The FE model of the concrete girders was developed using 3-D 8- and 6-node fully integrated solid elements. An elastic material model was used for analysis with properties for concrete obtained from cylinder testing of the girders by the FDOT Structures Research Laboratory.

Reinforcement of the girders included reinforcing bars and prestressing strands, which were modelled using 1-D beam and rod elements respectively.

Each AASHTO girder included two No. 9 strands at the top and 24 No. 13 strands at the bottom. One equivalent strand at the top and eleven equivalent strands at the bottom were modeled due to the discrete location of the nodes in the FE model cross section. Selected strands were grouped and their properties were lumped together as presented in Figure 5. The process was done to make sure that the FE model accurately behaved like the real beam.

A special material model (MAT_CABLE_DISCRETE_BEAM) was applied to the strands which allowed an introduction of prestressing forces, and allowed the cables to carry tensile loads without any stiffness for compression [8].

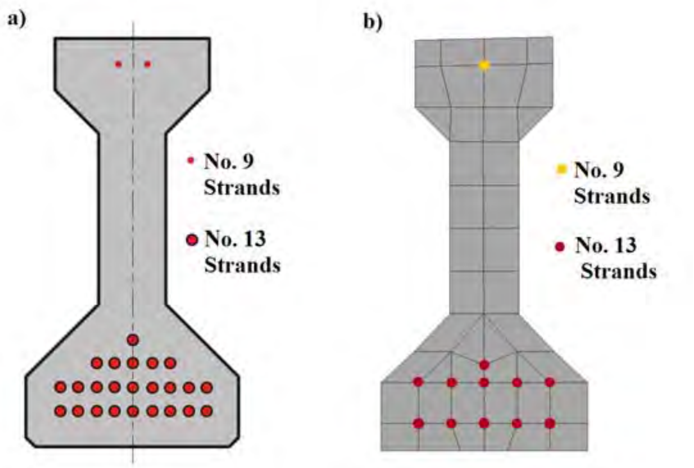

Figure 5: Prestressing strands: a) actual location in girder, b) equivalent location in FE model.

The FE model of the diaphragm, concrete deck, and bridge barriers were modelled using 3-D fully integrated solid elements. The elastic material model was selected for analysis, with their actual properties for concrete as tested. Reinforcement of these components was modelled using 1-D beam elements for the reinforcing bars. Elastic material models with specific properties for steel were used for the reinforcements according to the blueprint information.

The bridge approach surfaces of all three bridges were inspected and the surface with the worst deterioration of the three was selected. The surface of bridge #500133 exhibit an area characterized by two distinct ruts made in the asphalt by passing vehicles, with the adjacent stronger concrete deck not showing such wear and tear damage. As a result there was a difference in elevation between the asphalt and the concrete which was found to be around 15 to 20 mm. The approach surface was found to have a pronounced effect in the dynamic response of the bridge; therefore the same approach surface was used on all three bridges to make use of the worst conditions available. The bridge approach surface was modelled as is, with the exact geometry obtained using Optech’s ILRIS scanner. More detailed information on the development of the bridge approach surface model is available in [5].

The final FE model of the bridge consisted of 145,604 finite elements. A similar process was used for the development of the other two bridges. The final FE model of one of the bridges is presented in Figure 6.

Figure 6: An FE model of bridge #500133.

5. VALIDATION AND VERIFICATION OF FE BRIDGE MODELS

Validation of the concrete bridges was obtained by experimental testing of one of the selected bridges. All experimental tests were carried out on bridge #500133 on US 90 in north eastern Florida. This newer bridge was built in 1999 with three simply supported spans and with six AASHTO type III girders in each span. The bridge was tested twice, first in 2003 with an FDOT truck, and then in 2008, including two additional vehicles: the tractor trailer and the Terex crane. One span of the bridge was instrumented with two linear variable displacement transformers (LVDT), 38 strain gauges, and 14 accelerometers installed at the top of the bridge deck. Over 35 static and dynamic tests were carried out at speeds ranging from 48 to 80 km/h. Data obtained from the experimental testing allowed for calculation of DLA, and comparison to results from the numerical model. Detailed description of the tests carried out on the bridge and the results are available in [5].

The tests were virtually replicated, with strains and displacements obtained from the same points as in the experiment. Figure 7 shows result of the experiment and numerical analysis for one case, in which the tractor trailer crosses the bridge in the center of the westbound lane at a speed of 80 km/h.

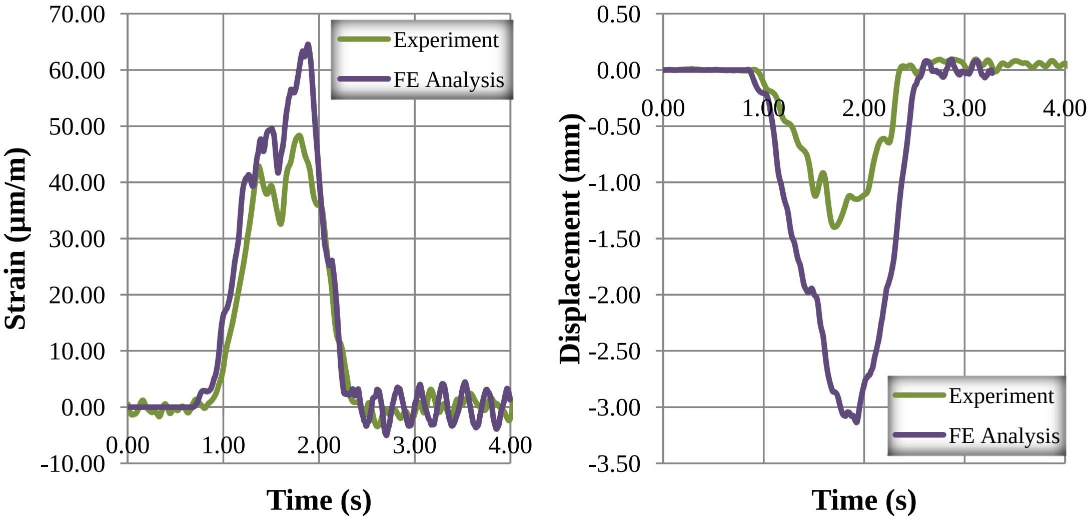

Figure 7: Time histories from experiment and FE analysis at 80 km/h over bridge #500133.

It is observed that the strain values are between ranges of measurement error. Results for displacements show a largest discrepancy which is attributed to the lack of zeroing of the displacement meters before each test. Still with some of the error observed, the values are accepted as qualitatively rather than quantitatively. The complete results of the tests are available in [5]. The same process was carried out with all three vehicles, and the FE model of the bridge was considered to be validated.

6. ANALYSIS OF DYNAMIC LOAD ALLOWANCE

DLA factors were calculated for all three bridges loaded with all three vehicles. DLAs were determined based on maximum displacement and strains in the bottom of the girder in the middle of the bridge span. DLA factors based on maximum strains proved to be more reliable, and closer to the experimental data, as well as recommended values by AASHTO [1]. The largest strains and displacements were recorded in girders no. 4 and 5 located directly underneath the path of the vehicle during the tests. Over ninety different tests with the numerical models were conducted to study the effect of the velocity on the DLA factor. As an illustration, DLA variation due to the vehicle speed is presented for one of the cases in Figure 8.

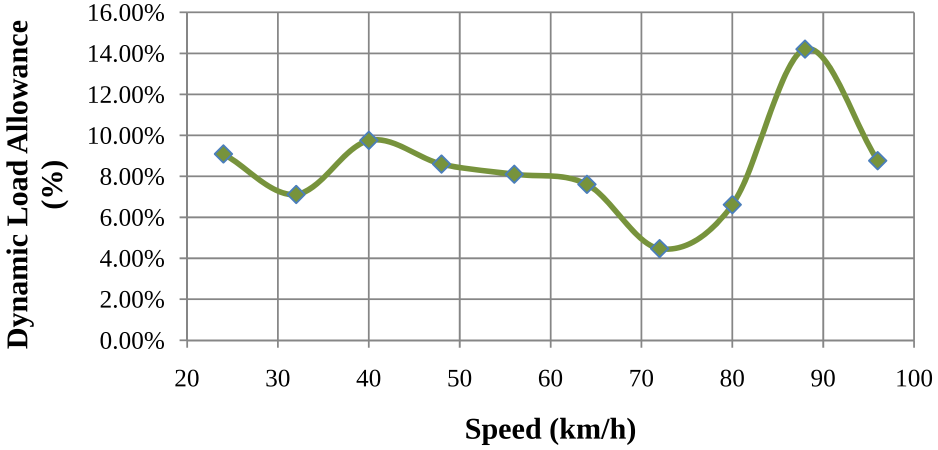

Figure 8: DLA factor vs. speed for the tractor trailer on bridge #500133.

Figure 8 illustrates the fact that DLA factors do not necessarily monotonically increase as vehicle speed increases. For this case of the tractor-trailer crossing over the bridge, the maximum DLA factor observed was at speed of about 88 km/h with a value of about 14%. DLA factors were calculated for every case with the same observation in all the cases.

The suspension system of the vehicles was one of the most influential characteristics that affected the dynamic response of the bridge. Results of DLA factors for the three vehicles crossing over bridge #500133 at a specified speed are presented in Table 6.

Vehicle	Speed (km/h)	DLA (%)
Tractor-trailer	80	6.6
Terex crane	80	32.7
FDOT truck	80	35.4

Table 6: Analysis of vehicles traveling over bridge #500133.

Another feature identified as triggering an increased DLA is a loosely attached cargo that is able to bounce on top of the trailer, producing a so called hammering effect. The tractor trailer model was modified to allow the bouncing of the cargo on top of the trailer. The cargo was detached from the trailer and seatbelt elements were introduced to act as tying chains. Final results of the testing of the tractor-trailer on bridge #500133 are presented in Figure 9.

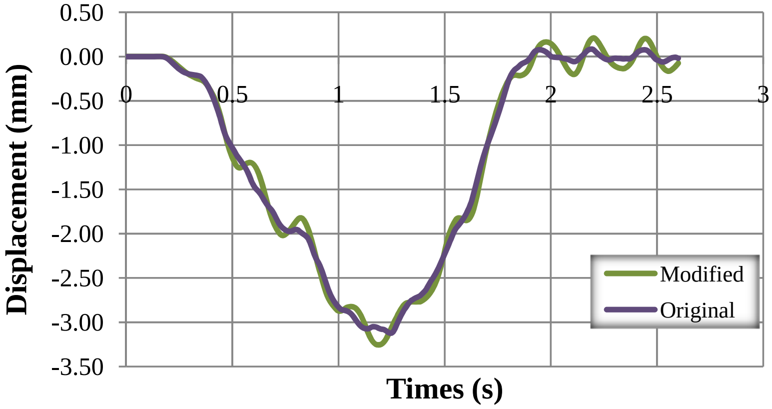

Figure 9: Deflection of the bridge girder #4 from FE analyses at 80 km/h.

It can be seen from Figure 9 that with the modifications made to the tractor-trailer model, the bridge was subjected to a larger displacement, which was caused by an additional pounding of the bouncing load on the bridge. Qualitatively both time histories look the same, but there is an additional frequency observed in the modified model of about f = 4.8 Hz. This pounding frequency was consistent with those observed earlier during the experimental testing of bridge #500133.

The quality of the bridge approach depression was also found to have a significant impact on the DLA factors calculated. The bridge approach depression of the FE model of bridge #500133 was replaced by a perfectly flat approach surface. The virtual experiment used the Terex crane travelling at a speed of 80 km/h. Strain measurements from the virtual tests are presented in Figure 10. The strain for the case in which the vehicle travels over the flat approach shows a decrease in magnitude.

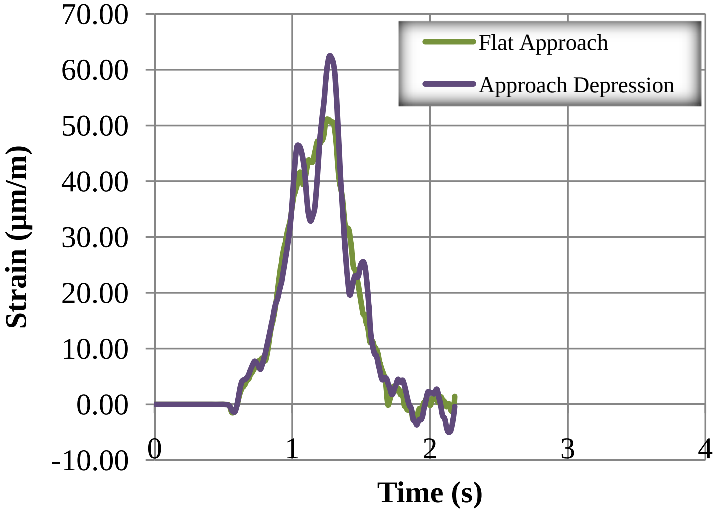

Figure 10: Longitudinal strains from FE analyses for girder #4 at 80 km/h.

7. CONCLUSIONS

This paper presented a comprehensive analysis of vehicle-bridge dynamic systems. The complete analysis consisted of computational mechanics and experimental parts. Three FE models of highway bridges and three FE models of heavy vehicles were used. Analysis of DLA factors was conducted for all bridges depending on vehicle speed and type. Efforts were made to develop realistic vehicle models for they account as much as 20% of the total mass of the vehicle-bridge system. Representing them as concentrated loads would not provide accurate data on the real system.

Considering the analysis was of dynamic nature, the vehicles springs and dampers were accounted for through a careful modelling process of the suspension systems. Rotating wheels and tires were also modelled carefully due to their influence on the vehicle-bridge dynamic system. The accuracy of the results obtained is credited to the development of the innovative finite element models and is supported with data from experimental tests. From the analysis several factors were found to have a significant influence on the DLA such as:

1. Vehicle suspension system: the very stiff suspension from FDOT resulted in the worst DLA factors in most of the cases.
2. Road surface condition: faults in the abutment joint and surface imperfections such as cracks and ruts; when compared to a flat surface result in a much higher DLA factor.
3. Loosely attached cargo which is able to bounce on top of the trailer: an additional pounding frequency is observed with a higher dynamic response on the bridge.

These were the factors that had the most influence on the magnitude of the DLA factors. From the variety of tests conducted in computational analysis, some other observations were also made, such as:

1. AASHTO recommendation value of DLA = 33% appeared to be a reasonable approximation with only five cases surpassing it, but at relatively high speeds as presented in Figure 11.

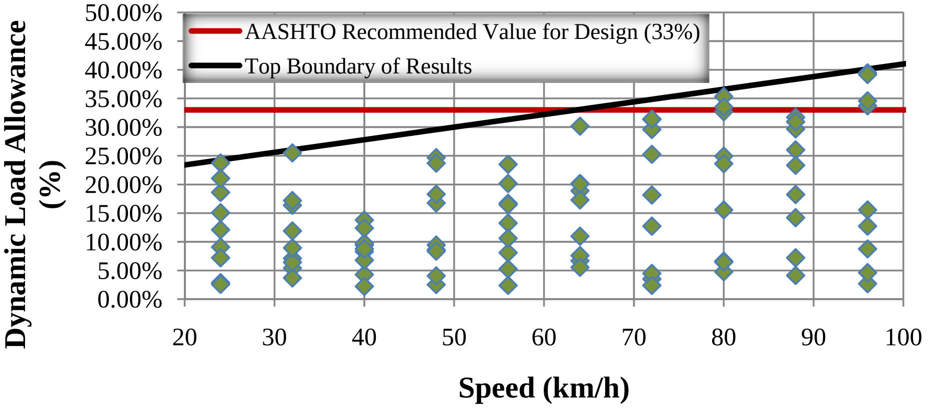

Figure 11: Summary of FE analyses of all the vehicle-bridge interactions.

2. The DLA factor does not monotonically increase as the vehicle speed increases; a lower vehicle speed in certain cases resulted in a higher DLA factor.
3. The bridge dynamic response is dependent on a combination of span length, width, and girder type which specifies the structure natural frequency.
4. The DLA factors also depend on the bridge natural frequency, and vibrations transferred in the interaction with the heavy vehicle.

ACKNOWLEDGEMENTS

This study was completed under direction and in cooperation with the Florida Department of Transportation Structures Laboratory. Thanks to all the professionals who helped in conducting all the experimental tests including Marc Ansley, Stephen Eudy, William Potter and Paul Tighe. All the comments, advice, guidance, and technical support provided by this group of professionals were essential in the development of the project and are highly appreciated. Thanks are also due to Blueprint 2000 office in Tallahassee for making Broadmoor Estate available free of charge for speed bump testing. Opinions and views expressed in this paper are those of the authors and not necessarily those of the sponsoring Agency.

REFERENCES

[1] *AASHTO LRFD* Bridge design specifications, *customary U.S. units, with 2008 and 2009 interim revisions, 4th Ed., Washington, D.C., 2009.*

[2] S. Earle, L. Kwasniewski, P. Szurgott, J.W. Wekezer, Dynamic Performance of Reinforced Concrete Bridges. Paper 1387, Session MS5. Complete paper on CD. Conference program, 60 and 96. *IV European Conference on Computational Mechanics. Solids, Structures and Coupled Problems in Engineering*. Paris, France, May 16-21, 2010.

[3] H. Li, L. Kwasniewski, J.W. Wekezer, Dynamic Response of a Highway Bridge Subjected to Moving Trucks. *ASCE Journal of Bridge Engineering*, **13-5,** 439-448, September – October 2008.

[4] H. Li, J. Wekezer, L. Kwasniewski, J. Malachowski, Numerical Assessment of Dynamic Response of Highway Bridges Subjected to Heavy Vehicles. *Advances in Transportation Studies*, *An International Journal.* Issue XII, Section B, 47-58. July, 2007.

[5] J.W. Wekezer, P. Szurgott, L. Kwasniewski, J. Siervogel, Investigation of Impact Factors for Permit Vehicles. *Final Report, FDOT Project BD543.* Structural Research Center, Florida Department of Transportation, 2008.

[6] P. Szurgott, L. Kwasniewski, J.W. Wekezer, J. Siervogel, M. Ansley, Experimental Assessment of Dynamic Responses Induced by Permit Vehicles. *ASCE Journal of Bridge Engineering*, Vol. 16, Iss. 1, pp. 108-116, 2011.

[7] J.W. Wekezer, H. Li, L. Kwasniewski, J. Malachowski, Analytical and Experimental Evaluation of Existing Florida DOT Bridges. *Final Report, FDOT BD493.* Structural Research Center, Florida Department of Transportation, 2004.

[8] LS-DYNA Keyword User's Manual, Version 971, *Livermore Software Technology Corporation.* May 2007.

COMPDYN 2011
III ECCOMAS Thematic Conference on
Computational Methods in Structural Dynamics and Earthquake Engineering
M. Papadrakakis, M. Fragiadakis, V. Plevris (eds.)
Corfu, Greece, 25–28 May 2011

NONLINEAR EFFECTS IN ELASTIC FLEXURAL – TORSIONAL VIBRATIONS OF BEAMS OF ARBITRARY CROSS SECTION

Evangelos J. Sapountzakis[1] and Ioannis C. Dikaros[2]

[1]Assoc. Professor
Institute of Structural Analysis and Antiseismic Research
School of Civil Engineering
National Technical University of Athens
Zografou Campus Gr-15780
Athens, GREECE
tel.: +30210-7721718; Fax.: +30210-7721720
e-mail: cvsapoun@central.ntua.gr

[2]PhD Student, Civil Engineer
Institute of Structural Analysis and Antiseismic Research
School of Civil Engineering
National Technical University of Athens
Zografou Campus Gr-15780
Athens, GREECE
tel.: +30210-7721620; Fax.: +30210-7721720
e-mail: dikarosgiannis@gmail.com

Key words: Flexural-Torsional Analysis, Dynamic analysis, Wagner's coefficients, Nonlinear analysis, Shortening Effect, Boundary element method.

Abstract. *In this paper a boundary element method is developed for the nonlinear flexural-torsional dynamic analysis of beams of arbitrary, simply or multiply connected, constant cross section, undergoing moderate large deflections and rotations under general boundary conditions, taking into account the effects of rotary and torsional warping inertia. Four boundary value problems are formulated with respect to the transverse displacements, to the axial displacement and to the angle of twist and solved using the Analog Equation Method, a BEM based method. The geometric, inertia, torsion and warping constants are evaluated employing the Boundary Element Method. The proposed model takes into account, both the Wagner's coefficients and the shortening effect. Numerical examples are worked out to illustrate the efficiency, wherever possible the accuracy, the range of applications of the developed method as well as the influence of the nonlinear effects to the response of the beam.*

1 INTRODUCTION

In engineering practice, we often come across the analysis of beam structures subjected to vibratory loading. This problem becomes much more complicated in the case the cross section’s centroid does not coincide with its shear center (asymmetric beams), leading to the formulation of the flexural-torsional vibration problem. Besides, when arbitrary torsional boundary conditions are applied either at the edges or at any other interior point of the bar due to construction requirements, this bar under the action of general twisting loading is leaded to nonuniform torsion. Moreover, since weight saving is of paramount importance, frequently used thin-walled open section beams have low flexural and/or torsional stiffness and their deformations can be of such magnitude that it is not adequate to treat the cross section displacements and its angle of rotation as small. In these cases, the study of nonlinear effects on these members becomes essential, where this non-linearity results from retaining the nonlinear terms in the strain–displacement relations (finite displacement – small strain theory). When finite displacements are considered, the flexural-torsional dynamic analysis of bars becomes much more complicated, leading to the formulation of coupled and nonlinear flexural, torsional and axial equilibrium equations.

When the displacement components of a member are small, a wide range of linear analysis tools, such as modal analysis, can be used and some analytical results are possible. As these components become larger, the induced geometric nonlinearities result in effects that are not observed in linear systems. In such situations the possibility of an analytical solution method is significantly reduced and is restricted to special cases of beam boundary conditions or loading.

During the past few years, the nonlinear dynamic analysis of beams undergoing large deflections has received a good amount of attention in the literature. More specifically, Rozmarynowski and Szymczak in [1] studied the nonlinear free torsional vibrations of axially immovable thin-walled beams with doubly symmetric open cross section, employing the Finite Element Method. In this research effort only free vibrations are examined, the solution is provided only at points of reversal of motion (not in the time domain), no general axial, torsional or warping boundary conditions (elastic support case) are studied, while some nonlinear terms related to the finite twisting rotations as well as the axial inertia term are ignored. Crespo Da Silva in [2-3] presented the nonlinear flexural-torsional-extensional vibrations of Euler-Bernoulli doubly symmetric thin-walled closed cross section beams, primarily focusing to flexural vibrations and neglecting the effect of torsional warping. Pai and Nayfeh in [4-6] studied also the nonlinear flexural-torsional-extensional vibrations of metallic and composite slewing or rotating closed cross section beams, primarily focusing to flexural vibrations and neglecting again the effect of torsional warping. Simo and Vu-Quoc in [7] presented a FEM solution to a fully nonlinear (small or large strains, hyperelastic material) three dimensional rod model including the effects of transverse shear and torsion-warping deformation based on a geometrically exact description of the kinematics of deformation. Qaisi in [8] obtained nonlinear normal modes of free vibrating geometrically nonlinear beams of various edge conditions employing the harmonic balance analytical method. Moreover, Pai and Nayfeh in [9] studied a geometrically exact nonlinear curved beam model for solid composite rotor blades using the concept of local engineering stress and strain measures and taking into account the in-plane and out-of-plane warpings. Di Egidio et al. in [10-11] presented also a FEM solution to the nonlinear flexural-torsional vibrations of shear undeformable thin-walled open beams taking into account in-plane and out-of-plane warpings and neglecting warping inertia. In this paper, the torsional-extensional coupling is taken into account but the inextensionality assumption leads to the fact that the axial boundary conditions are not general. Mohri et. al. in [12] proposed a FEM solution to the linear vibration analysis of pre- and post- buckled thin-walled open cross section beams, neglecting warping and axial inertia, considering geometrical nonlinearity only for the static loading and presenting examples of bars subjected to free vibrations and special boundary conditions. Machado and Cortinez in [13] presented also a FEM solution to the linear free vibration analysis of bisymmetric thin-walled composite beams of open shaped cross section, taking into account static initial stresses and deformations considering geometrical nonlinearity only for the static loading and presenting examples of bars subjected to special boundary conditions. Avramov et. al. [14-15] studied the free flexural-torsional vibrations of beams and obtained nonlinear normal modes by expansion of the equations of motion employing the Galerkin technique and neglecting the cross-section warping. Lopes and Ribeiro [16] studied also the nonlinear flexural-torsional free vibrations of beams employing a FEM solution and neglecting the longitudinal and rotary inertia as well as the cross-section warping. Duan [17] presented a FEM formulation for the nonlinear free vibration problem of thin-walled curved beams of asymmetric cross-section based on a simplified displacement field. Finally, the boundary element method has also been used for the nonlinear flexural [18-20] and torsional [21] dynamic analysis of only doubly symmetric beams. To the authors' knowledge the general problem of coupled nonlinear flexural – torsional free or forced vibrations of asymmetric beams has not yet been presented.

In this paper, a boundary element method is developed for the nonlinear flexural-torsional dynamic analysis of beams of arbitrary, simply or multiply connected, constant cross section, undergoing moderate large deflections and twisting rotations under general boundary conditions, taking into account the effects of rotary and warping inertia. The beam is subjected to the combined action of arbitrarily distributed or concentrated transverse loading in both directions as well as to twisting and/or axial loading. Four boundary value problems are formulated with respect to the transverse displacements, to the axial displacement and to the angle of twist and solved using the Analog Equation Method [22], a BEM based method. Application of the boundary element technique leads to a system of nonlinear coupled Differential – Algebraic Equations (DAE) of motion, which is solved iteratively using the Petzold-Gear Backward Differentiation Formula (BDF) [23], a linear multistep method for differential equations coupled to algebraic equations (DAE). The geometric, inertia, torsion and warping constants are evaluated employing the Boundary Element Method. The essential features and novel aspects of the present formulation compared with previous ones are summarized as follows.

i. The cross section is an arbitrarily shaped thin or thick walled one. The formulation does not stand on the assumption of a thin-walled structure and therefore the cross section's torsional and warping rigidities are evaluated "exactly" in a numerical sense.
ii. The beam is subjected to an arbitrarily distributed or concentrated transverse loading and bending moments in both directions as well as to axial loading.
iii. The beam is supported by the most general boundary conditions including elastic support or restraint.
iv. For the first time in the literature, the effects of rotary and warping inertia are taken into account on the nonlinear flexural-torsional dynamic analysis of asymmetric beams subjected to arbitrary loading and boundary conditions.

v. The transverse loading can be applied at any arbitrary point of the beam cross section. The eccentricity change of the transverse loading during the torsional beam motion, resulting in additional torsional moment is taken into account.

vi. The proposed model takes into account the coupling effects of bending, axial and torsional response of the beam as well as the Wagner's coefficients and the shortening effect.

vii. The proposed method employs a BEM approach (requiring boundary discretization for the cross sectional analysis) resulting in line or parabolic elements instead of area elements of the FEM solutions (requiring the whole cross section to be discretized into triangular or quadrilateral area elements), while a small number of line elements are required to achieve high accuracy.

Numerical examples are worked out to illustrate the efficiency, wherever possible the accuracy, the range of applications of the developed method as well as the influence of the nonlinear effects to the response of the beam.

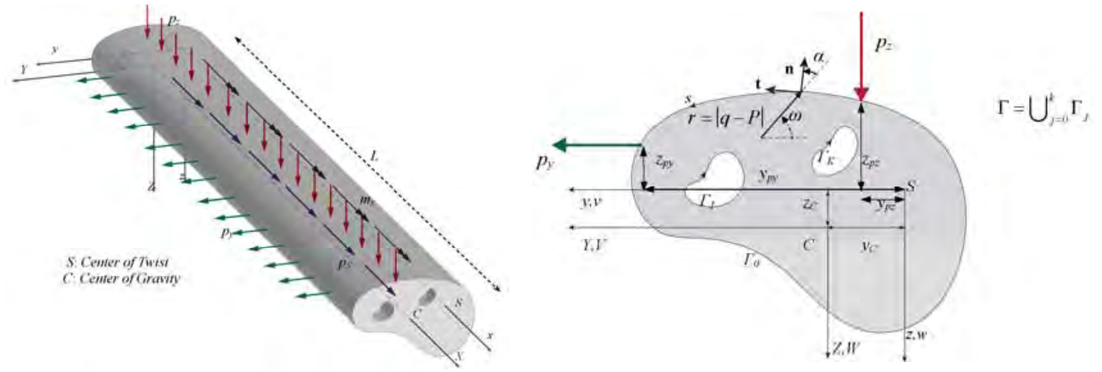

(a) (b)

Figure1: Prismatic beam in axial - flexural - torsional loading (a) of an arbitrary cross-section occupying the two dimensional region Ω (b).

3 STATEMENT OF THE PROBLEM

Let us consider a prismatic beam of length L (Fig.1), of constant arbitrary cross section of area A. The homogeneous isotropic and linearly elastic material of the beam's cross section, with modulus of elasticity E, shear modulus G and Poisson's ratio v occupies the two dimensional multiply connected region Ω of the y,z plane and is bounded by the Γ_j ($j=1,2,...,K$) boundary curves, which are piecewise smooth, i.e. they may have a finite number of corners. In Fig. 1 CYZ is the principal bending coordinate system through the cross section's centroid C, while y_C, z_C are its coordinates with respect to the Syz shear system of axes through the cross section's shear center S, with axes parallel to those of the CYZ system. The beam is subjected to the combined action of the arbitrarily distributed or concentrated, time dependent and conservative axial loading $p_X = p_X(X,t)$ along X direction, twisting moment $m_x = m_x(x,t)$ along x direction and transverse loading $p_y = p_y(x,t)$, $p_z = p_z(x,t)$ acting along the y and z directions, respectively, applied at distances y_{p_y}, z_{p_y} and y_{p_z}, z_{p_z}, with respect to the Syz shear system of axes (Fig. 1b). It is worth here noting that the aforementioned transverse loading can be applied at any arbitrary point of the beam's cross section and not necessarily at its centroid or at its shear center. In the case of a linear analysis, where the beam deflections and rotations are considered to be small, in order to overcome the fact that the external transverse loading is usually applied as tractions upon the surface of the beam, the superposition principle is adopted and the actual applied system of forces is replaced by a statically equivalent one, acting on the centroid or on the shear center of the beam (Fig. 2a). However in nonlinear analysis, where twisting rotations are considered to be large, the occurring change of eccentricity (Fig. 2b) may have substantial influence on the beam response and must be taken into account.

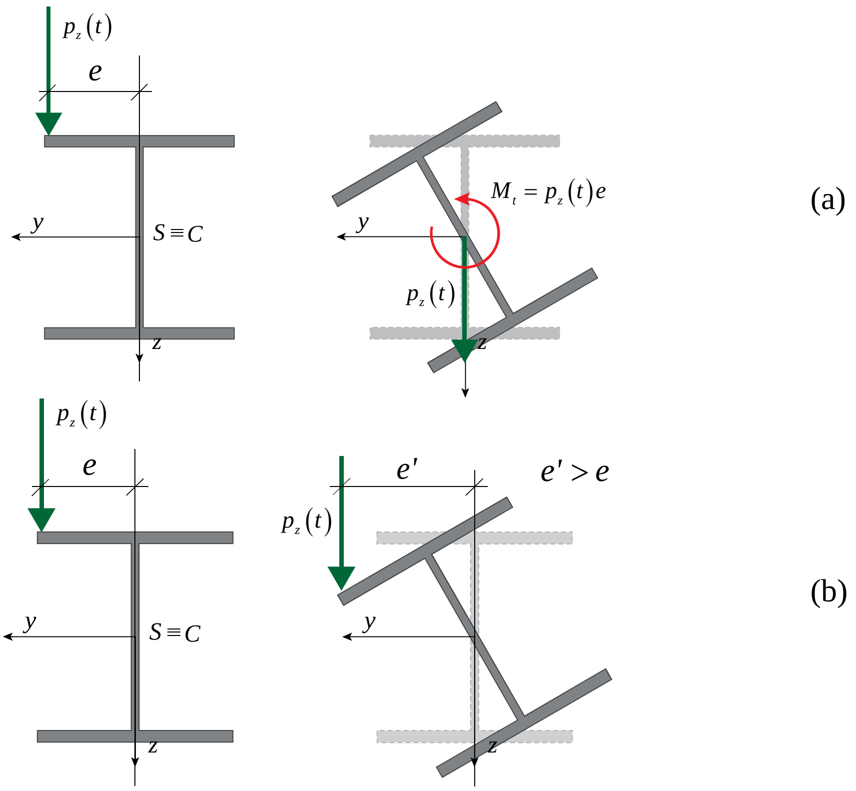

Figure 2: Superposition principle in linear analysis (a) and change of eccentricity of the transverse force p_z during the twisting motion of the cross section in nonlinear analysis (b).

Under the action of the aforementioned loading and employing the Euler-Bernoulli assumption, the displacement field of an arbitrary point of the cross section can be derived with respect to those of the shear center as [12]

$$\bar{u}(x,y,z,t)=u(x,t)-(y-y_C)\theta_Z(x,t)+(z-z_C)\theta_Y(x,t)+\theta_x'(x,t)\varphi_S^P(y,z) \tag{1a}$$

$$\bar{v}(x,y,z,t)=v(x,t)-z\sin\left(\theta_x(x,t)\right)-y\left[1-\cos\left(\theta_x(x,t)\right)\right] \tag{1b}$$

$$\bar{w}(x,y,z,t)=w(x,t)+y\sin\left(\theta_x(x,t)\right)-z\left[1-\cos\left(\theta_x(x,t)\right)\right] \tag{1c}$$

$$\theta_Y(x,t)=v'(x,t)\sin\left(\theta_x(x,t)\right)-w'(x,t)\cos\left(\theta_x(x,t)\right) \tag{1d}$$

$$\theta_Z(x,t)=v'(x,t)\cos\left(\theta_x(x,t)\right)+w'(x,t)\sin\left(\theta_x(x,t)\right) \tag{1e}$$

where $\bar{u}$, $\bar{v}$, $\bar{w}$ are the axial and transverse beam displacement components with respect to the Syz shear system of axes; $u(x,t)=\frac{1}{A}\int_A \bar{u}(x,y,z,t)\,dA$ denotes the average axial displacement of the cross section [24] and $v=v(x,t)$, $w=w(x,t)$ are the corresponding components of the shear center S ; $\theta_Y\left(x,t\right)$, $\theta_Z\left(x,t\right)$ are the angles of rotation of the cross section due to bending, with respect to its centroid; $\theta_x'\left(x,t\right)$ denotes the rate of change of the angle of twist $\theta_x\left(x,t\right)$ regarded as the torsional curvature and φ_S^P is the primary warping function with respect to the shear center S [25]. Employing the strain-displacement relations of the three-dimensional elasticity for moderate displacements [26, 27], the strain components can be written as

$$\begin{aligned}\varepsilon_{xx} &= u' + \left(z - z_C\right)\left(v''\sin\theta_x - w''\cos\theta_x\right) - \left(y - y_C\right)\left(v''\cos\theta_x + w''\sin\theta_x\right) + \\ &\quad + \theta_x''\phi_S^P - \theta_x'\left(z_C\left(v'\cos\theta_x + w'\sin\theta_x\right) + y_C\left(v'\sin\theta_x - w'\cos\theta_x\right)\right) + \\ &\quad + \frac{1}{2}\left(v'^2 + w'^2 + \left(y^2 + z^2\right)\left(\theta_x'\right)^2\right)\end{aligned} \tag{2a}$$

$$\gamma_{xy} = 2\varepsilon_{xy} = \left(\frac{\partial\phi_S^P}{\partial y} - z\right)\theta_x' \tag{2b}$$

$$\gamma_{xz} = 2\varepsilon_{xz} = \left(\frac{\partial\phi_S^P}{\partial z} + y\right)\theta_x' \tag{2c}$$

while considering strains to be small, the non vanishing stress components of the second Piola – Kirchhoff stress tensor are obtained as

$$\begin{aligned}S_{xx} &= E\Big[u' + \left(z - z_C\right)\left(v''\sin\theta_x - w''\cos\theta_x\right) - \left(y - y_C\right)\left(v''\cos\theta_x + w''\sin\theta_x\right) + \\ &\quad + \theta_x''\phi_S^P - \theta_x'\left(z_C\left(v'\cos\theta_x + w'\sin\theta_x\right) + y_C\left(v'\sin\theta_x - w'\cos\theta_x\right)\right) + \\ &\quad + \frac{1}{2}\left(v'^2 + w'^2 + \left(y^2 + z^2\right)\left(\theta_x'\right)^2\right)\Big]\end{aligned} \tag{3a}$$

$$S_{xy} = G\cdot\theta_x'\cdot\left(\frac{\partial\phi_S^P}{\partial y} - z\right) \tag{3b}$$

$$S_{xz} = G\cdot\theta_x'\cdot\left(\frac{\partial\phi_S^P}{\partial z} + y\right) \tag{3c}$$

In order to establish the nonlinear equations of motion, the principle of virtual work

$$\delta W_{\text{int}} + \delta W_{mass} = \delta W_{ex\text{t}} \tag{4}$$

where

$$\delta W_{\text{int}} = \int_V \left(S_{xx}\delta\varepsilon_{xx} + S_{xy}\delta\gamma_{xy} + S_{xz}\delta\gamma_{xz}\right)dV \tag{5a}$$

$$\delta W_{mass} = \int_V \rho\left(\ddot{\bar{u}}\delta\bar{u} + \ddot{\bar{v}}\delta\bar{v} + \ddot{\bar{w}}\delta\bar{w}\right)dV \tag{5b}$$

$$\delta W_{ext} = \int_L \left(p_X\delta\bar{u}_C + p_y\delta\bar{v}_{p_y} + p_z\delta\bar{w}_{p_z} + m_x\delta\theta_x\right)dx \tag{5c}$$

under a Total Lagrangian formulation, is employed. In the above equations, $\delta(\cdot)$ denotes virtual quantities, $(\dot{})$ denotes differentiation with respect to time, V is the volume of the beam, $\bar{u}_C$ is the axial displacement of the centroid and $\bar{v}_{p_y}$, $\bar{w}_{p_z}$ are the transverse displacements of the points where the loads p_y, p_z, respectively, are applied. It is worth here noting that the aforementioned relation of the external work δW_{ext} (eqn. (5c)) is expressed in terms of the applied external forces and virtual quantities of the kinematical components in the deformed configuration of the beam. This expression takes into account the change of the eccentricity of the external conservative transverse loading, arising from the cross section torsional rotation, inducing additional (positive or negative) torsional moment (Fig. 2b). Substituting the expressions of virtual quantities in eqn. (5c), the external work can be written as

$$\begin{aligned}\delta W_{ext} = \int_L \Big[& p_X \delta u + p_y \delta v + p_z \delta w + \Big(p_y \left(-z_{p_y} \cos\theta_x - y_{p_y} \sin\theta_x \right) + \\ & + p_z \left(y_{p_z} \cos\theta_x - z_{p_z} \sin\theta_x \right) + m_x \Big) \delta\theta_x \Big] dx\end{aligned} \tag{6}$$

Expanding the trigonometric functions in terms of Taylor series and keeping the first two terms [12], the following approximate expressions are obtained

$$\cos\theta_x = 1 - \frac{\theta_x^{\ 2}}{2!} = 1 - \frac{\theta_x^{\ 2}}{2} \tag{7a}$$

$$\sin\theta_x = \theta_x - \frac{\theta_x^{\ 3}}{3!} = \theta_x - \frac{\theta_x^{\ 3}}{6} \tag{7b}$$

Using equations (7), equation (6) can be written as

$$\begin{aligned}\delta W_{ext} = \int_L \Bigg[& p_X \delta u + p_y \delta v + p_z \delta w + \Bigg(p_y \left(-z_{p_y} - y_{p_y}\theta_x + \frac{1}{2}\theta_x^{\ 2} z_{p_y} + \frac{1}{6}\theta_x^{\ 3} y_{p_y} \right) + \\ & + p_z \left(y_{p_z} - z_{p_z}\theta_x - \frac{1}{2}\theta_x^{\ 2} y_{p_z} + \frac{1}{6}\theta_x^{\ 3} z_{p_z} \right) + m_x \Bigg) \delta\theta_x \Bigg] dx\end{aligned} \tag{8}$$

As it can be observed from equation (8), neglecting all the nonlinear terms leads to the well known linear expression of the external twisting moment, arising from the superposition principle. In the present study, these terms are retained, so that the change of eccentricity is taken into account. Moreover, the stress resultants of the beam can be defined as

$$N = \int_\Omega S_{xx} d\Omega \tag{9a}$$

$$M_Y = \int_\Omega S_{xx} Z d\Omega \tag{9b}$$

$$M_Z = -\int_\Omega S_{xx} Y d\Omega \tag{9c}$$

$$M_t^P = \int_\Omega \left[S_{xy} \left(\frac{\partial \varphi_S^P}{\partial y} - z \right) + S_{xz} \left(\frac{\partial \varphi_S^P}{\partial z} + y \right) \right] d\Omega \tag{9d}$$

$$M_w = -\int_\Omega S_{xx} \varphi_S^P d\Omega \tag{9e}$$

$$M_R = \int_\Omega S_{xx} \left(y^2 + z^2 \right) d\Omega \tag{9f}$$

where M_t^P is the primary twisting moment [25, 28] resulting from the primary shear stress distribution S_{xy}, S_{xz}, M_w is the warping moment due to torsional curvature and M_R is a higher order stress resultant. Substituting the expressions of the stress components (3) into equations (9a-9f), the stress resultants are obtained as

$$\begin{aligned} N = EA\Bigg[& u' + \frac{1}{2}\left(v'^2 + w'^2 + \frac{I_S}{A}\theta_x'^2 \right) - \\ & - \theta_x' \left(z_C \left(v' \cos\theta_x + w' \sin\theta_x \right) + y_C \left(v' \sin\theta_x - w' \cos\theta_x \right) \right) \Bigg] \end{aligned} \tag{10a}$$

$$M_Y = -EI_Y \left(w'' \cos\theta_x - v'' \sin\theta_x - \beta_Z \theta_x'^2 \right) \tag{10b}$$

$$M_Z = EI_Z \left(v'' \cos\theta_x + w'' \sin\theta_x - \beta_Y \theta_x'^2 \right) \tag{10c}$$

$$M_t^P = GI_t \theta_x' \tag{10d}$$

$$M_w = -EC_S \left(\theta_x'' + \beta_\omega \theta_x'^2 \right) \tag{10e}$$

$$\begin{aligned} M_R = {} & N\frac{I_S}{A} - 2EI_Z\beta_Y \left(v'' \cos\theta_x + w'' \sin\theta_x \right) - 2EI_Y\beta_Z \left(w'' \cos\theta_x - v'' \sin\theta_x \right) + \\ & + 2EC_S\beta_\omega\theta_x'' + \frac{1}{2}E\left(I_R - \frac{I_S{}^2}{A} \right)\theta_x'^2 \end{aligned} \tag{10f}$$

where the area *A*, the polar moment of inertia I_S with respect to the shear center *S*, the principal moments of inertia I_Y, I_Z with respect to the cross section's centroid, the fourth moment of inertia I_R with respect to the shear center *S*, the torsion constant I_t and the warping constant C_S with respect to the shear center S, are given as

$$A = \int_\Omega d\Omega \tag{11a}$$

$$I_S = \int_\Omega \left(y^2 + z^2 \right) d\Omega \tag{11b}$$

$$I_Y = \int_\Omega Z^2 d\Omega \tag{11c}$$

$$I_Z = \int_\Omega Y^2 d\Omega \tag{11d}$$

$$I_R = \int_\Omega \left(y^2 + z^2 \right)^2 d\Omega \tag{11e}$$

$$C_S = \int_\Omega \left(\varphi_S^P \right)^2 d\Omega \tag{11f}$$

$$I_t = \int_\Omega \left(y^2 + z^2 + y\frac{\partial \varphi_S^P}{\partial z} - z\frac{\partial \varphi_S^P}{\partial y} \right) d\Omega \tag{11g}$$

while the Wagner’s coefficients β_Z, β_Y and β_ω are given as

$$\beta_Z = \frac{1}{2I_Y}\int_\Omega \left(z - z_C\right)\left(y^2 + z^2\right) d\Omega \tag{12a}$$

$$\beta_Y = \frac{1}{2I_Z}\int_\Omega \left(y - y_C\right)\left(y^2 + z^2\right) d\Omega \tag{12b}$$

$$\beta_\omega = \frac{1}{2C_S}\int_\Omega \left(y^2 + z^2\right)\varphi_S^P d\Omega \tag{12c}$$

Employing the expressions of strain obtained in equations (2), the expressions of stress resultants given in equations (10) and applying the principle of virtual work (eqn. (4)), the equations of motion of the beam can be derived. The arising set of equations is coupled and highly complicated. Simplification can be achieved by neglecting the axial inertia of the beam, denoted by the term $\rho A\ddot{u}$, and employing the approximate expressions given in equations (7). Thus, using the aforementioned approximations and ignoring the nonlinear terms of the fourth or greater order [12], the governing partial differential equations of motion for the beam at hand can be written as

$$\begin{aligned} &-EA\left[u'' + w'w'' + v'v'' + \frac{I_S}{A}\theta_x{}'\theta_x{}'' - z_C\left(\theta_x\theta_x{}'w'' + \theta_x\theta_x{}''w' + \theta_x{}''v' + \theta_x{}'v'' + \theta_x{}'^2 w'\right) - \right. \\ &\quad \left. -y_C\left(\theta_x\theta_x{}''v' + \theta_x\theta_x{}'v'' - \theta_x{}''w' - \theta_x{}'w'' + \theta_x{}'^2 v'\right)\right] = p_X \end{aligned} \tag{13a}$$

$$\begin{aligned} &EI_Z v'''' - N\left[-z_C\theta_x{}'' - y_C\left(\theta_x{}'^2 + \theta_x{}''\theta_x\right) + v''\right] + \\ &\quad +\left(EI_Z - EI_Y\right)\left(w''''\theta_x + 2w'''\theta_x{}' + w''\theta_x{}'' - v''''\theta_x^2 - 4v'''\theta_x\theta_x{}' - 2v''\theta_x\theta_x{}'' - 2v''\theta_x{}'^2\right) + \\ &\quad +EI_Z\beta_Y\left(-2\theta_x{}'\theta_x{}''' - 2\theta_x{}''^2\right) + EI_Y\beta_Z\left(2\theta_x{}'\theta_x{}'''\theta_x + 2\theta_x{}''^2\theta_x + 5\theta_x{}'^2\theta_x{}''\right) + \rho A\ddot{v} + \\ &\quad +\rho\left[\left(I_Z - I_Y\right)\left(\theta_x v'' + \theta_x{}'v'\right) - I_Z w'' - A\left(y_C\theta_x + z_C - \frac{1}{2}z_C\theta_x^2\right)\right]\ddot{\theta}_x + \rho\left(I_Z - I_Y\right)\cdot \\ &\quad \cdot\left[2\theta_x\theta_x{}'\ddot{v}' + \theta_x^2\ddot{v}'' + 2\left(\theta_x{}'\dot{\theta}_x + \theta_x\dot{\theta}_x{}'\right)\dot{v}' + 2\theta_x\dot{\theta}_x\dot{v}'' - \theta_x{}'\ddot{w}' - \theta_x\ddot{w}'' + v'\theta_x\ddot{\theta}_x{}'\right] + \rho I_Z \cdot \\ &\quad \cdot\left[-w'\ddot{\theta}_x{}' - \ddot{v}'' - 2\dot{\theta}_x\dot{w}'' + v''\dot{\theta}_x^2 + 2v'\dot{\theta}_x\dot{\theta}_x{}' - 2\dot{\theta}_x{}'\dot{w}'\right] - \rho A\left(y_C - z_C\theta_x\right)\dot{\theta}_x^2 = p_y - \\ &\quad -p_X\left(v' - y_C\theta_x{}'\theta_x - z_C\theta_x{}'\right) \end{aligned} \tag{13b}$$

$$\begin{aligned} &EI_Y w'''' - N\left[w'' + y_C\theta_x{}'' - z_C\left(\theta_x{}'^2 + \theta_x\theta_x{}''\right)\right] + \\ &\quad +\left(EI_Z - EI_Y\right)\left(v''''\theta_x + 2v'''\theta_x{}' + v''\theta_x{}'' + w''''\theta_x{}^2 + 4w'''\theta_x\theta_x{}' + 2w''\theta_x\theta_x{}'' + 2w''\theta_x{}'^2\right) + \end{aligned}$$

$$
\begin{aligned}
&+EI_Z\beta_Y\left(-2\theta_x{}'\theta_x{}'''\theta_x-5\theta_x{}'^2\theta_x{}''-2\theta_x{}''^2\theta_x\right)+EI_Y\beta_Z\left(-2\theta_x{}'\theta_x{}'''-2\theta_x{}''^2\right)+\rho A\ddot{w}+\\
&+\rho\left[\left(I_Z-I_Y\right)\left(-\theta_x w''-\theta_x{}'w'\right)+I_Y v''+A\left(-z_C\theta_x+y_C-\frac{1}{2}y_C\theta_x^2\right)\right]\ddot{\theta}_x-\rho\left(I_Z-I_Y\right)\cdot\\
&\cdot\left[2\theta_x\theta_x{}'\ddot{w}'+\theta_x^2\ddot{w}''+2\left(\theta_x{}'\dot{\theta}_x+\theta_x\dot{\theta}_x{}'\right)\dot{w}'+2\theta_x\dot{\theta}_x\dot{w}''+\theta_x{}'\ddot{v}'+\theta_x\ddot{v}''+w'\theta_x\ddot{\theta}_x{}'\right]-\rho I_Y\cdot\\
&\cdot\left[-v'\ddot{\theta}_x{}'+\ddot{w}''-2\dot{\theta}_x\dot{v}''-w''\dot{\theta}_x^2-2w'\dot{\theta}_x\dot{\theta}_x{}'-2\dot{\theta}_x{}'\dot{v}'\right]-\rho A\left(z_C+y_C\theta_x\right)\dot{\theta}_x^2=p_z-\\
&-p_X\left(w'+y_C\theta_x{}'-z_C\theta_x{}'\theta_x\right)
\end{aligned}
\tag{13c}
$$

$$
\begin{aligned}
&EC_S\theta_x{}''''-GI_t\theta_x{}''-\frac{3}{2}E\left(I_R-\frac{I_S{}^2}{A}\right)\theta_x{}'^2\theta_x{}''-N\left[\frac{I_S}{A}\theta_x{}''+y_C\left(w''-v''\theta_x\right)-z_C\left(v''+w''\theta_x\right)\right]+\\
&+\left(EI_Z-EI_Y\right)\left(v''w''-v''^2\theta_x+w''^2\theta_x\right)+\\
&+EI_Z\beta_Y\left(2\theta_x{}''w''\theta_x+w''\theta_x{}'^2+2\theta_x{}'v'''+2\theta_x{}''v''+2\theta_x{}'w'''\theta_x\right)+\\
&+EI_Y\beta_Z\left(-2\theta_x{}''v''\theta_x+2\theta_x{}''w''+2\theta_x{}'w'''-v''\theta_x{}'^2-2\theta_x{}'v'''\theta_x\right)+\rho\left(v'^2I_Y+w'^2I_Z+I_S\right)\ddot{\theta}_x-\\
&-\rho A\left(z_C+y_C\theta_x-\frac{1}{2}z_C\theta_x^2\right)\ddot{v}+\rho A\left(y_C-z_C\theta_x-\frac{1}{2}y_C\theta_x^2\right)\ddot{w}+\rho\left(I_Z-I_Y\right)\theta_x\left(w'\ddot{w}'-v'\ddot{v}'\right)+\\
&+\rho I_Z\left(w'\ddot{v}'+2\dot{\theta}_x\dot{w}'w'\right)+\rho I_Y\left(-v'\ddot{w}'+2\dot{\theta}_x\dot{v}'v'\right)-\rho C_S\ddot{\theta}_x{}''=m_x+p_zy_{p_z}-p_yz_{p_z}+\\
&+\left(\frac{1}{2}\theta_x^2z_{p_y}+\frac{1}{6}\theta_x^3y_{p_y}-\theta_xy_{p_y}\right)p_y+\left(\frac{1}{6}\theta_x^3z_{p_z}-\frac{1}{2}\theta_x^2y_{p_z}-z_{p_z}\theta_x\right)p_z-\\
&-p_X\left(\frac{I_S}{A}\theta_x{}'-y_Cv'\theta_x-z_Cw'\theta_x-z_Cv'+y_Cw'\right)
\end{aligned}
\tag{13d}
$$

while the expression of N is given as

$$
N=EA\left[u'+\frac{1}{2}\left(v'^2+w'^2+\frac{I_S}{A}\theta_x{}'^2\right)-\theta_x{}'\left(z_C\left(w'\theta_x+v'\right)+y_C\left(v'\theta_x-w'\right)\right)\right]
\tag{14}
$$

The above governing differential equations (eqns. (13)) are also subjected to the initial conditions ($x\in\left(0,l\right)$)

$u\left(x,0\right)=u_0\left(x\right)$ $\qquad$ $\dot{u}\left(x,0\right)=\dot{u}_0\left(x\right)$ (15a,b)

$v\left(x,0\right)=v_0\left(x\right)$ $\qquad$ $\dot{v}\left(x,0\right)=\dot{v}_0\left(x\right)$ (16a,b)

$w\left(x,0\right)=w_0\left(x\right)$ $\qquad$ $\dot{w}\left(x,0\right)=\dot{w}_0\left(x\right)$ (17a,b)

$\theta_x\left(x,0\right)=\theta_{x0}\left(x\right)$ $\qquad$ $\dot{\theta}_x\left(x,0\right)=\dot{\theta}_{x0}\left(x\right)$ (18a,b)

together with the corresponding boundary conditions of the problem at hand, which are given as

$$a_1 u\left(x,t\right)+\alpha_2 N\left(x,t\right)=\alpha_3 \tag{19}$$

$$\beta_1 v\left(x,t\right)+\beta_2 V_y\left(x,t\right)=\beta_3 \qquad \bar{\beta}_1\theta_Z\left(x,t\right)+\bar{\beta}_2\mathrm{M}_Z\left(x,t\right)=\bar{\beta}_3 \tag{20a,b}$$

$$\gamma_1 w\left(x,t\right)+\gamma_2 V_z\left(x,t\right)=\gamma_3 \qquad \bar{\gamma}_1\theta_Y\left(x,t\right)+\bar{\gamma}_2\mathrm{M}_Y\left(x,t\right)=\bar{\gamma}_3 \tag{21a,b}$$

$$\delta_1\theta_x\left(x,t\right)+\delta_2 M_t\left(x,t\right)=\delta_3 \qquad \bar{\delta}_1\theta_x'\left(x,t\right)+\bar{\delta}_2 M_w\left(x,t\right)=\bar{\delta}_3 \tag{22a,b}$$

at the beam ends $x=0,l$, where V_y, V_z and M_Z, M_Y are the reactions and bending moments with respect to y, z or to Y, Z axes, respectively, given by the following relations (ignoring again the nonlinear terms of the fourth or greater order)

$$\begin{aligned}V_y = {} & N\left(v'-z_C\theta_x'-y_C\theta_x\theta_x'\right)+\\ & +EI_Z\left(v'''\theta_x^2-w''\theta_x'-w'''\theta_x-v'''+2v''\theta_x\theta_x'+2\beta_Y\theta_x'\theta_x''\right)+\\ & +EI_Y\left(w'''\theta_x+w''\theta_x'-2v''\theta_x\theta_x'-v'''\theta_x^2-\beta_Z\theta_x'^3-2\beta_Z\theta_x\theta_x'\theta_x''\right)\end{aligned} \tag{23a}$$

$$\begin{aligned}V_z = {} & N\left(w'+y_C\theta_x'-z_C\theta_x'\theta_x\right)+\\ & +EI_Y\left(w'''\theta_x^2+v'''\theta_x-w'''+v''\theta_x'+2w''\theta_x\theta_x'+2\beta_Z\theta_x'\theta_x''\right)-\\ & -EI_Z\left(v''\theta_x'+w'''\theta_x^2+v'''\theta_x+2w''\theta_x\theta_x'-2\beta_Y\theta_x\theta_x'\theta_x''-\beta_Y\theta_x'^3\right)\end{aligned} \tag{23b}$$

$$M_Z=EI_Z\left(w''\theta_x-\beta_Y\theta_x'^2+v''-v''\theta_x^2\right)+EI_Y\left(-w''\theta_x+v''\theta_x^2+\beta_Z\theta_x'^2\theta_x\right) \tag{23c}$$

$$M_Y=EI_Z\left(-w''\theta_x^2+\beta_Y\theta_x'^2\theta_x-v''\theta_x\right)+EI_Y\left(\beta_Z\theta_x'^2-w''+w''\theta_x^2+v''\theta_x\right) \tag{23d}$$

while M_t and M_w are the torsional and warping moments at the boundary of the bar, respectively, given as

$$\begin{aligned}M_t = {} & GI_t\theta_x'-EC_S\theta_x'''+N\left(-z_C w'\theta_x+y_C w'-y_C v'\theta_x-z_C v'+\frac{I_S}{A}\theta_x'\right)+\\ & +EI_Z\beta_Y\left(-2\theta_x'v''-2\theta_x'w''\theta_x\right)+EI_Y\beta_Z\left(-2\theta_x'w''+2\theta_x'v''\theta_x\right)+\frac{1}{2}E\left(I_R-\frac{I_S^2}{A}\right)\theta_x'^3\end{aligned} \tag{24a}$$

$$M_w=-EC_S\left(\theta_x''+\beta_\omega\theta_x'^2\right) \tag{24b}$$

Finally, α_k, β_k, $\bar{\beta}_k$, γ_k, $\bar{\gamma}_k$, δ_k, $\bar{\delta}_k$ $(k=1,2,3)$ are time dependent functions specified at the boundaries of the bar ($x=0,l$). The boundary conditions eqns. (19)-(22) are the most general boundary conditions for the problem at hand, including also the elastic support. It is apparent that all types of the conventional boundary conditions (clamped, simply supported, free or guided edge) can be derived from these equations by specifying appropriately these functions (e.g. for a clamped edge it is $\alpha_1 = \beta_1 = \gamma_1 = \delta_1 = 1$, $\overline{\beta}_1 = \overline{\gamma}_1 = \overline{\delta}_1 = 1$, $\alpha_2 = \alpha_3 = \beta_2 = \beta_3 = \gamma_2 = \gamma_3 = \delta_2 = \delta_3 = \overline{\beta}_2 = \overline{\beta}_3 = \overline{\gamma}_2 = \overline{\gamma}_3 = \overline{\delta}_2 = \overline{\delta}_3 = 0$). In a case of eccentric axial loading or additional concentrated or distributed bending or warping moments, additional terms in governing equations (13) would arise. These terms could be taken into account without any special difficulty, by modifying appropriately equations (5c), (6), (8).

4 INTEGRAL REPRESENTATIONS-NUMERICAL SOLUTION

4.1 Evaluation of the axial displacement $\mathrm{u}(\mathrm{x},\mathrm{t})$, the transverse displacements $\mathrm{v}(\mathrm{x},\mathrm{t})$, $\mathrm{w}(\mathrm{x},\mathrm{t})$ and the angle of twist $\theta_{\mathrm{x}}(\mathrm{x},\mathrm{t})$

According to the precedent analysis, the nonlinear flexural-torsional vibration problem of a beam reduces in establishing the axial displacement component $u(x,t)$ having continuous partial derivatives up to the second order and the transverse displacement components $v(x,t)$, $w(x,t)$ and the angle of rotation $\theta_x(x,t)$ having continuous partial derivatives up to the fourth order with respect to x and up to the second order with respect to t, satisfying the nonlinear initial boundary value problem described by the coupled governing differential equations of motion (eqns. (13)) along the beam, the initial conditions (eqns. (15)-(18)) and the boundary conditions (eqns. (19)-(22)) at the beam ends $x = 0, l$. Eqns. (13) and (15)-(22) are solved using the Analog Equation Method [22] as it is developed for hyperbolic differential equations in [29, 30].

5 NUMERICAL EXAMPLES

On the basis of the analytical and numerical procedures presented in the previous sections, a computer program has been written and representative examples have been studied to demonstrate the validation, the efficiency, wherever possible the accuracy and the range of applications of the developed method. The numerical results have been obtained employing 21 nodal points (longitudinal discretization) and 400 boundary elements (cross section discretization).

Example 1

In the first example, for comparison reasons, the forced vibrations of a steel-I beam (Fig. 3), ($E = 2{,}1 \times 10^8\, kN/m^2$, $G = 8{,}0769 \times 10^7\, kN/m^2$, $\rho = 7{,}85\, tn/m^3$, flange width $t_f = 0{,}03m$, web width $t_w = 0{,}012m$, total height $h = 0{,}56m$, total width $b = 0{,}30m$) having geometric constants presented in Table 1, under three load cases, are examined. In the first load case (case (a), Fig. 3a), a beam with hinged-hinged ends, of length $l = 10\, m$ is considered. The beam is subjected to a uniformly distributed 'static' loading $p_z(t) = p_{z0}(t/t_1)$ for $0 \le t \le t_1$ and $p_z(t) = p_{z0}$ for $t \ge t_1$ ($t_1 = 0{,}02 \sec$, $p_{z0} = 3000\, kN/m$), as this is shown in Fig. 3a. In Fig. 4 the time histories of the displacements $u(x_0,t)$, $w(x_0,t)$ at $x_0 = 6{,}9048\, m$ are presented, respectively, as compared with those obtained from a BEM solution [20], noting the accuracy of the proposed method.

$A = 2,4\times10^{-2}\,m^2$	$I_R = 1,14831\times10^{-4}\,m^6$
$I_Y = 1,39035\times10^{-3}\,m^4$	$I_t = 5,38871\times10^{-6}\,m^4$
$I_Z = 1,35072\times10^{-4}\,m^4$	$C_S = 9,48415\times10^{-6}\,m^6$
$I_S = 1,5254\times10^{-3}\,m^4$	

Table 1: Geometric constants of the beam of example 1.

	Linear Analysis	Nonlinear Analysis					
		Load case (b)			Load case (c)		
		Present study	FEM 960 solid elements [31]	FEM 2080 shell elements [31]	Present study	FEM 960 solid elements [31]	FEM 2080 shell elements [31]
$u(l)_{\max}$	0,0000	-0,0033	-0,0034	-0,0037	-0,0031	-0,0032	-0,0032
$v(l)_{\max}$	0,0000	0,0615	0,0603	0,0675	0,0331	0,0329	0,0328
$w(l)_{\max}$	0,2040	0,2045	0,2108	0,2114	0,2040	0,2108	0,2078

Table 2: Maximum values of the kinematical components $u(l,t)\ (m)$, $v(l,t)\ (m)$ and $w(l,t)\ (m)$ of the cantilever beam of example 1 for load cases (b), (c).

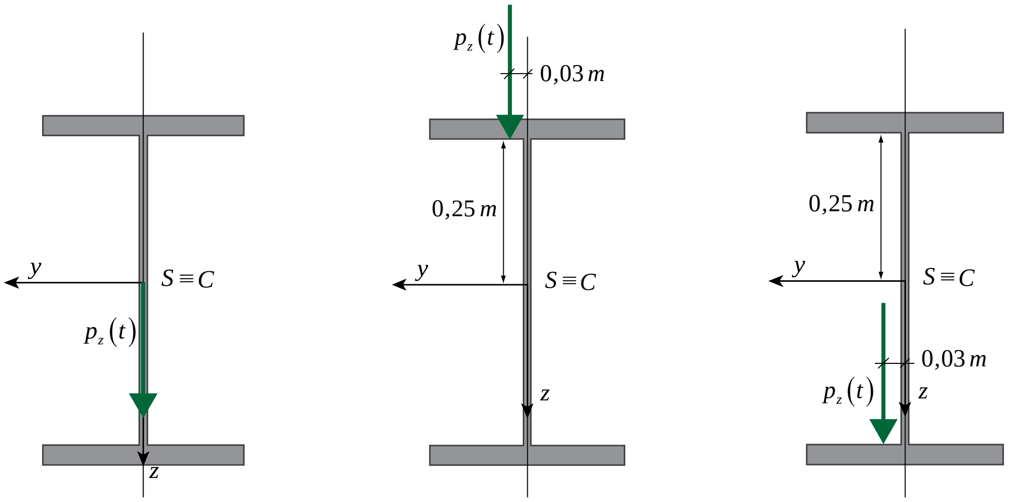

(a) (b) (c)

Figure 3: Transverse load applied on the centroid concerning the first load case (a) and on the flange concerning the second load case (b) and the third load case (c) of example 1.

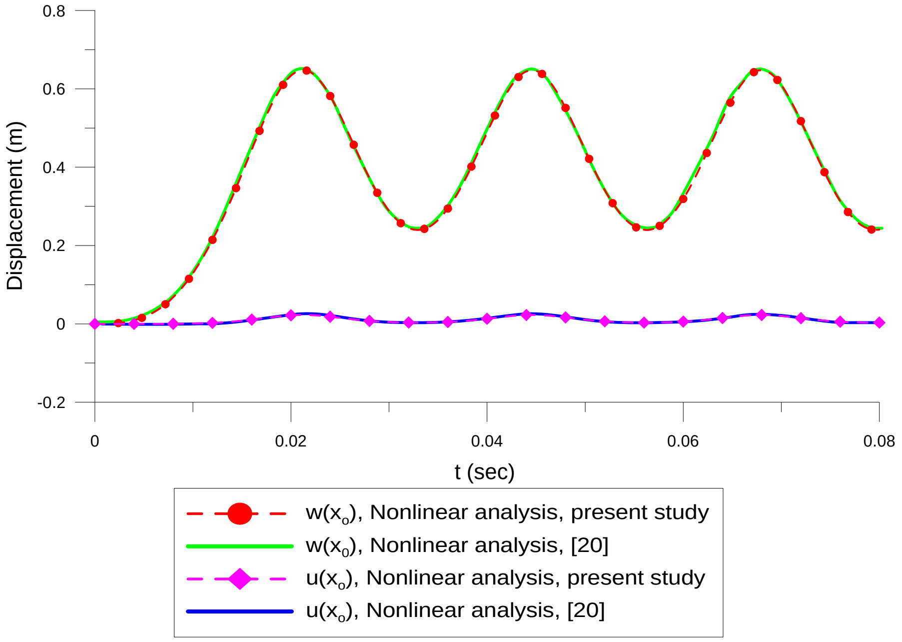

Figure 4: Time history of the displacements u and w at $x_0 = 6,9048\,m$ of the hinged-hinged beam of example 1 for load case (a).

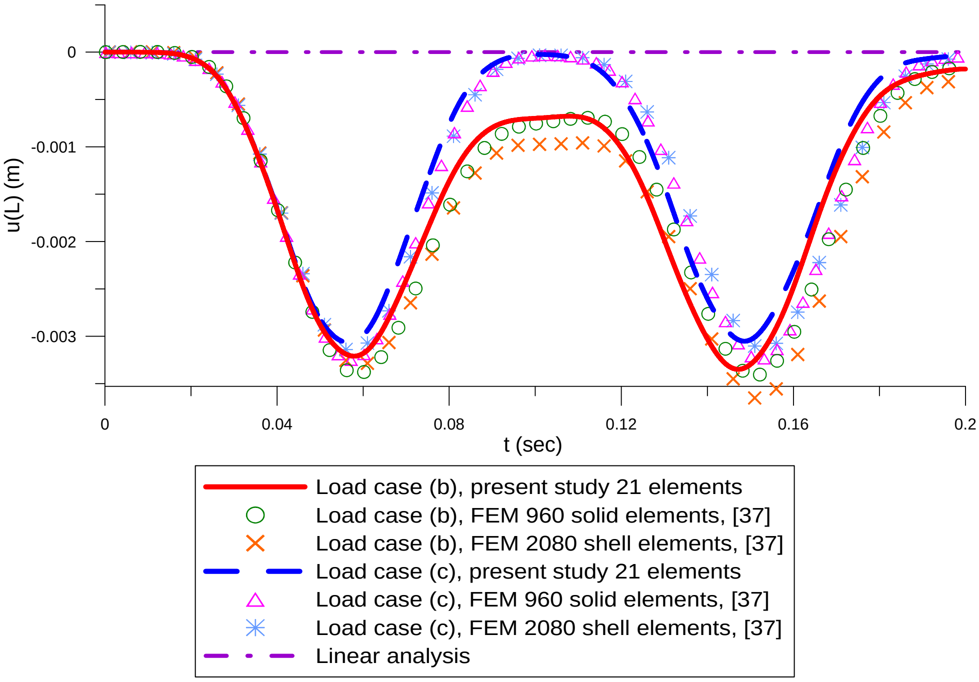

Figure 5: Time history of the displacement u at the tip of the cantilever beam of example 1 for load cases (b), (c).

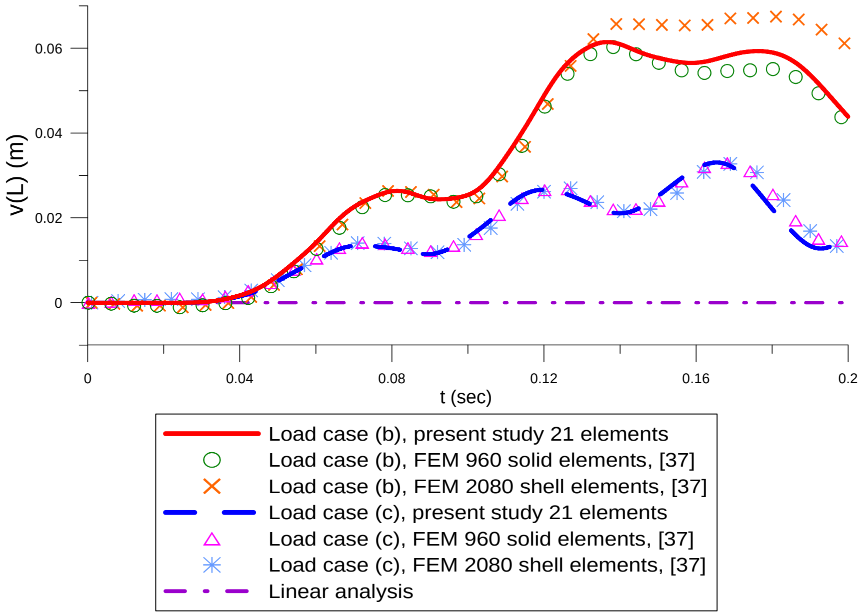

Figure 6: Time history of the displacement v at the tip of the cantilever beam of example 1 for load cases (b), (c).

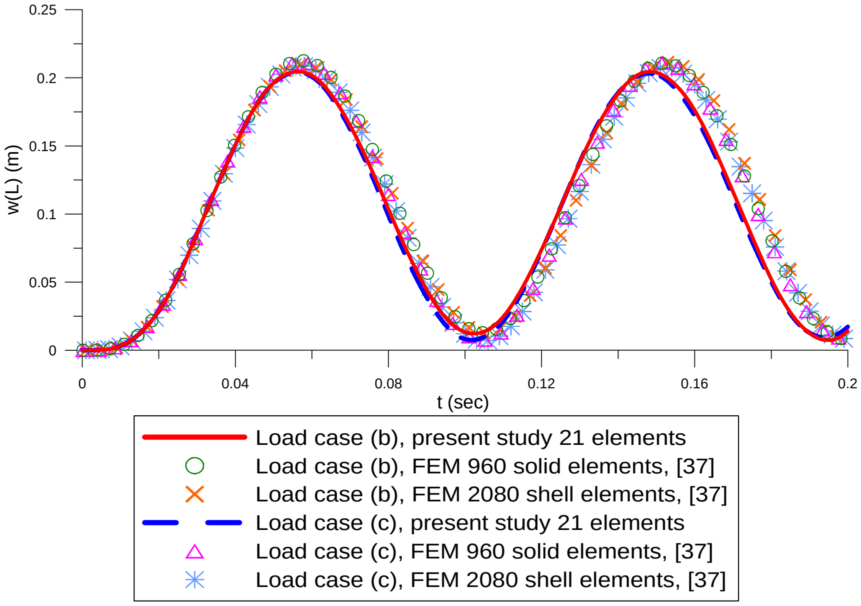

Figure 7: Time history of the displacement w at the tip of the cantilever beam of example 1 for load cases (b), (c).

Moreover, in order to demonstrate the influence of the loading position upon the cross section, a cantilever beam of the same cross section of length $l = 8\,m$, undergoing a uniformly distributed ‘static’ loading ($t_1 = 0{,}02\sec$, $p_{z0} = 60\,kN/m$) is examined for the load cases (b), (c) (Figs. 3b,c). In Figs. 5-7 the time histories of the kinematical components $u(l,t), v(l,t)$ and $w(l,t)$, respectively, at the tip cross section of the cantilever beam are presented as compared with those obtained from a FEM solution [31, 32], employing either shell or solid finite elements. In Fig. 8 the deformed configurations of the beam at the time instant $t = 0{,}1\sec$ for the load case (b) and at $t = 0{,}067\sec$ for the load case (c) are presented as compared with those obtained from a FEM solution [31, 32]. Finally, in Table 2 the maximum values of the kinematical components $u\left(l,t\right), v\left(l,t\right)$ and $w\left(l,t\right)$ of the present study are presented together with those obtained from the aforementioned FEM solutions [31, 32]. From these figures and table the accuracy of the proposed method is demonstrated. Moreover, as it can easily be observed, the loading position may have important influence on the dynamic response of the beam.

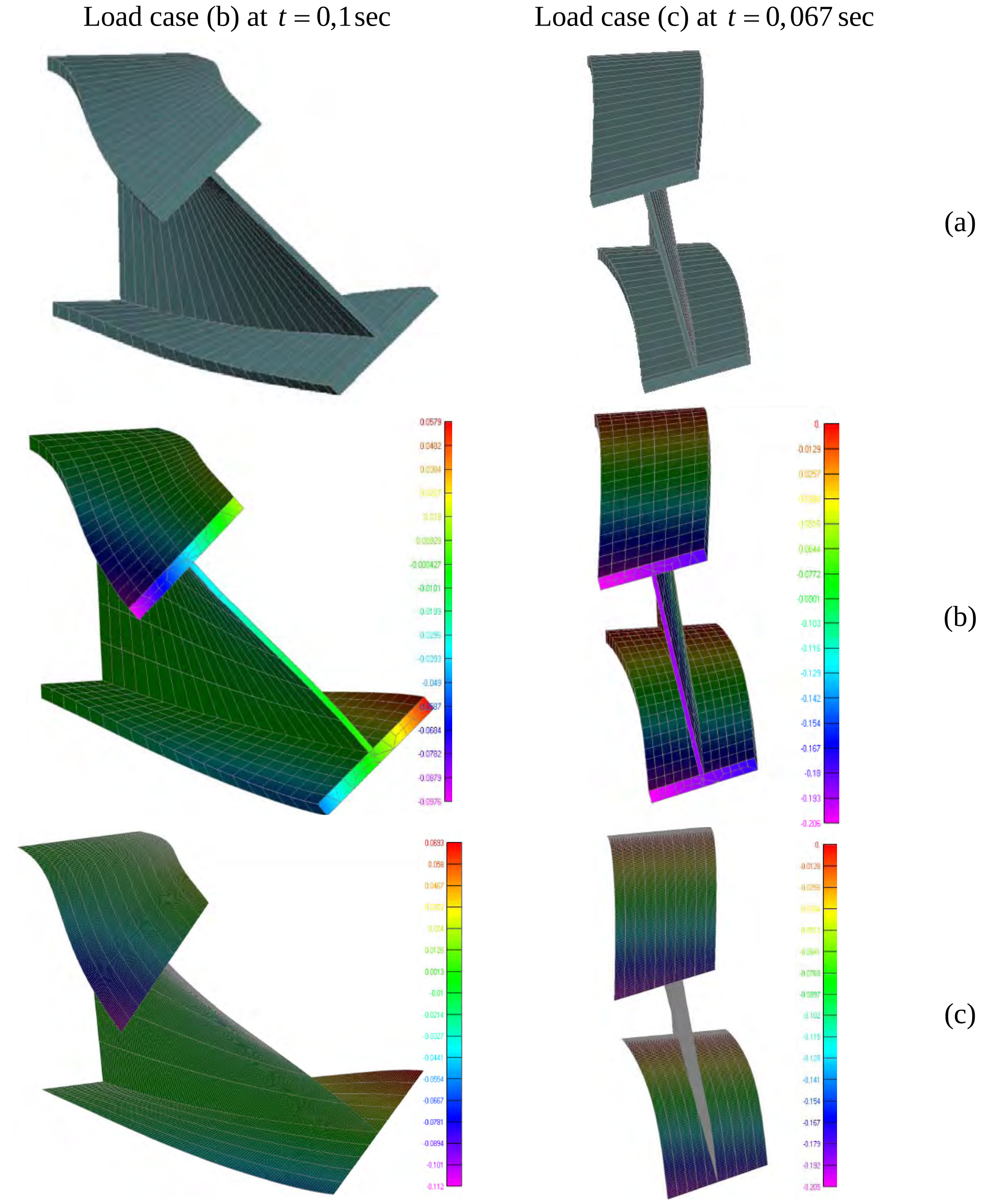

Figure 8: Deformed configurations of the cantilever beam of example 1 from the present study (a) and a FEM solution using solid elements (b) or shell elements (c).

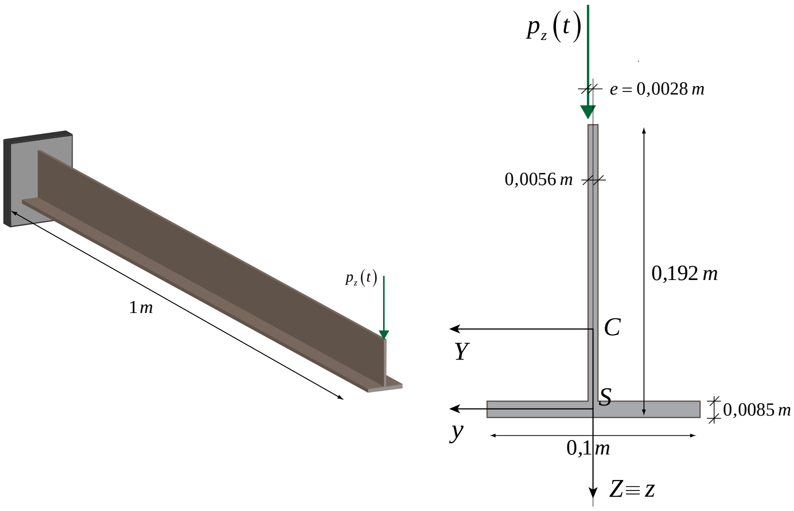

(a) (b)

Figure 9: Cantilever beam of example 2 (a) and load with eccentricity with respect to the shear center of its cross section (b).

$A = 1{,}878 \times 10^{-3}\, m^2$	$I_t = 3{,}049 \times 10^{-8}\, m^4$
$I_Y = 7{,}176 \times 10^{-6}\, m^4$	$C_S = 3{,}495 \times 10^{-11}\, m^6$
$I_Z = 7{,}110 \times 10^{-7}\, m^4$	$\beta_z = -7{,}276 \times 10^{-2}\, m$
$I_S = 1{,}295 \times 10^{-5}\, m^4$	$z_c = -5{,}2 \times 10^{-2}\, m$
$I_R = 2{,}581 \times 10^{-7}\, m^6$	

Table 3: Geometric constants of the beam of example 2.

	Linear Analysis	Nonlinear Analysis	
		Ignoring eccentricity change	Taking into account eccentricity change
$v(l)_{\max}$	0,0009	−0,0017	0,0021
$w(l)_{\max}$	0,0068	0,0068	0,0068
$\theta_x(l)_{\max}$	0,0304	0,0264	0,1090

Table 4: Maximum values of the kinematical components $v(l,t)$ (m), $w(l,t)$ (m) and $\theta_x(l,t)$ (rad) of the cantilever beam of example 2.

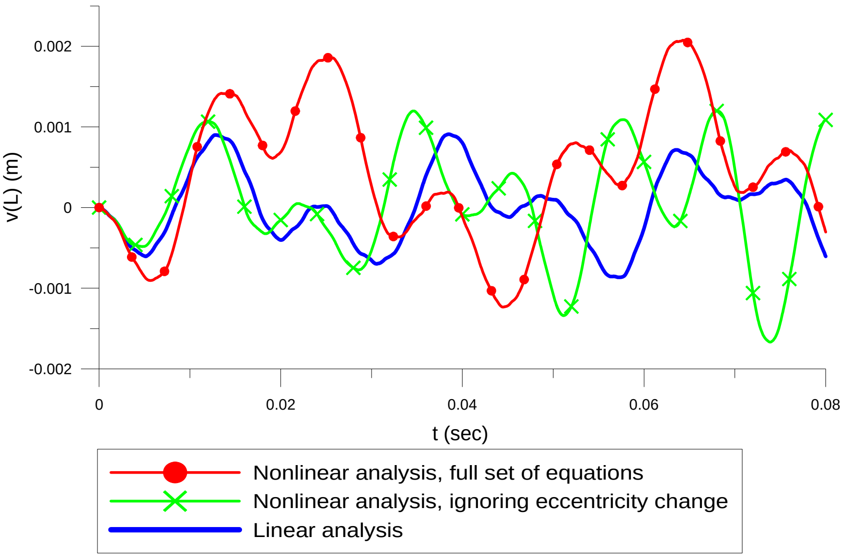

Figure 10: Time history of the displacement v at the tip of the cantilever beam of example 2.

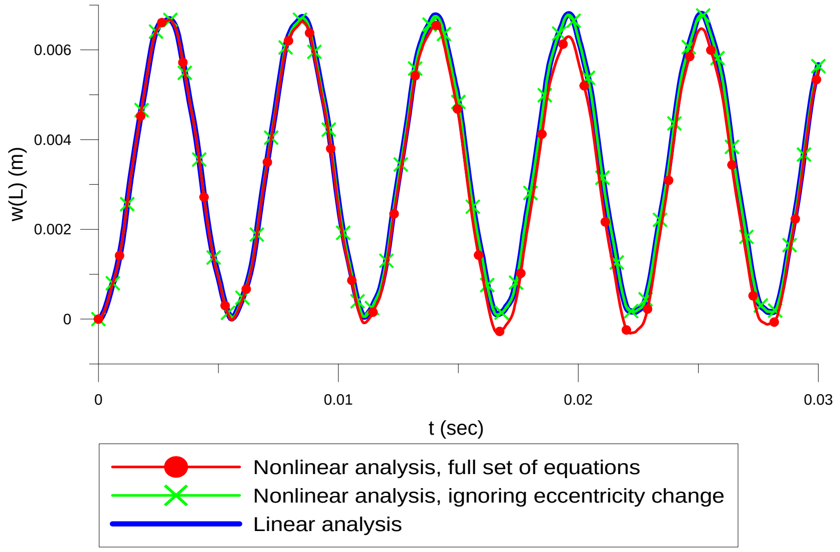

Figure 11: Time history of the displacement w at the tip of the cantilever beam of example 2.

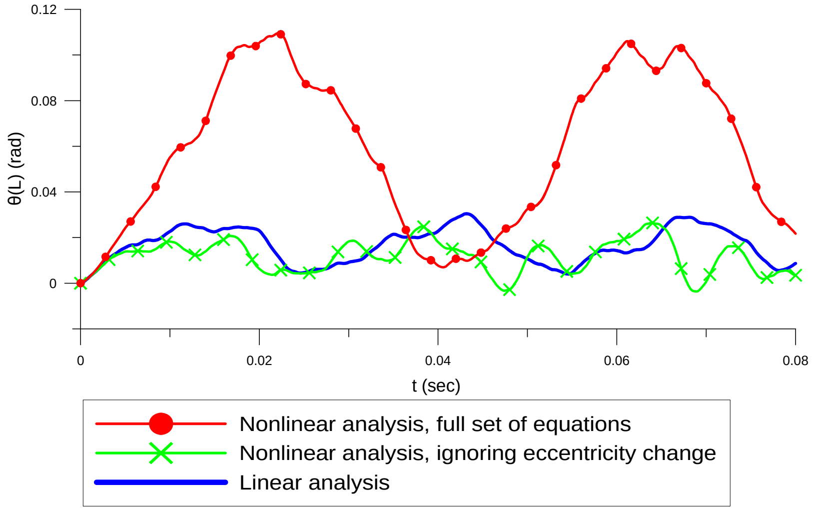

Figure 12: Time history of the angle of twist θ_x at the tip of the cantilever beam of example 2.

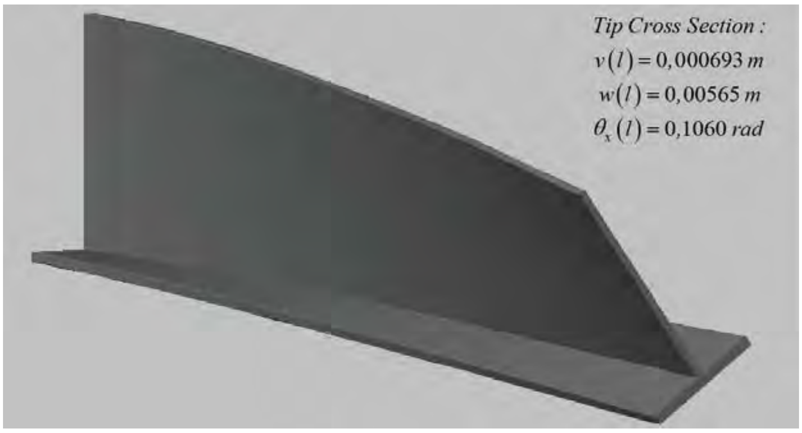

Figure 13. Deformation of the cantilever beam of example 2 at $t=0,02\,\sec$.

Example 2

In order to investigate the influence of eccentricity change of the transverse loading in nonlinear flexural-torsional vibrations, the forced vibration of a cantilever beam ($E=2,1\times10^8\ kN/m^2$, $G=8,0769\times10^7\ kN/m^2$, $\rho=7,85\,tn/m^3$, $l=1\,m$) of a monosymmetric thin-walled open shaped cross section (its geometric constants are presented in Table 3), as this is shown in Fig. 9, has been studied. More specifically, the beam is subjected to a suddenly applied concentrated force $P_z(t)=16\,kN$ having a slight eccentricity $e=0,0028\,m$ with respect to the shear center of the tip cross section (Fig. 9b). In Figs. 10-12 the time histories of the transverse displacements $v(l,t)$, $w(l,t)$ and the angle of twist $\theta_x(l,t)$ of the cantilever beam, respectively, in Table 4 the maximum values of its kinematical components and in Fig. 13 the deformation of the cantilever beam at the time instant $t=0,02\,\sec$, are presented. From these figures and table, the influence of the relatively small ‘imperfection’ of the application point of the transverse loading to the beam response is remarked.

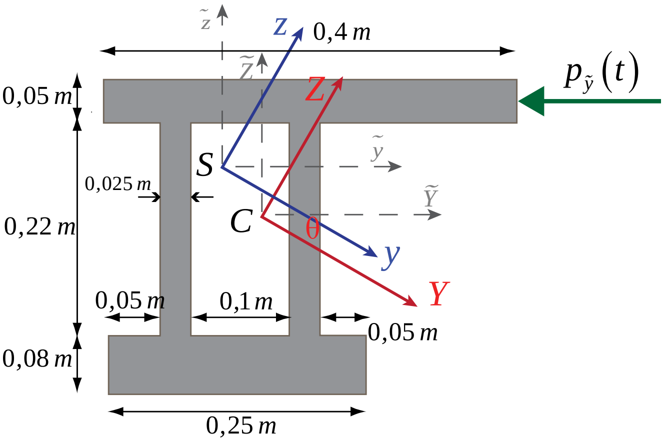

Figure 14: Cross section of the cantilever beam of example 3.

$A = 5{,}1 \times 10^{-2} m^2$	$\theta = -0{,}41330 rad$
$I_Y = 9{,}64614 \times 10^{-4} m^4$	$I_t = 2{,}6965 \times 10^{-4} m^4$
$I_Z = 3{,}90079 \times 10^{-4} m^4$	$C_S = 4{,}6911 \times 10^{-6} m^6$
$I_S = 1{,}58177 \times 10^{-3} m^4$	$\beta_y = 8{,}56633 \times 10^{-2} m$
$I_R = 7{,}14223 \times 10^{-5} m^6$	$\beta_z = -8{,}89913 \times 10^{-3} m$
$y_c = 6{,}20527 \times 10^{-2} m$	$\beta_\omega = 0{,}39404$
$z_c = -2{,}45329 \times 10^{-2} m$	

Table 5: Geometric constants of the beam of example 3.

Example 3

In order to demonstrate the range of applications of the developed method, in this final example the forced vibration of a hinged-hinged (axially immovable ends) beam of length $l = 3{,}5\, m$ ($E = 3{,}0 \times 10^7\, kN/m^2$, $G = 1{,}25 \times 10^7\, kN/m^2$, $\rho = 2{,}5\, tn/m^3$) having an asymmetric closed shaped cross section (its geometric constants are presented in Table 5), subjected to a uniformly distributed suddenly applied loading $p_{\tilde{y}} = 1000\, kN/m$, as this is shown in Fig. 14, is examined. In Figs. 15-17 the time histories of the transverse displacements $\tilde{v}(l/2,t)$, $\tilde{w}(l/2,t)$ and the angle of twist $\theta_x(l/2,t)$, respectively, in Table 6 the maximum values of its kinematical components and in Fig. 18 the deformation of the hinged-hinged beam at the time instant $t = 0{,}017 \sec$, are presented. As it can be observed, in this case, the eccentricity change did not affect significantly the dynamic response of the beam, while geometrical nonlinearity due to axially immovable ends had important influence, especially on the transverse displacements $\tilde{v}$, $\tilde{w}$.

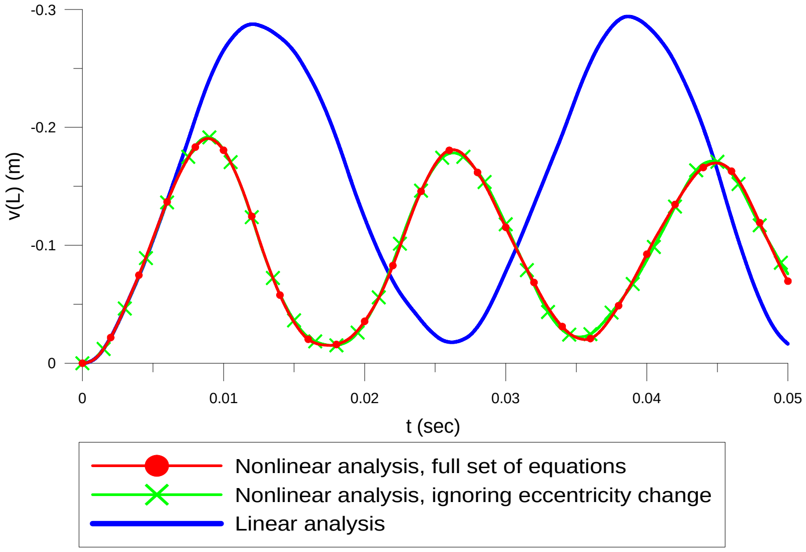

Figure 15: Time history of the displacement $\tilde{v}$ at the midpoint of the hinged-hinged beam of example 3.

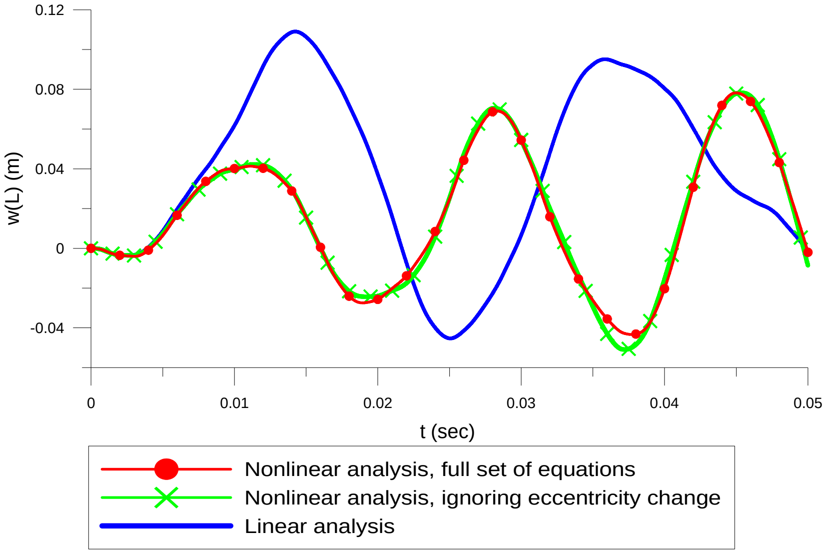

Figure 16: Time history of the displacement $\tilde{w}$ at the midpoint of the hinged-hinged beam of example 3.

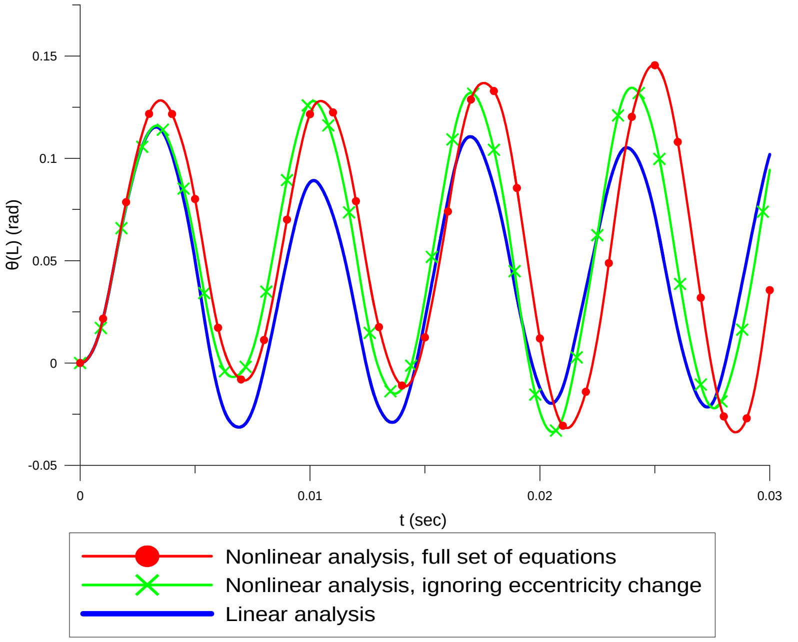

Figure 17: Time history of the angle of rotation θ_x at the midpoint of the hinged-hinged beam of example 3.

	Linear Analysis	Nonlinear Analysis	
		Ignoring eccentricity change	Taking into account eccentricity change
$\tilde{v}(l/2)_{\max}$	$-0{,}2940$	$-0{,}1920$	$-0{,}1910$
$\tilde{w}(l/2)_{\max}$	0,1090	0,0782	0,0782
$\theta_x(l/2)_{\max}$	0,1150	0,1340	0,1460

Table 6: Maximum values of the kinematical components $\tilde{v}(l/2,t)$ (m), $\tilde{w}(l/2,t)$ (m) and $\theta_x(l/2,t)$ (rad) of the fixed-fixed beam of example 3.

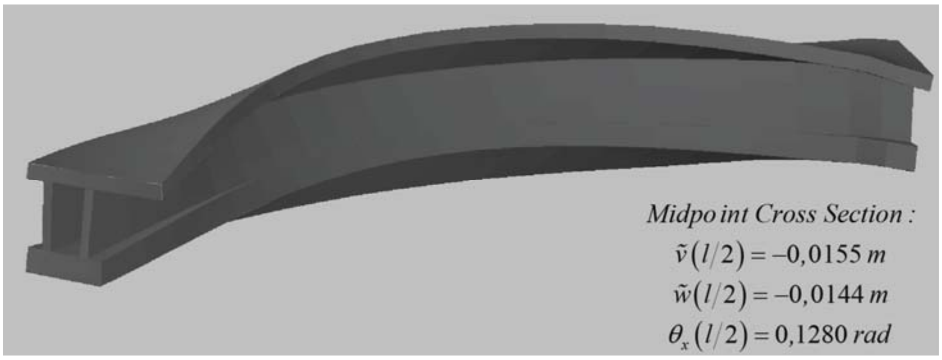

Figure 18: Deformation of the hinged-hinged beam of example 3 at $t = 0,017\,\sec$.

6 CONCLUSIONS

In this paper a boundary element method is developed for the nonlinear elastic flexural-torsional dynamic analysis of beams of arbitrary cross section, undergoing moderately large displacements and angles of twist, taking into account the effects of rotary and warping inertia and the change of eccentricity of transverse loads during torsional rotation. The main conclusions that can be drawn from this investigation are:

- The numerical technique presented in this investigation is well suited for computer aided analysis of beams of arbitrary simply or multiply connected cross section supported by the most general boundary conditions and subjected to the combined action of arbitrarily distributed or concentrated time dependent loading.
- The geometrical nonlinearity leads to strong coupling between the axial, torsional and bending equilibrium equations, resulting a significantly different response of the beam compared with this obtained from a linear analysis.
- The change of eccentricity of the transverse loading during the torsional rotation of the cross section affects significantly the torsional response of the beam
- Different loading positions upon the cross section may alter significantly the torsional response of the beam.
- Accurate results are obtained using a relatively small number of nodal points along the beam.
- The developed procedure retains most of the advantages of a BEM solution over a FEM approach, although it requires longitudinal domain discretization.

REFERENCES

[1] B. Rozmarynowski, C. Szymczak, Non-linear free torsional vibrations of thin-walled beams with bisymmetric cross-section. *Journal of Sound and Vibration*, **97**, 145-152, 1984.

[2] M.R.M. Crespo Da Silva, Non-linear flexural-flexural-torsional-extensional dynamics of beams--I. Formulation. *International Journal of Solids and Structures*, **24**, 1225-1234, 1988.

[3] M.R.M. Crespo Da Silva, Non-linear flexural-flexural-torsional-extensional dynamics of beams--II. Response analysis, *International Journal of Solids and Structures*, **24**, 1235-1242, 1988.

[4] P.F. Pai, A.H. Nayfeh, Three-dimensional nonlinear vibrations of composite beams--I. Equations of motion. *Nonlinear Dynamics*, **1**, 477-502, 1990.

[5] P.F. Pai, A.H. Nayfeh, Three-dimensional nonlinear vibrations of composite beams--II. flapwise excitations. *Nonlinear Dynamics*, **2**, 1-34, 1991.

[6] P.F. Pai, A.H. Nayfeh, Three-dimensional nonlinear vibrations of composite beams--III. Chordwise excitations. *Nonlinear Dynamics*, **2**, 137-156, 1991.

[7] J.C. Simo, L. Vu-Quoc, A Geometrically-exact rod model incorporating shear and torsion-warping deformation. *International Journal of Solids and Structures*, **27**, 371-393, 1991.

[8] M.I. Qaisi, Application of the Harmonic Balance Principle to the Nonlinear Free Vibration of Beams. *Applied Acoustics*, **40**, 141-151, 1993.

[9] P.F. Pai, A.H. Nayfeh, A fully nonlinear theory of curved and twisted composite rotor blades accounting for warpings and three-dimensional stress effects. *International Journal of Solids and Structures*, **31**, 1309-1340, 1994.

[10] A. Di Egidio, A. Luongo, F. Vestroni, A non-linear model for the dynamics of open cross-section thin-walled beams--Part I: formulation. *International Journal of Non-Linear Mechanics*, **38**, 1067-1081, 2003.

[11] A. Di Egidio, A. Luongo, F. Vestroni, A non-linear model for the dynamics of open cross-section thin-walled beams--Part II: forced motion. *International Journal of Non-Linear Mechanics*, **38**, 1083-1094, 2003.

[12] F. Mohri, L. Azrar, M. Potier-Ferry, Vibration analysis of buckled thin-walled beams with open sections. *Journal of Sound and Vibration*, **275**, 434-446, 2004.

[13] S.P. Machado, V.H. Cortinez, Free vibration of thin-walled composite beams with static initial stresses and deformations. *Engineering Structures*, **29**, 372-382, 2007.

[14] K.V. Avramov, C. Pierre, N. Shyriaieva, Flexural-flexural-torsional Nonlinear Vibrations of Pre-twisted Rotating Beams with Asymmetric cross-sections. *Journal of Vibration and Control*, **13**, 329-364, 2007.

[15] K.V. Avramov, O.S. Galas, O.K. Morachkovskii, Analysis of Flexural-Flexural-Torsional Nonlinear Vibrations of twisted rotating beams with cross-sectional deplanation. *Strength of Materials*, **41**, No. 2, 200-208, 2009.

[16] R. Lopes Alonso, P. Ribeiro, Flexural and torsional non-linear free vibrations of beams using a p-version finite element. *Computers and Structures*, **86**, 1189-1197, 2008.

[17] H. Duan, Nonlinear free vibration analysis of asymmetric thin-walled circularly curved beams with open cross section. *Thin-Walled Structures*, **46**, 1107-1112, 2008.

[18] E.J. Sapountzakis, J.A. Dourakopoulos, Nonlinear dynamic analysis of Timoshenko beams by BEM. Part I: Theory and numerical implementation. *Nonlinear Dynamics*, **58**, 295-306, 2009.

[19] E.J. Sapountzakis, J.A. Dourakopoulos, Nonlinear dynamic analysis of Timoshenko beams by BEM. Part II: Applications and validation. *Nonlinear Dynamics*, **58**, 307-318, 2009.

[20] J.T. Katsikadelis, G.C. Tsiatas, Non-linear dynamic analysis of beams with variable stiffness. *Journal of Sound and Vibration* **270**, 847-863, 2004.

[21] E.J. Sapountzakis, V.J. Tsipiras, Nonlinear nonuniform torsional vibrations of bars by the boundary element method. *Journal of Sound and Vibration*, **329**, 1853-1874, 2010.

[22] J.T. Katsikadelis, The analog equation method. A boundary-only integral equation method for nonlinear static and dynamic problems in general bodies. *Theoretical and Applied Mechanics*, **27**, 13-38, 2002.

[23] K.E. Brenan, S.L. Campbell L.R. Petzold, *Numerical Solution of Initial-value Problems in Differential-Algebraic Equations*. North-Holland, Amsterdam, 1989.

[24] M.M. Attard, Nonlinear theory of non-uniform torsion of thin-walled open beams. *Thin-Walled Structures*, **4**, 101-134, 1986.

[25] E.J. Sapountzakis, V.G. Mokos, Warping shear stresses in nonuniform torsion by BEM. *Computational Mechanics*, **30**, 131-142, 2003.

[26] E. Ramm, T.J. Hofmann, *Stabtragwerke, Der Ingenieurbau, Ed.G. Mehlhorn, Band Baustatik/Baudynamik*. Ernst & Sohn, Berlin, 1995.

[27] H. Rothert, V. Gensichen, *Nichtlineare Stabstatik, Springer–Verlag*. Berlin, 1987.

[28] E.J. Sapountzakis, J.A. Dourakopoulos, Flexural-torsional postbuckling analysis of beams of arbitrary cross section. *Acta Mechanica*, **209**, 67-84, 2010.

[29] E.J. Sapountzakis, V.G. Mokos, Analysis of Plates Stiffened by Parallel Beams. *International Journal for Numerical Methods in Engineering*. 70, 1209-1240, 2000.

[30] E.J. Sapountzakis, G.C. Tsiatas, Flexural – torsional buckling and vibration analysis of composite beams, *Computers, Materials and Continua*, **6**, No.2, 103-115, 2007.

[31] FEMAP for Windows. Finite element modeling and post-processing software. Help System Index, Version 10, 2008.

[32] Siemens PLM Software Inc., NX Nastran User’s Guide, 2008.

COMPDYN 2011
III ECCOMAS Thematic Conference on
Computational Methods in Structural Dynamics and Earthquake Engineering
M. Papadrakakis, M. Fragiadakis, V. Plevris (eds.)
Corfu, Greece, 25–28 May 2011

MODAL ANALYSIS OF THE FGM BEAMS WITH SPATIAL VARIATION OF MATERIAL PROPERTIES UNDER LONGITUDINAL VARIABLE ELASTIC WINKLER FOUNDATION

J. Murin[1], M. Aminbaghai[2], and V. Kutis[1]
[1] Department of Mechanics, Faculty of Electrical Engineering and Information Technology
of STU in Bratislava
Ilkovičová 3, 812 19 Bratislava, Slovakia
justin.murin@stuba.sk, vladimir.kutis@stuba.sk

[2] Vienna University of Technology, Institute for Mechanics of Materials and Structures
Karlsplatz 13, A-1040 Vienna, Austria
mehdi.aminbaghai@tuwien.ac.at

Keywords: Modal Analysis, Multilayer FGM Beams, 1st and 2nd Order Beam Theory, Shear Correction Function, Large Axial Force, Spatial Variation of Material Properties.

Abstract. *A differential equation of the homogenized functionally graded material (FGM) beam deflection will be presented which will be used for free vibration analysis of the beams with continuous longitudinal and transversal variation of material properties. The FGM beams with continuous spatial variation of material properties of double symmetric cross-section have been transformed into the multilayer FGM beams. Symmetrical layering according the neutral plane in transversal direction is assumed: the corresponding layers have the same height and material properties. The material properties vary continuously in longitudinal direction, but they are constant along the height and width of competent layers. The FGM beams are considered to be resting on longitudinal variable (Winkler) elastic foundation. The first and second order beam theories have been used for establishing the kinematics and kinetic equations. Not only the shear force deformation effect and the effect of consistent mass distribution and mass moment of inertia have been taken into account, but also the effect of large axial forces have been considered. Numerical experiments were performed to calculate the eigenfrequencies and corresponding eigenmodes of chosen FGM beams. The solution results are discussed and compared with those obtained using a very fine mesh of two-dimensional solid finite elements. The effects of material properties variation, layering fineness, the shear force correction factor and large axial forces have been evaluated and discussed.*

1 INTRODUCTION

Nowadays, the interaction between FGM beams and elastic foundations is an important issue in the study of beam behavior. Ying et al. [1] presented exact two-dimensional elasticity solution for the bending and free vibration of FGM beams on a Winkler – Pasternak foundation. The beam is assumed orthotropic at any point, and the material properties are taken as exponential functions of the thickness coordinate. The elastic foundation modules have been assumed as a constant. Pradhan et al. [2] presented thermo-mechanical vibration analysis of FGM beams resting on a variable Winkler foundation and two-parameter elastic foundation. The FGM material properties of these beams are assumed to be varying in thickness direction. In [3], the free vibration analysis of FGM beams has been presented. Spatial variation of material properties of these beams has been assumed. The shear force deformation effect and the effect of consistent mass distribution and mass moment of inertia have been taken into account. In [4], the paper [3] was extended by the effect of large axial forces. The solution results confirmed a very strong effect of large axial forces: the tensional axial force increased and the compression axial force decreased the level of eigefrequencies significantly. Many other authors investigate with free vibration of FGM beams with constant or transversal variation of material properties, e.g. [5], [6], [7]. In [8], the nonlinear dynamic analysis of partially supported beam-columns on non-linear elastic foundation including shear deformation effect has been discussed.

In [9], a differential equation of the homogenized functionally graded material (FGM) beam deflection has been proposed to be in a further free vibration analysis of multilayer and sandwich FGM beams of rectangular cross-section. The FGM beam was considered to be resting on longitudinal variable (Winkler) elastic foundation. In the contribution [10], an extension of paper [9] was presented, where not only the shear force deformation effect, the effect of consistent mass distribution as well as mass moment of inertia have been taken into account, but also the effect of large axial forces was considered.

In this contribution, which is a continuation of the paper [10], the differential equations of the 1st and 2nd order beam theory of the homogenized functionally graded material (FGM) beam deflection will be presented which will be used in the modal analysis of FGM beams with continuous longitudinal and transversal variation of material properties. The FGM beam with spatial variation of material properties will be transformed to multilayer beam. Symmetric layering along the neutral plane in transversal direction is assumed. The material properties vary continuously in longitudinal direction, but they are constant along the height and width of each layer. The multilayer beam will be then transformed to one layer homogenized beam with longitudinal variation of effective material properties. The FGM beams are considered to be resting on longitudinal variable (Winkler) elastic foundation. Numerical experiments were performed to calculate the eigenfrequencies and corresponding eigenmodes of chosen FGM beams with continuous spatial variation of material properties. The shear correction function has been derived from which the average shear correction factor has been calculated. The effects of the average shear correction factor, the large axial force, the variation of material properties and the layering fineness have been studied and compared with those obtained using a very fine mesh of a plane solid finite elements.

2 MATERIAL PROPERTIES HOMOGENIZATION AND DIFFERENTIAL EQUATION DERIVATION

Let as consider a two nodal straight beam element with predominantly rectangular cross-sectional area A and quadratic moment of inertia I (Fig. 1).

The composite material of this beam/link arises from mixing two components (matrix and fibres) that are approximately of the same geometrical form and dimensions (e.g. by powder metallurgy or plasma spraying).

Both, the fibre volume fraction $v_f(x,y)$ and the matrix volume fraction $v_m(x,y)$ are chosen as polynomial functions of x with continuous and symmetrical variation through its height h in respect to the neutral plane of the beam. The volume fractions are assumed constant through the cross-sectional depth b. At each point of the beam it holds: $v_f(x,y)+v_m(x,y)=1$. The values of the volume fractions at the nodal points are denoted by indices i and j.

The material properties of the constituents (fibres - $p_f(x,y)$ and matrix - $p_m(x,y)$) can vary analogically (in dependence on inhomogeneous temperature field for example) as defined by the variation of volume fractions. Homogenization of the material properties (the reference volume is the volume of the whole beam) will be done in two steps. In the first step, the real beam (Figure 1a) will be transformed to a multilayered beam (Figure 1b). Material properties of the layers will be calculated via the extended mixture rules [11]. Each layer will have constant volume fractions and material properties of the constituents through the beam height. They are calculated as an average value from boundary values of the respective layer. Polynomial variation of these parameters will appear in the longitudinal direction. Sufficient accuracy of the substitution of the continuous lateral variation of material properties with the layer-wise constant lateral distribution of material properties will be reached when the division to layers is fine enough. In the second step, the effective longitudinal material properties of the homogenized beam will be derived using laminate theory. These homogenized material properties are constant through the beam height but they vary continuously along the longitudinal beam axis. Finally, a differential equation for calculation of the effective beam variables for homogenized beam (Figure 1c) will be established.

One thin layer of the composite or FGM is depicted in Figure 2 with a constant rectangular cross-section considered. The layer length is L. Longitudinal variation of the constituent volume fractions and longitudinal variation of the constituent elasticity modules will be assumed. These parameters will be considered constant along the layer height and width. The fibers (constituent 1) volume fraction $v_f(x)$ is chosen as a polynomial function of x :

$$v_f(x)=1-v_m(x)=v_{fi}\eta_{vf}(x)=v_{fi}\left(1+\sum_k \eta_{vfk}x^k\right) \tag{1}$$

Then the matrix (constituent 2) volume fraction $v_m(x)$ is

$$v_m(x)=1-v_f(x)=v_{mi}\eta_{vm}(x)=v_{mi}\left(1+\sum_k \eta_{vmk}x^k\right) \tag{2}$$

where v_{fi} and v_{mi} are the fibre and the matrix volume fractions at node i and $\eta_{vf}(x)$ and $\eta_{vm}(x)$ are the polynomials of fibre and matrix volume fractions variation, respectively. Constants η_{vfk} and η_{vmk} , (k = 1,…,r), and the order r of these polynomials depends on the fibre and matrix volume fractions variation.

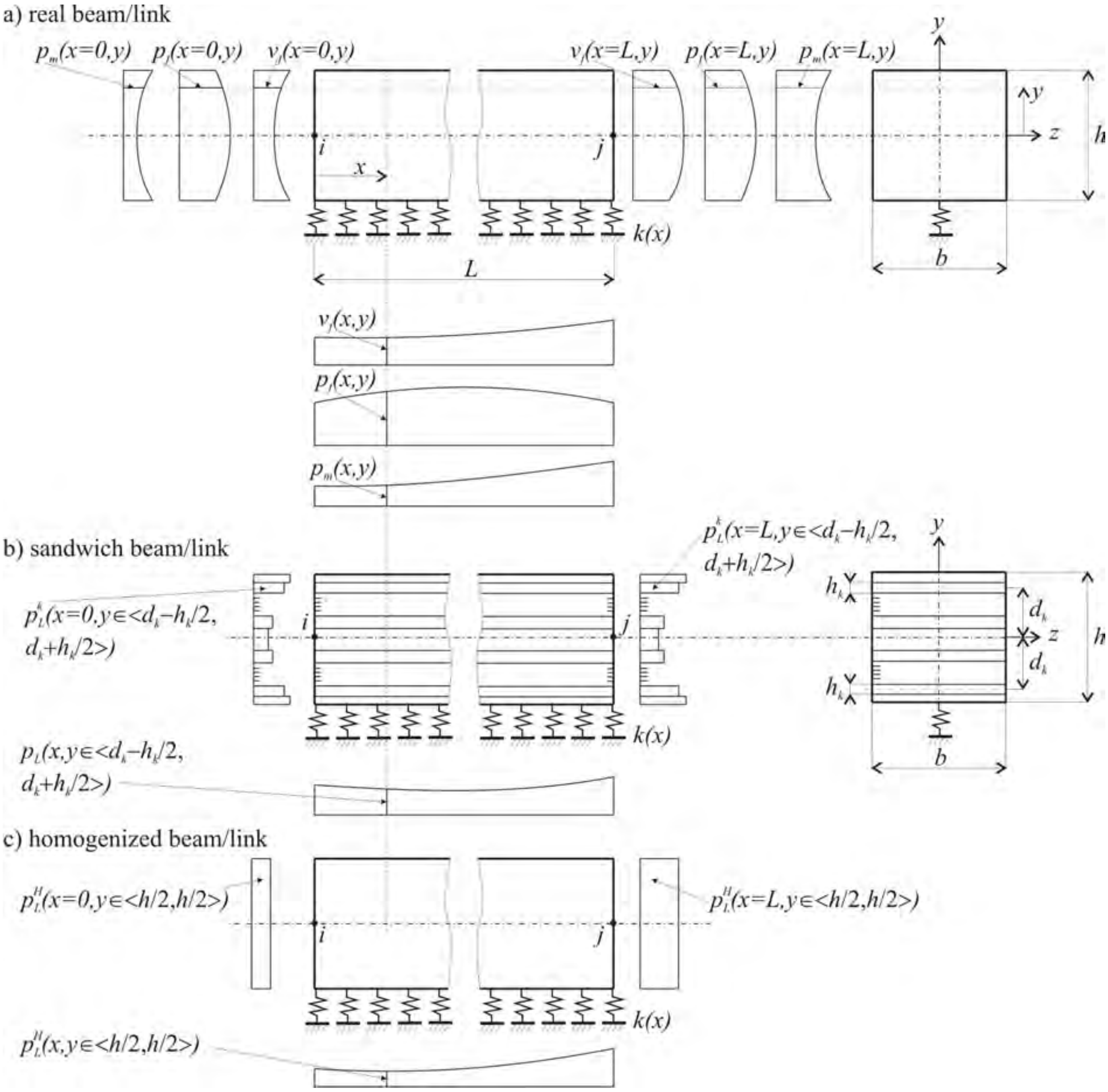

Figure 1: FGM beam with spatial variation of the material properties.

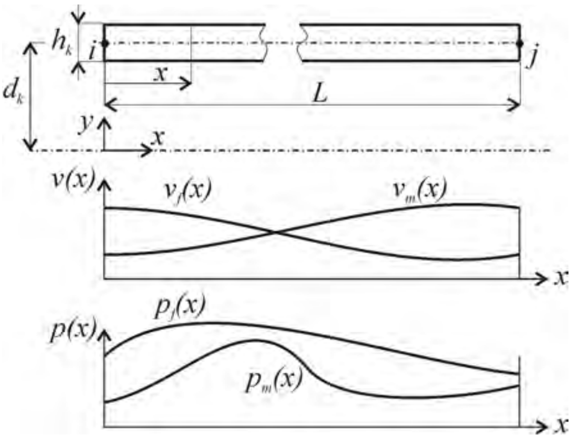

Figure 2: One thin layer of FGM.

Also the fibre material property $p_f(x)$ and the matrix material property $p_m(x)$ are chosen as polynomial functions of x :

$$p_f(x) = p_{fi}\eta_{pf}(x) = p_{fi}\left(1 + \sum_k \eta_{pfk} x^k\right) \tag{3}$$

$$p_m(x) = p_{mi}\eta_{pm}(x) = p_{mi}\left(1 + \sum_k \eta_{pmk} x^k\right) \tag{4}$$

where p_{fi} and p_{mi} are the fibre and matrix material properties at node *i* and $\eta_{pf}(x)$ is the polynomial of fibre material property variation. Its constants η_{pfk}, where *k* = 1,…, *r*, and the order *r* of this polynomial depend on the fibre material property variation. $\eta_{pm}(x)$ is the polynomial of matrix material property variation. The constants η_{pmk}, where *k* = 1,…, *s*, and the order *s* of this polynomial depend on the matrix material property variation.

Then the effective material property of the composite one-layer beam is given by

$$p_L(x) = v_f(x)\,p_f(x) + v_m(x)\,p_m(x) \tag{5}$$

Similarly to (4), we can write

$$p_L(x) = p_{Li}\eta_{p_L}(x) \tag{6}$$

Here, p_{Li} is the effective longitudinal material property at node *i*, and

$$\eta_{pL}(x) = \frac{p_L(x)}{p_{Li}} \tag{7}$$

is the polynomial of effective longitudinal material property variation.

The indices are: $p \equiv E$ and ρ - for elasticity modulus and mass density, respectively.

Expressions (5 - 7) can be used in the effective material properties calculation for single- layer FGM beams.

Let us replace the initial beam (Fig. 1a) by a multilayered beam (Fig. 1b). Lamination is symmetric according to the geometry of the layers and material properties as well. This symmetry allows the application of the elementary theory of the homogeneous isotropic beam for all solutions when the material properties are replaced by their effective values [12]. From the mechanical coupling point of view, axial loading is not coupled with transversal loading.

Individual layers are built of composite layers with longitudinal variation of volume fractions and material properties of the constituents as described above.

Homogenization of material properties of the multilayered beam will be done using the theory of laminates [12], [13], [14]. In this way we get one layer beam with longitudinal variation of homogenized longitudinal material properties. Main dimensions of the beam such as the length *L*, height *h* and width *b* remain conserved.

a) Homogenized elastic properties

If we denote the effective longitudinal elasticity modulus of a chosen layer with superscript *k*, then, according to (6), it holds

$$E_L^k(x) = E_{Li}^k \eta_{E_L^k}(x) \tag{9}$$

Index $k \in \langle 1, n \rangle$ represents the layer number in the upper and lower symmetrical part of the beam/link. The number of layers of the symmetrical part is *n*. If the cross-sectional area of the k^{th} layer is A^k, then the volume fraction of the pair of these symmetrical areas is $v^k = 2A^k/A$.

Then, the effective longitudinal elasticity modulus for axial loading of the homogenized sandwich can be derived using the expression

$$E_L^{NH}(x) = E_{Li}^{NH}\eta_{E_L^{NH}}(x) = \sum_{k=1}^{n} v^k E_L^k(x) \tag{10}$$

where $E_{Li}^{NH} = \sum_{k=1}^{n} E_{Li}^k v^k$ is the effective longitudinal elasticity modulus for axial loading of the homogenized beam at node *i*, and $\eta_{E_L^{NH}}(x) = E_L^{NH}(x)/E_{Li}^{NH}$ is the polynomial of its variation. This effective longitudinal elasticity modulus has to be used for calculation of an axial free vibration of the FGM beam.

According to the notation in Figure 1, the effective longitudinal elasticity modulus for flexural loading of the homogenized beam of rectangular cross-section has been derived [15]:

$$E_L^{MH}(x) = \frac{12}{h^3}\sum_{k=1}^{n}\left(\frac{h_k^3}{6} + 2d_k^2 h_k\right)E_L^k(x) = E_{Li}^{MH}\eta_{E_L^M}(x) \tag{11}$$

where E_{Li}^{MH} is the value of the effective longitudinal elasticity modulus for flexural loading of the homogenized beam/link at node *i*, and $\eta_{E_L^{MH}} = E_L^{MH}(x)/E_{Li}^{MH}$ is the polynomial of its longitudinal variation. This effective longitudinal elasticity modulus has to be used in the calculation of a flexural free vibration of the FGM beam.

In a similar way, the effective longitudinal elasticity modules can be derived for beams with different other types of cross-sections.

b) Homogenized mass density

If we denote ρ with superscript *k* the effective longitudinal mass density of a chosen layer *k*, then, according to (5), (6) and (7), it holds

$$\rho_L^k(x) = \rho_{Li}^k \eta_{\rho_L^k}(x) \tag{12}$$

Index *k*, the cross-sectional area of the the k^{th} layer A^k, and the volume fraction $v^k = 2A^k/A$ have the same meanings as in the elastic properties derivation.

Accordingly, the homogenized effective longitudinal mass density is

$$\rho_L^H(x) = \rho_{Li}^H \eta_{\rho_L^H}(x) = \sum_{k=1}^{n} v^k \rho_L^k(x) \tag{13}$$

where $\rho_{Li}^H = \sum_{k=1}^{n} \rho_{Li}^k v^k$ is the effective longitudinal mass density at node *i* of the homogenized beam, and $\eta_{\rho_L^H}(x) = \rho_L^H(x)/\rho_{Li}^H$ is the polynomial of its longitudinal variation.

All the homogenized effective longitudinal properties are denoted by upper right index *H* in this chapter. As assumed, their variation along the homogenized beam is polynomial.

Sufficient accuracy of substituting the continuous lateral variation of material properties by a layer-wise constant lateral distribution of material properties will be reached when the layer-division is fine enough. The constant value of the material property in the assumed layer at position *x* will be calculated as a mean value from its values at the top and the bottom of this layer. The same approach will be used in the calculation of the components volume fractions in the competent layer.

Variations of the homogenized beam properties and the loading are shown in Fig. 3.

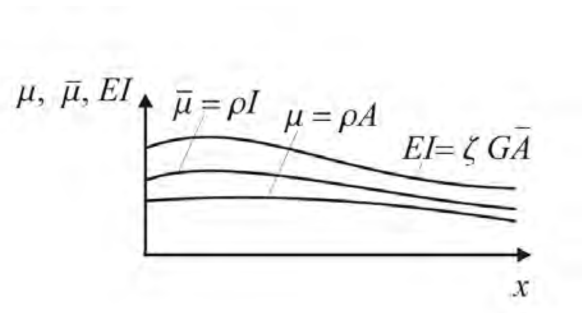

Figure 3: Variation of the beam parameters.

$\mu = \rho A$ is the mass distribution, $\bar{\mu} = \rho I$ is the mass moment of inertia distribution, $\rho = \sum_{j=0}^{p_\rho} \rho_j a_j = \rho_L^H(x)$ is the homogenized varying mass density (also defined by (13), indices *L, H* are omitted for simplicity), *A* is the cross-sectional area, *I* is the moment of inertia, $EI = \sum_{j=0}^{p_e} EI_j a_j = B$ is the varying bending stiffness caused by varying elasticity modulus $E \equiv E_L^{MH}(x)$, $G\bar{A} = \sum_{j=0}^{p_G} G\bar{A}_j\, a_j$ is the varying shear stiffness with $G = G_L^H(x)$, and $\varsigma = \frac{EI}{G\bar{A}} = const.$, $k(x)$ is the longitudinally varying Winkler elastic foundation modulus, and finally, $a_j = \frac{x^j}{j!}$ is the polynomial function. The same longitudinal polynomial variation of the homogenized shear modulus *G* has been assumed as stated by the homogenized elasticity modulus *E*. The assumption $\varsigma = \frac{EI}{G\bar{A}} = const.$ is a simplification which holds exactly only for single-layer FGM beams with only longitudinal variation of material properties. In addition, the condition $\frac{E}{G} = const.$ must be fulfilled. For the initial beam (Fig. 1a) both the shear correction factor $k^s = \frac{\bar{A}}{A} = k^s(x)$ and consecutive the factor $\varsigma = \varsigma(x)$ are functions of *x*. In our consideration, the parameters k^s and ς will be assumed as average values of their functional variation. The assumption $\varsigma = \varsigma(x)$ would make the differential equation of the beam deflection very complicated. In the following derivation of the differential equation, indices *L, M, H* have been also omitted for simplicity.

In Fig. 4 the distributed loads and the nodal internal forces are shown at the beam increment *dx* in the deformed configuration of the beam increment. In Fig. 5 the internal forces and nodal displacements at position *x* are shown.

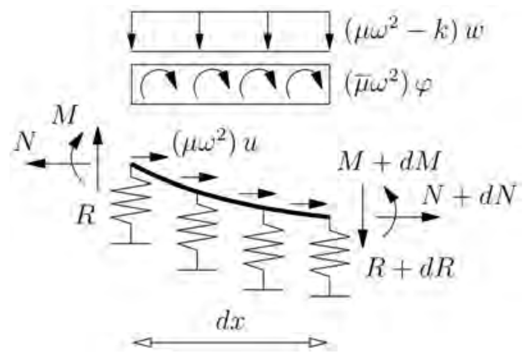

Figure 4: Distributed loads and internal forces in *R* – formulation.

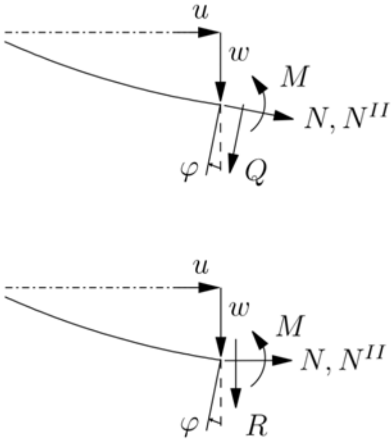

Figure 5: Internal forces and displacements at point *x* in *Q*- and *R* – formulation, respectively.

Here, *M* is the bending moment, *N* is the axial force, *Q* is the shear force, *R* is the transversal force, φ is the angle of cross-section rotation, *w* is the deflection perpendicular to the un-deformed longitudinal beam axis and *u* is the longitudinal displacement, ω is the circular frequency. The inertia forces in *x* – direction has not been assumed in the following considerations. N^{II} is the 2nd order beam theory constant axial force, which is of a system character and it is a known variable.

The differential equilibrium equations of a harmonic free vibration of 2nd order beam theory according to the un-deformed longitudinal beam axis (the *R* - formulation) are (the superscript “′“ denotes the differentiations *d/dx*):

$$R' = \left(k - \omega^2 \mu\right) w \tag{14}$$

$$M' = Q + \bar{\mu}\omega^2 \varphi \tag{15}$$

The dependence between the shear and transversal force can be expressed as [16]: $Q = R - N^{II} w'$.

The kinematical differential equations are:

$$\varphi' = -\frac{M}{B} \tag{16}$$

$$w' = \varphi + \frac{Q}{G\overline{A}} = \varphi + \varsigma \frac{Q}{B} \tag{17}$$

After some mathematical operations the homogeneous differential equation of the 4th order of the homogenized functionally graded material (FGM) beam deflection has been obtained. Its form is:

$$\eta_4 w'''' + \eta_3 w''' + \eta_2 w'' + \eta_1 w' + \eta_0 w = 0 \tag{18}$$

After the boundary conditions application, the equation (18) can be used for the modal analysis of the multilayer FGM beams resting on the elastic Winkler foundation, with above mentioned effects.
The non constant parameters of the differential equation of the 4th order (18) are:

$$\begin{gathered}
\eta_0 = \left(\omega^2 \mu - k\right)\left(\varsigma B\left(B'' - \omega^2 \overline{\mu}\right) - \varsigma B'^2 + B^2\right)^2 + \varsigma Bk\Omega B'' - \varsigma\omega^2 B\mu\Omega B'' + \varsigma B\Omega B'\left(\omega^2 \mu' - k'\right) \\
- \varsigma Bk\Gamma B' + \varsigma k\Omega B'^2 + \varsigma\omega^2 B\Gamma\mu B' - \varsigma\omega^2 \mu\Omega B'^2 - \varsigma B^2 \Omega k'' + \varsigma B^2 \Gamma\left(k' - \omega^2 \mu'\right) + \varsigma\omega^2 B^2 \Omega\mu''
\end{gathered}$$

$$\begin{gathered}
\eta_1 = -B\left(\Omega\left(B'\left(\omega^2\left(-\left(2\mu + \varsigma\mu\right)\right) + \varsigma k + 2N^{II}\right) + \varsigma N^{II}\left(B''' - \omega^2 \overline{\mu'}\right)\right) + \varsigma N^{II}\Gamma\Delta\right) + \\
\varsigma N^{II} B'\left(\Omega\left(\omega^2 \overline{\mu} + B''\right) - \Gamma B'\right) + B^2\left(\Gamma\left(\omega^2\left(-\left(\overline{\mu} + \varsigma\mu\right)\right) + \varsigma k + N^{II}\right) + \Omega\left(\omega^2\left(\overline{\mu'} + 2\varsigma\mu'\right) - 2\varsigma k'\right)\right)
\end{gathered}$$

$$\eta_2 = B\left(B\left(\Omega\left(\omega^2\left(\overline{\mu} + \varsigma\mu\right) + B'' - \varsigma k - N^{II}\right) - \Gamma B'\right) + \Omega\left(\varsigma N^{II} \omega^2 \overline{\mu} - 2\varsigma N^{II} B'' + 2B'^2\right) + \varsigma N^{II} \Gamma B'\right)$$

$$\eta_3 = B\left(\Omega B'\left(4B + \varsigma N^{II}\right) - B\Gamma\left(B + \varsigma N^{II}\right)\right) \tag{19}$$

$$\eta_4 = B^2 \Omega\left(B + \varsigma N^{II}\right)$$

$$\Gamma = \varsigma B'\left(\omega^2 \overline{\mu} + B''\right) + B\left(\varsigma\omega^2 \overline{\mu'} - \varsigma B''' - 2B'\right)$$

$$\Omega = \varsigma B\left(\omega^2 \overline{\mu} - B''\right) + \varsigma B'^2 - B^2$$

$$\Delta = \omega^2 \overline{\mu} - B''$$

After integration of the differential equation the transfer relations will be obtained for the vertical displacement, angle of cross-section rotation, bending moment and transversal force. The 4 transfer relations have been transformed to the transfer matrix method form:

$$\begin{bmatrix} w(x) \\ \varphi(x) \\ M(x) \\ R(x) \\ 1 \end{bmatrix} = \begin{bmatrix} A_{11} & A_{12} & A_{13} & A_{14} & 0 \\ A_{21} & A_{22} & A_{23} & A_{24} & 0 \\ A_{31} & A_{32} & A_{33} & A_{34} & 0 \\ A_{41} & A_{42} & A_{43} & A_{44} & 0 \\ 0 & 0 & 0 & 0 & 1 \end{bmatrix} \cdot \begin{bmatrix} w_i \\ \varphi_i \\ M_i \\ R_i \\ 1 \end{bmatrix} \tag{20}$$

The kinematical and kinetic variables at node *i* are denoted by index "*i*" in (20). The parameters of the transfer matrix are not expressed in detail here from space spending point of view. After implementation of the applied boundary conditions, the homogenous equations system will be obtained for the calculation of internal forces and deformations. Hence, eigenvalue problems can be solved for circular eigenfrequencies and subsequently, the eigenfrequencies $f_n = \omega_n / 2\pi$ can be obtained (index *n* denotes the frequency number).

If the axial force N^{II} is set to zero in equations (14) – (20), then $R = Q$ and the equation of the 1st order beam theory has been obtained.

3 NUMERICAL EXPERIMENTS

3.1 Modal analysis of the FGM beam: Case I

A FGM beam has been considered as shown in Fig. 6. Its square cross-section is constant with height h = 0.2 m and width b = 0.2 m. Length of the beam is L = 3 m. Material of the beam consists of two components: NiFe – named as a matrix and denoted with index *m* ; Tungsten – named as a fibre and denoted with index *f*.

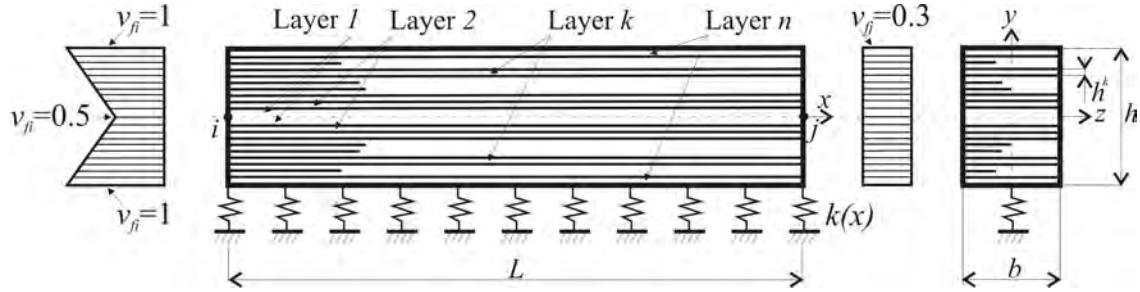

Figure 6: Composite beam with spatial variation of material properties.

Material properties of the components are constant and their values are: Tungsten (fibres) – elasticity modulus E_f = 400 GPa, mass density $\rho_f = 19300$ kg·m^{-3}; NiFe (matrix) – elasticity modulus E_m = 255 GPa, mass density $\rho_m = 9200$ kg·m^{-3} [11]. The cross-sectional area A = 0.04 m^2; the moment of inertia $I = bh^3/12 = 0.2^4/12$ m^4; and the reduced cross-sectional area $\overline{A} = k^s A$ [m^2]. The shear correction factor k^s can be computed so that the strain energy of the classical transverse shear stress equals the strain energy computed using the first order shear deformation theory [12], [17]]. According the notation in Fig. 1, it is possible to extend the calculation of shear stresses for a symmetrically layered beam with longitudinal variation of material properties of the layers [15]. The shear stress at point (*x,y*) of the relevant layer is a function of position of this point and it varies through the height and length of the layer. There is no jump of the shear stresses on the interface of the layers. Especially, for a rectangular cross-section – see Fig.1, the shear stress in the kth layer for $k \in \langle 1, n \rangle$ and $y \in \langle d_k - h_k/2, d_k + h_k/2 \rangle$ is

$$\tau_k(x,y) = \frac{Q(x)}{D(x)}\left(\frac{E_L^k(x)}{2}\left(\left(d_k + \frac{h_k}{2}\right)^2 - y^2\right) + \sum_{j=k}^{n} \frac{E_L^{j+1}(x)}{2}\left(\left(d_{j+1} + \frac{h_{j+1}}{2}\right)^2 - \left(d_j + \frac{h_j}{2}\right)^2\right)\right) \tag{21}$$

where $Q(x)$ is the shear force, $D(x)$ is the effective bending stiffness of the multilayer FGM beam at position x [15]. Using the expression (21) for the calculation of the strain energy in the cross-sectional area of the multilayered beam and putting it equal to the strain energy of the first order shear deformation theory, the shear correction factor function $k^s(x)$ (which is originally studied in [18]) can be calculated (because of longitudinal variation of the material properties in the layers, the shear correction factor is a function of x as well). Its average value

$$k^{sm} = \frac{1}{L}\int k^s(x)dx \tag{22}$$

has been used in calculation of the constant parameter ς included in the differential equation (19):

$$\varsigma = \frac{EI}{k^{sm}GA} \tag{23}$$

If the shear force effect is neglected, the factor $\varsigma = 0$. If the non-continuous distribution of the shear stresses (21) and the longitudinal variation of material properties in the layers is not accounted, then k^S = 0.833334. Otherwise, the shear correction function and the average shear correction factor (22) depend on the layering fineness. By increasing numbers of layers, the average shear correction factor will converge to the value which approximately fits the continuous variation of the material properties in transversal and longitudinal direction.

The fiber volume fraction, in this case, varies linearly and symmetrically according to the $x-z$ neutral plane in transversal direction at node i ($v_{fi} \in \langle 0.5, 1.0 \rangle$), and continues linearly in the longitudinal direction to the constant value at node j.

Both halves of the height h of this beam have been divided symmetrically to the beam neutral plane to n = 5, and n = 10 layers in such a way that all the layers have the same thickness h^k, where $k \in \langle 1, n \rangle$. The transversally constant fiber volume fractions of the assumed layers have been calculated from their values at the top and the bottom of the competent layer.

Pairs of the symmetrical layers in all cases were built as a mixture of the two components. The volume fraction of the components is constant along the height and width of the competent layer but it varies linearly along the layer length:

$$v_f^k(x) = v_{fi}^k\left(1 + \eta_1^k x\right) = 1 - v_m^k(x) \tag{24}$$

where index k is the number of the symmetrical layers, v_{fi}^k is the volume fraction of the fibres in the k^{th} layer at node i, and η_1^k is a parameter of variation of the fibres volume fraction. The list of these parameters for n = 5 is given in Table 1. The fibres volume fraction in the layers at node j is a constant and it is equal to $v_{fj}^k = 0.3$, $v_m^k(x)$ is the matrix volume fraction in layer k.

Layer k	1	2	3	4	5
v_{fi}^{k} (-)	0.55	0.65	0.75	0.85	0.95
η_1^{k} (-)	-4.545	-5.384	-6.000	-6.470	-6.842

Table 1: Parameters of the fibres volume fractions variation for n = 5.

With expressions (9) and (12) the effective longitudinal elasticity modules and the mass densities of the layers can be calculated. Subsequently, the effective elasticity modulus for transversal loading, the effective mass density and the average shear stress correction factor of the homogenized multilayer beam have been calculated by using of the expressions (10), (11) (13) and (22), and we have got:

a) for $n = 5$ layers
$E_L^{MH}(x) = 381.15 - 27.55x$ [GPa]; $\rho_L^{H}(x) = 16775.0 - 1515.0x$ [kgm^{-3}]; $k^{sm} = 0.836594$ [-];
b) for $n = 10$ layers
$E_L^{MH}(x) = 381.69 - 27.73x$ [GPa]; $\rho_L^{H}(x) = 16775.0 - 1515.0x$ [kgm^{-3}]; $k^{sm} = 0.836798$ [-].

The shear stress correction functions $k^{s}(x)$ have non-linear longitudinal distribution (see Fig. 9): its value is equal to 0.83934 for $n = 5$, and 0.839714 for $n = 10$ at point *i*; and it is equal to 0.833334 at point *j* for the both divisions (the material properties are the same at this point in each layer).

If the homogenized material properties have been calculated by direct integration method (without division into layers), following parameters have been obtained:

$$E_L^{MH} = 381.875 - 27.79x \text{ [GPa]} \qquad k^{sm} = 0.836868$$

As can be seen, the homogenized material properties converge very fast to the values obtained by the direct integration methods.

The ratio $\dfrac{E_L^{MH}(x)}{G_L^{H}(x)} = 2.6$ has been used for the effect of shear forces assumption in this example. Longitudinal distributions of the homogenized elasticity modulus and the effective elasticity modules in the respective layers for *n* = 5 are shown in Fig. 7.

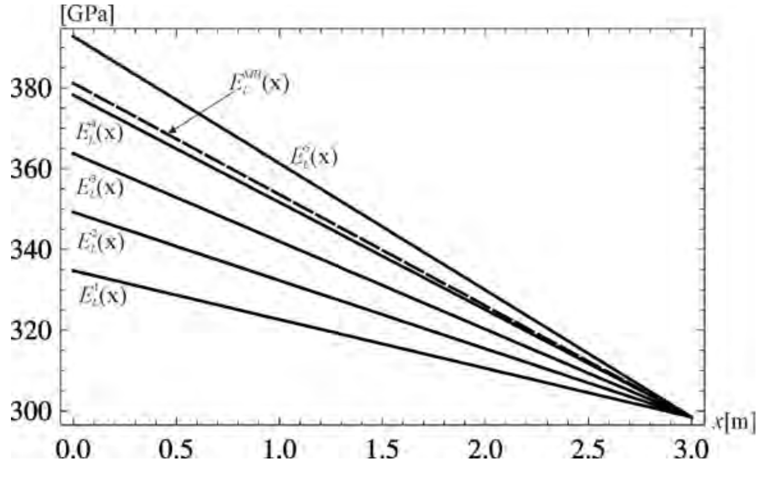

Figure 7: Longitudinal distributions of the homogenized elasticity modulus and the effective elasticity modules in respective layers for *n* = 5

Longitudinal distributions of the mass density in the homogenized beam and the effective mass densities distribution in respective layers of the multilayer beam for n = 5 are shown in Fig. 8.

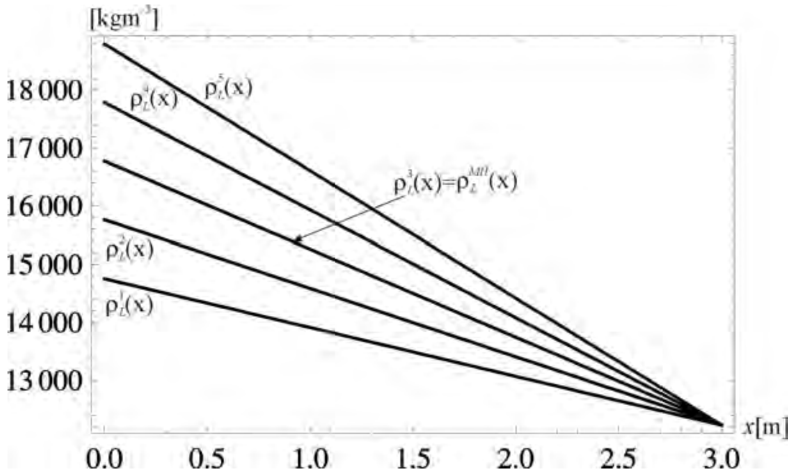

Figure 8. Effective mass density distribution along the homogenized beam and the effective elasticity mass density in respective layers for n = 5.

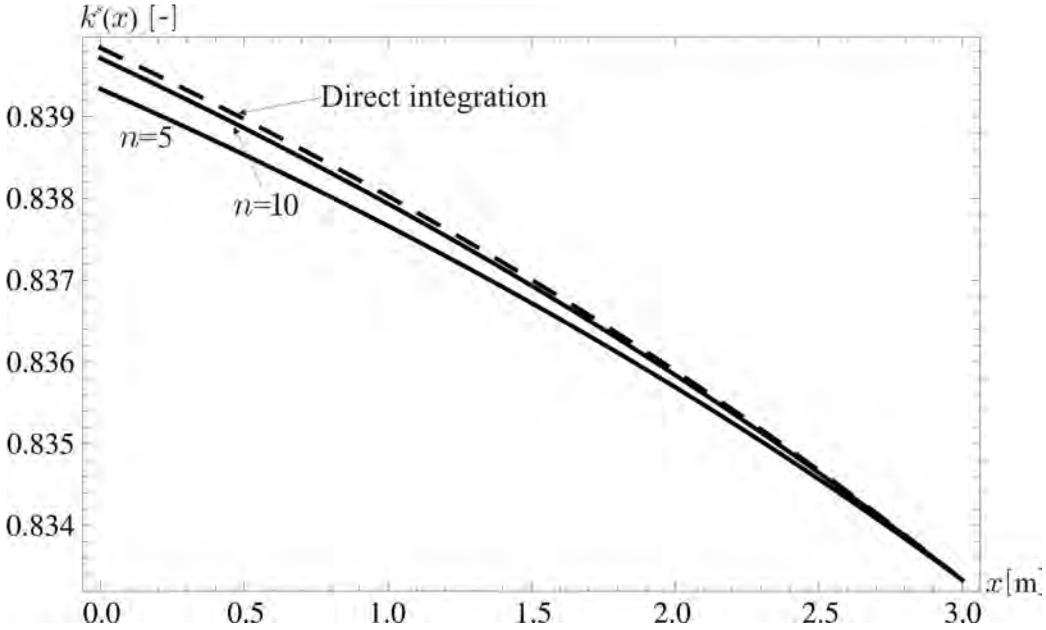

Figure 9**:** Shear correction function for n = 5 and n =10.

The varying Winkler elastic foundation modulus is chosen as a linear function: $k(x) = 5000 - 1000x$ [kN/m^2].

The homogenized simply supported beam (Fig. 6) has been studied by modal analysis. The first three bending eigenfrequencies have been found using the differential equation (18) and the appropriate boundary conditions. The buckling critical forces have been calculated by [19], and they are: $N_{Ki}^{II} = -52172.0$ kN for n = 5 layers; and $N_{Ki}^{II} = -52209.7$ kN for $n = 10$ layers. The axial force (tension and compression) $N^{II} \equiv N$ will be chosen as a part of the critical buckling force N_{Ki}^{II}. In all cases, the applied axial force N was smaller than the critical buckling force. The effects of the shear stress correction factor and the large axial force have been studied and evaluated.

The same problem has been solved using a very fine mesh – 12000 of 2D PLANE42 elements and 401 COMBIN14 elements of the FEM program ANSYS [20] where each element has material properties equal to their value at the (x,z) location of the element center. The results of ANSYS as well as the results of the differential equations solution (using the software MATHEMATICA [21] and denoted by DIF) are presented in Tables 2 – 5. The shear force deformation effect and the effect of axial force (tension and compression) on the eigefrequencies have been studied.

The Table 2 presents the eigenfrequency results for tensional axial force when the average shear correction factors k^{sm} have been considered by DIF solution. In the second column of this table, the 1st order beam theory results obtained by DIF solution are presented.

$N^{II} = N$ [kN]		1st order DIF $N = 0$	DIF $N =$ 13000	ANSYS $N =$ 13000	DIF $N =$ 26000	ANSYS $N =$ 26000	DIF $N =$ 39000	ANSYS $N =$ 39000
f_1 [Hz]	$n = 5$	49.93	55.81	56.33	61.11	61.58	66.00	66.41
	$n = 10$	49.95	55.82		61.13		66.01	
f_2 [Hz]	$n = 5$	190.10	196.49	197.50	202.68	203.63	208.68	209.58
	$n = 10$	190.18	196.56		202.75		208.75	
f_3 [Hz]	$n = 5$	413.10	419.69	418.34	426.18	424.81	432.57	431.17
	$n = 10$	413.27	419.85		426.34		432.72	

Table 2: Eigenfrequencies in the Case I for tensional axial force with the shear correction factors

The Table 3 presents the eigenfrequency results for compression axial force when the average shear correction factors k^{sm} have been considered by DIF solution.

$N^{II} = N$ [kN]		DIF –13000	ANSYS –13000	DIF –26000	ANSYS –26000	DIF –39000	ANSYS –39000
f_1 [Hz]	$n = 5$	43.27	43.95	35.37	36.19	25.09	26.21
	$n = 10$	43.29		35.40		25.13	
f_2 [Hz]	$n = 5$	183.49	184.60	176.63	177.78	169.49	170.69
	$n = 10$	183.57		176.71		169.58	
f_3 [Hz]	$n = 5$	406.41	405.08	399.60	398.27	392.67	391.33
	$n = 10$	406.57		399.77		392.84	

Table 3: Eigenfrequencies in the Case I for compression axial force with the shear correction factors

Table 4 and Table 5 show the DIF solution results when the shear correction has not been considered.

$N^{II} = N$ [kN]		1st order DIF $N = 0$	DIF $N =$ 13000	DIF $N =$ 26000	DIF $N =$ 39000
f_1 [Hz]	$n = 5$	50.20	56.04	61.33	66.00
	$n = 10$	50.22	56.06	61.35	66.21
f_2 [Hz]	$n = 5$	194.24	200.49	206.55	212.44
	$n = 10$	194.32	200.57	206.62	212.21
f_3 [Hz]	$n = 5$	432.49	438.76	444.93	451.02
	$n = 10$	432.66	438.92	445.09	451.18

Table 4: Eigenfrequencies in the Case I for tensional axial force without the shear correction factors

$N^{II} = N$ [kN]		DIF –13000	DIF –26000	DIF –39000
f_1 [Hz]	$n = 5$	43.58	35.75	25.62
	$n = 10$	43.60	35.77	25.66
f_2 [Hz]	$n = 5$	187.79	181.10	174.15
	$n = 10$	187.86	181.18	174.23
f_3 [Hz]	$n = 5$	426.14	419.68	413.13
	$n = 10$	426.31	419.85	413.30

Table 5: Eigenfrequencies in the Case I for compression axial force without the shear correction factors

Dependence of the 1st eigenfrequency on the applied axial force (with and without the shear correction factor and for $n = 10$) is shown in Fig. 9

As we can see in Tab. 2 to Tab. 5, and in Fig. 9, the solution results obtained by our new differential equation agree very well with the ones obtained by very fine mesh of the PLANE42 solid elements. As expected, inclusion of the shear force deformation effect makes the results more accurate. But this effect is not significant in this example. This effect will grow with higher variation of non-linearities in material properties in transversal and longitudinal direction. As expected, increasing compression axial force decreases the values of eigenfrequency and, on the other hand, increasing tensional force increases the eigenfrequency. The influence of the large axial force is significant in calculated cases. This fact can be utilized by the control and tuning of dynamic properties of beam structures.

Foundation elastic properties have not been studied in this contribution.

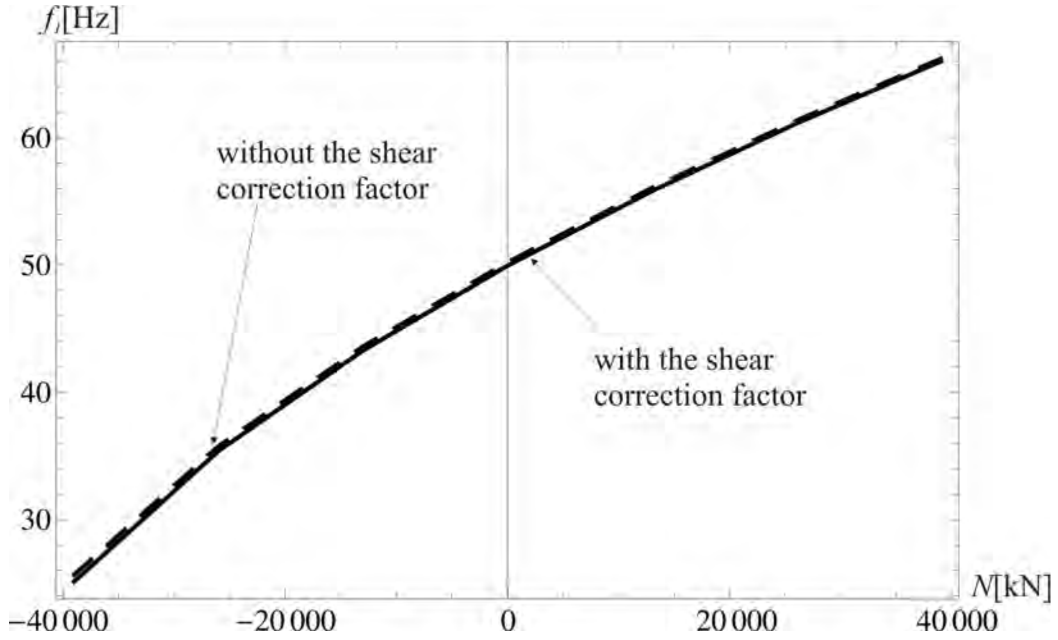

Figure 9: Dependence of the eigenfrequencies in the Case I for n = 10.

3.2 Modal analysis of the FGM beam: Case II

An FGM beam has been considered as shown in Fig. 10. Its geometry and material properties of the constituents are the same as in Case I. Only the variation of fibre volume fractions has been changed.

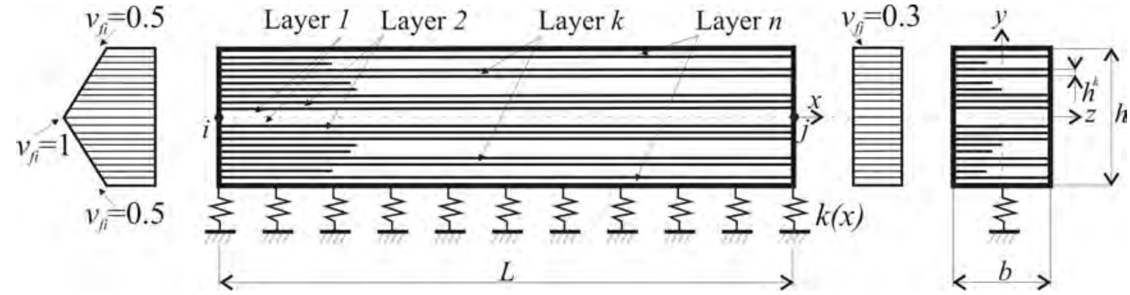

Fig. 10. FGM beam with spatial variation of material properties

The fibre volume fraction at node i varies linearly and symmetrically according to the neutral plane in the transversal direction ($v_{fi} \in \langle 1.0, 0.5 \rangle$) and continuous linearly in the longitudinal direction to the value $v_{fj} = 0.3$.

By the same approach described in chapter 2 the fibres volume fraction have been obtained - see Table 6.

Layer k	5	4	3	2	1
v_{fi}^k (-)	0.55	0.65	0.75	0.85	0.95
η_1^k (-)	-4.545	-5.384	-6.000	-6.470	-6.842

Table 6: Parameters of the fibres volume fractions variation for n = 5

With expressions (9) and (12) the effective longitudinal elasticity modules and the mass densities of the layers can be calculated. Following, the effective elasticity modulus for transversal loading, the effective mass density and the average shear stress correction factor of the homogenized multilayer beam have been calculated using expressions (10), (11) (13). The effective elasticity modulus and the average shear correction factor of the homogenized multilayer beams for transversal loading have been calculated via expressions (11) and (29), and we have got:

a) for $n = 5$ layers
$E_L^{MH}(x) = 345.88 - 15.79x$ [GPa]; $\rho_L^H(x) = 16775.0 - 1515.0x$ [kgm^{-3}]; k^{sm} = 0.828612 [-];
b) for $n = 10$ layers
$E_L^{MH}(x) = 345.74 - 15.74x$ [GPa]; $\rho_L^H(x) = 16775.0 - 1515.0x$ [kgm^{-3}]; k^{sm} = 0.829386 [-].

The shear stress correction function $k^s(x)$ has non-linear longitudinal distribution (see Fig. 11): its value is equal to 0.824329 for $n = 5$ and 0.82579 for $n = 10$ at point *i*; and it is equal to 0.833334 at point *j* for the both divisions (the material properties are the same at this point in each layer).

The ratio $\dfrac{E_L^{MH}(x)}{G_L^H(x)} = 2.6$ has been used to express the effect of shear forces assumption in this example.

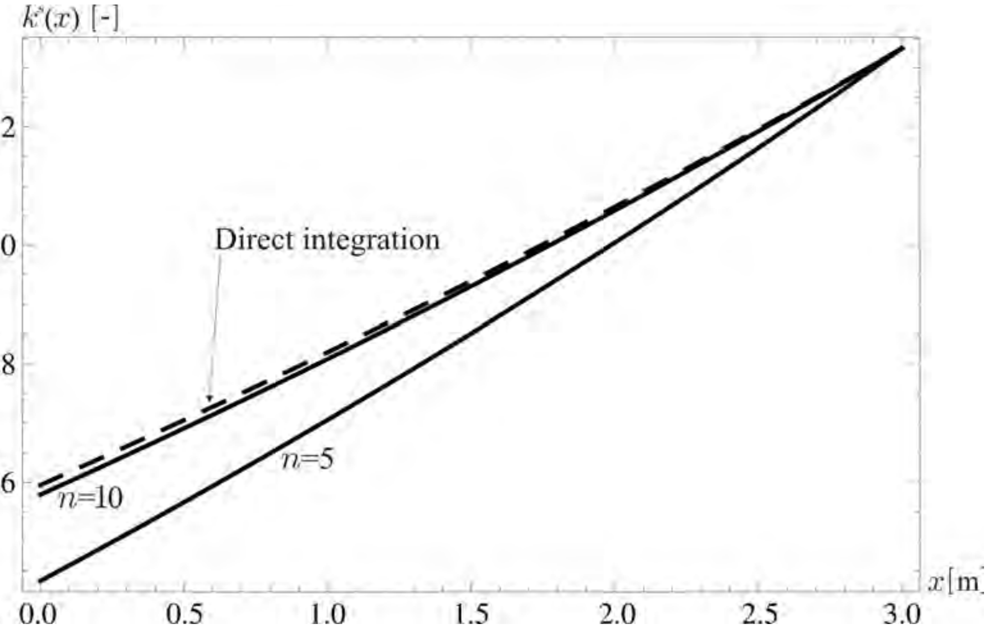

Figure 11: Shear correction function for n = 5 and n =10, and direct integration.

Homogenized material properties obtained by direct integration (without division into layers) give following parameters:

$$E_L^{MH}(x) = 345.625 - 15.70x \text{ [GPa]} \qquad k^{sm} = 0.829478$$

The above listed parameters show that the division of the beam into $n = 10$ layers gives enough accurate results which agree very well with the ones obtained by the direct integration method.

The ratio $\dfrac{E_L^{MH}(x)}{G_L^H(x)} = 2.6$ has been used to express the effect of shear forces assumption in this example.

Longitudinal distributions of the homogenized elasticity modulus and the effective elasticity modules in respective layers for $n = 5$ are shown in Fig. 12.

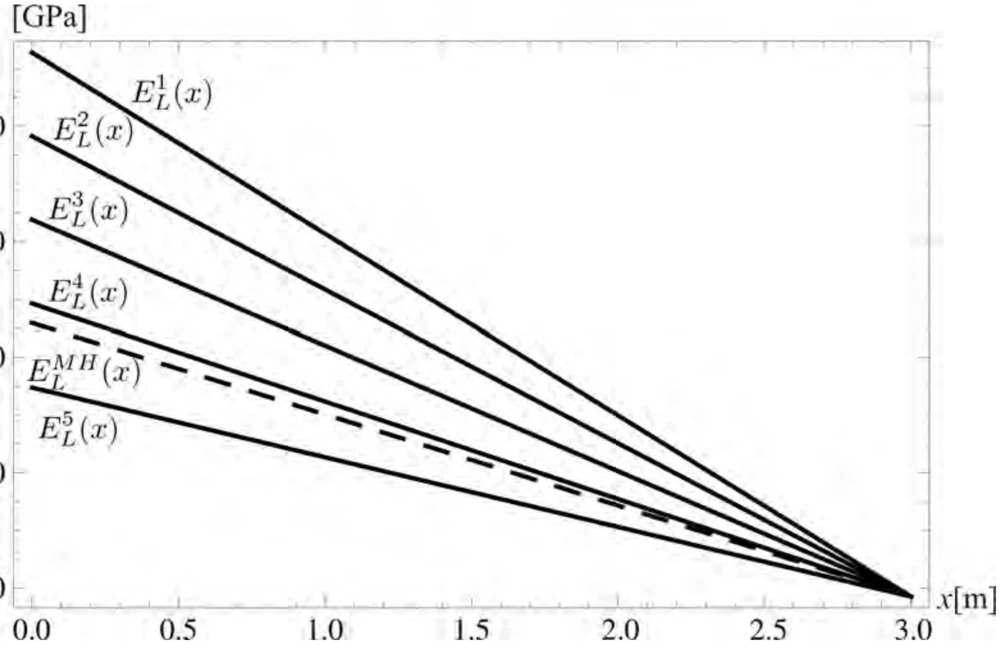

Fig. 12. Longitudinal distributions of the homogenized elasticity modulus and the effective elasticity modules in respective layers for *n* = 5.

Longitudinal distributions of the homogenized elasticity modules for division into n = 10 layers are shown in Fig. 13.

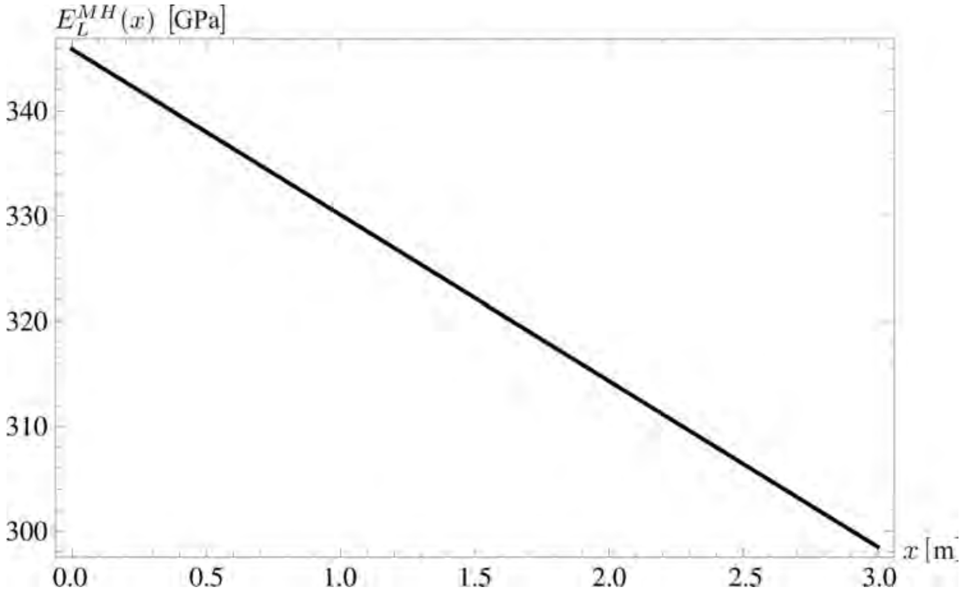

Fig. 13. Longitudinal distributions of the homogenized elasticity modules for *n* = 10 layers.

The homogenized mass density has been calculated by expressions (12) and (13): $\rho_L^H(x) = 16775.0 - 1515.0x$, [kg·m^{-3}]; this value is the same for any number of divisions n as it was in the Case I. Distribution of the mass density in the layers is similar to the one displayed in Fig. 8 but the ordering of layers is in contrary series. The same varying Winkler elastic foundation has been chosen as in the Case I.

The homogenized simply supported beam (Fig. 10) has been studied using modal analysis. The first three bending eigenfrequencies have been found using the differential equation (18) and the appropriate boundary conditions. The buckling critical forces have been calculated by [19], and they are: $N_{Ki}^{II} = -49711.3$ kN for $n = 5$ layers; and $N_{Ki}^{II} = -49701.6$ kN for $n = 10$ layers. The axial force (tension and compression) $N^{II} \equiv N$ will be chosen as a part of the critical buckling force N_{Ki}^{II}. In all cases, the applied axial force N was smaller than the critical buckling force. The effects of the shear stress correction factor and the large axial force have studied and evaluated. The same problem has been solved using a very fine mesh – 12000 of 2D PLANE42 elements and 401 COMBIN14 elements of the FEM software ANSYS [20] – with a variation of material properties (in competent layers) as displayed in Fig. 7 and Fig. 8. The results from ANSYS as well as the results of the differential equations solution (using the software MATHEMATICA [21] and denoted by DIF) are presented in Tables 7 – 10. The shear force deformation effect and the effect of axial force (tension and compression) on the eigefrequencies have been investigated.

The Table 7 presents the eigenfrequency results for tensional axial force when the average shear correction factors k^{sm} have been considered in the DIF solution. In the second column of this table, the 1st order beam theory results obtained by DIF solution are presented.

$N^{II} = N$ [kN]		1st order DIF $N = 0$	DIF $N =$ 13000	ANSYS $N =$ 13000	DIF $N =$ 26000	ANSYS $N =$ 26000	DIF $N =$ 39000	ANSYS $N =$ 39000
f_1 [Hz]	$n = 5$	48.72	54.72	55.27	60.12	60.620	65.07	65.525
	$n = 10$	48.71	54.71		61.12		65.07	
f_2 [Hz]	$n = 5$	185.18	191.72	193.22	198.05	199.49	204.17	205.56
	$n = 10$	185.16	191.71		198.04		208.75	
f_3 [Hz]	$n = 5$	402.31	409.06	409.96	415.70	416.58	422.24	423.09
	$n = 10$	402.28	409.03		415.68		422.22	

Table 7: Eigenfrequencies in the Case II for tensional axial force with the shear correction factors

The Table 8 presents the eigenfrequency results for compression axial force when the average shear correction factors k^{sm} have been considered in the DIF solution.

$N^{II} = N$ [kN]		DIF –13000	ANSYS –13000	DIF –26000	ANSYS –26000	DIF –39000	ANSYS –39000
f_1 [Hz]	$n = 5$	41.87	42.59	33.65	34.53	22.62	23.86
	$n = 10$	41.86		33.64		22.61	
f_2 [Hz]	$n = 5$	178.39	180.00	171.34	172.99	163.98	165.69
	$n = 10$	178.38		171.32		163.96	
f_3 [Hz]	$n = 5$	395.44	396.38	388.45	389.39	381.33	382.27
	$n = 10$	395.41		388.42		381.30	

Table 8: Eigenfrequencies in the Case II for compression axial force with the shear correction factors

Table 9 and Table 10 show the DIF solution results when the shear correction has not been considered.

$N^{II} = N$ [kN]		1st order DIF $N = 0$	DIF $N =$ 13000	DIF $N =$ 26000	DIF $N =$ 39000
f_1 [Hz]	$n = 5$	48.98	54.95	60.33	65.27
	$n = 10$	48.97	54.94	60.33	65.26
f_2 [Hz]	$n = 5$	189.25	195.65	201.85	207.86
	$n = 10$	189.23	195.63	201.83	207.84
f_3 [Hz]	$n = 5$	421.37	427.79	434.11	440.34
	$n = 10$	421.32	427.74	434.06	440.29

Table 9: Eigenfrequencies in the Case II for tensional axial force without the shear correction factors

$N^{II} = N$ [kN]		DIF –13000	DIF –26000	DIF –39000
f_1 [Hz]	$n = 5$	42.17	34.03	23.17
	$n = 10$	42.17	35.02	25.16
f_2 [Hz]	$n = 5$	182.62	175.75	168.59
	$n = 10$	182.60	175.72	168.56
f_3 [Hz]	$n = 5$	414.85	408.23	401.50
	$n = 10$	414.80	408.18	401.45

Table 10: Eigenfrequencies in the Case II for compression axial force without the shear correction factors

Dependence of the 1st eigenfrequency on the applied axial force (with and without the shear correction factor and for $n = 10$) is shown in Fig. 14.

As we can see in Tab. 7 to Tab. 10 and in Fig. 14, the effects and conclusions are similar to the ones in the previous Case I. In addition, also the changed variation of material properties influenced the eigenfrequencies of the FGM beams. The eigenfrequencies are higher in the Case I due a variation of material properties making the beam stiffer.

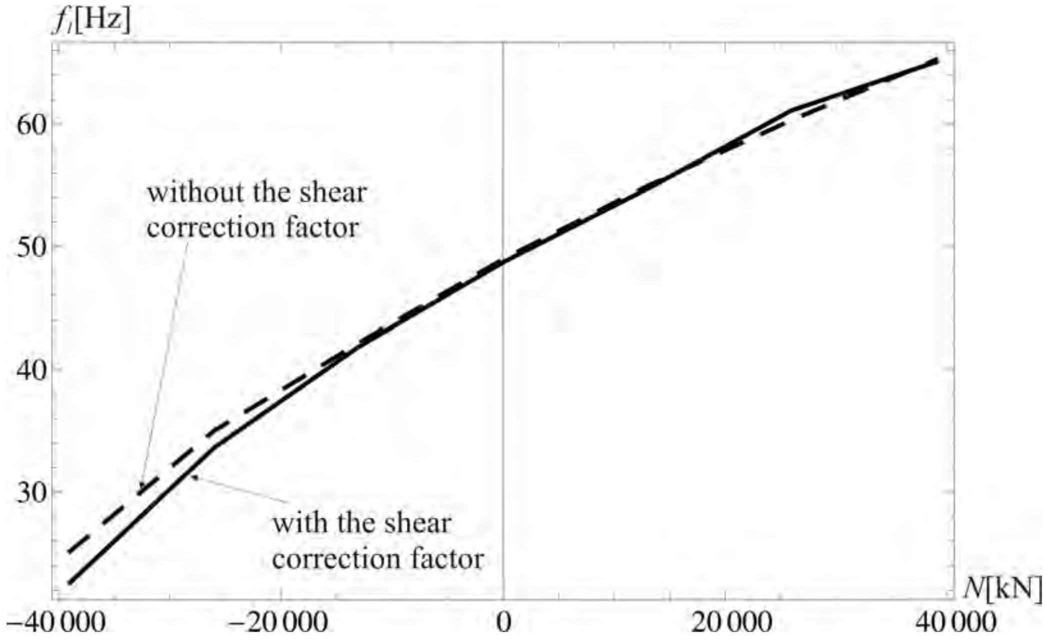

Figure 14: Dependence of the eigenfrequencies on the axial force in the Case II for n = 10.

4 CONCLUSIONS

Differential equation of the homogenized functionally graded material (FGM) beam deflection was established for 2^{nd} the order beam theory, which has been used in a modal analysis of FGM beams of rectangular cross-sections with continuous spatial variation of material properties. The FGM beams are considered to be resting on longitudinally variable (Winkler) elastic foundation. Homogenization of material properties has been done by the multilayer method and by direct integration. By the multilayer method, the FGM beam with continuous spatial variation of material properties has been transformed into a multilayer beam. Symmetrical layering along the neutral plane in transversal direction has been assumed: the corresponding layers having the same height and material properties variation. The material properties vary continuously in longitudinal direction but they are constant along the height and width of each layer. By the second one the direct integration of the varying material properties over the height and length of the beam has been used. Increasing numbers of layers make the homogenized material properties converge to the ones obtained by a direct integration.

Not only the shear force deformation effect and the effect of consistent mass distribution and mass moment of inertia but also the effect of a large axial force has been taken into account. Large axial force has a system character: if set to zero in the derived differential equation, the 1^{st} order beam theory differential equation will be obtained. The shear correction function has been derived and an average shear correction factor has been calculated to express the shear force effect. Effects of variation of elastic foundation properties are not subject of this contribution.

Numerical experiments were performed to calculate the eigenfrequencies of the chosen FGM beams. The solution results are discussed and compared with those obtained using a very fine mesh of two-dimensional solid finite elements.

The main conclusions that can be drawn from this investigation are:

- the large axial force has a significant effect on the eigenfrequency value also in the case of a beam resting on an elastic foundation;
- increasing compression axial force decreases the eigenfrequency and increasing tensional force increases the eigenfrequency;

- inclusion of the shear force deformation effect makes the results more accurate (the shear correction function has been derived for calculation of the average shear correction factor);
- not only transversal but also longitudinal variation of material properties affects the dynamic properties of the FGM beams;
- the results obtained by solution of the differential equation agree very well with these obtained by an FEM solution using a very fine mesh of the solid finite elements.

The presented differential equation is suitable for an effective modal analysis of beams with continuous spatial variation of material properties resting on a Winkler elastic foundation with longitudinally varying material properties. Results of such analyses can be used not only as a benchmark solution in comparison of results obtained by other numerical method but also in modal analysis of the real FGM beams.

Acknowlegement

This paper has been supported by Grant Agency VEGA (grant No. 1/0093/10).

REFERENCES

[1] J. Ying, C.F. Lu, W.Q. Chen, Two-dimensional elasticity solution for functionally graded beam resting on elastic foundations. *Composite Structures*, **86**, 209 – 219, 2008.

[2] S.C. Pradham, T. Murmu, Thermo-mechanical vibration of FGM sandwich beam under variable elastic foundations using differential quadrature method. *Journal of Sound and Vibration*, **321**, 342 – 362, 2009.

[3] J. Murín, M. Aminbaghai, V. Kutiš, Exact solution of the bending vibration problem of FGM beams with variation of material properties. *Engineering Structures*, **32**, 1631 – 1640, 2010.

[4] J. Murín,– M. Aminbaghai,– V. Kutiš, Free Vibration of the FGM-beams with Continuous Transversal Symmetric and Longitudinal Variation of Material Properties with Effect of Large Axial Force. In: *IV European Conference on Computational Mechanics. Solid, Structures and Coupled Problems in Engineering (ECCM 2010)*, Palais des Congres, Paris, France, May 16-21, 2010.

[5] L.S. Ma, D.W. Lee, A further discussion of nonlinear mechanical behaviour for FGM beams under in-plane loading. *Composite Structures*, **93**, 831 – 842, 2011.

[6] L.L. Ke, J. Yang, S. Kitipornchai, An anlytical study on nonlinear vibration of functionally graded carbon reinforced composite beams. *Composite Structures*, **92**, 676 – 683, 2010.

[7] S.A. Emamm, A.H. Nayfeh, Postbuckling and free vibrations of composite beams. *Composite Structures*, **88**, 636 – 642, 2009.

[8] E.S. Sapountzakis, A.E. Kampitsis, Nonlinear dynamic analysis of partially supported beam-column on nonlinear foundation including shear deformation effect. *Computational modelling and advanced simulations*, Springer Science + Business Media B.V., ISBN 978-94-007-0316-2, 364 p., 2011. http://dx.doi.org/10.1007/978-94-007-0317-9

[9] J. Murin, M. Aminbaghai, V. Kutis, Free Vibration of the Multilayer FGM Beams under Longitudinal Variable Elastic Foundation. *New Trends in Statics and Dynamics of*

Buildings : 8th International Conference. Bratislava, Slovak Republic, October 21.-22, 121-128, 2010.

[10] M. Aminbaghai, J. Murin, V. Kutis, Free Vibration of the Multilayer FGM Beams under Longitudinal Variable Elastic Foundation with Effect of Large Axial Force. *New Trends in Statics and Dynamics of Buildings* : 8th International Conference. Bratislava, Slovak Republic, October 21 – 22, 1-8, 2010.

[11] J. Murín, V. Kutiš, An Effective Solution of the Composite (FGM'S) Beam Structures. *Engineering Mechanics*, **15**, 115-132, 2008.

[12] H. Altenbach, J. Altenbach, W. Kissing, Mechanics of Composite Structural Elements. Engineerig - Monograph, Springer-Verlag, 463 p.,2003.

[13] J.Murin, V. Kutis, M. Masny, R. Duris, Composite (FGMs) beam finite elements. *Composites with Micro- and Nano-Structure*. Springer Science+Business Media B.V, 209 – 239, 2008.

[14] J. Murin, V. Kutis, Improved mixture rules for the composite (FGMs) sandwich beam finite element. *IX International Conference on Computational Plasticity (COMPLAS IX)*, CIMNE, Barcelona, 2007.

[15] J. Murin, V. Kutis, An effective multilayered sandwich beam-link finite element for solution of the electro-thermo-structural problems. *Int. J. Computers and Structures*, **87**, 23-24, 2009.

[16] H. Rubin, Analytische Lösung linearer Differentialgleichungen mit veränderlichen Koeffizienten und baustatische Anwendung. *Bautechnik*, **76**, 1999.

[17] H. Mang, G. Hoffstetter, Festigkeitslehre. *Springer-Verlag*, 2000.

[18] J. Murin, M. Aminbaghai, V. Kutis, Exact Solution of the Bending Vibration Problem of FGM Beams with Variation of Materials Properties. Engineering Structures, 32, 1631-1640, 2010.

[19] IQ – 100, Schneider Bautabellen für Ingenieure, 19. Auflage, 2010 Wolters Kluwer Deutschland GmbH, Luxemburger Straße 449, 50939 Köln. ISBN 978-3-8041-5242-7

[20] ANSYS Swanson Analysis System, Inc., 201 Johnson Road, Houston, PA 15342/1300, USA.

[21] S. Wolfram, MATHEMATICA 5, Wolfram research, Inc., 2003.

COMPDYN 2011
ECCOMAS Thematic Conference on
Computational Methods in Structural Dynamics and Earthquake Engineering
M. Papadrakakis, M. Fragiadakis, V. Plevris (eds.)
Corfu, Greece, 25-28 May 2011

PIEZOELECTRIC TORSIONAL SENSORS AND ACTUATORS - A COMPUTATIONAL STUDY

Christian Zehetner[1], **Markus Zellhofer**[1] **and Michael Krommer**[2]

[1]Linz Center of Mechatronics
Linz, Austria
e-mail: {christian.zehetner, markus.zellhofer}@lcm.at

[2] Institute for Technical Mechanics
Johannes Kepler University, Linz, Austria
e-mail: michael.krommer@jku.at

Keywords: Torsion, piezoelectric rod, piezoelectric actuation, piezoelectric sensor, macro fiber composites

Abstract. *This paper concerns a computational study on the realization of piezoelectric torsional actuators and sensors. Exemplarily, a rod with rectangular solid cross-section is considered consisting of a linear elastic substrate material on which orthotropic piezoelectric layers are bonded. On the one hand side, piezoelectric actuation is obtained by applying voltage to the electrodes of the piezoelectric layer. Secondly, the layers can be used as sensors by measuring the voltage on the electrodes which is caused by external torsional loads. Three material types are compared for possible realisations: ammonium dihydrogen phosphate (ADP) and two types of macro fiber composites (MFC). In the framework of Saint Venant's theory of torsion, the actuator and sensor equations are formulated: The actuating torsional moment is proportional to the applied voltage, and the sensor voltage is proportional to the torsional angle. Finally, the results are validated by means of three-dimensional Finite Element computations.*

1 INTRODUCTION

Recently, interest in active vibration compensation using piezoelectric materials has gained more and more. Possible applications can be found for instance in the fields of robotics and light-weight structures. Piezoelectric layers can either be integrated into structures, or applied on the surfaces of structures. Such layers can be used as sensors and actuators, utilizing the direct and converse piezoelectric effect, respectively, [1].

The topic of this paper is the application of piezoelectric materials for sensing and actuation of torsional rod vibrations. Exemplarily, a rod of rectangular cross-section made of aluminium is considered which is subject to an external torsional couple. On the top and bottom of the rod, piezoelectric layers are attached, such that a sandwich structure is obtained. Each layer can be used as a sensor by measuring the voltage on the electrodes, or as an actuator by prescribing the voltage. The main scope is the derivation of the sensor and actuator equations, and to perform numerical investigations in order to find a suitable configuration for an experimental setup.

Torsional actuation and sensing is either based on the piezoelectric extension or on the shear mode. In the first case, torsional actuation is obtained by piezoelectric normal strains acting at an angle of 45^o degrees to the rod axis, c.f. Park and Chopra [2]. In the second case, piezoelectric shear strains cause a resulting actuating torque, [3]-[9]. On the other hand, in torsional sensors the strains corresponding to the piezoelectric mode cause the sensor voltage at the electrodes. In this paper two types of materials are investigated: (a) Shear mode: Piezoceramic material ammonium dihydrogen phosphate (ADP) and (b) Extension mode: Macro fiber composites (MFC) consisting of lead zirconate titanate (PZT) fibers embedded within an epoxy-substrate. Two types of MFCs are compared utilizing eiter the transversal d_{31}-effect or the longitudinal d_{33}-effect of the PZT fibers. For the MFC transduceres effective homogenized material properties are used, which have been obtained by applying mixing rules according to Deraemaeker et al. [10].

In order to investigate the influence of piezoelectricity on torsion, Saint Venant's theory has been extended by Zehetner [5] and Zehetner and Krommer [7]. The main extension is the consideration of the additional cross-sectional warping caused by piezoelectric strains. In this paper, the theory is adapted for studying the behaviour of the three materials mentioned above. It turns out that for the three configurations the sensor and actuator equations only differ with respect to some coefficients referring to the material properties. It also turns out that for an experimental realization MFCs are more practicable because of higher sensitivity and efficiency of actuation. Finally, the theoretical results are validated by means of three-dimensional Finite Element computations performed with *ANSYS* and *ABAQUS* showing a good coincidence.

2 PIEZOELECTRIC SHEAR ACTUATORS AND SENSORS

In this paper two kinds of materials suitable for torsional sensing and actuation are investigated: Figure 1a shows a homogenous layer made of the piezoceramic ammonium dihydrogen phosphate (ADP), z is the thickness direction, and x is the axial direction of the rod. The second type of material is shown in Figure 1b, a macro fiber composite (MFC) consisting of piezoceramic fibers (lead zirconate titanate, PZT) which are embedded into an epoxy-substrate at an angle of 45^o with respect to the axial direction x of the rod.

The compliance matrices $\boldsymbol{S}$ of the two materials are stated in Eq. (1). In layers made of ADP, the shear strains correspond to the shear stresses only. The same behavior is obtained for MFC's, if the coordinate frame coincides with the axes of material symmetry. On the contrary, for the investigated case with a ply angle of 45^o, the shear strains are coupled to normal stresses by the compliance components S_{16} and S_{36}.

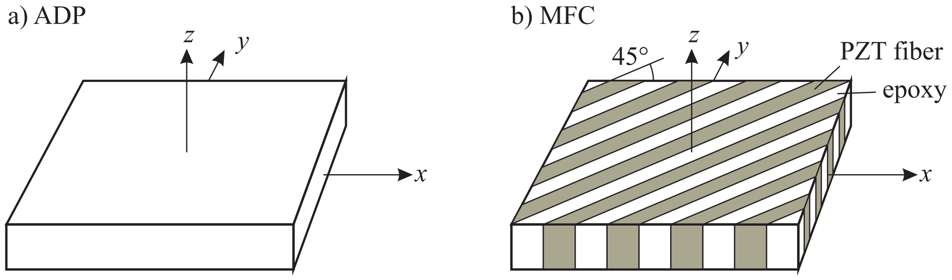
a) ADP

b) MFC

Figure 1: Piezoelectric materials

a) ADP　　　　　　b) MFC

$$\boldsymbol{S}=\begin{bmatrix} S_{11} & S_{12} & S_{13} & 0 & 0 & 0 \\ S_{12} & S_{11} & S_{13} & 0 & 0 & 0 \\ S_{13} & S_{13} & S_{33} & 0 & 0 & 0 \\ 0 & 0 & 0 & S_{55} & 0 & 0 \\ 0 & 0 & 0 & 0 & S_{55} & 0 \\ 0 & 0 & 0 & 0 & 0 & S_{66} \end{bmatrix}, \quad \boldsymbol{S}=\begin{bmatrix} S_{11} & S_{12} & S_{13} & 0 & 0 & S_{16} \\ S_{12} & S_{11} & S_{13} & 0 & 0 & S_{16} \\ S_{13} & S_{13} & S_{33} & 0 & 0 & S_{36} \\ 0 & 0 & 0 & S_{55} & S_{45} & 0 \\ 0 & 0 & 0 & S_{45} & S_{55} & 0 \\ S_{16} & S_{16} & S_{36} & 0 & 0 & S_{66} \end{bmatrix}. \tag{1}$$

Three configurations are considered as shown in Figure 2: (a,b) A layer made of ADP or MFC type 1 (d_{31}-effect) is polarized in thickness direction, and the electrodes are bonded on the top and bottom surfaces, (c) A layer made of MFC type 2 (d_{33}-effect) is polarized in longitudinal direction of the fibers, and the electrodes are normal to this direction.

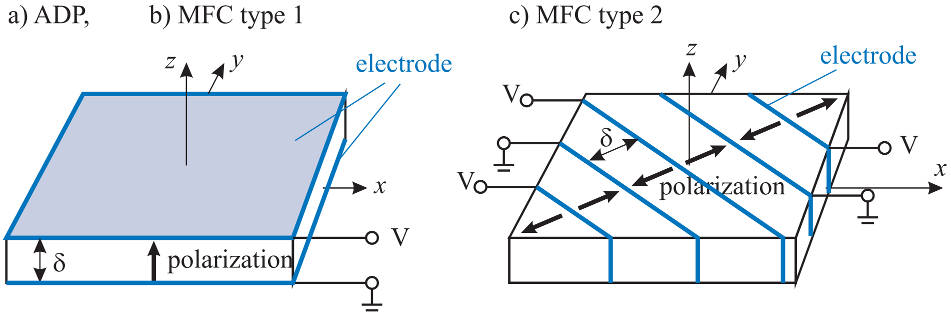
a) ADP, b) MFC type 1

c) MFC type 2

Figure 2: Electrodes and polarization direction

The matrices $\boldsymbol{d}$ of piezoelectric coefficients d_{ij} for the three configurations are specified in Eq. (2). In layers made of ADP only piezoelectric shear strains are induced, such that pure torsional actuation is possible. On the contrary, in MFC's also normal eigenstrains arise, which can excite elongation and bending modes of the rod. In the following, the bending mode is avoided due to a symmetrical set-up, and the elongation is neglected.

a) ADP　　　　　　b) MFC type 1　　　　　　c) MFC type 2

$$\boldsymbol{d}=\begin{bmatrix} 0 & 0 & 0 \\ 0 & 0 & 0 \\ 0 & 0 & 0 \\ d_{25} & 0 & 0 \\ 0 & d_{25} & 0 \\ 0 & 0 & d_{36} \end{bmatrix}, \quad \boldsymbol{d}=\begin{bmatrix} 0 & 0 & d_{13} \\ 0 & 0 & d_{13} \\ 0 & 0 & d_{33} \\ d_{25} & d_{15} & 0 \\ d_{15} & d_{25} & 0 \\ 0 & 0 & d_{36} \end{bmatrix}, \quad \boldsymbol{d}=\begin{bmatrix} d_{11} & d_{12} & 0 \\ d_{12} & d_{11} & 0 \\ d_{13} & d_{13} & 0 \\ 0 & 0 & d_{35} \\ 0 & 0 & d_{35} \\ d_{16} & d_{16} & 0 \end{bmatrix}. \tag{2}$$

3 TORSION OF PIEZO-LAMINATED RODS

Figure 3 shows the cross-section of a laminated rod with length L, width B and total height H. The rod consists of an isotropic aluminum layer with height h on which two piezoelectric layers with height h_L are ideally bonded. The rod is subject to the external torsional couple M_x^e. A Cartesian coordinate system is introduced such that the x-axis represents the longitudinal axis of the rod, and the axes y and z form the cross-sectional plane. The cross-sectional area of the piezoelectric layers is denoted as A_L, the interface between the layers i and j by ∂I_{ij}, A is the total cross-sectional area, and ∂A the boundary of the cross-section.

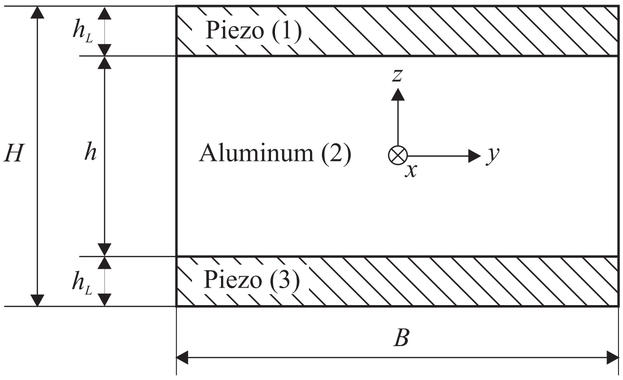

Figure 3: Cross-section of the laminated rod

3.1 Kinematical assumptions

According to Saint Venant's theory of torsion, the elastic deformation of the rod is composed of a rigid-body rotation of the cross-section about the torsional angle $\chi = \chi(x,t)$ and an axial displacement due to cross-sectional warping. It has been shown by Zehetner [5] that under the presence of piezoelectric shear strains the displacement components can be expressed by

$$u_x = \chi' \varphi + \phi^0, \quad u_y = -z\chi, \quad u_z = y\chi, \tag{3}$$

where $\varphi = \varphi(y,z)$ is Saint Venant's warping function, and the additional warping function $\phi^0 = \phi^0(y,z,t)$ represents the additive influence of the piezoelectric strains on the axial displacement. In order to obtain continuity at the interfaces, the warping functions have to satisfy the compatibility relations

$$\partial I_{ij}: \quad [\![\varphi(y,z)]\!] = 0, \quad [\![\phi^0(y,z)]\!] = 0, \tag{4}$$

where the notation $[\![\cdot]\!]$ stands for the jump of the respective quantity at the interface ∂I_{ij}. Note that due to the interface conditions the additional warping function is defined for the whole cross-section. With Eq. (3) and the assumption that $\chi'' = 0$ in case of unconstrained warping, the only non-vanishing linearized strain components are the shear angles

$$\gamma_{xz} = \chi' \left(\frac{\partial \varphi}{\partial z} + y \right) + \frac{\partial \phi^0}{\partial z}, \quad \gamma_{xy} = \chi' \left(\frac{\partial \varphi}{\partial y} - z \right) + \frac{\partial \phi^0}{\partial y}. \tag{5}$$

3.2 Constitutive Relations

The constitutive relations for the considered materials have been stated in section 2. Assuming, that the piezoelectric layers are thin, the normal stress σ_{zz} in thickness and the shear stress τ_{yz} are neglected, such that the mechanical consitutive relations can be written in the generalized form

$$\begin{bmatrix} \sigma_{xx} \\ \sigma_{yy} \\ \tau_{xz} \\ \tau_{xy} \end{bmatrix} = \begin{bmatrix} Q_{11} & Q_{12} & 0 & Q_{16} \\ Q_{12} & Q_{11} & 0 & Q_{16} \\ 0 & 0 & Q_{55} & 0 \\ Q_{16} & Q_{16} & 0 & Q_{66} \end{bmatrix} \left(\begin{bmatrix} \varepsilon_{xx} \\ \varepsilon_{yy} \\ \gamma_{xz} \\ \gamma_{xy} \end{bmatrix} - \begin{bmatrix} \varepsilon^0_{xx} \\ \varepsilon^0_{yy} \\ \gamma^0_{xz} \\ \gamma^0_{xy} \end{bmatrix} \right), \tag{6}$$

where Q_{ij} are the coefficients of the effective stiffness matrix, ε^0_{ii} and γ^0_{ij} are piezoelectric eigenstrains. From the kinematical assumptions in section 3.1 follows that $\varepsilon_{xx} = \varepsilon_{yy} = 0$, such that the constitutive equations reduce to

$$\tau_{xz} = Q_{55}(\gamma_{xz} - \gamma^0_{xz}), \qquad \tau_{xy} = Q_{66}(\gamma_{xy} - \bar{\gamma}^0_{xy}). \tag{7}$$

Note that the constitutive relations for the isotropic substrate (aluminium) follows from Eq. (7) by setting $\gamma^0_{xz} = \gamma^0_{xy} = 0$ and $Q_{55} = Q_{66} = G$. For the piezoelectric materials in section 2 we obtain the effective shear moduli

$$Q_{55} = S^{-1}_{55}, \quad Q_{66} = \begin{cases} S^{-1}_{66} & \text{for ADP}, \\ (S_{11} + S_{12})(S_{11}S_{66} - S^2_{16} + S_{12}S_{66})^{-1} & \text{for MFC}. \end{cases} \tag{8}$$

For the considered piezoelectric materials the effective eigenstrains can be expressed by

$$\gamma^0_{xz} = 0, \qquad \bar{\gamma}^0_{xy} = d_{xy}E_{\|}, \tag{9}$$

where $E_{\|}$ is the component of the electric field parallel to the polarization direction, and d_{xy} is the effective piezoelectric coefficient, which depends on the material type, i.e.

$$d_{xy} = \begin{cases} d_{36} & \text{for ADP}, \\ d_{36} - 2d_{31}S_{16}(S_{11} + S_{12})^{-1} & \text{for MFC type 1}, \\ \sqrt{2}d_{16} - \sqrt{2}(d_{11} + d_{12})S_{16}(S_{11} + S_{12})^{-1} & \text{for MFC type 2}. \end{cases} \tag{10}$$

Assuming that the distance δ between the electrodes is relatively small, the parallel electric field component is proportional to the applied voltage V, but the normal component vanishes,

$$E_{\|} = \frac{V}{\delta}, \quad E_{\perp} = 0. \tag{11}$$

The electrical constitutive relations for the piezoelectric materials are given by

$$D_{\|} \;=\; \eta_{\|}(E_{\|} - E^0_{\|}), \tag{12}$$

where $D_{\|}$ is the dielectric displacement component in direction of the polarization, $\eta_{\|}$ the permittivity, and $E^0_{\|}$ the electric eigenfield representing the direct piezoelectric effect,

$$E^0_{\|} = -\frac{d_{xy}}{\eta_{\|}}\tau_{xy}. \tag{13}$$

Inserting Eqs. (5), (9) and (11) into Eq. (7) yields the shear stresses in the piezoelectric layers as

$$\begin{aligned}\tau_{xz} &= Q_{55}\left[\left(\frac{\partial\varphi}{\partial z}+y\right)\chi'+\frac{\partial\phi^0}{\partial z}\right],\\ \tau_{xy} &= Q_{66}\left[\left(\frac{\partial\varphi}{\partial y}-z\right)\chi'+\frac{\partial\phi^0}{\partial y}-\frac{d_{xy}}{\delta}V\right].\end{aligned} \tag{14}$$

Note that the stresses in the isotropic substrate layer are obtained by setting $Q_{55}=Q_{66}=G$ and $V=0$. Integrating over the cross-sectional area yields the internal torsional moment

$$M_x = C_{11}\chi' - M_x^a \tag{15}$$

with the torsional stiffness C_{11} and the actuating torsional moment M_x^a,

$$C_{11} = \int_A \left[Q_{55}\left(\frac{\partial\varphi}{\partial z}+y\right)y - Q_{66}\left(\frac{\partial\varphi}{\partial y}-z\right)z\right]\,\mathrm{dA}, \tag{16}$$

$$M_x^a = -\int_A\left(Q_{55}\frac{\partial\phi^0}{\partial z}y - Q_{66}\frac{\partial\phi^0}{\partial y}\right)\mathrm{d}A - 2V\int_{A_L} Q_{66}\frac{d_{xy}}{\delta}z\,\mathrm{dA}. \tag{17}$$

3.3 Warping functions

Inserting Eq. (14) into the equilibrium equations of elastostatics,

$$\frac{\partial\tau_{xy}}{\partial y}+\frac{\partial\tau_{xz}}{\partial z}=0,\quad \partial A:\ \tau_n=0,\quad \partial I_{ij}:\ [\![\tau_n]\!]=0, \tag{18}$$

where τ_n is the projection of the shear stress on the outer normal of the boundary and interface, yields boundary value problems for the warping functions φ and ϕ^0, c.f. Zehetner [5]. For the cross-section in Figure 3 the Saint Venant warping function φ follows to

$$\begin{gathered} Q_{66}\frac{\partial^2\varphi}{\partial y^2}+Q_{55}\frac{\partial^2\varphi}{\partial z^2}=0, \\ \partial A_h:\ \frac{\partial\varphi}{\partial z}=-y,\quad \partial A_v:\ \frac{\partial\varphi}{\partial y}=z,\quad \partial I_{ij}:[\![Q_{55}\frac{\partial\varphi}{\partial z}]\!]=0,\quad [\![\varphi]\!]=0,\end{gathered} \tag{19}$$

where ∂A_h denotes the horizontal boundary at the top and bottom, and ∂A_v the vertical boundary. Solutions of Eq. (19) are given in Rand and Rovenski [11]. A similar boundary value problem is obtained for the additional warping function. Using the separation

$$\phi_0(y,z,V(t)) = \frac{d_{xy}}{\delta}V(t)\bar{\phi}^0(y,z) \tag{20}$$

yields the boundary value problem

$$\begin{gathered} Q_{66}\frac{\partial^2\bar{\phi}^0}{\partial y^2}+Q_{55}\frac{\partial^2\bar{\phi}^0}{\partial z^2}=0, \\ \partial A_h:\ \frac{\partial\bar{\phi}^0}{\partial z}=0,\quad \partial A_v:\ \frac{\partial\bar{\phi}^0}{\partial y}=1,\quad \partial I_{ij}:\ [\![Q_{55}\frac{\partial\bar{\phi}^0}{\partial z}]\!]=0,\quad [\![\bar{\phi}^0]\!]=0.\end{gathered} \tag{21}$$

A solution of Eq. (21) has been given in Zehetner [5]. Note that $\varphi(y,z)$ and $\bar{\phi}^0(y,z)$ only depend on geometric and material properties.

4 SENSOR AND ACTUATOR EQUATIONS

Inserting Eq. (20) into Eq. (17) yields the actuator equation

$$M_x^a(t) = c_A V(t), \tag{22}$$

i.e. the actuating moment is proportional to the applied voltage with the actuator constant

$$c_A = \int_A \left[Q_{55} \frac{\partial \bar{\phi}^0}{\partial z} y - Q_{66} \frac{\partial \bar{\phi}^0}{\partial y} \, z \right] \mathrm{d}A - 2 \int_{A_L} Q_{66} \frac{d_{xy}}{\delta} \, z \, \mathrm{d}A. \tag{23}$$

Following the strategy presented by Zehetner and Krommer [7] yields the sensor equation

$$V(t) = -c_S \, \chi_L(t), \tag{24}$$

i.e. the measured voltage is proportional to the tip torsional angle with the sensor constant

$$c_S = \frac{d_{xy} Q_{66} \delta}{L} \frac{\int\limits_{A_{el}} \left(\frac{\partial \varphi}{\partial y} - z \right) \mathrm{d}A}{\int\limits_{A_{el}} \left[\left(\frac{\partial \bar{\phi}^0}{\partial y} - 1 \right) d_{xy}^2 Q_{66} + \eta_{\|} \right] \mathrm{d}A}. \tag{25}$$

Note that the actuator constant depends on cross-sectional properties only, but the sensor constant is a function of the rod length.

5 NUMERICAL EXAMPLES

5.1 Results of rod theory

In this section the expressions for torsional stiffness, actuator and sensor constants given in Eqs. (16), (23) and (25) are evaluated using the numerical values of table 1, $\eta_0 = 8.854 \cdot 10^{-12}$ $\mathrm{F/m}$ is the permittivity of vacuum. The results are compared in table 2. The highest actuator constant is obtained for MFC type 2, and the highest sensor constant for ADP.

property	unit	ADP	MFC type 1	MFC type 2
Q_{55}	N/m^2	$8.6207 \cdot 10^9$	$2.3059 \cdot 10^9$	$2.2959 \cdot 10^9$
Q_{66}	N/m^2	$6.0241 \cdot 10^9$	$4.2484 \cdot 10^9$	$3.8188 \cdot 10^9$
d_{xy}	C/N	$5.17 \cdot 10^{-11}$	$1.7234 \cdot 10^{-10}$	$5.1495 \cdot 10^{-10}$
$\eta_{\|}/\eta_0$	1	15.4	307.12	307.12

Table 1: Material properties

constant	unit	ADP	MFC type 1	MFC type 2
C_{11}	Nm^2/rad	67.31	63.41	62.52
c_A	Nm/V	$8.5827 \cdot 10^{-5}$	$2.002 \cdot 10^{-4}$	$5.4028 \cdot 10^{-4}$
c_S	V/rad	$3.5443 \cdot 10^4$	$3.8773 \cdot 10^3$	$1.5235 \cdot 10^4$

Table 2: Rod Theory: Sensor and actuator constants

5.2 Finite Element Results

In the following these results of rod theory are verified by means of three dimensional Finite Element computations using the model presented in Zehetner [5]. The model has been implemented within *ABAQUS* and *ANSYS*. The following steps have been performed:

1. The torsional stiffness C_{11} is obtained by applying an external torsional couple $M_x^e = 100\ \mathrm{Nm}$ to the rod and evaluating the torsional tip angle χ_L for $V = 0$. The stiffness is then obtained from Eq. (15),
$$C_{11} = \frac{M_x^e L}{\chi_L}. \tag{26}$$
2. For evaluating the actuator constant c_A the external torsional couple is set to $M_x^e = 0$ and the voltage $V = 100\ \mathrm{V}$ is prescribed. Equation (15) yields
$$c_A = \frac{C_{11}}{V}\frac{\chi_L}{L}. \tag{27}$$
3. The sensor constant c_S is obtained by applying an external torsional couple M_x^e to the rod and evaluating the torsional angle and the sensor voltage V. From Eq. (24) follows that
$$c_S = \frac{V}{\chi_L}. \tag{28}$$

The deformed rod for load case 2 with an actuator voltage of $V = 100\ \mathrm{V}$ is shown in Figure 4, where the displacements have been scaled by a factor of 1000. The figure shows that the largest actuation is obtained for MFC type 2.

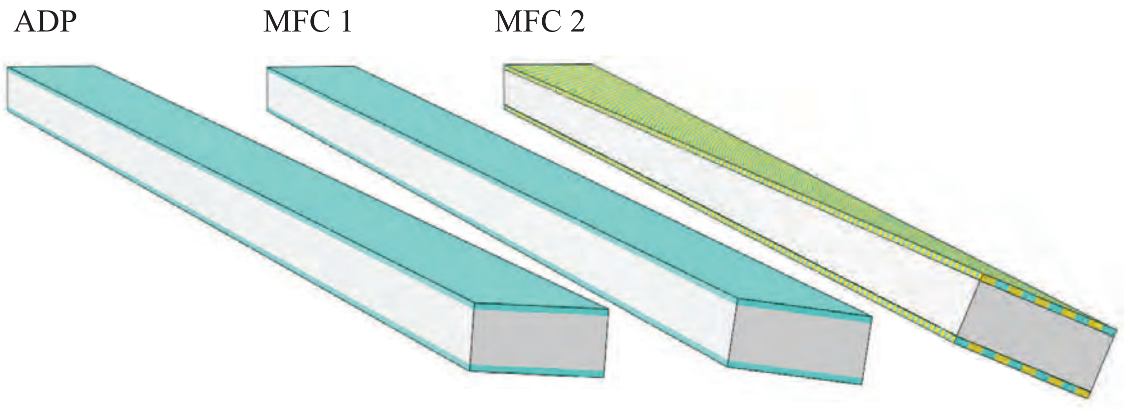

Figure 4: Deformed rod, displacements scaled by a factor of 1000

The results for Eqs. (26)-(28) obtained with *ABAQUS* and *ANSYS* are shown in Tables 3 and 4, respectively.

load case	constant	unit	ADP	MFC type 1	MFC type 2
1	M_x^e	Nm	0.01	0.01	0.01
stiffness	V	V	0	0	0
	χ_L	rad	$7.356 \cdot 10^{-5}$	$7.852 \cdot 10^{-5}$	$7.9380 \cdot 10^{-5}$
	C_{11}	Nm^2/rad	67.97	63.68	62.99
2	M_x^e	Nm	0	0	0
actuator	V	V	100	100	100
constant	χ_L	rad	$6.315 \cdot 10^{-5}$	$1.496 \cdot 10^{-4}$	$4.2620 \cdot 10^{-4}$
	c_A	Nm/V	$8.585 \cdot 10^{-5}$	$1.904 \cdot 10^{-4}$	$5.3691 \cdot 10^{-4}$
3	M_x^e	Nm	0.01	0.01	0.01
sensor	V	V	2.543	0.314	1.209
constant	χ_L	rad	$7.196 \cdot 10^{-5}$	$7.805 \cdot 10^{-5}$	$7.423 \cdot 10^{-5}$
	c_S	V/rad	$3.53 \cdot 10^4$	$4.023 \cdot 10^3$	$1.629 \cdot 10^4$

Table 3: Results of the ABAQUS analysis

load case	constant	unit	ADP	MFC type 1	MFC type 2
1	M_x^e	Nm	0.01	0.01	0.01
stiffness	V	V	0	0	0
	χ_L	rad	$7.39 \cdot 10^{-5}$	$7.842 \cdot 10^{-5}$	$7.538 \cdot 10^{-5}$
	C_{11}	Nm^2/rad	67.66	63.76	66.33
2	M_x^e	Nm	0	0	0
actuator	V	V	100	100	100
constant	χ_L	rad	$6.3 \cdot 10^{-5}$	$1.534 \cdot 10^{-4}$	$4.084 \cdot 10^{-4}$
	c_A	Nm/V	$8.53 \cdot 10^{-5}$	$1.956 \cdot 10^{-4}$	$5.418 \cdot 10^{-4}$
3	M_x^e	Nm	0.01	0.01	0.01
sensor	V	V	2.53	0.309	1.157
constant	χ_L	rad	$7.24 \cdot 10^{-5}$	$7.77 \cdot 10^{-5}$	$7.08 \cdot 10^{-5}$
	c_S	V/rad	$3.494 \cdot 10^4$	$3.976 \cdot 10^3$	$1.634 \cdot 10^4$

Table 4: Results of the ANSYS analysis

The results of rod theory in Section 5.1 are confirmed: The highest actuator constant is obtained for MFC type 2, and the highest sensor constant for ADP. The slight differences between *ABAQUS* and *ANSYS* result from some minor discrepancies in the Finite Element models. A better adjustment of the models is a topic for further investigations.

5.3 Comparison of rod theory and FEM

Finally, the results of rod theory and Finite Element computations are compared in Figure 5. The relative difference of Finite Element and rod theory solutions are shown in Table 5.

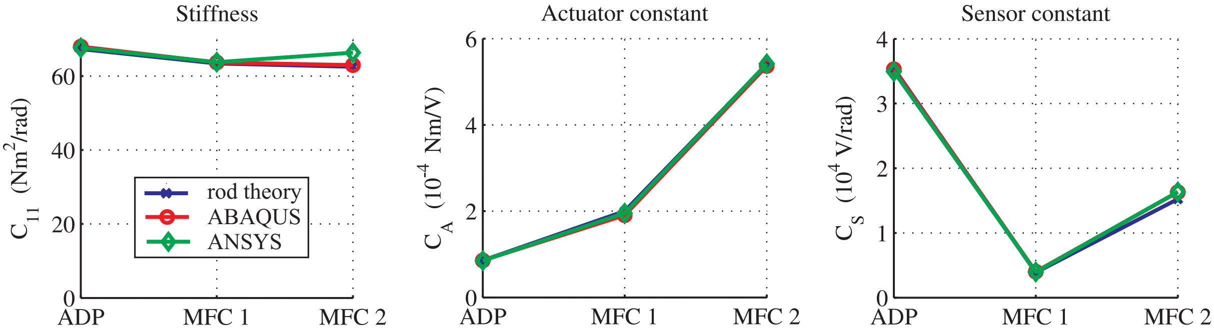

Figure 5: Comparison of the results for C_{11}, c_A and c_S

constant		ADP	MFC type 1	MFC type 2
C_{11}	*ABAQUS*	1.0 %	0.4 %	0.8 %
	ANSYS	0.5 %	0.6 %	6.1 %
C_A	*ABAQUS*	0.0 %	4.9 %	0.6 %
	ANSYS	0.6 %	2.3 %	0.3 %
C_S	*ABAQUS*	0.3 %	3.8 %	6.9 %
	ANSYS	1.4 %	2.5 %	7.3 %

Table 5: Comparison of theory and Finite Element solutions: Relative difference

The maximum difference of 7.3% is obtained for the sensor constant of MFC type 2. The differences in Table 5 result from the assumptions of the presented rod theory, e.g. the kinematical assumptions and the neglect of some coupling terms. All in all Figure 5 shows a good coincidence of the results, such that the presented rod theory can be utilized for finding a suitable configuration for the planned experimental verification.

6 CONCLUSIONS

In this paper it has been shown how three kinds of piezoelectric materials can be used for actuating and sensing of torsional vibrations. An extension of Saint Venant's theory of torsion has been used to derive sensor and actuator equations. A numerical evaluation has shown high sensitivity of the investigated configurations, but relative small efficiency for actuation. The highest sensor constant is obtained for the ADP layer, and the highest actuator constant for MFC type 2.

ACKNOWLEDGEMENTS

Support of the authors from the Austrian Center of Competence in Mechatronics (ACCM) and of M.Krommer & M.Zellhofer from the Austrian Science Fund (FWF Translational project L441-N41 *Sensor Systems for Structural and Health Monitoring*) is gratefully acknowledged.

REFERENCES

[1] W.P. Mason W.P, Piezoelectricity, its history and applications. *Journal of the Acoustical Society of America*, **6**, 1561-1566, 1981.

[2] C. Park, I. Chopra, Modeling piezoceramic actuation of beams in torsion. *AIAA Journal*, **34**, 2582-2589, 1996.

[3] C. Sung, V.V. Varadan, X. Bao, V.K. Varadan, Active torsional vibration control experiments using shear-type piezoceramic sensors and actuators. *Journal of Intelligent Materials Systems and Structures*, **4**, 436-442, 1994.

[4] L.R. Centolanza, E.C. Smith, B. Munsky, Induced-shear piezoelectric actuators for rotor blade trailing edge flaps. *Smart Materials and Structures*, **11**, 24-35, 2002.

[5] Ch. Zehetner, Compensation of Torsion in Rods by Piezoelectric Actuation, *Archive of Applied Mechanics*, **78**, 921-933, 2008.

[6] Ch. Zehetner, Compensation of torsional vibrations in rods by piezoelectric actuation. *Acta Mechanica*, **207**, 121-133, 2009.

[7] Ch. Zehetner, M. Krommer, Control of torsional vibrations by piezoelectric sensors and actuators, *Proceedings of COMPDYN 2009*, M. Papadrakakis, N.D. Lagaros, M. Fragiadakis (eds.), Rhodes, Greece, June 22-24, 2009.

[8] Ch. Zehetner, M.Krommer, Control of torsional vibrations in piezolaminated rods, *Structural Control and Health Monitoring*, accepted for publication, 2011.

[9] P. Berik, A. Benjeddou, Piezoelectric d_{15} shear response-based torsion actuation mechanism: An experimental benchmark and its 3D finite element simulation. *International Journal of Smart and Nano Materials*, **1**, 224-235, 2010.

[10] A. Deraemaeker, H. Nasser, A. Benjeddou, A. Preumont, Mixing Rules for the piezoelectric properties of macro fiber composites, *Journal of Intelligent Material Systems and Structures*, **20**, 1475-1482, 2009.

[11] O. Rand, V. Rovenski, *Analytical Methods in Anisotropic Elasticity*, Birkhäuser, Boston, 2005.

COMPDYN 2011
III ECCOMAS Thematic Conference on
Computational Methods in Structural Dynamics and Earthquake Engineering
M. Papadrakakis, M. Fragiadakis, V. Plevris (eds.)
Corfu, Greece, 25–28 May 2011

THEORETICAL ANALYSIS AND NUMERICAL MODELING OF ELASTIC WAVE PROPAGATION IN HONEYCOMB-TYPE THIN LAYER

B. –Y. Tian, B. Tie, D. Aubry

LMSSMat (CNRS UMR8579), Ecole Centrale Paris
Grande Voie des Vignes, 92295 Châtenay-Malabry Cedex, France
(biyu.tian, bing.tie, denis.aubry)@ecp.fr

Keywords: Honeycomb sandwich, Elastic wave propagation, periodic media, Bloch wave transformation.

Abstract. *The present work is devoted to a theoretical analysis and numerical modeling of the phenomena of high-frequency wave propagation in honeycomb-type periodic media. A one-dimensional periodic elastic rod model and a two-dimensional periodic elastic beam hexagonal model are considered. The Bloch wave direct and inverse transformations are applied to find general or particular solutions. By identifying eigenfrequencies and the corresponding eigenmodes of the periodic systems, important information, such as the frequency bandgaps and the diffracted waves caused by the periodic cells, is obtained. The aims are to improve our understanding of how HF waves are transmitted and attenuated in the studied periodic media and to link the theoretical analyses to our numerical assessments.*

1 INTRODUCTION

Sandwich shells using honeycomb-type core are very useful composite materials to design lightweight but high-strength structures, especially in aerospace and aeronautics industries, for the honeycomb core provides an efficient solution to increase bending stiffness without significant increase in structural weight. When high-frequency (HF) flexural waves propagating in such sandwich shells, the involved wavelengths are of the same order of the characteristic lengths of the honeycomb cells, or even shorter, the honeycomb cellular microstructure can interact with the waves and highly perturb the propagation phenomena, as they are governed by the geometry and the material properties of the cells. Indeed, due to the periodic geometric and material discontinuities within the cellular structure, waves can propagate completely or be attenuated even stopped, depending upon the involved frequencies and upon the spatial direction, so we observe the existence of passing and stop bands in frequency domain ([1]). As the classical homogenized models cannot take into account this kind of interaction, they fail to correctly describe the transient flexural behaviors of the sandwich shells in HF ranges ([2]). Therefore, relevant analytical and numerical models should be established by understanding how HF waves propagate in a honeycomb thin layer and interact with its cellular structure.

To simplify and optimize numerical models but still taking into account the detail characteristics of the cellular microstructure, the Bloch wave theory is more and more widely used now. The basic idea is to transform a non-periodic function defined in a periodic structure to a set of periodic functions having the same periodicity as the structure. Therefore the study of the original function in the whole structure can be replaced by considering the periodic functions in a unique cell. The theory was firstly applied in the quantum mechanics to solve the Schrödinger equation in periodic lattice of particles ([3]). Now it has been introduced to the structural mechanics. In the literature, the dispersion equations relating the frequency to the Bloch wave vector have been given for several types of honeycomb cells composed by beams and the effects of the cellular characteristics, for example the slenderness ratio and the internal angle, have been discussed in [4] and [5].

The honeycomb thin layer that we are interested is composed by thin-walled hexagonal regular cells, which give rise to an in-plane two-dimension periodic hexagonal cellular microstructure. Each hexagonal cell has two parallel sides whose thickness is doubled due to the manufacturing process, which forms ribbons with a semi-hexagonal profile and bonds them together in pairs to obtain hexagonal cells. These doubled thickness walls result in plane anisotropic properties of the honeycomb thin layer. Our first research works presented herein consist in the development of theoretical and numerical modeling tools based on the Bloch wave theory and then in their validation by application to a one-dimensional (1D) periodic elastic rod model and a two-dimensional (2D) elastic beam hexagonal model, for which the previously mentioned double thickness aspect is considered. The Bloch wave modes inside one cell are considered and the dispersion equations are obtained.

The paper is organized as follows: The section 2 introduces the direct and inverse Bloch wave transformations. The section 3 is devoted to the theoretical and numerical analyses of the wave propagation in a 1D periodic structure composed by elastic rods. The modeling of a more complex 2D periodic structure composed by elastic beams is then presented in the section 4, before some concluding remarks in the section 5.

2 BLOCH WAVE THEORY

Let us consider a periodic structure Ω of space dimension *N*, a *primitive cell* Q_0 and a set of basis vector $\mathbf{e}_i$ (i=1,...,N), called *direct cell basis*, are defined so that the entire structure Ω can be obtained by repeating the primitive cell along the direct cell basis. Dual to the primitive cell Q_0, a *reciprocal cell* Q_0^* and a *reciprocal cell basis*, $\mathbf{e}_j^*$, are defined, which satisfies the following relation:

$$\mathbf{e}_i . \mathbf{e}_j^* = \delta_{ij} \tag{1}$$

where δ_{ij} is the Kronecker delta. The reciprocal cell is also called the *first Brillouin zone* [6]. The areas of Q_0 and Q_0^*verify the following equation:

$$\text{volume}(Q_0)\text{volume}(Q_0^*) = 1 \tag{2}$$

For any non periodic function $\mathbf{V}(\mathbf{x})$ defined on Ω, the Bloch wave theory states that, for each wave vector $\mathbf{k}$ restricted in the first Brillouin zone Q_0^*, the Bloch transformation $\mathbf{V}^B(\mathbf{x},\mathbf{k})$ of $\mathbf{V}(\mathbf{x})$ is a periodic function having the same periodicity as the periodic structure, which is also called *Bloch wave function*:

$$\mathbf{V}^B(\mathbf{x},\mathbf{k}) = \sum_n \mathbf{V}\left(\mathbf{x} + n_i\lambda_i\mathbf{e}_i\right)e^{i\mathbf{k}.(\mathbf{x}+n_i\lambda_i\mathbf{e}_i)} \tag{3}$$

Then, $\mathbf{V}(\mathbf{x})$ can be recovered by the following inverse Bloch transformation:

$$\mathbf{V}(\mathbf{x}) = \frac{1}{\text{volume}(Q_0^*)}\int_{Q_0^*} \mathbf{V}^B(\mathbf{x},\mathbf{k})e^{-i\mathbf{k}.\mathbf{x}}d\mathbf{k} \tag{4}$$

By virtue of the Bloch wave transformation, the propagation phenomena of HF elastic waves, transmission, reflection, conversion and attenuation, through the periodic microstructure can be understood by investigating the Bloch wave modes within the primitive cell, which allows to save lots of the efforts when doing analysis and simulation.

3 WAVE PROPAGATION IN 1D ELASTIC ROD MODEL

The first periodic structure considered herein is a 1D elastic rod model, which is a topology of a primitive cell composed by two rigidly jointed elastic rods respectively of lengths l_1 and l_2, therefore the period of the 1D medium is $\lambda = l_1 + l_2$ (Figure 1).

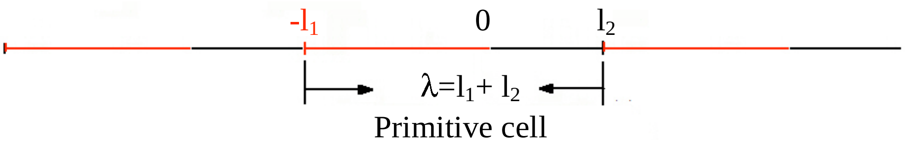

Figure 1: 1D elastic rod model

The equilibrium eigen equation of the i-th rod (i=1, 2) reads as:

$$\frac{d}{dx}\left[E_i\frac{dU(x)}{dx}\right] = -\rho_i\omega^2 U(x) \tag{5}$$

where (E_i, ρ_i) denote the Young's Modulus and the density, ω the eigenfrequency and U(x) the corresponding eigenmode. By applying Bloch wave transformation to (5), the following Bloch eigen equation is obtained:

$$E_i \frac{\partial^2 U^B(x,\ k)}{\partial x^2} - 2ikE_i \frac{\partial U^B(x,\ k)}{\partial x} - E_i k^2 U^B(x,\ k) = -\rho_i \omega^2 U^B(x,\ k) \tag{6}$$

with $k \in Q_0^* = [0, 2\pi/\lambda[$ the Bloch wave vector. Given k, the goal is to find the eigenvalue ω and the corresponding Bloch eigenmode U^B(x, k) of the eigen problem (6). It is straightforward that the general solution of (6) has the following analytical form:

$$U_i^B(x,\ k) = a_i e^{i\left(k + \frac{\omega}{c_i}\right)x} + b_i e^{i\left(k - \frac{\omega}{c_i}\right)x} \tag{7}$$

where, for the i-th rod, $c_i = \sqrt{E_i/\rho_i}$ is the wave velocity and (a_i, b_i) are four constants to be determined.

3.1 Dispersion equation

To calculate the four constants (a_i, b_i), (i=1, 2), we consider the following the interface conditions between the two rods inside the primitive cell and the periodic conditions on its extremities:

$$\begin{aligned} &U^B(0^-) = U^B(0^+),\ N^B(0^-) = N^B(0^+) \\ &U^B(-l_1) = U^B(l_2),\ N^B(-l_1) = N^B(l_2) \end{aligned} \tag{8}$$

where $N^B = dU^B/dx - ikU^B$ denotes the 1D Bloch axial force vector. Substituting the general solution form (7) to these conditions (8), a system of four linear equations is obtained. To ensure that system admits nontrivial solutions, its determinant must vanish, which finally gives a relation between k and ω, called *dispersion equation.*

For our 1D rod model, the following analytical dispersion equation can be obtained:

$$\cos(\lambda k) = \cos(\omega T_1)\cos(\omega T_2) - \left(\frac{Z_1}{2Z_2} + \frac{Z_2}{2Z_1}\right)\sin(\omega T_1)\sin(\omega T_2) \tag{9}$$

where $Z_i = \rho_i c_i$ denotes the characteristic acoustic impedance and $T_i = l_i / c_i$ the time for wave to propagate through the whole i-th rod. Using (9), for each given frequency ω, a Bloch wave vector $k = k_r + i\, k_{im}$ can be found and result in the following Bloch eigenmode in the i-th rod:

$$U_i^B(x,k) = a_i e^{i\left(k_r + \frac{\omega}{c_i}\right)x} e^{-k_{im}x} + b_i e^{i\left(k_r - \frac{\omega}{c_i}\right)x} e^{-k_{im}x} \tag{10}$$

Therefore, when k is real ($k_{im} = 0$), the Bloch wave mode U_i^B is a propagating mode, which is transmitted to the adjacent cells with the same amplitude and there is no energy losing when propagating through the periodic medium. Otherwise, when k is complex or pure imaginary ($k_{im} \neq 0$), U_i^B is an evanescent Bloch wave mode, it vanishes rapidly when propagating to the adjacent cells and the pure energy exchanging between periodic cells is equal to zero ([1]).

The frequency ranges that give real values of k is called *passing band* and the others *stop band*. The figure 2 gives the frequency bandgap of the 1D model: The red curves plot the two real solutions of k and so indicate the passing bands, while the blue curves present the stop bands, by plotting the imaginary part k_{im} of the two complex solutions of k: $\frac{j\pi}{\lambda} + i\,k_{im}$, (j=0,1). We remark that the location and the width of the stop bands mainly depend on the ratio between the two characteristic acoustic impedances Z_1/Z_2 ([7]).

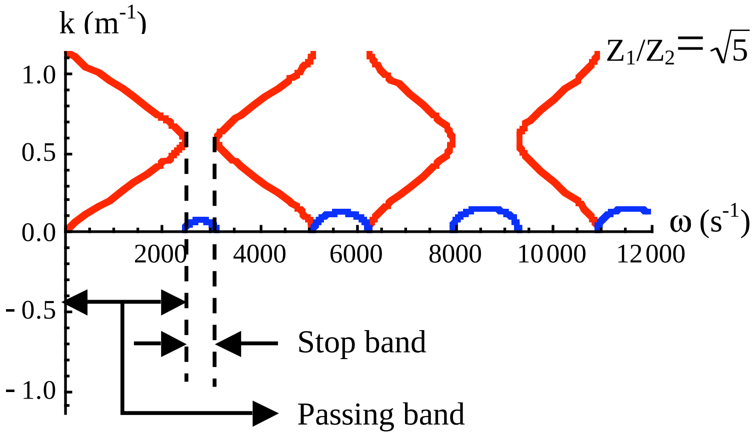

Figure 2: Dispersion relation of eigenfrequency on k, $Z_1/Z_2 = \sqrt{5}$

3.2 Diffracted wave analysis

Now, we consider an incident plane wave $u_0(x, t) = e^{i(k_0x-\omega_0t)}$ and investigate how its propagation through the 1D periodic structure that is perturbed by the periodic cells. To do this, the wave solution u(x, t) is decomposed into two parts:

$$u(x,\ t) = \left[e^{ik_0x} + u_d(x)\right]e^{-i\omega_0t} \tag{11}$$

where (k_0, ω_0) are the wave vector and the angular frequency of the incident wave. We are interested in finding $u_d(x)$, the diffracted wave caused by the periodicity of the cells, which indicate us in fact what's the difference between the wave motion in a periodic medium and in a homogenous medium.

By substituting the equation (11) in the equilibrium eigenequation (5), we get:

$$\frac{d}{dx}\left[E_i\frac{du_d(x)}{dx}\right] + \underbrace{\left\{\frac{d}{dx}\left[E_i\frac{du_0(x)}{dx}\right] + \rho_i\omega_0^2u_0(x)\right\}}_{f_e} = -\rho_i\omega_0^2u_d(x) \tag{12}$$

where the second term of the left member is considered as an external loading f_e due to the incident wave. By expanding $u_d(x)$ as a linear combination of eigenmode U(x):

$$u_d(x) = \sum\nolimits_n \alpha_n U_n(x) \tag{13}$$

the Bloch diffracted wave u_d^B reads as:

$$u_d^B(x,\ k) = \sum\nolimits_n \alpha_n(k) U_n^B(x,\ k) \tag{14}$$

where $U^B(x, k)$ is the Bloch eigenmode and $\alpha_n(k)$ the Bloch coefficient.

Since we have already calculated $U^B(x, k)$, we look for $\alpha_n(k)$ now. Applying the Bloch wave transformation to the equation (12) to get Bloch equilibrium eigenequation and substituting the equation (14) into it, we get:

$$\sum_n \rho_i(\omega^2 - \omega_0^2)\alpha_n(k)U_n^B(x, k) = f_e^B(x, k) \tag{15}$$

where f_e^B is the Bloch external loading that can be expanded using the same Bloch modes $U^B(x, k)$:

$$f_e^B(x, k) = \sum_n F_n(k)U_n^B(x, k) \tag{16}$$

Therefore α_k can be obtained in the following way:

$$\alpha_n(k) = \frac{F_n(k)}{\rho_i(\omega^2 - \omega_0^2)} \tag{17}$$

Subsequently the u_d^B is got using (14) and finally u_d is obtained using the inverse Bloch transformation (4).

The figure 3 illustrates the ratio of amplitude between u_0 and u_d with two incident waves with having respectively two different frequencies f_0=2.5 kHz and f_0=10 kHz, whose corresponding wave lengths in the first rod, λ_0, are respectively 0.3 and 0.075 times of the period. We observe an important amplification of wave propagation phenomena due to diffracted wave caused by the periodicity of the cells and the amplification level is not affected a lot by the frequency of the incident wave.

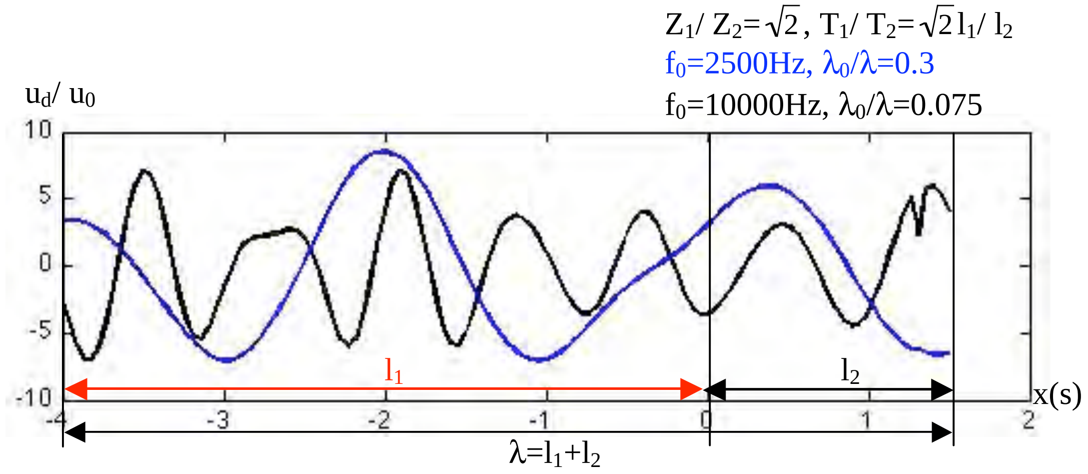

Figure 3: Diffracted wave inside the primitive cell.

4 WAVE PROPAGATION IN 2D ELASTIC BEAM MODEL

The second periodic structure considered here is a 2D elastic beam model (Figure 4). It is a topology of a primitive cell composed by three rigidly jointed elastic beams ([8]) with the same length s. The Lamé constants and the density of the beams are (λ, μ, ρ). The thickness of beam (1) is twice of the thickness of the other two beams (2) and (3) (see Figure 4). Each beam is firstly considered in its local basis (**s**, **n**), in which the unit vector **s** is parallel to the beam's axis and the unit vector **n** is perpendicular to the beam's axis. Then the entire model is considered in a global basis (**x**, **y**).

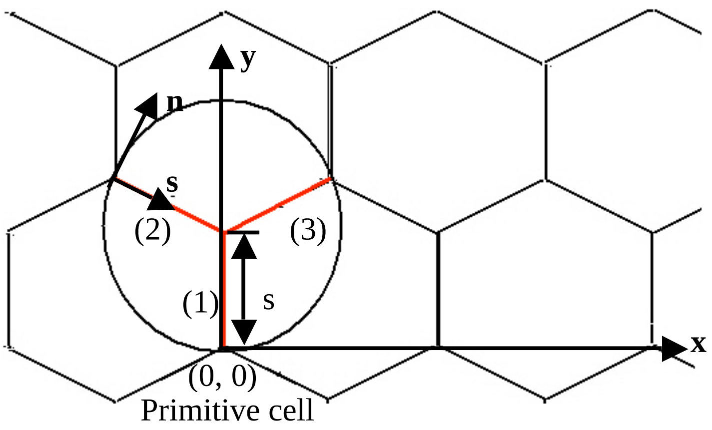

Figure 4: 2D elastic periodic structure composed by beams

4.1 Dispersion relation

The well-known Timoshenko kinetics for thick beams is used, so the displacement **u**(s, t) in each beam reads as:

$$\mathbf{u}(s,t) = u_{01}(s)\mathbf{s} + u_{02}(s)\mathbf{n} + t\, u_{13}(s)\mathbf{s} \tag{18}$$

where $u_{01}(s)$ and $u_{02}(s)$ are the displacement fields of the middle line in direction **s** and **n** and $u_{13}(s)$ is the rotation of the fibers.

For each beam, the Bloch equilibrium eigenequations of the 2D model are:

$$\begin{aligned}
&\frac{d^2U_{01}^B}{ds^2} - 2i(\mathbf{k}.\,\mathbf{s})\frac{dU_{01}^B}{ds} - (\mathbf{k}.\,\mathbf{s})^2U_{01}^B = -\frac{\rho\omega^2}{\lambda+2\mu}U_{01}^B \\
&\frac{d^2U_{02}^B}{ds^2} - 2i(\mathbf{k}.\,\mathbf{s})\frac{dU_{02}^B}{ds} - (\mathbf{k}.\,\mathbf{s})^2U_{02}^B + \frac{dU_{13}^B}{ds} = -\frac{\rho\omega^2}{\mu}U_{02}^B,\ (m=0,\ 1) \\
&\frac{d^2U_{13}^B}{ds^2} - 2i(\mathbf{k}.\,\mathbf{s})\frac{dU_{13}^B}{ds} - \left[(\mathbf{k}.\,\mathbf{s})^2 + \frac{12\mu}{(\lambda+2\mu)H_m^2}\right]U_{13}^B - \frac{12\mu}{(\lambda+2\mu)H_m^2}\frac{dU_{02}^B}{ds} = -\frac{\rho\omega^2}{\lambda+2\mu}U_{13}^B
\end{aligned} \tag{19}$$

with $(U_{01}^B,\ U_{02}^B, U_{13}^B)$ the Bloch eigenmode and $\mathbf{k} \in Q_0^*$ the Bloch wave vector. In this 2D model, the first Brillouin zone Q_0^* is also a hexagonal cell. Similar to the analysis we did for the 1D model, giving **k**, we look for the eigenvalues and the corresponding Bloch eigenmodes of the equation (19).

According to the interface conditions between the beams inside the primitive cell and the periodic conditions on their extremities as following:

$$\begin{aligned}
&U_{01}^{B(1)} + U_{02}^{B(1)} = U_{01}^{B(2)} + U_{02}^{B(2)} = U_{01}^{B(3)} + U_{02}^{B(3)} \\
&U_{13}^{B(1)} = U_{13}^{B(2)} = U_{13}^{B(3)} \\
&N^{B(1)} + Q^{B(1)} + N^{B(2)} + Q^{B(2)} + N^{B(3)} + Q^{B(3)} = 0 \\
&M^{B(1)} = M^{B(2)} = M^{B(3)}
\end{aligned} \tag{20}$$

where $\mathbf{N}^B$ is the Bloch axial force vector, $\mathbf{Q}^B$ is the Bloch transverse shear force vector and $\mathbf{M}^B$ is the Bloch bending moment, we get a system of 18 linear equations. Let the determinant of the system equal to zero, we can get finally the dispersion equations between **k** and ω. Unfortunately, in the 2D model, we are not able to explicit the dispersion equation and we can only plot the dispersion surface numerically (Figure 5). We find that the ratio of H_0/H_1 largely affects the width of the stop bands and the bandgap will move to HF range if we shorter the lengths of the beams.

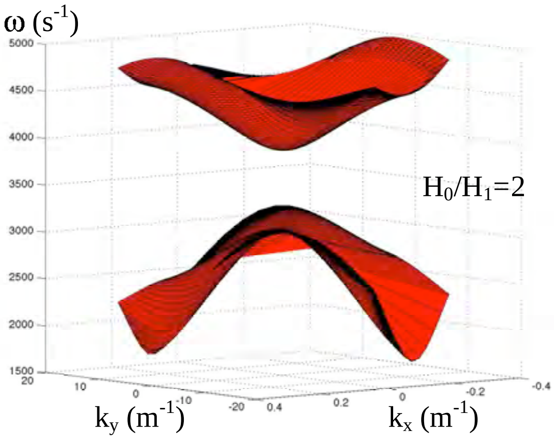

Figure 5: Dispersion surface of eigenfrequency upon Bloch wave vector.

5 CONCLUSIONS

The classical homogenized models fail to correctly describe the HF transient flexural behavior of the honeycomb-type sandwich shells. It is necessary to look into the effects coming from the periodic microstructure of the honeycomb thin layer. The Bloch wave theory has been adopted in order to take into account the characteristics of the honeycomb cells while optimizing numerical models and saving calculation costs.

Theoretical analyzing and numerical modeling tools base on the Bloch wave theory and the FE method has been developed. They are at first applied to a 1D periodic structure composed by elastic rods and validated. By considering only the primitive cell, the dispersion equation is obtained, which allows identifying the passing and stopping bands of frequency. With an incident plane wave, the diffracted wave due to the periodicity of the cells is calculated and amplification phenomena are observed independently from the frequency of the incident wave.

Then, a 2D periodic hexagonal regular structure composed by elastic beams is investigated. The first result of eigenfrequency bandgap is obtained.

Our current research work is to apply our theoretical and numerical tools to the honeycomb-type thin layer composed of periodic thin-walled hexagonal regular cells.

REFERENCES

[1] D. J. Mead, A general theory of harmonic wave propagation in linear periodic systems with multiply coupling. *Journal of Sound and Vibration*, **27**, 235-260, 1973.

[2] A. Grédé, B. Tie, D. Aubry, Elastic wave propagation in hexagonal honeycomb sandwich panels: Physical understanding and numerical modelling. *Journal de Physique*, **134**, 507–514, 2006.

[3] P. Atkins, R. Friedman, *Molecular quantum mechanics*. Oxford university press, New York, 2005.

[4] A. Srikantha, J. Woodhouse, N. A. Fleck, Wave propagation in two-dimensional periodic lattice. *J. Acoust. Soc. Am*, **119**(4), 1995-2005, 2006.

[5] S. Gonella, M. Ruzzene, Analysis of in-plane wave propagation in hexagonal and re-entrant lattices. *Journal of Sound and Vibration*, **312**, 125-139, 2008.

[6] L. Brillouin, *Wave propagation in the periodic structures*. Dover Publications, New York, 1946.

[7] B. –Y. Tian, B. Tie, D. Aubry, Théorie des Ondes de Bloch Appliquée à la Modélisation de la Propagation d'Ondes Elastiques dans des Milieux Périodiques. *10th Colloque National en Calcul des Structures (CSMA 2011),* Giens, France, May 9-13, 2011.

[8] C. Davini, F. Ongaro, A Homogenized Model for Honeycomb Cellular Materials. *Journal of Elasticity,* **Published online**, 2011.

COMPDYN 2011
III ECCOMAS Thematic Conference on
Computational Methods in Structural Dynamics and Earthquake Engineering
M. Papadrakakis, M. Fragiadakis, V. Plevris (eds.)
Corfu, Greece, 25–28 May 2011

Bi-hierarchical finite element for the analysis of the non-axisymmetric free vibration of shells of revolution

Mohammed Nabil Ouissi[1], Abderrahim Houmat[2]

[1] Abou Bekr Belkaïd University - Tlemcen Algeria

n_ouissi@mail.univ-tlemcen.dz

[2] Abou Bekr Belkaïd University - Tlemcen Algeria

a_houmat@ mail. univ-tlemcen.dz

Keywords: Bi-hierarchical finite element, double hierarchical increment, shells of revolution, linearly varying thickness, non – axisymmetric, free vibration.

Abstract. *A new hierarchical finite element is developed to analyze the free vibration of isotropic shells of revolution with linear varying thickness. It is a bi-hierarchical four nodes quadrilateral element with three degrees of freedom (three displacements) by node. The specificity of this element is a double increase of the hierarchical mode number independently according to both axial and radial directions. The advantage is that the solution is accurate for high ratio dimensions as well flattened axisymmetric (plates) shells that slim ones (high cylindrical shells) with different shapes and boundary conditions. The second advantage is the possibility of using only one element to idealize regular shape shells. Through the application of this element to some numerical examples, the comparisons with other studies show clearly that this element gives good results accuracy with simple idealization for axisymmetric and non-axisymmetric shells vibration (thick and thin).*

1 INTRODUCTION

The propose of this work is to present a new bi-hierarchical finite element to idealize isotropic shells of revolution with linear varying thickness. Shells of revolution can be of different shape and dimensions. Thin and thick plates and cylindrical shells cannot be idealized by the same finite elements in standard or hierarchical method. The dimensions ratio and the shape of the shell influence on the choice of the finite element and the mesh. For modeling for example a storage tank, one must have two elements, one for the cylinder and the other for the plate. The new proposed element can idealize the two shells.

The literature on finite element approximation of shells of revolution is huge. Let us just mention a few different approaches. Bodies of revolution compounds of thin shell segments, thick shell segments, and rings have been analyzed by using quadrilateral isoparametric elements of revolution of eight nodes [1] and Mindlin Reissner axisymetric finite elements which take in account the shearing strains and the rotational inertia effects [2]. Other methods were implemented of which a three-dimensional method of analysis to determine the frequencies and eigen modes of paraboloïd solids and paraboloïd shells of revolution with variable thickness [3] and a spline finite element method for the analysis of the free vibration of shells of revolution which is based on the theory of the thin shells [4].

The proposed element in this work is a four nodes volumetric and axisymetric bi-hierarchical finite element with only displacements as degrees of freedom. The word "bi-hierarchical" comes from the fact that this element has two hierarchical mode numbers, one in the axis direction and the second in the radius direction. These two hierarchical mode numbers increase independently. This element can than idealize flattened shells like plates and high shells like cylinders and conic shells (thins and thicks) or structures composed of them. For the first kind of shells, the radius direction hierarchical mode number is increased to have the accuracy of the results, and for the second kind, the axis hierarchical mode number is increased.

2 POTENTIAL ENERGY

The potential energy stored in the shell is in the form of strain energy due to the effect of both stretching and bending. The strain energy expression can be written as

$$U(t)=\frac{1}{2}\int_{R_i}^{R_e}\int_0^H\int_0^{2\pi}\left(\sigma_r\varepsilon_r+\sigma_z\varepsilon_z+\sigma_\theta\varepsilon_\theta+\tau_{rz}\gamma_{rz}+\tau_{r\theta}\gamma_{r\theta}+\tau_{z\theta}\gamma_{z\theta}\right).r.dr.dz.d\theta z \tag{1}$$

And in matrix form

$$U(t)=\frac{1}{2}\int_{R_i}^{R_e}\int_0^H\int_0^{2\pi}\left(\{\varepsilon\}^T.\{\sigma\}\right)r.dr.dz.d\theta \tag{2}$$

Where $\{\varepsilon\}=\begin{Bmatrix}\varepsilon_r\\ \varepsilon_z\\ \varepsilon_\theta\\ \gamma_{rz}\\ \gamma_{r\theta}\\ \gamma_{z\theta}\end{Bmatrix}$ (3-a) and $\{\sigma\}=\begin{Bmatrix}\sigma_r\\ \sigma_z\\ \sigma_\theta\\ \tau_{rz}\\ \tau_{r\theta}\\ \tau_{z\theta}\end{Bmatrix}$ (3-b) are the stain and stress vectors

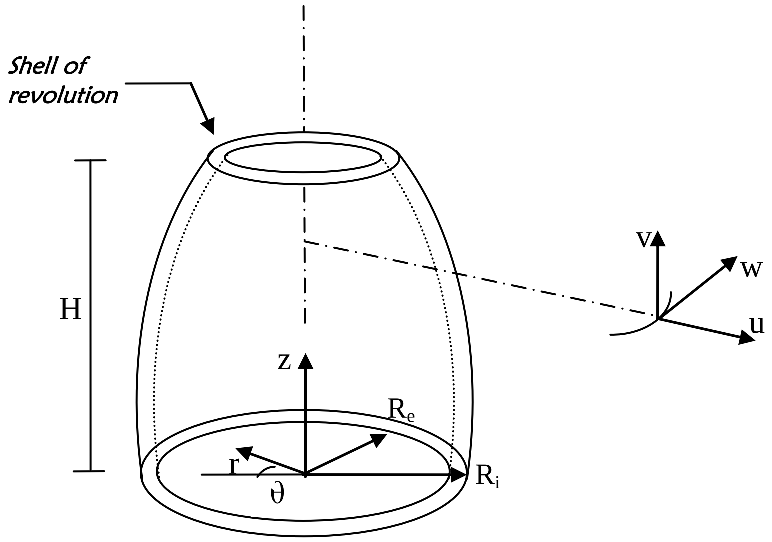

Figure 1: Shell of revolution

The constitutive relationship between stress and strain is the generalized Hooke's law. For an isotropic homogeneous structure, it is given as

$$\{\sigma\} = [D]\{\varepsilon\} \tag{4}$$

Where $[D]$ is the elasticity matrix, E is Young's modulus, and υ is Poisson ratio of the structure.

Eq. (4) into Eq. (2), the potential energy is given in terms of strain as

$$U(t) = \frac{1}{2}\int_{R_i}^{R_e}\int_0^H\int_0^{2\pi}\left(\{\varepsilon\}^T.[D]\{\varepsilon\}\right)r.dr.dz.d\theta \tag{5}$$

The strain-displacement relations are given by:

$$\{\varepsilon\} = \begin{Bmatrix} \varepsilon_r \\ \varepsilon_z \\ \varepsilon_\theta \\ \gamma_{rz} \\ \gamma_{r\theta} \\ \gamma_{z\theta} \end{Bmatrix} = \begin{Bmatrix} \dfrac{\partial u}{\partial r} \\ \dfrac{\partial v}{\partial z} \\ \dfrac{u}{r} + \dfrac{1}{r}\cdot\dfrac{\partial w}{\partial \theta} \\ \dfrac{\partial u}{\partial z} + \dfrac{\partial v}{\partial r} \\ \dfrac{1}{r}\cdot\dfrac{\partial u}{\partial \theta} + \dfrac{\partial w}{\partial r} - \dfrac{w}{r} \\ \dfrac{1}{r}\cdot\dfrac{\partial v}{\partial \theta} + \dfrac{\partial w}{\partial z} \end{Bmatrix} \tag{6}$$

The strain vector can be expressed in terms of the displacement vector as follows:

$$\{\varepsilon\} = [d]\{\delta\} \tag{7}$$

Where $\{\delta\} = \{u, v, w\}$ (8)

and $[d]$ is a differential operator matrix

The stress vector can be expressed in terms of the displacement vector, as:

$$\{\sigma\}=\frac{E}{(1+\nu).(1-2\nu)}.\begin{Bmatrix} (1-\nu).\dfrac{\partial u}{\partial r}+\nu.\left(\dfrac{\partial v}{\partial z}+\dfrac{u}{r}+\dfrac{1}{r}.\dfrac{\partial w}{\partial \theta}\right) \\ (1-\nu).\dfrac{\partial v}{\partial z}+\nu.\left(\dfrac{\partial u}{\partial r}+\dfrac{u}{r}+\dfrac{1}{r}.\dfrac{\partial w}{\partial \theta}\right) \\ (1-\nu).\left(\dfrac{u}{r}+\dfrac{1}{r}.\dfrac{\partial w}{\partial \theta}\right)+\nu.\left(\dfrac{\partial u}{\partial r}+\dfrac{\partial v}{\partial z}\right) \\ \dfrac{1-2\nu}{2}.\left(\dfrac{\partial u}{\partial z}+\dfrac{\partial v}{\partial r}\right) \\ \dfrac{1-2\nu}{2}.\left(\dfrac{1}{r}.\dfrac{\partial u}{\partial \theta}+\dfrac{\partial w}{\partial r}-\dfrac{w}{r}\right) \\ \dfrac{1-2\nu}{2}.\left(\dfrac{1}{r}.\dfrac{\partial v}{\partial \theta}+\dfrac{\partial w}{\partial z}\right) \end{Bmatrix} \tag{9}$$

3 KINETIC ENERGY

The kinetic energy of the shell can be written as

$$T(t)=\frac{1}{2}\int_{R_i}^{R_e}\int_{0}^{H}\int_{O}^{2\pi}\rho.\left[\left(\frac{\partial u(r,z,\theta,t)}{\partial t}\right)^2+\left(\frac{\partial v(r,z,\theta,t)}{\partial t}\right)^2+\left(\frac{\partial w(r,z,\theta,t)}{\partial t}\right)^2\right].r.dr.dz.d\theta \tag{10}$$

where ρ is the density. Equation can be written as follows

$$T(t)=\frac{1}{2}\int_{R_i}^{R_e}\int_{0}^{H}\int_{O}^{2\pi}\rho.\{\dot{\delta}\}^T.\{\dot{\delta}\}.r.dr.dz.d\theta \tag{11}$$

where $\{\delta\}$is the displacement vector defined by Eq. (8) , and differentiation is with respect to the time, t.

4 HIERARCHICAL FINITE ELEMENT FORMULATION

The hierarchical finite element method known under the name of the p-version of the finite element method is more precise and its convergence is faster than that of the h-method. Indeed, when the exact solution is analytical everywhere the rate of convergence is exponential, whereas that of the h-method is only algebraic. The quality of the solutions is not very sensitive to the distortions of the elements, which allows the use of flattened elements or great ratio on sides without penalizing the precision too much. In addition, as a hierarchical formulation is adopted for the representation of displacements, the matrix of stiffness relative to a given degree imbricates those of lower degrees. This makes it possible to obtain in an economic way a sequence of solutions instead of only one solution as it is the case of the h-method [5], [6] et [7].

The hp version of the finite element method has as a characteristic to increase the precision by increasing both the degree of the polynomial of interpolation and the number of finite elements as for the standard finite element method [7].

4.1 Idealization of the shell

The shell is divided into four nodes hierarchical axisymmetric quadrilateral isoparametric finite elements (Fig.1). The element size is arbitrary. They may all be of the same size or may all be different. The shell can also be idealized by only one element if the thickness of the shell is varying linearly or if it is constant.

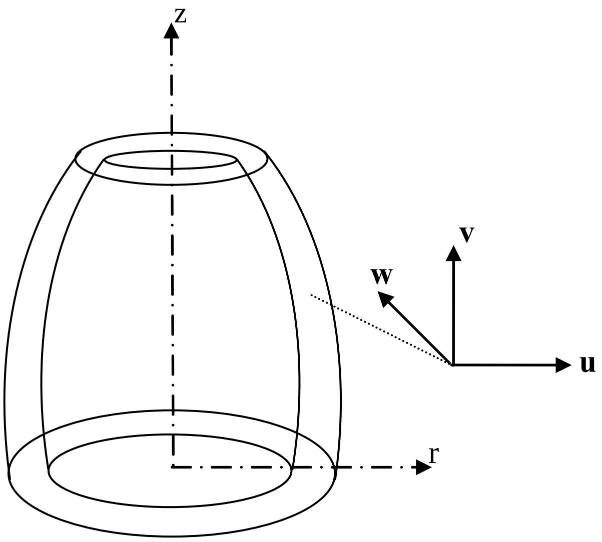

Figure 2: Displacements of a shell point

The equation of motion of the shell admit the representation of the Radial, circumferential and axial displacement components u, v, and w following respectively R, Z and θ in the following form

$$\begin{cases} u(r,z,\theta)=\overline{u}(r,z).\cos n\theta \\ v(r,z,\theta)=\overline{v}(r,z).\cos n\theta \\ w(r,z,\theta)=\overline{w}(r,z).\sin n\theta \end{cases} \tag{12}$$

The displacement functions $\overline{u}(r,z)$, $\overline{v}(r,z)$ and $\overline{w}(r,z)$ can be expressed in terms of the nodal displacements of the finite elements by means of an appropriate set of interpolation functions. title should be written centered, in 14pt, boldface Roman, all capital letters. It should be single spaced if the title is more than one line long.

4.2 Shape functions selection

The hierarchical shape functions are generally selected in the Serendipity space. In this paper, the shape functions are built from the shifted Legendre orthogonal polynomials introduced by [8]. They are so different from those introduced by [9]. These polynomials are defined in the interval [0,1].

They can be classified in three categories, nodal shape functions, side shape functions, internal shape functions. Their recurring form is:

$$\begin{cases} f_i(x)=1-x \\ f_i(x)=x \\ f_{i+2}(x)=\int_0^x P_i(\alpha).d\alpha \end{cases} \tag{13}$$

where $P_i(\alpha)$ are the shifted Legendre polynomials defined by :

$$\begin{cases} P_0(\alpha)=1 \\ P_1(\alpha)=2.\alpha-1 \\ P_{i+1}(\alpha)=\dfrac{1}{i+1}\cdot\left[(-2i-1+(4i+2)\alpha)\cdot P_i(\alpha)-i\cdot P_{i-1}(\alpha)\right] \end{cases} \tag{14}$$

i = 1,2,3,…

The shape functions are given on the basis of one-dimensional hierarchical finite element. The origin of the non-dimensional coordinates is at the left end of the element. For the C° continuous problems, the first two linear shape functions of the standard finite element method are retained. The higher order C° shape functions vanish at each end of the elements, they are used to describe the displacement function inside the element. These functions are generated by using the recursive formula (16).

Having the shape functions, the displacement functions $\overline{u}(r,z)$, $\overline{v}(r,z)$ and $\overline{w}(r,z)$ can be expressed:

$$\begin{cases} \overline{u}(r,z)=\sum_{1}^{n} N_i(r,z).u_i \\ \overline{v}(r,z)=\sum_{1}^{n} N_i(r,z).v_i \\ \overline{w}(r,z)=\sum_{1}^{n} N_i(r,z).w_i \end{cases} \tag{15}$$

where

$$N_i(r,z)=f_k(r).g_l(z) \tag{16}$$

with: k = 1,..,p+1 et l = 1,..,q+1

p: Hierarchical modes number according to ξ,
q: Hierarchical modes number according to η, f, g: Shape functions

The matrix form of the expression (15) is:

$$\{\overline{\delta}\}=[N].\{q\} \tag{17}$$

Where:

$$\{\overline{\delta}\}=\begin{Bmatrix} \overline{u}(r,z) \\ \overline{v}(r,z) \\ \overline{w}(r,z) \end{Bmatrix} \tag{18}$$

is the generalized displacement vector,

$$\{q\}=\{u_1,v_1,w_1,\ldots,u_i,v_i,w_i,\ldots\}^T \tag{19}$$

With i=1,…,(p+1)(q+1)

is the nodal displacement vector

$$[N]=[[N_1],[N_2],\ldots,[N_i],\ldots,[N_{(p+1)(q+1)}]] \tag{20}$$

is the shape functions matrix, where $\left[N_i\right]$ is a sub-matrix given by:

$$\left[N_i\right]=\begin{bmatrix} f_k(r).g_l(z) & 0 & 0 \\ 0 & f_k(r).g_l(z) & 0 \\ 0 & 0 & f_k(r).g_l(z) \end{bmatrix} \tag{21}$$

$f_k(r)$ and $g_l(z)$ are the nodal, edge and internal shape functions of the element.

4.3 Shell stiffness matrix

Defining the stiffness properties of the shell is reduced to evaluating the stiffness of a typical element.

Expression (12) can be written

$$\{\delta\}=[\theta_n].\{\bar{\delta}\} \tag{22}$$

Where

$$[\theta_n]=\begin{bmatrix} \cos n\theta & 0 & 0 \\ 0 & \cos n\theta & 0 \\ 0 & 0 & \sin n\theta \end{bmatrix} \tag{23}$$

Substitute Eq. (22) into Eq. (7), then one can write

$$\{\varepsilon\}=[d].\{\delta\}=[d].[\theta_n].\{\bar{\delta}\}=\left[\bar{d}\right].\{\bar{\delta}\} \tag{24}$$

Where $\left[\bar{d}\right]$ is an operator vector .Eq. (24) into Eq. (5), the potential energy can be written, as

$$U(t)=\frac{1}{2}\int_{R_i}^{R_e}\int_0^H\int_0^{2\pi}\left(\left(\left[\bar{d}\right].\{\bar{\delta}\}\right)^T.[D].\left[\bar{d}\right].\{\bar{\delta}\}\right).r.dr.dz.d\theta \tag{25}$$

To evaluate the stiffness matrix of an element, the global cylindrical coordinates (r , z) may be expressed in terms of the local non-dimensional coordinates (ξ , η) which are varying from 0 to 1 whose origin is the node lower right of the element.

After transformations, the potential energy can be written, as

$$U(t)=\frac{k\pi}{2}\int_0^1\int_0^1\left(\{q\}^T.[N]^T.\left[\bar{d}\right]^T.[D].\left[\bar{d}\right].[N].\{q\}\right).|J|.r.d\xi.d\eta=\frac{1}{2}\{q\}^T.[K].\{q\} \tag{26}$$

Where

$$[K_e]=k\pi\int_0^1\int_0^1\sum_{i=1}^{p+1}\sum_{j=1}^{q+1}\left([B_i]^T.[D].[B_j]\right).r.|J|d\xi.d\eta \tag{27}$$

is the element stiffness matrix.

$[B]=\left[\bar{d}\right].[N]$ and k = 2 for n = 0 and k = 1 for n = 1,2,… (n: circumferential wave number),

4.4 Mass matrix

The kinetic energy can be written

$$T(t)=\frac{1}{2}\int_{R_i}^{R_e}\int_{0}^{H}\int_{O}^{2\pi}\rho.\left\{\bar{\dot{\delta}}\right\}^T.[\theta_n]^T.[\theta_n].\left\{\bar{\dot{\delta}}\right\}r.dr.dz.d\theta=\frac{1}{2}\{\dot{q}\}^T.[M_e].\{\dot{q}\} \tag{28}$$

Where

$$[M_e]=k\pi.\int_0^1\int_0^1\rho.\sum_{i=1}^{p+1}\sum_{j=1}^{q+1}[N_i]^T.[N_j].|J|.r.d\xi.d\eta \tag{29}$$

is the element mass matrix

4.5 Numerical integration

The double integral appearing in the forms of the mass and stiffness matrices results in a numerical integration. For his implementation, one uses the Gauss quadrature expressed by:

$$\int_0^1 f(x)d(x)=\sum_{i=1}^{N}W_i.f(x_i) \tag{30}$$

Where N is the integration points number. After having tested several integration points numbers, the number which is a compromise between the computing time and the precision is:

$$N_{int}=p+2 \tag{31}$$

5 RESULTS AND DISCUSSIONS

The convergence and comparison studies must be carried out to ensure the reliability of the results. The vibration frequency ω is expressed in terms of the frequency parameter

$$\Omega=\omega\cdot\sqrt{\frac{2\rho(1+\nu)}{E}} \tag{32}$$

5.1 Convergence

The bi-hierarchical finite element is used for the first time, to study the free vibration of a very thin cylindrical shell with free boundary conditions. The external and internal radius are respectively $R_e=1$ and $R_i=0.99$, the shell height is H=2. Table 1 show the convergence study of the first six modes with an increasing of the two hierarchical mode numbers p and q following respectively the radius and the axis directions for two and four elements.

Element number	**q**	**p**	**DOF**	**Modes number**					
				1	**2**	**3**	**4**	**5**	**6**
2 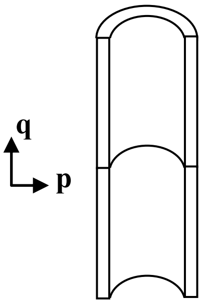	1	1	18	0.014	0.018	1.923	1.930	3.012	4.007
	2	1	30	0.014	0.018	1057	1.347	1.882	2.614
	2	2	45	0.013	0.017	1.057	1.346	1.882	2.614
	4	2	81	0.013	0.017	0.996	1.300	1.463	1.561
	4	3	108	0.013	0.017	0.996	1.300	1.463	1.561
	6	3	156	0.013	0.017	0.996	1.300	1.461	1.531
	8	3	189	0.013	0.017	0.996	1.300	1.461	1.530
	BCM			0.013	0.017	0.996	1.300	1.465	1.529
	ANSYS			0.013	0.017	0.996	1.303	1.463	1.533
4 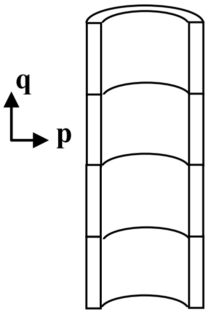	1	1	30	0.014	0.018	1.318	1.851	2.724	2.939
	2	1	54	0.014	0.018	0.998	1.310	1.529	1.576
	2	2	81	0.013	0.017	0.998	1.309	1.526	1.571
	4	2	153	0.013	0.017	0.996	1.300	1.461	1.531
	4	3	204	0.013	0.017	0.996	1.300	1.461	1.531
	6	3	300	0.013	0.017	0.996	1.300	1.461	1.530
	8	3	396	0.013	0.017	0.996	1.300	1.461	1.530
	BCM			0.013	0.017	0.996	1.300	1.465	1.529
	ANSYS			0.013	0.017	0.996	1.303	1.463	1.533

Table 1: Convergence and comparison study of frequency parameter Ω for a free cylindrical shell (Re =1, Ri=0.99, H=2)

The results are compared with those of the boundary collocation method [10] and those of ANSYS (20 harmonic and axisymmetric structural element solid with eight nodes). For the two idealization, two and four elements, an accuracy of three digits after the comma is reached for the first two modes for p=2 and q=2.

For modes 3, 4, 5; the convergence is reached for p=6 and q=3 for a 2 elements model, and for p=4 and q=2 for a 4 elements model. The sixth mode reaches the convergence for p=8 and q=3 for 2 elements, and p=6 and q=2 for 4 elements.

It is apparent that by increasing the number of elements, the hierarchical mode numbers p and q necessary to reach convergence are smaller. But the degrees of freedom number becomes more important. Indeed for mode 6 this number is of 300 for 4 elements whereas it is only of 189 for 2 elements.

The matrices size is smaller if one increases p and q rather than the elements number. Table (2) shows that the number of degrees of freedom can be easily decreased by modifying the values of p and q according to the shell geometry.

5.2 Comparison with other methods

In order to verify the accuracy of the bi-hierarchical finite element in solving the vibration of shells of revolution, a comparison study is conducted for different shells. A thick and a very thin cylindrical shells, a hollow cylindrical shell with varying thickness and a very thin plate. The results are compared with those of the boundary collocation method BCM, [10] and with those obtained by ANSYS where the harmonic and axisymmetric structural element solid with eight nodes is used.

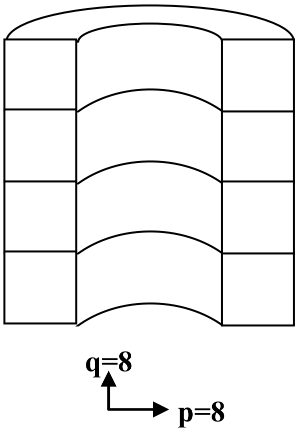

		Modes					
circumferential wave's number	**Method**	**1**	**2**	**3**	**4**	**5**	**6**
0	**Present**	2.298	2.512	3.237	4.138	4.502	6.352
	BCM	2.299	2.513	3.237	4.137	4.500	6.347
	ANSYS	2.300	2.514	3.239	4.141	4.508	6.368
1	**Present**	2.124	2.716	3.305	3.448	3.892	4.645
	BCM	2.123	2.716	3.304	3.447	3.890	4.645
	ANSYS	2.125	2.718	3.307	3.452	3.895	4.650
2	**Present**	1.371	1.444	3.142	3.143	4.195	4.626
	BCM	1.371	1.441	3.139	3.140	4.194	4.622
	ANSYS	1.370	1.442	3.142	3.143	4.199	4.630
3	**Present**	2.820	3.079	3.762	4.285	5.531	5.716
	BCM	2.818	3.071	3.758	4.279	5.526	5.711
	ANSYS	2.818	3.074	3.761	4.286	5.538	5.727

Table 2: Comparison of frequency parameters Ω for free thick cylindrical shell (Re =1/3, Ri=1, H=4/3,p=8,q=8)

The comparison of the frequency parameters Ω with those of the boundary collocation method [10] and ANSYS (32 harmonic and axisymmetric structural element solid with eight nodes) for a free thick cylindrical shell is given in table 1. The inner radius is R_i=1/3, the outer radius is $R_{e=}$1and the shell height is H=4/3. Considering that the results accuracy is quickly reached for a low number of elements if one increases the number of hierarchical modes, the shell is idealized by only four bi-hierarchical finite elements with the same hierarchical modes numbers p and q according to the axial and radial directions. For this very thick cylindrical shell, p=q=8.

The results given in table 2 are in good agreement with those of the two other methods, as well for the axisymmetric case as for the non-axisymmetric case. For the high frequencies the results approach more those of the BCM that those of ANSYS. The reason is that the warping of cross-sections is important and thus the interpolation polynomials degree must be larger to describe these modes. It is easily and automatically possible by using this bi-hierarchical finite element.

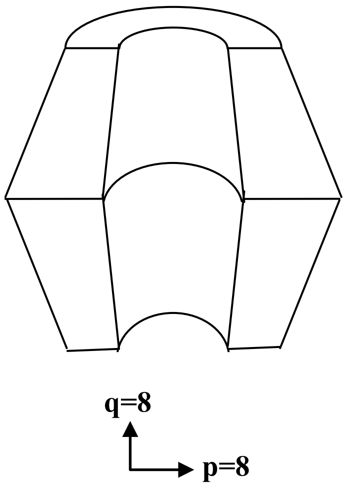

		Modes					
circumferential wave's number	**Method**	**1**	**2**	**3**	**4**	**5**	**6**
0	**Present**	2.006	2.193	2.366	2.844	3.273	3.880
	BCM	2.007	2.195	2.367	2.839	3.279	3.896
	ANSYS	2.007	2.193	2.367	2.846	3.275	3.889
1	**Present**	1.629	1.996	2.518	2.832	3.370	3.382
	BCM	1.627	2.002	2.518	2.835	3.370	3.384
	ANSYS	1.629	1.997	2.519	2.839	3.373	3.386
2	**Present**	0.644	0.761	1.853	2.466	2.967	3.309
	BCM	0.646	0.760	1.861	2.464	2.963	3.308
	ANSYS	0.644	0.761	1.855	2.468	2.976	3.312
3	**Present**	1.641	1.762	2.444	3.356	3.767	4.228
	BCM	1.641	1.755	2.449	3.348	3.761	4.228
	ANSYS	1.642	1.763	2.448	3.365	3.774	4.239

Tableau 3: Comparison of frequency parameters Ω for a free thick hollow cylindrical shell of varying thickness (R_e varying , R_i=0.6, H=2,p=8,q=8)

Finally, a thick free hollow cylindrical shell with varying thickness is considered. Along the axis the inner radius is R_i=0.6 and the outer radius is varying from R_e=0,8 at the edges to R_e=1 at the middle height . The height is H=2. The shell being thick, one takes the same hierarchical modes numbers the p=q= 8. Each half cylindrical shell is idealized by one bi-hierarchical finite. Comparison Results with those of the BCM [10] and those of ANSYS (16 elements) are given in table 3. The same observation is made as for the two other examples. The results agree very well with those of the BCM and those of ANSYS, which shows the power of this element.

6 CONCLUSION

The bi-hierarchical finite element presented in this study is able to give accurate frequencies for shells of revolution of an unspecified shape. The results show clearly that this element can be easily used for the extreme cases of very thin or very thick shells of revolution. With this element one is not constrained any more to have the same number of hierarchical modes in the two main directions of the radial and axial shells of revolution. Indeed, if the shapes and dimensions change (thick or thin shells) the hierarchical modes number can change very easily. This element can also be used to idealize a composed shell, plate linked to cylindrical shell for example. Finally this bi-hierarchical finite element allows triple increase in the accuracy, finite elements number, and radial and axial hierarchical modes numbers.

REFERENCES

[1] D. Bushnell, buckling and vibration of hybrid bodies of revolution, *Computers & Structures*, **7**, 517-537, 1977.

[2] M. Özakça, and E. Hinton, Free vibration analysis and optimization of axisymmetric plates and shells—I. Finite element formulation, *computers and structures*, **52**, 1181-1197, 1993.

[3] J. H. Kang, and A.W. Leissa, Free vibration of thick complete conical shells of revolution from a three-dimensional theory, *Journal of Applied Mechanics*, **72**, Issue 5, 797-800, 2005.

[4] M.H. Luah, and S.C. Fan, General free vibration analysis of shells of revolution using the spline finite element method , *computers and structures*, **33**, 1153-1162, 1989.

[5] I. Babuska, and B. Szabo, On the rates of convergence of the finite element method, *Int. J. Num. Meth. Engng.*, **18**, Issue 3, 323-341, 1982.

[6] B.A. Szabo, The use of a priori estimates in engineering computations, *Comp. Meth. Appli. Mech. Engng.*, **82**, Issues 1-3, 139-154, 1990.

[7] B.A. Szabo, and I. Babuska, , *Finite element analysis,* John Wiley, 1991.

[8] A. Houmat, Three dimensional hierarchical finite element free vibration analysis of annular sector plates, *Journal of Sound and Vibrations*, **276**, Issues 1-2, 181-193, 2004.

[9] A. G. Peano, *Hierarchies of conforming finite elements*, Ph.D. Thesis, Washington University, 1975.

[10] A. Houmat and J.R. Hutchinson, Free vibration of bodies of revolution by boundary collocation , *Journal of Sound and Vibrations*, 171, Issue 1, 35-48, 1994.

20 COMPDYN 2011
III ECCOMAS Thematic Conference on
Computational Methods in Structural Dynamics and Earthquake Engineering
M. Papadrakakis, M. Fragiadakis, V. Plevris (eds.)
Corfu, Greece, 25–28 May 2011

DISCRETE EQUIVALENCE PRINCIPLE FOR MODEL ORDER REDUCTION OF DYNAMIC STRUCTURES

Fikret Kamil CORBACI[1]
[1] STM
Savunma Teknolojileri Muhendislik Ticaret A.S.
Ankara Teknoloji Gelistirme Bolgesi
Bilkent Cyberpark E Blok 5.Cadde No: 6/A,
06800, Bilkent – Cankaya/Ankara, Turkey
e-mail: fcorbaci@stm.com.tr

Keywords: Finite Element Methods, Dynamic Analysis, Model Order Reduction, Discrete Equivalence

Abstract. *In dynamic structural analyses, in order to improve the analyses performance, model order reduction methods are applied to mathematical models obtained by computational techniques to reduce the size of the associated problems. There are various techniques for model order reduction with different performance levels applying to complex problems. In this study, model order reduction approaches based on discrete equivalent principle are compared with some methods given in literature.*

Newly developed discrete equivalent model order reduction approach is based on that the response of the original and reduced order model is equal to each other at discrete time steps. In the proposed model order reduction approach, the degrees-of-freedom (DOFs) that give responses conforming with the original system are the main criteria at the selection of the DOFs which are transferred into the reduced system as the active DOFs.

The developed model order reduction method was applied to create some sample structures by using some Matlab codes and the results of the model order reduction analyses are compared with the original system response. In the same Matlab codes, responses of some other model order reduction methods were also compared with the original system responses. Damping characteristics of the systems are taken into account in all these comparisons and the results of analyses with different model orders are evaluated in terms of calculation time and performance.

To develop computational models, finite element methods are employed. It is observed that as the damping of the original system decreases, the accuracy of the model order reduction process decreases. In simulation studies, the inputs for the sample systems are selected to be external forces applied to some nodes. If the input force is smooth enough then the performance of model order reduction process based on discrete equivalent methods improves substantially.

1 INTRODUCTION

Model order reduction methods have been the subject of significant number of recent studies, e.g., see [1] for an overview and discussion. Many techniques have been proposed to obtain reduced order finite element models by reducing the orders of mass and stiffness matrices. One class of techniques such as [2, 3, 4, 5, 6, 7, 8, 9, 10] uses a direct reduction of physical model coordinates by omitting some selected degrees-of-freedom (DOF), whose accuracy is very sensitive to the selection of active DOF. The second class of methods such as the works [11] and [12] is the modal methods having better accuracy, yielding decoupled equations and giving a better insight into the problems; however, they have the following disadvantages: computation of the modes may be costly if too many modes are needed in the analyses and their results may be unacceptable due to the effects of truncated modes. In order to overcome this drawback, quasi-static compensation (QSC) method studied in [13, 14, 15, 16, 17, 18] was developed. The third class of methods is the Ritz vector methods (e.g., see [1, 19, 20, 21, 22, 23, 24, 25, 27, 28]) developed to eliminate the need to compute costly eigenvalue problems and to improve the accuracy in cases where eigenvectors are not the best choice; these methods can be regarded as a generalized approach replacing the eigenvectors by more generally defined Ritz vectors. Juanmin Gu et. al. in [29] used the data recovery techniques in dynamic analyses to recover the physical response from the modal response obtained by using the mode-displacement method. In [30], the frequency and time domain responses of some popular model order reduction methods such as QSC, quasi-static mode synthesis (QSM) method [19], subspace based identification [31] and nonlinear least square (NLS) fit in frequency domain [32, 33] are compared.

In this paper, a family of model order reduction techniques is derived in time domain based on the principle that the exact solution of the semi-discrete equation of a system and the solution of the reduced order model match at discrete time steps. It is sufficient to pursue exact match at discrete time steps, i.e., discrete equivalence, since the solutions of semi-discrete equations are obtained only at the time steps. Numerical examples are presented to compare the performance of the proposed approach with that of exact solution. It is shown that proposed methods have certain advantages over conventional methods.

2 DEFINITIONS

A linear time-invariant discrete-time system is represented by the transfer function obtained by the ratio of the Z-transform of input to the Z-transform of output as follows

$$G_z(z) = \frac{D_z(z)}{F_z(z)} = \frac{num(z)}{den(z)} \tag{1}$$

where $D_z(z)$ and $F_z(z)$ are respectively Z-transforms of output and input, $num(z) = n_k z^k + n_{k-1} z^{k-1} + \ldots + n_1 z + n_0$, $den(z) = d_l z^l + d_{l-1} z^{l-1} + \ldots + d_1 z + d_0$ and z is the complex *Z*-transform variable [34]. For a signal having the discrete values $u_0, u_1, u_2, .. u_k$, the *Z*-transform is defined as follows

$$U(z) = Z\{u(k)\} = \sum_{k=-\infty}^{\infty} u_k z^{-k} \tag{2}$$

On the other hand, a linear time-invariant continuous-time system is represented by the transfer function in terms of the complex Laplace transform variable s as follows

$$G_s(s) = \frac{D_s(s)}{F_s(s)} = \frac{num(s)}{den(s)} \tag{3}$$

where $D_s(s)$ and $F_s(s)$ are respectively Laplace transforms of the output and input, $num(s) = n_k s^k + n_{k-1} s^{k-1} + \ldots + n_1 s + n_0$ and $den(s) = d_l s^l + d_{l-1} s^{l-1} + \ldots + d_1 s + d_0$. For a time varying signal $u(t)$, the Laplace transform is defined as follows

$$U(s) = L\{u(t)\} = \int_0^\infty u(t) e^{-st} dt \tag{4}$$

3 DISCRETE EQUIVALENCE PRINCIPLE

It is common to study a time integration algorithm by considering the single modal equation. Accordingly, the following continuous-time transfer function $G_s(s)$ of the first-order single modal equation of a parabolic problem is considered

$$G_s(s) = \frac{1}{s+\lambda} \tag{5}$$

where λ is the modal parameter. For the second-order structural systems, $G_s(s)$ is equal to

$$G_s(s) = \frac{1}{s^2 + 2\xi\Omega s + \Omega^2} \tag{6}$$

where Ω is the undamped natural frequency and ξ the damping ratio. Note that Ω and λ belong to the finite element discretization, and they are usually denoted by the superscript h in literature that is omitted in this article for brevity. Let $G_z(z)$ denote the discrete-time transfer function of a time integration method which is unknown to us. Suppose that we have a forcing term f(t) that is applied to the semi-discrete equation and we want to integrate the semi-discrete equation via the time integration method. Let $F_z(z) = \{f(k)\}$ and $F_s(s) = \{f(t)\}$ denote the *Z*-transform and Laplace transform of the forcing term *f(t)*, respectively. Then, if the solution of the time integration method is equal to the exact solution of the semi-discrete equation at discrete time steps, the following equation should hold:

$$Z^{-1}\{G_z(z)F_z(z)\} = L^{-1}\{G_s(s)F_s(s)\}_{t=k\Delta t} \tag{7}$$

Equivalently,

$$G_z(z) = \frac{1}{F_z(z)} Z\left\{L^{-1}\{G_s(s)F_s(s)\}_{t=k\Delta t}\right\} \tag{8}$$

where $Z^{-1}\{\cdot\}$ and $L^{-1}\{\cdot\}$ are, respectively, the inverse Z-transform and inverse Laplace transform operators, Δt time step and *k* an integer denoting the time step number. Note that (8) guarantees that the solution of the time integration method matches with the exact solution at discrete time steps no matter what the time step is; however, the frequency response of this time integration method cannot match with that of the original semi-discrete equation. Therefore, time integration methods obtained by using (8) are called discrete equivalent methods. Now, (8) can be used to find the unknown discrete-time transfer function $G_z(z)$ of the time integration method, e.g., see [30] for details.

4 DESIGN OF TIME INTEGRATION METHODS BY USING DISCRETE EQUIVALENCE PRINCIPLE

Consider two systems having the following semi-discrete equations

$$M\ddot{d} + C\dot{d} + Kd = f \tag{9}$$

$$\hat{M}\ddot{\hat{d}} + \hat{C}\dot{\hat{d}} + \hat{K}\hat{d} = \hat{f} \tag{10}$$

where (9) represents the original system and (10) represents the system obtained by a model order reduction method. It is noteworthy that in general the solutions *d(t)* and $\hat{d}(t)$ are different [35]. Suppose that even though (9) and (10) represent two different systems, certain outputs of these systems obtained by discrete equivalence principle (7) are equal to each other at discrete time steps. That is, at a discrete time step *t=kΔt*, we have

$$\hat{d}_k = Ed_k \quad \text{and} \quad \hat{f}_k = Ef_k \tag{11}$$

where *E* is the transformation matrix defined by

$$E = \begin{bmatrix} e_i^T \\ e_j^T \\ \vdots \\ e_k^T \end{bmatrix} \tag{12}$$

and e_i is the unit vector in the ith direction whose elements are zero except for the *i*th element which is 1 as follows

$$e_i = \begin{bmatrix} 0 & 0 & \dots & 0 & 1 & 0 & \dots\dots & 0 \end{bmatrix}^T \tag{13}$$

where superposed *T* denotes transpose. Thus, the outputs of systems represented by (9) and (10) that correspond to the unit vectors e_i in (12) are equal to each other at discrete time steps. Note that the transformation matrix is in general rectangular and by definition $EE^T = I$ due to $e_i e_j^{\ T} = \delta_{ij}$ is equal to the Kronecker delta function.

Consider the following semi-discrete equations of a parabolic problem

$$M\dot{d} + Kd = f \tag{14}$$

where M is the mass matrix, *K* stiffness matrix, *f* load vector, *d* displacement vector and $\dot{d}$ time derivative of *d*. Note that *M* and *K* are symmetric, *M* positive definite and *K* positive semidefinite. The load vector *f* is the function of time denoted by *f=f(t)* for $t \in [0,T]$. The purpose of the initial value problem defined by (14) is to find the solution *d=d(t)* satisfying the initial condition *d(0)=d*$_0$. Next, we will apply "response invariant" time integration methods to the system represented by (14).

Suppose that we would like to have that the impulse response of the original system represented by (9) obtained by IRI method [6] is equal to the exact solution of (9) at discrete time steps. Consider the following single DOF modal equation of (9)

$$\dot{d} + \lambda d = f \tag{15}$$

The discrete-time solution of the time integration method is equal to $f_d(k\Delta t) = Z^{-1}\{G_z(z)\}$, and the corresponding continuous-time impulse response of the semi-discrete equation is equal to $f_c(t) = L^{-1}\{G_s(s)\}$; then, $f_d(k\Delta t) = \Delta t f_c(t)\big|_{t=k\Delta t}$ [6]. On the other hand, since

$$G_z(z) = Z\{f_d(k\Delta t)\} = Z\{f_c(t)\}\Delta t = Z\{L^{-1}\{G_s(s)\}\}\Delta t \tag{16}$$

where $G_s(s)$ is given by (5); then, (16) yields

$$G_z(z) = \frac{D_z(z)}{F_z(z)} = Z\left\{L^{-1}\left\{\frac{1}{s+\lambda}\right\}\right\}\Delta t = \frac{z}{z - e^{-\lambda\Delta t}}\Delta t \tag{17}$$

where z is the time shift operator such that $z^n d_k = d_{k+n}$ where d_k is the output value at the kth time step, i.e., $t = k\Delta t$, then (12) yields that

$$d_{k+1} = e^{-\lambda\Delta t} d_k + \Delta t f_{k+1} \tag{18}$$

5 TOTAL ENERGY EQUIVALENCE METHOD

The main criteria in newly proposed model order reduction method is based on principal that "The total energy level of the model order reduced system should be equal to the total energy level of the original system.". In this approach, the main method accuracy criteria comes from the comparison of total energy levels of both systems. In order to reach the total energy, the kinetic and potential energy of the original system can firstly be given as,

$$\text{Kinetic energy: } \boldsymbol{H}_k = \frac{1}{2}\dot{\boldsymbol{d}}_k{}^T \boldsymbol{M}\dot{\boldsymbol{d}}_k \tag{19}$$

$$\text{Potential energy: } \boldsymbol{P}_k = \frac{1}{2}\boldsymbol{d}_k{}^T \boldsymbol{K}\boldsymbol{d}_k \tag{20}$$

By using (19) and (20), total energy is obtained as

$$\text{Total energy: } \boldsymbol{T}_k = \boldsymbol{H}_k + \boldsymbol{P}_k \tag{21}$$

To obtain the lowest deviation on the total energy error of both systems, system transformation formulation is developed and then system mass M and system stiffness K matrices by finite element methods are produced.

To calculate the total energy, forward difference integration method is applied to (21) by $\boldsymbol{d}_k$ and $\boldsymbol{d}_{k+1}$.

By using $\dot{\boldsymbol{d}}_k \cong \dfrac{\boldsymbol{d}_{k+1} - \boldsymbol{d}_k}{\Delta t}$ statement, kinetic energy of original model can be written,

$$H_k = \frac{1}{2\Delta t^2}\left(d_{k+1}^T - d_k^T\right) M \left(d_{k+1} - d_k\right) \tag{22}$$

and (21) equation can be orientated again by (20), original model total energy (22) yields,

$$T_k = H_k + P_k = \frac{1}{2} d_k^T K d_k + \frac{1}{2\Delta t^2}\left[d_{k+1}^T M d_{k+1} - d_{k+1}^T M d_k - d_k^T M d_{k+1} + d_k^T M d_k\right] \tag{23}$$

The matrix form of (23) is given by,

$$T_k = \frac{1}{2}\begin{bmatrix} d_k^T & d_{k+1}^T \end{bmatrix} \begin{bmatrix} K + \dfrac{M}{\Delta t^2} & -\dfrac{M}{\Delta t^2} \\ -\dfrac{M}{\Delta t^2} & \dfrac{M}{\Delta t^2} \end{bmatrix} \begin{Bmatrix} d_k \\ d_{k+1} \end{Bmatrix} \tag{24}$$

The total energy of the model order reduced system is similarly formed as,

$$\hat{T}_k = \frac{1}{2}\begin{bmatrix} \hat{d}_k^T & \hat{d}_{k+1}^T \end{bmatrix} \cdot \begin{bmatrix} \hat{K} + \dfrac{\hat{M}}{\Delta t^2} & -\dfrac{\hat{M}}{\Delta t^2} \\ -\dfrac{\hat{M}}{\Delta t^2} & \dfrac{\hat{M}}{\Delta t^2} \end{bmatrix} \begin{Bmatrix} \hat{d}_k \\ \hat{d}_{k+1} \end{Bmatrix} \tag{25}$$

If (25) is modified, below equation is obtained,

$$\hat{T}_k = \frac{1}{2}\begin{bmatrix} d_k^T & d_{k+1}^T \end{bmatrix} E^T \begin{bmatrix} \hat{K} + \dfrac{\hat{M}}{\Delta t^2} & -\dfrac{\hat{M}}{\Delta t^2} \\ -\dfrac{\hat{M}}{\Delta t^2} & \dfrac{\hat{M}}{\Delta t^2} \end{bmatrix} E \begin{Bmatrix} d_k \\ d_{k+1} \end{Bmatrix} \tag{26}$$

When the active DOFs of original and model order reduced systems is taken into consideraiton, because total energy equivalence $\boldsymbol{T}_k \equiv \hat{\boldsymbol{T}}_k$ is desired, the identical parameters of the matrices should be equal (energy saving algorithm). Thus,

$$\boldsymbol{E}^T \begin{bmatrix} \hat{\boldsymbol{K}} + \dfrac{\hat{\boldsymbol{M}}}{\Delta t^2} & -\dfrac{\hat{\boldsymbol{M}}}{\Delta t^2} \\ -\dfrac{\hat{\boldsymbol{M}}}{\boldsymbol{\Delta t^2}} & \dfrac{\hat{\boldsymbol{M}}}{\Delta t^2} \end{bmatrix} \boldsymbol{E} = \begin{bmatrix} \boldsymbol{K} + \dfrac{\boldsymbol{M}}{\Delta t^2} & -\dfrac{\boldsymbol{M}}{\Delta t^2} \\ -\dfrac{\boldsymbol{M}}{\Delta t^2} & \dfrac{\boldsymbol{M}}{\Delta t^2} \end{bmatrix} \tag{27}$$

and, the first elements of the matrices are considered equal as below,

$$\boldsymbol{E}^T \hat{\boldsymbol{K}} \boldsymbol{E} + \boldsymbol{E}^T \frac{\hat{\boldsymbol{M}}}{\Delta t^2} \boldsymbol{E} = \boldsymbol{K} + \frac{\boldsymbol{M}}{\Delta t^2} \tag{28}$$

the second parameters should be equal.

$$\boldsymbol{E}^T \frac{\hat{\boldsymbol{M}}}{\Delta t^2} \boldsymbol{E} = \frac{\boldsymbol{M}}{\Delta t^2} \tag{29}$$

On the other hand, if (29) is premultiplied by the transformation matrix E, and then also postmultiplied by the transpose of transformation matrix $\boldsymbol{E}^T$, and using the fact that $EE^T = I$, we obtain

$$\hat{\boldsymbol{M}} = \boldsymbol{E}\boldsymbol{M}\boldsymbol{E}^T \tag{30}$$

Similarly from the equality of the first parameters of (28), and by using pre and post multiplying, we get

$$\hat{\boldsymbol{K}} = \boldsymbol{E}\boldsymbol{K}\boldsymbol{E}^T \tag{31}$$

Note that (30) and (31) determine respectively the mass and stiffness matrices for the reduced order system whose certain outputs are equal to those of the exact solution at discrete time steps for which the Total Energy Equivalence Method is used as the time integration method; namely, their impulse responses should be identical at discrete time steps for certain outputs defined by the transformation matrix *E*. Note that the second order systems could be cast in the state space form by defining the state-space matrices appropriately.

6 NUMERICAL EXAMPLE

The results of the example system will be presented in this section such as a cantilever beam. More examples and argument can be found in [35]. By considering the cantilever planar beam, the model order reduction method is applied to the beam given in Figure 1 by using the programs developed in Matlab environment.

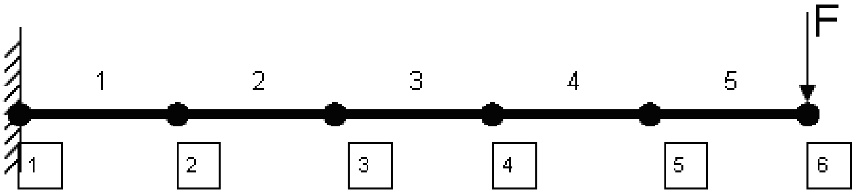

Figure 1: The Euler-Bernoulli beam system on which model order reduction is applied.

In the planar beam element, each node has 1 axial, 1 vertical and 1 rotational DOF. The length of the beam is 0.5 m, cross-sectional area is 4x10^{-4} m^2, beam height is 2x10^{-2} m, area moment of the cross-section is 1.33x10^{-8} m^4, density of the material of the beam is 7850 kg/m^3 and material elasticity modulus is 210 GPa (steel material). The loading is applied to the beam tip downward having the magnitude of 100 N as shown in Figure 1. By considering the proportional Rayleigh damping $C = \beta K$, the reduced model order system is created and then the analyses are repeated for different Rayleigh damping ratios as β =0, 0.00008, 0.001, 0.01 and 0.1.

Different element number combinations were studied as seen at Table 1. Through these studies, impulse and sinusoidal forces were separately loaded. The results of the beam having 5 elements are presented here. The impulse responses and forced responses for the input of *f(t)*=100*sin(2*time)+50*sin(5*time) are presented in Figures 2 and 3.

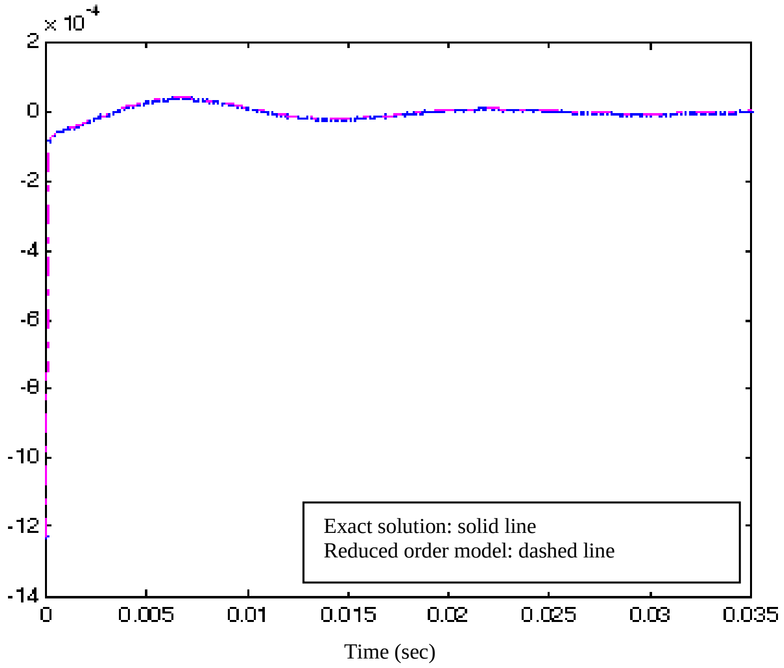

Figure 2: The beam tip displacement (in meter) for the impulse response where β =0.001.

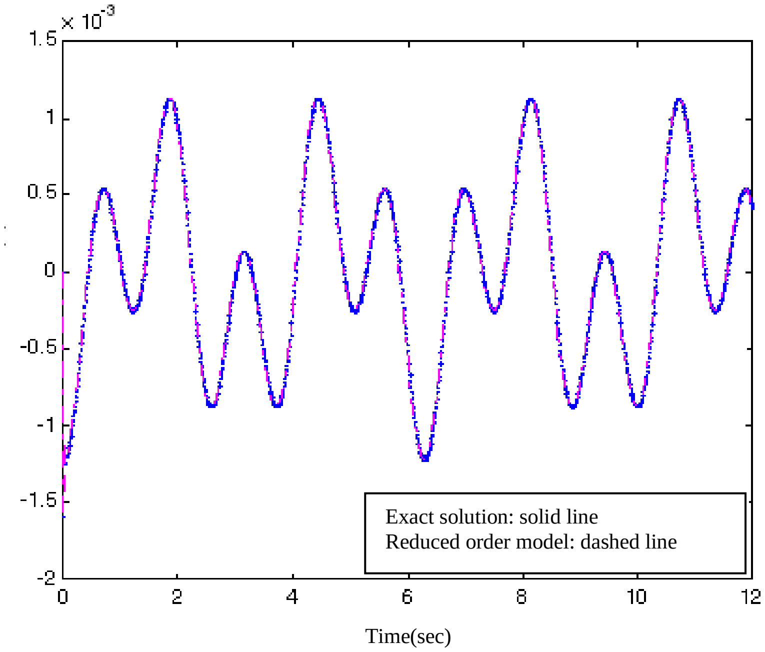

Figure 3: The beam tip displacement (in meter) for the sinusoidal input response where β =0.001.

Note that other simulation studies were also carried out whose results were not presented here for brevity. In sum, as the damping coefficient β reduces, the accuracy also reduces. Moreover, the accuracy of the response for the sinusoidal input is always superior to that of impulse response.

In order to compare the performance of the proposed model order reduction method, the CPU times of the original system and other systems obtained by using the existing model order reduction methods are listed in Table 1, where the damping coefficient β and number of elements are changing. In sum, creating the reduced order model is always beneficial by considerable time.

Number of Elements	Original DOF/Reduced DOF	Rayleigh stiffness proportional damping co-efficient	CPU time used by reduced order model by Total Energy Equivalence MOR method [sec.]	CPU time used by reduced order model by Forward difference MOR method [sec.]	CPU time used by reduced order model by Newmark MOR method [sec.]	CPU time for Original System [sec.]
5	15/10	0	0.001	0.001	0.001	0.037
		0.001	0.001	0.001	0.001	0.031
		0.01	0.001	0.001	0.001	0.032
		0.1	0.001	0.001	0.001	0.032
15	45/12	0	0.015	0.016	0.015	0.156
		0.001	0.015	0.032	0.016	0.141
		0.01	0.015	0.015	0.016	0.141
		0.1	0.015	0.015	0.016	0.141
100	300/148	0	0.175	0.527	0.175	1.531
		0.001	0.172	0.507	0.235	1.498
		0.01	0.172	0.515	0.235	1.525
		0.1	0.175	0.527	0.235	1.484
1000	3000/1000	0	2.579	16.515	3.906	1106.969
		0.001	2.578	15.671	3.813	1105.484
		0.01	2.515	16.375	4.093	1082.531
		0.1	2.408	16.453	3.906	1092.031

Table 1: CPU times while the number elements and damping coefficient β are changing.

7 CONCLUSIONS

A model order reduction techniques –Total Energy Equivalence Method- is derived in time domain based on the principle that the exact solution of the semi-discrete equation of a system and the solution of the reduced order model match at discrete time steps. It is sufficient to pursue exact match at discrete time steps, i.e., discrete equivalence, since the solutions of semi-discrete equations are obtained only at the time steps. A numerical example is presented to show the advantages of the pro-posed method and to compare the performance of them with that of some popular methods. The proposed method is applied to a sample problem and the results are compared with exact solutions. It is shown that proposed methods have certain advantages. It is concluded that characteristics of the responses of discrete equivalent reduced order models are similar as well no matter what the magnitude of the damping is. In order to improve the convergence, the DOFs neighboring the DOFs to which forces are applied and outputs are computed should be selected as active DOFs. It was determined that especially, in case of the sudden input force changes like impulse or step functions, performance of the model order reduction process based on discrete equivalent methods decreases. More examples and discussion about the presented approach can be found in [35]. In the future, this method would be applied to other kinds of problems and will be tested further.

REFERENCES

[1] J. Gu, *Efficient Model Reduction Methods for Structural Dynamics Analyses,* Doctoral Thesis, The University of Michigan, 2000.

[2] M. A. Blair, T. S. Camino and J. M. Dickens, An Iterative Approach to a Reduced Mass Matrix, *Proc. 9th International Modal Analysis Conference,* Florence, Italy (1991) 621-627.

[3] N. Bouhaddi and R. Fillod, Substructuring Using a Linearized Dynamic Condensation Method, *Computers and Structures,* **45**, 679-683, 1992.

[4] N. Bouhaddi and R. Fillod, Model Reduction by a Simplified Variant of Dynamic Condensation, *Journal of Sound and Vibration,* **191,** 233-250, 1996.

[5] M. I. Frishwell, S. D. Garvey and J. E. T. Penny, Model Reduction Using Dynamic and Iterated IRS Techniques, *Journal of Sound and Vibration,* **186,** 211-323, 1995.

[6] R. J. Guyan, Reduction Stiffness and Mass Matrices, *AIAA Journal,* **3**, 380, 1965.

[7] B. M. Irons, Structural Eigenvalue Problems: Elimination of Unwanted Variables, AIAA Journal, **3,** 961-962, 1965.

[8] R. L. Kidder, Reduction of Structural Frequency Equations, *AIAA Journal,* **11,** 892, 1973.

[9] A. Y. T. Leung, A Simple Dynamic Substructure Method, *Earthquake Engineering and Structural Dynamics,* **16,** 827-837, 1988.

[10] J. O'Callahan, A Procedure for an Improved Reduced System (IRS) Model, *Proc. 7th International Modal Analysis Conference,* Las Vegas, NV, USA (1989) 17-21.

[11] R. L. Bisplinghoff and H. Ashley, *Aeroelasticity,* Addison-Wesley, Reading, MA, 1995.

[12] N. R. Maddox, On the Number of Modes Necessary for Accurate Response and Resulting Forces in Dynamic Analysis, *ASME Journal of Applied Mechanics,* **42,** 516-517, 1975.

[13] Z. D. Ma and I. Hagiwara, Improved Mode-superposition Technique for Modal Frequency Response Analysis of Coupled Acoustic-Structural Systems, *AIAA Journal,* **29** 1720-1726, 1991.

[14] Z. D. Ma and I. Hagiwara, Sensitivity Analysis Methods for Coupled Acoustic-Structural System Part I: Modal Sensitivities, *AIAA Journal,* **29,** 1787-1795, 1991.

[15] Z. D. Ma and I. Hagiwara, Sensitivity Analysis Methods for Coupled Acoustic-Structural System Part II: Direct Frequency Response and its Sensitivities, *AIAA Journal,* **29,** 1796-1801, 1991.

[16] W. H. Shyu, *Quasi-Static Mode Compensation for Component Mode Synthesis of Dynamical Systems,* Doctoral Thesis, The University of Michigan, 1996.

[17] W. H. Shyu, Z. D. Ma and G. M. Hulbert, A New Component Mode Synthesis Method: Quasi-Static Mode Compensation, *Finite Elements in Analysis and Design,* **24,** 271-281, 1997.

[18] W. H. Shyu, J. Gu, G. M. Hulbert and Z. D. Ma, On the Use of Multiple Quasi-Static Mode Compensation Sets for Component Mode Synthesis of Complex Structures, *Finite Elements in Analysis and Design,* **35**, 119-140, 2000.

[19] J. Gu, Z. D. Ma and G. M. Hulbert, A New Load Dependent Ritz Vector Method for Structural Dynamic Analyses: Quasi-static Ritz Vector Method, *Finite Elements in Analysis and Design,* **36**, 261-278, 2000.

[20] K. J. Joo, E. L. Wilson and P. Leger, Ritz Vectors and Generation Criteria for Mode Superposition Analysis*, Earthquake Engineering and Structural Dynamics,* **18**, 149-167, 1989.

[21] C. Lanczos, An iteration Method for the Solution of the Eigenvalue Problem of Linear Differantial and Integral Operators, *Journal of Research of the National Bureau of Standards,* **45**, 252-282, 1950.

[22] P. Leger, E. L. Wilson and R. W. Clough, *The Use of Load Dependent Vectors for Dynamic and Earthquake Analyses*, Earthquake Engineering Reseach Center Report, University of California, Berkeley, UCB/EERC-86/04, 1986.

[23] P. Leger, Load Dependent Subspace Reduction Methods for Structural Dynamic Computations, *Computers and Structures,* **29**, 993-999, 1988.

[24] P. Leger, Application of Load-Dependent Vectors Bases for Dynamic Substructure Analysis, *AIAA Journal,* **28**, 177-179, 1989.

[25] B. Nour-Omid and R. W. Clough, Dynamic Analysis of Structures Using Lanczos Coordinates*, Earthquake Engineering and Structural Dynamics,* **12,** 565-577, 1984.

[26] B. Nour-Omid and R. W. Clough, Block Lanczos Method for Dynamic Analysis of Structures, *Earthquake Engineering and Structural Dynamics,* **13,** 271-275, 1985.

[27] E. L. Wilson, M. W. Yuan and J. M. Dickens, Dynamic Analysis by Direct Superposition of Ritz Vectors, *Earthquake Engineering and Structural Dynamics,* **10,** 813-821, 1982.

[28] E. L. Wilson and E. P. Bayo, Use of Special Ritz Vectors in Dynamic Substructure Analysis, *Journal of Structural Engineering,* **112**, 1944-1953, 1986.

[29] J. Gu, Z. D. Ma and G. M. Hulbert, Quasi-static Data Recovery for Dynamic Analyses of Structural Systems, *Finite Elements in Analysis and Design,* **37**, 825-841, 2001.

[30] A Mugan, Discrete equivalent time integration methods, for transient analysis, *International Journal for Numerical Methods in Engineering,* **57**, 2043-2075, 2003.

[31] T. McKelvey, H. Akçay and L. Ljung, Subspace-Based Multivariable System Identification from Frequency Response Data, *IEEE Trans. on Automatic cont.,* **41,** 960-979, 1996.

[32] J. Schoukens and R. Pintelon, *Identification of Linear Systems: a Practical Guideline for Accurate Modelling,* Pergamon Press, London, 1991.

[33] P. Van Overschee and B. De Moor, S*ubspace Identification for Linear Systems*, Kluwer Academic Publishers, Boston, 1996.

[34] Y. Cunedioglu, Analyses of Reduced Order Models of Structures and Superelement Techniques in Frequency Domain and Time Domain, Ph.D. thesis submitted to Istanbul Technical University, 2005.

[35] F. K. Corbaci, *The improvement of the responses obtained by finite element methods for the analyses of the structural dynamic problems by super elements and substructuring, Doctoral Thesis,* Istanbul Technical University, Turkey, 2009.

COMPDYN 2011
ECCOMAS Thematic Conference on
Computational Methods in Structural Dynamics and Earthquake Engineering
M. Papadrakakis, M. Fragiadakis, V. Plevris (eds.)
Corfu, Greece, 25-28 May 2011

A FAST METHOD FOR COMPUTING CONVOLUTIONS WITH STRUCTURAL GREEN'S FUNCTION : APPLICATION TO TIRE/ROAD CONTACT PROBLEMS

R. Meftah[1] **and D. Duhamel**[1]

[1] Université Paris-Est, UR Navier (ENPC/IFSTTAR/CNRS),
Ecole des Ponts ParisTech, 6 et 8 Avenue Blaise Pascal,
Cité Descartes, Champs sur Marne, 77455 Marne la Vallée, cedex 2, France
Tel: 33 1 64 15 37 36
Fax: 33 1 64 15 37 41
e-mail: {rabie.meftah,denis.duhamel}@enpc.fr

Keywords: Dynamic contact, Tire-road, Green function, Traffic noise, Road texture, Convolution

Abstract. *Tire/road contact represents the major source of traffic noise with driving speed above 50 km/h. One of the most important problems is to take into account the contact conditions and to calculate the contact forces in an accurate way. As a general approach, the dynamic response of the tire is calculated by convolving the contact forces with the Green function of the tire. The disadvantage of this method is that the computation can be time consuming. In this paper, an alternative which is a modal decomposition model is used. The developed method allows quicker calculations than the traditional convolution. It consists, at the first stage, on an approximation of the pre-calculated Green function on a series of modal contributions with the Least Square Complex Exponential (LSCE) algorithm then, on the calculation of the dynamic response in the time domain as a series of SDoF systems response. For verification, the approach is tested by using a Single Degree of Freedom (SDoF) oscillator where the system moves through a sinusoidal road profile with a constant speed. Then, it is applied to the Ring on Elastic Foundation (REF) Model.*

1 Introduction

In many advanced structures, the contact impact problems present an important interest. In numerical modeling of the effect of contact on structures, two classic approaches can be used. The Lagrange multiplier method [1] and the penalty method [2] are most commonly used in dynamic contact problems.

The dynamic contact problems can also be treated by using the Green's functions. In this approach the dynamic response is calculated by convolving the Green's functions with the contact forces. The convolution technique for contact problems is used by many authors : M. McIntyre al. [3] have applied the approach to the string/bow contact to study large-amplitude oscillations of musical instruments. C. Wang and J. Kim. [4],[5] have used the same approach for a thin beam impacting against a stop, A. Nordborq [6] for the wheel/rail contact problem and many other authors have used this technique in the tyre/road contact [7, 8, 9, 10].

The convolution technique for contact problems presents the advantage of simple implementation and is relatively less time consuming than classical methods. However, the time calculation for the convolution can be improved. G. Beylkin has developed [11] a fast convolution with free space Helmholtz Green's function. The convolution combines the spatial and Fourier domains. In the space domain, the Green's function is approximated by a sum of decaying Gaussians with positive coefficients and in the Fourier domain by a multiplication by a band-limited kernel.

In this paper, we present a fast convolution in which the Green's function in the frequency domain is approximated by a sum of modal contributions. The modal parameters are identified by LSCE algorithm and used in the time domain to construct a fast and accurate algorithm for computing convolutions with Green's functions. Two examples illustrate the efficiency of the method : first a SDoF system moving on a sinusoidal profile and in the second a MDoF on a random profile.

2 Structural Green's function

2.1 Standard convolution

A linear discretized dynamic problem can be generally expressed by a second order differential equation in the time domain:

$$\mathbf{M}\ddot{\mathbf{u}}(t) + \mathbf{C}\dot{\mathbf{u}}(t) + \mathbf{K}\mathbf{u}(t) = \mathbf{q}(t) \tag{1}$$

where **M**, **C** and **K** are the mass matrix, the damping matrix and the stiffness matrix, respectively. In the frequency domain, the problem can be written:

$$\left[-\omega^2\mathbf{M} + j\omega\mathbf{C} + \mathbf{K}\right]\mathbf{U}(\omega) = \mathbf{Q}(\omega) \tag{2}$$

The resolution of equation (1) first needs to search a general solution $\mathbf{u}_g(t)$ of the associated homogeneous equation and then to find a particular solution of the full equation. The computation of the Green's function $\mathbf{G}(\omega)$ is a systematic tool to get this particular solution. The traditional method when the time Green's function $\mathbf{g}(t)$ is known, is to calculate the dynamic response of the system by convolving the contact forces with the Green's function:

$$\mathbf{u}(t) = \mathbf{u}_g(t) + \int_0^t \mathbf{g}(t-\tau)\mathbf{q}(\tau)\mathrm{d}\tau \tag{3}$$

When the system is at rest until a certain time taken as origin $t = 0$, the solution of the homogeneous problem is null ($\mathbf{u}_g(t) = \mathbf{0}$), and the solution is reduced to the relation:

$$\mathbf{u}(t) = \int_0^t \mathbf{g}(t-\tau)\mathbf{q}(\tau)\mathrm{d}\tau \tag{4}$$

Equation (4) can be discretized as follows:

$$\mathbf{u}_k = \sum_{m=0}^{k} \mathbf{g}_{k-m}\mathbf{q}_m \tag{5}$$

Where $\mathbf{u}_k$ is the displacement at the time $k\Delta t$.

Let's note N_t the number of time steps used to calculate the displacement, and N_g the number of time steps for the influencing Green's function. The effect of the Green's function is neglected when the amplitudes of oscillation at time greater than $N_g\Delta t$ are hundred times smaller than the maximum of the Green's function $g(t)$.

Equation (5) is reduced to :

$$u_k = \sum_{m=0}^{\min(k,N_g)} g_{k-m}q_m \tag{6}$$

The number of arithmetic operations necessary to obtain the displacement until the time $N_t\Delta t$ is of the same order as N_tN_g.

2.2 Modal decomposition

The idea is to express the Green's function as a sum of modal contributions, and through numerical manipulations, the modal parameters can be identified. The Green's function $G(\omega)$ is supposed to be known, and $g(t)$ denotes its inverse Fourier transform. For the sake of simplicity, we restrict to one component for the displacement, in this case the Green's function $G(\omega)$ can be approximated as follows.

$$G(\omega) \simeq \sum_{k=1}^{k=N} \left[\frac{R_k}{j\omega - \lambda_k} + \frac{R_k^*}{j\omega - \lambda_k^*}\right] \tag{7}$$

One seeks to identify the modal parameters (residues A_k, damping ξ_k and frequencies ω_k). There exist several methods to deal with this kind of problems. The LSCE method

(Least Square Complex Exponential) remains the reference in the applications of experimental modal analysis. Equation (7) can be written in the equivalent form

$$G(\omega) \simeq \sum_{k=1}^{k=N} \frac{A_k}{-\omega^2 + 2j\xi_k\omega\omega_k + \omega_k^2} \tag{8}$$

The LSCE algorithm is used for the decomposition.

To check the accuracy of estimated modal data, the Green's function is regenerated. This method aims to find the best estimates of modal data that minimizes the error defined in equation (9)

$$E = \frac{\int_0^{\omega_{max}} |G(\omega) - \sum_{k=1}^{k=N} \frac{A_k}{-\omega^2 + 2j\xi_k\omega\omega_k + \omega_k^2}| \mathrm{d}\omega}{\int_0^{\omega_{max}} |G(\omega)| \mathrm{d}\omega} \tag{9}$$

3 Fast convolution

After finding the modal parameters A_k, ω_k and ξ_k, then truncating the decomposition to an order N, the Green's function in the time domain can be written in the form of a sum of the contribution of each mode:

$$g(t) = \sum_{k=1}^{k=N} \frac{A_k}{\omega_k^d} e^{-\xi_k\omega_k t} \sin(\omega_k^d\, t) \tag{10}$$

with

$$\omega_k^d = \omega_k\sqrt{1-\xi_k^2}$$

The displacement can be calculated by a convolution product

$$u(t) = \int_0^t g(\tau)q(t-\tau)\mathrm{d}\tau = \int_0^t g(t-\tau)q(\tau)\mathrm{d}\tau \tag{11}$$

Replacing $g(t)$ by its decomposition in equation (11) yields

$$u(t) = \int_0^t \sum_{k=1}^{k=N} \frac{A_k}{\omega_k^d}\, e^{-\xi_k\omega_k\ (t-\tau)} \sin\left(\omega_k^d\ (t-\tau)\right) q(\tau)\mathrm{d}\tau \tag{12}$$

By separating the variables t and τ, then rearranging the terms, we can write the displacement in the form

$$u(t) = \sum_{k=1}^{k=N} \frac{A_k}{\omega_k^d} e^{-\xi_k\omega_k t} \left[\sin\left(\omega_k^d\, t\right) \alpha^k(t) - \cos\left(\omega_k^d\, t\right) \beta^k(t)\right] \tag{13}$$

where $\alpha^k(t)$ and $\beta^k(t)$ are given as

$$\alpha^k(t) = \int_0^t e^{\xi_k \omega_k \tau} \cos(\omega_k^d \, \tau) q(\tau) \mathrm{d}\tau \tag{14}$$

$$\beta^k(t) = \int_0^t e^{\xi_k \omega_k \tau} \sin(\omega_k^d \, \tau) q(\tau) \mathrm{d}\tau \tag{15}$$

$$\tag{16}$$

At the time $n\Delta t$ the discrete displacement is written

$$u(n\Delta t) = \sum_{k=1}^{k=N} \frac{A_k}{\omega_k^d} e^{-\xi_k \omega_k n\Delta t} \left[\sin\left(\omega_k^d \, n\Delta t\right) \alpha^k(n\Delta t) - \cos\left(\omega_k^d \, n\Delta t\right) \beta^k(n\Delta t)\right] \tag{17}$$

The coefficients $\alpha^k(n\Delta t)$ and $\beta^k(n\Delta t)$ are calculated by the recurrence equations

$$\alpha^k((n+1)\Delta t) = \alpha^k(n\Delta t) + e^{\xi_k \omega_k n\Delta t} \cos(\omega_k^d \, n\Delta t) q(n\Delta t)\Delta t \tag{18}$$

$$\beta^k((n+1)\Delta t) = \beta^k(n\Delta t) + e^{\xi_k \omega_k n\Delta t} \sin(\omega_k^d \, n\Delta t) q(n\Delta t)\Delta t \tag{19}$$

The number of arithmetic operations necessary to obtain the displacement until the time $N_t\Delta t$ is of the same order than $N_t N_m$, where N_m is the number of modes used to represent the Green's function.

4 Contact models using Green's functions

4.1 General procedure

To illustrate the approach presented above, let us consider a simple dynamic contact problem. The purpose of this example is to test the fast convolution method and to compare it with the traditional convolution. So we consider a mechanical system represented by its Green's function. The system is moving with a constant speed on a surface without slipping.

The displacement $u(t)$ at time t, depends on the contact forces history $f_c(t)$ imposed by the texture of the surface. Two situations arise: either, there is a contact between the system and the surface and the displacement of the system equals the height of the surface $u_r(t)$, or there is no contact and in this case the contact force is null and the displacement of the system is strictly higher than that of the surface. Only vertical displacements are considered here.

The ideal conditions of unilateral contact are given by:

$$u(t) = u_r(t) \ ; \ f_c(t) > 0 \tag{20}$$

$$u(t) > u_r(t) \ ; \ f_c(t) = 0 \tag{21}$$

The procedure of the computation is described in the following.

1. First the displacement history $u^h(n\Delta t)$ is computed by assuming no contact $f_c(n\Delta t) = 0$.
$$u^h(n\Delta t) = \Delta t \sum_{k=0}^{n-1} f_c(k\Delta t) g((n-k)\Delta t) \tag{22}$$
2. The displacement history is compared with the profile altitude:
$$\Delta x(n\Delta t) = u_r(n\Delta t) - u^h(n\Delta t) \tag{23}$$
3. If the assumption of no contact ($\Delta x < 0$) is satisfied, the displacement is:
$$u(n\Delta t) = u^h(n\Delta t) \tag{24}$$
Then the procedure is repeated by assuming no contact for the next time step ($f_c((n+1)\Delta t) = 0$).
4. If $\Delta x \geq 0$, the contact force is computed from the cinematic conditions described below.
5. The procedure is repeated by assuming no contact condition for the next time step ($f_c((n+1)\Delta t) = 0$).

The same procedure is used for the modal decomposition model, but the displacement history $u^h(n\Delta t)$ is computed by

$$\begin{aligned} u^h(n\Delta t) \quad &= \sum_{k=1}^{k=N} \frac{A_k}{\omega_k^d} e^{-\xi_k \omega_k n\Delta t} \\ &\left[\sin\left(\omega_k^d\, n\Delta t\right) \alpha^k((n-1)\Delta t) - \cos\left(\omega_k^d\, n\Delta t\right) \beta^k((n-1)\Delta t)\right] \end{aligned} \tag{25}$$

4.1.1 Cinematic condition

The standard convolution can be written as following

$$\begin{aligned} u(t) \quad &= \int_0^{t-\Delta t} g(t-\tau)q(\tau)d\tau + \int_{t-\Delta t}^{t} g(t-\tau)q(\tau)d\tau \\ &= \underbrace{\int_0^{t-\Delta t} g(t-\tau)q(\tau)d\tau}_{u_h(t)} + \int_0^{\Delta t} g(\tau)q(t-\tau)d\tau \\ &= u_h(t) + \int_0^{\Delta t} g(\tau)q(t-\tau)d\tau() \end{aligned} \tag{26}$$

We derive the equation (26)

$$\begin{aligned} v(t) = u'(t) \quad &= \int_0^{t-\Delta t} g'(t-\tau)q(\tau)d\tau + \int_{t-\Delta t}^{t} g'(t-\tau)q(\tau)d\tau \\ &= \underbrace{\int_0^{t-\Delta t} g'(t-\tau)q(\tau)d\tau}_{v_h(t)} + \int_0^{\Delta t} g'(\tau)q(t-\tau)d\tau \\ &= v_h(t) + \int_0^{\Delta t} g'(\tau)q(t-\tau)d\tau \end{aligned} \tag{27}$$

let's note $\mathbf{Y} = [u(t) \;\; v(t)]^T$ and $\mathbf{Y}_h = [u_h(t) \;\; v_h(t)]^T$, we can write

$$\mathbf{Y} = \mathbf{Y}_h + \Psi(q) \tag{28}$$

where Ψ is an integral operator which reflects the influence of efforts at the present moment.

Where there is contact, the displacement is imposed by the rigid profile. We suppose that the contact point follows the profile. We can write the following contact conditions

$$u(t) \quad = u_r(t) \tag{29}$$

$$v(t) \quad = \frac{du_r(t)}{dt} \tag{30}$$

$$\tag{31}$$

In the vectorial form

$$\mathbf{Y} = \mathbf{Y}_r = [u_r(t) \;\; \frac{du_r(t)}{dt}]^T \tag{32}$$

Using the modal decomposition convolution we have

$$u(t) = \sum_{k=1}^{k=N} \frac{A_k}{\omega_k^d} e^{-\xi_k \omega_k t} \left[sin\left(\omega_k^d \, t\right) \alpha^k(t) - cos\left(\omega_k^d \, t\right) \beta^k(t) \right] \tag{33}$$

and

$$\begin{aligned} v(t) = \quad & - \sum_{k=1}^{k=N} \frac{A_k \xi_k \omega_k}{\omega_k^d} e^{-\xi_k \omega_k t} \left[sin\left(\omega_k^d \, t\right) \alpha^k(t) - cos\left(\omega_k^d \, t\right) \beta^k(t) \right] \\ & + \sum_{k=1}^{k=N} A_k e^{-\xi_k \omega_k t} \left[cos\left(\omega_k^d \, t\right) \alpha^k(t) + sin\left(\omega_k^d \, t\right) \beta^k(t) \right] \end{aligned} \tag{34}$$

Equations (33) and (34), can be written in the matrix form

$$\mathbf{Y} = \sum_{k=1}^{k=N} \mathbf{B}_k \mathbf{x}_k \tag{35}$$

where

$$\mathbf{x}_k = [\alpha^k(t) \;\; \beta^k(t)]^T \tag{36}$$

and

$$\mathbf{B}_k = A_k e^{-\xi_k \omega_k t} \begin{bmatrix} \frac{sin\left(\omega_k^d\, t\right)}{\omega_k^d} & -\frac{cos\left(\omega_k^d\, t\right)}{\omega_k^d} \\ cos\left(\omega_k^d\, t\right) - \frac{\xi_k \omega_k}{\omega_k^d} sin\left(\omega_k^d\, t\right) & sin\left(\omega_k^d\, t\right) + \frac{\xi_k \omega_k}{\omega_k^d} cos\left(\omega_k^d\, t\right) \end{bmatrix} \tag{37}$$

The contact conditions are

$$\mathbf{Y}_r = \mathbf{Y}^h + \Psi(\mathbf{q}) \tag{38}$$

The purpose is to find the contact force that verify simultaneously the conditions (32). Contact forces are related to displacements and velocities by the operator Ψ.

$$\begin{aligned} \Delta \mathbf{Y} &= \mathbf{Y}_r - \mathbf{Y}^h \\ &= \begin{bmatrix} \int_0^{\Delta t} g(t-\tau) q(\tau) d\tau \\ \int_0^{\Delta t} g'(t-\tau) q(\tau) d\tau \end{bmatrix} \end{aligned} \tag{39}$$

Integrals can be computed using two Gauss points. The values of the contact force at the two Gauss points are then calculated by inverting the operator Ψ

$$\mathbf{q} = \begin{bmatrix} q_1 \\ q_2 \end{bmatrix} \tag{40}$$

$$= \Psi^{-1}(t_1, t_2) \Delta \mathbf{Y} \tag{41}$$

The operator Ψ is given by

$$\Psi = \begin{bmatrix} g(t-t_1) & g(t-t_2) \\ g'(t-t_1) & g'(t-t_2) \end{bmatrix} \Delta t \tag{42}$$

where,

$$g(t) = \sum_{k=1}^{k=N} \frac{A_k}{\omega_k^d} e^{-\xi_k \omega_k t} sin\left(\omega_k^d\, t\right) \tag{43}$$

On a time interval $[t \;\; t+\Delta t]$, the contact force is the medium of its two values at the two Gauss points t_1 and t_2.

where

$$t_1 = t + \left(1 - \frac{1}{\sqrt(3)}\right) \frac{\Delta t}{2} \tag{44}$$

$$t_2 = t + \left(1 + \frac{1}{\sqrt(3)}\right) \frac{\Delta t}{2} \tag{45}$$

Knowing the values of the contact force at the Gauss points t_1 and t_2 we can compute the parameters $\alpha_k(t+\Delta t)$ and $\beta_k(t+\Delta t)$ by the recursion equations

$$\alpha^k(t+\Delta t) = \alpha_h^k(t) + \frac{f^c(t_1)q_1 + f^c(t_2)q_2}{2}\Delta t \tag{46}$$

$$\beta^k(t+\Delta t) = \beta_h^k(t) + \frac{f^s(t_1)q_1 + f^s(t_2)q_2}{2}\Delta t \tag{47}$$

where

$$f^s(t) \quad = e^{\xi_k \omega_k t} sin(\omega_k^d t) \tag{48}$$

$$f^c(t) \quad = e^{\xi_k \omega_k t} cos(\omega_k^d t) \tag{49}$$

5 Examples

5.1 Case of a single DoF system

The simplest dynamic system considered in vibration problems is the Single Degree of Freedom (SDoF) oscillator as shown in Figure (1). The analysis of this system is used to compare the standard convolution with the developed approach.

In this example, the system moves through a profile $u_r(x)$ with a constant speed $V_0 = 0.1$ m.s^{-1}. It is supposed that the displacement is done without slipping as shown in figure (1).

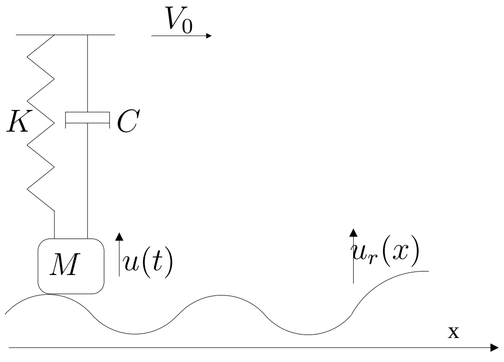

Figure 1: SDOF mass-spring system on a sinusoidal surface

Consider a sinusoidal profile

$$u_r = A_0 \sin(\omega_r x) = A_0 \sin(\frac{2\pi}{\lambda_r} V_0 t) \tag{50}$$

where $\lambda_r = 25\ mm$ is the wavelength of the profile and $A_0 = 5\ mm$ its amplitude.

The system verifies the equations:

$$M\ddot{u} + C\dot{u} + Ku = -Mg + F_c \tag{51}$$
$$u(t) \geq u_r(t) \tag{52}$$
$$F_c \geq 0 \tag{53}$$

with the initial conditions:

$$u_0 = u(0) = u_r(0) \tag{54}$$
$$v_0 = \frac{du(t)}{dt}|_{t=0} = 0 \tag{55}$$

If the mass is above the surface, there is no contact. The displacement and contact forces are given by

$$u(t) = e^{-\xi\omega_0(t-t_c)}\left[u_c\cos(\omega_d(t-t_c)) + \frac{v_c + \xi\omega_0 u_c}{\omega_d}\sin(\omega_d(t-t_c))\right] \tag{56}$$
$$F_c(t) = 0 \tag{57}$$

where u_c and v_c are respectively the displacement and velocity at the last contact moment t_c.

If the mass is below the surface, there is contact and the contact force is computed from the cinematic conditions described previously.

The parameters used in the model for the simulations are given in Table (1).

M[Kg]	K[N/m]	ξ
1	$4\ 10^5$	0.02

Table 1: SDoF parameters used in the simulations

Figures (2) and (3) show respectively the displacements $u(t)$ and the contact forces $F_c(t)$ calculated by the standard convolution method and the modal decomposition method. Both methods give the same result. In the part where there is contact, we notice that the displacement and contact force curves are fitting the shape of the surface. When this contact force is null, the system enters on a free vibration regime.

Using standard convolution is costly in terms of computing time, especially with a small time step. Indeed, from equations (5) and (17) we can see that in the case of a classical convolution, the number of calculation operations is proportional to the number of time steps N and to the size of the Green's functions N_g while in the modal decomposition it is proportional to N and to the approximation order. Table (2) shows a comparison of computing times between both methods.

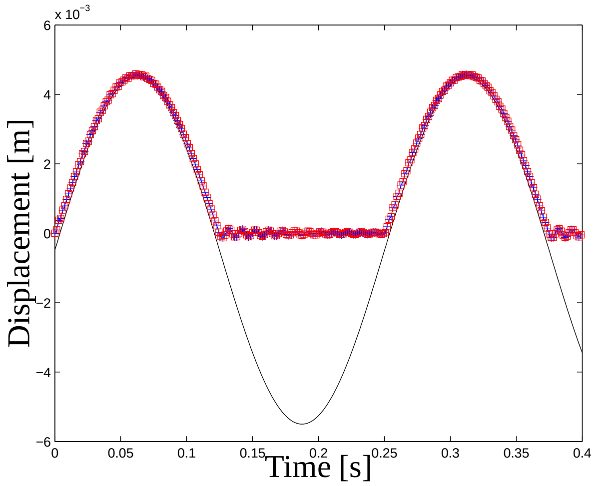

Figure 2: Displacement of a SDOF system on a sinusoidal surface : — profile, $-+-$ standard convolution, -□- modal decomposition

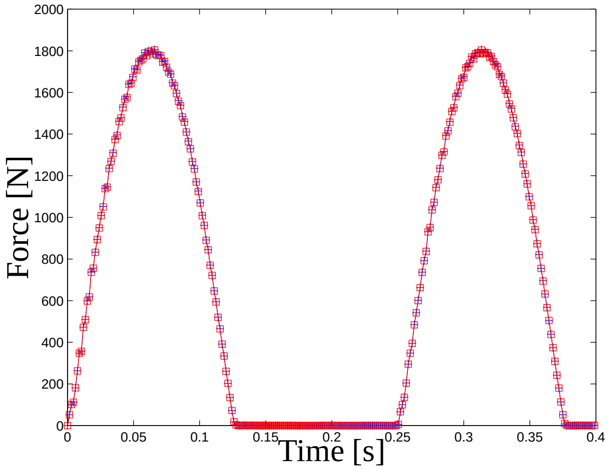

Figure 3: Contact force of a SDOF system on a sinusoidal surface :$-+-$ standard convolution, -□- modal decomposition

Time step [ms]	N_t	Standard convolution		Modal decomposition	
		N_g	Computing time [s]	N_m	Computing time [s]
0.1	2000	1900	0.06	1	0.03
0.1	20000	1900	1.01	1	0.17
0.01	20000	19000	5.50	1	0.26
0.01	200000	19000	105.14	1	2.80

Table 2: Comparison of the computing time: SDof system

5.2 Ring on Elastic Foundation Model

Modelling complex tire structures in details is a hard task. In the literature the ring on elastic foundation model was frequently used. In this model, the main dynamical properties of the tire are taken into account. The tread is modelled by a circular Euler-Bernoulli beam, the elastic properties of the sidewalls and the rim are modelled by distributed springs as shown in Figure (4).

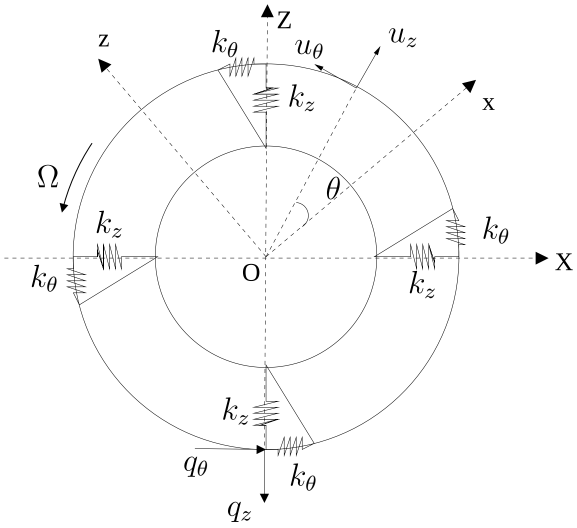

Figure 4: Ring on Elastic Foundation Model

The Green functions of the system is given by [12]:

$$\mathbf{G}(\omega) = \begin{bmatrix} G_{\theta\theta} & G_{\theta z} \\ G_{z\theta} & G_{zz} \end{bmatrix} = \sum_{n=-\infty}^{+\infty} \left[-\omega^2\mathbf{M} + j\omega\mathbf{C} + \mathbf{L}_n\right]^{-1} e^{jn\theta} \tag{58}$$

where **M** the mass matrix, **C** the gyroscopic matrix and $\mathbf{L}_n$ the matrix defined by equation (60):

$$\mathbf{M} = \rho S \begin{bmatrix} 1 & 0 \\ 0 & 1 \end{bmatrix} \; ; \; \mathbf{C} = 2\rho S\Omega \begin{bmatrix} 0 & 1 \\ -1 & 0 \end{bmatrix} \tag{59}$$

$$\mathbf{L}_n = \begin{pmatrix} \left(\frac{EI}{R^4} + \frac{K}{R^2} + \frac{pb}{R} + \rho S\Omega^2\right) n^2 + \frac{pb}{R} + k_\theta & -j\left[\frac{EI}{R^4}n^3 + \left(\frac{K}{R^2} + \frac{2pb}{R} + 2\rho S\Omega^2\right) n\right] \\ j\left[\frac{EI}{R^4}n^3 + \left(\frac{K}{R^2} + \frac{2pb}{R} + 2\rho S\Omega^2\right) n\right] & \frac{EI}{R^4}n^4 + \left(\frac{pb}{R} + \rho S\Omega^2\right) n^2 + \frac{K}{R^2} + \frac{pb}{R} + k_z \end{pmatrix} \tag{60}$$

Only the normal component G_{zz} of the Green function is computed for the contact problem. The parameters used for the simulation are given in Table (3).

We assume that the contact line contains three points $A(\theta = -\pi/100)$, $B(\theta = 0)$ and $C(\theta = \pi/100)$. The matrix of Green functions is calculated at these three points. Figure (5) shows the Green functions in the frequency rang $[0\ 1000Hz]$. The figures (6) and (7) show the displacements and the contact forces at the three contact points.

Parameters	Values	Unit
Young modulus(E)	10^8	Pa
Density (ρ)	2280	Kgm^{-3}
Mean radius(R)	0.285	m
Thickness(h)	0.01	m
Width(b)	0.16	m
Membrane stiffness(k_z)	1.6410^6	Nm^{-2}
Circumferential stiffness(k_θ)	2.1910^5	Nm^{-2}

Table 3: Parameters used for the numerical simulations

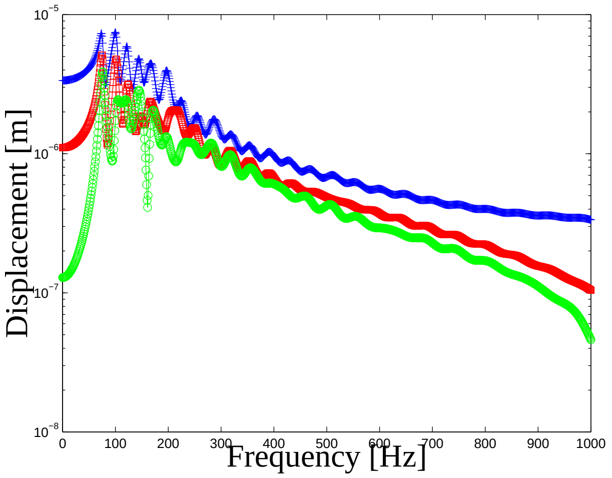

Figure 5: Green functions B : $-+-$ $G_{AA}=G_{BB}=G_{CC}$, -□- $G_{AB}=G_{BC}$, $-o-$ G_{AC}

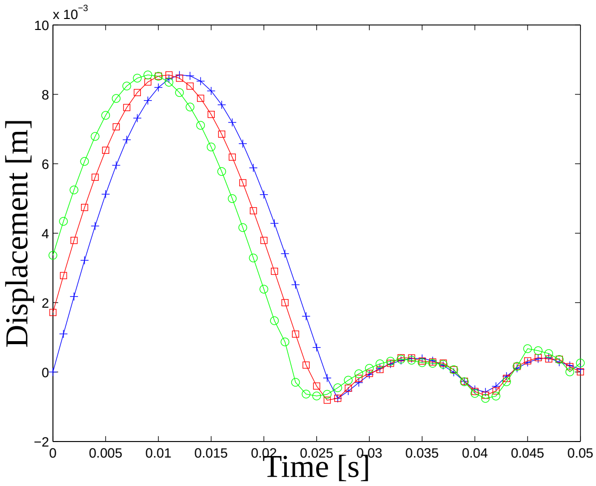

Figure 6: Displacements on the three contact points : — profile, $-+-$ point C, -□- point B , $-o-$ point A

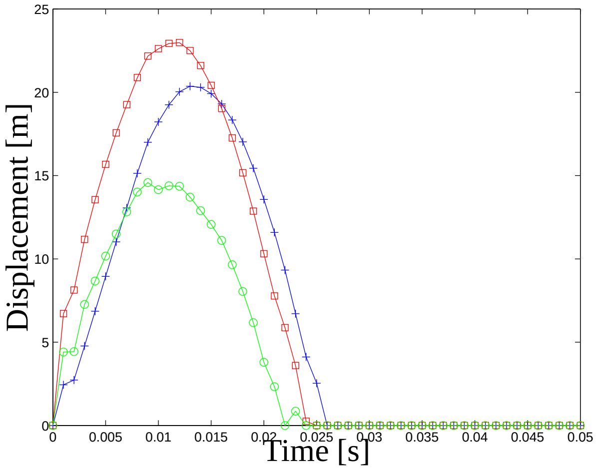

Figure 7: Contact forces on the three contact points : $-+-$ point C, -□- point B , $-o-$ point A

6 Conclusion

A unilateral contact dynamic model has been presented in this contribution. The model is based on a fast convolution using a modal decomposition of the Green functions. First, the Green function is approximated by a sum of a SDoF Green functions using the LSCE algorithm, then the identified modal parameters are used to constract a fast convolution. By exploiting the cinematic condition, the fast convolution can be inverted to calculate the contact forces when the contact occurs. Two examples are presented to prove the efficiency of the model.

REFERENCES

[1] K.J. Bathe and A.B. Chaudhary. A solution method for planar and axisymmetric contact problems. *International Journal for Numerical Methods in Engineering*, 21:65–88, 1985.

[2] Y. Kanto and G. Yakwa. A dynamic contact buckling analysis by the penalty finite element method. *International Journal for Numerical Methods in Engineering*, 29:755–774, 1990.

[3] M. McIntyre, R. Schumacher, and J. Woodhouse. On the oscillations of musical instruments. *Journal of the Acoustical Society of America*, 74 (1983):1325–1345, 1983.

[4] C. Wang and J. Kim. New analysis method for a thin beam impacting against a stop based on the full continuous mode. *Journal of Sound and Vibation*, 1996:809–823, 191.

[5] C. Wang and J. Kim. The dynamic analysis of a thin beam impacting against a stop of general three-dimensional geometry. *Journal of Sound and Vibation*, 203:237–249, 1997.

[6] A. Nordborg. Wheel/rail noise generation due to nonlinear effects and parametric excitation. *Journal of the Acoustical Society of America*, 111:1772–1781, 2002.

[7] W. Kropp. *Ein Modell zur Beschreibung des Rollgerusches eines unprofilierten Grtelreifens auf rauher Strassenoberflche (A model to describe the rolling noise of a smooth radial tire on a rough road surface)*. PhD thesis, T. U. Berlin, 1992.

[8] K. Larsson. *Modelling of dynamic contact-exemplified on tire/road interaction.* PhD thesis, Chalmers University of Technology, Goteborg, Sweden, 2002.

[9] F. Wullens. *Excitation of tyre vibration due to tyre/road interaction*. PhD thesis, Chalmers University of Technology, Goteborg, Sweden, 2004.

[10] P.B.U. Andersson and W. Kropp. Time domain contact model for tyre/road interaction including nonlinear contact stiffness due to small-scale roughness. *Journal of Sound and Vibration*, pages 296–312, 2008.

[11] G. Beylkin, C. Kurcza, and L. Monzona. Fast convolution with the free space Helmholtz Green's function. *Journal of Computational Physics*, 228:2770–2791, 2009.

[12] R. Meftah, D. Duhamel, J. Cesbron, F. Anfosso-Lde, H. Yin, and P. Argoul. Efficient computation of tire/road contact forces using an ARMA model of the Green function. In *XVIIth Symposium Vibrations, Chocs and Bruit, Ecole Centrale de Lyon*, 2010.

COMPDYN 2011
3rd ECCOMAS Thematic Conference on
Computational Methods in Structural Dynamics and Earthquake Engineering
M. Papadrakakis, M. Fragiadakis, V. Plevris (eds.)
Corfu, Greece, 25-28 May 2011

DISPERSION ERRORS OF B-SPLINE BASED FINITE ELEMENT METHOD IN ONE-DIMENSIONAL ELASTIC WAVE PROPAGATION

Radek Kolman[1], **Jiří Plešek**[1], **Miloslav Okrouhlík**[1] **and Dušan Gabriel**[1]

[1]Institute of Thermomechanics
Academy of Sciences of the Czech Republic
Dolejškova 5
182 00 Praha 8, Czech Republic
e-mail: {kolman,plesek,ok,gabriel}@it.cas.cz

Keywords: Wave Propagation, Dispersion Analysis, B-spline based finite element method.

Abstract. *The spatial discretization of elastic continuum by finite element method (FEM) introduces dispersion errors to numerical solutions of wave propagation tasks. For higher order Lagrangian as well as Hermitian elements there are optical modes in their frequency spectra leading to spurious oscillations of shock induced responses in a vicinity of propagating wavefronts. Furthermore, the behavior of classical higher order elements accounts for discontinuities in their spectra as well as for false representation of maximum frequency, the error of which increases with element order. For brevity this property is called the divergent behavior in the text. The recent innovations in finite element analysis rely on spline-based shape functions, taking inspiration in CAD (Computer Aided Design) approaches where the B-splines and mainly NURBS (non-uniform rational B-spline) representations are regularly employed. B-spline as well as NURBS curves are piecewise polynomial curves that are differentiable up to a prescribed order. The B-splines functions, employed as finite element shape functions, are examined in this paper, using the 1D stress wave modeling as a testing vehicle. It is shown that the employed approach leads to substantial minimization of dispersion errors; furthermore the errors decrease with increasing order of B-spline elements. It is believed that the B-spline based FE technology represents a promising tool allowing to increase reliability of numerical solutions of wave propagation problems.*

1 INTRODUCTION

The numerical solution of fast transient elastodynamics problems by the classical Lagrangian as well as Hermitian type of the finite element method (FEM) [1] is influenced by dispersion errors caused by both spatial and temporal discretizations [2]. A monochromatic harmonic stress wave propagates in unbounded elastic continuum regardless of its frequency and correspondingly a wave packet propagates without distortion. When these propagating phenomena are modeled by FEM the speed of a single harmonic wave depends on its frequency and thus a wave packet is distorted. The parasitic effects do not exist in 'ideal' unbounded continuum. The dispersive properties of one-dimensional Lagrangian and Hermitian elements were studied in Ref. [3]. Furthermore, the finite element (FE) mesh behaves as a frequency filter - higher frequencies are transfered with a strong attenuation.

The theoretical basis of the dispersion analysis of FEM for the solution of the hyperbolic partial differential equation has been laid in [4], where the Gibb's effect with the connection of FEM was observed. The oscillations near the wavefront or the stress jump change do not vanish for the fine-grained mesh. Fourier method as the dispersion analysis tool of the numerical solution of the hyperbolic partial differential equation is described in [5]. Very simple and efficient computational strategy of the complex wavenumber Fourier analysis of FEM is presented in Ref. [6].

In seismology the spectral finite elements [7] appeared recently. Spectral finite elements are of h-type finite elements, where nodes have special positions along the elements corresponding to the numerical quadrature schemes. But the displacements along element are approximated by the Lagrangian interpolation polynomials. The spectral finite elements improve dispersion errors for lower dispersion branches but not for upper ones.

A modern approach in the finite element analysis is the isogeometric analysis [8], where shape functions are based on varied types of splines. For example, Bézier representation, B-spline (basis spline), NURBS (non-uniform rational B-spline), PB-spline, T-spline and others are used for spatial discretization. This approach has an advantage that the geometry and approximation of the field of unknown quantities is prescribed by the same technique. Another benefit is that the approximation is smooth.

Dispersion of B-spline based finite elements was established for the same recurrent (uniform) B-spline basis functions [5] approximating one dimensional infinite domain. It was shown, that the optical modes did not exist and next, dispersion errors were reported to decrease with increasing order of B-spline shape functions [9]. This is a very good result for the explicit dynamics, where critical time step is bounded by the highest eigenfrequency of the whole system [10].

Generally, the B-spline or NURBS basis functions for bounded solids are not uniform. For this reason, the non-homogeneity of basis functions near the boundary of the domain produces the dispersion and attenuation behavior. These behavior can be controled by parameterization of B-spline entity, by order of piecewise polynomials, etc. In this paper, the dispersion of B-spline based finite element will be determined for a one-dimensional elastic wave propagation problem. Numerical parameters of B-spline representation will be tested to show their dispersion and attenuation.

2 PROPAGATION OF ELASTIC WAVES IN ONE-DIMENSIONAL CASE

In one-dimensional case the classical equation governing linear elastic wave propagation [11] is given by

$$c_0^2 \frac{\partial^2 u}{\partial x^2} - \frac{\partial^2 u}{\partial t^2} = 0, \quad \text{where} \quad x \in (-\infty, \infty),\ t \in [0, \infty), \tag{1}$$

where c_0 denotes the wave propagation speed, $u(x,t)$ is the displacement field, x is the position and t is the time. The unbounded one-dimensional continuum is assumed, therefore boundary conditions are not prescribed. The 1D continuum can be realized as a 'thin' elastic bar, the material of which is characterized by Young's modulus E and mass density ρ. For a 'thin' elastic bar, the wave speed is given by $c_0 = \sqrt{E/\rho}$. In case of constant E and ρ, the wave speed is as well constant. Moreover, the value of wave speed is independent of the wavenumber or frequency of wave. This continuum is called non-dispersive [11].

3 B-SPLINE BASED FINITE ELEMENT METHOD

Firstly, the B-spline basis functions will be mentioned, see details in Ref. [12]. For a given knot vector Ξ, the B-spline basis functions are defined recursively starting with piecewise constants ($p = 0$)

$$N_{i,0}(\xi) = \begin{cases} 1 & \text{if} \quad \xi_i \leq \xi \leq \xi_{i+1}, \\ 0 & \text{otherwise}. \end{cases} \tag{2}$$

The basis functions $N_{i,0}(\xi)$ are step functions, equal to zero everywhere except on the half-open interval $\xi = [\xi_i, \xi_{i+1})$, where ξ is parameter usually chosen so, that $\xi = [0, 1]$.

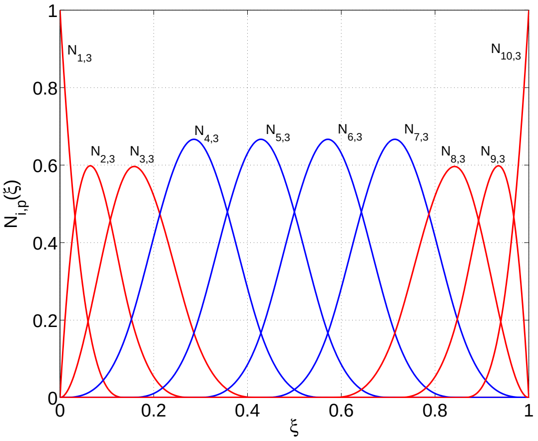

Figure 1: Example of cubic B-spline basis functions for ten control points $n = 10$ and uniform knot vector Ξ. Red lines correspond to non-uniform basis functions and blue lines correspond to uniform (homogeneous) basis functions. The number of non-uniform basis functions are depends on the polynomial order.

For $p = 1, 2, 3, ...$, they are defined by

$$N_{i,p}(\xi) = \frac{\xi - \xi_i}{\xi_{i+p} - \xi_i} N_{i,p-1}(\xi) + \frac{\xi_{i+p+1} - \xi}{\xi_{i+p+1} - \xi_{i+1}} N_{i+1,p-1}(\xi). \tag{3}$$

This is referred to as the Cox-de Boor recursion formula [12]. A knot vector in one dimensional case is a non-decreasing set of coordinates in the parameter space, written $\Xi = \{\xi_1, \xi_2, ..., \xi_m\}$, where $\xi_i \in R$ is the i-th knot, i is the knot index, $i = 1, 2, \ldots, m$, where $m = n + p + 1$, p is the polynomial order, and n is the number of basis functions used to construct a B-spline curve. Equation (3) can yield the quotient $0/0$, for this case the quotient is prescribed zero. The main properties of $N_{i,p}$, defined by (2) and (3), are introduced in Ref. [12]. Example of cubic B-spline basis functions for ten control points $n = 10$ and uniform knot vector is displayed in Fig. 1.

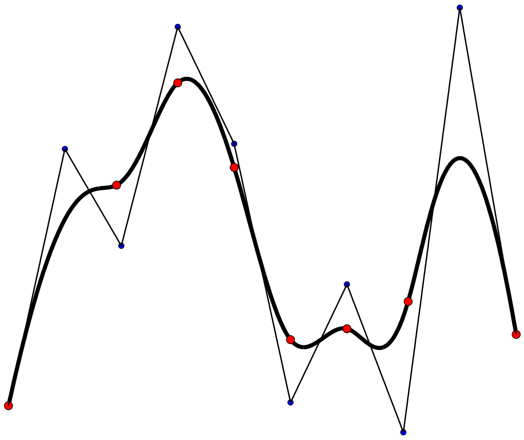

Figure 2: Example of cubic B-spline curve for ten control points and uniform knot vector. The corresponding control polygon is depicted.

In CAD technology [13] a B-spline curve is given by linear combination of B-spline basis functions $N_{i,p}$ [12]

$$\mathbf{C}(\xi) = \sum_{i=1}^{n} N_{i,p}(\xi)\, \mathbf{B}_i, \tag{4}$$

where $\mathbf{B}_i, i = 1, 2, \ldots, n$ are corresponding control points. Piecewise linear interpolation of control points gives the so-called control polygon. Example of cubic B-spline curve with its control polygon is shown in Fig. 2.

The open B-spline curve interpolating end points is used, where the knot vector is prescribed as

$$\Xi = \{a, \ldots, a, \xi_{p+2}, \ldots, \xi_n, b, \ldots, b\}, \tag{5}$$

where values are usually set as $a = 0$ and $b = 1$. The multiplicity of the first and last knot value is $p + 1$. If the values ξ_{p+1} up to ξ_{n+1} are chosen uniformly, the knot vector Ξ is called uniform knot vector, otherwise non-uniform, for more details see Ref. [12]. The B-spline curve for the knot vector given by (5) is passed through the end points of the control polygon.

Analogically, the spatial coordinate for a one-dimensional continuum can be approximated by linear combination of B-spline basis functions $N_{i,p}$

$$x(\xi) = \sum_{i=1}^{n} N_{i,p}(\xi)\, x_i^{\mathrm{B}}, \tag{6}$$

where $x_i^{\mathrm{B}}, i = 1, 2, \ldots, n$ are positions of control points in the x-direction. Furthermore, the approximation of the displacement field u^h by the B-spline approach is given by

$$u^h(\xi) = \sum_{i=1}^{n} N_{i,p}(\xi)\, u_i^{\mathrm{B}}, \tag{7}$$

where u_i^{B} is the component of the vector of control variables – displacements corresponding to the control points.

A scheme of a admissible dependence of a one dimensional displacement field based on B-spline representation is presented in Fig. 3. Generally, the displacement field discretized by B-spline technology in one-dimensional case can be controlled by following parameters:

- length of element patch h (*h-refinement*),
- polynomial order p (*p-refinement*),
- number of control points n (*k-refinement*),
- positions of control points x_i^{B}, $i = 1, 2, \ldots, n$, (choice of parameterization),
- components of the knot vector Ξ and their multiplicities,
- continuity between patches C^m, $m \leq p - 1$ order of continuity.

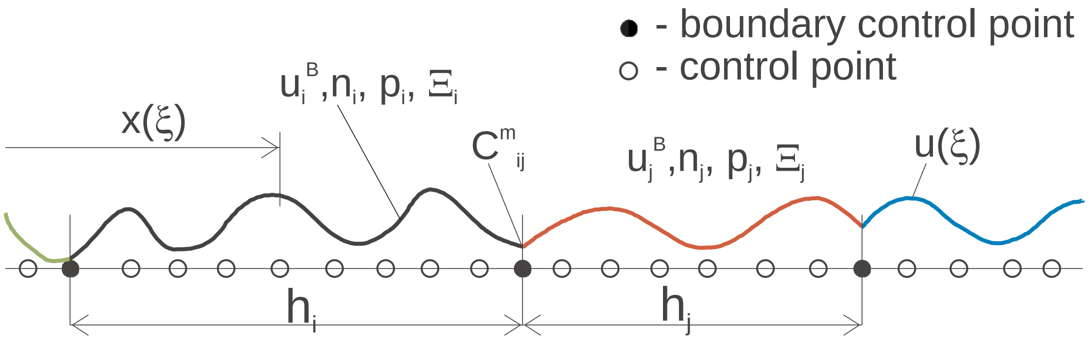

Figure 3: Scheme for permissible spatial discretization of a one-dimensional domain by B-spline based FE. h_i denotes a length of B-spline segment, u_i^{B} are control variables, n_i is number of control points, p_i denotes polynomial order, Ξ_i denotes a knot vector for i-th B-spline segment. C_{ij}^m marks order of continuity between i-th and j-th B-spline segment. Spatial coordinate $x(\xi)$ and corresponding displacement $u(\xi)$ are parametric functions of parameter ξ.

In this paper, C^0 continuity between B-spline segments with the identical length h is considered. The number of control points n, theirs positions and polynomial order p are the same. The knot value appears only once in the knot vector, but the first and last knot values appear $p + 1$ times. Of course, the continuity of the displacement field inside the B-spline segment is C^{p-1}.

In the following text, the continuous Galerkin's approximation method [1] for the solution of partial differential equations is employed. Spatial discretization of elastodynamics problems by finite elements leads to the second order ordinary differential system in the form [1]

$$\mathbf{M}\ddot{\mathbf{u}} + \mathbf{K}\mathbf{u} = \mathbf{R}. \tag{8}$$

Here, $\mathbf{M}$ is the mass matrix, $\mathbf{K}$ the stiffness matrix, $\mathbf{R}$ is the time-dependent load vector, $\mathbf{u}$ and $\ddot{\mathbf{u}}$ contain nodal displacements and accelerations. Neglecting the loading we have $\mathbf{R} = \mathbf{0}$. A lot of discrete time direct integration methods for the system (8) were developed [1]. However, the time is considered continuous in this work.

The element mass and stiffness matrices are given by

$$\mathbf{M}^e = \int_{h^e} \rho\, \mathbf{H}^T \mathbf{H}\, \mathrm{d}x \tag{9}$$

and

$$\mathbf{K}^e = \int_{h^e} E\, \mathbf{B}^T \mathbf{B}\; \mathrm{d}x \tag{10}$$

where h^e denotes the finite element length or length of B-spline segment, $\mathbf{B}$ is the strain-displacement matrix, $\mathbf{H}$ stores the displacement interpolation (shape) functions h_i [1]. For case of B-spline based FEM, shape functions are denoted $N_{i,p}$. Integrations (9) and (10) are carried over the element domain. If the theory of linear elastodynamics is considered, then mass matrix $\mathbf{M}^e$ (9) and stiffness matrix $\mathbf{K}^e$ (10) are constant. Global matrices are assembled in the usual fashion. Mass matrix defined by (9) is called consistent mass matrix and this mass matrix is employed in the following text. The stiffness matrix $\mathbf{K}$ and mass matrix $\mathbf{M}$ is computed numerically by the Gauss-Legendre quadrature formula [1].

4 DISPERSION ANALYSIS

The complex wavenumber dispersion analysis was performed for one-dimensional finite elements in Ref. [6]. In Fourier analysis [5], the displacement u_i^h corresponding to given spatial discretization is prescribed in the form of wave solution

$$u_i^h = A_i e^{\mathrm{i}\left(\omega t - \psi^h x_i\right)}, \tag{11}$$

where A_i is displacement amplitude, ω is angular velocity, imaginary unit $\mathrm{i} = \sqrt{-1}$ and x_i is the position. The discrete (numerical) wavenumber k^h equals to the real part of ψ^h, $k^h = \mathrm{Re}\,\psi^h$. Imaginary part $b^h = \mathrm{Im}\,\psi^h$ has a physical meaning of the attenuation intensity.

In Fourier analysis, the assumed solution of (11) is inserted to the equation (1) and the dispersion relation $\omega = f(k^h)$ is obtained. The dispersion errors can be measured by non-dimensional numerical phase speed c^h/c_0, where numerical phase speed is defined by the relationship $c^h = \omega/k^h$. Mostly, the dispersion errors are depicted as a function of the non-dimensional numerical wavenumber $k^h h$, where h is characteristic length of finite element domain or B-spline segment.

5 RESULTS OF DISPERSION ANALYSIS FOR B-SPLINE BASED FEM

In this section, the dispersion diagrams for B-spline based FEM are shown for different number of control points with linear or non-linear parameterization and for different polynomial order, respectively. These graphs are compared with results for classical Lagrangian finite elements.

5.1 Uniform B-spline FEM versus classical finite element

Dispersion of one-dimensional Lagrangian FE was been studied in [3], [6]. The normalized dispersion errors in phase speed are depicted in Fig. 4 (on the left). These errors are divergent with the polynomial order of approximation of a displacement field. In Fig. 4 (on the left), h denotes the length of Lagrangian finite element. Nevertheless, the distances between uniformly-spaced nodes are h/p. The wavenumbers are normalized, being divided by appropriate polynomial order p. Thus, the non-dimensional numerical wavenumbers are in the range $k^h h/p = [0, \pi]$. The horizontal jumps in the dispersion graph on Fig. 4 (on the left) correspond to the attenuating solution [14]. For higher order Lagrangian finite elements, the optical modes are occurred [2]. These vibration modes produce the spurious oscillations in numerical solutions of transient elastodynamics problems.

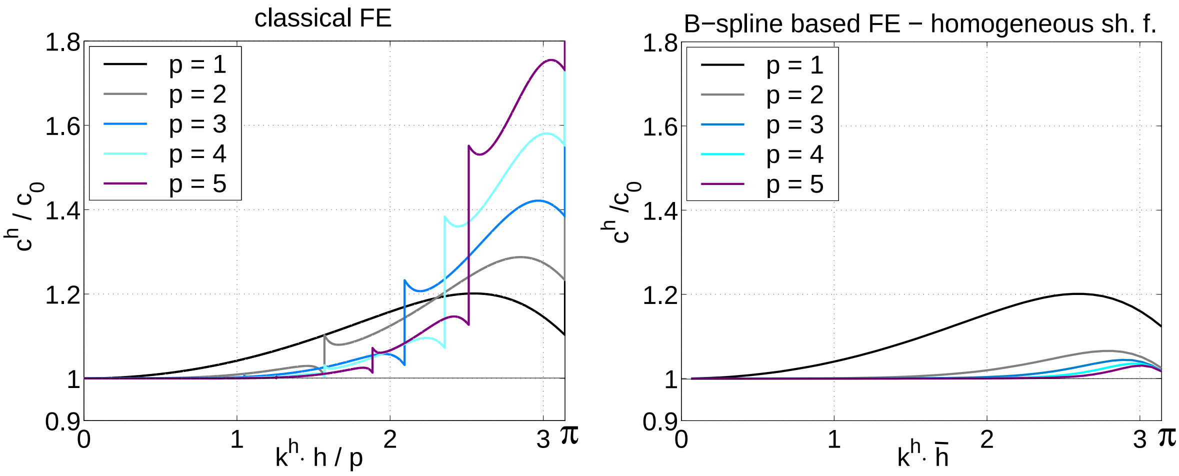

Figure 4: Dispersion errors for Lagrangian FE (on the left) [3], [6] and B-spline based FE (on the right) [9] for different polynomial order p. h denotes the finite element length, $\bar{h}$ is the distance of uniformly-spaced control points.

In Ref. [8], the errors of eigenfrequency of an elastic fixed-fixed bar computed by classical FEM and B-spline based FEM are compared. The dependence of eigenfrequence ω^h/ω on the corresponding counter has the same character as the dependence c^h/c_0 on the corresponding non-dimensional wavenumber $k^h h$. It is a consequence of the duality principle accomplished in Ref. [9].

The dispersion analysis of B-spline based FEM has been investigated in Ref. [5], where uniform basis shape functions are employed. This case is in agreement with a model of an infinite elastic 'thin' bar. The dispersion graph for uniform B-spline based FEM is presented in Fig. 4 (on the right), where the high mode behavior is convergent with the polynomial order p of B-spline approach. The dispersion errors are decreasing with increasing polynomial order. The permissible values of numerical wavenumber $k^h\bar{h}$ are in the range $[0, \pi]$. In Fig. 4 (on the right), $\bar{h}$ denotes distance of uniformly-spaced control points. The optical modes and attenuating solution in the right-open range $k^h\bar{h} = [0, \pi)$ do not exist, but for $k^h\bar{h} = \pi$ the attenuating solution arises. The spatial resolution limit corresponds to the numerical wavenumber is $k^h\bar{h} = \pi$, where positions of control points are in the 'saw tooth' oscillation form. The uniform B-spline based finite element for discretization of a one-dimensional domain produces better dispersion dependence without optical modes and band gaps [14] with respect to the Lagrangian classical FEM [9].

REMARK: Another solution of wave equation (1) discretized by uniform B-spline based FEM exists [9]. This solution is called evanescent solution [14]. This solution of discretized system is characteric by non-zero imaginary parts of ψ^h and for the numerical wavenumber is is valid $k^h\bar{h} \neq i\pi, i = 0, 1, 2, \ldots, p$, simultaneously. The number of the evanescent solutions is $p-1$, see Ref. [9]. The evanescent solutions do not have practically meaning in the numerical solution of wave equation due to their attenuating efect.

5.2 Non-linear parameterization - uniformly-spaced control points

This section deals with the dispersion analysis for B-spline segments with polynomial order p, different number of uniformly-spaced control points. And also with the uniform knot vector and for case, where individual B-spline segments are connected only with C^0 continuity with theirs neighbouring B-spline segments. In Fig. 5 (on the left), dispersion errors c^h/c_0 of the quadratic ($p = 2$) B-spline based FE are drawn. In Fig. 5 (on the right) there are presented the dispersion errors for cubic ($p = 3$) B-spline based FE with different number of control points, where h denotes the patch length of B-spline (see Fig. 3). For increasing number of control points, the dispersion errors are convergent to value of wave speed c_0 – i.e. to the exact solution for continuum.

The vertical jumps pertain to the decay solution with non-zero attenuation. These parts of the dispersion dependencies depict quantitatively the passing and band gaps in the frequency range [14]. Thereby, the band gaps exist also for the B-spline based element method with C^0 continuity between B-spline segments. With increasing number of control points the band gap range is decreasing and the maximal band gap range occurs in higher dispersion branches. It can be shown, that dispersion errors are influenced by shape (basis) functions $N_{i,p}$ defined in the vicinity of patch domain boundary, see Fig. 1. The corresponding shape functions are not homogeneous due the interpolation of end points [12].

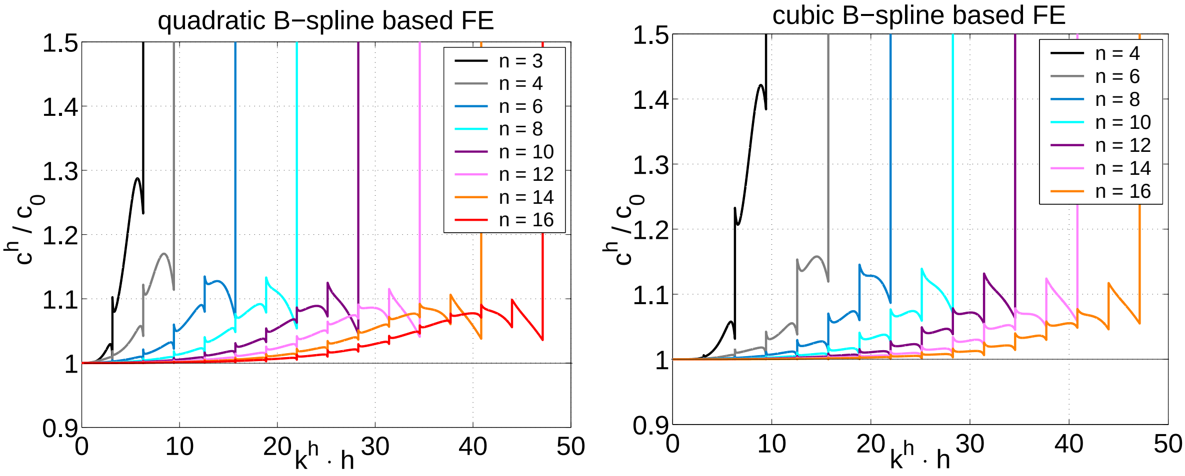

Figure 5: Dispersion errors for quadratic (on the left) and cubic (on the right) B-spline based FE with different number of control points. The red line corresponds to homogeneous shape functions [9].

The dispersion dependencies in Fig. 5 can be redrawn to the normalized non-dimensional wavenumber $k^h h/(n-1)$. Which means that the abscissa variables are divided by the appropriate number of distances of control points, i.e. $n-1$. The distance between uniformly-spaced control points is $\bar{h} = h/(n-1)$. It is the averaged distance of control points. The normalized numerical wavenumbers are in the range $k^h h/(n-1) \in [0, \pi]$. The normalized dispersion errors are depicted in Fig. 6, where corresponding dispersion errors for uniform B-spline shape functions (Fig.4 (on the right)) are added. The normalized dispersion errors for quadratic B-spline are shown in Fig. 6 (on the left) and for cubic B-spline are represented in Fig. 6 (on the right). For clarity the number of control points in Fig. 6 is different from that appearing in Fig. 5. It is of interest that the mentioned normalized dispersion errors are approaching to those of the uniformly (homogeneous) B-spline shape functions (Fig. 4).

For minimization of dispersion errors, the increasing number of control points (*k-refinement*) is better than the partition of the B-spline segments (*h-refinement*). The higher order of continuity inside the B-spline produces more reliable dispersion behavior.

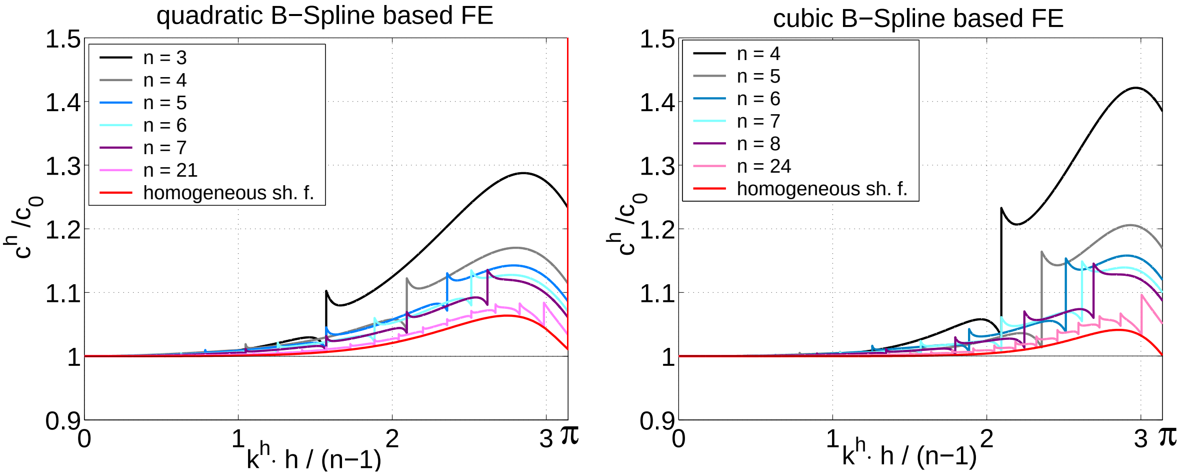

Figure 6: Normalized dispersion errors for quadratic (on the left) and cubic (on the right) B-spline based FE with different number of control points. The red line corresponds to homogeneous shape functions [9].

REMARK: For situations, where number of control points is $n = p + 1$ and B-spline segments are only connected with C^0 continuity, the dispersion dependencies are identical with those of Lagrangian finite elements (Fig. 4 (on the left)).

5.3 Linear parameterization - Graville abscissa

The simple modification of the previously shown B-spline non-linear parameterization is based on a choice of special positions of control points. Good interpolation properties of B-splines can also be obtained by so called Graville abscissa. In such a case the abscissa is associated with the knot vector Ξ. See [15] and [16] for details. Thus, the control points are given by the formula

$$x_i^*(\xi) = \frac{\xi_{i+1} + \ldots + \xi_{i+p}}{p}, \quad i = 1, 2, \ldots, n. \tag{12}$$

The set of control points positions obtained this way (12) is usually called the set of averaged collocation points or Greville collocation points. If the knot vector is chosen so, that $a = 0$, $b = 1$ in (5) and the outside knots are with $p + 1$ multiplicity, then the boundary control points are located on $x_1^* = 0$ and $x_n^* = 1$. B-spline displacement field is passed through end points. Therefore, the coordinates $x_i, i = 1, 2, \ldots, n$ of control points of B-spline segment with length h are given by

$$x(\xi) = x_i^*(\xi) \cdot h. \tag{13}$$

The fundamental property of this parameterization based on the Greville abscissa is such, that Jacobians of the transformation from the parametric space to the physical space are constant for arbitrary parameter ξ, i.e. $\frac{\mathrm{d}x(\xi)}{\mathrm{d}\xi} = const$ for $\forall \xi \in [0, 1]$ [16]. This parameterization is called linear.

The normalized dispersion errors c^h/c_0 versus non-dimensional wavenumber $k^h h/(n-1)$ for quadratic B-spline with linear parameterization are shown in Fig. 7 and for cubic B-spline with linear parameterization are in Fig. 8, where influence of the number of control points is displayed. The dispersion graphs are normalized with respect to the averaged distance between the control points prescribed by relationship (12) and (13), respectively. The details of $c^h - k^h$-curves presented in Figs. 7 (on the left) and 8 (on the left) are enlarged in Figs. 7 (on the right) and 8 (on the right). The band gap ranges for this parameterization are rapidly disappearing.

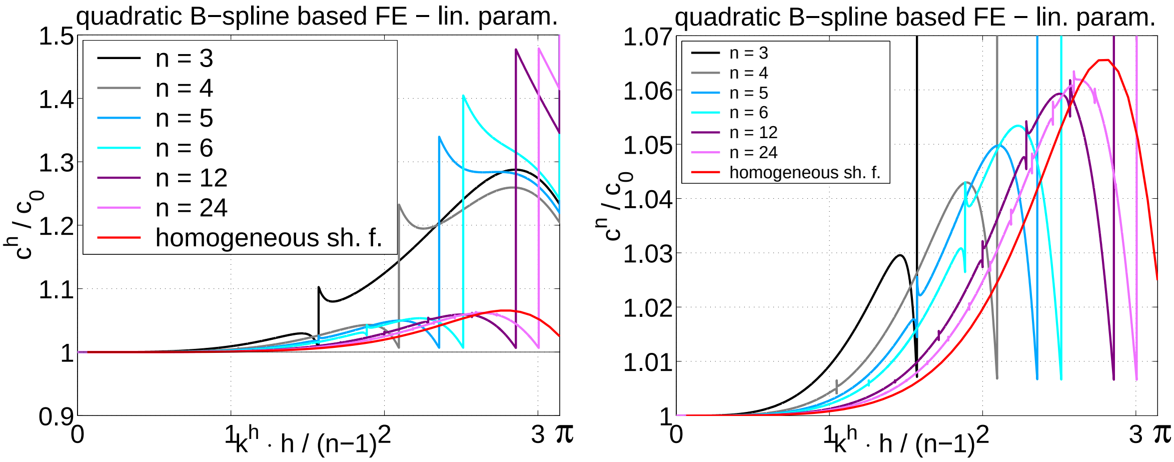

Figure 7: Normalized dispersion errors for quadratic B-spline based FE with linear parameterization. The red line corresponds to homogeneous shape functions [9].

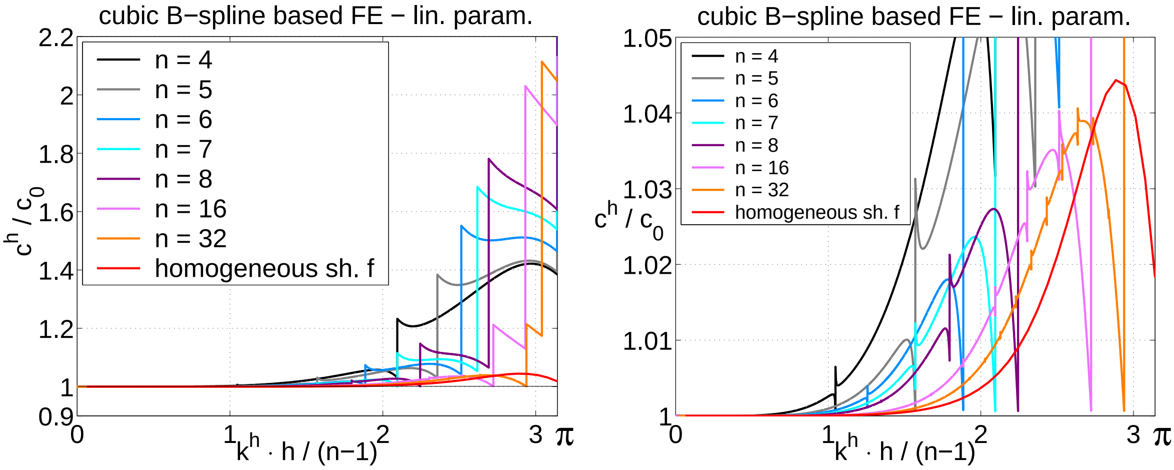

Figure 8: Normalized dispersion errors for cubic B-spline based FE with linear parameterization. The red line corresponds to homogeneous shape functions [9].

The dispersion curves for linear parameterization converge to the solution employing uniform (homogeneous) B-spline basis functions. For large number of control points, approximately $n \geq 10$, the $p-1$ highest dispersion branches ω versus k^h display a constant behavior. From it follows that the group speed $c_g^h = \mathrm{d}\omega/\,\mathrm{d}k^h = 0$ and the dependence of phase speed $c^h = \omega/k^h$ is a linear function with the negative slope. The wave corresponding to the last $p-1$ dispersion branches are not propagated through a elastic bar discretized by B-spline approach. The linear parameterization rapidly miminize the dispersion errors. The maximal error in phase speed for quadratic B-spline discretization is less than 7% and for cubic B-spline less than 4% thanks to the linear parametrization. This is very good property of B-spline based finite element method for case, where connection between several B-spline segments are only C^0.

6 CONCLUSIONS

It was shown that the dispersion errors of B-spline based finite element method for increasing number of control points converge to the continuum solution. The solution with high number of control points is near by the solution for uniform B-spline shape functions. On the other hand, its dependence is with jumps from the reason of existing of passing and band gaps. Moreover, the spurious modes are reduced by the B-spline based spatial discretization thanks to higher order of continuity of approximation of a unknown quantity (in this case displacement). Further, the dispersion errors and ranges of band gaps can be similarly eliminated by a special choice of positions of control points, for example, by the Greville abscissa. It is valid as well in the case, where individual B-spline segments are only connected with C^0 continuity. B-splines basis functions as shape functions have a potential for using in high performance and accurate finite element analysis of elastic wave propagation problems.

Acknowledgment

This work was supported by the grant projects GA ČR P101/10/P376, 101/09/1630, 101/07/1471 and P101/11/0288 under AV0Z20760514.

REFERENCES

[1] T.J.R. Hughes, *The Finite Element Method: Linear and Dynamic Finite Element Analysis*. New York: Prentice-Hall, Englewood Cliffs, 1983.

[2] T. Belytschko, R. Mullen, On dispersive properties of finite element solutions. J. Miklowitz eds. *Modern Problems in Elastic Wave Propagation*, John Wiley, 67–82, 1978.

[3] M. Okrouhlík, C. Höschl, A contribution to the study of dispersive properties of one-dimensional Lagrangian and Hermitian elements. *Computers* & *Structures*, **49**(5), 779–795, 1993.

[4] R.C.Y. Chin, Dispersion and Gibb's phenomenon associated with difference approximations to initial boundary-value problems. *J. Comp. Phys*, **18**, 233–247, 1975.

[5] R. Vichnevetsky, J.B. Bowles, *Fourier analysis of numerical approximations of hyperbolic equations*. SIAM, Philadelphia, 1982.

[6] L.L. Thompson, P.M. Pinky, Complex wave-number Fourier-analysis of the p-version finite element method. *Computational Mechanics*, **13**(4), 255–275, 1995.

[7] G. Seriani, S.P. Oliveira, Dispersion analysis of spectral element methods for elastic wave propagation. *Wave Motion*, **45**(6), 729–744, 2008.

[8] J.A. Cottrell, T.J.R. Hughes, Y. Bazilevs, *Isogeometric Analysis: Toward Integration of CAD and FEA*. John Wiley & Sons, New York, 2009.

[9] T.J.R. Hughes, A. Reali, G. Sangalli, Duality and Unified Analysis of Discrete Approximations in Structural Dynamics and Wave Propagation: Comparison of p-method Finite Elements with k-method NURBS. *Comput. Methods Appl. Mech. Engrg.*, **197**, 4104–4124, 2008.

[10] K.C. Park, Practical aspect of numerical time integration. *Computers* & *Structures*, **7**, 343–353, 1977.

[11] H. Kolsky, *Stress Wave in Solids*. New York: Dover Publications, 1963.

[12] L. Piegl,W. Tiller, *The NURBS Book, (Monographs in Visual Communication), Second Edition*. Springer-Verlag, 1997.

[13] G. Farin, *Curves and Surfaces for CAGD, A Practical Guide, Fifth Edition.* Morgan Kaufmann Publishers, 1999.

[14] L. Brillouin, *Wave propagation in Periodic Structures: Electric Filters and Crystal Lattices*. New York: Dover Publications, 1953.

[15] T.N.E. Greville, On the normalization of the B-splines and the location of the nodes for the case of unequally spaced knots. O. Shiska eds. *Inequalities*, Academic Press, New York, 1967

[16] H. Prautzsch, W. Boehm and M. Paluszny, *Bézier and B-Spline Techniques*. Springer Berlin Heidelberg, 2010.

COMPDYN 2011
ECCOMAS Thematic Conference on
Computational Methods in Structural Dynamics and Earthquake Engineering
M. Papadrakakis, M. Fragiadakis, V. Plevris (eds.)
Corfu, Greece, 25-28 May 2011

STUDIES IN NUMERICAL STABILITY AND CRITICAL TIME STEP ESTIMATION BY WAVE DISPERSION ANALYSIS VERSUS EIGENVALUE COMPUTATION

Jiří Plešek[1], **Radek Kolman**[1], **and Dušan Gabriel**[1]

[1]Institute of Thermomechanics
Dolejškova 5, Praha 8, 182 00, Czech Republic
e-mail: plesek@it.cas.cz

Keywords: Explicit integration, Courant number, Critical time step, Wave propagation, Dispersion.

Abstract. *The critical Courant number limiting the length of time step in explicit integration schemes is inversely proportional to the maximum natural frequency of a finite element mesh. The well known recommendation* $\mathrm{Co} = 1$ *for linear finite elements is deemed to be best. In fact, for some configurations this choice may dangerously overestimate the critical time step. It was shown in an earlier paper that by increasing the number of elements in the finite element mesh one will paradoxically improve the mesh's stability towards its theoretical limit. The present paper refines some details, presenting small scale numerical tests. The first test involves a long truss/bar consisting of one row of elements whose critical Courant number changes as elements are added one after another. Since this increases the critical number one may pick up a time step such that it is supercritical to a certain mesh but becomes subcritical by merely adding one element. In a similar fashion, a square area is tested in the second example, using different arrangements of edge supports. It turns out that the numerical solutions to wave propagation may be strongly influenced by small variation of distant boundary conditions, which should normally be physically insignificant.*

1 INTRODUCTION

Detailed analysis of accuracy and stability of finite element wave propagation solutions was presented in review paper [1] and references cited therein for various finite elements including consistent and lumped mass matrices. The critical Courant number limiting the length of the time step in explicit integration schemes, namely the central difference method, follows from the famous formula

$$\mathrm{Co}_{\mathrm{crit}} = \frac{2}{\bar{\omega}} \tag{1}$$

where $\bar{\omega}$ is the dimensionless frequency

$$\bar{\omega} = \frac{\omega_{\max} H}{c_1} \tag{2}$$

with $\omega_{\max}$ being the maximum natural frequency of a finite element mesh, H the element size, and c_1 the speed of the fasted wave propagating in a continuum, typically the longitudinal wave. Nearly equally famous recommendation $\mathrm{Co} = 1$ (or slightly less to be on the safe side) for linear finite elements, also known to engineers as "rule of thumb" is deemed to be best. In fact, this observation comes from dispersion analysis but, as it has been shown in Ref. [1], for some configurations it may dangerously overestimate the critical time step. It was also shown that by increasing the number of elements, N, in the finite element mesh one will improve the mesh's stability towards $\mathrm{Co}_{\mathrm{crit}} = 1$ as $N \rightarrow \infty$, which is rather a paradoxical finding.

The present paper refines these details, presenting small scale numerical tests, which exemplify some peculiarities. The first test involves a long truss/bar consisting of one row of elements whose critical Courant number changes as elements are added one after another. Since this increases the critical number one may pick up a time step such that it is supercritical to a certain mesh but becomes subcritical by merely adding one element. In a similar fashion, a square area is tested in the second example, using different arrangements of edge supports. It turns out that the numerical solutions to wave propagation may be strongly influenced by small variation of distant boundary conditions, which should normally be physically insignificant. Finally, the third illustration shows the direct numerical results relevant to the above mentioned choices of sub and supercritical times steps.

2 PROBLEM DESCRIPTION

This section concerns with essentials of wave propagation in homogeneous solids, finite element technology and dispersion computation.

2.1 Propagation of waves in an elastic isotropic continuum

The ith equation of motion in linear elastodynamics reads

$$(\Lambda + G) u_{j,ji} + G u_{i,jj} = \rho \ddot{u}_i \tag{3}$$

In this equation, Λ and G are Lamé's constants, ρ is the mass density and u_i is the ith component of the displacement vector. Furthermore, a comma placed before subscripts refers to spatial differentiation whereas the superimposed dots denote the time derivatives. The summation convention on repeated indices is assumed. The Lamé constants Λ, G may be related to engineering constants E, ν as

$$\Lambda = \frac{\nu E}{(1+\nu)(1-2\nu)}, \qquad G = \frac{E}{2(1+\nu)} \tag{4}$$

where E and ν are Young's modulus and Poisson's ratio.

In an unbounded isotropic continuum, two types of planar waves exist: the longitudinal wave and two transversal waves, featuring mutually orthogonal polarisation. The longitudinal wave propagates with the speed

$$c_1 = \sqrt{\frac{\Lambda + 2G}{\rho}} \tag{5}$$

The speed of the two transversal waves is

$$c_2 = \sqrt{\frac{G}{\rho}} \tag{6}$$

The standard continuum is said to be *non-dispersive*. This is, by d'Alembert's solution, because the wave profile (wavelength) does not affect the velocity of propagation.

As a special case, one may consider a plane harmonic solution to Eqn. (3) as

$$u_i = U_i(\mathbf{x}) \exp(\mathrm{i}k\ (\mathbf{p} \cdot \mathbf{x} \pm ct)) \tag{7}$$

or its equivalent form

$$u_i = U_i(\mathbf{x}) \exp(\mathrm{i}(\mathbf{k} \cdot \mathbf{x} \pm \omega t)) \tag{8}$$

where $\mathrm{i} = \sqrt{-1}$ is the imaginary unit; $\mathbf{x}$ is a position vector; t is time; k is the wave number; $\mathbf{p}$ is the unit normal to the wave front; $\mathbf{k}$ is the wave vector, $\mathbf{k} = k\mathbf{p}$; c is the phase velocity; ω is the angular velocity; and U_i is the ith component of the amplitude vector at the point defined by the position vector $\mathbf{x}$. For a given wavelength λ, the wave number k may be computed from

$$k = \frac{2\pi}{\lambda} \tag{9}$$

The phase velocity c is related to ω and k by

$$c = \frac{\omega}{k} \tag{10}$$

Finally, the group velocity c_g is defined as

$$c_g = \frac{\mathrm{d}\omega}{\mathrm{d}k} \tag{11}$$

In non-dispersive systems, c is a constant and since $\omega = ck$, we get $c_g = c$. Thus, in the absence of dispersion the group velocity equals the phase velocity. On the other hand, $c_g \neq c$ indicates dispersion.

2.2 Finite element method

Spatial discretization by the finite element of an elastodynamic problem introduces the ordinary differential system

$$\mathbf{M}\ddot{\mathbf{u}} + \mathbf{K}\mathbf{u} = \mathbf{R} \tag{12}$$

Here, $\mathbf{M}$ is the mass matrix, $\mathbf{K}$ the stiffness matrix, $\mathbf{R}$ is the time-dependent load vector, and $\mathbf{u}$ and $\ddot{\mathbf{u}}$ contain nodal displacements and accelerations. The element mass and stiffness matrices are given by

$$\mathbf{M}_e = \int_V \rho \mathbf{H}^T \mathbf{H} \, \mathrm{d}V \tag{13}$$

and

$$\mathbf{K}_e = \int_V \mathbf{B}^T \mathbf{C} \mathbf{B} \; \mathrm{d}V \tag{14}$$

where $\mathbf{C}$ is the elasticity matrix, $\mathbf{B}$ is the strain-displacement matrix, $\mathbf{H}$ stores the displacement interpolation functions and integration is carried over the element domain. Global matrices are assembled in the usual fashion. Under plane strain conditions, the elastic matrix $\mathbf{C}$ takes the form

$$\mathbf{C} = \frac{E}{1-\nu^2} \begin{bmatrix} 1 & \nu & 0 \\ \nu & 1 & 0 \\ 0 & 0 & \frac{1-\nu^2}{2(1+\nu)} \end{bmatrix} \tag{15}$$

The mass matrix defined by Eqn. (13) is called the consistent mass matrix.

Explicit integration methods, such as the central difference method discussed later, require the mass matrix inverted. Thus, it is advantageous to have it diagonal or *lumped.* In contrast to consistent matrices, which are uniquely defined by the variational formulation, lumping procedures are not strictly prescribed. The only common principle is the ability of FEM to assemble diagonal global matrix from the element mass matrices, thus, lumping may be performed on an element basis. Out of many methods rendering the mass matrix diagonal we shall refer to the simplest: the row sum method (RS) for bilinear elements and the Hinton-Rock-Zienkiewicz method (HRZ) for quadratic elements—see Ref [1].

In the subsequent analysis, a regular $H_x \times H_y$ mesh composed of plane rectangular elements is considered with H_x and H_y measuring the length of element edges aligned with coordinate axes. It proves useful to define reference matrices $\bar{\mathbf{M}}_e$, $\bar{\mathbf{K}}_e$ for a parent element having unit properties E and ρ, unit thickness b and unit length $H_x = 1$. Then performing integration over the reference domain $1 \times r$ one gets

$$\mathbf{M}_e = brH_x^2 \rho \bar{\mathbf{M}}_e \tag{16}$$

and

$$\mathbf{K}_e = bE\bar{\mathbf{K}}_e \tag{17}$$

Therefore, a class of problems is defined by two constants: the Poisson ratio ν and the aspect ratio $r = H_y/H_x$. Within this class, the reference stiffness matrix $\bar{\mathbf{K}}_e$ is a function of ν and r whereas the reference mass matrix $\bar{\mathbf{M}}_e$ is independent of both. Denote by $\bar{\omega}_e$ the maximum natural frequency of a *single* element described by these unit matrices. For example, one may compute $\bar{\omega}_e = 2.39$ for the bilinear RS elements or $\bar{\omega}_e = 7.61$ for the quadratic serendipity HRZ elements.

2.3 Dispersion computation

The smooth solutions, Eqn. (7) and (8), no longer apply to discretized system (12). In this case, the speed of propagation of an harmonic wave depends on its angular frequency. According to Ref. [1], such dependence may be manifested by the dispersion plot shown in Fig. 1. In general, dispersion behaviour is investigated by considering an harmonic wave train travelling through unbounded mesh, which may be accomplished by prescribing periodic boundary conditions. Thus, the normalized frequencies read off the plot actually represent the limit natural frequencies corresponding to a very large (theoretically infinite) finite element mesh.

As in the preceding section, denote by $\bar{\omega}_\lambda$ the supreme value of the normalized angular frequency in Fig 1, e.g. $\bar{\omega}_\lambda = 2.00$ for bilinear elements and $\bar{\omega}_\lambda = 7.37$ for quadratic elements. It is worth mentioning that $\bar{\omega}_\lambda < \bar{\omega}_e$ in every case. It should also be noted that the dispersion

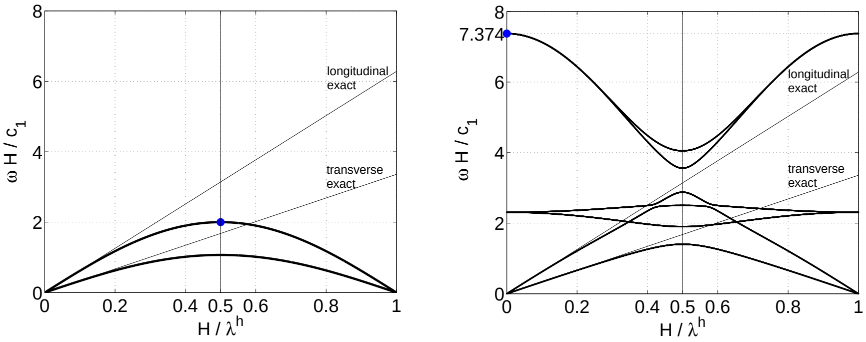

Figure 1: Dispersion curves for bilinear (left) and serendipity (right) elements.

diagrams discussed in this text are entirely due to spatial dispersion, neglecting effects of time integration—refer to paper [1] for complete treatise. This by no means oversimplifies actual problems since they are namely these theoretical values that enter stability criteria.

2.4 Explicit time integration and numerical stability

As a representative of explicit schemes, reviewed in Reference [2], the central difference method (CDM) will be discussed. Its discrete operator reads

$$\frac{1}{\Delta t^2}\mathbf{M}\mathbf{u}^{t+\Delta t} = \mathbf{R}^t - (\mathbf{K} - \frac{2}{\Delta t^2}\mathbf{M})\mathbf{u}^t - \frac{1}{\Delta t^2}\mathbf{M}\mathbf{u}^{t-\Delta t} \tag{18}$$

where $\mathbf{R}^t$ contains forces acting on the nodal points at time t. It is well known that CDM is only conditionally stable, Ref. [3], that is

$$\Delta t \leq \frac{2}{\omega_{\max}} \tag{19}$$

where $\omega_{\max}$ is the maximum eigenfrequency of the finite element mesh. The highest frequency can be computed by the standard FE software, aiming at the lowest eigenvalue with $\mathbf{K}$ and $\mathbf{M}$ swapped. This method was indeed employed in all the numerical computations presented here. Alternatively, the crititical time step may be estimated analytically as in Ref. [4].

At this point, it is convenient to introduce the Courant dimensionless number defined as

$$\mathrm{Co} = \frac{c_1 \Delta t}{H} \tag{20}$$

In elastodynamics, c_1 is the velocity of the longitudinal wave. Using the latter definition and that of $\bar{\omega}$ in Eqn. (2), the stability condition (19) can be rephrased as

$$\mathrm{Co} \leq \frac{2}{\bar{\omega}} \tag{21}$$

or, defining $\mathrm{Co}_{\mathrm{crit}}$, in the form of Eqn. (1). Inequality $\mathrm{Co} \leq 1$ then exactly manifests the Courant-Friedrichs-Levy stability condition for the linear truss element [2] but for other elements it may not be generally valid. On the other hand, we know, by Fried's theorem [5], which is a direct consequence of Sturm's polynomial separation property, that the maximum frequency is bounded by $\bar{\omega}_e$ obtained as the maximum eigevalue taken over all the elements in the FE mesh.

If the mesh is regular, composed only of rectangular elements of the same aspect ratio (the so-called structured mesh), one may devise another estimate of the critical time step, which lends some interesting insight into the problem of numerical stability in general. One asymptotic case arises for the infinite mesh, when $\omega_{\max}$ equals the supremum taken over all the dispersion curves for the particular element, i.e., $\bar{\omega}_\lambda$ is exploited. Tentatively, one may conjecture

$$\bar{\omega}_\lambda \leq \bar{\omega} \leq \bar{\omega}_e \tag{22}$$

This expression is indeed valid for an abitrary body with free boundary, $\Gamma_u = \emptyset$, but *does not hold* for a constrained mesh, for instance, if some displacement boundary conditions are prescribed. The meaning of the statement (22) will be clarified in full by examples shown in the next section.

Finally, it should be pointed out, that precisely because of the inequality (22), the true frequency of a real mesh will probably be higher than the estimate stemming from dispersion theory. Hence, the popular formula $c_1 \Delta t = H$ for the determination of time step length is not entirely safe.

3 NUMERICAL EXPERIMENTS

Unit dimensions were set in the numerical tests as follows: mass density $\rho = 1$, Poisson's ratio $\nu = 0.3$, and Young's modulus $E = 0.7428\ldots$ so that $c_1 = 1$ and $c_2 = 0.5345\ldots$. Furthemore, plane strain square bilinear elements with edge length $H = 1$ and unit thickness, $b = 1$, were employed. The reason for chosing linear rather than quadratic elements to illustrate stability properties is that the difference between $\bar{\omega}_\lambda = 2.00$ and $\bar{\omega}_e = 2.39$ is greater for these elements. Having N elements in the mesh, the total mass is $m = N\rho H^2 b = N$.

3.1 Plane strain bar

As the first example we consider a plane strain bar whose length is variable depending on the number of elements used. Fig 2 shows the eigenmode corresponding to the bar's maximum frequency for 40×1 discretization. The value of frequencies computed for various Ns are listed in Tab. 1.

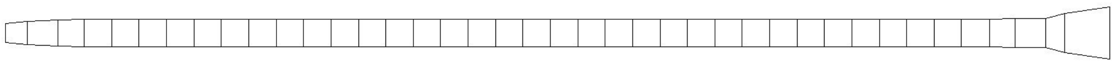

Figure 2: Eigenvector corresponding to the highest frequency of a bar with free ends.

One important observation following the inspection of Tab. 1 is that starting from the 20×1 bar, the maximum frequency does not change within the first 8 digits, which suggests an existence of the limit. Alas, this limit, $\bar{\omega} = 2.16$, differs from the theoretical value $\bar{\omega}_\lambda = 2.00$. On the one hand, our sequence correctly starts at $\bar{\omega}_e = 2.39$ for 1×1 discretization, but on the other, the asymptotics $\mathrm{Co}_{\text{crit}} = 1$ has never been reached. Why is it so? The answer lies in Fig 2. Since only the free ends vibrate, the maximum eigenvalue does not depend on the bar's length but solely on this boundary effect. The limit solution will not fit the periodical boundary conditions characteristic of the dispersion approach.

N	$\bar{\omega}$	$\mathrm{Co}_{\mathrm{crit}}$
1x1	2.3904568	0.8366602
2x1	2.1837346	0.9158622
3x1	2.1865457	0.9146848
4x1	2.1664669	0.9231620
5x1	2.1649080	0.9238268
6x1	2.1621023	0.9250256
7x1	2.1616266	0.9252292
8x1	2.1612303	0.9253988
9x1	2.1611334	0.9254403
10x1	2.1610747	0.9254654
20x1	2.1610454	0.9254780
40x1	2.1610454	0.9254780
80x1	2.1610454	0.9254780
100x1	2.1610454	0.9254780

Table 1: Critical Courant numbers for the bilinear finite element mesh of a free bar.

Another interesting observation follows from the graphical representation depicted in Fig. 3 on the log scale. Apart from the limit, there is a pronounced gap between the three and four element configurations. Selecting $\mathrm{Co} = 0.92$, the time step is stable for the 4×1 mesh but unstable for the smaller 3×1 mesh. This motivates the critical test defined in Fig. 4.

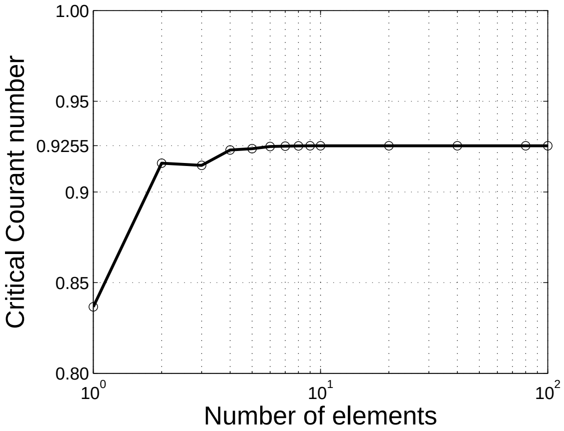

Figure 3: Distribution of the critical Courant number for the bar with free ends.

A three-element bar is loaded by the Heaviside step function $F(t) = 1$ for $t > 0$. Since $\mathrm{Co} = 0.92 > \mathrm{Co}_{\mathrm{crit}}$ one expects an incursion of instability after some time has elapsed but a stable solution if a four-element problem had been considered instead. In both the cases, parabolic displacement evolution

$$u(t) = \frac{F}{2m} t^2 = \frac{t^2}{2N} \tag{23}$$

applies to the motion of the whole body. The average acceleration, $1/N$, measured at the control point A for the 4×1 configuration equals 0.25. The existence of the stable solution is confirmed

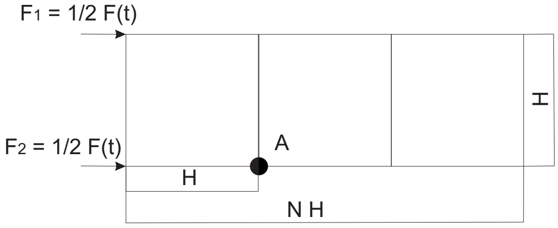

Figure 4: Transient problem with Heaviside load; unstable configuration.

by plots shown in Fig. 5. The oscillatory course of acceleration history is due to waves reflection about the mean value 0.25, which matches the rigid body motion. By contrast, the unstable 3×1 problem exhibits the solution's uncotrolled blow up at about $t = 3000$, see Fig. 6. The instability commences even much earlier after several wave reflections, which is nicely captured in Fig. 7.

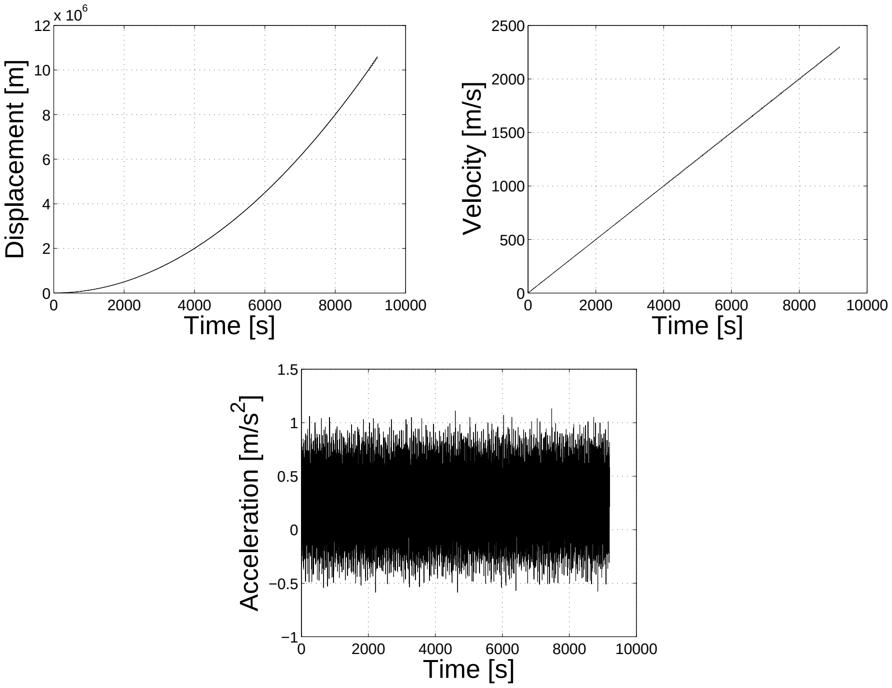

Figure 5: Displacement, velocity and acceleration in the stable 4×1 computation.

Let us return to the original eigenvalue problem shown in Fig. 2. This time the boundary conditions are modified by clamping the right end. The corresponding eigenvector and the frequencies computed are shown in Fig. 8 and Tab. 2, respectively. The same limit $\bar{\omega} = 2.16$ is reached already by the 8×1 discretization, which is not surprising. Indeed, the vibration modes roughly correspond to those of the free bar twice the length of the free-fixed bar. A more interesting fact is that the maximum frequency now *increases.* This is because the results converge to the same limit as before but for each N-element bar the constrained configuration has lower maximum frequency than the free one. The critical Courant number distribution is shown in Fig. 9

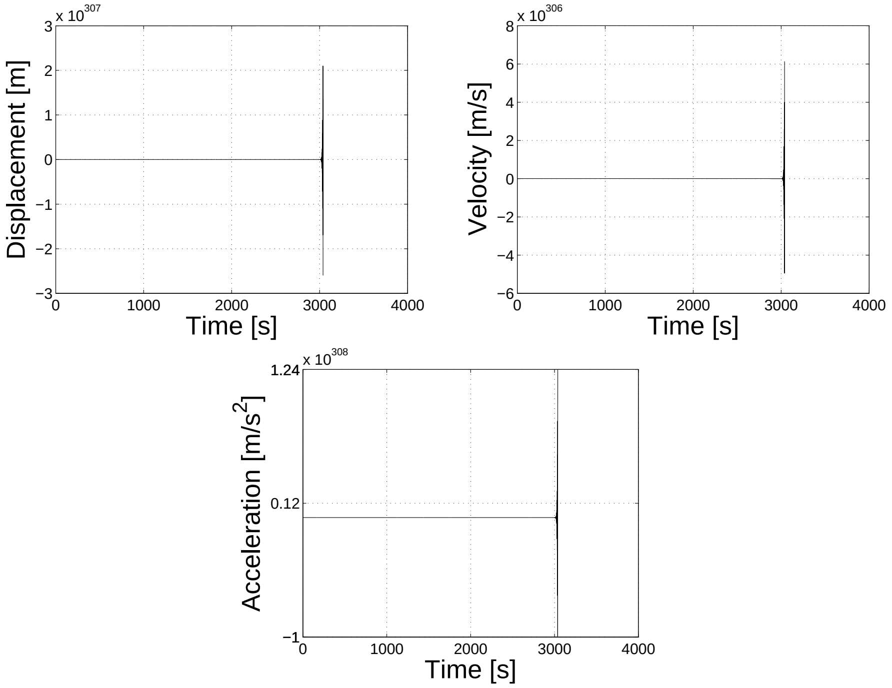

Figure 6: Displacement, velocity and acceleration in the unstable 3×1 computation.

N	$\bar{\omega}$	$\mathrm{Co}_{\mathrm{crit}}$
1x1	1.8403500	1.0867498
2x1	2.1530847	0.9288998
3x1	2.1587386	0.9264670
4x1	2.1608547	0.9255597
5x1	2.1609985	0.9254981
6x1	2.1610395	0.9254805
7x1	2.1610425	0.9254793
8x1	2.1610454	0.9254780
9x1	2.1610454	0.9254780
10x1	2.1610454	0.9254780
20x1	2.1610454	0.9254780
40x1	2.1610454	0.9254780
80x1	2.1610454	0.9254780
100x1	2.1610454	0.9254780

Table 2: Critical Courant numbers for the free-fixed bar.

We close our discussion concerning this example with the remark that the conjecture (22) does not hold for a constrained problem. For example, for the free-fixed bar $\bar{\omega}_\lambda > \bar{\omega}_{1\times1}$, because the maximu frequency has been reduced by the imposition of the boundary condition. Theoretically, one could even have had $\bar{\omega} = 0$ if all the nodes had been fixed. By contrast, $\bar{\omega}_e$ always forms the upper bound.

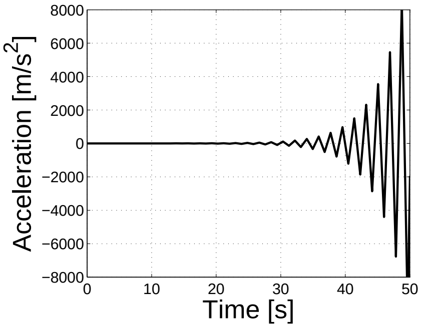

Figure 7: Detail of acceleration build up.

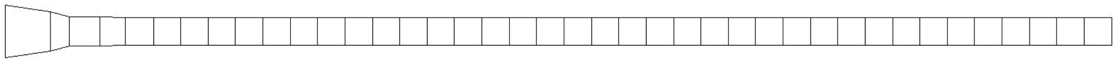

Figure 8: A free-fixed bar.

3.2 Plane strain square domain

Similar examples as in the preceding section may be analysed. Consider a plane strain square domain shown in Fig. 10 and the critical Courant number distributions for both (fixed and free) boundary configurations—Fig. 11.

In this case, convergence to the limit $\mathrm{Co}_{\mathrm{crit}} = 0.99$ is observed. Similarly as for the free bar this number is slightly less than the theoretical value $\mathrm{Co}_{\mathrm{crit}} = 1$. The reason can again been seen in Fig. 10, which suggests that it is the vibration of the corner elements that is responsible for the maximum frequency and is, in fact, independent of the mesh size.

A new phenomenon is detected with the constrained mesh. Comparing it with the free-fixed bar one notices that, here, zero displacements are prescribed along the whole boundary. This means that adding extra elements is merely equivalent to mesh refinement, which in turn implies the increase of the dimensionless maximum frequency. Since the mesh grading is regular and there are no boundary effects, monotonous convergence to the theoretical limit, $\mathrm{Co}_{\mathrm{crit}} = 1$, follows. It is interesting to note that also in this situation $\bar{\omega} < \bar{\omega}_{\lambda}$, which violates condition (22) as the present problem is fully constrained.

4 CONCLUSIONS

It might seem at first glance that, except illustrating certain mathematical principles, the present study bears little importance to real-world computation. On the one hand, todays engineering problems are extremely large (rendernig $N \to \infty$ effectively) and, on the other, one may safely use the upper bound by calculating the maximum eigenvalue of a single element.

It should be borne in mind that Fried's estimate, $\bar{\omega} \leq \bar{\omega}_e$, is only useful for a structured mesh when all the elements have the same spectrum. For an unstructured mesh, this information is hardly available and one must resort to other estimates. It is namely under such circumstances

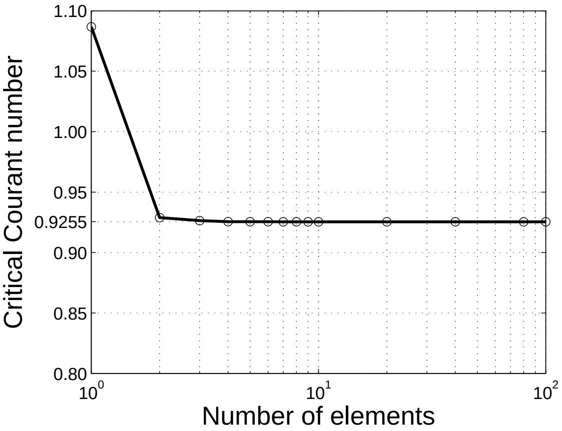

Figure 9: Distribution of the Critical Courant number for the free-fixed bar.

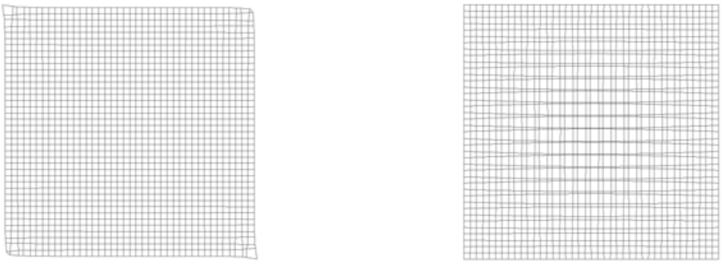

Figure 10: Maximum eigenmode of a free square domain (left) and the domain with fixed edges (right).

that the analysts use the $\bar{\omega}_\lambda$ limit derived from dispersion diagrams often unaware of its pitfalls. It must be emphasised that for the reasons exaplained in the paper the frequent recommendation $c_1\Delta t = H$ is not entirely safe.

The examples involving free bodies clearly demonstrated the way the vibration of corner elements changed the stability limits. Hence, we conclude that even distant boundary conditions, which should normally be physically insignificant, may considerably influence numerical solution.

ACKNOWLEDGEMENTS

Support by GACR 101/09/1630, 101/07/1471 and GPP101/10/P376 under AV0Z20760514 is acknowledged.

REFERENCES

[1] J. Plešek, R. Kolman, D. Gabriel, Dispersion errors of finite element discretizations in elastodynamics. *Computational Technology Reviews Vol. 1, Saxe-Coburg Publications,* 251–279, 2010.

[2] M.A. Dokainish, K. Subbaraj, A survey of direct time-integration methods in computational structural dynamics - I: Explicit methods. *Computers* & *Structures*, **32**, 1371–1386, 1989.

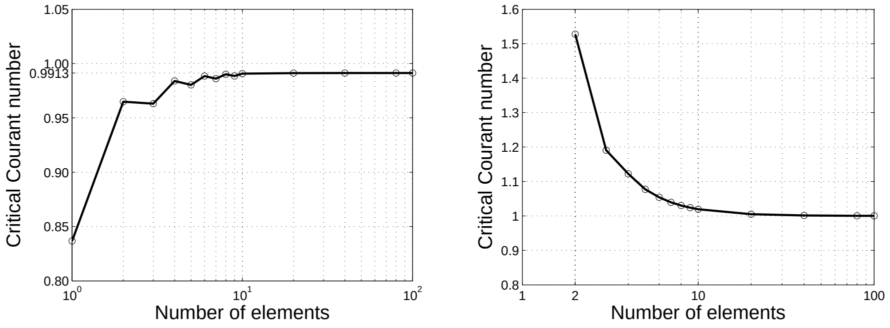

Figure 11: Critical Courant numbers for free (left) and fixed domain (right).

[3] K.C. Park, Practical aspect of numerical time integration. *Computers & Structures*, **7**, 343–353, 1977.

[4] D.P. Flanagan, T. Belytschko A uniform strain hexahedron and quadrilateral with orthogonal hourglass control. *Int. J. Num. Methods Engng.*, **17**, 679–706, 1981.

[5] I. Fried, Bounds on the extremal eigenvalues of the finite element stiffness and mass matrices and their spectral condition number. *Journal of Sound and Vibration*, **22**, 407–418, 1972.

COMPDYN 2011
3rd ECCOMAS Thematic Conference on
Computational Methods in Structural Dynamics and Earthquake Engineering
M. Papadrakakis, M. Fragiadakis, V. Plevris (eds.)
Corfu, Greece, 25-28 May 2011

ACCURATE NUMERICAL SOLUTIONS OF STRUCTURAL DYNAMICS AND WAVE PROPAGATION PROBLEMS BASED ON NEW DISPERSION-REDUCTION TECHNIQUE AND NEW TWO-STAGE TIME-INTEGRATION TECHNIQUE

A. Idesman

Texas Tech University
Box 41021, Lubbock, TX 79409, USA
e-mail: alexander.idesman@coe.ttu.edu

Keywords: time integration, spurious oscillations, numerical dispersion

Abstract. *There are the following issues with existing numerical methods for elastodynamics problems (including wave propagation and structural dynamics problems): a) a large dispersion error of space-discretization methods may lead to a great error in space, especially in the 2-D and 3-D cases; b) due to spurious high-frequency oscillations, the lack of reliable numerical techniques that yield an accurate solution of wave propagation in solids; c) the treatment of the error accumulation for long-term integration; d) the selection of an effective time-integration method among known ones; e) the selection of the size of a time increment for a time-integration method with numerical dissipation; f) the increase in accuracy and the reduction of computation time for real-world dynamic problems. A new numerical approach for computer simulation of the dynamic response of linear elastic structures is suggested, resolves the issues listed and includes two main components: a) a new dispersion reduction technique for linear finite elements based on the extension of the modified integration rule method to elastodynamics problems, and b) a new two-stage time-integration technique with the filtering stage. The suggested two-stage time-integration technique includes the stage of basic computations and the filtering stage, new first-, second- and high-order accurate time-integration methods for elastodynamics, and a new calibration procedure for the selection of the minimum necessary amount of numerical dissipation for time-integration methods, new criteria for the selection of time-integration methods for elastodynamics. In contrast to existing approaches, the new technique does not require guesswork for the selection of numerical dissipation and does not require interaction between users and computer codes for the suppression of spurious high-frequency oscillations. Different discretization methods in space such as the finite element method, the spectral element method, the boundary element method, and others can be used with the suggested two-stage time-integration approach. 1-D and 3-D numerical examples show that the new approach used with the finite element method yields an accurate non-oscillatory solution for impact and wave propagation problems and considerably reduces the number of degrees of freedom and the computation time in comparison with existing methods.*

1 INTRODUCTION

The application of finite elements in space to transient acoustics or transient linear elastodynamics problems leads to a system of ordinary differential equations in time

$$\mathbf{M}\,\ddot{\mathbf{U}} + \mathbf{C}\,\dot{\mathbf{U}} + \mathbf{K}\,\mathbf{U} = \mathbf{R}\,, \tag{1}$$

where $\mathbf{M}$, $\mathbf{C}$, $\mathbf{K}$ are the mass, damping, and stiffness matrices, respectively, $\mathbf{U}$ is the vector of the nodal displacement, $\mathbf{R}$ is the vector of the nodal load. The case of zero natural viscosity, $\mathbf{C} = \mathbf{0}$, is considered in the paper. It is known that even the exact solution to Eq. (1) contains the numerical dispersion error, which is also related to the space discretization error; e.g., see [1, 2, 3, 4, 5, 6, 7, 8, 9, 10] and others. The decrease in the space discretization error by the use of mesh refinement considerably increases computational costs. Therefore, several techniques have been proposed for the reduction in the numerical dispersion error. One simple approach for acoustic and elastic wave propagation problems is based on the use of the averaged mass matrix in Eq. (1) instead of the consistent or lumped mass matrix $\mathbf{M}$; see [5, 6, 7, 8] and others. For linear finite elements, this technique reduces the relative error in the wave velocity for harmonic waves from the second order to the fourth order of accuracy in the 1-D case. However, these results are not valid in the general case of harmonic wave propagation for 2-D and 3-D problems (nevertheless, in the 2-D and 3-D cases, the averaged mass matrix yields more accurate results compared with the standard mass matrix). Another simple technique for linear finite elements, which is suggested in [9] for acoustic waves in the 2-D case, is based on the modified integration rule for the mass and stiffness matrices. In contrast to the averaged mass matrix, this approach increases the accuracy for the phase velocity from the second order to the fourth order in the general multi-dimensional case of acoustic waves. However, the applicability of the modified integration rule to linear elastodynamics problems has not been studied.

As we mentioned above, the analysis of numerical dispersion is based on propagation of harmonic waves. In the general case of loading (boundary conditions), the numerical study of the effectiveness of the finite element formulations with the reduced dispersion error is difficult due to the presence of spurious high-frequency oscillations in numerical solutions; e.g., see [3, 5].

In the current paper, we will apply two dispersion reduction techniques for linear finite elements to 1-D and 3-D impact problems. Similar to the classical finite element technique for elastodynamics, the finite element formulations with reduced dispersion also suffer spurious high-frequency oscillations in numerical solutions (e.g., see below). Therefore, for obtaining accurate numerical results and for the numerical study of the effectiveness of the dispersion reduction techniques applied to elastodynamics problems with general loading, the two-stage time-integration technique with the filtering stage (developed in our previous papers [11, 12, 13]) is used along with the finite elements with reduced dispersion. This technique identifies and removes spurious high-frequency oscillations from numerical solutions. 1-D and 3-D impact problems for which all frequencies of the semi-discrete system, Eq. (1), are excited are solved with the standard and new techniques. Numerical results show that compared with the standard mass and stiffness matrices, the simple dispersion reduction techniques lead to a considerable reduction in the number of degrees of freedom and computation time at the same accuracy, especially for multi-dimensional problems.

2 NUMERICAL TECHNIQUE

2.1 Dispersion reduction of linear finite elements (see [14])

We will use two numerical techniques which reduce the dispersion error of linear finite elements at the space discretization. The first approach is based on the use of the mass matrix $\boldsymbol{M}$ calculated as a weighted average of consistent and lumped mass matrices with the weighting factor γ (similar to that used in [5, 6, 8])

$$\boldsymbol{M} \;=\; \boldsymbol{M}^{lump}\gamma + \boldsymbol{M}^{cons}(1-\gamma) \tag{2}$$

where γ is the parameter to be determined. The second technique is the extension of the modified integration rule to the case of elastodynamics suggested in our paper [14]. For the dispersion reduction of linear finite elements, the mass and stiffness matrices of each finite element are calculated with the modified integration rule (similar to those used in [9])

$$\boldsymbol{M}^e \;=\; \int_{-1}^{1} \boldsymbol{N}^T(s)\boldsymbol{N}(s)det(\boldsymbol{J})ds \approx \sum_{i=1}^{2} \boldsymbol{N}^T((-1)^i\alpha_M)\,\boldsymbol{N}((-1)^i\alpha_M)det(\boldsymbol{J})\,, \tag{3}$$

$$\boldsymbol{K}^e \;=\; \int_{-1}^{1} E\boldsymbol{B}^T(s)\boldsymbol{B}(s)det(\boldsymbol{J})ds \approx \sum_{i=1}^{2} E\boldsymbol{B}^T((-1)^i\alpha_K)\,\boldsymbol{B}((-1)^i\alpha_K)det(\boldsymbol{J}) \tag{4}$$

in the 1-D case,

$$\boldsymbol{M}^e \;=\; \int_{-1}^{1}\int_{-1}^{1}\int_{-1}^{1} \boldsymbol{N}^T(s,t,q)\boldsymbol{N}(s,t,q)det(\boldsymbol{J})dsdtdq$$

$$\approx \sum_{i=1}^{2}\sum_{j=1}^{2}\sum_{p=1}^{2} \boldsymbol{N}^T((-1)^i\alpha_M,(-1)^j\alpha_M,(-1)^p\alpha_M)\,\boldsymbol{N}((-1)^i\alpha_M,(-1)^j\alpha_M,(-1)^p\alpha_M)det(\boldsymbol{J})\,, \tag{5}$$

$$\boldsymbol{K}^e \;=\; \int_{-1}^{1}\int_{-1}^{1}\int_{-1}^{1} \boldsymbol{B}^T(s,t,q)\boldsymbol{D}\boldsymbol{B}(s,t,q)det(\boldsymbol{J})dsdtdq$$

$$\approx \sum_{i=1}^{2}\sum_{j=1}^{2}\sum_{p=1}^{2} \boldsymbol{B}^T((-1)^i\alpha_K,(-1)^j\alpha_K,(-1)^p\alpha_K)\,\boldsymbol{D}\boldsymbol{B}((-1)^i\alpha_K,(-1)^j\alpha_K,(-1)^p\alpha_K)det(\boldsymbol{J}) \tag{6}$$

in the 3-D case. Here, $\boldsymbol{N}$ and $\boldsymbol{B}$ are the standard finite element shape and B matrices; $\boldsymbol{D}$ is the matrix of elastic coefficients; $\boldsymbol{J}$ is the Jacobian matrix ($det(\boldsymbol{J}) = dx/2$; $dx^2/4$; $dx^3/8$ in the 1-D case, in the 2-D case for square elements and in the 3-D case for cubic elements, respectively; dx is the length of a finite element); E is Young's modulus; s, t, q are the isoparametric coordinates; α_M and α_K are the coordinates of the integration points for the mass and stiffness matrices to be determined (2 and $2 \times 2 \times 2 = 8$ integration points are used for linear elements in the 1-D and 3-D cases, respectively); e.g., see [15] for the derivation of finite element matrices. The integration error related to the application of the modified integration rule for the mass and stiffness matrices does not change the convergence rate of finite element solutions; see [9].

The analytical study of numerical dispersion shows (see our paper [14]) that the use of the averaged mass matrix with $\gamma = 0.5$ increases the accuracy in the calculation of the wave velocity from the second order to the fourth order in the 1-D case. Completely equivalent results for the numerical dispersion reduction are obtained with the modified integration rule in the 1-D case with $\alpha_M = \sqrt{\frac{2}{3}}$. However, in the multi-dimensional cases with the presence of compressional and shear waves, these results are valid only under some specific conditions. For example, for the averaged mass matrix ($\gamma = 0.5$), the increase in the order of accuracy for the phase velocity is valid only for the waves propagating along the coordinate axes of uniform meshes. The modified integration rule with $\alpha_M = \sqrt{\frac{2}{3}}$ and $\alpha_K = \sqrt{\frac{4(2\nu-1)}{3(4\nu-3)}}$ (ν is Poisson's ratios) additionally allows the extension of the results of the 1-D case only for the compressional waves or only for the shear waves propagating in any direction in the 2-D case and propagating in any direction within the coordinate planes of uniform meshes in the 3-D case.

2.2 The two-stage time-integration technique with filtering spurious oscillations (see [11, 12, 13])

The standard finite elements and the finite elements with reduced dispersion described in the previous section lead to the appearance of spurious high-frequency oscillations at time integration of Eq. (1) for wave propagation and impact problems. Below we briefly describe the approach developed in our previous papers [11, 12, 13] which, for the standard finite elements and for the finite elements with reduced dispersion, allows accurate numerical solutions of elastodynamics problems without spurious oscillations. It includes the two-stage time-integration technique with the stage of basic computations and the filtering stage, the implicit time-continuous Galerkin (TCG) method with large numerical dissipation and the calibration procedure for the selection of the minimum necessary amount of numerical dissipation (in terms of a time increment) for the implicit TCG method; see also the Appendix.

The idea of the two-stage time-integration technique is very simple. Because for linear elastodynamics problems there is no interaction between different modes during time integration (they are integrated independently of each other; e.g., see [12, 13]), the most accurate time-integration method (usually without numerical dissipation or artificial viscosity) should be used at the stage of basic computations, especially for a long-term integration. This means that all modes including high-frequency modes are integrated very accurately and the solution includes spurious high-frequency oscillations after basic computations. For the damping out of spurious high modes, a time-integration method with large numerical dissipation (or artificial viscosity) is used for a number of time increments for the filtering of spurious oscillations (the filtering stage). A small number of time increments for implicit time-integration methods is sufficient for the filtering stage, with negligible error accumulation at low modes (e.g., 10 time increments with the implicit TCG with large numerical dissipation is used with the proposed technique at the filtering stage for all elastodynamics problems; see [13]).

The main advantages of the developed approach are as follows. The suggested numerical technique: a) allows the selection of the best time-integration method for basic computations from simple criteria (the most important one being the accuracy of the method); b) includes pre-, or/and post-processing for filtering spurious high-frequency oscillations, which requires little computation time compared with that for the stage of basic computations (a small number of time increments with the implicit TCG method with large numerical dissipation is used for the filtering stage); c) yields no error accumulation due to numerical dissipation (or artificial viscosity) at the stage of basic computations; d) allows the calibration of spurious oscillations at different observation times (see [12, 13] and the Appendix below) and does not require any guesswork for the selection of numerical dissipation or artificial viscosity as do existing approaches. Thus, the approach can be easily incorporated in computer codes and does not require interaction with users for the suppression of spurious high-frequency oscillations.

Summarizing, in contrast to existing approaches with one time integration method, the described technique is based on the application two different time integration methods to Eq. (1): one method is used for accurate integration of a semi-discrete system at the stage of basic computations and allows spurious oscillations; another method is used for filtering spurious oscillations at the pre-, or/and post-processing stage. At mesh refinement, the numerical solutions obtained with the two-stage time-integration technique include more modes (because a finer mesh requires smaller numerical dissipation; see Eqs. (13)-(15) in the Appendix), exclude spurious high modes, and converge to exact solutions.

In the current paper, we will use the standard implicit trapezoidal rule with small time increments for basic computations in order to obtain an accurate solution of the semi-discrete elastodynamics problem, Eq. (1), with a negligible error in time (this solution contains spurious high-frequency oscillations). We should mention that other known implicit or explicit time-integration methods can also be used for basic computations with very small time increments (the trapezoidal rule is the most accurate second-order time-integration method). For filtering spurious oscillations, the implicit TCG method with large numerical dissipation developed in [12, 13] and briefly described in the Appendix is used at the filtering stage (the post-processing stage).

3 NUMERICAL MODELING

The new numerical approach is implemented into the finite element code FEAP [16]. 1-D and 3-D impact linear elastodynamics problems will be considered below. Due to spurious high-frequency oscillations, these problems cannot be accurately solved by existing time-integration methods based on the introduction of artificial viscosity (or numerical dissipation) at each time increment, especially in the case of long-term integration. For the filtering of spurious oscillations in the problems solved below, the filtering stage will be used with the TCG method with $N = 10$ time increments (5 positive plus 5 negative time increments) the size of which is calculated according to Eqs. (13) - (15) with $\Omega_{0.1}(N = 10) = 0.81$ (see [12, 13, 17] and the Appendix below).

3.1 1-D impact of an elastic bar against a rigid wall

First, the impact of an elastic bar of the length $L = 4$ against a rigid wall is considered in the 1-D case (see Fig. 1a). Young's modulus is chosen to be $E = 1$ and the density to be $\rho = 1$. The following boundary conditions are applied: the displacement $u(0, t) = t$ (which corresponds to the velocity $v(0, t) = v_0 = 1$) and $u(4, t) = 0$ (which corresponds to the velocity $v(4, t) = 0$). Initial displacements and velocities are zero; i.e., $u(x, 0) = v(x, 0) = 0$. The analytical solution to this problem includes the continuous variation of displacements $u_a(x, t) = t - x$ for $t \geq x$ and $u_a(x, t) = 0$ for $t \leq x$, and the piecewise continuous variation of velocities and stresses $v_a(x, t) = -\sigma^a(x, t) = 1$ for $t \geq x$ and $v_a(x, t) = \sigma^a(x, t) = 0$ for $t \leq x$ (at the interface $x = t$, jumps in stresses and velocities occur). The observation time is chosen to be $T = 18$. During this time the velocity pulse travels within the bar with two reflections from each end of the bar.

It is known that the application of traditional semi-discrete methods to this problem leads to oscillations in velocities and stresses due to the spurious high-frequency response [11, 18, 19]. As we will see (e.g., from Fig. 1b), finite elements with reduced numerical dispersion reduce these oscillations after basic computations but they do not completely remove them from the numerical solution. Therefore, the two-stage procedure with the filtering stage as described in

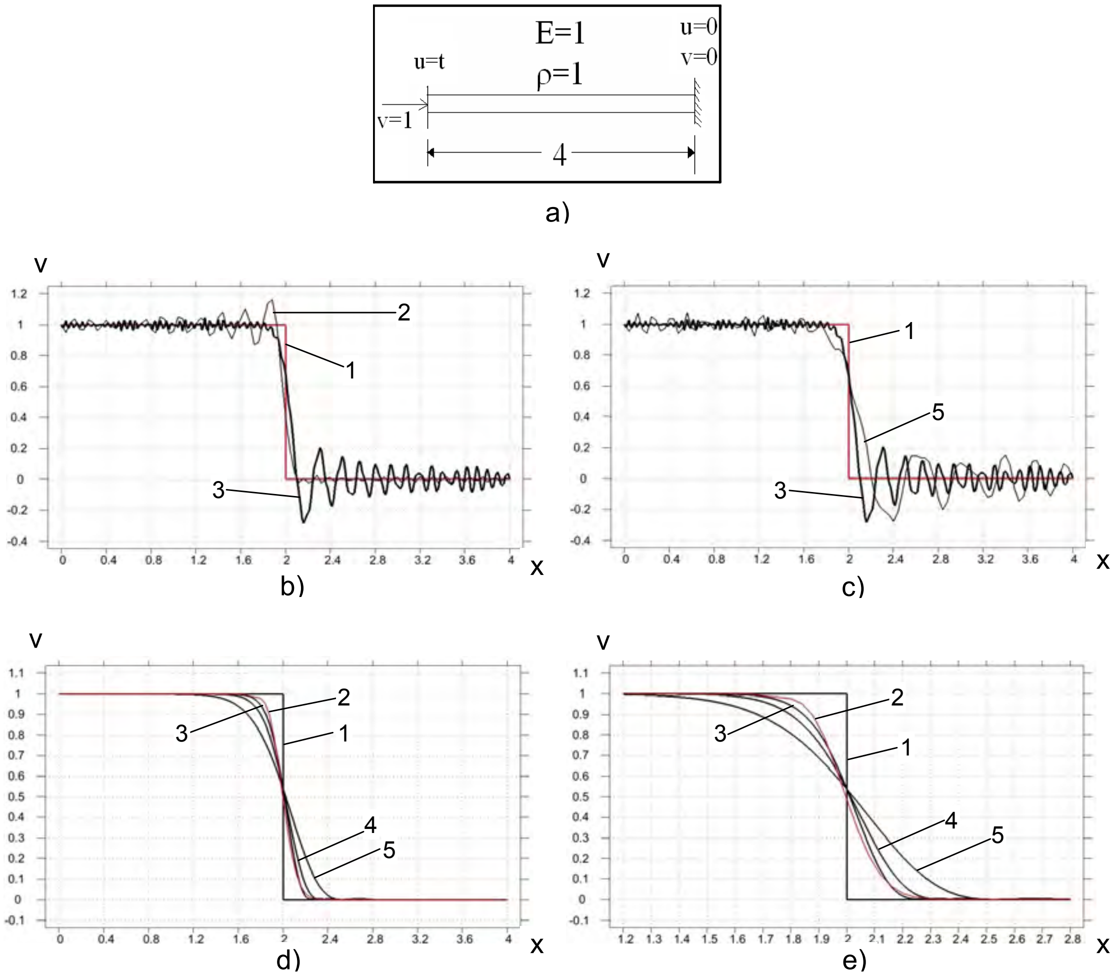

Figure 1: Impact of an elastic bar of length $L = 4$ against a rigid wall (a). Velocity distribution along the bar at observation time $T = 18$ after basic computations (b, c) and after post-processing (d, e). Curves 1 correspond to the analytical solution. Curves 2 correspond to the numerical solution with the averaged mass matrix ($\gamma = 0.5$) on a uniform mesh with 100 linear 2-node finite elements. Curves 3, 4, 5 correspond to the numerical solutions with the consistent mass matrix on uniform meshes with 300, 200 and 100 linear 2-node finite elements, respectively. e) shows the zoomed graph d) in the range $1.2 < x < 2.8$.

Section 2.2 will be applied for accurate and non-oscillatory solutions. The 1-D impact problem with propagating discontinuities in stresses and velocities can be considered a good benchmark problem for the testing of new numerical methods for wave propagation problems.

The problem is solved on uniform meshes with 100, 200 and 300 $Q2$ linear finite elements with the consistent and averaged ($\gamma = 0.5$) mass matrices as well as on uniform meshes with 50 and 70 $Q3$ quadratic finite elements with the consistent mass matrix. We should mention that the techniques based on the modified integration rule with $\alpha_M = \sqrt{2/3}$ and the averaged mass matrix with $\gamma = 0.5$ are completely equivalent and yield the same results in the 1-D case. Because in the paper we study the improvement of the spatial accuracy due to the reduction in the numerical dispersion error, for the time integration of Eq. (1) at basic calculations we will use the trapezoidal rule with very small time increments $\Delta t = 0.001$. A further reduction of time increments does not practically affect the numerical results for the meshes used; i.e., the error in time is very small and can be neglected.

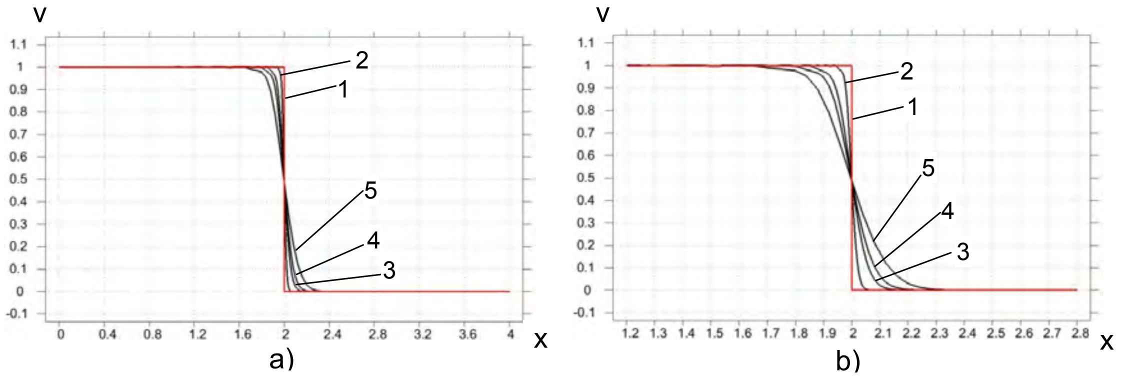

a) b)

Figure 2: Velocity distribution along the bar at observation time $T = 18$ after post-processing. Curve 1 corresponds to the analytical solution. Curves 2, 3, 4, 5 correspond to the numerical solutions with the averaged mass matrix ($\gamma = 0.5$) on uniform meshes with 1000, 300, 200 and 100 linear 2-node finite elements, respectively. b) shows the zoomed graph a) in the range $1.2 < x < 2.8$.

Fig. 1 shows the numerical results for linear elements obtained with the consistent and averaged mass matrices after basic computations and after the filtering stage (post-processing). The use of the formulation with the reduced dispersion error reduces the amplitudes of spurious oscillations (see curve 2 in Fig. 1b) and yields a more accurate slope of the wave front at $x = 2$ (see curve 2 in Fig. 1b and curve 5 in Fig. 1c for the consistent mass matrix obtained at the same numbers of elements). However, the presence of spurious high-frequency oscillations makes it difficult to compare numerical results. After the filtering of spurious oscillations, we can see that for the selected observation time and at the same accuracy, the use of the averaged mass matrix reduces the number of degrees of freedom by a factor of three as compared with the case with the standard consistent mass matrix (see curves 2 and 3 in Fig. 1d,e). We should also mention that after basic computations the slopes of the wave front in the numerical solutions obtained on a uniform mesh with 100 elements and the averaged mass matrix and obtained on a uniform mesh with 300 elements and the consistent mass matrix are approximately the same (see curves 2 and 3 in Fig. 1b). After the filtering stage, the numerical results obtained with the averaged mass matrix converge to the analytical solution at mesh refinement; see Fig. 2. These numerical results for the 1-D impact problem after the filtering stage are similar to those obtained in [18] by the use of special non-linear discontinuity-capturing operators.

Fig. 3 shows that for the standard mass and stiffness matrices, quadratic finite elements yield more accurate results than linear finite elements (e.g., compare curves 4 and 5 obtained on the meshes with the same numbers of degrees of freedom). However, at the same numbers of degrees of freedom, the linear elements with the averaged mass matrix (or the modified integration rule) are more accurate than the quadratic elements with the consistent mass matrix (e.g., compare curves 2 and 4 in Fig. 3 obtained on the meshes with the same numbers of degrees of freedom). The comparison of curves 2 and 3 in Fig. 3 also shows that for the selected observation time and at the same accuracy, the linear elements with the reduced dispersion error reduces the number of degrees of freedom by a factor of 1.4 as compared with the case of the quadratic elements with the consistent mass matrix. In addition to this advantage, numerical solutions with linear elements require less computation time compared with that for quadratic elements because at the same numbers of degrees of freedom, the bandwidth of the mass and stiffness matrices for quadratic elements is twice of that for linear elements.

Remark. It is interesting to note that the range of frequencies in numerical solutions after

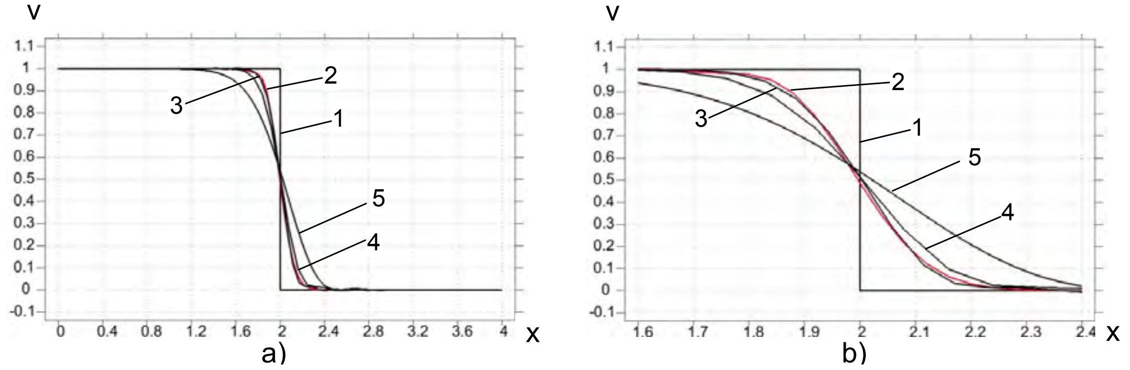

Figure 3: Velocity distribution along the bar at observation time $T = 18$ after post-processing. Curve 1 corresponds to the analytical solution. Curves 2 and 5 correspond to the numerical solutions on a uniform mesh with 100 linear 2-node finite elements with the averaged mass matrix ($\gamma = 0.5$) and with the consistent mass matrix, respectively. Curves 3 and 4 correspond to the numerical solutions with the consistent mass matrix on uniform meshes with 70 and 50 quadratic 3-node finite elements, respectively. b) shows the zoomed graph a) in the range $1.6 < x < 2.4$.

the filtering stage is indirectly determined by the size of the time increments calculated by Eqs. (13) - (14) (see the Appendix). The numerical results show that if the time increments calculated according to Eqs. (13) - (14) for the filtering stage are close to each other for the formulations with the consistent and averaged mass matrices on different uniform meshes, then the numerical solutions obtained on these different uniform meshes are close to each other. This means that Eqs. (13) - (14) allow the quantitative estimation of the advantage of the averaged mass matrix ($\gamma = 0.5$) compared with the consistent mass matrix. For example, for a uniform mesh with 100 linear finite elements and the averaged mass matrix ($\gamma = 0.5$), the size of the time increments at the filtering stage is $\Delta t_1 = 0.03447$ according to Eqs. (13) - (14). For a uniform mesh with 300 linear finite elements and the consistent mass matrix, the size of the time increments at the filtering stage is $\Delta t_2 = 0.03908$ according to Eqs. (13) - (14). Because Δt_2 is close to Δt_1, then curves 2 and 3 in Fig. 1d,e are close to each other (curve 2 is slightly more accurate because Δt_1 is slightly smaller than Δt_2); see also the analytical solution, curve 1. For a uniform mesh with 70 $Q3$ quadratic elements and the consistent mass matrix, the size of the time increments at the filtering stage is $\Delta t_3 = 0.03465$ according to Eqs. (13) - (14). Because Δt_3 is close to Δt_1, then curves 2 and 3 in Fig. 3 are close to each other.

3.2 3-D impact of an elastic bar against a rigid wall

A solid 3-D bar of length $L = 2$ with a square cross section $a \times a$ ($a = 2$) under impact loading at the left end $ACEM$ is considered; see Fig. 4. Due to symmetry, the problem is solved for a quarter of the bar $ACEMNFDB$ where planes $ABDC$ and $ABNM$ are the planes of symmetry. Young's modulus is chosen to be $E = 1$, Poisson's ratio to be $\nu = 0.3$, and the density to be $\rho = 1$. The following boundary conditions are applied: along the left end $ACEM$: $u_n = t$ (which corresponds to the instantaneous application of velocity $v_{load}(t) = v_0 = 1$) and $\tau_n = 0$; along planes $BDFN$, $CDEF$ and $EFNM$: $\sigma_n = 0$ and $\tau_n = 0$ (free surfaces); along planes $ABDC$, $ABNM$: $u_n = 0$ and $\tau_n = 0$ where u_n, v_n, and σ_n are the normal displacements, velocities and the tractive forces, respectively; τ_n are the tangential tractive forces. The observation time is chosen to be $T = 7$. During this time the velocity pulse travels within the bar with multiple reflections from the ends of the bar and from the external surfaces $CDFE$ and $EFNM$. We should mention that with the dimensionless coordinates $\tilde{x}$,

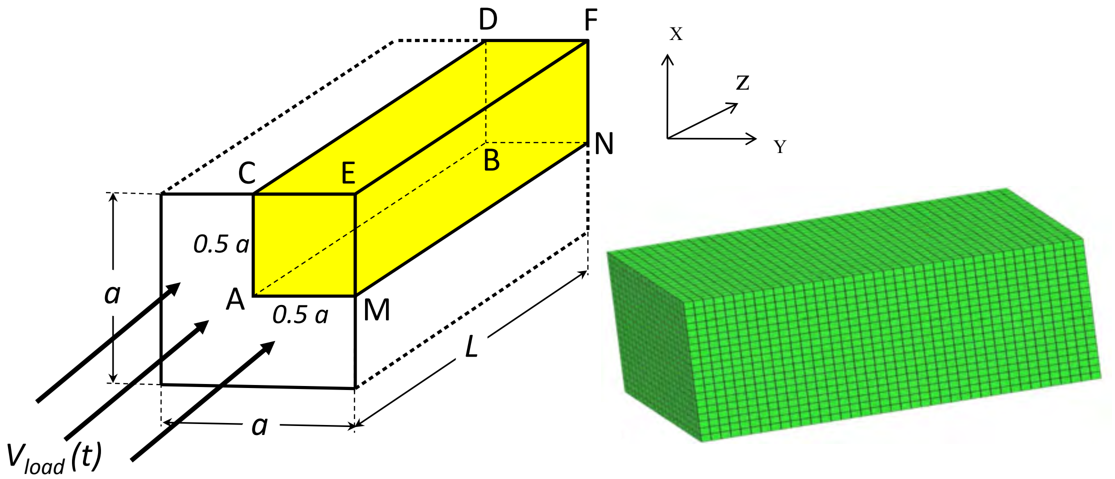

a) b)

Figure 4: Impact of an elastic 3-D square bar of length $L = 2$ and width $a = 2$ against a rigid wall (a). A uniform mesh with $20 \times 20 \times 40 = 16000$ linear $Q8$ finite elements (b).

$\tilde{y}$ and $\tilde{z}$ and the dimensionless time $\tilde{t}$

$$\tilde{x} = \frac{x}{a}, \qquad \tilde{y} = \frac{y}{a}, \qquad \tilde{z} = \frac{z}{a}, \qquad \tilde{t} = \frac{tc_0}{a},$$

and with the normalized displacements $\tilde{u}_i$, velocities $\tilde{v}_i$, stresses $\tilde{\sigma}_{ij}$ and strains $\tilde{\varepsilon}_{ij}$

$$\tilde{u}_i = \frac{u_i c_0}{a v_0}, \qquad \tilde{v}_i = \frac{v_i}{v_0}, \qquad \tilde{\varepsilon}_{ij} = \frac{\varepsilon_{ij} c_0}{v_0},$$

$$\tilde{\sigma}_{ij} = \frac{\sigma_{ij} c_0 \sqrt{(1+\nu)(1-\nu)(1-2\nu)}}{\sqrt{2}\nu E v_0}, \qquad i, j = x, y, z$$

numerical results are independent of Young's modulus, the density, the amplitude of the velocity v_0 and the size a of a cross-section, and depend on Poisson's ratio ν and the dimensionless length of the bar L/a. Here, $c_0 = \sqrt{\frac{E}{\rho}}$ is the wave velocity in the 1-D case.

The problem is solved on uniform meshes with $10 \times 10 \times 20 = 2000$ and $20 \times 20 \times 40 = 16000$ linear quadrilateral $Q8$ elements with the modified integration rule for the mass and stiffness matrices ($\alpha_M = \sqrt{\frac{2}{3}}$ and $\alpha_K = \sqrt{\frac{4(2\nu-1)}{3(4\nu-3)}}$) as well as with the consistent and averaged ($\gamma = 0.5$) mass matrices. Similar to the 1-D impact problem, for the time integration of Eq. (1) at basic calculations we use the trapezoidal rule with very small time increments ($\Delta t = 0.001$). A further reduction of time increments does not practically affect the numerical results for the meshes used; i.e., the error in time is very small and can be neglected.

Figs. 5 and 6 show the distribution of the axial velocity along lines EF and AB at observation time $T = 7$. Similar to the previous 1-D impact problem, the numerical results after basic computations with the standard mass and stiffness matrices and the formulations with reduced numerical dispersion contain spurious oscillations; see Fig. 5. Fig. 6 shows the convergence of numerical results at mesh refinement after the filtering stage for the cases of the modified integration rule and the averaged mass matrix (these results do not contain spurious oscillations).

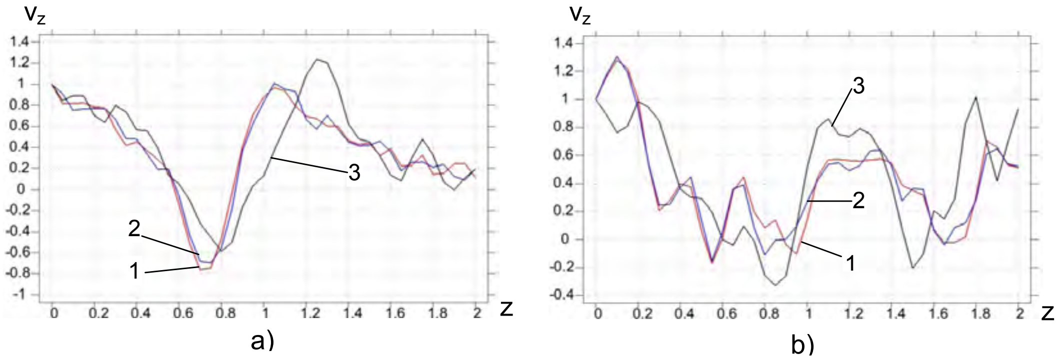

Figure 5: The distribution of the axial v_z (curves 1, 2, 3) velocity components along lines EF (a) and AB (b) (see Fig. 4) after basic computations at time $T = 7$ on a uniform mesh with $20 \times 20 \times 40 = 16000$ linear $Q8$ finite elements. The Poisson's ratios is $\nu = 0.3$. Curves 1, 2 and 3 correspond to the numerical solutions obtained by the use of the modified integration rule, the averaged mass matrix with $\gamma = 0.5$ and the consistent mass matrix, respectively.

The difference between the numerical results obtained with the modified integration rule and with the averaged mass matrix is small and can be neglected compared with the change in the numerical results at mesh refinement; see Fig. 6. Fig. 6 also shows that for the selected observation time $T = 7$, the use of the modified integration rule (or the averaged mass matrix) reduces the number of degrees of freedom by a factor of 8 (see curves 3, 4 and 5 in Fig. 6). Similar to the 1-D case, the size of the time increments at post-processing calculated by Eqs. (13) - (15) allows the quantitative estimation of the advantage of the modified integration rule (or the averaged mass matrix) compared with the consistent mass matrix. For example, for a uniform mesh with $10 \times 10 \times 20 = 2000$ finite elements and the modified integration rule (or the averaged mass matrix), the size of the time increments at the filtering stage is $\Delta t_1 = 0.084951$ according to Eqs. (13) - (15). For a uniform mesh with $20 \times 20 \times 40 = 16000$ finite elements and the consistent mass matrix, the size of the time increments at the filtering stage is $\Delta t_2 = 0.091410$ according to Eqs. (13) - (15). Because Δt_2 is close to Δt_1, then curves $3, 4$ and 5 in Fig. 6 are close to each other (curves $3, 4$ are slightly more accurate because Δt_1 is slightly smaller than Δt_2; see also curves 1 and 2 for the numerical solutions on a finer mesh).

4 CONCLUDING REMARKS

Two dispersion reduction techniques for linear finite elements has been applied to the to 1-D and 3-D impact problems, along with the filtering technique developed in our previous papers [11, 12, 13]. The considered finite element formulations with reduced numerical dispersion increase the accuracy of numerical solutions for elastodynamics problems; however, they do not remove all spurious high-frequency oscillations for wave propagation problems. These spurious oscillations make it difficult to estimate the effectiveness of the finite element formulations with reduced numerical dispersion applied to engineering elastodynamics problems. In the paper, this issue has been overcome by the use of the two-stage time-integration technique with the filtering stage [11, 12, 13], which identifies and removes spurious oscillations. Despite the fact that the modified integration rule yields a smaller numerical dispersion error compared with that for the averaged mass matrix, the numerical results after the filtering stage show that the difference between the numerical solutions obtained with the modified integration rule and with the averaged mass matrix is small and can be neglected compared with the change in

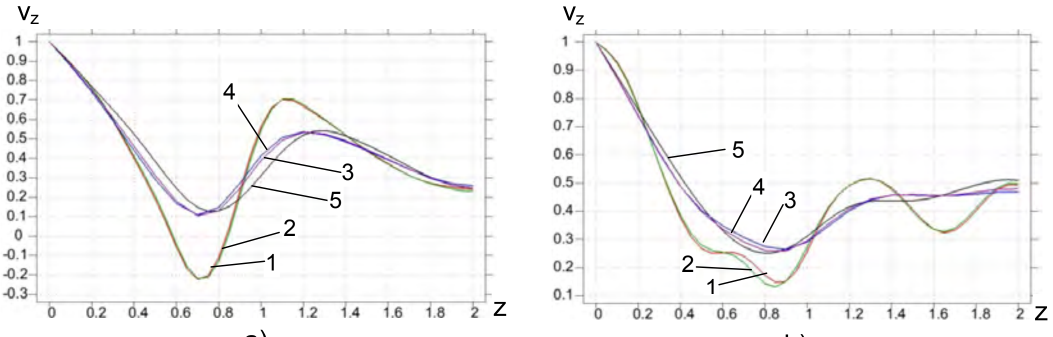

a) b)

Figure 6: The distribution of the axial v_z (curves 1, 2, 3) velocity components along lines EF (a) and AB (b) (see Fig. 4) after post-processing at time $T = 7$. The Poisson's ratios is $\nu = 0.3$. Curves 1, 2, 5 and 3, 4 correspond to the numerical solutions on uniform meshes with $20 \times 20 \times 40 = 16000$ and $10 \times 10 \times 20 = 2000$ linear $Q8$ elements, respectively. The modified integration rule (curves 1 and 3), the averaged mass matrix with $\gamma = 0.5$ (curves 2 and 4) and the consistent mass matrix (curves 5) are used.

the numerical results at mesh refinement. The numerical results after the filtering stage also show that compared with the use of linear finite elements with the consistent mass matrix and the standard stiffness matrix, the finite element formulations with reduced numerical dispersion reduce the number of degrees of freedom for uniform meshes by a factor of $n = 2 \sim 3$ in the 1-D case and $n = 8 \sim 27$ in the 3-D case depending upon the material properties and the observation time. This leads to a huge reduction in computation time, especially for multi-dimensional elastodynamics problems. We should also mention that for the standard mass and stiffness matrices, quadratic finite elements yield more accurate results than linear elements; e.g., see [3, 13] and the numerical results in Section 3.1. However, the linear elements with reduced dispersion are more accurate than the quadratic elements with the standard mass and stiffness matrices. It is interesting to note that the range of frequencies in numerical solutions after the filtering stage is indirectly determined by the size of the time increments calculated by Eqs. (13) - (15) (see the Appendix). Numerical experiments show that if for uniform meshes with different numbers of degrees of freedom and with different types of finite elements, the time increments calculated according to Eqs. (13) - (15) are close to each other then the numerical solutions obtained on these meshes after the filtering stage are close to each other as well. This means that Eqs. (13) - (15) allow the quantitative estimation of the effectiveness of the finite element formulations with reduced numerical dispersion compared with the standard mass and stiffness matrices (the effectiveness is different for different observation times).

Acknowledgments

The research has been supported in part by the Air Force Research Lab, Eglin (contract # FA8651-08-D-0108) and by Texas Tech University.

Appendix. The implicit TCG method for filtering spurious high-frequency oscillations and the selection of the minimum necessary amount of numerical dissipation

Let us describe the implicit TCG method with large numerical dissipation suggested in [12, 13] that is used for the step-by-step time integration of the semi-discrete elastodynamics equations (1) at the filtering stage of the two-stage time-integration technique. The method is based on the linear approximations of displacements $U(t)$ and velocities $V(t)$ within a time step Δt ($0 \leq t \leq \Delta t$)

$$\mathbf{U}(t) \,=\, \mathbf{U}_0 \,+\, \mathbf{U}_1\, t\,, \qquad \mathbf{V}(t) \,=\, \mathbf{V}_0 \,+\, \mathbf{V}_1\, t\,, \tag{7}$$

and has the first order of accuracy. Here $\mathbf{U}_0$ and $\mathbf{V}_0$ are the known initial nodal displacements and velocities, and the unknown nodal vector $\mathbf{V}_1$ can be expressed in terms of the unknown nodal vector $\mathbf{U}_1$ as follows:

$$\mathbf{V}_1 \,=\, \frac{1}{a_1}\mathbf{U}_1 \,-\, \frac{1}{a_1}\mathbf{V}_0\,. \tag{8}$$

Finally, the following system of algebraic equations is solved for the determination of $\mathbf{U}_1$

$$(\mathbf{M} \,+\, a_1\mathbf{C} \,+\, a_1^2\mathbf{K}\,)\mathbf{U}_1 \,=\, -\,a_1\mathbf{K}\,\mathbf{U}_0 \,+\, \mathbf{M}\,\mathbf{V}_0 \,+\, \mathbf{R}_1\,, \tag{9}$$

where

$$a_1 \,=\, \frac{m+2}{m+3}\Delta t\,, \tag{10}$$

$$\mathbf{R}_1 \,=\, \frac{(m+2)^2}{(m+3)\Delta t^{m+1}} \int_0^{\Delta t} \mathbf{R}(t) t^{m+1}\, dt\,. \tag{11}$$

The parameter m is responsible for the amount of numerical dissipation. After the calculation of $\mathbf{U}_1$ from Eq. (9), the values of displacements and velocities at the end of a time increment Δt are calculated using Eqs. (7) and (8) for $t = \Delta t$:

$$\mathbf{U}(\Delta t) \,=\, \mathbf{U}_0 \,+\, \mathbf{U}_1\, \Delta t\,, \qquad \mathbf{V}(\Delta t) \,=\, \mathbf{V}_0 \,+\, \mathbf{V}_1\, \Delta t\,. \tag{12}$$

The maximum numerical dissipation corresponds to $m = \infty$. For the case $m = \infty$, the parameter $a_1 = \Delta t$, and $\mathbf{R}_1$ should be calculated analytically; see Eqs. (11). However, in order to avoid the analytical calculation of $\mathbf{R}_1$ at $m = \infty$, a value $m \geq 15$ can be used in computations (the difference in numerical dissipation for $m = \infty$ and $m \geq 15$ is not very essential). Numerical examples show that the first-order accurate implicit TCG method suppresses spurious high-frequency oscillations for 10 time steps and retains good accuracy of a numerical solution at low modes. In order to have a numerical solution before and after the filtering stage at the same observation time, the first five uniform time increments are taken positive, and the last five uniform time increments are taken negative (the boundary conditions and external forces are zero during the filtering stage).

For the selection of minimum necessary amount of numerical dissipation for filtering spurious oscillations, a special calibration procedure was developed in [13]. The procedure was based on the analysis of spurious high-frequency oscillations for the 1-D impact problem for which the analytical solution is known (see [12, 13] for details). The following empirical formula for the selection of time increments for an implicit time-integration method with large numerical dissipation (the size of a time increment is related to the amount of numerical dissipation) is suggested in [12, 13] for 1-D elastodynamics problems:

$$\Delta t = \alpha(N_1)\frac{\Delta x \Omega_{0.1}(N)}{c}\,, \tag{13}$$

where $c = c_o = \sqrt{\frac{E}{\rho}}$ is the wave velocity; Δx is the size of a finite element; $\Omega_{0.1}(N)$ is the value of $\Omega = w\Delta t$ at which the spectral radius has the value 0.1 for the selected number N of time increments; w is the frequency of vibration for a system with a single degree of freedom; $\Omega_{0.1}$ is used to scale spectral radii calculated at different numbers of time increments N; $\alpha(N_1)$ is the empirical coefficient depending on the time-integration method, the order of finite elements, and on the number N_1 of elements which are passed through by the wave front (this number can be expressed as $N_1 = \frac{cT}{\Delta x}$; see [12, 13]). For example, for the first-order implicit TCG method ($m = 15$), the following explicit expression is suggested in [13] for the coefficient $\alpha(N_1)$:

$$\alpha(\frac{cT}{\Delta x}) = a_1 \left(\frac{cT}{\Delta x}\right)^{a_2} . \tag{14}$$

The coefficients a_1 and a_2 for linear and quadratic elements with the consistent mass matrix are calculated in [13]. Using the calibration procedure described in [13], we found the following coefficients for linear elements with the averaged ($\gamma = 0.5$) mass matrix: $a_1 = 0.2942$ and $a_2 = 0.2104$ (see [14]); for linear elements with the standard consistent mass matrix: $a_1 = 0.2986$ and $a_2 = 0.3461$ (see [13]); for quadratic elements with the standard consistent mass matrix: $a_1 = 0.1948$ and $a_2 = 0.234$ (see [13]).

For the selection of the size of time increments for the filtering stage of 2-D and 3-D problems, the following modification of Eq. (13) can be used

$$\begin{aligned}\Delta t &= \max_{i,j}\left[\alpha(\frac{c_i T}{\Delta x_j})\,\frac{\Delta x_j}{c_i}\right]\Omega_{0.1}(N) \;=\; \max_{i,j}\left[\frac{\Delta x_j}{c_i}\right]^{1-a_2} a_1\,T^{a_2}\,\Omega_{0.1}(N) \\ &= \left[\frac{\max\limits_{j}\,\Delta x_j}{\min\limits_{i}\,c_i}\right]^{1-a_2} a_1\,T^{a_2}\,\Omega_{0.1}(N) \;=\; \left[\frac{\Delta x_{max}}{c_2}\right]^{1-a_2} a_1\,T^{a_2}\,\Omega_{0.1}(N)\,,\end{aligned} \tag{15}$$

where $c_2 = \min\limits_{i}\, c_i$ ($i = 1, 2$) is the minimum value between the velocities of the compressional wave $c_1 = \sqrt{\frac{\lambda+2\mu}{\rho}}$ and the shear wave $c_2 = \sqrt{\frac{\mu}{\rho}}$, $\Delta x_{max} = \max\limits_{j}\, \Delta x_j$ is the maximum dimension of finite elements along the axes x_j ($j = 1, 2$ for 2-D problems and $j = 1, 2, 3$ for 3-D problems). Eq. (15) is based on Eqs. (13) and (14) with the selection of the maximum size of a time increment with respect to the compressional and shear waves, and the dimensions of a finite element along the coordinate axes. For 2-D and 3-D uniform meshes with linear quadrilateral elements, we use the coefficients a_1 and a_2 obtained for the 1-D case; see Eq. (14). As shown in [12], Eq. (15) is the necessary condition for the selection of the amount of numerical dissipation in the multi-dimensional case.

REFERENCES

[1] H. P. Cherukuri. Dispersion analysis of numerical approximations to plane wave motions in an isotropic elastic solid. *Computational Mechanics*, 25(4):317–328, 2000.

[2] W. Dauksher and A. F. Emery. Solution of elastostatic and elastodynamic problems with chebyshev spectral finite elements. *Computer Methods in Applied Mechanics and Engineering*, 188(1):217–233, 2000.

[3] D. Gabriel, J. Plesek, R. Kolman, , and F. Vales. Dispersion of elastic waves in the contactimpact problem of a long cylinder. *Journal of Computational and Applied Mathematics*, 234:1930–1936, 2010.

[4] M. N. Guddati and B. Yue. Modified integration rules for reducing dispersion error in finite element method. *Computer Methods in Applied Mechanics and Engineering*, 193:275–287, 2004.

[5] S. Krenk. Dispersion-corrected explicit integration of the wave equation. *Computer Methods in Applied Mechanics and Engineering*, 191:975–987, 2001.

[6] K. J. Marfurt. Accuracy of finite difference and finite element modeling of the scalar and elastic wave equation. *Geophysics*, 49:533–549, 1984.

[7] R. Mullen and T. Belytschko. Dispersion analysis of finite element semidiscretizations of the two-dimensional wave equation. *International Journal for Numerical Methods in Engineering*, 18:11–29, 1982.

[8] G. Seriani and S. P. Oliveira. Optimal blended spectral-element operators for acoustic wave modeling. *Geophysics*, 72(5):95–106, 2007.

[9] B. Yue and M. N. Guddati. Dispersion-reducing finite elements for transient acoustics. *Journal of the Acoustical Society of America*, 118(4):2132–2141, 2005.

[10] F. I. Zyserman and P. M. Gauzellino. Dispersion analysis of a nonconforming finite element method for the three-dimensional scalar and elastic wave equations. *Finite Elements in Analysis and Design*, 41(13):1309–1326, 2005.

[11] A. V. Idesman. A new high-order accurate continuous galerkin method for linear elastodynamics problems. *Computational Mechanics*, 40:261–279, 2007.

[12] A. V. Idesman. Accurate time integration of linear elastodynamics problems. *Computer Modeling in Engineering and Sciences*, pages 1–38, 2011 (accepted).

[13] A. V. Idesman, H. Samajder, E. Aulisa, and P. Seshaiyer. Benchmark problems for wave propagation in elastic materials. *Computational Mechanics*, 43(6):797–814, 2009.

[14] A. V. Idesman, M. Schmidt, and J. R. Foley. Accurate finite element modeling of linear elastodynamics problems with the reduced dispersion error. *Computational Mechanics*, pages 1–18, 2011 (accepted, DOI 10.1007/s00466-010-0564-3).

[15] T. J. R Hughes. *The Finite Element Method: Linear Static and Dynamic Finite Element Analysis*. Prentice- Hall, Englewood Cliffs, NJ,, 1987.

[16] O. C. Zienkiewicz and R. L. Taylor. *The Finite Element Method*. Butterworth-Heinemann, Oxford, UK, 2000.

[17] A. Idesman, K. Subramanian, M. Schmidt, J. R. Foley, Y. Tu, and R. L. Sierakowski. Finite element simulation of wave propagation in an axisymmetric bar. *Journal of Sound and Vibration*, 329:2851–2872, 2010.

[18] G. M. Hulbert. Discontinuity-capturing operators for elastodynamics. *Computer Methods in Applied Mechanics and Engineering*, 96(3):409–426, 1992.

[19] G. M. Hulbert and T. J. R. Hughes. Space-time finite element methods for second-order hyperbolic equations. *Computer Methods in Applied Mechanics and Engineering*, 84(3):327–348, 1990.

COMPDYN 2011
III ECCOMAS Thematic Conference on
Computational Methods in Structural Dynamics and Earthquake Engineering
M. Papadrakakis, M. Fragiadakis, V. Plevris (eds.)
Corfu, Greece, 25–28 May 2011

IMPACT MODELING BY MANIFOLD APPROACH IN EXPLICIT TRANSIENT DYNAMICS

Timo J. Saksala[1*], **Jari M. Mäkinen**[2],

[1,2] Department of Mechanics and Design,
Tampere University of Technology
P.O. Box 589, FI-33101 Tampere, Finland
[1]timo.saksala@tut.fi,
[2]jari.m.makinen@tut.fi

Keywords: Explicit dynamics, Contact mechanics, Lagrange multiplier method, Penalty method, Constraint manifold.

Abstract. *In this paper we study numerically different methods to impose contact constraints in explicit dynamics. The traditional methods, the penalty method and the more recent forward increment Lagrange multiplier method, are compared, in their performance and accuracy, to a direct elimination method based on the theory of manifolds. The idea of the method is that when a contact constraint is active the solution lies on the boundary of the contact manifold generated by contact constraints. Then the contact problem can be solved with the elimination of additional degrees of freedom. This elimination technique can be viewed as a parameterization of the contact manifold. We show numerically that in the case of a rigid impactor, the elimination method is highly more efficient than the forward Lagrange multiplier method since the latter leads to a coupled system of equations for solving the Lagrange multipliers while both methods produce similar results. In the present work the elimination method is also developed for the impact problem of deformable bodies and the performance of the different methods are compared in numerical simulations of the longitudinal impact of thick bars. The modified Euler method is employed in solving the equations of motion in time.*

1 INTRODUCTION

The traditional method to impose contact constraints in explicit transient dynamics is the penalty function method. It is, however, an approximate method and has an adverse effect on the numerical stability of explicit integration. For this reason, Carpenter et al. [1] introduced a modification of Lagrange multiplier method, called Forward Increment Lagrange Multiplier method (FILM), which is compatible with explicit time integrators and does not affect the stability of integration. The idea of the method is to refer the kinematic contact constraints one time step ahead of the equations of motion and the Lagrange multipliers. With general contact interfaces, this method leads to a coupled system of equations for the Lagrange multipliers. Therefore, if the number of contact pairs is large it is not effective.

In this paper we present an alternative and efficient method for impact modeling in explicit transient dynamics. The method, called here DME (Direct Manifold Elimination method) is based on the theory of manifolds. Contact constraints, i.e. the displacement inequalities, generate a constraint manifold with a boundary [2]. When a contact constraint is active the solution lies on the boundary of the contact manifold. This method was employed by Saksala & Mäkinen [3] in case of a rigid piston impacting an elasto-viscoplastic damaging domain. In that case, the contact constraints, i.e. the impenetrability conditions between the piston node and rock surface nodes, were eliminated. In the present paper, this formulation is also performed in the case of a deformable impactor and the node-to-node contact interface.

The developed technique is implemented in 2D (axisymmetric) case. In the numerical examples involving impacts between linear elastic bodies and dynamic indentation by a rigid indenter, the accuracy and efficiency of the manifold method is compared to the penalty function method and the forward increment Lagrange multiplier method. The modified Euler explicit integrator is used for solving the FE discretized equations of motion in time.

2 IMPOSITION OF CONTACT CONSTRAINTS

In this section we describe the traditional methods, the penalty method and the more recent forward increment Lagrange multiplier method, as well as the manifold method to impose kinematic contact constraints in explicit time integration setting. The background for the manifold method is elaborated only to the level required for understanding how the method arises. Linear elasticity and small displacements are assumed for simplicity.

2.1 Modified Euler method for explicit time integration

The explicit modified Euler time integrator is chosen for solving the equations of motion. The response of the system using this method is computed by [4]:

$$\begin{aligned}\ddot{\mathbf{u}}^{t} &= \mathbf{M}^{-1}\left(\mathbf{f}_{\text{ext}}^{t} - \mathbf{C}\dot{\mathbf{u}}^{t} - \mathbf{f}_{\text{int}}^{t}\right)\\ \dot{\mathbf{u}}^{t+\Delta t} &= \dot{\mathbf{u}}^{t} + \Delta t\ddot{\mathbf{u}}^{t}\\ \mathbf{u}^{t+\Delta t} &= \mathbf{u}^{t} + \Delta t\dot{\mathbf{u}}^{t+\Delta t}\end{aligned} \tag{1}$$

where $\mathbf{M}$ is the lumped mass matrix, $\mathbf{C}$ is the damping matrix (set zero here), $\mathbf{f}_{\text{int}}, \mathbf{f}_{\text{ext}}$ are the internal and external force vectors, respectively, and $\mathbf{u}$ is the displacement vector while a dot above it denotes time derivative.

2.2 Forward increment Lagrange multiplier and penalty method

The classical Lagrange multiplier method is incompatible with explicit time integrators. For this reason, Carpenter et al. [1] introduced a modification, called here forward increment

Lagrange multiplier method, which is compatible with explicit methods. The idea of the method is to refer the kinematic contact constraints one time step ahead of Lagrange multipliers as:

$$\begin{aligned}&\mathbf{M}\ddot{\mathbf{u}}^{t}+\mathbf{C}\dot{\mathbf{u}}^{t}+\mathbf{f}^{t}_{\mathrm{int}}=\mathbf{f}^{t}_{\mathrm{ext}}-\mathbf{G}^{\mathrm{T}}\boldsymbol{\lambda}^{t}\\&\mathbf{G}\mathbf{u}^{t+\Delta t}-\mathbf{b}=\mathbf{0}\end{aligned}\tag{2}$$

where **b** is the vector containing the initial distances between the contact node pairs (which are known in advance), **G** is the kinematic contact constraint matrix consisting, usually, of the normal vectors of the contact surfaces, and $\boldsymbol{\lambda}$ is the Lagrange multiplier vector having the physical interpretation of contact forces. On substituting (1) into (2) gives, after some algebra:

$$\begin{aligned}\ddot{\mathbf{u}}^{t}&=\tilde{\ddot{\mathbf{u}}}^{t}-\mathbf{M}^{-1}\mathbf{G}^{\mathrm{T}}\boldsymbol{\lambda}^{t}\\\dot{\mathbf{u}}^{t+\Delta t}&=\dot{\mathbf{u}}^{t}+\Delta t\ddot{\mathbf{u}}^{t}\\\mathbf{u}^{t+\Delta t}&=\mathbf{u}^{t}+\Delta t\dot{\mathbf{u}}^{t+\Delta t}\end{aligned}\tag{3}$$

where

$$\begin{aligned}\tilde{\ddot{\mathbf{u}}}^{t}&=\mathbf{M}^{-1}\left(\mathbf{f}^{t}_{\mathrm{ext}}-\mathbf{C}\dot{\mathbf{u}}^{t}-\mathbf{f}^{t}_{\mathrm{int}}\right)\\\tilde{\mathbf{u}}^{t+\Delta t}&=\mathbf{u}^{t}+\Delta t\dot{\mathbf{u}}^{t}+\Delta t^{2}\tilde{\ddot{\mathbf{u}}}^{t}\\\left(\Delta t^{2}\mathbf{G}\mathbf{M}^{-1}\mathbf{G}^{\mathrm{T}}\right)\boldsymbol{\lambda}^{t}&=\mathbf{G}\tilde{\mathbf{u}}^{t+\Delta t}-\mathbf{b}\rightarrow\boldsymbol{\lambda}^{t}\end{aligned}\tag{4}$$

This method belongs to the class of predictor-corrector methods in that, first, the acceleration and displacement of the system are predicted as if there were no contacts. Then, the contact forces are solved based on the virtual penetration. Finally, the acceleration is corrected by subtracting the contribution of the contact forces and the response of the system is updated.

It should be noted that this method is fully explicit only when the node-to-node contact interface is used. In this case, with the lumped mass matrix, the equations for solving the Lagrange multipliers in (4) are uncoupled, i.e. matrix $\Delta t^{2}\mathbf{G}\mathbf{M}^{-1}\mathbf{G}^{\mathrm{T}}$ is diagonal. With more general contact interfaces a coupled system of equations must be solved. Thus, computational efficiency of this method considerably depends on the type of contact interface. The efficiency can be, however, greatly increased, at the expense of accuracy and stability however, if the Penalty method is employed in the contact force calculation. Accordingly, the third equation in (4) and Lagrange multiplier in (3) is replaced by

$$\mathbf{f}^{t}_{\mathrm{cont}}=p\left(\mathbf{G}\tilde{\mathbf{u}}^{t+\Delta t}-\mathbf{b}\right)\tag{5}$$

where p is the problem dependent penalty coefficient. Other equations go unaltered.

2.3 Direct elimination method based on theory of manifolds

Different kinematic relations of constraint equations are shown in Figure 1, where geometric constraints include all holonomic and the unilateral constraints, which are given by inequality equations with the function of time and a generalized place vector only. Unilateral constraints arise when modeling a kinematic relation between bodies in contact.

Contact constraints, i.e. the displacement inequalities, generate a contact manifold with a boundary. When a contact constraint is active the solution lies on the boundary of the contact manifold. Next, the formal definition of the contact manifold is given.

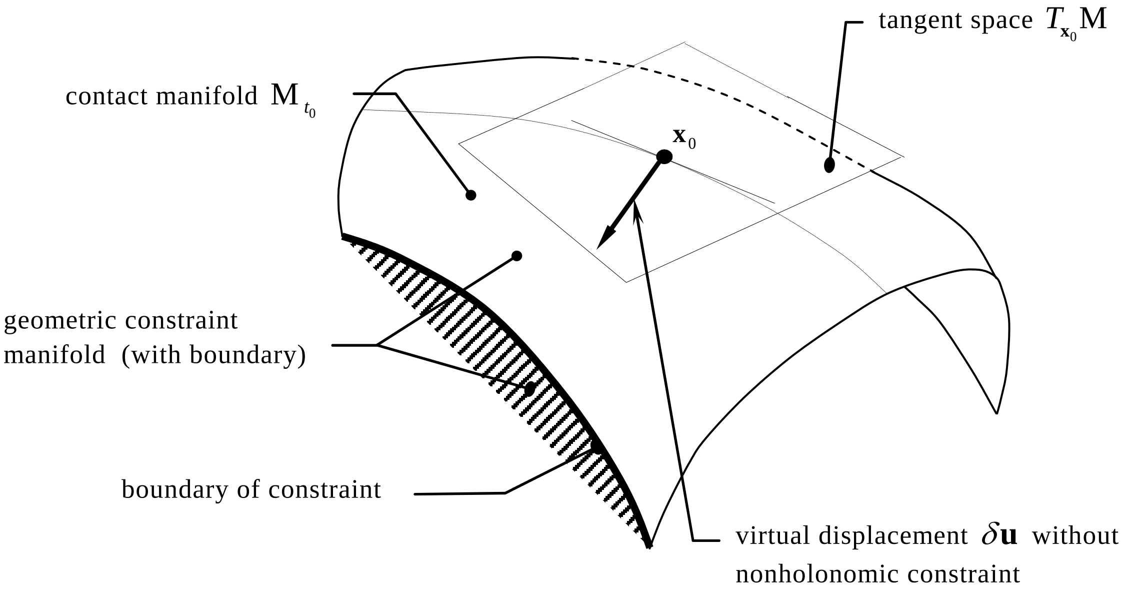

Figure 1: Geometric interpretation of constraints.

Definition for contact manifold: The geometric constraint equations induce a *d*-manifold that is defined by:

$$\mathrm{M} := \left\{ \mathrm{t} \times \mathbf{u} \in \mathbf{R} \times \mathrm{E}^n \mid \mathbf{h}(t,\mathbf{u}) \leq \mathbf{0} \in \mathrm{E}^{n-d} \right\} \tag{6}$$

The contact manifold is a *d*-dimensional smooth manifold with time as 1-parameter family. The contact manifold at fixed time $t = t_0$ is denoted by M_{t_0}.

In our case, the unilateral constraint equations are simply $\mathbf{h}(t,\mathbf{u}) = \mathbf{G}\mathbf{u}^t - \mathbf{b}$. The Lagrange multiplier method and the penalty method, described in the previous section, are conventional methods to impose the contact constraints. However, the contact problem can also be solved with the elimination of additional degrees of freedom. This elimination technique can be viewed as a parameterization of the contact manifold.

In the present paper, we have only node-to-node contacts with straight interfaces (lines) between bodies *A* and *B* and both bodies can be deformable or one of them can be rigid depending on the application. In both cases, the solution procedure begin with the detection of active contacts by checking the violation of the equation

$$\mathbf{G}\tilde{\mathbf{u}}^{t+\Delta t} - \mathbf{b} \geq \mathbf{0} \tag{7}$$

where the predicted displacement is as in Equation (4). Next, two different schemes to compute the nodal displacements, velocities and accelerations are presented. The first one is for the case in which the other body is rigid, thus representing usually a tool used for indentation, and the second is for the impact of deformable bodies.

Case 1 (B is a rigid body, say a punch): If any contact constraint is active, say *i*, then this nodal displacement u_i^A of the body *A* is eliminated by solving the active constraint equation (7) with respect to u_i^A as:

$$\begin{aligned} u_i^A &= u_i^B - b_i \\ \dot{u}_i^A &= \dot{u}_i^B \\ \ddot{u}_i^A &= \ddot{u}_i^B = \sum f_{\text{tot},i} / M_i \end{aligned} \tag{8}$$

where $\sum f_{\text{tot},i}$ and $M_i = \sum m_i$ are the total force and mass related to the active contact constraints, i.e. the summation is over the degrees of freedom of the active constraints *i*.

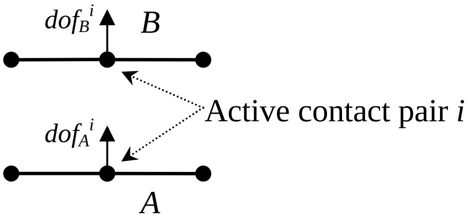

Figure 2: Illustration of node-to-node contact interface.

Case 2 (A and B are deformable bodies): When an active contact pair, say *i*, is detected according to Equation (7), the acceleration and displacement in the vertical degrees of freedom ($dof_B{}^i$ and $dof_A{}^i$ in Figure 2) of the nodes in contact are calculated as:

$$\begin{aligned} \hat{u}_i^B &= \hat{u}_i^A = \tfrac{1}{2}\left(u_i^B + u_i^A\right) \\ \ddot{\hat{u}}_i^B &= \ddot{\hat{u}}_i^A = f_{\text{tot},i} / (m_i^A + m_i^B) \end{aligned} \tag{9}$$

where $f_{\text{tot},i} = \mathbf{f}_{\text{tot}}(dof_A^i) + \mathbf{f}_{\text{tot}}(dof_B^i)$ and $m_i^A + m_i^B = \mathbf{M}(dof_A^i) + \mathbf{M}(dof_B^i)$ are the total force and mass related to the active contact pair *i* with m_i^A and m_i^B being the nodal point masses of the active constraint *i* for the body *A* and *B*, respectively.

As to the velocities, they can be solved from the equations provided by elementary physics of colliding rigid bodies:

$$\begin{aligned} m_i^A \dot{u}_i^A + m_i^B \dot{u}_i^B &= m_i^A \hat{\dot{u}}_i^A + m_i^B \hat{\dot{u}}_i^B \\ e(\dot{u}_i^A + \dot{u}_i^B) &= \hat{\dot{u}}_i^A + \hat{\dot{u}}_i^B \end{aligned} \tag{10}$$

where *e* is the coefficient of restitution with *e* = 1 for elastic collision and *e* = 0 for perfectly inelastic collision. By the elimination technique presented, the degrees of freedom of the problem reduce by one for each active constraint.

Finally, the detection of separation of the active contact constraint can be examined via the nodal internal forces. The separation occurs when the nodal internal force is a tractive force. The tractive force converts the active constraint inactive.

3 NUMERICAL EXAMPLES

In this section the performance of the different methods to impose contact constraints are compared in numerical simulations involving low-velocity impact. First, the performance of the manifold method is demonstrated in the rigid punch indentation problem with varying number of contact constraints. Then, the problem of longitudinal impact of thick cylindrical bars is simulated and the accuracy of the methods is compared with each other and to the analytical solution as well. The material is assumed rigid and/or linear elastic. All the simulations are performed with self-written Matlab (64-bit 2009a version) codes using a Windows Vista pc equipped with 2.60 GHz AMD Phenom™ II X3 710 processor and 8.0 GB of RAM.

3.1 Rigid punch indentation problem

The indentation problem with a rigid punch described in Figure 3 is solved with the FILM, DME and Penalty methods. Axisymmetry of the problem is exploited and CST elements are used in the mesh. The material of the indented domain is linear elastic. The punch is assumed rigid while it is modeled as a single node.

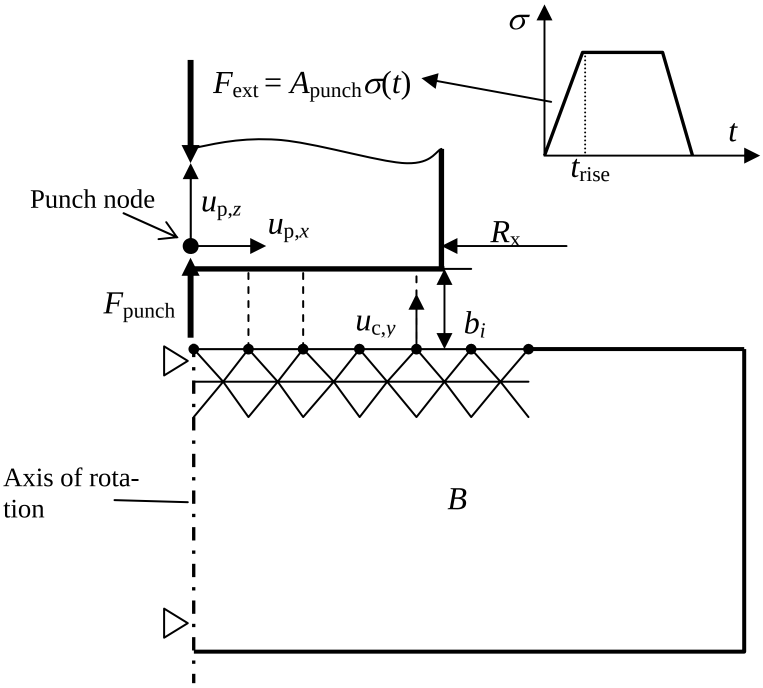

Figure 3: Indentation with a rigid punch.

The external stress pulse, $\sigma(t)$, is used to simulate the impact of the rigid punch to the deformable domain B. As multiplied by the cross sectional area of the indenter A_{punch}, an external force, F_{ext}, to be applied to the punch node is obtained. Moreover, the force that resists the punch penetration into domain B, the contact force F_{punch}, needs to be solved during the solution process. Thus, the equation of motion for the punch node, with its motional degrees of freedom $u_{p,x}$, $u_{p,z}$, to be added to the FE discretized equation of motion, can be written as:

$$m_p \ddot{u}_{p,z} = F_{\text{ext}} - F_{\text{punch}} \tag{11}$$

where m_p is a computational mass attached to the punch node. The value of this mass must be small enough so that it doesn't affect the solution and big enough to maintain the mass matrix well-conditioned.

The geometry of the punch (indenter) is defined as b_i, i.e. the distances between the punch node and the contact nodes on the indented domain boundary. Thus, using the notation in Figure 3, the kinematic contact constraints can be written in form:

$$u_{\mathrm{c},z} - u_{\mathrm{p},z} = b_i \tag{12}$$

Equations of this form are written for all contact nodes and, consequently, the constraint equation of form $\mathbf{Gu} = \mathbf{b}$ is obtained. As there is only one DOF (friction is not taken into account) associated to the punch node, the system of constraint equations is coupled. This system is solved (when using the FILM method) using the Matlab backslash operation. The contact computations are performed as explained in Section 2.

Next, the problem described in Figure 3 is simulated with varying number of contact constraints (achieved easily by different values of radius R_z) using the mesh consisting of 22060 CST elements shown in Figure 4.

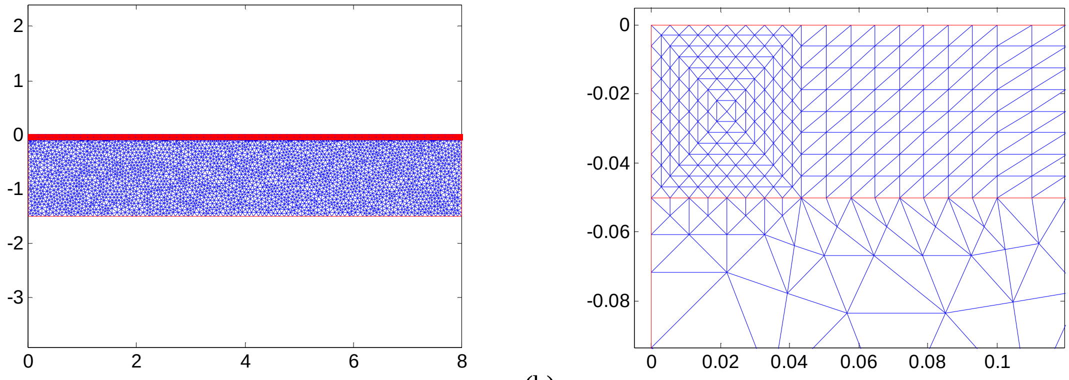

(a) (b)

Figure 4: CST mesh (a) and a detail (b).

The material parameters are: E = 200 GPa, ν = 0.3 and ρ = 7850 kg/m^3. A computational mass of 0.1 kg is used for the punch node mass m_p. A time step $\Delta t = 3.64\times10^{-7}$ s is chosen to keep the computations stable. Three different simulations are carried out in what follows, corresponding to three different number of contact constraints: Sim1 with 107 (R_z = 1 m), Sim2 with 308 (R_z = 3 m) and Sim3 with 610 (R_z = 6 m) contact constraints. The analysis time is $400\Delta t = 1.457\times10^{-4}$s. The stress pulse amplitude is 200 MPa while its duration, rise and descent times are 1×10^{-4}s, 1×10^{-5}s, respectively. The results of the simulations for Sim1 are presented in Figure 5.

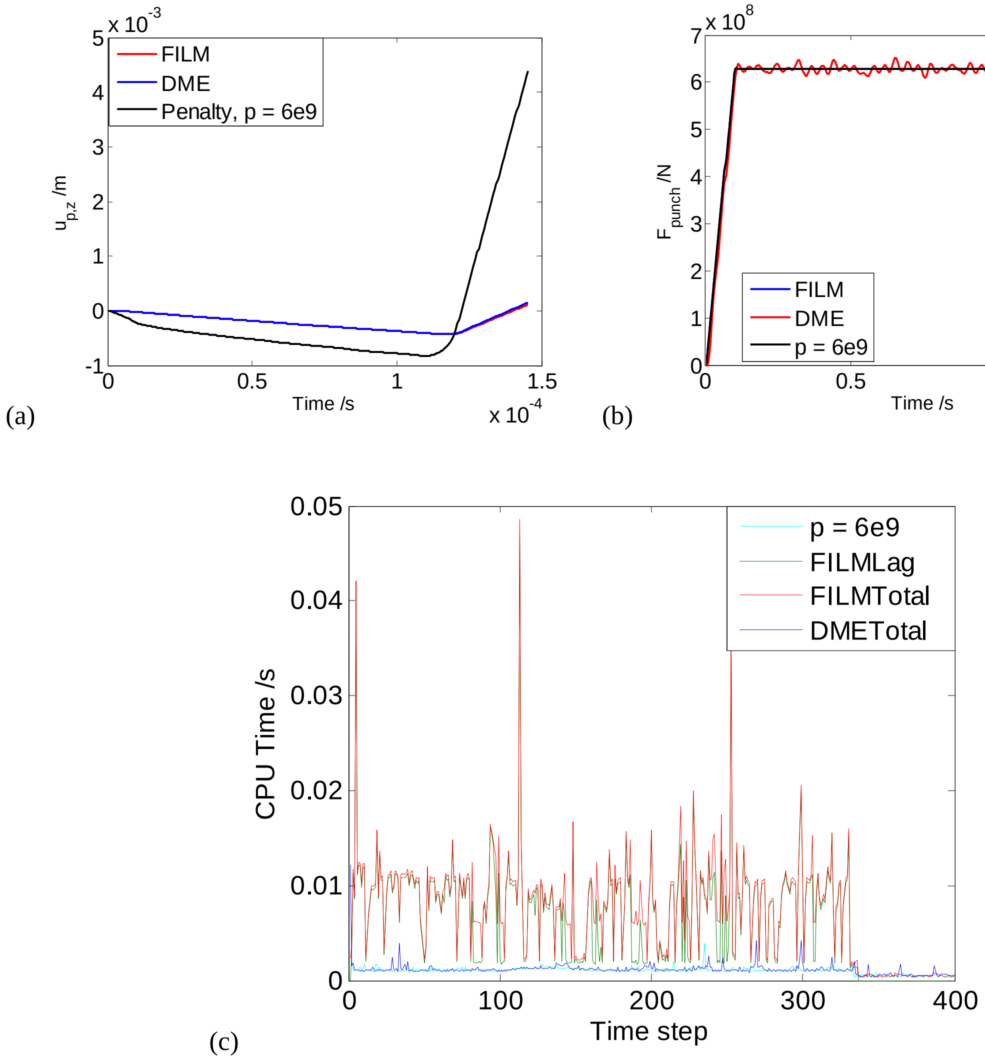

Figure 5: Punch penetration (a), contact force (b) and CPU times for contact solution (c) in Sim1.

According to Figure 5a the FILM and DME (Case 1) methods produce equal punch displacement during loading phase but slight, barely noticeable difference occurs during unloading. In contrast, the vertical displacement by Penalty method deviates considerably from the other methods. The value $p = 6\times10^9$, found by trial and error, gave the best results in this problem. The force resisting penetration, F_{punch}, is also quite similar to all methods besides the oscillations seen in the DME curve in Figure 5b. As for the CPU times (measured by Matlab tic function), it is seen that the time spend for contact computations by the DME and Penalty methods (DMETotal and p = 6e9) is about half of the lowest times by the FILM method. Moreover, most of the total time used by the FILM method is consumed in solving for the Lagrange multipliers from Equation (4), (compare the FILMLag and FILMTotal curves in Figure 5c). Finally, the FILM method displays heavy variations in CPU times which are attested by the high peaks in Figure 5c. Next, the results for Sim2 and Sim3 are shown in Figure 6.

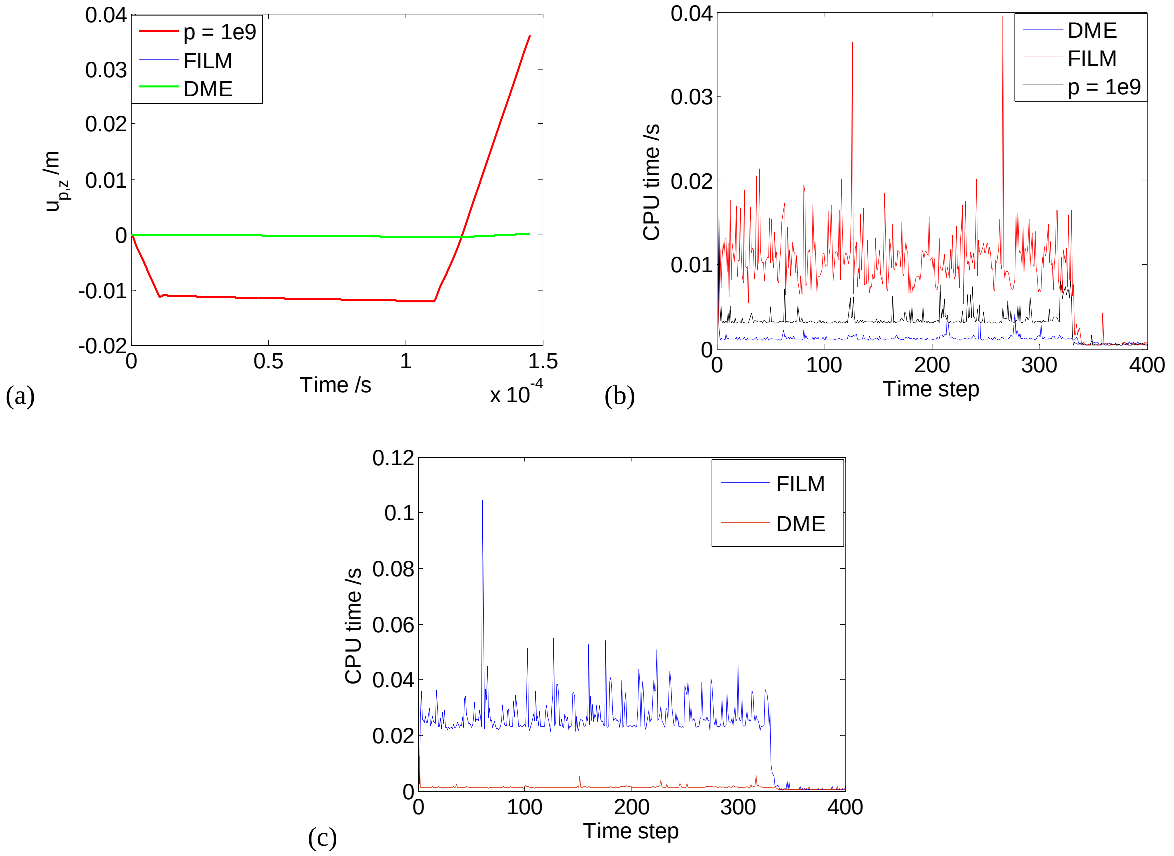

Figure 6: Punch penetration (a) and CPU times (b) in Sim2, and CPU times for contact solution (c) in Sim3

As the number of contact constraints increase, the Penalty method becomes more ill-behaving as seen in Figure 6a. In fact, no value of penalty coefficient giving reasonable results for punch displacement, $u_{p,z}$, was found in Sim3, i.e. when the number of contact constraints is 610. This deficiency of the penalty method is related to the relatively long contact interface in this problem: a value of the penalty coefficient giving good results close to the axis of symmetry is far too small, by many orders of magnitude, further away from it.

As to the CPU times spent in the contact computations, the DME method is clearly the most efficient one. Indeed, in Sim3, see Figure 6c, it is at least 20 times faster than the FILM method. It is also twice as fast as the Penalty method, as seen in Figure 6b.

In this specific problem, having 23036 DOFs, the second most time consuming operation during a time step is the computation of the internal force vector by $\mathbf{f}_{\text{int}} = \mathbf{Ku}$ where $\mathbf{K}$ is the global linear elastic stiffness (sparse) matrix. In the present simulations this time varied between 1 to 2 ms which is approximately of the same magnitude as the time needed to perform the contact computations with the DME method. Therefore, the efficiency of contact computations is crucial in this kind of explicit transient elasto-dynamics involving contact-impact.

3.2 Longitudinal impact of cylindrical bars

The problem of longitudinal impact of thick cylindrical bars described in Figure 7a is solved with the FILM, DME and Penalty methods in order to compare their performance. Axisymmetry of the problem is exploited and CST mesh shown for the left bar in Figure 7b is used. Relatively coarse mesh, with 406 for the left and 426 elements for the right bar is used.

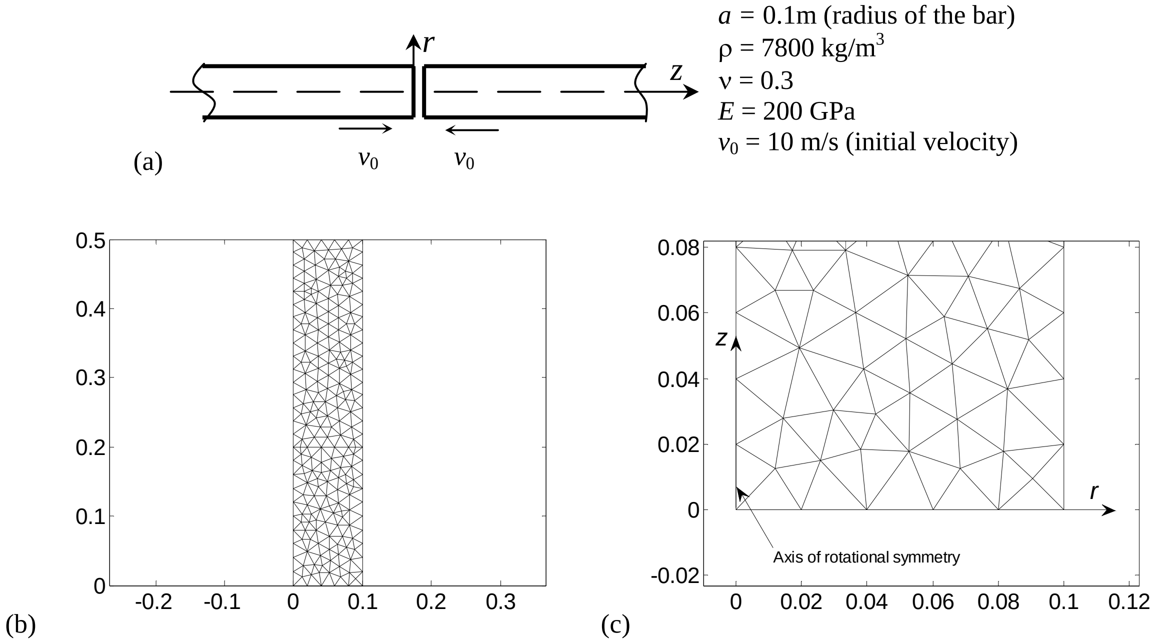

Figure 7: Longitudinal impact of thick bars (a), the CST mesh (b) and a detail (c).

The node-to-node contact interface is employed here and the contact computations are performed as explained in Section 2. The number of contact pairs is very small, 6 pairs, which is insignificant from the computational point of view. A time step $\Delta t = 1\times10^{-6}$ s is chosen to keep the computations stable. As the matrix $\Delta t^2\mathbf{G}\mathbf{M}^{-1}\mathbf{G}^{\mathrm{T}}$ is diagonal for the node-to-node contact interface, the average of its entries, 1.19×10^{10}, is taken for the penalty parameter. In the results in Figures 8-10, the gap computed as $\mathbf{G}\mathbf{u}^t - \mathbf{b}^t$ and contact forces are plotted at the contact nodes as a function of time for different methods.

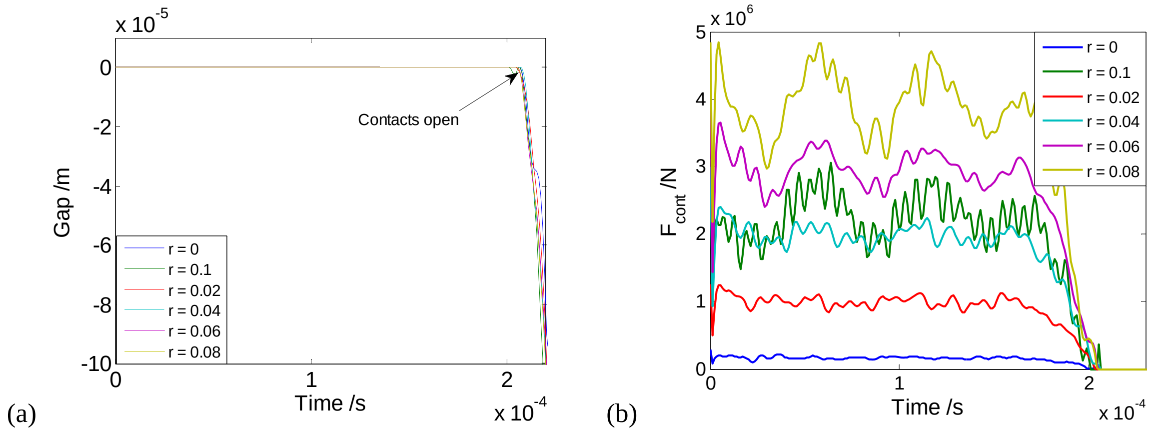

Figure 8: Simulation results with FILM method: gap (a), and contact forces (b).

According to the results in Figure 8, the impenetrability condition is accurately satisfied, i.e. the gap is zero all the time bars are in contact, with the FILM method. As the stress waves reflected at the free ends of the bars reach the contact surfaces, the contacts open and bars start to retreat. This event is indicated in Figure 8a. Next, the same results are presented for the Penalty method in Figure 9.

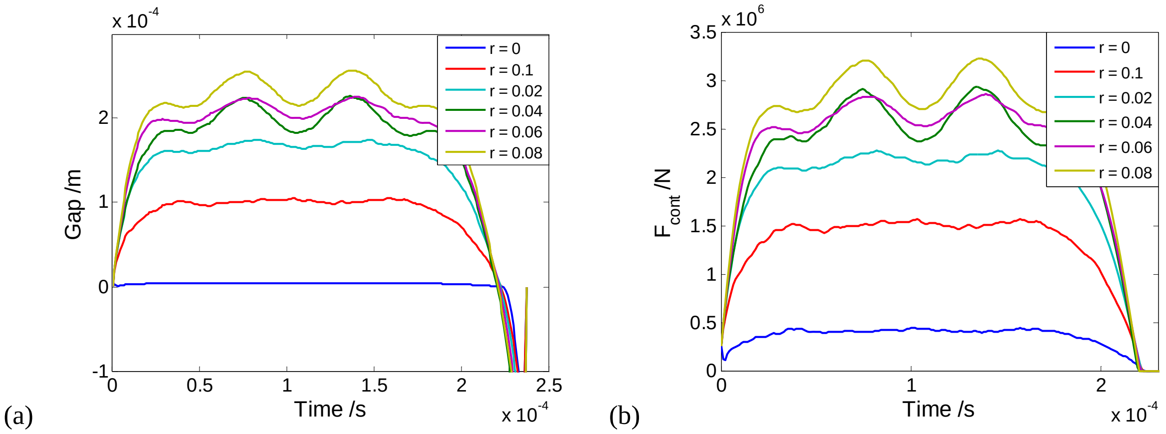

Figure 9: Simulation results with Penalty method (p = 1.19×10^{10}): gap (a), and contact forces (b).

As expected, the Penalty method does not satisfy the impenetrability condition. Indeed, penetration occurs and the contact force is based on this penetration. Finally, the same results are presented for the DME method with the perfectly inelastic collision scheme (e = 0) in Figure 10.

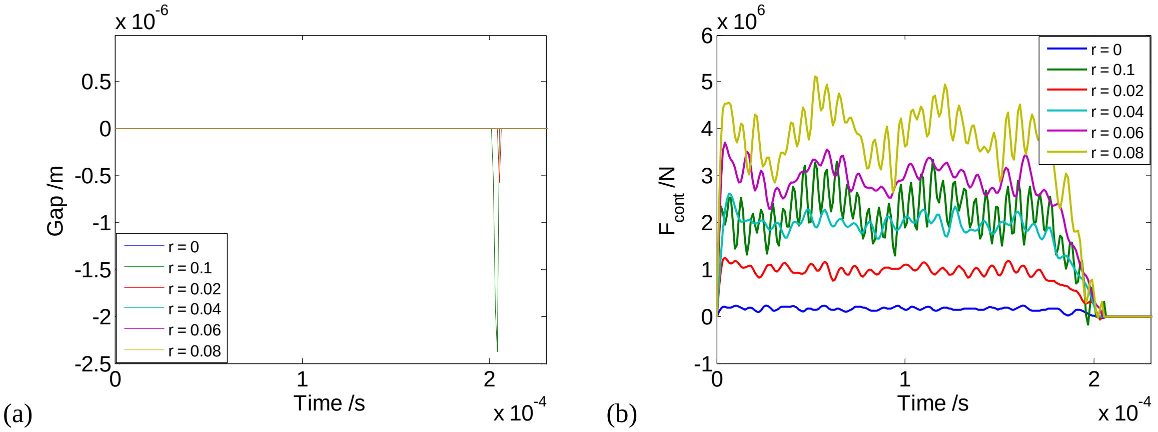

Figure 10: Simulation results with DME method: gap (a), and contact forces (b).

The results for the DME method with the perfectly inelastic collision assumption satisfy the impenetrability condition accurately, as attested by the zero gap values (see Figure 10a) until the arrival of the stress wave reflected from the free end of the bar. The contact forces in Figure 10b are somewhat similar to those produced with the FILM method.

Next, the methods are compared to the analytical solution of the problem by Valeš et al. [5]. The dimensionless axial stress at the location r = 0.1 m and z = 0.2 m, a location close enough to the contact surfaces so that the differences in the results between the methods are still visible (and not smoothed too much by the Saint-Venant principle). In addition, the different schemes for calculating the velocity of contact nodes with the DME method, Equation (10), are compared. The results are shown in Figure 11.

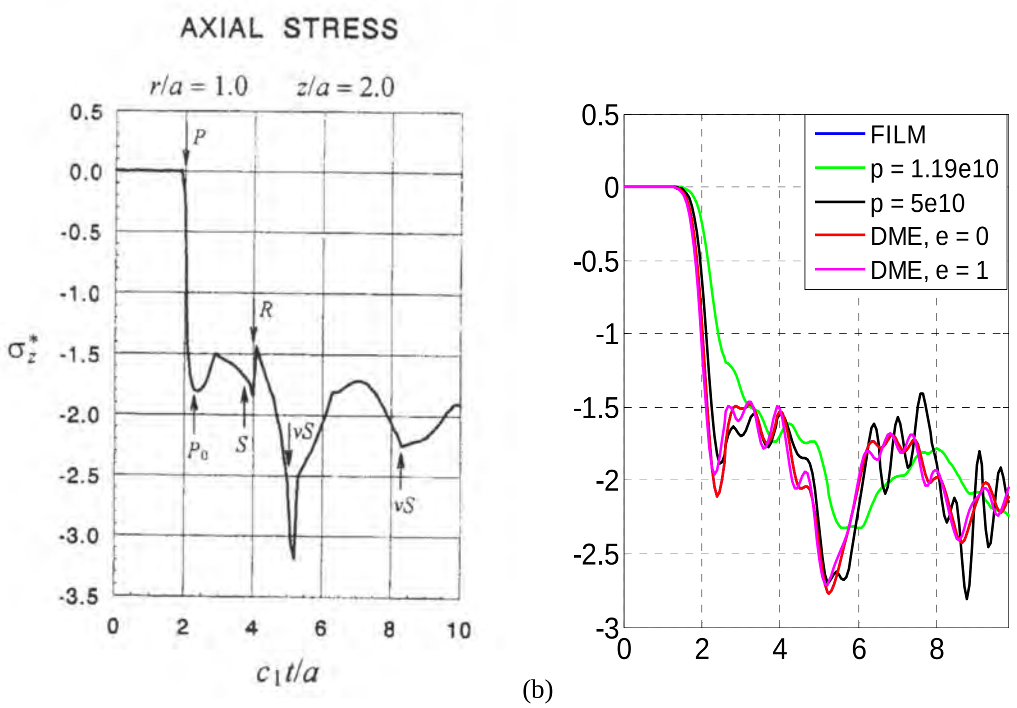

(a) (b)

Figure 11: Analytical solution for dimensionless axial stress [5] (a), simulation results with different methods (b) and results with different velocity schemes of DME method (c).

As seen in Figure 11b, the axial stress predicted with the FILM and DME (*e* = 0) methods are identical. The result with the elastic collision scheme for velocity (DME, *e* = 1) deviates slightly from these. These methods predict the analytical solution with a good accuracy. For example, the arrivals of the different wave types are clearly identifiable in the numerical results as well. In contrast, the Penalty method with the value $p = 1.19 \times 10^{10}$ is quite poor when compared to the analytical solution. With the higher value, $p = 5 \times 10^{10}$, the Penalty method seems to perform slightly better first but then, after time station $c_1t/a = 5$, overshooting oscillations develop in the response. Moreover, this value provided poor results at the contact nodes.

4 CONCLUSIONS

- Different methods, including the forward increment Lagrange multiplier method (FILM), the Penalty method and the direct manifold elimination method (DME), to impose contact constraints in transient explicit dynamics were numerically compared in this paper.
- A method based on direct elimination of the contact constraints was developed and tested for the node-to-node contact interface. The theoretical background of the method based on the theory of manifolds was elaborated with some detail.
- In the numerical simulation of the indentation problem with a rigid punch, the DME method was found to be overwhelmingly more efficient than the FILM method while both methods provided similar results. As to the Penalty method, while efficient, it failed to produce reasonable results when the contact interface was relatively wide. It is more suitable for point-like contact problems. Moreover, the Penalty method has an adverse effect on the numerical stability of the explicit integration and the problem specific pain to find the correct value of the parameter.

- In the impact problem of longitudinal bars, the FILM and DME methods predicted the analytical solution for axial stress with a good accuracy. These methods, the DME with the perfectly inelastic collision assumption, satisfied the impenetrability condition accurately and predicted identical results for axial stress. In contrast, the results with the Penalty method deviated from the analytical solution and from the other methods as well.
- Due to its efficiency and accuracy, the DME method can be regarded as superior to the FILM method in problems where the FILM method requires a solution of coupled system of equations for the Lagrange multiplier. These problems include the rigid punch indentation simulated in this paper and problems with a more general contact interface.
- In the future developments of the DME method, it will be formulated for more general node-to-segment contact interfaces.

REFERENCES

[1] N.J. Carpenter, R.L. Taylor M.G. Katona, Lagrange Constraints for Transient Finite Element Surface Contact. *International Journal for Numerical Methods in Engineering*, **32**, 103-128, 1991.

[2] J.M. Mäkinen, Manifolds on Continuum Mechanics. In: A. Koppel & J. Oja Eds. *Continuum Mechanics*, Nova Science Publishers. pp. 1-52, 2010.

[3] T.J. Saksala, J.M. Mäkinen, Numerical Modelling of Bit-Rock Interaction in Percussive Drilling by Manifold Approach, In: A. Eriksson and G. Tibert Eds. *Proceedings of the 23rd Nordic Seminar on Computational Mechanics*, KTH Stockholm, Sweden, October 21-22, 2010.

[4] G. D. Hahn, A Modified Euler Method for dynamical analyses. *International Journal for Numerical Methods in Engineering*, **32**, 943 – 955, 1991.

[5] F, Valeš et al., Wave Propagation in a Thick Cylindrical Bar Due to Longitudinal Impact. *JSME International Journal, Series A: Mechanics and Material Eng*, **39**, 60 – 70, 1996.

COMPDYN 2011
III ECCOMAS Thematic Conference on
Computational Methods in Structural Dynamics and Earthquake Engineering
M. Papadrakakis, M. Fragiadakis, V. Plevris (eds.)
Corfu, Greece, 25–28 May 2011

NONLINEAR MODELING AND ANALYSIS OF R.C. SPATIAL FRAMES TO STUDY THE EFFECTS OF THE VERTICAL COMPONENT OF NEAR-FAULT GROUND MOTIONS

F. Mazza[1] **and M. Mazza**[2]

[1] Department of Engineering Modeling, University of Calabria
87036, Rende (Cosenza), Italy
e-mail: fabio.mazza@unical.it

[2] Department of Engineering Modeling, University of Calabria
87036, Rende (Cosenza), Italy
e-mail: mirko.mazza@unical.it

Keywords: R.C. Spatial Frames, Lumped Plasticity Model, Axial Load-Biaxial Bending, Nonlinear Dynamic Analysis, Near-Fault Ground Motions.

Abstract. *Near-fault ground motions are characterized by high values of the ratio* α_{PGA} *between the peak value of the vertical acceleration,* PGA_V*, and the analogous value of the horizontal acceleration,* PGA_H*, which can notably modify the axial force demand in columns (e.g. producing both tension and high compressive forces larger than the balanced force) and the bending moment demand in girders (e.g. plastic hinges are expected along the span of r.c. girders, especially in the upper storeys). At present, the Italian seismic code (NTC08) does not consider the effects of near-fault ground motions in the design of a r.c. framed structure. In order to check the effectiveness of current code provisions, six- and twelve-storey r.c. spatial framed structures are designed according to the provisions of NTC08, considering the horizontal seismic loads acting alone or in combination with the vertical ones. A numerical investigation is carried out considering the nonlinear response of the test structures subjected to horizontal and vertical accelerograms, representative of near-fault ground motions with different values of the acceleration ratio* α_{PGA}*. A lumped plasticity model (LPM) based on the Haar-Kàrmàn principle is proposed to model the inelastic behaviour of the r.c. frame members. Specifically, the lumped plasticity model for a column (LPMC) includes a piecewise linearization of the bounding surface of the axial load-biaxial bending moment elastic domain, at the end sections where inelastic deformations are expected. On the other hand, the lumped plasticity model for a girder (LPMG) takes into account the potential plastic hinges along the span, due to the vertical ground motion, modifying the uniaxial plastic moments of the end-sections and so avoiding the computational effort required by the sub-discretization of the frame member.*

1 INTRODUCTION

Structural damage of reinforced concrete (r.c.) framed buildings, designed according to recent seismic codes and located in a near-fault area, has been observed during near-fault ground motions [1] and experimentally verified [2]. Generally, the design provisions of current seismic codes are not very accurate for assessing near-fault effects, because only far-fault ground motions are considered. At present, the Italian [3] and European [4] seismic codes do not consider the effects of the vertical component of near-fault ground motions in the design of a r.c. framed structure. These motions are characterized by high values of the ratio between the peak value of the vertical acceleration (PGA_V) and the analogous value of the horizontal acceleration (PGA_H) [5]. More specifically, high values of the acceleration ratio α_{PGA} can notably modify the axial load in r.c. columns, producing undesirable phenomena in these elements [6]: e.g., reduction in the shear capacity, buckling of the longitudinal bars, brittle failure in compression, bond deterioration or failure under tension. Moreover, plastic hinges are expected along the span of the girders, especially if rather long [7], and in the upper storeys, where the effects of the gravity loads generally prevail over those of the horizontal seismic loads and an amplification of the vertical motion is expected [8].

In order to establish if suitable additional code guidelines are needed, it is very important to study the nonlinear response of r.c. spatial frames subjected to near-fault ground motions. The high computational effort required to obtain accurate results by finite elements or fibre models has encouraged the development of simplified approaches [9]. In the present work, a lumped plasticity model (LPM) based on the Haar-Kàrmàn principle is proposed to model the inelastic behaviour of r.c. frame members. Specifically, the lumped plasticity model for a r.c. column (LPMC) includes a piecewise linearization of the bounding surface of the axial load-biaxial bending moment elastic domain, at the end sections where inelastic deformations are expected. Each flat surface corresponds to a plastic strain mechanism for the section, defined by axial strains and curvatures. This type of element represents a good choice for the response simulation of structural members, like columns, that may experience inelastic deformations at the end sections. On the contrary, the lumped plasticity model for a r.c. girder (LPMG) takes into account the potential plastic hinges along the span of the girders, due to the vertical ground motion, modifying the uniaxial plastic moments of the end-sections depending on the top and bottom plastic moments of selected critical intermediate sections and so avoiding the computational effort required by the sub-discretization of the frame member [10].

Six- and twelve-storey r.c. spatial frames are assumed as test structures and designed according to the provisions of the Italian seismic code (NTC08) considering (besides the gravity loads) the horizontal seismic loads acting alone or in combination with the vertical ones. Horizontal and vertical accelerograms, representative of near-fault ground motions with different values of the acceleration ratio α_{PGA}, are considered for the numerical investigation.

2 LUMPED PLASTICITY MODELING

The nonlinear dynamic analysis of a spatial framed structure can be carried out adopting a numerical step-by-step procedure based on an initial stress-like iterative procedure [11]. At each step of the analysis, the elastic-plastic behaviour of a beam element is described using the Haar-Kàrmàn principle, without satisfying nodal equilibrium conditions, once the initial state and the incremental load in the step are known. Then, an implicit two-parameter integration scheme is adopted in order to satisfy the global dynamic equilibrium of the overall structure. Each frame member is modeled by a LPM composed of two parallel elements, one elastic-perfectly plastic and the other linearly elastic, assuming a bilinear moment-curvature (M-χ) law, depending on the axial load in the case of a column. The elastic component is characterized by the flexural stiffness *pEI*, *p* being the hardening ratio of the (M-χ) law. Torsional strains are assumed to be fully elastic while shear strains are neglected. Distributed masses are considered along the girders to evaluate the influence of the vertical vibrations.

2.1 Frame members in biaxial bending with axial force

The nonlinear behaviour of r.c. structural elements under biaxial bending with axial force is generally based on the knowledge of the bounding surface of the cross-sections, resulting from the plastic moments obtained for different values of the axial force [12]. A lumped plasticity model, labelled as LPMC, is proposed for a r.c. column, assuming that the bounding surface of the elastic domain is described by means of flat surfaces. More specifically, the inelastic deformations, supposed as lumped at the end cross-sections, are represented by the axial strain ε_P, along the longitudinal axis *x*, and the curvatures χ_{Py} and χ_{Pz}, along the principal axes *y* and *z*, collected in the vector

$$\boldsymbol{\varepsilon}_P=\left[\varepsilon_P,\chi_{Py},\chi_{Pz}\right]^T \tag{1}$$

and referring to the (geometric) centroid of the cross-section. Denoting the corresponding generalized stresses at the end section by the vector

$$\boldsymbol{\sigma}=\left[N,M_y,M_z\right]^T \tag{2}$$

and the plastic stresses, related to $\boldsymbol{\varepsilon}_{Pk}=\boldsymbol{n}_k$, by $\boldsymbol{\sigma}_{Pk}$, the elastic domain $g(\boldsymbol{\sigma})=0$ can be approximated by n_{fs} flat surfaces $g_k(\boldsymbol{\sigma})$, each defined by a different (normal) direction $\boldsymbol{n}_k$.

As suggested in [13], a satisfactory representation of the axial load-biaxial bending moment bounding surface of the elastic domain can be obtained considering 26 flat surfaces, including: 6 surfaces normal to the principal axes *x*, *y* and *z* (Figure 1a); 12 surfaces normal to the bisections of the *y*-*z*, *x*-*y* and *x*-*z* principal planes (Figure 1b); 8 surfaces normal to the bisections of the octants (Figure 1c). The piecewise linearized elastic domain is characterized by the corresponding 26 columns of the matrix

$$\boldsymbol{N}=\left[\begin{matrix} 1 & -1 & 0 & 0 & 0 & 0 & 0 & 0 & 0 & 0 & c_{yx} & c_{yx} & -c_{yx} & -c_{yx} & c_{zx} & c_{zx} & -c_{zx} & -c_{zx} \\ 0 & 0 & 1 & -1 & 0 & 0 & 1 & -1 & 1 & -1 & 1 & -1 & 1 & -1 & 0 & 0 & 0 & 0 \\ 0 & 0 & 0 & 0 & 1 & -1 & c_{yz} & c_{yz} & -c_{yz} & -c_{yz} & 0 & 0 & 0 & 0 & 1 & -1 & 1 & -1 \end{matrix}\right.$$
$$\left.\begin{matrix} c'_{yz} & c'_{yz} & -c'_{yz} & -c'_{yz} & c'_{yz} & c'_{yz} & -c'_{yz} & -c'_{yz} \\ 1 & -1 & 1 & -1 & 1 & -1 & 1 & -1 \\ c_{yz} & c_{yz} & c_{yz} & c_{yz} & -c_{yz} & -c_{yz} & -c_{yz} & -c_{yz} \end{matrix}\right] \tag{3}$$

where each column represents a vector $\boldsymbol{n}_k$ defined starting from

$$c_{yx}=\frac{\left\|\boldsymbol{\sigma}_{P3}-\boldsymbol{\sigma}_{P4}\right\|}{\left\|\boldsymbol{\sigma}_{P1}-\boldsymbol{\sigma}_{P2}\right\|},\quad c_{zx}=\frac{\left\|\boldsymbol{\sigma}_{P5}-\boldsymbol{\sigma}_{P6}\right\|}{\left\|\boldsymbol{\sigma}_{P1}-\boldsymbol{\sigma}_{P2}\right\|},\quad c_{yz}=\frac{\left\|\boldsymbol{\sigma}_{P3}-\boldsymbol{\sigma}_{P4}\right\|}{\left\|\boldsymbol{\sigma}_{P5}-\boldsymbol{\sigma}_{P6}\right\|},\quad c'_{yz}=\frac{\left\|\boldsymbol{\sigma}_{P7}-\boldsymbol{\sigma}_{P10}\right\|}{\left\|\boldsymbol{\sigma}_{P1}-\boldsymbol{\sigma}_{P2}\right\|} \tag{4}$$

which refer to the plastic generalized stresses

$$\boldsymbol{\sigma}_{P1}=\begin{bmatrix} N_{P1} \\ 0 \\ 0 \end{bmatrix},\boldsymbol{\sigma}_{P2}=\begin{bmatrix} N_{P2} \\ 0 \\ 0 \end{bmatrix},\boldsymbol{\sigma}_{P3}=\begin{bmatrix} N_{P3} \\ M_{Py3} \\ 0 \end{bmatrix},\boldsymbol{\sigma}_{P4}=\begin{bmatrix} N_{P4} \\ M_{Py4} \\ 0 \end{bmatrix},\boldsymbol{\sigma}_{P5}=\begin{bmatrix} N_{P5} \\ 0 \\ M_{Pz5} \end{bmatrix},\boldsymbol{\sigma}_{P6}=\begin{bmatrix} N_{P6} \\ 0 \\ M_{Pz6} \end{bmatrix}$$
$$\boldsymbol{\sigma}_{P7}=\begin{bmatrix} N_{P7} \\ M_{Py7} \\ M_{Pz7} \end{bmatrix},\boldsymbol{\sigma}_{P8}=\begin{bmatrix} N_{P8} \\ M_{Py8} \\ M_{Pz8} \end{bmatrix},\boldsymbol{\sigma}_{P9}=\begin{bmatrix} N_{P9} \\ M_{Py9} \\ M_{Pz9} \end{bmatrix},\boldsymbol{\sigma}_{P10}=\begin{bmatrix} N_{P10} \\ M_{Py10} \\ M_{Pz10} \end{bmatrix} \tag{5}$$

In particular, once the plastic strain mechanism of the cross-section corresponding to the vector $\boldsymbol{n}_k$ ($k=1..n_{fs}$) is considered, the maximum compressive strain in concrete (ε_{cmax}) and the maximum tensile strain in longitudinal steel reinforcement (ε_{smax}) are evaluated, avoiding values greater than the corresponding ultimate ones (e.g. $\varepsilon_{cu}=0.35\%$ and $\varepsilon_{su}=1\%$). In this way, the position of the neutral axis and the area of the compressed concrete section (A_c) being known, the components of the generalized plastic stress vector $\boldsymbol{\sigma}_{Pk}$ can be evaluated by the equilibrium equations:

$$N_{Pk}=\int_{A_c}\sigma_c dA+\sum_{i=1}^{n_b}A_{si}\sigma_{si}, \quad M_{Pyk}=-\int_{A_c}\sigma_c z\, dA-\sum_{i=1}^{n_b}A_{si}\sigma_{si}z_i, \quad M_{Pzk}=\int_{A_c}\sigma_c y\, dA+\sum_{i=1}^{n_b}A_{si}\sigma_{si}y_i \qquad (6)$$

where $\sigma_c=\sigma_c(\varepsilon)$ and $\sigma_{si}=\sigma_{si}(\varepsilon)$. In Eq. (5) n_b is the number of longitudinal bars while (y_i, z_i) and A_{si} define, respectively, the position and area of each bar. Elastic-perfectly plastic constitutive laws are assumed for both concrete (σ_c–ε_c) and steel (σ_s–ε_s), assuming stresses and strains with the appropriate signs (i.e. negative for compression and positive for tension).

At each step of the analysis, the elastic-plastic behaviour of a column, once the initial state and the incremental load are known, can be obtained by using the Haar-Kàrmàn principle. It states that, among all the generalized stress fields $\boldsymbol{\sigma}$ satisfying equilibrium, the elastic-plastic solution $\boldsymbol{\sigma}_{EP}$ is that with minimum distance, in terms of complementary energy Π_c, from the elastic solution $\boldsymbol{\sigma}_E$ [11]

$$\Pi_c\left(\boldsymbol{\sigma}_{EP}\right)=\frac{L}{2}\int_0^1\left(\boldsymbol{\sigma}_{EP}-\boldsymbol{\sigma}_E\right)^T\boldsymbol{D}_c^{-1}\left(\boldsymbol{\sigma}_{EP}-\boldsymbol{\sigma}_E\right)d\xi=min. \qquad (7)$$

$\xi(=x/L)$ being a nondimensional abscissa, L the length of the beam element and $\boldsymbol{D}_c$ the elastic matrix of a column. The plastic admissibility conditions

$$g_k\left(\boldsymbol{\sigma}_{EP}\right)\leq 0 \ \ \text{for } k=1..n_{fs} \qquad (8)$$

also have to be satisfied at the end sections of the beam element. The elastic-plastic solution corresponds to the tangent point between a level curve of $\Pi_c(\boldsymbol{\sigma}_{EP})$ and the piecewise approximation of the bounding surface of the elastic domain. Moreover, when the elastic solution lies within the fan limited by the planes normal to the boundaries of the flat surfaces, the elastic-plastic solution corresponds to a point along the corner line resulting from the intersection between these surfaces.

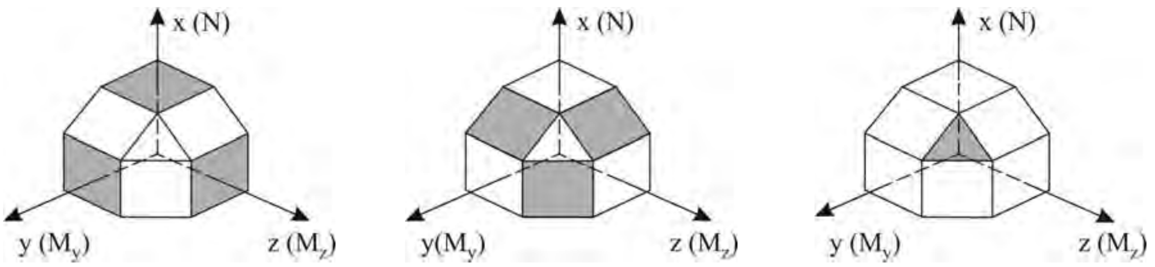

(a) Surfaces normal to the *x*, *y* and *z* axes.

(b) Surfaces normal to the bisections of the *y-z*, *x-y* and *x-z* planes.

Surface normal to the bisection of the octant.

Figure 1: Flat surfaces approximating the elastic domain for the end sections of a column.

2.2 Frame members in uniaxial bending without axial force

A lumped plasticity model, already proposed by the authors [10], is adopted for a r.c. girder and labelled as LPMG. The elastic-plastic solution is evaluated only at the end sections (*i* and *j*) in the vertical plane (i.e. *x-z* plane) of bending. Moreover, the potential inelastic deformations lumped at n_s intermediate sections along the span, due to the vertical ground motions, are also checked. In order to avoid the computational effort due to the sub-discretization of the frame member, the elastic solution at the end section i (j) is modified taking into account the possible inelastic effects occurring at an intermediate section s ($s=1..\ n_s$), besides those at the end section j (i). Specifically, when a plastic (flexural) distortion

$$\Delta\phi_{Pys} = \Delta M_{EPys}\left(\frac{4EI_y(1-p)}{L}\left(3\left(\frac{x_s}{L}\right)^2-3\left(\frac{x_s}{L}\right)+1\right)\right)^{-1} \tag{9}$$

consequent to an elastic-plastic moment M_{EPys} greater than the corresponding plastic moment occurs at an intermediate section of abscissa x_s, the corresponding moments at the end sections can be evaluated as

$$\Delta M^{(s)}_{EPyi} = \frac{2EI_y\left(1-p\right)}{L}\left(3\left(\frac{x_s}{L}\right)-2\right)\Delta\phi_{Pys},\ \ \Delta M^{(s)}_{EPyj} = \frac{2EI_y\left(1-p\right)}{L}\left(3\left(\frac{x_s}{L}\right)-1\right)\Delta\phi_{Pys} \tag{10a,b}$$

With reference to the bending moment along the principal axis y and neglecting the inflection along the principal axis z, the generalized stresses of a girder are denoted by the vector

$$\boldsymbol{\sigma}=\left[M_{yi},M_{yj}\right]^T \tag{11}$$

Then the elastic-plastic solution satisfying equilibrium is obtained, according to the Haar-Kàrmàn principle, minimizing the complementary energy

$$\Pi_c\left(\boldsymbol{\sigma}_{EP}\right)=\frac{L}{2}\int_0^1\left(\boldsymbol{\sigma}_{EP}-\boldsymbol{\sigma}_E-\Delta\boldsymbol{\sigma}^{(s)}_{EP}\right)^T\boldsymbol{D}_g^{-1}\left(\boldsymbol{\sigma}_{EP}-\boldsymbol{\sigma}_E-\Delta\boldsymbol{\sigma}^{(s)}_{EP}\right)d\xi=min. \tag{12}$$

where $\boldsymbol{D}_g$ is the elastic matrix of a girder. Moreover, the plastic admissibility condition

$$g\left(\boldsymbol{\sigma}_{EP}\right)\leq 0 \tag{13}$$

also has to be satisfied at the end sections of the beam element. Specifically, the (uniaxial) top (T) and bottom (B) plastic moments at the end sections

$$\boldsymbol{\sigma}_{P,T}=\left[M_{Pyi,T},M_{Pyj,T}\right]^T \quad , \quad \boldsymbol{\sigma}_{P,B}=\left[M_{Pyi,B},M_{Pyj,B}\right]^T \tag{14a,b}$$

are modified during the nonlinear analysis, assuming the following values when a plastic distortion occurs at an intermediate section (see Figure 2)

$$\bar{\boldsymbol{\sigma}}_{P,T}=\left[\bar{M}_{Pyi,T},\bar{M}_{Pyj,T}\right]^T \quad , \quad \bar{\boldsymbol{\sigma}}_{P,B}=\left[\bar{M}_{Pyi,B},\bar{M}_{Pyj,B}\right]^T \tag{15a,b}$$

The elastic-plastic solution of the problem defined by the Equations (12) and (13) can be obtained by a predictor-corrector procedure. It is triggered evaluating the elastic-plastic solution at an end section (e.g. end section i) by the formula:

$$M^{(0)}_{EPyi} = max\left(-\bar{M}_{Pyi,T},min\left(\bar{M}_{Pyi,B},M_{Eyi}+\sum\nolimits_{s=1}^{n_s}\Delta M^{(s)}_{EPyi}\right)\right) \tag{16}$$

Afterwards the elastic-plastic solution is alternately evaluated at the end section i (j) and j (i)

$$M^{(k)}_{EPyj} = max\left(-\bar{M}_{Pyj,B},min\left(\bar{M}_{Pyj,T},M_{Eyj}+\sum\nolimits_{s=1}^{n_s}\Delta M^{(s)}_{EPyj}-\frac{M_{Eyi}+\sum\nolimits_{s=1}^{n_s}\Delta M^{(s)}_{EPyj}-M^{(k-1)}_{EPyi}}{2}\right)\right) \tag{17}$$

$$M_{EPyi}^{(k+1)} = max\left(-\bar{M}_{Pyi,T}, min\left(\bar{M}_{Pyi,B}, M_{Eyi} + \sum\nolimits_{s=1}^{n_s} \Delta M_{EPyi}^{(s)} - \frac{M_{Eyj} + \sum\nolimits_{s=1}^{n_s} \Delta M_{EPyi}^{(s)} - M_{EPyj}^{(k)}}{2} \right)\right) \tag{18}$$

In cases where the intermediate sections experience inelastic deformations, Eqns. (17) and (18) are solved iteratively until, in these sections, at the iteration loop *k* the differences between the plastic moments and the elastic-plastic moments evaluated by the equilibrium, starting from the elastic-plastic solution at the end sections, become less than a prefixed tolerance.

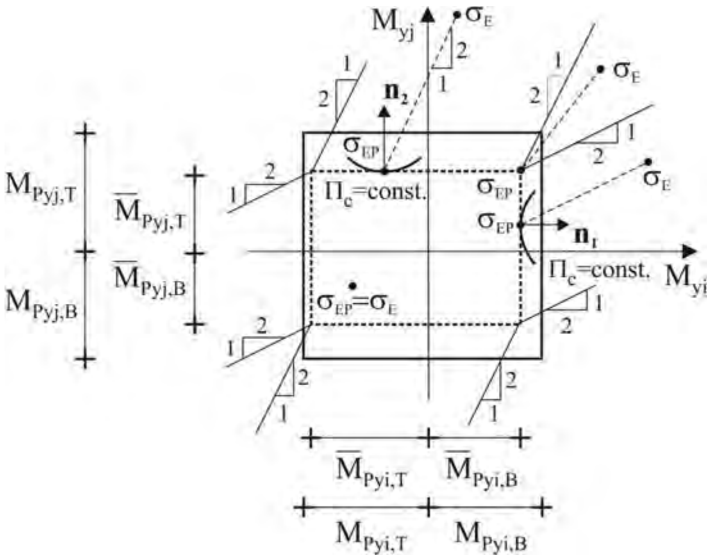

Figure 2: Bounding surface of the elastic domain for the end sections of a girder.

3 LAYOUT AND DESIGN OF THE R.C. FRAMED BUILDINGS

Typical six- and twelve-storey residential buildings with r.c. framed structures, whose symmetric plan is shown in Figure 3, are considered as test structures. Deep girders are placed along the perimeter of the building together with infilled walls assumed as non-structural elements regularly distributed in elevation; deep and flat girders, perpendicular and parallel to the floor slab direction, respectively, are assumed inside the building. Geometric dimensions of the girders and columns are shown in Table 1. Moreover, the vibration periods corresponding to the high-participation modes with prevailing components in the horizontal and vertical directions are: T_{1X}=0.576s, T_{1Y}=0.698s and T_{1Z}=0.064s, for the six-storey buildings; T_{1X}=0.993s, T_{1Y}=1.249s and T_{1Z}=0.103s, for the twelve-storey buildings. The gravity loads used in the design are represented by dead- and live-loads, equal respectively to: 4.8 kN/m^2 and 2 kN/m^2, for the top floor; 5.7 kN/m^2 and 2 kN/m^2, for the other floors. The weight of the perimeter masonry-infills is taken into account considering a gravity load of 2.7 kN/m^2. A cylindrical compressive strength of 25 N/mm^2 for the concrete and a yield strength of 450 N/mm^2 for the steel are considered.

The proportioning of the test structures has been done according to the Italian seismic code (Technical Regulations for Constructions 2008, NTC08 [3]) assuming, besides the gravity loads, the horizontal seismic loads acting alone or in combination with the vertical ones. Each building (B) is identified by two symbols: the first one (6 or 12) indicates the number of storeys, the second one refers to the design seismic loads which are considered (i.e.: H, when considering only the horizontal component of the seismic loads; HV, when also considering the vertical component of the seismic loads). The following assumptions have been made: medium subsoil (class B, subsoil parameters: S_{SH}=1.13 in the horizontal direction and S_{SV}=1 in the vertical one); flat terrain (class T1, topographic parameter: S_T=1).

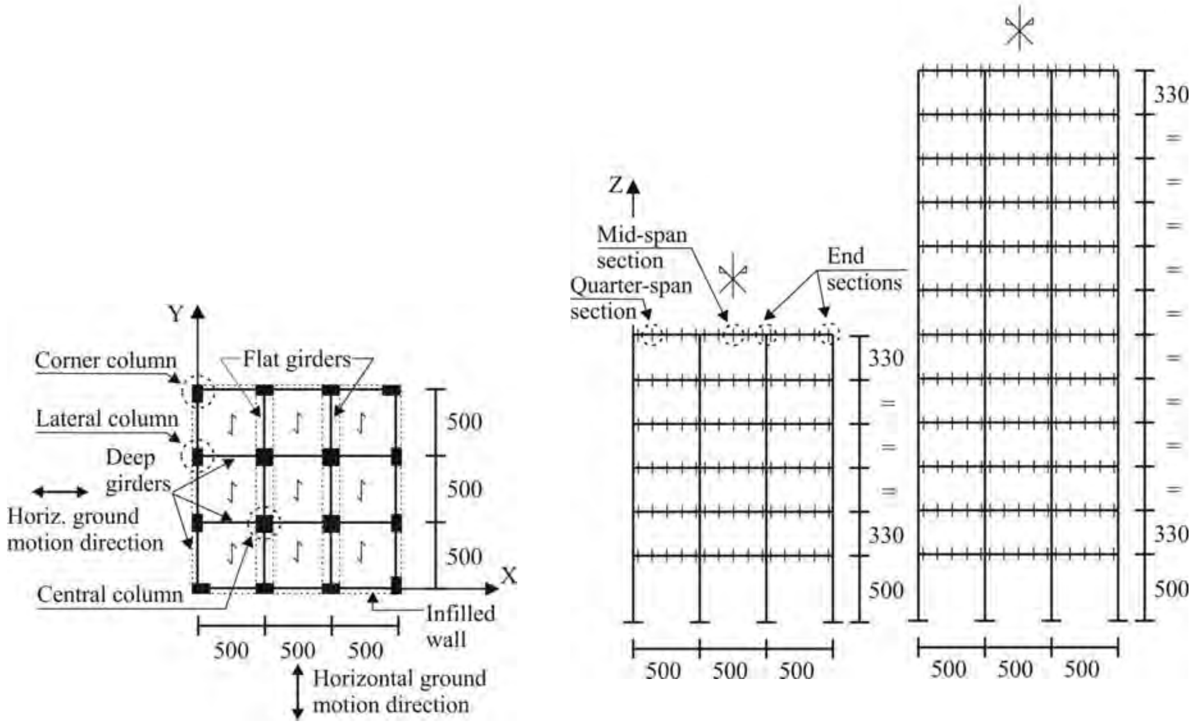

(a) Plan of the buildings. (b) Six-storey frames. (c) Twelve-storey frames.

Figure 3: R.c. test structures (dimensions in cm).

Storey	Corner columns	Lateral columns	Central columns	Deep girders	Flat girders
12	30x30	30x40	40x40	30x50	50x25
11	30x30	30x40	40x40	30x50	50x25
10	30x40	30x50	40x40	30x50	60x25
9	30x40	30x50	40x40	30x60	60x25
8	35x40	35x60	50x50	30x60	70x25
7	35x40	35x60	50x50	30x60	70x25
6	40x50 (30x50)	45x60 (30x50)	60x60 (40x40)	40x65 (30x50)	80x25 (50x25)
5	40x50 (30x50)	45x60 (30x50)	60x60 (40x40)	40x65 (30x50)	80x25 (50x25)
4	50x60 (30x60)	50x70 (40x60)	70x70 (50x50)	40x65 (30x60)	90x25 (60x25)
3	50x60 (30x60)	50x70 (40x60)	70x70 (50x50)	40x70 (30x60)	90x25 (60x25)
2	50x70 (40x70)	50x90 (50x80)	80x80 (60x60)	40x70 (40x60)	100x25 (70x25)
1	50x70 (40x70)	50x90 (50x80)	80x80 (60x60)	40x70 (40x60)	100x25 (70x25)

Table 1: Section dimensions (in cm) of the six- (in brackets) and twelve-storey r.c. buildings.

The design is carried out to comply with the ultimate limit state (ULS) of life safety, according to the horizontal and vertical elastic response spectra whose main data are reported in Table 2: i.e. return period (T_r) corresponding to a nominal life of the structure equal to 50 years; peak ground accelerations in the horizontal (PGA_H) and vertical (PGA_V) directions; amplification factors defining the maximum horizontal (F_o) and vertical (F_v) spectral acceleration on rock-site; upper limit of the period of the constant spectral acceleration branch in the horizontal direction (T^*_C). Six- and twelve-storey structures have to be classified as regular in plan and irregular in elevation, according to the criteria imposed by NTC08. As a consequence, a low ductility class is considered, assuming: behaviour factor for the horizontal seismic loads, q_H=3.12; behaviour factor for the vertical seismic loads, q_V=1.5. Finally, the serviceability limit state (SLS) of damage is also controlled, checking that, under the horizontal seismic loads corresponding to the elastic response spectra whose main parameters are shown in Table 2, the inter-storey drift is less than 0.5% of the storey height. Detailing for local ductility is also imposed to satisfy minimum conditions for the longitudinal bars of the r.c. frame members. Finally, capacity design rules regarding the beam-column moment ratio and shear forces and local ductility requirement of girders and columns are also satisfied.

Limit state	T_r (years)	PGA_H (g)	PGA_V (g)	F_o	F_v	T^*_C (s)
ULS (Life safety)	475	0.312	0.276	2.44	1.73	0.370
SLS (Damage)	50	0.108	-	2.28	-	0.301

Table 2: Main parameters of the horizontal elastic response spectra.

4 NUMERICAL RESULTS

In order to evaluate the effects produced by the combination of the horizontal and vertical components of near-fault ground motions on the response of r.c. spatial frames, a computer code has been implemented according to the LPMs proposed in Section 2. A bilinear moment-curvature law is adopted, assuming a hardening ratio p=5%. In the Rayleigh hypothesis, the damping matrix is assumed as a linear combination of the mass and stiffness matrices, assuming a viscous damping ratio equal to 5% or 2% with reference to the two vibration periods corresponding to high-participation modes with components prevailing in the Y (T_{1Y}) or Z (T_{1Z}) direction, respectively. In this way, an intermediate value of the damping ratio is achieved in the range of vibration periods T_{1Z}-T_{1Y}, while the higher frequency modes, which do not contribute significantly to the dynamic response, are practically eliminated due to their high damping ratio. Plastic conditions are checked at the end sections of the columns, considering an approximation with flat surfaces of the axial force-biaxial bending moment bounding surface of the elastic domain (see Section 2.1). Three intermediate sections (i.e. the two quarter-span sections and the mid-span section) are checked along the span of the girders, in addition to the end sections (Figure 3b) even if, according to the model proposed in Section 2.2, girders are discretized with only one element instead of four sub-elements, reducing the computational effort of the discretization by about 2/3.

The nonlinear dynamic response of the B6H, B6HV, B12H and B12HV test structures, which are described in Section 3, is studied with reference to the records of the Imperial Valley earthquake, available in the Pacific Earthquake Engineering Research center database [14]. More specifically, ground motions recorded at different stations placed at close range to one another and exhibiting high values of the acceleration ratio α_{PGA}(=PGA_V/PGA_H) are considered. It is worth mentioning that the accelerograms are characterized by a PGA_H value approximately comparable, for one of the two horizontal directions, with the one adopted in the design of the test structures (i.e. PGA_H=0.312g in Table 2). In Table 3 the main data of the selected near-fault ground motions are reported: recording station, closest distance to fault rupture (D); magnitude (M_s), peak ground acceleration for the horizontal components ($PGA_{H,1}$ and $PGA_{H,2}$) and the vertical one (PGA_V) and acceleration ratios ($\alpha_{PGA,1}$ and $\alpha_{PGA,2}$). As can be observed, α_{PGA} has a maximum value of 2.009 for the El Centro Differential Array (D.A.) station as opposed to the value 1.13 prescribed by NTC08 in the examined case (see Table 2).

Station	D	M_s	$PGA_{H,1}$	$PGA_{H,2}$	PGA_V	$\alpha_{PGA,1}$	$\alpha_{PGA,2}$
El Centro Array #5	1.0 km	6.9	0.379g	0.519g	0.537g	1.417	1.035
El Centro Array #7	0.6 km	6.9	0.338g	0.463g	0.544g	1.609	1.175
El Centro Differential Array	5.3 km	6.9	0.352g	0.480g	0.707g	2.009	1.473

Table 3: Main data of the selected near-fault ground motions (Imperial Valley, 15/10/1979).

The elastic (normalized) response spectra of acceleration in the horizontal ($S_{aH,1}$ and $S_{aH,2}$) and vertical (S_{aV}) directions are plotted in Figure 4, assuming an equivalent viscous damping ratio in the horizontal direction, ξ_H, equal to 5%, and an analogous ratio in the vertical direction, ξ_V, equal to 2% due to the low damping capacity of the structure expected in this direction [1]. The response spectra of these motions are compared with the corresponding target NTC08 response spectra for a high-risk seismic region and a medium subsoil class (class B): i.e. PGA_H=0.312g and PGA_V=0.276g. It is interesting to note that in the vertical direction the spectral values for the El Centro ground motions (Figure 4c) are much greater than those corresponding to NTC08, at least in the range of the vibration periods which are more relevant for the test structures.

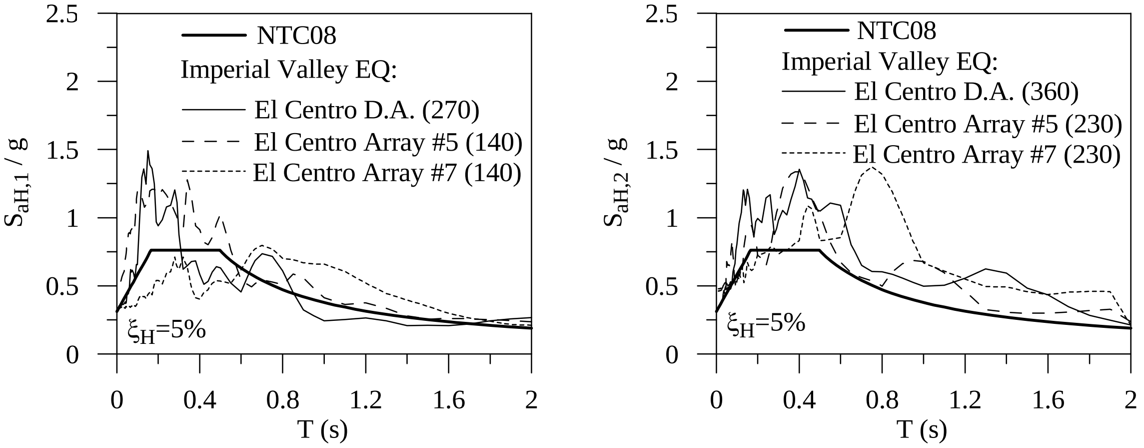

(a) Horizontal direction No. 1.

(b) Horizontal direction No. 2.

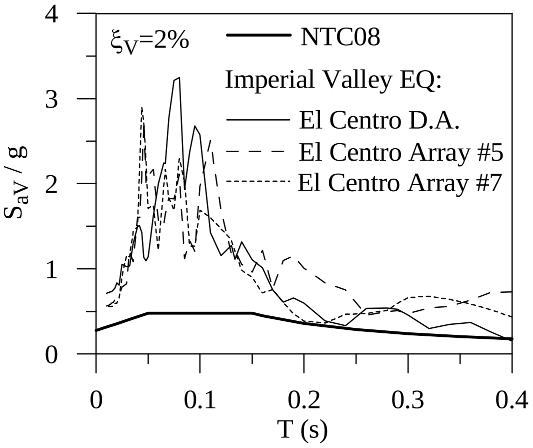

(c) Vertical direction.

Figure 4: Acceleration (elastic) response spectra.

To emphasize the importance of also considering the vertical ground motion, the main response parameters affected by this component are considered: i.e. curvature ductility demand at the potentially critical sections (i.e. end, quarter span and mid-span sections) of the girders, for each of the two loading directions; curvature ductility demand, at the end sections, and axial force demand for the columns. More specifically, the ductility demand for a column is evaluated with reference to the radial direction defined by the bending moment axis vector

$$\mu_{max,r} = \frac{\chi_{max,r}}{\chi_{Er}} = \frac{\sqrt{\left(\chi_{Ey} + \Sigma\, \Delta\chi_{Py}\right)^2 + \left(\chi_{Ez} + \Sigma\, \Delta\chi_{Pz}\right)^2}}{M_{Pr}\left[N_V\right] / \left(EI_r\right)} \qquad (19)$$

where $\chi_{max,r}$ and $\chi_{E,r}$ represent the maximum and yielding curvatures, respectively, in the radial direction. Plastic curvatures at each step of the analysis (i.e. $\Delta\chi_{Py}$ and $\Delta\chi_{Pz}$) are accumulated and added to the yielding curvatures at the current step (i.e. χ_{Ey} and χ_{Ez}). Finally, the plastic moment (M_{Pr}) is calculated considering the axial force due to the gravity loads only (N_V) and referring to the radial direction identified by $\chi_{max,r}$.

In order to compare the response of the test structures designed for the horizontal seismic loads only (i.e. B6H and B12H structures) with that of the analogous structures designed also for the vertical seismic loads (i.e. B6HV and B12HV structures), the mean values of the ductility demand of girders and columns are reported in Figures 5 and 6. The results below were obtained as an average of the maximum (local) curvature ductility demand attained at the most critical sections of the structures subjected to the selected Imperial Valley ground motions (see Table 3). The numerical investigation is carried out considering the horizontal components of motion acting alone (H), for B6H and B12H structures, or contemporaneously with the corresponding vertical component (H+V), for B6HV and B12HV structures. Moreover, the horizontal accelerogram with $PGA_{H,1}$ ($PGA_{H,2}$) is applied twice, once along the principal axis *X* (*Y*) and the other along the principal axis *Y* (*X*) of the building plan.

The curves in Figures 5a and 6a correspond to the mean ductility demand for the end sections and quarter-span sections of the interior deep girders, perpendicular to the floor slab direction shown in Figure 3a. As shown, the effects of the vertical component of ECDA, ECA#5 and ECA#7 ground motions proved to be more evident at the upper floors where bending moments due to vertical seismic loads are more important than those due to the horizontal seismic loads. More specifically, the end sections, at the top side, and quarter-span sections, at the bottom one, proved to be the more stressed sections. This kind of behaviour can be explained observing that the ductility demand at these sections, in contrast to the mid-span ones, already appears under the horizontal components of the Imperial Valley ground motions. Moreover, the bottom plastic moments of the quarter-span sections, at the upper floors, were less than or equal to those assumed at the mid-span sections. This result emphasizes the need to take into account the vertical ground motion in the design of the girders, especially at the upper storeys. Further results, omitted for the sake of brevity, highlighted that flat girders, parallel to the floor slab direction, exhibit plastic deformations at the end sections due to the horizontal components of the ground motion, but the intermediate sections are practically independent of the vertical component due to their small tributary mass.

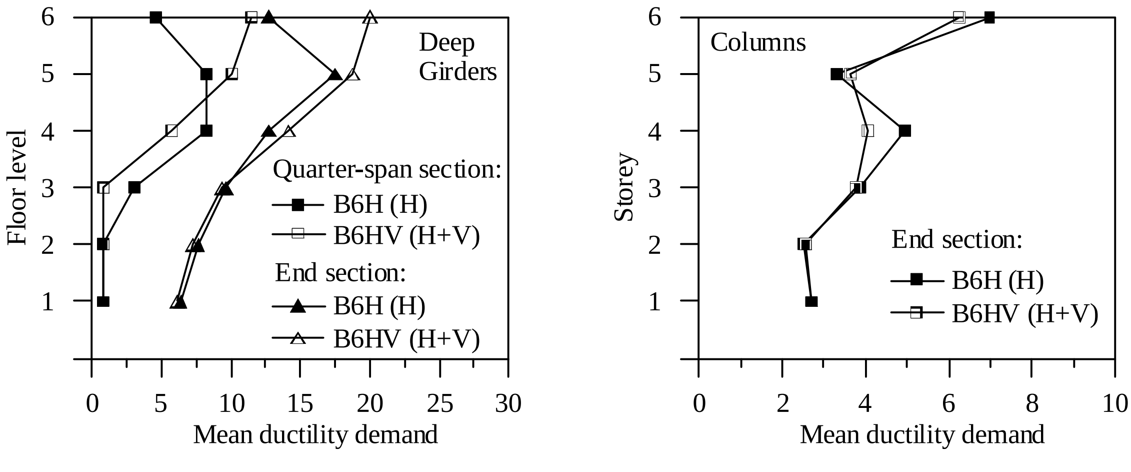

(a) (b)

Figure 5: Mean ductility demand of B6H and B6HV structures subjected, respectively, to the horizontal components (H) and horizontal and vertical components (H+V) of the Imperial Valley earthquakes.

Successively, the maximum values of the mean ductility demand at the end sections of the columns are evaluated with reference to the same cases as discussed above. As can be observed, the effects of the vertical ground motion are negligible for the B6HV structure (Figure 5b) and generally limited to the upper storeys for the B12HV structure (Figure 6b). However, note that the mean ductility demand at each storey is shown for the (central, lateral or corner) column section exhibiting the maximum value, but in many cases the section where the maximum ductility value is attained is different, when the horizontal ground motions alone (H) or in combination with the vertical ground motion (H+V) are considered. As expected, a "strong-column weak-beam" mechanism is achieved, with acceptable maximum values of the ductility demand for the columns of all the storeys.

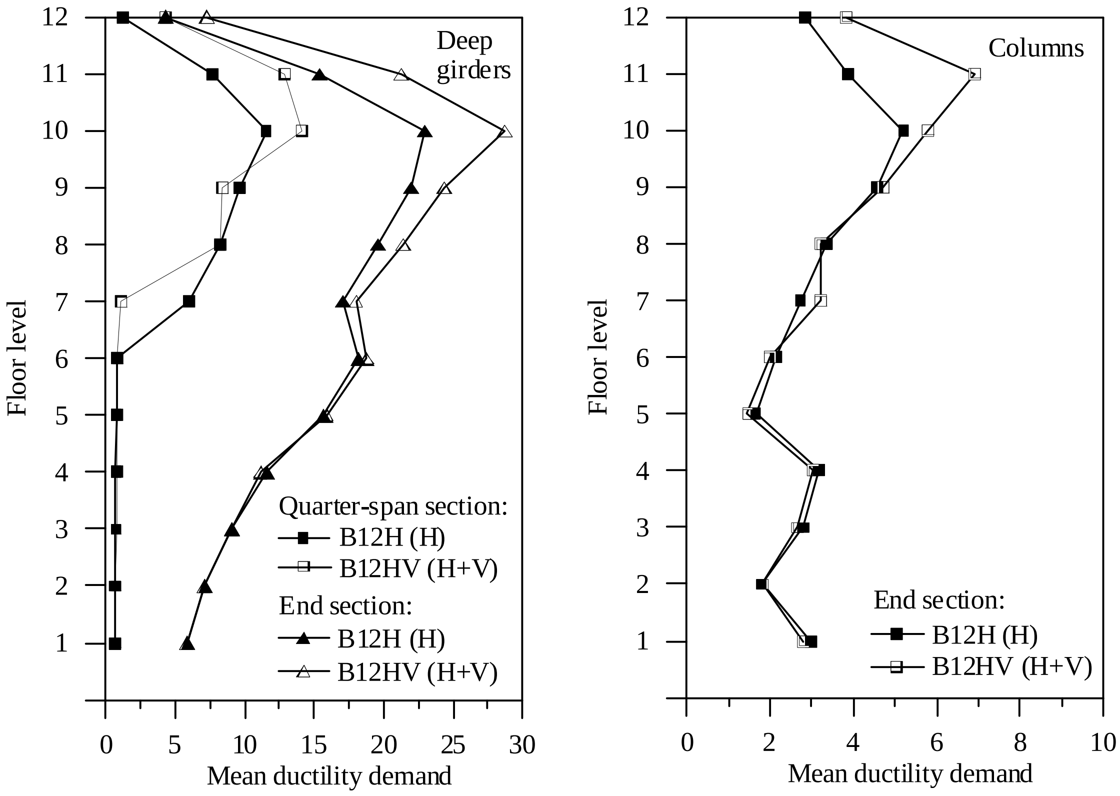

(a) (b)

Figure 6: Mean ductility demand of B12H and B12HV structures subjected, respectively, to the horizontal components (H) and horizontal and vertical components (H+V) of the Imperial Valley earthquakes.

Finally, attention was focused on the axial force attained by the columns, in order to check whether failure phenomena occur: i.e. failure under compression or tension, due to the attainment of the corresponding ultimate compressive load, N_{cu}, or tensile load, N_{tu}; brittle failure under a compressive load greater than the balanced load N_b. For this purpose, the minimum (N_{min}) and maximum (N_{max}) values attained by the axial load (assuming positive to be a compressive load) in the corner and central columns of B6H and B6HV structures subjected, respectively, to the horizontal (H) and horizontal and vertical (H+V) components of ECDA ground motion are plotted in Figure 7. Analogous curves are also plotted in Figure 8 with reference to B12H and B12HV structures subjected, respectively, to the H and H+V components of ECA#5 ground motion. As can be observed, the axial-force variation induced a rather high compressive force, which in many columns was greater than the balanced load, thus producing a reduction in both the ultimate bending moment and available ductility. It should be noted that a compressive load greater than N_b does not necessarily imply a brittle failure, because it depends on the value attained by the bending moment, which may be less than the ultimate moment corresponding to the current axial load. Nevertheless, caution is needed when the compressive load is greater than N_b. It is also useful to note that NTC08 requires that, in the case of medium ductility class, the maximum compressive load for the columns should not be greater than 65% of the corresponding ultimate load N_{cu}.

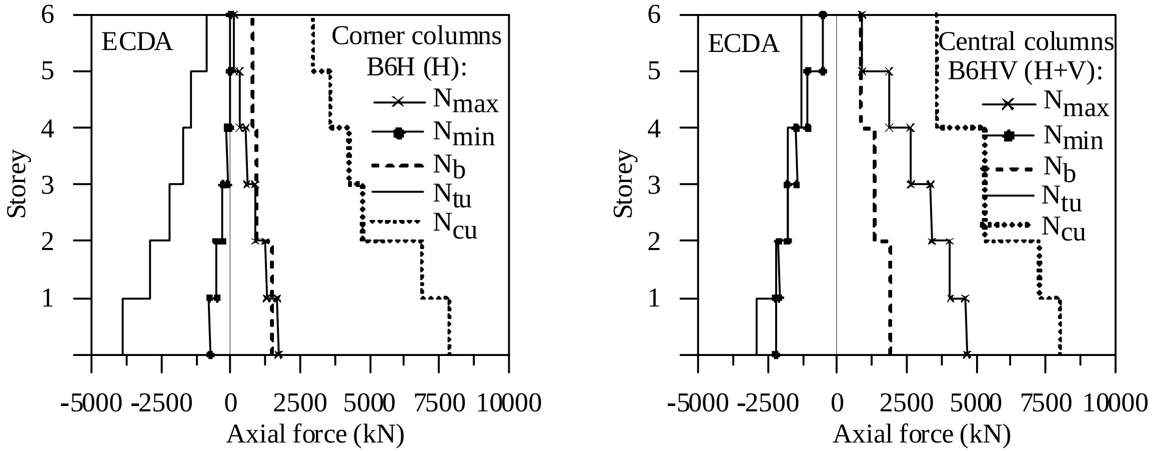

(a) (b)

Figure 7: Typical values of column axial forces for the corner and central columns of B6H and B6HV structures subjected to El Centro D.A. records.

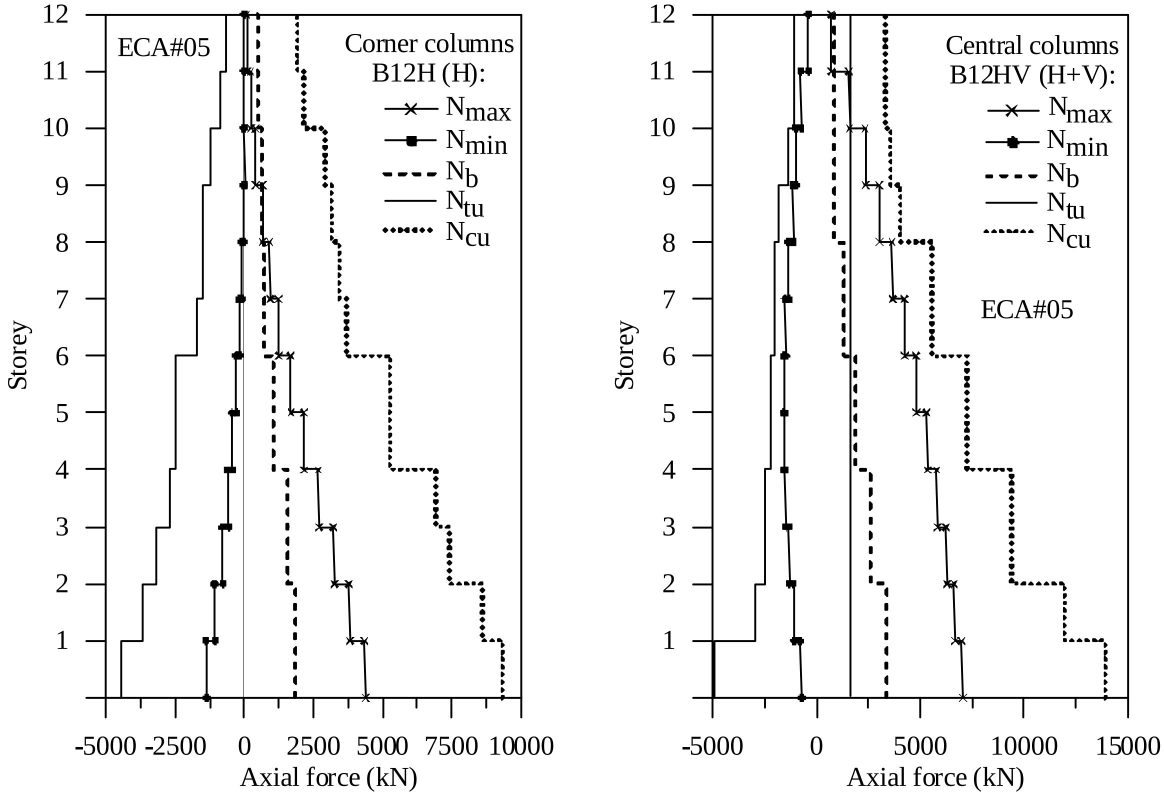

(a) (b)

Figure 8: Typical values of column axial forces for the corner and central columns of B12H and B12HV structures subjected to El Centro Array #5 records.

The overturning moment due to the horizontal components of ECDA and ECA#5 ground motions induced an evident variation of the axial load in the corner columns of B6H (Figure 7a) and B12H (Figure 8a) structures. On the other hand, for the central columns, having the greatest tributary mass (i.e. their tributary mass in a storey is about four times the analogous mass corresponding to the corner columns, respectively), the addition of the vertical ground motion produced an evident variation in the axial force giving rise even to a tensile force, which in many sections of B6HV (Figure 7b) and B12HV (Figure 8b) structures is very close to the ultimate tensile force N_{tu}.

5 CONCLUSIONS

An efficient nonlinear beam model based on the Haar–Kàrmàn principle has been proposed for the analysis of r.c. spatial frames subjected to the vertical component of near-fault ground motions. Specifically, the lumped plasticity model for a column (LPMC) includes a piecewise linearization of the bounding surface of the elastic domain corresponding to axial load-biaxial bending moment interaction. A satisfactory compromise between accuracy and computational efficiency has been attained considering 26 flat surfaces: i.e., 6 surfaces normal to the principal axes; 12 surfaces normal to the bisections of the principal planes; 8 surfaces normal to the bisections of the octants. Moreover, the lumped plasticity model for a girder (LPMG) takes into account the potential plastic hinges along the span of the girders, due to the vertical ground motion, modifying the uniaxial plastic moments of the end-sections depending on the top and bottom plastic moments of selected critical intermediate sections. LPMG allowed a reduction in the computational effort due to the sub-discretization of the girders by about 2/3.

Afterwards, a computer code was developed on the basis of the proposed LPMC and LPMG, in order to investigate the effects of the vertical component of near-fault ground motions on the inelastic behavior of r.c. spatial frames. To this end, six- and twelve-storey r.c. framed buildings were designed assuming, besides the gravity loads, the horizontal seismic loads acting alone or in combination with the vertical ones. In order to emphasize the effects due to the vertical component, the numerical investigation was carried out with reference to cases in which the considered horizontal components of the motion acted alone or contemporaneously with the corresponding vertical component. The numerical results showed that the frame members should be designed to also take into account the vertical ground motion. Specifically, the ductility demand increased in many end sections and quarter-span sections of deep girders, while for flat girders it did not depend on the vertical component due to their small tributary mass. As regards the columns, a large variation in the axial force occurred producing even tension (close to the ultimate tensile force) and high compressive forces (larger than the balanced force) which are more evident, respectively, at the upper and lower storeys of the test structures.

ACKNOWLEDGEMENTS

The present work was financed by the Italian Ministry of Education, University and Research.

REFERENCES

[1] A.J. Papazoglou, A.S. Elnashai, Analytical and Field Evidence of the Damaging Effect of Vertical Earthquake Ground Motion. *Earthquake Engineering and Structural Dynamics*, **25**, 1109-1137, 1996.

[2] S.J. Kim, A.S. Elnashai, Seismic assessment of rc structures considering vertical ground motion. University of Illinois at Urbana-Champaign, USA, *MAE Center Report* No. 08-03, 2008.

[3] Technical Regulations for Constructions. *Italian Ministry of the Infrastructures.*2008.

[4] Eurocode 8. Design of structures for earthquake resistance - part 1: general rules, seismic actions and rules for buildings. *UNI ENV 1998-1*, 2003.

[5] S. Li, L.-L. Xie, Progress and trend on near-field problems in civil engineering. *Acta Seismologica Sinica,* 20(1):105-114, 2007.

[6] L. Di Sarno, A.S. Elnashai, G. Manfredi, Effects of vertical earthquake ground motions on rc structures. *14th European Conference on Earthquake Engineering*, Skopije, Republic of Macedonia, CD-ROM, paper No. 289, 2010.

[7] R. Alaghebandian, S. Otani, H. Shiohara, Effect of distributed mass on earthquake response of reinforced concrete frames. *12th World Conference on Earthquake Engineering, Auckland, New Zealand,* paper No. 2230, 2000.

[8] F. Mazza, A. Vulcano, Nonlinear dynamic response of rc framed structures subjected to near-source ground motions: effects of the vertical component. *Fédération Internationale du Béton (FIB), 2nd International Congress*, paper No. 8-24, 2006.

[9] FIB. Practitioners' guide to finite element modeling of reinforced concrete structures. State-of-art report. *FIB Bulletin* No. 45, 2008.

[10] F. Mazza, M. Mazza, Modeling of spatial frames to study the effects of the vertical component of near-fault earthquakes. *14th European Conference on Earthquake Engineering*, Skopije, Republic of Macedonia, paper No. 293, 2010.

[11] F. Mazza, M. Mazza, Nonlinear analysis of spatial framed structures by a lumped plasticity model based on the Haar–Kàrmàn principle. *Computational Mechanics*, **45**, 647-664, 2010.

[12] G.M. Sfakianakis, Biaxial bending with axial force of reinforced, composite and repaired concrete sections of arbitrary shape by fiber model and computer graphics. *Advances in Engineering Software*, **33**, 227-242, 2002.

[13] M. Malena, R. Casciaro, Finite Element Shakedown Analysis of Reinforced Concrete 3D Frames. *Computers and Structures*, **86**, 1176-1188, 2008.

[14] Pacific Earthquake Engineering Research Center database. http://peer.berkeley.edu/smcat/search.html.

COMPDYN 2011
ECCOMAS Thematic Conference on
Computational Methods in Structural Dynamics and Earthquake Engineering
M. Papadrakakis, M. Fragiadakis, V. Plevris (eds.)
Corfu, Greece, 25-28 May 2011

SEARCHING FOR LOCAL CONTACT CONSTRAINTS BY THE QUASI-NEWTON METHODS IN THE FINITE ELEMENT PROCEDURES FOR CONTACT-IMPACT PROBLEMS

Dušan Gabriel[1], **Ján Kopačka**[1], **Jiří Plešek**[1] **and Miran Ulbin**[2]

[1]Institute of Thermomechanics
Academy of Sciences of the Czech Republic
Dolejškova 5
182 00 Praha 8, Czech Republic
e-mail: {gabriel,kopacka,plesek}@it.cas.cz

[2] Faculty of Mechanical Engineering
University of Maribor
Smetanova 17
2000 Maribor, Slovenia
e-mail: ulbin@uni-mb.si

Keywords: FEM, Contact-Impact Problems, Local Contact Search, Quasi-Newton Methods

Abstract. *The essential part of the solution of a contact problem in the finite element method is to locate probable contact areas reliably and efficiently. Most contact searching algorithms are based on the definition of master and slave contact surfaces, when the slave nodes/integration points are checked on against master segments for penetration. The present paper deals with the local search problem which comprises the calculation of the exact position of the slave node/integration point with respect to a given master segment. Since the analytical solution for finding the distance does not exist for a general quadrilateral contact segment, the iterative numerical procedure is solved. Several methods for the solution of non-linear algebraic systems are tested: the Newton-Raphson procedure, the least square projection, the steepest descent method, Broydens method, BFGS method, DFP method and the simplex method. The effectiveness of methods is tested by means of a contact-impact problem of two colliding thick plates, for which analytical solution is available.*

1 INTRODUCTION

The key issue in the numerical treatment of contact problem in the finite element method is to locate contact areas reliably and efficiently. Most contact algorithms are based on the master-slave concept, when the position of slave node is checked on against the master segment for penetration. The contact detection can be usually divided into two phases: the global search for finite elements/segments which actually intersect and the local search for projections of slave points (nodes/quadrature points) onto master surfaces.

An overview of global search algorithms might be found in Refs. [1, 2]. When the global search is successfully done, the local search is performed. There are several possibilities to deal with this problem.

The most frequently used approach for local contact searching is described in Ref. [3]. The contact point is defined on the master segment as the point closest to the slave point. Its parametric coordinates are calculated by solving the minimization problem. There is an analytical solution for linear triangular segments, however, a bilinear quadrilateral as well as higher order elements have to be solved numerically. The Newton-Raphson method is applied for solving the simple non-linear equations.

In order to increase efficiency, in Ref. [4] each quadrilateral segment is broken into four triangles with their common vertex at the centre of the master segment. The contact point is calculated by determining which triangle is closest to the slave node and projecting the slave node onto it. Although efficiency of this approach is undeniable, it is not adequate for distorted elements which can occur within post-buckling calculations [5].

For node-to-segment contact design the algorithm based on the definition of a mesh normal was proposed in Ref. [6]. The mesh normal vector of a node is defined as the average normal vector for all surfaces which adjacent to the node. The inside-outside algorithm [7] employs this vector to determine whether the projection of a node is located inside or outside of a surface. Since no iterations are involved the algorithm is very fast. However, a lack of continuity on the boundary of surfaces called the deadzone problem was observed. In order to overcome this drawback, the free-form-surface (FFS) algorithm was proposed in Ref. [2]. The contact area is approximated with the FFS patch, which ensures smoothness. The accuracy can be increased by subdividing of the surface patch.

In this paper, we focused on the solution of a minimization problem between slave integration (quadrature) point and the master segment of the three-dimensional quadratic serendipity element. The solution of resulting non-linear equations is not trivial, especially when higher order finite elements are taken into account. First, the formulation of a minimization problem is presented in Section 2. Various numerical methods for the solution of this problem are presented in Section 3. First, the convergence difficulties of the Newton-Raphson method are analyzed. Next, the least square projection constructed as the linearized Newton-Raphson scheme [5] is mentioned. Then, the line search strategy is presented [8], utilized in the steepest descent method, Broyden's method, BFGS and DFP method [9]. The last three methods belong to an alternative approach to the Newton-Raphson method, known as quasi-Newton methods. Finally, the Nelder-Mead simplex method [10] is discussed as an interesting alternative to preceding methods. The effectiveness of methods is compared in Section 3.9, followed by the numerical example of the longitudinal impact of two thick plates in Section 4.

2 FORMULATION OF THE MINIMIZATION PROBLEM

Let us consider the slave quadrature point $\mathbf{y}_s \in \mathbb{E}^3$ and the master segment γ_c. The aim of the local contact search is to calculate the parametric coordinates $\xi_1, \xi_2 \in [-1, 1]$ corresponding to projection $\bar{\mathbf{y}}\left(\xi_1, \xi_2\right) \in \mathbf{E^3}$ of the quadrature point $\mathbf{y}_s$ (see Fig. 1).

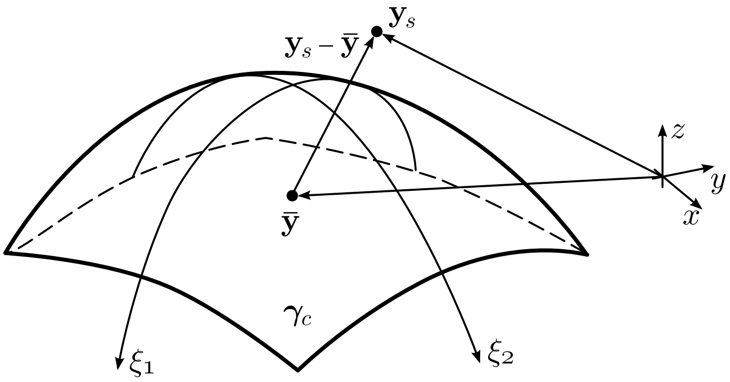

Figure 1: Formulation of the minimization problem.

Such a point has to satisfy

$$\bar{\mathbf{y}} = \min_{\mathbf{y} \in \gamma_c} \left\{ (\mathbf{y}_s - \mathbf{y}) \cdot (\mathbf{y}_s - \mathbf{y}) \right\} \tag{1}$$

where the minimization of the inner product on $\mathbb{E}^3$ instead of more natural Euclidean norm has been used. Hence, the minimized function is defined as

$$f = (\mathbf{y}_s - \mathbf{y}) \cdot (\mathbf{y}_s - \mathbf{y}) \tag{2}$$

The necessary condition for local extremum is

$$\begin{aligned} (\mathbf{y}_s - \mathbf{y}) \cdot \frac{\partial \mathbf{y}}{\partial \xi_1} &= 0 \\ (\mathbf{y}_s - \mathbf{y}) \cdot \frac{\partial \mathbf{y}}{\partial \xi_2} &= 0 \end{aligned} \tag{3}$$

The master segment γ_c is parametrized by

$$\mathbf{y}\left(\xi_1, \xi_2\right) = \sum_{i=1}^{n} N_i\left(\xi_1, \xi_2\right) \mathbf{Y}_i \tag{4}$$

where $N_i\left(\xi_1, \xi_2\right) : \mathbb{R} \times \mathbb{R} \rightarrow \mathbb{R}$ are the shape functions, n is the number of nodes and $\mathbf{Y}_i \in \mathbb{E}^3$ are the global coordinates of nodes. Note that the partial derivations are constant and Eqn. (3) is system of linear equations for linear triangular segments. If higher order elements are taken into account, Eqn. (3) results in the system of non-linear algebraic equations. The inequality constraints $\left|\xi_1\right|, \left|\xi_2\right| \leq 1$ for isoparametric segment γ_c are not explicitly imposed. The solution of the unconstrained problem lying outside the permissible range indicates that the integration point does not penetrate onto the master segment. Therefore, methods for unconstrained optimization can be employed [8, 9].

3 METHODS FOR UNCONSTRAINED OPTIMIZATION

For the purpose of this section, some notation will be introduced. First, the vector of the isoparametric coordinates is defined as

$$\mathbf{x}^k = \left\{ \begin{array}{c} \xi_1^k \\ \xi_2^k \end{array} \right\} \tag{5}$$

where the superscript k is the iteration counter. Then, the gradient of the minimized function is denoted by

$$\nabla f^k = \left\{ \begin{array}{c} (\mathbf{y}_s - \mathbf{y}) \cdot \dfrac{\partial \mathbf{y}}{\partial \xi_1} \\ \\ (\mathbf{y}_s - \mathbf{y}) \cdot \dfrac{\partial \mathbf{y}}{\partial \xi_2} \end{array} \right\} \tag{6}$$

and the Hessian matrix of second partial derivations is

$$\mathbf{H}^k = \left[\begin{array}{cc} \dfrac{\partial^2 f^k}{\partial \xi_1^2} & \dfrac{\partial^2 f^k}{\partial \xi_1 \partial \xi_2} \\ \\ \dfrac{\partial^2 f^k}{\partial \xi_1 \partial \xi_2} & \dfrac{\partial^2 f^k}{\partial \xi_2^2} \end{array} \right] \tag{7}$$

3.1 Newton-Raphson method

The numerical scheme of the Newton-Raphsons method is based on the first-order Taylor's series expansion of (3) about $\mathbf{x}^k$. The numerical scheme can be written in the form

$$\mathbf{x}^{k+1} = \mathbf{x}^k - \left(\mathbf{H}^k\right)^{-1} \cdot \nabla f^k \tag{8}$$

Generally, there are two constructions of the Newton-Raphson method. First, the method can be thought as the root-finding algorithm of the residuals (3). The matrix $\mathbf{H}^k$ is considered as the tangent matrix and the point $\mathbf{x}^k + 1$ is understood as the intersection of hyperplanes with constraint $f\left(\mathbf{x}^k\right) = 0$. Second, the Newton-Raphson is taken as an quadratic interpolation in point $\mathbf{x}^k$

$$Q = \frac{1}{2}\left(\mathbf{H}^k \cdot \Delta\mathbf{x}^k\right) \cdot \Delta\mathbf{x}^k + \nabla f^k \cdot \Delta\mathbf{x}^k + f^k, \qquad \Delta\mathbf{x}^k = \mathbf{x}^{k+1} - \mathbf{x}^k \tag{9}$$

Then, new iteration $\mathbf{x}^{k+1}$ is minimizer of this quadratic function

$$\mathbf{H}^k \cdot \Delta\mathbf{x}^k + \nabla f^k = 0 \tag{10}$$

Indeed, for convex functions the Newton-Raphson produces only positive definite matrices $\mathbf{H}^k$, for which the quadratic function (9) is paraboloid. Minimization of such interpolation embodies quadratic convergence [8]. On the other hand, for general non-linear functions the positive definiteness of $\mathbf{H}^k$ cannot be guaranteed. In case of indefinite Hessian matrix, next iteration $\mathbf{x}^k$ could bounce, because hyperbolic paraboloid, which represents indefinite matrix, could have the minimimum (saddle point) far from $\mathbf{x}^{k+1}$. Consequently, the solution could converge to another local minimum or even diverge. The necessary condition for the convergence of the Newton-Raphson method is positive definiteness of the Hessian matrix $\mathbf{H}^k$. The rigorous proof can be found in [8]. It should be pointed out that the convergence property of the Newton-Raphson iteration is difficult to achieve since the Hessian matrix of the distance function (2) to be minimized is not positive definite in general. Therefore, several methods will be discussed in the following sections.

3.2 Least squares projection

Whereas the Newton-Raphson linearizes the minimized function (2), the least squares projection linearizes the master contact segment (4)

$$\mathbf{y} = \mathbf{y}^k + \left.\frac{\partial \mathbf{y}}{\partial \mathbf{x}}\right|_{\mathbf{x}^k} \cdot \Delta \mathbf{x}^k \tag{11}$$

For given point $\mathbf{x}^k$ the necessary condition for local extremum (3) becomes linear

$$\left(\mathbf{y}_s - \mathbf{y}^k + \left.\frac{\partial \mathbf{y}}{\partial \mathbf{x}}\right|_{\mathbf{x}^k} \cdot \Delta \mathbf{x}^k\right) \cdot \left.\frac{\partial \mathbf{y}}{\partial \mathbf{x}}\right|_{\mathbf{x}^k} = 0 \tag{12}$$

By rearranging

$$\left.\frac{\partial \mathbf{y}}{\partial \mathbf{x}}\right|_{\mathbf{x}^k} \cdot \left.\frac{\partial \mathbf{y}}{\partial \mathbf{x}}\right|_{\mathbf{x}^k} \cdot \Delta \mathbf{x}^k = - \left.\frac{\partial \mathbf{y}}{\partial \mathbf{x}}\right|_{\mathbf{x}^k} \cdot \left(\mathbf{y}_s - \mathbf{y}^k\right) \tag{13}$$

and introducing the matrix notation, we obtain

$$\left\{ \begin{array}{c} \dfrac{\partial \mathbf{y}^k}{\partial \xi_1} \\ \\ \dfrac{\partial \mathbf{y}^k}{\partial \xi_2} \end{array} \right\} \cdot \left\{ \begin{array}{cc} \dfrac{\partial \mathbf{y}^k}{\partial \xi_1} & \dfrac{\partial \mathbf{y}^k}{\partial \xi_2} \end{array} \right\} \cdot \left\{ \begin{array}{c} \Delta \xi_1^k \\ \\ \Delta \xi_2^k \end{array} \right\} = - \left\{ \begin{array}{c} \dfrac{\partial \mathbf{y}^k}{\partial \xi_1} \\ \\ \dfrac{\partial \mathbf{y}^k}{\partial \xi_2} \end{array} \right\} \cdot \left\{ \mathbf{y}_s - \mathbf{y}^k \right\} \tag{14}$$

Benson et al. [5] recommends three iterations of this method to generate an initial guess for the Newton-Raphson. We try to use the least squares projection as fully-fledged method. The global convergence was attained for arbitrary initial guess [11]. Nevertheless, the global minimum lies outside the permissible range in most cases and therefore this method is not feasible for local search.

3.3 Line search strategy

In each iteration of a line search method a search direction is computed $\mathbf{p}^k \in \mathbb{R}^n$ and then decided how far to move along that direction. The iteration is given by

$$\mathbf{x}^{k+1} = \mathbf{x}^k + t^k \mathbf{p}^k \tag{15}$$

where the positive scalar $t^k \in \mathbb{R}$ is called the step length. The success of a line search method depends on the effective choices of both the direction $\mathbf{p}^k$ and the step length parameter t^k. Most line-search algorithms require $\mathbf{p}^k$ to be a descent direction for which $\mathbf{p}^k \cdot \nabla f^k < 0$. The search direction often has the form

$$\mathbf{p}^k = -\mathbf{D}^k \cdot \nabla f^k \tag{16}$$

where $\mathbf{D}^k \in \mathbb{R}^{n,n}$ is a suitable matrix. Let us consider that $\mathbf{D}^k$ is positive definite. Multiply Eqn. (16) by ∇f^k yields

$$\mathbf{p}^k \cdot \nabla f^k = - \left(\mathbf{D}^k \cdot \nabla f^k\right) \cdot \nabla f^k < 0 \tag{17}$$

Thus, the positive definiteness of $\mathbf{D}^k$ guarantee a descent direction of $\mathbf{p}^k$. The methods of computation of the matrix $\mathbf{D}^k$ will be discussed in following sections. Note that for $\mathbf{D}^k = \left(\mathbf{H}^k\right)^{-1}$ and $t^k = 1$ one can obtain the Newton-Raphson method. We now turn attention to the choice of the step length parameter t^k. Its computation is based on the restriction of the minimized function $f(\mathbf{x})$ to the ray from a point $\mathbf{x}^k$ in the search direction $\mathbf{p}^k$

$$\varphi(t) = f\left(\mathbf{x}^k + t\mathbf{p}^k\right), \quad t > 0 \tag{18}$$

Apparently, the exact minimization of this function is computationally expensive. In order to find even a local minimizer of $\varphi(t)$ it generally requires too many evaluations of the minimized function $f(\mathbf{x})$. In Ref. [8], more sophisticated strategies are mentioned to perform an inexact line search to identify a step length that achieves reductions of $f(\mathbf{x})$. In proposed algorithm the step length is computed analytically by the one-dimensional minimizer of the quadratic function along the direction $\mathbf{x}^k + t\mathbf{p}^k$

$$t^k = -\frac{\nabla f^k \cdot \mathbf{p}^k}{\left(\mathbf{p}^k \cdot \mathbf{H}^k\right) \cdot \mathbf{p}^k} \tag{19}$$

3.4 Steepest descent method

The steepest descent method is the simplest line search method, for which $\mathbf{D}^k$ is the identity matrix and so the search direction $\mathbf{p}^k$ is the negative gradient. Thus, the iteration scheme is

$$\mathbf{x}^{k+1} = \mathbf{x}^k - t^k \nabla f^k \tag{20}$$

Since the Hessian matrix is not employed the steepest descent method does not converge to the saddle points.

3.5 Broyden's method

The Broyden's method is a generalization of the 1D secant method to multiple dimensions as well as the Newton-Raphson is a generalization of the Newton's tangent method. The Broyden's sequence $\left\{\mathbf{x}^k\right\}$ is defined by the recurrent formula [9]

$$\mathbf{x}^{k+1} = \mathbf{x}^k - t^k \left(\mathbf{D}^k\right)^{-1} \nabla f^k \tag{21}$$

where the update of $\mathbf{D}^k$ is computed by

$$\mathbf{D}^{k+1} = \mathbf{D}^k + \frac{\left(\nabla f^{k+1} - \nabla f^k\right) - \mathbf{D}^k\left(\mathbf{x}^{k+1} - \mathbf{x}^k\right)}{\left(\mathbf{x}^{k+1} - \mathbf{x}^k\right) \cdot \left(\mathbf{x}^{k+1} - \mathbf{x}^k\right)} \otimes \left(\mathbf{x}^{k+1} - \mathbf{x}^k\right) \tag{22}$$

3.6 BFGS method

A very effective minimization method is the Broyden-Fletcher-Goldfarb-Shenno (BFGS) method. This method requires no evaluation of the Hessian matrix. Moreover, the BFGS method was developed so that the search direction $\mathbf{p}^k$ has always a descent direction. Thus, the positive definiteness of the matrix $\mathbf{D}^k$ is guaranteed. The BFGS iteration scheme is defined by the recurrence [9]

$$\mathbf{x}^{k+1} = \mathbf{x}^k - t^k \left(\mathbf{D}^k\right)^{-1} \nabla f^k \tag{23}$$

The update of $\mathbf{D}^k$ is computed by

$$\mathbf{D}^{k+1} = \mathbf{D}^k + \frac{\mathbf{y}^k \otimes \mathbf{y}^k}{\mathbf{d}^k \cdot \mathbf{y}^k} - \frac{\mathbf{D}^k\mathbf{d}^k \otimes \mathbf{D}^k\mathbf{d}^k}{\mathbf{d}^k \cdot \mathbf{D}^k\mathbf{d}^k} \tag{24}$$

where $\mathbf{d}^k = \mathbf{x}^{k+1} - \mathbf{x}^k$ and $\mathbf{y}^k = \nabla f^{k+1} - \nabla f^k$.

3.7 DFP method

Another famous method is the Davidon-Fletcher-Powell (DFP) method. Instead of updating the matrices $\mathbf{D}^k$

$$\mathbf{x}^{k+1} = \mathbf{x}^k - t^k \left(\mathbf{D}^k\right)^{-1} \nabla f^k \tag{25}$$

as in the BFGS method, the DFP method updates their inverses and retains the features of a secant method. The DFP method sequence $\left\{\mathbf{x}^k\right\}$ is defined by the recurrent formula

$$\mathbf{x}^{k+1} = \mathbf{x}^k - t^k \mathbf{D}^k \nabla f^k \tag{26}$$

The update of $\mathbf{D}^k$ is computed by

$$\mathbf{D}^{k+1} = \mathbf{D}^k + \frac{\mathbf{d}^k \otimes \mathbf{d}^k}{\mathbf{y}^k \cdot \mathbf{d}^k} - \frac{\mathbf{D}^k\mathbf{y}^k \otimes \mathbf{D}^k\mathbf{y}^k}{\mathbf{y}^k \cdot \mathbf{D}^k\mathbf{y}^k} \tag{27}$$

where $\mathbf{d}^k = \mathbf{x}^{k+1} - \mathbf{x}^k$, $\mathbf{y}^k = \nabla f^{k+1} - \nabla f^k$.

3.8 Nelder-Mead simplex method

In geometry context, the simplex is a generalization of the motion of a triangle or tetrahedron to arbitrary dimension. Specifically, an n-simplex is an n-dimensional polytope with $n+1$ vertices whereas the distance between each of them is equal. The examples of such a simplex is shown in Fig. 2. The minimized function is evaluated in all vertices of simplex. The algorithm of the simplex method is based on the three rules [10]. The first rule says that the vertex with the maximum value is released. Alternatively, it is replaced by new one according to Fig. 3. In case that the value in new vertex is maximum again, the second rule (see Fig. 4) holds. It is not allowed to return the vertex back in the subsequent iteration due to runaway loop. Instead, the

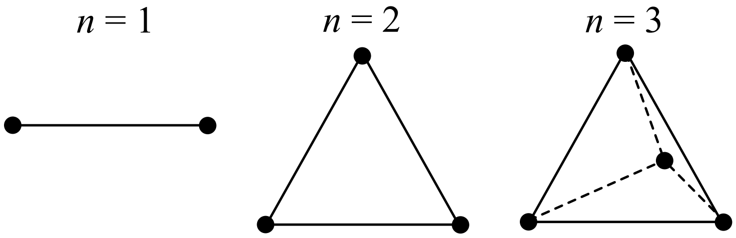

Figure 2: The examples of simplex.

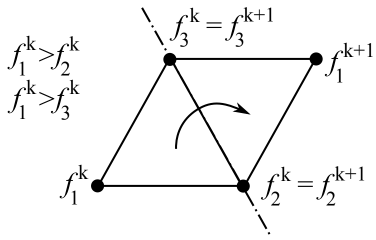

Figure 3: First rule of the simplex method.

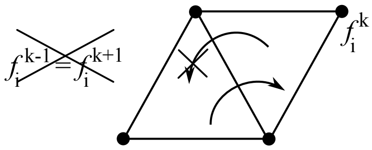

Figure 4: Second rule of the simplex method.

vertex with second highest value is released. Finally, the third rule treats the case when one of the vertices has still the same position. This situation indicates that the simplex rotates above a local extremum. Therefore, the simplex edge length a is halved after m iterations. The number of iteration m can be estimated by the empiric formula

$$m = 1.65n + 0.05n^2 \tag{28}$$

where n is the number of dimensions. Fig. 5 shows two-dimensional case ($n = 2$).

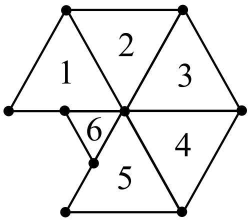

Figure 5: Third rule of the simplex method.

3.9 Comparison of methods for local contact search

A numerical test was performed for three different positions of slave point with respect to the deformed master segment topology. The first estimation was gained by one iteration of the least squares projection. Then, the origin of isoparametric coordinates was taken. Finally, the corners of the master segment were tested as the initial guesses. The results are summarized in Tab. 1, where the number of iterations n and normalized time t are shown. The normalized time is defined as the CPU time related to CPU time for the Newton-Raphson for the initial guess (0.83,-0.62). The criterion of convergence was set $\left\|\mathbf{x}^k - \mathbf{x}^{k-1}\right\| \leq 10^{-10}$. Note that the superscript *sp* denotes the solutions which converged to a saddle point.

	Initial guess											
	(0.83,-0.62)		(0,0)		(-1,-1)		(1,-1)		(1,1)		(-1,1)	
	n	t	n	t	n	t	n	t	n	t	n	t
N-R	28	1.00	5	0.20	12	0.45	17^{sp}	0.61	5^{sp}	0.20	12^{sp}	0.44
LSP	133	0.44	134	0.45	137	0.46	124	0.42	116	0.39	134	0.46
SD	51	4.50	71	6.10	28	2.52	14	1.22	29	2.60	1543	142.97
Broyden	9	0.48	11	0.58	10	0.51	9	0.46	11^{sp}	0.55	14900	819.15
BFGS	8	0.37	8	0.42	8	0.41	7	0.36	9^{sp}	0.48	23	1.22
DFP	7	0.35	8	0.39	8	0.40	7	0.36	9^{sp}	0.45	26	1.28
Simplex	190	6.75	200	7.13	192	6.75	184	6.84	210	7.61	196	6.91

Table 1: n - number of iteration, t - normalized CPU time.

It clear that the best results were obtained for BFGS and DFP methods. The Broyden's as well as the steepest descent methods gave only average results. Due to facts mentioned in Section 3.2 the least squares projection was not efficient for the solution of this problem. In comparison to other methods the advantage of the Nelder-Mead simplex method is insensitivity to the convergence to saddle points. Finally, it should be pointed out that the convergence property of the Newton-Raphson iteration was difficult to achieve in general. It is illustrated by the difference between NR iterations for the first and the second initial point.

In conclusion, the most fitting turned out the conjunction of the simplex method for coarse searching and the quasi-Newton solvers BFGS or DFP for fine tuning of numerical solution. The performance of new local contact search procedure was tested by means of a contact-impact problem of two colliding thick plates. The results are presented in following Section 4.

4 LONGITUDINAL IMPACT OF THICK PLATES

The longitudinal impact of two thick plates was studied, for which the analytical solution was available [12]. Despite the problem is two-dimensional one it could be used for testing three-dimensional local contact search procedure. The plates dimensions were: thickness $2d = 5$ mm, length 2.5 mm. Young's modulus, Poisson's ratio and density, respectively, were $E = 2.1 \times 10^5$ MPa, $\nu = 0.3$, $\rho = 7800\,\mathrm{kg/m^3}$. The plates made contact with initial velocity $v_0 = 1$ m/s prescribed at time $t = 0$ s (Fig. 6).

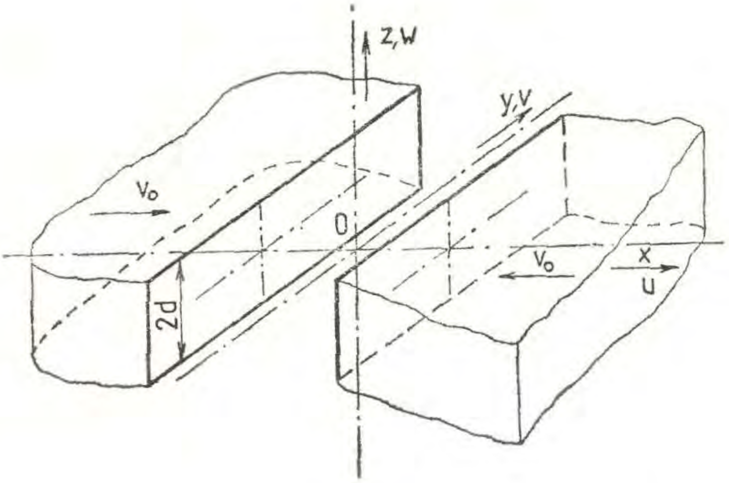

Figure 6: Longitudinal impact of two plates.

The analytical solution [12] utilizing the Laplace transform is rather complex. The distributions of displacements and stresses are cast in the form of infinite series of improper integrals which are evaluated numerically. For illustration, theoretical positions of wave fronts for a short time after impact are plotted in Fig. 7. At the instant the faces of the plates come into contact there are aroused elementary dilatation waves at all points of the contact area. The envelope of these waves is represented by a wave with a plane wave front, propagating in both directions at speed of dilatation waves c_1. From the boundary points A, D of the contact area emanates a reflected wave which continues propagating in perpendicular direction to x, y plane at speed c_1. Behind the dilatation wave the transversal waves proceeds at speed c_2. In the region bounded by plane wave fronts of the dilatation wave and by circular wave fronts of the wave starting from the points A and D, the state of stress is the same as that encountered by a longitudinal impact of half-spaces.

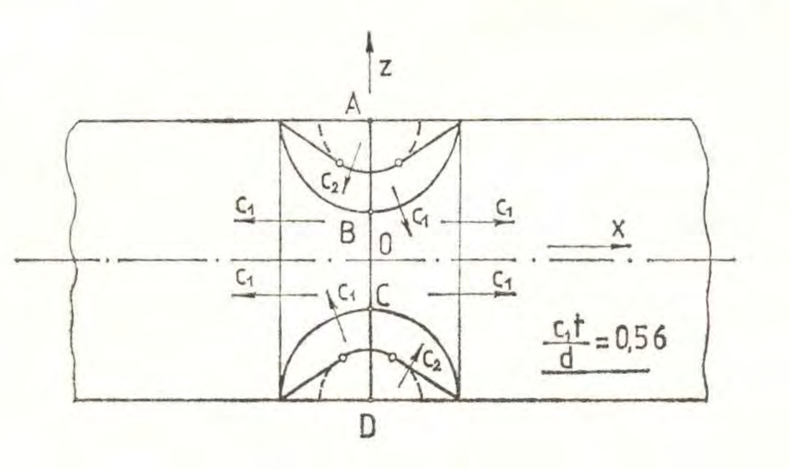

Figure 7: Theoretical position of wave fronts for $c_1 t/d = 0.56$ after [12].

In view of symmetry, only one half of the plates was discretized using 100×100 eight-node linear brick elements per each plate. For the integration of equilibrium equations, the central difference with the lumped mass matrix was employed. The time step was chosen very small corresponding to the dimensionless Courant number C$o = 0.125$.

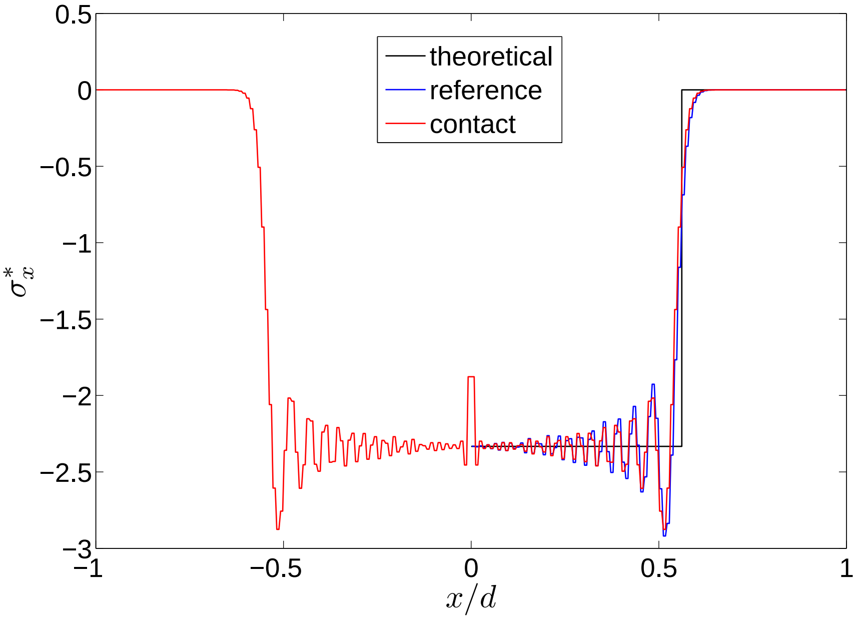

Figure 8: Longitudinal stress distribution σ_x^* along x-axis for $z/d = 0$.

The normalized longitudinal stress distribution $\sigma_x^* = \sigma_x c_1/\Lambda v_0$ (Λ is Lamé’s constant) along x-axis is drawn in Fig. 8. The results are plotted for normalized time $c_1 t/d = 0.56$ and coordinate $z/d = 0$, for which no reflections from boundaries occur. Except the contact analysis a symmetric reference calculation was performed, where the longitudinal displacements of the front-end nodes of the plate were fixed. In Fig. 8 the contact solution is plotted by red line while the solution based on the reference calculation is denoted by blue line. In addition, the theoretical solution corresponding to uniaxial strain condition is plotted by the black line in Fig. 8. It is clear that the numerical solution is influenced by dispersion errors caused by both FE spatial and time discretization. In comparions with the continuum solution the speed of the longitudinal wave is slower. This fact follows from the theoretical dispersion diagrams for the bilinear four-node and serendipity elements (e.g. Ref. [13]). Quite a good agreement between the contact and reference calculation was observed. Furthermore, it should be emphasized that the symmetry of longitudinal stress distributions was perfectly preserved in contact analysis.

The normalized transversal stress distribution $\sigma_z^* = \sigma_z c_1/\Lambda v_0$ along z-axis is drawn in Fig. 9. In contrast to graphs in previous Fig. 8 these distributions are strongly influenced by the longitudinal and transversal waves reflected from the boundary of plate. Before the arrival of these waves the solution is identical to the constant values $\sigma_z^* = -1$ corresponding to a half-space impact problem. Quite a good agreement between the contact and reference calculation versus the analytical solution was observed. It should be pointed out that the accuracy of analytical solution is strongly influenced by the number of terms included in the series of improper integrals [12]. The analytical solution plotted in this paper was derived from the summation of the first 300 terms of this series.

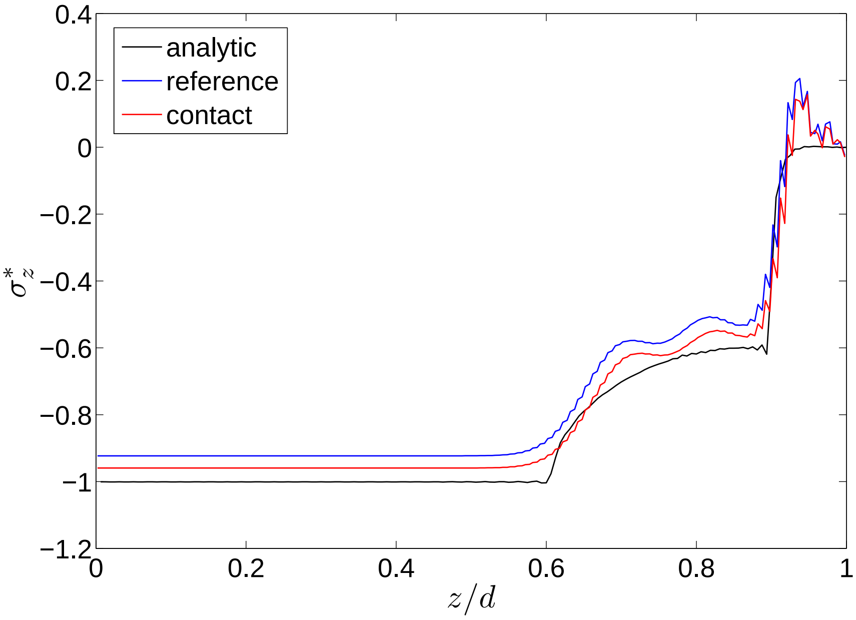

Figure 9: Transversal stress distribution σ_z^* along z-axis for $x/d = 0.4$.

ACKNOWLEDGEMENTS

This work was supported by projects ME10114, GA101/07/1471 and GA101/09/1630 in the framework of AV0Z20760514.

REFERENCES

[1] D. Gabriel, J. Plešek, M. Ulbin, Symmetry preserving algorithm for large displecement frictionless contact by the pre-discretization penalty method. *Int. J. Num. Met. Engng*, **61**, 2615–2638, 2004.

[2] F. Wang, J. Cheng, Z. Yao, FFS contact searching algorithm for dynamic finite element analysis. *Int. J. Num. Met. Engng*, **52**, 655–672, 2001.

[3] J. O. Hallquist, G.L. Goudreau, D. J. Benson, Sliding interfaces with contact-impact in large-scale Lagrangian computations. *Computer Methods in Applied Mechanics and Engineering*, **51**, 107–137, 1985.

[4] A. B. Chaudhary, K.J. Bathe, A solution method for static and dynamic analysis of three-dimensional contact problems with friction. *Computers and Structures*, **24**(6), 855–873, 1986.

[5] D. J. Benson, J. O. Hallquist, A single surface contact algorithm for the post-buckling analysis of shall structures. *Computer Methods in Applied Mechanics and Engineering*, **78**, 141–163, 1990.

[6] Y. T. Keum, E. Nakamachi, R. H. Wagoner, J. K. Lee, Compatible description of tool surfaces and FEM meshes for analysing sheet forming operations. *Int. J. Num. Met. Engng*, **30**(8), 1471–1502, 1990.

[7] S. P. Wang, E. Nakamachi, The inside-outside contact search algorithm for finite element analysis. *Int. J. Num. Met. Engng*, **40**, 3665–3685, 1997.

[8] J. Nocedal, S. J. Wright, *Numerical optimization*. Springer, 1999.

[9] A. L. Peressini, F. E. Sullivan, J. J. Uhl, Jr., *The mathematics of nonlinear programming*. Springer, 1988.

[10] J. A. Nelder, R. Mead, A simplex method for function minimization. *The Computer Journal*, **7**, 308–313, 1965.

[11] J. Kopačka, D. Gabriel, J. Plešek, Review of methods for local contact search. *3rd GACM Colloquium on Computational Mechanics (GACM 2009)*, Hannover, September 20-23, 2009.

[12] R. Brepta, F. Valeš, Longitudinal impact of bodies. *Acta Technica ČSAV*, **32**, 575–602, 1987.

[13] D. Gabriel, J. Plešek, R. Kolman, F. Valeš, M. Ulbin, Two benchmark problems for testing accuracy and stability of finite element solutions to wave propagation. M. Papadrakakis et al. eds., *COMPDYN 2009*, ECCOMAS 2009.

COMPDYN 2011
III ECCOMAS Thematic Conference on
Computational Methods in Structural Dynamics and Earthquake Engineering
M. Papadrakakis, M. Fragiadakis, V. Plevris (eds.)
Corfu, Greece, 25–28 May 2011

EFFECT OF HIGHER ORDER SHEAR DEFORMATION ON THE NONLINEAR DYNAMIC ANALYSIS OF LAMINATED COMPOSITE PLATE UNDER IN-PLANE LOADS

Dr. Haider K. Ammash

Iraq , Al-Qadissiya University , Engineering College ,Civil
Engineering

amashhk@gmail.com

Keywords: Dynamic analysis, Nonlinear analysis, Composite plate, Finite element method

Abstract: *A nonlinear finite element method is adopted for the large displacement dynamic analysis of anisotropic plates under in-plane compressive loads. The analysis is based on the two-dimensional layered approach with higher order shear deformation theory with five, seven, nine, and eleven degrees of freedom per node, nine-node Lagrangian isoparametric quadrilateral elements are used for the discretization of the laminated plates. A complete bond between the layers is assumed (no delamination occurs). A consistent mass matrix is used in the present study. Damping property is considered by using Rayleigh type damping which is linearly related to the mass and the stiffness matrices. Newmark integration method and Harmonic acceleration method are used for solving the dynamic equilibrium equations. The effects of number of layers, damping factor, and number of degree of freedom per node on the large displacement dynamic analysis are considered. From the present study, noticed that the central deflection increase with increasing the degree of freedom per node.*

1.GENERAL

Certain civil engineering structures are designed to carry their own dead load plus superimposed loads which are immovable and unvarying with time, that is, superimposed static loads. In such cases, the stress analysis involves only principles of statics. More often the design of a civil engineering structure involves not only static loads but also superimposed loads which are either moving or movable and may vary with time as in superimposed dynamic loads. In such cases, the stress analysis properly should involve principles of dynamics to determine the effect of dynamic loading. However, in many of these cases, experience has shown that the dynamic effect makes a minor contribution to the total load which must be provided for the design and therefore the dynamic effect need not be evaluated precisely. In such cases, the dynamic effect may be handled by the use of an equivalent static load, or by an impact factor or by a modification of the factor of safety(3).

There have been a number of developments which have led to growing interest in a more precise evaluation of the effects produced by the dynamic portion of the loading. Among these are the imposition of more severe live load conditions (that is, machinery and vehicles moving at high speeds), the construction of high towers and long bridges involving more severe and important wind-loading conditions, the necessity of developing blast resistant constructions, and the desire to improve earthquake resistance of constructions. These are some aspects where it may be necessary to consider more precisely the response produced by dynamic loading.

The ability of thin-walled structures to absorb the energy of dynamic transient loading has led to its utilization for several classes of important structures, such as aerodynamic structures, power plant structure, bridge structures, etc. These types of structures are designed under these loads to maintain the overall structural integrity with irreversible deformation analysis. In the present study a computational modeling is developed for the nonlinear dynamic analysis of laminated composite plates using finite element method. The dynamic equilibrium Equation and the derivation of mass and damping matrices will be presented. A Newmark direct time integration method is adopted. In [**1993**], **Kommineni** and **Kant** presented a C^o-continuous finite element formulation of a higher order displacement theory for predicting linear and geometrically nonlinear behavior in the sense of von-Karman transient response of composite and sandwich plates. **Azevedo** and **Awruch** [**1999**] presented a geometric nonlinear dynamic analysis of plates and shells using eight-node hexahedral isoparametric elements. The main features of their study are: (1) the element matrices were obtained by using reduced integrations with hourglass control; (2) an explicit Taylor-Galerkin scheme was used to carry out the dynamic analysis by solving the corresponding equations of motion in terms of velocity components. **Tao, et al.** [**2004**] presented a simple solution of the dynamic buckling of stiffened plates under impact loading. Based on large deflection theory, a discretely stiffened plate model had been used. The tangential stresses of stiffeners and their in-plane displacements were neglected.

2. LAMINATED PLATE THEORIES

A laminated plate is a series of laminas bonded together to act as an integral structural element. Thus, a laminate is not a material but instead a structural element with essential features of both material properties and geometry. The stiffness and strength of such a composite material with structural configuration are obtained from the properties of the constituent laminas, and thus the macromechanical behavior of a laminate is the main topic of this section. The lamination so described can be considered as a single layer with "rule of mixtures" representation of the interaction between the multiple laminas in a plate or shell(6).

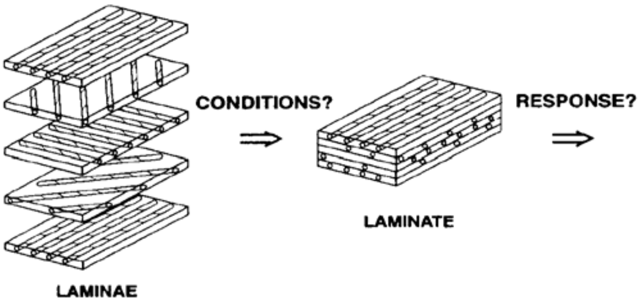

Figure (1): Laminated plate with several lamina orientations(6)

In the analysis of the laminated plates, there are two categories of theories, equivalent single layer and three dimensional elasticity theories. In the first category, the material properties of the constituent layer are smeared to form a hypothetical single layer whose properties are equivalent to through thickness integrated sum of its constituents, and this category contains classical lamination theory, first order shear deformation theory, and higher order shear deformation theory as will be given in the following section:

2.1 Classical lamination theory

Classical laminated plate theory is also often called "classical laminated theory (CLT)" which is based on the Kirchhoff-Love hypothesis for plates and shells (6). The assumptions of classical laminated plate theory are as follows:

1- The plate is thin. That is the thickness (***h***) is small compared to the other physical dimensions.
2- The displacements $u(x,y,z), v(x,y,z)$ and $w(x,y,z)$ are small compared to the plate thickness.
3- The in-plane strains $\varepsilon_x^o, \varepsilon_y^o$ and γ_{xy}^o are small compared to unity.
4- The transverse normal stress σ_z is negligible.
5- The transverse shear stresses τ_{xz}, τ_{yz} are negligible.

2.2 First order shear deformation theory (FSDT)

Timoshenko deep beam theory, which includes transverse shear deformation and rotary inertia effect, has been extended to isotropic plates by **Reissner** and **Mindlin**, and to laminate anisotropic plates by **Yang**, ***et. al***. and their theory, also called "First order shear deformation theory (FSDT)", takes into account the effect of transverse shear deformation and assume it constant through the plate thickness. Thus, a shear correction factor is used (3). The assumptions of First order shear deformation theory (FSDT) are as follows:

1- The in-plane displacements are linear functions of ***z*** (plane cross sections remaining plane after deflection).
2- The displacements $u(x,y,z), v(x,y,z)$ and $w(x,y,z)$ are small compared to the plate thickness.
3- The in-plane strains $\varepsilon_x, \varepsilon_y$ and γ_{xy} are small compared to unity.
4- The transverse normal stress σ_z is negligible.
5- The transverse shear stresses τ_{xz} , and τ_{yz} are considered to be constant through the plate thickness.

2.3 Higher order shear deformation theory (HSDT)

In general, a layered composite plate exhibits coupling between the in-plane displacements, transverse displacements and shear rotations. However, due to the low transverse shear modulus relative to the in-plane Young's modulus of each lamina, the transverse shear deformation effect is more pronounced in composite than in isotropic plates. Hence, several types of shear deformation theories have been introduced.

The higher order shear deformation theories are more efficient to represent the transverse shear deformation, through-thickness displacement and strains. The assumption of a higher order plate theory can also be used within the equivalent layer formulation $^{(6)}$.

The assumptions of higher order shear deformation are as follows:

1- The plate may be moderately thick.

2- The in-plane displacements $u(x,y,z), v(x,y,z)$ are cubic functions of z.

3- The transverse shear stresses τ_{xz} , and τ_{yz} are parabolic in z, no shear correction factor is necessary.

4- The in-plane stresses σ_x, σ_y, and τ_{xy} are cubic functions of z.

5- The normals to the mid-surface before deformation are straight, but not necessarily remain normal to it the mid-surface after deformation.

6- The transverse normal stress σ_z is negligible.

Figure (2) briefly shows, the basic difference between the classical and the first order theories with the higher order theories.

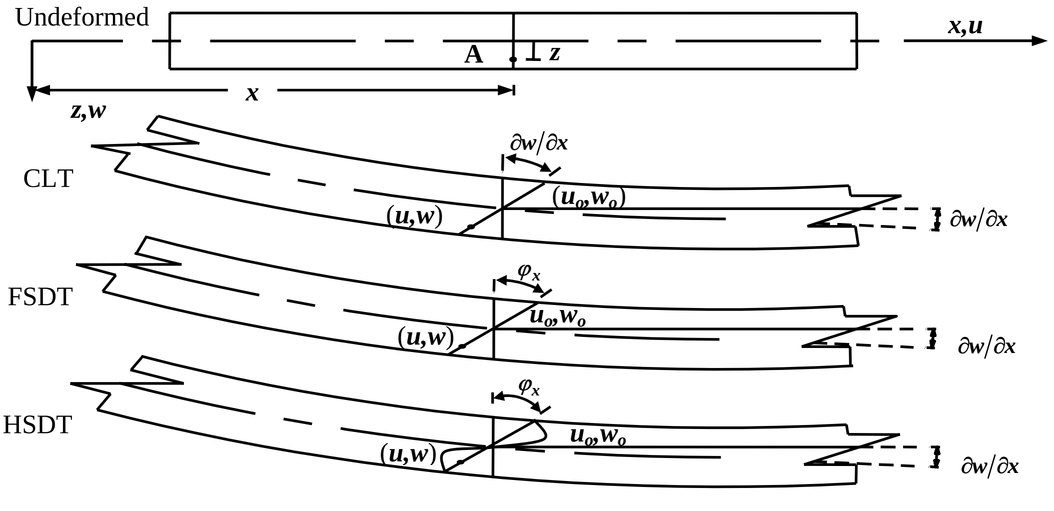

Figure (2): Kinematics of deformation of a plate in various plate theories$^{(1)}$

All the prescribed theories are considered in the present study in order to study the effect of these theories on the accuracy and the time consumption in the analysis. In the present study, three types of displacement equations were considered. Firstly the displacement representation for this theory with five degrees of freedom per node is as follows:

$$\begin{aligned} u(x,y,z,t) &= u_o(x,y,t) + z\theta_x(x,y,t) \\ v(x,y,z,t) &= v_o(x,y,t) + z\theta_y(x,y,t) \\ w(x,y,z,t) &= w_o(x,y,t) \end{aligned} \quad (1)$$

in which $\boldsymbol{t}$ denotes the time; and $\boldsymbol{u_o}$, $\boldsymbol{v_o}$, and $\boldsymbol{w_o}$ are the components of the mid-plane displacements for a generic point ($\boldsymbol{x,y,z}$) having displacements $\boldsymbol{u}$, $\boldsymbol{v}$, and $\boldsymbol{w}$ in $\boldsymbol{x}$, $\boldsymbol{y}$, and $\boldsymbol{z}$ directions, respectively. Here, θ_x and θ_y are rotations of transverse normals in the ($\boldsymbol{xz}$) and ($\boldsymbol{yz}$) planes, respectively.

The strain-displacement relations after differentiating Equation (1) are:

$$\begin{aligned}
\varepsilon_x &= \frac{\partial \boldsymbol{u}}{\partial \boldsymbol{x}} = \varepsilon_x^{o} + z\kappa_x \\
\varepsilon_y &= \frac{\partial \boldsymbol{v}}{\partial \boldsymbol{y}} = \varepsilon_y^{o} + z\kappa_y \\
\gamma_{xy} &= \frac{\partial \boldsymbol{u}}{\partial \boldsymbol{y}} + \frac{\partial \boldsymbol{v}}{\partial \boldsymbol{x}} = \gamma_{xy}^{o} + z\kappa_{xy} \\
\gamma_{xz} &= \frac{\partial \boldsymbol{u}}{\partial \boldsymbol{z}} + \frac{\partial \boldsymbol{w}}{\partial \boldsymbol{x}} = \varphi_x \\
\gamma_{yz} &= \frac{\partial \boldsymbol{v}}{\partial \boldsymbol{z}} + \frac{\partial \boldsymbol{w}}{\partial \boldsymbol{y}} = \varphi_y
\end{aligned} \tag{2}$$

where

$$\begin{aligned}
&\varepsilon_x^{o} = \frac{\partial \boldsymbol{u_o}}{\partial \boldsymbol{x}},\ \varepsilon_y^{o} = \frac{\partial \boldsymbol{v_o}}{\partial \boldsymbol{y}},\ \gamma_{xy}^{o} = \frac{\partial \boldsymbol{u_o}}{\partial \boldsymbol{y}} + \frac{\partial \boldsymbol{v_o}}{\partial \boldsymbol{x}} \\
&\kappa_x = \frac{\partial \theta_x}{\partial \boldsymbol{x}},\ \kappa_y = \frac{\partial \theta_y}{\partial \boldsymbol{y}},\ \kappa_{xy} = \frac{\partial \theta_x}{\partial \boldsymbol{y}} + \frac{\partial \theta_y}{\partial \boldsymbol{x}} \\
&\varphi_x = \theta_x + \frac{\partial \boldsymbol{w_o}}{\partial \boldsymbol{x}} \\
&\varphi_y = \theta_y + \frac{\partial \boldsymbol{w_o}}{\partial \boldsymbol{y}}
\end{aligned} \tag{3}$$

All the strains above are defined in the middle plane of the laminate and substitution these Equations into the stress-strain relations. Secondly the higher order shear deformation theory (HSDT) with seven degrees of freedom per node was considered. The strain expressions derived from the displacement field was considered by **Mallikarjuna,** and **Kant** [**1988**]**,** and by **Ali** [**2004**] with seven degrees of freedom per node as follows:

$$\begin{aligned}
\boldsymbol{u}(x,y,z,t) &= \boldsymbol{u_o}(x,y,t) + z\theta_x(x,y,t) + z^3\theta_x^*(x,y,t) \\
\boldsymbol{v}(x,y,z,t) &= \boldsymbol{v_o}(x,y,t) + z\theta_y(x,y,t) + z^3\theta_y^*(x,y,t) \\
\boldsymbol{w}(x,y,z,t) &= \boldsymbol{w_o}(x,y,t)
\end{aligned} \tag{4}$$

in which ($\boldsymbol{u}$, $\boldsymbol{v}$, $\boldsymbol{w}$, θ_x, and θ_y) are defined previously, θ_x^* and θ_y^* are the corresponding higher order terms in Taylor's series expression and also defined at the middle plane. The strain-displacement relations after differentiating Equation (4) are:

$$
\begin{aligned}
\varepsilon_x &= \frac{\partial u}{\partial x} = \varepsilon_x^o + z\kappa_x + z^3\kappa_x^* \\
\varepsilon_y &= \frac{\partial v}{\partial y} = \varepsilon_y^o + z\kappa_y + z^3\kappa_y^* \\
\gamma_{xy} &= \frac{\partial u}{\partial y} + \frac{\partial v}{\partial x} = \gamma_{xy}^o + z\kappa_{xy} + z^3\kappa_{xy}^* \\
\gamma_{xz} &= \frac{\partial u}{\partial z} + \frac{\partial w}{\partial x} = \varphi_x + z^2\varphi_x^* \\
\gamma_{yz} &= \frac{\partial v}{\partial z} + \frac{w}{\partial y} = \varphi_y + z^2\varphi_y^*
\end{aligned}
\tag{5}
$$

where the parameters ($\varepsilon_x^o, \varepsilon_y^o, \gamma_{xy}^o, \kappa_x, \kappa_y, \kappa_{xy}, \varphi_x, \varphi_y$) are defined previously.

$$
\begin{aligned}
&\kappa_x^* = \frac{\partial\theta_x^*}{\partial x},\ \kappa_y^* = \frac{\partial\theta_y^*}{\partial y},\ \kappa_{xy}^* = \frac{\partial\theta_x^*}{\partial y} + \frac{\partial\theta_y^*}{\partial x} \\
&\varphi_x^* = 3\theta_x^* \\
&\varphi_y^* = 3\theta_y^*
\end{aligned}
\tag{6}
$$

Also, all the strains above are defined in the middle-plane of the laminate and substitution these Equations into the stress-strain relations.

Thirdly, Higher order shear deformation theory (HSDT) with nine degrees of freedom per node was considered. The strain expressions derived from the displacement field were considered by [Ali, 2004] with nine degrees of freedom per node as follows:

$$
\begin{aligned}
u(x,y,z,t) &= u_o(x,y,t) + z\theta_x(x,y,t) + z^2 u_o^*(x,y,t) + z^3\theta_x^*(x,y,t) \\
v(x,y,z,t) &= v_o(x,y,t) + z\theta_y(x,y,t) + z^2 v_o^*(x,y,t) + z^3\theta_y^*(x,y,t) \\
w(x,y,z,t) &= w_o(x,y,t)
\end{aligned}
\tag{7}
$$

in which the parameters (u, v, w, θ_x, θ_y, θ_x^*, and θ_y^*) are defined previously, u_o^*, and v_o^* are the corresponding higher order terms in Taylor's series expression and they are also defined at the middle plane. The strain-displacement relations after differentiating Equation (7) are:

$$
\begin{aligned}
\varepsilon_x &= \frac{\partial u}{\partial x} = \varepsilon_x^o + z\kappa_x + z^2\varepsilon_x^{o*} + z^3\kappa_x^* \\
\varepsilon_y &= \frac{\partial v}{\partial y} = \varepsilon_y^o + z\kappa_y + z^2\varepsilon_y^{o*} + z^3\kappa_y^* \\
\gamma_{xy} &= \frac{\partial u}{\partial y} + \frac{\partial v}{\partial x} = \gamma_{xy}^o + z\kappa_{xy} + z^2\gamma_{xy}^{o*} + z^3\kappa_{xy}^* \\
\gamma_{xz} &= \frac{\partial u}{\partial z} + \frac{\partial w}{\partial x} = \varphi_x + z\gamma_{xz}^o + z^2\varphi_x^* \\
\gamma_{yz} &= \frac{\partial v}{\partial z} + \frac{\partial w}{\partial y} = \varphi_y + z\gamma_{yz}^o + z^2\varphi_y^*
\end{aligned}
\tag{8}
$$

where ($\varepsilon_x^o, \varepsilon_y^o, \gamma_{xy}^o, \kappa_x, \kappa_y, \kappa_{xy}, \kappa_x^*, \kappa_y^*, \kappa_{xy}^*, \varphi_x, \varphi_y, \varphi_x^*, \varphi_y^*$) are defined previously.

$$
\begin{aligned}
&\varepsilon_x^{o*} = \frac{\partial u_o^*}{\partial x}, \ \varepsilon_y^{o*} = \frac{\partial v_o^*}{\partial y}, \ \gamma_{xy}^{o*} = \frac{\partial u_o^*}{\partial y} + \frac{\partial v_o^*}{\partial x} \\
&\gamma_{xz}^{o*} = 2u_o^* \\
&\gamma_{yz}^{o*} = 2v_o^*
\end{aligned}
\tag{9}
$$

Also, all the strains above are defined in the middle-plane of the laminate. By substitution from Equation (8) into the stress-strain relations, after complete integration, the stress-resultant/strain relations of the laminate are as follows:

$$
\begin{bmatrix} N_x \\ N_y \\ N_{xy} \\ N_x^* \\ N_y^* \\ N_{xy}^* \\ M_x \\ M_y \\ M_{xy} \\ M_x^* \\ M_y^* \\ M_{xy}^* \end{bmatrix}
=
\begin{bmatrix}
A_{11} & A_{12} & A_{16} & D_{11} & D_{12} & D_{16} & B_{11} & B_{12} & B_{16} & E_{11} & E_{12} & E_{16} \\
A_{12} & A_{22} & A_{26} & D_{12} & D_{22} & D_{26} & B_{12} & B_{22} & B_{26} & E_{12} & E_{22} & E_{26} \\
A_{16} & A_{26} & A_{66} & D_{16} & D_{26} & D_{66} & B_{16} & B_{26} & B_{66} & E_{16} & E_{26} & E_{66} \\
D_{11} & D_{12} & D_{16} & F_{11} & F_{12} & F_{16} & E_{11} & E_{12} & E_{16} & G_{11} & G_{12} & G_{16} \\
D_{12} & D_{22} & D_{26} & F_{12} & F_{22} & F_{26} & E_{12} & E_{22} & E_{26} & G_{12} & G_{22} & G_{26} \\
D_{16} & D_{26} & D_{66} & F_{16} & F_{26} & F_{66} & E_{16} & E_{26} & E_{66} & G_{16} & G_{26} & G_{66} \\
B_{12} & B_{12} & B_{16} & E_{11} & E_{12} & E_{16} & D_{11} & D_{12} & D_{16} & F_{11} & F_{12} & F_{16} \\
B_{12} & B_{22} & B_{26} & E_{12} & E_{22} & E_{26} & D_{12} & D_{22} & D_{26} & F_{12} & F_{22} & F_{26} \\
B_{16} & B_{26} & B_{66} & E_{16} & E_{26} & E_{66} & D_{16} & D_{26} & D_{66} & F_{16} & F_{26} & F_{66} \\
E_{11} & E_{12} & E_{16} & G_{11} & G_{12} & G_{16} & F_{11} & F_{12} & F_{16} & H_{11} & H_{12} & H_{16} \\
E_{12} & E_{22} & E_{26} & G_{12} & G_{22} & G_{26} & F_{12} & F_{22} & F_{26} & H_{12} & H_{22} & H_{26} \\
E_{16} & E_{26} & E_{66} & G_{16} & G_{26} & G_{66} & F_{16} & F_{26} & F_{66} & H_{16} & H_{26} & H_{66}
\end{bmatrix}
\begin{bmatrix} \varepsilon_x^o \\ \varepsilon_y^o \\ \gamma_{xy}^o \\ \varepsilon_x^{o*} \\ \varepsilon_y^{o*} \\ \gamma_{xy}^{o*} \\ \kappa_x \\ \kappa_y \\ \kappa_{xy} \\ \kappa_x^* \\ \kappa_y^* \\ \kappa_{xy}^* \end{bmatrix}
\tag{10}
$$

and,

$$
\begin{bmatrix} Q_x \\ Q_y \\ S_x \\ S_y \\ Q_x^* \\ Q_y^* \end{bmatrix}
=
\begin{bmatrix}
A_{55} & A_{45} & B_{55} & B_{45} & D_{55} & D_{45} \\
A_{45} & A_{44} & B_{45} & B_{44} & D_{45} & D_{44} \\
B_{55} & B_{45} & D_{55} & D_{45} & E_{55} & E_{45} \\
B_{45} & B_{44} & D_{45} & D_{44} & E_{45} & E_{44} \\
D_{55} & D_{45} & E_{55} & E_{45} & F_{55} & F_{45} \\
D_{45} & D_{44} & E_{45} & E_{44} & F_{45} & F_{44}
\end{bmatrix}
\begin{bmatrix} \varphi_x \\ \varphi_y \\ \gamma_{xz}^{o*} \\ \gamma_{yz}^{o*} \\ \varphi_x^* \\ \varphi_y^* \end{bmatrix}
\tag{11}
$$

All coefficients in ***A***, ***B***, ***D***, ***E***, ***F***, ***G***, and ***H*** groups are defined as follows:

$$A_{ij} = \sum_{L=1}^{NL} Q_{ij}(h_L - h_{L-1}) \qquad i, j = 1, 2, 6 \text{ or } i, j = 4, 5 \tag{12 a}$$

$$B_{ij} = (1/2)\sum_{L=1}^{NL} Q_{ij}(h_L^2 - h_{L-1}^2) \qquad i, j = 1, 2, 6 \text{ or } i, j = 4, 5 \tag{12 b}$$

$$D_{ij} = (1/3)\sum_{L=1}^{NL} Q_{ij}(h_L^3 - h_{L-1}^3) \qquad i, j = 1, 2, 6 \text{ or } i, j = 4, 5 \tag{12 c}$$

$$E_{ij} = (1/4)\sum_{L=1}^{NL} Q_{ij}(h_L^4 - h_{L-1}^4) \qquad i, j = 1, 2, 6 \text{ or } i, j = 4, 5 \tag{12 d}$$

$$F_{ij} = (1/5)\sum_{L=1}^{NL} Q_{ij}(h_L^5 - h_{L-1}^5) \qquad i, j = 1, 2, 6 \text{ or } i, j = 4, 5 \tag{12 e}$$

$$G_{ij} = (1/6)\sum_{L=1}^{NL} Q_{ij}(h_L^6 - h_{L-1}^6) \qquad i, j = 1, 2, 6 \tag{12 f}$$

$$H_{ij} = (1/7)\sum_{L=1}^{NL} Q_{ij}(h_L^7 - h_{L-1}^7) \qquad i, j = 1, 2, 6 \tag{12 g}$$

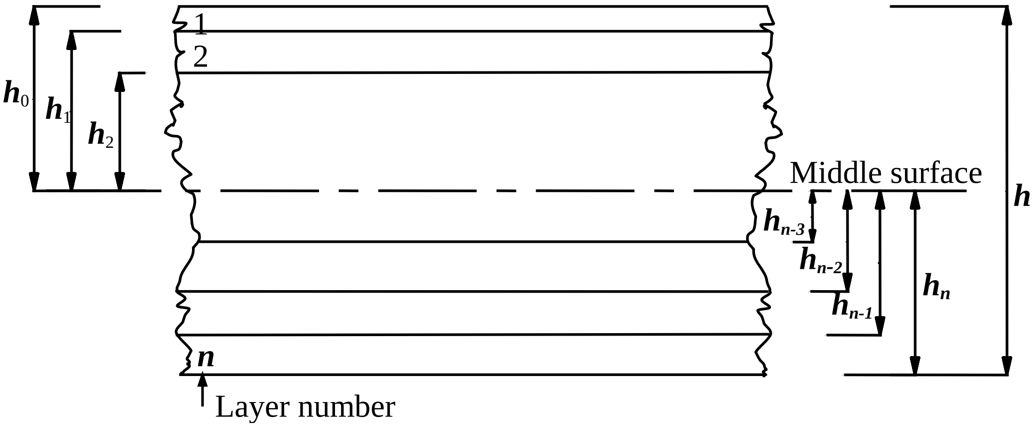

Figure (3): Geometry of an NL-layered laminate [Jones,1999]()

DYNAMIC EQUILIBRIUM EQUATION

The dynamic equilibrium Equations are obtained by using the principle of virtual work which states that for any arbitrary kinematically consistent set of displacements, the internal virtual work done by stresses through virtual strains must be equal to that done by the external forces irrespective of the material behavior as [**Cook**, **1995**](8):

$$\int_v (d\varepsilon)^T \sigma\, dv = \int_{s_t} (du)^T P_t\, ds + \int_v (du)^T (P_b - \rho\ddot{u} - C\dot{u})dv \tag{13}$$

where du is a vector of virtual displacements, $d\varepsilon$ is the vector of associated virtual strains and σ is the vector of actual stresses. The term P_t is a vector of surface tractions acting on the portion s_t of the boundary S . Vectors $P_b, \rho\ddot{u}$ and $C\dot{u}$ are the body, inertial and damping forces respectively. The symbol (˙) denotes differentiation with respect to time. ρ is the mass density and C is the damping parameter.

For the finite element representation, the displacements, velocities and accelerations $u, \dot{u}$ and $\ddot{u}$ can be defined in terms of the nodal variables $d, \dot{d}$ and $\ddot{d}$ by the expressions:

$$u = \sum_{i=1}^{m} N_i(\xi,\eta) d_i = Nd \quad , du = N\,\delta d \tag{14}$$

$$\dot{u} = \sum_{i=1}^{m} N_i(\xi,\eta)\dot{d}_i = N\dot{d} \tag{15}$$

$$\ddot{u} = \sum_{i=1}^{m} N_i(\xi,\eta)\ddot{d}_i = N\ddot{d} \tag{16}$$

where $u = \sum_{i=1}^{m} N_i(\xi,\eta) d_i = Nd$, N_i is the shape functions for i node, and m is the number of nodes.

With standard strain-nodal displacement matrix $[B]$, the virtual strain vector can be related to the nodal displacements as:

$$d\varepsilon = \sum_{i=1}^{m} [B]_i \delta d_i = [B]\delta d \tag{17}$$

Upon substitution of Equations (14-17) into Equation (13) then:

$$\delta d^T \left[[M]\ddot{d} + [C]\dot{d} + [K]d \right] = \delta d^T \{ f_e(t) \} \tag{18}$$

in which the mass matrix $[M]$, the damping matrix $[C]$, the stiffness matrix $[K]$ and the external applied vector $\{f_e(t)\}$ have the following element contributions:

$$[M_e] = \int_{Ve} N^T \rho \, N \, dV \tag{19}$$

$$[C_e] = \int_{Ve} N^T C \, N \, dV \tag{20}$$

$$[K_e] = \int_{Ve} [B]^T [D][B] dV \tag{21}$$

$$f_e(t) = \int_{se} N^T P_t \, ds + \int_{Ve} N P_b \, dV \tag{22}$$

where s_e and V_e denote the surface and volume of the element under consideration. As δd^T is arbitrary, then Equation (18) may be written as:

$$[M]\{\ddot{d}\} + [C]\{\dot{d}\} + [K]\{d\} = \{ f_e(t) \} \tag{23}$$

Equation (23) is the dynamic equilibrium Equation for a single or multi-degree of freedom system.

FORMULATION OF ELEMENT MASS MATRIX

The kinetic energy of the element (e) can be expressed as follows:

$$TI^e = \frac{1}{2} \int_A \{\dot{d}\}^T [m] \{\dot{d}\} dA \tag{24}$$

The velocity vector within an element is discretized such that:

$$\{\dot{d}\} = \sum_{i=1}^{NN} N_i \{\dot{d}\}, \text{ NN: number of nodes.} \tag{25}$$

By substituting Equation (25) into Equation (24), one gets:

$$TI^e = \frac{1}{2} \sum_{i=1}^{NN} \{\dot{d}\}^T \int_A N_i^T [m] N_i \, dA \{\dot{d}\} \tag{26}$$

Thus,

$$[M]^e = \int_A [N]^T [m][N] dA = \int_{-1}^{1}\int_{-1}^{1} [N]^T [M][N] |J| \, d\xi \, d\eta \tag{27}$$

The mass matrix for nine degrees of freedom per node is:

$$[\boldsymbol{m}]_{9\times 9} = \begin{bmatrix} \boldsymbol{I}_1 & & & & & & & & 0 \\ & \boldsymbol{I}_1 & & & & & & & \\ & & \boldsymbol{I}_1 & & & & & & \\ & & & \boldsymbol{I}_2 & & & & & \\ & & & & \boldsymbol{I}_2 & & & & \\ & & & & & \boldsymbol{I}_3 & & & \\ & & & & & & \boldsymbol{I}_3 & & \\ & & & & & & & \boldsymbol{I}_4 & \\ 0 & & & & & & & & \boldsymbol{I}_4 \end{bmatrix} \tag{28}$$

For layered plates, the element mass matrix can be written as follows:

$$[\boldsymbol{M}] = \sum_{L=1}^{NL} [\boldsymbol{M}]^{e} \tag{29}$$

where in the above Equation (28), $\boldsymbol{I}_1$, $\boldsymbol{I}_2$, $\boldsymbol{I}_3$, and $\boldsymbol{I}_4$ are translation inertia, rotary inertia, and respectively higher order inertia terms, and these are given by:

$$(\boldsymbol{I}_1, \boldsymbol{I}_2, \boldsymbol{I}_3, \boldsymbol{I}_4) = \sum_{L=1}^{NL} \int_{h_{L-1}}^{h_L} (1, z^2, z^4, z^6)\, \rho^{L} dz \tag{30}$$

where ρ^{L} is material density of L-th layer.

FORMULATION OF DAMPING PROPERTIES

The most common form for the representation of the damping matrix [$\boldsymbol{C}$] is the so-called Rayleigh-type damping(3) which was given as;

$$[\boldsymbol{C}] = \boldsymbol{a}_o [\boldsymbol{M}] + \boldsymbol{a}_1 [\boldsymbol{K}] \tag{31}$$

in which ($\boldsymbol{a}_o$ and $\boldsymbol{a}_1$) are arbitrary proportionality factors, which make the damping matrix satisfy the orthogonality condition with respect to the modal matrix [$\boldsymbol{\Phi}$] in the same way of the orthogonality conditions for the mass and stiffness matrices that is(5):

$$\begin{aligned} \{\Phi\}^{T} [\boldsymbol{M}] \{\Phi\} &= [\boldsymbol{I}] \\ \{\Phi\}^{T} [\boldsymbol{K}] \{\Phi\} &= [\Lambda] \\ \{\Phi\}^{T} [\boldsymbol{C}] \{\Phi\} &= 2[\gamma][\Lambda]^{1/2} \end{aligned} \tag{32}$$

where

$\{\Phi\}$**:** The modal matrix whose columns represent the natural modal shapes and the superscript ($\boldsymbol{T}$) denotes transpose.

$[\boldsymbol{I}]$**:** Identity matrix.

$[\Lambda]$ **:** Spectral matrix, which is a diagonal matrix with elements representing the squares of the natural frequencies (ω_i^2).

$[\gamma]$ **:** Modal damping matrix which is also a diagonal matrix with elements representing the damping ratios for the system modes (γ_i)

Premultiplying Equation (37) by $\{\Phi\}^T$ and postmultiplying it by $\{\Phi\}$ yields:

$$\{\Phi\}^T[C]\{\Phi\} = a_o\{\Phi\}^T[M]\{\Phi\} + a_1\{\Phi\}^T[K]\{\Phi\} \qquad (33)$$

Substituting Equations (38) into Equation (39) gives;

$$2[\gamma][\Lambda]^{1/2} = a_o[I] + a_1[\Lambda] \qquad (34)$$

The two factors, a_o and a_1 can be determined by specifying the damping ratios for two modes for example 1 and 2, and substituting into Equation (34) as(12):

$$2\gamma_1\omega_1 = a_o + a_1\omega_1^2 \qquad (35)$$

$$2\gamma_2\omega_2 = a_o + a_1\omega_2^2 \qquad (36)$$

where ω_1 and ω_2 are the natural frequencies for modes 1 and 2 respectively. By solving the above two Equations one can get:

$$a_o = \frac{2\omega_1\omega_2(\omega_2\gamma_1 - \omega_1\gamma_2)}{(\omega_2^2 - \omega_1^2)} \qquad (37)$$

$$a_1 = \frac{2(\omega_2\gamma_2 - \omega_1\gamma_1)}{(\omega_2^2 - \omega_1^2)} \qquad (38)$$

Then, the values of a_o and a_1 are substituted into Equation (31) to get the required damping matrix.

FORCED VIBRATION ANALYSIS

The calculation of the nonlinear dynamic response of structure of structures including instability or buckling phenomena has received considerable attention and a good amount of literature has appeared on this subject. The nonlinear dynamic analysis depends largely on solving the following Equations:

$$[M]\{\ddot{d}(t)\} + [C]\{\dot{d}(t)\} + [K_T]\{d(t)\} = \{F(t)\} \qquad (39)$$

in which $[K_T]$ is the tangent stiffness matrix of the plate (or structure) and depends on the current displacements and stresses. The most conventional implicit time integration procedures is **Newmark** method. After solving Equation (39) at time ($t+\Delta t$) for displacements, velocities, and accelerations, the following equation as:

$$\begin{aligned}([K_T] + a_o[M] + a_1[C])\{d\}_{t+\Delta t} = \{F(t)\}_{t+\Delta t} &+ [M]\left(a_2\{\dot{d}\}_t + a_3\{\ddot{d}\}_t\right) \\ &+ [C]\left(a_4\{\dot{d}\}_t + a_5\{\ddot{d}\}_t\right)\end{aligned} \qquad (40)$$

For convenience, the following is used:

$$[K_T]_{eff} = [K_T] + a_o[M] + a_1[C] \qquad (41)$$

and,

$$\{F(t)\}_{eff} = \{F(t)\}_{t+\Delta t} + [M]\left(a_2\{\dot{d}\}_t + a_3\{\ddot{d}\}_t\right) + [C]\left(a_4\{\dot{d}\}_t + a_5\{\ddot{d}\}_t\right) \qquad (42)$$

So, Equation (42) may be written in the form:

$$[K_T]_{eff}\{d\}_{t+\Delta t} = \{F(t)\}_{eff} \qquad (43)$$

For a linear system, $[K_T]_{eff}$ will be constant during the analysis at any time, while in the nonlinear analysis, $[K_T]_{eff}$ is a function of current displacement vector $\{d\}$. Therefore, an iterative procedure must be used to define $[K_T]_{eff}$. In the nonlinear analysis, it is more useful to put Equation (43) in increment form. For such purpose, Equation (43) may be rewritten as:

$$[\hat{K}_T]\{\Delta d\} = \{\Delta\hat{F}(t)\} \qquad (44)$$

in which $[\hat{K}_T]$ is the effective stiffness matrix and $\{\Delta\hat{F}(t)\}$ is the effective load vector. Equation (44) is solved by an iterative procedure like Equation (40). It may be noted that Equation (40) may be used for solving linear problems, while for nonlinear problems, Equation (44) should be used.

Solving Equation (44) for $\{\Delta d\}$, approximate values for accelerations, velocities and displacements may be given as:

$$\begin{aligned}\{\ddot{d}\}_{t+\Delta t} &= a_o\{\Delta d\} - a_2\{\dot{d}\}_t - a_3\{\ddot{d}\}_t\\ \{\dot{d}\}_{t+\Delta t} &= a_1\{\Delta d\} - a_4\{\dot{d}\}_t - a_5\{\ddot{d}\}_t \qquad (45)\\ \{d\}_{t+\Delta t} &= \{d\}_t + \{\Delta d\}\ ;\end{aligned}$$

where

$$a_o = \frac{1}{\beta(\Delta t)^2},\ a_1 = \frac{\gamma}{\beta(\Delta t)},\ a_2 = \frac{1}{\beta(\Delta t)},\ a_3 = \frac{1}{2\beta} - 1$$

$$a_4 = \frac{\gamma}{\beta} - 1,\ a_5 = \frac{\Delta t}{2}\left(\frac{\gamma}{\beta} - 2\right)$$

APPLICATIONS AND DISCUSSIONS

Several plates are analyzed to study the different effects on the large displacement dynamic behavior of plates with some comparison with other researchers.

Comparison with available theoretical investigation of composite plate

Clamped supported square angle-ply laminated plate under transverse suddenly applied constant dynamic loading

A square angle-ply (0°/45°/90°/core/90°/45°/30°/0°) sandwich laminated plate with clamped edges and subjected to a suddenly applied uniformly transverse load was analyzed and compared with **Kommineni** and **Kant** [**1993**]^0. The following layer material properties are used in the analysis: for face sheets (Graphite/epoxy prereg system) (E_1=130.8 GPa; E_2=10.6 GPa G_{12}=G_{13}=6 GPa; G_{23}=3.9 GPa; v_{12}=0.28; and ρ=15.8 kN.sec^2/m^4); for core sheet (US Commercial al. honeycomb, ¼ in cell size, 0.003 in foil) (G_{13}=0.5206 GPa; G_{23}=0.1772 GPa; ρ=1.009 kN.sec^2/m^4). The time step is (Δt=0.000025 sec),and applied load (q=50 kN/m^2). The geometry properties are (a=1.0 m, a/b=1, and h=0.01m, at top three stiff layers, thickness of each layer=0.025 h, at bottom four stiff layer, thickness of each layer=0.08125 h, and thickness of core=0.6 h). **Kommineni** and **Kant** used nine-node isoparametric Lagrangian elements with nine-node degrees of freedom per node and divided the full plate into (4×4) element mesh.

In the present study, the full laminated plate is modeled by (4×4) element mesh with nine-node isoparametric Lagrangian element and nine degrees of freedom per node. A consistent mass matrix and **Newmark** integration method with $\alpha=1/2$, and $\beta=1/4$ were used in the present study.

Figure (4) shows the time history curve for the clamped angle-ply laminated plate under transverse suddenly applied load. From this figure, it can be noticed that good agreement with other study exists with a difference not exceeding (1%).

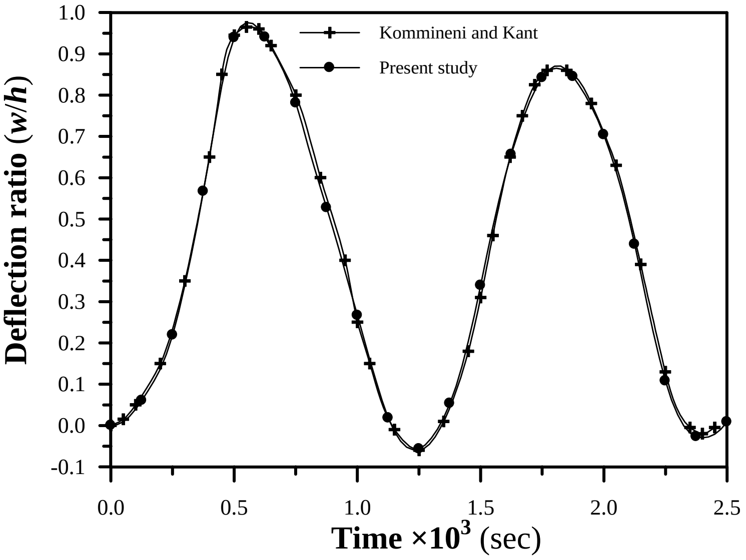

Figure (4): Central deflection ratio-time curve of a clamped square sandwich composite plate under transverse constant dynamic loading,($b/h=100$, $\Delta t=0.000025$sec, $q=50$ kN/m^2)

A simply supported square plate with slenderness ratio (***b***/***h***=100), and with symmetric cross-ply and antisymmetric cross-ply arrangements, were chosen to study the effect of number of layers on the large displacement dynamic behavior of a laminated composite plate under in-plane constant dynamic loading. The initial imperfection is ($w_o/h=0.1$) by which the shape is considered to be a sinusoidal curve.

Figures (5) and (6) present the time history curve and show that for the same volume of the plate, the response (deflection) will decrease about (15%) for the symmetric cross-ply and about (29%) for the antisymmetric cross-ply plates where with increasing the number of layers (3-10) for the symmetric cross-ply and (2-10) for the antisymmetric cross-ply arrangements, the stiffness increase may be related to the increase of the number of the reinforced layers. Thus, extension and bending stiffness will increase; and therefore, the amplitude will decrease. Also, the increase of the number of layers will give a better distribution of orthogonal stiffness through the depth. From these figures, it can be seen that the increase of the number of layers more than (8 layers) for the symmetric cross-ply and the antisymmetric cross-ply plates have slight effect on increasing the stiffness of the plate.

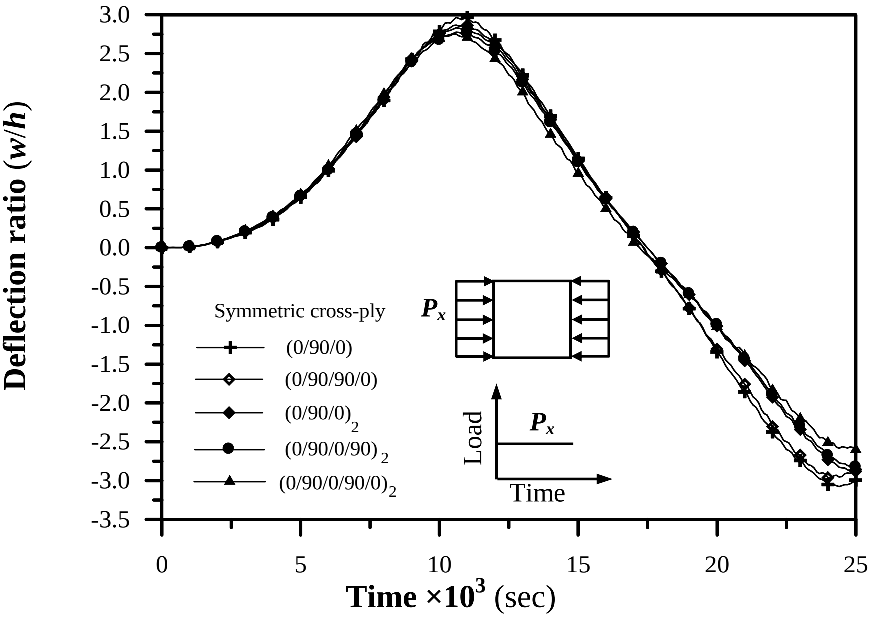

Figure (5): Effect of number of layers on the large displacement analysis of symmetric cross-ply laminated plate under in-plane constant dynamic loading ratio (P_x/P_u=0.4), (b/h=100, t=0.0001, w_o/h=0.1)

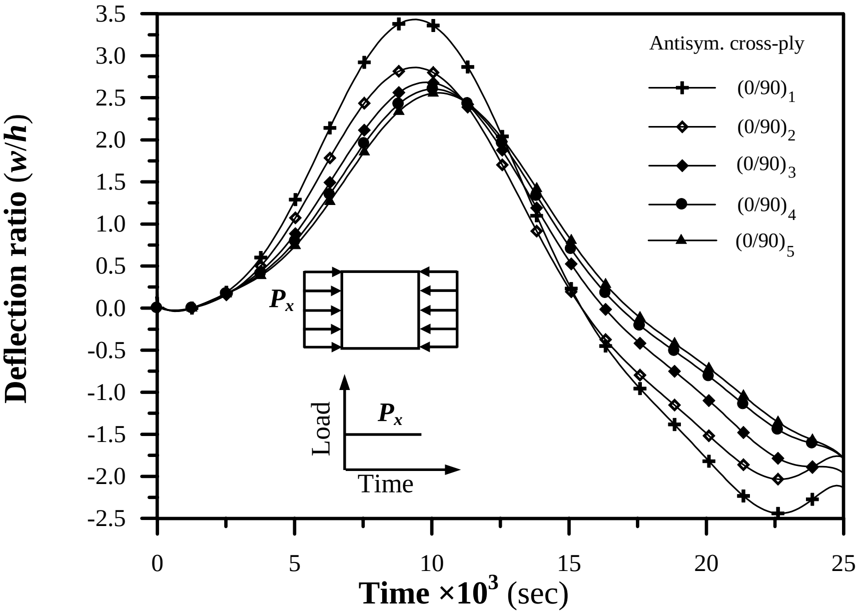

Figure (6): Effect of number of layers on the large displacement analysis of antisymmetric cross-ply laminated plate under in-plane constant dynamic loading ratio (P_x/P_u=0.4), (b/h=100, t=0.0001, w_o/h=0.1)

To study the effect of shear deformation on the large displacement dynamic analysis of a laminated composite plate under in-plane constant dynamic loading, a simply supported square plate with slenderness ratio (***b***/***h***=20), and with symmetric cross-ply antisymmetric cross-ply arrangements and with eight layers was analyzed. The initial imperfection is ($\boldsymbol{w_o/h}$= 0.1) by which the shape is considered to be a sinusoidal curve.

Figures (7) and (8) present the time history curves for the symmetric cross-ply, and for the antisymmetric cross-ply laminated composite plates by taking the through-thickness shear deformation through the degrees of freedom of the element. From these figures, it can be noticed that increasing the number of degrees of freedom per node from five degrees to nine degrees will increase the central deflection about (16%) for symmetric cross-ply and about (20%) for antisymmetric cross-ply plates.

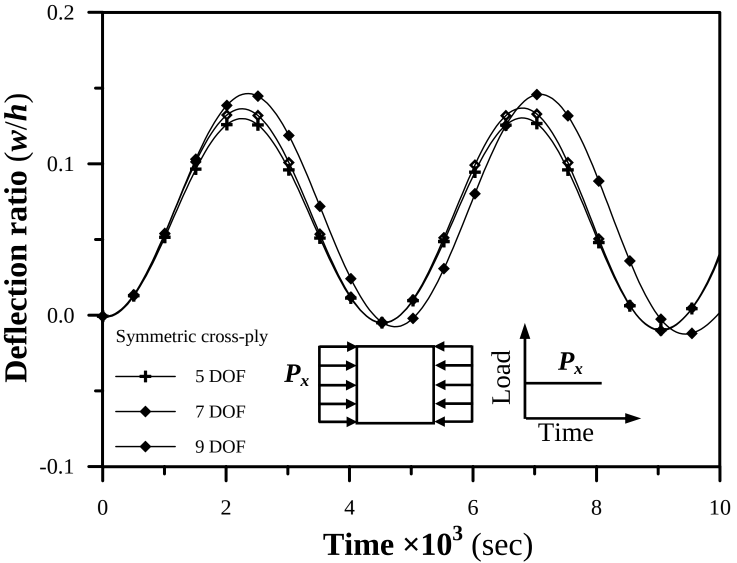

Figure (7): Effect of transverse shear deformation on the large displacement analysis of symmetric cross-ply laminated plate under in-plane constant dynamic loading ratio (P_x/P_u=0.3), (b/h=20, t=0.0001, w_o/h=0.1,P_u=18563 kN/m)

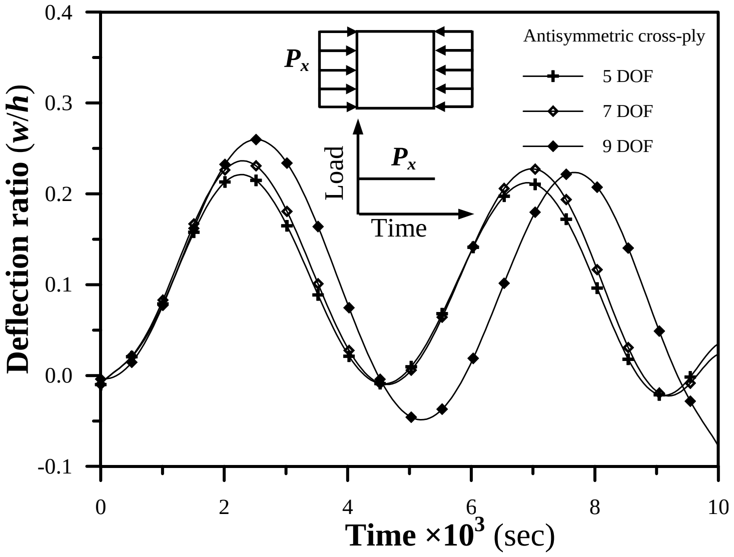

Figure (8): Effect of transverse shear deformation on the large displacement analysis of antisymmetric cross-ply laminated plate under in-plane constant dynamic loading ratio (P_x/P_u=0.3), (b/h=20, t=0.0001, w_o/h=0.1,P_u=16347 kN/m)

To study the effect of damping on the large displacement elastic-plastic dynamic behavior of composite plates, two examples are considered. The first one is a simply supported square plate with symmetric cross-ply lamination with eight layers and under in-plane dynamic loading. The second one is a simply supported square plate with antisymmetric cross-ply lamination with eight layers and under in-plane dynamic loading. Different values of damping factor (0.05-0.1) are considered in the present study. The initial imperfection shape is considered to be a sinusoidal curve. The following geometry and layer material properties of high graphite epoxy are used in the analysis: (E_1=172.5 GPa***;*** E_2=7.08 GPa; G_{12}=G_{13}=3.45 GPa, G_{23}=1.38 GPa; ρ=15.8 kN.sec^2/m^4)^0. The geometry properties are (***a***=1.0 m, ***a***/***b***=1).

Figure (9) and (10) present the time history curve for a simply supported square plate with symmetric and antisymmetric cross-ply lamination under in-plane constant loading. It is noticed that the response (deflection) decreases with the increase of the damping factor. Also, the plate shows no oscillation about the static deflection position, this means that the plate is under the critical damping ratio

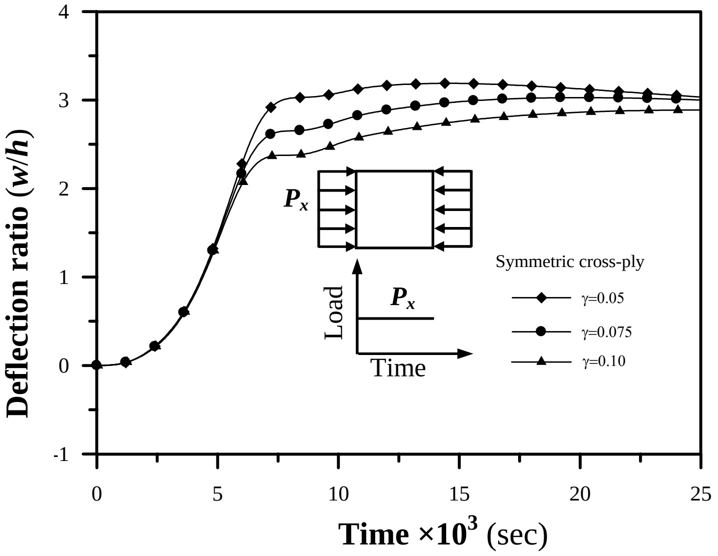

Figure (9):Effect of damping factor on the large displacement analysis of a simply supported square symmetric cross-ply plate under in-plane constant dynamic loading, (*b*/*h*=100,   *t*=0.0001, w_o/h=0.1, P_x/P_u=0.65, P_u=972.4 kN/m)

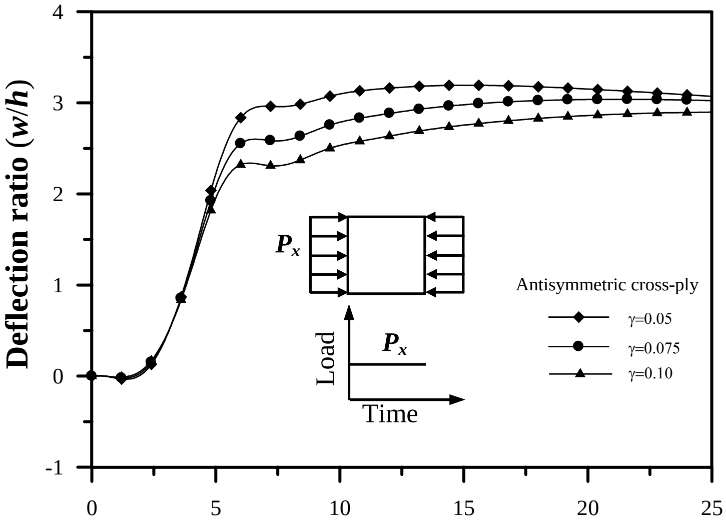

Figure (10):Effect of damping factor on the large displacement analysis of a simply supported square antisymmetric cross-ply plate under in-plane constant dynamic loading, (b/h=100, □ t=0.0001, wo/h=0.1, Px/Pu=0.65, Pu=960 kN/m)

CONCLUSIONS

A nonlinear finite element method is adopted for the large displacement dynamic analysis of anisotropic plates under in-plane compressive load. Damping property is considered by using Rayleigh type damping which is linearly related to the mass and the stiffness matrices. Newmark integration method is used for solving the dynamic equilibrium equations. The effects of initial imperfection, orthotropy of individual layers, fiber's orientation angle, type of loading, damping factor, and on the large displacement dynamic analysis are considered. The conclusion it is shown that the antisymmetric cross-ply laminated plate has a damping rate faster than the symmetric cross-ply laminated plate and if damping is considered and if the response of the plate shows no oscillation about the static deflection position, it means that the damping factor is below the critical damping factor. So, noticed that the central deflection increasing with increasing the degree of freedom per node.

REFERENCES

[1] Ali, N. H., "Finite Element Dynamic Analysis of Laminated Composite Plates Including Damping Effect", *M.Sc. Thesis*, University of Babylon, Hilla, Iraq, 2004.

[2] Akay, H. "Dynamic Large Deformation Analysis of Plates Using Mixed Finite Elements" *Comp. & Struct.*, Vol.11, 1980, pp1-11.

[3] Ammash, H. K., "Nonlinear Static and Dynamic Analysis of Laminated Plates Under In-plane Forces", *Ph.D. Thesis*, University of Babylon, Hilla, Iraq, 2008.

[4] Azevedo, R.L. and Awruch, A.M. "Geometric Nonlinear Dynamic Analysis of Plates and Shells Using Eight-Node Hexahedral Finite Element with Reduced Integration", *J. Braz. Soc. Mech. Sci.*, Vol.21, No.3, 1999, pp.1-22.

[5] Bathe, K.J., and Ozdemir, H. "Elastic-Plastic Large Deformation Static and Dynamic Analysis.", *Comp. & Struct.*, Vol.6, No.2, 1975, pp81-92.

[6] Jones, R.M., "Mechanics of Composite Materials", *Second Edition*, Taylor and Francis Inc., U.S.A., 1999.

[7] Kao, R., "Nonlinear Dyanmic Buckling of Spherical Caps with Initial Imperfections", *Comp. & Struct.*, Vol.12, 1980, pp49-63.

[8] Kaw, A., "Mechanics of Composite Materials", *Second Edition*, Taylor and Francis Group, LLC, 2006.

[9] Khante, S. N., Rode, V., and Kant, T., "Nonlinear Transient Dynamic Response of Damping Plates Using a Higher Order Shear Deformation Theory", *Nonlinear Dynamics*, Vol.47, 2007, pp38-403.

[10] Kommineni, J. R., and Kant, T. "Geometrically Non-linear Transient Co Finite Element Analysis of Composite and Sandwich Plates with a Refined Theory." *Struct. Eng. And Mech.*, Vol.1, No.1, 1993, pp87-102.

[11] Pica, A., Wood, R.D., and Hinton, E. "Finite Element Analysis of Geometrically Nonlinear Plate Behavior Using a Mindlin Formulation." *Comp. & Struct.*, Vol.11, 1979, pp.203-215.

[12] Pytet, M., "Introduction to Finite Element Vibration Analysis", 1990.

[13] Tao, Z., Tu-guang, L., Yao,Z., and Jio-zhi,L. "Nonlinear Dynamic Buckling of Stiffened Plates under In-plane Impact Load.", *J. Zhejiang University Science*, Vol.5, No.5, 2004, pp609-617.

[14] Weller, T., Abramovich, H., and Yaffe, R., "Dynamic Buckling of Beams and Plates Subjected to Axial Impact", *Comp. & Struct.*, Vol.32, No.3/4, 1989, pp835-851.

COMPDYN 2011
III ECCOMAS Thematic Conference on
Computational Methods in Structural Dynamics and Earthquake Engineering
M. Papadrakakis, M. Fragiadakis, V. Plevris (eds.)
Corfu, Greece, 25–28 May 2011

AN EFFICIENT *H*-ADAPTIVE SCALED BOUNDARY ELEMENT METHOD FOR TRANSIENT ELASTODYNAMICS

Zihua Zhang[1], Zhenjun Yang[2]*, Guohua Liu[1], Yunjin Hu[1]

[1]College of Civil Engineering and Architecture, Zhejiang University
Hangzhou, 310058, China
zhangzihua1984@googlemail.com

[2*]School of Engineering, the University of Liverpool
Brownlow Street, Liverpool, L69 3GQ, UK
zjyang@liv.ac.uk

Keywords: Scaled boundary finite element method, *h*-hierarchical adaptivity, subdivision of subdomains, mesh mapping, elastodynamics

Abstract. *This study develops a posterior h-hierarchical adaptive scaled boundary finite element method for transient elastodynamic problems using a mesh refinement procedure which subdivides subdomains. In a time step, the fields of displacement, stress, velocity and acceleration are all semi-analytical and the kinetic energy, strain energy and energy errors are all semi-analytically integrated in subdomains. This makes mesh mapping very simple but accurate. Mesh refinement is very simple, flexible and efficient because only a small number of subdomains are subdivided due to the high accuracy of the SBFEM. The results of an example with stress wave propagation were presented. It is shown that the developed method is capable of capturing the propagation of steep stress regions and calculating accurate dynamic responses, but only using a fraction of degrees of freedom required by adaptive finite element methods.*

1 INTRODUCTION

A few adaptive spatial discretisation methods based on finite element method (FEM) and *posteriori* error estimators have been developed to efficiently simulate elastodynamic problems with stress wave propagation [1, 2]. However, there still exist two major difficulties in adaptive finite element method (AFEM). First, automatic remeshing to capture the stress wave propagation usually involves complicated and time-consuming topological changes on a large number of small-sized elements, especially for large-scale problems. This may also lead to ill-shaped elements resulting in inaccurate responses. Second, mesh mapping after remeshing to transfer state variables from the old mesh to the new one is approximate, which may lead to high accumulative errors in later time steps. In addition, identifying the old element where a new node is located may be time-consuming as well because a large number of finite elements need to be checked.

The scaled boundary finite element method (SBFEM) developed in 1990s [3, 4] is a semi-analytical method combining the advantages of the FEM and the boundary element method (BEM). It models an analysis domain by a small number of large-sized subdomains and only the subdomain boundaries are discretised, and the modeled dimensions are reduced by one as the BEM, but no fundamental solutions or singular integrations are needed. Therefore, the FEM's wide applicability and the BEM's simplicity in remeshing are both retained.

This study aims to further extend the applicability of the SBFEM by developing an adaptive SBFEM (ASBFEM) for transient elastodynamic problems using a simple subdomain subdivision procedure. A simply-supported beam under impact was modeled to validate the developed ASBFEM.

2 METHODOLOGY

2.1 The scaled boundary finite element method

A domain of analysis is illustrated in Figure 1(a) as an example. The domain is divided into three subdomains whose geometry and dimensions are defined by a few vertices. Figure 1(b) shows the details of Subdomain 1. The subdomain is represented by scaling a defining curve *S* relative to a scaling centre. A normalized radial coordinate ξ is defined, varying from zero at the scaling centre and unit value on *S*. A circumferential coordinate η is defined around the defining curve *S*. A curve similar to *S* defined by ξ=0.5 is shown in Figure 1b. The coordinates ξ and η form a local coordinate system used in all the subdomains and simple transformation equations between the local and global coordinates can be identified with ease for each subdomain:

$$x = x_0 + \xi\left(\frac{x_1 + x_2 - 2x_0}{2} + \frac{(x_2 - x_1)\eta}{2}\right) \tag{1}$$

$$y = y_0 + \xi\left(\frac{y_1 + y_2 - 2y_0}{2} + \frac{(y_2 - y_1)\eta}{2}\right) \tag{2}$$

where (x_1, y_1) and (x_2, y_2) are nodal coordinates of a two-node element on the boundary and (x_0, y_0) are the coordinates of the scaling centre. The displacements of any point (ξ, η) in a subdomain are assumed as

$$\mathbf{u}(\xi,\eta) = \mathbf{N}(\eta)\mathbf{u}(\xi) \tag{3}$$

where $\mathbf{u}(\xi)$ are the displacements along the radial lines and are analytical with respect to ξ. $\mathbf{N}(\eta)$ is the shape function matrix in the circumferential direction.

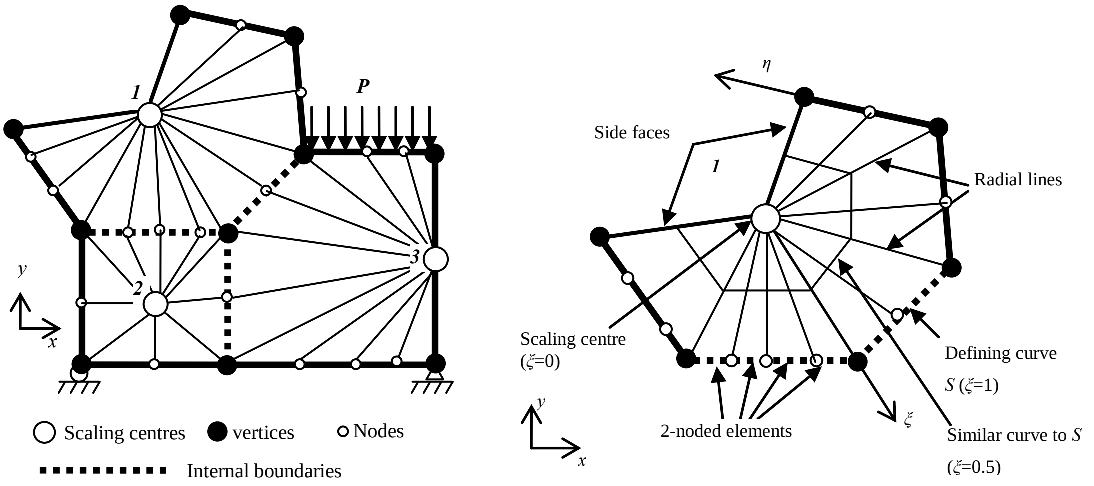

(a) Subdomaining of a domain (b) Subdomain 1

Figure 1 The concept of the scaled boundary finite element method

For linear elastic materials, the stress vector in a subdomain is calculated by

$$\boldsymbol{\sigma}(\xi,\eta) = \mathbf{DB}^1(\eta)\mathbf{u}(\xi)_{,\xi} + \frac{1}{\xi}\mathbf{DB}^2(\eta)\mathbf{u}(\xi) \tag{4}$$

where $\mathbf{B}^1(\eta)$ and $\mathbf{B}^2(\eta)$ are coefficient matrixes, and $\mathbf{D}$ is the elasticity matrix.

2.2 Solutions in time domain

In elastodynamics, the dynamic equilibrium equation of a subdomain is derived as [5]

$$\mathbf{M}_s\ddot{\mathbf{u}}_\mathbf{b} + \mathbf{K}_s\mathbf{u}_\mathbf{b} = \mathbf{p}_s \tag{5}$$

where $\mathbf{u}_\mathrm{b}$ is the displacement vector and $\ddot{\mathbf{u}}_\mathrm{b}$ is the acceleration vector on the subdomain boundary, $\mathbf{p}_\mathrm{s}$ the subdomain load vector, $\mathbf{K}_\mathrm{s}$ the subdomain stiffness matrix and $\mathbf{M}_\mathrm{s}$ the subdomain mass matrix.

Assembling Eq. (5) for all subdomains lead to the global equation system

$$\mathbf{M}\ddot{\mathbf{U}} + \mathbf{KU} = \mathbf{P} \tag{6}$$

where $\mathbf{M}$ and $\mathbf{K}$ are the assembled global mass and stiffness matrices, $\mathbf{P}$ is the global load vector, $\mathbf{U}$ and $\ddot{\mathbf{U}}$ are the nodal displacement and acceleration vectors respectively.

The Newmark integration scheme [6] is used to solve Eq. (6). At time step n, the state variables are calculated by

$$(a_1\mathbf{M} + \mathbf{K})\mathbf{U}_n = \mathbf{F}_n + \mathbf{M}(a_1\mathbf{U}_{n-1} + a_2\dot{\mathbf{U}}_{n-1} + a_3\ddot{\mathbf{U}}_{n-1}) \tag{7a}$$

$$\ddot{\mathbf{U}}_n = a_1(\mathbf{U}_{n-1} - \mathbf{U}_{n-1}) - a_2\dot{\mathbf{U}}_{n-1} - a_3\ddot{\mathbf{U}}_{n-1} \tag{7b}$$

$$\dot{\mathbf{U}}_n = \dot{\mathbf{U}}_{n-1} + a_4\ddot{\mathbf{U}}_{n-1} + a_5\ddot{\mathbf{U}}_n \tag{7c}$$

$$a_1 = \frac{1}{\beta(\Delta t)^2},\quad a_2 = \frac{1}{\beta\Delta t},\quad a_3 = \frac{1}{2\beta} - 1,\quad a_4 = \Delta t(1-\gamma),\quad a_5 = \gamma\Delta t \tag{8}$$

where Δt is the time increment, β and γ are the Newmark parameters. In this study, $\beta = 0.25$ and $\gamma = 0.5$ are used for all the examples with unconditional stability.

The subdomain displacement and stress field are

$$\mathbf{u}(\xi,\eta) = \mathbf{N}(\eta)\sum_{i=1}^{N} c_i\xi^{\lambda_i}\boldsymbol{\varphi}_i \tag{9}$$

$$\boldsymbol{\sigma}(\xi,\eta)=\mathbf{DB}^{1}(\eta)\left(\sum_{i=1}^{N}c_i\lambda_i\xi^{\lambda_i-1}\boldsymbol{\varphi}_i\right)+\mathbf{DB}^{2}(\eta)\left(\sum_{i=1}^{N}c_i\xi^{\lambda_i-1}\boldsymbol{\varphi}_i\right) \tag{10}$$

where λ_i and $\boldsymbol{\varphi}_i$ (i=1-N) are eigen values and eigen vectors from solving a standard eigen problems [7]. $\mathbf{c}=\{c_1, c_2, ..., c_N\}^T$ are constants dependent on boundary conditions, and N is the number of degrees of freedom (DOFs) of the subdomain.

The velocity and acceleration fields in a subdomain are calculated by differentiating Eq. (9) with respect to time

$$\dot{\mathbf{u}}(\xi,\eta)=\mathbf{N}(\eta)\sum_{i=1}^{N}\dot{c}_i\xi^{\lambda_i}\boldsymbol{\varphi}_i \tag{11}$$

$$\ddot{\mathbf{u}}(\xi,\eta)=\mathbf{N}(\eta)\sum_{i=1}^{N}\ddot{c}_i\xi^{\lambda_i}\boldsymbol{\varphi}_i \tag{12}$$

From Eqs. (9)-(12) it is clear that the displacements, stresses, velocities and accelerations in a subdomain are all analytical with respect to the radial coordinate ξ.

3 DYNAMIC ENERGY ERROR ESTIMATOR

The energy norm of the total energy is

$$\|\mathbf{u}\|=\left(\|\mathbf{u}\|_k^2+\|\mathbf{u}\|_s^2\right)^{1/2} \tag{13}$$

where

$$\|\mathbf{u}\|_k=\left(\sum_{s=1}^{NS}\int_{V_s}\dot{\mathbf{u}}(\xi,\eta)^T\rho\dot{\mathbf{u}}(\xi,\eta)dV\right)^{1/2} \tag{14}$$

$$\|\mathbf{u}\|_s=\left(\sum_{s=1}^{NS}\int_{V_s}\boldsymbol{\sigma}(\xi,\eta)^T\mathbf{D}^{-1}\boldsymbol{\sigma}(\xi,\eta)dV\right)^{1/2} \tag{15}$$

are the energy norm of the kinetic energy and the strain energy respectively. NS is the number of subdomains.

A recovered stress field can be used to calculate the strain energy semi-analytically [8]

$$\|\mathbf{u}\|_s\approx\left(\sum_{s=1}^{NS}\sum_{i=1}^{N}\sum_{j=1}^{N}\frac{c_ic_j}{\lambda_i+\lambda_j}\int_{S_s}\boldsymbol{\sigma}_i^*(\eta)^T\mathbf{D}^{-1}\boldsymbol{\sigma}_j^*(\eta)\,|\,J\,|\,d\eta\right)^{1/2} \tag{16}$$

And the kinetic energy is [9]

$$\|\mathbf{u}\|_k=\left(\sum_{s=1}^{NS}\sum_{i=1}^{N}\sum_{j=1}^{N}\frac{\rho\dot{c}_i\dot{c}_j}{\lambda_i+\lambda_j+2}\int_{S_s}\left(\dot{\mathbf{u}}_i(\eta)\right)^T\dot{\mathbf{u}}_j(\eta)|J|d\eta\right)^{1/2} \tag{17}$$

where $\boldsymbol{\sigma}_i^*$ is the recovered stresses of ith mode at the boundary nodes, $\dot{\mathbf{u}}_{\mathrm{i}}(\eta)$ is the velocity vector of ith mode along the subdomain boundary.

Substituting Eqs. (16) and (17) into Eq. (13) yields

$$\|\mathbf{u}\|=\left(\sum_{s=1}^{NS}\sum_{i=1}^{N}\sum_{j=1}^{N}\left(\frac{\rho\dot{c}_i\dot{c}_j}{\lambda_i+\lambda_j+2}\int_{S_s}\left(\dot{\mathbf{u}}_i(\eta)\right)^T\dot{\mathbf{u}}_j(\eta)|J|d\eta+\frac{c_ic_j}{\lambda_i+\lambda_j}\int_{S_s}\boldsymbol{\sigma}_i^*(\eta)^T\mathbf{D}^{-1}\boldsymbol{\sigma}_j^*(\eta)\,|\,J\,|\,d\eta\right)\right)^{1/2} \tag{18}$$

The domain energy error can be evaluated as [8]

$$\|\mathbf{e}\|\approx\left(\sum_{s=1}^{NS}\|\mathbf{e}\|_s^2\right)^{1/2} \tag{19}$$

where

$$\|\mathbf{e}\|_s\approx\sum_{i=1}^{N}\sum_{j=1}^{N}\frac{c_ic_j}{\lambda_i+\lambda_j}\int_{S_s}\mathbf{e}_{\sigma i}^*(\eta)^T\mathbf{D}^{-1}\mathbf{e}_{\sigma j}^*(\eta)\,|\,J\,|\,d\eta \tag{20}$$

is the energy error of a subdomain and

$$\mathbf{e}^{*}_{\sigma i}(\eta) = \mathbf{N}(\eta)\boldsymbol{\sigma}^{*}_{i} - \mathbf{D}(\lambda_i \mathbf{B}^{1}(\eta) + \mathbf{B}^{2}(\eta))\boldsymbol{\varphi}_{i} \tag{21}$$

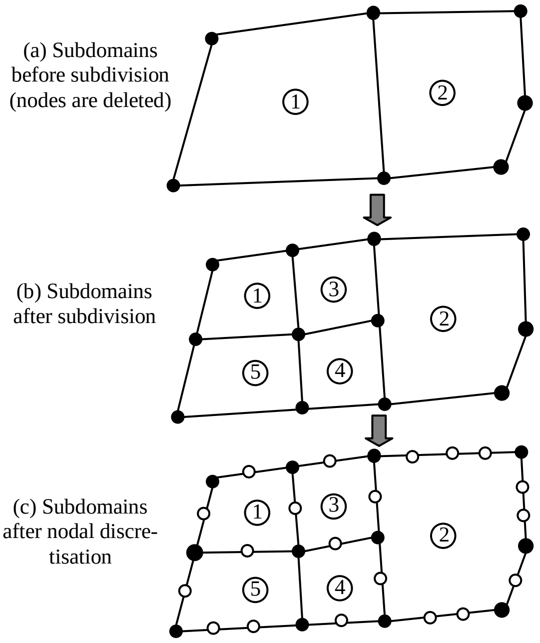

Figure 2 The remeshing procedure

The dynamic energy error estimator is defined as

$$\delta = \frac{\|\mathbf{e}\|}{\|\mathbf{u}\|} \times 100\% \tag{22}$$

4 THE ADAPTIVE PROCEDURE

4.1 Remeshing

The aim of the adaptive procedure is to make each subdomain contribute equally to the domain energy error. The average limit of the subdomain error is defined as

$$\|\mathbf{e}\|_{s}^{\lim} = \bar{\delta}\left(\frac{\|\mathbf{u}\|^{2}}{NS}\right)^{1/2} \tag{23}$$

where $\bar{\delta}$ is the target error estimator of the domain.

A parameter θ is employed to identify the subdomains that should be refined

$$\theta = \frac{\|\mathbf{e}\|_{s}}{\|\mathbf{e}\|_{s}^{\lim}} \tag{24}$$

In each time step, a very simple mesh refinement procedure applies to all subdomains with θ>1, as illustrated in Figure 2 where two subdomains in the whole domain are shown. Subdomain 1 needs to be refined and Subdomain 2 represents those connected with Subdomain 1. Figure 2a shows the two subdomains with vertices only after nodes are removed. Subdomain 1 is first subdivided into four smaller subdomains by adding a vertex at the scaling centre and a vertex at the middle point of each of the four edges, as shown in Figure 2b. The old subdomain 1 is then deleted and the topologies of the four smaller subdomains are generated. The topology of Subdomain 2 is updated with the addition of one vertex. A global seed of elemental size is then assigned to the five subdomains to generate nodes on their edges, resulting in Figure 2c for analysis.

The estimator is updated based on the new mesh until the following condition is satisfied

$$\delta < \bar{\delta} \tag{25}$$

4.2 Mesh mapping

Once a new mesh is obtained, nodal state variables, including displacement, velocity and acceleration, are transferred from the old mesh to the new one as initial conditions of the following time step. For a point or a node located at coordinates (x_0, y_0) in the new mesh after remeshing, the subdomain in the old mesh within which the point (x_0, y_0) is located is first found. The coordinates (x0, y0) are then easily transformed to SBFEM coordinates (ξ_0, η_0) by Eqs. (1) and (2) in this subdomain. Because the properties of this subdomain (eigenvalues λ_i, eigenvectors φ_i and constants c_i) are known, the displacements, velocities and accelerations at (ξ_0, η_0) in the old mesh or (x_0, y_0) in the new mesh can be calculated by Eq. (9), Eq. (11) and Eq. (12), respectively (ξ=ξ_0, η=η_0). This procedure is also very accurate because Eqs (9, 11-12) are semi-analytical. In addition, because the SBFEM discretises a domain by a few large-sized subdomains, it takes little time to locate the old subdomain for the newly-generated nodes.

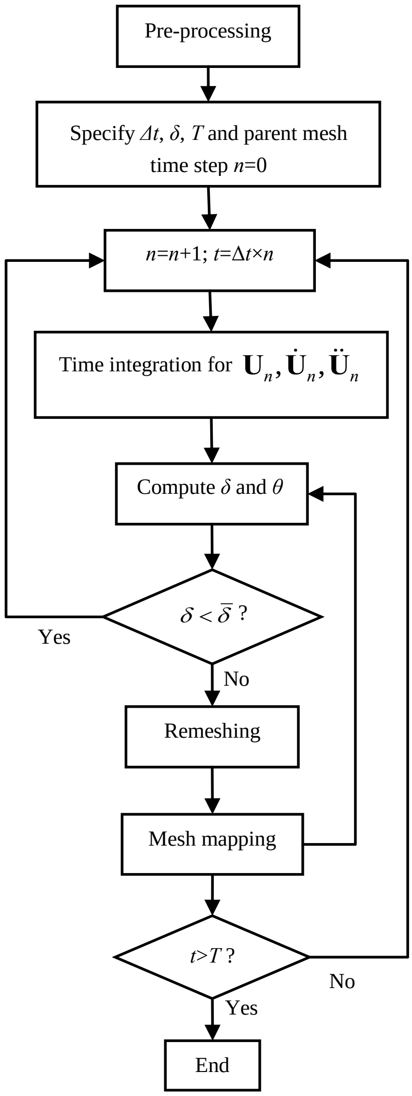

Figure 3 Flow chart of the adaptive procedure

4.3 The flow chart

Figure 3 illustrates the flow chart of the adaptive procedure. A parent mesh consisting of relatively large-sized subdomains and a target error estimator $\bar{\delta}$ are input first. At time step n, the state variables $\mathbf{U}_n, \dot{\mathbf{U}}_n, \ddot{\mathbf{U}}_n$ are solved by the Newmark integration method using the old mesh at the end of time step (n-1) and the error estimator δ is calculated. If δ exceeds the target, the adaptive procedure is triggered to identify a new mesh, starting from the parent mesh. The nodal state variables are then mapped from the old mesh to the new mesh as the initial conditions. After the state variables are solved, Eq. (25) is checked again. This iteration is repeated until an optimal adaptive mesh satisfying Eq. (25) is identified.

5 NUMERICAL EXAMPLE

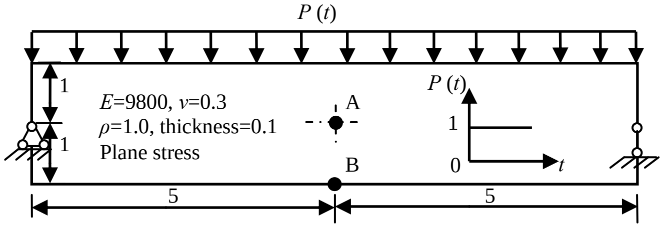

Figure 4 Dimensions of the simply-supported beam

The numerical example examined is a simply-supported beam subjected to an impact loading on the beam top face. The dimensions and material properties are shown in Figure 4. The dynamic responses in a time period of (0, 1.2s) were calculated with a constant time increment Δt=0.02s. A regular mesh (mesh 1) and an irregular mesh (mesh 2) are employed as the parent mesh, as shown in Figure 5. The target error estimator is $\bar{\delta}$ =15%. The same example was modeled in [2] using AFEM.

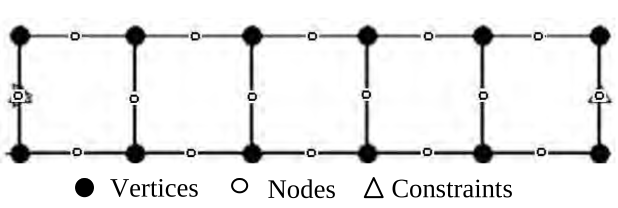

a. Mesh 1 (DOFs=56)

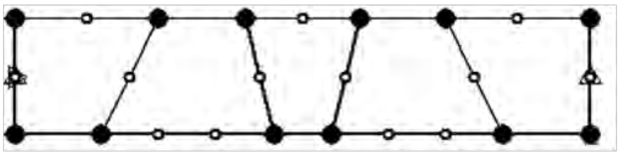

b. Mesh 2 (DOFs=50)

Figure 5 Parent meshes of the beam

Figures 6(a) and 6(b) show the horizontal stress contours and corresponding adaptive meshes at t=0.04s & 0.10s respectively. It can be observed that, with the stress wave propagation, the mesh is refined from the ends to the mid-span of the beam.

Figure 7 shows the histories of vertical displacement at point A. It can be seen that the results of non-adaptive SBFEM for both meshes gradually deviate away from the results of FEM [2] using a very fine mesh which can be considered as exact.

The results of the developed ASBFEM are better than AFEM reported in [2] and very close to FEM. Figure 8 shows the horizontal stress at point B. It can also be seen that the results of the present method agree well with FEM and better than the non-adaptive SBFEM.

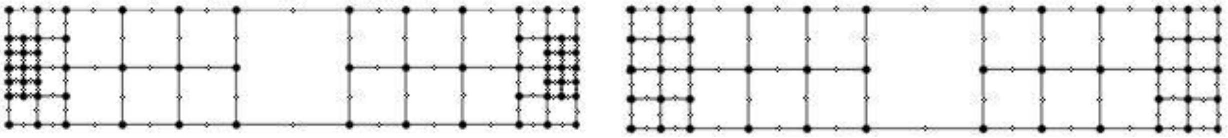

Based on mesh 1, DOFs=344 Based on mesh 1, DOFs=248

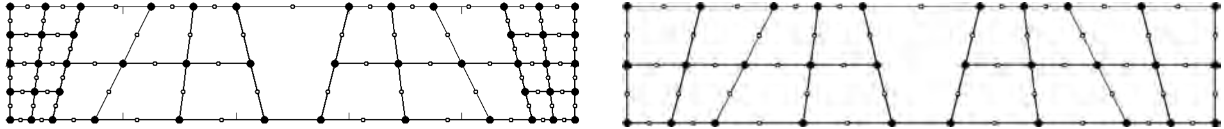

Based on mesh 2, DOFs=246 Based on mesh 2, DOFs=150

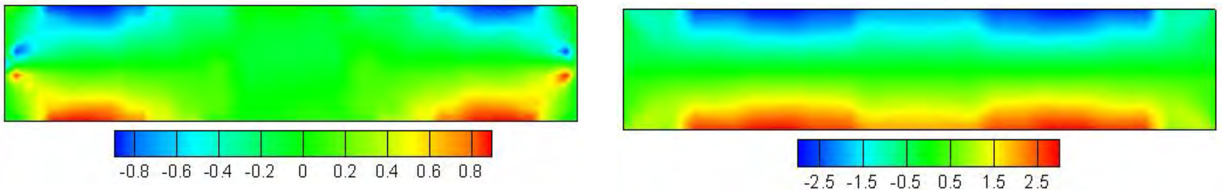

(a) *t*=0.04s (b) *t*=0.10s

Figure 6 Adaptive meshes and the horizontal stress contours

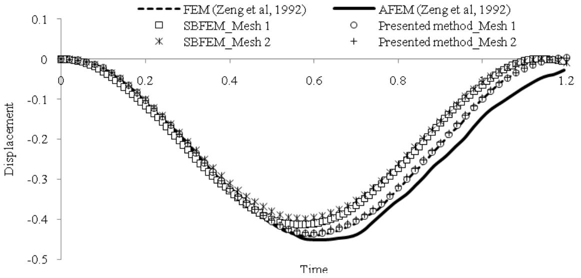

Figure 7 Histories of the vertical displacement at A

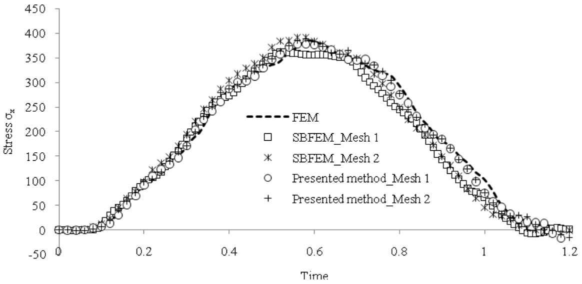

Figure 8 Histories of horizontal stress at B

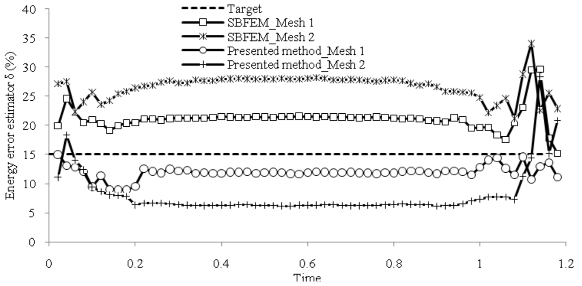

Figure 9 Histories of the energy error estimator δ

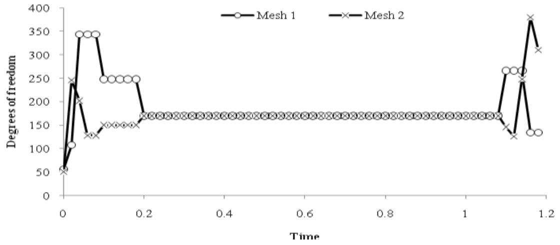

Figure 10 Histories of degrees of freedom

Figure 9 shows the histories of the energy error estimator calculated by non-adaptive SBFEM and the present method. It can be observed that the present method is able to control the estimator under the target 15% in most stages, while the estimators of the former are around 20% based on mesh 1 and 25% based on mesh 2 respectively.

Figure 10 shows the degrees of freedom used in the present ASBFEM. For this example, 150 DOFs are used in most stages while about 2,000 DOFs were used in AFEM [2].

6 CONCLUSIONS

An adaptive scaled boundary finite element method subdividing subdomains has been developed for elastodynamic problems in this study. It uses a semi-analytically integrated posteriori error estimator, and a simple and efficient mesh refinement procedure with accurate mesh mapping to adaptively identify an optimal mesh that captures stress wave propagation. An example under impact load was modelled. It has been demonstrated that the developed method is capable of computing accurate dynamic responses and effectively capturing stress wave propagation while using a fraction of degrees of freedom that are needed by adaptive finite element methods. The developed method thus provides a strong competitor in adaptive modelling of elastodynamic problems.

REFERENCES

[1] N. E. Wiberg, L. F. Zeng and X. D. Li. A postprocessed error estimate and an adaptive procedure for the semidiscrete finite element method in dynamic analysis. International Journal for Numerical Methods in Engineering, 37(21): 3585-3603, 1994.

[2] L. F. Zeng, N. E. Wiberg and L. Bernspång. An adaptive finite element procedure for 2D dynamic transient analysis using direct integration. International Journal for Numerical Methods in Engineering, 34(3): 997-1014, 1992.

[3] J. P. Wolf and C. M. Song. The scaled boundary finite-element method-a primer: derivations. Computers and Structures, 78(1-3): 191-210, 2000.

[4] C. M. Song and J. P. Wolf. The scaled boundary finite-element method-a primer: solution procedures. Computers and Structures, 78(1-3): 211-225, 2000.

[5] E. T. Ooi and Z. J. Yang. Modelling dynamic crack propagation using scaled boundary finite element method. International Journal for Numerical Methods in Engineering, in press.

[6] N. M. Newmark. A method of computation for structural dynamics. ASCE Journal of the Engineering Mechanics Division, 85: 67-94, 1959.

[7] A. J. Deeks and J. P. Wolf. A virtual work derivation of the scaled boundary finite-element method for elastostatics. Computational Mechanics, 28: 489-504, 2002.

[8] A. J. Deeks and J. P. Wolf. Stress recovery and error estimation for the scaled boundary finite-element method. International Journal for Numerical Methods in Engineering, 54(4): 557-583, 2002.

[9] Z. J. Yang, A. H. Zhang, G. H. Liu and E. T. Ooi. An *h*-hierarchical adaptive scaled boundary finite element method for elastodynamics, *Computers and Structures*, under review.

COMPDYN 2011
3^{rd} ECCOMAS Thematic Conference on
Computational Methods in Structural Dynamics and Earthquake Engineering
M. Papadrakakis, M. Fragiadakis, V. Plevris (eds.)
Corfu, Greece, 25-28 May 2011

NONCLASSICAL MODELS IN THE SHELL THEORY WITH APPLICATIONS TO MULTILAYERED NANOTUBES

Svetlana M. Bauer, Andrei M. Ermakov, Stanislava V. Kashtanova, Nikita F. Morozov[1]

[1] St. Petersburg State University, St. Petersburg, Russia
s_bauer@mail.ru, khopesh_ra@mail.ru, kastasya@yandex.ru, morozov@nm1016.spb.edu

Keywords: Theory of anisotropic shells, Shell theory of Paliy-Spiro, Shell theory of Rodionova-Titaev-Chernykh.

Abstract. *In [1] the stiffness of bridges and cantilevers made of natural chrysotile asbestos nanotubes has been studied by means of scanning probe microscopy. The stiffness is defined as a ratio the value of local load (applied to the tube) to the value of the displacement. The nanotubes with different materials for fillings are analyzed. The experiments show that the stiffness of the tube depends on the materials for filling. The tubes with water are softer than the tubes without filling materials and the tubes filled with mercury are more rigid than tubes without filling materials. It was shown in [1] that the classical theory of beam bending can not explain the experimental results, but the experimental results well agree with the Timoshenko-Reissner theory (at least qualitatively), when interlaminar shear modulus of elasticity changes for different filling materials. When additional factors such as lamination of structure and cylindrical anisotropy are taken into account [2] the theory of Rodionova-Titaev-Chernykh (RTC) permits to obtain much more reliable results. In this work the authors also applied one more nonclassical shell theory, namely the shell theory of Paliy-Spiro (PS) developed for medium - thickness shells and considered radial pressure. The comparison of nonclassical shell theories (RTC and PS) with experimental data and FEM calculations are presented in the report.*

1 INTRODUCTION

It is known [3] that mechanical characteristics corresponding to nano-dimensional structure elements such as beams, plates and shells can differ from mechanical characteristics corresponding to structures of the same material, which have ”normal” geometrical sizes. There is a possibility of appearance of the anisotropy of nanoobjects. In [1], [2] results of experiments, which examined mechanical properties of nanotubes made of natural chrysolite asbestos are discussed. The diameter of nanotubes is approximately equal to 30nm, internal diameter is 5nm. The inner cavity of a tube was filled with water, mercury or tellurium under pressure. The rigidity of nanotubes was measured with the use of scanning probing microscopy. The rigidity was understood as the ratio between applied strain and value of bridge deflection formed by the nanotube, which blocked an opening in porous bottom layer. (Conditions of the experiment are described in detail in [1]). The experiments showed that tube filled with water is substantially softer than a ”dry” tube (tube without any filler) and tubes filled with mercury are slightly more rigid than ”dry” tubes. In [1] experimental data and the results of modeling were compared. The simplest classical models of isotropic beams and non-classical transversal isotropic models were considered. In [2] the problem of nanotubes deformation was solved with the use of the Rodionova-Titaev-Chernykh (RTCH) theory of anisotropic shells [4] , which permits to take into account layered structure of asbestos and cylindrical anisotropy as well. In this work deformation of a multilayered tube under locally applied load (Fig. 1) is found with the use of the theory of anisotropic shells of moderate thickness, which is developed in [5]. There was made a comparison of the results obtained with the use of the Timoshenko-Reissner (TR) theory [6] , RTCH theory, the Paliy-Spiro theory and FEM calculations in ANSYS code.

2 PROBLEM DEFINITION

Let α and β be cylindrical coordinates on a shell surface, α — the polar angle, β — coordinate along the tube's generatrix, $h^{(i)}$ — thicknesses, $R^{(i)}$ — radiuses of medium surfaces of the shell layers, and L — tube's length. For definition of coefficients we will use symbol $A_j^{(i)}$. Low index j denotes curvilinear coordinate corresponding to the value A, upper index i — denotes to which layer it corresponds, i.e. if $i = 1$ then A corresponds to the first inner layer, if $i = N$ then A corresponds to the last outer layer. $E_1^{(i)}, E_2^{(i)}, E_3^{(i)}$ are modules of elasticity in tangential and normal directions, $\nu_{jk}^{(i)}$ are the Poisson's ratios.

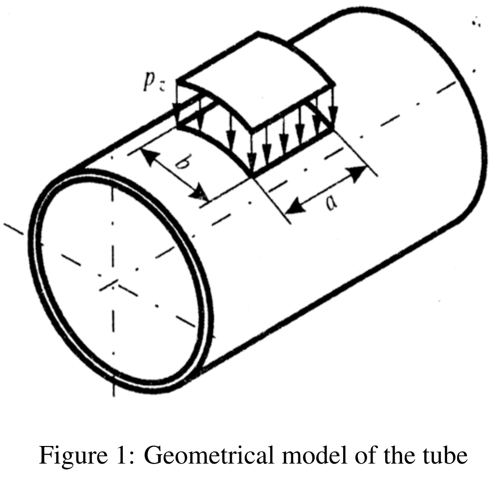

Figure 1: Geometrical model of the tube

We studies the stress-strain state of a multilayered tube under locally applied load with the use of the new improved iterative theory of anisotropic shells of Rodionova-Titaeva-Chernykh [4], the theory by Paliy-Spiro suggested in [5], the Timoshenko-Reissner theory.

The improved iterative RTCH theory is based on the following hypotheses:

1. transverse tangential and normal stresses are distributed on shell's thickness according to quadratic and cubic laws respectively;
2. tangential and normal components of the displacement vector are distributed on the shell thickness according to quadratic and cubic laws respectively.

This theory takes into account turns of fibers, their deviation and change of their length.

Functions which describe displacement of the shell's layer $u_1(\alpha,\beta,z)$, $u_2(\alpha,\beta,z)$, $u_3(\alpha,\beta,z)$ according to the Rodionova-Chernykh theory are suggested to be found as series of Legendre polynomials $P_0,\ P_1,\ P_2,\ P_3$ in normal coordinate $z\in\left[-\frac{h}{2},\frac{h}{2}\right]$

$$\begin{aligned}
u_1(\alpha,\beta,z) &= u(\alpha,\beta)P_0(z)+\gamma_1(\alpha,\beta)P_1(z)+\theta_1(\alpha,\beta)P_2(z)+\varphi_1(\alpha,\beta)P_3(z),\\
u_2(\alpha,\beta,z) &= v(\alpha,\beta)P_0(z)+\gamma_2(\alpha,\beta)P_1(z)+\theta_2(\alpha,\beta)P_2(z)+\varphi_2(\alpha,\beta)P_3(z),\\
u_3(\alpha,\beta,z) &= w(\alpha,\beta)P_0(z)+\gamma_3(\alpha,\beta)P_1(z)+\theta_3(\alpha,\beta)P_2(z),
\end{aligned}\tag{1}$$

$$P_0(z)=1,\quad P_1(z)=\frac{2z}{h},\quad P_2(z)=\frac{6z^2}{h^2}-\frac{1}{2},\quad P_3(z)=\frac{20z^3}{h^3}-\frac{3z}{h},\tag{2}$$

where u,v,w are the components of the displacement vector for points of the middle surface of the shell, γ_3 and θ_3 characterize change in length of the normal to this surface, γ_1 and γ_2 are angles of rotation of the normal in planes $(\alpha,z),(\beta,z)$ correspondingly. The variables θ_1 and φ_1, describe normal curvature of the fiber in plane (α,z), quantities θ_2 φ_2, normal curvature in plane (β,z) before deformation they were perpendicular to the shell middle surface.

The Paliy-Spiro shells theory [5] is a theory of shells of moderate thickness, which assumes the following hypotheses:

1. straight fibers of the shell, which are perpendicular to its middle surface before deformation, remain also straight after deformation;
2. cosine of the slope angle of these fibers shell's slope to the middle surface of the deformed shell is equal to the averaged angle of transverse shear.

Mathematical formulation of these hypotheses gives following equalities:

$$\begin{aligned}
&u_1(\alpha,\beta,z)=u(\alpha,\beta)+\phi(\alpha,\beta)z, && u_2(\alpha,\beta,z)=v(\alpha,\beta)+\psi(\alpha,\beta)z,\\
&u_3(\alpha,\beta,z)=w(\alpha,\beta)+F(\alpha,\beta,z), &&\\
&\phi(\alpha,\beta)=\gamma_1(\alpha,\beta)+\phi_0(\alpha,\beta), && \psi(\alpha,\beta)=\gamma_2(\alpha,\beta)+\psi_0(\alpha,\beta),\\
&\phi_0(\alpha,\beta)=-\frac{1}{A_1}\frac{\partial w(\alpha,\beta)}{\partial\alpha}+k_1u(\alpha,\beta), && \psi_0(\alpha,\beta)=-\frac{1}{A_2}\frac{\partial w(\alpha,\beta)}{\partial\alpha}+k_2v(\alpha,\beta),
\end{aligned}\tag{3}$$

where ϕ and ψ are angles of normal's rotation in planes $(\alpha,z),(\beta,z)$; ϕ_0, ψ_0,γ_1 and γ_2 — are angles of normal's rotation to the median surface and angles of displacement in the same planes. The function $F(\alpha,\beta,z)$ characterizes change of length of the normal to the median surface.

The Lamé's coefficients and curvature coefficients, which determine geometry of the cylindrical shell have the following form

$$A_1^{(i)}=R^{(i)},\quad A_2^{(i)}=1,\quad k_1^{(i)}=\frac{1}{R^{(i)}},\quad k_2^{(i)}=0\tag{4}$$

Let us introduce the following dimensionless variables:

$$\begin{aligned}
&\tilde{R}^{(i)} = \frac{A_1^{(i)}}{A_2^{(i)}}, \quad \tilde{h}^{(i)} = \frac{h}{R^{(i)}},\\
&\left\{\tilde{u}^{(i)}, \tilde{v}^{(i)}, \tilde{w}^{(i)}, \tilde{\gamma}_{1,2,3}^{(i)}, \tilde{\theta}_{1,2,3}^{(i)}, \tilde{\varphi}_{1,2}^{(i)}, \tilde{\phi}_{,0}^{(i)}, \tilde{\psi}_{,0}^{(i)}\right\}\\
&= \frac{1}{h}\left\{u^{(i)}, v^{(i)}, w^{(i)}, \gamma_{1,2,3}^{(i)}, \theta_{1,2,3}^{(i)}, \varphi_{1,2}^{(i)}, \phi_{,0}^{(i)}, \psi_{,0}^{(i)}\right\},\\
&\tilde{E}_{2,3} = \frac{E_{2,3}}{E_1}, \quad \tilde{G}_{13,12,23} = \frac{G_{13,12,23}}{E_1},\\
&\tilde{Pin}_{1,2,3}{}^{(i)} = \frac{Pin_{1,2,3}^{(i)}}{E_1}, \; \tilde{Pout}_{1,2,3}{}^{(i)} = \frac{Pout_{1,2,3}^{(i)}}{E_1},\\
&\left\{\tilde{T}_{0,1,2}^{(i)}, \tilde{Q}_{1,2}^{(i)}, \tilde{m}_{1,2,3}^{(i)}\right\} = \frac{\left\{T_{0,1,2}^{(i)}, Q_{1,2}^{(i)}, m_{1,2,3}^{(i)}\right\}}{R^{(i)}E_1},\\
&\left\{\tilde{M}_{0,1,2}^{(i)}\right\} = \frac{\left\{M_{0,1,2}^{(i)}\right\}}{R^{(i)}E_1 h}, \left\{\tilde{q}_{1,2,3}^{(i)}\right\} = \frac{\left\{q_{1,2,3}^{(i)}\right\}}{E_1},
\end{aligned} \tag{5}$$

where $Pout_x$, Pin_x are the values of the pressure on the internal and external shell surfaces. For simplicity we introduce the following parameters:

$$\begin{aligned}
&E_{11} = \frac{1}{1-\nu_{12}\nu_{21}}, \quad E_{12} = \frac{\tilde{E}_2}{1-\nu_{12}\nu_{21}}, \quad E_{22} = \frac{\nu_{12}}{1-\nu_{12}\nu_{21}},\\
&E_z = \frac{\tilde{E}_3}{1-\nu_{13}\mu_1-\nu_{23}\mu_2}, \quad \mu_1 = \frac{\nu_{31}+\nu_{21}\nu_{32}}{1-\nu_{12}\nu_{21}}, \quad \mu_2 = \frac{\nu_{32}+\nu_{21}\nu_{31}}{1-\nu_{12}\nu_{21}},\\
&K_{11} = -E_{11}\tilde{h}^{(i)}, \quad K_{12} = E_{22}\tilde{h}^{(i)}, \quad K_{21} = \frac{3}{2}E_{11}\tilde{h}^{(i)}\mu_1, \quad K_{22} = \frac{3}{2}E_{22}\tilde{h}^{(i)}\mu_2,\\
&K_{13} = E_{11}\frac{\tilde{h}^{(i)}}{2}(\mu_2+2\nu_{12}\mu_1), \quad K_{23} = E_{11}\frac{\tilde{h}^{(i)}}{2}(\nu_{12}\mu_1+2\mu_2),\\
&\tilde{m}_x^{(i)} = \frac{\tilde{h}^{(i)}}{2}\tilde{Pout}_x{}^{(i)}\left(1+\frac{\tilde{h}^{(i)}}{2}\right) + \frac{\tilde{h}^{(i)}}{2}\tilde{Pin}_x{}^{(i)}\left(1-\frac{\tilde{h}^{(i)}}{2}\right), \quad (x=1,2,3),\\
&\tilde{q}_x^{(i)} = \tilde{Pout}_x{}^{(i)}\left(1+\frac{\tilde{h}^{(i)}}{2}\right) - \tilde{Pin}_x{}^{(i)}\left(1-\frac{\tilde{h}^{(i)}}{2}\right), \quad (x=1,2,3)
\end{aligned} \tag{6}$$

3 CORRELATIONS OF THE RODIONOVA-TITAEV-CHERNYKH SHELL THEORY AND THE PALIY-SPIRO THEORY

Shell deformations of the theories under consideration are expressed through the components of displacements with the use of the following equations.

Deformation components those are different for the theories are underlining. Below we present the relations for moments, strains and deformation components for the RTCH theory, which were converted for the case of a cylindrical shell. Substituting the given dependencies in expression (7), we can receive an equation, which characterizes their connection to components of the displacement.

Rodionova-Titaev-Chernykh theory	Paliy-Spiro theory
$\tilde{\varepsilon}_1^{(i)} = \tilde{h}^{(i)}(\frac{\partial \tilde{u}^{(i)}}{\partial \alpha^{(i)}} + \tilde{w}^{(i)}), \quad \tilde{\varepsilon}_2^{(i)} = \frac{\partial \tilde{v}^{(i)}}{\partial \beta^{(i)}},$	$\tilde{\varepsilon}_1^{(i)} = \tilde{h}^{(i)}(\frac{\partial \tilde{u}^{(i)}}{\partial \alpha^{(i)}} + \tilde{w}^{(i)}), \quad \tilde{\varepsilon}_2^{(i)} = \frac{\partial \tilde{v}^{(i)}}{\partial \beta^{(i)}},$
$\tilde{\eta}_1^{(i)} = \tilde{h}^{(i)}(\frac{\partial \tilde{\gamma}_1^{(i)}}{\partial \alpha^{(i)}} + \tilde{\gamma}_3^{(i)}), \quad \tilde{\eta}_2^{(i)} = \frac{\partial \tilde{\gamma}_2^{(i)}}{\partial \beta^{(i)}},$	$\underline{\tilde{\eta}_1^{(i)} = \tilde{h}^{(i)}(\frac{\partial \tilde{\phi}^{(i)}}{\partial \alpha^{(i)}})}, \quad \underline{\tilde{\eta}_2^{(i)} = \frac{\partial \tilde{\psi}^{(i)}}{\partial \beta^{(i)}}},$
$\tilde{\varepsilon}_{13}^{(i)} = \tilde{h}^{(i)} \frac{\partial \tilde{w}^{(i)}}{\partial \alpha^{(i)}} - \tilde{h}^{(i)} \tilde{u}^{(i)} + 2\tilde{\gamma}_1^{(i)},$	$\underline{\tilde{\varepsilon}_{13}^{(i)} = 0},$
$\tilde{\varepsilon}_{23}^{(i)} = \frac{\partial \tilde{w}^{(i)}}{\partial \beta^{(i)}} + 2\tilde{\gamma}_2^{(i)},$	$\underline{\tilde{\varepsilon}_{23}^{(i)} = 0},$
$\tilde{\omega}_1^{(i)} = \tilde{h}^{(i)} \frac{\partial \tilde{v}^{(i)}}{\partial \alpha^{(i)}}, \quad \tilde{\omega}_2^{(i)} = \frac{\partial \tilde{u}^{(i)}}{\partial \beta^{(i)}},$	$\tilde{\omega}_1^{(i)} = \tilde{h}^{(i)} \frac{\partial \tilde{v}^{(i)}}{\partial \alpha^{(i)}}, \quad \tilde{\omega}_2^{(i)} = \frac{\partial \tilde{u}^{(i)}}{\partial \beta^{(i)}},$
$\tilde{\tau}_1^{(i)} = \tilde{h}^{(i)} \frac{\partial \tilde{\gamma}_2^{(i)}}{\partial \alpha^{(i)}}, \quad \tilde{\tau}_2^{(i)} = \frac{\partial \tilde{\gamma}_1^{(i)}}{\partial \beta^{(i)}},$	$\underline{\tilde{\tau}_1^{(i)} = \tilde{h}^{(i)} \frac{\partial \tilde{\psi}^{(i)}}{\partial \alpha^{(i)}}}, \quad \underline{\tilde{\tau}_2^{(i)} = \frac{\partial \tilde{\phi}^{(i)}}{\partial \beta^{(i)}}},$
$\tilde{\tau}^{(i)} = \tilde{\tau}_1^{(i)} + \tilde{\tau}_2^{(i)}, \tilde{\omega}^{(i)} = \tilde{\omega}_1^{(i)} + \tilde{\omega}_2^{(i)}$	

Table 1: Deformation components in two theories

$$
\begin{aligned}
&\tilde{T}_1^{(i)} = E_{11}\tilde{h}^{(i)}\varepsilon_1^{(i)} + E_{12}\tilde{h}^{(i)}\varepsilon_2^{(i)} + \mu_1^{(i)}\tilde{T}_0^{(i)}, \tilde{T}_2^{(i)} = E_{12}\tilde{h}^{(i)}\varepsilon_1^{(i)} + E_{22}\tilde{h}^{(i)}\varepsilon_2^{(i)} + \mu_2^{(i)}\tilde{T}_0^{(i)},\\
&\tilde{M}_1^{(i)} = \tfrac{\tilde{h}^{(i)}}{6}(E_{11}\eta_1^{(i)} + E_{12}\eta_2^{(i)}) + \mu_1^{(i)}\tilde{M}_0^{(i)}, \tilde{M}_2^{(i)} = \tfrac{\tilde{h}^{(i)}}{6}(E_{12}\eta_1^{(i)} + E_{22}\eta_2^{(i)}) + \mu_2^{(i)}\tilde{M}_0^{(i)},\\
&\tilde{T}_{12}^{(i)} = \tilde{T}_{21}^{(i)} = \tilde{G}_{12}^{(i)}\tilde{h}^{(i)}\tilde{\tau}^{(i)}, \tilde{M}_{12}^{(i)} = \tilde{M}_{21}^{(i)} = \tfrac{1}{6}\tilde{G}_{12}^{(i)}\tilde{h}^{(i)}\tilde{\omega}^{(i)},\\
&\tilde{Q}_1^{(i)} = \tfrac{5\tilde{h}^{(i)}\tilde{G}_{13}^{(i)}}{6}\varepsilon_{13}^{(i)} + \tfrac{\tilde{m}_1^{(i)}}{6} - (\tilde{h}^{(i)})^2\tfrac{\tilde{G}_{13}^{(i)}}{6}\tfrac{\partial\theta_3^{(i)}}{\partial\alpha^{(i)}},\\
&\tilde{Q}_2^{(i)} = \tfrac{5\tilde{h}^{(i)}\tilde{G}_{23}^{(i)}}{6}\varepsilon_{23}^{(i)} + \tfrac{\tilde{m}_2^{(i)}}{6} - \tilde{h}^{(i)}\tfrac{\tilde{G}_{23}^{(i)}}{6}\tfrac{\partial\theta_3^{(i)}}{\partial\beta^{(i)}},\\
&\tilde{T}_0^{(i)} = \tilde{m}_3^{(i)} + \tfrac{(\tilde{h}^{(i)})^2}{12}\left(\tfrac{\partial\tilde{q}_1^{(i)}}{\partial\alpha^{(i)}} + \tilde{R}^{(i)}\tfrac{\partial\tilde{q}_2^{(i)}}{\partial\beta^{(i)}}\right) - \tilde{h}^{(i)}\tilde{M}_1^{(i)},\\
&M_0^{(i)} = \tfrac{(\tilde{h}^{(i)})^2}{10}\tilde{q}_3^{(i)} + \tfrac{\tilde{h}^{(i)}}{60}\left(\tfrac{\partial\tilde{m}_1^{(i)}}{\partial\alpha^{(i)}} + \tilde{R}^{(i)}\tfrac{\partial\tilde{m}_2^{(i)}}{\partial\beta^{(i)}}\right) - \tfrac{\tilde{h}^{(i)}}{60}\tilde{T}_1^{(i)}
\end{aligned}
\tag{7}
$$

Let us substitute the following relations (8) for six components of the displacement in formulas (7). Thus we reduce them to dependence on the five main components of the displacement $u, v, w, \gamma_1, \gamma_2$:

$$
\begin{aligned}
&\tilde{\theta}_1^{(i)} = \tfrac{\tilde{q}_1^{(i)}}{12G_{13}} - \tfrac{\tilde{h}^{(i)}}{6}\tfrac{\partial\tilde{\gamma}_3^{(i)}}{\partial\alpha^{(i)}}, && \tilde{\varphi}_1^{(i)} = \tfrac{m_1{}^{(i)} - \tilde{Q}_1^{(i)}}{10\tilde{h}^{(i)}\tilde{G}_{13}^{(i)}} - \tfrac{\tilde{h}^{(i)}}{10}\tfrac{\partial\tilde{\theta}_3^{(i)}}{\partial\alpha^{(i)}},\\
&\tilde{\theta}_2^{(i)} = \tfrac{\tilde{q}_2^{(i)}}{12G_{23}} - \tfrac{\tilde{h}^{(i)}}{6\tilde{R}^{(i)}}\tfrac{\partial\tilde{\gamma}_3^{(i)}}{\partial\beta^{(i)}}, && \tilde{\varphi}_2^{(i)} = \tfrac{m_2{}^{(i)} - \tilde{Q}_2^{(i)}}{10\tilde{h}^{(i)}\tilde{G}_{23}^{(i)}} - \tfrac{\tilde{h}^{(i)}}{\tilde{R}^{(i)}}\tfrac{\partial\tilde{\theta}_3^{(i)}}{\partial\beta^{(i)}},\\
&\tilde{\gamma}_3^{(i)} = \tfrac{1}{2\tilde{h}^{(i)}}\tfrac{\tilde{T}_0^{(i)}}{\tilde{E}_z^{(i)}} - \tfrac{1}{2}\left(\mu_1\varepsilon_1^{(i)} + \mu_2^{(i)}\varepsilon_2^{(i)}\right), && \tilde{\theta}_3^{(i)} = \tfrac{1}{\tilde{h}^{(i)}}\tfrac{\tilde{M}_0^{(i)}}{\tilde{E}_z^{(i)}} - \tfrac{1}{6}\left(\mu_1\eta_1^{(i)} + \mu_2\eta_2^{(i)}\right)
\end{aligned}
\tag{8}
$$

The same transformation for Paliy-Spiro theory gives:

$$
\begin{array}{l}
\tilde{T}_1^{(i)} = E_{11}\tilde{h}^{(i)}\varepsilon_1^{(i)} + E_{12}\tilde{h}^{(i)}\varepsilon_2^{(i)} + \underline{\tfrac{\tilde{h}^{(i)}}{12}((K_{11}-K_{12})\tilde{\eta}_1^{(i)} - K_{13}\tilde{\eta}_2^{(i)}) + \mu_1^{(i)}\tfrac{q_3^i}{2}\tilde{h}^{(i)}},\\
\tilde{T}_2^{(i)} = E_{12}\tilde{h}^{(i)}\varepsilon_1^{(i)} + E_{22}\tilde{h}^{(i)}\varepsilon_2^{(i)} + \underline{\tfrac{\tilde{h}^{(i)}}{12}((K_{21}-K_{22})\tilde{\eta}_2^{(i)} - K_{23}\tilde{\eta}_1^{(i)}) + \mu_2^{(i)}\tfrac{q_3^i}{2}\tilde{h}^{(i)}},\\
\tilde{T}_{12}^{(i)} = \tilde{G}_{12}^{(i)}\tilde{h}^{(i)}\left(\tilde{\omega}_1^{(i)} + \tilde{\omega}_2^{(i)} - \underline{\tfrac{(\tilde{h}^{(i)})^2}{12}}\tilde{\tau}_1^{(i)}\right),\\
\tilde{T}_{21}^{(i)} = \tilde{G}_{12}^{(i)}\tilde{h}^{(i)}\left(\tilde{\omega}_1^{(i)} + \tilde{\omega}_2^{(i)} + \underline{\tfrac{(\tilde{h}^{(i)})^2}{12}}\tilde{\tau}_2^{(i)}\right),\\
\tilde{M}_1^{(i)} = \tfrac{\tilde{h}^{(i)}}{6}(E_{11}\eta_1^{(i)} + E_{12}\eta_2^{(i)} + \underline{(K_{11}-K_{12})\tilde{\varepsilon}_1^{(i)} - K_{23}\tilde{\varepsilon}_2^{(i)}) + \mu_1^{(i)}\tfrac{q_3^i}{8}\tilde{h}^{(i)}},\\
\tilde{M}_2^{(i)} = \tfrac{\tilde{h}^{(i)}}{6}(E_{12}\eta_1^{(i)} + E_{22}\eta_2^{(i)} + \underline{(K_{21}-K_{22})\tilde{\varepsilon}_2^{(i)} - K_{13}\tilde{\varepsilon}_1^{(i)}) + \mu_2^{(i)}\tfrac{q_3^i}{8}\tilde{h}^{(i)}},\\
\underline{\tilde{M}_{12}^{(i)} = \tilde{G}_{12}^{(i)}\tfrac{\tilde{h}^{(i)}}{12}\left(\tilde{\tau}_1^{(i)} + \tilde{\tau}_2^{(i)} - (\tilde{h}^{(i)})^2\tilde{\omega}_1^{(i)}\right)},\\
\underline{\tilde{M}_{21}^{(i)} = \tilde{G}_{12}^{(i)}\tfrac{\tilde{h}^{(i)}}{12}\left(\tilde{\tau}_1^{(i)} + \tilde{\tau}_2^{(i)} + (\tilde{h}^{(i)})^2\tilde{\omega}_2^{(i)}\right)},\\
\underline{\tilde{Q}_1^{(i)} = \tilde{G}_{13}^{(i)}\tilde{h}^{(i)}\gamma_1^{(i)}}, \qquad \underline{\tilde{Q}_2^{(i)} = \tilde{G}_{23}^{(i)}\tilde{h}^{(i)}\gamma_2^{(i)}},\\
\sigma_{33} = \dfrac{\tilde{P}out_3{}^{(i)}\left(1+\frac{\tilde{h}^{(i)}}{2}\right)\left(0.5+\frac{z}{h^{(i)}}\right) - \tilde{P}in_3{}^{(i)}\left(1-\frac{\tilde{h}^{(i)}}{2}\right)\left(0.5-\frac{z}{h^{(i)}}\right)}{1+\frac{z}{R^{(i)}}},\\
\tilde{F}(\alpha,\beta,z)^{(i)} = \int\limits_0^z \tfrac{\sigma_{33}}{E_z}dz - (\mu_1\varepsilon_1 + \mu_2\varepsilon_2)z - \left[\mu_1\left(\eta_1 - \tfrac{\varepsilon_1}{R^{(i)}}\right) + \mu_2\eta_2\right]\tfrac{z^2}{2} + \left(\tfrac{\mu_1\eta_1}{R^{(i)}}\right)\tfrac{z^3}{3}.
\end{array}
\tag{9}
$$

By using Table 1 we obtain moments and strains as functions of the displacement $u, v, w, \gamma_1, \gamma_2$. By substituting these relations into equilibrium equation of the cylindrical shell

$$
\begin{array}{l}
\frac{\partial\tilde{T}_1^{(i)}}{\partial\alpha^{(i)}} + \tilde{R}^{(i)}\frac{\partial\tilde{T}_{21}^{(i)}}{\partial\beta^{(i)}} + \tilde{Q}_1^{(i)} + \tilde{q}_1^{(i)} = 0, \quad \frac{\partial\tilde{T}_{12}^{(i)}}{\partial\alpha^{(i)}} + \tilde{R}^{(i)}\frac{\partial\tilde{T}_2^{(i)}}{\partial\beta^{(i)}} + \tilde{q}_2^{(i)} = 0,\\
\frac{\partial\tilde{Q}_1^{(i)}}{\partial\alpha^{(i)}} + \tilde{R}^{(i)}\frac{\partial\tilde{Q}_2^{(i)}}{\partial\beta^{(i)}} - \tilde{T}_1^{(i)} + \tilde{q}_3^{(i)} = 0,\\
\frac{1}{\tilde{h}^{(i)}}\left(\frac{\partial\tilde{M}_1^{(i)}}{\partial\alpha^{(i)}} + \tilde{R}^{(i)}\frac{\partial\tilde{M}_{21}^{(i)}}{\partial\beta^{(i)}}\right) - \tilde{Q}_1^{(i)} + \tilde{m}_1^{(i)} = 0,\\
\frac{1}{\tilde{h}^{(i)}}\left(\frac{\partial\tilde{M}_{12}^{(i)}}{\partial\alpha^{(i)}} + \tilde{R}^{(i)}\frac{\partial\tilde{M}_2^{(i)}}{\partial\beta^{(i)}}\right) - \tilde{Q}_2^{(i)} + \tilde{m}_2^{(i)} = 0
\end{array}
\tag{10}
$$

one can get a system of five partial differential equations with five unknown functions for both theories. For the Rodionova-Titaev-Chernykh theory this system of equations is 14 order, and for the Paliy-Spiro theory is of 10 order. Substituting corresponding components of the deformation in formulas (1)-(3) one can get all components of the stress-deformed state of the shells under consideration.

4 TIMOSHENKO-REISSNER THEORY

In the first approximation the nanotube could be considered as a beam. If we use the Timoshenko-Reissner theory then the solution for beams with the freely supported edges has the following [6] form

$$
w(L_v) = \frac{F{L_v}^2(L-L_v)^2}{3LEJ}\left(1 + \frac{1}{GS}\frac{3nEJ}{L_v(L-L_v)}\right). \tag{11}
$$

where L_v is a coordinate of the load application, $J = \frac{\pi R^4}{4}$ is moment of inertia for circular cross-section, $n = 5/6$ is coefficient in the formula Zhuravsky, $S = \pi R^2$ is cross-sectional area.

5 NUMERICAL METHOD

For solving the system of equations (10) in the displacements we will use the following series:

$$\begin{array}{lll} (u^{(i)}(\alpha,\beta)),(\gamma_1^{(i)}(\alpha,\beta)) & = & \sum_{n=0}^{\infty}\sum_{m=0}^{\infty}(u_{nm}^{(i)}),(\gamma 1_{nm}^{(i)})\sin[n\alpha]\sin[\bar{m}\beta], \\ (v^{(i)}(\alpha,\beta)),(\gamma_2^{(i)}(\alpha,\beta)) & = & \sum_{n=0}^{\infty}\sum_{m=0}^{\infty}(v_{nm}^{(i)}),(\gamma 2_{nm}^{(i)})\cos[n\alpha]\cos[\bar{m}\beta], \\ w^{(i)}(\alpha,\beta) & = & \sum_{n=0}^{\infty}\sum_{m=0}^{\infty} w_{nm}^{(i)}\cos[n\alpha]\sin[\bar{m}\beta], \qquad \bar{m}=(\pi m)/L, \end{array} \tag{12}$$

These formulas take into account the symmetry of the shell deformation in regard to plane $\alpha = 0$ and provide zero displacements u, γ_1 and w while $\beta = 0, L$. Expressions for v, γ_2 do not satisfy zero boundary conditions but this displacements are small. External and internal forces, which act on the shell surface can be represented as a product of sectional forces expanded in series. Let $X1_{mn}^{(i+1)}, X2_{mn}^{(i+1)}, X3_{mn}^{(i+1)}$ — be components of the pressure on the external surface of i^{th} shell, and $X1_{mn}^{(i)}, X2_{mn}^{(i)}, X3_{mn}^{(i)}$ pressure on its internal surface. Then expressions for the load and moments become:

$$\begin{array}{l} \tilde{m}_1^{(i)}(\alpha,\beta) = \sum_{n=0}^{\infty}\sum_{m=0}^{\infty}\frac{\tilde{h}^{(i)}}{2}\left(X1_{nm}^{(i+1)}\left(1+\frac{\tilde{h}^{(i)}}{2}\right)+X1_{nm}^{(i)}\left(1-\frac{\tilde{h}^{(i)}}{2}\right)\right)\sin[n\alpha]\sin[\bar{m}\beta], \\ \tilde{q}_1^{(i)}(\alpha,\beta) = \sum_{n=0}^{\infty}\sum_{m=0}^{\infty}\left(X1_{nm}^{(i+1)}\left(1+\frac{\tilde{h}^{(i)}}{2}\right)-X1_{nm}^{(i)}\left(1-\frac{\tilde{h}^{(i)}}{2}\right)\right)\sin[n\alpha]\sin[\bar{m}\beta], \\ \tilde{m}_2^{(i)}(\alpha,\beta) = \sum_{n=0}^{\infty}\sum_{m=0}^{\infty}\frac{\tilde{h}^{(i)}}{2}\left(X1_{nm}^{(i+1)}\left(1+\frac{\tilde{h}^{(i)}}{2}\right)+X1_{nm}^{(i)}\left(1-\frac{\tilde{h}^{(i)}}{2}\right)\right)\cos[n\alpha]\cos[\bar{m}\beta], \\ \tilde{q}_2^{(i)}(\alpha,\beta) = \sum_{n=0}^{\infty}\sum_{m=0}^{\infty}\left(X1_{nm}^{(i+1)}\left(1+\frac{\tilde{h}^{(i)}}{2}\right)-X1_{nm}^{(i)}\left(1-\frac{\tilde{h}^{(i)}}{2}\right)\right)\cos[n\alpha]\cos[\bar{m}\beta], \\ \tilde{m}_3^{(i)}(\alpha,\beta) = \sum_{n=0}^{\infty}\sum_{m=0}^{\infty}\frac{\tilde{h}^{(i)}}{2}\left(X1_{nm}^{(i+1)}\left(1+\frac{\tilde{h}^{(i)}}{2}\right)+X1_{nm}^{(i)}\left(1-\frac{\tilde{h}^{(i)}}{2}\right)\right)\cos[n\alpha]\sin[\bar{m}\beta], \\ q_3^{(i)}(\alpha,\beta) = \sum_{n=0}^{\infty}\sum_{m=0}^{\infty}\left(X1_{nm}^{(i+1)}\left(1+\frac{\tilde{h}^{(i)}}{2}\right)-X1_{nm}^{(i)}\left(1-\frac{\tilde{h}^{(i)}}{2}\right)\right)\cos[n\alpha]\sin[\bar{m}\beta] \end{array} \tag{13}$$

Index $i = 1$ corresponds to the internal, and $i = N+1$ to the external surface of the tube, which consists of N layers. Following [4], we accept the condition of rigidly bound layers:

$$\tilde{u}_k^{(i)}(\alpha,\beta,h/2) \;=\; \tilde{u}_k^{(i+1)}(\alpha,\beta,-h/2), \qquad k=1,2,3 \tag{14}$$

The load localized in a small rectangular area can be represented in the form of a product of the Fourier series of two loading functions in cross-section and longitudinal section:

$$Pa[\alpha] = P(\frac{C}{L}+\frac{2}{L}\sum_{n=0}^{\infty}\frac{L}{n\pi}\sin(\frac{n\pi}{L}C)\cos(\frac{n\pi}{L}\alpha)) \tag{15}$$

Pressure in longitudinal section of the tube is equal to

$$Pb[\beta] = P(\frac{4}{L}\sum_{m=0}^{\infty}\frac{L}{m\pi}\sin(\frac{m\pi}{L}C)sin(\frac{m\pi}{L}L_v)\sin(\frac{m\pi}{L}\beta)), \tag{16}$$

where L_v is a center of load application, $2C$ is a size of load application area, P is pressure in the area. Pressure area is described by function of the product of the series:

$$Pd[\alpha,\beta] = Pa[\alpha] * Pb[\beta] \tag{17}$$

The load is applied to the outer surface of the tube:

$$X1_{nm}^{(N+1)} = 0, \quad X2_{nm}^{(N+1)} = 0, \quad X3_{nm}^{(N+1)} = Pd[\alpha,\beta] \tag{18}$$

Pressure on the internal surface of the tube is absent:

$$X1^{(1)}_{nm} = 0, \quad X2^{(1)}_{nm} = 0, \quad X3^{(1)}_{nm} = 0 \tag{19}$$

Substituting dependencies (11),(12) and (16) in the system (10) and in conditions (13) we obtain a system of $8N-3$ linear algebraic equations for $5N$ deformation components and $3N-3$ forces of interaction between layers of shells. Each of the obtained coefficients $u^{(i)}_{nm}$, $v^{(i)}_{nm}$, $w^{(i)}_{nm}$, $\gamma 1^{(i)}_{nm}$, $\gamma 2^{(i)}_{nm}$, $X1^{(i)}_{mn}$, $X2^{(i)}_{mn}$, $X3^{(i)}_{mn}$ is a member of the Fourier series of functions of deformation and loading functions.

For realization of the aforementioned numerical method we developed a program based on code Mathematica 7.0.

6 NUMERICAL RESULTS

In [4] deformation of a nanotube was considered with the following parameters: thickness of each of the 100 layers $h = 0,135$ nm, inner tube radius R=2.5 nm, outer R=16 nm, length of the tube L=500 nm. For values of the modulus of elasticity of the shell $E_{1,2,3} = 1.75 * 10^{11}$ Pa, and relatively small value of the shear modulus $G_{13} = G_{12} = G_{23} = 2.3 * 10^7$ Pa. Poisson ratios $\nu_{12} = \nu_{21} = \nu_{32} = \nu_{31} = \nu_{23} = \nu_{13} = 0.3$.

The table 2 shows the values of deflection of the described tube, obtained by RTCH, TR theory and theory of PS. Calculation of the functions of displacement was done with external force $F_v = 10$ nN. The area of applied load is $[40 * 40]$ nm^2. For comparison we present values of deflections of a transversal-isotropic tube, which were received in code Ansys 11 where 3-dimensional 20 knots element Solid 186 was used. Lines ”TR1”, ”Ansys1” correspond to tube with a hole; lines ”TR2”, ”Ansys2” correspond to solid tube.

L_v	250	220	200	170	150	120	100	70	40
TR1	60.61	59.7	58.07	54.14	50.52	43.65	38.12	28.47	17.24
TR2	59.2	58.31	56.72	52.87	49.34	42.62	37.22	27.79	16.82
RTCH	57.79	56.86	55.21	51.22	47.56	40.62	35.07	25.45	14.4
PS	57.54	56.62	54.97	51	47.35	40.45	34.92	25.34	14.34
Ansys1	54.11	53.26	51.7	48.3	45.1	39.02	34.07	25.37	15.37
Ansys2	52.39	52.38	50.12	46.77	43.71	37.81	33.02	24.6	14.91

Table 2: Deflection of the many-layer nanotube.

Let us compare results obtained by the three-dimensional theory that is used in code Ansys 11 with results obtained by the aforementioned non-classical theories of shells for single-layer cylindrical shell. We consider a shell with constant outer radius and gradually increase the thickness of the shell (and consequently reduce a radius of the middle surface of the shell). The following table lists the values of deflections at the center of considered shells.

Figures 2 present functions of the upper layer displacement of the shell when the load is applied to the center of the tube.

Table 3 gives the values of the deflections of shells. Other values that characterize the stress-strain state of shells are also similar. With increasing the relative thickness of the shell, values of deflection obtained with the PS theory are closer to the values obtained with the finite element method.

h/R	1/15	1/10	1/5	1/4	1/3	1/2
TR1	46.33	31.91	17.55	14.71	11.88	9.13
RTCH	78.09	52.64	27.14	22.13	17.31	12.98
PS	75.28	49.82	24.29	19.26	14.39	9.9
Ansys1	76.36	46.44	20.37	15.9	11.95	8.92

Table 3: Deflection of a single-layer shell with constant outer radius

REFERENCES

[1] A.V. Ankudinov, S.M. Bauer, S.V. Kashtanova, N.F. Morozov, I.A. Nyapshaev, Study of mechanical stiffness of a solitary asbestos nanotub. *Bulletin of Higher Educational Institutions. The North Caucasus Region.* Series Natural Sciences 7-9 (2009).

[2] A.V. Ankudinov, S.M. Bauer, A.M. Ermakov, S.V. Kashtanova, N.F. Morozov, On mechanical properties of asbestos nanotubes. *XIV International Conference Modern Problems of the Mechanics of Solid Media*. Azov, Russia, 2010. Conference Proceedings, Vol. 1, Pp. 35-38.

[3] A.M. Krivtsov, N.F. Morozov, Anomalies in the mechanical properties of nano sized objects, *Dokl. Akad. Nauk*, 381 (3), 345-347 (2001).

[4] V.A. Rodionova, B.F. Titaev, K.F Chernykh, *Applied Theory of Anisotropic Plates and Shells*. St. Peterburg University Press, St. Petersburg (1996) (in Russian).

[5] O.M. Paliy, V.E. Spiro, *Anisotropic Shells in Shipbuilding. Theory and Analysis*. Sudostroenie, Leningrad (1977) (in Russian).

[6] L.H. Donnell, *Beams, Plates and Shells*. McGraw-Hill Book Company, 1976.

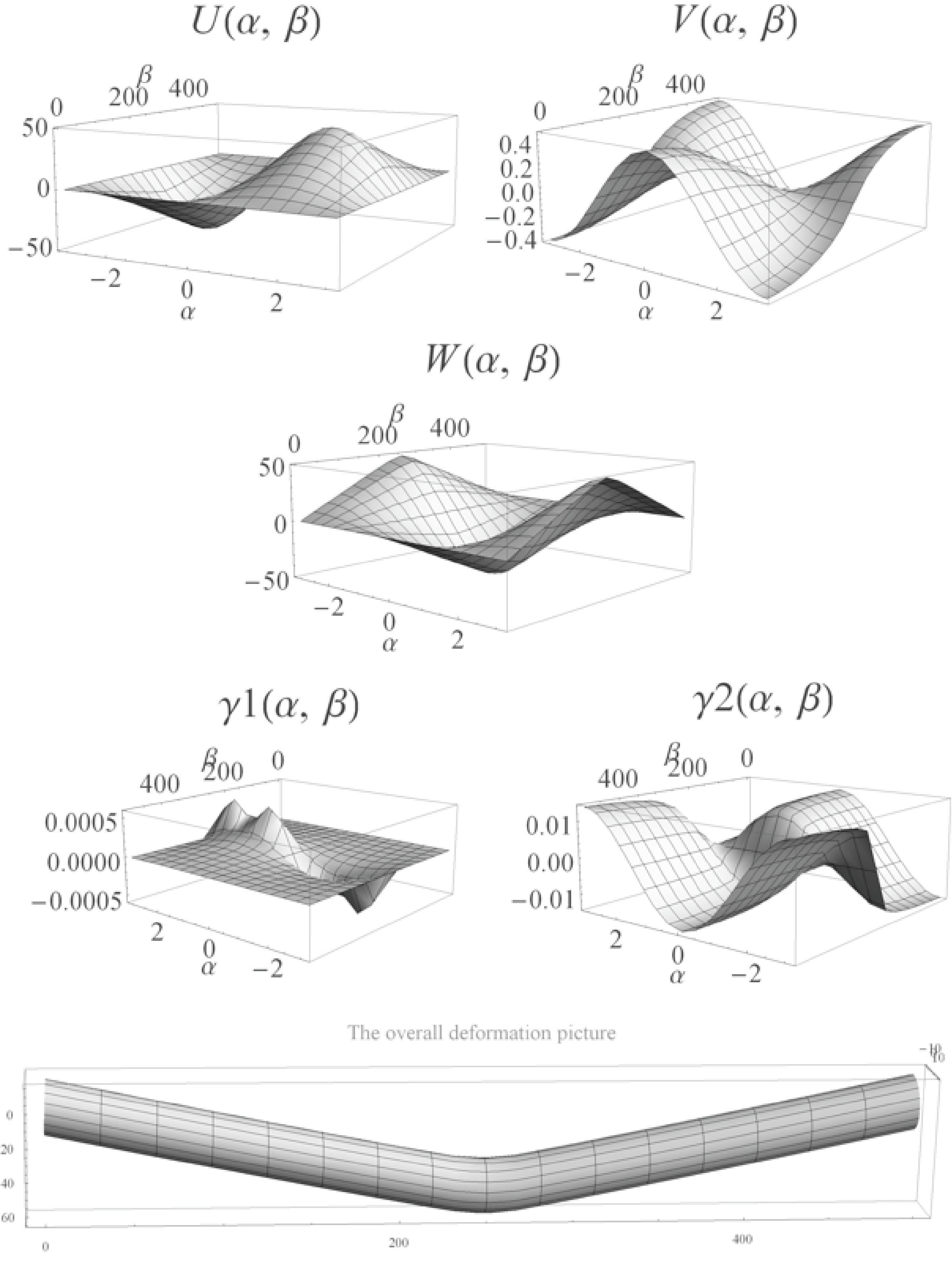

Figure 2: Deformed tube

COMPDYN 2011
ECCOMAS Thematic Conference on
Computational Methods in Structural Dynamics and Earthquake Engineering
M. Papadrakakis, M. Fragiadakis, V. Plevris (eds.)
Corfu, Greece, 25-28 May 2011

NONLINEAR DEFORMATION OF AN INFLATABLE ANISOTROPIC TOROIDAL MEMBRANE

Sergei B. Filippov

St. Petersburg State University
28 Universitetskiy pr., 198504 St. Petersburg, Russia
e-mail: s_b_filippov@mail.ru

Keywords: Pneumatic Textile Structures, Anisotropic Toroidal Membrane, Nonlinear Deformation, Asymptotic and Numerical Solutions.

Abstract. *Nonlinear axisymmetric deformation of a toroidal shell under action of internal pressure is considered. The shell is made of neo-Hookean material and is reinforced by two system of threads located on parallels and meridians. The nonlinear theory of membranes is used. For the evaluating deformations and displacements of a membrane the system of the ordinary differential equations of the fourth order is obtained. The method of asymptotical integration in the case when the meridian radius is much smaller than the parallel one is elaborated. Comparison of asymptotic and numerical results is performed.*

1 INTRODUCTION

Textile composites and pneumatic structures have become increasingly popular for a variety of applications in a civil engineering, architecture, aerospace engineering, etc. [1]. Typical examples of inflatable toroidal shells include tires, pneumatic jacks and inflatable pools. In this paper the axisymmetric nonlinear deformation under internal pressure of the toroidal shell reinforced of fibers is studied. The bending of an inflatable cylindrical membrane was considered in the paper [2].

2 MAIN ASSUMPTIONS

It is supposed that the toroidal shell is made of a cylindrical textile composite pipe which contains two systems of threads located on parallels and meridians. The lengths of not deformed threads are equal accordingly L and l (see Figure 1a).

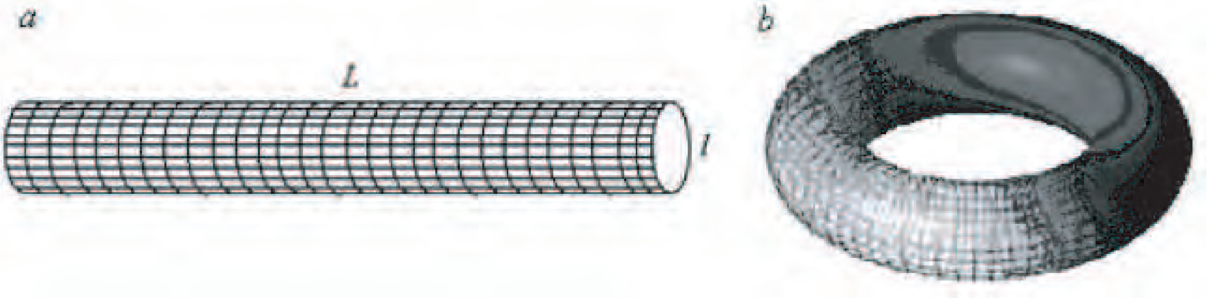

Figure 1: Transformation of the cylindrical pipe into toroidal membrane.

We assume that the fibers are disposed frequently enough. After averaging we get the two-dimensional elastic medium. This medium we consider as an anisotropic membrane. Let's close end faces of a pipe and create inside of it the pressure q. Connecting end faces of a pipe, we get a membrane like the toroidal one (see Figure 1b).

All fibers going on membrane meridians are stretched, but some fibers going on parallels are compressed if $q < q_*$, where q_* is the minimal value of pressure at which all parallels are stretched. A membrane can not hold the compression stresses. Therefore in case $q < q_*$ the part of its surface is covered by folds. If the internal pressure q increases then the area covered by folds decreases. At $q = q_*$ all shell will be stretched.

3 BASIC EQUATIONS

The theory of elastic membranes is a particular case of nonlinear theory of shells developed in the work of W.T. Koiter, W. Pietraszkiewicz, K.Z. Galimov, A. Libai and J.G. Simmonds [3]. The nonlinear membrane theory has the satisfactory accuracy for sufficiently thin shells.

For a toroidal membrane the following geometrical relations are valid:

$$\begin{gathered}\lambda_1 = \frac{ds}{ds_0}, \qquad \lambda_2 = \frac{r}{R}, \qquad R = \frac{L}{2\pi}, \\ \frac{dr}{ds} = -\sin\theta, \qquad \frac{d\hat{z}}{ds} = \cos\theta, \qquad \frac{1}{R_1} = \frac{d\theta}{ds}, \qquad \frac{1}{R_2} = \frac{\cos\theta}{r},\end{gathered} \tag{3.1}$$

where $s_0 \in [0, l]$ and $s(s_0)$ are the length of the meridian arch before and after deformation, $r(s_0)$ is the radius of a parallel, $\hat{z}(s_0)$ is the height of a parallel above a point O, $\lambda_1(s_0)$ and

$\lambda_2(s_0)$ are the stretch ratios of meridians and parallels, R_1 and R_2 are the radiuses of curvature of a surface, θ is the angle between a tangent to a meridian and the vertical direction (see Figure 2).

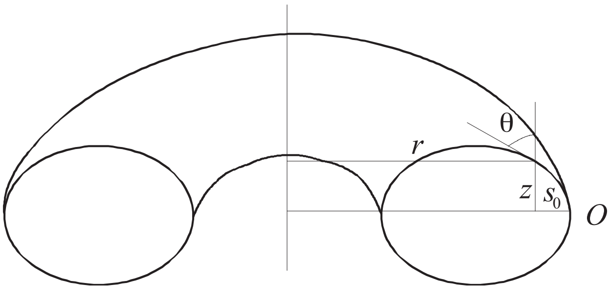

Figure 2: Toroidal membrane.

The equilibrium equations in a projection to the tangent to a meridian and the normal to the membrane give

$$\frac{d(rT_1)}{ds} + T_2 \sin\theta = 0, \qquad \frac{T_1}{R_1} + \frac{T_2}{R_2} = q, \tag{3.2}$$

where q is the internal pressure, T_1 and T_2 are stress resultants.

Assume that the shell and threads are made of incompressible homogeneous isotropic materials with elastic potentials

$$G_i \Phi_i(\lambda_1, \lambda_2, \lambda_3), \quad i = 1, 2, 3, \tag{3.3}$$

where G_i are constants of a material. For the threads going on meridians and parallels $i = 1$ and $i = 2$ accordingly, and $i = 3$ for a material of the shell. In case of small deformations G_i is the shear modulus.

Whereas the material is incompressible, equality $\lambda_1\lambda_2\lambda_3 = 1$ is valid. Besides for the threads going on meridians $\lambda_2 = \lambda_3$. Therefore the potential (3.3) becomes

$$G_1\Phi_1(\lambda_1, \lambda_1^{-1/2}, \lambda_1^{-1/2}) = G_1\Psi_1(\lambda_1).$$

For the threads going on parallels $\lambda_1 = \lambda_3$ and

$$G_2\Phi_2(\lambda_2, \lambda_2^{-1/2}, \lambda_2^{-1/2}) = G_2\Psi_2(\lambda_2).$$

For the shell potential (3.3) have the form

$$G_3\Phi_3(\lambda_1, \lambda_2, (\lambda_1\lambda_2)^{-1}) = G_3\Psi_3(\lambda_1, \lambda_2).$$

The stress resultants entering into equations (3.2) are the sums of the tensile thread forces and the stresses arising as result of a deformation of the shell:

$$T_1 = \frac{G_1 N_1 S_1}{\lambda_2}\frac{d\Psi_1}{d\lambda_1} + \frac{G_3 h_0}{\lambda_2}\frac{\partial\Psi_3}{\partial\lambda_1}, \qquad T_2 = \frac{G_2 N_2 S_2}{\lambda_1}\frac{d\Psi_2}{d\lambda_2} + \frac{G_3 h_0}{\lambda_1}\frac{\partial\Psi_3}{\partial\lambda_2}, \tag{3.4}$$

where N_1, N_2 and S_1, S_2 are numbers of threads on unit of length in a cross-sectional direction and the areas of cross-section of threads in the state before deformation for meridians and parallels correspondingly, h_0 is the thickness of the shell before deformation.

If at $\varphi \in [\varphi_*, \pi]$ formula (3.4) gives $T_2 < 0$ then according to membrane hypotheses it is necessary to put $T_2 = 0$ in system (3.2) when $\varphi \in [\varphi_*, \pi]$.

4 DIMENSIONLESS VARIABLES

Let’s enter dimensionless variables by formulas

$$\begin{gathered}
z = \frac{\hat{z}}{R}, \quad s_0 = \rho\varphi, \quad \rho = \frac{l}{2\pi}, \quad \mu = \frac{\rho}{R}, \quad Q = \frac{qR}{G_0 h_0}, \\
t_1 = \frac{T_1 \lambda_2}{G_0 h_0}, \quad t_2 = \frac{T_2 \lambda_1}{G_0 h_0}, \quad g_i = \frac{G_i N_i S_i}{G_0 h_0}, \quad i = 1, 2, \quad g_3 = \frac{G_3}{G_0},
\end{gathered} \tag{4.1}$$

where G_0 is any number, $\mu < 0.5$, and parameters g_i characterize relative stiffness of treads in comparison with one of the shell. Due to a choice G_0 any of values g_i can be taken equal 1.

Using formulas (3.1), (3.2) and (4.1) we get the following system for unknown variables $\theta(\varphi)$, $t_1(\varphi)$, $\lambda_2(\varphi)$ and $z(\varphi)$

$$\begin{aligned}
&\frac{d\theta}{d\varphi} = \frac{\mu}{t_1}(\lambda_1\lambda_2 Q - \hat{t}_2 \cos\theta), \quad \frac{dt_1}{d\varphi} = -\mu \hat{t}_2 \sin\theta, \\
&\frac{d\lambda_2}{d\varphi} = -\mu\lambda_1 \sin\theta, \quad \frac{dz}{d\varphi} = \mu\lambda_1 \cos\theta, \\
&\hat{t}_2 = \max\{t_2, 0\}, \quad 0 \le \varphi \le 2\pi.
\end{aligned} \tag{4.2}$$

The function

$$\Phi(\lambda_1, \lambda_2, \lambda_3) = \frac{1}{2}(\lambda_1^2 + \lambda_2^2 + \lambda_3^2 - 3)$$

corresponds to neo-Hookean material. Assume that $\Phi_1 = \Phi_2 = \Phi_3 = \Phi$. Then after the introduction of dimensionless variables (4.1) formulas (3.4) take the form

$$t_1 = g_3\left(\lambda_1 - \frac{1}{\lambda_1^3\lambda_2^2}\right) + g_1\left(\lambda_1 - \frac{1}{\lambda_1^2}\right), \quad t_2 = g_3\left(\lambda_2 - \frac{1}{\lambda_1^2\lambda_2^3}\right) + g_2\left(\lambda_2 - \frac{1}{\lambda_2^2}\right). \tag{4.3}$$

Owing to the symmetry of the problem to the plane $z = 0$, to find its periodic solution it is enough to find the solution of system (4.2), (4.3) satisfying the boundary conditions

$$\theta(0) = 0, \quad z(0) = 0, \quad \theta(\pi) = \pi, \quad z(\pi) = 0. \tag{4.4}$$

5 THE APPROXIMATE SOLUTION FOR COMPLETELY STRETCHED MEMBRANE

Assume that $\mu \ll 1$, $t_2 \ge 0$ for $\varphi \in [0, \pi]$ and introduce the new variables

$$\alpha = \mu^{-1} t_1, \quad \beta = \mu^{-1}(\lambda_1 - 1), \quad \gamma = \mu^{-1}(\lambda_2 - 1), \quad \delta = \mu^{-1} t_2, \quad \zeta = \mu^{-1} z. \tag{5.1}$$

Equations (4.2), (4.3) and boundary conditions (4.4) take the form

$$\begin{aligned}
&\frac{d\alpha}{d\varphi} = -\mu\delta \sin\theta, \quad \frac{d\theta}{d\varphi} = \frac{1}{\alpha}[(1 + \mu\beta)(1 + \mu\gamma)Q - \mu\delta\cos\theta], \\
&\frac{d\zeta}{d\varphi} = (1 + \mu\beta)\cos\theta, \quad \frac{d\gamma}{d\varphi} = -(1 + \mu\beta)\sin\theta.
\end{aligned} \tag{5.2}$$

$$\begin{aligned}
\mu\alpha &= (g_1 + g_3)(1 + \mu\beta) - \frac{g_1}{(1 + \mu\beta)^2} - \frac{g_3}{(1 + \mu\beta)^3(1 + \mu\gamma)^2} \\
\mu\delta &= (g_2 + g_3)(1 + \mu\gamma) - \frac{g_2}{(1 + \mu\gamma)^2} - \frac{g_3}{(1 + \mu\gamma)^3(1 + \mu\beta)^2}
\end{aligned} \tag{5.3}$$

$$\theta(0) = \zeta(0) = \zeta(\pi) = 0, \quad \theta(\pi) = \pi. \tag{5.4}$$

Substitute into (5.2)–(5.4) the asymptotic expansions

$$\begin{aligned} &\alpha = \alpha_0 + \mu\alpha_1, \quad \beta = \beta_0 + \mu\beta_1, \quad \gamma = \gamma_0 + \mu\gamma_1, \\ &\delta = \delta_0 + \mu\delta_1, \quad \theta = \theta_0 + \mu\theta_1, \quad \zeta = \zeta_0 + \mu\zeta_1. \end{aligned} \tag{5.5}$$

In the zeroth approximation we get

$$\begin{aligned} &\alpha_0 = Q, \quad \theta_0 = \varphi, \quad \zeta_0 = \sin\varphi, \quad \gamma_0 = \cos\varphi + a_0, \\ &\beta_0 = A_1 - A_2\gamma_0, \quad \delta_0 = A_3\gamma_0 + A_4, \end{aligned} \tag{5.6}$$

where a_0 is the arbitrary constant which can be found at the construction of the first approximation,

$$A_1 = \frac{Q}{4g_3 + 3g_1}, \quad A_2 = \frac{2g_3A_1}{Q}, \quad A_3 = 4g_3 + 3g_2 - 2g_3A_2, \quad A_4 = QA_2.$$

It follows from formulas (4.1), (5.1) and (5.6) that in the zeroth approximation a cross-section of the membrane is the circumference of the radius ρ. The distance between the center of this circumference and the center of the torus is equal to $R + a_0\rho$.

The solutions of equations of the first approximation

$$\begin{aligned} &\frac{d\alpha_1}{d\varphi} = -\delta_0\sin\varphi, \quad \frac{d\theta_1}{d\varphi} = \beta_0 + \gamma_0 - \frac{\alpha_1}{Q} - \frac{\delta_0}{Q}\cos\varphi, \\ &\frac{d\zeta_1}{d\varphi} = \beta_0\cos\varphi - \theta_1\sin\varphi, \quad \frac{d\gamma_1}{d\varphi} = -\beta_0\sin\varphi - \theta_1\cos\varphi, \end{aligned} \tag{5.7}$$

satisfy the boundary conditions

$$\theta_1(0) = \zeta_1(0) = \theta_1(\pi) = \zeta_1(\pi) = 0. \tag{5.8}$$

First equation (5.7) has solution

$$\alpha_1 = (A_3a_0 + A_4)\cos\varphi + \frac{A_3}{2}\cos^2\varphi + a_1Q, \tag{5.9}$$

where a_1 is the arbitrary constant. Substitution expressions (5.9) in second equation (5.7) and taking first condition (5.8) into account we get

$$\theta_1 = (A - 3c)\varphi + B\sin\varphi - \frac{c}{2}\sin 2\varphi,$$

where

$$A = A_1 + a_0(1 - A_2) - a_1, \quad B = 1 - A_2 - \frac{2(a_0A_3 + A_4)}{Q}, \quad c = \frac{A_3}{4Q}.$$

Equality $\theta_1(\pi) = 0$ holds if

$$A = 3c. \tag{5.10}$$

The solution of the third equation (5.7) satisfying the boundary condition $\zeta_1(0) = 0$ has the form

$$\zeta_1 = -\frac{1}{2}(B + A_2)\varphi + (A_1 - a_0A_2)\sin\varphi + \frac{B - A_2}{4}\sin 2\varphi + c\sin^3\varphi.$$

Taken into account the condition $\zeta_1(\pi) = 0$ we get equality $B + A_2 = 0$. Hence

$$a_0 = \frac{Q - 2A_4}{2A_3}.$$

The substitution of the expression for a_0 in formula (5.10) allows one to find a_1:

$$a_1 = A_1 + \frac{(1 - A_2)(Q - 2A_4)}{2A_3} - 3c.$$

The expression for the function γ_1 contains the constant term a_2 which can be found at the construction of the second approximation.

The condition $t_2 \geq 0$ at $\varphi \in [0, \pi]$ is necessary for a correctness of the obtained solution. After the substitution into the inequality $t_2 \geq 0$ the approximate expression $t_2 \simeq \mu\delta_0$, we get $Q \geq Q_0$, where $Q_0 = 2A_3$. The number Q_* for which by means of the asymptotic method the approximate expression Q_0 is obtained, represents a characteristic value of dimensionless pressure Q. In case of $Q < Q_*$ the part of the membrane is covered by folds, and at $Q > Q_*$ the membrane is completely stretched.

6 THE APPROXIMATE SOLUTION FOR PARTLY STRETCHED MEMBRANE

Assume that $t_2 > 0$ when $\varphi \in [0, \varphi_*]$ and $t_2 < 0$ when $\varphi \in [\varphi_*, \pi]$. Then in the area $\varphi \in [0, \varphi_*]$ all fibers going on parallels are streched and the part of the membrane surface $\varphi \in [\varphi_*, \pi]$ is covered by folds. At these assumptions equalities

$$t_2(\varphi_*) = 0, \quad \delta(\varphi_*) = 0 \tag{6.1}$$

take place.

At $\varphi \in [0, \varphi_*]$ the axisymmetric deformation of a toroidal membrane describe equation (5.2), (5.3). The function α', β', γ', θ' and ζ' define on the interval $\varphi \in [\varphi_*, \pi]$ satisfy the following equation

$$\begin{aligned} &\frac{d\alpha'}{d\varphi} = 0, \quad \frac{d\theta'}{d\varphi} = \frac{Q}{\alpha'}[(1 + \mu\beta')(1 + \mu\gamma'), \\ &\frac{d\zeta'}{d\varphi} = (1 + \mu\beta')\cos\theta', \quad \frac{d\gamma'}{d\varphi} = -(1 + \mu\beta')\sin\theta'. \end{aligned} \tag{6.2}$$

$$\mu\alpha' = (g_1 + g_3)(1 + \mu\beta') - \frac{g_1}{(1 + \mu\beta')^2} - \frac{g_3}{(1 + \mu\beta')^3(1 + \mu\gamma')^2} \tag{6.3}$$

We search the solutions of equations (5.2), (5.3) and (6.2), (6.3) satisfying boundary conditions

$$\theta(0) = \zeta(0) = 0, \quad \theta'(\pi) = \pi, \quad \zeta'(\pi) = 0, \tag{6.4}$$

$$\alpha(\varphi_*) = \alpha'(\varphi_*), \quad \theta(\varphi_*) = \theta'(\varphi_*), \quad \gamma(\varphi_*) = \gamma'(\varphi_*), \quad \zeta(\varphi_*) = \zeta'(\varphi_*), \tag{6.5}$$

in the form (5.5). To find the approximate value of the unknown number φ_* we use the asymptotic expansion $\varphi_* = \varphi_0 + \mu\varphi_1$.

In the zeroth approximation we get the same results, as in case when the toroidal membrane is completely stretched:

$$\alpha_0 = \alpha_0' = Q, \quad \theta_0 = \theta_0' = \varphi, \quad \zeta_0 = \zeta_0' = \sin\varphi,$$

$$\gamma_0 = \gamma_0' = \cos\varphi + a_0, \quad \beta_0 = \beta_0' = A_1 - A_2\gamma_0.$$

It follows from second equality (6.1) that

$$a_0 = -\cos\varphi_0 - \frac{A_4}{A_3}.$$

The number φ_0 will be found at the construction of the first approximation.

If $\varphi \le \varphi_0$ then for the construction of the first approximation we can use equations (5.7). In case $\varphi \ge \varphi_0$ equations of the first approximation have the form

$$\begin{aligned} &\frac{d\alpha_1'}{d\varphi} = 0, \quad \frac{d\theta_1'}{d\varphi} = \beta_0 + \gamma_0 - \frac{\alpha_1'}{Q}, \\ &\frac{d\zeta_1'}{d\varphi} = \beta_0\cos\varphi - \theta_1'\sin\varphi, \quad \frac{d\gamma_1'}{d\varphi} = -\beta_0\sin\varphi - \theta_1'\cos\varphi. \end{aligned} \tag{6.6}$$

The solutions of equations (5.7) and (6.6) satisfy the boundary conditions

$$\theta_1(0) = \zeta_1(0) = \theta_1'(\pi) = \zeta_1'(\pi) = 0, \tag{6.7}$$

$$\alpha_1(\varphi_0) = \alpha_1'(\varphi_0), \quad \theta_1(\varphi_0) = \theta_1'(\varphi_0), \quad \zeta_1(\varphi_0) = \zeta_1'(\varphi_0), \quad \gamma_1(\varphi_0) = \gamma_1'(\varphi_0). \tag{6.8}$$

In a considered case formulas (5.7) and (5.8) suit for the definition of the functions $\alpha_1(\varphi)$ and $\theta_1(\varphi)$. Taken into account first equation (6.6) and first condition (6.8) we get

$$\alpha_1' = \alpha_1(\varphi_0) = -\frac{A_3}{2}\cos^2\varphi_0 + a_1 Q.$$

It follows from second equation (6.6) and third condition (6.7) that

$$\theta_1' = \left(A + 2c\cos^2\varphi_0\right)(\varphi - \pi) + (1 - A_2)\sin\varphi, \tag{6.9}$$

The substitution of expressions (5.8) and (6.9) into second condition (6.8) gives the equality

$$(A/c + 2\cos^2\varphi_0)\pi = 3\varphi_0 - 5\sin\varphi_0\cos\varphi_0 + 2\varphi_0\cos^2\varphi_0. \tag{6.10}$$

Whereas for partly stretched toroidal membrane equality (5.9) is not valid, the expression for the function $\zeta_1(\varphi)$ differs from the expression obtained in the previous section:

$$\zeta_1 = (A_1 - a_0A_2)\sin\varphi + (A - 3c)(\varphi\cos\varphi - \sin\varphi) - \frac{1}{2}(B + A_2)\varphi + \frac{B - A_2}{4}\sin 2\varphi + c\sin^3\varphi. \tag{6.11}$$

The solution $\zeta_1'(\varphi)$ of the third equation (6.6) satisfying last boundary condition (6.7) has the form

$$\zeta_1 = (A_1 - a_0A_2)\sin\varphi + \left(A - 2c\cos^2\varphi_0\right)[(\varphi - \pi)\cos\varphi - \sin\varphi) + \frac{1}{2}(\pi - \varphi) + \frac{1 - 2A_2}{4}\sin 2\varphi. \tag{6.12}$$

Substitute equalities (6.11) and (6.12) into third condition (6.8). Taking in account formula (6.10) after transformations we obtain the following equation for the evaluating φ_0:

$$\sin\varphi_0 - \varphi_0\cos\varphi_0 = \pi p, \quad p = \frac{Q}{Q_0}. \tag{6.13}$$

Equation (6.13) has no an explicit solution, however its root $\varphi_0 \in [0, \pi]$ depends only on one parameter $p \in [0, 1]$. Therefore for the estimation of the value of this root it is possible to use Figure 3.

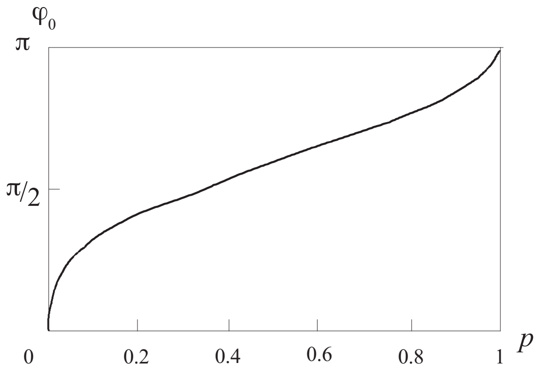

Figure 3: Plot of the functions $\varphi_0(p)$.

7 RESULTS

Consider three cases:

$$1)\quad g_1 = g_2 = 1,\ g_3 = 0; \quad 2)\quad g_1 = g_2 = g_3 = 1/2; \quad 3)\quad g_1 = g_2 = 0,\ g_3 = 1.$$

In the first case the stiffness of the threads only is taken into account, influence of the stiffness of the threads and the shell in the second case are equal and in the third case the threads are absent.

Table 1 lists the values of the dimensionless characteristic pressure Q_* for these cases. The second and third columns contain the values calculated by a numerical solution of equations (4.2) and (4.3) for $\mu = 0.1$ and $\mu = 0.01$. The last column contains the values $Q_0 = 2A_3$ found by the asymptotic approach. The error of the asymptotic formula $Q_* \simeq Q_0$ decreases with the parameter μ.

Case	Q_*		
	$\mu = 0.1$	$\mu = 0.01$	Asymptotics
1)	4.12	5.71	6.00
2)	4.59	6.15	6.43
3)	4.71	5.78	6.00

Table 1: The values of Q_* for three cases.

The boundaries φ_* of the area covered by folds for the case $g_1 = g_2 = g_3 = 1/2$ and for the different values of the dimensionless pressure Q are given in Table 2. The second and third columns contain the values calculated by a numerical solution of equations (4.2) and (4.3). The last column contains the root φ_0 of equation (6.13). The error of the asymptotic results decreases with the μ and Q.

8 CONCLUSIONS

The application of the asymptotic approach to the problem of the toroidal membrane deformation under internal pressure permits to obtain the simple approximate solution. In particular, the explicit expression Q_0 for the minimal dimensionless pressure Q_* at which folds on the shell are not formed is found. It is shown that the relative stiffness of treads influences value of the characteristic pressure Q_* a little.

Q	φ_*		
	$\mu = 0.1$	$\mu = 0.01$	Asymptotics
1	1.28	1.20	1.19
2	1.67	1.58	1.56
3	2.04	1.87	1.85
4	2.51	2.16	2.12

Table 2: The values of φ_* for the different Q.

The equation for the evaluating the boundary of the membrane area covered by folds φ_* is derived. This equation contains only one non-dimensional parameter Q/Q_0. For $\mu = 0.1$ and $Q < 3$ the error of the asymptotic results for the boundary φ_* in comparison with numerical ones is less than 10%.

9 ACKNOWLEDGEMENTS

This work was supported by RFBR (grant 10-01-00244) which is gratefully acknowledged. Thanks to Petr E. Tovstik for the formulation of the problem and the algorithm of the numerical integration.

REFERENCES

[1] E. Oñate, B. Kröplin, *Textile composites and inflatable structures*. Springer, 2005.

[2] A.M. Kolesnikov, L.M. Zubov, Pure bending of a cylindrical membrane with internal pressure. W. Pietraszkiewicz, C. Szymczak eds. *Shell Structures: Theory and Applications, Proceedings of the eighth SSTA Conference, Jurata*, 129–133, Balkema, 2005.

[3] A. Libai, J.G. Simmonds, *The Nonlinear Theory of elastic shells*. Cambridge: Univ. Press, 1998.

COMPDYN 2011
III ECCOMAS Thematic Conference on
Computational Methods in Structural Dynamics and Earthquake Engineering
M. Papadrakakis, M. Fragiadakis, V. Plevris (eds.)
Corfu, Greece, 25–28 May 2011

NONLINEAR VISCOELASTIC ANALYSIS OF A PNEUMATIC 2D STRUCTURE INTERPOSED BETWEEN A COUPLE OF RIGID MOVING PLANES

Andrea De Simone[1], **Angelo Luongo**[2]

[1]Università degli Studi dell'Aquila
Dipartimento di Ingegneria delle Strutture, delle Acque e del Terreno
Via Giovanni Falcone 25, 67100 Coppito (AQ), Italy
andrea.desimone@univaq.it

[2]Università degli Studi dell'Aquila
Dipartimento di Ingegneria delle Strutture, delle Acque e del Terreno
Via Giovanni Falcone 25, 67100 Coppito (AQ) , Italy
angelo.luongo@univaq.it

Keywords: Balloon Mechanics, Contact Problem, Balloon Squeezing, Visco-elasticity, Fender-ship Model.

Abstract. *A nonlinear planar model of visco-elastic balloon, interposed between a couple of moving rigid bodies, is formulated. The pneumatic structure is modeled as an initially circular cable, pre-stressed by an internal pressure, and constrained to remain in a planar domain. External pressure is assumed to be zero. The pushing bodies are modeled as a couple of frictionless rigid parallel bars, approaching each other normally, and causing squeezing of the pneumatic body. Motion is assumed slow, in such a way any inertial effects are negligible. Both cases of long and short bars are considered, the latter entailing the possibility of puncture of the deformable body. A thermoplastic polyurethane material behavior is considered, and proper constitutive relationships adopted. Several models are formulated, which differ for constitutive laws (inextensible, elastic, linearly or non linearly visco-elastic) and/or for kinematic analysis (small strains and displacements or finite kinematics). The governing mixed differential-algebraic equations are analytically or numerically integrated for several impressed motion time-histories and the main features of the phenomenon are investigated.*

1 INTRODUCTION

Pneumatic structures have many applications in different technical fields. Often, they consist in balloons interposed between bodies of higher stiffness, that cause their squeezing or puncture. Examples are given by fender-devices, gaskets, balloons for bulkheads control, blood vessels and angioplastic balloons. Fender-devices are used in nautical, as peer-fenders, ship-fenders and rollers; pressurized gaskets are interposed between bodies in contacts; ballons are used to lift-up bulkheads, to create artificial rapids for rafting; balloons are also extensively used for biomedical applications, e.g. to free narrowed arteries obstructed by cholesterol and fats in general.

In all these application, it is of interest to predict the evolution in time of the geometry of the balloon, of its stress, its strain and its internal pressure. Of course, the response of the balloon depends on several causes: (a) the stiffness and geometry of the in-contact bodies, (b) the type of friction at the contact, (c) the law of relative motion of the bodies, (d) the geometry of the balloon, (e) the constitutive law of the material of which the balloon is made. Here, a first attempt is made to approach the problem in a simple way, by using simple models, leading to analytical or semi-analytic solutions. The goal is to gain insights into the physics of the phenomenon, and to highlight the implications of different levels of approximation in the analysis. A long cylindrical balloon under internal pressure is considered, interposed between two rigid planar surfaces, slowly approaching each other normally. External pressure is assumed zero. By ignoring boundary effects, the problem is studied as planar, in the plane orthogonal to the cylinder axis. The structural model consists therefore in an initially circular cable, pre-stressed by an internal pressure, squeezed by two rigid and parallel bars, assumed frictionless [1]. Due to the prescribed motion of the bars, quasi-static variations of geometry, stress, and internal pressure occur. The configuration history is sketched in Fig 1, for both cases of ‘long’ (Fig 1a) and ‘short’ (Fig 1b) bars. Contact initially occurs at one point on each bar (phase I in Fig 1a,b), then it extends over a segment during the loading process (phases II in Fig 1a,b), while the free part of the cable keeps its circular shape, with modified unknown radius. These two phases are common to both kind of bars. If the bar are long, however, the process ends with a complete adhesion of cable to the bodies (phase III in Fig 1a). If the bars are short, in contrast, a critical configuration is observed (phases III in Fig 1b), in which a part of the cable is adherent to the bars for their entire length, but a remaining part is still free. Then, a partial puncture of the deformable body occurs (phase IV in Fig 1b) ending with a complete puncture (phase V in Fig 1b).

Different models are adopted for the balloon material behavior, namely (1) inextensible, (2) elastic, (3) linear visco-elastic, (4) large-strain visco-elastic, (5) fully non-linear visco-elastic. Models (3)-(5) differ in kinematic description (small strains and displacements regime, or finite kinematics) and in stress-strain-rate relationships (linear or nonlinear). In model (5), a thermoplastic polyurethane material is considered, and a properly simplified constitutive relationship adopted, deduced by the literature [2,3]. The five models are aimed to highlight the influence of the constitutive law and large displacements and strain on the overall response. For all the models considered, the formulation is illustrated, and the solution, analytical or numerical, given. Numerical results, relevant to different loading time-histories, are finally displayed and commented.

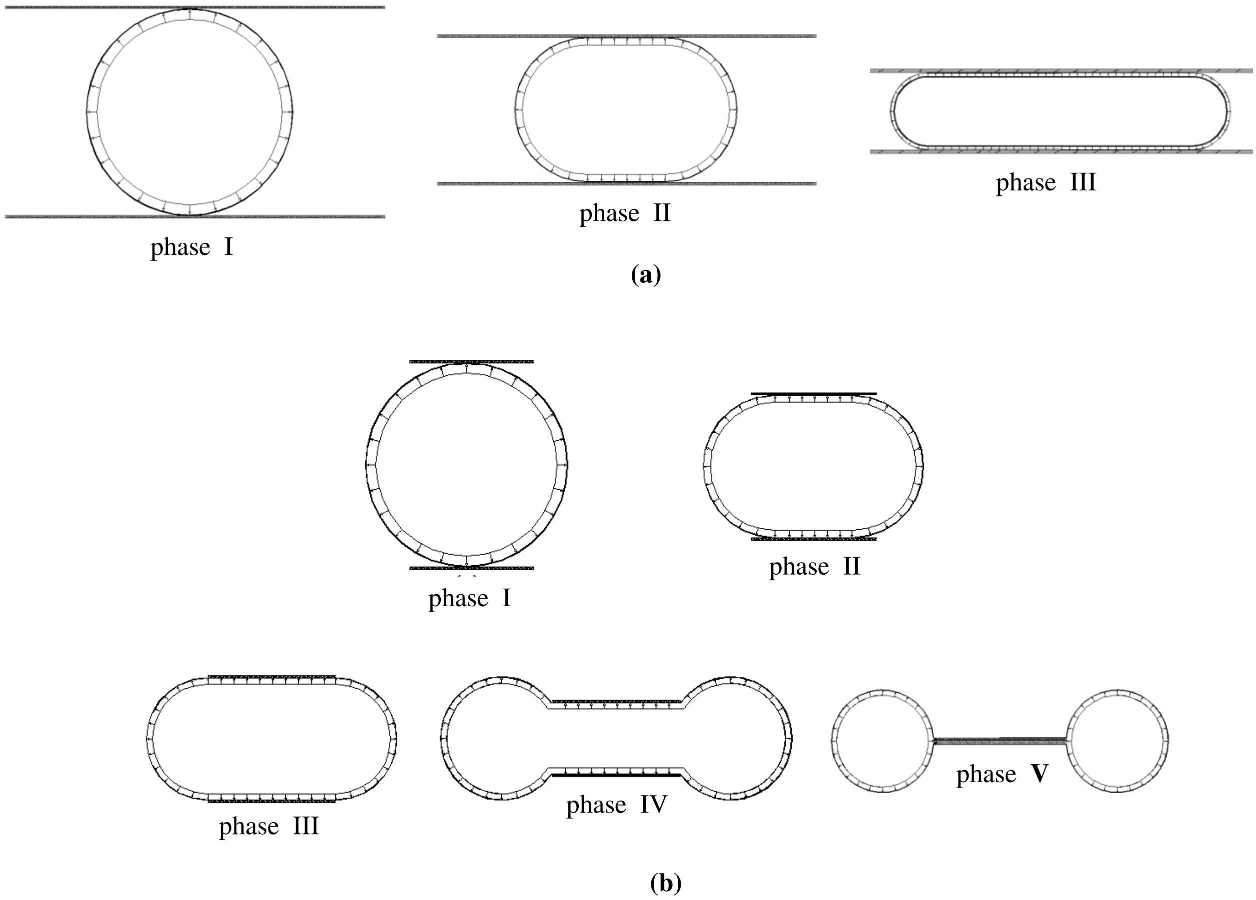

Figure 1: Evolution of the cable configuration: (a) long bars: (I) initial contact, (II) partial contact, (III) advanced configuration (close to total adhesion); (b) short bars: (I) initial contact, (II) partial contact, (III) critical configuration, (IV) punctured configuration, (V) final configuration (totally punctured).

2 MODEL FORMULATION

2.1 State-variables, pre- and post-critical states

The physical system is made of two components, the cable and the insufflated air. Its mechanical state is defined by quantities able to describe (a) the actual shape of the system (by configuration variables), (b) the state of strain (by extensive variables) and (c) the state of stress (by dual intensive variables). As it will be explained soon, since the cable is made of rectilinear and circular parts, two configuration variables are sufficient to describe the geometry. However, one of them must be taken as control parameter for the loading process, so that just one geometrical variable is unknown; it is convenient to take it as the radius R of the circular part. On the other hand, the state of the air is defined by its pressure P and by the volume V instantaneously included in the cable. The state of the cable is determined by the stress T and the strain ε, this latter measured with respect to a reference (or *initial*) configuration $\mathcal{C}_I$. Due to geometry, both these quantities are constant along the cable. By summarizing, the state is described by five scalar quantities (state-variables), $\mathbf{x} := (R, P, V, T, \varepsilon)$, all depending on time.

The state of first-contact between cable and rods (phase I in Fig 1) is taken as initial configuration. Here $\mathbf{x}_I := (R_I, P_I, V_I, T_I, \varepsilon_I)$ are assumed to be known quantities. Their evaluation, of course, calls for solving a *pre-contact evolution problem*, in which the circular cable is free. This transformation leads the body from its natural state to the initial state, as a consequence of its own visco-elastic properties.

By accounting for the double symmetry of the system, only a quarter of the cable is considered, as shown in Fig 2, for the two cases of long bars (Fig 2a,b) and short bars (Fig 2c,d). In the initial configuration (Fig 2a,c) the cable is circular, of center *O*, and delimited by the (material) contact point *A* and the symmetry point *C*; the volume subtended by this arc is $V_I = \pi R_I^2 / 4$. In the actual (or *varied*) configuration $\mathcal{C}_V$ (Fig 2b,c), a third point *B* is of interest, which separates the contact portion of cable (*AB* segment) from the circular part (*BC* arc). The projection of *B* on the horizontal symmetry axis is the new center O' of the arc. The varied configuration is determined once the radius *R* and the angle $\theta = A\hat{O}B$ are known. Although *R* coincides with the (assigned) semi-distance a between the two rods, it appears computationally more convenient to take the angle θ, instead of R, as control parameter for the loading process, by leaving to *R* the meaning of configuration variable. This state, that also occurs for short bars, will be referred to as *pre-critical.*

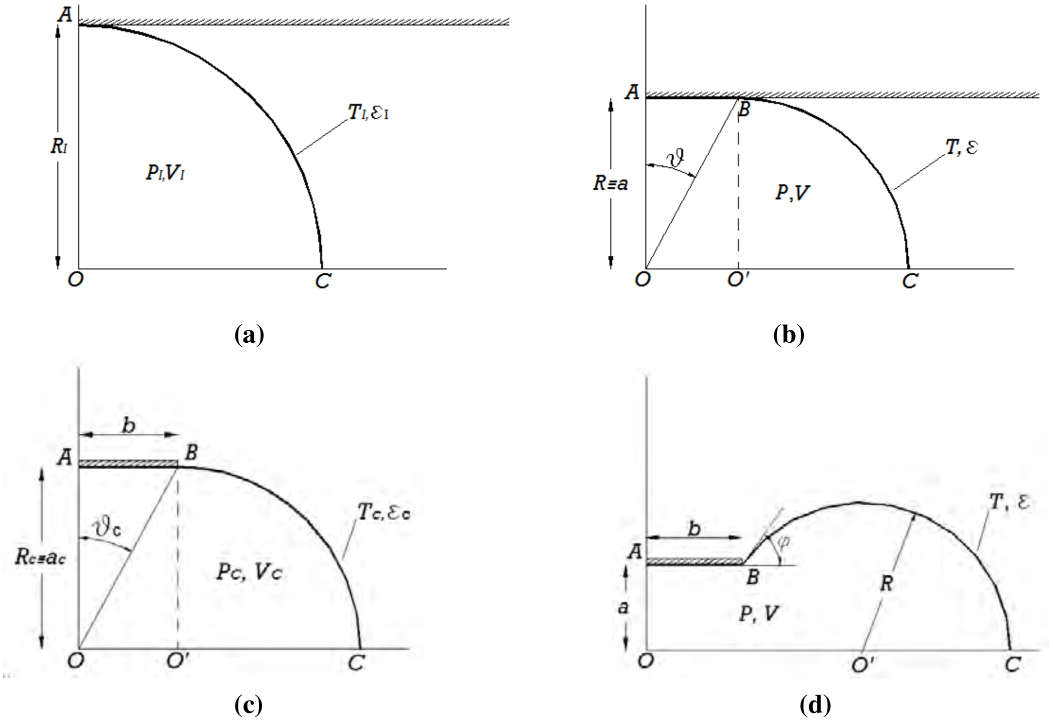

(a) **(b)**

(c) **(d)**

Figure 2: Configurations and state variables for long (a,b) and short (c,d) bars: (a) initial state; (b) actual state; (c) critical state; (d) actual (post-critical) configuration. θ, φ are control parameters.

If the bars are short, the system experiences a *critical state* $\mathcal{C}_C$ in which the contact point *B* coincides with an end of the bar (Fig 2c); in this configuration the quantities previously introduced assume the values $\mathbf{x}_C := (R_C, P_C, V_C, T_C, \varepsilon_C)$. A further approach between the bars causes the new geometrical structure of Fig 2d (punctured configuration). In order to describe how the phenomenon evolves, the new control parameter φ is chosen, which is the angle that the tangent at the circular arc at point *B* forms with the horizontal axis. The center of the arc, O', is no more the projection of *B*, and therefore a and *R* are no more coincident, but $a = R\cos\varphi$.

In this phase, the state-variables will be still denoted by $\mathbf{x}:=(R,P,V,T,\varepsilon)$, but the state will be referred to as *post-critical*. The history of these quantities, as well as the instant at which the system reaches the critical configuration, now depends on the bar semi-length b.

2.2 Governing equations

The formulation of the problem calls for establishing balance equations, geometric compatibility and constitutive equations. The balance equation expresses the equilibrium of an elementary material element belonging to the circular portion of the cable, namely:

$$T = PR \tag{1}$$

Equilibrium of the rectilinear part, indeed, is guaranteed by the fact that $T=\text{const}$ along the cable. Indeed, the internal pressure is balanced by the reactions normal to the contact, while no tangential forces act on the cable, since friction has been neglected.

As regards the constitutive laws, air is assumed to behave as perfect gas, and transformations are considered isothermal, for which:

$$PV = P_I V_I \tag{2}$$

The cable behavior, instead, is modeled in several ways. In the more general, visco-elastic case, the constitutive law assumes the form:

$$f(T,\dot{T},\varepsilon,\dot{\varepsilon})=0 \tag{3}$$

where the dot denotes time-differentiation, and the initial conditions $T(0)=T_I$, $\varepsilon(0)=\varepsilon_I$ are prescribed.

The kinematics of the system requires writing two additional compatibility equations, expressing the two extensive variables, V,ε, in terms of the unique configuration variable R. They will be named the *volumetric* and *extensional* compatibility equations, respectively. Concerning volume, elementary calculations relevant to the shape assumed by the cable in Fig 2b,d, lead to:

$$V=\begin{cases} R^2\left(\tan\theta+\dfrac{\pi}{4}\right) & \text{in pre-critical phase} \\ \dfrac{R^2}{4}\left(\sin 2\varphi+\pi+2\varphi\right)+bR\cos\varphi & \text{in post-critical phase} \end{cases} \tag{4}$$

where, of course, the post-critical phase exists only if the bars are short. Concerning the strain, and defining it as the specific elongation $\varepsilon:=(l/l_I)-1$, with l and l_I being the total length of the cable in the actual and initial configuration, it follows, that:

$$\varepsilon=\begin{cases} \dfrac{R}{R_I}\left(1+\dfrac{2}{\pi}\tan\theta\right)-1 & \text{in pre-critical phase} \\ \dfrac{R}{R_I}\left(1+\dfrac{2}{\pi}\varphi\right)+\dfrac{2b}{\pi R_I}-1 & \text{in post-critical phase} \end{cases} \tag{5}$$

In the critical state is: $\tan\theta=b/R$, $\varphi=0$, so that both the alternative expressions in Eqs (4) and (5) furnish $\varepsilon_C=R/R_I+(2b)/(\pi R_I)$ and $V_C=bR+\pi R^2/4$.

3 SPECIALIZED CONSTITUTIVE MODELS

The governing equations (1)-(5) are specialized ahead to different constitutive models of cable. Non-dimensional quantities are used, according to the following definitions:

$$\begin{gathered} p := P / P_I, \quad \tau = T / T_I, \quad v := V / V_I, \quad r := R / R_I \\ \alpha = a / R_I, \quad \beta = b / R_I \end{gathered} \tag{6}$$

in which $T_I = P_I R_I$ holds, since $\mathcal{C}_I$ is equilibrated.

3.1 Inextensible cable

The simplest model of material behavior is the inextensible model. Accordingly, the cable is considered perfectly flexible, but axially indeformable. In this case, no a constitutive law like Eq (3) exists, since the stress T assumes a reactive character. On the other hand, compatibility requires $\varepsilon = 0$, so that Eq (5) simplifies. Therefore, the relevant mechanical problem is governed by four equations in four unknowns. By using non-dimensional quantities, they read:

$$\tau = pr, \quad pv = 1, \quad v = \begin{cases} r^2 \left(1 + \dfrac{4}{\pi} \tan\theta \right) \\ r^2 \left(1 + \dfrac{2}{\pi}\varphi + \dfrac{1}{\pi}\sin 2\varphi \right) + \dfrac{4}{\pi}\beta r \cos\varphi \end{cases}, \quad \begin{cases} r\left(1 + \dfrac{2}{\pi}\tan\theta\right) = 1 \\ r\left(1 + \dfrac{2}{\pi}\varphi\right) + \dfrac{2}{\pi}\beta = 1 \end{cases} \tag{7}$$

in the pre-critical and post-critical phase, respectively.

3.2 Elastic cable

An improved model accounts for elasticity of the cable. By assuming that the body obeys to the Hooke law, and considering the initial stress, the constitutive relationship reads:

$$T = T_I + EA_I \varepsilon \tag{8}$$

where EA_I is the axial stiffness evaluated at $\mathcal{C}_I$. In non-dimensional form, the elastic problem (1)-(5) reads:

$$\begin{gathered} \tau = pr, \quad pv = 1, \quad \tau = 1 + k\varepsilon, \\ v = \begin{cases} r^2 \left(1 + \dfrac{4}{\pi}\tan\theta\right) \\ r^2 \left(1 + \dfrac{2}{\pi}\varphi + \dfrac{1}{\pi}\sin 2\varphi\right) + \dfrac{4}{\pi}\beta r\cos\varphi \end{cases}, \quad \varepsilon = \begin{cases} r\left(1 + \dfrac{2}{\pi}\tan\theta\right) - 1 \\ (r + 2\beta)\left(1 + \dfrac{2}{\pi}\varphi\right) - 1 \end{cases} \end{gathered} \tag{9}$$

in the two phases, respectively. In Eqs (9) the following non-dimensional elastic stiffness has been introduced:

$$k := EA_I / T_I \tag{10}$$

3.3 Linear visco-elastic cable

To account for slow-time effects and for internal energy dissipation of the cable, a visco-elastic constitutive model must be used. As a first, simplest approach to the problem, the well-known *linear* standard model (also called ‘three parameter model’, Fig 3) is adopted.

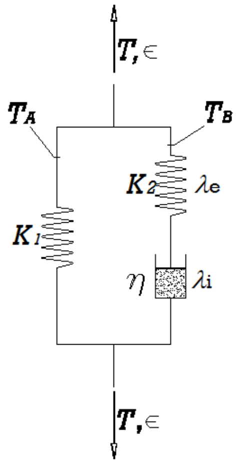

Figure 3: Standard visco-elastic model

The relevant constitutive relationship is:

$$\begin{cases} \dot{T} + \dfrac{K_2}{\eta} T = (K_1 + K_2)\dot{\varepsilon} + \dfrac{K_1 K_2}{\eta}\varepsilon \\ T(0) = T_I, \quad \varepsilon(0) = \varepsilon_I \end{cases} \tag{11}$$

where K_1, K_2, are elastic moduli, and η a viscosity coefficient. In non-dimensional form, it reads:

$$\begin{cases} \dot{\tau} + \tau = (k_1 + k_2)\dot{\varepsilon} + k_1\varepsilon \\ \tau(0) = 1, \quad \varepsilon(0) = \varepsilon_I \end{cases} \tag{12}$$

where:

$$\tilde{t} := (K_2 / \eta)t, \quad k_1 := K_1 / T_I, \quad k_2 := K_2 / T_I \tag{13}$$

have been introduced, and where the dot now denotes differentiation with respect the non-dimensional time $\tilde{t}$ (tilde dropped ahead). The visco-elastic problem for the system is therefore governed by:

$$\tau = pr, \quad pv = 1, \quad v = \begin{cases} r^2\left(1 + \dfrac{4}{\pi}\tan\theta\right) \\ r^2\left(1 + \dfrac{2}{\pi}\varphi + \dfrac{1}{\pi}\sin 2\varphi\right) + \dfrac{4}{\pi}\beta r\cos\varphi \end{cases}, \quad \varepsilon = \begin{cases} r\left(1 + \dfrac{2}{\pi}\tan\theta\right) - 1 \\ (r + 2\beta)\left(1 + \dfrac{2}{\pi}\varphi\right) - 1 \end{cases} \tag{14}$$

$$\dot{\tau} + \tau = (k_1 + k_2)\dot{\varepsilon} + k_1\varepsilon, \quad \tau(0) = 1, \quad \varepsilon(0) = \varepsilon_I$$

It is therefore a mixed differential-algebraic problem, whose solution calls for a numeric integration. It can be recast in the matrix form:

$$\begin{cases} \mathbf{A}(\mathbf{y}(t))\dot{\mathbf{y}}(t)+\mathbf{B}(\mathbf{y}(t))\mathbf{y}(t)=\mathbf{f}(t) \\ \mathbf{y}(0)=\mathbf{y}_0 \end{cases} \tag{15}$$

where $\mathbf{A}$ and $\mathbf{B}$ are 6×6 matrices, $\mathbf{y}=(\mathbf{x};\theta)$ or $\mathbf{y}=(\mathbf{x};\varphi)$ is an extended 6-vector of state variables, including the control parameter, and $\mathbf{f}(t)=(1,1,0,-1,0;f(t))$ is a 6-vector of know-terms, in which $f(t)$ denotes the impressed time-history for $\theta(t)$ or $\varphi(t)$. Moreover $\mathbf{y}_0=(r_I,p_I,v_I,\tau_I,\varepsilon_I;f(0))$. Equations (15) have been integrated by using a solver for singular and sparse matrices.

3.4 Large strain visco-elastic cable

An enhanced visco-elastic model is introduced, in which large strains are accounted for. The stretch $\lambda:=1+\varepsilon$ (whose logarithm is known as the 'true strain') instead of the (engineering) elongation ε, is used as the strain measure, since this latter is not additive in finite kinematics[1]. Reference is made again to the three-parameter model of Fig 3, in which *A* is the elastic part and *B* the visco-elastic part. Compatibility for the two parts requires $\lambda_A=\lambda_B=:\lambda$, while compatibility for part *B* calls for $\lambda=\lambda_i\lambda_e$, where $\lambda_{i,e}$ are the stretches of the in-series inelastic and elastic devices, respectively. Equilibrium requires that $T=T_A+T_B$ and $T_i=T_e=:T_B$. By still assuming linear constitutive laws for the single devices, namely:

$$T_A=K_1(\lambda-1),\quad T_B=K_2(\lambda_e-1),\quad T_B=\eta\dot{\lambda}_i \tag{16}$$

the following nonlinear stress-strain law is finally derived, with relevant initial conditions:

$$\begin{cases} \lambda\dot{T}-(K_1+K_2+T)\dot{\lambda}+\dfrac{K_2}{\eta}\left[T-K_1(\lambda-1)\right]\left[1-\dfrac{K_1}{K_2}(\lambda-1)+\dfrac{T}{K_2}\right]^2=0 \\ T(0)=T_I,\quad \lambda(0)=\lambda_I \end{cases} \tag{17}$$

It should be noted that, for small strain and $T<<K_2$, the squared bracket in Eq (17) tends to 1, so that Eq. (11) is recovered. In nondimensional variables, Eq. (17) reads:

$$\begin{cases} \lambda\dot{\tau}-(k_1+k_2+\tau)\dot{\lambda}+\left[\tau-k_1(\lambda-1)\right]\left[1-\dfrac{k_1}{k_2}(\lambda-1)+\dfrac{\tau}{k_2}\right]^2=0 \\ \tau(0)=\tau_I,\quad \lambda(0)=\lambda_I \end{cases} \tag{18}$$

The visco-elastic problem for the large-strain cable model is therefore governed by the following set of equations:

---

[1] Indeed, if $\Delta l_1,\Delta l_2$ are two successive deformations of a segment of initial length l, then the final strain $\dfrac{\Delta l_1+\Delta l_2}{l}$ differs from the sum of the two strains: $\varepsilon_1\dfrac{\Delta l_1}{l}$, $\varepsilon_2=\dfrac{\Delta l_2}{l+\Delta l_1}$. In contrast, since $\lambda=\dfrac{l+\Delta l_1+\Delta l_2}{l}$, $\lambda_1=\dfrac{l+\Delta l_1}{l}$, $\lambda_2=\dfrac{l+\Delta l_1+\Delta l_2}{l+\Delta l_1}$, then $\lambda=\lambda_1\lambda_2$.

$$\tau = pr, \quad pv = 1, \quad v = \begin{cases} r^2\left(1+\dfrac{4}{\pi}\tan\theta\right) \\ r^2\left(1+\dfrac{2}{\pi}\varphi+\dfrac{1}{\pi}\sin 2\varphi\right)+\dfrac{4}{\pi}\beta r\cos\varphi \end{cases}, \quad \varepsilon = \begin{cases} r\left(1+\dfrac{2}{\pi}\tan\theta\right)-1 \\ (r+2\beta)\left(1+\dfrac{2}{\pi}\varphi\right)-1 \end{cases} \tag{19}$$

$$\lambda\dot{\tau}-(k_1+k_2+\tau)\dot{\lambda}+[\tau-k_1(\lambda-1)]\left[1-\frac{k_1}{k_2}(\lambda-1)+\frac{\tau}{k_2}\right]^2=0, \quad \tau(0)=\tau_I, \quad \lambda(0)=\lambda_I$$

The whole system is then rearranged as in Eqs (15), to be numerically integrated.

3.5 Fully-nonlinear visco-elastic cable

Although the previous model accounts for large strains, the constitutive laws (16) of the single components are still linear. To formulate a fully-nonlinear visco-elastic model (i.e. large-strain and mechanically nonlinear), it needs to more accurately describe the stress-strain-rate law. Here, reference is made to a thermoplastic polyurethane material, for which a proper 3D-constitutive law has been proposed in [2], still based on the model of Fig. 3. It involves all the eigenvalues $\lambda_1, \lambda_2, \lambda_3$ of the deformation gradient **F**. To reduce the model to 1D, two hypotheses were introduced: (a) *each* parts *A* and *B* are incompressible, and (b) the material is transversally isotropic, these entailing $\lambda_2 = \lambda_3 = \pm 1/\sqrt{\lambda}$, with $\lambda := \lambda_1$ the longitudinal stretch. Although hypothesis (a) is quite strong (since isochoricity is more likely to hold on the two parts as a whole, rather than separately), it has been introduced here to keep the model the simplest possible. Based on this approximations, the following five-parameter visco-elastic, 1D-model were obtained in [1] (quite involved details are omitted here):

$$T_A = c_1\left(\lambda^2-\frac{1}{\lambda}\right), \quad T_B = c_2\frac{\ln\lambda_e}{\lambda_e}, \quad T_B = c_3\left(\lambda_e\sqrt{1+\frac{2}{\lambda_e^3}}-1\right)^{c_4}\left(\frac{\dot{\lambda}_i}{\lambda_i}\right)^{c_5} \tag{20}$$

in which c_i are constant materials. By using compatibility and equilibrium as in the previous model, the final constitutive equation was derived. Together with Eqs ($19_{1\text{-}4}$), they govern the fully-nonlinear visco-elastic problem for the cable.

4 PRELIMINARY NUMERICAL RESULTS

The simplest inextensible and elastic models, governed by the algebraic Eqs (7) and (9), respectively, admit a closed-form solution, which is reported in the Appendix. In contrast, the mixed algebraic differential equations, governing all the visco-elastic models, call for numerical integrations. A sample numerical integration is shown here, in order to illustrate a typical time-history of a balloon (Fig 4). Three models have been considered, and the relevant results compared, namely elastic (*E*), linear visco-elastic (*LVE*) and fully nonlinear viscoelastic (*NLVE*). A fourth model, the large-strain visco-elastic, was disregarded, since it gave results very similar to the linear one. Figure 4 shows, for the three models, the strain (Fig 4a) and the stress (Fig 4b) time-histories. When $t < t_0$, the cable is at rest in its natural (unstressed, unstrained) configuration. At $t = t_0$ an internal pressure is instantaneously applied, by insufflating air, so that the cable undergoes the strain ε_0 and the tension T_0. It should be noted that these state-variables relevant to *NLVE* differ from those relevant to *E* and *LVE*, due to the different elastic law adopted for the former. With the air-flow stopped, a time-interval $[t_0, t_I]$ is waited, in which, due to viscosity, the strain increases, while the stress decreases. In contrast, strain and stress remain constant in the elastic model. At the instant t_I, two (long) bars are juxtaposed to the balloon, touching it each in a single point, and a constant-rate motion approach is imposed to them. Both strain and stress decrease, up the critical configuration is reached at a point *C*, at an instant t_C which is different for each model. After that, the constant-rate motion is continued for an additional time interval, sufficient to move the system far from the critical condition. Then, at point *P*, a pulsating bar movement is started, of amplitude such that the balloon remains in post-critical phase. A remarkable different behavior is also appreciated in this phase for the three models.

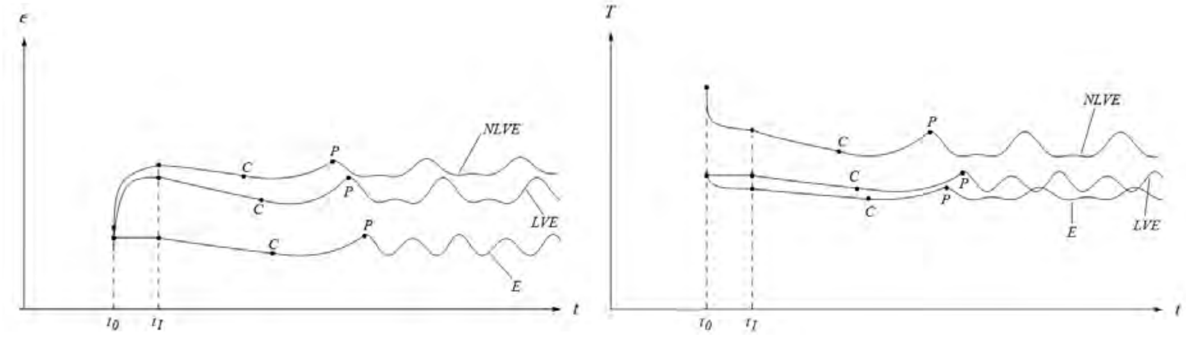

(a) **(b)**

Figure 4: Time-histories of (a) strain and (b) stress; *E*:elastic, *LVC*: linear visco-elastic, *NLVE*: nonlinear visco-elastic; t_I start of the constant-rate motion; *C*: critical point; *P*: start of the pulsating motion.

5 CONCLUSIONS

A nonlinear planar model of visco-elastic balloon, interposed between two moving rigid bars, has been formulated. The problem has been found to be governed by five algebraic-ode equations in five state-variables (radius, strain, volume, stress, internal pressure), expressing equilibrium, compatibility and stress-strain-rate relationships. The distance between the two bars (or an equivalent geometrical magnitude) is taken as loading parameter, and an arbitrarily selected time-history, assigned. According to the ratio between the radius of the balloon and the length of the bars, a one-phase evolution problem (only squeezing, for long bars) or a two-phases evolution problems (squeezing and puncture, for short bars), occur. Five specific models have been derived, of increasing complexity: inextensible, linearly elastic, linear visco-elastic, large-strain visco-elastic, fully-nonlinear visco-elastic. Preliminary analytical and numerical results have been obtained, comparing the models for a sample time-history. More extended parametric analysis will be presented at the conference.

REFERENCES

[1] A. De Simone, A non linear viscoelastic pneumatic 2D structure interposed between a couple of rigid moving surfaces, University of L'Aquila, Phd Thesis, 2010.

[2] H.J. Qi, M.C. Boyce, Stress-strain behavior of thermoplastic polyurethan. *Mechanics of materials*, 37, 817-839, 2005.

[3] McCrum N.G., Buckley C.P. and Bucknall C.B., *Principles of Polymer Engineering*. Oxford University Press, 1997.

APPENDIX: Solution to the inextensible and elastic models

Equations (7), relevant to the inextensible model, admit a unique solution, that can be obtained in closed-form. It reads:

$$r=\frac{\pi}{\pi+2\tan\theta},\quad v=\frac{\pi\left(4\tan\theta+\pi\right)}{\left(2\tan\theta+\pi\right)^2},\quad p=\frac{\left(2\tan\theta+\pi\right)^2}{\pi\left(4\tan\theta+\pi\right)},\quad \tau=1-\frac{2}{4+\pi\cot\theta} \tag{21}$$

in the pre-critical phase, and:

$$\begin{gathered} r=\frac{\pi-2\beta}{\pi+2\varphi},\quad v=\frac{(\pi-2\beta)\left(4\beta(\pi+2\varphi)\cos\varphi+(\pi-2\beta)(\pi+2\varphi+\sin2\varphi)\right)}{\pi(\pi+2\varphi)^2},\\ p=\frac{\pi(\pi+2\varphi)^2}{(\pi-2\beta)\left(4\beta(\pi+2\varphi)\cos\varphi+(\pi-2\beta)(\pi+2\varphi+\sin2\varphi)\right)},\quad \tau=\frac{\pi(\pi+2\varphi)}{4\beta(\pi+2\varphi)\cos\varphi+(\pi-2\beta)(\pi+2\varphi+\sin2\varphi)} \end{gathered} \tag{22}$$

in the post-critical phase.

Equations (9), relevant to the elastic model, can be solved analytically as well. Two distinct solutions were found; one of them, however, had to be disregarded, since physically not admissible ($\tau<0$)(see [1]). The admissible solution, instead, is:

$$\begin{gathered} \tau=\frac{1}{2}\left(1-k+\frac{\cos\theta\sqrt{\pi+4\tan\theta}\sqrt{(1+k)^2\pi+4\left(1+k^2\right)\tan\theta}}{\pi\cos\theta+4\sin\theta}\right),\\ p=\frac{\left(1+k^2\right)\pi+4\left(1+(k-1)k\right)\tan\theta-(k-1)\sqrt{\pi+4\tan\theta}\sqrt{(1+k)^2\pi+4\left(1+k^2\right)\tan\theta}}{2\pi},\\ \varepsilon=\frac{1}{2}\left(-1+\frac{-1+\sqrt{\dfrac{(1+k)^2\pi+4\left(1+k^2\right)\tan\theta}{\pi+4\tan\theta}}}{k}\right),\\ v=\frac{\pi\left(\left(1+k^2\right)\pi+4\left(1+(k-1)k\right)\tan\theta+(k-1)\sqrt{\pi+4\tan\theta}\sqrt{(1+k)^2\pi+4\left(1+k^2\right)\tan\theta}\right)}{2k^2\left(\pi+2\tan\theta\right)^2},\\ r=\frac{\pi\left(-1+k+\sqrt{\dfrac{(1+k)^2\pi+4\left(1+k^2\right)\tan\theta}{\pi+4\tan\theta}}\right)}{2k\left(\pi+2\tan\theta\right)} \end{gathered} \tag{23}$$

in the pre-critical phase, and**:**

$$\begin{gathered} \tau=\frac{\beta(\pi+2\varphi)-2\beta(\pi+2\varphi)\cos\varphi+\beta\sin2\varphi+\frac{1}{2}A}{\pi(\pi+2\varphi+\sin2\varphi)},\\ p=\frac{1}{\pi^3-8\pi\beta^2\cos\varphi}\left(\pi^3+2\pi^2\varphi+2\beta^2\pi(1-2\cos\varphi)+2\beta^2\left(2\varphi-4\varphi\cos\varphi+\sin2\varphi\right)+\beta A\right),\\ \varepsilon=\frac{(\beta-\pi)(\pi+2\varphi)-2\beta(\pi+2\varphi)\cos\varphi+(\beta-\pi)\sin2\varphi+\frac{1}{2}A}{\pi(\pi+2\varphi+\sin2\varphi)},\\ v=\frac{1}{\pi(\pi+2\varphi)^2}\left(\pi^3+2\pi^2\varphi+2\beta^2\pi(1-2\cos\varphi)+2\beta^2\left(2\varphi-4\varphi\cos\varphi+\sin2\varphi\right)-\beta A\right),\\ r=\frac{1}{(\pi+2\varphi)(\pi+2\varphi+\sin2\varphi)}\left(-\beta\pi(1+2\cos\varphi)-2\beta\left(\varphi+\cos\varphi(2\varphi+\sin\varphi)\right)+\frac{1}{2}A\right) \end{gathered} \tag{24}$$

in the post-critical phase, where the following constant has been defined:

$$A=\sqrt{4(\pi+2\varphi)\left(\pi^2-8\beta^2\cos\varphi\right)(\pi+2\varphi+\sin2\varphi)+4\beta^2\left((\pi+2\varphi)(1+2\cos\varphi)+\sin2\varphi\right)^2} \tag{25}$$

COMPDYN 2011
3rd ECCOMAS Thematic Conference on
Computational Methods in Structural Dynamics and Earthquake Engineering
M. Papadrakakis, M. Fragiadakis, V. Plevris (eds.)
Corfu, Greece, 25–28 May 2011

QUASI-STATIC SIMULATIONS OF THIN SPACE MEMBRANES, AIMING AT STABILITY ANALYSES OF BALLOON-LIKE STRUCTURES

Anders Eriksson

KTH Mechanics, Royal Institute of Technology
Osquars backe 18, SE-100 44 Stockholm, Sweden
e-mail: anderi@kth.se

Keywords: Space membranes, Inflation, Compressible medium, Quasi-static equilibrium, Stability, Path-following.

Abstract. *This paper discusses the evaluation of quasi-static equilibrium solutions for inflatable space membrane structures, such as balloons. A flat linearly interpolated triangular element is used for simulations, with a Mooney-Rivlin hyper-elastic material model, with variable constitutive constants. A compressible medium is used to introduce a one-parametric over-pressure loading within the membrane. Complex path-following procedures are used to find generalized equilibrium paths, with different parameterizations. Numerical examples show that the methods developed can give information on the stability of the structures, but that the medium and means for introducing the internal pressure is of importance for the interpretation of stability.*

1 INTRODUCTION

A large variety of thin three dimensional inflatable structures, i.e., balloons, are used in several engineering and medical contexts, e.g., [1, 2, 3]. These structures often show large deformations when subjected to distributed pressures. The bending stiffness can often be neglected and only a membrane state considered. Several analytical and numerical treatments for more or less general situations are available in literature, [4, 5, 6, 7, 8]. The treatment of these structures also leads to several accompanying aspects, such as the load descriptions, [9], contact formulations, [10], and instability aspects, [11, 12, 13].

Simulations of very thin membranes are often based on shell models, but these show important drawbacks in situations where the bending stiffness almost vanishes. The main problems lie in the treatment of large rotations, the aspect ratios of the elements, and the stiffness differences in membrane and bending action. As one remedy, rotation-free shell elements have been suggested by many researchers, [14, 15, 16, and others]. The main efforts have been related to non-local evaluation of the element curvatures, and to degenerated solid elements, [17]. Advantages and disadvantages of rotation-free shell elements are described in [18, 19].

For the balloon-like structures considered in the present work, an assumption has been that simulations of the inflation process can be based purely on the membrane behavior, disregarding the bending stiffness. This assumption will remove the numerical problems associated with shell formulations when thickness tends to zero, and also leads to efficient simulations. Some space membrane elements have been developed in literature for special applications. An interesting recent development is discussed by Pargana et al., [20], where an initially flat, quadratically interpolated 6-node membrane element is developed for ‘Tensioned Fabric’ structures. The element uses a total Lagrangian approach, and Green strains, but considers only cases where strains can be assumed as small.

The problems considered here, i.e., the inflation of balloon-like structures, are both geometrically non-linear due to finite deformations and materially non-linear through the constitutive relationship. A co-rotational (‘CR’) finite element form was developed in [21], where the local element is purely in an in-plane state. It was concluded that the CR formulation can be relevant and efficient for problems where the local behavior is sufficiently well described by an elastic formulation, but that the formulation became inefficient when hyper-elastic material models were introduced. In the present work, a hyper-elastic flat triangular membrane element based on a total Lagrangian (‘TL’) formulation was used for the analysis of thin space membrane structures, allowing different hyper-elastic forms.

The restrictions of the current formulation are primarily that all elements connecting to a node can not be co-planar at any stage, and that only surface-normal pressure loads are present. For physical relevance, the elements in the mesh must also be under tensile states at any solution. We also only consider quasi-static equilibrium situations, hypothesizing that he dynamics of a real inflation process is not primarily related to the inertia properties of the structure, but to the loading situations. The quasi-static assumption in this work means that any combination of pressure and volume can be immediately introduced, without dynamic or thermal effects.

The element formulation was tested for the structural class considered, noting that the present problems demand sophisticated path-following algorithms, with several aspects of instability detection and classification included. In particular, the generalized path-following in a parameter space with not just a single load factor was shown to be useful for the analyses.

2 COMPUTATIONAL MODELING

The basic quasi-static structural equilibrium situation is based on a one-parametric pressure loading. The formulation is thereby aimed at seeking a set of combinations $(\boldsymbol{u}, \psi)$ satisfying:

$$\boldsymbol{F}(\boldsymbol{u}, \psi) \equiv \boldsymbol{f}(\boldsymbol{u}) - \boldsymbol{p}(\psi, \boldsymbol{u}) = \boldsymbol{0} \tag{1}$$

where $\boldsymbol{f}$, $\boldsymbol{p}$, and $\boldsymbol{u}$ are vectors containing internal forces, external forces, and displacements, respectively, in the degrees of freedom of the structure considered. Also, ψ is a scalar value representing the over-pressure in the transversal direction. Element displacements $\boldsymbol{u}^g$ are extracted from $\boldsymbol{u}$ based on a topology defined, while $\boldsymbol{f}$ and $\boldsymbol{p}$ are assembled from element contributions $\boldsymbol{f}^g$ and $\boldsymbol{p}^g$, respectively. The super-index g indicates that the element components are measured in the common degrees of freedom of the structure, which in the present case are translations in the three global axis directions.

The differential relation corresponding to Eq. (1) is:

$$\delta\boldsymbol{F} = \frac{\partial \boldsymbol{f}}{\partial \boldsymbol{u}}\delta\boldsymbol{u} - \frac{\partial \boldsymbol{p}}{\partial \boldsymbol{u}}\delta\boldsymbol{u} - \frac{\partial \boldsymbol{p}}{\partial \psi}\delta\psi = (\mathbf{K} - \mathbf{K}_p)\,\delta\boldsymbol{u} - \delta\psi\frac{\partial \boldsymbol{p}}{\partial \psi} \tag{2}$$

which gives a tangential stiffness matrix containing a load-dependent term, since the pressure load is acting on the deformed geometry.

2.1 Element formulation

The element used for large deflection space membrane simulations is based on the linearly interpolated constant strain triangle, ‘CST’, for in-plane analysis. When seen in a three-dimensional context, the nodes (i, j, k) are defined by initial coordinates $\boldsymbol{x}_I^g,\ (I = i, j, k)$. The global displacement components are similarly $\boldsymbol{u}_I^g$. The element is assumed to be flat, and the initial nodal positions define a plane in space, with three initial element coordinate axes in an orthogonal matrix $\mathbf{R}_0$, the third axis being an outwards normal direction to the flat element. Using the initial position of node i as the origin for a local coordinate system, the initial shape of the element is defined by local coordinates:

$$\boldsymbol{x}_I^e = \mathbf{R}_0^T\,(\boldsymbol{x}_I^g - \boldsymbol{x}_i^g) \qquad (I = i, j, k) \tag{3}$$

where the third coordinate is zero for the three nodes, by construction. Relative to this initial element coordinate system, the displacements are:

$$\boldsymbol{u}_I^e = \mathbf{R}_0^T\ \boldsymbol{u}_I^g \qquad (I = i, j, k) \tag{4}$$

The displacements of a point p within the element is interpolated as:

$$\boldsymbol{u}_p^e = \sum_I N_I(x_{p,1}^e, x_{p,2}^e)\boldsymbol{u}_I^e \tag{5}$$

with common shape functions for the CST element, representing a linear interpolation of all three local displacement components related to the initial element plane.

Corresponding to the element displacements $\boldsymbol{u}_I^e$, element internal forces $\boldsymbol{f}_I^e$ are evaluated, which are then transformed into internal force contributions in global coordinate directions as:

$$\boldsymbol{f}_I^g = \mathbf{R}_0\ \boldsymbol{f}_I^e \qquad (I = i, j, k) \tag{6}$$

The evaluation of the internal forces in the element is assuming an incompressible isotropic hyper-elastic material model. Strains are described by the the right Cauchy-Green deformation tensor:

$$\mathbf{C} = \begin{bmatrix} C_{11} & C_{12} & 0 \\ C_{21} & C_{22} & 0 \\ 0 & 0 & C_{33} \end{bmatrix} \tag{7}$$

where the incompressibility condition $J = \det(\mathbf{C}) = 1$ relates C_{33} to the other components, and where initial element coordinates are used. Stresses are represented by the second Piola-Kirchhoff stress tensor:

$$\mathbf{S} = \begin{bmatrix} S_{11} & S_{12} & 0 \\ S_{21} & S_{22} & 0 \\ 0 & 0 & S_{33} \end{bmatrix} \tag{8}$$

where the assumption of a local plane-stress situation demands $S_{33} = 0$.

Introducing the constraints above, a convenient form can be derived based on considering the four components C_{11}, C_{22}, C_{12} and C_{21}, and the corresponding stress components. It is noted that the strains are non-linearly dependent on nodal displacements but constant over the element area. An incremental strain operator $\mathbf{B} = \mathbf{B}(\boldsymbol{x}_I^e, \boldsymbol{u}_I^e)$ gives variations in strain components from variations in element displacements.

The hyper-elastic model is characterized by a strain-energy relation, [22, 23]:

$$\mathbf{S} = -\rho\,\mathbf{C}^{-1} + 2\frac{\partial W}{\partial \mathbf{C}} \tag{9}$$

where W is a strain energy function, and ρ a hydro-static pressure, which can also be seen as a Lagrange multiplier enforcing the strain and stress constraints above. With the incompressibility assumption, $I_3(\mathbf{C}) = 1$, the strain energy function is written:

$$W = W(I_1(\mathbf{C}), I_2(\mathbf{C})) \tag{10}$$

with the first and second invariants of the tensor $\mathbf{C}$. A Mooney-Rivlin form, [22] defines the stress-strain relation from two constitutive constants:

$$W = c_1(I_1(\mathbf{C}) - 3) + c_2(I_2(\mathbf{C}) - 3) \tag{11}$$

The above expressions were used to describe the relation between the stress and strain components considered:

$$\mathbf{S} = \mathbf{S}(\mathbf{C}, c_1, c_2) \tag{12}$$

and also the differential relation between increments in stress and strain. These give the internal force vector and the tangential stiffness matrix for the element at a current state of displacement; as all quantities are constant within each element, the required integration is simple.

A neo-Hookean form is a further specialization of the above expression, where a single constitutive constant is $c_1 = \mu/2$, half the shear modulus. A general demand on the constants is that the sum $c_1 + c_2 = \mu/2$, [22]. Different relations between the two constitutive constants were tested for the numerical examples below, and are in the examples represented as a ratio n_1/n_2, where:

$$c_1 = \frac{n_1}{n_1 + n_2}\frac{\mu}{2} \tag{13}$$

$$c_2 = \frac{n_2}{n_1 + n_2}\frac{\mu}{2} \tag{14}$$

2.2 Loading assumptions

A membrane can be pressurized in several different ways. One important aspect is the medium introducing the pressure on the membrane. Typically, a gas is compressible and can be assumed to have zero density, whereas a liquid is incompressible and has a density. In particular for gases, the mechanism for introducing the medium into the membrane is of importance, where it is assumed that either a specified pressure can be introduced independent of the resulting volume, or a specific amount of gas is introduced leading to a balance between pressure and volume.

In the present work, it has been assumed that the pressure is introduced by a compressible gas, with zero density. This means that a one-parameter description of the over-pressure can be used, and this pressure is acting in a normal, outwards direction on all surfaces, with only positive over-pressures considered. The over-pressure ψ is seen as related to a constant surrounding pressure of the membrane ψ_0. The total pressure within the membrane is thereby $\Psi = \psi_0 + \psi$.

The local displacement-dependent loading due to normal uniform over-pressure is evaluated as:

$$\boldsymbol{p}_I^e = \psi \frac{A}{3} (0, 0, 1)^{\mathrm{T}}, \quad (I = i, j, k) \tag{15}$$

where ψ is the current surface pressure, and $A = A(\boldsymbol{x}_I^e, \boldsymbol{u}_I^e)$ is the current element area. The element contribution is transformed to global degrees of freedom and assembled to the structural pressure load vector.

The stiffness term $\mathbf{K}_p$ in Eq. (2) is related to the displacement-dependent pressure loads. This aspect is extensively discussed in [11], and must be considered when simulating large deformations of a pressure-loaded structure. Assembled from element contributions $\mathbf{K}_p^g$, rather simple geometric consideration show that for the present formulation:

$$\mathbf{K}_p^g = \mathbf{R}_0 \begin{bmatrix} \mathbf{k}_{p,ii} & \mathbf{k}_{p,ij} & \mathbf{k}_{p,ik} \\ \mathbf{k}_{p,ji} & \mathbf{k}_{p,jj} & \mathbf{k}_{p,jk} \\ \mathbf{k}_{p,ki} & \mathbf{k}_{p,kj} & \mathbf{k}_{p,kk} \end{bmatrix} \mathbf{R}_0^{\mathrm{T}} \tag{16}$$

where the submatrices are formulated in displaced local coordinates:

$$\mathbf{k}_{p,IJ} = \frac{\psi}{6} \begin{bmatrix} 0 & 0 & y_{d(J-1)} - y_{d(J+1)} \\ 0 & 0 & x_{d(J+1)} - x_{d(J-1)} \\ y_{d(J+1)} - y_{d(J-1)} & x_{d(J-1)} - x_{d(J+1)} & 0 \end{bmatrix} \tag{17}$$

The indices i, j, k are thereby introduced cyclically, and the coordinates are

$$\boldsymbol{x}_{dI} = \begin{pmatrix} x_{dI} \\ y_{dI} \\ z_{dI} \end{pmatrix} = \boldsymbol{x}_I^e + \boldsymbol{u}_I^e \tag{18}$$

The amount of gas contained by the membrane can be evaluated from the equation for an ideal gas, stated as:

$$\Psi V = NT \tag{19}$$

where Ψ is the total gas pressure, V the volume enclosed by the membrane, N an amount measure and T the absolute temperature. This expression can be used in different ways in the evaluation of membrane behavior, as indicated by the examples below.

2.3 Quasi-static equilibrium solutions

The pressurized membranes often show complicated non-linear responses to loading, with different instability states being important aspects. The solution of quasi-static equilibrium states thereby demands rather sophisticated solution algorithms. The present work has utilized one-dimensional path-following techniques based on variable parameterizations along the solution path, changing both the parameterizing component and the step length as functions of the path traversed, [24, 25]. The isolation of critical instability states is based on sequential bisections along the parameterized path, [26]. The response variables can also be seen as functions of, e.g., geometric or material parameters in the model, [27], where augmenting equations specify a subset of equilibrium states under variation of the additional parameters. In particular, the dependence of the critical states on the added parameters can be evaluated by methods from [28]. An interesting possibility, not yet utilized, is also to to evaluate two-dimensional solution surfaces, where parametric combinations leading to certain response aspects can be evaluated and visualized, [29]. The general setting is thereby:

$$\boldsymbol{G}(\boldsymbol{u},\boldsymbol{\lambda}) \equiv \begin{pmatrix} \boldsymbol{f}(\boldsymbol{u}) - \boldsymbol{p}(\lambda_1,\boldsymbol{u}) \\ \boldsymbol{g}(\boldsymbol{u},\boldsymbol{\lambda}) \end{pmatrix} = \boldsymbol{0} \tag{20}$$

where Eq. (1) gives the equilibrium equations between the displacements and the load-describing variable $\lambda_1 = \psi$, and the N_g augmenting equations $\boldsymbol{g}(\boldsymbol{u},\boldsymbol{\lambda})$ define some extra relations for the interesting subset of equilibrium solutions, under the variations of the variables $\lambda_1,\ldots,\lambda_{N_\lambda}$. The dimension of the solutions to the augmented system is then $N_\lambda - N_g$.

3 NUMERICAL EXAMPLES

We have performed some test with a spherical membrane, and a balloon-shaped membrane, both subjected to internal over-pressures. In both cases, we used an initial thickness of 0.1 mm, and a material with shear modulus $\mu = 0.4225$ MPa.

3.1 A sphere

A sphere with radius $r = 10$ mm under internal pressure was considered, [4, 22]. Boundary conditions were chosen to allow uniform expansion, cf Fig. 1. A mesh of the whole sphere with 5120 triangular elements was considered, based on successive subdivisions of a 20-corner icosahedron mesh; all nodes were moved radially to be placed on the sphere. The example was used to show the properties of the hyper-elastic formulation, with different ratios between c_1 and c_2 coefficients in the Mooney-Rivlin constitutive relation Eq. (11), described by (n_1, n_2) as in Eqs. (13)–(14).

The results from hyper-elastic models are given in Fig. 2. Re-drawn with the radial expansion u_D expressed as a stretch, the results visually agree with the analytical results given in [22], for $c_1 = 0.5\mu, c_2 = 0$ ('neo-Hookean') and for $c_1 = \frac{7}{16}\mu, c_2 = \frac{1}{16}\mu$ ('Mooney-Rivlin'). No instabilities were noted in addition to the turning points with respect to pressure, [4].

Solutions with a sufficiently low c_2 constant show a maximum pressure state for small expansions. Even for very small non-zero values of c_2, there will also be a (local) minimum pressure state, but the pressures will eventually increase with radial expansion; this was verified for a case with $(n_1/n_2) = 1023/1$, where the minimum limit pressure was found as $p = 0.528$ kPa at a radial expansion $u_D \approx 310$ mm. The pair of limit pressure states disappear between calculated solutions for $n_1/n_2 = 5/1$ and $n_1/n_2 = 4/1$.

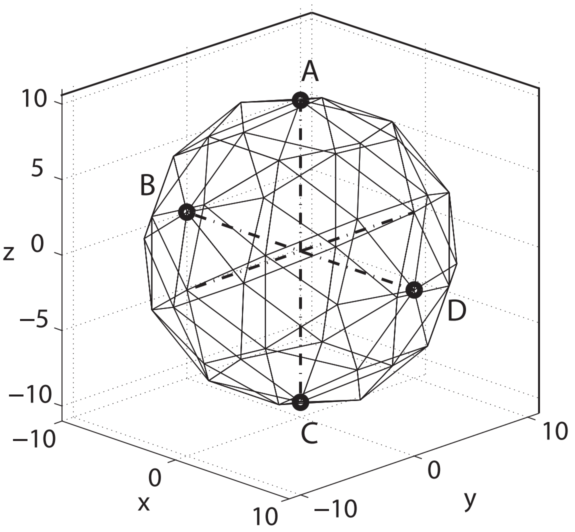

Figure 1: Sphere under internal pressure. The figures shows an eighty element model, and sample points, but calculations were performed with an 5120 element mesh. Supports were given as: $u_A = v_A = v_B = u_C = v_C = w_C = 0$, with (u, v, w) the translations in global (x, y, z) directions.

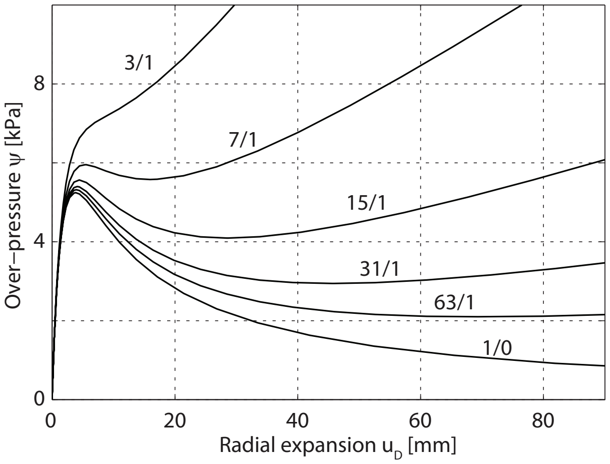

Figure 2: Sphere under internal pressure. Radial expansion and internal over-pressure for different parameters in a Mooney-Rivlin model. Curve notation n_1/n_2 according to Eqs. (13)–(14).

3.2 A long balloon

Figure 3 shows a model with 672 triangular elements of an inflated balloon which is completely fixed in one end, $x = 0$, constrained to only axial movement of the farthest end (A), and subjected to a uniform internal pressure ψ, assuming a surrounding pressure of $\psi_0 = 100\,\text{kPa}$. The initial geometry of the balloon was composed of a $L = 95\,\text{mm}$ cylinder with radius $r = 10\,\text{mm}$ and an end half-sphere. Sample points for deflections are marked in Fig. 3. Quasi-static equilibrium simulations were performed for refined models with 2688 and 10752 elements.

The pressure-expansion sequence was followed by a displacement-based iteration sequence for a 10752 element mesh, and different hyper-elastic material model, described by the ratio n_1/n_2 in Eqs. (13)–(14). The result is represented by the radial expansion v_D related to the internal over-pressure ψ in Fig. 4. A set of longitudinal sections through the inflated balloon are shown in Fig. 5. The profiles show the section of the balloon at $z = 0$, but the section $y = 0$

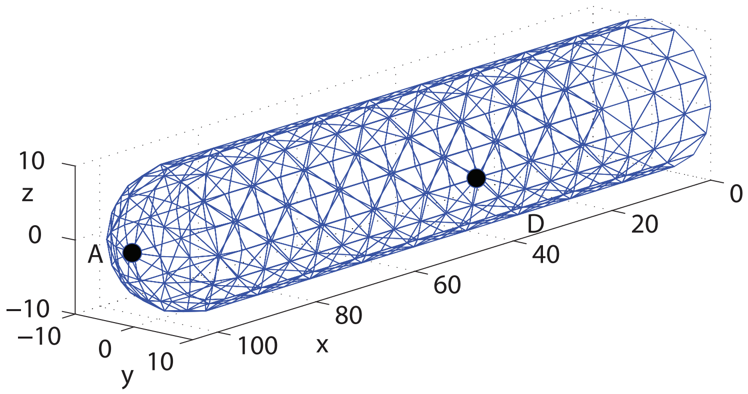

Figure 3: Inflation of balloon, 672 element model with sample points. All nodes at $x = 0$ were considered fully fixed in the simulations, the node at A could only move axially; all other nodes were completely free. Calculations were made with refined models (2688, 10752 elements), obtained from successive divisions of the figure elements into four triangles.

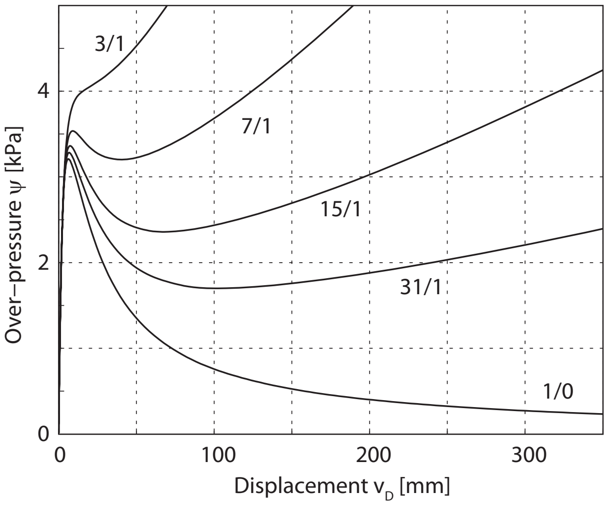

Figure 4: Inflation of balloon. Hyper-elastic material models, and 10752 element mesh. Quasi-static equilibrium paths, represented by internal over-pressure ψ and radial expansion at sample point D, v_D, Fig. 3. Curve notation n_1/n_2 according to Eqs. (13)–(14).

gives completely identical figures, as all solutions are rotationally symmetric. The sections were chosen when the radial expansion $v_D \approx 300$ mm for the different material models; the position of sample point D is marked by a circle in the figures. It is noted that these solutions refer to significantly different pressures ψ, cf. Fig. 4.

The dots on the sections in Fig. 5 show the displaced positions of the nodes on the symmetry line, which were close to evenly distributed initially. It is obvious that the neo-Hookean model $n_1/n_2 = 1/0$ will give a considerably different behavior than the other models, as it localizes the strains to the central parts of the balloon. This is an effect of the softening behavior with strain, whereas a non-zero c_2 coefficient will give a final stiffening of the material. This localization of the straining means that the mesh must be finer for the neo-Hookean material, in order to avoid behavior artifacts from the discretization. The 2688 element model was shown to be essentially free from such artifacts even for the neo-Hookean case.

Several of the material models showed a limit state with respect to internal over-pressure: a maximum load point, which was isolated to high accuracy. This limit state existed for all tested

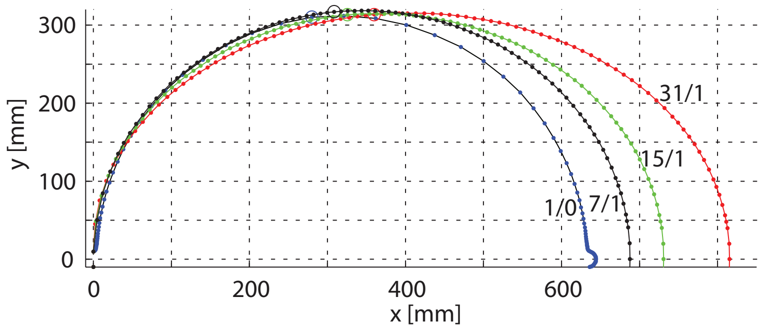

Figure 5: Inflation of balloon. Hyper-elastic material models, and 10752 element mesh. Sections through inflated balloon, for solutions with $v_D \approx 300\,\text{mm}$, for different parameters in a Mooney-Rivlin model. Curve notation n_1/n_2 according to Eqs. (13)–(14).

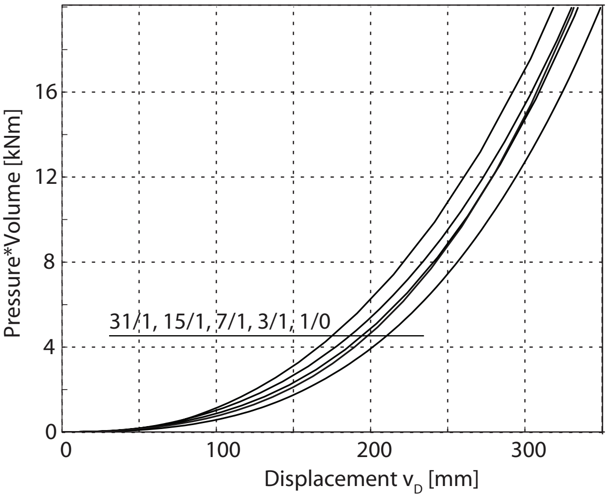

Figure 6: Inflation of balloon. Hyper-elastic material models, and 10752 element mesh. Radial expansion v_D related to the amount of gas injected, represented by product $(\psi_0 + \psi)V(\boldsymbol{u})$, for different parameters in a Mooney-Rivlin model. Curve notation n_1/n_2 according to Eqs. (13)–(14). Surrounding pressure $\psi_0 = 100\,\text{kPa}$.

material models with ratios $n_1/n_2 \geq 5$, whereas no (local) maximum pressure state was found for $n_1/n_2 \leq 4$. Except for the neo-Hookean model, the maximum pressure state corresponded to a (local) minimum before the pressure started to increase monotonically with expansion. A loading situation where the pressure can be regulated would thus show a dynamic snap-through behavior in the inflation process for such materials.

The models showed bifurcation states for very large expansions. For the $n_1/n_2 = 7/1$ model with 10752 elements, this occurred at an overpressure $\psi = 43.9\,\text{kPa}$, and a radial expansion $v_D = 2139\,\text{mm}$ with a mode corresponding to a torsion of the balloon. The same bifurcation was found for $\psi = 59.0\,\text{kPa}$, $v_D = 1435\,\text{mm}$ when $n_1/n_2 = 3/1$. It is noted that some possible instability modes are restrained by the adopted kinematic constraints.

The results in Fig. 4 are represented as radial expansion v_D and product $(\psi_0 + \psi)V(\boldsymbol{u})$ in Fig. 6, for the assumed $\psi_0 = 100\,\text{kPa}$, and the volume V calculated from the current displacements $\boldsymbol{u}$. For all material models, the expansion is monotonically increasing together with the injected amount of gas, so no instability would occur in the process for a loading situation where the inflow of gas is regulated. It is noted, however, that the evaluation of the injected amount of gas is significantly dependent on the assumed surrounding pressure.

As an alternative to the above solution, the solution of the inflation problem can also be

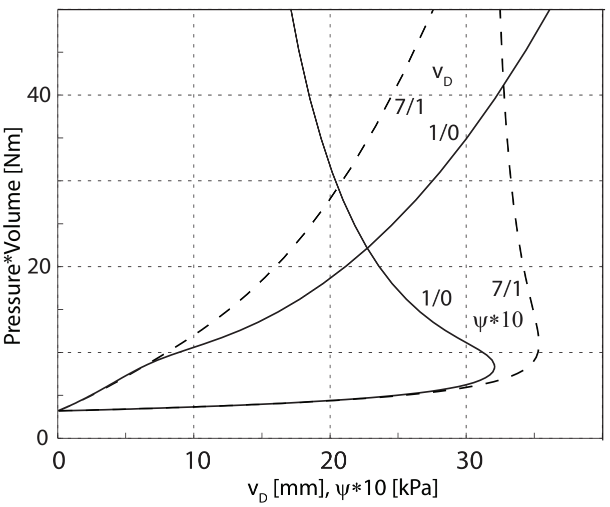

Figure 7: Inflation of balloon. Hyper-elastic material models, and 2688 element mesh. Solutions parameterized by amount measure, for different parameters in a Mooney-Rivlin model. Radial expansion v_D and internal over-pressure ψ, Fig. 3. Curve notation n_1/n_2 according to Eqs. (13)–(14). Surrounding pressure $\psi_0 = 100\,\mathrm{kPa}$.

parameterized by the amount of gas injected. Assuming isothermal conditions, a second control variable $\lambda_2 = N_t$ was used in addition to the over-pressure $\lambda_1 = \psi$, together with an augmenting equation:

$$g(\boldsymbol{u}, \boldsymbol{\lambda}) = (\psi_0 + \lambda_1)V(\boldsymbol{u}) - \lambda_2 = 0 \tag{21}$$

Driving the path-following with the λ_2 variable gave the results presented in Fig. 7, for different constitutive parameters c_1, c_2. The solutions are identical to the ones obtained without the amount parameter.

The augmenting equation method was used to study the behavior of an inflated balloon under change of temperature. The problem was set up with three control variables $\boldsymbol{\lambda}^{\mathrm{T}} = (\psi, N, T)$, with two augmenting equations beside the equilibrium equations:

$$\boldsymbol{g}(\boldsymbol{u}, \boldsymbol{\lambda}) = \begin{pmatrix} (\psi_0 + \lambda_1)V(\boldsymbol{u}) - \lambda_2\,(\lambda_3 + 273) \\ \lambda_2 - N_0 \end{pmatrix} = \boldsymbol{0} \tag{22}$$

where N_0 is a constant, defined in each material model case from the primary solutions in Fig. 4 for an over-pressure of $\psi = 3.0\,\mathrm{kPa}$, and assuming that this situation was first achieved at $T = 20°\mathrm{C}$, whereafter the balloon was sealed. The solutions obtained for variable temperature are shown in Fig. 8

4 CONCLUDING REMARKS

In this paper, a faceted triangular membrane space element is used for the analysis of pressurized membrane structures, using a class of hyper-elastic, Mooney-Rivlin, material models. The loading was seen as a uniform over-pressure, representing a gas loading. Quasi-static conditions were assumed, neglecting dynamic effects primarily coming from the flow velocities within the volume. It is emphasized by examples that the pressurizing mechanism is of importance for the response, even when the analysis is restricted to gas as the pressurizing medium. Two simple ‘balloon-type’ membranes show that limit points can occur when the pressure variable is seen as the parameter for the inflation, whereas these limit states can disappear when the injected gas

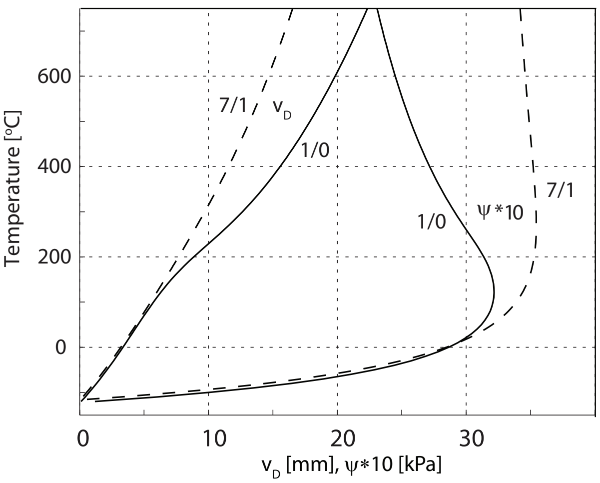

Figure 8: Inflation of balloon. Hyper-elastic material models, and 2688 element mesh. Solutions parameterized by temperature, for different parameters in a Mooney-Rivlin model. Radial expansion v_D and internal over-pressure ψ, Fig. 3. Curve notation n_1/n_2 according to Eqs. (13)–(14). Surrounding pressure $\psi_0 = 100\,\text{kPa}$.

volume is seen as the parameter. This difference thus has significance for the dynamic response of the membrane.

The results from the numerical examples indicate that the proposed formulation can be used for analysis of space membrane problems showing large displacements and large strains. The present study has been limited to uniform internal over-pressures, but other media or methods for introduction of the pressure, as well as partially filled structures, are interesting continuations of the project reported. A requirement for the model to be useful in the analysis of realistic structures is the development and verification of other non-linear material models.

A sophisticated path-following algorithm is needed for following the complex generalized equilibrium paths, which are used for the simulations. It is believed that the two-dimensional equilibrium surfaces discussed in [29] can be used for an improved understanding of membrane behavior under different classes of loadings.

REFERENCES

[1] J. A. Main, S. W. Peterson, A. M. Strauss, Load-deflection behavior of space-based inflatable fabric beams, J. Aerospace Eng. 7 (2) (1994) 225–238.

[2] D. K. Liang, D. Z. Yang, M. Qi, W. Q. Wang, Finite element analysis of the implantation of a balloon-expandable stent in a stenosed artery, Int. J. cardiol. 104 (3) (2005) 314–318.

[3] B. Bénech, A. Ezcurra, M. Lothon, F. Saïd, B. Campistron, F. Lohou, P. Durand, Constant volume balloons measurements in the urban Marseille and Fos-Berre industrial ozone plumes during ESCOMPTE experiment, Atm. Env. 42 (22) (2008) 5589–5601.

[4] A. Needleman, Inflation of spherical rubber balloons, Int. J. Solids Struct. 13 (5) (1977) 409–421.

[5] P. D. Gosling, W. J. Lewis, Optimal structural membranes — I. Formulation of a curved quadrilateral element for surface definition, Comput. Struct. 61 (5) (1996) 871–883.

[6] D. T. Berry, H. T. Y. Yang, Formulation and experimental verification of a pneumatic finite element, Int. J. Numer. Meth. Eng. 39 (7) (1996) 1097–1114.

[7] J. Bonet, R. D. Wood, J. Mahaney, P. Heywood, Finite element analysis of air supported membrane structures, Comput. Methods Appl. Mech. Engrg. 190 (5-7) (2000) 579–595.

[8] F. Cirak, M. Ortiz, Fully C^1-conforming subdivision elements for finite deformation thin-shell analysis, Int. J. Numer. Meth. Eng. 51 (7) (2001) 813–833.

[9] K. Schweizerhof, E. Ramm, Displacement dependent pressure loads in nonlinear finite element analyses, Comput. Struct. 18 (6) (1984) 1099–1114.

[10] D. E. Kiousis, T. C. Gasser, G. A. Holzapfel, Smooth contact strategies with emphasis on the modeling of balloon angioplasty with stenting, Int. J. Numer. Meth. Eng. 75 (7) (2008) 826–855.

[11] T. Rumpel, K. Schweizerhof, Volume-dependent pressure loading and its influence on the stability of structures, Int. J. Numer. Meth. Eng. 56 (2) (2003) 211–238.

[12] A. N. Gent, Elastic instabilities in rubber, Int. J. Numer. Meth. Eng. 40 (2-3) (2005) 165–175.

[13] L. M. Kanner, C. O. Horgan, Elastic instabilities for strain-stiffening rubber-like spherical and cylindrical thin shells under inflation, Int. J. Non-lin. Mech. 42 (2) (2007) 204–215.

[14] R. Phaal, C. R. Calladine, Simple class of finite elements for plate and shell problems. II: An element for thin shells, with only translational degrees of freedom, Int. J. Numer. Meth. Eng. 35 (5) (1992) 979–996.

[15] J. K. Hampshire, B. H. V. Topping, H. C. Chan, Three node triangular bending elements with one degree of freedom per node, Eng. Comput. 9 (1) (1992) 49–62.

[16] E. Oñate, M. Cervera, Derivation of thin plate bending elements with one degree of freedom per node: a simple three node triangle, Eng. Comput. 10 (6) (1993) 543–561.

[17] R. Hauptmann, K. Schweizerhof, A systematic development of 'solid-shell' element formulations for linear and non-linear analyses employing only displacement degrees of freedom, Int. J. Numer. Meth. Eng. 42 (1) (1998) 49–69.

[18] E. Oñate, F. Zárate, Rotation-free triangular plate and shell elements, Int. J. Numer. Meth. Eng. 47 (1-3) (2000) 557–603.

[19] M. Gärdsback, G. Tibert, A comparison of rotation-free triangular shell elements for unstructured meshes, Comput. Methods Appl. Mech. Engrg. 196 (49-52) (2007) 5001–5015.

[20] J. B. Pargana, D. Lloyd-Smith, B. A. Izzuddin, Fully integrated design and analysis of tensioned fabric structures: Finite elements and case studies, Eng. Struct.(doi: 10.1016/j.engstruct.2009.12.032).

[21] A. Eriksson, S. Farughi, Quasi-static inflation simulations based on a co-rotational triangular space membrane element, Int. J. Struct. Stab. Dyn.(submitted).

[22] G. A. Holzapfel, Nonlinear solid mechanics. A continuum approach for engineering, Wiley, Chichester, 2000.

[23] C. Truesdell, The elements of continuum mechanics, Springer, Berlin, 1966.

[24] A. Eriksson, On linear constraints for Newton-Raphson corrections and critical point searches in structural F. E. problems, Int. J. Numer. Meth. Eng. 28 (1989) 1317–1334.

[25] A. Eriksson, R. Kouhia, On step size adjustments in structural continuation problems, Comput. Struct. 55 (1995) 495–506.

[26] A. Eriksson, Equilibrium subsets for multi-parametric structural analysis, Comput. Methods Appl. Mech. Engrg. 140 (1997) 305–327.

[27] A. Eriksson, Structural instability analyses based on generalised path-following, Comput. Methods Appl. Mech. Engrg. 156 (1998) 45–74.

[28] A. Eriksson, Fold lines for sensitivity analyses in structural instability, Comput. Methods Appl. Mech. Engrg. 114 (1994) 77–101.

[29] A. Eriksson, C. Pacoste, Solution surfaces and generalised paths in non-linear structural mechanics, Int. J. Struct. Stab. Dyn. 1 (2001) 1–30.

COMPDYN 2011
3rd ECCOMAS Thematic Conference on
Computational Methods in Structural Dynamics and Earthquake Engineering
M. Papadrakakis, M. Fragiadakis, V. Plevris (eds.)
Corfu, Greece, 25–28 May 2011

INTERFACE TREATMENT IN COMPUTATIONAL FLUID-STRUCTURE INTERACTION

Thomas Klöppel, Alexander Popp and Wolfgang A. Wall

Institute for Computational Mechanics, Technische Universität München
Boltzmannstr. 15, 85748 Garching b. München, Germany
e-mail: {kloeppel,popp,wall}@lnm.mw.tum.de

Keywords: Fluid-Structure Interaction, Non-Matching Meshes, Mortar Method, Dual Lagrange Multipliers, Finite Elements.

Abstract. *Computational approaches for the simulation of fluid-structure interaction (FSI) problems have received much attention in recent years and their importance is still continuously growing. The main reason for this is that FSI problems are of great relevance in all fields of engineering (civil, mechanical, aerospace, bio, etc.) as well as in the applied sciences. In order to develop robust, reliable and efficient methods a number of challenges have to be met. This contribution focuses on the important question of how to treat the interface between solid and fluid. The topic is addressed by reviewing our novel, recently proposed method for dealing with non-matching grids in the context of moving grid FSI schemes. In contrast to available approaches in the literature, the proposed formulation is based on a mortar method with so-called dual Lagrange multipliers and handles the additional complexity of coupling non-matching interface meshes at negligible computational cost. Owing to its generality, the resulting FSI framework does not introduce any restriction on the particular choice of finite element formulations neither for fluid, ALE nor structure. It allows for the application of state-of-the-art iterative solution methods to the resulting system matrices in a straightforward manner and shows an excellent performance within monolithic FSI coupling algorithms.*

1 INTRODUCTION

The numerical simulation of fluid-structure interaction (FSI) phenomena has long been a field of intensive research owing to its many applications in civil, mechanical, aerospace and biomechanical engineering. Of particular interest is the interaction of incompressible flow with flexible structures undergoing finite deformations. We discuss here the most important features of our recently proposed dual mortar finite element method for dealing with non-matching interface meshes in the context of moving grid FSI schemes and monolithic coupling algorithms. The present contribution is thus a shortened version of our article [1] to which we refer for full technical details, more profound discussion of the methods and further numerical examples.

Possible solution strategies for FSI problems range from weakly coupled partitioned over strongly coupled partitioned to monolithic schemes. It could be shown that for some challenging numerical problems such as collapsible tubes [2], thin-walled structures in the hemodynamic or respiratory system [3] or balloon-like problems of human red blood cells [4], monolithic coupling schemes outperform partitioned approaches or are even the only feasible schemes to solve the problem at all. The issue of efficient and robust solvers for monolithic FSI scheme has among others been addressed in [5] where a novel algebraic multigrid preconditioner has been proposed. In general and also in [5], monolithic schemes are derived based on the assumption of a conforming interface discretization, i.e. fluid and structure share a common interface mesh. But only in very rare cases, this assumption will hold. Due to a manifold of reasons one generally has to deal with non-matching grids at the fluid-structure interface. Most often different resolution requirements in the different physical domains or quite simply the presence of complex interface geometries (e.g. in patient-specific biomechanics modeling) make the creation of matching fluid and structure meshes cumbersome or even impossible.

A possible remedy is provided by the mortar method, which has originally been introduced in the context of non-overlapping domain decomposition [6]. A characteristic feature of the mortar method is the imposition of interface constraints in a variationally consistent manner based on Lagrange multipliers. This approach has seen a great thrust of research over the past decade. New fields of application such as finite deformation contact analysis [7, 8, 9, 10] have been established and the mathematical understanding concerning the choice of adequate discrete Lagrange multiplier spaces has been deepened [11, 12, 13, 14].

Different other coupling methods for non-conforming interfaces in the framework of fluid-structure problems have been discussed for example in [15, 16, 17, 18, 19]. However, those contributions are limited to 2D analysis [16, 18] or only consider partitioned coupling schemes. The mortar method is referred to as a method with desirable mathematical and numerical properties [15, 17], but it has not yet been used for FSI computations in a competitive manner. It is obvious that a straightforward application of the standard mortar method will raise numerical issues in the case of monolithic FSI schemes. The Lagrange multiplier degrees of freedom lead to a global system matrix with increased size and saddle point structure. Especially the latter limits the practical use of this approach, since most iterative solvers rely on a matrix structure with only non-zero diagonal entries. A condensation could remedy this problem but would necessitate the inversion of a large matrix and is hence not feasible for practical purposes.

To overcome the numerical issues of the standard mortar method discussed above, we employ a so-called dual mortar method [11, 12, 13, 14] with discrete Lagrange multipliers that are constructed based on a biorthogonality relation with the primal shape functions at the fluid-structure interface. In contrast to standard mortar methods, the dual mortar approach allows for an elimination of the additional degrees of freedom by condensation at negligible computational cost in the monolithic setting. This ensures that there are only non-zero diagonal entries in the global system matrix. We show that state-of-the-art iterative solvers for monolithic FSI systems with matching interface meshes as proposed in [5] can be applied to the resulting global system matrices without any conceptual changes.

The remainder of this article is organized as follows: The next section briefly introduces the mechanical problem and states the governing equations as well as the weak forms. In section 3 the resulting monolithic system of equations after discretization and consistent linearization is presented and we give some details on dual mortar coupling as well as on condensation of the Lagrange multiplier degrees of freedom. Section 4 demonstrates the validity of the proposed approach with a representative numerical example, and in section 5 we conclude the findings.

2 PROBLEM DESCRIPTION

FSI problems can formally be described as four field problems. To begin with, there are two physical fields, fluid and structure. Furthermore, to account for deformations of the fluid domain, an arbitrary Lagrangian-Eulerian (ALE) approach is employed, constituting a third, non-physical mesh field later also called ALE field. Fluid and structure share a common FSI interface Γ, but not necessarily a common finite element discretization of Γ. Therefore, coupling conditions are applied in a weak sense, introducing a field of Lagrange multipliers on Γ.

2.1 Fluid

The present FSI approach is not limited to a specific flow description. For the sake of brevity we assume a fluid field governed by the instationary, incompressible Navier-Stokes equations for a Newtonian fluid on a deformable fluid domain Ω^{F}. The unknown fluid domain deformation $\mathbf{d}^{\mathrm{G}}$ is defined by a unique mapping $\boldsymbol{\varphi}$ given by

$$\mathbf{d}^{\mathrm{G}}(\mathbf{x},t) = \boldsymbol{\varphi}\left(\mathbf{d}_{\Gamma}^{\mathrm{G}},\mathbf{x},t\right) \quad \text{in} \quad \Omega^{\mathrm{F}} \times (0,T), \tag{1}$$

based on the mesh interface displacement $\mathbf{d}_{\Gamma}^{\mathrm{G}}$, that will later be related to the structure interface displacement $\mathbf{d}_{\Gamma}^{\mathrm{S}}$. This mapping (1) is arbitrary and defines the domain velocity $\mathbf{u}^{\mathrm{G}}$ by

$$\mathbf{u}^{\mathrm{G}} = \frac{\partial \boldsymbol{\varphi}}{\partial t} \quad \text{in} \quad \Omega^{\mathrm{F}} \times (0,T), \tag{2}$$

which has to match the fluid velocity $\mathbf{u}_{\Gamma}^{\mathrm{F}}$ at the interface Γ, i.e.

$$\mathbf{u}_{\Gamma}^{\mathrm{F}} = \mathbf{u}_{\Gamma}^{\mathrm{G}} \quad \text{in} \quad \Gamma \times (0,T). \tag{3}$$

Equation (2) allows for the definition of the ALE convective velocity $\mathbf{c} = \mathbf{u}^{\mathrm{F}} - \mathbf{u}^{\mathrm{G}}$, representing the fluid velocity relative to the arbitrarily moving fluid domain. The Navier-Stokes equations of the fluid field hence read

$$\frac{\partial \mathbf{u}^{\mathrm{F}}}{\partial t} + \mathbf{c} \cdot \boldsymbol{\nabla} \mathbf{u}^{\mathrm{F}} - 2\nu \boldsymbol{\nabla} \cdot \boldsymbol{\varepsilon}(\mathbf{u}^{\mathrm{F}}) + \nabla p^{\mathrm{F}} = \mathbf{b}^{\mathrm{F}}, \tag{4}$$

$$\boldsymbol{\nabla} \cdot \mathbf{u}^{\mathrm{F}} = 0, \tag{5}$$

both valid in $\Omega^{\mathrm{F}} \times (0,T)$, where fluid velocity $\mathbf{u}^{\mathrm{F}}$ and kinematic fluid pressure p^{F} are unknown. In the momentum equation (4), $\mathbf{b}^{\mathrm{F}}$ denotes a body force, $\boldsymbol{\varepsilon}(\mathbf{u}^{\mathrm{F}}) = \frac{1}{2}\left(\boldsymbol{\nabla}\mathbf{u}^{\mathrm{F}} + (\boldsymbol{\nabla}\mathbf{u}^{\mathrm{F}})^{\mathrm{T}}\right)$ the strain rate tensor of the Newtonian fluid and ν its kinematic viscosity. Equation (5) states the fluid's incompressibility deduced from the conservation of mass and a constant density ρ^{F}. The fluid system is completed by the usual Dirichlet and Neumann boundary conditions and an initial divergence-free velocity field $\mathbf{u}_0^{\mathrm{F}}$.

The weak form of the incompressible Navier-Stokes equations (4) and (5) is obtained by testing these equations with test functions $\delta\mathbf{u}^{\mathrm{F}}$ for velocity and δp^{F} for pressure and subsequent integration by parts

$$\begin{aligned}0 = &\left(\delta\mathbf{u}^{\mathrm{F}}, \frac{\partial\mathbf{u}^{\mathrm{F}}}{\partial t}\right)_{\Omega^{\mathrm{F}}} + \left(\delta\mathbf{u}^{\mathrm{F}}, \mathbf{c}\cdot\boldsymbol{\nabla}\mathbf{u}^{\mathrm{F}}\right)_{\Omega^{\mathrm{F}}} + \left(\boldsymbol{\nabla}\delta\mathbf{u}^{\mathrm{F}}, 2\nu\boldsymbol{\varepsilon}(\mathbf{u}^{\mathrm{F}})\right)_{\Omega^{\mathrm{F}}} - \left(\boldsymbol{\nabla}\cdot\delta\mathbf{u}^{\mathrm{F}}, p^{\mathrm{F}}\right)_{\Omega^{\mathrm{F}}}\\ &- \left(\delta\mathbf{u}^{\mathrm{F}}, \mathbf{b}^{\mathrm{F}}\right)_{\Omega^{\mathrm{F}}} - \left(\delta p^{\mathrm{F}}, \boldsymbol{\nabla}\cdot\mathbf{u}^{\mathrm{F}}\right)_{\Omega^{\mathrm{F}}} + \left(\delta\mathbf{u}^{\mathrm{F}}, \bar{\mathbf{h}}^{\mathrm{F}}\right)_{\Gamma_{\mathrm{N}}^{\mathrm{F}}} + \delta W_{\Gamma}^{\mathrm{F}},\end{aligned} \tag{6}$$

where $\Gamma_{\mathrm{N}}^{\mathrm{F}}$ denotes the Neumann boundary and $\delta W_{\Gamma}^{\mathrm{F}}$ denotes a contribution of the FSI interface that will be deduced in section 2.3.

2.2 Structure

In this work we assume a structure field governed by the nonlinear elastodynamics equation

$$\rho^{\mathrm{S}}\frac{\mathrm{d}^2\mathbf{d}^{\mathrm{S}}}{\mathrm{d}t^2} = \boldsymbol{\nabla}\cdot(\mathbf{FS}) + \rho^{\mathrm{S}}\mathbf{b}^{\mathrm{S}} \quad \text{in} \quad \Omega^{\mathrm{S}}\times(0,T), \tag{7}$$

which states an equilibrium between the forces of inertia, internal forces and an external body force $\mathbf{b}^{\mathrm{S}}$ in the undeformed structural configuration Ω^{S}. Given the structural density ρ^{S} defined per unit undeformed volume, equation (7) has to be solved for the unknown structural displacements $\mathbf{d}^{\mathrm{S}}$. The internal forces are expressed in terms of the second Piola-Kirchhoff stress tensor $\mathbf{S}$ and the deformation gradient $\mathbf{F}$.

Different constitutive relations can be employed in this context, but for the sake of simplicity a hyperelastic material behavior with strain energy function Ψ is considered in the remainder of this paper. The second Piola-Kirchhoff stress tensor $\mathbf{S}$ is thus defined as

$$\mathbf{S} = 2\frac{\partial\Psi}{\partial\mathbf{C}}, \tag{8}$$

where the right Cauchy-Green tensor $\mathbf{C} = \mathbf{F}^{\mathrm{T}}\mathbf{F}$ has been introduced. Dirichlet and Neumann boundary conditions as well as the usual initial boundary conditions, given initial displacements and velocities $\mathbf{d}_0^{\mathrm{S}}$ and $\dot{\mathbf{d}}_0^{\mathrm{S}}$, respectively, have to be additionally satisfied.

Testing (7) with the virtual displacements $\delta\mathbf{d}^{\mathrm{S}}$ and integration by parts yield the weak form

$$0 = \left(\delta\mathbf{d}^{\mathrm{S}}, \rho^{\mathrm{S}}\frac{\mathrm{d}^2\mathbf{d}^{\mathrm{S}}}{\mathrm{d}t^2}\right)_{\Omega^{\mathrm{S}}} + \left(\boldsymbol{\nabla}\delta\mathbf{d}^{\mathrm{S}}, \mathbf{FS}\right)_{\Omega^{\mathrm{S}}} - \left(\delta\mathbf{d}^{\mathrm{S}}, \rho^{\mathrm{S}}\mathbf{b}^{\mathrm{S}}\right)_{\Omega^{\mathrm{S}}} - \left(\delta\mathbf{d}^{\mathrm{S}}, \bar{\mathbf{h}}^{\mathrm{S}}\right)_{\Gamma_{\mathrm{N}}^{\mathrm{S}}} + \delta W_{\Gamma}^{\mathrm{S}}, \tag{9}$$

where $\Gamma_{\mathrm{N}}^{\mathrm{S}}$ denotes the Neumann boundary. The influence of the interface on the structure field is accounted for by $\delta W_{\Gamma}^{\mathrm{S}}$, which will be discussed in the following subsection.

2.3 Fluid-Structure Interface

Coupling of the different fields is realized by enforcing kinematic and dynamic constraints at the fluid-structure interface Γ. Usually, the no-slip boundary condition

$$\frac{\partial\mathbf{d}_{\Gamma}^{\mathrm{S}}}{\partial t} = \mathbf{u}_{\Gamma}^{\mathrm{F}} \quad \text{in} \quad \Gamma\times(0,T) \tag{10}$$

is applied, which prohibits both a mass flow across and a relative tangential movement of fluid and structure at the fluid-structure interface. In combination with (3) this condition (10) is equivalent to

$$\mathbf{d}_\Gamma^\mathrm{S} = \mathbf{d}_\Gamma^\mathrm{G} \quad \text{in} \quad \Gamma \times (0,T), \tag{11}$$

stating that structural deformation and fluid movement (represented by the ALE based fluid domain deformation $\mathbf{d}_\Gamma^\mathrm{G}$) must match on Γ. In addition, equilibrium of forces requires the surface tractions of fluid and structure to be equal, yielding

$$\mathbf{h}_\Gamma^\mathrm{S} = -\mathbf{h}_\Gamma^\mathrm{F} \quad \text{in} \quad \Gamma \times (0,T). \tag{12}$$

In preparation of the mortar finite element discretization to follow, the method of weighted residuals is applied to the interface conditions. By introducing the Lagrange multiplier field $\boldsymbol{\lambda}$ and corresponding test functions $\delta\boldsymbol{\lambda}$ on the fluid-structure interface Γ, we obtain the weak form

$$\left(\delta\boldsymbol{\lambda}, \mathbf{d}_\Gamma^\mathrm{S} - \mathbf{d}_\Gamma^\mathrm{G}\right)_\Gamma = 0. \tag{13}$$

This adds an integral version of the continuity constraint (11) to the general problem definition. Furthermore, the unknown surface tractions introduced in (12) have to be imposed in a weak sense on the respective physical field, yielding the missing coupling terms in fluid weak form (6) and structure weak form (9)

$$\delta W_\Gamma^\mathrm{F} = \left(\mathbf{h}_\Gamma^\mathrm{F}, \delta\mathbf{u}_\Gamma^\mathrm{F}\right)_\Gamma, \tag{14}$$

$$\delta W_\Gamma^\mathrm{S} = \left(\mathbf{h}_\Gamma^\mathrm{S}, \delta\mathbf{d}_\Gamma^\mathrm{S}\right)_\Gamma. \tag{15}$$

Identifying the Lagrange multiplier field $\boldsymbol{\lambda}$ with the unknown surface traction $\mathbf{h}_\Gamma^\mathrm{S} = -\mathbf{h}_\Gamma^\mathrm{F}$, these coupling terms can be expressed as

$$\delta W_\Gamma^\mathrm{F} = -\left(\boldsymbol{\lambda}, \delta\mathbf{u}_\Gamma^\mathrm{F}\right)_\Gamma, \tag{16}$$

$$\delta W_\Gamma^\mathrm{S} = \left(\boldsymbol{\lambda}, \delta\mathbf{d}_\Gamma^\mathrm{S}\right)_\Gamma. \tag{17}$$

Thus, fluid-structure coupling is established in a weak sense, which formally leads to a four field FSI system.

3 DISCRETIZATION AND SOLUTION ALGORITHM

3.1 The monolithic FSI system

To derive the monolithic FSI system of equations, the governing equations stated above are discretized in space and time and the resulting non-linear equations are linearized consistently in order to apply a Newton-Raphson algorithm. Note that the presented algorithm is not limited to a particular choice of these discretizations. In general, we use finite element discretizations for fluid, ALE and structure fields and implicit time integration schemes.

The final linear system of equation for timestep $n+1$ and iteration step i then emerges as

$$\begin{bmatrix} \mathbf{S}_{\mathrm{II}} & \mathbf{S}_{\mathrm{I\Gamma}} & & & & \\ \mathbf{S}_{\mathrm{\Gamma I}} & \mathbf{S}_{\mathrm{\Gamma\Gamma}} & & & & \mathbf{C}_{\mathrm{S}}^{\mathrm{T}} \\ & & \mathbf{F}_{\mathrm{II}} & \mathbf{F}_{\mathrm{I\Gamma}} + \frac{\Delta t}{2}\mathbf{F}^{\mathrm{G}}_{\mathrm{I\Gamma}} & \mathbf{F}^{\mathrm{G}}_{\mathrm{II}} & \\ & & \mathbf{F}_{\mathrm{\Gamma I}} & \mathbf{F}_{\mathrm{\Gamma\Gamma}} + \frac{\Delta t}{2}\mathbf{F}^{\mathrm{G}}_{\mathrm{\Gamma\Gamma}} & \mathbf{F}^{\mathrm{G}}_{\mathrm{\Gamma I}} & -\mathbf{C}_{\mathrm{F}}^{\mathrm{T}} \\ & & \mathbf{0} & \frac{\Delta t}{2}\mathbf{A}_{\mathrm{I\Gamma}} & \mathbf{A}_{\mathrm{II}} & \\ & \mathbf{C}_{\mathrm{S}} & & -\frac{\Delta t}{2}\mathbf{C}_{\mathrm{F}} & & \end{bmatrix} \begin{bmatrix} \Delta\mathbf{d}^{\mathrm{S},n+1}_{\mathrm{I},i} \\ \Delta\mathbf{d}^{\mathrm{S},n+1}_{\Gamma,i} \\ \Delta\mathbf{u}^{\mathrm{F},n+1}_{\mathrm{I},i} \\ \Delta\mathbf{u}^{\mathrm{F},n+1}_{\Gamma,i} \\ \Delta\mathbf{d}^{\mathrm{G},n+1}_{\mathrm{I},i} \\ \boldsymbol{\lambda}^{n+1}_{i} \end{bmatrix} = \\ - \begin{bmatrix} \mathbf{f}^{\mathrm{S},n+1}_{\mathrm{I},i} \\ \mathbf{f}^{\mathrm{S},n+1}_{\Gamma,i} \\ \mathbf{f}^{\mathrm{F},n+1}_{\mathrm{I},i} \\ \mathbf{f}^{\mathrm{F},n+1}_{\Gamma,i} \\ \mathbf{0} \\ \mathbf{0} \end{bmatrix} - \delta_{i0}\Delta t \begin{bmatrix} \mathbf{0} \\ \mathbf{0} \\ \mathbf{F}^{\mathrm{G}}_{\mathrm{I\Gamma}}\mathbf{u}^{\mathrm{F},n}_{\Gamma} \\ \mathbf{F}^{\mathrm{G}}_{\mathrm{\Gamma\Gamma}}\mathbf{u}^{\mathrm{F},n}_{\Gamma} \\ \mathbf{A}_{\mathrm{I\Gamma}}\mathbf{u}^{\mathrm{F},n}_{\Gamma} \\ \mathbf{C}_{\mathrm{F}}\mathbf{u}^{\mathrm{F},n}_{\Gamma} \end{bmatrix}, \tag{18}$$

where δ_{i0} denotes the Kronecker delta. In equation (18) the vector of unknowns and the right-hand side are split in quantities defined on the FSI interface denoted by $\cdot_{\Gamma}$ and in the interior field denoted by $\cdot_{\mathrm{I}}$. This split then propagates to the matrix block structure. The block structure of the structure stiffness matrix $\mathbf{S}$ is defined as $\mathbf{S}_{\alpha\beta} = \partial\mathbf{f}^{\mathrm{S}}_{\alpha}/\partial\mathbf{d}^{\mathrm{S}}_{\beta}$, $\alpha,\beta \in \{\mathrm{I},\Gamma\}$, where $\mathbf{f}^{\mathrm{S}}$ denotes the residual vector and $\mathbf{d}^{\mathrm{S}}$ the vector of discretized nodal displacements. To shorten the notation for the fluid part, we have merged the pressure degrees of freedom into the vector of fluid interior unknowns. Fluid entries are then defined as $\mathbf{F}_{\alpha\beta} = \partial\mathbf{f}^{\mathrm{F}}_{\alpha}/\partial\mathbf{u}^{\mathrm{F}}_{\beta}$ and shape derivatives as $\mathbf{F}^{\mathrm{G}}_{\alpha\beta} = \partial\mathbf{f}^{\mathrm{F}}_{\alpha}/\partial\mathbf{d}^{\mathrm{G}}_{\beta}, \alpha,\beta \in \{\mathrm{I},\Gamma\}$. Here, $\mathbf{f}^{\mathrm{F}}$ denotes the fluid residual, $\mathbf{u}^{\mathrm{F}}$ the vector of discretized fluid unknowns and $\mathbf{d}^{\mathrm{G}}$ the vector of fluid grid displacements. The ALE system matrix $\mathbf{A}$ is split accordingly into blocks $\mathbf{A}_{\mathrm{I\Gamma}}$ and $\mathbf{A}_{\mathrm{II}}$.

The system is completed by coupling matrices $\mathbf{C}_{\mathrm{S}}$ and $\mathbf{C}_{\mathrm{F}}$. The last row of (18) weakly imposes the continuity constraint (11) and thus represents the discrete version of (13). The contributions of the vector of discretized Lagrange multiplier values $\boldsymbol{\lambda}$, i.e. $-\mathbf{C}^{\mathrm{F}}\boldsymbol{\lambda}$ and $\mathbf{C}^{\mathrm{S}}\boldsymbol{\lambda}$, account for the additional surface tractions on the fluid and structure field, respectively, which result from the coupling at the FSI interface and correspond to (16) and (17).

3.2 Dual mortar coupling

Non-conforming finite element discretization brings about that fluid and structure surfaces at the FSI interface Γ do not match any more, as it is the case when using node-matching interface meshes. For making the following derivations more general, we define so-called *slave* and *master* sides Γ^{sl} and Γ^{ma}, introduce the displacement fields $\mathbf{d}^{\mathrm{sl}}_{\Gamma}$ and $\mathbf{d}^{\mathrm{ma}}_{\Gamma}$ and derive the dual mortar method as an abstract coupling strategy for two non-conforming meshes. The general form of slave and master displacement interpolation then reads

$$\mathbf{d}^{\mathrm{sl}}_{\Gamma} = \sum_{k=1}^{n^{\mathrm{sl}}} N^{\mathrm{sl}}_{k}\mathbf{d}^{\mathrm{sl}}_{k}, \quad \mathbf{d}^{\mathrm{ma}}_{\Gamma} = \sum_{l=1}^{n^{\mathrm{ma}}} N^{\mathrm{ma}}_{l}\mathbf{d}^{\mathrm{ma}}_{l}, \tag{19}$$

where shape functions N^{sl}_{k}, N^{ma}_{l} are obtained based on their trace space relationship with the underlying discretizations of the domains ‘behind‘ the mortar interface (in this context fluid

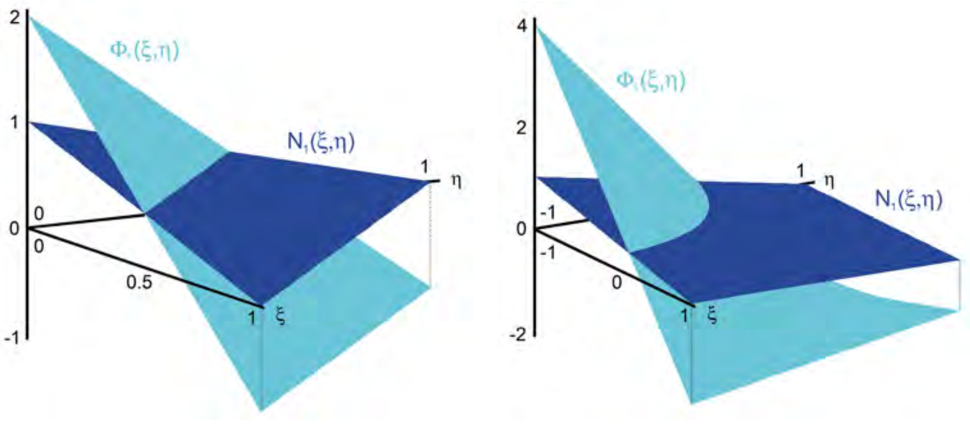

(a) 3-node triangular surface elements (b) 4-node quadrilateral surface elements

Figure 1: Exemplary shape functions $N_1(\xi,\eta)$ and dual shape functions $\Phi_1(\xi,\eta)$.

and structure domains). Nodal displacements are represented by $\mathbf{d}_k^{\mathrm{sl}}$, $\mathbf{d}_l^{\mathrm{ma}}$. The total number of slave and master nodes is given by n^{sl} and n^{ma}, respectively.

Within the *dual* mortar method considered here, the Lagrange multiplier interpolation on the slave side of the interface is based on so-called dual shape functions Φ_j as

$$\boldsymbol{\lambda} = \sum_{j=1}^{n^{\mathrm{sl}}} \Phi_j \boldsymbol{\lambda}_j \,, \tag{20}$$

with discrete nodal Lagrange multipliers $\boldsymbol{\lambda}_j$. The dual shape functions are constructed such that a biorthogonality condition, as introduced in [20, 13, 14], is satisfied, yielding

$$\int_{\Gamma^{\mathrm{sl}}} \Phi_j N_k^{\mathrm{sl}} \mathrm{d}\Gamma = \delta_{jk} \int_{\Gamma^{\mathrm{sl}}} N_k^{\mathrm{sl}} \mathrm{d}\Gamma, \tag{21}$$

where δ_{jk} is the Kronecker delta. Note that (21) demands an evaluation of shape function integrals on the actual (possibly distorted) surface element geometry in the reference configuration. Therefore, an *a priori* definition of dual shape functions is not possible in general, but these ansatz functions for Lagrange multiplier interpolation become element-specific. Fig. 1 exemplarily shows (standard) displacement shape functions and (dual) Lagrange multiplier shape functions for a 3-node triangular and for an undistorted 4-node quadrilateral surface element. For a more detailed overview and exemplary local calculations of element-specific dual shape functions for 3D mortar coupling, we refer to [11, 8].

For the sake of clarity, we temporarily ignore the weak continuity condition (13) already derived for the concrete FSI setting and instead consider the more general form

$$\left(\delta\boldsymbol{\lambda}, \mathbf{d}_\Gamma^{\mathrm{sl}} - \mathbf{d}_\Gamma^{\mathrm{ma}}\right)_\Gamma = 0 \tag{22}$$

in the following, which couples slave and master displacements of an abstract non-conforming interface. When the interpolations (19) and (20) are substituted into (22), the nodal blocks of two mortar integral matrices $\mathbf{D}$ and $\mathbf{M}$ emerge as

$$\mathbf{D}[j,k] = \mathrm{D}_{jk}\mathbf{I}_3 = \int_{\Gamma^{\mathrm{sl}}} \Phi_j N_k^{\mathrm{sl}} \mathrm{d}\Gamma \, \mathbf{I}_3 \,, \tag{23}$$

$$\mathbf{M}[j,l] = \mathrm{M}_{jl}\mathbf{I}_3 = \int_{\Gamma^{\mathrm{sl}}} \Phi_j N_l^{\mathrm{ma}} \mathrm{d}\Gamma \, \mathbf{I}_3 \,, \tag{24}$$

with the 3×3 identity matrix $\mathbf{I}_3$. Herein, $\mathbf{D}$ is a square $3n^{\mathrm{sl}} \times 3n^{\mathrm{sl}}$ matrix, whereas the definition of $\mathbf{M}$ generally yields a rectangular matrix of dimensions $3n^{\mathrm{sl}} \times 3n^{\mathrm{ma}}$. Inserting the biorthogonality relation (21) into (23) allows for the advantageous simplification of $\mathbf{D}$ to become a diagonal matrix with nodal blocks

$$\mathbf{D}[j,k] = \mathrm{D}_{jk}\mathbf{I}_3 = \delta_{jk} \int_{\Gamma^{\mathrm{sl}}} N_k^{\mathrm{sl}} \mathrm{d}\Gamma\, \mathbf{I}_3 \,. \tag{25}$$

Finally, the discrete form of the general weak continuity condition (22) reads

$$\mathbf{D}\mathbf{d}_\Gamma^{\mathrm{sl}} - \mathbf{M}\mathbf{d}_\Gamma^{\mathrm{ma}} = \mathbf{0}, \tag{26}$$

which naturally defines a discrete projection from master to slave displacements as

$$\mathbf{d}_\Gamma^{\mathrm{sl}} = \mathbf{D}^{-1}\mathbf{M}\mathbf{d}_\Gamma^{\mathrm{ma}}. \tag{27}$$

Equation (27) illustrates one major advantage of the dual mortar approach as compared with standard mortar schemes. The discrete projection operator $\mathbf{P} = \mathbf{D}^{-1}\mathbf{M}$ at a non-conforming interface can be applied locally based on the trivial inversion of the diagonal matrix $\mathbf{D}$. Thus, evaluating (27) does not require the solution of a possibly large linear system of equations. This evades the high computational cost associated with standard mortar coupling of two non-conforming grids. Note that depending on the choice of structure or fluid as slave side for the mortar approach, the discrete coupling matrices $\mathbf{C}_\mathrm{S}$ and $\mathbf{C}_\mathrm{F}$ in (18) can be identified with the mortar matrices $\mathbf{D}$ and $\mathbf{M}$.

3.3 Condensed linear system

The four-field linear system in (18) is in general very hard to solve numerically with parallel iterative linear solvers, because of the saddle point type structure of the problem. Since larger model sizes necessitate this type of solvers, the linear system is transformed into the same block-structure as the standard monolithic FSI system for conforming discretizations shown in [5]. The transformation is based on condensation of the Lagrange multipliers, which is only possible due to the dual mortar approach discussed in section 3.2.

Of course both choices for master and slave side of the mortar coupling are possible and result in viable algorithms as has been shown in great detail in [1]. For the sake of brevity, in this contribution only one possibility is discussed: we assume that the structure side of the FSI interface Γ serves as slave side for the mortar coupling. Thus the coupling matrices in (18) can be identified as $\mathbf{C}_\mathrm{F} = \mathbf{M}$ and $\mathbf{C}_\mathrm{S} = \mathbf{D}$.

The second row of (18) is solved for the Lagrange multipliers $\boldsymbol{\lambda}_i^{n+1}$, involving a trivial inversion of the diagonal matrix $\mathbf{D}$. The result can then be substituted into the fourth row of (18), so that the Lagrange multipliers are fully eliminated from the system. A further reduction can be obtained by a transformation of the last row of (18), which allows to express the structure interface displacement updates $\boldsymbol{\Delta}\mathbf{d}_{\Gamma,i}^{\mathrm{S},n+1}$ in terms of fluid interface velocity updates $\boldsymbol{\Delta}\mathbf{u}_{\Gamma,i}^{\mathrm{F},n+1}$.

Subsequent substitution and reordering yield the final reduced system of equations

$$\begin{bmatrix} \mathbf{S}_{\mathrm{II}} & \frac{\Delta t}{2}\mathbf{S}_{\mathrm{I}\Gamma}\mathbf{P} & & \\ \mathbf{P}^{\mathrm{T}}\mathbf{S}_{\Gamma\mathrm{I}} & \frac{\Delta t}{2}\mathbf{P}^{\mathrm{T}}\mathbf{S}_{\Gamma\mathrm{I}}\mathbf{P}+\mathbf{F}_{\Gamma\Gamma}+\frac{\Delta t}{2}\mathbf{F}^{\mathrm{G}}_{\Gamma\Gamma} & \mathbf{F}_{\Gamma\mathrm{I}} & \mathbf{F}^{\mathrm{G}}_{\Gamma\mathrm{I}} \\ & \mathbf{F}_{\mathrm{I}\Gamma}+\frac{\Delta t}{2}\mathbf{F}^{\mathrm{G}}_{\mathrm{I}\Gamma} & \mathbf{F}_{\mathrm{II}} & \mathbf{F}^{\mathrm{G}}_{\mathrm{II}} \\ & \frac{\Delta t}{2}\mathbf{A}_{\mathrm{I}\Gamma} & \mathbf{0} & \mathbf{A}_{\mathrm{II}} \end{bmatrix} \begin{bmatrix} \mathbf{\Delta d}^{\mathrm{S},n+1}_{\mathrm{I},i} \\ \mathbf{\Delta u}^{\mathrm{F},n+1}_{\Gamma,i} \\ \mathbf{\Delta u}^{\mathrm{F},n+1}_{\mathrm{I},i} \\ \mathbf{\Delta d}^{\mathrm{G},n+1}_{\mathrm{I},i} \end{bmatrix} =$$

$$\begin{bmatrix} \mathbf{f}^{\mathrm{S},n+1}_{\mathrm{I},i} \\ \mathbf{f}^{\mathrm{F},n+1}_{\Gamma,i}+\mathbf{P}^{\mathrm{T}}\mathbf{f}^{\mathrm{S},n+1}_{\Gamma,i} \\ \mathbf{f}^{\mathrm{F},n+1}_{\mathrm{I},i} \\ \mathbf{0} \end{bmatrix} + \delta_{i0}\,\Delta t \begin{bmatrix} \mathbf{S}_{\mathrm{I}\Gamma}\mathbf{P}\,\mathbf{u}^{\mathrm{F},n}_{\Gamma} \\ \left(\mathbf{P}^{\mathrm{T}}\mathbf{S}_{\Gamma\Gamma}\mathbf{P}+\mathbf{F}^{\mathrm{G}}_{\Gamma\Gamma}\right)\mathbf{u}^{\mathrm{F},n}_{\Gamma} \\ \mathbf{F}^{\mathrm{G}}_{\mathrm{I}\Gamma}\mathbf{u}^{\mathrm{F},n}_{\Gamma} \\ \mathbf{A}_{\mathrm{I}\Gamma}\mathbf{u}^{\mathrm{F},n}_{\Gamma} \end{bmatrix}. \qquad (28)$$

4 EXAMPLE

To demonstrate the efficiency of the proposed method, different discretizations of the same fluid filled circular pipe with traveling pressure wave are considered. The example is motivated by [5, 21]. The tube is 0.1 m long, has an inner radius of 0.01 m and an outer radius of 0.011 m. The structure is described with a Neo-Hookean material law with Young's modulus $E = 10^5\,\mathrm{Pa}$, Poisson's ratio $\nu = 0.3$ and a density of $\rho^{\mathrm{S}} = 1{,}200\,\mathrm{kg/m^3}$. The Newtonian fluid inside the tube has a dynamic viscosity of $\mu = 0.003\,\mathrm{Pa\,s}$ and a density of $\rho^{\mathrm{F}} = 1{,}000\,\mathrm{kg/m^3}$. The inflow surface is loaded with a surface traction of 1,000 Pa for 0.003 s. For the computation a timestep size of $\Delta t = 1.0\times 10^{-4}\,\mathrm{s}$ is used and 250 timesteps are performed. The fluid is discretized with stabilized hexahedral finite elements, the structure with hexahedral solid shell elements proposed in [22].

We concentrate on four fluid discretizations denoted by A, B, C and D with different mesh sizes, which range from 2,080 to 130,560 elements. For all fluid mesh sizes corresponding conforming and non-conforming structure discretizations are considered. In the non-conforming versions the structure mesh is rotated such that the meshes overlap in circumferential direction by approximately a third of an element length, see Fig. 2(a). Furthermore, it contains two elements less than the fluid discretization across the length of the tube. The coarsest non-conforming model can be seen in Fig. 2.

Computations are performed in parallel on up to 12 processors. In order to study efficiency and scalability of the proposed approach, we distinguish not only between conforming and non-conforming (NC), but consider two solution methods for the conforming case: with mortar

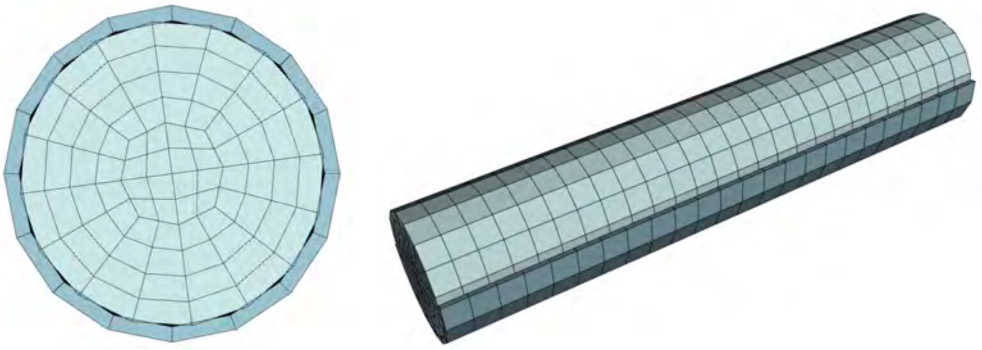

(a) front view (b) side view

Figure 2: Coarse, non-conforming mesh A for pressure wave example.

Table 1: Characteristics for the numerical solver averaged over timestep and number of processors used.

Mesh		n_{dof}	n_{pr}	Newton	GMRES	time
A	(C)	19,413	4	2.97	29.2	4.44
A	(CM)	19,413	4	2.97	29.2	4.56
A	(NC)	19,221	4	2.97	36.1	6.09
B	(C)	140,291	8	2.98	30.0	22.99
B	(CM)	140,291	8	2.98	30.0	23.59
B	(NC)	139,715	8	2.98	32.8	27.1
C	(C)	377,857	12	2.97	30.9	41.09
C	(CM)	377,857	12	2.97	30.9	41.43
C	(NC)	376,705	12	2.97	37.1	50.68
D	(C)	1,045,553	12	2.78	33.9	99.44
D	(CM)	1,045,553	12	2.78	33.9	101.12
D	(NC)	1,043,663	12	2.78	42.7	121.68

coupling (CM) and with the standard approach (C) presented in [5]. In all cases the AMG(BGS) preconditioner introduced in [5] is employed to solve the linear system (28). The numerical behavior is assessed by the average number of Newton iterations, the average number of GMRES iterations and the average computation time per timestep. These quantities and the total number n_{dof} of degrees of freedom are listed in Tab. 1.

As could be expected the number of Newton iterations and linear iterations of the GMRES algorithm for the two conforming meshes coincide. The mortar approach and the corresponding explicit matrix-matrix products, which are needed to eliminate the discrete Lagrange multipliers and to set up the condensed system matrices, affect the numerical costs only very slightly. The average time spent for a timestep increases by less than 2% in all cases considered, which indicates the numerical efficiency of the proposed approach. Having to deal with non-conforming meshes (rows marked with 'NC' in Tab. 1) leads to an increase in computation time of approximately 25% for this example. This is completely due to linear systems of equations that are apparently harder to solve, which becomes obvious by comparing the average number of GMRES steps and Newton steps. The relative increase of iteration steps needed in the GMRES corresponds exactly to the relative increase in computation time, whereas the number of Newton iterations is unchanged. While this increase can not be neglected, it is however important to point out that the preconditioners have not been optimized for the non-conforming case but are simply carried over from the conforming case. The computational cost associated with the evaluation of dual mortar coupling itself is virtually zero. This is above all due to the fact that the mortar integrals (i.e. matrices **D** and **M**) only need to be evaluated once during problem initialization and remain unchanged during all FSI timesteps afterwards.

5 CONCLUSION

A novel mortar-based approach to efficiently simulate fluid-structure interaction phenomena allowing for independent discretization of fluid and structure domains has been presented. Owing to its generality, the proposed FSI framework does not introduce any restriction on the particular choice of finite element formulations neither for fluid, ALE nor structure. Implicit time integration is employed for all three physical fields. Consistent linearization within a Newton-Raphson scheme provides the fundamental building blocks of the monolithic system.

In contrast to available approaches in literature, the proposed formulation is based on a dual mortar method and handles the additional complexity of non-matching interface meshes at negligible computational cost. The complete four-field monolithic system initially has a saddle point type structure, but is then transformed into a three-field system by condensation of the Lagrange multiplier degrees of freedom. The transformation requires the inversion of one of the coupling matrices, which is trivial due to its diagonal shape. This diagonality is a key feature of the dual mortar approach as opposed to standard mortar coupling schemes. Because of the transformation the application of state-of-the-art iterative solution methods to the resulting system matrices is straightforward.

In particular, block-specific preconditioners tailored for conforming monolithic FSI show excellent performance also in the non-conforming case, which is demonstrated with the well-known pressure wave example. It also shows that computational cost associated with the evaluation of dual mortar coupling itself and with the additional matrix-matrix multiplication necessary in some sub-blocks of the monolithic system is very low.

REFERENCES

[1] T. Klöppel, A. Popp, U. Küttler, W.A. Wall, Fluid-structure interaction for non-conforming interfaces based on a dual mortar formulation. *Computer Methods in Applied Mechanics and Engineering*, submitted, 2010.

[2] M. Heil, An efficient solver for the fully coupled solution of large-displacement fluid–structure interaction problems. *Computer Methods in Applied Mechanics and Engineering*, **193**, 1–23, 2004.

[3] U. Küttler, M. Gee, Ch. Förster, A. Comerford, W.A. Wall, Coupling strategies for biomedical fluid-structure interaction problems. *International Journal for Numerical Methods in Biomedical Engineering*, **26**, 305–321, 2010.

[4] T. Klöppel, W.A. Wall, A novel two-layer, coupled finite element approach for the nonlinear elastic and viscoelastic behavior of human erythrocytes. *Biomech. Model. Mechan.*, DOI: 10.1007/s10237-010-0246-2, 2010.

[5] M. W. Gee, U. Küttler, W. A. Wall, Truly monolithic algebraic multigrid for fluid-structure interaction. *Int. J. Numer. Meth. Engng.*, **85**(8), 987–1016, 2011.

[6] C. Bernardi, Y. Maday, A.T. Patera, A new nonconforming approach to domain decomposition: the mortar element method. H. Brezis, J.L. Lions eds. *Nonlinear partial differential equations and their applications*, Pitman/Wiley: London/New York, 1994.

[7] A. Popp, M.W. Gee, W.A. Wall, A finite deformation mortar contact formulation using a primal-dual active set strategy. *International Journal for Numerical Methods in Engineering*, **79**, 1354–1391, 2009.

[8] A. Popp, M. Gitterle, M.W. Gee, W.A. Wall, A dual mortar approach for 3D finite deformation contact with consistent linearization. *International Journal for Numerical Methods in Engineering*, **83**, 1428–1465, 2010.

[9] M.A. Puso, T.A. Laursen, A mortar segment-to-segment contact method for large deformation solid mechanics. *Computer Methods in Applied Mechanics and Engineering*, **193**, 601–629, 2004.

[10] M.A. Puso, T.A. Laursen, A mortar segment-to-segment frictional contact method for large deformations. *Computer Methods in Applied Mechanics and Engineering*, **193**, 4891–4913, 2004.

[11] B. Flemisch, B.I. Wohlmuth, Stable lagrange multipliers for quadrilateral meshes of curved interfaces in 3D. *Computer Methods in Applied Mechanics and Engineering*, **196**, 1589–1602, 2007.

[12] M.A. Puso, A 3D mortar method for solid mechanics. *International Journal for Numerical Methods in Engineering*, **59**, 315–336, 2004.

[13] B.I. Wohlmuth, A mortar finite element method using dual spaces for the Lagrange multiplier. *SIAM Journal on Numerical Analysis*, **38**, 989–1012, 2000.

[14] B.I. Wohlmuth, *Discretization methods and iterative solvers based on domain decomposition.* Springer-Verlag Berlin Heidelberg, 2001.

[15] A. de Boer, A.H. van Zuijlen, H. Bijl, Review of coupling methods for non-matching meshes. *Computer Methods in Applied Mechanics and Engineering*, **196**, 1515–1525, January 2007.

[16] W. Dettmer, D. Peric, A computational framework for fluid-structure interaction: Finite element formulation and applications. *Computer Methods in Applied Mechanics and Engineering*, **195**, 5754–5779, 2006.

[17] C. Farhat, M. Lesoinne, P. Le Tallec, Load and motion transfer algorithms for fluid/structure interaction problems with non-matching discrete interfaces: Momentum and energy conservation, optimal discretization and application to aeroelasticity. *Computer Methods in Applied Mechanics and Engineering*, **157**, 95–114, 1998.

[18] H.-G. Kim, A new coupling strategy for fluid-solid interaction problems by using the interface element method. *International Journal for Numerical Methods in Engineering*, **81**, 403–428, 2010.

[19] M.R. Ross, M.A. Sprague, C.A. Felippa, K.C. Park, Treatment of acoustic fluid-structure interaction by localized lagrange multipliers and comparison to alternative interface-coupling methods. *Computer Methods in Applied Mechanics and Engineering*, **198**, 986–1005, 2009.

[20] S. Hüeber, B.I. Wohlmuth, A primal-dual active set strategy for non-linear multibody contact problems. *Computer Methods in Applied Mechanics and Engineering*, **194**, 3147–3166, 2005.

[21] J.F. Gerbeau, M. Vidrascu, A quasi-Newton algorithm based on a reduced model for fluid-structure interaction problems in blood flow. *Mathematical Modelling and Numerical Analysis*, **37**(4), 631–647, 2003.

[22] L. Vu-Quoc, X.G. Tan, Optimal solid shells for non-linear analyses of multilayer composites. i. statics. *Computer Methods in Applied Mechanics and Engineering*, **192**, 975–1016, 2003.

COMPDYN 2011
III ECCOMAS Thematic Conference on
Computational Methods in Structural Dynamics and Earthquake Engineering
M. Papadrakakis, M. Fragiadakis, V. Plevris (eds.)
Corfu, Greece, 25–28 May 2011

DYNAMIC CHARACTERISTICS OF STRUCTURES WITH VISCOELASTIC DAMPERS MODELED BY MEANS OF GENERALIZED RHEOLOGICAL MODELS

R. Lewandowski[1] **and A. Bartkowiak**[1]

[1] Poznan University of Technology
60-965 Poznan, ul. Piotrowo 5, Poland
e-mail: roman.lewandowski@put.poznan.pl, aleksandra.a.bartkowiak@gmail.com

Keywords: Dynamics of Frames, VE Dampers, Rheological Models, Dynamic Characteristics.

Abstract. *Frame structures with viscoelastic (VE) dampers mounted on them are considered in this paper. Generalized rheological models are used to model the VE dampers. The finite element method is used to derive the equations of motion of a structure with dampers and such equations are written in terms of both physical and state-space variables. A solution to motion equations in the frequency domain is provided and the dynamic properties of the structure with VE dampers are determined as a solution to the appropriately defined eigenvalue problem. The dynamic characteristics of a relatively large structure with VE are determined and discussed.*

1 INTRODUCTION

Viscoelastic (VE) dampers are a passive type of energy dissipation devices, frequently used to mitigate excessive vibrations of structures due to winds or earthquakes. The properties of VE dampers, such as the possibility of energy dissipation and stiffness, are frequency and temperature dependent and are commonly defined in terms of experimentally obtained storage and loss modules. The frequency dependence of the properties of VE dampers can be accurately described by means of rheological models. Both the classical rheological models and the so-called rheological models with the fractional derivative are used [1, 2].

The dynamic analysis of frame or building structures with viscous and/or viscoelastic dampers are presented in a number of papers [3 - 14]. The most popular models of VE dampers are the simple rheological models, i.e., the Kelvin model and the Maxwell model. In papers [6 – 8] the simple Maxwell model was used. Moreover, in papers [7, 9, 13] the simple Kelvin model is used to describe the dynamic behavior of dampers. These simple models are used in [7, 12, 13] to solve the problem of optimum design of structures with VE dampers. However, as shown in [15], the simple Maxwell or Kelvin models cannot accurately approximate the frequency dependence of the storage modulus and the loss modulus of VE dampers. Recently, more advanced models of VE dampers have also been used when considering the dynamic analysis of structures with VE dampers. The dynamics of structures with VE dampers modeled by means of the generalized rheological models is very rarely discussed in the literature. These models are used in papers [4, 16] only. In papers [3, 5, 14] a three-parameter rheological model with the fractional-derivative model is used to model the VE dampers’ behavior. Moreover, rational polynomial approximation modeling is used in paper [17] for an analysis of structures with VE dampers.

In this paper, frame structures equipped with VE dampers are considered. The frame is treated as a linear system while the generalized Kelvin model and the generalized Maxwell model are used to accurately describe the dynamic behaviour of VE dampers. The considered generalized models of VE dampers contain more parameters than the rheological models with the fractional derivative but lead to traditional differential equations of motion. The finite element method is adopted to write the equation of motion of the considered system in terms of both physical and state nodal variables. In particular, the solution of motion equation of a whole system in the frequency domain is considered and the dynamic properties of structure with VE dampers are determined. The frequencies of vibration, the non-dimensional damping ratios together with the corresponding eigenvectors are determined as a solution to the appropriately defined linear eigenvalue problem. Moreover, the frequency response functions are also determined. The results of typical calculations are presented and discussed.

Up to now, the dynamic characteristics of structures with VE dampers modeled by means of the generalized rheological models have not been considered or discussed in the available literature. Moreover, it was found that the VE damper model is not unique, i.e., both of the considered models can be used for modeling accurately the real damper for a sufficiently great number of model parameters.

2 THE GENERALIZED RHEOLOGICAL MODELS OF VE DAMPERS

The frequency dependence of the properties of VE dampers can be captured using generalized rheological models. The generalized Kelvin model and the generalized Maxwell model, as shown in Figs. 1 and 2, are used for modeling the VE dampers in this paper. The generalized Kelvin model is built of a spring and a set of the m Kelvin elements connected in series (see Fig.1). The Kelvin element is build of a spring and a dashpot connected in parallel. The generalized Maxwell model is built of the spring and a set of the m Maxwell elements connected in parallel (see Fig.2). The Maxwell element is the classical Maxwell rheological model, i.e., the spring and dashpot connected in series. As shown in [18], the frequency dependence of the properties of VE dampers can be accurately taken into account using the generalized rheological models.

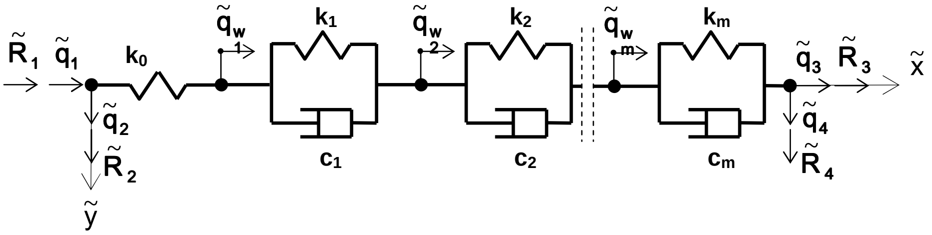

Figure 1: A schematic of the generalized Kelvin model

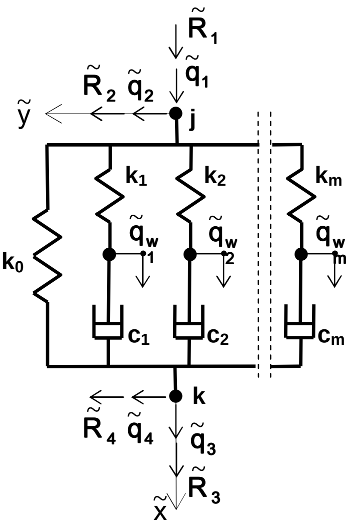

Figure 2: A schematic of the generalized Maxwell model

The concept of superelement and the concept of so-called internal variables have been used in describing both models. The dynamic behavior of the Kelvin damper can be described by means of the following equations:

$$u_0(t) = k_0(\tilde{q}_{w,1}(t) - \tilde{q}_1(t)) \ , \tag{1}$$

$$u_i(t) = k_i(\tilde{q}_{w,i+1}(t) - \tilde{q}_{w,i}(t)) + c_i(\dot{\tilde{q}}_{w,i+1}(t) - \dot{\tilde{q}}_{w,i}(t)) \ , \tag{2}$$

$$u_m(t) = k_m(\tilde{q}_3(t) - \tilde{q}_{w,m}) + c_m(\dot{\tilde{q}}_3(t) - \dot{\tilde{q}}_{w,m}) \ , \tag{3}$$

where $u_i(t)$ is the force in the *i-th* element of the model ($i = 0,1,..,m$), k_i and c_i are the spring stiffness and the damping factor of the dashpot of the *i-th* element of the model, respectively, and symbols $\tilde{q}_1(t)$ and $\tilde{q}_3(t)$ denote the external nodes displacements given in the local coordinate system (compare Fig.1). Moreover, the dot denotes differentiation with respect to time t and the symbol $\tilde{q}_{w,i}(t)$ denotes the internal variable ($i = 1,..,m$).

After introducing the vector of external reactions $\tilde{\mathbf{R}}_z(t) = col(\tilde{R}_1(t), \tilde{R}_2(t), \tilde{R}_3(t), \tilde{R}_4(t))$ (see Figure 1) and utilizing the equilibrium conditions of the external nodes: $\tilde{R}_1(t) = -u_0(t)$, $\tilde{R}_2(t) = 0$, $\tilde{R}_1(t) = u_m(t)$ and $\tilde{R}_4(t) = 0$ we can write the following matrix equation:

$$\tilde{\mathbf{R}}_z(t) = \tilde{\mathbf{K}}_{zz}\tilde{\mathbf{q}}_z(t) + \tilde{\mathbf{K}}_{zw}\tilde{\mathbf{q}}_w(t) + \tilde{\mathbf{C}}_{zz}\dot{\tilde{\mathbf{q}}}_z(t) + \tilde{\mathbf{C}}_{zw}\dot{\tilde{\mathbf{q}}}_w(t) \ , \tag{4}$$

where $\tilde{\mathbf{q}}_z(t) = col(\tilde{q}_1(t), \tilde{q}_2(t), \tilde{q}_3(t), \tilde{q}_4(t))$, $\tilde{\mathbf{q}}_w(t) = col(\tilde{q}_{w,1}(t), \ldots\ldots, \tilde{q}_{w,m}(t))$. The matrices $\tilde{\mathbf{K}}_{zz}$, $\tilde{\mathbf{K}}_{zw}$, $\tilde{\mathbf{C}}_{zz}$ and $\tilde{\mathbf{C}}_{zw}$ are defined in Appendix A.

Moreover, the equilibrium conditions of the internal nodes, i.e., $u_{i-1}(t) - u_1(t) = 0$ for $i = 1,..,m$ lead to the following matrix equation:

$$\tilde{\mathbf{K}}_{wz}\tilde{\mathbf{q}}_z(t) + \tilde{\mathbf{K}}_{ww}\tilde{\mathbf{q}}_w(t) + \tilde{\mathbf{C}}_{wz}\dot{\tilde{\mathbf{q}}}_z(t) + \tilde{\mathbf{C}}_{ww}\dot{\tilde{\mathbf{q}}}_w(t) = \mathbf{0} \ , \tag{5}$$

where $\tilde{\mathbf{K}}_{wz} = \tilde{\mathbf{K}}_{zw}^T$, $\tilde{\mathbf{C}}_{wz} = \tilde{\mathbf{C}}_{zw}^T$ and the matrices $\tilde{\mathbf{K}}_{ww}$, $\tilde{\mathbf{C}}_{ww}$ are defined in Appendix A.

The equation of motion of the Kelvin model of a VE damper written in the local coordinate system can be finally presented in the form:

$$\tilde{\mathbf{R}}_d(t) = \tilde{\mathbf{K}}_d\tilde{\mathbf{q}}_d(t) + \tilde{\mathbf{C}}_d\dot{\tilde{\mathbf{q}}}_d(t) \ , \tag{6}$$

where $\tilde{\mathbf{R}}_d(t) = col(\tilde{\mathbf{R}}_z(t),\ \mathbf{0})$, $\tilde{\mathbf{q}}_d(t) = col(\tilde{\mathbf{q}}_z(t),\ \tilde{\mathbf{q}}_w(t))$,

$$\tilde{\mathbf{K}}_d = \begin{bmatrix} \tilde{\mathbf{K}}_{zz} & \tilde{\mathbf{K}}_{zw} \\ \tilde{\mathbf{K}}_{wz} & \tilde{\mathbf{K}}_{ww} \end{bmatrix}, \qquad \tilde{\mathbf{C}}_d = \begin{bmatrix} \tilde{\mathbf{C}}_{zz} & \tilde{\mathbf{C}}_{zw} \\ \tilde{\mathbf{C}}_{wz} & \tilde{\mathbf{C}}_{ww} \end{bmatrix}. \tag{7}$$

Transforming nodal parameters to the global coordinate system, the usual transformation of displacements of the external nodes of the damper is used while the internal variables of the damper are still defined in the local coordinate system. This means that the transformation matrix is:

$$\mathbf{T}_d = \begin{bmatrix} \tilde{\mathbf{T}}_d & \mathbf{0} \\ \mathbf{0} & \mathbf{I} \end{bmatrix}, \tag{8}$$

where

$$\tilde{\mathbf{T}}_d = \begin{bmatrix} \tilde{\mathbf{T}} & \mathbf{0} \\ \mathbf{0} & \tilde{\mathbf{T}} \end{bmatrix}, \qquad \tilde{\mathbf{T}} = \begin{bmatrix} c & s \\ -s & c \end{bmatrix}, \tag{9}$$

$c = \cos\alpha$, $s = \sin\alpha$, α is the angle between the global and local coordinate systems and $\mathbf{I}$ is the $(m \times m)$ identity matrix.

In the global coordinate system the generalized Kelvin model equation has the form:

$$\mathbf{R}_d(t) = \mathbf{K}_d\mathbf{q}_d(t) + \mathbf{C}_d\dot{\mathbf{q}}_d(t) \ , \tag{10}$$

where

$$\mathbf{R}_d(t) = col(\mathbf{R}_z(t),\ \mathbf{0}) = \mathbf{T}_d^T\tilde{\mathbf{R}}_d\mathbf{T}_d \ , \qquad \mathbf{R}_z(t) = col(R_1(t), R_2(t), R_3(t), R_4(t)) \ ,$$

$$\mathbf{q}_d(t) = col(\mathbf{q}_z(t),\ \mathbf{q}_w(t) = \tilde{\mathbf{q}}_w(t)) = \mathbf{T}_d^T\tilde{\mathbf{q}}_d\mathbf{T}_d \ , \quad \mathbf{q}_z(t) = col(q_1(t), q_2(t), q_3(t), q_4(t)) \ , \tag{11}$$

are the vector of nodal reactions and the vector of nodal parameters, respectively, in the global coordinate system. The explicit forms of matrices $\mathbf{K}_d$ and $\mathbf{C}_d$ are given in Appendix A.

The dynamic behavior of the Maxwell damper could be described in a similar way. Using the internal variables defined in Fig. 2, the following equations can be written:

$$u_0(t) = k_0(\tilde{q}_3(t) - \tilde{q}_1(t)) \ , \tag{12}$$

$$u_{is}(t) = k_i(\tilde{q}_{w,i}(t) - \tilde{q}_1(t)) \ , \tag{13}$$

$$u_{id}(t) = c_i(\dot{\tilde{q}}_3(t) - \dot{\tilde{q}}_{w,i}(t)) \ , \tag{14}$$

for the spring element and for the *i-th* Maxwell element ($i = 1,..,m$), respectively. The symbols $u_0(t)$, $u_{is}(t)$ and $u_{id}(t)$ in the above relationships denote the force in the spring element, the force in the spring of the *i-th* Maxwell element, and the force in the dashpot of the *i-th* Maxwell element, respectively.

The nodal reactions in the local coordinate system are:

$$\tilde{R}_1(t) = -u_0(t) - \sum_{i=1}^{m} u_{is}(t) \ , \quad \tilde{R}_2(t) = 0 \ , \quad \tilde{R}_3(t) = u_0(t) + \sum_{i=1}^{m} u_{id}(t) \ , \quad \tilde{R}_4(t) = 0 \ . \tag{15}$$

After introducing relationships (12) – (14) into Eqns (15) we obtain again Eqn (4) though its matrices are defined in Appendix B. Moreover, in the global coordinate system, Eqn (10) is also valid with the matrices $\mathbf{K}_d$ and $\mathbf{C}_d$ given in Appendix B.

Many particular rheological models described in the literature can be obtained by varying the number of elements in the generalized models mentioned above.

However, the simple Kelvin and Maxwell models, which contain only one Kelvin or Maxwell element, respectively, are not particular instances of the generalized models being discussed because the spring element with stiffness k_0 is not present. For the reader’s convenience, a brief description of the above-mentioned simple models is also presented. In the matrix notation the equation of both models could be written in the form of Eqns (6) and (10). The matrices and vectors appearing in these equations are defined in Appendix C.

3 EQUATION OF MOTION AND DYNAMIC CHARACTERISTICS OF STRUCTURES WITH VE DAMPERS

Planar frame structures with VE dampers are modeled using the finite element method. A typical two-node bar element with six nodal parameters is used to describe the structure treated as the elastic system. The mass and stiffness matrices together with the vector of nodal forces of the element can be found in many books. The equation of motion of the structure with VE dampers modeled using the generalized rheological models can be written in the following form:

$$\mathbf{M}_{ss}\ddot{\mathbf{q}}_s(t) + \mathbf{C}_{ss}\dot{\mathbf{q}}_s(t) + \mathbf{C}_{sd}\dot{\mathbf{q}}_d(t) + \mathbf{K}_{ss}\mathbf{q}_s(t) + \mathbf{K}_{sd}\mathbf{q}_d(t) = \mathbf{p}_s(t) \ , \tag{16}$$

$$\mathbf{C}_{ds}\dot{\mathbf{q}}_s(t) + \mathbf{C}_{dd}\dot{\mathbf{q}}_d(t) + \mathbf{K}_{ds}\mathbf{q}_s(t) + \mathbf{K}_{dd}\mathbf{q}_d(t) = \mathbf{0} \ , \tag{17}$$

where the symbols $\mathbf{M}_{ss}$, $\mathbf{C}_{ss}$, $\mathbf{C}_{sd} = \mathbf{C}_{ds}^T$, $\mathbf{C}_{dd}$, $\mathbf{K}_{ss}$, $\mathbf{K}_{sd} = \mathbf{K}_{ds}^T$ and $\mathbf{K}_{dd}$ denote the mass, damping, and stiffness matrices of the system (i.e., structure with dampers), respectively, written in the global coordinate system. The dimension of matrices $\mathbf{M}_{ss}$, $\mathbf{C}_{ss} = \mathbf{C}_{ss}^{(s)} + \mathbf{C}_{ss}^{(d)}$

and $\mathbf{K}_{ss} = \mathbf{K}_{ss}^{(s)} + \mathbf{K}_{ss}^{(d)}$ is ($n \times n$). The matrices $\mathbf{M}_{ss}$, $\mathbf{C}_{ss}^{(s)}$ and $\mathbf{K}_{ss}^{(s)}$ describe the inertia, damping, and elastic properties of the structure without dampers, while the matrices $\mathbf{C}_{ss}^{(d)}$, $\mathbf{K}_{ss}^{(d)}$ and the ($n \times r$) matrices $\mathbf{C}_{sd} = \mathbf{C}_{ds}^{T}$, $\mathbf{K}_{sd} = \mathbf{K}_{ds}^{T}$ represent the effect of the coupling of dampers with the structure. The ($r \times r$) matrices $\mathbf{C}_{dd}$ and $\mathbf{K}_{dd}$ describe the damping and stiffness properties of dampers with braces, respectively. Moreover, $\mathbf{q}_s(t)$, $\mathbf{q}_d(t)$ and $\mathbf{p}_s(t)$ are the global vectors of nodal generalized displacements, internal variables and nodal excitation forces, respectively. The concept of proportional damping is used to model the damping properties of the structure, i.e.: $\mathbf{C}_{ss}^{(s)} = \alpha \mathbf{M}_{ss} + \kappa \mathbf{K}_{ss}^{(s)}$ where α and κ are proportionality factors.

The equation of motion written in terms of state variables will also be useful. After introducing the following state vector $\mathbf{x}(t) = col(\mathbf{q}_s(t),\ \dot{\mathbf{q}}_s(t),\ \mathbf{q}_d(t))$ and adding the equation:

$$\mathbf{M}_{ss}\dot{\mathbf{q}}_s(t) - \mathbf{M}_{ss}\dot{\mathbf{q}}_s(t) = \mathbf{0}\,, \tag{18}$$

to the system of Eqns (16) and (17) the following state equation could be written

$$\mathbf{A}\dot{\mathbf{x}}(t) + \mathbf{B}\mathbf{x}(t) = \mathbf{s}(t)\ , \tag{19}$$

where

$$\mathbf{A} = \begin{bmatrix} \mathbf{C}_{ss} & \mathbf{M}_{ss} & \mathbf{C}_{sd} \\ \mathbf{M}_{ss} & \mathbf{0} & \mathbf{0} \\ \mathbf{C}_{ds} & \mathbf{0} & \mathbf{C}_{dd} \end{bmatrix}, \qquad \mathbf{B} = \begin{bmatrix} \mathbf{K}_{ss} & \mathbf{0} & \mathbf{K}_{sd} \\ \mathbf{0} & -\mathbf{M}_{ss} & \mathbf{0} \\ \mathbf{K}_{ds} & \mathbf{0} & \mathbf{K}_{dd} \end{bmatrix}, \qquad \mathbf{s}(t) = \begin{Bmatrix} \mathbf{p}(t) \\ \mathbf{0} \\ \mathbf{0} \end{Bmatrix}. \tag{20}$$

Please note that the matrices $\mathbf{A}$ and $\mathbf{B}$ are symmetrical and the matrix $\mathbf{B}$ is non-singular.

The solution to the homogenous state equation, i.e., when $\mathbf{s}(t) = \mathbf{0}$, is assumed in the form:

$$\mathbf{x}(t) = \mathbf{a}\exp(st)\ . \tag{21}$$

Introducing (21) into the state equation (19) we obtain the following eigenvalue problem:

$$(s\mathbf{A} + \mathbf{B})\,\mathbf{a} = \mathbf{0}\ . \tag{22}$$

The linear eigenvalue problem (22) must be solved to determine the ($2n + r$) eigenvalues s_i and eigenvectors $\mathbf{a}_i$. In the case of an undercritically damped structure the $2n$ eigenvalues (eigenvectors) are complex and conjugate numbers (vectors) while the remaining r eigenvalues (eigenvectors) are real numbers (vectors).

The dynamic behavior of a frame with VE dampers is characterized by the natural frequencies ω_i and the non-dimensional damping parameters γ_i . The above-mentioned quantities are defined as:

$$\omega_i^2 = \mu_i^2 + \eta_i^2\ , \qquad \gamma_i = -\mu_i / \omega_i\ , \tag{23}$$

where $\mu_i = \mathrm{Re}(s_i)$, $\eta_i = \mathrm{Im}(s_i)$. The formulae (23) refer to complex eigenvalues only.

The third dynamic characteristic of the considered system are the frequency response functions. Before determination of these functions it is useful to rewrite equations of motion (16) and (17) in the form of the following one matrix equation:

$$\mathbf{M}\ddot{\mathbf{q}}(t) + \mathbf{C}\dot{\mathbf{q}}(t) + \mathbf{K}\mathbf{q}(t) = \overline{\mathbf{p}}(t)\ , \tag{24}$$

where

$$\mathbf{M} = \begin{bmatrix} \mathbf{M}_{ss} & \mathbf{0} \\ \mathbf{0} & \mathbf{0} \end{bmatrix}, \quad \mathbf{C} = \begin{bmatrix} \mathbf{C}_{ss} & \mathbf{C}_{sd} \\ \mathbf{C}_{ds} & \mathbf{C}_{dd} \end{bmatrix}, \quad \mathbf{K} = \begin{bmatrix} \mathbf{K}_{ss} & \mathbf{K}_{sd} \\ \mathbf{K}_{ds} & \mathbf{K}_{dd} \end{bmatrix}, \quad \mathbf{q}(t) = \begin{Bmatrix} \mathbf{q}_s(t) \\ \mathbf{q}_d(t) \end{Bmatrix}, \quad \overline{\mathbf{p}}(t) = \begin{Bmatrix} \mathbf{p}(t) \\ \mathbf{0} \end{Bmatrix}. \tag{25}$$

To determine the frequency response functions the steady state harmonic responses of the system are considered. If the excitation forces vary harmonically in time, i.e., when

$$\overline{\mathbf{p}}(t) = \overline{\mathbf{P}} \exp(\mathrm{i}\lambda t) \ , \tag{26}$$

then the steady state response of the system under consideration can be described by:

$$\mathbf{q}(t) = \mathbf{Q} \exp(\mathrm{i}\lambda t) \ , \tag{27}$$

where $\mathrm{i} = \sqrt{-1}$ is an imaginary unit.

After substituting Eqns (26) and (26) into Eqn (24) the following standard formula describes the matrix of the frequency response functions:

$$\mathbf{H}(\lambda) = (-\lambda^2 \mathbf{M} + \mathrm{i}\lambda \mathbf{C} + \mathbf{K})^{-1} \ . \tag{28}$$

If the structure with dampers modeled by the simple Maxwell model is considered, then all of the relationships presented above in this section are valid provided that the matrices given in Appendix C are used to generate the global matrices appearing in Eqns (16) and (17).

The vector of internal variables $\mathbf{q}_d(t)$ does not exist in the case of a structure with dampers modeled by the simple Kelvin model, and the motion equation (16) takes the form:

$$\mathbf{M}_{ss} \ddot{\mathbf{q}}_s(t) + (\mathbf{C}_{ss} + \mathbf{C}_{dd})\, \dot{\mathbf{q}}_s(t) + (\mathbf{K}_{ss} + \mathbf{K}_{dd})\, \mathbf{q}_s(t) = \mathbf{p}_s(t) \ . \tag{29}$$

The matrices $\mathbf{C}_{dd}$ and $\mathbf{K}_{dd}$ appearing in (29) are built from the matrices $\mathbf{C}_d$ and $\mathbf{K}_d$, respectively, given by formulae (C.4).

The state equation has the form of Equation (19) where, now

$$\mathbf{x}(t) = \begin{Bmatrix} \mathbf{q}_s(t) \\ \dot{\mathbf{q}}_s(t) \end{Bmatrix}, \quad \mathbf{A} = \begin{bmatrix} \mathbf{C}_{ss} + \mathbf{C}_{dd} & \mathbf{M}_{ss} \\ \mathbf{M}_{ss} & \mathbf{0} \end{bmatrix}, \quad \mathbf{B} = \begin{bmatrix} \mathbf{K}_{ss} + \mathbf{K}_{dd} & \mathbf{0} \\ \mathbf{0} & -\mathbf{M}_{ss} \end{bmatrix}, \quad \mathbf{s}(t) = \begin{Bmatrix} \mathbf{p}(t) \\ \mathbf{0} \end{Bmatrix}. \tag{30}$$

Moreover, the matrix of frequency response functions must be defined as

$$\mathbf{H}(\lambda) = \left[-\lambda^2 \mathbf{M}_{ss} + \mathrm{i}\lambda(\mathbf{C}_{ss} + \mathbf{C}_{dd}) + \mathbf{K}_{ss} + \mathbf{K}_{dd} \right]^{-1} \ . \tag{31}$$

4 RESULTS OF TYPICAL CALCULATIONS

4.1 Description of a representative structure and VE dampers

An eight-storey RC frame with three-bays is selected to determine the dynamic characteristics of a structure with dampers. The frame is designed according to the EC8 Part 1 for class B soils. The height of the columns is 3.0 m, the span of the beams is 5.0 m and Young's modulus for concrete is 31.0 GPa. The dimensions of the cross-section of the structural elements are presented in Table 1 while the unit masses of the frame elements are given in Table 2.

Table 3 shows the natural frequencies of vibration of the frame without dampers. The dynamic properties of the structure are obtained by way of a two-dimensional analysis of the frame. Any axial deformations and internal damping of the structure are neglected.

The dampers are attached in the middle bay on all floors of the structure. The dampers are modeled using the following rheological models: i) the simple Kelvin model; ii) the simple

Maxwell model; iii) the generalized Kelvin model with seven parameters, and iv) the generalized Maxwell model also with seven parameters.

Storey level	Lateral column [cm]	Central column [cm]	Beams [cm]
7, 8	35×35	40×40	30×40
5, 6	40×40	45×45	30×45
3, 4	45×45	53×53	30×50
1, 2	50×50	60×60	30×50

Table 1: Dimensions of eight-storey frame elements

Storey level	Unit lateral column mass [kg/m]	Unit central column mass [kg/m]	Unit beam mass [kg/m]
7, 8	306.2	400.0	15000.0
5, 6	400.0	506.2	15000.0
3, 4	506.2	702.2	15000.0
1, 2	625.0	900.0	15000.0

Table 2: Unit mass of eight-storey frame elements

Natural frequencies [rad/sec]			
3.1311	8.6582	15.4268	23.7804
31.2647	40.1148	42.1251	51.1550
52.3598	57.6067	65.6532	69.9862

Table 3: Natural frequencies of frame without dampers

Data from the real experiment are not adopted in this paper. Instead, the storage and loss modulus of dampers are calculated from the formulae:

$$K'(\lambda) = k + c\lambda^{\alpha}\cos(\alpha\pi/2)\ , \qquad K''(\lambda) = c\lambda^{\alpha}\sin(\alpha\pi/2)\ , \tag{32}$$

which are the analytical formulae of the fractional-derivative Kelvin model of dampers. The chosen parameters of the fractional-derivative Kelvin model are: $\alpha = 0.63$, $k = 0.4\times10^6\, N/m$ and $c = 3.6\times10^6\, N\sec^{\alpha}/m$. The value of the parameter α is similar to the one used in papers [1, 4], but the original values of k and c are divided by 2.0.

In paper [1] the parameters of generalized models are obtained by minimizing the mean square norm of the differences between the targeted modules and the analytical modules of the considered model. The parameters of the generalized Kelvin model and the generalized Maxwell model, both with seven parameters and used in this paper, are given in Table 4.

	Stiffness $(\times10^6)\,[N/m]$			Damping factor $(\times10^6)\,[N\sec/m]$	
	Kelvin model	Maxwell model		Kelvin model	Maxwell model
k_0	57.650	0.1065		–	–
k_1	18.350	33.385	c_1	2.729	1.478
k_2	6.160	3.310	c_2	6.190	1.732
k_3	0.5545	1.443	c_3	8.675	8.305

Table 4: Parameters of generalized Kelvin and Maxwell models

The energy dissipated by the damper was calculated assuming that the amplitude of a harmonically varying vibration of the damper is equal to $0.01\,m$ in all of the considered cases. From this calculation, it can be concluded that the loss modulus and dissipation energy of the fractional-derivative Kelvin model and both generalized models are approximately equal in the range 0 – 15.0 rad/sec of excitation frequency. This range of frequency covers the range of the first three natural frequencies of vibration of the structure considered.

The values of the parameters of the simple Kelvin model are: $k = 0.74637\times10^7\; N/m$, $c = 0.134420\times10^7\; N\sec/m$ and the values of the parameters of the simple Maxwell model are: $k = 1.90392\times10^7\; N/m$ and $c = 0.338669\times10^7\; N\sec/m$. These parameters are calculated by minimizing the mean square norm of difference between the target modules, given by (32), and the analytical modules of the respective model. However, the dissipation energy of simple models and the dissipation energy of the fractional-derivative model are not equal and, as expected, the differences are significant, especially for the simple Maxwell model.

Chevron braces are used to connect the dampers with the structure. The braces are made of HEB 200 stainless steel profiles of which the parameters are: $EA = 1.60105\times10^9$ N and $EJ = 1.1685\times10^7$ Nm^2.

4.2 Comparison of dynamic characteristics of considered frame

Results of the solution to the eigenvalue problems are presented in Tables 5 – 10. The real and the complex conjugate numbers are obtained as eigenvalues. In Table 5 the values of the first three complex conjugate eigenvalues are given for all of the considered models (the two parameter model denotes the simple Kelvin or Maxwell model).

Kelvin model of damper with		Maxwell model of damper with	
7 parameters	2 parameters	7 parameters	2 parameters
-0.18461 ± i 3.30499	-0.1224 ± i 3.3754	-0.18260 ± i 3.30439	-0.25113 ± i 3.31731
-0.99448 ± i 9.39577	-0.9846 ± i 9.28452	-1.01395 ± i 9.50962	-0.58872 ± i 9.83667
-2.09561 ± i 16.8189	-2.4740 ± i 16.0635	-1.76745 ± i 17.2242	-0.56505 ± i 17.0933

Table 5: The first three complex conjugate eigenvalues of frame with dampers

Kelvin model of damper with 7 parameters $[\sec^{-1}]$		Maxwell model of damper with 7 parameters $[\sec^{-1}]$	
-0.377771	-2.90147	-0.166298	-1.83572
-0.382183	-2.93738	-0.167949	-1.85359
-0.383780	-2.95781	-0.168588	-1.86274
-0.386515	-3.01417	-0.169621	-1.89241
-0.389423	-27.3841	-0.170717	-15.3707
-0.391331	-28.5853	-0.171435	-16.1435
-0.392254	-29.2224	-0.171781	-16.6836
-0.395517	-30.4773	-0.173008	-17.2797
-2.72596	-31.9943	-1.73882	-17.9245
-2.80627	-33.8003	-1.78531	-18.8592
-2.84271	-35.3870	-1.78985	-20.0361
-2.85854	-36.0392	-1.80968	-20.5792

Table 6: Real eigenvalues of frame with dampers

Given in Tables 6 and 7 are all real eigenvalues obtained for all of the models considered. The real eigenvalues for both of the generalized models could be divided into three groups, each with eight elements. The values of elements in one group are of the same order as the eigenvalues of the eigenproblem obtained for one separate damper. For the generalized Kelvin model of damper with seven parameters the above-mentioned problem has the following form:

$$\left(\begin{bmatrix} k_0+k_1 & -k_1 & 0 \\ -k_1 & k_1+k_2 & -k_2 \\ 0 & -k_2 & k_2+k_3 \end{bmatrix} + s\begin{bmatrix} c_1 & -c_1 & 0 \\ -c_1 & c_1+c_2 & -c_2 \\ 0 & -c_2 & c_2+c_3 \end{bmatrix}\right)\begin{Bmatrix} x_1 \\ x_2 \\ x_3 \end{Bmatrix} = \begin{Bmatrix} 0 \\ 0 \\ 0 \end{Bmatrix}, \qquad (33)$$

from which we obtain: $s_1 = -0.3975\,\text{sec}^{-1}$, $s_2 = -3.0518\,\text{sec}^{-1}$ and $s_3 = -41.418\,\text{sec}^{-1}$. In the case of the generalized Maxwell model the equations of the above-mentioned eigenproblem are uncoupled and the real eigenvalues are approximately equal to the inverse of the relaxation time of the Maxwell element (with a minus sign), i.e., in the case under consideration, $s_1 = -k_1/c_1 = -22.588\,\text{sec}^{-1}$, $s_2 = -1.911\,\text{sec}^{-1}$ and $s_3 = -0.1738\,\text{sec}^{-1}$. A similar remark is true for the real eigenvalues of the frame with dampers modeled using the simple Kelvin model and presented in Table 7.

The reason why real eigenvalues exist for the frame with dampers modeled by the simple Kelvin model, given in Table 8, is completely different. The loss factor of the simple Kelvin model is a linear function of excitation frequency. This means that higher modes of vibration are more strongly damped, compared with lower ones, and could be overdamped, which happens in the case under consideration where eight modes of vibration are overcritically damped. In other cases, all modes are undercritically damped. It is a qualitative difference, compared with other damper models.

Maxwell model of damper with 2 parameters $[\text{sec}^{-1}]$	
-3.75157	-4.57767
-4.09211	-4.79722
-4.27776	-4.98507
-4.53600	-5.32095

Table 7: Real eigenvalues for frame with dampers modeled by the simple Maxwell model

Kelvin model of damper with 2 parameters $[\text{sec}^{-1}]$			
-231.120	-254.940	-14840.1	-14847.5
-240.435	-258.708	-14845.1	-14848.7
-245.480	-261.561	-14846.0	-14849.6
-250.975	-262.479	-14846.9	-14855.5

Table 8: Real eigenvalues for frame with dampers modeled by the simple Kelvin model

The first three natural frequencies of the frame with dampers modeled using different models are presented in Table 9. As is easily verified, the damper model does not significantly change the first three natural frequencies of the frame. The maximal difference is 6.1%. However, as is obvious from Table 10, the influence of the damper model on the non-dimensional damping ratios is substantial because the maximal difference is of the order of 80%.

Natural frequency	Kelvin model of damper with		Maxwell model of damper with	
	7 parameters [rad/sec]	2 parameters [rad/sec]	7 parameters [rad/sec]	2 parameters [rad/sec]
ω_1	3.31014	3.37757	3.30944	3.32681
ω_2	9.44825	9.33658	9.56352	9.85427
ω_3	16.9490	16.2529	17.3146	17.1026

Table 9: The natural frequencies of frame with dampers

Damping ratio	Kelvin model of damper with		Maxwell model of damper with	
	7 parameters	2 parameters	7 parameters	2 parameters
γ_1	0.0557702	0.0362529	0.0551757	0.0754865
γ_2	0.105256	0.105455	0.106023	0.0597427
γ_3	0.123642	0.152223	0.102078	0.0330390

Table 10: Non-dimensional damping ratios of frame with dampers

A comparison of the first and second modes of vibration is shown in Figures 3. The dashed lines represent the shape of vibration of frame without dampers while the real and imaginary parts of eigenvector for the frame with dampers are shown by the solid line and the solid line with crosses, respectively. Moreover, the imaginary part of eigenvectors is multiplied by 10 in order to show this quantity in detail. The calculation is done for dampers modeled using the Kelvin model with seven parameters. It is easy to observe that the real part of both eigenvectors is very similar to the respective mode of vibration of the frame without dampers.

The frequency response functions are also calculated and one example is shown in Figures 4 where the frequency response function corresponding to the horizontal displacement of the eighth storey is shown. The frequency response curve for the frame with dampers modeled using the generalized Kelvin model (the solid line) and the simple Kelvin model (the dashed line) is shown.

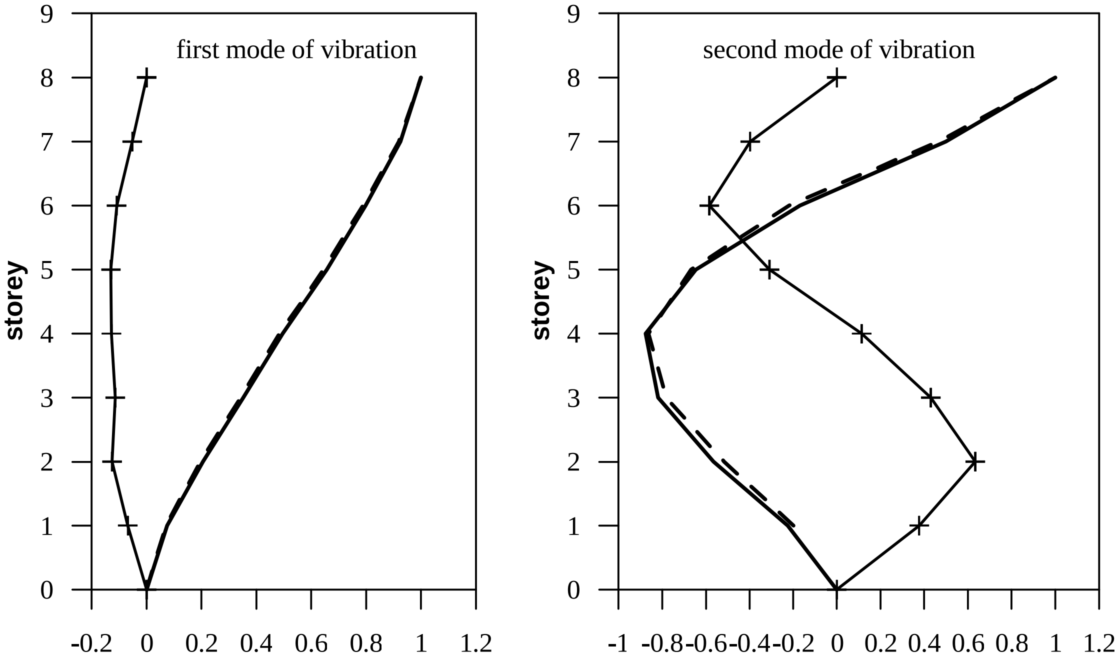

Figure 3: A comparison of modes of vibration for a frame without dampers (the dashed lines) with the real part of eigenvector for frame with dampers modeled by the generalized Kelvin model (the solid line). The imaginary part of the eigenvector is multiplied by 10 and shown by the solid line with crosses

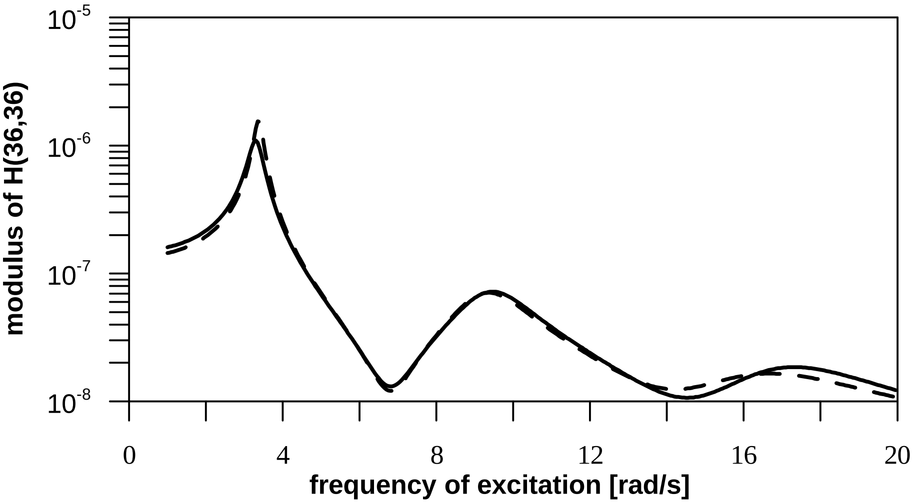

Figure 4: Frequency response function of frame with dampers modeled by the generalized Kelvin model (the solid line) and by the simple Kelvin model (the dashed line)

5 CONCLUSIONS

Several models of dampers are used in this paper to describe the dynamic behaviour of frame structures with VE dampers. A family of generalized rheological models, including the very often used simple Kelvin and Maxwell models, are compared in detail. The comparison is made in the frequency domain for a carefully selected frame structure with VE dampers. The finite element method is used to derive equations of motion.

Several conclusions can be formulated on the basis of the results of numerical analysis presented above. The most important ones are listed below.

- Different models are able to correctly describe the dynamic behaviour of VE dampers. The seven-parameter Kelvin model and the seven-parameter Maxwell model provide almost identical results. This conclusion is in agreement with the results presented by Singh and Chang [4] where the generalized Kelvin and Maxwell models are used as models of VE dampers.
- The simple Kelvin and the simple Maxwell models are not able to correctly describe, in the frequency domain, the dynamic behavior of frames with VE dampers. In particular, relative differences concerning the non-dimensional damping ratios are large.
- The linear eigenvalue problems must be solved in order to determine the dynamic characteristics of the frame with VE dampers. The solution procedure for this problem is much simpler than the solution procedure for the nonlinear eigenvalue problem obtained when the fractional-derivative Kelvin model or the complex modulus model are used as the VE damper model.
- There are some qualitative differences between the results obtained. For the frame with a fixed number of VE dampers the total number of eigenvalues and eigenvectors depends on the selected model of dampers and the number of parameters of the models. Both the real and complex eigenvalues are obtained. The number of real eigenvalues depends on dampers model.

Acknowledgments

The first author wishes to acknowledge the financial support received from the Poznan University of Technology (Grant No. **DS 11 - 068/11**) in connection with this work.

6 APPENDIX A

In this appendix the explicit form of the matrices used to describe the generalized Kelvin model of the VE damper is given.

$$\tilde{\mathbf{K}}_{zz} = \begin{bmatrix} k_0 & 0 & 0 & 0 \\ 0 & 0 & 0 & 0 \\ 0 & 0 & k_m & 0 \\ 0 & 0 & 0 & 0 \end{bmatrix}, \qquad \tilde{\mathbf{C}}_{zz} = \begin{bmatrix} 0 & 0 & 0 & 0 \\ 0 & 0 & 0 & 0 \\ 0 & 0 & c_m & 0 \\ 0 & 0 & 0 & 0 \end{bmatrix}, \tag{A.1}$$

$$\tilde{\mathbf{K}}_{zw} = \begin{bmatrix} -k_0 & 0.....0.......0 \\ 0 & 0.....0.......0 \\ 0 & 0.....0.....-k_m \\ 0 & 0.....0.......0 \end{bmatrix}, \qquad \tilde{\mathbf{C}}_{zw} = \begin{bmatrix} 0 & 0.....0.......0 \\ 0 & 0.....0.......0 \\ 0 & 0.....0.....-c_m \\ 0 & 0.....0.......0 \end{bmatrix}, \tag{A.2}$$

$$\tilde{\mathbf{K}}_{ww} = \begin{bmatrix} k_0+k_1 & -k_1.............0 & 0 & 0.............0 & 0 \\ -k_1 & k_1+k_2..........0 & 0 & 0.............0 & 0 \\ \multicolumn{5}{c}{\dots\dots\dots\dots\dots\dots\dots\dots\dots\dots\dots\dots\dots\dots\dots\dots} \\ 0 & 0............-k_{i-1} & k_{i-1}+k_i & -k_i...........0 & 0 \\ \multicolumn{5}{c}{\dots\dots\dots\dots\dots\dots\dots\dots\dots\dots\dots\dots\dots\dots\dots\dots} \\ 0 & 0................0 & 0 & 0.......-k_{m-1} & k_{m-1}+k_m \end{bmatrix}, \tag{A.3}$$

$$\tilde{\mathbf{C}}_{ww} = \begin{bmatrix} c_1 & -c_1 \ldots\ldots\ldots\ldots 0 & 0 & 0 \ldots\ldots\ldots 0 & 0 \\ -c_1 & c_1 + c_2 \ldots\ldots\ldots 0 & 0 & 0 \ldots\ldots\ldots 0 & 0 \\ \ldots\ldots\ldots & \ldots\ldots\ldots & \ldots\ldots\ldots & \ldots\ldots\ldots & \ldots\ldots\ldots \\ 0 & 0 \ldots\ldots\ldots -c_{i-1} & c_{i-1} + c_i & -c_i \ldots\ldots\ldots 0 & 0 \\ \ldots\ldots\ldots & \ldots\ldots\ldots & \ldots\ldots\ldots & \ldots\ldots\ldots & \ldots\ldots\ldots \\ 0 & 0 \ldots\ldots\ldots\ldots 0 & 0 & 0 \ldots\ldots -c_{m-1} & c_{m-1} + c_m \end{bmatrix}, \tag{A.4}$$

$$\mathbf{K}_d = \mathbf{T}_d^T \tilde{\mathbf{K}}_d \mathbf{T}_d = \begin{bmatrix} \mathbf{K}_{zz} & \mathbf{K}_{zw} \\ \mathbf{K}_{wz} & \mathbf{K}_{ww} \end{bmatrix}, \qquad \mathbf{C}_d = \mathbf{T}_d^T \tilde{\mathbf{C}}_d \mathbf{T}_d = \begin{bmatrix} \mathbf{C}_{zz} & \mathbf{C}_{zw} \\ \mathbf{C}_{wz} & \mathbf{C}_{ww} \end{bmatrix}, \tag{A.5}$$

$$\mathbf{K}_{zz} = \begin{bmatrix} c^2 k_0 & csk_0 & 0 & 0 \\ csk_0 & s^2 k_0 & 0 & 0 \\ 0 & 0 & c^2 k_m & csk_m \\ 0 & 0 & csk_m & s^2 k_m \end{bmatrix}, \qquad \mathbf{C}_{zz} = \begin{bmatrix} 0 & 0 & 0 & 0 \\ 0 & 0 & 0 & 0 \\ 0 & 0 & c^2 c_m & \mathrm{csc}_m \\ 0 & 0 & \mathrm{csc}_m & \mathrm{csc}_m \end{bmatrix}, \tag{A.6}$$

$$\mathbf{K}_{zw} = \mathbf{K}_{wz}^T = \begin{bmatrix} -ck_0 & 0 \ldots\ldots 0 \ldots\ldots\ldots & 0 \\ -sk_0 & 0 \ldots\ldots 0 \ldots\ldots\ldots & 0 \\ 0 & 0 \ldots\ldots 0 \ldots\ldots & -ck_m \\ 0 & 0 \ldots\ldots 0 \ldots\ldots & -sk_m \end{bmatrix}, \quad \mathbf{C}_{zw} = \mathbf{C}_{wz}^T = \begin{bmatrix} 0 & 0 \ldots\ldots 0 \ldots\ldots\ldots & 0 \\ 0 & 0 \ldots\ldots 0 \ldots\ldots\ldots & 0 \\ 0 & 0 \ldots\ldots 0 \ldots\ldots & -cc_m \\ 0 & 0 \ldots\ldots 0 \ldots\ldots & -sc_m \end{bmatrix}, \tag{A.7}$$

$$\mathbf{K}_{ww} = \tilde{\mathbf{K}}_{ww}, \qquad \mathbf{C}_{ww} = \tilde{\mathbf{C}}_{ww}. \tag{A.8}$$

7 APPENDIX B

In this Appendix the explicit form of matrices used to describe the generalized Maxwell model of the VE damper is given.

$$\tilde{\mathbf{K}}_{zz} = \begin{bmatrix} k_0 + \sum_{i=1}^{m} k_i & 0 & -k_0 & 0 \\ 0 & 0 & 0 & 0 \\ -k_0 & 0 & k_0 & 0 \\ 0 & 0 & 0 & 0 \end{bmatrix}, \qquad \tilde{\mathbf{C}}_{zz} = \begin{bmatrix} 0 & 0 & 0 & 0 \\ 0 & 0 & 0 & 0 \\ 0 & 0 & \sum_{i=1}^{m} c_i & 0 \\ 0 & 0 & 0 & 0 \end{bmatrix}, \tag{B.1}$$

$$\tilde{\mathbf{K}}_{zw} = \begin{bmatrix} -k_1 & -k_2 \ldots\ldots -k_i \ldots\ldots\ldots & -k_m \\ 0 & 0 \ldots\ldots\ldots\ 0 \ldots\ldots\ldots & 0 \\ 0 & 0 \ldots\ldots\ldots\ 0 \ldots\ldots\ldots & 0 \\ 0 & 0 \ldots\ldots\ 0 \ldots\ldots\ldots & 0 \end{bmatrix}, \qquad \tilde{\mathbf{C}}_{zw} = \begin{bmatrix} 0 & 0 \ldots\ldots\ldots\ 0 \ldots\ldots\ldots & 0 \\ 0 & 0 \ldots\ldots\ldots\ 0 \ldots\ldots\ldots & 0 \\ -c_1 & -c_2 \ldots\ldots -c_i \ldots\ldots\ldots & -c_m \\ 0 & 0 \ldots\ldots\ 0 \ldots\ldots\ldots & 0 \end{bmatrix}, \tag{B.2}$$

$$\tilde{\mathbf{K}}_{ww} = diag(k_1,\ k_2, \ldots\ldots\ldots\ldots, k_m,), \qquad \tilde{\mathbf{C}}_{ww} = diag(c_1,\ c_2, \ldots\ldots\ldots\ldots, c_m,), \tag{B.3}$$

$$\mathbf{K}_d = \mathbf{T}_d^T \tilde{\mathbf{K}}_d \mathbf{T}_d = \begin{bmatrix} \mathbf{K}_{zz} & \mathbf{K}_{zw} \\ \mathbf{K}_{wz} & \mathbf{K}_{ww} \end{bmatrix}, \qquad \mathbf{C}_d = \mathbf{T}_d^T \tilde{\mathbf{C}}_d \mathbf{T}_d = \begin{bmatrix} \mathbf{C}_{zz} & \mathbf{C}_{zw} \\ \mathbf{C}_{wz} & \mathbf{C}_{ww} \end{bmatrix}, \tag{B.4}$$

$$\mathbf{K}_{ww} = \tilde{\mathbf{K}}_{ww}, \qquad \mathbf{C}_{ww} = \tilde{\mathbf{C}}_{ww}, \tag{B.5}$$

$$\mathbf{K}_{zz} = \begin{bmatrix} c^2\left(k_0 + \sum_{i=1}^{m} k_i\right) & cs\left(k_0 + \sum_{i=1}^{m} k_i\right) & -c^2 k_0 & -csk_0 \\ cs\left(k_0 + \sum_{i=1}^{m} k_i\right) & s^2\left(k_0 + \sum_{i=1}^{m} k_i\right) & -csk_0 & -s^2 k_0 \\ -c^2 k_0 & -csk_0 & c^2 k_0 & csk_0 \\ -csk_0 & -s^2 k_0 & csk_0 & s^2 k_0 \end{bmatrix} , \tag{B.6}$$

$$\mathbf{C}_{zz} = \begin{bmatrix} 0 & 0 & 0 & 0 \\ 0 & 0 & 0 & 0 \\ 0 & 0 & c^2 \sum_{i=1}^{m} c_i & cs \sum_{i=1}^{m} c_i \\ 0 & 0 & cs \sum_{i=1}^{m} c_i & s^2 \sum_{i=1}^{m} c_i \end{bmatrix} , \qquad \mathbf{K}_{zw} = \mathbf{K}_{zw}^T = \begin{bmatrix} -ck_1 - ck_2 \ldots\ldots - ck_i \ldots\ldots\ldots - ck_m \\ -sk_1 - sk_2 \ldots\ldots - sk_i \ldots\ldots\ldots - sk_m \\ 0 \quad 0\ldots\ldots\ldots \quad 0 \ldots\ldots\ldots \quad 0 \\ 0 \quad 0\ldots\ldots\ldots \quad 0 \ldots\ldots\ldots \quad 0 \end{bmatrix} , \tag{B.7}$$

$$\mathbf{C}_{zw} = \mathbf{C}_{zw}^T = \begin{bmatrix} 0 \quad 0\ldots\ldots\ldots \quad 0 \ldots\ldots\ldots \quad 0 \\ 0 \quad 0\ldots\ldots\ldots \quad 0 \ldots\ldots\ldots \quad 0 \\ -cc_1 - cc_2 \ldots\ldots - cc_i \ldots\ldots\ldots - cc_m \\ -sc_1 - sc_2 \ldots\ldots - sc_i \ldots\ldots\ldots - sc_m \end{bmatrix} . \tag{B.8}$$

8 APPENDIX C

The explicit form of the vectors and matrices used to describe the simple Kelvin model of VE damper is:

$$\tilde{\mathbf{q}}_d(t) = \tilde{\mathbf{q}}_z(t) = col(\tilde{q}_1(t), \tilde{q}_2(t), \tilde{q}_3(t), \tilde{q}_4(t)) \ , \tag{C.1}$$

$$\tilde{\mathbf{K}}_d = \tilde{\mathbf{K}}_{zz} = k_1 \begin{bmatrix} 1 & 0 & -1 & 0 \\ 0 & 0 & 0 & 0 \\ -1 & 0 & 1 & 0 \\ 0 & 0 & 0 & 0 \end{bmatrix} , \qquad \tilde{\mathbf{C}}_d = \tilde{\mathbf{C}}_{zz} = c_1 \begin{bmatrix} 1 & 0 & -1 & 0 \\ 0 & 0 & 0 & 0 \\ -1 & 0 & 1 & 0 \\ 0 & 0 & 0 & 0 \end{bmatrix} , \tag{C.2}$$

$$\mathbf{q}_d(t) = \mathbf{q}_z(t) = col(q_1(t), q_2(t), q_3(t), q_4(t)) \ , \tag{C.3}$$

$$\mathbf{K}_d = \mathbf{K}_{zz} = k_1 \begin{bmatrix} c^2 & cs & -c^2 & -cs \\ cs & s^2 & -cs & -s^2 \\ -c^2 & -cs & c^2 & cs \\ -cs & -s^2 & cs & s^2 \end{bmatrix} , \quad \mathbf{C}_d = \mathbf{C}_{zz} = c_1 \begin{bmatrix} c^2 & cs & -c^2 & -cs \\ cs & s^2 & -cs & -s^2 \\ -c^2 & -cs & c^2 & cs \\ -cs & -s^2 & cs & s^2 \end{bmatrix} , \tag{C.4}$$

The explicit form of the matrices used to describe the simple Maxwell model of VE damper is:

$$\tilde{\mathbf{q}}_d(t) = col(\tilde{\mathbf{q}}_z(t), \ \tilde{\mathbf{q}}_w(t)) \ , \tag{C.5}$$

$$\tilde{\mathbf{q}}_z(t) = col(\tilde{q}_1(t), \tilde{q}_2(t), \tilde{q}_3(t), \tilde{q}_4(t)) \ , \qquad \tilde{\mathbf{q}}_w(t) = col(\tilde{q}_{w,1}(t)) \ , \tag{C.6}$$

$$\tilde{\mathbf{K}}_{zz} = \begin{bmatrix} k_1 & 0 & 0 & 0 \\ 0 & 0 & 0 & 0 \\ 0 & 0 & 0 & 0 \\ 0 & 0 & 0 & 0 \end{bmatrix}, \quad \tilde{\mathbf{K}}_{zw} = \tilde{\mathbf{K}}_{wz}^{T} = \begin{bmatrix} -k_1 \\ 0 \\ 0 \\ 0 \end{bmatrix}, \quad \tilde{\mathbf{K}}_{ww} = [\,k_1\,], \tag{C.7}$$

$$\tilde{\mathbf{C}}_{zz} = \begin{bmatrix} 0 & 0 & 0 & 0 \\ 0 & 0 & 0 & 0 \\ 0 & 0 & c_1 & 0 \\ 0 & 0 & 0 & 0 \end{bmatrix}, \quad \tilde{\mathbf{C}}_{zz} = \tilde{\mathbf{C}}_{wz}^{T} = \begin{bmatrix} 0 \\ 0 \\ -c_1 \\ 0 \end{bmatrix}, \quad \tilde{\mathbf{C}}_{ww} = [\,c_1\,], \tag{C.8}$$

$$\mathbf{q}_d(t) = col(\mathbf{q}_z(t),\ \mathbf{q}_w(t)), \tag{C.9}$$

$$\mathbf{q}_z(t) = col(q_1(t), q_2(t), q_3(t), q_4(t)), \quad \mathbf{q}_w(t) = col(q_{w,1}(t)), \quad \mathbf{K}_d = \begin{bmatrix} \mathbf{K}_{zz} & \mathbf{K}_{zw} \\ \mathbf{K}_{wz} & \mathbf{K}_{ww} \end{bmatrix}, \tag{C.10}$$

$$\mathbf{K}_d = \begin{bmatrix} \mathbf{K}_{zz} & \mathbf{K}_{zw} \\ \mathbf{K}_{wz} & \mathbf{K}_{ww} \end{bmatrix}, \quad \mathbf{C}_d = \begin{bmatrix} \mathbf{C}_{zz} & \mathbf{C}_{zw} \\ \mathbf{C}_{wz} & \mathbf{C}_{ww} \end{bmatrix}, \tag{C.11}$$

$$\mathbf{K}_{zz} = k_1 \begin{bmatrix} c^2 & cs & 0 & 0 \\ cs & s^2 & 0 & 0 \\ 0 & 0 & 0 & 0 \\ 0 & 0 & 0 & 0 \end{bmatrix}, \quad \mathbf{K}_{zw} = \mathbf{K}_{zw}^{T} = k_1 \begin{bmatrix} -c \\ -s \\ 0 \\ 0 \end{bmatrix}, \quad \mathbf{K}_{ww} = [\,k_1\,], \tag{C.12}$$

$$\mathbf{C}_{zz} = c_1 \begin{bmatrix} 0 & 0 & 0 & 0 \\ 0 & 0 & 0 & 0 \\ 0 & 0 & c^2 & cs \\ 0 & 0 & cs & s^2 \end{bmatrix}, \quad \mathbf{C}_{zw} = \mathbf{C}_{zw}^{T} = c_1 \begin{bmatrix} 0 \\ 0 \\ -c \\ -s \end{bmatrix}, \quad \mathbf{C}_{ww} = [\,c_1\,]. \tag{C.13}$$

REFERENCES

[1] T.S. Chang, M.P. Singh, Mechanical model parameters for viscoelastic dampers. *Journal of Engineering Mechanics*, **135**, 581-584, 2009.

[2] R. Lewandowski, B. Chorążyczewski, Identification of the parameters of the Kelvin-Voigt and the Maxwell fractional models, used to modeling of viscoelastic dampers. *Computers and Structures*, **88**, 1-17, 2010.

[3] Chang T.S. and Singh M.P., Seismic analysis of structures with a fractional derivative model of viscoelastic dampers. *Earthquake Engineering and Engineering Vibration*, **1**, 251-260, 2002.

[4] Singh M.P. and Chang T.S., Seismic analysis of structures with viscoelastic dampers. *Journal of Engineering Mechanics*, **135**, 571-580, 2009.

[5] R. Lewandowski and Z. Pawlak, Dynamic analysis of frames with viscoelastic dampers modelled by rheological models with fractional derivatives. *Journal of Sound and Vibration,* **330**, 923-936, 2011.

[6] Hatada T., Kobori T., Ishida M.A. and Niwa N., Dynamic analysis of structures with Maxwell model. *Earthquake Engineering and Structural Dynamics Earthquake*, **29** 159-176, 2000.

[7] Singh M.P. and Moreschi L.M., Optimal placement of dampers for passive response control. *Earthquake Engineering and Structural Dynamics,* **31**, 955-976, 2002.

[8] Singh M.P., Verma N.P., and Moreschi L.M., Seismic analysis and design with Maxwell dampers. *Journal of Engineering Mechanics,* **129**, 273-282, 2003.

[9] Matsagar V.A. and Jangid R.S., Viscoelastic damper connected to adjacent structures involving seismic isolation. *Journal of Civil Engineering and Management*, **11**, 309-322, 2005.

[10] Zhang W.S. and Xu Y.L., Vibration analysis of two buildings linked by Maxwell model-defined fluid dampers. *Journal of Sound and Vibration,* **233**, 775-796, 2000.

[11] Shukla A.K. and Datta T.K., Optimal use of viscoelastic dampers in building frames for seismic force. *Journal of Structural Engineering*, **125**, 401–409, 1999.

[12] Park J.H., Kim J. and Min K.W., Optimal design of added viscoelastic dampers and supporting braces. *Earthquake Engineering and Structural Dynamics*, **33**, 465-484, 2004.

[13] Lee S.H., Son D.I., Kim J. and Min K.W., Optimal design of viscoelastic dampers using eigenvalue assignment. *Earthquake Engineering and Structural Dynamics*, **33**: 521-542, 2004.

[14] Tsai M.H. and Chang K.C., Higher-mode effect on the seismic responses of buildings with viscoelastic dampers. *Earthquake Engineering and Engineering Vibration*, **1**, 119-129, 2002.

[15] R. Lewandowski and B. Chorążyczewski, Remarks on modelling of passive viscoelastic dampers. *Proceedings of the 9th International Conference "Modern Building Materials, Structures and Technique"*, 16-18 May, 2007, Vilnius, Lithuania.

[16] Palmeri, A, Ricciardelli, F., De Luca, A., Muscolino, G., State space formulation for linear viscoelastic dynamic systems with memory. *Journal of Engineering Mechanics,* **129**, 715–724, 2003.

[17] Okada R., Nakata N., Spencer B.F., Kasai K., Kim B.S., Rational polynomial approximation modeling for analysis of structures with VE dampers. *Journal of Earthquake Engineering*, **10**, 97–125, 2006.

[18] Park S.W., Analytical modeling of viscoelastic dampers for structural and vibration control. *International Journal of Solids and Structures*, **38**, 8065-8092, 2001.

COMPDYN 2011
3rd ECCOMAS Thematic Conference on
Computational Methods in Structural Dynamics and Earthquake Engineering
M. Papadrakakis, M. Fragiadakis, V. Plevris (eds.)
Corfu, Greece, 25–28 May 2011

THE ROCKING RESPONSE OF SEISMICALLY ISOLATED, FREE-STANDING RIGID BLOCKS.

Michalis F. Vassiliou and Nicos Makris

Department of Civil Engineering University of Patras, Patras GR26500, Greece
email: mfvassiliou@gmail.com
nmakris@upatras.gr

Keywords: Rocking Columns, Seismic Isolation, Spherical Sliding Bearings, Earthquake Engineering

Abstract. This paper examines the rocking response and stability of rigid blocks standing free on an isolated base supported on linear viscoelastic bearings and bearings that exhibit bilinear behavior. The investigation concludes that seismic isolation is beneficial only for small blocks. This happens because while seismic isolation increase the “static” value of the minimum overturning acceleration, this acceleration value remains nearly constant as we move towards larger blocks or higher frequency pulses; therefore seismic isolation removes drastically from the dynamics of rocking blocks the beneficial property of increasing stability as their size increases or as the excitation pulse period decreases. This remarkable result suggests that freestanding ancient classical columns exhibit superior stability as they are built (standing free on a rigid foundation) rather than if they were seismically isolated even with isolation systems with very long isolation periods. The study further confirms this finding by examining the seismic response of the columns from the peristyle of two ancient Greek temples when subjected to historic records.

1 INTRODUCTION

Under base shaking slender objects and tall rigid structures may enter into rocking motion that occasionally results in overturning. Early studies on the rocking response of a rigid block supported on a base undergoing horizontal accelerated motion were presented by Housner (1963) [1]. His pioneering work uncovered a size-frequency scale effect which explained why: (a) the larger of two geometrically similar blocks can survive the excitation that will topple the smaller block; and (b) out of two same acceleration-amplitude pulses the one with the longer duration is more capable to induce overturning.

As the size of the block increases, the duration of the coherent pulse of the base motion plays a dominant role in inducing overturning. For instance, Figure 1, plots the rocking response of a rigid block that is 2.0m tall and 0.5m wide when subjected to an intense (a_p=0.5g) but short duration (T_p=0.5s) one-sine acceleration pulse (left–no overturning) and a less intense (a_p=0.29g), yet longer duration pulse (T_p=2s) one sine acceleration pulse (right – overturning). Interestingly, this 2.0m×0.5m rigid block survives the intense, short duration pulse; yet overturns when subjected to the lower acceleration amplitude, long-duration pulse. The above example shows that reducing the base acceleration while lengthening the period of the excitation (what seismic isolation does) is not a beneficial approach for all combinations of block size and frequency content of the base excitation.

The rocking response of slender rigid objects standing free on a seismically isolated base is a subject that has received attention during the last two decades mainly from the need to protect slender art objects within museums (Augusti et al. 1992 [2], Vestroni and Di Cinto 2000 [3], Calio and Marletta 2003 [4], Roussis et al. 2008 [5], Contento and Egidio 2009 [6]

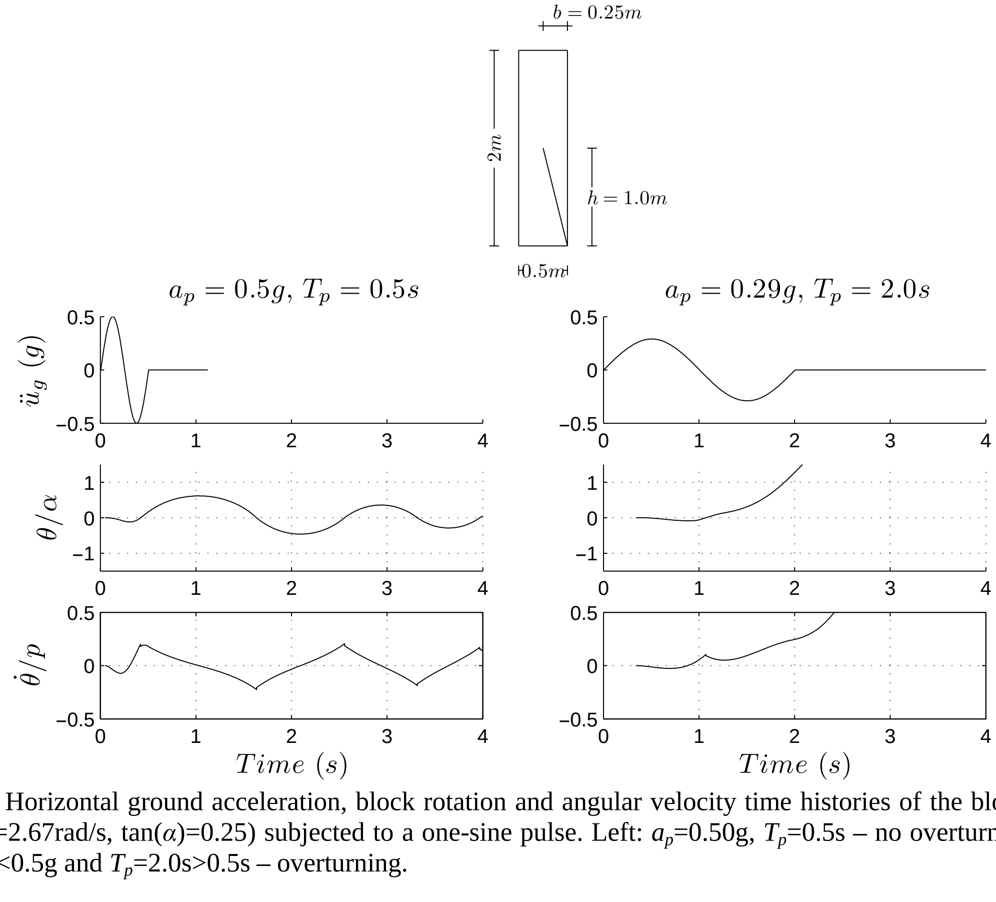

Figure 1. Horizontal ground acceleration, block rotation and angular velocity time histories of the block shown above (p=2.67rad/s, tan(α)=0.25) subjected to a one-sine pulse. Left: a_p=0.50g, T_p=0.5s – no overturning, Right a_p=0.29g<0.5g and T_p=2.0s>0.5s – overturning.

among others). These studies primarily focused on the seismic protection of relative small size blocks such as art objects up to human-size statues and they invariably concluded that seismic isolation suppresses the rocking response and protects such objects from overturning. Given, however, the results of Figure 1, this paper investigates in depth up to what size of free standing objects the application of seismic isolation is beneficial and concludes that larger free-standing structures like ancient columns of temples have superior stability as they stand free atop their massive foundations compare to if they were seismic isolated. Furthermore, this study settles the matter of conservation of linear momentum of the entire system (the rocking – translating block and the translating isolated base) during the impact of the rocking block – a matter that has been overlooked by other investigators.

2 REVIEW OF THE ROCKING RESPONSE OF A RIGID BLOCK.

With reference to Figure 2 and assuming that the coefficient of friction is large enough so that there is no sliding, the equation of motion of a rocking block with size $R=\sqrt{h^2+b^2}$ and slenderness α=atan(b/h) for rotation around O and O' respectively is (Yim et al. 1980 [7], Makris and Roussos 2000 [8], Zhang and Makris 2001 [9] among others)

$$I_o\ddot{\theta}(t)+mgR\sin[-\alpha-\theta(t)]=-m\ddot{u}_g(t)R\cos[-\alpha-\theta(t)], \quad \theta(t)<0 \tag{1}$$

$$I_o\ddot{\theta}(t)+mgR\sin[\alpha-\theta(t)]=-m\ddot{u}_g(t)R\cos[\alpha-\theta(t)], \quad \theta(t)>0\,. \tag{2}$$

For rectangular blocks, $I_o=(4/3)mR^2$ and the above equations can be expressed in the compact form

$$\ddot{\theta}(t)=-p^2\left\{\sin\left[\alpha\,\mathrm{sgn}\left(\theta(t)\right)-\theta(t)\right]+\frac{\ddot{u}_g}{g}\cos\left[\alpha\,\mathrm{sgn}\left(\theta(t)\right)-\theta(t)\right]\right\}\,. \tag{3}$$

The oscillation frequency of a rigid block under free vibration is not constant, because it strongly depends on the vibration amplitude (Housner 1963 [1]). Nevertheless, the quantity

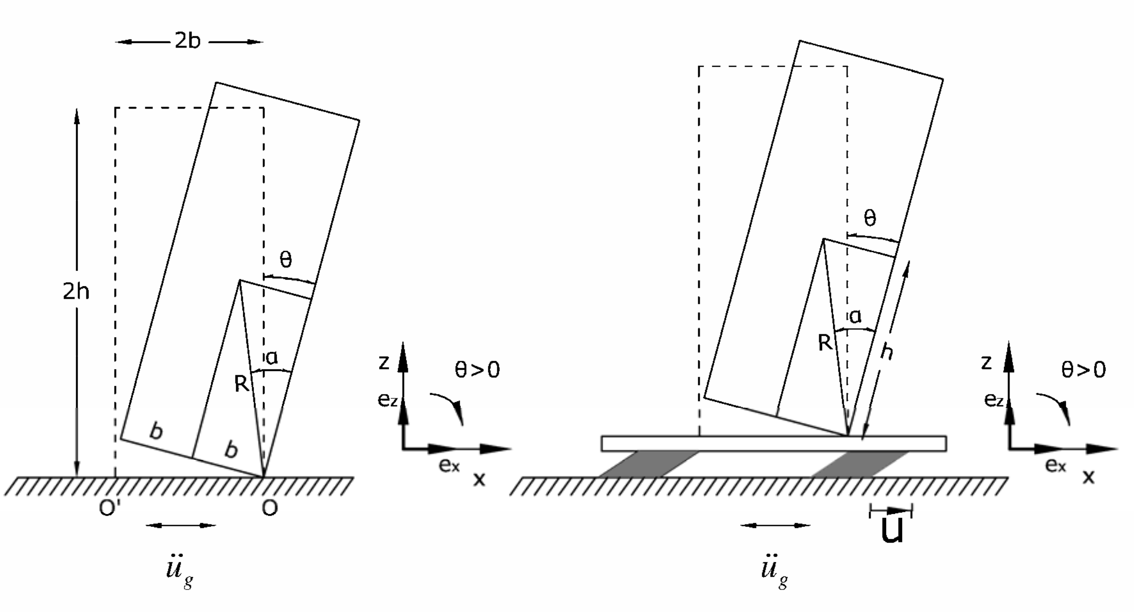

Figure 2. Geometric characteristics of the model considered. Left: Rigid block subjected to ground shaking. Right: Rigid block on isolated base.

$p=\sqrt{\frac{3g}{4R}}$ is a measure of the dynamic characteristics of the block. For the 2.0m×0.5m block shown in Figure 1 (say an modern refrigerator), $p = 2.67\ rad/s$, and for a household brick, $p \approx 8\ rad/s$.

Figure 3 shows the moment-rotation relationship during the rocking motion of a free-standing block. The system has infinite stiffness until the magnitude of the applied moment reaches the value $mgR\sin\alpha$, and once the block is rocking, its restoring force decreases monotonically, reaching zero when $\theta = \alpha$. During the oscillatory rocking motion, the moment-rotation curve follows this curve without enclosing any area. Energy is lost only during impact, when the angle of rotation reverses. When the angle of rotation reverses, it is assumed that the rotation continues smoothly from points *O* to *O'* and that the impact force is concentrated at the new pivot point, *O'*. With this idealization, the impact force applies no moment around *O'*, hence the angular momentum around *O'* is conserved. Conservation of angular momentum about point *O'* just before the impact and right after the impact gives

$$I_o\dot{\theta}_1 - m\dot{\theta}_1 2bR\sin(\alpha) = I_o\dot{\theta}_2 \tag{4}$$

where $\dot{\theta}_1$ = angular velocity just prior to the impact; and $\dot{\theta}_2$ = angular velocity right after the impact. The ratio of kinetic energy after and before the impact is

$$r = \frac{\dot{\theta}_2^2}{\dot{\theta}_1^2} \tag{5}$$

which means that the angular velocity after the impact is only $\sqrt{r}$ times the velocity before the impact. Substitution of (4) into (5) gives

$$r = [1-\frac{3}{2}\sin^2\alpha]^2 \tag{6}$$

The value of the coefficient of restitution given by (6) is the maximum value of *r* under which a block with slenderness α will undergo rocking motion. Consequently, to observe rocking motion, the impact has to be inelastic. The less slender a block (larger α), the more plastic is the impact, and for the value of $\alpha = \sin^{-1}\sqrt{2/3} = 54.73^o$, the impact is perfectly plastic.

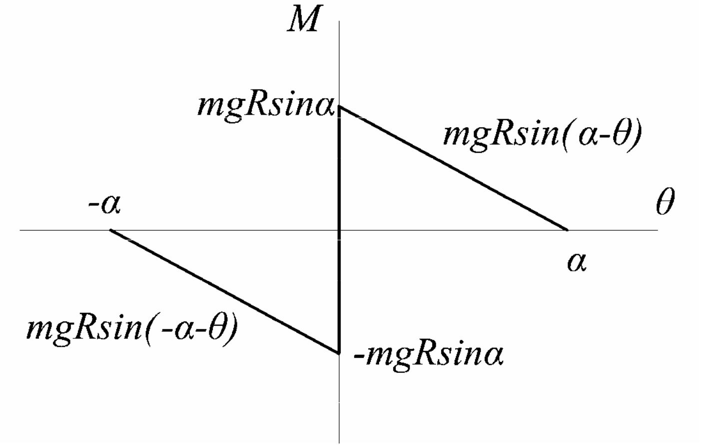

Figure 3. Moment rotation diagram of a rocking object

During rocking motion of slender blocks, if additional energy is lost due to the inelastic behavior at the instant of impact, the value of the true coefficient of restitution *r* will be less than the one computed from equation (6).

3 TIME SCALE AND LENGTH SCALE OF PULSE-LIKE GROUND MOTIONS

The relative simple form, yet destructive potential of near source ground motions has motivated the development of various closed form expressions which approximate their leading kinematic characteristics. The early work of Veletsos et al. [10] was followed by the papers of Hall et al. [11], Heaton et al. [12], Makris [13], Makris and Chang [14], Alavi and Krawinkler [15] and more recently by the paper of Mavroeidis and Papageorgiou [16]. Some of the proposed pulses are physically realizable motions with zero final ground velocity and finite accelerations whereas some other idealizations violate one or both of the above requirements. Physically realizable pulses can adequately describe the impulsive character of near-fault ground motions both qualitatively and quantitatively. The input parameters of the model have an unambiguous physical meaning. The minimum number of parameters is two, which are either the acceleration amplitude, a_p, and duration, T_p, or the velocity amplitude, v_p, and duration, T_p (Makris 1997[13], Makris and Chang 2000[14]). The more sophisticated model of Mavroeidis and Papageorgiou [16] involves 4 parameters, which are the pulse period, the pulse amplitude as well as the phase and number of half cycles, and was found to describe a large set of velocity pulses generated due to forward directivity or permanent translation effect. The pulse period, T_p, of the most energetic pulse of strong ground motions is strongly correlated with the moment magnitude, M_w, of the event. For a given moment magnitude, the duration of pulses produced by strike-slip faults is on average larger than the duration of pulses generated by reverse faults. Assuming that the time scale T_p is independent of the source–station distance, for stations located within ~10km from the causative fault, the pulse period and moment magnitude are related through the following empirical relationship which also satisfies a self-similarity condition [16, 17, 18]:

$$\ln T_p = -2.9 + 0.5 M_w \tag{7}$$

Furthermore, seismological data indicate that the amplitude of the velocity pulses recorded within a distance of 7 km from the causative fault varies from 60 to 120 cm/s. This observation is in good agreement with the typical slip velocity value of 90 cm/s frequently considered by seismologists (Brune 1970 [19], Aki 1983[20]).

The current established methodologies for estimating the pulse characteristics of a wide class of records are of unique value since the product, $a_p T_p^2 = L_p$, is a characteristic length scale of the ground excitation and is a measure of the persistence of the most energetic pulse to generate inelastic deformations (Makris and Black 2004 [21]). It is emphasized that the persistence of the pulse is a different characteristic than the strength of the pulse which is measured with the peak pulse acceleration. The reader should recall that among two pulses with different acceleration amplitude (say $a_{p1} > a_{p2}$) and different pulse duration (say $T_{p1} < T_{p2}$), the inelastic deformation does not scale with the peak pulse acceleration (most intense pulse) but with the stronger length scale (larger $a_p T_p^2$ = most persistent pulse), Makris and Black 2004a,b [21],[22], Karavassilis et al. 2010 [23].

The heavy line in Figure 4 (top) which approximates the long-period acceleration pulse of the NS component of the 1992 Erzinkan, Turkey, record is a scaled expression of the second derivative of the Gaussian distribution, $e^{-\frac{t^2}{2}}$, known in the seismology literature as the symmetric Ricker wavelet (Ricker 1943[24], 1944[25]) and widely referred as the "Mexican Hat" wavelet, Addison 2002[26])

$$\ddot{u}_g(t) = a_p(1 - \frac{2\pi^2 t^2}{T_p^2})e^{-\frac{1}{2}\frac{2\pi^2 t^2}{T_p^2}} \tag{8}$$

The value of $T_p = \frac{2\pi}{\omega_p}$, is the period that maximizes the Fourier spectrum of the symmetric Ricker wavelet.

Similarly, the heavy line in Figure 4 (center) which approximates the long-period acceleration pulse of the Pacoima Dam motion recorded during the February 9, 1971 San Fernando, California earthquake is a scaled expression of the third derivative of the Gaussian

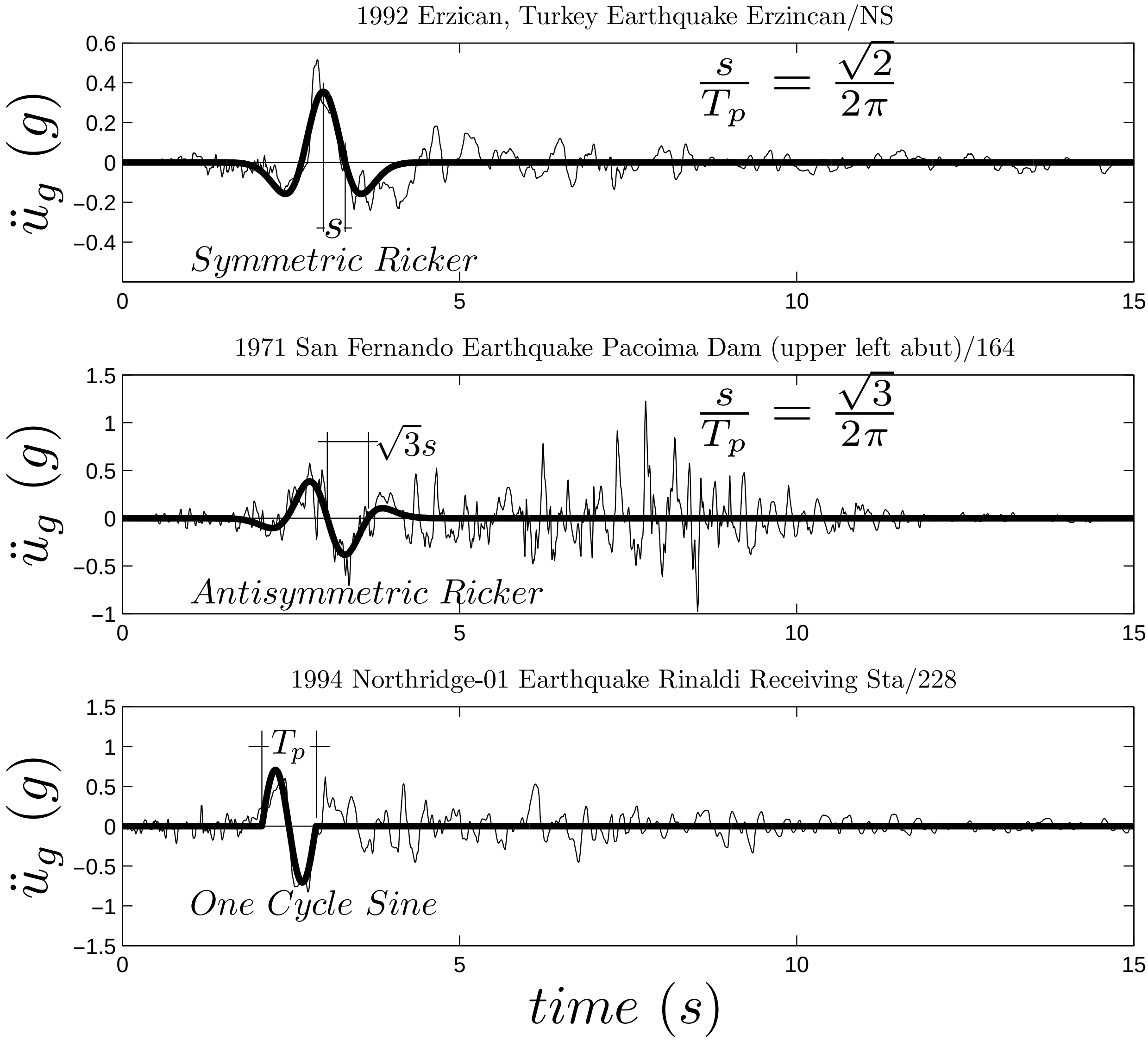

Figure 4. Acceleration time histories recorded during the: (Top) 1992 Erzincan, Turkey earthquake together with a symmetric Ricker wavelet; (Center) 1971 San Fernando earthquake – fault normalcomponent of the Pacoima Dam record together with an antisymmetric Ricker wavelet; and (bottom) 1994 Northridge earthquake – 228 Rinaldi station together with a one cycle sine pulse.

distribution $e^{-\frac{t^2}{2}}$. Again, in equation (18) the value of $T_p = \frac{2\pi}{\omega_p}$ is the period that maximizes the Fourier spectrum of the antisymmetric Ricker wavelet.

$$\ddot{u}_g(t) = \frac{a_p}{\beta}\left(\frac{4\pi^2 t^2}{3T_p^2} - 3\right)\frac{2\pi t}{\sqrt{3}T_p} e^{-\frac{1}{2}\frac{4\pi^2 t^2}{3T_p^2}} \tag{9}$$

in which β is a factor equal to 1.38 that enforces the above function to have a maximum – a_p.

The choice of the specific functional expression to approximate the main pulse of pulse–type ground motions has limited significance in this work. In the past simple trigonometric pulses have been used by the senior author (Makris 1997[13], Makris and Chang 2000[14], Makris and Black 2004[21],[22]) to extract the time scale and length scale of pulse-type ground motions. For instance the heavy line in Figure 4 (bottom) which approximates the strong coherent acceleration pulse of the 228 component at the Rinaldi receiving station of the 1994 Northridge earthquake is a one-sine acceleration pulse

$$\ddot{u}_g(t) = a_p \sin(\omega_p t), \qquad 0 < t < T_p \tag{10}$$

A mathematically rigorous and easily reproducible methodology based on wavelet analysis to construct the best matching wavelet on a given record (signal) has been recently proposed by Vassiliou and Makris (2009)[27,28].

5 OVERTURNING SPECTRA – SELF-SIMILAR RESPONSE

Consider a free standing rigid block subjected to an acceleration pulse (like those shown in Figure 4) with acceleration amplitude a_p and pulse duration $T_p = \frac{2\pi}{\omega_p}$. From equation (3) it results that the response of a rocking block subjected to an acceleration pulse is a function of five variables

$$\theta(t) = f\left(p, \alpha, g, a_p, \omega_p\right) \tag{11}$$

The six (6) variables appearing in Equation (11), $\theta \doteq [\ ]$, $a_p \doteq [\mathrm{L}][\mathrm{T}]^{-2}$, $\omega_p \doteq [\mathrm{T}]^{-1}$, $p \doteq [\mathrm{T}]^{-1}$, $\alpha \doteq [\ ]$, $g \doteq [\mathrm{L}][\mathrm{T}]^{-2}$ involve only two reference dimensions; that of length [L] and time [T]. According to Buckingham's Π-theorem the number of dimensionless products with which the problem can be completely described is equal to [number of variables in Eq. (11)= 6] – [number of reference dimensions = 2]. Herein we select as repeating variables the characteristics of the pulse excitation, a_p and ω_p. The four independent Π-terms are

$$\Pi_\theta = \theta \tag{12}$$

$$\Pi_\omega = \frac{\omega_p}{p} \tag{13}$$

$$\Pi_\alpha = \tan(\alpha) \tag{14}$$

$$\Pi_g = \frac{a_p}{g} \tag{15}$$

With the four dimensionless Π-Terms established equation (11) reduces to

$$\theta(t) = \varphi\left(\frac{\omega_p}{p}, \tan\alpha, \frac{\alpha_p}{g}\right) \tag{16}$$

The rocking response of a rigid block when subjected to a horizontal base acceleration, $\ddot{u}_g(t)$, is computed by solving equation (3) in association with the minimum energy loss expressions given by equation (6) which takes place at every impact. The solution of the nonlinear differential equation given by (3) is computed numerically by means of a state-space formulation. The state vector of the system shown in Figure 2 (left) is merely

$$\mathbf{y(t)} = \begin{bmatrix} \theta(t) \\ \dot{\theta}(t) \end{bmatrix} \tag{17}$$

and the time-derivative vector $\mathbf{f(t) = \dot{y}(t)}$ is

$$\mathbf{\dot{y}(t)} = \begin{bmatrix} \dot{\theta}(t) \\ -p^2[\sin[\alpha\,\mathrm{sgn}[\theta(t)] - \theta(t)] + \dfrac{\ddot{u}_g(t)}{g}\cos[\alpha\,\mathrm{sgn}[\theta(t)] - \theta(t)] \end{bmatrix} \tag{18}$$

The numerical integration of (18) is performed with standard Ordinary Differential Equations (ODE) solvers available in MATLAB (The Mathworks, 1992) [29].

Figure 5 shows the overturning acceleration spectrum of a rigid block with slenderness α = 14^{o} due to a one sine acceleration pulse (left) , a symmetric Ricker wavelet (center) and an antisymmetric Ricker wavelet (right). Figure 5 indicates that as $\Pi_\omega = \dfrac{\omega_p}{p}$ increases the acceleration needed to overturn the object becomes appreciably larger than the one needed to uplift it.

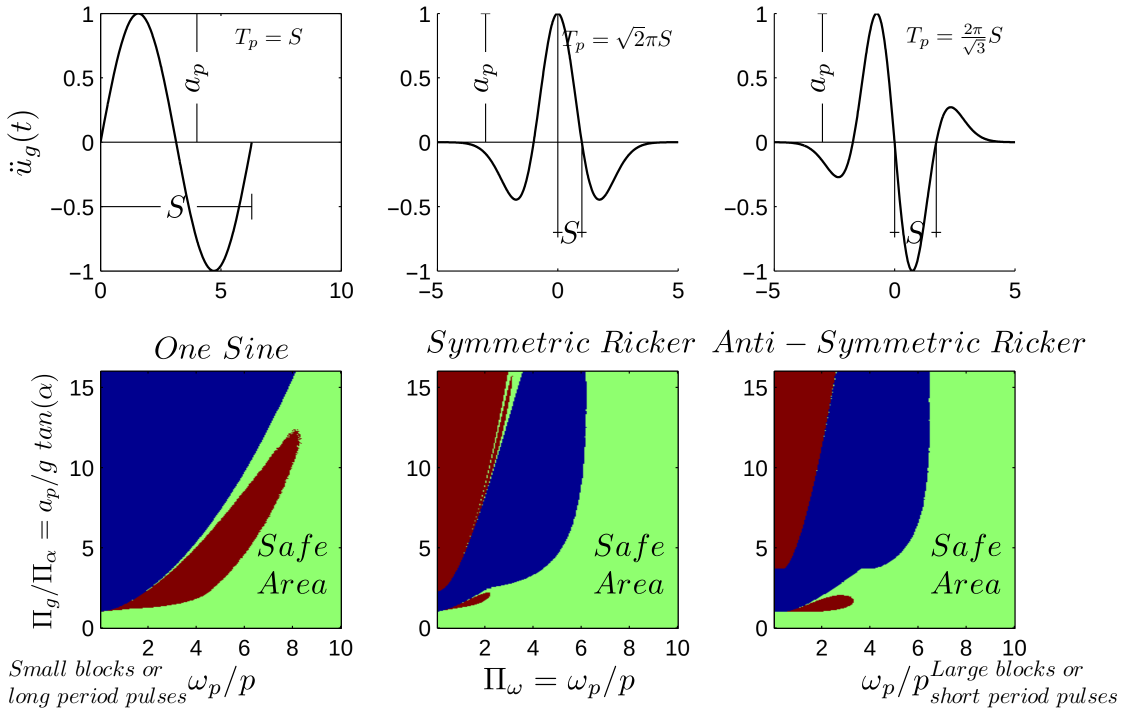

Figure 5 Overturning acceleration spectra of a free standing block with slenderness α=14^{o} subjected to a one-sine acceleration pulse (left); a symmetric Ricker wavelet (center) and an antisymmetric Ricker wavelet (right)

The light grey (green in the colored version) area in all three bottom plots corresponds to stability (no overturning). Note that all three plots show that there are safe areas above the minimum overturning acceleration – a behavior that results from the strong nonlinear nature of the problem. Most importantly is that as the ratio $\Pi_\omega = \omega_p/p$ increases (shorter duration pulses or larger blocks) the minimum overturning acceleration needed to overturn the block increases appreciably.

6 ROCKING RESPONSE OF A RIGID BLOCK STANDING FREE ON A SEISMICALLY ISOLATED BASE

6.1 Linear Viscoelastic Isolation System

We consider a rigid block with mass, m, slenderness α, and frequency parameter p, standing free on a seismically isolated base with mass m_b, horizontal linear stiffness k_b and viscous damping c_b, as shown in Figure 2 (right). The equation of motion can be derived from equation (3) by substituting $\ddot{u}_g$ with $\ddot{u}_g + \ddot{u}$ where u is the displacement of the isolated base relative to the ground. Then equation (3) becomes

$$\ddot{\theta}(t) = -p^2 \left\{ \sin\left[\alpha \operatorname{sgn}\left(\theta(t)\right) - \theta(t)\right] + \frac{\ddot{u}_g(t) + \ddot{u}(t)}{g} \cos\left[\alpha \operatorname{sgn}\left(\theta(t)\right) - \theta(t)\right] \right\} \tag{19}$$

Moreover, given that there is no sliding, horizontal force equilibrium of the isolated base below isolators gives

$$-k_b u - c_b \dot{u} = m_b \left(\ddot{u}_g + \ddot{u}\right) + m\left(\ddot{u}_g + \ddot{u} + \ddot{x}\right) \tag{20}$$

where x is the horizontal, relative to the base translation of the center of mass of the rigid block given by

$$x(t) = \operatorname{sgn}\left(\theta(t)\right) R \sin(a) - R \sin\left(\operatorname{sgn}\left(\theta(t)\right)\alpha - \theta(t)\right) \tag{21}$$

Equations (19) and (20) are expressed in terms of $\ddot{u}$ and $\ddot{\theta}$ which are explicit expressions of the four states of the system, $u(t), \dot{u}(t), \theta(t), \dot{\theta}(t)$ in order to solve the system of equations explicitly. Accordingly,

$$\ddot{u}(t) = \frac{-\omega_b^2 u(t) - 2\xi\omega_n \dot{u}(t) - \gamma R\left(\dot{\theta}(t)\right)^2 \sin A(t) + \gamma R p^2 \cos A(t) \sin A(t)}{1 - \dfrac{\gamma R p^2 \cos^2 A(t)}{g}} - \ddot{u}_g(t) \tag{22}$$

$$\ddot{\theta}(t) = -p^2 (\sin A(t) + \cos A(t) (\frac{-\omega_n^2 u(t) - 2\xi\omega_n \dot{u}(t) - \gamma R\left(\dot{\theta}(t)\right)^2 \sin A(t) + \gamma R p^2 \cos A(t) \sin A(t)}{g - \gamma R p^2 \cos^2 A(t)})) \tag{23}$$

where the term $A(t) = \alpha \operatorname{sgn}\theta(t) - \theta(t)$ and $\gamma = \dfrac{m}{m_b + m}$ and $\omega_b = \sqrt{\dfrac{k_b}{m_b + m}}$

Again, in this case we assume that when the angle of rotation reverses, the rotation of the block continues smoothly from point O to O’ and that the impact force is concentrated as a point force which applies on the new pivot point O’. The subtle difference between a rocking block impacting a base with finite mass, m_b, and a rocking block impacting a rigid foundation with infinite mass, is that the translational velocity of the isolated base also experiences a finite jump during impact; whereas the translational velocity of the rigid foundation with infinite mass remains the same during impact.

With reference to Figure 6, conservation of angular momentum around point O' gives

$$\int_{block} \mathbf{r}\times\left(\dot{\mathbf{v}}_1+\dot{\mathbf{u}}_1\right)dm=\int_{block} \mathbf{r}\times\left(\dot{\mathbf{v}}_2+\dot{\mathbf{u}}_2\right)dm \tag{24}$$

where $\dot{\mathbf{v}}_1$ and $\dot{\mathbf{v}}_2$ are the velocities (with respect to the isolated base) of a point mass due to rotation before and after the impact and $\dot{\mathbf{u}}_1$ and $\dot{\mathbf{u}}_2$ are the translational velocities of the base (with respect to the ground) before and after the impact. Equation (24) gives

$$\left(I_o\dot{\theta}_1-2mRb\sin\alpha\dot{\theta}_1\right)\mathbf{e}_y+\int_{block}\mathbf{r}\times\dot{\mathbf{u}}_1dm=I_o\dot{\theta}_2\mathbf{e}_y+\int_{block}\mathbf{r}\times\dot{\mathbf{u}}_2dm \tag{25}$$

or

$$I_o\dot{\theta}_1-2mRb\sin\alpha\dot{\theta}_1+mhu_1=I_o\dot{\theta}_2+mhu_2\,. \tag{26}$$

For a rectangular block $I_o=\dfrac{4}{3}mR^2$ and the above expression reduces to

$$4R^2\dot{\theta}_1-6Rb\sin\alpha\dot{\theta}_1+3h\dot{u}_1=4R^2\dot{\theta}_2+3h\dot{u}_2 \tag{27}$$

Equation (27) indicates that because of the finite mass of the isolation base one has to determine the translational velocity of the base $\dot{u}_2$ after the impact. The extra equation that is needed to relate $\dot{u}_1$ and $\dot{u}_2$ is the conservation of the linear momentum of the entire system(the rocking – translating block together with the translating base) along the horizontal direction. Accordingly

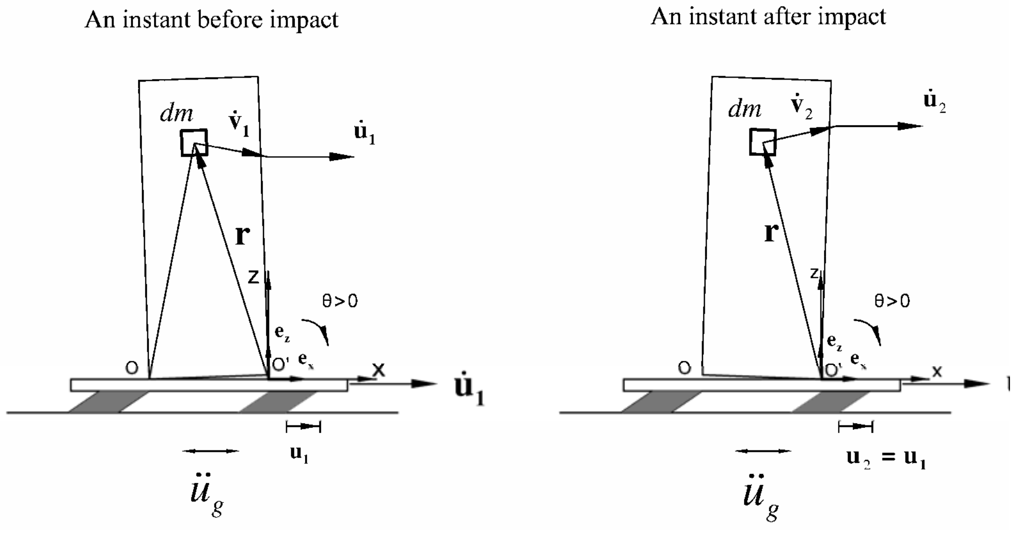

Figure 6. Rigid block rocking on an isolated base before (left) and after (right) the impact.

$$\left(m+m_b\right)\dot{u}_1+mh\dot{\theta}_1=\left(m+m_b\right)\dot{u}_2+mh\dot{\theta}_2 \tag{28}$$

or

$$\left(\gamma+1\right)\dot{u}_1+\gamma h\dot{\theta}_1=\left(\gamma+1\right)\dot{u}_2+\gamma h\dot{\theta}_2 \tag{29}$$

From equations (27) and (29) one obtains

$$\dot{\theta}_2=\frac{\left(\gamma+4\right)\cot^2\alpha-2\left(\gamma+1\right)}{\left(\gamma+4\right)\cot^2\alpha+4\left(\gamma+1\right)}\dot{\theta}_1 \tag{30}$$

and

$$\dot{u}_2=\dot{u}_1+\frac{6\gamma h}{\left(\gamma+4\right)\cot^2\alpha+4\left(\gamma+1\right)}\dot{\theta}_1 \tag{31}$$

Note that in the limiting case of a very havy base ($m_b\rightarrow\infty$ or $\gamma\rightarrow 0$) equation (30) reduces to equation (6); while $\dot{u}_1=\dot{u}_2$; therefore the situation of a block rocking on a rigid foundation is recovered. From equation (30) the maximum value of the coefficient of restitution that allows rocking motion of a block rocking on an isolated base is

$$r=\left(\frac{\dot{\theta}_2}{\dot{\theta}_1}\right)^2=\left(\frac{\left(\gamma+4\right)\cot^2\alpha-2\left(\gamma+1\right)}{\left(\gamma+4\right)\cot^2\alpha+4\left(\gamma+1\right)}\right)^2. \tag{32}$$

The expression of the coefficient of restitution given by (32) is in agreement with an equivalent expression presented by Roussis et al. [5], which, to our knowledge is the only past publication that treats this problem correctly.

Figure 7 plots the expression given by equation (32) for three values of $\gamma=m/m_b$=0.01, 0.1 and 1. Figure 7 indicates that when the mass of the base is finite, the rocking block looses additional energy during impact (compared to the same block rocking on a rigid foundation) due to the reason that the translational velocity of the isolated base experiences a finite jump at the instant of the impact.

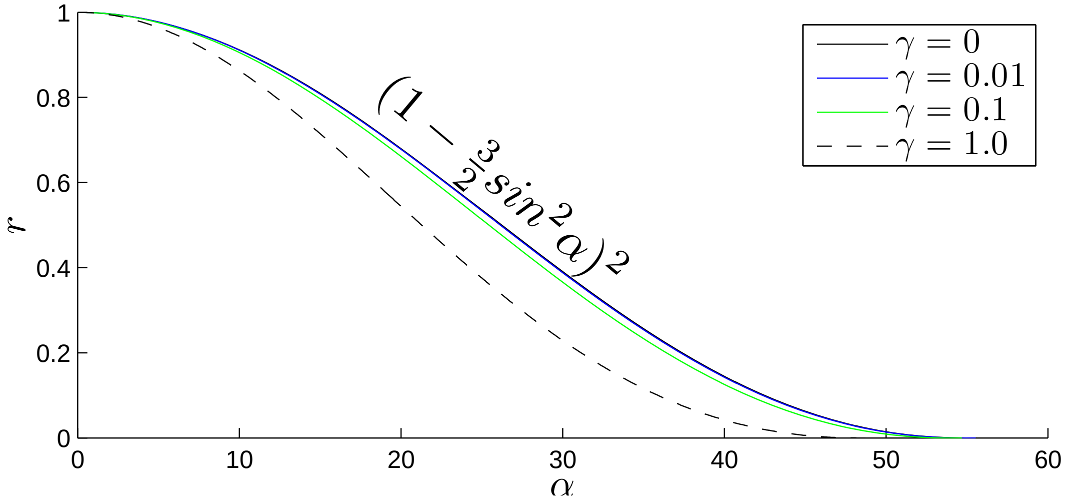

Figure 7. Coefficient of restitution, r, vs slenderness, α, for different values of $\gamma=m/m_b$.

6.2 Overturning Spectra – Self-Similar Response

We consider again that the ground excitation of the system shown in Figure 2 is characterized by a coherent acceleration pulse with amplitude a_p and pulse duration ($T_p = \frac{2\pi}{\omega_p}$). From equations (22) and (23) it results that the response of a rocking block standing free on an isolated base subjected to an acceleration pulse is a function of eight (8) variables

$$u(t) = f\left(p,\alpha,g,\omega_b,\xi,\gamma,\alpha_p,\omega_p\right) \tag{33}$$

$$\theta(t) = f\left(p,\alpha,g,\omega_b,\xi,\gamma,\alpha_p,\omega_p\right) \tag{34}$$

Each of the coupled Equations (20) and (21) $\theta \doteq [\ ]$, $u \doteq [L]$, $a_p \doteq [L][T]^{-2}$, $T_p \doteq [T]$, $T_b \doteq [T]$, $\zeta \doteq [\ ]$, $p \doteq [T]^{-1}$, $\alpha \doteq [\ ]$, $g \doteq [L][T]^{-2}$, $\gamma \doteq [\ ]$ involves only two reference dimensions; that of length [L] and time [T]. According to Buckingham's Π-theorem the number of dimensionless products (Π-Terms) = [number of variables in Eq. (20) and (21) = 10] – [number of reference dimensions = 2]; therefore for the 2 DOF system described above, there are 10-2 = 8 Π–terms

$$\Pi_m = \frac{u_{\max}\omega_p^2}{a_p} \tag{35}$$

$$\Pi_\theta = \theta \tag{36}$$

$$\Pi_\omega = \frac{\omega_b}{\omega_p} \tag{37}$$

$$\Pi_\xi = \xi \tag{38}$$

$$\Pi_\gamma = \gamma \tag{39}$$

$$\Pi_p = \frac{\omega_p}{p} \tag{40}$$

$$\Pi_a = \tan(\alpha) \tag{41}$$

$$\Pi_g = \frac{a_p}{g} \tag{42}$$

The rocking response of a rigid block standing free on an isolated base subjected to a horizontal base acceleration is computed by solving equations (21) and (22) in association with the minimum energy loss expression given by equation (32) which takes place at every impact. In this case, the state vector of the system shown in Figure 2 (right) for linear viscoelastic bearings is

$$\mathbf{y}(t) = \begin{bmatrix} u(t) \\ \dot{u}(t) \\ \theta(t) \\ \dot{\theta}(t) \end{bmatrix} \tag{43}$$

and the time derivative vector $\mathbf{f}(t) = \dot{\mathbf{y}}(t)$ is

$$\dot{\mathbf{y}}(t)=\begin{bmatrix} \dot{u}(t) \\ \dfrac{-\omega_b^2 u(t)-2\xi\omega b\dot{u}(t)-\gamma R\left(\dot{\theta}(t)\right)^2\sin A(t)+\gamma R\cos A(t)\,p^2\sin A(t)}{1-\dfrac{\gamma Rp^2\cos^2 A(t)}{g}}-\ddot{u}_g(t) \\ \ddot{\theta}(t) \\ -p^2\left(\sin A(t)+\cos A(t)\left(\dfrac{-\omega_b^2 u(t)-2\xi\omega b\dot{u}(t)-\gamma R\left(\dot{\theta}(t)\right)^2\sin A(t)+\gamma R\cos A(t)\,p^2\sin A(t)}{g-\gamma Rp^2\cos A(t)}\right)\right) \end{bmatrix} \tag{44}$$

Figure 8 plots the overturning acceleration spectra for a rigid block with slenderness α=10^o (top) and α=20^o (bottom) when it is standing free on a rigid foundation (left), and when it is isolated (center and right) and subjected to a symmetric Ricker wavelet. The viscous damping ratio of the bearings is ξ=5% and the mass ratio is γ=0.01 (heavy base). Figure 8 indicates that the presence of the isolation base increases the "static" overturning acceleration; however, for isolated rigid blocks this "static" value remains nearly constant as the ratio ω_p / p increases (moving to larger blocks or high frequency pulses). Consequently, the presence of an isolation base removes appreciably from the dynamics of rocking blocks the fundamental property of increasing stability as their size increases or as the excitation pulse-period decreases.

The findings of Figure 8 together with results due to an antisymmetric Ricker excitation are summarized in Figure 9 in terms of minimum acceleration overturning spectra. In all configurations the free-standing block on a rigid base (heavy dark line) beyond a certain value of ω_p/p exhibits superior stability than the same block when isolated. Note also that for both symmetric (left plots) and antisymmetric (right plots) Ricker wavelets, the minimum overturning acceleration of the free standing block on a rigid foundation exceeds the overturning acceleration of the isolated configuration at smaller values of ω_p/p as the slenderness of the block decreases (larger values of α).

The practical use of the results shown in Figure 9 is illustrated by considering the dominant pulses that capture the coherent component of the two earthquake records shown in Figure 10 – that of the fault parallel component of the OTE record from the 1995 Aigio, Greece earthquake (top) and that of the Gilroy – Array #6 record from the 1979 Coyote Lake , USA earthquake (bottom). For the FP OTE record shown in Figure 10 (top), T_p=0.6s while for the Coyote Lake record (bottom), T_p=0.9s. The corresponding values of the semidiagonal, R, beyond which non-isolated free standing blocks exhibit more stability than when seismic isolated are offered in Table 1 for two values of slenderness α=10^o and α=20^o and three values of T_b/T_p 2, 3 and 4.

Table 1 indicates that free-standing objects appreciably smaller than ancient classical columns R≈(3.5m – 5.0m) are more stable when they stand free on a rigid foundation while seismic isolation would have been detrimental.

The influence of the mass ratio $\gamma=\dfrac{m}{m+m_b}$ (m = mass of the rocking block, m_b = mass of the isolated base) is shown in Figure 11 for a block with slenderness α=12^o, two values of T_b/T_p=2 and 3 and five values of γ. Figure 11 indicates that for values of ω_p/p<6 (the range when it makes sense to isolate rocking blocks) all response curves for γ≤0.1 tend to the finite

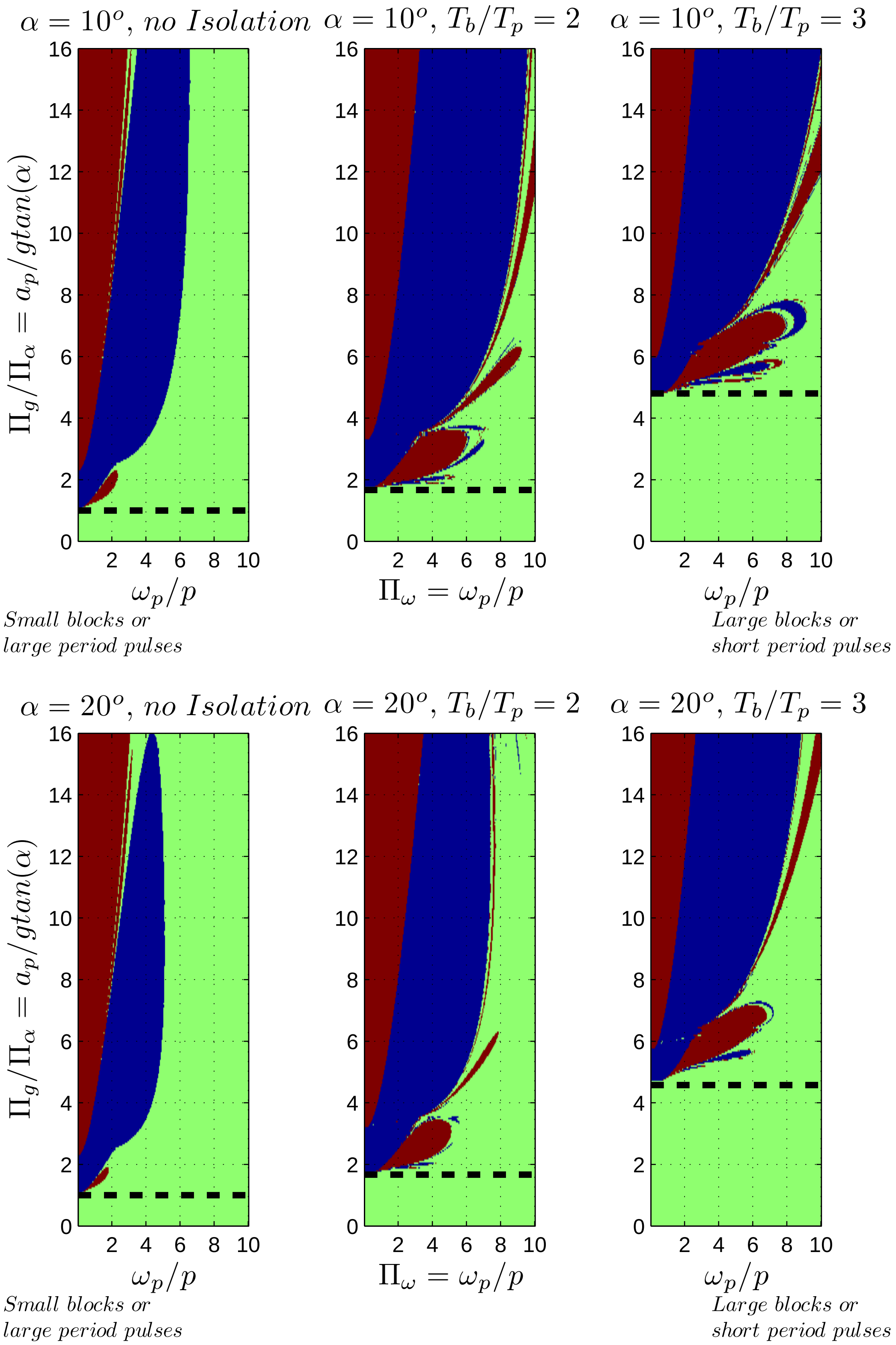

Figure 8. Overturning spectra for rigid block without isolation (left), and with linear isolation with T_b/T_p=2 (center) and T_b/T_p=3 for slenderness α=10° (top) and α=20° (bottom) for a symmetric Ricker excitation.

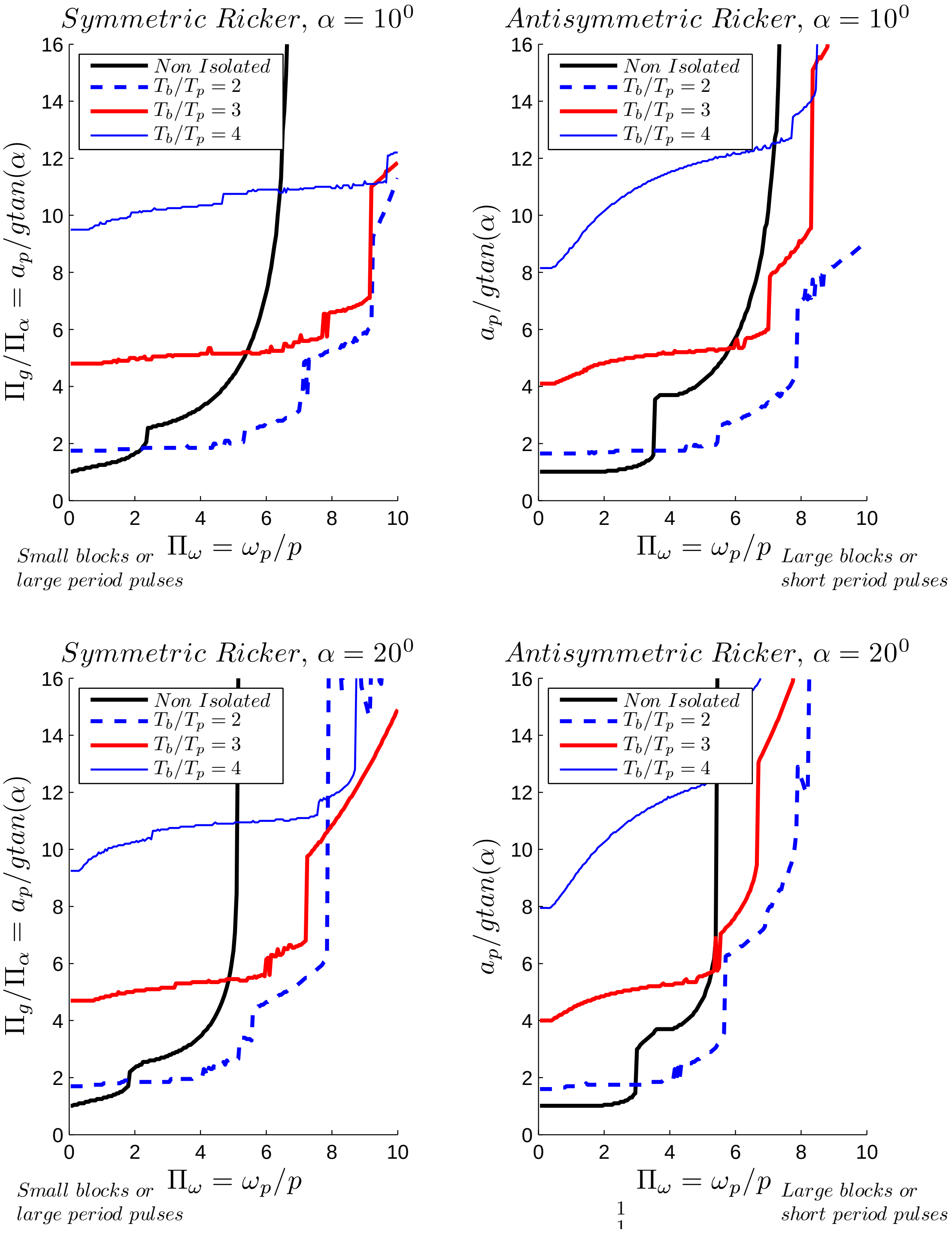

Figure 10. Comparison of the minimum acceleration needed to overturn a rigid block of slenderness α=10° (top) and α=20° (bottom) resting on rigid ground and on an isolated bases whith various isolation frequencies when excited by a symmetric Ricker pulse (left) or an antisymmetric Ricker pulse (right).

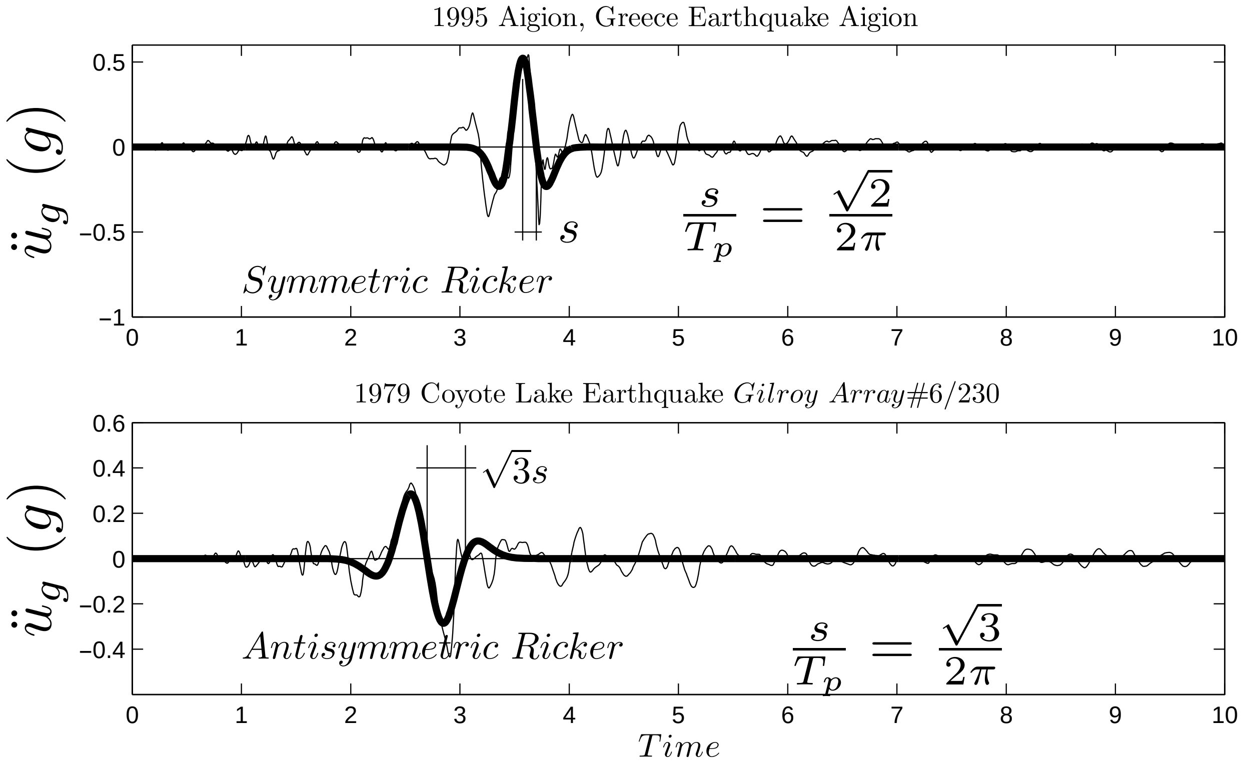

Figure 11 Acceleration time histories during the (Top) 1995 Aigion, Greece earthquake – fault parallel component of the OTE record together with a symmetric Ricker wavelet; and (bottom) 1979 Coyote Lake earthquake – 230 component of the Gilroy Array #6 record together with an antisymmetric Ricker wavelet.

		T_b/T_p=2			T_b/T_p=3			T_b/T_p=4		
			$R_{critical}$ (m)			$R_{critical}$ (m)			$R_{critical}$ (m)	
	T_p (s)	T_b (s)	10°	20°	T_b (s)	10°	20°	T_b (s)	10°	20°
Aigio, OTE FP, 1995	0.6	1.2	0.32	0.22	1.8	1.96	1.58	2.4	2.79	1.78
Coyote Lake, Gilroy #6 230, 1979	0.9	1.8	1.85	1.31	2.7	5.08	4.24	3.6	7.83	4.48

Table 1. Length of the semidiagonal, *R*, of rigid blocks beyond which they exhibit superior stability when they stand free on a rigid base (no isolation).

limit where the response of the heavy base is not influenced by the response of the light rocking block (decoupled system). Consequently for the case where $\gamma \leq 0.1$ the mass ration γ drops out of consideration (γ=0) and it can be eliminated from equations (33) and (34) – a conclusion that shows that the rocking response of a rigid block standing free on an isolated base exhibits a “complete similarity” in terms of the mass ratio $\gamma = \dfrac{m}{m + m_b}$.

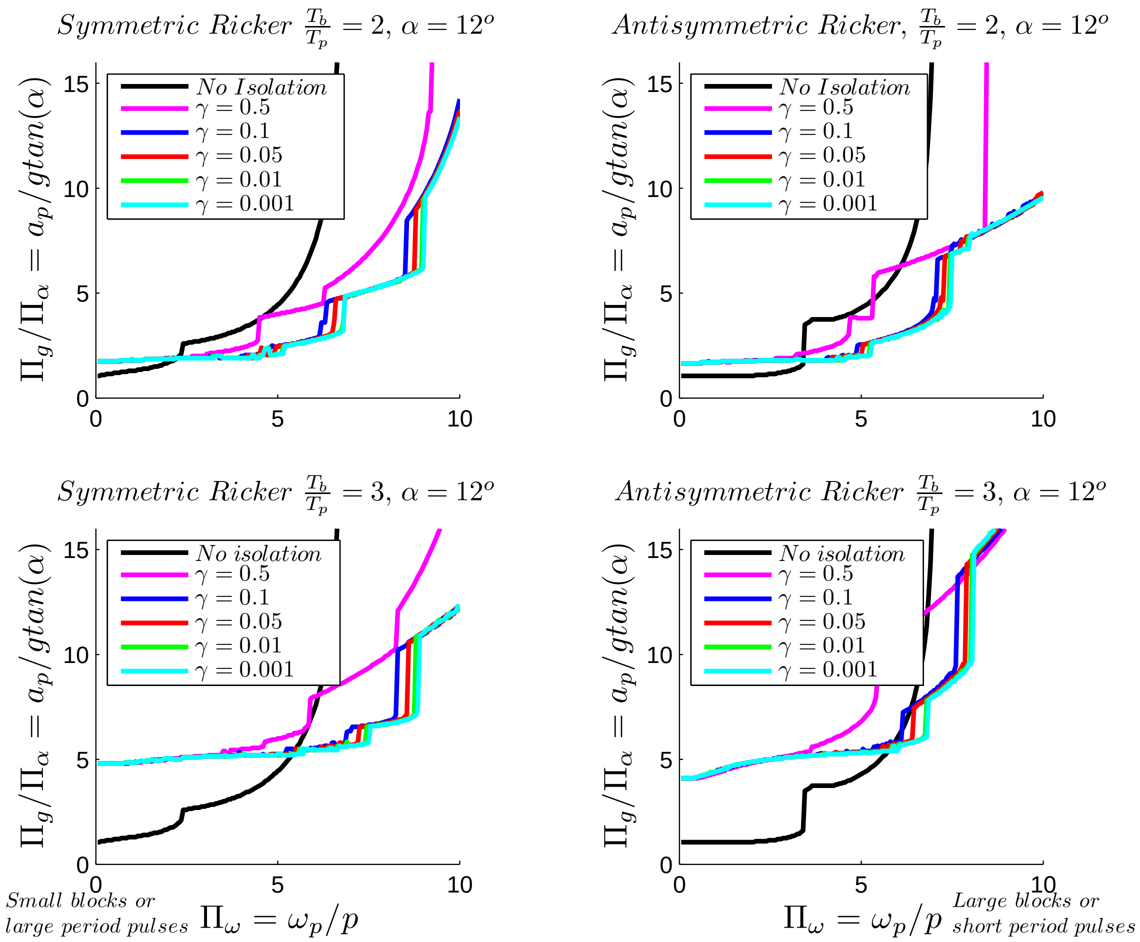

Figure 12 Comparison of the minimum acceleration needed to overturn a rigid block of slenderness α=12° resting on a linear viscoelastic isolated base subjected to a symmetric Ricker wavelet (left) and an antisymmetric Ricker wavelet (right). Results for five values of mass ratio $\gamma = \dfrac{m}{m+m_b}$ are used showing that for values of γ<0.1 the overturning acceleration does not depend on the mass ratio $\gamma = \dfrac{m}{m+m_b}$

6.3 Bilinear isolation system

When the behavior of the isolation system is bilinear – a very good idealization for the behavior of spherical sliding bearings and lead rubber bearings, the equation of the rocking block is again given by equation (19) whereas, horizontal equilibrium of the isolated base below isolators gives

$$-k_b u(t) - Q\cdot z(t) = m_b\left(\ddot{u}_g(t) + \ddot{u}(t)\right) + m\left(\ddot{u}_g(t) + \ddot{u}(t) + \ddot{x}(t)\right) \tag{45}$$

where k_b is the second slope of the bilinear idealization, Q is the strength of the system (force at zero displacement), $x(t)$ is the horizontal relative to the base translation of the center of mass of the rigid block and $z(t)$ is a dimensionless parameter of the Bouc-Wen model given by

$$\dot{z}(t) = \frac{1}{u_y}\left(\dot{u}(t) - \gamma\left|\dot{u}(t)\right| z(t)\left|z(t)\right|^{n-1} - \beta\dot{u}(t)\left|z(t)\right|^{n}\right), \tag{46}$$

where u_y is the yield displacement of the bilinear behavior.

In this paper our study concentrates in the case where u_y is very small ($u_y \approx 0.25$mm). In this case the bilinear model is the mathematical description of the spherical sliding bearing with coefficient of friction μ, in which case the strength $Q=\mu(m+m_b)g$. Recent studies (Makris and Chang [14], Makris and Vassiliou [30]), have demonstrated that the response of isolated structures is merely indifferent to the exact value of the yield displacement, therefore the results obtained in this paper are also valid for isolation systems that use lead rubber bearings (larger values of u_y) as long as they experience the same second slope and the same strength. Given equations (45) and (46), together with equation (19) the state vector of the system shown in Figure 2 (right) with spherical sliding bearings is:

$$\mathbf{y}(t)=\begin{bmatrix} u(t) \\ \dot{u}(t) \\ z(t) \\ \theta(t) \\ \dot{\theta}(t) \end{bmatrix} \tag{47}$$

$$\dot{\mathbf{y}}(t)=\begin{bmatrix} \dot{u}(t) \\ \dfrac{-\omega_b^2 u(t)-\mu g z(t)-\gamma R\left(\dot{\theta}(t)\right)^2 \sin A(t)+\gamma R\cos A(t)\, p^2 \sin A(t)}{1-\dfrac{\gamma R p^2 \cos^2 A(t)}{g}}-\ddot{u}_g(t) \\ \dfrac{1}{u_y}\left(\dot{u}(t)-\gamma\left|\dot{u}(t)\right| z(t)\left|z(t)\right|^{n-1}-\beta\dot{u}(t)\left|z(t)\right|^{n}\right) \\ \dot{\theta}(t) \\ -p^2\left(\sin A(t)+\cos A(t)\left(\dfrac{-\omega_b^2 u(t)-\mu g z(t)-\gamma R\left(\dot{\theta}(t)\right)^2 \sin A(t)+\gamma R\cos A(t)\, p^2 \sin A(t)}{g-\gamma R p^2 \cos A(t)}\right)\right) \end{bmatrix} \tag{48}$$

In the case where the base is isolated on lead rubber bearings exhibiting a strength Q, the term μg in the 1st and 5th component of the $\dot{\mathbf{y}}(t)$ vector is replaced with $\dfrac{Q}{m+m_b}$.

Figure 12 plots overturning spectra of a rigid block with slenderness $\alpha=16^{\circ}$ standing free on a base that is isolated on single concave spherical sliding bearings with coefficient of friction $\mu=5\%$ when subjected to a symmetric Ricker wavelet next to the overturning acceleration spectra when the base is isolated on linear viscoelastic bearings with coefficient $\xi=5\%$. The response between the two isolation configurations is very similar. For completeness, Figure 12 (bottom) shows the minimum overturning acceleration associated with the two isolation configurations together with the corresponding spectrum of a rigid block rocking on a rigid foundation (heavy dark line). The near-vertical growth of the heavy dark line indicates that regardless how flexible the isolation system is, for values of $\omega_p/p>6$, the rigid block rocking on a rigid foundation has superior stability. The seismic response of a rigid block standing free on a base that is isolated on double concave spherical sliding bearings is presented in the paper by Vassiliou and Makris [32].

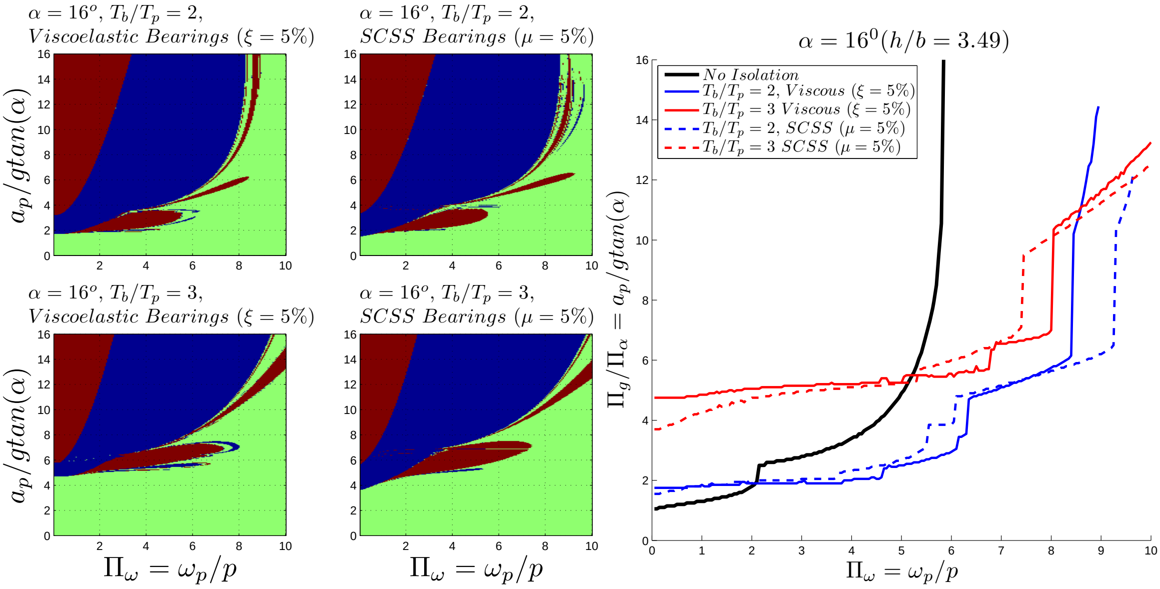

Figure 13. Comparison of overturning spectra (top) and minimum acceleration overturning spectra (bottom) of a rigid body with slenderness `α=16^o when the supporting base is isolated on viscoelastic bearings with damping ratio ξ=5% (left) and single concave spherical sliding bearings with coefficient of friction 5% (right). The excitation is a symmetric ricker wavelet and the mass ratio γ= 0.01

7 THE EFFECT OF SEISMIC ISOLATION ON ANCIENT CLASSICAL COLUMNS

The seismic response analysis of rocking blocks standing free on an isolated base has been studied in this paper by using as ground excitation, acceleration pulses described either by the symmetric or the antisymmetric Ricker wavelets. The acceleration amplitude, a_p, and duration T_p of any distinct acceleration pulse allow the use of the dimensional analysis presented in this work and the derivation of the associated Π-products which improve appreciably the understanding of the physics that governs the problem together with the organization and presentation of the response quantities in a most meaningful way. Nevertheless, in order to stress the main finding of this study – that for large blocks (say $\omega_p/p > 6$) the use of seismic isolation reduces the seismic stability of free-standing rocking structures – we examine the seismic response of two free standing slender blocks which have the dimensions of the columns of the peristyle of the Temple of Appolo at Bassae and the Temple of Zeus at Nemea, both located in Peloponese, Greece.

The Temple of Apollo at Bassae is a fifth Century BC doric style structure. The columns of the temple are 5.95m high, the diameter of the base drum is 1.11m (resulting in slenderness α=0.1844 and in size R=3.03m). The number of drums in each column is not constant for all the columns and is controlled by the size of the sound rock that was available in the ancient limestone quarry. The temple is still standing but has suffered from erosion of the building material caused by the adverse climatic conditions at the site (1000m altitude a.s.l.) and from the tilting of some columns due to differential settlement of the foundations [32].

The Temple of Zeus at Nemea was built in the late fourth century BC. The columns of this temple are much taller and more slender than the ones of the temple at Bassae, reaching a height of 10.33 m. All columns consist of 13 drums and the base drum diameter is 1.52 m. The resulting slenderness is α=0.1461 and R=5.22m. This slenderness ratio is the smallest among the ancient Greek temples of continental Greece. Only one column of the peristyle and two columns of the pronaos of the Temple of Zeus remain standing from the ancient times.

While the columns from the two abovementioned Temples are multidrum, this investigation proceeds by considering that they are monolithic free standing blocks. Past studies led by the senior author (Konstantinidis and Makris, 2005 [33]) have shown that multidrum columns exhibit slightly more controlled response than the equal size monolithic configuration.

Our investigation proceeds by examining the response of the two abovementioned columns when subjected to the 11 historic records shown in Table 2. The columns are considered to stand free on a rigid foundation, or standing free on a seismic isolated base with isolation periods T_b=2s, 2.5s and 3s and linear viscous damping ξ_b=0.1.

Table 3 summarizes the results from the nonlinear time history analysis. The column from the Temple of Apollo at Bassae (R=3.03m α=0.1844) when standing free on a rigid foundation survives all the induced records, while when isolated on bearings that offer an isolation period, T_b=2.0s, it topples in all but one records. As the period of the isolation system increases the column survives additional records. Similarly, the column for the Temple of Zeus a Nemea (R=5.22m, α=0.1461) when standing free on a rigid foundation survives 9 out of the 11 records, while when isolated on bearings that offer an isolation period

Table 2. Earthquake records used for the dynamic response analysis of the column.

Earthquake	Record Station	Magnitude (Mw)	Distance (km)	PGA (g)	PGV (m/s)	a_p (g)	T_p (s)
1966 Parkfield	CO2/065	6.1	0.1	0.48	0.75	0.41	0.6
1977 Vrancea	Bucharest	7.2	160	0.20	0.74	0.20	2.1
1979 Imperial Valley	El Centro #6 / 230	6.5	9.3	0.41	0.65	0.14	3.1
1980 Irpinia, Italy	Sturno/270	6.5	32	0.36	0.52	0.11	3.0
1986 San Salvador	Geotech Investig. Center	5.4	4.3	0.48	0.48	0.34	0.8
1987 Superstition Hills	Parachute Test Site/225	6.7	0.7	0.45	1.12	0.30	2.0
1992 Erzican,	Erzincan/EW	6.9	13	0.50	0.64	0.34	0.9
1994 Northridge	Jensen Filter Plant/022	6.7	6.2	0.57	0.76	0.39	0.5
1995Kobe	Takarazuka/000	6.9	1.2	0.69	0.69	0.50	1.1
1999 Chi-Chi Taiwan	CHY101/E	7.6	11.2	0.35	0.71	0.10	3.5
1999 Chi-Chi Taiwan	CHY128/N	7.6	9.7	0.17	0.69	0.09	4.5

Table 3. Stability results for the rigid blocks corresponding to the columns of the Temples of Bassae and Nemea when subjected to the 11 earthquakes. (✓ = no overturn, ✗ = overturn)

		Columns from the Temple of Apollo at Bassae (R=3.03m α=0.1844)				Columns from the Temple of Zeus at Nemea (R=5.22m, α=0.1461)			
Earthquake	Record Station	Non-Isolated	T_I=2s	T_I=2.5s	T_I=3s	Non-Isolated	T_I=2s	T_I=2.5s	T_I=3s
1966 Parkfield	CO2/065	✓	✗	✓	✓	✓	✗	✗	✓
1977 Bucharest		✓	✗	✗	✓	✓	✗	✗	✗
1979 Imperial Valley	El Centro #6 / 230	✓	✗	✗	✗	✓	✗	✗	✗
1980 Irpinia, Italy	Sturno/270	✓	✗	✗	✗	✓	✗	✗	✗
1986 San Salvador	Geotech Investig. Center	✓	✗	✓	✓	✓	✗	✓	✓
1987 Superstition Hills	Parachute Test Site/225	✓	✗	✗	✗	✗	✗	✗	✗
1992 Erzican,	Erzincan/EW	✓	✗	✗	✓	✗	✗	✗	✗
1994 Northridge	Jensen Filter Plant/022	✓	✗	✗	✗	✓	✗	✗	✗
1995Kobe	Takarazuka/000	✓	✗	✓	✓	✓	✗	✗	✓
1999 Chi-Chi Taiwan	CHY101/E	✓	✓	✗	✗	✓	✗	✗	✗
1999 Chi-Chi Taiwan	CHY128/N	✓	✗	✓	✓	✓	✗	✗	✗

T_b=2.0s it topples in all records

Again, as the isolation period increases the column survives additional records; however, even when the isolation period is T_b=3.0s the column from the Temple of Zeus at Nemea survives only 3 out of the 11 records. The reason that seismic isolation is so detrimental to the stability of tall slender blocks is because the presence of the isolation system lengthens the duration of the pulses while at the same time increases the number of the significant induced cycles.

As an example, Figure 13 plots the response of a rigid block with the dimensions of a column of a column from the peristyle of the Temple of Zeus at Nemea subjected to the 022 component of the Jensen Filter Plant record from the 1994 Northridge earthquake when is standing free on a rigid foundation (left) and when standing free on an isolated base with T_b=3.0s (right).

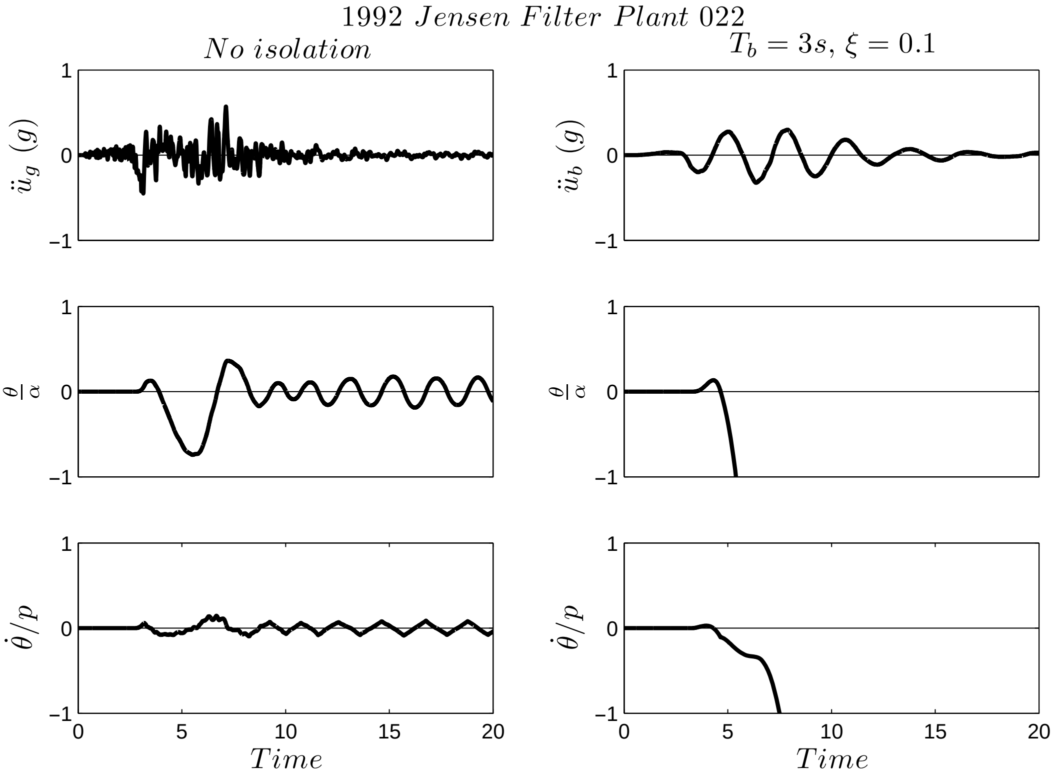

Figure 14. Comparison of the response of a rigid block with the dimensions of a column from the peristyle of the Temple of Zeus at Nemea subjected to the 022 component of the Jensen Filter Plant record from the 1994 Northridge earthquake when is standing free on a rigid foundation (left) and when standing free on an isolated base with T_b=3.0s (right).

8 CONCLUSIONS

In this paper the seismic response analysis and stability of slender rigid blocks standing free on a seismically isolated base is investigated in depth. The paper examines the rocking response when the isolated base is supported: (a) on linear viscoelastic bearings, (b) on single concave and (c) on double concave spherical sliding bearings. Our study revisits the equations of motion and settles the matter of conservation of linear momentum of the entire moving system that is the rocking – translating block together with the translating isolated base. This analysis leads to a closed form expression (eq. (32)) for the maximum value of the coefficient of restitution during impact that allows rocking motion of a block rocking on an isolated base and is concluded that this value is always smaller (more energy is dissipated) than the maximum value, $r = \left(1 - \frac{3}{2}\sin^2\alpha\right)^2$ which is associated with a rigid block rocking on a rigid (non-isolated) foundation. Our extended parametric analysis concludes that seismic isolation is beneficial for small blocks. This happens because seismic isolation increases the “static” overturning acceleration; however for isolated rigid blocks this “static” value remains nearly constant as the ratio ω_p/p increases (moving to longer blocks or higher frequency pulses). Consequently, while the presence of an isolation base increases the “static” overturning acceleration it removes appreciably from the dynamics of rocking blocks the fundamental property of increasing stability as their size increases or the excitation pulse period decreases. This behavior prevails regardless whether the rocking block is supported on an isolated base with linear viscoelastic or spherical sliding bearings with single or double curvaruture.

The longer the isolation period of the supporting base is, the more stability is offered to the rocking blocks; however large blocks subjected to moderate period pulses (say ω_p/p>6) exhibit superior stability when they stand free on a rigid base (non-isolated) rather when they are isolated even on isolation systems with very long periods. This remarkable result suggests that free standing ancient classical columns exhibit superior stability as they are built (standing free on a rigid foundation) rather than if they were seismic isolated. Consequently, seismic isolation is not recommended as a technology to improve the seismic stability of ancient Greek or Roman temples.

ACKNOWLEDGEMENTS

Partial financial support has been provided by the EU research project “DARE” (“Soil-Foundation-Structure Systems Beyond Conventional Seismic Failure Thresholds: Application to New or Existing Structures and Monuments”), which is funded through the 7th Framework Programme “Ideas”, Support for Frontier Research – Advanced Grant, under contract number ERC-2—9-AdG 228254-DARE to Professor G. Gazetas.

Partial financial support has been provided to the second author by the Alexander S. Onassis Public Benefit Foundation.

REFERENCES

1.Housner, G. W. The behaviour of inverted pendulum structures during earthquakes. *Bulletin of the Seismological Society of America.* 1963; **53(2)**: 404–417.

2. G. Augusti, M. Ciampoli and L. Airoldi, ‘Mitigation of seismic risk for museum contents’, *Proceedings of the 10th world conference in earthquake engeineering,* Madrid 1992, pp.5995-6000

3. Vestroni F, Di Cinto S. Base isolation for seismic protection of statues. *Twelfth World Conference on Earthquake Engineering,* New Zealand, 2000.

4. Calio I, Marletta M. Passive control of the seismic response of art objects. *Engineering Structures* 2003; **25**: 1009–1018.

5. Roussis, PC, Pavlou, EA, Pisiara, EC. Base-isolation technology for earthquake protection of art objects, *14th World Conference on Earthquake Engineering: Innovation Practice Safety. 2008*

6. Contento A and Di Egidio A. Investigations into benefits of base isolation for non-symmetric rigid blocks, *Earthquake Engineering and Structural Dynamics* **38**(2009), pp. 849–866

7. Yim CS, Chopra AK, Penzien J. Rocking response of rigid blocks to earthquakes. *Earthquake Engineering and Structural Dynamics* 1980; **8**(6):565–587.

8. Makris N, Roussos Y. Rocking response of rigid blocks under near-source ground motions. *Geotechnique* 2000; **50**(3):243–262.
9. Zhang J, Makris N. Rocking response of free-standing blocks under cycloidal pulses. *Journal of Engineering Mechanics,* ASCE 2001; 127(5):473–483.
10. Veletsos AS, Newmark NM, Chelepati CV. Deformation spectra for elastic and elastoplastic systems subjected to ground shock and earthquake motions. *Proceedings of the 3rd World Conference on Earthquake Engineering,* vol. II, Wellington, New Zealand, 1965; 663–682.
11. Hall JF, Heaton TH, Halling MW, Wald DJ. Near-source ground motion and its effects on flexible buildings. *Earthquake Spectra* 1995; **11**(4):569 –605.
12. Heaton TH, Hall JF, Wald DJ, Halling MW. Response of high-rise and base-isolated buildings to a hypothetical Mw 7.0 blind thrust earthquake. *Science* 1995; **267**:206–211.
13. Makris N. Rigidity–plasticity–viscosity: can electrorheological dampers protect base-isolated structures from near-source ground motions? *Earthquake Engineering and Structural Dynamics* 1997; **26**:571–591.
14. Makris N, Chang S-P. Effect of viscous, viscoplastic and friction damping on the response of seismic isolated structures. *Earthquake Engineering and Structural Dynamics 2000*; **29**(1):85–107.
15. Alavi B, Krawinkler H. Effects of near-source ground motions on frame-structures. *Technical Report No. 138,* The John A. Blume Earthquake Engineering Center, Stanford University, 2001.
16. Mavroeidis GP, Papageorgiou AS. A mathematical representation of near-fault ground motions. *Bull. Seism. Soc. Am. 2003;* **93**(3):1099 –1131.
17. Aki K, Bouchon M, Chouet B, Das S. Quantitative prediction of strong motion for a potential earthquake fault. *Annali di Geofisica* 1977; 30:341–368.
18. Papageorgiou AS, Aki K. A specific barrier model for the quantitative description of inhomogeneous faulting and the prediction of strong ground motion. II. Applications of the model. *Bull. Seism. Soc. Am.* 1983; **73**:953–978.
19. Brune JN. Tectonic stress and the spectra of seismic shear waves from earthquakes. *Journal of Geophysical Research* 1970; **75**:4997–5009.
20. Aki K. Strong-motion seismology. In Earthquakes: Observation, Theory and Interpretation, Kanamori H, Boschi E (eds). *Proceedings of the International School of Physics, Enrico Fermi, Course 85*. North-Holland: Amsterdam, 1983; 223–250.
21. Makris N, Black CJ. Dimensional analysis of rigid-plastic and elastoplastic structures under pulse-type excitations. *Journal of Engineering Mechanics* (ASCE) 2004; **130**(9):1006–1018.
22. Makris N, Black CJ. Dimensional Analysis of Bilinear Oscillators under Pulse-Type Excitations *Journal of Engineering Mechanics* (ASCE) 2004 **130**(9) 1019-1031.
23. Karavasilis TL, Makris N, Bazeos N, Beskos DE Dimensional Response Analysis of Multistory Regular Steel MRF Subjected to Pulselike Earthquake Ground Motions, *J. Struct. Engrg.* 2010 **136**, 921-932 .
24. Ricker N. Further developments in the wavelet theory of seismogram structure. *Bulletin of the Seismological Society of America* 1943; **33,** 197-228.
25. Ricker N. Wavelet functions and their polynomials, *Geophysics* 1944 **9,** 314–323.
26. Addison P. *The Illustrated Wavelet Transform Handbook: Introductory Theory and Applications in Science, Engineering, Medicine and Finance,* Institute of Physics, London, UK, 2002.

27. Vassiliou MF, Makris N, Estimating time scales and length scales in earthquake acceleration records with the extended wavelet transform Report No. EEAM 2009-01, University of Patras, Greece, 2009.

28. Vassiliou MF, Makris N, Estimating time scales and length scales in pulselike earthquake acceleration records with wavelet analysis., *Bulletin of the Seismological Society of America.* 2011; **101(2)** DOI:10.1785/0120090387

29. MATLAB Version 2007b. *The Language of Technical Computing*. The Mathworks, Inc.: Natick, MA, 1999.

30. Makris N, Vassiliou MF. The existance of "complete similarities" in the response of seismic isolated structures subjected to pulse like ground motions and their implications in analysis. *Earthquake Engineering and Structural Dynamics* DOI:10.1002/eqe.1072

31. Psycharis IN, Papastamatiou DY, Alexandris AP. Parametric investigation of the stability of classical columns under harmonic and earthquake excitations. *Earthquake Engineering and Structural Dynamics* 2000; 29(8): 1093–1109.

32. Vassiliou MF, Makris N, Analysis of the rocking response of rigid blocks standing free on a seismically isolated base. *Earthquake Engineering and Structural Dynamics* (accepted for publication)

33. Konstantinidis D, Makris N. Seismic response analysis of multidrum classical columns. *Earthquake Engineering and Structural Dynamics* 2005; **34**(10):1243–1270.

P

COMPDYN 2011
III ECCOMAS Thematic Conference on
Computational Methods in Structural Dynamics and Earthquake Engineering
M. Papadrakakis, M. Fragiadakis, V. Plevris (eds.)
Corfu, Greece, 25–28 May 2011

SEISMIC DESIGN METHODOLOGY FOR CONTROL OF 3D BUILDINGS BY MEANS OF MULTIPLE TUNED-MASS-DAMPERS

Yael Daniel[1] **and Oren Lavan**[2]

[1] Faculty of Civil and Environmental Engineering, Technion – Israel Institute of Technology
Technion City, Haifa 32000, Israel
e-mail: ~~yaeldan@tx.technion.ac.il~~

[2] Faculty of Civil and Environmental Engineering, Technion – Israel Institute of Technology
Technion City, Haifa 32000, Israel
e-mail: ~~lavan@tx.technion.ac.il~~

Keywords: Seismic Control, Tuned-Mass-Dampers, Dynamic Vibration Absorbers, Fully-Stressed Design, Multiple Mode Vibration.

Abstract. *This paper presents a methodology for the optimal design of multiple Tuned Mass Dampers (TMDs) in 3D irregular buildings. The objective function minimizes the total mass of all added TMDs. Constraints are added to limit the total accelerations experienced at the edges of the floors in the direction parallel to each edge. The formulation of the design methodology relies on optimality criteria conjectured herein, hence, a two stage iterative analysis/redesign procedure that is based on analysis tools only is resulted. This allows the application of the methodology in a practical design process.*

1 INTRODUCTION

Seismic protection of structures is an important issue in structural design due to its threatening consequences. Often, it is required that the design of a structure provide even more than life safety, promising a certain level of serviceability following a severe earthquake, while allowing for a defined level of damage, i.e. performance-based design. Damage to structural components is often linked to inter-story drifts, when considering damage due to maximal responses, and to energy dissipation when considering damage due to cumulative actions. When considering damage to acceleration sensitive non-structural elements, total accelerations (which are accelerations in respect to an inertial frame of reference, also referred to as absolute accelerations) produced during the ground-motion are of most interest. Total acceleration levels are also very important when considering the comfort level of human occupancy. In addition, total accelerations have an effect on base-shear and overturning moments [1].

There is ample literature on the control of these responses through control devices that reduce the energy dissipation demand of the structure. Several passive damping devices are available, including viscous and visco-elastic dampers, and metallic and friction hysteretic dampers [1, 2]. Another device to be used herein is the Tuned-Mass-Damper (TMD). Details about TMDs and their applications may be found in the fine works [1, 3, 4, 5, 6], only to name a few.

The use of TMDs for the reduction of responses of tall buildings due to wind loadings became widespread [7, 8, 9]. With efficient seismic design strategies, those devices may be attractive for multi-hazard mitigation of both winds and earthquakes. While wind-induced vibrations are usually dominated by a single mode, using TMDs for seismic structural protection is more complicated. In seismic vibrations, no single distinct frequency dominates the behavior, but rather many frequencies, including the ones of higher modes. Many researchers are therefore hesitant in using TMDs for seismic structural applications [10, 11, 12, 13, 14]. It should be noted that most of those works use only a single TMD tuned to a fundamental frequency. In addition, a TMD relies on tuning the device's natural frequency as to suppress the vibration of the structure, based on the structure’s natural frequencies. However, if detuning occurs, the device loses much of its efficiency.

One solution to these drawbacks may be found in active or semi-active TMDs (ATMDs or SATMDs), whose frequencies may be altered at each moment [15, 16, 17, 18]. Active control, however, requires an external power source to be activated, which may be costly and may force a reliability issue during an actual earthquake. Another possible solution may be achieved using multiple TMDs (MTMDs), each tuned to a different frequency. This may lead to a solution that controls various frequencies for various modes of the structure. Those TMDs could also be distributed along the structure and located at locations which will optimize the control of the structure. In addition, each TMD that is aimed at controlling a certain mode of the structure could be split to several TMDs, each tuned to a slightly different frequency within a bandwidth close to the natural frequency of the main system, thus reducing the detuning effect and allowing design robustness (for example [19]). The idea of using MTMDs tuned to various natural frequencies of the structure and distributed along its height is not new. Clark [20] indicated that a single TMD can not significantly reduce the motion created due to seismic excitations, while MTMDs can substantially reduce motion. Moon [21, 22] shows a practical application of vertically-distributed MTMDs in tall buildings for reducing wind-induced vibrations, and offers a method of distributing them by mode shape. In his work, dampers are located at the perimeter in the space between the inner and outer façade layers in double skin façade systems, as their vibrations are in the direction perpendicular to the edge of the floor. In the methodology presented herein a somewhat different approach is taken, as the dampers' vibrations are in parallel to the floor edge. This allows a better control of torsional response as well as larger strokes for the dampers.

Several methodologies for the optimal design of a single passive TMD for MDOF structures exist, each using a different objective function [8, 23, 24, 25]. Hadi and Arfiadi [26] use an H_2 performance index to retrieve the optimal parameter of a TMD added to a MDOF structure. H_2 and H_∞ optimization criteria are also widely used in ATMD problems (for example [27]). The H_2 approach minimizes a weighted average of the weighted sum of responses at various locations, and the control energy input. In the case of passive control, however, the control energy input is not a relevant cost measure. The H_∞ approach, on the other hand, minimizes the worst case energy attenuation of the controlled output with respect to an excitation of a given energy. Here, however, the characteristics of the input motion expected at the site where the structure is located are not considered. It should be emphasized that both approaches make use of smeared measures of the controlled responses rather than limiting each local response separately. In buildings in general, however, (see for example [28, 29]), and in the case of irregular buildings in particular, it is highly important to limit each local response separately. In addition, both approaches do not target an allowable response limit. In the context of the last two highly important issues, Bounded State Control (BSC) seems more appropriate since local states are each bounded to allowable limits [28, 29].

Bounded State Control algorithms can be roughly categorized into two groups. The first relies on a train of high energy pulses of control forces (e.g. [29, 30] and references therein) while the second makes use of a continuous control law (e.g. [31, 32, 33). While may be attractive in the application of an active control system, the pulse control strategies are not likely to be implemented by passive means. The methods that make use of continuous control laws, on the other hand, usually require formal optimization.

There are not many methodologies available for the design of MTMDs of various frequencies and locations in seismic application. In their pioneering work, Chen and Wu [34] use a frequency based transfer function as a response measure of the multi-modal vibration problem of structures. Rather than solving a formal optimization problem, they use a sequential search technique in order to allocate multi-modal MTMDs. A pre-assumed number of TMDs is sequentially added at locations where the location index (which, for example, can be the location of maximal root-mean-square (RMS) acceleration prior to placement of each damper) is optimal in each sequence. Luo et al. [35] also dealt with the multi-modal vibration problem of structures using MTMDs. In their work, a dynamic magnification factor (DMF) of the first mode obtained based on the transfer function of the structure's response in frequency domain is minimized. Constraints on the DMFs of other modes are also considered. Lin et al. [36] proposed a two-stage frequency-domain based optimal design of MTMDs taking into consideration both the structural response and the TMD stroke, and found that there is a good balance between limiting the TMD stroke and not substantially compromising on structural response. Fu and Johnson [37] suggest using passive MTMDs with a vertical distribution of mass, where each story is assigned with one TMD of which its' parameters (mass, stiffness and inherent damping) are optimized as to minimize the sum of inter-story drifts. The optimization problem is solved using a pattern-search, and a local minimum is obtained. While the above methodologies present a huge step forward, there is still no methodology that leads to a desired performance under a realistic representation of the ground motion hazard, in small computational efforts while using analysis tools only.

This paper presents a simple frequency-domain performance-based methodology for solving the allocation and sizing problem of multi-modal MTMDs in structures undergoing seismic excitations. The objective function minimizes the total mass of all added TMDs. Constraints are added to limit the total accelerations experienced at the edges of the floors in the direction parallel to each edge. The methodology is based on a simple iterative analysis/redesign procedure where first, an analysis is performed for a given design and then redesign of the TMDs is performed according to recurrence relations. The redesign first determines the mass of all dampers at a given location based on RMS acceleration (peak acceleration could be indirectly used). Then this mass is distributed between dampers tuned to various frequencies. The methodology is based on the simple optimal design parameters of TMDs presented by Den-Hartog [3] and Warburton [4] to successfully reduce the acceleration demands within the structure. The advantages of the proposed methodology is its simplicity, relaying on analyses tools only, it is performance-based - catered to serve any desirable performance, and its fast convergence.

2 PROBLEM FORMULATION

2.1 Equations of motion

Following Soong [29], the equations of motion of a MDOF system can be represented in state-space notation as:

$$\begin{aligned} \dot{\hat{\mathbf{x}}}(t) &= \mathbf{A}\cdot\hat{\mathbf{x}}(t)+\mathbf{B}\cdot a_g(t) \\ \mathbf{y}(t) &= \mathbf{CC}\cdot\hat{\mathbf{x}}(t) \end{aligned} \tag{1}$$

where $\hat{\mathbf{x}}^{\mathrm{T}} = \left[\mathbf{x}^{\mathrm{T}} \quad \dot{\mathbf{x}}^{\mathrm{T}}\right]$; $\mathbf{x}\in R^N$, $\hat{\mathbf{x}}\in R^{2N}$ is the state variable vector, $\mathbf{x}(t)$ is the displacement vector between the DOFs and the ground, $a_g(t)$ is the ground-motion's acceleration, a dot represents the derivative with respect to time, and $\mathbf{y}(t)$ is the output vector of the system, whose entries are responses of interest. Those responses are a linear combination of the state variables and the input forces (in our case $\mathbf{y}(t)=\mathbf{x}(t)$). The matrices **A**, **B** and **CC** are defined as following:

$$\mathbf{A}=\begin{bmatrix} \mathbf{0}_{N\times N} & \mathbf{I}_{N\times N} \\ -\mathbf{M}^{-1}\mathbf{K} & -\mathbf{M}^{-1}\mathbf{C} \end{bmatrix} \quad \mathbf{B}=\begin{bmatrix} \mathbf{0}_{N\times 1} \\ -\mathbf{e} \end{bmatrix} \quad \mathbf{CC}=\left[\mathbf{I}_{N\times N} \quad \mathbf{0}_{N\times N}\right] \tag{2}$$

where **M**, **C** and **K** are the mass, inherent damping and stiffness matrices of the structure according to the chosen *N* degrees-of-freedom (DOFs), respectively, **e** is the excitation direction vector with values of zero and one, **I** is the identity matrix and **0** is a zero matrix of appropriate dimensions, as noted.

It should be noted that for the sake of presentation, Eq. (1) and the following methodology are presented using a single input (component of the ground motion). An extension to the case of multiple inputs simultaneously, or multiple components of the ground motion in different directions, is straightforward.

2.2 Performance measures

Sensitivity of equipment within the structure, as well as human discomfort is found to be most dependent on total accelerations produced within the structure during an earthquake [1, 34]. The acceleration serviceability limit of structures is thus a suitable performance criterion for design. Reducing the drift levels within the structure is also a goal that should be reckoned with, as drifts are the main source of structural damage. This criterion is not directly taken into consideration in the present work; however, as will be seen in the example, using the proposed methodology leads to a considerable reduction of peak drifts as well. Moreover, some structures are expected to lead to acceptable, or close to acceptable, drifts even without retrofitting, but to be sensitive to total accelerations. One example for that is buildings for which wind loads dictate the design for lateral loads. Here, earthquakes may still lead to high total accelerations. Hence, total accelerations serve in this paper as the performance measure of the structure.

Added TMDs help control the responses of the structure, and the measure of cost of this controlling system is by the amount of added mass. As more mass is added to the structure, the retrofit is said to be more expensive and thus less cost-effective.

2.3 Problem formulation

The problem at hand is formulated as an optimization problem for which the objective function minimizes the total amount of added masses in the TMDs under constraints of maximal performance measures. The total accelerations at all peripheral locations of all floors are taken as the performance measures, as they are the largest accelerations expected within story limits. Those locations are shown in Fig. 1 as: $(\mathbf{x}_{\text{pyl}})_n$, $(\mathbf{x}_{\text{pyr}})_n$, $(\mathbf{x}_{\text{pxt}})_n$ and $(\mathbf{x}_{\text{pxb}})_n$, and are the peripheral coordinates in the "y", "y", "x" and "x" directions, at the left, right, top and bottom edges of floor n, respectively. The remaining variables will be explained subsequently. That is, the constraints are on the total accelerations at the edges of all floors in the directions parallel to each edge. The optimization problem is thus formulated as:

$$\begin{aligned}
&\min J = \sum_{l}^{\substack{\text{all}\\\text{locations}}} \sum_{f}^{\substack{\text{all}\\\text{frequencies}}} \left(\mathbf{m}_{\text{TMD}}\right)_{l,f} \\
&s.t. \\
&\frac{\max\limits_{eq}\left(\max\limits_{t}\left(\left(\ddot{\mathbf{x}}_{\text{p}}^{\text{t}}(t)\right)_l\right)\right)}{a_{\text{all}}^{\text{t}}} \leq 1.0 \qquad \forall l = 1,2,\ldots,N_{locations}
\end{aligned} \tag{3}$$

where $(\mathbf{m}_{\text{TMD}})_{l,f}$ is the mass of the TMD located at peripheral location l tuned to frequency f, $\max\limits_{eq}\left(\max\limits_{t}\left(\left(\ddot{\mathbf{x}}_{\text{p}}^{\text{t}}(t)\right)_l\right)\right)$ is the envelope of peak total acceleration in time at each location, l, under all considered earthquakes, $a_{\text{all}}^{\text{t}}$ is the allowable total acceleration, and $N_{locations}$ is the number of locations to be constrained (=$4N_{floors}$ where N_{floors} is the number of floors). The peripheral locations, l, are ordered such that the vector of peripheral coordinates is $\mathbf{x}_{\text{p}}=[\mathbf{x}_{\text{pyl}}^{\text{T}}\ \mathbf{x}_{\text{pyr}}^{\text{T}}\ \mathbf{x}_{\text{pxt}}^{\text{T}}\ \mathbf{x}_{\text{pxb}}^{\text{T}}]^{\text{T}}$ (see also Fig. 1). It should be noted that with a slight modification, the methodology to follow could also constrain the total accelerations of the floors' corners in any direction, if desired.

Rather than directly solving the time-domain representation of the problem (Eq. (3)), the proposed methodology uses an equivalent frequency-domain representation, introducing peripheral RMS total accelerations rather than peripheral peak total accelerations. The allowed values for the RMS total accelerations are properly scaled so as to lead to the desired allowable peak accelerations in time of Eq. (3). In frequency-domain, Eq. (3) is transformed into:

$$\begin{aligned}
&\min J = \sum_{l}^{\substack{\text{all}\\\text{locations}}} \sum_{f}^{\substack{\text{all}\\\text{frequencies}}} \left(\mathbf{m}_{TMD}\right)_{l,f} \\
&s.t. \\
&\frac{RMS\left(\left(\ddot{\mathbf{x}}_{\text{p}}^{\text{t}}\right)_l\right)}{a_{\text{all}}^{\text{RMS}}} \leq 1.0 \qquad \forall l = 1,2,\ldots,N_{locations}
\end{aligned} \tag{4}$$

where $a_{\text{all}}^{\text{RMS}}$ is the allowable RMS total acceleration and $RMS\left(\left(\ddot{\mathbf{x}}_{\text{p}}^{\text{t}}\right)_l\right)$ is the root mean square of the total acceleration at location l (the l^{th} term of $RMS\left(\ddot{\mathbf{x}}_{\text{p}}^{\text{t}}\right)$). Such reference to a component of a vector or a matrix, i.e. $(\cdot)_l$, will be used throughout the paper.

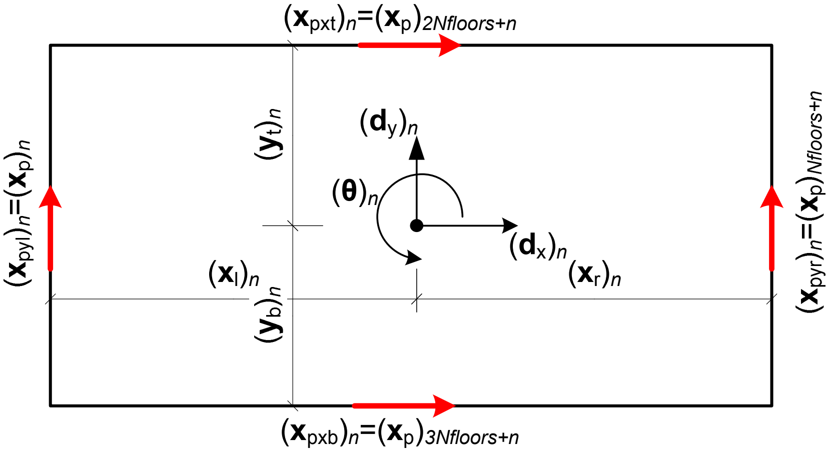

Figure 1: Definition of dynamic DOFs and peripheral coordinates of the n$^{\text{th}}$ floor.

3 PROPOSED SOLUTION SCHEME

3.1 Fully-stressed design (FSD)

Designs that are based on fully stressed characteristics go back to the classical design of trusses under static loads, whereby the weight is minimized for a given allowable stress. For that problem, it had been widely accepted that the optimal design yields a: statically determinate fully stressed design, with members out of the design having strains smaller than the allowable. This result appeared in the literature as early as 1900 as: “A statically determined framework of included figure is the most economic form of a framework of given indeterminate figure for the support of a given loading” [38]. It was later shown that this design is a Karush-Kuhn-Tucker point and therefore, an optimal design [39].

Recently, it was shown that some dynamic optimal designs also possess "fully stressed" characteristics. Levy and Lavan [40] considered the minimization of total added viscous damping to frame structures subjected to ground accelerations, while constraining various inter-story responses. Their optimal solutions attained by formal optimization indicated that: "At the optimum, damping is assigned to stories for which the local performance index has reached the allowable value. Stories with no assigned damping attain a local performance index which is lower or equal to the allowable." That is, the optimal solutions attained "fully stressed" characteristics.

Based on past experience of the authors in similar problems, it is conjectured here that the optimal solution to MTMD allocation and sizing in structures (the solution of Eq. (4)) possesses FSD characteristics, i.e.:

At the optimum, TMDs are assigned to peripheral locations for which the RMS total acceleration has reached the allowable value under the considered input acceleration PSD. In addition, at each location to which TMDs are added, TMDs of a given frequency are assigned only to frequencies for which the output spectral density is maximal.

Potential locations for TMDs are located at the edges of the floors, as their lines of action are in direction parallel to the edges (Fig. 2). Those are actually the same locations where total accelerations are to be limited. The coordinates "**z**" in Fig. 2 will be explained subsequently.

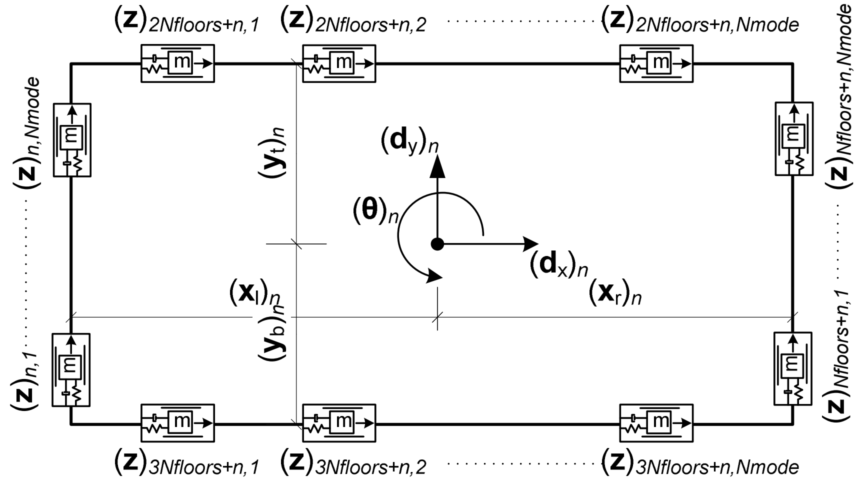

Figure 2: Locations of TMDs at the floor n and their associated z DOFs.

Stage one of the conjecture, imposes that for all peripheral locations with masses within the design, the total acceleration equals the allowable one, while all peripheral locations with zero masses (outside the design) have an acceleration equal to or less than the allowable. This is illustrated on the left-hand side of Fig. 3, which presents the concept on a selected peripheral frame. Here, the 5th floor is the only on to be dampened ($\sum_{f}\left(\mathbf{m}_{\mathrm{TMD}}\right)_{5,f} \neq 0$), as it is the only floor to reach the allowable RMS acceleration. The second stage of the conjecture imposes that for all dampers at a peripheral location where the acceleration equals the allowable one, and are within the design, the output spectral densities are maximal (with respect to ω) and equal. As for masses outside of the design at this DOF, the output spectral density is less than maximal. This is illustrated on the right-hand side of Fig. 3 where $\left(\mathbf{R}_{\ddot{\mathbf{x}}_{\mathrm{p}}^{\mathrm{t}}}(\omega)\right)_{l}$ is the output spectral density for the total acceleration at the location l (=5 in Fig. 3). As can be seen, $\left(\mathbf{m}_{\mathrm{TMD}}\right)_{5,1}$ and $\left(\mathbf{m}_{\mathrm{TMD}}\right)_{5,2}$ are the only ones with a mass larger than zero as their output spectral densities, $\left(\mathbf{R}_{\ddot{\mathbf{x}}_{\mathrm{p}}^{\mathrm{t}}}(\omega)\right)_{5}$, are largest. It should be noted that if the desired constraints are on the corners' total accelerations in any direction, dampers would be added to the direction that contributes more to the acceleration (between x and y).

The above conjecture suggests that the tuning frequency of each TMD is searched for amongst all possible frequencies. However, for practical reasons, it is reasonable to assume that these frequencies are in the vicinity of the bare structure's frequencies, and thus the tuning of TMDs could be in relation to the bare structure's natural frequency.

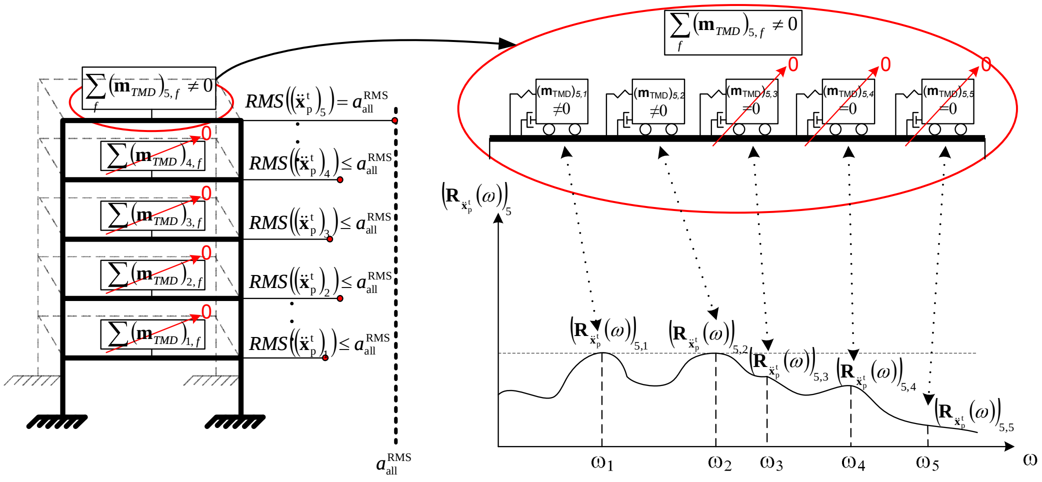

Stage 1

Stage 2

Figure 3: Illustrations of the first part of the conjecture (left) and the second part of the conjecture (right).

3.2 Analysis/Redesign algorithm

Solutions to optimization problems, which possess fully stressed characteristics, are efficiently achieved iteratively using a two step algorithm in each iteration cycle. In the first step, an analysis is performed for a given preliminary design, whereas in the second step the design is changed using a recurrence relationship that targets fully stressedness. The recurrence relation can be generally written as:

$$x_l^{(n+1)} = x_l^{(n)} \cdot \left(\frac{pi_l^{(n)}}{pi_{allowable}} \right)^P \tag{5}$$

where x_l is the value of the design variable associated with the location l, pi_l is the performance measure of interest for the location l, $pi_{allowable}$ is the allowable value for the performance measure, n - the iteration number and P - a convergence parameter. Fully stressedness is obtained from using Eq. (5) since upon convergence one of the following must take place. Either $x_l^{(n+1)} = x_l^{(n)}$ giving $pi_l^{(n)} = pi_{allowable}$, or $x_l^{(n+1)} = x_l^{(n)} = 0$ giving $pi_l^{(n)} \leq pi_{allowable}$.

In the optimal design of trusses, for example, the engineer would assume initial values for the cross sections as design variables (x_l's in Eq. (5)) and run an analysis. Then, based on the attained stresses as the performance measures (pi_l's in Eq. (5)), and their allowable values, the cross section of each bar could be redesigned using Eq. (5). The process could be repeated until convergence. The advantages of the analysis/redesign algorithm include its simplicity, the need to use analysis tools only, and the fairly small computational effort that lies in the small number of analyses required for convergence. Such analysis/redesign procedure will be utilized here to attain fully stressed designs where the mass, frequency and locations of MTMDs within framed structures is to be determined.

4 DESIGN METHODOLOGY

The proposed design methodology relies on the analysis/redesign procedure which leads to the FSD criteria presented above. The proposed methodology is summarized in the following flowchart. Following the flowchart is an extensive elaboration of each step, including the equations referred to within the flowchart.

4.1 Stepwise flowchart

Initial actions

1. Determine the mass, stiffness and inherent damping matrices of the structure. Decide on allowable RMS accelerations, which should represent the desired peak total acceleration.
2. Determine the natural frequencies and mode shapes of the structure.
3. Decide on an input PSD, which should represent an ensemble of chosen ground-motions (see example). For each DOF, evaluate the total acceleration transfer function in frequency domain using Eq. (8), transform this transfer function into peripheral coordinates using Eq. (10) and determine the peripheral output spectral density using Eq. (11). The peripheral RMS acceleration is derived from Eq. (12).
4. Add N_{mode} (N_{mode} being the number of modes potentially damped) TMDs at each peripheral coordinate, each tuned to one frequency of the structure, with the initial properties described in Eqs. (14), (17) and (19).

Iterative action

5. Update the mass, stiffness and damping matrices of the structure with the added damping system, using Eqs. (20) - (25).
6. Re-evaluate the RMS accelerations excited within the structure using Eqs. (8) - (12). Notice that for Eq. (8) the expressions $\mathbf{M}^{-1}\mathbf{K}$ and $\mathbf{M}^{-1}\mathbf{C}$ are taken from Eqs. (26) and (27), to avoid singularity.
7. Redesign the mass of each TMD according to the recurrence formulas given in Eqs. (28) and (29). Accordingly, reevaluate the stiffness and damping coefficient of each TMD using Eqs. (15) - (19).
8. Repeat steps 5 to 7 until convergence of the mass is reached.
9. Validate the results using time-history analysis and the selected set of ground-motions.
10. If desired, the allowable RMS acceleration may be scaled according to the reduction of envelope peak acceleration determined in step 9 and the allowable peak acceleration in time domain, using Eq. (30), followed by repeating steps 5-9 until fully satisfied.

Step 1: A desired maximal RMS acceleration (representing the desired peak total acceleration) is chosen. The mass, damping and stiffness matrices of the structure are assembled according to the relevant dynamic DOFs, which in the case of the simplest n^{th} floor of a 3D structure are two perpendicular displacements of a chosen coordinate and the floor's rotation, as noted in Fig. 1 by "$(\mathbf{d}_x)_n$", "$(\mathbf{d}_y)_n$" and "$(\boldsymbol{\theta})_n$". As it is desired to control peripheral responses (which include the largest responses within floor limits in the "x" and "y" directions), a coordinate transformation from floor DOFs to peripheral coordinates is performed as follows:

$$\mathbf{x}_p = \mathbf{T} \cdot \mathbf{x} \tag{6}$$

where $\mathbf{x} = \left[\mathbf{d}_x^{\mathrm{T}} \quad \mathbf{d}_y^{\mathrm{T}} \quad \boldsymbol{\theta}^{\mathbf{T}}\right]^{\mathrm{T}}$ and the transformation matrix $\mathbf{T}$ is:

$$\underset{(4 \cdot N_{floors} x 3 \cdot N_{floors})}{\mathbf{T}} = \begin{bmatrix} \underset{(N_{floors} x N_{floors})}{\mathbf{0}} & \underset{(N_{floors} x N_{floors})}{\mathbf{I}} & \underset{(N_{floors} x N_{floors})}{diag(\mathbf{x_l})} \\ \underset{(N_{floors} x N_{floors})}{\mathbf{0}} & \underset{(N_{floors} x N_{floors})}{\mathbf{I}} & \underset{(N_{floors} x N_{floors})}{diag(\mathbf{x_r})} \\ \underset{(N_{floors} x N_{floors})}{\mathbf{I}} & \underset{(N_{floors} x N_{floors})}{\mathbf{0}} & \underset{(N_{floors} x N_{floors})}{-diag(\mathbf{y_t})} \\ \underset{(N_{floors} x N_{floors})}{\mathbf{I}} & \underset{(N_{floors} x N_{floors})}{\mathbf{0}} & \underset{(N_{floors} x N_{floors})}{-diag(\mathbf{y_b})} \end{bmatrix} \tag{7}$$

where N_{floors} is the number of floors, N is the number of DOFs and $\mathbf{x_l}$, $\mathbf{x_r}$, $\mathbf{y_t}$, and $\mathbf{y_b}$ are the distances from the DOFs' coordinate system's origin to the left, right, top and bottom edges, ordered from first to top floor, as shown for the story *n* in Fig. 1.

Step 2: Solution of the eigenvalue problem determines the structure's natural frequencies and mode shapes.

Step 3: A power spectral density (PSD) for the input acceleration is chosen. Examples of such input spectrums are stationary white-noise, which gives a constant PSD, and the Kanai-Tajimi PSD [41]. Additional PSDs for ground-motional modeling can be found in Nagarajaiah and Narasimhan [42] and in Agrawal et al. [43]. The PSD is fitted to represent real ground-motions. This is done by fitting its parameters to a frequency-based spectrum, representing the decomposition of earthquakes into frequency components (for example, a FFT spectrum). For each DOF, the transfer function of total acceleration of the bare frame is evaluated using Eq. (8). This transfer function represents the ratio between the sinusoidal output amplitude to a sinusoidal input amplitude with frequency ω.

For total accelerations it can be shown that the appropriate transfer vector, $\mathbf{H}_{\ddot{\mathbf{x}}^{\mathrm{t}}}(j\omega)$, is:

$$\mathbf{H}_{\ddot{\mathbf{x}}^{\mathrm{t}}}(j\omega) = -\mathbf{M}^{-1} \cdot (j\omega\mathbf{C} + \mathbf{K}) \cdot \mathbf{H}_{\mathbf{x}}(j\omega) \tag{8}$$

where $j = \sqrt{-1}$ and $\mathbf{H}_{\mathbf{x}}(j\omega)$ is the displacement transfer vector [44], given by:

$$\mathbf{H}_{\mathbf{x}}(j\omega) = \mathbf{CC} \cdot (j\omega\mathbf{I} - \mathbf{A})^{-1} \cdot \mathbf{B} \tag{9}$$

This transfer function is transformed to peripheral coordinates using:

$$\mathbf{H}_{\ddot{\mathbf{x}}_{\mathrm{p}}^{\mathrm{t}}}(j\omega) = \mathbf{T} \cdot \mathbf{H}_{\ddot{\mathbf{x}}^{\mathrm{t}}}(j\omega) \tag{10}$$

where $\mathbf{H}_{\ddot{\mathbf{x}}_{\mathrm{p}}^{\mathrm{t}}}(j\omega)$ is the structure's transfer function of total accelerations in peripheral coordinates. The output spectral densities of the peripheral accelerations, $\left(\mathbf{R}_{\ddot{\mathbf{x}}_{\mathrm{p}}^{\mathrm{t}}}(\omega)\right)_l$, are evaluated using:

$$\left(\mathbf{R}_{\ddot{\mathbf{x}}_{\mathrm{p}}^{\mathrm{t}}}(\omega)\right)_l = \left|\left(\mathbf{H}_{\ddot{\mathbf{x}}_{\mathrm{p}}^{\mathrm{t}}}(j\omega)\right)_l\right|^2 \cdot S(\omega) \tag{11}$$

where $S(\omega)$is the input PSD, $\left|\left(\mathbf{H}_{\ddot{\mathbf{x}}_{\mathrm{p}}^{\mathrm{t}}}(j\omega)\right)_l\right|^2 = \left(\mathbf{H}_{\ddot{\mathbf{x}}_{\mathrm{p}}^{\mathrm{t}}}(j\omega)\right)_l \cdot \left(\mathbf{H}^*_{\ddot{\mathbf{x}}_{\mathrm{p}}^{\mathrm{t}}}(j\omega)\right)_l$ where $\left(\mathbf{H}_{\ddot{\mathbf{x}}^{\mathrm{t}}}(j\omega)\right)_l$ is the l^{th} term of $\mathbf{H}_{\ddot{\mathbf{x}}^{\mathrm{t}}}(j\omega)$, $\left(\mathbf{H}^*_{\ddot{\mathbf{x}}^{\mathrm{t}}}(j\omega)\right)_l$ is its complex conjugate.

The area under the output spectral density curve equals the mean-square response [45], and thus, the root-mean-square (RMS) of total accelerations at peripheral coordinate *l*, $RMS\left(\ddot{\mathbf{x}}_{\mathrm{p}}^{\mathrm{t}}\right)_l$,taking into consideration the contribution of all frequencies to the total response, is derived using:

$$RMS\left(\ddot{\mathbf{x}}_{\mathrm{p}}^{\mathrm{t}}\right)_l = \sqrt{2 \cdot \int_0^\infty \left(\mathbf{R}_{\ddot{\mathbf{x}}_{\mathrm{p}}^{\mathrm{t}}}(\omega)\right)_l d\omega} \tag{12}$$

Step 4: If for any peripheral coordinate, *l*, the RMS acceleration obtained is larger than the allowable RMS acceleration, MTMDs are added to suppress the acceleration produced. Each TMD of mass $(\mathbf{m}_{\mathrm{TMD}})_{l,f}$ is assigned with a DOF for its displacement relative to the ground, $(\mathbf{z})_{l,f}$. Here, the subscript *l* stands for its location while the subscript *f* stands for its frequency. The location, *l*, is corresponding to the peripheral coordinate $(\mathbf{x}_{\mathrm{p}})_l$ the TMD is attached to. At each location, N_{mode} TMDs are added, to suppress N_{mode} original frequencies of the structure, where N_{mode} is the number of modes to potentially be controlled. Thus, generally a total of $N_{mode} \cdot N_{locations}$ dampers are potentially added (Fig. 2). Note that the order of DOFs in the damped structure is:

$$\tilde{\mathbf{x}} = \begin{bmatrix} \mathbf{d}_x^{\mathrm{T}} & \mathbf{d}_y^{\mathrm{T}} & \boldsymbol{\theta}^{\mathbf{T}} & (\mathbf{z})_{1,1} & (\mathbf{z})_{2,1} & \cdots & (\mathbf{z})_{N_{locations},1} & \cdots & (\mathbf{z})_{1,N_{mode}} & (\mathbf{z})_{2,N_{mode}} & \cdots & (\mathbf{z})_{N_{locations},N_{mode}} \end{bmatrix}^{\mathbf{T}} \tag{13}$$

Note the difference between the coordinates $(\mathbf{x}_{\mathrm{p}})_l$ to the coordinates $(\mathbf{z})_{l,f}$. While the coordinates $(\mathbf{x}_{\mathrm{p}})_l$ relate to peripheral displacements of the floors themselves, $(\mathbf{z})_{l,f}$ relate to displacements of the masses of TMDs relative to the ground. Note also that those two vectors are organized such that the component *l* of **z** relates to the displacement of a TMD that is attached to the floor at the location of the component *l* of $\mathbf{x}_{\mathrm{p}}$, i.e. the locations *l* are corresponding in those two vectors.

The initial properties of each such damper are obtained based on a SDOF system representing the damped mode. In this work, Den-Hartog's properties [3] were chosen. These properties were derived for the optimal reduction of mass displacement of a SDOF system under external sinusoidal loading. They were later shown to also reduce the maximum total acceleration response of the mass of a SDOF system undergoing a harmonic base excitation [4]. It should be noted that any different set of chosen properties (mass, stiffness and inherent damping of each TMD) can be easily used with the proposed scheme instead of Den-Hartog. In the case of optimal Den-Hartog properties:

1. For each peripheral coordinate, the initial mass of all TMDs located at that coordinate is taken as certain predetermined percentage of the structure's mass (say 1%). It is divided equally between the dampers situated at the same location:

$$\left(\mathbf{m}_{\mathrm{TMD}}\right)_{l,f} = \frac{0.01}{N_{mode}} \cdot M_{structure} \tag{14}$$

where *l* represents the damper's location, *f* represents the mode dampened and $M_{structure}$ is the structure's total mass. The mass ratio $\left(\boldsymbol{\mu}_{\mathrm{TMD}}\right)_f$ of all TMDs tuned to frequency *f* equals the ratio between the effective TMD mass of all TMDs tuned to frequency *f* and the f^{th} modal mass of the structure. This mass ratio is defined as:

$$\left(\boldsymbol{\mu}_{\mathrm{TMD}}\right)_f = \frac{\phi_f^{\mathrm{T}} \cdot \mathbf{T}^{\mathrm{T}} \cdot \mathfrak{D}\left(\left(\mathbf{m}_{\mathrm{TMD}}\right)_f\right) \cdot \mathbf{T} \cdot \phi_f}{\phi_f^{\mathrm{T}} \cdot \mathbf{M}_{\mathbf{original}} \cdot \phi_f} \tag{15}$$

where ϕ_f is the f^{th} mode-shape of the bare structure, $\lfloor \mathbf{M}_{\mathbf{original}} \rfloor$ is the bare frame's mass matrix, **T** is the transformation matrix of Eq. (7), and $\mathfrak{D}\left(\left(\mathbf{m}_{\text{TMD}}\right)_f\right)$ is a diagonal matrix with the terms $\left(\mathbf{m}_{\text{TMD}}\right)_{1:Nlocations,f}$ sitting on the diagonal in the order of TMD DOFs, as in Eq. (13).

2. Each TMD's stiffness is determined according to the frequency of the mode which is dampened by the TMD. The frequency is tuned to:

$$\left(\boldsymbol{\omega}_{\text{TMD}}\right)_f = \frac{\left(\boldsymbol{\omega}_{\text{n}}\right)_f}{1+\left(\boldsymbol{\mu}_{\text{TMD}}\right)_f} \tag{16}$$

where $\left(\boldsymbol{\omega}_{\text{n}}\right)_f$ is the frequency f to be dampened. The compatible stiffness is:

$$\left(\mathbf{k}_{\text{TMD}}\right)_{l,f} = \left(\mathbf{m}_{\text{TMD}}\right)_{l,f} \cdot \left(\left(\boldsymbol{\omega}_{\text{TMD}}\right)_f\right)^2 \tag{17}$$

3. Each TMD's modal damping ratio is determined according to:

$$\left(\boldsymbol{\xi}_{\text{TMD}}\right)_f = \sqrt{\frac{3\cdot\left(\boldsymbol{\mu}_{\text{TMD}}\right)_f}{8\cdot\left(1+\left(\boldsymbol{\mu}_{\text{TMD}}\right)_f\right)^3}} \tag{18}$$

and the matching damping coefficient:

$$\left(\mathbf{c}_{\text{TMD}}\right)_{l,f} = 2\cdot\left(\mathbf{m}_{\text{TMD}}\right)_{l,f} \cdot \left(\boldsymbol{\xi}_{\text{TMD}}\right)_f \cdot \left(\boldsymbol{\omega}_{\text{n}}\right)_f \tag{19}$$

<u>**Step 5:**</u> The mass, damping and stiffness matrices of the damped frame are formulated, using the following. The new mass matrix is:

$$\mathbf{M} = \begin{bmatrix} \left\lfloor \mathbf{M}_{\mathbf{original}} + \mathbf{B}_{\mathbf{dm}}{}^{\mathbf{T}} \mathbf{m}_{\mathbf{TMD}} \mathbf{B}_{\mathbf{dm}} \right\rfloor & \mathbf{0} \\ \mathbf{0} & \left\lfloor \mathbf{m}_{\mathbf{TMD}} \right\rfloor \end{bmatrix} \tag{20}$$

where $\lfloor \mathbf{M}_{\mathbf{original}} \rfloor$ is the bare frame's mass matrix and $\lfloor \mathbf{m}_{\mathbf{TMD}} \rfloor$ is a diagonal matrix with the terms $\left(\mathbf{m}_{\text{TMD}}\right)_{l,f}$ sitting on the diagonal in the order of TMD DOFs, as in Eq. (13). The matrix $\mathbf{B}_{\mathbf{dm}}$ is a transfer matrix, used to add the mass of TMDs to the mass of the structure perpendicular to their original DOF (i.e. if a certain damper is used to reduce vibration in the "y" direction, and thus its DOF is in the "y" direction, the mass of that TMD is added to the mass of the structure in the "x" direction of the story where it is situated). It is given by:

$$\mathbf{B}_{\mathbf{dm}}{}^{\mathbf{T}} = \begin{array}{c} \begin{array}{ccccccc} 1 & . & . & . & . & . & N_{mode} \end{array} \\ \left[\begin{array}{ccccccc} \mathbf{T}_{\mathbf{m}}{}^{\mathbf{T}} & . & . & . & . & . & \mathbf{T}_{\mathbf{m}}{}^{\mathbf{T}} \end{array} \right] \end{array} \tag{21}$$

where:

$$\underset{(4\cdot N_{floors} x 3\cdot N_{floors})}{\mathbf{T}_{\mathbf{m}}} = \begin{bmatrix} \underset{(N_{floors} x N_{floors})}{\mathbf{I}} & \underset{(N_{floors} x N_{floors})}{\mathbf{0}} & \underset{(N_{floors} x N_{floors})}{\mathbf{0}} \\ \underset{(N_{floors} x N_{floors})}{\mathbf{I}} & \underset{(N_{floors} x N_{floors})}{\mathbf{0}} & \underset{(N_{floors} x N_{floors})}{\mathbf{0}} \\ \underset{(N_{floors} x N_{floors})}{\mathbf{0}} & \underset{(N_{floors} x N_{floors})}{\mathbf{I}} & \underset{(N_{floors} x N_{floors})}{\mathbf{0}} \\ \underset{(N_{floors} x N_{floors})}{\mathbf{0}} & \underset{(N_{floors} x N_{floors})}{\mathbf{I}} & \underset{(N_{floors} x N_{floors})}{\mathbf{0}} \end{bmatrix} \tag{22}$$

The damping matrix of the damped frame is constructed as:

$$\mathbf{C} = \begin{bmatrix} \left[\mathbf{C}_{\mathbf{original}} + \mathbf{B_d}^{\mathbf{T}} \mathbf{c}_{\mathbf{TMD}} \mathbf{B_d}\right] & \left[-\mathbf{B_d}^{\mathbf{T}} \mathbf{c}_{\mathbf{TMD}}\right] \\ \left[-\mathbf{c}_{\mathbf{TMD}} \mathbf{B_d}\right] & \left[\mathbf{c}_{\mathbf{TMD}}\right] \end{bmatrix} \tag{23}$$

where $\left[\mathbf{C}_{\mathbf{original}}\right]$ is the bare frame's inherent damping matrix and $\left[\mathbf{c}_{\mathbf{TMD}}\right]$ is a diagonal matrix with the terms $\left(\mathbf{c}_{\mathrm{TMD}}\right)_{l,f}$ sitting on the diagonal in the order of DOFs as in Eq. (13). The matrix $\mathbf{B_d}$ is a transfer matrix, used to assign the TMDs within the structure.

$$\begin{array}{cccccccc} & 1 & . & . & . & . & . & N_{mode} \\ \mathbf{B_d}^{\mathbf{T}} = \Big[& \mathbf{T}^{\mathrm{T}} & . & . & . & . & . & \mathbf{T}^{\mathrm{T}} \ \Big] \end{array} \tag{24}$$

The stiffness matrix of the damped frame is constructed similarly as:

$$\mathbf{K} = \begin{bmatrix} \left[\mathbf{K}_{\mathbf{original}} + \mathbf{B_d}^{\mathbf{T}} \mathbf{k}_{\mathbf{TMD}} \mathbf{B_d}\right] & \left[-\mathbf{B_d}^{\mathbf{T}} \mathbf{k}_{\mathbf{TMD}}\right] \\ \left[-\mathbf{k}_{\mathbf{TMD}} \mathbf{B_d}\right] & \left[\mathbf{k}_{\mathbf{TMD}}\right] \end{bmatrix} \tag{25}$$

where $\left[\mathbf{K}_{\mathbf{original}}\right]$ is the bare frame's stiffness matrix and $\left[\mathbf{k}_{\mathbf{TMD}}\right]$ is a diagonal matrix with the terms $\left(\mathbf{k}_{\mathrm{TMD}}\right)_{l,f}$ sitting on the diagonal in the order of DOFs as in Eq. (13).

<u>Step 6:</u> The peripheral RMS accelerations of the damped frame at all coordinates are evaluated using frequency-domain analysis based on Eqs. (8) - (12), using the newly-updated matrices (note that in Eq. (12) it is needed to take only the first *N* components of the extended vector $\mathbf{H}_{\ddot{\mathbf{x}}^{\mathrm{t}}}(j\omega)$ as now DOFs of TMDs are included in this vector). As earlier mentioned, this requires the evaluation of each DOF's transfer function. As the computation of the transfer function involves inversion of the mass matrix, and some TMD masses may get very small during the design process, singularity issues may occur. To avoid those, the expressions $\mathbf{M}^{-1}\mathbf{K}$ and $\mathbf{M}^{-1}\mathbf{C}$ used in Eq. (2) are evaluated as follows:

$$\mathbf{M}^{-1}\mathbf{K} = \begin{bmatrix} \left(\mathbf{M}_{\mathbf{original}} + \mathbf{B_{dm}}^{\mathbf{T}} \mathbf{m}_{\mathbf{TMD}} \mathbf{B_{dm}}\right)^{-1} \cdot \left(\mathbf{K}_{\mathbf{original}} + \mathbf{B_d}^{\mathbf{T}} \mathbf{k}_{\mathbf{TMD}} \mathbf{B_d}\right) & -\left(\mathbf{M}_{\mathbf{original}} + \mathbf{B_{dm}}^{\mathbf{T}} \mathbf{m}_{\mathbf{TMD}} \mathbf{B_{dm}}\right)^{-1} \mathbf{B_d}^{\mathbf{T}} \mathbf{k}_{\mathbf{TMD}} \\ -\mathbf{\Omega}^{\mathbf{2}}_{\mathbf{TMD}} \mathbf{B_d} & \mathbf{\Omega}^{\mathbf{2}}_{\mathbf{TMD}} \end{bmatrix} \tag{26}$$

where $\mathbf{\Omega}^{\mathbf{2}}_{\mathbf{TMD}}$ is a diagonal matrix with the terms $\left(\left(\boldsymbol{\omega}_{\mathrm{TMD}}\right)_{l,f}\right)^2$ sitting on the diagonal in the order of DOFs given in Eq. (13), and:

$$\mathbf{M}^{-1}\mathbf{C} = \begin{bmatrix} \left(\mathbf{M}_{\mathbf{original}} + \mathbf{B_{dm}}^{\mathbf{T}} \mathbf{m}_{\mathbf{TMD}} \mathbf{B_{dm}}\right)^{-1} \cdot \left(\mathbf{C}_{\mathbf{original}} + \mathbf{B_d}^{\mathbf{T}} \mathbf{c}_{\mathbf{TMD}} \mathbf{B_d}\right) & -\left(\mathbf{M}_{\mathbf{original}} + \mathbf{B_{dm}}^{\mathbf{T}} \mathbf{m}_{\mathbf{TMD}} \mathbf{B_{dm}}\right)^{-1} \mathbf{B_d}^{\mathbf{T}} \mathbf{c}_{\mathbf{TMD}} \\ -\mathbf{\Omega}\boldsymbol{\xi}_{\mathbf{TMD}} \mathbf{B_d} & \mathbf{\Omega}\boldsymbol{\xi}_{\mathbf{TMD}} \end{bmatrix} \tag{27}$$

where $\mathbf{\Omega}\boldsymbol{\xi}_{\mathbf{TMD}}$ is a diagonal matrix with the terms $2 \cdot \left(\boldsymbol{\xi}_{\mathrm{TMD}}\right)_{l,f} \cdot \left(\boldsymbol{\omega}_{\mathrm{TMD}}\right)_{l,f}$ sitting on the diagonal in the order of DOFs given in Eq. (13).

<u>Step 7:</u> The TMD's mass is re-determined using two stages; the total mass of all dampers located at a given location is determined, followed by the distribution of that mass between all

TMDs at that location, having various tuning frequencies. This is done according to the recurrence relationships described below. Following the change in mass, the stiffness and modal damping ratio of each TMD are also updated while keeping the Den-Hartog principles intact, using Eqs. (15) - (19). The two-stage analysis/redesign procedure is carried out iteratively, in the following way.

Stage 1: The first stage of redesign includes the evaluation of the total mass of all TMDs at a certain location, which promises the existence of the first part of the conjecture. This is formulated using:

$$\left(\mathbf{m}^{(n+1)}_{\text{TMD,total}}\right)_l = \sum_{f=1}^{\substack{\text{all}\\ \text{frequencies}}} \left(\mathbf{m}^{(n+1)}_{\text{TMD}}\right)_{l,f} = \sum_{f=1}^{\substack{\text{all}\\ \text{frequencies}}} \left(\mathbf{m}^{(n)}_{\text{TMD}}\right)_{l,f} \cdot \left(\frac{RMS\left(\left(\ddot{\mathbf{x}}_{\text{p}}^{\text{t}\,(n)}\right)_l\right)}{a^{\text{RMS}}_{\text{all}}}\right)^P \tag{28}$$

where $(\cdot)^{(n)}$ is the value at iteration *n*, $\left(\mathbf{m}^{(n+1)}_{\text{TMD,total}}\right)_l$ is the total mass of all dampers at location *l*, and *P* is a constant which influences the convergence and convergence rate. A large *P* will result in a faster but less stable convergence of the above equation. Based on the authors' experience, a *P* in the range of 0.1-2.0 should be satisfying in terms of stability, convergence and fair amount of iterations.

Stage 2: In the second stage of redesign, the total mass obtained at each location is distributed between N_{mode} dampers (dampening modes $\left(\boldsymbol{\omega}_{\text{n}}\right)_f$) at that same location *l*, promising the existence of the second part of the conjecture, using the following:

$$\left(\mathbf{m}^{(n+1)}_{\text{TMD}}\right)_{l,f} = \left(\mathbf{m}^{(n)}_{\text{TMD}}\right)_{l,f} \left(\frac{\sqrt{\left(\mathbf{R}^{(n)}_{\ddot{\mathbf{x}}_{\text{p}}^{\text{t}}}\left(\left(\boldsymbol{\omega}_{\text{n}}\right)_f\right)\right)_l}}{\max\limits_f\left(\sqrt{\left(\mathbf{R}^{(n)}_{\ddot{\mathbf{x}}_{\text{p}}^{\text{t}}}\left(\left(\boldsymbol{\omega}_{\text{n}}\right)_f\right)\right)_l}\right)}\right)^P \cdot \frac{\left(\mathbf{m}^{(n+1)}_{\text{TMD,total}}\right)_l}{\sum\limits_{f=1}^{\substack{\text{all}\\ \text{frequencies}}} \left(\mathbf{m}^{(n)}_{\text{TMD}}\right)_{l,f} \left(\frac{\sqrt{\left(\mathbf{R}^{(n)}_{\ddot{\mathbf{x}}_{\text{p}}^{\text{t}}}\left(\left(\boldsymbol{\omega}_{\text{n}}\right)_f\right)\right)_l}}{\max\limits_f\left(\sqrt{\left(\mathbf{R}^{(n)}_{\ddot{\mathbf{x}}_{\text{p}}^{\text{t}}}\left(\left(\boldsymbol{\omega}_{\text{n}}\right)_f\right)\right)_l}\right)}\right)^P} \tag{29}$$

where $\left(\mathbf{R}^{(n)}_{\ddot{\mathbf{x}}_{\text{p}}^{\text{t}}}\left(\left(\boldsymbol{\omega}_{\text{n}}\right)_f\right)\right)_l$ is the component of $\mathbf{R}^{(n)}_{\ddot{\mathbf{x}}_{\text{p}}^{\text{t}}}(\omega)$ at the location *l* evaluated at $\omega = \left(\boldsymbol{\omega}_{\text{n}}\right)_f$.

The analysis/redesign procedure is continued until convergence. It shall be noted that each iteration cycle may result in either a bigger or smaller mass.

Rational: Upon convergence, i.e when values at the iteration *n+1* are equal to the corresponding values at the iteration *n*, Eq. (28) is satisfied under one of two conditions. That is, either $\sum_{f=1}^{\substack{\text{all}\\ \text{frequencies}}} \left(\mathbf{m}^{(n+1)}_{\text{TMD}}\right)_{l,f} = \sum_{f=1}^{\substack{\text{all}\\ \text{frequencies}}} \left(\mathbf{m}^{(n)}_{\text{TMD}}\right)_{l,f} \neq 0$ and thus $RMS\left(\left(\ddot{\mathbf{x}}_{\text{p}}^{\text{t}\,(n+1)}\right)_l\right) = RMS\left(\left(\ddot{\mathbf{x}}_{\text{p}}^{\text{t}\,(n)}\right)_l\right) = a^{\text{RMS}}_{\text{all}}$, or $RMS\left(\left(\ddot{\mathbf{x}}_{\text{p}}^{\text{t}\,(n+1)}\right)_l\right) = RMS\left(\left(\ddot{\mathbf{x}}_{\text{p}}^{\text{t}\,(n)}\right)_l\right) \leq a^{\text{RMS}}_{\text{all}}$ and then $\sum_{f=1}^{\substack{\text{all}\\ \text{frequencies}}} \left(\mathbf{m}^{(n+1)}_{\text{TMD}}\right)_{l,f} = \sum_{f=1}^{\substack{\text{all}\\ \text{frequencies}}} \left(\mathbf{m}^{(n)}_{\text{TMD}}\right)_{l,f} = 0$. This portrays fully-stressedness in total accelerations, i.e. the first part of the conjecture. Eq. (29), on the other hand, portrays fully-stressedness in frequency response. Here, taking the sum of each side of the equation with respect to *f* implies that the sum of masses of TMDs at the location *l* and iteration *n+1* equals the desired total mass from the first stage, $\left(\mathbf{m}^{(n+1)}_{\text{TMD,total}}\right)_l$, or $\sum_{f=1}^{\substack{\text{all}\\ \text{frequencies}}} \left(\mathbf{m}^{(n+1)}_{\text{TMD}}\right)_{l,f} = \left(\mathbf{m}^{(n+1)}_{\text{TMD,total}}\right)_l$. This is actually attained using the fraction on the right-hand side of Eq. (29), which is constant for all *f*'s. The remaining part of Eq. (29) has a similar structure to that of Eq. (28). That is, upon convergence, either $\left(\mathbf{m}_{\mathrm{TMD}}^{(n+1)}\right)_{l,f} = \left(\mathbf{m}_{\mathrm{TMD}}^{(n)}\right)_{l,f} \neq 0$ and thus $\sqrt{\left(\mathbf{R}_{\ddot{\mathbf{x}}_{\mathrm{p}}^{\mathrm{t}}}^{(n)}\left((\boldsymbol{\omega}_{\mathrm{n}})_f\right)\right)_l} = \max_f\left(\sqrt{\left(\mathbf{R}_{\ddot{\mathbf{x}}_{\mathrm{p}}^{\mathrm{t}}}^{(n)}\left((\boldsymbol{\omega}_{\mathrm{n}})_f\right)\right)_l}\right)$, or $\sqrt{\left(\mathbf{R}_{\ddot{\mathbf{x}}_{\mathrm{p}}^{\mathrm{t}}}^{(n)}\left((\boldsymbol{\omega}_{\mathrm{n}})_f\right)\right)_l} \leq \max_f\left(\sqrt{\left(\mathbf{R}_{\ddot{\mathbf{x}}_{\mathrm{p}}^{\mathrm{t}}}^{(n)}\left((\boldsymbol{\omega}_{\mathrm{n}})_f\right)\right)_l}\right)$ and then $\left(\mathbf{m}_{\mathrm{TMD}}^{(n+1)}\right)_{l,f} = \left(\mathbf{m}_{\mathrm{TMD}}^{(n)}\right)_{l,f} = 0$. This portrays fully-stressedness in frequency response, i.e. the second part of the conjecture. It should be noted that the normalization of $\sqrt{\left(\mathbf{R}_{\ddot{\mathbf{x}}_{\mathrm{p}}^{\mathrm{t}}}^{(n)}\left((\boldsymbol{\omega}_{\mathrm{n}})_f\right)\right)_l}$ with respect to $\max_f\left(\sqrt{\left(\mathbf{R}_{\ddot{\mathbf{x}}_{\mathrm{p}}^{\mathrm{t}}}^{(n)}\left((\boldsymbol{\omega}_{\mathrm{n}})_f\right)\right)_l}\right)$ has no effect on the results of this equation and is done here only for clarification of the rational behind Eq. (29).

Step 8: Repeat steps 5 to 7 until convergence of the mass is reached.

Step 9: After the process converges, the retrofitted frame's response is validated using time history analysis for all ground-motions within the chosen ensemble.

Step 10: The percent of reduction in RMS acceleration and the percent of reduction of envelope peak accelerations in time domain may not be entirely compatible. Thus, a modification of the allowable RMS acceleration may be performed as to scale these two frequency/time domain measures, using the following:

$$a_{\mathrm{all},l}^{\mathrm{RMS}} = a_{\mathrm{all}}^{\mathrm{t}} \cdot \frac{RMS\left(\left(\ddot{\mathbf{x}}_{\mathrm{p}}^{\mathrm{t}}\right)_l\right)}{\max\limits_{eq}\left(\max\limits_{t}\left(\left(\ddot{\mathbf{x}}_{\mathrm{p}}^{\mathrm{t}}(t)\right)_l\right)\right)} \qquad \forall l = 1,2,.......,N_{locations} \tag{30}$$

where: $a_{\mathrm{all},l}^{\mathrm{RMS}}$ is the modified allowable RMS acceleration to be used in the frequency-domain analysis.

Once the allowable RMS acceleration is re-scaled, steps 5-9 are repeated until the reduction in peak acceleration is as desired in the performance-based design.

5 EXAMPLE

The following 8-story asymmetric RC frame structure (Fig. 4) introduced by Tso and Yao [46] is retrofitted using MTMDs for an excitation in the "y" direction. A uniform distributed mass of 0.75 ton/m^2 is taken. The column dimensions are 0.5m by 0.5m for frames 1 and 2 and 0.7m by 0.7m for frames 3 and 4. The beams are 0.4m wide and 0.6m tall. 5% Rayleigh damping for the first and second modes is used. A 40% reduction of the peripheral peak total acceleration obtained in the bare structure is desired. Hence, initially, an allowable peripheral RMS acceleration of 60% of the maximal peripheral RMS acceleration of the bare structure is adopted. The response is analyzed under a Kanai-Tajimi PSD with parameters fitted to the average FFT values of a chosen ensemble of ground-motions (SE 10 in 50). The design variables are the locations and properties of the individual tuned mass dampers. The dampers are to potentially be located in the peripheral frames, where they are most effective, and as the excitation is in the "y" direction only, dampers will be assigned only to peripheral frames 1 and 4, to dampen frequencies of modes which involve "y" and "θ". The ‘stepwise flowchart’ described above is closely followed to optimally design the MTMDs.

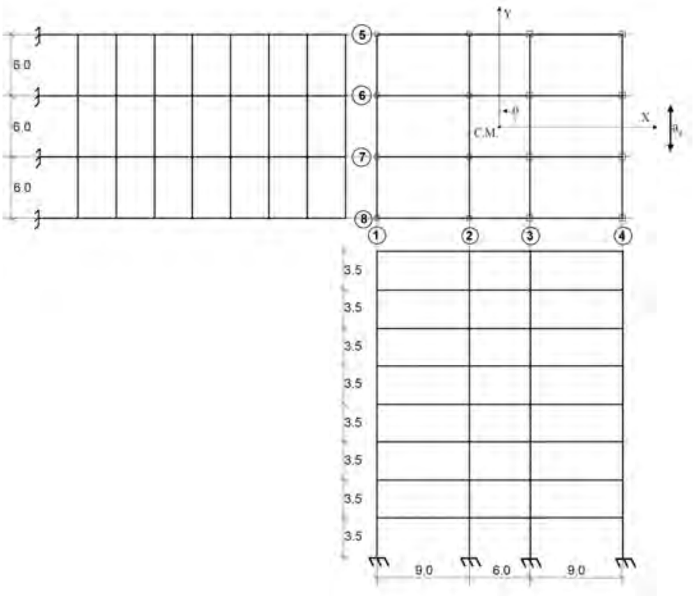

Figure 4: eight-story asymmetric structure.

Step 1: The mass, inherent damping and stiffness matrices of the frame in the dynamic DOFs shown in Fig. 1 were constructed.

Step 2: The natural frequencies, of the structure were determined. The first 10 frequencies are presented in Table 1.

Mode no.	Angular frequency (rad/sec)	Mode direction	Mode no.	Angular frequency (rad/sec)	Mode direction
1	5.135	x	6	22.407	y,θ
2	5.463	y,θ	7	29.649	x
3	7.087	y,θ	8	29.876	y,θ
4	16.240	x	9	40.918	y,θ
5	16.938	y,θ	10	44.770	y,θ

Table 1: Frequencies of the structure.

Step 3: The RMS accelerations of the undamped building at the peripheral frames in the "y" direction are presented in Fig. 5. Those were obtained using the Kanai-Tajimi PSD with parameters: $\omega_g = 13 \,{}^{rad}\!/_{\sec}$, $\xi_g = 0.98$ and $S_0 = 1$. Those parameters were determined by fitting the parameters ω_g and ξ_g to a spectrum of mean FFT values of the SE 10 in 50 ground-motion ensemble, scaled to S_0=1.0 (see Fig. 6). The actual value of S_0 has no effect since the allowable RMS acceleration is determined by the percentage of reduction desired. The allowable RMS acceleration for all peripheral accelerations was earlier adopted as 60% of the maximum peripheral RMS acceleration of the bare frame, giving: $a_{\mathrm{all}}^{\mathrm{RMS}} = 15.95$. It is assumed, as a first guess, that a similar reduction would be achieved in the envelope peak acceleration in time domain.

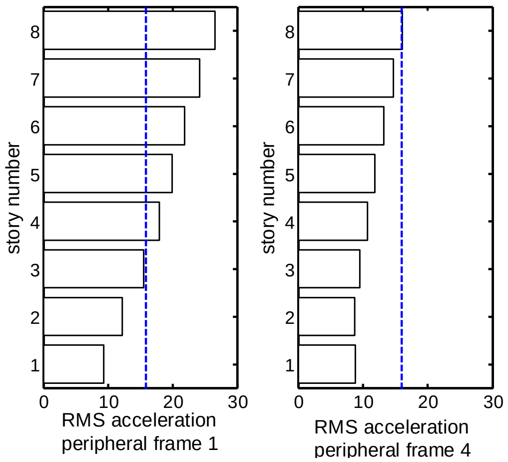

Figure 5: Peripheral RMS accelerations of bare structure (continuous) and allowable values (dashed).

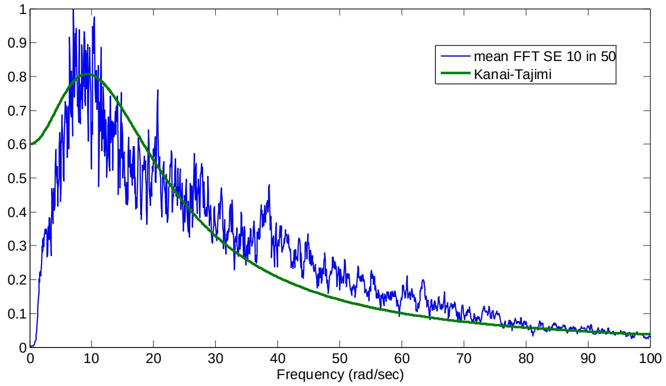

Figure 6: chosen input power-spectral-density.

Step 4: 160 TMDs were added, as a first guess, with initial properties as given in Table 2. Those are comprised of 10 dampers each tuned to a different mode frequency (of modes related to "y" and "θ") at each of the 16 peripheral locations of frames 1 and 4.

No. TMD	mode to dampen	Initial mass (ton)	Initial natural frequency (rad/sec)	Initial damping ratio
1-16	2	2.592	5.37	0.0788
17-32	3	2.592	6.89	0.1004
33-48	5	2.592	16.64	0.0795
49-64	6	2.592	21.78	0.0998
65-80	8	2.592	29.34	0.0805
81-96	9	2.592	39.79	0.0989
97-112	11	2.592	43.94	0.0816
113-128	12	2.592	60.28	0.0822
129-144	13	2.592	62.30	0.0983
145-160	15	2.592	77.55	0.0826

Table 2: Initial properties of TMDs.

Step 5: The mass, stiffness and damping matrices were updated using Eqs. (20) - (25).

Step 6: With the newly-updated matrices and the same PSD input, new peripheral RMS accelerations, shown in Fig. 7 (for frames 1 and 4), were evaluated using Eq. (8) – (12). Peripheral accelerations smaller than the allowable, were attained for all floors of frames 5 and 8 (see Fig, 4 for frame numbering).

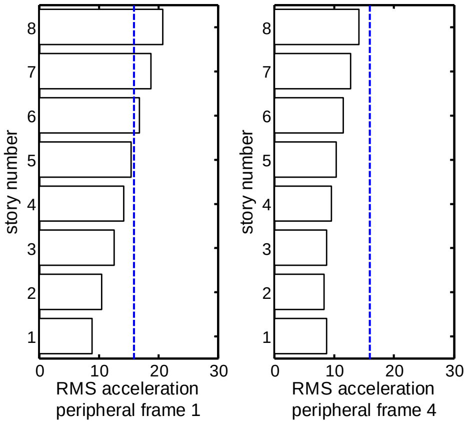

Figure 7: Peripheral RMS accelerations of structure with initial TMDs (continuous) and allowable values (dashed).

Step 7: The problem has not converged, and thus the TMDs' properties were altered, using the recurrence relations of Eqs. (28) and (29), while using ***P***=2 as the convergence parameter, giving updated total masses at each DOF. For example, the newly updated mass of all TMDs at floor 1 of peripheral frame 1 is: $m_{TMD,1}^{(1)} = 2.592 \cdot \left(\frac{9.41}{15.92}\right)^2 = 0.906$ for a RMS total acceleration of 9.41 at that location (frame 1, 1st floor) after adding initial TMDs (Fig. 7). The total mass of each peripheral coordinate was then distributed between the 10 dampers at the same location using Eq. (29).

Step 8: Iterative analysis/redesign as described in Eqs. (28) and (29) while altering the mass of the damper is carried out until convergence to allowable levels. Upon convergence the dampers’ total mass at each location are shown in Table 3.

TMDs with non-zero properties were located at frames number 1 and 4 at, both at the 8th floor, which is the top floor of each peripheral frame. The final properties of each added TMD are shown in Table 4. For frame number 1, the TMDs are set to dampen mode 2, while for frame number 4, the TMDs are set to dampen modes 2 and 3.

floor	Total mass frame 1	Total mass frame 4
1-7	0	0
8	112.69	6.25

Table 3: Total mass of TMDs upon convergence

frame	floor	mode to dampen	Final mass (ton)	Final stiffness (kN/m)	Final damping ratio
1	8	2	112.69	2472.15	0.1983
4	8	2	5.69	124.89	0.1983
4	8	3	0.55	27.72	0.0209

Table 4: Final properties of added TMDs

Finally, an analysis of the retrofitted structure yields the peripheral RMS accelerations shown in Fig. 8.

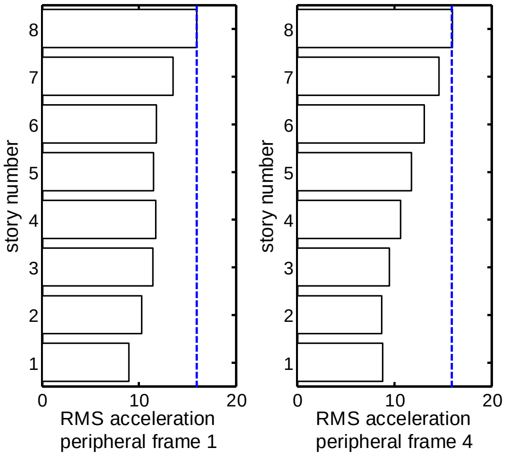

Figure 8: Peripheral RMS accelerations of structure with final TMDs (continuous) and allowable values (dashed).

All 4 assigned TMDs add up to 4.59% of the original structure's mass. As can be seen, only floors who had reached the maximum allowable RMS total acceleration (Fig. 8) were assigned with added absorbers (Table 4), making the solution obtained a FSD.

Fig. 9 presents the convergence of the design variables (masses) and the performance measure (acceleration). As can be seen in Fig. 9, although the initial guess was very far from optimum, convergence is practically reached within less than 40 iterations.

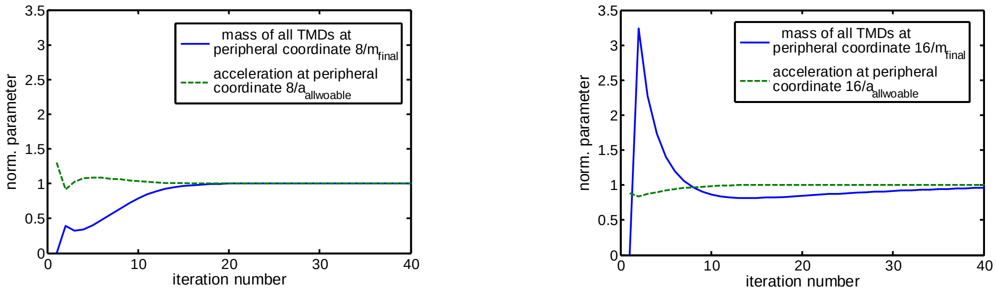

(a) (b)

Figure 9: Convergence of sum of masses and RMS acceleration at (a) 8th floor of peripheral frame number 1 and (b) 8th floor of peripheral frame number 4.

Step 9: The retrofitted structure was examined using time-history analysis under the SE 10 in 50 ensemble of real recorded earthquakes, scaled by a factor of 0.8, to check the validity of the solution obtained. The results of the envelope peak peripheral total accelerations and inter-story drifts of frames 1 and 4 obtained using time-history analysis are shown in Fig. 10. Smaller accelerations were attained in frames 5 and 8.

The results reveal that for this ensemble, the envelope maximum total acceleration of all locations of the bare structure was at the 8th floor of frame number 1, equaling 1.34g, while the envelope maximum total acceleration of all locations of the damped structure was 1.11g

(8th floor of frame 4). This represents a 17% reduction in acceleration response, not so close to the desired reduction of 40% in maximum response.

Although reducing the drifts was not part of the design process, it can be seen that these too were appreciably reduced. The maximum peripheral drift of all locations was reduced from 1.95% in the bare structure to 1.30% in the damped structure.

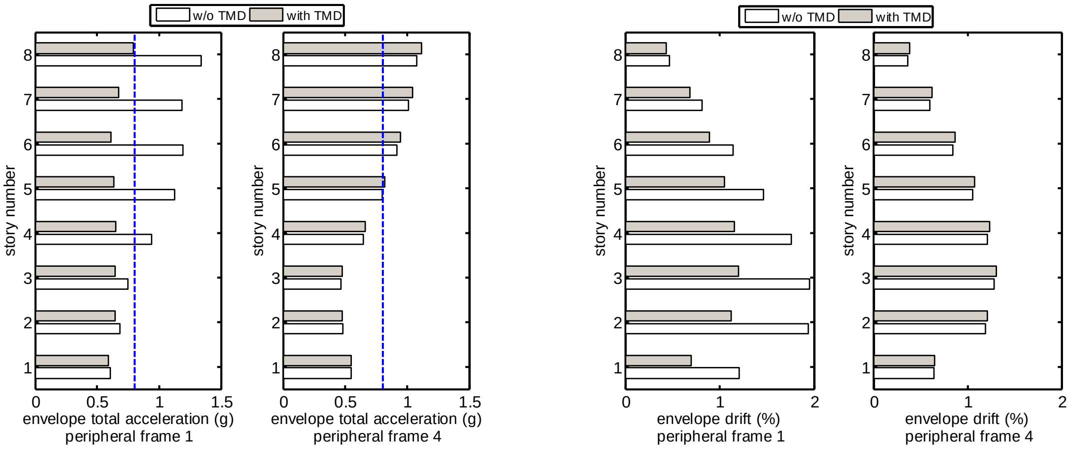

(a)

(b)

Figure 10: Peripheral envelope (a) accelerations and allowable values (dashed) and (b) drifts of the bare and damped structure under the SE 10 in 50 ground motion ensemble.

<u>Step 10:</u> For a more accurate design, the allowable RMS total acceleration of each story is modified to better reflect the allowable peak acceleration, using Eq. (30).

In this case, a 40% reduction in envelope peak acceleration is desired, thus $a_{\mathrm{all}}^{\mathrm{t}} = 0.6 \cdot \max_{l} \left(\max_{eq} \left(\max_{t} \left(\left(\ddot{\mathbf{x}}_{\mathrm{p}}^{\mathrm{t}}(t)_{bare-frame} \right)_{l} \right) \right) \right) = 0.6 \cdot 1.34 = 0.804g$). For example, for location 8 (frame 1, 8th floor): $a_{\mathrm{all},8}^{\mathrm{RMS}} = 0.804 \cdot \frac{15.952}{0.795} = 16.15$. Using this modification, the analysis/redesign process (steps 5-9) is repeated until convergence is once again reached. After convergence, the total mass was increased to 8.36% of the structure's mass. The modified retrofitted structure was again examined using time-history analysis under the SE 10 in 50 ensemble scaled by a factor of 0.8. The reduction between maximal envelope acceleration of all floors of the bare and damped structure was increased to 34.8%. The results can be modified yet again using step 10. After the third modification, the added mass of all TMDs increased to 8.87% (see Table 5), while the envelope peak total acceleration equaled 0.82g, representing a 39.0% reduction in response, which is very close to the desired reduction of 40%. The results of the envelope peak peripheral total accelerations and inter-story drifts of frames 1 and 4 obtained using time-history analysis are shown in Fig. 11.

frame	floor	mode to dampen	Final mass (ton)	Final stiffness (kN/m)	Final damping ratio
1	8	2	114.18	2397.4	0.2062
4	8	2	115.81	2431.7	0.2062

Table 5: Final properties of added TMDs after 3rd modification

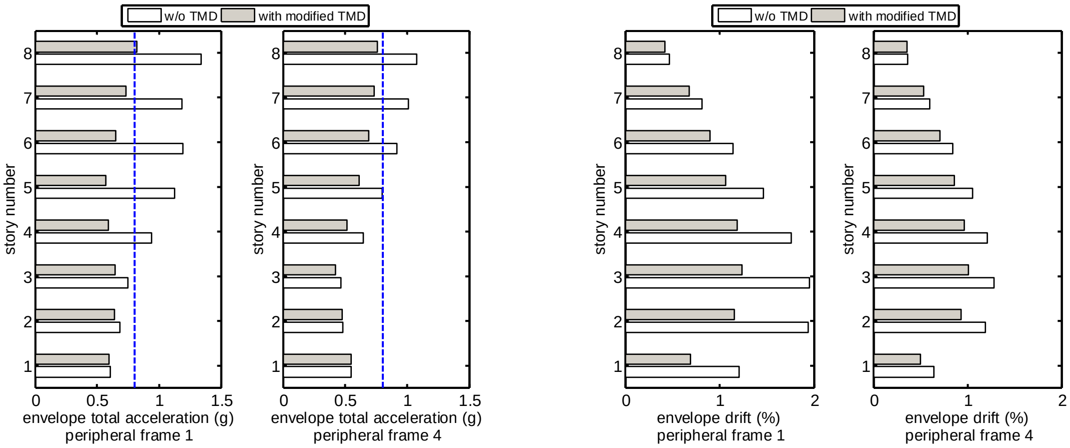

(a)

(b)

Figure 11: Peripheral envelope (a) accelerations and allowable values (dashed) and (b) drifts of the bare and 3rd-time modified damped structure under the SE 10 in 50 ground motion ensemble.

6 CONCLUSIONS

An analysis/redesign frequency-domain-based methodology for optimally allocating and sizing MTMDs in 3D irregular structures was presented. The proposed methodology considers the possible dampening of all modes of the structure, at all peripheral frames, thus eliminating the decision of what modes to dampen and where the TMDs should be allocated. As shown, using MTMDs tuned to various frequencies can efficiently reduce total accelerations within the structure and bring them to a desired level, allowing for performance based design. The advantages of this methodology are its simplicity of use and relying solely on analysis tools to solve the allocation and sizing problem, with no assumptions or pre-selection of any design variable. These advantages make the proposed methodology very attractive and efficient for practical use.

The methodology is based on the following conjecture: *At the optimum, TMDs are assigned to peripheral locations for which the RMS total acceleration has reached the allowable value under the considered input acceleration PSD. In addition, at each location to which TMDs are added, TMDs of a given frequency are assigned only to frequencies for which the output spectral density is maximal.* And the designs are attained using a very simple analysis/redesign based methodology suggested.

As previously mentioned, detuning of the TMDs may cause major deterioration to the passive control system. Depending on the level of detuning expected, a TMD located at location *l* tuned to dampen mode *f* can be split into several smaller TMDs, each with a slightly different frequency within a bandwidth close to the natural frequency *f* of the main system. Thus reduction of the detuning effect and design robustness could be achieved. This could be done a-priori and taken into account in the design methodology. In cases where the damped structure is not brought to behave linearly, and damage to the structural system is apparent, the natural frequencies of the structure may change considerably. In those cases, a design according to the proposed scheme, combined with the use of semi-active TMDs (for example, [15, 16, 17]) which allow the simple change of the TMD's tuning, while still keeping the control system's low-cost, could be beneficial.

REFERENCES

[1] T.T. Soong, G.F. Dargush, *Passive Energy Dissipation Systems in Structural Engineering*. John Wiley & Sons Ltd., Chichester, England, 1997.

[2] C. Christopoulos, A. Filiatrault, *Principles of Supplemental Damping and Seismic Isolation*. Milan, Italy ,IUSS Press, 2006.

[3] J.P. Den-Hartog, *Mechanical Vibrations 2nd edition*. McGraw-Hill Book Company, Inc, 1940.

[4] G.B. Warburton, Optimum Absorber Parameters for Various Combinations of Response and Excitation Parameters. *Earthquake Engineering and Structural Dynamics*, **10**, 381-401, 1982.

[5] G.W. Housner, L.A. Bergman, T.K. Caughey, A.G. Chassiakos, R.O. Claus, S.F. Masri, R.E. Skelton, T.T. Soong, B.F. Spencer, J.T.P. Yao, Structural Control: Past, Present and Future. *Journal of Engineering Mechanics*, **123:9**, 897-971, 1997.

[6] S.G. Kelly, *Fundamentals of Mechanical Vibrations 2nd edition*. McGraw-Hill, Boston, 2000.

[7] R.J. McNamara, Tuned Mass Dampers for Buildings. *ASCE Journal of Structural Division*, **103**, 1785-1798, 1977.

[8] R.W. Luft, Optimum Tuned Mass Dampers for Buildings. *ASCE Journal of Structural Division*, **105**, 2766-2772, 1979.

[9] K.B. Wiesner, Tuned Mass Dampers to Reduce Building Wind Motion. *ASCE Convention and Exposition*, Boston, Mass, 1-21, 1979.

[10] Y.P. Gupta, A.R. Chandrasekaran, Absorber System for Earthquake Excitation. *Proceedings of the 4th world Conference on Earthquake Engineering*, Santiago, Chile, **II**, 139-148, 1969.

[11] A.M. Kaynia, D. Veneziano, J.M. Biggs, Seismic Effectiveness of Tuned Mass Dampers. *ASCE Journal of Structural Division*, **107**, 1465-1484, 1981.

[12] J.K. Sladek, R.E. Klingner, Effect of Tuned-Mass Dampers on Seismic Response. *ASCE Journal of Structural Division*, **109**, 2004-2009, 1983.

[13] A.H. Chowdhury, M.D. Iwuchukwu, J.J. Garske, The Past and Future of Seismic Effectiveness of Tuned Mass Dampers. *Proceedings of the Second International Symposium on Structural Control*, Ontario, Canada, 105-127, 1985.

[14] S.K. Rasouli, M. Yahyai, Control of Response of Structures with Passive and Active Tuned Mass Dampers. *The Structural Design of Tall Buildings*, **11**, 1-14, 2002.

[15] S. Nagarajaiah, E. Sonmez, Structures with Semiactive Variable Stiffness Single/Multiple Tuned Mass Dampers. *Journal of Structural Engineering*, **133:1**, 67-77, 2007.

[16] S. Nagarajaiah, Adaptive Passive, Semiactive, Smart Tuned Mass Dampers: Identification and Control using Empirical Mode Decomposition, Hilbert Transform, and Short-Term Fourier Transform. *Structural Control and Health Monitoring*, **16**, 800-841, 2009.

[17] A.J. Roffel, R. Lourenco, S. Narasimhan, Experimental Studies on an Adaptive Tuned Mass Dampers with Real-time Tuning Capability. *ASCE 19th Analysis & Computation Specialty Conference*, 314-324, 2010.

[18] M. Abdel-Rohman, Optimal Design of Active TMD for Buildings control. *Building and Environment*, **19:3**, 191-195, 1984.

[19] K. Xu, T. Igusa, Dynamic Characteristics of Multiple Substructures with Closely Spaced Frequencies. *Earthquake Engineering and Structural Dynamics*, **21**, 1059-1070, 1992.

[20] A.J. Clark, Multiple Passive Tuned Mass Dampers for Reducing Earthquake Induced Building Motion. *Proceedings of the 9th World Conference on Earthquake Engineering*, Tokyo-Kyoto, Japan, **V**, 779-784, 1988.

[21] K.S. Moon, Vertically Distributed Multiple Tuned Mass Dampers in Tall Buildings: Performance Analysis and Preliminary Design. *The Structural Design of Tall and Special Buildings*, **19**, 347-366, 2010.

[22] K.S. Moon, Integrated Damping Systems for Tall Buildings: Vertically Distributed TMDs. *2010 ASCE Structures Congress*, 3122-3131, 2010.

[23] P.H. Wirsching, G.W. Campbell, Minimal Structural Response under Random Excitations using Vibration Absorber. *Earthquake Engineering and Structural Dynamics*, **2**, 303-312, 1974.

[24] F. Sadek, B. Mohraz, A.W. Taylor, R.M. Chung, R.M., A Method of Estimating the Parameters of Tuned Mass Dampers for Seismic Applications. *Earthquake Engineering and Structural Dynamics*, **26**, 617-635, 1997.

[25] C.L. Lee, Y.T. Chen, L.L. Chung, Y.P. Wang, Optimal Design Theories and Applications of Tuned Mass Dampers. *Engineering Structures*, **28**, 43-53, 2006.

[26] M.N.S Hadi, Y. Arfiadi, Optimum Design of Absorber for MDOF Structures. *Journal of Structural Engineering*, **124: 11**, 1272-1280, 1998.

[27] B.F. Spencer, J. Suhardjo, M.K. Sain, Frequency Domain Optimal Control Strategies for Aseismic Protection. *Journal of Engineering Mechanics*, **120:1**, 135-158, 1994.

[28] T.T. Soong, State of the Art Review – Active Structural Control in Civil Engineering. *Engineering Structures*, **10**, 74-84, 1988.

[29] T.T. Soong, *Active Structural Control: Theory and Practice*. Harlow, England: Longman Scientific & Technical, 1990.

[30] Z. Prucz, T.T. Soong, A.M. Reinhorn, An Analysis of Pulse Control for Simple Mechanical Systems. *ASME Journal of Dynamic* Systems, Measurement and Control, **107**, 123-131, 1985.

[31] C.H. Chuang, D.N. Wu, Optimal Bounded-State Control with Applications to Building Structure. *Optimal Control Applications and Methods*, **17**, 209-230, 1996.

[32] C.H. Chuang, D.N. Wu, Q. Wang, LQR for State-Bounded Structural Control. *ASME Transactions Journal of Dynamic Systems, Measurement and Control*, **118**, 113-119, 1996.

[33] A. Del Grosso, A. Zucchini, Bounded-State Active Control of Structures: a Set-Theoretic Approach. *Smart Materials and Structures*, **4**, A15-A24, 1995.

[34] G. Chen, J. Wu, Optimal Placement of Multiple Tune Mass Dampers for Seismic Structures. *Journal of Structural Engineering*, **127:9**, 1054-1062, 2001.

[35] X. Luo, R. Ma, G. Li, D. Zhao, Parameter Optimization of Multi-Mode Vibration Control System. *International Conference of Measuring Technology and Mechatronics Automation*, IEEE Computer Society, 685-688, 2009.

[36] C.C. Lin, J.F. Wang, C.H. Lien, H.W. Chiang, C.S. Lin, Optimum Design and Experimental Study of Multiple Tuned Mass Dampers with Limited Stroke. *Earthquake Engineering and Structural Dynamics*, **39**, 1631-1651, 2010.

[37] T.S. Fu, E.A. Johnson, Distributed Mass Damper System for Integrating Structural and Environmental Control in Buildings. *Journal of Engineering Mechanics*, in press (doi:10.1061/(ASCE)EM.1943-7889.0000211), 2011 .

[38] F.H. Cilley, The Exact Design of Statically Indeterminate Frameworks, An Exposition of its Possibility but Futility. *ASCE Transactions,* **43**, 353-407, 1990.

[39] R. Levy, On the Optimal Design of Trusses under One Loading Condition. *Quarterly of Applied Mathematics*, **43:2**, 129-134, 1985.

[40] R. Levy, O. Lavan, Fully Stressed Design of Passive Controllers in Framed Structures for Seismic Loadings. *Journal of Structural and Multidisciplinary Optimization*, **32**, 485-498, 2006.

[41] K. Kanai, Semi-Empirical Formula for the Seismic Characteristics of the Ground. *Bulletin of Earthquake Research Institute*, University of Tokyo, **35**, 309-325, 1957.

[42] S. Nagarajaiah, S. Narasimhan, Smart Base-Isolated Benchmark Building. Part II: Phase I Sample Controllers for Linear Isolation Systems. *Structural Control and Health Monitoring,* **12**, 589-604, 2006.

[43] A.K. Agrawal, Z. Xu, W.L. He, Ground Motion Pulse-Based Active Control of a Linear Base-Isolated Benchmark Building. *Structural Control and Health Monitoring*, **13**, 792-808, 2006.

[44] H. Kwakernaak, R. Sivan, *Modern Signals and Systems*. Englewood Cliffs, NJ, Prentice Hall Inc., 1991.

[45] D.E. Newland, *An Introduction to Random Vibrations, Spectral & Wavelet Analysis.* Prentice Hall, Harlow, England, 1993.

[46] W.K. Tso, S. Yao, Seismic Load Distribution in Buildings with Eccentric Setback. *Canadian Journal of Civil Engineering*, **21**, 50-62, 1994.

COMPDYN 2011
3rd ECCOMAS Thematic Conference on
Computational Methods in Structural Dynamics and Earthquake Engineering
M. Papadrakakis, M. Fragiadakis, V. Plevris (eds.)
Corfu, Greece, 26-28 May 2011

NON-LINEAR DYNAMIC BEHAVIOUR OF A BALL VIBRATION ABSORBER

Jiří Náprstek[1], **Cyril Fischer**[1], **Miroš Pirner**[1] **and Ondřej Fischer**[1]

[1]Institute of Theoretical and Applied Mechanics, v.v.i.
Prosecká 76, Prague 9, Czech Republic.
e-mail: {naprstek,fischerc,pirner,fischero}@itam.cas.cz

Keywords: Vibration ball absorber, Dynamic stability, Nonlinear vibration.

Abstract. *Wind excited vibrations of slender structures such as towers, masts or certain types of bridges can be reduced using passive or active vibration absorbers. If there is available only a limited vertical space to install such a device, a ball type of absorber can be recommended. In general, it is a semi-spherical horizontal dish in which a ball of a smaller diameter is rolling. Ratio of both diameters, mass of the rolling ball, quality of contact surfaces and other parameters should correspond with characteristics of the structure. The ball absorber is modeled as a holonomous system. Using Lagrange equations of the second type, governing non-linear differential system is derived. The solution procedure combines analytical and numerical processes. As the main tool for dynamic stability investigation the 2nd Lyapunov method is used. The function and effectiveness of the absorber identical with those installed at the existing TV towers was examined in the laboratory of the Institute of Theoretical and Applied Mechanics. The response spectrum demonstrates a strongly non-linear character of the absorber. The response amplitudes at the top of a TV tower with ball absorber were reduced to* $15 \div 40\%$ *of their original values.*

1 INTRODUCTION

Passive vibration absorbers of various types are very widely used in civil engineering, especially when wind induced vibration should be suppressed. TV towers, masts and other slender structures exposed to wind excitation are usually equipped by such devices. Conventional passive absorbers are of the pendulum type. Although they are very effective and reliable, they have several disadvantages limiting their application. First of all, they have certain requirements to space, particularly in a vertical direction. These requirements cannot be satisfied any time when an absorber should be installed as a supplementary equipment. Also horizontal construction, like foot bridges, cannot accept any absorber of the pendulum type. Another disadvantage represents a need of a regular maintenance.

Both above shortcomings can be avoided using the absorber of ball type. The basic principle comes out of a rolling movement of a metallic ball of a radius r inside of a metallic rubber coated dish of a radius $R > r$. This system is closed in an airtight case. Such a device is practically maintenance free. Its vertical dimension is relatively very small and can be used also in such cases where a pendulum absorber is inapplicable due to lack of vertical space or difficult maintenance. First papers dealing with the theory and practical aspects of ball absorbers have been published during the last decade, see [1] and [2].

Dynamics of the ball absorber is more complicated in comparison with the pendulum one. Its movement can be hardly described in a linear state although for the first view its behavior is similar to the pendulum absorber type. A number of problems are still open being related with movement stability, bifurcations, auto-parametric resonances and at least but not last with dish and ball surface imperfections. This paper presents basic mathematical model in 2D together with its numerical evaluation and practical application as far as to the state of the realization including some results of long-term measurements.

2 MATHEMATICAL MODEL IN TWO DIMENSIONS

The dish is fixed to a vibrating structure. Their dynamic character is represented by a linear SDOF system represented by a mass M. Inside of a dish an internal ball m in a vertical plane is moving, i.e. 2DOF system should be investigated, as it is outlined in the Fig. 1. It follows from geometric relations:

$$R \cdot \varphi = r(\psi + \varphi) \Rightarrow r\psi = \varrho\varphi \tag{1}$$

where $\varrho = R - r$. It holds for vertical, or horizontal components of a displacement and velocity of the internal ball centre:

$$\left.\begin{array}{lrcr} \text{horiz.:} & u + \varrho \cdot \sin\varphi & \Rightarrow & \dot{u} + \varrho\dot{\varphi}\cos\varphi \\ \text{vert.:} & \varrho \cdot \cos\varphi & \Rightarrow & -\varrho\dot{\varphi}\sin\varphi \end{array}\right\} \quad (2)$$

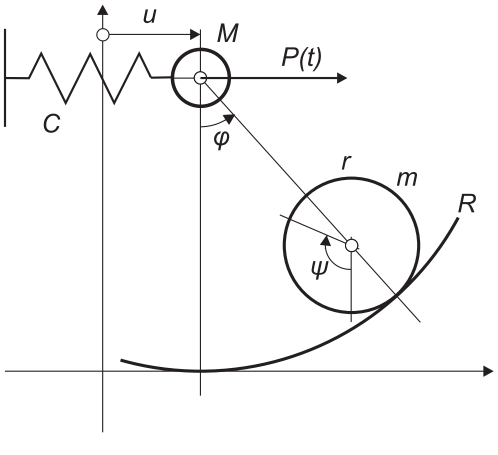

Figure 1: Basic scheme of a system

Kinetic energy of a moving system of balls m, M can be written in a form:

$$T = \frac{1}{2}m[(\dot{u} + \varrho\dot{\varphi}\cos\varphi)^2 + \varrho^2\dot{\varphi}^2\sin^2\varphi] + \frac{1}{2}J\dot{\psi}^2 + \frac{1}{2}M\dot{u}^2 = \frac{1}{2}(m+M)\dot{u}^2 + m\varrho\dot{u}\dot{\varphi}\cos\varphi + \frac{m}{2\kappa}\varrho^2\dot{\varphi}^2 \tag{3}$$

$m/\kappa = m + J/r^2 \;\Rightarrow\; \kappa = 5/7$, while the potential energy is given by an expression:

$$V = mg\varrho(1-\cos\varphi) + \frac{1}{2}Cu^2 \tag{4}$$

The damping should be introduced in a form of a simple Rayleigh function:

$$B = \frac{1}{2}(Mb_u\dot{u}^2 + mb_\varphi\varrho^2\dot{\varphi}^2) \tag{5}$$

m – mass of the ball m;
J – inertia moment of the ball m;
b_u, b_φ – damping coefficients (logarithmic decrements);

Expressions (3), (4), (5) should be put into the Lagrange equations of the second type, see e.g. [3]:

$$\sum_{r=1}^{n}\left\{\frac{d}{dt}\left(\frac{\partial T}{\partial \dot{q}_r}\right) - \frac{\partial T}{\partial q_r} + \frac{\partial V}{\partial q_r} + \frac{\partial B}{\partial \dot{q}_r}\right\}\delta q_r = P_r(t) \tag{6}$$

$$q_1 = u = \zeta\cdot\varrho\;; \quad q_2 = \varphi\;; \quad P_u(t) = p(t)\cdot M\varrho\;; \quad P_\varphi(t) = 0$$

which give the governing equations of the system:

$$\begin{array}{rcll} \ddot{\varphi} + \kappa b_\varphi\dot{\varphi} + \kappa\omega_m^2\sin\varphi + \kappa\ddot{\zeta}\cdot\cos\varphi & = & 0 & (a) \\ \mu\ddot{\varphi}\cos\varphi - \mu\dot{\varphi}^2\sin\varphi + (1+\mu)\ddot{\zeta} + b_u\dot{\zeta} + \omega_M^2\zeta & = & p(t) & (b) \\ \mu = m/M\;; \quad \omega_M^2 = C/M\;; \quad \omega_m^2 = g/\varrho & & & (c) \end{array} \tag{7}$$

Eq. (7) describes 2D movement of a ball absorber under excitation by the force $P(t)$ at any arbitrary deviation amplitudes including incidental transition through a limit cycle towards an open regime.

3 THEORETICAL ANALYSIS OF THE ABSORBER

Theoretical efficiency of the absorber will be assessed using its frequency characteristics for excitation of the mass M by harmonic force $p(t) = p_0\cdot\sin\omega t$ simulating influence of external loading or for kinematic excitation of the same mass M. In the later case the movement of the ball m rolling inside of the dish is fully described by Eq. (7a). Should we solve the deviation $\varphi(t)$, Eq. (7b) can serve us subsequently for an evaluation of the force $p(t)$, which is necessary when the deviation $u(t) = \varrho\cdot\zeta(t)$ should be achieved. To obtain frequency characteristics the harmonic excitation $\zeta(t) = \zeta_o\cos(\omega t)$ should be introduced into Eq. (7), which yields:

$$\begin{array}{rcll} \ddot{\varphi} + \kappa b_\varphi\dot{\varphi} + \kappa\omega_m^2\sin\varphi - \kappa\omega^2\cos\varphi\cdot\zeta_o\cos\omega t & = & 0 & (a) \\ \mu\ddot{\varphi}\cos\varphi - \mu\dot{\varphi}^2\sin\varphi + (-(1+\mu)\omega^2 + \omega_M^2)\zeta_o\cos\omega t - b_u\omega\cdot\zeta_o\sin\omega t & = & p(t) & (b) \end{array} \tag{8}$$

Eq. (8a). corresponds to the equation of a mathematical pendulum excited in a point of suspension. Its effective mass is increased due to a moment of inertia of the ball m by the factor $1/\kappa = 7/5$. Even in practice the movement amplitudes of this ball do not admit to linearize the Eq. (8a). At least a simple Duffing non-linear form should be retained:

$$\ddot{\varphi} + \kappa b_\varphi\dot{\varphi} + \kappa\omega_m^2(\varphi - \frac{1}{6}\varphi^3) - \kappa\omega^2(1 - \frac{1}{2}\varphi^2)\cdot\zeta_o\cos\omega t = 0 \tag{9}$$

Let us concentrate in this paper to the prior case when the excitation of a harmonic force is taken into account. As the resulting system is auto-parametric, the corresponding methods can be applied, see e.g. [4]. Expecting a single mode response, following approximate expressions for excitation and response can be written (c.f. e.g. [5]):

$$\begin{aligned} p(t) = &\ \ p_0 \sin(t\omega) \\ \varphi(t) = &\ \ \alpha \sin(t\omega) + \beta \cos(t\omega) \\ \zeta(t) = &\ \ \gamma \sin(t\omega) + \delta \cos(t\omega)\} \end{aligned} \tag{10}$$

Having four new variables $\alpha = \alpha(t), \beta = \beta(t), \gamma = \gamma(t), \delta = \delta(t)$ instead of two original unknowns $\varphi(t), \zeta(t)$, two additional conditions can be freely chosen:

$$\dot{\alpha} \sin(t\omega) + \dot{\beta} \cos(t\omega) = 0, \qquad \dot{\gamma} \sin(t\omega) + \dot{\delta} \cos(t\omega) = 0 \tag{11}$$

After substitution (10) and (11) into (7) and substituting the sin and cos functions by two terms of Taylor expansion, the harmonic balance procedure gives differential system for unknown amplitudes $\mathbf{X} = (\alpha, \beta, \gamma, \delta)^T$, see e.g. [6] or [7].

$$\mathbf{M}(\mathbf{X})\dot{\mathbf{X}} = \mathbf{F}(\mathbf{X}) \tag{12}$$

The system (12) for amplitudes $\mathbf{X}(t)$ is meaningful if they are functions of a "slow time", in other words if their changes within one period $2\pi/\omega$ are small or vanishing and individual steps of the harmonic balance operation are acceptable. The matrix $\mathbf{M}$ and right hand side vector $\mathbf{F}$ have the following form

$$\mathbf{M} = \begin{pmatrix} 0 & -\omega & -\frac{1}{4}\alpha\beta\kappa\omega & \frac{1}{8}\kappa\omega A_\alpha \\ \omega & 0 & -\frac{1}{8}\kappa\omega A_\beta & \frac{1}{4}\alpha\beta\kappa\omega \\ -\frac{1}{8}\mu\omega A_\beta & \frac{1}{4}\alpha\beta\mu\omega & (\mu+1)\omega & 0 \\ -\frac{1}{4}\alpha\beta\mu\omega & \frac{1}{8}\mu\omega A_\alpha & 0 & -(\mu+1)\omega \end{pmatrix} \tag{13}$$

$$\mathbf{F} = \frac{1}{48} \begin{pmatrix} 6A_0\kappa\left(3\gamma\omega^2 - \alpha\omega_m^2\right) + 12\omega^2\left(\kappa\left(\alpha\beta\delta + \left(8-\beta^2\right)\gamma\right) - 4\alpha\right) - 48\beta\kappa\omega b_\varphi \\ 6A_0\kappa\left(\delta\omega^2 - \beta\omega_m^2\right) + 12\omega^2(\alpha\gamma\kappa + \beta\delta\kappa - 4)\beta + 48\alpha\kappa\omega b_\varphi \\ \omega^2\left(A_0\left(A_0+22\right)\beta\mu - 16(3\delta(\mu+1) - 4\beta\mu)\right) + 48\left(\gamma\omega b_u + \delta\omega_M^2\right) \\ \omega^2\left(A_0\left(A_0+22\right)\alpha\mu - 16(3\gamma(\mu+1) - 4\alpha\mu)\right) - 48\left(\delta\omega b_u - \gamma\omega_M^2 + p_0\right) \end{pmatrix} \tag{14}$$

where

$$A_0 = \alpha^2 + \beta^2 - 8, \ \ A_\alpha = 3\alpha^2 + \beta^2 - 8, \ \ A_\beta = \alpha^2 + 3\beta^2 - 8$$

Determinant of the system matrix $\mathbf{M}$ can be easily evaluated:

$$\det(\mathbf{M}) = -\frac{\omega^4}{4096}\left(64(\kappa-1)\mu + \kappa\mu\Delta_1 R^2 - 64\right)\left(64(\kappa-1)\mu + \kappa\mu\Delta_3 R^2 - 64\right) \tag{15}$$

$$\Delta_1 = \left(R^2 - 16\right), \qquad \Delta_3 = 3\left(3R^2 - 16\right)$$

where $R^2 = R^2(t) = \alpha^2 + \beta^2$ is the amplitude of φ. Polynomial (15) has four roots $R_1^2, \ldots, R_4^2$:

$$3R_1^2 = R_2^2 = 8\left(1 - \frac{\mu+1}{\sqrt{\kappa\mu(\mu+1)}}\right), \ 3R_3^2 = R_4^2 = 8\left(1 + \frac{\mu+1}{\sqrt{\kappa\mu(\mu+1)}}\right) \tag{16}$$

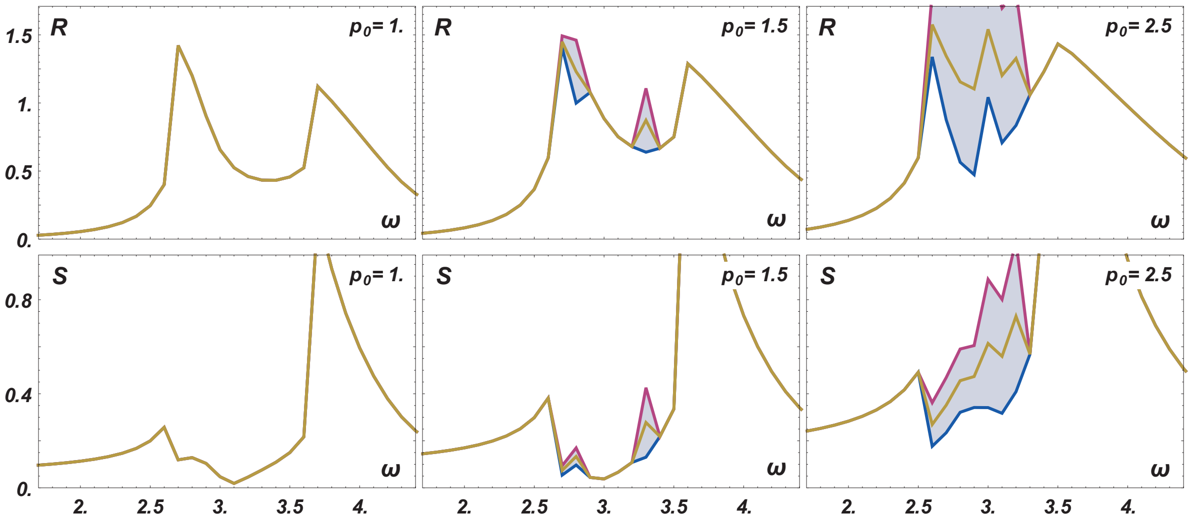

Figure 2: Stabilized numerical solution Eq. (12) . Values of the amplitude $R = \sqrt{\alpha^2 + \beta^2}$ (variable φ, first row) and $S = \sqrt{\gamma^2 + \delta^2}$ (variable ζ, second row) are shown for three selected excitation amplitudes $p_0 = 1, 1.5, 2.5$. The excitation frequency ω is on the horizontal axis. Greyed areas correspond to the frequency region of non-stationary response.

For positive μ and $0 < \kappa < 1$ are the first two roots negative, the last two roots are positive. The negative roots have not any physical meaning, whereas the positive roots form strictly decreasing functions of parameter μ. For $\kappa = 5/7$ (see (3)) it holds:

$$\lim_{\mu\to\infty} R_3^2 = \frac{8}{15}\left(5 + \sqrt{35}\right) \approx 5.82191, \qquad \lim_{\mu\to\infty} R_4^2 = 8\left(1 + \sqrt{\frac{7}{5}}\right) \approx 17.4657 \tag{17}$$

With respect to the meaning of variable φ, even the lower value should not be reached in any real case.

Knowing the exact form and regularity properties of the system matrix $\mathbf{M}$, its inverse could be easily derived and then the normal form of the differential equation (12) can be established. However, as long as the matrix $\mathbf{M}$ is regular, the original right hand side $\mathbf{F}$ can be studied equivalently.

Let us consider stationary response of the system. In this case, the derivatives $\mathrm{d}\mathbf{X}/\mathrm{d}t$ vanish and the right hand side $\mathbf{M}$ has to vanish too. Eq. (12) degenerates to the form of:

$$\mathbf{F}(\mathbf{X}) = 0 \tag{18}$$

Thus, to identify the stationary solutions, the zero solution points of $\mathbf{F}$, depending on the excitation frequency and amplitude, should be traced. In the same time, the signum and the zero points of the Jacobian $\det(\mathbf{JF})$ have to be checked. Negative value of the Jacobian for a particular point indicates that the corresponding solution is stable, whereas when Jacobian vanishes a bifurcation could occur.

The curve $\mathbf{F}(\alpha, \beta, \gamma, \delta, \omega) = 0$, projected into the planes (ω, R) or (ω, S) (for $S^2 = \gamma^2 + \delta^2$), forms the resonance curves known from the analysis of linear oscillators. However, correspondence of this curve to the original equation (7) is limited to the case of stationary response. It is necessary to remind, that limits of stationarity of the response cannot be determined from properties of Eq. (18) itself. The complete Eq. (12) has to be take into account for this purpose.

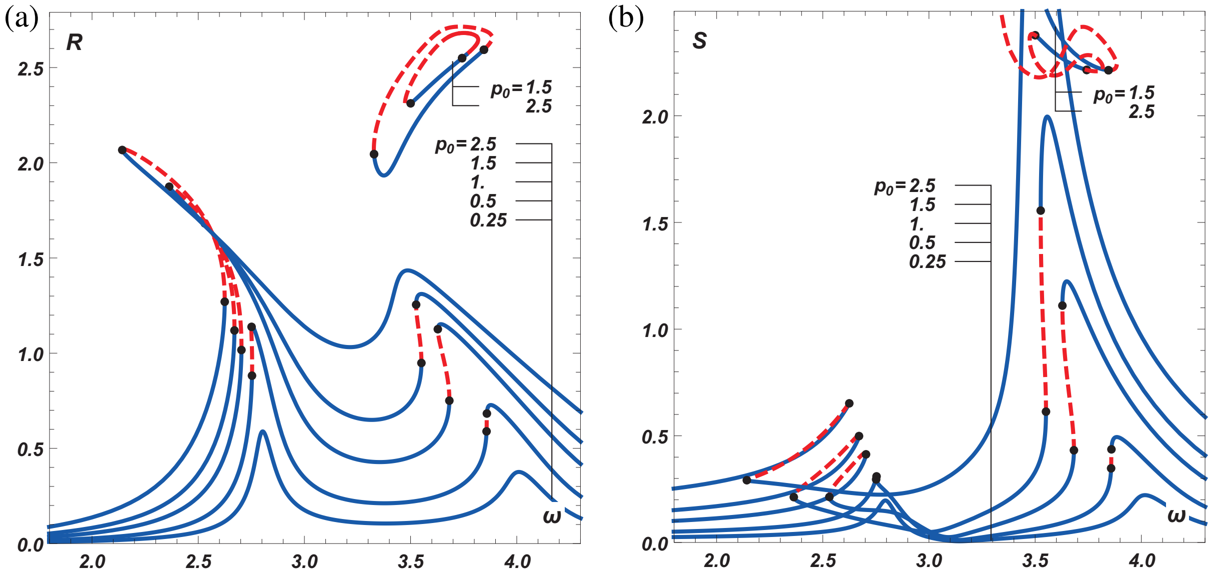

Figure 3: Non-linear resonance curves describing the stationary response of the system computed as zero solutions of Eq. (18) for excitation amplitudes $p_0 = 0.25, 0.5, 1, 1.5, 2.5$. Stable branches are shown as solid blue curves, unstable parts are indicated as the red dashed curves. Amplitudes $R = \sqrt{\alpha^2 + \beta^2}$ are shown in the left part of the figure, amplitudes $S = \sqrt{\gamma^2 + \delta^2}$ are on the right.

4 NUMERICAL ANALYSIS

The aim of this study is a basic engineering approach demonstrating the problem as a whole from the theoretical background until realization in practice. Thus, the numerical analysis has been selected as it leads the most quickly to a basic overview about dynamic properties of a ball absorber.

With respect to actual experiences regarding passive vibration absorbers and some interesting properties of the system (7), following reference input data have been introduced:

$$M = 10.0\ ;\ m = 2.0\ ; \varrho = 0.71\ ;\ b_\varphi = 0.1\ ;\ b_u = 0.2\ ; C = 140\ ;\ p_o = 0.5 \div 2.5 \qquad (19)$$

Several analysis procedures have been performed:
(a) Numerical integration of Eq. (7) shows the response characteristics of the system.
(b) Numerical solution of Eq. (12) can help to decide if the response is stable or unstable.
(c) Analysis of the term $\mathbf{F}(\mathbf{X})$ given by Eq. (18) gives the resonance curve including the unstable branches.

Frequency response characteristics of the Eq. (12) for the particular data is shown in the Fig. 2. This non-linear equation has to be solved numerically. Starting from non-trivial initial conditions solution $\alpha(t), \beta(t), \gamma(t), \delta(t)$ stabilizes after certain time. Mean value and standard deviation of the stabilized amplitudes $R = \sqrt{\alpha^2 + \beta^2}$ (variable φ, first row) and $S = \sqrt{\gamma^2 + \delta^2}$ (variable ζ, second row) depending on the excitation frequency ω are shown in Fig. 2. The variance of the amplitudes is shown as greyed area around the mean curve. Thus, the greyed areas indicate regions where a non-stationary solution should be expected (amplitudes R and S are not constant). It should be emphasized here, that validity of the Eq. (12) in non-stationary case is limited, as it was derived with an assumption of slow time change of the amplitudes.

Utilizing the Eqs. (18) and (14), the non-linear resonance curves describing the stationary response of the system (7) can be obtained. A set of such curves for excitation amplitudes $p_0 = 0.25, 0.5, 1, 1.5, 2.5$ is shown in the Fig. 3. It is obvious for the first view the non-linear

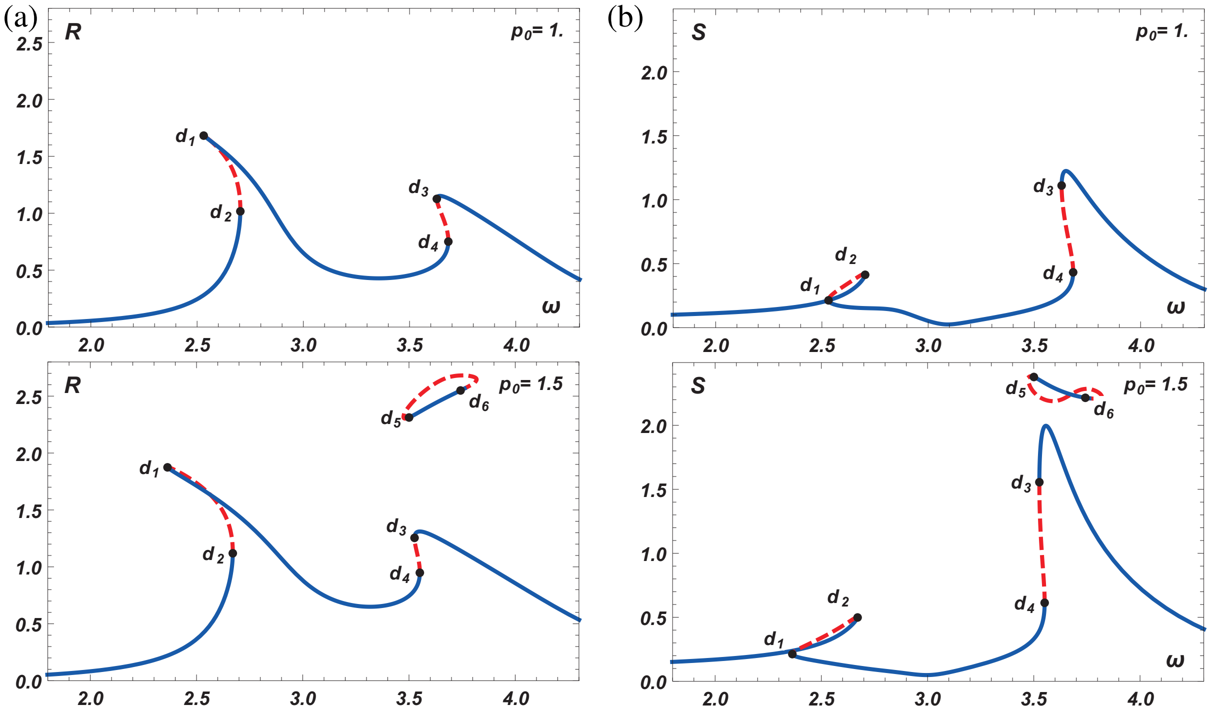

Figure 4: Selected non-linear resonance curve for $p_0 = 1$ and $p_0 = 1.5$. (a) The case for $R = \sqrt{\alpha^2 + \beta^2}$ is on the left, (b) case for $S = \sqrt{\gamma^2 + \delta^2}$ is in the right part of the figure. Points $d_1, ..., d_6$ correspond to zero points of Jacobian $\mathbf{JF}$ and indicate change of stability properties of the curve.

character manifesting oneself by a dependence of a position of extreme points on an amplitude of excitation force. This effect is visible predominantly in a neighbourhood of a conventional ”linear” natural frequency of the absorber although also the second natural frequency corresponding to the original natural frequency of the structure is affected. The resonance curves are typical for a system with ”softening” non-linearities. It turns out that the non-linear element represented by a ball absorber can be more effective when broad band random response should be reduced. Even better results can be expected in case of non-stationary excitation when amplitude spectrum is significantly variable in time. In such a case no doubt non-linear absorber should be preferred, while the linear one works better in cases of strong narrow band excitation mostly of deterministic character.

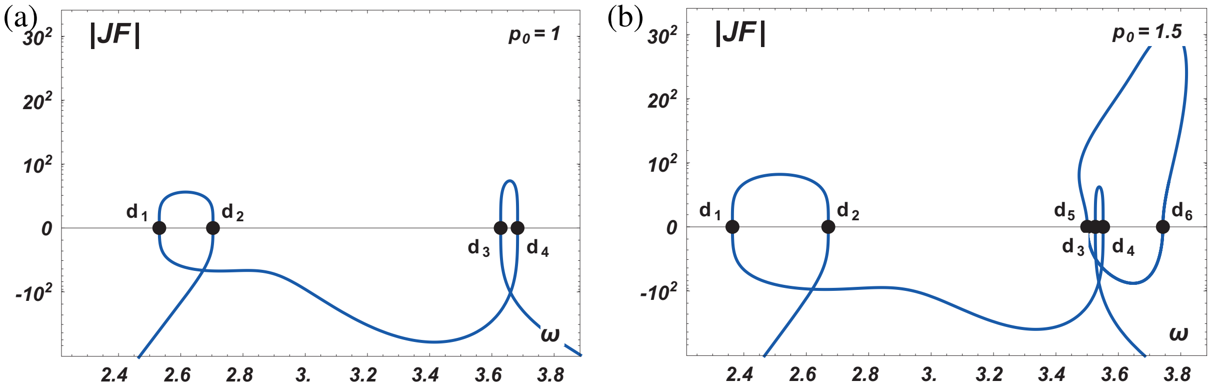

Figure 5: Values of Jacobi determinant $\det(\mathbf{JF})$ corresponding to the stationary resonance curve for $p_0 = 1$ (a) and $p_0 = 1.5$ (b). Negative values indicate stable branches of the resonance curve and vice versa. Closed curve in the right part of fig. (b) correspond to the isolated part of the resonance curve, c.f. second row of Fig. 4.

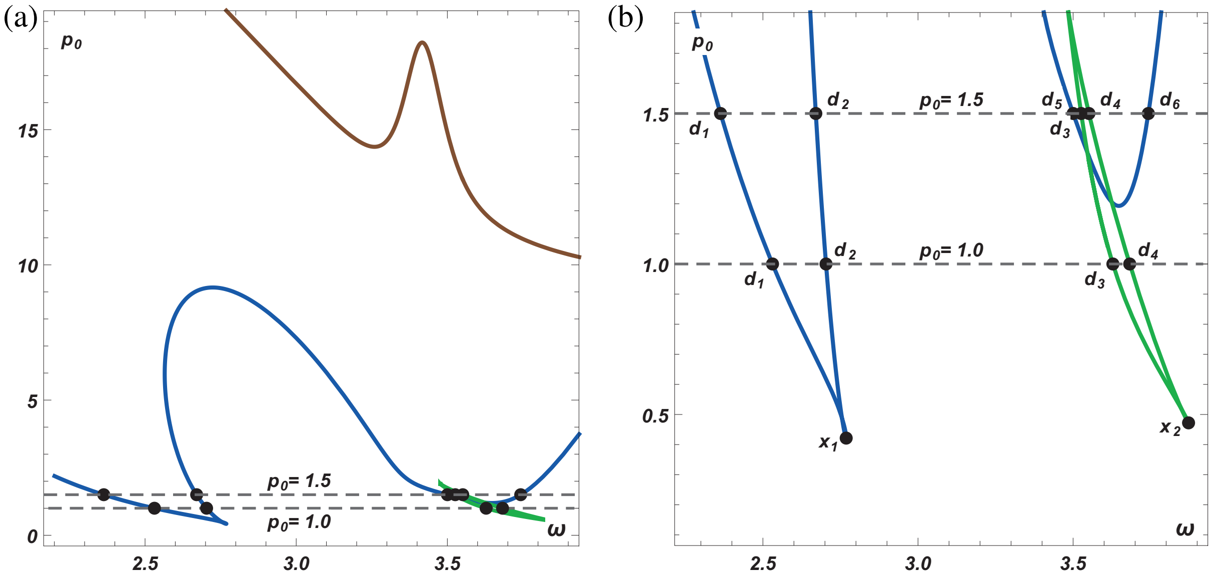

Figure 6: (a) Position of zeroes of the Jacobian in the (ω, p_0) plane. (b) Zoomed view of the interesting area for $p_0 \in (0, 2)$ of the figure (a). Points $d_1, ..., d_6$ are indicated on the level of $p_0 = 1$ and $p_0 = b$, c.f. figures 4 and 5. Points x_1 and x_2 show the critical values of p_0 computed using Eq. (20-21).

Let us comment the isolated curves indicating high amplitudes of response for $p_0 = 2$ and 3. Limit value for R, as it results from the roots of the $\det(\mathbf{M})$ (Eq. (15)) is for data (19) $R < 3.22$. This limit is for the high curves in Fig. 3 still not violated. However, these curves have not any physical meaning in this case: (i) such high amplitudes of R are unrealistic, (ii) Eq. (12) was derived utilizing two terms of Taylor expansions for sin and cos functions and thus assuming only ”small” amplitudes.

Let us study in more detail the stability of one particular curve from Fig. 3, the one for $p_0 = 1$. The both R and S (or φ and ζ respectively) resonance dependencies are shown in the first row of Fig. 4. The solid parts of the curves correspond to the stable solution, whereas the red dashed sections correspond to the unstable solution of Eq. (18). Second row of Fig. 4 shows similar curves for higher excitation amplitude $p_0 = 1$. The islolated part of the response curve is present in this case.

Response of a real system cannot be expected to reach values of a unstable part of resonance curve. The stability of the individual sections of the curves follows from the sign of the Jacobian. Course of this value, corresponding to the curves in Fig. 4 is shown in Fig. 5a for $p_0 = 1$ and in Fig. 5b for $p_0 = 1.5$. Here the points $d_1, ..., d_4$ or $d_1, ..., d_6$ correspond to zero points of Jacobian $\mathbf{JF}$ and indicate change of stability properties of the curve, c.f. all parts of Fig. 4. Closed curve in the right part of Fig.5b correspond to the isolated part of the resonance curve.

Existence of the unstable branches could serve as a characteristic of the system from the engineering point of view. It can be stated, that until the system properties (structural parameters) and the expected excitation amplitude are such that no unstable part of the resonance curve occurs, almost linear and stationary behaviour of the system can be expected. Positions of the dangerous values of the excitation amplitude p_0 depending on the excitation frequency are shown in Fig. 6. The overall situation for the system defined by values (19) is shown in the left part of the figure (a), whereas the part of realistic expected amplitudes is shown in the part (b). Positions of points $d_1, ..., d_4$ corresponding to the excitation amplitude $p_0 = 1$ and $d_1, ..., d_6$ for $p_0 = 1.5$ are shown in the both parts of the Fig. 6.

The curves from the Fig. 6 can be relatively easily computed from the algebraic system

$$\begin{aligned} \det(\mathbf{JF}(\mathbf{X},\omega) &= 0 \\ \mathbf{F}(\mathbf{X},\omega,p_0) &= 0 \end{aligned} \tag{20}$$

Having a solution of (20) for any particular value of ω and p_0 the curves can be considered as parameter dependent $\omega(s)$ and $p_0(s)$ and traced e.g. using the arc-length method. The extremal values are then such points $(\omega(s), p_0(s))$ that

$$\partial_s\omega(s_0) = \partial_s p_0(s_0) = 0 \tag{21}$$

To cover all the extremes, the relation (21) has to be used for all interesting solutions obtained from the system (20). For data defined by (19) are the critical values of the amplitude p_0 shown in the Fig. 6 as points x_1 and x_2. Corresponding critical values of p_0 are $p_{0,x_1} = 0.421$ and $p_{0,x_2} = 0.472$ for $\omega_{x_1} = 2.77$ and $\omega_{x_2} = 3.87$.

For sake of comparison, the non-linear resonance curve for $p_0 = 1$ is shown together with result of the frequency response relation, which has been obtained using numerical integration of the original system (7) for excitation amplitude $p_0 = 1$. As it can be seen from the Fig. 7, the agreement is rather good. Relatively low non-stationarity can be seen as the greyed areas of the curve for ω just above points d_2 and d_4. For other excitation amplitudes the graphs resemble the Fig. 3 and thus are not shown here.

It appears, that increasing the excitation amplitude over a certain limit a domain of unstable chaotic response to deterministic excitation emerges. It does not reveal that this domain increases significantly when random instead of deterministic excitation is applied. Nevertheless a presence of chaotic response domain is for the sake of the structure, as the effective response amplitudes are decreasing under these circumstances due to the rapid increase of the entropy of the response probability density.

On the other hand it is necessary to remain realistic. During testing in laboratory many effects corresponding to various critical and post-critical effects have been observed which are not yet described and quantified theoretically.

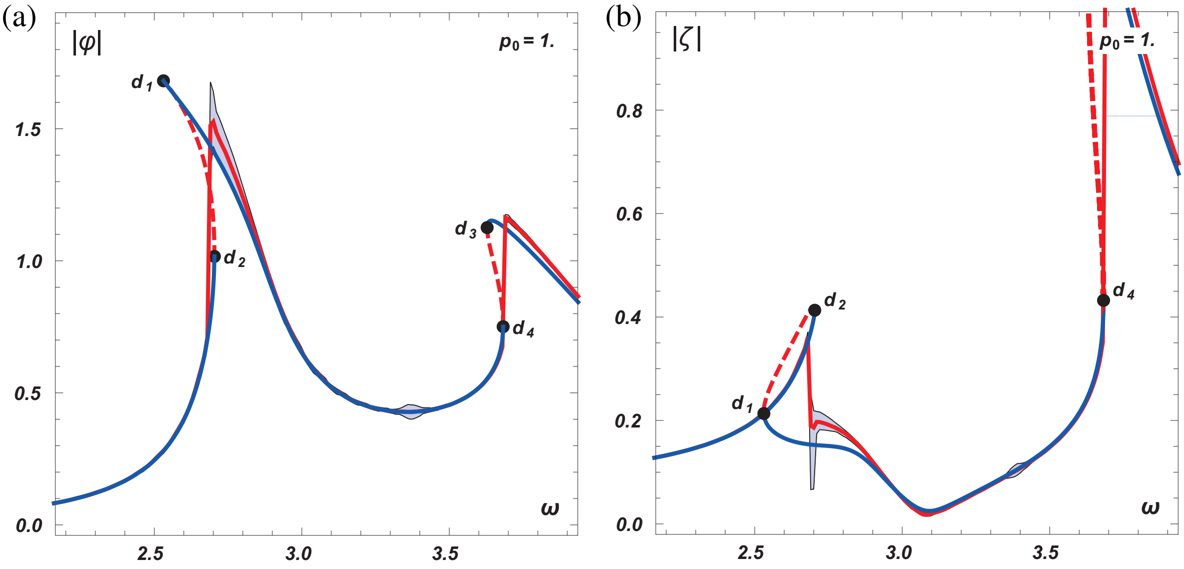

Figure 7: Example of correspondence between stationary resonance curves computed using (14) (blue curves) and response characteristics obtained via numerical integration of Eq. (7) (show in red). Absolute values of the maximum, minimum and mean peak responses of φ are shown on the left and for ζ on the right. Greyed area between minima and maxima curves shows the regions of non-stationary response.

5 APPLICATION OF BASIC THEORY AND EXPERIMENT

First of all two practical knowledge resulting from laboratory experiments and in situ measurements should be mentioned.

As regards the damping, the use of the logarithmic decrement as the measure of damping does not correspond very well to the non-linear nature of the phenomenon. However, a comparison of the behaviour of different physical models which were examined is very useful. Fig. 8 shows the value of the logarithmic decrement b_φ of the model plotted against the absorber - mass ratio μ, see Eq. (7c). The model was put into vibration by initial deflection from its equilibrium position. In this figure diagrams for several values of initial displacement have been plotted. It can be seen that the model without ball ($\mu = 0$) has the damping nearly 0.02 (the point on the horizontal axis $\mu = 0$), while adding ball the damping reaches 0.17-0.25 (the points on the horizontal axis $\mu = 0.2$, curves valid for simple motion) i.e. nearly 8 times more. Similar effect appears also on conventional pendulum absorbers. For details, see [1].

The influence of inclination was also tested on the model, involving the case when the dish of the absorber exercises the rotation about the horizontal axis, coupled with its horizontal translation. The most unfavourable case was tested, i.e. when the frequency of dish inclination approaches the natural frequency of the ball rolling inside the dish (ω_m). No unfavourable increase of the amplitudes of the ball was observed.

The function and effectiveness of vibration ball absorber was described in detail in [2]. Now we shall describe the experiments made in the laboratory. The dish was fastened to a table supported by nine steel balls enabling the excitation of its movement by one, possibly two mutually perpendicular forces. The forces were supplied by one (uniaxial excitation) or two (biaxial excitation) MTS cylinders (jacks) via arms. The ”position control” regime was selected in which the excited movement displacement was constant within a frequency range $\omega \in (4.40 \div 9.40 s^{-1})$. Excitation force amplitude was variable being a function of excitation frequency. Two series of experiments have been done. The first one with the internal side of the dish with rubber covering layer and the second one without this covering.

During the excitation by one harmonic force, the excitation frequency was varied within the range $\omega \in (4.40 \div 9.40 s^{-1})$ in steps of $\Delta\omega = 0.5$, and in the resonance domain in steps of

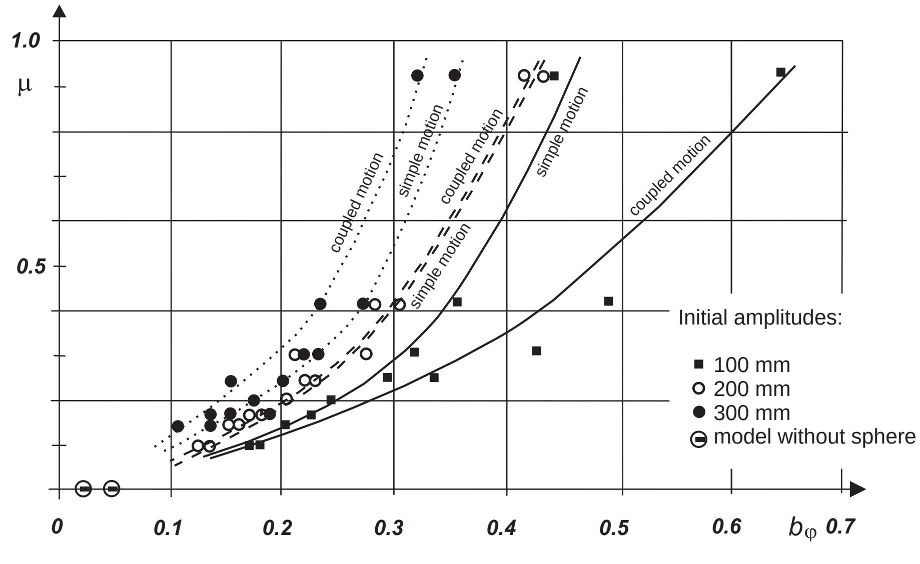

Figure 8: Logarithmic decrement b_φ plotted against the mass-ratio μ for different initial amplitudes

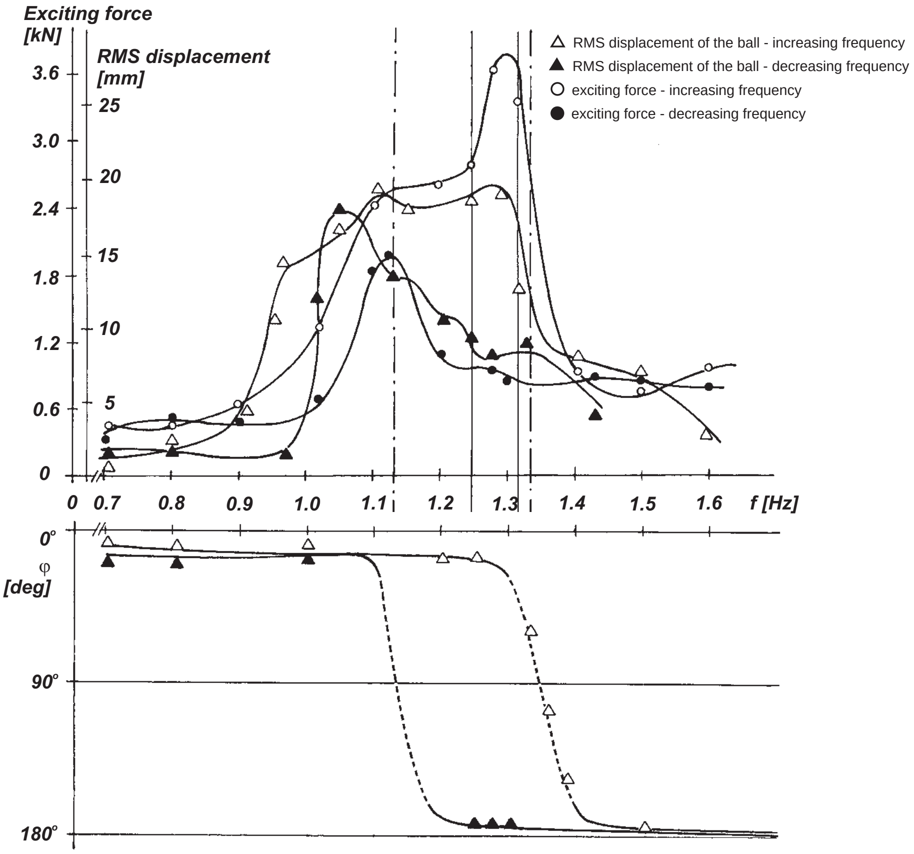

Figure 9: Experimental resonance curves of exciting force and of ball m response

$\Delta\omega = 0.25$. The duration of one step was 30 seconds, the transition from one step to another 15 seconds. Seven amplitudes of table displacements ranging from $1mm$ to $7mm$ were applied. As an example (table displacement amplitude $u_o = 4mm$), Fig. 9 shows the resonance curves of the ball m and dish movement depending on frequency of the excitation force, when the dish is without rubber coating (another plot applies for the state with coating). Fig. 9 shows also the phase shift of the ball and the dish displacement in the excitation direction, once again for the increasing as well as decreasing excitation frequency, see the bottom part in the Fig. 9. Two jumps of phase shift (increase or decrease) within the range $(0 - 2\pi)$ can be observed in a neighborhood of the frequency corresponding with the biggest excitation force values.

The ball, although subjected to uniaxial excitation, performed a movement which comprised also a component deviating from the direction of excitation. This complex 3D ball movement appeared in the dish without rubber lining. The response spectrum contains peaks different from excitation frequency, particularly outside the resonance domain and corresponding rather with multiples of the natural frequency of the linearized system. It is another evidence of significant non-linear character of the system, which manifests this time by super-harmonics of the response.

Relation of logarithmic decrement of the damping and the amplitude $\varphi_o \cdot \varrho$ of the dish is presented in the Fig.10a,b, while the relationship of the natural frequency of the ball (moving on steel and on rubber coating respectively) on the amplitude $\varphi_o \cdot \varrho$ has been outlined in the Fig. 10c.

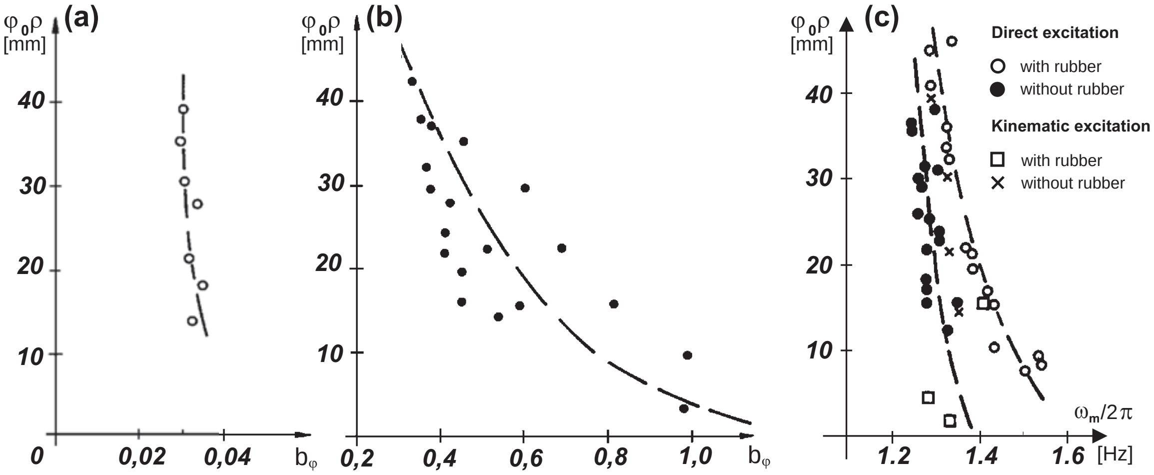

Figure 10: (a) and (b): Relation of logarithmic decrement b_φ and amplitude $\varphi_o \cdot \varrho$ of the ball m,
(c) Relation of natural frequency ω_φ and amplitude $\varphi_o \cdot \varrho$ of the ball m

6 PRACTICAL REALIZATION

The ball absorber was used recently on two TV towers in the Czech Republic to suppress wind excited vibration (Figs 11a, 11b) . Both towers under observation showed two dominant natural frequencies before absorber has been installed $\omega_{(1)} = 7.98s^{-1}, \omega_{(2)} = 10.68s^{-1}$ (nearly identical for both towers). Corresponding natural modes and the amplitude of vibration in wind of mean velocity $8 - 15m/s$ are plotted in the Fig. 11c. The response amplitude at the top of the tower is $10.65mm$, while that at the RC platform level $0.273mm$. Four legs of the steel lattice part were recently strengthened.

The ball absorber before the mounting on the top of the tower presents the photo at the Fig. 12. The most important numerical results demonstrating the absorber efficiency in dimensionless values are outlined in the Tab. 1. The efficiency has been evaluated for the most important

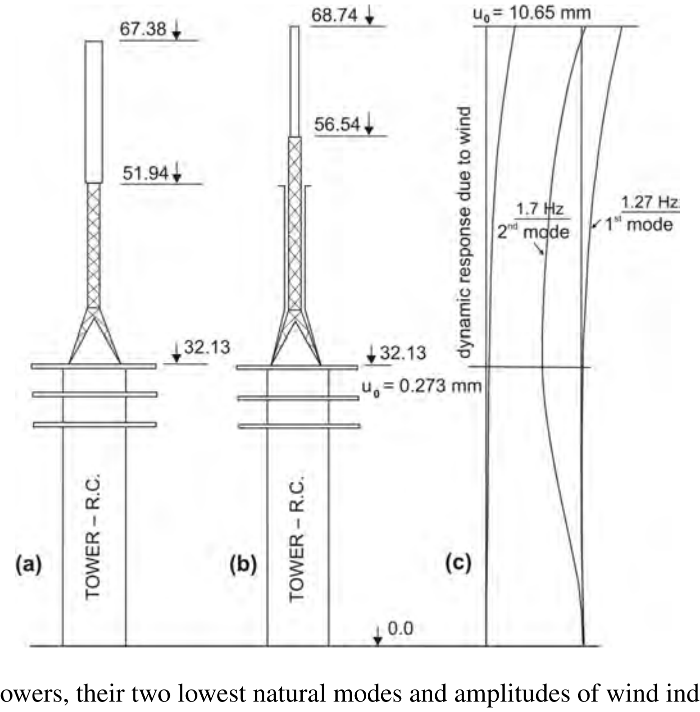

Figure 11: TV towers, their two lowest natural modes and amplitudes of wind induced vibrations

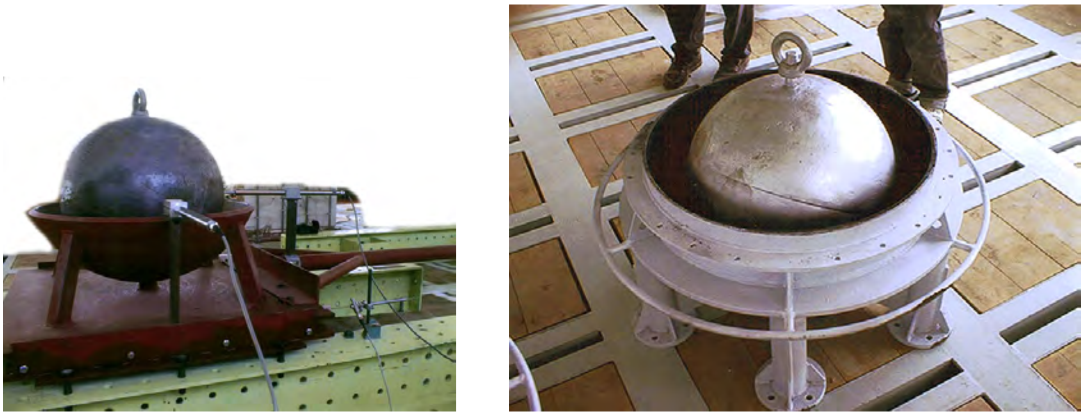

Figure 12: Ball absorber intended for a TV tower

Table 1: Ball absorber efficiency

	without absorber		with absorber		ratio with/without absorber	
Frequency $[Hz/s^{-1}]$	X	Y	X	Y	X	Y
0.90/5.65	0	0.0948	0	0.2031	-	2.14
1.27/7.98	19.064	3.279	0.271	0	0.0142	-
1.70/10.68	0	7.382	0	0.466	-	0.0632

$$X = f \cdot G_x(f)/\sigma_x^2\ ; \quad Y = f \cdot G_y(f)/\sigma_y^2$$

frequencies using records of the long term measurements. For evaluation of absorber efficiency the following parameters has been introduced:

$$\varepsilon_x = \frac{f \cdot G_x(f)}{\sigma_x^2}\ ; \quad \varepsilon_y = \frac{f \cdot G_y(f)}{\sigma_y^2} \qquad (f = \omega/2\pi)$$

$G_x(f)$, or $G_y(f)$ – power spectral density of the tower top displacement in directions x, or y;

σ_x^2, or σ_y^2 – RMS of the tower top displacement in respective directions x, or y;

The scale of the response is presented in a form of a comparison of the values $\varepsilon_x, \varepsilon_y$ valid for the state without absorber (columns 2 and 3) and with absorber (columns 4 and 5), while columns 6 and 7 represent ratio of with/without absorber for respective directions. In particular, both columns 6 and 7 demonstrate high efficiency of the installed vibration absorber of ball type.

7 CONCLUSIONS

The vibration absorber of a ball type has been introduced. The basic Lagrangian analytical theory of non-linear behaviour has been done. Very wide numerical investigation reveals that the non-linear character of this device is an important factor influencing significantly its dynamic properties and practical efficiency. It turns out, that the non-linear character making the form of resonance curves dependent on the excitation amplitude leads to better efficiency in comparison with linear mechanism. For the same reason also chaotic component of the response can occur in certain frequency domains which increases significantly the efficiency of this device due to higher energy loss. Laboratory tests of a ball vibration absorber with the dish without and with rubber coating have demonstrated several aspects of real operation of the damper . They have also proved the effectiveness of the damper and the influence of the rubber coating. With respect to laboratory tests and long-term in situ measurements can be concluded that the ball vibration absorber is a simple nearly maintenance free low cost device with very small vertical dimensions. For these properties it is very convenient for application especially in cases when broad band excitation of random character prevails and when very limited space is available.

The same experiments gave many results demonstrating various processes of stability loss and transition into various post-critical states under certain conditions. These phenomena remained without adequate theoretical explanation and without any assessment of influence onto damping properties. Therefore an intensive theoretical investigation should be provided. Detailed stability analysis is necessary to enable a reliable description of post-critical regimes, bifurcation points and corresponding transition effects involving the damping process. Also random parametric excitation and stochastic imperfection influence should be carefully studied.

ACKNOWLEDGEMENT

The kind support of the Czech Science Foundation project No. 103/09/0094, Grant Agency of the ASCR (projects No. IAA200710902, No. IAA200710805) and of the research plan AV OZ720710524 are gratefully acknowledged.

REFERENCES

[1] Pirner, M., Dissipation of kinetic energy of large-span bridges. *Acta Technica, CSAV*, **39**, 407-418, 1994.

[2] Pirner, M., Fischer, O., The development of a ball vibration absorber for the use on towers. *Jour.Int.Assoc.for Shell and Spatial Structures*, **41**(2), pp 91-99, 2000.

[3] Hamel, G., *Theoretische Mechanik*, Springer, Berlin, 1978.

[4] A. Tondl, A., *Quenching of Self-Excited Vibrations*. Academia, Prague, 1994.

[5] Xu Z., Cheung Y.K. (1994) Averaging method using generalized harmonic functions for strongly non-linear oscillators. *Journal of Sound and Vibration*, **174**(4), 563-576, 1994.

[6] Ren, Y., Beards, C.F., A new receptance-based perturbative multi-harmonic balance method for the calculation of the steady state response of non-linear systems. *Journal of Sound and Vibration*, **172**(5), 593-604, 1994.

[7] Náprstek, J., Fischer, C. (2009) Auto-parametric semi-trivial and post-critical response of a spherical pendulum damper *Computers and Structures*, **87**(19-20), 1204-1215, 2009.

[8] Náprstek, J., Pirner, M., Non-linear behaviour and dynamic stability of a vibration spherical absorber. In: *Proc. 15th ASCE Engineering Mechanics Division Conference* (A. Smyth et al. eds). Columbia Univ., New York, CD ROM, paper #150, 2002.

COMPDYN 2011
III ECCOMAS Thematic Conference on
Computational Methods in Structural Dynamics and Earthquake Engineering
M. Papadrakakis, M. Fragiadakis, V. Plevris (eds.)
Corfu, Greece, 26–28 May 2011

MAXWELL NONLINEAR SLIDER MODEL FOR SEISMIC RESPONSE PREDICTION OF SEMI-ACTIVE CONTROLLED MAGNETO-RHEOLOGICAL DAMPERS

Yunbyeong Chae[1], **James M. Ricles**[1], **and Richard Sause**[1]

[1] Lehigh University, 117 ATLSS Drive, Bethlehem, PA 18015 USA
e-mail: yuc206@lehigh.edu, jmr5@lehigh.edu, rs0c@lehigh.edu

Keywords: Magneto-Rheological (MR) damper, Structural Dynamics, Real-Time Hybrid Simulation, Dynamics of Electromagnetism

Abstract. *Magneto-rheological (MR) dampers are a promising device for seismic hazard mitigation of structural systems due to their ability to adaptively vary their damping characteristics using an appropriate control law. A majority of past research has involved small-scale MR dampers. In order to investigate the dynamic behavior of large-scale MR dampers, characterization tests have been conducted on large-scale MR dampers at the Lehigh NEES equipment site. A new MR damper model, called the Maxwell Nonlinear Slider Model (MNS), was developed using the data from these tests. The new MR damper model can independently describe the pre-yield and post-yield behavior of an MR damper, making it easier to identify the model parameters. The new damper model utilizes the Hershel-Bulkley visco-plasticity formulation to describe the post-yield behavior of the damper, and possesses the characteristics of a non-Newtonian fluid, i.e., shear thinning and thickening behavior of MR fluid. The effects of the dynamics of an MR damper associated with variable current input from a semi-active control law is integrated into the model by a nonlinear differential equation describing the eddy current effect and the magnetization behavior of damper materials. The accuracy of the new MR damper model is compared with other existing models, such as the Bouc-Wen and hyperbolic tangent models. Experimental studies are performed involving real-time hybrid simulations of complete structural systems, where MR dampers in the structure are subjected to realistic demands associated with the design basis and maximum considered earthquakes. Comparisons of the measured hysteretic response of the large-scale dampers in the tests with the predicted behavior by the MNS damper model show that the new model is able to achieve a high degree of accuracy compared to existing MR damper models under earthquake loading conditions. The MNS model enables accurate nonlinear time history analysis for the response prediction of structural systems with MR dampers to be performed.*

1 INTRODUCTION

Magneto-rheological (MR) dampers are devices which can have their characteristics vary by changing the input current to the damper. The MR damper force depends on the yield stress of the MR fluid inside the damper, which is a function of the input current to the damper. When an MR fluid is subjected to a magnetic field, the iron particles in the fluid are aligned and form linear chains parallel to the field, changing the state of the fluid to a semi-solid, which in turn increases the fluid viscosity and restricts the fluid movement through the orifices in an MR damper. This results in changing the yield stress of the MR fluid. MR dampers can be used for seismic hazard mitigation by incorporating these devices into structures. Dyke et al. [1] studied the feasibility of an MR damper as a means of suppressing vibrations in a structure using a clipped optimal controller algorithm. Thereafter, numerous researchers have studied the behavior of structures with passively or semi-actively controlled MR dampers [2-4]. Most of those studies involved small-scale MR dampers.

Large-scale MR dampers have been experimentally investigated by numerous researchers [5-8]. Numerous damper models have been developed to predict the behavior of MR dampers [9-11]. Among these models, the Bouc-Wen model [9] and hyperbolic tangent model [11] are popular, and have been used by Yang et al. [12] and Bass and Christenson [8] to model large-scale MR dampers. Both the Bouc-Wen model and the hyperbolic tangent model can accurately predict the frequency dependent behavior and roll-off phenomenon that occurs at low velocities in MR dampers. However, due to the complexity of these nonlinear models the estimation of the model parameters can be difficult. Moreover, it is difficult for these models to accurately describe the shear thinning or thickening behavior that occurs in the MR fluid [6] during the post yield response when high velocities can develop in the damper. In both the Bouc-Wen and hyperbolic tangent models the post-yield behavior is predominantly described by a linear dashpot; hence, the post-yield behavior of these models is a Newtonian fluid motion where the damper force is proportional to velocity. This can result in an inaccurate prediction of damper force at large amplitudes and high velocities, where under these conditions a non-Newtonian fluid behavior is experimentally observed to occur in the MR fluid.

This paper describes called the newly developed *Maxwell Nonlinear Slider* (MNS) model for modeling large-scale MR dampers. Characterization tests are conducted on a large-scale damper to identify the parameters for the MNS model. Comparisons are subsequently made between the behavior predicted by the MNS model and that measured while subjecting large-scale dampers to varying displacement and current histories. The results are shown to have better accuracy than existing models when applied toward the modeling of large-scale MR dampers.

2 MAXWELL NONLINEAR SLIDER MR DAMPER MODEL

The components of the MNS model are shown in Figure 1. The model has two modes: pre-yield and post-yield. In Figure 1, x is the degree of freedom of the model that is associated with the deformation of the damper, while y and z are variables associated with the pre-yield mode of the model. x and $\dot{x}$ are referred to as the *damper displacement* and the *damper velocity*, respectively, for simplicity. The variables x and y are related through the velocities $\dot{x}$ and $\dot{y}$ as well as the force f in the damper. The variables y and z are related through equilibrium with the damper force f applied to the model. One of the advantages of the MNS model is that the pre- and post-yield modes of response can be separated from each other, enabling the model parameters that describe these two modes of behavior to be independently identified. This makes it easier to identify the parameters for the model compared to other existing MR damper models.

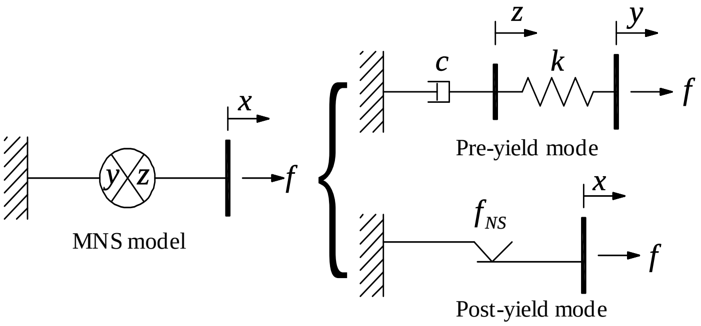

Figure 1. Proposed phenomenological MR damper model: Maxwell Nonlinear Slider (MNS) MR damper model

2.1 Pre-Yield Mode

During the pre-yield mode, the behavior of the damper is described by a Maxwell element, hence, the damper force f is determined by solving the following differential equation

$$f = k(y - z) = c\dot{z} \tag{1}$$

When the damper is in pre-yield mode, $\dot{y}$ is equal to the damper velocity $\dot{x}$. The initial value of y is set to be equal to x; thus Eq. 1 can be solved in terms of z for a given x and the damper force is then determined. The values of c and k for the Maxwell element are obtained from the force-velocity relationship observed in damper characterization tests, selecting two appropriate points on the hysteretic response curve and then applying visco-elasticity theory. Assuming the Maxwell element is subjected to a harmonic motion with an amplitude of u_0 and circular excitation frequency of ω, the coefficients c and k are calculated as follows:

$$c = \frac{1}{u_0\omega}\frac{f_0^2 + f_m^2}{f_m}, \qquad k = \frac{1}{u_0}\frac{f_0^2 + f_m^2}{f_0} \tag{2}$$

where f_0 and f_m are the damper force when the damper velocity is zero and a maximum value, respectively.

2.2 Post-Yield Mode

The post-yield behavior of the MNS model is described by the nonlinear slider which a frictional force defined by a set of post-yield curves that are pre-defined trajectories of the damper force on the force-velocity plane. In the post-yield mode the force is based on considering the damper velocity, i.e., $\dot{x}$. Figure 2 shows the post-yield curves for the MNS model, where a curve is defined for both a positive and negative force and referred to as the ***positive*** and ***negative force post-yield curves***, respectively. Each post-yield curve is based on the Herschel-Bulkley model [13] and a linear line that is tangential to this curve at the velocity of $\dot{x}_t^+$ or $\dot{x}_t^-$, as shown in Figure 2. Since the Herschel-Bulkley model is incorporated into the MNS model, the property of a non-Newtonian fluid can be easily described by the MNS model. The mathematical representation of the positive force post-yield curve for the MNS model is given by

$$f_{py}^{+}(\dot{x}) = \begin{cases} a + b|\dot{x}|^{n} & \text{if } \dot{x} \geq \dot{x}_t^{+} \\ a_t(\dot{x} - \dot{x}_t^{+}) + f_t^{+} & \text{if } \dot{x} < \dot{x}_t^{+} \end{cases} \tag{3}$$

where a, b, n, and $\dot{x}_t^{+}$ are parameters to be identified from damper characterization tests; and $a_t = bn|\dot{x}_t^{+}|^{n-1}$and $f_t^{+} = a + b|\dot{x}_t^{+}|^{n}$. The negative force post-yield curve, $f_{py}^{-}(\dot{x})$, can be defined in a similar manner as $f_{py}^{+}(\dot{x})$ using the appropriate values for the negative force post-yield curve parameters. The simplicity of the Herschel-Bulkley model enables values for the model parameters to be readily obtained from characterization tests since the post-yield behavior is independent of the identification of the Maxwell element parameters c and k that describe the pre-yield mode of the MNS model.

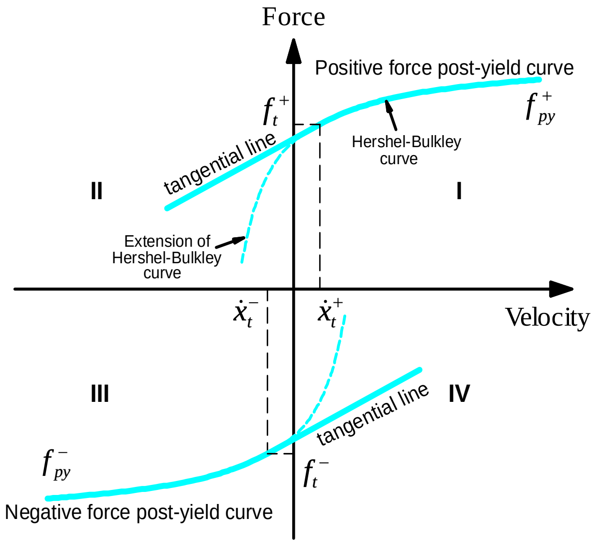

Figure 2. Pre-defined post-yield curves for MNS model

The post-yield curve is composed of two phases in the MNS model, namely, an *increasing phase* and *decreasing phase*. If the magnitude of the damper force is increasing during the post-yield mode, the damper is in the increasing phase. On the contrary, the damper is in the decreasing phase if the magnitude of the damper force is decreasing. Experimental data from the characterization tests show the trajectory of damper forces can be slightly different during the increasing and decreasing phase [14]. To account for this behavior, an inertial term is added to the post-yield damper force for the MNS model, whereby the force f in the damper is:

$$f = \begin{cases} f_{py}^{+}(\dot{x}) & \ddot{x} \geq 0; \text{increasing phase} \\ f_{py}^{+}(\dot{x}) + m_0\ddot{x} & \ddot{x} < 0; \text{decreasing phase} \end{cases} \tag{4}$$

where m_0 is a mass to account for the force discrepancy. When the damper force is on the negative force post-yield curve, the damper force is

$$f = \begin{cases} f_{py}^{-}(\dot{x}) & \ddot{x} < 0; \text{increasing phase} \\ f_{py}^{-}(\dot{x}) + m_0\ddot{x} & \ddot{x} \geq 0; \text{decreasing phase} \end{cases} \tag{5}$$

The value for the parameter m_0 can be obtained by equating the product of the measured acceleration and m_0 to the discrepancy between the post-yield mode measured damper force and the predicted force by the MNS model without the inertia term, where the measured quantities are from damper characterization tests.

2.3 Criteria for Mode Change

When the damper force f from the Maxwell element reaches the post-yield curve, the nonlinear slider is activated and the mode changes from the pre-yield to the post-yield state. Mathematically, this condition is expressed as

$$|f| = \left|f_{py}(\dot{x})\right| \tag{6}$$

Equation 6 implies that the generated damper force is always bounded by the positive and negative force post-yield curves in the MNS model. The transition from the post-yield mode to the pre-yield mode occurs when the following velocity equation is satisfied during the post-yield mode

$$\dot{x} = \dot{y} \tag{7}$$

where, $\dot{y}$ is calculated from

$$\dot{y} = \frac{\dot{f}}{k} + \frac{f}{c} \tag{8}$$

Equation (8) is obtained by solving for y from Eq. (1) and then taking the time derivative of y. The value for $\dot{y}$ is then calculated by substituting the damper force f and the time derivative of the damper force, $\dot{f}$, from the post-yield mode into Eq. (8). To obtain a smooth transition from the post-yield mode to the pre-yield mode, during the post-yield mode the pre-yield mode variables y and z of the model are continuously updated by solving Eq. (1) for z and y using the force f developed in the damper during the post-yield mode.

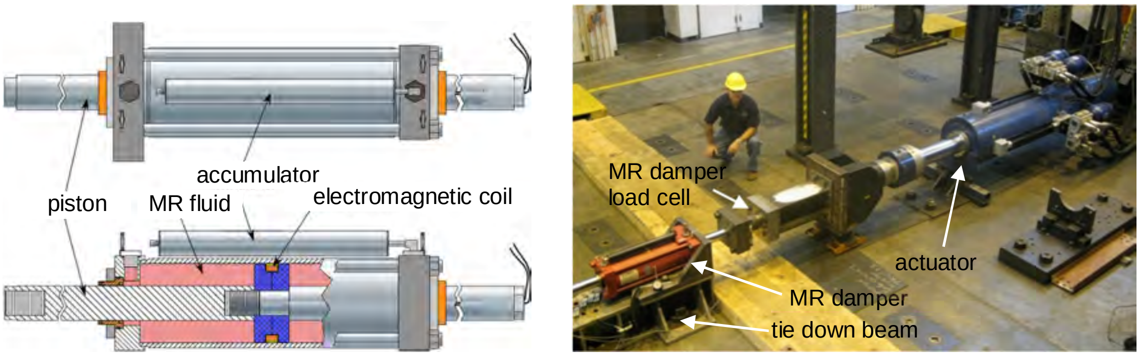

(a) (b)

Figure 3. (a) Schematic of a large-scale MR damper by Lord Corporation (after Bass and Christenson 2007); (b) experimental setup for the characterization test of MR damper

3 DAMPER CHARACTERIZATION TESTS

Characterization tests were performed at the Lehigh NEES equipment site on a large-scale MR damper. The damper is manufactured by Lord Corporation and is similar to the MR dampers used by Bass and Christenson [8] in their research. The damper is shown schematically in Figure 3(a). The length and available stroke of the damper are 1.5m and ±279mm, respectively. The electromagnetic coil consists of 368 turns of 18 AWG magnet wire with an annular gap of 1.0 mm between the piston head and the inside diameter of the cylinder. The damper is filled with approximately 19 liters of MRF-132DG type MR fluid manufactured by Lord Corporation.

The experimental setup for the characterization test consists of primary two parts: i) a hydraulic actuator to control the movement of the MR damper; and ii) electrical hardware to supply an appropriate current to the damper for the control of the damper force. Figure 3(b) shows the test setup for the characterization test of the MR damper. The MR damper is connected to the hydraulic actuator through a stiff horizontal steel section. This is done in order to extend the arm of the actuator piston to accommodate the spacing of anchor locations for threaded rods that secure the damper and actuator to the laboratory strong floor. The maximum force capacity of the actuator is 1,700kN; with the actuator having the ability to generate approximately 500kN of force at a piston velocity of 1.0m/sec. A 534kN load cell is installed between the horizontal steel section and the damper piston to directly measure the force developed in the damper.

The current going into the damper is controlled by a pulse width modulation (PWM) type current driver manufactured by Advanced Motion Controls (30A8). The PWM servo-amplifier can supply the current to the electrical circuit up to 30A by driving the DC motor at a high rate of switching frequency (22kHz). To reduce the noise from the electrical power source, a Schaffner line filter is deployed in front of the DC power supply that provides 72 DC voltage to the PWM servo-amplifier. The command current is transferred to the PWM servo-amplifier through voltage signals from -10V to +10V to produce the desired current utilizing pulse width modulation. The current going into the MR damper is monitored by a current probe (CR Magnetics current transformer).

Table 1. Identified parameters for MNS damper model

Current, I (Amps)	c (kN s/m)	k (kN/m)	Positve force post-yield curve				Negative force post-yield curve				m_0 (kN s^2/m)
			a (kN)	b (kN s/m)	n	$\dot{x}_t^+$ (m/s)	a (kN)	b (kN s/m)	n	$\dot{x}_t^-$ (m/s)	
0.0	10,000	100,000	7.5	243.5	1.62	0.010	-7.3	-235.6	1.60	-0.010	0.50
0.5	11,000	100,000	53.1	162.5	0.85	0.010	-53.1	-162.5	0.85	-0.010	0.50
1.0	12,000	118,000	91.5	122.5	0.52	0.010	-96.0	-134.9	0.60	-0.010	1.60
1.5	12,000	118,000	126.7	152.1	0.58	0.010	-126.7	-152.1	0.58	-0.010	1.50
2.0	11,491	110,030	148.5	166.3	0.66	0.003	-146.8	-182.1	0.71	-0.003	1.05
2.5	12,278	112,890	138.5	161.8	0.46	0.017	-133.5	-171.8	0.46	-0.012	1.04

The parameters for the MNS damper model are identified in such a manner that a minimal error is achieved between the damper force predicted by the model and that measured during the characterization tests. In this paper the particle swarm optimization (PSO) algorithm by Kennedy and Eberhart [15] is used for the identification of the damper model parameters. The normalized root mean square (RMS) error by Gavin [11] is used as the objective function that is minimized to establish the values of the model parameters. The parameters are obtained for a range of selected currents from various characterization tests involving sinusoidal displacement histories. For each current level, four different sinusoidal tests with the amplitude of 25.4mm and frequencies of 0.5Hz, 1.0Hz, 2.0Hz, and 3.0Hz were conducted for the identification of the model parameters. Table 1 shows the identified parameters of the MNS model for the various current levels. To compare the performance of the MNS model with the Bouc-Wen and hyperbolic tangent models the parameters for these other models are also identified using the PSO applied to the same experimental data set.

4 EXPERIMENTAL EVALUATION OF MNS MODEL UNDER CONSTANT CURRENT

The MNS model was evaluated by comparing the damper response predicted by the model with that recorded in tests where the displacement history was based on selected Gaussian white noise (see Figure 4(a) and Table 2). The comparisons are shown in Figure 4(b), (c) and (d), where the damper force time history, damper force-displacement, and damper force-velocity are given, respectively. The current input, I, for the damper is constant and equal to 2.5A for the results shown in Figure 4. Good agreement between the MNS model and the test results is evident in Figure 4.

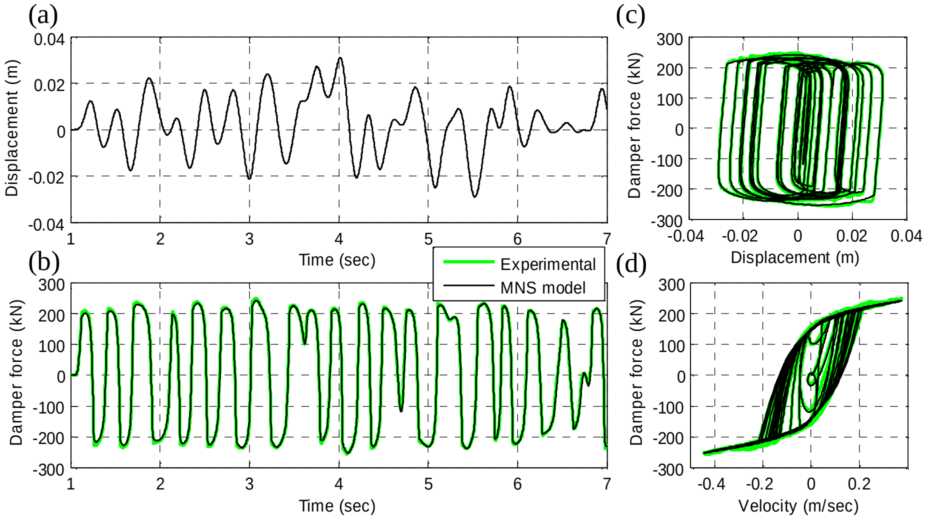

Figure 4. Comparison of predicted damper force by MNS model with experimental data (I=2.5A): (a) time history of input displacement; (b) time history of damper force; (c) force-displacement relationship; (d) force-velocity relationship.

Table 2. Comparison of normalized RMS error of MR damper models with band-limited Gaussian white noise

Damper Current I (Amps)	Gaussian white noise (displacement input)			Normalized RMS error		
	Max. disp. (m)	Max. velocity (m/s)	Bandwidth (Hz)	Bouc-Wen model	Hyperbolic tangent model	MNS model
0.0	0.050	0.452	2.0	0.1291	0.0992	0.0688
2.5	0.030	0.445	4.0	0.0420	0.0409	0.0370

Table 2 presents a comparison of the normalized RMS error [11] for the MNS, Bouc-Wen, and hyperbolic-tangent damper models for two cases involving a constant current input of I=0.0A and 2.5A. For the cases with I=0.0A and 2.5A the displacement history is based on Gaussian white noise with a bandwidth of 2Hz and 4Hz, respectively. As can be seen in Table 2, the MNS model shows better agreement with the test data than with the Bouc-Wen and hyperbolic-tangent models.

5 DYNAMICS OF MR DAMPER ASSOCIATED WITH VARIABLE CURRENT

5.1 Dynamics of Current Driver (PWM Servo-Amplifier)

Due to the inductance of the electro-magnetic coil that generates the magnetic field in the damper, the current within the electro-magnetic circuit changes slowly if a voltage driven power supply is used [12]. To overcome this problem, a PWM servo-amplifier with a PI controller is often used. Yang presented a governing differential equation for the electro-magnetic circuit based on the duty cycle of a PWM servo-amplifier and PI controller [6]. In this paper the same governing equation is used, from which a transfer function ***G(s)*** between the current output to the damper and current command signal for the current driver is derived:

$$G(s) = \frac{235s + 44522}{s^2 + 302s + 44522} \tag{9}$$

5.2 Dynamics of Electromagnetism

As noted previously, numerous semi-active control algorithms have been developed for MR dampers. These control laws involve supplying a variable current command to the damper. To understand the dynamics of an MR damper, it is necessary to investigate the dynamic behavior of the magnetic field in the damper associated with variable current. When the current changes inside the electromagnetic coil, a magnetic flux that is proportional to the current in the coil is generated. The magnetic flux induces eddy currents in the material around the coil (e.g., the piston head, cylinder housing), which opposes the magnetic flux generated by the coil according to Lenz's law. This results in the development of a time delay in the MR damper force under a variable current input [16]. The hysteresis of the magnetization of the MR damper fluid makes it difficult to predict the damper force, for the piston head and cylinder housing around the coil can develop a residual magnetic field after the applied magnetic field has been removed. This nonlinear hysteretic behavior not only can affect the induction of eddy currents, but it can also disturb the formation of the total magnetic field and the damper force. Therefore, the use of a first order filter [9] for the description of the dynamics of a MR damper may not be sufficient to explain the complex behavior of an MR damper under a variable current input. To obtain a better prediction of the damper force under variable current, this paper proposes a model based on the following nonlinear differential equation to relate the coil current to an equivalent static current:

$$\dot{I}_{eq} = \alpha\left(\dot{I}_r\right)\left(I - I_{eq}\right) \tag{10}$$

The function $\alpha()$ is determined from the Eqs. (11) and (12):

$$\alpha\left(\dot{I}_r\right) = \begin{cases} a^+\dot{I}_r + \alpha_1 & \text{if } \dot{I}_r \geq 0 \\ a^-\dot{I}_r + \alpha_1 & \text{if } \dot{I}_r < 0 \end{cases} \tag{11}$$

$$\dot{I}_r = \alpha_0(I - I_r) \tag{12}$$

where, α_0, α_1, a^+ and a^- are constants which are obtained by utilizing nonlinear optimization theory to minimize the error between the predicted and experimental response of the damper force. I is the current in the coil, which is generated by the current driver. I_{eq} is an equivalent static current that can generate the same magnetic flux as the resultant magnetic flux at time t created by I, the eddy currents, residual magnetic fields, and other phenomena that affect the formation of the magnetic flux.

The MNS model with the Eqs. (9) and (10) to account for the effect of variable current input is referred to as the *variable current MNS model*. Figure 5 shows the block diagram for the variable current MNS model. With I_{eq} obtained from the solution to Eq. (10), the parameter sets in Table 1 can be interpolated or directly used under variable current inputs to specify the damper parameters for the model which enables the damper force to be calculated using the MNS model.

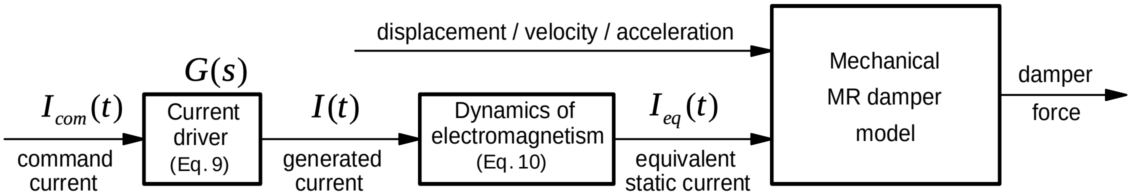

Figure 5. Block diagram for MR damper model under variable current

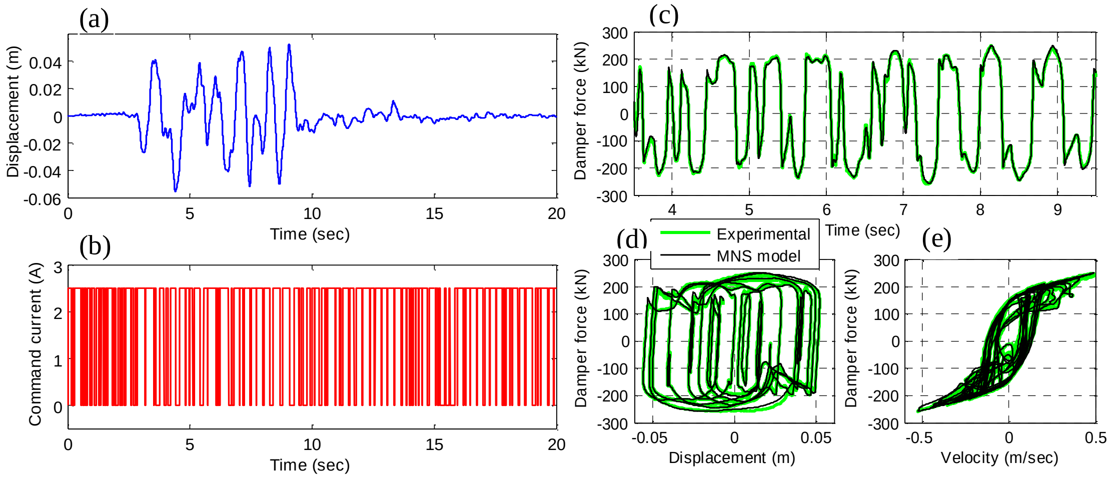

Figure 6. Response of large-scale MR damper under variable current: (a) time history of input displacement; (b) time history of input current; (c) time history of damper force; (d) force-displacement relationship; (e) force-velocity relationship.

To assess the model, tests with variable displacement and current were performed, where the variation in current simulated that from the clipped optimal controller algorithm with a maximum current of 2.5A. Figure 6 (a) and (b) show the pre-defined displacement and current time histories for the MR damper. The experimental response and MNS model prediction of the MR damper are shown in Fig. 6 (c) through (e). The values for the parameters for Eqs. 10, 11, and 12 are: $\alpha_0 = 24.96$, $\alpha_1 = 3.57$, $a^+ = 0.31$, $a^- = -0.30$. As can be observed in Figure 6, the MNS model can accurately predict the response of the MR damper under variable current.

In order to further validate the variable current MNS model, a real-time hybrid simulation of a 3-story building with the large-scale MR damper was conducted [17]. The experimental response of the damper was compared with the results from a numerical simulation involving the variable current MNS model. The building was subjected to the 1989 Loma Prieta earthquake ground motion scaled to the design basis earthquake (DBE) having about a 475 year return period [18]. The sliding mode control (SMC) [19] was used for the semi-active control of the MR damper. As can be observed in Figure 7, the damper force predicted by the variable current MNS model in the numerical simulation (denoted as *Numerical* in Figure 7) matches well with the measured experimental damper force obtained from the real-time hybrid simulation (denoted as *RTHS* in Figure 7); the command current from the numerical simulation also shows good agreement with that from the real-time hybrid simulation. The results shown in Figure 6 and 7 demonstrate the robustness and accuracy of the variable current MNS MR damper model.

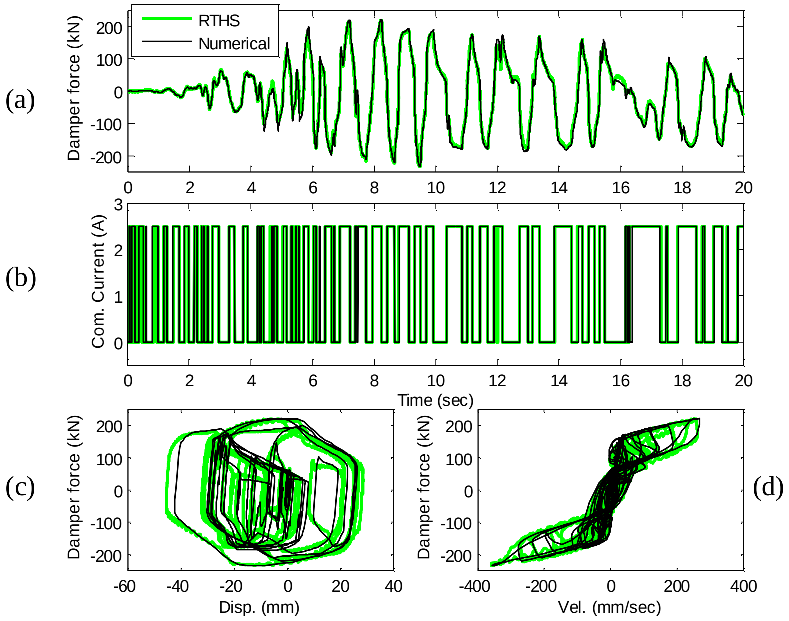

Figure 7 Comparison of damper response under the 1989 Loma Prieta earthquake ground motion with sliding mode controller: (a) time history of damper force; (b) time history of command current; (c) force-displacement relationship; (d) force-velocity relationship

6 CONCLUSIONS

A newly developed formulation called the variable current Maxwell Nonlinear Slider model was presented for the prediction of the dynamic behavior of large-scale MR dampers under variable current. In the Maxwell Nonlinear Slider model, the pre-yield and post-yield behaviors of an MR damper are independently described. This simplifies the identification of the model parameters from characterization tests. The Maxwell Nonlinear Slider model utilizes the Hershel-Bulkley model to describe the post-yield behavior, thereby enabling the property of a non-Newtonian fluid to be readily included in the Maxwell Nonlinear Slider model and the effects of shear thinning and thickening behavior of the MR fluid to be accounted for. The solution to a nonlinear differential equation is used to account for the time lag response of the MR damper force that occurs under with a variable current input. Predictions made by the Maxwell Nonlinear Slider model under constant and variable current inputs show good agreement with experimental results. Further studies of the dynamics of MR dampers needs to be conducted in order to evaluate and calibrate the formulation over a wider range of variable current inputs, as well as frequencies and amplitudes in the displacement history than those presented in this paper.

ACKNOWLEDGEMENTS

This paper is based upon work supported by grants from the Pennsylvania Department of Community and Economic Development through the Pennsylvania Infrastructure Technology Alliance, and by the National Science Foundation under Grant No. CMS-1011534 within the George E. Brown, Jr. Network for Earthquake Engineering Simulation Research (NEESR) program, Award No. CMS-0612661, and Award No. CMS-0402490 NEES Consortium Operation.. The MR fluid dampers were provided by Dr. Richard Christenson at the University of Connecticut. The authors appreciate his support.

REFERENCES

[1] Dyke, S.J., Spencer Jr., B.F., Sain, M.K. and Carlson, J.D., Modeling and control of magneto-rheological dampers for seismic response reduction, *Smart Materials and Structures*, **5**, 565-575, 1996.

[2] Jansen, L.M. and Dyke, S.J., Semi-active control strategies for MR dampers: comparison study, *Journal of Engineering Mechanics*, **126**(8), 795-803, 2000.

[3] Schurter, K. C. and Roschke, P. N., Neuro-fuzzy control of structures using acceleration feedback, *Smart Materials and Structures*, **10**, 770-779, 2001.

[4] Ribakov, Y. and Gluck, J., Selective controlled base isolation system with magneto-rheological dampers, *Earthquake Engineering and Structural Dynamics*, **31**, 1301-1324, 2002.

[5] Carlson, J. D., and Spencer, B. F., Jr., Magneto-rheological fluid dampers for semi-active seismic control, *Proc., 3rd Int. Conf. on Motion and Vibration Control*, **3**, Chiba, Japan, 35–40, 1996.

[6] Yang, G., Large-Scale Magneto-rheological fluid damper for vibration mitigation: modeling, testing and control, *Ph.D. Dissertation*, Department of Civil Engineering and Geological Sciences, University of Notre Dame, Notre Dame, Indiana, 2001.

[7] Sodeyama, H., Suzuki, K. and Sunakoda, K., Development of large capacity semi-active seismic damper using magneto-rheological fluid, *Journal of Pressure Vessel Technology*, **126**, 105-109, 2004.

[8] Bass, B. J., and Christenson, R. E., System identification of a 200 kN, magneto-rheological fluid damper for structural control in large-scale smart structures, *Proc., Amer. Control Conf.*, NY, 2007.

[9] Spencer, B. F., Dyke, S. J., Sain, M. K. and Carlson, J. D., Phenomenological model for magneto-rheological dampers, *Journal of Engineering Mechanics*, **123**(3), 230-238, 1997.

[10] Butz, T and Von Stryk, O., Modelling and simulation of electro- and magneto-rheological fluid dampers, *ZAMM - Journal of Applied Mathematics and Mechanics*, **82**, 3-20, 2002.

[11] Gavin, H.P., Multi-duct ER dampers, *Journal of Intelligent Material Sys and Structures*, **12**, 353-366, 2001.

[12] Yang, G., Spencer Jr., B. F., Carlson, J. D., Sain, M. K., Large-scale MR fluid dampers: modeling and dynamic performance considerations, *Engineering Structures*, **24**, 309-323, 2002.

[13] Herschel, W.H. and Bulkley, R., Konsistenzmessungen von Gummi-Benzollösungen, Kolloid Zeitschrift, **39**, 291–300, 1926.

[14] Chae, Y., Seismic hazard mitigation of building structures using magneto-rheological dampers, *Ph.D. Dissertation*, Lehigh University, Bethlehem, PA, 2011.

[15] Kennedy, J. and Eberhart, R. C., Particle swarm optimization, *IEEE Int. Conf. on Neural. Networks (Perth)* , **4**, 1942–1949, 1995.

[16] Takesue, N., Furusho, J. and Kiyota, Y., Fast response MR-fluid actuator, *JSME International Journal Series C,* **47**(3), 783-791, 2004.

[17] Chae, Y., Ricles, J.M., Sause, R., Dong, B., Chen, C., Christenson, R., Dyke, S.J., Agrawal, A., and Spencer, B.F., Experimental studies on control strategies for steel frames with MR dampers for earthquake hazard reduction, *5th World Conference on Structural Control and Monitoring*, Japan, 2010.

[18] Federal Emergency Management Agency *NEHRP Recommended Provisions for Seismic Regulations for New Buildings and Other Structures, Part 1- Provisions and Part 2 – Commentary,* Report No. FEMA-450, Washington, D.C., 2003.

[19] Utkin, V.I. *Sliding Modes in Control Optimization* Springer-Verlag, New York, 1992.

COMPDYN 2011
III ECCOMAS Thematic Conference on
Computational Methods in Structural Dynamics and Earthquake Engineering
M. Papadrakakis, M. Fragiadakis, V. Plevris (eds.)
Corfu, Greece, 25–28 May 2011

A TWO STAGE APPROACH FOR THE SEISMIC ANALYSIS OF BASE-ISOLATED STRUCTURES

G. Muscolino[1], **A. Palmeri**[2], **and C. Versaci**[1]
[1] Department of Civil Engineering, University of Messina
C.da Di Dio, Villaggio S. Agata, 98166 Messina, Italy
{muscolin, claudia.versaci}@ingegneria.unime.it

[2] Department of Civil and Building Engineering, Loughborough University
Sir Frank Gibb Building, Loughborough LE11 3TU, United Kingdom
a.palmeri@lboro.ac.uk

Abstract. *Base Isolation System (BIS) is a very effective strategy for reducing the effects of earthquakes on building structures. The classical Response Spectrum Method (RSM) continues to be the most common approach for the design of base-isolated buildings. This paper offers a new strategy of seismic analysis and design for such structures in conjunction with the RSM. The main advantages of the proposed approach are: first, reduced computational effort with respect to an exact complex-valued modal analysis, which is obtained through a two-stage transformation of coordinates, both involving real-valued eigenproblems; second, accurate representation of the damping, which is pursued by consistently defining different viscous damping ratios for the modes of vibration of the coupled dynamic system made of superstructure and BIS; third, ease of use, since a convenient reinterpretation of the combination coefficients leads to a novel Damping-Adjusted Combination (DAC) rule, in which just a single response spectrum is required for the reference value of the viscous damping ratio.*

Keywords: BIS (Base Isolation System); CQC (Complete Quadratic Combination) rule; DCF (Damping Correction Factor); random vibration theory; RSM (Response Spectrum Method).

1 INTRODUCTION

Different types of Base Isolation System (BIS) have been developed over the years in the attempt of mitigating seismic effects on building structures, lowering structural and non-structural damages and reducing the risk for the occupants [1,2].

The main result of a BIS is to increase the fundamental period of vibration of the isolated structure, which is permitted by large deformations at the isolation level. This effect is contrasted either by providing isolators with high inherent damping, or by coupling them with additional fluid and/or metallic dampers. This combination of large period of vibration and high damping capabilities tremendously reduces the earthquake-induced forces in the superstructure, which in turn can be designed to remain in the elastic range, even in the case of strong ground motions. As a consequence, less energy is dissipated in the superstructure. It follows that, from a mathematical point of view, a seismically isolated structure is a non-classically damped system [3-6], with most of the energy being dissipated at the isolators' level, although this point is often overlooked in practice [7-10].

The classical Response Spectrum Method (RSM) continues to be the most common approach for the design of base-isolated buildings. This technique requires the following steps: (i) solve an eigenproblem for the undamped structure, i.e. frequencies, participation factors and deformed shapes for the first modes of vibration; (ii) select the appropriate viscous damping ratio for each mode; (iii) take from the pertinent design spectrum the maximum value for each modal response; (iv) combine the modal maxima to get the sought design response of the structure.

The last two steps introduce the main sources of inaccuracy in the practical application of the RSM. Indeed, most seismic codes furnish the response spectrum just for a reference value of the viscous damping ratio, which is typically $\zeta_0 = 0.05$, and thus quite different from the usual values assumed for BIS and superstructure. This circumstance motivates the use of a Damping Correction Factor (DCF), for which various expressions have been proposed [11-13]. It has been recently shown that such expressions can be quite different from each other [14], and they are not effective for seismically isolated structure [15,16].

In parallel, the combination rules available in the literature are not fully adequate. The so-called CQC (Complete Quadratic Combination) rule [17] is generally adopted by practitioners. This formula combines the ordinates of the given response spectrum by using the cross-correlation coefficients of the modal oscillators [18,19]. It has been recognized that the conventional expressions of CQC are unsuitable for analyzing non-classically damped structures, and hence alternative techniques have been proposed [20-22]. Unfortunately, the additional computational burden associated with the solution of complex-valued eigenproblems continues to limit the practical applications of these methods.

It follows that a new combination rule would be required for the analysis and design of base-isolated structures. To be effective in practice, and overcome the main shortcomings of existing techniques, an improved RSM should embed the following features: first, reduced computational effort; second, accurate representation of the damping; third, ease of use, requiring a single response spectrum for the reference value of the viscous damping ratio. These practical needs constitute the motivation of the present study.

The proposed DAC rule, which is alternative to the classical CQC rule and incorporates the features highlighted above, can be viewed as a special variant of the method originally developed by Falsone and Muscolino [23,24] for non-classically damped structures, and recently improved by Muscolino and Palmeri [25] for the seismic analysis of primary structures with light secondary appendages. The numerical results included in this contribution demonstrate the accuracy of the proposed method of analysis.

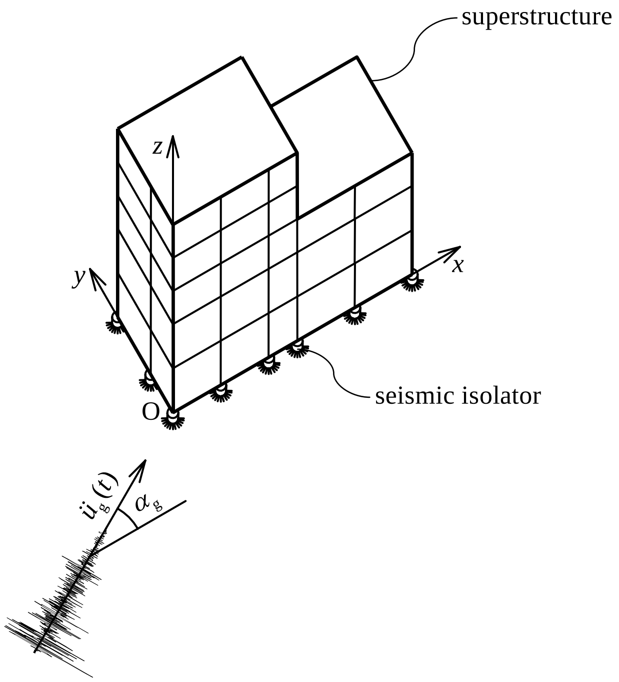

Figure 1. 3D sketch of a base-isolated building subjected to ground acceleration $\ddot{u}_{\mathrm{g}}(t)$ with angle of attack α_{g}.

2 EQUATIONS OF MOTION OF COUPLED BIS-SUPERSTUCTURE

Let us consider the n-floor base-isolated building depicted in Figure 1, subjected to the horizontal ground acceleration $\ddot{u}_{\mathrm{g}}(t)$ in the generic line of action defined by the angle α_{g}. Assuming diaphragmatic constraint for slabs and masses lumped at the storey's level, the building possesses $3(n+1)$ Degrees of Freedom (DoFs). The isolation level has three DoFs, listed in the array $\mathbf{u}_{\mathrm{b}}(t) = \left\{ u_{\mathrm{x}}^{(\mathrm{b})}(t) \quad u_{\mathrm{y}}^{(\mathrm{b})}(t) \quad u_{\varphi}^{(\mathrm{b})}(t) \right\}^{\mathrm{T}}$, the superscript T denoting the transpose operator; these DoFs can be respectively defined as horizontal displacements along x and y directions of the origin O and rotation of the base about the vertical axis z, all taken with respect to the ground. The superstructure has $3n$ DoFs, listed in the n-dimensional block array $\mathbf{u}_{\mathrm{s}}^{\mathrm{T}}(t) = \left\{ \mathbf{u}_{1}^{\mathrm{T}}(t) \mid \mathbf{u}_{2}^{\mathrm{T}}(t) \mid \cdots \mid \mathbf{u}_{n}^{\mathrm{T}}(t) \right\}^{\mathrm{T}}$, where the i-th three-dimensional array $\mathbf{u}_{i}(t) = \left\{ u_{\mathrm{x}}^{(i)}(t) \quad u_{\mathrm{y}}^{(i)}(t) \quad u_{\varphi}^{(i)}(t) \right\}^{\mathrm{T}}$ collects origin's displacements and storey's rotation for the i-th level, with $i = 1, \cdots, n$, all taken with respect to the isolation level. Since BIS (Base Isolation System) and superstructure are characterised by a high contrast of mechanical properties, the substructure approach is resorted to. Accordingly, BIS and superstructure are handled as two interconnected substructures, and the equations ruling the seismic motion of the coupled dynamic system can be posed in the form:

$$\hat{\mathbf{M}} \cdot \ddot{\mathbf{u}}(t) + \hat{\mathbf{C}} \cdot \dot{\mathbf{u}}(t) + \hat{\mathbf{K}} \cdot \mathbf{u}(t) = \hat{\mathbf{G}} \cdot \boldsymbol{\tau}_{\mathrm{b}}(\alpha_{\mathrm{g}})\, \ddot{u}_{\mathrm{g}}(t)\,, \tag{1}$$

where the dot symbol $(\cdot)$ means matrix product; $\mathbf{u}(t) = \left\{ \mathbf{u}_{\mathrm{s}}^{\mathrm{T}}(t) \mid \mathbf{u}_{\mathrm{b}}^{\mathrm{T}}(t) \right\}^{\mathrm{T}}$ is the super-array of the DoFs of the base-isolated building; $\boldsymbol{\tau}_{\mathrm{b}}(\alpha_{\mathrm{g}}) = \left\{ \cos(\alpha_{\mathrm{g}}) \quad \sin(\alpha_{\mathrm{g}}) \quad 0 \right\}^{\mathrm{T}}$ is the three-dimensional array listing the influence coefficients of the ground shaking; the matrices of mass $\hat{\mathbf{M}}$, viscous damping $\hat{\mathbf{C}}$ and elastic stiffness $\hat{\mathbf{K}}$ are those of the whole structure, and can be assembled from the corresponding matrices of superstructure and isolation level:

$$\hat{\mathbf{M}} = \left[\begin{array}{c|c} \mathbf{M}_{\mathrm{s}} & \mathbf{M}_{\mathrm{s}} \cdot \mathbf{R}_{\mathrm{sb}} \\ \hline \mathbf{R}_{\mathrm{sb}}^{\mathrm{T}} \cdot \mathbf{M}_{\mathrm{s}} & \mathbf{m}_{\mathrm{r}} \end{array}\right]; \quad \hat{\mathbf{C}} = \left[\begin{array}{c|c} \mathbf{C}_{\mathrm{s}} & \mathbf{O}_{3n,3} \\ \hline \mathbf{O}_{3,3n} & \mathbf{c}_{\mathrm{b}} \end{array}\right]; \quad \hat{\mathbf{K}} = \left[\begin{array}{c|c} \mathbf{K}_{\mathrm{s}} & \mathbf{O}_{3n,3} \\ \hline \mathbf{O}_{3,3n} & \mathbf{k}_{\mathrm{b}} \end{array}\right]; \quad \hat{\mathbf{G}} = -\left[\begin{array}{c} \mathbf{M}_{\mathrm{s}}\,\mathbf{R}_{\mathrm{sb}} \\ \hdashline \mathbf{m}_{\mathrm{r}} \end{array}\right], \tag{2}$$

in which the symbol $\mathbf{O}_{p,q}$ stands for a zero matrix having p rows and q columns, while $\mathbf{R}_{\mathrm{sb}} = \left[\mathbf{I}_3 \mid \mathbf{I}_3 \mid \cdots \mid \mathbf{I}_3\right]^{\mathrm{T}}$ is a Boolean matrix of dimensions $3n \times 3$, the symbol $\mathbf{I}_p$ being the identity matrix of size p ; $\mathbf{M}_{\mathrm{s}}$, $\mathbf{C}_{\mathrm{s}}$ and $\mathbf{K}_{\mathrm{s}}$ in Eqs. (2) are the $(3n)$-dimensional symmetric matrices of mass, damping and stiffness of the superstructure, assumed to be fixed to its own base; $\mathbf{c}_{\mathrm{b}}$ and $\mathbf{k}_{\mathrm{b}}$ in Eqs. (2) are the three-dimensional symmetric matrices collecting the effective values of viscous damping and elastic stiffness for the BIS, respectively; finally, $\mathbf{m}_{\mathrm{r}}$ is the three-dimensional symmetric mass matrix of the whole structure assumed as a rigid body moving on top of the seismic isolators:

$$\mathbf{m}_{\mathrm{r}} = \mathbf{m}_{\mathrm{b}} + \mathbf{R}_{\mathrm{sb}}^{\mathrm{T}} \cdot \mathbf{M}_{\mathrm{s}} \cdot \mathbf{R}_{\mathrm{sb}} \,, \tag{3}$$

in which $\mathbf{m}_{\mathrm{b}}$ is the three-dimensional mass matrix of the isolated base. One can easily verify that even though the mass, damping and stiffness matrices of two substructures separately taken satisfy the well-known condition due to Caughey-O'Kelly [26] the coupled BIS-superstructure assembly is in general a non-classically damped dynamic system.

3 TWO-STAGE TRANSFORMATION OF COORDINATES FOR THE MODAL EQUATIONS OF MOTION

The main difficulty in the direct use of Eq. (1) lies in the non classical nature of the energy dissipation for the whole structural system, which does not allow diagonalising together the matrices of mass, damping and stiffness in the real space. To overcome this drawback, a convenient two-stage transformation of coordinates is introduced in this section.

3.1 Stage 1

Two independent transformations of coordinates are initially operated on the base-isolated buildings, i.e. on superstructure and BIS, which can be written in compact form:

$$\left\{\begin{array}{c} \mathbf{u}_{\mathrm{s}}(t) \\ \hdashline \mathbf{u}_{\mathrm{b}}(t) \end{array}\right\} = \left[\begin{array}{c;c} \boldsymbol{\Phi}_{\mathrm{s}} & \mathbf{O}_{3n,3} \\ \hdashline \mathbf{O}_{3,m} & \boldsymbol{\Phi}_{\mathrm{b}} \end{array}\right] \cdot \left\{\begin{array}{c} \mathbf{q}_{\mathrm{s}}(t) \\ \hdashline \mathbf{q}_{\mathrm{b}}(t) \end{array}\right\}, \tag{4}$$

where the arrays $\mathbf{q}_{\mathrm{s}}(t) = \left\{q_{\mathrm{s},1}(t) \;\; \cdots \;\; q_{\mathrm{s},m}(t)\right\}^{\mathrm{T}}$ and $\mathbf{q}_{\mathrm{b}}(t) = \left\{q_{\mathrm{b},1}(t) \;\; q_{\mathrm{b},2}(t) \;\; q_{\mathrm{b},3}(t)\right\}^{\mathrm{T}}$ list the first $m \le 3n$ modal coordinates of the base-fixed superstructure and the three modal coordinates of the BIS, respectively; and where the $3n \times m$ tall matrix $\boldsymbol{\Phi}_{\mathrm{s}}$ and the 3×3 square matrix $\boldsymbol{\Phi}_{\mathrm{b}}$ are the associated real-valued modal matrices of the two subsystems, which can be evaluated along with the corresponding spectral matrices $\boldsymbol{\Omega}_{\mathrm{s}} = \operatorname{diag}\left\{\omega_{\mathrm{s},1}, \cdots, \omega_{\mathrm{s},m}\right\}$ and $\boldsymbol{\Omega}_{\mathrm{b}} = \operatorname{diag}\left\{\omega_{\mathrm{b},1}, \omega_{\mathrm{b},2}, \omega_{\mathrm{b},3}\right\}$ as solution of two decoupled real-valued eigenproblems:

$$\mathbf{K}_{\mathrm{s}}^{-1} \cdot \mathbf{M}_{\mathrm{s}} \cdot \boldsymbol{\Phi}_{\mathrm{s}} = \boldsymbol{\Phi}_{\mathrm{s}} \cdot \boldsymbol{\Omega}_{\mathrm{s}}^{-2} \,; \quad \mathbf{k}_{\mathrm{b}}^{-1} \cdot \mathbf{m}_{\mathrm{r}} \cdot \boldsymbol{\Phi}_{\mathrm{b}} = \boldsymbol{\Phi}_{\mathrm{b}} \cdot \boldsymbol{\Omega}_{\mathrm{b}}^{-2} \,, \tag{5}$$

with the respective ortho-normalization conditions

$$\boldsymbol{\Phi}_{\mathrm{s}}^{\mathrm{T}} \cdot \mathbf{M}_{\mathrm{s}} \cdot \boldsymbol{\Phi}_{\mathrm{s}} = \mathbf{I}_m \,; \quad \boldsymbol{\Phi}_{\mathrm{b}}^{\mathrm{T}} \cdot \mathbf{m}_{\mathrm{r}} \cdot \boldsymbol{\Phi}_{\mathrm{b}} = \mathbf{I}_3 \,. \tag{6}$$

Upon substitution of Eqs. (4) into Eq.(1), after some simple algebra, the equations of motion take the form:

$$\bar{\mathbf{m}} \cdot \ddot{\mathbf{q}}(t) + \bar{\mathbf{c}} \cdot \dot{\mathbf{q}}(t) + \bar{\mathbf{k}} \cdot \mathbf{q}(t) = \bar{\mathbf{g}}(\alpha_\mathrm{g})\,\ddot{u}_g(t)\,, \tag{7}$$

in which $\mathbf{q}(t) = \left\{ \mathbf{q}_\mathrm{s}^\mathrm{T}(t) \;\vdots\; \mathbf{q}_\mathrm{b}^\mathrm{T}(t) \right\}^\mathrm{T}$ is $(m+3)$-dimensional array collecting the modal coordinates of both superstructure and BIS. The other quantities appearing in Eq. (7) are so defined:

$$\begin{gathered}
\bar{\mathbf{m}} = \left[\begin{array}{c:c} \mathbf{I}_m & \mathbf{\Phi}_\mathrm{s}^\mathrm{T} \cdot \mathbf{M}_\mathrm{s} \cdot \mathbf{R}_\mathrm{sb} \cdot \mathbf{\Phi}_\mathrm{b} \\ \hdashline \mathbf{\Phi}_\mathrm{b}^\mathrm{T} \cdot \mathbf{R}_\mathrm{sb}^\mathrm{T} \cdot \mathbf{M}_\mathrm{s} \cdot \mathbf{\Phi}_\mathrm{s} & \mathbf{I}_3 \end{array} \right]; \\
\bar{\mathbf{c}} = \left[\begin{array}{c:c} 2\zeta_\mathrm{s}\mathbf{\Omega}_\mathrm{s} & \mathbf{O}_{m,3} \\ \hdashline \mathbf{O}_{3,m} & 2\zeta_\mathrm{b}\mathbf{\Omega}_\mathrm{b} \end{array} \right]; \quad \bar{\mathbf{k}} = \left[\begin{array}{c:c} \mathbf{\Omega}_\mathrm{s}^2 & \mathbf{O}_{m,3} \\ \hdashline \mathbf{O}_{3,m} & \mathbf{\Omega}_\mathrm{b}^2 \end{array} \right]; \quad \bar{\mathbf{g}}(\alpha_\mathrm{g}) = -\left[\begin{array}{c} \mathbf{\Phi}_\mathrm{s}^\mathrm{T}\,\mathbf{M}_\mathrm{s}\,\mathbf{R}_\mathrm{sb} \\ \hdashline \mathbf{\Phi}_\mathrm{b}^\mathrm{T}\,\mathbf{m}_\mathrm{r} \end{array} \right] \cdot \boldsymbol{\tau}_\mathrm{b}(\alpha_\mathrm{g})\,.
\end{gathered} \tag{8}$$

3.2 Stage 2

The reduced matrices $\bar{\mathbf{m}}$, $\bar{\mathbf{c}}$ and $\bar{\mathbf{k}}$ specified in Eq.(8), as the corresponding matrices of Eqs.(1) , do not satisfy the Caughey-O'Kelly condition [26]. Hence, the practical difficulty persists that the conventional formulation of the RSM is not applicable. This drawback can be overcome by using a further transformation of coordinates:

$$\mathbf{q}(t) = \tilde{\mathbf{\Phi}} \cdot \tilde{\boldsymbol{\gamma}}(\alpha_\mathrm{g}) \cdot \tilde{\boldsymbol{\theta}}(t)\,, \tag{9}$$

where $\tilde{\boldsymbol{\theta}}(t) = \left\{ \tilde{\theta}_1(t) \;\; \cdots \;\; \tilde{\theta}_{m+3}(t) \right\}^\mathrm{T}$ is the $(m+3)$-dimensional array of the modal coordinates obtained by combining superstructure and BIS; the square transformation matrix $\tilde{\mathbf{\Phi}}$, along with the diagonal spectral matrix $\tilde{\mathbf{\Omega}} = \operatorname{diag}\left\{ \tilde{\omega}_1, \cdots, \tilde{\omega}_{m+3} \right\}$, can be obtained as solution of the new real-valued eigenproblem:

$$\bar{\mathbf{k}}^{-1} \cdot \bar{\mathbf{m}} \cdot \tilde{\mathbf{\Phi}} = \tilde{\mathbf{\Phi}} \cdot \tilde{\mathbf{\Omega}}^{-2}\,, \tag{10}$$

with the ortho-normalization condition $\tilde{\mathbf{\Phi}}^\mathrm{T} \cdot \bar{\mathbf{m}} \cdot \tilde{\mathbf{\Phi}} = \mathbf{I}_{m+3}$; $\tilde{\boldsymbol{\gamma}}(\alpha_\mathrm{g}) = \operatorname{diag}\left\{ \tilde{\gamma}_1(\alpha_\mathrm{g}), \cdots, \tilde{\gamma}_{m+3}(\alpha_\mathrm{g}) \right\}$ is the diagonal matrix collecting the $(m+3)$ modal participation coefficients $\tilde{\gamma}_i(\alpha_\mathrm{g}) = \left\{ \tilde{\mathbf{\Phi}} \right\}_i^\mathrm{T} \cdot \bar{\mathbf{g}}(\alpha_\mathrm{g})$, $\left\{ \tilde{\mathbf{\Phi}} \right\}_i$ being the i-th column of the matrix $\tilde{\mathbf{\Phi}}$; and where the over-tilde denotes all the quantities associated with the proposed stage-2 transformation of coordinates. In doing so, the reduced equations of motion in the modal space take the alternative form:

$$\ddot{\tilde{\boldsymbol{\theta}}}(t) + \tilde{\Xi} \cdot \dot{\tilde{\boldsymbol{\theta}}}(t) + \tilde{\mathbf{\Omega}}^2 \cdot \tilde{\boldsymbol{\theta}}(t) = \mathbf{1}_{m+3}\,\ddot{u}_g(t)\,, \tag{11}$$

in which the symbol $\mathbf{1}_s$ stands for a unit array of size s, while $\tilde{\Xi} = \tilde{\mathbf{\Phi}}^\mathrm{T} \cdot \bar{\mathbf{c}} \cdot \tilde{\mathbf{\Phi}}$ is the matrix of viscous damping in the transformed modal space. Given the non-classical nature of the energy dissipation in base-isolated buildings, this matrix is generally sparse, but with off-diagonal terms much less than the diagonal ones. Hence, from an engineering point of view, the modal coupling in terms of damping forces can be neglected, so that the time evolution of i-th modal coordinate $\tilde{\theta}_i(t)$ is ruled by:

$$\ddot{\tilde{\theta}}_i(t) + 2\,\tilde{\zeta}_i\tilde{\omega}_i\,\dot{\tilde{\theta}}_i(t) + \tilde{\omega}_i^2\,\tilde{\theta}_i(t) = \ddot{u}_g(t)\,. \tag{12}$$

where $\tilde{\zeta}_i = \tilde{\Xi}_{ii} / 2\tilde{\omega}_i$. In this equation $\tilde{\Xi}_{ii}$ and $\tilde{\omega}_i = \tilde{\Omega}_{ii}$ are the elements on principal diagonal of the matrices $\tilde{\Xi}$ and $\tilde{\mathbf{\Omega}}$, respectively. It is worth emphasizing that the additional computational burden required by the proposed two-stage transformation of coordinates is very low. Indeed, in real applications the size of the second eigenproblem (Eq. (10)) is much less than the size of the eigenproblem required for a conventional modal analysis, being very often $m+3 \ll 3(n+1)$.

Remarkably, only two approximations have been introduced so far, namely:

i) modal truncation for the superstructure, since only the first m modes of vibration are retained for the base-fixed superstructure;

ii) modal decoupling, since the off-diagonal terms in modal matrix of viscous damping are neglected.

Both approximations are acceptable in the vast majority of practical design situations.

4 CONVENTIONAL RESPONSE SPECTRUM METHOD

Before proceeding with the formulation of the proposed Response Spectrum Method (RSM), let us summarize the conventional implementation of the RSM as formulated in EC8 [27], for base-isolated buildings, which requires the following steps:

1. Select the number $\hat{m}$ of vibrational modes to be retained for the superstructure-BIS coupled dynamic system (in practice, $\hat{m} \ll 3(n+1)$);

2. Compute modal matrix $\hat{\boldsymbol{\Phi}}$, whose columns are the real-valued modal shapes of the superstructure-BIS combined system, and the associated spectral matrix $\hat{\boldsymbol{\Omega}} = \operatorname{diag}\left\{\hat{\omega}_1, \cdots, \hat{\omega}_{\hat{m}}\right\}$, which are solution of the real-valued eigenproblem:

$$\hat{\mathbf{K}}^{-1} \cdot \hat{\mathbf{M}} \cdot \hat{\boldsymbol{\Phi}} = \hat{\boldsymbol{\Phi}} \cdot \hat{\boldsymbol{\Omega}}^{-2} , \tag{13}$$

   with the normalization condition $\hat{\boldsymbol{\Phi}}^{\mathrm{T}} \cdot \hat{\mathbf{M}} \cdot \hat{\boldsymbol{\Phi}} = \mathbf{I}_{\hat{m}}$, where $\hat{\mathbf{M}}$ and $\hat{\mathbf{K}}$ are the block matrices of mass and stiffness introduced in Eq. (2).

3. Define the equivalent viscous damping ratio ζ_{b} for the BIS and ζ_{s} for the superstructure.

4. For the generic structural response of interest, $y(t)$, define the set of influence coefficients $\hat{e}_i$ of the $\hat{m}$ modal coordinates $\hat{q}_i(t)$, with $i = 1, \cdots, \hat{m}$, so that:

$$y(t) \cong \hat{y}(t) = \sum_{i=1}^{\hat{m}} \hat{e}_i\, \hat{q}_i(t) , \tag{14}$$

   where the hat means the use of conventional approach. Notice that in the influence coefficients $\hat{e}_i$.

5. Evaluate the design value of $\hat{y}(t)$ according to the Complete Quadratic Combination (CQC) rule (Wilson et al. 1981):

$$\hat{Y} = \sqrt{\sum_{i=1}^{\hat{m}} \sum_{k=1}^{\hat{m}} \hat{\rho}(i,k)\, \hat{e}_i\, \hat{g}_i(\alpha_{\mathrm{g}})\, \hat{e}_k\, \hat{g}_k(\alpha_{\mathrm{g}}) \frac{A_{\mathrm{e}}\left(\hat{T}_i, \hat{\zeta}_i\right)}{\hat{\omega}_i^2} \frac{A_{\mathrm{e}}\left(\hat{T}_k, \hat{\zeta}_k\right)}{\hat{\omega}_k^2}} , \tag{15}$$

   where $\hat{g}_i(\alpha_{\mathrm{g}}) = \left\{\hat{\boldsymbol{\Phi}}\right\}_i^{\mathrm{T}} \cdot \hat{\mathbf{G}} \cdot \boldsymbol{\tau}_{\mathrm{b}}(\alpha_{\mathrm{g}})$ is the i-th participation factor; $\hat{\rho}(i,k)$ is the correlation coefficient between i-th and k-th modes of vibration, usually computed under the assumption that the seismic acceleration is a zero-mean stationary Gaussian white noise [17-19]; and $A_{\mathrm{e}}\left(\hat{T}_i, \hat{\zeta}_i\right)$ is the i-th ordinate of the elastic response spectrum in terms of pseudo-acceleration. This quantity depends in turn on periods of vibration $\hat{T}_i = 2\pi/\hat{\omega}_i$ and viscous damping ratios $\hat{\zeta}_i$ of the $\hat{m}$ modes of vibration. It is generally assumed that the modal viscous damping ratios for the BIS-superstructure combined system take the values $\hat{\zeta}_i = \zeta_{\mathrm{b}}$ for $i \le 3$ and $\hat{\zeta}_i = \zeta_{\mathrm{s}}$ for $i \ge 4$. Indeed, the first three modes of vibrations are those associated with large deformations of the seismic isolators, and hence the energy dissipation of the

> BIS dictates the damping, while higher modes of vibration mainly involves the deformation of the superstructure, which dissipates less energy.

It may be useful to remember that Eq. (15) is consistent with the random vibration theory, so that the sought design value $\hat{Y}$ is defined as the expected extreme value of the structural response $\hat{y}(t)$ during the seismic motion, that is:

$$\hat{Y} = \mathrm{E}\left\langle \max\left|\hat{y}(t)\right|\right\rangle = \mathrm{PF}\left\langle \hat{y}(t)\right\rangle \mathrm{SD}\left\langle \hat{y}(t)\right\rangle , \tag{16}$$

where the symbols $\mathrm{E}\langle\cdot\rangle$, $\mathrm{PF}\langle\cdot\rangle$ and $\mathrm{SD}\langle\cdot\rangle$ denote Expectation (E) operator, dimensionless Peak Factor (PF) and Standard Deviation (SD), respectively; and where the notation $|x|$ stands for the modulus of the scalar *x*. In the conventional CQC rule it is also made the additional simplifying assumption that PFs of structural response $\hat{y}(t)$ and modal coordinates $\hat{q}_i(t)$ are approximately equal.

5 PROPOSED DAMPING-ADJUSTED COMBINATION RULE

Aim of this section is to then formulate a Damping-Adjusted Combination (DAC) rule in which a new set of combination and correction coefficients, consistently based on the random vibration theory, enables one to make use of a single response spectrum in combining the modal maxima. The particularization of the proposed DAC rule in the case of white noise excitation, leading to handy closed-form expressions, is presented in the next section. The equivalence of dimensionless PF for structural response and PFs for the contributing modal responses (i.e. one of the main assumptions of CQC rule) is also removed.

Let $y(t)$ be the time history of a generic structural quantity of interest for the purposes of designing a base-isolated building. Without loss of generality, this structural response can be expressed as linear combination of the DoFs of the system:

$$y(t) = \mathbf{d}_\mathrm{s}^\mathrm{T} \cdot \mathbf{u}_\mathrm{s}(t) + \mathbf{d}_\mathrm{b}^\mathrm{T} \cdot \mathbf{u}_\mathrm{b}(t) , \tag{17}$$

where the arrays $\mathbf{d}_\mathrm{s} = \left\{ d_{\mathrm{s},1} \quad \cdots \quad d_{\mathrm{s},3n} \right\}^\mathrm{T}$ and $\mathbf{d_b} = \left\{ d_{\mathrm{b},1} \quad d_{\mathrm{b},2} \quad d_{\mathrm{b},3} \right\}^\mathrm{T}$ collect the influence coefficients of superstructure and isolation level, respectively. Once the suggested two-stage transformation of coordinates is adopted, the generic structural response $y(t)$ can be expressed by a linear combination of the modal responses:

$$y(t) \cong \tilde{y}(t) = \tilde{\boldsymbol{\varepsilon}}^T \, \tilde{\boldsymbol{\theta}}(t) = \sum_{i=1}^{m+3} \tilde{\varepsilon}_i \, \tilde{\gamma}_i(\alpha_\mathrm{g}) \, \tilde{\theta}_i(t) , \tag{18}$$

in which $\tilde{\boldsymbol{\varepsilon}} = \left\{ \tilde{\varepsilon}_1 \quad \cdots \quad \tilde{\varepsilon}_{m+3} \right\}^\mathrm{T}$ is the array listing the influence coefficients of the $m+3$ modal coordinates for structural response under consideration, and can be assembled as:

$$\tilde{\boldsymbol{\varepsilon}} = \tilde{\boldsymbol{\Phi}}^\mathrm{T} \cdot \left\{ \begin{array}{c} \boldsymbol{\Phi}_\mathrm{s}^\mathrm{T} \cdot \mathbf{d}_\mathrm{s} \\ \hdashline \boldsymbol{\Phi}_\mathrm{b}^\mathrm{T} \cdot \mathbf{d}_\mathrm{b} \end{array} \right\}^\mathrm{T} . \tag{19}$$

By assuming that structural response $\tilde{y}(t)$ and modal responses $\tilde{\theta}_i(t)$, with $i = 1, \cdots, (m+3)$, are zero-mean Gaussian random processes, the standard deviation $\mathrm{SD}\left\langle \tilde{y}(t) \right\rangle$ can be expressed in the form:

$$\mathrm{SD}\left\langle \tilde{y}(t)\right\rangle = \sqrt{\sum_{i=1}^{m+3}\sum_{k=1}^{m+3}\tilde{\rho}(i,k)\,\tilde{\varepsilon}_i\,\tilde{\gamma}_i(\alpha_\mathrm{g})\,\tilde{\sigma}_i\,\tilde{\varepsilon}_k\,\tilde{\gamma}_k(\alpha_\mathrm{g})\,\tilde{\sigma}_k}\ , \tag{20}$$

where $\tilde{\rho}(i,k)$ is the following correlation coefficient:

$$\tilde{\rho}(i,k) = \tilde{\sigma}_{i,k} \big/ \left(\tilde{\sigma}_i\,\tilde{\sigma}_k\right), \tag{21}$$

in which $\tilde{\sigma}_i$ and $\tilde{\sigma}_{i,k}$ stand for Standard Deviation (SD) of the i-th stationary modal response $\tilde{\theta}_i(t)$ and steady-state covariance between $\tilde{\theta}_i(t)$ and $\tilde{\theta}_k(t)$, respectively:

$$\tilde{\sigma}_i = \mathrm{SD}\left\langle \tilde{\theta}_i(t)\right\rangle = \sqrt{\mathrm{E}\left\langle \tilde{\theta}_i(t)^2\right\rangle}\ ; \tag{22}$$

$$\tilde{\sigma}_{i,k} = \mathrm{E}\left\langle \tilde{\theta}_i(t)\,\tilde{\theta}_k(t)\right\rangle . \tag{23}$$

Following now the same strategy recently proposed by Muscolino and Palmeri [25] for the seismic analysis of light secondary substructures, let us rewrite the modal correlation coefficient in the equivalent form:

$$\tilde{\rho}(i,k) = \frac{\tilde{\sigma}_{i,k}}{\tilde{\sigma}_i\,\tilde{\sigma}_k} = \tilde{r}(i,k)\frac{\tilde{\sigma}_i^{(0)}\,\tilde{\sigma}_k^{(0)}}{\tilde{\sigma}_i\,\tilde{\sigma}_k}\ , \tag{24}$$

in which the novel combination coefficient $\tilde{r}(i,k)$ is so defined:

$$\tilde{r}(i,k) = \frac{\mathrm{E}\left\langle \tilde{\theta}_i(t)\,\tilde{\theta}_k(t)\right\rangle}{\tilde{\sigma}_i^{(0)}\,\tilde{\sigma}_k^{(0)}}\ , \tag{25}$$

where the denominator $\tilde{\sigma}_i^{(0)} = \mathrm{SD}\left\langle \tilde{\theta}_i^{(0)}(t)\right\rangle$ denotes the standard deviation of the stationary seismic response of a dummy SDoF oscillator associated with the i-th mode of vibration of the base-isolated building. This dummy oscillator has unit mass, a reference value of the viscous damping ratio, ζ_0, for which the elastic response spectrum in known, and undamped period of vibration $\tilde{T}_i = 2\pi/\tilde{\omega}_i$. Therefore, the dynamic response of this dummy oscillator is ruled by:

$$\ddot{\tilde{\theta}}_i^{(0)}(t) + 2\,\zeta_0\tilde{\omega}_i\,\dot{\tilde{\theta}}_i^{(0)}(t) + \tilde{\omega}_i^2\,\tilde{\theta}_i^{(0)}(t) = \ddot{u}_g(t)\,. \tag{26}$$

Interestingly, Eq. (26) can be simply derived from Eq. (12) by substituting the viscous damping ratio (i.e., the reference value ζ_0 instead of the actual modal value $\tilde{\zeta}_i$).

Once the new set of combination coefficients has been introduced, substitution of Eq. (24) into Eq.(20), and the result into Eq. (16), gives:

$$\tilde{Y} = \mathrm{PF}\left\langle \tilde{y}(t)\right\rangle \sqrt{\sum_{i=1}^{m+3}\sum_{k=1}^{m+3}\tilde{r}(i,k)\,\tilde{\varepsilon}_i\,\tilde{\gamma}_i(\alpha_\mathrm{g})\ \tilde{\varepsilon}_k\,\tilde{\gamma}_k(\alpha_\mathrm{g})\,\tilde{\sigma}_i^{(0)}\,\tilde{\sigma}_k^{(0)}}\ . \tag{27}$$

This formula can be further manipulated by multiplying and dividing each term in the double summation by the PF of the corresponding dummy oscillator, and by introducing the dimensionless correction coefficient $\tilde{\chi}_i^{(0)}$ so defined:

$$\tilde{\chi}_i^{(0)} = \mathrm{PF}\left\langle \tilde{y}(t)\right\rangle \big/ \mathrm{PF}\left\langle \tilde{\theta}_i^{(0)}(t)\right\rangle . \tag{28}$$

Indeed, according to Eq. (16) and to the conventional CQC rule, the expected extreme value of the dynamic response of a dummy oscillator can be assumed to be equal to the maximum displacement given by the pertinent elastic response spectrum:

$$\left\{\mathrm{PF}\left\langle\tilde{\theta}_i^{(0)}(t)\right\rangle\tilde{\sigma}_i^{(0)}\right\} = \mathrm{E}\left\langle\max\left|\tilde{\theta}_i^{(0)}(t)\right|\right\rangle = \frac{A_e\left(\tilde{T}_i,\zeta_0\right)}{\tilde{\omega}_i^2}\,. \tag{29}$$

Therefore, Eq. (27) gives:

$$\tilde{Y} = \sqrt{\sum_{i=1}^{m+3}\sum_{k=1}^{m+3}\tilde{r}(i,k)\frac{\tilde{\varepsilon}_i\,\tilde{\gamma}_i(\alpha_{\mathrm{g}})\,\tilde{\chi}_i^{(0)}}{\tilde{\omega}_i^{\,2}}\frac{\tilde{\varepsilon}_k\,\tilde{\gamma}_k(\alpha_{\mathrm{g}})\,\tilde{\chi}_k^{(0)}}{\tilde{\omega}_k^{\,2}}A_e\left(\tilde{T}_i,\zeta_0\right)A_e\left(\tilde{T}_k,\zeta_0\right)}\,, \tag{30}$$

which is formally similar to the CQC rule of Eq. (15). However, there are three fundamental novelties in the proposed formula:

1. The combination coefficient $\tilde{r}(i,k)$, defined by Eq.(25), is no more the correlation coefficient between i-th and k-th modal oscillators of the base-isolated building, and requires the evaluation in the frequency domain of the following quantities:

$$\tilde{\sigma}_i^{(0)} = 2\int_0^{+\infty}\left|\tilde{H}_i^{(0)}(\omega)\right|^2 S_g(\omega)\,d\omega\,; \tag{31}$$

$$\mathrm{E}\left\langle\tilde{\theta}_i(t),\tilde{\theta}_k(t)\right\rangle = 2\int_0^{+\infty}\tilde{H}_i^*(\omega)\,\tilde{H}_k(\omega)\,S_g(\omega)\,d\omega\,. \tag{32}$$

   in which $S_{\mathrm{g}}(\omega)$ is the Power Spectral Density (PSD) function simulating the energy distribution of the design ground shaking and:

$$\tilde{H}_i^{(0)}(\omega) = \left[\left(\tilde{\omega}_i^2-\omega^2\right)+j\left(2\,\zeta_0\,\tilde{\omega}_i\,\omega\right)\right]^{-1}\,; \tag{33}$$

$$\tilde{H}_i(\omega) = \left[\left(\tilde{\omega}_i^2-\omega^2\right)+j\left(2\,\tilde{\zeta}_i\,\tilde{\omega}_i\,\omega\right)\right]^{-1}\,. \tag{34}$$

2. The correction coefficient $\tilde{\chi}_i^{(0)}$ is introduced with respect to the i-th dummy oscillator (Eq.(28)), so that the hypothesis of equivalence between dimensionless PFs for structural response and contributing modal responses is removed;

3. Most importantly, only the elastic response spectrum for the reference value ζ_0 of the viscous damping ratio is required. It follows that the use of a semi-empirical DCF is avoided, and the effects of different viscous damping ratios in the actual modal oscillators are consistently taken into account by the novel combination ($\tilde{r}$) and correction ($\tilde{\chi}^{(0)}$) coefficients introduced in the double summation of Eq.(30). For this reason the formula has been termed Damping-Adjusted Combination (DAC) rule.

It is worth mentioning that all the quantities appearing in the proposed DAC rule of Eq. (30) can be easily evaluated in practice, so that the computational effort is just slightly higher with respect to the traditional CQC rule. Indeed, the modal parameters ($\tilde{\varepsilon}_i$, $\tilde{\gamma}_i$, $\tilde{\omega}_i$ and $\tilde{T}_i$) simply require the application of the two-stage transformations of coordinates presented in the third section, while the novel coefficients $\tilde{r}$ and $\tilde{\chi}_i^{(0)}$ introduced for the DAC rule just depend on the first spectral moments of both actual modal oscillators and dummy oscillators, which in turn can be easily computed by using traditional techniques of the random vibration theory.

6 CLOSED FORM EXPRESSION UNDER WHITE NOISE ASSUMPTION

The traditional CQC rule is usually applied under the simplified assumption that the ground acceleration is a stationary white noise, i.e. with energy uniformly distributed over the frequencies. The same assumption is considered in this section with the purpose of deriving simple closed-form expressions for the new coefficients introduced in the proposed Damping-Adjusted Combination (DAC) rule, in so reducing the computational burden. Indeed, when the Power Spectral Density (PSD) function of the input is constant, it is possible to evaluate the exact solution of the following integrals appearing in previous expressions. In particular by assuming that $S_g(\omega)=1$ the new combination coefficients of Eq. (25) becomes:

$$\tilde{r}(i,k)=\frac{\zeta_0}{\sqrt{\tilde{\zeta}_i\,\tilde{\zeta}_k}}\,\tilde{\rho}(i,k)\,, \tag{35}$$

where $\tilde{\rho}(i,k)$ is the correlation coefficient between i-th and k-th modes of vibration evaluated assuming the seismic excitation as a white noise process [18,19]:

$$\tilde{\rho}(i,k)=\frac{8}{\tilde{C}_{i,k}}\sqrt{\tilde{\zeta}_i\,\tilde{\zeta}_k}\;\tilde{\omega}_i\,\tilde{\omega}_k\sqrt{\tilde{\omega}_i\,\tilde{\omega}_k}\left(\tilde{\zeta}_i\,\tilde{\omega}_i+\tilde{\zeta}_k\,\tilde{\omega}_k\right), \tag{36}$$

and

$$\tilde{C}_{i,k}=\tilde{B}_{i,k}^2+4\,\tilde{A}_{i,k}\,\tilde{\zeta}_i\,\tilde{\zeta}_k\,\tilde{\omega}_i\,\tilde{\omega}_k+4\left(\tilde{\zeta}_i^2+\tilde{\zeta}_k^2\right)\tilde{\omega}_i^2\,\tilde{\omega}_k^2\ , \tag{37}$$

$$\tilde{A}_{i,k}=\tilde{\omega}_i^2+\tilde{\omega}_k^2\ ;\quad \tilde{B}_{i,k}=\tilde{\omega}_i^2-\tilde{\omega}_k^2\ . \tag{38}$$

Under the white noise approximation, an additional simplification arises in the computation of the coefficient $\tilde{\chi}_i^{(0)}$ defined in Eq. (28) by introducing the Vanmarcke's PF [28,29], for the structural response of interest $\mathrm{PF}\left\langle \tilde{y}(t)\right\rangle$ and for the dummy responses $\mathrm{PF}\left\langle \tilde{\theta}_i^{(0)}(t)\right\rangle$:

$$\mathrm{PF}\left\langle \tilde{y}(t)\right\rangle=\sqrt{2\ln\left\{2.89\,N^+\left\langle \tilde{y}(t)\right\rangle\left[1-\exp\left(-1.77\,q\left\langle \tilde{y}(t)\right\rangle^{1.20}\sqrt{\ln\left(2.89\,N^+\left\langle x(t)\right\rangle\right)}\right)\right]\right\}}\,; \tag{39}$$

$$\mathrm{PF}\left\langle \tilde{\theta}_i^{(0)}(t)\right\rangle=\sqrt{2\ln\left\{0.4601\,\tilde{\omega}_i\,T_\mathrm{g}\left[1-\exp\left(-0.3283\sqrt{\ln\left(0.4601\,\tilde{\omega}_i\,T_\mathrm{g}\right)}\right)\right]\right\}}\ . \tag{40}$$

Importantly, $\mathrm{PF}\left\langle \tilde{\theta}_i^{(0)}(t)\right\rangle$ depends only on the dimensionless quantity $\tilde{\omega}_i\,T_\mathrm{g}$, T_g being the duration of the strong-phase of the ground motion, while $\mathrm{PF}\left\langle \tilde{y}(t)\right\rangle$ depends on the expected number of upcrossings of the time axis, $N^+\left\langle \tilde{y}(t)\right\rangle$, and on the bandwidth parameter $q\left\langle \tilde{y}(t)\right\rangle$. These quantities can be evaluated as:

$$N^+\left\langle \tilde{y}(t)\right\rangle=\frac{1}{2\pi}\sqrt{\frac{\lambda_2\left\langle \tilde{y}(t)\right\rangle}{\lambda_0\left\langle \tilde{y}(t)\right\rangle}}\,T_\mathrm{g}\ ; \tag{41}$$

$$q\left\langle \tilde{y}(t)\right\rangle=\sqrt{1-\frac{\lambda_1\left\langle \tilde{y}(t)\right\rangle^2}{\lambda_0\left\langle \tilde{y}(t)\right\rangle\lambda_2\left\langle \tilde{y}(t)\right\rangle}}\ . \tag{42}$$

The symbol $\lambda_\ell\left\langle \tilde{y}(t)\right\rangle$ in Eqs. (41) and (42) is the spectral moments of order $\ell=0,1,2$ of the structural response $\tilde{y}(t)$, which under the white noise approximation can be evaluate in closed form as:

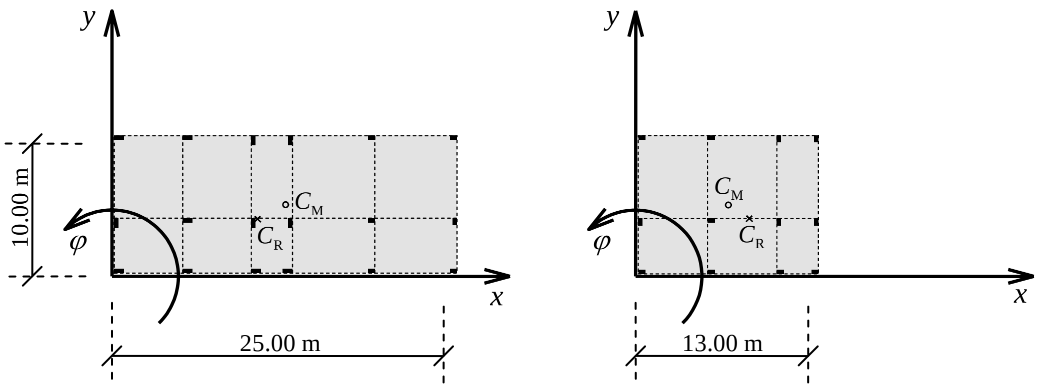

Figure 2. Bottom (left) and top (right) plan layouts of the base-isolated building considered in the numerical applications; circle (o) and cross (x) identify centre of mass (C_{M}) and centre of rigidity (C_{R}), respectively.

$$\lambda_0\left\langle \tilde{y}(t)\right\rangle=\sum_{i=1}^{m+3}\sum_{k=i+1}^{m+3}\frac{4\pi\,\tilde{\varepsilon}_i\,\tilde{\varepsilon}_k}{\tilde{C}_{i,k}}\tilde{\gamma}_i\,\tilde{\gamma}_k\left(\tilde{\zeta}_i\,\tilde{\omega}_i+\tilde{\zeta}_k\,\tilde{\omega}_k\right); \tag{43}$$

$$\lambda_1\left\langle \tilde{y}(t)\right\rangle=\sum_{i=1}^{m+3}\sum_{k=i+1}^{m+3}\frac{2\tilde{\varepsilon}_i\,\tilde{\varepsilon}_k}{\tilde{C}_{i,k}}\tilde{\gamma}_i\,\tilde{\gamma}_k\Big[\left(\tilde{\zeta}_i\,\tilde{A}_{i,k}+2\zeta_k\,\tilde{\omega}_i\,\tilde{\omega}_k\right)\tilde{D}_i+\left(\tilde{\zeta}_k\,\tilde{A}_{i,k}+2\zeta_i\,\tilde{\omega}_i\,\tilde{\omega}_k\right)\tilde{D}_k-\tilde{B}_{i,k}\ln\left(\tilde{\omega}_i/\tilde{\omega}_k\right)\Big]; \tag{44}$$

$$\lambda_2\left\langle \tilde{y}(t)\right\rangle=\sum_{i=1}^{m+3}\sum_{k=i+1}^{m+3}\frac{4\pi\,\tilde{\varepsilon}_i\,\tilde{\varepsilon}_k}{\tilde{C}_{i,k}}\tilde{\gamma}_i\,\tilde{\gamma}_k\,\tilde{\omega}_i\,\tilde{\omega}_k\left(\tilde{\zeta}_i\,\tilde{\omega}_k+\tilde{\zeta}_k\,\tilde{\omega}_i\right), \tag{45}$$

in which:

$$\tilde{D}_i=\frac{1}{\sqrt{1-\tilde{\zeta}_i^2}}\arctan\left(\frac{\sqrt{1-\tilde{\zeta}_i^2}}{\tilde{\zeta}_i}\right). \tag{46}$$

7 NUMERICAL APPLICATIONS

7.1 Objective structure

Aimed at validating the proposed method of analysis and design, the seismic response of a representative 5-storey base-isolated building $(n=5)$ has been investigated. A superstructure with irregular distributions of mass and stiffness in plan and elevation has been chosen (see Figure 1). The first three storeys have dimensions of $25\,\mathrm{m}$ by $10\,\mathrm{m}$, which reduce to $13\,\mathrm{m}$ by $10\,\mathrm{m}$ for the last two storeys. The floor layouts are sketched in Figure 2, where the position of centres

Table I. Exact ($\hat{T}_i$) and approximate ($\tilde{T}_i$) periods of vibration for the base-isolated building.

Mode i	$\hat{T}_i$ (s)	$\tilde{T}_i$ (s)	Inaccuracy (%)	Mode i	$\hat{T}_i$ (s)	$\tilde{T}_i$ (s)	Inaccuracy (%)
1	2.086	2.086	–0.002	5	0.244	0.243	–0.555
2	2.077	2.077	–0.005	6	0.214	0.208	–2.592
3	1.809	1.808	–0.011	7	0.143	0.141	–1.288

Table II. Analysis cases considered for validation purposes.

Case	Ground type	Duration of stationary part	Damping ratios		superstructure's modes
		T_{g} (s)	superstructure ζ_{s}	BIS ζ_{b}	m
(1)	A	15	0.02	0.12	8
(2)	A	30	0.02	0.012	8
(3)	C	30	0.02	0.012	8
(4)	C	30	0.01	0.18	8
(5)	C	30	0.01	0.18	13

of mass C_{M} (o) and rigidity C_{R} (x) is also shown. Their relative distance is $2.31\,\mathrm{m}$ for the first three storeys and $1.82\,\mathrm{m}$ for the last two storeys. The total mass of the base-isolated building is $M_{\mathrm{tot}} = 1{,}106\,\mathrm{Mg}$ and the lateral stiffness of the BIS is $K_{\mathrm{lat}}^{(\mathrm{b})} = 10{,}370\,\mathrm{kN/m}$, so that the nominal value of the isolation period is $T_{\mathrm{iso}} = 2\pi\sqrt{M_{\mathrm{tot}}/K_{\mathrm{lat}}^{(\mathrm{b})}} = 2.05\,\mathrm{s}$.

7.2 Modal analysis

Aimed at investigating the accuracy of the proposed two-stage transformation of coordinates against the conventional modal analysis, exact ($\hat{T}_i = 2\pi/\hat{\omega}_i$) and approximate ($\tilde{T}_i = 2\pi/\tilde{\omega}_i$) periods of vibration for the first 8 modes of the undamped structure have been evaluated by using the full eigenproblem of Eq. (13) and the reduced one of Eq. (10), respectively. As shown in Table I, exact and approximate values are in excellent agreement, in so confirming the validity of the novel two-stage modal analysis for base-isolated buildings, which in turn is adopted for the proposed DAC rule.

7.3 Seismic analyses

Five methods of analysis have been applied and compared, namely: i) Response Spectrum Method (RSM), as formulated in EC8 [27]; ii) Monte Carlo Simulation (MCS), with 400 samples of artificially generated time histories of ground acceleration consistent with the response spectrum; iii) direct application of the random vibration theory with a consistent PSD function of the accelerograms; iv) proposed Damping-Adjusted Combination (DAC) rule; v) simplified version of the DAC rule under White Noise input (DAC-WN), as presented in Section 6. For each analysis, the angle of attack $\alpha_{\mathrm{g}} = 90°$ has been used.

In order to test the performances of the proposed approach in different design situations, five cases have been analysed, which differ in seismic input and/or damping properties and/or number of retained modes. As summarized in Table II, two different soil conditions have been considered, i.e. ground types A (rocks) and C (deep deposits of dense sands or stiff clay) as defined in EC8 [27], along with two durations of the stationary part of the accelerogram, i.e. $T_{\mathrm{g}} = 15\,\mathrm{s}$ and $30\,\mathrm{s}$; two sets of viscous damping ratios have been used for superstructure and BIS, i.e. $\{\zeta_{\mathrm{s}} = 0.02,\ \zeta_{\mathrm{b}} = 0.12\}$ and $\{\zeta_{\mathrm{s}} = 0.01,\ \zeta_{\mathrm{b}} = 0.18\}$; either $m = 8$ or 13 modes of vibration have been retained for the superstructure.

Figure 3 depicts the profiles of inter-storey drifts along the epicentral direction of the ground shaking for the five design situations summarized in Table IV and for angle of attack $\alpha_{\mathrm{g}} = 90°$, which is the weakest direction of the 3D frame. In the pictures, the mean value of the MCS with 400 samples is shown with a solid black line, and the corresponding interval of confidence (mean value ± standard deviation) is delimited by a pair of dashed thin lines; the prediction of the random vibration theory is shown with a dashed gray line, while the values consistent with

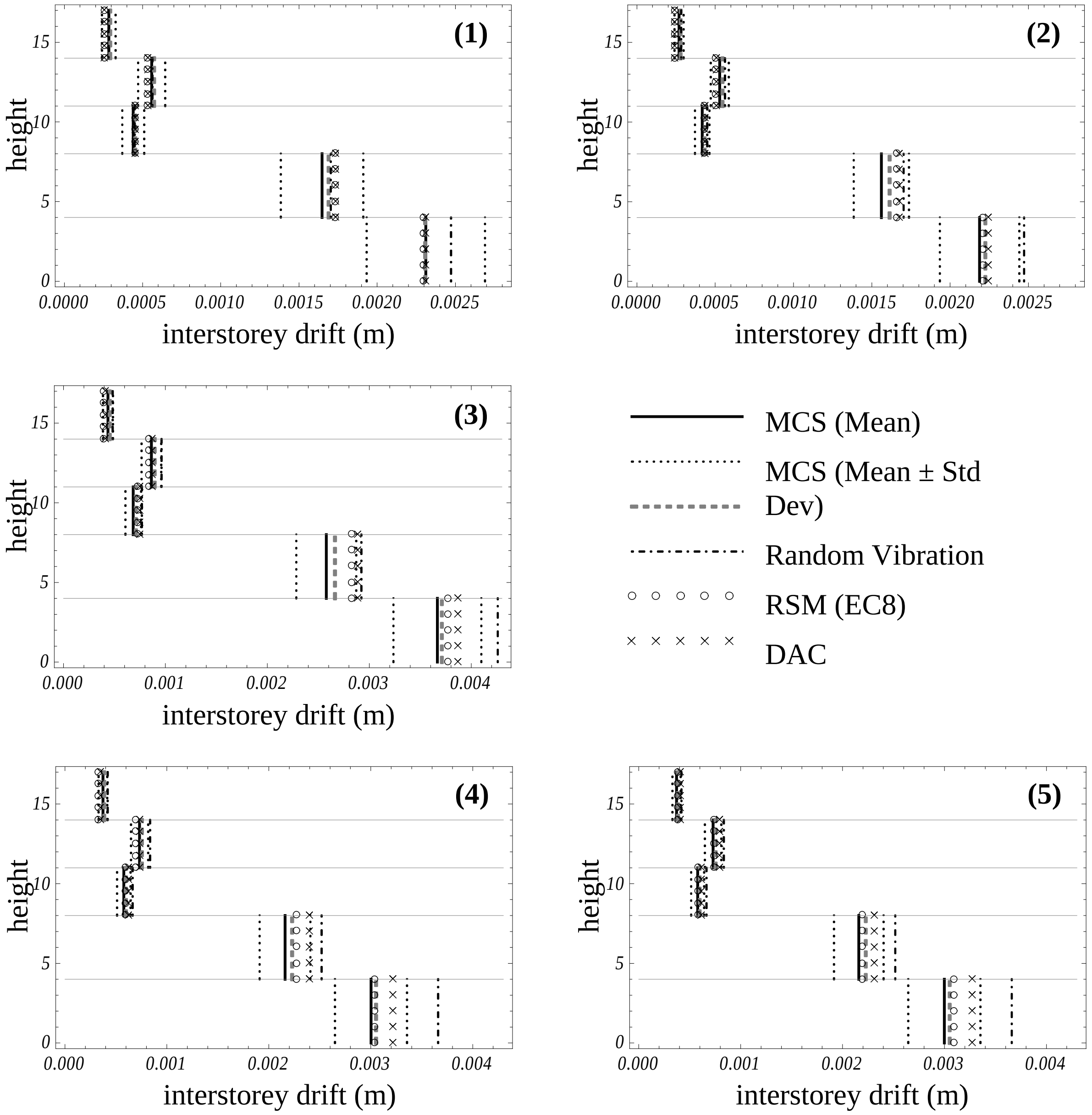

Figure 3. Profiles of superstructure's interstorey drifts for the five cases of Table IV when the agle of attack of the ground motion is $\alpha_g = 90°$ (weakest superstructure's direction).

RSM as formulated in EC8 are those with dot-dashed thin lines; DAC and DAC-WN results are reported with circles and crosses, respectively.

The inspection of these graphs reveals that:

- The proposed DAC and DAC-WN rules are always in good agreement with the results of MCS and random vibration theory.
- The results of the RSM (EC8) very often show large inaccuracies, falling most of the times outside the interval of confidence of the MCS.
- The larger is the stationary duration of the accelerogram, the smaller is the interval of confidence of the MCS (comparison of cases (1) and (2)), i.e. the more deterministic is the mean value of the generated response spectra.

- The predictions of the RSM (EC8) are less accurate when the viscous damping ratios ζ_s and ζ_b become smaller for superstructure and larger for BIS, respectively (comparison of cases (3) and (4)), i.e. when the discrepancy increases with respect to the reference value $\zeta_0 = 0.05$.(3)).
- The results' trend is not significantly affected by soil type (comparison of cases (2) and (3)) and number of modes retained in the analysis (comparison of cases (4) and (5)).

8 CONCLUSIONS

The two main sources of inaccuracy of the classical Response Spectrum Method (RSM) in the practical analysis and design of base-isolated buildings have been pointed out. First, the use of elastic response spectra for different values of the viscous damping ratio, although the seismic action is defined for just a single reference value; second, the use of combination rules not fully adequate for non-conventional structures. This is confirmed by the numerical results included in this paper, where the inaccuracy of the conventional RSM with DCF (Damping Correction Factor) and CQC (Complete Quadratic Combination) rule can be as large as 27%, which is unacceptable from an engineering point of view.

Aimed at overcoming these shortcomings, an improved RSM has been presented and validated. The proposed technique consists of a two-stage transformation of coordinates in parallel with a novel Damping-Adjusted Combination (DAC) rule. The following features have been embedded in the formulation: first, light computational effort, since the calculation of the exact complex-valued eigenproperties of base-isolated buildings is avoided; second, accurate representation of the damping for both superstructure and Base Isolation System (BIS); third, ease of use, requiring a single response spectrum for the reference value of the viscous damping ratio, i.e. the only spectrum which defines the seismic action. Numerical investigations for a realistic structure confirm the improved accuracy of the proposed method, leading toward more economical and/or dependable design of base-isolated buildings. The closed-form expressions derived under the white noise assumption for the ground acceleration allow reducing the computation burden in the proposed DAC rule, and hence they are particularly suitable for practical applications.

REFERENCES

[1] J.M. Kelly, *Earthquake-Resistant Design with Rubber*. Springer-Verlag: London, 1997.

[2] F. Naeim, J.M. Kelly, *Design of Seismic Isolated Structures: From Theory to Practice*. John Wiley & Sons: New York, 1999.

[3] H.C. Tsai, J.M. Kelly, Seismic response of heavily damped base isolation systems. *Earthquake Engineering and Structural Dynamics*, **22**, 633–645, 1993.

[4] J.M. Kelly, The role of damping in seismic isolation. *Earthquake Engineering and Structural Dynamics*, **28**, 3–20, 1999.

[5] J.F. Hall, Discussion: The role of damping in seismic isolation. *Earthquake Engineering and Structural Dynamics*, **28**, 1717–1720, 1999.

[6] Y. Du, H. Li, B.F. Jr Spencer, Effect of non-proportional damping on seismic isolation. *Journal of Structural Control*, **9**, 205–236, 2002.

[7] N. Makris, S.P. Chang, Effect of viscous, viscoplastic and friction damping on the response of seismic isolated structures. *Earthquake Engineering and Structural Dynamics*, **29**, 85-107, 2000.

[8] C.S. Tsai, T.C. Chiang, B.J. Chen, S.B. Lin, An advanced analytical model for high damping rubber bearings. *Earthquake Engineering and Structural Dynamics*, **32**, 1373-1387, 2003.

[9] M. Dicleli, S. Buddaram, Comprehensive evaluation of equivalent linear analysis method for seismic-isolated structures represented by sdof systems. *Engineering Structures*, **29**, 1653-1663, 2007.

[10] K.L. Ryan, J. Polanco, Problems with Rayleigh damping in base-isolated buildings. *Journal of Structural Engineering*, **134**, 1780-1784, 2008.

[11] N.M. Newmark, W.J. Hall, *Earthquake Spectra and Design*. EERI Monograph Series: Oakland, CA, 1982.

[12] J.P. Wu, R.D. Hanson, Inelastic response spectra with high damping. *Journal of the Structural Division (ASCE)*, **115**, 1412–1431, 1989.

[13] O.M. Ramirez, M.C. Constantinou, A.S. Whittaker, C.A. Kircher, C.Z. Chrysostomou, Elastic and inelastic seismic response of buildings with damping systems. *Earthquake Spectra*, **18**, 531–547, 2002.

[14] Y.Y. Lin, K.C. Chang, A study on damping reduction factor for buildings under earthquake ground motions. *Journal of Structural Engineering*, **129**, 206–214, 2003.

[15] Y.Y. Lin, E. Miranda, K.C. Chang, Evaluation of damping reduction factors for estimating elastic response of structures with high damping. *Earthquake Engineering and Structural Dynamics*, **34**, 1427–1443, 2005.

[16] R. Weitzmann, M. Ohsaki, M. Nakashima, Simplified methods for design of base-isolated structures in the log-period high-damping range. *Earthquake Engineering and Structural Dynamics*, **35**, 497-515, 2006

[17] E.L. Wilson, A. Der Kiureghian, E.P. Bayo, A replacement for the SRSS method for seismic analysis. *Earthquake Engineering and Structural Dynamics*, **9**, 187–192, 1981.

[18] A. Der Kiureghian, Structural response to stationary excitation. *Journal of the Engineering Mechanics Division (ASCE)*, **106**, 1195-213, 1980.

[19] A. Der Kiureghian, A response spectrum method for random vibration analysis of MDF systems. *Earthquake Engineering and Structural Dynamics*, **9**, 419– 435, 1981.

[20] M.P. Singh. Seismic response by SRSS for nonproportional damping. *Journal of the Engineering Mechanics Division (ASCE)*, **106**, 1405–1419, 1980.

[21] R. Sinha, T. Igusa, CQC and SRSS methods for non-classically damped structures. *Earthquake Engineering and Structural Dynamics*, **24**, 615–619, 1995.

[22] R. Villaverde, Rosenblueth’s modal combination rule for systems with non-classical damping. *Earthquake Engineering and Structural Dynamics*, **16**, 931-942, 1988.

[23] G. Falsone, G. Muscolino, Cross-correlation coefficients and modal combination rules for non-classically damped systems. *Earthquake Engineering and Structural Dynamics*, **28**, 1669–1684, 1999.

[24] G. Falsone, G. Muscolino, New real-value modal combination rules for non-classically damped structures. *Earthquake Engineering and Structural Dynamics*, **33**, 1187-209, 2004.

[25] G. Muscolino, A. Palmeri, An earthquake response spectrum method for linear light secondary substructures. *ISET Journal of Earthquake Technology*, **44**, 193-211, 2007.

[26] T.K. Caughey, M.E.J. O'Kelly, Classical normal modes in damped linear dynamic systems. *Journal of Applied Mechanics (ASME)*, **32**, 583-588, 2007, 1965.

[27] European Committee for Standardization, *Eurocode 8: Design of Structures for Earthquake Resistance*, 2004 Edition.

[28] E.H. Vanmarcke, On the distribution of the first-passage time for normal stationary random processes. *Journal of Applied Mechanics (ASME)*, **42**, 215-220, 1975.

[29] E.H. Vanmarcke, Structural response to earthquakes. In: *Seismic Risk and Engineering Decisions, Chapter 8 (Lomnitz C. and E. Rosenblueth Eds)*, Elsevier: Amsterdam, 1976.

COMPDYN 2011
III ECCOMAS Thematic Conference on
Computational Methods in Structural Dynamics and Earthquake Engineering
M. Papadrakakis, M. Fragiadakis, V. Plevris (eds.)
Corfu, Greece, 26–28 May 2011

COLLAPSE RESISTANCE OF BUILDINGS WITH LARGE-SCALE MAGENTO-RHEOLOGICAL (MR) DAMPERS

Yunbyeong Chae[1], James M. Ricles[1], and Richard Sause[1]

[1] Lehigh University, 117 ATLSS Drive, Bethlehem, PA 18015 USA
e-mail: yuc206@lehigh.edu, jmr5@lehigh.edu, rs0c@lehigh.edu

Keywords: Magneto-Rheological (MR) damper, Semi-Active Control, Incremental Dynamic Analysis, Collapse Fragility

Abstract. *Supplemental damping systems are known to improve the performance of structures under the design basis earthquake (DBE) and maximum considered earthquake (MCE). In this paper, the seismic collapse potential of a 3-story building with large-scale MR dampers is investigated for extreme levels of ground motion beyond the MCE, where the MR dampers are controlled by various control algorithms. The control algorithms include: i) passive control; ii) linear quadratic regulator (LQR) semi-active control; iii) sliding model control (SMC) semi-active control; iv) decentralized bang-bang (DBB) semi-active control; and v) phase angle control (PAC) semi-active control. The collapse fragility curves of the building with these structural control strategies are obtained using the incremental dynamic analysis (IDA) procedure with an ensemble of ground motions recommended by FEMA P695. The nonlinear time history analysis for the IDA is conducted using OpenSees, where a phenomenological based model to account for strength deterioration in beam plastic hinge regions subject to cyclic loading is incorporated into OpenSees. The collapse fragility curves for various structural control strategies are compared and discussed to assess the performance of the building structure with MR dampers in mitigating structural collapse under extreme earthquake ground motions.*

1 INTRODUCTION

In earthquake engineering, collapse implies that a structural system, or a part of it, is incapable of maintaining gravity load carrying capacity in the presence of seismic effects [1]. When a building is subjected to large story drifts, it is vulnerable to dynamic instability due to P-Δ effects and deterioration in strength and stiffness of its structural components that can lead to collapse of the system. Collapse prevention has always been a major concern in the design of structures. The recently developed FEMA P695 [2] document provides a methodology for seismic collapse assessment of structures.

While several studies have been conducted to assess the performance of supplemental damping systems and their effectiveness in mitigating the seismic hazard of structures under the design basis earthquake (DBE) and maximum considered earthquake (MCE), the collapse resistance of buildings with Magneto-Rheological (MR) dampers has not been investigated. The seismic collapse potential of structures with passive supplemental damping systems has been investigated by a few researchers using the incremental dynamic analysis (IDA) method [4-6]. In this paper, the collapse resistance capacity of a 3-story building with moment resisting frames (MRFs) and braced frames with MR dampers designed to achieve specified performance levels under the DBE and MCE is assessed for seismic collapse using the procedure given in FEMA P695. The nonlinear time history analyses used in the IDA method are conducted using OpenSees [6]. A phenomenological-based model developed by Ibarra and Krawinkler [1] and modified by Lignos [7] for modeling deterioration in beam plastic hinge regions in MRFs is incorporated into OpenSees. IDA are performed on the building for cases involving five different controllers [8]: i) passive control; ii) linear quadratic regulator (LQR); iii) sliding mode control (SMC); iv) decentralized bang-bang control (DBB); and v) phase angle control (PAC). Collapse fragility curves are obtained using the ensemble of 22 recorded far-field ground motion pairs (i.e., 44 far-field ground motions) recommended by FEMA P695. The collapse fragility curves for the various control strategies are compared in order to assess the performance of the MR damper control strategies in mitigating structural collapse under extreme earthquake ground motions.

2 BEAM PLASTIC HINGE DETERIORATION MODEL

The P-Δ effect and the strength and stiffness deterioration of structural components are considered to be the major contributors to the collapse of a structural system under seismic loading. The P-Δ effect is well-understood and mathematical models have been formulated for use in linear and nonlinear structural analysis, while the modeling of strength and stiffness deterioration under seismic loading is an on-going research topic. For the accurate evaluation of the collapse of a structure, it is necessary to construct a model that is capable of capturing the strength and stiffness deterioration of structural components under seismic loading. In this section, recently developed deterioration models for plastic hinges in steel beams of MRFs are introduced. The models are used for the IDA presented later in this paper.

Ibarra and Krawinkler developed a hysteretic inelastic deterioration model to describe the moment-rotation behavior in the plastic hinge region of a steel or concrete beam [1]. The model is based on a backbone curve that defines a reference skeleton behavior of a non-deteriorated system. A set of rules are used to define the basic characteristics of the hysteretic behavior between the bounds defined by the backbone curve as well as deterioration in strength and stiffness with respect to the backbone curve.

Lignos modified the Ibarra-Krawinkler model based on observations from data from several hundred tests that had been conducted on steel and reinforced concrete beams [7]. Lignos modified the backbone curve and the cyclic deterioration formulation in the original Ibarra-

Krawinkler model, where the new backbone curve proposed by Lignos is shown in Figure 1. In Figure 1, δ_c is the cap deformation (deformation associated with capacity F_c for monotonic loading); F_y is the effective yield strength; δ_y is the effective yield deformation (=F_y/K_e); K_e is the effective elastic stiffness; F_r is the residual strength capacity; δ_r is the deformation at the residual strength; δ_u is the ultimate deformation capacity; δ_p is the plastic deformation capacity associated with monotonic loading; δ_{pc} is the post-capping deformation capacity associated with monotonic loading; and κ is the residual strength ratio (=F_r/F_y). The capacity F_c mentioned above is the strength cap associated with the maximum strength incorporating average strain hardening. The strain hardening ratio α_s and the post-capping stiffness ratio α_c are defined as $\alpha_s = K_s/K_e = [(F_c/F_y)/\delta_p]/K_e$ and $\alpha_c = K_{pc}/K_e = (F_c/\delta_{pc})/K_e$, respectively. The reference energy dissipation capacity E_t, which is used to describe the cyclic deterioration, is defined as $E_t = \Lambda\delta_p$, where Λ denotes the reference cumulative deformation capacity.

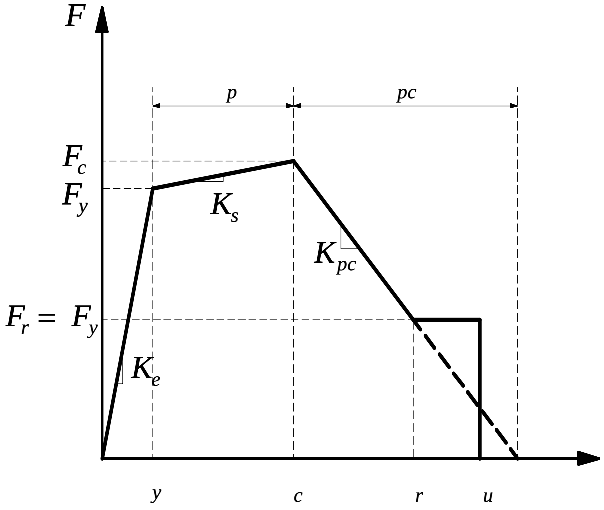

Figure 1 Modified backbone curve of Ibarra-Krawinkler model

3 MODELING OF 3-STORY BUILDING

The 3-story building shown in plan and elevation in Figures 2 and 3, respectively, was used for the study. The building has two perimeter MRFs along each of its sides and braced internal bays with MR dampers (called *damped brace frames* (DBFs)) at the 2nd and 3rd floors. The structure was designed using the simplified design procedure developed by Chae et al. [8] to achieve a performance objective of 1.5% story drift and 2.6% story drift under the DBE and MCE, respectively. The 3-story building was scaled down using a scale factor of 0.6 for the study since a reduced scale model of the building will be constructed and tested in the laboratory in future research studies. The members of the MRF are proportioned using a weak beam-strong column design. Yielding is expected to occur predominately at the ends of the MRF beams and at the base of the columns in the first story of the MRF and DBF under the DBE. The beams and diagonal bracing members in the DBF have pin-ended connections. The beams are axially restrained in the DBF by the floor diaphragm (which is assumed to be rigid in-plane) at each floor level. The inertial force due to the floor mass is transferred to the MRF and DBF through the rigid floor diaphragm connected to the lean-on column depicted in Figure 4. The diagonal bracing is expected to remain elastic up to 135% story drift [9].

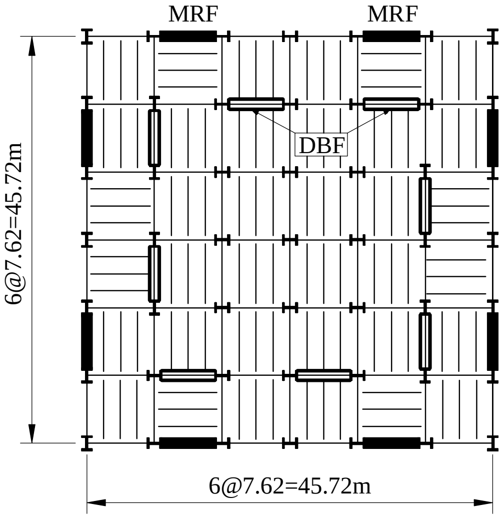

Figure 2 Floor plan of prototype building

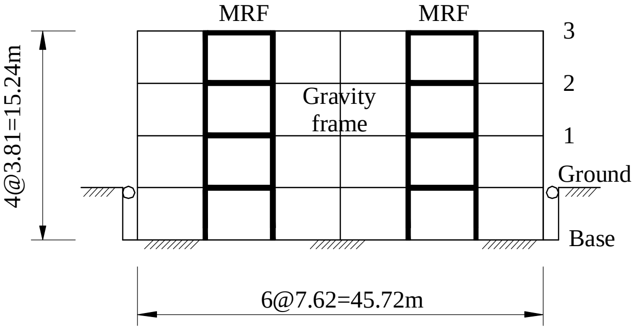

Figure 3 Exterior elevation of prototype building

Table 1 Member sizes for MRFs and gravity frames

Story (or Floor Level)	MRFs		Gravity Frames	
	Column	Beam	Column	Beam
1	W8X67	W18X46	W8X48	W10X30
2	W8X67	W14X38	W8X48	W10X30
3	W8X67	W10X17	W8X48	W10X30

Table 2 Member sizes for DBFs

Story (or Floor level)	Column	Beam	Diagonal bracing
1	W10X33	W10X30	-
2	W10X33	W10X30	W6X20
3	W10X33	W10X30	W6X20

Tables 1 and 2 summarize the member sizes for the 0.6-scale building. The OpenSees model for the scaled building is shown in Figure 4. Symmetry in the floor plan and ground motions along only one principal axis of the building were considered in the analysis. Hence, only one-quarter of the building was modeled consisting of one MRF, one DBF, and the gravity frames that are within the tributary area of the MRF and DBF.

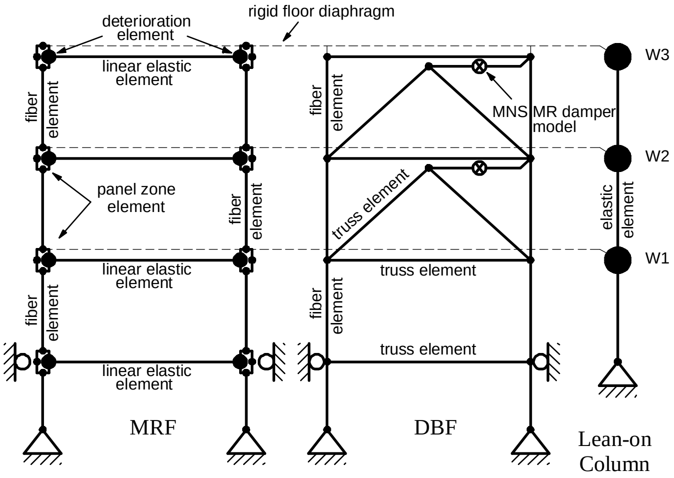

Figure 4 OpenSees model of the 3-story structure for the incremental dynamic analysis

Each beam of the MRF in the model consists of three elements: two inelastic deterioration elements with zero length at the column faces based on the modified Ibarra-Krawinkler model; and one linear elastic element between the deterioration elements. The parameters for the deterioration element are summarized in Table 3, where M_y, θ_p and θ_{pc} denote the yield moment, plastic rotation capacity and the post-capping rotation capacity, respectively. The values of these parameters are based on Lignos and Krawinkler [10] for the beam sections used in the MRF.

Table 3 Parameters for deterioration element for MRF beams

Beam size	Deterioration element parameters						
	K_e (kN-m/m)	M_y (kN-m)	α_s	θ_p (rad)	θ_{pc} (rad)	Λ	κ
W10X17	103531	116	0.002	0.062	0.207	1.244	0.01
W14X38	462520	383	0.002	0.043	0.171	1.084	0.01
W18X46	855748	564	0.002	0.033	0.186	1.104	0.01

The columns of the MRF and DBF are modeled using a nonlinear distributed plasticity force-based beam-column element. Each fiber is modeled with a bilinear stress-strain relationship with a post-yielding stiffness that is 0.01 times the elastic stiffness. The columns extend below the ground level in the model to the base, where they are pinned. The beam-to-column joints in the MRF are modeled using a nonlinear panel zone element, where shear and symmetric column bending deformation modes are considered [11]. Doubler plates in the panel zones of the MRF are included in the model. The beams and braces of the DBF are modeled using linear elastic truss elements. The gravity frames are idealized using the concept of a lean-on column, where an elastic beam-column element with geometric stiffness is used to model the lean-on column. The section properties of the lean-on column are obtained by taking the sum of the section properties of each column of the gravity frames within the tributary area (i.e., one quarter of the floor plan) of the MRF and the DBF.

The structural model in Figure 4 has two major structural components that can lead to dynamic instability under extreme earthquake ground motions: (1) negative stiffness induced by the gravity loads acting on the lean-on column (the P-Δ effect); and (2) strength deterioration in the inelastic deterioration elements in the beams of the MRF. The columns of the MRF and DBF are assumed to have sufficient strength and compactness of their cross-sections such that no deterioration in strength or stiffness of the columns is expected to occur.

To model a rigid floor diaphragm at each floor level the top node of each panel zone element in the MRF and the beam-column joint in the DBF are horizontally constrained together with the node of the lean-on column, while the vertical and rotational DOFs are released. The MR damper is assumed to be located between the top of the diagonal bracing and beam-to-column joint of the DBF. The variable current MNS model developed by Chae [9] is used to model the MR dampers for the nonlinear time history analysis.

Large-scale MR dampers were used for the study which can generate a 200kN damper force at a velocity of 0.1m/sec. [12]. The damper has a stroke limit of ±279mm. The story height of the 3-story building is 2.286m, implying that the dampers will reach their stroke limit at 12.2% story drift. Since large story drifts can be expected in a collapse simulation, the MR damper may bottom out with respect to the damper stroke limit under extreme earthquake ground motions. In this case, a gap or the hook element should be included in the model to account for the dynamic behavior associated with reaching the stroke limit, as suggested by Miyamoto et al. [5]. The MR dampers in this study are assumed to have sufficient stroke limit to accommodate the large story drifts during a collapse simulation since no experimental data exists that can be used to model the effect of bottoming out of the dampers.

4 GROUND MOTIONS

As noted previously, the far-field ground motion record set recommended by FEMA P695 (ATC 2009) was selected as ground motions for the IDA. These ground motions were selected to permit evaluation of the record-to-record (RTR) variability of the structural response and calculation of the median of the intensity of spectral acceleration at which collapse occurs. Among the 22 earthquakes, 14 occurred in the United States and 7 in other countries. Event magnitudes range from M6.5 to M7.6, with an average magnitude of M7.0. Each earthquake has two horizontal components so that a total of 44 ground motions are used for the IDA.

FEMA P695 recommends the use of spectral acceleration at the fundamental period of a structure, S_{aT_1}, as the intensity measure (IM). The ground motions are scaled up (or down) based on the spectral acceleration at the fundamental period of the structure. The MR damper stiffness depends on its displacement amplitude [9]. Hence, the effective fundamental period of the structure is dependent on the amplitude of the damper displacements, which is a function of the intensity of ground motion. In this paper, the fundamental period of the structure without MR dampers is used to determine the spectral acceleration corresponding to the IM, rather than using the effective fundamental period of the structure with the dampers. The fundamental period without the MR dampers is 0.94 sec [9], and the scaling of ground motions is performed based on the spectral acceleration at this period.

5 CONTROLLERS

As noted previously, five different control strategies for MR dampers are used in this study, namely: i) passive control; ii) linear quadratic regulator (LQR); iii) sliding mode control (SMC); iv) decentralized bang-bang control (DBB); and v) phase angle control (PAC). More details on these controllers can be found in Chae [9]. A constant current with I=2.5A is supplied to the MR dampers for passive control, while for the semi-active controllers the current switched from I=0.0A to 2.5A based on the semi-active control law.

6 INCREMENTAL DYNAMIC ANALYSIS

The incremental dynamic analysis (IDA) curves are a set of plots that correlate a damage measure (DM) with the IM that characterizes the applied scaled accelerograms [13]. The roof drift ratio of the building, θ_{roof}, is selected as the DM for this study. A ground motion is scaled up until dynamic instability occurs, where an IDA curve becomes a flat line, i.e., at collapse. Each selected ground motion is gradually scaled up until θ_{roof} reaches 17% or collapse occurs. For the 44 ground motions in the ensemble, the IDA curves all became flat indicating collapse before θ_{roof} reached 17%. The median roof drift when the IDA curves become flat is approximately 14%.

Figures 5 through 10 show the IDA curves for the structure with various control strategies. These results are for the 44 ground motions. The collapse margin ratio (CMR) was determined for each case, where the CMR is defined by FEMA P695 as the ratio of the median value for the collapse spectral acceleration, $\hat{S}_{CT}$, to the spectral acceleration of the MCE, S_{MT}, at the fundamental period of the structural system:

$$\mathrm{CMR} = \frac{\hat{S}_{CT}}{S_{MT}} \tag{1}$$

$\hat{S}_{CT}$ for each control case is calculated from the IDA curves and marked in Figures 5 through 10 along with the S_{MT}. Table 4 shows the CMR values for each control strategy. Since the purpose is to evaluate the collapse capacity of a structure with MR dampers with various control strategies, the further adjustment of the CMR values based on the spectral shape factor (SSF) [2] is not considered in this study. The results in Table 4 show that when passive control is used that the CMR value increases by about 26% compared to the no damper case, demonstrating the benefit of using MR dampers. The overall performance of each semi-active controller is similar to that of the passive control case, except for the LQR controller. The LQR controller shows the highest CMR value, where the improvement over passive control is about 7%.

7 COLLAPSE FRAGILITY CURVES

A collapse fragility curve is the cumulative distribution function (CDF) which relates the intensity of ground motion to the probability of collapse, and is constructed utilizing the results of the IDAs. For a prescribed level of spectral acceleration S_{aT_1}, the number of cases, N_{SaT1}, where collapse occurs for a spectral acceleration equal to or less than this value of S_{aT_1} among the IDA curves for the various ground motions is counted. The probability of collapse associated with this value of S_{aT_1} is N_{SaT1}/N_{tot}, where N_{tot} is the total number of IDA curves (i.e., ground motions).

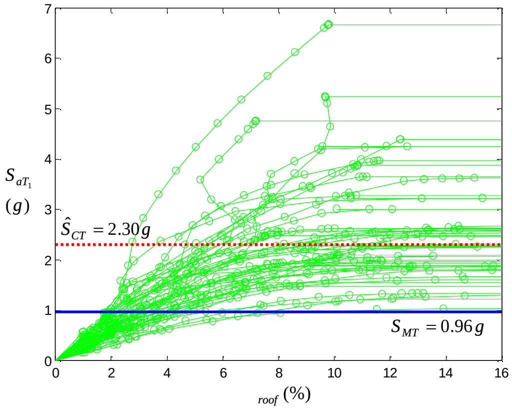

Figure 5 IDA curves: no damper case

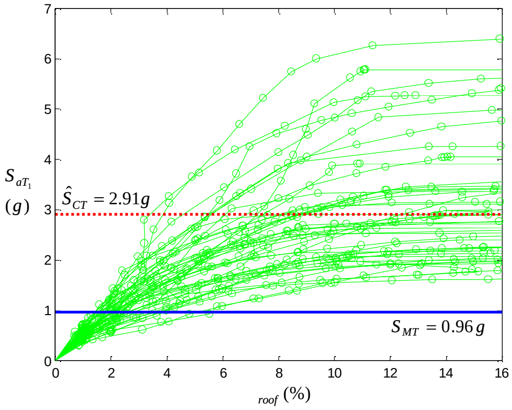

Figure 6 IDA curves: passive control

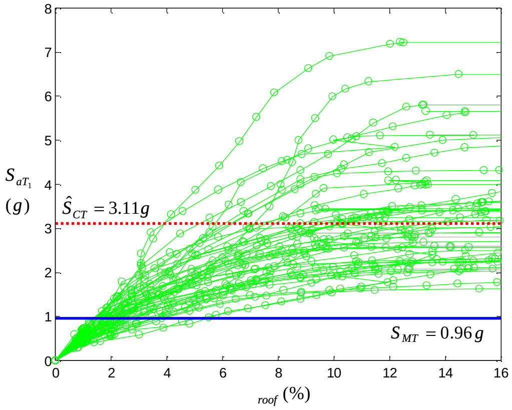

Figure 7 IDA curves: LQR control

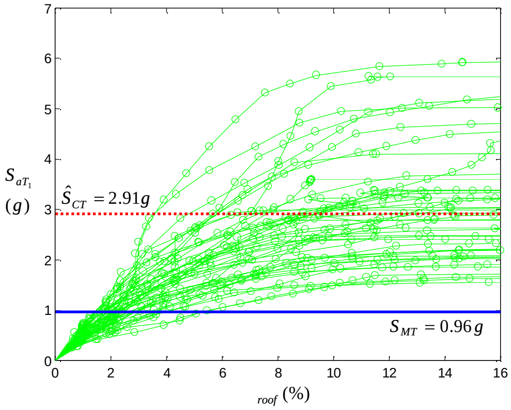

Figure 8 IDA curves: SMC

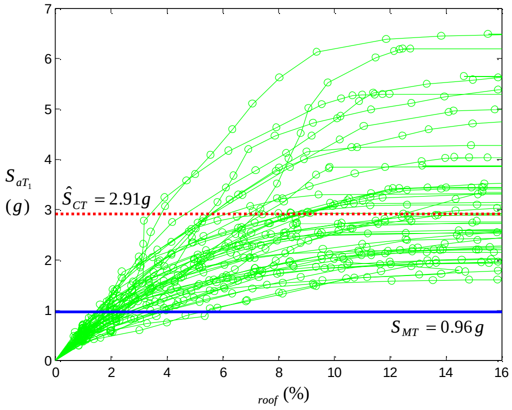

Figure 9 IDA curves: DBB control

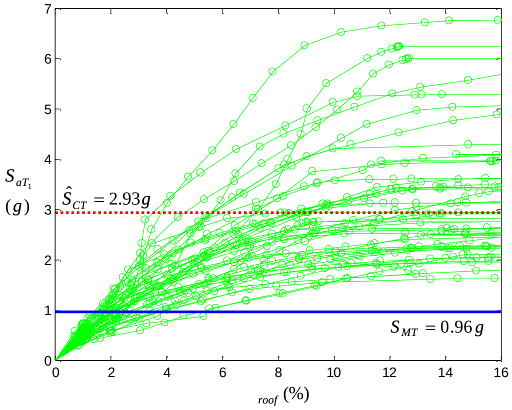

Figure 10 IDA curves: PAC

The probability of collapse typically follows a lognormal distribution. A set of collapse data points can thus be fitted using the lognormal distribution to construct the collapse fragility curve. The fitted lognormal distribution is defined by two parameters, namely, the median collapse spectral acceleration ($\hat{S}_{CT}$), and the standard deviation of the natural logarithm of the collapse spectral accelerations (ζ). The CDF with a lognormal distribution, $F(x)$, is mathematically expressed as

$$F(x) = \int_0^x \frac{1}{s\zeta\sqrt{2\pi}} \exp\left[-\frac{(\ln s-\lambda)^2}{2\zeta^2}\right] ds = \Phi\left(\frac{\ln x-\lambda}{\zeta}\right) \tag{2}$$

where, Φ is the cumulative distribution function of the standard normal distribution and $\lambda = \ln \hat{S}_{CT}$. Figure 11 compares the collapse fragility curves for passive control with the no damper case. The fragility curve for passive control is located to the right of the fragility curve for the no damper case, which means the collapse potential of the structure with passive control is lower than that for the structure with no dampers. This result is also illustrated in Table 4 by a comparison of the CMR values, where passive control has a higher CMR value. The collapse fragility curve for various semi-active control strategies are compared to the collapse fragility curve for passive control in Figures 12 through 15. The collapse fragility curves for the semi-active control strategies are shown to be similar to passive control, except for the LQR controller. The collapse fragility curve for the building with the LQR controller is more notably to the right of that for the passive control case (Figure 12) than for the other comparisons, indicating a lower probability of collapse compared to passive control, and consistent with having a higher CMR value in Table 4.

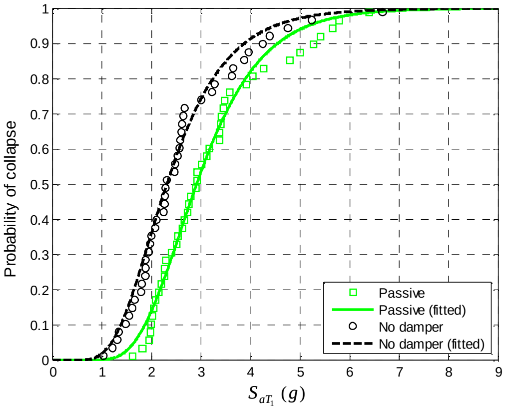

Figure 11 Collapse fragility curves where no damper case is compared with passive control

Table 4 Collapse margin ratio (CMR) for 3-story building with various control strategies

	No damper	Passive	LQR	SMC	DBB	PAC
CMR	2.39	3.02	3.23	3.03	3.02	3.05

8 COLLAPSE MODE

The collapse mode of the building studied is characterized by the formation of plastic hinges in the beams and columns leading to a collapse mechanism. A soft story mechanism, where both ends of all columns at a particular story level develop plastic hinges, did not occur in any of the cases. The design methodology based on a strong column-weak beam design appears to enable a soft story collapse mechanism to be avoided.

Figure 16 shows the deformed shape of the building with passively controlled MR dampers at the time of maximum drift under the 1994 Northridge earthquake (Canyon country, 000 component), where the ground motion was scaled to a spectral acceleration of S_{aT_1}=2.25g. Collapse for this ground motion occurs when S_{aT_1}=2.27g. Both ends of each beam in the 1st through 3rd floors in the MRF and the ground level of the 1st story columns for both the MRF and DBF form plastic hinges during the earthquake.

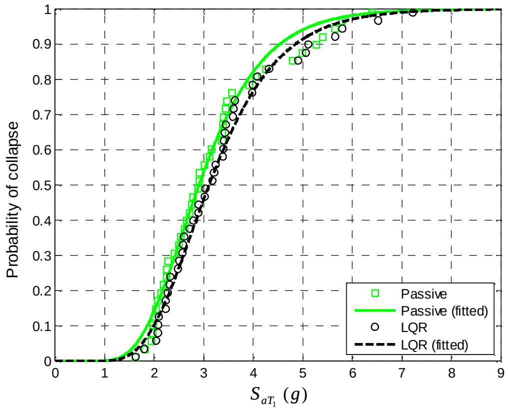

Figure 12 Collapse fragility curves where LQR controller is compared with passive control

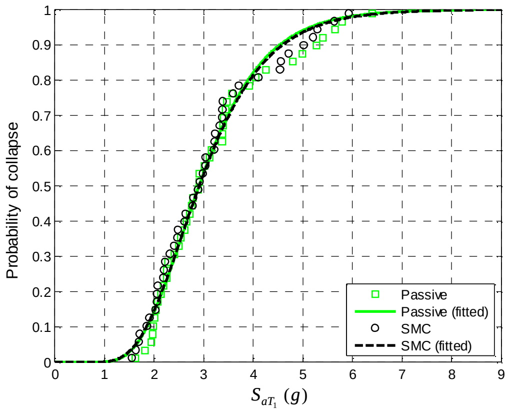

Figure 13 Collapse fragility curves where SMC controller is compared with passive control

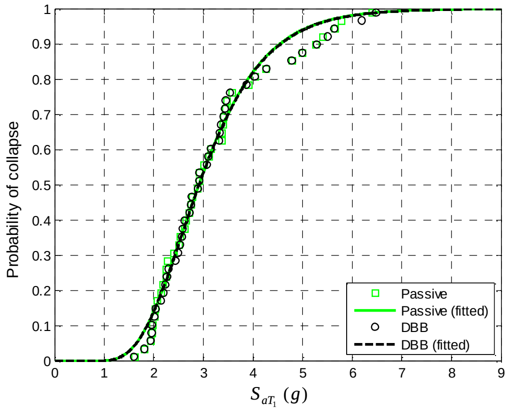

Figure 14 Collapse fragility curves where DBB controller is compared with passive control

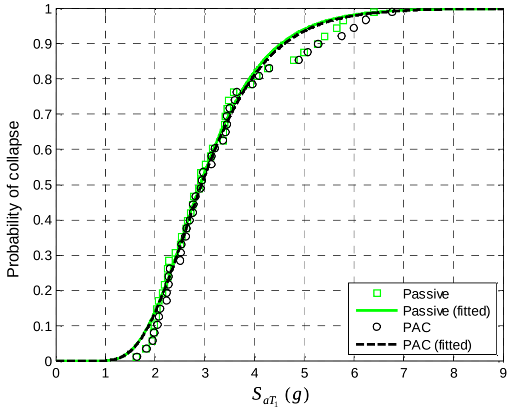

Figure 15 Collapse fragility curves where PAC controller is compared with passive control

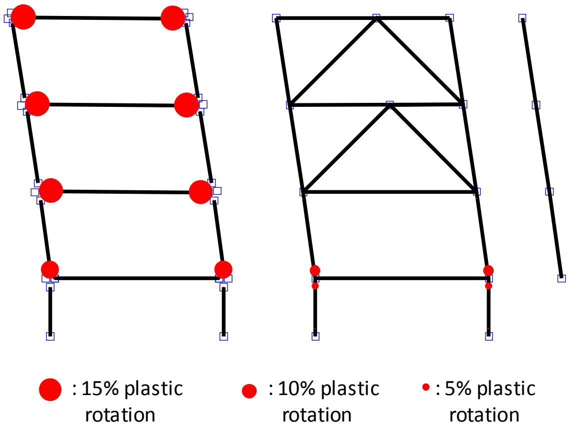

Figure 16 Deformed shape of building at incipient collapse; the solid circles represent the location of plastic hinges and their size denotes the magnitude of plastic rotation

9 CONCLUSIONS

In this paper, the collapse potential of a 3-story steel frame building with MR dampers controlled by various control strategies was investigated. A model of the structure was developed using OpenSees that included strength and stiffness deterioration along with the P-Δ effect. Incremental dynamic analyses based on nonlinear time history earthquake simulations were performed to obtain the statistical response and collapse margin ratios (CMRs) for the structure. Five different control strategies for the MR dampers were used, and the collapse potential for each case was compared. The passive control of MR dampers with a 2.5A constant current input improved the CMR value by about 26% compared to the structure without MR dampers. The collapse fragility curves for sliding mode control, decentralized bang-bang control, and phase angle control resulted in almost the same collapse potential as passive control, while the LQR controller provided a reduction in the collapse potential. The CMR is about 7% greater for the structure with an LQR controller compared to passive control.

The LQR and SMC controllers require control gains to be specified. To reach more general conclusions about the seismic collapse potential of buildings with semi-active controlled MR dampers it is recommended that the effect of the control gains on the collapse potential be further investigated. In addition, other semi-active controllers and various structural geometries (e.g. the height of the building) should be included. The effect of a damper bottoming out on the collapse potential of structures with MR dampers also needs to be investigated.

ACKNOWLEDGEMENTS

This paper is based upon work supported by grants from the Pennsylvania Department of Community and Economic Development through the Pennsylvania Infrastructure Technology Alliance, and by the National Science Foundation under Award No. CMMI-1011534, within the George E. Brown, Jr. Network for Earthquake Engineering Simulation Research (NEESR) program, Award No. CMS-0612661, and Award No. CMS-0402490 NEES Consortium Operation.

REFERENCES

[1] Ibarra, L.F. and Krawinkler, H., Global collapse of frame structures under seismic excitations, *John A. Blume Earthquake Engineering Center, Report No. 152*, 2005.

[2] Applied Technology Council, *Quantification of building seismic performance factors*, ATC-63 Project Report (FEMA P695), Redwood City, CA, 2009.

[3] Solberg, K., Bradley, B., Rodgers, G., Mander, J., Dhakal, R., and Chase, J., Multi-level seismic performance assessment of a damage-protected beam-column joint with internal lead dampers, *New Zealand Society for Earthquake Engineering Annual Conference (NZSEE 07)*, Palmerston North, New Zealand, 2007.

[4] Marshall, J.D. and Charney, F.A., A hybrid passive control device for steel structures, I: development and analysis, *Journal of Constructional Steel Research*, **66**, 1278-1286, 2010.

[5] Miyamoto, H.K., Gilani, A.S.J., Ariyaratana, Ch., and Wada, A., Probabilistic evaluation of seismic performance of steel moment framed buildings incorporating damper limit states, *ASCE Structures Congress*, Orlando, FL, 2010.

[6] OpenSees, *Open system for earthquake engineering simulation*, Pacific Earthquake Engineering Research Center, University of California, Berkeley, 2009.

[7] Lignos, D., Sidesway collapse of deteriorating structural systems under seismic excitations, *Ph.D. Dissertation*, Stanford University, Stanford, CA, 2008.

[8] Chae, Y., Dong, B., Ricles, J.M., and Sause, R., Development of simplified design procedure for structures with magneto-rheological (MR) dampers, *8th International Conference on Urban Earthquake Engineering*, Tokyo, Japan, 2011.

[9] Chae, Y., Seismic hazard mitigation of building structures using magneto-rheological dampers, *Ph.D. Dissertation*, Lehigh University, PA, 2011.

[10] Lignos, D., and Krawinkler, H., Sidesway collapse of deteriorating structural systems under 17 seismic excitations, *John A. Blume Earthquake Engineering Center Report No. TR 172*, Department of Civil Engineering, Stanford University, 2009.

[11] Seo, C.Y., Lin, Y.C., Sause, R, and Ricles, J.M., Development of analytical models for 0.6 scale self-centering MRF with beam web friction devices, *6th International Conference for Steel Structures in Seismic Area (STESSA)*, Philadelphia, 2009.

[12] Chae, Y., Ricles, J.M., and Sause, R., Development of a large-scale MR damper model for seismic hazard mitigation assessment of structures, *9th US National and l10th Canadian Conference on Earthquake Engineering*, Toronto, Canada, 2010.

[13] Vamvatsikos, D. and Cornell, C.A., Incremental dynamic analysis, *Earthquake Engineering and Structural Dynamics*, **31**, 491-514, 2002.

COMPDYN 2011
3^{rd} ECCOMAS Thematic Conference on
Computational Methods in Structural Dynamics and Earthquake Engineering
M. Papadrakakis, M. Fragiadakis, V. Plevris (eds.)
Corfu, Greece, 25-28 May 2011

MODEL UNCERTAINTIES IN SMART STRUCTURES

Amalia J. Moutsopoulou[1], **Georgios E. Stavroulakis**[2], **and Anastasios T. Pouliezos**[2]

[1]Department of Civil Engineering, Technological Educational Institute of Crete
Estavromenos, 71004, Heraklion
e-mail: amalia@staff.teicrete.gr

[2] Department of Production Engineering and Management, Technical University of Crete
Kounoupidiana, 73100, Chania
e-mail: gestavr@dpem.tuc.gr, tasos@dpem.tuc.gr

Keywords: Uncertainty, Smart beam, Strochastic load, Robust performance, Robust analysis, Robust synthesis.

Abstract. *This paper deals with the incorporation of model uncertainties and the usage of robust control techniques in active vibration suppression of smart structures. The used advanced control techniques are based on the* H_∞ *criterion and m-analysis. Both techniques allow us to take into account the worst case scenario of uncertain disturbances and noise of the system. The presented results demonstrate remarkable efficiency of the proposed techniques.*

1 INTRODUCTION

The field of smart structures has been an emerging area of research for the last few decades [2, 3, 4, 5, 9]. Smart structures are equipped with sensors, actuators and controlunits, and are able to respond in a smart way to external stimuli. The importance of this field is supported by developments in the field of materials science and technology and in the fiels of control and electronics. In materials science, new smart materials are developed that can be used for sensing and actuation in an efficient and controlled manner. These smart materials can be integrated into structures so they can be employed as actuators and sensors for the resulting smart composite structure. On the other hand the applicability of a smart structure strongly depends on the efficient design and implementation of the control systems. Critical issues, like deviation of the structure or the environment from their nominal values or time-delay, must be addressed. In this paper we focus our attention on the existence of uncertainties in smart structures. A finite element based model of a smart beam equipped with uncertainties is used. Based on this model an H_∞ and a μ-controller are designed which effectively suppress the vibrations of the smart beam under stochastic wind-type loading. The advantage of the H_∞ criterion is its ability to take into account the worst influence of uncertain disturbances or noise in the system. By using this technique it is possible to synthesize a H_∞ controller which will be robust with respect to a prespecified number of errors in the model.

Uncertainties in a structural model may arise from non-linearities which are not taken into account in a linear model, from inaccurate knowledge of certain parameters (for example, damping), from unmodelled dynamics in higher frequencies, as well as from their variations over the life of the structure. On the structural model with uncertainties a robust μ-controller is analyzed and synthesized, using the $D - K$ iterative method. The results are compared and commented upon using the various controllers. The results are very good: the oscillations were suppressed even for a real aeolian load, with the required voltages of the piezoelectric components taking values within their endurance limits.

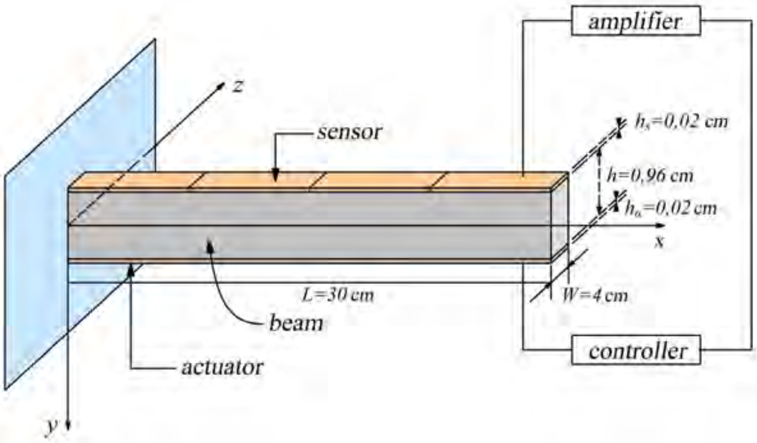

Figure 1: Beam with piezoelectric sensors/actuators.

2 MATHEMATICAL MODELLING

A cantilever slender beam with rectangular cross-section is considered. Four pairs of piezoelectric patches are embedded symmetrically at the top and the bottom surfaces of the beam, as shown in Fig. 1. The beam is made from graphite- epoxy $T300-976$ and the piezoelectric patches are $PZTG1195N$. The top patches act like sensors and the bottom like actuators. The resulting composite beam is modelled by means of the classical laminated technical theory of bending. Furthermore, we assume that the mechanical properties of both the piezoelectric material and the host beam are independent in time. The thermal effects are considered to be negligible as well [9].

The beam has length L, width b and thickness h. The sensors and the actuators have width b_S and b_A and thickness h_S and h_A, respectively. The electromechanical parameters of the beam used for the application of the method in this paper are given in the table.

Parameters	Values
Beam length, L	$0.3m$
Beam width, W	$0.04m$
Beam thickness, h	$0.0096m$
Beam density, ρ	$1600kg/m$
Youngs modulus of the beam, E	$1.5 \times 10^{11} N/m^2$
Piezoelectric constant, d_{31}	$254 \times 10^{-12} m/V$
Electric constant, ξ_{33}	$11.5 \times 10^{-3} Vm/N$
Young's modulus of the piezoelectric element	$1.5 \times 10^{11} N/m^2$
Width of the piezoelectric element	$b_S = b_a = 0.04m$
Thickness of the piezoelectric element	$h_S = h_a = 0.0002m$

Table 1: Parameters of the composite beam.

2.1 Piezoelectric equations

In order to derive the basic equations for piezoelectric sensors and actuators (S/As), we assume that:

- The piezoelectric S/A are bonded perfectly on the host beam;
- The piezoelectric layers are much thinner then the host beam;
- The piezoelectric material is homogeneous, transversely isotropic and linearly elastic;
- The piezoelectric S/A are transversely polarized (in the z-direction)[9].

Under these assumptions the three-dimensional linear constitutive equations are given by [8],

$$\left\{ \begin{array}{c} \sigma_{xx} \\ \sigma_{xz} \end{array} \right\} = \left[\begin{array}{cc} Q_{11} & 0 \\ 0 & Q_{55} \end{array} \right] \left(\left\{ \begin{array}{c} \varepsilon_{xx} \\ \varepsilon_{xz} \end{array} \right\} - \left[\begin{array}{c} d_{31} \\ 0 \end{array} \right] E_z \right) \tag{1}$$

$$D_z = Q_{11} d_{31} \varepsilon_{xx} + \xi_{xx} E_z \tag{2}$$

where σ_{xx}, σ_{xz} denote the axial and shear stress components, D_z, denotes the transverse electrical displacement; ε_{xx} and ε_{xz} are axial and shear strain components; Q_{11}, and Q_{55}, denote elastic constants; d_{31}, and ξ_{33}, denote piezoelectric and dielectric constants, respectively. Equation 1 describes the inverse piezoelectric effect and equation 2 describes the direct piezoelectric effect. E_z, is the transverse component of the electric field that is assumed to be constant for the piezoelectric layers and its components in the xy-plain are supposed to vanish. If no electric field is applied in the sensor layer, the direct piezoelectric equation 2 is fermed like this,

$$D_z = Q_{11} d_{31} \varepsilon_{xx} \tag{3}$$

and it is used to calculate the output charge created by the strains in the beam.[7]

2.2 Equations of motion

We assume that:

- The beam centroidal and elastic axis coincides with the x-coordinate axis so that no bending-torsion coupling is considered;
- The axial vibration of the host beam is considered negligible;
- The displacement field $\{u\} = (u_1, u_2, u_3)$ is obtained based on the usual Timoshenko assumptions [1],

$$\begin{aligned} u_1(x,y,z) &\approx z\phi(x,t) \\ u_2(x,y,z) &\approx 0 \\ u_3(x,y,x) &\approx \mathrm{w}(x,t) \end{aligned} \tag{4}$$

where ϕ is the rotation of the beam's cross-section about the positive y-axis and w is the transverse displacement of a point of the centroidal axis $(y = z = 0)$.
The strain displacement relations can be applied to equation 4 to give,

$$\varepsilon_{xx} = z\frac{\vartheta\phi}{\vartheta x} \quad \varepsilon_{xz} = \phi + \frac{\vartheta \mathrm{w}}{\vartheta x} \tag{5}$$

We suppose that the transverse shear deformation ε_{xx} is equal to zero[2].
In order to derive the equations of the motion of the beam we use Hamilton's principle,[11]

$$\int_{t_2}^{t_1} (\delta T - \delta U + \delta W)dt = 0, \tag{6}$$

where T is the total kinetic energy of the system, U is the potential (strain) energy and W is the virtual work done by the external mechanical and electrical loads and moments. The first variation of the kinetic energy is given by,

$$\begin{aligned} \delta T &= \frac{1}{2}\int_V \rho \left\{\frac{\vartheta u}{\vartheta t}\right\}^r \left\{\frac{\vartheta u}{\vartheta t}\right\} dV \\ &= \frac{b}{2}\int_0^L \int_{-\frac{h}{2}-h_a}^{\frac{h}{2}+h_s} \rho \left(z\frac{\vartheta\phi}{\vartheta t}\delta\frac{\vartheta\phi}{\vartheta t} + \frac{\vartheta \mathrm{w}}{\vartheta t}\delta\frac{\vartheta \mathrm{w}}{\vartheta t}\right) dz dx \end{aligned} \tag{7}$$

The first variation of the kinetic energy is given by,

$$\begin{aligned} \delta U &= \frac{1}{2}\int_V \delta\{\epsilon\}^T\{\sigma\}dV \\ &= \frac{b}{2}\int_0^L \int_{-\frac{h}{2}-h_a}^{\frac{h}{2}+h_s} \left[Q_{11}\left(z\frac{\vartheta \mathrm{w}}{\vartheta x}\delta\right)\left(z\frac{\vartheta \mathrm{w}}{\vartheta x}\right)\right] dzdx \end{aligned} \tag{8}$$

If the load consists only of moments induced by piezoelectric actuators and since the structure has no bending twisting couple then the first variation of the work has the form [11],

$$\delta W = b\int_0^L M^a \delta\left(\frac{\vartheta\phi}{\vartheta x}\right)dx \tag{9}$$

where M^a is the moment per unit length induced by the actuator layer and is given by,

$$\begin{aligned} M^a = \int_{-\frac{h}{2}-h_a}^{-\frac{h}{2}} z\sigma^a_{xx}dz \quad &= \textstyle\int_{-\frac{h}{2}-h_a}^{-\frac{h}{2}} zQ_{11}d_{31}E^a_z dz \\ \left(E^a_z = \frac{V_a}{h_a}\right) \end{aligned} \tag{10}$$

2.3 Finite element formulation

We consider a beam element of length L_e, which has two mechanical degrees of freedom at each node: one translational ω_1 (respectively ω_2) in direction y and one rotational ψ_1 (respectively ψ_2), as it is shown in Fig. 2. The vector of nodal displacements and rotations q_e is defined as [8],

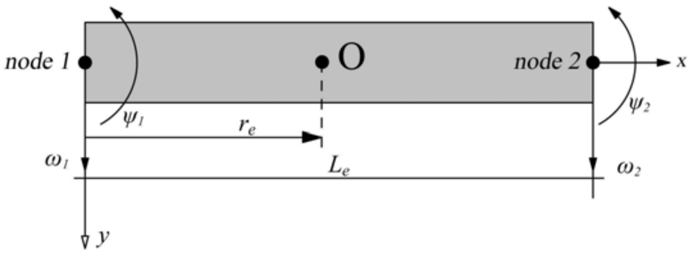

Figure 2: Beam finite element.

$$q_e = [\omega_1, \psi_1, \omega_2, \psi_2] \tag{11}$$

The transverse deflection $\omega(x,t)$ and rotation $\psi(x,t)$ along the beam are continuous and they are interpolated by Hermitian linear shape functions H_i^ω and H_i^ψ as follows[5],

$$\begin{aligned} \omega(x,t) &= \sum_{i=1}^{4} H_i^\omega(x)q_i(t) \\ \psi(x,t) &= \sum_{i=1}^{4} H_i^\psi(x)q_i(t) \end{aligned} \tag{12}$$

This classical finite element procedure leads to the approximate (discretized) problem. For a finite element the discrete differential equations are obtained by substituting the discretized expressions 13 into equations 8 and 9 to evaluate the kinetic and strain energies. Integrating over spatial domains and using the Hamilton's principle 6 the equation of motion for a beam element are expressed in terms of nodal variable q as follows [2, 6, 8],

$$M\ddot{q}(t) + D\dot{q}(t) + Kq(t) = f_m(t) + f_e(t) \tag{13}$$

where M is the mass matrix, D is the viscous damping matrix, K is the stiffness matrix, f_m is the external loading vector and f_e is the generalized control force vector produced by electromechanical coupling effects. The independent variable vector $q(t)$ is composed of transversal deflections ω_i and rotations ψ_i, i.e.,[4]

$$q(t) = \begin{bmatrix} \omega_1 \\ \psi_1 \\ \vdots \\ \omega_n \\ \psi_n \end{bmatrix} \tag{14}$$

where n is the number of nodes used in the analysis. Vectors w and f_m are positive upwards. For the state-space control transformation,we are presented with,

$$\dot{x}(t) = \begin{bmatrix} q(t) \\ \dot{q}(t) \end{bmatrix} \tag{15}$$

Furthermore to express $f_e(t)$ in the form of $Bu(t)$ we write it as the product $f_e^* u$, where f_e^* is the piezoelectric force for a unit applied on the corresponding actuator, and u represents the voltages on the actuators. Finally, $d(t) = f_m(t)$ is the disturbance vector[3]. Then,

$$\dot{x}(t) = \begin{bmatrix} 0_{2n\times 2n} & I_{2n\times 2n} \\ -M^{-1}K & -M^{-1}D \end{bmatrix} x(t) + \begin{bmatrix} 0_{2n\times n} \\ M^{-1}f_e^* \end{bmatrix} u(t) + \begin{bmatrix} 0_{2n\times 2n} \\ M^{-1} \end{bmatrix} \tag{16}$$

$$= Ax(t) + Bu(t) + Gd(t) = Ax(t) + \begin{bmatrix} B & G \end{bmatrix} \begin{bmatrix} u(t) \\ d(t) \end{bmatrix} = Ax(t) + \tilde{B}\tilde{u}(t) \tag{17}$$

The previous description of the dynamical system will be augmented with the output equation (*displacements* only measured)[5],

$$y(t) = [x_1(t) \quad x_3(t) \quad \ldots \quad x_{n-1}(t)]^T = Cx(t) \tag{18}$$

In this formulation u is $n \times 1$ (at most, but can be smaller), while d is $2n \times 1$. The units used are compatible for instance m, rad, sec and N. [6, 8]

3 DESIGN OBJECTIVES AND SYSTEM SPECIFICATIONS

The structured singular value of the transfer function to what matrix is defined as,

$$\mu(M) = \begin{cases} \frac{1}{\min_{k_m}\{det(I - k_m M\Delta)=0,\ \bar{\sigma}(\Delta)\leq 1\}} \\ 0,\ \Delta\ det(I - M\Delta) = 0 \end{cases} \tag{19}$$

This quantity defines the smallest structured $\mu(M)$(measured in terms of $\bar{\sigma}(\Delta)$)which makes $det(I - M\Delta) = 0$: then $\mu(M) = \frac{1}{\bar{\sigma}(\Delta)}$. It follows that values of μ smaller than 1 are desired [12, 13]

The design objectives fall into two categories:

1. Stability of closed loop system (plant+controller).
   (a) Disturbance attenuation with satisfactory transient characteristics (overshoot, settling time).
   (b) Small control effort.
2. Robust performance

Stability of closed loop system (plant+controller) should be satisfied in the face of modelling errors. [10]

In order to obtain the required system specifications with respect to the above objectives we need to represent our system in the so-called - Δ structure. Let us start with the simple typical diagram of Fig. 3. [14, 15]

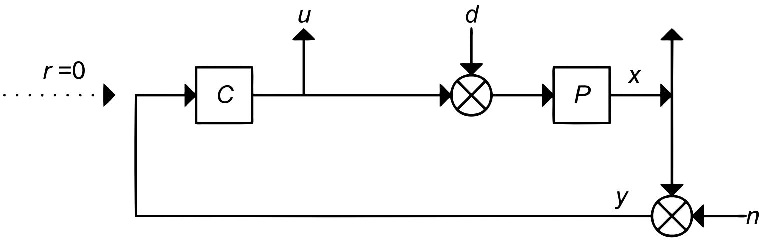

Figure 3: Classical control block diagram (P: plant dynamical system, C: controller)

In this diagram there are two inputs, d and n, and two outputs, u and x. In what follows it is assumed that,

$$\left\| \begin{matrix} d \\ n \end{matrix} \right\|_2 \leq 1, \quad \left\| \begin{matrix} x \\ u \end{matrix} \right\|_2 \leq 1 \tag{20}$$

If this is not the case, appropriate frequency-dependent weights can transform original signals so that the transformed signals have this property. The details of the system are given in Fig.4:

In this description,

$$z = \begin{bmatrix} u \\ x \end{bmatrix}, \quad \mathrm{w} = \begin{bmatrix} d \\ n \end{bmatrix} \tag{21}$$

where z are the output variables to be controlled, and w the exogenous inputs.

Given that P has two inputs and two outputs it is, as usual, naturally partitioned as,

$$\begin{bmatrix} z(s) \\ y(s) \end{bmatrix} = \begin{bmatrix} P_{z\mathrm{w}}(s) & P_{zu}(s) \\ P_{y\mathrm{w}}(s) & P_{yu}(s) \end{bmatrix} \begin{bmatrix} \mathrm{w}(s) \\ u(s) \end{bmatrix} = P(s) \begin{bmatrix} \mathrm{w}(s) \\ u(s) \end{bmatrix} \tag{22}$$

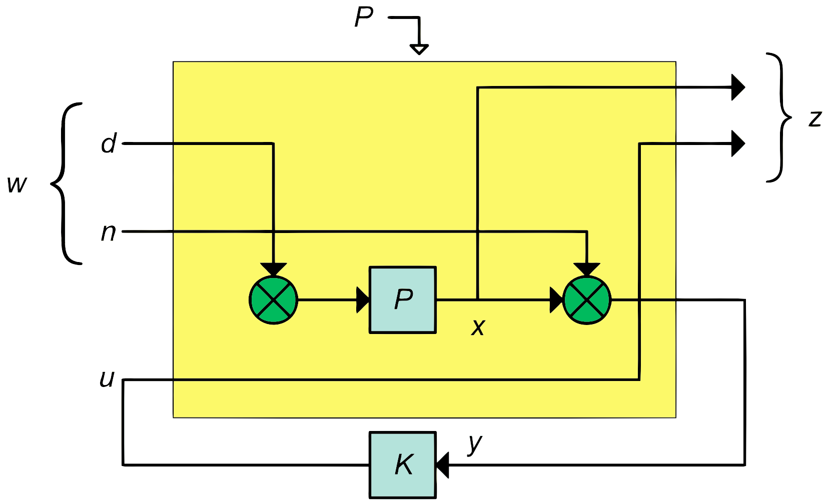

Figure 4: Detailed two-port diagram (with a linear feedback control K)

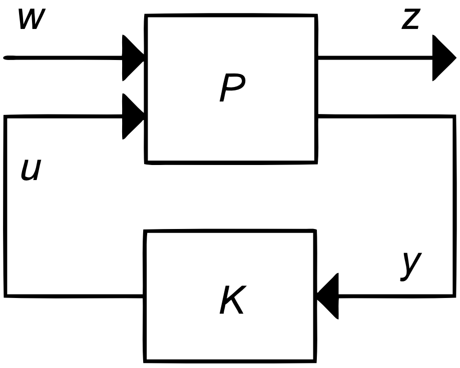

Figure 5: Two-port diagram

In addition the controller is written,

$$u(s) = K(s)y(s) \tag{23}$$

Substituting (22) in (23) gives the closed loop transfer function $N_{zw}(s)$,

$$N_{zw}(s) = P_{zw}(s) + P_{zu}(s)K(s)(I - P_{yu}(s)K(s))^{-1}P_{yw}(s) \tag{24}$$

To deduce robustness specifications one more diagram is needed, namely that of Figure 6: where N is defined by (24) and the uncertainty modelled in Δ satisfies $||\Delta||_\infty \leq 1$ (details are given later on in this paper). Here,

$$z = \mathcal{F}_u(N, \Delta)w = [N_{22} + N_{21}\Delta(I - N_{11}\Delta)^{-1}N_{12}]w = Fw \tag{25}$$

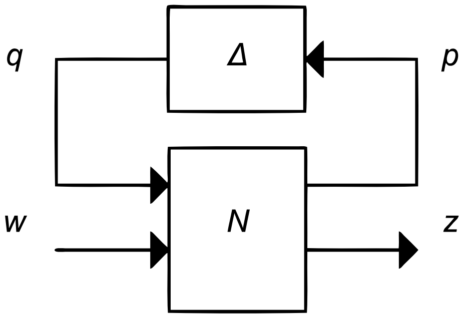

Figure 6: Two port diagram with uncertainty

Given this structure we can state the following definitions:

$$\begin{gathered}\text{Nominal stability } (NS) \Leftrightarrow N \text{ internally stable}\\ \text{Nominal performance } (NP) \Leftrightarrow ||N_{22}(j\omega)||_\infty \leq 1 \; \forall\omega \text{ and } NS\\ \text{Robust stability } (RS) \Leftrightarrow F = \mathcal{F}_u(N,\Delta) \text{ stable } \forall\Delta,\; ||\Delta||_\infty < 1 \text{ and } NS\\ \text{Robust performance } (RP) \Leftrightarrow ||F||_\infty < 1,\; \forall\Delta,\; ||\Delta||_\infty < 1 \text{ and } S\end{gathered} \tag{26}$$

It has been proved that the following conditions hold in the case of block-diagonal real or complex perturbations Δ:

1. The system is nominally stable if M is internally stable.
2. The system exhibits nominal performance if $\bar{\sigma}(N_{22}(j\omega)) < 1$
3. The system (M, Δ) is robustly stable if and only if,

   $$\sup_{\omega\in\mathbb{R}} \mu_\Delta(N_{11}(j\omega)) < 1 \tag{27}$$

   where μ_Δ is the structured singular value of N given the structured uncertainty set Δ. This condition is known as the generalized small gain theorem.
4. The system (N, Δ) exhibits robust performance if and only if,

   $$\sup_{\omega\in\mathbb{R}} \mu_{\Delta_a}(N(j\omega)) < 1 \tag{28}$$

   where,

   $$\Delta_a = \begin{bmatrix}\Delta_p & 0\\ 0 & \Delta\end{bmatrix} \tag{29}$$

   and Δ_p is full complex, has the same structure as Δ and dimensions corresponding to w, z. [15]
   Unfortunately, only bounds on μ can be estimated.

3.1 Controller synthesis

All the above results support the analysis problem and provide tools to judge the performance of any controller or to compare different controllers. However it is possible to approximately synthesize a controller that achieves given performance in terms of the structured singular value μ.

In this procedure, which is called $(D, G-K)$ iteration [20] the problem of finding an μ-optimal controller K such that $\mu(\mathcal{F}_u(F(j\omega)), K(j\omega)) \leq \beta$, $\forall \omega$ is transformed into the problem of finding transfer function matrices $D(\omega) \in \mathcal{D}$ and $G(\omega) \in \mathcal{G}$, such that,

$$\sup_{\omega} \bar{\sigma} \left[\left(\frac{D(\omega)\mathcal{F}_u(F(j\omega), K(j\omega))D^{-1}(\omega)}{\gamma} - jG(\omega) \right) \left(I + G^2(\omega)\right)^{-\frac{1}{2}} \right] \leq 1, \quad \forall \omega \tag{30}$$

Unfortunately this method does not guarantee even finding local maxima. However for complex perturbations a method known as $D-K$ iteration is available (implemented in MATLAB). [20] It combines H_∞ synthesis and μ-analysis and often yields good results. The starting point is an upper bound on μ in terms of the scaled singular value,

$$\mu(N) \leq \min_{D \in \mathcal{D}} \bar{\sigma}(DND^{-1}) \tag{31}$$

The idea is to find the controller that minimizes the peak over the frequency range namely,

$$\min_{K} \left(\min_{D \in \mathcal{D}} ||DN(K)D^{-1}||_\infty \right) \tag{32}$$

by alternating between minimizing $||DN(|K)D^{-1}||_\infty$ with respect to either K or D (while holding the other fixed).

1. **K-step**. Synthesize an $\mathcal{H}_\infty$ controller for the scaled problem $\min_K ||DN(K)D^{-1}||_\infty$ with fixed $D(s)$.
2. **D-step**. Find $D(j\omega)$ to minimize at each frequency $\bar{\sigma}(DND^{-1}(j\omega))$ with fixed N.
3. Fit the magnitude of each element of $D(j\omega)$ to a stable and minimum phase transfer function $D(s)$ and got to Step 1. [20]

3.2 System uncertainty

Let us assume uncertainty in the mass M and K matrices of the form,

$$\begin{aligned} K &= K_0(I + k_p I_{2n\times 2n}\delta_K) \\ M &= M_0(I + m_p I_{2n\times 2n}\delta_M) \end{aligned} \tag{33}$$

Alternatively, since in general the Reyleigh damping assupmtion is,

$$D = aK + \beta M \tag{34}$$

D could be expressed similarly to K, M, as,

$$D = D_0(I + d_p I_{2n\times 2n}\delta_D) \tag{35}$$

In this way we introduce uncertainty in the form of percentage variation in the relevant matrices. More detailed correlation of uncertainty with certain properties of the structures (e.g., material constants, flexibility of joints, cracks or delaminations) is possible and will be investigated in the future.

Here it will be assumed,

$$||\Delta||_\infty \overset{def}{=} \left\| \left[\begin{array}{c|c} I_{n\times n}\delta_K & 0_{n\times n} \\ \hline 0_{n\times n} & I_{n\times n}\delta_M \end{array}\right] \right\|_\infty < 1 \tag{36}$$

hence m_p, k_p are used to scale the percentage value and the zero subscript denotes nominal values (it is reminded here that the norm for a matrix $A_{n\times n}$ is calculated through $||A||_\infty = \max_{1\leq j\leq m} \sum_{j=1}^{n} |a_{ij}|$)

With these definitions Eq. 13 becomes,

$$\begin{aligned} &M_0(I + m_p I_{2n\times 2n}\delta_M)\ddot{\mathrm{w}}(t) + K_0(I + k_p I_{2n\times 2n}\delta_K)\mathrm{w}(t) \\ &+[D_0 + 0.0005[K_0 k_p I_{2n\times 2n}\delta_K + M_0 m_p I_{2n\times 2n}\delta_M]]\dot{w}(t) = f_m(t) + f_e(t) \\ &\Rightarrow M_0\ddot{\mathrm{w}}(t) + D_0\dot{q}(t) + K_0\mathrm{w}(t) = \\ &-[M_0 m_p I_{2n\times 2n}\delta_M \ddot{\mathrm{w}}(t) + 0.0005[K_0 k_p I_{2n\times 2n}\delta_K + M_0 m_p I_{2n\times 2n}\delta_M]\dot{\mathrm{w}}(t) + \\ &K_0 k_p I_{2n\times 2n}\delta_K \mathrm{w}(t)] \\ &= f_m(t) + f_e(t) \\ &\Rightarrow M_0\ddot{\mathrm{w}}(t) + D_0\dot{\mathrm{w}}(t) + K_0\mathrm{w}(t) = \tilde{D}q_u(t) + f_m(t) + f_e(t) \end{aligned} \tag{37}$$

where,

$$q_u(t) = \begin{bmatrix} \ddot{\mathrm{w}}(t) \\ \dot{\mathrm{w}}(t) \\ \mathrm{w}(t) \end{bmatrix} \tag{38}$$

$$\begin{aligned} \tilde{D} &= -\begin{bmatrix} M_0 m_p & K_0 k_p \end{bmatrix} \left[\begin{array}{c|c} I_{2n\times 2n}\delta_M & 0_{2n\times 2n} \\ \hline 0_{2n\times 2n} & I_{2n\times 2n}\delta_K \end{array}\right] \begin{bmatrix} I_{2n\times 2n} & 0.0005 I_{2n\times 2n} & 0_{2n\times 2n} \\ 0_{2n\times 2n} & 0.0005 I_{2n\times 2n} & I_{2n\times 2n} \end{bmatrix} \\ &= G_1 \cdot \Delta \cdot G_2 \end{aligned} \tag{39}$$

Writing (37) in state space form, gives,

$$\begin{aligned} \dot{x}(t) &= \begin{bmatrix} 0_{2n\times 2n} & I_{2n\times 2n} \\ -M^{-1}K & -M^{-1}D \end{bmatrix} x(t) + \begin{bmatrix} 0_{2n\times 2n} \\ M^{-1}f_e^* \end{bmatrix} u(t) + \begin{bmatrix} 0_{2n\times 2n} \\ M^{-1} \end{bmatrix} d(t) + \begin{bmatrix} 0_{2n\times 6n} \\ M^{-1}F_1 \cdot \Delta \cdot G_2 \end{bmatrix} q_u(t) \\ &= Ax(t) + Bu(t) + Gd(t) + G_u G_2 q_u(t) \end{aligned} \tag{40}$$

In this way we treat uncertainty in the original matrices as an extra uncertainty term. To express our system in the form of Fig. 6, consider Fig. 7.

The matrices E_1, E_2 are used to extract,

$$q_u(t) \overset{def}{=} \begin{bmatrix} \ddot{\mathrm{w}}(t) \\ \dot{\mathrm{w}}(t) \\ \mathrm{w}(t) \end{bmatrix} \tag{41}$$

Since,

$$\gamma = \begin{bmatrix} \dot{\mathrm{w}}(t) \\ \ddot{\mathrm{w}}(t) \end{bmatrix} \qquad \beta = \int \begin{bmatrix} \dot{\mathrm{w}}(t) \\ \ddot{\mathrm{w}}(t) \end{bmatrix} dt = \begin{bmatrix} \mathrm{w}(t) \\ \dot{\mathrm{w}}(t) \end{bmatrix} \tag{42}$$

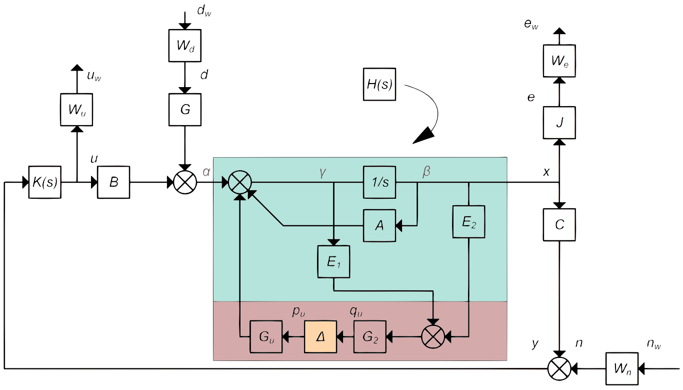

Figure 7: Uncertainty block diagram.

appropriate choices for E_1, E_2 are,

$$E_1 = \begin{bmatrix} 0_{2n\times 2n} & \vdots & I_{2n\times 2n} \\ \cdots & \vdots & \cdots \\ I_{2n\times 2n} & \vdots & 0_{2n\times 2n} \\ \cdots & \vdots & \cdots \\ 0_{2n\times 2n} & \vdots & 0_{2n\times 2n} \end{bmatrix}, \quad E_2 = \begin{bmatrix} 0_{2n\times 2n} & \vdots & 0_{2n\times 2n} \\ \cdots & \vdots & \cdots \\ 0_{2n\times 2n} & \vdots & 0_{2n\times 2n} \\ \cdots & \vdots & \cdots \\ I_{2n\times 2n} & \vdots & 0_{2n\times 2n} \end{bmatrix} \tag{43}$$

The idea is to find an N such that,

$$\begin{bmatrix} q_u \\ \cdots \\ e_{\mathrm{w}} \\ u_{\mathrm{w}} \end{bmatrix} = N \begin{bmatrix} p_u \\ \cdots \\ d_{\mathrm{w}} \\ n_{\mathrm{w}} \end{bmatrix}, \quad N = \begin{bmatrix} N_{p_u q_u} & \vdots & N_{d_w q_u} & N_{n_w q_u} \\ \cdots & \vdots & \cdots & \cdots \\ N_{p_u e_w} & \vdots & N_{d_w e_w} & N_{n_w e_w} \\ N_{p_u u_w} & \vdots & N_{d_w u_w} & N_{n_w u_w} \end{bmatrix} = \begin{bmatrix} N_{11} & N_{12} \\ N_{21} & N_{22} \end{bmatrix} \tag{44}$$

or in the notation of Fig. 6

$$\begin{bmatrix} q_u \\ \mathrm{w} \end{bmatrix} = N \begin{bmatrix} p_u \\ z \end{bmatrix} \tag{45}$$

Now $N_{d_w e_w}$, $N_{n_w e_w}$, $N_{n_w u_w}$ are known. For the rest we will use a methodology known as “pulling out the Δ's”. To this end, break the loop at points p_u, q_u (which will be used as additional inputs/outputs respectively) and use the auxiliary signals a, β, γ. To get the transfer function $N_{d_w q_u}$ (from d_{w} to q_u):

$$q_u = G_2(E_2\beta + E_1\gamma) = G_2(E_2\frac{1}{s} + E_1)\gamma \tag{46}$$

$$\gamma = GW_d d_{\mathrm{w}} + Bu + A\frac{1}{s}\gamma = GW_d d_{\mathrm{w}} + BKC\frac{1}{s}\gamma + A\frac{1}{s}\gamma \tag{47}$$

$$\Rightarrow \gamma = (I - BKC\frac{1}{s} - A\frac{1}{s})^{-1} GW_d d_{\mathrm{w}} \tag{48}$$

Hence,

$$N_{d_w q_u} = G_2(E_2\frac{1}{s} + E_1)(I - BKC\frac{1}{s} - A\frac{1}{s})^{-1}GW_d \tag{49}$$

Now, $N_{p_u q_u}$, $N_{p_u e_w}$, $N_{p_u u_w}$, are similar to $N_{d_w q_u}$, $N_{d_w e_w}$, $N_{d_w u_w}$, with GW_d replaced by G_u, i.e.,

$$\begin{aligned} N_{p_u q_u} &= G_2(E_2\frac{1}{s} + E_1)(I - BKC\frac{1}{s} - A\frac{1}{s})^{-1}G_u \\ N_{p_u e_w} &= W_y JH[I + B[K(I - CHBK)^{-1}CH]]G_u \\ M_{p_u u_w} &= W_u K(I - CHBK)^{-1}CHG_u \end{aligned} \tag{50}$$

Finally to find $N_{n_w q_u}$,

$$q_u = G_2(E_2\beta + E_1\gamma) = G_2(E_2\frac{1}{s} + E_1)\gamma \tag{51}$$

$$\gamma = Bu + A\frac{1}{s}\gamma = BK(W_n n_\mathrm{w} + y) + A\frac{1}{s}\gamma = BKW_n n_\mathrm{w} + BKC\frac{1}{s}\gamma + A\frac{1}{s}\gamma \tag{52}$$

$$\Rightarrow \gamma = (I - BKC\frac{1}{s} - A\frac{1}{s})^{-1}BKW_n n_\mathrm{w} \tag{53}$$

Hence,

$$N_{n_w q_u} = G_2(E_2\frac{1}{+}E_1)(I - BKC\frac{1}{s} - A\frac{1}{s})^{-1}BKW_n \tag{54}$$

Collecting all the above yields N:

$$N =$$

$$\begin{bmatrix} G_2\left(E_2\frac{1}{s}+E_1\right)\left(I-BKC\frac{1}{s}-A\frac{1}{s}\right)^{-1}G_u & G_2\left(E_2\frac{1}{s}+E_1\right)\left(I-BKC\frac{1}{s}-A\frac{1}{s}\right)^{-1}GW_d & G_2\left(E_2\frac{1}{s}+E_1\right)\left(I-BKC\frac{1}{s}-A\frac{1}{s}\right)^{-1}BKW_u \\ W_e JH\left[I+BK(I-CHBK)^{-1}CF\right]G_u & W_e J(I-HBKC)^{-1}HGW_d & W_e J(I-HBKC)^{-1}HBKW_u \\ W_u K(I-CHBK)^{-1}CFG_u & W_u(I-KCHB)^{-1}KCHGW_d & W_u(I-KCHB)^{-1}KW \end{bmatrix} \tag{55}$$

Having obtained N for the beam problem, all proposed controllers $K(s)$ can be compared using the structured singular value relations. [18, 19, 21]

4 ROBUSTNESS ISSUES

The superiority of H_∞ control lies in its ability to take explicitly into account the worst effect of unknown disturbances and noise in the system. Furthermore, at least in theory, it is possible to synthesize an H_∞ controller that is robust to a prescribed amount of modeling errors. Unfortunately, this last possibility is not implementable in some cases, as it will be subsequently illustrated.[16, 17]

In what follows, the robustness to modeling errors of the designed H_∞ controller will be analyzed. Furthermore an attempt to synthesize a μ-controller will be presented, and comparisons between the two will be made.

In all simulations, routines from Matlab's Robust Control Toolbox will be used. In particular:

1. For uncertain elements,

2. To calculate bounds on the structured singular value,

3. To calculate a μ-controller,

Numerical models used in all simulations, are implemented in three ways:

1. Through Eq. 56

$$\begin{aligned} K &= K_0(I + k_p I_{2n\times 2n}\delta_K) \\ M &= M_0(I + m_p I_{2n\times 2n}\delta_M) \\ D &= D_0 + 0,0005[K_0 k_p I_{2n\times 2n}\delta_K + M_0 m_p I_{2n\times 2n}\delta_M] \end{aligned} \tag{56}$$

   and subsequent evaluation of matrix N for specific values of k_p, m_p.

2. By use of Matlab's "uncertain element object". As explained, this form is needed in the D-K robust synthesis algorithm.

3. By Simulink implementation of Fig. 8.

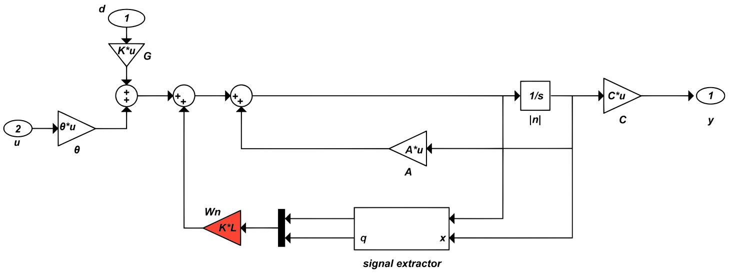

Figure 8: Simulink diagram of uncertain plant

4.1 Robust analysis - Results

Robust analysis is carried out through the relations:

$$\sup_{\omega\in\mathbb{R}} \mu_\Delta(N_{11}(j\omega)) < 1 \tag{57}$$

for robust stability, and,

$$\sup_{\omega\in\mathbb{R}} \mu_{\Delta_a}(N(j\omega)) < 1 \tag{58}$$

for robust performance.

In all the simulations that follow the disturbance is the mechanical load, i.e. $10N$ at the free end. For the H_∞ found, robust analysis was performed for the following values of m_p, k_p.

1. $m_p = 0$, $k_p = 0.9$. This corresponds to a ±90% variation from the nominal value of the stiffness matrix K.

   In Fig. 9 the displacement responses for this controller for the mechanical input are shown. In Fig. 10 are shown the bounds on the μ values. As seen the system remains

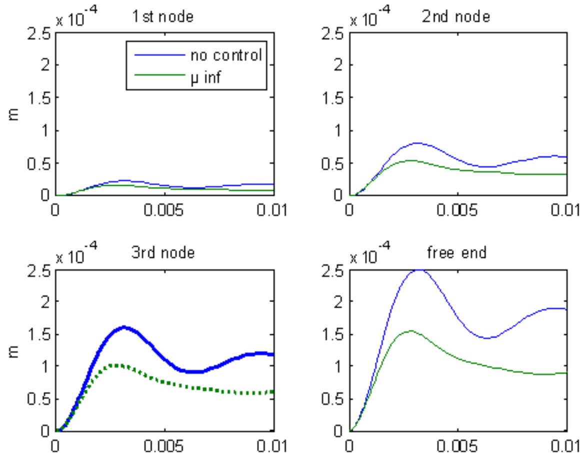

Figure 9: Displacement response loading equal to 10N at free end, μ-controller for $m_p = 0$, $k_p = 0.9$

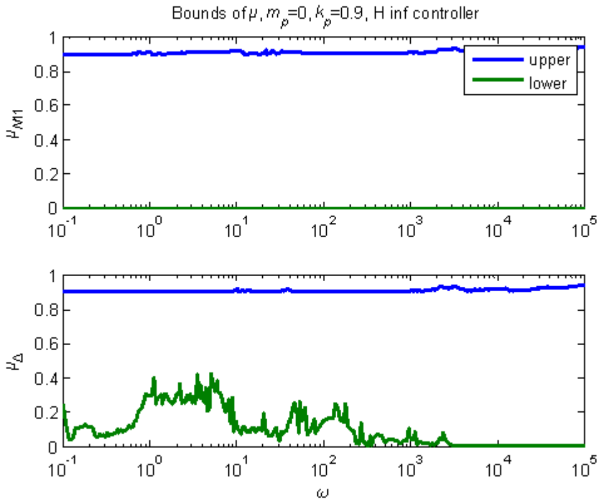

Figure 10: μ-bounds of the H_∞ controller for $m_p = 0$, $k_p = 0.9$

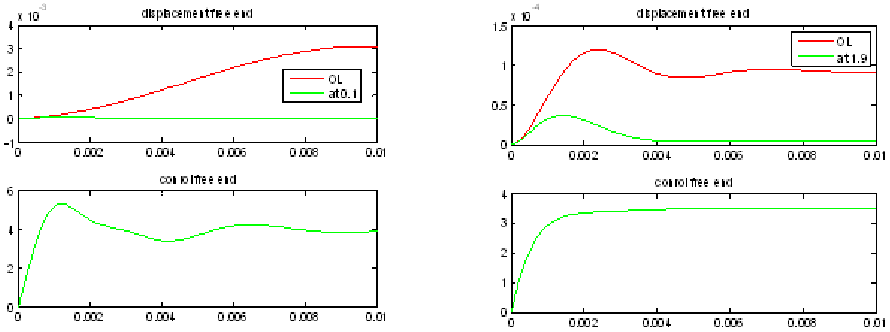

Figure 11: Displacement and control at free end for the H_∞ controller with $m_p = 0$, $k_p = 0.9$ (extreme values)

stable and exhibits robust performance, since the upper bounds of both values remain below 1 for all frequencies of interest. This result is validated in Fig. 11, where the displacement of the free end and the voltage applied are shown at the extreme uncertainty. Comparison with the open loop response for the same plant shows the good performance of the nominal controller.

2. $m_p = 0.9$, $k_p = 0$. This corresponds to a ±90% variation from the nominal value of the mass matrix M.

   In Fig. 12 are shown the bounds on the μ values. As seen the system remains stable and exhibits robust performance, since the upper bounds of both values remain below 1 for all frequencies of interest. This result is validated in Fig. 13, where the displacement of the free end and the voltage applied are shown. Comparison with the open loop response for the same plant shows the good performance of the nominal controller.

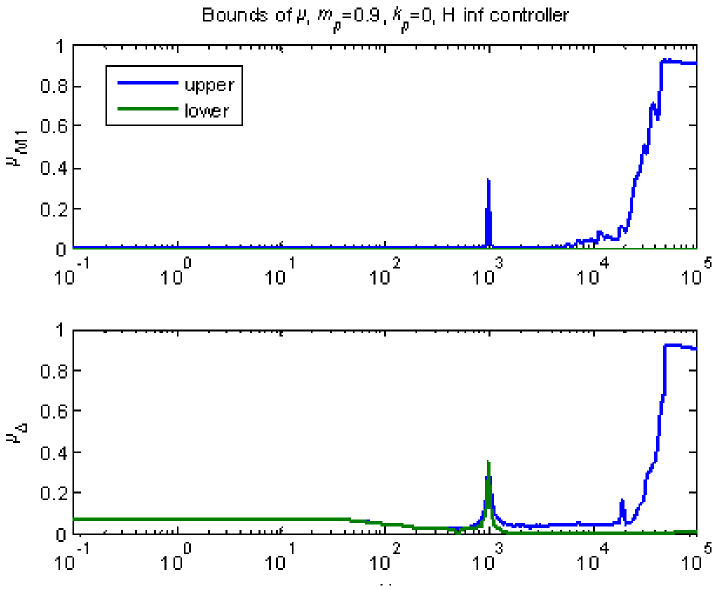

Figure 12: μ-bounds of the H_∞ controller for $m_p = 0.9$, $k_p = 0$

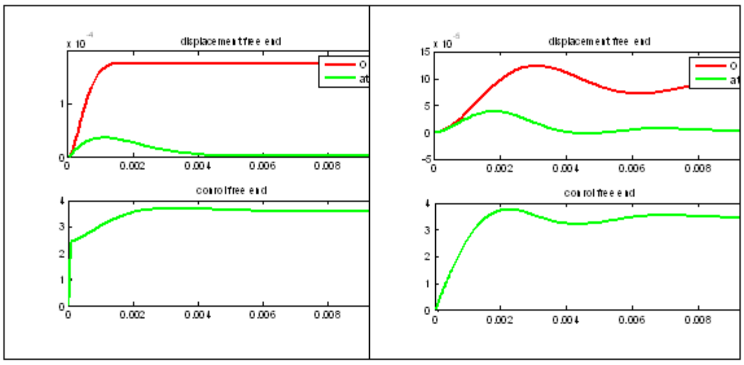

Figure 13: Displacement and control at free end for the H_∞ controller with $m_p = 0.9$, $k_p = 0$(extreme values)

3. $m_p = 0.9$, $k_p = 0.9$. This corresponds to a ±90% variation from the nominal values of both the mass and stiffness matrices M, K.

   In Fig. 14 are shown the bounds on the μ values. As seen the system remains stable and exhibits robust performance, since the upper bounds of both values remain below 1 for all frequencies of interest. This result is validated in Fig. 15, where the displacement of the free end and the voltage applied are shown. Comparison with the open loop response for the same plant shows the good performance of the nominal controller.

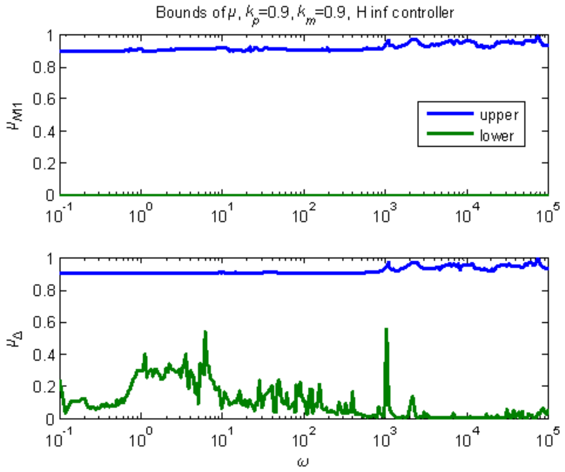

Figure 14: Displacement and control at free end for the H_∞ controller with $m_p = 0.9$, $k_p = 0$(extreme values)

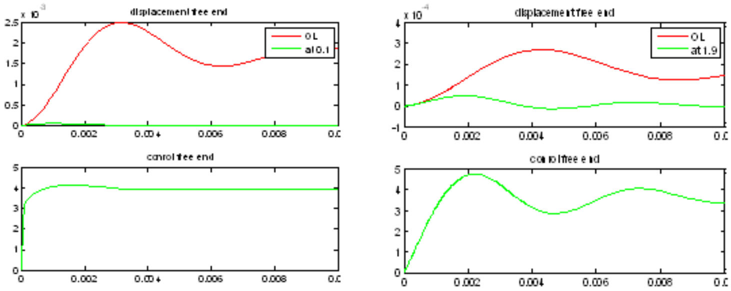

Figure 15: Displacement and control at free end for the H_∞ controller with $m_p = 0.9$, $k_p = 0$(extreme values)

5 CONCLUSIONS

In this paper advanced control techniques, like criterion H_∞ and m-analysis, have been applied for the suppression vibrations of smart structures. Under the assumption of an uncertainty introduced at the level of matrices in the structural analysis of the system the robust characteristics of the H_∞ controller and m-analysis were checked. There was a complete suppression of the oscillation and rigidity of the beam up to and including 90% variation from the nominal values.

An effort was made to find a robust μ-controller, using the recurring method $D - K$. In this case the resulting order of the controller as well as the required calculation requirements was very large. The performance of the robust μ-controller was not the one expected, something that most likely is due to the numerical properties of the system tables. Contrary to the H_∞ controller, the results are quite satisfactory and prove that the H_∞ control can suppress the oscillation of the smart beam taking into account the modelling uncertainties, external disturbances and the noise of the measurements.

In summary, the scientific fields which this paper has contributed to are:

- Application of the control in suppressing the oscillation of structural models.
- Introduction of the uncertainties in the mathematic model of structural elements.
- Suppression of oscillation and rejection of disturbances, by taking into account the modelling error, using the criterion of the robust H_∞ control.

- Reduction of the calculation requirements of the control using optimisation algorithms.
- Finding of a robust μ-controller

Experimental verification of the very good results that were found in this work as well as further detailed correlation of uncertainties with the real parameters of the mechanical system (material parameters, joints, cracks and delaminations etc) remain open for future investigations.

REFERENCES

[1] J. Friedman, K. Kosmatka, *An improved two node Timoshenko beam finite element*, Computer and Structures, vol. 47, pp. 473-481, 1993.

[2] G. Foutsitzi, D. Marinova, E. Hadjigeorgiou and G. Stavroulakis, *Robust H2 vibration control of beams with piezoelectric sensors and actuators*, Proceedings of Physics and Control Conference (PhyCon03), St. Petersburg, Russia, 20-22 August, Vol. I, pp. 158-163, 2003.

[3] C. Sisemore, A. Smaili, R. Houghton, *Passive damping of flexible mechanism system: experimental and finite element investigation*, The 10^{th} World Congress of the Theory of Machines and Mechanisms, Oulu, Finland, Vol. 5, pp. 2140-2145, 1999.

[4] N. Zhang, I. Kirpitchenko, *Modelling dynamics of a continuous structure with a piezoelectric sensor/actuator for passive structural control*, Journal of Sound and Vibration, vol. 249, pp. 251-261, 2002.

[5] B. Miara, G. Stavroulakis, V. Valente (Eds.), *Topics on mathematics for smart systems*. Proceedings of the European Conference, Rome, Italy, 26-28 October 2006, World Scientific Publishers, Singapore, International, 2007.

[6] B. Shahian, M. Hassul, *Control system design using MATLAB*, Prentice-Hall, NJ, 1994.

[7] W.S. Huang, H.C. Park, *Finite element modelling of piezoelectric sensors and actuators*, American Institute of Aeronautics and Astronautics Journal, vol.31, pp. 930-937, 1993.

[8] G. Foutsitzi, D. Marinova, E. Hadjigeorgiou, G. Stavroulakis, *Finite element modelling of optimally controlled smart beams*, 28Ih Summer School: *Applications of Mathematics in Engineering and Economics*, Sozopol, Bulgaria, 2002.

[9] G.E. Stavroulakis, G. Foutsitzi, E. Hadjigeorgiou, D. Marinova, C.C. Baniotopoulos, *Design and robust optimal control of smart beams with application on vibrations suppression* Advances in Engineering Software, Volume 36, Issues 11-12, Pages 806-813, November-December 2005.

[10] J.V. Burke, D. Henrion, M.L. Lewis, *Overton.HIFOO-a MATLABpackage for fixed-order controller design and Hinf. optimization.* Proceedings of the IFAC Symbosium on Robust Control Design, Toulouse, France, 2006. www.cs.nyu.edu/overton/software/hifoo

[11] H.F. Tiersten, *Linear Piezoelectric Plate Vibrations*, Plenum Press New York, 1969.

[12] J.V. Burke, D. Henron, A.S. Kewis and M.L. Overton, *Stabilization via Nonsmooth, Nonconvex Optimization*, Automatic Control IEE Volume 5 Issue11 page1760-1769 November 2006.

[13] O. Bosgra, H. Kwakernaak, *Design methods for control systems*, Course notes, Dutch Institute for Systems and Control, p.69, 2001.

[14] M. Hou and P.C. Muller, *Design of observers for linear systems with unknown inputs*, IEEE Trans. on Automatic Control, 37: 871-875, 1992.

[15] A. Packard, J. Doyle, and G. Balas, *Linear, multivariable robust control with a perspective,* ASME Journal of Dynamic Systems, Measurement and Control, 50th Anniversary Issue, Vol. 115, no. 2b, p. 310-319, 1993.

[16] A. Pouliezos (2008). *MIMO control systems*, class notes. http://pouliezos.dpem.tuc.gr

[17] D. Marinova, G.E. Stavroulakis, D. Foutsitzi, E. Hadjigeorgiou, and E.C. Zacharenakis, *Robust design of smart structures taking into account structural defects*, Summer School Conference Advanced Problems in Mechanics Russian Academy of Sciences, Editor: D.A. Indeitsev, 288-292, 2004.

[18] A.L. Tits and Y. Yang, *Globally convergent algorithms for robust pole assignment by state feedback*, IEEE Trans. on Automatic Control, 41: 1432-1452, 1996.

[19] R.C. Ward, *Balancing the generalized eigenvalue problem*, SIAM J. Sci. Stat. Comput., 2: 141-152, 1981.

[20] P. Young, M. Newlin, and J. Doyle, *Practical computation of the mixed problem,* Proceedings of the American Control Conference, pp. 2190-2194, 1992.

[21] K.G. Arvanitis, E.C. Zacharenakis, A.G. Soldatos and G.E. Stavroulakis, *New trends in optimal structural control*, Selected Topics in Structronic and Mechatronic System, World Scientific Publishers 321-415 chapter 8, Singapore, 2003.

COMPDYN 2011
3rd ECCOMAS Thematic Conference on
Computational Methods in Structural Dynamics and Earthquake Engineering
M. Papadrakakis, M. Fragiadakis, V. Plevris (eds.)
Corfu, Greece, 25–28 May 2011

VIBRATION CONTROL OF STRUCTURES WITH A NOVEL SEMI-ACTIVE TUNED MASS DAMPER USING WAVELET TRANSFORM

S. S. Feizabadi-Sani [1], A. K. Ghorbani-Tanha [2]

[1]School of Civil Engineering, University of Tehran
P.O. Box 11155-4563, Tehran, Iran
e-mail: {s_feizabadi, ghtanha}@ut.ac.ir

Keywords: Vibration control, Semi-active tuned mass damper, Variable stiffness, Wavelet Transform

Abstract. *An innovative design for a semi-active tuned mass damper (SATMD) with variable stiffness has been proposed for structural vibration control. The stiffness of the device can be continuously varied within a certain range using the variations of moment of inertia of an area. This adaptive tuned mass damper (TMD) is capable of real-time retuning and operates effectively in broad band frequency excitations. Employing the numerical simulations, the responses of a SDOF model coupled with the SATMD subjected to a seismic record are obtained. Wavelet transform is used to detect the instantaneous frequency of the excitation. The control effectiveness of the proposed SATMD is evaluated by comparing the results with those of the system coupled with a TMD. It is found that, the vibration suppression by the proposed SATMD is significantly superior to that of a conventional passive TMD.*

1 INTRODUCTION

Semi-active tuned mass damper (SATMD) is a semi-active vibration control device which basically originates from a passive tuned mass damper (TMD). TMD is a simple, inexpensive and reliable device to attenuate the undesired vibrations of systems. The principal drawback of TMDs, however, is that they are only effective over a narrow frequency band and their performance can be highly degraded due to changes in excitation frequency.

In an effort to improve the effectiveness of TMDs, active tuned mass dampers (ATMDs) have been introduced [1]. Although the ATMDs demonstrate better performance than the TMDs, the active system is more costly, more complex and needs careful maintenance. Besides, injection of energy into the controlled system by active control mechanisms enhances the potential for system destabilization.

Considering the advantages and limitations of the active system, the concept of a semi-active vibration control has been introduced. SATMD is the semi-active counterpart of TMD which has been subsequently modified to allow for the adjustment of damping [2, 3] and/or stiffness properties [4-8]. Compared to ATMDs, a smaller amount of active energy is required to modulate the damping or stiffness of such devices.

Most of the variable stiffness devices which have been proposed, involve several moving parts and mechanical and electrical components, which may put limits on the usage of these devices. Moreover, they may do not allow for the quick adjustment of stiffness, and their complicated design may cause manufacturing and maintenance difficulties.

In present study, in an effort to overcome the disadvantages of the above-mentioned variable stiffness devices, an innovative semi-active variable stiffness (SAVS) has been proposed This beam-like device is capable of altering its stiffness in a smooth manner between minimum and maximum levels using the variations of the moment of inertia of an area as it rotates about a normal axis passing through its centroid. Theoretical expressions for the change of device stiffness as a function of rotation angle are developed underlying the concept of unsymmetrical bending of beams. A semi-active tuned mass damper (SATMD) is developed based on the proposed SAVS device. This adaptive vibration absorber is capable of real-time retuning and operates effectively in broad band frequency excitations. The excitation is assumed to be an earthquake record. Wavelet transform is employed to detect the instantaneous frequency of excitation and online tuning of the SATMD. The control effectiveness of the proposed SATMD is evaluated by comparing the results with those of the system coupled with a TMD.

2 THE INNOVATIVE SAVS DEVICE

The innovative variable stiffness device proposed in this paper is based on the variation of moment of inertia as an area rotates about a normal axis passing through its centroid. The formulations are developed using the well-known theory of skew bending or unsymmetrical bending of beams. The details are discussed in the following sub-sections.

2.1 Theory: Unsymmetrical bending of beams

Consider a cantilever prismatic elastic beam loaded at the end of the span with a concentrated force P as shown in Figure 1(a). The cross-sectional area of the beam is assumed to be rectangular with height h and width b, as shown in Figure 1(b). In this figure z and y are the principal axes passing through the centroid of the cross-sectional area. The downward deflection at the end of the beam is [9]

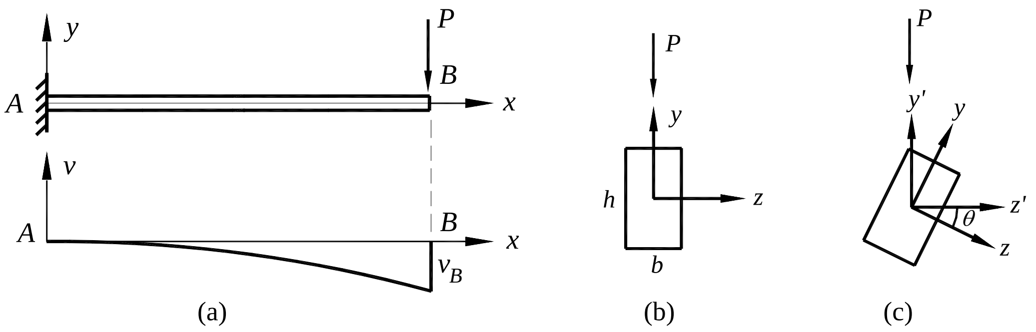

Figure 1: (a) Fixed-end beam loaded with a concentrated force at the end of the span and its deflected curve; (b) Cross-sectional area; (c) Rotated cross-section.

$$v_B = \frac{PL^3}{3EI_z} \tag{1}$$

where L, E and I_z are the length of the beam, modulus of elasticity of the beam material and moment of inertia of the cross-sectional area about principal axis z. It can be said that the effective stiffness at the end of the beam in y-direction is

$$k_{yB} = \frac{3EI_z}{L^3} \tag{2}$$

Now consider the case in which the beam is rotated clockwise about x-axis through an angle θ as shown in Figure 1(c). The new horizontal and vertical axes are denoted as z' and y'. The deflection at the end of the beam in y' and z'-directions can be expressed, respectively, as [10]

$$\bar{v}_B = \frac{PL^3 I_{y'}}{3E(I_{z'}I_{y'} - I_{z'y'}^2)} \tag{3a}$$

$$\bar{w}_B = \frac{PL^3 I_{z'y'}}{3E(I_{z'}I_{y'} - I_{z'y'}^2)} \tag{3b}$$

where I_y is the moment of inertia of the cross section about principal axis y and $I_{z'y'}$ is the product of inertia of the cross section in the new $z'y'$-coordinates. $\bar{v}_B$ is downward; and $\bar{w}_B$ is rightward for $0 < \theta < \pi/2$ and leftward for $\pi/2 < \theta < \pi$. It can be concluded that the equivalent stiffness at the end of the beam in y'-direction is

$$k_{y'B} = \frac{3E(I_{z'}I_{y'} - I_{z'y'}^2)}{L^3 I_{y'}} \tag{4}$$

Using the well-known equations which relate $I_{z'}$, $I_{y'}$ and $I_{z'y'}$ to I_z and I_y [11], gives

$$k_{y'B} = \frac{6EI_z I_y}{L^3[(I_z + I_y) - (I_z - I_y)\cos 2\theta]} \tag{5}$$

which shows the variation of the stiffness at the end of the rotated beam in vertical directions as a function of θ.

2.2 The proposed SAVS device

The proposed device is composed of a mass which is connected to the main structure by the use of two co-axial cantilever beams, located in two opposite sides of the mass as shown in Figure 2. The beams are hinged together at their free ends (point *B*) and their other ends are clamped to the main structure (points *A* and *C*). The rotational degrees of freedom at the clamped ends are released, so it is possible for the beams to be rotated about their neutral axes. The mass is perpendicularly connected to the hinge point through a rigid truss element. The beams are rotated through the same angle but in the opposite directions, Figure 2(b), as the result, point *B* and hence the mass will move just in horizontal direction. (the external excitation is assumed to be applied to the main structure horizontally). By rotating the beams, the effective stiffness of point *B* in horizontal direction will smoothly vary from its minimum value, Figure 2(a) to its maximum value, Figure 2(c). Electric motors mounted at two ends of the beams may rotate the beams about their neutral axes to the desired angle according to a signal which is supplied through control algorithm.

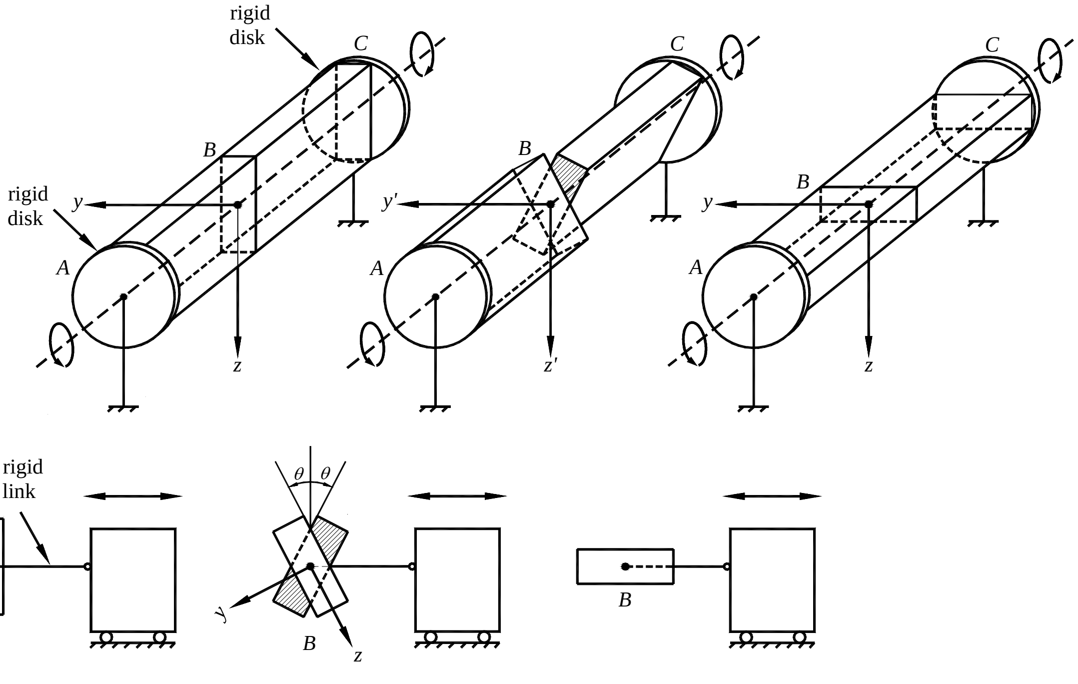

(a) (b) (c)

Figure 2: Variable stiffness device (a) θ = 0; (b) $0<\theta<90^\circ$; (c) θ = 90°.

Since the beams behave like parallel springs, the effective stiffness at point *B* equals the sum of each beam's stiffness at their end points. Employing the same procedure as [7], it can be shown that

$$\bar{k}_{y'B}=\frac{6EI_{z'}}{L^3} \tag{6}$$

or

$$\bar{k}_{y'B}=\frac{3E}{L^3}[(I_z+I_y)+(I_z-I_y)\cos 2\theta] \tag{7}$$

It should be noted that due to opposite rotation of the beams through the same angle, their vertical deflections will cancel out.

3 VIBRATION CONTROL OF A SDOF SYSTEM BY THE PROPOSED SATMD

As a case study, the efficacy of the proposed SATMD for suppression of vibrations of a SDOF system under earthquake excitation is investigated.

3.1 Analysis of the model

Consider a SDOF system equipped with a SATMD. This integrated system can be modeled as a 2DOF system, as schematically shown in Figure 3. The governing equations of motion of the system are

$$\begin{aligned} &m_1\ddot{x}_1(t)+(c_1+c_2)\dot{x}_1(t)-c_2\dot{x}_2(t)+(k_1+k_2(t))x_1(t)-k_2(t)x_2(t)=-m_1\ddot{x}_g \\ &m_2\ddot{x}_2(t)-c_2\dot{x}_1(t)+c_2\dot{x}_2(t)-k_2(t)x_1(t)+k_2(t)x_2(t)=-m_2\ddot{x}_g \end{aligned} \tag{8}$$

where m_1, c_1 and k_1 are the mass, damping capacity and stiffness of the primary system, respectively; m_2, c_2 and $k_2(t)$ are the mass, damping capacity and adjustable stiffness of the mass damper, respectively; $x_1(t)$ and $x_2(t)$ represent, respectively, primary and mass damper displacement relative to the ground; and $\ddot{x}_g$ is the ground acceleration.

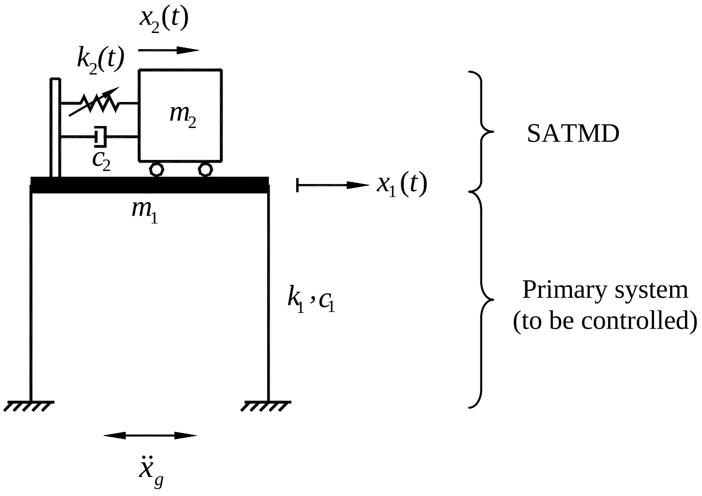

Figure 3: SDOF system equipped with a SATMD.

3.2 Tuning algorithm

In order to attenuate undesirable vibrations during earthquake, the stiffness of the mass damper is varied to tune the damper to the excitation frequency. However, in practice the semi-active stiffness coefficient is limited by both an upper bound, k_{max}, and lower bound, k_{min}. The instantaneous frequency of the excitation is detected using complex morlet wavelet transform and the stiffness of SATMD is altered to keep it tuned to the excitation in real time.

When the calculated tuning stiffness for the mass damper, $m_2\omega^2(t)$, lies within the range specified by the lower and upper limit parameters, the damper stiffness is set to this value. When the calculated stiffness is outside these bounds, the damper stiffness is clipped to the upper or lower bound. The stiffness is then related to an angle θ according to Equation (7).

3.3 Developed model and parameter values used

In the system considered, the damper's stiffness varies nonlinearly with time. Therefore, the system response is to be obtained through numerical integration of equations of motion, in which the damper's stiffness is to be calculated at each step. For this purpose a SIMULINK model is developed. The assumed parameters of the primary system and SATMD are summarized in Table 1. In present study, the variable spring is assumed to be massless and there is thus no kinetic energy associated with its motion.

The results are obtained and compared to those of the system equipped with a conventional TMD. For this case, the mass and damping coefficient of the TMD are the same as SATMD and the stiffness has a constant value such that the natural frequency of the TMD equals the steady-state excitation frequency.

Table 1: Primary system and SATMD parameters**.**

Primary system		SATMD	
Parameter	Value	Parameter	Value
m_1	10000 kg	b	4 mm
f_1	1 Hz	h	22 mm
ξ_1	0.02	L	48 cm
		E	2×10^{11} Pa
		ξ_2	0.01
		m_2	100 kg

3.4 Numerical results

In this study, 1968 Hachinohe earthquake signal is used as the excitation (Fig 4). Fig. 5 shows the instantaneous frequency of the earthquake which is detected by wavelet transform. The system's response is obtained numerically using the SIMULINK model. To evaluate the control system performance, maximum displacement, velocity and acceleration of the primary system for the system controlled by TMD (passive control) and by SATMD (semi-active control) are calculated. Since the performance of the controlled system may not be provided solely by the peak responses, normed system responses (RMS) are obtained as well. The norm, denoted $\|\cdot\|$, is defined as

$$\|\cdot\| = \sqrt{\frac{1}{t_f}\int_0^{t_f} [\cdot]^2 dt} \tag{9}$$

where t_f is the simulation time.

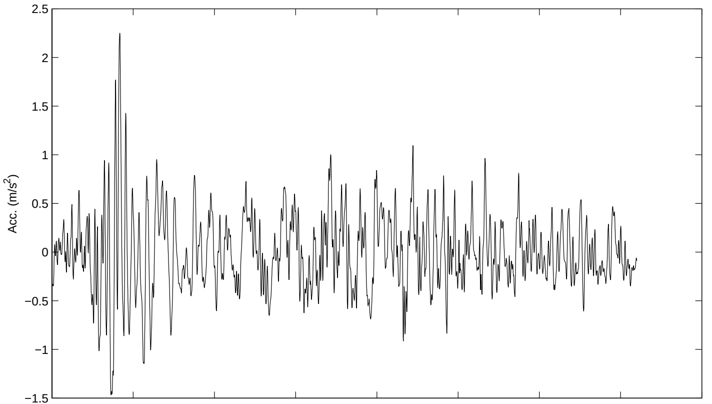

Figure 4: Hachinohe earthquake signal.

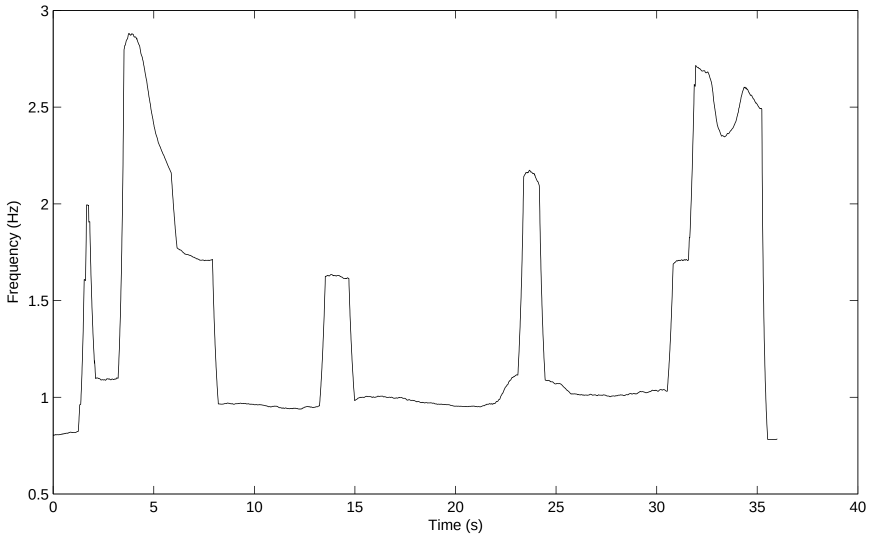

Figure 5: Instantaneous frequency of the excitation.

The primary system and mass damper's response for both TMD and SATMD cases are shown in Figures 6 to 8. The peak and RMS values of the primary system are summarized in Table 2. It can be observed that the maximum displacement response reduction in the case of SATMD compared to the TMD case is about 15%. This reduction for the maximum velocity and acceleration responses are about 13% and 4%, respectively. Furthermore, the reduction in RMS of displacement, velocity and acceleration responses is, respectively, about 39%, 39% and 36%.

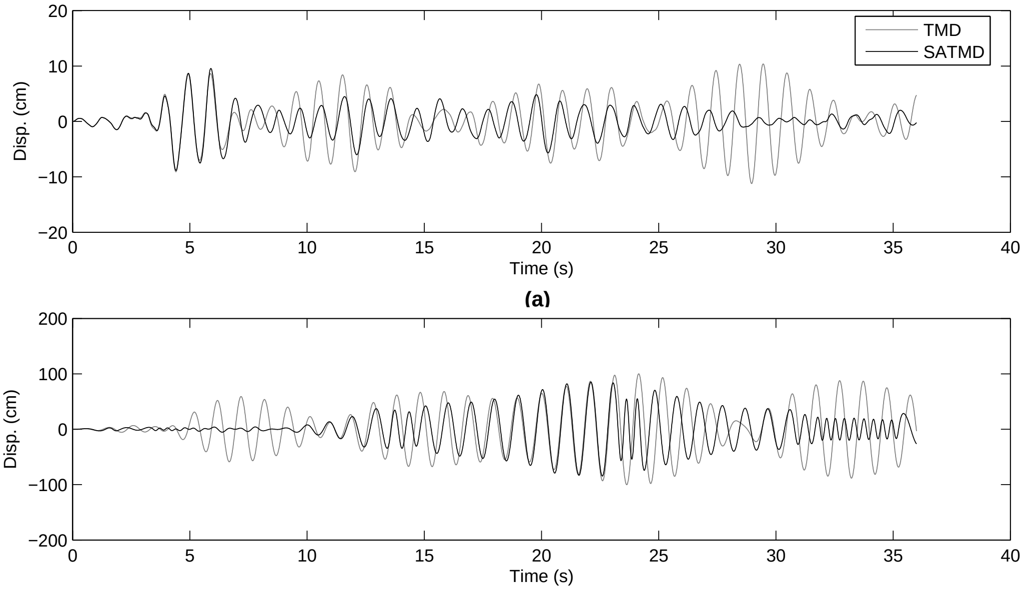

(b)

Figure 6: Displacement response of (a) primary system; (b) vibration absorber.

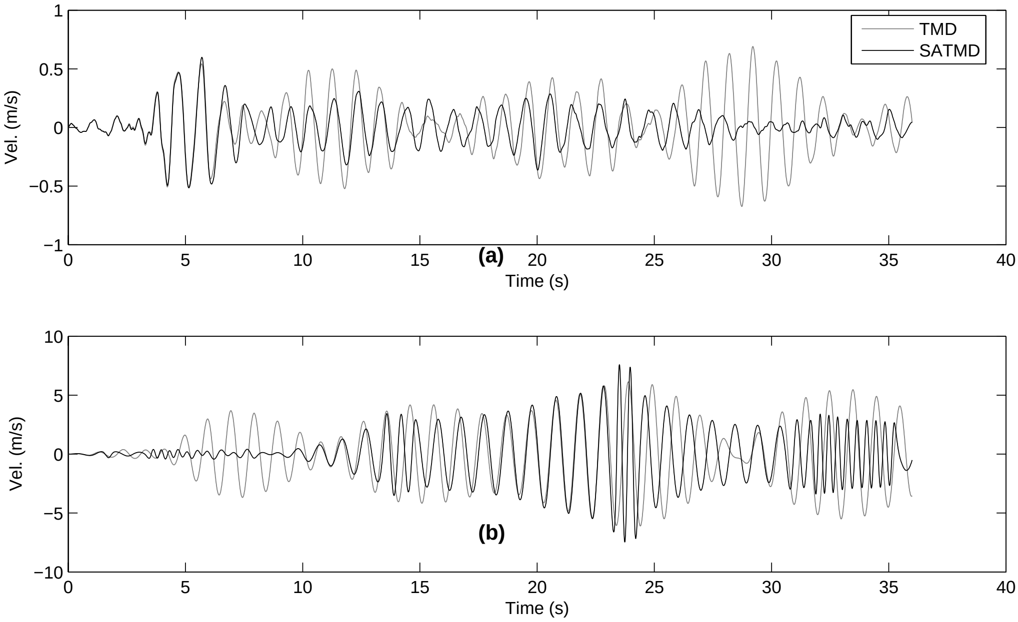

Figure 7: Velocity response of (a) primary system; (b) vibration absorber.

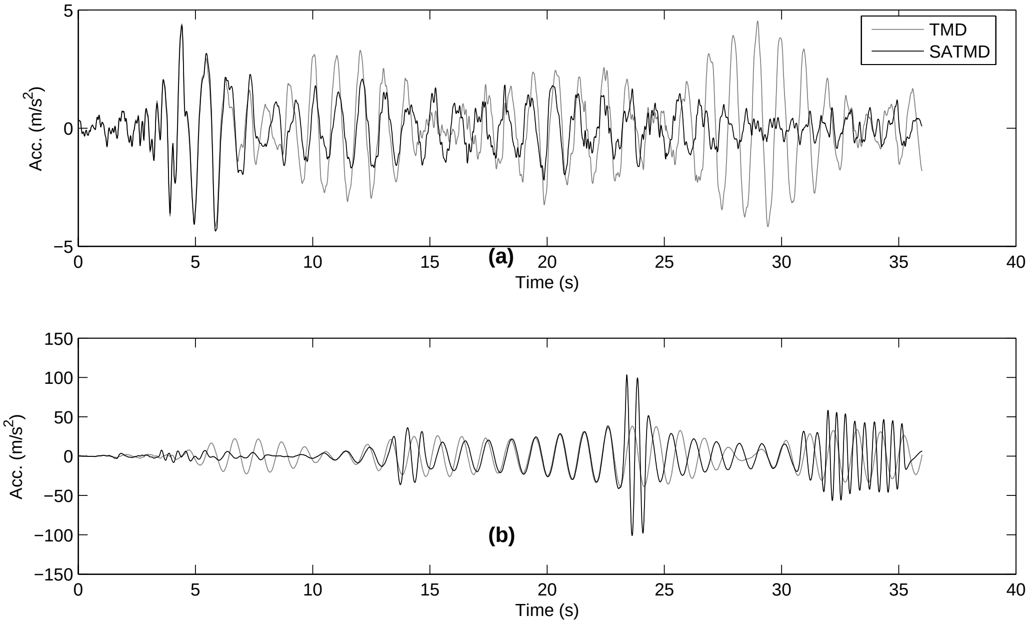

Figure 8: Acceleration response of (a) primary system; (b) vibration absorber.

Table 2: max and RMS values of the primary system response.

Control System	$\max(x_1(t))$ (m)	$\max(\dot{x}_1(t))$ (m/s)	$\max(\ddot{x}_1(t))$ (m/s^2)	$\mathrm{RMS}(x_1(t))$ (m)	$\mathrm{RMS}(\dot{x}_1(t))$ (m/s)	$\mathrm{RMS}(\ddot{x}_1(t))$ (m/s^2)
TMD	0.11	0.69	4.54	0.04	0.25	1.61
SATMD	0.10	0.60	4.35	0.02	0.15	1.02

According to the cross-sectional dimensions of the beam given in Table 1, the minimum and maximum values of the moment of inertia are 117.33 mm^4 and 3549.3 mm^4, respectively. Therefore, the stiffness of SAVS device can vary between certain minimum and maximum values of 1273.1 N/m and 38513 N/m. Figure 9 shows the variation of SATMD's stiffness as a function of time. Figure 10 shows the angle of rotation of the each beams from the principal axis about which the moment of inertia is a maximum. The figure demonstrates that the angle varies between 79.94° to 23.11° to provide the required stiffness.

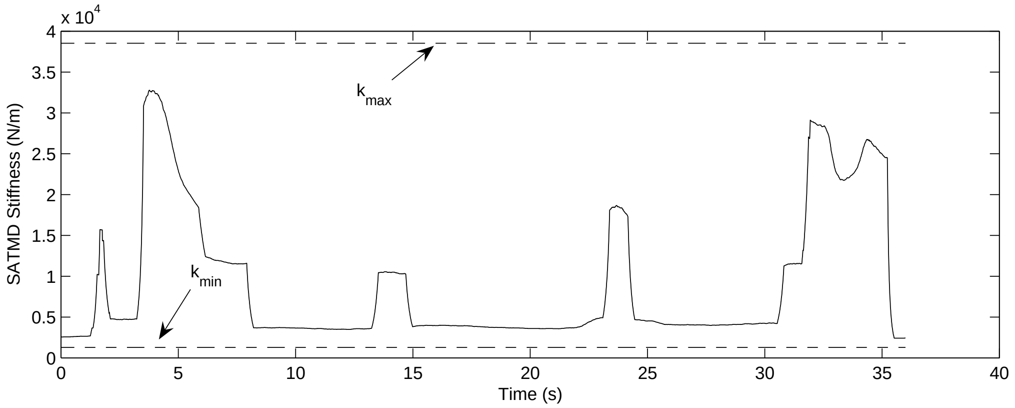

Figure 9: Variations of SATMD's stiffness versus time.

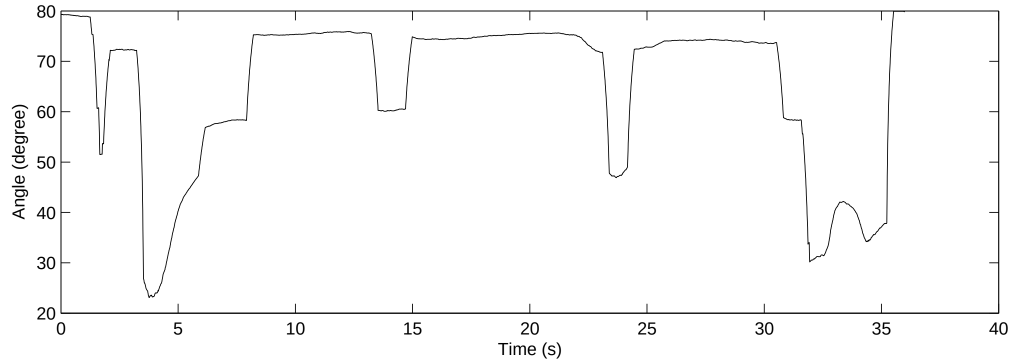

Figure 10: Angle of rotation of SAVS.

4 CONCLUSIONS

The design and formulations of a novel SAVS device is presented. The main advantages of this device can be enumerated as: simple structure, low power requirement, ease of design and manufacturing, quick adjustment of stiffness from minimum to maximum, low moving parts. A new SATMD is developed based on the SAVS device which is capable of adjusting its frequency in real-time. The effectiveness of the SATMD for suppression of a SDOF system under earthquake excitation is investigated. Wavelet transform is used to detect instantaneous frequency of the excitation and online tuning of SATMD. It was shown that the SATMD reduces the maximum and RMS displacement response of the primary system about 15% and 39%, respectively, compared to the passive TMD tuned to the operating frequency. A reduction of 13%, 4%, 39% and 36% is also observed for the maximum velocity, maximum acceleration and RMS of velocity and acceleration of the system, respectively.

REFERENCES

[1] J.C.H. Chang, T.T. Soong, Structural control using active tuned mass dampers. *Journal of Engineering Mechanics Division*, **106**, 1091-1098, 1980.

[2] D. Hrovat, P. Barak, M. Rabins, Semi-active versus passive or active tuned mass dampers for structural control. *Journal of Engineering Mechanics*, **109**, 691-705, 1983.

[3] T. Pinkaew, Y. Fujino, Effectiveness of semi-active tuned mass dampers under harmonic excitation. *Engineering Structures*, **23**, 850-856, 2001.

[4] P.L. Walsh, J.S. Lamancusa, A variable stiffness vibration absorber for minimization of transient vibration. *Journal of Sound and Vibration*, **158**, 195-211, 1992.

[5] M.A. Franchek, M.W. Ryan, R.J. Bernhard, R.J. Adaptive passive vibration control. *Journal of Sound and Vibration*, **189**, 565-585, 1995.

[6] S. Nagarajaiah, Structural vibration damper with continuously variable stiffness. US Patent No. 6098969, 2000.

[7] A.K. Ghorbani-Tanha, M. Rahimian, A. Noorzad, A novel semi-active variable device and its application in a new semi-active vibration absorber. *Journal of Engineering Mechanics*, Accepted for publication.

[8] A.K. Ghorbani-Tanha, Development of a novel semi-active tuned mass damper for vibration control of structures. *5th World Conference on Structural Control and Monitoring*, Tokyo, Japan, 12-14 July 2010.

[9] M. Rahimian, A.K. Ghorbani-Tanha, *Structural analysis*, Sanjesh Publications, Tehran, 2003. (In Persian).

[10] S. Timoshenko, *Strength of materials, part I: elementary theory problems*, W.D. Ten Broeck, New Delhi, 1965.

[11] E.P. Popov, *Mechanics of materials*, Prentice-Hall Inc., Englewood Cliffs, NJ, 1978.

COMPDYN 2011
3rd ECCOMAS Thematic Conference on
Computational Methods in Structural Dynamics and Earthquake Engineering
M. Papadrakakis, M. Fragiadakis, V. Plevris (eds.)
Corfu, Greece, 25–28 May 2011

SEMI-ACTIVE CONTROL OF AN EXPERIMENTAL FRAME USING MR DAMPERS: NUMERICAL RESULTS AND EXPERIMENTAL VALIDATION

Manuel T. Braz-César[1], Rui C. Barros[2]

[1] Polytechnic Institute of Bragança
Campus de Santa Apolónia – Apt. 134 - 5301-857 Bragança - Portugal
e-mail: brazcesar@ipb.pt

[2] Faculty of Engineering of the University of Porto
Rua Dr. Roberto Frias, s/n 4200-465 Porto PORTUGAL
rcb@fe.up.pt

Keywords: Response control, Clipped optimal control, MR dampers, Semi-active control.

Abstract. *The present work describes part of the R&D on using a semi-active structural control technique in a civil engineering experimental model frame equipped with a MR damper, developed within COVICOCEPAD project approved in the framework of Eurocores program S3T. Some results are provided associated with the calibration of a magneto-rheological (MR) damper at FEUP (Faculdade de Engenharia da Universidade do Porto) as well as on the experimental modal identification of the dynamic properties of a small-scale metallic frame, with and without the inclusion of a specific MR device. Some numerical results of the controlled frame under simulated earthquakes are given, to be later compared with the experimental results of such frame installed in a Quanser shaking table.*

1 INTRODUCTION

In the last two decades R&D of structural vibration control devices for buildings and bridges has been intensified in order to answer the construction market needs that demand more effective systems to reduce the damage caused on structures by seismic and wind loadings. Although the main purpose of a seismic design is to protect the population from the consequences of a severe earthquake, the protection of the building stock may also be regarded as an important option during the conception and design process.

Seismic isolation and passive energy dissipation are two well-established techniques validated by a huge amount of real applications [1, 2]. Magneto-rheological fluid based devices have the appropriate features justifying their relevance for possible civil engineering applications and therefore the attention of researchers to study its potential as vibration control hardware [3, 4]. The control strategy for these devices is based on semi-active control that may be more reliable and stable than active control.

In this paper is addressed some on-going R&D on the vibration control of a three degree-of-freedom (3-DOF) scaled metallic frame with a MR damper [5].

An equivalent device was tested in the laboratory to obtain the main rheological characteristics in order to develop a numerical model to simulate its behavior. Then a 3-DOF scaled frame was assembled and system identification techniques using an impact hammer procedure were performed to obtain the experimental dynamic properties of this structural system. Based on these results a numerical model was created to initiate the semi-active control research process in order to investigate and calibrate the frame behavior with the MR damper.

2 SEMI-ACTIVE CONTROL OF MR DAMPERS

MR fluids have become an extensively studied “smart” fluid and some experimental research has been done in the last years to produce a “smart” control device. The MR damper performance is often characterized by using the force versus velocity relationship. MR dampers have the possibility to change the damping characteristics based on a force versus velocity envelope, which can be described as an area rather than a line in the force-velocity plane.

Many authors have developed modeling techniques for the MR dampers. The Bouc-Wen model shown in Fig. 1 allows modeling nonlinear hysteretic systems and is frequently used to model MR dampers [3].

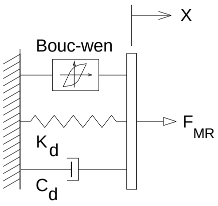

Figure 1: Bouc-Wen model for a MR damper.

The MR force of the device can be computed by

$$F_{MR} = c_0 + k_0 \left(X - X_0 \right) + \alpha z \tag{1}$$

In this equation FMR is the predicted damping force, *k₀* is the accumulator stiffness, *c₀* is the viscous damping and *z* is the evolutionary variable of the first order nonlinear differential equation

$$\dot{z} = -\gamma \left| \dot{x} \right| z \left| z \right|^{n-1} - \beta \dot{x} \left| z \right|^{n} + A\dot{x} \tag{2}$$

The parameters *β*, *γ* and *A* allow controlling the linearity in the unloading and the smoothness of the transition from the pre-yield to the post-yield region.

The equation of motion that describes the behavior of a controlled building under an earthquake load [6] is given by:

$$M\ddot{x}+C\dot{x}+Kx=-\Gamma f-M\lambda\ddot{x}_g \tag{3}$$

where *M* is the mass matrix, *C* is the damping matrix, *K* is the stiffness matrix, *x* is the vector of floors displacements, $\dot{x}$ and $\ddot{x}$ are the floor velocity and acceleration vectors respectively, *f* is the measured control force, *λ* is a vector of ones and *Γ* is a vector that accounts for the position of the MR damper in the structure. This equation can be rewritten in the state-space form as

$$\begin{cases}\dot{z}=Az+Bf+E\ddot{x}_g\\ y=Cz+Df+v\end{cases} \tag{4}$$

where *z* is the state vector, *y* is the vector of measured outputs and *v* is the measurement noise vector. The other matrix quantities are defined by

$$\begin{gathered}A=\begin{bmatrix}0 & I\\ -M^{-1}K & -M^{-1}C\end{bmatrix}\qquad B=\begin{bmatrix}0\\ M^{-1}\Gamma\end{bmatrix}\quad E=-\begin{bmatrix}0\\ \lambda\end{bmatrix}\\ C=\begin{bmatrix}-M^{-1}K & -M^{-1}C\\ I & 0\end{bmatrix}\qquad D=\begin{bmatrix}M^{-1}\Gamma\\ 0\end{bmatrix}\end{gathered} \tag{5}$$

To perform the numerical analysis a single bay three-storey frame (three degree of freedom in shear frame configuration) was designed. The columns at the corners, having the same stiffness, are made of aluminum with an average cross section of 1.5mm by 50mm and the diaphragm floors are made of polycarbonate plates monolithically attached to the columns. The frame mass is around 19 kg and each floor has an average mass of 3.65 kg. The stiffness of the experimental frame was designed to keep the fundamental frequency near to 2 Hz.

Assuming a three storey shear frame, the frame mass (*M*) and the stiffness matrix (*K*) are obtained as:

$$M=\begin{bmatrix}3.65 & 0 & 0\\ 0 & 3.65 & 0\\ 0 & 0 & 3.65\end{bmatrix}(kg) \tag{6}$$

$$K=\begin{bmatrix}5820 & -2910 & 0\\ -2910 & 5820 & -2910\\ 0 & -2910 & 2910\end{bmatrix}(N/m) \tag{7}$$

The three natural frequencies obtained with the above mass and stiffness matrices are: 2.00Hz, 5.60Hz and 8.09Hz. A damping of 0.5% along with the above mass and stiffness matrices formed the initial parameters for the modal analysis.

The frame was then assembled (Fig. 2) to perform experimental research and calibration of the numerical model.

Figure 2: Metallic scaled frame at the shaking table.

After calibrating the MR damper numerical model it is necessary to select a proper control algorithm to efficiently use this device in reducing the dynamic response of structural systems. The fundamental condition to operate the MR damper is based on a generated damping force that is related with the input voltage; the control strategy is selected so that the damping force can track a desired command damping force.

In the last few years several approaches have been proposed for better selection of the input voltage that must be applied to the MR damper to achieve the maximum performance [7-9]. In the present numerical study a Clipped Optimal control will be used as shown in Fig. 3.

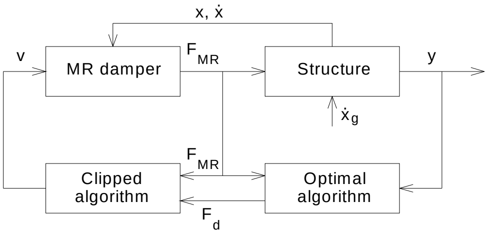

Figure 3: Clipped Optimal controller.

This strategy consists of a Bang-Bang (on-off) controller that causes the damper to generate a desirable control force that is determined by an “ideal” active controller (in state feedback form). A force feedback is used to produce the desired control force f_d, which is determined by a linear optimal controller $K_{k(s)}$, based on the measured structural responses y and the measured damper force fc.

Only applied voltage v_a can be commanded (and not the damper force) that is selected by $v_a = v_{max}\, H\,(f_d - f_c)\, f_c$ in which vmax is the voltage level associated with the saturation of the magnetic field in the MR damper and $H(.)$ is the Heaviside step operator.

The following voltage selection algorithm is applied: When the actual force being generated by the damper f_c equals the desirable force f_d, the voltage applied remains the same. When the magnitude of the force f_c is smaller than the magnitude of f_d and both forces have the same sign, then the voltage applied is set to its maximum level to increase the damper force. Otherwise, voltage is set to zero.

The selected optimal controller is based on a Linear Quadratic Optimal Control. In this numerical study the linear controller is obtained with a Linear Quadratic Regulator (LQR) strategy that will be used in a state feedback control.

The main objective to design the optimal controller is to obtain an optimal control vector $f_c(t)$ that minimizes a performance index J. In this case a quadratic performance index in $z(t)$ and $f_c(t)$ is used and represented by:

$$J = \int_0^{t_f} \left[z^T(t) \cdot Q \cdot (t) + f(t) \cdot R \cdot f(t) \right] dt \tag{8}$$

In eq. 8 Q and R are weighting matrices associated with the state variables and with the input variables respectively. The magnitudes of these matrices are defined according to the importance that is given to the state variables and the control forces on the minimization process. Increasing the values of Q matrix elements implies the prioritization of the response reduction over the control forces. On other hand, increasing the values of the elements of R implies the prioritization of the control forces over the response reduction.

The solution of the LQR problem is based on the analysis of the algebraic Riccati equation

$$PA + A^T P - PBR^{-1}B^T P + Q = 0 \tag{9}$$

and the LQR problem can be solved using a linear state feedback with a constant gain G according to

$$u(t) = -G \cdot x(t) = \left[R^{-1} B^T P \right] \cdot x(t) \tag{10}$$

To select the appropriate values for Q and R the following procedure was used in this study: it was assumed that R matrix has the following form

$$R = r \cdot I \tag{11}$$

where I is the identity matrix and r is a multiplier, and that Q matrix assumes the following form

$$Q = \begin{bmatrix} K & 0 \\ 0 & 0 \end{bmatrix} \tag{12}$$

A parametric study was carried out by changing the value of the multiplier (10^{-1}, 10^{-3}, 10^{-5}, 10^{-7}, 10^{-9}, 10^{-11}, 10^{-13} and 10^{-15}) and then verifying the efficiency of (reduction of floor displacements, accelerations and also the control force on the actuator). It was verified that decreasing this value implies a more marked reduction of the response.

In this case a significant reduction (up to 90% of the floor displacements and accelerations) was obtained with $r=10^{-9}$.

3 EXPERIMENTAL SETUP

According to the scheduled research program [10], the next stage was related to the study of the experimental dynamic behavior of a 3DOF scaled metallic load frame equipped with a semi-active device. The experimental frame located at FEUP-Covicocepad Lab, can be forced dynamically using the Quanser shaking table II as the dynamic loading actuator.

To study the semi-active control strategy a small MR damper was placed at the first floor level attached to the frame and rigidly attached to the shaking table as shown in Fig 4. To measure the damping force values generated during the experimental tests a load cell was placed in the MR damper support system.

a) b)

Figure 4: a) MR damper attached to the experimental metallic frame; b) RD-1097-01 MR Damper.

The parameters of the MR damper shown in Fig. 5 are: minimum force in passive-off mode < 9 N (for current 0.0A at piston velocity 200 mm/s), maximum force 100 N (for current 1.0A and piston velocity 51 mm/s), stroke ±25 and response time < 25 ms (time required to reach 90% of the steady-state value of force under a step change of the current from 0.0 to 1.0A, for 51 mm/s).

3.1 Experimental MR Damper Behavior

To study the behavior of a MR damper some experiments were carried out on a MTS universal testing machine (Mechanical Engineering Laboratory at FEUP) with two MR dampers: RD-1005-03 and RD-1097-01 supplied by LORD Corporation.

After assemblage the MR dampers were forced with a sinusoidal signal at a fixed frequency, amplitude and current supply. To obtain the response under several combinations of frequencies, amplitudes and current supplies a series of tests were carried out. Therefore, a set of frequencies (0.5, 1.0, 1.5 and 2.0 Hz), amplitudes (2, 4, 6, 8 and 10 mm) and current supplies (0.0, 0.1, 0.2, 0.25, 0.5, 0.75, 1.0 and 1.5 A) were used to complete the test program [6].

The variable current tests demonstrate that increasing the input current implies an increase in the force required to yield the MR fluid and a plastic-like behavior is observed in the hysteretic loop. In the frequency dependent test, it was observed that the maximum damping force increases with the frequency due to large plastic viscous force at higher speeds.

The same procedure was used to obtain the rheological behaviour of the RD-1097-01 MR damper. This was the selected device to be used in this analysis due to the small range of forces involved in the scaled frame dynamic analysis. In order to use the Bouc-Wen model, the following current (I) dependent parameters were used:

$$\begin{cases} \alpha(I) = 72.80I^3 - 42.88I^2 + 14.83I + 0.29 \\ c_d(I) = -9.37I^4 + 10.22I^3 - 4.33I^2 + 0.89I + 0.02 \end{cases} \tag{13}$$

And the current independent parameters are: k_0= 0.0, β= -7.078, γ=10.614, A=36.21 and n= 1.0. These are approximate values that probed to capture very well the hysteretic behaviour of the MR damper [11].

3.2 System Identification

An impulse hammer test was carried out in order to obtain the modal parameters of the structure. The structural response was measured with a piezoelectric accelerometer (Bruel & Kjaer type 4393 with measuring amplifier type 2525) placed at the first floor and a portable real-time analyzer (OROS 35 real-time multi-analyzer) that was used to perform the necessary mathematical rationing on input and response signals to produce the desired transfer function.

The desired frequency response functions (magnitude) for each input/output measurements are shown in Figs. 6-8.

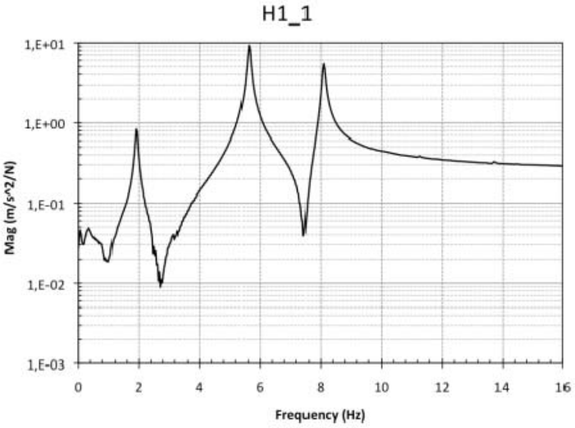

Figure 6: Frequency Response Function of H1_1.

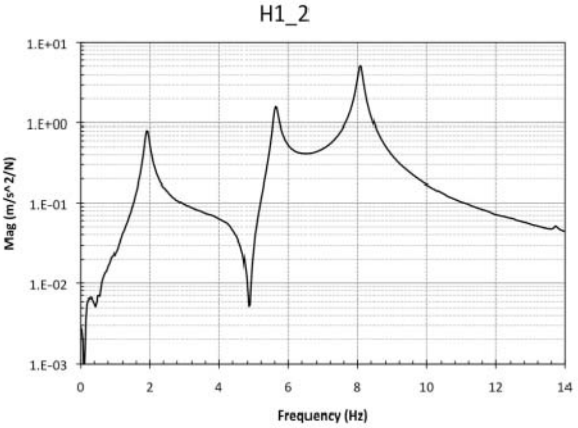

Figure 7: Frequency Response Function of H1_2.

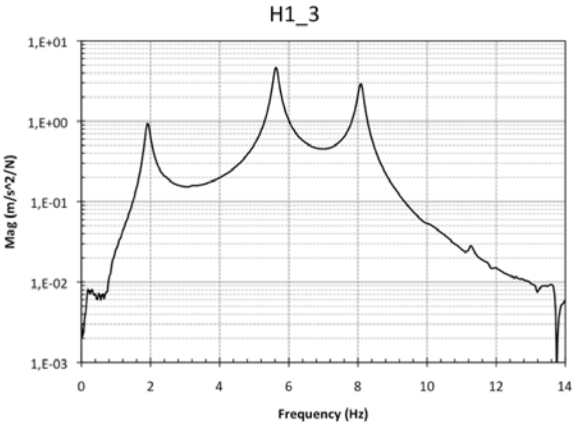

Figure 8: Frequency Response Function of H1_3.

The parameters of the scaled frame were then obtained based on the data provided by these functions and are tabulated in Table 1.

Frequency	Damping	Modal Participation
1,913986 (1st mode)	0.03157	34.43248
5,627778 (2nd mode)	0.01198	35.25975
8,086245 (3rd mode)	0.00899	30.30777

Table 1: Parameters of the scaled frame.

4 RESULTS

To study the response of the structure with the semi-active controller, a few characteristic earthquake records were considered; those will be also input in the Quanser shaking table of FEUP-Covicocepad laboratorial facilities, in order to experimentally calibrate and numerically compare different control strategies. The results considered herein are just for the El Centro earthquake record selected as input.

The three horizontal floor displacements were selected as the parameters (output) to verify the efficiency of the control law. Some results of this numerical analysis are plotted in Figs. 11-14 for uncontrolled and semi-active controlled scenarios.

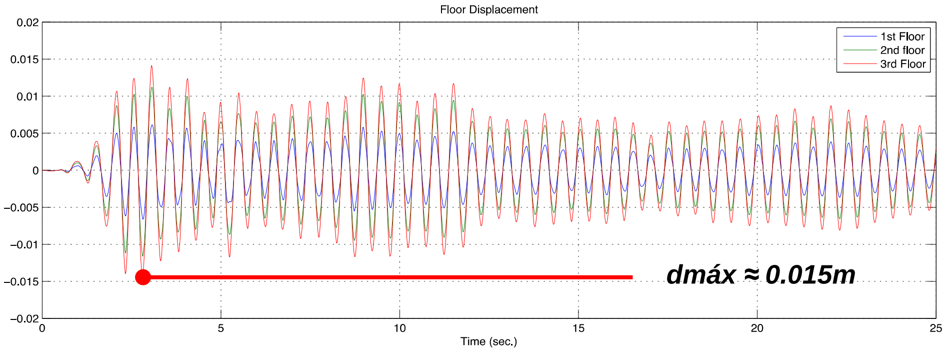

Figure 9: Uncontrolled response without MR damper.

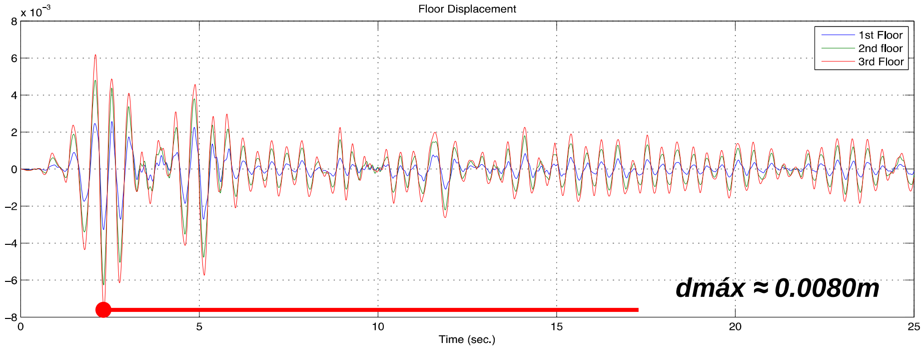

Figure 10: Uncontrolled response with MR damper @ 0.00A.

The structure response plot shown in Fig. 9 was obtained without any device connected to the scaled frame (non-controlled response). Then, the MR damper was attached to the 1st floor in a passive configuration (without current applied) and a new displacement response plot was obtained as shown in Fig. 10. It is clear that a significant displacement reduction is obtained even with the MR damper in passive mode.

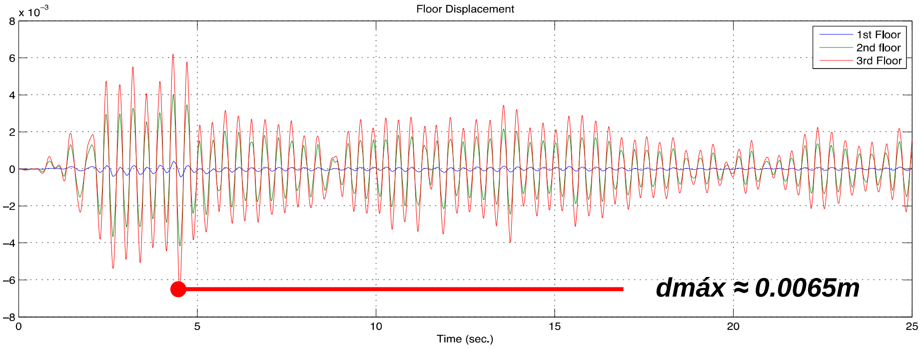

Figure 11: Uncontrolled response with MR damper @ 0.25A.

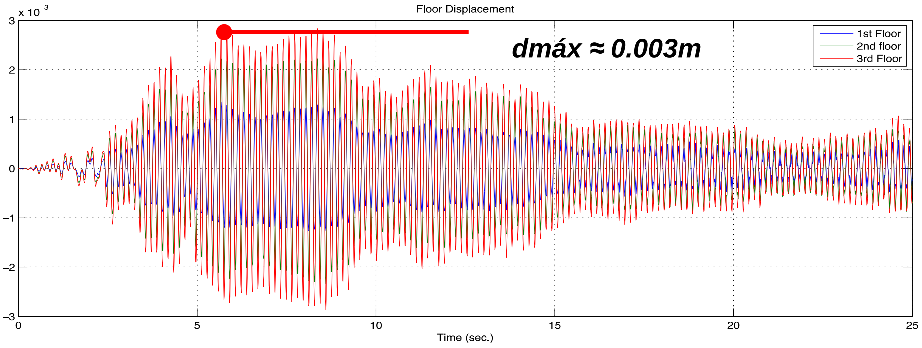

Figure 12: Semi-active control response.

A new analysis was carried out with the MR damper acting as a passive device but with a constant current of 0.25A. As it can be verified in Fig. 11, the three floor displacements were considerably reduced (from 0.008 to 0.006 m) due to the increase of damping and stiffness at this level. This means that the MR damper introduces a partial constraint and as consequence the frame behaves like a 2 DOF system above the first floor level. Finally, the semi-active controller was activated and the horizontal floor displacements were again plotted as shown in Fig. 12.

As expected, the semi-active control based on the Clipped Optimal algorithm was successfully applied. The lateral displacements of the building floors were reduced significantly during the earthquake duration, as visible by the maximum displacement of the top floor reaching a value of about 0.003 m. This value corresponds to 20% of what was reached initially without control; and to 40% of what was reached with passive control.

Although the main objective of this analysis is to validate the efficiency of the Clipped Optimal algorithm, it is clear that further numerical and experimental research must be carried out. Since this is an ongoing research program, the next step will be the implementation of new control strategies.

5 CONCLUSIONS

This paper addresses the vibration control of a 3-DOF experimental metallic frame with a MR damper. The MR damper was tested to find the dynamic properties and a numerical model was developed to simulate its behaviour. System identification allowed obtaining the dynamic response of this structural system. In a numerical example the three-story structure was controlled using a MR damper on the first floor. The simulated results show that the Clipped Control algorithm resulted in an improvement over the uncontrolled system.

6 ACKNOWLEGMENTS

This work is integrated in the thematic and activities of the international collaborative research project COVICOCEPAD approved by the European Science Foundation (ESF) within the Smart Structural Systems Technologies (S3T) Program. It was sponsored in Portugal until last December 2010 by FCT (Fundação para a Ciência e a Tecnologia) project PPPCDT-05-S3T-FP054-COVICOCEPAD, fact that is herein acknowledged.

REFERENCES

[1] F. Naeim, J. Kelly, *Design of Seismic Isolated Structures: from Theory to Practice,* New York: John Wiley & Sons Inc., 1989.

[2] M. Cesar, R. Barros, *Influence of Resistant Cores Location on the Seismic Response of a R/C 3D-Frame Equipped with HDRB Base Isolation Devices*, in Proceedings of the Eleventh International Conference on Civil Structural and Environmental Engineering Computing, Editor: B.H.V. Topping, Paper 199 - 20 pages, Civil-Comp Press, Stirlingshire, Scotland, 2007.

[3] S. Dyke, B. Spencer, M. Sain , J. Carlson, *Modeling and Control of Magneto-Rheological Dampers for Seismic Response Reduction*, Smart Materials and Structures, Vol. 5, pp. 565-575, 1996.

[4] V. Gattulli, M. Lepidi, F. Potenza, *Mitigation of Seismic Vibration by Semi-Active Control*, in School and Symposium on Smart Structural System Technologies (S3T-2010), Editors: R. Barros and A. Preumont, pp. 347-367. Faculty of Engineering of the University of Porto (FEUP), Porto, Portugal, 2010.

[5] M. Cesar, R. Barros, *Semi-Active Control of a Metallic Scalled Frame with a MR Damper: Numerical and Experimental Research.* in School and Symposium on Smart Structural System Technologies (S3T-2010), Editors: R. Barros and A. Preumont, pp. 419-440. Faculty of Engineering of the University of Porto (FEUP), Porto, Portugal, 2010.

[6] R. Barros, A. Baratta, O. Corbi, M. Cesar, M. Paredes, *Some Research on Control of Vibrations in Civil Engineering under COVICOCEPAD Project*, in Proceedings of the Third International Conference on Integrity Reliability & Failure (IRF 2009), Editors: J.F. Silva Gomes and Shaker A. Meguid, Ref: S2606-A0583, Edicoes INEGI, Portugal, 2009.

[7] S. Dyke, B. Spencer Jr., *A Comparison of Semi-Active Control Strategies for the MR Damper,* in Proceedings of the IASTED International Conference, Intelligent Information Systems, The Bahamas, 1997.

[8] L. Jansen, S. Dyke, *Semi-active control strategies for MR dampers: a comparative study*. ASCE Journal of Engineering Mechanics, Vol. 126, No. 8, pp. 795-803, 1999.

[9] C. Oliveira, R. Bairrão, R. Barros, L. Guerreiro, *The New Generation of Seismic Semi-Active and Active Protection Systems*, in Proceedings of the 4th European Conference on Structural Control (4ECSC), Paper 227, Russia, 2008.

[10] R. Barros, *Project COVICOCEPAD under Smart Structural Systems Technologies of Program Eurocores*, in Smart Materials and Smart Structures Technology, Editors: B.F. Spencer, M. Tomizuka, C.B. Yun, W.M. Chen, R.W. Chen, London: Taylor & Francis Group, 2008.

[11] Y. Shen, M. Golnaraghi, G. Heppler, *Load-Leving suspension system with a magnetorheological damper*, Vehicle System Dynamics, 45:4, 297-312, 2007.

COMPDYN 2011
3rd ECCOMAS Thematic Conference on
Computational Methods in Structural Dynamics and Earthquake Engineering
M. Papadrakakis, M. Fragiadakis, V. Plevris (eds.)
Corfu, Greece, 25–28 May 2011

THE USE OF TMD'S WITH HEAVY MASS TO MITIGATE THE SEISMIC RESPONSE OF STRUCTURES

José E. Barros[1], Carlos Moutinho[2], and Rui C. Barros[2]

[1] MSc Engineer, Metalogalva, Trofa, Portugal
e-mail: j.ed.barros@hotmail.com
[2] Assistant Prof. and Associate Prof. with Habilitation, Department of Civil Engineering
FEUP-Faculdade de Engenharia Universidade do Porto, Portugal
moutinho@fe.up.pt , rcb@fe.up.pt

Keywords: Passive Control, TMD, Earthquake Engineering, Structural Dynamics.

Abstract. *This document demonstrates the usefulness, operation and design of Tuned Mass Dampers (TMDs) in the structural control of seismic response. This vibration control system, which main asset is the introduction of additional damping on structural system, can improve the structural behavior particularly in terms of forces and displacements, in case of seismic loads. This paper describes some practical situations using TMDs and the theoretical approach of their operation. Then, design graphics are presented as a result of the research work developed at FEUP and the effectiveness of this type of solution is demonstrated by an illustrative example.*

1 INTRODUCTION

Tuned Mass Dampers have been widely used to control the dynamic response of structures in Civil Engineering. This devices consisting in an additional mass connected to the structure by a spring and a damper, and demonstrate effectiveness in the mitigation of harmonic vibrations. In this kind of vibrations, a well-tuned device behaves in a correct phase opposition to the response of the controlled system, reducing its vibrations [1]. Usually in these cases, the TMD mass represents 1 or 2% of the modal mass associated at the vibration mode in analysis, which results in a small control system, easily integrated architecturally or even hidden.

However, if the structure contains a non-harmonic response, as usually happens in Earthquake Engineering, the mechanism used by TMDs to reduce movement of the main system is no longer based on phase compensation to the movement. Thus, the main advantage is based on the effect of adding supplementary damping to the structure (Paredes, Barros and Cunha [2]). In these cases, the mobilization of considerable damping values which increase significantly the structural damping ratios and hence reduce the dynamic response of the system, is only possible through the use of additional heavy masses.

In this context, this paper aims to expose the research work that has been developed at FEUP about the possibility of using TMDs with heavy mass in structures, using as an additional mass a part of the own structure to control the remaining. This idea was inspired by some real applications in buildings such as the case "Applause Tower" located in Osaka, Japan. In this building, the mass associated with a helipad on the roof was used to act as control system of the remaining structure, using hydraulic actuators, which cause inertial forces between platform and building (Figure 1).

In the case of the control system proposed in this paper, the idea is use a passive system mobilizing a heavier mass. To realize a practical system of this kind will be necessary to use a portion of the structure less commonly used, such as roof and technical floor. Thus, it is possible to materialize the high amount of mass required for the passive system to become efficient. Figure 2 presents some possible solutions (Barros [3]).

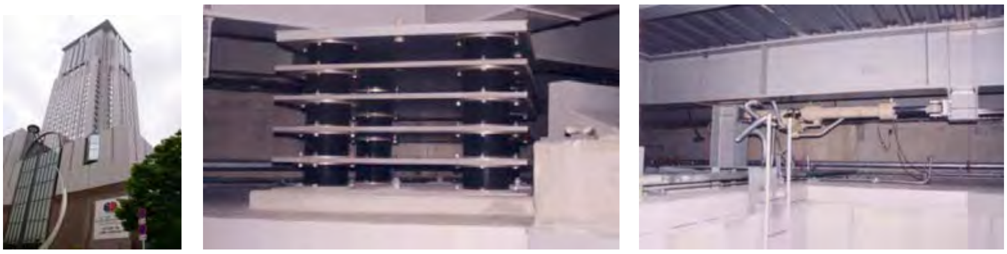

Figure 1 – a) Overview of the "Applause Tower"; b) Support equipment of the platform; c) Hydraulic actuators

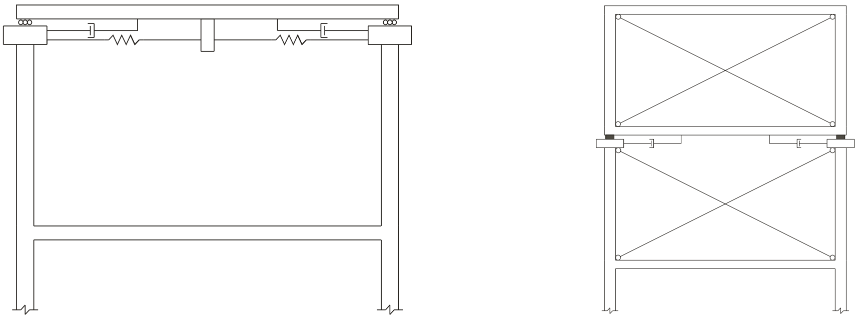

Figure 2 – Examples of use of part of the structure to function as the control system (Barros [3])

2 ANALYSIS OF THE TMD'S OPERATION

2.1 Application to structures with low damping under harmonic solicitations

The structural model usually used to the analyses of the TMD's operation in structures under harmonic solicitations is indicated in Figure 3, where m_1, k_1 and c_1 are the variables that define respectively the characteristics of mass, stiffness and damping of the initial structure, and m_2, k_2 and c_2 define the same characteristics in TMD. When this device is optimally designed, the Frequency Response Function (FRF) presents two peaks corresponding to the natural frequencies of the system of two degrees of system. The FRF curve should be determined so that the two peaks are flat and have de lowest possible value of the amplification of the initial system (Figure 4). In these circumstances it is said that the TMD is tuned optimally.

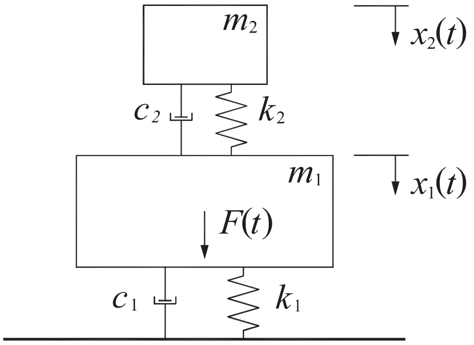

Figure 3 – One degree of freedom model with a TMD

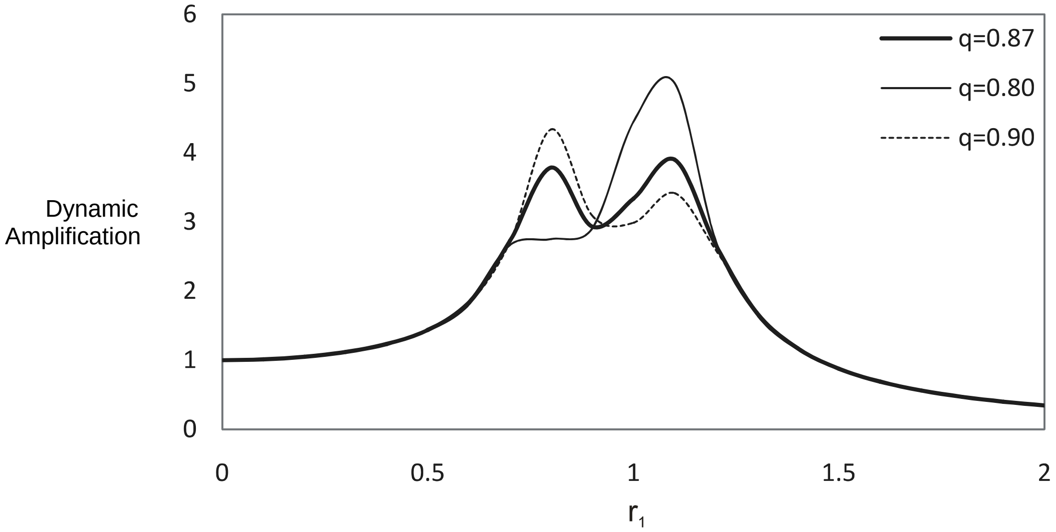

Figure 4 – FRF curves for three different TMDs in the same system $(q_{opt} = 0{,}87)$

In the particular case where the structural damping is null $(c_1 = 0)$, the TMD's design may be done by the following expressions proposed by Den Hartog [1]:

$$q_{opt} = \frac{1}{1+\mu} \tag{1}$$

$$\xi_{2opt} = \sqrt{\frac{3\mu}{8(1+\mu)^3}} \tag{2}$$

where

$$\mu = \frac{m_2}{m_1} \;\; ; \;\; q = \frac{\omega_2}{\omega_1} \;\; ; \;\; \omega_1 = \sqrt{\frac{k_1}{m_1}} \;\; ; \;\; \omega_2 = \sqrt{\frac{k_2}{m_2}} \;\; ; \;\; \xi_2 = \frac{c_2}{2m_2\omega_2}$$

In this situation, the design process begins through the quantification of μ which corresponds to the maximum dynamic amplification (D) imposed to the main system, and this parameter can be obtained by the following expression.

$$D = \sqrt{\frac{2+\mu}{\mu}} \tag{3}$$

After calculating the TMD's mass, using the parameter μ, the optimal frequency and damping of the device are given by the expressions (1) and (2).

The previous expressions can still be used on TMD's design in structures with low structural damping, typically less than 1% (Bachmann and Weber [4]). However, in structures with a higher level of damping, the assumptions used in obtaining such expressions are no longer valid, requiring a different methodology for the determination of the ideal characteristics of these devices. In this case, one should resort to numerical methods to obtain design graphics where to find the values of q_{opt} and ξ_{2opt} (or ξ_{TMD}) corresponding to a particular value of μ, which can minimize the dynamic amplification of the main structure.

2.2 Methodology used in the case of seismic actions

The implementation of a properly tuned TMD to a structure has as a result the introduction of a certain level of additional damping to the system. According to Villaverde [5], for one degree of freedom system with a damping ratio ξ_1 which is installed a small TMD optimally designed with damping ratio ξ_2, the final damping ratio of the system with TMD is approximately

$$\xi_{Final} \cong \frac{\xi_1 + \xi_2}{2} \tag{4}$$

This expression clearly indicates that the inclusion of a TMD in a structure may increase the final damping to a defined level required for the system, which TMD damping is given by the previous equation. This approach is clearly appropriate to the context of seismic design of structures, since effect of structural damping in the response is quantified in the regulations. So, if you need the structural behavior remains within certain limits, which is associated with a given damping required to achieve it, this level of damping can be achieved with the installation of a Tuned Mass Damper.

However, the design procedure of these devices is different in these cases. Indeed, the classical definition based on the mass of the TMD that corresponds to a certain level of reduction of structural response and subsequent determination of the stiffness and damping is no longer valid. In seismic design, to obtain a certain final damping in the structure, first it's need to fix the value of TMD's damping and then his mass and stiffness.

An important aspect in determining the optimal parameters of a TMD is that you can only mobilize high levels of damping in the use of additional high mass values. Due to this fact arises the need for TMDs with heavy mass. Notice for example the FRF curves shown in Figure 5 (Paredes [6] , Barros [3]) which correspond to a structure with an initial damping ratio of 5% associated with a TMD which mass represents 5% of the mass of the initial system. The continuous curve corresponds to the situation where the device is optimally tuned (lower maximum possible dynamic amplification) resulting in a device with a damping of 14%. The attempt to increase the TMD's damping without changing its mass results in the loss of efficiency of the device. Nevertheless, until a certain amount of increased damping it is possible to keep the peaks with the same ordinate. For increasing damping ratio values, the TMD begins to behave like it is "clinging" to the structure and the set begins to converge to a system without TMD.

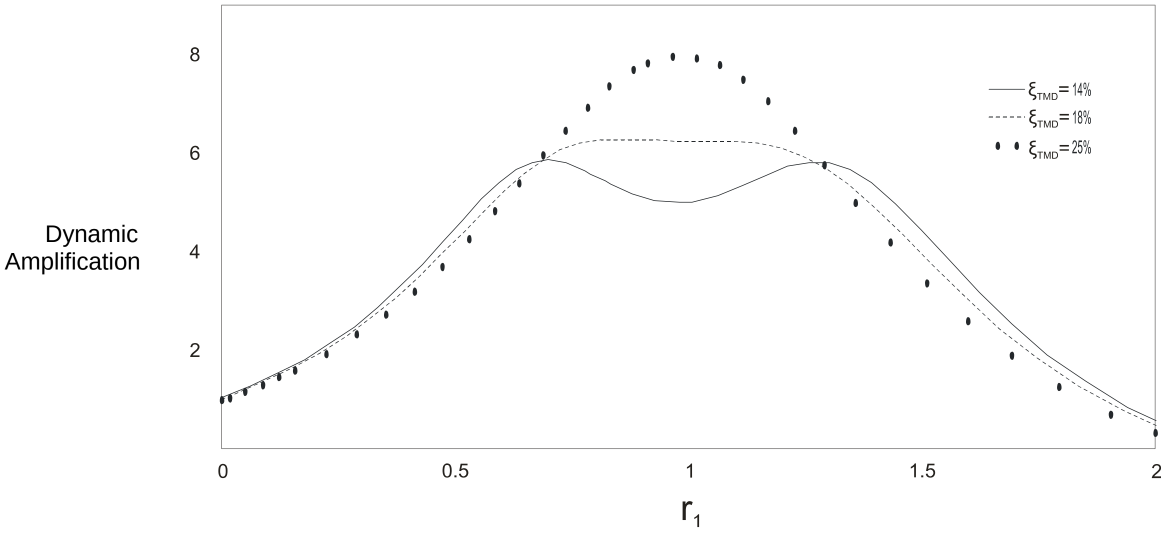

Figure 5 – FRF curves for three different TMDs in the same system $\left(\xi_{2opt} = 14\%\right)$

3 DESIGN GRAPHICS

3.1 Process for obtaining the TMD design graphs

In order to obtain the parameters of a TMD which can introduce a certain level of damping to the system, can be used a structural model similar to that shown in Figure 3. In this case, the values of m_1, k_1 and c_1 as well as m_2, k_2 and c_2 have the same physical meaning presented above. The m_2 parameter has to take several values fixed in corresponding to several values of μ , and the system was studied so that the initial damping ratio takes value of 1%, 3% and 5%, thus resulting in three curves in each graph. Then, for various values of μ up to 0,50 was determinate the value of q_{opt} that flat the two peaks of the FRF curves for various damping values installed on TMD. The damping installed on the control system that corresponds to a lower dynamic amplification, is the optimum damping of the TMD (ξ_{2opt}).

After the addition of Tuned Mass Damper, the two resulting vibration modes have almost the same modal damping, so their average is presented in a third graphic, depending on the value of μ . This reasoning is repeated for each one of the three initial structural damping considered (Barros [3]).

3.2 Design graphics for determination of the TMD’s parameters

Following the procedure presented above, it is possible to compile all the values of optimal parameters for the design of TMDs, for the three initial structural damping of 1%, 3% and 5%. Thus, the values of q_{opt} and ξ_{2opt} for a given value of the μ , can be obtained from the graphs presented in the following Figures 6 and 7.

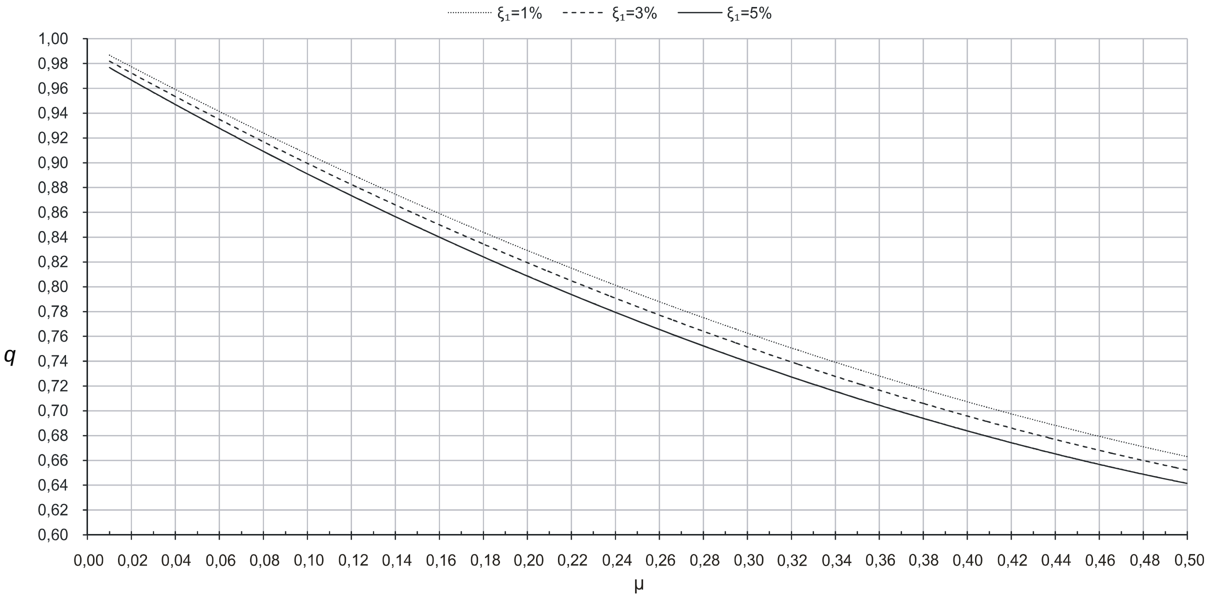

Figure 6 – q_{opt} for values of μ up to 0,50 , (Barros [3])

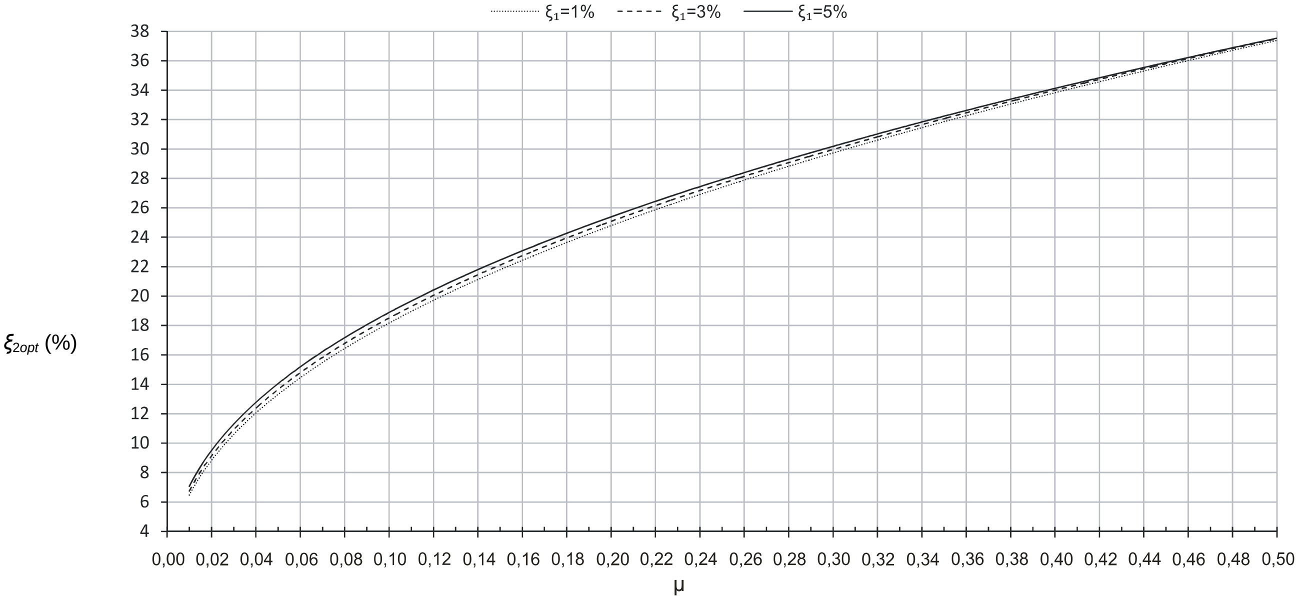

Figure 7 – ξ_{2opt} for values of μ up to 0,50 , (Barros [3])

As already mentioned, have been made a third graphic that reflects the average value of the two final modal damping achieved, and this has an additional utility as the input of the query graph can be given by any one of its axes. In other words, you can set up the final damping achieved for a given μ , or otherwise, can determine the value of μ and thus the mass of the TMD necessary to achieve a given final damping desired, from an initial damping significantly lower. This second way of using this graphic is particularly interesting for the cases of structural control under seismic actions. This third graph is represented in Figure 8.

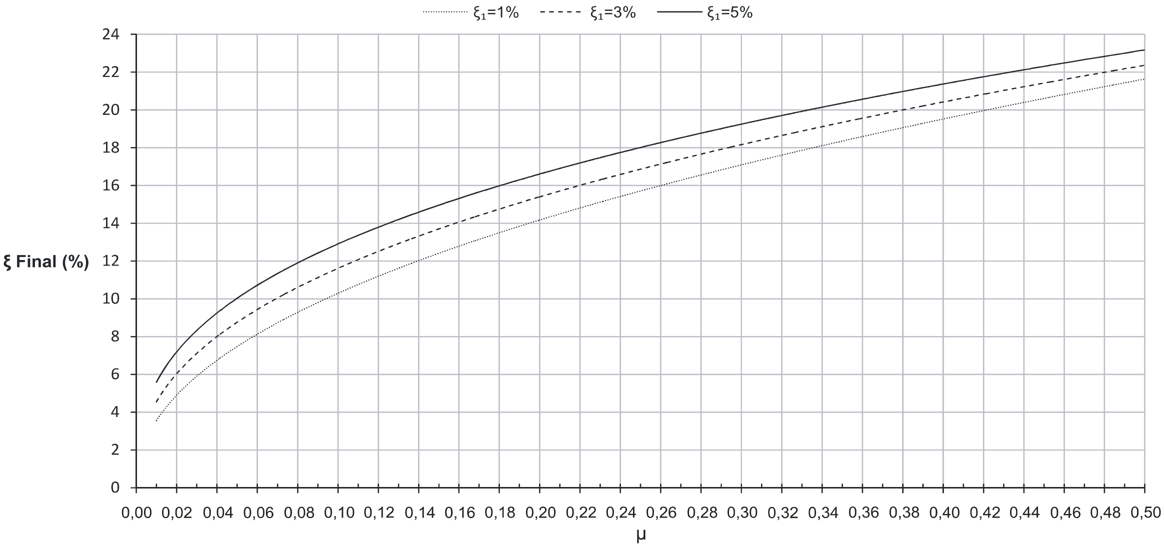

Figure 8 – Final structural damping for values of μ up to 0,50 , (Barros [3])

Comparing the final damping achieved with the inclusion of a Tuned Mass Damper in a system with an initial damping of, for example, 5% with the final damping proposed by Villaverde [5] (that would be approximately the average of both dampings in question), it appears that this formula is a good approximation for values of μ up to about 0,04. For higher values of μ , this match begins to lose its accuracy, thus corroborating the idea in the Villaverde's method that this approximation is valid for low values of μ and damping of TMD. The following Figure 9 represents the two curves referring to both final damping concerned and identifies the similarity to a range of μ up to 0,04 as well as the evolution of loss of accuracy of the approach suggested by Villaverde [5] for higher values of μ .

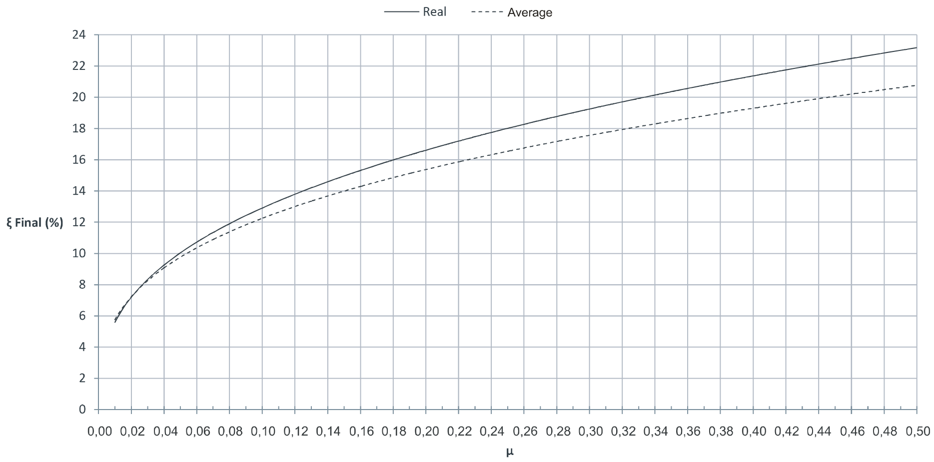

Figure 9 – Comparison between the real final damping achieved and the average of Villaverde's method [5]

4 EXAMPLE OF APPLICATION

4.1 Description of the problem

The application example presented consists in a fifteen storey reinforced concrete frame located in Portimão, Algarve. This case's study aims to compare the behavior of the structure in terms of displacements and applied forces resulting from seismic activity present in the regulatory response spectra of Eurocode 8 (EC8) [6], when the structure has or has not control system through a TMD. Also, when there is no TMD, the structure was studied as having two distinct behavior factors of 1,5 and 2,5, enabling the comparison of the effectiveness of the application of TMD into structures more or less ductile (Barros [3]).

This study was performed through a modal analysis by response spectrum which consists in a linear elastic analysis. This procedure is a simplified analysis by which, according to regulation FEMA 356 [7], when the structure is under control must behave elastically to the seismic action considered, although the EC8 does not refer such approach.

To realizing the TMD, was considered the two top floors of the frame structure as a mass to be used by the control system. The choice of the number of floors to behave as a mass of TMD was based on the final damping achieved in each scenario.

So, consider the structural scheme shown in Figure 10, which represents the frame structure treated, regular in height and plant and set on a ground classified as type C.

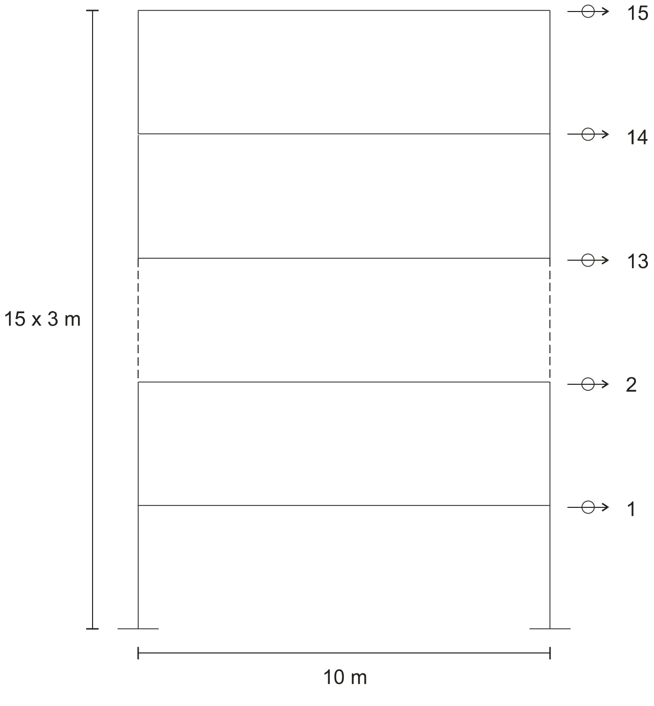

Figure 10 – Schematic structure of the frame in study (Barros [3])

Neglecting the contribution of the pillar's mass when compared with the floor's mass, it is assumed that in the almost permanent combination of actions the mass of each degree of freedom is worth 10 tones. With regard to the stiffness of the structure, the slabs are considered infinitely rigid in bending when compared with the pillars. It is also assumed that the section of the columns is constant in all the framed structures, with approximate dimensions of 0,30 x 0,40 square meters (C25/30 concrete), resulting in a fundamental frequency of vibration in the order of 1 Hertz.

4.2 Main results

In order to control the first vibration mode of the main structure (thirteen storeys), a TMD was installed consisting of two floors which should behave as a single mass, which is why the structure now has fourteen degrees of freedom. The TMD's characteristics were obtained from the design graphics presented and are shown in Table 1. The structural damping ratio of the frame structure increases from 5% to about 19%, consisting in a significant amplification of this parameter.

μ	q_{opt}	ξ_{TMD} (%)	ξ_{Final} (%)
0,295	0,741	30	19

Table 1 – TMD's characteristics and final damping achieved

As noted above, the structure without TMD is studied with two distinct behavior factors. The natural frequencies of vibration given bellow correspond to the frame structure without TMD (regardless of the behavior factor) and with TMD.

Vibration Mode	Natural frequency without TMD (rad/s)	Natural frequency with TMD (rad/s)
1	6,73	5,19
2	20,11	8,43
3	33,29	23,20
4	46,12	38,16
5	58,48	52,64
6	70,25	66,42
7	81,29	79,31
8	91,49	91,13
9	100,76	101,73
10	109,00	110,95
11	116,11	118,67
12	122,04	124,79
13	126,71	129,22
14	130,08	131,90
15	132,12	-

Table 2 – Natural frequencies of the structure with and without TMD

Regarding the effect of seismic accelerations in the structure are only shown the parameters for the type 1 earthquake, since the type 2 is not so onerous, being of course the type 1 that affects the design of the structure. Thus, Table 3 outlines the structure's displacements for the three cases of study, for each degree of freedom.

As can be seen by consulting Table 3, all degrees of freedom have strong reductions in their displacements after the installation of the control system. The exception is the two top floors, because they are associated with TMD have their movements increased, as expected. Another aspect that can be seen from the analysis of this table is that the final displacements of the structure without TMD are practically the same for both cases of different behavior factors.

Degree of freedom	Displacements for behavior factor of 2,5 (m)	Displacements for behavior factor of 1,5 (m)	Displacements for the structure with TMD (m)
1º	0,01506	0,01505	0,00566
2º	0,02993	0,02991	0,01114
3º	0,04444	0,04440	0,01633
4º	0,05842	0,05836	0,02113
5º	0,07172	0,07165	0,02553
6º	0,08424	0,08416	0,02953
7º	0,09586	0,09577	0,03315
8º	0,10651	0,10641	0,03639
9º	0,11610	0,11599	0,03924
10º	0,12455	0,12443	0,04171
11º	0,13177	0,13164	0,04374
12º	0,13768	0,13755	0,04530
13º	0,14220	0,14207	0,04635
14º	0,14526	0,14512	0,16487
15º	0,14681	0,14667	

Table 3 – Structure’s displacements for the three studied cases

Likewise the seismic forces associated with each degree of freedom, for the two structural behavioral factors of 1.5 and 2.5, are tabulated in Table 4.

Degree of freedom	Applied forces for behavior factor of 2,5 (kN)	Applied forces for behavior factor of 1,5 (kN)	Applied forces for the structure with TMD (kN)
1º	4,90	8,17	14,59
2º	9,47	15,79	26,24
3º	13,43	22,38	33,15
4º	16,57	27,61	35,31
5º	18,79	31,31	34,57
6º	20,14	33,56	33,35
7º	20,84	34,71	32,59
8º	21,21	35,33	31,51
9º	21,68	36,11	29,99
10º	22,58	37,60	30,27
11º	24,00	39,97	34,41
12º	25,77	42,92	40,41
13º	27,56	45,89	39,02
14º	28,98	48,28	94,63
15º	29,77	49,59	

Table 4 – Applied forces to the structure for the three studied cases

In examining Table 4 it appears that when compared with the initial structure provided with a behavior factor of 2,5, the installation of a TMD does increase the seismic forces in the structure markedly. Moreover, when compared the seismic forces after docking the TMD with the forces arising from the same phenomenon in the structure with the behavior factor of 1,5, it appears that the addiction of forces is much less significant, as there are a few degrees of freedom whose forces diminish its value.

5 CONCLUSIONS

The numerical study conducted on this issue has enabled the development of design graphs for TMDs with a heavy mass, which allow an easy practical and quick way to obtain the optimal parameters of such passive system of vibration control, which can be of important use for both buildings and bridges (Paredes and Barros [9]).

As can be understood through the analysis of Table 3, the displacements checked in the structure due to seismic accelerations are practically equal in both cases of different ductility characteristics. Thus it appears that the displacements do not depend on the behavior factors of the structure. Because of this, the effectiveness of the use of TMDs in displacements values is similar in both cases so that these parameters are a little more than a third of what they were initially. This proves that this control system is quite effective in terms of displacements under seismic actions.

With regard to seismic forces that arise in the structure (Table 4), and not forgetting the obligatory of the structure remains in elastic regime when it has control system (imposed by FEMA 356), the influence of the installation of TMD has strongly depends on the characteristics of ductility concerned. Indeed, when the structure is characterized by a behavior factor of 2,5, there is a significant increase of forces, there are even a few degrees of freedom increased to more than double its initial value, resulting in an increase of almost 60% in foundation’s bending moments. When the structure is less ductile, having a behavior factor of 1,5, the seismic forces installed in most of the degrees of freedom reduce its value. In the remaining degrees of freedom, the increase is much less significant when compared with the situation of more ductile structure, leading to a reduction in the bending moments at the foundations of around 4%. Due to this scenario, the use of TMDs to control the seismic response of structures is more interesting in more rigid structures, and in the more ductile the extra efforts may undermine the feasibility of using this damping system.

ACKNOWLEDGEMENTS

This work is integrated in the thematic and activities of the international collaborative research project COVICOCEPAD approved by the European Science Foundation (ESF) within the Smart Structural Systems Technologies (S3T) Program. It was sponsored in Portugal until last December 2010 by FCT (Fundação para a Ciência e a Tecnologia) project PPPCDT-05-S3T-FP054-COVICOCEPAD, fact that is herein acknowledged.

REFERENCES

[1] Den Hartog, J. (1940), *Mechanical Vibrations*. McGraw-Hill, New York.

[2] Paredes, M.M., Barros, R.C. and Cunha, A.F. (2009). *A Parametric Study of TMD’s for Regular Buildings under Earthquakes*. Computational Methods in Structural Dynamics and Earthquake Engineering (COMPDYN 2009), M. Papadrakakis, N.D. Lagaros, M. Fragiadakis (eds.), Rhodes, Greece, 22–24 June 2009.

[3] Barros, J.E. (2010). *Utilização de TMDs de Grandes Dimensões no Controlo da Resposta Dinâmica de Estruturas de Edifícios*. Dissertação de Mestrado, Faculdade de Engenharia da Universidade do Porto, Porto, Portugal.

[4] Bachmann, H. and Weber, B. (1995). *Tuned Vibration Absorbers for Lively Structures*. Journal of IABSE, Structural Engineering International, vol. **5**, nº1.

[5] Villaverde, R. (1985). *Reduction in Seismic Response with Heavily-Damped Vibration Absorbers*. Earthquake Engineering and Structural Dynamics. Vol. **13**, pp 33-42, John Wiley & Sons, Ltd.

[6] Paredes, M.M. (2008). *Utilização de Amortecedores de Massas Sintonizadas no Controlo de Vibrações em Estruturas*, Dissertação de Mestrado, Faculdade de Engenharia da Universidade do Porto, Porto, Portugal.

[7] Instituto Português da Qualidade (2009). *Eurocódigo 8: projecto de estruturas para resistência aos sismos*. NP EN 1998-1: 2009. Caparica: IPQ, Portugal.

[8] American Society of Civil Engineers. (2000). *Federal Emergency Management Agency, FEMA 356*, Pre-standard and Commentary for the Seismic Rehabilitation of Buildings. Washington D.C., USA.

[9] Paredes, M.M. and Barros, R.C. (2009). *The Use of TMDs for Structural Vibration Control: Numerical Studies of Shear Buildings under Earthquakes and of a Pedestrian Bridge*. Proceedings of the Twelfth International Conference on Civil Structural and Environmental Engineering Computing, Edited by: B.H.V. Topping, L.F. Costa Neves and R.C. Barros. Civil-Comp Press, Paperback: 316 pages, CD-ROM: 293 papers, ISBN 978-1-905088-32-4, 2009.

COMPDYN 2011
3rd ECCOMAS Thematic Conference on
Computational Methods in Structural Dynamics and Earthquake Engineering
M. Papadrakakis, M. Fragiadakis, V. Plevris (eds.)
Corfu, Greece, 25–28 May 2011

COMPARISONS OF A TALL BUILDING WIND RESPONSE WITH AND WITHOUT A TMD

Nuno A.C. Ferreira[1], **Rui C. Barros**[2], **Raimundo Delgado**[2]

[1] GEG, Engineering Design Consultants, Porto, Portugal
[2] Faculty of Engineering of the University of Porto
Rua Dr. Roberto Frias, s/n 4200-465 Porto PORTUGAL
rcb@fe.up.pt

Keywords: Wind response, Tall buildings, Vibration control, TMD, Eurocode 1.

Abstract. *This work addresses basic concepts regarding the wind effects on tall buildings and their subsequent wind responses. The methodology proposed in Eurocode 1 for quantification of the wind actions, is compared with the methodology still in force in the Portuguese legislation, to assess the pros and cons of each towards a more realistic building design. Using commercial software for the structural calculations, a specific study of a given tall building is performed by the actions associated with the two regulations, with the intention of comparing stress resultants and generalized displacements. A simplified method for quantifying the dynamic action on these structures is adopted, with the purpose of studying techniques for vibration control of the along-wind response in terms of displacements and accelerations. For the tall building case under study, a realistic comparison is made between the building's response under dynamic wind action with and without a TMD.*

1 INTRODUCTION

The wind action on towers (Almeida and Barros [1]) and masts (Barros [5]) and on a tall building (Ferreira [11], Taranath [21]) is of paramount importance to their design, which can influence the structural system to be adopted or even lead to the needed implementation of control systems to reduce vibrations caused by wind dynamic phenomena.

After a comparative analysis between the Portuguese Regulation on Safety and Actions for Building Structures and Bridges (RSAEEP) [18] and Eurocode 1 (EC1) [10] it can be concluded that there are differences in these methods here considered to quantify the wind actions, with an improvement for design inherent to the European regulation.

Using the World Trade Center (WTC) as reference tall building type, a parametric study was performed on the variation of shear forces and bending moments as a function of height, as evaluated by the RSAEEP and by EC1. An equivalent frame structure to the reference World Trade Center was modeled, based upon matching fundamental mode contribution, leading to a structural behavior very close to the three-dimensional modeled behavior found in available references.

For modeling the dynamic wind action reference is made to a method of generating sets of synthetic wind, called the method of Shinozuka. The dynamic response of the reference building, in the longitudinal along-the-wind direction, permits to assess occupants comfort level with regards to accelerations. A theoretical implementation of TMD will be studied and proven to be effective for this tall building under harmonic or under wind loads. The reductions of the responses were found to be more effective on accelerations than on displacements.

2 WIND ACTIONS UNDER TWO DESIGN CODES

For better understanding of the case of study that will be analyzed, some considerations and synthesis of the methodologies are given concerning the two used regulations, in this paper, for wind effects: Portuguese Regulation on Safety and Actions for Building Structures and Bridges (RSAEEP) [18] (still in use) and Eurocode 1 (EC1) [10] (in view of its implementation at European level).

2.1 Wind actions according to Portuguese Regulation RSAEEP

2.1.1 Zoning of territory

RSAEEP [18] admits the differentiation of Portuguese territory in two zones (A and B) based on the analyses of existing meteorological records that, for the same occurrence probability of occurrence, attributes wind intensities sufficiently differentiated.

	Zoning of territory
Zone A	Practically all Portugal except regions belonging to zone B
Zone B	Azores and Madeira; Coastal strip 5 km width; Places of altitude above 600 m; Places on zone A but subjected to particularly unfavorable wind conditions

Table 1 Zoning of Portuguese territory

2.1.2 Aerodynamic roughness of the terrain profile

RSAEEP [18] proposes the differentiation of the terrain profile roughness in two types: type I and type II. The variation of the wind speed with height depends strongly on the dimensions and distribution of existing obstacles in the terrain that affect the air flow in the neighborhood. Notice that the consideration of just two roughness types is a bit schematic and it results from the difficulty of characterizing objectively the multiplicity of the wind situations.

	Aerodynamic roughness of the terrain profile
Type I	Places inside urban zones where medium and tall buildings prevail
Type II	Remaining places: rural zones and periphery of urban zones

Table 2 Distinction between the two types of roughness at RSAEEP

Since roughness of type I is greater, to it will correspond lower wind speed and therefore lower dynamic wind pressures.

2.1.3 Quantification of wind speeds

The wind action on structures depends on the greatness and distribution of the wind speed and of its characteristics; therefore, it is necessary to define the characteristic values and the reduced values of the wind speed in function of the height above the soil.

The average wind speed is defined in function of the height above the soil and is referred to time intervals of 10 minutes. The variation with height h of the characteristic value of the mean wind velocity v (m/s) is given by equation (1). In this formula, h_0 is the height above the soil for which the roughness of the soil is no longer felt; v_0 is the average wind speed at the height h_0; and α is a parameter that depends on the soil roughness. For terrain roughness of type I, v_0 is equal to 18 m/s and $1/\alpha$ takes the value 0,28 ; for terrain roughness of type II, v_0 is equal to 25 m/s and $1/\alpha$ takes the value 0,20.

$$v = v_0 \left(\frac{h}{h_0} \right)^{1/\alpha} \tag{1}$$

Given the imprecision of the definition of the wind speeds in the immediate neighborhood of the terrain, it is advisable to admit a constant value of the wind speed: (i) of 20 m/s up to a height of 15 m, for terrain roughness of type I; (ii) of 25 m/s up to a height of 10 m, for terrain roughness of type II.

For the case of structures identically loaded by the wind in any direction (as is the case of structures with symmetry of revolution), the values of the wind speed to consider should be multiplied by $\sqrt{3}$.

To take into account the fluctuations of wind velocity resulting from the flow turbulence, RSAEEP [18] contemplates a constant value of 14 m/s to be added to equation (1) regardless of the terrain roughness type. RSAEEP [18] also contemplates that the characteristic value of the average wind velocity for zone B, are 10% higher than those of zone A. Table 3 synthesizes all the previous considerations. Additionally RSAEEP [18] contemplates situations on how to consider the height of ground in inclined terrains.

		Zone A		Zone B	
		Roughness Type I	Roughness Type II	Roughness Type I	Roughness Type II
Height (m)	≤ 10	$v_A = 20+14$	$v_A = 25+14$	$v_B = 1.1\ v_A$	$v_B = 1.1\ v_A$
	$10 \leq h \leq 15$	$v_A = 20+14$	$v_A = 25\left(\frac{h}{10}\right)^{0.20} + 14$		
	>15	$v_A = 18\left(\frac{h}{10}\right)^{0.28} + 14$			

Table 3 Characteristic values of wind velocity (m/s)

2.1.4 Determination of Wind Actions on Buildings

For determining the wind actions on buildings, RSAEEP [18] is based on a simplified method that consists on the application of a static pressure on the surface of the structure. The static pressure p is obtained multiplying the dynamic wind pressure w_k (dependent on the wind speed and therefore also on height or elevation along the structure) by shape coefficients δ that are characteristic of the aerodynamic shape of the structure, as given by equation (2).

$$p = w_k\,\delta \tag{2}$$

It should be enhanced that this process does not lead to correct results for flexible structures, since they are dynamically excited by the flow and therefore generating a fluid-structure interaction (FSI) difficult to quantify. Nevertheless, on this section, wind actions are evaluated according to RSAEEP [18] methodology, for comparison with the results that will be obtained through the EC1. Although the latter also calculates the actions based in equivalent static loads, it presents however a structural factor contemplating dynamic effects.

The dynamic wind pressure w_k (N/m^2 or Pa), corresponding to a specific or volumetric air mass density of 1,225 kg/m^3, is given by equation (3) with the wind speed v in m/s.

$$w_k = 0.613\,v^2 \tag{3}$$

For determining the characteristic values of the wind dynamic pressure along height above ground, RSAEEP [18] presents a graph for zone A (Figure 1) coherent with Table 3.

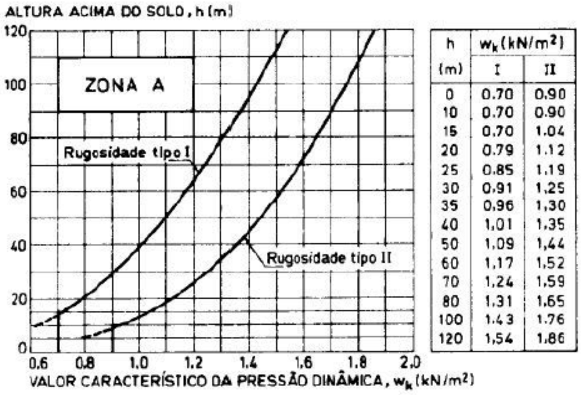

h	w_k (kN/m^2)	
(m)	I	II
0	0.70	0.90
10	0.70	0.90
15	0.70	1.04
20	0.79	1.12
25	0.85	1.19
30	0,91	1,25
35	0,96	1,30
40	1,01	1,35
50	1,09	1,44
60	1,17	1,52
70	1,24	1,59
80	1,31	1,65
100	1.43	1.76
120	1,54	1,86

Figure 1 Characteristic values of the dynamic pressure w_k (kN/m^2) for zone A

The values corresponding to zone B are obtained multiplying by 1.2 the values indicated for zone A (since wind speed for zone B is 10% higher than that of zone A, and in the equation for dynamic pressure the speed is raised to the power exponent 2). According to regulation RSAEEP [18], the reduced values of the wind dynamic pressures should be obtained through the following coefficients: $\Psi_0 = 0.4$, $\Psi_1 = 0.4$ and $\Psi_2 = 0.4$. Also, depending on the building typology, Ψ_0 can reach the value of 0.6.

The shape coefficients can be: (exterior and interior) pressure coefficients and force coefficients. The pressure coefficients permit to determine the wind pressure perpendicularly to the building surfaces, in agreement with equation (2). The acting force on a surface will be given by the product of the pressure by the respective area. The resulting force of the wind action is obtained through the summation of the (interior and exterior) forces applied to each considered surface. Figure 2, taken literally from RSAEEP [18], gives the exterior pressure coefficients for building facades.

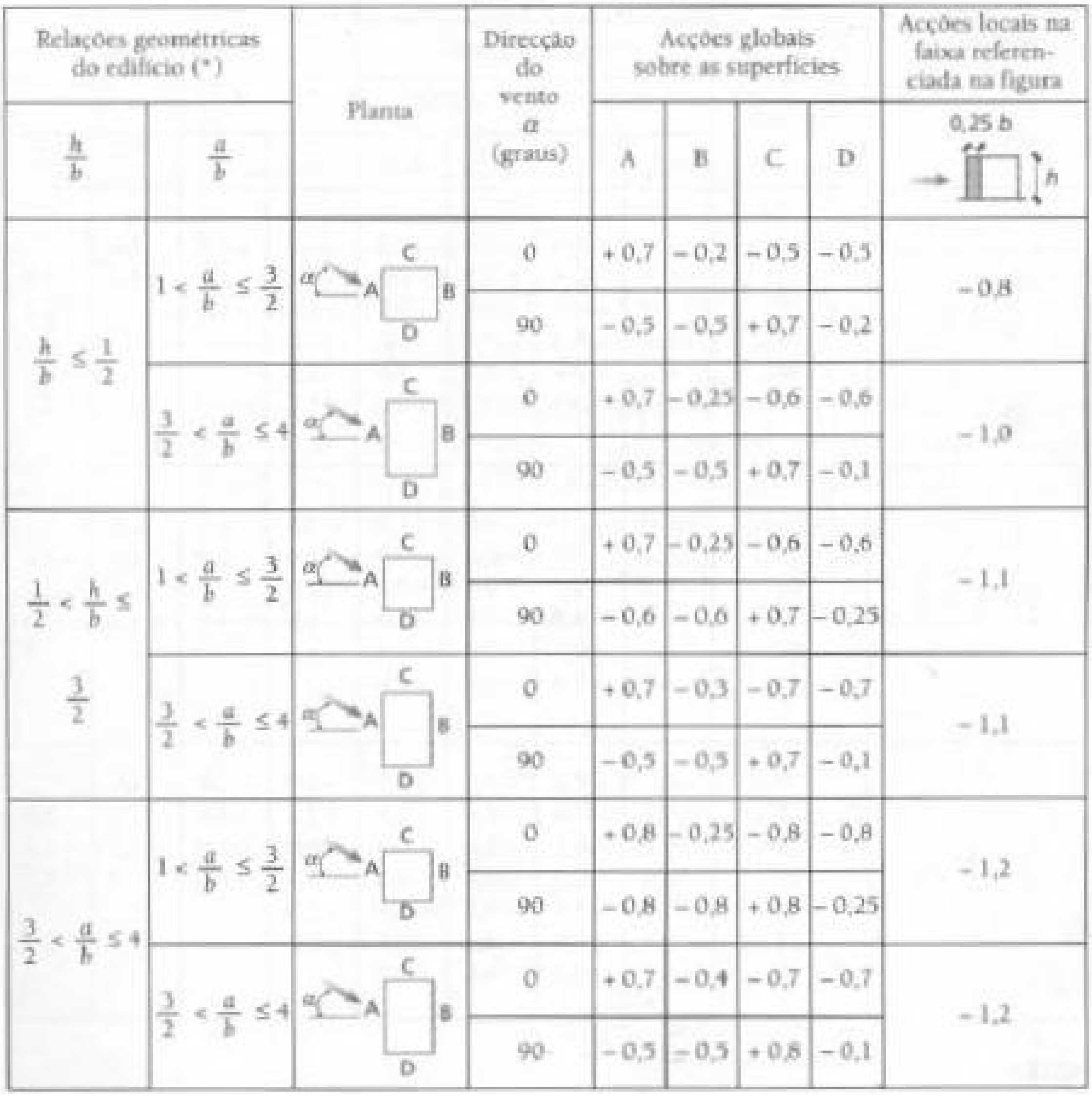

Relações geométricas do edifício (*)		Planta	Direcção do vento α (graus)	Acções globais sobre as superfícies				Acções locais na faixa referenciada na figura
$\frac{h}{b}$	$\frac{a}{b}$			A	B	C	D	0,25 b h
$\frac{h}{b} \leq \frac{1}{2}$	$1 < \frac{a}{b} \leq \frac{3}{2}$		0	+ 0,7	− 0,2	− 0,5	− 0,5	− 0,8
			90	− 0,5	− 0,5	+ 0,7	− 0,2	
	$\frac{3}{2} < \frac{a}{b} \leq 4$		0	+ 0,7	− 0,25	− 0,6	− 0,6	− 1,0
			90	− 0,5	− 0,5	+ 0,7	− 0,1	
$\frac{1}{2} < \frac{h}{b} \leq \frac{3}{2}$	$1 < \frac{a}{b} \leq \frac{3}{2}$		0	+ 0,7	− 0,25	− 0,6	− 0,6	− 1,1
			90	− 0,6	− 0,6	+ 0,7	− 0,25	
	$\frac{3}{2} < \frac{a}{b} \leq 4$		0	+ 0,7	− 0,3	− 0,7	− 0,7	− 1,1
			90	− 0,5	− 0,5	+ 0,7	− 0,1	
$\frac{3}{2} < \frac{a}{b} \leq 4$	$1 < \frac{a}{b} \leq \frac{3}{2}$		0	+ 0,8	− 0,25	− 0,8	− 0,8	− 1,2
			90	− 0,8	− 0,8	+ 0,8	− 0,25	
	$\frac{3}{2} < \frac{a}{b} \leq 4$		0	+ 0,7	− 0,4	− 0,7	− 0,7	− 1,2
			90	− 0,5	− 0,5	+ 0,8	− 0,1	

Figure 2 Values of the external pressure coefficients for the facades of buildings

The force coefficients allow to determine directly the resulting force F of the wind pressures on a certain structure (or on part of it) according to the equation (4), where A is the area of the surface (or portion) of the structure and d_f is the force coefficient.

$$F = w_k \, d_f \, A \tag{4}$$

2.2 Wind actions according to Eurocode EC1

The Eurocode 1 Part 1-4 (EC1) [10] gives characteristic values of wind actions for the global structure, and for parts of it (for example, walls and roofs) or for elements linked to the structure (for example, chimneys).

The calculation is based in a model using a peak factor. The basic idea of this model is that the maximum wind action in a static analysis or the dynamic response of the structure, can be described by the sum of an average component (constant part of the action) with a turbulent component (not constant). The development of this calculation model and its promotion is attributed to Davenport [8].

The wind action calculated according to the EC1 [10] gives characteristic values, that are obtained from base values of wind speed and wind pressure, corresponding to a probability of annual exceedence of 2% (ie, 0.02) that is equivalent to a return period of 50 years. The return period (R) for a set of generic value of a random variable (U) is the reciprocal or inverse of the probability of exceedence, and it corresponds to the number of samples that it is necessary to consider, on the average, so that a sample is registered with a value higher than U.

The effect of the wind in the structure depends on the size, shape and dynamic properties of the structure. The response of the structure should be calculated from the peak velocity pressure q_p at a reference height and in the undisturbed wind field. Also the coefficients of pressure and/or of force should be considered, as well as the contribution of a structural factor $c_s\, c_d$. Peak velocity pressure depends on the wind climate, the terrain roughness and orography, and the reference height; such pressure is equal to the mean velocity pressure plus a contribution from short-term pressure fluctuations.

2.2.1 Zoning of territory by categories

EC1 characterizes and distinguishes between five categories of terrain roughness according to Table 4, which also gives terrain parameters (roughness length z_0 and minimum height $z_{\min}$).

Terrain category	z_0 (m)	$z_{\min}$ (m)
0 Sea or coastal area exposed to the open sea	0,003	1
I Lakes or flat and horizontal area with negligible vegetation and without obstacles	0,01	1
II Area with low vegetation such as grass and isolated obstacles (trees, buildings) with separations of at least 20 obstacle heights	0,05	2
III Area with regular cover of vegetation or buildings or with isolated obstacles with separations of maximum 20 obstacle heights (such as villages, suburban terrain, permanent forest)	0,3	5
IV Area in which at least 15 % of the surface is covered with buildings and their average height exceeds 15 m	1	10

Table 4 Terrain categories and terrain parameters

2.2.2 Basic values

The fundamental value of the basic wind velocity $v_{b,0}$ is the characteristic 10 minutes mean wind velocity, irrespective of wind direction and time of year, at 10 m above ground level in open country terrain with low vegetation such as grass and isolated obstacles with separations of at least 20 obstacle heights (terrain category II).

The basic wind velocity v_b (defined as a function of wind direction and time of year at 10m above ground of terrain category II) shall be calculated from the following equation

$$v_b = c_{dir}\ c_{season}\ v_{b,0} \tag{5}$$

where c_{dir} is the directional factor, c_{season} is a season factor and $v_{b,0}$ is the fundamental value of the basic wind velocity. In some situations it is advantageous to consider a fundamental velocity with a probability of annual exceedence (*p*) different from 0,02 (or 2%). The method used by EC1 is based in the statistical treatment of European wind pressure data. The basic velocity is then obtained multiplying the previous equation (5) by a probably factor c_{prob} (given below) and dependent of the desired or intended probability (*p*).

$$c_{prob} = \left(\frac{1-K \ \ln(-\ln(1-p))}{1-K \ \ln(-\ln(0.98))} \right)^{n} \tag{6}$$

The shape parameter K, depending on the coefficient of variation of the extreme-value distribution, and the exponent n, are parameters that should be quantified in the respective national annexes and whose recommended values are 0,2 and 0,5, respectively.

2.2.3 Mean wind

The mean wind velocity varies with height and is defined as the average value of wind speed for a 10 minutes period at an appropriate height above ground. The variation of the mean wind velocity $v_m(z)$ at a height z above the terrain depends on the terrain roughness (Houghton and Carruthers [13]) and orography and on the basic wind velocity v_b and should be determined according to:

$$v_m(z) = c_r(z) \ c_o(z) \ v_b \tag{7}$$

where $c_r(z)$ is the roughness factor and $c_o(z)$ is the orography factor (usually taken as 1). The roughness factor accounts for the influence of the ground roughness of terrain (upwind of the structure in the wind direction considered) in the vertical distribution of the mean wind velocity at the site (profile along the height above ground level). It is given by:

$$c_r(z) = \begin{cases} k_r \ln(\frac{z}{z_0}) \ , \ \mathit{for} \ \ z_{\min} \le z \le z_{\max} \\ \\ c_r\,(z_{\min}) \ , \ \mathit{for} \ \ z \le z_{\min} \end{cases} \tag{8}$$

where the roughness length z_0 and the minimum height $z_{\min}$ depend on the terrain categories and assume the recommended values given in Table 4. The terrain factor k_r depends on the roughness length z_0 and is calculated using

$$k_r = 0.19 \ (\frac{z_0}{z_{0,II}})^{0.07} \tag{9}$$

where $z_{0,II}$ = 0.05 m (terrain category II), $z_{\min}$ is the minimum height (Table 4, according to terrain categories) and $z_{\max}$ is to be taken as 200 m.

The category of roughness which should be used for a given wind direction depends on the distance at which the roughness is constant, called the reference distance (small areas presenting different roughness of the terrain can be ignored), and within a sector angle of 15 degrees to each side of the fixed wind direction. The reference distance must be specified in the National Annex and in case of choice between two or more terrain categories it should be chosen the area corresponding to the lower roughness. The orographic factor takes into account the existence of mountains, hills or cliffs, where their existence results in an increase in wind speed by more than 5%. The regulation indicates that the procedure for determining this factor should be given in the national annex of each country.

Nevertheless, the effects of orography can be overlooked when the theoretical slope (average slope of terrain) upstream is less than 3. Although this is not usually a problem for tall buildings, it should be noted that for considering the wind effects on lower building structures, it must be taken into account that these may be affected by strong winds led to the near-ground due to the existence of higher neighboring structures. Annex A.4 of the Eurocode EC1 proposes a methodology for taking into account these effects on structures.

2.2.4 Wind turbulence

According to Cook [7], because the standard deviation of the turbulence near the ground is relatively constant with height, EC 1 [10] adopts a simplified model where the turbulence intensity decreases with height in inverse proportion to the growth of average wind speed between heights $z_{\min}$ and $z_{\max}$, and taking a constant value for heights below $z_{\min}$.

The turbulence intensity $I_v(z)$ at height z is defined as the standard deviation of the turbulence σ_V divided by the mean wind velocity, as given in equation (10).

$$\begin{cases} I_v(z) = \dfrac{\sigma_v}{v_m(z)} = \dfrac{k_l}{c_0(z)\ln(\dfrac{z}{z_0})} & \text{for } z_{\min} \le z \le z_{\max} \\ I_v(z) = I_v(z_{\min}) & \text{for } z \le z_{\min} \end{cases} \tag{10}$$

The turbulent component of wind velocity has a mean value of 0 and a standard deviation σ_v determined - in terms of the terrain factor k_r, basic wind velocity v_b and for the turbulence factor k_I - by:

$$\sigma_v = k_r \; v_b \; k_l \tag{11}$$

The value of the turbulence factor k_I may be given in the National Annex of each country. The recommended value for k_I is 1. Cook [7] proposes a better balance of turbulence factor values, as given in Figure 3 where k_I values are also a function of the height. Figure 4 shows the evolution of turbulence intensity as a function of height for different terrain categories, using the values recommended by the Eurocode EC1 EC 1 [10] for k_I and c_o.

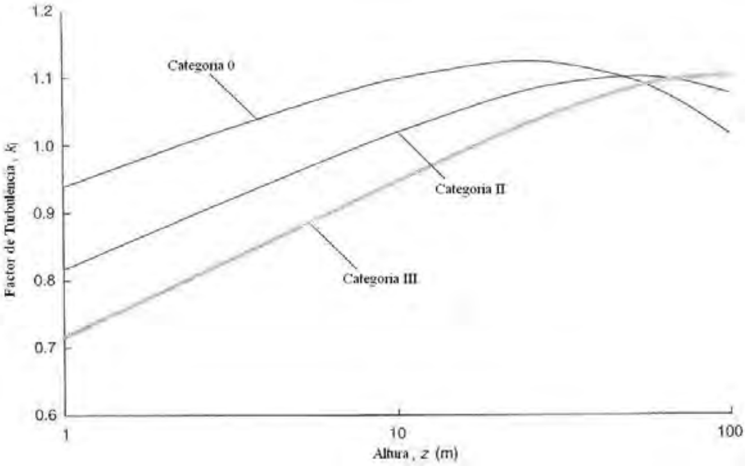

Figure 3 Alternative values for turbulence factor k_I

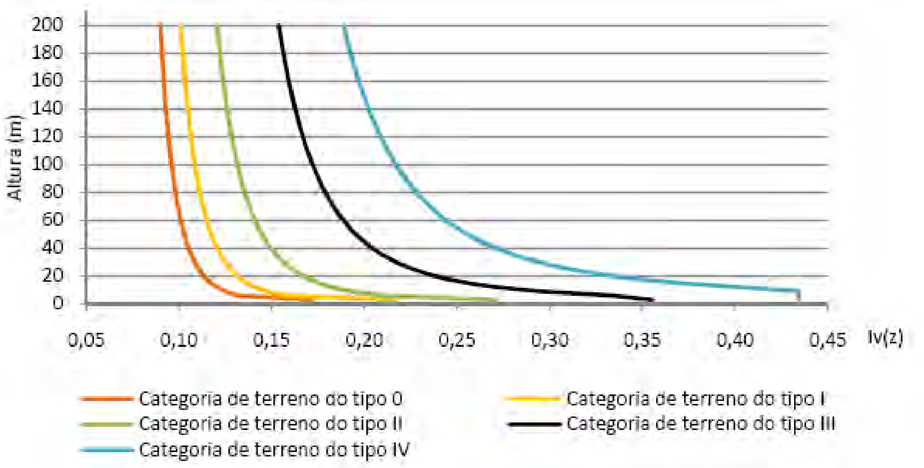

Figure 4 Profiles of turbulence intensities according to EC1

2.2.5 Wind dynamic pressure for peak velocity

The calculation of wind dynamic pressure by EC1 is based on the method of the “gust loading factor”, assuming that the response of the structure can be obtained through the sum of an average (constant) component with a fluctuating (dynamic) component; the latter component is expressed through a peak gust factor *g(t)* (Kappos [15], Almeida and Barros [1], Cook [7]). In this situation the peak velocity can be given by

$$\hat{v} = v_m(z) + g(t)\,\sigma_v(z) = v_m(z)\left[1 + g(t)\,I_v(z)\right] \tag{12}$$

As the dynamic wind pressure is $½\,\rho\, v(z)^2$, the peak pressure is given by:

$$q_p(z) = \frac{1}{2}\rho\left(\hat{v}(z)\right)^2 = \frac{1}{2}\rho\left(v_m(z)\right)^2\left[1 + 2\,g(t)\,I_v(z) + \left(g(t)\right)^2\left(I_v(z)\right)^2\right] \tag{13}$$

As last term in the previous equation is negligible with comparison with the others, EC1 suggests the following equation for determining the wind dynamic pressure for peak velocity:

$$q_p(z) = \frac{1}{2}\rho\left(\hat{v}(z)\right)^2 \approx \left[1 + 7\,I_v(z)\right]\frac{1}{2}\rho\left(v_m(z)\right)^2 = c_e(z)\,q_b \tag{14}$$

where ρ is the specific mass air density varying with height, temperature and barometric pressure (recommended value is 1.25 kg/m^3), q_b is the basic velocity pressure given by $½\,\rho\, {v_b}^2$ and $c_e(z)$ is the exposure factor interpreted as the ratio

$$c_e(z) = q_p(z)\,/\,q_b = 1 + 7\,I_v(z) \tag{15}$$

The value 7 in the previous equation corresponds to a gust peak factor of 3.5 for an average period of 10 minutes.

2.2.6 Actions due to wind

The wind pressures on external surfaces w_e are obtained by multiplying a pressure coefficient of external pressure c_{pe} by the dynamic pressure for peak velocity $q_p(z_e)$ evaluated at a certain reference height for the external pressure z_e (section 7 of EC1), according to the equation:

$$w_e = q_p(z_e)\ .\ c_{pe} \tag{17}$$

Similarly, the wind pressures on internal surfaces w_i are obtained by multiplying a pressure coefficient of external pressure c_{pi} by the dynamic pressure for peak velocity $q_p(z_i)$ evaluated at a certain reference height for the external pressure z_i, according to a similar equation. The actuating pressure on a given area will be given by the difference pressure between the exterior and interior, taking into account the signs. The reference heights to adopt as well as the coefficients of external and internal pressure for different structures are recommended in Section 7 of EC1.

According to EC1 and with respect to buildings, the pressure coefficient of external pressure depends on the size of the area where wind action is applied. The coefficient of external pressure for loaded areas smaller than 1 m^2 ($c_{pe,1}$) and greater than 10 m^2 ($c_{pe,10}$) are provided in tables for appropriate settings of buildings. Table V presents the recommended values for pressure coefficients of external pressure on the windward and leeward sides of the vertical walls of buildings rectangular in plan. Figure illustrates the reference height z_e to consider for the same type of structures on the windward side.

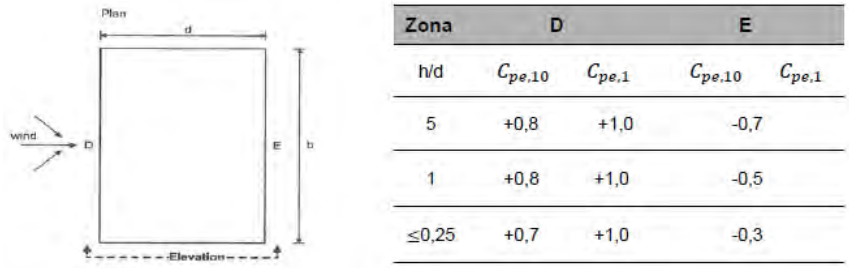

Zona	D		E	
h/d	$c_{pe,10}$	$c_{pe,1}$	$c_{pe,10}$	$c_{pe,1}$
5	+0,8	+1,0	-0,7	
1	+0,8	+1,0	-0,5	
≤0,25	+0,7	+1,0	-0,3	

Table 5 Coefficients of external pressure on the windward and leeward sides of the vertical walls of buildings rectangular in plan

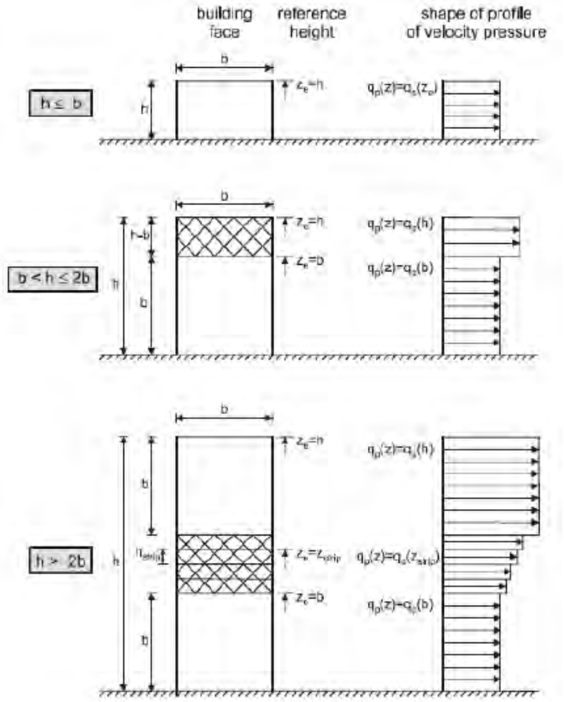

Figure 5 Reference height for the external pressure and corresponding pressure profile in the windward side

According with EC1, the wind forces acting in the entire structure (or on a structural component) can be determined directly through the: (i) appropriate force coefficients applied to the whole structure or on the structural component; (ii) vectorial sum of the components of pressure (external and internal forces in structural members evaluated from surface external and internal pressures) and frictional stresses acting on the structure resulting from the friction of the wind parallel to the external surfaces.

When using force coefficients, the wind force F_w acting on a structure or a structural component may be determined directly by

$$F_w = c_s \ c_d \ c_f \ q_p(z_e) \ A_{ref} \tag{18}$$

or by vectorial summation over the individual structural elements using the expression

$$F_w = c_s \ c_d \sum_{elements} c_f \ q_p(z_e) \ A_{ref} \tag{19}$$

where the product $c_s \, c_d$ is the structural factor, c_f is the force coefficient for the structure or structural element (Section 7 of EC1), $q_p(z_e)$ is the peak velocity pressure evaluated at the reference height z_e, and A_{ref} is the reference area of the structure or structural element (Section 7 of EC1).

Wind forces obtained by the sum of the components of external and internal pressure and frictional forces are given by:

$$F_w = c_s \ c_d \sum_{surfaces} w_e \ A_{ref} + \sum_{surfaces} w_i \ A_{ref} + c_{fr} \ q_p(z_e) \ A_{fr} \tag{20}$$

where w_e is the external pressure on the individual surface at height z_e, w_i is the internal pressure on the individual surface at height z_i, c_{fr} is the friction coefficient and A_{fr} is the area of external surface parallel to the wind.

The frictional forces act only on the surfaces parallel to the wind and are small when compared with the forces of pressure, so that only become significant when the area of surfaces parallel to the flow is considerable. The EC 1 [10] states that the effects of friction surfaces may be waived when the area of all surfaces parallel to the wind flow (or that do the least angle with this) is equal to or less than four times the area of all exterior surfaces perpendicular to the flow.

It is important to also emphasize that the dynamic effects and the effects related to the size of the structure, due to the structural factor $c_s \, c_d$, are restricted to the external components because the code standard assumes that the internal pressures and the frictional forces are static values that are fully distributed along the surfaces.

According to Cook [7] this assumption is correct with respect to the internal pressures, which depend on the volume inside, but it is not quite correct with respect to the friction forces. If in fact the structural factor takes into account fluctuations of pressure normal to the surfaces (due to wind gusts not acting simultaneously along a large surface), then the friction effects caused by these blasts also do not act simultaneously.

2.2.7 Structural factor

The structural factor $c_s\,c_d$ takes into account the combined effect of: (i) No simultaneous occurrence of the peak pressure of wind on the facades of the structure, often called the size effect (size factor c_s); (ii) Vibration of the structure in its fundamental mode due to the turbulence action, commonly called dynamic response (dynamic factor c_d).

The Eurocode defines a number of situations for which the value of the structural factor can be used as 1, avoiding the detailed process of calculation. These situations correspond to small structures or structural elements, for which the effect of size and the dynamic effect are both small. In the case of structures which are not suitable for the direct consideration of this factor as a unit value, this can be obtained using two different procedures specified in the code standard. In Annex D, EC1 provides indicative figures of the structural factor for different types of structures and their characteristics. Figure shows the values of the structural factors (taken from Annex D), with respect to reinforced concrete buildings.

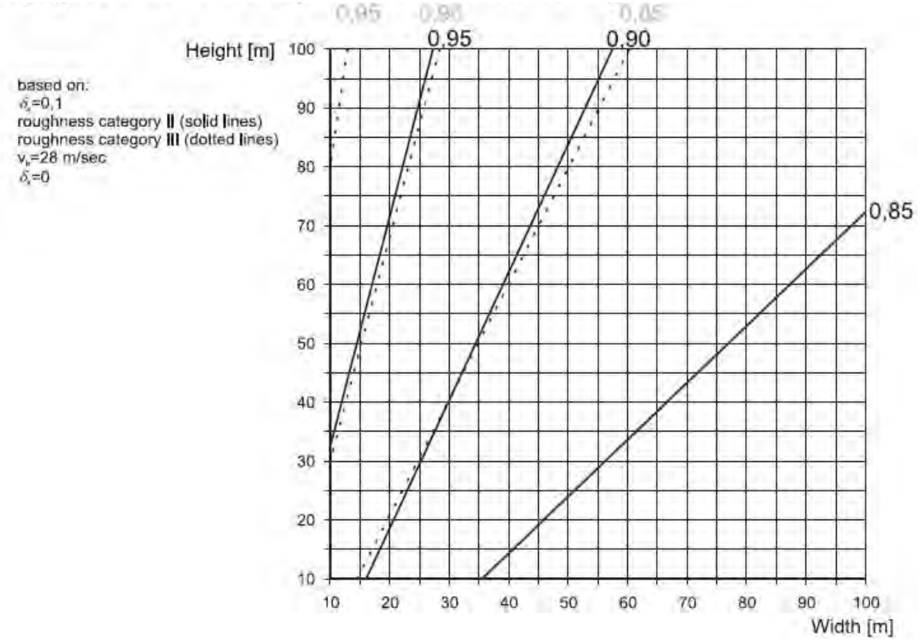

Figure 6 Structural factor for multistory concrete buildings

For the case of vertical structures such as buildings, or horizontal structures such as bar members or beams or point-like structures as signboards, and for the case where the vibration of the structure in wind direction occurs only in its fundamental mode of vibration, the structural factor is given by equation (21):

$$c_s\,c_d = \frac{1 + 2\,K_p\,I_v(z_s)\,\sqrt{B^2 + R^2}}{1 + 7\,I_v(z_s)} \tag{21}$$

where z_s is the reference height, K_p is the peak factor defined as the ratio of the maximum value of the fluctuating part of the response to its standard deviation, $I_v(z_s)$ is the turbulence intensity, B^2 is the background factor allowing for the lack of full correlation of the pressure on the structure surface, R^2 is the resonance response factor allowing for turbulence in resonance with the vibration mode.

This procedure then estimates the dynamic response of the structure as the square root of the sum of one resonance component and another background component. According to EC1 the evaluation of component parcels (K_p, B^2, R^2) can be made according to two procedures suggested in separate annexes B and C of the code standard. Both annexes indicate that it is conservative to take $B^2 = 1$. As an indication it is suggested that the values obtained by these two procedures should not differ by more than 5%.

In the following paragraph a comparative study of these procedures will be presented, here labeled *Procedure 1* and *Procedure 2* and evaluated respectively in agreement with Annexes B and C of EC1. A synthetic description of these is given in Table 6, outlining the calculation the main parameters.

Procedure 1 – Annex B (EC1)	**Procedure 2 – Annex C (EC1)**
$B^2 = \dfrac{1}{1 + 0{,}9\left(\dfrac{b+h}{L(z_s)}\right)^{0{,}63}}$	$B^2 = \dfrac{1}{1 + \dfrac{3}{2}.\sqrt{\left(\dfrac{b}{L(z_s)}\right)^2 + \left(\dfrac{h}{L(z_s)}\right)^2 + \left(\dfrac{b}{L(z_s)}.\dfrac{h}{L(z_s)}\right)^2}}$
$R^2 = \dfrac{\pi^2}{2.\delta}.S_L(z_s, n_{1,x}).R_h(\eta_h).R_b(\eta_b)$	$R^2 = \dfrac{\pi^2}{2.\delta}.S_L(z_s, n_{1,x}).K_s(n_{1,x})$
$K_p = \sqrt{2.\ln(\upsilon.T)} + \dfrac{0{,}6}{\sqrt{2.\ln(\upsilon.T)}}$	$K_p = \sqrt{2.\ln(\upsilon.T)} + \dfrac{0{,}6}{\sqrt{2.\ln(\upsilon.T)}}$
$\sigma_{a,x}(z) = \dfrac{c_f.\rho.b.I_v(z_s).v_m{}^2(z_s)}{m_{1,x}}.R.K_x.\phi_{1,x}(z)$	$\sigma_{a,x}(z) = c_f.\rho.I_v(z_s).v_m{}^2(z_s).R.\dfrac{K_y.K_z.\phi(y,z)}{\mu_e.\phi_{max}}$

Table 6 Two procedures for calculating parameters of the structural factor

In both procedures the turbulence length scale *L(z)*, representing the average gust size for natural winds, is given by equation (22); the non-dimensional power spectral density function $S_L(z,n)$ given by equation (23) is illustrated in Figure 7.

$$\begin{cases} L(z) = L_t\left(\dfrac{z}{z_t}\right)^{\alpha} & ,\ for\quad z \geq z_{\min} \\ L(z) = L(z_{\min}) & ,\ for\quad z \leq z_{\min} \end{cases} \tag{22}$$

$$S_L(z,n) = \frac{6{,}8\ f_L(z,n)}{(1+10{,}2\ f_L(z,n))^{5/3}} \qquad \text{with} \quad f_L(z,n) = \frac{n\ L(z)}{v_m(z)} \tag{23}$$

In these equations the reference height z_t = 200 m, the reference length scale L_t =300 m, the exponent $\alpha = 0{,}67 + 0{,}05 \ln(z_0)$, where the roughness length z_0 (m) and the minimum height $z_{\min}$ (m) are given in Table IV.

Also the non-dimensional frequency f_L is determined by the natural fundamental frequency *n* of the structure (in *Hz*) by the mean velocity $v_m(z)$ and by the turbulence length scale $L(z)$, as detailed in equation (23) above.

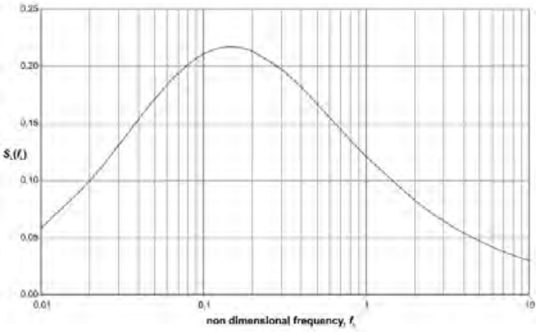

Figure 7 Power spectral density function $S_L(f_L)$

Annex F of EC1 presents the considerations for calculating the dynamic characteristics of some structures and for the case of buildings, with height *h* above 50 m, the fundamental frequency can be approximately calculated according to equation (24):

$$n = \frac{46}{h} \qquad (Hz, \text{with height in } m) \tag{24}$$

For the use of Table VI: *b* and *h* are the width and height of the building, respectively; δ is the logarithmic decrement of the damping, given by the sum of the structural logarithmic decrement δ_s with the aerodynamic logarithmic decrement δ_a and the logarithmic decrement due to the existence of special damping systems (tuned mass dampers TMD, sloshing tanks TLD, etc) δ_d; the calculation of δ is specified in Annex F of the code standard EC1; the variables $R_h(\eta_h)$ and $R_b(\eta_b)$ are aerodynamic admittance functions and $K_s(n_{1x})$ is a size reduction function (expressed in terms of the natural frequency of the structure n_{1x}, which may be determined using Annex F), given in Annexes B and C of EC1; T is the averaging time for the mean wind velocity (*T* = 600 seconds); the up-crossing frequency ν should be obtained from equation (25); $\sigma_{a,x}(z)$ is the standard deviation of the characteristic along-wind acceleration of the structural point at height *z* (Annex B of EC1); $\Phi_{1,x}(z)$ is the fundamental along wind modal shape (first approximation expressions are given in Annex F); $m_{1,x}$ is the along wind fundamental equivalent mass; K_x K_y and K_z are coefficients defined in Annexes B and C.

$$\nu = n_{1,x}\sqrt{\frac{R^2}{B^2+R^2}} \qquad (\nu \geq 0,08\,Hz) \tag{25}$$

3 COMPARATIVE ANALYSIS BETWEEN RSAEEP AND EC1

As summarized in previous chapters, it can be seen that although both code regulations RSAEEP [18] and EC 1 [10] detail calculation methods for the actions of wind on buildings through consideration of equivalent static loads, these two regulations are quite distinct.

In short, EC 1 [10] departs from a basic wind velocity from which the mean wind velocity is calculated, and thereafter the turbulence intensity. The dynamic pressure for peak velocity is obtained from the turbulence intensity and from the mean wind velocity. The wind pressure exerted on the surfaces is then calculated by multiplying the pressure peak velocity by their pressure coefficients, specific to each zone. The forces are finally obtained multiplying the wind pressure by the reference area, introducing corrections taken into account by the structural factor.

In RSAEEP [18] the quantification of the wind forces results from the multiplication of the dynamic pressures (function of the gust velocity, at the height of the floor in analysis) by the coefficient of external pressure (depending on wind direction and dimensions of the building) and by the area of influence corresponding to the application of force on each floor.

In order to understand and compare the procedures adopted by both code regulations for evaluating the shear forces and the bending moments at the base of a building due to wind actions, the results obtained for these generalized actions on a reference tall building are given herein; the considered reference building has a square cross section of 20 m x 20 m and a variable height ranging from 3 m to 200 m. It is also intended with this analysis to have an idea of the variation of wind forces along the height of the reference buildings, as evaluated by these two independent design code regulations.

The EC1 refers to the national annex defining the reference point for calculating the pressures at the leeward side. Since RSAEEP allows the distribution of pressure on this face equal to the face of windward, it is adopted here this same assumption; in this way taking the coefficients of internal pressure the same value, the corresponding forces in opposite directions due to internal pressure shall be cancelled. The wind was considered acting solely in one direction, the topography of the terrain is considered flat and horizontal and were not considered the effects of the possible interferences in the wind flow due to existing structures in the vicinity of the building under review.

The building was considered as being situated in zone A and all the types of terrain roughness available in each design code were considered (as a way to interpret its influence in the results).

To analyze this problem under RSAEEP, equation (1) was used to calculate the mean wind velocity with the appropriate parameters for terrain roughness of type I or type II.

To calculate the mean wind velocity according to EC1 equation (5) was used with $V_{b,0}$ equal to 28 m/s, since up to now there is no recommendation for this value in the national annex. The choice of this basic value is in accordance with the established for the zone A in an earlier version of EC1.

The velocity profiles for the two types of roughness considered in RSAEEP and for the five different categories of terrain considered in EC1 are represented in Figure 8.

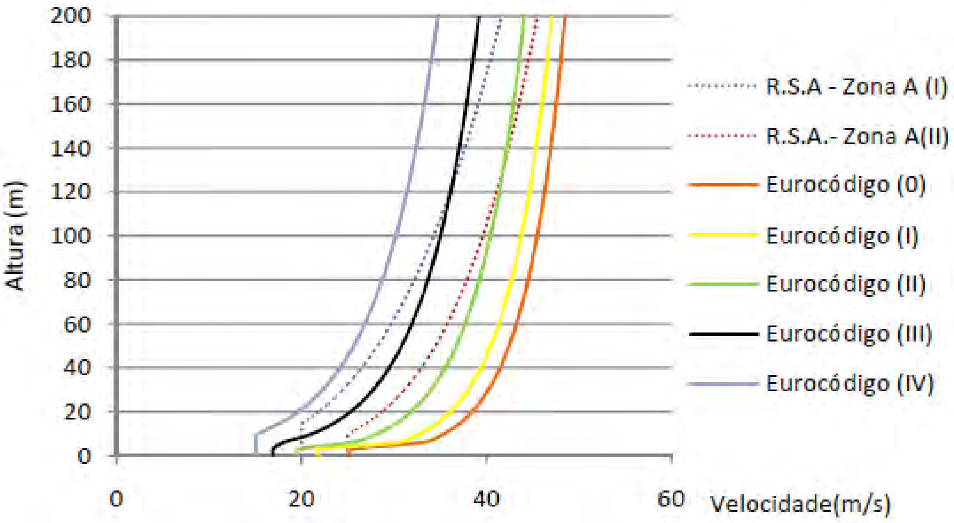

Figure 8 Profiles of mean wind velocities for two design codes and different types of terrain roughness

From the analysis of Figure 8 it is seen that the growth of wind velocity with height is more enhanced when calculated by RSAEEP than when it is calculated according to EC1: the gradient or slope of the curve is bigger. This can be justified and understood because the law used to calculate the wind velocity by the Portuguese code RSAEEP is a power law, while the one of EC1 is a logarithmic law. It was refered by Cook [7] that the logarithmic law, in the EC1 design code, for a height near the ground reveals to be a good approximation while for bigger heights it becomes non-conservative compared with the power law used by older design code regulations (such as RSAEEP). It should be noted however that considering a larger number of terrain categories (as in EC1) leads to a better differentiation of the ground types reflected in the velocity profile. According to the same Figure 8, it appears that as the terrain category evolves from the category 0 to the category IV (EC1) or from type II to type I (RSAEEP), the velocity values decrease for a given height. This would be expected since the terrain category IV or the terrain profile type I corresponds to a bigger terrain roughness, therefore lower wind speed.

Based on the calculation method proposed in the design code RSAEEP previously outlined, the variations with the height of the buildings of the shear forces and bending moments at the base of the buildings were determined for the two terrain profile types (Figures 9 and 10, for RSAEEP).

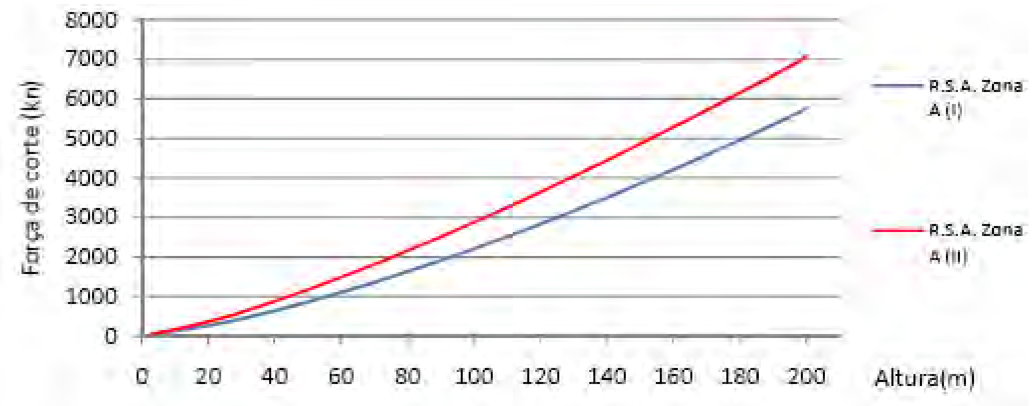

Figure 9 Total shear force at the base of buildings according to RSAEEP

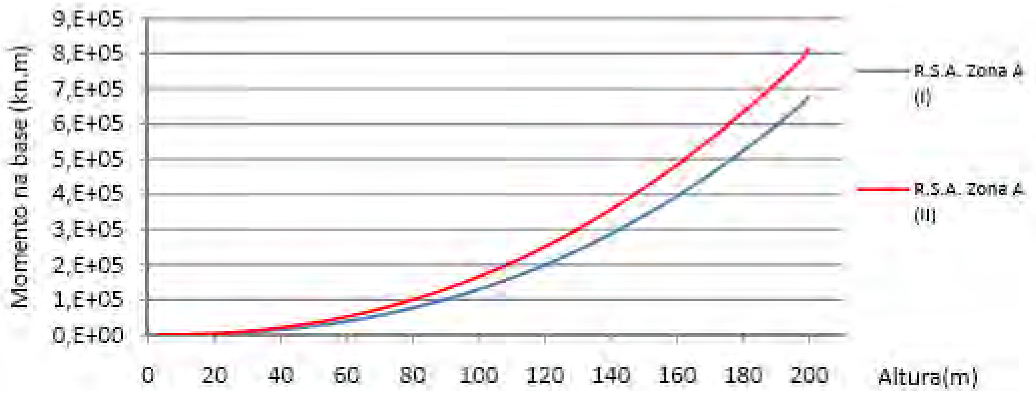

Figure 10 Total bending moment at the base of buildings according to RSAEEP

As shown in Figures 9 and 10 (RSAEEP), a terrain profile corresponding to roughness of type II leads to higher shear forces and bending moments at the base. This situation can be understood because a profile of type II is associated with a roughness smaller than that of a terrain profile of Type I; therefore, type II corresponds to higher mean wind velocity and consequently higher dynamic pressure and greater generalized forces at the base of the buildings.

For a building 200 m height and with the square cross section considered earlier, the shear forces and the bending moments at the base are about 13% higher when calculated for a terrain profile with roughness of type II than when calculated for a terrain profile with roughness of the type I.

Now by using the calculation method proposed in EC1, the wind forces on a structure can be determined by the sum of forces acting on each one of the facades multiplied by a structural factor $c_s c_d$ that can be calculated by two procedures (Procedure 1 and Procedure 2, in Table 6), for the five different categories of terrain roughness.

The left part of Figures 11 and 12 detail the variations with the height of the buildings of the shear forces and bending moments at the base of the buildings determined for the categories of terrain roughness, using EC1 – Procedure 1. Seemingly, the right part of Figures 11 and 12 detail the variations of the shear forces and bending moments at the base of the buildings determined for the categories of terrain roughness, using EC1 – Procedure 2.

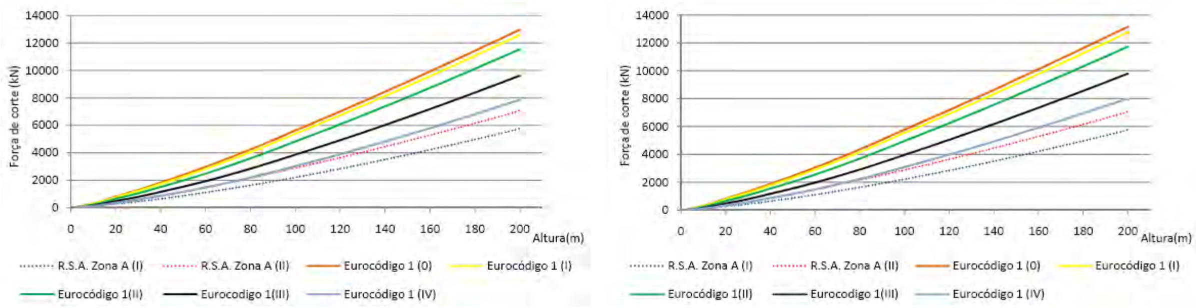

Figure 11 Base shear force as a function of height and terrain category, for structural factor calculated by Procedure 1 (left) and Procedure 2 (right)

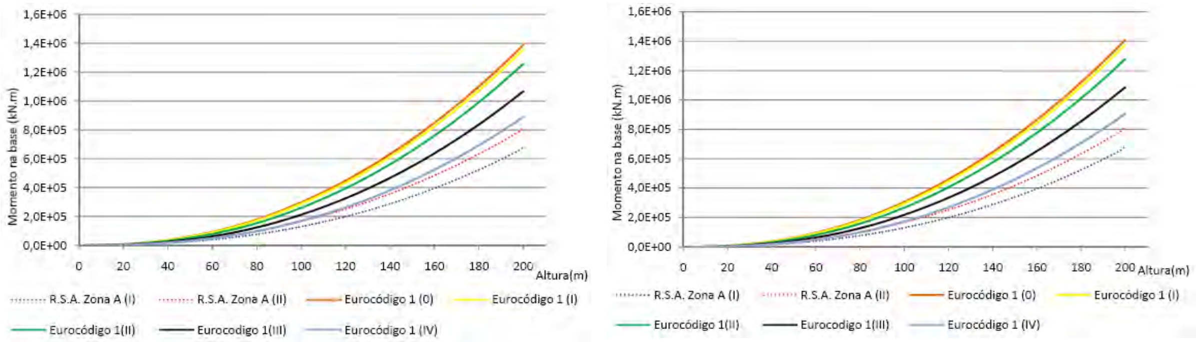

Figure 12 Base bending moment as a function of height and terrain category, for structural factor calculated by Procedure 1 (left) and Procedure 2 (right)

Figures 11-12 show that for the considered basic velocity (28 m/s) the values obtained by the calculation Procedures (1 and 2) described in EC1 are generally higher than those obtained by applying the current Portuguese design code RSAEEP. The difference in the results is due to the pressure coefficients adopted by each design code for the leeward facade of the building. While for the conditions analyzed Portuguese design code allows for the coefficient of external pressure a value of -0.25 (Figure 2), the EC1 admits this coefficient varies as a function of building height and may take values of -0.7 for h/d >5 (Table 5).

By this study and for the building situations examined, it is understood that EC1 is based in the method of the Gust Loading Factor, to quantify the wind actions. Also EC1 considers the non-simultaneity of occurrence of pressures over the building as well as possible dynamic phenomena that may occur.

As regards to this aspect it is seen that the values obtained by each of the proposed procedures (Procedure 1 and Procedure 2) do not differ considerably; also, for lower building heights it seems conservative to use this factor with the unit value.

With EC1 it is possible to estimate the acceleration of the building along the wind longitudinal direction (Table 6), while the Portuguese design code RSAEEP has no indication to that effect. It is also noted that EC1 considers coefficients that take into account the wind direction, season of the year, presence of structures in the vicinity of the building, which constitute factors that are not properly contemplated in RSAEEP. The use and definition in EC1 of a higher number of terrain categories, also allows quantification of more realistic wind actions.

Therefore it seems to exist a considerable evolution in the way of handling the wind actions on buildings by the Eurocode EC1, as compared with RSAEEP especially when dealing with larger tall buildings.

4 NUMERICAL MODELING OF A REAL STRUCTURE UNDER WIND ACTION

This chapter begins by describing the structure of the tall building chosen for case study and how it was modeled computationally. The building chosen was tower-1 of World Trade Center (WTC) and the program used for structural calculations was the “ROBOT MILLENNIUM v16.5” available at FEUP. [It was so chosen WTC because of its significant structural importance, but also majorly *as of public homage to all the innocent victims of the ignominious attack and consequent destruction of this structural icon*].

For use of this program a frame was modeled with specific characteristics that reproduce the structural behavior of the chosen building. The wind loads were calculated according to RSAEEP and to EC1, and its application in the equivalent frame permitted to compare generalized displacements and stresses.

It is also addressed the way the dynamic wind action was modeled to obtain the structural response of the building. Mathematical modeling of turbulent flow is complex and the possibility of interaction between the flow and the tall building structure (FSI) may lead to changes in dynamic pressure and in the response of the building along time. This chapter also addresses the simplifications used to consider this dynamic action.

4.1 Structural description of the building case-study (Tower 1 of WTC)

Each of the twin towers of WTC had 110 floor level above ground zero plaza and 7 underground sub-caves. With a 417 m height and a 64 m x 64 m base, tower-1 owned then the title of tallest building in the world.

The building weighed an average of about 420 ton/m [39] but despite the huge gravitational weight the wind action was the most significant action affecting its structural system (Eagar and Musco [9]). Rigidly connected to each other, the walls of the facades that formed the structure consisted of 240 tubular square hollow columns (tubular pillars) spaced about 1 meter apart (Figure 13) and with varying thickness every 22 floors (Santos [19]). With square section 36 cm x 36 cm, the pillars played a key role in the building structural strength to resist the wind action. The adjacent pillars were connected by a deep beam 1.3 m high (Figure 13).

The wall acted by the incident wind behaved as the tensile flange of the tube, and the opposite wall behaved as the compression flange. The side walls behaved like the web of the tube, and transferred the wind actions between the windward and the leeward walls.

The stiffness of the deep beams, created by the combined effect of reduced span and significant beam height, created a structural system that was rigid laterally and vertically.

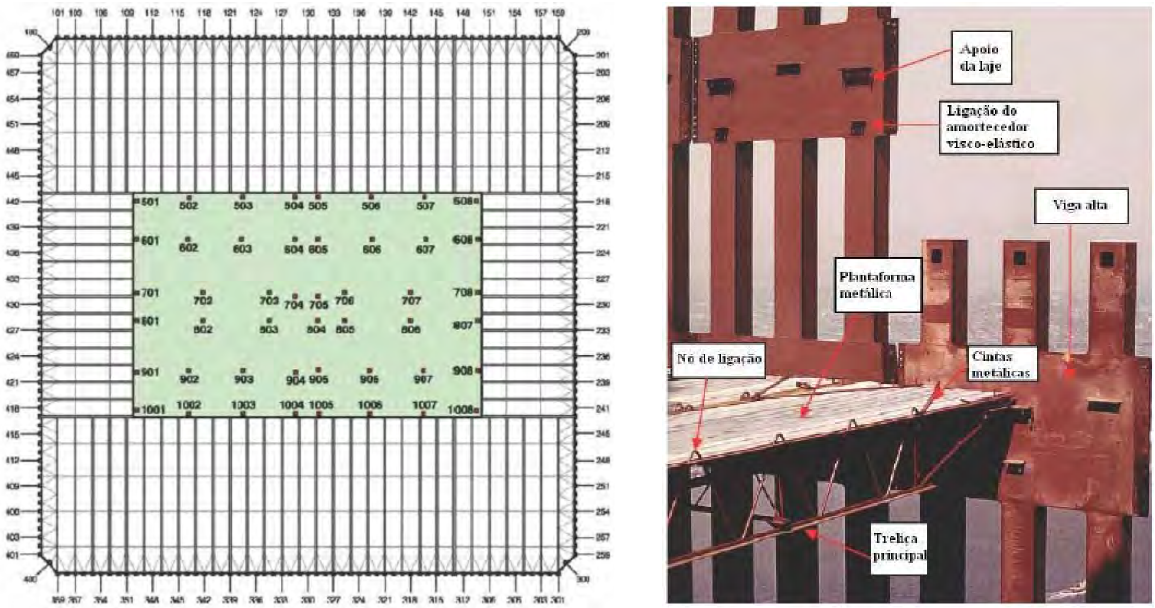

Figure 13 Structural plan of WTC tower-1 and detail of facade pillars with deep beam and metallic truss

The construction of the exterior walls was achieved using prefabricated modules, each consisting of three pillars with a height of three floors, connected by deep beams, and welding all the elements. At the base of the building each set of three adjacent pillars were gathered to form a bigger pillar in a formation like that in a “fork”. According to Eagar and Musco [9] this building was designed to withstand a wind lateral pressure of about 2 kPa.

In the center of the building there was a core that supported most of the building weight. Some of the constitutive pillars were very thick, with sections of 356 mm by 915 mm, converting themselves at the upper floors into large laminated profiles. The building slabs had the behavior of a mixed composite structure, consisting of 10 cm lightweight concrete slabs (13 cm in the core zone) and a metal lattice platform (Wilkinson [24]). Outside the core the platform floor was supported by a series of trusses which were placed between the outer wall and core (Figure 14) and which gave great torsional stiffness to the building.

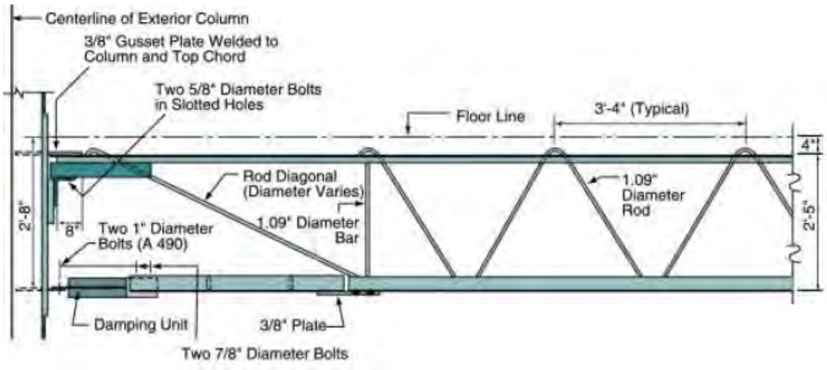

Figure 14 Metallic truss supporting the floor slabs (detail of connection floor-outer facade column)

Between floors 106 and 110 there were a series of diagonal bars in the frames of the building. These diagonals, together with the columns and slabs, formed a space truss extending between the exterior walls and passing through the core of the building. This system reinforced the framework for wind resistance, mobilizing some of the weight supported by the core itself to ensure stability against overturning.

The proximity of the two towers caused that the wind action in each one was conditioned by change in flow caused by such proximity. The quantification of wind action was made through a wind tunnel test, developed at the University of Colorado using a scale model of 1:500 [39]. About 10000 visco-elastic dampers were used, placed between the bottom of the main truss of the slab and the columns of the outer wall, from the 7th to the 107th floor. These dampers, designed by Mahmoodi (Santos [19]), were first applied in skyscrapers with the purpose of reducing building movement induced by wind and earthquakes. Figure 14 also details their location and connection with the outer columns.

4.2 Modeling a frame equivalent to WTC

In the software ROBOT MILLENNIUM v.16.5 was computationally modeled a frame that would reproduce the behavior of the structural system of the WTC tower-1, having stiffness and mass that would approximately describe the behavior of the building under the horizontal wind action. Each of the side columns of the equivalent frame has inertia equivalent to the total inertia of the columns on a plane façade perpendicular to the wind direction. The central column of the frame has an inertia equivalent to the sum of inertias of the two plane facades along lateral wind direction added with the inertia due to the core contribution. A schematic illustration is given in Figure 15.

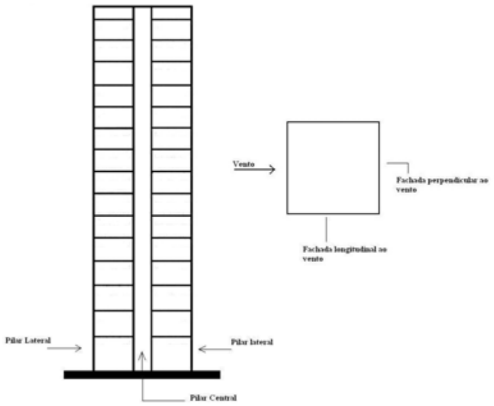

Figure 15 Schematic equivalent frame to WTC

According to Santos [19], the contribution of inertia of the facades along with core is given approximately by the values in Table 7, taking into account the variation in thickness of the columns every 22 floors. The average building mass is 420 ton/m, and the considered steel elasticity modulus and damping ratio were 200 GPa and 2% respectively.

Adopting a rectangular section 1 m wide, the dimensions of the central column were calculated so that the equivalent inertia of inertia would correspond to the inertia of each group. The equivalent sections adopted are presented in Table 5.2. The contribution of the side columns in terms of inertia is small as compared with that the central column.

Structural Group	***WTC structural data***				***Modeled equivalent frame***	
	M (ton/m)	I_{FAC} (m^4)	(%) Core	I_{Total} (m^4)	Lateral Columns	Central Column
Until 22nd floor	454,16	2831,57	34	3794,30	1 m x 1 m	1 m x 36 m
Until 44nd floor	436,32	2165,73	30	2815,44	1 m x 1 m	1 m x 33 m
Until 66nd floor	413,52	1666,18	27	2116,04	1 m x 1 m	1 m x 30 m
Until 88nd floor	392,19	1333,08	21	1613,02	1 m x 1 m	1 m x 27 m
Until 110nd floor	368,80	999,90	15	1149,88	1 m x 1 m	1 m x 24 m

Table 7 Structural data of WTC tower-1 and of the modeled equivalent frame

Regarding to the simulation of the floors, an equivalent beam was simulated equivalent to the metallic lattice truss that supports the slab of lightweight concrete. The center of gravity of the truss and the inertia of the metallic truss bars to that center were determined, corresponding to a value of 3.86 x10^{-2} m^4 for such total inertia of floor. Choosing a beam of rectangular area with an area approximately equal to the area of the main members of the truss, and with the calculated inertia given above, it was found an equivalent beam size with dimensions b=0.55 m and h=0.95 m.

Table 8 shows the values of the natural frequencies and natural periods found for the first six modes of vibration of the equivalent structure. Figure 16 depicts the first two modes of vibration of the structure modeled by the equivalent frame to WTC tower-1.

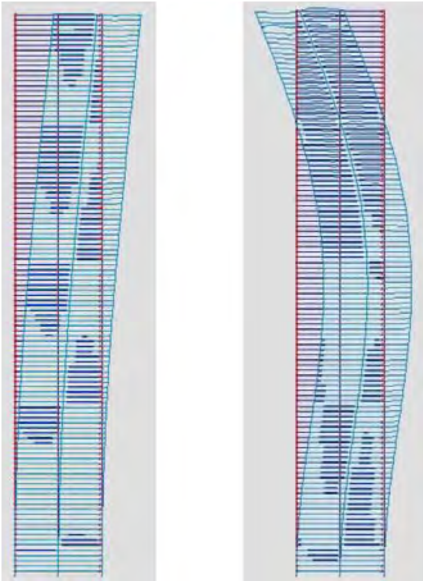

Figure 16 First two modes of vibration of the equivalent frame modeled

The vibration frequency of the first mode was evaluated as f_1=0.132 Hz, quite close to the fundamental frequency given by Santos [19] and relative to a three-dimensional modeling of the building in the program SAP2000. It is seen that the structure had two modes whose frequencies of vibration were less than 1 Hz, but the first mode clearly displays a lower frequency corresponding to a very flexible structure.

Mode	Mode 1	Mode 2	Mode 3	Mode 4	Mode 5	Mode 6
Frequency (Hz)	0,132	0,692	1,831	3,496	5,550	8,104
Period (s)	7,577	1,446	0,546	0,286	0,180	0,123

Table 8 Natural frequencies and natural periods of the first six vibration modes of the equivalent frame

4.3 Modeling wind dynamic action

Although it is recognized the great complexity in modeling turbulent flow around buildings, even with scaled physical models in wind tunnels, some simplifications will be considered herein with regards to the quantification of dynamic pressures and generalized forces due to wind action in a tall building along the time. For that, the FSI is considered negligible and the correlations of the velocity fluctuations in height are considered in a simplified manner. Firstly it is addressed the methodology for generating time series of wind to be used latter in the calculation of the instantaneous dynamic pressures and therefore in the quantification of the generalized wind forces acting at every floor level of the equivalent frame.

The methodology used to generate synthetic time series is commonly referred as the Method of Shinozuka, which bases the generation of time series in the calculation of the inverse function of the Fourier Transform of the amplitude of the random process (given by a spectral density function of the energy of a process). Such generation of synthetic series of wind occurs in the range of wavelengths corresponding to fluctuations of wind velocity with an approximately Gaussian distribution of the atmospheric wind flow (Saraiva and Silva [20]).

The purpose of the method is to obtain a realization of a stochastic process (for example: a time series of the fluctuations of the longitudinal component of wind velocity) from the spectral density function that characterizes the process.

The method uses this function to perform a weighted sum of sinusoidal functions (in this case of cosines). The contribution of each of the N waves is given by the amplitude of the spectrum ($S_L(z,n)$, real function) for each corresponding natural frequency (*n*). The phases are obtained (for the case of one-dimensional spectrum of simple non-correlated series) by pseudo-random number generation in the interval [0, 2π].

According to the Method of Shinozuka, in the simplest case of one-dimensional univariate stochastic processes, a realization of the random process may be obtained (Barbat and Canet [4], Saraiva and Silva [20]) by equation (26).

$$u(t) = \sqrt{2}\sum_{k=1}^{n} A_k \cos(\omega_k t + \phi_k) \quad \text{with } A_k = \sqrt{S(\omega_k)\,\Delta\omega} \text{ and } \Delta\omega = \frac{\omega_{\max} - \omega_{\min}}{N} \qquad (26)$$

In the previous expression N is the number of frequencies of the discretization of the spectrum, and $\omega = 2\pi n$ is the angular frequency. To generate the synthetic time series of wind velocity it is necessary to define a spectral density function of the fluctuations of longitudinal velocity of the wind; the spectral density function given in EC1 is used herein in the dimensionless form of equation (23) and the description of Figure 7.

For the generation of the synthetic series to be considered an ergodic process, according to [40] the number N of frequencies for discretization of the spectrum should be sufficiently high. However, not having an indication of the number of discrete frequencies to use, a study of the generation of wind series was made discretizing the spectrum into a different number of frequency ranges. Herein five processes for five frequency intervals were studied, corresponding to the division of the spectral density function in 50, 100, 500, 1000 and 5000 intervals respectively; for each case, fluctuations of longitudinal wind velocity were obtained according with the process described.

These fluctuations were calculated for an elevation *H*=100 m, and considering that the WTC was located on a terrain of class IV according to EC1 to which corresponds a roughness length z_0=1 m. The basic velocity assumed for a return period of 50 years was 30 m/s (based on the recorded data in 3 meteorological stations close to New York city) and in these conditions, according to EC1, standard deviation of the turbulent component of wind velocity was $\sigma_v = 7.03$ (Santos [19]). Figure 17 represents the time series of the fluctuations of wind velocity, evaluated with the previous data, for the four higher discretizations.

As the spectral density function has high values for low frequencies but reduces rapidly with increasing frequency (Figure 7), from the analysis of previous figures it is noted that when choosing a lower number of frequencies of discretization (lower N) for generation of the synthetic time series of wind, these are clearly more affected by low frequency components (where the spectrum has more energy) resulting in a value numerically higher.

Herein was adopted a reference number of discretization frequencies of around 500, for which it is no longer noticeable the influence of low frequency components; also, although for discretizations with 1000 and 5000 intervals the greater number of sinusoids would induce a better defined process, there seems not to exist large differences between the time series associated with these divisions of the wind spectrum.

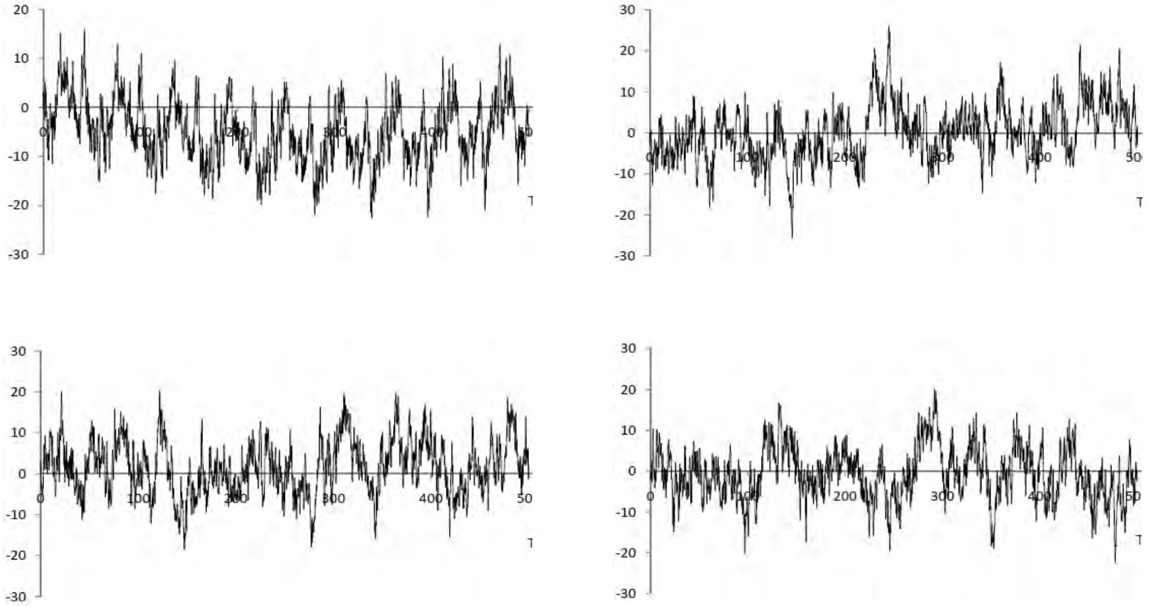

Figure 17 Time series of fluctuations of wind velocity for wind spectrum with 100-500-1000-5000 intervals

For the instantaneous wind velocity *U(t)* at any height given by the sum of a constant mean component $\overline{U}$ with a dynamic fluctuation component *u(t)*, the instantaneous wind force *F(t)* on any surface *A* is given by:

$$F(t)=\tfrac{1}{2}\rho c_f\, A\left[\overline{U}+u(t)\right]^2=\tfrac{1}{2}\rho c_f\, A\overline{U}^2+\rho c_f\, A\overline{U}\,u(t)+\tfrac{1}{2}\rho c_f\, A\left(u(t)\right)^2 \qquad (27)$$

where c_f is the force coefficient for the structure or structural element.

The fluctuations of wind velocity along time also have a spatial variability, which for a first approximation is herein neglected. For the case of tall buildings whereas the response is majorly due to the contribution of the first mode of vibration (which is also a condition imposed for the calculation of the structural factor $c_s\,c_d$ by EC1), modeled as a structural system with one degree of freedom, the passage or conversion of the power spectrum of the wind velocity fluctuations into structural response spectrum is given by:

$$S_X(n)=\frac{4\,\overline{X}}{\overline{U}^2}\left|H(n)\right|^2\left(\chi(n)\right)^2\,S_u(n) \qquad (28)$$

where $\left|H(n)\right|^2$ represents the mechanical admittance function given by equation (29) and $\left(\chi(n)\right)^2$ represents an aerodynamic admittance function (Vickery and Kao [22]) given approximately by equation (30).

According to Holmes [12], in a frequency domain analysis for tall large structures, it is this latter function that takes into account the non-simultaneous occurrence of the fluctuations of wind velocity. It is explicitly stated that: "*For larger structures, the velocity fluctuations do not occur simultaneously over the windward face and their correlation over the whole area must be considered. To allow for this effect, an aerodynamic admittance* $\left(\chi(n)\right)^2$ *is introduced*".

$$\left|H(n)\right|^2 = \frac{1}{\left(1-\left(\frac{n}{n_1}\right)^2\right)^2+\left(2\xi\frac{n}{n_1}\right)^2} \qquad (29)$$

$$\chi(n) = \frac{1}{1+\left(\frac{2n\sqrt{A}}{\overline{U}}\right)^{4/3}} \qquad (30)$$

According to EC1 for tall structures with the shape and conditions equivalent to the case-study under consideration, the parameters of the spectral density function for calculating the structural factor should be determined for a reference height of approximately 0.6 times the height of the building. Given this indication, for generating sets of time series, the height chosen was 250 meters that is about 60% of the height of tower-1 of the World Trade Center.

So, for the dynamic analysis of this case-study, ten random sets of fluctuation velocities were generated. The applied wind generated forces were obtained according to equation (27) taking account the acting dynamic pressures and the influence area for each floor, considering the mean wind velocity depending on the height (given by the expression of EC1) and the fluctuation velocities given by the random series generated.

As an example, Figure 18 (left) presents one series (called Series 1) for the fluctuations of wind velocity generated in these conditions at a height of 250m and using wind power spectrum of EC1. Figure 18 (right) shows the same series, that is adopting the same phase angles for the harmonics, but generated from the wind power spectrum multiplied by the previously mentioned aerodynamic admittance function $\chi^2(n)$.

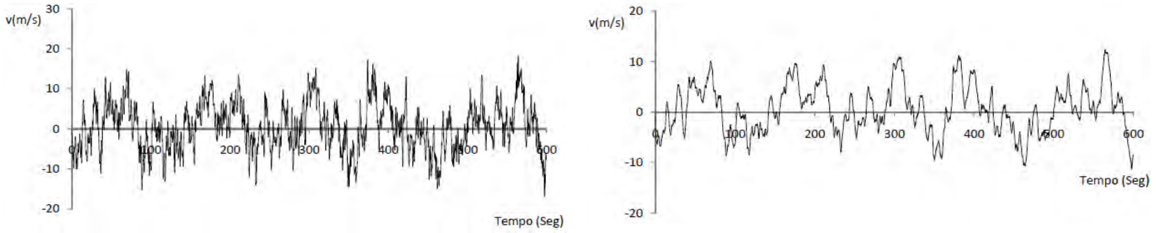

Figure 18 Fluctuation velocity time series for: height of 250 m, basic velocity 30 m/s, terrain roughness of category IV, using EC1 wind power spectrum (at left, not multiplied by the aerodynamic admittance function; at right, already multiplied by aerodynamic admittance function)

4.4 Modeling a TMD for passive control of vibrations

The tuned mass dampers (TMD) can be used to control one or more vibration modes of structures excited by external actions. However, in many cases, control of the first mode is sufficient to reduce significantly the level of vibrations recorded. Except for cases in which it is intended to simultaneously monitor the contribution of more than one mode of vibration, the use of a single TMD may be satisfactory. Examples of application of this system in tall buildings are listed in the literature, namely: John Hancock Tower Building (with 60 floors) in Boston (USA) and the building Chiba Port Tower (with 125 m) in Japan, where large-scale measurements were performed to evaluate the efficiency these systems (Holmes [12]).

The building tower Taipei 101 (with 508 m) in Taiwan, has the largest (so far) TMD mass (about 730 ton mass) placed on top of the building to control excessive vibrations due to wind and earthquakes; according to [14], the accelerations would be reduced by about 40% to 45%.

The behavior of TMD in tall buildings under wind action was studied by Kwok and Samali [17]. The design of a TMD for application to structures without damping is based on two parameters – mass ratio μ and frequency ratio q – as detailed in Kelly [16]. The optimum frequency ratio q_{opt} (corresponding to the fixed points at the same level or with the same displacement amplitude), the maximum amplitude of the controlled principal system, and the inherent optimal damping $\xi_{2,opt}$ of the TMD, are given in the set of equations (31).

$$q_{opt} = \frac{1}{1+\mu} \ , \qquad \frac{X_1}{X_{1,static}} = \sqrt{\frac{2+\mu}{\mu}} \ , \qquad \text{and} \qquad \xi_{2,opt} = \sqrt{\frac{3\mu}{8(1+\mu)^3}} \tag{31}$$

For the design of a TMD tuned for application to structures with damping, it is still possible to use these equations provided the damping is less or equal to 1%. For higher damping, the use of such equations will lead to a non optimized tuning of the TMD. For such cases, the design of the TMD can be done with design graphs associated with the numerical solution of the expression of maximum amplitude of the controlled principal system (Barros, Moutinho and Barros [6]).

The considerations made previously focused its application to a structure with a single degree of freedom which was associated with a second mass, thus resulting in a system of two degrees of freedom. However, in the case of real structures with various degrees of freedom, it becomes essential to consider a system of one degree of freedom that translates roughly the dynamic behavior of the structure under analysis.

The reduction of structural vibrations using the vibration control theory can be addressed either through modal control or through optimal control (Yao [25]). In the former, a predetermined structural mode of vibration is controlled; in the case of long slender metallic towers under wind actions, tuned mass dampers (TMDs) are frequently the choice but tuned liquid dampers (TLDs) or tuned liquid column dampers (TLCDs) can also be used with equivalent efficiency. In the latter, structural performance criteria are controlled such as the minimization of the structural deflections (top tip displacement and/or top section rotation).

Kwok and Samali [17] studied the behavior of TMD's in tall buildings subjected to the action of wind and, according to the authors, the considerations presented here about the effectiveness of a TMD in response of a system of one degree of freedom can be extended to solid structures such as in the case of tall buildings, leading to a modal analysis. Kwok and Samali [17] indicated that while there were large decreases in response for the modes controlled by the TMD’s installed, the higher order modes were not affected. For such higher modes to be less contributive to the structural response would require implementing new TMD’s tuned according to their frequency.

Thus, using modal analysis, for each vibration mode whose contribution to the overall response of the structure is important, and that one wishes control, it is necessary to determine the corresponding values of stiffness, of mass and of modal damping. According to Villaverde [23], for the determination of the dynamic characteristics of the equivalent system, should be adopted a mode normalization criteria based on attributing a unit value to the mode component associated to the degree of freedom where TMD would be applied.

Since the fundamental frequency of the WTC tower-1 is very low (0.132 Hz) and because the wind action has a spectral density function with strong content for low frequencies, it is possible that the response is conditioned by the harmonic of the fundamental frequency. It is therefore assumed herein, for control of vibrations purposes, that the response is only dependent on the first vibration mode, with which the TMD solutions were designed with the expressions available for harmonic vibration with frequency equal to the first vibration frequency of the overall structure.

Accordingly, the value of the modal mass corresponding to the first mode of vibration was determined (with the structural software used: Robot Millennium) as 41378.414 ton and the corresponding modal stiffness of 28463kN/m, values quite close to the ones found in a three-dimensional modeling of the building (Santos [19]). For the case-study structure with the deployment of TMD's, two different mass ratios of μ=0.01 and μ=0.005 were used, for which with design charts (Barros, Moutinho and Barros [6]) it was possible to determine the optimal parameters to be adopted for each TMD situation. In Table 9 the values adopted are systematized.

TMD mass ratio	q_{opt}	$\xi_{TMD, opt}$	m_{TMD} (ton)	ω_{TMD} (rad/s)	k_{TMD} (kN/m)		Size (cm) of square section steel bar E=210 GPa , L=2 m
μ = 0.01	0,987	0,046	413,78	0,81860	277,2764		8,1 x 8,1
μ = 0.005	0,993	0,036	206,89	0,82357	140,3284		6,8 x 6,8

Table 9 Optimal parameters of TMD in WTC tower-1 case-study, for two mass ratios μ

Since the structural software used does not have an intrinsic function that allows the direct introduction of dampers, herein for the simulation of the TMD's were determined the dimensions of a square section bar with a lateral stiffness equivalent to that required for the damper placed on top. Acting as a vibrating bar (built in end – free end) with a concentrated mass that would give the frequency obtained for the sizing of the TMD with the damping introduced in the material parameters constitutive of the bar.

Assuming a bar length L=2 m, made of steel with elasticity module E=210 GPa, from the bar stiffness $3EI/L^3$ is obtained the equivalent inertia I of the square section bar. Table 10 also indicates the dimensions required for such bar, for the two mass ratios considered in the design of the TMD. Table 10 shows the first six natural frequencies of the vibration modes of the case-study structure (WTC tower-1) incorporating the two TMD solutions; some changes occur as compared with Table 8 of the structure without any TMD.

Mode	Mode 1	Mode 2	Mode 3	Mode 4	Mode 5	Mode 6
Frequency (Hz) for WTC using TMD with μ=0.01	0,125	0,138	0,692	1,831	3,496	5,550
Frequency (Hz) for WTC using TMD with μ=0.005	0,127	0,136	0,692	1,831	3,496	5,550

Table 10 Natural frequencies of first six vibration modes of the equivalent frame with TMD vibrating bar

5 ANALYSIS OF RESULTS BY DESIGN CODES

This chapter begins by comparing the results obtained for the forces acting on each floor due to wind action, obtained by applying each of the two regulations addressed in this case-study of the WTC tower-1. The corresponding displacements were also evaluated and compared with the computer software used herein, applied to the computational structural model addressed earlier.

The wind was considered actuating perpendicular to the facade of the building and for the implementation of RSAEEP, the building was considered as implanted in Zone B with terrain roughness of type 1 corresponding to an urban area.

For application of EC1 the building was considered on a terrain category of type IV, with a basic velocity of 30 m/s, with unit orography factor and with frictional forces neglected (since the total area of the facades of the building parallel to the wind direction is less than 4 times the area of the facades perpendicular to the wind direction. Since the ratio between the height of building *h* and its width *d* is greater than 5, the EC1 indicates that the forces due to wind on buildings should be based on force coefficients. For the building under study, the value obtained for the force coefficient was 1.428 . The structural factor calculated according to EC1, by the two procedures (Procedure 1 and Procedure 2) contemplated in that design code as outlined in the previous paragraph (2.2.7), was 0.95 (Procedure 1) or 0.97 (Procedure 2).

Table 11 compares the results for the wind forces, along the height of the case-study building, evaluated by the two design codes. Figure 19 compares the results for the shear forces and bending moment due to wind pressures, along the height of the case-study building, evaluated by the two design codes.

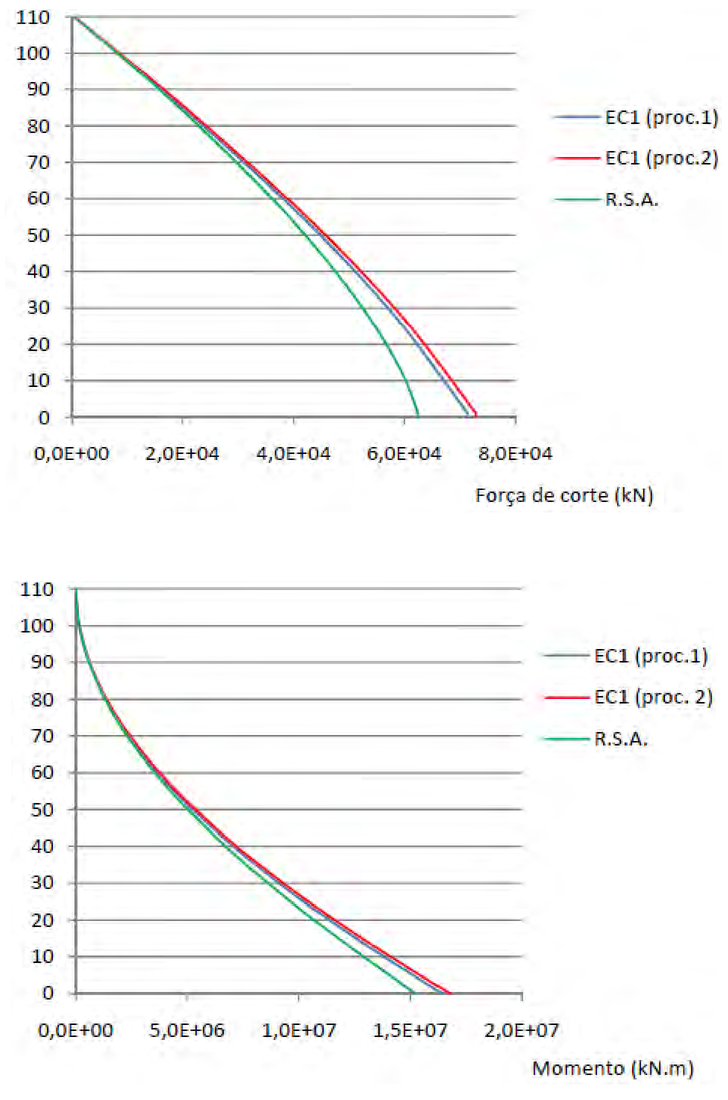

Figure 19 Shear forces (top graph) and bending moments (bottom graph) at every floor of WTC, evaluated by the two design codes: RSAEEP and EC1

Floor	RSAEEP	EC1(Pr.1)	EC1(Pr.2)
1	218,8	472,9	482,9
2	218,8	472,9	482,9
3	218,8	472,9	482,9
4	218,8	472,9	482,9
5	239,1	472,9	482,9
6	254,5	472,9	482,9
7	268,8	472,9	482,9
8	281,6	472,9	482,9
9	293,8	472,9	482,9
10	305,2	472,9	482,9
11	316,1	472,9	482,9
12	326,4	472,9	482,9
13	336,3	472,9	482,9
14	345,8	472,9	482,9
15	354,9	472,9	482,9
16	363,7	472,9	482,9
17	372,2	472,9	482,9
18	380,5	483,3	493,5
19	388,5	491,9	502,2
20	396,3	500,0	510,6
21	403,9	507,9	518,5
22	411,3	515,3	526,2
23	418,6	522,5	533,6
24	425,7	529,5	540,6
25	432,6	536,2	547,5
26	439,4	542,6	554,0
27	446,0	548,9	560,4
28	452,5	554,9	566,6
29	458,9	560,8	572,6
30	465,2	566,4	578,4
31	471,4	571,9	584,0
32	477,5	577,3	589,5
33	483,5	582,5	594,8
34	489,3	587,6	600,0
35,0	495,1	592,5	605,0
36,0	500,8	597,4	609,9
37,0	506,5	602,1	614,8
38,0	512,0	606,7	619,5
39,0	517,5	611,2	624,0
40,0	522,9	615,6	628,5
41,0	528,3	619,9	632,9
42,0	533,5	624,1	637,2
43,0	538,7	628,2	641,4
44,0	543,9	632,2	645,5
45,0	549,0	636,2	649,6
46,0	554,0	640,0	653,5
47,0	559,0	643,8	657,4
48,0	563,9	647,6	661,2
49,0	568,7	651,2	664,9
50,0	573,6	654,8	668,6
51,0	578,3	658,4	672,2
52,0	583,0	661,8	675,8
53,0	587,7	665,3	679,3
54,0	592,3	668,6	682,7
55,0	596,9	671,9	686,1
56,0	601,5	675,2	689,4
57,0	606,0	678,4	692,7
58,0	610,4	681,5	695,9
59,0	614,8	684,6	699,0
60,0	619,2	687,7	702,2
61,0	623,6	690,7	705,2
62,0	627,9	693,7	708,3
63,0	632,2	696,6	711,2
64,0	636,4	699,5	714,2
65,0	640,6	702,3	717,1
66,0	644,8	705,1	720,0
67,0	648,9	707,9	722,8
68,0	653,0	710,6	725,6
69,0	657,1	713,3	728,3
70,0	661,2	716,0	731,0
71,0	665,2	718,6	733,7
72,0	669,2	721,2	736,4
73,0	673	724	739
74,0	677,1	726,3	741,6
75,0	681,0	728,8	744,1
76,0	684,9	731,3	746,7
77,0	688,7	733,7	749,2
78,0	692,6	736,1	751,6
79,0	696,4	738,5	754,1
80,0	700,2	740,9	756,5
81,0	703,9	743,2	758,9
82,0	707,7	745,5	761,2
83,0	711,4	747,8	763,5
84,0	715,1	750,1	765,9
85,0	718,8	752,3	768,1
86,0	722,4	754,5	770,4
87,0	726,0	756,7	772,6
88,0	729,6	758,9	774,8
89,0	733,2	761,0	777,0
90,0	736,8	763,1	779,2
91,0	740,3	765,2	781,4
92,0	743,9	767,3	783,5
93,0	747,4	769,4	785,6
94,0	750,9	801,3	818,1
95,0	754,3	801,3	818,1
96,0	757,8	801,3	818,1
97,0	761,2	801,3	818,1
98,0	764,6	801,3	818,1
99,0	768,0	801,3	818,1
100,0	771,4	801,3	818,1
101,0	774,8	801,3	818,1
102,0	778,1	801,3	818,1
103,0	781,4	801,3	818,1
104,0	784,8	801,3	818,1
105,0	788,1	801,3	818,1
106,0	791,3	801,3	818,1
107,0	794,6	801,3	818,1
108,0	797,9	801,3	818,1
109,0	801,1	801,3	818,1
110,0	401,7	400,6	409,1
TOTAL	**62446**	**71347**	**72849**

Table 11 Forces on every floor due to wind, under the two design codes RSAEEP and EC1

For both generalized forces, the two EC1 procedures gave higher values than the one's obtained by RSAEEP. In fact the basal bending moment by RSAEEP was evaluated as 15231856 kNm while by the procedures in EC1 was 16612740 kNm and 16962482 kNm.

Applying the previous wind design forces on every floor in the computational model of the case-study WTC, the following lateral displacements were obtained (Figure 20) leading to top floor lateral displacements of 0.99 m (with RSAEEP forces) and 1,05 m and 1,07 m (with the two procedures of EC1 for the determination of the structural factor). These lateral displacements, obtained with the simplified equivalent computational model proposed, slightly overpass the recommended maximum value of top displacement given by the building height/500 (0.85 m, for this WTC tower with a height of 417 m) as suggested by the *Subcommittee on Wind Bracing* of ASCE [2].

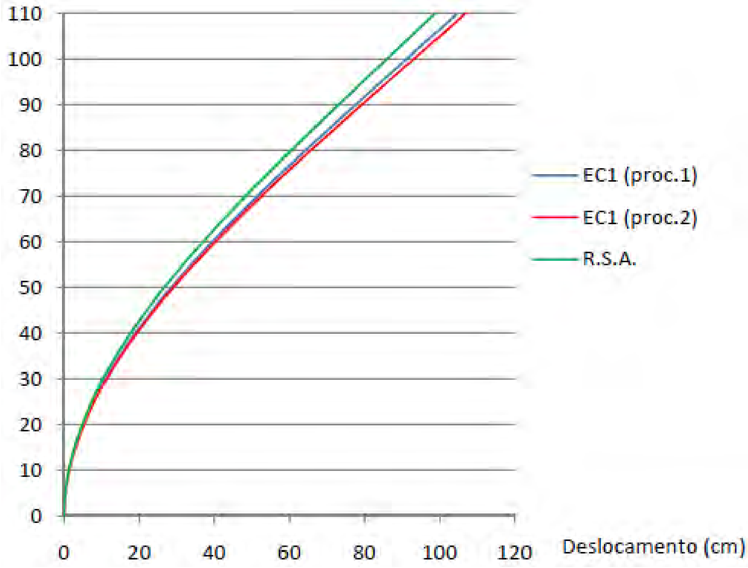

Figure 20 Lateral displacements in every floor by the application of the design forces on the considered computational model

As regards to the determination of the maximum acceleration on the top of this building, according to the two procedures in EC1 described earlier (paragraph 2.2.7) for multiplying the standard deviation of the acceleration by the peak factor, the values obtained were 0.27 m/s2 (Procedure 1) and 0.32 m/s2 (Procedure 2). Comparing these acceleration values due to wind action with the limits of human perception, it was clear that the lateral top acceleration lies between the threshold of perception and discomfort (Bachmann [3]); therefore no problems are expected to the level of human comfort due to the wind horizontal direction analyzed.

It should be noted that if the aerodynamic damping would not have been considered, the acceleration values would be ranging from 0.38 m/s2 to 0.45 m/s2 and that would lead to discomfort for human occupants. This shows once more that, in the longitudinal along the wind direction, the aerodynamic damping plays an important role in vibration control, and therefore its correct evaluation is really important for a good design.

6 ANALYSIS OF RESULTS EVALUATED COMPUTATIONALLY

Based on the methodology adopted for consideration of the dynamic wind action (using a set of 10 time series, for frequencies in the wind spectral density function evaluated with 500 frequency intervals), the results in terms of displacements and accelerations were evaluated and compared for the computational structural model, without and with installed TMD vibrating bar (with an hypothetical vibrating mass with appropriate stiffness and damping properties).

Using the mentioned structural software with modal superposition, a damping ratio of 2% and an integration time step of Δt=0.25 sec, ten series of wind dynamic loads were applied and their average results obtained in terms of displacements and accelerations. As an example Figure 21 shows the time variations of displacement and acceleration on the top of WTC, for the wind loads evaluated using equation (27), with velocity fluctuations corresponding to wind series 1.

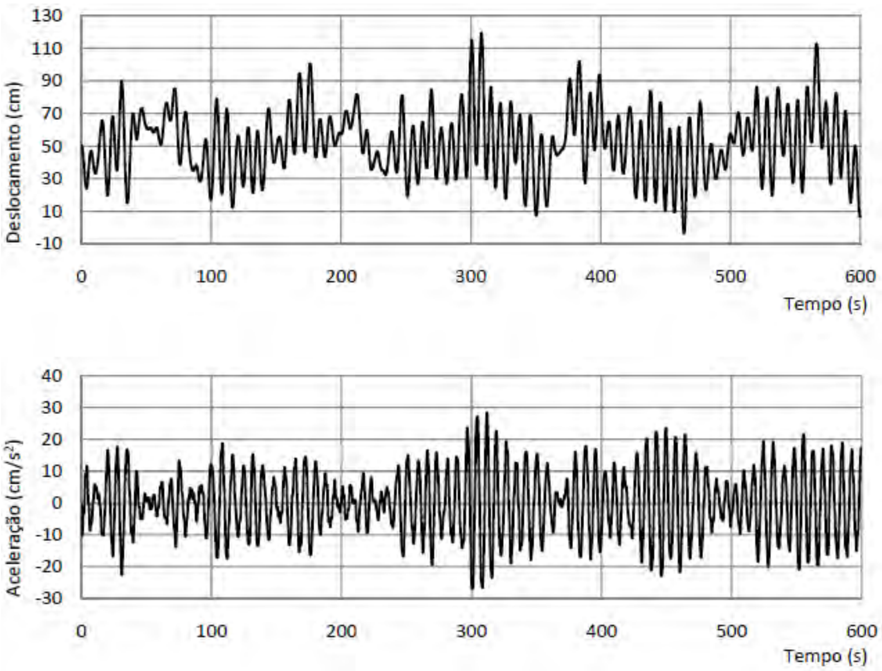

Figure 21   Displacement and acceleration on the top of WTC, for the wind loads corresponding to wind series 1

Table 12 presents a summary of maximum values of displacements and accelerations on top of the building, for each of the time series. It also presents the maximum values of the same variables but which are calculated (Holmes [12]) by multiplying the standard deviation of the responses by the peak factor of 3.16 (evaluated conservatively for the natural frequency of the structure of 0.11 Hz and for a time interval of 600 seconds, during which the maximum value is evaluated (Davenport [8]).

SÉRIE	1	2	3	4	5	6	7	8	9	10	Média
Deslocamento máximo obtido directamente da resposta (m)	1,19	1,32	1,03	1,09	1,09	1,33	1,05	1,15	1,22	1,27	**1,17**
Aceleração máxima obtida directamente da resposta (m/s^2)	0,28	0,35	0,32	0,27	0,36	0,32	0,35	0,29	0,36	0,37	**0,33**
Deslocamento máximo obtido através do factor de pico (m)	1,12	1,16	1,21	1,16	1,18	1,20	1,09	1,10	1,24	1,25	**1,17**
Aceleração máxima através do factor de pico (m/s^2)	0,32	0,34	0,37	0,30	0,36	0,31	0,33	0,30	0,39	0,38	**0,34**

Table 12   Maximum displacements and accelerations on top of WTC, for each of the wind time series (without TMD)

As regards to the use of a TMD on the top floor, and as an earlier comparison with the building subjected to a harmonic excitation in resonance with the fundamental frequency, the Figure 22 shows such comparison of displacements (left) and accelerations (right) of top floor, along the time, without and with TMD with mass ratios of 1% and 0,5%.

Table 13 shows the comparison of the maximum displacements and maximum accelerations of the top floor in such circumstances; to it correspond attenuation of displacements of 58% and 68% respectively.

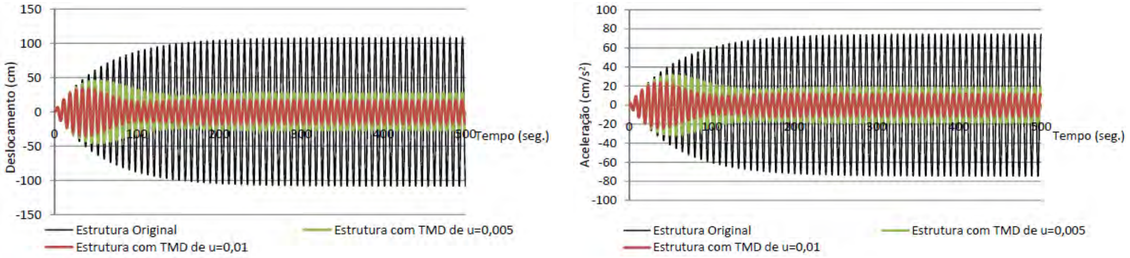

Figure 22 Displacements and accelerations of the top floor, under a harmonic fundamental resonant excitation, without and with TMD's

	Maximum displacement (m)	Maximum acceleration (m/s^2)
Building without TMD	1,08	0,75
Building with TMD (μ=0,005)	0,45	0,31
Building with TMD (μ=0,01)	0,35	0,24

Table 13 Maximum displacements and accelerations of the top floor, under a harmonic fundamental resonant excitation, without and with TMD's

Figure 23 shows the time variations of displacement and acceleration on the top of WTC, equipped with the TMD modeled before with mass ratio of 1%, for the wind loads evaluated using equation (27), with velocity fluctuations corresponding to wind series 1. Table 14 presents a summary of maximum values of displacements and accelerations on top of the building, for each of the time series. It also presents the maximum values of the same variables, multiplying the standard deviation of the responses by the peak factor.

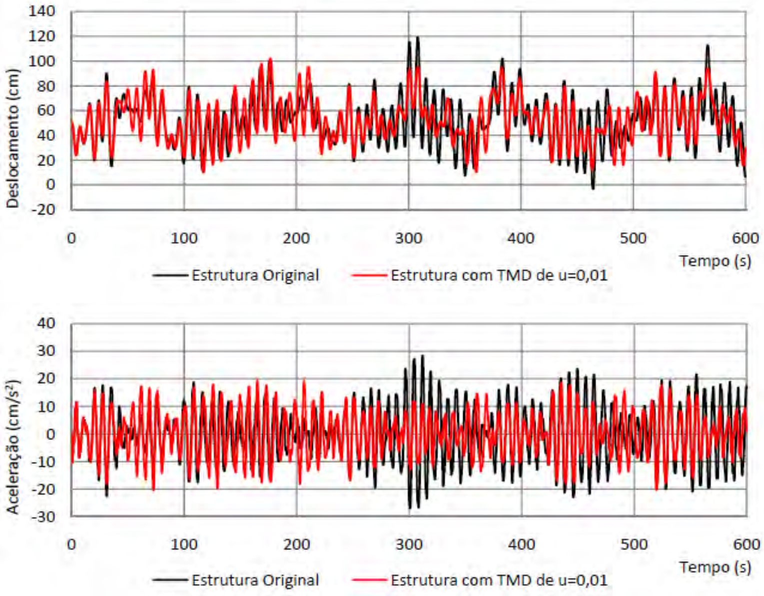

Figure 23 Displacement and acceleration on the top of WTC, equipped with the TMD modeled with mass ratio of 1%, for the wind loads corresponding to wind series 1

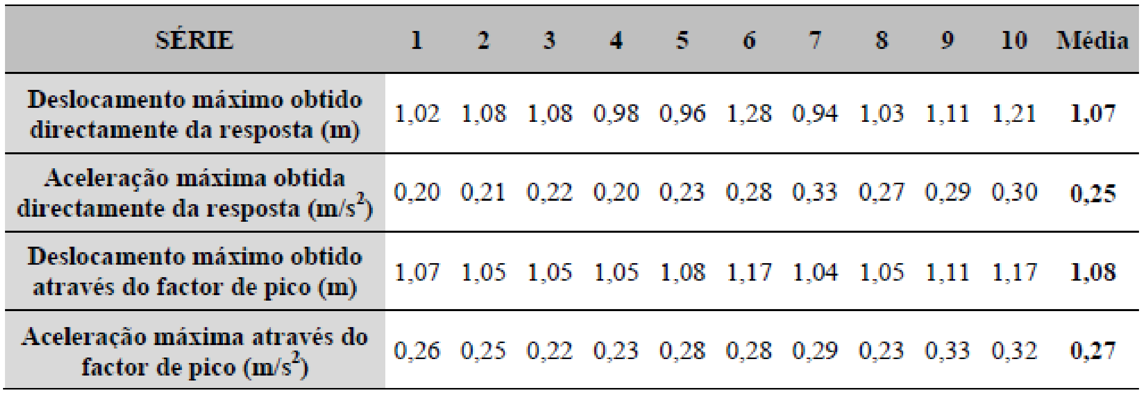

SÉRIE	1	2	3	4	5	6	7	8	9	10	Média
Deslocamento máximo obtido directamente da resposta (m)	1,02	1,08	1,08	0,98	0,96	1,28	0,94	1,03	1,11	1,21	**1,07**
Aceleração máxima obtida directamente da resposta (m/s^2)	0,20	0,21	0,22	0,20	0,23	0,28	0,33	0,27	0,29	0,30	**0,25**
Deslocamento máximo obtido através do factor de pico (m)	1,07	1,05	1,05	1,05	1,08	1,17	1,04	1,05	1,11	1,17	**1,08**
Aceleração máxima através do factor de pico (m/s^2)	0,26	0,25	0,22	0,23	0,28	0,28	0,29	0,23	0,33	0,32	**0,27**

Table 14 Maximum displacements and accelerations on top of WTC, for each of the wind time series (using TMD with mass ratio of μ=0,01)

The efficiency on the use of the modeled TMD on top of building can be interpreted by the results of Table 15, here associated with mass ratio of 1%: reduction of maximum displacements and accelerations on the order of 10% and 20%, respectively. Quite similar conclusions, with less efficiency, were obtained for the TMD with mass ratio of 0,5%.

	Building w°/ TMD	Building w/ TMD (μ=0,01)	Reduction relative to building w°/ TMD
Average max displacement evaluated from response	1,17 m	1,07 m	9%
Average max acceleration evaluated from response	0,33 m/s^2	0,25 m/s^2	24%
Average max displacement evaluated from peak factor	1,17 m	1,08 m	8%
Average max acceleration evaluated from peak factor	0,34 m/s^2	0,27 m/s^2	21%

Table 15 Efficiency of using the modeled top TMD for mass ratio of 1%

7 CONCLUSIONS

After a comparative analysis between the Portuguese Regulation on Safety and Actions for Building Structures and Bridges (RSAEEP) [18] and Eurocode 1 (EC1) [10], it can be concluded that there are differences in these methods here considered to quantify the wind actions with an improvement of the European regulation. Eurocode 1 is based on the method of “Gust Loading Factor” for the quantification of wind action and that takes into account a structural factor that considers the non-simultaneity of the occurrence of the pressures along the facade of the building where potential dynamic phenomena may occur.

Comparing the two procedures suggested by EC1 to quantify this structural factor, it can be concluded that the difference in values obtained by each of them is less than 5%; since it is dependent on the frequency of vibration of the structure, a decrease of same frequency leads to an increase in the value of the structural factor. With a variation of vibration frequency of the structure of 25% over the value obtained by the expression recommended for buildings by EC1, the difference in the value of the structural factor as calculated by the two procedures continues to be no more than 5%, thus leading both of the procedures adopted to very similar results.

A parametric study on the variation of the design wind shear forces and design wind bending moments as a function of height, as evaluated by the RSAEEP and by EC1, was performed using the World Trade Center (WTC) as the reference tall building type.

It can be concluded that for the considered base velocity (28m/s), the values obtained for these generalized forces by EC1 are generally higher than those obtained by RSAEEP, a fact that is related to differences in the coefficient of external pressure evaluated by each code standard adopted for the along the wind façade. Also the definition of a greater number of terrain categories inherent to EC1, allows a more realistic quantification of the wind actions as compared with RSAEEP.

Regarding the modeling of an equivalent frame structure equivalent to the reference World Trade Center, it can be concluded that the value of the structural parameters found for the frequency, mass and stiffness corresponding to the first mode of vibration led to a structural behavior very close to the three-dimensional modeling performed earlier by Santos [19].

For modeling the dynamic wind action reference is made to a method of generating sets of synthetic wind – called the method of Shinozuka – and for which the number of discretization intervals to adopt is discussed; the greater the number of intervals to adopt, the better the process, but with divisions over 1000 intervals results are already quite acceptable.

The simplified methodology adopted for the evaluation of the effects of the dynamic wind action, consisted of varying forces over time at each floor, following the same law of variation. This law is obtained, from each generated time series based on the power spectrum previously multiplied by the aerodynamic admittance function.

Through the generation of ten different series, it was concluded that the dynamic results obtained in terms of average values of maximum displacements, were about 10% higher than those results obtained by applying EC1. Also, the dynamic response of the structure is greatly influenced by the wind series of load considered.

The dynamic response of the building, in the longitudinal along-the-wind direction, indicates that the dynamic phenomena for the case study are not significant with regards to the occupants comfort level since the accelerations obtained are within the limits considered acceptable. It should be emphasized that for this situation the aerodynamic damping, added to the structural damping, appears to contribute significantly in controlling the response under service conditions in this direction.

Regarding the implementation of TMD, it was concluded that these are proving very effective in terms of displacements and in terms of acceleration when the structure is subjected to a harmonic action with frequency equal to the fundamental frequency of vibration of the building. The application of these devices for vibration control can therefore be very effective for control resonances in the transverse direction to the flow caused by the formation of vortices.

However, the attenuation found for the structure equipped with a modeled top floor TMD, when subjected to the wind action modeled as representative, depends greatly on the wind series generated; it is not as effective as before, under perfect harmonic action at resonance.

For the TMD modeled with the parameters calculated, it was concluded that in terms of maximum accelerations reductions of the order of 24% can be achieved for a TMD with 1% mass ratio, and reductions of the order of 18% can be achieved for a TMD with a 0.5% mass ratio. With regard to maximum displacements it was concluded that the structural reference system has proved less effective, achieving reductions of only 9% for a TMD with 1% mass ratio, and of the order of 7% for a TMD with 0,5% mass ratio.

ACKNOWLEDGEMENTS

This work is integrated in the thematic and activities of the international collaborative research project COVICOCEPAD approved by the European Science Foundation (ESF) within the Smart Structural Systems Technologies (S3T) Program. It was sponsored in Portugal until last December 2010 by FCT (Fundação para a Ciência e a Tecnologia) project PPPCDT-05-S3T-FP054-COVICOCEPAD, fact that is herein acknowledged.

REFERENCES

1. Almeida, R. F., and Barros, R. C., *Analysis of the Wind Dynamic Response of Towers and Metallic Masts*, Eighth Internatonal Conference on Computacional Structures Technology, Las Palmas de Gran Canaria, Spain, 12-15 September 2006.
2. ASCE Subcommittee No. 31, *Wind Bracing in Steel Buildings*, Final Report, Transactions of the American Society of Civil Engineers, **105**, pp. 1713-1738, New York, 1940.
3. Bachmann, H., *Vibration Problems in Structures - practical guidelines*. Birkhäuser Verlag, 1997.
4. Barbat, A., and Canet, J., *Estructuras Sometidas a Acciones Sísmicas – Cálculo por Ordenador*, CIMNE, Barcelona, 1994.
5. Barros, R. C., *Dimensionamento Estrutural de Mastros*, Revista Internacional de Métodos Numéricos para Cálculo y Deseño en Ingenieria (RIMNCDI), Ed. E. Oñate (España) and J.C. Heinrich (USA), Universitat Politecnica de Catalunya (UPC), Vol. **18**, Nº 3, pp. 351-365, Barcelona, 2002.
6. Barros, J.E., Moutinho, C., Barros, R.C., *Utilização de TMDs de Grandes Dimensões na Atenuação da Resposta Sísmica de Estruturas*, Sismica 2010 - 8º Congresso Nacional de Sismologia e Engenharia Sísmica, Universidade de Aveiro, Sociedade Portuguesa de Engenharia Sísmica, Portugal, 2010.
7. Cook, N., *Designer's guide to EN 1991-1-4 : Eurocode 1: actions on structures, general actions*. Part 1-4, Wind actions, Thomas Telford, London, 2007.
8. Davenport, A.G., *How can we simplify and generalize wind loads*, Journal of Wind Engineering and Industrial Aerodynamics, Vol. **54/55**, pp. 657-669, 1995.
9. Eagar, T., and Musso, C., *Why Did the World Trade Center Collapse? Science, Engineering and Speculation*. 2001. http://www.tms.org/pubs/journals/JOM/0112/Eagar/Eagar-0112.html .
10. *EN 1991-1-4: Eurocode 1: actions on structures, general actions*. Part 1-4, Wind actions, CEN, Brussels; April 2005.
11. Ferreira, N.A.C., *Efeito do Vento em Edifícios Altos: aplicação a um caso concreto*, Dissertação de Mestrado (Especialização em Estruturas), Faculdade de Engenharia da Universidade do Porto (FEUP), Porto, 2008.
12. Holmes, J.D., *Wind Loading of Structures*, Spon Press, London; 2001.
13. Houghton, E., Carruthers N., *Wind forces on buildings and structures: an introduction*, London, 1976.
14. http://www.sky-scrapers.org/Structural_Facts/index.php/Taipei_101:_Engineering .
15. Kappos, A.J. (editor), *Dynamic Loading and Design of Structures*, Chapter 3: Wind Loading, Spon Press, Taylor & Francis Group, London, 2002.
16. Kelly, S., *Fundamentals of Mechanical Vibrations*, McGraw-Hill International Editions, Singapore, 1993.
17. Kwok, K., and Samali, B., *Performance of tuned mass dampers under wind loads*. Engineering Structures, 1995, pp. 655-667, Elsevier Science Ltd., Great Britain.
18. *Regulamento de Segurança e Acções para Estruturas de Edifícios e Pontes*, Porto Editora, Porto, August 2000.
19. Santos, E., *Atenuadores Visco-Elásticos para Redução de Oscilações Aeroelásticas de Edifícios Altos*. Dissertação de Mestrado, Universidade Federal do Rio de Janeiro, Rio de Janeiro, 2003.
20. Saraiva, J., and Silva, F., *A Interacção do Vento com Grandes Estruturas*, Métodos Computacionais em Engenharia, 31 May- 4 June 2004, Lisbon, Portugal.

21. Taranath, B.S., *Steel Concrete and Composite Design of Tall Buildings*, 2nd edition, McGraw-Hill Book Company, New York, 1998.
22. Vickery, B.J. and Kao, K.H., *Drag of Along-Wind Response of Slender Structures,* J. Structural Division, ASCE, **98**, ST1, Proc. Paper 8635, 21-36, New York, 1972.
23. R. Villaverde, Reduction in Seismic Response with Heavily-Damped Vibration Absorbers”. *Earthquake Engineering and Structural Dynamics*, Vol. **13**, pp. 33-42, John Wiley & Sons, Chichester, 1985.
24. Wilkinson, T., *The World Trade Center and 9/11: A Discussion on Some Engineering Design Issues*. Safe Buildings of this Century, Australian Institute of Building Surveyors National Conference, 12-13 August 2002, Sydney, Australia.
25. Yao, J., *Concept of Structural Control*, Journal of the Structural Division, Proceedings of the American Society of Civil Engineers, Vol. **98**, pp. 1567-1573, New York, U.S.A., 1972.

COMPDYN 2011
3^{rd} ECCOMAS Thematic Conference on
Computational Methods in Structural Dynamics and Earthquake Engineering
M. Papadrakakis, M. Fragiadakis, V. Plevris (eds.)
Corfu, Greece, 25–28 May 2011

NEURAL NETWORK BASED SEMI-ACTIVE CONTROL STRATEGY FOR STRUCTURAL VIBRATION MITIGATION WITH MAGNETORHEOLOGICAL DAMPER

SUBRATA BHOWMIK

Department of Mechanical Engineering, Technical University of Denmark
403 Nils Koppens Allé, Lyngby, Denmark 2800
e-mail: subho@mek.dtu.dk

Keywords: Magnetorheological damper, neural network, semi-active control.

Abstract. *This paper presents a neural network based semi-active control method for a rotary type magnetorheological (MR) damper. The characteristics of the MR damper are described by the classic Bouc-Wen model, and the performance of the proposed control method is evaluated in terms of a base exited shear frame structure. As demonstrated in the literature effective damping of flexible structures is obtained by a suitable combination of pure friction and negative damper stiffness. This damper model is rate-independent and fully described by the desired shape of the hysteresis loops or force-displacement trajectories. The proposed neural network controller is therefore trained based on data derived from these desired force-displacement curves, where the optimal relation between friction force level and response amplitude is determined explicitly by simply maximizing the damping ratio of the targeted vibration mode of the structure. The neural network control is then developed to reproduce the desired force based on damper displacement and velocity as network input, and it is therefore referred to as an amplitude dependent model reference control method. An inverse model of the MR damper is needed to determine the damper current based on the derived optimal damper force. For that reason an inverse MR damper model is also designed based on the neural network identification of the particular rotary MR damper. The performance of the proposed controller is compared to that of an optimal pure viscous damper. The top floor displacement and acceleration of the base excited shear frame structure are selected as the performance parameters of this comparison. It is found by the simulations that the proposed control design yields a reduction in the structural response compared to the viscous case.*

1 INTRODUCTION

As large scale structures become increasingly slender and flexible the magnitude of dynamic response due to loading from wind, traffic and even earthquakes may increase beyond the acceptable level. Thus, the need for additional external damping is pronounced, where in particular the concept of semi-active control has received a great amount of attraction during the most recent decades. The Magnetorheological (MR) damper is one of the most popular types of semi-active devices. It is inherently dissipative and thereby stable, and it behaves roughly as a friction damper, where the friction force level can be altered real-time by simply changing the applied damper current. Thus, the MR damper is a cost effective device that combines some of the adaptability of active control with the low power requirements and reliability of pure passive dampers.

The main challenges arising in connection with the use of most semi active damping devices lies in the development of effective control laws, and in the subsequent digital and real-time implementation. Most control strategies for semi-active structural control fall into two main categories. The first one consists of control strategies that require accurate mathematical formulation for the plant model. Examples in this category are the H2/LQG, H_∞ and the sliding mode control, where any active parts are simple clipped. Conversely, the second category contains control strategies that do not require an accurate mathematical model of the plant. Neural network and fuzzy control fall into this category. Several neural network based control strategies [1-3], neuro-fuzzy network based strategies [4,5] or neuro-predictive control methods [6] have been developed for different control aspects of MR dampers. The advantage of neural network based methods is that they mainly excel in the handling of uncertainties in nonlinear applications, which makes them suitable for both modeling and control of the inherently nonlinear MR damper.

It has been demonstrated in [7,8] that for semi-active control of flexible structures the combination of pure friction and a negative stiffness component yields very effective damping of structural vibrations. Therefore, this paper considers the development of a model reference neural network, which will track the desired hysteresis behavior of an ideal friction damper with negative stiffness. The proposed controller performance is compared with performance of an optimal viscous damper, and for the response of a simple shear frame structure subjected to harmonic base excitation the good performance of the proposed method is verified.

2 STRUCTURAL MODEL AND MR DAMPER PROPERTIES

The performance of the semi-active control strategies for the MR damper is in this paper assessed by the harmonic response of a base excited five-storey shear frame structure. The MR damper is collocated at the first floor of the shear frame, where the measuring data is collected. To apply the semi-active control strategy on the MR damper, an inverse model of the damper is needed to predict the damper current associated with the desired MR damper force. The equation of motion of the shear frame structure with MR damper and inverse MR damper model are discussed in the following sub-sections.

2.1 Equation of motion

In dynamic analysis of flexible structures the structural model is typically modeled by finite elements or determined by experimental modal analysis, whereby the equation of motion can be written in the form

$$\mathbf{M}_c\ddot{\mathbf{x}}+\mathbf{C}_c\dot{\mathbf{x}}+\mathbf{K}_c\mathbf{x}=-\boldsymbol{\lambda}f+\mathbf{M}_c\,\mathbf{I}\left(-\ddot{x}_g\right) \tag{1}$$

where $\mathbf{M}_c$, $\mathbf{C}_c$ and $\mathbf{K}_c$ are the mass, damping and stiffness matrices in Cartesian coordinates, $\mathbf{x}$ is the displacement vector containing the displacements of the five concentrated masses, the dot represents the time derivative, f is the force of the external MR damper, $\boldsymbol{\lambda} = [1, 0, 0, 0, 0]^T$ is the connectivity vector that applies the semi-active force f to the first mass, $\mathbf{I} = [1,1,1,1,1]^T$ is the unity vector and $\ddot{x}_g$ is the ground acceleration. The schematic illustration of the shear frame structure with rotational MR damper is shown in Fig. 1.

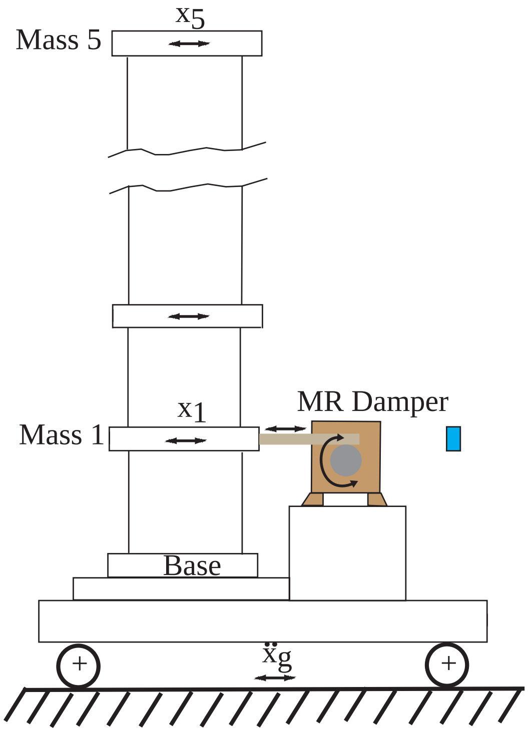

Figure 1: Shear Frame Structure with MR damper

2.2 MR damper model

The rotational MR damper is modeled using the classical Bouc-Wen hysteresis model. The parameters of the model have been calibrated by experiments, where the damper has been driven harmonically in a testing machine at various frequency-amplitude combinations. The modified Bouc-Wen model by Spencer et al. [9] was formulated for the cylindrical type MR damper. In the present case this model is slightly simplified, mainly because the cylindrical damper concept has no need for an accumulator chamber, which for the many cylindrical type dampers introduce an additional stiffness component. Figure 2 shows the close up of the rotary type damper at the Swiss Federal Laboratory of Material Science and Research (EMPA) and the schematic diagram of the classical Bouc-Wen model. For more information on the characteristics and modeling of the rotary MR damper please see Boston et al. [10].

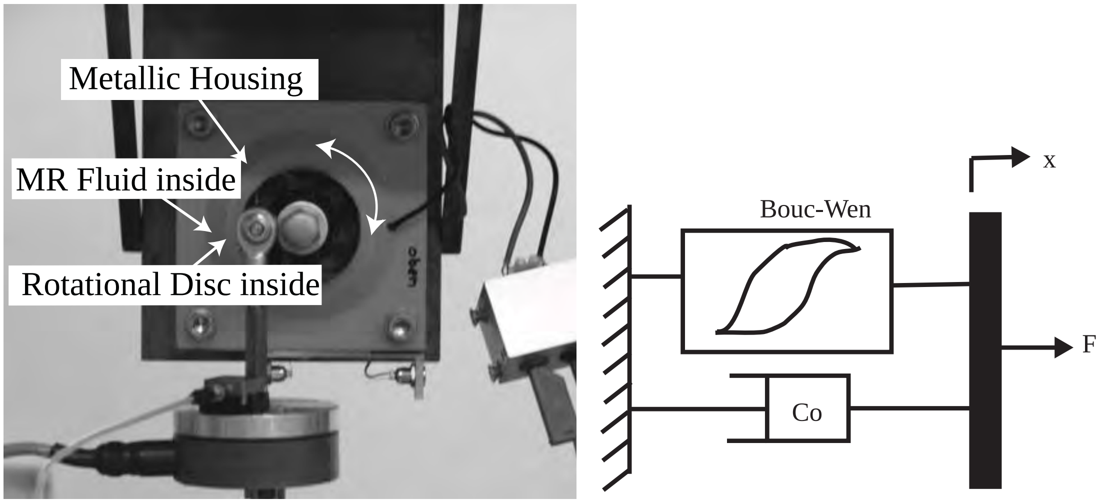

Figure 2: Rotational MR Damper and Bouc-Wen damper model

The governing equations for the damper force *f* predicted by the classical Bouc-Wen model can be written as follows:

$$f = \left(\alpha z + c_0 \dot{x}\right) \tag{2}$$

where the hysteresis effect follows from the evolutionary variable *z* controlled by the Bouc-Wen equation

$$\dot{z} = -\gamma \left|\dot{x}\right| z \left|z\right|^{n-1} - \beta(\dot{x}) \left|z\right|^{n} + A(\dot{x}) \tag{3}$$

The gain parameters on the hysteresis effect and the viscous effect are in the present case described by cubic and linear functions of the applied current, respectively:

$$\alpha = \alpha_a + \alpha_b u + \alpha_c u^2 + \alpha_d u^3 \quad , \quad c_0 = c_{0a} + c_{0b} u \tag{4}$$

The applied current *u* is described with a time delay relative to the desired current *I* by the following first order filter:

$$\dot{u} = -\eta(u - i) \tag{5}$$

The estimated parameters of the simplified Bouc-Wen model for the rotational MR damper are given in Table. 1.

MR Damper Parameters			
α_a	4.038	η	100
α_b	1.984	γ	410
α_c	7.901	β	410
α_d	-0.704	A	1000
c_{0a}	10	c_{0b}	100

Table 1: Parameters for Bouc-Wen Model

Typical force-displacement and force-velocity hysteresis loops for the rotational MR damper are shown in Fig. 3. It is seen that the MR damper behaves approximately as a friction damper, where the friction force level can be altered by changing the applied damper current. The opening of the force-velocity loops indicates some form of stiffness or inertia effects.

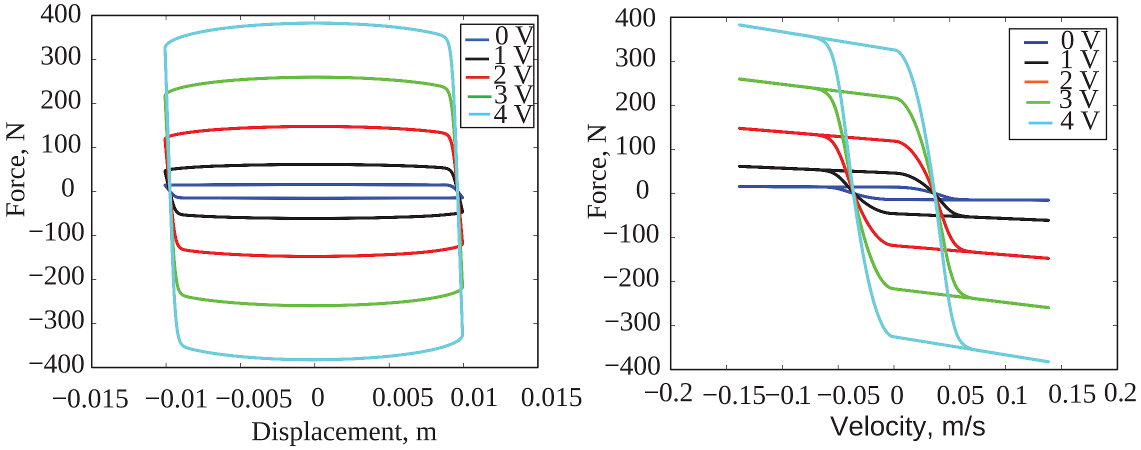

Figure 3: Force Displacement /Velocity hysteresis loops.

2.3 Inverse MR damper

The inverse model modeling for rotary MR damper is a quite complicated task due to high nonlinearity in MR damper dynamics. This work can be done by using parametric [10] such as Evolutionary Algorithm and also non-parametric system identification methods such as neural network identification approach [11, 12]. The inverse MR damper behavior is modeled to solve the force tracking task by MR damper in closed loop cycle. The training and validation data are generated by dynamic tests of the MR damper mounted on a hydraulic testing machine. The inverse modeling training data are absolute velocity and absolute force and the current is the target. This approach has been chosen because current is always positive and thereby leads to a small modeling error independently of the sign of velocity. The inverse model of the MR damper is verified with totally independent set of input-output data. The model validation is thoroughly described in Bhowmik et al [14].

The inverse MR damper behaviour, i.e. the input states at time instant k are the damper velocity $\dot{x}_1(k)$ and desired control force $f_{des}(k)$ and the output state is current $I(k)$, is modelled by a neural network with the following architecture

$$I(k) = NN\begin{bmatrix} |\dot{x}_1(k)| & |\dot{x}_1(k-1)| & |\dot{x}_1(k-2)| & |\dot{x}_1(k-3)| \\ |f_{des}(k)| & |f_{des}(k-1)| & |f_{des}(k-2)| & |f_{des}(k-3)| \end{bmatrix} \tag{6}$$

The neural network based inverse MR damper model is used to solve the force tracking task.

3 CONTROL STRATEGIES

The present paper describes a neural network based model reference control strategy for the prediction of the desired force to control structural vibrations. To evaluate the performance of the proposed model reference controller, the optimal pure viscous damper force is also applied to the structure.

For linear damper models the characteristics of the damper are conveniently formulated in the frequency domain as

$$f(\omega) = gH(\omega)x \tag{7}$$

where g is the control gain and $H(\omega)$ is the associated frequency dependent transfer function.

The effective damping of the structure is evaluated in terms of its modal damping ratio, where the presence of the external damper generates a non-proportional damping with corresponding complex valued natural frequencies and mode shapes. The analysis of the damper modal vibrations is described by the two-component system reduction technique introduced by Main and Krenk [13]. In that formulation the response of the structure is represented by a linear combination of the two limiting mode shapes for the structure without damper $\mathbf{u}_0$ and for the structure with the damper fully locked $\mathbf{u}_\infty$, respectively. The linear combination can then be written as:

$$\mathbf{x} = \mathbf{u}_0 \mathrm{r}_0 + \mathbf{u}_\infty \mathrm{r}_\infty \tag{8}$$

The first term represents the classical undamped case, while the second term introduces the local effect of the damper described in terms of its ability to lock the structure at its location. The undamped mode shape is governed by the classical generalized eigenvalue problem

$$\left(\mathbf{K} - \omega_0^2 \mathbf{M}\right)\mathbf{u}_0 = \mathbf{0} \tag{9}$$

A similar eigenvalue problem exists for the case where the damper link is fully locked, defining ω_∞ and $\mathbf{u}_\infty$. The locked mode shape $\mathbf{u}_\infty$ is by construction orthogonal to the connectivity vector which yields the identity $\boldsymbol{\lambda}^T \mathbf{u}_\infty = 0$.

The two-component representation reduces the full dimensional problem to a two-dimensional problem, where the associated characteristic equation can be solved explicitly, providing expressions for the complex valued natural frequency and the corresponding modal damping ratio. Optimal calibration of the damper model is based on the maximization of the damping ratio. For the general damper format in (7) it is demonstrated in [14] that the optimal gain can be determined by the expression:

$$g_{opt} = \frac{1}{|H|} \frac{\left(\omega_\infty^2 - \omega_0^2\right)}{u_0^2} \tag{10}$$

where u_0 is the amplitude of the undamped mode shape at damper location. This expression is in the following used to calibrate the control strategies.

3.1 Viscous damping strategy

The prototype damper model is the pure viscous model. For this model the damper force is directly proportional to the collocated velocity of the damper motion,

$$f = c\dot{x} \tag{11}$$

where c is the viscous parameter. When compared with the linear frequency representation of the damper force in Eq. 7, the damper transfer function for the viscous damper is

$$H(\omega) = i\omega \simeq i\omega_0 \tag{12}$$

while the gain value is

$$g = c \tag{13}$$

Substitution of (12) and (13) into (10) gives the following expression for the optimal viscous parameter:

$$c_{opt} \approx \frac{2(\omega_{\infty} - \omega_0)}{u_0^2} \tag{14}$$

where $\omega_{\infty} + \omega_0 \approx 2\omega_0$

The optimal viscous damper is without stiffness and is therefore a suitable benchmark example for damper models with negative stiffness.

3.2 Proposed Neural network based model reference control strategy

The proposed controller is developed based on a neural network model identification technique, where the neural network model is trained by a reference damper model. In this paper, the characteristics of the damper model are described by the desired shape of the hysteresis loop, which combines an amplitude dependent friction damper with a negative stiffness component. The optimal shape of this hysteresis loop has originally been identified and verified by Boston et al. [7]. The hysteresis loop is based on the assumption of pure harmonic displacement and velocity, which is used as the input to the proposed neural model, while the damper force based on the desired hysteresis loop is used as the output of the neural controller. The optimal shape of the force-displacement trajectory is shown in fig. 4.

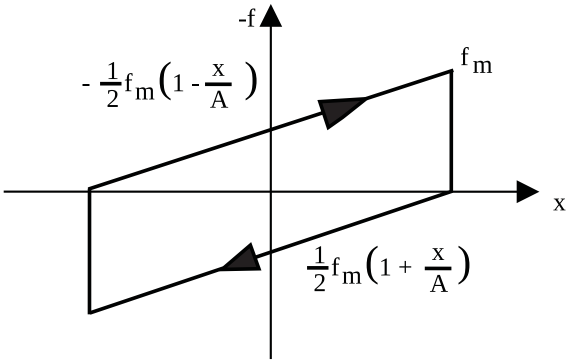

Figure 4: Force-Displacement Hysteresis model for Friction Damper with negative stiffness

The hysteresis model is inherently nonlinear, whereas the calibration formulation in (10) requires a linear damper model. Thus, an equivalent linear model is assumed to contain a viscous and a stiffness component,

$$f = c\dot{x} + kx \tag{15}$$

If x is a sinusoidal signal, the parameters of the linear equivalent model in (15) can be determined by equivalence over a full vibration period, see [14]. The yields the following equivalent linear model for the hysteresis loop in Fig. 4:

$$f = \frac{2f_{\mathrm{m}}}{\pi\omega A}\dot{x} - \frac{f_{\mathrm{m}}}{2A}x \tag{16}$$

where A is the amplitude of the damper displacement, k is negative stiffness and f_{m} is maximum force of the hysteresis loop. In frequency domain the model is expressed as

$$f = \frac{f_{\mathrm{m}}}{A}\left(-\frac{1}{2} + i\frac{2}{\pi}\right)x \tag{17}$$

Comparison with the frequency representation in Eq. 7 gives the following expression for the transfer function of the linear equivalent hysteretic damper model:

$$H(\omega) = \left(-\frac{1}{2} + i\frac{2}{\pi} \right) \tag{18}$$

and the corresponding gain value:

$$g = \frac{f_{\mathrm{m}}}{A} \tag{19}$$

From Eq.10 the optimal value of g is determined as

$$g_{opt} = 1.24\frac{\left(\omega_{\infty}^{2} - \omega_{0}^{2}\right)}{u_{0}^{2}} \tag{20}$$

The optimal value f_m is determined as

$$f_{\mathrm{m}} = g_{opt} A \tag{21}$$

where A is the amplitude of the displacement.

In this paper, a four-layer feed forward neural network is adopted which consists of one input, two hidden layers and a single output layer. The displacement and velocity with current state and five preceding values are taken as input and force at current state is output in the proposed neural network. The neural network controller is trained with training data generated at different amplitudes and at different frequencies of both the displacement response and the corresponding force data from the optimal friction model. The trained model is verified with independent data set and subsequently used in a closed loop implementation. The training algorithm used in the feed forward back propagation neural network is the Levenberg-Marquardt (LM) algorithm based on a least-square curve fitting.

4 NUMERICAL EXAMPLES

To evaluate the effectiveness of the proposed control strategy for the structural vibration mitigation with rotary MR damper, two numerical examples are considered. The first one is based on pure viscous damping strategy and the second one is our proposed neural network based model reference control (NN-MRC). Both the examples are discussed below

4.1 Viscous Damper

The viscous damping strategy using MR damper in closed loop is simulated for five storied shear frame structure with harmonic base excitation. The force-velocity and force-displacement hysteresis plots of the damper force and desired force from control law are compared for optimal viscous damping strategy and the result is quite satisfactory. The force tracking task by MR damper is quite well. From fig. 3, it is visible that MR damper has a force limit at zero current. For that reason it is not possible for MR damper to follow the desired force below the force limit at zero current. Here for this damper, force limit is 24 N.

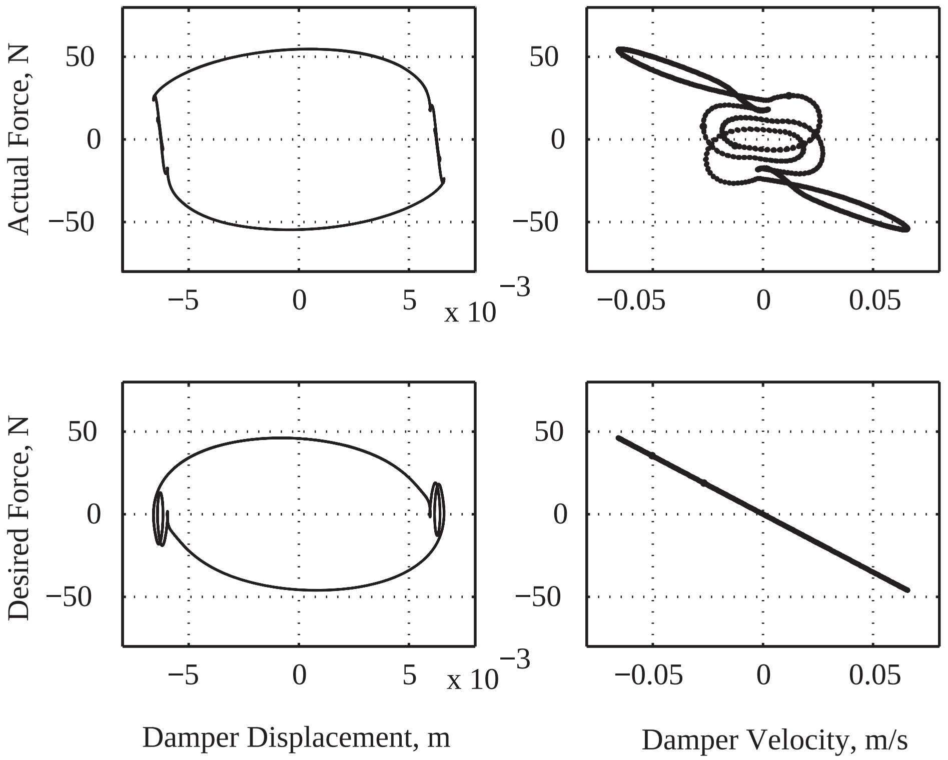

Figure 5: Force-Displacement and Force Velocity hysteresis diagram for viscous damper

The top floor displacement and damper displacement are shown in fig. 6.

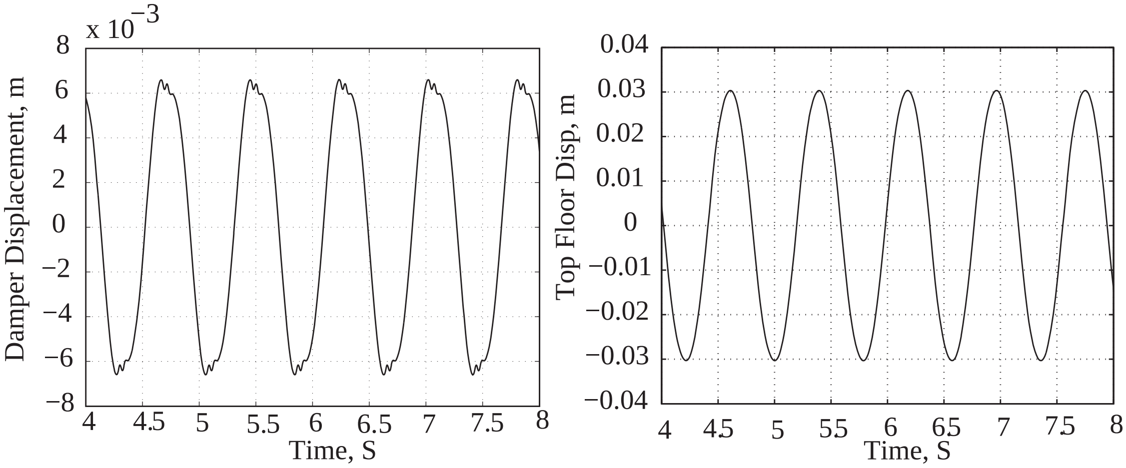

Figure 6: Time history of damper and top floor displacement for viscous damper

The viscous damping strategy is also applied directly on structure without MR damper and compared the change in performance.

4.2 Model Reference Neural Controller

The proposed neural control strategy is applied for structural vibration reduction based on harmonic base excitation using MR damper in closed loop simulation. The Time history of damper displacement and top floor displacement are shown below.

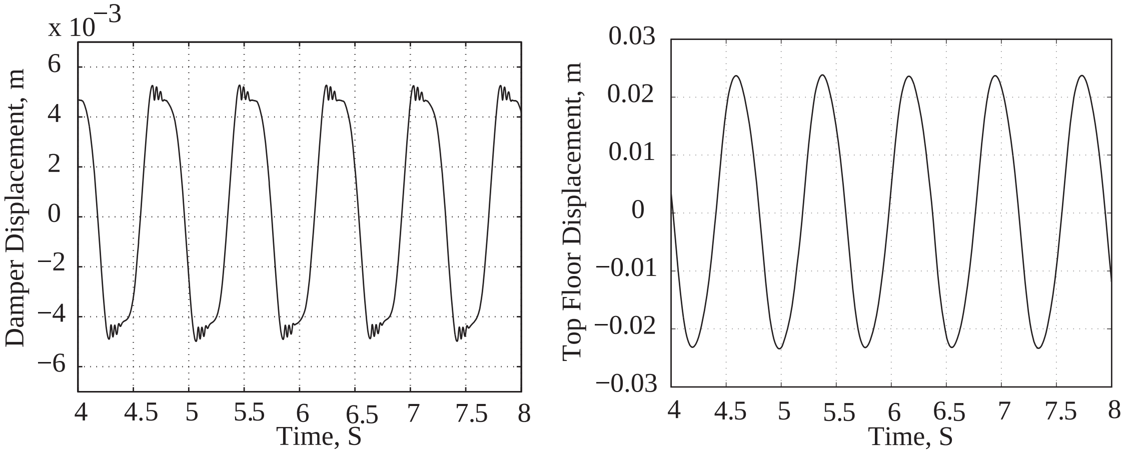

Figure 7: Force-Displacement and Force Velocity hysteresis diagram for neural controller

The hysteresis plots for force-displacement and force-velocity trajectories are shown in fig.8.

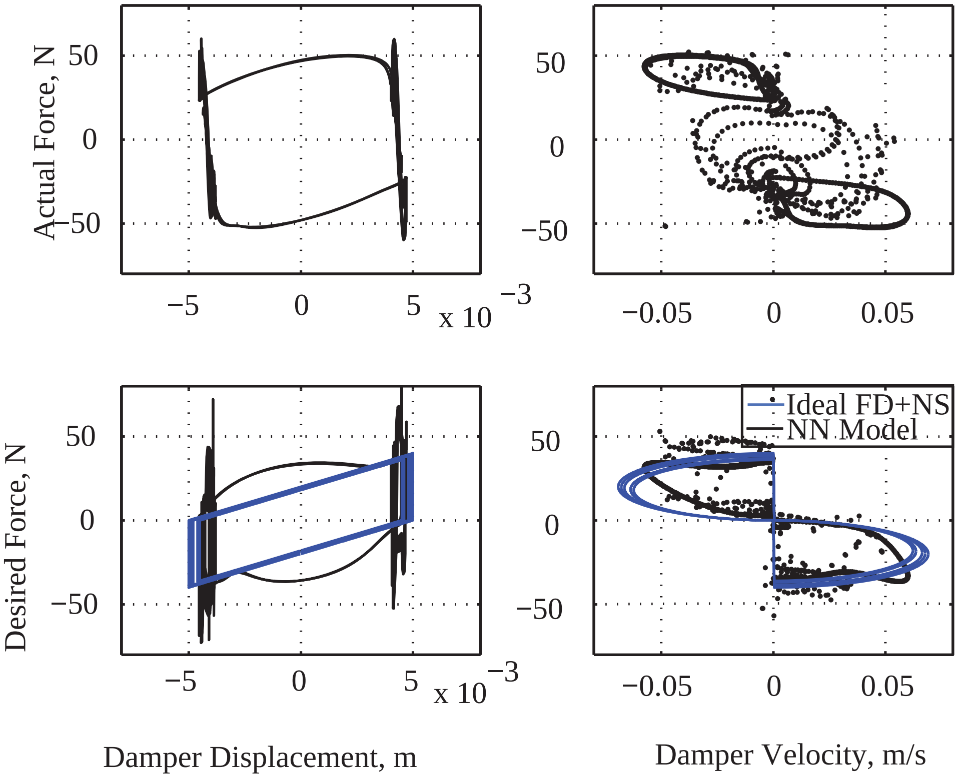

Figure 8: Time history of damper and top floor displacement for neural controller

The schematic diagram for the closed loop simulation is shown below

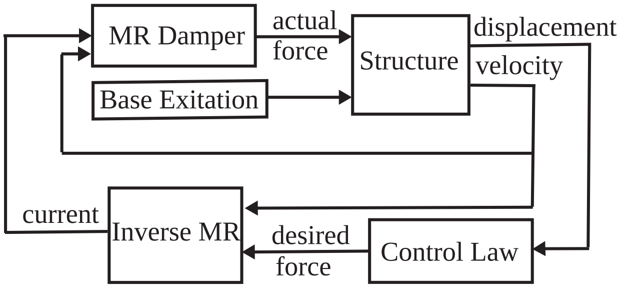

Figure 9: Schematic diagram for closed loop simulation

Force from an optimal friction damper with negative stiffness are calculated by analytical method and compared with the desired force prediction from neural network. Desired force from neural controller and the analytical force have some deviation because the slope of the desired force is not linear due to change in the motion of the damper. The damper displacement is slightly changed from pure sinusoidal due to some spiky effect in current output from inverse MR damper model. The current from inverse MR damper model is shown in fig. 10

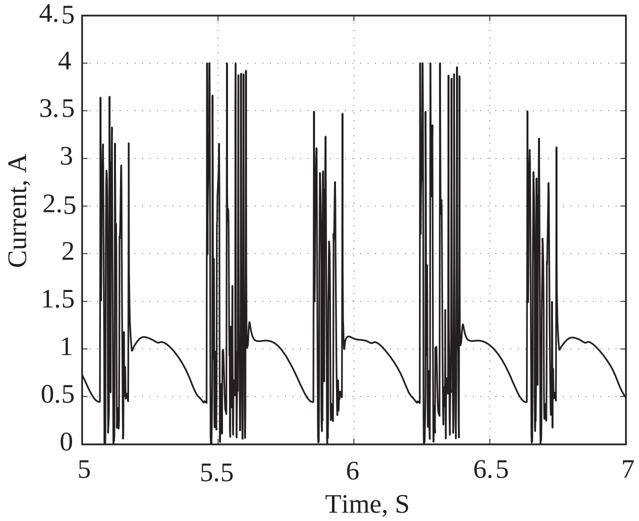

Figure 10: Time history of current from inverse MR model

The force-displacement and force-velocity diagram are shown in Fig. 8. The diagrams are quite satisfactory with compared with identical one. There is some deviation in the force prediction due to non-sinusoidal behaviour of the structural response. This is mainly due to some spiky current prediction by inverse MR model but overall the force tracking is quite satisfactory.

	Passive Viscous	Viscous with MR damper	NN-MRC
RMS(x_1^{max})	0.0091 m	0.0066 mm	0.0044 mm
RMS(x_5^{max})	0.036 m	0.030 m	0.024 m
RMS(a_1^{max})	0.64 m/s^2	0.81 m/s^2	0.80 m/s^2
RMS(a_5^{max})	2.02 m/s^2	1.81 m/s^2	1.76m/s^2

Table 1: Performance Parameters

5 CONCLUSIONS

In the closed loop simulation, two neural network models are used. One is for force tracking which is an inverse MR damper model and another is used for tracking reference damper model which is following hysteresis force-displacement behaviour for optimal friction damper with negative stiffness. RMS of the peak displacement and peak acceleration of each cycle for top floor and damper location are taken as performance parameters. From the performance parameters chart, it is clearly visible that proposed control method can reduce around 35% in damper displacement and 30% in top floor displacement. The damper displacement for viscous damping strategy with and without MR damper has deviation due to limitation MR damper force realization at zero current when MR damper is attached. The response of the top floor using semi active neural controller gives is quite satisfactory with compared to pure viscous damping. There is also significant improvement in acceleration term and but the acceleration contains some noise. The major advantage of the proposed controller is it is inherritently modeled with amplitude dependency and the inherent time-delay problem which is an important drawback of model based control can be solved in neural based control. In general, a neural network is trained under certain condition which can be used in a slightly modified but similar nature of the training state. The important feature of neural network is that it can handle nonlinearity so well that it can apply to nonlinear structural control also based on linearly trained neural model. This is the reason why neural network is used in this paper for structural control. The numerical study revealed that proposed neural based model reference controller can track the desired hysteresis behaviour of optimal friction damper with negative stiffness satisfactorily and the performance is better than optimal viscous damper.

ACKNOWLEDGEMENT

This research is financially supported by the Danish Agency for Science, Innovation and Research. The major part of the work has been done at Swiss Federal laboratory for Material Science and Research, Switzerland with collaboration with Dr. Felix Weber. These supports are gratefully acknowledged.

REFERENCES

[1] Z.D. Xu, Y.P. Shen, Y. Q. Guo, Semi-active control of structures incorporated with magnetorheological dampers using neural network. *Smart materials and Structure*, **12**, 80-87, 2003.

[2] K.A. Bani-Hami, M.A. Sheban, Semi-active neuro-control for base-isolation system using magnetorheological (MR) dampers. *Earthquake Engineering and Structural Dynamics*, **35**, 1119-1144, 2006.

[3] D.H. Kim, S.N. Seo, I. W. Lee, Optimal neurocontroller for nonlinear benchmark structure. *Journal of Engineering Mechanics*, **130**, 424-429, 2004.

[4] Z.Q. Gu, S.O. Oyadiji, Application of MR damper in structural control using ANFIS method. *Computers and Structures*, **86**, 427-436, 2008.

[5] Z.D. Xu, Y. Q. Guo, Neuro-fuzzy control strategy for earthquake-exited nonlinear magnetorheological structures. *Soil Dynamics and Earthquake Engineering*, **28**, 717-727, 2008.

[6] A.K. Karamodin, M.H. Kazemi, Semi-active control of structures using neuro-predictive algorithm for MR dampers. *Structural Control and Health Monitoring,* **DOI: 10.1002/stc.278**, 2008.

[7] C. Boston, F. Weber, L. Guzzella, Optimal semi-active damping of cables: evolutionary algorithms and closed-form solutions, *Smart Material and Structures*, **18**, 055006 (9 pp), 2009

[8] H. Iemura, M.H. Pradono, Advances in the development of pseudo-negative-stiffness dampers for seismic response control, *Structural Control & Health Monitoring*, **16**, 784-799, 2009

[9] B.F. Spencer, S.J. Dyke, M.K. Sain, J.D. Carlson, Phenomenological model for magnetorheological dampers. *Journal of Engineering Mechanics*, **123**, 230-238, 1997.

[10] C. Boston, F. Weber, L. Guzzella, Modeling of a disc-type magnetorheological damper, *Smart Material and Structures*, **19**, 045005 (12 pp), 2010

[11] H. Metered, P. Bonello, S. Oyadiji, The experimental identification of magnetorheological dampers and evaluation of their controllers, *Mechanical Systems and Signal Processing*, **24**, 976-994, 2010

[12] S.Bhowmik, J. Høgsberg, F. Weber, Neural Network Modeling of forward and inverse behaviour of rotary MR damper. 23*rd* *Nordic Seminar on Computation Mechanics (NSCM23),* Stockholm, Sweden, October 14-15, 2010.

[13] J.A. Main, S. Krenk, Efficiency and tuning of viscous dampers on discrete systems, *Journal of Sound and vibration,* **286,** 97-122, 2005

[14] J. Høgsberg, Modeling of Dampers and Damping in Structures, *PhD Thesis*, Technical University of Denmark, 2005

COMPDYN 2011
3rd ECCOMAS Thematic Conference on
Computational Methods in Structural Dynamics and Earthquake Engineering
M. Papadrakakis, M. Fragiadakis, V. Plevris (eds.)
Corfu, Greece, 25–28 May 2011

DYNAMIC PERFORMANCE OF EXISTING HIGH-SPEED RAILWAY BRIDGES UNDER RESONANT CONDITIONS, RETROFITTED WITH FLUID-VISCOUS DAMPERS SUPPORTED ON CLAMPED AUXILIARY BEAMS

J. Lavado[1], **M.D. Martinez-Rodrigo**[2], **and P. Museros**[3]

[1] University of Granada, Dept. of Structural Mechanics and Hydraulic Engineering
18071 Granada, Spain
e-mail: jlavado@ugr.es

[2] University Jaume I, Dept. of Mechanical Engineering and Construction
12071 Castellon, Spain
e-mail: Lola.Martinez@emc.uji.es

[3] University Polytechnic of Valencia, Dept. of Cont. Medium Mechanics and Theory of Structures
46022 Valencia, Spain
e-mail: pmuseros@mes.upv.es

Keywords: Resonance in Railway Bridges, Passive Control of Structures, Double-beam System, Moving Loads, Dynamics of Bridges, Fluid-viscous Dampers.

Abstract. *In this contribution the application of Passive Control techniques is applied to reduce the severe transverse vibrations that railway bridges of moderate lengths may experiment under resonance conditions. The proposed solution consists on connecting the slab to a series of auxiliary beams with partially restrained rotational end conditions through a set of fluid-viscous dampers. A particular configuration minimizing the space occupied under the bridge deck by the devices and the auxiliary beams is proposed for slabs and girder bridges, typical typologies in the aforementioned range of lengths. First, the dynamic response of the double-beam system at resonance is obtained in closed-form under harmonic excitation in order to detect the main governing parameters of the bridge response. Then conditions for the optimal dampers constants and minimum beam sizes that minimize the bridge dynamic amplification at resonance are obtained using a planar analytical model. Finally the effectiveness of the solution and the adequacy of the expressions derived from the harmonic case are proven under railway traffic excitation. Special attention is given to the beneficial effect of partially restraining the auxiliary beam supports throughout the study.*

1 INTRODUCTION

The extensive construction of new High-Speed railway lines and the use of conventional lines for higher operating train velocities require the continuous upgrading of railway infrastructure and, in particular, of bridge structures. Even though modern trains' axle loads are not higher than old-time vehicles transmitted forces, higher design velocities may lead to the appearance of resonance phenomena. Resonance, in a railway bridge, takes place when the exciting frequency of the train's periodic loading becomes close to the natural frequency of the bridge. If this is the case, the loads enter the bridge in phase with the natural oscillations of the structure leading to a progressive increase of the deck transverse oscillations. If structural damping is low, as it usually is the case in railway bridges [1], and the number of axles is sufficient severe transverse vibrations at the platform area could build up causing the failure of the Serviceability Limit State of vertical acceleration [2]. Specially critical structures in this regard are short-to-medium-span bridges (12 to 25 m) where the main structural elements are simply-supported (S-S) beams or plates. In these structures resonance phenomena may cause not only impact or fatigue related damage but also failure of ballast-beds due to relaxation and scattering of ballasts. This can compromise the running safety of the trains, the ride comfort of passengers, and ultimately increase the bridge maintenance costs [1, 3, 4].

In existing bridges that experiment this kind of behavior, due to either an increase in the Maximum Line Speed at the site or to structural degradation with time, classical solutions could be applied such as increasing the mass of the deck and therefore reducing its acceleration or augmenting its stiffness and consequently raising its natural frequencies and critical velocities. Nevertheless in many circumstances it is not possible to preserve the original structure and the deck needs to be demolished and replaced with the subsequent interruption of the line services. Alternatively, in this contribution the reduction of the bridge dynamic response by artificially increasing the overall damping of the structure applying Passive Control techniques and, in particular, retrofitting the bridge deck with Fluid Viscous Dampers (FVDs) is proposed and evaluated.

Despite the fact that vibration control systems have been applied to reduce the dynamic response of structures since the 1960s, only a few authors have addressed the practical application of these technologies to bridges under the action of moving vehicles. The application of Tuned Mass Dampers (TMDs) to the train-induced vibration problem has been addressed by Kwon et al. [5], Wang et al. [6], Yau et al. [7, 8, 9] and Li et al. [10]. These authors investigate the dynamic performance of bridges using planar models retrofitted with single or multiple TMDs. TMDs are tuned to a single frequency of the superstructure (usually the fundamental one) or several frequencies which contributions need to be reduced. From these works it can be inferred that the vehicle passage time on the bridge is, in many circumstances, too short to build up the needed TMD vibrating regime that effectively mitigates the bridge excessive vibrations; besides, detuning problems may arise if the devices are tuned to the bridge natural frequency, due to the variability of this magnitude over time associated to vehicle-bridge interaction effects, changing environmental parameters (e.g. temperature), or to the decay of the TMD stiffness with time. Nevertheless this second drawback may be partially overcome with multiple TMDs tuned in a frequency interval [8, 10] or with the string-type TMD presented in [9]. Recently Samani [11] has compared the vibration reduction capability of nonlinear TMDs when compared to linear elements connected to simply-supported beams under moving loads concluding that the vibration reduction achieved levels are very similar.

Minsili et al. [12] suggest the installation of supplemental diagonal elements in truss bridges connected to the original braces through Slotted Friction Connections, in order to mitigate traffic and earthquake induced vibrations. The authors point out that with this alternative structural displacements can be reduced to a great extent, but vertical accelerations may exceed their initial values due to the nature of the new forces introduced in the bridge deck. The appearance of residual displacements in the structure after the devices activation is an additional inconvenient of the proposed system.

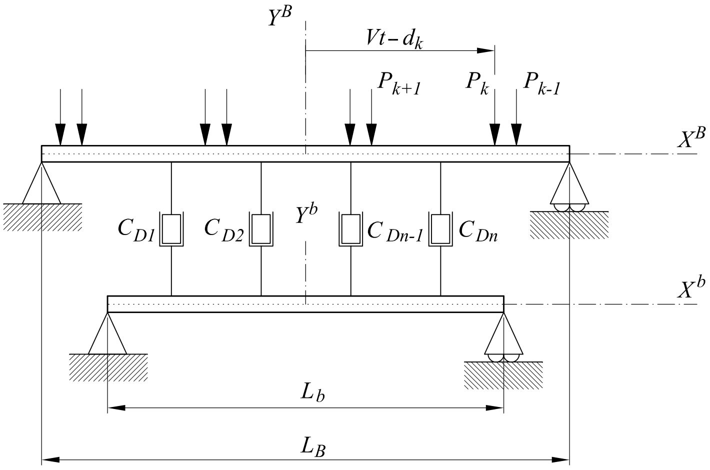

Figure 1: Simply-supported double beam system connected through FVDs and (b) simply-supported-partially-clamped double beam system connected through FVDs.

The use of viscoelastic (VE) materials to improve the dynamic performance of railway bridges has been addressed by a number of researchers. Choo et al. [13] propose the introduction of acrylic rubber patches connected to S-S beams deforming in shear when the main elements bend. The authors carry out an experimental program and adjust a numerical constitutive model for this material. They finally conclude that the proposed design could reduce to permitted levels the structural response of long span bridges which experience inadmissible vertical accelerations. A few authors have investigated the applicability of Continuous Dynamic Vibration Absorbers (CDVAs) combined with viscoelastic materials, to the vibration control of beams under harmonic and moving loads. Vu et al. [14] and Abu-Hilal [15] study the possibility of reducing the dynamic response of a Bernoulli-Euler (B-E) beam by connecting it to an identical element through a continuous layer of VE material. Onsizczuk analyses the dynamic behaviour of double-beam [16, 17] and double plate systems [18, 19] linked through continuous Winkler media focusing on the relative properties of the three elements that control the oscillations of the main element. Recently, Moliner et al. [20, 21] have investigated the dynamic performance of the double-beam system connected by discrete Kelvin elements and have evaluated its applicability in reducing the resonant response of short S-S railway bridges. A few authors have addressed the use of pure viscous dampers to reduce the amplification in beams traversed by moving vehicles. Oliveto et al. [22] and Greco et al. [23] solve the dynamic problem of a continuous beam with two end rotational viscous dampers under the circulation of a single load, by using an extension of the complex mode superposition method. Nevertheless, to the authors' knowledge, this type of damper has never been previously applied in the context of High-Speed railway traffic.

FVDs have been selected, as compared to other Passive Control devices for this application, because they dissipate energy at a wide scope of frequency ranges, and not only at narrow ranges like TMDs. As a consequence, they do not present relevant tuning and detuning drawbacks. A further advantage is the fact that dissipative devices based on friction or yielding increase replacement operations and maintenance costs. In contrast, some FVDs are equipped with labyrinth seals which eliminate mechanical friction [24], allowing them to undergo an enormous number of cycles before they have to be replaced. Moreover, since in FVDs the maximum force and maximum displacement are out of phase, additional forces introduced in the structure are small when compared to other techniques.

The authors of this contribution have investigated in the past the dynamic behaviour of a double-beam system as the one shown in Fig. 1 linked through a distribution of pure FVDs under the circulation of moving loads [25, 26].

It consists of a *main beam*, which represents the bridge, and an *auxiliary beam* with simply-supported end conditions connected to the bridge by means of FVDs. Closed-form expressions for the optimal dampers minimising the bridge response have been provided, and a methodology for the auxiliary beam design has been developed based on the overall damping needs. This study has been completed accounting for the contribution of three-dimensional modes of the bridge, which cannot be neglected in multi-track decks or when the deck has a skew geometry. To this end the dynamic performance of orthotropic plates connected to auxiliary beams distributed along the deck width with, again, simply-supported end conditions through FVDs has been analysed in detail [25, 27, 28].

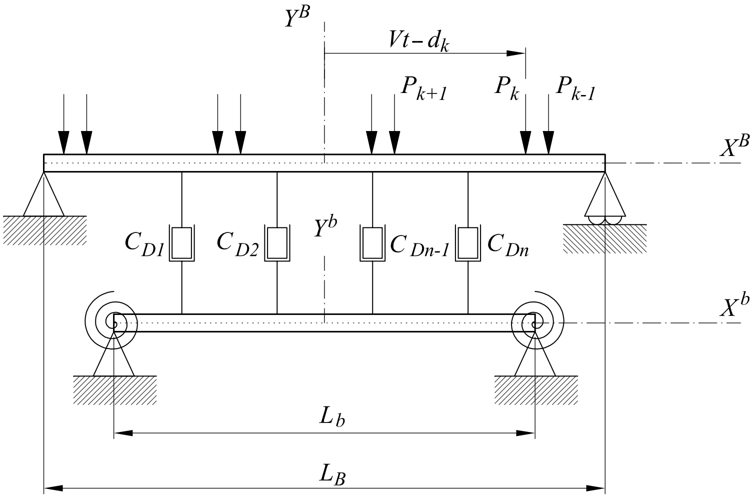

Figure 2: Simply-supported-partially-clamped double beam system connected through FVDs.

One of the main conclusions derived from the previous works by the authors is that in order for the FVDs to effectively reduce the deck vibratory response, the fundamental frequency of the auxiliary beam (lower beam in Fig. 1) needs to exceed the bridge or main beam highest frequency which contribution is to be controlled. Moreover, as the auxiliary beam frequency increases, the dissipative capacity of the system raises. Due to this condition the secondary beam needs always to be oversized when compared to the minimum beam that would accomplish resistance requirements under the dampers forces. As the proposed configuration, that is presented in section 2, consists on installing the retrofitting system below the slab the needed auxiliary beams may occupy an excessive portion of the free space under the deck. Furthermore, as current design standards [2, 29] prescribe to account for frequency contents up to 30 Hz in the computation of the deck transverse acceleration, modes close to 30 Hz are almost impossible to control with the proposed system because beams with fundamental frequencies exceeding 30 Hz require enormous section heights for spans in the neighborhood of 20-25 m. To overcome this problem a variation on the configuration of the retrofitting system already studied by the authors is proposed which consists on transforming the original simply-supported boundary conditions of the auxiliary beam restraining the extreme sections rotation. In an ideal case if the beam could be perfectly clamped at the ends the natural frequency of the fundamental mode would increase approximately 2.27 times with respect to simply-supported end conditions. As perfect clamping is not possible the system shown in Fig. 2 is analyzed. This way the efficiency of the solution can be investigated in terms of the partial rotational restriction of the beam supports.

The objectives of the present study are (i) to propose a methodology to select the minimum size of the auxiliary beam and optimum FVDs constants minimizing the dynamic response of the main simply-supported beam at resonance; (ii) to prove that with the proposed solution severe levels of vertical acceleration may be drastically reduced without exceeding the devices maximum bearing capacity, the maximum admissible stress in the beams nor the punching force in the slab, and (iii) to evaluate the beneficial effect of partially clamping the auxiliary beam supports when compared to the previously analyzed simply-supported case.

2 CONFIGURATION OF THE DAMPING SYSTEM

The dissipative system to be installed on the beam supporting the passage of the loads consists of two main elements. The first element is an auxiliary, partially clamped beam which in typical applications is generally located underneath the main one.

The second element is a set of FVDs linking the vertical motion of certain sections of the main beam and the auxiliary one. Our attention here is focused on mitigating the flexural vibrations of the main beam when the train of moving loads induces a resonance situation. For this reason, the planar model shown in Fig. 2 is used to analyse the performance of the proposed retrofit alternative. For the sake of simplicity two Cartesian coordinate systems are introduced with origins located at both beams mid-span sections.

The loads acting on the structure are assumed to be constant-valued, i.e. vehicle–bridge interaction effects are neglected. Also, the main beam is assumed to rest directly on the abutments without any intermediate elastic bearing.

The torsional oscillations experienced by beams subjected to eccentric moving loads are not accounted for in the analytical formulation and optimisation of this study. Consequently, the results presented in sections 2 and 3 are not applicable to either multi-track or single-track skewed railway bridges. However, it should be emphasised that single-track non-skewed bridges, and in particular, medium to short-span ones are some of the most unfavourable cases found in practice. As a consequence of their low total mass, this type of structures may undergo severe resonant oscillations under the passage of fast trains, thus generating highly demanding situations for any dissipative system.

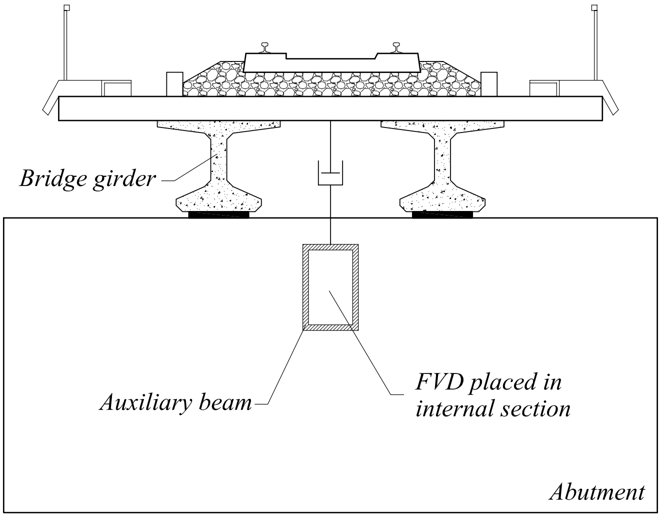

Figure 3: Retrofit configuration for a concrete girders bridge deck.

Fig. 3 shows a possible configuration of the auxiliary beam and dampers installed in a single-track railway bridge. The dampers link the lower side of the slab and the upper flange of an auxiliary beam with hollow rectangular cross-section. The auxiliary beam is clamped on the abutments at the outermost sections of the bridge. Other suitable configurations could be adopted for different auxiliary beams geometries and deck typologies with an essential dynamic behaviour as that represented in Fig. 2.

3 GOVERNING PARAMETERS AND INFLUENCE ON THE RESPONSE

3.1 Equations of motion of a simple beam under moving loads

The partial differential equation governing the flexural behaviour of a simply supported beam (main beam of the system) subjected to a train of concentrated loads can be found in the works of several authors such as Frýba [30, 31], Olsson [32], Yang et al. [33] and Museros and Alarcón [34]. Neglecting the effects of shear deformation and rotary inertia, and considering that the loads are aligned with the axis of symmetry of the cross-section (*Y* axis), the governing equation can be written as

$$m\frac{\partial^2 y}{\partial y^2}+\frac{\partial^2}{\partial x^2}\left(EI\frac{\partial^2 y}{\partial x^2}\right)=q\left(x,t\right). \tag{1}$$

In Eq. (1) the following notation is used: *m* is the mass per unit length, $y = y(x,t)$ the transverse displacement of any beam section at time *t*, *x* refers to the longitudinal coordinate, *E* is the Modulus of Elasticity, *I* the second moment of area of the cross-section and $q(x,t)$ stands for the distributed load per unit length acting at time *t* (positive if directed upwards).

The deformed shape is expressed as a linear combination of a family of sines and cosines $\phi_j(x)$ as in Eq. (2), where N_{mod} stands for the number of modes considered, $\xi_j(t)$ is the amplitude of the *j*th mode, and *L* is the length of the beam.

$$y(x,t)=\sum_{j=1}^{N_{\mathrm{mod}}}\xi_j(t)\cdot\phi_j(x)\quad\text{where}\quad\phi_j(x)=\begin{cases}\cos\left(\dfrac{j\pi x}{L}\right) & if\quad j=odd\ number\\ \sin\left(\dfrac{j\pi x}{L}\right) & if\quad j=even\,number\end{cases} \tag{2}$$

The loads are represented by means of Dirac delta functions acting at $x = Vt–d_k$, where *V* is the constant train speed, and d_k is the original distance from the *k*th load to the mid-span section of the beam. Thus, $q(x,t)$ may be expressed as follows:

$$q\left(x,t\right)=-\sum_{k=1}^{N_P}\left(H\left(t-\frac{d_k}{V}\right)-H\left(t-\frac{d_k+L}{V}\right)\right)P_k\delta\left(x-\left(Vt-d_k\right)\right), \tag{3}$$

where N_P is the total number of axle loads; P_k is the value of the *k*th load; and $H(t–t_0)$ is the Heaviside unit function acting at time t_0. When Eqs. (2) and (3) are introduced in Eq. (1), and multiplication by the *n*th function $\phi_n(x)$ and integration along the span *L* are carried out, the *n*th modal equation of motion is obtained. To this end, the mass per unit length *m* and the flexural stiffness *EI* are assumed to be constant along the beam. Introducing a modal viscous damping ratio ζ_n, the modal equation of motion is expressed as

$$\ddot{\xi}_n\left(t\right)+2\zeta_n\omega_n\dot{\xi}_n\left(t\right)+\omega_n^2\xi_n\left(t\right)=\frac{-2}{mL}\sum_{k=1}^{N_P}\left(H\left(t-\frac{d_k}{V}\right)-H\left(t-\frac{d_k+L}{V}\right)\right)P_k\cos\frac{n\pi\left(Vt-d_{k)}\right)}{L}, \tag{4}$$

where over-dots indicate differentiation with respect to time, and ω_n represents the *n*th circular frequency of the main beam in rad/s

$$\omega_n = \left(\frac{n\pi}{L}\right)^2 \sqrt{\frac{EI}{m}}. \tag{5}$$

3.2 Governing equations of the beam equipped with fluid viscous dampers and subjected to moving loads

In this section the equations of motion of the double-beam system are formulated as the auxiliary beam is connected to the main one through the dampers distribution.

The auxiliary beam is partially clamped, therefore, the boundary conditions of the secondary beam are considered to be simply supported with two identical rotational springs at both ends. The partial differential equation governing the flexural behaviour of the auxiliary beam has the same general expression than that of a simply supported element Eq. (1).

When the auxiliary beam is connected to the main one by means of the FVDs, the equations of motion must be suitably modified. In practical applications, resonance induced by constant moving loads is a problem of bridges subjected to the passage of fast trains. Museros and Alarcón [34] show that resonance of the second bending mode can take place in certain cases but, in single-track bridges it is most likely that resonance will be related to oscillations of the first bending mode. This is a consequence of the maximum speed attainable by modern high-speed trains. Under such circumstances, the influence of modes other than the one undergoing resonance can be disregarded for the computation of the main beam response.

The oscillations of the first mode of the main beam at resonance tend to create a symmetric distribution of dampers forces with respect to the mid-span section. These forces excite the movement of the auxiliary beam which, consequently, can be initially analysed only taking into account the contribution of its first bending mode as well. The viability of disregarding the second and higher modes of the beams in the calculation of the optimal parameters of the damping system is subsequently verified in section 5.

If the deformed shape of the auxiliary beam is expressed as the product of a modal amplitude times its first modal shape:

$$y(x,t) = \xi_1(t)\cdot\phi_1(x) = \xi_1(t)\cdot\left(\frac{\cosh\left(\frac{\beta\cdot L}{2}\right)\cdot\cos(\beta\cdot x)}{\cosh\left(\frac{\beta\cdot L}{2}\right)-\cos\left(\frac{\beta\cdot L}{2}\right)} - \frac{\cos\left(\frac{\beta\cdot L}{2}\right)\cdot\cosh(\beta\cdot x)}{\cosh\left(\frac{\beta\cdot L}{2}\right)-\cos\left(\frac{\beta\cdot L}{2}\right)}\right) \tag{6}$$

where β is:

$$\beta = \sqrt[4]{\frac{\omega_1^{\ 2}\cdot m}{E\cdot I}}. \tag{7}$$

In expression (7) ω_1 represents the first circular frequency of a simply-supported beam with rotational springs, in rad/s, which can be computed from the lowest root of the frequency equation:

$$\begin{aligned} &-\frac{(\beta L)^2}{4}\sinh(\beta L)\sin(\beta L) + \bar{K}\beta L\sinh(\beta L)\cos(\beta L) - \\ &\qquad -\bar{K}\beta L\cosh(\beta L)\sin(\beta L) + 2\bar{K}^2\cosh(\beta L)\cos(\beta L) - 2\bar{K}^2 = 0 \end{aligned} \tag{8}$$

being $\bar{K}$ a stiffness ratio between the rotational springs constants and the beam bending stiffness defined as

$$\bar{K} = \frac{KL}{4EI}. \tag{9}$$

Considering therefore only the contribution of the fundamental modes of both beams, the resulting equations of motion of the double-beam system linked by the distribution of the dampers in modal space are as follows:

$$\tilde{m}_B\ddot{\xi}_B(t)+2\zeta_B\omega_B\tilde{m}_B\dot{\xi}_B(t)+C_D^{BB}\dot{\xi}_B(t)-C_D^{Bb}\dot{\xi}_b(t)+\tilde{K}_B\xi_B(t)=q(x,t) \tag{10a}$$

$$\tilde{m}_b\ddot{\xi}_b(t)+2\zeta_b\omega_b\tilde{m}_b\dot{\xi}_b(t)+C_D^{bb}\dot{\xi}_b(t)-C_D^{Bb}\dot{\xi}_B(t)+\tilde{K}_b\xi_b(t)=0 \tag{10b}$$

$$q(x,t)=-\sum_{k=1}^{N_p}\left(H\left(t-\frac{d_k}{V}\right)-H\left(t-\frac{d_k+L_B}{V}\right)\right)P_k\cos\frac{n\pi(Vt-d_k)}{L_B} \tag{10c}$$

The notation in Eq. (10) is analogous to previous equations but with superscripts and subscripts *B* and *b*, which are included to indicate magnitudes associated to the main and auxiliary beam, respectively. Moreover, in equation (10):

$\tilde{m}_B=\dfrac{m_BL_B}{2}$ is the first modal mass for the main beam (11)

$\tilde{K}_B=\dfrac{\omega_B^2m_BL_B}{2}$ is the first modal stiffness for the main beam (12)

$\tilde{m}_b=m_b\cdot c$ is the first modal mass for the auxiliary beam, where: (13)

$$c=\frac{L_b\cdot\left[2\gamma+\gamma\cos\gamma+\cosh\gamma(\gamma-\sin\gamma)-\sin\gamma-(1+\cos\gamma)\sinh\gamma\right]}{4\gamma\left[\cos\left(\frac{\gamma}{2}\right)-\cosh\left(\frac{\gamma}{2}\right)\right]^2} \tag{14}$$

$$\gamma=\beta L_b \tag{15}$$

$$\tilde{K}_b=\left(\frac{\gamma}{L_b}\right)^4\cdot c\cdot E_b\cdot I_b \tag{16}$$

$$C_D^{BB}=\sum_{i=1}^{N_D}C_{Di}\cdot\left(\cos\left(\frac{\pi x_{Di}^B}{L_B}\right)\right)^2 \tag{17}$$

$$C_D^{Bb}=\sum_{i=1}^{N_D}C_{Di}\cdot\cos\left(\frac{\pi x_{Di}^B}{L_B}\right)\cdot\left[A\cdot\cosh\left(\frac{\gamma\cdot x_{Di}^b}{L_b}\right)+B\cdot\cos\left(\frac{\gamma\cdot x_{Di}^b}{L_b}\right)\right] \tag{18}$$

$$C_D^{bb}=\sum_{i=1}^{N_D}C_{Di}\cdot\left[A\cdot\cosh\left(\frac{\gamma\cdot x_{Di}^b}{L_b}\right)+B\cdot\cos\left(\frac{\gamma\cdot x_{Di}^b}{L_b}\right)\right]^2 \tag{19}$$

Notice that parameter γ is a function of the quotient between the auxiliary partially clamped beam circular frequency and the same beam frequency with simply-supported end conditions:

$$\gamma=\beta L_b=\pi\sqrt{\frac{\omega_b}{\omega_{b,ss}}} \tag{20}$$

In expressions (17), (18) and (19), C_{Di} is the constant of the *i*th damper. The location of the *i*th damper is designated as x^B_{Di} along the X^B axis of the main beam, and as x^{b}_{Di} along the X^b axis of the auxiliary beam. The significance of parameters A and B is:

$$A = \frac{-\cos\left(\frac{\gamma}{2}\right)}{\cosh\left(\frac{\gamma}{2}\right) - \cos\left(\frac{\gamma}{2}\right)} \qquad B = \frac{\cosh\left(\frac{\gamma}{2}\right)}{\cosh\left(\frac{\gamma}{2}\right) - \cos\left(\frac{\gamma}{2}\right)} \tag{21}$$

From Eqs. (10) it can be seen that, if the modal system of equations is written in matrix form, the load term associated to the forces exerted by the FVDs gives rise, in general, to a full damping matrix.

3.3 Nondimensional formulation of the system under harmonic excitation

This article focuses on the reduction of the resonant response of beams or bridges, and therefore the system shown in Fig. 2 will first be analysed under the action of a harmonically varying force applied at the mid-span section of the main beam (see Fig. 4a). This kind of excitation captures the essential features of the system response at resonance.

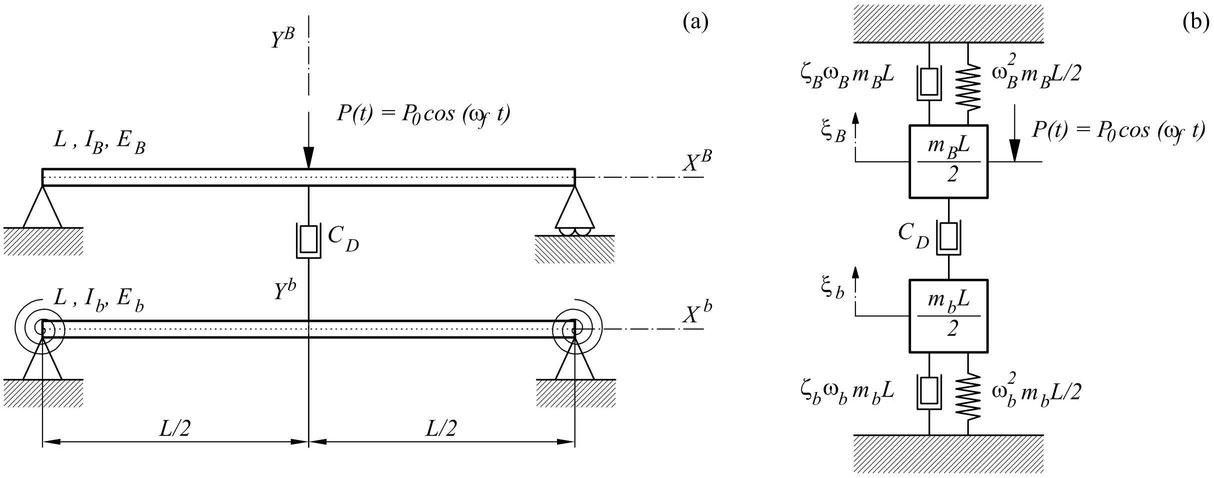

Figure 4: (a) Double-beam system under harmonic excitation applied at mid-span. (b) Equivalent 2dof system in modal space.

In what follows, it will be assumed that the lengths of both beams are equal, $L_B = L_b = L$ and the main and auxiliary beams are vertically aligned so that $x^B_{Di} = x^b_{Di}$, $i = 1, 2, \ldots N_D$. These hypotheses are the most relevant ones for real applications because it is most likely that in actual bridges, the auxiliary beam or beams are supported at the original abutments or close to them. If only the first mode of both beams is taken into account, any number of FVDs located at different sections is equivalent to a single equivalent FVD located at mid-span with equivalent damping constant:

$$C_D = \sum_{i=1}^{N_D} C_{Di} \cdot \left(\cos\left(\frac{\pi x^B_{Di}}{L_B}\right)\right)^2 \tag{22}$$

Under the aforementioned circumstances, the response in terms of modal amplitudes corresponds to that of the two-degree-of-freedom (2dof) system shown in Fig. 4b, where ξ_B and ξ_b, are the first modal amplitudes of the main and auxiliary beam, respectively.

The equations of motion of the system may be expressed as:

$$\begin{bmatrix} \tilde{m}_B & 0 \\ 0 & \tilde{m}_b \end{bmatrix} \cdot \begin{pmatrix} \ddot{\xi}_B \\ \ddot{\xi}_b \end{pmatrix} + \begin{bmatrix} 2\zeta_B \omega_B \tilde{m}_B + C_D^{BB} & -C_D^{Bb} \\ -C_D^{Bb} & 2\zeta_b \omega_b \tilde{m}_b + C_D^{bb} \end{bmatrix} \cdot \begin{pmatrix} \dot{\xi}_B \\ \dot{\xi}_b \end{pmatrix} + \begin{bmatrix} \tilde{K}_B & 0 \\ 0 & \tilde{K}_b \end{bmatrix} \cdot \begin{pmatrix} \xi_B \\ \xi_b \end{pmatrix} = \begin{pmatrix} -P_0 \cos\left(\omega_f t\right) \\ 0 \end{pmatrix} \tag{23}$$

In Eq. (23) P_0 and ω_f are the amplitude and the forcing frequency of the excitation, respectively. In order to solve Eq. (23) the following dimensionless ratios are defined:

$$\text{Frequency ratio: } \eta = \omega_b / \omega_B \tag{24a}$$

$$\text{Excitation frequency ratio: } \Omega = \omega_f / \omega_B \tag{24b}$$

$$\text{Mass ratio: } \mu = m_b / m_B \tag{24c}$$

$$\text{Supplemental damping ratio: } \zeta_D = C_D / \left(m_B L \omega_B\right) \tag{24d}$$

Moreover, when there is only a single equivalent FVD located at mid-span, with $x_D^B = x_D^b = 0$ parameters C_D^{BB}, C_D^{Bb} and C_D^{bb} become equal:

$$C_D^{BB} = \sum_{i=1}^{N_D} C_{Di} \cdot \left(\cos\left(\frac{\pi x_{Di}^B}{L_B} \right) \right)^2 = C_D \tag{25}$$

$$C_D^{Bb} = \sum_{i=1}^{N_D} C_{Di} \cdot \cos\left(\frac{\pi x_{Di}^B}{L_B} \right) \cdot \left[A \cdot \cosh\left(\frac{\gamma \cdot x_{Di}^b}{L_b} \right) + B \cdot \cos\left(\frac{\gamma \cdot x_{Di}^b}{L_b} \right) \right] = C_D \cdot \left[A + B\right] = C_D \tag{26}$$

$$C_D^{bb} = \sum_{i=1}^{N_D} C_{Di} \cdot \left[A \cdot \cosh\left(\frac{\gamma \cdot x_{Di}^b}{L_b} \right) + B \cdot \cos\left(\frac{\gamma \cdot x_{Di}^b}{L_b} \right) \right]^2 = C_D \cdot \left[A + B\right]^2 = C_D \tag{27}$$

Rewriting Eq. (23) in terms of the dimensionless ratios defined in Eqs. (24) yields

$$\begin{bmatrix} 1 & 0 \\ 0 & \mu \end{bmatrix} \cdot \begin{pmatrix} \ddot{\xi}_B \\ \ddot{\xi}_b \end{pmatrix} + 2\omega_B \begin{bmatrix} \zeta_B + \zeta_D & -\zeta_D \\ -\zeta_D & \zeta_b \eta \mu + \zeta_D \end{bmatrix} \cdot \begin{pmatrix} \dot{\xi}_B \\ \dot{\xi}_b \end{pmatrix} + \omega_B^2 \begin{bmatrix} 1 & 0 \\ 0 & \eta^2 \mu \end{bmatrix} \cdot \begin{pmatrix} \xi_B \\ \xi_b \end{pmatrix} = \begin{pmatrix} \dfrac{-2P_0}{m_B L} \cos\left(\omega_f t\right) \\ 0 \end{pmatrix} \tag{28}$$

Equation (28) written in terms of the nondimensional parameters is equivalent to that of the double-beam system with simply-supported end conditions in both beams previously analysed by the authors in reference [26]. Assuming again that the maximum response of the main beam will take place at resonance the transient solution is neglected and the dynamic amplification of the response is obtained for both beams as:

$$\begin{pmatrix} \bar{\xi}_B \\ \bar{\xi}_b \end{pmatrix} = \left(-\omega_f^2 \mathbf{M} + i \omega_f \mathbf{C} + \mathbf{K} \right)^{-1} \cdot \begin{pmatrix} \dfrac{-2P_0}{m_B L} \\ 0 \end{pmatrix} \tag{29}$$

where $\bar{\xi}_B$ and $\bar{\xi}_b$ are the complex amplitudes, **M**, **C** and **K** are the mass, damping and stiffness modal matrices from Eq. (28), and $i = \sqrt{-1}$. The moduli of $\bar{\xi}_B$ and $\bar{\xi}_b$ give the amplitudes of the response. In order to obtain a dimensionless representation of the beams response, two modal amplifications are defined as the modulus of $\bar{\xi}_B$ and $\bar{\xi}_b$ divided by the static deflection caused by the concentrated load P_0 acting on the main beam

$$A_B = \frac{\left|\bar{\xi}_B\right|}{2P_0 / \left(\omega_B^2 m_B L\right)} \tag{30a}$$

$$A_b = \frac{\left|\bar{\xi}_b\right|}{2P_0 / \left(\omega_B^2 m_B L\right)} \tag{30b}$$

After some algebraic manipulation, the modal amplifications are obtained

$$A_B = \sqrt{\frac{4\Omega^2\left(\zeta_b \eta \mu + \zeta_D\right)^2 + \mu^2\left(\eta^2 - \Omega^2\right)}{E^2 + 4\Omega^2 F^2}} \tag{31a}$$

$$A_b = \frac{2\Omega\zeta_D}{\sqrt{E^2 + 4\Omega^2 F^2}} \tag{31b}$$

being

$$E = \mu\left(1-\Omega^2\right)\left(\eta^2-\Omega^2\right) + 4\Omega^2\left(\zeta_D^2 - \left(\zeta_B + \zeta_D\right)\left(\zeta_b \eta \mu + \zeta_D\right)\right) \tag{31c}$$

$$F = \left(1-\Omega^2\right)\left(\zeta_b \eta \mu + \zeta_D\right) + \mu\left(\zeta_B + \zeta_D\right)\left(\eta^2 - \Omega^2\right) \tag{31d}$$

The main beam modal acceleration is also of great interest because of its relation with ballast stability, as mentioned in section 1. In the steady-state the amplitude of the acceleration a_B is

$$a_b = \left|\overline{\xi}_B\right| \omega_f^2 = \frac{2P}{m_B L}\Omega^2 A_B \tag{32}$$

Eq. (31) shows that the amplification of the main beam response A_B, depends on the following six parameters: Ω, η, μ, ζ_D, ζ_b, ζ_B. Additionally, from Eq. (32) it can be seen that the modal acceleration of the main beam is inversely proportional to its total mass $m_B L$. The behaviour of the system in terms of these parameters is analysed in detail in the following section.

4 RETROFITTING SYSTEM OPTIMISATION

4.1 Optimal value of the supplemental damping ratio

The key variables of the problem that should be minimised are the main beam dynamic amplification and modal acceleration, A_B and a_B. In order to visualise how the governing parameters affect these magnitudes and determine what is the best selection of the auxiliary beam and damper for a particular bridge, a number of plots are included in Fig. 5.

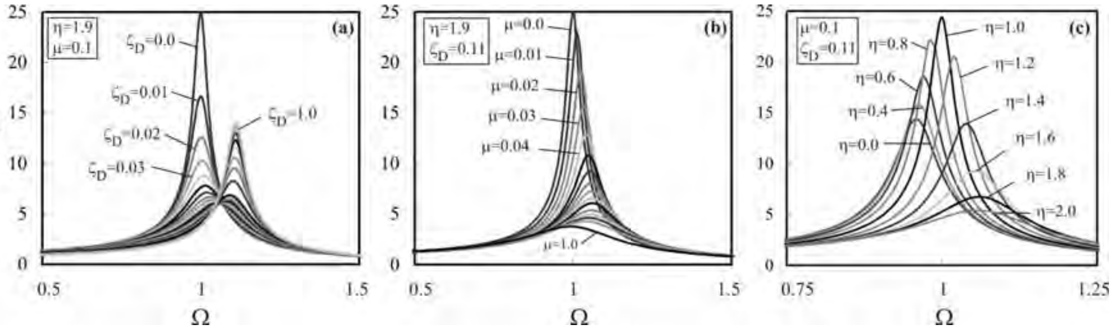

Figure 5: Main beam amplification A_B versus Ω for different values of ζ_D, μ and η.

The plots illustrate the evolution of the main beam resonant amplification with μ, η, and ζ_D. In all the cases structural dampings of the main and secondary beams are 2% and 0.5%, respectively. In Fig. 5a μ and η are fixed and equal to 0.1 and 1.9, respectively. In this plot, for a particular bridge and auxiliary beam the resonant response of the former is analyzed as the damper constant increases. As it can be seen, there is an optimum value of the damper constant which, for a particular auxiliary beam, leads to the minimum response of the main element. In Fig. 5b it is shown how the main beam amplification at resonance monotonically diminishes with the auxiliary beam mass for fixed values of this element natural frequency and damper constant. Finally, in Fig. 5c the evolution of A_B with the frequency ratio η of the two beams fundamental frequency is evaluated. From the analysis of this plot it can be concluded that in order for the retrofitting system to effectively reduce the dynamic response of the main beam, η has to be higher than one, that is, the secondary beam natural frequency must exceed the main beam frequency. The system hardly dissipates energy when $\eta=1$. For values of $\eta<1$ the secondary beam and damper behave in a certain way as a Tuned Mass Damper and the main beam resonant response partially reduces but this reduction can reach much higher levels for values of $\eta>1$. When η tends to infinity, A_B monotonically decreases as in this case the damper lower end tends to be attached to a fixed reference (the same occurs when $\mu\rightarrow\infty$). From this situation the clear advantage of partially clamping the auxiliary beam ends is evident as it leads to an increase of the secondary beam frequency and a reduction of the main beam resonant response.

In conclusion, as there are not optimal values of η and μ, or in other words, the dissipation capacity of the system increases with increasing values of any of these two parameters, the design strategy should be to select the smallest auxiliary beam such that with its associated optimal damper provides enough energy dissipation to achieve the desired target performance. In what follows, a closed form expression for the optimal supplemental damping ratio ζ_D is obtained.

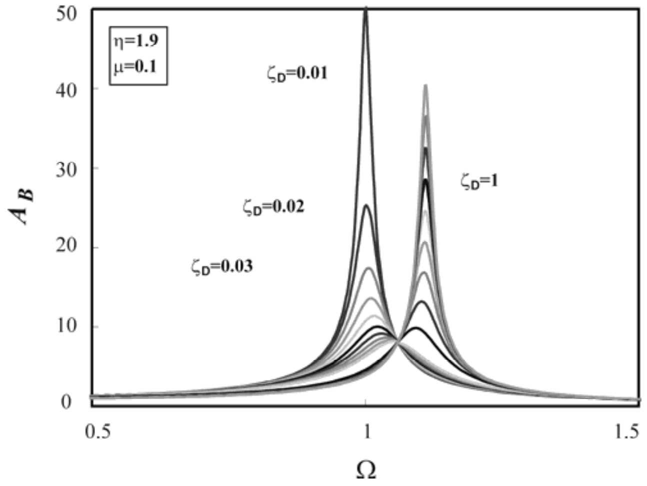

Figure 6: Main beam amplification A_B versus Ω for different values of ζ_D neglecting structural damping.

From the works of the European Rail Research Institute [1] it can be concluded that damping ratios in modern railway bridges are usually small, of the order of 1% or 2%, or even smaller in composite or metallic bridges. Therefore, in most practical cases an approximate solution to the problem can be obtained by assuming that structural damping is negligible in comparison with the dissipation introduced by the external FVD. This hypothesis allows the computation of a closed form expression for the optimal value of ζ_D. The subsequent numerical examples will prove the soundness of this approach. Neglecting structural damping, that is $\zeta_B = \zeta_b = 0$, Eqs. (31a), (31c) and (31d) transform into

$$A_B = \sqrt{\frac{4\Omega^2\zeta_D^2 + \mu^2\left(\eta^2-\Omega^2\right)^2}{\left(1-\Omega^2\right)^2\mu^2\left(\eta^2-\Omega^2\right)^2 + 4\Omega^2\zeta_D^2\left[1-\Omega^2+\mu\left(\eta^2-\Omega^2\right)\right]^2}} \tag{33}$$

Comparing Figs. 5a and 6 the effect of structural damping on the response can be observed.

The maximum amplification for low and high values of ζ_D at resonance reaches a much higher level when structural damping is neglected as in Fig. 6, but two important facts must be highlighted. First, the difference between the maximum amplifications is much lower when ζ_D takes the optimal value. This fact reveals that, if structural damping is low and the optimal value of ζ_D is selected, the greater part of the energy at resonance is dissipated through the FVD. Secondly, if structural damping is neglected as in Fig. 6, A_B is independent of ζ_D at the value of Ω corresponding to the minimum maximum. This fact permits the computation of the excitation frequency ratio at the minimum maximum Ω_R^*:

$$\Omega_R^* = \frac{1}{2+\mu}\sqrt{\left(2+\mu\right)\left(2+\mu\eta^2\right)} \tag{34}$$

and the subsequent derivation of closed-form expressions for the optimal damping ratio ζ_D minimising the main beam amplification and acceleration responses:

$$\frac{\partial A_B}{\partial\Omega}\left(\Omega=\Omega_R^*, \zeta_D=\zeta_{D,A}^*\right)=0 \quad \rightarrow \quad \zeta_{D,A}^* = \frac{\left(\eta^2-1\right)\mu}{\sqrt{4+6\mu+2\mu^2+2\mu\eta^2+3\mu^2\eta^2+\mu^3\eta^2}} \tag{35a}$$

$$\frac{\partial a_B}{\partial\Omega}\left(\Omega=\Omega_R^*, \zeta_D=\zeta_{D,a}^*\right)=0 \quad \rightarrow \quad \zeta_{D,a}^* = \frac{\left(\eta^2-1\right)\mu}{\sqrt{4+2\mu+6\mu\eta^2+3\mu^2\eta^2+2\mu^2\eta^4+\mu^3\eta^4}} \tag{35b}$$

Substituting the damping ratios given by Eqs. (35) into Eq. (24d), the associated optimal damper constants are obtained when structural damping is neglected. These equations provide optimum *equivalent* dampers, which are related to a particular longitudinal distribution of FVDs as per (22). In reference [26] a comprehensive analysis proving the adequacy of expressions (35) when structural damping is not neglected has been performed under harmonic conditions. Finally, in the example of a bridge retrofitted with the system proposed herein that is included in section 5 it is proven that these expressions predict dampers constants real optima with a great degree of accuracy under railway traffic, accounting for modal contributions higher than the fundamental one and including the presence of structural damping.

4.2 Effect of partial rotational restriction at the auxiliary beam supports

In this section the effect of partially restraining the auxiliary beam ends is analysed in terms of the reduction of the main beam resonant response attained as that obtained with a simply-supported auxiliary element. In order to isolate the boundary conditions alteration effect from the secondary beam size, the frequency ratio η is expressed as:

$$\eta = \frac{\omega_{b,ss}}{\omega_B}\left(\frac{\gamma}{\pi}\right)^2 = \eta_{ss,B}\left(\frac{\gamma}{\pi}\right)^2 \tag{36}$$

where $\omega_{b,ss}$ is the auxiliary beam circular frequency with hypothetical simply-supported end conditions and γ varies from π in the simply-supported case to 4.73004074 in the clamped case. In Fig. 7a curves of A_B associated to optimal values of the damping ratio $\zeta_{D,A}^*$ versus Ω have been plotted for a particular pair of beams (μ=0.1, $\eta_{ss,B}$=1.2, ζ_B=2% and ζ_b=0.5%) for increasing levels of rotational restriction of the secondary beam.

In order to measure these levels, instead of using the frequency parameter γ, the increase experimented by the auxiliary beam fundamental frequency with respect to the simply-supported case is employed defining to this end the following ratio:

$$\eta_{b,ss} = \frac{\omega_b}{\omega_{b,ss}} = \left(\frac{\gamma}{\pi}\right)^2 \tag{37}$$

Values of $\eta_{b,ss}$ increase from unity when the beam is simply supported towards 2.267 in the ideal case of a perfectly clamped beam. In order to be conservative it is considered that with nowadays constructive technologies and materials the maximum increase in the secondary beam frequency that can be attained clamping it is 1.5 times. In Fig. 7a $A_B(\Omega)$ has been plotted in the unretrofitted case for comparison purposes. The remaining curves correspond to the minimum response of the main beam at resonance (for optimal damping values $\zeta^*_{D,A}$) for a particular pair of beams and increasing values of γ (and therefore $\eta_{b,ss}$). The amplification at resonance is reduced from 25 to 16.3 when the auxiliary beam is simply supported, which entails a 34.8% reduction with respect to the unretrofitted case. This reduction increases with the restriction of the beam end rotations achieving 73.4% for $\eta_{b,ss}$=1.5. In other words, the main beam response is reduced in more than twice when, due to the auxiliary beam rotational springs stiffenning, the fundamental frequency of this element increases 50%. As we move towards the ideal case of a doubly clamped beam, this reduction tends to 88.6%. The interesting side of this alternative when compared to the simply-supported case previously analysed by the authors, is that the auxiliary beam size if partially clamped can be drastically reduced for the same main beam dynamic performance. If the beams are to be installed under the bridge deck in a practical application this is a crucial issue in order to minimise the free space occupied with the retrofit. Fig. 7b is similar to Fig. 7a but in this case the natural frequency of the secondary beam without restraining the ends rotations is higher ($\eta_{ss,B}$ = 1.6).

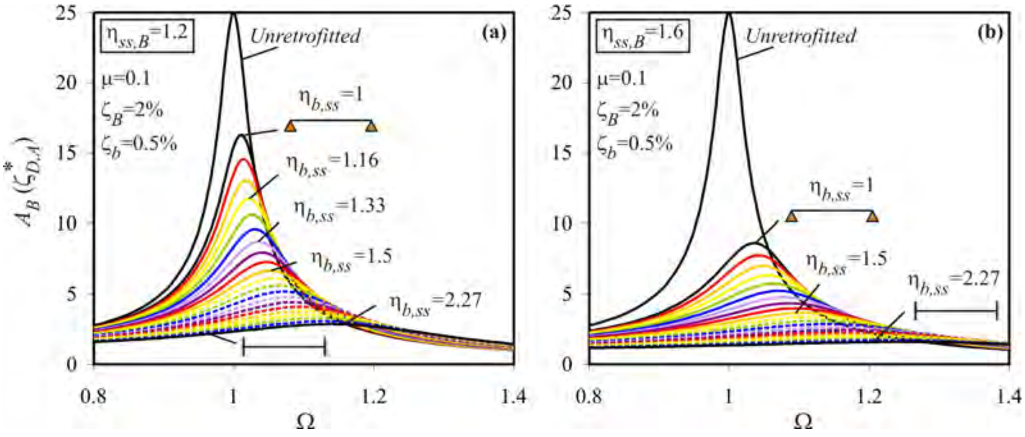

Figure 7: Main beam amplification A_B associated to the optimal damping ratio versus Ω for different clamping states of the auxiliary beam.

In order to visualize how the main beam response at resonance evolves with a particular auxiliary beam, always combined with the optimal equivalent damper, as the end rotational stiffness increases for different values of $\eta_{ss,B}$ the ratio R_{max} is defined measuring the reduction of the main beam maximum response achieved with the retrofit when compared to the unretrofitted case:

$$R_{max}(\%) = \frac{A^{\max}_{B,unret} - A^{\max}_{B}\left(\zeta_D = \zeta^*_{D,A}\right)}{A^{\max}_{B,unret}} \cdot 100 \tag{38}$$

where $A^{\max}_{B,unret}$ is the amplification of the main beam at resonance in the unretrofitted case and $A^{\max}_{B}\left(\zeta_D = \zeta^*_{D,A}\right)$ is the amplification of the main beam retrofitted with a particular auxiliary beam in the optimal case. In other words, $A_B^{\max}\left(\zeta_D=\zeta_{D,A}^*\right)$ is the minimum response of the main beam at resonance that can be obtained with a particular auxiliary beam. This variable is calculated fixing the value of $\eta_{ss,B}$, i.e. for a particular auxiliary beam with a particular natural frequency and lineal mass and recalculated as the rotational restriction at the beam ends increases towards the fully clamped case. Therefore only the degree of clamping of the auxiliary beam is modified. In Fig. 8, plots (a), (b), (c) and (d) correspond to values of $\eta_{ss,B}$ {1, 1.2, 1.4, 1.6}and in each graph each curve has been calculated with a different level of the main beam structural damping.

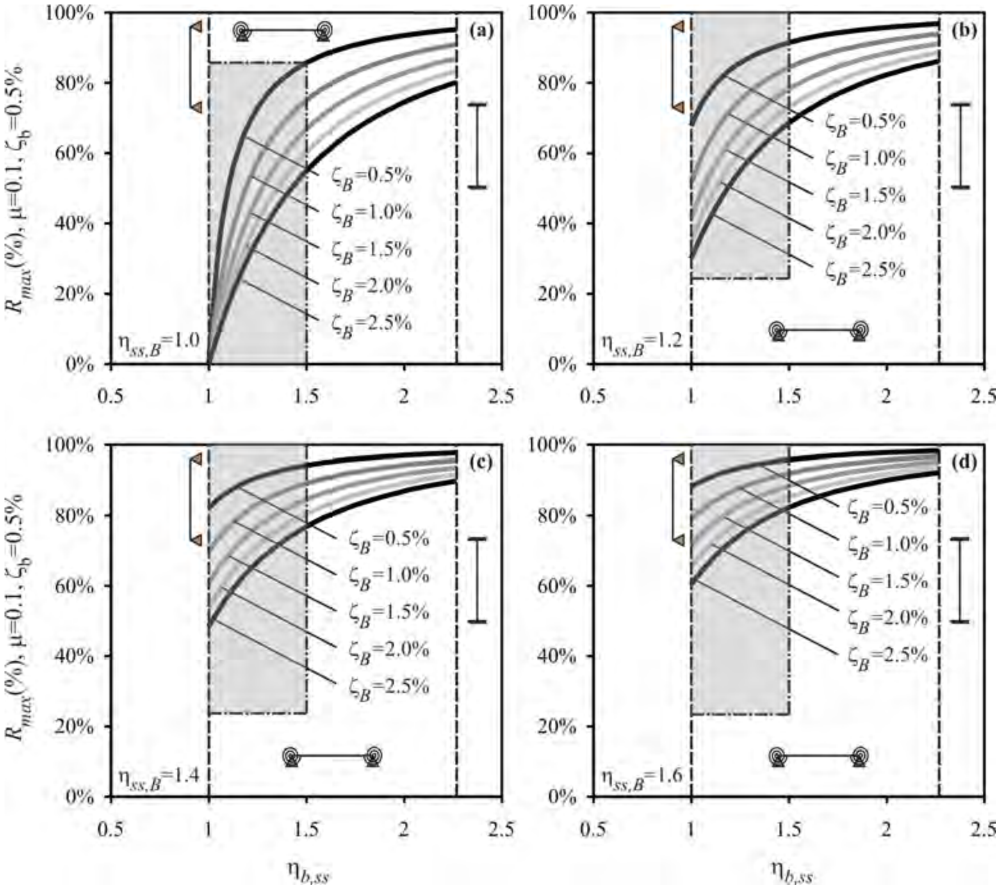

Figure 8: Maximum reduction with respect to the unretrofitted case vs. auxiliary beam frequency increase $\eta_{b,ss}$ due to supports rotational restriction.

In graph (a) $\eta_{ss,B}$=1, therefore prior to starting to clamp the secondary beam both beams have the same natural frequency. Due to this fact the retrofitting system efficiency is practically inexistent (see Fig. 5c) and the reduction of the main beam response is almost null. That is why for $\eta_{b,ss}$=1 (auxiliary beam simply-supported) all the curves tend to R_{max}=0. As the rotational restriction at the ends increases and therefore $\eta_{b,ss}$ raises from 1 towards 2.267 (perfectly clamped case) the reduction of the main beam maximum response with respect to the unretrofitted situation drastically increases, especially for low levels of structural damping of the super-structure. In fact if ζ_B=0.5% R_{max} increases from zero reduction in the simply-supported case to approximately 87% for $\eta_{b,ss}$=1.5, that is, when the natural frequency of the auxiliary beam is increased 1.5 times its initial value thanks to restraining the end rotations. In the remaining three cases a similar tendency is observed although the results are less impressive as the retrofitting system effect on the main beam is already better in the simply-supported case.

5 INTRODUCTION OF RAILWAY TRAFFIC EXCITATION

In the present section the effectiveness of the proposed solution and the adequacy of expressions (35) which provide the optimal dampers for a particular auxiliary beam are evaluated under railway traffic. To this end the dynamic performance of a single track bridge retrofitted with the partially clamped auxiliary beam system is investigated under the circulation of trains of moving loads which excite resonance situations in the superstructure.

In what follows the dynamic performance of a 15 m bridge is investigated using a planar FE model as the one shown in Fig. 2. The upper beam, which represents the deck, has a fundamental frequency f_{B1}=8.92 Hz and a linear mass m_B=10000 kg/m. The auxiliary beam is considered a steel element with a hollow rectangular cross-section, having $L_B=L_b=L$ and $E_b=2.1\cdot10^{11}$ N/m^2. The external dimensions of the auxiliary beam are $b \times h$ (width × height) and its constant thickness is e. Thus, the second moment of area is $I=(bh^3-(b-2e)(h-2e)^3)/12$. The mass per unit length is $m_b=\rho_b(bh-(b-2e)(h-2e))$, where ρ_b=7850 kg/m^3 is the mass density of steel. Respectively, linear and quadratic variations of b and e in terms of h are adopted

$$b(h) = a \times h \qquad \text{for } a = 0.6 \tag{39}$$

$$e(h) = e_0 + e_1 \times h + e_2 \times h^2 \quad \text{for } \; e_0 = 2.14\times10^{-2}\,\text{m},\; e_1 = 7.86\times10^{-3},\; e_2 = 1.07\times10^{-2}\,\text{m}^{-1} \tag{40}$$

The dynamic response of the bridge retrofitted with a particular auxiliary beam with h=0.80 m is evaluated under the circulation of the eighth train of the High Speed Load Model –A (HSLM-A8) defined in Eurocode [35] using a moving load model. The degree of partial restriction of the auxiliary beam end section rotations is considered to be such that the fundamental frequency of the element is increased 1.5 times with respect to the simply-supported case. This corresponds to a rotational stiffness of $K=4.5\cdot10^8$ Nm leading to a fundamental frequency of the auxiliary beam f_{b1}=15.87 Hz. Three dampers are introduced linking the vertical motion of corresponding sections of the main and auxiliary beams. The response of the system is computed by Modal Superposition of the first three modes of the bridge and the first three modes of the auxiliary beam. Structural damping ratios of ζ_{Bi}=1.35% and ζ_{bi}=0.5% for i=1,2,3 are assumed for each element.

In first place the adequacy of the expressions derived in the harmonic case for the external optimal damping ratios (35) is evaluated. To this end the maximum vertical acceleration at the mid-span section of the bridge is calculated under the HSLM-A8 train for circulating velocities in the range [40, 125] m/s in steps of 0.5 m/s ([144, 450] km/h in steps of 1.8 km/h). The maximum response of the bridge retrofitted with the previously described beam is computed for several values of the dampers constants and plotted in terms of accelerations in Fig. 9. The bridge in the bare case (ζ_D=0%) experiments a second and a third resonance of its fundamental mode at the theoretical velocities

$$V^{RES}_{m=1,n=2} = \frac{d_k \cdot f_{B1}}{n}\cdot 3.6 = \frac{18\cdot 8.92}{2}\cdot 3.6 = 401.4 \text{ km/h} \tag{41}$$

$$V^{RES}_{m=1,n=3} = \frac{d_k \cdot f_{B1}}{n}\cdot 3.6 = \frac{18\cdot 8.92}{3}\cdot 3.6 = 267.6 \text{ km/h} \tag{42}$$

being d_k=18 m the characteristic distance (or distance causing resonance) of train HSLM-A8, m the mode number, n the resonance order (or number of oscillations completed by the upper beam between the passage of repetitive groups of axle loads separated d_k). The response of the bridge has been recalculated for increasing values of the external damping ratio and, therefore, of the individual dampers constants. If the three dampers are located at 0.25L, 0.5L and 0.75L the relation between the constants and ζ_D is given by

$$C_{Di} = \frac{1}{2} m_B L_B \omega_{B1} \zeta_D \quad \text{for} \quad i = 1, 2, 3 \tag{43}$$

being ω_{B1} the circular frequency of the bridge fundamental mode. As ζ_D increases the bridge response decreases, especially at resonance, and the resonant or critical velocity slightly shifts towards higher values. This kind of behaviour was already detected in the harmonic case (see Fig. 5a). When ζ_D reaches certain value the amplification at resonance starts to increase again. The theoretical optimal external damping ratio associated to the minimum acceleration at resonance has been calculated applying equation (35b) for η=1.779 and μ=0.066 (frequency and mass ratio for the particular case h=0.80 m and K=4.5·10^8 Nm) providing a value of $\zeta^*_{D,a} = 6.1\%$. In Fig. 9 the maximum acceleration of the bridge has been represented for this particular retrofitting level in red trace.

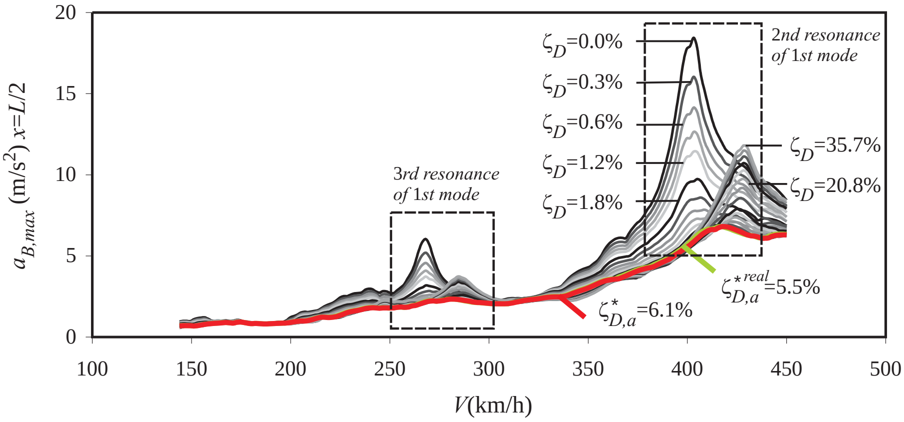

Figure 9: Maximum acceleration at bridge mid-span vs. velocity of train HSLM-A8 for different values of ζ_D.

As it can be observed equation (35b) provides a good estimate of the dampers constants real optima under the circulation of moving loads, accounting for the contribution of three modes of each beam and considering structural damping. Regarding the difference between optimal damping ratios $\zeta^*_{D,A}$ and acceleration $\zeta^*_{D,a}$ provided by equations (35a) and (35b) respectively, the former provides better estimates for the optimal dampers minimising the bridge response in terms of displacements and the latter does the same in terms of accelerations. Nevertheless the difference between both values is very small. Finally, the real value of the optimal external damping, $\zeta^{*real}_{D,a}$, has been obtained numerically as the one minimising the acceleration at the second resonance of the bridge fundamental mode being as $\zeta^{*real}_{D,a} = 5.5\%$. The bridge acceleration at mid-span for the real optimal dampers has been represented as well in green trace in Fig. 9. Even though there is a difference of 0.6% between the real and the theoretical optimal damping the difference in the bridge response is practically negligible as it can be seen when comparing the red and green curves in Fig. 9. In particular the maximum response of the bridge at the second resonance when retrofitted with the theoretical optimal dampers $a_{B,\max}\left(\zeta^*_{D,a} = 6.1\%\right) = 6.809\, m/s^2$ and when retrofitted with the real optimal dampers $a_{B,\max}\left(\zeta^{*real}_{D,a} = 5.5\%\right) = 6.801\, m/s^2$.

Finally, the possibility of retrofitting the 15 m bridge so that the structure accomplishes the Serviceability Limit State of vertical acceleration (3.5 m/s^2 for ballasted tracks) is envisaged. To this end two possibilities are considered and compared: (i) connecting to the bridge deck to a simply-supported auxiliary beam with its corresponding optimal dampers located at 0.25 L, 0.5 L and 0.75 L, and (ii) installing a partially clamped auxiliary beam with the same configuration of dampers. The aim of this analysis is to determine what would be the minimum size of the auxiliary beam needed to reduce the maximum acceleration of the bridge below 3.5 m/s^2 in each case. In the unretrofitted case the maximum acceleration of the bridge under the circulation of the HSLM-A8 train in the range of velocities [144, 450] km/h reaches 18.4 m/s^2. The steel box section beam previously described is considered for the retrofit. Beam section heights starting from 1.0 m and increasing in 10 cm increments are first considered in the simply-supported case. For each beam, nondimensional parameters μ and η are calculated and the theoretical optimal damping ratio $\zeta^*_{D,a}$ is obtained as per Eq. (35b). From this value the dampers constants are determined and the bridge dynamic response after the retrofit is computed. In Table 1 a summary of the retrofitting system parameters along with the maximum response of the bridge that takes place for each particular retrofit has been included.

h (m)	BC	K (Nm)	f_{b1} (Hz)	η	μ	$\zeta^*_{D,a}$ (%)	$a_{B,max}$ (m/s^2)
1.3	SS	---	17.20	1.928	0.155	14.21%	3.52
1.2	SS	---	15.87	1.779	0.155	10.61%	4.41
1.1	SS	---	14.54	1.630	0.155	7.45%	5.99
1.0	SS	---	13.20	1.480	0.155	4.80%	7.72
1.3	EC	2.80E+09	25.90	2.904	0.155	28.38%	2.59
1.2	EC	2.00E+09	23.80	2.668	0.155	23.23%	2.85
1.1	EC	1.47E+09	21.91	2.457	0.155	18.43%	3.17
1.0	EC	1.02E+09	19.90	2.231	0.155	13.72%	3.56

Table 1: Retrofit parameters.

In Table 1 BC, SS and EC stand for *Boundary Conditions*, *Simply-Supported* and *Elastically-Clamped*, respectively.

In Fig. (10a) the maximum acceleration of the bridge at mid-span for a simply-supported auxiliary beam of section heights varying from 1.0 m to 1.3 m has been represented.

It is important to stress that each auxiliary beam is combined with the dampers that lead to the super-structure minimum response, that is, with the optimal dampers. As it is shown a minimum height of 1.3 m is needed for the maximum acceleration to reduce until the limit 3.5 m/s^2 if the beam is simply-supported. The same calculations are repeated considering that the beam is partially clamped. The rotational stiffness is supposed to be the same at both ends and such that the fundamental frequency of the auxiliary beam increases 1.5 times its corresponding value in the simply-supported case. In Fig. (10b) the maximum acceleration of the bridge is plotted for each particular beam size in the elastically-clamped case. The response of the bridge drastically reduces for a particular retrofit if the auxiliary beam ends rotations are restrained. It can be observed that if the beam is partially clamped a beam with a section height of 1 m would be sufficient for the bridge to accomplish the Serviceability State of vertical acceleration, while in the simply-supported case a 1.3 m beam was needed.

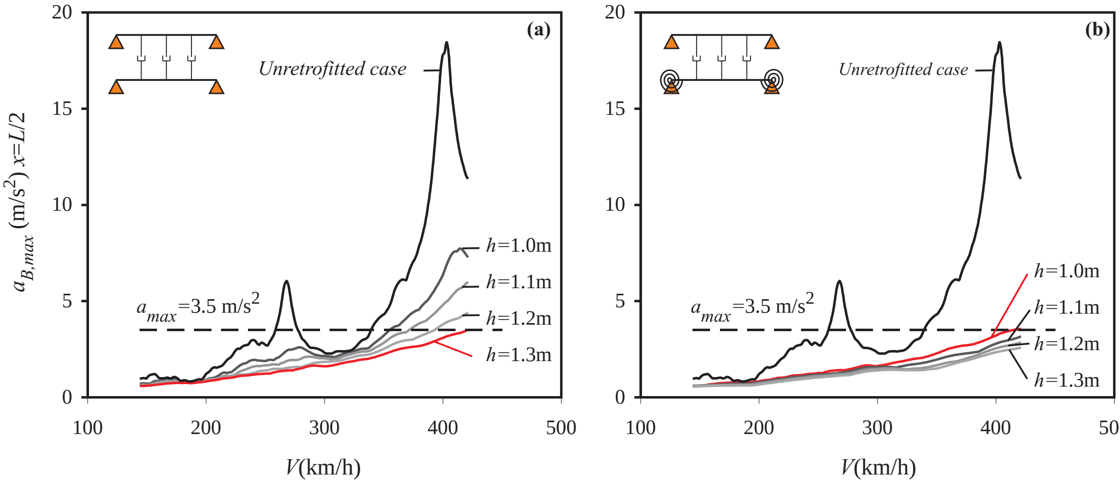

Figure 10: Maximum acceleration at bridge mid-span vs. velocity of train HSLM-A8 for different auxiliary beam sizes in the (a) simply-supported and (b) elastically clamped cases.

6 CONCLUSIONS

The dynamic performance of simply supported beams retrofitted with FVDs and subjected to moving loads has been evaluated. The main beam, which supports the passage of the loads, is connected to an auxiliary beam placed parallel to the former through a set of dampers linking the vertical motion of corresponding sections of the elements. The auxiliary beam is considered to be partially clamped at both ends. From the results obtained herein, the following conclusions can be derived:

- (i) The resonant vibrations that may appear in simply supported beams when subjected to moving loads can be drastically reduced with the damping system proposed herein.
- (ii) For a particular auxiliary beam, there exists an optimum value of the FVD constants that minimise the main beam response.
- (iii) The main beam response monotonically reduces with the auxiliary beam mass and natural frequency, but, in order for the dampers to effectively dissipate energy, the auxiliary beam fundamental frequency must exceed the main beam modal frequency which contribution is to be reduced.
- (iv) The design strategy should be to select the smallest auxiliary beam such that when associated with its corresponding optimal FVDs leads to the desired system performance.
- (v) Partially restraining the rotation of the auxiliary beam supports leads to an important reduction of the main beam response at resonance when compared to the simply-supported case. This permits to reduce the size of these elements which are to be installed underneath the deck in general applications.
- (vi) Analytical expressions for the optimal damper constants are provided which provide very accurate results as long as the maximum response of the main beam in the range of evaluated velocities occurs at resonance.

- (vii) With the system proposed in this article the FVDs need not interact with the upper side of the bridge. This allows existing railway bridges to be retrofitted while keeping the line in operation.
- (viii) The damping system and optimal damper expressions presented here may apply to other situations where simply supported beams vibrate at resonance due to different causes.

REFERENCES

[1] European Rail Research Institute, *PontsRails pour vitesses > 200 km/h. Rapport final*. ERRI D-214/RP9, 2000.

[2] Ministerio de Fomento, *Instrucción sobre las acciones a considerar en el proyecto de puentes de ferrocarril* (IAPF-07). Ministerio de Fomento, 2007.

[3] Fryba L. *Dynamics of bridges under moving loads. Past, present and future*. Workshop: Dynamics of High-Speed railway bridges, R. Delgado, R. Calçada, J.M. Goicolea and F. Gabaldón eds., Porto, 2005; 25–44.

[4] Mancel F. *Cedypia: Analytical software for calculating dynamic effects on railway bridges*. In: Proc. Fourth European conference on Structural Dynamics (Eurodyn’99), Vol. 2, Prague, 1999; 675–680.

[5] Kwon HC, Kim MC, Lee IW. *Vibration control of bridges under moving loads*. Comput Struct 1998; 66:473–480.

[6] Wang JF, Lin CC, Chen BL, *Vibration suppression for High-Speed railway bridges using tuned mass dampers*. Int J Solids Struct 2003; 40:465–491.

[7] Yau JD, Yang YB. *Vibration reduction for cable-stayed bridges travelled by High-Speed trains*. Finite Elem Anal Des 2004; 40:341–359.

[8] Yau JD, Yang YB. *A wideband MTMD system for reducing the dynamic response of continuous truss bridges to moving train loads*. Eng Struct 2004; 26:1795–1807.

[9] Yau JD. *Train-induced vibration control of simple beams using string-type tuned mass dampers*. J Mech 2007; 4:329–340.

[10] Li J, Su M, Fan L. *Vibration control of railway bridges under High-Speed trains using multiple tuned mass dampers*. J Bridge Eng 2005; 10:312–320.

[11] Samani F.S., Pellicano F., *Vibration reduction on beams subjected to moving loads using linear and nonlinear dynamic absorbers*. J Sound Vib 2009; 325:742–754.

[12] Minsili LS, Zhong T, Xia H, Manguelle DE. *Design and vibration control by friction dampers in truss bridges*. In: Proc. of the Second International Conference on Construction in Developing Countries: Challenges Facing the Construction Industry in Developing Countries 2002.

[13] Choo JF, Koh HM, Kang SC, Kim BS. *Vibration control of long-span High-Speed railway bridges under periodic moving loading using viscoelastic damper*. In: Structures for High-speed Railway Transportation, International Association for Bridge and Structural Engineering 2003.

[14] Vu HV, Ordóñez AM, Karnopp BH. *Vibration of a double-beam system*. J Sound Vib 2000; 229:807–822.

[15] Abu-Hilal M. Dynamic response of a double Euler-Bernoulli beam due to a moving constant load. J Sound Vib 2006; 297:477–491.

[16] *Oniszczuk Z. Free transverse vibrations of elastically connected simply supported double-beam complex system*. J Sound Vib 2000; 232:387–403.

[17] Oniszczuk Z. *Forced transverse vibrations of an elastically connected complex simply supported double-beam system*. J Sound Vib 2003; 264:273–286.

[18] Oniszczuk Z. *Free transverse vibrations of an elastically connected rectangular simply supported double-beam plate system*. J Sound Vib 2000; 236:595–608.

[19] Oniszczuk Z. *Forced transverse vibrations of an elastically connected complex rectangular simply supported double-beam plate system*. J Sound Vib 2004, 270:997–1011.

[20] Moliner E, Martínez-Rodrigo MD, Lavado J. *Vibration control of high-speed railway bridges using viscoelastic dampers*. In: Proc. of the Eleventh International Conference on civil, Structural and Environmental Engineering Computing 2007.

[21] Moliner E, Museros P, Martínez-Rodrigo MD. *Vibration control of high-speed railway bridges using viscoelastic dampers modelled by means of fractional derivatives*. In: Proc. of the International conference on noise and vibration engineering 2008, 2867-2877.

[22] Oliveto G, Santini A, Tripodi E. *Complex modal analysis of a flexural vibrating beam with viscous end conditions*. J Sound Vib 1997; 200:327–345.

[23] Greco A, Santini A. *Dynamic response of a flexural non-classically damped continuous beam under moving loadings*. Comput Struct 2002; 80:1945–1953.

[24] Taylor DP, Lee DA. *Frictionless damper*. United States Patent number 4.815.574, 1989.

[25] Martínez-Rodrigo MD. *Atenuación de vibraciones resonantes en puentes de ferrocarril de Alta Velocidad mediante amortiguadores fluido-viscosos*. PhD Thesis. Universidad Politénica de Valencia, 2009.

[26] Museros P, Martinez-Rodrigo MD. *Vibration control of simply supported beams under moving loads using fluid viscous dampers*. J Sound Vib 2007; 300:292–315.

[27] Martinez-Rodrigo MD, Museros P. *Optimal design of passive viscous dampers for controlling the resonant response of orthotropic plates under high-speed moving loads*. J Sound Vib 2010; doi:10.1016/j.jsv.2010.10.017.

[28] Martínez-Rodrigo MD, Lavado J, Museros P. *Dynamic performance of existing high-speed railway bridges under resonant conditions retrofitted with fluid viscous dampers*. Eng Struct 2010; 32:808–828.

[29] European Committee for Standardisation (CEN). *Eurocode: Basis of structural design. Annex A2: Application for bridges*. Final Draft prEN 1990 prAnnex A2 (pre-European Standard) 2002.

[30] Frýba L. *A rough assessment of railway bridges for high speed trains*. Eng Struct 2001; 23:548–556.

[31] Frýba L. *Dynamics of solids and structures under moving loads*. Thomas Telford, 1999.

[32] Olsson M. *On the fundamental moving load problem*. J Sound Vib 1991; 145: 299–307.

[33] Yang YB, Yau JD, Hsu LC. *Vibration of simple beams due to trains moving at high speeds*. Eng Struct 1997; 19: 936–944.

[34] Museros P, Alarcón E. *Influence of the second bending mode on the response of high-speed bridges at resonance*. J Struct Eng-ASCE 2005; 131:405–415.

[35] European Committee for Standardisation (CEN). *Eurocode 1: Actions on structures. Part 2: traffic loads on bridges*. Final Draft prEN 1991-2 (pre-European Standard) 2002.

COMPDYN 2011
ECCOMAS Thematic Conference on
Computational Methods in Structural Dynamics and Earthquake Engineering
M. Papadrakakis, M. Fragiadakis, V. Plevris (eds.)
Corfu, Greece, 25-28 May 2011

VERIFICATION OF AN EMPIRICAL PREDICTION METHOD FOR GROUND BORNE VIBRATIONS IN BUILDINGS DUE TO HIGH SPEED RAILWAY TRAFFIC

H. Verbraken[1], **S. François**[1], **G. Degrande**[1], **G. Lombaert**[1]

[1]Department of Civil Engineering, K.U.Leuven
Kasteelpark Arenberg 40, B-3001 Leuven, Belgium
e-mail: {hans.verbraken,stijn.francois,geert.degrande,geert.lombaert}@bwk.kuleuven.be

Keywords: Railway induced vibration, Empirical predictions; Dynamic soil–structure interaction

Abstract. *Ground borne vibration in buildings due to railway traffic is a major concern in densely built up areas. In practice, railway induced vibration is often predicted by means of empirical methods such as the Detailed Vibration Assessment developed by the U.S. Federal Railroad Administration (FRA). The vibration velocity level in a building is predicted based on a separate characterization of the source, the wave propagation and the receiver. They are characterized by a force density, a line transfer mobility and a coupling loss factor, respectively. While the line transfer mobility is determined directly with in situ measurements of transfer functions, the force density and the coupling loss factor are obtained indirectly. In this paper, a numerical model is used to simulate the experimental FRA procedure. The influence of the soil properties on the coupling loss factor is investigated by computing the coupling loss factor on three sites with different soil conditions. Each coupling loss factor is used to predict the vibration velocity level and the result is compared to a numerical prediction such that the accuracy of the procedure can be investigated. It turns out that the soil has a large influence on the coupling loss factor, as the reduction of the vibration velocity level between the free field and the foundation is affected by the relative stiffness of the building and the soil. Furthermore, the coupling loss factor strongly depends on the position of the point where it has been measured.*

1 Introduction

Ground borne vibration in buildings due to railway traffic is a major concern in densely built up areas. At low frequencies (1–80 Hz), vibration in buildings is perceived by the occupants as mechanical vibration, whereas at higher frequencies (16–250 Hz), it is perceived as re-radiated noise. An accurate prediction of this vibration is required so that effective mitigation measures can be taken.

The numerical modeling of vibration in building is a problem of dynamic soil–structure interaction. Generally, the coupling between the source and the receiver can be neglected such that a prediction in two steps is possible. First, the dynamic load is determined at the source and the vibration in the free field is computed. Second, the free field vibration is imposed as the incident wave field and the building response is computed. Several numerical models have been developed for the prediction of free field vibration due to railway traffic at grade [1, 2] at the source side and the building response at the receiver side. The validation of these models show that a good knowledge of all relevant input parameters is necessary to obtain reliable predictions. In practice, empirical predictions where these parameters are inherently taken into account are therefore often used. The Federal Railroad Administration (FRA) and the Federal Transit Administration (FTA) of the U.S. Department of Transportation have developed a set of empirical procedure to predict vibration levels due to railway traffic [3, 4]. Three different levels of assessment are described: the Screening procedure, the Generalized Vibration Assessment and the Detailed Vibration Assessment. The first two levels are used for general screening purposes. The third level is based on a prediction technique developed by Bovey [5] and Nelson and Saurenman [6] and presents a more elaborate method based on field measurements.

The Detailed Vibration Assessment predicts the vibration velocity level $\mathrm{L_v}$ $[\mathrm{dB\,ref\,10^{-8}\,m/s}]$ (root mean square in one-third octave bands) with the following equation:

$$\mathrm{L_v} = \mathrm{L_F} + \mathrm{TM_L} + \mathrm{C_{build}} \tag{1}$$

The first term in equation (1) is the force density $\mathrm{L_F}$ $[\mathrm{dB\,ref\,1\,N/\sqrt{m}}]$ and is a measure for the power per unit length radiated by the source. The second term is the line transfer mobility $\mathrm{TM_L}$ $[\mathrm{dB\,ref\,10^{-8}\,\frac{m/s}{N/\sqrt{m}}}]$ and is a measure for the vibration energy that is transmitted through the soil relative to the power per unit length radiated by the source. The third term is the coupling loss factor $\mathrm{C_{build}}$ $[\mathrm{dB}]$ and is a measure for the modification of vibration spectrum due to the dynamic interaction between the foundation and the soil. Each term in equation (1) is determined experimentally.

The line transfer mobility $\mathrm{TM_L}$ is determined with an experimental measurement of transfer functions between the track and the free field (Figure 1). The point transfer mobility TMP_k $[\mathrm{dB\,ref\,10^{-8}\,\frac{m/s}{N}}]$ is measured as the transfer function between the applied force in a single impact point k and the velocity in the free field. The line transfer mobility $\mathrm{TM_L}$ is obtained as the superposition of different point transfer mobilities, determined along the track alignment:

$$\mathrm{TM_L} = 10\log_{10}\left(L_\mathrm{a}\sum_{k=1}^{n}10^{\frac{\mathrm{TMP}_k}{10}}\right) \tag{2}$$

where L_a is the distance between the impact points and n is the total number of impact points.

The force density $\mathrm{L_F}$ is determined indirectly based on equation (1). The vibration velocity level during a train passage is measured in the free field (without the presence of a building). The line transfer mobility $\mathrm{TM_L}$ is determined experimentally and is subtracted from the free

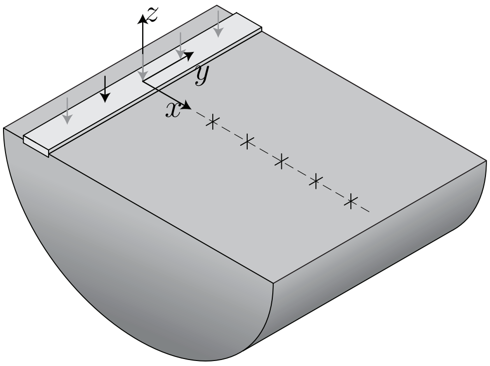

Figure 1: The experimental setup for the determination of the line transfer mobility $\mathrm{TM_L}$.

field vibration velocity level, resulting in a normalized force density $\mathrm{L_F}$ of the train passage. The force density is not only determined, however, by the dynamic characteristics of the train and the track, but also depends on the subsoil conditions.

The coupling loss factor $\mathrm{C_{build}}$ is determined indirectly as the relation between the vibration velocity level in the free field and the vibration velocity level at the foundation of a building. The coupling loss factor depends on the building and foundation type, but also on the subsoil conditions. In the FRA manual, a frequency dependent coupling loss factor is proposed for several building and foundation types.

In a prediction with the FRA procedure, each term in equation (1) is determined experimentally. When a new building is constructed in the neighborhood of an existing track, the vibration velocity level in the building is predicted as follows. The force density $\mathrm{L_F}$ and the line transfer mobility $\mathrm{TM_L}$ are measured on site. The advantage is that the source and the local transfer of vibration are correctly accounted for. The coupling loss factor $\mathrm{C_{build}}$ cannot be determined on site, however, as no building is present yet. It can be obtained from a database that contains previous measurements of the coupling loss factor of several building types. Examples of coupling loss factors are also given in de FRA manual [3]. The coupling loss factor is not only determined by the building or foundation type but also by the subsoil conditions, however. It is therefore important that the conditions of the soil are similar at the site where the coupling loss factor has been determined and at the site where it will be applied.

When a prediction is needed on a site with an existing building and a new track, the line transfer mobility $\mathrm{TM_L}$ and the coupling loss factor $\mathrm{C_{build}}$ are determined on site, whereas the force density $\mathrm{L_F}$ has to be determined at another site with similar conditions for the train, the track and the soil.

In the present paper, the influence of the soil characteristics on the coupling loss factor is investigated by numerical simulations to assess possible inaccuracies in the prediction due to a mismatch in the soil conditions. The influence of the soil conditions on the force density has been investigated previously [7]. In section 2, the numerical model is introduced. The vibration velocity level in the free field and in the building is computed numerically on three different soils in section 4 and section 5. In section 6, the coupling loss factor at each soil type is obtained from these results. Finally, in section 7, a prediction of the vibration velocity level in the building is made by combining the computed coupling loss factors for each soil type with the free field vibration velocity level at another site. The predictions are compared to the exact solution and the accuracy of the FRA procedure is evaluated.

2 Numerical model

A numerical model is used to compute the vibration velocity in a building due to a train passage on a railway track. The source and receiver are considered to be weakly coupled such that a prediction in two steps is possible. First, the vibration velocity in the free field due to moving loads is computed. Therefore, the axle loads of the moving train and the transfer functions from the track to the free field need to be determined. Second, the response of the building is computed based on the incident wavefield.

2.1 Source model

Figure 2 shows the coupled track–soil domain Ω of the source system, which is subdivided into the soil subdomain Ω_{s} and the track subdomain Ω_{b}, connected at the interface Σ_{bs}. Tractions $\bar{\mathbf{t}}_{\mathrm{b}}$ are imposed at the boundary $\Gamma_{\mathrm{b}\sigma}$. In case of a train passage, these tractions represent the axle loads.

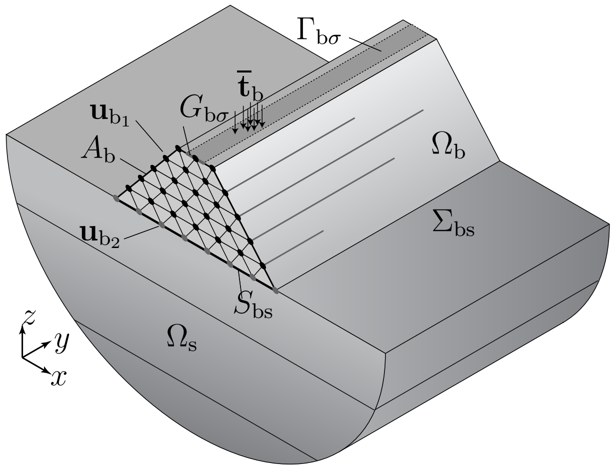

Figure 2: The geometry of the coupled track–soil system.

The vibration velocity $\mathbf{v}(\mathbf{x}', t)$ at a point $\mathbf{x}'$ in the free field due to k moving axle loads $\mathbf{g}_k(t)$ is calculated with the following convolution integral [1, 8]:

$$\mathbf{v}(\mathbf{x}', t) = \sum_{k=1}^{n_{\mathrm{a}}} \int_{-\infty}^{t} \mathbf{H}^{\mathrm{T}}(\mathbf{x}_k(\tau), \mathbf{x}', t-\tau)\mathbf{g}_k(\tau)d\tau \tag{3}$$

Each element $h_{ij}(\mathbf{x}', \mathbf{x}, t)$ of the matrix $\mathbf{H}(\mathbf{x}', \mathbf{x}, t)$ represents the velocity at a point $\mathbf{x}$ in the direction $\mathbf{e}_j$ at time t due to an impulsive load at a point $\mathbf{x}'$ in the direction $\mathbf{e}_i$ at time $t = 0$. In equation (3), dynamic reciprocity is used to replace the matrix $\mathbf{H}(\mathbf{x}', \mathbf{x}, t)$ by $\mathbf{H}^{\mathrm{T}}(\mathbf{x}, \mathbf{x}', t)$.

In the following, a longitudinal invariant track and a horizontally layered soil are assumed such that the geometry of the domain Ω is invariant in the longitudinal direction $\mathbf{e}_y$. In this case, the transfer function is unaffected by an arbitrary translation $l\mathbf{e}_y$ of the source and the receiver position. If l equals $y_{k0} + v\tau$, the source position $\mathbf{x}_k(\tau) - l\mathbf{e}_y = \{x_{k0}, 0, z_{k0}\}^{\mathrm{T}}$ no longer depends on the time τ and can be omitted in the argument of the transfer function. Furthermore, the coordinates x' and z' of the receiver position $\mathbf{x}' = \{x', y', z'\}^{\mathrm{T}}$ are assumed to be fixed, so that equation (3) is rewritten as follows:

$$\mathbf{v}(y',t) = \sum_{k=1}^{n_\mathrm{a}} \int_{-\infty}^{t} \mathbf{H}^\mathrm{T}(y' - y_{k0} - v\tau, t-\tau)\mathbf{g}_k(\tau)d\tau \tag{4}$$

Because the domain is longitudinally invartiant, a double forward Fourier transform from the space–time domain (y',t) allows for an expression of the vibration velocity in the wavenumber–frequency domain (k_y,ω):

$$\tilde{\mathbf{v}}(k_y,\omega) = \sum_{k=1}^{n_\mathrm{a}} \tilde{\mathbf{H}}^\mathrm{T}(k_y,\omega)\hat{\mathbf{g}}_k(\omega - k_y v)\exp(+ik_y y_{k0}) \tag{5}$$

where a hat denotes the representation in the space–frequency domain and a tilde the representation in the wavenumber–frequency domain. An inverse wavenumber transform results in the frequency content $\hat{\mathbf{v}}(y',\omega)$ of the vibration velocity.

The transfer matrix $\tilde{\mathbf{H}}^\mathrm{T}(k_y,\omega)$ in equation (5) is formulated in the wavenumber–frequency domain. It is computed with a 2.5D coupled finite element – boundary element method [9], where the longitudinal invariance of the domain is exploited by a Fourier transform from the direction y' to the wavenumber k_y. A finite element model for the track is coupled to a boundary element model for the soil.

The dynamic axle loads $\hat{\mathbf{g}}_k(\omega)$ in equation (5) are the result of the interaction between the vehicle, the track and the soil. They are computed in the frequency domain by means of a compliance formulation in a moving frame of reference [8], based on a perfect contact between the wheels and the track.

2.2 Receiver model

Figure 3 shows the coupled soil–structure domain Ω of the receiver system, which is subdivided into the soil subdomain Ω_s and the structure subdomain Ω_b, connected at the interface Σ_bs.

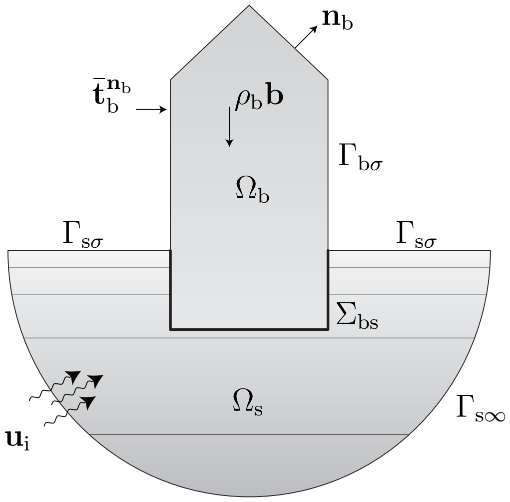

Figure 3: The geometry of the coupled soil–structure system.

The calculation of the vibration velocity in the building due to an incident wavefield is a problem of dynamic soil–structure interaction. The problem is assumed to be linear and all equation are elaborated in the frequency domain.

For any virtual displacement field $\hat{\mathbf{v}}_{\rm b}$ imposed on the structure $\Omega_{\rm b}$, the sum of the virtual work of the internal and the inertial forces is equal to the virtual work of the external loads:

$$
\begin{aligned}
&-\omega^2 \int_{\Omega_{\rm b}} \hat{\mathbf{v}}_{\rm b} \cdot \rho_{\rm b} \hat{\mathbf{u}}_{\rm b} d\Omega + \int_{\Omega_{\rm b}} \hat{\boldsymbol{\epsilon}}_{\rm b}(\hat{\mathbf{v}}_{\rm b}) : \hat{\sigma}_{\rm b}(\hat{\mathbf{u}}_{\rm b}) d\Omega \\
&\qquad = \int_{\Omega_{\rm b}} \hat{\mathbf{v}}_{\rm b} \cdot \rho_{\rm b} \hat{\mathbf{b}} d\Omega + \int_{\Gamma_{{\rm b}\sigma}} \hat{\mathbf{v}}_{\rm b} \cdot \hat{\bar{\mathbf{t}}}_{\rm b}^{\mathbf{n}_{\rm b}} d\Gamma + \int_{\Sigma_{\rm bs}} \hat{\mathbf{v}}_{\rm b} \cdot \hat{\mathbf{t}}_{\rm b}^{\mathbf{n}_{\rm b}}(\hat{\mathbf{u}}_{\rm b}) d\Gamma \qquad (6)
\end{aligned}
$$

where $\hat{\mathbf{u}}_{\rm b}$ is the displacement vector in the structure, $\rho_{\rm b}\hat{\mathbf{b}}$ denotes the body force in the domain $\Omega_{\rm b}$, and $\hat{\mathbf{t}}_{\rm b}^{\mathbf{n}_{\rm b}} = \hat{\sigma}_{\rm b} \cdot \mathbf{n}_{\rm b}$ is the traction vector on a boundary with unit outward normal vector $\mathbf{n}_{\rm b}$. Tractions $\hat{\bar{\mathbf{t}}}_{\rm b}^{\mathbf{n}_{\rm b}}$ are imposed on the boundary $\Gamma_{{\rm b}\sigma}$.

When equation (6) is discretized by means of 3D finite elements and the equilibrium of stresses on the interface $\Sigma_{\rm bs}$ is accounted for, the following expression is obtained [9]:

$$\left(\mathbf{K}_{\rm bb} - \omega^2 \mathbf{M}_{\rm bb} + \hat{\mathbf{K}}_{\rm bb}^{\rm s}(\omega)\right) \hat{\mathbf{u}}_{\rm b} = \hat{\mathbf{f}}_{\rm b}(\omega) + \hat{\mathbf{f}}_{\rm b}^{\rm s}(\omega) \qquad (7)$$

where $\mathbf{K}_{\rm bb}$ and $\mathbf{M}_{\rm bb}$ are the finite element stiffness and mass matrix, $\hat{\mathbf{K}}_{\rm bb}^{\rm s}(\omega)$ is the dynamic soil stiffness matrix, $\hat{\mathbf{f}}_{\rm b}(\omega)$ is the external load vector and $\hat{\mathbf{f}}_{\rm b}^{\rm s}(\omega)$ is the force vector due to the incident wavefield. The dynamic soil stiffness matrix $\hat{\mathbf{K}}_{\rm bb}^{\rm s}(\omega)$ and the force vector $\hat{\mathbf{f}}_{\rm b}^{\rm s}(\omega)$ account for the interaction with the soil and for the incident wavefield, respectively, and are computed by means of the boundary element method.

3 Case

In the following sections, the vibration velocity level in the free field and in a building due to a train passage is computed by means of the numerical models introduced in section 2. The coupling loss factor can be determined numerically from these results. By considering different soil types, the influence of a mismatch in the soil conditions on the coupling loss factor and the resulting prediction is investigated. In this section, the characteristics of the train, track, soil and building are discussed.

In the present case, a classical ballasted track [1] is considered with UIC 60 rails supported every 0.60 m by rubber pads on monoblock concrete sleepers. The rails are continuously welded and are fixed with a Pandrol E2039 rail fastening system and supported by resilient studded rubber rail pads (type 5197) with a thickness of 11 mm. Each rail pad is preloaded with a clip toe load of about 20 kN per rail seat. The prestressed concrete monoblock sleepers have a length $l_{\rm sl} = 2.50\,{\rm m}$, a width $b_{\rm sl} = 0.235\,{\rm m}$, a height $h_{\rm sl} = 0.205\,{\rm m}$ and a mass $m_{\rm sl} = 300\,{\rm kg}$. The track is supported by a porphyry ballast layer (calibre $25/50$, thickness $d = 0.35\,{\rm m}$) and a limestone sub-ballast layer (thickness $d = 0.60\,{\rm m}$). The density of these ballast layers is $1700\,{\rm kg/m^3}$.

The track is modeled as a longitudinally invariant track [1] by means of the 2.5D finite element method, where the dynamics of the rail pads and the mass of the sleepers are uniformly distributed along the track. It has been shown that continuously and discretely supported tracks have similar dynamic behaviour up to about 500 Hz [10]. The rails are modeled as Euler–Bernoulli beams and the rail pads are modeled as continuous spring–damper connections. The sleepers are assumed to be rigid in the plane of the cross section and are modeled as a uniformly distributed mass along the track. The ballast bed is modeled as a set of distributed, independent linear springs and dampers. Figure 4 shows the cross section of the ballasted track model.

The track is supported by a homogeneous halfspace. In order to investigate the influence of the soil properties on the prediction of the vibration velocity level, three sites are considered

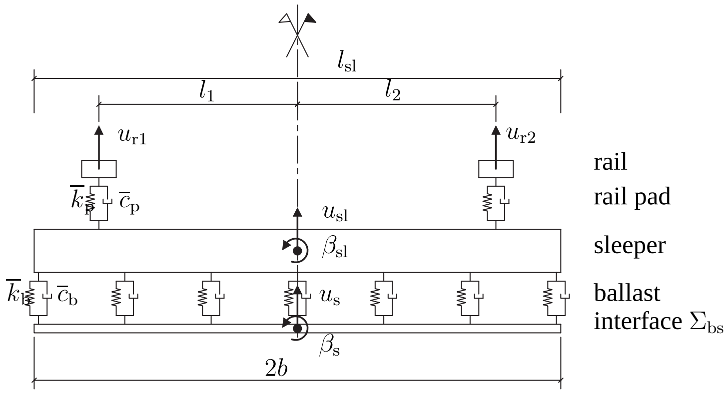

Figure 4: Cross section of a ballasted track model.

with different soil characteristics representing a soft, medium and stiff soil. The dynamic soil characteristics are summarized in Table 1.

Table 1: Dynamic soil characteristics.

Type	C_{s} $[\mathrm{m/s}]$	C_{p} $[\mathrm{m/s}]$	ν [-]	ρ $[\mathrm{kg/m^3}]$	β [-]
Soft	100	200	0.33	1800	0.025
Medium	150	300	0.33	1800	0.025
Stiff	300	600	0.33	1800	0.025

The Thalys HST consists of two locomotives and eight carriages and has a total of 26 axles [8]. Each axle has an unsprung mass $M_{\mathrm{u}} = 2027\,\mathrm{kg}$. The length l of the train equals 200.18 m. The train is modeled as a series of individual axles, as the coupling between different axles through the vehicle can be neglected. The mechanical model of the train therefore only takes into account the unsprung mass M_{u} of each axle.

At 30 m from the track, a masonry building with dimensions $12\,\mathrm{m} \times 6\,\mathrm{m} \times 6\,\mathrm{m}$ is assumed to be present (figure 5a) [11]. The structure has two stories, each subdivided into 4 rooms. The interior and exterior walls have a thickness $t_{\mathrm{w}} = 0.10\,\mathrm{m}$, and consist of clay brick masonry. The floors are concrete slabs with a thickness $t_{\mathrm{fl}} = 0.20\,\mathrm{m}$. All floors are simply supported, corresponding to hinged joints at the slab edges. The structure is founded on a concrete strip foundation with a width $w_{\mathrm{fou}} = 0.60\,\mathrm{m}$ and a thickness $t_{\mathrm{fou}} = 0.20\,\mathrm{m}$. Figure 5b shows the foundation of the building and indicates the location of points A, B, C and D where the response in the free field and in the building will be computed.

The building is modeled with the finite element method. The strip foundation, the walls and the floors are modeled by means of shell elements, using isotropic properties for the foundation and the floors and orthotropic properties for the masonry walls [11]. The lintels above the door and the windows are modeled by means of beam elements.

4 Vibration velocity level in the free field

In this section, the free field response due to the passage of the Thalys HST on the track at a speed of 150 km/h is computed with the source model described in section 2.1. Figure 6 shows the computed time history and the frequency content of the free field vibration velocity in point A due to the passage of the Thalys HST at a speed $v = 150\,\mathrm{km/h}$ on a site with medium soil.

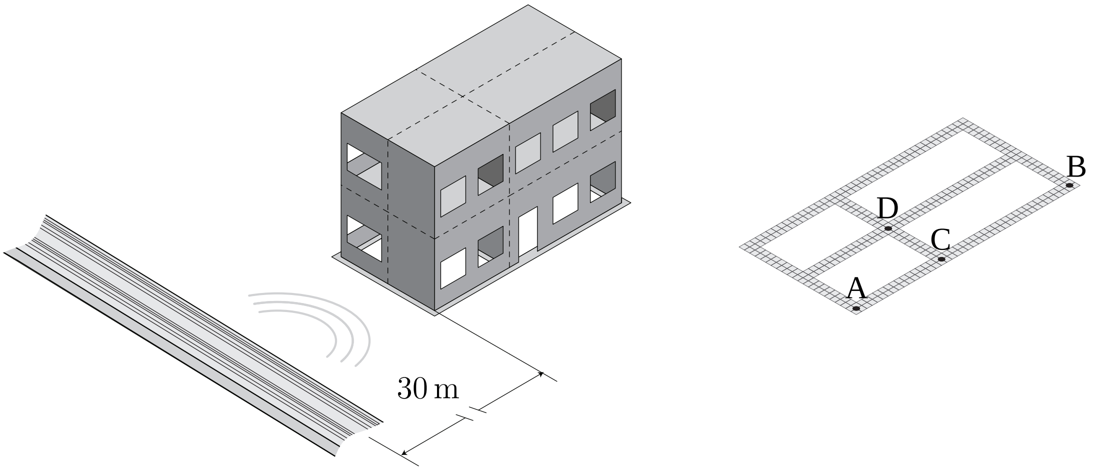

(a) (b)

Figure 5: (a) Geometry and location of the building and (b) foundation of the building and location of the measurement points.

The duration of the passage is about 4.8 s which is approximately equal to the length l of the train divided by the train speed v. The time history can be divided in three parts: an increasing vibration level when the train approaches, a nearly stationary part when the train passes and a decreasing vibration level when the train moves away. The stationary part of the response is selected by means of the DIN selection procedure [12] based on the time T_2 and is indicated in black in Figure 6a. The vibration velocity level $\mathrm{L_v}$ is then defined as the one-third octave band RMS spectrum of the stationary part of the vibration velocity.

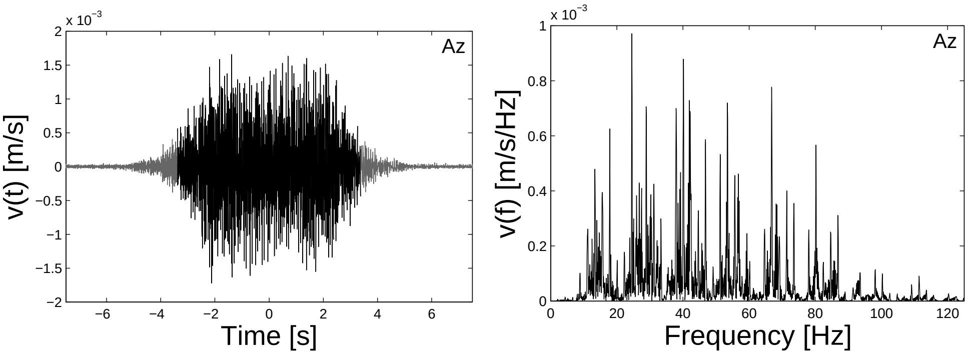

(a) (b)

Figure 6: (a) Time history and (b) frequency content of the vertical velocity at 30 m from the track in the free field due to the passage of a Thalys HST at a speed of 150 km/h on a site with medium soil (stationary part of the time history is indicated in black).

Figure 7 shows the vibration velocity level $\mathrm{L_v}$ at the three different sites in the free field in the points corresponding to point A and point B (Figure 5b). In the response on the stiff soil, a peak around 63 Hz is found. This is due to the resonance of unsprung mass of the wheelsets on the track. In the low frequency range, the highest response is obtained for the soft soil. The response is increasingly attenuated, however, not only at larger distances from the track but also with increasing frequency. As this attenuation is stronger for softer soils, the peak at 63 Hz is no longer observed in the response on the soft and the medium soil and the highest response in the high frequency range is obtained for the stiff soil.

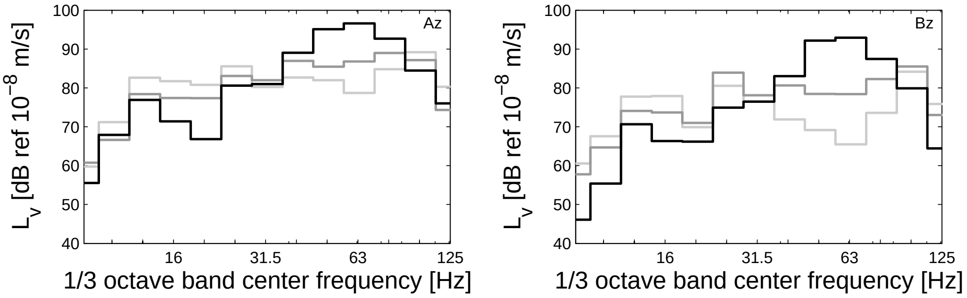

(a) (b)

Figure 7: Free field vibration velocity level at (a) 30 m and (b) 42 m on a soft (light grey line), medium (dark grey line) and stiff (black line) soil.

5 Vibration velocity level in a building

In this section, the response of the building to the passage of the Thalys train on the track is computed with the receiver model described in section 2.2. In Figure 8, the vibration velocity levels at the foundation of the building determined on three different soils are compared. The response is shown at the front side (point A) and at the back side (point B) of the building (Figure 5b), corresponding to the points where the free field response is shown in Figure 7. At low frequencies the highest response is obtained for the soft and the medium soil, whereas at higher frequencies the highest response is obtained for the stiff soil, corresponding to the observation of the vibration velocity level in the same points in the free field. It can be observed, however, that the response at the foundation differs from the response in the free field due to the dynamic soil–structure interaction. This modification is described by the coupling loss factor, discussed in the next section.

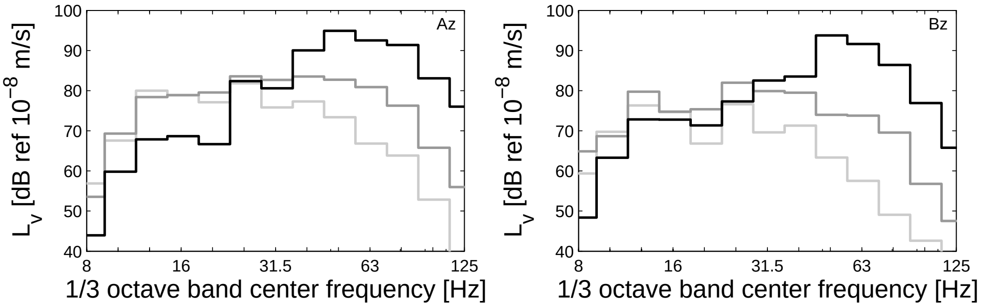

(a) (b)

Figure 8: Vibration velocity level of the foundation in (a) point A and (b) point B on a soft (light grey line), medium (dark grey line) and stiff (black line) soil.

6 Coupling loss factor

The coupling loss factor $\mathrm{C_{build}}$ is determined by subtracting the vibration velocity level $\mathrm{L_F} + \mathrm{TM_L}$ in the free field from the vibration velocity level $\mathrm{L_v}$ at the foundation of the building:

$$\mathrm{C_{build}} = \mathrm{L_v} - (\mathrm{L_F} + \mathrm{TM_L}) \tag{8}$$

Figure 9 shows the coupling loss factors in point A and point B, determined at the three different soil types. These values are compared to coupling loss factor proposed in the FRA manual for a 2 to 4 story masonry building. A negative value of the coupling loss factor C_{build} implies a reduction of the vibration velocity level from the free field to the foundation, while a positive value means an increase of the vibration velocity level.

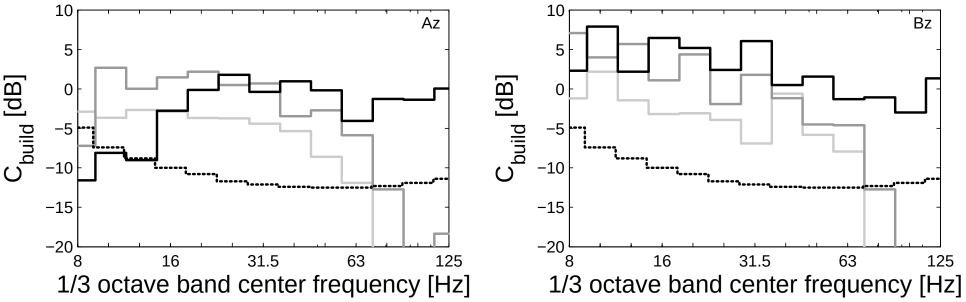

(a) (b)

Figure 9: Coupling loss factor C_{build} in (a) point A and (b) point B on a soft (light grey line), medium (dark grey line) and stiff (black line) soil compared to the curve proposed in the FRA manual for a 2 to 4 story masonry building (dotted line).

In the high frequency range, a zero value is observed for the coupling loss factor for the stiff soil. Due to the high relative stiffness of the soil, the ground vibration is imposed to the building and is transmitted almost unaffectedly to the foundation. A large reduction is observed, however, for the coupling loss factor in the case of the soft and the medium soil. Due to the lower relative stiffness, the ground vibration is transmitted at a reduced level to the foundation. The interaction between the soil and the structure is determined by the characteristic wavelength of the vibration. As the wavelength decreases with increasing frequency and for softer soils, a higher reduction is obtained at high frequencies for the soft and the medium soil.

In the low frequency range, a difference up to 15 dB is observed between the coupling loss factor at the front side (point A) and the back side (point B) of the building. This can be due to the fact that the building response at low frequencies is an average response to the incident wavefield. As the incident wavefield itself is attenuated with increasing distance from the track, a reduction is found at the front side wereas an increase is found at the back side. This effect is more pronounced for the case of the stiff soil.

From the previous discussion it can be concluded that the soil conditions significantly affect the values obtained for the coupling loss factor. Furthermore, it is observed that the computed values for the coupling loss factor overestimate the values proposed by the FRA. The coupling loss factor is also strongly dependent, however, on the location of the measurement point. Figure 10 shows the coupling loss factor determined on the three soils in point C along the edge of the building and in point D in the centre of the building (Figure 5b). The reduction in point D is generally around 10 dB higher than the reduction in point C. The foundation response in a point is affected by the kinematics of the complete building as well as by the local geometry. When torsional and rotational modes of the building are excited, the response at the centre of the foundation is lower. As the incident wavefield is similar in point C and point D, the reduction is higher in point D.

Figure 11a shows the spatial variation over the foundation of the coupling loss factor at 63 Hz, confirming that a higher reduction is obtained in the centre of the building. Furthermore, it is observed that the reduction is generally higher at the front of the building (left side) than

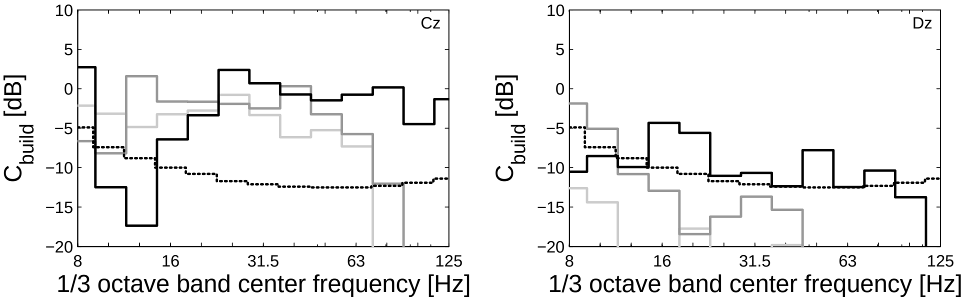

(a) (b)

Figure 10: Coupling loss factor C_{build} in (a) point C and (b) point D on a soft (light grey line), medium (dark grey line) and stiff (black line) soil compared to the curve proposed in the FRA manual for a 2 to 4 story masonry building (dotted line).

at the back (right side). Figure 11b shows the average value of the coupling loss factor over all points in the foundation and the 90 % interval of the coupling loss factor values over the foundation. The coupling loss factor is strongly dependent on the location of the measurement point, as a large spread, up to 20 dB, can be observed. The conclusion still holds in case of the average coupling loss factor, however, that the reduction is stronger for softer soils, particularly at higher frequencies.

7 Prediction of the vibration velocity

In this section, a prediction is made for the vibration velocity level at the foundation of a building on a medium soil. In order to investigate the influence of the soil properties on the prediction accuracy, the free field vibration velocity level on a medium soil is therefore combined with the coupling loss factors obtained in section 6. As the coupling loss factor is affected by the position of the measurement point, the average value over the foundation is used. Figure 12 shows the prediction of the response in point A and point B (Figure 5b), compared to a 12 dB region around the exact solution for the medium soil. In case of a coupling loss factor determined on a medium soil, the prediction is generally within 6 dB of the exact solution. In case of a coupling loss factor determined on a soft or a stiff soil, however, the accuracy is significantly less good at higher frequencies. An overestimation of the response up to approximately 20 dB is obtained with the coupling loss factor of the stiff soil, whereas an underestimation up to approximately 15 dB is obtained with the coupling loss factor of the soft soil.

The prediction of the response in point A and B is relatively accurate with an average coupling loss factor determined on the same soil type. Due to the spatial variability, however, it can be expected that the accuracy of the prediction will be less good in other points of the building. Figure 13 shows the prediction of the response for point C and point D (Figure 5b) compared to a 12 dB region around the exact solution. The prediction of the response in point C, located at the edge of the foundation, is relatively accurate when the coupling loss factor of the medium soil is used. The prediction in point D, located in the centre of the foundation, however, is overestimating the response, even when the medium soil coupling loss factor is used.

From the previous analysis, it can be concluded that the coupling loss factor should be determined from data obtained at sites where the conditions for the building, the foundation and the subsoil are similar in order to obtain an accurate prediction. Furthermore, it can be concluded that the location of the measurement point strongly affects the coupling loss factor and

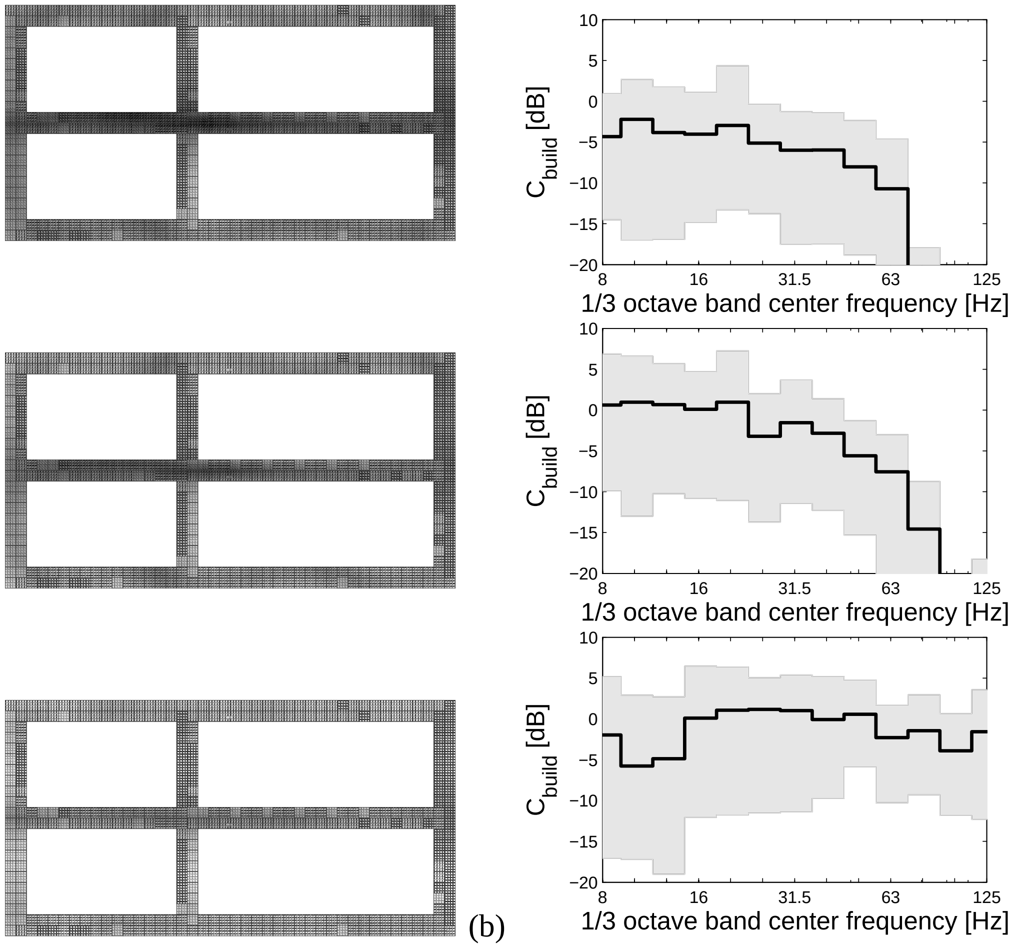

(a) (b)

Figure 11: (a) Spatial variation at 63 Hz and (b) average value (black line) and 90 % interval (grey region) of the coupling loss factor $\mathrm{C_{build}}$ on a soft (top), medium (middle) and stiff (bottom) soil.

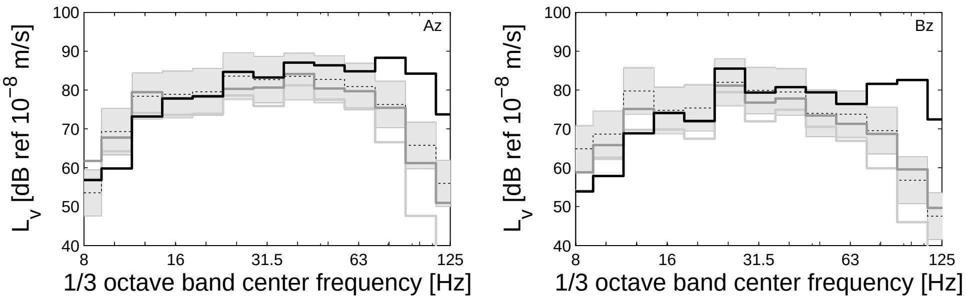

(a) (b)

Figure 12: Predicted vibration velocity level in (a) point A and (b) point B using the average coupling loss factor determined on a soft (light grey line), medium (dark grey line) and stiff (black line) soil compared to a 12 dB region (grey region) around the exact solution (dotted black line).

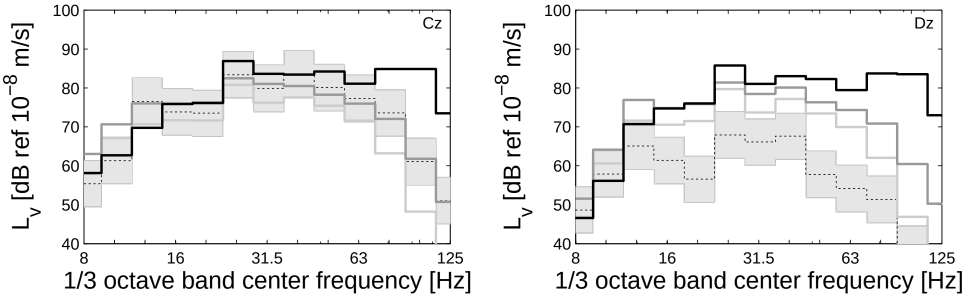

(a) (b)

Figure 13: Predicted vibration velocity level in (a) point C and (b) point D using the average coupling loss factor determined on a soft (light grey line), medium (dark grey line) and stiff (black line) soil.

the resulting prediction of the vibration velocity level. In a prediction with the FRA procedure, an experimental value obtained from previous measurements of the coupling loss factor of a similar building type postis used. As the prediction is affected as well by parameters such as the subsoil conditions and the measurement point, however, an accurate experimental prediction is not possible in every situation. The accuracy of the prediction could be improved by providing predictions of the coupling loss factor by means of numerical simulation, as has been shown in this paper. The advantage of the numerical prediction of the coupling loss factor is the greater flexibility in dealing with different building and founation configurations and soil properties, while the advantage of using experimental data of the source and the transfer of vibration is that the local conditions are correctly accounted for. A hybrid experimental–numerical prediction combines both advantages.

8 Conclusions

The FRA procedure is an empirical procedure for the prediction of railway induced vibration in buildings. The source, the wave propagation and the receiver are characterized experimentally by a force density, a line transfer mobility and a coupling loss factor, respectively. The line transfer mobility is determined directly based on wave propagation tests. The force density and the coupling loss factor are determined indirectly, however, and they are influenced by several parameters such as the subsoil conditions. Previously, the influence of the soil conditions and other parameters on the force density and the resulting prediction accuracy has been investigated [7]. In this paper, the influence of the soil conditions and the location of measurement points on the coupling loss factor of a specific building type has been investigated by means of a numerical simulation of the FRA procedure.

The coupling loss factor characterizes the modification of the vibration velocity level due to the dynamic soil–structure interaction at the receiver side. This effect, however, is dependent on the conditions of the subsoil. Generally, a higher reduction is obtained at a higher frequency and for softer soils. The dependency of the coupling loss factor on the soil conditions leads to an overestimation of the response in case of a coupling loss factor determined on a stiffer soil and an underestimation in case of a coupling loss factor determined on a softer soil. Furthermore, a large spatial variation is observed in the coupling loss factors determined at different points in the foundation of a building due to the kinematics of the building and local variations of the geometry.

As the coupling loss factor is influenced by several parameters such as the soil conditions and the location of the measurement point, it is important that experimental data of the coupling loss factor is used on sites with similar conditions. An appropriate experimental coupling loss factor may not be available, making an accurate empirical prediction impossible. It has been shown in this paper that the coupling loss factor can also be predicted by means of numerical simulations and combined with an experimental prediction of the free field vibration velocity level. A hybrid experimental–numerical prediction method is then obtained that combines the advantages of both methods.

Acknowledgements

The first author is a Research Assistant of the Research Foundation - Flanders (FWO). Their financial support is gratefully acknowledged.

REFERENCES

[1] G. Lombaert, G. Degrande, J. Kogut, and S. François, "The experimental validation of a numerical model for the prediction of railway induced vibrations," *Journal of Sound and Vibration*, vol. 297, no. 3-5, pp. 512–535, 2006.

[2] X. Sheng, C.J.C. Jones, and M. Petyt, "Ground vibration generated by a load moving along a railway track," *Journal of Sound and Vibration*, vol. 228, no. 1, pp. 129–156, 1999.

[3] C.E. Hanson, D.A. Towers, and L.D. Meister, "High-speed ground transportation noise and vibration impact assessment," HMMH Report 293630-4, U.S. Department of Transportation, Federal Railroad Administration, Office of Railroad Development, October 2005.

[4] C.E. Hanson, D.A. Towers, and L.D. Meister, "Transit noise and vibration impact assessment," Report FTA-VA-90-1003-06, U.S. Department of Transportation, Federal Transit Admininistration, Office of Planning and Environment, May 2006.

[5] E.C. Bovey, "Development of an impact method to determine the vibration transfer characteristics of railway installations," *Journal of Sound and Vibration*, vol. 87, no. 2, pp. 357–370, 1983.

[6] J.T. Nelson and H.J. Saurenman, "A prediction procedure for rail transportation groundborne noise and vibration," *Transportation Research Record*, vol. 1143, pp. 26–35, 1987.

[7] H. Verbraken, H. Eysermans, E. Dechief, S. François, G. Lombaert, and G. Degrande, "Verification of an empirical prediction method for railway induced vibration," in *Proceedings of the 10th International Workshop on Railway Noise IWRN10*, Nagahama, Japan, October 2010, pp. 229–236.

[8] G. Lombaert and G. Degrande, "Ground-borne vibration due to static and dynamic axle loads of InterCity and high speed trains," *Journal of Sound and Vibration*, vol. 319, no. 3-5, pp. 1036–1066, 2009.

[9] S. François, M. Schevenels, G. Lombaert, P. Galvín, and G. Degrande, "A 2.5D coupled FE-BE methodology for the dynamic interaction between longitudinally invariant structures and a layered halfspace," *Computer Methods in Applied Mechanics and Engineering*, vol. 199, no. 23-24, pp. 1536–1548, 2010.

[10] K. Knothe and S.L. Grassie, “Modelling of railway track and vehicle/track interaction at high frequencies,” *Vehicle Systems Dynamics*, vol. 22, pp. 209–262, 1993.

[11] S. François, *Nonlinear modelling of the response of structures due to ground vibrations*, Ph.D. thesis, Department of Civil Engineering, K.U.Leuven, 2008.

[12] Deutsches Institut für Normung, *DIN 45672 Teil 2: Schwingungsmessungen in der Umgebung von Schienenverkehrswegen: Auswerteverfahren*, 1995.

COMPDYN 2011
III ECCOMAS Thematic Conference on
Computational Methods in Structural Dynamics and Earthquake Engineering
M. Papadrakakis, M. Fragiadakis, V. Plevris (eds.)
Corfu, Greece, 25–28 May 2011

HIGH-SPEED RAILWAY TRACKS OF A SURFACE, BRIDGE AND TUNNEL LINE AND SOME EFFECTS ON THE TRAIN-INDUCED BRIDGE AND GROUND VIBRATIONS

Lutz Auersch[1]

[1] Federal Institute for Materials Research and Testing,
D 12200 Berlin, Germany
e-mail: lutz.auersch-saworski@bam.de

Keywords: Track compliance, surface line, bridge track, tunnel track, ground vibration, layered soil, bridge resonance, train speed, axle sequence, track irregularities.

Abstract. *Different high-speed railway tracks have been analysed theoretically and experimentally, a ballasted track at a surface line, a slab track in a tunnel, and a ballasted track on a concrete bridge. Vehicle, track and ground vibration as well as their interaction are considered in a combined finite-element boundary-element (FEBEM) approach. The layered soil is calculated in frequency wavenumber domain and the solution for fixed or moving point or track loads follow as wavenumber integrals. The comparison of the dynamic compliances of the different tracks leads to an improved understanding of the different track elements. Certain maxima have been observed for certain train speeds and certain eigenmodes of the bridge. These maxima correlate with some maxima of the ground vibrations. The bridge and the ground vibrations are discussed with the axle-sequence of the train. The ground vibrations strongly depend on the regular and random inhomogeneity of the soil. The regular layering of the soil yields a cut-on and resonance phenomenon whereas the random inhomogeneity yields a scattering of the axle impulses which proved to be important for high-speed trains. All theoretical results are compared with measurements at a high-speed line.*

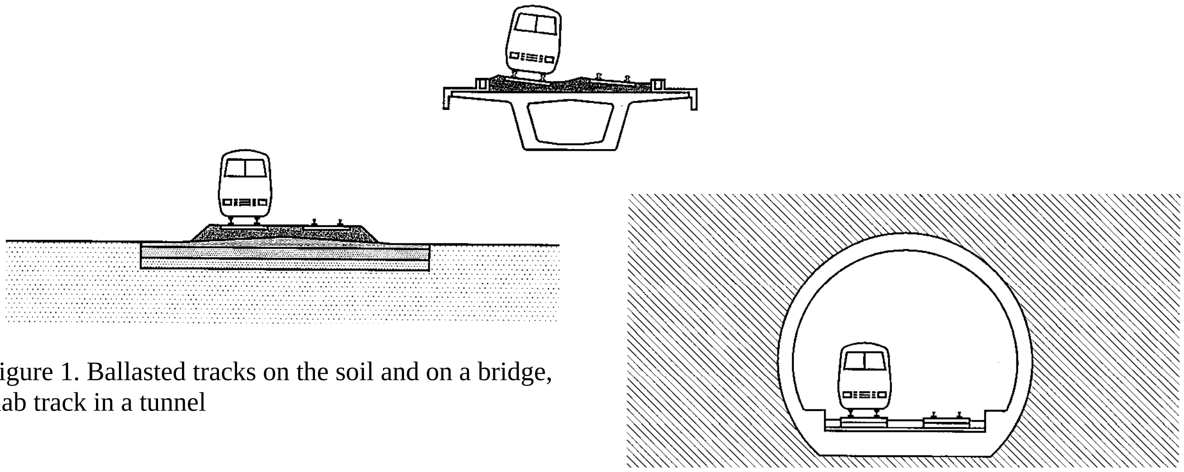

Figure 1. Ballasted tracks on the soil and on a bridge, slab track in a tunnel

1 FINITE-ELEMENT BOUNDARY ELEMENT METHOD FOR THE DYNAMIC COMPLIANCE OF TRACKS ON LAYERED SOILS

A 3-dimensional track model is combined with the boundary element formulation of the soil. That means, that the Greens' functions of a homogeneous or layered soil are used to establish a fully coupling soil matrix which is added to the FEM matrix of the track.

1.1 Green's functions of the soil

The soil is a homogeneous or horizontally layered elastic half-space, which is excited at its surface by dynamic forces **F**, and the displacements **u** have to be calculated for surface points, too. The relation between the displacements **u** and the force **F** can be described in cylindrical (transversal, radial and vertical) components as

$$\begin{bmatrix} u_t \\ u_r \\ u_z \end{bmatrix} = \begin{bmatrix} f_{tt} & 0 & 0 \\ 0 & f_{rr} & f_{rz} \\ 0 & -f_{rz} & f_{zz} \end{bmatrix} \begin{bmatrix} F_t \\ F_r \\ F_z \end{bmatrix} \tag{1}$$

The four functions $f_{ij}(r,\omega)$ of distance and circular frequency can be calculated by integration in wavenumber domain [1], for example as

$$f_{zz} = \frac{1}{2\pi} \int_0^\infty H_{zz}(k) \mathrm{J}_0(kr) k dk \tag{2}$$

for the simplest case of the vertical component. J_0 is the Bessel function of the first kind and the vertical compliance H_{zz} in wavenumber domain k can be given explicitly for the homogeneous half-space

$$H_{\mathrm{zz}} = \frac{k_S{}^2 \sqrt{k_{\mathrm{P}}{}^2 - k^2}}{iG\left[(k_S{}^2 - 2k^2)^2 + 4k^2 \sqrt{k_{\mathrm{S}}{}^2 - k^2} \sqrt{k_{\mathrm{P}}{}^2 - k^2} \right]} \tag{3}$$

with the abbreviations (v_S, v_P the shear and compressional wave velocities)

$$k_S = \omega / v_S \qquad k_P = \omega / v_P \tag{4}$$

or calculated by matrix methods for a layered soil [1, 2]. Similar formulas hold for the other components and the complete set of Green's functions (1) is used in the present boundary element method of the soil.

1.2 The stiffness matrix of the discretized soil

First, the soil has to be defined by a set of m surface points with coordinates $\mathbf{x}_\alpha$. A certain portion A_α of the surface area belongs to each surface point. A force **F** at a point $\mathbf{x}_\alpha$ of the surface of the soil is considered. By using the Green's functions (of the preceding section), the displacements at all other points $\mathbf{x}_\beta$ are calculated

$$\begin{bmatrix} u_x \\ u_y \\ u_z \end{bmatrix} = \begin{bmatrix} f_{rr} x_r{}^2 + f_{tt} y_r{}^2 & (f_{rr} - f_{tt}) x_r y_r & f_{rz} x_r \\ (f_{rr} - f_{tt}) x_r y_r & f_{rr} y_r{}^2 + f_{tt} x_r{}^2 & f_{rz} y_r \\ -f_{rz} x_r & -f_{rz} y_r & f_{zz} \end{bmatrix} \begin{bmatrix} F_x \\ F_y \\ F_z \end{bmatrix} \tag{5}$$

with

$x_r = (x_\alpha - x_\beta)/r \qquad\qquad y_r = (y_\alpha - y_\beta)/r$

Equation (5) is the same as equation (1), but transformed into the cartesian coordinate system.

For the point of excitation $\mathbf{x}_\alpha$ itself, the Green's function cannot be evaluated because the solution is singular at this point. This difficulty can be overcome by calculating the mean value over the corresponding surface area. This leads to the mean values of the scalar functions $f_{ii}(r)$

$$\overline{f}_{ii} = \frac{2}{r_\alpha^{\;2}} \int_0^{r_\alpha} f_{ii}(r)\, r\, dr \tag{6}$$

where r_α is the radius of area A_α. So the compliance relation at the excited point of the soil is

$$\begin{bmatrix} u_x \\ u_y \\ u_z \end{bmatrix} = \begin{bmatrix} \dfrac{\overline{f}_{rr} + \overline{f}_{tt}}{2} & 0 & 0 \\ 0 & \dfrac{\overline{f}_{rr} + \overline{f}_{tt}}{2} & 0 \\ 0 & 0 & \overline{f}_{zz} \end{bmatrix} \begin{bmatrix} F_x \\ F_y \\ F_z \end{bmatrix} \tag{7}$$

The flexibility matrix of the soil is assembled of all these 3x3 matrices $\mathbf{f}_{\beta\alpha}$

$$\begin{bmatrix} \mathbf{u_1} \\ \vdots \\ \mathbf{u_\beta} \\ \vdots \\ \mathbf{u_m} \end{bmatrix} = \begin{bmatrix} \mathbf{f_{11}} & \cdots & \mathbf{f_{1\alpha}} & \cdots & \mathbf{f_{1m}} \\ \vdots & & \vdots & & \vdots \\ \mathbf{f_{\beta 1}} & \cdots & \mathbf{f_{\beta\alpha}} & \cdots & \mathbf{f_{\beta m}} \\ \vdots & & \vdots & & \vdots \\ \mathbf{f_{m1}} & \cdots & \mathbf{f_{m\alpha}} & \cdots & \mathbf{f_{mm}} \end{bmatrix} \begin{bmatrix} \mathbf{F_1} \\ \vdots \\ \mathbf{F_\alpha} \\ \vdots \\ \mathbf{F_m} \end{bmatrix} \tag{8}$$

with m the number of points, or in short form

$$\mathbf{u} = \mathbf{f}\,\mathbf{F} \tag{8'}$$

The inversion of this equation

$$\mathbf{F} = \mathbf{f}^{-1}\,\mathbf{u} =: \mathbf{K_S}\,\mathbf{u} \tag{9}$$

gives the dynamic stiffness matrix $\mathbf{K_S} = \mathbf{f}^{-1}$ of the soil which is introduced in the finite element procedure for the structure [3].

1.3 Combined finite-element boundary-element method

Now the coupling of both sub-systems, track and soil, is done by introducing the soil into the finite element code as a new type of element. The points of the soil define one special element of which the dynamic stiffness matrix $\mathbf{K_S}$ is calculated by the boundary element method. The track structure is described by the conventional finite element method. Local stiffness matrices as well as local mass matrices are assembled in a global stiffness matrix $\mathbf{K_0}$ and a global mass matrix $\mathbf{M}$ respectively. Combining these matrices, the frequency-dependent dynamic stiffness matrix $\mathbf{K_F}(\omega)$ of the track structure

$$\mathbf{K_F} = \mathbf{K_0} - \omega^2\mathbf{M} \tag{10}$$

is obtained. Then the coupling of the boundary element and finite element part of the system can be expressed in terms of global representations of the matrices and

$$\mathbf{F} = (\mathbf{K_F}(\omega) + \mathbf{K_S}(\omega))\,\mathbf{u} \tag{11}$$

is the equation of the whole track-soil system, that has to be solved for given external forces $\mathbf{F}$, for example the wheel-set forces.

2 CALCULATED COMPLIANCES OF BALLASTED AND SLAB TRACKS

Three different tracks, a ballasted surface track, a ballast track on a bridge and a slab track in a tunnel are considered (Fig. 1). All tracks have the same UIC60 rails with bending stiffness EI_R = 6.4 10^6 Nm^2 and mass per length m' = 60 kg/m, and the same concrete sleepers with EI_S = 5.2 10^6 Nm^2 and m = 338 kg. For each track, the stiffness of the material under the track (the ballast or the subsoil of the slab) is varied.

2.1 Ballasted track on a homogeneous soil

The surface track consists of a 0.35 m ballast layer. The sub-soil has a shear wave velocity of v_S = 300 m/s. The rail pads are rather stiff with k_P = 300 kN/m. The ballast is varied as

v_S = 100, 150, 200, 300 m/s.

The dynamic compliances of the rails are given as amplitude and phase in Figure 2. Although the ballast stiffness is varied by a factor of 9, the static compliance of the rail is in the narrow range of u/P = 1.8 to 3.2 10^{-9} m/N. That means 0.2 to 0.3 mm displacement under a 100 kN axle load. The stiff ballast yields an almost constant compliance and only a small phase delay of 20°. All softer ballast materials result in a stronger phase delay and a related amplitude reduction at a certain frequency which is lower for the softer ballast. The softest ballast has a strong phase and amplitude decay at about 60 Hz. The softest ballast with v_S = 100 m/s has the strongest contrast with the underlying soil v_S = 300 m/s and this results in moderate amplifications of the track amplitudes.

2.2 Ballasted track on a bridge (rigid base)

The ballasted track is the same on the bridge as for the surface line. The bottom of the ballast layer is fixed. The same variation of the ballast stiffness is analysed in Figure 2b. The rigid base reduces the static compliances of the ballasted tracks to values between u/P = 1.4 to 2.9 10^{-9} m/N. No radiation damping of the soil is present and only small phase values due to the material damping can be observed. Clear resonances occur for the softer ballast materials at f = 95 and 135 Hz for v_S = 100 and 150 m/s. These resonance frequencies are lower than the layer frequencies $f = v_P/4d$ = 200/1.4 = 140 or 300/1.4 = 210 Hz due to the influence of the track mass. The phase decay at the resonance is stronger than for the surface line.

2.3 Slab track in a tunnel (on a layer over bedrock)

The slab track in the tunnel has a 0.6 m thick concrete plate which lies on a 1.5 m layer of softer soil material. The base is the tunnel floor which is assumed to be rigid. Medium soft rail pads of k_P = 60 kN/m are used to compensate the stiff track plate. The compliance of the rail is ruled by these soft rail pads and is constant if the stiffness of the sub-soil is varied between v_S = 100 and 300 m/s. Moreover it does not change its static value of u/P = 3.7 10^{-9} m/N with increasing frequency (see Fig. 2d). The influence of the sub-soil can be clearly seen for the plate compliance under the axle load (Fig. 2c). The massive plate yields low resonance frequencies of f = 20, 30, 40 and 60 Hz with the compliances of the different sub-soils. These resonance frequencies are far below the layer resonances at f = 33, 50, 66 and 100 Hz. The amplitudes of the plate are much smaller than those of the rail. It is 20 or 10 % for the soft sub-soils and even less for the stiff sub-soils.

Figure 2d shows the rail compliances of the three tracks, surface track with soft ballast, bridge track with soft ballast, and tunnel track with a thick plate over a stiff sub-soil. The rail compliance of the tunnel is increasing at 150 Hz, the end of the frequency range. The resonance of the rail on the soft rail pads is expected at 205 Hz. While the ballasted tracks show a

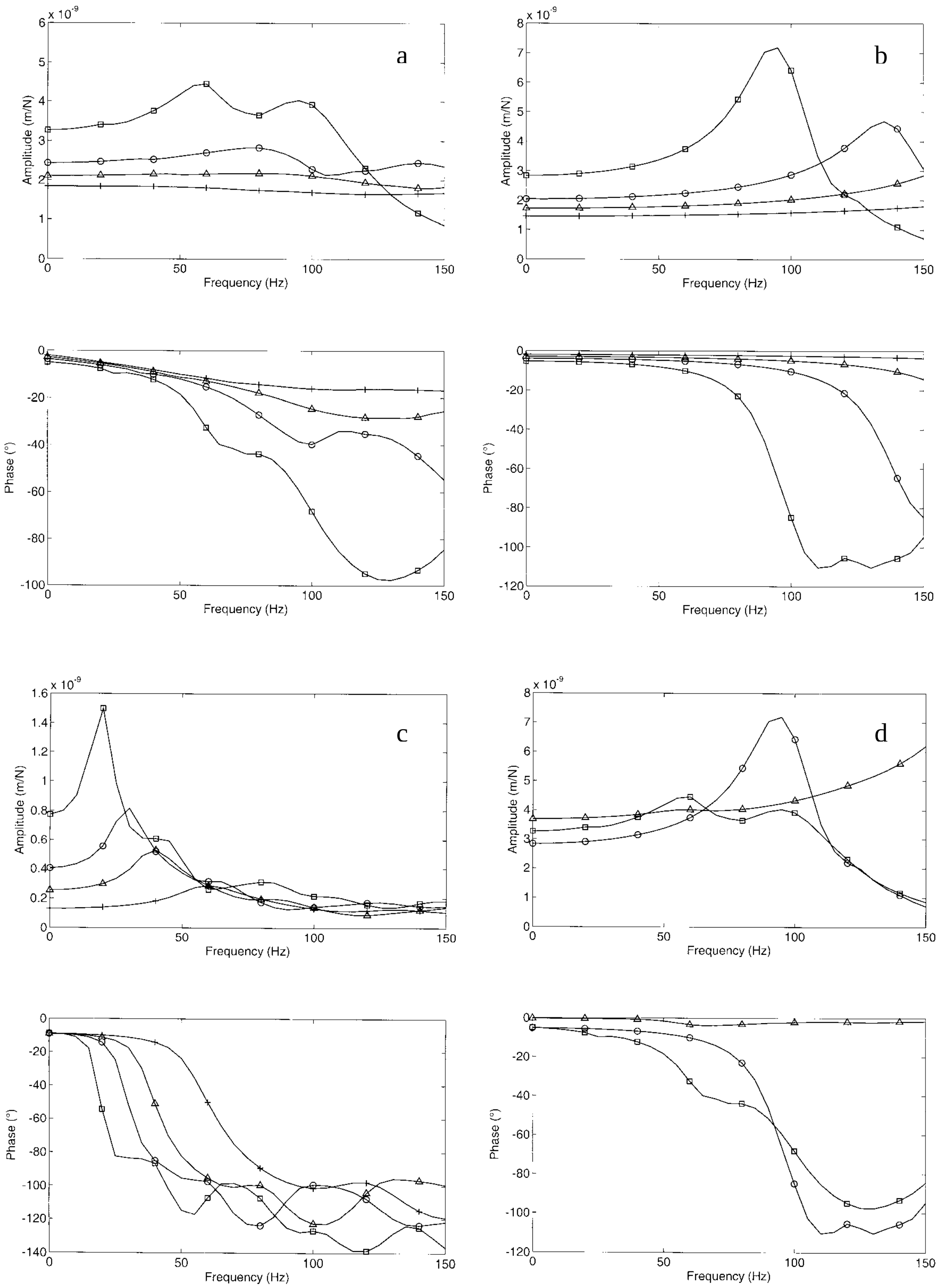

Figure 2: Compliances of different tracks, a) ballasted track on the soil, b) ballasted track on the bridge, c) slab track on a sub-soil layer (compliance of the plate) variation of the ballast or subsoil □ 100, ○ 150, △ 200 +300 m/s in a, b, c. Comparison of the rail compliances (d) for the ballasted track on the soil □, the ballasted track on the bridge ○, and the slab track △.

phase drop below 100 Hz, the rail of the tunnel track shows almost no phase delay. Such strong differences between rail and sleeper displacements are only found for the tunnel track. The sleeper to rail displacement ratio of the ballasted tracks is at 33 to 67 % for the bridge track line and at 50 to 77 % for the surface line. The differences increase with a stiffer ballast material, but also with a softer rail pad.

3 TRAIN INDUCED GROUND VIBRATION

3.1 Calculation in wavenumber domain

An alternative method to the FEBEM is the calculation of an infinite track in frequency-wavenumber domain. This method yields the track behaviour and the ground vibration due to moving or fixed loads [4]. The dynamic stiffness of the soil under the track in frequency wavenumber domain is calculated as the wavenumber integral

$$\smile(k_y,\omega)=\frac{1}{2\pi}\int_{-\infty}^{+\infty}H(k_x,k_y,\omega)p_1(k_x)dk_x=\frac{1}{K_S(k_y,\omega)} \qquad (12)$$

The dynamic stiffness K_S of the soil is combined with the stiffness $K_T = EIk^4 - m'\omega^2$ of the track

$$H_{TS}(k_y,\omega)=\frac{1}{K_T+K_S} \qquad T_{TS}(k_y,\omega)=\frac{K_S}{K_T+K_S} \qquad (13)$$

and these track-soil transfer functions are used to calculate the displacements of the track and the soil

$$u_T(\omega)=\frac{F}{2\pi}\int_{-\infty}^{+\infty}H_{TS}(k_y,\omega-k_y v)dk_y \qquad (14)$$

$$u_S(x,y^*,\omega)=\frac{F}{(2\pi)^2}\int_{-\infty}^{+\infty}\int_{-\infty}^{+\infty}H(k_x,k_y,\omega-k_y v)T_{TS}(k_y,\omega-k_y v)p_1(k_x)e^{i(k_x x+k_y y^*)}dk_x dk_y$$

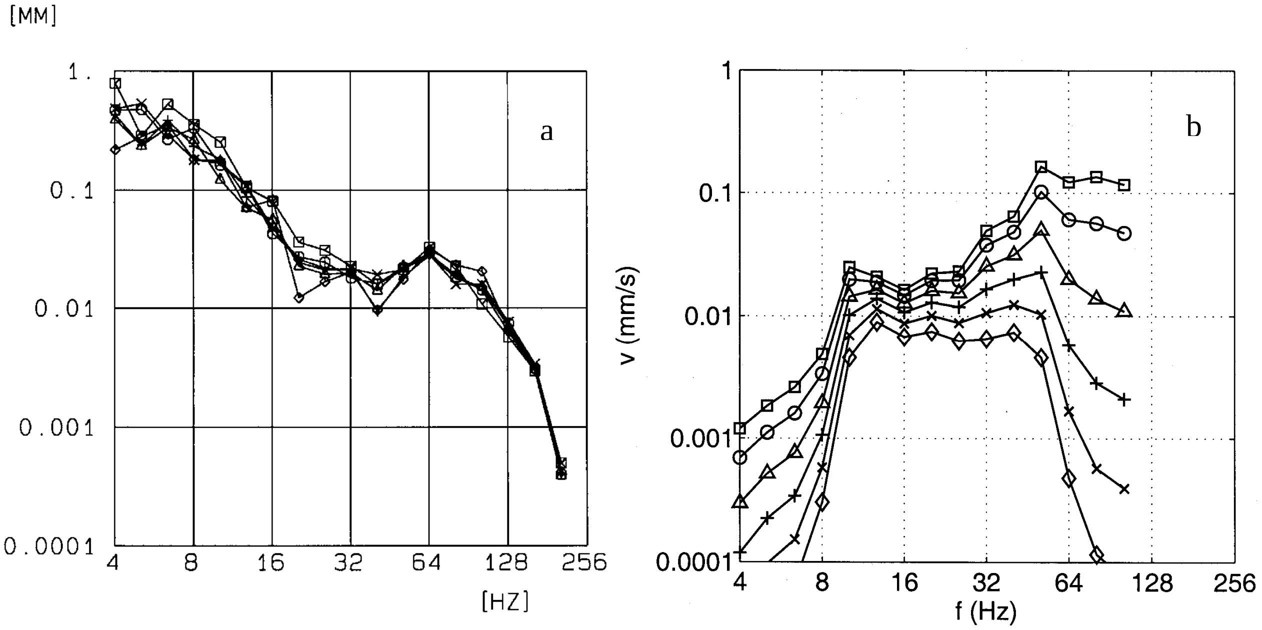

Figure 3: a) Third-of-octave spectra of the irregularities of the ballasted track at six different places of the 3 km long testing section: b) calculated ground vibration at the layered site; at □ 2.5, ○ 7.5, △ 12.5, + 20, × 30, ◇ 50 m distance from the track.

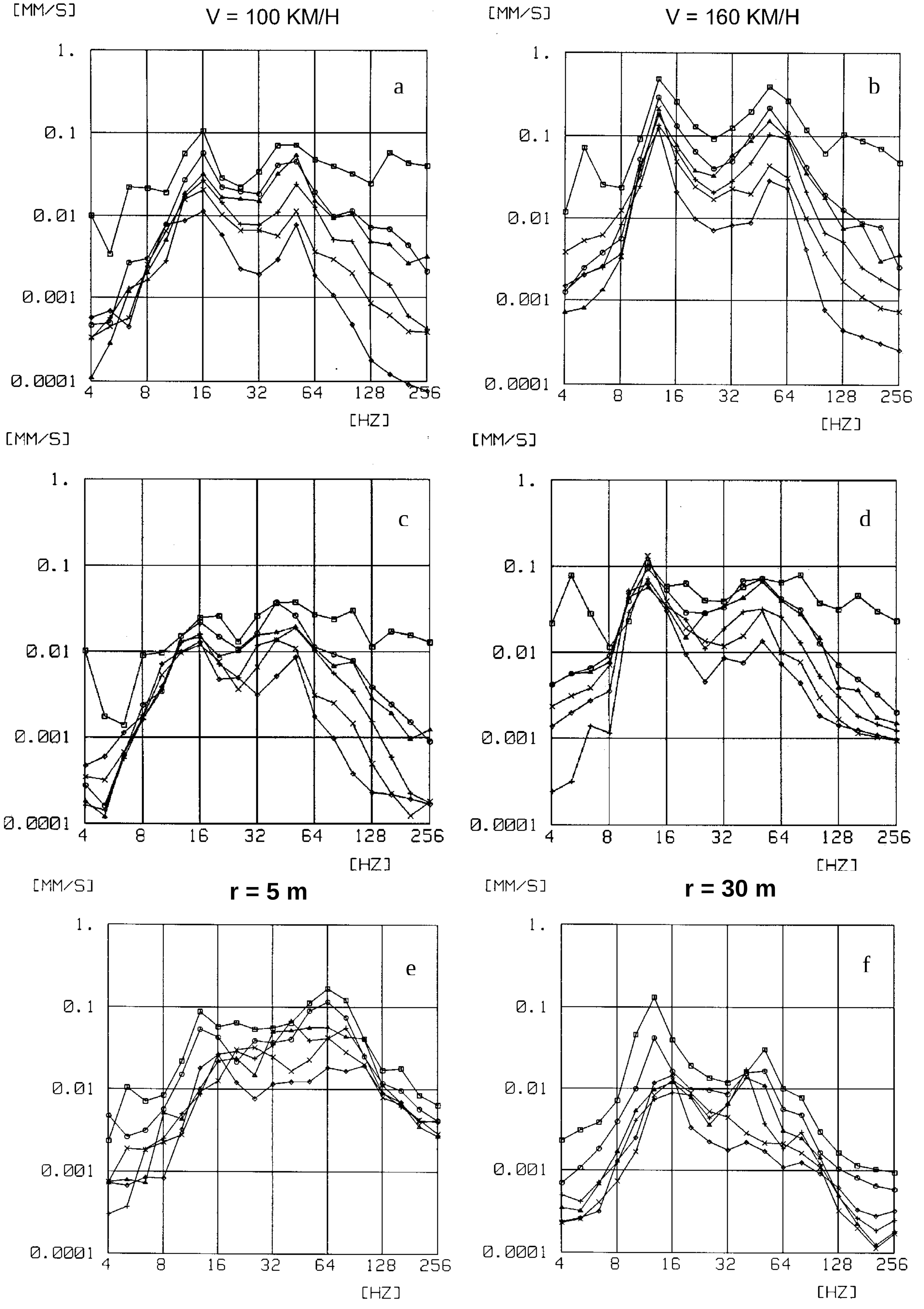

Figure 4: Train induced ground vibration, a), b) passage of a locomotive with v_T = 100 and 160 km/h, c), d) passage of a passenger car with v_T = 100 and 160 km/h, measured at □ 2.5, ○ 7.5, △ 12.5, + 20, × 30, ◇ 50 m, e), f) results at r = 5 and 30 m with train speeds v_T = □ 160, ○ 125, △ 100, + 80, × 63, ◇ 40 km/h.

The spectrum of vibration amplitudes $v(x,\omega)$ at a fixed point for an excitation frequency ω_E is calculated as [5]

$$v(x,\omega,\omega_E) = \frac{F}{2\pi v_T} T_{BS}\left(\frac{\omega_E-\omega}{v_T},\omega\right)\int_{-\infty}^{+\infty} H\left(k_x,\frac{\omega_E-\omega}{v_T},\omega\right)p_1(k_x)\exp(ik_x x)dk_x \,. \qquad (15)$$

The excitation of the ground vibration is a force spectrum $F(\omega)$ which is due to the irregularities s of the track. The irregularity spectrum $s(\omega)$ of the ballasted track is shown in Figure 3a for different places of the 3 km long test section. The soil consists of a layer with $v_S = 250$ m/s and $h = 10$ m on a rock half-space of $v_S = 1000$ m/s. The material damping of the soil is increasing from $D = 1$ % at 10 Hz to $D = 10$ % at 100 Hz, see [6] for more details. The calculated response of the soil is shown in Figure 3b for distances between 2.5 to 50 m.

While the irregularities are decreasing with frequency, the resulting excitation forces are almost constant, and the ground vibration amplitudes are mainly increasing with frequency. There is a strong cut-off for the frequencies below 12.5 Hz, which is the resonance frequency of the soil layer. The increase of the amplitudes is very strong below the cut-off, and moderate above. Frequencies above 63 Hz are reduced considerably due to the strong material damping. The two cut-off phenomena yield a specific frequency range of the ground vibration between 10 and 63 Hz which is due to the soil and not to the train excitation. All these theoretical characteristics are in good agreement with the experimental results in Figure 4c.

3.2 Experimental observations

The measured ground vibrations of different distances, different train speeds and different trains are shown on Figure 4, [7] where the spectra due to the locomotive display stronger and clearer characteristics than those of the passenger cars. A sharp resonance is observed for the layer frequency at 12.5 Hz in case of a train speed of 160 km/h. The same excitation frequency would be at 8 Hz for the lower train speed of $v_T = 100$ km/h, but no resonance is observed. The frequency is in the cut-off region of the soil, and therefore only small amplifications can be seen in the near field which indicate some specific train excitation. The characteristics of the layered and strongly damped soil are so dominant that the spectra of the different train speeds (Fig. 4e and f) are very similar. At a near-field distance of 5 m, the characteristic frequency range from 10 to 63 Hz has an almost constant level whereas the low frequencies are more dominant in the far field at 30 m. An increase of the amplitudes with increasing train speed can be observed. Especially the increase for $v_T = 160$ km/h due to the resonance at $f = 12.5$ Hz is very strong in the far field.

4 TRAIN INDUCED BRIDGE VIBRATION

4.1 Experimental observations

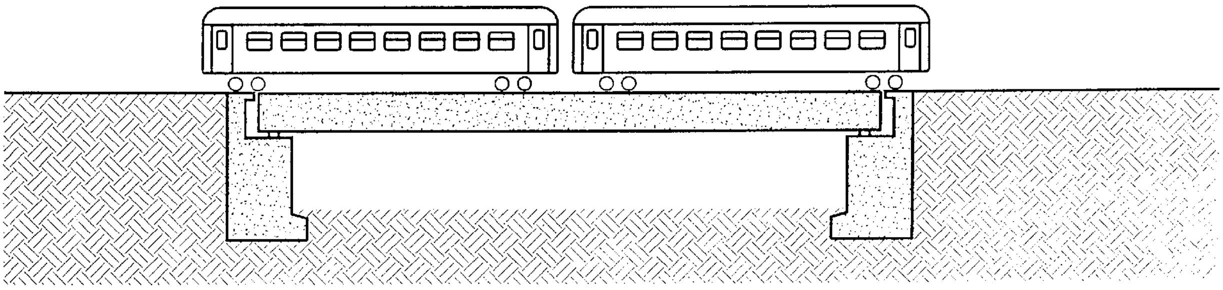

Figure 5: 45 m long concrete bridge on elastic bearings

A 45 m long concrete bridge has been analysed and measured (Fig. 5), [7]. The cross section can be seen on Figure 1. The bridge is simply supported on elastic bearings. The first four modes and eigenfrequencies are shown on Figure 6. The first bending mode fits perfectly the mode shape of a simply supported bridge. The first torsional mode has a contribution of the elastic bearings. During the passage of the test train, a clear excitation of the 7 Hz resonance has been observed for a train speed of $v_T = 100$ km/h and of the 11 Hz resonance for $v_T = 160$ km/h (see Figure 11 in Appendix A), [7]. These frequencies are close to those observed on the soil.

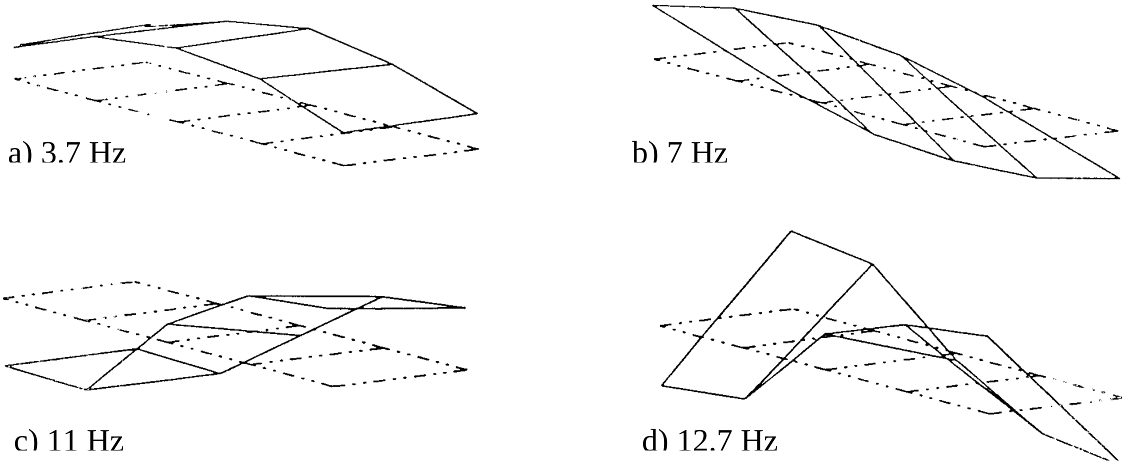

Figure 6: The first four eigenmodes of the concrete railway bridge a) first bending mode, b) first torsional mode, c) second bending mode, d) second torsional mode.

4.2 Modal excitation of railway bridges by sequence of axle loads

To examine the effect of passing trains, first a single axle passage over the bridge is considered. (The moving load concept is used here which is conservative compared to the more detailed train-bridge interaction, see for example [8]).

The excitation of mode j with circular eigenfrequency ω_j and normalized eigenform $v_j(x)$ can be determined from the Fourier transformed differential equation of this mode

$$m_j(\omega_j^2 + 2Di\omega_j^2 - \omega^2)u_j = F_j(\omega) \tag{16}$$

where

$$F_j(\omega) = \mathrm{FFT}\{F(\mathrm{t})\mathrm{v}_\mathrm{j}(x = v_T t)\} \tag{17}$$

is the transformed modal force component. The static load F_S yields

$$F_j(\omega) = F_S\,\mathrm{FFT}\{v_j(x = v_T t)\} = F_S V_j(\omega) \tag{18}$$

and a harmonic dynamic load F_D of frequency ω_j yields

$$F_j(\omega_j) \approx F_D V_j(0)\,. \tag{19}$$

Figure 8 shows the forces of the first and second mode as time histories and spectra. The low frequencies have always high amplitudes which are related to the slow impulse of the total passage of the static force. These frequencies are much lower than the resonance frequencies of the bridge. A resonance due to the bridge passage impulse is only possible for the high-speed passage over a short bridge.

The higher frequencies are due to the irregularities when the static load is entering and leaving the bridge. The simply supported bridge yields a sudden bend at the beginning of the bridge. If the bridge is on an elastic support, as in the present situation, there is an additional step. Both cases, the simply supported bridge on a rigid or elastic support are shown in Figure

8. The additional step of 15 % of the maximum displacement for the elastic support yields high-frequency amplitudes which are up to five times higher than for the bridge on rigid support. There is a strong variation with frequency due to the constructive or destructive superposition of the entering and leaving of the bridge. As the resonance curve has some bandwidth, a smoothed curve of the modal force $F_j(\omega)$ is better suited to discuss possible resonances.

Another excitation of the bridge is due to the irregularities s of the track. The measured irregularities of the ballasted track on the bridge are shown in Figure 7a. From the irregularities at the resonance frequencies 7 and 11 Hz, $s = 2$ and 1 mm, dynamic forces of approximately $F_7 = F_{11} = 1$ kN are deduced. Their effects on the modes of the bridge are shown in Figure 8c and d. The amplitudes of the modal forces are almost the same as the amplitudes due to the entering and leaving of the simply supported bridge (Fig. 8a and 8b).

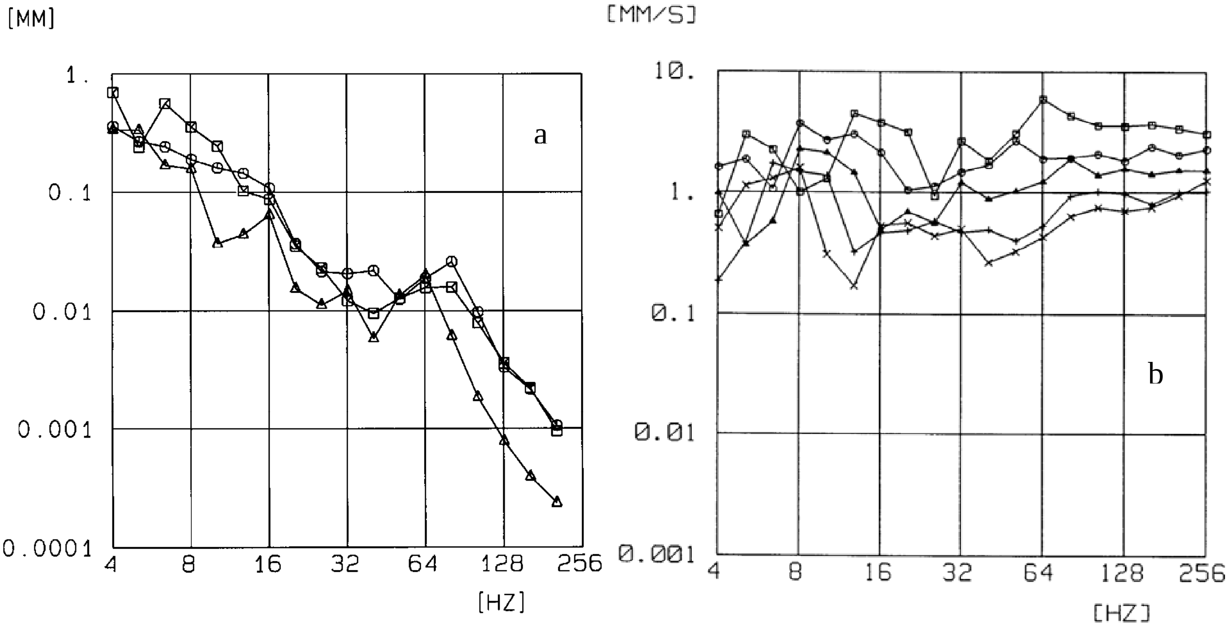

Figure 7: a) Irregularities of the track □ on the soil, ○ on the bridge, △ in the tunnel (slab track), b) vibration spectra of the bridge track during the passage of the passenger car with v_T = □ 160, ○ 125, △ 100, + 80, × 63 km/h.

So far, no reason for the different excitation of different modes could be found. It should be due to the specific axle sequence of the train which is shown on Figure 9 for the two interesting train speeds and on Figure 7b in a third-of-octave version for all train speeds. A maximum is found at 7 Hz for 100 km/h and at 11 Hz for 160 km/h close to the excited eigenfrequencies. Each maximum is the highest peak in a wider frequency band with several peaks. At the same time there are minima and a range of reduced amplitudes around 7 Hz for the train speed of 160 km/h and around 11 Hz for 100 km/h. Moreover, these minima are also found for a single car or a single locomotive (Fig. 9c-d). So it is concluded, that the axle sequence is important for the excitation of the eigenfrequencies of the bridge. The axle sequence yields maxima and minima which are suitable to the experimental observation, and the cancellation due to the sequence of the axles seems to be more important [9]. Isolated peaks of the axle sequence spectrum are only found for specific, very regular trains [10].

The axles-sequence spectra discussed here are in relation to the signatures of trains in the UIC rules [11] which are expressed as the axle loads as a function of the wave length. But the axle sequence spectra also include higher frequencies which are important for the train-bridge situation discussed here.

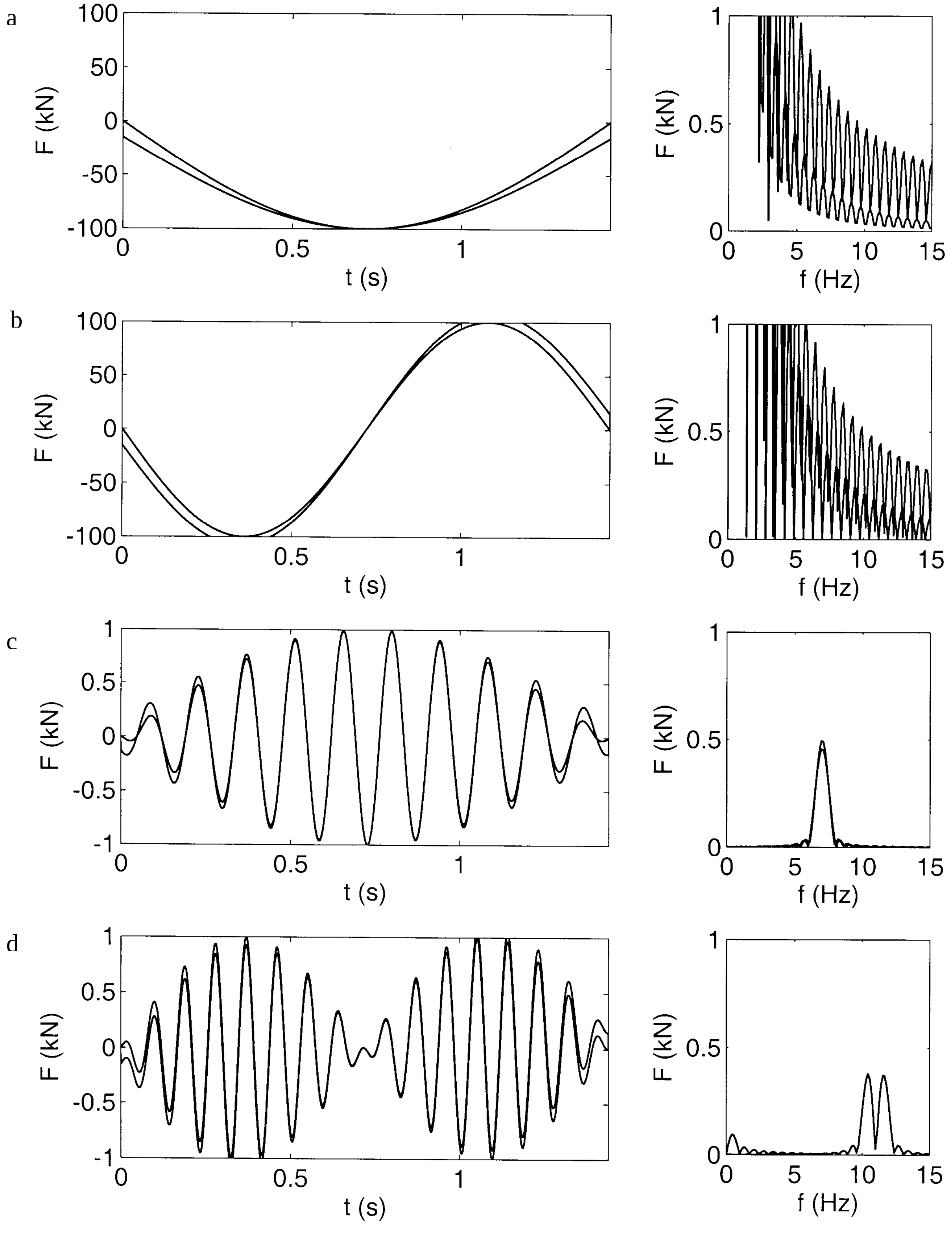

Figure 8: Modal forces as time history and spectra, due to the passage of a static load, a) first and b) second mode, and due to harmonic loads of f = c) 7 Hz for the fist mode and d) 11 Hz for the second mode, all results are given for rigid and elastic support.

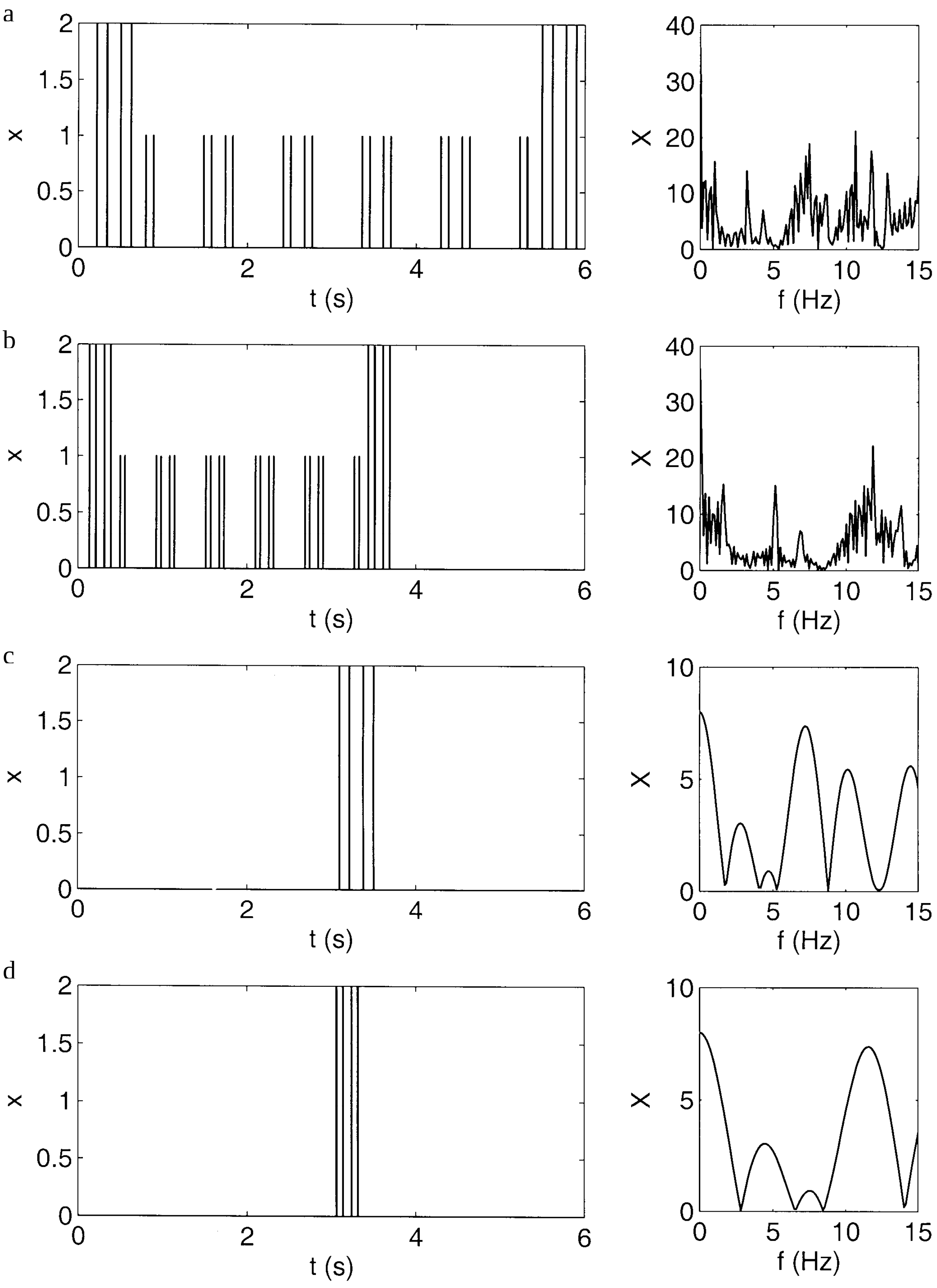

Figure 9: Axles sequence of the test train with v_T = a) 100 and b) 160 km/h, time histories and spectra, c) and d) of the locomotive with 100 and 160 km/h respectively.

5 CONCLUSIONS

- The calculated compliances of different ballasted and slab tracks on layered soils show some typical characteristics, resonances, amplitude and phase delays, rail to sleeper amplitude ratios, which can also be found in the measurements.
- Dominant frequencies, which have been measured on the ground, are close to the resonance frequencies of the bridge that are excited by trains of the same speed.
- The excitation of the modes of the bridge can be due to the passing over the bridge, the entering and leaving of the bridge or the random irregularities of the track.
- All these excitations are modified by the axle sequence of the whole train. In the present case the axle sequence spectrum has a maximum at the excited eigenfrequency and a minimum at the other eigenfrequency of the bridge.
- The maximum of the axle sequence spectrum also excites the layer resonance of the soil for a train speed of 160 km/h whereas the same excitation is in the cut-off region of the soil for a train speed of 100 km/h.

REFERENCES

[1] L. Auersch, Wave propagation in layered soil: theoretical solution in wavenumber domain and experimental results of hammer and railway traffic excitation. *Journal of Sound and Vibration*, **173**, 233-264, 1994.

[2] L. Auersch, Wave propagation in the elastic half-space due to an interior load and its application to ground vibration problems and buildings on pile foundations. *Soil Dynamics and Earthquake Engineering*, **30**, 925-936, 2010.

[3] L. Auersch, Dynamics of the railway track and the underlying soil: the boundary-element solution, theoretical results and their experimental verification. *Vehicle System Dynamics*, **43**, 671-695, 2005.

[4] L. Auersch, The effect of critically moving loads on the vibrations of soft soils and isolated railway tracks. *Journal of Sound and Vibration*, **310**, 587-607, 2008.

[5] L. Auersch, Train induced ground vibrations – different amplitude-speed relations for different layered soils. *Journal of Rail and Rapid Transit*, submitted 2010.

[6] L. Auersch, M. Maldonado, Interaction véhicule-voie-sol et vibrations dues aux trains: modélisations et vérifications expérimentales. *Revue Européenne de Mécanique Numérique*, submitted 2009.

[7] L. Auersch, S. Said, W. Rücker, *Das Fahrzeug-Fahrweg-Verhalten und die Umgebungserschütterungen bei Eisenbahnen*. Forschungsbericht 243, BAM, Berlin, 2001.

[8] K. Liu, *Analysis and monitoring of dynamic effects of train-bridge interaction*. PhD Thesis, KU Leuven, 2010.

[9] M. Martínez Rodrigo, *Atenuación de vibraciones resonantes en puentes de ferrocarril de alta velocidad mediante amortiguadores fluido-viscosos*. PhD Thesis, Universitad Politecnica, Valencia, 2009.

[10] L. Auersch, Ground vibration due to railway traffic - The calculation of the effects of moving static loads and their experimental verification. *Journal of Sound and Vibration*, **293**, 599-610, 2006.

[11] UIC Code 776-2: *Design requirements for rail-bridges based on interaction phenomena between train, track and bridge*. 2009

APPENDIX A - MEASURED COMPLIANCES OF THE DIFFERENT TRACKS

The compliances of the different tracks of the surface, bridge and tunnel line have been measured by impulse tests and are shown on Figure 10 for a wide frequency range. The slab track in the tunnel has a high compliance up to 200 Hz (Fig. 10c) whereas the ballasted tracks drop down below 100 Hz (Figs. 10a and b). The bridge and tunnel track show a resonance, the ballasted track on the soil has no resonance amplification. The slab track in the tunnel has two resonances, the strongest at 205 Hz is due to the rail mass on the rail pad stiffness, and the minor resonance at about 100 Hz is due to the plate mass on the sub-soil stiffness. The displacements of the rail on the medium soft rail pad are ten times higher than those of the plate (Fig. 10c). The sleeper to rail amplitude ratios of the ballasted tracks are at about 70 %. All these details are in agreement with the theoretical results.

The experimental results can be used to choose the ballast and sub-soil parameters. The low–frequency decay of the ballasted tracks means a low stiffness of the ballast during the impulse tests. A higher stiffness of the ballast is expected under train loading. The sub-soil stiffness in the tunnel is stiff, but a thinner layer or a thinner plate could also explain the high plate-subsoil resonance frequency.

APPENDIX B – MEASURED TRAIN PASSAGE OVER THE DIFFERENT TRACKS

The behaviour of the different tracks under train passages is shown in Figure 11. The time histories on the left show the displacements of the rail and the sleeper which are calculated from the measured velocities [3]. The third of octave spectra on the right are for the original velocity measurements and compare several rail, sleeper and environmental measuring points. The displacements under a 100 kN axle load is about 0.3 mm for the ballasted track. The displacement of the slab track with softer rail pads are somewhat higher, but the displacements of the plate are considerably smaller as can be observed at the time histories and the spectra.

APPENDIX C – MEASURED TRAIN PASSAGE OVER THE BRIDGE

Figure 12 shows the time histories of two train passages over the bridge. One passage is with a train speed of v_T = 100 km/h, the other with v_T = 160 km/h. The time segment, when the middle of the train passes the bridge, is selected. A clear resonance is observed for both passages. For the lower train speed, all measuring points on the bridge are in phase, so it is a first symmetric mode of the bridge. For the higher train speed the north and south end of the bridge are in anti-phase and the middle of the bridge has the lowest amplitude. That means that a second antimetric mode is excited by the train at 160 km/h. The eigenfrequencies which are clearly dominating for each train passage are also different, f = 7 Hz for v_T = 100 km/h and f = 11 Hz for v_T = 160 km/h.

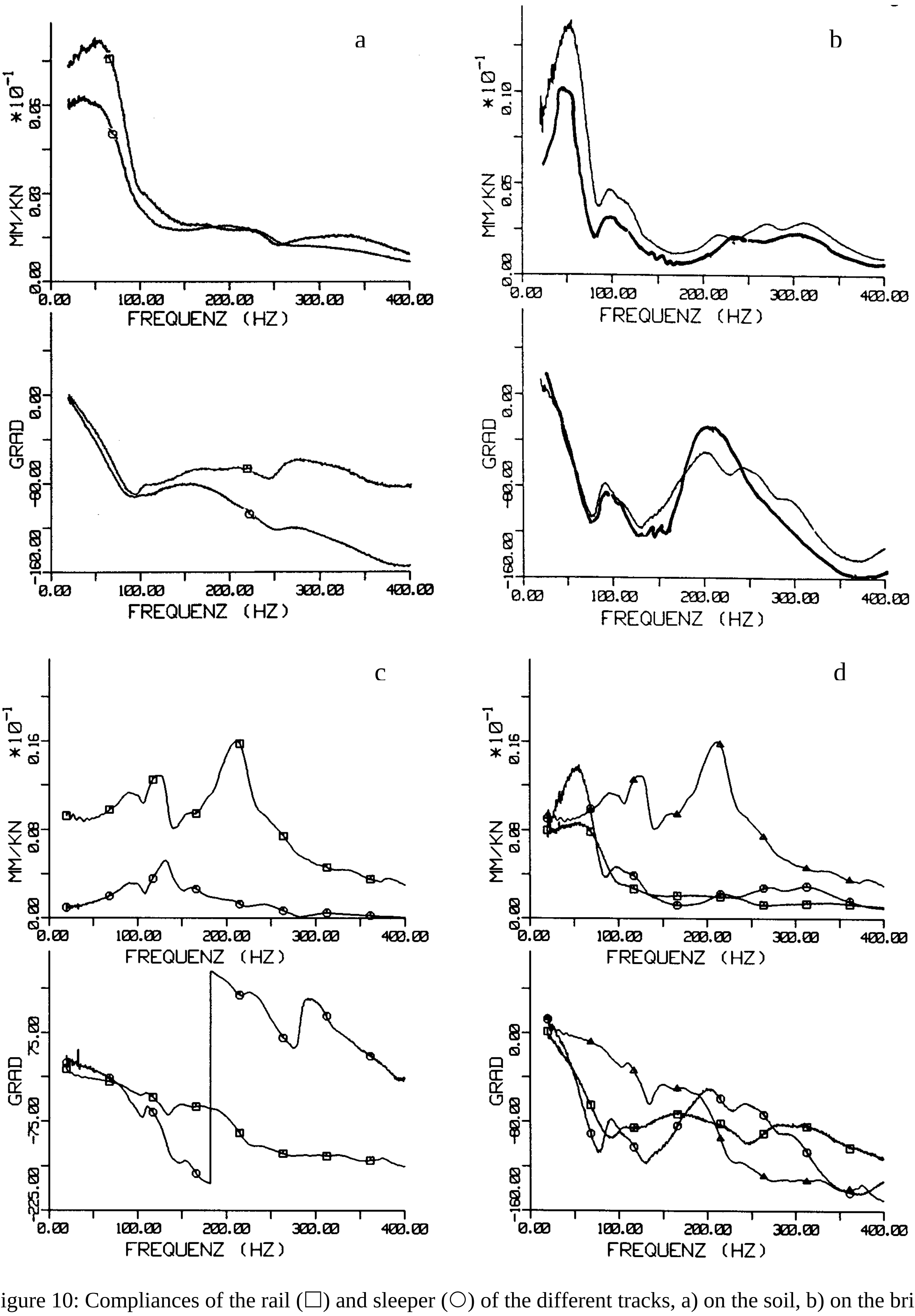

Figure 10: Compliances of the rail (☐) and sleeper (○) of the different tracks, a) on the soil, b) on the bridge, c) in the tunnel, d) comparison of the rail compliance for the ballasted track ☐ on the soil, ○ on the bridge, and △ the slab track in the tunnel.

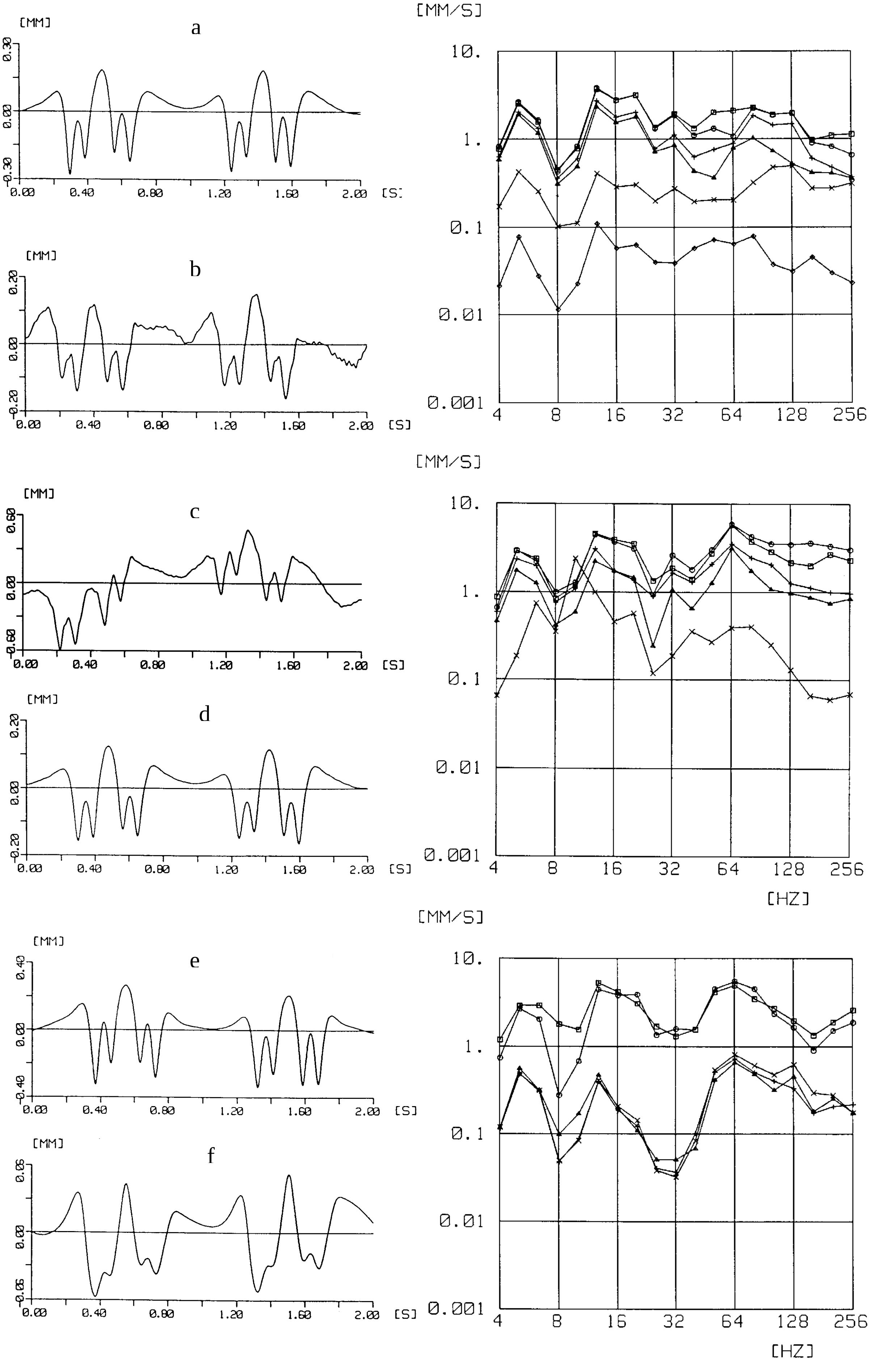
a
[MM]
0.30
0.00
-0.30
0.00 0.40 0.80 1.20 1.60 2.00 [S]
b
[MM]
0.20
0.00
-0.20
0.00 0.40 0.80 1.20 1.60 2.00 [S]
[MM/S]
10.
1.
0.1
0.01
0.001
4 8 16 32 64 128 256
c
[MM]
0.60
0.00
-0.60
0.00 0.40 0.80 1.20 1.60 2.00 [S]
d
[MM]
0.20
0.00
-0.20
0.00 0.40 0.80 1.20 1.60 2.00 [S]
[MM/S]
10.
1.
0.1
0.01
0.001
4 8 16 32 64 128 256
[HZ]
e
[MM]
0.40
0.00
-0.40
0.00 0.40 0.80 1.20 1.60 2.00 [S]
f
[MM]
0.05
0.00
-0.05
0.00 0.40 0.80 1.20 1.60 2.00 [S]
[MM/S]
10.
1.
0.1
0.01
0.001
4 8 16 32 64 128 256
[HZ]

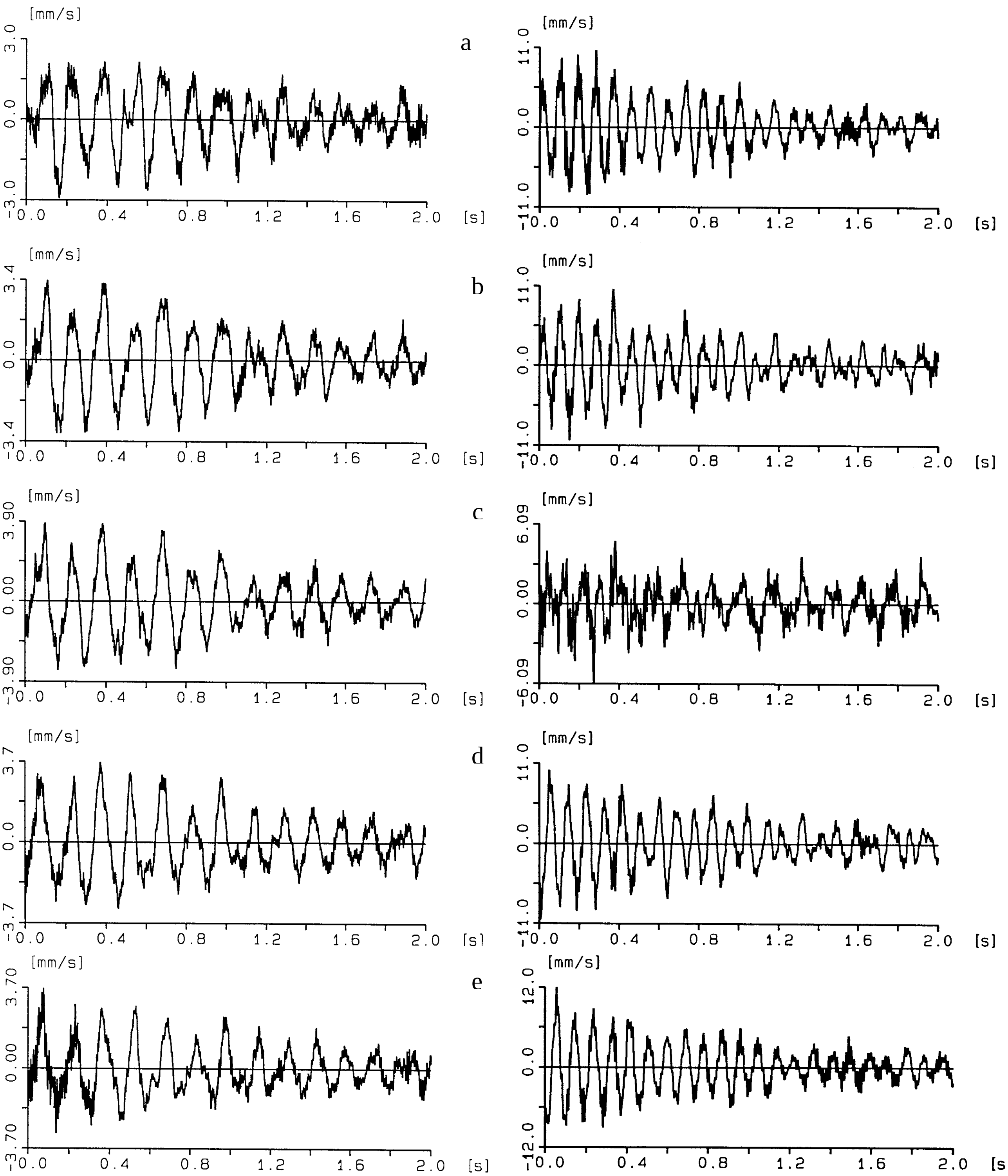

Figure 12: Time histories of the passage of the train with v_T = 100 km/h (left) and 160 km/h (right) at x = a) 7.5, b) 15, c) 22.5, d) 30, e) 37.5 m

Figure 11 (previous page): Passage of the train over the different tracks surface line (top), bridge (middle) and tunnel (bottom), time histories of the displacements of the rail (a, c, e) and the sleeper (b, d, f), third-of octave spectra of the rail (□, ○), the sleeper (△, +) and the soil, bridge or plate (×).

COMPDYN 2011
3rd ECCOMAS Thematic Conference on
Computational Methods in Structural Dynamics and Earthquake Engineering
M. Papadrakakis, M. Fragiadakis, V. Plevris (eds.)
Corfu, Greece, 25-28 May 2011

DYNAMIC EFFECTS OF RAILWAY TRAFFIC DUE TO LATERAL MOTION IN LONG VIADUCTS WITH HIGH PIERS

Jos M. Goicolea and Pablo Antolín

Dept. of Mechanics and Structures, School of Civil Engineering
Technical University of Madrid
e-mail: `jose.goicolea@upm.es`

Keywords: Instructions, ECCOMAS Thematic Conference, Structural Dynamics, Earthquake Engineering, Proceedings.

Abstract. *The layout of new high-speed railway lines often requires long slender viaducts, including continuous decks with lengths of 1000 m or more, and high piers or arches with heights over* 70 *m. These structures generally exhibit a high lateral compliance. The fundamental mode of vibration usually corresponds to this lateral motion, with frequencies lower than* 1 *Hz and associated to long wavelengths. Current experience on lateral behavior of bridges under traffic includes research work carried out by ERRI D181 committee [1], which considered problems in European bridges for conventional rail with steel open decks, and of much shorter length and deformation wavelengths. According to the conclusions from ERRI minimum lateral vibration frequencies of spans are required to be higher than* 1.2 *Hz in the new design codes [2]. However, this case does not correspond to the high speed rail viaducts described above, for which there is so far not enough evidence on the behavior nor sufficient knowledge of the relevant mechanisms. In this work we present newly developed models for considering the coupled dynamic behavior of vehicles and structure in railway viaducts. The structure is discretised with finite elements of beam and shell type, and vehicles are considered with 3D multibody models, within ABAQUS [3]. A novel technique for considering contact between wheels and rails has been developed. This model includes both vertical and lateral contact, incorporating an implementation of Kalker's FASTSIM solution technique [4], providing adequate simulation of lateral nosing motion of railway vehicles.*

The models developed are applied to a representative case, the "Arroyo de Las Piedras" viaduct [5] with a total length of 1209 m and piers of 94m height. Several simulation scenarios are compared, considering track alignment irregularities or not as well as full interaction models or simpler moving load models.

1 INTRODUCTION

A considerable investment has been done in new high speed railway lines in Spain, having in operation as of today over 2000 km of new lines with UIC gauge. Due to the orography in the Iberian peninsula, often these lines have to cross deep valleys, necessitating tunnels and viaducts. Generally these viaducts must be supported on tall piers or arches, of the order of 100 m or more, and will consist of long continuous decks, of the order of 1000 m or more. As a consequence they will generally have very low lateral stiffness and associated low natural frequencies of vibration.

Figure 1: Viaducto “Arroyo las Piedras” in Córdoba–Málaga HS line: first mode of vibration 0.313 Hz

In some cases bridges with low lateral frequencies have been seen to develop considerable vibrations, causing concern for the safety of circulation of railway vehicles. Addressing this problem was the objective of the ERRI committee D181 [1], whose work included a number of European bridges. These bridges were generally steel structures with open decks and low lateral bending stiffness. Following the conclusions of this work several limitations for lateral deformability of decks and minimum natural frequencies have been introduced in the Eurocodes [2] and national codes [6].

In principle the types of bridges considered in the ERRI report are not of the same type here considered. Although the lateral compliance is high in both cases, the long and tall viaducts typical of high speed lines have a much longer wavelength of deformation and of vibration modes, of the order of several hundreds of meters or more, whereas the ERRI bridges had lateral deformation wavelengths of the order of tens of meters. It may be expected that with these latter wavelengths it is possible to produce some resonance or dynamic amplification of the vehicles lateral movement, whose kinematic wavelengths are also in this order of magnitude. On the other hand, for a long wavelength which will be generally longer than the complete train it may be more unlikely to obtain synchronous amplification in all vehicles, as well as with nosing motion.

However, there remain important uncertainties as the lateral dynamic coupled vibrations of vehicles and bridges have not been throughly studied and the possibilities of obtaining high amplifications or resonance may lead to tragic results for the safety of passengers. Furthermore, external actions such as high lateral winds or earthquake may make these matters worse.

In this work we present a description of a model to consider in a realistic manner vehicle-bridge interaction models, in order to apply to the type of long tall slender viaducts as described above. As will be described below, models for coupled lateral dynamics of railway vehicle–bridge interaction are considerable more complex in nature than those for vertical dynamic actions, due to the specific nature of the wheel–rail contact which admits some lateral relative movement.

The model for vehicle–bridge interaction consists of five main ingredients: 1) dynamic model for structure subsystem; 2) dynamic model for vehicle subsystem; 3) geometrical description of track including irregularities; 4) wheel–rail contact model and 5) a numerical solution algorithm for the equations.

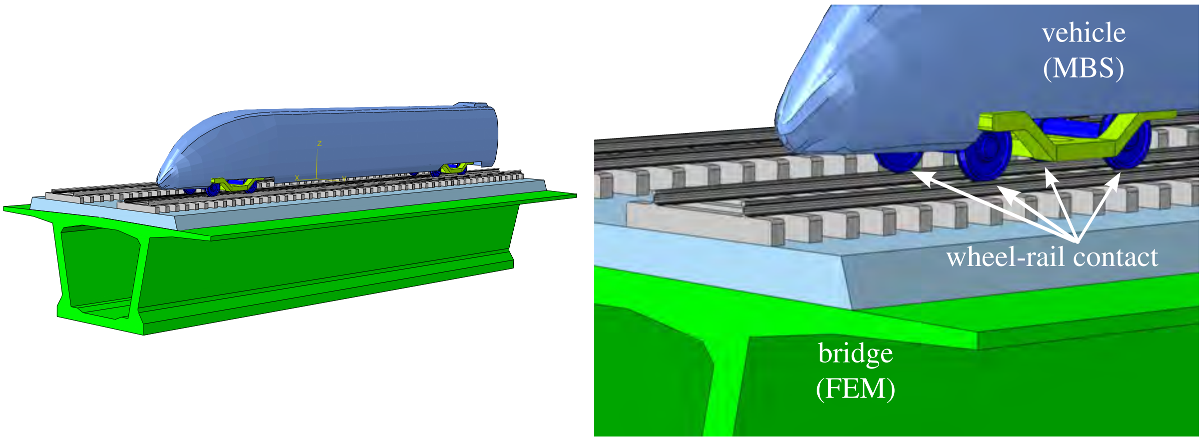

Figure 2: The basic ingredients of vehicle-structure interaction: vehicles, bridge and the interaction forces

The structure is usually discretised with finite elements, either beam type as in [7], [8], [9] or shell type as in [10] or solid [11]. Vehicle models may be assembled from rigid bodies with joints and/or constraints as *multibody dynamic models*, including discrete springs or dampers. In railway vehicle–structure dynamics generally linear models are employed [7], [8], [12], [9], [13]. More complete models with nonlinear effects are used in [14] and [15].

A key point of the vehicle-bridge interaction for lateral dynamics is to establish the geometric and dynamic relationships between both subsystems (Figure 2). For establishing these relationships wheel-rail contact theories are used.

The simplest approach for modeling the wheel-rail contact is to consider a perfectly guided path, i.e. contact points between wheels and rails share positions and velocities, approach followed in [16], [10], [13]. This approach neglects nosing relative movement between wheelsets an rails. A relatively simple option to introduce this lateral movement is to prescribe a sinusoidal relative displacement between the wheelset and the track, as in [17], [16], [12]. This procedure permits consideration of a worst case of fully developed hunting motion, thus providing a hypothetical upper bound for these effects, but is a relatively simplistic solution and does not take into account the real dynamic coupling in lateral motion. This was also the approach followed in our previous work reported in [18].

In order to include the dynamic effects from lateral motion in the wheel-rail contact the relative displacements between wheels and rails must be considered, subject to the geometric constraints and dynamic contact laws. The first basic ingredient of any such procedure is a geometric model of wheel and rail profiles. Once the position is well determined it is necessary to introduce the normal and tangential forces. For normal contact, the well established nonlinear Hertz theory [19] is probably the best option, see [7], [20], [14] and [15]. Often a linearization of this theory is applied, as in [9]. The full solution of tangential contact, including precise local slip limits at each point within every contact area requires a high amount of computer resources. For this reason Kalker's linear theory [21] is often applied in vehicle-bridge interaction models as in [7], [8], [9]. Other works more focused on the dynamic behaviour of vehicles [14], [15] introduce more realistic and complex tangential contact models, such as Kalker's variational theory [22] or the simplification of this in FASTSIM [4]. A practical alternative is the USETAB tables [23], is based on Kalker Variational Theory [22], which is the approach followed in this work.

In addition, it must be considered that tracks do not follow perfectly the ideal geometry. The alignment irregularities are an essential ingredient for excitation of laterl vibrations of vehicles. For considering a hypothetical upper bound scenario Irregularity profiles can be generated using power spectral density functions as defined in [24]. This approach is followed in [9], [18] and also in this work. Another option is of course to employ irregularity profiles measured directly from the track, as in [17], [8] and [16].

The last ingredient for the model is the strategy for numerical solutiona t each time-step. An option is to integrate separately both subsystems and establish at each time-step an iteration loop for achieving force and displacement compatibility at contact points, as in [17], [9], [25] and [26]. Another option is to form a global set of coupled equations including both subsystems can be solved directly, as in [8], [16], [12], [13] and [27]. In this work the approach followed is similar to this latter option, including both subsystems within the same dynamic model, with special emphasis on the contact interface.

In the remaining of this work firstly the details of the numerical model employed will be discussed. Following, this will be applied for the Las Piedras viaduct [5] in the spanish high-speed railway Cordoba–Malaga, which has piers of 94 m and length of 1209 m. The results obtained show that, for the scenarios considered, no adverse lateral vibration effects are foreseable.

2 NUMERICAL MODEL

The vehicle-bridge interaction system is composed of the vehicle and bridge subsystems and the contact interface between them. The model is constructed within ABAQUS simulation system [3], employing multibody capabilities for the vehicles, finite elements for the bridge, and user-developed algorithms for the compatibility between both and the contact interface.

Common cartesian coordinates are used in both subsystems: x along the bridge's lontigudinal direction, z pointing upwards and y laterally. The corresponding rotations around each of these axes will be called θ_x, θ_y and θ_z (Figure 3).

2.1 Vehicle model

The vehicle is considered as a multibody system. Car body, bogies and wheelsets are considered as rigid bodies. The primary and secondary suspensions are defined using linear springs and dampers (figure 4). Anti-yaw dampers are included in the model with appropriate definition of viscoelastic properties. For the vehicle model, the following assumptions are considered:

(A1) Small displacements are considered here (except for the wheel-rail contact interface). However this is not a limitation of the model, there is no restriction for nonlinear multibody dynamics effects should they be necessary, as a full nonlinear solution is performed at each time-step.

(A2) The train is supposed to cross the bridge at a constant speed v.

(A3) The train is composed of independent cars: no connection between cars is considered.

(A4) A constant velocity v along the x axis is considered for all the bodies of each car, therefore the degrees of freedom of car-bodies and bogies are y, z, θ_x, θ_y and θ_z. For wheelsets, θ_y is prescribed as $\dot{\theta}_y = v/r_0$, being r_0 the nominal rolling radius of wheels.

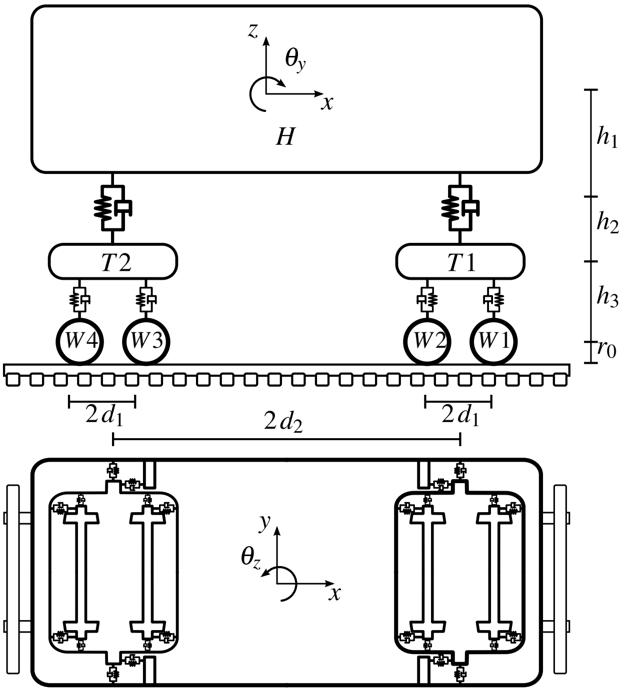

Figure 3: Vehicle schema and coordinates.

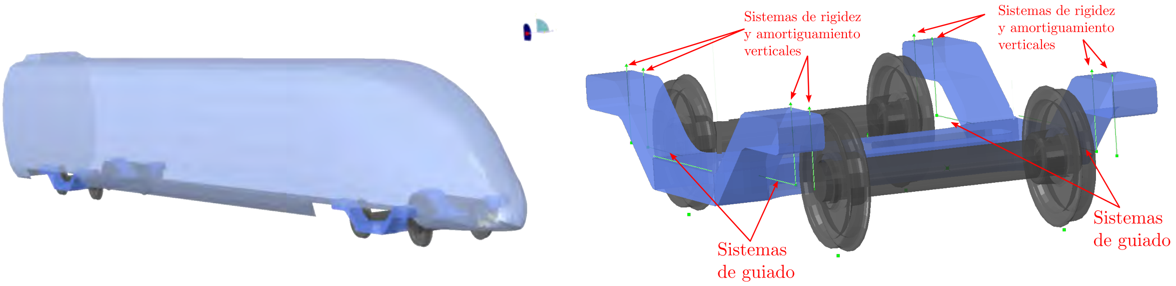

Figure 4: Multibody model showing vehicle box and bogies

(A5) The coordinates used for each of the rigid bodies are absolute inertial coordinates, not relative coordinates with respect to the bridge.

The multibody capabilities within ABAQUS program [3] are employed in this work to obtain the vehicle multibody dynamic models.

2.2 Bridge model

The bridge is modeled with finite elements through the finite element library provided within ABAQUS [3]. In general, any type of finite elements can be employed (continuum, shell, beam or truss). In this case the model has been built using 3D beam elements for the deck and the piers of the viaduct. The assumptions that have been made are:

(A6) Small displacements and linear elastic materials are considered in this case (except for the wheel-rail contact interface). However this is not a limitation of the model, there is no restriction for nonlinear effects should they be necessary, as a full nonlinear solution is performed at each time-step.

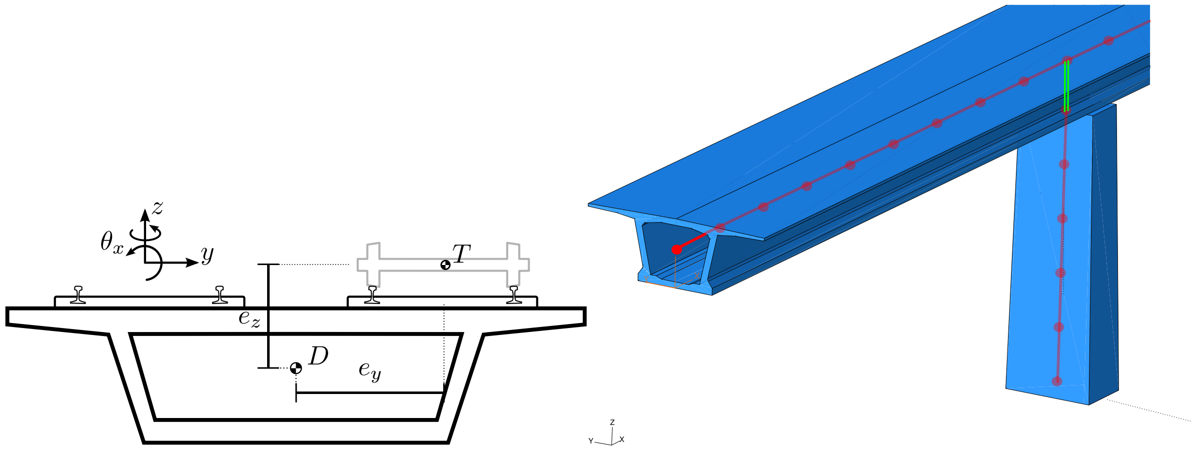

Figure 5: Schematic representation of bridge deck and 3D beam finite elements.

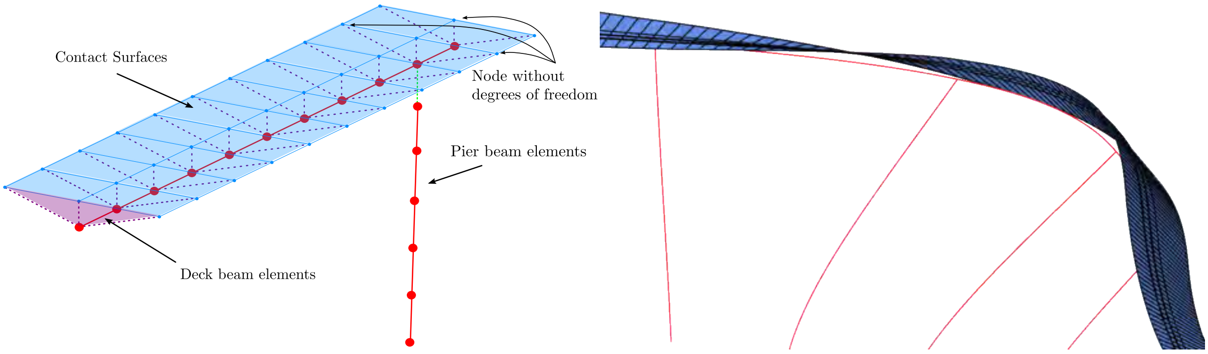

Figure 6: Kinematic constraints for wheelset position on bridge deck: schema and deformed view of rigid contact surfaces

(A7) The rails are supposed to be rigidly attached to the deck section, with the appropriate offsets and eccentricities.

(A8) Elastic effects for rail deformation are neglected.

The points on the rails corresponding to each wheelset are derived by interpolation and kinematical constraints with the beam degrees of freedom. For this purpose, special rigid contact surfaces are defined in the finite element model, linked kinematically to the structural beams (figure 6).

2.3 Track alignment irregularities

An essential ingredient for proper consideration of the vehicle dynamic effects are the track irregularities. For this work irregularities for horizontal alignment and vertical profile were considered as these will be the most important for lateral dynamics. In order to provide probabilistic upper bounds, irregularities were generated from a power spectral density spectrum adjusted to upper bounds of deviations to be expected in the wavelength between 3 and 25 m from maintenance operations (figure 7). The procedure used here is similar to that followed in [24]

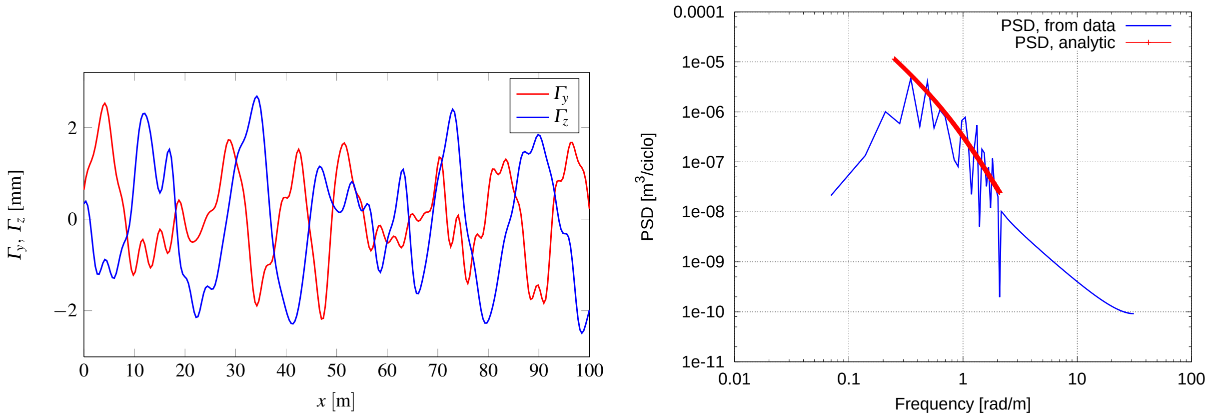

Figure 7: Profile of generated alignment irregularities and check for fit to PSD spectrum

2.4 Vehicle-bridge interaction

The final ingredient are the forces for establishing the interaction between the vehicle and the structure. This is achieved through contact models, including geometric and dynamic components. The coupled system of equations may be represented as:

$$\begin{pmatrix} \boldsymbol{\mathsf{M}}^V & \mathbf{0} \\ \mathbf{0} & \boldsymbol{\mathsf{M}}^B \end{pmatrix} \begin{Bmatrix} \ddot{\mathbf{X}}^V \\ \ddot{\mathbf{X}}^B \end{Bmatrix} \begin{pmatrix} \boldsymbol{\mathsf{C}}^V & \mathbf{0} \\ \mathbf{0} & \boldsymbol{\mathsf{C}}^B \end{pmatrix} \begin{Bmatrix} \dot{\mathbf{X}}^V \\ \dot{\mathbf{X}}^B \end{Bmatrix} \begin{pmatrix} \boldsymbol{\mathsf{K}}^V & \mathbf{0} \\ \mathbf{0} & \boldsymbol{\mathsf{K}}^B \end{pmatrix} \begin{Bmatrix} \mathbf{X}^V \\ \mathbf{X}^B \end{Bmatrix} = \begin{Bmatrix} \mathbf{F}^V + \mathbf{F}_c^V \\ \mathbf{F}^B + \mathbf{F}_c^B \end{Bmatrix}, \tag{1}$$

where superscripts $(\cdot)^V$ and $(\cdot)^B$ refer to the vehicle and bridge subsystems respectively. Additionally, $\mathbf{F}_c^V$ is the vector of forces applied on the vehicle as a consequence of the interaction with the structure, and $\mathbf{F}_c^B$, on the structure, which will be computed from the vehicle and bridge displacements, velocities and time. The components of the contact forces are described in Section 2.5.

Equation (1) will be solved directly in time using the HHT Method [28], which is an implicit algorithm. The tangent matrices of contact forces are needed for the numerical solution:

$$\boldsymbol{\mathsf{K}}_c = \frac{\mathrm{d}\mathbf{F}_c}{\mathrm{d}\mathbf{X}}, \quad \boldsymbol{\mathsf{C}}_c = \frac{\mathrm{d}\mathbf{F}_c}{\mathrm{d}\dot{\mathbf{X}}}, \tag{2}$$

where $\mathbf{F}_c = (\mathbf{F}_c^V, \mathbf{F}_c^B)^{\mathrm{T}}$. The expressions of the tangential forces applied in this work do not have analytical derivatives and hence the tangent matrices are computed using numerical jacobians.

2.5 Nonlinear contact forces

The wheel-rail contact forces are developed in this Section. Considering some assumptions, that are expossed below, this problem can be split in three main parts:

Geometric problem: it consists on computing the main geometric variables which depend on the relative displacements between wheel and rail.

Normal problem: considering the geometric variables obtained before, the contact ellipse dimensions and the normal stress distribution is calculated using the Hertz theory [19].

Tangential problem: the tangential forces, which depend on the contact geometry, normal stresses and relative velocities between wheel and rail, are computed.

According to [22], if the wheel and rail materials have the same mechanical properties, the three problems can be studied separately: geometric problem is solved firstly, normal problem secondly and tangential problem thirdly.

2.5.1 Geometric contact problem

For obtaining the main geometric variables of the contact problems serveral assumptions are made:

(A9) Separations between wheel and rail are not allowed.

(A10) The wheel-rail contact appears only in one area.

(A11) Only rigid body movements perpendicular to x axis are considered for the wheelset and the track.

Considering that the distance between two wheelset of the same wheelset is $2d_W$, the geometric variables can be computed as a function of only variable: the lateral displacement of the wheelset relative to the track Δy_W. These geometric variables for wheels A and B (Figure 9) are (see Figure 8):

- r_A and r_B: the rolling radii of both wheels at the contact point.
- γ_A and γ_B: the angle between horizontal and contact plane (the plane where the contact ellipse is contained).
- k_A^a, k_A^b, k_B^a and k_B^b : ellipse dimension coefficients that depend on the curvatures of wheel and rail in the two main directions at the contact point (see [19]). a is the ellipse semiaxis along x_c, and b along y_c.
- $\Delta\hat{z}_W$ and $\Delta\hat{\theta}_{x,W}$: relative vertical displacement and rotation between the wheelset and the track, considering only geometric conditions.

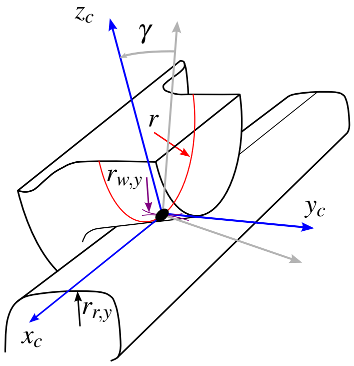

Figure 8: Main variables of the contact geometry.

In this article, realistic wheel and rail profiles are considered (biconic profiles are avoided), due to that, when the relative lateral displacements of the wheelset respect to the track are small, the variation of the previous variables is linear. However, when the displacements become larger, contact between the flange of the wheel and the rail occurs, and the variation becomes nonlinear.

The relative displacements of the wheelset of vehicle respect to the track are:

$$\Delta y_W = y_W - y_T^B(x)\,, \tag{3a}$$

$$\Delta z_W = z_W - z_T^B(x)\,, \tag{3b}$$

$$\Delta \theta_{x,W} = \theta_{x,W} - \theta_{x,T}^B(x)\,, \tag{3c}$$

$$\Delta \theta_{z,W} = \theta_{z,W} - \theta_{z,T}^B(x)\,, \tag{3d}$$

being y_W, z_W, $\theta_{x,W}$ and $\theta_{z,W}$ the absolute displacements and rotations of the wheelset.

2.5.2 Normal contact problem

The Hertz theory [19], for solving the shape and dimensions of the contact surface and the normal stress distribution, take into consideration the following assumptions:

(A12) At contact point, contact surfaces are continuous and nonconformal.

(A13) No plastic deformation is considered and strains are supposed to be small and elastic.

(A14) Stresses are neglected far from contact point.

(A15) Friction between surfaces does not affect to normal problem.

(A16) Quadratic functions of two variables can be used to define the wheel and rail surfaces near to contact point.

With these assumptions, contact area is considered an ellipse and normal stress distribution an ellipsoid.

The ellipse semiaxes can be computed as:

$$a^k = k_k^a(\Delta y_W)\left(\frac{1-\nu}{G}N^k\right)^{1/3} \tag{4a}$$

$$b^k = k_k^b(\Delta y_W)\left(\frac{1-\nu}{G}N^k\right)^{1/3} \tag{4b}$$

where $k = \{A, B\}$, G is the shear stress modulus, ν the Poisson coefficient of wheels and rails and N^k the contact normal force in wheel-rail pair (it is explained below how to compute these normal forces). The coefficients k_k^a and k_k^b, which depend on Δy_W, are computed before the calculation and depend on the main curvatures of wheel and rail at contact point (see [4]).

2.5.3 Tangential contact problem

In this problem the tangential contact forces are computed. They appear as a consequence of a rolling and sliding motion between wheels and rails. In each point of the contact surface the shear stress value can not be greater than the normal stress times friction coefficient. Thus, in the contact ellipse adhesion and slip areas could appear.

The main variables of the tangential contact are the creepages, which are defined as the non dimensional relative velocities between wheel and rail. ζ_x^k, ζ_y^k and ζ_R^k are, respectively, longitudinal, lateral and rotational creepages of wheel-rail pair k and can be expressed as:

$$\zeta_x^k = 1 - \frac{r_k}{r_0} \pm \frac{\Delta\dot{\theta}_{z,W}}{v} d_W \tag{5a}$$

$$\begin{aligned}\zeta_y^k = \frac{1}{v} \, \big[& \big(\Delta\dot{y}_W + \Delta\dot{\theta}_{x,W}\, r_k\big) \cos\gamma_k \\ & + \big(\Delta\dot{z}_W \pm \Delta\dot{\theta}_{x,W}\, d_W\big) \sin\gamma_k \big]\end{aligned} \tag{5b}$$

$$\zeta_R^k = -\frac{\sin\gamma_k}{r_0} \tag{5c}$$

where the upper sign of ± and ∓ in the above equations corresponds to the wheel-rail pair A, and the lower, to B (see Figure 9).

Depending on the assumed hypothesis, different methods for solving tangential contact exist. The Kalker Variational Method [22] is a very accurate method for computing tangential forces, however, due to it is computationally very expensive, it can not be applied in an analysis like that. The USETAB approximation [23], proposed by Kalker, is used in this work. This method obtains the tangential forces in a pre-calculated table whose input variables are the contact normal force, the ellipse semiaxes, the friction coefficient and the creepages, and the output variables are the tangential forces in longitudinal T_x^k and lateral T_y^k local directions and moment around normal direction M_z^k. The values of this table have been computed using the Kalker Variational method for different values of the input variables.

2.5.4 Vehicle-structure interaction forces

As it has been seen above, vertical relative displacement Δz_W and relative rotation $\Delta\theta_{x,W}$ can be computed as geometric variables, without regard to dynamic aspects. Thus, the relative displacements computed as geometric variables and those obtained from the dynamic response of vehicle and structure must be equal:

$$\Delta z_W = \Delta\hat{z}_W(\Delta y_W)\,, \tag{6a}$$

$$\Delta\theta_{x,W} = \Delta\hat{\theta}_{x,W}(\Delta y_W)\,. \tag{6b}$$

For imposing these constraints, a penalty force and moment are introduced in wheelsets gravity centre:

$$F_c^z = k_z\,\left(\Delta\hat{z}_W(\Delta y_W) - \Delta z_W\right)^{3/2}\,, \tag{7a}$$

$$M_c^x = k_\theta\,\left(\Delta\hat{\theta}_{x,W}(\Delta y_W) - \Delta\theta_{x,W}\right)^{3/2}\,. \tag{7b}$$

These nonlinear penalty expresions derive from the approach expression bewtween two bodies of the Hertz theory. Stiffness coefficients k_z and k_θ depend on Δy_W and N_W^k, but in order to simplify the equations, they are computed considering only the train own weight in a static case and $\Delta y_W = 0$.

The forces applied on the wheelset gravity centre, shown in Figure 9, can be written as:

$$F_c^y = -N^A \sin\gamma_A + T_y^A \cos\gamma_A - N^B \sin\gamma_B + T_y^B \cos\gamma_B \,, \tag{8a}$$

$$F_c^z = N^A \cos\gamma_A + T_y^A \sin\gamma_A + N^B \cos\gamma_B + T_y^B \sin\gamma_B \,, \tag{8b}$$

$$\begin{aligned} M_c^x = \Big(&-N^A \cos\gamma_A - T_y^A \sin\gamma_A + N^B \cos\gamma_B \\ &+ T_y^B \sin\gamma_B\big)\, d_W + \Big(T_y^A \cos\gamma_A - N^A \sin\gamma_A\Big)\, r_A \\ &+ \big(-N^B \sin\gamma_B + T_y^B \cos\gamma_B\big)\, r_B \,, \end{aligned} \tag{8c}$$

$$M_c^z = \Big(T_x^A - T_x^B\Big)\, d_W + M_z^A \cos\gamma_A + M_z^B \cos\gamma_B \,. \tag{8d}$$

Using equations (7), (8b) and (8c), normal forces N^A and N^B, which are needed to compute the tangential forces and moments, can be obtained and applied to compute the values of F_c^y and M_c^z. Thus, the equation set (8) is nonlinear and, in order to solve a linear system, as it is proposed in [14], the normal forces computed in the previous time step are used for computing the tangential forces in the current time step. Before obtaining F_c^y and M_c^z, the contact forces T_y^A, T_x^B, T_y^B and moments M_z^A and M_z^B must be computed using normal forces of the previous time step and the creepages of current step.

3 Application

3.1 Models for viaduct “Arroyo las Piedras”

The above numerical model has been applied to a bridge representative of the type discussed in this work, the “Arroyo las Piedras” viaduct, in operation in the Córdoba–Málaga high speed line. The viaduct is a double-track composite steel-concrete continuous deck beam, supported on concrete piers with pot-type bearings. The spans of the deck are of 65 m, and the section has upper and lower concrete slabs performing a so-called double composite action, with adequate torsional stiffness. The tallest piers are of 94 m height. The first natural frequency oc this viaduct is 0.313 Hz and corresponds to a lateral deformation mode (figure 1). More complete details of the structure may be seen in [5].

As described above, the model for the viaduct is based on 3D beams with appropriate kinematic constraints. The Rayleigh method has been used for the damping matrix of the structure subsystem, with a 0.5% damping centered in the two first natural frequencies. The train that has been used in the calculations is an approximation of the Siemens ICE 3 composed of 8 cars, each of 24.775 m length. The ICE3 is a distributed power train, and, for that reason, all cars ares supposed to have the same geometrical and mechanical properties.

Calculations have been carried out for train speeds of 250, 300 and 350 km/h, in several different models:

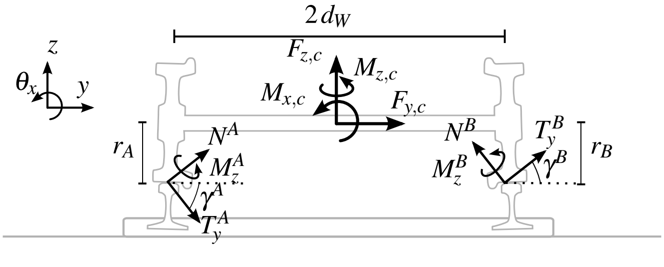

Figure 9: Wheelset equilibrium.

(1) *Bridge only model with moving loads*, consisting only of the bridge dynamic subsystem, with the vehicle wheelsets simplified as moving loads of fixed magnitude. This amounts to neglecting the dynamic effects of vehicle vibration, and serves as a basic result with which to compare the influence of the vehicle vibration on the results. It also serves the purpose of obtaining a so-called *virtual path* for the wheelsets of the vehicles, which can be later applied to these in a decoupled approach to the vehicle-bridge dynamics: the bridge history of displacements is obtained in a first step, and these histories are then applied in a second step to the vehicle wheelsets to obtain the response of the train.

(2) *Vehicle model*, consisting only of the vehicle subsystem, in two different scenarios:

  (a) Vehicle on rigid platform (i.e. no bridge) with prescribed profiles of irregularities. This model will enable to compare the influence of the bridge deformation on the vibrations of the vehicle.

  (b) Vehicle on *virtual path*, as described above, this path results from previous analysis of the bridge with moving loads. The geometric track irregularities are added to the *virtual path* in order to consider their effect on the vehicle.

(3) *Bridge-Vehicle model*, performing the calculation for the global system with the wheel-rail contact interaction. In this case, two scenarios have been considered:

  (a) Model with interaction but without track irregularities

  (b) Model with interaction and with track irregularities

3.2 Results for bridge and vehicle response

Following we show only the results for train speed of $v = 350$ km/h, as they correspond to the greatest effects. Firstly we present results for the deformation of the bridge deck. The displacements and rotations at the center of span 11, corresponding to the tallest pier, are shown in figure 10. These correspond to the three different scenarios defined in section 3.1, the cases enumerated as 1, 3a and 3b. It may be clearly seen that the influence of the vehicle vibration and of the track irregularities on the bridge deformation is negligible. It is also seen that these deformations are small, with maximum lateral displacement of 9 mm, which for a viaduct of 1209 m length is very small.

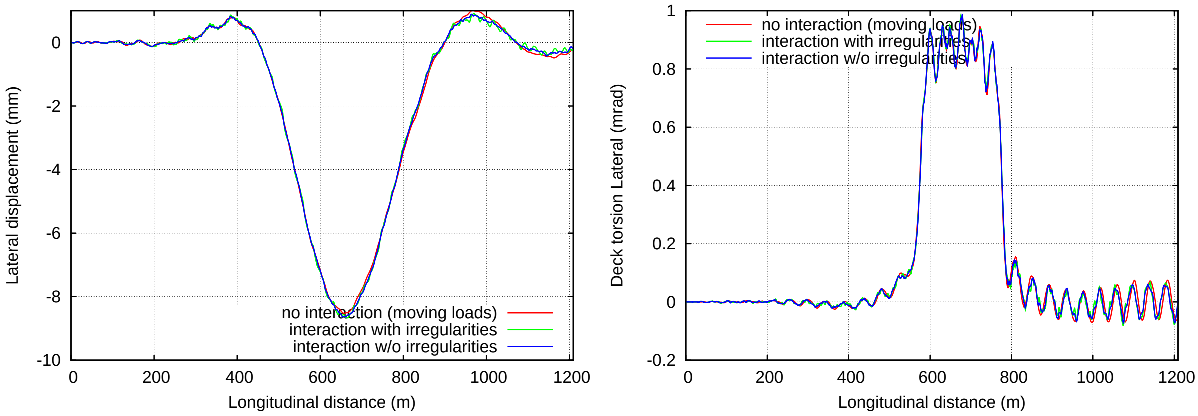

Figure 10: Displacements and torsional rotation of bridge deck at center of span 11, $v = 350$ km/h.

Regarding the response of the vehicle, the accelerations of vehicle body on coach 4 are shown in figure 11. Four scenarios are shown, as defined in section 3.1, the cases enumerated as 2a, 2b, 3a and 3b. Maximum accelerations experienced are in the order of $0.2 – 0.3\,\mathrm{m/s^2}$. First we remark that very clearly irregularities are the main cause responsible for vehicle vibrations, as in the case 2a accelerations are negligible compared to other cases with irregularities. In other words, the vehicle body accelerations attributable to deformation of the bridge are of the order of $0.05\,\mathrm{m/s^2}$. In figure 12 the lateral loads exerted by one of the wheels of the vehicle on the rail are shown. These achieve maximum values of the order of 15 kN.

4 CONCLUSIONS

The following remarks are concluded from the above work:

- Lateral dynamic effects in tall and long railway viaducts are an important issue with high lateral compliance must be studied in order to consider adequately the safety of the traffic.
- In this paper a model considering the dynamics of the bridge, the vehicle and the geometric and dynamic aspects of wheel-rail contact has been developed and validated. This model includes multibody subsystems for the vehicles, a structural finite element subsystem for the viaduct, and a specially developed wheel-rail contact interface between them.
- The case of HS viaduct on “Arroyo las Piedras” [5] has been studied as a representative case. The loading considered includes only the vertical effects from the traffic, considering track alignment irregularities, but not other possible actions such as lateral wind or earthquake. For the cases studied it is shown that the lateral effects on the viaduct are small and do not compromise in any way its safety.
- The lateral vibration of the vehicle is originated mainly from the assumed irregularities of the track, with a small contribution from the bridge deformation and interaction. The level of acceleration obtained as well as the loads transmitted by vehicle wheels to the rails are small and well within acceptable limits.
- The above procedure could be applied to evaluate realistically the effect of high lateral winds on the vehicles as they traverse the viaduct, as well as the earthquake actions.

Acknowledgments

The authors are grateful for support from Ministerio de Fomento of Spanish Government in the project *Efectos del viento transversal sobre la circulación de vehículos ferroviarios. Determinación de valores límite* (PT-2007-024-17CCP) and the Technical University of Madrid, Spain.

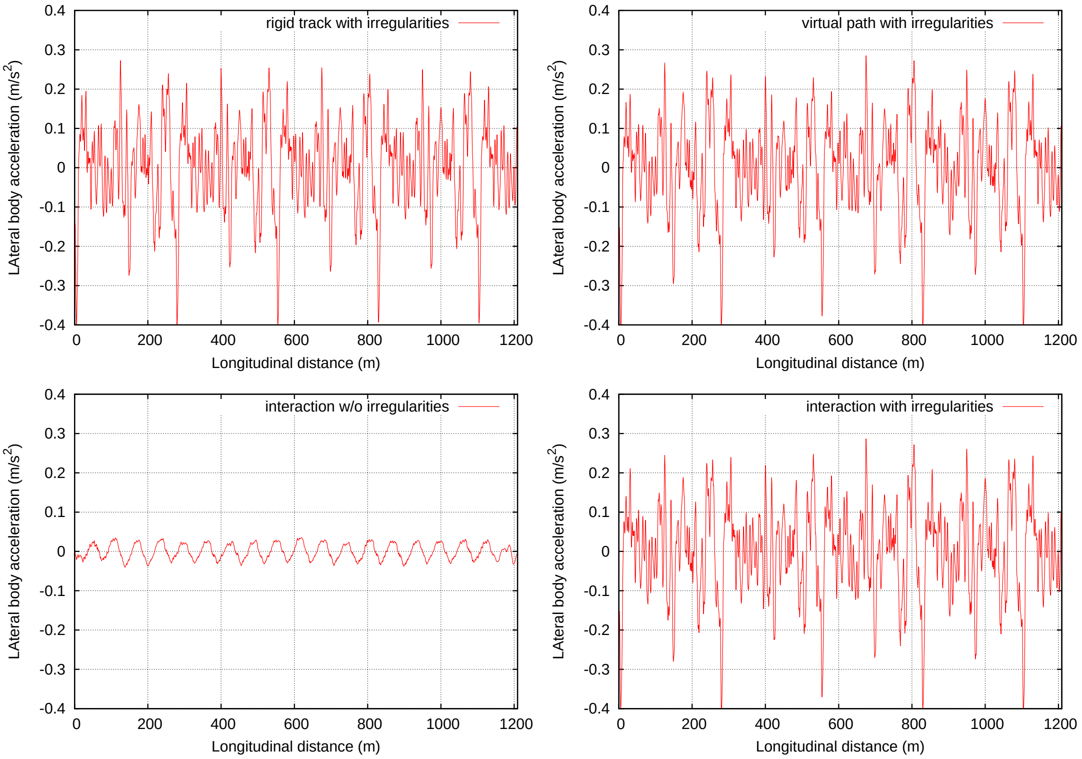

Figure 11: Acceleration of coach body, $v = 350$ km/h

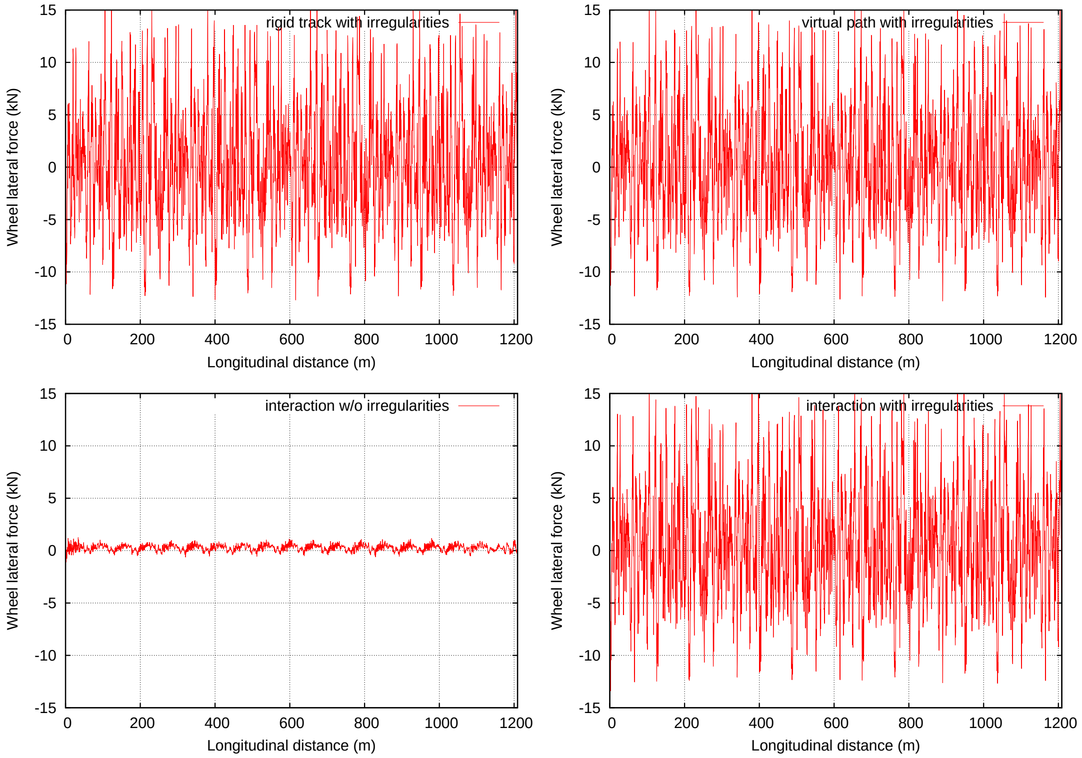

Figure 12: Lateral wheel force (for a single wheel), $v = 350$ km/h

REFERENCES

[1] ERRI, *Forces Latérales sur les Ponts Ferroviaires. Rapport final RP6*, European Railway Research Institute, 1996.

[2] European Committee for Standardization, *EN1990-A1: EUROCODE 0 – Basis of Structural Design, Ammendment A1: Annex A2, Application for bridges*, European Union, 2005.

[3] SIMULIA, 166 Valley Street Providence, RI 02909 USA, *Abaqus/Standard 6.9*, 2010, www.simulia.com.

[4] J J Kalker, *Three-Dimensional Elastic Bodies in Rolling Contact (Solid Mechanics and Its Applications)*, Springer, 1990.

[5] F. Millanes, J. Pascual, and M. Ortega, "'Arroyo las Piedras' viaduct: The first composite steel–concrete high speed railway bridge in spain," *Structural Engineering International*, vol. 17, no. 4, pp. 292–297, 2007.

[6] Ministerio de Fomento, *IAPF-07: Instrucción sobre las acciones a considerar en el proyecto de puentes de ferrocarril*, Government of Spain, 2007.

[7] M Tanabe, H Wakui, N Matsumoto, H Okuda, M Sogabe, and S Komiya, "Computational model of a Shinkansen train running on the railway structure and the industrial applications," *Journal of Materials Processing Technology*, vol. 140, no. 1-3, pp. 705–710, 2003.

[8] N Zhang, H Xia, W W Guo, and G De Roeck, "A Vehicle-Bridge Linear Interaction Model and Its Validation," *International Journal of Structural Stability and Dynamics*, vol. 10, no. 02, pp. 335, 2010.

[9] D V Nguyen, K D Kim, and P Warnitchai, "Simulation procedure for vehicle-substructure dynamic interactions and wheel movements using linearized wheelrail interfaces," *Finite Elements in Analysis and Design*, vol. 45, no. 5, pp. 341–356, 2009.

[10] M K Song, H C Noh, and C K Choi, "New three-dimensional finite element analysis model of high-speed train-bridge," *Engineering Structures*, vol. 25, pp. 1611–1626, 2003.

[11] L Kwasniewski, H Li, J Wekezer, and J Malachowski, "Finite element analysis of vehicle-bridge interaction," *Finite Elements in Analysis and Design*, vol. 42, no. 11, pp. 950–959, 2006.

[12] H Xia and N Zhang, *Dynamic Interaction of Vehicles and Structures*, Science Press, Beijing, China, 2nd edition, 2005.

[13] Y B Yang and J D Yau, "Vehicle-bridge interaction element for dynamic analysis," *Journal of Sound and Vibration*, vol. 123, no. 11, pp. 1512–1518, 1997.

[14] A A Shabana, K E Zaazaa, and H Sugiyama, *Railroad Vehicle Dynamics: A Computational Approach*, CRC Press, 2008.

[15] K Popp and W Schiehlen, *Ground Vehicle Dynamics*, Springer Berlin Heidelberg, Chennai, 1st edition, 2010.

[16] H Xia, N Zhang, and G D Roeck, “Dynamic analysis of high speed railway bridge under articulated trains,” *Computers & Structures*, vol. 81, pp. 2467–2478, 2003.

[17] N Zhang, H Xia, and W Guo, “Vehicle-bridge interaction analysis under high-speed trains,” *Journal of Sound and Vibration*, vol. 309, no. 3-5, pp. 407–425, 2008.

[18] R. Dias, J.M. Goicolea, F. Gabaldon, M. Cuadrado, J. Nasarre, and P. Gonzalez, “A study of the lateral dynamic behaviour of high speed railway viaducts and its effect on vehicle ride comfort and stability,” in *Bridge Maintenance, Safety, Management, Health Monitoring and Informatics*, Koh & Frangopol, Ed., Seoul, 14-16 jul 2008, IABMAS08: Fourth International Conference on Bridge Maintenance, Safety and Management, pp. 724–735, Taylor & Francis Group London, ISBN 978-0-415-46844-2.

[19] H Hertz, “Über die berührung fester elasticher körper and über die härtean,” *J. für reine und agewandte Mathematik*, vol. 92, pp. 156–171, 1882.

[20] D V Nguyen, K D Kim, and P Warnitchai, “Dynamic analysis of three-dimensional bridge-high-speed train interactions using a wheelrail contact model,” *Engineering Structures*, vol. 31, no. 12, pp. 3090–3106, 2009.

[21] J J Kalker, *On the rolling contact of two elastic bodies in the presence of dry friction*, Ph.D. thesis, Delft Unversity of Technology, 1967.

[22] J J Kalker, “The computation of three-dimensional rolling contact with dry friction,” *International Journal for Numerical Methods in Engineering*, vol. 14, no. 9, pp. 1293–1307, 1979.

[23] J J Kalker, “Book of tables for the Hertzian creep-force law,” in *Proceedings of the 2nd Mini Conference on Contact Mechanics and Wear of Wheel/Rail Systems*, I Zobory, Ed., Budapest: Technical University of Budapest, 1996, pp. 11–20.

[24] H Claus and W Schiehlen, “Modeling and Simulation of Railway Bogie Structural Vibrations,” *Vehicle System Dynamics*, vol. 29, no. 1, pp. 538–552, Aug. 1997.

[25] Y L Xu, N Zhang, and H Xia, “Vibration of coupled train and cable-stayed bridge systems in cross winds,” *Engineering Structures*, vol. 26, pp. 1389–1406, 2004.

[26] G De Roeck, J Maeck, and A Teughels, “Train-bridge interaction: Validation of numerical models by experiments on high-speed railway bridge in Antoing,” in *TIVC’2001*, Beijing, 2001, pp. 283–294.

[27] J D Yau and Y B Yang, “Vibration reduction for cable-stayed bridges traveled by high-speed trains,” *Finite Elements in Analysis and Design*, vol. 40, pp. 341–359, 2004.

[28] H M Hilber, T J R Hughes, and R L Taylor, “Improved numerical dissipation for time integration algorithms in structural dynamics,” *Earthquake Engineering & Structural Dynamics*, vol. 5, pp. 283–292, 1977.

COMPDYN 2011
3rd ECCOMAS Thematic Conference on
Computational Methods in Structural Dynamics and Earthquake Engineering
M. Papadrakakis, M. Fragiadakis, V. Plevris (eds.)
Corfu, Greece, 25–28 May 2011

DYNAMICS OF A PRECAST SYSTEM FOR HIGH-SPEED RAILWAY TRACKS

Vale C.[1], Ribeiro N. [1], Calçada R. [1] and Delgado R.[1]

[1] Faculdade de Engenharia da Universidade do Porto
R. Dr. Roberto Frias s/n 4200-465 Porto, Portugal
e-mail: cvale@fe.up.pt, nribeiro@fe.up.pt , ruiabc@fe.up.pt , rdelgado@fe.up.pt

Keywords: Railway tracks, Dynamics, Precast slabs

Abstract. *As far as slab tracks are concerned, UIC [1] considers seven different families of structures, regarding the type of slab supporting (punctual or continuous), the construction method (in situ or precast), the number of resilient levels and also the type of the foundation material (plain concrete or bituminous material).*

This paper begins with a brief description of precast slab systems currently available for high-speed railway lines. A research work on the dynamic behavior of precast slab tracks is being undertaken in order to identify the dynamic effects of high-speed traffic in this type of systems. In this paper some of the results attained so far in the numerical calculations are presented and discussed. Calculations are performed in 2D with the finite element program Ansys, considering several vehicle speeds and also different types of vehicle models. The dynamic response of the track is evaluated in terms of track displacement, force at the fastening systems, bending moment on the slab and also on the support concrete layer. Also the influence of the track foundation and the track geometrical quality on its response is studied.

1 INTRODUCTION

According to the Technical Specification for Interoperability (TSI) relating to the infrastructure [2], there are three types of high speed railways: new lines for speed higher than 250 km/h; specially upgrade lines for speed higher around 200 km/h; new or upgrades lines with technical constraints.

In general, railway tracks can be categorized in ballasted systems and ballastless or slab systems. Nowadays, there are two currents of opinion on the track concept for high speed railway lines. The first one defends the ballasted track -the traditional permanent-way. The second current considers that slab tracks can meet the exigent demands of a modern railway track for high speed lines with reduced maintenance actions.

As far as slab tracks are concerned, UIC [1] considers seven different families of structures, regarding the type of slab supporting (punctual or continuous), the construction method (in situ or precast), the number of resilient levels and also the type of the foundation material (plain concrete or bituminous material), which are:

1. systems without punctual fixing of the rail;
2. systems with punctual fastening of the rail and independent stretches of rail;
3. systems with punctual fastening of the rail on sleepers incorporated in structure by infill concrete;
4. systems with punctual fastening of the rail on sleepers incorporated in structure by vibration;
5. systems with punctual fastening of the rail on sleepers laid and anchored on a supporting structure;
6. systems with punctual fastening of the rail on sleepers separated from supporting structure by a resilient level;
7. systems with punctual fastening of the rail on prefabricated slabs.

Currently commercial prefabricated slabs present a wide variety of dimensions, materials and configurations. These prefabricated slabs may be reinforced or prestressed into which fastening systems and rails are incorporated.

Figures 1 to 3 present the most known precast slabs used in high speed railways lines: the Bogl, the OBB-Porr and the Shinkansen systems.

Figure 1: Bogl system

Figure 2: OBB-Porr system

Figure 3: Shinkansen system

The Bogl system (Figure 1) consists in prestressed slabs in the transversal direction fixed with spindles on a stabilised layer in the earthworks case, on a tunnel base or on a bridge deck [3]. The OBB-Porr system (Figure 2) is a conventionally-reinforced precast concrete slab with two rectangular openings from where concrete is introduced during construction in the site. This concrete block ensures the transfer of forces in the horizontal direction. The joints between adjacent slabs are no filled. The Shinkansen system (Figure 3) is used by the Japanese National Railways and it has provided excellent performance by maintaining track geometry and reducing maintenance costs of the track. The geometrical configuration of this system is more complex than the two previous ones, because of the slab geometry and also because of the existence of stoppers between adjacent slabs. Complete descriptions of these precast systems and others (in situ) slab systems may be found in [1, 3, 4, 5].

2 VEHICLE TRACK INTERACTION MODEL

In general, the simulation of train-track interaction implies that the whole system is divided into two subsystems, the vehicle and the track, and between them a physical wheel-rail contact. Until recently the behavior of these dynamic subsystems were investigated separately but the increase of train speed demands a better understanding of the dynamic phenomena, considering the vehicle and the track together as an unique system. In the present study a time domain methodology is adopted to calculate the interaction forces between the wheel and the rail and the track vibrations, in the vertical direction.

2.1 Vehicle model

Assuming loading to be symmetrically distributed on the two rails, 2D models can be adopted to represent the vehicle, such as the models presented in Figures 4 to 6.

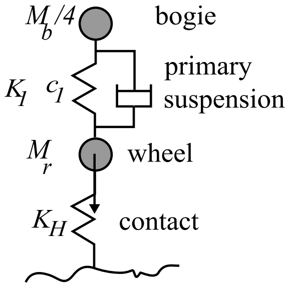

Figure 4: Quarter bogie model

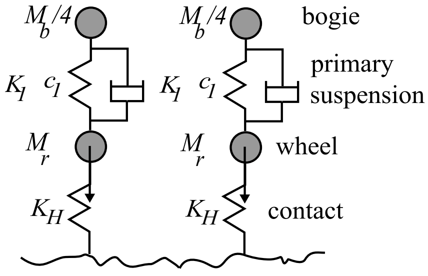

Figure 5: Two independent quarter bogie model

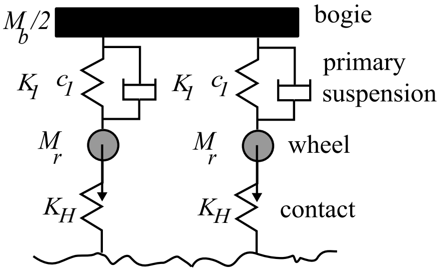

Figure 6: Half bogie model

In all these models, the vehicle is characterized by the wheel and the bogie masses and by the primary suspension represented by a linear spring in parallel to a dashpot. The two independent quarter bogie model (Figure 5) and the half bogie model (Figure 6) allow to consider the superposition of the action of the two bogie axles in the track response. In the half bogie model, the two axles are connected by the bogie, which is more realistic than the two independent quarter bogie model.

2.2 Track model

A rail track is a complex structure and in the case of slab track it is composed by rails, pads, sleepers, slab, concrete support layer and foundation.

To represent the precast slab track in study the model indicated in Figure 7 may be used. The rail is modeled as a continuous beam discretely supported on sleepers. The fastening systems and the pads are represented by springs in parallel with dashpots; theirs masses are disregarded. The slab and the concrete support layer are modeled by plain stress finite elements. The foundation is modeled by distributed springs in parallel to dashpots with no interaction between them (Winker foundation with damping). The joint between adjacent slabs are filled with an elastic material with the same mechanical characteristics of the interface layer between the slab and the concrete support layer.

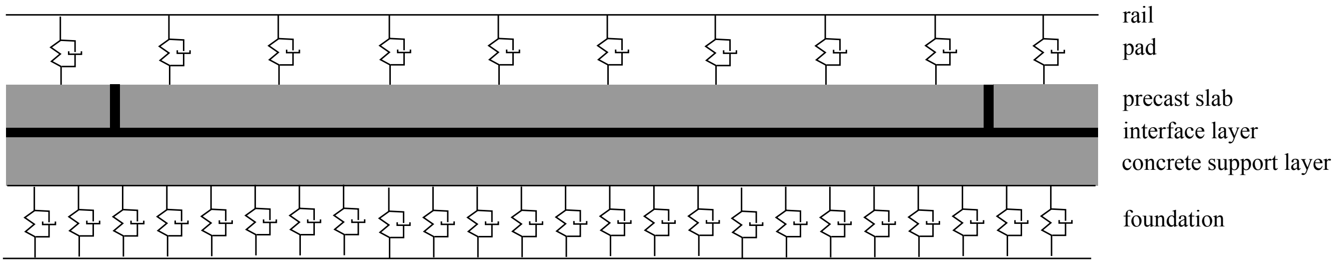

Figure 7: Track model

2.3 Contact model

The contact interaction force between the wheel and the rail is determined by the contact theory. For normal contact between two bodies with no tangential forces and at the contact area, the nonlinear Hertzian model is usually adopted. According to the Hertz model, the interaction (contact) load is given by Equation (1):

$$F = \begin{cases} C_H(x - y - \overline{r})^{3/2} & \text{if } x - y - \overline{r} \geq 0 \\ 0 & \text{if } x - y - \overline{r} \leq 0 \end{cases} \tag{1}$$

where x is the wheel vertical displacement; y is the rail displacement; $\overline{r}$, the rail profile; C_H, the Hertzian stiffness.

However a linearized model can be adopted when the variation of the dynamic load is not considerable. In this situation, the linearized stiffness can be evaluated by Equation (2):

$$k_H = \frac{dF}{d\delta} = \frac{3}{2}C_H\delta^{1/2} = \frac{3}{2}C_H(F/C_H)^{1/3} = \frac{3}{2}C_H^{2/3}F^{1/3} \tag{2}$$

where: $\delta = x - y - \overline{r}$ is the relative displacement between the wheel and the rail; F is the load adopted for the linearization.

3 NUMERICAL ANALYSIS

In this section of the paper, the dynamic response of a precast tracks is evaluated in order to study:

- the influence of the vehicle model and the train speed;
- the influence of the mechanical characteristics of the interface layer between the slab and the concrete support layer;
- the influence of the track foundation;
- the influence of the slab dimension;
- the influence of the geometrical quality of the track.

The numerical assumptions considered for calculations are:

- 2D track model;
- track composed by 20 slabs;
- segment track in a straight alignment;
- ICE 2 train;
- train speed varying from 200 to 420 km/h in steps of 20 km/h.

In all calculations, except for the analysis of the influence of slab dimension on the track response, the total length of the model is 20×5.15 m = 104.0 m .

3.1 Track and train characteristics

In Table 1, the characteristics of the track are presented. Usually the foundation is characterized by the elastic modulus and the Poisson coefficient. To define the foundation stiffness and damping parameters to include in the track model the methodology proposed by Vale et al. [6] is used.

Component	Type of element	Parameter
Rail UIC 60	Euler Bernoulli beam	$E = 210$ GPa; $I = 3055$ cm^4 ; $\nu = 0.3$; $A_t = 76.84$ cm^2 ; $\rho = 60.34$ kg/m
Pad + fastening system	spring and dashpot in parallel	$k_p = 40$ kN/mm; $c_p = 8$ kNs/m
Prefabricated slab	plain stress finite elements	$E = 34$ GPa; $\nu = 0.2$; $H_s = 0.24$ m; $L_s = 5.15$ m; $W_s = 2.8$ m; $\rho = 2500$ kg/m^3
Interface layer	plain stress finite elements	$E = 300$ MPa; $\nu = 0.3$; $H_i = 0.06$ m; $L_i = 104$ m;
Joint	plain stress finite elements	$E = 300$ MPa; $\nu = 0.3$; $w = 0.05$ m;
Concrete support layer	plain stress finite elements	$E = 10$ GPa; $\nu = 0.3$; $H_c = 0.30$ m; $L_c = 104$ m; $W_c = 3.4$ m; $\rho = 2500$ kg/m^3
Foundation	Winkler foundation	$k_f = 50$ kN/mm; $c_f = 492$ kNs/m

Table 1: Mechanical and geometrical properties of the track elements

In this Table, E is the elasticity modulus; I, the moment of inertia; ν, the Poisson coefficient; A_t, the area of the transversal section of the rail; ρ, the density; k_p, the stiffness of the pad; c_p, the damping of the pad; H_s, the thickness of the precast slab; L_s, the longitudinal length of the slab; W_s, the width of the slab; H_i, the thickness of the interface layer; L_i, the longitudinal length of the interface layer; w, the width of the joint; H_c, the thickness of the concrete support layer; L_c, the longitudinal length of the concrete support layer; W_c, the width of the concrete support layer; k_p, the stiffness of the foundation; c_f, the damping of the foundation.

The vehicle characteristics are indicated in Table 2.

Bogie	Mass - M_b [kg]	5600
Primary suspension	Stiffness - k_1 [N/m]	2.40×10^6
	Damping - c_1 [Ns/m]	5.4×10^4
Wheel	Mass - M_r [kg]	1001.5
	Axle load - P [N]	0.981×10^5
Contact	Stiffness - k_H [N/m]	1.588×10^9

Table 2: Mechanical and geometrical parameters of ICE2 - 2D model ([7])

In Figure 8, the complete load model of the ICE2 train is presented.

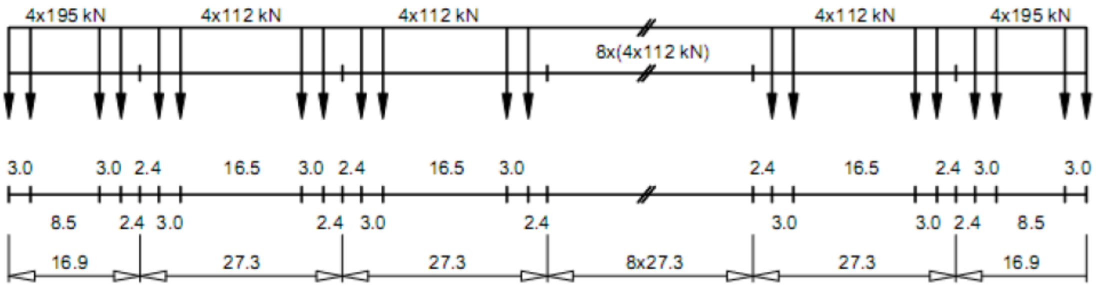

Figure 8: Load model of the ICE2 train [7]

3.2 Results and discussion

3.2.1 Influence of the vehicle model and the train speed

For studying the influence of the vehicle model and the train speed, the response of a perfect track is evaluated for train speeds varying from 220 to 420 km/h in steps of 20 km/h and considering the three vehicle models indicated in Section 2.1.

In Figures 9 and 10, the maximum vertical displacement in the rail and in the slab are presented for the three models together with the results attained with the complete load model of the ICE2 train (Figure 8).

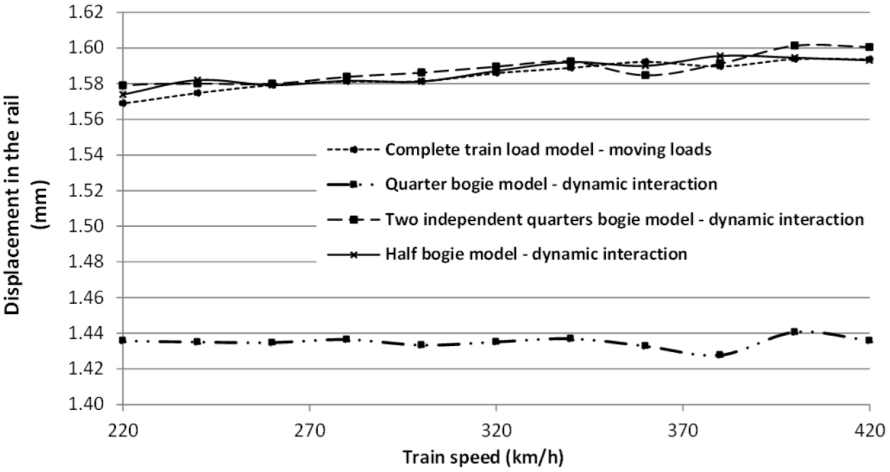

Figure 9: Maximum vertical displacement in the rail for different vehicle model and train speed

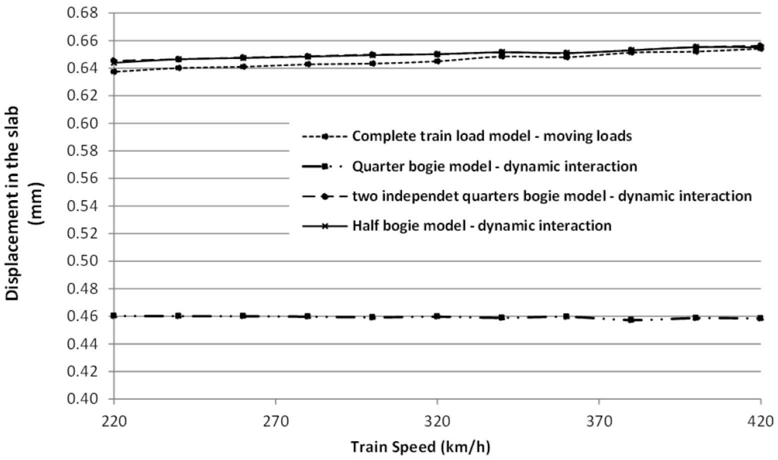

Figure 10: Maximum vertical displacement in the slab for different vehicle model and train speed

The maximum moments in the slab is presented in Figure 11, for the same scenarios.

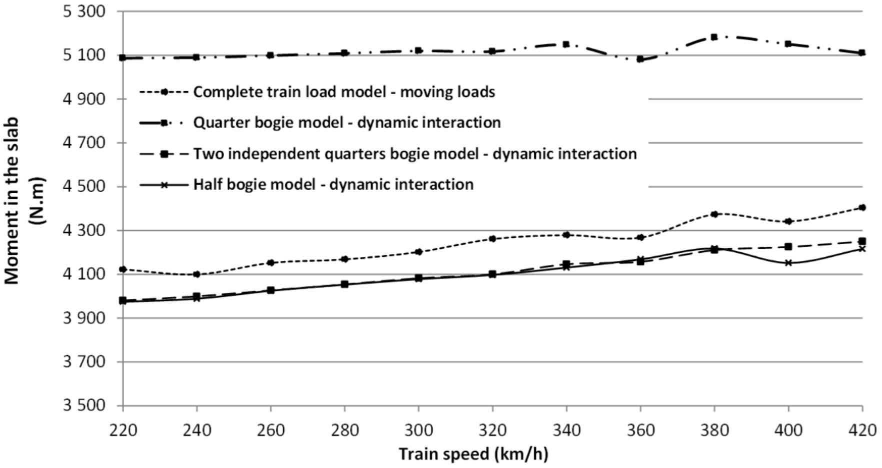

Figure 11: Maximum moments in the slab for different vehicle model and the train speed

The results presented in Figures 9 to 11 show that the quarter bogie is insufficient to represent the correct response of the track due to the passage of the bogie, because the load of the quarter bogie model is $1/2$ to the load of the half bogie model and also because the influence of the wheel spacing of the same bogie is relevant in this type of track models. Although the moving load model gives similar response to the ones attained with the two quarter bogie and the half bogie models, the moving load model is no suitable in the case of track with irregularities. In this analysis the results are similar for these three vehicle models, because the track has no irregularity.

Based on these results the following calculations are performed considering the half bogie model.

3.2.2 Influence of the interface characteristics between the slab and the concrete support layer

For the analysis of the influence of the characteristics of the interface layer between the slab and the concrete layer, elastic modulus varying from 0 to 10000 MPa with $\nu = 0.5$. The simulation of a sliding interface between the slab and the underlying concrete layer corresponds to an elastic modulus equal to zero with a Poisson coefficient equal to 0.5. In this study, a vehicle speed of 360 km/h is adopted. Although the value of the Poisson coefficient ($\nu = 0.5$) is different from $\nu = 0.3$, the value indicated in Table 1 and used for the other parametric analysis, this fact does not influence the system elasticity for the numerical application presented here, as Figures 12 and 13 show.

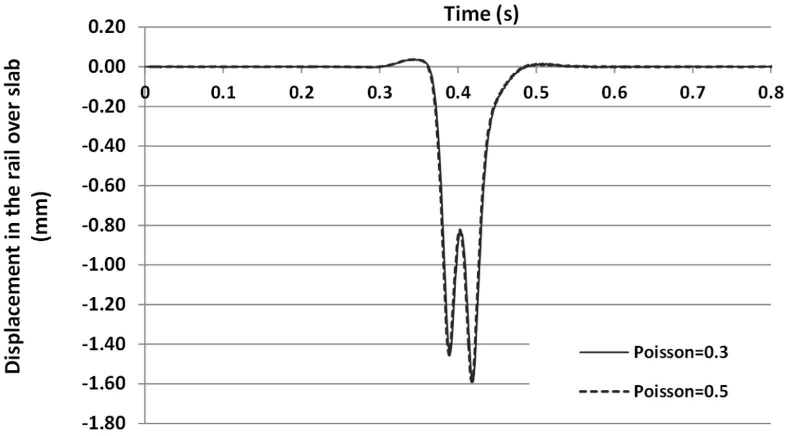

Figure 12: Rail displacement over the slab

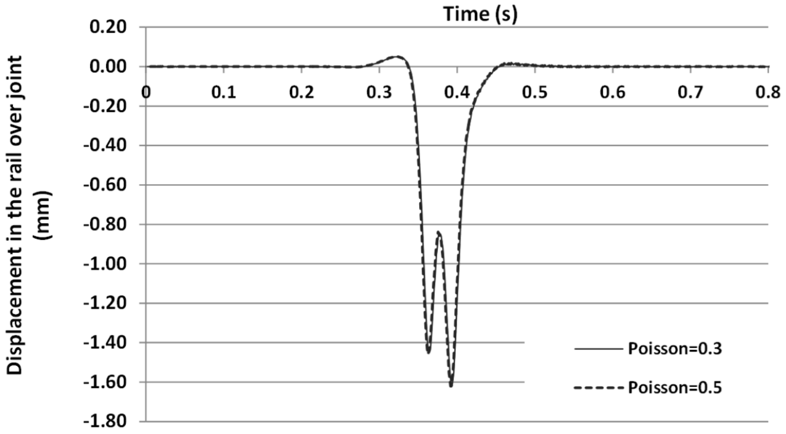

Figure 13: Rail displacement over the joint

In Figures 14 and 15, the maximum dynamic loads at the front and at the rear vehicle axles are presented for different elastic modulus of the interface layer.

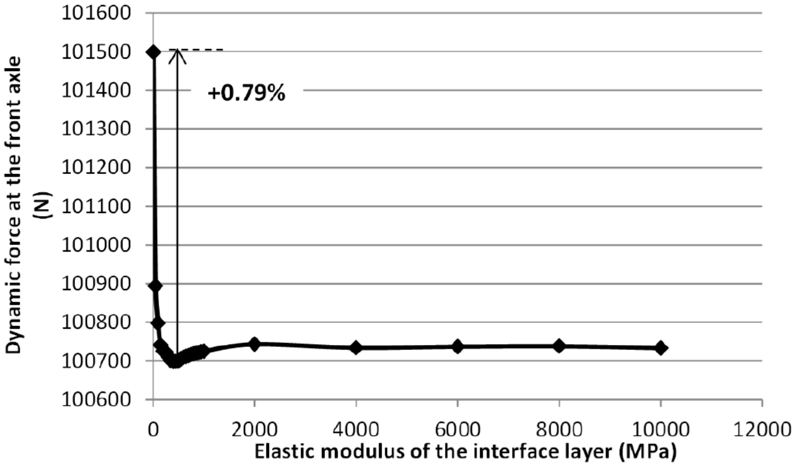

Figure 14: Maximum dynamic load at the front axle

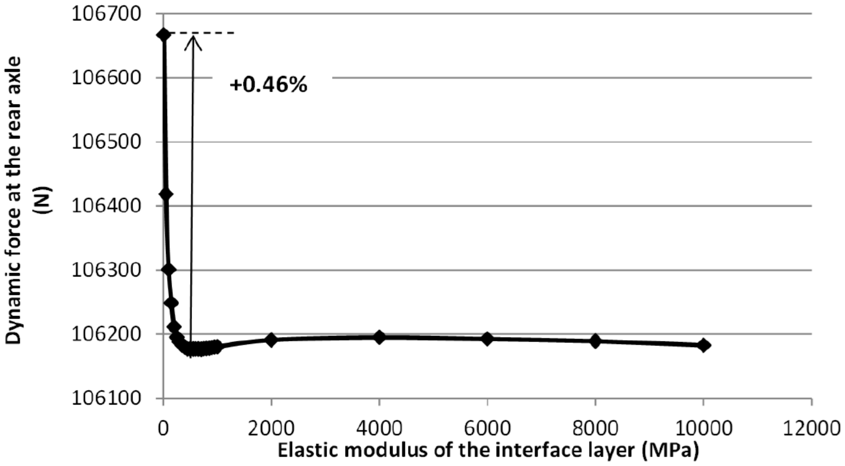

Figure 15: Maximum dynamic load at the rear axle

These figures show that the maximum dynamic load is independent of the interface elastic modulus. However, the elastic properties of the interface layer between the slab and the concrete layer may influence the track dynamic behavior.

In Figures 16 to 21, the maximum track response in terms of vertical displacement in the rail, in the slab and in the concrete sub-base are presented for an increasing interface elastic modulus.

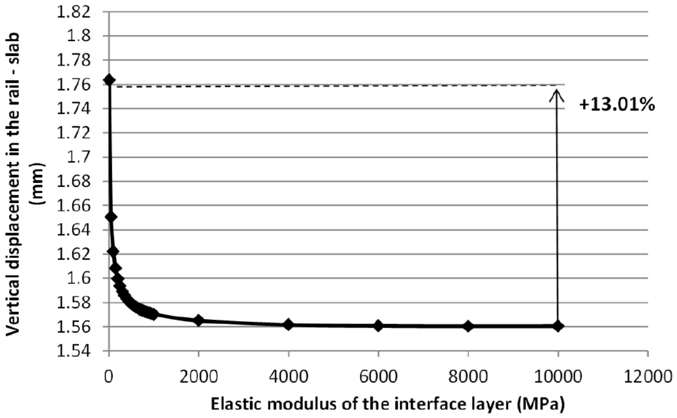

Figure 16: Maximum vertical displacement in the rail over the middle point of the slab

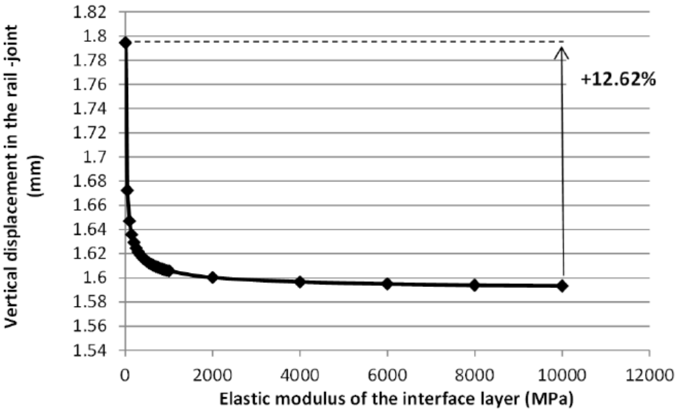

Figure 17: Maximum vertical displacement in the rail over the joint between slabs

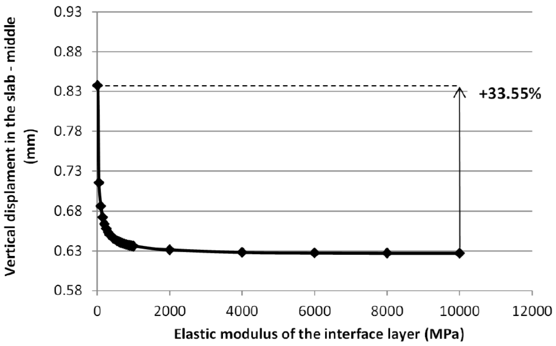

Figure 18: Maximum vertical displacement in the middle point of the slab

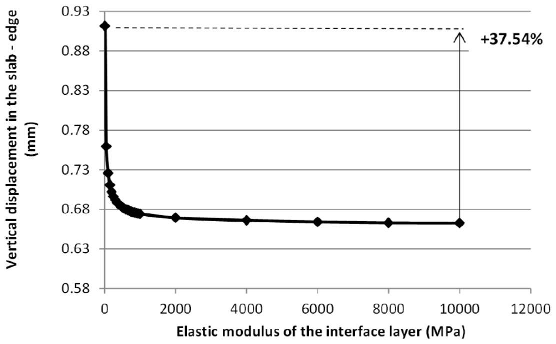

Figure 19: Maximum vertical displacement in the edge of the slab

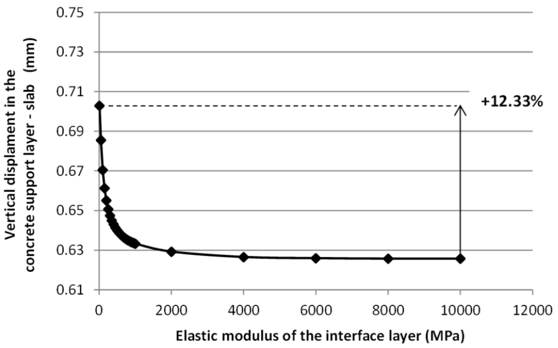

Figure 20: Maximum vertical displacement in the concrete support layer under the middle point of the slab

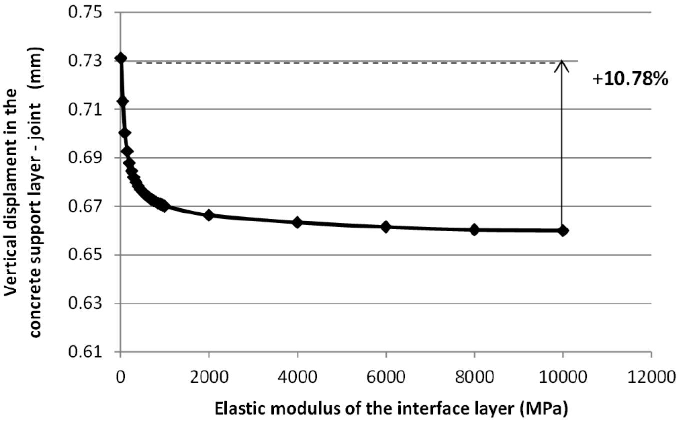

Figure 21: Maximum vertical displacement in the concrete support layer under the joint between slabs

The results evidence that the vertical displacement of the rail decreases with the increase of the elastic modulus of the interface layer. Varying this elastic modulus from zero to 10000 MPa, the decrease of the slab vertical displacement is around 33-37% and the vertical displacement of the concrete support layer is slighty lower, around 10-12% (Figures 18 to 21). For elastic modulus of the interface higher than 1000 MPa, the displacements of the track elements tend to a constant value.

Figure 22 shows that increasing the interface elastic modulus also the maximum dynamic force in the fastening increases with a decreasing rate.

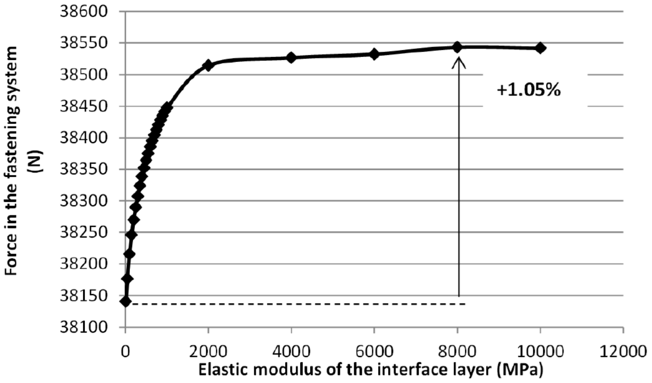

Figure 22: Maximum dynamic force in the fastening systems

Figure 23 and 24 present the maximum bending moments in the rail and in the slab for different characteristics of the interface material.

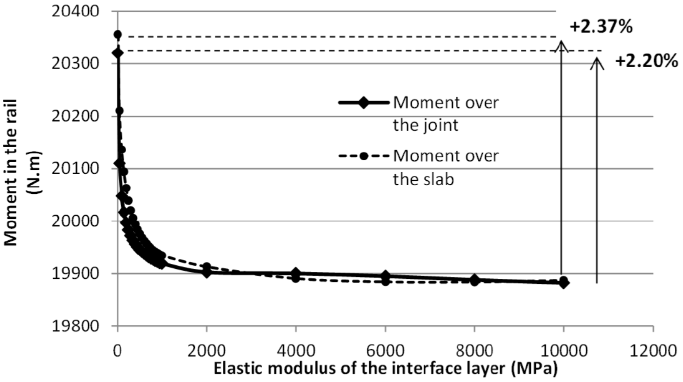

Figure 23: Maximum moment in the rail

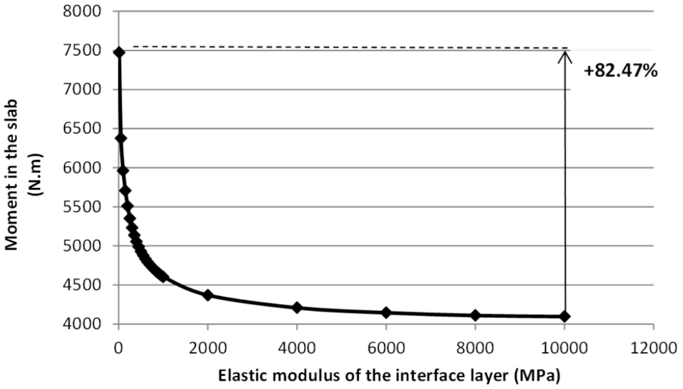

Figure 24: Maximum moment in the slab

The moments in the rail and in the slab decrease with the increase of the elastic modulus of the interface layer. In the rail the reduction is insignificant ($\approx 2\%$); in the slab the reduction of the moments is considerable (around 82%).

3.2.3 Influence of the track foundation

Figures 25 and 26 present, respectively, the maximum vertical displacements in the rail and in the slab, for a vehicle speed of 360 km/h and for four elastic modulus of foundation: 50, 80, 130 and 200 MPa.

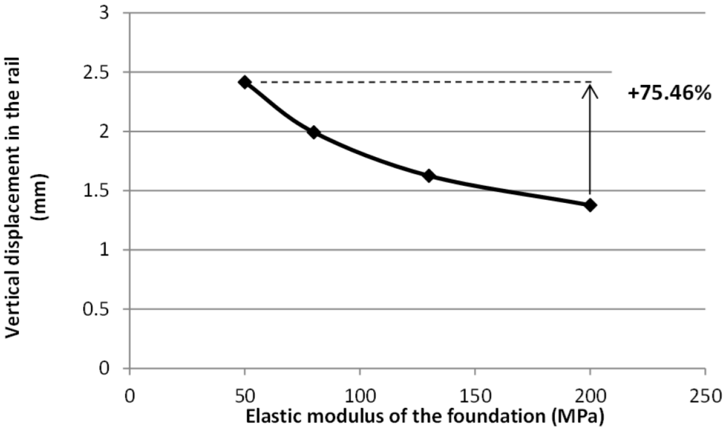

Figure 25: Maximum vertical displacement in the rail

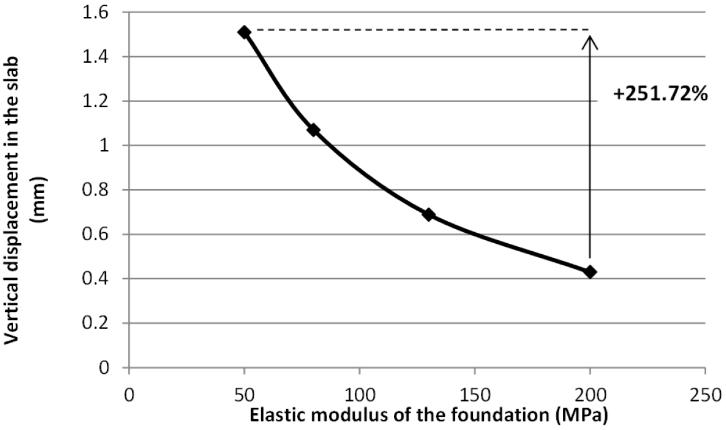

Figure 26: Maximum vertical displacement in the slab

The maximum moments in the rail and in the slab for the same traffic and foundation scenarios are shown in Figures 27 and 28.

From the Figures, the increase of the elastic modulus of the foundation causes a reduction of the maximum values of displacements and bending moments on both the rail and the slab. The influence of the foundation characteristics is more pronounced in the slab than in the rail.

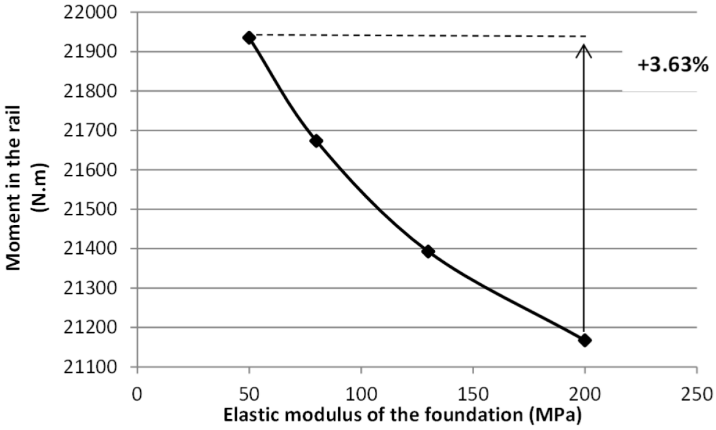

Figure 27: Maximum moments in the rail

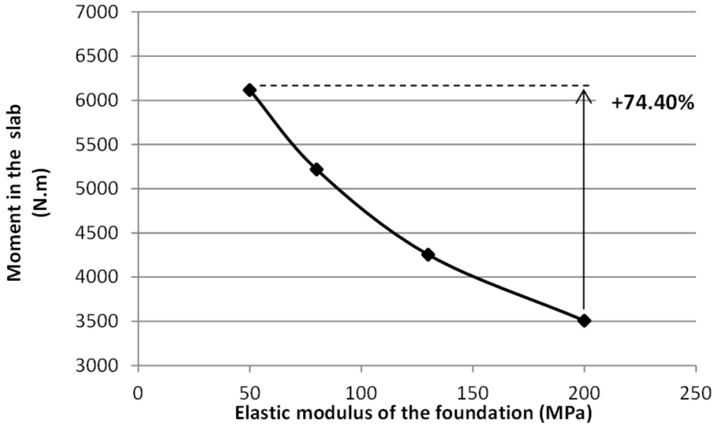

Figure 28: Maximum moments in the slab

In Figure 29, the percentage of the global displacement in each one of the track elements is presented for different elastic modulus of the foundation. As it can be seen, the displacement of the concrete support layer decreases with the increase of the elastic modulus of the foundation.

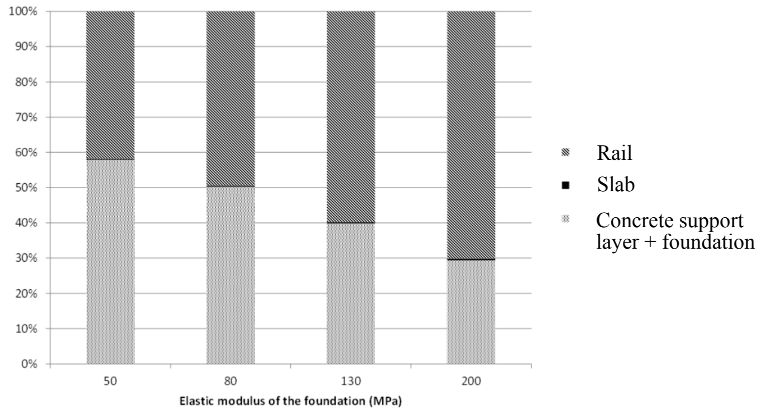

Figure 29: Percentage of displacement in the track elements for different elastic modulus foundation

3.2.4 Influence of the slab dimension

In this paper, the influence of the slab dimension is analyzed for a vehicle speed of 360 km/h. In calculations the width of the slab is considered to be constant (2.4 m). The length of the slab varies between 3.2 and 7.75 m in steps of 0.65 m.

Figures 30 and 31 illustrate that the length of the slab do not influence significantly the maximum vertical displacement of the rail and the slab.

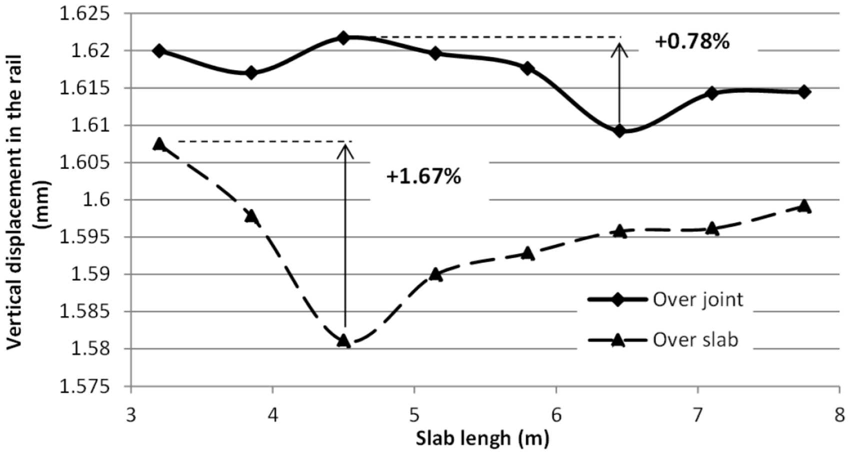

Figure 30: Maximum vertical displacement in the rail

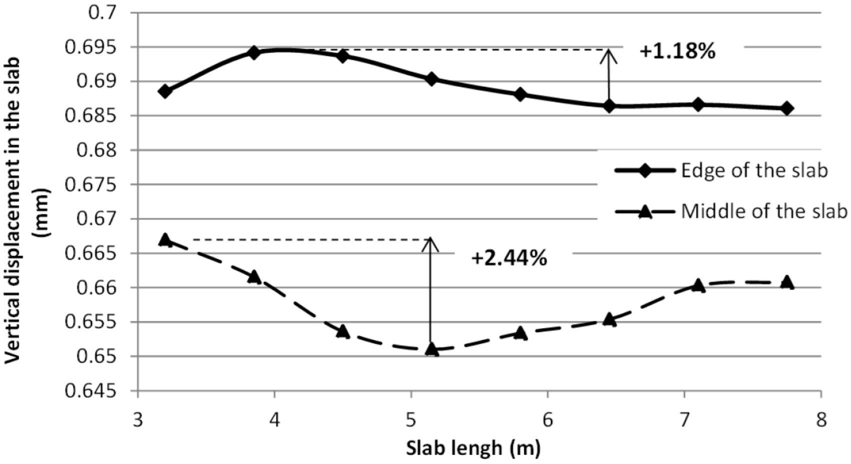

Figure 31: Maximum vertical displacement in the slab

From figure 32, increasing the length of the slab, the moments in this track element also increase, which shows that bigger slabs behave almost as continuous elements.

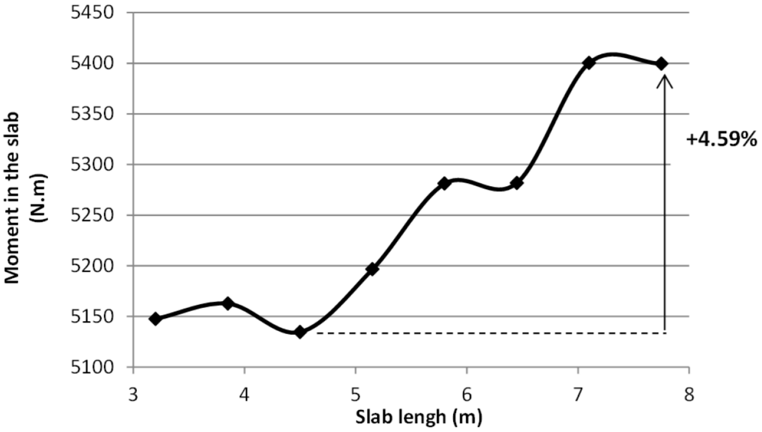

Figure 32: Maximum moments in the slab

3.2.5 Influence of the geometrical quality of the track

Although slab tracks may present a low level of irregularities, in this research the influence of the geometrical quality of the track on its response is also evaluated for train speeds from 220 to 420 km/h.

In Figure 33, the longitudinal level adopted in calculations is indicated. This track profile presents a standard deviation of 1.25 mm, which is near the alert limit for preventive maintenance according to the European Standard EN 13848-5 [8] for wavelengths between 3 and 25 m.

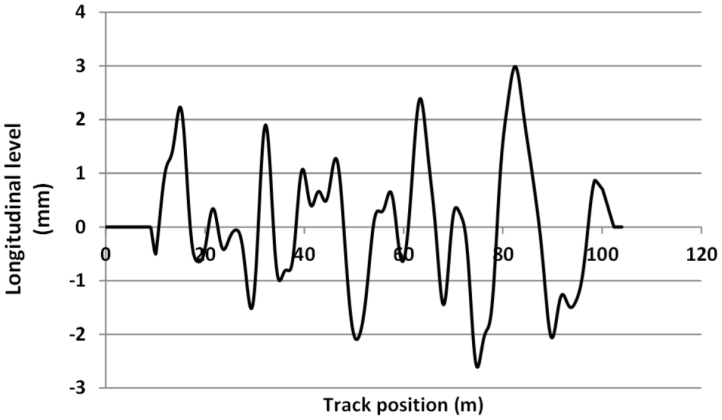

Figure 33: Longitudinal level of the track

The dynamic load for perfect and rough track is presented in Figure 34 together with the static load.

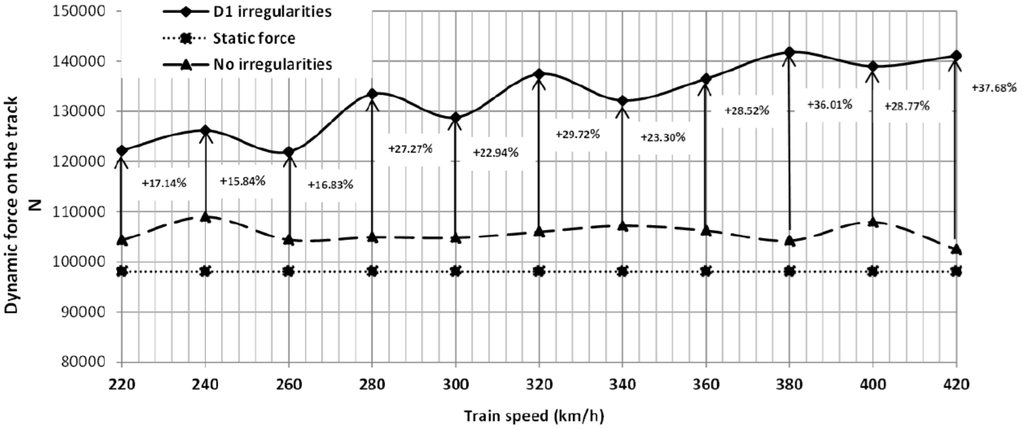

Figure 34: Static load and dynamic load for perfect and rough track

The results reveal that dynamic load in the track is higher in a rough track than in a perfect one and the ratio between these two dynamic loads increase with the increase of the train speed.

4 CONCLUSIONS

A numerical study on the dynamics of a precast track for high speed railways is presented in order to evaluate in the track response the influence of the vehicle model and the train speed, the influence of the interface characteristic between the slab and the concrete support layer, the influence of the track foundation elastic properties, the influence of the slab dimension and also the influence of the track geometrical quality. Calculations are performed in 2D, with Ansys software, in the time domain, considering no dynamic interaction between the wheel of the ICE 2 and the rail (load model) and dynamic interaction between these two elements. For second case, three vehicle models are used: the quarter bogie model, two independent quarter bogie model and half bogie model.

The results show that:

- the half bogie model is the most suitable simplified vehicle model to be used when assessing numerically in 2D the dynamic behavior of slabs tracks composed by precast elements;
- the characteristics of the interface layer between the precast slab and the concrete support layer mainly influence the slab response;
- the rail displacements and bending moments are higher over the slab joint than in the middle point of this element;
- the vertical displacement of the concrete support layer decreases with the increase of the elastic properties of the foundation;
- the elastic properties of the foundation strongly influence the slab response in terms of displacements and bending moments;
- the influence of the slab length in the track response seems to be insignificant;
- the track irregularity induces higher dynamic loads on the track, that increase with the vehicle speed.

In the authors' opinion, more numerical and experimental research is needed on this topic for a better understanding of precast systems for high speed railway lines.

ACKNOWLEDGMENTS

The present work has been funded by the Portuguese Foundation for Science and Technology (FCT). The authors wish to acknowledge to the support of the project ”SI IDT - 3440/2008 - SIPAV - Soluções Inovadoras Pré-fabricadas para Vias-Férreas de Alta Velocidade (Innovative precast solutions for high speed railway lines)”.

REFERENCES

[1] UIC *Feasibility Study Ballastless Track*. UIC, 2002.

[2] TSI *Technical specification for interoperability relating to the infrastructure subsystem of the trans-European high-speed rail system*, Official Journal of the European Communities, L 245 - 12 september 2002.

[3] UIC *Ballastless track. Application and experience with ballastless track*. UIC, 2008.

[4] K. Ando, M. Sunaga, Development of slab tracks for Hokuriku Shinkansen line, *Quarterly Report of RTRI*, vol. 42, n1, Mar. 2001.

[5] Y. C. Shiau, M.T. Wang, C. M. Huang; L. T. Lu, New model of cement product - precast slab track for THSR (Taiwan High Speed Rail), *The 25th International Symposium on Automation and Robotics in Construction*, June 26-29, 2008, Vilnius, Lithuania.

[6] C. Vale, N. Ribeiro, P. Costa, R. Calçada, Numerical estimation of track foundation stiffness and damping by receptance analysis using simplified models: an application to continuous slab track, *International Conference on Railways and Environment*, 16 and 17 December 2010, Delft, the Netherlands.

[7] ERRI-D214/RP9 *Railway Bridges for Speed > 200 km/h - Final Report*. European Rail Research Institute (ERRI), 2001.

[8] CEN *EN13848-5 Railway Applications - Track - Track geometry quality - Part 5: Geometric quality levels*, European Committee for Standardization (CEN), 2008.

COMPDYN 2011
ECCOMAS Thematic Conference on
Computational Methods in Structural Dynamics and Earthquake Engineering
M. Papadrakakis, M. Fragiadakis, V. Plevris (eds.)
Corfu, Greece, 25-28 May 2011

ANALYSIS OF THE VEHICLE-TRACK-STRUCTURE-SOIL DYNAMIC INTERACTION OF RAILWAY BRIDGES FOR HST

A. Romero, J. Domínguez, P. Galvín

Escuela Técnica Superior de Ingenieros. Universidad de Sevilla.
Camino de los Descubrimientos, 41092 Sevilla, Spain
aro@us.es, jose@us.es, pedrogalvin@us.es

Keywords: High speed train (HST), Soil structure interaction, Railway bridge, Resonant vibration.

Abstract. *The dynamic vehicle-track-bridge-soil interaction is studied on high speed lines. The analysis is carried out using a general and fully three dimensional multi-body-finite element-boundary element model, formulated in the time domain to predict vibrations due to the train passage over the bridge. The vehicle is modelled as a multi-body system, the track and the bridge are modelled using finite elements and the soil is considered as a homogeneous half-space by the boundary element method. Usually, moving force model and moving mass model are employed to study the dynamic response of bridges. In this work, the multi-body system allows one to consider the quasi-static and dynamic excitation mechanisms. Soil-structure interaction is taken into account on the dynamic behaviour on simply-supported short span bridges. The influence of soil-structure interaction is analysed in both resonant and non-resonant regimes.*

1 INTRODUCTION

Resonance phenomenon on railway bridges occurs when the loading frequency is close to a multiple of a natural frequency of the structure. In short-span bridges, actual operation velocity could be higher than resonance velocities. In that case, high level vibrations reached on resonance regime can result in problems to the security, passenger comfort and track stability. Therefore, the dynamic behaviour of railway bridges becomes an important design issue. Bridge behaviour is influenced by many factors such as the axle load, successive load passage and track irregularities. These effects are evaluated by dynamic amplification factors on railway bridge standards, which represent the amplification in the dynamic response in relation with the static response for a single moving load [1]. However, the dynamic amplification factors do not account for the resonance effects and its use is limited to trains speed below 220 km/h. In other cases, it is required further analysis.

References about the dynamic response of railway bridges are quite extensive. Frýba [2] presented a theoretical model of a bridge using the integral transformation method. An estimation of the amplitude of the free vibration was given. Li et al. [3] investigated the influence of the vehicle-bridge interaction on resonant vibrations. They concluded that the maximum response in resonant regime is reached at the first resonance velocity. Ju et al. [4] suggested a three-dimensional finite element model to study resonant effects on multi-span bridges, concluding that loading frequencies and natural frequencies of bridges should be as different as possible to avoid resonance phenomenons. Xia et al. [5] investigated the resonance mechanisms and conditions of train-bridge system, analysing the resonant regimens according to their excitation mechanisms.

One of the first steps in the study of railway bridge vibrations is to develop an accurate model of the induced force by the train. Different vehicle-bridge interaction models have been used: moving load model, moving mass model and moving oscillators models. The moving force model is the simplest vehicle-bridge interaction model. The model can be used if the train speed is low enough to neglect its inertia. The model has been widely employed by the scientific comunity [6, 7, 8, 9]. Most sophisticated model is the moving mass model. This model takes into account the mass of the vehicle, but the model does not consider the effect of the suspension. Finally, comprehensive moving oscillator models have been used by several authors [3, 4, 5, 10, 11]. Pesterev et al. [10] examined the asymptotic behaviour of the moving oscillator for large and small values of the suspension. For infinite spring stiffness, the moving oscillator model is not equivalent to the moving mass model. Liu et al. [11] studied under which conditions dynamic train-bridge interaction must be considered for the dynamic analysis of railway bridges. They have concluded that the dynamic vehicle-bridge interaction is more important for large train-bridge mass ratio. Li and Su [3] established that the dynamic vehicle-bridge interaction leads a lower level dynamic response of the bridge than the moving force model.

The number of publications about the influence of soil-structure interaction (SSI) on railway bridges vibrations is reduced. Takemiya et al. [12, 13] studied the soil-foundation-bridge interaction under moving loads using a dynamic substructure method in the frequency domain. Recently, Ülker-Kaustell et. al [14] presented a qualitative analysis of dynamic the soil-structure interaction on a frame railway-bridge. That work is based on Takemiya's work.

In this work, a three dimensional numerical model is developed to study vehicle-track-structure-soil interaction (Fig. 1). The numerical model is based on the three dimensional finite element and boundary element formulation in the time domain. The articulated train configuration is modelled as a multi-body system. Therefore, quasi-static and dynamic excitation mechanisms are considered.

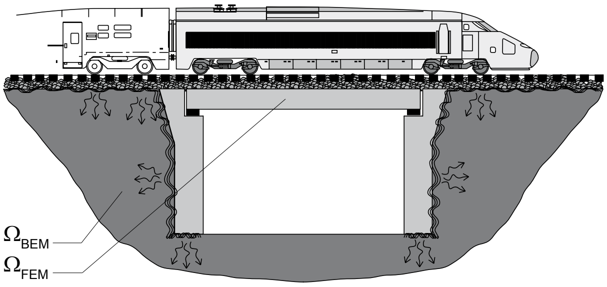

Figure 1: Vehicle-track-structure-soil interaction.

The outline of this papers is as follows. First, the numerical model is presented, including a brief summary of finite element and boundary element time domain formulation, and the multi-body model used to represent the vehicle-track-structure-soil interaction. Second, the influence of soil-structure interaction on the dynamic properties of the bridge is analysed. Third, the contribution of the dynamic excitation mechanisms due to high speed train passage are studied. Finally, induced vibrations on a simply-supported short span bridge are computed for several train speeds. Resonant and non-resonant regimes are studied. The influence of soil-structure interaction in the vibrations of railway bridge is considered.

2 Soil-structure interaction model

The model is based on the three-dimensional finite element [15] and boundary element [16] time domain formulations.

The boundary element method system of equations can be solved step-by-step to obtain the time variation of the boundary unknowns; i.e. displacements and tractions. Piecewise constant time interpolation functions are used for tractions and piecewise linear functions for displacements. Nine node rectangular quadratic elements are used for spatial discretization. Explicit expressions of the fundamental solution of displacements and tractions corresponding to an impulse point load in a three dimensional elastic full-space can be seen in reference [17].

Once the spatial and temporal discretizations are carried out it is obtained the following equation for each time step:

$$\begin{aligned}&\mathbf{H}^{nn}\mathbf{u}^{n} = \mathbf{G}^{nn}\mathbf{p}^{n}+\\&\sum_{m=1}^{n-1}(\mathbf{G}^{nm}\mathbf{p}^{m} - \mathbf{H}^{nm}\mathbf{u}^{m})\exp\left[-2\pi\alpha(n-m)\Delta t\right]\end{aligned} \tag{1}$$

where, $\mathbf{u}^n$ is the displacement vector and $\mathbf{p}^n$ is the traction vector at the end of the time interval n, and $\mathbf{H}^{nn}$ and $\mathbf{G}^{nn}$ are the full unsymmetrical boundary element system matrices, in the time interval n, α is the soil attenuation coefficient and Δt is the time step. An approach based on the classical Barkan expression [18] is employed to account for the material damping in the soil; the right hand side term derived from previous steps is damped by an exponential coefficient α using a linearly increasing exponent with time.

The equation which results from the finite element method can be expressed symbolically as follows if an implicit time integration Newmark method is applied [19]:

$$\mathbf{D}^{nn}\mathbf{u}^{n} = \mathbf{f}^{n} + \mathbf{f}^{n-1} \tag{2}$$

where $\mathbf{D}^{nn}$ is the dynamic stiffness matrix, $\mathbf{u}^n$ the displacement vector and $\mathbf{f}^n$ the equivalent force vector, in the time interval n.

In this paper, damping matrix **C** is considered proportional to mass matrix **M** and stiffness matrix **K**:

$$\mathbf{C} = \alpha_0 \mathbf{M} + \alpha_1 \mathbf{K} \tag{3}$$

α_0 and α_1 are obtained from i^{th} and j^{th} modal damping ratios (ζ_i and ζ_j, respectively). The n^{th} modal damping ratio is [20]:

$$\zeta_n = \frac{\alpha_0}{2\omega_n} + \frac{\alpha_1 \omega_n}{2} \tag{4}$$

The i^{th} and j^{th} modes should be chosen to obtain the damping ratios for all modes that contribute at the response. If both modes have the same damping ratio ζ, it is obtained:

$$\alpha_0 = \zeta \frac{2\omega_i \omega_j}{\omega_i + \omega_j} \quad \alpha_1 = \zeta \frac{2}{\omega_i + \omega_j} \tag{5}$$

Coupling boundary element and finite element sub-regions entails satisfying equilibrium and compatibility conditions at the interface between both regions [21].

3 Vehicle model

The multi-body model used to represent the vehicle-structure-soil dynamic interaction is shown in figure 2.(a). Axles and car bodies are considered rigid parts. Primary and secondary suspensions are represented by spring and damper elements [22].

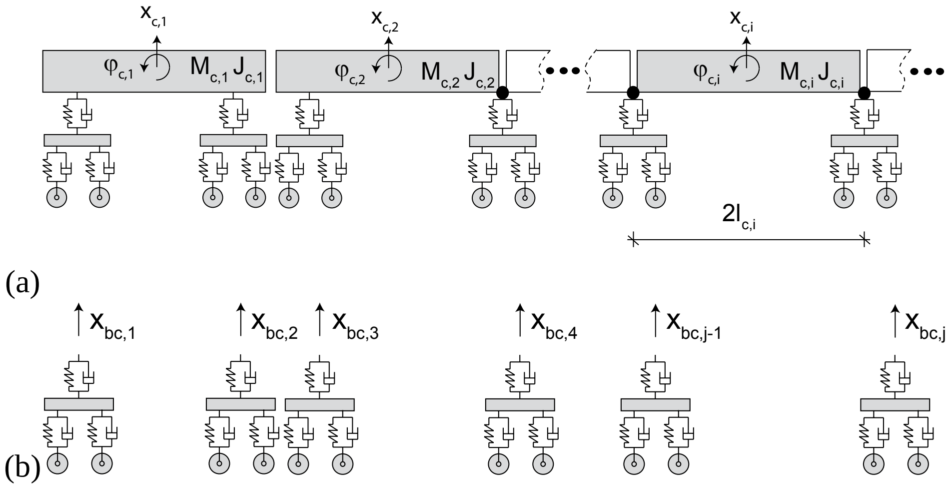

Figure 2: (a) The multi-body model for an articulated HST. (b) Uncoupled bogies.

The equations of motion for the uncoupled multi-body system shown in Fig. 2.(b) can be written as follows:

$$\tilde{\mathbf{M}}\ddot{\mathbf{x}} + \tilde{\mathbf{C}}\dot{\mathbf{x}} + \tilde{\mathbf{K}}\mathbf{x} = \tilde{\mathbf{F}} \tag{6}$$

where, $\tilde{\mathbf{M}}$, $\tilde{\mathbf{C}}$ and $\tilde{\mathbf{K}}$ are the mass, damping and stiffness matrices, respectively. Vehicle response is described by the displacement x_c and rotation φ_c of the body, the displacement x_b and rotation φ_b of the bogies, and the displacement of the wheels x_{wr} and x_{wf}.

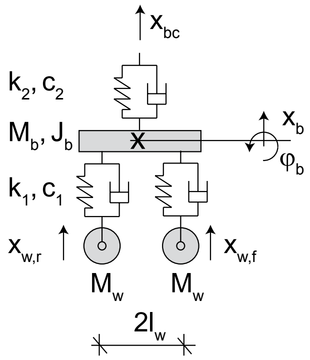

Figure 3: The multi-body model for a bogie.

The mass matrix of each bogie (Eq. 7) is composed of the bogie mass M_b, the bogie inertia moment J_b and wheel masses M_w:

$$\mathbf{M}_b = diag\left(0\ M_b\ J_b\ M_w\ M_w\right) \tag{7}$$

The stiffness and damping matrices of a bogie can be written as:

$$\mathbf{K}_b = \begin{pmatrix} k_2 & -k_2 & 0 & 0 & 0 \\ -k_2 & 2k_1+k_2 & 0 & -k_1 & -k_1 \\ 0 & 0 & 2k_1 l_w^2 & -k_1 l_w & k_1 l_w \\ 0 & -k_1 & -k_1 l_w & k_1 & 0 \\ 0 & -k_1 & k_1 l_w & 0 & k_1 \end{pmatrix} \tag{8}$$

$$\mathbf{C}_b = \begin{pmatrix} c_2 & -c_2 & 0 & 0 & 0 \\ -c_2 & 2c_1+c_2 & 0 & -c_1 & -c_1 \\ 0 & 0 & 2c_1 l_w^2 & -c_1 l_w & c_1 l_w \\ 0 & -c_1 & -c_1 l_w & c_1 & 0 \\ 0 & -c_1 & c_1 l_w & 0 & c_1 \end{pmatrix} \tag{9}$$

where, k_1 and c_1 are the stiffness and damping of the primary suspension, k_2 and c_2 are the stiffness and damping of the secondary suspension, and $2l_w$ is the distance between axles of a bogie.

The equation of motion of the whole train can be obtained from displacement relationships between car bodies and bogies. The relationshisp to obtain the equation of motion of the front traction car [22] are:

$$\begin{aligned} x_{bc,1} &= x_{c,1} - \varphi_{c,1} l_c \\ x_{bc,2} &= x_{c,1} + \varphi_{c,1} l_c \end{aligned} \tag{10}$$

where, $x_{c,1}$ and $\varphi_{c,1}$ represent vertical displacement and rotation of the car body, respectively, and $2l_c$ the bogie distance in a vehicle. Similar expression can be drawn for the first passenger car (Fig. 2). The vertical displacement $x_{bc,n}$ for the m^{th} vehicle can be written as follows:

$$x_{bc,n} = 2\sum_{i=3}^{m}\left((-1)^{n+i} x_{c,i}\right) + (-1)^n \left(x_{c,2} + l_{c,2}\varphi_{c,2}\right) \tag{11}$$

The relationships for the whole train can be expressed as:

$$\mathbf{x}_{bc} = \mathbf{L}\mathbf{x}_c \tag{12}$$

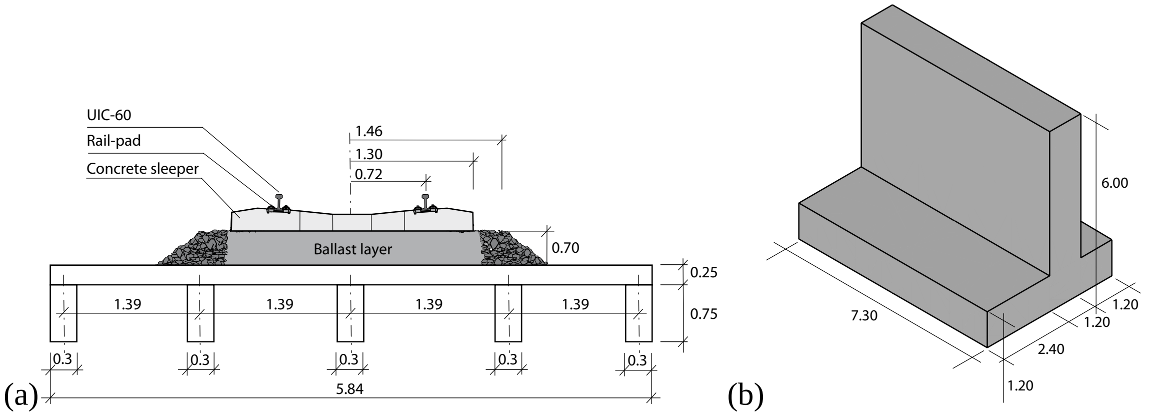

Figure 4: (a) Deck cross-section. (b) Abutment geometry.

Introducing Eq. (12) into Eq. (6) lead to:

$$\mathbf{M}\ddot{\mathbf{x}} + \mathbf{C}\dot{\mathbf{x}} + \mathbf{K}\mathbf{x} = \mathbf{F} \tag{13}$$

where, **M**, **C** and **K** are the mass, damping and stiffness matrices of the articulated HST (Fig. 2.(a)). The mass matrix is obtained by assembling car body mass matrix:

$$\mathbf{M}_c = diag\left(M_c\ J_c\right) \tag{14}$$

where M_c is the mass of the car body and J_c the inertia moment of the car body. The degree of freedom of rotation of the vehicle allows us to consider the pitch car inertia moment.

Finally, the equation of motion of the vehicle is introduced in the soil-structure interaction equation imposing equilibrium and compatibility conditions at each wheel-rail contact point. A Hertzian contact spring is considered between wheels and rails [22, 23]. As vehicle moves along the track according to its speed, contact points between wheels and rails change as time goes on. A moving node is created at each wheel-rail contact point in the rail to couple vehicles and track. So the track mesh including rail changes at each time step. Then, mass, damping and stiffness matrices vary at each time step and the obtained finite element system of equations becomes non-linear. Nevertheless, the time domain formulation allows one to solve the non-linear system of equations using, for example, the methodology presented in reference [24].

4 Dynamic behaviour of simply-supported short span bridge

In this section, the dynamic behaviour of a simply-supported short span bridge under HST passage is studied. First, the modal properties are obtained account for soil-structure interaction. Second, the quasi-static and the dynamic load contribution are studied. Finally, the dynamic response of the bridge due to HST passage is analysed taken into account soil-structure interaction.

4.1 Soil-structure dynamic interaction

In this paper a railway bridge with a single suported slab bay of $12\,\mathrm{m}$ is studied. The deck (Fig. 4.(a)) is composed of a $0.25\,\mathrm{m}$ thickness concrete slab. The slab resting over five pre-stressed concrete beams with a $0.75 \times 0.3\,\mathrm{m}$ rectangular cross-section. A distance $1.39\,\mathrm{m}$ between beams is considered. The concrete has a density $\rho = 2500\,\mathrm{kg/m^3}$, a Poisson ratio $\nu = 0.2$, and a Young's modulus $E = 31 \times 10^9\,\mathrm{N/m^2}$.

The deck leans over two concrete abutments (Fig. 4.(b)) with density $\rho = 2500\,\mathrm{kg/m^3}$, a Poisson ratio $\nu = 0.3$, and a Young's modulus $E = 20 \times 10^9\,\mathrm{N/m^2}$. Beams resting on laminated rubber bearings. The bearings have a thickness of $20\,\mathrm{mm}$ and the stiffness and damping values are $k_b = 560 \times 10^6\,\mathrm{N/m}$ and $c_{rp} = 50.4 \times 10^3\,\mathrm{Ns/m}$.

A single ballast track is located over the deck. The track is composed of two UIC60 rails with a bending stiffness $EI = 6.45 \times 10^6\,\mathrm{Nm^2}$ and a mass per unit length $m = 60.3\,\mathrm{kg/m}$ for each rail. The rail-pads have a $10\,\mathrm{mm}$ thickness and their stiffness and damping values are $k_{rp} = 150 \times 10^6\,\mathrm{N/m}$ and $c_{rp} = 13.5 \times 10^3\,\mathrm{Ns/m}$, respectively. The prestressed concrete monoblock sleepers have a length $l = 2.50\,\mathrm{m}$, a width $w = 0.235\,\mathrm{m}$, a height $h = 0.205\,\mathrm{m}$ (under the rail) and a mass $m = 300\,\mathrm{kg}$. A distance $d = 0.6\,\mathrm{m}$ between the sleepers is considered. The ballast has a density $\rho = 1800\,\mathrm{kg/m^3}$, a Poisson ratio $\nu = 0.2$, and a Young's modulus equal to $E = 209 \times 10^6\,\mathrm{N/m^2}$. The width of the ballast equals $2.92\,\mathrm{m}$ and the height $h = 0.7\,\mathrm{m}$.

The structure is assumed to be located at the surface of a homogeneous half-space that represents a stiff soil, with a S-wave velocity $C_s = 400.0\,\mathrm{m/s}$, a P-wave velocity $C_p = 799.4\,\mathrm{m/s}$, and a Rayleigh wave velocity $C_R = 372.6\,\mathrm{m/s}$.

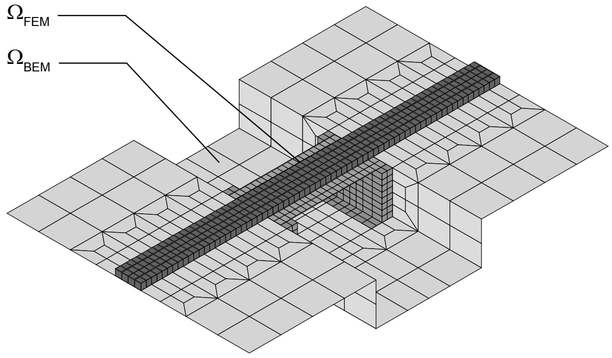

Figure 5: Soil-structure discretization.

Fig. 6 shows the first four mode shapes, corresponding with the first bending (symmetric), the first torsional, the first bending of cross-section (symmetric) and the first antisymmetric bending deck mode shapes, respectively.

Fig. 7 shows the vertical displacement at the center of the mid-span deck due to an impulsive load $P(t) = -1\,\mathrm{N}\,(H(t) - H(t - 0.045\,\mathrm{s}))$ acting in both rails. The response is governed by the first bending (symmetric) deck mode. The same structural damping is considered for all modes that contribute significantly to the response of the structure $\zeta = 2\,\%$. Damping matrix (Eq. 2) is obtained considering $\omega_i = \omega_1$ and $\omega_j = \omega_4$, being $\alpha_0 = 2.3$ and $\alpha_1 = 1.24 \times 10^{-4}$. Fig. 7 shows that the resonant frequency moves to $\tilde{f}_1 = 11.06\,\mathrm{Hz}$ and an amplification in the response when SSI is considered. This effect is due to the additional level of flexibility between the abutments and the soil. The damping can be obtained from the free vibration response. Its value increases to $\tilde{\zeta} = 3.9\,\%$ when SSI is considered.

4.2 Quasi-static and dynamic excitation mechanisms

Induced vibrations due to HST passage are generated by several excitation mechanisms: the quasi-static contribution, the parametric excitation due to the discrete support of the rails and the dynamic contribution due to wheel and rail unevenness. In this section, the different excitation mechanisms are studied.

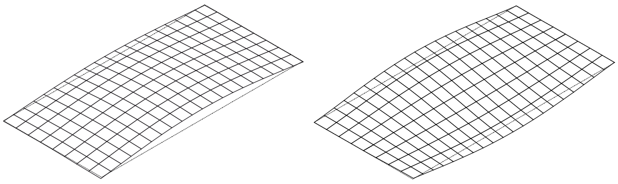

(a) $f_1 = 11.96\,\mathrm{Hz}$ (b) $f_2 = 21.90\,\mathrm{Hz}$

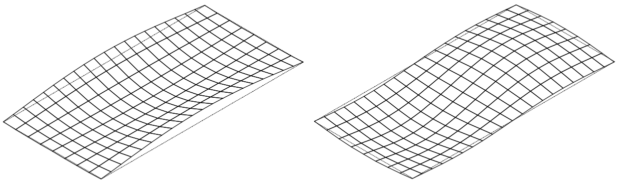

(c) $f_3 = 29.99\,\mathrm{Hz}$ (d) $f_4 = 47.82\,\mathrm{Hz}$

Figure 6: First four modes of vibrations of the structure.

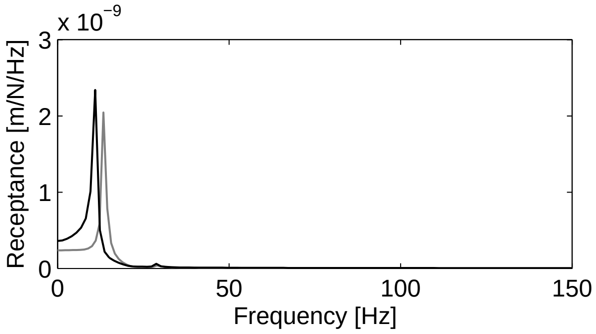

Figure 7: Track-structure-soil and track-structure receptance

Usually, the quasi-static contribution is modelled as moving constant forces and inertia effects of the vehicle are neglected. In this paper, the proposed multi-body system allows one to consider the sprung masses and the vehicle's suspension. Fig. 8 shows the articulated HST studied in this work. The train system consists of one front traction car, eight passenger cars and one rear traction car. Passenger cars adjacent to traction cars share one bogie with the neighbouring passenger car, while central passenger cars share both bogies with the neighbouring cars. Bogie distances, l_b, and axle distances, l_a, are shown in Fig. 8. The mechanical properties of the HST are summarized in table 1.

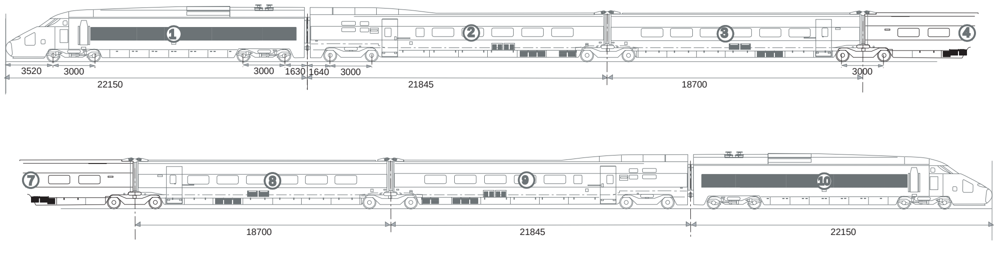

Figure 8: HST configuration.

Description	Name	Unit	Traction cars	Passenger cars
Mass of car-body	M_c	kg	55790	24000
Mass of bogie	M_b	kg	2380	3040
Mass of wheel-axle	M_w	kg	2048	2003
Car-body inertia moment	J_c	$kg\,m^2$	1.15×10^3	1.48×10^3
Bogie inertia moment	J_b	$kg\,m^2$	1.48×10^6	2.68×10^3
Primary suspension stiffness	k_1	N/m	2.45×10^6	1.4×10^6
Secondary suspension stiffnessa	k_2	N/m	2.45×10^6	0.82×10^6
Primary suspension damping	c_1	Ns/m	20×10^3	10×10^3
Secondary suspension damping	c_2	Ns/m	40×10^3	48×10^3

Table 1: Mechanical properties of HST

The transmitted load by an axle can be computed as the elastic interaction force F_H at wheel-rail contact point as follows:

$$F_H = -2k_H(u_c - u_w) \tag{15}$$

where, u_c is the rail displacement at contact point, u_w represents the wheel displacement and $k_H = 1.4 \times 10^9$ N/m is a Hertzian contact spring between wheels and rail [23]. Fig. 9 shows the one-third octave band spectra of the transmitted load for train speed $v = 80\,$m/s and $V_{1,2} = 110.14\,$m/s. $V_{1,2}$ is resonant resonant speed of the bridge (see section 4.3). The computed results are compared with those obtained using a moving force model. Both models lead to the same results at the bogie passing frequency, $f_b = v/l_b$, and the axle passing frequency, $f_a = v/l_a$. However, the computed transmitted forces present differences at higher frequencies due to inertia effects are neglected in the moving force model.

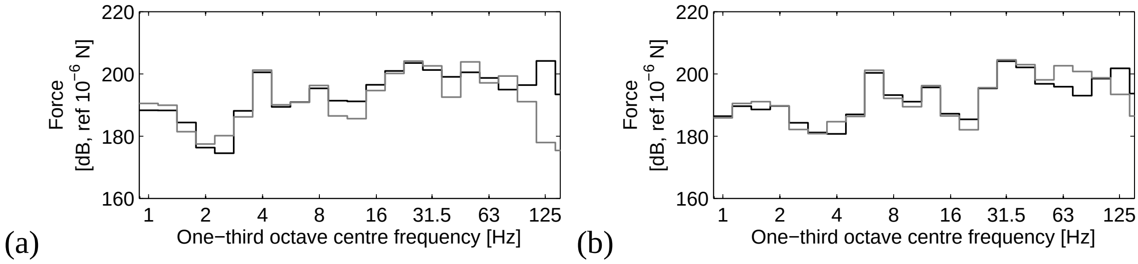

Figure 9: Excitation force on the track computed with a moving force model (grey line) and the multi-body system (black line) for a HST travelling at (a) $v = 80\,$m/s and (b) $V_{1,2} = 110.14\,$m/s

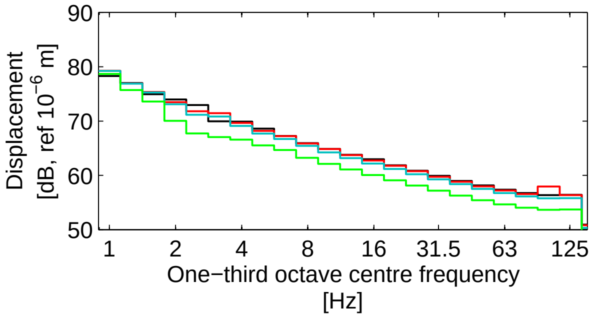

Figure 10: One-third octave band spectra of the vertical displacement at the wheel (red line), bogie (blue line) and the car body (green line) due to the track unevenness (black line) for a HST travelling at $v = 80$ m/s.

The dynamic contribution account for track and wheel irregularities. The displacement vector u_c is equal to the sum of rail displacement u_r and rail unevenness $u_{w/r}$ perceived by an axle [25, 26]:

$$u_c = u_r + u_{w/r} \tag{16}$$

In this paper, random track unevenness $u_{w/r}(x)$ is modelled as a stationary Gaussian random process characterized by its one-sided PSD function $\tilde{S}_{u_{w/r}}(k_y)$. The spectral representation theorem is used to generate samples of track unevenness $u_{w/r}(x)$ as a superposition of harmonic functions with random phase angles [25, 26]:

$$u_{w/r}(x) = \sum_{m=1}^{n} \sqrt{2\tilde{S}_{u_{w/r}}(k_{ym})\Delta k_y} \cos(k_{ym}y - \theta_m) \tag{17}$$

where $k_{ym} = m\Delta k_y$ is the wavenumber sampling used only to compute the artificial profile, Δk_y the wavenumber step and θ_m are independent random phase angles uniformly distributed in the interval $[0, 2\pi]$. The artificial track profile is generated from PSD function according to ISO 8608 [27]:

$$\tilde{S}_{u_{w/r}}(k_y) = \tilde{S}_{u_{w/r}}(k_{y0}) \left(\frac{k_y}{k_{y0}}\right)^{-w} \tag{18}$$

An artificial profile is obtained from the PSD function with $k_{y0} = 1$ rad/m and $\tilde{S}_{u_{w/r}}(k_{y0}) = 2\pi \times 10^{-8}\, m^3$. $w = 3.5$ is commonly assumed for wheel-rail unevenness in current high speed lines.

Fig. 10 shows the one-third octave band spectra of the vertical displacement at the wheel, bogie and body car due to the unevenness profile shown in the same figure. Primary and secondary suspensions system isolate body car and bogie at frequencies higher than 1.2 Hz y 5.5 Hz, respectively.

Figs. 11(a),(b) show the one-third octave band spectra of the vertical acceleration at the center of the mid-span deck for a train passage at $v = 80$ m/s and $V_{1,2} = 110.14$ m/s, respectively. The quasi-static contribution are represented in these figures. The deck response is governed by the quasi-static contribution.

4.3 Induced vibrations due to HST

In this section, SSI effect on induced vibrations due to HST passage is studied. Resonant and non resonant regimes are analysed. The geometry and the mechanical properties of the bridge have been described in previous sections.

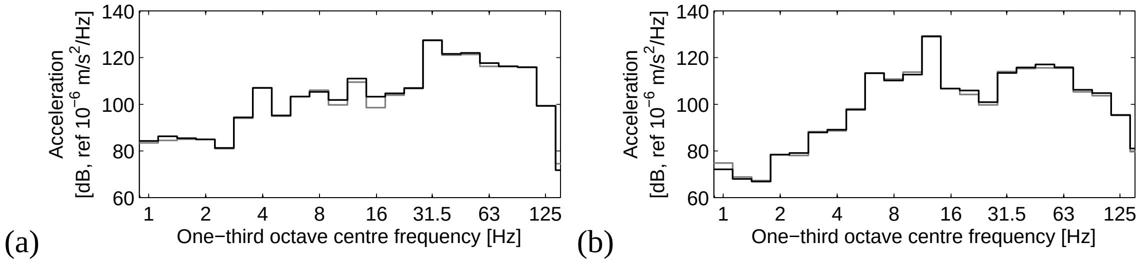

Figure 11: The computed total response (black line) and the computed quasi-static (grey line) one-third octave band spectra of the vertical acceleration at the center of the mid-span deck for a HST travelling at (a) $v = 80\,$m/s y (b) $V_{1,2} = 110\,$m/s.

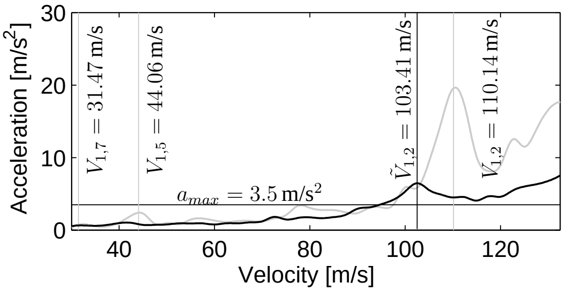

Figure 12: Maximum vertical acceleration at the mid-span center deck computed from SSI model (black line) and non-SSI model (grey line).

The resonant condition of a bridge excited by a row of moving forces can be expressed as follows [2, 5]:

$$V_{n,i} = \frac{f_n d}{i} \quad (n = 1, 2, ..., \; i = 1, 2, ...) \tag{19}$$

where, $V_{n,i}$ is the train speed, f_n is the n^{th} resonant frequency of the bridge and d is a characteristic distance of the moving loads.

Fig. 12 shows the maximum vertical acceleration at the center of mid-span deck in relation to the train speed passage. There is an increase of deck acceleration when the speed increases. Maximum levels are reached at resonant velocities of the first bending (symmetric) mode shape, considering the distance between bogies $d = 18.7\,$m. Figure 12 shows the resonant velocities $V_{1,2} = 110.14\,$m/s, $V_{1,5} = 44.06\,$m/s and $V_{1,7} = 31.47\,$m/s. The Spanish Standard [1] sets a limit state of vertical accelerations at $a_{max} = 3.5\,$m/s^2, plotted in Fig. 12. The maximum acceleration at the center of the mid-span deck is below this limit in the range of operating speeds on current high speed lines. The response of the structure varies substantially when SSI is considered. Resonant velocities decrease due to variation of the dynamic behaviour of the structure. The maximum response occurs at $\tilde{V}_{1.2} = 103.41\,$m/s. Moreover, it is observed that the maximum level of acceleration achieved in resonant regime is significantly lower when the soil-structure interaction is considered. The structural damping varies from $\zeta = 2\,\%$ to $\tilde{\zeta} = 3.9\,\%$.

Fig. 13 shows the time histories and frequency content of the vertical acceleration at the center of mid-span deck for three train speed passage: $v = 80\,$m/s, $\tilde{V}_{1,2} = 103.41\,$m/s and $V_{1,2} = 110.14\,$m/s. In the first case, the response obtained with both models corresponds with a non-resonant regime. The time history shows similar levels in both cases and the differences are not significant. The response is governed by the bogie passing frequency, for the first bending (symmetric) mode and the first bending mode of the cross-section. The SSI produces an amplification of the response at the bogie passing frequency. In addition, the frequency response associated with the natural frequencies of the structure decreases. In resonant regime, the response of the structure shows a gradually increase of the vibrations with the successive bogie passage at the resonant velocities $\tilde{V}_{1,2}$ and $V_{1,2}$ (Fig. 13.(c),(e), respectively). The predominant frequency in the response are asociated with the first bending mode (Fig. 13.(d),(f)). The model without SSI does not estimate accurately the bridge response as can be seen in Fig. 13.(c),(d). Since the amplitude of the resonant vibration depend inversely on damping [2], the model without soil overestimates the response, as can be seen in Figs. 13.(e),(f).

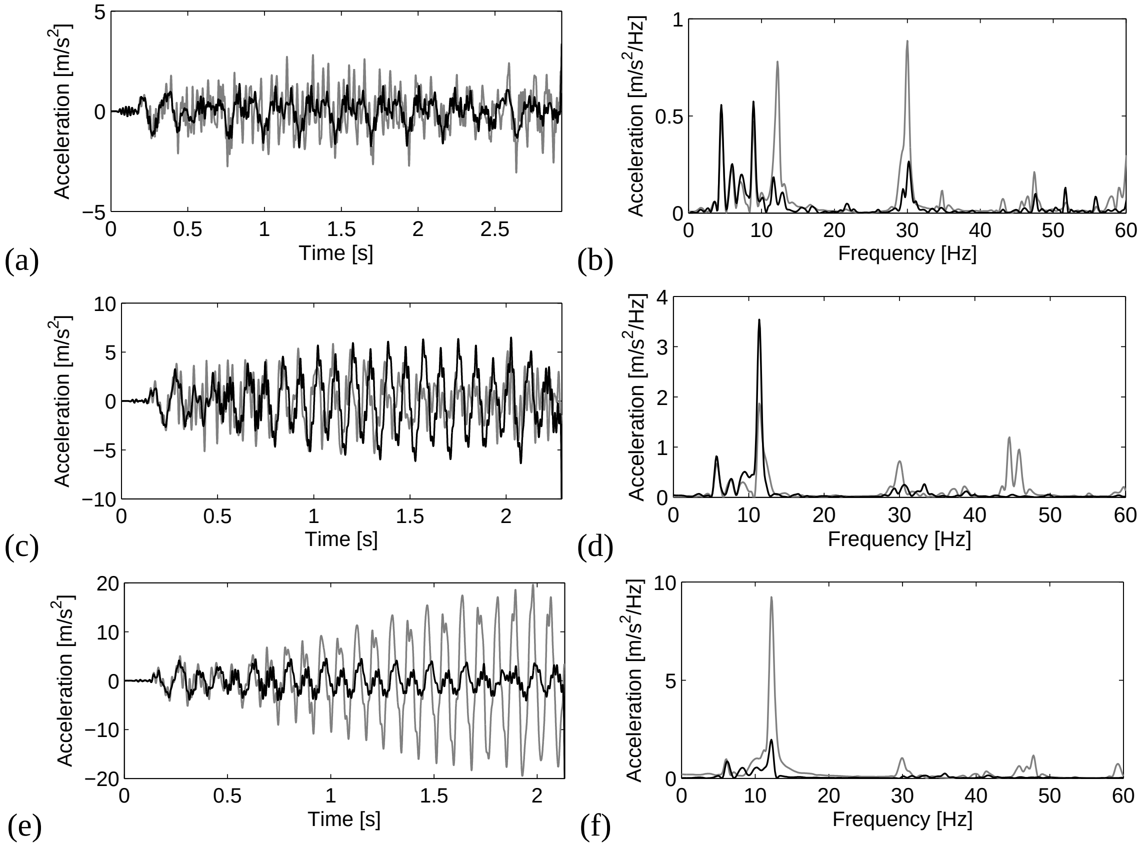

Figure 13: (a,c,e) Time histories and (b,d,f) frequency contents of the vertical acceleration at the mid-span center deck for a HST travelling at (a,b) $v = 80$ m/s, (c,d) $\tilde{V}_{1,2} = 103.41$ m/s y (e,f) $V_{1,2} = 110.14$ m/s, computed from the SSI model (black line) and the non-SSI model (grey line).

5 Conclusions

In this paper, a numerical model to predict vibrations on railway bridges has been presented. The numerical model is based on the three dimensional finite element and boundary element formulations in time domain. The articulated HST is modelled as a multi-body system. Therefore, the different excitation mechanisms can be considered accurately. The following conclusions can be drawn from the obtained results:

1. Transmitted force has a high frequency content that the moving force model does not

reproduce accurately due to vehicle's inertia effects are neglected.

2. Structure soil interaction produces a reduction in the natural frequencies and an increase of structural damping due to the additional flexibility level between the abutment and the soil.
3. Therefore, the resonant behaviour occurs at speeds lower than those predicted by the model without soil.
4. The amplitude of the resonant response regime depends on the structural damping ratio. So, it is necessary to take into account the influence of the SSI to estimate correctly the response.

Acknowledgments

This research is financed by the Ministerio de Ciencia e Innovación of Spain under the research project BIA2010-14843. The financial support is gratefully acknowledge. The support give by the Andalusian Scientific Computing Centre (CICA) is gratefull.

REFERENCES

[1] Ministerio de Fomento, *Instrucción sobre las acciones a considerar en el proyecto de puentes de ferrocarril IAPF07,* Ministerio de Fomento 2007

[2] L. Frýba, A rough assessment of railway bridges for high speed trains, *Engineering Structures* 23 (2001) 548-556.

[3] J. Li, M. Su, The resonant vibration for a simply supported girder bridge under high-speed trains, *Journal of Sound and Vibration* 224 (1999) 897-915

[4] S.H. Ju, H.T. Lin, Resonance characteristics of high-speed trains passing simply supported bridges, *Journal of Sound and Vibration* 267 (2003) 1127-1141

[5] H. Xia, N. Zhang, W.W. Guo, Analysis of resonance mechanism and conditions of train-bridge system, *Journal of Sound and Vibration* 297 (2006) 812-822.

[6] P. Museros, E. Alarcón, E, Influence of the second bending mode on the response of high-speed bridges at resonance, *Journal of Structural Engineering* 131 (2005) 405-415.

[7] P. Museros, M.D. Martinez-Rodrigo, Vibration control of simply supported beams under moving loads using fluid viscous dampers, *Journal of Sound and Vibration* 300 (2007) 292-315.

[8] M.D. Martínez-Rodrigo, J. Lavado, P. Museros, Transverse vibrations in existing railway bridges under resonant conditions: Single-track versus double-track configurations , *Engineering Structures* 32 (2010) 1861-1875.

[9] M.D. Martínez-Rodrigo, P. Museros, Optimal design of passive viscous dampers for controlling the resonant response of orthotropic plates under high-speed moving loads, *Journal of Sound and Vibration* (2010), doi:10.1016/j.jsv.2010.10.017

[10] A.V. Pesterev, L.A. Bergman, C.A. Tan, T.-C. Tsao, B. Yang, On the asymptotics of the solution of the moving oscillator problem, *Journal of Sound and Vibration* 260 (2003) 519-536.

[11] K. Liu, G. De Roeck, G. Lombaert, The effect of dynamic train-bridge interaction on the bridge response during a train passage, *Journal of Sound and Vibration* 325 (2009) 240-251.

[12] H. Takemiya, X.C. Bia, Shinkansen high-speed train induced ground vibratios in view of víaduct-ground interaction, *Soil Dynamics and Earthquake Engineering* 27 (2007) 506-520.

[13] H. Takemiya, Analyses of wave field from high-speed train on víaduct at shallow/deep soft grounds, *Journal of Sound and Vibration* 310 (2008) 631-649.

[14] M. Ülker-Kaustell, R. Karoumi, C. Pacoste, Simplified analysis of the dynamic soil-structure interaction of a portal frame railway bridge, *Engineering Structures* 32 (2010) 3692-3698.

[15] O.C. Zienkiewicz, *The Finite Element Method*, McGraw-Hill Company, London, 1977.

[16] J. Domínguez, *Boundary elements in dynamics*, Computational Mechanics Publications and Elsevier Applied Science, Southampton, 1993.

[17] P. Galvín, J. Domínguez, Analysis of ground motion due to moving surface loads induced by high-speed trains, *Engineering analysis with boundary elements* 30 (2007) 931–941.

[18] D.D. Barkan, *Dynamics of Bases and Foundations*, McGraw-Hill, New York, 1962.

[19] N.M. Newmark, A method of computation for structural dynamics, *ASCE Journal of the Engineering Mechanics Division* 85 (1959) 67–94.

[20] R.W Clough, J. Penzien *Dynamic of Structures*, McGraw-Hill, New York, 1975.

[21] P. Galvín, A. Romero, J. Domínguez, Fully three-dimensional analysis of high-speed train-track-soil-structure dynamic interaction , *Journal of Sound and Vibration* 329 (2010) 5147–5163.

[22] X. Sheng, C.J.C. Jones, D.J. Thompson, A theoretical model for ground vibration from trains generated by vertical track irregularities, *Journal of Sound and Vibration* 272 (2004) 937–965.

[23] C. Esveld, *Modern Railway Track*, MRT Productions,Zaltbommel, 2001.

[24] S.Y. Chang, Nonlinear error propagation analysis for explicit pseudodynamics algorithm, *Journal of engineering mechanics ASCE* 123 (2003) 841–850.

[25] G. Lombaert, G. Degrande, J. Kogut, S. François, The experimental validation of a numerical model for the prediction of railway induced vibrations, *Journal of Sound and Vibration* 297 (2006) 512–535.

[26] G. Lombaert, G. Degrande, Ground-borne vibration due to static and dynamic axle loads of InterCity and high-speed trains, *Journal of Sound and Vibration* 319 (2009) 1036–1066.

[27] International Organization for Standardization ISO 8608:1995, *Mechanical vibration road surface profiles-reporting of measured data*, 1995.

COMPDYN 2011
3rd ECCOMAS Thematic Conference on
Computational Methods in Structural Dynamics and Earthquake Engineering
M. Papadrakakis, M. Fragiadakis, V. Plevris (eds.)
Corfu, Greece, 25–28 May 2011

EXPERIMENTAL VALIDATION OF A 2.5D FEM-BEM MODEL FOR THE ASSESSMENT OF VIBRATIONS INDUCED BY TRAFFIC

Alves Costa, P.[1], **Calçada, R**[2], **and Silva Cardoso, A.**[3]

[1,2,3] University of Porto, Faculty of Engineering
R. Dr. Roberto Frias, Porto, Portugal
pacosta@fe.up.pt[1]; ruiabc@fe.up.pt[2]; scardoso@fe.up.pt[3]

Keywords: Track-ground vibrations induced by railway traffic; numerical modeling; experimental validation

Abstract. This paper presents two main parts, encompassing the experimental assessment and the numerical modelling of vibrations induced by railway traffic. Firstly, a global description of an experimental trial field developed in the Portuguese railway network is presented. In that trial field several tests were performed in order to obtain a reasonable mechanical characterization of the main elements involved in the process of generation and propagation of waves induced by traffic. So as to reach the proposed goal, a geotechnical characterization campaign was performed, including cross-hole tests and specific tests to estimate the ground damping properties. Concerning the track properties, receptance tests and a campaign of measurement of irregularities were conducted. After the global characterization of the site and of the track, vibrations induced by the railway traffic were then measured both in the railway track and in the free-field.

The results of the tests are used in the validation of a 2.5D FEM/BEM model developed by the authors. The model fully accounts for the dynamic interaction between the train, the track and the layered ground. The railway track and embankment, assumed to be invariant in the longitudinal direction, are modelled with 2.5D finite elements [1]. On the other hand, the layered ground below the embankment is simulated by a 2.5D boundary elements formulation. This formulation allows an efficient solution of the track-ground dynamic interaction problem in the frequency-wavenumber domain, as recently explained by François et al. [2]. Regarding the modelling of the rolling stock, a multi-body model is adopted, where the main masses and suspensions of the train are incorporated.

The study, involving experimental and numerical techniques, revealed to be very useful, allowing not only the experimental validation of the numerical model proposed by the authors, but also a deep understanding of the influence of several aspects who determine the problem's solution.

1 INTRODUCTION

The railway is one the most efficient transport systems. Nowadays, it is well known that for middle distances, i.e., lower than 500 km, the energetic efficiency and the comfort associated to the rail transportation turns this transportation system very competitive when compared with the air traffic or with the road transit [3]. However, the sustainable development of modern railway networks should take into account several aspects, few of them neglected in the past.

One particular and important concern is related with the environmental impact that the railway traffic can present on the facilities near to the track, mainly in urban environment, comprising the noise and vibration induced by the train passage. Apart from other issues, the railway traffic can cause discomfort to inhabitants or affect the regular use of sensitive equipments in surrounding buildings. Although structural damage in building is not commonly related to traffic, it is not so unusual the occurrence of some cosmetic damages, which are also unacceptable in the case of important and historical heritage. Therefore, the prediction and assessment of train induced ground vibration is becoming increasingly important, and much attention has been given to this challenge during the last decade, since proposals of empirical prediction models to advanced numerical models. As result, several numerical and semi-analytical models have been proposed. The semi-analytical approaches present a clear supremacy in terms of computation efficiency and capability to the understanding of the phenomena. Many research studies about this subject were carried out since the introduction of the pioneer concept of equivalent stiffness of the ground by Dieterman and Metrikine [3, 4]. An efficient and comprehensive three dimensional model that takes into account the fully interaction train-track-ground was presented by Sheng et al [5]. Despite of the effort dedicated by many researchers in order to improve the semi-analytical models for the incorporation of more complex geometries, the strictness generally found on these solutions does not allow the consideration of the complex geometries usually found in practical applications [6].

The above mentioned limitations, intrinsic to the semi-analytical approaches, combined with the development of computational capabilities, has leaded to the development of numerical approaches specially designed for the simulation of large domains subjected to moving loads. An efficient approach to the modeling of the dynamic track-ground response can be reached taking advantage of some properties commonly assumed, namely: the linearity and the invariability of the domain along the track direction [7]. These properties allow solving the 3D problem by an efficient computational scheme, usually called 2.5D, which only requires the cross section discritization since the spatial coordinate along the track development is subjected to a domain transformation by a Fourier transform. This procedure is becoming very popular, and several researchers have applied this concept to the formulation of models based on the finite elements approach, and more recently also to the boundary elements approach [1, 8-12]. Recently, François et al [2] presented an efficient and comprehensive approach for coupling between both methods, which was also applied in a study performed by Galvín et al. [13].

Apart from the matters related with the modeling of track-ground response, a lack of experimental validation of proposed models remains. In fact, the number of case studies reported in the bibliography remains very scarce, contributing to the difficulty generally found on the experimental validation of the numerical models.

The aim of this paper is twofold. The first objective is to present a numerical model for the assessment of track-ground vibrations induced by railway traffic. This model was developed by the authors and implemented on the numerical platform Matlab 2009, taking advantage of this platform for the use of parallel computation schemes.

The second objective is to present a set of experiments, developed on a site of the Portuguese railway network, which are used for the validation of this particular numerical model, but can also be used for the validation of further models proposed by other authors.

2 NUMERICAL MODEL

2.1 Generalities

The proposed numerical model is divided into two main modulus: the former includes the track-ground structure, modeled by a 2.5D approach where the tridimensionality of the domain is taken into account: the latter concerns to the simulation of the dynamic of the structural behavior of the train, which is simulated by a multi-body formulation taking into account the main masses and suspensions of the vehicles.

Both formulations are integrated by a compliance formulation in order to take into account the train-track interaction. In following sections the main aspects and assumptions of both methods are described.

2.2 Track-ground simulation by 2.5D FEM-BEM

The track-ground dynamic response induced by train passage is computed by a numerical procedure based on the coupling between finite elements and boundary elements methods, both formulated in the 2.5D domain. Since it is assumed that the dynamic problem is linear, the formulation can be developed in the wavenumber-frequency domain, employing Fourier expansions for space (only in the track development direction) and time. This procedure, called 2.5D, allows obtaining the 3D solutions without the need of numerical discretization along the development direction of the track. A similar model was recently presented by François et al. [2] and Galvín et al. [13].

Domain decomposition is used to solve the dynamic problem, being the track modeled by the 2.5D FEM and the layered ground simulated through 2.5D BEM, as shown in Figure 1.

The coupling between both domains is done by a finite elements formulation, comprising the transformation of the flexibility matrix that governs the dynamic behavior of the BEM domain into a dynamic stiffness matrix.

Following the inner formalism of the 2.5D FEM, the dynamic equilibrium equations of the medium can be reached by the formulation in the variation form. So, for a conservative system, the sum of the virtual work of the internal forces and of the inertial forces is equal to the virtual work of the external forces. After introducing the discretization of the cross-section into 2.5D finite elements and applying a Fourier transform regarding the x coordinate, the dynamic equilibrium can be described by the following system of equations:

$$(K_1^{global} + ik_1 K_2^{global} + k_1^2 K_3^{global} + k_1^4 K_4^{global} - \omega^2 M^{global} + K_5^{global}(k_1, \omega))\tilde{u}_n(k_1, \omega) = \tilde{p}_n(k_1, \omega) \tag{1}$$

where K_1^{global} to K_4^{global} are stiffness matrices of the domain described by finite elements, M^{global} is the mass matrix, k_1 is the Fourier image of the coordinate x, ω is the frequency, u_n is the vector of the nodal displacements, p_n is the vector of the external forces, and, finally K_5^{global} is the matrix that collects the impedance terms of the layered ground.

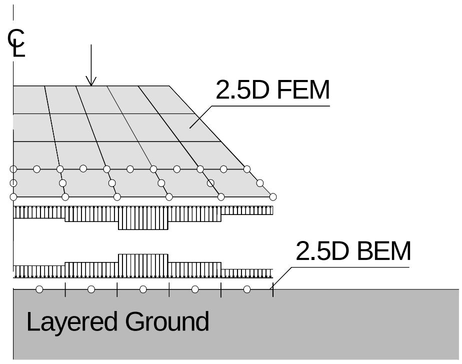

Figure 1 - 2.5D FEM-BEM coupling.

The continuous medium, i.e., the embankment and the granular layers of the track are simulated by 8 nodes finite elements, with exception of the elements that establish the connection between the FEM domain with the BEM domain. In the latter, 7 nodes elements are adopted in order to have two nodes along the side of connection FEM-BEM. Regarding to particular elements of the track, as for instance the sleepers and the rails, a comprehensive description of the modeling strategy can be found on Alves Costa et al. [1]

Since the 2.5D FEM is well explained in several technical documents, including in one paper previously presented by the authors, the deduction of the above mentioned matrices is not presented here again; the reader is advised to consult the following references: [1, 2, 13]. In following, the attention is focalized on the coupling between 2.5 FEM-BEM, which is described by the matrix K_5.

Several 2.5D boundary integral equations have been proposed during the recent years. Sheng et al. [14] have proposed a 2.5D boundary integral equation based on the reciprocity theorem. More recently, François et al. [2] proposed a new approach based on a regularized version of the boundary integral equation in order to avoid the analytical integration of singular terms. However, the version here presented is simpler, since it is assumed that the coupling between the FEM and BEM domains occurs along the ground surface, not being allowed the embedment of the finite element mesh in the BEM domain. In that case, taking into account the reciprocity theorem and the Somigliana identity, the boundary integral equation assumes the following aspect:

$$u_j\left(\mathbf{x},\omega\right)=\int_{\Sigma} u_{ji}^{G}\left(\mathbf{x},\mathbf{y},\omega\right)p_i\left(\mathbf{y},\omega\right)d\Sigma \qquad (2)$$

where uj corresponds to the displacement of the point with coordinates x when a pressure, p_i, is applied along the surface Σ (belonging to the ground surface). On the other hand u_{ji}^{G} is the tensor of the Green's functions of the displacements.

For the computation of the displacement Green's function several methodologies can be followed. Since the objective is to find the BEM matrices in the 2.5D domain, it looks be natural and, apparently more efficient, the option by the 2.5D Green's function proposed by Tadeu and António [15] for a halfspace instead of other methodology. However, in order to avoid the discretization of the interface between distinct layers, in the present study 3D Green's functions are adopted, which are computed in the transformed domain by resource to a hybrid formulation of Thin-layer method, as proposed by Kausel [16].

The introduction of the ground surface discretization is anteceded by some simplifications that must be mentioned and clarified. In approach followed in the present work, only linear boundary elements are used, with one point of collocation (in the middle of the element) and its dimension is defined by the side length of the neighbor finite element. It should be remembered that the neighbor finite element only presents two nodes along the side of connection FEM-BEM, which means that some error of approximation is allowed between the displacements computed by both methods along the connection surface.

In sum, considering the 2.5D discretization and the schematic representation presented in Figure 2, the BEM equilibrium equation can be described by:

$$u_n\ (k_1, y_1, 0, \omega) = \left[G(k_1, y_j - y_i, z_1, \omega)\right] p_n(k_1, \omega) \tag{3}$$

where u_n is the vector of that collects the displacements of the collocation points; p_n is the vector of the applied pressures along each boundary element and, finally the matrix G corresponds to the flexibility matrix of the domain.

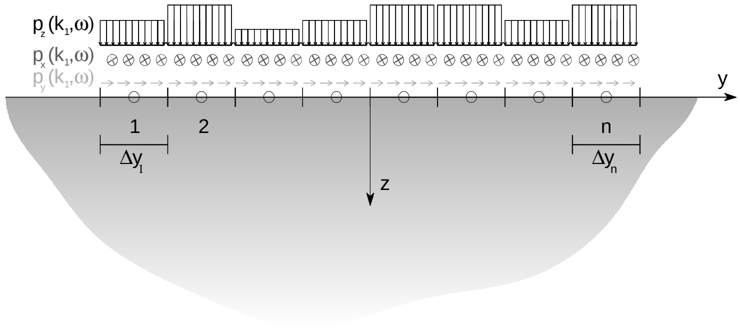

Figure 2- 2.5D ground surface discritization.

The FEM-BEM coupling can be performed by several approaches. In the present study the coupling is done in FEM sense, being the flexibility matrix G transformed into the dynamic stiffness K_5, trough the following relashionship:

$$K_5 = \left[T_q\right]\left[G(k_1, \omega)\right]^{-1}[T] \tag{4}$$

where T is a matrix that relates nodal displacements with the homologous evaluated in the collocation points and, T_q is a matrix resulting from the integration of the shape functions (of the finite elements) along the coupling boundary.

Since the motion and equilibrium of the domain is formulated by a 2.5D approach, where Fourier transform are applied over the x coordinate and time, the simulation of moving loads is easy, and can be found in several paper related with this matter .

Solving the equations system presented in (1), the nodal displacements in the transformed domain are obtained, as well as the traction along the coupling boundary. Once these tractions and the Green's functions of the displacements are known, the computation of the free field response is trivial.

2.3 Track-Train interaction

The load applied by the train on the track can be divided into two components: i) the static load, resulting from the weight of the train; ii) the dynamic load, due to the dynamic interaction between the train and the track. As the first component is an input data and not an unknown variable, its consideration on a numerical model is trivial. Unfortunately, the same statement cannot be extended for the latter component, which demands for the solution of the dynamic train-track interaction problem. In the present study, this problem is solved by a compliance procedure formulated in a referential that moves with the train, as suggested by several authors [10, 11, 17, 18].

Assuming perfect contact between both structures, the following relationship must be adhered to at any temporal instant for all connection points between the train and the track:

$$u_{c,i} = u_r\left(x = ct + a_i\right) + \Delta u\left(t + \frac{a_i}{c}\right) \tag{5}$$

where u_c represents the vector of vertical displacements of the vehicle in the connection points, ur is the vector of vertical displacements of the track at the same location; Δu is the rail unevenness; t is the time; a_i is the location of contact point i at t=0 s and c is the vehicle speed.

Since the wheelsets are simulated by rigid bodies, the displacement of any axle is equal to the sum of the displacement of the corresponding connection point with the deformation of the Hertzian spring introduced in order to take into account the contact deformation:

$$u_{c,i} = u_r\left(x = ct + a_i\right) + \Delta u\left(t + \frac{a_i}{c}\right) + \frac{P_i(t)}{k_H} \tag{6}$$

where k_H is the Hertzian stiffness and P_i is the dynamic interaction force developed at the connection point i.

Equation 5 can be written in matrix form in the frequency domain using the transformation of the unevenness for that domain. So, the train-track interaction force in the frequency domain is given by:

$$P(\Omega) = -\left([F] + [F]^H + [A]\right)^{-1} \Delta u(\Omega) \tag{7}$$

where [F] is the train compliance at the contact points with the track, $[F]^H$ is a diagonal matrix where the terms are equal to $1/k_H$ and [A] is the compliance matrix of the track. All matrices are square with a dimension equivalent to the number of wheelsets and its deduction can be found in Alves Costa et al. [19]

Analyzing equation 7, one can conclude that the influence of the vehicle properties and of the modeling strategy used only affects matrix [F]. A simple but general vehicle model, which takes into account the main structural aspects of the train dynamics, was proposed by Zhai e Cai [20] (Figure 3).

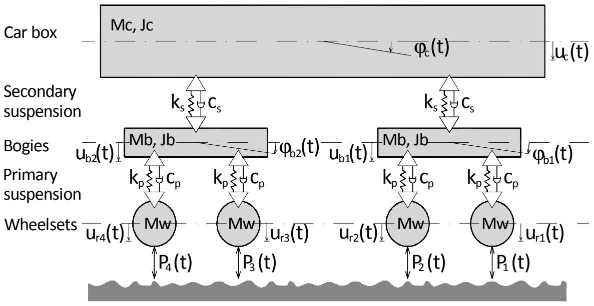

Figure 3 - Complete 2D vehicle model.

However, the difficulty generally found in the determination of the mechanical properties of the vehicle, gave rise to proposals of simplified models where the motion of the car body and, sometimes, also the motion of the semi-sprung masses (bogies) are disregarded [10, 21]. A parametric study developed by the authors in order to discern the influence of the sprung and semi-sprung masses on the global dynamic response of the system, revealed that the vehicle model must comprise, at least, the dynamic behavior of the bogies and wheelsets [19].

3 EXPERIMENTAL ACTIVITIES

3.1 General description and objectives

In order to validate the numerical models developed by the authors, an experimental test site was selected and implemented in the Portuguese railway network (between Lisbon and Oporto), near to Carregado site.

Regarding the main aspects of the site, it must be referred that the track presents a straight alignment, corresponding to a renewed part of the railway connection between Porto and Lisbon. The line is composed by a double track on ballast, as illustrated in Figure 4, and distinct types of traffic are allowed in this line, ranging from freight trains up to passenger trains that circulate at speeds close to 220 km/h.

Figure 4 – General view of the site.

Two sets of experiments were performed: i) the first, to evaluate the dynamic properties of the track and of the ground; ii) the second, to measure the vibrations induced by the passage of the Alfa-Pendular train. Additionally, the track unevenness, key parameter for performing a dynamic train-track interaction analysis, was also measured.

The first set of experiments is used for the calibration of the numerical model and for a deeper understanding of the dynamic behavior of the track-ground system. On the other hand, the second set of experiments, comprising the response of the track-ground system during the passage of Alfa-Pendular train, is used for the experimental validation of the numerical model presented above.

3.2 Geodynamic characterization of the ground

Due to the uncertainty generally attributed to the ground properties, a detailed attention must be addressed to the geotechnical characterization of the ground. Following this logic three types of tests were performed in the site: i) one bore-hole with SPT tests spaced 1,50 m into depth; ii) two CPT tests; iii) two cross-hole tests.

Concerning the geotechnical scenario, the SPT and CPT tests allowed to find four main formations: i) up to 1.80 m to 2.00 m, the ground is mainly constituted by fine soil, overconsolidated; ii) between 1.80 m to 5.40 m, a relatively homogeneous formation is found, comprising clayey soils; iii) below 5.40 m and above 7.2 m, the ground is constituted by very soft organic layers intercalated with sand layers; iv) finally, for depths below 7.20 m, the ground is very homogeneous, corresponding to a thick layer of clays. Figure 5, shows the classification chart of the soil from the CPT tests, according the proposal of Robertson. The laboratorial tests confirmed this layering.

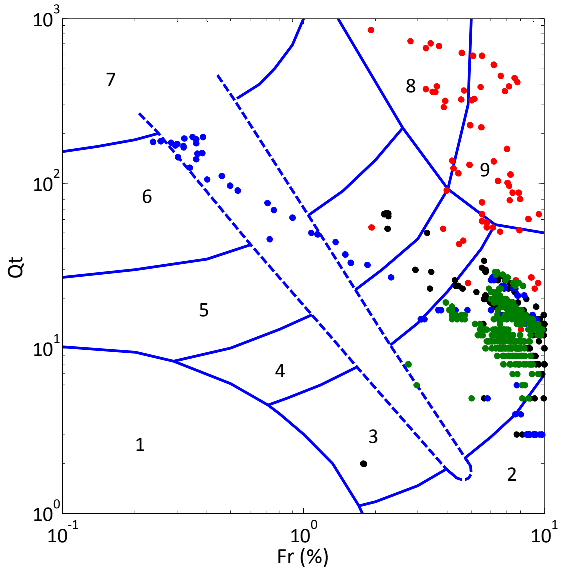

Figure 5 – Soil classification from the CPT test (red dots – 0 m <z<1.8 m; black dots – 1.8 m <z<5.4 m; blue dots – 5.4 m<z<7.2 m; green dots – z>7.2 m)..

The device used to perform the cross-hole tests enables to generate polarized S waves, allowing the measurement of P and S wave velocities. Figure 4 shows the measured wave velocities profile as well as the values adopted in the numerical model.

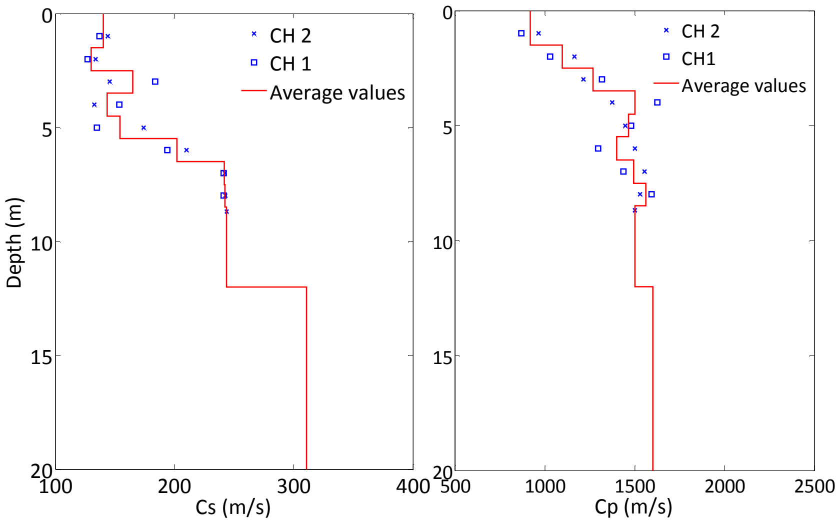

Figure 6 – Seismic wave velocities profile: a) Shear wave; b) Compressive wave.

A complete geodynamic characterization, for the purpose of the present study, should attend not only to the elastic properties of the ground but also to an estimation of the damping profile in depth.

In the present study, the damping profile was estimated from an inversion procedure based on the calibration of the numerical model in order to obtain a reasonable fit between measured and computed mobilities of the ground due to an excitation induced by a controlled source. The experimental setup adopted is shown on Figure 7.

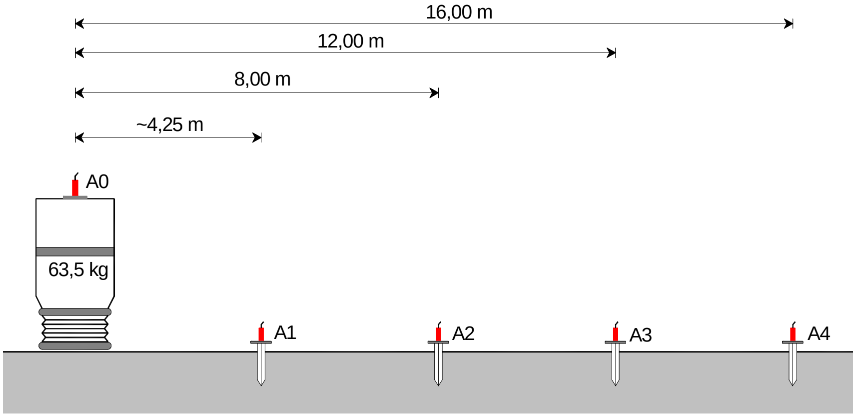

Figure 7 – Damping evaluation tests. Experimental setup.

From the acquired data, the experimental mobility is computed for the set of measuring points. On the other hand, a theoretical model was developed, taking into account the ground layering and stiffness properties described in Figure 6, where the damping profile is adjusted in order to obtain a reasonable fit between the measured and computed mobilities. Therefore, the only unknown variable in the numerical model is the damping of the ground, which gives rise to a simple inversion procedure. Figure 8 shows the modulus of the mobility measured and computed, for the 4 points of analysis. It is well patent in the figures that a reasonable fit between measured and computed results is achieved when the damping profile illustrated in Figure 9 is adopted.

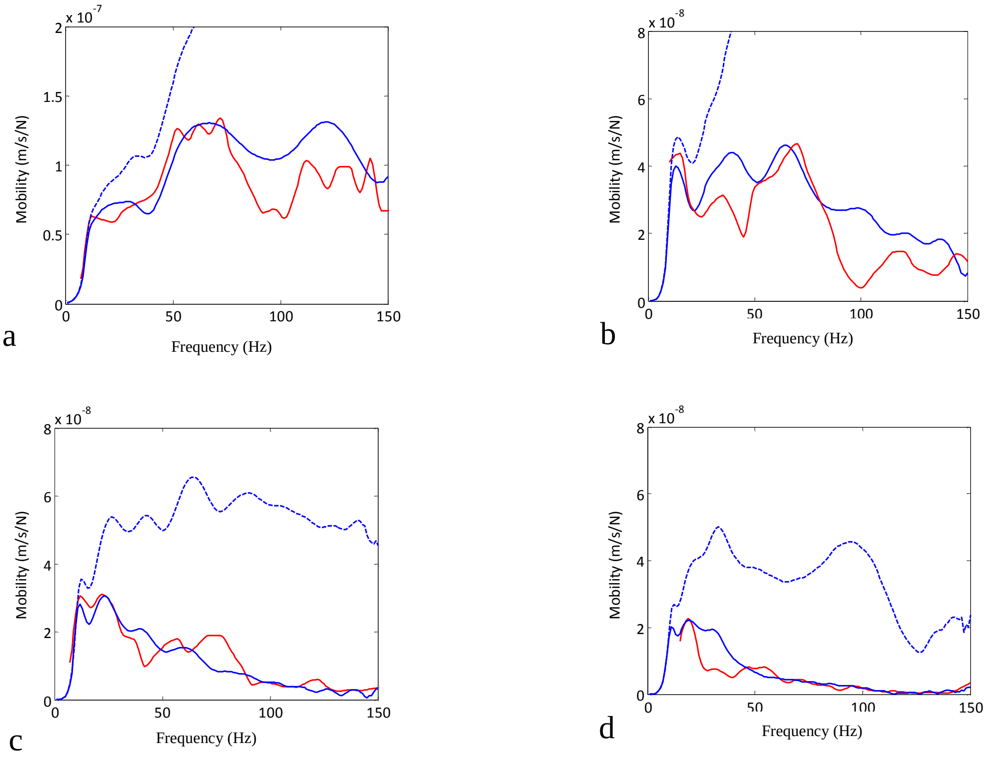

Figure 8 – Experimental and numerical mobility at different distances receiver-source: a) 4.25 m; b) 8.00 m; c) 12.00 m; d) 16.00 m.

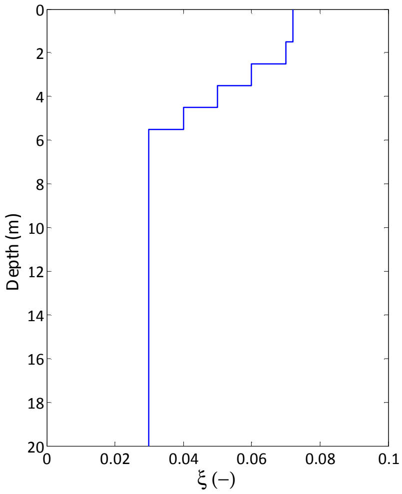

Figure 9 – Damping profile.

3.3 Assessment of the track mechanical properties

Another challenging usually found in the numerical analysis of railway tracks is due to the difficulty in the assessment of the properties of this complex structural system. If, by one hand, the properties of the rail and sleepers are well defined, the same statement cannot be extended to the other components such as the ballast or the railpads. In order to minimize the uncertainty related to properties of those elements, receptance tests were performed and the numerical model was calibrated, by an inversion procedure, in order to obtain a reasonable fit between the measured and computed receptances.

The adopted setup for the receptance tests is shown in Figure 10. As can be seen, the impact load (provided by an impulse hammer) is applied in the mid span of the sleeper and the response is measured by accelerometers installed on the sleeper extremities and on the rails.

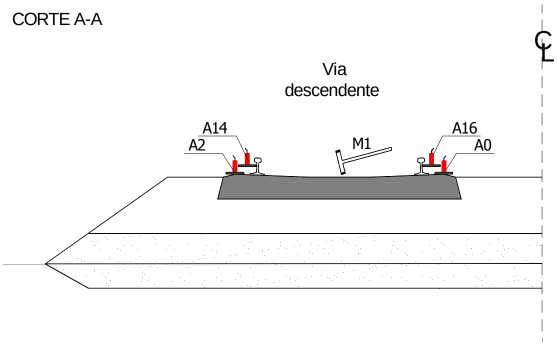

Figure 10 – Receptance tests setup.

A preliminary examination of the receptance of the rails enabled to confirm that very stiff railpads are used in this railway track. Through a simplified analysis it was found that the resonance frequency of the rails over the sleepers is related to a railpad stiffness of 700 kN/m, which is in correspondence with the value previously pointed out by the railpad manufactor.

Despite of the mentioned above, several variables (properties of the track elements) remain unknown, namely: the stiffness, the damping and the mass of the ballast and of subballast.

These properties are determined by the solution of a nonlinear least squares optimization problem with a residual that is a function of the track characteristics.

Figure 11 shows the geometry adopted for the numerical model, as well as the properties adopted after the optimization solution (see Figure 12). It should be noticed that the rail and sleepers were simulated according to the above mentioned properties of the materials. The layered ground was simulated by the 2.5D BEM procedure taking into account the stiffness, mass and damping provided by the set of tests described in the latter section.

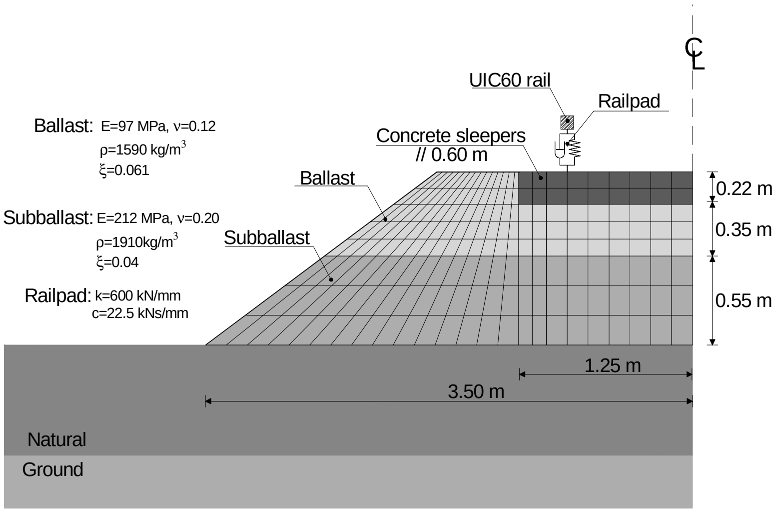

Figure 11 – Numerical model geometry and mechanical properties.

As is well patent is Figure 12, a reasonable agreement was found between measured and computed receptances, mainly for frequencies in the range between 70 Hz and 250 Hz.

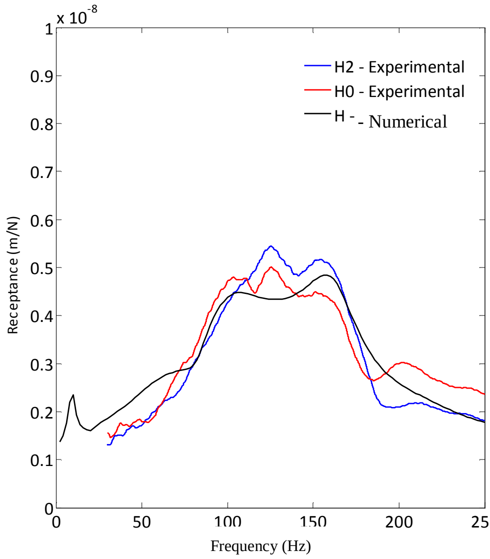

Figure 12 – Numerical and experimental sleeper receptance.

3.4 Measurement of track unevenness

As shown by equation 4, the knowledge of the track unevenness is a key parameter for the analysis of the dynamic excitation mechanism. Unlike other case studies, where the track unevenness is artificially generated, in the present study it was measured. Distinct equipments were used in order to have a reliable unevenness profile comprising the frequency bandwidth relevant to the analyses of vibrations induced by traffic. The recording car used by the Portuguese Railway Company (REFER) enables to measure the unevenness for wavelengths between 1.0 m and 25.0 m (Figure 13a). Therefore, for moderate running velocities, it is also necessary to know the short wavelength unevenness (also called rail corrugation) in order to take into account excitation frequencies up to 150 Hz. So, it was used a device that enabled the measurement of the wavelengths range between 0.4m and 1.0m. Both equipments are illustrated in Figure 13.

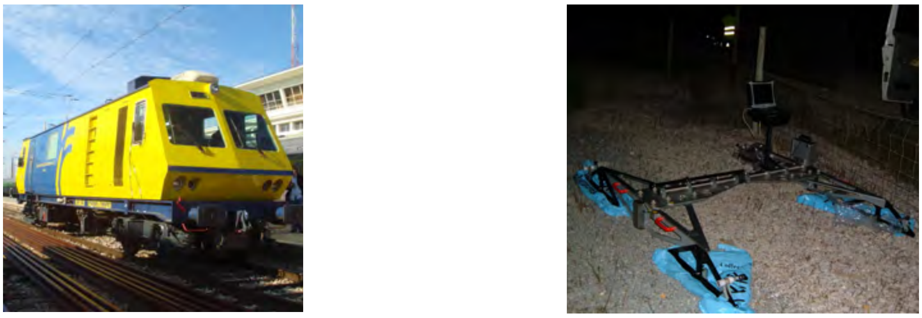

a b

Figure 13 – Equipments for measuring the track unvenness: a) recording car; b) device for measuring the rail corrugation.

Figure 14 shows the measured unevenness profile of the right rail for the range of wavelengths between 0.4m and 25m. At a train speed of 212 km/h this range of wavelengths corresponds to an excitation frequency range of the vehicles between 2.1 Hz and 147 Hz. The reference section, i.e., the cross-section of the track and of the ground that was instrumented during the train passage, is also indicated in Figure 14.

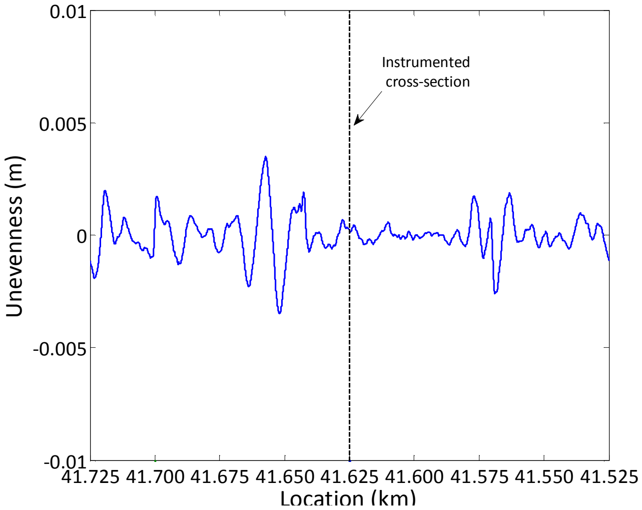

Figure 14 – Track uneveness profile.

3.5 Experimental assessment of vibrations induced by traffic

After the initial characterization experiments, focus was given to the measurement of track and free-field vibrations induced by traffic. Bearing this in mind, the setup illustrated in Figure 15 was implemented in order to experimentally evaluate the track-ground response due to traffic. As can be seen, the experimental setup comprised the measurement of vertical accelerations on the sleepers and on the ground surface, the latter at several distances from the track along a cross section. Complementarily, the displacement of the rail induced by the traffic was also measured by a laser device.

Although the huge amount of data acquired in this experimental test, subsequent to the passage of several distinct trains running at different speeds, in the following analysis only a fraction of the collected data was used, always regarding to the passage of the train Alfa-Pendular at a running speed of 212 km/h.

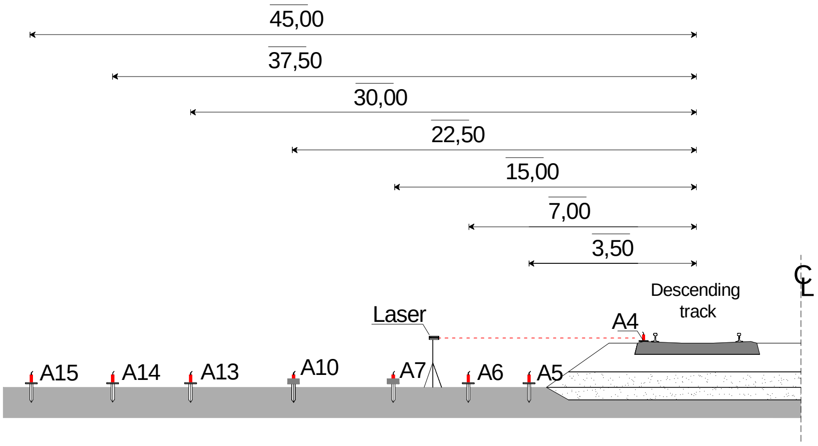

Figure 15 – Experimental setup.

4 EXPERIMENTAL VALIDATION

4.1 Model description

As emphasized before, the main objective of the study is the experimental validation of the numerical model presented in the initial sections of the paper. Thus, a numerical model comprising the train-track-ground dynamic interaction was constructed, in accordance to the formulation previously described.

The numerical model for the track-ground system is consistent with the information illustrated in Figure 11, reason why do not deserve more commentaries or justifications. Only a small remark must be done concerning to the difference between the real double-track geometry and the homologous adopted in the numerical modeling. In fact, as is well patent in Figure 11, the numerical model introduces a false plane of symmetry, crossing the mid span of the sleepers. An earlier sensibility study performed by the authors allowed concluding that this simplification is reasonable and doesn’t give rise to an appreciable loss of accuracy in the prediction. Moreover, the numerical model was calibrated taking into account this “false” symmetry, reason why it is expected to obtain a good description of the physical reality through this model.

Concerning the rolling stock properties and the interaction mechanisms, in the following sections is considered the passage of train Alfa-Pendular at the speed of 212 km/h. The track unevenness, in accordance to the results of the measurements presented in previous section, is included in the modeling procedure.

The Alfa-Pendular is the fastest train operating in Portugal. It is a conventional train composed by 6 vehicles, as indicated in Figure 16.

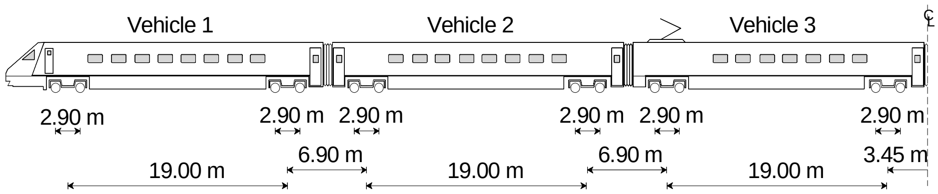

Figure 16 – Alfa Pendular geometry.

The main mechanical properties of the train were provided by the operator. In spite of this information, some identification modal tests for the structural characterization of the train were also developed and the properties adopted in the numerical model were adjusted in order to obtain a good fit between numerical and experimental natural frequencies. Table 1 summarizes the main properties of the train, in correspondence with the values adopted in the numerical analyses. The vehicles of the train are not exactly equal; Table 1 indicates the range of values found for the distinct vehicles of the train.

Table 1 – Train properties

Axles	Mw (kg)	1538-1884
Primary suspension	Kp (kN/m)	34200
	Cp (kNs/m)	36
Bogies	Mb (kg)	4712-4932
	Jb (kg/m^2)	5000-5150
Car body	Mc (kg)	32900-35710

A simplified structural model for the train was adopted. In that model, the motion of the sprung mass (car boby) is discarded. However, this suffices for the purpose of the present study due to the fact that secondary suspension of the Alfa-Pendular train is soft enough to guarantee an efficient isolation of the car body for frequencies higher than few hertz.

4.2 The track dynamic response

Figure 17 compares the computed rail displacement with the measurement supplied by the laser device. In order to minimize the noise present in the measured signal, a low-pass filter with a cut-off frequency of 80 Hz was applied to both results.

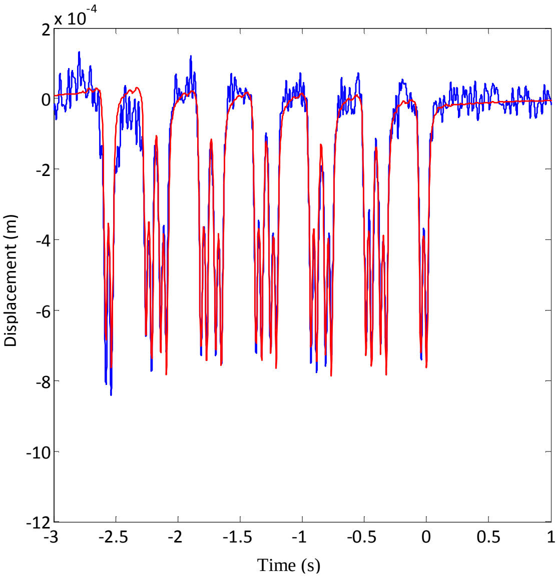

Figure 17 – Time record of the rail displacement (blue line – measurement; red line-computation).

As can be seen a splendid fit between rail displacement prediction and measurement was achieved. In fact, excluding a little discrepancy found during the passage of the first vehicle, the ability showed by the numerical model in the reproduction of the rail displacement is notorious.

Concerning the sleeper response, Figure 18 compares experimental and numerical time histories of the vertical velocity of the sleeper induced by the passage of the train Alfa-Pendular at 212 km/h.

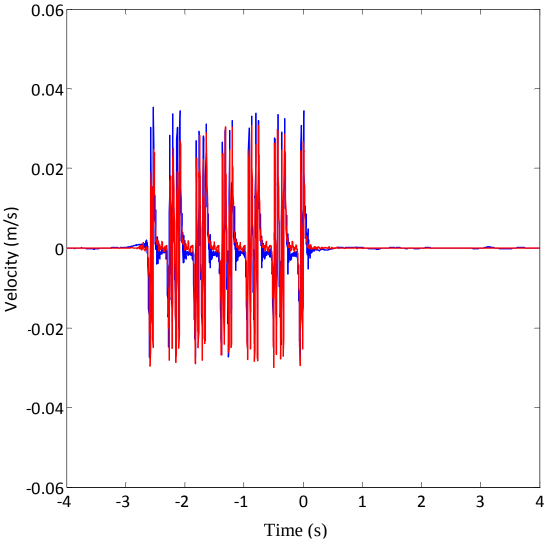

Figure 18 – Time record of the sleeper velocity (blue line – measurement; red line-computation).

Once again, a very good match between both results is emphathized by Figure 18. A clear distinction of the passage of each bogie is identified in the record, and a very good agreement between numerical and experimental results is found. Despite of the high quality of the results, it must be noticed that slight differences between measurement and prediction are found for frequencies above 75 Hz.

4.3 The free-field dynamic response

Fulfilling the requirements of synthesis of this paper, only the results concerning the points of the ground closer to the track are here analyzed. The reader is invited to consult Alves Costa et al. [19] where complementary results are shown.

Figure 19 shows the time records of the vertical velocity of those points induced by the passage of train Alfa-Pendular at 212 km/h. The numerical prediction is overlapped to the experimental record.

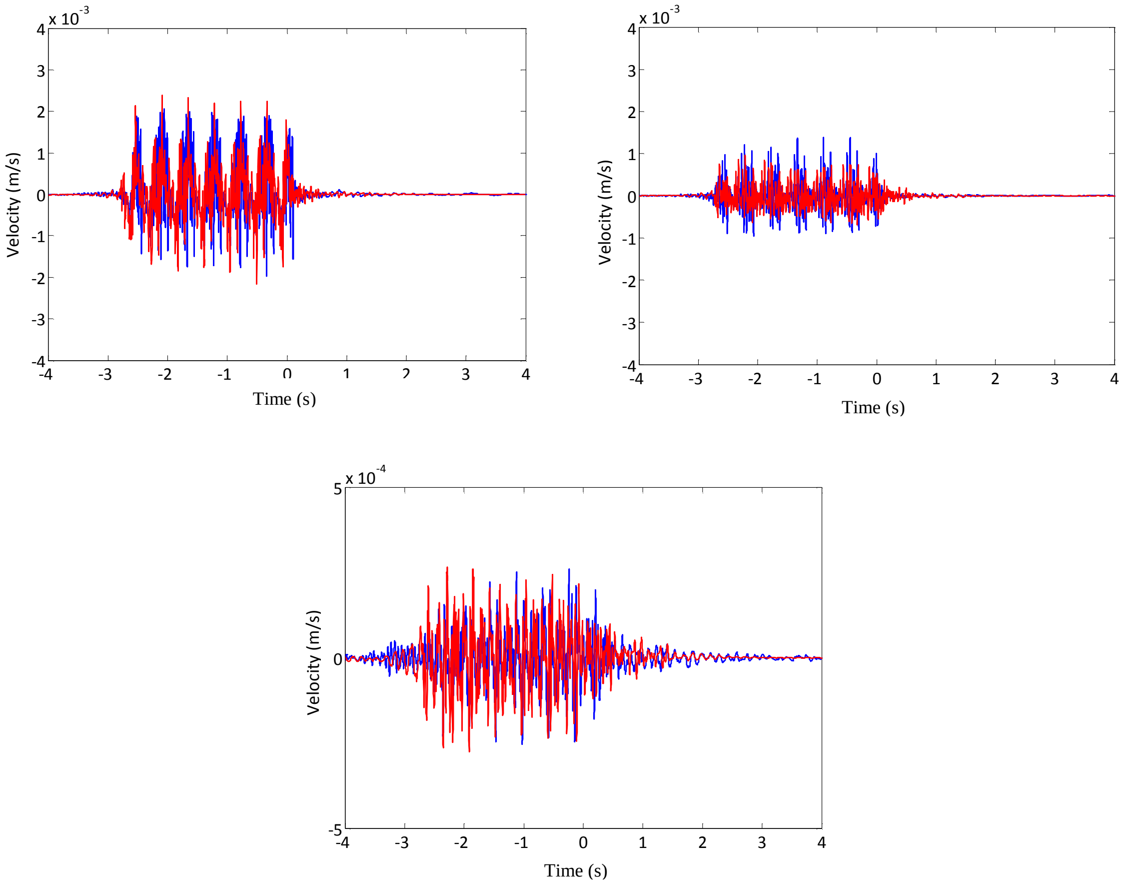

Figure 19 – Vertical velocity record at diferent distances from the track: a) 3.5 m; b) 7.0 m; c) 15.0 m (bue line – experimental; red line – computed).

Despite some differences between predicted and measured free-field vertical velocities, a reasonable agreement between simulation and physical reality was found. In fact, the numerical model was able to simulate the main aspects of the time record. However, a better discernment can be achieved by the analysis of the frequency content of the records, as illustrated in Figure 20.

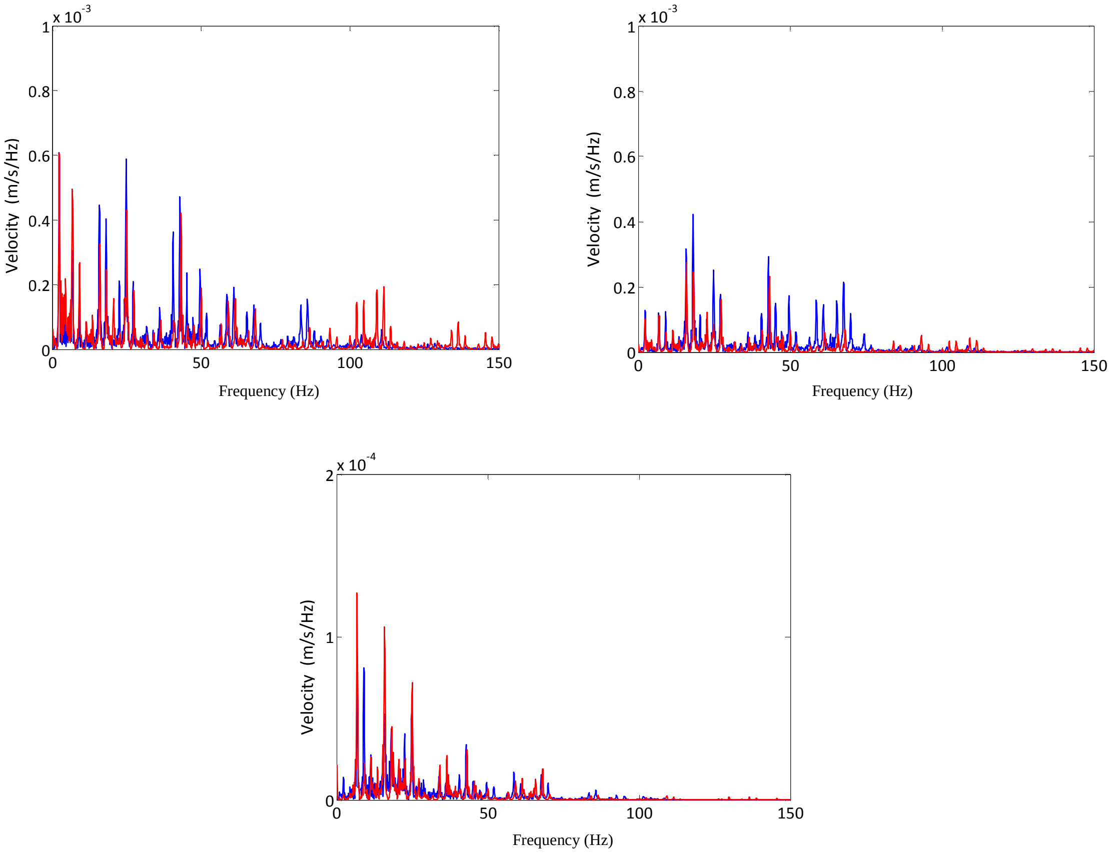

Figure 20 – Frequency content of the vertical velocity at diferent distances from the track: a) 3.5 m; b) 7.0 m; c) 15.0 m (bue line – experimental; red line – computed).

From the results exposed in Figure 20, one can conclude that the main characteristics of the frequency content were also well reproduced by the numerical model. Despite of this global good fit, for the point at a distance of 7.0 m, a more evident discrepancy between prediction and measurement is observed. Probably this difference is due to a local geotechnical condition of the ground that is distinct from the average scenario assumed in the simulation.

Despite of the successful obtained in the experimental validation of the model, it should be noticed that the discrepancy between prediction and measurement is much more evident when the analysis is focused on the dynamic response of the free-field than when the attention is dedicated to the track response. This fact shows well the complexity of the mechanisms of the wave propagation and the difficulty usually found in its numerical modeling.

5 CONCLUSIONS

In this paper, an experimental validation procedure of a 2.5D FEM-BEM model for the prediction of vibrations induced by railway traffic was shown.

The guidelines of the numerical model, implemented in Matlab 2009, were revealed, with special emphasis for the coupling procedure between the domains simulated by the 2.5 D FEM and the 2.5D BEM. Moreover, the model is able to perform train-track interaction analysis, aspect that was also described in the paper.

Bearing in mind the objective of the paper, an experimental test field, which was implemented in the Portuguese railway network, is described with emphasis to the experiments developed in order to calibrate the numerical model.

Finally, the vibrations measured during the passage of Alfa-Pendular train are compared with the prediction. The comparison between both results revealed a very good agreement for the track response and also for ground vibrations.

In the authors' opinion, the successful of this prediction is intrinsically related with a reliable characterization of the soil and of the track. Despite of the good fit reached between measurements and prediction, it should be noticed that the discrepancies between both results increases when the attention is focused on the prediction of free-field vibrations instead of track vibrations. This evidence is justified by the strong influence that local soil properties and inhomogenities of stiffness and damping can present on the waves propagation mechanisms.

ACKNOWLEDGMENTS

This paper reports research developed under the financial support of "FCT - Fundação para a Ciência e Tecnologia", Portugal, namely from the research project - PTDC/ECM/114505/2009. The first author wishes to thank FCT for the financial support provided by the grant SFRH / BD / 29747 / 2006.

The authors also wish to acknowledge the support of the project “Risk Assessment and Management for High-Speed Rail Systems” of the MIT – Portugal Program Transportation Systems Area.

The collaboration of REFER, CP and LNEC was also appreciated by the authors of the present work.

REFERENCES

1. Alves Costa, P., R. Calçada, A. Silva Cardoso, and A. Bodare, *Influence of soil nonlinearity on the dynamic response of high-speed railway tracks.* Soil Dynamics and Earthquake Engineering, 2010. **30**(4): p. 221-235.
2. François, S., M. Schevenels, P. Galvín, G. Lombaert, and G. Degrande, *A 2.5D coupled FE–BE methodology for the dynamic interaction between longitudinally invariant structures and a layered halfspace.* Computer Methods in Applied Mechanics and Engineering, 2010. **199**(23-24): p. 1536-1548.
3. Dieterman, H.A. and A. Metrikine, *The equivalent stiffness of a half-space interacting with a beam. Critical velocities of a moving load along the beam.* European Journal of Mechanics A/Solids, 1996. **15**(1): p. 67-90.
4. Dieterman, H.A. and A. Metrikine, *Steady-state displacements of a beam on an elastic half-space due a uniformly moving constant load.* European Journal of Mechanics A/Solids, 1997. **16**(2): p. 295-306.
5. Sheng, X., C. Jones, and D. Thompson, *A comparison of a theoretical model for quasi-statically and dynamically induced environmental vibration from trains with measurements.* Journal of Sound and Vibration, 2003. **267**(3): p. 621-635.

6. Kausel, E., *Commentaries on methods to estimate ground vibrations elicited by fast moving loads*, in *Noise and Vibration on high-speed railways*, R.D. Calçada, R.; Carvalho, A., Degrande, G., Editor. 2008: Porto.
7. Yang, Y.B. and H.H. Hung, *A 2.5D finite/infinite element approach for modelling visco-elastic body subjected to moving loads.* International Journal for Numerical Methods in Engineering, 2001. **51**: p. 1317-1336.
8. Yang, Y., H. Hung, and D. Chang, *Train-induced wave propagation in layered soils using finite/infinite element simulation.* Soil Dynamics and Earthquake Engineering, 2003. **23**: p. 263-278.
9. Yang, Y. and H. Hung, *Soil Vibrations Caused by Underground Moving Trains.* Journal of Geotechnical and Geoenvironmental Engineering, 2008. **134**(11): p. 1633-1644.
10. Lombaert, G., G. DeGrande, J. Kogut, and S. François, *The experimental validation of a numerical model for the prediction of railway induced vibrations.* Journal of Sound and Vibration, 2006. **297**: p. 512-535.
11. Lombaert, G. and G. Degrande, *Ground-borne vibration due to static and dynamic axle loads of InterCity and high-speed trains.* Journal of Sound and Vibration, 2008. **----**(-----): p. -------.
12. Alves Costa, P., R. Calçada, J. Couto Marques, and A. Cardoso, *A 2.5D finite element model for simulation of unbounded domains under dynamic loading*, in *7th European Conference on Numerical Methods in Geotechnical Engineering*, T.B.a.S. Nordal, Editor. 2010: Trondheim. p. (aceite para publicação).
13. Galvín, P., S. François, M. Schevenels, E. Bongini, G. Degrande, and G. Lombaert, *A 2.5D coupled FE-BE model for the prediction of railway induced vibrations.* Soil Dynamics and Earthquake Engineering, 2010. **30**(12): p. 1500-1512.
14. Sheng, X., C. Jones, and D. Thompson, *Responses of infinite periodic structures to moving or stationary harmonic loads.* Journal of Sound and Vibration, 2005. **282**: p. 125-149.
15. Tadeu, A., J. Antonio, and L. Godinho, *Green's function for two-and-a-half dimensional elastodynamic problems in a half-space.* Computational Mechanics, 2001. **27**: p. 484-491.
16. Kausel, E., *An explicit solution for the green functions for dynamic loads in layered media*, R.R. R81-13, Editor. 1981, MIT: Boston.
17. Lopes, P., P. Alves Costa, R. Calçada, and A. Silva Cardoso, *Análise numérica de vibrações induzidas por tráfego ferroviário em túneis baseada em modelos 2.5D*, in *12º Congresso Nacional de Geotecnia*. 2010: Guimarães.
18. Sheng, X., C. Jones, and D. Thompson, *A theoretical study on the influence of the track on train-induced ground vibration.* Journal of Sound and Vibration, 2004. **272**: p. 909-936.
19. Alves Costa, P., R. Calçada, and A. Silva Cardoso, *Vibrations induced by railway traffic: influence of the mechanical properties of the train on the dynamic excitation mechanism*, in *EURODYN 2011*. 2011.
20. Zhai, W. and Z. Cai, *Dynamic Interaction between a lumped mass vehicle and a discretely supported continuous rail track.* Computers and Structures, 1997. **63**(5): p. 987-997.
21. Lombaert, G. and G. Degrande, *Ground-borne vibration due to static and dynamic axle loads of InterCity and high-speed trains.* Journal of Sound and Vibration, 2009. **319**(3-5): p. 1036-1066.

COMPDYN 2011
3rd ECCOMAS Thematic Conference on
Computational Methods in Structural Dynamics and Earthquake Engineering
M. Papadrakakis, M. Fragiadakis, V. Plevris (eds.)
Corfu, Greece, 25–28 May 2011

EFFECT OF THE TYPE OF TRACK ON THE DYNAMIC BEHAVIOUR OF HIGH SPEED RAILWAY BRIGDES

J. M. Proença[1*], H. Casal[1], and M. Neves[2]

[1] ICIST/IST, Department of Civil Engineering and Architecture, Instituto Superior Técnico, T U Lisbon, Portugal
Av. Rovisco Pais, Nº 1, 1049-001, Lisbon, Portugal
e-mail: jmiguel@civil.ist.utl.pt

hugobaleiacasal@gmail.com
mdsneves@gmail.com

Keywords: Rheda 2000® ballastless track, ballasted track, high-speed railway bridge, dynamic analysis, moving loads, finite element numerical models.

Abstract. *This paper presents a study performed with the purpose of providing a comparison between the effects of the two types of railway track – ballasted and ballastless – in the dynamic behaviour of a bridge. This study also addresses the different methods to model the various types of track, as well as their consequences for the parameters defining the dynamic behaviour of the bridge structure.*

Initially, an overview of the different types of track systems is presented, comprising the more traditional solution of ballasted track, and, alternatively, the ballastless track solution, with an emphasis on the wide range of options currently available for both of these track systems.

At a later stage, the presented study is focused in how the dynamic behaviour of a bridge is affected by the type of track and what might be the consequences for the dynamic response parameters (vertical acceleration, displacement and internal stresses). This work is complemented by a comparative analysis of various numerical models, in which the different types of railway track systems are considered with varying degrees of refinement of the track mechanical models. This comparative analysis is carried out with the hypothetical case study of the São Martinho Viaduct, near Alcácer do Sal, in Portugal, a viaduct that was recently designed and built for conventional rail traffic (design speed of 220 km/h). A comparative *analysis of four types of finite element models of the bridge – solid, shell and frame (grid and single bar) elements – is also presented.*

At the end, some conclusions based on parametric analysis of the case study are drawn, highlighting the different results concerning the modelling and the use of these two different railway track systems.

1 INTRODUCTION

The high-speed railway network has imposed stringent new demands on the structure of railway bridges. These demands are, in part, a reaction to the dynamic effects due to the passage of vehicles. As a consequence, the study of the dynamic behaviour of railway bridges subjected to moving vehicles gained a substantial importance in the design of such structures. It is crucial to question the assumptions under which all the study is based, which will largely determine its degree of reliability. It should be noted, for example, the degree of representation and detail desired for a possible numerical model of a bridge. A better representation of the railway track through finite elements may have influence on the dynamic response of the structure. And given this representation, it is interesting to see how some of the components of the track interfere in the dynamic behaviour. Finally, it is important to assess how the type of railway track, i.e. ballasted track or ballastless track, influences such dynamic behaviour.

2 TYPES OF RAILWAY TRACK

2.1 Ballasted track

2.1.1. Track characterization

The ballasted track, Figure 1, is a solution with more than two centuries of existence and has been used in a vast number of high speed tracks. In railway bridges, this typology is composed by the superstructure (rails, sleepers and fastening systems) and by the substructure (ballast).

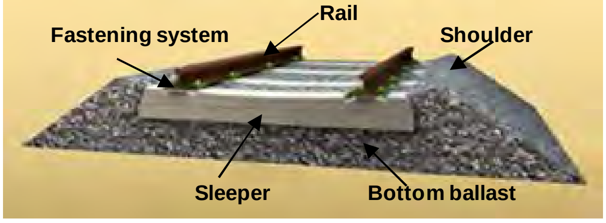

Figure 1 - Ballasted track.

Besides the fact that this typology is the most commonly used nowadays, the definition of its geometry as well as the properties of the elements used has some variability.

Rails

The rails are the first elements in contact with the vehicle wheels and its main functions are the transmission and distribution of the vertical and horizontal forces by the sleepers and guidance of the vehicle wheels. The choice of the UIC60 rail is justified in high speed lines by technical and economical reasons as referred by Gil [1].

Fastening Systems

The choice of the type of fastening system depends essentially on the railway and sleeper type used and on the stiffness of the granular layers which support the sleepers. These elements should guarantee a good connection between the rail and the sleeper. The rail pads may also be used to limit the stiffness of the railway track in order to reduce the dynamic effects resulted by the circulation of the trains. Teixeira [2] states that, in high-speed railways, the stiffness of the rail pads varies between 30 and 500 kN/mm. In spite of these values being generally attributed to a certain type of pad, these may not consider the pre-loading effect which has relevant influence in the dynamic properties of the rail pads.

Sleepers

The sleepers are elements of considerable stiffness and allow the distribution of stresses coming from the rail to the layer which supports them. The most common typology is the monoblock sleeper and those elements are generally placed at a distance which can vary between 50 and 70 cm.

Ballast layer

The ballast layer is designed in order to guarantee the capacity of spreading and conveniently transmitting the loads that are transmitted to the supporting structure. In the EN 1991-2 [3], it is referred that, to be assured a good distribution of this stresses without damaging the surface of a bridge or of an eventual ballast mats, a depth not inferior to 250 mm should be adopted. In general, a depth of 350 mm is adopted, which allows an efficient maintenance of the track.

2.1.2. Modelling of the ballasted track

The numeric or analytic modelling of the railway track has been used together with field experiments to study its behaviour as well as its element characterization, its properties and also the vehicle-track-bridge interaction.

Facing the desired goals, more or less detailed models can be used.

The Ballasted Track can be modelled as a simple dead load, distributed over the deck, or by means of intermediate complexity models, in which the physical properties of the track are defined. In this paper, 2D simplified models are presented, based on studies of previous authors, to represent the effect of the various elements of the track:

- **Non-vibrating ballast model**: Calçada [4] and De Man [5] used a model in their studies which considers the rails represented as a beam with an Euler-Bernoulli or Timoshenko behaviour and with such a length that the edge restrictions do not affect the structural behaviour. The sleepers are modelled as suspended masses connected to the beam, in the top, through parallel systems of spring-damper which represents the pads' properties, and to the subsoil/bridge, in the bottom, through parallel spring-damper systems which represent the ballast properties. In this model, the distance between elements is defined by the spacing between sleepers.

- **Vibrating ballast model**: The Specialists' Committee D214 of the ERRI [6] presents a similar model to the one presented beforehand, but which considers the ballast modelled as suspended masses. These masses are connected to the sleepers, in the top, and to the subsoil/bridge, in the bottom, through parallel spring-damper systems which respectively represent the pads' properties and the connection between the ballast and the bridge subsoil.

Figure 2 presents schematically this two simplified models:

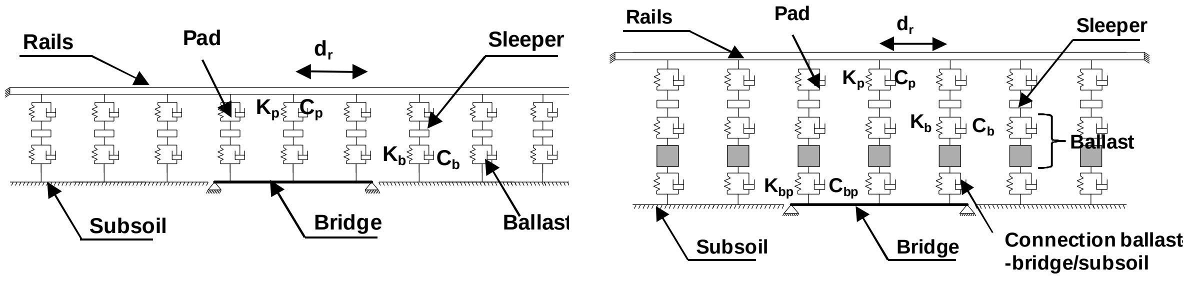

(a) (b)

Figure 2 - 2D simplified models of ballasted track: considering the ballast without a vibrating mass (a) and considering the ballast as a vibrating mass (b).

Some properties that characterize elements such as rails, pads and sleepers, can be found in catalogues of suppliers. In this paper, the characterization of the ballast layer may be more ambiguous.

Zhai [7] presents various equations which allow the calculation of the vibrating mass and the vertical stiffness as a function of the geometry of the ballast layer and the distance between sleepers.

The computation of each vibrating mass that corresponds to the influence of a half-sleeper is related to the attenuation angle (α) as presented in Figure 3 and expressed by the following equation.

$$M_b=\rho_b h_b\left[l_e l_b+(l_e+l_b)h_b tg\alpha+\frac{4}{3}h_b^2 tg^2\alpha\right] \tag{1}$$

In which ρ_b is the ballast density, h_b is the depth of ballast, l_e is the effective supporting length of half sleeper and l_b is the width of sleeper underside.

The vertical stiffness for each vibrating mass of the ballast is computed by:

$$K_b=\frac{2(l_e-l_b)tg\alpha}{\ln(l_e/l_b)\,(l_b+2h_b tg\alpha)/(l_e+2h_b tg\alpha)}E_b \tag{2}$$

where E_b is the elastic modulus of the ballast. These equations assume that there is no overlapping over the adjacent cone regions of ballast.

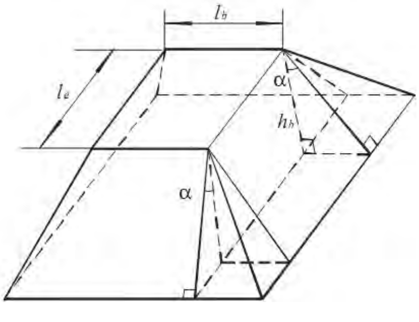

Figure 3 – Model of the ballast under one rail support point.

2.2 Ballastless track

2.2.1. Track characterization

The ballastless track is already at the forefront of the Railway Engineering, presenting a wide range of advantages when compared to the conventional ballasted track. The high demands imposed by high speed railway traffic have provided conditions to invest in a new kind of track with increased performance levels.

Actually, it is especially at high speed that greater benefits can result from the resource to ballastless tracks. This innovative type of railway track stands out mainly for its performance, leading to substantial reductions in maintenance costs and also in maintenance work like tamping, ballast cleaning or track lining. Despite the high initial construction costs, these expenses may be offseted over the service life of the track, creating a more economical and competitive solution when one assesses a broader dimension of time.

Additionally, the problem with drag forces at ballast due to the passage of high speed trains is no more a reason for concern. Indeed, this feature, together with others, has increasingly been providing the application of ballastless tracks on high speed railway lines.

The wide range of different solutions developed by different countries, such as Germany, Japan or even the Netherlands, may eventually hamper the selection process by the designer. In fact, there is a high technical, economical, or even functional ambiguity among the different solutions available.

Nevertheless the Rheda® system may be considered a benchmark for proving its performance and efficiency over the years, having already presented a wide range of applications since its origin.

The cross-section of Rheda 2000® ballastless track used on the Hollandsch Diep Bridge, in the Netherlands, on which this study was also based, is depicted in Figure 4.

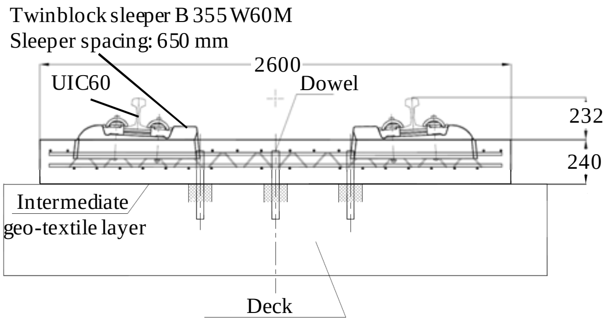

Figure 4 – Cross-section of Rheda 2000 ballastless track used on the Hollandsch Diep Bridge (in millimetres). Adapted from [8].

The Rheda 2000® slab is anchored to the bridge structure in pre-designated free-drilling zones by means of high quality stainless steel dowels with a diameter of 40 mm [8]. An important feature of this connexion is its capacity to allow movements in the longitudinal direction. Thus, the overloading of dowels, as a result of expansion or shrinkage of deck or even track's concrete, can be avoided [9]. The ballastless track is composed by segmented slabs with a length of 3.50 to 6.40 m. The Rheda 2000® slab used concrete of C35/45 grade for its construction.

2.2.2. Modelling of the track

The ballastless track was considered according to two different approaches:

- consideration of the track by means of linear distributed forces;
- consideration of the track by means of a finite element model, which reproduces the characteristics of several components of the track.

The first procedure was very simple and easy to perform. The inclusion of the ballastless track in the grid model through its equivalent weight was the basis for this type of representation.

The second procedure, i.e. the numerical modelling, was inspired by the double beam model, a type of representation suggested by several authors [10], [5] and [11] and depicted in Figure 5:

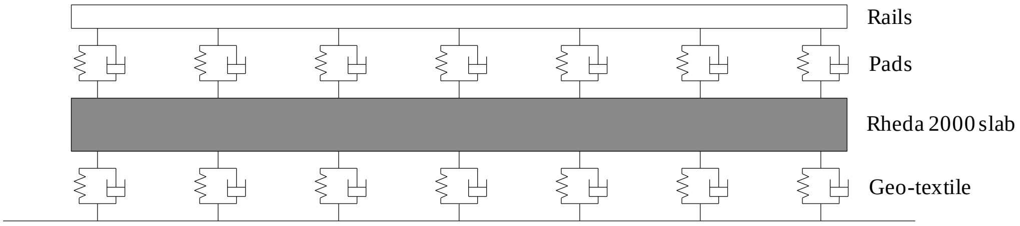

Figure 5 – Schematic representation of the ballastless track model.

The UIC60 rails and the Rheda 2000 slab were modelled using frame elements, while the remainder components were modelled using finite elements that reflect the properties of a viscoelastic material characterized by stiffness and damping values. The longitudinal alignment of the frame elements of the Rheda 2000® slab is not continuous but segmented, with segments of 6.5 m length.

3 PRESENTATION OF THE CASE STUDY

3.1 Presentation of the bridge

The case study for the bridge was based on the São Martinho Viaduct, located in the Natural Reserve of the Sado river estuary, near Alcácer do Sal. This structure is designed to accommodate rail traffic on ballasted track, with a design speed of 220 km/h.

From the structural point of view, the Viaduct is composed of 8 continuous segments, 7 with 4 spans of 28.4 m length each, giving a total length of 113.6 m, and another segment with 56.8 m, consisting of 2 spans of 28.4 m. Only the structural portion of 113.6 m in length will be modelled to study its dynamic behaviour.

The Viaduct cross-section (Figure 6) consists of a prestressed concrete deck, composed of two main beams connected by the railway platform concrete slab. At supports there is a diaphragm with 0.60 m width.

The weight of the deck advocated for this viaduct, including the other permanent loads (except the weight of the railway track), corresponds to 248 kN/m.

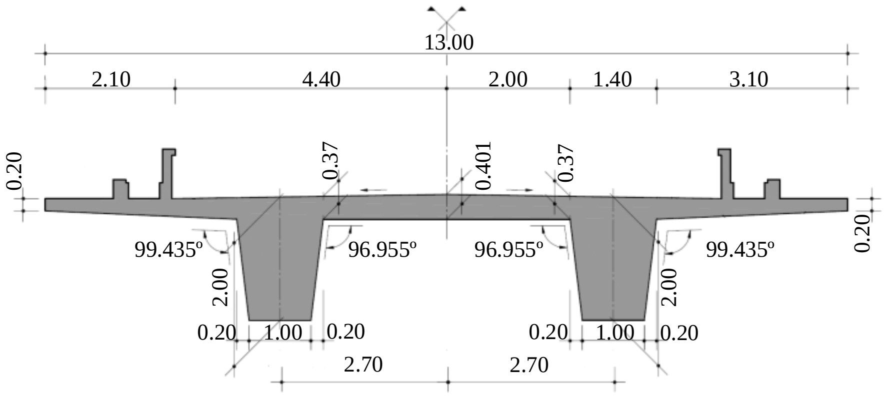

Figure 6 – São Martinho Viaduct cross-section (in meters). Adapted from [12].

3.2 Numerical modelling of the bridge

São Martinho Viaduct was represented using 4 different numerical models based on finite elements. These 4 models have undergone a process of evaluation and comparison to indentify which is the best suited for the present study. The models created were:

- A numerical model with solid finite elements;
- A grid numerical model with frame finite elements;
- A numerical model with shell finite elements;
- A bar numerical model with frame finite elements.

3.2.1. Model with solid elements

This model is composed by solid elements with 8 nodes each. Each node has 3 degrees of freedom of translation, providing a total of 24 degrees of freedom per element. The size of these finite elements was cleared to ensure a high degree of discretization. In total, 60 530 nodes and 37 540 solid finite elements were used.

This model was considered a reference for the calibration of the remaining models, given its high degree of reliability and given the impossibility of conducting an experimental campaign. For such calibration several static and modal analyses were performed.

This model was not selected to perform the planned dynamic analyses because of the unreasonable calculation times that would otherwise greatly extent the duration this task. This situation would persist even if a coarser discretization was used.

3.2.2. Grid model

Regarding the grid model, the Viaduct was modelled in a three-dimensional configuration with frame finite elements.

The two beams were modelled making use of two longitudinal alignments of frame elements with an appropriate cross-section identical to the beam. The frame elements representing the cantilevers and the top slab between beams were calibrated and transversely aligned, being replicated to a constant value of 0.65 m. Finally, the diaphragms were modelled resorting to the use of frame elements with 0.60 m thick. In total, 3002 nodes and 3243 frame finite elements were used.

Figure 7 represents graphically two fundamental mode shapes obtained from modal analysis:

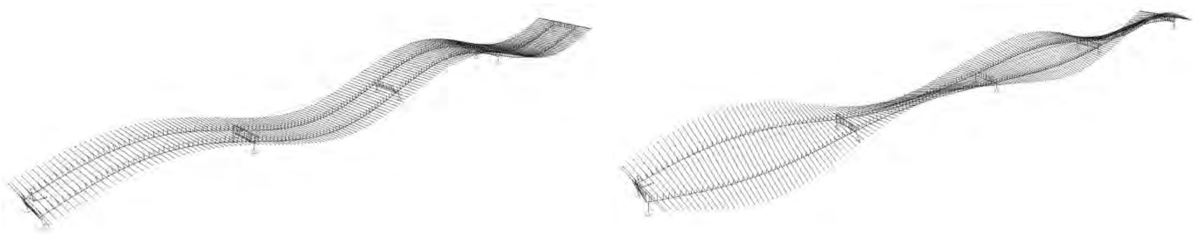
(a)
(b)

Figure 7 – Graphical representation of the vertical fundamental mode shape (f=4.0271 Hz)(a) and of the torsional fundamental mode shape (f=7.0443 Hz)(b).

The grid model was selected to perform the desired dynamic study and subsequent dynamic analyses. With a performance very similar to the shell model, regarding the comparison criteria used, this model proved to be a strong option for the realization of dynamic analyses. In addition, the calculation times of this model were likely to be lower than those from the shell model, which did not show other significant advantages. The grid model is the most appropriate, among the four models, to conduct the remaining stages of the desired dynamic study.

3.2.3. Bar model and shell model

These models have interesting features and the results are similar to those obtained from the two models presented above.

Regarding the bar (frame) model, the deck was modelled making use of frame finite elements longitudinally aligned and with an average length of 0.3 m. In order to represent deck areas on piers and on half span, two different cross sections for frame finite elements were defined. In total, 400 nodes and 399 frame finite elements were used.

The bar model was not used to perform dynamic analyses because it is completely unable to effectively represent the torsional behaviour of the Viaduct and, therefore, its torsional mode shapes. This model is not appropriate for the concerned dynamic study since it is not possible to represent, in a reliable way, the effect of the eccentricity of rails.

Regarding the shell model, the beams are represented making use of two longitudinal alignments of shell finite elements classified as “thick” and with a non-constant thickness in order to consider the differences between the bottom and the top of the beam. The top slab between beams and the cantilevers were modelled in a similar way using shell finite elements classified as “thin” and with a non-constant thickness. The diaphragms are represented with shell elements classified as “thin” and with a constant thickness.

In total, this model contains 6825 nodes and 6554 shell finite elements.

The shell model could be a viable option, if the grid model did not exist, thanks to the high degree of reliability of its performance, very close to the model with solid elements. The criteria used for comparison showed few parameters with deviations exceeding 5%. Moreover there is a clear similarity between the first 9 mode shapes and those obtained from the reference model. This option was not used to perform the desired dynamic analyses since it could cause high calculation times. Indeed, as one may know, using shell elements could lead sometimes to a more complex model.

3.3 Railway track models

3.3.1. Ballasted track models

The dynamic analyses of the viaduct can be conducted considering the track as a uniformly distributed load along the deck or considering a simplified model.

Regarding a ballasted track, the EN1991-2 [3] refers that the dynamic analyses should be performed considering the minimum density of a clean ballast with a minimum depth and a maximum saturation density to a dirty ballast taking into account the probable increase on depth of ballast layer. The present study was performed considering a depth of ballast of 350 mm and two different ballast densities $\rho_{ballast}$ = 17 kN/m^3 and $\rho_{ballast}$ = 20kN/m^3. Table 1 presents the weight of the ballasted track on the Viaduct.

Typology	Properties	Weight (kN/m)
Ballasted track (double track)	Model BT1 ($\rho_{ballast}$=17 kN/m^3)	95
	Model BT2 ($\rho_{ballast}$=20 kN/m^3)	112

Table 1 – Different typologies of ballasted track considered and its weight per linear meter on the Viaduct.

Regarding the models of ballasted track, Table 2 shows the parameters used on the study of the influence of the various elements of this type of track in the dynamic behaviour of the structure. The geometry of the ballasted track as well as the ballast properties are related to the properties of model BT2.

3.3.2. Ballastless track models

In similarity to the ballasted track, the dynamic analyses were also performed considering the ballastless track by means of linear distributed forces and by means of a simplified finite element model.

The Rheda 2000® ballastless track (double track) highlighted in this paper has a weight per linear meter of 35 kN/m [8].

With regard to the track model, the properties of the frame elements are shown in Table 2:

	Parameters of the railway track	Symbology	Value		
			Non-vibrating ballast	**Vibrating ballast**	**Ballastless track**
UIC60 Rail	Cross section	S_r [cm^2]	76,86	76,86	76,86
	Mass	m_r [kg/m]	60,34	60,34	60,34
	Elasticity modulus	E_r [GPa]	210,00	210,00	210,00
	Poisson's ratio	ν_r [-]	0,30	0,30	0,30
	Vertical bending inertia	I_{xx} [cm^4]	3050	3050	3050
	Lateral bending inertia	I_{yy} [cm^4]	515,60	515,60	515,60
Pad	Dynamic stiffness	K_p (MN/m)	65 [13]	65	Variable
	Damping	C_p (kNs/m)	5,50 [13]	5,50	Variable
Sleeper	Mass	M_s [kg]	300	300	-
	Spacing	l_s [m]	0,60	0,60	0,65
Ballast	Vertical stiffness	Kb [N/m]	3,30E08	3,30E08	-
	Damping	C_b [Ns/m]	1,20E05 [6]	1,20E05	-
	Vibrating mass	M_b [kg]	-	770,94	-
Connexion	Vertical stiffness	K_{bp} [N/m]	-	1000E06 [6]	-

	Parameters of the railway track	**Symbology**	**Value**		
			Non-vibrating ballast	**Vibrating ballast**	**Ballastless track**
ballast/deck	Damping	C_{bp} [Ns/m]	-	50E03 [6]	-
Rheda2000® slab	Specific weight	ρ_L [kN/m^3]	-	-	26,37
	Length x Height	Lxh [mxm]	-	-	2,60x0,24
	Elasticity modulus	E_L [GPa]	-	-	34,00
	Poisson's ratio	ν_L [-]	-	-	0,20
Geo-textile	Vertical stiffness	K_{Gt} [GN/m/m]	-	-	20E03
	Damping	C_{Gt}[GNs/m/m]	-	-	20

Table 2 – Parameters used in the ballasted and ballastless models.

4 DYNAMIC ANALYSES

4.1 General considerations

The dynamic analyses were performed according to the following assumptions:

- The method of modal superposition was applied, considering a number of frequencies and associated mode shapes on the analysis up to the greater of 30 HZ, as recommended in EN1990-A2 [14];
- The structural damping was simulated using the Rayleigh damping;
- The used time step was $\Delta t = 0.005$ s;
- The range of speeds used was 140 km/h to 420 km/h with a speed step of $\Delta v=10$ km/h;
- Only the 4th span of the Viaduct was assessed.

4.2 Results of the ballasted track models

This subsection presents the results of the dynamic analyses performed, making use of the grid model with and without the ballasted track model. The load models were regarded as moving loads. The realized parametric study aims to assess the effect of the various components of the track in the dynamic behaviour of the support structure.

4.2.1. Grid model without the ballasted track model

The envelope of accelerations and displacements, depicted in Figure 8, were obtained for all the ten HSLM-A defined in EN1991-2 [3] and making use of the grid model without the track model (BT1).

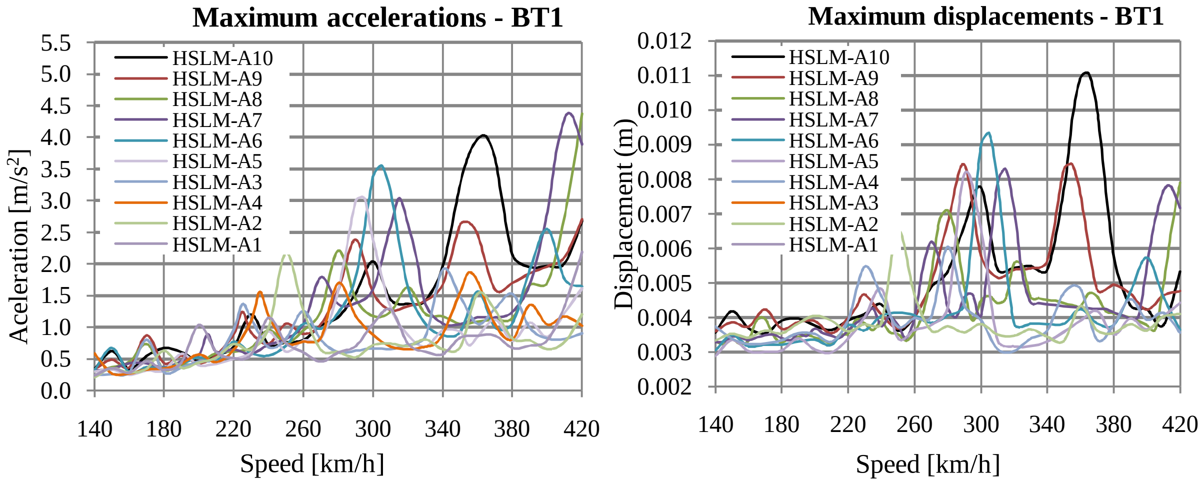

(a) (b)

Figure 8 – Envelope of accelerations (a) and envelope of displacements (b) for the passage of the HSLM-A

The following conclusions were drawn:

- a maximum vertical acceleration peak of a_v=4,38 m/s^2 occurs for the load model HSLM-A7;
- a maximum vertical displacement peak of δ_v = 0,0111 m occurs for the load model HSLM-A10;
- the limit of 3,5 m/s^2 for the acceleration of ballasted tracks, defined in EN1990-A2 [14], was exceeded;
- the maximum limit of δ_{lim}=L/600 for the vertical displacement, defined in EN1990-A2 [14], was never exceeded.

With regard to the model BT2 and in comparison with the results obtained for the model BT1, a maximum vertical acceleration is obtained with a lower value but occurring also for a lower resonance speed. On the contrary, the maximum vertical displacement is not influenced by the variation of the weight of the track.

4.2.2. Grid model with the ballasted track models

The results presented in Table 3 correspond to the values of the first 5 natural frequencies of the structure with and without consideration of the ballasted track models. There are minor variations of the values in each vibration mode shape and on the first mode shapes this variation is barely perceptible. Such results do not demonstrate a contribution of the ballasted track properties for the overall behaviour of the structure. Analyzing the Figure 9 it is of clear understanding that a superposition of the obtained results exists, not only for the maximum vertical accelerations but also for the maximum vertical displacements along the load path, to the considered speed range. It is concluded, though, that the consideration of the ballasted track models does not change the structural response when the dynamic analysis are limited to lower than 30 Hz mode shapes. To the viaduct modelled with a span length of L=28.4m the distribution of the loads along various sleepers resulting from the track models, does not contribute to the acceleration reduction nor to the structures' displacements.

Mode shape of vibration	Vibration frequency[Hz]		
	BT2 Model	Vibrating ballast	Non-vibrating ballast
1	3,058	3,059	3,059
2	3,600	3,600	3,600
3	4,653	4,653	4,654
4	5,132	5,146	5,147
5	5,222	5,236	5,237

Table 3 - Comparison of the vibrating frequencies of the viaduct with and without the consideration of the ballasted track models.

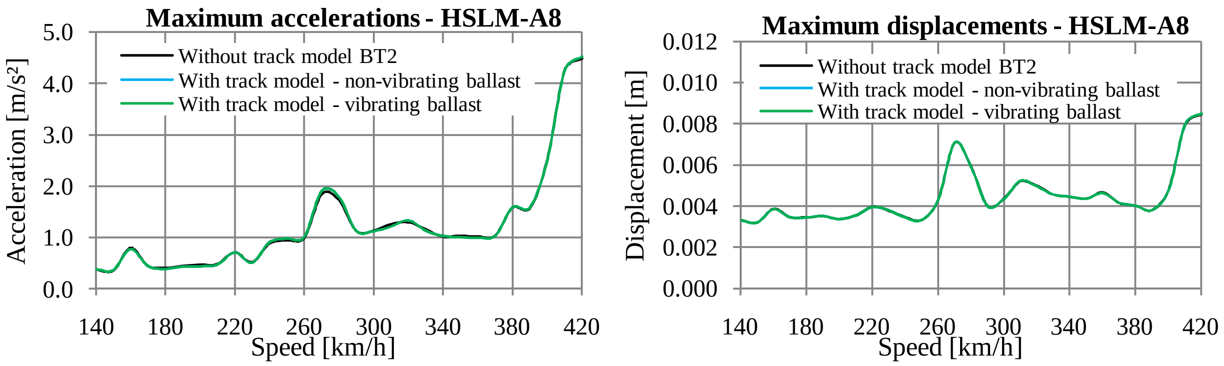

(a) (b)

Figure 9 – Envelope of accelerations (a) and envelope of displacements (b) for the HSLM-A8, considering three different possibilities for the inclusion of the ballasted track

In fact, calculating the vibration fundamental frequencies of the ballasted track and assuming a simplified SDOF model graphically represented in Figure 10, a fundamental frequency of vibration of 115Hz has been computed, thus largely exceeding the 30 Hz limit of vibration mode shapes to be considered in the dynamic analyses. Barbero [15] has reached similar conclusions and noticed that the railway vibrates jointly with the bridge when the vibration frequencies of the track are much higher than those of of the bridge.

Dynamic analyses considering a more flexible ballasted track were also performed. Nevertheless, the obtained results did not show different variations.

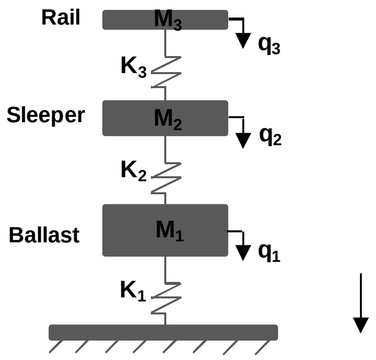

Figure 10 – Model with three degrees of freedom representative of the behaviour of the ballasted track.

4.3 Results of the ballastless track model

This subsection presents a comparative study that aims at evaluating the dynamic behaviour of the Viaduct taking into account the type of representation chosen for the ballastless track

4.3.1. Grid model without the ballastless track model

The envelope of accelerations and displacements, depicted in the Figure below, were obtained for all the ten HSLM-A defined in EN1991-2 [3] and making use of the grid model without the track model:

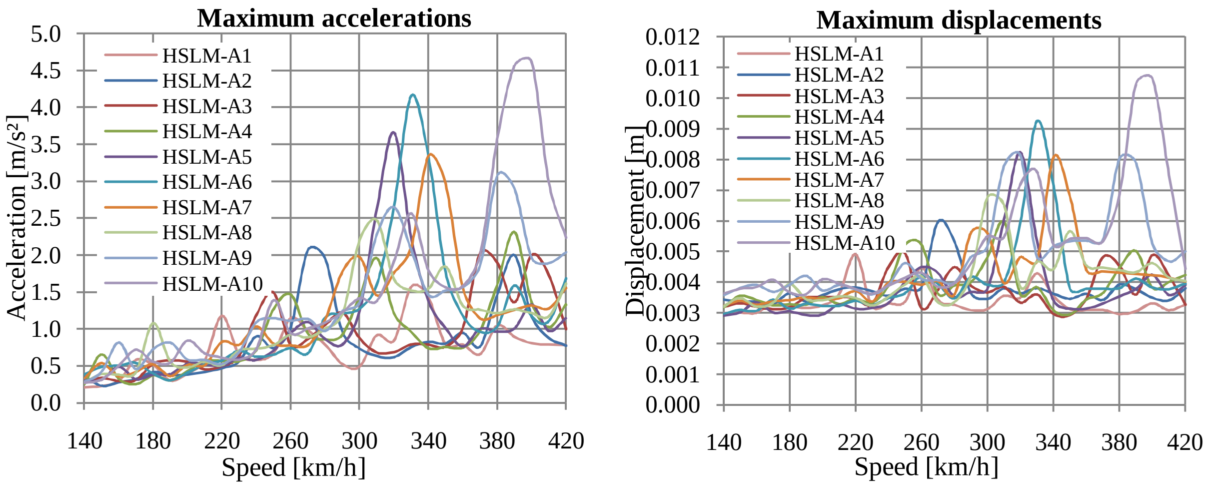

(a) (b)

Figure 11 – Envelope of accelerations (a) and envelope of displacements (b) for the passage of the HSLM-A.

As it can be observed:

- the maximum acceleration and displacement occur for the HSLM-A10, which induces dynamic responses with quite significant resonance peaks;
- a maximum acceleration of 4.613 m/s^2 and a maximum displacement of 0.01062 m were computed;
- the serviceability limit of 5 m/s^2 for the acceleration of ballastless tracks, defined in EN1990-A2 [14], was never exceeded;
- the maximum limit of δ_{lim}=L/600 for the vertical displacement, defined in EN1990-A2 [14], was never exceeded.

4.3.2. Grid model with the ballastless track model

Regarding the grid model with the track model, a parametric study was performed considering the properties of the pads, such as the dynamic stiffness and damping, assigned with the values present in Table 4.

Grid model	Pads	
	Dynamic stiffness $k_{d,p}$ [kN/m]	Damping c_p [kNs/m]
With track model 1	100000	15
With track model 2	100000	75
With track model 3	100000	500
With track model 4	30000	15
With track model 5	30000	75
With track model 6	30000	500
With track model 7	∞	—

Table 4 – List of models tested with distinct properties for the pads.

Figure 12 shows the results obtained from the dynamic analyses performed for the HSLM-A10:

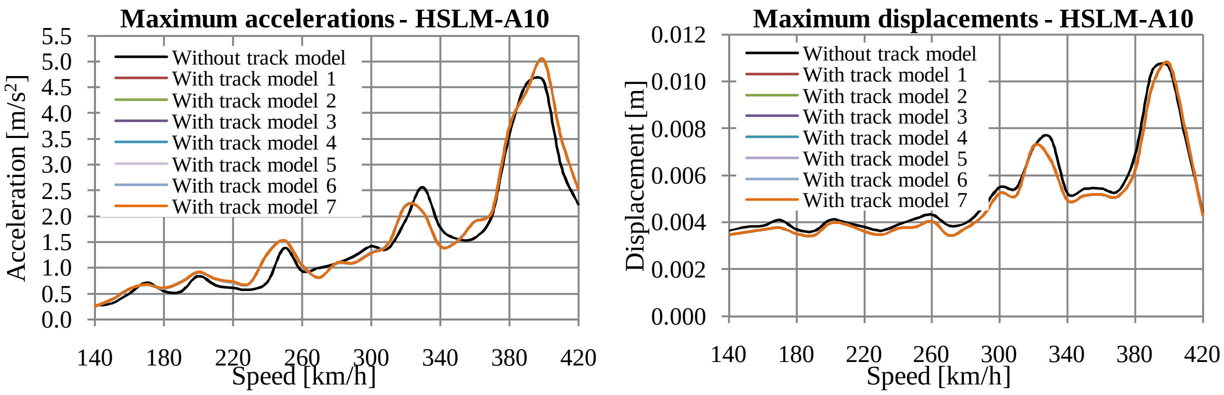

(a) (b)

Figure 12 – Envelope of accelerations (a) and displacements (b) for the passage of the HSLM-A10, obtained from the grid model with track model 1-7 and from the grid model without the track model.

As it can be observed, and regarding the 7 models tested, the graphical representations of the envelopes are indistinguishable from each other. The variation of the properties of the pads between the different proposed values does not cause any substantial change in the response of the global structure.

Furthermore, the envelope of accelerations and displacements display deviations when compared to those obtained from the grid model without the track model. However, the configuration of these envelopes still exhibits an obvious similarity.

Similar conclusions were drawn after a parametric study assessing the influence of the geo-textile.

By comparing the dynamic responses of the grid model without the track model and the grid model with the track model it can be concluded that the main differences recorded are due to the frame elements used to represent the rails and the Rheda 2000® slab. In fact, these elements add an extra stiffness in the structure. Naturally, such stiffness is not taken into account in the grid model without the track model. This extra stiffness will appreciably change the dynamic response of the structure since these elements absorb some of the load of the vehicles.

Consequently, it is useful to assess the degree of stiffness of the ballastless track since such stiffness might influence the dynamic response of the structure.

4.4 Comparative assessment of the type of track

Aiming for a comparative analysis of the two types of track, it will be taken into account the influence of the weight of the tracks and the influence of the modelling of the tracks in the dynamic response of the structure.

To assess the influence of the weight of the tracks, two grid models without the ballasted track model (BT1 and BT2 with different weights) and the grid model without the ballastless track model (BLT), were considered.

Figure 13 shows the results obtained from the dynamic analyses performed for the HSLM-A10:

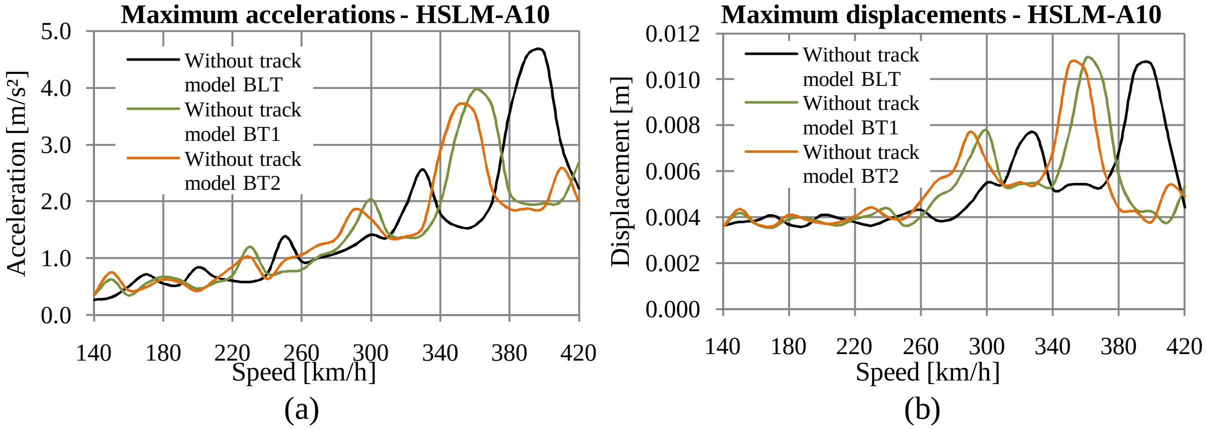

Figure 13 – Envelope of accelerations (a) and displacements (b) for the passage of the HSLM-A10, obtained from the grid model without ballastless track model (BLT) and from the grid models without ballasted track model (BT1 and BT2).

As it can be observed, the envelopes of accelerations and displacements are lagged, despite the obvious similarity in their configurations. Thus, the lighter the track is, the more to the right the resonance peaks will be shifted, which will correspond to higher speeds. Furthermore, the lighter the track is, the higher the accelerations peaks will be. In structures with a lighter track one might avoid resonance peaks recorded in structures with heavier tracks if such peaks occur outside the range of speeds analysed.

With Figure 9 and Figure 12 the influence of the modelling of the tracks may be assessed. As can be seen, and contrarily to what occurs in the case of the ballastless track, the ballasted track considered by means of a track model with vibrating ballast or non-vibrating ballast does not cause significant changes in the dynamic response obtained from the grid model without the track model.

This happens because the models with vibrating and non-vibrating ballast are prone to vibrate for frequencies above the limit of 30 Hz, imposed by the EN1990-A2 [14] to determine the dynamic response. Furthermore, it is not considered the shear stiffness of the ballast. Therefore, the ballasted track models added just a small extra stiffness in structure. Such stiffness is related to the rails. This small stiffness increment causes virtually no effect in the dynamic response of the structure.

The ballastless track models also tend to vibrate for high frequencies. However, the Rheda 2000® slab adds a significant stiffness in structure.

5 CONCLUSIONS

By assessing the influence of the type of railway track in the dynamic response of the bridge, some conclusions can be drawn:

- When a lighter track is used, the resonance peaks will occur at higher speeds. It is possible to avoid resonance peaks occurring in structures with heavier tracks if a lighter track is used and if such peaks occur outside the range of speeds analysed;
- The lighter the track is, the higher the resonance peaks will be;
- The modelling of the ballasted track does not significantly influence the dynamic response of the global structure when obtained from a grid model without a ballasted track model. On the contrary, such dynamic response may be affected if a ballastless track model is used;
- The increment of stiffness provided by the track is an important feature distinguishing the models of the two types of railway track;
- The railway track models presented tend to vibrate for frequencies above the limit of 30 Hz, advocated by the EN1990-A2 [14] to determine the dynamic response.

6 ACKNOWLEDGMENTS

This study was developed under the co-operation protocol celebrated between IST and Rave in May 2007 and renewed in April 2010. The purpose of this protocol is to support the Portuguese national high-speed railway project with a set of recommendations for the structural design, particularly in what concerns the railway track.

The authors would like to thank GRID, specially Professor António Reis and Eng. Nuno Lopes, for supplying valuable data related to the case study. They would also like to send their appreciation to Eng João Francisco Henriques for his generosity in handing out his pre-process computation, which has proved to be very useful for the dynamic analysis. The opinion and relevant published work of Professor Rui Calçada are also gratefully acknowledged.

7 REFERENCES

1 Gil, A.F. and Fernández, M. G. *Track Performance on New High Speed Lines in Spain.* In Track for High-Speed Railways, Porto: Feup, 2006.

2 Teixeira, P. F. *Contribución a la Reducción de los costes de Mantenimiento de Vías de Alta Velocidad Mediante la Optimización de su Rigidez Vertical*. Universidade Politécnica de Catalunha, Barcelona, 2003.

3 EN1991-2. *Eurocode 1: Actions on structures - Part2: Traffic loads on bridges*. European Committee for Standardization (CEN), Brussels, 2003.

4 Calçada, R. *Efeitos dinâmicos em pontes resultantes do tráfego ferroviário a alta velocidade*. FEUP: Faculdade de Engenharia do Porto, Porto, 1996. MSc. Thesis.

5 De Man, Amnon P. *A survey of dynamic railway track properties and their quality*. Technische Universiteit Delft, Delft, 2002. PhD thesis.

6 ERRI Specialists' Committee D214/RP 9. *Final Report - Rail Bridges for Speeds > 200 km/h.* European Rail Research Institute , Utrecht, 2001.

7 Zhai, W., Wang, K., and Lin, J. Modelling and experiment of railway ballast vibrations (2004), 673-683.

8 Tünnissen, Joep T. F. M. Dynamic Aspects of the High-Speed railway Bridge Across the Hollandsch Diep. In *Workshop Track-Bridge Interaction on High-Speed Railways*. FEUP, Universidade do Porto, Porto, 2007.

9 Infraspeed. *High Speed in the Low Lands*. Infraspeed, Zoetermeer, 2006.

10 Esveld, Coenraad. *Modern Railway Track*. MRT-Productions, Technische Universiteit Delft, 2001.

11 Varandas, José, Dimitrovová, Zuzana, Palácio, Alberto, and da Silva, Manuel. *Influência da rigidez da fundação no valor da velocidade crítica de uma carga móvel. Aplicação a vias ferroviárias*. UNIC Centro de Investigação em estruturas e Construção da UNL, 2007.

12 Reis, A. J., Lopes, N. T., and Ribeiro, D. Track-Structure Interaction in Long Railway Bridges. In *Workshop Track-Bridge Interaction on High-Speed Railways*. FEUP, Universidade do Porto, porto, 2007.

13 Kaewunruen, S. and Remennikov, A.M. An Alternative Rail Pad Tester for Measuring Dynamic Properties of Rail Pads Under Large Preloads. *Experimental Mechanics*, 48 (2007), 55–64.

14 EN1990-A2. *Eurocode: Basis of structural design - Annex A2: Applications for bridges (Normative)*. European Committee for Standardization (CEN), Brussels, 2005.

15 Barbero, J. D. *Dinámica de puentes de ferrocarril para alta velocidad: métodos de cálculo y estudio de la resonancia*. Escuela Técnica Superior de Ingenieros de Caminos, Canales y Puertos de Madrid, Madrid, 2001. Tesis Doctoral.

16 Casal, Hugo. *Comportamento Dinâmico de Pontes Ferroviárias de Alta Velocidade com Via Não Balastrada*. IST, Lisboa, 2010b. Dissertação de mestrado integrado em Engenharia Civil.

17 Neves, Marco. *Comportamento Dinâmico de Pontes Ferroviárias de Alta Velocidade com Via Balastrada*. IST, Lisboa, 2010. Dissertação de mestrado integrado em Engenharia Civil.

COMPDYN 2011
III ECCOMAS Thematic Conference on
Computational Methods in Structural Dynamics and Earthquake Engineering
M. Papadrakakis, M. Fragiadakis, V. Plevris (eds.)
Corfu, Greece, 25–28 May 2011

ON ANALYSIS OF LIQUEFACTION-INDUCED DISPLACEMENT IN A CAISSON QUAY WALL

Majid T. Manzari[1], Karma Yonten[1], Mohamed El Ghoraiby[1], and Christine Z. Beyzaei[2]

[1] The George Washington University
801 22nd Street, NW, Washington, DC 20052
manzari@gwu.edu

{kyonten, ghoraiby}@gwmail.gwu.edu

[2] Formerly at the George Washington University
zbeyzaei@berkeley.edu

Keywords: Caisson, Earthquake, Elastoplasticity, Displacement, Finite Element, Liquefaction, Quay Wall.

Abstract. *A series of finite element analyses have been conducted to assess the capability of en open source finite element code in dynamic analysis of a caisson quay wall with liquefiable backfill and foundation soils. A typical quay wall of Rokko island that suffered large displacements and rotations during the 1995 Earthquake in Kobe was considered as a case study. The nonlinear fully-coupled finite element analyses led to the following observations. Earthquake-induced excess pore water pressures have caused significant stiffness degradation in the backfill and foundation soil. This is a likely cause of large lateral displacements and settlements of the caisson wall and the backfill soil. Vertical displacements of the wall and the backfill soil were under-predicted by the finite element simulations. However the numerical simulations produced correct displacement modes, and the order of magnitude of lateral displacement was also correctly simulated.*

1 INTRODUCTION

In the past two decades, there has been considerable progress in development of advanced constitutive and numerical modeling techniques for seismic analysis of geostructures containing liquefiable granular soils. An accurate estimation of earthquake-induced permanent deformations in these structures is an essential component of a performance-based design approach that is currently becoming the prevailing design concept in geotechnical earthquake engineering. In this paper, a caisson quay wall that suffered large displacements and rotations during the 1995 Earthquake in Kobe (Iganaki, et al., 1996) is considered as a case study (Figure 1). The wall is sitting on rubble material underlain by a medium dense sandy soil. The backfill soil is also a sandy soil underlain by an alluvial clay layer. Iganaki et al. (1996) have presented a detailed study of the engineering properties of the backfill and foundation soils.

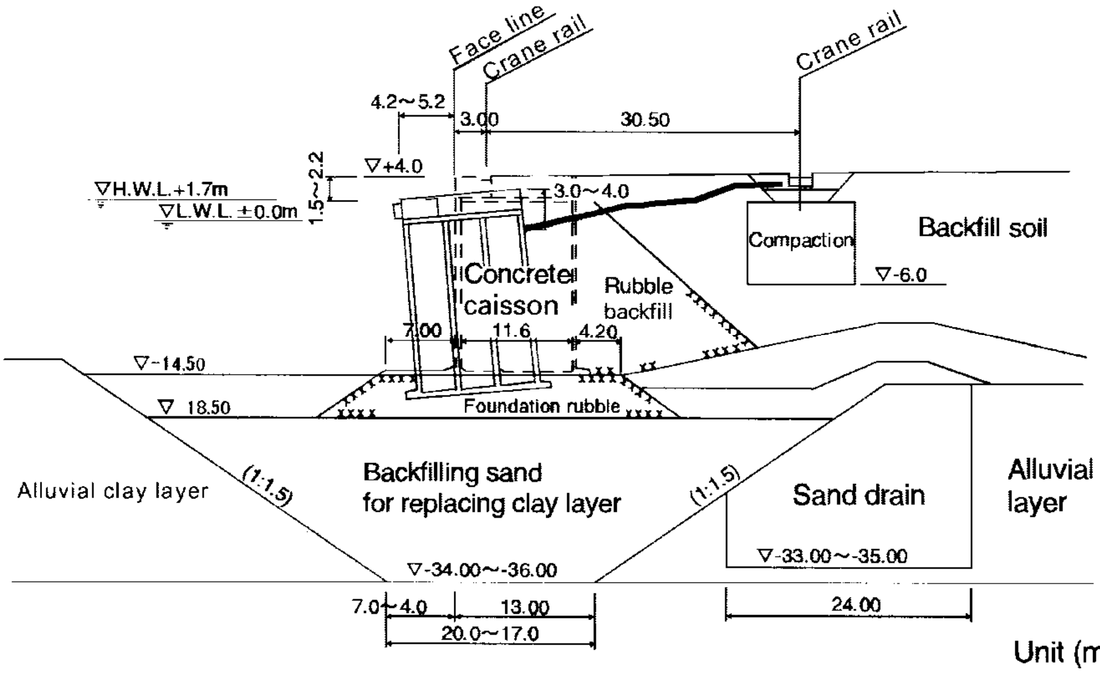

Figure 1. A typical section of the caisson quay-wall in Rokko Island that sustained significant damage and permanent deformations during 1995 Kobe Earthquake (Iganaki, et al., 1996)

Iai et al. (1996) conducted detailed finite element simulations of this quay-wall structure by using a multi-mechanism strain-space plasticity model. The results presented by Iai et al. (1996) show good agreement with the observed response of the wall. In this paper, the results of a series of fully-coupled nonlinear finite element analyses are used to examine the capabilities and limitations of an advanced constitutive and numerical modeling platform (Opensees, http://opensees.berkeley.edu/index.php) in seismic analysis of this quay wall system that contains liquefiable soils as backfill and foundation soils. An outline of the numerical simulations and the results obtained in these analyses is presented in this paper.

2 FINITE ELEMENT MODEL

A detailed finite element model of the wall, its foundation and the surrounding soil was developed, and the material models used for different parts of the model were calibrated based on the experimental data available for the site (Iganaki, et al., 1996). A typical finite element mesh used in the analyses is shown in Figure 2. In order to consider wall-water interaction, the body of water in front of the wall was also included in the finite element model (elements shown in red).

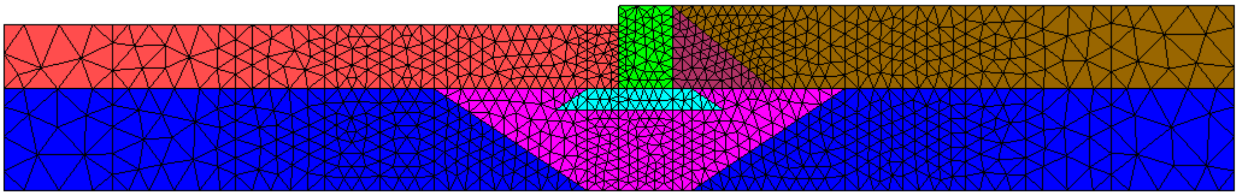

Figure 2. A Typical Finite Element Mesh used in the Analyses

Interfaces of the quay wall with the foundation and backfill soils were also modeled using appropriate interface elements. No-tension zero-length elements were used in the interface between the wall and foundation rubble, the wall and backfill rubble, and the wall and water. No friction was considered between the wall and backfill. Friction between the wall and foundation rubble was modeled using zero-length elements.

3 CONSTITUTIVE MODELS

The multi-surface plasticity models implemented in Opensees platform (Elgamal et al., 2003) were used in the finite element simulations. The pressure dependent multi-surface plasticity model was used for sands and rubbles while the pressure-independent multi-surface plasticity model was used for the alluvial clay. The models were calibrated against the results of the triaxial tests conducted on the soil samples obtained from the site (Iganaki et al., 1996). Calibration efforts showed that it was difficult to match the observed response of the soil at all strain levels and for all shear stress ratios.

Figure 3 shows a typical comparison of the model predictions with the experimental data. In this Figure, the number of cycles to reach a double amplitude axial strain of 5% is plotted against shear stress ratio (i.e. deviatoric stress, τ_d, divided by initial vertical effective stress in the specimen). The calibration efforts showed that it is possible to match the experimental data for any specific level of shear stress ratio. However, when the applied stress ratio is changed to a different level, the predicted number of cycles using the same model constants (parameters) shows some discrepancies with the observed response in the experiments.

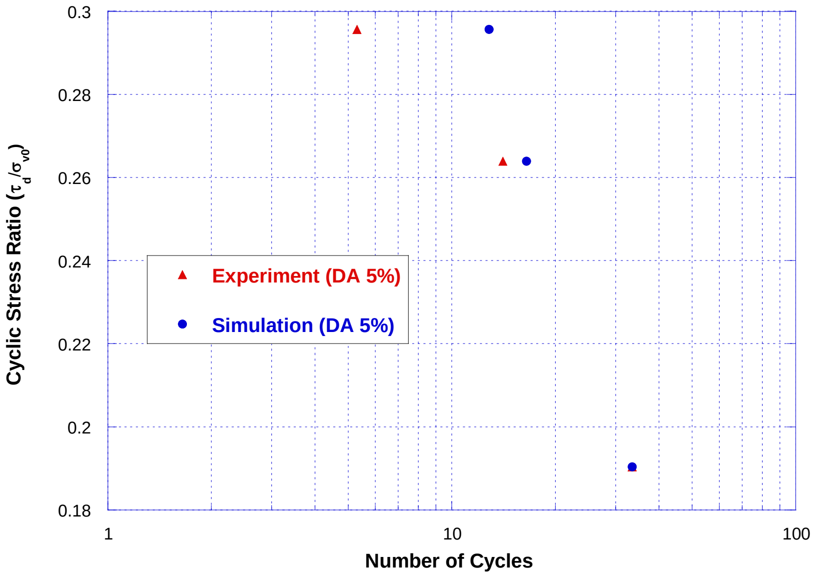

Figure 3. Comparison of the Number of Cycles Predicted by the Calibrated Constitutive Model against the Experimental Data Reported by Iganaki et al., (1996) for the Foundation Sand.

4 ANALYSIS STEPS

The finite element simulations were conducted in two steps. First, initial stresses and internal variables of the constitutive models were initialized by using an incremental gravity turn-on technique. Since the site consisted of both cohesionless and cohesive soils, a quasi-static fully-coupled effective stress analysis was conducted to ensure that both the initial pore water pressure and initial effective stresses were fully accounted for before the system was subjected to seismic loading.

Next, the complete soil-wall-water system was subjected to the horizontal and vertical ground motions recorded near the site during the 1995 earthquake (Iganaki, et al., 1996). Mesh sensitivity analyses were conducted to evaluate the accuracy of the numerical solutions. All the simulations were conducted by using the same parameters that were obtained from calibration of the constitutive models.

5 RESULTS

The numerical simulations showed that the earthquake caused significant pore water pressure generation in the backfill sand (Figure 3) and created a near liquefaction state in the foundation sand (Figure 4).

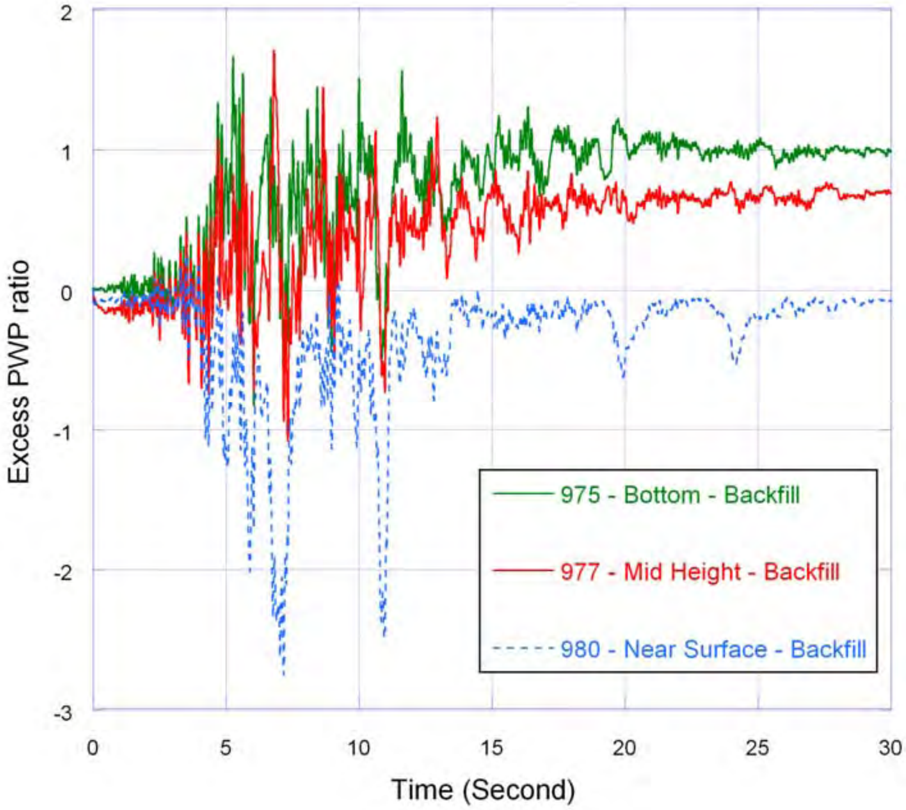

Figure 3. Excess Pore Pressure Ratios Computed at Different Elevations in the Backfill Soil

Figure 3 shows that very large negative excess pore pressure ratio is developed at a soil element located near ground surface in the backfill soil. This is mainly caused by the low confining stress in the soil which makes the soil highly dilative. Much less dilative response is seen in the mid height and bottom of the backfill sand (i.e., near the interface with the alluvial clay) where the higher initial confining stresses make the soil more contractive. It is also observed that the large excess pore pressure at the bottom of the backfill soil brings the soil to a near liquefaction state. The excess pore pressure ratio remains at its high level even when the earthquake ceases.

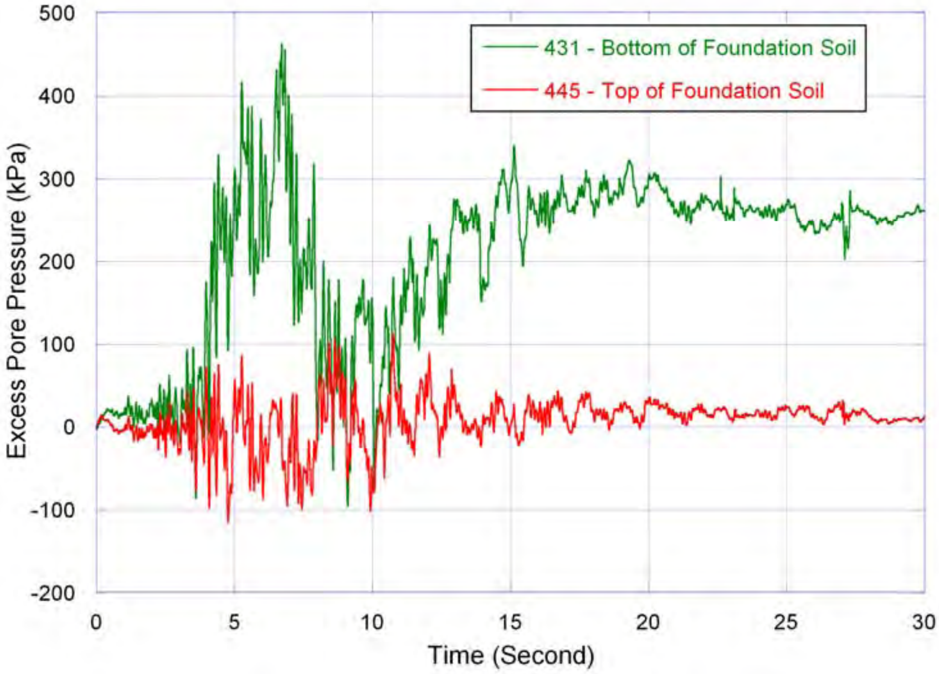

Figure 4. Excess Pore Pressure Computed at Different Elevations in the Foundation Soil

Figure 4 shows that large positive excess pore pressure is generated at an element near the bottom of the foundation sand. This excess pore pressure significantly degrades the stiffness of the foundation soil and contributes to the rotation of the quay wall. A soil element near the top of the foundation soil (just below the foundation rubble), however, shows highly dilative response. This is likely due to the large shear stresses imposed by the movement of the wall on a soil element that is under a modest confining stress.

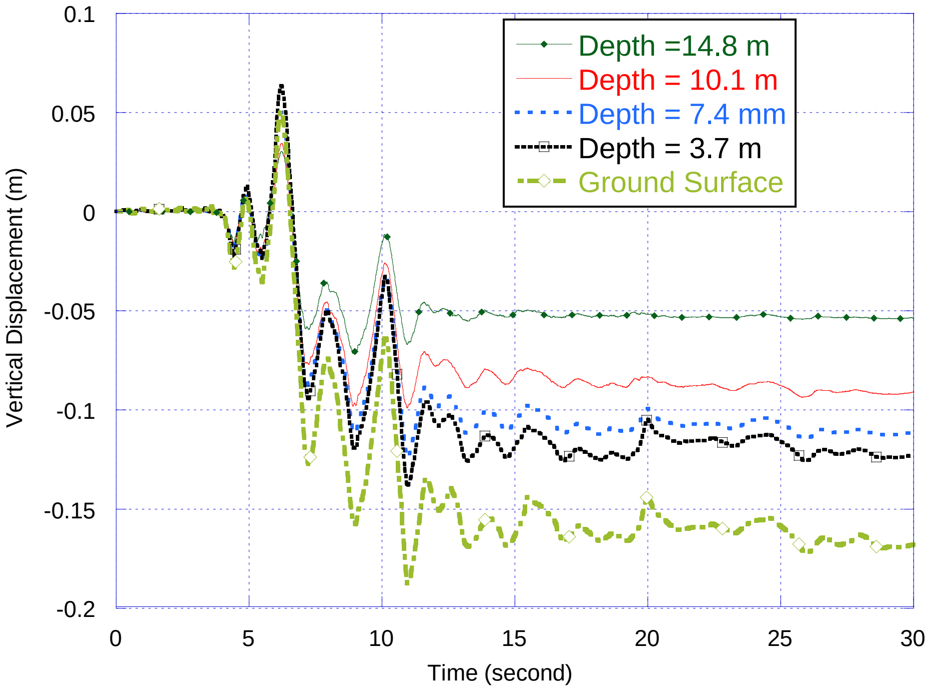

Figure 5. Vertical displacements in the backfill soil far away from the wall

Figure 5 shows the computed vertical displacements in a column of the backfill soil far away from the wall. The backfill soil has experienced significant settlements due to the large excess pore pressure generation caused by the earthquake.

The analysis results also indicate that despite the significant pore pressure generation in the foundation soil, the soil has amplified the base motion and the wall has experienced large horizontal accelerations at its crest. Figure 6 shows a comparison of the acceleration time histories computed at the ground surface and at the wall crest with the assumed base acceleration.

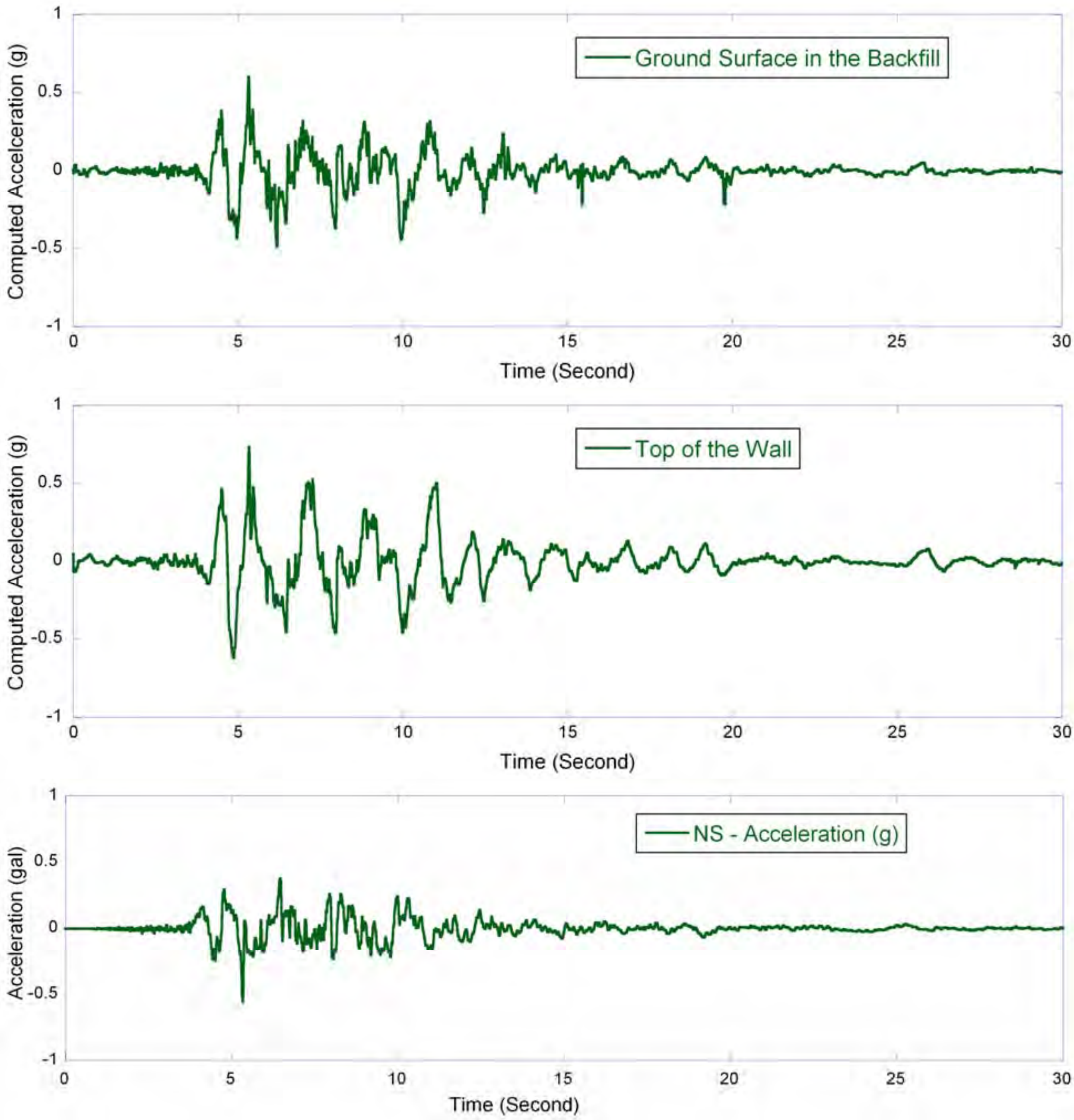

Figure 6. Comparison of the Acceleration Time Histories Computed at the Ground Surface in the Backfill (top) and at the Wall Crest (middle) with the Base Acceleration Time History (bottom).

The finite element simulations show a lateral displacement of about 2 meters for the wall and a settlement of 1 meter in the backfill soil. The wall tilted about 2.5^o counter-clockwise.

The simulated displacements and deformation patterns are in general agreement with the observed response of the wall in the field. However both lateral and vertical displacements are under-predicted. Figure 7 shows the earthquake-induced displacements of the quay wall and its surrounding soils at the end of the earthquake loading.

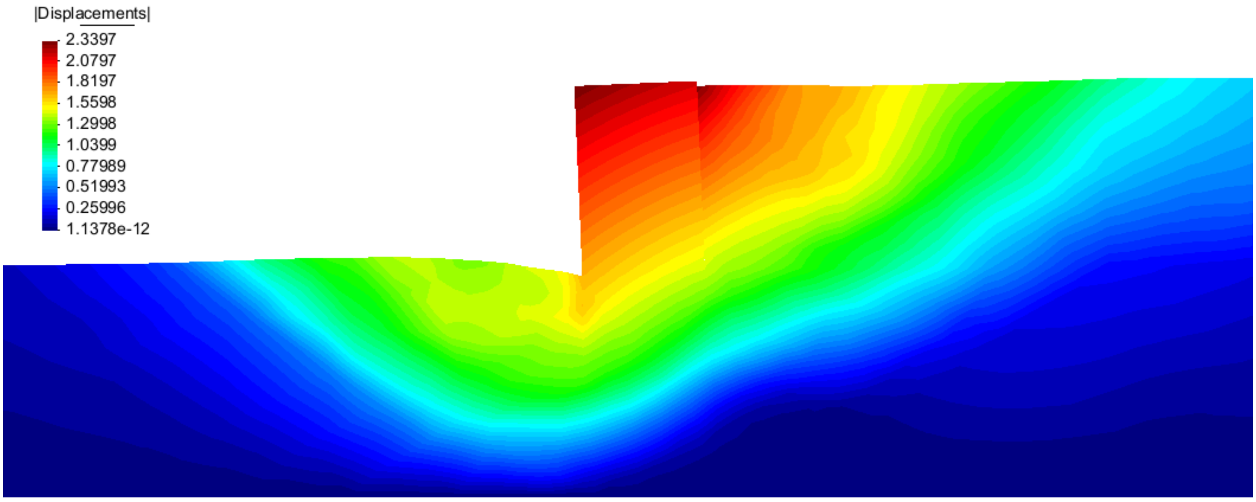

Figure 7. Earthquake-induced Permanent Displacements in the Quay Wall and Surrounding Soils

6 CONCLUDING REMARKS

Based on the finite element simulations presented in this paper, the following observations are made:

- Relatively large excess pore water pressures were developed in the backfill and foundation soils. These excess pore pressures have likely led to significant stiffness degradation in these soils. This is a likely cause of large lateral and vertical displacements and in the caisson quay wall and the backfill soil.
- Vertical displacements of the wall and backfill were under-predicted by the finite element simulations. However, the numerical simulations produced correct displacement patterns, and the order of magnitude of lateral displacements was also correctly simulated.

A key factor contributing to the large rotation of the wall appears to be the local failure of the foundation soil. Given the inherent deficiency of classical continuum formulation in capturing the post-failure response of granular soils, it is difficult to model the local failure in the foundation soil by using the constitutive models that are based on classical continuum mechanics. An enhanced constitutive model with an internal length scale (e.g., Manzari, 2004) is necessary for proper modeling of the settlements and rotations caused by the local failure in the foundation soil.

7 ACKNOWLEDGMENT

The authors are grateful for the support provided by the National Science Foundation via Geomechanics and Geohazard programs directed by Dr. Richard Fragaszy. The first and fourth authors wish to acknowledge the REU supplemental funds for the participation of the fourth author during her undergraduate studies at the George Washington University. Professor Susumu Iai, Dr. Atsushi Nozu, Port and Airport Research Institute, and the Kobe City Government graciously provided the ground motion records used in the simulations.

REFERENCES

[1] Inagaki, H., S. Iai, T. Sugano, H. Yamazaki, and Inatomi, T. (1996). "Performance of caisson type quay walls at Kobe Port," *Soils and Foundations*, Special Issue on Geotechnical Aspects of the January 17 1995 Hyogoken Nanbu Earthquake, Japanese Geotechnical Society, pp.119-136.

[2] Iai S., Sugano T., Ichii K., Morita T., Inagaki H., and Inatomi T. (1996). "Performance of Caisson Type Quay Walls." The 1995 Hyogo-ken Nanbu Earthquake-Investigation into Damage to Civil Engineering Structures. Japan Society of Civil Engineers, 181-207.

[3] Elgamal, A., Yang, Z., Parra, E., and Ragheb, A., (2003). "Modeling of Cyclic Mobility in Saturated Cohesionless Soils," *International Journal of Plasticity*, Pergamon, Elsevier Science Ltd., 19(6): 883-905.

[4] Manzari, M.T. (2004). "Application of Micropolar Plasticity to Post-failure Analysis in Geomechanics Problems." International Journal of Numerical and Analytical Methods in Geomechanics, 28(10), 1011-1032.

COMPDYN 2011
III ECCOMAS Thematic Conference on
Computational Methods in Structural Dynamics and Earthquake Engineering
M. Papadrakakis, M. Fragiadakis, V. Plevris (eds.)
Corfu, Greece, 25–28 May 2011

THE DECOUPLING OF LINEAR DYNAMICAL SYSTEMS

Matthias Morzfeld, Fai Ma[2]

[1] Department of Mechanical Engineering
University of California
Berkeley, California 94720
e-mail: mmo@berkeley.edu

[2] Department of Mechanical Engineering
University of California
Berkeley, California 94720
e-mail: fma@me.berkeley.edu

Keywords: Modal Analysis, Quadratic Eigenvalue Problem, Coordinate Coupling.

Abstract. *The purpose of this paper is report on a recently developed methodology to decouple any linear dynamical system. The decoupling transformation is time-varying and reduces to the well known time-invariant modal transformation for linear systems that are undamped or classically damped.*

1 INTRODUCTION

It has long been recognized that coordinate coupling in damped linear systems is a considerable barrier to analysis and design. In the absence of damping, a linear system possesses classical normal modes, which constitute a linear time-invariant coordinate transformation that decouples the system. This process of decoupling the equation of motion of a dynamical system is a time-honored procedure termed modal analysis. A damped linear system cannot be decoupled by modal analysis unless it also possesses a full set of classical normal modes, in which case the system is said to be classically damped. Rayleigh [1] showed that a system is classically damped if its damping matrix is a linear combination of its inertia and stiffness matrices. Practically speaking, classical damping means that energy dissipation is almost uniformly distributed throughout the system. In general, there is no reason why this condition should be satisfied and thus damped linear systems cannot be decoupled by modal analysis [2-6]. In addition, it has been shown [7] that no time-invariant linear transformations in the configuration space can decouple all damped systems. Even partial decoupling, i.e. simultaneous transformation of the coefficient matrices of the equation of motion to upper triangular forms, cannot be ensured with time-invariant linear transformations [8].

It was shown in [9, 10] that a non-classically damped system in free vibration can be transformed into one with classical damping by synchronizing the phase angles in its non-classically damped modes. This process, termed phase synchronization, generates a real time-varying transformation that decouples the system in configuration space. Furthermore, the decoupling procedure reduces to modal analysis under classical damping. When additional time shifts induced by external forces are accounted for, the decoupling transformation for free vibration can be extended to decouple forced vibration [10]. The purpose of this paper is to summarize the decoupling of all linear systems concisely.

2 PROBLEM STATEMENT

The equation of motion of an n-degree-of-freedom viscously damped linear system can be written as

$$\mathbf{M}\ddot{\mathbf{q}} + \mathbf{C}\dot{\mathbf{q}} + \mathbf{K}\mathbf{q} = \mathbf{f}(t) \tag{1}$$

where **M**, **C** and **K** are real symmetric and positive definite square matrices of order n. The generalized coordinate $\mathbf{q}$ and the excitation $\mathbf{f}(t)$ are real n-dimensional vectors. Unless the three coefficient matrices are diagonal, Eq. (1) is coupled. Coupling is not an inherent property of a system but depends on the generalized coordinates used. The “classical decoupling problem” is concerned with the transformation of Eq. (1) into

$$\ddot{\mathbf{p}} + \mathbf{D}_1\dot{\mathbf{p}} + \mathbf{\Omega}_1\mathbf{p} = \mathbf{g}(t) \tag{2}$$

where $\mathbf{D}_1$, $\mathbf{\Omega}_1$ are real diagonal matrices of order n, and $\mathbf{p}$ and $\mathbf{g}(t)$ are also real. Over the years, various types of decoupling approximation were employed in the analysis of damped systems [11-20]. Different indices of coupling were also introduced to quantify coordinate coupling [21-29]. However, a solution to the “classical decoupling problem” has not been reported in the open literature.

2.1 The quadratic eigenvalue problem

Associated with system (1) is the quadratic eigenvalue problem [30-33]

$$(\mathbf{M}\lambda^2 + \mathbf{C}\lambda + \mathbf{K})\mathbf{v} = \mathbf{0} \tag{3}$$

There are $2n$ eigenvalues λ_j but there cannot be more than n linearly independent eigenvectors $\mathbf{v}_j$, where $j = 1,\ldots,2n$. Because the matrices **M**, **C** and **K** are real, any complex eigenvalues must occur in complex conjugate pairs. The quadratic eigenvalue problem plays a key role in decoupling system (1). In fact, all required parameters for the decoupling transformation can be obtained from the solution of the quadratic eigenvalue problem (3).

2.2 Assumptions and possible relaxation

It will be assumed that the 2*n* eigenvalues λ_j of Eq. (3) are distinct. This assumption is made to streamline the introduction of new concepts and it can be readily relaxed. There will be little change to the exposition of decoupling under the less restrictive condition that eigenvectors associated with repeated eigenvalues are independent. When an eigenvalue is repeated *m* times and a full complement of *m* independent eigenvectors cannot be found, the eigenvalue problem (3) is said to be defective [30]. Decoupling of systems with defective eigenvalue problems is of a purely theoretical nature but is still relatively straightforward [see 9, 10 for more details].

2.3 Classical modal analysis

To set up the necessary terminology and notation, the decoupling of classically damped systems will be concisely surveyed. Since **M**, **K** are positive definite, solution of the symmetric eigenvalue problem

$$\mathbf{Ku} = \lambda\mathbf{Mu} \tag{5}$$

generates *n* positive eigenvalues λ_i and *n* real eigenvectors $\mathbf{u}_i$ that are orthogonal with respect to either **M** or **K**. Upon mass normalization, the eigenvectors constitute the columns of a modal matrix $\mathbf{U} = [\mathbf{u}_1 \,|\, \mathbf{u}_2 \,|\cdots|\, \mathbf{u}_n]$. Define a modal transformation by

$$\mathbf{q} = \mathbf{Up} \tag{6}$$

In terms of the principal coordinate **p**, Eq. (1) takes the canonical form

$$\ddot{\mathbf{p}} + \mathbf{D}\dot{\mathbf{p}} + \mathbf{\Omega p} = \mathbf{U}^T\mathbf{f}(t) \tag{7}$$

where $\mathbf{\Omega} = \mathrm{diag}[\lambda_1, \lambda_2, \ldots, \lambda_n]$ is the spectral matrix and $\mathbf{D} = \mathbf{U}^T\mathbf{CU}$ is the modal damping matrix. A system is classically damped if it can be decoupled by classical modal analysis, whereby **D** is diagonal. A necessary and sufficient condition [34] for classical damping is $\mathbf{CM}^{-1}\mathbf{K} = \mathbf{KM}^{-1}\mathbf{C}$. There is, of course, no particular reason why this condition should be satisfied. In general, a damped linear system cannot be decoupled by classical modal analysis.

Classical modal analysis utilizes real coordinate transformations and is amenable to physical interpretation. Foss and others [35-37] extended classical modal analysis to a process of complex modal analysis in the state space to treat non-classically damped systems. However, complex modal analysis still cannot decouple all damped linear systems. A condition of non-defective eigenvectors in the state space must be satisfied in order for complex modal analysis to achieve complete decoupling. Furthermore, upon state-space transformation it is generally not possible to classify the 2*n* state variables as displacements and velocities. Physical insight is thus greatly diminished. Perhaps it is even fair to say that decoupling in configuration space renders decoupling in state space unnecessary; the state of a system can always be obtained from displacements and their time derivatives.

3 THE DECOUPLING OF FREE VIBRATION

Suppose all eigenvalues of Eq. (3) are complex and distinct. The eigenvalues λ_j of Eq. (3) and the corresponding eigenvectors $\mathbf{v}_j$ occur in *n* pairs of complex conjugates. Let

$$\lambda_j = \alpha_j + i\omega_j \tag{8}$$

$$\mathbf{v}_j = [r_{j1}e^{-i\varphi_{j1}} \quad r_{j2}e^{-i\varphi_{j2}} \quad \cdots \quad r_{jn}e^{-i\varphi_{jn}}]^T \tag{9}$$

where α_j, ω_j, r_{jk} and φ_{jk} are real parameters for $j,k = 1,\ldots,n$. The $2n$ complex conjugate eigensolutions $\mathbf{v}_j e^{\lambda_j t}$ are sometimes referred to as the complex modes in configuration space [30, 38, 39]. Two eigensolutions $\mathbf{v}_j e^{\lambda_j t}$ and $\overline{\mathbf{v}}_j e^{\overline{\lambda}_j t}$ combine to generate a non-classically damped mode of vibration [9]. A characteristic of a non-classically damped mode is a constant phase drift between system components in each mode. If suitable phase shifts are introduced into each mode, various components of the system vibrate in a synchronous manner, passing through their equilibrium positions at the same instant of time. In other words, the system is transformed into one with classical damping. A basic objective of a process termed phase synchronization is to do just that [9, 10]. Upon phase synchronization, the resulting classically damped system can be decoupled by modal analysis. When $\mathbf{f}(t) = \mathbf{0}$ and all eigenvalues λ_j of Eq. (3) are complex, Eq. (1) can always be converted into Eq. (2), for which

$$\mathbf{D}_1 = -\mathrm{diag}[\lambda_j + \overline{\lambda}_j] = -\mathrm{diag}[2\alpha_1, 2\alpha_2, ..., 2\alpha_n] \tag{11}$$

$$\mathbf{\Omega}_1 = \mathrm{diag}[\lambda_j \overline{\lambda}_j] = \mathrm{diag}[\alpha_1^2 + \omega_1^2, \alpha_2^2 + \omega_2^2, ..., \alpha_n^2 + \omega_n^2] \tag{12}$$

and $\mathbf{g}(t) = \mathbf{0}$. The free response $\mathbf{q}(t)$ of Eq. (1) can be recovered from the free response $\mathbf{p}(t)$ of Eq. (2) by

$$\mathbf{q}(t) = \sum_{j=1}^{n} \mathrm{diag}[p_j(t - \varphi_{j1}/\omega_j), p_j(t - \varphi_{j2}/\omega_j), \ldots, p_j(t - \varphi_{jn}/\omega_j)]\mathbf{z}_j \tag{13}$$

where

$$\mathbf{z}_j = [r_{j1}e^{\alpha_j \varphi_{j1}/\omega_j} \quad r_{j2}e^{\alpha_j \varphi_{j2}/\omega_j} \quad \cdots \quad r_{jn}e^{\alpha_j \varphi_{jn}/\omega_j}]^T \tag{14}$$

If system (1) is non-oscillatory, both real and complex eigenvalues λ_j of Eq. (3) occur simultaneously. Free vibration with mixed eigenvalues can be decoupled by dividing its eigensolutions into two groups: one associated with the real eigenvalues and the other with complex eigenvalues. The complex eigensolutions are treated by complex conjugation and the real ones by real quadratic conjugation [10].

Specifically, let $2c$ eigenvalues be complex and $2r = 2(n - c)$ be real. Separate the distinct eigenvalues into two disjoint sets so that

$$\{\lambda\} = \{2c \text{ complex } \lambda\} \cup \{2r \text{ real } \lambda\} \tag{15}$$

The complex eigenvalues occur as *c* pairs of complex conjugates and the real eigenvalues can be classified into primary eigenvalues (the *r* smallest ones) and secondary eigenvalues (the *r* largest ones). Enumerate the eigenvalues in such a way that

$$\{2c \text{ complex } \lambda\} = \{\lambda_1, ..., \lambda_c, \lambda_{n+1} = \overline{\lambda}_1, \ldots, \lambda_{n+c} = \overline{\lambda}_c\} \tag{16}$$

$$\{2r \text{ real } \lambda\} = \{\lambda_{c+1} < ... < \lambda_n < \lambda_{n+c+1} = \widetilde{\lambda}_{c+1} < ... < \lambda_{2n} = \widetilde{\lambda}_n\} \tag{17}$$

The above indexing means that the first *c* eigenvalues are complex and the next $r = n - c$ are the real secondary eigenvalues. These are followed by *c* complex conjugates of the first set and finally by *r* real primary eigenvalues. Simultaneous phase synchronization of all damped modes [9, 10] produces a decoupled system (2) for which

$$\mathbf{D}_1 = -\mathrm{diag}[\lambda_j + \overline{\lambda}_j,\ \lambda_k + \widetilde{\lambda}_k] = -\mathrm{diag}[\lambda_1 + \lambda_{n+1},\ \lambda_2 + \lambda_{n+2}, \ldots, \lambda_n + \lambda_{2n}] \tag{18}$$

$$\mathbf{\Omega}_1 = \mathrm{diag}[\lambda_j \overline{\lambda}_j,\ \lambda_k \widetilde{\lambda}_k] = \mathrm{diag}[\lambda_1 \lambda_{n+1},\ \lambda_2 \lambda_{n+2}, \ldots, \lambda_n \lambda_{2n}] \tag{19}$$

The decoupling transformation is given by Eq. (13). See [10] for details on how to compute the parameters α_j, ω_j, r_{jk} and φ_{jk} using the concept of real quadratic conjugation.

4 DECOUPLING OF FORCED VIBRATION

It has been shown [9, 10] that a damped system in free vibration can be decoupled if suitable phase shifts are introduced into each damped mode of vibration so that all components are either in phase or out of phase. This process is termed phase synchronization, and its purpose is to compensate for the time drifts caused by viscous damping. The required phase drifts are constant; that is why the time-varying decoupling transformation for free vibration in Eq. (13) is merely time-shifting. In the presence of an external excitation $\mathbf{f}(t)$, the interplay between these time drifts and $\mathbf{f}(t)$ generates a genuinely time-varying decoupling transformation for forced vibration [10].

Postulate that system (1) is decoupled into the form (2), where the diagonal matrices $\mathbf{D}_1$, $\mathbf{\Omega}_1$ are still given by Eqs. (18) and (19). What is the relationship between $\mathbf{f}(t)$ and $\mathbf{g}(t)$? How is the decoupling transformation (13) generalized? While it is possible to investigate these issues in the configuration space, with the theoretical framework that has been set up it is more efficient to perform additional manipulations in state space.

Let $2c$ eigenvalues be complex, $2r = 2(n - c)$ be real and enumerate the eigenvalues as in Eqs. (16) – (17). Without loss of generality, normalize the eigenvectors according to

$$2\lambda_j \mathbf{v}_j^T \mathbf{M} \mathbf{v}_j + \mathbf{v}_j^T \mathbf{C} \mathbf{v}_j = \lambda_j - \lambda_{n+j} \tag{20}$$

$$2\lambda_{n+j} \mathbf{v}_{n+j}^T \mathbf{M} \mathbf{v}_{n+j} + \mathbf{v}_{n+j}^T \mathbf{C} \mathbf{v}_{n+j} = \lambda_{n+j} - \lambda_j \tag{21}$$

for $j = 1, \ldots, n$. The above normalization reduces to mass normalization if system (1) is undamped or classically damped [6, 9, 10]. Cast Eq. (1) in state space in the symmetric form

$$\begin{bmatrix} \mathbf{C} & \mathbf{M} \\ \mathbf{M} & \mathbf{0} \end{bmatrix} \begin{bmatrix} \dot{\mathbf{q}} \\ \ddot{\mathbf{q}} \end{bmatrix} + \begin{bmatrix} \mathbf{K} & \mathbf{0} \\ \mathbf{0} & -\mathbf{M} \end{bmatrix} \begin{bmatrix} \mathbf{q} \\ \dot{\mathbf{q}} \end{bmatrix} = \begin{bmatrix} \mathbf{f}(t) \\ \mathbf{0} \end{bmatrix} \tag{22}$$

Define a state transformation by

$$\begin{bmatrix} \mathbf{q} \\ \dot{\mathbf{q}} \end{bmatrix} = \begin{bmatrix} (\mathbf{V}\overline{\mathbf{\Lambda}} - \overline{\mathbf{V}}\mathbf{\Lambda})(\overline{\mathbf{\Lambda}} - \mathbf{\Lambda})^{-1} & (\overline{\mathbf{V}} - \mathbf{V})(\overline{\mathbf{\Lambda}} - \mathbf{\Lambda})^{-1} \\ (\mathbf{V} - \overline{\mathbf{V}})\mathbf{\Lambda}\overline{\mathbf{\Lambda}}(\overline{\mathbf{\Lambda}} - \mathbf{\Lambda})^{-1} & (\overline{\mathbf{V}\mathbf{\Lambda}} - \mathbf{V}\mathbf{\Lambda})(\overline{\mathbf{\Lambda}} - \mathbf{\Lambda})^{-1} \end{bmatrix} \begin{bmatrix} \mathbf{p}_1 \\ \mathbf{p}_2 \end{bmatrix} \tag{23}$$

where

$$\mathbf{V} = [\mathbf{v}_n \,|\cdots|\, \mathbf{v}_n],\ \mathbf{V}^* = [\mathbf{v}_{n+1} \,|\cdots|\, \mathbf{v}_{2n}] \tag{24}$$

$$\mathbf{\Lambda} = \mathrm{diag}[\lambda_1, \ldots, \lambda_n],\ \mathbf{\Lambda}^* = \mathrm{diag}[\lambda_{n+1}, \ldots, \lambda_{2n}] \tag{25}$$

Equation (22) becomes

$$\begin{bmatrix} \mathbf{D}_1 & \mathbf{I} \\ \mathbf{I} & \mathbf{0} \end{bmatrix} \begin{bmatrix} \dot{\mathbf{p}}_1 \\ \dot{\mathbf{p}}_2 \end{bmatrix} + \begin{bmatrix} \mathbf{\Omega}_1 & \mathbf{0} \\ \mathbf{0} & -\mathbf{I} \end{bmatrix} \begin{bmatrix} \mathbf{p}_1 \\ \mathbf{p}_2 \end{bmatrix} = \begin{bmatrix} \mathbf{T}_1^T \mathbf{f} \\ \mathbf{T}_2^T \mathbf{f} \end{bmatrix} \tag{26}$$

where $\mathbf{T}_1$ and $\mathbf{T}_2$ are given by

$$\mathbf{T}_1 = (\mathbf{V}\mathbf{\Lambda}^* - \mathbf{V}^*\mathbf{\Lambda})(\mathbf{\Lambda}^* - \mathbf{\Lambda})^{-1} \tag{27}$$

$$\mathbf{T}_2 = (\mathbf{V}^* - \mathbf{V})(\mathbf{\Lambda}^* - \mathbf{\Lambda})^{-1} \tag{28}$$

and where $\mathbf{D}_1$, $\mathbf{\Omega}_1$ are given by Eqs. (18)–(19) (see [10] for details of the calculation). The upper and lower halves of Eq. (26) are

$$\mathbf{q} = \mathbf{T}_1\mathbf{p} + \mathbf{T}_2\dot{\mathbf{p}} - \mathbf{T}_2\mathbf{T}_2^T\mathbf{f} \tag{29}$$

$$\mathbf{q} = \mathbf{T}_1\mathbf{p}_1 + \mathbf{T}_2\mathbf{p}_2 \tag{30}$$

Eliminate $\mathbf{p}_2$ from the above two equations to get

$$\ddot{\mathbf{p}}_1 + \mathbf{D}_1\dot{\mathbf{p}}_1 + \mathbf{\Omega}_1\mathbf{p}_1 = \mathbf{T}_1^T\mathbf{f} + \mathbf{T}_2^T\dot{\mathbf{f}} \tag{31}$$

When Eqs. (2) and (31) are compared, it becomes obvious that $\mathbf{p}_1$ can be identified with $\mathbf{p}$. Therefore, the relationship between $\mathbf{f}(t)$ and $\mathbf{g}(t)$ is

$$\mathbf{g}(t) = \mathbf{T}_1^T\mathbf{f}(t) + \mathbf{T}_2^T\dot{\mathbf{f}}(t) \tag{32}$$

Observe that $\mathbf{T}_1$, $\mathbf{T}_2$, and hence $\mathbf{g}(t)$ can be readily obtained from the solution of the quadratic eigenvalue problem (3). Upon substitution of Eq. (32) in (2), forced vibration with complex eigenvalues is decoupled in the configuration space.

The relationship between the solution $\mathbf{p}(t)$ of Eq. (2) and solution $\mathbf{q}(t)$ of the original system (1) can be deduced from Eqs. (23), (30) and (31)

$$\mathbf{q} = \mathbf{T}_1\mathbf{p} + \mathbf{T}_2\dot{\mathbf{p}} - \mathbf{T}_2\mathbf{T}_2^T\mathbf{f} \tag{33}$$

The above expression represents a time-varying decoupling transformation in the configuration space. A closer examination of Eq. (33) reveals that it consists of two parts. The first part, $\mathbf{T}_1\mathbf{p} + \mathbf{T}_2\dot{\mathbf{p}}$, accounts for time drifts caused by viscous damping in free vibration. The second part, $\mathbf{T}_2\mathbf{T}_2^T\mathbf{f}$, accounts for time drifts induced by the excitation $\mathbf{f}(t)$. When $\mathbf{f}(t) = \mathbf{0}$, Eq. (33) reduces to $\mathbf{q} = \mathbf{T}_1\mathbf{p} + \mathbf{T}_2\dot{\mathbf{p}}$ which, by direct manipulations, is the same as Eq. (13). Thus, the decoupling transformation (33) generalizes the decoupling transformation (13) for free vibration and, therefore, represents **a general decoupling transformation for all non-defective linear dynamical systems**.

To cast Eq. (33) in state space, simply rewrite Eq. (23) in the form

$$\begin{bmatrix}\mathbf{p}(t)\\ \dot{\mathbf{p}}(t)\end{bmatrix} = \begin{bmatrix}\mathbf{I} & \mathbf{I}\\ \mathbf{\Lambda} & \overline{\mathbf{\Lambda}}\end{bmatrix}\begin{bmatrix}\mathbf{V} & \overline{\mathbf{V}}\\ \mathbf{V\Lambda} & \overline{\mathbf{V\Lambda}}\end{bmatrix}^{-1}\begin{bmatrix}\mathbf{q}(t)\\ \dot{\mathbf{q}}(t)\end{bmatrix} + \begin{bmatrix}\mathbf{0}\\ \mathbf{T}_2^T\mathbf{f}(t)\end{bmatrix} \tag{34}$$

Initial conditions of $\mathbf{p}(t)$ in Eq. (2) and $\mathbf{q}(t)$ in the original system (1) can be connected by putting $t = 0$ in Eq. (34). A flowchart depicting the decoupling method is shown in Fig. 1.

5 REDUCTION TO CLASSICAL MODAL ANALYSIS

The decoupling methodology developed herein is a direct generalization of classical modal analysis. Without loss of generality, assume that all eigenvectors are normalized in accordance with either Eqs. (20)-(21). When real and complex eigenvalues of Eq. (3) occur simultaneously, and the system is classically damped, $\mathbf{V} = \mathbf{V}^* = \mathbf{U}$ [10]. Using Eqs. (27) and (28), it can now be shown that the transformation of excitation in Eq. (32) reduces to $\mathbf{g}(t) = \mathbf{U}^T\mathbf{f}(t)$, while the decoupling transformation in Eq. (33) simplifies to the classical modal transformation $\mathbf{q} = \mathbf{U}\mathbf{p}$. Thus, the decoupling method presented reduces to classical modal analysis for systems that are classically damped.

6 EFFICIENCY OF SOLUTION BY DECOUPLING

Response calculation is probably not the most important reason for decoupling. It is the possibility, for example, of modal reduction and of an investigation of energy distribution among independent coordinates that would make decoupling worthwhile. Nevertheless, it may still be instructive to examine the efficiency of solution of Eq. (1) by decoupling. It will be assumed that the excitation $\mathbf{f}(t)$ and response $\mathbf{q}(t)$ are sufficiently smooth (adequate if twice differentiable).

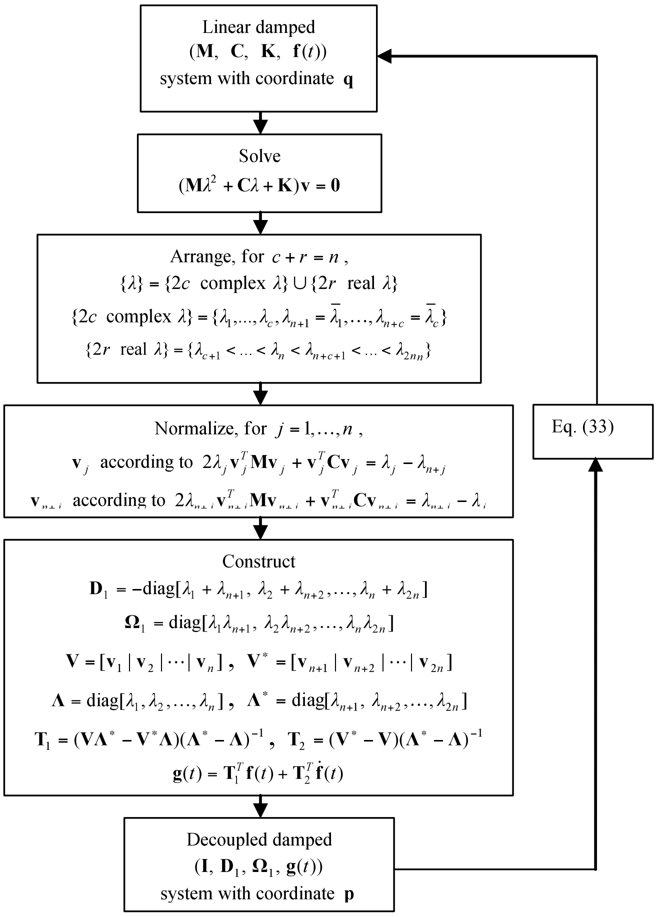

Figure 1: Algorithm for decoupling all linear systems.

One measure of the performance of an algorithm is the number of flops (floating point operations) required to evaluate the response at m points within a given time window. The flops associated with two procedures are compared. (a) In direct numerical integration, a standard procedure is to recast the second-order Eq. (1) in state space as a first-order system of dimension $2n$. The state equation is then discretized, and the resulting difference equation is solved by matrix computations [40]. The estimate of flops of this procedure at m instants is [9, 10, 41-43] $N_1 = 160n^3 + 16mn^2$, where n is the number of degrees of freedom and $m >> n$ in general. (b) In solving Eq. (1) by decoupling, Eq. (2) is obtained through solution of Eq. (3) and evaluation of Eq. (32). Each independent decoupled system in Eq. (2) is then solved numerically at m instants with the same algorithm used in procedure (a). Subsequently, Eq. (33) is employed to compute the response $\mathbf{q}(t)$. The estimate of flops is [9, 10, 41-43] $N_2 = 10mn^2 + 16mn + 213n^3 + 4n^2$. The variations of N_1 and N_2 with n are illustrated in Fig. 2 for a window containing $m = 10^6$ instants.

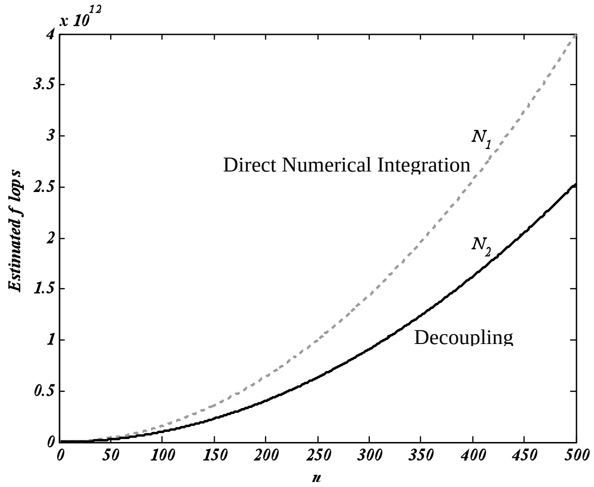

Figure 2: Comparison of efficiency in response calculation.

It is observed that response calculation by decoupling generally reduces the flops and therefore economizes on both core memory and computing time.

In fact, Fig. 2 is rather conservative because N_2 has been estimated by using the same time step in the integration of all decoupled equations. If an optimal time step is individually chosen for each decoupled equation, N_2 may decrease substantially. Moreover, each decoupled equation may be solved exactly in many applications. On the other hand, the efficiency of response calculation by decoupling depends on the size of the time window. In addition, validity of the flop estimates requires that the excitation is $\mathbf{f}(t)$ sufficiently smooth. Distributional excitation such as an impulse leading to weak solutions ($\mathbf{q}(t)$ less than twice differentiable) are excluded [44, 45]. Thus Fig. 2 should be interpreted as indicative rather than absolute in the comparison of efficiency.

7 NUMERICAL EXAMPLE

A four-degree-of-freedom system possessing both real and complex eigenvalues is decoupled to illustrate the method. The example is taken from [10]. In Eq. (1), let $\mathbf{M} = \mathbf{I}$,

$$\mathbf{C} = \begin{bmatrix} 0.1 & -0.1 & 0 & 0 \\ -0.1 & 0.2 & -0.1 & 0 \\ 0 & -0.1 & 0.2 & -0.1 \\ 0 & 0 & -0.1 & 1.35 \end{bmatrix}, \quad \mathbf{K} = \begin{bmatrix} 1 & -1 & 0 & 0 \\ -1 & 2 & -1 & 0 \\ 0 & -1 & 2 & -1 \\ 0 & 0 & -1 & 1.1 \end{bmatrix} \tag{35}$$

and $\mathbf{f}(t) = [0,0,0,1]^T te^{-0.3t} \sin 2t$ and assume zero initial conditions $\mathbf{q}(0) = \mathbf{0}$, $\dot{\mathbf{q}}(0) = \mathbf{0}$. This system is non-classically damped and, therefore, can only be decoupled by the method presented herein. Solution of the quadratic eigenvalue problem (3) yields $c = 3$ pairs of complex conjugate and $r = 1$ pairs of real quadratic conjugate eigenvalues and eigenvectors [10]. From Eqs. (27) and (28),

$$\mathbf{T}_1 = \begin{bmatrix} -0.38 & 0.53 & 0.30 & 0.70 \\ -0.05 & -0.45 & -0.70 & 0.68 \\ 0.52 & -0.66 & 0.64 & 0.64 \\ 1.11 & 0.37 & -0.16 & 0.57 \end{bmatrix} \tag{36}$$

$$\mathbf{T}_2 = \begin{bmatrix} 0.49 & -0.07 & -0.02 & 0.53 \\ 0.71 & -0.07 & 0.03 & 0.31 \\ 0.90 & 0.15 & 0.02 & -0.17 \\ 0.70 & 0.27 & -0.09 & -0.93 \end{bmatrix} \tag{37}$$

It can be checked that the decoupled $(\mathbf{I},\ \mathbf{D}_1,\ \mathbf{\Omega}_1,\ \mathbf{g}(t))$ system is given by

$$\mathbf{D}_1 = -\mathrm{diag}[\lambda_j + \bar{\lambda}_j\,(j=1,2,3), \lambda_4 + \tilde{\lambda}_4] = \mathrm{diag}[0.65, 0.40, 0.39, 0.41] \tag{38}$$

$$\mathbf{\Omega}_1 = \mathrm{diag}[\lambda_j \bar{\lambda}_j\,(j=1,2,3), \lambda_4 \tilde{\lambda}_4] = \mathrm{diag}[0.46, 1.75, 3.32, 0.04] \tag{39}$$

$$\mathbf{g}(t) = e^{-0.3t} \begin{bmatrix} 1.4t\cos(2t) + (0.70 + 0.90t)\sin(2t) \\ 0.54t\cos(2t) + (0.27 + 0.29t)\sin(2t) \\ -0.18t\cos(2t) - (0.09 + 0.13t)\sin(2t) \\ -1.86t\cos(2t) + (-0.93 + 0.85t)\sin(2t) \end{bmatrix} \tag{40}$$

\with initial conditions $\mathbf{p}(0) = \mathbf{0}$, $\dot{\mathbf{p}}(0) = \mathbf{0}$. The decoupled system can be readily solved and solution $\mathbf{q}(t)$ of the original $(\mathbf{M},\ \mathbf{C},\ \mathbf{K},\ \mathbf{f}(t))$ system can be recovered from $\mathbf{p}(t)$ by Eq. (33). As shown in Fig. 3, $\mathbf{g}(t)$, $\mathbf{p}(t)$, and $\mathbf{q}(t)$ are all oscillatory.

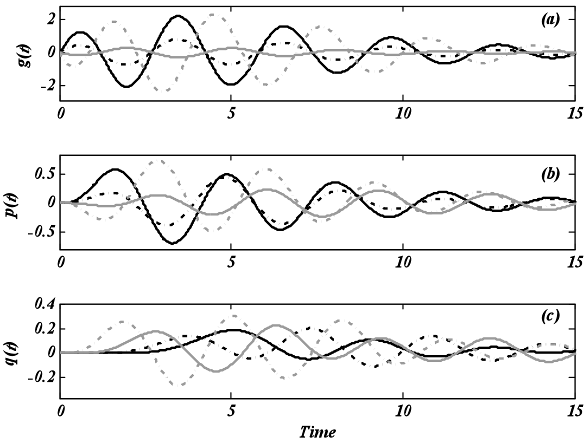

Figure 3: Simulation results.

It can be verified that $\mathbf{q}(t)$, whether generated by decoupling or by direct numerical integration, is the same.

8 CONLUSIONS

A method has been presented to decouple all linear dynamical systems under viscous damping. The decoupling methodology developed herein possesses ample physical insight and it also lends itself to numerical computations. If the linear system is in free vibration, the time varying decoupling transformation in Eq. (33) reduces to a time shifting transformation in Eq. (13). Under classical damping, the decoupling method reduces to modal analysis. Major findings of this paper are summarized in the following statements.

1. In free or forced vibration, all parameters required for the decoupling of a linear system are obtained through the solution of a quadratic eigenvalue problem.

2. Any viscously damped linear system (no restrictions) can be completely decoupled. A flowchart outlining the decoupling procedure is given in Fig. 1.
3. While damped linear systems are decoupled in the configuration space, transformations of initial conditions are prescribed in state space (otherwise initial values are connected at different time instants due to phase synchronization).

To streamline the introduction of new concepts, most formulas have been established with the assumption that eigenvalues of the quadratic eigenvalue problem (3) are distinct. These formulas remain unchanged when Eq. (3) is non-defective (each repeated eigenvalue possesses a full complement of independent eigenvectors). However, a system for which Eq. (3) is defective can still be decoupled by the method presented herein. Due to the lack of practical importance of defective systems (a system is non-defective with probability 1) and because the mathematics becomes quite involved, details on the decoupling of defective systems are deferred to a future paper on general mode-by-mode transformations

REFERENCES

[1] Strutt, J. W., Lord Rayleigh, 1945, *The Theory of Sound*, Vol. I, Dover, New York (reprint of the 1894 edition).

[2] Clough, R. W., and Mojtahedi, S., 1976, “Earthquake Response Analysis Considering Non-Proportional Damping,” *Earthquake Engineering and Structural Dynamics*, **4**, 489-496.

[3] Tsai, H. C., and Kelly, J. M., 1988, “Non-Classical Damping in Dynamic Analysis of Base-Isolated Structures with Internal Equipment,” *Earthquake Engineering and Structural Dynamics*, **16**, 29-43.

[4] Tsai, H. C., and Kelly, J. M., 1989, “Seismic Response of the Superstructure and Attached Equipment in a Base-Isolated Building,” *Earthquake Engineering and Structural Dynamics*, **18**, 551-564.

[5] Itoh, T., 1973, Damped Vibration Mode Superposition Method for Dynamic Response Analysis, *Earthquake Engineering and Structural Dynamics* 2, 47-57.

[6] Sestieri, A., Ibrahim, S. R., 1994, Analysis of Errors and Approximations in the Use of Modal Co-ordinates, *Journal of Sound and Vibration* 177 (2) 145-157.

[7] Ma, F., Caughey, T. K., 1995, Analysis of Linear Nonconservative Vibrations, *ASME Journal of Applied Mechanics* 62 685-691.

[8] Caughey, T. K., Ma, F., 1993, Complex Modes and Solvability of Nonclassically Damped Linear Systems, *ASME Journal of Applied Mechanics* 60 26-28.

[9] Ma,, F., Imam, A., Morzfeld, M., 2009, The Decoupling of Damped Linear Systems in Oscillatory Free Vibration, *Journal of Sound and Vibration* 324 (1-2) 408-428.

[10] Ma,, F., Morzfeld, M., Imam, A., 2010, The Decoupling of Damped Linear Systems in Free or Forced Vibration, *Journal of Sound and Vibration* 329 (15), 3182-3202.

[11] Cronin, D. L., 1976, Approximation for Determining Harmonically Excited Response of Nonclassically Damped Systems, *ASME Journal of Engineering for Industry* 98 43-47.

[12] Chung, K. R., Lee, C. W., 1986, Dynamic Reanalysis of Weakly Non-proportionally Damped Systems, *Journal of Sound and Vibration* 111 (1) 37-50.

[13] Shahruz, S. M., Ma, F., 1988, Approximate Decoupling of the Equations of Motion of Linear Underdamped Systems, *ASME Journal of Applied Mechanics* 55 716-720.

[14] Udwadia, F. E., Esfandiari, R. S., 1990, Nonclassically Damped Dynamic Systems: an Iterative Approach, *ASME Journal of Applied Mechanics* 57 423-433.

[15] Felszeghy, S. F., 1993, On Uncoupling and Solving the Equations of Motion of Vibrating Linear Discrete Systems, *ASME Journal of Applied Mechanics* 60 456-462.

[16] Hwang, J. H., Ma, F., 1993, On the Approximate Solution of Nonclassically Damped Linear Systems, *ASME Journal of Applied Mechanics* 60 695-701.

[17] Bhaskar, A., 1995, Estimates of Errors in the Frequency Response of Non-classically Damped Systems, *Journal of Sound and Vibration* 184 (1) 59-72.

[18] Gawronski, W. K., 1998, *Dynamics and Control of Structures: A Modal Approach*, Springer, New York.

[19] Knowles, J. K., 2006, On the Approximation of Damped Linear Dynamical Systems, *Structural Control and Health Monitoring* 13 324-335.

[20] Chopra, A. K., 2007, *Dynamics of Structures: Theory and Applications to Earthquake Engineering*, 3*rd* ed., Prentice Hall, Upper Saddle River, New Jersey.

[21] Prater, G., Singh, R., 1986, Quantification of the Extent of Non-proportional Viscous Damping in Discrete Vibratory Systems, *Journal of Sound and Vibration* 104 (1) 109-125.

[22] Nair, S. S., Singh, R., 1986, Examination of the Validity of Proportional Approximations and two further Numerical Iindices, *Journal of Sound and Vibration* 104 (2) 348-350.

[23] Bellos, J., Inman, D. J., 1990, Frequency Response of Nonproportionally Damped, Lumped Parameter, Linear Dynamic Systems, *ASME Journal of Vibration and Acoustics* 112 194-201.

[24] Xu, K., Igusa, T., 1991. Dynamic Characteristics of Non-classically Damped Structures, *Earthquake Engineering and Structural Dynamics* 20 1127-1144.

[25] Park, I. W., Kim, J. S., Ma, F., 1994, Characteristics of Modal Coupling in Nonclassically Damped Systems under Harmonic Excitation, *ASME Journal of Applied Mechanics* 61 77-83.

[26] Tong, M., Liang, Z., Lee, G. C., 1994, An Index of Damping Non-proportionality for Discrete Vibratory Systems, *Journal of Sound and Vibration* 174 (1) 37-55.

[27] Liu, K., Kujath, M. R., Zheng, W., 2000, Quantification of Non-proportionality of Damping in Discrete Vibratory Systems, *Computers and Structures* 77 (5) 557-569.

[28] Liu, K., Kujath, M. R., Zheng, W., 2001, Evaluation of Damping Non-proportionality using Iidentified Modal Information, *Mechanical Systems and Signal Processing* 15 (1) 227-242.

[29] Morzfeld, M., Ajavakom, N., Ma, F., 2009, Diagonal Dominance of Damping and the Decoupling Approximation in Linear Vibratory Systems, *Journal of Sound and Vibration*, 320 (1-2) 406-420.

[30] Lancaster, P., 1966, “Lambda-Matrices and Vibrating Systems,” Pergamon Press, Oxford, United Kingdom.

[31] Gohberg, I., Lancaster P., and Rodman, L., 1982, *Matrix Polynomials*, Academic Press, New York.

[32] Lancaster, P., 1991, “Quadratic Eigenvalue Problems,” *Linear Algebra and its Applications*, **150**, 499-506.

[33] Tisseur, F., and Meerbergen, K., 2001, “The Quadratic Eigenvalue Problem,” *SIAM Review*, **43**(2), 235-286.

[34] Caughey, T. K., and O'Kelly, M. E. J., 1965, “Classical Normal Modes in Damped Linear Dynamic Systems,” *ASME Journal of Applied Mechanics*, **32**, 583-588.

[35] Foss, K. A., 1958, “Co-Ordinates Which Uncouple the Equations of Motion of Damped Linear Dynamic Systems,” *ASME Journal of Applied Mechanics*, **25**, 361-364.

[36] Velestos, A. S., and Ventura, C. E., 1986, “Modal Analysis of Non-Classically Damped Linear Systems,” *Earthquake Engineering and Structural Dynamics*, **14**, 217-243.

[37] Vigneron, F. R., 1986, “A Natural Mode Model and Modal Identities for Damped Linear Dynamic Structures,” *ASME Journal of Applied Mechanics*, **53**, 33-38.

[38] Meirovitch, L., 1967, *Analytical Methods in Vibrations*, Macmillan, New York.

[39] Woodhouse, J., 1998, Linear Damping Models for Structural Vibration, *Journal of Sound and Vibration* 215 (3) 547-569.

[40] Brogan, W. L., 1991, *Modern Control Theory*, 3*rd* ed., Prentice Hall, Upper Saddle River, New Jersey.

[41] Anderson, E., Bai, Z., Bischof, C., Blackford, S., Demmel, J., Dongorra, J., Du Croz, J., Greenbaum, A., Hammerling, S., McKenney, A., Sorensen, D., 1999 *LAPACK Users' Guide*, 3*rd* ed., SIAM, Philadelphia, Pennsylvania.

[42] Demmel, J. W., 1997, *Applied Numerical Linear Algebra*, SIAM, Philadelphia, Pennsylvania.

[43] Golub, G. H., Van Loan, C. F., 1996, *Matrix Computations*, 3*rd* ed., Johns Hopkins University Press, Baltimore, Maryland.

[44] Schwartz, L., 1966, *Mathematics for the Physical Sciences*, Hermann, Paris, 1966.

[1] Stakgold, I., 1998, *Green's Functions and Boundary Value Problems, 2nd ed.,* Wiley, Hoboken, New Jersey.

[2] J.T. Oden, T. Belytschko, I. Babuska, T.J.R. Hughes, Research directions in computational mechanics. *Computer Methods in Applied Mechanics and Engineering*, **192**, 913-922, 2003.

[3] J.H. Argyris, M. Papadrakakis, L. Karapitta, Elastoplastic analysis of shells with the triangular element TRIC. M. Papadrakakis, A. Samartin, E. Oñate eds. *4th International Colloquium on Computation of Shell and Spatial Structures (IASS-IACM 2000),* Chania, Crete, Greece, June 4-7, 2000.

COMPDYN 2011
3^{rd} ECCOMAS Thematic Conference on
Computational Methods in Structural Dynamics and Earthquake Engineering
M. Papadrakakis, M. Fragiadakis, V. Plevris (eds.)
Corfu, Greece, 25-28 May 2011

HYBRID LAPLACE-TIME DOMAIN APPROACH FOR NONLINEAR DYNAMIC SOIL-STRUCTURE INTERACTION PROBLEMS

A. Nieto Ferro[1,2], **D. Clouteau**[1], **N. Greffet**[2] **and G. Devésa**[2]

[1]LMSSMat (CNRS UMR 8579) - Ecole Centrale Paris
Grande Voie des Vignes, 92295 Châtenay-Malabry, France
e-mail: {didier.clouteau,alex.nieto-ferro}@ecp.fr

[2]Electricité de France R&D - Dept. AMA
Avenue du Général de Gaulle 1, 92141 Clamart, France
e-mail: {nicolas.greffet, georges.devesa}@edf.fr

Keywords: Dynamic soil-structure interaction, impedance matrix, hybrid Laplace-time domain approach, Convolution Quadrature Method, nonlinear analysis.

Abstract. *Nonlinear dynamic soil-structure interaction problems are usually solved by a substructuring technique where the soil-structure system is decomposed into two sub-domains: the nonlinear structure, which can also include a part of the soil showing a nonlinear behavior, and the linear unbounded soil. The present work considers the case where the problem is localized on the building. The effects of the unbounded soil are then represented as a particular type of boundary condition by means of the so-called impedance operator, assumed to be known in the Laplace domain. In this framework, since nonlinearities are taken into account, the problem has to be solved in the time domain. Consequently, the interaction forces are expressed in terms of the Laplace-domain impedance results as a convolution integral between the time impedance coefficients and the nodal displacements located on the interface. In order to compute this convolution product a hybrid Laplace-time domain approach based on a Convolution Quadrature Method is introduced. It allows to express this convolution not only in terms of displacements but also in terms of accelerations and velocities convolutions. The proposed method is finally tested on a soil-structure application modeled with a lumped-parameter system. Satisfactory results are obtained when an elasto-plastic behaviour is accounted for.*

1 INTRODUCTION

The classical dynamic soil-structure interaction method is based on a domain decomposition technique, where the whole soil-structure domain is decomposed into two subdomains: the soil and the structure. Both subdomains lead to a local problem that is solved separately, warranting in a conformal approach that the traction equilibrium and displacement continuity are verified on the soil-structure interface. The main reason for this decomposition is that different numerical methods can be used for the soil and for the structure. On the one hand, the bounded subdomain of the structure can be modeled by means of a Finite Element method which allows to take into account nonlinear phenomena in a straightforward way. On the other, the unbounded linear elastic soil can be computed using a Boundary Element method, the radiation conditions being thus implicitly satisfied. When the soil shows a nonlinear behaviour, the corresponding part of this subdomain should be incorporated to the structure subdomain.

Since engineers are usually more interested in the structural response, the global problem is solved directly in the building and the effect of the soil is taken into account as a particular type of boundary condition. This condition is expressed by means of the so-called impedance operator which, in the present work, is assumed to be known in the Laplace domain. The matrix impedance $s \mapsto \hat{\boldsymbol{Z}}(\boldsymbol{s}), s \in \mathbb{C}$, i.e. the discretized version of the impedance operator, maps any displacement vector of the soil-structure interface to its corresponding force vector on the same boundary.

When nonlinearities are accounted for, the problem have to be formulated in the time domain. Consequently, the interaction forces on the soil-structure interface denoted by Γ result in a convolution product between the time dynamic impedance coefficients $t \mapsto \boldsymbol{Z}(t)$ and the degrees-of-freedom of the nodes located on the interface $t \mapsto \boldsymbol{u}_\Gamma(t), t \in \mathbb{R}$:

$$\left(\boldsymbol{Z} * \boldsymbol{u}_\Gamma\right)(t) = \int_0^t \boldsymbol{Z}(t-\tau)\boldsymbol{u}_\Gamma(\tau)\, d\tau, \quad 0 \le t \le T \tag{1}$$

where the impedance is assumed to satisfy causality properties.

In order to compute this kind of convolution integrals, literature proposes different numerical methods, such as the frequency-time method [1, 2] or the hidden variables method [3], which are based on a frequency domain formulation of the impedance operator. Similarly, some authors have focused on formulations in the Laplace domain [4, 5], showing a special interest when coupled to a Convolution Quadrature Method (CQM) [6].

The approach presented in this article is in essence an extension of the work originally proposed by Moser and al. [7, 8] and Pereira and Beer [9]. A hybrid Laplace-time domain technique is therefore introduced in the following sections in order to numerically evaluate Equation 1. Time is discretized by means of a CQM, so the Laplace transform of the convolution kernel is supposed to be analytic on the complex half-plane $\Re e(s) > \sigma_0$ and polynomially bounded for large $|s|$:

$$||\hat{\boldsymbol{Z}}(s)|| \le D|s|^\mu \tag{2}$$

for $D, \mu \in \mathbb{R}$. Particularly, the dynamic impedance matrix will be assumed of the following form:

$$\hat{\boldsymbol{Z}}(s) = \boldsymbol{M}_\Gamma s^2 + \boldsymbol{C}_\Gamma s + \boldsymbol{K}_\Gamma + \hat{\boldsymbol{Z}}_{ns}(s) \tag{3}$$

where $\boldsymbol{K}_\Gamma$,$\boldsymbol{C}_\Gamma$ and $\boldsymbol{M}_\Gamma$ are the matrices which correspond to the inertial, damping and stiffness effects and where $\hat{\boldsymbol{Z}}_{ns}(s)$ denotes a non-singular function vanishing for large $|s|$.

2 HYBRID LAPLACE-TIME DOMAIN APPROACH

In this framework, the CQM approximates the convolution integral in Equation 1 by a discrete convolution (time step $\Delta t > 0$):

$$(\boldsymbol{Z} * \boldsymbol{u})(n\Delta t) = \sum_{0 \leq n\Delta t \leq t} \boldsymbol{\Phi_k} \boldsymbol{u}(t - n\Delta t) \;\; , \quad t = \Delta t, 2\Delta t, 3\Delta t, ... \tag{4}$$

where coefficients $\boldsymbol{\Phi_k}$ correspond to the weights of the generating power series:

$$\sum_{k=0}^{+\infty} \Phi_k \zeta^k = \hat{\boldsymbol{Z}}\left(s_{\Delta t}\right) \tag{5}$$

The complex sampled values $s_{\Delta t}$ of the dynamic soil impedance are given by a rational function of a linear multistep method of order p satisfying strong A-stability conditions. For instance, let $s_{\Delta t}$ be $\frac{\delta(\zeta)}{\Delta t}$ where $\delta(\zeta)$ is the backward differentiation formula of $p = 2$ reading $\delta(\zeta) = \frac{3}{2} - 2\zeta + \frac{1}{2}\zeta^2$.

Nevertheless, paying attention to the physical units of Equation 1, it seems natural to express the convolution not only in terms of displacements, but also in terms of accelerations and velocities. To that end, the polynomial part $\hat{\boldsymbol{P}}(s)$ of the impedance is factorized yielding to:

$$\hat{\boldsymbol{Z}}(s) = \hat{\boldsymbol{Z}}_m(s)\hat{\boldsymbol{P}}(s) = \hat{\boldsymbol{Z}}_m(s)\left(\tilde{\boldsymbol{M}}_\Gamma s^2 + \tilde{\boldsymbol{C}}_\Gamma s + \tilde{\boldsymbol{K}}_\Gamma\right) \tag{6}$$

where $\tilde{\boldsymbol{K}}_\Gamma$, $\tilde{\boldsymbol{C}}_\Gamma$ and $\tilde{\boldsymbol{M}}_\Gamma$ are respectively the estimators of the matrices $\boldsymbol{K}_\Gamma$,$\boldsymbol{C}_\Gamma$ and $\boldsymbol{M}_\Gamma$ presented in Equation 3.

Therefore, the convolution can be written in terms of the Laplace transform as follows:

$$(\boldsymbol{Z} * \boldsymbol{u})(t) = \frac{1}{2\pi i}\int_{\sigma_0 + i\mathbb{R}} \hat{\boldsymbol{Z}}_m(s)\hat{\boldsymbol{P}}(s)\hat{\boldsymbol{u}}(s)\; e^{st} ds \tag{7}$$

The polynomial function $\hat{\boldsymbol{P}}(s)$ acts thus over the displacement as a differential operator and Equation 1 finally reads:

$$(\boldsymbol{Z} * \boldsymbol{u})(t) = (\boldsymbol{Z}_m * \tilde{\boldsymbol{M}}_\Gamma \ddot{\boldsymbol{u}})(t) + (\boldsymbol{Z}_m * \tilde{\boldsymbol{C}}_\Gamma \dot{\boldsymbol{u}})(t) + (\boldsymbol{Z}_m * \tilde{\boldsymbol{K}}_\Gamma \boldsymbol{u})(t) \tag{8}$$

where the interaction force vector (denoted hereafter by $\boldsymbol{R}_\Gamma(t)$) involves in its calculation the evaluation of displacement, velocity and acceleration convolutions.

If a time step $\Delta t > 0$ is chosen, the convolution integral can be discretized again as in Equation 4 leading to:

$$\boldsymbol{R}_{\Gamma,n} = (\boldsymbol{Z} * \boldsymbol{u})(n\Delta t) = \sum_{k=1}^{n}\left(\boldsymbol{\Psi}_2^{n-k+1}\ddot{\boldsymbol{u}}_k + \boldsymbol{\Psi}_1^{n-k+1}\dot{\boldsymbol{u}}_k + \boldsymbol{\Psi}_0^{n-k+1}\boldsymbol{u}_k\right) \tag{9}$$

where matrices multiplying displacement vectors $\boldsymbol{u}_k$, velocity vectors $\dot{\boldsymbol{u}}_k$ and acceleration vectors $\ddot{\boldsymbol{u}}_k$ are given by:

$$\begin{aligned} \boldsymbol{\Psi}_0^k &= \boldsymbol{Z}_m^k \tilde{\boldsymbol{K}}_\Gamma \\ \boldsymbol{\Psi}_1^k &= \boldsymbol{Z}_m^k \tilde{\boldsymbol{C}}_\Gamma \\ \boldsymbol{\Psi}_2^k &= \boldsymbol{Z}_m^k \tilde{\boldsymbol{M}}_\Gamma \end{aligned} \tag{10}$$

From a numerical point of view, *sub-convolutions* are just unknown at $t = n\Delta t$, since all previous time steps have already been computed. Therefore, Equation 9 can be written by isolating instant n as:

$$\boldsymbol{R}_{\Gamma,n} = \boldsymbol{\Psi}_2^1 \ddot{\boldsymbol{u}}_n + \boldsymbol{\Psi}_1^1 \dot{\boldsymbol{u}}_n + \boldsymbol{\Psi}_0^1 \boldsymbol{u}_n + \boldsymbol{R}_{\Sigma(n-1)} \tag{11}$$

Consequently, coefficients $\boldsymbol{\Psi}_i^1 (i = 0, 1, 2)$ are respectively related to instantaneous stiffness, damping and inertia terms and $\boldsymbol{R}_{\Sigma(n-1)}$ depends only on previous time steps:

$$\boldsymbol{R}_{\Sigma(n-1)} = \sum_{k=1}^{n-1} \left(\boldsymbol{\Psi}_2^{n-k+1} \ddot{\boldsymbol{u}}_k + \boldsymbol{\Psi}_1^{n-k+1} \dot{\boldsymbol{u}}_k + \boldsymbol{\Psi}_0^{n-k+1} \boldsymbol{u}_k \right) \tag{12}$$

3 NUMERICAL APPLICATION

A lumped-parameter model is considered in the following in order to represent the soil-structure system. The nonlinear behaviour is introduced by an elastoplastic spring with one end attached to the upper mass m_1 and the other, to the smaller mass m_2. A square surface foundation layering on a homogeneous half-space is connected to mass m_2 by means of a rigid body constraint (see Figure 1). The soil impedance seen from the foundation is then computed with a boundary element method in the Laplace domain. For the sake of simplicity, the foundation is modeled to give an impedance in the form of inertial, damping and stiffness terms so that a time reference solution can be straightforwardly obtained. In order to illustrate some properties of the soil-structure system considered in an elastic regime, Table 1 gives the main eigenfrequencies of the structure clamped at its base.

	Pumping	Shaking	Torsional	Rocking
Eigenfrequencies [Hz]	5.43	7.95	99.86	405.34

Table 1: Main eigenfrequencies of the structure clamped at its base.

The soil can be characterized by its shear velocity $C_s = 505 m.s^{-1}$ and the elastoplastic behaviour of the spring is modeled with the linear kinematic work hardening law sketched in Figure 1. The elastic deformation is characterized here by the elastic stiffness matrix $\boldsymbol{K}_e$ which, after reaching the yield of plasticity $\boldsymbol{F}_y$, becomes $\boldsymbol{K}_p = 0.1\boldsymbol{K}_e$.

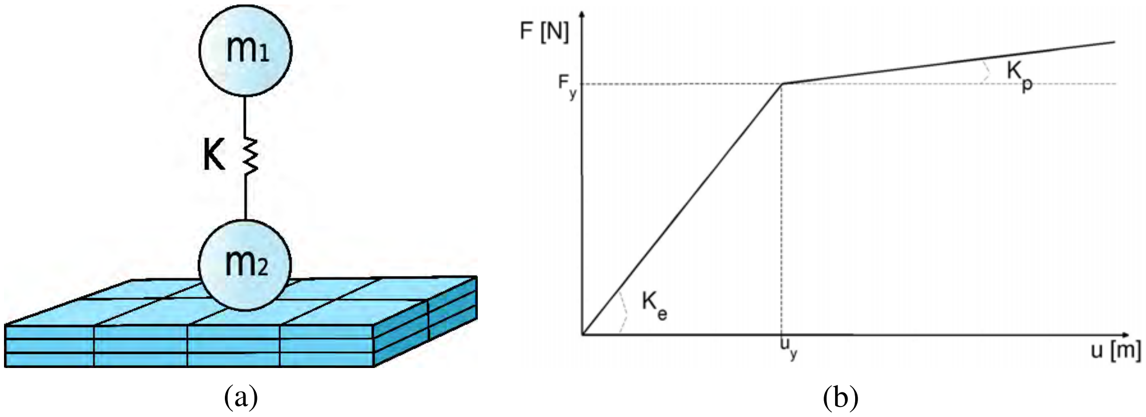

(a) (b)

Figure 1: (a) Simplified model of a structure on a square surface foundation. (b) Linear kinematic work hardening law of the nonlinear spring K.

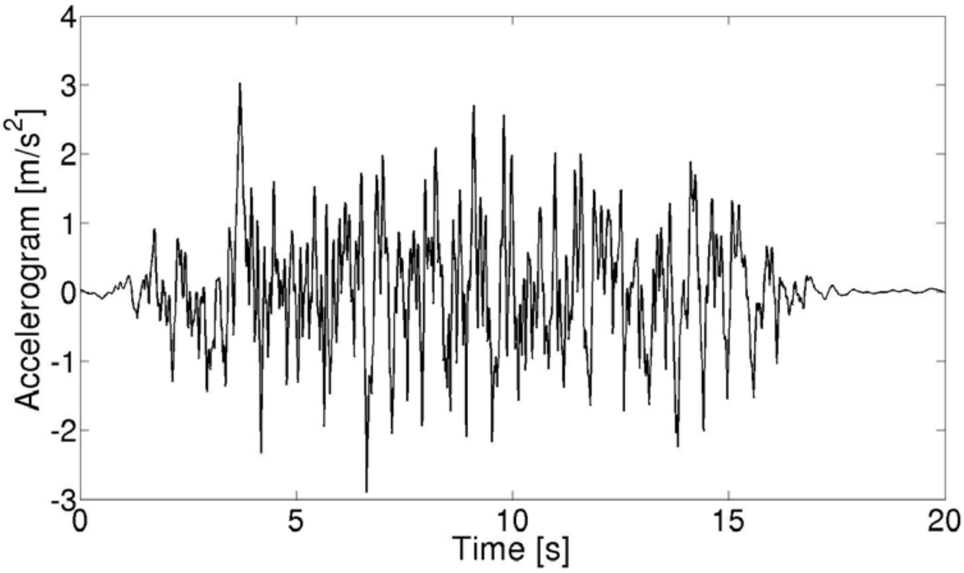

Figure 2: Free-field accelerogram applied to m_2 as a representation of the seismic loading.

The loading applied to m_2 in the x-direction $\boldsymbol{e}_x$ corresponds to the earthquake giving the free-field accelerogram $\gamma(t)$ shown in Figure 2, whose maximal acceleration is around $0.3g$.

The governing equations of this numerical model from the non-inertial frame of reference of the structure can be written at $t = n\Delta t$ as follows:

$$\begin{bmatrix} \boldsymbol{M}_{11} & \boldsymbol{0} \\ \boldsymbol{0} & \boldsymbol{M}_{22} + \boldsymbol{\Psi}_2^1 \end{bmatrix} \begin{bmatrix} \ddot{\boldsymbol{u}}_{1,n} \\ \ddot{\boldsymbol{u}}_{2,n} \end{bmatrix} + \begin{bmatrix} \boldsymbol{F}_{1,n}^{int} \\ \boldsymbol{F}_{2,n}^{int} \end{bmatrix} = \begin{bmatrix} -\boldsymbol{M}_1 \boldsymbol{e}_x \gamma_n \\ -\boldsymbol{M}_2 \boldsymbol{e}_x \gamma_n \end{bmatrix} + \begin{bmatrix} \boldsymbol{0} \\ -\boldsymbol{R}_{\Sigma(n-1)} \end{bmatrix} \tag{13}$$

where $\boldsymbol{F}_{\alpha}^{int}(t)$ $(\alpha \in \{1, 2\})$ denote the nonlinear internal efforts in the structure and depend on both displacement and velocity vectors. The interaction forces $\boldsymbol{R}_{\Gamma,n}$ have been directly substituted by Equation 11. It has to be noticed that the application considered here is particularized to the case where $\tilde{\boldsymbol{K}}_{\Gamma} = \tilde{\boldsymbol{C}}_{\Gamma} = \boldsymbol{0}$, that is the case where only inertial terms are taken into account for the computation of the convolution integral:

$$\boldsymbol{R}_{\Gamma,n} = \sum_{k=1}^{n} \boldsymbol{\Psi}_2^{n-k+1} \ddot{\boldsymbol{u}}_{2,k} = \boldsymbol{\Psi}_2^1 \ddot{\boldsymbol{u}}_{2,n} + \sum_{k=1}^{n-1} \boldsymbol{\Psi}_2^{n-k+1} \ddot{\boldsymbol{u}}_{2,k} \tag{14}$$

where $\boldsymbol{\Psi}_2^k = \boldsymbol{Z}_m^k \tilde{\boldsymbol{M}}_{\Gamma}$. The coefficients corresponding to $\boldsymbol{Z}_m^k$ can be efficiently computed by using Fast Fourier Transforms (FFT) [10]:

$$\boldsymbol{Z}_{\boldsymbol{m}}^{\boldsymbol{k}} = \frac{\rho^{-n}}{L} \sum_{l=0}^{L-1} \hat{\boldsymbol{Z}}_m(s_l) e^{-\frac{2\pi i n l}{L}}, \; n = 0, 1, .., N \tag{15}$$

where ρ represents the radius of a circle in the analyticity domain of $\hat{\boldsymbol{Z}}_m(s) = s^{-2} \hat{\boldsymbol{Z}}(s) \tilde{\boldsymbol{M}}_{\Gamma}^{-1}$ and $s_l = \frac{\delta(\rho e^{2\pi i l/L})}{\Delta t}$ with $\delta(\zeta)$ the polynomial of the underlying linear multistep method. Assuming that the values of $\hat{\boldsymbol{Z}}_m$ are computed with precision ϵ_{CQM}, one gets that the error in $\boldsymbol{Z}_{\boldsymbol{m}}^{\boldsymbol{k}}$ is $O(\sqrt{\epsilon_{CQM}})$ when $L = N$ and $\rho^N = \sqrt{\epsilon_{CQM}}$. In addition, the FFT algorithm allows to compute the weights in $O(L \log L)$ operations.

The governing equations are finally solved for displacement by using the modified average acceleration time integration scheme of the Newmark family. This time integration scheme allows to introduce numerical damping by means of the parameter α. Two different yields of plasticity $\boldsymbol{F}_{y1}$ and $\boldsymbol{F}_{y2}$ with $\boldsymbol{F}_{y1} >> \boldsymbol{F}_{y2}$. For both cases, Equations 13 have been solved for different accuracies ϵ_{CQM}. In the following, normalized errors during the first T seconds of the earthquake are calculated using the expression $e_T = \frac{RMS(\boldsymbol{u}-\boldsymbol{u}_{ref})}{max(\boldsymbol{u}_{ref})}$ where RMS and $\boldsymbol{u}_{ref}$ denote respectively the Root Mean Square and the reference solution. Table 2 presents the errors $e_{10}(\%)$ on the displacement of m_1 in the x-direction. No numerical damping is introduced ($\alpha = 0$).

ϵ_{CQM}	$e_T(\%)$
10^{-04}	5.81
10^{-06}	0.76
10^{-08}	1.29
10^{-10}	1.51
10^{-12}	1.53

(a)

ϵ_{CQM}	$e_T(\%)$
10^{-04}	62.82
10^{-06}	2.59
10^{-08}	2.73
10^{-10}	3.29
10^{-12}	3.34

(b)

Table 2: Relative errors for different precisions ϵ_{CQM} when the displacement at the top of the structure is computed during $T = 10s$ for (a) $\boldsymbol{F}_{y1}$ and (b) $\boldsymbol{F}_{y2}$, with $\boldsymbol{F}_{y1} >> \boldsymbol{F}_{y2}$ and $\alpha = 0$.

Results presented in Tables 2 show that better agreements with the reference solution are obtained for a precision of $\epsilon_{CQM} = 10^{-06}$ with both yields of plasticity. In addition, it seems that the more nonlinear the response, the larger the error. In fact, if numerical damping is introduced ($\alpha = 0.1$) for the reference solution computed with $\boldsymbol{F}_{y2}$ and $\epsilon_{CQM} = 10^{-06}$, the measured relative error reduces to $e_{10} = 1.59\%$. The observed dissipation is less important for $\boldsymbol{F}_{y1}$. Therefore, the numerical damping introduced by the proposed approach may come from the Newton nonlinear solver.

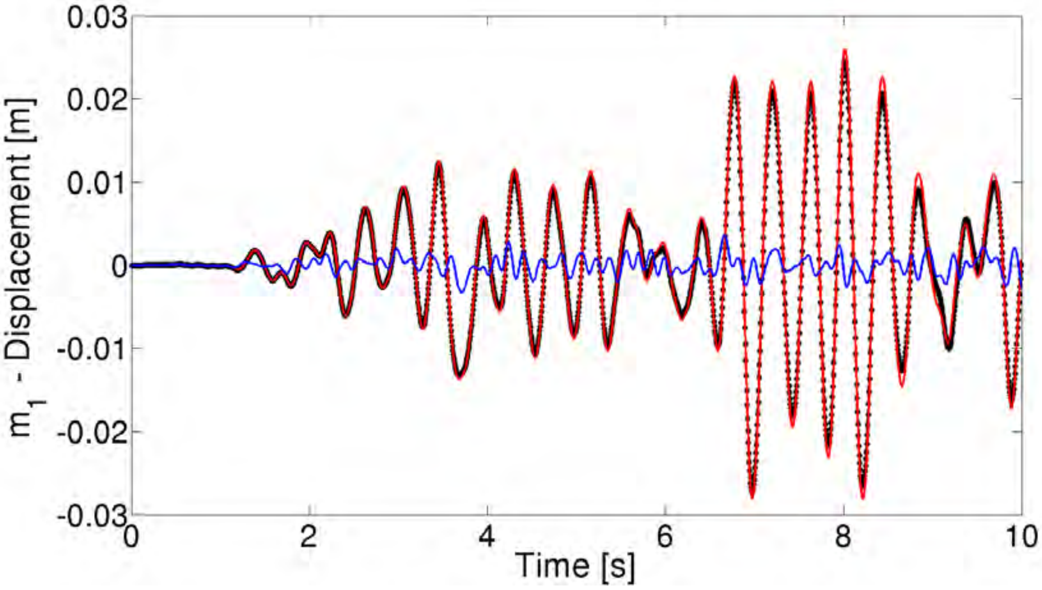

Figure 3: Displacement at m_1 in the x-direction computed with the hybrid time-Laplace domain approach (black markers) and compared to the reference solution (red line) and to the linear response (blue line) for $\boldsymbol{F}_{y2}$.

It should be remarked that if the plasticity yield is chosen sufficiently large, the entire calculation remains linear. Therefore, linear and nonlinear responses can easily be compared using a fixed precision, for example $\epsilon = 10^{-06}$. Figure 3 shows thus the displacement at m_1 in the x-direction compared to the reference solution and also to the linear solution for $\boldsymbol{F}_{y2}$. It is then observed that the amplitude of displacements is increased as expected. In addition, when the elastoplastic effects are taken into account, the structural response is clearly shifted to the low frequencies because of the reduction in stiffness ($\boldsymbol{K}_{e,i} > \boldsymbol{K}_{p,i}$). However, only one fundamental frequency seems to stand out in the response as if just one equivalent stiffness were present in the system. Hence, the effects of both stiffness $\boldsymbol{K}_e$ and $\boldsymbol{K}_p$ on the response can be highlighted by increasing the yield of plasticity. The response with a larger $\boldsymbol{F}_y$, plotted in Figure 4, is significantly different from the one plotted in Figure 3 showing in particular a higher frequency content.

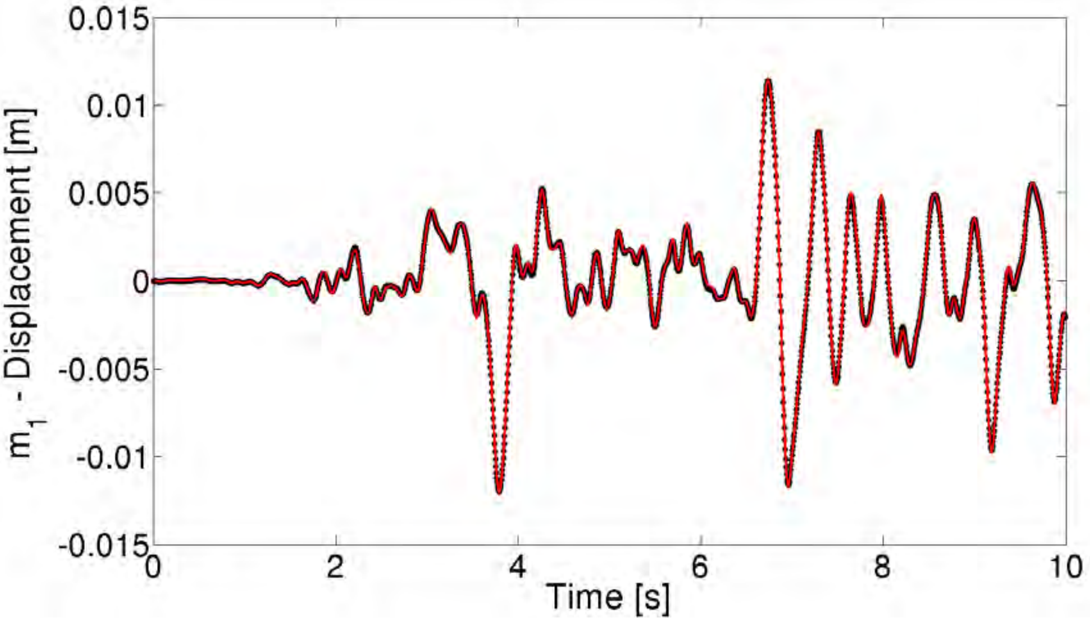

Figure 4: Displacement at m_1 in the x-direction computed with the hybrid time-Laplace domain approach (black markers) and compared to the reference solution (red line) for $\boldsymbol{F}_{y1}$.

Further research has to be pursued in order to investigate if the numerical response is improved when the damping and stiffness parts of the dynamic impedance are also factorized.

4 CONCLUSIONS

The soil-structure interaction problem is solved directly in the building and the impedance operator, defined on the boundary, is used as a particular type of boundary conditions that accounts for the unbounded soil. When nonlinearities are taken into account, the problem is solved in the time domain. Therefore, the influence of the soil is accounted for as a load (interaction forces) computed as a convolution integral in the time domain.

The proposed approach based on the Laplace domain presents some interesting features. On the one hand, it can be combined with IFFT algorithms yielding to small computational costs. On the other hand, it allows to express the convolution integral in terms of inertial, damping and stiffness quantities.

A numerical application considering nonlinear phenomena in the structure has been studied. The convolution integral has been transform to a convolution depending only on acceleration quantities. Very satisfactory results have been obtained when compared to a reference solution. However, it seems that the proposed approach introduces numerical damping when strong elastoplastic behaviour is taken into account.

REFERENCES

[1] G. R. Darbre and J. P. Wolf, Criterion of stability and implementation issues of hybrid frequency time domain procedure for non-linear dynamic analysis. *Earthquake Engineering and Structural Dynamics*, **16** (4), 569–581, 1988.

[2] J. P. Wolf, *Soil-Structure-Interaction Analysis in Time Domain*. Prentice-Hall, NJ, USA, 1988.

[3] R. Cottereau, D. Clouteau, C. Soize and S. Cambier, Probabilistic nonparametric models of impedance matrices. Application to the seismic design of a structure. *European Journal of Computational Mechanics*, **15**, 131–142, 2006.

[4] L. Gaul and M. Schanz, A comparative study of three boundary element approaches to calculate the transient response of viscoelastic solids with unbounded domains, *Computer Methods in Applied Mechanics and Engineering*, **179**, 111–123, 1999.

[5] M. Schanz and H. Antes, Aplication of 'Operational Quadrature Methods' in Time Domain Boundary Element Methods, *Meccanica*, **32** (3), 179–186, 2006.

[6] C. Lubich, Convolution quadrature and discretized operational calculus I. *Numerische Mathematik*, **52**, 129–145, 1988.

[7] W. Moser and H. Antes and G. Beer, A Duhamel integral based approach to one-dimensional wave propagation analysis in layered media, *Computational Mechanics*, **35**, 115–126, 2005.

[8] W. Moser and H. Antes and G. Beer, Soil-structure interaction and wave propagation problems in 2D by a Duhamel integral based approach and the convolution quadrature method, *Computational Mechanics*, **36**, 431–443, 2005.

[9] A. Pereira and G. Beer, Interface dynamic stiffness matrix approach for three-dimensional transient multi-region boundary element analysis. *International Journal for Numerical Methods in Engineering*, **80**, 1463–1495, 2009.

[10] C. Lubich, Convolution quadrature and discretized operational calculus II. *Numerische Mathematik*, **52**, 413–425, 1988.

COMPDYN 2011
ECCOMAS Thematic Conference on
Computational Methods in Structural Dynamics and Earthquake Engineering
M. Papadrakakis, M. Fragiadakis, V.Plevris (eds.)
Corfu, Greece, 25-28 May 2011

INFLUENCE OF TYPE OF WAVE AND ANGLE OF INCIDENCE ON THE SEISMIC RESPONSE OF PILE FOUNDATIONS AND PILE SUPPORTED STRUCTURES

José M. Zarzalejos, Juan J. Aznárez, Luis A. Padrón, and Orlando Maeso

Universitary Institute SIANI, Universidad de Las Palmas de Gran Canaria
Edif. Central del Parque Científico, Campus Universitario de Tafira, 35017
Las Palmas de Gran Canaria, Spain
e-mail: {jmzarzalejos,jjaznarez,lpadron,omaeso}@siani.es

Keywords: Structural Dynamics, Earthquake Engineering, Angle of Incidence, SSI

Abstract. *The dynamic response of pile foundations and pile supported structures has been extensively studied during the last four decades. Even though, there exists yet the need of achieving a better understanding on different aspects of the problem, such as the response of inclined piles, the influence of the presence of nearby structures, the importance of various kinds of non-linearities, or the influence of the different parameters of the soil-foundation-structure system on the seismic response of the superstructure and on the internal efforts arising along the piles.*

The type of seismic waves impinging on the site, and the angle of incidence of the waves, are important parameters of the seismic excitation. However, vertical incidence of waves is usually assumed in the analysis of the seismic response of piles, and only a small percentage of the large amount of works related to this topic take the angle of incidence into account.

In this work, the influence of the type of wave and its angle of incidence on the seismic response of pile foundations and pile supported structures is investigated using a direct approach. To this end, a frequency-domain boundary element - finite element formulation is used, being the Boundary Element Method used to model the soil as a homogeneous, isotropic, viscoelastic, semi-infinite region; and the Finite Element Method used to model both piles (as Euler-Bernoulli beams) and superstructure (formed by horizontal rigid slabs and extensible vertical elastic piers). The code is able to model the incidence of Rayleigh waves, and also P, SH and SV body waves with a general angle of incidence.

The formulation is briefly presented at the beginning of the paper. Some validation results, in terms of kinematic interaction factors of pile foundations, are presented. Then, different results in terms of internal efforts in piles and inter-storey drift in the superstructure are presented for different types of waves. It is shown that the angle of incidence has a great influence on the structural response, especially in the case of the SV wave, where the critical angle (at which there is a change in the nature of the reflected waves, and whose value depends exclusively on the Poisson's ratio) plays a very important role, as the seismic response of the structure increases greatly around such angle. It is also shown that, in general, the vertical incidence is not the most unfavourable situation.

1 INTRODUCTION

The study presented herein is integrated on a research line focused on the development of numerical models used to determine the dynamic response of structures of different typology. The dynamic response of both deep foundations and piled structures is a topic deeply studied. However, improvements in the comprehension of some aspects of the problem, such as the influence of the direction of propagation of the waves defining the excitation, are still needed.

The numerical methods used to solve the equations of the problem are both the Boundary Element Method (BEM) and the Finite Element Method (FEM). The former allows the treatment of infinite or semi-infinite regions since it implicitly verifies the radiation conditions. Therefore, the BEM is used to model the soil as a homogeneous, isotropic, viscoelastic, semi-infinite region. On the other hand, the FEM is used to model both piles (as Euler-Bernoulli beams) and superstructure (formed by horizontal rigid slabs and extensible vertical elastic columns). The dynamic interaction between the different regions is rigorously formulated using equilibrium and compatibility conditions, leading to a system of equations including unknowns on displacements and tractions on the boundaries of the regions. The system loads are seismic waves of different nature (P, SH and SV waves) with a generic angle of incidence impinging the structural system.

2 MAIN OBJECTIVES

This work investigates the influence of the type of the incident wave and its angle of incidence on the dynamic response of pile foundations and piled buildings in terms of internal efforts in piles and inter-storey drift amplitudes in the superstructure. It also looks into the influence of parameters such as the slenderness of the building on the magnitudes mentioned above. To this end, volumetric P, SH and SV waves propagating through a homogeneous, semi-infinite domain with a generic angle of incidence are taken into account.

3 PROBLEM DEFINITION

3.1 General aspects

In this work, a frecuency-domain boundary element - finite element formulation [1] is used, being the Boundary Element Method used to model the soil as a homogeneous, isotropic, viscoelastic semi-infinite region; and the Finite Element Method used to model piles (as Euler-Bernoulli beams) and superstructure (formed by horizontal rigid slabs and extensible vertical columns). A more detailed description of both the numerical aspects of the Boundary Element Method and its use on dynamical problems can be found in [2], while a proper description of the Finite Element Method can be seen in [3].

Once this process is done, the system of equations arising from applying the Boundary Element Method to the soil is coupled with that one coming from the use of the Finite Element Method to model the equations of motion of beams, columns and piles (as seen in [1]), leading to a single system of equations describing the behaviour of the entire problem.

The loads taken into account in the problem are seismic loads. Total displacements and tractions due to the seismic action can be found as the superposition of those caused by the so-called incident field (representing the original waves, coming from a far source) and the scattered field (representing the one produced by the reflection and refraction phenomena). This way, a matrix equation can be written for every domain Ω (see [1, 4]) as:

$$H^{ss}\, u^s - G^{ss}\, p^s - \sum_{j=1}^{n_p} G^{sp_j}\, q^{sj} + \sum_{j=1}^{n_p} \delta_j\, \Psi^{sj}\, F_{p_j} = H^{ss}\, u_I^s - G^{ss}\, p_I^s \tag{1}$$

being H^{ss}, G^{ss} and G^{sp_j} the influence coefficients, u^s and p^s the displacements and tractions of the total field, n_p the number of piles on the domain, q^{sj} the tractions on piles due to the soil, δ_j a parameter taking a unitary value if the jth load line contains the tip of a floating pile and zero otherwise, Ψ^{sj} a three-component vector representing the contribution of the axial force F_{p_j} on the tip of the jth load line and u_I^s and p_I^s the displacements and tractions of the reflected field. The expressions of the latter two values can be found for a generic angle of incidence in [5] (in terms of displacements and tractions) or in [6] (in terms of Lame's potentials).

3.2 Incident field equations

Let $\boldsymbol{s}$ be a vector defining the direction of propagation of a certain wave and $\boldsymbol{d}$ a vector defining the direction of the particle displacements. These directions are perpendicular in S waves and coincident in P waves. It should also be taken into account that when a wave reaches the free surface of the halfspace, a reflection phenomenon occurs, leading to the propagation of a number of new waves depending on the nature of the incident one. Thus, when an SH wave reaches the free surface, the reflected wave is a single SH wave. If the incident wave is a P or an SV one, then after the process of reflection there appears both a P and an SV waves (see figure 1).

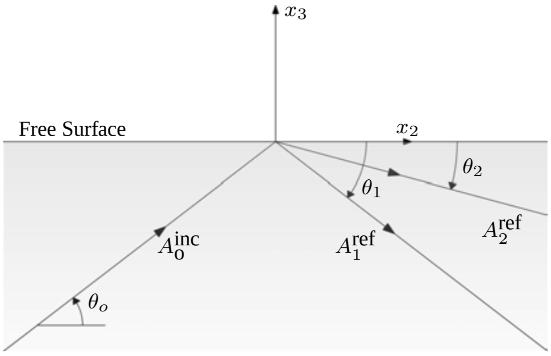

Figure 1: Incident and reflected waves. Incident field

The displacements on the ith direction (x_i, $i = 1, 2, 3$) can be written as:

$$u_i = \sum_{j=1}^{n} d_i^j\, A_j\, \mathrm{e}^{-\mathrm{i}\, k_j\, \left(\mathbf{s}^{(j)} \cdot \mathbf{r}\right)} \tag{2}$$

being u_i the component on the ith direction of the total displacement, n the total number of waves of the problem (i.e., the incident plus the reflected waves), d_i^j the component on the ith direction of the vector containing the direction cosines of the displacements produced by the jth wave, A_j the amplitude of the jth wave, k_j the wave number of the jth wave (defined as the ratio between the excitation frequency ω and the velocity of propagation of the wave) and $\mathbf{s}^{(j)} \cdot \mathbf{r}$ the dot product of the vector defining the direction of propagation of the jth wave and the vector containing the coordinates of the point where the displacements are calculated.

Once the expressions of the field of displacements are obtained for a point, it is easy to determine the small strain tensor using the compatibility equations. In addition, and provided that the soil is a linear, elastic, homogeneous, isotropic solid, the stress tensor can be obtained using the Hooke's Law.

The boundary conditions of the problem are free surface conditions. Thus, σ_{33} and σ_{23} should be zero in points located on the surface (i.e., those with zero value of their x_3 coordinate). As a consequence of the application of boundary conditions, the angle θ_o of incidence of a wave is equal to the angle θ_1 of the reflected wave of the same kind of the incident one.

Another aspect of interest is that the incidence of an SV wave with a smaller angle than a so-called critical one (directly proportional to the ratio between the velocity of S and P waves on the medium) causes the reflection of both an SV wave and an additional wave. This wave is a P wave in the complex field but represents a surface wave with motions along two perpendicular directions out of phase in the real field. This fact remarkably influences the dynamic response of structures submitted to these types of waves.

4 VALIDATION RESULTS

Once the problem has been briefly explained, it is time to validate the formulation and its computational implementation. To this end, some selected results, in terms of kinematic interaction factors on displacements and rotations at pile caps of different pile foundations are presented.

Some selected results taken from [7] are used to validate the formulation. In these numerical examples, the soil internal damping is $\beta = 0.05$, the ratio between the material modulae is $E_p/E_s = 10^2$ or $E_p/E_s = 10^3$, the ratio between densities is $\rho_p/\rho_s = 1.5$, the piles aspect ratio is $L/d = 20$, and the Poisson's ratios are $\nu_s = 1/3$ (for the soil) and $\nu_p = 0.25$ (for the piles). Results are presented for single piles and groups of 3×3 and 4×4 piles submitted to SH, SV and P waves whose direction of propagation is contained in the x_2x_3 plane.

Figure 2 shows the results obtained using the BEM-FEM model compared with those obtained by Kaynia and Novak using a discrete layer matrix approach. Results of kinematic interaction factors on displacements are presented in terms of the modulus of the horizontal displacement at the pile head ($|u|$) with respect to the modulus of the corresponding free field motion ($|u_{ff}|$). Alternatively, the results of kinematic interaction factors on rotations are presented as the ratio between the modulus of the rotation measured at the pile cap times the pile diameter ($|\phi|\ d$) and the modulus of the corresponding free field motion. All the results are plotted against the dimensionless frequency, defined as the ratio between the excitation frequency times the pile diameter and the soil shear-wave velocity (i.e., $a_o = \omega d/c_s$). It can be seen that the agreement between the results is very good, with differences reaching 5 or 6 per cent.

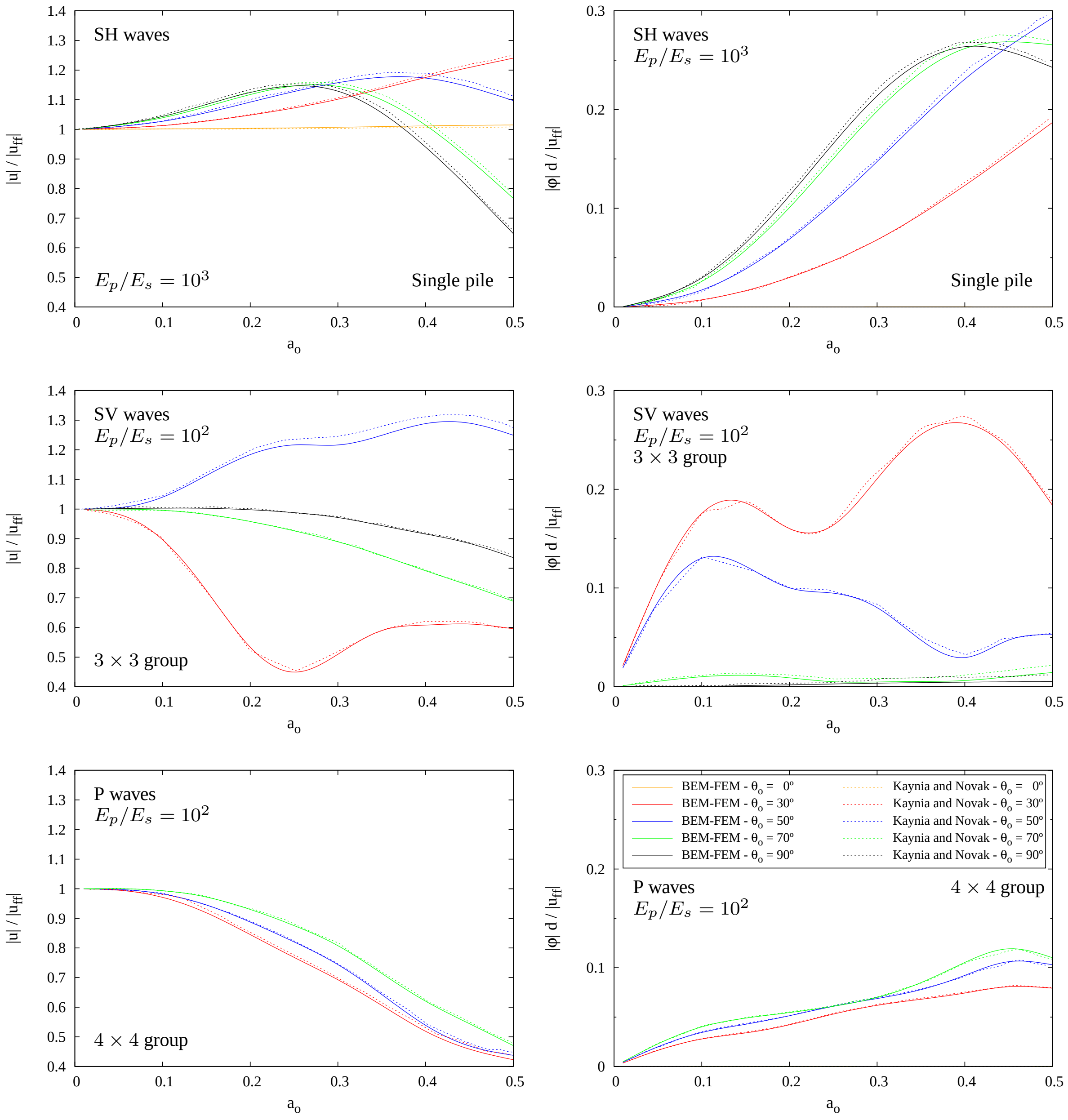

Figure 2: Kinematic interaction factors on displacements (left) and rotations (right) of some different foundations. Comparison with Kaynia and Novak [7]

5 INFLUENCE OF THE TYPE OF WAVE AND ANGLE OF INCIDENCE ON THE SEISMIC RESPONSE OF PILE FOUNDATIONS AND PILE SUPPORTED STRUCTURES

5.1 Problem definition

The problem studied from now on is sketched in figure 3. The main objective of this example is illustrating the influence of the type of wave and its angle of incidence on the seismic response of pile foundations and pile supported structures. The behaviour of a piled structure is studied. To this end, the superstructure is depicted with a single rigid slab supported by massless flexible columns. This system can represent both a single degree of freedom system (like a one-storey shear building) or an equivalent system defining the behaviour of a multimodal structure according to a specific mode of vibration.

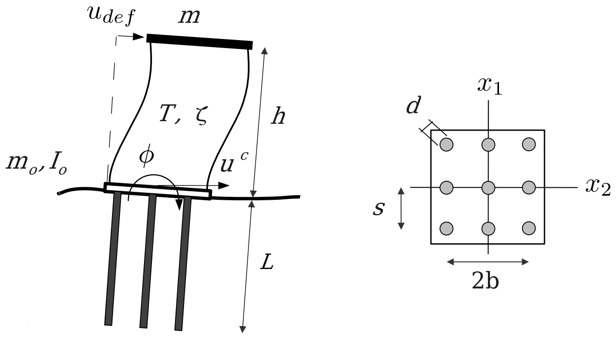

Figure 3: Problem definition

The dynamic behaviour of the structure can be defined by its rigid base fundamental period T, the height h of the resultant of the inertia forces for the first mode, the mass m participating on the first mode and the corresponding structural damping ζ. The horizontal stiffness of the structure is $\mathcal{K} = 4\pi^2 m/T^2$, with a hysteretic damping given by a complex stiffness of the type $k = \mathcal{K}\,(1 + 2\mathrm{i}\zeta)$. The structure is founded on a square 3×3 pile group embedded in a viscoelastic halfspace. Pile groups are defined by the length L and diameter d of the piles, the distance s between adjacent piles, the pile cap mass m_o and its moment of inertia I_o with respect to a horizontal axis going through its center of gravity and by a parameter b measuring half of the width of the foundation. Thus, the movement of the system can be expressed by three degrees of freedom. These degrees of freedom represent horizontal and rocking movements at the rigid pile cap and inter-storey drift in the superstructure.

5.2 Parameters of the problem

Mechanical and geometric properties of soil and foundation are defined by the soil damping ratio $\beta = 0.05$, the Young's modulus ratio $E_p/E_s = 10^2$, the pile-soil densities ratio $\rho_s/\rho_p = 0.7$, the slenderness ratio of the piles $L/d = 15$, the soil Poisson's ratio $\nu_s = 0.4$ and the separation between adjacent piles $s/d = 5$.

The parameters used to depict the dynamic behaviour of the superstructure are the aspect ratios $h/b = 2$ and 4, the ratio between the stiffnesses of structure and soil $h/\left(T\ c_s\right) = 0.3$, being c_s the shear waves velocity, and the structural damping $\zeta = 0.05$. It is also of interest to know the moment of inertia of the foundation, taken as the 5% of the mh^2 factor, the structure-soil mass ratio $m/\left(4\ \rho_s\ b^2\ h\right) = 0.2$ and the foundation-structure mass ratio $m_o/m = 0.25$. The values chosen for these three last parameters are considered to be representative for typical constructions.

5.3 Variation of horizontal free-field motion with the angle of incidence

As the following results will be adimensionalized with the horizontal free-field motion at ground surface, it is interesting to study its evolution with the angle of incidence. For this purpose, it is worth noting that the horizontal free-field motion at ground surface is constant with the angle of incidence when the incident wave is an SH one. On the other hand, the variation of such a magnitude divided by the corresponding amplitude is shown on figure 4 for SV or P incident waves. Note the sharp variation of the values around the critical angle on SV waves ($\theta_{cr} = 52.24^o$ for $\nu_s = 0.2$, $\theta_{cr} = 57.69^o$ for $\nu_s = 0.3$ and $\theta_{cr} = 65.91^o$ for $\nu_s = 0.4$) and the smooth but marked change in the case of P waves.

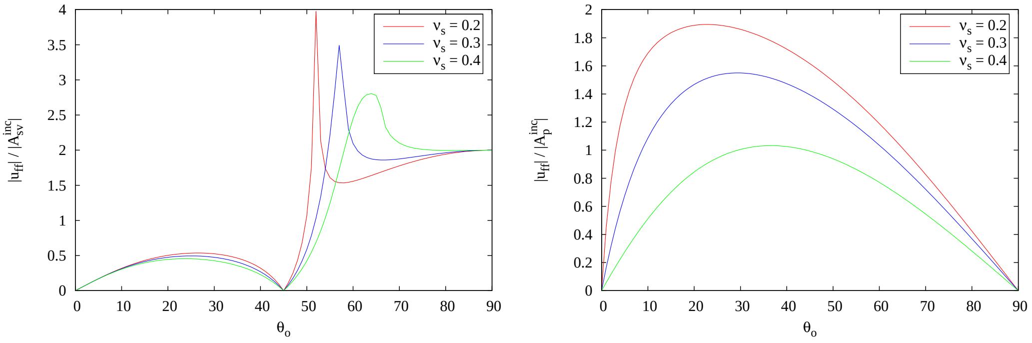

Figure 4: Variation of horizontal free-field motion at ground surface with the angle of incidence and the Poisson's ratio of the soil. Incident SV and P waves

5.4 Lateral deflection of the building

In this case, deflection amplitude can be defined in terms of variables shown on figure 3 as:

$$u_{def} = u - u_c - \phi\, h \tag{3}$$

being u the absolute displacement of the vibrating mass. This way, this deflection relates the shear forces F on the base of the structure with the stiffness k of the system ($F = k\, u_{def}$).

The first set of results is shown on figures 5 and 6. They represent the evolution of the inter-storey drift amplitude with the dimensionless frequency for SH, SV and P incident waves. Results for five different angles of incidence (30, 50, 60, 70 and 90 degrees) are shown. As expected, the deflection shows a maximum around the fundamental frequency of the structure taking SSI into account. For SH, but specially of P waves, the angle of incidence has little influence on the deflection. On the contrary, it shows a very strong influence for the SV wave. Note that u_{def} is normalized by u_{ff}, which for $\theta_o = 30^o$ and 50 has significantly smaller values than for the rest of angles. This variation of u_{ff} with θ_o (shown above in figure 4) is in part responsible for the great increment of the deflection for $\theta_o = 30^o$. In addition, rotations at pile cap are substantially greater for $\theta_o = 30^o$ than for the rest of angles, and since u_{def} depends on such a value (see equation 3), the observed values are justified.

5.5 Internal efforts in piles

This last set of results represents axial, shear forces and bending moments at the pile head of the four representative piles. Two different aspect ratios are considered ($h/b = 2$ and 4) and results are normalized by the corresponding stiffness of a Euler-Bernoulli beam with the properties of the pile.

The results shown on figures from 7 to 15 have a general trend of increasing efforts with the aspect ratio. Like on deflection drift amplitudes, these results also have a peak value around the fundamental frequency of the building taking SSI into account.

It is worth noting that the axial forces arising from the incidence of an SH wave are null on the central piles of the group. This is because the vertical displacement of the center of gravity of the pile cap is also null, rotating the pile cap around an axis passing through the central piles of the group. Therefore, central piles are unloaded.

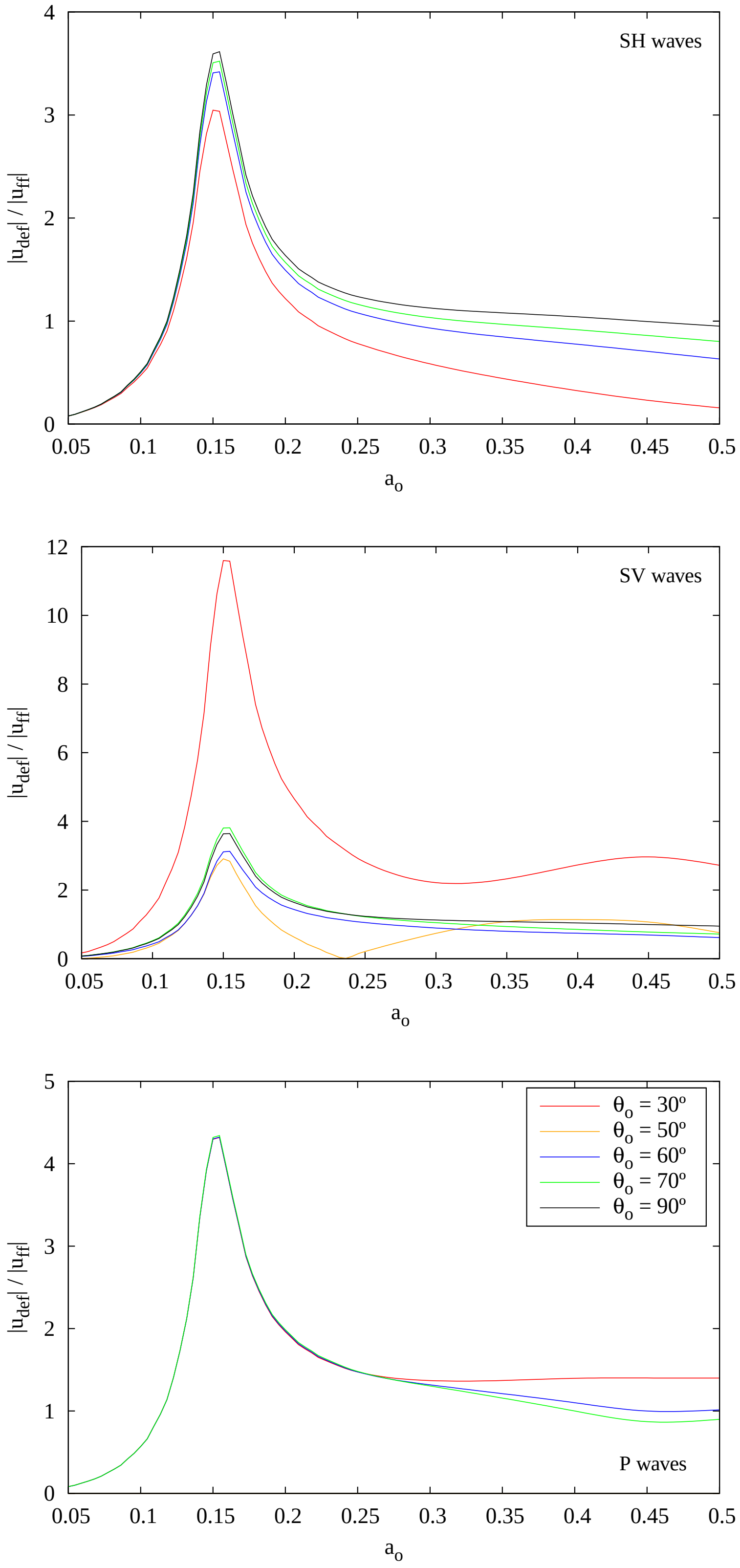

Figure 5: Inter-storey drift amplitudes. Aspect ratio $h/b = 2$

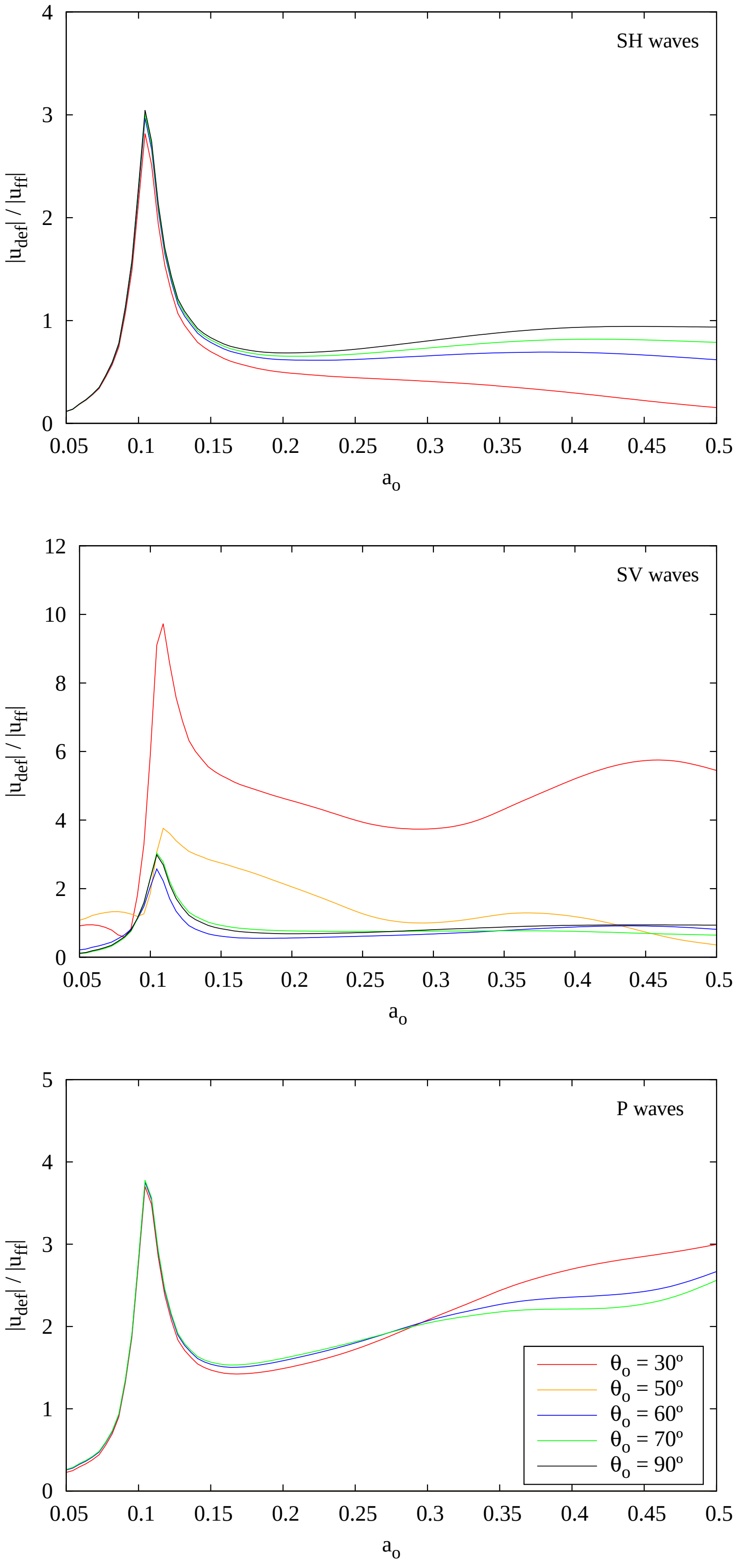

Figure 6: Inter-storey drift amplitudes. Aspect ratio $h/b = 4$

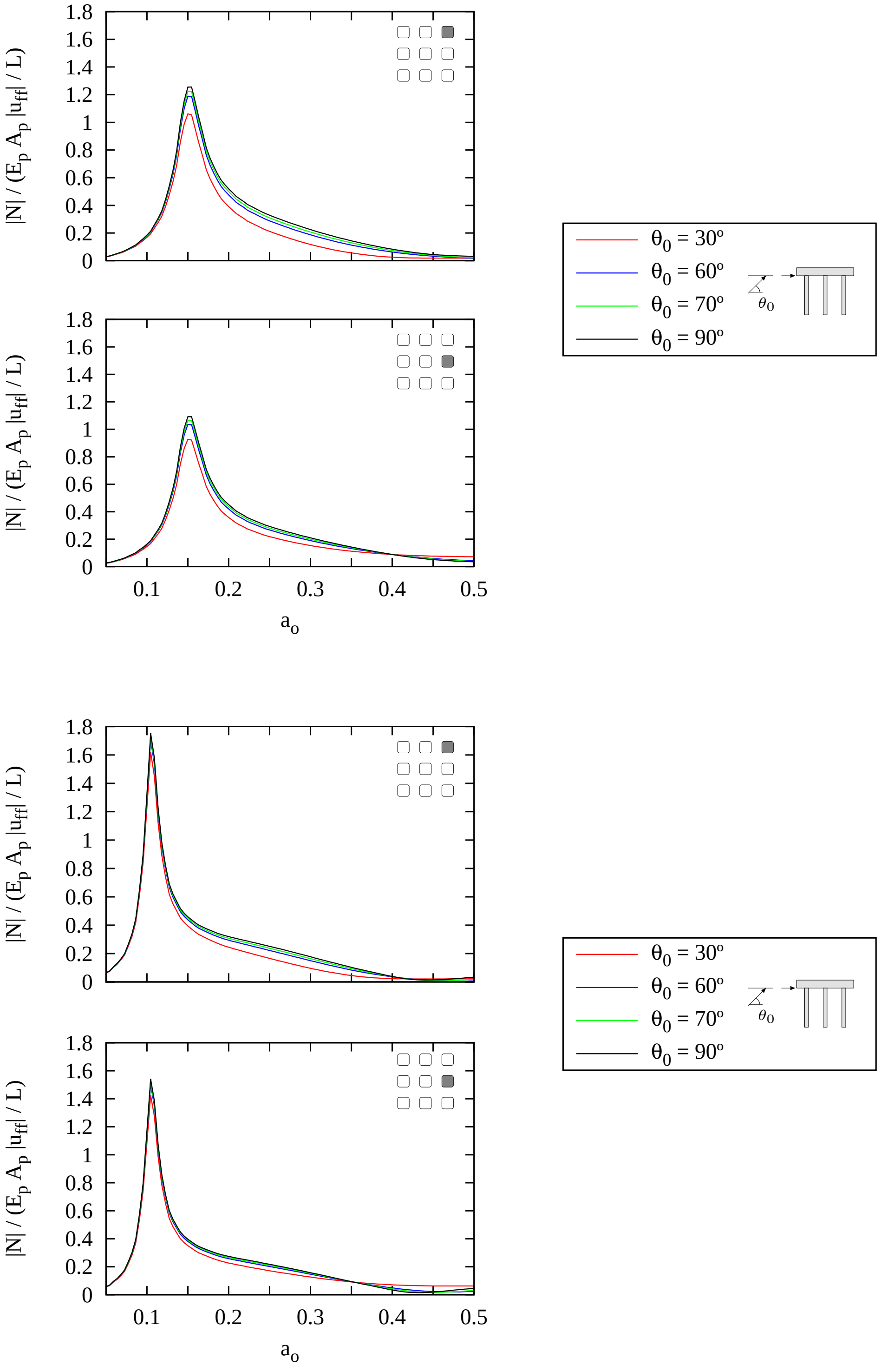

Figure 7: Axial forces at pile heads. Incident SH waves. Aspect ratios $h/b = 2$ (up) and $h/b = 4$ (down). Analysed pile of the group indicated by the sketch (central right and right top piles)

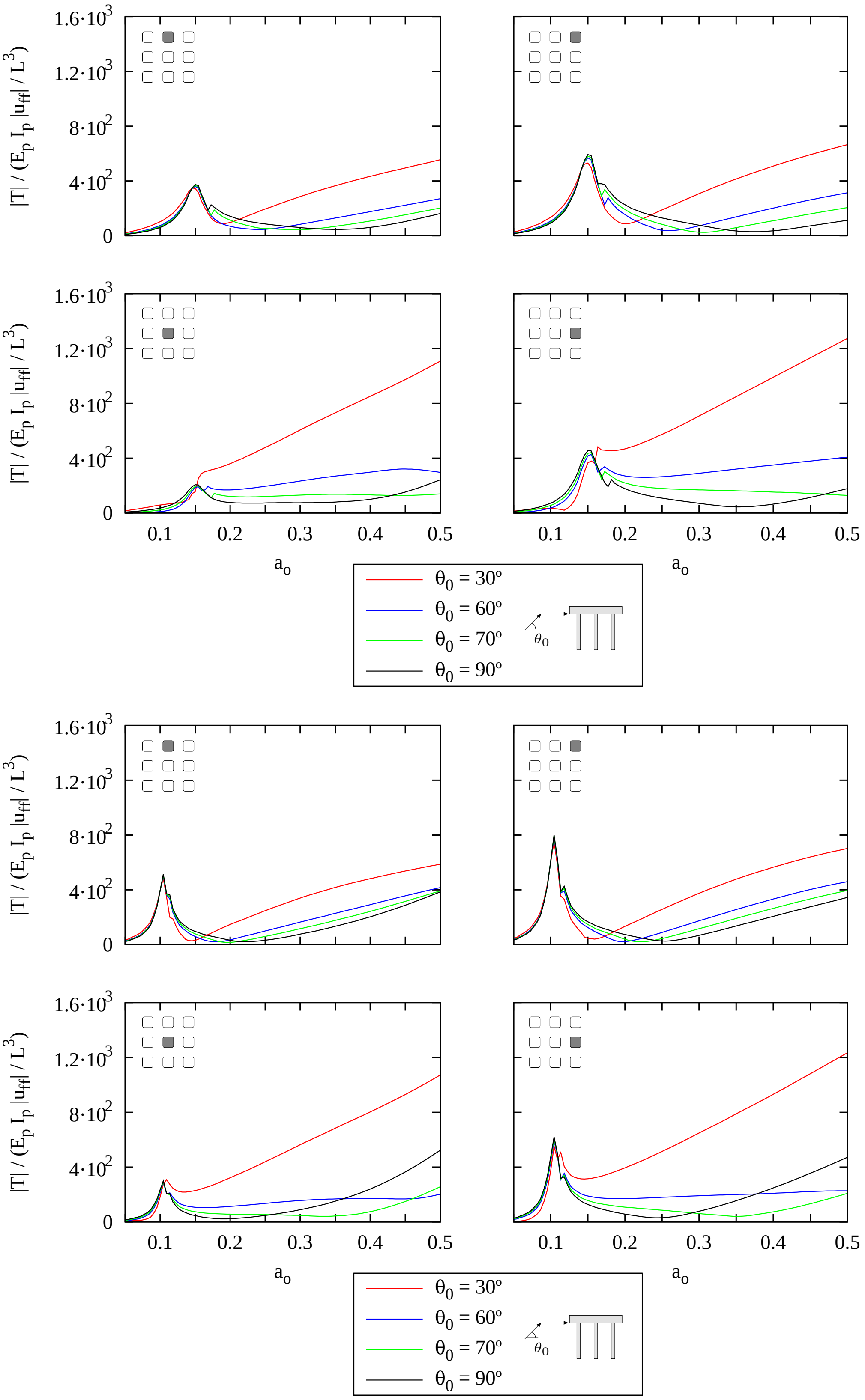

Figure 8: Shear forces at pile heads. Incident SH waves. Aspect ratios $h/b = 2$ (up) and $h/b = 4$ (down). Analysed pile of the group indicated by the sketch (central, central top, central right and right top piles)

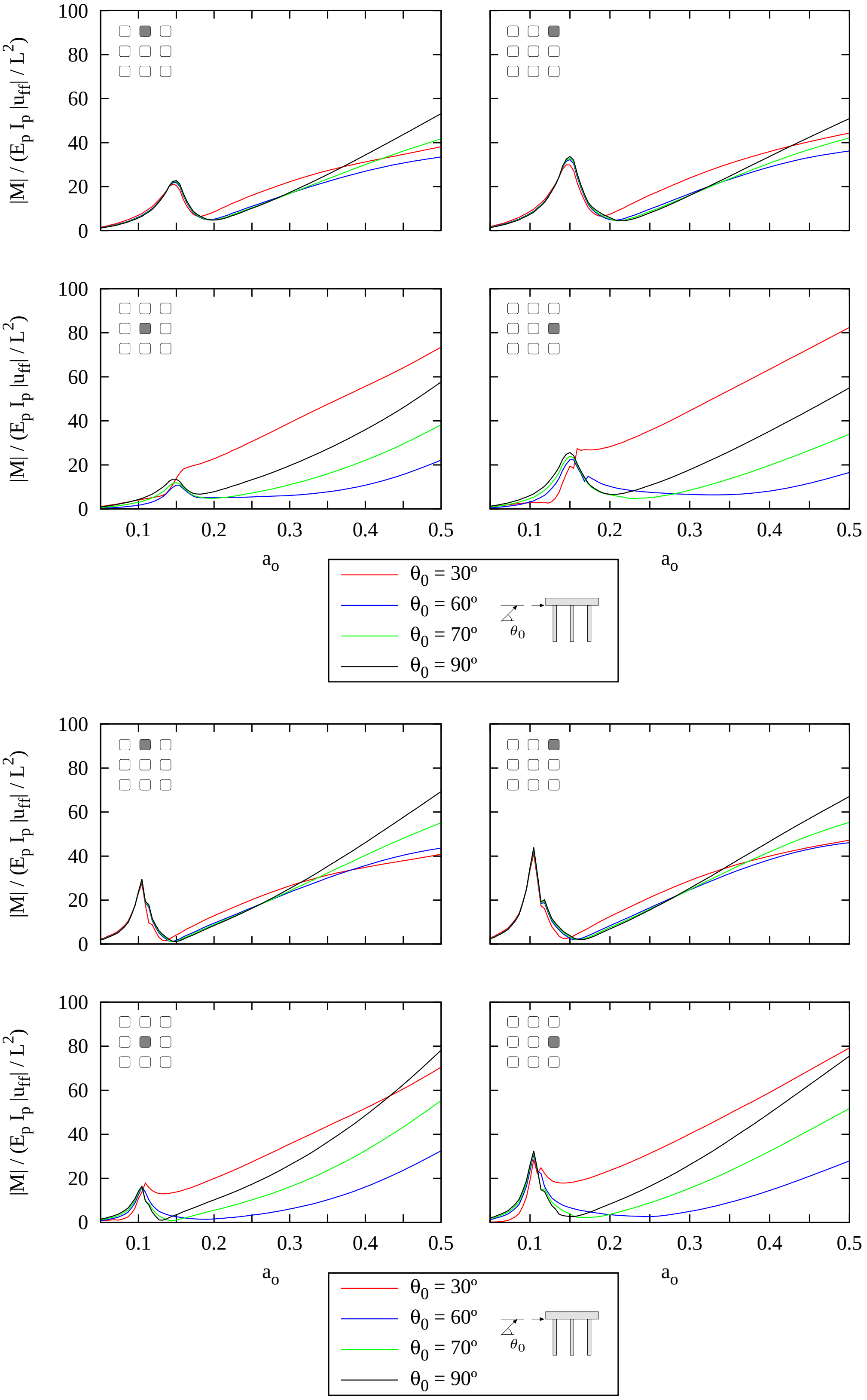

Figure 9: Bending moments at pile heads. Incident SH waves. Aspect ratios $h/b = 2$ (up) and $h/b = 4$ (down). Analysed pile of the group indicated by the sketch (central, central top, central right and right top piles)

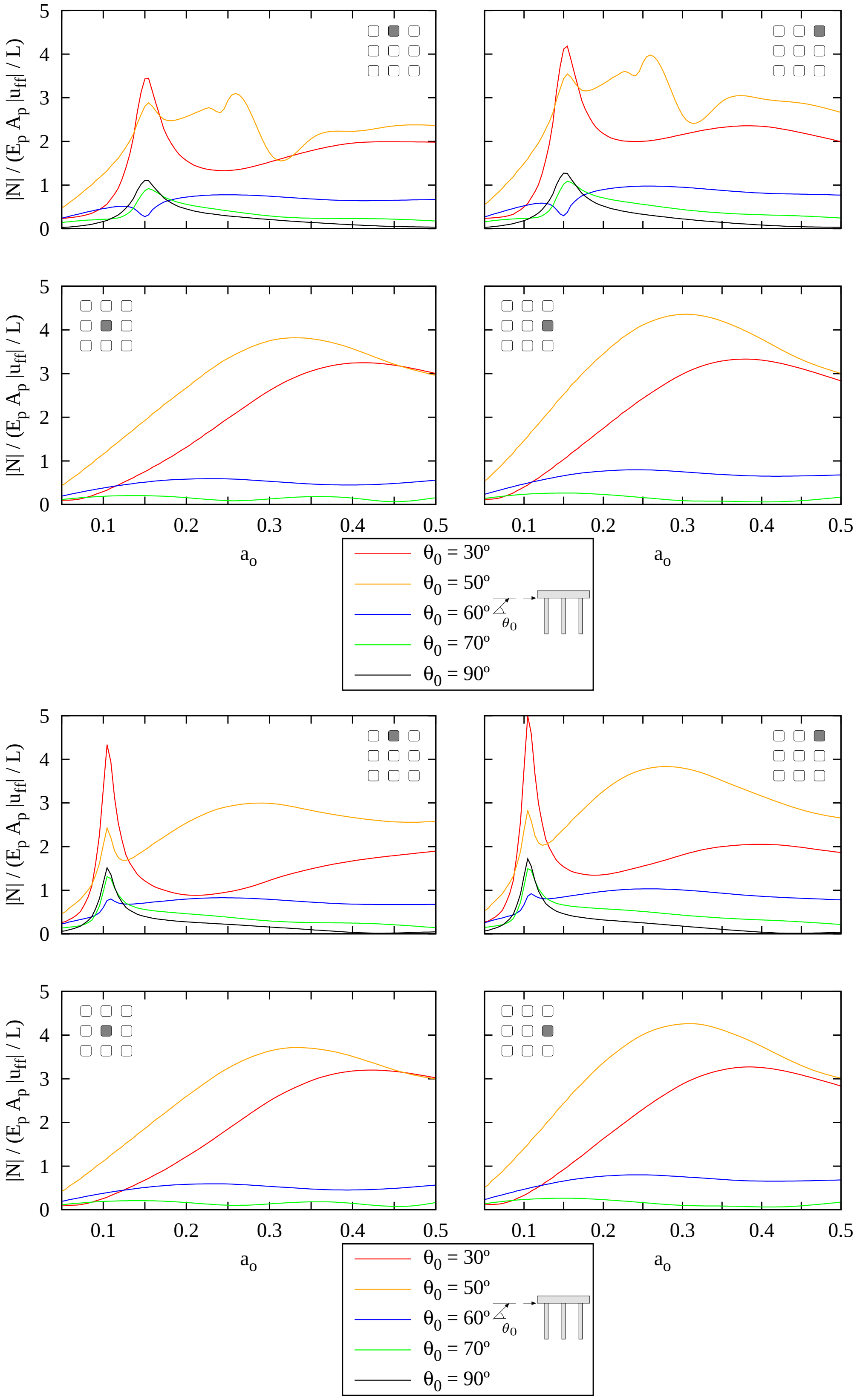

Figure 10: Axial forces at pile heads. Incident SV waves. Aspect ratios $h/b = 2$ (up) and $h/b = 4$ (down). Analysed pile of the group indicated by the sketch (central, central top, central right and right top piles)

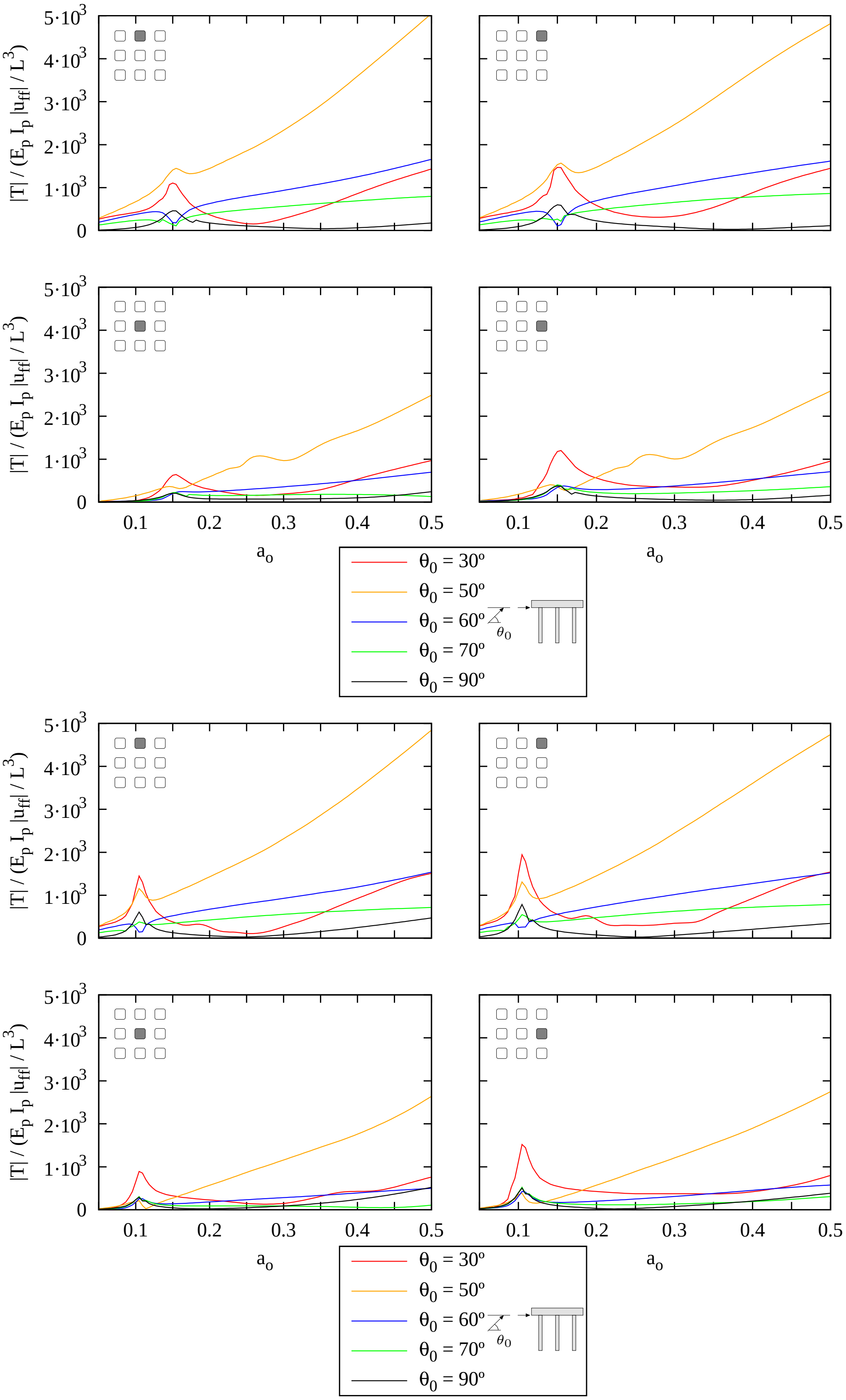

Figure 11: Shear forces at pile heads. Incident SV waves. Aspect ratios $h/b = 2$ (up) and $h/b = 4$ (down). Analysed pile of the group indicated by the sketch (central, central top, central right and right top piles)

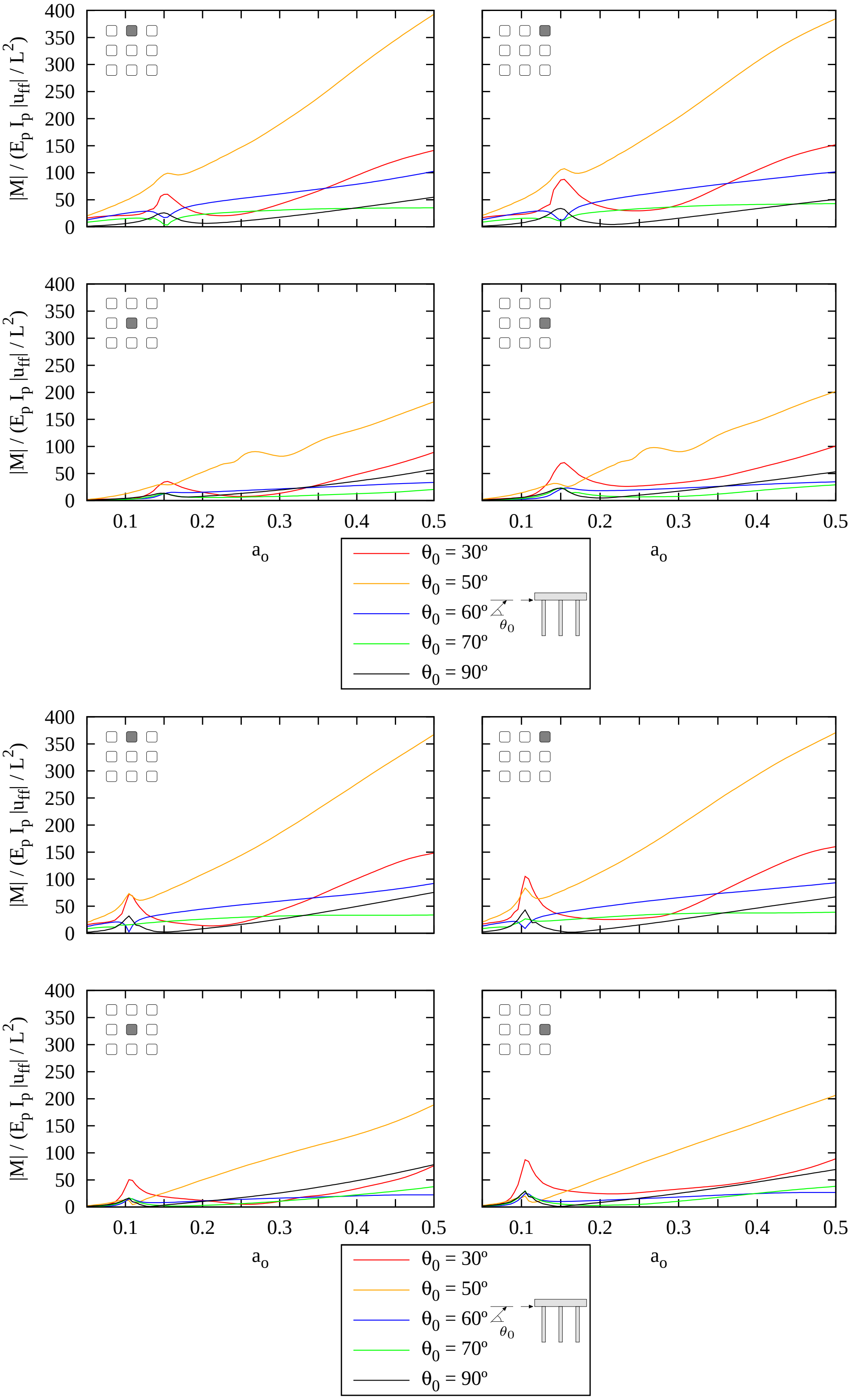

Figure 12: Bending moments at pile heads. Incident SV waves. Aspect ratios $h/b = 2$ (up) and $h/b = 4$ (down). Analysed pile of the group indicated by the sketch (central, central top, central right and right top piles)

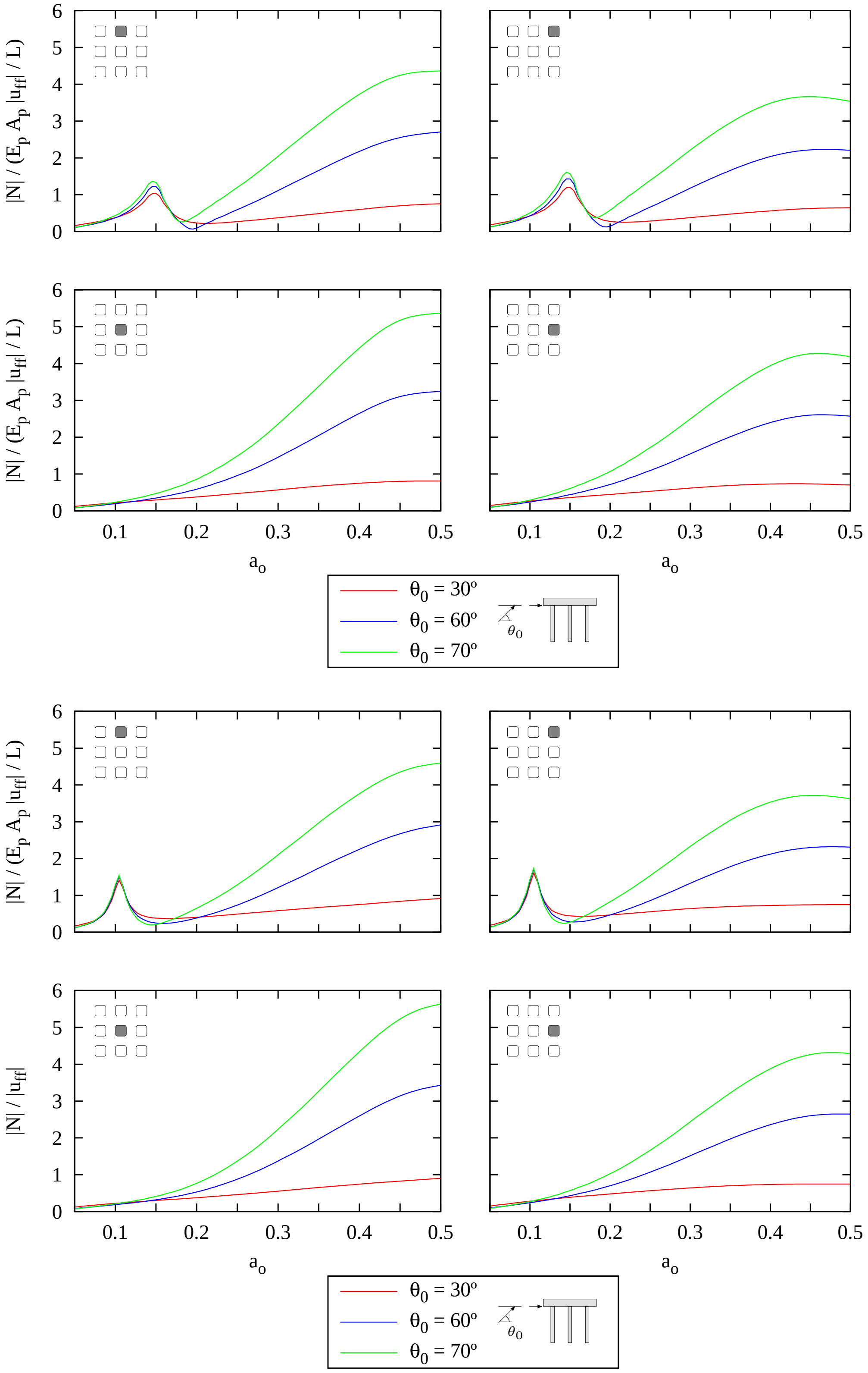

Figure 13: Axial forces at pile heads. Incident P waves. Aspect ratios $h/b = 2$ (up) and $h/b = 4$ (down). Analysed pile of the group indicated by the sketch (central, central top, central right and right top piles)

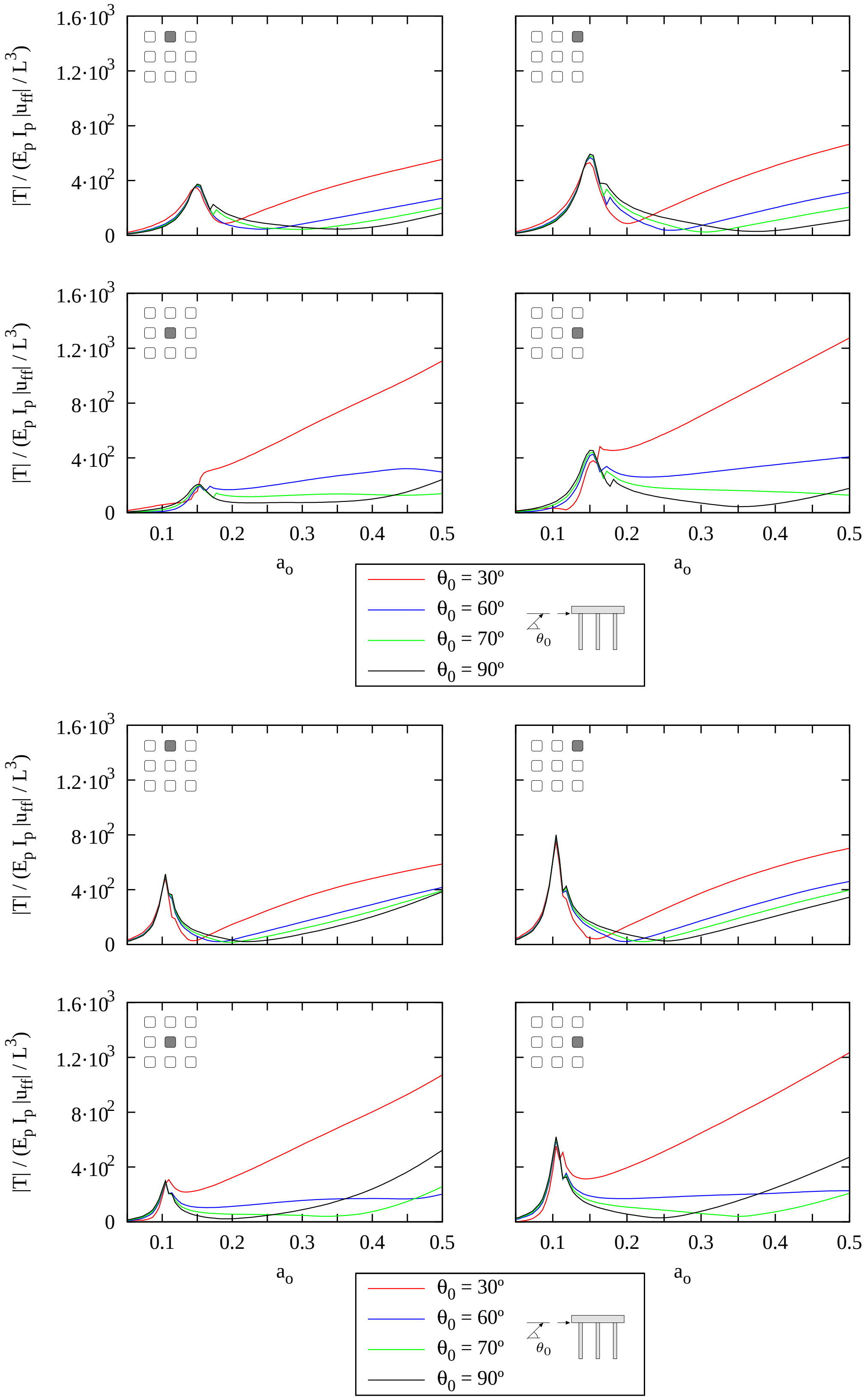

Figure 14: Shear forces at pile heads. Incident P waves. Aspect ratios $h/b = 2$ (up) and $h/b = 4$ (down). Analysed pile of the group indicated by the sketch (central, central top, central right and right top piles)

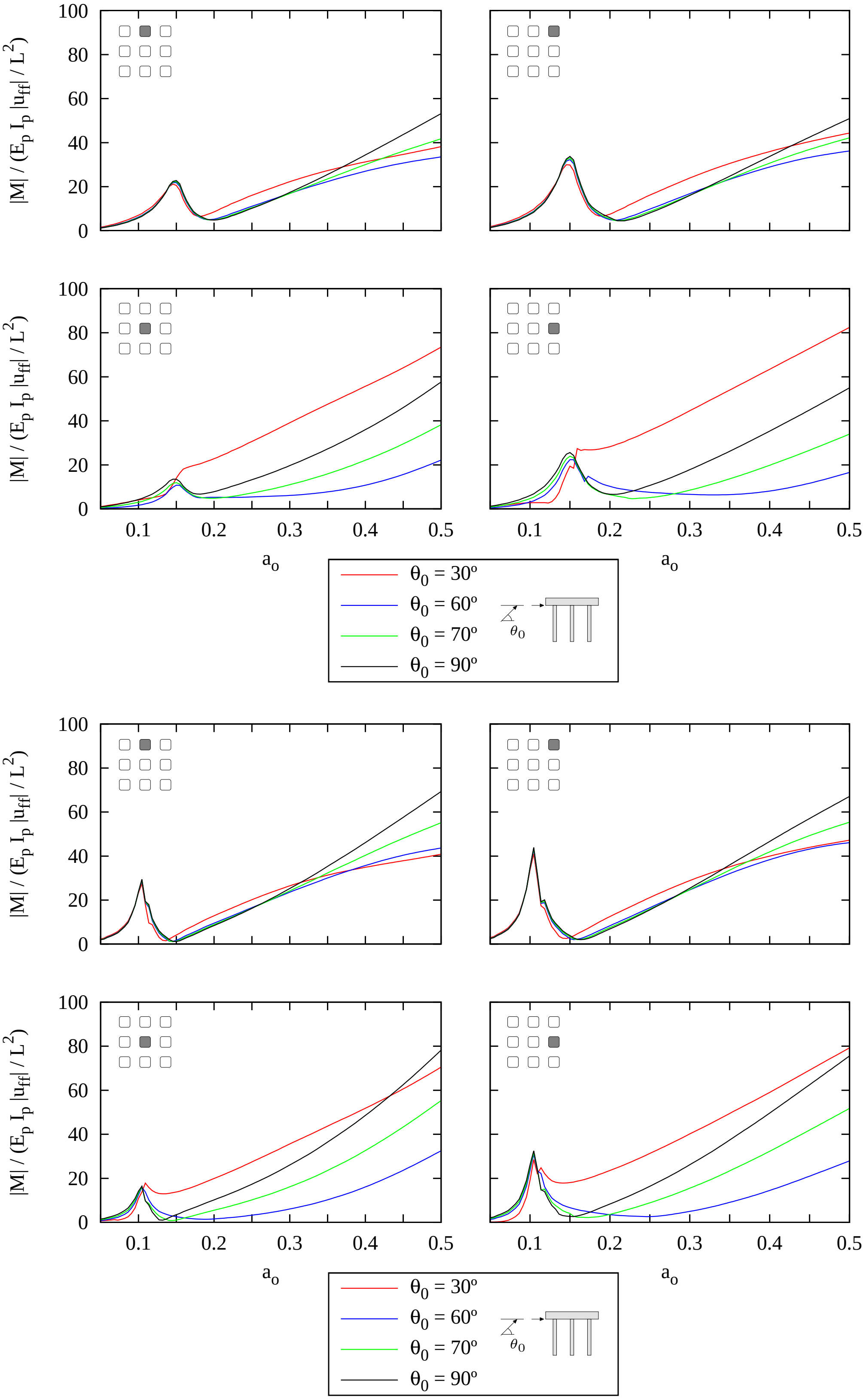

Figure 15: Bending moments at pile heads. Incident P waves. Aspect ratios $h/b = 2$ (up) and $h/b = 4$ (down). Analysed pile of the group indicated by the sketch (central, central top, central right and right top piles)

6 CONCLUSIONS

The influence of the type of wave and its angle of incidence on the dynamic response of pile foundations and superstructures has been studied throughout this work. To this end, the inter-storey drift amplitude and the internal efforts in piles of a piled building modelled as a single degree of freedom system are determined using a BEM-FEM approach. Results are presented in this work for three different incident volumetric waves (P, SH and SV) and two ratios between the height of the superstructure and half the width of the pile cap.

The angle of incidence has a strong influence on the behaviour of piled structures. This effect is particularly marked when the incident wave is an SV one. There exist great differences between the displacements and efforts arising from incident waves of the same amplitude but with angles slightly different from the critical angle. Then, the widely accepted hypothesis of vertical incidence of the waves does not have to necessarily be the most unfavorable situation from the point of view of both piled foundations or superstructures.

REFERENCES

[1] L.A. Padrón, J.J. Aznárez, O. Maeso, 3-D boundary element - finite element method for the dynamic analysis of piled buildings. *Engineering Analysis with Boundary Elements*, **35(3)**, 465–477, 2011.

[2] J. Domínguez, *Boundary elements in dynamics*. Computational Mechanics Publications & Elsevier Applied Science, Southampton, NY, 1993.

[3] O.C. Zienkiewicz, R.C. Taylor, *The finite element method, Vol. I, 4th Edition*. McGraw Hill, 1989.

[4] L.A. Padrón, *Numerical model for the dynamic analysis of pile foundations*. PhD. Thesis. University of Las Palmas de Gran Canaria. Available for download at: http://acceda.ulpgc.es/handle/10553/2841, 2009.

[5] J.D. Achembach, *Wave propagation in elastic solids*. North-Holland, Amsterdam. 1973.

[6] A.C. Eringen, E.S. Suhubi, *Elastodynamics, Vol. 2 – Linear Theory*. Academic Press, NY.

[7] A.M. Kaynia, M. Novak, Response of pile foundations to Rayleigh waves and obliquely incident body waves. *Earthquake Engineering and Structural Dynamics*, **21**, 303–318, 1992.

COMPDYN 2011
III ECCOMAS Thematic Conference on
Computational Methods in Structural Dynamics and Earthquake Engineering
M. Papadrakakis, M. Fragiadakis, V. Plevris (eds.)
Corfu, Greece, 25–28 May 2011

ON INTENSITY MEASURE SELECTION FOR NONLINEAR DYNAMIC ANALYSIS OF SOIL-MDOF STRUCTURE INTERACTING SYSTEMS

Abedi Nik Farhad[1], **Khoshnoudian Faramarz** [1]

[1] Department of Civil and Environmental Engineering, Tehran Polytechnic University, Iran

Farnikan@aut.ac.ir

Keywords: Soil-Structure Interaction, Intensity Measure, Ground Motion Scaling, Multi Degree of Freedom Structure

Abstract. *A major source of variability in seismic responses of structures arises from selecting the earthquake Intensity Measure (IM), for conducting nonlinear dynamic analysis, relative to the damaging effects of earthquakes on structures. In this paper, the capability of the six most common IMs on estimation of Engineering Demand Parameters (EDPs) of Soil-MDOF Structure Interacting (SMSI) systems is investigated. Two-dimensional structural models of 5, 10 and 20 stories shear buildings are studied, using elasto-plastic MDOF stick models, whereas the underlying soil is considered as a homogeneous elastic half space and is modeled using the cone model concept. Then, the systems are subjected to 60 representative ground motions. The analyses are done directly in time domain using direct step-by-step integration method. This paper attempts to elucidate the accuracy and efficiency of considered methods for the evaluation of EDPs, in SMSI systems, and to find the most effective IM. For this purpose, two criteria are examined: (a) the median of EDPs in comparison with the predicted values, obtained from regression analyses, and (b) coefficient of variations of EDPs. The results show that a suitable IM for an EDP may differ from one to another in terms of accuracy and efficiency. Finally, the appropriate IM is proposed for each of the considered EDPs.*

1 INTRODUCTION

The selection of the measure of ground motion intensity challenges researchers, since an appropriate intensity measure (IM), can significantly decrease the runtime of the estimation of engineering demand parameter (EDP). This may lead to more reliable evaluations of the seismic performance of the facilities. Researchers have suggested various measure of ground motion intensity. Shome et al. (1998) [1] recommended that scaling of ground motions to a given level of spectral ordinate at the fundamental period of vibration significantly decrease the variability in the maximum demand observed in the structural system. In another study, Cordova et al.(2000) [2] proposed an intensity measure that accounts for period softening to reduce variability at large levels of maximum interstory drift ratio, drift demands larger than 5%, for composite structures. Luco and Cornell (2001) [3] investigated the effects of six different intensity measures on the estimation of the maximum interstory drift ratio for moderate-to-long period buildings using the concepts of efficiency and sufficiency for an intensity measure. Baker and Cornell (2005) [4] proposed a vector IM containing two or three parameters as opposed to the scalar IMs that contain only a single parameter.

Almost all previous studies on IM selection have either dealt only with the response of fixed base SDOF or MDOF structures. The objective in this study is to evaluate six different measures of ground motion intensity using the results of response history analyses in the context of Soil-MDOF Structure Interaction (SMSI) problem. Two types of structural responses are investigated; maximum roof drift ratio (MRDR) and peak floor acceleration, (PFA), may occur anywhere in the height of structure.

2 SOIL-MDOF STRUCTURE NUMERICAL MODEL

As shown in Figure 1, the system under consideration consists of an N-story building and a foundation resting on a soil medium. The structure is modeled as a shear building with equivalent circular plan. Let $\mathrm{m_i}$, $\mathrm{I_i}$, $\mathrm{r_i}$ and $\mathrm{H_i}$ denote the mass, the mass moment of inertia around its geometric center, the radius of the equivalent circular plan and the height of the mass in the $\mathbf{i}^{th}$ story from the foundation surface, respectively.

This research assumes that the characteristics of all stories are the same. The foundation is treated as a circular rigid disk and the flexibility of the foundation is not taken into account. The mass and mass moment of inertia of foundation are expressed by $\mathrm{m_0}$ and $\mathrm{I_0}$, respectively. The mass of foundation is considered so that foundation uplift does not occur due to design earthquake load, and with considering the empirical relationship between the ratio of $\mathrm{m_0}$ and total mass of structure for typical buildings. In this case, $0.05 \leq (\mathrm{m_0}/\mathrm{M}) \leq 0.5$ is selected for the considered structures, where M is the total mass of the superstructure.

In order to model soil beneath the structure, a lumped-parameter model is adopted to represent the soil and the interaction mechanisms. The soil beneath the foundation is assumed a homogenous half-space and replaced by a simplified 3DOF system based on the concept of Cone Models. Cone model was proposed by Meek and Wolf (1993) [5] and Wolf (1994) [6] for evaluating the dynamic stiffness and the effective input motion of a foundation on the ground.

To consider the frequency dependency of the rotational spring and dashpot coefficients, the additional internal rotational degree of freedom θ, is assigned to a polar mass moment of inertia, $\mathrm{M_\theta}$, and connected to the foundation node using a rotational dashpot, with the high frequency limit of the radiation damping. For the motions in the case of nearly incompressible and incompressible soil, corresponding modifications are performed for the soil with Poisson’s ratio greater than 0.3, Wolf (2004) [7].

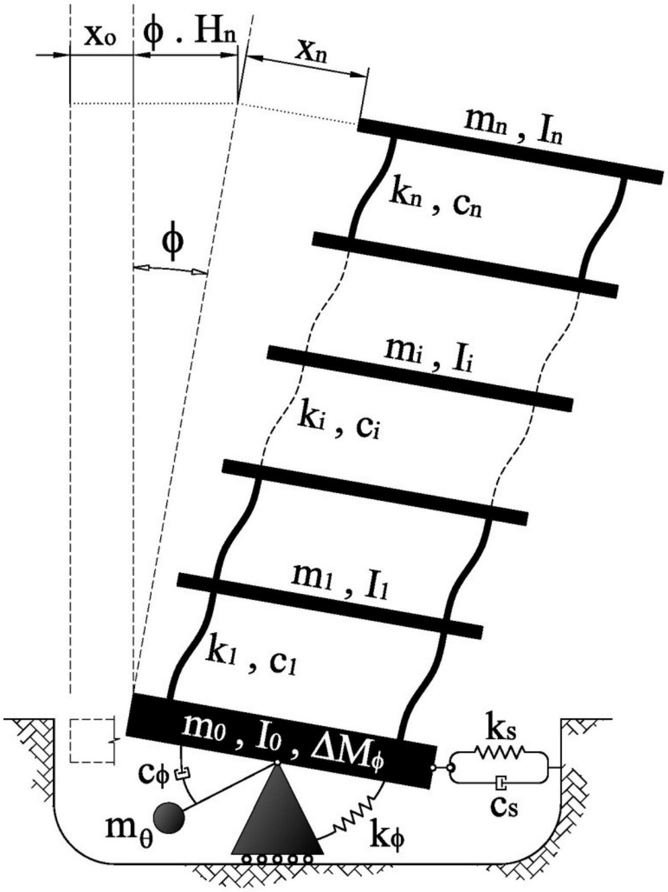

Figure 1: Soil-MDOF structure interacting system and displacement components

3 SOIL-MDOF STRUCTURE SYSTEMS CONSIDERED

Table 1 briefly summarizes the interacting system models evaluated in this paper. These specific three buildings are chosen to capture some variation in number of stories and first-mode period of system. The story shear force-interstory drift relationship is modeled by a normal bilinear hysteretic rule with 5% strain hardening ratio. All of the considered structures have the same value of aspect ratio, $\mathrm{H_n/r} = 3$, and viscous damping coefficient $\xi_{\mathrm{str}} = 5\%$.

For the superstructure, nonuniform distribution of lateral stiffness and yielding strength along the height of the structure are considered. For this purpose, the vertical distribution coefficient in accordance with ASCE7 (2010) [9] method is calculated. The yield strength of structure is determined in basis of the response modification coefficient and the overstrength factor equal to 8 and 2, respectively ($R = 8 \; and \; \Omega_0 = 2$).

In order to comparison of soil flexibility condition in the studied systems, dimensionless frequency parameter, $\mathrm{a_0}$, is introduced as an index for the Structure-to-Soil stiffness ratio:

$$\mathrm{a_0} = \frac{\omega_{\mathrm{fix}} \mathrm{H_n}}{\mathrm{V_s}} \tag{1}$$

Where, ω_{fix} is the circular frequency of the fixed base structure.

It should be noted that two different base fixity conditions are considered base on values of dimensionless frequency. $\mathrm{a_0} = 0$ and $\mathrm{a_0} = 3$ which are representative of the fixed base structure and predominant SSI effect, respectively.

Stories	Fundamental Period	
	Interacting System ($a_0 = 3$)	Fixed Base Structure ($a_0 = 0$)
5	0.75	0.55
10	1.20	0.90
20	2.00	1.50

Table 1: Period of systems in flexible and fixed base conditions

4 REGRESSION ANALYSIS AND POINT OF COMPARISON

To evaluate the prediction accuracy of the various IM methods, it may be helpful to establish an estimate of the true response limit. Because of uncertainty in knowledge of ground motion behavior, this prediction is termed the Point of Comparison (POC) [10].

In order to estimate the POC values of response parameters of interest (MRDR and PFA), a large number of SMSI systems analyses are performed. For this purpose, 60 representative ground motions are scaled by 16 incremental scale factor (a total of 5760 independent nonlinear analyses for SMSI systems) and MRDRs and PFAs are recorded for each analysis, along with spectral acceleration at periods of interest, $S_a(\beta_i T_1)$.

To create a predictive equation that relates the spectral accelerations to the observed structural response, regression analysis is used. For this study, the following functional form is selected to model the EDPs of interest.

$$\mathrm{Ln(EDP)} = a_0 + \sum_{i=1}^{11} \left[a_i \left(\mathrm{Ln}\, S_a(\beta_i T_1) \right) + b_i \left(\mathrm{Ln}\, S_a(\beta_i T_1) \right)^2 \right] \tag{2}$$

Where β_i coefficients are selected in eleven different levels to consider the spectral shape of each record, including $\beta = \{0, 0.1, 0.2, 0.4, 0.6, 0.8, 1.0, 1.5, 2.0, 2.5, 3.0\}$. Then, a_i and b_i coefficients are determined using least-squares regression.

The values of POC and coefficients of determination, R^2, of predictive equation obtained from this procedure are shown in Table 2. In general, the selected regression model has good predictive ability as indicated by its R^2 values greater than 90% in the most cases, which indicates that the predictive equation explains more than 90% of variance in $\mathrm{Ln(EDP)}$ observed in the raw data.

	MRDR		**PFA**	
Structure / System	**POC**	**R^2**	**POC**	**R^2**
5-Story / SSI	0.023	0.945	14.60	0.907
10-Story / SSI	0.016	0.921	17.96	0.903
20-Story / SSI	0.011	0.921	19.85	0.881
5-Story / Fixed	0.020	0.877	16.00	0.932
10-Story / Fixed	0.018	0.906	17.32	0.918
20-Story / Fixed	0.010	0.922	18.70	0.897

Table 2: Values of point of comparison and R^2 of predictive equation

5 EVALUATION OF INTENSITY MEASURE METHODS

The objective in this study is to evaluate capability of six common Intensity Measures (IMs) on estimation of EDPs of SMSI systems. As expressed in introduction, Maximum Roof Drift Ratio (MRDR) and peak floor acceleration (PFA), occurring anywhere in the structure, are the focuses on this current paper as EDPs.

Many different methods for scaling to specified severity are proposed in the literature. In this study, the following methods are explored:

IM-1: Scaling the ground motions to a constant peak ground acceleration, PGA.

$$\mathrm{IM}_1 = \mathrm{S_a}(\mathrm{T} = 0) \tag{3}$$

IM-2: Scaling the ground motions to the spectral acceleration measured at the fundamental period of vibration.

$$\mathrm{IM}_2 = \mathrm{S_a}(\mathrm{T}_1) \tag{4}$$

IM-3: Scaling the ground motions to a two-parameter intensity index proposed by Cordova et. al (2000) [2].

$$\mathrm{IM}_3 = \sqrt{\mathrm{S_a}(\mathrm{T}_1)\mathrm{S_a}(2\mathrm{T}_1)} \tag{5}$$

IM-4: Scaling the ground motions to the intensity measure proposed by Cornell and Luco (2001) [3], base on the ratio of inelastic spectral displacement to the corresponding elastic spectral displacement and participation factors.

$$\mathrm{IM}_4 = \frac{\mathrm{S_d^I}(\mathrm{T}_1, \xi_1, \mathrm{d_y})}{\mathrm{S_d}(\mathrm{T}_1, \xi_1)} \sqrt{\left[\mathrm{PF}_1^{[2]}\mathrm{S_d}(\mathrm{T}_1, \xi_1)\right]^2 + \left[\mathrm{PF}_2^{[2]}\mathrm{S_d}(\mathrm{T}_2, \xi_2)\right]^2} \tag{6}$$

IM-5: Scaling the ground motions to three-parameter intensity measure proposed by Vamvatsikos and Cornell (2005) [11].

$$\mathrm{IM}_5 = \sqrt[3]{\mathrm{S_a}(\tau_a)\mathrm{S_a}(\tau_b)\mathrm{S_a}(\tau_c)} \tag{7}$$

IM-6: Scaling the ground motions in accordance with the provisions of seismic codes such as NEHRP 2003 [12]. In this case, the ground motions are scaled such that for each period between $0.2\mathrm{T}_1$ and $1.5\mathrm{T}_1$ the avarega of the five-percent damped response spectra for the suit of ground motion is not less than the corresponding ordinate of the target response spectrum.

Where

T_1	:	Fundamental period of the Soil-MDOF Structure system
$\mathrm{S_d^I}(\mathrm{T}_1, \xi_1, \mathrm{d_y})$	:	The spectral displacement of an elastic-perfectly-plastic oscillator with period T_1, damping ratio ξ_1, and yield-displacement $\mathrm{d_y}$
$\mathrm{S_d}(\mathrm{T}_1, \xi_1)$	:	Elastic spectral displacement with period T_1 and damping ratio ξ_1
$\mathrm{PF}_1^{[2]}$	:	The first-mode participation factor for the story corresponding to the first-two-mode SRSS estimate of EDP.
τ_a, τ_b and τ_c	:	Arbitrary periods, which are selected in this research equal to T_2 , T_1 and $1.5\mathrm{T}_1$

More descriptions and information about the parameters used in the mentioned intensity measure can be reached in the relevant references.

The Maximum Considered Earthquake (MCE) spectrum, introduced in current building code provisions (ASCE 2010 [9]), is selected as target spectrum. For each of applied ground motion records, a scale factor is calculated so that the same values of intensity measure is obtained from target spectrum (MCE) and each of the individual ground motion response spectrum.

Three selected structures are analyzed using 60 ordinary ground motion records in the fixed and flexible base conditions. In each case, the quality of distribution of results, their averages and coefficient of variation (COV) are shown in Figure 2 to 4.

6 CONCLUSIONS

The objective of this study was to gain an insight on capability of the six different methods of scaling earthquake ground motions required for nonlinear dynamic analysis of MDOF structure in context of soil-structure interaction problem. For this purpose, two criteria are examined: (a) the mean value of EDPs in comparison with the predicted values, obtained from regression analyses, and (b) dispersion of the response. As shown in figure 2 and 4, the following conclusions can be drawn from the investigation of MRDR results:

- In most cases, with increasing number of stories, the dispersion of MRDR tendency to decrease and concentration of mean of results around POC values increases .In this regard, as indicated in figure 4, IM-3 and IM-5 indicate the lowest values of dispersion in comparison with other methods.
- IM-1 and IM-6 can lead to conservative mean for 5-story and all building considered in comparison with POC value, respectively. The values of COV are between about 50% and 65% for IM-1 and between about 30% and 70% for IM-6, in the considered systems, which may not be desirable.
- Mean of the results obtained through IM-4 represents the least values of response. Accordingly, IM-4 might be taken as an unsafe method in accordance with POC values.
- In comparison with the other methods, e.g. IM-2, 3 and 5, for the case of maximum roof drift ratio (MRDR), IM-3 may be better measure of intensity in terms of estimating the dispersion and mean of the responses, both at fixed and flexible base conditions.

As indicated in figure 3 and 4, for the case of PFA response, the conclusion may be summarized as follows:

- Except for IM-1, in the other cases, along with increasing number of stories, the dispersion of PFA is increasing.
- In general, for the case of the peak floor acceleration, PFA, the dispersion of results due to IM-1 has the lowest values. Therefore, PGA is the best measure of intensity in terms of estimating the dispersion and mean of the response, both at fixed and flexible base structures. Similar conclusion had been presented by Aslani and Miranda (2005) [13] for fixed base structures.

Finally, it can be noted that base on engineering demand parameter of interest, the type of the appropriate measure of ground motion intensity (IM) may be changed. It should be recall that the results presented here are based on a suite of soil-structure models and these models are by no means representative of all classes of systems in existence. It is believed that further work is needed to consider more different types of EDPs and IMs.

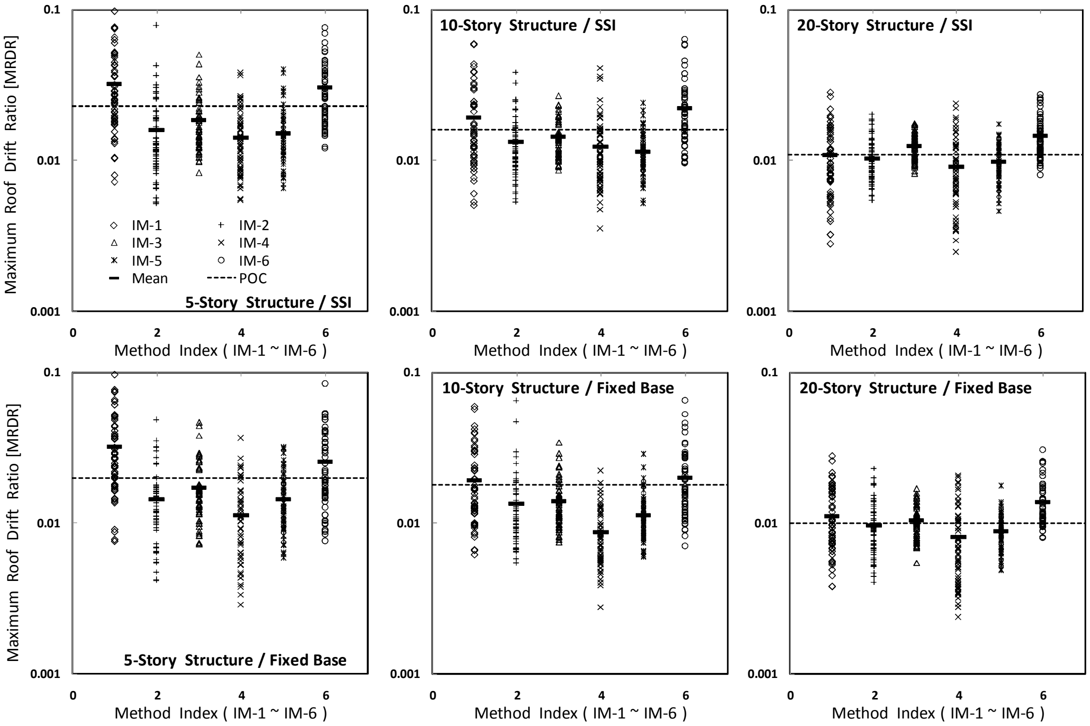

Figure 2: Comparison of Mean of MRDRs from different IM methods and POC values in fixed and flexible base conditions

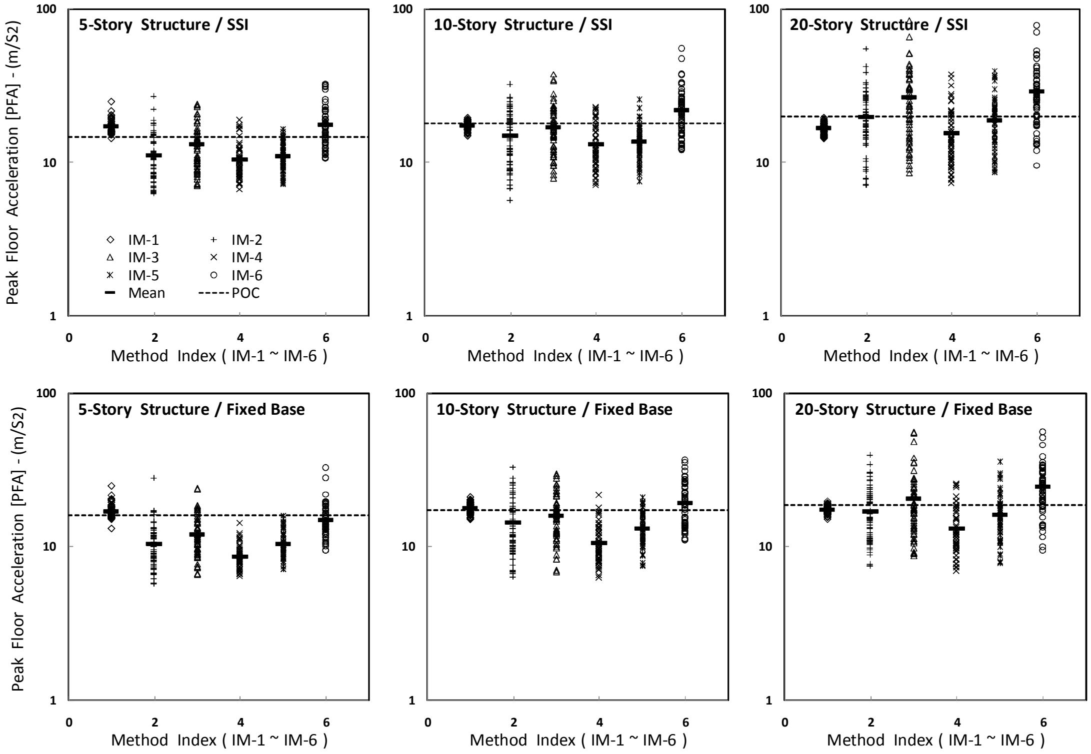

Figure 3: Comparison of Mean of PFAs from different IM methods and POC values in fixed and flexible base conditions

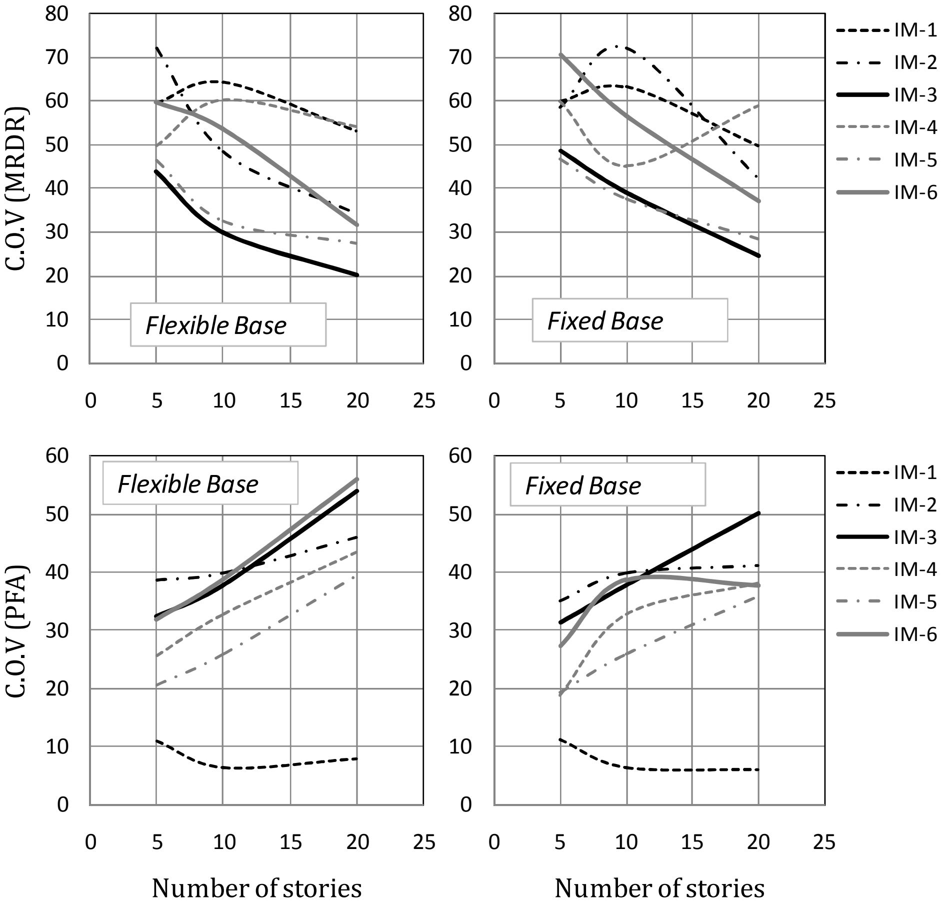

Figure 4: Comparison of COV (EDP) of different IM methods in flexible and fixed base conditions

REFERENCES

[1] Shome, N., C. A. Cornell, P. Bazzurro, and J. E. Carballo (1998). Earthquakes, records and nonlinear responses, *Earthquake Spectra* 14 (3), 469-500.

[2] Cordova P., Deierlein G., Mehanny S.F., Cornell C.A., 2000, Development of a Two-Parameter Seismic Intensity Measure and Probabilistic Assessment Procedure, *The second U.S.-Japan workshop on performance-based earthquake engineering methodology for reinforced concrete building structures, Hokkaido, Japan.*

[3] Luco N., Cornell C.A., 2001, Structure-Specific Scalar Intensity Measures for Near-Source and Ordinary Earthquake Ground Motions, *Submitted to Earthquake Spectra in April*, 2001.

[4] Baker, J.W., and Cornell, C.A. (2005). A vector-valued ground motion intensity measure consisting of spectral acceleration and epsilon. *Earthquake Engineering and Structural Dynamics*, 2005; 34:1193-1217.

[5] Meek W, Wolf JP. Why cone models can represent the elastic half-space. *Earthquake Engineering and Structural Dynamics* 1993; 22:759–771.

[6] Wolf JP. Foundation vibration analysis using simple physical models. *Englewood Cliffs (NJ): Prentice-Hall*; 1994.

[7] Wolf, J.P., Foundation Vibration Analysis: A Strength-of-Materials Approach, 2004

[8] Meek W, Wolf JP. Material Damping for Lumped-Parameter Models of Foundation. *Earthquake Engineering and Structural Dynamics* 1994; 23:349–362.

[9] ASCE/SEI 7-10, Minimum Design Loads for Buildings and Other Structures. *Published by American Society of Civil Engineeris.*

[10] Stewart P., Chiou J., Bray D., Graves R., Somerville P., 2001, Ground Motion Evaluation Procedures for Performance-Based Design , *PEER report 2001/09, Pacific Earthquake Engineering Research Center, College of Engineering, University of California, Berkeley.*

[11] Vamvatsikos D., Cornell C.A., 2005, SEISMIC PERFORMANCE, CAPACITY AND RELIABILITY OF STRUCTURES AS SEEN THROUGH INCREMENTAL DYNAMIC ANALYSIS, *the John A. Blume Earthquake Engineering Center, Department of Civil and Environmental Engineering, Stanford University, Report No. 151.*

[12] NEHRP (2003) Recommended Provisions for the Development of Seismic Regulations for New Buildings and Other Structures.

[13] Aslani H., Miranda E., 2005, PROBABILISTIC EARTHQUAKE LOSS ESTIMATION AND LOSS DISAGGREGATION IN BUILDINGS, *the John A. Blume Earthquake Engineering Center, Department of Civil and Environmental Engineering, Stanford University, Report No. 157.*

COMPDYN 2011
III ECCOMAS Thematic Conference on
Computational Methods in Structural Dynamics and Earthquake Engineering
M. Papadrakakis, M. Fragiadakis, V. Plevris (eds.)
Corfu, Greece, 25–28 May 2011

SEISMIC EVALUATION OF EXISTING BASEMENT WALLS

Alireza Ahmadnia, Mahdi Taiebat, W.D. Liam Finn, and Carlos E. Ventura

Department of Civil Engineering, University of British Columbia, Vancouver, BC, Canada
(ahmadnia, mtaiebat, finn, ventura)@civil.ubc.ca

Keywords: Basement wall, seismic, lateral earth pressure.

Abstract. *Structural and geotechnical engineers have long relied upon the use of the popular Mononobe-Okabe (M-O) method for determining seismic lateral pressures acting on retaining walls. This limit equilibrium-based method was originally developed for rigid retaining walls with sufficient rigid body displacements to mobilize the active wedge in the backfill soil. In reality, however, certain types of retaining walls, such as basement walls, have variable degrees of flexibility and deformation at different depths. Recently, the Structural Engineers Association of British Columbia (SEABC) initiated a task force to review the problem. The authors are members of this task force committee and have carried out series of dynamic numerical analyses to study lateral earth pressures against basement walls taking into account the flexibility and potential yielding of the wall components. This paper outlines a part of the findings in this study.*

1 INTRODUCTION

Basement walls constitute an integral part of tall buildings. These walls should be designed to resist the static and seismically induced lateral earth pressures. Since no guideline exists that specifically addresses seismic design of basement walls, designers use the Coulomb theory to find the static active lateral thrust from soil to the wall and the Mononobe and Okabe (M-O) method [1] to find the total (static and earthquake induced) active lateral thrust during seismic loading. Based on the Coulomb theory and the M-O method the active static and the total (static and earthquake induced) active lateral thrusts on a wall are given by $P_A = \gamma H^2 K_A / 2$ and $P_{AE} = \gamma H^2 K_{AE} / 2$, respectively, where P_A and P_{AE} are the active earth pressure coefficient without and with the earthquake effect, γ is the soil density, and H is the retaining wall height. For a straight wall with level backfill, K_A and K_{AE} are mainly functions of the friction angle of the soil and the angle of wall friction. The K_{AE} is also a function of the horizontal and vertical coefficients of Peak Ground Acceleration (PGA). These limit equilibrium-based methods were originally developed for rigid retaining walls with sufficient rigid body displacements to mobilize the active wedge in the backfill soil. Basement walls, on the other hand, have variable degrees of flexibility and deformation at different depths. The M-O method also assumes that the movement of basement wall will be sufficient to produce minimum active pressure. It also assumes that the soil behind the wall acts as a rigid body and does not account for flexibility of the soil-structure system. The M-O method only provides the total lateral earth pressure, P_{AE}. It does not explicitly indicate anything about the distribution of lateral earth pressure from seismic events. Several studies have been conducted for investigating the distribution of the lateral earth pressures and the point of application of the resultant lateral forces, depending on the mode of deformation of the wall (e.g., see [2–4]).

The current state of practice for design of basement walls is using the Coulomb theory and the M-O method for finding the static and total lateral thrusts, P_A and P_{AE}. It is also the current state of practice to use the PGA for application of the M-O method in the basement wall problems. In this method the soil is assumed to behave as a rigid mass and consequently the inertial force is equally distributed throughout the soil mass. However, wave scattering analyses by Segrestin and Bastick [5] show that for walls in excess of 20 or 30 ft, it is more justified to use an equivalent seismic coefficient. AASHTO LRFD Bridge Design Specification [6] provides a useful guideline for the conventional gravity and semi-gravity cantilever walls, non-gravity walls, and anchor walls. The guideline suggests the use of M-O method to estimate equivalent static force for gravity walls. However for non-gravity walls the guideline is not explicit and suggests the use of the M-O method with a factor for adjusting the PGA as a function of the wall height. For finding the distribution of the total lateral thrust, the P_A is distributed linearly along the wall height as a triangle with zero pressure at the surface and a pressure equivalent to $\gamma H K_A$ at the base. The total active thrust can be divided into the static component, P_A, and a dynamic component $\Delta P_{AE} = P_{AE} - P_A$. It is the current state of practice to distribute the dynamic component ΔP_{AE} as an inverse triangle along the height of the wall with zero pressure at the base of the wall and a pressure equivalent to $\gamma H(K_{AE} - K_A)$ at the ground surface. This distribution of lateral earth pressures is then used for finding the resulting moments in the walls and eventually simplified design of the walls.

The seismic hazard level in the 1995 edition of the National Building Code of Canada [7] for design of buildings had a probability of exceedance of 10% in 50 years. The related PGA hazard under NBCC1995 is 0.24g for Vancouver area. The designers were using the M-O method, as explained above, with this PGA for estimating the seismic lateral pressures and eventually designing the basement walls. The 2005 edition of the National Building Code of Canada [8] suggest a higher seismic hazard level for design of buildings that is probability of exceedance of 2% in 50 years. For Vancouver, the related PGA hazard under NBCC2005 is as big as 0.46g. Using the M-O method with this high PGA results in a high demand in designing the basement walls and this has raised some concerns for the design engineers on the applicability of the M-O method for the basement walls.

Recently, the Structural Engineers Association of British Columbia (SEABC) initiated a task force to review the problem. The authors are members of this task force committee and have carried out series of dynamic numerical analyses that take into account the flexibility and potential yielding of the wall components, as an effective procedure to study the lateral earth pressures against basement walls. To this end a specific type of wall, designed by the structural engineers using the current state of practice to withstand a seismic event in Vancouver with 10% probability of exceedance in 50 years, has been numerically analyzed in this study. Performance of this wall has been studied for three seismic events with 2% probability of occurrence in 50 years in Vancouver, a higher seismic demand enforced by the NBCC2005. In addition, the dynamic analysis results are compared to the standard methods of determining lateral earth pressures on the wall. The results to date indicate that flexibility of the walls has important effects on the distribution of the seismic lateral pressures on the walls. This paper outlines a part of the findings in this study.

2 PROPERTIES OF WALL

A specific basement wall designed by the structural engineers for this study based on the current state of practice, as explained in the previous section. A PGA of 0.24g was used in M-O equation for design of the wall. This corresponds to a probability of exceedance of 10% in 50 years (NBCC1995), although the current PGA for design is 0.46g (NBCC 2005).

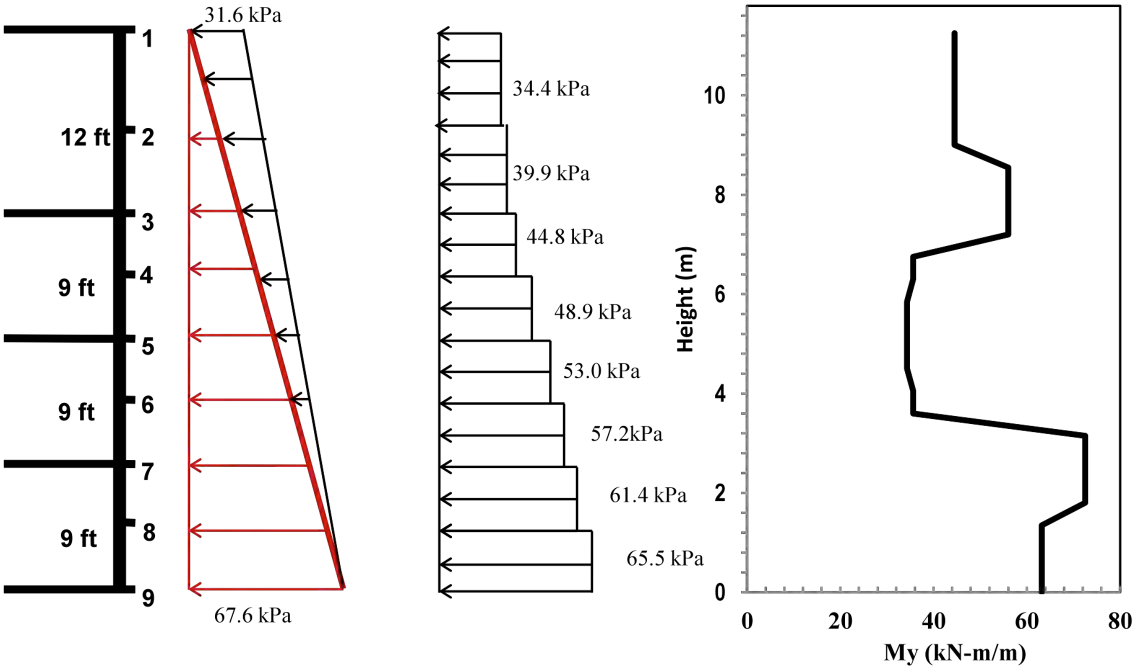

(a) (b)

Figure 1: (a) Distribution of the design lateral pressure along the height of the wall for based on the current state of practice for a seismic event with PGA=0.24g and a backfill soil with friction angle of 33°; (b) Resulting designed moment resistance distribution along the height of the wall.

The structural engineers were interested in how the basement wall designs based on the 1995 standard would behave under the 2005 loading. Figure 1(a) depicts the design lateral earth pressure distribution for the basement wall for a friction angle of 33 degrees and seismic coefficient of PGA=0.24g. The required moment resistance of the wall is the calculated along its height, as shown in Fig. 1(b), based the distributed pressures on the wall. In this design the structural engineer has not used any load reduction factor or ductility factor for the applied pressures on the wall. Uniform properties of I= 0.0013 m^4, A=0.25 m^2, and E=2.74×10^7 kN/m^2 are considered along the height of the basement wall.

3 DESCRIPTION OF THE MODEL

3.1 Model building

Non-linear seismic response of the basement wall is analyzed by using the two-dimensional finite difference computer program FLAC 6.00 [9]. Different stages of the modeling procedure are presented in Fig. 2. In order to ensure the proper initial stress distribution on the basement the actual construction sequence is modeled. First, a 24.3 m deep and 150 m wide layer of soil is created and brought to equilibrium under gravity forces. The model consists of two soil layers that will be discussed further in the next section. A part of the upper soil layer is then excavated in lifts to a depth of 11.7 m and a width 30m as shown in Fig. 2(a). As each lift was excavated, lateral pressures (shoring) are applied to retain the soil. Then as depicted in Fig. 2(b) the basement wall is constructed and global equilibrium is re-established. In the next stage, as shown in Fig. 2(c), the shoring pressures are removed, and load from the soil is transferred to the basement wall. The flexural behavior of the walls is modeled by elastic-perfectly plastic beam model with yield moments equal to the corresponding moment resistance values as shown in Fig. 1(b).

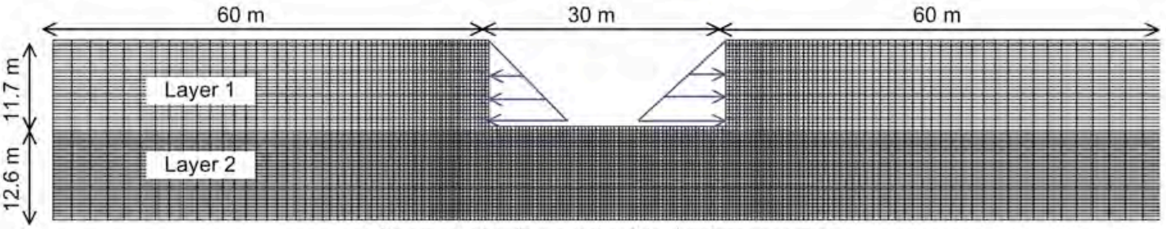

a) Excavated soil model with shoring pressures

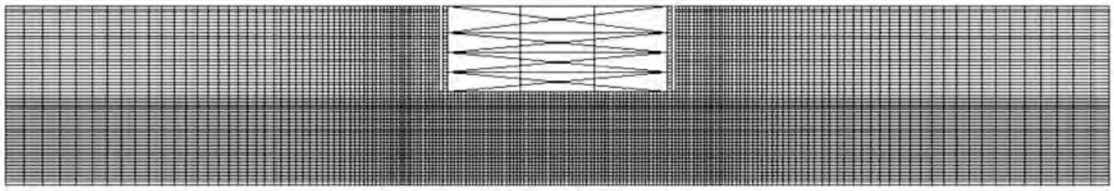

b) Construction of basement walls

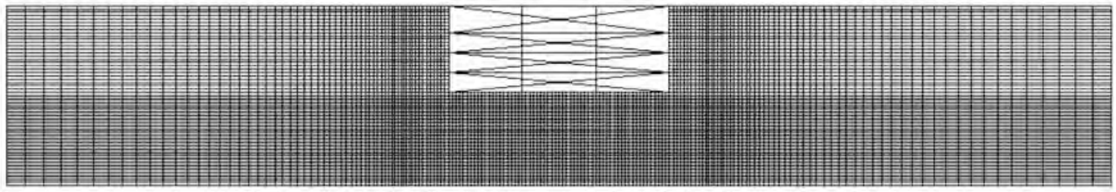

c) Removing shoring pressures, and applying the earthquake

Figure 2: Different stages of modeling procedure in FLAC.

3.2 Properties of soil

Constitutive response of the soil is modeled by a Mohr-Coulomb material model. The required model parameters are elastic bulk and shear moduli, cohesion, and friction and dilation angles of soil. The properties used in conjunction with the Mohr-Coulomb model for layers 1 and 2 of soil, as depicted in Figure 1, are presented in Table 1. Based on the results of a Shake analysis [10] for the present soil profile, the selected ground motions in this study, and a representative modulus reduction curve for the soil, an equivalent shear modulus equal to 30% of elastic shear modulus, i.e. G=0.3 G_{max}, was adopted for analysis.

Soil layer	Density (kg/m^3)	Bulk modulus (kPa)	G_{max} (kPa)	G/G_{max}	Cohesion (kPa)	Friction angle (degrees)	Dilations angle (degrees)
1	1950	1×10^5	5×10^4	0.3	0	33	0
2	1950	1×10^5	5×10^4	0.3	20	40	0

Table 1: Example of the construction of one table.

3.3 Ground motions

Ground motions for the analyses are selected from Pacific Earthquake Engineering Research (PEER) strong ground motion database. Based on the results of de-aggregation of the NBCC Uniform Hazard Spectrum (UHS), site class C for Vancouver, candidate input motions are selected in the magnitude range M=6.5–7.5 and the distance range 10–30 km using the program Design Ground Motion Library, DGML [11]. Table 2 shows the list of three ground motions selected for this study.

Ground motion	NGA #	Event	Year	Station	Magnitude
G1	162	Imperial Valley	1979	Calexico Fire	6.53
G2	987	Northridge	1994	LA-Centinela	6.69
G3	778	Loma Prieta	1989	Hollister	6.93

Table 2: List of selected ground motions.

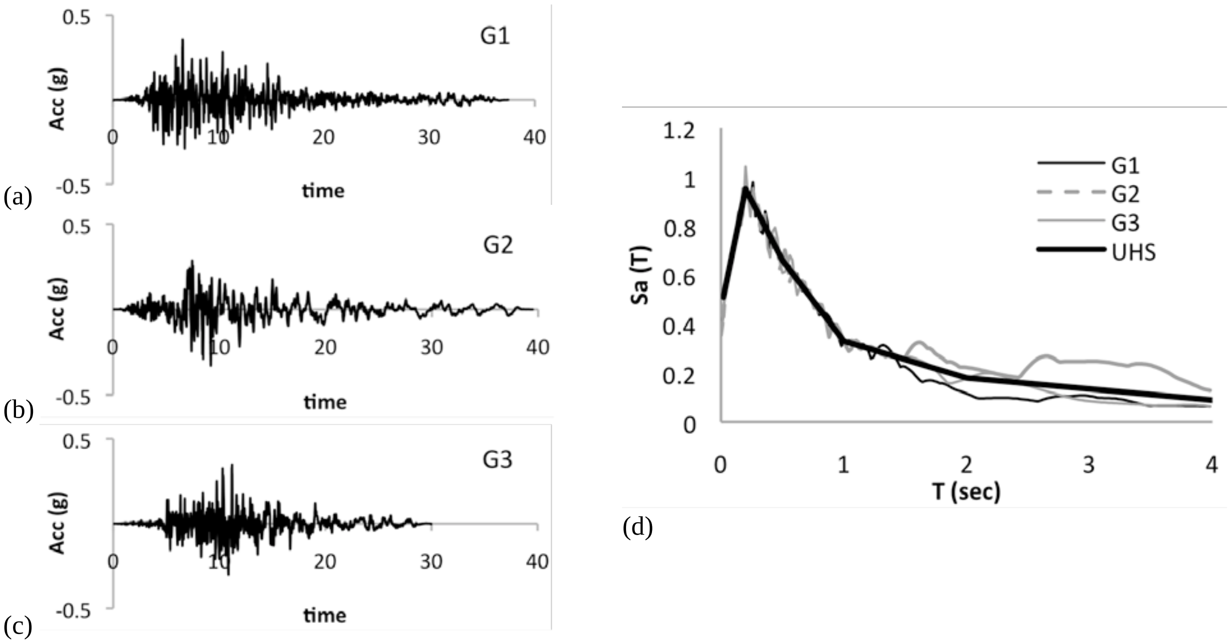

Figure 3: Time histories (a–c) and response spectra (d) of ground motions G1–G3 spectrally matched to UHS in periods 0.02–1.7 sec.

The selected ground motions are linearly scaled to match UHS using the computer program DGML and then spectrally matched to UHS in the period range of 0.02–1.7 sec, as shown in Fig. 3, using computer program SeismoMatch [12]. Figures 3(a-c) show the acceleration time histories of the three spectrally match ground motions and Fig. 3(d) shows the resulting response spectra compared to the UHS.

4 RESULT OF ANALYSIS

Numerical studies are conducted to evaluate the seismic response of basement walls which were designed for a PGA=0.24g that corresponds to a probability of exceedance of 10% in 50 years. The main seismic response parameters of the conducted analyses are: (a) the magnitude and distribution of lateral earth pressures, (b) the resultant lateral forces and the corresponding centers of application of the resultant force, (c) the basement wall bending moment and shear envelopes, and (d) the basement wall deflection envelopes, residual deflections, and drift ratio envelopes. These results are presented and discussed in this section.

Figure 4 shows lateral earth pressure time histories at three different levels along the height of the basement wall due to earthquake G1. The larger amount of stress produced at point 3 is due the existence of the basement floor at this level. In each one of these three elevations the initial static lateral pressures (before the earthquake) are lower than the residual static lateral pressure (after the earthquake).

The resultant lateral earth force at each time is obtained by integrating the lateral stresses along the height of the basement wall at that time. In addition, the moment arm at each time is calculated to track the center of application of the resultant force. The values of the resultant lateral earth force and its center of application are calculated for each time to generate the corresponding time histories for these two quantities during the dynamic simulation.

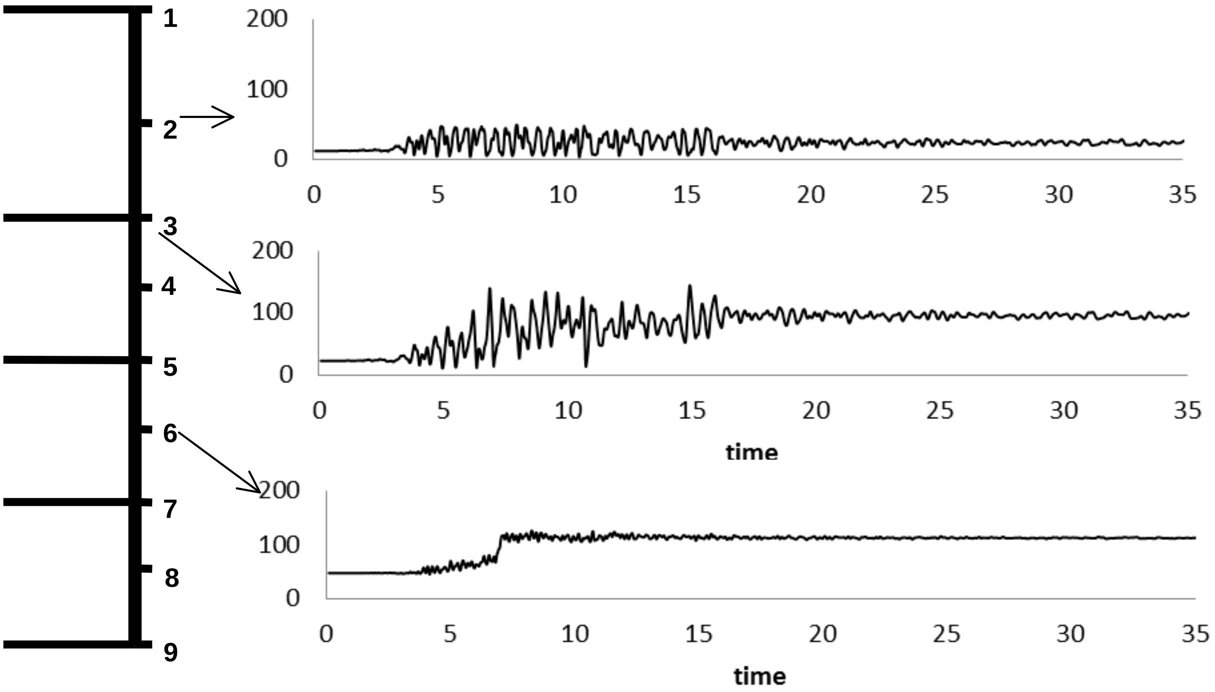

Figure 4: Numerical results of the lateral earth pressure time histories at different locations along the wall under ground motion G1.

Figure 5 shows the time histories of the resultant lateral earth force and the distance of its center of application from the base of the wall normalized with respect to the wall height (*H*) for three earthquakes. The corresponding results of a simplified method currently used in practice are also shown in this figure for comparison. In the simplified method, the resultant force (P_{AE}) is obtained by the M-O equation based on a design PGA level and the center of application of the resultant force is calculated assuming that the resulting ΔP_{AE} is applied approximately at a distance of 0.6H from the base of the wall. The simplified method is used for the hazard levels of PGA=0.24g (NBCC 1995), for which this wall is designed, and also for PGA=0.46g (NBCC 2005) which corresponds to the UHS that is used for spectral matching of the selected three ground motions in this study. Figures 5(a,c,e) show that the M-O method with PGA=0.46g reasonably predicts the maximum resultant force on the basement wall. Figures 5(b,d,f) show that with PGA=0.46g the simplified method for calculation of the center of application of the results force slightly over-predicts the elevation of the application center of the resultant lateral earth force on the wall at the instance of the maximum resultant force.

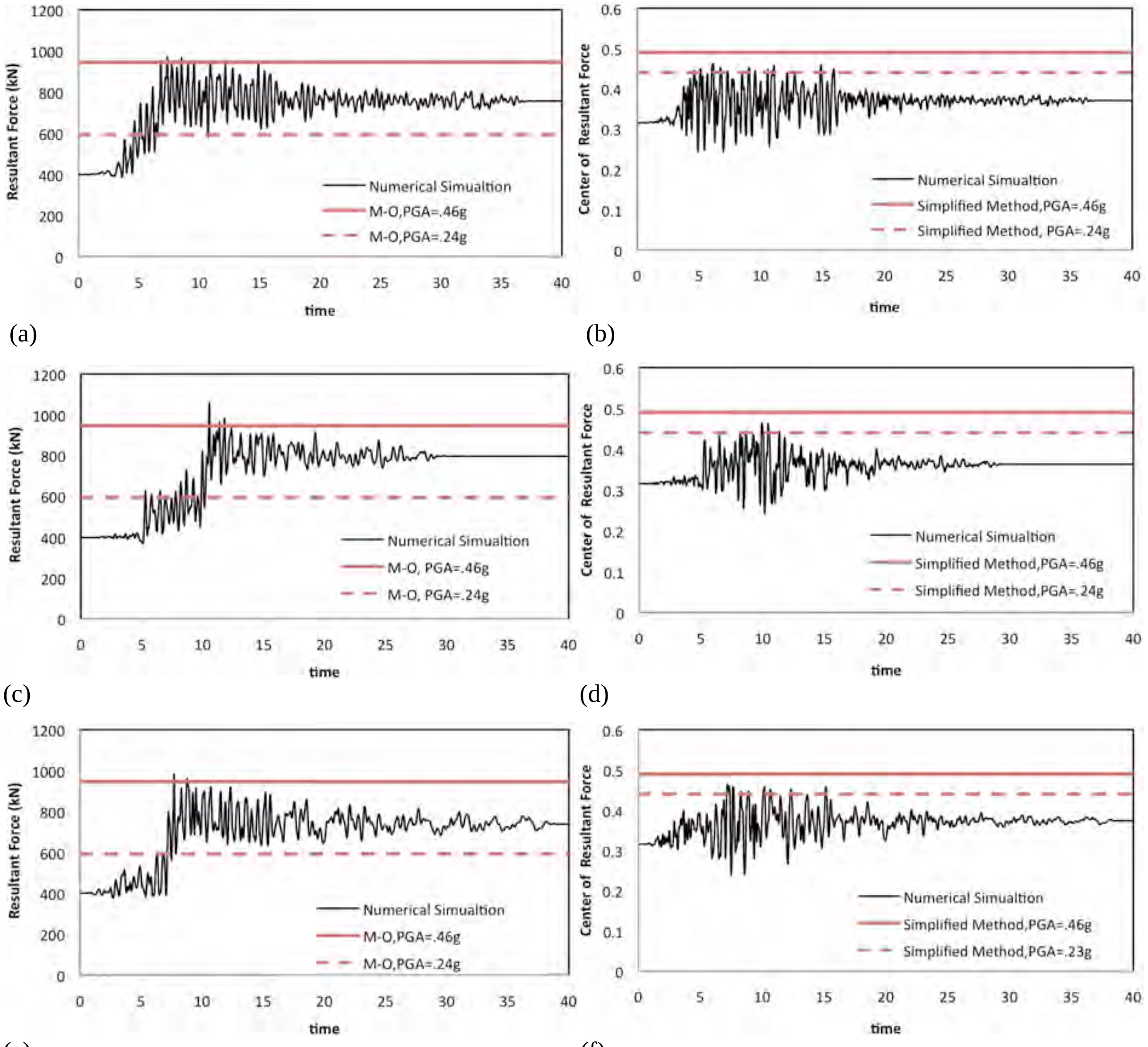

(a) (b)

(c) (d)

(e) (f)

Figure 5: Time histories of the resultant lateral earth forces and the normalized center of the resultant forces for ground motions G1 (a,b), G2 (c,d), and G3 (e,f).

The dashed lines that correspond to the simplified method using PGA=0.24g are presented in Fig. 5 only as baselines for comparison.

Snapshots of the computed lateral earth pressure distribution along the height of the basement wall at different times are shown in Fig. 6. The results are for the analysis with ground motion G1. The results of numerical analysis are presented at four different times during the analysis. Figure 6(a) shows the analysis results at the beginning of dynamic analysis (symbols) and compares those to the suggested distribution of lateral pressures from Coulomb's theory (solid red line). The numerical analysis results at t=0 sec adequately match to those obtained from the Coulomb's theory for static lateral earth pressure distribution. Figures 6(b) and 6(c) present the numerical analysis results at t=7.7sec (the instance of occurrence of maximum lateral earth force on the wall) and t=10 sec (an arbitrary time during the shaking phase). These figures also show the suggested results from the simplified design procedure. By comparing the lateral earth pressures at t=7.7 sec or t=10 sec with the suggested distribution of the simplified method, it is evident that the simplified method cannot predict the lateral earth pressure adequately. The simplified method underestimates the lateral earth pressures at each floor slab level. In addition, for the most of the basement stories in this example, the simplified method overestimates the lateral earth pressures on the walls in between the floor slab levels. In other words, the numerical simulation results indicate that the lateral earth pressures are higher at the proximities of the floor slab locations (due to higher lateral stiffness of the floor slabs) and are lower on the mid height of the walls in between different floor levels (due to higher lateral stiffness of the walls compared to the slabs).

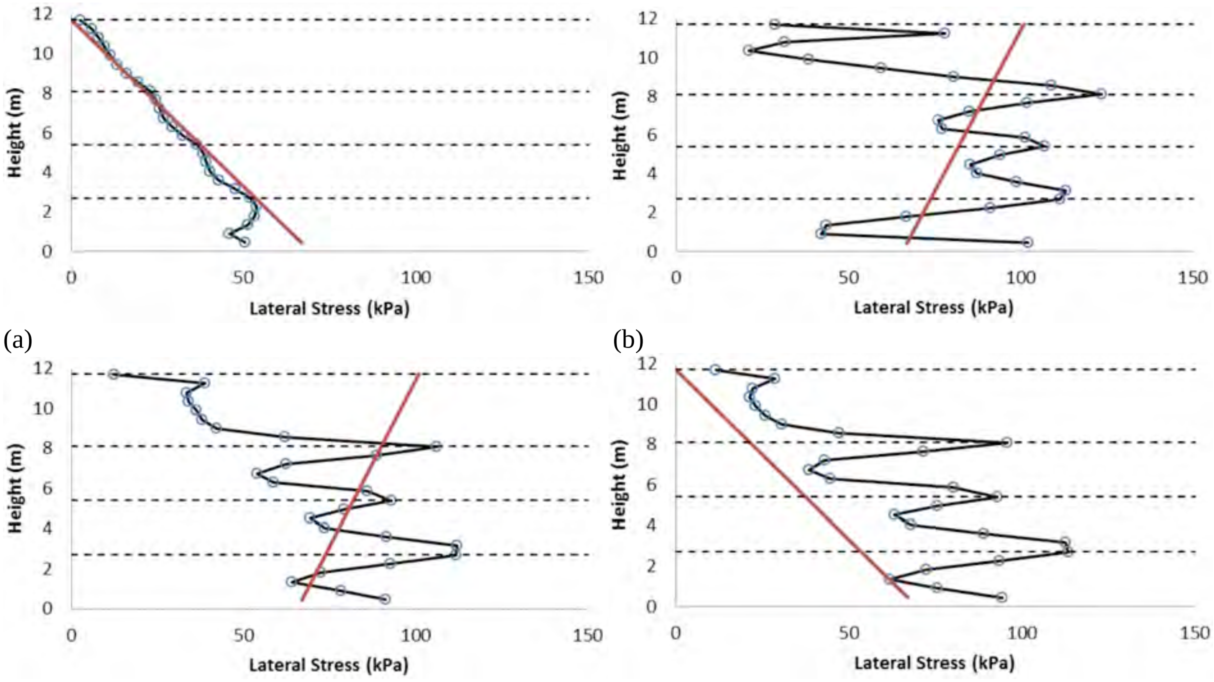

(a) (b)

(c) (d)

Figure 6: Lateral earth pressure distribution along the height of the basement wall for ground motion G1; symbols representing the results of numerical analysis at (a) t=0 sec (initial static pressures), (b) t=7.7 sec (the instance of occurrence of maximum lateral earth force on the wall), (c) t=10 sec (an arbitrary time during the shaking phase), and (d) t=42 sec (residual static pressures), and solid red lines representing the prediction from Coulomb's theory [for (a) and (d)] and the simplified design method [for (b) and (c)].

Finally Fig. 6(d) compares the numerical analysis results after the end of shaking (t=42 sec) with the suggested distribution of lateral pressures from Coulomb's theory. Numerical analysis results show a significant increase in the residual static earth pressure at the end of shaking. The significant difference between the two sets for distribution profiles of pressures can be attributed to the wall deformation.

The resulting bending moment and shear envelopes (maximum and minimum) over the wall height during the analysis with ground motion G1 are presented in Figs. 7(a) and 7(b), respectively. It is found that the resulting bending moment and shear envelopes for the three analyzed earthquakes are almost the same, and therefore only the analysis results of the basement wall subjected to ground motion G1 are shown here. In this figure, the limiting values of M_y and V_y correspond to nominal [designed] yield moment and yield shear of the wall sections, respectively. As shown in Fig. 7, the basement walls designed for a hazard level of 10% probability of exceedance in 50 years yields in moment at the mid-height of each basement story and also at each floor level. The shear diagram shows that the shear demand is considerably less than the shear capacity along the height of the wall.

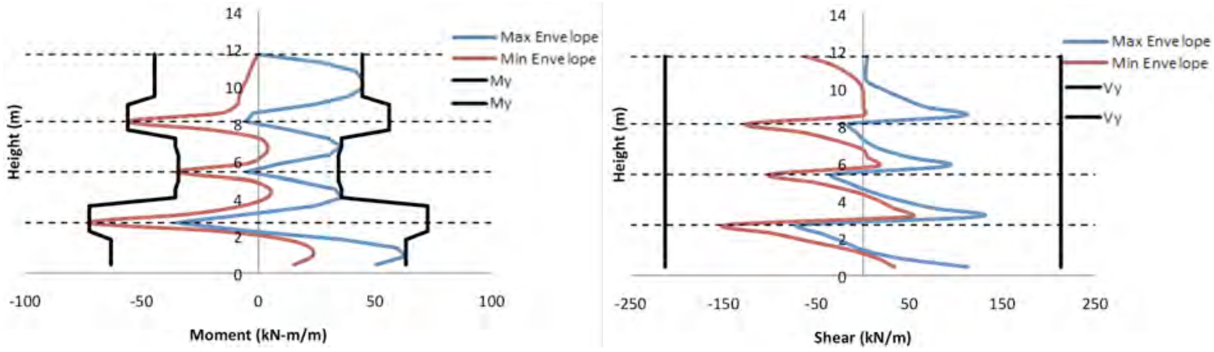

(a) (b)

Figure 7: The analysis results for bending moment and shear envelopes for the basement wall subjected to ground motion G1 and the nominal [designed] yield moments and yield shears of the basement wall.

Given that the wall yields at many different levels in the conducted analyses, it is very important to monitor the resulting deformations and drift ratios of the wall. The deformation or the relative displacement of the wall at each level is calculated as the difference between the displacement of the wall at that level and the displacement of the wall at its base. Drift ratio for each story is calculated as shown in Fig. 8. The resulting drift ratio from this figure is a useful indicator to determine the amount of damage to the wall. In this figure h_i is the floor height, $u_{\mathrm{floor,top}}$ and $u_{\mathrm{floor,bottom}}$ are the wall deformations at the floor levels and u_{wall} is the deformation at the mid height of the wall (between the two floors).

The envelopes of relative maximum and minimum displacements along with the residual relative displacements for the analysis with the three ground motions are shown in Fig. 9(a,c,e). The relative displacements are larger between the floors and are smaller at each floor level. The results of relative residual displacement show that the residual relative displacement of the wall at each floor level is approximately zero while in between different floor levels the wall shows some permanent deformations. The envelopes of drift ratios are shown in Figure 9(b,d,f). Maximum displacement and maximum drift ratio occur in the topmost story of the basement.

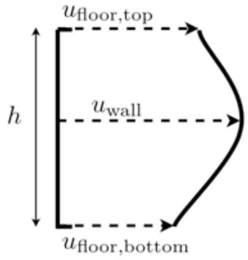

$$\text{Drift ratio} = \left[u_{\text{wall}} - \frac{u_{\text{floor,top}} + u_{\text{floor,bottom}}}{2}\right] / (0.5h)$$

Figure 8: Definition of drift ratio for each story of the basement wall.

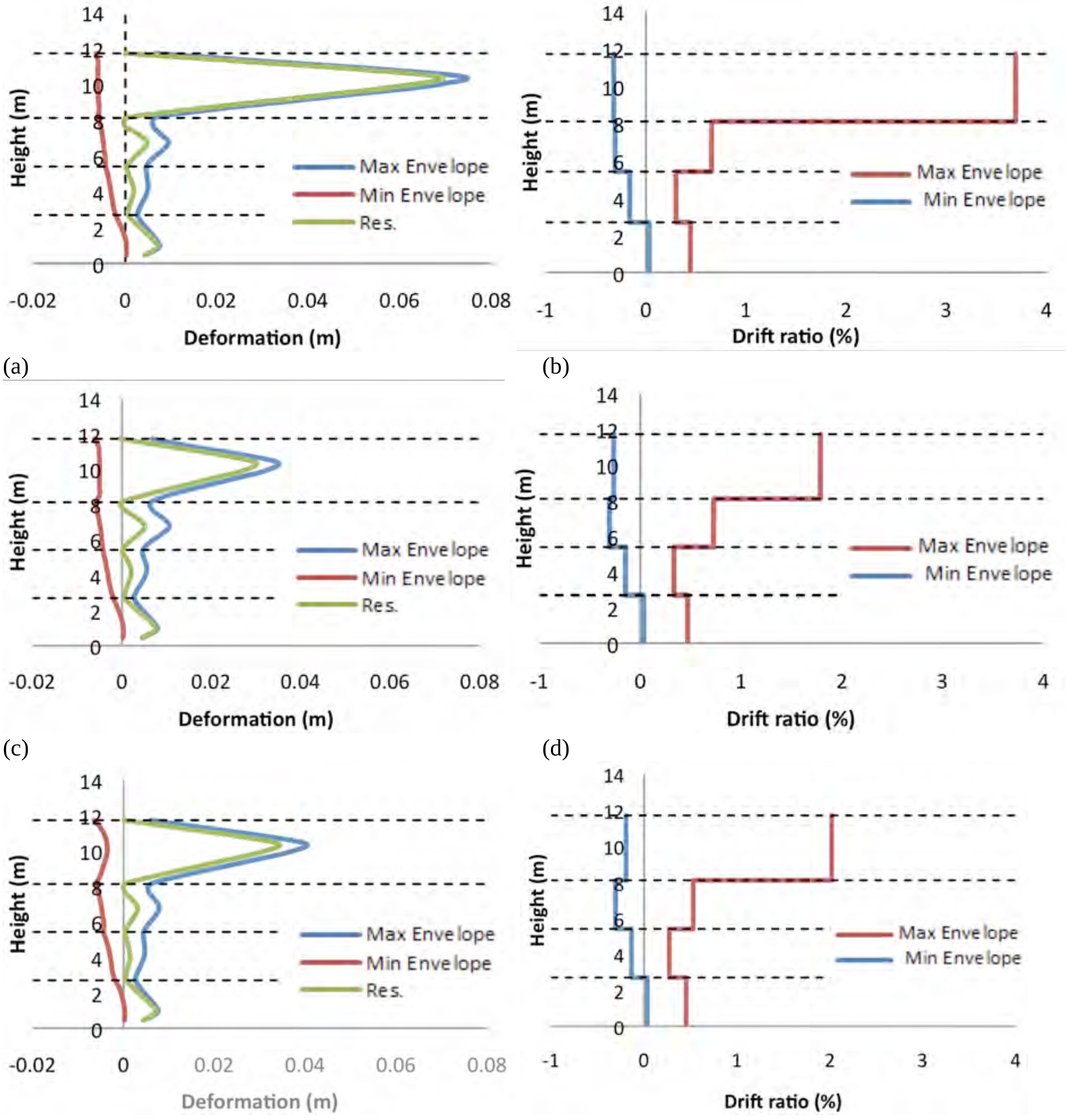

(a)
(b)
(c)
(d)
(e)
(f)

Figure 9: Envelops of maximum, envelopes of minimum, and values of residual wall deformations (displacements relative to the base of the basement wall) and envelop of maximum and envelopes of envelopes of minimum story drift ratios for ground motions G1 (a,b), G2 (c,d), and G3 (e,f).

5 SUMMARY AND CONCLUSION

One of the aims of this study was to assess whether existing basement walls designed for a hazard level with 10% probability of exceedance in 50 years (NBCC1995) in Vancouver would be safe when subjected to the higher seismic hazard level of 2% in 50 years which is mandated by the NBCC2005. The seismic pressures against the wall for design were calculated using the M-O procedure. The walls were designed to behave elastically under these pressures. The response of the walls to higher hazard level mandated by NBCC2005 was evaluated using the computer program FLAC.

The M-O pressures for the higher hazard are approximately double the pressures used for the original design. Therefore it was expected that the wall might yield under these elevated pressures and so a nonlinear analysis was carried out including nonlinear soil behavior and yielding of the wall. The analysis was conducted using three different input motions, all of them matched to Vancouver Uniform Hazard Spectrum in the period range 0.05–1.5 sec. The analyses show that M-O accurately predicts the peak resultant force on the wall and the point of application of the resultant force on the wall is consistently at about 0.55H from the base of the wall. This is the location usually assumed in British Columbia for application of M-O resultant force. However, the pressure distribution from the dynamic analysis was radically different from the linear distribution typically assumed in the practice. The total pressure during the earthquake against the top basement level is much smaller than estimated by M-O. At the end of earthquake, the residual pressure are significantly greater the Coulomb’s theory.

It was found in Fig. 7(a) that in all levels the wall yields roughly at mid elevation and also yields at the floor levels on the opposite side. The behavior under shear is shown in Fig. 7(b) and it is shown that the shear demand is considerably less than the shear capacity along the height of the wall.

Figure 9 shows the deformations that occur in the wall in terms of displacement relative to the base of the wall and also in terms of drift ratios. The maximum drift ratio in the first level is approximately 4% for one of the motions. For the other motions the drift ratio is 2% in the top level. For the lower three basement levels the drift ratio is less than 1%. These results suggest that apart from the results for motion G1 the drift ratios are in acceptable limits so the elastic design under the seismic hazard of 10% in 50 years is almost adequate to carry the higher hazard of 2% in 50 years, except possibly in the upper basement level. More detailed study on this topic is underway by the authors.

ACKNOWLEDGEMENT

The materials presented in this paper are part of an ongoing study conducted by the authors as members of a task force committee for evaluation of seismic pressure on basement walls; struck by the Structural Engineers Association of British Columbia (SEABC). The authors are grateful for many constructive discussions with the Chairman of the Committee, Dr. Ron DeVall, and the committee members, Ali Amini, Don Anderson, Michael Belfry, Peter Byrne, Mat Kokan, Jim Mutrie, Ernest Naesgaard, Rob Simpson, and Doug Wallis.

REFERENCES

[1] Mononobe, N., and Matsuo, H. (1929). On the Determination of Earth Pressures During Earthquakes, *Proceedings of World Engineering Conference*, 9, 176-182.

[2] Seed, H.B., and Whitman, R.V. (1970). Design of Earth Retaining Structure of Dynamic Loads, *Proceedings, Specialty Conference on Lateral Stresses in the Ground and Design of Earth Retaining Structure*, ASCE, 103-147.

[3] Sherif, M.A. , Ishibashi, I. , and Lee, C.D. (1982). Earth Pressure Against Rigid Retaining Walls, *Journal of the Geotechnical Engineering Division*, ASCE, 108, GT5, 679-696.

[4] Sherif, M.A., and Fang, Y. S. (1984). Dynamic Earth Pressure on Walls Rotating about Top, *Soil and Foundations*, 24, 4, 109-117.

[5] Segrestin, P. and Bastick M. L. (1988). “Seismic Design of Reinforced Earth Retaining Walls , The Contribution of Finite Element Analysis.” *International Geotechnical Symposium on Theory and Practice of Earth Reinforcement*, Fukuoka, Japan, October.

[6] American Association for State Highway and Transportation Officials, AASHTO (2010). LRFD bridge design specification (5nd ed.), Washington D. C.

[7] NRCC (1995). National building code of Canada 1995. *Institute for Research in Construction, National Research Council of Canada*, Ottawa, Ont.

[8] NRCC (2005). National building code of Canada 2005. *Institute for Research in Construction, National Research Council of Canada*, Ottawa, Ont.

[9] Itasca Consulting Group, Inc. (2008). FLAC: Fast Lagrangian Analysis of Continua, User Manual, Version 6.0, Minneapolis.

[10] Idriss, I. M. and Sun, J. I. (1992). "User's Manual for SHAKE91, A computer Program for Conducting Equivalent Linear Seismic Response Analyses of Horizontally Layered Soil Deposits Program Modified based on the Original SHAKE Program Published in December 1972 by Schnabel, Lysmer and Seed."

[11] SeismoMatch 1.0.3, Educational Version, SeismoSoft Company.

[12] Wang G., Power M., and Youngs R. (2009). Design Ground Motion Library (DGML), AMEC Geomatrix, Inc., Oakland, California, Project 10607.000.

COMPDYN 2011
ECCOMAS Thematic Conference on
Computational Methods in Structural Dynamics and Earthquake Engineering
M. Papadrakakis, M. Fragiadakis, V. Plevris (eds.)
Corfu, Greece, 25-28 May 2011

FUZZY AND FUZZY STOCHASTIC METHODS FOR THE NUMERICAL ANALYSIS OF REINFORCED CONCRETE STRUCTURES UNDER DYNAMICAL LOADING

F. Steinigen[1], **J.-U. Sickert**[1], **W. Graf**[1] **and M. Kaliske**[1]

[1]Technische Universität Dresden
Institute for Structural Analysis
01062 Dresden, Germany
e-mail: frank.steinigen@tu-dresden.de

Keywords: Structural Dynamics, Reinforced Concrete, Fuzzy Stochastic Analysis.

Abstract. *This paper is mainly devoted to enhanced computational algorithms to simulate the load-bearing behavior of reinforced concrete structures under dynamical loading. In order to take into account uncertain data of reinforced concrete, fuzzy and fuzzy stochastic analyses are presented. The capability of the fuzzy dynamical analysis is demonstrated by an example in which a steel bracing system and viscous damping connectors are designed to enhance the structural resistance of a reinforced concrete structure under seismic loading.*

1 INTRODUCTION

The numerical analysis of reinforced concrete (RC) structures under dynamical loads requires realistic nonlinear structural models and computational algorithms. Furthermore, the engineer/designer has to deal with uncertainty which result from variations in material parameters as well as incomplete knowledge about further excitations and the quality of the numerical model itself. The variations in material parameters may be assessed by the uncertainty measure probability. However, the stochastic model cannot be determined precisely because of rare information in most cases. Therefore, an imprecise probability approach is suggested in this contribution bases on the uncertainty measure fuzzy probability resulting in a set of probability models which assessed by membership values. Using this approach, input variables may be also modeled as fuzzy quantities and considered as a special case, if only subjective or linguistic assessments are available.

The incorporation of uncertain input variables within a dynamic structural analysis leads to uncertain structural responses representing the uncertain structural performance close to reality. The uncertain structural responses are determined using fuzzy stochastic dynamic analysis. Thereby, fuzzy stochastic processes result because of the specific dynamic actions. The fuzzy stochastic structural analysis of practical problems requires high performance computational tools in order to deal with a large number of uncertain input variables as well as complex nonlinear structural models. An efficient approach is introduced which is based on α-level optimization and Monte-Carlo simulation using meta-models which partly replace the dynamic structural analyses.

2 UNCERTAINTY IN STRUCTURAL DYNAMICS

2.1 Data models

The input variables – for geometry, material, load etc. – of the numerical simulations of structural behavior are generally uncertain. To describe this uncertainty, traditional stochastic and non-stochastic models are available [6]. In Fig. 1, the models randomness, fuzziness and fuzzy randomness are displayed. The choice of the model depends on the available data.

If sufficient statistical data exist for a parameter and the reproduction conditions are constant, the parameter may be described stochastically. Thereby, the choice of type of probability distribution function affects the result considerably.

Overcoming the traditional probabilistic uncertainty model enables the suitable consideration of imprecision (epistemic uncertainty). Thereby, epistemic uncertainty is associated with human cognition, which is not limited to a binary measure. Advanced uncertainty concepts allow a gradual assessment of intervals. This extension can be realized with the uncertainty characteristic fuzziness. The combination of fuzziness and probabilistic leads to the generalized model fuzzy randomness.

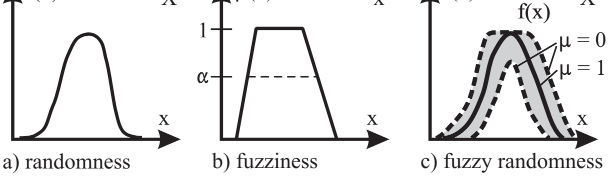

a) randomness b) fuzziness c) fuzzy randomness

Figure 1: Models of uncertainty.

2.1.1 Fuzzy variables

Often, the uncertainty description for parameters is based on pure expert judgment or samples which are not validated statistically. Then, the description by the uncertainty model fuzziness is recommended. The model comprehends both objective and subjective information. The uncertain parameters are characterized with the aid of a membership function $\mu(x)$ (see Fig. 1b) and Eq. (1)). The membership function $\mu_x(x)$ assesses the gradual membership of elements to a set. Fuzzy variables

$$\tilde{x} = \{(x;\, \mu_x(x)) \mid x \in X\}; \quad \mu_x(x) \geq 0 \,\forall\, x \in X \tag{1}$$

may be utilized to describe the imprecision of structural parameters directly as well as to specify the parameters of fuzzy random variables.

2.1.2 Fuzzy random variables

If, e.g. reproduction conditions vary during the period of observation or if expert knowledge completes the statistical description of data, an adequate uncertainty quantification succeeds with fuzzy random variables. The theory of fuzzy random variables is based on the uncertain data model fuzzy randomness representing a generalized model due to the combination of stochastic and non-stochastic characteristics. A fuzzy random variable $\tilde{X}$ is defined as the fuzzy set of their originals, whereby each original is a real-valued random variable X.

The representation of fuzzy random variables presented in this paper is based on [12]. The space of the random elementary events Ω is introduced. Here, e.g. the measurement of a structural parameter may be an elementary event ω. Each elementary event $\omega \in \Omega$ generates not only a crisp realization but a fuzzy realization $\tilde{x}(\omega) = \tilde{x}$, in which $\tilde{x}$ is an element of the set $\mathbf{F}(\mathbb{R})$ of all fuzzy variables on $\mathbb{R}$. Each fuzzy variable is defined as a convex, normalized fuzzy set, whose membership function $\mu_x(x)$ is at least segmentally continuous. Accordingly, a fuzzy random variable $\tilde{X}$ is a fuzzy result of the mapping given by

$$\tilde{X} : \Omega \mapsto \mathbf{F}(\mathbb{R}). \tag{2}$$

Based on this formal definition, a fuzzy random variable is described by its fuzzy cumulative distribution function (fuzzy cdf) $\tilde{F}(x)$. The function $\tilde{F}(x)$ is defined as the set of real-valued cumulative distribution functions F(x) which are gradually assessed by the membership $\mu_F(F(x))$. F(x) is the cdf of the original X and is referred to as trajectory of $\tilde{F}(x)$. As result, a fuzzy functional value $\tilde{F}(x_i)$ belongs to each value x_i (see Fig. 2). Thus, $\tilde{F}(x)$ represents a fuzzy function as defined in Section 2.2.1. A fuzzy probability density function

$$\tilde{f}(x) = \{(f(x);\, \mu_f(f(x))) \mid f \in \mathbf{f}\}\,; \quad \mu_f(f(x)) \geq 0 \;\forall\; f \in \mathbf{f} \tag{3}$$

is defined accordingly. In that, **f** represents the set of all probability density functions defined on X.

2.2 Uncertain functions and processes

2.2.1 Fuzzy function

In case that fuzzy parameters depend on crisp or uncertain conditions, they are modeled as fuzzy functions $\tilde{x}(\underline{\tilde{t}}) = \tilde{x}(\underline{\tilde{\theta}},\, \tilde{\tau},\, \underline{\tilde{\varphi}})$ or in the special case of pure time dependency as fuzzy

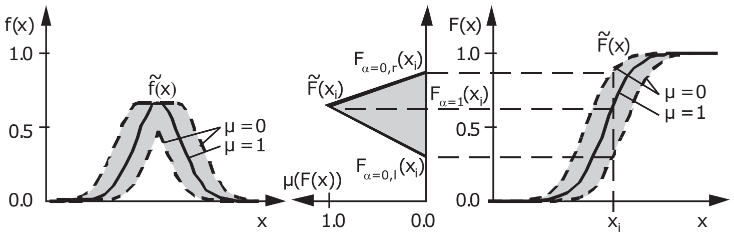

Figure 2: Fuzzy probability density and cumulative distribution function.

processes $\tilde{x}(\tilde{\tau})$. Arguments may be the time $\tilde{\tau}$, the spatial coordinates $\underline{\tilde{\theta}}$ and further parameters $\underline{\tilde{\varphi}}$, e.g. temperature. A fuzzy function $\tilde{x}(\underline{\tilde{t}})$ enables the formal description of at least piecewise continuous uncertain structural parameters in $\mathbb{R}$. In the following, a definition of fuzzy functions is introduced. Given are

- the fundamental sets $\mathbf{T} \subseteq \mathbb{R}$ and $\mathbf{X} \subseteq \mathbb{R}$,
- the set **F(T)** of all fuzzy variables $\underline{\tilde{t}}$ on the fundamental set **T**,
- the set **F(X)** of all fuzzy variables $\tilde{x}$ on the fundamental set **X**.

Then, the uncertain mapping of **F(T)** into **F(X)** that assigns exactly one $\tilde{x} \in \mathbf{F}(\mathbf{X})$ to each $\underline{\tilde{t}} \in \mathbf{F}(\mathbf{T})$ is referred to as a fuzzy function denoted by

$$\tilde{x}(\underline{\tilde{t}}): \quad \mathbf{F}(\mathbf{T}) \overset{\sim}{\mapsto} \mathbf{F}(\mathbf{X}), \tag{4}$$

$$\tilde{x}(\underline{\tilde{t}}) = \left\{ \tilde{x}_t = \tilde{x}(\underline{\tilde{t}}) \quad \forall\, \underline{\tilde{t}} \mid \underline{\tilde{t}} \in \mathbf{F}(\mathbf{T}) \right\}. \tag{5}$$

In Fig. 3, a fuzzy process $\tilde{x}(\tau)$ is presented, which assigns a fuzzy quantity $\tilde{x}(\tau_i)$ to each time τ_i. For the numerical simulation, a bunch parameter representation of a fuzzy function

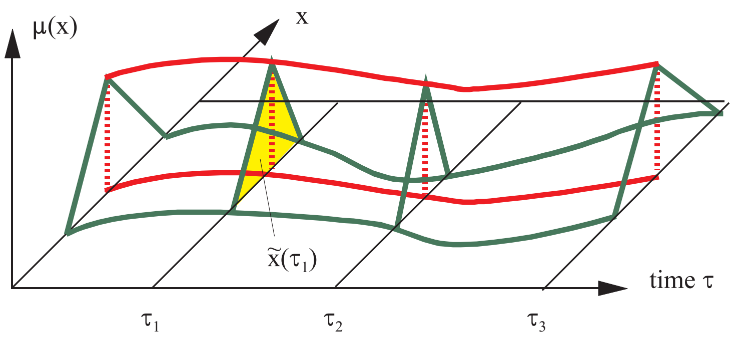

Figure 3: Fuzzy process $\tilde{x}(\tau)$.

$$x(\underline{\tilde{s}},\, \underline{t}) = \tilde{x}(\underline{\tilde{t}}) \tag{6}$$

is applied. Therewith, the fuzziness of both $\tilde{x}$ and $\tilde{t}$ is concentrated in the bunch parameter vector $\underline{\tilde{s}}$.

For each crisp bunch parameter vector $\underline{s} \in \underline{\tilde{s}}$ with the assigned membership value $\mu(\underline{s})$, a crisp function $x(\underline{t}) = x(\underline{s},\, \underline{t}) \in \tilde{x}(\underline{t})$ with $\mu(x(\underline{t})) = \mu(\underline{s})$ is obtained. The fuzzy function

$$\tilde{x}(\underline{t}) = \tilde{x}(\underline{\tilde{s}},\, \underline{t}) = \{(x(\underline{s},\, \underline{t}),\, \mu(x(\underline{s},\, \underline{t}))) \mid \mu(x(\underline{s},\, \underline{t})) = \mu(\underline{s}) \;\; \forall\, \underline{s} \mid \underline{s} \in \underline{\tilde{s}}\} \tag{7}$$

may thus be represented by the fuzzy set of all real valued functions $x(\underline{s},\, \underline{t})$ which may be generated from all possible real vectors $\underline{s} \in \tilde{\underline{s}}$. For every $\underline{t} \in \mathbf{T}$, each of the crisp functions $x(\underline{s},\, \underline{t})$ yields values x_t which are contained in the associated fuzzy functional values $\tilde{x}_t$. The real functions $x(\underline{s},\, \underline{t})$ of $\tilde{x}(\underline{t})$ are referred to as trajectories. Numerical processing of fuzzy functions $\tilde{x}(\underline{t}) = x(\tilde{\underline{s}},\, \underline{t})$ demands the discretization of their arguments $\underline{t}$ in space and time.

2.2.2 Fuzzy random function

According to Eqs. (2) and (4), a fuzzy random function is the result of an uncertain mapping

$$\tilde{X}(\underline{t}):\ \mathbf{F}(\mathbf{T}) \times \Omega \rightarrow \mathbf{F}(\mathbb{R}). \tag{8}$$

Thereby, **F(X)** and **F(T)** denote the sets of all fuzzy variables in **X** and **T** respectively [14]. At a specific point $\underline{t}$, the mapping of Eq. (8) leads to the fuzzy random variable $\tilde{X}_t = \tilde{X}(\underline{t})$. Therefore, fuzzy random functions are defined as a family of fuzzy random variables

$$\tilde{X}(\underline{t}) = \{\tilde{X}_t = \tilde{X}(\underline{t})\,\forall\,\underline{t} \mid \underline{t} \in \mathbf{T}\}. \tag{9}$$

For the numerical simulation, again the bunch parameter representation of a fuzzy random function is applied. For each crisp bunch parameter vector $\underline{s} \in \tilde{\underline{s}}$ with the assigned membership value $\mu(\underline{s})$, a real random function $X(\underline{t}) = X(\underline{s},\, \underline{t}) \in \tilde{X}(\underline{t})$ with $\mu(X(\underline{t})) = \mu(\underline{s})$ is obtained. The fuzzy random function $\tilde{X}(\underline{t})$ may thus be represented by the fuzzy set of all real random functions $X(\underline{t}) \in \tilde{X}(\underline{t})$

$$X(\tilde{\underline{s}},\, \underline{t}) = \{(X(\underline{t}),\, \mu(X(\underline{t}))) \mid X(\underline{t}) = X(\underline{s},\, \underline{t}); \mu(X(\underline{t})) = \mu(\underline{s})\ \ \forall\,\underline{s} \mid \underline{s} \in \tilde{\underline{s}}\} \tag{10}$$

which may be generated from all possible real vectors $\underline{s} \in \tilde{\underline{s}}$. The real random function $X(\underline{t}) \in \tilde{X}(\underline{t})$ is defined for all $\underline{t} \in \mathbf{T}$ and referred to as original function. A numerical processing of a fuzzy random function $\tilde{X}(\underline{t}) = X(\tilde{\underline{s}},\, \underline{t})$ requires the discretization of their arguments $\underline{t}$ in space and time.

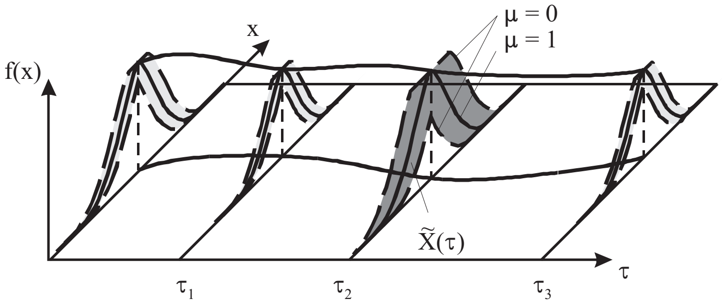

Figure 4: Fuzzy random process $\tilde{X}(\underline{\theta}_j,\, \tau)$.

3 Fuzzy stochastic analysis

Fuzzy stochastic analysis is an appropriate computational model for processing uncertain data using the uncertainty model fuzzy randomness. Basic terms and definitions related to fuzzy randomness have been introduced, inter alia, by [12]. The formal description of fuzzy randomness chosen by [12] is however not suitable to formulating uncertainty encountered in engineering tasks. A suitable form of representation with the scope of numerical engineering tasks is given with the so-called α-discretization by [6] and [7].

The numerical simulation under consideration of fuzzy variables and fuzzy functions (fuzzy analysis) may formally be described by the mapping

$$F_{FA}(d): \quad \underline{\tilde{x}}(\underline{t}) \mapsto \underline{\tilde{z}}(\underline{t}). \tag{11}$$

According to Eq. (11), the fuzzy variables $\underline{\tilde{x}}$ and the fuzzy functions $\underline{\tilde{x}}(\underline{t})$ are mapped onto the fuzzy results $\underline{\tilde{z}}(\underline{t})$ with aid of the crisp analysis algorithm d. Every arbitrary deterministic fundamental solution may be used as algorithm d. On the basis of space and time discretization, fuzzy functional values $x(\underline{\tilde{s}}, \underline{\theta}_j, \tau_i, \underline{\varphi_k})$ of the function $x(\underline{\tilde{s}}, \underline{\theta}, \tau, \underline{\varphi})$ are determined at points in space $\underline{\theta}_j$, time τ_i, and a realization of $\underline{\varphi}_k$.

The numerical simulation is carried out with the aid of the α-level optimization [7]. For fuzzy variables $\tilde{x}$ and fuzzy bunch parameter $\underline{\tilde{s}}$ of the fuzzy functions $x(\underline{\tilde{s}}, \underline{\theta}, \tau, \underline{\varphi})$, an input subspace $\underline{E}_\alpha$ is formed assigned to the level α. By multiple application of the deterministic analysis, the extreme values $z_{\alpha,l}(\underline{\theta}_j, \tau_i, \underline{\varphi}_k)$ and $z_{\alpha,r}(\underline{\theta}_j, \tau_i, \underline{\varphi}_k)$ of the fuzzy result variable $\tilde{z}(\underline{\theta}_j, \tau_i, \underline{\varphi}_k)$ are computed. These points are interval bounds of the α-level sets and enable the numerical description of the convex membership function of the fuzzy result variable $\tilde{z}(\underline{\theta}_j, \tau_i, \underline{\varphi}_k)$. For the computation of $\tilde{z}(\underline{\theta}_j, \tau_{i+1}, \underline{\varphi}_k)$ at the time point τ_{i+1}, the procedure must be restarted at $\tau = 0$ due to the interaction within the mapping model.

Fuzzy stochastic analysis allows the mapping of fuzzy random input variables onto fuzzy random result variables. The fuzzy stochastic analysis can be applied for static and dynamic structural analysis and for assessment of structural safety, durability as well as robustness. Two different approaches for computation of the fuzzy random result variables have been developed. The first variant (Fig. 5) bases on the bunch parameter representation of fuzzy random variables by [14]. The second variant utilizes the $l_\alpha r_\alpha$-representation of fuzzy random variables. The variant to be preferred depends on the engineering task, the available uncertain data and the wanted results [9].

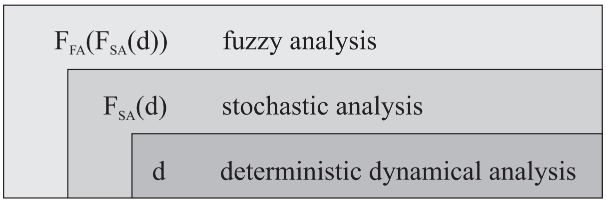

Figure 5: Fuzzy stochastic analysis (FSA).

The fuzzy stochastic analysis is called fuzzy stochastic finite element method (FSFEM), if the deterministic dynamical analysis is based on a finite element (FE) model.

4 DETERMINISTIC DYNAMICAL ANALYSIS OF RC STRUCTURES

4.1 1D – Beams

Plane and spatial beam structures are called 1D-structures. For the physical nonlinear analysis, the cross-sections of the beams are subdivided into layers (plane structures) or fibers (spatial structures). In contrast to the widespread finite element formulations, solutions based on the differential equations for the straight or imperfectly straight beam also exist. A respective approach for plane beam structures is presented here.

The geometrical and physical nonlinear analysis of plane reinforced concrete, prestressed concrete, and steel beam structures is chosen as fundamental model [13]. The beams are subdivided into integration sections, the cross-sections are subdivided into layers. On this basis an incrementally formulated system of second order differential equations for the straight or imperfectly straight beam is solved.

$$\left[\frac{d\Delta\underline{z}(\theta_1)}{d\theta_1}\right]_{(n)}^{[k]} = \underline{A}(\theta_1,\underline{z})_{(n-1)}\cdot\Delta\underline{z}(\theta_1)_{(n)}^{[k]} + \Delta\underline{b}(\theta_1)_{(n)}^{[k-1]} + \underline{d}(\theta_1)_{(n-1)}\cdot\Delta\underline{\dot{z}}(\theta_1)_{(n)}^{[k]} + \underline{m}(\theta_1)_{(n-1)}\cdot\Delta\underline{\ddot{z}}(\theta_1)_{(n)}^{[k]} \tag{12}$$

where $[k]$ – counter of iteration steps; (n) – counter of increments; θ_1 – bar coordinate; Δ – increment; $\underline{z} = \{\underline{z}_1, \underline{z}_2\} = \{u\,v\,\phi; N\,Q\,M\}$ – vector of structural responses; $\underline{A}$ – matrix of coefficients (constant within the increment); $\underline{b}$ – "right hand side" of the system of differential equations with loads and varying parts resulting from geometrical and physical nonlinearities as well as with forces from unbonded prestressing; $\underline{d}$ – damping matrix; and $\underline{m}$ – mass matrix.

The implicit nonlinear system of differential equations for the differential beam sections is linearized by increments. All geometrically and physically nonlinear components in the $\Delta\underline{b}$-vector are recalculated after every iteration step, and the $\underline{A}$-, $\underline{d}$-, and $\underline{m}$-matrix are recalculated after the completion of the iteration within the increment.

The solution of the system of differential equations by a Runge-Kutta integration results in the system of differential equations

$$\underline{K}_{T\,(n-1)}\cdot\Delta\underline{v}_{(n)}^{[k]} + \underline{D}_{T\,(n-1)}\cdot\Delta\underline{\dot{v}}_{(n)}^{[k]} + \underline{M}_{T\,(n-1)}\cdot\Delta\underline{\ddot{v}}_{(n)}^{[k]} = \Delta\underline{P}_{(n)} - \Delta\overset{o}{\underline{F}}{}_{(n)}^{[k]} + \Delta\Delta\underline{F}_{(n-1)} \tag{13}$$

of the unknown incremental displacements $\Delta\underline{v}$, velocities $\Delta\underline{\dot{v}}$, and accelerations $\Delta\underline{\ddot{v}}$ of the nodes.

4.2 2D – folded plate RC structures

Shells, folded plates, shear panels and plates are called 2D-structures. Here, we focus on folded plates which represent the general case for plane 2D structures. They can further be applied to approximate the shape of slightly curved structures. The internal forces are related to the reference plane, which is not stringently the midplane. The cross-section is subdivided into layers to describe the physical nonlinear behavior of reinforced concrete. Over the past years, a new strengthening technology for damaged RC structures has been developed. The thin strengthening layers consist of fine-grained concrete reinforced with textiles made of AR-glass or carbon. The classical layered model with one reference plane for folded plate structures is enhanced to take into account the later applied strengthening layers.

An extended layer model with specific kinematics, the so-called multi-reference-plane model (MRM), is used to describe the load-bearing behavior of RC constructions with textile strengthening. The MRM consists of concrete layers and steel reinforcement layers of the old construction, the strengthening layers comprised of the inhomogeneous material textile concrete (TRC), and the interface layers (Fig. 6). This multilayer continuum has the following kinematic peculiarities. Due to the fact that the modification of the concrete layer thickness is very small and can be neglected, we have $\varepsilon_{33} = 0$. Furthermore, the transverse shear stresses in the concrete layers have no significant influence on the deformation, which means that $\varepsilon_{13} = 0$ and $\varepsilon_{23} = 0$ can be set to zero. The deformation state of the concrete layers may be described by Kirchhoff

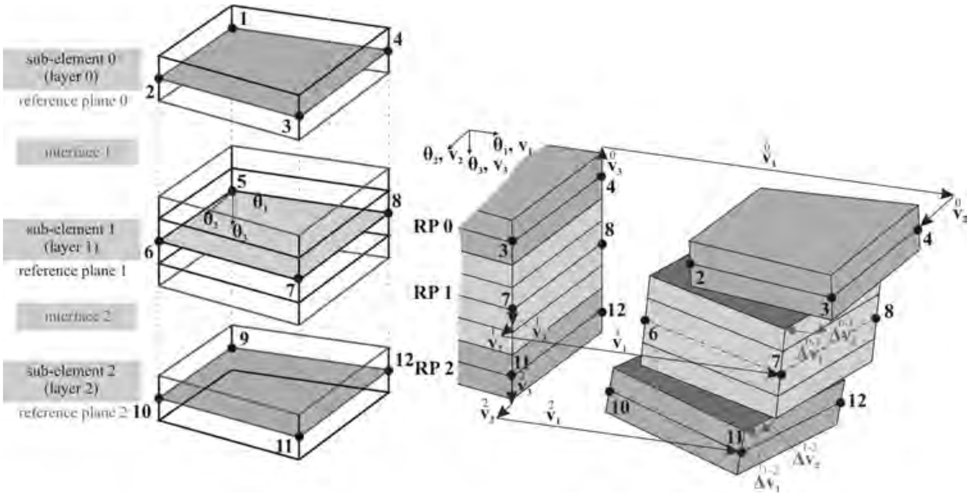

Figure 6: MRM discretization and kinematics.

kinematics. The independent degrees of freedom are assigned to a reference plane which can be selected arbitrarily.

The very thin strengthening layers are subject to the same kinematic assumptions. Kirchhoff kinematics with a reference plane are also assigned to each strengthening layer. The independent degrees of freedom of the strengthening layer lie in the reference plane. The bond between the layers of reinforced concrete and an arbitrary strengthening layer is modeled by an interface. The interface is an immaterial layer of zero thickness. The bonding state is assessed with the help of the relative displacements $\Delta v_1,\ \Delta v_2,\ \Delta v_3$ between the contact surfaces. In conjunction with a bonding matrix, the relative displacements enable assumptions regarding delamination and shear failure.

The FE discretization of the MRM is based on the functional of the complementary energy extended by the static transition conditions $\Delta \underline{p} - \overset{+}{\underline{p}} = 0$ to O^r_p and the equilibrium conditions $\underline{G} \cdot \underline{\sigma}^e_{el} + \overset{+}{\underline{p}}^e - \rho^e \cdot \underline{\ddot{v}}^e = 0$ in V^e

$$\begin{aligned} \Pi_{mh} \;=\; & \int\limits_{\tau_1}^{\tau_2} \sum_{e=1}^{n} \left\{ \int\limits_{V^e} \left[w_c(\underline{\sigma}^e_{el}) + (\underline{G} \cdot \underline{\sigma}^e_{el} + \overset{+}{\underline{p}}^e - \rho^e \cdot \underline{\ddot{v}}^e)^T \cdot \underline{v}^e \right] dV + \int\limits_{V^e} (\underline{\sigma}^e_{el})^T \cdot \underline{\varepsilon}^e_0 \, dV \right. \\ & \left. - \int\limits_{O^{r,e}_p} (\underline{p}^{r,e} - \overset{+}{\underline{p}}^{r,e})^T \cdot \underline{v}^{r,e} dO - \int\limits_{O^{r,e}_v} (\underline{p}^{r,e})^T \cdot \overset{+}{\underline{v}}^{r,e} dO \right\} d\tau \end{aligned} \tag{14}$$

with $w_c(\underline{\sigma}^e_{el})$ – internal complementary energy; $\underline{G}$ - matrix of differential operators; $\overset{+}{\underline{p}}$ – external forces in V^e ; ρ^e – density in ; $\underline{\ddot{v}}^e$ – internal acceleration in V^e ; ρ^e ; $\underline{\varepsilon}^e_0$ – initial strain; $\underline{p}^{r,e}$ – internal forces in the boundary surface $O^{r,e}_p$; $\overset{+}{\underline{p}}^{r,e}$ – external forces along the boundary surface $O^{r,e}_p$; $\underline{v}^{r,e}$ – displacements of the boundary surface $O^{r,e}_p$; $\overset{+}{\underline{v}}^{r,e}$ – prescribed displacements of the boundary surface $O^{r,e}_v$; τ – time.

After some transformations, the quasi-static part of the equilibrium conditions $(\underline{G} \cdot \underline{\sigma}^e_{el} + \overset{+}{\underline{p}}^e)$

and the kinetic energy become visible in the mixed hybrid functional

$$
\begin{aligned}
\Pi_{mh} \;=\; \int\limits_{\tau_1}^{\tau_2} \sum_{e=1}^{n} \Bigg\{ & \int\limits_{V^e} \left[w_c(\underline{\sigma}_{el}^{e}) + (\underline{G} \cdot \underline{\sigma}_{el}^{e} + \overset{+}{\underline{p}}{}^{e})^T \cdot \underline{v}^{e} + \frac{1}{2} \rho^{e} \cdot (\dot{\underline{v}}^{e})^T \cdot \dot{\underline{v}}^{e} \right] dV \\
& + \int\limits_{V^e} (\underline{\sigma}_{el}^{e})^T \cdot \underline{\varepsilon}_0^{e} \, dV - \int\limits_{O_p^{r,\,e}} (\underline{p}^{r,\,e} - \overset{+}{\underline{p}}{}^{r,\,e})^T \cdot \underline{v}^{r,\,e} \, dO \\
& - \int\limits_{O_v^{r,\,e}} (\underline{p}^{r,\,e})^T \cdot \overset{+}{\underline{v}}{}^{r,\,e} dO \Bigg\} \, d\tau.
\end{aligned} \tag{15}
$$

In extension to the static case [8], [18], this functional may be applied to a layered continuum with dynamic loads. Following the procedure described in [8], [18], the steady-state condition of the mixed hybrid functional

$$
\delta\Pi_{mh,\,NC} = \frac{1}{2}\,\delta(d^2\Pi_{mh}) = \sum_{i=0}^{k} \delta\left(d^2({}^{(R_i)}\Pi_{mh,\,NC})\right) + \sum_{j=1}^{k} \delta\left(d^2({}^{(I_j)}\Pi_{mh,\,NC})\right) = 0 \tag{16}
$$

with

$$
\begin{aligned}
{}^{(R_i)}\Pi_{mh,\,NC} \;=\; \int\limits_{\tau_1}^{\tau_2} \Bigg\{ \sum_{e_i=1}^{n} \Bigg(\frac{1}{2} \sum_{m=0}^{s_i-1} \Bigg[& \int\limits_{V^{e_i,\,m}} (d\underline{\sigma}_{el}^{e_i,\,m})^T \cdot d\underline{\varepsilon}_{el}^{e_i,\,m} dV \\
& + 2 \int\limits_{V^{e_i,\,m}} (\underline{G} \cdot d\underline{\sigma}_{el}^{e_i,\,m} + d\,\overset{+}{\underline{p}}{}^{e_i,\,m})^T \cdot d\underline{v}^{e_i,\,m} dV \\
& + \int\limits_{V^{e_i,\,m}} \rho^{e_i,\,m} \cdot (d\dot{\underline{v}}^{e_i,\,m})^T \cdot d\dot{\underline{v}}^{e_i,\,m} dV \\
& + 2 \int\limits_{V^{e_i,\,m}} (d\underline{\sigma}_{el}^{e_i,\,m})^T \cdot d\underline{\varepsilon}_0^{e_i,\,m} dV \Bigg] \\
& - \int\limits_{{}^{(R_i)}O_p^{r,\,e_i}} (d\underline{p}^{r,\,e_i} - d\,\overset{+}{\underline{p}}{}^{r,\,e_i})^T \cdot d\underline{v}^{r,\,e_i} dO \\
& - \int\limits_{{}^{(R_i)}O_v^{r,\,e_i}} (d\underline{p}^{r,\,e_i})^T \cdot d\,\overset{+}{\underline{v}}{}^{r,\,e_i} dO \Bigg) \Bigg\} \, d\tau
\end{aligned} \tag{17}
$$

$$
{}^{(I_j)}\Pi_{mh,\,NC} = \int\limits_{\tau_1}^{\tau_2} \Bigg\{ \sum_{e_j=1}^{n} \int\limits_{{}^{(I_j)}O_p^{e_j}} (d^I\underline{\sigma}^{e_j})^T \cdot \left({}^{(j|j)}d\underline{v}^{r,\,e_j} - {}^{(j-1|j)}d\underline{v}^{r,\,e_{j-1}}\right) dO \Bigg\} \, d\tau \tag{18}
$$

for a layered continuum with k layers is obtained from Eq. (15). Eq. (17) describes the functional for the sub-element R_i whereas Eq. (18) depicts the functional for the interface I_j. Compared to [8], [18] Eqs. (16), (17) and (18) are extended by inertial forces. In order to account for physical nonlinearities of the layered continuum, the layer i with the reference plane R_i is subdivided into s_i sub-layers in Eq. (17).

On the basis of Eq. (16), the differential equation of motion can be derived. Thereby, the same stress shape functions, the same boundary displacement shape functions and the same element displacement shape function are chosen within all layers of the continuum.

The stress shape functions are chosen in such a way, that they fulfil strongly the quasi-static part of the equilibrium conditions

$$\underline{G} \cdot d\underline{\sigma}_{el}^{e_i,m} + d\,\overset{+}{\underline{p}}{}^{\,e_i,m} = 0. \tag{19}$$

The evaluation of the steady-state condition, Eq. (16) yields the MRM element and leads to the differential equation of motion

$$\underline{K}_T \cdot d\underline{q} + \underline{M} \cdot d\underline{\ddot{q}} - d\underline{R} - d\underline{R}_K = 0 \tag{20}$$

with $\underline{K}_T$ – tangential system stiffness matrix, $\underline{M}$ – system mass matrix, $d\underline{R}$, $d\underline{R}_K$ – differential load contributions, and $\underline{q}$ – nodal displacement degrees of freedom. The matrix $\underline{K}_T$ and the vectors $d\underline{R}$, and $d\underline{R}_K$ are identical to the corresponding values of the hybrid procedure in [8]. The system mass matrix $\underline{M}$ is specified in [17].

4.3 3D – compact RC structures

Hybrid eight-node hexagonal solid elements for the physical linear static analysis are described in [11]. For the physically nonlinear analysis of reinforced concrete and textile reinforced concrete (TRC), respectively, two kinds of reinforcement are introduced – single fibers and fiber layers (see Fig. 7). The formulation of the hybrid eight-node hexagonal solid element with embedded (textile) reinforcement is outlined in the following.

Starting point is the functional of Hellinger-Reissner

$$\Pi_{HR} = \int\limits_V \left(\underline{\sigma}^T \cdot (\underline{G} \cdot \underline{v}) - \frac{1}{2}\underline{\sigma}^T \cdot \underline{\varepsilon} - \overset{+}{\underline{p}}{}_V^T \cdot \underline{v} \right) dV - \int\limits_{O_p} \overset{+}{\underline{p}}{}^T \cdot \underline{v}\; dO \tag{21}$$

with $\underline{\sigma}$, $\underline{\varepsilon}$, $\underline{v}$ – stresses, strains and displacements in the volume V, $\overset{+}{\underline{p}}{}_V^T$ – external forces in V and $\overset{+}{\underline{p}}{}^T$ – external forces along the boundary surface O_p, and the matrix of differential operators $\underline{G}$.

Based on it, the Hamilton functional is build

$$H = \delta \int\limits_{\tau_1}^{\tau_2} (K - \Pi_{HR})\; d\tau = \delta \int\limits_{\tau_1}^{\tau_2} \left(\frac{1}{2} \int\limits_V \rho \cdot (\dot{v})^T \cdot \dot{v}\, dV - \Pi_{HR} \right) d\tau \tag{22}$$

with the kinetic energy K.

The physical nonlinear analysis of reinforced concrete is a non-conservative problem arising e.g. from crack formation, nonlinear material behavior, bonding and damage. In order to solve this non-conservative problem, a differential load change is considered. Under such load change, the existence of a potential is assumed. The differential load change leads to a transition of the structure from the basic condition to a differentially adjacent neighboring condition (NC). The steady-state condition of the neighboring condition is therefore

$$\delta H_{NC} = \frac{1}{2}\delta(d^2 H) = 0 \tag{23}$$

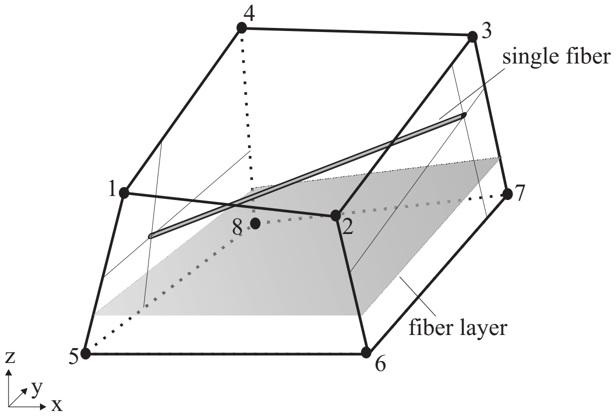

Figure 7: Eight-node solid element with embedded reinforcements.

with

$$
\begin{aligned}
H_{NC} \;=\; & \int\limits_{\tau_1}^{\tau_2} \left(\frac{1}{2} \int\limits_{V} \rho \cdot (d\dot{v})^T \cdot d\dot{v}\, dV - \int\limits_{V} \left(d\underline{\sigma}^T \cdot (\underline{G} \cdot d\underline{v}) - \frac{1}{2} d\underline{\sigma}^T \cdot d\underline{\varepsilon} - d\overset{+}{\underline{p}}{}_V^{\,T} \cdot d\underline{v} \right) dV + \right. \\
& \left. \int\limits_{O_p} d\overset{+}{\underline{p}}{}^{\,T} \cdot d\underline{v}\; dO \right) d\tau. \qquad (24)
\end{aligned}
$$

The continuum is subdivided into n finite 3D elements. The volume V^e of one finite 3D element e consists of the matrix volume V_m^e and the reinforcement volume V_b^e. Single fibers (sf) and fiber layers (fl) are taken into account. The volume of the reinforcement V_b^e consists then of n_{sf} single fibers and n_{fl} fiber layers. For a function F (e.g. stresses, strains, displacements) holds

$$
\begin{aligned}
\int\limits_{V^e} F dV \;=\; & \int\limits_{V_m^e} F_m dV + \int\limits_{V_b^e} F_b dV = \int\limits_{V^e} F_m dV + \int\limits_{V_b^e} F_b dV - \int\limits_{V_b^e} F_m dV \qquad (25) \\
=\; & \int\limits_{V^e} F_m dV + \sum_{i=1}^{n_{sf}} \int\limits_{V_{sf}^{e,i}} F_{sf}^{e,i} dV + \sum_{j=1}^{n_{fl}} \int\limits_{V_{fl}^{e,j}} F_{fl}^{e,j} dV - \sum_{i=1}^{n_{sf}} \int\limits_{V_{sf}^{e,i}} F_m^{e,i} dV - \sum_{j=1}^{n_{fl}} \int\limits_{V_{fl}^{e,j}} F_m^{e,j} dV.
\end{aligned}
$$

With Eq. (25), the reinforcement is taken into account in Eq. (24)

5 MODEL REDUCTION

The computational cost of a fuzzy stochastic structural analysis of RC structures under dynamic loads is almost completely caused by the nonlinear FE analysis. Thus, the most effective measure to increase the numerical efficiency is to replace the costly deterministic computational model (innermost loop in Fig. 5) by a fast approximation solution based on a reasonable amount of initial deterministic computational results. The fuzzy stochastic analysis can then be performed with that surrogate model, which enables the utilization of an appropriate sample size for the simulation. The surrogate model is designed to describe a functional dependency between the structural parameters $\underline{\mathrm{x}}$ and the structural responses $\underline{\mathrm{z}}$ in the form of a response surface approximation

$$
\underline{z} = f_{RS}(\underline{x}). \qquad (26)
$$

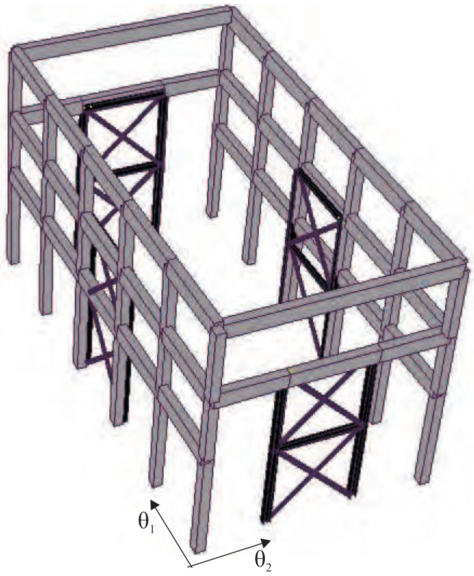

Figure 8: 3D pictorial view of the upgraded structure with scheme of the bracing system configuration.

For response surface approximation a variety of options exist (see [10], [16]). The suitability of the particular developments primarily depends on the properties of the computational model. Due to the very general properties of the FE analysis in structural analysis of textile strengthened RC structures, which can hardly be limited to convenient cases, a high degree of generality and flexibility of the approximation is demanded. In this context, an artificial neuronal network provides a powerful basis for response surface approximation. This approach can extract information from initial deterministic computational results and can subsequently reproduce the structural response based on the extracted information only. According to the universal function approximation theorem, artificial neural networks are capable of uniformly approximating any kind of nonlinear functions over a compact domain of definition to any degree of accuracy. There is virtually no restriction for a response surface approximation with the aid of artificial neural networks.

In the case, that the global structural behavior is dominated from few eigen modes, the number of degrees of freedom can be reduced. In the following example, a simplified 2-DOF model is used as equivalent system for the whole structure.

6 EXAMPLE

6.1 Investigated structure

The investigated building (Fig. 8) has a rectangular plan whose dimensions are $10.80 \times 20.40\,\mathrm{m}^2$. The elevation of the first floor is 7.40 m, whereas the second one is at 11.10 m. It is characterized by a RC structure framed in the longitudinal direction only and is designed against vertical loads without account for seismic action. Columns and beams have rectangular $40 \times 50\,\mathrm{cm}^2$ and $40 \times 70\,\mathrm{cm}^2$ cross-sections, respectively. The T-shaped hollow tile RC floors have a 6 cm thick concrete slab, so that the total depth of the first floor is 36 cm, whereas the second, at the roof level, is 30 cm.

In [4], the results of the vulnerability evaluation have been published. Thereby, a three-dimensional FEM model with beam elements of the structure has been created considering

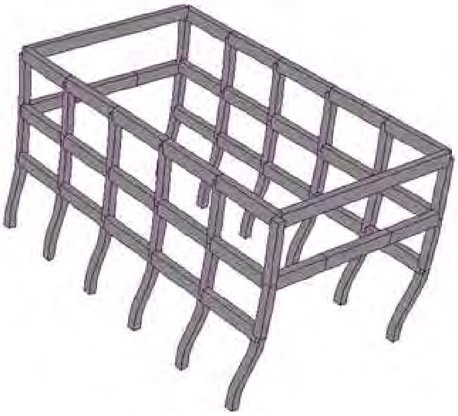

Figure 9: Deformed shapes of the fundamental vibration modes for one principal directions.

floors like rigid diaphragms in the horizontal plane. Two nonlinear static analyses and a set of linear and nonlinear time history analyses have allowed to evaluate the vulnerability of the structure in the as-built condition and the effectiveness of the upgrading interventions. First of all, a calculation of the natural frequencies of the system has been carried out. Relevant values are 2.075 s^{-1} in Θ_1 direction (longitudinal, see Fig. 9) and 0.796 s^{-1} in Θ_2 direction (transverse). The mass participation factors are higher than 95% for such modes, so that the structure can be assumed as a matter of fact as made of two mutually independent SDOF systems in both Θ_1 and Θ_2 direction. This consideration assumes relevance in the determination of the optimal value of the damping devices. In fact, a design procedure for viscous devices based on simplified 2-DOF system can be used when the structural dynamic behavior can be interpreted through two SDOF systems [1], [5].

A peak ground acceleration (PGA) of 0.25 g has been assumed in the analysis, considering the combination of site effect and the importance of the structure regard to collapse.

The time history analysis has shown an excessive deformability of the original structure, not compatible with the structural safety and immediate occupancy requirement after seismic events [2], [3]. The assumed upgrading interventions are aimed at reducing the lateral floor displacements of the structure by means of steel braces fitted with additional energy dissipation devices. Such devices connect the original structure at the first floor level with rigid steel braces and act due to the relative displacements occurring between the original structure and the steel braces. The study, presented in this paper, has been carried out considering the connection with purely viscous devices. As shown in [4], the reduction of horizontal floor displacements obtained thanks to the addition of this kind of devices is greater than the one obtained with a rigid connection of the original structure to the steel braces.

6.2 Uncertain input parameters

No technical documentation regarding the history of the structure is available, apart from the period of erection, which can be dated at the end of the 60s of XX century, on the basis of oral testimony.

Because of the lack of technical data and in order to find information about, the quality of structural materials, some characterization tests have been carried out on concrete core bored specimens and steel bars taken out of the structure. In result of the tests, the mechanical resistance of concrete is evaluated by means of fuzzy quantities. The concrete compressive and

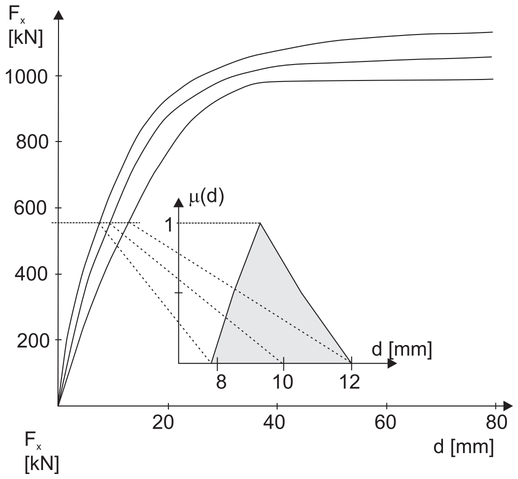

Figure 10: Fuzzy load-displacement dependency of the existing RC frame structure.

tensile strength are modeled as fuzzy triangular numbers $\tilde{\mathrm{f}}_{\mathrm{ck}} = \langle 14,\, 16.5,\, 20\rangle\, \mathrm{N/mm^2}$ and $\tilde{\mathrm{f}}_{\mathrm{t}} = \langle 1.5,\, 2.0,\, 2.5\rangle\, \mathrm{N/mm^2}$, respectively. A magneto-metric survey has been also carried out in order to locate the position and the diameter of steel bars in beams and columns. For the numerical study, twelve steel bars with a fuzzy cross-sectional area $\tilde{\mathrm{A}} = \langle 2.69,\, 3.14,\, 3.21\rangle\, \mathrm{cm^2}$ are considered. In order to assess the seismic vulnerability of the existing structure, nonlinear static analyses have been carried out under consideration of fuzzy resistance variables. The response of the as-built structure along both principal directions has then been evaluated in terms of fuzzy capacity curves F-d (Fig. 10). These curves have been represented in an approximate way by means of equivalent SDOF nonlinear relationships. Thereby, the kernel curve with $\mu\left(d(F)\right) = 1$ is scaled according to

$$\tilde{d}(F) = {}_{1.0}d(F) + \tilde{a} \cdot F \tag{27}$$

with $\tilde{\mathrm{a}} = \langle -3.3,\, 0.0,\, 6.0\rangle\, 10^{-3}$. The steel braces are also modeled as SDOF system with fuzzy stiffness $\tilde{\mathrm{K}}$ and fuzzy mass $\tilde{\mathrm{M}}$. Two variants are investigated especially: Variant 1 $\tilde{\mathrm{K}}_1 = \langle 39,\, 40.8,\, 43\rangle$ MN/m with $\tilde{\mathrm{M}}_1 = \langle 1.1,\, 1.3,\, 1.5\rangle$ t and Variant 2 $\tilde{\mathrm{K}}_1 = \langle 50,\, 52.5,\, 55\rangle$ MN/m with $\tilde{\mathrm{M}}_1 = \langle 1.2,\, 1.55,\, 1.8\rangle$ t. The uncertainty of the viscosity $\mathrm{c_x}$ of the connecting devices is with a fuzzy scaling factor according to $\tilde{\mathrm{c}} = \tilde{\mathrm{b}} \cdot \mathrm{c_x}$ with $\tilde{\mathrm{b}} = \langle 0.9,\, 1.0,\, 1.1\rangle$.

6.3 Fuzzy structural analysis

Nonlinear time-history analyses of the simplified 2-DOF system have then been performed considering the seismic input of Taiwan (1999) earthquake, scaled to PGA value of 0.25 g. Fig. 11 displays the time-history of the ground acceleration of the Taiwan earthquake. The fuzzy maximum displacement $\tilde{v}_{TD}$ at the top of the structure has been calculated on the basis of the fuzzy displacement-time dependency, as shown for one realization in Fig. 12. The parameter study with variation of the viscosity of damping devices yields a fuzzy function $\tilde{v}_{TD}(c_x)$ as presented in Fig. 13 for the Taiwan earthquake.

ACKNOWLEDGMENTS

Authors gratefully acknowledge the support of the German Research Foundation (DFG) within the framework of the Collaborative Research Center (SFB) 528 and the contribution of Alberto Mandara (Second University of Naples).

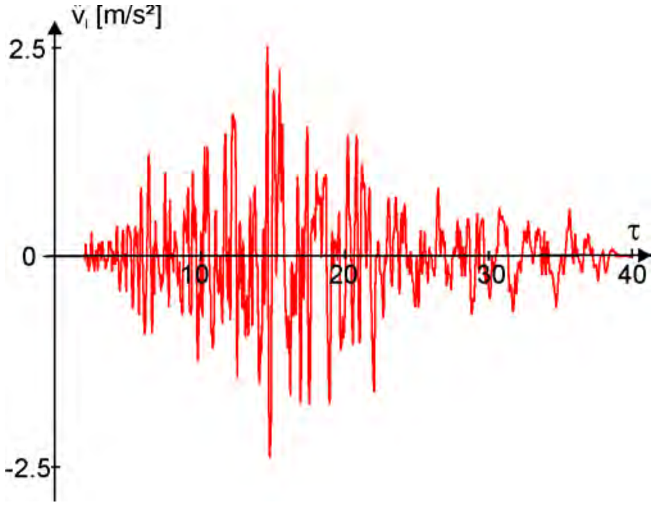

Figure 11: Acceleration of the Taiwan earthquake scaled to PGA value of 0.25 g.

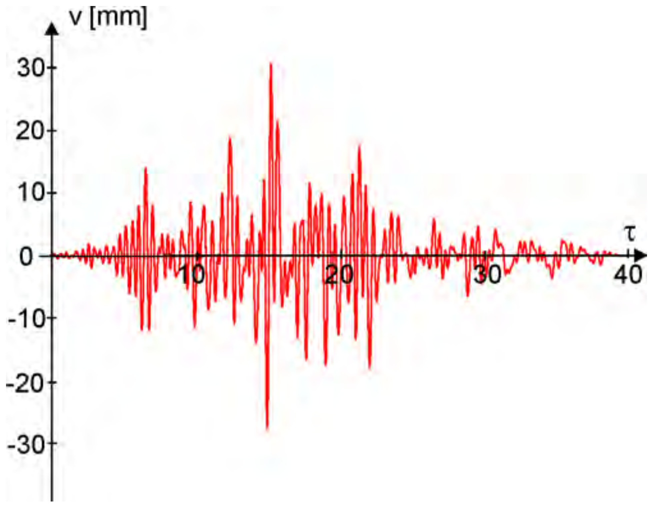

Figure 12: Realization of the fuzzy displacement-time dependency due to the Taiwan earthquake.

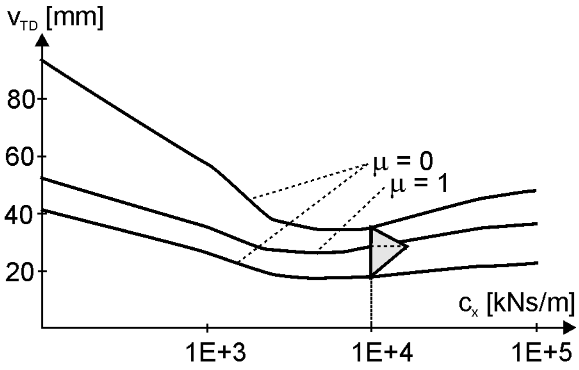

Figure 13: Fuzzy top displacement in dependency of the viscosity.

REFERENCES

[1] A. Mandara, F.M. Mazzolani, On the Design of Retro-fitting by means of Energy Dissipation Devices. *7th International Seminar on Seismic Isolation, Passive Energy Dissipation and Active Control of Vibrations of Structures*, Assisi, 2001.

[2] A. Mandara, F. Ramundo, G. Spina, Seismic up-grading of an existing r.c. building by steel braces and energy dissipation devices. *XXI National Congress of CTA*, Catania, 2007.

[3] A. Mandara, F. Ramundo, G. Spina, Steel Bracing for the Optimal Seismic Control of Existing r.c. Structures. *5th European Conference on Steel and Composite Structures*, Graz, 2008.

[4] A. Mandara, F. Ramundo, G. Spina, Seismic up-grading of r.c. structures with innovative bracing systems. *Proceedings of PROHITEC*, London, 2009.

[5] F.M. Mazzolani, A. Mandara, Seismic up-grading of an Old Industrial Building by Dissipative Steel Roofing. *International Seminar on Structural Analysis of Historical Constructions*, Padova, 2004.

[6] B. Möller, M. Beer, *Fuzzy Randomness – Uncertainty in Civil Engineering and Computational Mechanics*, Springer, Berlin, 2004.

[7] B. Möller, W. Graf, M. Beer, *Fuzzy structural analysis using α-level optimization*. Computational Mechanics, **26**, 547–565, 2000.

[8] B. Möller, W. Graf, A. Hoffmann, F. Steinigen, *Numerical simulation of RC structures with textile reinforcement*. Computers and Structures, **83**, 1659–1688, 2005.

[9] B. Möller, W. Graf, J.-U. Sickert, U. Reuter, *Numerical simulation based on fuzzy stochastic analysis*. Mathematical and Computer Modelling of Dynamical Systems, **13**, 349–364, 2007.

[10] R. H. Myers, D. C. Montgomery, *Response Surface Methodology: Process and Product Optimization Using Designed Experiments*, Wiley, New York, 1995.

[11] H.H.T. Pian, C.-C. Wu, *Hybrid and incompatible finite element methods,* Champman and Hall, Boca Raton, 2006.

[12] M.L. Puri, D. Ralescu, *Fuzzy random variables*. Journal of Mathematical Analysis and Applications, **114**, 409–422, 1986.

[13] R. Schneider, *Stochastische Analyse und Simulation des nichtlinearen Verhaltens ebener Stabtragwerke mittels M-N-Q-Interaktionsmodell*. Dissertation, Technische Universität Dresden, Veröffentlichungen des Lehrstuhls für Statik, Heft 2, 2001.

[14] J.-U. Sickert, M. Beer, W. Graf, B. Möller, *Fuzzy probabilistic structural analysis considering fuzzy random functions. 9th International Conference on Applications of Statistics and Probability in Civil Engineering,* Rotterdam, Millpress, 2003.

[15] J.-U. Sickert, *Fuzzy-Zufallsfunktionen und ihre Anwendung bei der Tragwerksanalyse und Sicherheitsbeurteilung*. Dissertation, Technische Universität Dresden, Veröffentlichungen Institut für Statik und Dynamik der Tragwerke, Heft 9, 2005.

[16] T. Simpson, J. Poplinski, P. N. Koch, J. Allen, *Metamodels for computer-based engineering design: Survey and recommendations.* Engineering with Computers, **17**, 129-150, 2001.

[17] F. Steinigen, B. Möller, W. Graf, A. Hoffmann, *Numerical simulation of textile reinforced concrete considering dynamic loading process*. J. Hegger, W. Brameshuber, N. Will, editors, *Textile Reinforced Concrete Proceedings of the 1st International RILEM Conference*, Aachen, 2006.

[18] F. Steinigen, *Numerische Simulation des Tragverhaltens textilverstärkter Bauwerke*. Dissertation, Technische Universität Dresden, Veröffentlichungen Institut für Statik und Dynamik der Tragwerke, Heft 11, 2006.

COMPDYN 2011
III ECCOMAS Thematic Conference on
Computational Methods in Structural Dynamics and Earthquake Engineering
M. Papadrakakis, M. Fragiadakis, V. Plevris (eds.)
Corfu, Greece, 25–28 May 2011

PERIODIC SHEAR BEAM AS A MODEL OF A HIGH BUILDING UNDER FUZZY NON-STATIONARY EXCITATION

K. Mazur-Sniady[1], R. Sieniawska[2], P. Sniady[2] and S. Zukowski[2]

[1] Institute of Civil Engineering, Wroclaw University of Technology
Wyb. Wyspianskiego 27, 50-370 Wroclaw, Poland
e-mail: krystyna.mazur-sniady@pwr.wroc.pl

[2] Institute of Civil Engineering, Wroclaw University of Technology
Wyb. Wyspianskiego 27, 50-370 Wroclaw, Poland
{roza.sieniawska,pawel.sniady,stanislaw.zukowski}@pwr.wroc.pl

Keywords: Shear vibration, periodic composite beam, fuzzy non-stationary stochastic excitation, uncertain parameters of structure

Abstract. *In the paper the problem of the shear vibration of a finite periodic composite beam with uncertain parameters as the model of a high building under a stochastic excitation is considered. The solution of the problem was found using the random dynamic influence function which allows applying the perturbation method while the average tolerance approach allows passing from differential equations with periodic variable coefficients to differential equations with constant coefficients. Different types of uncertainty of the structure parameters and the excitation process have been considered, namely: fuzzy numbers, random variables, random functions, fuzzy random variables, fuzzy random functions and fuzzy stochastic processes. This allows a wide analysis of complex problems of the shear vibrations of periodic composite beams with fuzzy random parameters under fuzzy stochastic excitations. Much attention has been focused on for obtaining the solution in the most genera case.*

1 INTRODUCTION

The dynamics response of the sheared beams or sheared plates as models of multistorey buildings was subjects of research by some authors [1-4]. In all the cases the homogeneous models have been assumed which do not exactly describe the real structure. Each storey of the building consists of two parts with different stiffnesses and masses. For this reason as a model of the building we can consider a sheared periodic beam. In most cases it is assumed that the parameters of the structure are deterministic. On the other hand, the structural parameters like geometry characteristics, material and damping properties might be uncertain to some extent. Their uncertainty may have a strong influence on the reliability of the structure in the dynamic context and be the crucial factor which determines the safety of the structure. Dynamic analysis of structures often involves two kinds of uncertainty. One of them is the randomness and the other one is the fuzziness which describe imprecision. The random variability is described by use of probability theory and the imprecision by use of fuzzy sets. Very often sufficient statistical data are not available in this case a fuzzy function (fuzzy process) or fuzzy random variable (fuzzy stochastic process) is possible to employ for modeling purposes. The concept of fuzzy random variables allows to combine both randomness and imprecision.

In the paper the problem of the shear vibration of a finite periodic composite beam as the model of high building with uncertain parameters (fuzzy random variables) under a fuzzy stochastic excitation is considered. The solution of the problem was found based on the fuzzy random dynamic influence function while the average tolerance approach allows passing from differential equations with periodic variable coefficients into differential equations with constant coefficients. The tolerance averaging method proposed by Woźniak [5-7] has several advantages and may be used as an alternative to the well-known homogenization method. The idea of random dynamic influence function has been presented in [8-10]. The fuzzy set theory was initiated by Zadeh [11]. The concept of fuzzy random variables was introduced by Kwarkernaak [12], Puri and Ralescu [13] and combines both randomness and imprecision. The dynamic response of the system with deterministic parameters under fuzzy stochastic excitation has been considered among other in the papers [14-20]. The definition of the variance of fuzzy random variables can be found in the papers [21-23]. The application of the uncertain forecasting in engineering and computational mechanics based on fuzzy stochastic processes is presented in the monographs [24,25].

2 GENERAL SOLUTION

Let us consider stochastic vibrations of a periodic straight cantilever beam of length h with a varying cross-section as a model of the building. The differential equation of motion of the sheared beam has the form

$$-[K(\mathbf{b}_\alpha,x)u_{\alpha,x}(\mathbf{b}_\alpha,x,t)]_{,x}+c(\mathbf{b}_\alpha,x)\dot{u}_\alpha(\mathbf{b}_\alpha,x,t)+m(\mathbf{b}_\alpha,x)\ddot{u}_\alpha(\mathbf{b}_\alpha,x,t)=p_\alpha(x,t), \tag{1}$$

where $u_\alpha(\mathbf{b}_\alpha,x,t)$ denotes the vertical displacement of the beam, $K(\mathbf{b}_\alpha,x)=(\kappa FG)_\alpha(x)$, $m(\mathbf{b}_\alpha,x)$, $c(\mathbf{b}_\alpha,x)$ are, respectively, the shear rigidity of the beam, mass of the beam per unit length and the damping coefficient, all of which are random functions of the spatial coordinate x, $x\in[0,h]$. Furthermore, G is the shear modulus of elasticity, κ is the shear stiffness factor that depends on the cross-sectional shape and F is the cross-sectional area. The function $p_\alpha(x,t)$ represents the excitation process of the beam in space and time. The symbol $(\cdot)_{,x}$ and the superimposed dot denote differentiation in space and time, respectively. The fuzzy random parameters of the beam are presented as a vector $\mathbf{b}_\alpha=[b_{\alpha 1},b_{\alpha 2},...b_{\alpha r}]^T$, where the superscript T denotes the transposition operation. It is assumed that the expected value $E[\mathbf{b}_\alpha]$ and the covariance matrix $\mathbf{C}_{\mathbf{b}_\alpha\mathbf{b}_\alpha} = [\mathrm{cov}(b_{\alpha i}, b_{\alpha j})]_{rxr} = E\ [\mathbf{b}_\alpha \mathbf{b}_\alpha^T] - E\ [\mathbf{b}_\alpha]\, E\, [\mathbf{b}_\alpha^T]$ are known. The symbol $E[\,\cdot\,]$ is the expectation operation. Possible random beam parameters include: the Kirchhoff modulus, the damping coefficient and the dimensions of the beam cross-section. It is assumed that the excitation process of the structure is a fuzzy stochastic process. Additionally, we assume that the structural and load parameters are mutually independent. The solution will be found within the correlation theory; therefore exact knowledge of the probability distributions of these random variables is not required.

In particular cases we can consider different types of the uncertainties of the structure and load parameters. They are fuzzy numbers, random variables (random functions) or in most general cases fuzzy random variables (fuzzy random function - fuzzy stochastic processes).

The boundary conditions of the cantilever beam have the form

$$u_\alpha(\mathbf{b}_\alpha, 0, t) = 0, \quad u_{\alpha,x}(\mathbf{b}_\alpha, h, t) = 0. \tag{2}$$

In the particular case when $K(\mathbf{b}_\alpha, x) = K(\mathbf{b}_\alpha) = (\kappa GF)_\alpha = const,$ $c(\mathbf{b}_\alpha, x) = c(\mathbf{b}_\alpha) = const$ and $m(\mathbf{b}_\alpha, x) = m(\mathbf{b}_\alpha) = const,$ Eq. (1) has the form

$$K(\mathbf{b}_\alpha)u_{\alpha,xx}(\mathbf{b}_\alpha, x, t) + c(\mathbf{b}_\alpha)\dot{u}_\alpha(\mathbf{b}_\alpha, x, t) + m(\mathbf{b}_\alpha)\ddot{u}_\alpha(\mathbf{b}_\alpha, x, t) = p_\alpha(x)\, f_\alpha(t). \tag{3}$$

The standard methods of analyzing the rod dynamics are effective only if the coefficients in Eq. (1) are constant. The quantities $K(\mathbf{b}_\alpha, x),$ $c(\mathbf{b}_\alpha, x)$ and $m(\mathbf{b}_\alpha, x)$ in this study are modeled as periodic fields and are rapidly varying *l*-periodic functions

$$K(\mathbf{b}_\alpha, x) = K(\mathbf{b}_\alpha, x+l), \quad c(\mathbf{b}_\alpha, x) = c(\mathbf{b}_\alpha, x+l), \quad m(\mathbf{b}_\alpha, x) = m(\mathbf{b}_\alpha, x+l). \tag{4}$$

The length l is the height of a single storey of the building and is small as compared with the height h of the building $(l << h)$.

It is difficult to find the solution of Eq. (1) because the coefficients are strongly periodic. We solve Eq. (1) basing on the concepts of the tolerance-averaged model [5-7]. Using this procedure it is possible to transform Eq. (1) to the form of a system of averaged differential equations with constant coefficients. This approximation describes the effect of the structural length parameter of the beam. We define $\Omega = (0,\ \mathrm{h})$, $\Delta(x) = (x - l/2, x + l/2)$, $l << h,$, $x \in \Omega^0$, $\Omega^0 = \{x \in \Omega^0 : \Delta x \in \Omega\}$. The periodic functions will be averaged by means of the formula

$$< g(x,t) >= \frac{1}{l}\int_{x-\frac{l}{2}}^{x+\frac{l}{2}} g(\xi, t)d\xi, \quad x \in \Omega^0, \tag{5}$$

where $g(x,t)$ is an arbitrary function defined on $\Omega = (0, h)$.

We base on Conformability Assumption [5-7] that the function $u(x,t)$ conforms to the *l*-periodic structure of the beam and together with all its derivatives it is periodic-like. Let us introduce the following decomposition of this function:

$$u_\alpha(\mathbf{b}_\alpha, x, t) = w_\alpha(\mathbf{b}_\alpha, x, t) + v_\alpha(\mathbf{b}_\alpha, x, t), \tag{6}$$

where $w(\mathbf{b}_\alpha, x, t)$ is the averaged part of the function $u(\mathbf{b}_\alpha, x, t)$ and $v(\mathbf{b}_\alpha, x, t)$ will be referred to as the fluctuating part of the function $u(\mathbf{b}_\alpha, x, t)$.

The modeling decomposition from Eq. (6) makes it possible to introduce two kinds of basic unknowns, namely function $w(\mathbf{b}_\alpha, x, t)$ which is a slowly varying function and $v(\mathbf{b}_\alpha, x, t)$ is an oscillating *l*-periodic-like function. Using Galerkin approximation we obtain the fluctuating function in the form

$$v_\alpha(\mathbf{b}_\alpha, x, t) = g^A(x) v_\alpha^A(\mathbf{b}_\alpha, x, t), \tag{7}$$

(the summation convention over *A*=1,2,... holds), where $g^A(x)$ are a priori known oscillating *l*-periodic-like functions and the new unknown amplitudes $v_\alpha^A(\mathbf{b}_\alpha, x, t)$ are sufficiently regular and slowly varying functions.

The functions $g^A(x)$ should satisfy conditions

$$< g^A(x) >= \frac{1}{l} \int_{x-\frac{l}{2}}^{x+\frac{l}{2}} g^A(x) dx = 0 \tag{8}$$

and

$$< m(\mathbf{b}_\alpha, x) g^A(x) >= \frac{1}{l} \int_{x-\frac{l}{2}}^{x+\frac{l}{2}} m(\mathbf{b}_\alpha, x) g^A(x) dx = 0 \tag{9}$$

Using the decomposition of Eqs. (6) and (7) and taking into account the Tolerance Averaging Approximation [5-7] after some manipulations we obtain the following system of $\mathrm{N}+1$ equations with constant coefficients for unknown functions $w(\mathbf{b}_\alpha, x, t)$ and $v^A(\mathbf{b}_\alpha, x, t)$, for $x \in \Omega_0$

$$\begin{aligned}
&-< K(\mathbf{b}_\alpha, x) > w_{\alpha,xx}(\mathbf{b}_\alpha, x, t) - < K(\mathbf{b}_\alpha, x) g_{,x}^A(x) > v_{\alpha,x}^A(\mathbf{b}_\alpha, x, t) \\
&+ < c(\mathbf{b}_\alpha, x) > \dot{w}_\alpha(\mathbf{b}_\alpha, x, t) + < m(\mathbf{b}_\alpha, x) > \ddot{w}_\alpha(\mathbf{b}_\alpha, x, t) =< p_\alpha(x, t) >, \\
&< K(\mathbf{b}_\alpha, x) g_{,x}^B(x) > w_{\alpha,x}(\mathbf{b}_\alpha, x, t) + < K(\mathbf{b}_\alpha, x) g_{,x}^B(x) g_{,x}^A(x) > v_\alpha^A(\mathbf{b}_\alpha, x, t) \\
&+ < c(\mathbf{b}_\alpha, x) g^B(x) g^A(x) > \dot{v}_\alpha^A(\mathbf{b}_\alpha, x, t) + \\
&< m(\mathbf{b}_\alpha, x) g^B(x) g^A(x) > \ddot{v}_\alpha^A(\mathbf{b}_\alpha, x, t) =< p_\alpha(x, t) g^A(x) >,
\end{aligned} \tag{10}$$

where $A,\ B = 1, 2, \ldots, N$.

It has been assumed that the damping coefficient fulfills $c(\mathbf{b}_\alpha, x) = 2\beta m(\mathbf{b}_\alpha, x)$, where β=*const* and hence $< c(\mathbf{b}_\alpha, x) g^A(x) >= 0$. The derivation of the beam equations (10) is analogous to the derivation of the rod equations [8].

2.1 Eigenvalue problem

Let us consider a deterministic eigenvalue problem. It this case we assume

$$< m(\mathbf{b}_\alpha, x) g^A(x) > = \frac{1}{l} \int_{x-\frac{l}{2}}^{x+\frac{l}{2}} m(\mathbf{b}_\alpha, x) g^A(x) dx = 0 \tag{11}$$

and

$$p_\alpha(x,t) = 0, \quad c(x) = 0 \tag{12}$$

After introducing (11) to equations (10) and taking into account (12) we obtain for $A = B = 1$

$$\begin{aligned} &< K(x) > W_{,xx}(x) + < K(x) g^1_{,x}(x) > V^1_{,x}(x) + \omega^2 < m(x) > W(x) = 0, \\ &< K(x) g^1_{,x}(x) > W_{,x}(x) + < K(x)[g^1_{,x}(x)]^2 > V^1(x) + \\ &-\omega^2 < m(x)[g^1(x)]^2 > V^1(x) = 0. \end{aligned} \tag{13}$$

From the second of Eqs. (13) one obtains

$$V^1(x) = \frac{< K(x) g^1_{,x}(x) >}{\omega^2 < m(x) g^1(x) g^1(x) > - < K(x) g^1_{,x}(x) g^1_{,x}(x) >} W_{,x}(x). \tag{14}$$

Introducing relationship (14) to the first of Eqs. (13) one obtains the differential equation in the following form

$$\begin{aligned} &[< K(x) > + \frac{[< K(x) g^1_{,x}(x) >]^2}{\omega^2 < m(x) g^1(x) g^1(x) > - < K(x) g^1_{,x}(x) g^1_{,x}(x) >}] W_{,xx}(x) \\ &+\omega^2 < m(x) > W(x) = 0, \end{aligned} \tag{15}$$

which can be written shortly as

$$W_{,xx}(x) + \lambda^2 W(x) = 0, \tag{16}$$

where

$$\lambda^2 = \frac{\omega^4 < m(x) >< m(x)(g^1(x))^2 > -\omega^2 < m(x) >< K(x)(g^1_{,x}(x))^2 >}{\omega^2 < K(x) >< m(x)(g(x))^2 > - < K(x) >< K(x)(g^1_{,x}(x))^2 > + (< K(x) g^1_{,x}(x) >)^2} \tag{17}$$

The solution of the equation (16) has the form

$$W(x) = A \sin \lambda x + B \cos \lambda x \tag{18}$$

Boundary conditions for cantilever beam have the form

$$W(0) = 0, \quad W_{,x}(h) = 0 \tag{19}$$

Therefore the eigenfunctions and eigenvalues are given by

$$W_n(x) = \sin \lambda_n x, \quad \lambda_n = \frac{\pi}{h}(n - \frac{1}{2}), \quad n = 1, 2, 3, \tag{20}$$

From the relationship (14) one obtains

$$V^1_n(x) = \frac{< K(x) g^1_{,x}(x) > \lambda_n}{\omega_n^2 < m(x) g^1(x) g^1(x) > - < K(x) g^1_{,x}(x) g^1_{,x}(x) >} \cos \lambda_n x, \tag{21}$$

and the eigenfrequencies

$$\begin{aligned}\omega^2_{n1/2} &= \frac{1}{2}\{\frac{<K(x)(g^1_{,x}(x))^2>}{<m(x)(g^1(x))^2>} + \lambda^2_n \frac{<K(x)>}{<m(x)>} \pm \\ &\pm \sqrt{[\frac{<K(x)(g^1_{,x}(x))^2>}{<m(x)(g^1(x))^2>} - \lambda^2_n \frac{<K(x)>}{<m(x)>}]^2 + 4\lambda^2_n \frac{(<K(x)g^1_{,x}(x)>)^2}{<m(x)><m(x)(g^1(x))^2>}}\}.\end{aligned} \tag{22}$$

In the case of a uniform beam ($K(x) = K = const.,\ m(x) = m = const.$) the eigenfrequencies have the form

$$\omega_n = \lambda_n \sqrt{\frac{K}{m}} = \lambda_n v_s. \tag{23}$$

The quantity $v_s = \sqrt{K/m}$ represents the shear wave velocity in the beam.

2.2 Forced vibration of the beam

The aim of this chapter is to find the general solution for probabilistic characteristics of the system response for arbitrary excitation stochastic process $p_\alpha(x,t) = q_\alpha(x) f_\alpha(t),$ where $q_\alpha(x)$ is a fuzzy deterministic function. The problem is being solved within the correlation theory. When the parameters of Eqs. (10) are random the problem can be solved only if the right sides of the equations (10) are deterministic. To overcome these difficulties we introduce the random dynamic influence function $H_\alpha(\mathbf{b}_\alpha, x, t) = H_{w\alpha}(\mathbf{b}_\alpha, x, t) + g^A(x) H^A_{v\alpha}(\mathbf{b}_\alpha, x, t)$ (RDIF) [8,9] which satisfies the following equations

$$\begin{aligned}&-<K(\mathbf{b}_\alpha, x)> H_{w\alpha,xx}(\mathbf{b}_\alpha, x, t) - <K(\mathbf{b}_\alpha, x) g^A_{,x}(x)> H^A_{v\alpha,x}(\mathbf{b}_\alpha, x, t) + \\ &+ <c(\mathbf{b}_\alpha, x)> \dot{H}_{w\alpha}(\mathbf{b}_\alpha, x, t) + <m(\mathbf{b}_\alpha, x)> \ddot{H}_{w\alpha}(\mathbf{b}_\alpha, x, t) =< q_\alpha(x)> \delta(t), \\ &<K(\mathbf{b}_\alpha, x) g^B_{,x}(x)> H_{w\alpha,x}(\mathbf{b}_\alpha, x, t) + <K(\mathbf{b}_\alpha, x) g^B_{,x}(x) g^A_{,x}(x)> H^A_{v\alpha}(\mathbf{b}, x, t) + \\ &+ <c(\mathbf{b}_\alpha, x) g^B(x) g'^A(x)> \dot{H}^A_{v\alpha}(\mathbf{b}_\alpha, x, t) + <m(\mathbf{b}_\alpha, x) g^B(x) g^A(x)> \ddot{H}^A_{v\alpha}(\mathbf{b}_\alpha, x, t) = 0,\end{aligned} \tag{24}$$

with initial conditions

$$H_{w\alpha}(\mathbf{b}_\alpha, x, 0) = 0,\ \dot{H}_{w\alpha}(\mathbf{b}_\alpha, x, 0) = 0,\ H^A_{v\alpha}(\mathbf{b}_\alpha, x, 0) = 0,\ \dot{H}^A_{v\alpha}(\mathbf{b}_\alpha, x, 0) = 0. \tag{25}$$

If the random dynamic influence function $H(\mathbf{b}, x, t) = H_w(\mathbf{b}, x, t) + g^A(x) H^A_v(\mathbf{b}, x, t)$ is known then the response of the beam to be found can be presented in the following form:

$$\begin{aligned}u_\alpha(\mathbf{b}_\alpha, x, t) &= w_\alpha(\mathbf{b}_\alpha, x, t) + g^A(x) v^A_\alpha(\mathbf{b}_\alpha, x, t) = \int_{t_0}^{t} H_\alpha(\mathbf{b}_\alpha, x, t-\tau) f_\alpha(\tau) d\tau = \\ &= \int_{t_0}^{t} H_{w\alpha}(\mathbf{b}_\alpha, x, t-\tau) f_\alpha(\tau) d\tau + g^A(x) \int_{t_0}^{t} H^A_{v\alpha}(\mathbf{b}_\alpha, x, t-\tau) f_\alpha(\tau) d\tau.\end{aligned} \tag{26}$$

where if $t_0 = 0$ then one considers transition vibrations and for $t_0 = -\infty$ one considers the steady-state vibration case.

On the basis of the relationship (26) we can obtain the expected value of the beam response

$$\begin{aligned} E[u_\alpha(\mathbf{b}_\alpha,x,t)]_\alpha &= E[w_\alpha(\mathbf{b}_\alpha,x,t)]_\alpha + g^A(x)E[v_\alpha^A(\mathbf{b}_\alpha,x,t)]_\alpha = \\ &= \int_{t_0}^{t} E[H_\alpha(\mathbf{b}_\alpha,x,t-\tau)]_\alpha E[f_\alpha(\tau)]_\alpha d\tau = \\ &= \int_{t_0}^{t} E[H_{w\alpha}(\mathbf{b}_\alpha,x,t-\tau)]_\alpha E[f_\alpha(\tau)]_\alpha d\tau + g^A(x)\int_{t_0}^{t} E[H_{v\alpha}^A(\mathbf{b}_\alpha,x,t-\tau)]_\alpha E[f_\alpha(\tau)]_\alpha d\tau, \end{aligned} \tag{27}$$

and the covariance of the displacement

$$\begin{aligned} &Cov_{uu_\alpha}\left[x_1,x_2,t_1,t_2\right]_\alpha = \\ &= \int_{t_0}^{t_1}\int_{t_0}^{t_2} E\left[H_\alpha\left(\mathbf{b}_\alpha,x_1,t_1-\tau_1\right)H_\alpha\left(\mathbf{b}_\alpha,x_2,t_2-\tau_2\right)\right]_\alpha Cov_{ff_\alpha}\left[\tau_1,\tau_2\right]_\alpha d\tau_1 d\tau_2 + \\ &+\int_{t_0}^{t_1}\int_{t_0}^{t_2} Cov_{HH_\alpha}\left[x_1,x_2,t_1-\tau_1,t_2-\tau_2\right]_\alpha E\left[f_\alpha\left(\tau_1\right)\right]_\alpha E\left[f_\alpha\left(\tau_2\right)\right]_\alpha d\tau_2 d\tau_2, \end{aligned} \tag{28}$$

where the covariance of RDIF can be estimated from

$$\begin{aligned} Cov_{HH_\alpha}\left[x_1,x_2,t_1,t_2\right]_\alpha &= E\left[H_\alpha\left(\mathbf{b}_\alpha,x_1,t_1\right)H_\alpha\left(\mathbf{b}_\alpha,x_2,t_2\right)\right]_\alpha + \\ &-E\left[H_\alpha\left(\mathbf{b}_\alpha,x_1,t_1\right)\right]_\alpha E\left[H_\alpha\left(\mathbf{b}_\alpha,x_2,t_2\right)\right]_\alpha \end{aligned} \tag{29}$$

and $Cov_{ff_\alpha}\left[\tau_1,\tau_2\right]_\alpha$ denotes the time covariance of the excitation force. The variance of the beam displacement is equal to

$$\begin{aligned} &\sigma_{u_\alpha}^2(x,t) = Cov_{uu_\alpha}\left[x,x,t,t\right]_\alpha = \\ &= \int_{t_0}^{t}\int_{t_0}^{t} E\left[H_\alpha\left(\mathbf{b}_\alpha,x,t-\tau_1\right)H_\alpha\left(\mathbf{b}_\alpha,x,t-\tau_2\right)\right] Cov_{ff_\alpha}\left[\tau_1,\tau_2\right]_\alpha d\tau_1 d\tau_2 + \\ &+\int_{t_0}^{t}\int_{t_0}^{t} Cov_{HH_\alpha}\left[x,x,t-\tau_1,t-\tau_2\right]_\alpha E\left[f_\alpha\left(\tau_1\right)\right]_\alpha E\left[f_\alpha\left(\tau_2\right)\right]_\alpha d\tau_2 d\tau_2. \end{aligned} \tag{30}$$

Due to the relationship (27) one obtains

$$\begin{aligned} E[u_\alpha(\mathbf{b}_\alpha,x,t)]_{\alpha l} &= \min\{\int_{t_0}^{t} E[H_{w\alpha}(\mathbf{b}_\alpha,x,t-\tau)]_\alpha E[f_\alpha(\tau)]_\alpha d\tau + \\ &+g^A(x)\int_{t_0}^{t} E[H_{v\alpha}^A(\mathbf{b}_\alpha,x,t-\tau)]_\alpha E[f_\alpha(\tau)]_\alpha d\tau\}, \end{aligned} \tag{31}$$

and

$$\begin{aligned} E[u_\alpha(\mathbf{b}_\alpha,x,t)]_{\alpha r} &= \max\{\int_{t_0}^{t} E[H_{w\alpha}(\mathbf{b}_\alpha,x,t-\tau)]_\alpha E[f_\alpha(\tau)]_\alpha d\tau + \\ &+g^A(x)\int_{t_0}^{t} E[H_{v\alpha}^A(\mathbf{b}_\alpha,x,t-\tau)]_\alpha E[f_\alpha(\tau)]_\alpha d\tau\}. \end{aligned} \tag{32}$$

Using *α-level* optimization procedure [24] for arbitrary $\alpha = \alpha_k \in [0,1]$ or the max-min in the extension principle [11], the smallest and the largest expected values at an established point x and time t can be found.

The lower and upper endpoints of the covariance could be defined using (28) as

$$\begin{aligned} &Cov_{uu_\alpha}\left[x_1,x_2,t_1,t_2\right]_{\alpha l} = \\ &= \min\{\int_{t_0}^{t_1}\int_{t_0}^{t_2} E\left[H_\alpha\left(\mathbf{b}_\alpha,x_1,t_1-\tau_1\right)H_\alpha\left(\mathbf{b}_\alpha,x_2,t_2-\tau_2\right)\right]_\alpha Cov_{ff_\alpha}\left[\tau_1,\tau_2\right]_\alpha d\tau_1 d\tau_2 + \\ &+\int_{t_0}^{t_1}\int_{t_0}^{t_2} Cov_{HH_\alpha}\left[x_1,x_2,t_1-\tau_1,t_2-\tau_2\right]_\alpha E\left[f_\alpha\left(\tau_1\right)\right]_\alpha E\left[f_\alpha\left(\tau_2\right)\right]_\alpha d\tau_2 d\tau_2\}, \end{aligned} \tag{33}$$

and

$$\begin{aligned} &Cov_{uu_\alpha}\left[x_1,x_2,t_1,t_2\right]_{\alpha r} = \\ &= \max\{\int_{t_0}^{t_1}\int_{t_0}^{t_2} E\left[H_\alpha\left(\mathbf{b}_\alpha,x_1,t_1-\tau_1\right)H_\alpha\left(\mathbf{b}_\alpha,x_2,t_2-\tau_2\right)\right]_\alpha Cov_{ff_\alpha}\left[\tau_1,\tau_2\right]_\alpha d\tau_1 d\tau_2 + \\ &+\int_{t_0}^{t_1}\int_{t_0}^{t_2} Cov_{HH_\alpha}\left[x_1,x_2,t_1-\tau_1,t_2-\tau_2\right]_\alpha E\left[f_\alpha\left(\tau_1\right)\right]_\alpha E\left[f_\alpha\left(\tau_2\right)\right]_\alpha d\tau_2 d\tau_2\}. \end{aligned} \tag{34}$$

In the particular case if the load of the beam is a “white-noise” stationary stochastic process then $C_{ff_\alpha}(\tau_1-\tau_2)_\alpha = \sigma^2_{f\alpha}\delta(\tau_1-\tau_2)$ and the variance is given by the formula

$$\begin{aligned} \sigma^2_{u_\alpha}(x,t)_\alpha &= \sigma^2_{f\alpha}\int_{t_0}^{t} E[H^2_\alpha(\mathbf{b}_\alpha,x,t-\tau)]_\alpha d\tau + \\ &+E[f^2_\alpha]_\alpha \int_{t_0}^{t}\int_{t_0}^{t} Cov_{HH_\alpha}(x,x,t-\tau_1,t-\tau_2)_\alpha d\tau_1 d\tau_2. \end{aligned} \tag{35}$$

Accordingly, we have obtained the formulas for the second-order probabilistic moments of the response of the structure.

We look for solutions of the system of Eqs. (24) in the form

$$H_{w\alpha}(\mathbf{b}_\alpha,x,t) = \sum_{n=1}^{\infty} y_{n\alpha}(\mathbf{b}_\alpha,t)\sin\lambda_n x, \tag{36}$$

and

$$H^A_{v\alpha}(\mathbf{b}_\alpha,x,t) = \sum_{n=1}^{\infty} z^A_{n\alpha}(\mathbf{b}_\alpha,t)\cos\lambda_n x \tag{37}$$

where $\lambda_n = \pi(n-1/2)/h, \quad n = 1,2,3,.$

In the particular case of $A=1$ one obtains from Eqs. (24):

$$\begin{aligned}
&\ddot{y}_{n\alpha}(\mathbf{b}_\alpha,t)+2\beta_\alpha(\mathbf{b}_\alpha)\dot{y}_{n\alpha}(\mathbf{b}_\alpha,t)+\omega^2_{n\alpha}(\mathbf{b}_\alpha)y_{n\alpha}(\mathbf{b}_\alpha,t)+\\
&+\lambda_n\frac{<K(\mathbf{b}_\alpha,x)g^1_{,x}(x)>}{<m(\mathbf{b}_\alpha,x)>}z^1_{n\alpha}(\mathbf{b}_\alpha,t)=\frac{2}{H\lambda_n}\delta(t),\\
&\ddot{z}^1_{n\alpha}(\mathbf{b}_\alpha,t)+2\beta_{v\alpha}(\mathbf{b}_\alpha)\dot{z}^1_{n\alpha}(\mathbf{b}_\alpha,t)+\omega^2_{v\alpha}(\mathbf{b}_\alpha)z^1_{n\alpha}(\mathbf{b}_\alpha,t)+\\
&+\lambda_n\frac{<K(\mathbf{b}_\alpha,x)g^1_{,x}(x)>}{<m(\mathbf{b}_\alpha,x)(g^1(x))^2>}y_{n\alpha}(\mathbf{b}_\alpha,t)=0.
\end{aligned}\tag{38}$$

where $2\beta_\alpha(\mathbf{b}_\alpha)=\dfrac{<c(\mathbf{b}_\alpha,x)>}{<m(\mathbf{b}_\alpha,x)>}$, $\quad \omega^2_{n\alpha}(\mathbf{b}_\alpha)=\lambda_n^2\dfrac{<K(\mathbf{b}_\alpha,x)>}{<m(\mathbf{b}_\alpha,x)>}=\lambda_n^2\bar{v}^2_{s\alpha}(\mathbf{b}_\alpha)$,

$2\beta_{v\alpha}(\mathbf{b})=\dfrac{<c(\mathbf{b}_\alpha,x)(g^1(x))^2>}{<m(\mathbf{b}_\alpha,x)(g^1(x))^2>}$, $\quad \omega^2_{v\alpha}(\mathbf{b}_\alpha)=\dfrac{<K(\mathbf{b}_\alpha,x)(g^1_{,x}(x))^2>}{<m(\mathbf{b}_\alpha,x)(g^1(x))^2>}$.

The initial conditions have the form

$$y_{n\alpha}(\mathbf{b}_\alpha,0)=0,\quad \dot{y}_{n\alpha}(\mathbf{b}_\alpha,0)=0,\quad z^1_{n\alpha}(\mathbf{b}_\alpha,0)=0,\quad \dot{z}^1_{n\alpha}(\mathbf{b}_\alpha,0)=0 \tag{39}$$

Let us consider the steady-state vibration ($t_0=-\infty$) of the beam under stationary, stochastic excitation. In this case the solutions (26-30) have the following form: for the expected value

$$\begin{aligned}
&E[u_\alpha(\mathbf{b}_\alpha,x,\infty)]_\alpha=E[w_\alpha(\mathbf{b}_\alpha,x,\infty)]_\alpha+g^A(x)E[v^A_\alpha(\mathbf{b}_\alpha,x,\infty)]_\alpha=\\
&=E[f_\alpha]_\alpha\int_0^\infty E[H_\alpha(\mathbf{b}_\alpha,x,\tau)]_\alpha d\tau=\\
&=E[f_\alpha]\int_0^\infty E[H_{w\alpha}(\mathbf{b}_\alpha,x,\tau)]_\alpha d\tau+g^A(x)E[f_\alpha]\int_0^\infty E[H^A_{v\alpha}(\mathbf{b}_\alpha,x,\tau)]_\alpha d\tau,
\end{aligned}\tag{40}$$

for the covariance:

$$\begin{aligned}
&Cov_{uu_\alpha}\left[x_1,x_2,\infty,\infty\right]_\alpha=\\
&=\int_0^\infty\int_0^\infty E\left[H_\alpha\left(\mathbf{b}_\alpha,x_1,\tau_1\right)H_\alpha\left(\mathbf{b}_\alpha,x_2,\tau_2\right)\right]_\alpha Cov_{ff_\alpha}\left[\tau_1-\tau_2\right]_\alpha d\tau_1 d\tau_2+\\
&+E^2[f_\alpha]_\alpha\int_0^\infty\int_0^\infty Cov_{HH_\alpha}\left[x_1,x_2,\tau_1,\tau_2\right]_\alpha d\tau_2 d\tau_2,
\end{aligned}\tag{41}$$

and for the variance:

$$\begin{aligned}
&\sigma^2_{u_\alpha}(x,\infty)_\alpha=Cov_{uu_\alpha}\left[x,x,\infty,\infty\right]_\alpha=\\
&=\int_0^\infty\int_0^\infty E\left[H_\alpha\left(\mathbf{b}_\alpha,x,\tau_1\right)H_\alpha\left(\mathbf{b}_\alpha,x,\tau_2\right)\right]_\alpha Cov_{ff_\alpha}\left[\tau_1-\tau_2\right]_\alpha d\tau_1 d\tau_2+\\
&+E^2[f_\alpha]_\alpha\int_0^\infty\int_0^\infty Cov_{HH_\alpha}\left[x,x,\tau_1,\tau_2\right]_\alpha d\tau_2 d\tau_2.
\end{aligned}\tag{42}$$

The lower and upper endpoints of the expected value and variance can be found based on the relationships (40) and (42)

$$\begin{aligned} E[u_\alpha(\mathbf{b}_\alpha,x,\infty)]_{\alpha l} &= \min\{E[f_\alpha]_\alpha \int_0^\infty E[H_\alpha(\mathbf{b}_\alpha,x,\tau)]_\alpha d\tau\} = \\ &= \min\{E[f_\alpha]\int_0^\infty E[H_{w\alpha}(\mathbf{b}_\alpha,x,\tau)]_\alpha d\tau + g^A(x)E[f_\alpha]\int_0^\infty E[H^A_{v\alpha}(\mathbf{b}_\alpha,x,\tau)]_\alpha d\tau\}, \end{aligned} \tag{43}$$

$$\begin{aligned} E[u_\alpha(\mathbf{b}_\alpha,x,\infty)]_{\alpha r} &= \max\{E[f_\alpha]_\alpha \int_0^\infty E[H_\alpha(\mathbf{b}_\alpha,x,\tau)]_\alpha d\tau\} = \\ &= \max\{E[f_\alpha]\int_0^\infty E[H_{w\alpha}(\mathbf{b}_\alpha,x,\tau)]_\alpha d\tau + g^A(x)E[f_\alpha]\int_0^\infty E[H^A_{v\alpha}(\mathbf{b}_\alpha,x,\tau)]_\alpha d\tau\}, \end{aligned} \tag{44}$$

and

$$\begin{aligned} \sigma^2_{u_\alpha}(x,\infty)_{\alpha l} &= \min\{\int_0^\infty\int_0^\infty E\left[H_\alpha(\mathbf{b}_\alpha,x,\tau_1)H_\alpha(\mathbf{b}_\alpha,x,\tau_2)\right]_\alpha Cov_{ff_\alpha}\left[\tau_1-\tau_2\right]_\alpha d\tau_1 d\tau_2 + \\ &+E^2[f_\alpha]_\alpha \int_0^\infty\int_0^\infty Cov_{HH_\alpha}\left[x,x,\tau_1,\tau_2\right]_\alpha d\tau_2 d\tau_2\}, \end{aligned} \tag{45}$$

$$\begin{aligned} \sigma^2_{u_\alpha}(x,\infty)_{\alpha r} &= \max\{\int_0^\infty\int_0^\infty E\left[H_\alpha(\mathbf{b}_\alpha,x,\tau_1)H_\alpha(\mathbf{b}_\alpha,x,\tau_2)\right]_\alpha Cov_{ff_\alpha}\left[\tau_1-\tau_2\right]_\alpha d\tau_1 d\tau_2 + \\ &+E^2[f_\alpha]_\alpha \int_0^\infty\int_0^\infty Cov_{HH_\alpha}\left[x,x,\tau_1,\tau_2\right]_\alpha d\tau_2 d\tau_2\}. \end{aligned} \tag{46}$$

In the case of the “white noise” excitation the variance has the form

$$\sigma^2_{u_\alpha}(x,\infty)_\alpha = \sigma^2_{f\alpha}\int_0^\infty E[H^2_\alpha(\mathbf{b}_\alpha,x,\tau]_\alpha d\tau + E^2[f_\alpha]_\alpha \int_0^\infty\int_0^\infty Cov_{HH_\alpha}(x,x,\tau_1,\tau_2)_\alpha d\tau_1 d\tau_2. \tag{47}$$

The randomness of the structural parameters is included in the random dynamic influence function $H_\alpha(\mathbf{b}_\alpha,x,t) = H_{w\alpha}(\mathbf{b}_\alpha,x,t) + g^A(x)H^A_{v\alpha}(\mathbf{b}_\alpha,x,t)$ which depends on the uncertain parameter vector $\mathbf{b}$. Here, another difficulty arises in the determination of the expected values and the second moment (covariance) of the RDIF which are in Eqs. (27-35) and (40-47). This problem can be solved using the perturbation method [8,9] or the Monte Carlo Method.

If the excitation process is of the type of non-stationary kinematic excitation following relationships should be introduced in the above general solution $<q_\alpha(x)>=<m_\alpha(x)>$, $f_\alpha(t) = -\ddot{z}_\alpha(t) = e_\alpha(t)X_\alpha(t)$, where $e_\alpha(t)$ is a fuzzy deterministic envelope and $X_\alpha(t)$ is a fuzzy stationary stochastic process.

3 MODEL OF THE BUILDING

Each storey of the building consists of two parts with different stiffnesses and masses. For this reason as a model of the buiding we can consider a beam composed of a periodic array of two linearly elastic, homogeneous and isotropic constituents with perfect interfaces. Let us assume that the Kirchhoff moduli $G(x)$ are fuzzy random variables and are equal to $b_{1\alpha} = G_{1\alpha}$ on $(0,a)$ and $b_{2\alpha} = G_{2\alpha}$ on (a,l). The fuzzy random variables $G_{1\alpha}$ and $G_{2\alpha}$ are assumed to be mutually independent. The other variables are deterministic and are equal to, respectively,

F_1, κ_1, ρ_1 on $(0,a)$ and F_2, κ_2, ρ_2 on (a,l) where ρ_1 and ρ_2 are denote mass density. One introduces only one ($N=1$) shape function $g^1(x)$, which is piecewise linear, Fig.1.

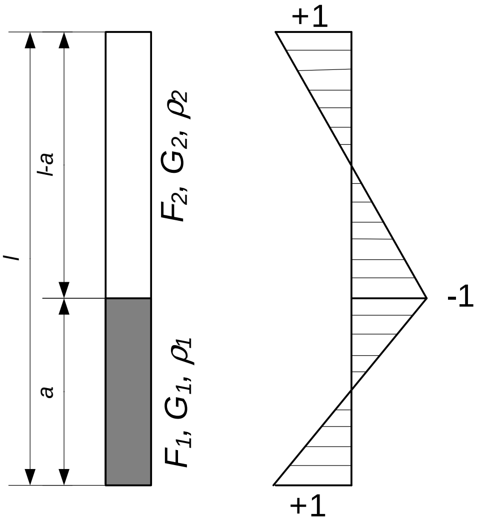

Figure 1:

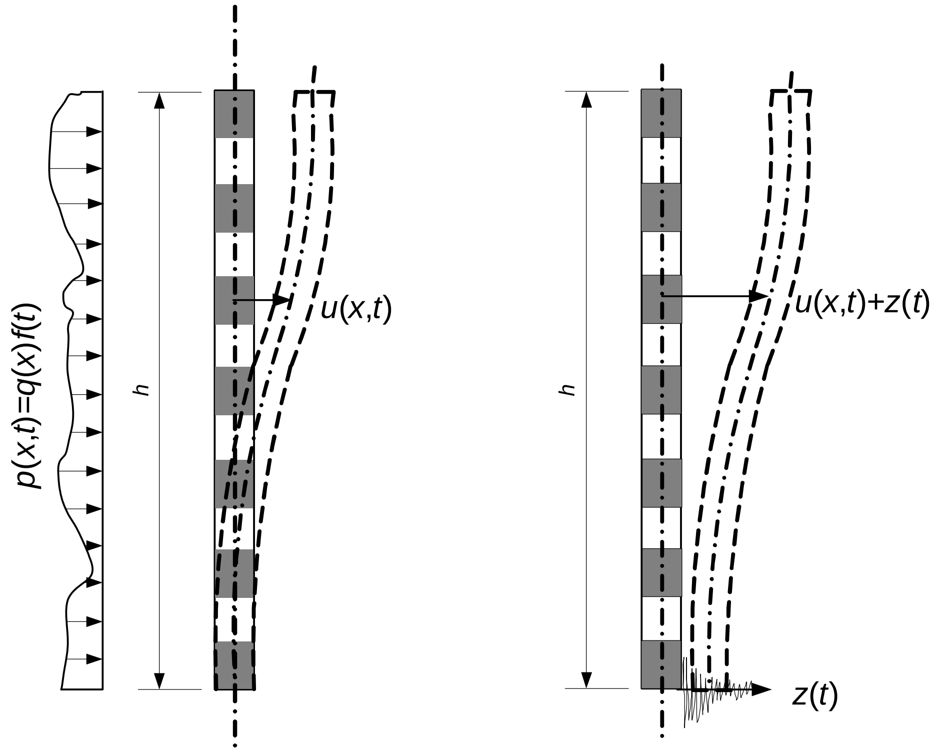

Figure 2:

In this case we have

$$
\begin{aligned}
&< K(x) >_\alpha = G_{1\alpha}\kappa_1 F_1 \frac{a}{l} + G_{2\alpha}\kappa_2 F_2 (1-\frac{a}{l}),\\
&< K(x) g^1_{,x}(x) >_\alpha = G_{1\alpha}\kappa_1 F_1 \frac{a}{l} - G_{2\alpha}\kappa_2 F_2 (1-\frac{a}{l}),\\
&< K(x) g^1_{,x}(x) g^1_{,x}(x)) >_\alpha = \frac{1}{3}[G_{1\alpha}\kappa_1 F_1 \frac{a}{l} - G_{2\alpha}\kappa_2 F_2 (1-\frac{a}{l})],\\
&< m(x) > = F_1\rho_1 \frac{a}{l} + F_2\rho_2 (1-\frac{a}{l}),\\
&< m(x) g^1(x) g^1(x) > = \frac{1}{3}[F_1\rho_1 \frac{a}{l} + F_2\rho_2 (1-\frac{a}{l})],\\
&< c(x) > = 2\beta[F_1\rho_1 \frac{a}{l} + F_2\rho_2 (1-\frac{a}{l})],\\
&< c(x) g^1(x) g^1(x) > = \frac{2\beta}{3}[F_1\rho_1 \frac{a}{l} + F_2\rho_2 (1-\frac{a}{l})].
\end{aligned}
\tag{48}
$$

For the particular case $a = l/2$ it is

$$
\begin{aligned}
&< K(x) >_\alpha = \frac{1}{2}(G_{1\alpha}\kappa_1 F_1 + G_{2\alpha}\kappa_2 F_2),\\
&< K(x) g^1_{,x}(x) >_\alpha = \frac{1}{2}(G_{1\alpha}\kappa_1 F_1 - G_{2\alpha}\kappa_2 F_2),\\
&< K(x) g^1_{,x}(x) g^1_{,x}(x)) >_\alpha = \frac{1}{6}(G_{1\alpha}\kappa_1 F_1 - G_{2\alpha}\kappa_2 F_2),\\
&< m(x) > = \frac{1}{2}(F_1\rho_1 + F_2\rho_2),\\
&< m(x) g^1(x) g^1(x) > = \frac{1}{6}(F_1\rho_1 + F_2\rho_2),\\
&< c(x) > = \beta(F_1\rho_1 + F_2\rho_2),\\
&< c(x) g^1(x) g^1(x) > = \frac{\beta}{3}(F_1\rho_1 + F_2\rho_2).
\end{aligned}
\tag{49}
$$

Using the perturbation method [8, 9] we obtain the following set of differential equations:
- Zeroth order equations

$$
\begin{aligned}
&-\frac{(\bar{G}_{1\alpha}\kappa_1 F_1 + \bar{G}_{2\alpha}\kappa_2 F_2)}{F_1\rho_1 + F_2\rho_2} H^0_{w\alpha,xx}(x,t) - \frac{4(\bar{G}_{2\alpha}\kappa_2 F_2 - \bar{G}_{1\alpha}\kappa_1 F_1)}{F_1\rho_1 + F_2\rho_2} H^{10}_{v\alpha,x}(x,t) +\\
&+2\beta \dot{H}^0_{w\alpha}(x,t) + \ddot{H}^0_{w\alpha}(x,t) = \frac{2 < q(x) >}{F_1\rho_1 + F_2\rho_2}\delta(t),\\
&\frac{12(\bar{G}_{2\alpha}\kappa_2 F_2 - \bar{G}_{1\alpha}\kappa_1 F_1)}{l^2(F_1\rho_1 + F_2\rho_2)} H^0_{w\alpha,x}(x,t) + \frac{48(\bar{G}_{1\alpha}\kappa_1 F_1 + \bar{G}_{2\alpha}\kappa_2 F_2)}{l^2(F_1\rho_1 + F_2\rho_2)} H^{10}_{v\alpha}(x,t) +\\
&+2\beta \dot{H}^{10}_{v\alpha}(x,t) + \ddot{H}^{10}_{v\alpha}(x,t) = 0.
\end{aligned}
\tag{50}
$$

- First order equations (for i=1,2.)

$$
\begin{aligned}
&-\frac{(\bar{G}_{1\alpha}\kappa_1 F_1+\bar{G}_{2\alpha}\kappa_2 F_2)}{F_1\rho_1+F_2\rho_2}H^{I}_{wi\alpha,xx}(x,t)-\frac{4(\bar{G}_{2\alpha}\kappa_2 F_2-\bar{G}_{1\alpha}\kappa_1 F_1)}{F_1\rho_1+F_2\rho_2}H^{1I}_{vi\alpha,x}(x,t)+\\
&+2\beta\dot{H}^{I}_{wi\alpha}(x,t)+\ddot{H}^{I}_{wi\alpha}(x,t)=\frac{1}{F_1\rho_1+F_2\rho_2}R_{1i\alpha}(x,t),\\
&\frac{12(\bar{G}_{2\alpha}\kappa_2 F_2-\bar{G}_{1\alpha}\kappa_1 F_1)}{l^2(F_1\rho_1+F_2\rho_2)}H^{I}_{wi\alpha,x}(x,t)+\frac{48(\bar{G}_{1\alpha}\kappa_1 F_1+\bar{G}_{2\alpha}\kappa_2 F_2)}{l^2(F_1\rho_1+F_2\rho_2)}H^{1I}_{vi\alpha}(x,t)+\\
&+2\beta\dot{H}^{1I}_{vi\alpha}(x,t)+\ddot{H}^{1I}_{vi\alpha}(x,t)=\frac{1}{F_1\rho_1+F_2\rho_2}R_{2i\alpha}(x,t),
\end{aligned}
\tag{51}
$$

where

$$
\begin{aligned}
&R_{11\alpha}(x,t)=H^{0}_{w\alpha,xx}(x,t)-4H^{10}_{v\alpha,x}(x,t),\\
&R_{21\alpha}(x,t)=\frac{12}{l^2}H^{0}_{w\alpha,x}(x,t)-\frac{48}{l^2}H^{10}_{v\alpha}(x,t),\\
&R_{12\alpha}(x,t)=H^{0}_{w\alpha,xx}(x,t)+4H^{10}_{v\alpha,x}(x,t),\\
&R_{22\alpha}(x,t)=-\frac{12}{l^2}H^{0}_{w\alpha,x}(x,t)-\frac{48}{l^2}H^{10}_{v\alpha}(x,t).
\end{aligned}
\tag{52}
$$

In particular case if $G_{1\alpha}=G_{2\alpha}=G_{\alpha}$ than the equations 47-50 have the forms

$$
\begin{aligned}
&<K(x)>_{\alpha}=G_{\alpha}[\kappa_1 F_{1\alpha}\frac{a}{l}+\kappa_2 F_{2\alpha}(1-\frac{a}{l})],\\
&<K(x)g^{1}_{,x}(x)>_{\alpha}=G_{\alpha}[\kappa_1 F_{1\alpha}\frac{a}{l}-\kappa_2 F_{2\alpha}(1-\frac{a}{l})],\\
&<K(x)g^{1}_{,x}(x)g^{1}_{,x}(x))>_{\alpha}=\frac{1}{3}G_{\alpha}[\kappa_1 F_{1\alpha}\frac{a}{l}-\kappa_2 F_{2\alpha}(1-\frac{a}{l})].
\end{aligned}
\tag{47a}
$$

for the particular case $a=l/2$

$$
\begin{aligned}
&<K(x)>_{\alpha}=\frac{G_{\alpha}}{2}(\kappa_1 F_{1\alpha}+\kappa_2 F_{2\alpha}),\\
&<K(x)g^{1}_{,x}(x)>_{\alpha}=\frac{1}{2}G_{\alpha}(\kappa_1 F_{1\alpha}-\kappa_2 F_{2\alpha}),\\
&<K(x)g^{1}_{,x}(x)g^{1}_{,x}(x))>_{\alpha}=\frac{1}{6}G_{\alpha}(\kappa_1 F_{1\alpha}-\kappa_2 F_{2\alpha}).
\end{aligned}
\tag{48a}
$$

- Zeroth order equations

$$\begin{aligned}&-\frac{\bar{G}_\alpha(\kappa_1F_{1\alpha}+\kappa_2F_{2\alpha})}{F_{1\alpha}\rho_1+F_{2\alpha}\rho_2}H^{0}_{w\alpha,xx}(x,t)-\frac{4\bar{G}_\alpha(\kappa_2F_{2\alpha}-\kappa_1F_{1\alpha})}{F_{1\alpha}\rho_1+F_{2\alpha}\rho_2}H^{10}_{v\alpha,x}(x,t)+\\&+2\beta\dot{H}^{0}_{w\alpha}(x,t)+\ddot{H}^{0}_{w\alpha}(x,t)=\frac{2<q(x)>}{F_{1\alpha}\rho_1+F_{2\alpha}\rho_2}\delta(t),\\&\frac{12\bar{G}_\alpha(\kappa_2F_{2\alpha}-\kappa_1F_{1\alpha})}{l^2(F_{1\alpha}\rho_1+F_{2\alpha}\rho_2)}H^{0}_{w\alpha,x}(x,t)+\frac{48\bar{G}_\alpha(\kappa_1F_{1\alpha}+\kappa_2F_{2\alpha})}{l^2(F_{1\alpha}\rho_1+F_{2\alpha}\rho_2)}H^{10}_{v\alpha}(x,t)+\\&+2\beta\dot{H}^{10}_{v\alpha}(x,t)+\ddot{H}^{10}_{v\alpha}(x,t)=0.\end{aligned}\tag{49a}$$

- First order equations (for i=1,2.)

$$\begin{aligned}&-\frac{\bar{G}_\alpha(\kappa_1F_{1\alpha}+\kappa_2F_{2\alpha})}{F_{1\alpha}\rho_1+F_{2\alpha}\rho_2}H^{I}_{w\alpha,xx}(x,t)-\frac{4\bar{G}_\alpha(\kappa_2F_{2\alpha}-\kappa_1F_{1\alpha})}{F_{1\alpha}\rho_1+F_{2\alpha}\rho_2}H^{1I}_{v\alpha,x}(x,t)+\\&+2\beta\dot{H}^{I}_{w\alpha}(x,t)+\ddot{H}^{I}_{w\alpha}(x,t)=\frac{1}{F_{1\alpha}\rho_1+F_{2\alpha}\rho_2}R_{1\alpha}(x,t),\\&\frac{12\bar{G}_\alpha(\kappa_2F_{2\alpha}-\kappa_1F_{1\alpha})}{l^2(F_{1\alpha}\rho_1+F_{2\alpha}\rho_2)}H^{I}_{w\alpha,x}(x,t)+\frac{48\bar{G}_\alpha(\kappa_1F_{1\alpha}+\kappa_2F_{2\alpha})}{l^2(F_{1\alpha}\rho_1+F_{2\alpha}\rho_2)}H^{1I}_{v\alpha}(x,t)+\\&+2\beta\dot{H}^{1I}_{v\alpha}(x,t)+\ddot{H}^{1I}_{v\alpha}(x,t)=\frac{1}{F_{1\alpha}\rho_1+F_{2\alpha}\rho_2}R_{2\alpha}(x,t),\end{aligned}\tag{50a}$$

Let us consider the shear vibration of a homogeneous beam. The random influence function has the form

$$H_\alpha(x,t)=\frac{2}{hm_\alpha}\sum_{n=1}^{\infty}\frac{q_n}{\Omega_{n\alpha}}e^{-\beta t}\sin\Omega_{n\alpha}t\sin\lambda_n x,\tag{53}$$

where $2\beta=\frac{c}{m}$, $(\Omega_{n\alpha})^2=\lambda_n^2\frac{G_\alpha F}{m}-\beta^2=(\omega_{n\alpha})^2-\beta^2$, $\lambda_n=\frac{\pi}{h}(n-\frac{1}{2})$, $\omega_n^2=\lambda_n^2\frac{K}{m}=\lambda_n^2v_s^2$,
$q_n=\int_0^h q(x)\sin\lambda_n x dx.$

We assume that the Kirchhoff modulus G_α is a fuzzy random variable. The other beam parameters are assumed to be deterministic. The random functions describing the load were assumed to be fuzzy weakly stationary stochastic processes, $E[f_\alpha(t)]_\alpha=E[f_\alpha]_\alpha=const.$, $C_{ff_\alpha}(t_1,t_2)=C_{ff_\alpha}(t_1-t_2)=C_{ff_\alpha}(t).$ Let us assume that the time and space correlation of the load process is of the "white noise" type, namely that the covariance functions has the form $C_{ff_\alpha}=\sigma^2_{f_\alpha}\delta(t).$ The solution will be found for the steady-state, i.e. $t_0=-\infty.$ The expected value is equal to

$$E[u_{\alpha\beta}(\mathbf{b}_\alpha,x,\infty)]_{\alpha\beta}=E[f_\alpha]_\alpha\int_{-\infty}^{t}E[H_\alpha(x,t-\tau)]d\tau=\frac{2E[f_\alpha]}{Fh}E[\frac{1}{G_\alpha}]_\alpha\sum_{n=1}^{\infty}\frac{q_n}{\lambda_n^2}\sin\lambda_n x.\tag{54}$$

In order to find the probabilistic characteristics the function of the random variables has been expanded into Taylor series around the mean value and restricted to three first items (components) of the expansion. The expected value of the response has form

$$E[u_\alpha(\mathbf{b}_\alpha, x, \infty)]_\alpha = \frac{2E[f_\alpha]_\alpha}{Fh}\frac{(1+v_{G\alpha}^2)}{E[G_\alpha]_\alpha}\sum_{n=1}^{\infty}\frac{q_n}{\lambda_n^2}\sin\lambda_n x, \tag{55}$$

where v_{G_α} is standard deviation of the Kirchhoff modulus.

The variance of the beam displacement for the steady-state vibrations (t→∞) can be shown in the form

$$\sigma_{u_\alpha}^2(x,\infty)_\alpha = \sigma_{f\alpha}^2\int_0^\infty E[h_\alpha^2(\mathbf{b}_\alpha, x,\tau]_\alpha d\tau + E^2[f_\alpha]_\alpha\int_0^\infty\int_0^\infty Cov_{hh_\alpha}(x,x,\tau_1,\tau_2)_\alpha d\tau_1 d\tau_2. \tag{56}$$

After calculating the integrals in the equation (56) one obtains

$$\begin{aligned}\sigma_{u_\alpha}^2(x,\infty)_\alpha &= \frac{\sigma_{f_\alpha}^2(1+v_{G_\alpha}^2)}{Fh^2 m\beta E[G_\alpha]_\alpha}\sum_{n=1}^{\infty}\frac{q_n^2}{\lambda_n^2}\sin^2\lambda_n x + \\ &+\frac{16\sigma_{f_\alpha}^2\beta}{h^2m^2}\sum_{n=1}^{\infty}\sum_{\substack{k=1\\ n\neq k}}^{\infty}q_n q_k E[\frac{1}{(2\beta^2+\omega_{n\alpha}^2+\omega_{k\alpha}^2)^2-4\Omega_{n\alpha}^2\Omega_{k\alpha}^2}]_\alpha \sin\lambda_n x\sin\lambda_k x.\end{aligned} \tag{57}$$

4 NUMERICAL EXAMPLE

For the testing the approach presented the shape functions of the expected value and standard deviation of the displacements on a top of multistorey tall building with averaged structure parameters have been calculated. The calculations have been done assuming that the expected value of the shear stiffness is a fuzzy number of triangular shape functions. Other quantities are being treated as deterministic parameters. The results obtained for the coefficient of variation of the shear stiffness equal to 0.1 are shown in the Figures 3 and 4.

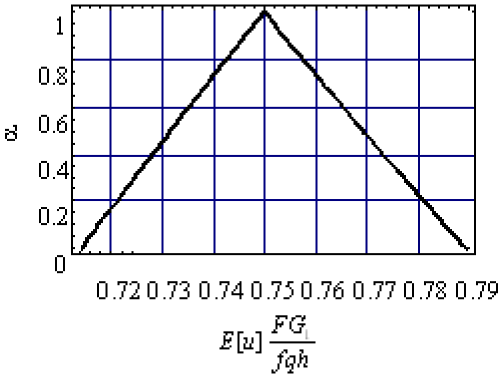

Figure 3. The shape function of the expected value of the displacement

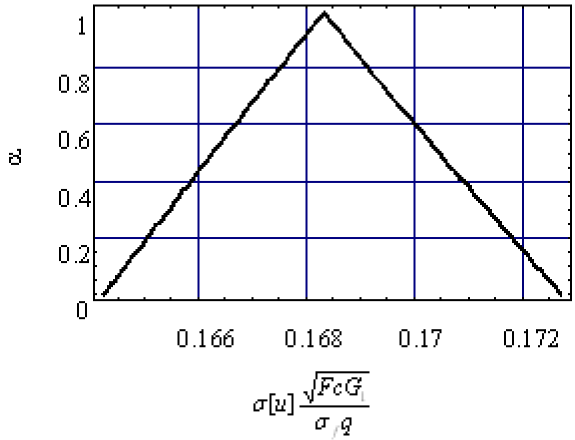

Figure 4. The shape function of the standard deviation of the displacement

5 SUMMARY AND CONCLUSIONS

- The model of a vibrating shear beam has been generalized on the finite periodic composite beam with uncertain parameters. Different types of uncertainty of the structure parameters and the excitation process have been considered, namely: fuzzy numbers, random variables, random functions, fuzzy random variables, fuzzy random functions and fuzzy stochastic processes. This allows for investigating a wide analysis of complex problems of the shear vibrations of periodic composite beams with fuzzy random parameters under fuzzy stochastic excitations. Much attention has been focused on for obtaining the solution in the most general case. Presented model of the finite periodic composite beam with uncertain parameters has been proposed as a model of multistory building. It has been assumed, that each storey has two different stiffnesses: one for the part without windows and doors and another one with windows and doors.

- For obtaining the solution within the correlation theory the fuzzy random dynamic influence function has been introduced, which allows for applying the perturbation method or Monte Carlo simulation.

- The difficulty connected with solving the differential equations with periodic variable coefficients has been overcame by applying the average tolerance approach, which transforms the differential equations with periodic variable coefficients into the averaged differential equations with constant coefficients.

- For the steady-state vibration of the beam with fuzzy random parameters under stationary stochastic excitation the expressions for calculating the expected value and variance of the beam displacements are given.

REFERENCES

[1] M.I.Todorovska, M.D. Trifunac, Antiplane earthquake waves in long structures. Journal of Engineering Mechanics, ASCE, 115, 12, 2687-2708, 1989.

[2] M.I.Todorovska, V.W. Lee, Seismic waves in buildings with walls or central core. Journal of Engineering Mechanics, ASCE, 115, 12, 2669-2686, 1989.

[3] E.Safak, Wave-propagation formulation of seismic response of multistory buildings. Journal of Structural Engineering, ASCE, 125, 4, 426-437, 1999.

[4] Z. Zembaty, Non-stationary random vibrations of a shear beam under high frequency sesmic effects. Soil Dynamics and Earthquake Engineering, 27, 1000-1011, 2007.

[5] Cz. Woźniak, Macro-dynamics of elastic and visco-elastic microperiodic composites. *Journal of Theoretical and Applied mechanics*, 39, 763-770, 1993.

[6] Cz. Woźniak, *A model for of micro-heterogeneous solid*, Mechanik Berichte, 1, Institut fur Allgemeine Mechanik, 1999.

[7] Cz. Woźniak, E. Wierzbicki, *Averaging techniques in thermomechanics of composite solids.* Wydawnictwo Politechniki Świętokrzyskiej, 2000.

[8] K. Mazur-Śniady, P. Śniady, W. Zielichowski-Haber, Dynamic response of micro-periodic composite rods with uncertain parameters under moving random load. Journal of Sound and Vibration, 320, 273-288, 2009.

[9] P. Śniady, R. Adamowski, G. Kogut, W. Zielichowski-Haber, Spectral stochastic analysis of structures with uncertain parameters, Probabilistic Engineering Mechanics, 23, 76-83, 2008.

[10] G. Adomian, Stochastic Systems, Academic Press; 1983.

[11] L.A. Zadeh, Fuzzy sets. Information Control, 8, 338-353, 1965.

[12] Kwarkernaak H. Fuzzy random variables (I). Information Sciences 1978; 15: 1-29.

[13] Puri M.I, Ralescu D.A. Fuzzy random variables. Journal of Mathematical Analysis and Application 1986; 114: 409-422.

[14] Zhang Y, Wang G, Su F, Zhong Q. The theory of response analysis of fuzzy stochastic dynamical systems with a single degree of freedom. Earthquake Engineering and Structural Dynamics 1996; 25: 235-251.

[15] Zhang Y, Wang G, Su F, Song Y. Response analysis for fuzzy stochastic dynamical systems with multiple degrees of freedom. Earthquake Engineering and Structural Dynamics 1997; 26: 151-166.

[16] Y. Zhang, G. Wang, F. Su F, The general theory for response analysis of fuzzy stochastic dynamical systems. *Fuzzy Sets and Systems,* **83**, 369-405, 1996.

[17] L. Chen, S. S. Rao, Fuzzy finite-element approach for the vibration analysis of imprecisely-defined systems. *Finite Elements in Analysis and Design,* **27**, 69-83, 1997.

[18] Y. Zhang, X. Liu, Theory of response analysis for continuous fuzzy stochastic dynamical systems I. Normal mode method. *Civil Engineering and Environmental Systems,* **15** (1): 23-44, 1998.

[19] Y. Zhang, X. Lium Theory of response analysis for continuous fuzzy stochastic dynamical systems II. Influence function method. *Civil Engineering and Environmental Systems,* **15** (1): 45-66, 1998.

[20] Feng Y. The solutions of linear fuzzy stochastic differential systems. *Fuzzy Sets and Systems*, **140**, 541-554, 2003.

[21] R. Körner, On the variance of fuzzy random variables. *Fuzzy Sets and Systems,* **92**, 83-93, 1997.

[22] Y. Feng, L. Hu, H. Shu, The variance and covariance of fuzzy random variables and their applications. *Fuzzy Sets and Systems,* **120**, 487-497, 2001.

[23] L, Hu, R. Wu, S. Shao, Analysis of dynamical systems whose inputs are fuzzy stochastic processes. *Fuzzy Sets and Systems*, **129**, 111-118, 2002.

[24] B. Möller, M. Beer, *Fuzzy randomness. Uncertainty in civil engineering and computational mechanics.* Springer; 2004.

[25] B. Möller B, U. Reuter, *Uncertainty forecasting in engineering*. Springer-Verlag; 2007.

COMPDYN 2011
III ECCOMAS Thematic Conference on
Computational Methods in Structural Dynamics and Earthquake Engineering
M. Papadrakakis, M. Fragiadakis, V. Plevris (eds.)
Corfu, Greece, 25–28 May 2011

ROBUST DESIGN OF TUNED LIQUID COLUMN DAMPERS UNDER STOCHASTIC GROUND MOTION CONSIDERING FUZZY UNCERTANTIES

G. Quaranta[1], **S. Chakraborty**[2], **and G. C. Marano**[3]

[1] Dept. of Civil and Environmental Engineering, University of California Davis
One Shields Avenue, Davis, CA 95616, U.S.A.
gquaranta@ucdavis.edu

[2] Dept. of Civil Engineering, Bengal Engineering and Science University
Shibpur, Howrah, 711103, India
schak@civil.becs.ac.in

[3] Dept. of Environmental Engineering and Sustainable Development, Technical University of Bari
viale del Turismo 10, 74100, Taranto, Italy
g.marano@poliba.it

Keywords: Credibility Theory, Fuzzy Uncertainty, Optimization, Robust Design, Stochastic Ground Motion, Tuned Liquid Column Damper.

Abstract. *The tuned liquid column dampers (TLCDs) have been shown to be effective vibration control devices for flexible structures subjected to long-duration, periodic or harmonic excitations. Their potential applications for seismic protection and retrofitting were recently explored. The optimum TLCD parameters are normally obtained based on the implicit assumption that the involved variables are deterministic. However, it is well known that the efficiency of TLCDs may be jeopardized if its parameters are not properly tuned to the vibrating mode of interest, for instance as consequence of the unavoidable presence of uncertain variables. Thus, the optimization of damper parameters considering model uncertainties has attracted a great deal of interest. The robust design of TLCDs for the passive control of mechanical systems under random ground motion is investigated in the present paper by coupling random vibration analysis and credibility theory in order to take into account fuzzy uncertainties. In doing so, two antithetical objective functions are considered, and they are the expected value and the variance of an appropriate displacement-based fuzzy structural index. Specifically, this latter one is introduced to characterize the performance variability due to the existence of fuzzy uncertainties affecting, both the system and random loading parameters. A numerical study is performed to demonstrate the applicability of the developed approach.*

1 INTRODUCTION

Base isolation, passive energy dissipation and active control are three current philosophies for enhancing structural performances and safety against natural and manmade hazards. Among the most popular passive control devices, the tuned mass dampers and the tuned liquid dampers are commonly used. A tuned mass damper (TMD) consists of a large mass attached to the structure through a spring and a dashpot, and dissipates energy when it is tuned to the frequency of the structure. The tuned liquid damper (TLD) consists of a container which is partially filled with liquid which dissipates energy through the sloshing action of a liquid in the container. For optimum results, the sloshing frequency is tuned to the frequency of the structure. Tuned liquid column dampers (TLCDs) are a class of tuned liquid dampers that impart indirect damping to the primary structure through oscillations of the liquid column in a U-shaped container which includes at least one orifice. It has been also investigated a type of TLCD that have different cross-sections in the horizontal and vertical columns, termed liquid column vibration absorbers (LCVAs). These devices are summarized in Fig. 1.

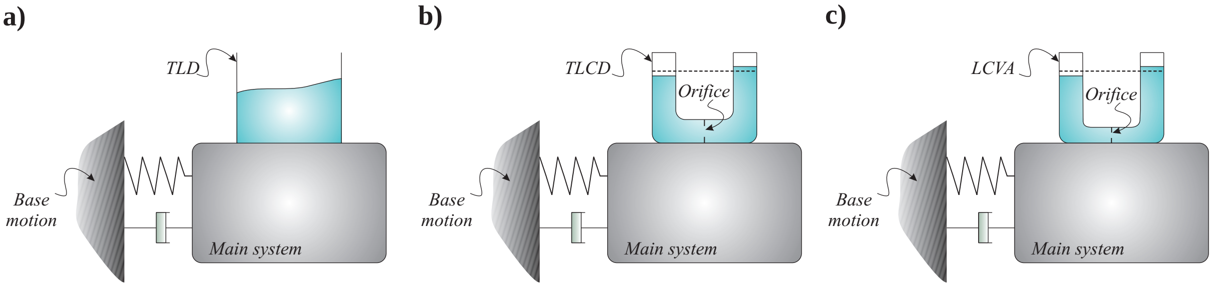

Figure 1: Tuned liquid damper (a), Tuned liquid column damper (b) and Liquid column vibration absorber (c).

Potential advantages of TLCDs over the conventional inertial devices (e.g., TMDs) are that the system is inexpensive and requires minimum maintenance and its vibration characteristics (e.g., tuning and damping) are well defined and can be easily modified. For instance, its natural frequency is only determined by the length of the liquid column, and its damping can be overall accounted for by the so-called head loss coefficient that depends on the orifice size in the horizontal column. Additionally, water storage already available in tall buildings can be utilized without introducing excessively extra large mass. The effectiveness of TLCD as protection strategy was primarily addressed for controlling the wind-induced vibration of towers [1] and tall buildings [2]. In doing this, the most of the studies consider a single-degree-of-freedom (SDOF) model of primary system equipped with a TLCD and subject to white noise type of wind loading [3]. On the contrary, the assessment of the TLCD performances for protecting structural systems subject to earthquake load is comparatively less. In this field, the effectiveness of the TLCD performances was investigated in [4] with regard to non-stationary random vibrations simulating an earthquake loading.

All mechanical parameters governing the adopted passive protection strategy have to be properly optimized in order to meet the maximum possible protection level. In doing so, the analysis of all sources of uncertainty is a crucial step of the design process. In this regard, it may be noted that earlier studies were mainly conducted by assuming deterministic protected mechanical systems subject to uncertain dynamic loads, i.e. [3][4][5]. However, this simplification may jeopardize the effectiveness of the adopted protection strategy. In fact, it was reported that the uncertainty in mechanical system parameters might have equal or sometimes even greater influence on the response than the uncertainty in the dynamic excitations [6]. Since passive protection systems do not have any feedback from the structural response, improved design strategies should be preferred for taking into account all possible sources of uncertainty and their effects on the expected performances. For instance, Marano and co-authors [7][8] investigated the effects due to uncertain mechanical systems parameters for robust optimum design strategies of TMDs. In doing this, the authors considered SDOF systems subject to stationary filtered white noise process and the sensitivity of a performance index against the fluctuations of the uncertain structural parameters is considered via direct perturbation method. The application of low-order perturbation methods allow a probabilistic analysis by considering few statistical moments of the uncertain parameters (e.g., mean and variance) and do not require full statistical descriptions (e.g., the joint probability density functions). Although researchers and practitioners are familiar with stochastic calculus, a pure probabilistic standpoint in designing these devices may present several limitations.

Since fuzziness is frequently involved in modeling random processes and variables, it is not so reasonable to take into account randomness while ignoring the existence of fuzziness aprioristically [9]. On the contrary, more consistent analysis may be carried out by relaxing conventional probabilistic-based methods in order to include non-probabilistic forms of uncertainty appropriately [10][11]. For instance, the reliability based optimum design of TMDs in seismic vibration control of structures with bounded uncertain parameters was presented in [12]. The optimum design of TLCDs under stochastic earthquake considering uncertain bounded system parameters was discussed in [13]. A procedure for the analysis of structural systems subject to random vibrations considering fuzzy variables was proposed in [14]. A robust-based optimization problem for TMDs was illustrated in [15] which take into account stochastic ground motion and fuzzy variables.

This paper addresses the robust design of TLCDs under stochastic ground motion considering fuzzy uncertainties. In detail, the dynamic loading is modeled as a stationary filtered white noise process whereas both load and system parameters are considered as fuzzy variables. As a consequence, a general performance index is affected by fuzziness itself. Therefore, we propose the application of the credibility measure in order to extract two representative crisp measures. The first one is based on the expected operator for fuzzy variables which needs to be minimized in order to improve the effectiveness of the TLCD. The second one, based on the variance operator for fuzzy variables, must be minimized in order to increase the robustness against fuzzy uncertainties. As these measures have an opposite behavior within typical design solution spaces, a multi-objective optimization problem can be formulated in order to define a collection of solutions (in Pareto sense) which are capable of ensuring a satisfactory trade-off between mechanical performances and robustness against the variability due to the uncertain (fuzzy) parameters. Numerical examples at the end will demonstrate the feasibility of the proposed approach of designing TLCDs.

2 DYNAMIC RESPONSE OF TLCD-STRUCTURE SYSTEM

The description of a SDOF system equipped with a TLCD under stochastic ground motion is provided in this section. The stochastic dynamic response analysis of the combined TLCD-structure is evaluated as in [13], by using the state space formulation in time domain and by solving the final Lyapunov equation.

2.1 TLCD system and liquid motion equation

The TLCD considered in the present study is a U-shaped pipe attached to the main system which is modeled as a SDOF system with properties in accordance with the specified mode of vibration. A schematic diagram of a SDOF system equipped with a TLCD under base excitation is shown in Fig. 2.

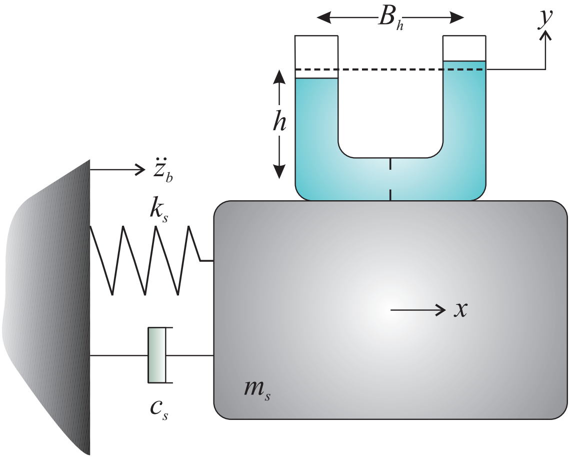

Figure 2: Layout of a SDOF system equipped with a TLCD.

The main geometrical and physical data for the TLCD are: cross-sectional area A, the length of the horizontal portion of the tube B_h, the vertical height of the liquid inside the tube h and the density of the liquid ρ. The main system to be protected has a mass equal to m_s, a linear stiffness k and a viscous damping c_s. The total length of the liquid column is $L_e=2h+B_h$. The mass of the liquid $m_l=\rho AL_e$ can be considered as part of m_s. An orifice is installed in the horizontal portion of the pipe and ξ denotes the coefficient of head loss which depends on its opening ratio. The orifice is typically placed at the centre of the horizontal portion of the tube. The combined TLCD-structure is subject to base acceleration (see Fig. 2), for instance due to an earthquake. The relative horizontal displacement of the SDOF system is x whereas the displacement of the liquid surface (with reference to the unperturbed original configuration) is denoted as y (the time variable is omitted throughout the paper to improve the readability of various equations). In order to derive the motion equation of the liquid within the U-shaped pipe, the following hypotheses are used: (*i*) the sloshing behavior on the liquid surface is negligible; (*ii*) the flow is incompressible (i.e., the flow rate is constant); (*iii*) the dimension of the column cross-section is much smaller than the horizontal length of a TLCD. The equation of motion of the liquid column is [16]:

$$\rho AL_e\ddot{y}+\frac{1}{2}\rho A\xi\left|\dot{y}\right|\dot{y}+2\rho gAy=-\rho AB_h\left(\ddot{x}+\ddot{z}_b\right) \tag{1}$$

In the above, g is the gravitational acceleration. It is evident in the second term of Eq. (1) that the TLCD response is non-linear as a result of the drag-type forces induced by the orifice. Within the framework of random vibration theory, the motion equation in Eq. (1) is usually linearized via stochastic equivalent linearization technique. First, a linear system is chosen to represent the original non-linear system:

$$\rho AL_e\ddot{y}+2\rho Ac_p\dot{y}+2\rho gAy=-\rho AB_h\left(\ddot{x}+\ddot{z}_b\right) \tag{2}$$

in which c_p is the equivalent damping coefficient for the TLCD after linearization. By minimizing the mean-square error between Eq. (1) and Eq.(2), it can be found:

$$c_p=\frac{\xi\left\langle\left|\dot{y}\right|\dot{y}\right\rangle}{4\left\langle\dot{y}^2\right\rangle} \tag{3}$$

where $\left\langle\bullet\right\rangle$ is the operator of expectation. If x is a zero-mean stationary Gaussian process, c_p is:

$$c_p = \frac{\xi \sigma_{\dot{y}}}{\sqrt{2\pi}} \quad \left(\sigma_{\dot{y}} : standard\ deviation\ of\ the\ liquid\ velocity\right) \tag{4}$$

In Eq. (4), the standard deviation of the liquid velocity is not known a priori: therefore, the dynamic analysis is performed by assuming an initial value for c_p (i.e., c_p=0) and is updated once the motion equation is solved. This implies an iterative procedure that will be stopped once a convergence criterion is fulfilled (the exact value of c_p is achieved after few iterations). The error due to this linearization depends on the head loss coefficient (the error increases as ξ grows): however, for the most part of engineering applications, Eq. (4) provides very good results. By normalizing Eq. (2) with respect to the mass of the liquid in the container, one obtains:

$$\ddot{y} + \frac{2c_p}{L_e}\dot{y} + \frac{2g}{L_e}y + p\ddot{x} = -p\ddot{z}_b \tag{5}$$

where $p=B_h/L_e$ is the length ratio.

2.2 Motion equation of the SDOF system equipped with a TLCD

The TLCD is used to protect a SDOF linear system as shown in Fig. 2. The equation of motion of the main system equipped with TLCD is:

$$\left(m_s + \rho A B_h + 2\rho h A\right)\ddot{x} + c_s\dot{x} + k_s x = -\left(m_s + \rho A B_h + 2\rho h A\right)\ddot{z}_b - \rho A B_h \ddot{y} \tag{6}$$

If the variable $m_l=\rho AB_h+\rho Ah$ is considered, then above equation can be expressed as:

$$\left(m_s + m_l\right)\ddot{x} + c_s\dot{x} + k_s x = -\left(m_s + m_l\right)\ddot{z}_b - \rho A p L_e \ddot{y} \tag{7}$$

The normalization of Eq. (7) with respect to m_s yields:

$$\left(1+\mu\right)\ddot{x} + \frac{c_s}{m_s}\dot{x} + \frac{k_s}{m_s}x = -\left(1+\mu\right)\ddot{z}_b - \mu p \ddot{y}\,, \tag{8}$$

in which $\mu=(\rho AL_e)/m_s$ is the so-called mass ratio. By introducing the notations of the natural frequency $\omega_s=\sqrt{(k_s/m_s)}$ and the damping coefficient $\xi_s=c_s/(2m_s\omega_s)$ for the main system, Eq. (8) can be rewritten as follows:

$$\left(1+\mu\right)\ddot{x} + 2\xi_s\omega_s\dot{x} + \omega_s^2 x + \mu p\ddot{y} = -\left(1+\mu\right)\ddot{z}_b \tag{9}$$

The tuning ratio $\gamma=\omega_l/\omega_s$ will be also used, where $\omega_l=\sqrt{(2g/L_e)}$ is the frequency of the liquid. Eq. (5) and Eq. (9) can be also expressed in matrix form:

$$\begin{bmatrix} 1 & p \\ \mu p & (1+\mu) \end{bmatrix}\begin{Bmatrix} \ddot{y} \\ \ddot{x} \end{Bmatrix} + \begin{bmatrix} \frac{2c_p}{L_e} & 0 \\ 0 & 2\xi_s\omega_s \end{bmatrix}\begin{Bmatrix} \dot{y} \\ \dot{x} \end{Bmatrix} + \begin{bmatrix} \frac{2g}{L_e} & 0 \\ 0 & \omega_s^2 \end{bmatrix}\begin{Bmatrix} y \\ x \end{Bmatrix} = -\ddot{z}_b\begin{Bmatrix} p \\ (1+\mu) \end{Bmatrix} \tag{10}$$

If the state space vector **u** is introduced:

$$\mathbf{u} = \left\{ y \quad x \quad \dot{y} \quad \dot{x} \right\}^T \tag{11}$$

then Eq. (10) is reduced to a standard first-order form:

$$\dot{\mathbf{u}} = \mathbf{A}_*\mathbf{u} + \mathbf{r}\ddot{z}_b \tag{12}$$

where

$$\mathbf{A}_* = \begin{bmatrix} \mathbf{0}_{2\times 2} & \mathbf{I}_{2\times 2} \\ \mathbf{M}^{-1}\mathbf{K} & \mathbf{M}^{-1}\mathbf{C} \end{bmatrix} \tag{13}$$

and $\mathbf{r}=\{0\ 0\ 1\ 1\}^T$. In Eq. (13), $\mathbf{0}$ and $\mathbf{I}$ are the null and the unit matrix, respectively (the subscripts denote their size).

2.3 Stochastic model for the ground motion

For base random accelerations, a usual model is obtained via second-order linear filtering of the white noise process. As in several previous studies – see for instance [7] and [13] – the stationary Kanai-Tajimi model is considered in this paper [17][18]. So doing, the excitation at the base is described as follows:

$$\begin{aligned} \ddot{x}_f + 2\xi_f\omega_f\dot{x}_f + \omega_f^2 x_f &= -w \\ \ddot{z}_b = \ddot{x}_f + w = 2\xi_f\omega_f\dot{x}_f &+ \omega_f^2 x_f \end{aligned} \tag{14}$$

In which w is a stationary Gaussian zero mean white noise process whose power spectral density (PSD) is S_0 which can be evaluated as follows

$$S_0 = \frac{2\xi_f\sigma_{\ddot{z}_b}^2}{\pi\left(1+4\xi_f^2\right)\omega_f} \tag{15}$$

The standard deviation of the base motion is related to the peak ground acceleration (PGA):

$$\text{PGA} = 3\sigma_{\ddot{z}_b} \tag{16}$$

Therefore, the dynamic loading model in Eq. (14) depends on two parameters, named the filter frequency ω_f and the filter damping ξ_f.

2.4 Response covariance analysis

The following algebraic matrix equation of order six – the so-called Lyapunov equation – is obtained by taking into account both Eq. (12) and Eq. (14):

$$\mathbf{AR} + \mathbf{RA}^T + \mathbf{B} = \mathbf{0}_{6\times 6} \tag{17}$$

In Eq. (17) the state space matrix $\mathbf{A}$ and $\mathbf{B}$ are, respectively:

$$\mathbf{A} = \begin{bmatrix} 0 & 0 & 0 & 1 & 0 & 0 \\ 0 & 0 & 0 & 0 & 1 & 0 \\ 0 & 0 & 0 & 0 & 0 & 1 \\ -2m_{11}g/L_e & m_{12}\omega_s^2 & 0 & -2m_{12}c_p/L_e & 2m_{12}\xi_s\omega_s & 0 \\ 2m_{21}g/L_e & -m_{22}\omega_s^2 & \omega_f^2 & 2m_{21}c_p/L_e & -2m_{22}\xi_s\omega_s & 2\xi_f\omega_f \\ 0 & 0 & -\omega_f^2 & 0 & 0 & -2\xi_f\omega_f \end{bmatrix} \tag{18}$$

$$\mathbf{B}=\begin{bmatrix} 0 & 0 & 0 & 0 & 0 & 0 \\ 0 & 0 & 0 & 0 & 0 & 0 \\ 0 & 0 & 0 & 0 & 0 & 0 \\ 0 & 0 & 0 & 0 & 0 & 0 \\ 0 & 0 & 0 & 0 & 0 & 0 \\ 0 & 0 & 0 & 0 & 0 & 2\pi S_0 \end{bmatrix}, \tag{19}$$

with

$$d_e=(1+\mu)-\mu p^2 \quad m_{11}=\frac{1+\mu}{d_e} \quad m_{21}=\frac{\mu p}{d_e} \quad m_{12}=\frac{p}{d_e} \quad m_{22}=\frac{1}{d_e} \tag{20}$$

And the global state space vector is:

$$\mathbf{z}=\left\{ y \quad x \quad x_f \quad \dot{y} \quad \dot{x} \quad \dot{x}_f \right\}^T \tag{21}$$

The space state covariance matrix **R** in Eq. (17) takes the form:

$$\mathbf{R}=\begin{bmatrix} \mathbf{R}_{\mathbf{zz}} & \mathbf{R}_{\mathbf{z}\dot{\mathbf{z}}} \\ \mathbf{R}_{\dot{\mathbf{z}}\mathbf{z}} & \mathbf{R}_{\dot{\mathbf{z}}\dot{\mathbf{z}}} \end{bmatrix}, \tag{22}$$

and each sub-matrix has a size 2×2. Our main interest is focused in the following quantities:

$$\sigma_x=\sqrt{\mathbf{R}_{\mathbf{zz}}(2,2)} \tag{23}$$

$$\sigma_{\dot{y}}=\sqrt{\mathbf{R}_{\dot{\mathbf{z}}\dot{\mathbf{z}}}(1,1)}, \tag{24}$$

that are the standard deviation of the main system displacement equipped with a TLCD and the standard deviation of the liquid velocity, respectively. Eq. (24) is needed to evaluate c_p in Eq. (4).

3 ROBUST DESIGN OPTIMIZATION CONSIDERING FUZZY UNCERTANTIES

Once the covariance response analysis is completed, the structural performance index under investigation is presented. Thus, the adopted uncertain parameters' model is introduced. Consequently, the robust design optimization problem of the TLCD is formalized within the framework of the credibility theory.

3.1 Structural performance index

In order to assess the effectiveness of the TLCD, the response covariance analysis is performed for the unprotected main system. In this case, the covariance matrix $\mathbf{R}_0$ has size 4×4 and can be evaluated as follows:

$$\mathbf{A}_0\mathbf{R}_0+\mathbf{R}_0\mathbf{A}_0^T+\mathbf{B}_0=\mathbf{0}_{4\times 4}, \tag{25}$$

where

$$\mathbf{A}_0 = \begin{bmatrix} 0 & 0 & 1 & 0 \\ 0 & 0 & 0 & 1 \\ -\omega_s^2 & \omega_f^2 & -2\xi_s\omega_s & 2\xi_f\omega_f \\ 0 & -\omega_f^2 & 0 & -2\xi_f\omega_f \end{bmatrix} \tag{26}$$

$$\mathbf{B}_0 = \begin{bmatrix} 0 & 0 & 0 & 0 \\ 0 & 0 & 0 & 0 \\ 0 & 0 & 0 & 0 \\ 0 & 0 & 0 & 2\pi S_0 \end{bmatrix}, \tag{27}$$

And the global state space vector is:

$$\mathbf{z}_0 = \left\{ x_0 \quad x_f \quad \dot{x}_0 \quad \dot{x}_f \right\}^T \tag{28}$$

Finally, the standard deviation of the unprotected main system displacement is:

$$\sigma_{x_0} = \sqrt{\mathbf{R}_{\mathbf{z}_0\mathbf{z}_0}(1,1)} \tag{29}$$

Given a set of TLCD parameters, i.e. $\mathbf{d}=\{\gamma, \xi\}$, a dimensionless performance index to assess the efficiency of the TLCD is [7]:

$$\psi(\mathbf{d}) = \frac{\sigma_x(\mathbf{d})}{\sigma_{x_0}} \tag{30}$$

This function represents a direct stochastic displacement-based performance index: in fact, the designed TLCD is effective in seismic protection as $\psi(\mathbf{d})$ tends to zero.

3.2 Consideration of non-probabilistic uncertainties

The performance index in Eq. (30) is carried out under the assumption that the dynamic loading is the only source of uncertainty, and it is assumed as a pure random process. The effects of uncertain structural parameters are generally considered via direct perturbation method in a probabilistic format by considering few statistical moments of the uncertain parameters. Unfortunately, a pure probabilistic standpoint may be an important limitation for some practical applications. This is because few experimental data are available in many cases and, sometimes, literature or expert opinions are the only supports for handling uncertainties. In this perspective, alternative (non-probabilistic) uncertain models should be included.

Several studies – see for instance [12][13][14][15] – demonstrated that non-probabilistic sources of uncertainty can play a significant role in the analysis of structural systems subject to random vibration. For instance, the natural frequency of the main system ω_S is quite difficult to predict accurately (its real value is usually defined by a full-scale field dynamic testing) and is subject to non-structural induced variations (i.e., due to the temperature). Moreover, different numerical techniques for extracting the natural frequencies from dynamic records may lead to dissimilar numerical values. However, the most relevant source of uncertainty in the main system is usually due to the way by which it dissipates energy when subject to dynamic loading and, in turn, in the numerical evaluation of ξ_S. The most important sources of indeterminateness can be detected in the assessment of the filter parameters [15] for which probabilistic models (e.g., probability density functions) are not typically available to designers. On the contrary, expert opinions and existing literature data base are often adopted to select appropriate values for ω_f and ξ_s. Unfortunately, the variability of the filter parameters does not observe a specific statistical model because of the lack of accurate and consistent information for a statistical treatment. Their numerical values generally depend on the soil type, which is defined using a linguistic-based criterion (stiff, medium or soft soil). Since fuzziness is usually involved in random variables modeling, it is not so reasonable to take into account randomness while ignoring the existence of fuzziness aprioristically [19]. Therefore, an appropriate design of TLCDs needs a more complicated analysis regarding the (different) sources of uncertainty. In this paper ω_s, ξ_s, ω_f and ξ_s are considered as fuzzy variables. The use of fuzzy variables for structures subject to random vibrations was proposed in [14] and [15]. Since each interval is an equally possible fuzzy variable, this approach is a generalized version of that in [12] and [13] based on uncertain bounded system parameters.

3.3 Credibility measure, expected value and variance of fuzzy variables

In order to introduce the robust design optimization problem considering fuzzy variables, some definitions from the credibility theory are required. The credibility space is mathematically defined by the triplet (Θ, $P(\Theta)$,Cr), where Θ is the nonempty set representing the sample space, $P(\Theta)$ the power set of Θ and Cr the credibility measure. In order to define the credibility measure, we consider an event Q, its possibility Pos$\{Q\}$ (a crisp number indicating the possibility that this event will occur) and its necessity Nec$\{Q\}$ (another crisp number denoting the impossibility of the opposite set Q^{opp}). The credibility of the fuzzy event Q (denoted as Cr$\{Q\}$) is defined as the average between its possibility and necessity of Q:

$$\mathrm{Nec}\{Q\} = 1 - \mathrm{Pos}\{Q^{opp}\} \tag{31}$$

$$\mathrm{Cr}\{Q\} = \frac{1}{2}\left(\mathrm{Pos}\{Q\} + \mathrm{Nec}\{Q\}\right) \tag{32}$$

A fuzzy variable $\tilde{b}$ is a measurable function from a credibility space (Θ, $P(\Theta)$,Cr) to the set of real numbers. For each fuzzy variable, it is possible to define its membership function (MF) $\pi(b)$ as follows [20]:

$$\pi(b) = \min\left\{2\mathrm{Cr}\left\{\tilde{b} = b\right\}, 1\right\} \quad \forall b \in \mathbb{R} \tag{33}$$

Throughout the paper we will suppose that it is possible to define a fuzzy variable by means of its α-cuts. Specifically, we assume that the generic α-cut of a fuzzy variable is the following closed interval:

$$\bar{b}^{\alpha} = \left[b^{\alpha_-}, b^{\alpha_+}\right] = \left\{b \in \mathbb{R} \middle| \pi(b) \geq \alpha\right\} \ \forall \alpha \in (0,1] \tag{34}$$

and the fuzzy variable $\tilde{b}$ is:

$$\tilde{b} = \bigcup_{\alpha \in (0,1]} \alpha \left[b^{\alpha_-}, b^{\alpha_+}\right] \tag{35}$$

The representation of the expected value for a fuzzy variable is identical to that for a random variable [21]. Based on the Choquet integral, the definition of the expected value of a fuzzy variable proposed in [21] is the following:

$$\mathrm{E}\left[\tilde{b}\right] = b_E = \int_0^{+\infty} \mathrm{Cr}\left\{\tilde{b} \geq s\right\} \mathrm{d}s - \int_{-\infty}^{0} \mathrm{Cr}\left\{\tilde{b} \leq s\right\} \mathrm{d}s \tag{36}$$

and

$$\mathrm{Cr}\left\{\tilde{b} \le b\right\} = \frac{1}{2}\left(\sup_{v \le b}\left\{\pi\left(v\right)\right\} + 1 - \sup_{v > b}\left\{\pi\left(v\right)\right\}\right) \quad \forall b \in \mathbb{R} \tag{37}$$

$$\mathrm{Cr}\left\{\tilde{b} \ge b\right\} = \frac{1}{2}\left(\sup_{v \ge b}\left\{\pi\left(v\right)\right\} + 1 - \sup_{v < b}\left\{\pi\left(v\right)\right\}\right) \quad \forall b \in \mathbb{R} \tag{38}$$

The variance of a fuzzy variable measures the spread of the distribution around its expected value. In perfect analogy with the probabilistic case, the credibility-based definition of the variance of a fuzzy variable is [20]:

$$\mathrm{V}\left[\tilde{b}\right] = \mathrm{E}\left[\left(\tilde{b} - b_E\right)^2\right] \tag{39}$$

In this paper, the expected value operator in Eq. (36) will be performed to obtain the likelihood of an event from fuzzy-type information. Since fuzzy-type outputs can have a different spread around the expected value, the variance operator in Eq. (39) will be adopted to discriminate their degree of indeterminateness. Both information will be important to formalize the robust design of TLCDs. Some closed form expressions of mean and variance for common MFs are available in [20].

3.4 Robust design optimization of TLCD

The following vector of fuzzy variables (that is, a fuzzy vector) is introduced in order to take into account non-probabilistic uncertainties in the optimum design of the TLCD:

$$\tilde{\mathbf{b}} = \left\{\tilde{b}_{i=1,\ldots,4}\right\} = \left\{\tilde{\omega}_s \quad \tilde{\xi}_s \quad \tilde{\omega}_f \quad \tilde{\xi}_f\right\} \tag{40}$$

As a consequence, Eq. (30) is a deterministic function involving fuzzy variables (that is, a type of fuzzy function) and whose output is fuzzy itself:

$$\tilde{\psi}\left(\mathbf{d}\right) = \frac{\tilde{\sigma}_x\left(\mathbf{d}\right)}{\tilde{\sigma}_{x_0}} \tag{41}$$

with

$$\tilde{\psi}\left(\mathbf{d}\right) = \psi\left(\mathbf{d};\tilde{\mathbf{b}}\right) \quad \tilde{\sigma}_x\left(\mathbf{d}\right) = \sigma_x\left(\mathbf{d};\tilde{\mathbf{b}}\right) \quad \tilde{\sigma}_{x_0} = \sigma_{x_0}\left(\tilde{\mathbf{b}}\right) \tag{42}$$

Since fuzzy uncertainties are involved in the proposed analysis, the original displacement-based performance index in Eq. (30) is uncertain (fuzzy) itself. Therefore, instead of aiming to find a single ‘‘best’’ design solution, it may be more interesting to carry out a set of ‘‘good’’ compromise between TLCD performance and sensitivity against fuzziness. This is the key-idea in robust-based design strategies and would be a more consistent way for supporting designers and decision makers. Because “performance” and “sensitivity” are often conflicting objectives, a multi-objective optimization problem has to be solved. In this paper, the robust design optimization of the TLCD is performed by solving the following multi-objective optimization problem

$$\begin{gathered}\min_{\mathbf{d}}\left\{f_1\left(\mathbf{d};\tilde{\mathbf{b}}\right),\, f_2\left(\mathbf{d};\tilde{\mathbf{b}}\right)\right\} \\ s.t. \quad \mathbf{d}_{max} \le \mathbf{d} \le \mathbf{d}_{min}\end{gathered} \tag{43}$$

in which

$$f_1\left(\mathbf{d};\tilde{\mathbf{b}}\right)=\mathrm{E}\left[\tilde{\psi}\left(\mathbf{d}\right)\right] \tag{44}$$

and

$$f_2\left(\mathbf{d};\tilde{\mathbf{b}}\right)=\sqrt{\mathrm{V}\left[\tilde{\psi}\left(\mathbf{d}\right)\right]} \tag{45}$$

The minimization of the first objective function f_1 in Eq. (44) aims at improving the effectiveness of the TLCD in seismic protection. On the other hand, the robustness of the protection system against fuzziness is improved by minimizing f_2 in Eq. (45). Moreover, $\mathbf{d}_{min}$ and $\mathbf{d}_{max}$ in Eq. (43) are the lower and upper bound of the candidate design solutions, respectively.

4 COMPUTATIONAL ISSUES

The proposed strategy of the fuzzy-based robust design of TLCDs needs the analysis of two important computational issues. The first one deals with the resolution strategy for solving the multi-objective optimization in Eq. (43). The second aspect is related to the evaluation of the fuzzy performance index in Eq. (41).

4.1 Solving the multi-objective optimization problem

Since Eq. (44) and Eq. (45) involve crisp outputs only, all existing algorithms for solving multi-objective optimization problems can be used. Therefore, a standard genetic algorithm based multi-objective optimization algorithm [22] is used in this paper. Having so done, all solutions within the Pareto set are equally optimal: it is up to the designer to select a solution in this set depending on the application. The initial population is uniformly generated, the population size is 200, the maximum number of iterations is 500. The multi-objective genetic algorithm is stopped once the average change in the spread of Pareto solutions is less than 1.0×10^{-4}. The fitness scaling rank strategy has been chosen as fitness scaling function and the tournament selection (with tournament size equal to 4) as selection operator. The arithmetic crossover with a crossover fraction equal to 80% is selected as crossover operator. An adaptive feasible strategy is performed as mutation operator.

4.2 Calculation of the fuzzy performance index

An approximation of the output MF in Eq. (41) for a given design vector **d** can be obtained by repeating a interval analysis at a number of cuts, see for instance [23]. So doing, the interval analysis at each α-cut becomes the central point for computing the MF of the fuzzy performance index in Eq. (41). In this paper, the Taylor series expansion based approach is chosen [12][13] because of its competitiveness from a computational standpoint.

Let be an α-cut of the ith fuzzy variable in the following form:

$$\overline{b}_i^{\alpha}=\left[b_i^{\alpha_-},b_i^{\alpha_+}\right]=\left[b_i^c-\Delta b_i,b_i^c+\Delta b_i\right] \tag{46}$$

with

$$b_i^c=\frac{b_i^{\alpha_+}+b_i^{\alpha_-}}{2} \tag{47}$$

and $\mathbf{b}^c=\{b_i^c\}$ for i=1,…,4. By making use of interval extension in interval mathematics and assuming a monotonic behavior as in [12] and [13], the α-cut of the fuzzy performance index is:

$$\bar{\psi}^{\alpha} = \left[\psi^{\alpha_-}, \psi^{\alpha_+} \right] \tag{48}$$

where

$$\psi^{\alpha_-} = \psi^{c} - \sum_{i=1}^{4} \left| \psi_{b_i}^{c} \right| \Delta b_i \quad \psi^{\alpha_-} = \psi^{c} + \sum_{i=1}^{4} \left| \psi_{b_i}^{c} \right| \Delta b_i \tag{49}$$

in which the superscript c denotes that the corresponding quantity is evaluated at $\mathbf{b}=\mathbf{b}^c$

$$\psi^{c} = \psi\left(\mathbf{b}^{c}\right) = \frac{\sigma_{x}\left(\mathbf{b}^{c}\right)}{\sigma_{x_0}\left(\mathbf{b}^{c}\right)} = \frac{\sigma_{x}^{c}}{\sigma_{x_0}^{c}} \tag{50}$$

$$\psi_{b_i}^{c} = \psi_{b_i}\left(\mathbf{b}^{c}\right) = \left.\frac{\partial \psi}{\partial b_i}\right|_{\mathbf{b}=\mathbf{b}^{c}} \tag{51}$$

Taking into account the above definitions, the computational procedure is based on the following steps that must be repeated as many times as the number of α-cuts.

At the beginning, the following Lyapunov equations have to be solved:

$$\mathbf{A}^{c}\mathbf{R}^{c} + \mathbf{R}^{c}\left(\mathbf{A}^{c}\right)^{T} + \mathbf{B}^{c} = \mathbf{0}_{6\times 6} \tag{52}$$

$$\mathbf{A}_0^{c}\mathbf{R}_0^{c} + \mathbf{R}_0^{c}\left(\mathbf{A}_0^{c}\right)^{T} + \mathbf{B}_0^{c} = \mathbf{0}_{4\times 4} \tag{53}$$

from which

$$\sigma_{x}^{c} = \sqrt{\mathbf{R}_{\mathbf{zz}}^{c}\left(2,2\right)} \quad \sigma_{x_0}^{c} = \sqrt{\mathbf{R}_{\mathbf{z}_0\mathbf{z}_0}^{c}\left(1,1\right)} \tag{54}$$

The central point of the α-cut of fuzzy performance index ψ^c which appears in Eq. (49) is obtained by introducing the results of Eq. (54) in Eq. (50).

Now, Eq. (49) needs the calculation of the following quantity:

$$\psi_{b_i}^{c} = \frac{\sigma_{x,b_i}^{c}\sigma_{x_0}^{c} - \sigma_{x}^{c}\sigma_{x_0,b_i}^{c}}{\left(\sigma_{x_0}^{c}\right)^{2}} \tag{55}$$

where

$$\sigma_{x,b_i}^{c} = \frac{1}{2}\frac{\mathbf{R}_{\mathbf{zz},b_i}^{c}\left(2,2\right)}{\sqrt{\mathbf{R}_{\mathbf{zz}}^{c}\left(2,2\right)}} \quad \sigma_{x,b_i}^{c} = \frac{1}{2}\frac{\mathbf{R}_{\mathbf{z}_0\mathbf{z}_0,b_i}^{c}\left(1,1\right)}{\sqrt{\mathbf{R}_{\mathbf{z}_0\mathbf{z}_0}^{c}\left(1,1\right)}} \tag{56}$$

The quantities in Eq. (56) are evaluated by solving the first-order Lyapunov equations:

$$\mathbf{A}^{c}\mathbf{R}_{b_i}^{c} + \mathbf{R}_{b_i}^{c}\left(\mathbf{A}^{c}\right)^{T} + \left(\mathbf{A}_{b_i}^{c}\mathbf{R}^{c} + \mathbf{R}^{c}\left(\mathbf{A}_{b_i}^{c}\right)^{T} + \mathbf{B}_{b_i}^{c}\right) = \mathbf{0}_{6\times 6} \tag{57}$$

$$\mathbf{A}_0^{c}\mathbf{R}_{0,b_i}^{c} + \mathbf{R}_{0,b_i}^{c}\left(\mathbf{A}_0^{c}\right)^{T} + \left(\mathbf{A}_{0,b_i}^{c}\mathbf{R}_0^{c} + \mathbf{R}_0^{c}\left(\mathbf{A}_{0,b_i}^{c}\right)^{T} + \mathbf{B}_{0,b_i}^{c}\right) = \mathbf{0}_{4\times 4} \tag{58}$$

The calculation of the derivates for the matrices in Eq. (57) and Eq. (58) is straightforward and thus omitted for sake of conciseness. The procedure is summarized in Fig. 3.

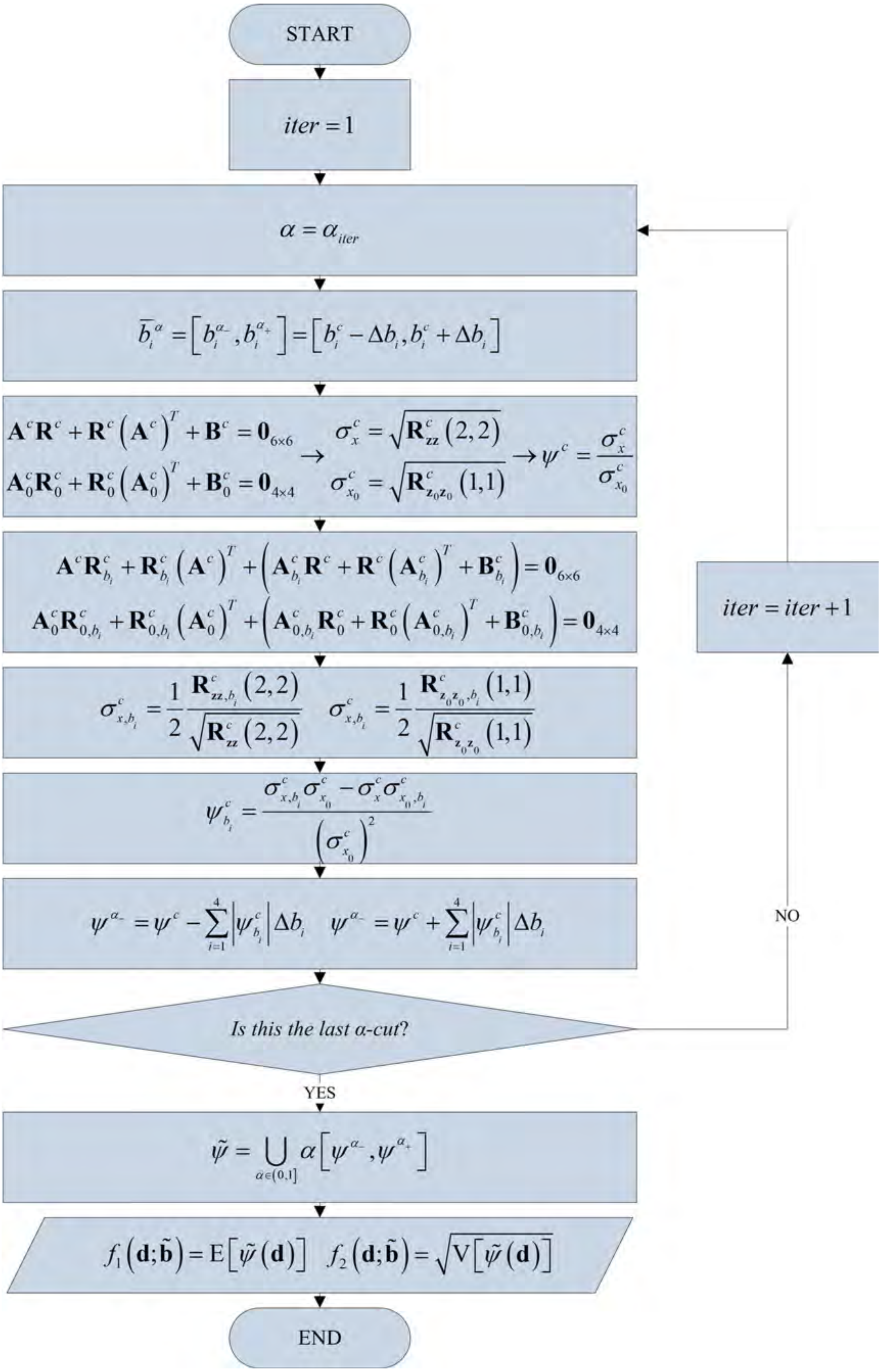

Figure 3: Flow-chart of the resolution strategy to compute fuzzy performance index and objective functions.

The monotonic response assumption over the range of uncertain parameter values ensures that no turning points exist on the performance index surface in the parameter space. As a consequence, the upper and lower bounds of the considered α-cut exist at some combination of the end points of the α-cuts of the uncertain parameters. Some preliminary numerical investigations verified that the performance index in Eq. (30) has a monotonic behavior over a range of numerical values of practical interest, as those in the following applications.

5 NUMERICAL APPLICATIONS

This section provides results of numerical study in order to demonstrate the applicability of the proposed design strategy of TLCDs.

5.1 Example

Since the design variable is a 2D vector, a graphical visualization of the objective functions can be obtained, thus showing the conflict between TLCD performance – as evaluated by means of f_1 in Eq. (44) and robustness against fuzzy uncertainties, as evaluated by means of f_2 in Eq. (45). A list of the adopted numerical values is given in Tab. 1. Fuzzy variables in Tab. 1 have a triangular MF ($e_1/e_2/e_3$) in which e_2 denotes the core value ($\mu(e_2)=1$) and the closed interval $[e_1,e_3]$ the support ($\mu(e_1)\to 0^+$ and $\mu(e_3)\to 0^+$).

Problem data	Numerical value
$\tilde{\omega}_s$	$(1.0\pi/1.5\pi/2.0\pi)$ rad/s
$\tilde{\xi}_s$	(0.02/0.03/0.04)
μ	0.01
p	0.70
$\tilde{\omega}_f$	$(4.5\pi/9\pi/13.5\pi)$ rad/s
$\tilde{\xi}_f$	(0.40/0.60/0.80)

Table 1: Numerical data.

The considered search space is $\mathbf{d}_{min}$={0.85,0.01} and $\mathbf{d}_{max}$={1.15,1.20}. The surfaces representing all values of the objective functions over the design space are shown in Fig. 4 and Fig. 5 (the mesh grid size is 50×50). Looking at the performances only (Fig. 4), acceptable results are obtained by selecting the tuning ratio close to 1 – i.e. γ within [0.96,1.00] – and by taking the coefficient of head loss values ξ within [0.40,0.90]. Therefore, it seems that designers can choose the final solution which best fit their (practical, economical, etc.) needs within a quite large number of alternatives. However, looking at the robustness of the final performances (Fig. 5), the designers should note some issues to be addressed in selecting the candidate solutions space. In fact, a very large variability of the final performances is observed in Fig. 5 for ξ within [0.40,0.90] and γ within [0.95,1.02]. In ξ approaches 0.50 and $\gamma\to 1.03$, then the final standard deviation up to one order of magnitude. Therefore, it is expected that the performance variability strongly influences the design strategy for ξ. Where the best values for the tuning ratio occur, if ξ is chosen to met the best performance – that is, within [0.40,0.90] – then a very small variation for γ may lead to a non-proportional and very large worsening of the robustness because the gradient in that zone of the search space is very high. On the other hand, if ξ falls between 0.12 and 0.30, then unexpected variations for γ (i.e. manufacturing errors, bad estimation of the MF for ω_s) will not cause an excessive worsening of the TLCD's robustness.

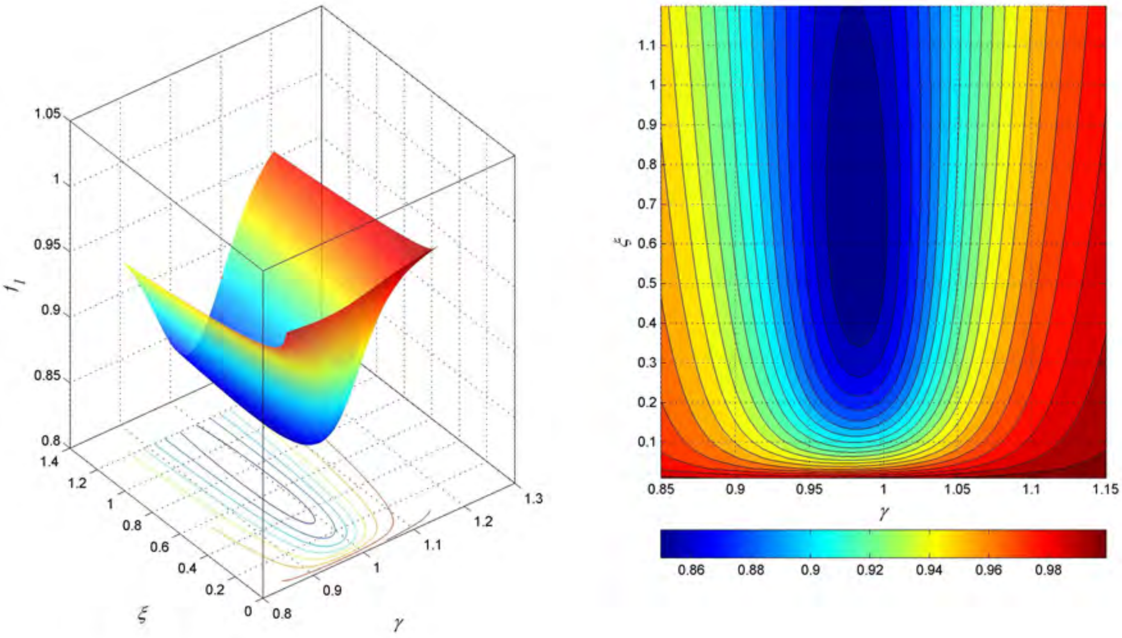

Figure 4: Objective function f_1 over the design space.

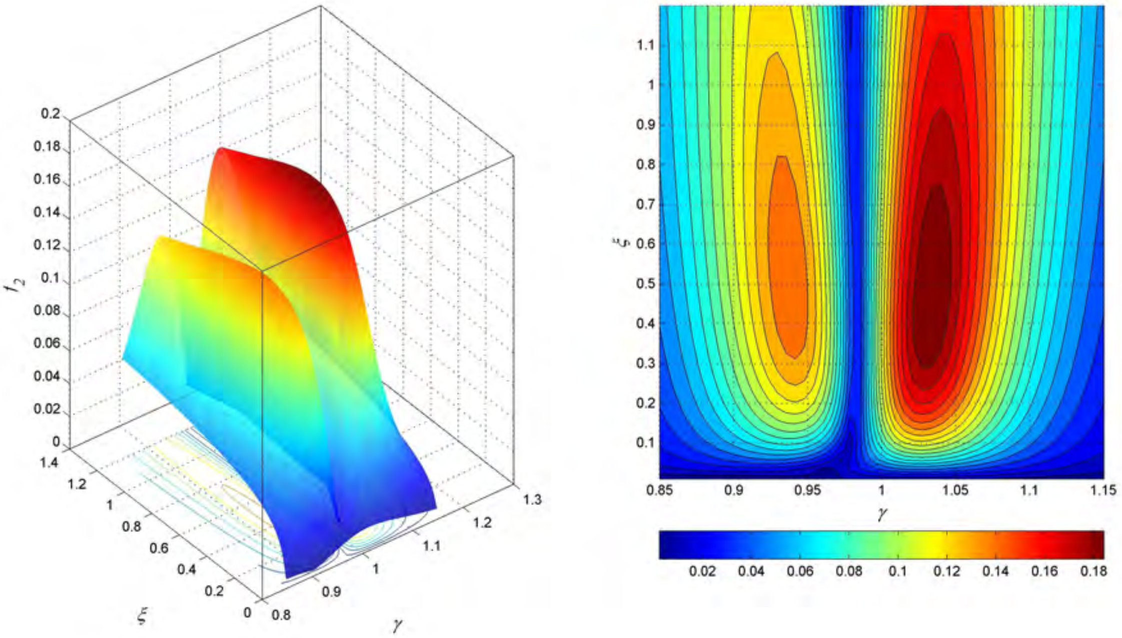

Figure 5: Objective function f_2 over the design space.

The Pareto front and the set of non-dominated solutions in Fig. 6 and Fig. 7 confirm the above analysis. A linear trade-off exists between f_1 and f_2 (Fig. 6, on the left). The most of the non-dominated solutions are the couples $(\gamma,\xi)\in[0.960.0.981]\otimes[0.025,0.30]$.

Although better performances can be obtained by increasing the coefficient of head loss (γ close to 0.985 and ξ between 0.60 and 0.70), the final performance will be more susceptible to large variations due to unexpected errors affecting γ.

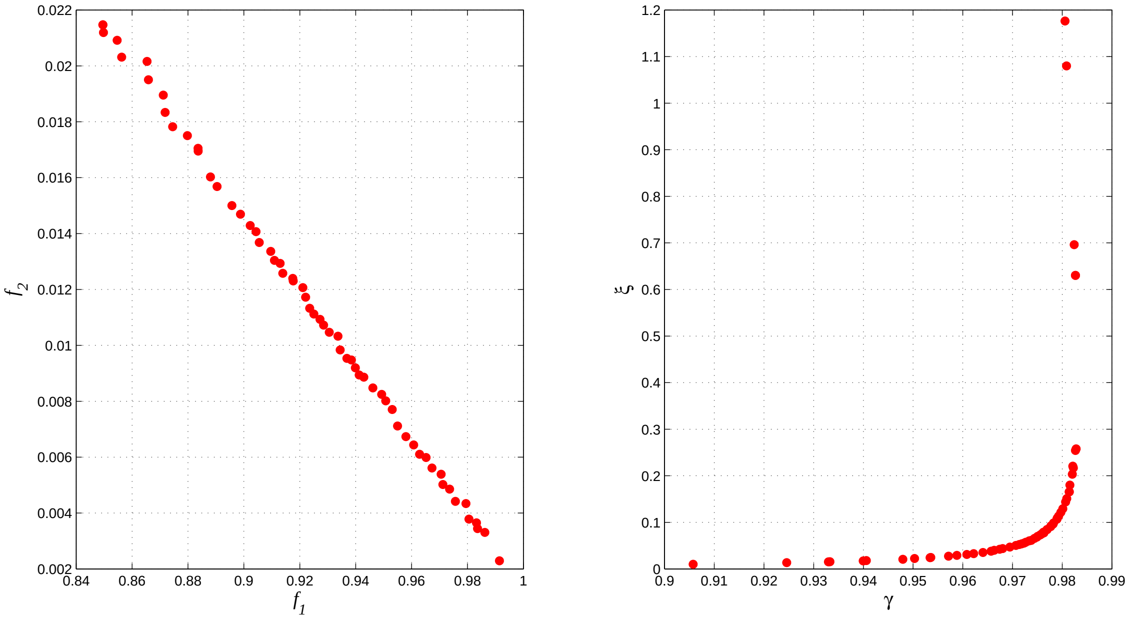

Figure 6: Pareto front and optimal solutions.

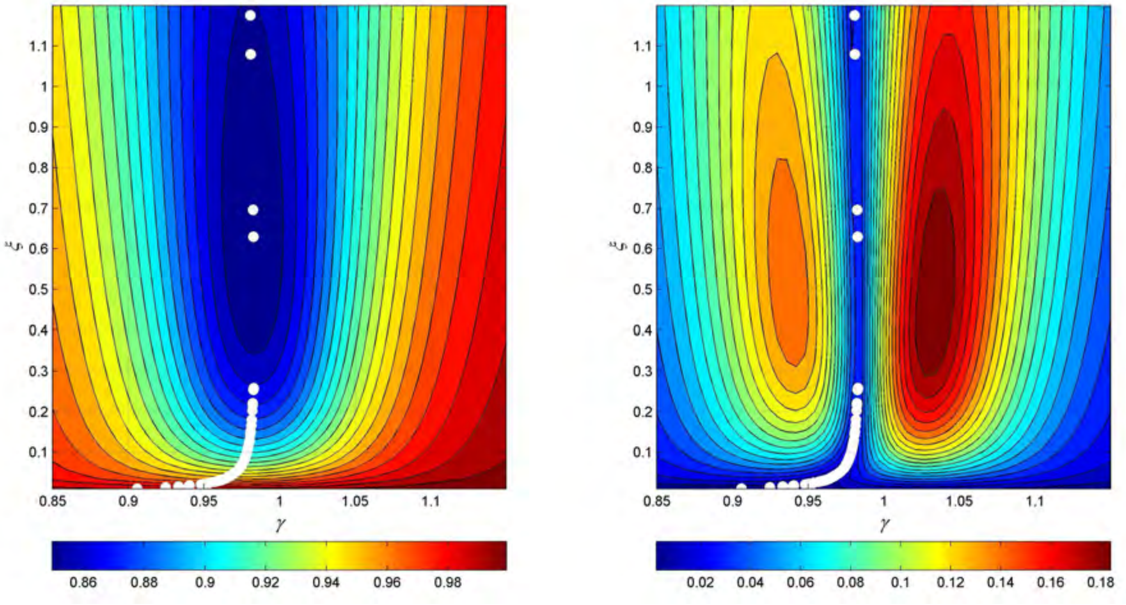

Figure 7: Distribution of the Pareto optimal solutions over the search space.

5.2 Sensitivity analyses

Two parameters – the mass ratio μ and the length ratio p – were considered as deterministic input data in Tab. 1. A sensitivity analysis may be carried out for them in order to understand their effects on the selection of the best TLCD parameters.

Different Pareto fronts and non-dominated solutions sets for varying mass ratio are depicted in Fig. 8. As expected, the optimal tuning ratio decreases as μ grows. Moreover, better performances are achieved when μ increases. For medium and high performances, the robustness decreases as μ grows. The trade-off between performance and robustness is still linear. The three Pareto front in Fig. 8 have some common points, which indicates that it is possible to obtain the same performance as well as robustness under different mass ratios scenarios by properly tuning the TLCD parameters.

The effects of the length ratio p on the final set of the non-dominated solutions are less evident. As the length ratio increases, the optimal value for γ decreases. It seems that the Pareto fronts are stretched and rotate on the worst performance point ($f_1 \rightarrow 1$) as p increases.

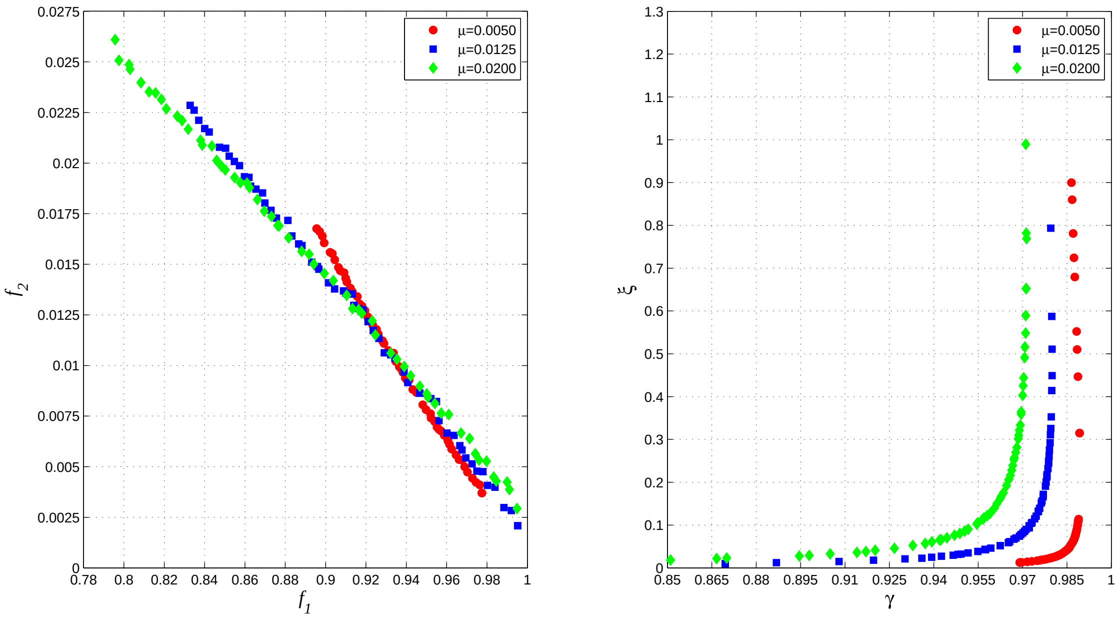

Figure 8: Pareto fronts and optimal solutions with varying mass ratio μ.

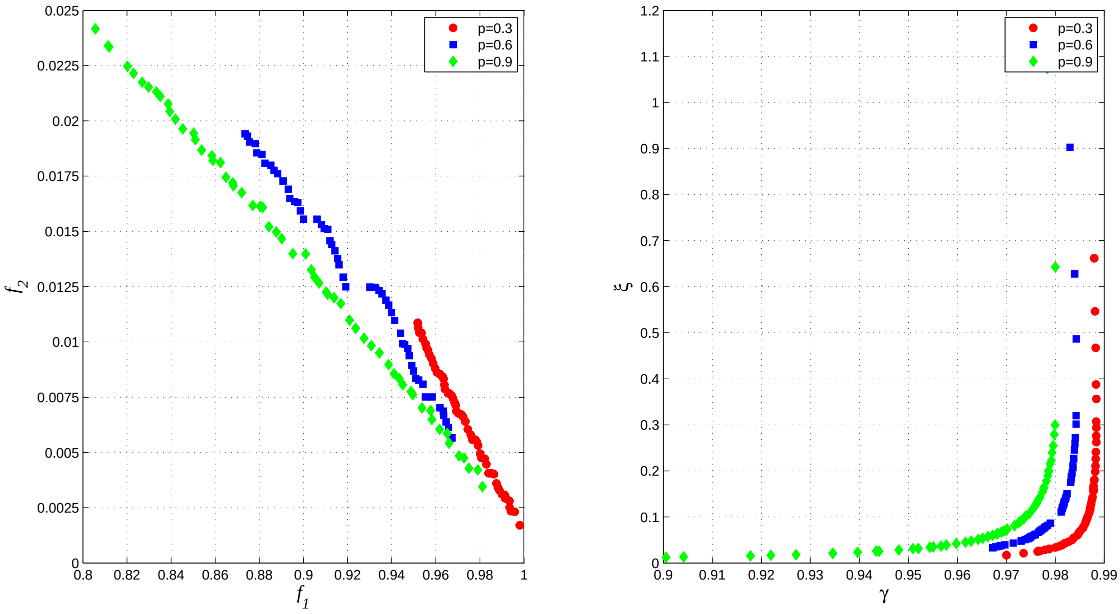

Figure 9: Pareto fronts and optimal solutions with varying length ratio p.

6 CONCLUSIONS

The paper presented an approach for incorporating fuzziness in the optimum design of TLCDs subject to stochastic ground motion. The main features of the proposed approach are: (*i*) the use of the Taylor series expansion for computing the final fuzzy performance index and (*ii*) the application of the credibility theory to define the objective functions of the final multi-objective optimization problem. The main advantage of the proposed procedure deals with its versatility in considering different sources of uncertainties in the robust design of TLCDs.

Numerical applications confirm the important role of non-probabilistic sources of uncertainty in random vibrations problems and the effectiveness of our approach in supporting the design of TLCDs. From a practical standpoint, numerical results show that the robustness against (fuzzy) uncertainties influences typical parameters for TLCDs whit respect to the case when they are designed taking into account random dynamic loadings only. In fact, we found that smaller values for the coefficient of head loss may be preferred to avoid an excessive variability of the final performances as consequence of unexpected fluctuations of the tuning ratio.

REFERENCES

[1] T. Balendra, C. M. Wang, H.F. Cheong, Effectiveness of tuned liquid column dampers for vibration control of towers. *Engineering Structures*, **17**, 668-675, 1995.

[2] K.W. Min, H.S. Kim, S.H. Lee, H. Kim, S.K., Ahn, Performance evaluation of tuned liquid column dampers for response control of a 76-story benchmark building. *Engineering structures*, **27**, 1101-1112, 2005.

[3] J.C. Wu, M.H. Shih, U.Y. Lin, Y.C. Shen, Design guidelines for tuned liquid column damper for structures responding to wind. *Engineering Structures*, **27**, 1893-1905, 2005.

[4] A.Y.J. Won, J.A. Pirest, M.A. Harount, Performance assessment of tuned liquid column dampers under random seismic loading. *International Journal of Non-linear Mechanics*, **32**, 745-758, 1997.

[5] G.C. Marano, R. Greco, F. Trentadue, B. Chiaia, Constrained reliability-based optimization of linear tuned mass dampers for seismic control. *International Journal of Solids and Structures*, **44**, 7370-7388, 2007.

[6] T. Igusa, A. Der Kiureghian, Response of uncertain systems to stochastic excitation. *Journal of Engineering Mechanics*, **114**, 812-832, 1988.

[7] G.C. Marano, S. Sgobba, R. Greco, M. Mezzina, Robust optimum design of tuned mass dampers devices in random vibrations mitigation. *Journal of Sound and Vibration*, **313**, 472-492, 2008.

[8] G.C. Marano, R. Greco, S. Sgobba, A comparison between different robust design approaches: Application to tuned mass dampers. *Probabilistic Engineering Mechanics*, **25**, 108-118, 2010.

[9] R.K. Reddy, A. Haldar, A random-fuzzy reliability analysis. *Proceedings of the first international symposium on uncertainty modeling and analysis*, B. M. Ayyub (Ed.), pp. 161–166, Los Alamitos: IEEE Computer Society Press, 1990.

[10] S. Chakraborty, P. C. Sam, Probabilistic safety analysis of structures under hybrid uncertainty. *International Journal of Numerical Methods in Engineering*, **70**, 405-422, 2007.

[11] G. Quaranta, Finite element analysis with uncertain probabilities. *Computer Methods in Applied Mechanics and Engineering*, accepted for publication, 2010.

[12] S. Chakraborty, B.K. Roy, Reliability based optimum design of Tuned Mass Damper in seismic vibration control of structures with bounded uncertain parameters. *Probabilistic Engineering Mechanics*, article in press, 2010.

[13] R. Debbarma, S. Chackraborty, S.K. Ghosh, Optimum design of tuned liquid column dampers under stochastic earthquake load considering uncertain bounded system parameters. *International Journal of Mechanical Sciences*, **52**, 1385-1393, 2010.

[14] G.C. Marano, E. Morrone, G. Quaranta, Analysis of randomly vibrating structures under hybrid uncertainty. *Engineering Structures*, **31**, 2677-2686, 2009.

[15] G.C. Marano, G. Quaranta, Robust optimum criteria for tuned mass dampers in fuzzy environments. *Applied Soft Computing*, **9**, 1232-1243, 2009.

[16] F. Sakai, S. Takaeda, T. Tamaki, Tuned liquid column damper – new type device for suppression of building vibrations. *Proceeding of the International Conference on High-rise Buildings*, Nanjing, China, March 25-27, 1989.

[17] K. Kanai, Semi-empirical formula for the seismic characteristics of the ground. *Bulletin of the Earthquake Research Institute*, University of Tokyo, **35**, 309-25, 1957.

[18] H. Tajimi, A statistical method of determining the maximum response of a building during earthquake. *Proceedings of the of second world conference on Earthquake engineering*, Tokyo, Japan, 1960.

[19] R.K. Reddy, A. Haldar, A random-fuzzy reliability analysis. *Proceedings of the first international symposium on uncertainty modeling and analysis*, College Park, MD, USA, December 3-5, 1990.

[20] Liu B, *Uncertainty theory - An Introduction to its Axiomatic Foundations*. Springer-Verlag, 2004.

[21] B. Liu, Y.K. Liu, Expected value of fuzzy variable and fuzzy expected value models. *IEEE Transactions on Fuzzy Systems*, **10**, 445-450, 2002.

[22] K. Deb, *Multi-Objective Optimization Using Evolutionary Algorithms*. John Wiley & Sons, 2001.

[23] D. Moens, D. Vandepitte, A survey of non-probabilistic uncertainty treatment in finite element analysis. *Computer Methods in Applied Mechanics and Engineering*, **194**, 1527-1555, 2005.

COMPDYN 2011
3^{rd} ECCOMAS Thematic Conference on
Computational Methods in Structural Dynamics and Earthquake Engineering
M. Papadrakakis, M. Fragiadakis, V. Plevris (eds.)
Corfu, Greece, 25-28 May 2011

APPLICATION OF INTERVAL FIELDS FOR UNCERTAINTY MODELING IN A GEOHYDROLOGICAL CASE

Wim Verhaeghe[1], Wim Desmet[1], Dirk Vandepitte[1], Ingeborg Joris[2], Piet Seuntjens[2,3] and David Moens[1,4]

[1]Department of Mechanical Engineering K.U.Leuven
Afdeling PMA, Celestijnenlaan 300B, B3001 Heverlee, Belgium
e-mail: wim.verhaeghe@mech.kuleuven.be

[2] VITO, Boeretang 200, B2400 Mol, Belgium
e-mail: piet.seuntjens@vito.be

[3] Department of Soil Management, Ghent University
Coupure Links 653, B9000 Gent, Belgium
Department of Bioscience Engineering, University of Antwerp
Groenenborgerlaan 171, B2020 Antwerpen, Belgium

[4] Dept. of Applied Engineering, Lessius Hogeschool - Campus De Nayer, K.U.Leuven Association
J. De Nayerlaan 5, B2860 Sint-Katelijne-Waver, Belgium
Associated professor, Department of Mechanical Engineering K.U.Leuven
e-mail: david.moens@mech.kuleuven.be

Keywords: Spatial uncertainty, interval analysis, input uncertainty elasticity of the output.

Abstract. *In situ soil remediation requires a good knowledge about the processes that occur in the subsurface. Groundwater transport models are needed to predict the flow of contaminants. Such a model must contain information on the material layers. This information is obtained from in situ point measurements which are costly and thus limited in number. The overall model is thus characterised by uncertainty. This uncertainty has a spatial character, i.e. the value of an uncertain parameter can vary based on the location in the model itself. In other words the uncertain parameter is non-uniform throughout the model. On the other hand the uncertain parameter does have some spatial dependency, i.e. the particular value of the uncertainty in one location is not totally independent of its value in a location adjacent to it. To deal with such uncertainties the authors have developed the concept of interval fields. The main advantage of the interval field is its ability to represent a field uncertainty in two separate entities: one to represent the uncertainty and one to represent the spatial dependency. The main focus of the paper is on the application of interval fields to a geohydrological problem. The uncertainty taken into account is the material layers' hydraulic conductivity. The results presented are the uncertainties on the contaminant's concentration near a river. The second objective of the paper is to define an input uncertainty elasticity of the output. In other words, identify the locations in the model, whose uncertainties influence the uncertainty on the output the most. Such a quantity will indicate where to perform additional in situ point measurements to reduce the uncertainty on the output the most.*

1 INTRODUCTION

In recent years, the study of uncertainties in numerical modeling has gained a lot of attention. Probabilistic and non-probabilistic methods were developed for dealing with scalar parameter uncertainties. However, scalar parameter uncertainties are not the only kind of uncertainties influencing numerical models. Often scalar parameter uncertainties represent uncertainties that have uncertainty on a smaller scale spatial dimension too. The spatial influence of such uncertainties is often neglected, as it is assumed captured by assumptions of uniformity and homogeneity. This neglect is not without reasons, for a thorough discretisation of an uncertain property over the spatial domain would result in an explosion of independent uncertainties and thus a drastic increase in the computation time for the uncertainty analysis. However, a go-between approach is possible when certain patterns describing the spatial behaviour of an uncertainty are available. Taking into account the patterns reduces the explosion of uncertainties in going from one spatially uniform uncertainty to a thorough discritisation of the spatial domain. The authors have developped an interval field approach [1] to formalize these notions.

The paper first presents the general problem of interval finite element analysis and the interval field approach to it. Secondly, a section details the choice of certain spatial patterns in the interval field approach, based on random field analogies. Next, the concept of input uncertainty elasticity of the output is introduced in the context op spatial uncertainties. In the next section the geohydrological problem is introduced and the obtained results are presented. The paper concludes with some suggestions for further research.

2 INTERVAL AND INTERVAL FIELD ANALYSIS

This section first describes the general concept of Interval Finite Element (IFE) analysis and the method used to deal with it. Next the interval field concept is introduced to deal with dependent uncertain quantities.

2.1 Interval Finite Element analysis

Generally an IFE problem can be represented by [2]:

$$\mathbf{y}^s = \{\mathbf{y} \mid (\mathbf{x} \in \mathbf{x}^I)(\mathbf{y} = f(\mathbf{x}))\} \tag{1}$$

with $\mathbf{x}^I$ the interval vector representing the bounds on the input uncertainties and $f(\mathbf{x})$ the function representing the input-output relationship. The solution is expressed as a set $\mathbf{y}^s$, rather than an interval vector $\mathbf{y}^I$ to stress that certain value combinations of components within a hypercubic approximation of the uncertain vector result $\mathbf{y}$ are not necessarily physically coherent. However in most cases the individual ranges of only some components of $\mathbf{y}$ are really of interest. Several implementation strategies for interval numerical analysis have been proposed. Because global optimisation based strategies yield physically correct results, they are more and more acknowledged as the standard approach for non-intrusive IFE analysis. The core of this analysis (the $f(\mathbf{x})$) is a black-box FE calculation which can roughly be any analysis (for example a static or dynamic structural analysis, but also a heat-conductivity problem, hydrogeological problem or vibro-accoustic problem), limited only by the capabilities of the FE solver. The global optimisation based solution strategies actively search in the non-deterministic input interval space for the combination that results in the minimum or maximum value of an output quantity. In theory, the global optimisation approach results in the exact interval vector.

However, despite the smooth behaviour of typical objective functions, the computational cost of the global optimisation based approach remains high. Hence, most research on this method focuses on fast approximate optimisation techniques. The approximating technique used in this paper starts by building a Kriging response surface based on a number of initial sample points. From this preliminary response surface the optimal additional samples are determined by focusing on the location of the possible extremes of the approximated output quantity in the uncertainty space [3]. The response surface is thus improved by additionally sampling the core FE-model till a pre-specified maximum number of samples are taken. Subsequently, global optimisation and anti-optimisation is performed on this response surface model to yield the bounds on the considered output quantity. For a thorough discussion of this adaptive response surface optimisation method, the interested reader is referred to [4].

For completeness the extension of an interval number to a fuzzy set is presented. A fuzzy set [5] is a set in which every member has a degree of membership, represented by the membership function $\mu_x(x)$, associated with it. If $\mu_x(x) = 1$, x is definitely a member of the fuzzy set. If $\mu_x(x) = 0$, x is definitely not a member of the fuzzy set. Analysis using fuzzy sets is very often done by using so-called α-cuts. An α-cut contains all the x for which $\mu_x(x) > \alpha$ is true. These α-cuts are essentially classical intervals, which means that the interval analysis is the basis of a fuzzy analysis.

2.2 Interval fields

The interval field framework as developped in [1] has an explicit and an implicit implementation. For the application presented here the explicit implementation is needed.

For a spatially dependent uncertainty, the interval vector $\mathbf{x}^I$ containing an independent interval component for every spatial location is not a realistic description. Furthermore, it would result in an infeasibly high dimensional optimisation problem. To describe spatially dependent variation, numerical modelling approaches often use some type of shape functions (e.g. the modes used to represent the dynamic behaviour of a structure using the modal superposition technique). The actual solution is a linear combination of these shape functions.

Accordingly, the explicit interval field $\mathbf{x}^F$ is defined as a superposition of n_b base vectors $\boldsymbol{\psi}_i$ using interval factors α_i^I:

$$\mathbf{x}^F = \sum_{i=1}^{n_b} \alpha_{x,i}^I \boldsymbol{\psi}_{x,i} \tag{2}$$

The base vectors represent a limited set of reference patterns over the spatial domain, each of which is scaled by an interval factor. The components of the interval fields themselves (the local value of the uncertainty) are coupled through the reference patterns. Once the reference patterns are chosen, the definition of the interval field requires the specification of the interval factors that define the field on x, which can be assembled in a classical (hypercubic) interval vector $\boldsymbol{\alpha}_x^I$. In matrix notation, the interval field is denoted as:

$$\mathbf{x}^F = [\boldsymbol{\psi}_x]\, \boldsymbol{\alpha}_x^I \tag{3}$$

The application of an explicit interval field on the input side of an analysis is rather straightforward. Since expert knowledge about the modelled system dominates the definition of the uncertainties, the freedom in choosing the base vectors is ideal to reflect this knowledge (for example: the sinusodal (= base vector) deviation of the thickness of a rolled plate with uncertain amplitude (= interval factor)). The main limitation of the explicit interval field is that its definition only allows a linear relation between the base vectors and the interval factors.

The application of an explicit interval field on the output side of an analysis is less straightforward. The base vectors and interval factors are determined by the analysis itself. Furthermore, in order to obtain an explicit interval field that introduces no conservatism in its derived response variables (i.e. derivatives of the primary response variables), the output interval factors should be completely independent. An analysis of the application of the interval field approach to the output of static FE analysis is presented in [6].

Once the spatially dependent uncertainty on the input side of an analysis is defined by means of an explicit interval field, the dimensions of the uncertainty space are drastically reduced. This allows for the use of the adaptive response surface technique as described in the above subsection.

3 THE CHOICE OF BASE VECTORS

The use of the explicit interval field on the input side of an analysis requires the selection of appropriate base vectors and interval factors. This section first presents the factors influencing the selection of these base vectors and interval factors. The choice for base vectors and interval factors based on random field expansions is explained in the next subsection.

3.1 Factors influencing the choice of base vectors

- The bounds on the uncertainty on a model parameter $\mathbf{x}$ are specified by two functions of the spatial coordinate $\mathbf{r}$, one function for the upper bound $\overline{x}(\mathbf{r})$ and one for the lower bound $\underline{x}(\mathbf{r})$ of the uncertainty. The linear combination of the base vectors with the interval factors that makes up an interval field must remain within these bounds for any value of the interval factors.
- The base vectors must represent the expert's knowledge of the spatial dependency of the model parameter. Most often knowledge about this dependency is limited and the set of base vectors preferably allows for a range of small and large scale dependency.
- The number of base vectors and corresponding interval factors to represent the input uncertainty will influence the calculation time to get the output uncertainty.

3.2 Base vectors derived from random field expansion

In an attempt to construct a base vector set that takes into account the above described factors, the expansion of a random field is studied.

The objective of a random field is to represent a spatial variation of a specific model property by a stochastic variable defined over the region on which the variation occurs [7]. A random field can thus be denoted as $H(\mathbf{r}, \theta)$ with $\mathbf{r}$ the spatial coordinate and θ the outcome of a random phenomenon. A random field is a random variable for a given $\mathbf{r_0}$ and is a realization of the field for a given θ_0. The specification of a random field generally comes down to the specification of the spatial evolution of the first two statistical moments of the field variable and a corresponding covariance function, expressing the spatial dependency of the field variable. In most cases the random field is considered to be weakly stationary, resulting in a constant for the first few statistical moments throughout the spatial domain (i.e. zero mean and unit variance). Furthermore the covariance function for weakly stationary random fields depends only on the distance between observation points, not on their actual location.

The application of the concept of random fields in a numerical modelling framework requires some sort of discretisation of the spatially varying stochastic field over the defined geometry. A good overview of methods can be found in the report by Sudret and Der Kiureghian [8]. The technique studied here is the Karhunen-Loève expansion [9] that has gained particular attention in literature. This approach is based on the spectral decomposition of the autocovariance function $C_{HH}(\mathbf{r_1}, \mathbf{r_2})$. The set of deterministic functions over which any realization of the field $H(\mathbf{r}, \theta_0)$ is expanded is defined by the eigenvalue problem:

$$\int_{\omega} C_{HH}(\mathbf{r_1}, \mathbf{r_2}) \varphi_i(\mathbf{r_2}) d\omega_{\mathbf{r_2}} = \lambda_i \varphi_i(\mathbf{r}) \tag{4}$$

with ω the spatial domain and $i = 1, \ldots$. Once the eigenfunctions are found the random field can be expressed as:

$$H(\mathbf{r}, \theta) = \sum_{i=1}^{\infty} \sqrt{\lambda_i} \xi_i(\theta) \varphi_i(\mathbf{r}) \tag{5}$$

with $\{\xi_i\}$ a set of orthonormal random variables. In stochastic analysis, this expansion is truncated after N terms to reduce the computational costs.

Several features of the random field expansion can be used in the interval field implementation after some adaptations. To begin, an off-set function $f_{mid}(\mathbf{r})$ to describe the mid value of the model parameter throughout the spatial domain is calculated

$$x_{mid}(\mathbf{r}) = \frac{\overline{x}(\mathbf{r}) + \underline{x}(\mathbf{r})}{2} \tag{6}$$

The eigenfunctions $\varphi_i(\mathbf{r})$ of the covariance function are then used as base vectors $\boldsymbol{\psi}_i(\mathbf{r})$ for the interval field with

$$\boldsymbol{\psi}_i(\mathbf{r}) = \lambda_i \varphi_i(\mathbf{r}) |\varphi_i(\mathbf{r})| \tag{7}$$

and replacing the orthonormal random variables $\{\xi_i\}$ by interval factors $\alpha_i^I \in \lfloor -1 \; 1 \rceil$. These adaptations make sure that for $N \to \infty$ the interval field will assign a value from the interval $\lfloor -1 \; 1 \rceil$ to the model parameter throughout the spatial domain. This unit interval is then scaled by the difference function

$$x_{dif}(\mathbf{r}) = \overline{x}(\mathbf{r}) - \underline{x}(\mathbf{r}) \tag{8}$$

describing the actual range of uncertainty on the model paramater for every location in the model. The description of the model parameter by the interval field is thus

$$\mathbf{x}^F = x_{mid}(\mathbf{r}) + \sum_{i=1}^{N} (\lambda_i \; \varphi_i(\mathbf{r}) \; |\varphi_i(\mathbf{r})| \; \alpha_i^I) \; (x_{dif}(\mathbf{r})) \tag{9}$$

With this equation the considerations from the first and last item in the list of influencing factors is accounted for. Next is the issue of uncertainty about the spatial dependency.

The base vectors taken from the expansion of a random field with a given autocovariance function only take into account the given correlation length L. In [10] a method is described to take into account interval correlation lengths with interval fields. Essentially the method relies on building an interval field description for the base vectors themselves in the correlation length space using a limited number of autocovariance expansions. In this way the base vectors are depending on the correlation length and can be calculated by a simple matrix vector product. The resulting interval field for the model parameter can thus be summarised by

$$\mathbf{x}^F = x_{mid}(\mathbf{r}) + \sum_{i=1}^{N} (\lambda_i(L) \; \varphi_i(\mathbf{r}, L) \; |\varphi_i(\mathbf{r}, L)| \; \alpha_i^I) \; (x_{dif}(\mathbf{r})) \quad L \in \lfloor L_{min} \; L_{max} \rceil \tag{10}$$

This approach only introduces one additional interval to represent the uncertainty about the amount of spatial dependency. The solution strategy to find the uncertainty on the output remains the same, for example a response surface based optimisation and anti-optimisation, with only one additional dimension in the uncertainty space.

4 INPUT UNCERTAINTY ELASTICITY OF THE OUTPUT

To assess the relative importance of an input uncertainty on an output uncertainty, the concept of input uncertainty elasticity of the output is introduced in general terms and then applied to the case of spatial uncertainty.

4.1 General concept

As in economics, an elasticity R is defined as the ratio of the relative change (more precisely, the derivative with respect to some quantity) in one parameter Y to the relative change in an other parameter X

$$R_X^Y = \frac{\Delta Y}{\Delta X}\frac{X}{Y} \tag{11}$$

Let Y be the range of the uncertain output and X be the range of the uncertain input. The reduction (i.e. the Δ) on the range of the interval for the input X, will affect the range of the interval for the output Y to a greater or lesser extent. The relative magnitude of this influence is described by the input uncertainty elasticity of the output R_X^Y.

4.2 Spatial uncertainty context

In the context of spatial uncertainty, the influence of an input uncertainty on an output uncertainty has a spatial component. The influence of an uncertain input parameter will depend on the spatial distribution of its uncertainty. Figure 1 shows in a generic way the influence of the spatial uncertainty distribution. For an investigated spatial location the amount of uncertainty $x_{dif}(\mathbf{r})$ is reduced and some sort of coherent distribution of the uncertainty is assumed over the spatial domain (as illustrated at the top left in the figure). The uncertainty analysis is carried out for this spatial uncertainty distribution and a resulting uncertainty (an interval) for the output is found (bottom left). By repeating this for other investigated spatial locations, one finds the combined result which is shown at the right of the figure. It presents the different output uncertainties for several investigated spatial locations. This data is then used to calculate the input uncertainty elasticity of the output over the spatial domain. In this context the R_X^Y is in particular usefull to identify the spatial location where an input uncertainty influences the output uncertainty the most. In allocating resources to reduce the uncertainty, the spatial location with the highest R_X^Y should get priority.

An appropriate selection of the $\overline{x}(\mathbf{r})$ and $\underline{x}(\mathbf{r})$ is needed to make a study over the spatial domain to give a scalar field of input uncertainty elasticities of the output. Important choices to be made in the selection of $\overline{x}(\mathbf{r})$ and $\underline{x}(\mathbf{r})$ to investigate a particular spatial location's uncertainty influence are listed below. Figure 2 shows $\overline{x}(\mathbf{r})$ and $\underline{x}(\mathbf{r})$ for three cases. The first case, at the left on the figure, is the reference case. The two other cases illustrate particular choices for $\overline{x}(\mathbf{r})$ and $\underline{x}(\mathbf{r})$ explained in the list below.

Important choices to be made in the selection of $\overline{x}(\mathbf{r})$ and $\underline{x}(\mathbf{r})$:

- the magnitude of the reduction of $x_{dif}(\mathbf{r})$ for the investigated spatial location. The second case in figure 2 shows a reduction of 50% for $x_{dif}(0.2)$, the third case shows a reduction of 90% for $x_{dif}(0.7)$.

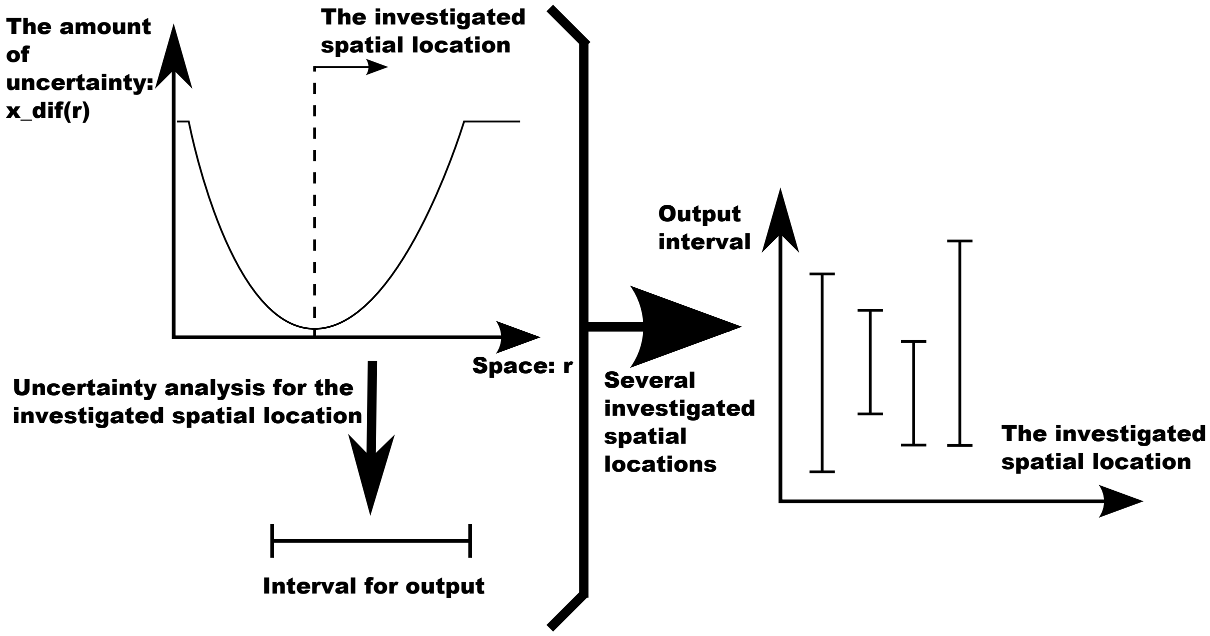

Figure 1: Concept to determine R_X^Y in a spatial context

- the magnitude of the reduction of $x_{dif}(\mathbf{r})$ in the local influence zone of the investigated spatial location. By reducing the amount of uncertainty for the investigated spatial location, the amount of uncertainty for the region around the investigated spatial location is also affected. In this so called local influence zone, a transition from the reduced amount of uncertainty to the reference amount of uncertainty is needed. In this paper a quadratic transition is suggested.

- the magnitude of the local influence zone of the investigated spatial location. The second case in figure 2 shows a zone of influence from -0.1 to $+0.1$ around the investigated spatial location 0.2. The third case shows a zone of influence from -0.3 to $+0.3$ around the investigated spatial location 0.7.

- the change in $x_{mid}(\mathbf{r})$. If $\overline{x}(\mathbf{r})$ and $\underline{x}(\mathbf{r})$ are not changed symmetrically with respect to $x_{mid}(\mathbf{r})$ in the reference case, then $x_{mid}(\mathbf{r})$ is affected as well. For simplicity this influence is not presented here.

These notions are explained further in the case study.

5 GEOHYDROLOGICAL CASE STUDY

A geohydrological case study was chosen to apply the above presented techniques. The case study deals with a groundwater pollution problem where benzene was spilled and is now being transported in groundwater to a river. To characterize the flow and transport of the benzene spill, a groundwater flow and transport model was built in HYDRUS3D. First, the problem together with its uncertainty is described and the results of a fuzzy analysis without taking into account the spatial dependency are presented. Next, the spatial dependency is introduced and an investigation of the input uncertainty elasticity of the output is performed.

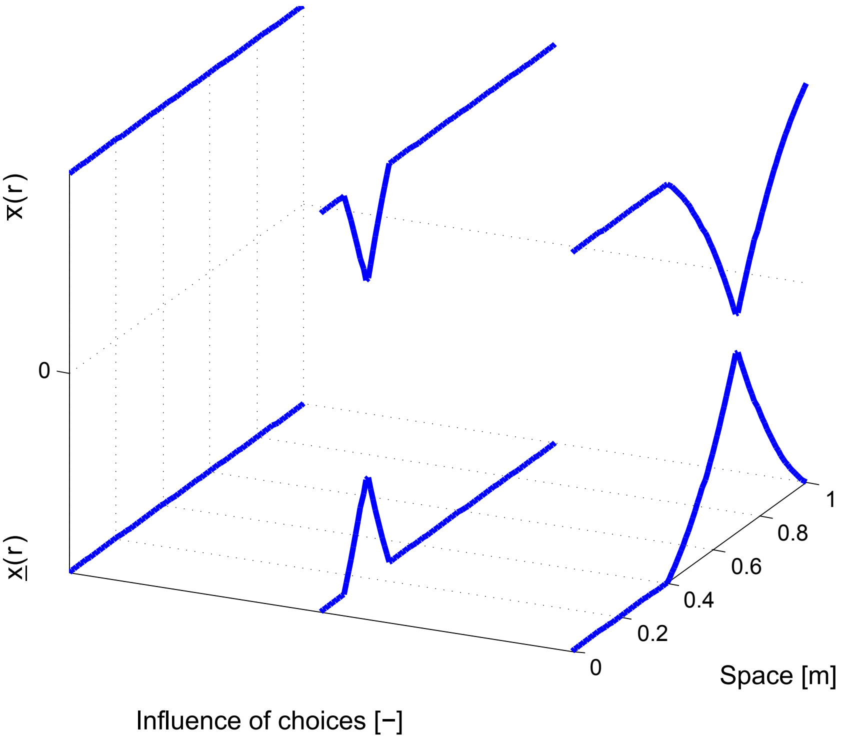

Figure 2: Choices in the selection of $\overline{x}(\mathbf{r})$ and $\underline{x}(\mathbf{r})$

Material Layer	Minimum K	Maximum K
1	1.4	2.1
2	8	12
3	3.6	5.4
4	2.6	3.9
5	4	6

Table 1: Intervals for the hydraulic conductivity K [m/day], ordered from top to bottom.

5.1 Problem description

The governing equation for solute transport in groundwater is a convection-diffusion equation based on conservation of mass. Convection is determined by groundwater flow which is based on the constitutive equation for variably saturated flow in porous media, called the Darcy Buckingham equation. For the solute (the contaminant: Benzene) and ground water flow problem at hand the following input was given:

- FE-model (14661 nodes) for the HYDRUS3D [11] solver (see figure 3). The dimensions of the problem are 1100 m in the length direction and between 32 and 36.5 m in the depth direction. In the time domain a period of 11000 days (approximately 30 years) is calculated. A deterministic run of this model takes 10 minutes.
- Intervals for the material properties, i.e. the saturated hydraulic conductivity K (see table 1) of the five different material layers.

A river is situated at the left side of the domain (see the red ellipse on figure 3) and the two sources of the contaminant are in the middle of the domain (see the red arrows on figure 3).

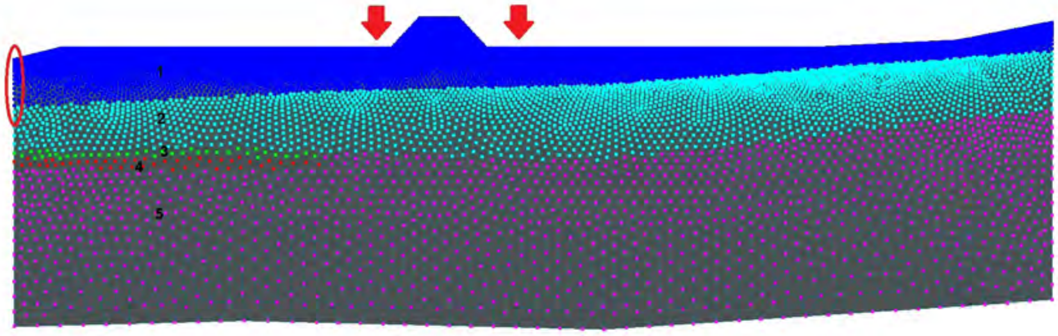

Figure 3: FE-model for solute and ground water flow showing the five different material layers.

The requested output is the concentration of the contaminant over time at the river given the uncertainties on the material properties.

5.2 Fuzzy analysis without spatial uncertainty

In the first fuzzy analysis, the uncertainty on the material properties is represented by fuzzy numbers. The hydraulic conductivity of each layer is considered independent and modelled as a triangular fuzzy number with the given intervals (see table 1) as base and the mid value as the top of the triangle. In each material layer the hydraulic conductivity is considered homogeneous through space. Figure 4 shows for example the spatial fuzzy number in blue and a possible sample of the fuzzy number in red for the hydraulic conductivity of material layer 1. Two types of fuzzy analyses were performed:

- Reduced Transformation Method (TM) [12] with 5 alpha-cuts, resulting in 161 samples.
- An optimisation on a Kriging response surface (ARSM) [4] that was built using 32 initial latinhypercube samples and 32 additional samples.

Additionally, a reference Monte Carlo Simulaion using 200 samples was performed at each alpha-level, based on a uniform distribution within the interval at each alpha-level Figure 5 shows the fuzzy concentration through time for location 11 (at the river, 3 m below the surface). In blue is the result of the reduced transformation method ($5 * 32 + 1$ samples); in green is the result of the optimisation on a Kriging response surface (32 initial + 32 additional samples); in red is the result of the Monte Carlo Simulation ($5 * 200$ samples). From these results it is clear that the TM and ARSM results are close to each other. The MCS result, despite being the computationally most expensive, does not yield good results for the maxima: the value given by the TM is an actual solution of the problem (i.e. a genuine sample) and results in higher maxima. The ARSM has problems identifying the proper minima since it tends to give negative (non-physical) results.

5.3 Fuzzy analysis with spatial uncertainty

In this fuzzy analysis, only the uncertainty on the hydraulic conductivity in material layer 1 is taken into account. The other hydraulic conductivities are set at their minimal value. To model the spatial uncertainty for the hydraulic conductivity of material layer 1, the following assumptions are made:

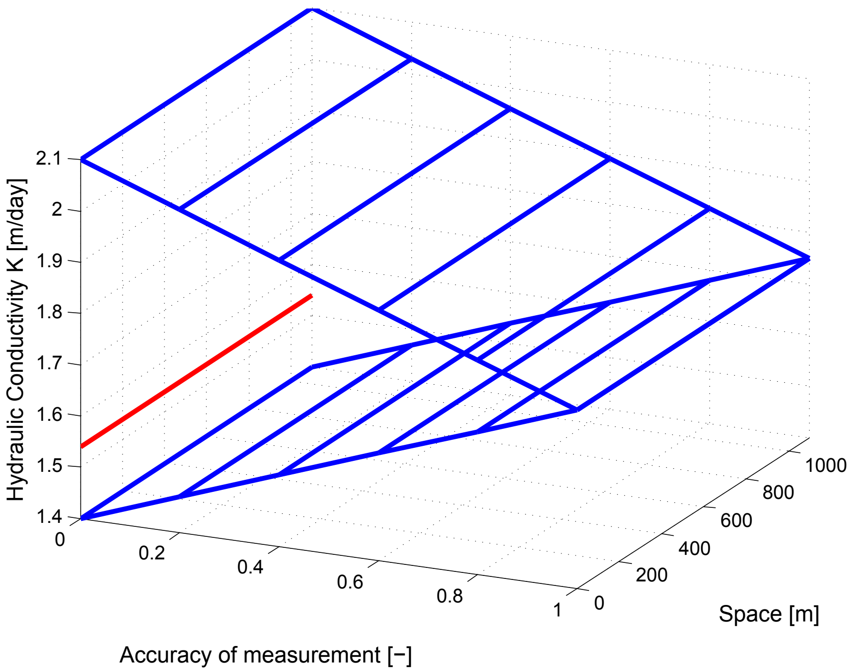

Figure 4: The spatial fuzzy number in blue and a sample of it in red for the hydraulic conductivity of material layer 1, assuming homogeneity.

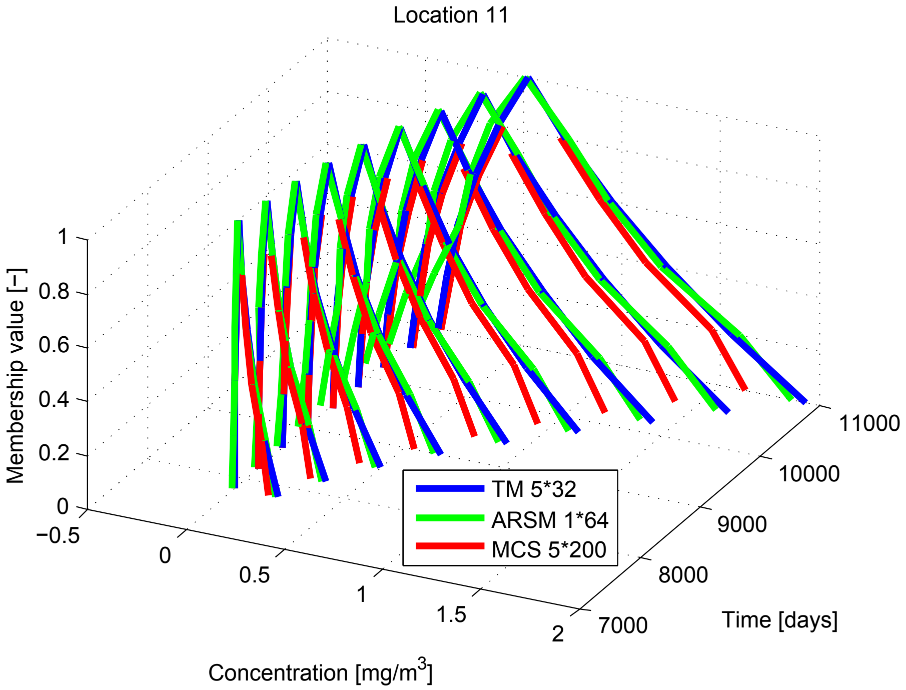

Figure 5: The fuzzy concentration at the river, 3 m below the surface.

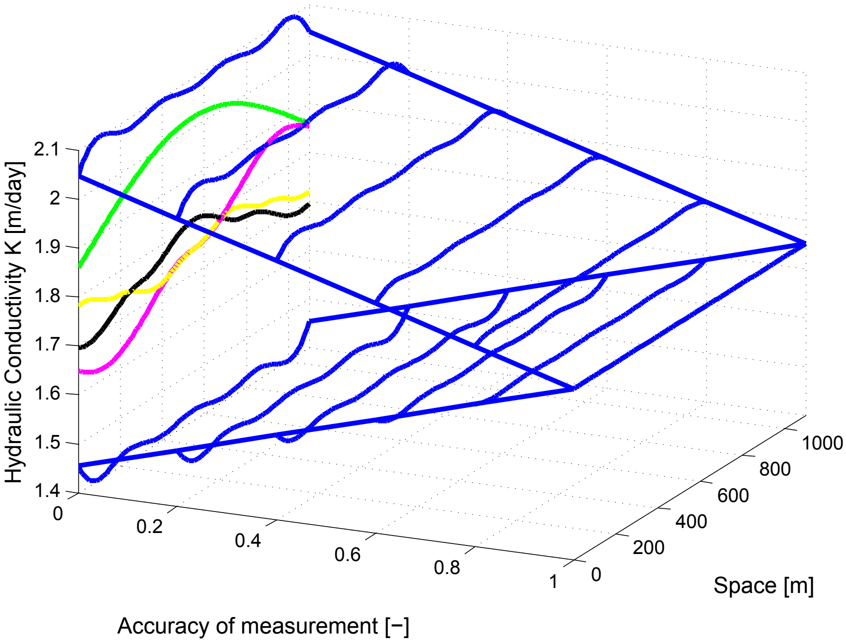

Figure 6: The spatial fuzzy number in blue and the four base vectors for membership level 0 in colours for the hydraulic conductivity of material layer 1, including spatial uncertainty.

- The upper bound $\overline{x}(\mathbf{r})$ and lower bound $\underline{x}(\mathbf{r})$ are given by a constant, namely the maximum and minimum of the interval given in table 1.
- The base vectors are derived from an exponential autocovariance function

$$C_{HH}(x_1, x_2) = e^{-\frac{|x_1 - x_2|}{L}} \tag{12}$$

as described in section 3.2. The first four eigenfunctions are used. Since a limited number of base vectors is used, the upper and lower bound on the uncertainty are not exactly satisfied throughout the domain. A scaling factor to adjust the maximal possible value of the interval field in the spatial domain to the requested bounds is applied. For a correlation length $L = 500$ m, the resulting base vectors are shown in 6.

To check the influence of taking into account the spatial uncertainty, two analyses (TM and ARSM) with the non-spatial uncertainty (i.e. uncertain, but homogeneous hydraulic conductivity of material layer 1) are performed as well. In total, the following types of analyses were performed:

- non-spatial uncertainty, Reduced Transformation Method (TM) with 5 alpha-cuts, resulting in 11 samples.
- non-spatial uncertainty, optimisation on a Kriging response surface (ARSM) that was built using 6 initial latinhypercube samples and 12 additional samples.
- spatial uncertainty, with correlation length between 500 and 2000 m, optimisation on a Kriging response surface (ARSM) that was built using 20 initial latinhypercube samples and 30 additional samples.

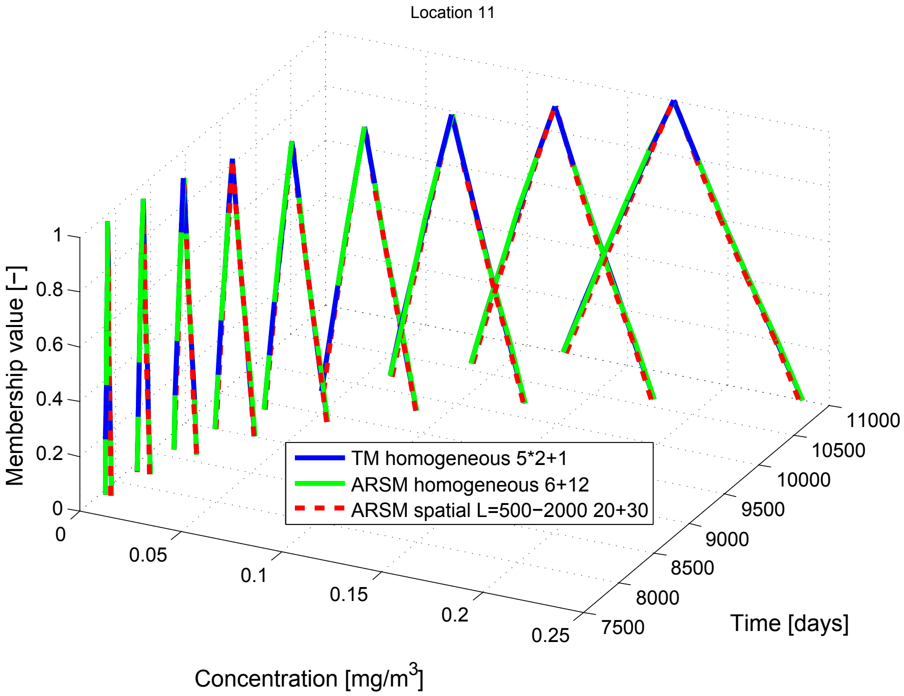

Figure 7: The fuzzy concentration at the river, 3 m below the surface.

Figure 7 shows the fuzzy concentration through time for location 11 (at the river, 3 m below the surface). The influence of taking into account the spatial uncertainty results in slightly narrower fuzzy numbers. This suggests that assuming homogeneity for the hydraulic conductivity of material layer 1 gives conservative bounds on the contaminant's concentration for the studied case.

5.4 Input uncertainty elasticity of the output

By performing an additional point measurement to determine the hydraulic conductivity in one location, the uncertainty on the contaminant's concentration will be reduced. To determine the optimal measurement location an input uncertainty elasticity of the output is calculated. The following assumptions, referring to section 4.2 and figure 8, are made:

- The magnitude of the reduction of the uncertainty for the considered measurement location is a design parameter. By selecting a more accurate measurement device, the uncertainty remaining after measurement is a choice of the expert. In figure 8 the influence of an increasing measurement accuracy on the bounds and the base vectors is shown.
- The magnitude of the reduction of the uncertainty in the local influence zone is an uncertainty. $f_{dif}(\mathbf{r})$ increases from the value at the measurement location to the reference value at the end of the local influence zone. In the presented analysis a quadratic function of the distance to the measurement location is chosen.
- The magnitude of the local zone of influence is an uncertainty. What is the extent of the influence of a measurement in one location on the rest of the spatial domain? Since a comparison between the input uncertainty elasticities of the output for different locations is of interest, the magnitude of this local zone of influence is chosen to be a fixed value. In

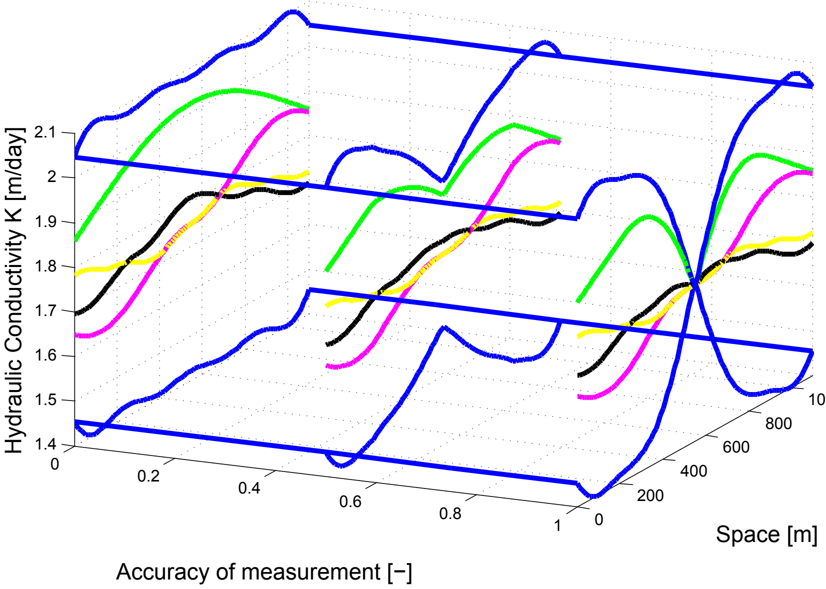

Figure 8: The influence of a measurement in the middle of the domain on the bounds of the uncertainty (in blue) and the base vectors (in colours), with a zone of influence of 330 m to both sides of the measurement location.

Design Parameter	Sampled values
Measurement location	110, 330 and 550 m from river
Measurement accuracy	50% reduction and 100% reduction of uncertainty
Uncertain Parameter	Range
Extent of influence	value chosen is 330 m.
Correlation length	$\lfloor 500\ 2000 \rceil$ m

Table 2: Parameters in the input uncertainty elasticity of the output analysis.

figure 8 the bounds and base vectors for an influence up to 330 m to both sides is shown, as it is used in the analysis.

- The actual outcome of the measurement gives a value for $f_{mid}(\mathbf{r})$ in the measurement location. Untill the measurement is done, this is also an uncertainty that influences the actual bounds on the output uncertainty. In the presented analysis the value of $f_{mid}(\mathbf{r})$ is considered a constant and unchanged by a measurement.

To summarize: the measurement location and the accuracy of the measurement are design parameters, whereas the influence of the measurement and the spatial correlation length are uncertainties. For the influence of the measurement a fixed magnitude is assumed and the correlation length is modelled as an interval. The values used in the analysis are presented in table 2. For a choice of the design parameters, the uncertainty analysis was carried out using the ARSM method with 20 inital samples and 30 additional samples. The results are presented in figure 9. The bounds on the contaminant's concentration are presented for location 11 (at the river, 3 m below the surface) at the end time of the simulation (approx. 30 years) as a function of the measurement location and the accuracy of the measurement. Based on this information the input uncertainty elasticity of the output is calculated using equation (11) with X and Y respectively the range on the hydraulic conductivity and the range on the contaminant's concentration. The results are presented in table 3, the reference is the range on the uncertainty

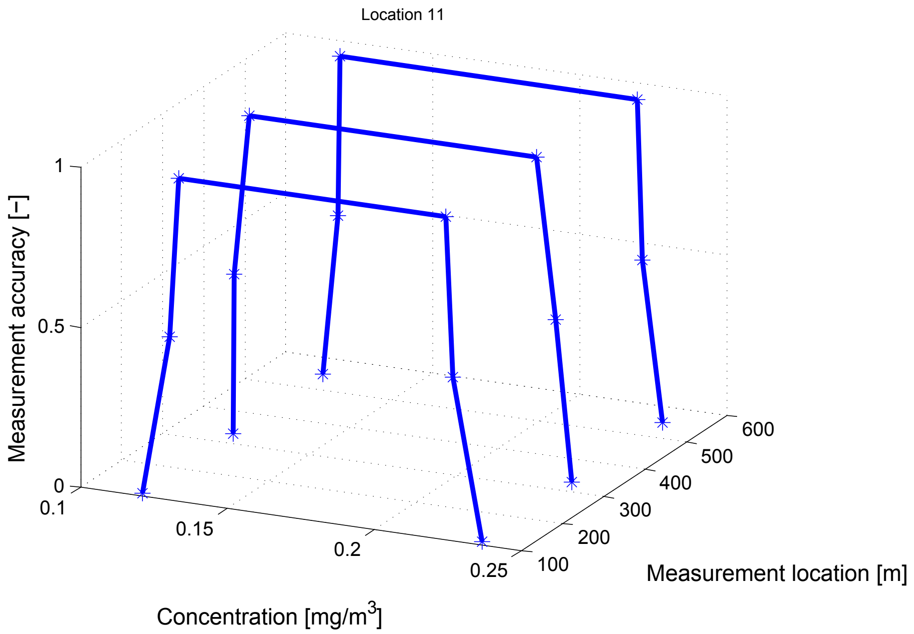

Figure 9: The results of the uncertainty analysis to determine the input uncertainty elesticity of the output

Measurement location [m]	110	330	550
Measurement accuracy [-]			
0.5	0.33	0.10	0.20
1.0	0.21	0.15	0.13

Table 3: The input uncertainty elasticity of the output.

before measurement. From this table 3 it becomes clear that performing an input uncertainty reduction (i.e. a measurement of the hydraulic conductivity in material layer 1) at 110 m from the river provides the greatest reduction in uncertainty on the output (i.e. the concentration of the contaminant at the considered location and time). Furthermore, for this measurement location increasing the uncertainty reduction from 50% to 100% will not decrease the uncertainty on the output with the same amount. In other words, a measurement with an uncertainty reduction of 50% will have a $\frac{0.33}{0.21} \simeq 1.5$ times higher relative uncertainty reduction on the output than a measurement with an uncertainty reduction of 100%. For a measurement at 330 m from the river the inverse is true: the extra effort of reducing the input uncertainty from 50% to 100% gives a 1.5 times higher relative uncertainty reduction on the output. Based on this information and knowledge of the actual costs of a measurement campaign an informed decision can be made concerning where and how accurate to measure.

6 CONCLUSION

From a methodological point of view, the paper introduces interval fields as an easy conceptual tool to deal with spatial uncertainty. The implementation of the interval field based on correlation length is made possible by deriving certain base vectors from the random field expansion technique. This allows for taking into account uncertainty on the correlation length. Furthermore, the concept of input uncertainty elasticity of the output is introduced in a spatial uncertainty context.

From an applied point of view, the paper shows the applicability of the interval field to a geohydrological problem of realistic complexity. The adaptive response surface technique proves to be very useful in practice. Certainty on the value of the correlation length often is a problem. The feasibility of dealing with the correlation length as an interval is shown. The concept of input uncertainty elasticity of the output in a spatial uncertainty context is proven to be usefull to determine the optimal location of a measurement (i.e. an uncertainty reduction) to reduce uncertainty on the output.

The support of the Flemish Governement through IWT-SBO project no. 060043: Fuzzy Finite Element Method is gratefully acknowledged.

REFERENCES

[1] D. Moens, M. De Munck, W. Desmet, D. Vandepitte, Numerical dynamic analysis of uncertain mechanical structures based on interval fields *IUTAM Symposium on Vibration Analysis of Structures with Uncertainties*, Saint Petersburg, 2009.

[2] D. Moens, M. De Munck, L. Farkas, H. De Gersem, W. Desmet, D. Vandepitte, Recent advances in interval finite element analysis in applied mechanics *Proceedings of the first Leuven Symposium on Applied Mechanics in Engineering LSAME.08*, Leuven, 2008.

[3] M. De Munck, D. Moens, W. Desmet, D. Vandepitte, An efficient response surface based optimisation method for non-deterministic harmonic and transient dynamic analysis *CMES: Computer Modeling in Engineering & Sciences*, **47**, 119–166, 2009.

[4] M. De Munck, Efficient optimization approaches for interval and fuzzy finite element analysis *PhD thesis, K.U.Leuven*, 2009.

[5] L.A. Zadeh, Fuzzy Sets *Information and Control*, **8**, 338–353, 1965.

[6] W. Verhaeghe, A. Rousounelos, W. Desmet, D. Vandepitte, D. Moens, Interval fields to represent uncertainty on input and output side of a FE analysis *Proceedings of ISMA2010 International Conference on Noise and Vibration Engineering including USD2010*, Leuven, 2010.

[7] E. Vanmarcke, Random fields: analysis and synthesis *MIT Press*, Cambridge, 1993.

[8] B. Sudret, and A. Der Kiureghian, Stochastic Finite Element Methods and Reliability: A State-of-the-Art Report *Department of Civil & Environmental Engineering, University of California, Berkley, Institute of Structural Engineering, Mechanics and Materials*, 2010.

[9] R. Ghanem and P.D. Spanos, Stochastic finite elements: a spectral approach *Springer-Verlag*, New-York, 1991.

[10] W. Verhaeghe, W. Desmet, D. Vandepitte, D. Moens, Uncertainty assessment in random field representations: an interval approach *Proceedings of the NAFIPS 2011 conference*, El Paso, 2011.

[11] HYDRUS Software package for simulating water, heat and solute movement in two- and three-dimensional variably saturated media. *Dr. M. Sejna, Dr. J. Simunek and Dr. R. Van Genuchten*, PC-Progress s.r.o, Prague, www.hydrus3D.com

[12] M. Hanss, Applied Fuzzy Arithmetic - An Introduction with Engineering Applications *Springer*, Berlin, 2005.

COMPDYN 2011
3rd ECCOMAS Thematic Conference on
Computational Methods in Structural Dynamics and Earthquake Engineering
M. Papadrakakis, M. Fragiadakis, V. Plevris (eds.)
Corfu, Greece, 25–28 May 2011

SEISMIC STRUCTURAL ANALYSIS USING INTERVAL RESPONSE SPECTRUM

Mehdi Modares[1] **and Adam Venezia**[2]
[1]Illinois Institute of Technology
3201 S. Dearborn St. AM213
Chicago, IL 60616
e-mail: mmodares@iit.edu

[2] Illinois Institute of Technology
3201 S. Dearborn St. AM213
e-mail: avenezia@iit.edu

Keywords: Structural Dynamics, Seismic Engineering, Interval Analysis, Response Spectrum.

Abstract. *Seismic analysis is an essential procedure to design a structure subjected to a system of suddenly applied loads due to earthquake excitations. However, throughout conventional seismic analyses, the structure is subjected to a limited number of recorded earthquake excitations. Moreover, the presence of variations and uncertainties in the recorded excitations from different earthquakes is not considered in current seismic analysis procedures. One of the methods to quantify the impreciseness and uncertainty is the interval or unknown-but-bounded representation.*

In this work, a new computationally feasible method for seismic structural analysis with interval uncertainty in the response spectrum is developed, which is capable of obtaining the bounds on the structure's dynamic response. Using this method, first, the response spectra from various recorded earthquakes are combined as an interval function and the interval earthquake response spectrum is constructed. Then, using the developed interval function, the response spectrum analysis is performed and the structure's dynamic response is obtained. This method shows that calculating the bounds on the dynamic response does not require a Monte-Carlo simulation procedure. An example problem that illustrates the developed algorithm with comparison to the different solutions is presented.

1 INTRODUCTION

In structural engineering, design of an engineered system requires that the performance of the system is guaranteed over its lifetime. In the case where the structure is subjected to loads induced by earthquake excitations, seismic analysis is a crucial procedure for reliable design. Using conventional seismic analysis procedures, the structure is subjected to a limited number of recorded earthquake excitations. However, the conventional procedures do not simultaneously consider the presence of variations and uncertainties in the recorded excitations in the analysis.

Treating uncertainty in the seismic analysis of a structure requires two major considerations: first, quantification of variations and uncertainties in the earthquake response spectra; and second, development of schemes that are capable of considering the presence of uncertainty throughout the solution process. Those developed schemes must be consistent with the structure's physical behavior and must also be computationally feasible.

The set-theoretic (unknown-but-bounded), or interval representation of vagueness is one possible method to quantify the uncertainty. The interval representation of uncertainty in the parametric space has been motivated by the lack of detailed probabilistic information on possible distributions of parameters and computational issues in obtaining solutions.

In this work, a new method for seismic structural analysis with interval uncertainty in the response spectrum is developed which is capable of bounding the structure's dynamic response. Using this method, first, the response spectra from various recorded earthquakes are combined as an interval function (with respect to frequency or period) and the interval earthquake response spectrum is constructed. Then, response spectrum analysis is performed using the constructed interval function to obtain the structure's upper-bounds of dynamic response.

This work represents the synthesis of two historically independent fields, seismic structural analysis and interval analysis. In order to represent the background for this work, a review of development of both fields is presented. First, a background and the analytical procedure for seismic structural analysis are presented. Next, a background and fundamentals of interval uncertainty analysis are presented. Following that, the new method for seismic analysis with response spectrum is introduced. Next, the upper-bounds on dynamic response of the structure are determined. Finally, exemplar and numerical results are presented that are followed by observations and conclusions.

2 DETERMINISTIC SEISMIC STRUCTURAL ANALYSIS

2.1 Historical background

Modern theories of structural dynamics were introduced mostly in mid 20th century. Biot (1932) [1] introduced the concept of earthquake response spectra and Housner (1941) [2] was instrumental in the widespread acceptance of this concept as a practical means of characterizing ground motions and their effects on structures. Newmark (1952) [3] introduced computational methods for structural dynamics and earthquake engineering. Anderson (1952) [4] developed methods for considering the effects of lateral forces on structures induced by earthquake and wind. Also, Hudson (1956) [5] developed techniques for response spectrum analysis in engineering seismology. Veletsos (1957) [6] determined natural frequencies of continuous flexural members. Rosenblueth (1959) [7] introduced methods for combining modal responses and characterizing earthquake analysis. Biggs (1964) [8] developed dynamic analyses for structures subjected to blast loads. Moreover, Penzien and Clough (1993) [9] further developed numerical methods for dynamics of structures and modal analysis.

2.2 Review of response spectrum analysis

The method of response spectrum analysis for computing the dynamic response of a multiple degree-of-freedom structure to a system of dynamic loads can be sequenced as following:

1. Define the structural properties.
    - Determine the stiffness matrix $[K]$ and mass matrix $[M]$.
    - Assume the modal damping ratio ζ_n.
2. Perform a generalized eigenvalue problem between the stiffness and mass matrices.
    - Determine natural circular frequencies (ω_n).
    - Determine mode shapes $\{\varphi_n\}$.
3. Compute the maximum modal response.
    - Determine the maximum modal coordinate $D_{n,\max}$ using the excitation response spectrum for the corresponding natural circular frequency and modal damping ratio.
    - Determine the modal participation factor Γ_n.
    - Compute the maximum modal response as a product of maximum modal coordinate, modal participation factor and mode shape.
4. Combine the contributions of all maximum modal responses to determine the maximum total response using square root of sum of squares (SRSS) or other combination methods.

3 INTERVAL ANALYSIS

3.1 Historical background

The concept of representation of an imprecise real number by its bounds is quite old. In fact, Archimedes (287-212 B.C.) [10] defined the irrational number (π) by an interval, $(3+10/71<\pi<3+1/7)$ which he found by approximating the circle with the inscribed and circumscribed 96-side regular polygons. The introduction of digital computers in the 1950's provided impetus for further interval analysis as discrete representations of real numbers with associated truncation error. Interval mathematics was further developed by Sunaga (1958) [11] who introduced the theory of *interval algebra* and its applications in numerical analysis. Also, Moore (1966) [12] introduced *interval analysis*, interval vectors and interval matrices as a set of techniques that provides error analyses for computational results.

Interval analysis provides a powerful set of tools with direct applicability to important problems in scientific computing. Alefeld and Herzberger (1983) [13] presented an extensive treatment of interval linear and non-linear algebraic equations and interval methods for systems of equations. Moreover, Neumaier (1990) [14] investigated the methods for solution of interval systems of equations.

The concept of interval systems has been further developed in analysis of structures with interval uncertainty. Muhanna and Mullen (1999) [15] developed fuzzy finite-element methods for solid mechanics problems. For the solution of interval finite element method (IFEM) problems, Muhanna and Mullen (2001) [16] introduced an Element-by-Element interval finite element formulation, in which a guaranteed enclosure for the solution of interval linear systems of equations was achieved. The research in interval eigenvalue problem began to emerge as its wide applicability in science and engineering was realized. Modares and Mullen (2004) [17] introduced a method for the solution of the parametric interval eigenvalue problem resulting from semi-discretization of structural dynamics which determines the exact bounds of the natural frequencies of a structure with uncertainties in their mechanical characteristics.

3.2 Interval (convex) variable

A real interval is a closed set defined by extreme values as (Figure 1):

$$\tilde{Z} = [z^l, z^u] = \{z \in \Re \mid z^l \le z \le z^u\} \tag{1}$$

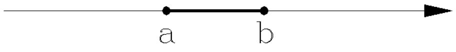

$$\tilde{x} = [a, b]$$

Figure 1: An interval quantity.

One interpretation of an interval number is a random variable whose probability density function is unknown but non-zero only in the range of interval. Another interpretation of an interval number includes intervals of confidence for α -cuts of fuzzy sets.

This interval representation transforms the point values in the deterministic system to inclusive set values in the system with bounded uncertainty. Interval arithmetic is a computational tool that can be used to represent uncertainty as 1) a set of probability density functions, 2) In Dempster-Shafer models for epistemic probability and, 3) α - cuts in fuzzy sets, etc. In this work, the symbol (~) represents an interval quantity.

3.3 Interval arithmetic operations

Considering $\tilde{X} = [a, b]$ and $\tilde{Y} = [c, d]$ as two interval numbers, the basic interval arithmetic operations are:

Addition: $$\tilde{X} + \tilde{Y} = [a + c, b + d] \tag{2}$$

Subtraction: $$\tilde{X} - \tilde{Y} = [a - d, b - c] \tag{3}$$

Multiplication: $$\tilde{X} \times \tilde{Y} = [\min(ac, ad, bc, bd), \max(ac, ad, bc, bd)] \tag{4}$$

Division: $$\frac{\tilde{X}}{\tilde{Y}} = [a, b] \times [\frac{1}{d}, \frac{1}{c}], (0 \notin [c, d]) \tag{5}$$

Interval Vector (2-D):

$$\tilde{V} = \begin{Bmatrix} \tilde{X} \\ \tilde{Y} \end{Bmatrix} = \begin{Bmatrix} [a, b] \\ [c, d] \end{Bmatrix} \tag{6}$$

which represents a “box” in 2-D space as the enclosure (Figure 2).

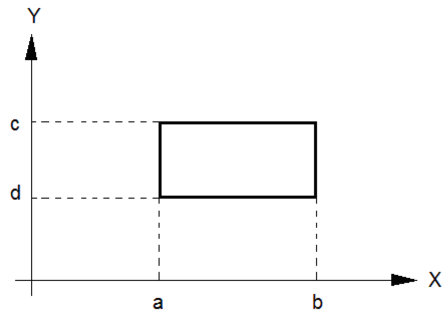

Figure 2: An interval vector

3.4 Functional dependency and sharpness considerations of interval operations

Considering $\tilde{X} = [-2,2]$ and $\tilde{Y} = [-2,2]$ as two independent interval numbers, the functional dependent interval multiplication results in:

$$\tilde{X} \times \tilde{X} = [0,4]$$

In contrast, the functional independent interval multiplication results in:

$$\tilde{X} \times \tilde{Y} = [-4,4]$$

In interval operations, the functional dependency of intervals must be considered in order to attain sharper results. In fact, the issue of sharpness and overestimation in interval bounds is the key limitation in the application of interval methods. Naïve implementation of interval arithmetic algorithms (substituting interval operations for their scalar equivalence) will yield bounds that are not useful for engineering design. Therefore, there is a need to develop algorithms to calculate sharp or nearly sharp bounds to the underlying set theoretic interval problems.

4 SEISMIC ANALYSIS USING INTERVAL RESPONSE SPECTRUM

The developed method for seismic analysis of structures using interval response spectrum enhances the conventional dynamic response spectrum analysis by: a) introducing an interval response spectrum constructed from a cluster of recorded excitation and, b) obtaining the bounds on the structure's dynamic response. The method is composed of following steps:

1. Define the physical or geometrical characteristics.
    - Determine the stiffness matrix $[K]$ and mass matrix $[M]$.
    - Assume the modal damping ratio ζ_n.
2. Perform an interval eigenvalue problem between the stiffness and mass matrices.
    - Determine the natural circular frequencies ω_n.
    - Determine the mode shapes $\{\varphi_n\}$.
3. Construct interval response spectrum.
    - Create a cluster of response spectra obtained from various recorded earthquakes.
    - Determine interval response spectrum as an interval function of excitation frequency.
4. Compute the interval modal response.
    - Determine the interval modal coordinate $\tilde{D}_n$ using the interval response spectrum for the corresponding natural circular frequency and assumed modal damping ratio.
    - Determine the modal participation factor Γ_n.
    - Compute the interval modal response as the product of interval modal coordinate, modal participation factor and mode shape.
5. Combine and maximize the contributions of all interval modal responses to determine the maximum total response using SRSS or other combination methods.

4.1 Interval Response Spectrum

In order to construct interval response spectrum, first, a cluster of response spectra obtained from various recorded earthquake excitations is combined. Then, by enclosing all the response spectra, an interval response spectrum function is determined which is an interval function of frequency or period. Moreover, additional uncertainties in response spectra can also be considered. Figure 3 depicts an example for an interval response spectrum.

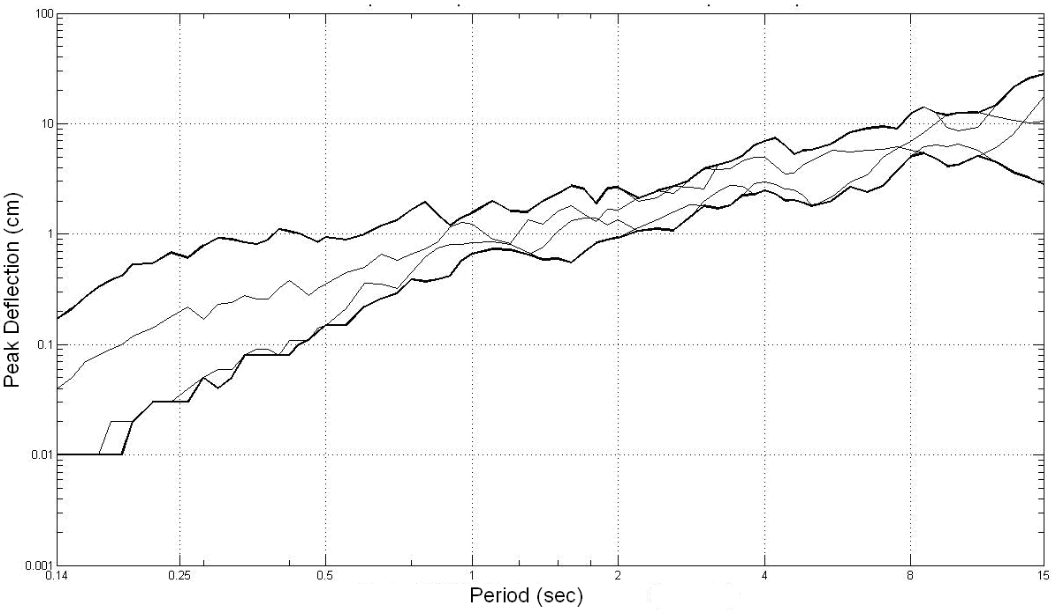

Figure 3: An interval response spectrum

4.2 Bounding Dynamic Response

The interval modal coordinate $\tilde{D}_n$ is determined using the interval response spectrum evaluated for the corresponding natural circular frequency ω_n and assumed modal damping ratio (Figure 4).

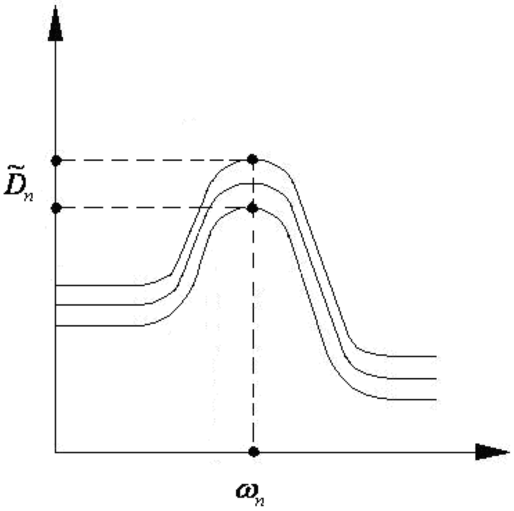

Figure 4: Determination of $\tilde{D}_n$ corresponding to a ω_n from an interval response spectrum.

If excitation is proportional, the modal participation factor is obtained as:

$$\Gamma_n = \frac{\{\varphi_n\}^T [M]\{r\}}{\{\varphi_n\}^T [M]\{\varphi_n\}} \qquad (7)$$
$$\{r\} = \{1 \quad 1 \quad \ldots \quad 1\}^T$$

The interval modal response is determined as the product of interval modal coordinate, modal participation factor and mode shape as:

$$\{\tilde{U}_n\} = (\tilde{D}_n)(\Gamma_n)\{\varphi_n\} \qquad (8)$$

Finally, the contributions of all interval modal responses are combined and maximized to determine the maximum total response using SRSS or other combination methods as:

$$\{U_{\max}\} = \max\left(\sqrt{\sum_{n=1}^{N} \{\tilde{U}_n^2\}}\right) \qquad (9)$$

in which the upper-bounds of response due to presence of variations and uncertainty in the response spectra is obtained.

5 NUMERICAL EXAMPLE

In this example, the bounds of the dynamic response of a 2-D truss structure subjected to multiple ground-motions are obtained using the developed method (Figure 5.)

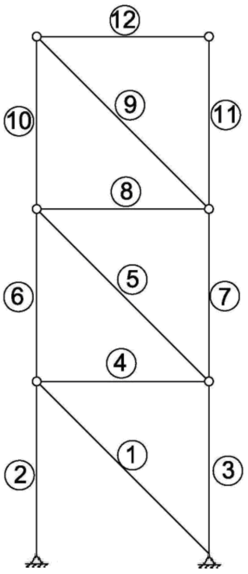

Figure 5: The structure of 2-D truss

The Young's moduli for all elements is $E = 200\ GPa$. The load on first floor, second floor and roof are 10,000 *kN*, 10,000 *kN* and 8,000 *kN*, respectively. The length of all horizontal and vertical members is 4*m*. The areas of the members are: $A_1 = A_6 = A_7 = A_8 = A_{12} = 65\ cm^2$, $A_2 = A_3 = 100\ cm^2$, $A_4 = 75\ cm^2$, $A_{10} = A_{11} = 35\ cm^2$.

5.1 Construction of interval response spectrum

For this example, ten recorded seismic response spectra are used which are obtained from five recent major earthquakes (two spectra per each earthquake measured in perpendicular directions). Table 1 summarizes the earthquakes' information. Figure 6 depicts the ten historical response spectra, and the bounding interval response spectrum.

Earthquake Location	Earthquake Date	Recording Location	Distance from Epicenter
Chile	Feb. 27, 2010	Concepcion, Chile	109 km
Samoa	Nov. 29, 2009	Afimalu, Samoa	179 km
Sumatra	Nov. 9, 2007	Sikuai Island, West Sumatra	392 km
Sumatra (aftershock)	Nov. 12, 2007	Sikuai Island, West Sumatra	165 km
Haiti	Jan. 12, 2010	Presa de Sabaneta, Dominican Republic	144 km

Table 1: Information for the earthquakes used in the example problem.

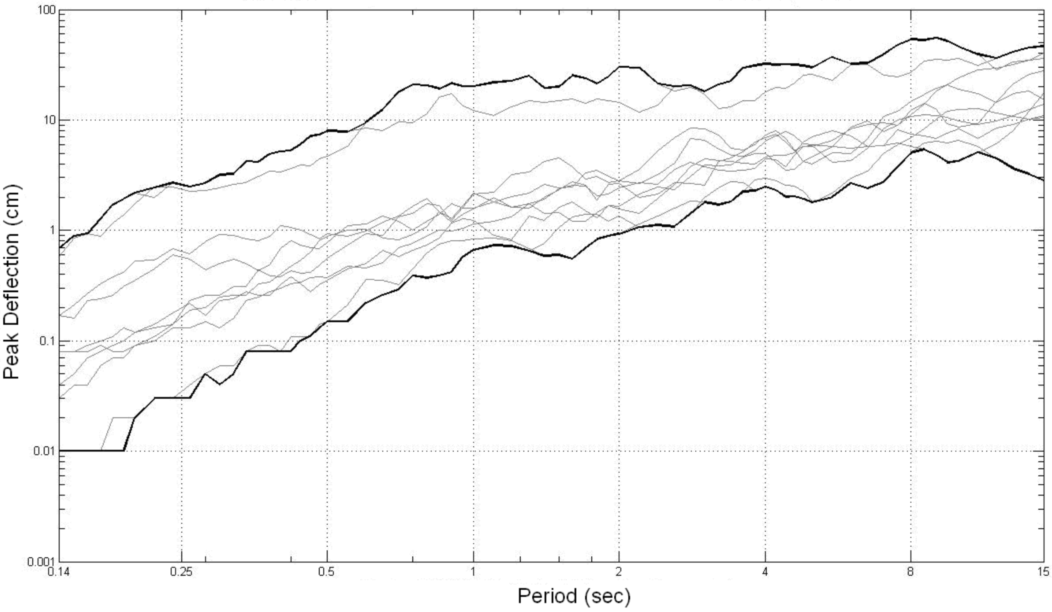

Figure 6: Constructed interval response spectrum for the example problem.

5.2 Solution

The problem is solved using the present method and the results are compared with solutions for 10^4 Monte Carlo Simulations using uniformly distributed random variables. The structure's degrees-of-freedom are statically condensed to only three lateral degrees-of-freedom (one per floor).

Using the obtained interval response spectrum, interval modal coordinates $\tilde{D}_n$ for structure's natural periods are determined. The results are shown in Figure 7 and summarized in Table 2.

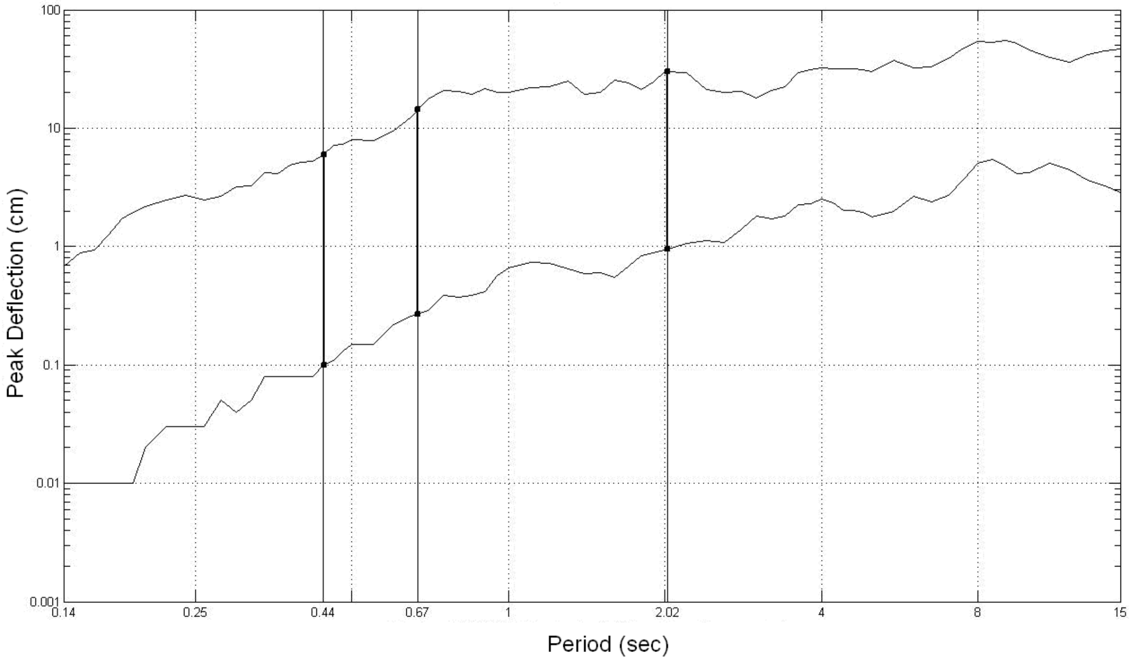

Figure 7: Determination of interval modal coordinates from interval response spectrum

Mode	Natural period T_n (sec)	Interval modal coordinate $\tilde{D}_n$ (cm)
1	0.44	[0.10 , 5.97]
2	0.67	[0.27 , 14.52]
3	2.02	[0.95 , 30.14]

Table 2: Interval modal coordinates

Next, the upper-bounds of modal responses are determined. Then, the dynamic response for each floor is obtained by combining modal responses using SRSS method. The analysis procedure is performed using both present method and Monte-Carlo simulations and the results are compared. Table 3 summarizes the results.

Mode	Maximum Response $U_{\max}$ (cm) (*present method*)	Maximum Response $U_{\max}$ (cm) (*simulation*)
1	10.64	10.50
2	25.53	25.42
3	40.56	40.48

Table 3: The structure's upper-bounds of dynamic responses

Figure 8 depict the structure's response obtained from both present method and Monte-Carlo simulation solution geometrically.

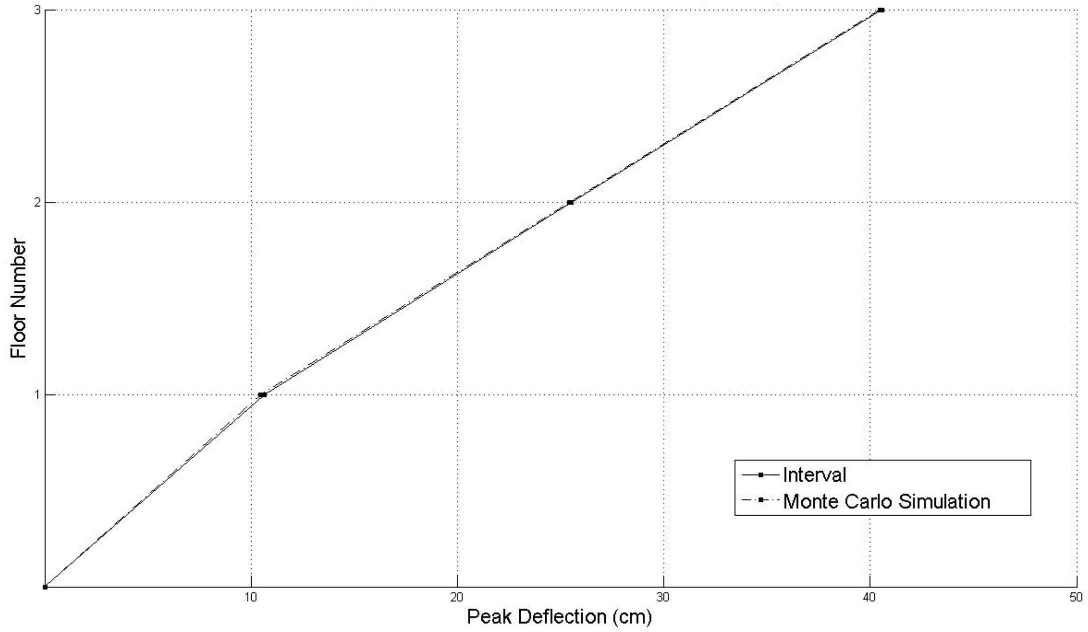

Figure 8: Geometric depiction of the structure's upper-bounds of dynamic responses

5.3 Observations

The results show that using the present method, the obtained sharp solutions are upper-bounds to solutions obtained by methods that produce inner-bound results such as Monte-Carlo simulation. Moreover, the proposed method is computationally feasible because of its non-iterative process.

6 CONCLUSIONS

- In this work, a finite-element based method for seismic structural analysis with interval uncertainty in the response spectrum is developed.
- This method enhances the conventional response spectrum analysis for considering the presence of variation and uncertainty in the ground excitation.
- For a given set of recorded ground motions for various earthquakes, the response spectra are combined as an interval response spectrum used in the analysis procedure defined in the developed methodology.
- The method is capable of obtaining sharp results for the structure's dynamic response.
- This method is computationally feasible and it shows that the bounds on the dynamic response can be obtained without any iterative procedure such as Monte-Carlo simulation procedure.
- The computational efficiency of the proposed method makes it attractive to introduce uncertainty into seismic analysis of structures.

REFERENCES

[1] M. A. Biot, *Vibrations of Buildings during Earthquake*, Chapter II in Ph.D. Thesis No. 259 entitled *Transient Oscillations in Elastic System*, Aeronautics Department, Calif. Inst. of Tech., Pasadena, California, U.S.A., 1932.

[2] G. W. Housner, *Behavior of Structures during Earthquake* Proc. ASCE Vol. 85, No. EM 4 p. 109, 1959.

[3] N. M. Newmark, *A Method of Computation for Structural Dynamics*, Trans. ASCE, Vol. 127, pt.1, pp. 1406-1435 (1962).

[4] A.W. Anderson et al., *Lateral Forces on Earthquake and Wind*", Trans. ASCE, Vol. 117, p. 716, 1952.

[5] D. E. Hudson, *Response Spectrum Techniques in Engineering Seismology*, Proc. World Conference on Earthquake Eng. Earthquake Engineering Research Institute, Berkeley, California, 1956.

[6] A. S. Veletsos, N. M. Newmark, , *Natural Frequencies of Continuous Flexural Members*, Trans. ASCE, Vol. 122, p. 249, 1957.

[7] E. Rosenblueth, & Bustamente, J. I., *Distribution of Structural Response to Earthquakes*, Proc. ASCE, Vol. 88, No. EM 3 p. 75, 1962.

[8] J. M Biggs, *Introduction to Structural Dynamics*, McGraw-Hill, Inc, 1964.

[9] R.W Clough, J. Penzien, *Dynamics of Structures*, McGraw-Hill, New York, 1993.

[10] Archimedes (287-212 B.C.); by T.L. Heath, *The Works of Archimedes*, Cambridge, Cambridge University Press, 1897.

[11] T. Sunaga, *Theory of an Interval Algebra and its Application to Numerical Analysis*, RAAG Memoirs II 2, 547-565. Tokyo, Japan, 1958.

[12] Ramon E. Moore, *Interval Analysis*, Prentice Hall, Englewood, NJ, 1966.

[13] G. Alefeld, J. Herzberger, *Introduction to Linear Computation*, New York, Academic Press, 1983.

[14] A. Neumaier, *Interval Methods for Systems of Equations*, Cambridge University Press, Cambridge, 1990.

[15] R. L Muhanna, R. L. Mullen, *Formulation of Fuzzy Finite Element Methods for Mechanics Problems*, Computer-Aided Civil and Infrastructure Engineering, 14, pp. 107-117, 1999.

[16] R. L. Muhanna, R. L. Mullen, *Uncertainty in Mechanics Problems-Interval-Based Approach*, Journal of Engineering Mechanics June-2001, pp.557-566, 2001.

[17] M. Modares, R. L. Mullen, *Free Vibration of Structures with Interval Uncertainty*, 9th ASCE Specialty Conference on Probabilistic Mechanics and Structural Reliability, 2004.

COMPDYN 2011
III ECCOMAS Thematic Conference on
Computational Methods in Structural Dynamics and Earthquake Engineering
M. Papadrakakis, M. Fragiadakis, V. Plevris (eds.)
Corfu, Greece, 25–28 May 2011

CLASSIFICATION OF SEISMIC DAMAGES IN BUILDINGS USING FUZZY LOGIC PROCEDURES

Anaxagoras Elenas[1], Eleni Vrochidou[2], Petros Alvanitopoulos[3], Ioannis Andreadis[4]

[1]Institute of Structural Mechanics and Earthquake Engineering, Democritus University of Thrace
GR-67100 Xanthi, Greece
e-mail: elenas@civil.duth.gr

[2,3,4]Laboratory of Electronics, Department of Electrical and Computer Engineering, Democritus University of Thrace, 67100 Xanthi, Greece
e-mail: [2]evrochid@ ee.duth.gr, [3]palvanit@ee.duth.gr, [4]iandread@ee.duth.gr

Keywords: Seismic Parameters, Damage Indices, Seismic Ground Motion, Damage Potential, Reinforced Concrete, Adaptive Neuro-Fuzzy Inference System.

Abstract. *It is well known that damage observations on buildings after severe earthquakes exhibit interdependence with the seismic intensity parameters, like peak ground acceleration, response-spectra, Arias intensity and strong motion duration. Numerical elaboration of structural systems quantified the interrelation degree by correlation coefficients. In addition, the seismic response of buildings is directly depended on the ground excitation. Consequently, the seismic response of buildings evaluated by a numerical analysis is directly depended on the used accelerogram and its intensity parameters. Among the several response quantities, the focus is on the overall damage indices (DIs) because they summarize the post-earthquake status of buildings on a single value, which can be easily handled. The Maximum Inter-Storey Drift Ratio (MISDR) and the damage index as defined by Park/Ang ($DI_{G,PA}$) characterize effectively the structural damages caused to buildings during earthquakes. Intervals for the values of the damage indices are defined to classify the damage degree in low, medium, large and total. This paper presents an Adaptive Neuro-Fuzzy Inference System (ANFIS) for the classification of seismic damages. The structural damage is presented by means of the two previously mentioned damage indices (MISDR and $DI_{G,PA}$). The seismic excitations are simulated by a set of artificial accelerograms and their intensity is described by a set of well-known seismic parameters. The proposed system was trained (using nonlinear dynamic analyses) and tested on an eighth-story reinforced concrete structure. The numerical results have shown that the fuzzy technique that is implemented in the proposed method contributes to the development of an efficient blind prediction of the seismic damage potential that an accelerogram possesses. The recognition scheme achieves correct classification rates over 90%.*

1 INTRODUCTION

Seismic accelerograms are records of ground acceleration versus time during earthquakes that cannot be described analytically. However, several seismic parameters have been presented in the literature during the last decades that can be used to express the intensity of a seismic excitation and to simplify its description. Post-seismic field observations and numerical investigations have indicated the interdependency between the seismic parameters and the damage status of buildings after earthquakes [1, 2]. The latter can be expressed by proper damage indices. The Maximum Inter-Storey Drift Ratio (MISDR) and the global damage index as defined by Park/Ang ($DI_{G,PA}$) characterize effectively the structural damage caused to buildings during earthquakes and thus, are used as metrics to classify the damage degree into 4 categories, low, medium, large and total. In this context, the damage degrees denote undamaged or minor damage-repairable damage-irreparable damage-partial or total collapse of the building, respectively.

This paper suggests a technique based on an Adaptive Neuro-Fuzzy Inference System (ANFIS) for seismic structural damage classification. A total set of 200 artificial accelerograms has been used and were correctively assigned to one of the above four categories with performances up to 90% and 87% of accuracy, for MISDR and $DI_{G,PA}$, respectively. High classification rates indicate that the proposed methodology is suitable for adaptive predictive control of the behavior of the concrete construction used, for any unknown seismic signal. The proposed method is applied to an eight-story reinforced concrete frame building, designed after the rules of the recent Eurocodes.

2 DAMAGE INDICES

MISDR is an overall structural damage index (OSDI) that can define the level of post-seismic corruption in a building [3, 4] and can be evaluated by the following equation:

$$MISDR=\frac{|u|_{max}}{h}100\left[\%\right] \tag{1}$$

Where $|u|_{max}$ is the maximum absolute inter-storey drift and h the inter-storey height.

Additionally, the OSDI after Park/Ang ($DI_{L,PA}$) is used to describe the structural damage [5]. First, the local damage index according to Park/Ang is calculated. The local damage index is a linear combination of the damage caused by excessive deformation and that contributed by the repeated cyclic loading effect that happens during an earthquake. The local DI is given by the relation:

$$DI_{L,PA}=\frac{\theta_m-\theta_r}{\theta_u-\theta_r}+\frac{\beta}{M_y\theta_u}E_T \tag{2}$$

Where θ_m is the maximum rotation during the load history, θ_u is the ultimate rotation capacity of the section, θ_r is the recoverable rotation at unloading, β is a strength degrading parameter (0.1-0.15), M_y is the yield moment of the section and E_T is the dissipated hysteric energy. The global damage index after Park/Ang is a linear combination of the maximum ductility and the hysteretic energy dissipation demand forced by the earthquake on the structure. Thus, the global damage index after Park/Ang ($DI_{G,PA}$) is given by:

$$DI_{G,PA} = \frac{\sum_{i=0}^{n} DI_L E_i}{\sum_{i=0}^{n} E_i} \tag{3}$$

where E_i is the energy dissipated at location i and n is the number of locations at which the local damage is calculated.

The two aforementioned global DIs are well known and used extensively in earthquake engineering, as they are experimentally proved to express the behavior of a structure [5-10]. In Table 1, intervals for the values of the DIs are defined to classify the damage degree in low, medium, large and total [11]. These categories refer to minor, reparable damage, irreparable damage and severe damage or breakdown of the building, respectively.

Structural Damage Indices	Structural Damage Degree			
	Low	Medium	Large	Total
MISDR	≤ 0.5	$0.5 < MISDR \leq 1.5$	$1.5 < MISDR \leq 2.5$	> 2.5
$DI_{G,PA}$	≤ 0.3	$0.3 < DI_{G,PA} \leq 0.6$	$0.6 < DI_{G,PA} \leq 0.8$	> 0.8

Table 1: Structural damage classification according to MISDR and $DI_{G,PA}$.

3 SEISMIC INTENSITY PARAMETERS

An accelerogram is the recording of the acceleration of the ground during an earthquake. Accelerograms exist in variant forms, and thus their similarity cannot be extracted directly. Therefore, a computer supported analysis has been done and a set of 20 features has been produced to describe the destructiveness of seismic excitations.

No	Seismic Intensity Parameter	References
1	Peak Ground Acceleration (PGA)	[13, 14]
2	Peak Ground Velocity (PGV)	[13, 14]
3	PGA to PGV ratio (PGA / PGV)	[13, 14]
4	Spectral Velocity (SV)	[13, 14]
5	Spectral Acceleration (SA)	[13, 14]
6	Spectral Displacement (SD)	[13, 14]
7	Central Period (CP)	[15]
8	Seismic Energy Input (E_{inp})	[16]
9	Arias Intensity (I_A)	[17]
10	Strong Motion Duration after Trifunac/Brady (SMD_{TB})	[18]
11	Power ($P_{0.90}$)	[19]
12	Root Mean Square Acceleration (RMS_a)	[13]
13	Seismic Intensity after Fajfar/Vidic/Fischinger (I_{FVF})	[20]
14	Spectrum Intensity after Housner (SI_H)	[21]
15	Spectrum Intensity after Kappos (SI_K)	[22]
16	Spectrum Intensity after Martinez-Rueda (SI_{MR})	[23]
17	Effective Peak Acceleration (EPA)	[24, 25]
18	Cumulative Absolute Velocity (CAV)	[26]
19	Maximum EPA (EPA_{max})	[24,25]
20	Destructiveness Potential after Araya/Saragoni (DP_{AS})	[27]

Table 2: Seismic intensity parameters.

In this study the parameters that have been selected are the following: peak ground acceleration PGA, peak ground velocity PGV, the term PGA/PGV, spectral acceleration (SA), spectral velocity (SV), spectral displacement (SD), central period (CP), absolute seismic input energy (E_{inp}), Arias intensity (I_A), strong motion duration after Trifunac/Brady (SMD_{TB}), seismic power ($P_{0.90}$), root mean square acceleration (RMS_a), intensity after Fajfar/Vidic/Fischinger (I_{FVF}), spectral intensities after Housner (SI_H), after Kappos (SI_K) and after Martinez-Rueda (SI_{MR}), Maximum EPA (EPA_{max}), cumulative absolute velocity (CAV), effective peak acceleration (EPA) and destructiveness potential after Araya/Saragoni (DP_{AS}). Table 2 presents the examined intensity parameters and their literature references, respectively.

4 STRUCTURAL MODEL

Figure 1 presents the examined reinforced concrete structure. The eigenfrequency of the frame is 0.85 Hz. The design of the 8-storey building is based on the recent Eurocode rules EC2 and EC8 [28, 29]. The cross-sections of the beams are T-beams with 40 cm width, 20 cm slab thickness, 60 cm total beam height and 1.45 m effective slab width. The distance between the frames of the structure is 6 m. The structure has been characterized as an “importance class II-ductility class medium” structure according to the EC8 Eurocode. The subsoil is of type C and the region seismicity of category 2 after the EC8 Eurocode (design around acceleration value equal to 0.24 g). External loads are taken under consideration and are incorporated into load combinations due to the rules of EC2 and EC8.

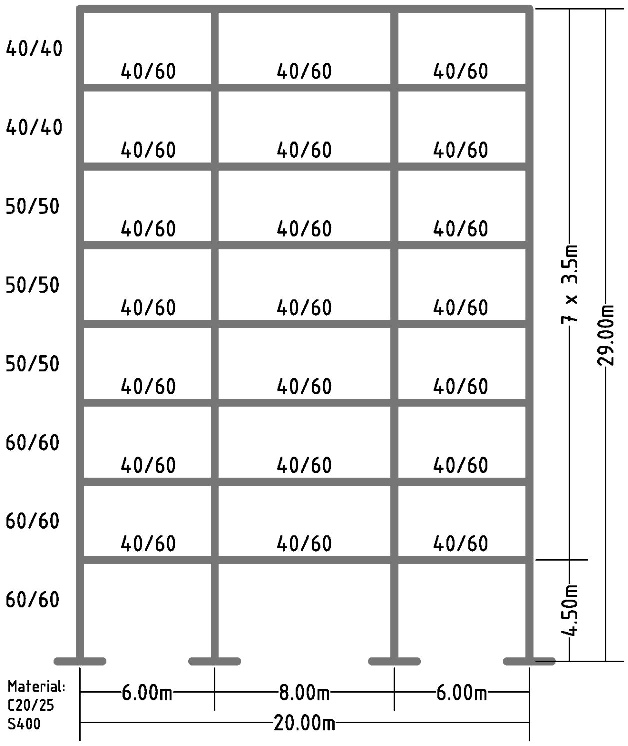

Figure 1: Reinforced concrete frame structure.

With the help of the IDARC software, the characteristics of the building are inserted into the program and a dynamic analysis is taking place, so as to estimate the structural behaviour of the building [7, 30].

5 ANFIS ALGORITHM

ANFIS was introduced in1993. ANFIS is able to extract a set of fuzzy “if-then” rules and define the membership functions in order to establish the association between inputs and outputs. Its structure is shown in Figure 2. Basically, ANFIS suggests a method that, through the training procedure, can estimate the membership function parameters that serve the fuzzy inference system (FIS) to consequently specify the desired output for a certain given input [31].

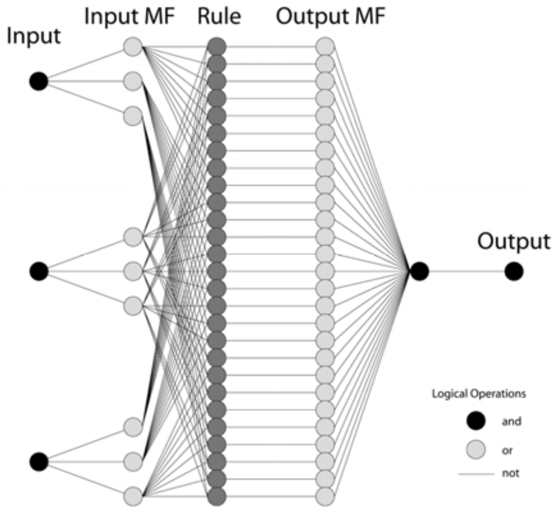

Figure 2: ANFIS structure.

ANFIS creates a fuzzy inference system in order to relate a certain input to the appropriate output. FIS interprets inputs into a set of fuzzy membership values and similarly the output membership functions to outputs. During the learning process, all parameters which define the membership functions will change. In order to optimize the model, these parameters are evaluated. Usually a gradient vector is used and an optimization routine could be applied in order to tune the parameters, so as to lead the model to a better generalization performance.

In this work, 20 seismic parameters are used as input data to describe the damage caused by one seismic event, and a total of 200 seismic events are used to train the system. All 20 seismic features have been normalized to belong in the interval [0, 1]. The 200 seismic events are distributed equally to all four damage categories in order to create a uniform data set.

First, inputs are related to membership functions (MFs), (Figure 3 shows the initial MF for one of the seismic parameters), to rules to outputs MFs, by using Fuzzy C-Means (FCM) technique [32, 33], which is analyzed later in this section. Next, the input/output data, which is a uniform set of 100 accelerograms, is used for training the model. The membership function parameters are tuned through the training process.

After the training, a model validation procedure is performed. During this procedure, an unknown input data set is presented to the trained fuzzy model for simulation. Thus, it can be evaluated the efficiency of the model. When a checking data set is presented to ANFIS, the fuzzy model selects the appropriate parameters associated with the minimum checking data model error. One crucial point with model validation, is selecting a suitable data set. This set must be representative of the data that the model is trying to simulate, and at the same time distinguishable from the training data. If a large amount of samples is collected, then all possible cases are contained and thus, the training set is more representative. In our case, a total number of 200 seismic excitations are considered as the data set.

FCM is a wildly used data clustering technique. Each data point is assigned to a cluster with a membership grade that is specified by a membership grade. It provides a method that shows how to group data points that populate some multidimensional space into a specific number of different clusters.

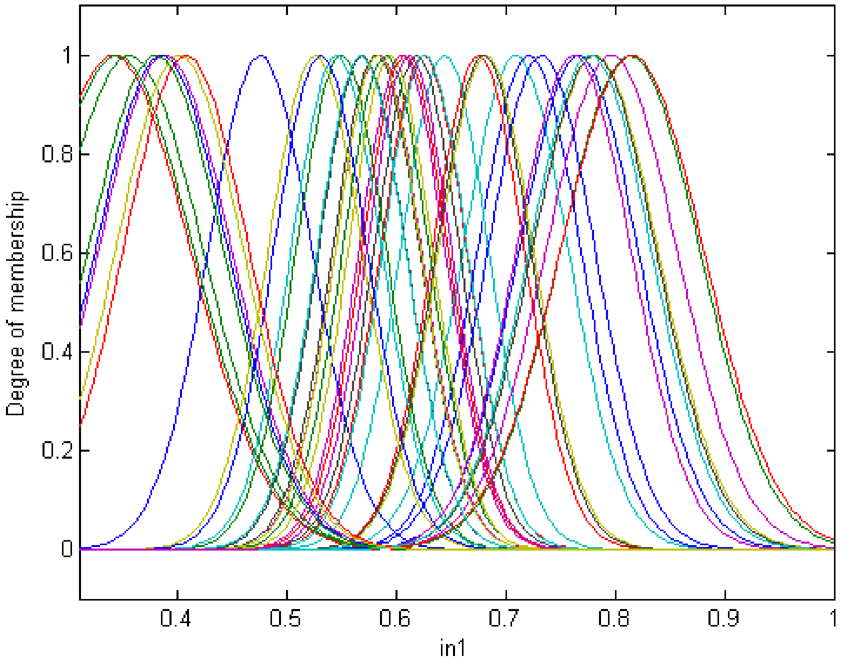

Figure 3: Initial membership function on input 1.

The purpose of data clustering is to discover similarities between input patterns from a large data set, in order to design an effective classification system.

At first, the FCM algorithm selects randomly the cluster centers. This initial choice for these centers is not always the appropriate. Furthermore, the variation of the cluster centers leads to different membership grades for each one of the clusters. Through the iteration process of the FCM algorithm, the cluster centers are gradually moved towards to their proper location. This is achieved by minimizing the weighted distance between any data point and the cluster centre. Finally, FCM function defines the cluster centers and the membership grades for every data point.

6 RESULTS

Simulation results are summarized in Table 3. The structural damage is presented by means of the two previously mentioned damage indices, MISDR and $DI_{G,PA}$, and the algorithm was tested for both damage indices. Experimental results indicate that using MISDR as metric for structural damage leads to higher performance, up to 90%, compared with the results when using $DI_{G,PA}$ which rates up to 87%.

Structural Damage Index	MISDR	$DI_{G,PA}$
Correct Classification Percentage (%)	90%	87%

Table 3: Comparative table for classification according to structural damage with MISDR and $DI_{G,PA}$.

In Figures 4 and 5, blue circles represent the seismic signals that have been misclassified with ANFIS algorithm using MISDR and $DI_{G,PA}$ respectively.

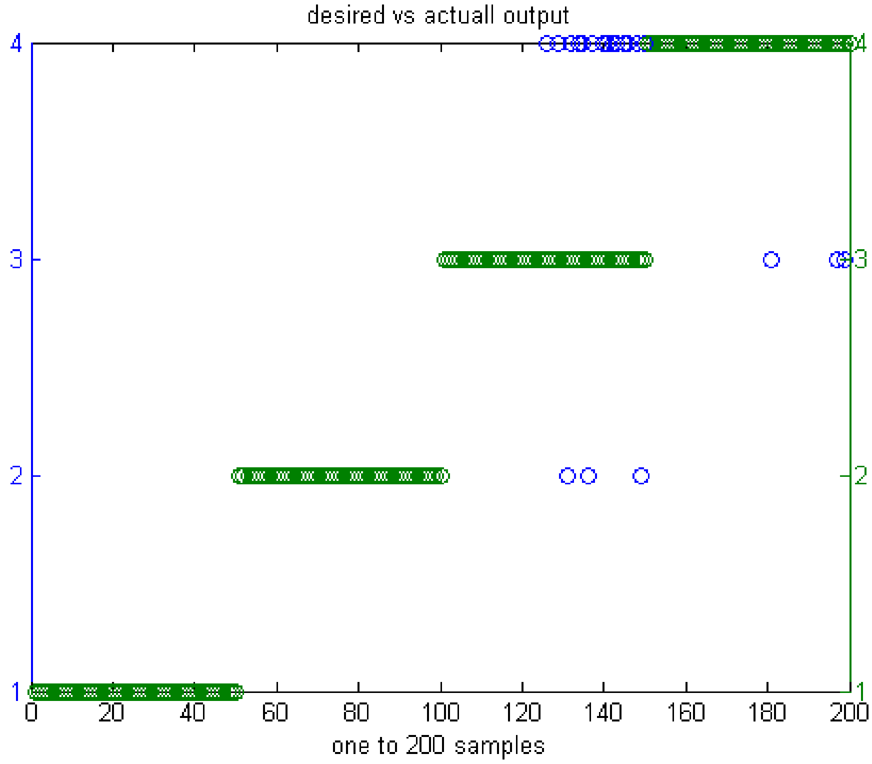

Figure 4: Classification of 200 seismic signals into 4 damage classes with MISDR as metric. Correct classification percentage: 90%.

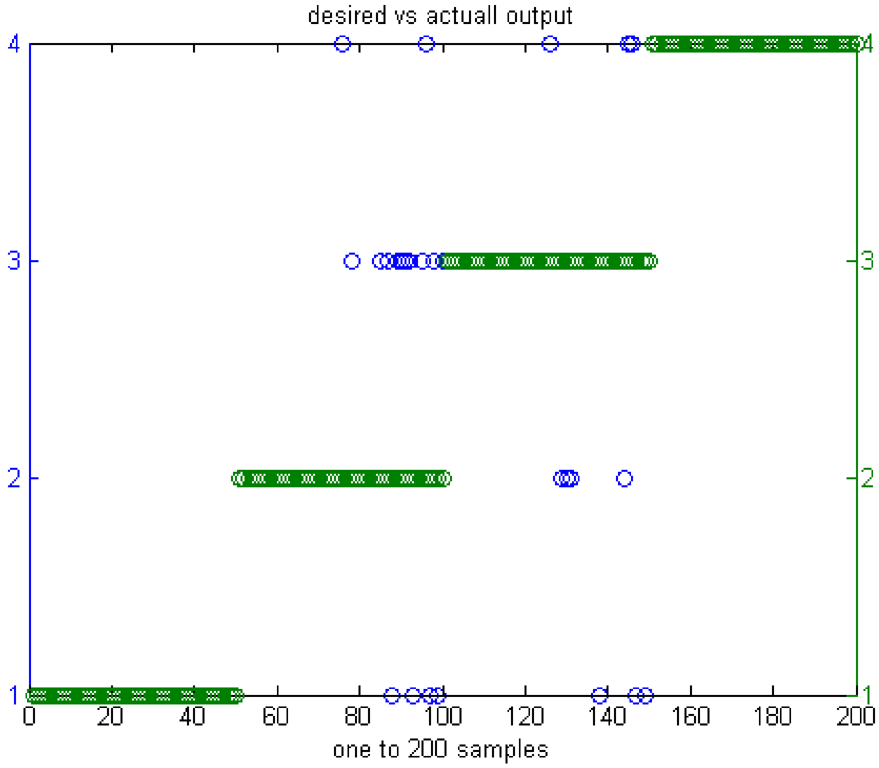

Figure 5: Classification of 200 seismic signals into 4 damage classes with $DI_{G,PA}$ as metric. Correct classification percentage: 87%.

7 CONCLUSIONS

This paper presents an efficient algorithm based on ANFIS techniques for seismic signal classification. A number of 20 seismic parameters and a set of 200 artificial accelerograms with known damage effects were used. For each seismic excitation the induced structural damage of the examined building is estimated and quantified according to two widely used damage indices, MISDR and $DI_{G,PA}$. The structural damage is expressed in the form of 4 damage categories. The 4 damage categories (classes) are defined through threshold values of the used damage indices. An ANFIS model is trained and tested. The classification results reveal the effectiveness of the proposed system to estimate the earthquake's impact (damage category) on the examined structure. Classification rates up to 90% in the case of MISDR and 87% in the case of $DI_{G,PA}$ are achieved. The high percentage of correct classification in both cases, prove the efficiency of the method and show that the fuzzy technique that is implemented, contributes to the development of a competent blind prediction of the seismic damage potential that an accelerogram possesses.

REFERENCES

[1] A. Elenas, Correlation between seismic acceleration parameters and overall structural damage indices of buildings, *Soil Dynamics and Earthquake Engineering*, **20**, 93-100, 2000.

[2] A. Elenas, K. Meskouris, Correlation study between seismic acceleration parameters and damage indices of structures, *Engineering Structures*, **23**, 698-704, 2001.

[3] Structural Engineers Association of California (SEAOC), *Vision 2000: Performance based seismic engineering of buildings*, Sacramento, California, 1995.

[4] S. Rodriguez-Gomez, A.S. Cakmak, Evaluation of seismic damage indices for reinforced concrete structures, *Technical Report NCEER-90-0022*, State University of New York, Buffalo, 1990.

[5] Y.J. Park, A.H.-S. Ang, Mechanistic seismic damage model for reinforced concrete, *Journal of Structural Engineering*, **111**, 722-739, 1985.

[6] A. Altoontash, Simulation and damage models for performance assessment of reinforced concrete beam-column joints, *PhD Dissertation*, Department of Civil and Environmental Engineering, Stanford University, Stanford, CA, 2004.

[7] R. Valles R, A.M. Reinhorn, S.K. Kunnath, C. Li, A. Madan, IDARC 2D version 4.0: a program for the inelastic damage analysis of buildings *Technical Report NCEER-96-0010*, State University of New York (Buffalo), 1996.

[8] S.A. Freeman, Drift limits: are they realistic, *Earthquake Spectra*, **1,** 355–62, 1985.

[9] CEB-FIP, Displacement-based design of reinforced concrete buildings, *State-of-Art report*, Fédération Internationale du Béton, Lausanne, 2003.

[10] S. Toussi, J.T.P. Yao, Assessment of structural damage using the theory of evidence *Structural Safety*, **1,** 107–21, 1982.

[11] S.K.V. Gunturi, H.C. Shah, Building specific damage estimation, *Proceedings of the l0th World Conference on Earthquake Engineering*, 6001–6006, Madrid, 1992.

[12] I. Andreadis, Y. Tsiftzis, A. Elenas, Intelligent seismic acceleration signal processing for structural damage classification, *IEEE Transactions on Instrumentation and Measurement*, 56, 1555-1564, 2007.

[13] K. Meskouris, *Structural Dynamics*, Ernst & Sohn, Berlin, 2000.

[14] A.K. Chopra, *Dynamics of Structures*, Prentice Hall International Inc, New Jersey, 1995.

[15] E.H. Vanmarcke, S.-S.P. Lai, Strong-motion duration and RMS amplitude of earthquake records, *Bulletin of the Seismological Society of America*, **70**, 1293-1307, 1980.

[16] C.M. Uang, V.V. Bertero, Evaluation of seismic energy in structures, *Earthquake Engineering and Structural Dynamics*, **19**, 77-90, 1990.

[17] A. Arias, A measure of earthquake intensity, In *Seismic Design for Nuclear Power Plants*, R.J. Hansen (ed.). MIT Press, Cambridge, MA, 438–483, 1970.

[18] M.D. Trifunac, A.G. Brady, A Study on the Duration of Strong Earthquake Ground Motion, *Bulletin of the Seismological Society of America*, **65**, 581-626, 1975.

[19] P.C. Jennings, Engineering Seismology, In *Earthquakes: observation, theory and interpretation*, H. Kanamori, E. Boschi (eds). Italian Physical Society, Varenna, 138-173, 1982.

[20] P. Fajfar, T. Vidic, M. Fischinger, A measure of earthquake motion capacity to damage medium-period structures, *Soil Dynamics and Earthquake Engineering*, **9**, 236-242, 1990.

[21] G.W. Housner, Spectrum intensities of strong motion earthquakes, *Proceedings of Symposium on Earthquake and Blast Effects on Structures*, EERI, Oakland California, 20-36, 1952.

[22] A.J. Kappos, Sensitivity of calculated inelastic seismic response to input motion characteristics, *Proceedings of the 4th U.S. National Conference on Earthquake Engineering*, EERI, Oakland California, 25-34, 1990.

[23] J.E. Martinez-Rueda, Definition of spectrum intensity for the scaling and simplified damage potential evaluation of earthquake records, *CD-ROM Proceedings of the 11th European Conference on Earthquake Engineering*, Balkema, Rotterdam, 1998.

[24] ATC 3-06 Publication, *Tentative Provisions for the Development of Seismic Regulations for Buildings*, DC: U.S. GPO, Washington, 1978.

[25] D. Lungu, A. Aldea, A. Zaicenco, T. Cornea, PSHA and GIS technology tools for seismic hazard macrozonation in Eastern Europe, *Proceedings of the 11th European Conference on Earthquake Engineering*, Balkema, Rotterdam, The Netherlands, 1998.

[26] L. Cabanas, B. Benito, M. Herraiz, *An approach to the measurement of the potential structural damage of earthquake ground motions, Earthquake Engineering and Structural Dynamics*, **26**, 79-92, 1997.

[27] R. Araya, G.R. Saragoni, Earthquake accelerograms destructiveness potential factor, *Proceedings of the 8th World Conference on Earthquake Engineering*, EERI, 835-842, San Francisco, CA, 1984.

[28] EC2, *Eurocode 2: Design of Concrete Structures - Part 1: General Rules and Rules for Buildings*, European Committee for Standardization, Brussels, Belgium, 2000.

[29] EC8, *Eurocode 8: Design of Structures for Earthquake Resistance - Part 1: General Rules, Seismic Actions, and Rules for Buildings*, European Committee for Standardization, Brussels, Belgium, 2004.

[30] A.M. Reinhorn, S.K. Kunnath, R. Valles Mattox, IDARC 2D Version 4.0: User's Manual. Buffalo, NY: Dept. Civil Eng., SUNY, 1996.

[31] R.O. Duda, P.E. Hart, D.G. Stock, *Pattern classification,* 2nd edition, John Wiley and Sons, New York, 2001.

[32] C.P. Kurian, V.I. George, J. Bhat, R.S. Aithal, ANFIS Model For Time Series Prediction of Interior Daylight Illluminance, *AIML Journal*, **6**(3), 35-40, 2006.

[33] S. Theodoridis, K. Koutroumbas, *Pattern Recognition*, 4th edition, Academic Press, 2009.

COMPDYN 2011
ECCOMAS Thematic Conference on
Computational Methods in Structural Dynamics and Earthquake Engineering
M. Papadrakakis, M. Fragiadakis, V. Plevris (eds.)
Corfu, Greece, 25-28 May 2011

A PROBABILISTIC APPROACH TO FUZZY METHODS

Mária Kuková

Faculty of Natural Sciences, Matej Bel University
Tajovského 40, Banská Bystrica, Slovakia
e-mail: kukova@fpv.umb.sk

Keywords: Probability, Effect Algebras, D-posets, Law of Large Numbers

Abstract. *Effect algebras ([1], [2]) and D-posets ([3]) are equivalent systems important in quantum structures. In the paper an independent sequence of observables on these structures is defined by such a way that a very general version of the law of large numbers may be proved.*

1 INTRODUCTION

In multi valued logic the MV algebras play the same role as Boolean algebras in two valued logic. Therefore probability theory on MV algebras seems to be very important (see ([6]). Of course, there are interesting generalizations of MV algebras: D-posets ([3]) and equivalent effect algebras ([1], [2]). Again probability theory can be constructed on D-posets and particularly on D-posets with product ([4]).

In the paper the law of large numbers is proved for very general D-posets.

In Section 2 some basic notions are defined. The key for the law of large numbers is the new formulation of independence. It is motivated and presented in Section 3. Also the sum of independent observables is defined there. The general law of large numbers is formulated and proved in Section 4. Similarly as in [6] a local representation of a sequence of independent observables by a sequence of random variables seems to be the main idea of the proof.

2 EFFECT ALGEBRAS AND D-POSETS

The concept of an effect algebra was introduced by Foulis and Bennet [1]. We will work with an equivalent algebraic structure, called D-poset introduced by Kôpka and Chovanec ([3]).

Definition 2.1. *Effect algebra is a system* $(E, +, 0, 1)$*, where* $0, 1$ *are distinguished elements of* E *and* $+$ *is a partial binary operation on* E *such that*

1. $x + y = y + x$ *if one side is defined,*
2. $(x + y) + z = x + (y + z)$ *if one side is defined,*
3. *for every* $x \in E$ *there exists a unique* x' *with* $x' + x = 1$*,*
4. *if* $x + 1$ *is defined then* $x = 0$*.*

Every effect algebra bears a natural partial ordering given by $x \leq y$ if and only if $y = x + z$ for some $z \in E$. The poset $(E, \leq)$ is bounded, 0 is the smallest element and 1 is the largest element. In every effect algebra, a partial subtraction $-$ can be defined as follows:

$x - y$ exists and is equal to z if and only if $x = y + z$.

The system $(E, \leq, -, 0, 1)$ so obtained is a D-poset defined by Kôpka and Chovanec [3].

Definition 2.2. *The structure* $(D, \leq, -, 0, 1)$ *is called D-poset if the relation* $\leq$ *is a partial ordering on D,* 0 *is the smallest and* 1 *is the largest element on* D *and*

1. $b - a$ *is defined if and only if* $a \leq b$*,*
2. *if* $a \leq b$ *then* $b - a \leq b$ *and* $b - (b - a) = a$*,*
3. $a \leq b \leq c \Longrightarrow c - b \leq c - a, (c - a) - (c - b) = b - a$*.*

To build a probability theory we need two important mappings equivalent to probability measure and random variable. In our concept we call them state and observable.

Definition 2.3. *A state on a D-poset D is any mapping* $m : D \to [0, 1]$ *satisfying the following properties:*

1. $m(1) = 1,\ m(0) = 0,$

2. $a_n \nearrow a \Longrightarrow m(a_n) \nearrow m(a), \forall a_n, a \in D$,

3. $a_n \searrow a \Longrightarrow m(a_n) \searrow m(a), \forall a_n, a \in D$.

Definition 2.4. *Let* $J = \{(-\infty, t); t \in R\}$. *An observable on* D *is any mapping* $x : J \to D$ *satisfying the following conditions:*

1. $A_n \nearrow R \Longrightarrow x(A_n) \nearrow 1$,

2. $A_n \searrow \emptyset \Longrightarrow x(A_n) \searrow 0$,

3. $A_n \nearrow A \Longrightarrow x(A_n) \nearrow x(A)$.

Theorem 2.5. *Let* $x : \mathcal{J} \to D$ *be an observable,* $m : D \to [0, 1]$ *be a state. Define a mapping* $F : R \to [0, 1]$ *by the formula*

$$F(t) = m(x((-\infty, t))).$$

Then F is a distribution function.

Proof. If $t_n \nearrow t$, then $(-\infty, t_n) \nearrow (-\infty, t)$, hence $x((-\infty, t_n)) \nearrow x((-\infty, t))$ by 3 of Def. 4, and

$$F(t_n) = m(x((-\infty, t_n))) \nearrow m(x((-\infty, t))) = F(t)$$

by 2 of Def. 2.3, hence F is left continuous in any point $t \in R$. Similarly

$$t_n \nearrow \infty \Longrightarrow F(t_n) \nearrow 1$$

by 1 of Def. 2.4 and 1 and 2 of Def. 2.3. Moreover

$$t_n \searrow -\infty \Longrightarrow F(t_n) \searrow 0$$

by 2 of Def. 2.4 and 1 and 3 of Def. 2.3. $\square$

Denote by $\mathcal{B}(R)$ the family of all Borel subsets of the real line R. Since F is a distribution function, there exists exactly one probability measure $\lambda_F : \mathcal{B}(R) \to [0, 1]$ such that

$$\lambda_F([a, b)) = F(b) - F(a)$$

for any $a, b \in R, a < b$.

Recall that in the Kolmogorov theory the mean value $E(\xi)$ of a random variable $\xi : (\Omega, \mathcal{S}, P) \to R$ is defined as an integral

$$E(\xi) = \int_\Omega \xi dP$$

Let $g : R \to R$ be a Borel measurable function. The transformation formula states

$$E(g \circ \xi) = \int_\Omega g \circ \xi dP = \int_R g dP_\xi = \int_R g(t) dF(t),$$

where F is the distribution function of ξ. It motivates the following definition.

Definition 2.6. *An observable* $x : \mathcal{J} \to D$ *is integrable, if there exists*

$$E(x) = \int_R t dF(t),$$

where F *is the distribution function of* x.

3 INDEPENDENCE

As a motivation consider a probability space $(\Omega, \mathcal{S}, P)$, where Ω is a non-empty set, $\mathcal{S}$ is a σ-algebra of subsets of Ω and $P : \Omega \to [0,1]$ is a probability measure. Two random variables $\xi, \eta : \Omega \to R$ are independent, if

$$P(\xi^{-1}(A) \cap \eta^{-1}(B)) = P(\xi^{-1}(A)).P(\eta^{-1}(B))$$

for any Borel sets $A, B \in \mathcal{B}(R)$. Let F_1 or F_2 be distribution functions of ξ or η resp., i.e.

$$F_1(t) = P(\{\omega; \xi(\omega) < t\}),$$

$$F_2(t) = P(\{\omega; \eta(\omega) < t\}).$$

Define Borel probability measures $\lambda_{F_1}, \lambda_{F_2} : \mathcal{B}(R) \to [0,1]$ by such a way that

$$\lambda_{F_1}([a,b)) = F_1(b) - F_1(a)$$

$$\lambda_{F_2}([a,b)) = F_2(b) - F_2(a)$$

for any $a, b \in R, a \leq b$. It is very well known that there exists exactly one probability measure

$$\lambda_{F_1} \times \lambda_{F_2} : \mathcal{B}(R^2) \to [0,1]$$

such that

$$\lambda_{F_1} \times \lambda_{F_2}(A \times B) = \lambda_{F_1}(A).\lambda_{F_2}(B)$$

for any $A, B \in \mathcal{B}(R)$. We need to characterize the probability distribution of the sum $\xi + \eta$, i.e.

$$P(\{\omega; \xi(\omega) + \eta(\omega) < t\}), t \in R.$$

Theorem 3.1. *Let $\xi, \eta : \Omega \to R$ be independent random variables, $\Delta_t = \{(u,v) \in R^2; u+v < t\}, t \in R, T = (\xi, \eta) : \Omega \to R^2$. Then*

$$P(T^{-1}(\Delta_t)) = \lambda_{F_1} \times \lambda_{F_2}(\Delta_t)$$

for any $t \in R$.

Proof. We have

$$P(T^{-1}(\Delta_t)) =$$

$$= P\left(\bigcup_{n=1}^{\infty} \bigcup_{i=-\infty}^{\infty} \xi^{-1}([\frac{i-1}{2^n}, \frac{i}{2^n})) \cap \eta^{-1}((-\infty, t - \frac{i}{2^n}))\right) =$$

$$= \lim_{n\to\infty} \sum_{i=-\infty}^{\infty} P\left(\xi^{-1}([\frac{i-1}{2^n}, \frac{i}{2^n})) \cap \eta^{-1}((-\infty, t - \frac{i}{2^n}))\right) =$$

$$= \lim_{n\to\infty} \sum_{i=-\infty}^{\infty} P\left(\xi^{-1}([\frac{i-1}{2^n}, \frac{i}{2^n}))\right) P\left(\eta^{-1}((-\infty, t - \frac{i}{2^n}))\right) =$$

$$= \lim_{n\to\infty} \sum_{i=-\infty}^{\infty} \lambda_{F_1}\left([\frac{i-1}{2^n}, \frac{i}{2^n})\right) \lambda_{F_2}\left((-\infty, t - \frac{i}{2^n})\right) =$$

$$= \lim_{n\to\infty} \sum_{i=-\infty}^{\infty} \lambda_{F_1} \times \lambda_{F_2} \left([\frac{i-1}{2^n}, \frac{i}{2^n}) \times (-\infty, t - \frac{i}{2^n}) \right) =$$

$$= \lim_{n\to\infty} \lambda_{F_1} \times \lambda_{F_2} \left(\bigcup_{i=-\infty}^{\infty} [\frac{i-1}{2^n}), \frac{i}{2^n} \times (-\infty, t - \frac{i}{2^n}) \right) =$$

$$= \lambda_{F_1} \times \lambda_{F_2} \left(\bigcup_{n=1}^{\infty} \bigcup_{i=-\infty}^{\infty} [\frac{i-1}{2^n}, \frac{i}{2^n}) \times (-\infty, t - \frac{i}{2^n}) \right) =$$

$$= \lambda_{F_1} \times \lambda_{F_2}(\Delta_t).$$

If $T = (\xi, \eta) : \Omega \to R^2$ is a random vector, then $T^{-1} : \mathcal{B}(R^2) \to \mathcal{S}$ is a mapping such that

$$P(T^{-1}(\Delta_t)) = \lambda_{F_1} \times \lambda_{F_2}(\Delta_t), t \in R.$$

The idea may be realized also in our general case.

Definition 3.2. *Let* $x_1, ..., x_n : \mathcal{J} \to D$ *be observables,* $\Delta_t^n = \{(u_1, ..., u_n) \in R^n; u_1 + ... + u_n < t\}, \mathcal{M}_n = \{\Delta_t^n; t \in R\}$. *The observables are called to be independent, if there exists a mapping* $h_n : \mathcal{M}_n \to D$ *with the following properties:*

1.$t_i \nearrow t \Longrightarrow h_n(\Delta_{t_i}^n) \nearrow h_n(\Delta_t^n)$.
2.$h_n(\bigcup_{t=1}^{\infty} \Delta_t^n) = 1$.
3.$h_n(\bigcap_{t=-1}^{-\infty} \Delta_t^n) = 0$.
4.$m(h_n(\Delta_t^n)) = \lambda_{F_1} \times ... \times \lambda_{F_n}(\Delta_t^n), t \in R$.

Theorem 3.3. *Define* $y_n : \mathcal{J} \to D$ *by the equality* $y_n((-\infty, t)) = h_n(\Delta_t^n)$. *Then* y_n *is an observable.*

Proof. It follows by properties 1 - 3 of the previous Definition.

Definition 3.4. *Let* $x_1, ..., x_n : \mathcal{J} \to D$ *be independent observables. Then the observable* $y_n : \mathcal{J} \to D$ *defined in previous Theorem is called the sum of observables* $x_1, ..., x_n, y_n = \sum_{i=1}^{n} x_i$, *i.e.*

$$(\sum_{i=1}^{n} x_i)((-\infty, t)) = h_n(\Delta_t^n), t \in R.$$

Remark. There has been proved in [5] that in so-called Kôpka D-posets there exists the mapping $h_n : \mathcal{M}_n \to D$ satisfying the properties stated in previous Definition.

4 THE LAW OF LARGE NUMBERS

Recall first the classical weak law of large numbers.

Theorem 4.1. *Let* (Ω, S, P) *be a probability space. Let* $(\zeta_n)_{n=1}^{\infty}$ *be a sequence of independent random variables having the same distribution function. Let* $a = E(\zeta_1) = E(\zeta_2) = \ldots$. *Then the sequence of random variables*

$$\frac{\zeta_1 + \ldots + \zeta_n}{n} - a \ \ (n = 1, 2, \ldots)$$

converges in measure P *to* 0.

Of course, we haven't told yet, what does convergence in measure mean. In classical probability space (Ω, S, P) a sequence of random variables $(\zeta_n)_{n=1}^{\infty}$ converges to 0 in measure P, if for each real $\varepsilon > 0$

$$\lim_{n\to\infty} P\left(\zeta_n^{-1}([-\varepsilon, \varepsilon))\right) = 1.$$

In our case, the definition is similar, but at first we need to define an expression $x((a,b))$, where x is an observable and $a, b \in R$.

Definition 4.2. *Let $x : \mathcal{J} \to D$ be an observable on a D-poset D and $\alpha, \beta \in R$. Then*

$$x([a,b)) = x((-\infty, b)) - x((-\infty, a)).$$

Definition 4.3. *Let $(x_n)_{n=1}^{\infty}$ be a sequence of independent observables on a D-poset D with a state m. We say that this sequence converges in measure m to 0 if for each $0 < \varepsilon \in R$*

$$\lim_{n\to\infty} m\left(x_n([-\varepsilon, \varepsilon))\right) = 1.$$

We are able now to formulate and prove the main result of the paper. We shall use the following notation. If $y : \mathcal{J} \to D$ is an observable and α, β are real numbers, $\alpha \neq 0$, then $\alpha y + \beta : \mathcal{J} \to D$ is defined by the formula

$$(\alpha y + \beta)((-\infty, t)) = y((-\infty, \frac{1}{\alpha}(t - \beta))).$$

Theorem 4.4. *Let D be a D-poset with a state $m : D \to [0,1]$, let $(x_n)_{n=1}^{\infty}$ be an independent sequence of integrable observables having the same probability distribution, $E(x_n) = a$, $(n = 1, 2, ...)$. Then the sequence*

$$\frac{\sum_{i=1}^{n} x_i}{n} - a$$

converges in measure m to 0.

Proof. Denote $P_n = \lambda_{F_1} \times ... \times \lambda_{F_n} : \mathcal{B}(R^n) \to [0,1]$. Then $(P_n)_n$ presents a consistent system of probability measures:

$$P_n(A \times R) = P_{n-1}(A), A \in \mathcal{B}(R), n \in N$$

We will use the projection $\pi_n : R^N \to R^n$:

$$\pi_n((u_i)_{i=1}^{\infty}) = (u_1, u_2, \ldots, u_n).$$

Let's take a family of all cylinders $\mathcal{C}$, i. e. sequences with a finite number of members being fixed:

$$\mathcal{C} = \{A \subset R^N; A = \pi_n^{-1}(B), B \in \mathcal{B}(R_n), n \in N\}$$

By the Kolmogorov consistence theorem there exists a probability measure $P : \sigma(\mathcal{C}) \to [0,1]$ such that

$$P(\pi_n^{-1}(B)) = P_n(B) = \lambda_{F_1} \times ... \times \lambda_{F_n}(B) \tag{1}$$

for any $B \in \mathcal{B}(R^n), n \in N$. Define $\xi_n : R^N \to R$ by the formula

$$\xi_n((u_i)_{i=1}^{\infty}) = u_n.$$

We have obtained a Kolmogorov probability space $(R^N, \sigma(\mathcal{C}), P)$, where the mapping ξ_n presents a random variable. The next formula will serve as a tool for "translating" the law of large numbers to D-posets:

$$P(\xi_1+\ldots+\xi_n<t)=P(\pi_n^{-1}(\Delta_n^t))=P_n(\Delta_n^t)\underbrace{=}_{(1)}\lambda_{F_1}\times\ldots\times\lambda_{F_n}(\Delta_n^t)\underbrace{=}_{3.2}m(h_n(\Delta_n^t))\underbrace{=}_{3.4}$$

$$=m\left((\sum_{i=1}^{n}x_i)((-\infty,t))\right)$$

For simpler notation, let's introduce new two mappings: a random variable $\eta_n : R^N \to R$ and an observable $y_n : \mathcal{M}_n \to D$.

$$\eta_n=\frac{1}{n}(\sum_{i=1}^{n}\xi_i)-a.$$

$$y_n=\frac{1}{n}(\sum_{i=1}^{n}x_i)-a=(\sum_{i=1}^{n}x_i)((-\infty,n(t+a))),$$

Then

$$m\left(y_n((-\infty,t))\right)=m\left((\sum_{i=1}^{n}x_i)((-\infty,n(a+t)))\right)=P(\xi_1+\ldots+\xi_n<n(a+t))=P(\eta_n^{-1}((-\infty,t)))$$

The last thing we need before we can use the Theorem 4.1 is to prove, that ξ_i are independent and $E(\xi_i)=E(x_i)=a\ \forall i$.

$$P((\xi_1,\ldots,\xi_n)\in((-\infty,t_1)\times\ldots\times(-\infty,t_n)))=P(\pi_n^{-1}((-\infty,t_1)\times\ldots\times(-\infty,t_n)))=$$

$$=\lambda_{F_1}\times\ldots\times\lambda_{F_n}((-\infty,t_1)\times\ldots\times(-\infty,t_n))=\lambda_{F_1}((-\infty,t_1)).\ldots.\lambda_{F_n}((-\infty,t_n))=$$

$$=P(\xi_1<t_1).\ldots.P(\xi_n<t_n)$$

$$E(x_n)=\int_{-\infty}^{\infty}t\,d\lambda_{F_n}(t)$$

$$E(\xi_n)=\int_{R^N}\xi_n(u)dP(u)=\int_{R^n}u_n dP_n((u_1,\ldots,u_n))=$$

$$=\int_{R^n}u_n d\lambda_{F_1}\times\ldots\times\lambda_{F_n}((u_1,\ldots,u_n))=\int_{R}u_n d\lambda_{F_n}(u_n)=E(x_n)$$

Now all the assumptions of Theorem 4.1 are satisfied, so for all real $\varepsilon>0$ there holds:

$$1=\lim_{n\to\infty}P\left(\eta_n^{-1}([-\varepsilon,\varepsilon))\right)=\lim_{n\to\infty}P\left(\eta_n^{-1}((-\infty,\varepsilon))\right)-\lim_{n\to\infty}P\left(\eta_n^{-1}((-\infty,-\varepsilon))\right)=$$

$$=\lim_{n\to\infty}m\left(y_n((-\infty,\varepsilon))\right)-\lim_{n\to\infty}m\left(y_n((-\infty,-\varepsilon))\right)=\lim_{n\to\infty}m\left(y_n([-\varepsilon,\varepsilon))\right)=$$

$$=\lim_{n\to\infty}m\left((\frac{1}{n}(\sum_{i=1}^{n}x_i)-a)([-\varepsilon,\varepsilon))\right)$$

Hence,

$$\frac{1}{n}(\sum_{i=1}^{n}x_i)-a\longrightarrow 0$$

in measure m and

$$\frac{1}{n}(\sum_{i=1}^{n}x_i)\longrightarrow a$$

in measure m. □

Acknowledgment
This paper was supported by Grant VEGA 1/0621/11.

REFERENCES

[1] D. J. Foulis, M. K. Bennet, The difference poset of monotone functions. *Found. Phys.*, **24**, 1325 – 1346, 1994.

[2] J. Chajda, R. Halaš, J. Kuhr, Every effect algebra can be made into a total algebra. *Algebra universalis*, **61(2)**, 133 – 150, 2009.

[3] F. Kôpka, F. Chovanec, D-posets. *Math. Slovaca*, **44**, 21 – 34, 1994.

[4] M. Kuková, B. Riečan, Strong law of large numbers on the Kôpka D-posets. *11th International Conference on Applications of Statistics and Probability in Civil Engineering(ICASP11)*, ETH Zurich, Switzerland, August 1-4, 2011 (to appear)

[5] B. Riečan, L. Lašová, On the probability theory on the Kôpka D-posets. *Developments in Fuzzy Sets, Intuitionistic Fuzzy Sets, Generalized Nets and Related Topics. Volume I: Foundations*, Systems Research Institute, Polish Academy of Sciences, Warsaw, 167 – 176, 2010.

[6] B. Riečan, D. Mundici, Probability on MV-algebras. *Handbook of Measure Theory* (E. Pap. ed.), Elsevier Science, Amsterdam, 869 – 909, 2002.

[7] B. Riečan, T. Nebrunn, *Integral, Measure, and Ordering*. Kluwer, Dordrecht, 1997.

COMPDYN 2011
III ECCOMAS Thematic Conference on
Computational Methods in Structural Dynamics and Earthquake Engineering
M. Papadrakakis, M. Fragiadakis, V. Plevris (eds.)
Corfu, Greece, 25–28 May 2011

A MODIFIED TRUNCATION METHOD FOR PRESSURE RECONSTRUCTION IN CASE OF NON PONCTUAL IMPACT ON AN ELASTIC PLATE

F. El Khannoussi[1], **A. Hajraoui**[1], **A. Khamlichi**[1], **A. Elbakari**[1],
A. Limam[2] **and E. Jacquelin**[2]

[1] Modeling and Analysis of Systems laboratory, Faculty of Sciences at Tetouan
B.P. 2121 M'Hannech, Tetouan 93002, Morocco
fadoua_845@hotmail.com

[2] Université Claude Bernard Lyon I
69622 Villeurbanne cedex, France
ali.limam@insa-lyon.fr

Keywords: Inverse Problem, Identification, Impact, Regularization, Truncation Method, Plates

Abstract. *This work deals with reconstruction of distributed force signal resulting from a non punctual object impacting perpendicularly an elastic homogeneous and isotropic rectangular plate. The impacting force is assumed to be uniformly distributed over a rectangular patch of the plate. The direct problem was solved by using modal decomposition method with explicit analytical modes. A discrete problem was written for that by sampling the obtained convolution integral. To extract the pressure signal by deconvolution of the dynamic response measured at a given point of the plate, solution of an inverse problem had been considered. Since this type of problem is known to be ill-posed due to bad conditioning of the involved Toeplitz like matrix, regularization is needed to obtain a physically meaningful solution. A new regularization technique based on truncation filtering was examined. This technique uses as a first step the generalized decomposition of Toeplitz matrix on singular values. Then, regularization of the decomposed form through a truncation filter is performed. The truncation consists in eliminating the first low index terms up to an optimal rank representing the contribution of low amplitude generalized singular values. If the impact force signal has a half sine like standard form, the index corresponding to time instant where the maximum displacement response is obtained was found to be the optimal order of truncation. This technique has proved to be effective in reconstruction of impact pressures through various cases of study and the computational cost was found to be much lower than that of the classical truncation method based on L-curve criterion.*

1 INTRODUCTION

To perform structural health monitoring or reliability analysis of structures, it is essential to provide accurate characterization of input forces experienced during service operation. In common practice, the input force is measured by using a force transducer that is positioned in the load path. On many circumstances, such as a high-speed impact of an object onto a structure, it is difficult to apply this technique such as a bird impacting an aeroplane fuselage. Another technique that has been widely employed for the impact-force signal reconstruction is based on analysis of the inverse problem. This means that the dynamic force is recovered from the data of the measured elastic response. When the impact point is known, the problem is equivalent to operating deconvolution of two signals: the measured response and the transfer function characterizing the dynamics of the structure. In many cases, the deconvolution results in an ill-posed problem in which the data noise strongly affects the solution accuracy. Therefore, it is difficult to obtain an accurate solution for such problems, so that, regularization is needed to obtain a physically meaningful solution.

There are a number of publications which deal with the impact-force reconstruction. In [1, 2, 3] the impact force profile had been reconstructed by using spectral analysis. The proposed method had utilized the convolution theorem that expresses the time domain deconvolution as a simple division in the frequency domain. Later on, various authors [4, 5, 6, and 7] adopted a more systematic approach to regularize the deconvolution problem by using either the singular value decomposition method (SVD) or the generalized singular value decomposition method (GSVD). These authors had considered the problem of a localized impact where the object could be approximated as a single point. In many cases, however, the impacting object is massive and the impact zone could not be approximated as a single point and the impacting force takes the form of a distributed pressure over the impact zone. In more recent works [8, 9, 10, 11] the problem of reconstruction of distributed dynamic loads on structures like Euler beam, thin plates or cylindrical shells had been tackled. The authors had used either the modified modal method or the mode-selection method. Though these methods are robust in comparison with Tikhonov based methods some problems such as the improvement of the selection criterion and the relative high errors on boundaries are still open [11].

Certain researchers have indicated that a major drawback of the Tikhonov-GSVD method is the expensive computational cost associated to GSVD and consequently the method is only suitable for small scale problems.

In the present work, we consider the impact pressure reconstruction problem in the case where a uniform distributed force is applied onto a homogeneous and isotropic elastic rectangular plate. The impacting zone is assumed to be a rectangular patch. For this purpose, the direct solution has been computed at first by using an analytical formula. Then, the regularization method based on GSVD method with truncation filtering was used. The truncation regularization method [12] is a particular case of the general filter factor regularization method and looks a lot like Tikhonov regularization [13], but it is simpler to implement. Here, a new technique of constructing the filter is examined. It is based on an a priori defined truncation order which reduces considerably the computational cost. This new method was tested on several case studies and the obtained results have shown that it is well suited in regularizing pressure reconstruction problems wherever the impact pressure profile is not too different from a half sine shape.

2 MATERIALS AND METHODS

We consider a rectangular plate as shown in figure 1 which has the dimensions a , b and e representing respectively the length, width and thickness. It is assumed to be simply supported on its ends. The plate is assumed to be made of a homogeneous and isotropic elastic material with Young's modulus E, Poisson's ratio υ and density ρ. The applied force modeling impact is assumed to be uniformly distributed over a rectangular patch of the plate. The dynamic response in terms of displacement, velocity, acceleration or strains is considered at a point which is located at a given distance away from the centre of the loading rectangle, figure 1.

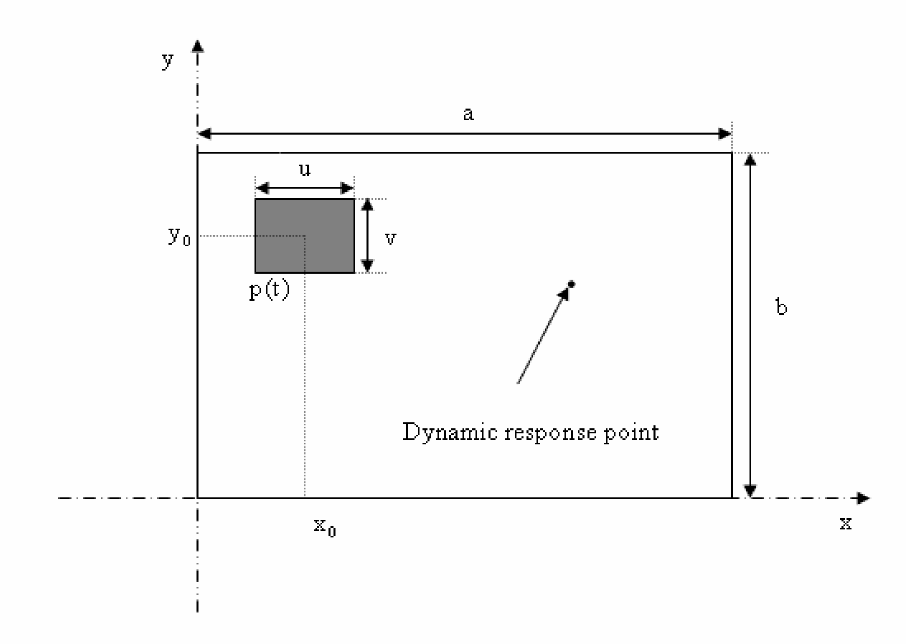

Figure 1: Simply supported rectangular plate showing the loading conditions and the point of response measurement

The equation of motion of a simply supported rectangular plate [14], can be expressed under the following form

$$D\Delta\Delta w(x,y,t)+c\dot{w}(x,y,t)+\rho h\ddot{w}(x,y,t)=q(x,y,t) \tag{1}$$

where x is the horizontal coordinate, y the vertical coordinate, t the time, $w(x,y,t)$ the transverse displacement, $q(x,y,t)=p(t)\Im_{[x_0-u/2,x_0+u/2]\times[y_0-v/2,y_0+v/2]}(x,y)$ the applied loading with $\Im$ the indicative function taking the value one on the domain shown in subscript and zero elsewhere, c the damping coefficient, $D=Ee^3/(12(1-\upsilon^2))$ the plate flexural rigidity modulus and $\Delta\Delta w(x,y,t)=\frac{\partial^4 w}{\partial x^4}+2\frac{\partial^2 w}{\partial x^2\partial y^2}+\frac{\partial^4 w}{\partial y^4}$.

The above governing equation is assumed to be subjected to the following boundary conditions

$$\begin{aligned} &w=0 \quad \text{and} \quad \frac{\partial^2 w}{\partial x^2}=0 \quad \text{for } x=0 \text{ and } x=a \\ &w=0 \quad \text{and} \quad \frac{\partial^2 w}{\partial y^2}=0 \quad \text{for } y=0 \text{ and } y=b \end{aligned} \tag{2}$$

By applying the modal superposition technique, the displacement $w(x,y,t)$ can be shown to be expressed under the following form

$$w(x,y,t)=\int_0^t h(x_0,y_0,u,v,x,y,t-\tau)p(\tau)d\tau \tag{3}$$

where h is the transfer function given by

$$\begin{aligned}h(x_0,y_0,u,v,x,y,\tau) = \frac{16}{\rho h\pi^2}\sum_{m=1}^{\infty}\sum_{n=1}^{\infty}\frac{1}{mn\gamma_{mn}}\sin(\frac{m\pi x_0}{a})\sin(\frac{n\pi y_0}{b})\sin(\frac{m\pi u}{a})\\ \sin(\frac{n\pi v}{b})\sin(\frac{m\pi x}{a})\sin(\frac{n\pi y}{b})\sin(\gamma_{mn}\tau)e^{-\xi_{mn}\omega_{mn}\tau}\end{aligned} \tag{4}$$

in which ω_{mn}, γ_{mn} and ξ_{mn} are respectively the circular eigenfrequency, the damped circular eigenfrequency ($\gamma_{mn}=\omega_{mn}\sqrt{1-\xi_{mn}^2}$) and the damping ratio for a given eigenmode (m,n).

In many practical circumstances it is possible to represent realistically the impact-force such as a half-sine function, figure 2. Shape of real impact force signal is not too different from this standard profile.

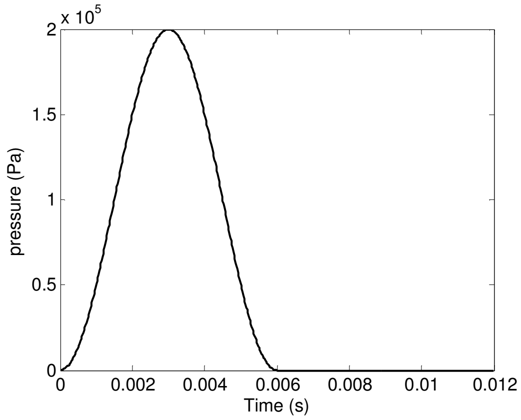

Figure 2: Pressure signal profile defined on the period time $T=0.006\,s$

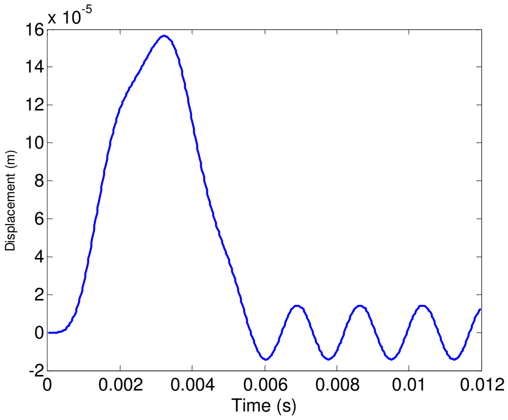

Figure 3: Calculated displacement at point $(x=0.041\,m, y=0.041\,m)$

The elastic response $w(x,y,t)$ can be computed over the considered time interval $[0,T_c]$ by integrating explicitly equation (3) where x_0, y_0, u, v , x, y take fixed values. In this work, the selected configuration of the impacted plate is defined by the following parameters values: $a=2.05$ m , $b=2.05$ m , $e=5\times10^{-3}$ m , $\xi_{mn}=0$, $x_0=y_0=0.1025$ m , $u=v=0.0342$ m , $x=y=0.041$ m and $T_c=0.012$ s.

Figure 3 gives the displacement calculated at the point $(x=0.041\,m, y=0.041\,m)$. The direct elastic response in terms of displacement which is given in figure 3 is stored and will be used in the following to reconstruct the impact-force signal.

To identify the impact-force acting on the plate over the rectangular domain of impact, the transfer function based approach is used. In more general problems, transfer functions can be determined analytically [15], experimentally [16], or numerically. Here, the transfer function is evaluated analytically through time integration of equations (3) and (4).

To solve the deconvolution problem associated to equation (3), a discrete problem must be written by sampling the convolution integral. This leads in the time domain to the following system of algebraic equations

$$W = HP \tag{5}$$

with

$$H = \begin{pmatrix} H(\Delta t) & 0 & & & 0 \\ H(2\Delta t) & H(\Delta t) & \ddots & & \\ H(3\Delta t) & H(2\Delta t) & \ddots & \ddots & \\ \vdots & \vdots & \ddots & \ddots & 0 \\ H(N\Delta t) & H((N-1)\Delta t) & \dots & \dots & H(\Delta t) \end{pmatrix} \quad \begin{matrix} W = \left[w(\Delta t) \quad w(2\Delta t) \quad \cdots \quad w(N\Delta t) \right]^t \\ P = \left[p(\Delta t) \quad p(2\Delta t) \quad \cdots \quad p(N\Delta t) \right]^t \end{matrix} \tag{6}$$

where H is the Toeplitz like transfer matrix, Δt is the sampling rate and N the total number of samples.

The sampling rate must be selected in order to recover a predefined cut-off frequency in the pressure signal. The matrix H is always ill-conditioned. This means that it can lead to an unstable solution which has no physical meaning. Therefore, to find a physically acceptable solution the deconvolution problem defined by equations (5) and (6) should be regularized.

Here, the regularization technique based on the generalized singular value decomposition (GSVD) is considered. It should be mentioned that the simpler SVD method has failed to regularize the actual problem. The GSVD-regularized solution of problem defined by equations (5) and (6) can be written as follows

$$[P] = [X][\Phi][\Delta]^{-1}[U]^t[W] = \left[H^*\right][W] \tag{7}$$

where (X, Δ, U) being the singular factors of H, $[\Phi]$ is the filter factor and $\left[H^*\right] = [X][\Phi][\Delta]^{-1}[U]^t$ is the regularized pseudo-inverse of H.

The filter factors goal is to minimize the influence of the low amplitude generalized singular values. Many techniques have been considered in the literature for that purpose. Among them, one finds the regularization techniques: Tikhonov method [13] and GSVD truncation method [5]. In the following the truncation based regularisation technique is used.

The truncation consists of eliminating the first low index terms up to the rank k. This index is called the regularization parameter. The index k should be selected in order to eliminate the small generalized singular values as well as the oscillating singular vectors.

The filter Φ defined by the truncation method writes:

$$\Phi_{ij} = f_i \, \delta_{ij} \quad i, j = 1, \dots, N \tag{8}$$

To build the filter Φ within the framework of truncation method, the rank k should be specified. The optimal rank should minimize the error between the identified pressure and the real pressure. Classically, the L-Curve method has been applied in order to determine the regularization parameter k by means of a graphical based method. This technique was developed in reference [5]. It is based on searching the optimum of a functional composed of two terms, a residue called $RN = \|W - HP\|_2$ (Residual Norm) and the norm of the solution, designated by $SN = \|P\|_2$ (Semi-Norm). When the k parametric curve defining SN versus RN is plotted, the optimal regularization parameter corresponds to the point of maximum curvature, the corner.

However, in practice, this method is often problematic; for measured data the L-curve is discrete and the determination of such point is delicate, because it is not distinguishable on the graph.

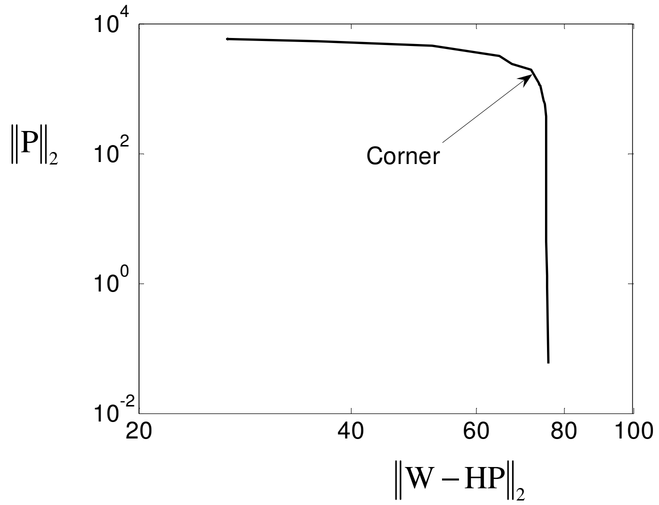

Figure 4. The L-curve associated to truncation filter design showing the corner point defining the optimal truncation order

Here a new heuristic method is proposed to determine the optimal rank truncation. Through various numerical tests conducted on pressure signals having half sine form, the rank defined as the index of the maximum value of the calculated displacement was found to yield a closer form of the real pressure input signal.

3 RESULTS AND DISCUSSION

Figure 5 presents the superposition of the real impact pressure with the pressure profile as obtained by the inverse problem solution for the impact centre zone given by $(x_0 = 0.0683\,\mathrm{m}, y_0 = 0.0683\,\mathrm{m})$ and the point of measurement located at $(x = 0.041\,\mathrm{m}, y = 0.041\,\mathrm{m})$. The pulse period considered is $T = 6\,\mathrm{ms}$. The truncation order which is defined as the index of the maximum value of the calculated displacement is found to be 160. The associated CPU time is 68.94.

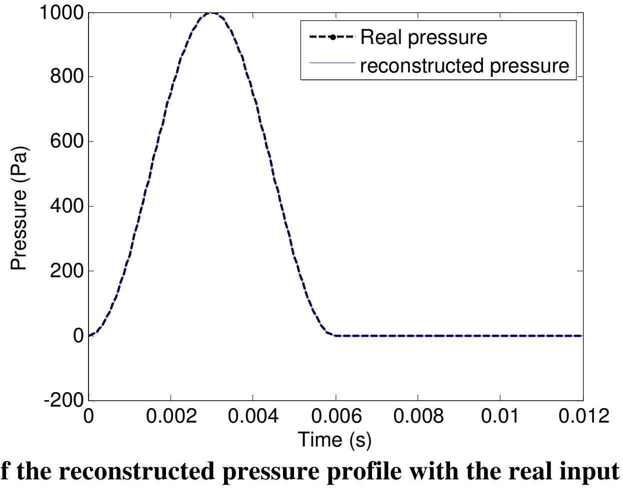

Figure 5: Comparison of the reconstructed pressure profile with the real input pressure for the input signal shown in figure 2 with period $T = 0.006\,\mathrm{s}$

Figure 6 presents the superposition of the real impact pressure with the pressure profile as obtained by the inverse problem solution for the case where $(x_0 = 0.0683\,\mathrm{m}, y_0 = 0.0683\,\mathrm{m})$, $(x = 0.041\,\mathrm{m}, y = 0.041\,\mathrm{m})$ and a pulse period $T = 4\mathrm{ms}$. The associated truncation order is 179.

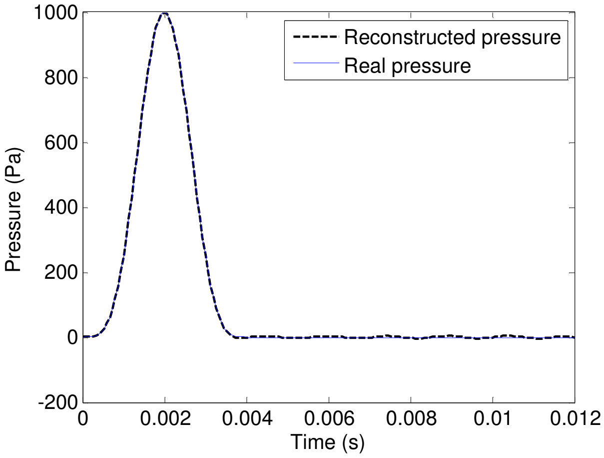

Figure 6: Comparison of the reconstructed pressure profile with the real input pressure having the form of figure 2 but with a period $T = 0.004\,\mathrm{s}$

It is clear that the new proposed method and the L-curve based method permit the exact reconstruction of the signal. However in the new heuristic method for which the order of truncation is defined a priori as the index of the maximum value of the calculated displacement, a lower computational cost is reached. The gain is about 47%. This methodology was proven to yield results that are independent from the impact location, the measurement point and the pulse period. But, it is necessary that the profile of the impacting force should have a half sine like form. This is not a real limitation since most of the impacting force signals have this general form in practice.

4 CONCLUSION

A new heuristic method for reconstruction of distributed force in case of non punctual object impacting an elastic rectangular plate was proposed. This method is based on generalized singular value decomposition of Toeplitz like matrix obtained for the discrete convolution problem relating the displacement dynamical response at a given point and the impact pressure signal. This last was assumed to be uniform over a rectangular patch of the plate and to have a half sine profile. To build the filter needed for regularization of the inverse problem, the truncation based method was used. The order of truncation corresponding to the index of time associated to the maximum measured displacement was found to yield good results. This was proven to be the case independently from the impact location, the measurement point and the pulse period. Even when the signal is not a half sine one, good results are also obtained. The computational cost of this method is lower than that of the classical truncation method, which makes it as a relevant alternative to better build the truncation filter needed for regularising the deconvolution in inverse problems.

5 REFERENCES

[1] J.F. Doyle, Further developments in determining the dynamic contact law. *Experimental Mechanics* **24**, 265–270, 1984.

[2] J.F Doyle, Experimentally determining the contact force during the transverse impact of an orthotropic plate. *Journal of Sound and Vibration* **118**, 441–448, 1987.

[3] M.T. Martin, J.F. Doyle, Impact force identification from wave propagation responses. *International journal of Impact Engineering* **18**, 65-77, 1996.

[4] R. Adams, J.F. Doyle, Multiple force identification for complex structures, *Experimental Mechanics* **42**, 25-37, 2000.

[5]P.C. Hansen, *Rank-Deficient and Discrete Ill-posed Problems*, SIAM, Philadelphia, PA, 1998.

[6)] E Jacquelin, A. Bennani, P. Hamelin, Force reconstruction analysis and regularization of a deconvolution problem. *Journal of Sound and Vibration* **265**, 81-107, 2003.

[7] Y. Liu, S. Shepard, Dynamic force identification based on enhanced least- squares schemes in the frequency domain. *Journal of Sound and Vibration* **282**, 37-60, 2005.

[8]Y. Liu, W.S. Shepard Jr. An improved method for the reconstruction of a distributed force acting on a vibrating structure. *Journal of Sound and Vibration* **291**, 369-387, 2006.

[9]M.C. Djamaa, N. Ouelaa, C. Pezerat, J.L. Guyader, Reconstruction of a distributed force applied on a thin cylindrical shell by an inverse method and spatial filtering. *Journal of Sound and Vibration* **301**, 560-575, 2007.

[10] X.Q. Jiang, H.Y. Hu, Reconstruction of distributed dynamic loads on an Euler beam via mode-selection and consistent spatial expression, *Journal of Sound and Vibration* **316**, 122-136, 2009.

[11] X.Q. Jiang, H.Y.Hu, Reconstruction of distributed dynamic loads on a thin plate via mode-selection and consistent spatial expression. *Journal of Sound and Vibration* **323**, 626-644, 2009.

[12] B.A Mair, Tikhonov regularization for finitely and infinitely smoothing operators. SIAM *Journal of Mathematical Analysis* **25**, 135–147, 1994.

[13] A.N. Tikhonov, V. Y. Arsenin, *Solutions of ill-posed problems*, Wiley, New York, 1977.

[14] S. Timoshenko, Woinovsky-Krieger, *Theory of plates and shells*, McGraw-Hill Book Co., Eng. Mech. Series collection, 1940 (reprinted 1959), 580 p.

[15] L. Meirovitch, *Dynamics and Control of Structures.* John Wiley, New York, 1990.

[16] P.C. Hansen, *The L-curve and its use in the numerical treatment of inverse problems*, Tech. Report, IMM-REP 99-15, Dept. of Math. Model. Tech. Univ. of Denmark, 1999.

.

COMPDYN 2011
III ECCOMAS Thematic Conference on
Computational Methods in Structural Dynamics and Earthquake Engineering
M. Papadrakakis, M. Fragiadakis, V. Plevris (eds.)
Corfu, Greece, 25–28 May 2011

FATIGUE ASSESSMENT OF PANARO BRIDGE: PRELIMINARY RESULTS

Francesco V. Lippi[1], **Walter Salvatore**[2]

[1] Consorzio Pisa Ricerche
Corso Italia, 116 - 56125 Pisa, Italy
e-mail: f.lippi@cpr.it

[2] Department of Civil Engineering - University of Pisa
Via Carlo F. Gabba, 22 - 56122 Pisa, Italy
email: walter@ing.unipi.it

Keywords: Railway bridges, vibration and distortion fatigue, steel structures, experimental tests, numerical modelling, dynamic identification.

Abstract. *The functionality maintenance of European infrastructures like bridges is acquiring more and more importance due to the huge economic losses related to the interruption of their regular service. In particular, fatigue represents one of the most diffused failure modes occurred in steel and composite steel-concrete bridges: in fact about 80/90% of failures in steel structures are related to fracture and fatigue. Railway bridges endure million of stress cycles during their life and they are expected to be highly vulnerable to such phenomena. Moreover, phenomena like "vibration induced" and "distortion induced" fatigue are still partially uncovered by actual design codes and represent a critical aspects for the assessment of existing bridge remaining life and for the design of new bridges.*

The European research project FADLESS "Fatigue damage control and assessment for railways bridges", funded by the European Research Found for Coal and Steel (RFCS), aims to define innovative technical guidelines for the assessment and control of existing and new bridges with regard to fatigue phenomena induced by vibrations and distortions produced by train passage. To this purpose, the Project combines experimental and numerical techniques in order to evaluate properly the fatigue damages on critical details induced by vibration and distortion phenomena, taking into account the dynamic train-bridge interaction effects and the actual traffic spectra on European railway lines.

In this paper, preliminary studies performed on the Italian case study, the Panaro Bridge, are reported. In particular, results of the standard fatigue assessment according to Eurocode rules were compared with the actual fatigue damages occurred to deck secondary components to obtain a preliminary critical review of adopted fatigue assessment methodologies. Moreover, experimental tests were designed and performed on the bridge in order to identify global and local vibration modes and to evaluate the strain time-histories under train passages of critical details. Finally, experimental global/local mode shapes were compared to numerical results of the preliminary FE bridge model.

1 INTRODUCTION

Fatigue is a very important failure mode for steel structures. In fact about 80/90% of failures in steel structures are related to fracture and fatigue. In particular, railway bridges endure million of stress cycles during their life and they are expected to be highly vulnerable to such phenomena. Obviously, if a bridge survive to the construction phase without any fractures occurring, fatigue will almost always precede fracture so that, in most practical cases, controlling fatigue is more important than controlling fracture. However, it is also important to design for fracture resistance because fatigue cracks eventually can grow to a critical size at which the member undergoes fracture. Several studies were performed in the past in order to assess the fatigue resistance of steel and steel-concrete composite bridges; such studies were the base of modern codes and standards [1; 2; 3; 4]. Despite of these efforts, the fatigue assessment of railway bridges both considering the design of new bridges and the assessment of existing ones is one of the main issues in current practice.

Such eventuality is due to concurrent events as for example the rapid development of the European railway networks according to the directives of the European Commission [5] the increase of passenger and freight railway traffic, the introduction of new high strength materials, the influence of particular effects like distortion and local vibration not actually covered by fatigue assessment procedures proposed by current codes and standards.

On the other hand, by 2020, new Trans-European Transport Network (TEN-T Project) will include 94 000 km of railways, including around 20 000 km of high-speed rail lines suitable for speeds of at least 200 km/h. Completing the network by 2020 involves the construction of the so-called „missing links" which will increase the existing rail by 12 500 km. In addition, 12 300 km of rail lines will be substantially upgraded [5].

Completing the networks will have a huge impact in reducing journey time for passengers and goods. For interregional traffic alone the benefits are estimated to be almost EUR 8 billion per year. In addition, freight transport in the EU is expected to increase by more than two thirds between 2000 and 2020, and to double in the new Member States. Freight transport among Member States is expected to show the largest increase overall. Without TEN-T this increase in transport would be impossible to handle, and our rate of economic growth significantly slowed.

An important aspect in design of new lines or in the evaluation of upgrading operations is the convenience that the railway lines will not be restricted to their use by a limited family of trains. On the contrary, they should allow the transit of all vehicle typologies (both traditional, high speed and freight trains), enabling interoperability of the infrastructure by all possible trains. This issue is not only essential from a social and economical point of view, but has also other implications, such as to separate the business of the infrastructure from that of the transport operators, as suggested by the new European directive [6].

The possible presence of new train typologies, characterized by several layouts of weights and axels distributions, introduces new uncertainties on the expected traffic loads and the consequent loading spectra to be adopted in fatigue verification. As a consequence, new operating conditions of European Railway Networks require the assessment of adequacy and effectiveness of actual loading spectra provided by design codes and regulations for fatigue verification purposes. Such spectra, derived from previous studies performed on old railway lines, could lead to an underestimation of actual railway traffic effects.

The knowledge of past and current load spectra, together with predicted future loads, is essential in the evaluation and fatigue analysis of existing bridges. In particular, the information concerning actual loads is very important during rating operations according to the procedures adopted by main Railway Administrator. Therefore, there is a need for accurate and inexpensive methods to determine the actual loads, the strength of the bridge, and its remaining life. There is also a need for verification of live load used for the development of a new generation of bridge design codes.

The increase of circulation speed, the change of the vehicles geometry and masses and the increase of loads that were observed led to a concern in the understanding of dynamic phenomena and in their quantification, and therefore to the improvement of safety checking procedures in structural codes. In particular, the evaluation of effective capability of existing bridges to guarantee the necessary safety level under actual traffic conditions requires the improvement of available design procedures. Figure 1 shows a general framework [7] to be adopted for the fatigue assessment of existing steel structures. Such an approach suggests the use of three different levels of assessment methodologies:

- *Simplified methods*: preliminary evaluation should be conducted by using current codes and recommendations and making conservative assumptions when information is lacking or doubtful; simplified models are adopted for the structures and their details;
- *Enhanced methods*: a detailed investigation should be performed, adopting a refined representation of the structure and of the loads/actions; anyway input data for model analysis can be adopted from current codes;
- *Advanced methods*: advanced evaluation should be carried out to analyze, by means of both numerical and experimental tools, the effective remaining fatigue life of all relevant details.

The application of different evaluation methodologies requires an increasing level of knowledge and information concerning the behaviour of structural components and details. In particular the use of advanced methodologies is actually limited to specialized laboratories and scientific research groups.

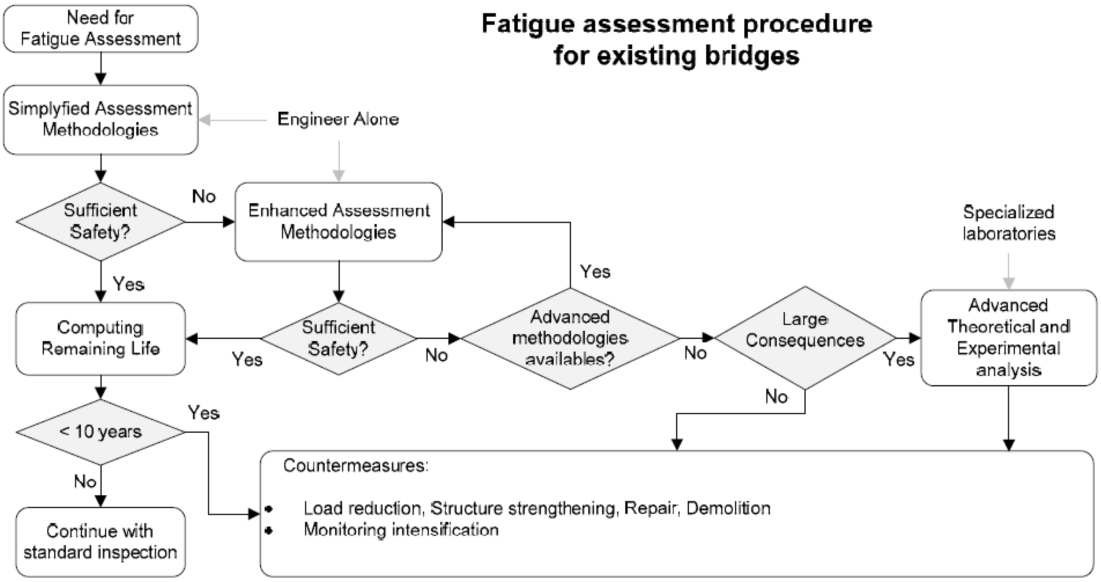

Figure 1: Fatigue assessment procedure for existing steel bridges [7].

Such an approach is mainly due to the fact that, traditionally, it was assumed that the need for the application of advanced analysis methodologies in design of steel and steel-concrete composite bridges can be limited adopting proper detailing that remove the secondary stresses. Such objectives were reached introducing an high number of global and local stiffeners, necessary to guarantee the verifications of static requirements against instability as well. On the contrary, several fatigue problems affected and still affect steel bridges due to several reasons.

Previous experience shows that most cracks found in bridges were caused by distortion of member cross sections and out-of-plane deformation of webs that induced localized bending stresses [8]. In older bridges, transverse stiffeners and attachment plates were not welded to the tension flange of welded I-girders and box girders for fear that a fatigue crack initiating in the flange would lead to a brittle fracture. This well-intended but outdated practice originated in Europe in the 1930‟s from unexpected brittle fracture in the oldest welded bridges, and it was at first attributed to welding details, but it was primarily due to the poor quality of steel.

This practice has been the main cause of distortion-induced cracking, which can sometime be prevented by welding stiffeners to the web and to the flanges. Figure 2 shows a crack which formed along the fillet weld attaching a diaphragm connection plate to the web of a plate girder [9]. The fatigue cracking in these gaps typically occurs in a longitudinal direction along the fillet weld toe of the longitudinal web-to-flange joint, at the termination of the vertical fillet weld, or at both locations, as shown in Figure 3 [9].

Figure 2: Examples of distortion induced fatigue crack progression [9].

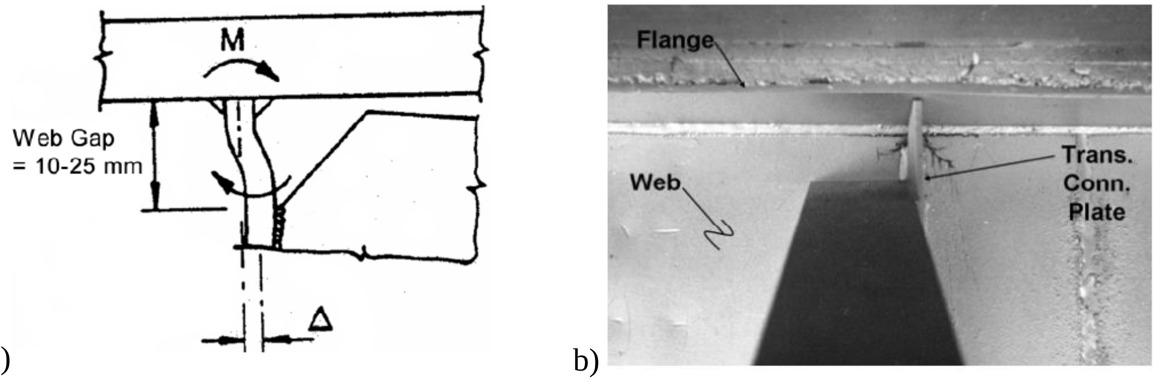

a)

b)

Figure 3: Web gap distortion: a) scheme of the effects; b) example in real bridge [9].

In many cases, the displacement causing this distortion is limited and the cracking arrests as the compliance of the gap increases and the stresses are reduced. Because most of the cracks are longitudinally oriented, there is typically no reason to be concerned about fracture of the girder unless the cracks turn downward and propagate across the web. It is typically a mistake to try to weld repair such cracks, as this restores the high stresses which originally caused the cracking and will certainly restart the cracking at the weld repair [9].

Besides, distortion and vibration induced fatigue phenomena, typically due to low local stiffness distribution in correspondence of critical details, can affect steel and composite bridges. Such phenomenon allows the presence of local vibration modes characterized by low frequencies (0-30 Hz) typically excited during train passages which could produce high local “modal” stresses causing relevant fatigue damages and reducing the remaining fatigue life.

As previously stated, distortion induced or vibration induced fatigue cracking in the web gaps may be solved by a proper detailing which eliminates the secondary stresses causing these cracks. In most cases, the web-gap-cracking can be prevented by rigidly connecting the attachment plates to the tension flange. Where the distortion is displacement controlled, the stresses can be reduced by increasing the flexibility of the connection. If distortion is limited, holes may be drilled or cored at the crack tips to temporarily arrest propagation [9].

Modern design methodologies for steel and steel-concrete composite bridges adopt new materials with very high performances allowing for very slender structures. Such solutions, characterized by improved performance against static loadings, revealed to be exposed to vehicle-bridge interaction effects which influence fatigue behavior.

High structural slenderness implies that non-structural elements, such as ballast, retaining walls and tracks, can affect bridges dynamic behavior caused by train passage. Moreover, the high local slenderness caused by the reduction of plate thickness and stiffeners number, can increase the possibility of obtaining local vibration modes characterized by low frequencies. As a consequence, such local modes can increase the possibility of observing “vibration induced” fatigue damage phenomena. By the way, actual codes and regulations appear inadequate to provide effective tools in order to obtain thorough information about such phenomena.

Moreover, the use of High Performance Steel does not modify the results of fatigue verifications since fatigue behavior does not depend on mechanical or dynamical properties of materials.

Local vibration and distortion phenomena do not affect only steel details/elements. In fact, both in steel-concrete connection systems (such as studs) and concrete slabs between the main girders in steel-concrete composite solutions result highly affected by such phenomena as well. In particular, it will be useful to evaluate the effective load spectra affecting reinforcement bars in concrete slabs directly subjected to the load induced by train passage and the consequent free vibrations.

Main object of the European research project FADLESS "*Fatigue damage control and assessment for railways bridges*", funded by the European Research Found for Coal and Steel (RFCS) and in course of realization, is to investigate the aforementioned uncertainties on the structural behaviour and integrity of steel and composite steel-concrete bridges with particular attention to the fatigue phenomena. To this aim, a modern procedure for the evaluation of the actual fatigue load and resistance of principal elements and critical details will be assessed for selected case studies representative of the bridge typologies most exposed to such damages.

In particular, the actual fatigue loading spectra will be evaluated taking into account the real and the expected traffic flows, also because of possible reclassification of railway lines, of the global dynamic train-bridge interaction effects and of the local dynamic vibration and distortional effects. Moreover, actual fatigue resistance of the main elements / critical details subjected to distortion induced effects will be evaluated. In such a way, it will also be possible to setup suitable strategies for the evaluation of vibration induced and distortion induced fatigue damaging in steel and composite steel-concrete railway bridges, as well for the control of the crack growth.

In this paper some preliminary results obtained for the Panaro bridge, a study case of FADLESS Project, are illustrated. In particular, standard modelling and fatigue assessment, experimental tests, model updating and advanced fatigue assessment of Panaro bridge will be described. Objectives of such activities were to: i) investigate the actual dynamic behaviour of the structure; ii) compare the fatigue assessment results obtained by standard and advanced approaches; iii) define preliminary observations to the fatigue assessment methodologies currently adopted in European design codes. Moreover, this first part of the Project will constitute the base for future developments of the research, leading to better comprehension of vibration and distortion fatigue phenomena induced by real traffic on steel and steel-composite railway bridges.

2 THE PANARO BRIDGE

The bow-string steel bridge on the Panaro river, along Bologna-Verona railway line, is the very first Italian railway bridge constructed adopting welded components (Figure 4). This particular bridge, supporting two tracks, has experienced an intense passenger and freight traffic since its construction in the 70's.

The bridge has a span length equal to 75.6 meters and its cross section height varies from 7 to 11 meters (Figure 5). All main components such as lower and upper strings, vertical and diagonal beams, main cross girders, lower and upper bracing diagonals at deck ends are built-up welded members (Figures 6 and 7). All joints are constituted by riveted solutions, thus realizing a very particular structure among steel railway bridges, an uncommon mix between welded components and riveted joints. Lower and upper main bracings are present, together with secondary longitudinal beams, directly supporting the rails, and local track bracings (Figures 8 and 9). End supports are constituted by steel bearings directly in contact with lower main strings (Figures 10 and 11).

Figure 4: Picture of Panaro bridge (Courtesy of RFI).

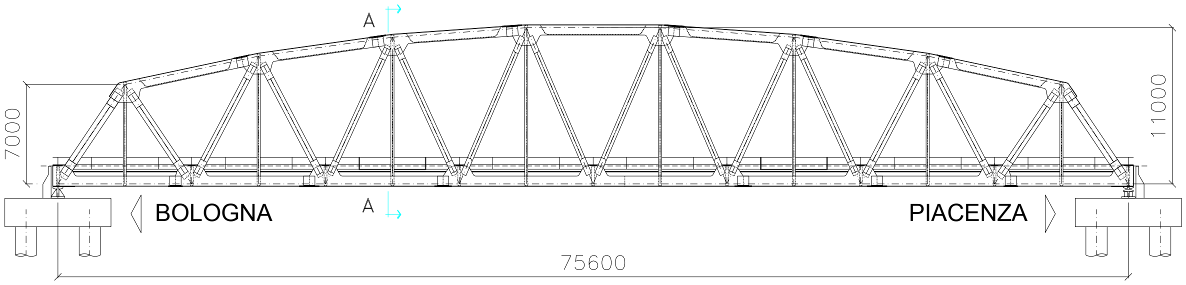

Figure 5: Drafting of Panaro bridge (Courtesy of RFI).

Figure 6: General view of Panaro bridge

Figure 7: Riveted diagonal-lower string joint of Panaro bridge

Figure 8: General view of deck structure

Figure 9: General view of lower and track bracings

Figure 10: General view of unidirectional bearing

Figure 11: General view of fixed bearing

During its exercise life, some of the secondary elements of the structures showed fatigue damages induced by distortion and vibration phenomena, as reported in Figures 12 and 13. In particular, almost all cross beams of track local bracings (originally fully fixed to the secondary longitudinal girders) experienced the same fatigue damage at the end restraints. Italian authority decided to cut the profiles in order to stop the crack propagation and changed beam end connections into pin joints removing the external bolts, in order to reduce the bending forces induced by distortion phenomena (Figure 12). Moreover, the connection between sleepers and longitudinal girders, obtained by catch bolts anchored to steel plates welded to the upper girder flanges, experienced fatigue damages in the longitudinal plate-flange welding due to vibration effects (Figure 13).

Figure 12: Typical fatigue damage and repair of track bracing cross beams

Figure 13: Sleepers-longitudinal girder connection by catch bolts

3 STANDARD MODELLING AND FATIGUE ASSESSMENT

Two FE beam models were developed by ANSYS® software for the standard fatigue assessment of Panaro bridge. The first model represented the bridge original resistant scheme, with track bracing cross beams fully fixed to the longitudinal girders (Full Fixed FE Model). The second model represented the actual situation as a results of the local repair interventions, with track bracing cross beams connected by hinge joints to the longitudinal girders (Hinge FE Model) (Figures 14 and 15).

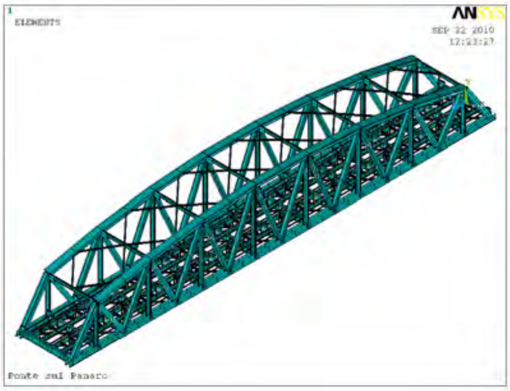

Figure 14: FEM model of the Panaro bridge

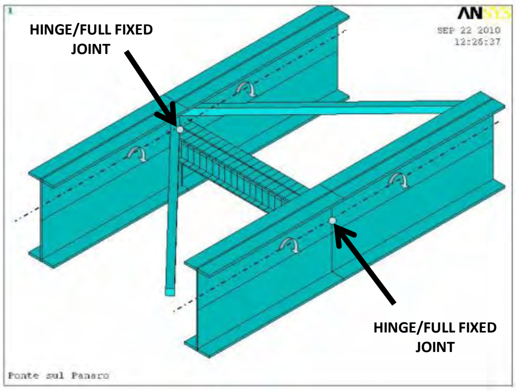

Figure 15: Track bracing cross beam connection to secondary longitudinal girders by full fixed/pin joints

All girders were represented by beam elements (BEAM188), except bracing diagonals represented by truss elements (LINK8). All elements were defined according to their actual geometrical axis and connected, where necessary, by proper internal constraints [10]. Those components characterized by variable end cross sections, as longitudinal girders, track and upper bracing cross beams, were represented by I section element in central parts and T sections elements at the ends. This approach was necessary to model properly the bridge stiffness and to obtain reliable force/stress values, as end stiffness greatly influence the intensity of in-plane and out of plane actions induced by distortion phenomena and, consequently, the intensity of local stresses (Figures from 16 to 19).

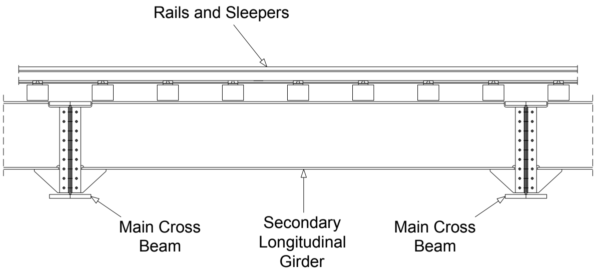

Figure 16: Side view of secondary longitudinal girders with variable end cross sections

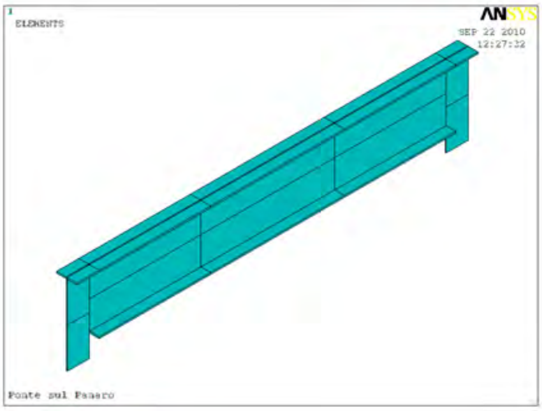

Figure 17: Local view of elements representing secondary longitudinal girders

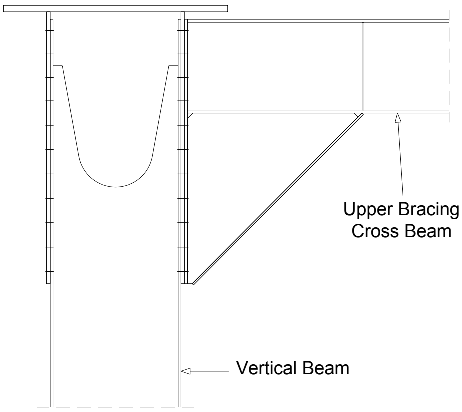

Figure 18: Side view of upper bracing cross beams with variable end cross sections

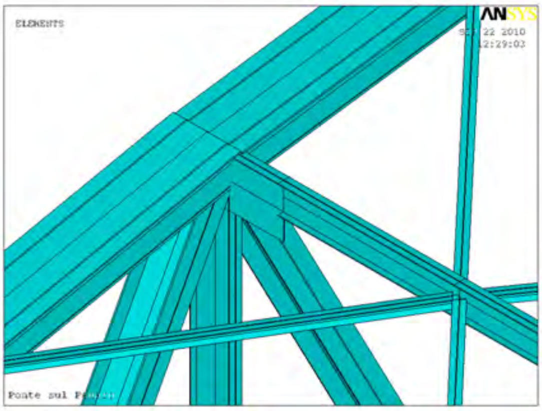

Figure 19: Local view of elements representing upper bracing cross beams

The evaluation of dynamic forces induced by train passages into the bridge components was performed according to the Eurocode rules. In particular, element stresses were calculated by incremental dynamic analysis of bridge models subjected to the moving loads of Standard and Heavy train traffic mixes [11]. The total number of train passages was calculated assuming a life cycle of 100 years.

As Eurocode fatigue train models are characterized by different lengths and velocities, the passage of each model was simulated assuming different sampling frequency in order to optimize the calculation times. In particular, analysis frequencies were calculated in such a way that the distance covered by loads between two subsequent steps was equal to 1/10 of secondary longitudinal girder length for each train velocity (Table 1).

In the dynamic analysis, damping characteristics of bridge components were represented assigning to each element a proper value of material damping, calculated as a function of length as specified by Eurocode [11]. Calculated girder material damping varied in the range 0.5% - 2.81%.

Beam element stresses were extracted from the FE models and elaborated in order to calculate the stress time-histories acting on net cross sections. In particular, the four possible combinations of normal stresses induced by the axial force and the two bending moments were considered for each element section. Moreover, vertical and transverse shear stresses acting at end restraint sections of main cross girders and upper bracing cross beams were also considered.

Normal and shear stress spectra were evaluated by rainflow counting technique. Fatigue damages were calculated independently adopting the linear damage accumulation rule of Palmgren-Miner. Fatigue classes of welded built-up members were assumed according to the indications of Eurocode [11], while for riveted components the fatigue classes proposed by Taras and Greiner were considered [12]. Fatigue classes of all bridge components are reported in Table 2.

Train Type	**Vel [Km/h]**	**Length [m]**	**Analysis Frequency [Hz]**
1	200	262.1	120
2	160	281.1	95
3	250	385.52	150
4	250	237.6	150
5	80	270.3	50
6	100	333.1	60
7	120	169.5	75
8	100	212.5	60
9	120	134.8	75
10	120	129.6	75
11	120	198.5	75
12	100	212.5	60

Table 1: Values of frequencies adopted in the dynamic analysis

Constructional detail	**Bridge Components**	**Fatigue Class**
One-shear joint with gusset plate	Main Lower and Upper Strings; Main Vertical Beams; Main Diagonals Beams; Main Cross Beams at end sections; Lower and Upper Bracing Diagonals	85 for normal stresses
Structural element with holes subject to bending and axial forces	Main Cross Beams at intermediate sections; Secondary Longitudinal Girders at end sections; Upper Bracing Cross Beams at intermediate Sections	90 for normal stresses
Built-up sections with automatic fillet weld	Secondary Longitudinal Girders at intermediate sections; Track cross beams at intermediate sections	125 for normal stresses
Tee-butt joints with fillet welds	Track cross beams at end sections; Upper Bracing Cross Beams at End Sections	36 for normal stresses 80 for shear stresses

Table 2: Fatigue classes adopted for Panaro bridge components

For each element section, the fatigue damage D_i induced by the i train type was calculated adopting the following simplified approach [1]:

$$D_i = D_{\sigma,\max} + D_{\tau v} + D_{\tau h} \tag{1}$$

where $D_{\sigma,\max}$ is the maximum damage induced by normal stresses considering the combinations of axial force and bending moments, D_{tv} is the vertical shear damage and D_{th} is the horizontal shear damage. Total fatigue damages obtained from Full Fixed and Hinge Model FE models for Standard and Heavy traffic mixes are reported in Figures from 20 and 24.

Considering the Full Fixed FE Model, that represents the original resistance scheme of Panaro Bridge, it is possible to observe that a significant number of elements showed a fatigue damage greater than 0.1 both for Heavy and Standard traffic mixes. Damage values between 0.1 and 1 were observed on almost all vertical beams while more severe damages, greater than 1, occurred at the end cross sections of track bracing cross beams (as really occurred) and at the connection joints of vertical beams with lower/upper stringers (actually undamaged) (Figure 22). From this point of view, more refined analysis of identified critical details seemed to be necessary for a proper evaluation of actual stress spectra.

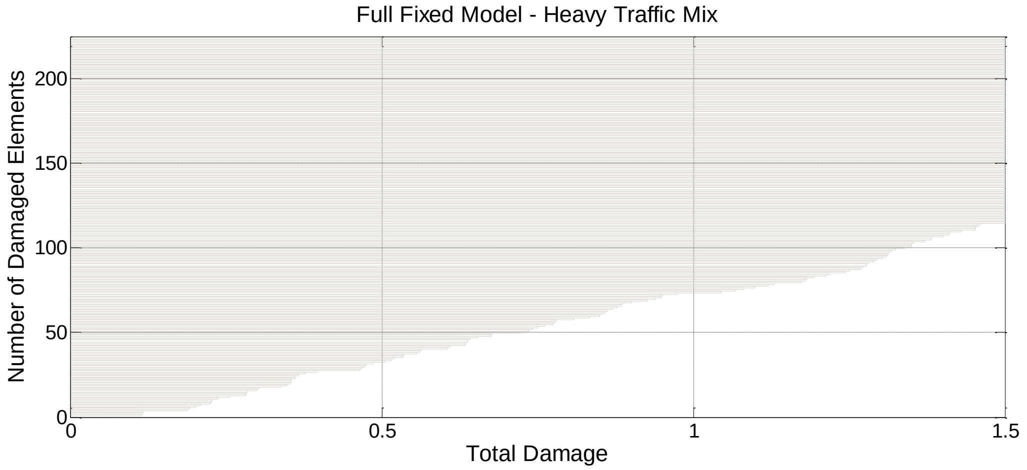

Figure 20: Full fixed FE model - Heavy Traffic Mix Damage

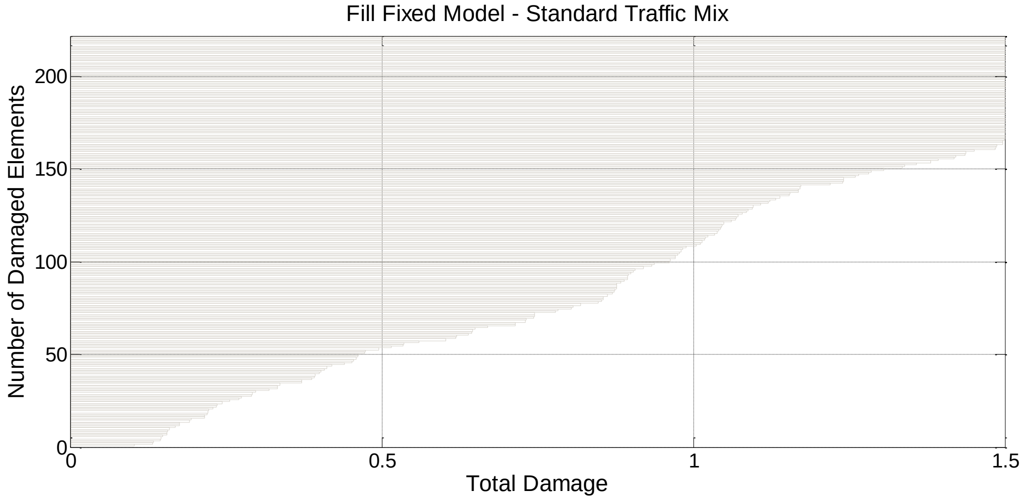

Figure 21: Full fixed FE model - Standard Traffic Mix Damage

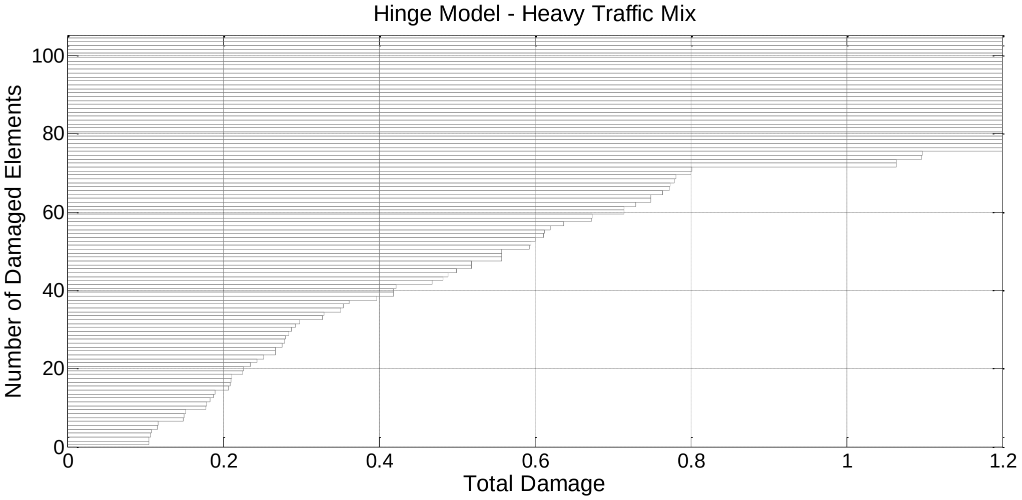

Figure 23: Hinge FE Model - Heavy Traffic Mix Damage

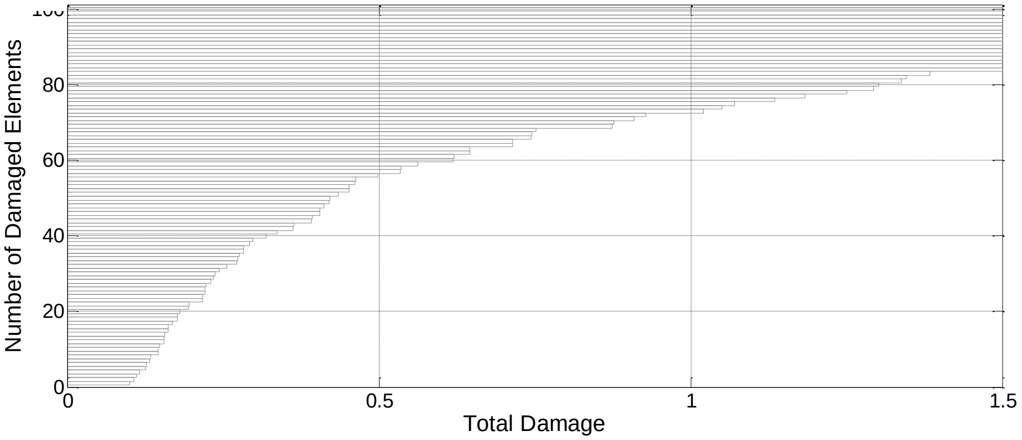

Figure 24: Hinge FE Model - Standard Traffic Mix Damage

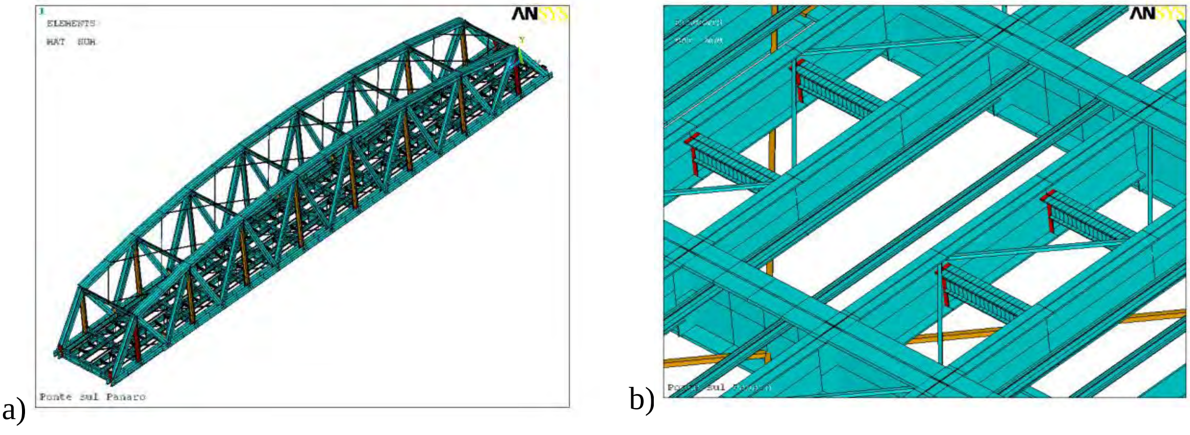

Figure 25: Full Fixed FE Models - Heavy Traffic Mix: general (a) and detailed (b) graphical representation of damaged components (Yellow elements: -0.1 < Damage < 1 --- Red elements: Damage > 1)

Also for the Hinge FE Model a great number of damaged components was observed for Heavy and Standard traffic mixes. Vertical beams showed damage values between 0.1 and 1 and more severe damages, greater than 1, occurred at the connection joints of vertical beams with lower/upper stringers. Nevertheless in the Hinge Model case, that represents the actual resistant scheme of Panaro bridge, the elements representing the end sections of track bracing cross beams did not show any fatigue damage. From these results, it is possible to observe that the local modification of the track bracing cross beams practically cancelled the distortion induced local forces while did not introduce significant variations in the global structural response of the bridge.

It is important to notice in both the Full Fixed and Hinge FE Models the reliability of calculated results is unknown, as expected fatigue damages in some cases really occurred but in others didn't. So, advanced FE models of critical details are necessary in order to obtain a correct evaluation of local stresses. From this point of view, the modelling experience of Panaro bridge confirmed the necessity of advanced analysis approaches in the design of new complex structures and in the assessment of older ones, as the use of standard techniques only could lead to an erroneous evaluation of local effects.

4 EXPERIMENTAL TESTS

Usually steel bridges show a real structural behaviour different from the theoretical one, as every modelling and analysis technique actually available is necessary a simplified representation of more complex structures. From this point of view, experimental tests are very effective tools for the evaluation of real forces and stresses acting into bridge steel components and, consequently, can be adopted as a useful base for a reliable evaluation of fatigue performance.

The experimental tests on Panaro bridge were focused on the structure dynamic identification and on evaluation of the effects induced by train passages. In particular, global and local vibration modes were identified by operative modal analysis technique (OMA) using the ambient vibrations (white noise) as excitation source. Moreover, the effects of train passages were investigated directly recording the strain time-histories on critical details and the horizontal displacement time-histories of the deck unidirectional bearings. Such tests permitted to improve the knowledge of the real structural behaviour and constituted the base for the numerical updating of FE bridge model.

4.1 Global/Local Experimental Dynamic Tests

The experimental dynamic analysis on Panaro bridge was performed in order to obtain the identification of the global vibration modes and, moreover, to evaluate the dynamic characteristics of track bracing cross beams. To this aim, accelerations in the vertical, horizontal and longitudinal directions of suitable structure key points were recorded assuming the ambient vibration as excitation source.

In particular for the identification of global vibration modes, structure accelerations were recorded on eleven sections adopting a multi-step approach, that consists of acquiring data by moving sensors along the structure and keeping some of them fixed as "reference" (Figures 25, 26 and 27). Such "reference" sensors are adopted as common base for merging the vibration modes identified by different recording configurations, thus providing the global identification of the structure [13]. Accelerations were recorded by PCB sensors and LMS Scadas acquisition unit adopting a sampling frequency of 400 Hz for time periods of 15 minutes at least. Some train passages occurred during the acquisition of ambient sources, nevertheless such noises were afterwards cleared from recorded signals before the numerical identification of natural vibration modes, obtained by PolyMAX algorithm [13].

Seven global modes of vibration were clearly identified during the experimental tests. Modal frequencies, damping values and mode shapes are reported in Table 3, together with the mode phase collinearity values (MPC) that is equal to the unity when the complex modal displacement of all recorded nodes have the same phase (i.e. the mode is real). The modal shape extracted for the identified modes are reported in Figure 28.

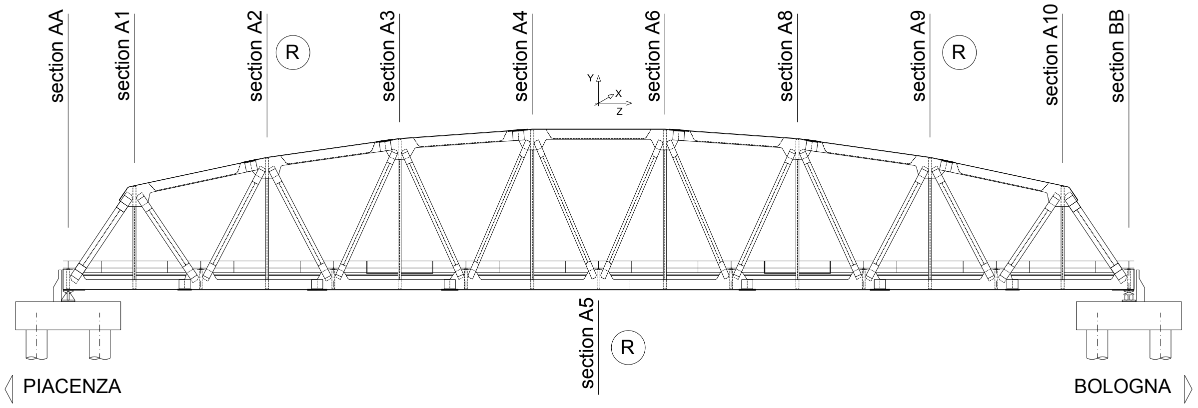

Figure 25: Global dynamic test of Panaro Bridge: test layout

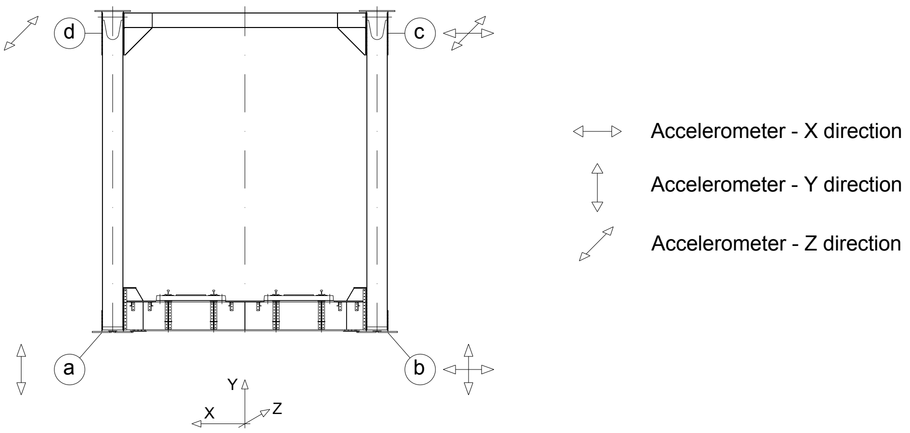

Figure 26: Global dynamic test of Panaro Bridge - position and orientation of sensors on the typical cross section

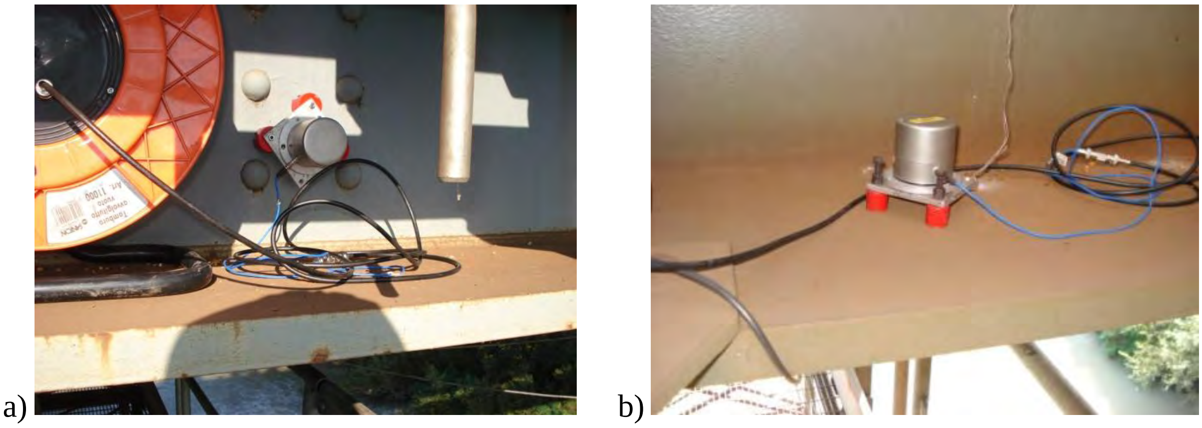
a)
b)

Figure 27: Horizontal (a) and certical (b) accelerometers on main lower string

Mode n°	Frequency [Hz]	Damping [%]	MPC	Mode Shape
1	1.77	0.49		Lateral Bending
2	3.65	0.15		Torsional
3	3.68	0.65		Vertical Bending
4	4.08	0.29		Lateral Bending
5	6.86	0.15		Distortional
6	10.93	0.24		Torsional
7	12.35	0.25		Vertical Bending

Table 3: Identified global vibration mode of Panaro bridge.

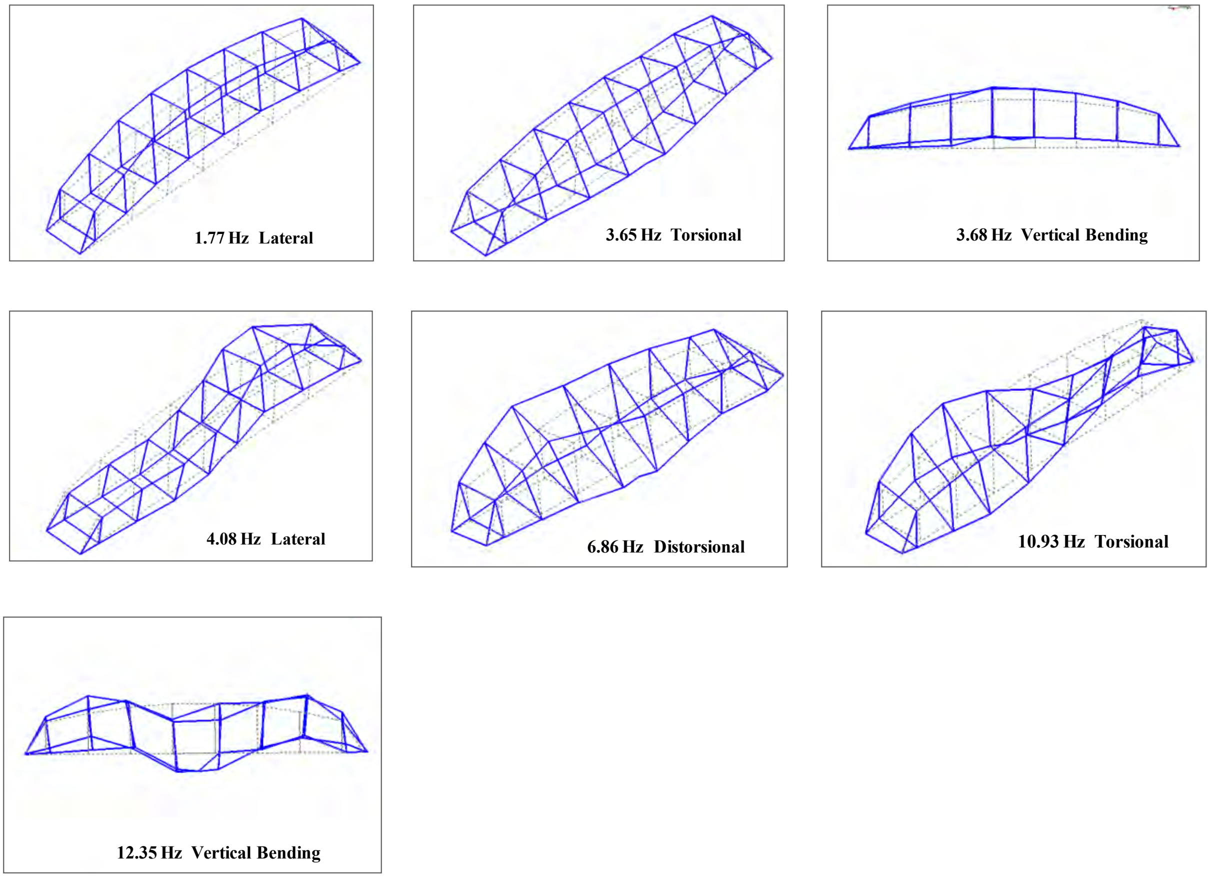

Figure 28: Panaro bridge - shapes of identified global vibration mode

Local dynamic tests were performed on a track bracing cross beam, recording vertical and transverse accelerations of upper flange at midspan and lateral sections (Figure 29). In this case, a single acquisition of all instrumented sections, realized adopting the same recording settings of global tests, permitted to identified clearly three local vibration modes of the cross beam. Modal parameters are reported in Table 4 while the calculated modal shapes are illustrated in Figure 30.

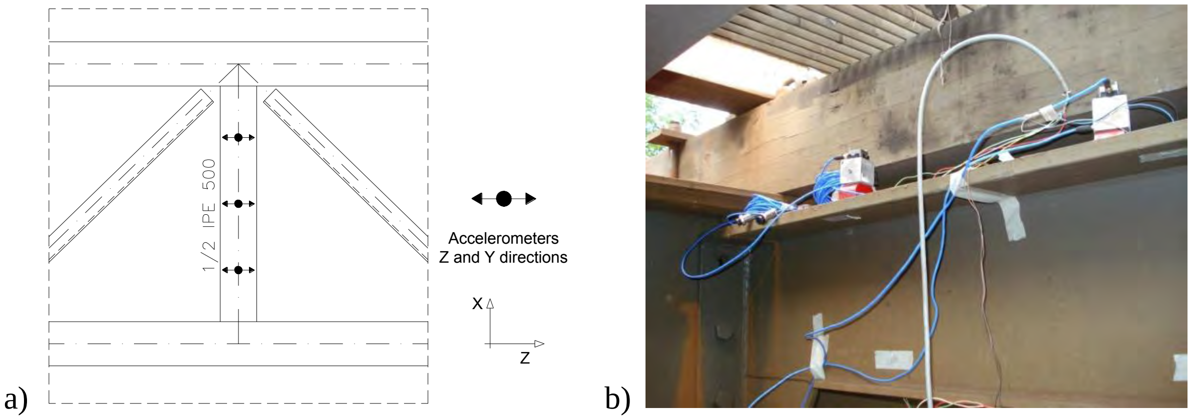

Figure 29: Instrumented sections (a) and sensors positioning (b) for the local cross beam dynamic tests.

Mode n°	Frequency [Hz]	Damping [%]	MPC	Mode Shape
1	15.65	0.82		Vertical Bending
2	44.18	0.46		Lateral Bending
3	97.22	0.56		Lateral Bending

Table 3: Identified local vibration modes of track bracing cross beam.

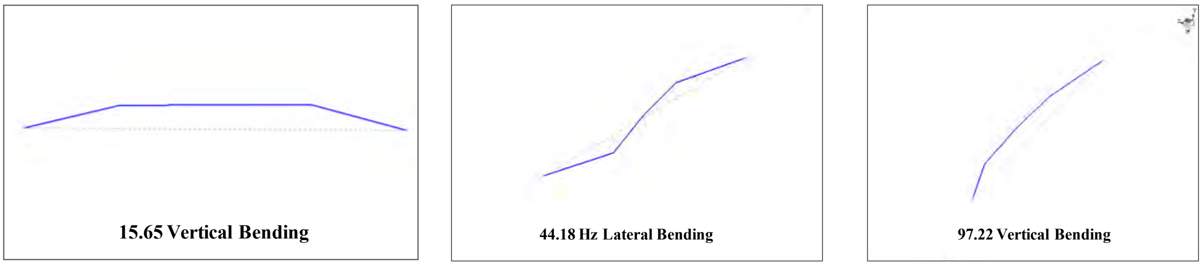

Figure 30: Panaro bridge - vibration mode shapes of track bracing cross beam

4.2 Strain/Displacement Experimental Tests

The effects of train passages were investigated analyzing strains of local details and displacements of external bearings.

In particular, strain time-histories were recorded on the track bracing cross beams and on the steel plates connecting sleepers to the secondary longitudinal girders (Figure 31). It was so possible to investigate the stresses actually induced into track cross beams by distortion phenomena, indirectly evaluating also the effects on internal forces of end restraint modifications from full fixed to hinge joints. Moreover, stress cycles acting into sleeper supporting steel plates were investigated as such secondary components showed extensive fatigue damages due to the vibration of track sleepers.

Stresses induced by train passages into the track bracing cross beam are very low, thus confirming that actually this component is not particularly subjected to distortion phenomena. On the contrary, more intensive actions are present into the sleeper supporting plates, due to distortion and vibration effects induced by sleeper movements under train passages. Such stresses caused extensive fatigue damages on the longitudinal welding connecting supporting steel plates to the upper flange of secondary longitudinal girders. Stress time-histories recorded at midspan section of track bracing cross beam (CH 4) and at the sleeper supporting plate (CH 10) are reported in Figures 32 and 33.

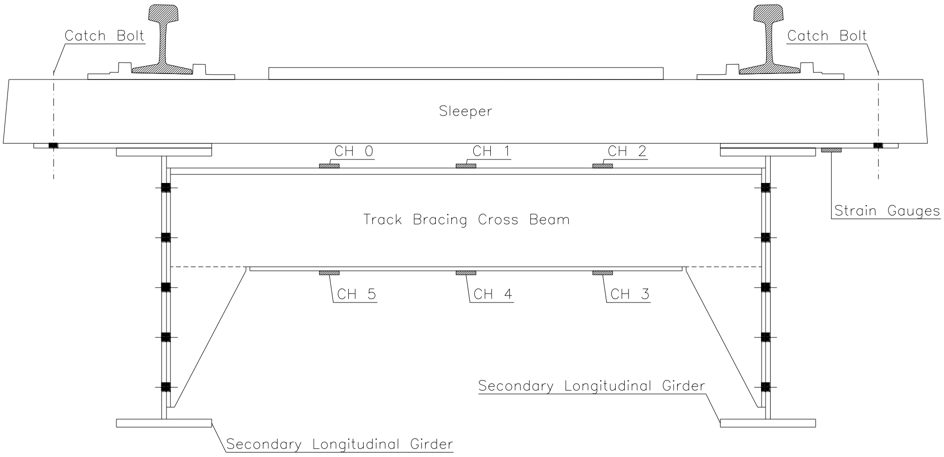

Figure 31: Strain gauge position on track bracing cross beam and sleeper supporting plates.

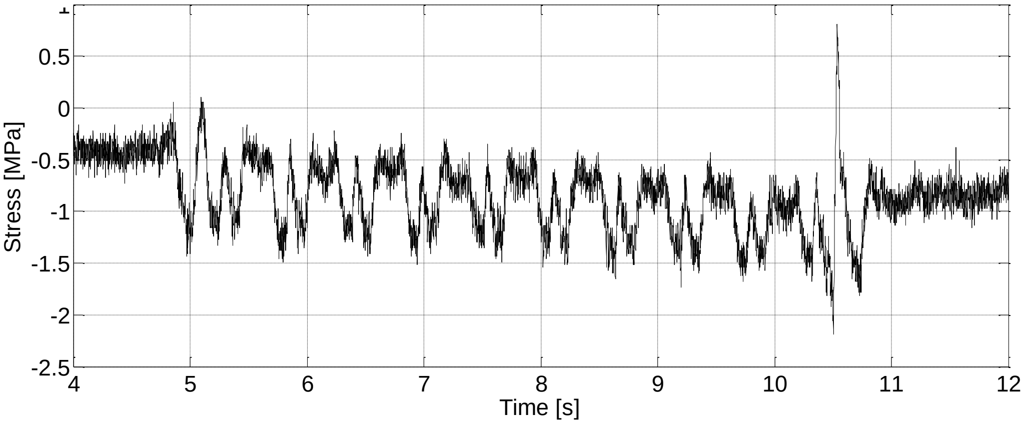

Figure 32: Midspan section of track bracing cross beam: strain time-history (CH 4)

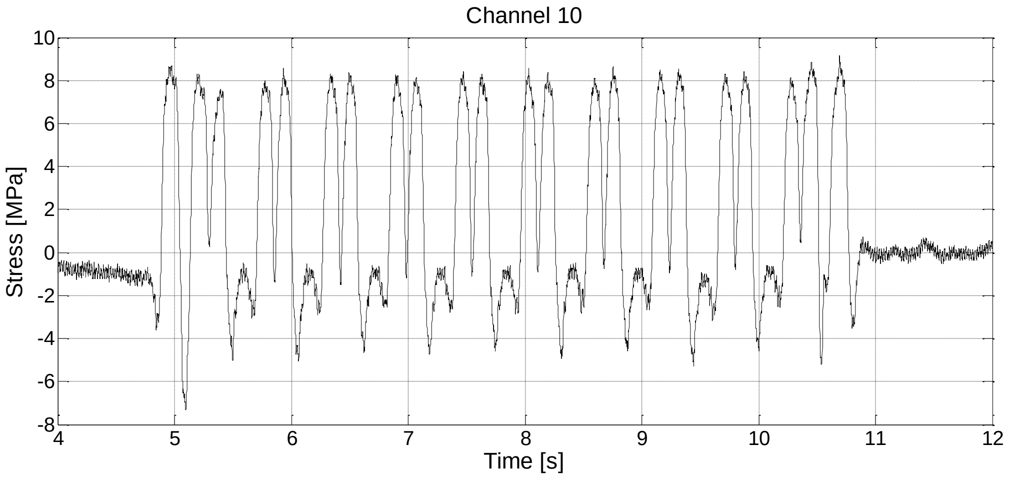

Figure 33: Strain time-history of sleeper supporting plate (CH 10)

Longitudinal movements of the two unidirectional external bearings were recorded using dynamic optoNCDT laser transducers (Figure 34). It was so possible to investigate the actual horizontal displacement time-histories of Panaro bridge under the passage of different train typologies (an example of recorded signals is reported in Figure 35). The different values of longitudinal displacements recorded for the two external bearings are probably due to torsional/lateral movements induced by asymmetric train passages on the bridge deck. The entity of such lateral bending and torsion depends on train composition, axle loads and speed. From this point of view, such results confirmed the need of considering not only vertical bending but also lateral bending and torsion in order to obtain a reliable evaluation of the dynamic structural response of such complex structures.

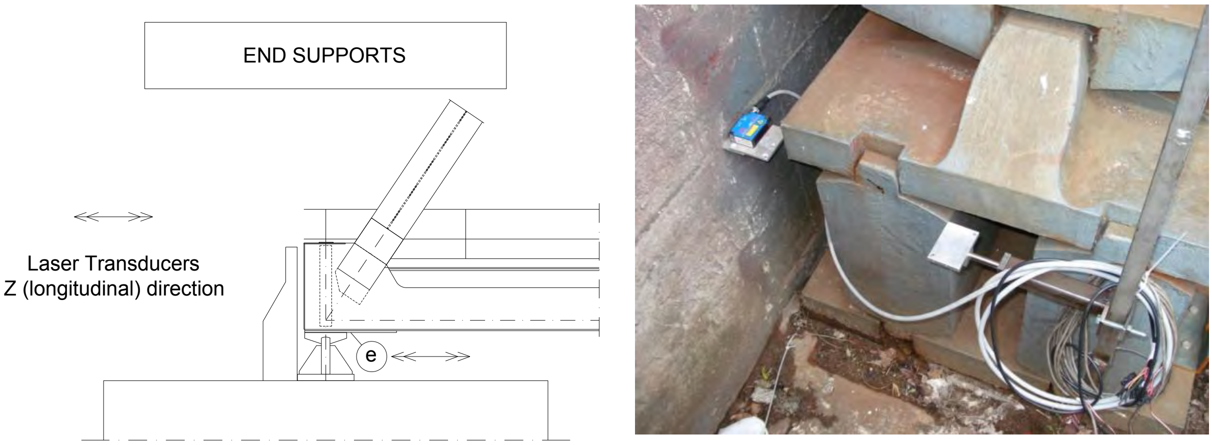

Figure 34: Laser transducers for the analysis of longitudinal bearing movements under train passages

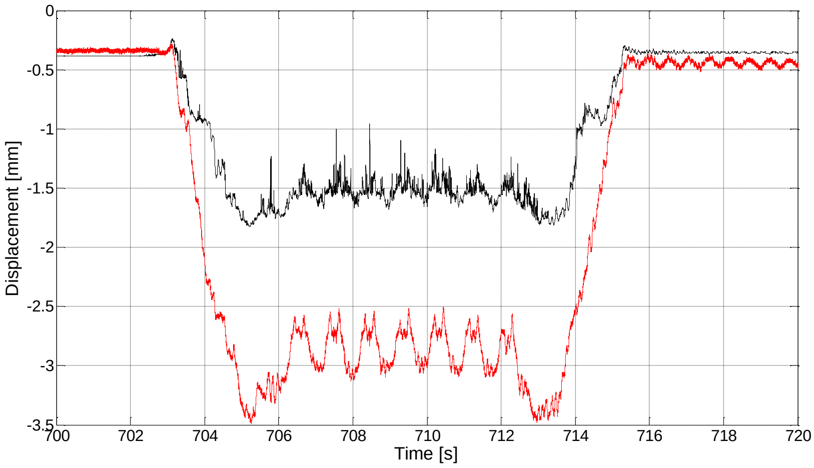

Figure 35: Example of bearing longitudinal displacements under train passages

5 NUMERICAL UPDATING

The global vibration modes identified in the experimental dynamic tests were adopted as reference for the numerical updating of the FE Hinge model of Panaro bridge, that represents the actual resistant scheme of the structure. To this aim, an automatic optimization procedure was implemented by MODEFRONTIER software (Figure 36). Objective of developed procedure was to minimize simultaneously and independently the differences between experimental and numerical eigenfrequencies by the variation of suitable parameters.

In each sequence cycle, parameter values were changed according to the MOGA-II optimization algorithm and transferred to the ANSYS FE model, in order to extract the first twenty eigenfrequencies and vibration mode shapes [14]. Calculated results were then elaborated by MATLAB to match experimental and numerical mode of vibrations. Mode matching between i^{th} experimental and j^{th} numerical vibration modes was obtained searching the highest MAC_{ij} value, where MAC_{ij} is the modal assurance criterion calculated for ϕ_i and ϕ_j mode shapes normalized to the unity.

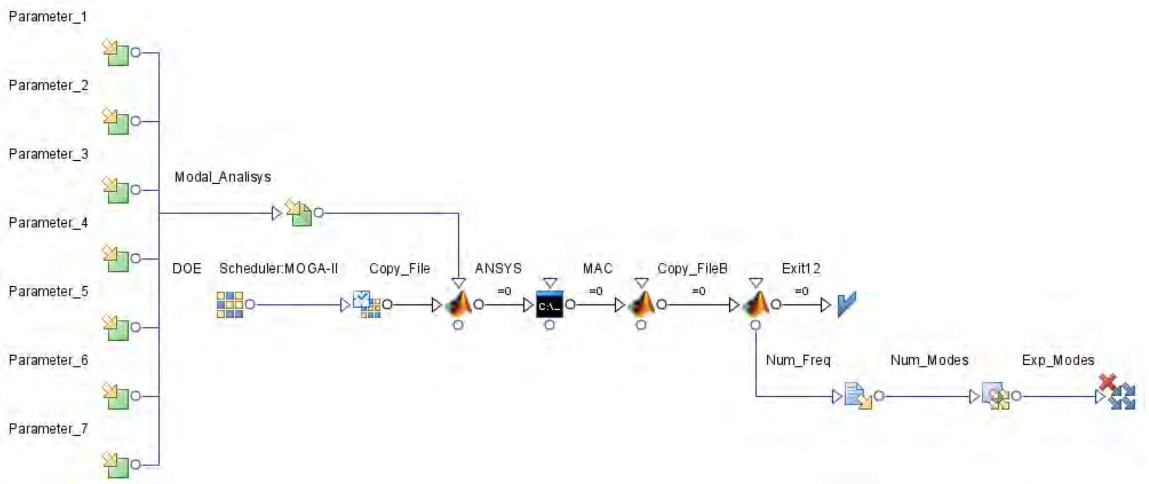

Figure 36: Optimization scheme developed for the FE model updating

After the optimization procedure was calibrated, suitable mechanical parameters had to be selected before the updating of Panaro bridge FE Hinge model. From a preliminary comparison between numerical and experimental vibration modes, a large difference between frequency values was observed, especially for those modes that involve transverse movements (lateral bending and torsion), as reported in Table 4. Some modifications were so introduced into the FE Hinge model before updating, in order to improve the numerical representation of bridge dynamic properties (Table 4).

The rotation center of end bearings, originally assumed at the contact point with the main lower stringers, was moved in the downward direction, using a mass less point element (MASS21), and its position was assumed as an optimization parameter. This modification was due to the observation that the upper bearing surfaces have a circular shape with a unknown radius, with the consequence that the rotation center is lower than the contact point.

Moreover, bearing stiffness were also represented into the FE model by spring elements (COMBIN14). In particular, longitudinal and torsional (rotation along the vertical axis) stiffness of fixed vertical bearings were modeled, while for unidirectional bearings only torsional spring elements were considered. Bearing stiffness were assumed as optimization parameters and their initial values were estimated by two FE models of fixed and unidirectional bearings subjected to unit longitudinal displacement or unit vertical rotation (Figure 37). Spring elements were directly connected to the point elements representing the rotation center of bearings. Vertical/transverse and longitudinal rotation DOFs of point elements representing the rotation center of unidirectional bearings were fixed, while for fixed bearing the longitudinal DOF was also fixed.

At least, also the values of dead loads, represented by equivalent densities of bridge components supporting secondary structures, were assumed as optimization parameters for the FE model updating. All selected optimization parameters are reported in Table 5.

Mode n°	Exp. [Hz]	Mode Shape	FE Hinge Model [Hz]	Δ [%]	Modified FE Hinge Model [Hz]	Δ_M [%]
1	1.77	Lateral Bending	2.284	29.0	1.96	10.5
2	3.65	Torsional	3.844	5.3	3.56	2.4
3	3.68	Vertical Bending	3.989	8.4	3.69	0.4
4	4.08	Lateral Bending	4.864	19.2	4.15	1.8
5	6.86	Distortional	7.377	7.5	6.65	3.0
6	10.93	Torsional	11.829	8.2	10.56	3.4
7	12.35	Vertical Bending	13.763	11.4	12.92	4.6

Table 4: Comparison between numerical and experimental modal frequencies

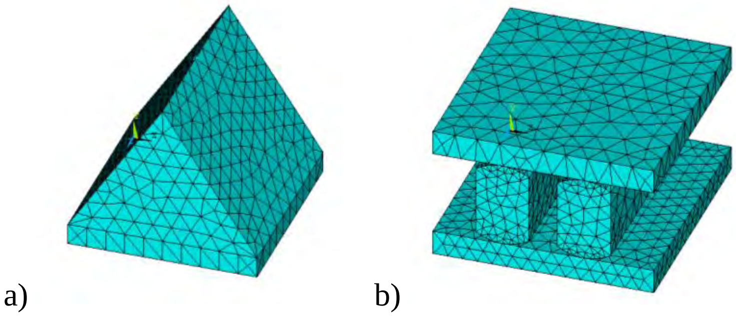

Figure 37: FE models of fixed (a) and unidirectional (b) bearings

Parameter n°	Description	Value
1	General material density of beam elements (dead weight of components, rivets and connecting plates)	9027.5 kg/m³
2	Material density of upper stringer elements (dead weight of components, rivets, connecting plates, suspended upper runaways)	17477 kg/m³
3	Material density of secondary longitudinal elements (dead weight of components, rivets, connecting plates, rails, sleepers, walking grates)	16854.6 kg/m³
4	Distance between lower stringer axis and bearing centre of rotation	0.174 m
5	Torsional stiffness of fixed bearing	124860 kN*m/rad
6	Torsional stiffness of unidirectional bearing	230690 kN*m/rad
7	Longitudinal stiffness of fixed bearing	1068800 kN/m

Table 5: Selected optimization parameters for numerical updating of Panaro FE model

The sensitivity functions of parameters n° 1-2-3 calculated for the 1st, 3rd and 4th vibration modes are reported in Figures 38a, 38b and 38c. The variation of such density parameters have a great influence on numerical values of the eigenfrequencies, while a variation of bearing stiffness parameters (n° 5-6-7) lower than 25% did not induced significant variations.

The distance of the bearing rotation centers from lower stringer axis influenced the eigenfrequencies of modes n° 1-3-5-6-7 in the range 0-20 m, while for greater values the frequencies of aforementioned vibration modes could be considered as constant (Figure 38d).

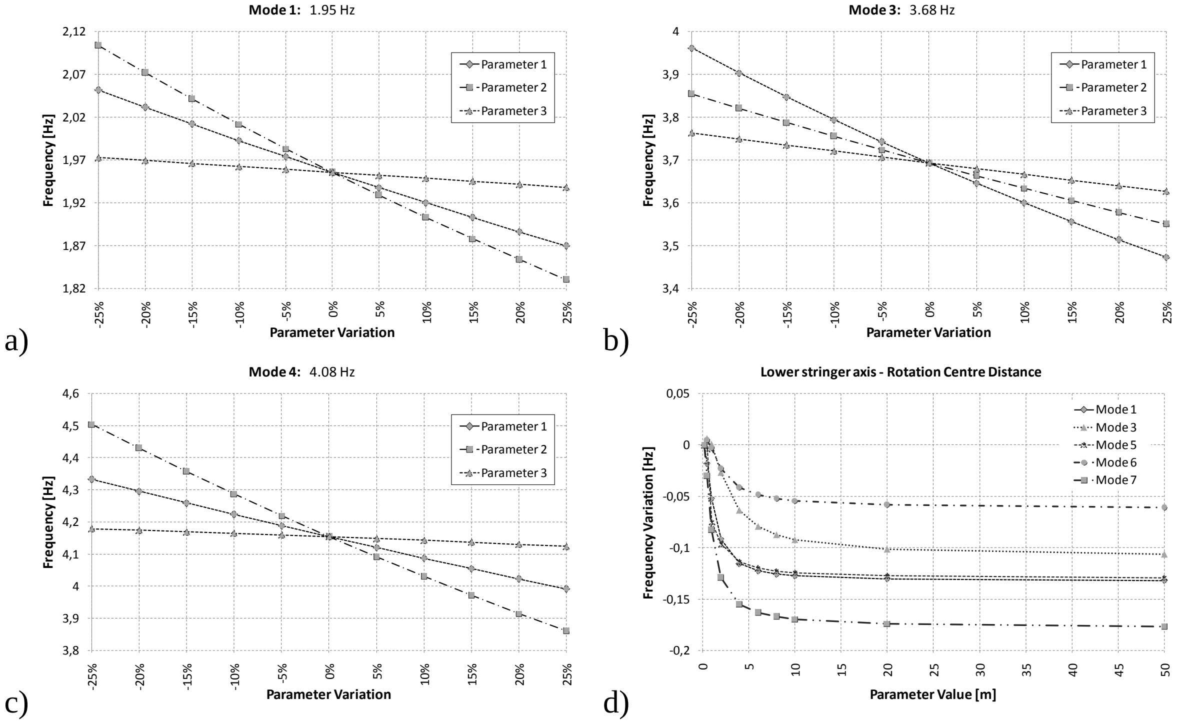

Figure 38: Sensitivity functions of parameter n° 1-2-3-5-6-7 calculated for vibration modes n° 1-3-4

The modeFRONTIER procedure converged to stable parameter configurations after 3560 cycle iterations, taking less than 15 seconds for each cycle for a total computation time equal to 15 hours. The numerical optimization permitted to obtain an updated model characterized by numerical eigenfrequencies very similar to the experimental results (maximum difference of about 4.5%) and high MAC values, reported in Table 6. The complete MAC matrix is reported in Figure 39.

Parameter n°	Initial Value	Final Value	Mode n°	Numerical Freq. [Hz]	Experimental Freq. [Hz]	Δ [%]	MAC
1	9027 kg/m³	7897 kg/m³	1	1.82	1.77	2.73	98.7%
2	17477 kg/m³	18735 kg/m³	2	3.64	3.65	0.33	98.3%
3	16854 kg/m³	18068 kg/m³	3	3.64	3.68	1.06	82.7%
4	0.17 m	76.00 m	4	4.13	4.08	1.27	72.7%
5	124860 kN*m	93645.00 kN*m	5	6.59	6.86	4.00	72.0%
6	230690 kN*m	183270 kN*m	6	10.66	10.93	2.52	75.9%
7	1068800 kN/m	1068800 kN/m	7	12.91	12.35	4.53	68.4%

Table 6: Updated FE Model: initial/final values of parameters and numerical/experimental frequencies

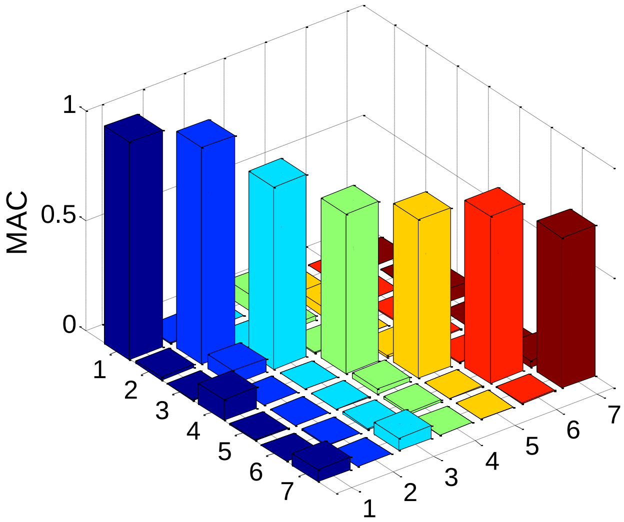

Figure 39: Graphical representation of numerical/experimental MAC matrix

6 ADVANCED FATIGUE ASSESSMENT

The Updated FE Hinge model of Panaro bridge was used for a further fatigue assessment of case study, comparing results obtained from an advanced modeling/updating approach with standard methodologies. Indeed, one main objective of Fadless Project is the critical review of standard approaches currently adopted for the fatigue assessment of complex structures like bridges. In particular, the Project aims also at evaluating the effectiveness of standard FE modeling techniques and fatigue load models, comparing theoretical results obtained from current design rules with experimental data. From this point of view, the comparison between fatigue damages calculated by an updated model and a standard one constitute a preliminary results in such critical review process.

The number (Figures 39 and 40) and distribution (Figure 41) of damaged components is similar to the standard results calculated by the Hinge Model, while damage intensities are a little lower. From the fatigue assessment point of view, the updating process didn't showed to vary significantly the results obtainable from a global FE model, thus confirming the necessity of refined local analysis of critical details in order to catch properly the actual stress spectra induced by distortion and vibration phenomena.

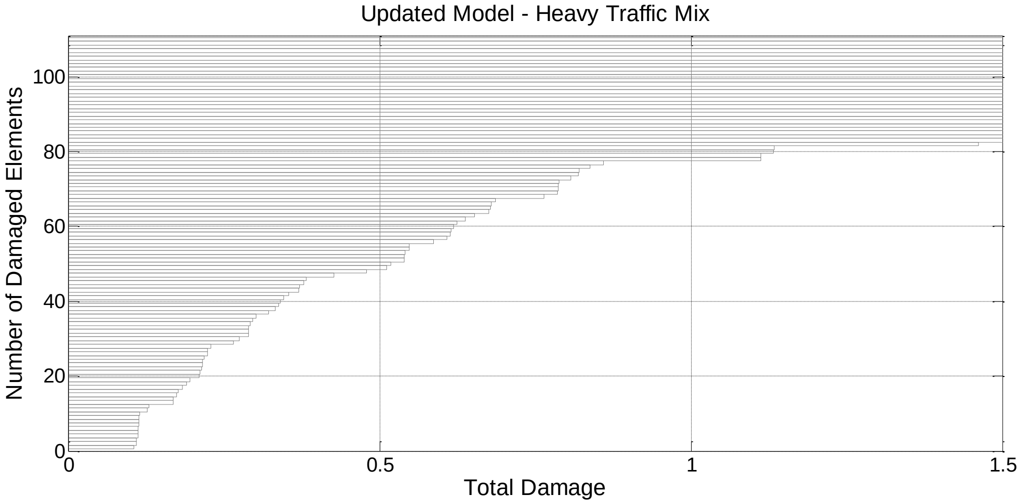

Figure 39: Updated Model - Standard Traffic Mix Damage

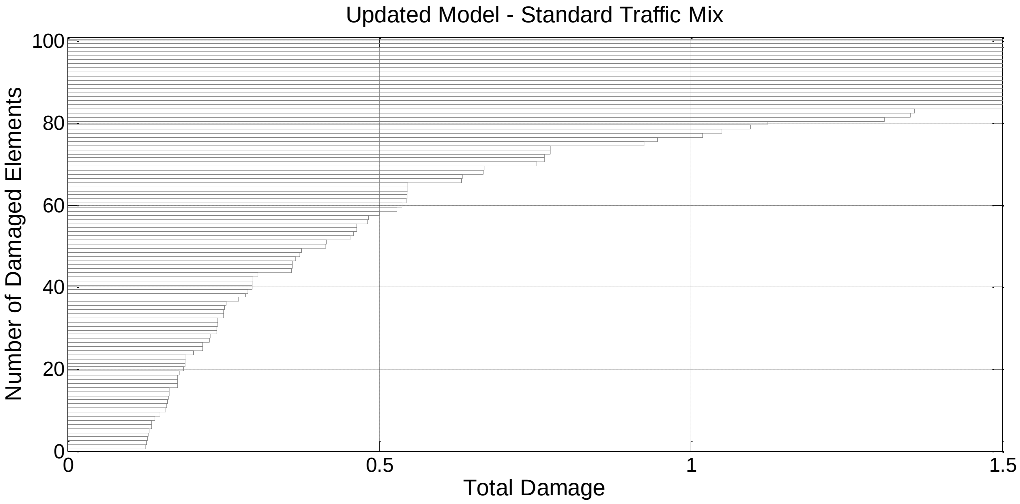

Figure 40: Updated Model - Standard Traffic Mix Damage

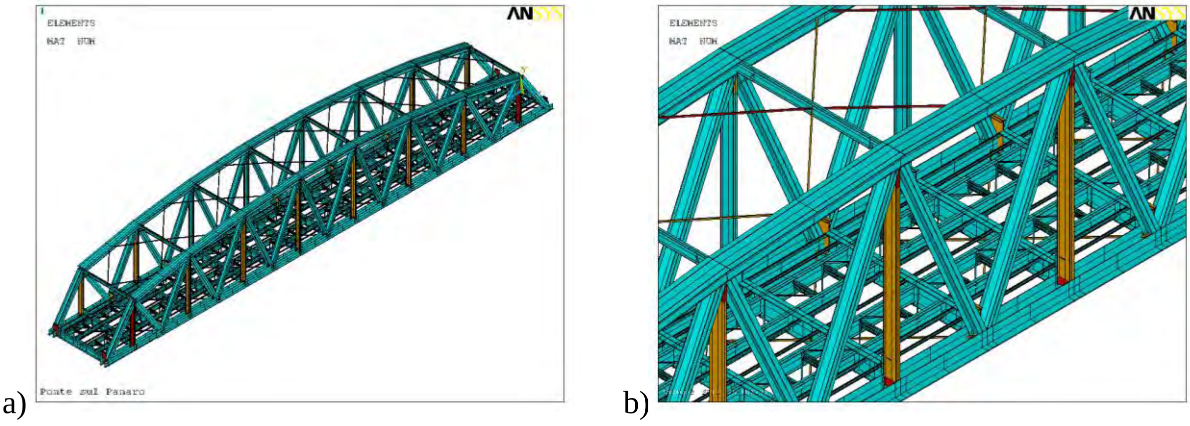

Figure 41: Updated FE Models - Heavy Traffic Mix: general (a) and detailed (b) graphical representation of damaged components (Yellow elements: -0.1 < Damage < 1 --- Red elements: Damage > 1)

7 SOME PRELIMINARY REMARK

Main objective of FADLESS Project are the development of enhanced approaches for the correct evaluation of fatigue damages on steel railway bridges considering in particular the distortion and vibration effects.

The theoretical and experimental analysis performed on Italian case study, the Panaro bridge, permitted to obtain very interesting preliminary results concerning the actual dynamic behavior of such complex structures and the effectiveness of currently adopted modeling approaches at representing the internal distribution of forces/stresses. In particular, standard FE models were used for the fatigue assessment of the bridge, realized according to Eurocode rules. Experimental dynamic analysis permitted to identify global/local vibration modes and to constitute a suitable base for the subsequent numerical updating of developed FE model, obtained by an automatic optimization procedure. Advanced fatigue assessment was performed on the updated FE model and related results were compared to standard ones.

Moreover, critical details concerning the distortion/vibration induced fatigue damages were identified; such details, in the second part of the project, will be the object of further studies including the development of local FE models and the realization of sub-structuring analysis.

At last, suitable long-term monitoring systems will be designed and installed on all case studies in order to indentify the actual railway traffic spectra on European bridges, providing the necessary base for a critical review of actually adopted fatigue load models.

REFERENCES

[1] EN 1993-1-9, 2002. Eurocode 3: Design of steel structures - Part 1.9: Fatigue strenght of steel structures. CEN European Committee for Standarsization.

[2] AREMA, 2005. Manual of railway engineering. Washington D.C: American Railway Engineering and Maintenance of Way Association (AREMA).

[3] Ferrovie dello Stato, 1992. Istruzione n. 44f del 30.01.1992: Verifiche a fatica dei ponti ferroviari metallici. Ente Ferrovie dello Stato (in Italian).

[4] Ferrovie dello Stato, 1997. Istruzione n. I/SC/PS-OM/2298 del 2.6.1995 "Sovraccarichi per il calcolo dei ponti ferroviari - Istruzioni per la progettazione, l"esecuzione ed il collaudo". Ente Ferrovie dello Stato (in Italian).

[5] European Commission, Energy and Transport DG, 2005. TEN-T Trans-European Transport Network: priority axes and projects 2005. Technical report, European Commission. (ec.europa.eu).

[6] Goicolea, J., 2004. "Dynamic loads in new engineering codes for railway bridges in Europe and Spain". In Bridges for High-Speed Railways, June 3-4; Porto.

[7] Kühn, B., Lukić, M., Nussbaumer, A., Günter, H.P., Helmerich, R., Herion, S., Kolstein, M.H., Walbridge, S., Androic, B., Dijkstra, O., Bucak., 2008. Assessment of Existing Steel Structures: Recommendations for Estimation of Remaining Fatigue Life. Report EUR 23252 EN - 2008, European Community.

[8] Fisher, J.W., 1984. Fatigue and fracture in steel bridges: case studies. John Wiley.

[9] Fisher, J.W. and Roy, S., 2008. "Fatigue of steel infrastructure". Proc. of Bridge Maintenance, Safety Management, Health Monitoring and Informatics IABMAS08 Conference, July 13 17 2008, Seoul. Korea.

[10] ANSYS Inc. (2005). ANSYS User Manuals Version 10. ANSYS Inc. Global Headquarters, Canonsburg, PA.

[11] UNI EN 1991-2, 2005. Eurocode 1: Actions on structures - Part 2: Traffic loads on bridges. CEN European Committee for Standardization.

[12] Taras, A. and Greiner, R., 2009. Development and Application of a Fatigue Class Catalogue for Riveted Bridge Components. Report ECCS TC6 - 2009 - xxx, Institute for Steel Structures and Shell Structures - Graz University of Technology, Graz. Austria.

[13] LMS International (2005). LMS TestLab Rev6A: Operational Modal Analysis User Manual

[14] ESTECO srl (2007). modeFRONTIER User Manual Version 4.0b.

COMPDYN 2011
ECCOMAS Thematic Conference on
Computational Methods in Structural Dynamics and Earthquake Engineering
M. Papadrakakis, M. Fragiadakis, V. Plevris (eds.)
Corfu, Greece, 25-28 May 2011

JOINT ESTIMATION OF STATES AND INPUT IN LINEAR STRUCTURAL DYNAMICS

Eliz-Mari Lourens[1], **Geert Lombaert**[1], **Costas Papadimitriou**[2] **and Guido De Roeck**[1]

[1]K.U. Leuven
Department of Civil Engineering, Kasteelpark Arenberg 40, B-3001 Leuven, Belgium
e-mail: elizmari.lourens@bwk.kuleuven.be

[2] University of Thessaly
Department of Mechanical Engineering, Volos 38334, Greece

Keywords: State estimation, Response prediction, Input estimation, Kalman filter, Force identification.

Abstract. *The problem of jointly estimating the input forces and states of a structure from a limited number of acceleration measurements is addressed. Utilizing a model-based joint input-state estimation algorithm originally developed for optimal control problems, minimum-variance unbiased estimates of the modal displacements and velocities of a structure as well as the dynamic forces causing these responses, are obtained. The proposed algorithm requires no prior information on the dynamic evolution of the input forces, is easy to implement, and allows online application. Its accuracy and effectiveness are demonstrated using data from a laboratory experiment on an instrumented steel beam and an in situ experiment on a footbridge.*

1 INTRODUCTION

In civil engineering state estimation refers to a model-based identification of quantities (e.g. displacements) that allow a complete description of the state of a structure from vibration response data. State estimators, among which the well-known Kalman filter and its variants, have been proposed for structural systems behaving both linearly and nonlinearly. A small survey is given by Ching et al. in [3]. The state estimates can be used for a variety of purposes including the prediction of stresses and fatigue loading, real-time structural health monitoring, structural control, the determination of response in critical joints, the verification of design calculations, etc. Examples include the work by Papadimitriou et al. [11], in which the Kalman filter is used as part of a methodology for estimating the damage accumulation in a structure due to fatigue from output-only vibration measurements at a limited number of locations. Ching and Beck [2] estimated the unknown states of a structure using a Kalman smoother in an application concerning reliability estimation for serviceability limit states. Smyth and Wu [15] proposed a multi-rate Kalman filter for the fusion of measured displacement and acceleration data sampled at different rates. The filter is designed to circumvent problems related to the integration of accelerometer or the differentiation of displacement data in situations where both these response quantities are available for system monitoring or damage detection. Hernandez and Bernal [9] designed a state estimator for structural dynamic systems based on the assumption that the primary source of uncertainty in the predicted state derives from errors in the matrices of the state-space model. Their estimator distinguishes itself from the related robust Kalman filter (RKF) in that it is derived on deterministic grounds, assumes no process/measurement noise and is significantly simpler to implement. It has been used as part of an iterative scheme for model updating in [7], and has been extended to nonlinear systems in [8], where it was used to estimate the states in a damaged seven-story building from a limited number of acceleration measurements.

In this contribution a joint input-state estimation algorithm is used to identify modal displacements, velocities and input forces using data from a laboratory experiment on an instrumented steel beam as well as an in situ experiment on a footbridge. The algorithm, developed by Gillijns and De Moor [6], has the structure of a Kalman filter, except that the true value of the input is replaced by an optimal estimate. It distinguishes itself from the state estimation methods mentioned above in that the excitation is assumed unknown, whilst there are also no assumptions made about its dynamic evolution (e.g. broadband, so that it can be modeled as a zero mean stationary white process). When the positions of the applied forces are known, the algorithm can be used to jointly estimate the states and input forces. Conversely, when the positions of the applied forces are unknown, a set of equivalent forces is identified. In the latter case the points of application of the forces are randomly chosen and equivalent forces, that would produce the same measured response, are identified at all chosen locations. It is this latter case, corresponding to pure state estimation in the absence of any a priori information regarding the positions or frequency characteristics of the input forces, that will be considered in this paper.

2 MATHEMATICAL FORMULATION

2.1 Equations of motion

Consider the continuous-time governing equations of motion for a linear system discretized in space:

$$\mathbf{M}\ddot{\mathbf{u}}(t) + \mathbf{C}\dot{\mathbf{u}}(t) + \mathbf{K}\mathbf{u}(t) = \mathbf{f}(t) = \mathbf{S}_{\mathrm{p}}(t)\mathbf{p}(t) \tag{1}$$

where $\mathbf{u}(t) \in \mathbb{R}^{n_{\mathrm{DOF}}}$ is the vector of displacement, $\mathbf{M}$, $\mathbf{C}$ and $\mathbf{K} \in \mathbb{R}^{n_{\mathrm{DOF}} \times n_{\mathrm{DOF}}}$ denote the mass, damping and stiffness matrix, respectively, and $\mathbf{f}(t)$ is the excitation vector. The excitation is factorized into an input force influence matrix $\mathbf{S}_{\mathrm{p}}(t) \in \mathbb{R}^{n_{\mathrm{DOF}} \times n_{\mathrm{p}}}$, and the vector $\mathbf{p}(t) \in \mathbb{R}^{n_{\mathrm{p}}}$ representing the n_{p} force time histories. Each column of the matrix $\mathbf{S}_{\mathrm{p}}$ gives the spatial distribution of the load time history in the corresponding element of the vector $\mathbf{p}$. In the case of a point load, the column of $\mathbf{S}_{\mathrm{p}}$ has only a limited number of non-zero entries corresponding to the distribution of the load over the degrees of freedom of the FE mesh. In the case of stochastic loading e.g. due to wind, the columns of the matrix $\mathbf{S}_{\mathrm{p}}$ may result from the decomposition of the load in uncorrelated contributions, e.g. by applying a Karhunen-Loève decomposition [5]. The undamped eigenvalue problem corresponding to (1) reads:

$$\mathbf{K\Phi} = \mathbf{M\Phi\Omega}^2$$

where $\mathbf{\Phi} \in \mathbb{R}^{n_{\mathrm{DOF}} \times n_{\mathrm{DOF}}}$ collects as columns the eigenvectors $\mathbf{\Phi}_j$, and $\mathbf{\Omega}$ is a diagonal matrix containing the eigenfrequencies ω_j in $\mathrm{rad/s}$. Introducing the coordinate transformation $\mathbf{u}(t) = \mathbf{\Phi z}(t)$ and premultiplying by $\mathbf{\Phi}^{\mathrm{T}}$ yields:

$$\mathbf{\Phi}^{\mathrm{T}}\mathbf{M\Phi}\ddot{\mathbf{z}}(t) + \mathbf{\Phi}^{\mathrm{T}}\mathbf{C\Phi}\dot{\mathbf{z}}(t) + \mathbf{\Phi}^{\mathrm{T}}\mathbf{K\Phi z}(t) = \mathbf{\Phi}^{\mathrm{T}}\mathbf{S}_{\mathrm{p}}(t)\mathbf{p}(t). \tag{2}$$

These equations can be decoupled by using the orthogonality conditions corresponding to a set of mass-normalized eigenvectors, $\mathbf{\Phi}^{\mathrm{T}}\mathbf{M\Phi} = \mathbf{I}$ and $\mathbf{\Phi}^{\mathrm{T}}\mathbf{K\Phi} = \mathbf{\Omega}^2$, and assuming proportional damping:

$$\mathbf{\Phi}^{\mathrm{T}}\mathbf{C\Phi} = \mathbf{\Gamma}$$

where $\mathbf{\Gamma}$ is a diagonal matrix containing the terms $2\xi_j\omega_j$, and ξ denotes a modal damping ratio. The decoupled governing equations of motion in modal coordinates then become:

$$\ddot{\mathbf{z}}(t) + \mathbf{\Gamma}\dot{\mathbf{z}}(t) + \mathbf{\Omega}^2\mathbf{z}(t) = \mathbf{\Phi}^{\mathrm{T}}\mathbf{S}_{\mathrm{p}}(t)\mathbf{p}(t). \tag{3}$$

2.2 Continuous-time state-space model

By introducing the state vector $\mathbf{x}(t) \in \mathbb{R}^{n_{\mathrm{s}} \times n_{\mathrm{s}}}$, $n_{\mathrm{s}} = 2n_{\mathrm{DOF}}$:

$$\mathbf{x}(t) = \begin{pmatrix} \mathbf{u}(t) \\ \dot{\mathbf{u}}(t) \end{pmatrix}$$

and utilizing the superficial identity $\mathbf{M}\dot{\mathbf{u}} - \mathbf{M}\dot{\mathbf{u}} = \mathbf{0}$, the second-order equations of motion (1) can be written as a first-order continuous-time state equation:

$$\dot{\mathbf{x}}(t) = \mathbf{A}_{\mathrm{c}}\mathbf{x}(t) + \mathbf{B}_{\mathrm{c}}\mathbf{p}(t) \tag{4}$$

where the system matrices $\mathbf{A}_{\mathrm{c}} \in \mathbb{R}^{n_{\mathrm{s}} \times n_{\mathrm{s}}}$ and $\mathbf{B}_{\mathrm{c}} \in \mathbb{R}^{n_{\mathrm{s}} \times n_{\mathrm{p}}}$ are defined as:

$$\mathbf{A}_{\mathrm{c}} = \begin{bmatrix} \mathbf{0} & \mathbf{I} \\ -\mathbf{M}^{-1}\mathbf{K} & -\mathbf{M}^{-1}\mathbf{C} \end{bmatrix}, \ \mathbf{B}_{\mathrm{c}} = \begin{bmatrix} \mathbf{0} \\ \mathbf{M}^{-1}\mathbf{S}_{\mathrm{p}} \end{bmatrix}.$$

Consider next the measurement data vector $\mathbf{d}(t) \in \mathbb{R}^{n_{\mathrm{d}}}$, containing the n_{d} observed quantities expressed as a linear combination of the displacement, velocity and acceleration vectors as follows:

$$\mathbf{d}(t) = \mathbf{S}_{\mathrm{a}}\ddot{\mathbf{u}}(t) + \mathbf{S}_{\mathrm{v}}\dot{\mathbf{u}}(t) + \mathbf{S}_{\mathrm{d}}\mathbf{u}(t) \tag{5}$$

where $\mathbf{S}_\mathrm{a}$, $\mathbf{S}_\mathrm{v}$ and $\mathbf{S}_\mathrm{d} \in \mathbb{R}^{n_\mathrm{d} \times n_\mathrm{DOF}}$ are selection matrices for acceleration, velocity and displacement, respectively, in which the locations of the measurements and/or difference relations can be specified. Using equation (1) and the definition of the state vector, equation (5) can be transformed into its state-space form:

$$\mathbf{d}(t) = \mathbf{G}_\mathrm{c}\mathbf{x}(t) + \mathbf{J}_\mathrm{c}\mathbf{p}(t) \tag{6}$$

with the output influence matrix $\mathbf{G}_\mathrm{c} \in \mathbb{R}^{n_\mathrm{d} \times n_\mathrm{s}}$ and direct transmission matrix $\mathbf{J}_\mathrm{c} \in \mathbb{R}^{n_\mathrm{d} \times n_\mathrm{p}}$ defined as:

$$\mathbf{G}_\mathrm{c} = \left[\begin{array}{cc} \mathbf{S}_\mathrm{d} - \mathbf{S}_\mathrm{a}\mathbf{M}^{-1}\mathbf{K} & \mathbf{S}_\mathrm{v} - \mathbf{S}_\mathrm{a}\mathbf{M}^{-1}\mathbf{C} \end{array}\right], \; \mathbf{J}_\mathrm{c} = \left[\mathbf{S}_\mathrm{a}\mathbf{M}^{-1}\mathbf{S}_\mathrm{p}\right].$$

Equations (4) and (6) together form the continuous-time state-space model for the full-order system described by equation (1). If a model reduction is performed, i.e. if the dynamics of the system are represented by a reduced number n_m of modal coordinates $\mathbf{z}(t) \in \mathbb{R}^{n_\mathrm{m}}$ as $\mathbf{u}(t) = \mathbf{\Phi}_\mathrm{r}\mathbf{z}(t)$, $\mathbf{\Phi}_\mathrm{r} \in \mathbb{R}^{n_\mathrm{DOF} \times n_\mathrm{m}}$, the state vector is transformed accordingly:

$$\mathbf{x}(t) = \begin{bmatrix} \mathbf{\Phi}_\mathrm{r} & \mathbf{0} \\ \mathbf{0} & \mathbf{\Phi}_\mathrm{r} \end{bmatrix} \boldsymbol{\zeta}(t).$$

The modal state vector $\boldsymbol{\zeta}(t) \in \mathbb{R}^{2n_\mathrm{m}}$ now collects the modal coordinates:

$$\boldsymbol{\zeta}(t) = \begin{pmatrix} \mathbf{z}(t) \\ \dot{\mathbf{z}}(t) \end{pmatrix}$$

and the expressions for the reduced-order continuous-time system matrices $\mathbf{A}_\mathrm{c} \in \mathbb{R}^{2n_\mathrm{m} \times 2n_\mathrm{m}}$, $\mathbf{B}_\mathrm{c} \in \mathbb{R}^{2n_\mathrm{m} \times n_\mathrm{p}}$, $\mathbf{G}_\mathrm{c} \in \mathbb{R}^{n_\mathrm{d} \times 2n_\mathrm{m}}$ and $\mathbf{J}_\mathrm{c} \in \mathbb{R}^{n_\mathrm{d} \times n_\mathrm{p}}$ in the modal state-space model:

$$\begin{aligned} \dot{\boldsymbol{\zeta}}(t) &= \mathbf{A}_\mathrm{c}\boldsymbol{\zeta} + \mathbf{B}_\mathrm{c}\mathbf{p}(t) && (7) \\ \mathbf{d}(t) &= \mathbf{G}_\mathrm{c}\boldsymbol{\zeta}(t) + \mathbf{J}_\mathrm{c}\mathbf{p}(t) && (8) \end{aligned}$$

can be shown to reduce to:

$$\begin{aligned} \mathbf{A}_\mathrm{c} &= \begin{bmatrix} \mathbf{0} & \mathbf{I} \\ -\mathbf{\Omega}^2 & -\mathbf{\Gamma} \end{bmatrix} && (9) \\ \mathbf{B}_\mathrm{c} &= \begin{bmatrix} \mathbf{0} \\ \mathbf{\Phi}^\mathrm{T}\mathbf{S}_\mathrm{p} \end{bmatrix} && (10) \\ \mathbf{G}_\mathrm{c} &= \left[\begin{array}{cc} \mathbf{S}_\mathrm{d}\mathbf{\Phi} - \mathbf{S}_\mathrm{a}\mathbf{\Phi}\mathbf{\Omega}^2 & \mathbf{S}_\mathrm{v}\mathbf{\Phi} - \mathbf{S}_\mathrm{a}\mathbf{\Phi}\mathbf{\Gamma} \end{array}\right] && (11) \\ \mathbf{J}_\mathrm{c} &= \left[\mathbf{S}_\mathrm{a}\mathbf{\Phi}\mathbf{\Phi}^\mathrm{T}\mathbf{S}_\mathrm{p}\right]. && (12) \end{aligned}$$

2.3 Discrete-time state-space model

Using a sampling rate of $1/\Delta t$, the state-space model of equations (4) and (6) - or the modal model of equations (7) and (8) - can be discretized to yield its discrete-time equivalent:

$$\begin{aligned} \mathbf{x}_{k+1} &= \mathbf{A}\mathbf{x}_k + \mathbf{B}\mathbf{p}_k && (13) \\ \mathbf{d}_k &= \mathbf{G}\mathbf{x}_k + \mathbf{J}\mathbf{p}_k && (14) \end{aligned}$$

where $\mathbf{x}_k = \mathbf{x}(k\Delta t)$, $\mathbf{d}_k = \mathbf{d}(k\Delta t)$, $k = 1, \ldots, N$ and:

$$\mathbf{A} = e^{\mathbf{A}_\mathrm{c}\Delta t},\ \mathbf{B} = [\mathbf{A} - \mathbf{I}]\mathbf{A}_\mathrm{c}^{-1}\mathbf{B}_\mathrm{c},\ \mathbf{G}_\mathrm{c} = \mathbf{G},\ \mathbf{J}_\mathrm{c} = \mathbf{J}.$$

3 JOINT INPUT-STATE ESTIMATION

In this section the joint input-state estimation algorithm developed by Gillijns and De Moor for linear systems with direct feedthrough of the unknown input to the output [6] is presented. Having direct feedthrough corresponds, from a structural dynamics point of view, to the situation where the measured quantities are accelerations, which is commonly the case. More details on the derivation of this algorithm and a proof of optimality, in a minimum-variance unbiased sense, can be found in [6].

The linear system under consideration is the discrete-time state-space system of equations (13) and (14), supplemented with random variables $\boldsymbol{w}_k$ and $\boldsymbol{v}_k$ representing the stochastic system and measurement noise, respectively:

$$\begin{aligned} \mathbf{x}_{k+1} &= \mathbf{A}\mathbf{x}_k + \mathbf{B}\mathbf{p}_k + \boldsymbol{w}_k && (15)\\ \mathbf{d}_k &= \mathbf{G}\mathbf{x}_k + \mathbf{J}\mathbf{p}_k + \boldsymbol{v}_k. && (16) \end{aligned}$$

The noise vectors $\boldsymbol{w}_k \in \mathbb{R}^{n_\mathrm{s}}$ and $\boldsymbol{v}_k \in \mathbb{R}^{n_\mathrm{d}}$ are assumed to be mutually uncorrelated, zero-mean, white signals with known covariance matrices $\mathbf{Q} = \mathbb{E}\{\boldsymbol{w}_k\boldsymbol{w}_l^T\} \geq \mathbf{0}$ and $\mathbf{R} = \mathbb{E}\{\boldsymbol{v}_k\boldsymbol{v}_l^T\} > \mathbf{0}$. Results can easily be generalized to the case where $\mathbf{w}_k$ and $\mathbf{v}_k$ are correlated by applying a preliminary transformation to the system [1, 6]. Results can also be generalized to systems with both known and unknown inputs [6].

A state estimate $\hat{\mathbf{x}}_{k|l}$ is defined as an estimate of $\mathbf{x}_k$ given $\{\mathbf{d}_n\}_{n=0}^{l}$ and its error covariance matrix $\mathbf{P}_{k|l}$ as $\mathbb{E}[(\mathbf{x}_k - \hat{\mathbf{x}}_{k|l})(\mathbf{x}_k - \hat{\mathbf{x}}_{k|l})^T]$. An initial unbiased state estimate $\hat{\mathbf{x}}_{0|-1}$ and its covariance matrix $\mathbf{P}_{0|-1}$ is assumed known. The initial state estimate $\hat{\mathbf{x}}_0$ is assumed independent of $\mathbf{w}_k$ and $\mathbf{v}_k$ for all k. Finally, it is assumed that the rank of the direct transmission matrix $\mathbf{J}$ equals the number of applied forces n_p, and that the pair $(\mathbf{A}, \mathbf{G})$ is observable. It can be proven that the latter two assumptions are almost always valid when dealing with structural dynamic systems.

The filter is initialized using the initial state and its variance, $\hat{\mathbf{x}}_{0|-1}$ and $\mathbf{P}_{0|-1}$; hereafter it computes the force and state estimates recursively in three steps: the input estimation, the measurement update, and the time update:

Input estimation:

$$\begin{aligned} \tilde{\mathbf{R}}_{[k]} &= \mathbf{G}\mathbf{P}_{[k|k-1]}\mathbf{G}^\mathrm{T} + \mathbf{R} && (17)\\ \boldsymbol{\mathcal{M}}_{[k]} &= \left(\mathbf{J}^\mathrm{T}\tilde{\mathbf{R}}_{[k]}^{-1}\mathbf{J}\right)^{-1}\mathbf{J}^\mathrm{T}\tilde{\mathbf{R}}_{[k]}^{-1} && (18)\\ \hat{\mathbf{p}}_{[k|k]} &= \boldsymbol{\mathcal{M}}_{[k]}\left(\mathbf{d}_{[k]} - \mathbf{G}\hat{\mathbf{x}}_{[k|k-1]}\right) && (19)\\ \mathbf{P}_{\mathbf{p}[k|k]} &= \left(\mathbf{J}^\mathrm{T}\tilde{\mathbf{R}}_{[k]}^{-1}\mathbf{J}\right)^{-1} && (20) \end{aligned}$$

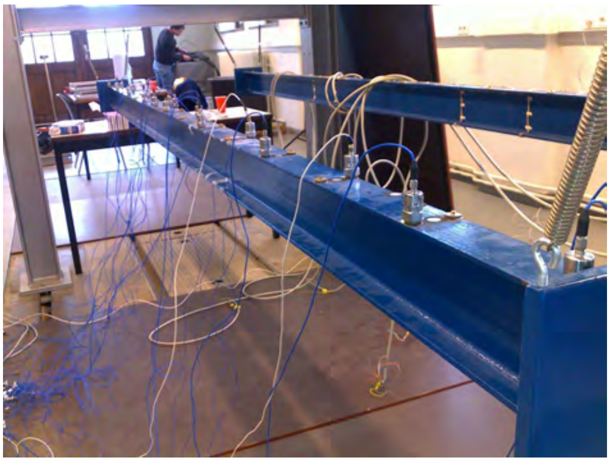

Figure 1: The measurement setup

Measurement update:

$$\mathbf{L}_{[k]} = \mathbf{P}_{[k|k-1]}\mathbf{G}^{\mathrm{T}}\tilde{\mathbf{R}}_{[k]}^{-1} \tag{21}$$

$$\hat{\mathbf{x}}_{[k|k]} = \hat{\mathbf{x}}_{[k|k-1]} + \mathbf{L}_{[k]}\left(\mathbf{d}_{[k]} - \mathbf{G}\hat{\mathbf{x}}_{[k|k-1]} - \mathbf{J}\mathbf{p}_{[k|k]}\right) \tag{22}$$

$$\mathbf{P}_{[k|k]} = \mathbf{P}_{[k|k-1]} - \mathbf{L}_{[k]}\left(\tilde{\mathbf{R}}_{[k]} - \mathbf{J}\mathbf{P}_{\mathbf{p}[k|k]}\mathbf{J}^{\mathrm{T}}\right)\mathbf{L}_{[k]}^{\mathrm{T}} \tag{23}$$

$$\mathbf{P}_{\mathbf{xp}[k|k]} = \mathbf{P}_{\mathbf{px}[k|k]}^{\mathrm{T}} = -\mathbf{L}_{[k]}\mathbf{J}\mathbf{P}_{\mathbf{p}[k|k]} \tag{24}$$

Time update:

$$\mathbf{x}_{[k+1|k]} = \mathbf{A}\hat{\mathbf{x}}_{[k|k]} + \mathbf{B}\hat{\mathbf{p}}_{[k|k]} \tag{25}$$

$$\mathbf{P}_{[k+1|k]} = \begin{bmatrix} \mathbf{A} & \mathbf{B} \end{bmatrix} \begin{bmatrix} \mathbf{P}_{[k|k]} & \mathbf{P}_{\mathbf{xp}[k|k]} \\ \mathbf{P}_{\mathbf{px}[k|k]} & \mathbf{P}_{\mathbf{p}[k|k]} \end{bmatrix} \begin{bmatrix} \mathbf{A}^{\mathrm{T}} \\ \mathbf{B}^{\mathrm{T}} \end{bmatrix} + \mathbf{Q} \tag{26}$$

It is mentioned that when $\mathbf{B} = \mathbf{J} = \mathbf{0}$, the Kalman filter is obtained. In the above, the system matrices are for ease of notation not indexed. The algorithm can, however, also be applied to time-variant systems by simply adding the appropriate subscripts, i.e. $\mathbf{A}_k$, $\mathbf{B}_k$, $\mathbf{G}_k$ and $\mathbf{J}_k$.

4 EXPERIMENTAL RESULTS

In this section the effectiveness of the proposed algorithm is illustrated by means of a laboratory experiment on an instrumented steel beam as well as an in situ experiment on a footbridge.

4.1 Laboratory experiment on a steel beam

A steel beam with an IPE100 cross section, a length of 3m, and plates of 150x150x15 mm welded to its ends, is suspended at both ends from a steel frame using flexible springs to simulate free-free boundary conditions. A series of accelerometers is placed along the beam to record its response to an impact force, applied with an instrumented hammer. The aim here is to use a subset of the measured accelerations to identify the remaining (measured) accelerations.

Vertical accelerations on the top flange of the beam were measured at 17 different cross sections using 19 accelerometers (PCB 338B35, sensitivity $\pm$ 100 $\mathrm{mV/g}$). The force was applied eccentrically with an impact hammer (PCB 086C03, mass 0.136 kg) at one of the free-free beam

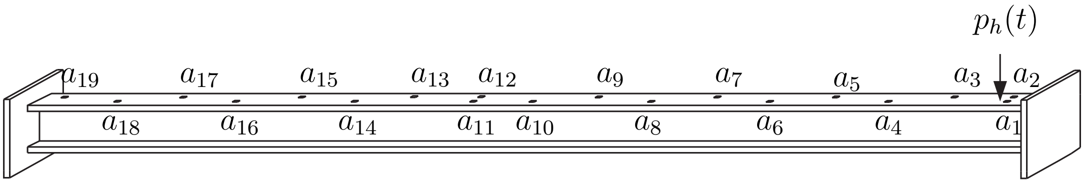

Figure 2: Positions of the sensors and applied force.

ends. The measurement setup and positions of the sensors and applied force are shown in figures 1 and 2. The modal parameters of the beam were identified in a Operational Modal Analysis with eXogenous inputs (OMAX) test [13] for the frequency range $0 - 900$ Hz. More details on this test and its results can be found in [10]. The identified modal parameters were used to tune the Young's modulus of the steel and the stiffness of the springs in a FE model. A comparison between the identified and computed eigenmodes is shown in table 1. Except for the torsional modes, whose contribution to the acceleration response considered is almost negligible, a good correspondence is found between the measured and experimental eigenfrequencies. All modes are very lightly damped with damping ratios below 0.5 % of critical.

	FEM	Experimental		
No.	f_{udi} [Hz]	f_{udi} [Hz]	ξ_i [%]	MAC [−]
1	1.780	1.771	0.36	0.99
2	2.787	2.701	0.19	1.00
3	3.106	4.917	0.41	0.99
4	31.56	30.81	0.12	0.99
5	61.51	60.90	0.05	1.00
6	74.94	71.20	0.32	0.98
7	136.0	128.1	0.15	0.99
8	174.6	173.9	0.04	1.00
9	216.9	200.5	0.12	0.98
10	319.1	293.5	0.13	0.97
11	341.9	341.0	0.02	1.00
12	443.3	402.6	0.11	0.98
13	589.8	535.4	0.12	0.95
14	557.4	556.7	0.03	1.00
15	807.1	805.6	0.04	1.00

Table 1: Comparison between the undamped eigenfrequencies f_{udi} of the FE model of the beam and those that were experimentally obtained. The experimental damping ratios ξ_i and MAC values between the measured mass-normalized mode shapes and the ones obtained from the FE model, are shown as well.

The 15 modes from the FE model, consisting of 3 rigid body, 5 bending and 7 torsional modes, are used to construct a reduced-order modal state-space model of the beam. Originally sampled at 10 kHz, all data used in the inverse calculations are resampled at a lower rate in order to include only frequencies within the range of the identified modes. Using a decimation factor of 5, the data is low-pass filtered using a Chebychev Type I filter at 800Hz and subsequently resampled at 2 kHz.

Of the 19 measured accelerations, 10 are used to identify the modal states and input forces, from which the acceleration (or displacement, strain, etc.) at any other point in the structure can be calculated as $\hat{\mathbf{d}} = \mathbf{G}\hat{\mathbf{x}} + \mathbf{J}\hat{\mathbf{p}}$. It is assumed that no a priori information on the positions of the forces is available and a set of equivalent forces are assumed to act at all measurement locations used for the identification, i.e. at positions a_1, a_3, a_4, a_6, a_9, a_{11}, a_{15}, a_{17}, a_{18} and a_{19}. The accelerations identified at the remaining locations are compared to the measured data during a period of 1 s. The covariance matrices $\mathbf{Q}$, $\mathbf{R}$ and $\mathbf{P}_{0|-1}$ are assigned values of $1e^{-10}$, $1e^{-1}$ and $1e^{-10}$ on the diagonal, respectively. In accordance with what they represent, these values are chosen so as to have the order of the square roots of the diagonal elements of $\mathbf{R}$ and $\mathbf{Q}$ corresponding to a small percentage of the highest peaks in the measured response and the states (displacements/velocities), respectively. The small values in $\mathbf{P}_{0|-1}$ indicate a low level of uncertainty regarding the initial state estimate. It is mentioned that the results are, however, not strongly influenced by these values and similar results are obtained for a large range of $\mathbf{Q}$, $\mathbf{R}$ and $\mathbf{P}_{0|-1}$.

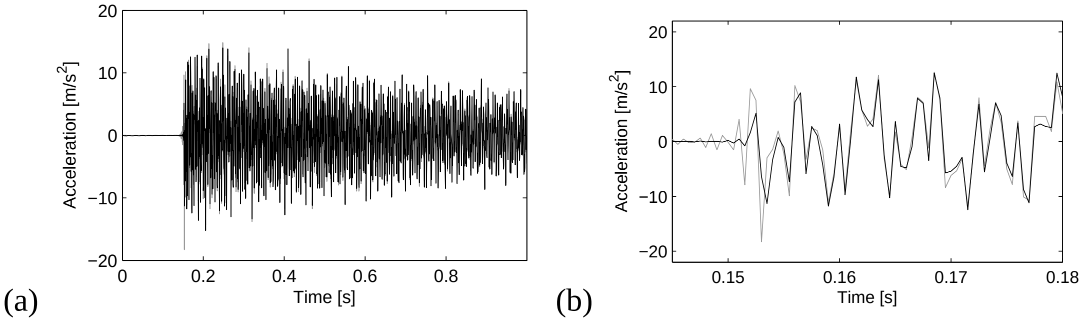

Figure 3: a) Complete and b) detail of the measured (black) and identified (grey) time history of the acceleration at sensor a_7.

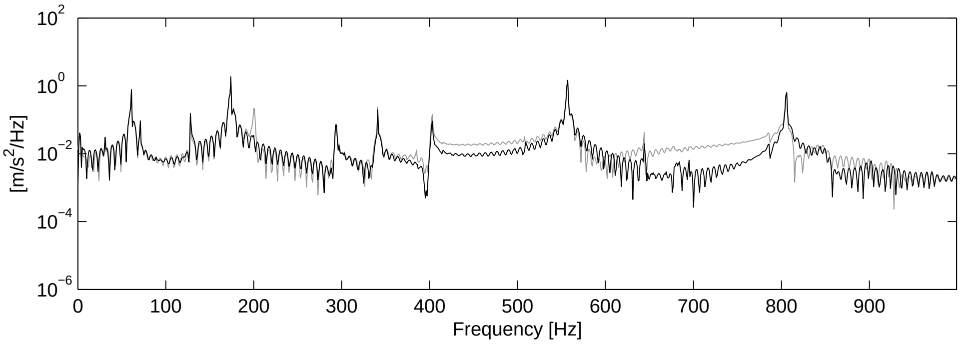

Figure 4: Frequency spectrum of the measured (black) and identified (grey) acceleration at sensor a_7.

Figures 3 to 8 show the results obtained when the beam is excited with the hammer at $t = \pm 0.15s$. Measured accelerations are plotted against those identified for three randomly chosen locations, namely a_7, a_{13} and a_{16}. The accelerations are compared in the time as well as in the frequency domain, and a detail of the acceleration time history at the time of impact is presented as well. A good reconstruction is obtained at all 3 locations.

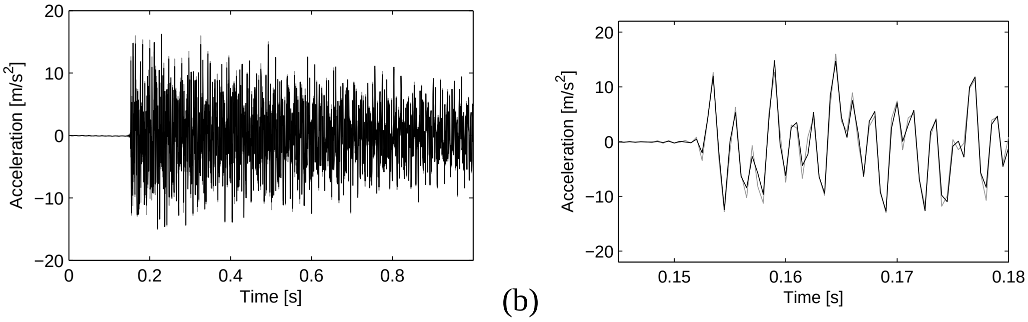

(a) (b)

Figure 5: a) Complete and b) detail of the measured (black) and identified (grey) time history of the acceleration at sensor a_{13}.

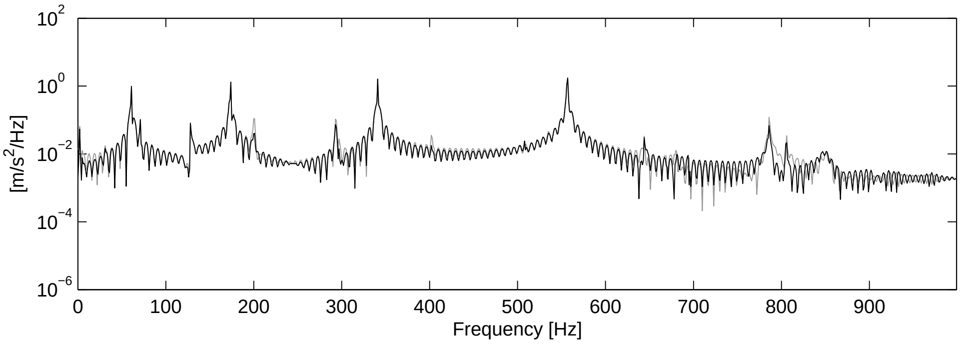

Figure 6: Frequency spectrum of the measured (black) and identified (grey) acceleration at sensor a_{13}.

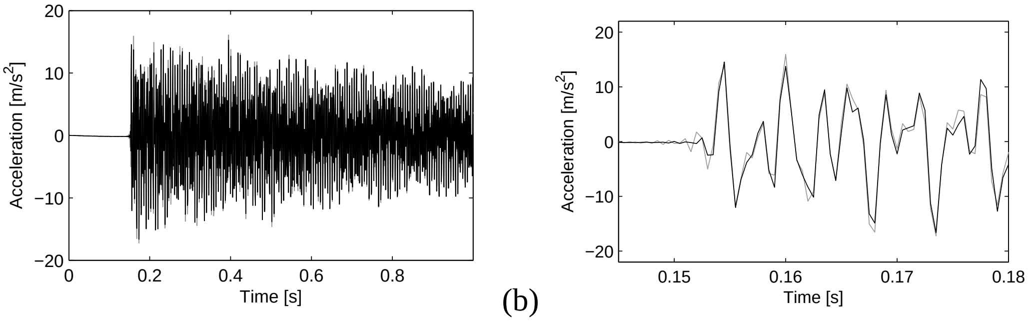

(a) (b)

Figure 7: a) Complete and b) detail of the measured (black) and identified (grey) time history of the acceleration at sensor a_{16}.

4.2 In situ experiment on a footbridge

Analogous to the previous test case, a subset of the accelerations measured during an in situ test on a footbridge is used to identify modal states and a set of equivalent forces. The identified modal states and forces are subsequently used to calculate the accelerations at the remaining measured positions and a comparison is made. The footbridge, depicted in figure 9, is located in Wetteren (Belgium), and has been used as an in situ test case for Operational Modal Analysis (OMA) [12] and previously mentioned OMAX techniques. It is a steel bridge that crosses the E40 highway between Brussels and Ghent at Wetteren, with a short and long bow-string span of 30.33m and 75.23m, respectively.

For the OMAX tests, measurements have been performed in a total number of 72 channels

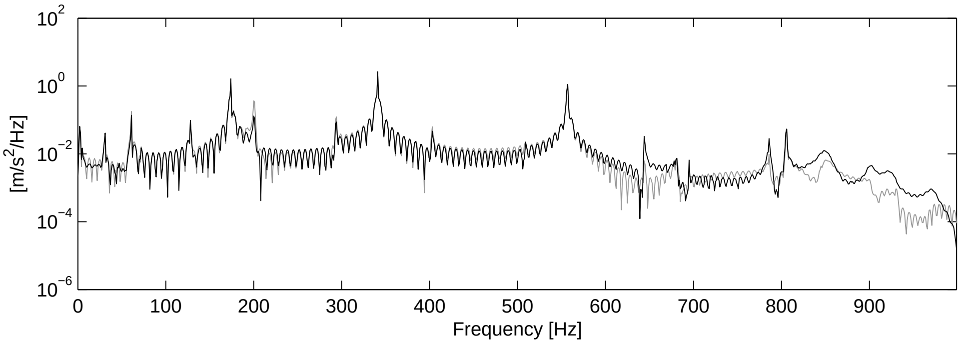

Figure 8: Frequency spectrum of the measured (black) and identified (grey) acceleration at sensor a_{16}.

Figure 9: The footbridge in Wetteren, Belgium.

during different setups. The locations of the sensors are shown in figure 10. The data used in the current example was obtained during excitation of the bridge by means of a drop weight system. The drop weight was applied at point 34, in the vertical direction, and during the setup accelerations were measured in 16 channels. In the following, 8 of the measured accelerations will be used to identify the modal states and to reconstruct the accelerations at the 8 remaining locations. Equivalent loads are assumed to act in the directions and at the locations of the 8 measured accelerations. The actual load on the structure consists of the drop weight as well as a high level of ambient excitation due to traffic underneath the bridge and wind.

Of the 16 measured accelerations, 4 vertical and 4 lateral accelerations were identified as optimal for the identification. These are the vertical accelerations in points 2, 3, 24 and 34 on the bridge deck, the lateral accelerations on the bridge deck at points 14 and 19, and the lateral accelerations of the bow at points 45 and 48. With the optimal 8 accelerations as input, the proposed algorithm is used to identify 7 ‘unmeasured’ vertical accelerations at points 8, 12, 14, 25, 30, 36 and 41 on the bridge deck, and the lateral acceleration at point 12 on the bow.

The system matrices are constructed from an updated finite element (FE) model of the bridge. In the FE model, developed using the FE program ANSYS, the bridge deck is modeled using the ANSYS shell element SHELL63. The longitudinal and transversal beams of the bridge deck, as well as the bows, connections of the bows, and supports, are modeled using the beam element BEAM188. A 3D truss element, LINK8, is used to model the cables, taking into account the effective stiffness E_{eff} of the cable based on the tensile cable force. The model has a total of

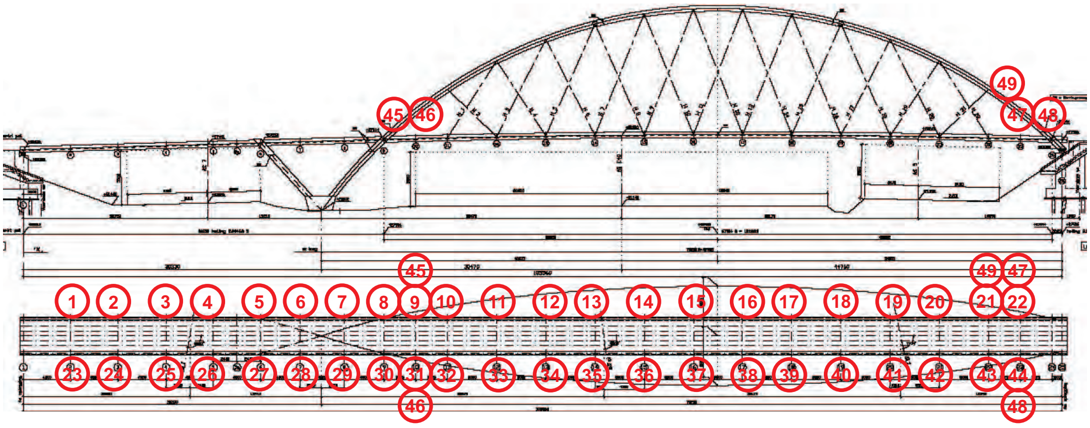

Figure 10: Positions of the sensors.

16007 nodes and 2210 elements. The first 4 modes calculated with the model are shown in figure 11.

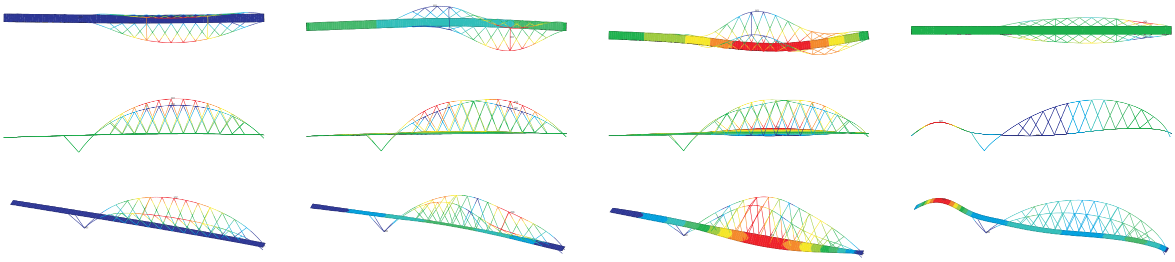

Figure 11: Results from the FE modal analysis for the first 4 modes. Top: transversal displacements, middle: vertical displacements, bottom: displacement vector sum.

The FE model is updated using a set of experimental modal parameters obtained during an OMAX test [14] in which the actuator was a pneumatic artificial muscle (PAM) developed by the Acoustics and Vibration Research Group of the Vrije Universiteit Brussel [4]. Table 2 presents a comparison between the eigenfrequencies of the updated FE model and those that were identified experimentally. The experimental damping ratios as well as the MAC values between the mass-normalized mode shapes and the ones obtained from the FE model are shown in the table. The 22 eigenmodes of the FE model, in conjunction with the corresponding identified modal damping ratios, are used to construct a reduced-order modal state-space model of the structure. As before, all data used in the inverse calculations are resampled at a lower rate. Using a decimation factor of 23, the data is low-pass filtered using a Chebychev Type I filter at 17.39 Hz and subsequently resampled at 43.48 Hz. A period of 9 s, in which the impact from the drop-weight is applied at $t = 2.3\ s$, is analysed.

As in the previous examples equivalent forces are assumed to act at all measurement locations. The covariance matrices $\mathbf{Q}$, $\mathbf{R}$ and $\mathbf{P}_{0|-1}$ are assigned values of $1e^{-10}$, $1e^{-1}$ and $1e^{-10}$ on the diagonal, respectively. In figures 12 to 15, 4 of the 8 identified accelerations are compared to those measured. The results are for the vertical accelerations at points 12, 25 and 41 (figures 12 to 14), and the lateral acceleration at point 12 (figure 15).

The identified accelerations are of lesser quality than those in the laboratory experiment, which can partly be explained by the fact that the updated FE model of the footbridge represents the structure considerably less accurately than the one used in the laboratory experiment (cfr.

	FEM	Experimental				FEM	Experimental		
No.	f_{udi} [Hz]	f_{udi} [Hz]	ξ_i [%]	MAC [$-$]	No.	f_{udi} [Hz]	f_{udi} [Hz]	ξ_i [%]	MAC [$-$]
1	0.739	0.693	1.05	0.92	12	8.599	8.307	1.18	0.79
2	1.739	1.669	0.23	0.87	13	10.395	9.967	1.10	0.65
3	2.363	2.195	0.50	0.98	14	11.397	10.475	0.64	0.76
4	3.250	3.731	0.55	0.71	15	11.864	11.214	0.78	0.85
5	3.833	3.838	0.49	0.80	16	11.625	11.821	1.68	0.79
6	4.897	4.480	0.76	0.84	17	13.147	12.728	0.35	0.70
7	5.370	5.154	0.44	0.86	18	13.255	12.863	0.72	0.89
8	6.377	6.117	0.27	0.88	19	14.479	13.530	0.72	0.62
9	6.662	6.321	0.50	0.92	20	15.312	14.810	0.41	0.80
10	6.991	6.605	0.58	0.88	21	16.648	16.502	0.53	0.82
11	8.028	7.488	0.70	0.82	22	18.358	17.833	0.28	0.88

Table 2: Comparison between the undamped eigenfrequencies f_{udi} of the updated FE model and those that were experimentally obtained in an OMAX test using the PAM. The experimental damping ratios ξ_i and MAC values between the measured mass-normalized mode shapes and the ones obtained from the FE model, are shown as well.

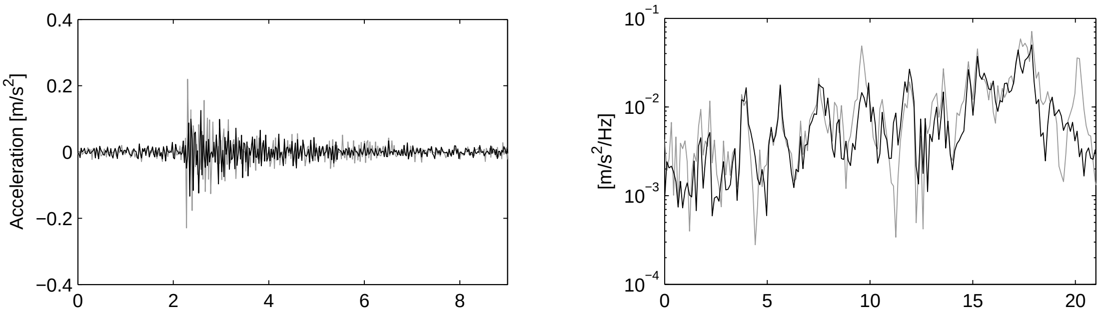

(a) (b)

Figure 12: a) Time history and b) frequency spectrum of the measured (black) and identified (grey) vertical acceleration at point 12.

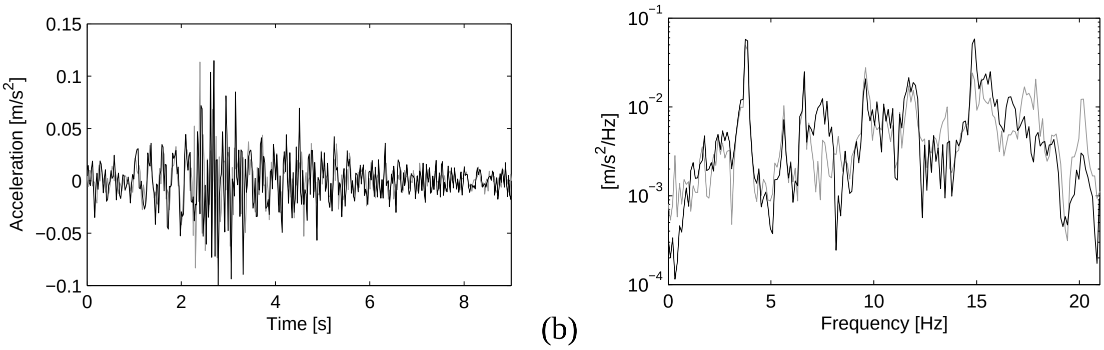

(a) (b)

Figure 13: a) Time history and b) frequency spectrum of the measured (black) and identified (grey) vertical acceleration at point 25.

MAC values in tables 1 and 2). Also, the number of sensors used is small compared to the geometrical and modal complexity of the footbridge. Taking these circumstances into account

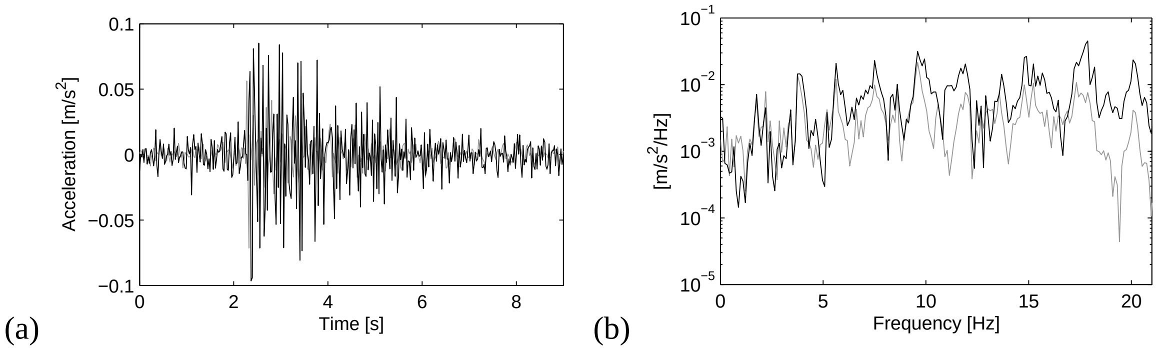

Figure 14: a) Time history and b) frequency spectrum of the measured (black) and identified (grey) vertical acceleration at point 41.

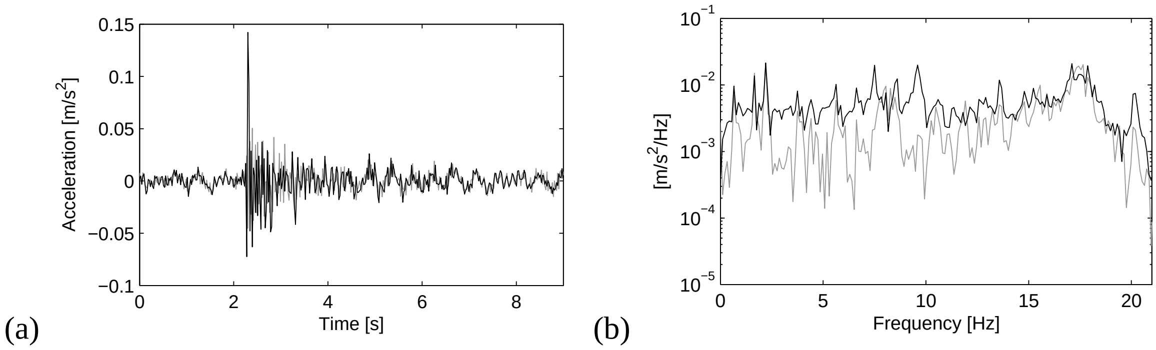

Figure 15: a) Time history and b) frequency spectrum of the measured (black) and identified (grey) lateral acceleration at point 12.

the identification is in fact very reasonable, especially those in the vertical direction. Moreover, the accuracy of the identification is similar for both the ambient part of the acceleration from $t = 0 - 2.3\ s$, where the vibrations are caused by low amplitude traffic loads, and the remaining stronger intensity part of the acceleration caused by the drop weight. The identification of the lateral acceleration is considerably less good between the resonance frequencies (cfr. figure 15b), but the dominant frequency components are still well identified. It can be concluded that the proposed algorithm performs well even when a significant amount of modeling error is present.

5 CONCLUSIONS

An existing model-based joint input-state estimation algorithm requiring no prior information on the dynamic evolution of the input forces, was used to estimate the state of a structure from a limited number of acceleration measurements. The algorithm's accuracy and applicability were tested using data from a laboratory experiment on an instrumented steel beam as well as an in situ experiment on a footbridge. It is concluded that the algorithm is capable of accurately estimating the state of a structure from a limited number of noise-contaminated acceleration measurements, also when a relatively high level of modeling error is present and no prior information on the positions or nature of the input forces is available.

REFERENCES

[1] B.D.O. Anderson and J.B. Moore. *Optimal filtering*. Prentice Hall, Englewood Cliffs, New Jersey, 1979.

[2] J. Ching and J.L. Beck. Real-time reliability estimation for serviceability limit states in structures with uncertain dynamic excitation and incomplete output data. *Probabilistic Engineering Mechanics*, 22:50–62, 2007.

[3] J. Ching, J.L. Beck, and K.A. Porter. Bayesian state and parameter estimation of uncertain dynamical systems. *Probabilistic Engineering Mechanics*, 21:81–96, 2006.

[4] K. Deckers, P. Guillaume, D. Lefeber, G. De Roeck, and E. Reynders. Modal testing of bridges using low-weight pneumatic artificial muscle actuators. In *Proceedings of IMAC 26, the International Modal Analysis Conference*, Orlando, FL, February 2008. CD-ROM.

[5] R.G. Ghanem and P.D. Spanos. *Stochastic finite elements: a spectral approach*. Springer-Verlag, New York, 1991.

[6] S. Gillijns and B. De Moor. Unbiased minimum-variance input and state estimation for linear discrete-time systems with direct feedthrough. *Automatica*, 43:934–937, 2007.

[7] E.M. Hernandez and D. Bernal. An observer-based approach for model updating. In *Proceedings of IMAC XXIV International Modal Analysis Conference*, 2006.

[8] E.M. Hernandez and D. Bernal. State estimation in nonlinear structural systems with model uncertainties. In *Proceedings of IMAC XXV International Modal Analysis Conference*, 2007.

[9] E.M. Hernandez and D. Bernal. State estimation in structural systems with model uncertainties. *ASCE Journal of Engineering Mechanics*, 134(3):252–257, 2008.

[10] E. Lourens, E. Reynders, G. Lombaert, G. De Roeck, and G. Degrande. Dynamic force identification by means of state-augmentation: a combined deterministic-stochastic approach. In *Proceedings of ISMA2010 International Conference on Noise and Vibration Engineering*, pages 2069–2080, Leuven, Belgium, September 2010.

[11] C. Papadimitriou, C.-P. Fritzen, P. Kraemer, and E. Ntotsios. Fatigue predictions in entire body of metallic structures from a limited number of vibration sensors using kalman filtering. *Structural Control and Health Monitoring*, 2011. Published online in Wiley InterScience (www.interscience.wiley.com). DOI:10.1002/stc.395.

[12] B. Peeters and G. De Roeck. Reference-based stochastic subspace identification for output-only modal analysis. *Mechanical Systems and Signal Processing*, 13(6):855–878, 1999.

[13] E. Reynders and G. De Roeck. Reference-based combined deterministic-stochastic subspace identification for experimental and operational modal analysis. *Mechanical Systems and Signal Processing*, 22(3):617–637, 2008.

[14] E. Reynders, D. Degrauwe, G. De Roeck, F. Magalhães, and E. Caetano. Combined experimental-operational modal testing of footbridges. *ASCE Journal of Engineering Mechanics*, 136(6):687–696, 2010.

[15] A. Smyth and M. Wu. Multi-rate kalman filtering for the data fusion of displacement and acceleration response measurements in dynamic system monitoring. *Mechanical Systems and Signal Processing*, 21:706–723, 2007.

COMPDYN 2011
3rd ECCOMAS Thematic Conference on
Computational Methods in Structural Dynamics and Earthquake Engineering
M. Papadrakakis, M. Fragiadakis, V. Plevris (eds.)
Corfu, Greece, 25–28 May 2011

SYSTEM IDENTIFICATION OF A R/C BRIDGE BASED ON AMBIENT VIBRATIONS AND 3D NUMERICAL SIMULATIONS OF THE ENTIRE SOIL-STRUCTURE SYSTEM

A. Sextos[1], P. Faraonis[2], C. Papadimitriou[3], P. Panetsos[4]

[1] Aristotle University of Thessaloniki
54124, Thessaloniki, Greece
e-mail: asextos@civil.auth.gr

[2] Aristotle University of Thessaloniki
54124, Thessaloniki, Greece
e-mail: pfaraonis@civil.auth.gr

[3] University of Thessaly
38334, Volos, Greece
e-mail: costasp@uth.gr

[4] Egnatia Odos S.A.
57001, Thermi, Greece
e-mail: ppane@egnatia.gr

Keywords: system identification, model updating, ambient vibrations, soil-structure interaction, 3D finite element modeling, computational dynamics.

Abstract. *The scope of this paper is to identify the parameters affecting the dynamic response of an existing R/C bridge, based on low ambient amplitude vibration measurements and numerical predictions using complex finite element models. For this purpose, the instrumented, 2nd Kavala Bypass Ravine Bridge constructed along the Egnatia Motorway Greece is studied and a refined three- dimensional (3D) FEM is developed that takes into consideration the coupling and dynamic interaction of the overall superstructure-foundation-soil and deck-abutment-embankment system. The instrumentation schemes and the necessary algorithms applied for computing the modal characteristics of the bridge are discussed, while the modelling assumptions made for the soil-structure system are comparatively assessed and justified for various models of different levels of complexity. Given the large number of the system's degrees of freedom, a manual, modal-based FEM updating method is also presented. The results show good agreement between the measured and computationally predicted dynamic characteristics of the structure. They also show that the accurate estimation of the pier, deck and bearings stiffness is a key parameter for reliable system identification.*

1 INTRODUCTION

Structural health monitoring and identification of structural modes of existing civil engineering projects is nowadays a major component of system maintenance and management especially for highway transportation networks. The modal characteristics of structures can be evaluated either by identification systems that are based on ambient (i.e., due to traffic and wind) and earthquake-induced vibrations or by modal analysis of finite element models (FEMs). Important information can be derived by the comparative assessment between the results of the two methodologies as scientists can investigate the structural integrity of structures and also validate the reliability of the FEMs that are developed for the analysis, design and assessment of structures.

An identification system based on ambient vibrations involves the presence of factors imposing ambient vibrations to a structure, monitoring of the structural response (measured acceleration time histories) and the development of an appropriate mathematical algorithm. Such an algorithm uses the measured output data as an input for the prediction of the modal frequencies, modal damping ratios and mode shapes through classically damped or non-classically damped modal models**.** A significant number of methods [1] and the respective software have been developed for the identification of modal properties, based on ambient vibrations, both in the time and frequency domain. The methods, based on output measurements only, make the assumption that the input can be well represented by a vector white noise process. Recent developments are also reported in Peeters and De Roeck [2] and Basseville et al. [3] using time domain stochastic subspace identification methods, in Beck et al. [4] using time domain least-squares methods based on correlation functions of the output time histories, in Verboven [5], Gauberghe [6] and Brincker et al. [7] using frequency domain least-squares methods based on full cross-power spectral densities (CPSD), and in Peeters and Van der Auweraer [8] based on half spectra. Bayesian and maximum likelihood statistical methods have also been proposed, for example, in Katafygiotis and Yuen [9], Guillaume et al. [10] and Verboven [5].

On the other hand, the estimation of dynamic characteristics using modal-based analysis of finite element models requires appropriate software to carry out dynamic analysis. However, in the case of extended structures such as bridges, the compliance and damping of the supporting soil has to be taken into consideration as it may affect significantly both the dynamic characteristics of the soil-foundation-superstructure and the embankment-abutment-superstructure system. An efficient way to account for this phenomenon is to de-couple the problem into a kinematic and an inertial sub-structure (Mylonakis and Gazetas [11]). Alternatively, a holistic numerically modelling of the entire soil, structure and foundation system is also feasible (i.e. Wolf [12]).

Despite above advances, it is still quite common to observe differences between the measured dynamic characteristics of the structure and the dynamic characteristics predicted numerically by FEMs. For that reason, mathematical algorithms have been developed based on the identified modal characteristics (e.g. Mottershead and Friswell [13], Bohle and Fritzen [14], Teughels et al. [15], Lam et al. [16], Christodoulou and Papadimitriou [17]) that permit the re-estimation of the structural parameters of the finite element models and the minimization of the induced error. These algorithms use the identified modal data and formulate them as weighted least-squares problems in which the optimal values of the structural parameters of a FEM are obtained by minimizing a measure of the residuals between the measured and numerically predicted modal characteristics. Alternatively, the structural parameters of the finite element model can be automatically updated, based on the identified modal data, without the development of a mathematical algorithm. This automatic model updating procedure solely consists of a sequential parametric analysis for different values of the structural parameters, until the percentage of error between the measured and predicted modes is minimized. Both the aforementioned calibration procedures for model updating provide an insight into the epistemic uncertainties related to the simplified assumptions and idealizations inevitably made during the development of FEMs. These uncertainties include the uncertainty in the model topology, the uncertainty in the boundary conditions of the model and the uncertainty in the material properties.

Along these lines, the scope of this paper is to qualitatively and quantitatively validate the uncertainties associated with the modeling assumptions made and to estimate which of them influences most the reliability of the results, at least for the particular bridge studied. For that purpose, a modal identification approach based on ambient vibrations, three FEMs of different modeling complexity and two model updating methods (automatic and manual) were implemented. The description of the bridge, the methodology adopted and the comparative assessment of the results obtained are presented in the following.

2 DESCRITION OF THE BRIDGE STUDIED

2.1 Structural system

The 2nd Kavala Bypass Ravine Bridge, shown in Figure 1, is a newly built bridge located in Section 13.7 of Egnatia, a major 670km highway constructed on the traces of the ancient Roman path, crossing northern Greece from its western to its eastern border. Its overall length is 170m and comprises two statically independent branches, with four identical simply supported spans of 42.5m. Each span is built with four precast post-tensioned I-beams of 2.80m height that support a continuous deck of 26cm thickness and 13m width. The I-beams are supported by 2 abutments (A1 and A2) and by 3 piers (M1, M2 and M3) through laminated elastomeric bearings. Each abutment has 4 cyclic bearings and each pier has 8 rectangular bearings. The piers have a 4×4m hollow cross-section, 40cm wall thickness and heights equal to 30m (M1, M3) and 50m (M2), all supported with large caissons on relatively stiff soil (corresponding to soil class “A” according to both the Greek Seismic Code and the Eurocode 8 soil classification). The four spans of the deck are interconnected through a 2-m long 20-cm thick continuity slab over the piers.

2.2 Instrumentation

Between the two identical branches of the 2nd Kavala Bypass Ravine Bridge only the southern branch is instrumented. The instrumentation consists of a 24-accelerometer array [1], one at each deck side and located at the middle of each bridge span. More specifically, the accelerometers are installed both on the external sidewalk of the deck and on the internal New Jersey barrier of the deck. As shown in Figure 2, 18 of the 24 sensors are installed on the deck and two at the top of each of the three piers (six in all) next to the laminated elastomeric bearings so that adequate information is provided to distinguish between the pier and bearing stiffness. The sensors on the deck have a 3-letter label that follow the above explained convention: The last letter denotes the orientation of the uniaxial sensor (L: longitudinal, T: transverse, V: vertical). The previous one denotes the side of the bridge deck on which the sensor lies (R: right, L: left). Finally, the first letter denotes the bridge section that the sensor lays on (A1, B1, C1 or D1). The numbers next to each sensor label denotes the length of the cable used to connect the sensor to each recording unit. The sensors on the piers follow the same convention used for the sensors on the deck with the exception that the letters U1, U2 and U3 refer to the top of the piers. The particular layout of the instrumentation permits the recording of the dynamic response of the bridge under ambient loads.

This recording system has start/common trigger capabilities to enable synchronous data acquisition. The trigger threshold can be set independently for each sensor, and the user can define the sensors that will cause a system trigger. The systems are equipped with GPS boards as well as with external GSM/GPRS cellular modems that allowed telematic control and data transfer to the user offices.

Figure 1: General overviews of the 2nd Kavala Ravine Bypas Bridge.

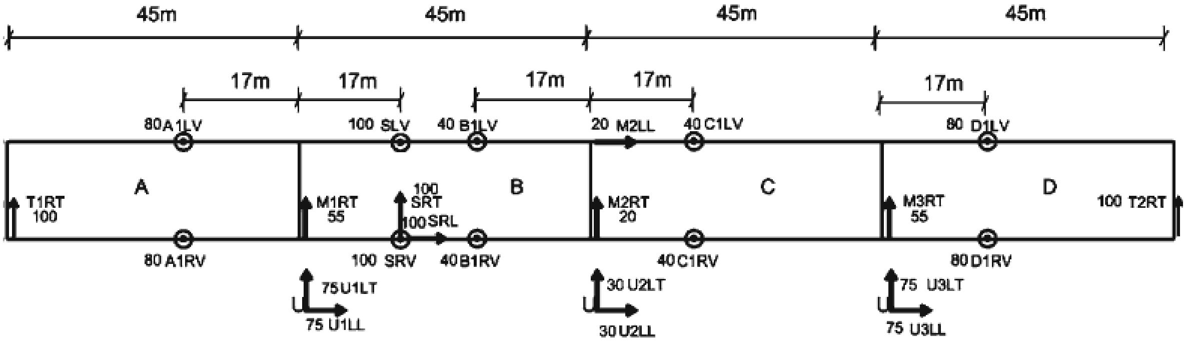

Figure 2: Instrumentation of the 2nd Kavala Ravine Bypas Bridge [1].

3 IDENTIFICATION OF STRUCTURAL MODES VIA AMBIENT VIBRATIONS

The methodology of identifying structural modes via ambient vibrations is based [1] on a least squares minimization of the measure of fit between the cross power spectral density (CPSD) matrix $\hat{S}(k\Delta\omega)\in C^{N_0\times N_0}$ and the CPSD matrix $S(k\Delta\omega;\psi)\in C^{N_0\times N_0}$. The $\hat{S}(k\Delta\omega\ )$ matrix is estimated from the measured output acceleration time histories and the $S(k\Delta\omega;\psi)$ matrix is predicted by a modal model. In Equation 1 N_0 is the number of measured degrees of freedom (DOF), $\Delta\omega$ is the discretization step in the frequency domain, $k = \{1, . . . , N\omega\}$ is the index set corresponding to frequency values $\omega = k\Delta\omega$, $N\omega$ is the number of data in the indexed set, and ψ is the parameter set to be estimated.

$$E(\psi)=\sum_{k=1}^{N_\omega}\mathrm{tr}\left[S(k\Delta\omega;\psi)-\hat{S}(k\Delta\omega))^{*T}\left(S(k\Delta\omega;\psi)-\hat{S}(k\Delta\omega)\right)\right] \qquad [1]$$

Gauberghe [6], as described in Equation 2, gives the CPSD matrix $S(k\Delta\omega;\psi)$ with the assumption of general non-classically damped modes. In Equation 2 m is the number of contributing modes in the frequency range of interest, λ_r is equal to $(-\zeta_r\omega_r \pm j\omega_r\_1 - \zeta\ ^2{}_r)$ and is the complex eigenvalue of the r-th contributing mode. In Equation 2 ω_r is the r–th modal frequency, ζ_r is the r–th modal damping ratio, $\varphi_r\in C^{N_0\times N_0}$ is the complex mode shape of the r-th mode, $A\in C^{N_0\times N_0}$, $B\in C^{N_0\times N_0}$ are real symmetric matrices accounting for the contribution of the out-of-bound modes to the selected frequency range of interest, and $g_r\ C^{N_0\times N_0}$ are vector quantities that depend on the characteristics of the modal model and the CPSD of the white noise input vector, while the symbol u^* denotes the complex conjugate of a complex number u.

$$S(\omega;\psi)=\sum_{r=1}^{m}\left[\frac{\phi_r g_r^T}{(j\omega)-\lambda_r}+\frac{\phi_r^* g_r^{*T}}{(j\omega)-\lambda_r^*}+\frac{g_r\phi_r^T}{-(j\omega)-\lambda_r}+\frac{g_r^*\phi_r^{*T}}{-(j\omega)-\lambda_r^*}\right] \qquad [2]$$

$$+\frac{1}{(j\omega)^4}A+B$$

The CPSD matrix in Equation 2 is defined by the parameters ω_r, ζ_r, φ_r, g_r, $r = 1, . . . ,m$, A and B. The modal parameter set ψ contains the above mentioned parameters and has to be identified. For non-classically damped modal models, the total number of parameters is $2m(1 + 2N_0) + N^2{}_0 + N_0$.

The objective is the minimization of Equation 1 and that can be carried out efficiently [18], significantly reducing computational cost, by recognizing that the error in Equation 1 is quadratic with respect to the complex modeshapes φ_r and the elements in the matrices A and B. This observation is used to develop explicit expressions that relate the parameters φ_r , A and B to the vectors g_r, the modal frequencies ω_r and the damping ratios ζ_r, so that the number of parameters involved in the optimization is reduced from $2m(1 + 2N_0) + N^2{}_0 + N_0$ to $2m\ (N_0 + 1)$. This reduction is considerable for a relatively large number of measurement points. Applying the optimality conditions in Equation 1 with respect to the components of φ_r, A and B, a linear system of equations results for obtaining φ_r, A and B with respect to the g_r, ω_r and ζ_r, $r = 1, . . . ,m$. The resulting nonlinear optimization problem with respect to the remaining variables g_r, ω_r and ζ_r, where $r = 1, . . . ,m$, is solved in Matlab using available gradient-based optimisation algorithms.

The starting values required in the optimization are obtained from a two-step approach as follows. In the first step, conventional least squares complex frequency algorithms [5] are employed, along with stabilization diagrams, to obtain estimates of the modal frequencies ω_r and modal damping ratios ζ_r and distinguish between the physical and the mathematical modes. These values in most cases are very close to the optimal values. In the second step, given the values of ω_r and ζ_r, the values of the residue matrices $R_r = \varphi_r g T_r \in C^{N_0 \times N_0}$ in Equation 2 are obtained by first recognizing that the objective in Equation 1 is quadratic with respect to R_r, A and B, then formulating and solving the resulting linear system of equations for R_r, A and B, and finally applying singular value decomposition to obtain estimates of φ_r and g_r from R_r. Usually, this two-step approach gives results that are very close to the optimal estimates. However, for closely spaced and overlapping modes it is often recommended to solve the original nonlinear optimization problem with respect to g_r, ω_r and ζ_r, $r = 1, \ldots, m$, using the estimates of the two-step approach as starting values.

4 ALTERNATIVE FINITE ELEMENT MODELS DEVELOPED

Three FEMs of increasing modeling complexity were created based on the exact geometrical and material properties that were used for design. The first model is an one-dimensional (i.e., frame type), fixed-base model (hereafter called “1D-Fixed”), the second is a three-dimensional, fixed-base (“3D-Fixed”) and the third is a model for which the whole soil-foundation-structure system has been simulated in 3D space (“3D-3D Soil”). The numerical simulation of the 1D-Fixed model was carried out with the computer program COMSOL 2005 multi-physics, while the numerical simulation of the other two 3D models was carried out with ABAQUS 6.8.

The 1D-Fixed model of the Kavala bridge [1] was simulated using three-dimensional, two node, beam-type finite elements for the modeling of the structural elements (deck, I-beams, piers and bearings). This model is shown in Figure 3 and has 900 degrees of freedom. The cross-sectional parameters of each one of the longitudinal beam elements are those of an equivalent cross-section that accounts for the section of the post-tensioned beam, as well as the corresponding effective width of the deck plate. The transverse beams at the two ends of the span correspond to the existing cross-beams above the bearings, whereas the other four transverse beams represent the coupling of the longitudinal beams in the transverse direction due to the presence of the deck. Adjacent spans are interconnected with a 20-cm thick 2-m long plate. The piers and the abutments bearing are assumed fixed at their base.

Figure 3: Overview of the fixed base, 1D superstructure finite element model (1D-Fixed).

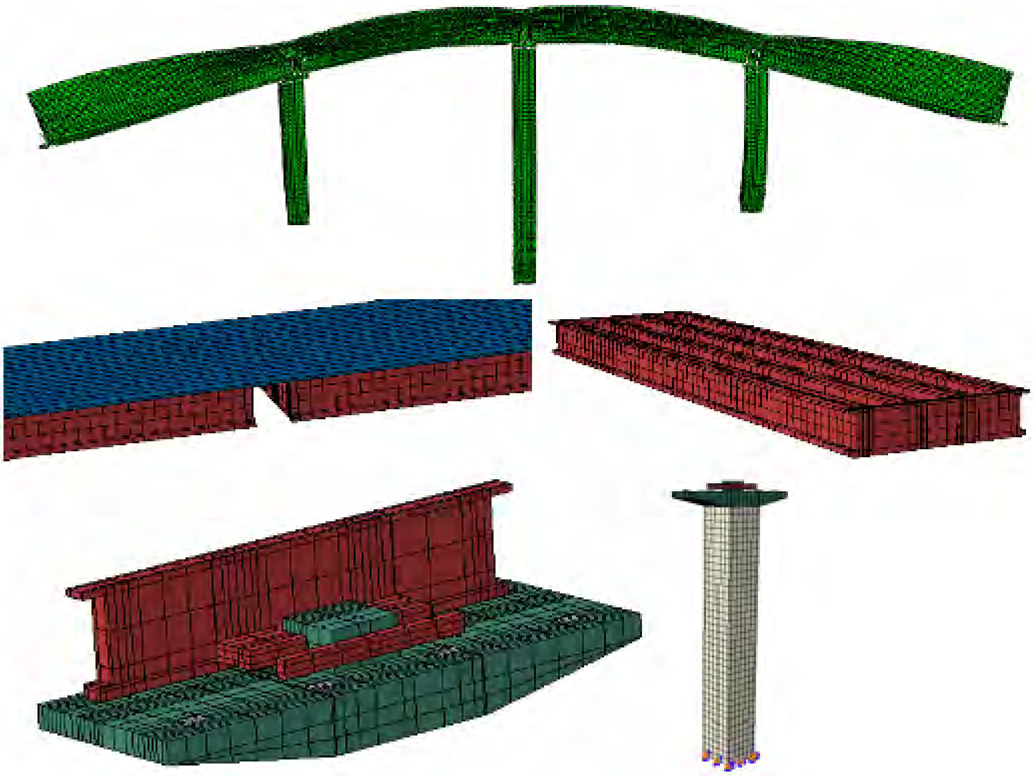

Figure 4: Overview and fundamental mode in the transverse direction (top) of the fixed base, 3D superstructure finite element model (3D-Fixed), as well as modelling details of the deck, stoppers and bearings (bottom).

The 3D-Fixed model of the Kavala bridge was simulated using three-dimensional eight node brick-type finite elements to model the entire superstructure. This model is shown in Figure 4 and has approximately 241,000 degrees of freedom. The mesh size of the elements used for bearing modeling was 0.25x0.25m while an average mesh size for the concrete sections was 0.75x0.75m. In this refined 3D FEM the deck, the I-beams, the piers, the bearings and the stoppers were modeled in maximum detail in 3D space. The abutments are considered as non-deformable, whereas the piers are assumed to be rigidly connected to the foundation, ignoring, in this version of the model, soil-structure interaction effects. Similarly, the piers and the abutment bearings are assumed fixed at their base.

The 3D-3D Soil model of the Kavala bridge is shown in Figure 5 and has approximately 960,000 degrees of freedom. In a similar fashion to the previous model, the superstructure is modeled in maximum possible detail. In addition, the entire soil-foundation-superstructure system is simulated, considering the exact geometry of the abutment-backfill-embankment system and the middle piers-caisson-soil substructure system. Mesh size for the superstructure was taken identical to the previous 3D-Fixed model and was also set equal to 2x2m for the surrounding and supporting soil. In order to reduce the computational time required, an additional, equivalent model of the 3D-3D Soil was also developed, after establishing a level of agreement between the two models by ensuring identical dynamic characteristics. This model is shown in Figure 6, 407,000 degrees of freedom and considered a smaller, though, adequate part of the soil volume. Given the compatibility of the two latter models in terms of system stiffness and damping, most analyses cases were carried out with this model instead of the initial 3D-3D Soil model.

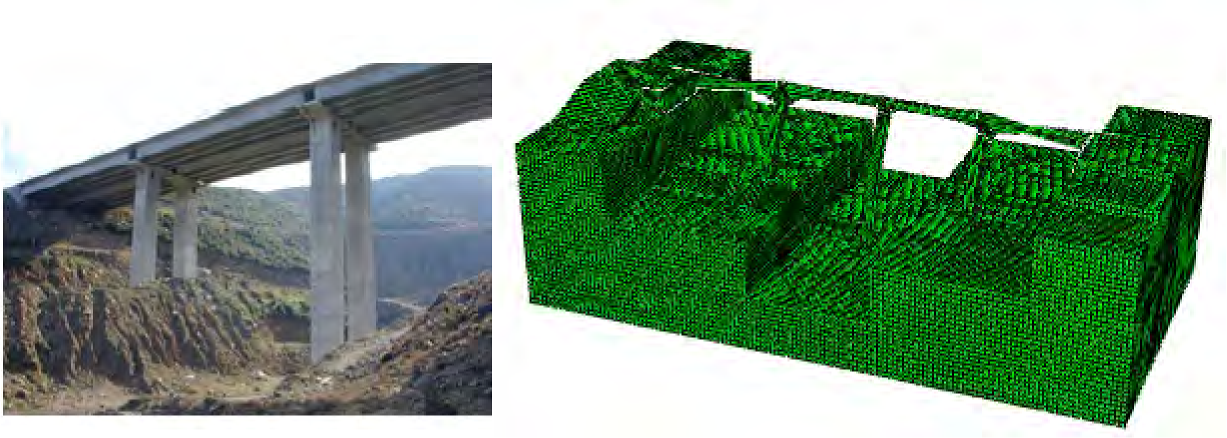

Figure 5: Overview and fundamental mode in the transverse direction of the 3D soil-foundation-superstructure finite element model (3D-3D Soil).

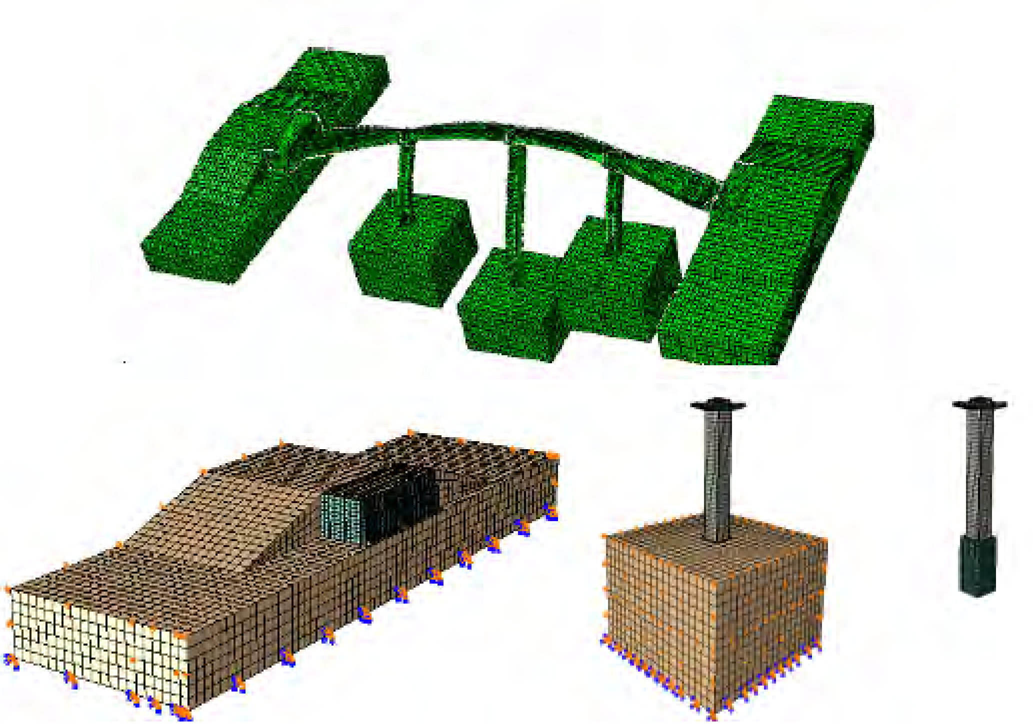

Figure 6: Overview and fundamental mode in the transverse direction of the equivalent 3D-3D Soil model as well as modelling details of the abutment-embankment system and the pier foundation subsoil.

5 FINITE ELEMENT MODEL UPDATING METHODOLOGY

The objective in a FEM updating methodology is to estimate the values of the structural parameter set $\theta \in R^{N_\theta}$ of a class of linear FEMs so that the modal frequencies and modeshapes $\{\omega_r(\theta), \varphi_r(\theta) \in R^{N_0}, r = 1, \ldots, m\}$ predicted by the linear class of models best matches, in some sense, the experimentally obtained modal data $\{\hat{\omega}_r, \hat{\varphi}_r \in R^{N_0}, r = 1, \ldots, m\}$ contained in the set ψ, where m is the number of observed modes, and N0 is the number of recorded DOFs. The optimal values of the parameter set θ are obtained by minimizing the weighted modal residuals [17].

$$J(\theta;w)=\sum_{r=1}^{m}\left[w_{w_r}\frac{\left[w_r(\theta)-\hat{w}_r\right]^2}{\left[\hat{w}_r\right]^2}+w_{\phi_r}\frac{\left\|\beta_r\phi_r(\theta)-\hat{\phi}_r\right\|^2}{\left\|\hat{\phi}_r\right\|^2}\right] \qquad [3]$$

The first norm in Equation 3 represents the difference between the measured and the model predicted frequency for the r-th mode, while the second norm represents the difference between the measured and the model predicted modeshape components for the r-th mode, where $\beta_r = \hat{\varphi}_r^T \varphi_r(\theta) / \varphi_r^T(\theta)\varphi_r(\theta)$ is a normalizing scalar guaranteeing that the measured $\hat{\varphi}_r$ is closest to $\varphi_r(\theta)$ for given θ. The weighting factors $w_{\omega r} \geq 0$ and $w_{\varphi r} \geq 0$, r = 1, . . . ,m, satisfy the condition $\Sigma^m{}_r=1[w_{\omega r}+ w_{\varphi r}] = 1$. The objective function J (θ;w) represents an overall measure of fit between the measured and the model predicted modal characteristics. Herein, conventional weighted least squares methods are used which assume equal weight values. Finally, the optimization of J (θ;w) in Equation 3with respect to θ can readily be carried out numerically using any available gradient-based algorithms for optimizing a nonlinear function of several variables. This procedure is described more detailed in Ntotsios et al. [19].

The above mentioned mathematical algorithm was applied for the updating of the 1D-Fixed model of the Kavala bridge. For that purpose, a Matlab code was developed in interaction with the computer program COMSOL, wherein the structure was simulated. In contrast, given the large number of degrees of freedom of the 3D-Fixed model and the 3D-3D Soil model of the Kavala bridge, their model updating was performed manually through a sequential parametric analysis scheme. The concept behind this simplified, manual updating approach for the 3D finite element models is described in detail in Section 6.

6 COMPARATIVE ASSESMENT OF THE PREDICTED AND MEASURED RESPONSE

6.1 Measured and predicted structural modes of Kavala Bridge

The accelerometers installed along the deck and at the top of the three piers recorded the bridge’s response and the acceleration time histories were then used as input to the model updating mathematical algorithm described in Section 3. Through this procedure, two transverse, one longitudinal and four bending modes were identified, whose modal frequencies are summarized in Table 1. Since the scope of the present research work was to validate, both qualitatively and quantitatively, the modeling assumptions made and to identify their relative impact on the numerically predicted structural response, the three finite element models developed were assessed comparatively.

The first comparison was made between the 1D-Fixed and 3D-Fixed models and aimed to identify the differences that arise by the inherent simplifications of the one dimensional modeling in contrast to the refined three dimensional modeling of the piers, I-beams, bearings and stoppers. For this reason, the soil compliance was deliberately not accounted for. The results of the predicted modal frequencies from the above models (i.e., 1D-Fixed and 3D-Fixed) are shown in Table 1. It can be seen that the agreement between the two models was very good (it is only the first two bending modes where the difference exceeds 10%), a fact that reveals that the assumptions made for the simplified 1D-Fixed model were reasonable. Despite their agreement though, it was evident that both models fail to predict well the actual, measured response as they exhibit large deviations from the identified modal frequencies that exceed 55% in the longitudinal direction and 34% and 58% respectively for the first two modes, in the transverse direction. In general, it is observed that the modes measured via ambient vibrations are on average 32% higher than those predicted by the two finite element modes, thus, the real structure is identified as significantly stiffer than predicted using the 1D and 3D fixed-base models.

A second comparison was made between the 3D-Fixed and the 3D-3D Soil models in order to quantify the importance of soil compliance on the predicted dynamic characteristics of the structure. The results of this analysis are shown in Table 2. It has to be noted herein that in case that the soil volume is modeled along with the superstructure, the identification of the modal frequencies of the entire soil-structure system is not as straightforward as it is in the case of a fixed structure, due to the enormous amount of the vibrating soil volume and the strong coupling among the structural and the soil modes. As a result, the characterization of modes as “transversal” or “bending” has to be made very carefully on the basis of both modal participation factors and modal shape visualization.

In terms of the predicted modal frequencies (Table 2), as anticipated, the refined consideration of abutment-backfill-embankment and pier-foundation-soil flexibility leads to lower values of modal frequencies. In particular, the 1st longitudinal mode is found 10% more flexible while the reduction of bending modal frequencies varies between 20-30%. However, compared to the identified modal frequencies, the particular 3D-3D soil model leads to an even more flexible (36% on average) prediction of structural response. This result clearly indicates that model refinement and soil-structure interaction simulation alone, cannot guarantee reliable representation of system stiffness unless appropriate model updating is performed in advance.

	AV	1D-Fixed		3D-Fixed	
Modes	ω(Hz)	ω(Hz)	Δω(%)	ω(Hz)	Δω(%)
1st Transverse	0.81	0.53	34.57	0.52	35.80
1st Longitudinal	1.29	0.57	55.81	0.56	56.59
2nd Transverse	1.61	0.67	58.39	0.67	58.39
1st Bending	3.40	2.78	18.24	2.69	20.88
2nd Bending	3.46	2.82	18.50	2.75	20.52
3rd Bending	3.47	2.82	18.73	2.84	18.16
4th Bending	3.51	2.83	19.37	2.87	18.23
Average Δω(%)			31.94		32.65

Table 1: Modal frequencies identified via Ambient Vibrations (AV) and numerical modeling (1D-Fixed vs. 3D-Fixed) and respective error (Δω%).

	AV	3D-Fixed		3D-3D Soil	
Modes	ω(Hz)	ω(Hz)	Δω(%)	ω(Hz)	Δω(%)
1st Transverse	0.81	0.52	35.80	0.49	39.51
1st Longitudinal	1.29	0.56	56.59	0.54	58.14
2nd Transverse	1.61	0.67	58.39	0.65	59.63
1st Bending	3.40	2.69	20.88	2.48	27.06
2nd Bending	3.46	2.75	20.52	2.55	26.30
3rd Bending	3.47	2.84	18.16	2.71	21.90
4th Bending	3.51	2.87	18.23	2.73	22.22
Average Δω(%)			32.65		36.39

Table 2: Modal frequencies identified via Ambient Vibrations (AV) and numerical modeling (3D-Fixed vs. 3D-3D soil) and respective error (Δω%).

Structural parameter	Model Updating Method
	Algorithmic
	Model Updating Case 1
E bearings	9.07
E deck	1.57
E piers	1.63

Table 3: Modal updating results for the 1D-Fixed FEM through a proposed mathematical algorithm.

	AV	1D-Fixed M.U. Case 1		3D-Fixed M.U. Case 1	
Modes	ω(Hz)	ω(Hz)	Δω(%)	ω(Hz)	Δω(%)
1st Transverse	0.81	0.86	-6.17	0.84	-3.70
1st Longitudinal	1.29	1.24	+3.88	1.19	+7.75
2nd Transverse	1.61	1.44	+10.56	1.55	+3.73
1st Bending	3.40	3.52	-3.53	3.62	-6.47
2nd Bending	3.46	3.56	-2.89	3.65	-5.49
3rd Bending	3.47	3.60	-3.75	3.73	-7.49
4th Bending	3.51	3.61	-2.85	3.80	-8.26
Average Δω(%)			+4.80		+6.13

Table 4: Modal frequencies identified via Ambient Vibrations (AV) and predicted by updated 1D-Fixed and 3D-Fixed FEMs for Case 1, as well as their in between percentage of error Δ(ω).

6.2 Finite element model updating

As mentioned earlier, for low amplitude vibrations, the structure was found to be much stiffer as one could numerically predict, regardless of model refinement. Given the fact that the finite element model used was indeed as complex and refined as possible, the model-induced (i.e., epistemic) uncertainty can be deemed as relatively low. As a result, the deviations between the identified and numerically predicted modal frequencies can be attributed primarily to the uncertainty in the material properties, which seem to be a key parameter for the reliable estimation of the dynamic characteristics of the structure.

Initially, the updating of model 1D-Fixed was carried out according to the procedure outlined in Section 5. For the case of the 3D models though, this procedure was not feasible for two main prohibitive reasons; due to the large number of the degrees of freedom of the soil-structure system but also because there was no communication protocol between the software ABAQUS used for the 3D simulations and the Matlab program running the model updating algorithm. For that reason, a different strategy was developed the manual updating of the 3D models towards the identification of the nearly-optimal fit between the identified and numerically predicted response. The workflow of this strategy is illustrated in Figure 7 and can be summarized into the following steps:

(a) Automatic model updating was performed for the case of the 1D-Fixed model. The results of the updated structural properties [1] of the 1D-Fixed model are presented in Table 3 (hereafter called “model updating Case 1”.

(b) The above identified properties were used as the first, best guess for the case of the 3D-Fixed model. Table 4 shows that the average percentage of error between the measured and the predicted modal frequencies has decreased from 31.94% to 4.8% for the 1D-Fixed model and from 32.65% to 6.13% for the 3D-Fixed verifying the trend of manual model updating was correct. It was also observed that both models predict higher values of frequencies to all modes compared with the ones identified via ambient vibrations, with the exception of the 1st longitudinal and the 2nd transverse mode.

(c) Given the refinement of the 3D-3D soil model and its capabilities to consider superstructure-foundation-soil and deck-abutment-embankment interaction, it was evident that the model updating factors predicted in step (b) would not necessarily be valid. For this reason, the 3D-3D Soil model was only initially updated based on the "Case 1" combination of structural parameters (Table 5). It can be seen that the average percentage of error between the measured and the predicted modal frequencies was decreased from 36.39% to 5.55%. In order to improve the convergence, sequential parametric analysis was conducted. The idea was to gradually modify specific structural parameters through a step-by-step parametric analysis scheme, until a nearly-optimal fit was achieved (Figure 7).

	AV	1D-Fixed M.U. Case 1		3D-Soil M.U. Case 1	
Modes	ω(Hz)	ω(Hz)	Δω(%)	ω(Hz)	Δω(%)
1st Transverse	0.81	0.86	-6.17	0.78	-3.85
1st Longitudinal	1.29	1.24	+3.88	1.13	-14.16
2nd Transverse	1.61	1.44	+10.56	1.50	-7.33
1st Bending	3.40	3.52	-3.53	3.47	+2.02
2nd Bending	3.46	3.56	-2.89	3.52	+1.70
3rd Bending	3.47	3.60	-3.75	3.65	+4.93
4th Bending	3.51	3.61	-2.85	3.69	+4.88
Average Δω(%)			+4.80		+5.55

Table 5: Modal frequencies identified via Ambient Vibrations (AV) and numerical modeling of the updated 1D-Fixed and 3D-3D Soil FEMs for structural parameter combination Case 1, and respective error (Δω%).

structural parameter	Model Updating Method Manual Case 2
E bearings	12.0
E deck	1.45
E piers	1.63

Table 6: Modal updating results for the 3D-3D Soil FEM through a proposed manual procedure.

The results of this parametric analysis resulted in the "Case 2" combination of updated structural parameters, summarized in Table 6. Table 7 shows the improvement of the modal frequencies predicted by the 3D-3D Soil for structural parameters combination "Case 2", compared to the modal frequencies predicted by the 1D-Fixed for "Case 1". By comparing Cases 1 and 2 (Tables 3 and 6), as well as the final modal frequencies predicted by the initial 1D-Fixed and the refined 3D-3D soil models, it is clear that the accurate soil-structure interaction modeling is a key parameter for reliable modal updating of the system.

It is also observed that both updated procedures (algorithmic and manual) showed that the Young Modulus of Elasticity for the bearings, the deck and the piers had to be significantly increased compared to the values assumed in the initial design. In particular, the bearing stiffness has to be increased by a factor of 12, while the concrete modulus of elasticity by a factor of 1.43 for the deck and 1.63 for the piers. With respect to the bearings, this can be clearly attributed to the low deformation (strain) levels that are developed under ambient vibrations at which the bearing stiffness is significantly lower than that assumed during design.

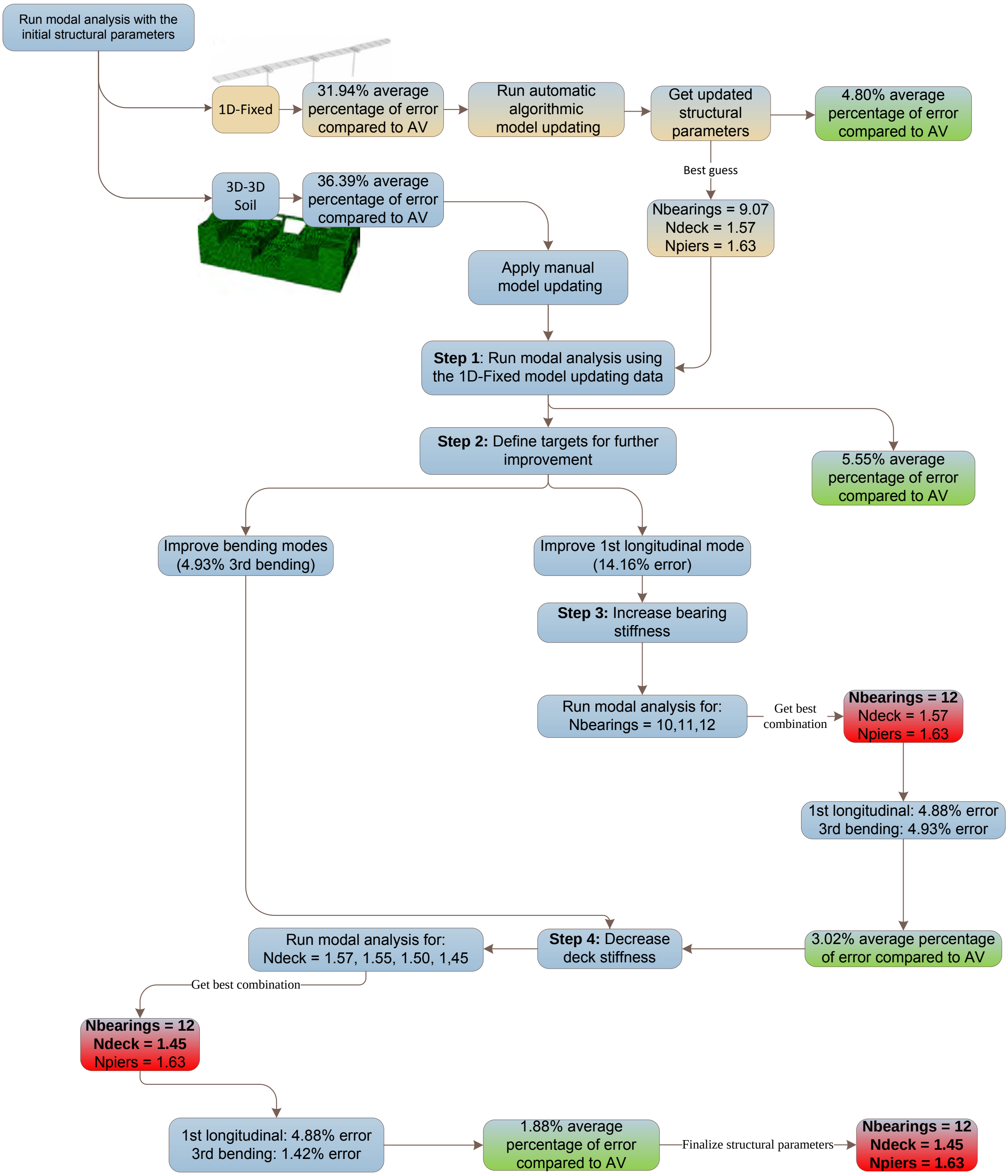

Figure 7: Manual model updating strategy.

The differences in the material properties of concrete can also be attributed to a series of contributing factors such as: (a) the definition of the modulus of elasticity according to the code used, which is calculated at strains higher than the ones imposed by ambient vibrations, (b) strengthening of concrete due to aging, (c) friction mechanisms that were activated at low levels of strain and (d) construction practices and quality control issues related to the casting of concrete. It is interesting to notice though, that similar deviations have been computed in numerous studies (i.e., [1]) and hence it is an issue that has to be investigated further.

	AV	1D-Fixed M.U. Case 1		3D-Soil M.U. Case 2	
Modes	ω(Hz)	ω(Hz)	Δω(%)	ω(Hz)	Δω(%)
1st Transverse	0.81	0.86	-6.17	0.79	-2.53
1st Longitudinal	1.29	1.24	+3.88	1.23	-4.88
2nd Transverse	1.61	1.44	+10.56	1.59	-1.26
1st Bending	3.40	3.52	-3.53	3.43	+0.87
2nd Bending	3.46	3.56	-2.89	3.46	+0.00
3rd Bending	3.47	3.60	-3.75	3.52	+1.42
4th Bending	3.51	3.61	-2.85	3.59	+2.23
Average Δω(%)			+4.80		+1.88

Table 7: Modal frequencies identified via Ambient Vibrations (AV) and numerical modeling of the updated 1D-Fixed for structural parameter combination Case 1and 3D-3D Soil FEMs for Case 2, and respective error (Δω%).

7 CONCLUSIONS

This paper aimed to identify the parameters that affect the dynamic response of the instrumented, 2nd Kavala Bypass Ravine Bridge constructed along the Egnatia Motorway Greece. Using alternative finite element models of various levels of complexity and modeling refinement in terms of consideration the dynamic interaction of the overall superstructure-foundation-soil and deck-abutment-embankment system, the modal frequencies of the bridge are computer and compared with the ones identified using ambient vibrations. The main conclusions drawn from this study can be summarized as follows:

- A good agreement was observed, on the basis of the predicted modal frequencies of the bridge, between the 1D-Fixed and the 3D-Fixed models, thus indicating that the simplifying assumptions made for the first were reasonably accurate. However, the initial prediction of the two models leads to considerably lower (34%-58%) modal frequencies than the ones identified, hence yielding model updating inevitable.
- Introduction of the soil compliance through the more refined 3D-3D soil model which simulated the overall soil-structure system led to a further reduction of the modal frequencies, by 10% in the 1st longitudinal direction and by 25% on average in the transverse direction.
- The model updating strategy that was followed for the case of the most complex and comprehensive 3D-3D soil model, eventually led to good agreement of the predicted modal frequencies with the identified ones and the average error was reduced to 1.88% (without exceeding 4.9% at any mode). The updated FEMs revealed that the differences

initially computed, were due to the higher actual stiffness of the elastomeric bearings, the piers and the deck as compared to the values that were assumed during design.

- The differences between the design assumptions and the actual structural properties under ambient vibrations can attributed to the low deformation (strain) levels, the definition of the modulus of elasticity according to the code used, which is calculated at strains higher than the ones imposed by ambient vibrations, strengthening of concrete due to aging, friction mechanisms as well as to construction practices during concrete casting.
- Consideration and numerical modeling of soil-structure interaction, abutment-backfill-embankment and pier-foundation-soil geometry and properties, may not affected the dynamic characteristics drastically in terms of their absolute values, but due to significant modal coupling, had a considerable effect on the prediction of the final, modified structural parameters. This effect is anticipated to be further pronounced in case of softer soil profiles. As a result, the accurate soil-structure interaction modeling is deemed to be a key parameter for reliable modal updating of extended bridge-soil systems.

REFERENCES

[1] E. Ntotsios, C. Caracostas, V. Lekidis, P. Panetsos, I. Nikolaou, C. Papadimitriou, T. Salonikos, Structural identification of Egnatia Odos Bridges based on ambient and earthquake-induced vibrations, *Bulletin of Earthquake Engineering*, 2008.

[2] B. Peeters, G. De Roeck, Stochastic system identification for operational modal analysis: a review, *ASME Journal of Dynamic Systems, Measurement and Control*, **123**(4), 659–667, 2001.

[3] M. Basseville, A. Benveniste, M. Goursat, L. Hermans, L. Mevel, H. Van der Auweraer, Output-only subspace-based structural identication: from theory to industrial testing practice, *ASME Journal of Dynamic Systems, Measurement and Control*, 123(4), 668–676, 2001.

[4] J.L. Beck, B.S. May, D.C. Polidori, Determination of modal parameters from ambient vibration data for structural health monitoring, *Proceedings of the 1st World Conference on Structural Control*, Los Angeles, USA, 1395–1402, 1994.

[5] P. Verboven, *Frequency domain system identification for modal analysis.* PhD Thesis, Vrije Universiteit Brussel, Belgium, 2002.

[6] B. Gauberghe, *Applied frequency-domain system identification in the field of experimental and operational modal analysis.* PhD Thesis, Vrije Universiteit Brussel, Belgium, 2004.

[7] R. Brincker, L. Zhang, P. Andersen, *Modal identification of output-only systems using frequency domain decomposition*. Smart Materials & Structures, **10**, 441–445, 2001.

[8] B. Peeters, H. Van der Auweraer, Recent developments in operational modal analysis. In: Soize C, Schueller GI (eds) *EURODYN 2005*, Millpress, Rotterdam, pp 149–154, 2005.

[9] L.S Katafygiotis, K.V. Yuen, Bayesian spectral density approach for modal updating using ambient data, Earthquake Engineering and Structural Dynamics, **30**(8),1103–1123, 2001.

[10] P. Guillaume, L. Hermans, H. Van der Auweraer, Maximum likelihood identification of modal parameters from operational data, *Proceedings of the international modal analysis conference—IMAC 2*, 1887–1893, 1999.

[11] G. Mylonakis, G. Gazetas, Seismic soil-structure interaction: Beneficial or detrimental?, *Journal of Earthquake Engineering*, **4**(3), 277-301, 2000.

[12] J.P. Wolf, *Soil-Structure-Interaction Analysis in Time Domain*. Prentice-Hall, Eng. Cliffs, N.J, 1988.

[13] J.E. Mottershead, M.I. Friswell, Model updating in structural dynamics: a survey, *Journal of Sound and Vibration*, **167**, 347–375, 1993.

[14] K. Bohle, C.P. Fritzen, Results obtained by minimizing natural frequencies and MAC-value errors of a plate model, *Mechanical Systems and Signal Processing*, **17**, 55–64, 2003.

[15] A. Teughels, G. DeRoeck, JAK Suykens, Global optimization by coupled local minimizers and its application to FE model updating, *Computers and Structures*, **81**(24–25), 2337–2351, 2003.

[16] H.F Lam, L.S Katafygiotis, N.C Mickleborough, Application of a statistical model updating approach on phase I of the IASC-ASCE structural health monitoring benchmark study, Journal of Engineering Mechanics, **130**(1), 34–48, 2004.

[17] K. Christodoulou, C. Papadimitriou, Structural identification based on optimally weighted modal residuals, Mechanical Systems and Signal Processing, **21**, 4–23, 2007.

[18] C. Papadimitriou, E. Ntotsios, E. (2009). Structural Model Updating using Vibration Measurements, *ECCOMAS Thematic Conference on Computational Methods in Structural Dynamics and Earthquake Engineering*, M. Papadrakakis, N.D. Lagaros, M. Fragiadakis (eds.), Rhodes, Greece, 22-24 June, 2009.

[19] E. Ntotsios, Papadimitriou, C. Multi-objective Optimization Algorithms for Finite Element Model Updating, *ISMA2008 International Conference on Noise and Vibration Engineering*, September 15-17, Leuven, 1895-1909, 2008.

COMPDYN 2011
III ECCOMAS Thematic Conference on
Computational Methods in Structural Dynamics and Earthquake Engineering
M. Papadrakakis, M. Fragiadakis, V. Plevris (eds.)
Corfu, Greece, 25–28 May 2011

ROBUST STRUCTURAL HEALTH MONITORING USING A POLYNOMIAL CHAOS BASED SEQUENTIAL DATA ASSIMILATION TECHNIQUE

George A. Saad[1], and Roger G. Ghanem[2]

[1] American University of Beirut
Beirut, Lebanon
george.saad@aub.edu.lb

[2] University of Southern California
Los Angeles, California, USA
ghanem@usc.edu

Keywords: Structural Health Monitoring, Sequential Data Assimilation, Kalman Filter, Uncertainty Quantification, Polynomial Chaos.

Abstract. *With the recent technological advances and the evolution of advanced smart systems for damage detection and signal processing, Structural Health Monitoring (SHM) emerged as a multidisciplinary field with wide applicability throughout the various branches of engineering, mathematics and physical sciences. However, significant challenges associated with modeling the physical complexity of systems comprising these structures remain. This is mainly due to the fact that numerous uncertainties associated with modeling, parametric and measurement errors could be introduced. In cases where these uncertainties are significant, standard identification and damage detection techniques are either unsuitable or inefficient. This study presents a robust data assimilation approach based on a stochastic variation of the Kalman Filter where polynomial functions of random variables are used to represent the inherent process uncertainties. The presented methodology is combined with a non-parametric modeling technique to tackle structural health monitoring of a four-story shear building. The structure is subject to a base motion specified by a time series consistent with the El-Centro earthquake and undergoes a preset damage in the first floor. The purpose of the problem is localizing the damage in both space and time, and tracking the state of the system throughout and subsequent to the damage time. The application of the introduced data assimilation technique to SHM enhances the latter's applicability to a wider range of structural problems with strongly nonlinear dynamical behavior and with uncertain and complex governing laws.*

1 INTRODUCTION

With the recent technological advances and the evolution of advanced smart systems for damage detection and signal processing, Structural Health Monitoring (SHM) emerged as a multidisciplinary field with wide applicability throughout the various branches of engineering, mathematics and physical sciences. Typically, the SHM problem can be addressed as a statistical pattern recognition paradigm with three main components:

1) A numerical model that accurately represents the governing system dynamics
2) Real-time data acquisition and management system
3) A sequential data assimilation technique that relies on a set of observational data to calibrate and update the underlying dynamic principles governing the system under observation.

In such context, numerous uncertainties associated with modeling, parametric and measurement errors could be introduced. In cases where these uncertainties are significant, standard identification and damage detection techniques are either unsuitable or inefficient. Therefore, the need rises for robust system identification algorithms that can tackle the aforementioned challenges. This has been a very active research area over the past decade [3, 4, 6, 8, 9, 11, 12].

Sequential data assimilation has been widely used for structural health monitoring and system identification problems. Many extensions of the Kalman Filter were developed as adaptations to important classes of these problems. While the Extended Kalman Filter may fail in the presence of high non-linearities, Monte Carlo based Kalman Filters usually give satisfactory results. The Ensemble Kalman Filter (EnKF) [1, 2] was recently used for damage detection in strongly nonlinear systems [4], where it is combined with non-parametric modeling techniques to tackle structural health monitoring for non-linear systems. The EnKF uses a Monte Carlo Simulation scheme for characterizing the noise in the system, and therefore allows representing non-Gaussian perturbations. Although this combination gives good results, it requires a relatively accurate representation of the non-linear system dynamics. It also requires a large ensemble size to quantify the non-Gaussian uncertainties in such systems and consequently imposes a high computational cost.

This study presents a system identification approach based on coupling robust non-parametric non-linear models with the Polynomial Chaos methodology in the context of the Kalman Filtering techniques [10]. The proposed approach uses a Polynomial Chaos expansion [7] of the nonparametric representation of the system's non-linearity to statistically characterize the system's behavior. A filtering technique that allows the propagation of a stochastic representation of the unknown variables using Polynomial Chaos is used to identify the chaos coefficients of the unknown parameters in the model. The introduced filter is a modification of the EnKF that uses the Polynomial Chaos methodology to represent uncertainties in the system. This allows the representation of non-Gaussian uncertainties in a simpler, less taxing way without the necessity of managing a large ensemble. It also allows obtaining the probability density function of the model state or parameters at any instant in time by simply simulating the Polynomial Chaos basis.

2 THE POLYNOMIAL CHAOS KALMAN FILTER (PCKF)

The Kalman Filter is an optimal sequential data assimilation method for linear dynamics and measurement processes with Gaussian error statistics. The PCKF builds on the mathematics of the original Kalman Filter to allow the propagation of a stochastic representation of the unknown variables using Polynomial Chaos. In the PCKF, the model state is given by,

$$x = \sum_{i=0}^{P} x_i \psi_i(\xi), \tag{1}$$

where, $P + 1$, is the number of terms in the Polynomial expansion of the state vector, $\{\psi_i\}$ is set of Hermite polynomials function of the Gaussian random variable, ξ. Consequently, the covariance matrix of the model state is defined around the mean, the zero order term, of the stochastic representation,

$$\begin{aligned} P &\approx \left\langle \left(\sum_{i=0}^{P} x_i \psi_i - x_0 \right) \left(\sum_{i=0}^{P} x_i \psi_i - x_0 \right)^T \right\rangle \\ &\approx \left\langle \left(\sum_{i=1}^{P} x_i \psi_i \right) \left(\sum_{i=1}^{P} x_i \psi_i \right)^T \right\rangle \\ &\approx \sum_{i=1}^{P} x_i x_i^T \left\langle \psi_i^2 \right\rangle, \end{aligned} \tag{2}$$

where, P is the covariance matrix, and $\langle\ \rangle$ denotes the mathematical expectation. The Polynomial Chaos representation depicts all the information available through the complete probability density function, and therefore allows the propagation of all the statistical moments of the unknown parameters and variables.

The observations are also treated as random variables represented via a Polynomial Chaos expansion with a mean equal to the first-guess observations. Since the model and measurement errors are assumed to be independent, the latter is represented as a Markov process

2.1 Analysis Scheme

For computational efficiency, the dimensionality and order of the Polynomial Chaos expansion are homogenized through out the solution. These parameters are initially defined based on the uncertainty within the problem at hand and are assumed to be constant thereafter. Since the model state and measurement vectors are assumed independent, the Polynomial Chaos representation of these variables has a sparse structure.

Let $\boldsymbol{A}$ be the matrix holding the chaos coefficients of the state vector $y \epsilon R^n$,

$$\mathbf{A} = (x_0, x_1, ..., x_P) \in R^{n\times(P+1)}, \tag{3}$$

where $P + 1$ is the total number of terms in the Polynomial Chaos representation of x and n is the size of the model state vector. The mean of x is stored in the first column of $\boldsymbol{A}$ and is denoted by x_0. The state perturbations are given by the higher order terms stored in the remaining columns. Consequently, the state error covariance matrix $\boldsymbol{P} \epsilon R^{n\times n}$is defined as:

$$\mathbf{P} = \sum_{i=1}^{P} x_i x_i^T \left\langle \psi_i^2 \right\rangle \tag{4}$$

Given a vector of measurements $d \epsilon R^m$, with m being the number of measurements at each occurrence, a Polynomial chaos representation of the measurements is defined as

$$d = \sum_{j=0}^{P} d_j \psi_j(\xi), \tag{5}$$

where the mean d_0 is given by the actual measurement vector, and the higher order terms represent the measurement uncertainties. The representation d can be stored in matrix form as:

$$\mathbf{B} = (d_0, d_1, \ldots., d_P) \in R^{m \times (P+1)}. \tag{6}$$

Based on Eq. 5, the measurement error covariance matrix, $\boldsymbol{R}$, is defined as:

$$\mathbf{R} = \sum_{i=1}^{P} d_i d_i^T \left\langle \psi_i^2 \right\rangle \in R^{m \times m} \tag{7}$$

The Kalman Filter forecast step is carried out by employing a stochastic Galerkin scheme, and the assimilation step consists if the traditional Kalman Filter correction step applied on the Polynomial Chaos expansion of the model state vector,

$$\sum_{i=0}^{P} x_i^a \psi_i = \sum_{i=0}^{P} x_i^f \psi_i + \mathbf{PH}^T (\mathbf{HPH}^T + \mathbf{R})^{-1} \left(\sum_{i=0}^{P} d_i \psi_i - \mathbf{H} \sum_{i=0}^{P} x_i^f \psi_i \right) \tag{8}$$

where, $\mathbf{H}$ is the observation matrix, and the superscripts f and a represent the forecast and analysis states respectively. Projecting the above equation on an approximating space spanned by the Polynomial Chaos $\{\psi_i\}_{i=0}^{P}$ yields,

$$x_i^a = x_i^f + \mathbf{PH}^T (\mathbf{HPH}^T + \mathbf{R})^{-1} \left(d_i - \mathbf{H} x_i^f \right) \qquad for \quad i = 0, 1, \ldots., P. \tag{9}$$

In matrix form, the assimilation step is expressed as:

$$\mathbf{A}^a = \mathbf{A}^f + \mathbf{PH}^T \left(\mathbf{HPH}^T + \mathbf{R} \right)^{-1} \left(\mathbf{B} - \mathbf{HA}^f \right) \tag{10}$$

3 NUMERICAL EXAMPLE

The efficiency of the presented method is assessed by applying it to the structural health monitoring of the four-story shear building shown in Figure 1. This model has a constant stiffness on each floor and a 5% damping ratio in all modes. All structural elements of this frame are assumed to involve hysteretic behavior, and it is supposed that a change in the hysteretic loop of the first floor element occurs at some point. It is of utmost importance to localize that point in time and track the state of the system throughout and subsequent to that point.

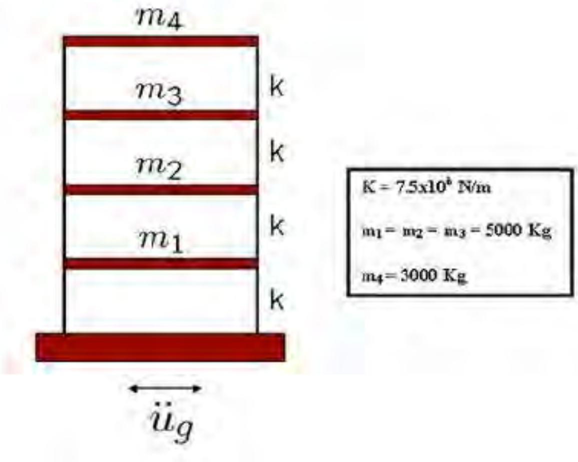

Figure 1: Shear Building Under Analysis

A synthetically generated dataset representing measurements of the displacements and velocities at each floor is obtained by representing the hysteretic restoring force by the Bouc-Wen model, which is therefore considered as the exact hysteretic behavior of the system. Thus, the equation of motion of the system is given by,

$$M\ddot{u}(t)+C\dot{u}(t)+K_{el}u(t)+(1-\alpha)K_{in}z(x,t)=-M\tau\ddot{u}_g(t) \tag{11}$$

where, M, C, K_{el}, and K_{in} are the mass, damping, elastic and inelastic stiffness matrices respectively; α is the ratio of the post yielding stiffness to the elastic stiffness, τ is the influence vector, u is the displacement vector, x is the inter-story drift vector, and z is an n-dimensional evolutionary hysteretic vector whose i^{th} component is give by the Bouc-Wen model as,

$$\dot{z}_i = A_i\dot{x}_i - \beta|\dot{x}_i||z_i|^{n_i-1} - \gamma_i\dot{x}_i|z_i|^{n_i}, \qquad i=1,\dots,n \tag{12}$$

A, β, and ϒ are the Bouc-Wen model parameters. The adopted values for these parameters are shown in Table 1.

Model Coef.	Pre-Change	Post-Change
α	0.15	0.15
β	0.1	10
n	1	1
γ	0.1	10
A	1	1

Table 1: Bouc-Wen Model Coefficients

The structure is subject to a base motion specified by a time series consistent with the El-Centro earthquake shown in Figure 2, and a change of the first floor hysteric behavior is assumed to take place five seconds after the excitation. A monitoring scenario where it is assumed that measurements are available every 5 time steps is adopted. A nonparametric representation of the system nonlinearity is adopted, and the filtering technique is used to characterize the latter representation in order to capture any ambiguous behavior of the structure examined.

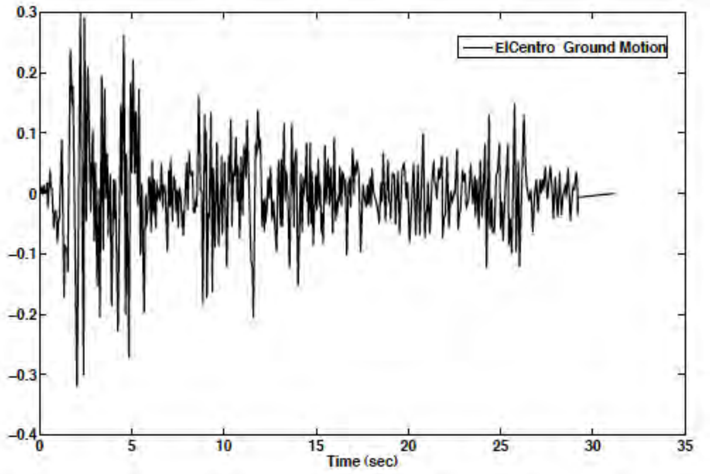

Figure 2: The Elcentro Excitation Applied to the Structure

4 NON-PARAMETRIC REPRESENTATION OF THE NON-LINEARITY

The proposed filtering methodology is combined with a non-parametric modeling technique to tackle structural health monitoring of non-linear systems but instead of adopting a deterministic nonparametric representation of the non-linearity, a stochastic representation via Polynomial Chaos is used. The basic idea behind the non-parametric identification technique used is to determine an approximating analytical function $\hat{F}$ that approximates the actual system non-linearities, with the form of $\hat{F}$ including suitable basis functions that are adapted to the problem at hand [8]. For general non-linear systems, a suitable choice of basis would be the list of terms in the power series expansion in the doubly indexed series,

$$S = \sum_{i=0}^{i_{\max}} \sum_{j=0}^{j_{\max}} u^i \dot{u}^j, \tag{13}$$

where u and $\dot{u}$ are used to represent the system's displacement and velocity respectively. Therefore, if $i_{max} = 3$ and $j_{max} = 3$, the basis functions become:

$$basis = \left\{1, \dot{u}, \dot{u}^2, \dot{u}^3, u, u\dot{u}, u\dot{u}^2, u\dot{u}^3, u^2, u^2\dot{u}, u^2\dot{u}^2, u^2\dot{u}^3, u^3, u^3\dot{u}, u^3\dot{u}^2, u^3\dot{u}^3\right\} \tag{14}$$

In the proposed method the displacements and velocities are stochastic processes represented by their Polynomial Chaos expansion. Thus, the approximating function is also expressed as a stochastic process via a Polynomial Chaos representation. The model adopted within the Kalman Filter is hence given by

$$M\ddot{u}(t) + F(u,\dot{u}) = -M\tau\ddot{u}_g(t) \tag{15}$$

where, F is the non-parametric representation of the non-linearity whose i^{th} floor component is given by

$$\begin{aligned}
F^i &\approx \sum_j F_j^i(u,\dot{u})\psi_j \\
F^i &\approx \sum_j a_j^i \psi_j \left(\sum_k (u_k - u_k^{i-1})\psi_k \right) + \sum_j a_j^{i+1} \psi_j \left(\sum_k (u_k^i - u_k^{i+1})\psi_k \right) \\
&+ \sum_j b_j^i \psi_j \left(\sum_k (u_k^i - u_k^{i-1})\psi_k \right)^2 + \sum_j b_j^{i+1} \psi_j \left(\sum_k (u_k^i - u_k^{i+1})\psi_k \right)^2 \\
&+ \sum_j c_j^i \psi_j \left(\sum_k (\dot{u}_k^i - \dot{u}_k^{i-1})\psi_k \right) + \sum_j c_j^{i+1} \psi_j \left(\sum_k (\dot{u}_k^i - \dot{u}_k^{i+1})\psi_k \right) \\
&+ \sum_j d_j^i \psi_j \left(\sum_k (u_k^i - u_k^{i-1})\psi_k \right) \left(\sum_l (\dot{u}_l^i - \dot{u}_l^{i-1})\psi_l \right) \\
&+ \sum_j d_j^{i+1} \psi_j \left(\sum_k (u_k^i - u_k^{i+1})\psi_k \right) \left(\sum_l (\dot{u}_l^i - \dot{u}_l^{i+1})\psi_l \right)
\end{aligned} \tag{16}$$

In the above equation, $\{a_j\}, \{b_j\}, \{c_j\}$, and $\{d_j\}$ represent the chaos coefficients of the unknown parameters to be identified. The fourth order Runge-Kutta method is used for the time stepping and a stochastic Galerkin approach is employed to solve the system at each time step.

5 RESULTS

In the numerical example, it is assumed that observations of displacements and velocities from all floors are available. The noise signals perturbing both the model and measurements are modeled as first order, one dimensional, independent, Polynomial Chaos expansions having zero-mean and an RMS of 0.05 and 0.001 respectively. The parametric uncertainties on the other hand, are modeled as second order, one dimensional, Polynomial Chaos expansions whose coefficients are to be determined in accordance with the available observations. This is done to incorporate the possibility that the unknown parameters may deviate from Gaussianity. Furthermore, it is assumed that the first floor undergoes a change in its hysteretic behavior 5 seconds after the ground excitation. The purpose of the application is to detect this behavioral change.

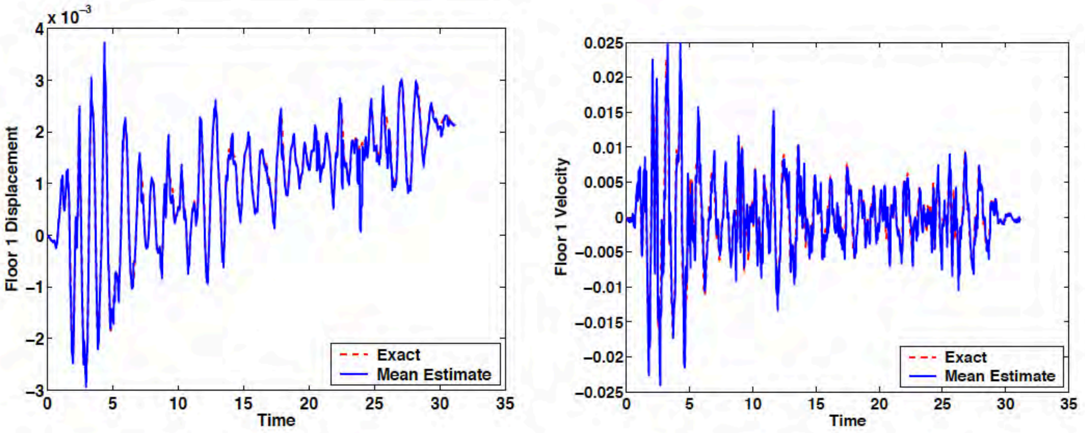

(a) (b)

Figure 3: Estimate of the first floor parameters, (a) displacement, (b) velocity

Figure 3 and Figure 4 describe the tracking of the displacement and velocity for the first and fourth floor respectively. Excellent match between the results estimated using the Polynomial Chaos based Kalman Filter and the true state is observed.

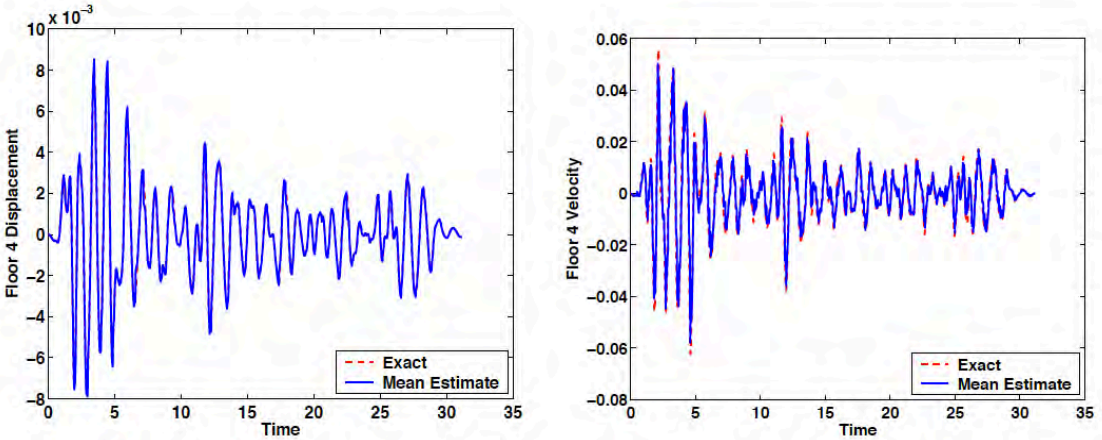

(a) (b)

Figure 4: Estimate of the fourth floor parameters, (a) displacement, (b) velocity

Figure 5 presents the evolution of the mean of the unknown parameters identified by the proposed filtering technique. Error bars representing the scatter in the estimated parameters are also present in Figure 5. The different jumps within the parameters are associated with the perks in the corresponding excitation.

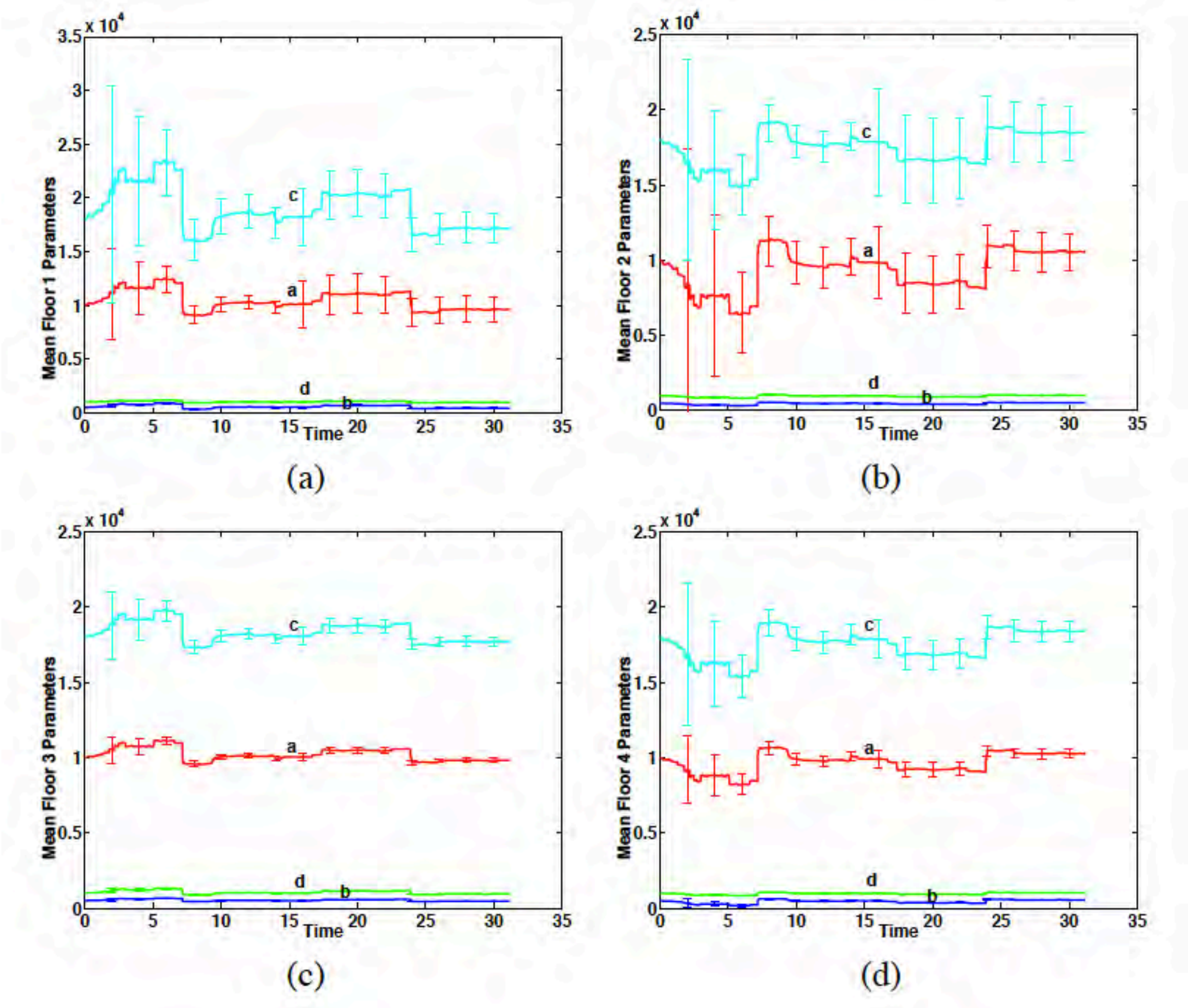

(a)

(b)

(c)

(d)

Figure 5: Estimate of the mean floor parameters

Further investigation of the parameters indicates that the main changes take place in the first floor following the 5sec time interval. Note that the parameters a and c in floors 1 and 2 undergo the greatest jumps since they are associated with inter-story drift and velocity, respectively. One of the main advantages of using the Polynomial Chaos Kalman filter is that is provides a scatter around the estimated parameters. This is represented by the probability density functions corresponding to each of the estimated parameters. Figure 6 presents the probability density functions of the estimated floor 1 parameters.

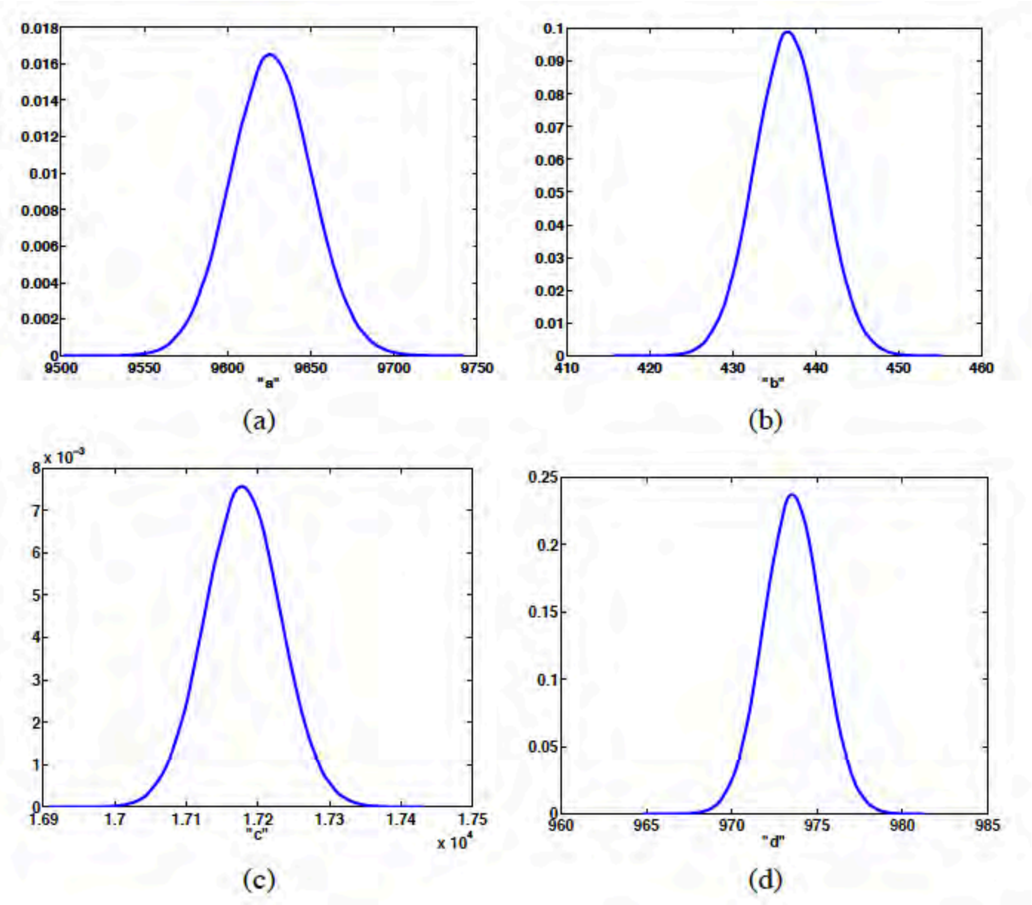

(a) (b)

(c) (d)

Figure 6: Probability density functions of the estimated floor 1 parameters

6 CONCLUSIONS

The combination of Polynomial Chaos with the Ensemble Kalman Filter renders an efficient data assimilation methodology that competes with other Kalman Filtering techniques while maintaining a relatively low computational cost. Although the proposed method employs traditional Kalman Filter updating schemes, it preserves all the error statistics, and hence allows the computation of the probability density function of the uncertain parameters and variables at all time steps. This is achieved by simply simulating the Polynomial Chaos representation of these parameters. Together with the non-parametric representation of the nonlinearities, the approach constitutes an effective system identification technique that accurately detects any changes in the systems behavior. The Polynomial Chaos representation of the non-parametric model for the nonlinearities is a robust innovative approach that permits damage identification and tracking the dynamical state beyond that point. Using Polynomial Chaos, the uncertainty associated with the assumed non-parametric model is inherently present and thus represents the actual nonlinearity in a more accurate way.

REFERENCES

[1] Evensen G., Sequential Data Assimilation with a nonlinear quasi-geostrophic model using Monte Carlo to forecast error statistics, *Journal of Geophysical Research,* **99**: 10143-10162, 1994

[2] Evensen G., The Ensemble Kalman Filter: Theoretical formulation and practical implementation, *Ocean Dynamics*, **53**:343–367, 2003

[3] Franco G., R. Betti, and S. Lus, Identification of structural systems using an evolutionary strategy, *Journal of Engineering Mechanics*, **130**:1125–1139, 2005

[4] Ghanem R. and G. Ferro, Health Monitoring for strongly non-linear systems using the ensemble Kalman filter, *Structural Control and Health Monitoring,* **13:** 245-259, 2002

[5] Ghanem R., G. Saad, and A. Doostan, Efficient Solution of stochastic systems: application to the embankment dam problem, *Structural Safety,* **29**: 238-251, 2007

[6] Ghanem R. and M. Shinozuka, Structural systems identification I, Theory, *Journal of Engineering Mechanics*, **121**: 255-264, 1995

[7] Ghanem R. and P. Spanos, *Stochastic Finite Elements: A Spectral Approach*, Dover Publications, Inc., revised edition, 2003

[8] Masri S., J.P. Caffrey, T.K. Caughey, A.W. Smyth, and A.G. Chassiakos, Identification of the state equation in complex non-linear systems, *International Journal of Non-Linear Mechanics*, **39**:1111–1127, 2004

[9] Masri S., R. Ghanem, F. Arrate, and J.P. Caffrey, A data based procedure for analyzing the response of uncertain nonlinear systems, *Structural Control and Health Monitoring,* **16**: 724-750, 2009

[10] Saad G. and R. Ghanem, Characterization of reservoir simulation models using a polynomial chaos based ensemble Kalman filter, *Water Resources Research,* **45**: W04417, 2009

[11] G. Saad, R. Ghanem, and S. Masri, Robust System Identification of Strongly Non-linear Dynamics Using a Polynomial Chaos-Based Sequential Data Assimilation Technique, 48th AIAA/ASME/ASCE/AHS/ASC Structures, Structural Dynamics, and Materials Conference, Honolulu, Hawaii, April 2007

[12] Zhang H., G. Foliente, Y. Yang, and F. Ma, Parametric identification of elastic structures under dynamic loads, *Earthquake Engineering and Structural Dynamics,* **31:**1113-1130, 2002

COMPDYN 2011
III ECCOMAS Thematic Conference on
Computational Methods in Structural Dynamics and Earthquake Engineering
M. Papadrakakis, M. Fragiadakis, V. Plevris (eds.)
Corfu, Greece, 25–28 May 2011

FULL-SCALE SHAKE TABLE EXPERIMENTS AND VIBRATION TESTS FOR ASSESSING THE EFFECTIVENESS OF TEXTILE MATERIALS FOR RETROFITTING MASONRY BUILDINGS

Paul Michelis[1], Costas Papadimitriou[2], Grigoris K. Karaiskos[2], and Dimitra-Christina P. Papadioti[2]

[1]Institute of Mechanics of Material & Geostructures S.A.
22 Askiton str., Penteli , 152 36, Greece
e-mail: immg@otenet.gr

[2]University of Thessaly, Department of Mechanical Engineering
Volos 38334, Greece
e-mail: {costasp, gkaraiskos, dxpapadioti}@uth.gr

Keywords: Masonry structures, FRP reinforcement, Shake table tests, Structural identification, Damage assessment.

Abstract. *Full-scale shake table seismic experiments and low amplitude vibration tests on a masonry building are carried out to assess its seismic performance as well as study the effectiveness of a new textile material for retrofitting masonry structures against earthquakes. The un-reinforced and the retrofitted with glass fiber reinforced polymer (GFRP) strips masonry buildings were subjected to a series of earthquake excitations of increasing magnitude in order to progressively induce various small, moderate and severe levels of damage to the masonry walls. The performance of the original and retrofitted building states is evaluated. Changes in the dynamic characteristics (lowest four modal frequencies and damping ratios) of the building are used to assess and quantify the damage states of the masonry walls. For this, the dynamic modal characteristics of the structure states after each earthquake event were estimated by performing low-amplitude impulse hammer and sine-sweep forced vibration tests. The retrofitting actions restored the stiffness characteristics of the reinforced masonry structure to the levels of the original undamaged un-reinforced structure. The results show that the despite a similar dynamic behavior identified, corresponding to reduction of the modal frequencies, the un-reinforced masonry building was severely damaged, while the reinforced masonry building was able to withstand, without visual damage, the induced strong seismic excitations. The GFRP textile material, optimally wrapped along the masonry walls following existing guidelines, was proven to be very effective in reinforcing the masonry building to withstand earthquake events significantly larger in magnitude than the ones caused severe damage to the un-reinforced building.*

1 INTRODUCTION

A large number of masonry structures exist in high seismicity regions throughout the world. Most masonry structures have been designed without following design procedures recommended by modern seismic codes. Such structures are vulnerable to damage and collapse due to moderate and large earthquakes. Un-reinforced brick masonry buildings perform poorly under (lateral) seismic forces, failing in out-of-plane bending, in-plan bending and shear. Although being the most widely used type of construction in the world it is not capable of dissipating energy through inelastic deformation. They are designed to resist primarily gravity and wind loads. Retrofitting techniques provide the means of stiffening and strengthening these structures to withstand earthquakes. Several retrofitting strategies have been proposed in the past. A large number of tests on the components of the masonry structures have been also performed to study the effectiveness of the retrofitting on the component level. Among the retrofitting techniques, repair technologies based on fiber-reinforced polymer (FRP) are effective and practical alternatives for stiffening and strengthening masonry building. Tests on complete masonry structures also have been performed on shake tables and the performance of masonry structures has been evaluated under the action of earthquakes. These tests have provided valuable information on the seismic performance of full scale masonry buildings or the components of the masonry.

A major problem in classical reinforced textile structure is their low working capacity due to missing dissipative plastic deformation capacity. In a large number of recent publications [1-17] on masonry reinforcement by fiber reinforced plastics, it is reported that masonry fails in a brittle manner with the load capacity dropping substantially and suddenly. This is in agreement with the field observations of specialized engineers working in high seismicity regions. Premature bonding of FRP occurs due to high concentration of interface shear stresses and normal peeling stress in the vicinity of the reinforcement. The brittle mode of failure is reflected in the low strains at failure and therefore in a minimum energy absorption. In addition, the mode of deformation, including the crack pattern, depends on the wall boundary conditions and reaction zones, which were not real in most of the cases examined in the Laboratory. These observations are particularly valid for dynamic (cyclic) loading, in-plane and out-of-plane, developing during earthquakes. At the same time reinforcement by FRP (mainly externally bonded carbon or glass fiber reinforced polymer) increases substantially the masonry load capacity, the static bending capability and the overall stiffness. This could be separated into two components: the nonlinear one representing the stiffness contribution of the masonry materials and a rather linear part representing the stiffness contribution of the fibre reinforcement.

Experimental and field data should be assessed to improve the masonry wall reinforcement design in order to increase the overall stiffness, strength and ductility (energy absorption capability) under real boundary conditions that prevail on full scale structures. The aim is to optimize strength and deformability in a synergistic interaction in order the reinforcement to become an integral structural part. The reinforcement design should ensure, through strengthening and deformability, that highly stressed zones are not developing in the reinforced masonry and also in the surrounding un-reinforced masonry and that the building will resist: out-of-plane bending, in-plane bending, in-plane shear, combined with axial load.

The objective of this study is twofold. The first objective is to experimentally investigate the seismic performance of full-scale, single room, un-reinforced masonry buildings and to validate the effectiveness of glass FRP strips as retrofitting techniques in an effort to improve the masonry wall stiffness, strength and ductility to withstand earthquakes. The second objective is to investigate and monitor the health of the structure through low amplitude dynamic testing and correlate the change in the dynamic characteristics of the structure to the intensity of ground shaking, the damages observed and the retrofitting actions carried using repair techniques and strengthening with glass fiber reinforced polymer (GFRP) material bands. The change of the dynamic characteristics, such as modal (resonant) frequencies and modal damping ratios, with damage and strengthening actions on the building are useful damage or strengthening index indicators. These indicators can be used for evaluating the degree of damage induced under seismic actions and the level of retrofitting steps required in order to restore the stiffness of the structure.

A series of shake table tests followed by low amplitude vibration tests were performed on a masonry building at its un-reinforced and reinforced configurations. The masonry building was designed in full scale to resemble typical brick masonry building types, encountered in countryside. The un-reinforced masonry building was subjected to a series of progressively intensified earthquakes until it was severely damaged, evident by the large crack openings in the four walls of the building. Then it was repaired, strengthened with GFRP strips until its original stiffness is recovered and re-tested with a similar second series of progressively intensified earthquakes to evaluate the effectiveness of the reinforcement. A new multifunctional GFRP textile material, developed under the European research project POLYTECT [18], is considered as retrofitting solution for un-reinforced masonry structures. Appropriate damage indices based on the observed evolution of the modal frequencies are introduced to monitor the health of the masonry structure and evaluate the effectiveness of retrofitting actions. Three different building and reinforcement configurations have been studied. The present study reports results from the third building and reinforcement configuration which was optimally designed based on existing guidelines and the experience from the tests on the first two masonry structures. The full-scale experimental tests are aimed to improve design retrofitting guidelines for masonry structures, taking into account realistic boundary conditions at the sides of the masonry walls, wall continuity at the corners and wall openings from windows and doors.

This study is organized as follows. Section 2 introduces the masonry building, the geometrical characteristics, the material properties identified from component tests, and the finite element model based on simplified assumptions on composite brick-mortal wall behavior. Details for the shake table facility and the building instrumentation are provided in Section 3. Section 4 presents the experimental set-up, giving details about the series of seismic experiments performed on the un-reinforced and the reinforced building along with the observed damages during the tests. Section 5 concentrates on the post-earthquake low-amplitude vibration tests performed to trace the modal characteristics of the masonry structure under the progressively intensified seismic events and retrofitting actions. It presents and discusses results for the correlation of the identified resonant frequencies and damping ratios with intensity of seismic excitation and stiffness degradations due to damage caused from the applied seismic events or stiffness restoration resulted from strengthening actions. Conclusions are summarized in Section 6.

2 DESCRIPTION OF MASONRY BUILDING AND MODELING

2.1 Building description with geometry

A full-scale single-story (one-room) brick-masonry building is designed and constructed in the laboratory. The un-reinforced brick building is representative of existing masonry buildings in Greece, particularly in the countryside. A picture of the intact building resting on the shake table is shown in Figure 1. The geometry of the masonry structure is shown in Figure 2. The masonry structure consists of four single masonry brick walls with two opposite doors and windows, and a reinforced concrete roof. The four walls of the masonry building are anchored on the shake table. The top view dimensions are 3.19m parallel to the X-axis and 2.78m parallel to the Y-axis. The structure height is 2.26m (including 10 cm concrete roof thickness). The door's width and height is 0.70m and 1.64m, respectively and it is placed on the center of the two opposite wall's width. The window's width and height is 0.70m and 0.70m, respectively and it is placed on the center of the two opposite wall's width. The layout of the door and window openings results in a symmetric building, avoiding eccentricities as much as possible. All the surrounding walls are 8.5 cm thick, determined by the width dimension of the bricks.

Figure 1: A picture of the intact masonry building.

2.2 Building materials and component tests

The construction of the masonry wall panels was based on common practices in Greece. The bricks used were common bricks used for the construction of masonry structures. The building brick is a rectangular, hollow multicored, clay prism of long dimension 187mm (parallel to the holes), height 112mm (perpendicular to the holes and along the vertical direction) and width 85mm (perpendicular to the holes and along the horizontal direction), weighting about 1.70 Kg.

Components tests were conducted separately on bricks, mortal and brick-mortal assemblies in order to understand their mechanical behavior and obtain their mechanical properties. These tests were performed using the mechanical testing equipment available on the Institute of Mechanics of Materials and Geostructures (IMMG). The tests included compression tests along directions parallel and perpendicular to the brick holes, as well as shear tests. In particular, based on the tests carried out on brick-mortal assemblies, consisted of a small number of building bricks bonded by mortal, the constitutive parameters in compression, tension and shear of the brick-mortar panels were experimentally measured. Compression tests on panels with the loading direction parallel to the brick holes confirmed higher peak strength values (nominal value of 4 MPa at 0.4% strain) but lower stiffness in comparison with loading of bricks normal to the holes where a nominal peak strength value of 3 MPa at 0.17% strain was measured. The mortal joint shear strength was found to be 0.7 to 0.75 MPa. Each compression tests was repeated for several speciment and a significant variation in the stiffness was observed. For example, the stiffness for the compression test with loading of bricks normal to the holes varied from 2.3 to 3.5 GPa. Similar ranges of variations were observed for the compression tests with loading parallel to the brick holes.

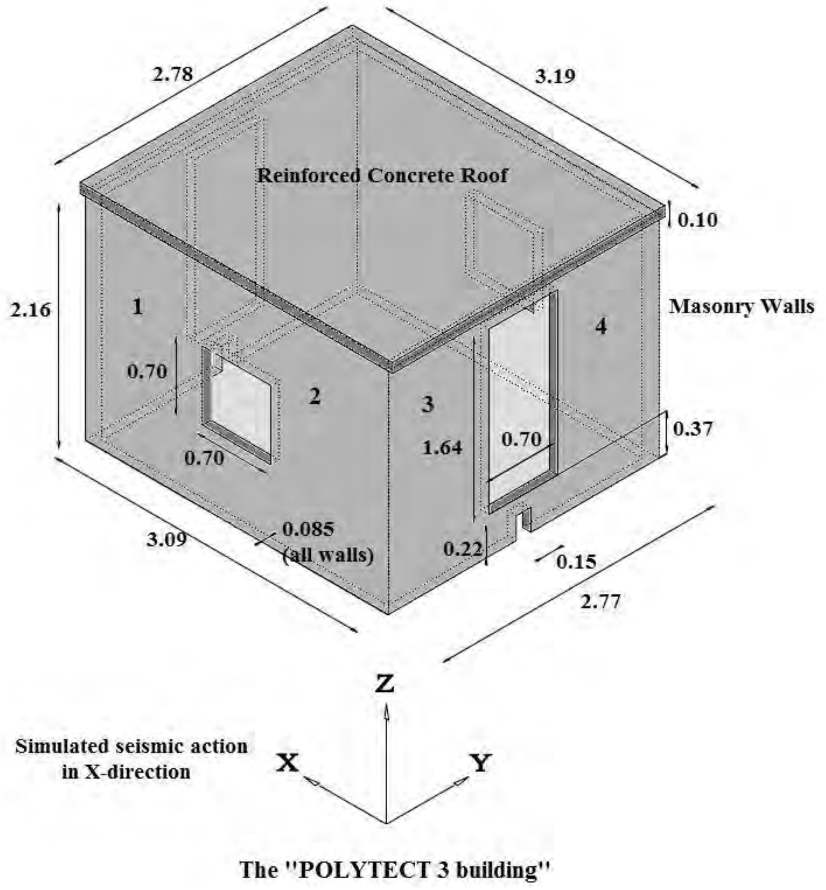

Figure 2: Geometric of masonry building.

2.3 Finite element model of the masonry building

A detailed finite element model of the masonry building at its undamaged un-reinforced state was created based on the geometric details and the material properties of the reinforced concrete roof and the masonry walls. The structure was designed in the COMSOL Multiphysics [19] finite element modelling environment. The finite element model for the structure was created using three-dimensional tetrahedral solid finite elements to model the whole structure. The elements along the basement are fixed in the direction of motion and the same applies for those linking the four walls and the concrete roof. The nominal values of the mechanical properties of the brick-mortal components and the reinforced concrete roof are used to construct a nominal linear finite element model of the masonry structure from the behavior of its components. Based on existing mechanical tests and the low strain levels expected to be experienced by the reinforced concrete roof during low-amplitude vibration tests, the roof was assumed to be homogeneous isotropic with material properties as follows: elasticity modulus E = 30 GPa, Poisson ratio n = 0.2 and density r = 2500 Kg/m^3. A homogeneous orthotropic material was assumed for the masonry walls to roughly account for the periodic structure of the brick-mortal elements. Based on the experimentally obtained stress-strain relationships, the following nominal values for the mechanical properties were assumed for the composite brick-mortal units: elasticity modulus parallel to the brick's holes E_1 = 1.8 GPa, elasticity modulus vertical to the brick's holes E_2 = 2.3 GPa, shear moduli G_1 = 0.64 GPa and G_2 = 0.82 GPa, Poisson ratio $n_1 = n_2 = 0.4$ and average density r = 1000 Kg/m^3. The finite element model is shown in Figure 3. It consists of 8341 solid finite elements and has 50553 degrees of freedom.

The linear finite element model of the building was constructed as a reference model in order to understand the dynamic behavior of the building under the various low intensity seismic excitations and gain an insight into the modal characteristics (modal frequencies and mode shapes) of the building. The model constitutes a simplified modeling of the complex behavior of the composite brick-mortal system. A more accurate modeling based on homogenization theories is expected to yield a much better description of the behavior of the masonry walls. In addition, the reinforcement using GFRP strips introduced extra modeling complications. However, such modeling is out of the scope of the present study.

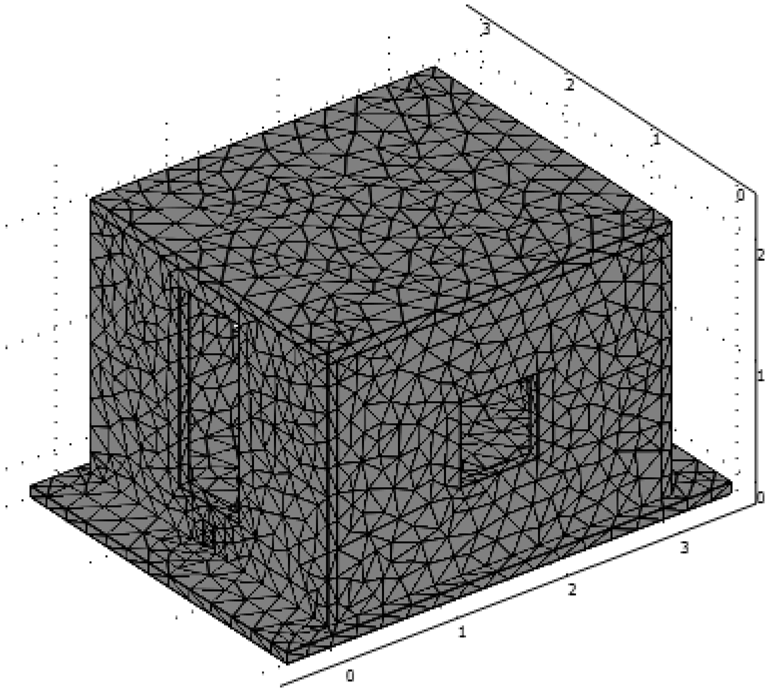

Figure 3: Finite element model of the masonry building using tetrahedral solid elements.

3 SHAKE TABLE FACILITY AND BUILDING INSTRUMENTATION

3.1 Shake table description

The tests were performed at IMMG. A unidirectional textile shake table was designed and constructed at IMMG for carrying out the seismic test campaign. The dimensions of the shaking table are 4m by 3m. The table is accelerated using a displacement controlled servo-hydraulic system, developed and validated within the European Research Project "POLYTECT" [18]. The table has the following two original characteristics. It is not metallic but textile table, produced by a honeycomb panel (glass reinforced PEEK), manufactured by IMMG based on the patented DIRIS architecture (Directionally Reinforced, Integrated, Stretched, Sing yarn) [20]. This panel is light, weighting only 210 Kg and extremely stiff, exhibiting the highest shear strength in in-plane and out-of-plane loading [21]. The actuation-control mechanism of the servofvalve is piezoelectric, reacting much faster and more precisely than the ones available in the market. Exploiting the previous capabilities, the shaking table possesses the following characteristics. It is capable of sinusoidal, random, shock and arbitrary time history excitation, it has a maximum payload of 10 Ton, maximum displacement of ±120 mm, maximum acceleration of 4 g (with 10 Tons payload), and frequency limit of 100 Hz. The reaction-actuating unit of the shake table facility is shown in Figure 4. The previous technical characteristics classify the facility as one of the few operating in Europe but with one distinction: its very low cost of construction (<10% of the equivalent European facilities) and operation.

Figure 4: The reaction-actuating unit of the shake table facility (left) with a masonry structure (right).

3.2 Building instrumentation

As many as twelve (12) uni-axial accelerometers, six (6) piezo beam and six (6) K-beam capacitive accelerometers, were mounted on the shake table and the structure in order to record the severity of the seismic excitation and the vibration levels experienced by the structure along all three directions, as well as to identify the structural modal characteristics from low amplitude vibration tests. The sensor locations along with the monitoring directions are shown in Figure 5. The sensor configurations depend on the series of the two tests conducted on the un-reinforced and reinforced masonry building. Only six (6) sensors were placed on the structure as shown in Figure 5(a) during the series of tests conducted for the un-reinforced masonry structure. Twelve (12) sensors were placed on the structure as shown in Figure 5(b) during the series of tests conducted for the reinforced masonry structure. For the reinforced structure, three different sensor configurations were employed based on the series of tests conducted and the experience gained from previous tests on similar reinforced masonry structures.

In general, up to as many as five sensor locations on the base of the structure were activated during the tests in order to monitor the acceleration of the shake table in all directions. Two of the acceleration positions (sensors 4 and 7) measure the horizontal base acceleration along the x-direction of the motion of the shake table. One sensor (sensor 12) measures along the horizontal y-direction perpendicular to the direction of motion and two sensors (sensors

11 and 13a) measure along the vertical z -direction in order to check possible rocking effects during the motion of the shake table.

A group of sensors was placed at the roof level to monitor the global motion of the masonry unit, and another group was placed at approximately the mid-height of the front wall to monitor in-plane and out-of-plane vibrations of the wall. A set of sensors was also placed on the roof to monitor the vibrations along its vertical direction and the out-of-plane motion of the roof. The sensor location was carefully designed so that all the response of the structure during the excitations from the earthquakes imposed by the shake table is carefully monitored and the important low frequency modes are identified during the low amplitude forced vibration tests performed after each seismic event. Experience from tests performed on very similar structures were used to design the sensor locations and directions.

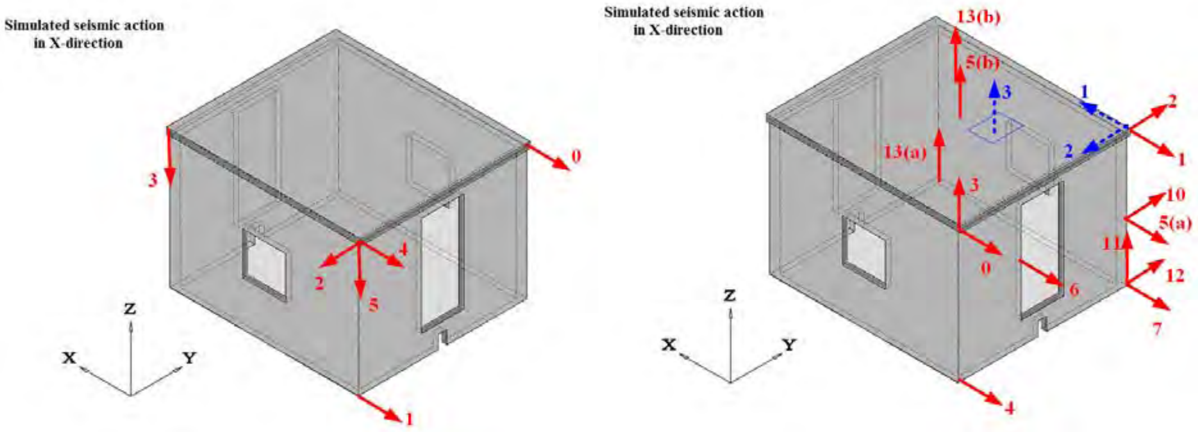

(a) (b)

Figure 5: Sensor configurations (positions) and hammer impact points on the masonry structure, (a) un-reinforced building, (b) reinforced building.

4 SHAKE TABLE SEISMIC EXPERIMENTS AND DAMAGE RESULTS

The objectives of the experiments are twofold. The first objective is to study the seismic performance of the un-reinforced masonry building and to evaluate the effectiveness of GFRP strips for retrofitting the structure to withstand earthquakes. The second objective is to investigate the change in the dynamic characteristics of the structure in terms of the intensity of ground shaking and correlate this change with the intensity of the shaking and the damage observed.

The un-reinforced masonry building was subjected to a series of progressively intensified earthquake events until it was severely damaged, evident by the large crack openings in the four walls of the building. Then it was repaired, strengthened with glass fiber reinforced polymer (GFRP) strips and re-tested using a second series of progressively intensified seismic events. The objective of the seismic experiments is to investigate the vulnerability of the un-reinforced building and then investigate the effectiveness of the GFRP reinforcement on the masonry building to withstand the second series of seismic events.

Section 4.1 describes the series of shake table strong motion tests performed on the un-reinforced masonry structure and reports the damages induced in terms of crack formation and openings in the masonry walls. Section 4.2 describes the repair procedure for the damaged masonry structure followed by the reinforcement of the masonry walls by GFRP strips. The results of second series of shake table tests performed on the retrofitted structure are presented in Section 4.3. The correlation of damage with the dynamic characteristics of the masonry structure during the various excitation phases is presented in Section 5.

4.1 Shake table tests of the un-reinforced masonry building

The seismic excitations exerted by the shake table were generated by scaling the intensity and the time of an artificial accelerogram, compatible with the elastic spectrum provided by the European Code EC8 for acceleration level $a_g =$ 0,15g. The artificial accelerogram is shown in Figure 6(a). The shake table command displacement time histories are obtained by double integration of the artificial accelerations. Figure 4(b) compares the corresponding command displacement time history fed to the shake table with the real displacement time history actually induced and measured at the shake table.

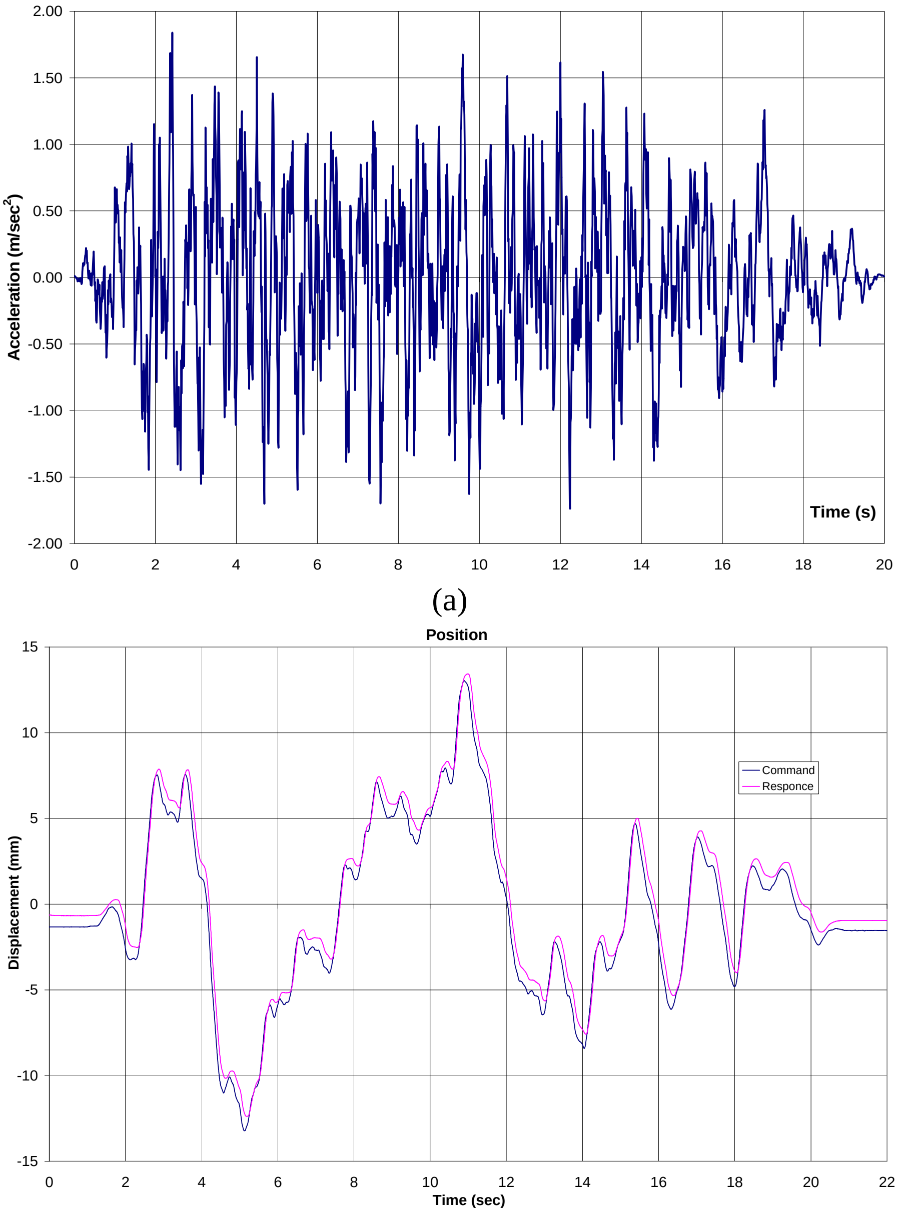

(a)

(b)

Figure 6: (a) Artificial earthquake shaking compatible with elastic spectrum provided by EC8 for $a_g =$ 0,15g, (b) Comparison between the command and the recorded displacement time history at the shake table.

A series of six (6) seismic excitation events were conducted that correspond to various peak ground acceleration (PGA) values selected to represent various levels of seismic intensity. These intensity levels were accomplished at the shake table by either scaling the intensity of the command displacement in the table, or scaling the time over which the earthquake was applied, or a combination of intensity and time scaling. Table 1 reports the information on the six seismic events, including the corresponding scale in intensity and time, and the actual PGA values recorded by the acceleration sensor placed on the shake table. In addition to the peak ground accelerations (PGA) along the direction of motion, the theoretical PGA values are also reported normalized so that they coincide with the measured PGA values for the unscaled earthquake excitation. It can be seen that the acceleration at the base has exceeded 2.5g.

The un-reinforced masonry building sustained the first five seismic events without suffering any serious visible damage. The last seismic event, which was theoretically intensified almost 8 times the original seismic event, heavily damaged the building with large crack openings developed along the walls and propagated mainly through the mortal. The four sides of the masonry building after the application of the sixth seismic event are shown in Figure 7. Based on visual inspection, the sixth seismic event generated shear failure of many bricks and mortar, diagonal cracking on the walls, extensive flexural faults and measurable shear sliding in the walls 1, 2, 5 and 6. Larger crack opening were observed on the two sides of the wall with the window openings that extend along the direction of motion. The other two sides of the building walls, with the door openings that extend along the perpendicular direction of motion, also sustained serious damage. All the walls were damaged but it seems that the in-plane shearing (walls 1-2 and 5-6) produced more damage than the out of plane loading (walls 3-4 and 7-8). Overall, during the action of the sixth seismic event, the masonry building sustained serious visual damage, with the walls loosing their structural integrity and posing increased threat to occupants due to high risk of collapse to future seismic excitations.

Seismic Event	**Intensity Scale (% of European Earthquake)**	**Time Scale (sec)**	**PGA Recorder Values (g)**	**PGA Theoretical Values (g)**
1st	20%	20	0.10	0.06
2nd	60%	20	0.29	0.19
3rd	100%	20	0.32	0.32
4th	100%	15	0.52	0.57
5th	100%	10	0.99	1.28
6th	100%	7	2.50	2.56

Table 1: Excitation characteristics of the seismic events applied on the un-reinforced building.

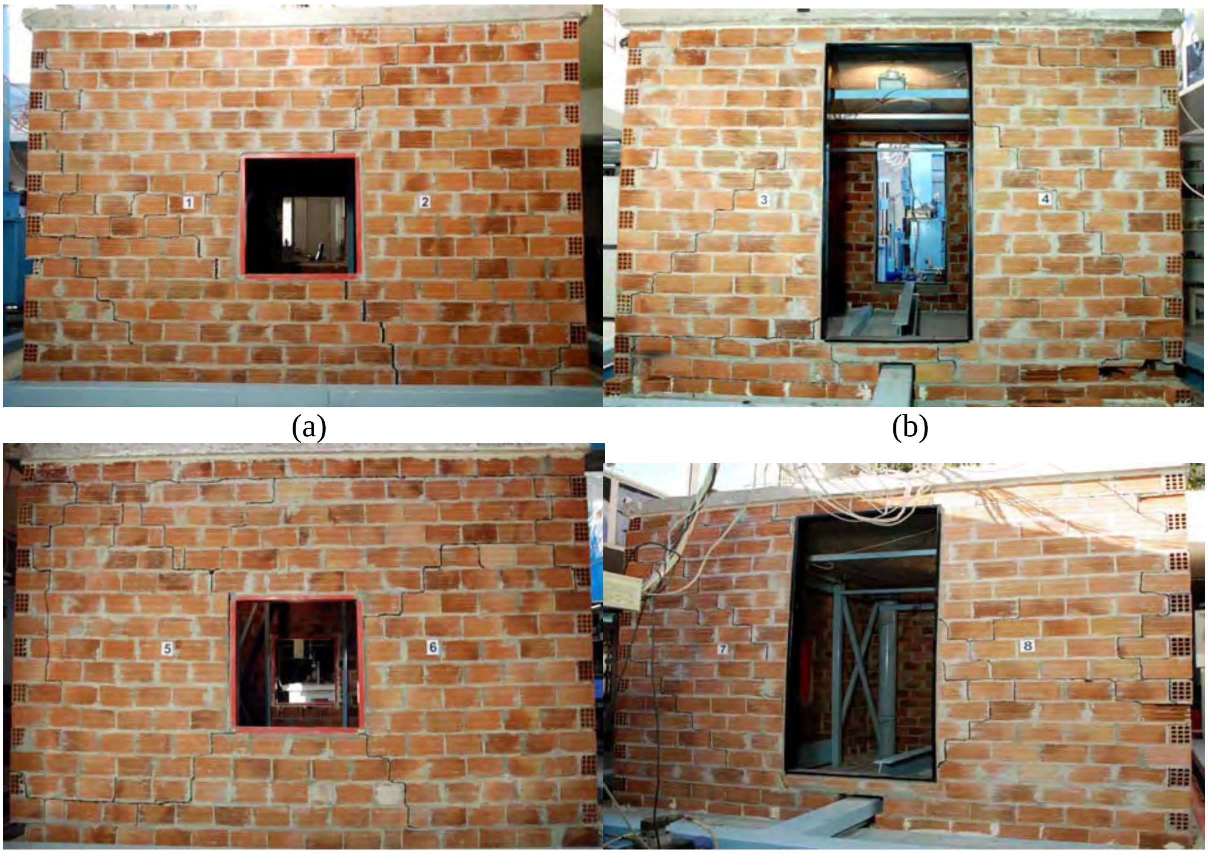

(a) (b)

(c) (d)

Figure 7: The masonry building damaged after the application of the sixth seismic event. (a) Walls 1 and 2, (b) Walls 3 and 4, (c) Walls 5 and 6, (d) Walls 7 and 8.

4.2 Repair of damaged masonry building and reinforcement with GFRP strips

The heavily damaged masonry building walls were repaired and strengthened. The restoration event refers to retrofitting of the damaged parts and application of an optimally designed GFRP strip reinforcement. Specifically, for retrofitting the damaged parts, the concrete roof was lifted, the cracked mortal and broken bricks along all four side walls of the building were removed and new mortal and bricks were placed. At the end the roof was bonded on the brick walls, as previously. The walls were carefully examined and small open cracks were cleaned with pressurized air and filled with pressurized epoxy in order to repair the structure and provide the necessary continuity between the different components.

The repairing design consists also of external reinforcement by bonding peripherically, tensioned glass fibre thermoplastic (GFRP) strips, with spacing in agreement with the CNR-DT/2004 guidelines [22]. Specifically, after the repair work was completed, the masonry walls were reinforced by GFRP strips against out-of-plane and in-plane loading, according to the CNR-DT/2004 guide. Figure 8 show the GFRP strip reinforcement along the masonry building walls 1-2 and 3-4. Exactly the same reinforcement patterns were applied along the masonry building walls 5-6 and 7-8. A schematic diagram of the reinforcement is also shown in Figure 9 and covers all four sides of the masonry walls along horizontal, vertical and diagonal directions. The GFRP strips are 150 mm wide, 3 mm thick and have 4 kN tensile strength.

(a) (b)

Figure 8: A picture of the repaired masonry building with reinforced GFRP strips; (a) sides 1-2, (b) sides 3-4.

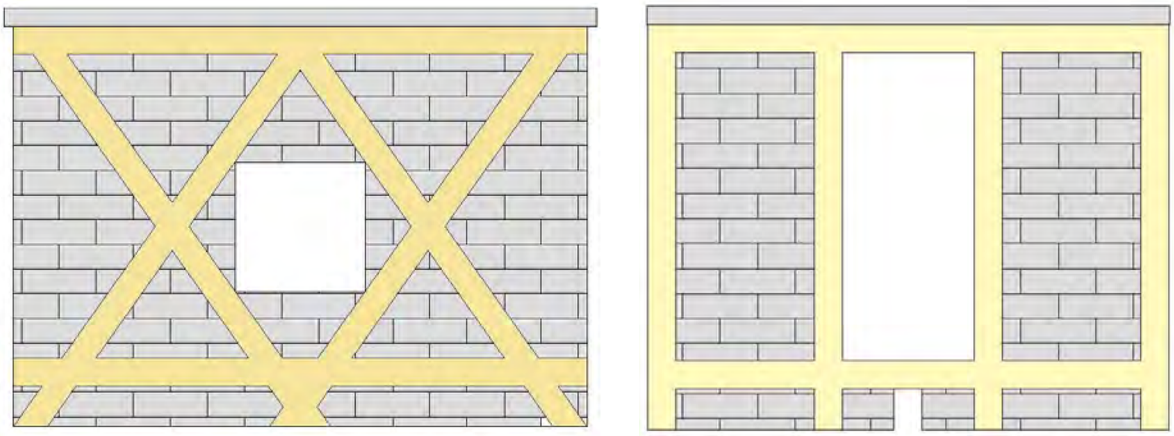

(a) (b)

Figure 9: A schematic diagram of the reinforcement on the masonry building; (a) sides 1-2 and 5-6, (b) sides 3-4 and 7-8.

The GFRP strips were bonded on the bricks, initially by polymer and then by polymer-cement plaster of B.G. Polymers. The patterns – positioning of the strips were designed to maximize the out-of-plane resistance for the walls with the doors (sides 3, 4, 7 and 8) and the in-plane resistance to shear for the walls with the windows (sides 1, 2, 5 and 6) along the direction of loading. To this end the strips are parallel in the walls with the doors and diagonal in the remaining walls with windows. The thin and flexible strips allow the masonry to move (to micro-slide) and therefore to mobilize more effectively reaction mechanisms to absorb energy. Also the symmetry of the strip layout prevents eccentric stiffness and strengthening that may cause twisting.

It should be noted that the retrofitting actions are expected to partly restore the stiffness of the structure. The degree of stiffness restoration will be examined in the next section. In addition, the ultimate strength of the reinforced structure is expected to be much higher since the structure was retrofitted with the GFRP strips. Also, the existence of the GPFR reinforcement provides the reinforced structure with ductility and higher capability of absorbing energy at low strains.

4.3 Shake table tests of masonry building repaired and reinforced with GFRP strips

A new series of earthquake excitation tests were conducted on the retrofitted building by scaling the intensity and time of the 2009 L’ Aquila W-E earthquake accelerogram, shown in Figure 10. Thirteen (13) seismic excitation events were included in the new series of tests. The thirteen excitations correspond to various intensity levels of the L’ Aquila earthquake. As before, the different intensity levels were accomplished at the shake table by either changing the intensity of the command displacement in the table or scaling the time over which the earthquake was applied. Table 2 reports the information on the thirteen seismic excitation events, including the corresponding scale in intensity and time. It also gives the PGA values along the direction of motion.

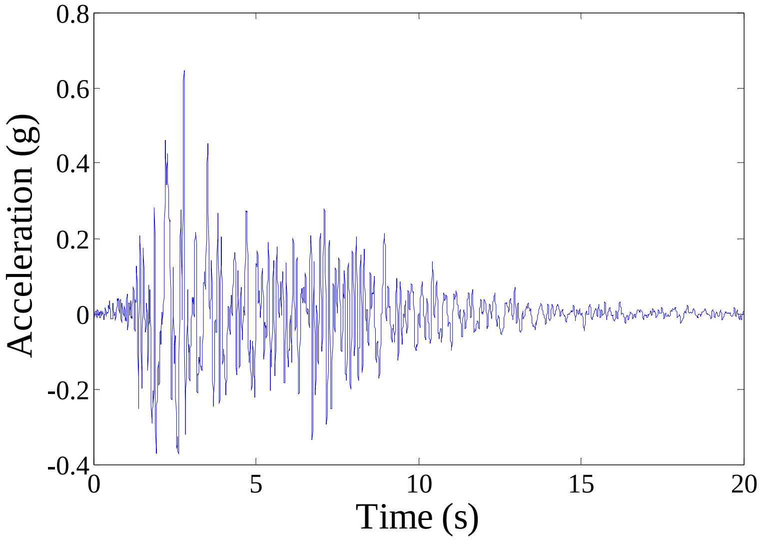

Figure 10: 2009 W-E component of L’ Aquila earthquake shaking.

Seismic Event	Intensity Scale (% L’ Aquila Earthquake)	Time Scale (sec)	PGA Recorded Values (g)	PGA Theoretical Values (g)
1st	20%	20	0.15	0.07
2nd	60%	20	0.29	0.21
3rd	100%	20	0.35	0.35
4th	100%	15	0.41	0.62
5th	100%	12	0.93	0.97
6th	100%	11	0.61	1.15
7th	100%	10	1.16	1.40
8th	100%	9	1.39	1.73
9th	100%	8	1.50	2.19
10th	100%	7	2.90	2.85
11th	100%	6	3.90	3.89
12th	100%	6	3.90	3.89
13th	100%	7	4.00	2.80

Table 2: Excitation characteristics of the seismic events applied on the reinforced building

In contrast to the severe damage observed for the un-reinforced building at the end of the sixth seismic event, no damage was observed in terms of visible cracks on the mortal, the bricks or the interfaces between them. The integrity of the masonry walls, seeing as a unit of bricks and mortal, and the integrity at the interface between the masonry walls and the table or the roof, was preserved. Comparing the characteristics of the two series of shake table seismic tests applied on the un-reinforced and reinforced building in Tables 1 and 2, respectively, it is obvious that in the case of the reinforced building, higher peak ground accelerations are recorded. Specifically, the last earthquake applied on the reinforced building has a ground shaking with PGA almost two times the PGA of the base shaking for the sixth earthquake applied on the un-reinforced building. Despite this stronger shaking of the reinforced building, the reinforced masonry performed very well and withstood the very strong ground shaking with no visible damage. It can be concluded that the reinforcement was sufficient to maintain the structural integrity of the masonry walls.

5 DAMAGE EVALUATION BASED ON DYNAMIC CHARACTERISTICS

The health state of the structure after each shake table test was evaluated by monitoring the modal dynamic characteristics such as modal (resonant) frequencies and modal damping ratios. These characteristics were identified by carrying out very low-amplitude forced vibration tests after each seismic event. These low-amplitude vibration tests, described in Section 5.1, are used to measure the modal characteristics and correlate the evolution of these characteristics with the stiffness degradation and observed damage caused by the seismic events. The reduction of the lower modal frequencies of the masonry structure after the application of each earthquake event is used as a damage index [23] to provide an overall measure of the damage state of the masonry structure at its un-reinforced and reinforced configurations.

5.1 Post-earthquake low amplitude forced vibration tests

The low amplitude vibration tests were performed with a PCB086D20 impulse hammer equipped with a medium tip head in order to excite the important lower modes of the masonry structure needed for the evaluation of its dynamic characteristics, such as modal frequencies, modal damping ratios and mode shapes. The vibration tests were performed before the shaking table tests were initiated and immediately after each earthquake event was inflicted by the shaking table on the structure. The purpose of the impulse hammer tests was to identify the dynamic characteristics of the structure and mainly to trace the change in the modal frequencies and the damping ratios as a function of the severity of the seismic excitation and the observed damage.

After each earthquake event, a total of 6 impulse hammer tests were contacted. The impact force was inflicted along the two horizontal directions and one vertical direction in order to excite all lower important modes of the structure. The impact points and directions are shown in Figure 5(b) with blue (broken) arrows. Two independent tests per each excitation direction were performed. Each impulse hammer test lasted only a few seconds allowing to speed up considerably the whole procedure of acquiring data from the structure.

During the first four (4) seismic tests (1st, 2nd, 3rd, and 4th) the building was instrumented with 10 sensors (sensors 0, 1, 2, 3, 4, 5, 10, 11, 12 and 13 in Figure 5(b)). During the 5th, 6th and 7th seismic tests the building was instrumented with 12 sensors: sensors were added at positions 6 and 7 in Figure 5(b) and the sensors 5(a) and 13(a) in the set up shown in Figure 5(b) were re-positioned (at locations (5b) and 13(b) in Figure 5(b)) on the roof of the building as shown in Figure 5(c). This sensor relocation was necessary in order to monitor the z-direction and take more accurate measurements of the out-of-plane mode of the concrete roof where strong motion was detected. During the final six (6) seismic events (8th to 13th events) the building was again instrumented with 12 sensors. The location of sensor 13(b) in sensor configuration shown in Figure 5(b) was changed to its original location 13(a).

To verify the reliability and accuracy of the dynamic characteristics obtained by analyzing the very low vibration results obtained from the impulse hammer tests, a sine sweep test campaign was also independently conducted using a eccentric mass shaker mounted at the top of the concrete roof. The roof shaker was used to excite the structure and compute the modal frequencies from the power spectral densities of the recorded acceleration signals. Complete frequency sweeps from 1 to 50 Hz with increasing step of 0.1 Hz were carried out. The low vibration levels that resulted from these tests were significantly higher than the vibration tests resulted from the impulse hammer tests. In contrast to the impulse hammer series of 6 tests lasting a couple of minutes after each earthquake event, each sine sweep test lasted a period of half an hour. Such experiments were performed only for the initial un-reinforced structure and yielded the same natural frequencies as the impulse hammer tests. Thus, it was not deemed necessary to perform these time-consuming sine sweep experiments for the reinforced masonry structure.

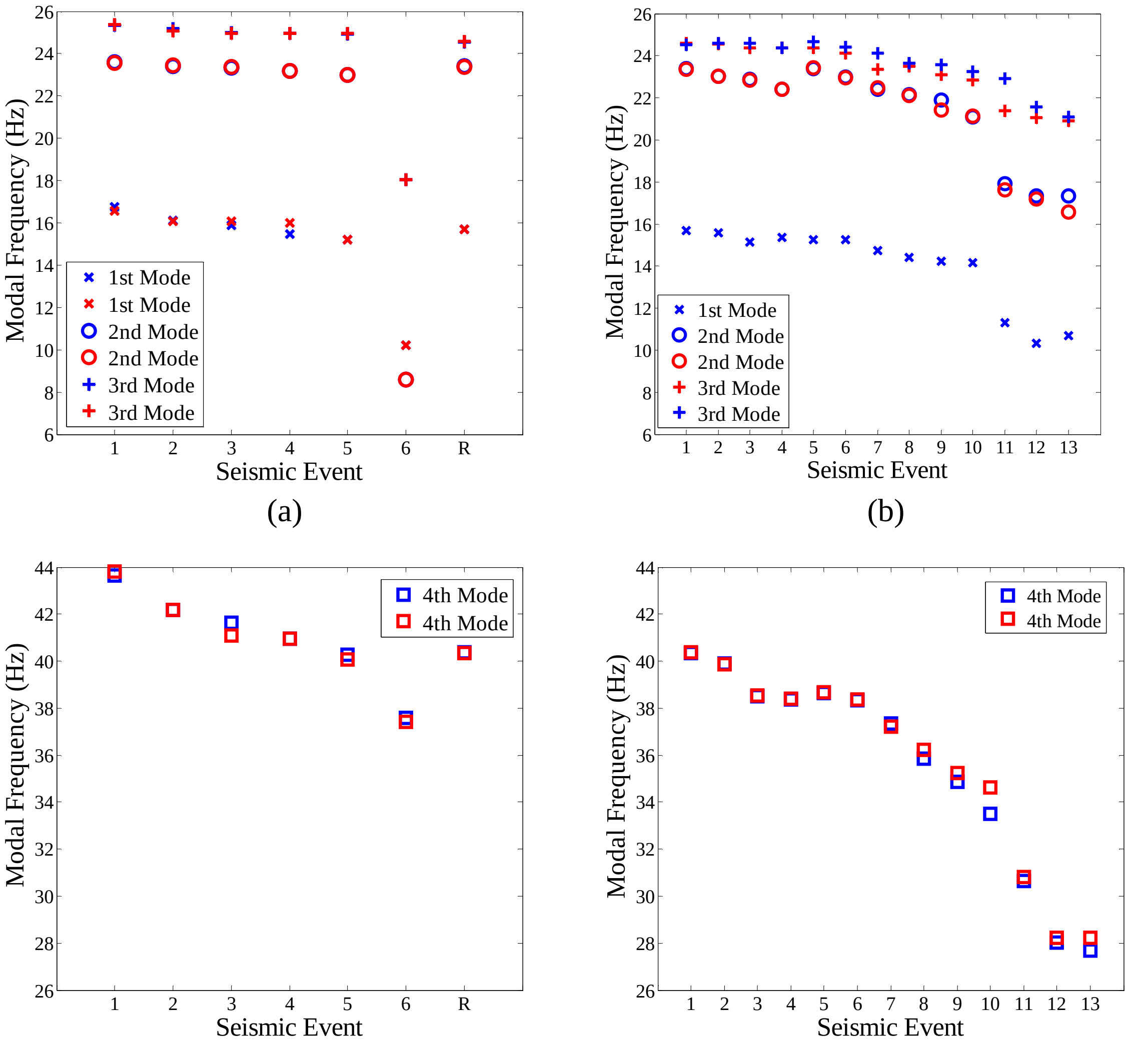

(a) (b)

(c) (d)

Figure 11: Evolution of modal frequencies as a function of the seismic events (a,c) un-reinforced building, (b,d) reinforced building.

The recorded acceleration time histories and the impulse force for each test were used to obtain the frequency response functions and then the PolyMAX frequency domain method [24] was applied to identify the modal characteristics of the structure. For this, the modal identification, graphical user interface, toolbox MI-Tool developed in SDLab of the University of Thessaly [25] was conveniently used to estimate the modes. The identified modal frequencies and modal damping ratios for the lowest four modes are reported in Figures 11 and 12 as a function of the seismic event for both the un-reinforced and the reinforced building. For each seismic event, more than one modal frequencies may be shown that results from the analysis of multiple vibration tests available. Representative mode shapes identified by the measurements are shown in Figure 13 and should be compared to the mode shapes in Figure 14 predicted by the nominal finite element model developed in Section 2.3. The length of the arrows in Figure 13 denotes the magnitude of each component of the mode shape along the measured DOF. It is clear that the first lowest mode in Figure 13(a) corresponds to the first shear mode in the horizontal y-direction perpendicular to the direction of the shake table motion, the second lowest mode in Figure 13(b) corresponds to the first shear mode in the horizontal x directions which is along the direction of the shake table motion, the third mode in Figure 13(c) is dominated by the first bending mode (out-of-plane mode) of the concrete roof, while the fourth mode in Figure 13(d) corresponds to a torsional mode of the building that arise from the rotation of the roof with respect to the vertical z-direction.

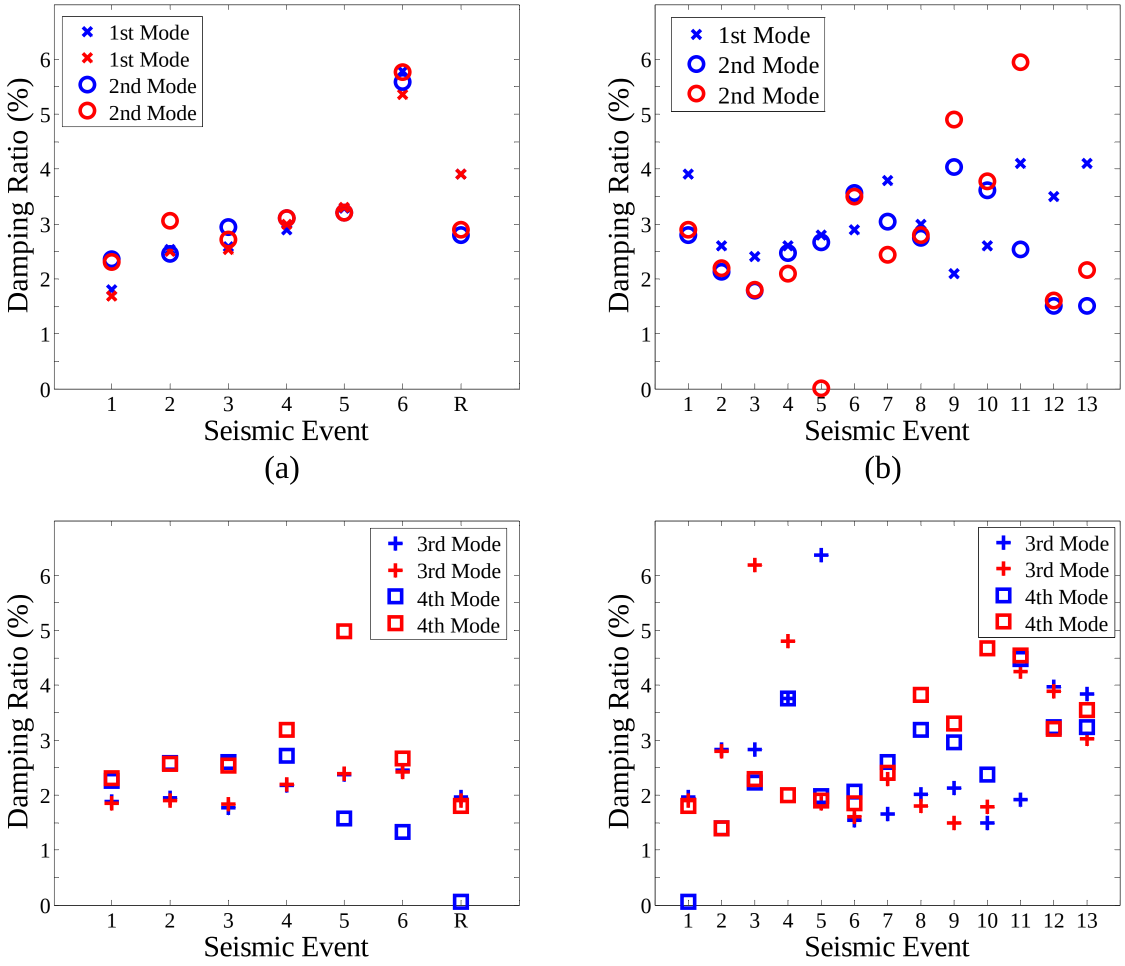

(a) (b)

(b) (d)

Figure 12: Evolution of modal damping ratios as a function of the seismic events (a,c) un-reinforced building, (b,d) reinforced building.

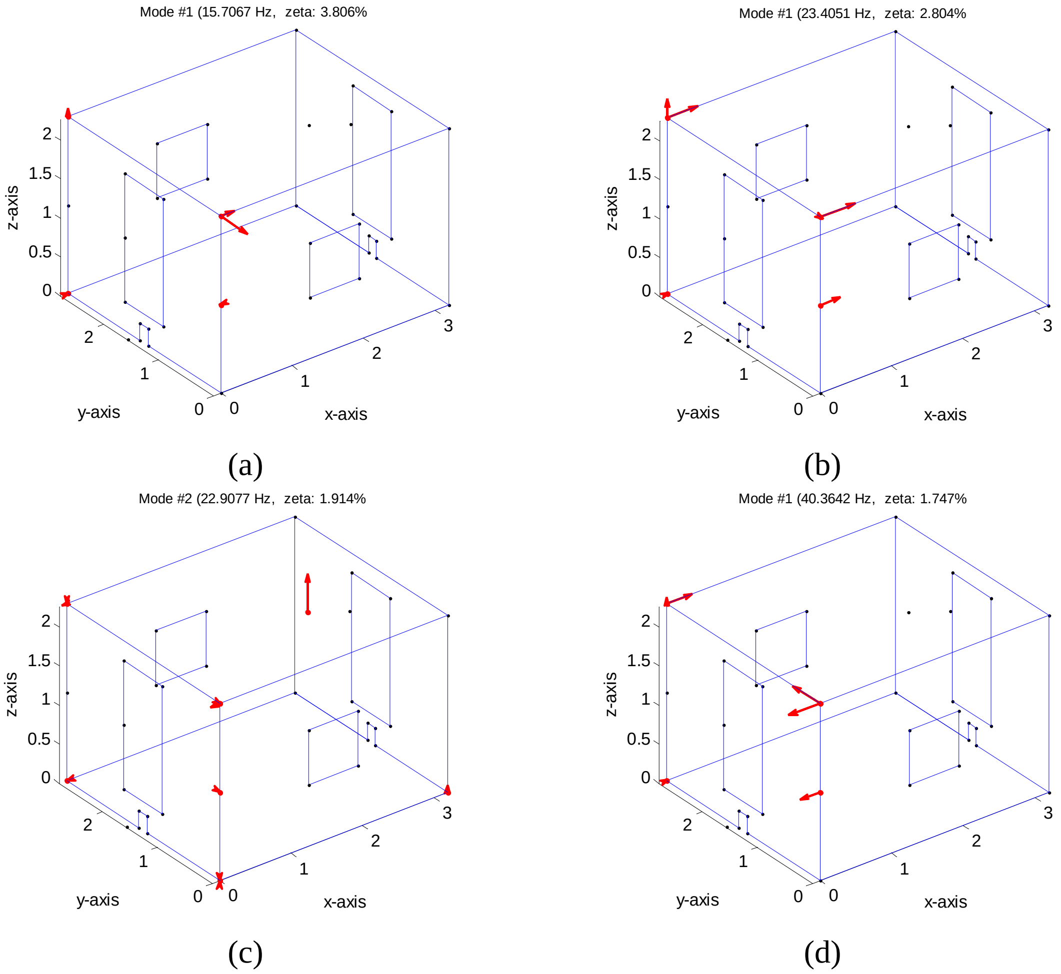

(a) (b)

(c) (d)

Figure 13: Identified mode shapes (a) first mode, (b) second mode, (c) third mode, (d) fourth mode.

5.2 Correlation of dynamic characteristics with seismic intensity, building damage and retrofitting actions

The change (reduction or increase) of the lowest four modal frequencies observed in Figure 11 is due to the change in stiffness of the masonry building caused by damage under the applications of the seismic events or by the retrofitting actions. The results in Figure 11 confirm that the identified values of the modal frequencies are highly dependent on the intensity levels of the seismic events and the corresponding health state of the building. The PGAs of the seismic events are shown as a functions of the seismic events in Figures 15(a) and 15(b) for the un-reinforced and the reinforced building, respectively.

Specifically, from the results in Figures 11(a) and 11(c), one clearly observes that earthquake shaking damages internally the structure causing a stiffness degradation, manifested as a reduction in the values of the modal frequencies. As the intensity of the earthquake event increases the values of all four modal frequencies reduce. However, for the first five seismic events no visible cracking in the masonry walls was evident for the case of the un-reinforced masonry structure. The small reduction of the modal frequencies observed is an indication of internal damage caused by non-visible micro cracking in the mortal and the interface between the mortal and the bricks. A large reduction in the modal frequency is observed after the sixth earthquake event which is due to significant stiffness deterioration caused by the severe damage in the masonry walls. As mentioned before, under the action of the sixth seismic event all four masonry walls sustained large crack openings, shown in Figure 7.

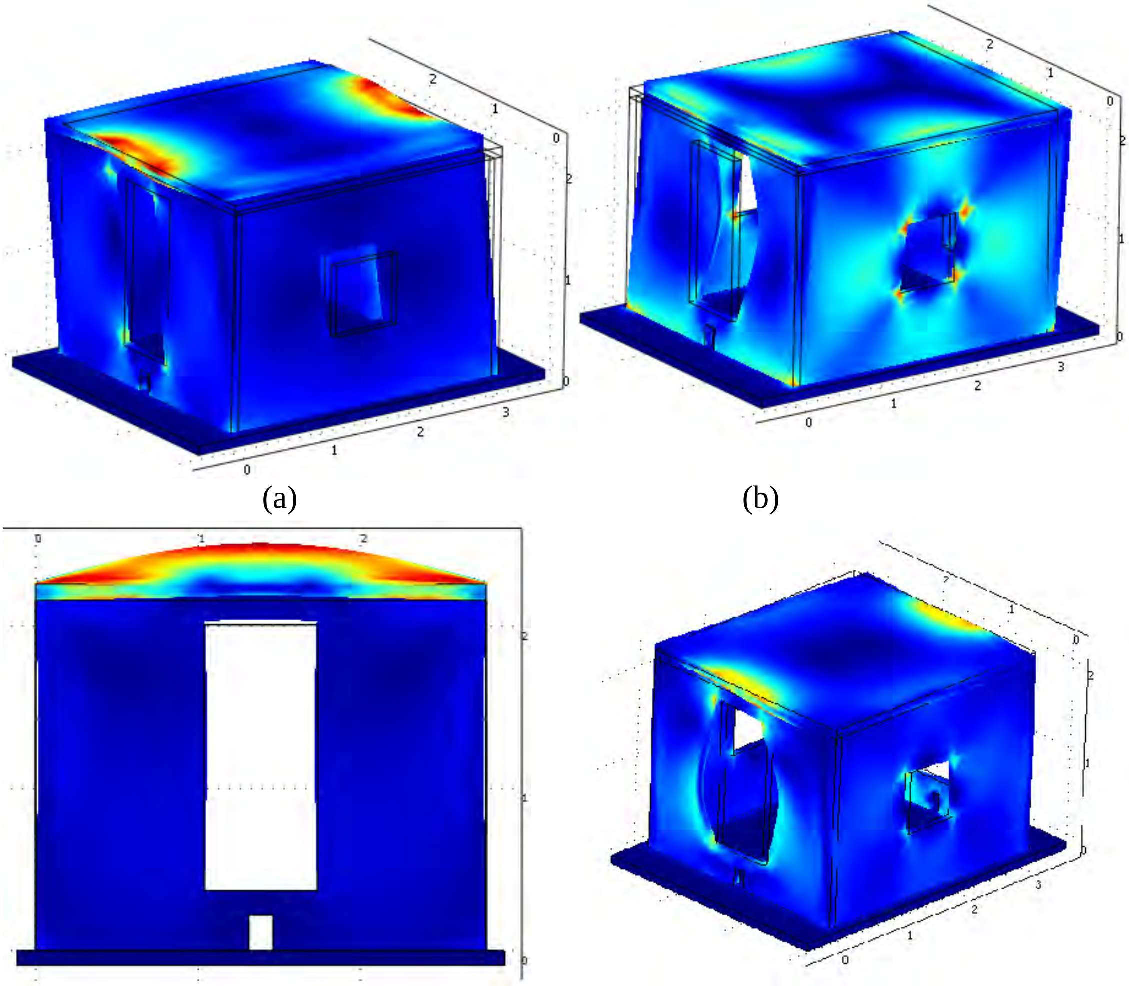

(a) (b)

(c) (d)

Figure 14: Model predicted mode shapes (a) first mode, (b) second mode, (c) third mode, (d) fourth mode.

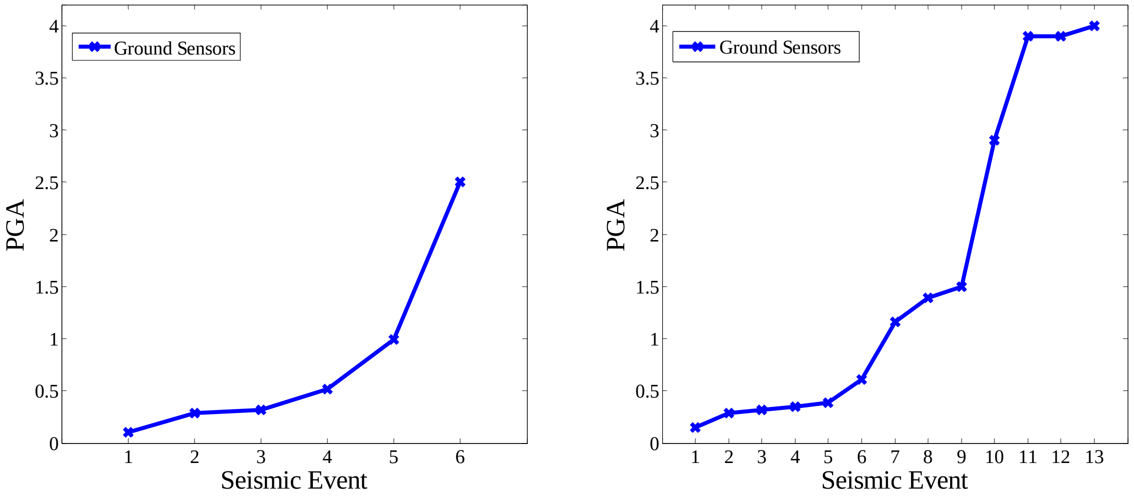

(a) (b)

Figure 15: Evolution of PGA as a function of the seismic events (a) un-reinforced building, (b) reinforced building.

After the building was repaired and reinforced with the GFRP strips, the identified modal frequencies of the retrofitted structure shown as the reinforcement event "R" in Figures 11(a) and 11(c) have increased substantially to almost the initial values of the modal frequencies of the un-reinforced building at its original un-damaged state. Thus the strengthening resulted in recovering the original stiffness levels of the un-reinforced building.

Based on the results obtained in Figures 11(b) and 11(d) for the re-tested reinforced masonry building, a similar reduction in the modal frequency values is observed as the intensity of the seismic events increases. The first ten seismic events reduced slightly the modal frequencies, while the last three strong seismic events reduced the modal frequencies considerably. However, no visible cracking in the reinforced masonry walls was evident for all earthquake tests for the case of reinforced masonry structure. The reduction in modal frequencies is again due to stiffness degradation and it is an indication of internal damage caused by micro cracking in the mortal and the interface between the mortal and the bricks. Such reduction was also observed for the first five seismic events for the un-reinforced building and it seems to indicate that the same damage mechanism was triggered even for the reinforced structure. This is consistent with similar results observed in [26].

The aforementioned results provide clear evidence that the changes in modal frequency are correlated with (a) stiffness degradation in the structure caused by damage after a seismic event, or (b) stiffness improvement caused by the retrofitting and strengthening actions using GFRP strips. This evolution (reduction or increase) of the modal frequencies can be used as a damage or strengthening index indicator. In addition, the availability of the modal frequency values of the undamaged building is useful for stiffness restoration of the damaged building using repair and strengthening actions. When the modal frequencies of a building are available using vibration measurements before a damaging event, then the restoration steps for a damaged building can be continued up to the level where the modal frequencies of the retrofitted structure reach (or even exceed) the original values of the undamaged building. This is a safe, validated procedure confirming that the initial stiffness of the structure is restored. However, if the modal frequencies of the undamaged building are not known and the building is damaged after an earthquake, the level of repairing cannot be defined with sufficient precision. Numerically predicted modal frequencies of the undamaged building based only on simplified finite element models for masonry walls, provide only qualitative information and not accurate quantitative information about the actual dynamic characteristic of the building. To provide a more accurate quantitative prediction of the building dynamic properties, numerical models should be developed that properly take into account the highly complex composite nature of the masonry walls and the boundary conditions resulting from the presence of window and door openings, the connections of the walls at the corners as well as the connections of the walls with the table and the roof.

Based on the results in Figure 12, the damping ratios of the lowest four modes at low vibration levels under which the post-earthquake vibration tests were conducted range from 1% to 6%. The damping ratio values for the lowest three modes of the un-reinforced building tend to increase with the intensity of the seismic event. This indicates that damage causes the damping ratios of the structure to increase in general. The overall increase of damping ratios with damage is consistent with results reported for other structures. However, a certain increasing tendency is not clear for the reinforced building. The use of the evolution of the damping ratio values as a damage index indicator is not suitable partly due to the fact that the fluctuation in the estimates of the modal damping ratios from repeated vibration tests using experimental modal analysis techniques is relatively high and this fluctuation may mask the real correlation that may exist between the modal damping ratios and the damage or strengthening actions on the structure.

Concluding, progressively increasing the intensity of the seismic event has an effect on the stiffness of the un-reinforced and reinforced structure as it is observed by the reduction in the modal frequencies. The un-reinforced brittle masonry walls sustained/suffered severe damage, losing structural integrity and posing increasing threat to occupants. The GFRP strips, however, maintained the integrity of the structure, causing no visible damage. GFRP strips are considered as one of the promising retrofitting strategies for protections of seismically excited masonry structures.

6 CONCLUSIONS

A series of progressively intensified shake table seismic vibration tests were performed on an un-reinforced and a reinforced and re-tested full-scale masonry structure in order to evaluate its seismic vulnerability and to validate the effectiveness of the reinforcement to withstand earthquakes. Low amplitude vibration tests were carried out to monitor the evolution of the dynamic characteristics of the structure after each seismic test. The un-reinforced masonry building was severely damaged with large visible crack openings manifested at all masonry walls. The retrofitted masonry building was obtained from the severely damaged un-reinforced masonry building by fixing the cracked masonry walls and bonding on the masonry walls specially designed GFRP bands. Despite the larger amplitude earthquake events applied on the reinforced building, no visible cracks were observed. The GFRP material, covering 20% of the masonry wall surfaces, was proven to be very effective in reinforcing the masonry building to withstand earthquake events significantly larger in magnitude than the ones caused severe damage to the un-reinforced building.

It was demonstrated that changes in modal frequency are correlated with stiffness degradation caused by minor to severe damage in the masonry walls after a seismic event, as well as correlated with stiffness improvement caused by repair and GFRP strip strengthening actions. The reduction or increase of the modal frequencies identified from low-amplitude vibration tests can be respectively used as damage or strengthening index indicators. Severe damage due to large crack formations along the un-reinforced masonry walls, is associated with significant stiffness reduction manifested as substantial shift in the lowest four modal frequency values, especially for the mode with the dominant deflections in the direction of shaking. Repair and strengthening with GFRP strips can restore and even exceed the stiffness to the original values of the un-damaged un-reinforced structure. The identified modal frequency reductions of the reinforced building under the series of earthquake tests were of similar level as the un-reinforced building. The observed reductions in modal frequencies of the reinforced masonry structure are attributed to the formation of non-visible micro-cracks between the brick and the mortal material which affected the stiffness of the masonry walls and thus the building’s global dynamic characteristics. The damping ratios of the lowest four modes identified from low amplitude vibration tests also show a general increasing tendency with the intensity of seismic excitation and the level of damage. However, such tendency may be hidden by the large fluctuations in the identified values of the modal damping ratios.

The shift of identified modal (resonant) frequencies with the intensity of excitation using low-amplitude vibration tests allows the assessment of the stiffness degradation after each loading event or improvement after a strengthening event. This procedure seems sufficient for developing a vibration–based damage or repairing assessment technique.

It was experimentally demonstrated that reinforcement based on the proposed GFRP material bands significantly stiffness and strengthens the structure. The proposed reinforcement applied before or after a damaging seismic event is useful for reducing the vulnerability and seismic risk of brick masonry structures. Optimally placed GFRP strips are thus considered as one of the promising retrofitting strategies for protections of seismically excited masonry structures.

ACKNOWLEDGEMENTS

This research is funded by the European research project POLYTECT. This support is gratefully acknowledged.

REFERENCES

[1] G.D. Wight, M.J. Kowalsky, J.M. Ingham, Shake table testing of post-tensioned concrete masonry walls with openings. *Journal of Structural Engineering*, **133**, 1551-1559, 2007.

[2] G. Marcari, G. Manfredi, A. Prota, M. Pecce, In-plane shear performance of masonry panels strengthened with FRP. *Composites Part B: Engineering*, **38**, 887-901, 2007.

[3] A.S. Mosallam, Out-of-plane flexural behavior of unreinforced red brick walls strengthened with FRP composites. *Composites Part B: Engineering*, **38**, 559-574, 2007.

[4] C.-H. Huang , Y.-C. Sung, C.-H. Tsai, Experimental study and modeling of masonry-infilled concrete frames with and without CFRP jacketing. *Structural Engineering and Mechanics*, **22**, 449-467, 2006.

[5] J. Liu, M. Liu, Y. Song, Experimental investigation on flexural performance of masonry walls reinforced with GFRP. *Journal Wuhan University of Technology, Materials Scince Edition*, **22**, 82-84, 2007.

[6] M. Turek, C.E. Ventura, S. Kuan, In-plane shake-table testing of GFRP-strengthened concrete masonry walls. *Earthquake Spectra*, **23**, 223-237, 2007.

[7] F. Bastianini, M. Corradi, A. Borri, A.D. Tommaso, Retrofit and monitoring of an historical building using ‘smart’ CFRP with embedded fibre optic Brillouin sensors. *Constructions and Building Materials*, **19**, 525-535, 2005.

[8] A. Gabor, E. Ferrier, E. Jacquelin, P. Hamelin, Analysis of the in-plane shear behaviour of FRP reinforced hollow brick masonry walls. *Structural Engineering and Mechanics*, **19**, 237-260, 2005.

[9] P. Agarwal, S.K. Thakkar, A comparative study of strengthening and retrofitting measures for unreinforced brick masonry model under cyclic testing. *Journal of Earthquake Engineering*, **8**, 839-863, 2004.

[10] J. Paquette, M. Bruneau, S. Brzev, Seismic testing of repaired unreinforced masonry building having flexible diaphragm. *Journal of Structural Engineering*, **130**, 1487-1496, 2004.

[11] A.C. Burr, Recent developments in the use of FRP anchors and masonry wall strengthening techniques. *Structural Engineer*, **82**, 20-21, 2004.

[12] A. Fam, D. Musiker, M. Kowalsky, S. Rizkalla, In-plane testing of damaged masonry wall repaired with FRP. *Advanced Composites Letters*, **11**, 275-281, 2002.

[13] K.H. Tan, M.K.H. Patoary, C.S.K. Roger, Anchorage systems for masonry walls strengthened with FRP composite laminates. *Journal of Reinforced Plastics and Composites*, **22**, 1353-1371, 2003.

[14] R.M. Kiss, L.P. Kollar, J. Jai, H. Krawinkler, Masonry strengthened with FRP subjected to combined bending and compression. Part II: Test Results and Model Predictions. *Journal of Composite Materials*, **36**, 1049-1063, 2002.

[15] R.M. Kiss, L.P. Kollar, J. Jai, H. Krawinkler, FRP strengthened masonry beams. Part I: Model. *Journal of Composite Materials*, **36**, 521-536, 2002.

[16] M.L. Albert, A.E. Elwi, J.J.R. Cheng, Strengthening of unreinforced masonry walls using FRPs. *Journal of Composites for Construction*, **5**, 76-84, 2001.

[17] T.C. Triantafillou, Strengthening of masonry structures using epoxy-bonded FRP laminates. *Journal of Composites for Construction*, **2**, 96-104, 1998.

[18] POLYTECT, 6 FP project of the E.C., Contract NMP2-CT-2006-026789.

[19] COMSOL AB, *COMSOL Multiphysics User's Guide*, (http://www.comsol.com/), 2005.

[20] P. Michelis, European Patent No EP08386002.3.

[21] IMMG, Final Report, ESA Contract No 21102/07/NL/PA, 2008.

[22] CNR-DT 200/2004, Guide for the Design and Construction of Externally Bonded FRP Systems for Strengthening Existing Structures, *National Research Council*, Rome, July 2004.

[23] S. Casciati, K. Hamdaoui, Experimental and numerical studies toward the implementation of shape memory alloy ties in masonry structures. *Smart Structures and Systems*, **4**, 153-169, 2008.

[24] B. Peeters, H. Van der Auweraer, P. Guillaume, J. Leuridan, The PolyMAX frequency-domain method: A new standard for modal parameter estimation?. *Shock and Vibration*, **11**, 395-409, 2004.

[25] E. Ntotsios, *Modal Identification of Structures using Ambient Vibrations: Theory, Software and Applications.* MSc Thesis, University of Thessaly, Department of Mechanical Engineeirng, 2009.

[26] D. Benedetti, P. Carydis, P. Limongelli, Evaluation of the seismic response of masonry buildings based on energy functions. *Earthquake Engineering and Structural Dynamics*, **30**, 1061-1081, 2001.

COMPDYN 2011
3rd ECCOMAS Thematic Conference on
Computational Methods in Structural Dynamics and Earthquake Engineering
M. Papadrakakis, M. Fragiadakis, V. Plevris (eds.)
Corfu, Greece, 25–28 May 2011

PERFORMANCE INDICATOR OF A BRIDGE EXPANSION JOINT

Ivo M. Kalkman[1], Sven S.K. Lentzen[1], Wim M.G. Courage[1], Oswaldo Morales Napoles[1], and Flavio M.B. Galanti[1]

[1] TNO Built Environment and Geosciences
Van Mourik Broekmanweg 6, 2628 XE Delft, the Netherlands
e-mail: (ivo.kalkman, sven.lentzen, wim.courage, oswaldo.moralesnapoles, flavio.galanti)@tno.nl

Keywords: Structural Health Monitoring, Expansion Joint, Inverse Modeling, Failure Parameters, Damage Prediction, Maintenance Planning.

Abstract. *In general the condition of a structure can be assessed in terms of a performance indicator. For example, this can be the strength of a structure. An asset manager is concerned with ensuring that the performance of a structure does not fall below a given minimum level. This can be achieved by inspecting or monitoring the structure. As the performance indicator decreases with time, the asset manager can decide to take pre-emptive measures to restore the condition to its initial level, thus avoiding getting too close to the minimum required level. In order to work this way, it is important to define a reliable performance indicator. Following an inventory of structures which are prone to some form of degradation over time, a modular bridge expansion joint was selected as a case to be considered in this investigation.*

In order to determine the observability of known failure mechanisms in terms of modal and spectral data an experiment is set up which can simulate the construction under these circumstances. Further, a Finite Element Model of the construction is made, which is tuned to the experimental setup. This model is used to validate the applied inverse modeling technique to identify the failure parameters. The inverse modeling is performed using a genetic algorithm.

Through inverse modeling of the monitor data, changes over time of the identified failure parameters are obtained. In order to predict the development of the observed failure parameters in the future, these changes over time are incorporated in a prediction model. Taking uncertainties into account, stochastic processes are used to describe the degradation process. Thus, different types of processes can be used, e.g. Markov chains for discrete state changes in time or Gamma processes for continuous quantities in time. By continuously updating the prediction model with the monitor data, a risk based maintenance management tool is obtained by which pro-active and well-planned maintenance actions can be decided on. The developed methodology is applied to a full scale monitoring system of a real bridge in the Netherlands.

1 INTRODUCTION

Bridge expansion joints generally require a lot of maintenance. Replacing an expansion joint usually requires closing off (part of) the bridge which, together with the cost of the joint itself, makes this type of maintenance very expensive and a possible cause of major traffic disruptions. In order to determine the best moment to perform maintenance it is advantageous to be able to continuously monitor the state of the expansion joint. At the moment the condition of joints is normally checked by carrying out visual inspections at regular intervals. These visual inspections rely heavily on the experience and judgement of the inspector while some types of damage may not be visible at all. This introduces a relatively large uncertainty which, given the cost of replacement of the expansion joint, is highly undesirable. If the remaining serviceable lifetime can be estimated in a non-invasive manner with greater certainty the cost savings involved could therefore be substantial.

In this paper the non-invasive detection of damages to a modular bridge expansion joint by ambient vibration monitoring will be discussed as a possible alternative to visual inspection. The theoretical background behind this technique is presented in section 2. The current investigation consists of four distinct parts: lab tests on part of a joint, damage detection by inverse modeling, extrapolation of detected damages using a degradation model and extraction of guidelines for ambient vibration measurements. These are subsequently discussed in sections 3 through 6. In section 7 the ongoing effort of validation of these techniques using a real bridge are briefly discussed. A summary and conclusions are given in section 8.

2 THEORY

2.1 Damage detection

From experience it is known that structural damage can manifest itself through changes in natural frequencies, modal shapes and damping factors [1]. Changes in the frequencies and modal shapes of lower eigenmodes are generally an indication of global damage whereas changes at higher eigenmodes are often indicative of local damage. In the case of localized damage the amount of change in modal shape is usually highly frequency dependent and especially pronounced near the damaged part of the structure and behind it (as observed from the direction of the excitation source).

When trying to solve the inverse problem of determining damage parameters from a measured dynamic system response several practical problems are encountered [2]. One of these is the relatively limited amount of sensors in any practical measurement setup, as a result of which the observation of local changes in mode shapes due to local damage becomes a matter of chance. This might be mediated somewhat by the placement of sensors in positions where damage is most likely (i.e. near welds or areas of high stress) but it doesn't solve the problem completely.

More serious are the problems related to ill-conditioning, such as the question of uniqueness: it is conceivable that different types of damage have very similar effects on the observables monitored in the experiment, in which case the type of damage that has occurred can only be extracted from the measurement data with great difficulty, if at all. Among the possible solutions to this problem are the judgemental placement of sensors (ideally based on model calculations done before the actual measurements), the use of high precision sensors, placing a large number of sensors and measuring over long periods of time.

In addition to all of the above the number of parameters that can be varied in a typical (FEM) model of even a single joint is very large. This means that it is impossible to try and fit all of them to the measurement data. Therefore a small number of possible damages has to be selected and only the parameters involved in those damage mechanisms are used as model input. However, it is obvious that any damage mechanism not considered beforehand will thus be overlooked. For these types of damage the model will therefore only be able to detect that a change has occurred, without being able to specify its cause.

2.2 Ambient vibration monitoring

In lab tests both the static and the dynamic response of the joint to a known excitation are measured (see section 3). However, for the purpose of monitoring real-life systems the use of artificial excitation sources has several drawbacks, for instance:

- The size of real-life systems is usually large, which means powerful excitation devices are needed. These devices are expensive and cumbersome, requiring a lot of time for their installation. Furthermore, in certain situations their size may be prohibitive
- The excitation of the structure due to traffic is generally much stronger than that due to (powerful) artificial excitation devices. Therefore, in order to perform sufficiently sensitive measurements, the bridge normally has to be closed off

As a result it has become common practice to monitor the dynamic response of a structure to ambient excitations (i.e. road traffic, wind, earthquakes etc.) instead. In the analysis these ambient forces are usually modeled as white noise. Although this assumption may introduce a modeling error and, given the statistical nature of the ambient forces, measurements have to be taken over a sufficiently large period of time, these shortcomings are normally outweighed by the advantages over artificial excitation.

2.3 Evolutionary algorithms

The solution process for any inverse problem is inherently iterative in nature. Many different algorithms have been developed for this purpose. Inverse modeling of damages is a global optimization problem where many local minima in solution space might exist. A global optimizer therefore has to be chosen, such as Monte Carlo methods, swarm-based optimization algorithms or neural networks. For the current investigation genetic algorithms were chosen, which belong to the more general class of evolutionary algorithms.

While many different implementations of evolutionary algorithms exist they are all based on the same general principles, inspired by the processes of reproduction and natural selection in nature. The concepts common to these implementations will briefly be discussed.

An individual is a trial solution to the problem and therefore consists of a complete set of parameter values that is necessary for the description of such a solution. In a first step the value of every parameter is chosen at random, each within a range set by the user. A given number of individuals (called a population) is generated this way, after which the quality of each individual is evaluated. This evaluation proceeds through a fitness function which quantifies the agreement between the trial solution and the target solution. The general idea is now to use the information contained in the best solution(s) (called parent(s)) in the generation of a new set of trial solutions (offspring). The creation of new trial solutions in each generation based on the best solution(s) from last generation ensures that the best solution will progressively improve. This process continues cyclically until the fit has converged.

The most popular evolutionary algorithm is probably the genetic algorithm. In this method the parameter values from two parents are randomly combined to create the offspring. To protect the algorithm from getting stuck in a local minimum of the error landscape some parameter values are changed at random for a small number of solutions, called a mutation. To make sure that the best solutions do not deteriorate between generations they are allowed to survive unaltered from one generation to the next (elitism). The solution process is depicted in figure 1.

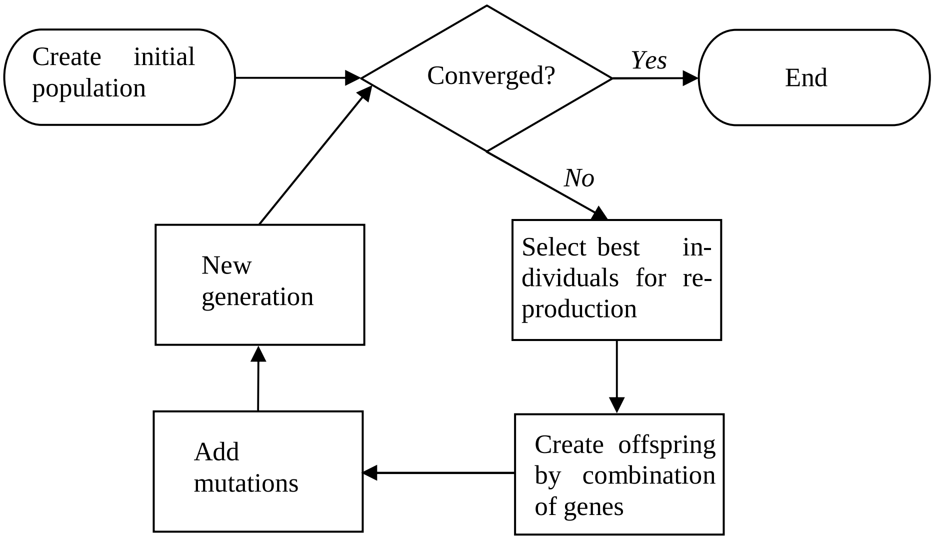

Figure 1: Genetic algorithm flowchart

As can be concluded from the above the genetic algorithm is basically stochastic in nature. This means that, depending on the complexity of the parameter space under investigation, convergence will be harder to achieve with increasing size of the parameter space. Although this effect can be countered by increasing the population size this will also increase the computational cost. For this reason it is very important to restrict parameter space as much as possible before a calculation is started. Unless the fitness function values for different possible solutions are suspected to be very close to each other it is therefore good practice to only include the parameters the final solution is most sensitive to in an initial fit and include the remaining parameters in a second, independent fit where the parameter range for the first set of parameters is much reduced.

3 LAB TESTS

3.1 Test setup

The full-size expansion joint mimicked in the lab tests is depicted in Figure 2. It is comprised of an edge beam, three center beams and a second edge beam arranged in the longitudinal direction of the joint with interposed elastomeric strip seals. The center beams are supported on cross bars (support bars) which bridge the structural gap. Each center beam has an individual set of support bars ensuring an independent movement of the center beams relative to each other. Support bars are placed at about 2m intervals and are grouped in sets of three. Each such set of support bars is inserted within a metal box which is fixed to the main structure. Each support bar rests on two sliding bearings.

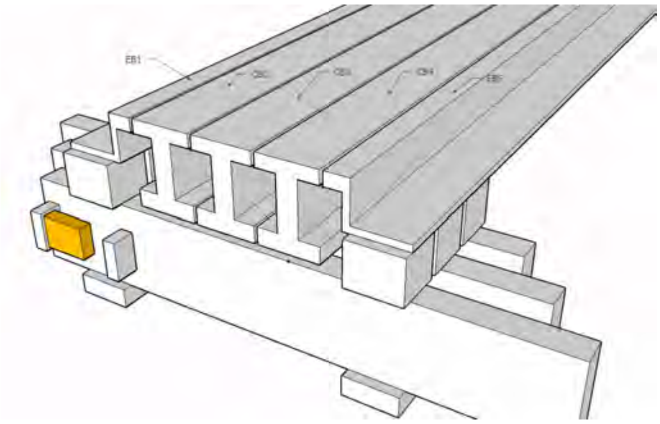

Figure 2: An example of a modular bridge expansion joint

The type of joint investigated can be prone to a number of different damage mechanisms as observed in the past:

- Wear and tear of sliding supports
- Wear and tear of control springs
- Failure of center beams or support bars
- Failure of weld joints between support bar and center beam
- Misalignment or breaking off of sliding supports
- Defects in strip seals

The experimental model consists of one single center beam on 5 support bars. The selected center beam is the first of the three center beams and is therefore located asymmetrically with respect to the support bar. The center beam is modelled using a HEM100 profile which has similar section properties as the beam used in the real expansion joint. The support bars on the other hand have identical dimensions as the real ones. The same sliding supports (sliding bearing and sliding spring) are used as in the real joint. The whole structure rests on two concrete plates placed in a bed of mortar of about 2 cm thickness on top of the laboratory floor. The sliding bearings and sliding springs are kept in place by a top steel plate which is fixed to the concrete plate via two threaded rods. The sliding bearing and spring can be positioned in such a way to simulate a closed joint as well as an open joint. Details of the lab model of the joint can be seen in Figures 3 and 4. The configuration depicted is that of a closed joint.

Figures 3 and 4 show side and top views of the lab model, respectively. The lab model has a total length of 7.5m, with support bars at intervals of approximately 1.8m. For reference purposes, a grid is defined consisting of 5 vertical lines numbered 1 to 5 and two horizontal lines indicated by ‘a’ and ‘b’. The 5 vertical lines correspond to the positions of the support bars. Lines ‘a’ and ‘b’ correspond to the long and short ends of the support bar, respectively. A Cartesian coordinate system is chosen such that the x-axis is parallel to the center beam, the y-axis is perpendicular to the center beam and the z-axis points upwards.

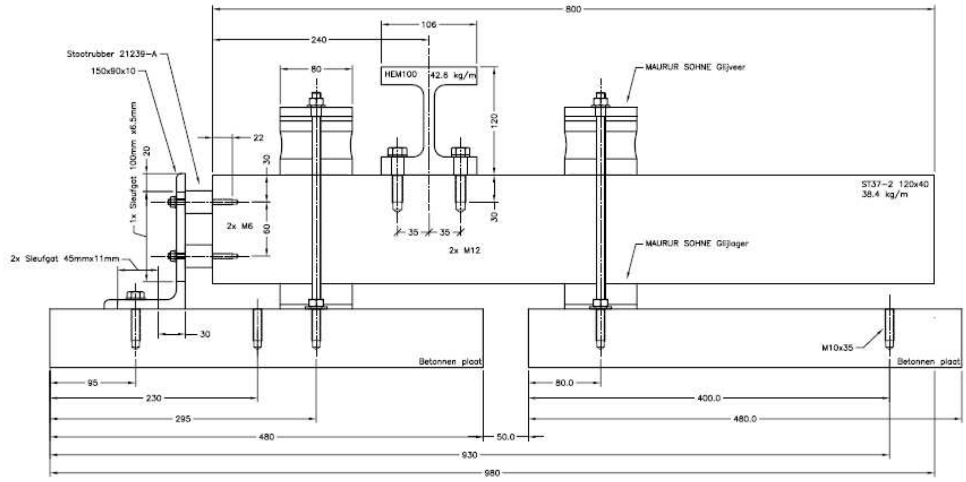

Figure 3: Side view of the lab model

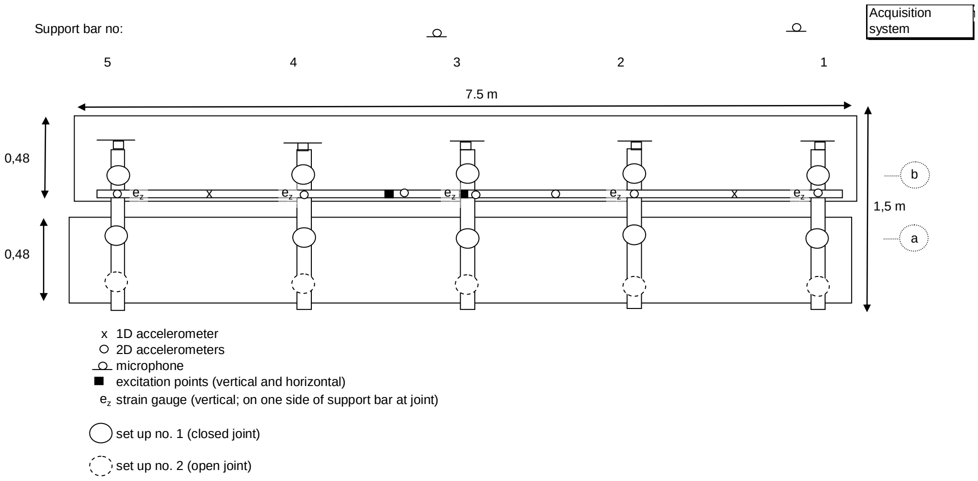

Figure 4: Top view of the lab model (schematic)

In the lab tests the objective is the reverse of that in the subsequent parts of the project: to investigate the effect of damage to the joint on measurable parameters in order to determine which quantities should be monitored. Several different observables were therefore monitored in the lab tests: accelerations of the center beam parallel and perpendicular to the road surface, strains and deflections of the support bars in the vertical direction (w.r.t. the road surface) and sound at some distance from the joint. An extensive set of measurements of both the static and dynamic response of the lab joint was carried out using accelerometers, strain gauges, microphones and laser triangulation sensors. The lab model allowed mimicking of all known damages mentioned in the previous section apart from the first (wear and tear of sliding supports) and the last (defects in strip seals).

3.2 Results

For lack of space only a small part of the tests which were performed are presented here. A single dynamic excitation of a 1000 kg weight impacting the center beam in vertical (negative *z*) direction between support bars 3 and 4 was therefore selected. Some of the recorded responses will be presented in section 4: here only the conclusions are discussed.

Control spring failure was not detected with the chosen observation quantities. This holds for any excitation position and any excitation direction.

A half saw cut in the support bar can be detected, though the effects are not significant. The main change is increased damping in the damaged support.

A half saw cut in the center beam can be detected with the investigated observation parameters. Compared to the effects of a half saw cut in one of the support bars the effects of a cut in the center beam are similar but more pronounced.

Loose joints can only be detected with the chosen observation parameters when the central beam is excited in *y*-direction and the dynamic parameters are determined in the same direction. In this case the main changes are larger displacements above the supports and different bending moments in the support bars. For the excitation considered in this paper, which is in the *z*-direction, no significant change is observed.

The failure of a support is very easily detectable: in the case of a single support this leads to the occurrence of a low frequency mode at about 25 Hz. At this mode the support bar vibrates at high amplitudes and low damping.

The effects of combined failures can roughly be superimposed.

4 INVERSE MODELING

4.1 Model definition

A finite element model of the bridge joint was constructed in Matlab. The model is very flexible, allowing the number of structural members (beams and support bars), the joint geometry and all material parameter values each to be set by a single variable. For a given set of parameter values it will then calculate eigenfrequencies, eigenmodes and the system response to a given input. This setup was chosen because it gives optimization routines written in Matlab direct access to all relevant parameters. An example of a bridge joint created with this Matlab script is given in Figure 5. In the following all relevant components of the model will be discussed in more detail.

First the number of beams and support bars, their sizes and their positions relative to each other and to the joint supports need to be specified. The number of elements to be used for each joint section is also selected. Based on this geometric information the script will construct a global coordinate system as well as local coordinate systems for both the beams and support bars; however, in this paper the global axis system indicated in Figure 4 will be referred to exclusively. It will then derive the coordinates of each element. In addition, in order to be able to fully specify how beams and support bars are connected, a small connection element which also carries its own local axis system is introduced between beams and support bars.

After this is done the material parameters for the beams, support bars and connection elements need to be specified: Young's Modulus (*E*), shear modulus (*G*), mass per unit length (*Mu*) and torsional mass per unit length (*J*). The connections between support bars and joint supports, which are made of rubber, are modeled as a spring-damper system in all 6 degrees of freedom (translations and rotations around all three local axes), corresponding with a total of 12 degrees of freedom (i.e. 6 for the springs and 6 for the dampers).

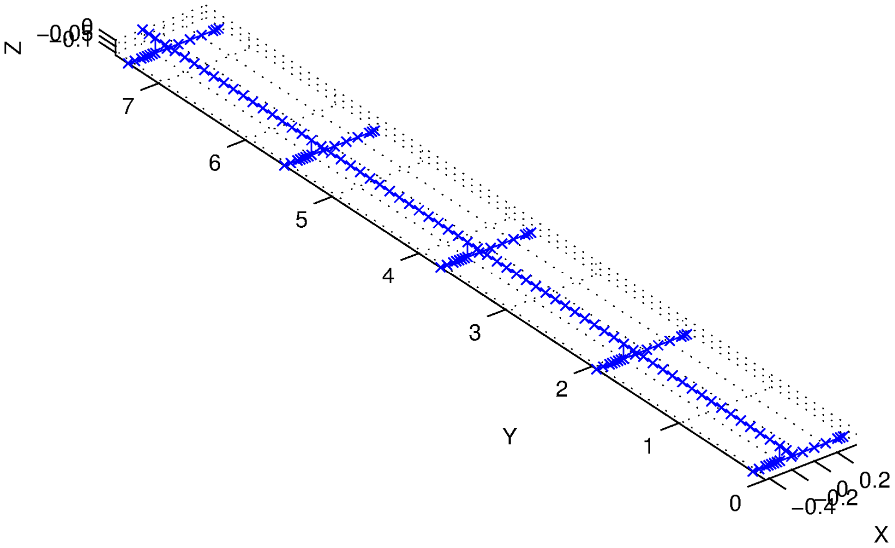

Figure 5: An example of a bridge joint model with a single beam and five support bars generated with the joint Matlab script. Each cross indicates a node of the FEM model. Also indicated is the axis system.

Each section of the joint is modeled as a Timoshenko beam with independent bending along the local y- and z-axes and torsion along the local x-axis. To this end the script has to be provided with five additional geometric parameters each for the beams, support bars and connections: cross sectional area, shear cross sectional area, bending inertia about the local y- and z-axes and torsional inertia about the local x-axis.

After the model has been defined the system matrices are set up and the eigenmodes and eigenfrequencies are calculated. When a time-dependent force acting on the system is now defined the response in each mode can be derived using the Newmark routine, after which all modal responses are added to yield the total system response. In this process a modal damping factor can be specified for each individual mode. Since the number of modes involved is usually so large that it is impractical to actually do so, in practice the damping values are obtained by interpolation from a table containing damping factors at a number of fixed frequencies.

4.2 Model tuning

Before a start can be made with the modeling of damages, the parameter values which are not precisely known from the experiment have to be fit by comparison of measured and calculated system responses for the undamaged joint. This process, termed model tuning, will be discussed in the following.

The model presented here contains 22 parameters for which their values were deemed to be uncertain enough to be included in the tuning process: the cross sectional area, shear cross sectional area, bending inertia about the x- and y-axes and torsional inertia about the z-axis for the connection element between beam and support bars; the six spring stiffnesses for the connection between support bars and joint supports; and eleven modal damping values at various frequencies.

For the tuning of the model a single measurement from the experiment was chosen, namely a dynamic excitation in z-direction (vertical), in the middle between support bars 3 and 4 (hereafter denoted as position 3.5). Even though the time trace of the corresponding excitation force is available from the measurements, in environmental vibration monitoring this excitation force is often unknown and therefore modeled as white noise (see section 2.2). For this reason the excitation force time trace was used as input for the Matlab model, in order to enable a comparison with the lab data which is as good as possible, but not in the comparison itself. Instead, the mobilities at different positions on the beam were chosen as the monitoring variables, as these contain information about the system as a whole yet are independent of the excitation force. Since the mobility becomes singular for zero force only those mobilities were used in the fitting procedure for which the corresponding force was at least 1% of its maximum value. As a result the mobility spectra throughout this paper feature gaps at those frequencies where this condition doesn't hold.

The parameter optimization problem at hand is clearly complex: it contains many variables (22) and the parameter ranges for most of these variables are very large, spanning several orders of magnitude. Such a parameter space can be very wild and erratic containing many local minima. In order to ensure the stability of the optimization process a global optimizatizer should therefore be used. For the present investigation a genetic algorithm (see section 2.3) was considered most appropriate and was therefore used throughout. As a fitness function the weighted normalized difference between measured and calculated mobilities was chosen:

$$fitness = \sum_i w_i \, \| mob_c^{\ i} - mob_m^{\ i} \| / \| mob_m^{\ i} \|, \tag{1}$$

where mob_c and mob_m indicate the calculated and measured mobility, respectively, and the sum runs over all measurement positions that are included in the evaluation. The relative weights w_i of the measured spectra are chosen to be proportional to the maximum mobility values in these spectra with $\sum w_i = 1$. From this definition it can be deduced that for trial solutions of comparable norm as the measured mobility ($\| mob_c^{\ i} \| \approx \| mob_m^{\ i} \| \forall i$) the given fitness function is approximately normalized, with a value ~1 meaning no correspondence whatsoever and 0 indicating perfect agreement. Correspondingly, it can be viewed as a measure of discrepancy between calculated and measured spectra, with for example a value of 0.18 indicating a mismatch of roughly 18%.

In a first attempt to fit the model output to measurement data six response traces were selected, at beam positions 2.5, 3 and 3.5, each in both the *x* and *z* direction of the axis system. Using initial estimates for the model parameters the sensitivity of the fitness function to a change in each of these parameters was investigated. The average change in the fitness function value to a change in parameter value by an order of magnitude in either direction was required to be at least $1 \cdot 10^{-4}$. This requirement was not met by two parameters, namely the damping values at both extreme ends of the specified frequency range (75 and 3000 Hz). The remaining 20 parameters were included in a genetic algorithm fit in the frequency range 0-500 Hz with a population size of 1000 and 40% elitism (400 individuals). On an average PC (a 3 GHz dual-core machine with 3GB internal memory) this calculation ran for approximately 48 hours before finishing at generation 57. A comparison between measured and fitted spectra showed some discrepancies, especially where the responses in the *x*-direction and at higher frequencies (> 350 Hz) were concerned. This may be because the excitation may not have been purely in the *z*-direction, because no direct coupling between the bending modes in both orthogonal directions has been included in the model or (in the case of the high-frequency modes) because the element size is too coarse for an accurate description.

Given the above result and the fact that most features which are indicative of damage are expected to be observable in the response curve in the *z*-direction at lower frequencies (≤ 350 Hz) a second global fit was made using only the mobilities in the *z*-direction and a frequency range of 0-350 Hz. All 22 parameters were included in the fit, which again had a population size of 1000 with 40% elitism, ran for another 48 hours and finished at generation 58. This fit converged to roughly the same corner of parameter space as the previous one, indicating that the global optimum had indeed been reached. In a third and last optimization step a local optimizer including all 22 parameters was run on the obtained solution to give the global minimum. The result, with a fitness function value of 0.2780, is displayed in Figures 6 through 8. As can be seen the correspondence is rather good, especially given the fact that the absolute response in Figure 7 is over 2 orders of magnitude smaller than at the other two positions and measurement noise may therefore be relevant here.

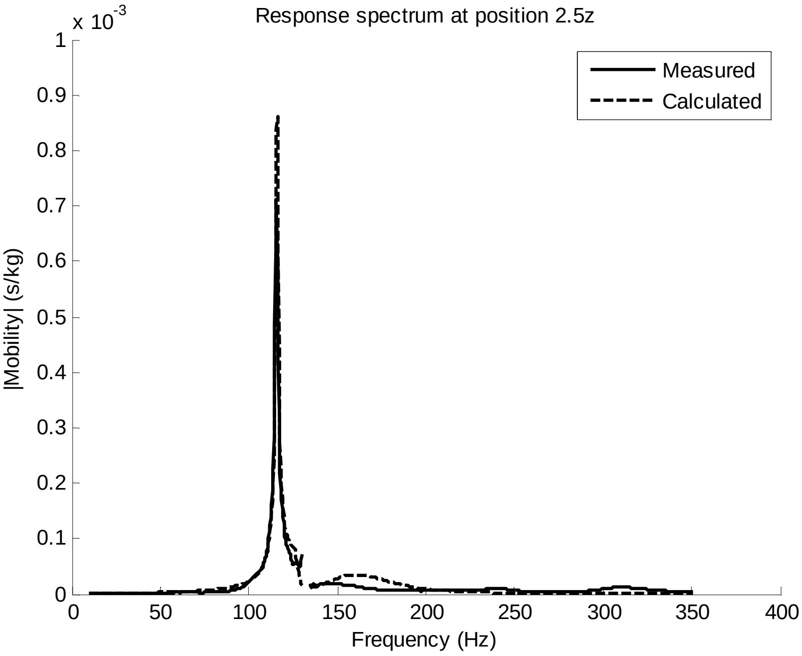

Figure 6: Measured and calculated mobilities in the *z*-direction in the middle between support bars 2 and 3 for an excitation force in *z*-direction between support bars 3 and 4

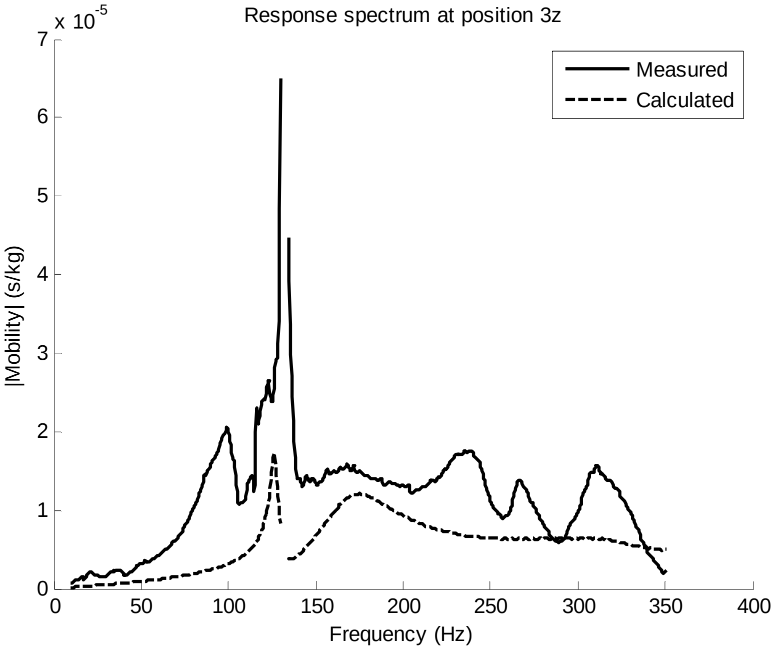

Figure 7: Measured and calculated mobilities in the *z*-direction above support bar 3 for an excitation force in *z*-direction between support bars 3 and 4

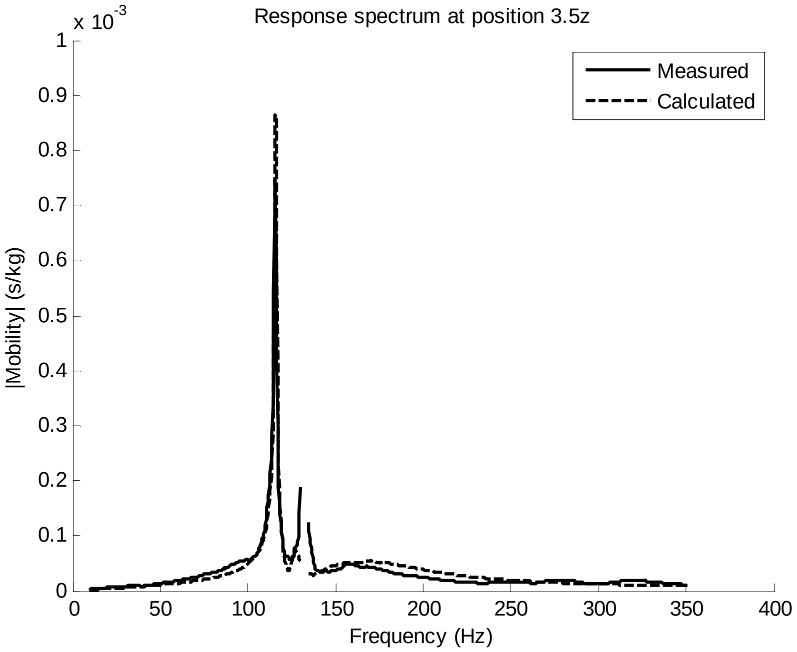

Figure 8: Measured and calculated mobilities in the *z*-direction in de middle between support bars 3 and 4 for an excitation force in the same direction and position

4.3 Damage detection

As mentioned in section 2.1 in the current measurement setup the total number of parameters in the model is much larger than the number of available measurement traces. Given the possibe non-uniqueness of a solution to the inverse problem it is unwise to try and unambiguously fit all parameters to the available data. The effects of the types of damage, to be considered by the model, on the model parameters should therefore be estimated before a fit is attempted. Here the same damages as investigated in the lab test (section 3.2) were included.

Control spring failure

This type of damage was modeled as zero support bar spring stiffness in the *x*-direction, the effect of which was not visible on any of the spectra observed here. This type of damage will therefore not be discussed further.

Support failure

In the lab tests the effects of sliding supports breaking off was investigated by removing a single sliding support of the third support bar, on the side furthest away from the beam, as well as by removing both sliding supports for the same support bar in a second test. This was modeled by setting all support bar spring stiffnesses for the respective sliding support(s) equal to zero. For the missing support on a single side it was also found that the best agreement between model and experiment could be found if the modal damping factor at 75 Hz was reduced from 15 % to 9 % while the damping factor at 118 Hz was increased from 0.3164 % to 0.65 %. The spectrum at position 3 for this one-sided damage case is given in Figure 9.

From this spectrum it can be deduced that a new mode has appeared at around 26 Hz which is especially strong over the support bar. Although the frequency of this mode is slightly overpredicted by the model (28 Hz) the agreement in position and relative mode intensities is very good. Even more subtle effects are reproduced very well: at all frequencies apart from the new mode the response is observed to be slightly higher at position 2.5, slightly lower at position 3.5 and significantly lower at position 3, and the peak at around 118 Hz which for the undamaged case is present at position 3 has disappeared for the damaged case, all in accordance with model predictions. A decreased response in the main mode at 118 Hz in the spectra at positions 2.5 and 3.5 is fitted by the aforementioned increased modal damping factor at this frequency. It can therefore be concluded that this type of damage is clearly visible in the spectra presented here and identification of this damage mode should therefore be possible.

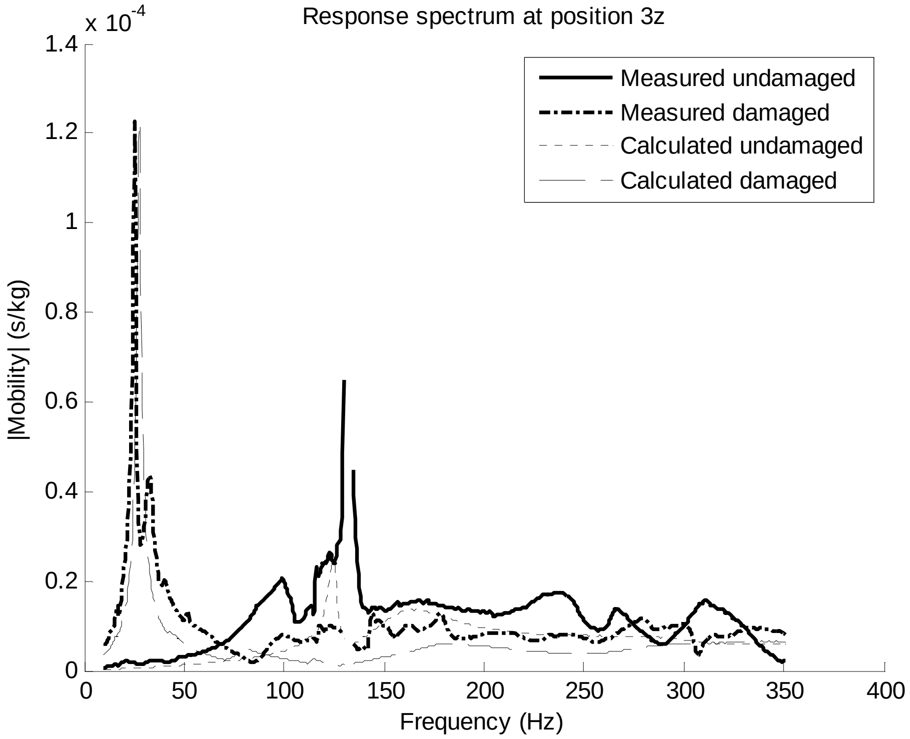

Figure 9: Effect of a single sliding support breaking off on the mobility spectrum at position 3

Half saw cut in a support bar

In the lab experiments this type of damage to a support bar was tested by making a cut in the vertical direction (the long axis of its cross section) over the full width of the support bar. In this configuration the cross sectional area, shear cross sectional area, bending inertia about the z-axis and torsional inertia about the x-axis all decrease linearly with increasing depth of the cut while the bending inertia about the y-axis decreases with the third power of this depth. For a different type of cut or different geometries like that of the beam, however, these dependencies could be different. Nevertheless, the same dependency was assumed for the beam as well (with x- and y-axes interchanged following its different orientation).

The effect the cut in support bar number 3 has on the measured mobilities is displayed in Figure 10. The only effect that can be observed at positions 2.5 and 3.5 is an increased damping in the main mode at 118 Hz. It was found that the measured spectra could best be reproduced using a modal damping value of 0.7% at this frequency. At position 3 the response at all frequencies up to about 250 Hz is significantly higher for the damaged case, most notably in the 118 Hz-mode. All these effects are accurately predicted by the model used here. Nevertheless, the absolute changes in the measured responses are relatively small, especially when considering the fact that a 50% cut was used for this experiment. Normally, actual cracks will of course be much smaller and their effects therefore even less visible than observed here.

Additionally, comparing the observed changes to the mobility spectra with other damage mechanisms considered in the current investigation, the question of uniqueness of the effects of this type of damage to a support bar arises once again. In a real life situation it is therefore unlikely that the existence of a crack in a support bar can be deduced from the mobilities observed here.

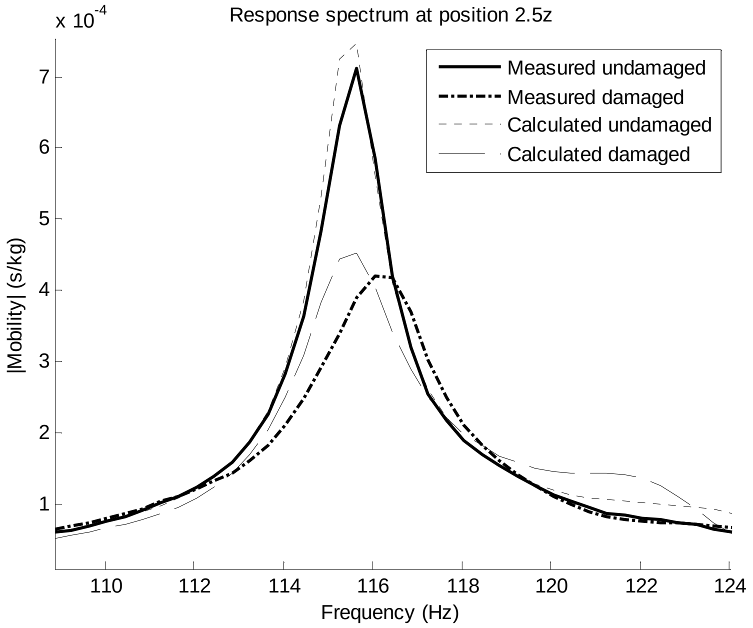

Figure 10: Effect of a 50% cut in support bar 3 on the mobility spectrum at position 2.5

Half saw cut in center beam

From the measured spectra (see Figures 11 and 12) it can be decuded that, most interestingly, the frequency of the main mode at positions 2.5 and 3.5 has descreased by 6 Hz and the intensity has decreased considerably as well. These effects are reproduced very well by the model, although the actual intensity of the responses for positions 2.5 and 3.5 is somewhat underestimated. Around the same frequency the peak in the mobility spectrum at position 3 seems to have split up into two separate peaks, one at a slightly lower and another at a slightly higher frequency. Whereas this splitup and the resulting frequencies are again reproduced by the model the intensity of the lower frequency mode (corresponding with the main peak at positions 2.5 and 3.5) is severely underestimated. It can be concluded nevertheless that the effect of a 50% cut in the beam can be observed very well and can clearly be distinguished from the effects of other types of damage. However, as with the crack in a support bar discussed above, it is questionable whether a clear reponse will be visible for a more real-life situation where the expected crack depth is small.

Loose joint

A weld failure between beam and support bar was reproduced in the model by setting all moments of inertia for the connection element to zero. Simultaneously the cross sectional area and shear cross sectional area for this element should be lowered. The actual value to be used is hard to predict since it is an effective value: upward motion of the beam is unhindered in case the connection between beam and support bar has failed, corresponding with zero area for the connection element. Downward motion of the beam, however, is unaltered since the support bar itself is still present. The reduction factor to be used for the cross sectional area and shear cross sectional area was therefore deduced from a comparison between the model and experiment. A value of 1e-3 was found to give the best correspondence. Lastly, the modal damping factor for the main mode at 118 Hz was increased to 0.5%. The resulting model calculations and a comparison with experiment are given in Figure 13.

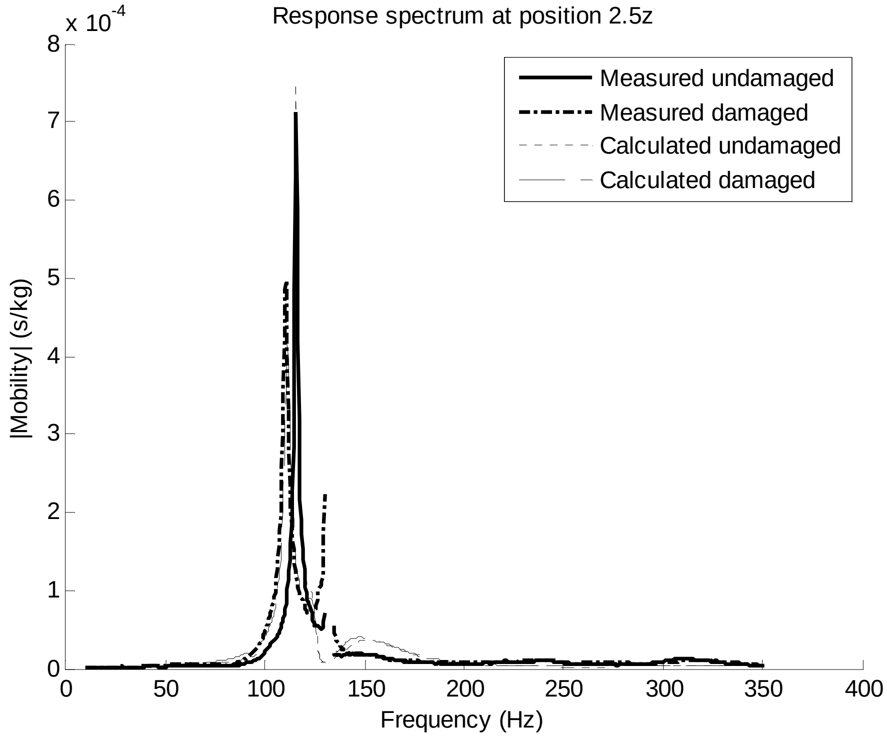

Figure 11: Effect of a 50% cut in the beam on the mobility spectrum at position 2.5

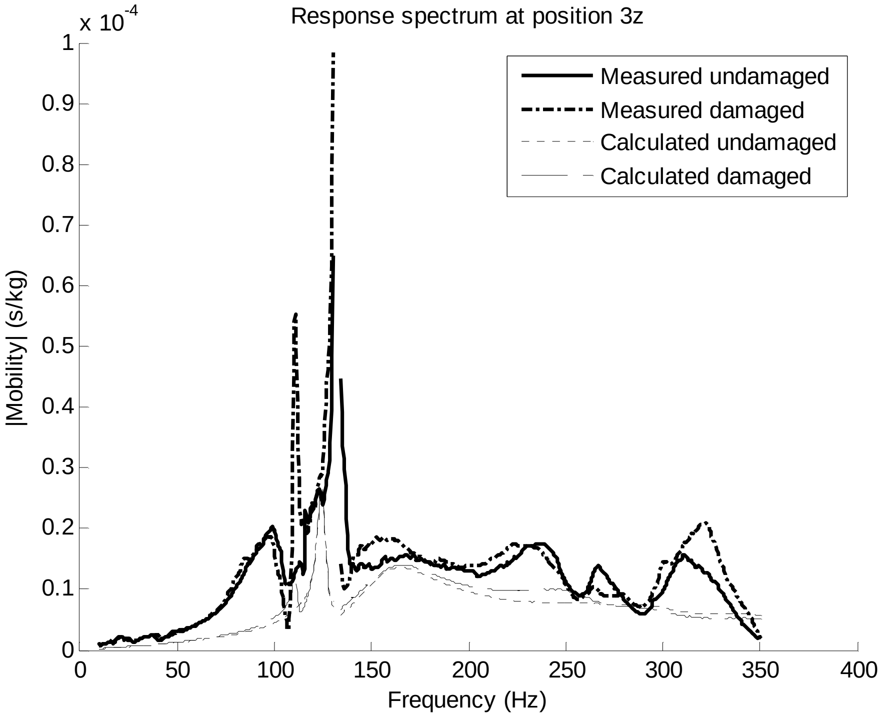

Figure 12: Effect of a 50% cut in the beam on the mobility spectrum at position 3

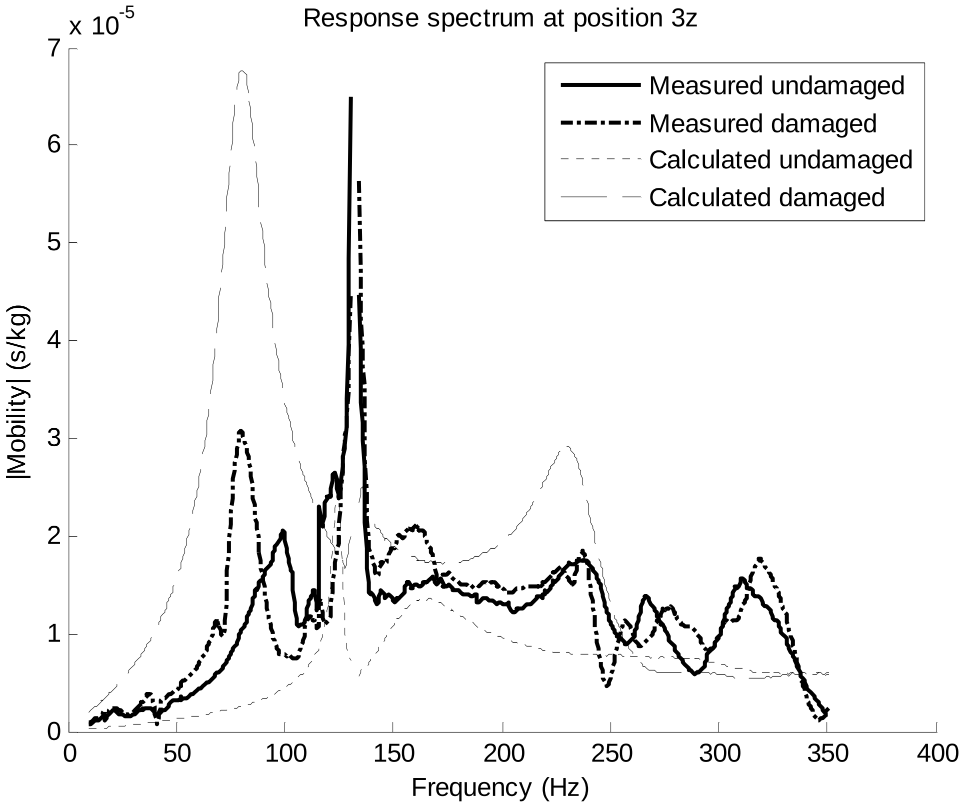

Figure 13: Effect of failure of a weld between beam and support bar at position 3 on the mobility spectrum at this position

Not surprisingly the largest effect for this type of damage can be observed above the support bar, where a very strong mode has appeared at a frequency of 79 Hz. The same mode is also present in the other two spectra, although much more weakly. Furthermore the intensity distributions are changed in all spectra, most notably above the support bar where it is much stronger in the range 0-250 Hz than for the undamaged case. All these effects, including even the minor changes in relative mode intensities at positions 2.5 and 3.5, are predicted perfectly by the model. The only blemish is the fact that in the damaged case the intensity for the new mode at 79 Hz is overestimated, in contrast with the underestimated response for the undamaged case. The predicted effects can also clearly be distinguished from those of other damages. Combined with the fact that weld failure is a binary effect which will always lead to the same amount of damage it can be safely concluded that this type of damage can easily be detected and identified. However, the fact that the cross sectional area and shear cross sectional area had to be fitted to the experimental data rather than determined from first principles is somewhat disappointing. It might be that the value of 1e-3 used here is different for other joint geometries or even other types of excititation and should therefore be redetermined for every analysis.

Combined damages

With respect to combined damages the inverse modeling confirms the conclusions obtained from the experiments: the effects of combined damages can well be approximated by adding the effects of each separate type of damage.

5 DEGRADATION MODEL

5.1 Defect initiation and growth

The process of degradation can often be well described as random due to poor inspection, lack of data or other sources of uncertainty. Stochastic processes have been widely used in order to investigate inspection strategies under stochastic degradation (see for example [3] and [4]). When the degradation process is to be modeled by continuous quantities in time, for example wall thickness loss or corrosion growth in time, then the gamma process is more natural [5]. When the degradation process is modeled by changes of one state to another in time then Markov chains are more suitable [6]. According to [5] the gamma process has been successfully fitted to data on creep of concrete, fatigue crack growth, corroded steel gates, thinning due to corrosion and chloride ingress into concrete. On the basis of the gamma deterioration process, case studies have been performed to determine optimal dike heightening, optimal sand nourishment sizes, optimal decisions for steel coatings and optimal inspection intervals for high speed railway tracks, berm breakwaters, steel pressure vessels, automobile brake pads, and block mats and rock dumping of the Eastern-Scheldt barrier in the Netherlands. In this paper a tool that investigates deterioration through the gamma process is introduced. The model is taken from [7]. The Poisson process is used to model initiation times while the gamma process is used to model deterioration growth.

The Poisson process is a counting process. This is a random function N: $\mathbb{R}^+ \rightarrow \mathbb{R}$ such that:

- $N(0) = 0$ and $N(t) \in \{0, 1, 2, 3, \dots\}$ for all t
- if $s < t$ then $N(s) < N(t)$

Following [8] the homogeneous Poisson process will be defined by equation (2). $N(a_i, b_i]$ denotes the number of events (degradation initiation in our case) falling in the half-open interval $(a_i, b_i]$ with $a_i < b_i \leq a_{i+1}$.

$$P\{N(a_i,b_i) = n_i,\ i = 1,\dots,k\} = \prod_{i=1}^{k} \frac{[\lambda(b_i - a_i)]^{n_i}}{n_i} e^{-\lambda(b_i - a_i)} \tag{2}$$

The parameter λ can be interpreted as the mean rate of occurrence or intensity. The non-homogeneous Poisson process with time dependent rate λ(t) can be defined exactly as in equation (2) with the quantities $\lambda(b_i - a_i) = \int_{a_i}^{b_i} \lambda dx$ replaced whenever they occur by quantities:

$$\Lambda(a_i, b_i) = \lambda \int_{a_i}^{b_i} m(x) dx \tag{3}$$

In this case, the parameter λ will be referred to as the proportionality constant. In a general framework this parameter may be used in a Bayesian analysis. It will be considered uncertain and in order to update the model we could use the number of defect observed in a given time interval.

In a gamma process a random variable X has a gamma distribution with shape parameter $v>0$ and scale parameter $u>0$ if its probability density function is given by:

$$ga(x \mid v(t), u) = \frac{u^{v(t)}}{\Gamma(v(t))} x^{v(t)-1} e^{-ux} I_{(0,\infty)}(x) \tag{4}$$

where $I_A(x) = 1$ for $x \in A$ and $I_A(x) = 0$ for $x \notin A$, and $\Gamma(a) = \int_{z=0}^{\infty} z^{a-1} e^{-z} dz$ is the gamma function for $a>0$. If $v(t)$ now is a non-decreasing, right continuous, real valued function for

$t \geq 0$ with $v(0) \equiv 0$ then the gamma process with shape function $v(t)>0$ and scale parameter $u>0$ is a continuous-time stochastic process $\{X(t);\, t \geq 0\}$ such that:

- $X(0) = 0$ with probability one
- $X(s) - X(t) \sim ga(\cdot|v(s) - v(t);\, u)$ for all $s > t \geq 0$
- X(t) has independent increments

From this definition the first hitting time distribution can be derived, which is the distribution of the first time at which the defect size is larger than a given defect size y. It is denoted by T_y and it is given by

$$F_{T_y}(t) = P(T_y \leq t) = P(X(t) \geq y) = \int_y^{\infty} ga(x, v(t), u)dx \tag{5}$$

5.2 Deterioration process

The deterioration process will be defined following [7] as a combination of defect initiation and defect growth. Defects will initiate according to a Poisson process (homogeneous or not) and will grow independently according to the gamma process. The probability density function (pdf) of the k^{th} arrival time ($S_k : 1 \leq k \leq n$) conditional on n defect initiations up to time t (for fixed t) is given by

$$f_{S_k|N(t)} = n(s) = \frac{n!}{(k-1)!(n-k)!}\left(\frac{\Lambda(s)}{\Lambda(t)}\right)^{k-1}\left(1-\frac{\Lambda(s)}{\Lambda(t)}\right)^{n-k}\frac{\lambda(s)}{\Lambda(t)} \tag{6}$$

The depth D_k of the k^{th} defect at time t will be defined as the growth according to a gamma process in the time interval between its initiation and t, that is, $D_k = X(t-S_k)$. Assuming that the process $X(\cdot)$ is independent of the arrival times S_k and using equation (6) we obtain:

$$P(D_k \leq x \mid N(t) = n) = \int_0^t P(X(t-s) \leq x) f_{S_k|N(t)=n}(s)ds \tag{7}$$

Under our assumption that we have knowledge that n defects have initiated up to time t we could ask what the distribution is of the size of a randomly selected defect at time t. This is given in the equation below.

$$P(D_k \leq x \mid N(t) = n) = \int_0^t P(X(t-s) \leq x)\frac{\lambda(s)}{\Lambda(t)}ds \tag{8}$$

5.3 Failure probability

We assume that our component fails as soon as a defect is deeper than a certain defect size y. Let $N_x(t)$ denote the number of defects deeper than x for $x > 0$ up to time t. Then the probability that no system failure occurs up to t is given by $P(N_y(t) = 0)$. It may be shown that the process $N_x(t)$ is also a Poisson process with intensity given by

$$\Lambda_x(t) = \lambda\int_0^t F_{T_x}(t-s)m(s)ds \tag{9}$$

We define the event $A_x(t)$ as the event of observing at least one defect larger than x within the time interval $(0, t]$. Since the event $N_x(t)$ is also a Poisson process then

$$P(A_x(t)) = 1 - e^{\Lambda_x(t)} \tag{10}$$

5.4 Structural assessment

The idea behind full-scale measurements is that ambient vibrations measured by e.g. strain meters are used as input for the damage detection model described in section 4. This will result in information regarding the number of defects present in the joint, the types of defects and the extent of each. These data could then be used to continuously update estimates of the degradation model parameters described above: the proportionality constant λ describing the rate of occurrence of defect initiation and the shape parameter *v* and scale parameter *u* describing the progression of defects after initiation. In absence of sufficient data to deteremine reliable values for the latter two parameters they can be estimated by structural experts from typical times after which certain levels of degradation are expected to be reached. With increasing measurement time the defect parameter estimates will become more accurate, enabling the asset manager to reliably determine when specified minimum performance criteria will be reached and maintenance should be planned.

6 SETTING UP AN EXPERIMENT

In the previous sections all aspects of damage detection using inverse analysis have been discussed in theory and checked against lab experiments on a bridge joint. It was found that under these controlled conditions at least some types of damage can indeed be detected and the corresponding damage parameters derived. This result shows that the more general approach to inverse analysis also applies to a bridge joint. The success or failure of a certain type of experiment can often be reliably predicted before the actual experiment is even performed.

When setting up an experiment for an inverse problem one should in general follow the procedure outlined in Figure 14, which starts with a definition of the parameters that are to be determined in the analysis (for the case discussed in this paper the different types of damage which are to be distinguished). A model of the problem can then be set up and its response to different types of input (for example the different damage types) analyzed. This will provide the user with information about the number of detectors that has to be used as well as their optimal placement in order to avoid ill-conditioning. The amount of detail used at this stage is of critical importance. This is also the point where, in the case of environmental vibration monitoring, the question should be answered which (prefarably force-independent) parameters should be monitored (for example mobilities). Lastly, the effect of the excitation location(s) and possible locations of damage should be considered, since for many types of damage changes in observables are mainly visible near these locations.

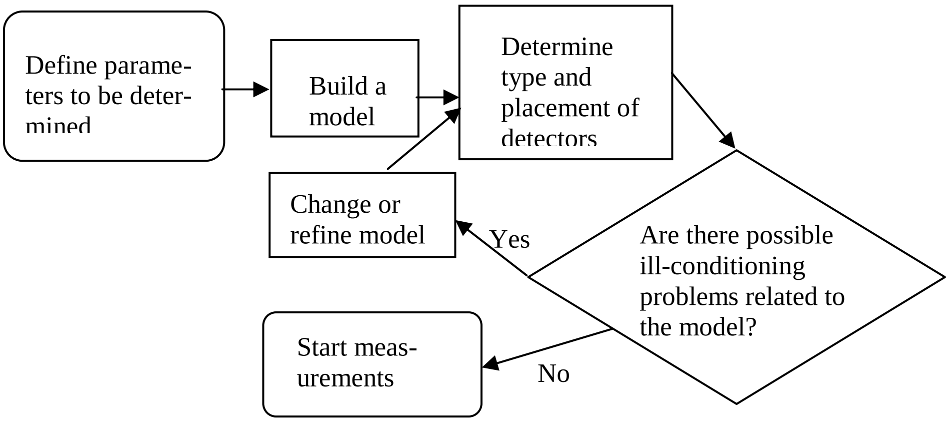

Figure 14: Procedure for setting up an inverse detection experiment

Using the information obtained above the user should be able to assess from calculated sensitivities whether any ill-conditioning is to be expected and whether all parameters of interest can be uniquely determined. If not the user can attempt to change or refine the model based on these observations in order to remedy the situation. Only when all issues have been solved can the experiment be started. If a problem persists despite changes to the model and/or detector placement it has to be concluded that it is not possible to reliably detect the parameters the user is interested in with the type of experiment under consideration.

After an experiment has been conducted the system response as predicted by the model needs to be fit to the actual response by variation of model parameters which are not well known (tuning of the model). In the current investigation it was found that in practical situations a model response (such as for the FEM model used here) quickly becomes so complex that a local optimization routine can no longer be used. A genetic algorithm was therefore chosen, which performed very well. As a good alternative neural networks could also be considered but their use was not explored here. The genetic algorithm might also be used to determine the optimal detector placement as part of the setup of an experiment as outlined in the previous paragraph.

In the case of continuous measurements the response of the tuned model can be compared with the measurement data at every timestep. When the discrepancy is greater than a predetermined threshold it is concluded that damage has occured and a refit of the model will be requested to determine the type of damage and the corresponding damage parameters. Since the model will usually contain far too many parameters to be able to determine all of them possible damages will have to be explicitly specified and included in the model refit as possible causes for the observed change in system response. This does mean that the damage detection system will only be able to identify those damages which have been considered at the outset of the experiment.

For the types of damage which occur gradually it is also important to determine at which point damage becomes visible as a change in variables. The answer to this question obviously depends on many different factors such as the level of detail of the model used in the analysis and the measurement noise. The threshold on the fitness function used to identify damages should be set accordingly. If, for example, a change in the fitness function value of 0.01 is taken as an indication of damage and the cause of this change is a crack in a beam, then for the model considered here a crack with a minimum depth of 1.5% of the beam height, corresponding with 1.8 mm, should be observable. Depending on the cause for the formation of this crack this may or may not coincide with the moment of crack appearance.

7 FULL-SCALE TESTS

In order to test the models described above full-scale measurements are performed on a bridge in the Netherlands. From mid to end June 2010 a monitoring system was installed in order to measure strain deformation in steel parts. However, given the recent installation of these strain gauges as compared to the bridge design lifetime insufficient information has yet been obtained to derive the necessary defect parameters. Detailed results of this ongoing effort will be presented in future publications.

8 CONCLUSIONS

In this paper lab measurements of the dynamic response of a damaged bridge expansion joint were discussed. It was found that several of the more common types of damage could reliably be discriminated and quantified through the use of genetic algorithms for the determination of key parameters in a FEM model. Given these promising results full-scale tests were started on an actual bridge expansion joint installed in a highway bridge in the Netherlands. Since no results from the full-scale tests are available yet thought should be given to the question as to how far the results obtained for the lab model can be extended to a full-size bridge joint. The number of model parameters for a full-sized joint is obviously larger than that for the lab model, but this is offset by the fact that the overall geometry of a joint is very regular. This means that, although larger, the model for the full-sized joint will most likely not be any more complex. The same types of spectra and effects can therefore be expected. Moreover, since lateral movement of the actual joint will be much more constricted than was the case for the lab model, unlike the lab model case it might even be possible to use the mobility spectra in this direction in the fitting procedures, which might help to alleviate some of the ill-posedness which was observed in the lab tests.

The quality of data from the actual bridge joint depends on many factors such as the number, type and sensitivity of the detectors used in the experiment, their placement and the amount of traffic across the bridge. However, given suitably large averaging times there is principally no reason to assume that data obtained for the full-sized joint should be of lower quality than those obtained from the lab tests. Since in the lab tests mobilities were observed, which are independent of the excitation force, the use of ambient vibrations as an excitation source should also not affect the suitability of the method investigated here. In conclusion, damage detection by environmental vibration monitoring is a feasible method for use with a bridge expansion joint.

REFERENCES

[1] H. Wenzel, D. Pichler, *Ambient Vibration Monitoring*, Wiley, 2005.

[2] G.R. Liu, X. Han, *Computational Inverse Techniques in Nondestructive Evaluation,* CRC Press, 2003.

[3] J.M. van Nortwijk, *Optimal Maintenance Decisions for Hydraulic Structures under Isotropic Deterioration*, Phd thesis, TU Delft, 1996.

[4] M.J. Kallen, *Markov Processes for Maintenance Optimization of Civil Infrastructure in the Netherlands,* Phd thesis, TU Delft, 2007.

[5] J.M. van Noortwijk. *A Survey of the Application of Gamma Processes in Maintenance,* Reliability Engineering & System Safety, 94(1):2 – 21, 2009.

[6] M.J. Kallen, *A Comparison of Statistical Models for Visual Inspection Data*, Proceedings of the Tenth International Conference on Structural Safety and Reliability (ICOSSAR), pages 3235 – 3242, Osaka, Japan, 2010.

[7] S.P. Kuniewski, J.A.M. van der Weide, J.M. van Noortwijk, *Sampling Inspection for the Evaluation of Time-dependent Reliability of Deteriorating Systems under Imperfect Defect Detection,* Reliability Engineering & System Safety, 94(9):1480 – 1490, 2009.

[8] D.J. Daley, D. Vere-Jones, *An Introduction to the Theory of Point Processes, Volume 1,* Springer, 2nd edition, 2002.

COMPDYN 2011
III ECCOMAS Thematic Conference on
Computational Methods in Structural Dynamics and Earthquake Engineering
M. Papadrakakis, M. Fragiadakis, V. Plevris (eds.)
Corfu, Greece, 26–28 May 2011

BAYESIAN SPECTRAL DECOMPOSITION METHOD FOR OPERATIONAL MODAL IDENTIFICATION IN WIRELESS SENSOR NETWORK

Zhouquan Feng[1], **Lambros S. Katafygiotis**[2]

[1] The Hong Kong University of Science and Technology
Clear Water Bay, Hong Kong, China
e-mail: simonce@ust.hk

[2] The Hong Kong University of Science and Technology
Clear Water Bay, Hong Kong, China
lambros@ust.hk

Keywords: Bayesian, Operational Modal Identification, Wireless Sensor Network, Spectral Decomposition.

Abstract. *Structural health monitoring (SHM) employing wireless sensor networks (WSN) is becoming increasingly popular in recent years. A Bayesian spectral decomposition (BSD) method employing a distributed computing strategy is presented for structural modal identification in WSN using output-only response data. This method uses the statistical properties of the largest eigenvalue of the output spectral matrix to obtain not only the optimal values of the updated modal frequencies and damping ratios but also their associated uncertainties by calculating the posterior joint probability distribution of these parameters. Mode shapes are obtained by singular value decomposition (SVD) of the output spectral matrix at corresponding discrete frequencies closest to their optimal values. This method identifies each mode, the modal frequency and damping ratio and the mode shape separately, which takes advantage of variable separation and can distribute the computational effort to several computational units, thus becoming suitable for implementation in wireless sensor network that provides such distributed computing environment. In addition, energy is conserved through the use of a novel distributed computing strategy. The efficacy and efficiency of the proposed methodology is demonstrated using numerical simulations.*

1 INTRODUCTION

Experimental modal analysis (EMA) using vibration data has been widely used over the years because of its importance in model updating, response prediction, vibration control and health monitoring. Many modal identification algorithms, both in the time and frequency domain, have been developed in the past three decades. Particularly, much attention has been devoted to the identification of modal parameters in the case where no input but only response measurements are available. These techniques, referred to as operational modal analysis or output-only modal identification or ambient modal identification, provide an in-operation testing solution for modal parameter identification with no need for external artificial excitations and take advantage of the ambient excitations such as micro-tremors, traffic, wind, waves and earthquakes, etc. Operational modal identification is proved to be very useful in civil engineering, where it is very difficult and expensive to excite infrastructures such as buildings and bridges with actuators to obtain artificially induced vibrations.

In recent years, the emerging wireless sensor networks (WSN) for structural health monitoring (SHM) have attracted a lot of attention from both the academic and industrial communities [1]. Wireless sensor networks have the potential to improve SHM dramatically with onboard computation and wireless communication capabilities. Compared with traditional wired structural monitoring systems, wireless sensors can locally process measured data and transmit only the important information through wireless communication, allowing for the distribution of the computation burden across the network. Moreover, there is no extensive wiring between sensors and data acquisition system, which arrows for a fast and flexible implementation, and easier maintenance. Inspired by these advantages, WSN are becoming immensely popular in structural health monitoring in recent years.

Though the wireless sensor network has the potential to improve SHM dramatically, limited resources on wireless sensors preclude direct application of existing algorithms in wireless sensor networks [2]. For example, the wireless sensors have limited computation speed, limited memory space and limited energy powered by batteries. Algorithms designed to be implemented in WSN should take account of such limitations, and it is preferable to process the data in a decentralized way. On the other hand, uncertainties are abundant in civil engineering and statistical methods for modal identification based on output-only measurements have been well developed and have been attracting more attention recently. Statistical methods are very powerful because they explicitly treat uncertainties entering the mathematical models of the structure and the excitations. Bayesian statistical approaches for modal identification have been proposed by Katafygiotis and Yuen [3-4] using ambient data under a Bayesian statistical framework. As a result, they not only obtain the optimal values of the updated parameters by maximizing the posterior probability density function (PDF), but also allow for the quantification of uncertainties associated with the identified parameters of interest. However, the critical issue that always remains is the efficient determination of optimal values and their covariance matrix. Usually, the optimal values are solved by multidimensional numerical optimization and the covariance matrix is determined by finite difference. When the number of identified parameters is moderate to large, which is typical in modal identification of civil infrastructures, numerical optimization in maximizing the posterior PDF is very challenging and requires lots of computation effort to obtain the optimal values, which would preclude such algorithms from being implemented in wireless sensor networks. A method that not only has most of the advantages related to Bayesian statistical algorithms for uncertainty treatment but also reduces much of the computation effort is desirable.

Au (2011) developed a fast Bayesian FFT method for ambient modal identification with separate modes [5], which allows for fast computation of the optimal values and covariance matrix. In this work, we present a Bayesian spectral decomposition (BSD) method for modal identification using ambient data which is based on the statistical properties of the largest eigenvalue of the output spectral matrix. This method identifies each mode, the modal frequency and damping ratio and the mode shape separately. As a result, the number of parameters to be identified by numerical optimization reduces to four for each mode. After the optimal modal frequencies have been obtained, mode shapes are determined by singular value decomposition of the output spectral matrix at corresponding frequencies. Moreover, a distributed computing strategy is proposed for energy conversation in WSN. A numerical example is presented to demonstrate its procedures and features.

2 THEORETICAL ASPECTS

Some of the theoretical aspects related to the presented work are briefly discussed in the following sections.

2.1 Bayesian spectral density method

Let the acceleration time history measured at N_s DOFs of a structure be $\mathbf{Y}_N=\{\mathbf{y}(m)\in\mathbb{R}^{N_s}, m=1,\ldots,N\}$, where N is the number of samples per channel. Herein, the measured acceleration is modeled as $\mathbf{y}(\mathrm{m})=\mathbf{x}(\mathrm{m})+\mathbf{n}(\mathrm{m})$, where $\mathbf{x}(\mathrm{m})$ is the acceleration response of the structural model defined by a set of model parameters $\boldsymbol{\theta}$, the parameters to be identified; $\mathbf{n}(\mathrm{m})$ is the prediction error which accounts for the difference between the model response and measured data, due to measurement noise and modeling error. Based on $\mathbf{Y}_N$ we introduce the following discrete estimator of the spectral density matrix

$$\mathbf{S}_{y,N}(\omega_k)=\mathcal{Y}_N(\omega_k)\mathcal{Y}_N(\omega_k)^H \tag{1}$$

where the superscript H denotes conjugate transpose, $\mathcal{Y}_N(\omega_k)$ denotes the (scaled) Fourier transform of the vector process $\mathbf{y}(t)$ at frequency ω_k, as follows:

$$\mathcal{Y}_N(\omega_k)=\sqrt{\frac{\Delta t}{2\pi N}}\sum_{m=0}^{N-1}\mathbf{y}(m)e^{-j\omega_k m\Delta t} \tag{2}$$

where $j^2=-1$, Δt is the sampling interval, $\omega_k=k\Delta\omega$, $k=0,\ldots,N_1-1$ with $N_1=INT(N/2)$, $\Delta\omega=2\pi/T$, and $T=N\Delta t$. The scaling factor of the FFT in Eq(2) is defined such that the spectral density is two-sided with respect to the circular frequency in rad/s.

For a liner classically damped structure subjected to white noise excitation and independent and identical distributed (i.i.d.) Gaussian prediction error, Katafygiotis and Yuen (2001) derived the PDF for the spectral density matrix and applied it to Bayesian modal identification [3]. Consider a set of independent, identically distributed, time histories $\mathbf{Y}_N^{(1)},\ldots\mathbf{Y}_N^{(M)}$. Assuming that $N\to\infty$, the corresponding Fourier transforms $\mathcal{Y}_N^{(m)}(\omega_k), m=1,\ldots,M$ are independent and follow an identical complex N_s-variate normal distribution with zero mean, and the average spectral density estimate

$$\mathbf{S}_{y,N}^{M}(\omega_k)=\frac{1}{M}\sum_{m=1}^{M}\mathbf{S}_{y,N}^{(m)}(\omega_k)=\frac{1}{M}\sum_{m=1}^{M}\mathcal{Y}_{y,N}^{(m)}(\omega_k)\mathcal{Y}_{y,N}^{(m)}(\omega_k)^H \tag{3}$$

follows a central complex Wishart distribution of dimension N_s with M degrees of freedom. The PDF of this distribution is given by:

$$p(\mathbf{S}_{y,N}^{M}(\omega_k)) = \frac{\pi^{-N_s(N_s-1)/2} M^{N_s(M-N_s)} \left|\mathbf{S}_{y,N}^{M}(\omega_k)\right|^{M-N_s}}{(\prod_{p=1}^{N_s}(M-p)!)\left|E[\mathbf{S}_{y,N}(\omega_k)]\right|^{M}} \exp(-M\mathrm{tr}[E[\mathbf{S}_{y,N}(\omega_k)]^{-1}\mathbf{S}_{y,N}^{M}(\omega_k)]) \quad (4)$$

where $\left|A\right|$, tr[A] and E[A] denote the determinant, the trace and the expectation, respectively, of a matrix A. Note that this PDF exists only when $M \geq N_s$. Furthermore, it can be shown that in the limit when $N \to \infty$ the matrices $\mathbf{S}_{y,N}^{M}(\omega_k)$ and $\mathbf{S}_{y,N}^{M}(\omega_l)$ are independently Wishart distributed for $k \neq l$.

On the other hand, for a high sampling rate and long duration of data, the term $E[\mathbf{S}_{y,N}(\omega_k)]$ in Eq(4) can be expressed as

$$E[\mathbf{S}_{y,N}(\omega_k)] = \mathbf{\Phi}\mathbf{H}_k\mathbf{\Phi}^T + \mathbf{S}_{n0} \quad (5)$$

where $\mathbf{\Phi} \in \mathbb{R}^{N_s \times N_m}$ is the mode shape matrix confined to the measured DOFs (the *i*-th column corresponds to the *i*-th mode shape); $\mathbf{S}_{n0}$ is the spectral density matrix (constant) of the prediction error; $\mathbf{H}_k$ is the spectral density matrix of the modal response with (*i*, *j*) element given by

$$H_k(i,j) = \frac{S_{ij}\omega_k^4}{[(\omega_i^2 - \omega_k^2) + 2j\omega_k\omega_i\zeta_i][(\omega_j^2 - \omega_k^2) - 2j\omega_k\omega_j\zeta_j]} \quad (6)$$

It should be noted that this is only valid for acceleration response, and the exponential of ω_k in the numerator will be the values 0 or 2 when the response corresponds to displacement or velocity, respectively.

In the context of modal identification the set of modal parameters $\boldsymbol{\theta}$ consists of the natural frequencies, damping ratios, mode shapes, spectral density matrix of modal excitations and spectral density of the prediction error. Assuming a non-informative prior distribution, the posterior PDF of $\boldsymbol{\theta}$ given the spectral density data is proportional to the likelihood function

$$p(\boldsymbol{\theta}\left|\mathbf{S}_{y,N}^{M,k_1,k_2}\right.) \propto p(\mathbf{S}_{y,N}^{M,k_1,k_2}\left|\boldsymbol{\theta}\right.) \simeq c_1 \prod_{k=k_1}^{k_2} \frac{\left|\mathbf{S}_{y,N}^{M}(\omega_k)\right|^{M-N_s}}{\left|E[\mathbf{S}_{y,N}(\omega_k)]\right|^{M}} \exp(-Mtr[E[\mathbf{S}_{y,N}(\omega_k)]^{-1}\mathbf{S}_{y,N}^{M}(\omega_k)]) \quad (7)$$

where c_1 is a normalizing constant.

The most probable parameters $\hat{\boldsymbol{\theta}}$ are obtained by minimizing the log-likelihood function $L(\boldsymbol{\theta})$

$$p(\boldsymbol{\theta}\left|\mathbf{S}_{y,N}^{M,k_1,k_2}\right.) \propto \exp[-L(\boldsymbol{\theta})] \quad (8)$$

where

$$L(\boldsymbol{\theta}) = M\sum_{k=k_1}^{k_2}\left[\ln\left|E[\mathbf{S}_{y,N}(\omega_k)]\right| + tr[E[\mathbf{S}_{y,N}(\omega_k)]^{-1}\mathbf{S}_{y,N}^{M}(\omega_k)]\right] \quad (9)$$

Furthermore, with a sufficient large amount of data, the posterior PDF of the parameters $\boldsymbol{\theta}$ can be well-approximated by a Gaussian distribution $N(\hat{\boldsymbol{\theta}}, \mathbf{H}^{-1}(\hat{\boldsymbol{\theta}}))$ with mean $\hat{\boldsymbol{\theta}}$ and covariance matrix $\mathbf{H}^{-1}(\hat{\boldsymbol{\theta}})$, where $\mathbf{H}(\hat{\boldsymbol{\theta}})$ denotes the Hessian of $L(\boldsymbol{\theta})$ calculated at $\boldsymbol{\theta} = \hat{\boldsymbol{\theta}}$. Consider a second order expansion for the log-likelihood function

$$L(\boldsymbol{\theta}) \simeq L(\hat{\boldsymbol{\theta}}) + \mathbf{J}(\hat{\boldsymbol{\theta}})(\boldsymbol{\theta}-\hat{\boldsymbol{\theta}}) + \frac{1}{2}(\boldsymbol{\theta}-\hat{\boldsymbol{\theta}})^T \mathbf{H}(\hat{\boldsymbol{\theta}})(\boldsymbol{\theta}-\hat{\boldsymbol{\theta}}) \tag{10}$$

Note that the first term is a constant, and the second term vanishes since the gradient vector $\mathbf{J}(\hat{\boldsymbol{\theta}})$ equals to zero due to the minimization nature. Substituting Eq.(10) into Eq.(8), the posterior PDF can be approximated by a Gaussian distribution

$$p(\boldsymbol{\theta}\big|\mathbf{S}_{y,N}^{M,k_1,k_2}) \propto \exp[-\frac{1}{2}(\boldsymbol{\theta}-\hat{\boldsymbol{\theta}})^T \mathbf{C}(\hat{\boldsymbol{\theta}})^{-1}(\boldsymbol{\theta}-\hat{\boldsymbol{\theta}})] \tag{11}$$

where $\mathbf{C}(\hat{\boldsymbol{\theta}}) = \mathbf{H}(\hat{\boldsymbol{\theta}})^{-1}$ is the posterior covariance matrix, inverse of the Hessian matrix.

The critical issue that remains is the efficient determination of the most probable parameters and their covariance. In the original method, the optimal values are solved by numerical optimization and the Hessian is determined by finite difference. In particular, the objective function is a nontrivial nonlinear function of the modal parameters, so the determination of most probable parameters is computationally very demanding. In addition, the inverse of $E[\mathbf{S}_{y,N}(\omega_k)$ is ill-conditioned in a resonance frequency band. If all the most probable parameters were to be found by numerical optimization then the computational effort grows with the number of measured DOFs N_s and the number of contributed modes N_m. By noting the symmetry of the spectral density matrix of modal excitations and the normalization characteristic of mode shapes, there are $2N_\mathrm{m} + N_\mathrm{m}(N_\mathrm{s}\text{-}1) + N_\mathrm{m}(N_\mathrm{m}+1)/2 + N_\mathrm{s} = O(N_\mathrm{m}^2 + N_\mathrm{m}N_\mathrm{s})$ parameters to be identified. The growth of the dimension with N_s is a major issue because it can be moderate or large in typical civil engineering applications (e.g., $N_\mathrm{s}>10$). The growth of the dimension with N_m, although quadratic, is not significant because one can focus on a resonance frequency band dominated by a small number of modes. For well-separate modes one can identify each mode separately and $N_\mathrm{m}=1$ in this case.

In the next section we shall analyze the statistical property of the largest eigenvalue of the output spectral matrix and utilize it to effectively determine the optimal values of modal frequency and damping ratio and their covariance matrix when the structure has separated modes.

2.2 Modal identification with single mode

Assume that in a resonance frequency band the response is dominated by a single mode and only the spectral density data in this band are used for modal identification. For simplification, the spectral density of the prediction error is assumed to be the same for all measured DOFs. In this case, the parameters $\boldsymbol{\theta}$ consist of the natural frequency ω, damping ratio ζ, mode shape $\Phi \in \mathbb{R}^{N_s}$, spectral density S_f of the modal excitation and the prediction error S_n. Here the modal index is omitted for simplification. It is assumed that the mode shape is normalized to have unit norm, i.e., $\|\Phi\|^2 = 1$.

We start by examming the mathematical structure of $E[\mathbf{S}_{y,N}(\omega_k)]$ in Eq.(5). In this case,

$$E[\mathbf{S}_{y,N}(\omega_k)] = \alpha_k \Phi\Phi^T + S_n \mathbf{I}_{N_s} \tag{12}$$

where

$$\alpha_k = \frac{S_f}{(\beta_k^2 - 1)^2 + (2\zeta\beta_k)^2} = S_f A_k \tag{13}$$

where $\beta_k = \omega/\omega_k$, and $A_k = 1/[(\beta_k^2 - 1)^2 + (2\zeta\beta_k)^2]$ is the modal dynamic amplification. To facilitate deriving the analytical form of largest eigenvalue, we shall express $E[\mathbf{S}_{y,N}(\omega_k)]$ in a more suitable form. The key is to express $E[\mathbf{S}_{y,N}(\omega_k)]$ via a suitable eigendecomposition. Define a set of orthonormal bases E = {$e_j \in \mathbb{R}^{N_s}$: j = 1, …, N_s}, where $e_1 = \Phi \in \mathbb{R}^{N_s}$ and {e_2, e_3, …, e_{Ns}} form an orthonormal basis in the complement subspace. Using this basis, the identity matrix can be represented as $\mathbf{I}_{N_s} = \sum_{j=1}^{N_s} e_j e_j^T$, so the Eq.(12) can be rewritten as

$$E[\mathbf{S}_{y,N}(\omega_k)] = \alpha_k e_1 e_1^T + S_n \sum_{j=1}^{N_s} e_j e_j^T = (\alpha_k + S_n) e_1 e_1^T + S_n \sum_{j=2}^{N_s} e_j e_j^T \tag{14}$$

The eigenvalues of $E[\mathbf{S}_{y,N}(\omega_k)]$ are $\alpha_k + S_n$, S_n, …, S_n, with corresponding eigenvector e_1, e_2, …, e_{Ns}, and the largest eigenvalue d_k of $E[\mathbf{S}_{y,N}(\omega_k)]$ is

$$d_k = \alpha_k + S_n = \frac{S_f}{(\beta_k^2 - 1)^2 + (2\zeta\beta_k)^2} + S_n \tag{15}$$

A considerable amount of mathematical effort has been devoted on finding distributions for the eigenvalues of a Wishart matrix. Let s_k be the largest eigenvalue of $\mathbf{S}_{x,N}^M(\omega_k)$. According to Ref. [6], the largest eigenvalue s_k are asymptotically independently normally distributed with

$$E(s_k) = d_k, \quad \mathrm{var}(s_k) = \frac{2d_k^2}{M} \tag{16}$$

In the context of modal identification, assuming a non-informative prior distribution, the posterior PDF of $\boldsymbol{\theta}$ given the eigenvalue data is proportional to the likelihood function

$$p(\boldsymbol{\theta} | \mathbf{s}_k^{k_1,k_2}) \propto p(\mathbf{s}_k^{k_1,k_2} | \boldsymbol{\theta}) \simeq \prod_{k=k_1}^{k=k_2} \frac{\sqrt{M}}{\sqrt{4\pi} d_k} \exp\left(-\frac{M(s_k - d_k)^2}{4d_k^2} \right) \tag{17}$$

In the context of wireless sensor network, in order to utilize the distributed computing capacity, the whole network may be divided into *n* clusters of sensors. In this case, each cluster can determine a posterior PDF based on its own data, and *n* sets of posterior PDF will be obtained. The fusion of all the information obtained by various clusters can be conducted in Bayesian manner. Take one cluster as a priori, continuously include the data in other clusters, then the final posterior PDF $p(\boldsymbol{\theta} | \mathbf{s}_k^{n,k_1,k_2})$ will be a product of the *n* posterior PDFs corresponding to all clusters,

$$p(\boldsymbol{\theta} | \mathbf{s}_k^{n,k_1,k_2}) \propto p(\mathbf{s}_k^{n,k_1,k_2} | \boldsymbol{\theta}) \simeq \prod_n \prod_{k=k_1}^{k=k_2} \frac{\sqrt{M}}{\sqrt{4\pi} d_k} \exp\left(-\frac{M(s_k - d_k)^2}{4d_k^2} \right) \tag{18}$$

The most probable parameters $\hat{\boldsymbol{\theta}}$ are obtained by maximizing the posterior PDF $p(\boldsymbol{\theta} | \mathbf{s}_k^{n,k_1,k_2})$. This is equivalent to minimizing $L(\boldsymbol{\theta}) = -\ln[p(s_k^{n,k_1,k_2} | \boldsymbol{\theta})]$. Various optimization algorithms can be employed to minimize $L(\boldsymbol{\theta})$ and obtain the optimal parameters $\hat{\boldsymbol{\theta}}$, and then central difference or analytical formulas can be used to calculate the Hessian matrix $\mathbf{H}(\hat{\boldsymbol{\theta}})$.

Furthermore, it is found that the updated PDF of the parameters $\boldsymbol{\theta}$ can be well approximated by a Gaussian distribution $N(\hat{\boldsymbol{\theta}}, \mathbf{H}^{-1}(\hat{\boldsymbol{\theta}}))$ with mean $\hat{\boldsymbol{\theta}}$ and covariance matrix $\mathbf{H}^{-1}(\hat{\boldsymbol{\theta}})$.

2.3 Mode shape identification and assembling

The mode shapes can be identified as follows: since the modal frequency ω is identified in the previous section, the nearest discrete frequency $\omega_k \to \omega$ can be obtained. From Eq. (14), we know that the corresponding singular vector $\mathbf{u}_k$ is an estimate of the r^{th} mode shape Φ with unitary normalization. The principle for mode shape identification is the same as that of FDD method [9].

The mode shapes extracted from a particular cluster of sensors are referred to as local mode shapes. The local mode shapes have to be rescaled and assembled to global mode shapes. Consider the global mode shape Φ^{Ω} for the r^{th} mode, along with local mode shapes Φ^{Ω_1}, $\Phi^{\Omega_2}, \ldots \Phi^{\Omega_n}$ associated with respective clusters of sensors $\Omega_1, \Omega_2, \ldots \Omega_n$. The local mode shapes Φ^{Ω_i} and Φ^{Ω_j} associated with two neighboring clusters with overlapped sensors can be expressed as

$$\Phi^{\Omega_i} = \begin{pmatrix} \phi_{i1} \\ \phi_{i2} \\ \vdots \\ \phi_{ip} \\ \phi_{i1} \\ \vdots \\ \phi_{io} \end{pmatrix} \text{ and } \Phi^{\Omega_j} = \begin{pmatrix} \phi_{j1} \\ \phi_{j2} \\ \vdots \\ \phi_{jq} \\ \phi_{j1} \\ \vdots \\ \phi_{jo} \end{pmatrix} \tag{19}$$

where o is the number of overlapping nodes, and p and q are the number of non-overlapping nodes in the i^{th} and j^{th} clusters, respectively. To allow assembly, the mode shapes in Equation (19) should be rescaled to have the same values at the overlapping nodes, i.e.

$$\begin{pmatrix} \phi_{i1} \\ \vdots \\ \phi_{io} \end{pmatrix} = R_j \begin{pmatrix} \phi_{j1} \\ \vdots \\ \phi_{jo} \end{pmatrix} \tag{20}$$

where R_j is a rescaling factor for the mode shape Φ^{Ω_j}. The global mode shape is the union of the local mode shapes as

$$\Phi^{\Omega} = \bigcup_{i=1}^{n} R_i \Phi^{\Omega_i} \tag{21}$$

In the presence of noise, the rescaling factors to Equation (20) for any $o>1$ does not exist in general. Therefore, the rescaling factors R_i (i=1,2,…n) must be approximately determined, for example as a solution in the least-square sense [7-8]. Using the rescaling factors, the local mode shapes are scaled and assembled to obtain the global mode shape. At the overlapping nodes, the local mode shapes are averaged to obtain the associated values of the global mode shape.

3 APPLICATION IN WIRELESS SENSOR NETWORKS

In this section, a distributed computing strategy is adopted to implement this algorithm. This distributed computing strategy can reduce the data amount of wireless transmission and take advantage of decentralized computing capacity of the wireless sensor networks (WSN). Because wireless communication often consumes more energy than other parts, algorithms which require transmission of long time history records should be avoided. Pre-processing data locally will not only make it possible to transmit smaller amount of important information but also take advantage of the autonomous computing capacity of smart sensors. A two-level hierarchical architecture is proposed for the application of WSN for Bayesian modal identification. There are three types of sensors classified by their functions in the network: gateway node, cluster head nodes and leaf nodes. The schematic network architecture is shown in Figure1.

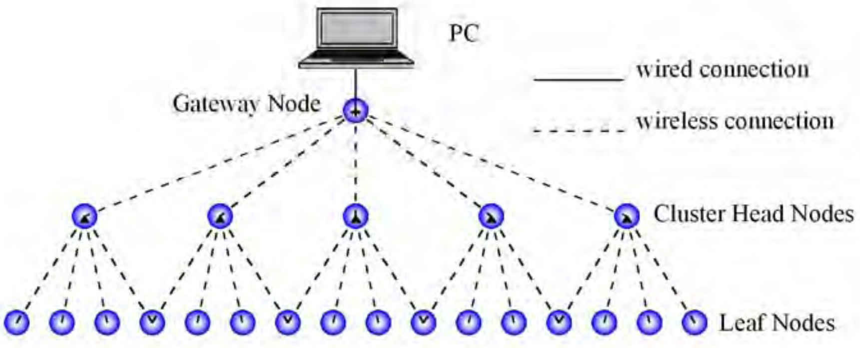

Figure 1. Two-level hierarchical architecture of WSN

Both the leaf nodes and cluster head nodes perform data acquisition, and each node calculates the FFT and then the auto-spectral density. Using Peak-Picking method, the potential modal frequencies can be obtained. Once all the local modal frequencies from leaf nodes and cluster head nodes are collected centrally in the gateway node, the first task is to pick out the true modes. The true modes should be identified obviously in the majority of clusters, while the noise modes will randomly appear. Thus, if a specific natural frequency is identified in a substantial number of clusters, it is considered as a true mode. FFT data around these modal frequencies are sent to cluster head nodes, and then cross-spectrum around these frequencies can be calculated in the cluster head node. In the cluster head node, SVD is performed in the vicinity of the modes to be identified, and then corresponding singular values (eigenvalues) are sent to the gateway node. Using Bayesian inference, modal frequencies and damping ratios together with their uncertainties are obtained in the gateway node and then the gateway node returns modal frequencies to each cluster head node. Thus, local mode shapes in each cluster can be obtained using SVD at the corresponding closest discrete frequencies. Finally, each cluster head node reports local mode shapes to the gateway node. A global mode shape is assembled in the gateway node by comparing the overlapping nodes in each cluster. After that, finalized modal parameters and their uncertainties are sent to PC via USB cable.

4 NUMERICAL EXAMPLE

In this example, we use simulated data from an 8-story shear building shown in Figure 2. It is assumed that this building has a uniformly distributed floor mass m=1×10^5kg and interstorey stiffness k=2.5×10^8N/m, and Rayleigh's damping with corresponding damping ratios $\zeta_1 = \zeta_2 = 1\%$ is assumed. The structure is assumed to be subjected to a base acceleration given by stationary Gaussian white noise with a spectral density of $0.0025\,m^2 s^{-3} rad^{-1}$. It is assumed that the accelerations at each floor were measured using a sampling interval ΔT=0.01sec. The time duration for one data set is 1000s and 10 data sets are collected. The measurement noise at different sensors is assumed to be i.i.d. Gaussian white noise with RMS=0.1 ms^{-2}. Therefore, the spectral density estimation calculated by Eq. (3) follows a Wishart distribution with M=10 degrees of freedom and their eigenvalues asymptotically follows a Gaussian distribution.

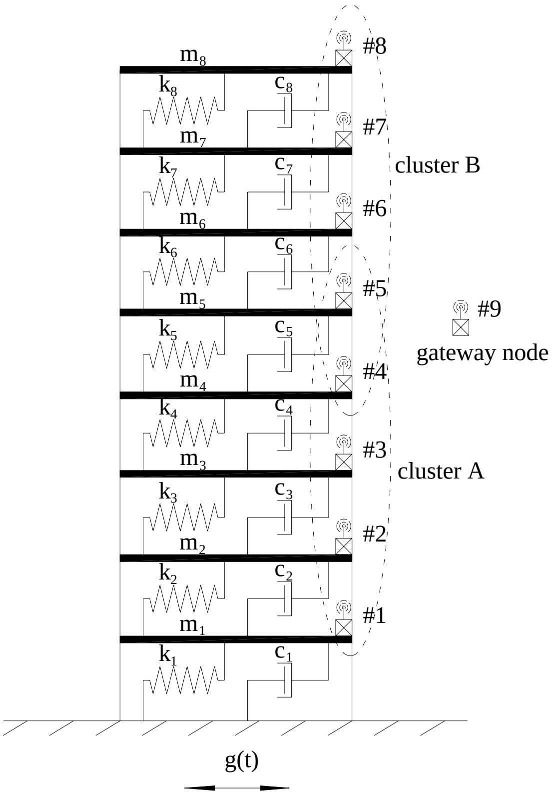

Figure 2. 8-storey shear building

The measurements can be taken by wireless sensors, which are grouped into two clusters: cluster A and cluster B. Cluster A consists of sensor #1, #2, #3, #4 and #5, one of which (excluding the overlapping nodes) is served as cluster head. Cluster B consists of sensor #4, #5, #6, #7 and #8, one of which (excluding the overlapping nodes) serves as cluster head. The overlapping nodes for these two clusters are sensor #4 and #5, which are used for global mode shape assembling. From the auto-spectrum in each sensor node, we know that there are three significant modes.

Table 1 shows the identified results from the output measurements. It shows the estimated optimal values $\hat{\boldsymbol{\theta}}$, the calculated standard deviations σ, coefficient of variance (COV), the value of a 'normalized distance' β. The parameter β represents the absolute value of difference between the identified optimal and actual value, normalized with respect to the corresponding calculated standard deviation. Thus, β expresses how many standard deviations away the identified value of a given parameter is from the target value. It can also be seen that the COV of damping is larger than that of natural frequency, which means it contains more uncertainty.

The mode shapes are identified using SVD of the output spectral matrix at the nearest discrete frequencies, and the corresponding singular vector $\mathbf{u}_k$ is an estimate of the r^{th} mode shape Φ with unitary normalization. The global mode shapes are assembled using least square method. The identified results are tabulated in table 2. The modal assurance criterion (MAC) values between theoretical values and identified ones are listed in the end column. The MAC values shows that the identified results closely match the theoretical ones.

	Actual θ	Optimal $\hat{\theta}$	S.D. σ	C.O.V	$\beta = \lvert\theta - \hat{\theta}\rvert / \sigma$
ω_1	6.2851	6.2831	0.0022	0.0004	0.8948
ω_2	18.6413	18.649	0.0064	0.0003	1.2129
ω_3	30.3626	30.312	0.0095	0.0003	5.3203
ζ_1	0.01	0.0102	0.0004	0.0416	0.4323
ζ_2	0.01	0.0104	0.0013	0.123	0.328
ζ_3	0.0137	0.0134	0.001	0.0763	0.3528

Table 1. Identified modal frequencies and damping ratios

mode	DOF	#1	#2	#3	#4	#5	#6	#7	#8	MAC
1st	Th*	-0.0891	-0.1752	-0.2554	-0.3268	-0.3871	-0.4342	-0.4666	-0.483	1.0000
	Id*	-0.0891	-0.1754	-0.2554	-0.3267	-0.3872	-0.4341	-0.4664	-0.4831	
2nd	Th	-0.2554	-0.4342	-0.483	-0.3871	-0.1752	0.0891	0.3268	0.4666	0.9999
	Id	-0.2568	-0.4363	-0.4862	-0.3893	-0.1781	0.0849	0.3217	0.4619	
3rd	Th	-0.3871	-0.4666	-0.1752	0.2554	0.483	0.3268	-0.0891	-0.4342	0.9977
	Id	-0.3998	-0.4739	-0.177	0.2726	0.4894	0.3283	-0.0683	-0.3976	

Note: * “Th” & “Id” denotes theoretical and identified values, respectively.

Table 2. Identified mode shapes

5 CONCLUSIONS

A Bayesian spectral decomposition (BSD) method for identifying modal parameters using output-only data is presented. This method takes advantage of the Bayesian spectral density approach (BSDA) and frequency domain decomposition (FDD) method, and avoids their limitations. Comparing with BSDA, this method reduces the dimension of identified parameters in the optimization problem to only four for each mode. It can identify each mode separately, which renders the method suitable for implementation in wireless sensor networks. Comparing with FDD, this method considers the uncertainty in a Bayesian statistical framework. It avoids the subjective peak-picking procedures for modal frequency identification and the accuracy of damping ratio is also remarkable. It obtains not only the optimal values of the modal frequencies and damping ratios but also their associated uncertainties by calculating the posterior joint probability of these parameters. The quantification of these uncertainties is very important when one plans to use modal parameters estimates for further processing.

The proposed method along with the distributed computing strategy may be suitable to be implemented in wireless sensor networks by utilizing the autonomous computing capacity of each wireless sensor. The proposed distributed computing strategy can reduce the amount of wireless communication and thus conserve the energy in an efficient manner.

6 ACKNOWLEDGEMENTS

This research has been supported by the Hong Kong Research Grants Council under grant 614406. This support is gratefully acknowledged.

REFERENCES

[1] J. P. Lynch, K. J. Loh, A summary review of wireless sensors and sensor networks for structural health monitoring. *Shock Vib Dig,* 38(2), 91-128, 2006.

[2] T. Nagayama, S. H. Sim, Y. Miyamori & B. F. Spencer Jr., Issues in structural health monitoring employing smart sensors. *Smart Structures and Systems,* 3(3), 299-329, 2007.

[3] L. S. Katafygiotis, K.-V. Yuen, Bayesian spectral density approach for modal updating using ambient data. *Earthquake Engineering and Structural Dynamics*, 30(8), 1103-1123, 2001.

[4] K-V. Yuen, L. S. Katafygiotis, Bayesian fast Fourier transform approach for modal updating using ambient data. *Adv.Struct.Eng.,* 6(2), 81-95, 2003.

[5] S.K. AU, Fast Bayesian FFT method for ambient modal identification with separated modes. *Journal of Engineering Mechanics, ASCE*, DOI:10.1061/(ASCE)EM.1943-7889.0000213, 2011.

[6] Y. Fujikoshi, R. Shimizu, & V. V. Ulyanov, *Multivariate statistics: high-dimensional and large-sample approximations*. Wiley, Hoboken, N.J., 2010.

[7] S.H. Sim, B.F. Spencer Jr., M. Zhang & H. Xie, Automated decentralized modal analysis using smart sensors. *Struct. Control Health Monit.,* Published Online, DOI: 10.1002/stc.348, 2009.

[8] S.K. AU, Assembling mode shapes by least squares. *Mechanical Systems and Signal Processing*, 25(1), 163-179, 2011.

[9] R. Brincker, L. Zhang & P. Andersen, Modal identification of output-only systems using frequency domain decomposition. *Smart Mater.Struct.,* 10(3), 441-445, 2001.

COMPDYN 2011
3rd ECCOMAS Thematic Conference on
Computational Methods in Structural Dynamics and Earthquake Engineering
M. Papadrakakis, M. Fragiadakis, V. Plevris (eds.)
Corfu, Greece, 25-28 May 2011

MASS, STIFFNESS AND DAMPING IDENTIFICATION OF A TWO-STORY BUILDING MODEL

D. Guida[1], **F. Nilvetti**[1], **C. M. Pappalardo**[1]

[1] University of Salerno
via Ponte don Melillo, Fisciano (Salerno), 84084, Italy
e-mail: {guida,nilvetti,cpappalardo}@unisa.it

Keywords: System Identification, Markov Parameters, ERA/DC, OKID, Modal Testing.

Abstract. *In this paper we propose the results of an experimental investigation addressed to identify mass, stiffness and damping matrices of a two-story building model. The goal of our research is to set up a quick procedure to design control laws for mitigating structural vibrations and/or detecting damage of structure itself. We placed on each floor a* 4507 *Bruel & Kjaer accelerometer connected to* 6160 *Bruel & Kjaer Pulse spectrum analyzer, then we excited the structure by* 8202 *Bruel & Kjaer impact hammer and through the recorded I/O data we identified the modal model. Once obtained the system modal parameters, we identified mass, stiffness and damping matrices of the structure. We are going to exploit these experimental results for designing a virtual passive controller. This apparatus is composed of an electric actuator placed on the top of the building connected to a NI-CompactRio System.*

1 INTRODUCTION

System identification is the art of determining a mathematical model of a physical system by combining information obtained from experimental data with that derived from an a priori knowledge. There are several types of system identification algorithms in relation to different goals one wants to pursue. In mechanical engineering, applied system identification allows to get modal parameters of a dynamical system using force and vibration measurements. These parameters are typically used to design optimal control laws whereas in the field of structural health monitoring they are used to detect and evaluate system damage. A very powerful algorithm to perform system identification is Eigensystem Realization Algorithm with Data Correlation using Observer/Kalman Filter Identification (ERA/DC OKID) [1, 2, 3, 4]. This numerical procedure is able to construct a state-space representation of a mechanical system starting from input and output measurements even in presence of process and measurement noise. On the other hand, when all degrees of freedom are instrumented with a force and/or an acceleration transducer, an efficient numerical procedure can be implemented to construct a second-order model of the mechanical system starting from state-space representation (MKR) [5, 6, 7]. Experimental investigations show that ERA/DC OKID correctly determines system natural frequencies and damping ratios whereas MKR method properly identifies mass and stiffness matrices but it fails in esteeming damping matrix because actual measurements are never noise-free. Nevertheless, if the real system is lightly damped, authors propose an efficient procedure [8, 9] for identifying in a direct way system damping matrix from state-space realization by assuming proportional damping hypothesis.

2 MATHEMATICAL BACKGROUND

2.1 System Modelling

Consider a multiple degrees of freedom mechanical system. Let $\mathbf{M} \in R^{n_2 \times n_2}$, $\mathbf{K} \in R^{n_2 \times n_2}$ and $\mathbf{R} \in R^{n_2 \times n_2}$ be the mass, stiffness and damping matrices, respectively. The system equations of motion can be expressed in matrix notation as:

$$\mathbf{M}\,\ddot{\mathbf{x}}(t) + \mathbf{R}\,\dot{\mathbf{x}}(t) + \mathbf{K}\,\mathbf{x}(t) = \mathbf{F}(t) \tag{1}$$

where $\mathbf{x}(t) \in R^{n_2}$, $\dot{\mathbf{x}}(t) \in R^{n_2}$, $\ddot{\mathbf{x}}(t) \in R^{n_2}$ are vectors of generalized displacement, velocity and acceleration, respectively, and $\mathbf{F}(t) \in R^{n_2}$ is the vector of forcing functions.

On the other hand, if the response of the dynamic system is measured by the $m \in N$ output quantities in the output vector $\mathbf{y}(t) \in R^m$, then the output equations can be written in a matrix form as follows:

$$\mathbf{y}(t) = \mathbf{C}_d\,\mathbf{x}(t) + \mathbf{C}_v\,\dot{\mathbf{x}}(t) + \mathbf{C}_a\,\ddot{\mathbf{x}}(t) \tag{2}$$

where $\mathbf{C}_d \in R^{m \times n_2}$, $\mathbf{C}_v \in R^{m \times n_2}$ and $\mathbf{C}_a \in R^{m \times n_2}$ are respectively the output influence matrices for displacement, velocity and acceleration. These output influence matrices simply describe the relation between the vectors $\mathbf{x}(t)$, $\dot{\mathbf{x}}(t)$, $\ddot{\mathbf{x}}(t)$ and the measurement vector $\mathbf{y}(t)$, which in general can be a linear combination of system generalized displacement, velocity and acceleration.

Let $\mathbf{z}(t) \in R^n$ be the state vector of the system:

$$\mathbf{z}(t) = \begin{bmatrix} \mathbf{x}(t) \\ \dot{\mathbf{x}}(t) \end{bmatrix} \tag{3}$$

where $n \in N$ is the dimension of the system state vector. The forcing function $\mathbf{F}(t)$ over the period of interest at a certain specific location can be expressed using a vector $\mathbf{u}(t) \in R^{r}$ containing $r \in N$ input quantities according to this relation:

$$\mathbf{F}(t) = \mathbf{B}_2\,\mathbf{u}(t) \tag{4}$$

where $\mathbf{B}_2 \in R^{n_2 \times r}$ is an input influence matrix characterizing the locations and type of inputs. The equations of motions and the output equations can both be respectively rewritten in terms of the state vector as follows:

$$\dot{\mathbf{z}}(t) = \mathbf{A}_c\,\mathbf{z}(t) + \mathbf{B}_c\,\mathbf{u}(t) \tag{5}$$

$$\mathbf{y}(t) = \mathbf{C}\,\mathbf{z}(t) + \mathbf{D}\,\mathbf{u}(t) \tag{6}$$

where $\mathbf{A}_c \in R^{n \times n}$ is the state transition matrix, $\mathbf{B}_c \in R^{n \times r}$ is the state influence matrix, $\mathbf{C} \in R^{m \times n}$ is the measurements influence matrix and $\mathbf{D} \in R^{m \times r}$ is the direct transmission matrix. These matrix can be computed in this way:

$$\mathbf{A}_c = \begin{bmatrix} \mathbf{O} & \mathbf{I} \\ -\mathbf{M}^{-1}\,\mathbf{K} & -\mathbf{M}^{-1}\,\mathbf{R} \end{bmatrix} \tag{7}$$

$$\mathbf{B}_c = \begin{bmatrix} \mathbf{O} \\ \mathbf{M}^{-1}\,\mathbf{B}_2 \end{bmatrix} \tag{8}$$

$$\mathbf{C} = \begin{bmatrix} \mathbf{C}_d - \mathbf{C}_a\,\mathbf{M}^{-1}\,\mathbf{K} & \mathbf{C}_v - \mathbf{C}_a\,\mathbf{M}^{-1}\,\mathbf{R} \end{bmatrix} \tag{9}$$

$$\mathbf{D} = \mathbf{C}_a\,\mathbf{M}^{-1}\,\mathbf{B}_2 \tag{10}$$

Equations (5) and (6) constitute a continuous-time state-space model of a multiple degrees of freedom dynamical system. Using the preceding definitions, the state-space complex eigenvalues problem can be stated as follows:

$$(\mathbf{A}_c - \lambda_c\,\mathbf{I})\psi = \mathbf{0} \tag{11}$$

where $\lambda_{c,j} \in C \;,\; j = 1, 2, \ldots, n$ and $\psi_j \in C^{n} \quad , \quad j = 1, 2, \ldots, n$ will be referred as system modal parameters. State-space model eigenvectors can be usefully grouped according to the following matrix notation:

$$\boldsymbol{\Psi} = \begin{bmatrix} \psi_1 & \psi_2 & \ldots & \psi_n \end{bmatrix} \tag{12}$$

where $\boldsymbol{\Psi} \in C^{n \times n}$ is a matrix constituted of system eigenvectors stacked by columns. Multibody model eigenvectors $\mathbf{W} \in C^{n_2 \times n}$ obtained from equation (1) and state-space model eigenvectors $\boldsymbol{\Psi} \in C^{n \times n}$ obtained from equation (5) are mathematically interconnected by the following formula:

$$\boldsymbol{\Psi} = \begin{bmatrix} \mathbf{W} \\ \mathbf{W}\,\boldsymbol{\Lambda}_c \end{bmatrix} \tag{13}$$

where $\boldsymbol{\Lambda}_c \in C^{n \times n}$ is a diagonal matrix whose elements are system eigenvalues.

2.2 Eigensystem Realization Algorithm with Data Correlation (ERA/DC) using Observer/Kalman Filter Identification (OKID)

The basic development of the state-space realization is attributed to Ho and Kalman. The Ho-Kalman procedure uses the generalized Hankel matrix to construct a state-space representation of a linear system form noise-free data. This methodology has been modified and substantially extended by Juang [1, 2] to develop the Eigensystem Realization Algorithm with Data Correlation (ERA/DC) to identify modal parameters from noisy measurement data. Recently, a method named Observer/Kalman Filter Identification (OKID) has been developed by Juang [3, 4] to compute the Markov parameters of a linear system from which the state-space model and a corresponding observer are determined simultaneously. This method is entirely formulated in time-domain and it is capable of handling general response data.

Conventional time-domain system identification methods use only the system Markov parameters [4] to determine $\mathbf{A}$, $\mathbf{B}$, $\mathbf{C}$ and $\mathbf{D}$. On the other hand, OKID uses the combined system and observer gain Markov parameters [4]. These parameters are computed directly from time-domain input and output measurements and are used to identify $\mathbf{A}$, $\mathbf{B}$, $\mathbf{G}$, $\mathbf{C}$ and $\mathbf{D}$ by the time-domain method named ERA/DC [4].

Basically, the ERA/DC OKID procedure consists in three steps: 1) computation of Markov parameters; 2) realization of state-space model; 3) modal parameters identification.

2.3 Modal Parameters Identification

The ERA/DC OKID procedure is a time-domain identification method which compute a minimum realization of system and the observer gain matrix starting from the combined system and observer gain Markov parameters [4]. A realization is a triplet of matrices $\left\{\hat{\mathbf{A}}\,,\hat{\mathbf{B}}\,,\hat{\mathbf{C}}\right\}$ that satisfies the discrete-time state-space equations. Obviously, the same system has an infinite set of realizations which will predict the identical response for any particular input. Minimum realization means a model with the smallest state space dimension among all the realizable systems that have the same input-output relations.

All minimum realizations have the same set of eigenvalues and eigenvectors, which are the modal parameters of the system itself. Assume that the state matrix $\hat{\mathbf{A}}$ has a complete set of linearly independent eigenvectors $\hat{\psi}_j\ ,\ j = 1, 2, \ldots, n$ with corresponding eigenvalues $\hat{\lambda}_j\ ,\ j = 1, 2, \ldots, n$:

$$\hat{\mathbf{A}}\,\hat{\mathbf{\Psi}} = \hat{\mathbf{\Psi}}\,\hat{\mathbf{\Lambda}} \tag{14}$$

where $\hat{\mathbf{\Lambda}} \in R^{n\times n}$ is the diagonal matrix of the eigenvalues and $\hat{\mathbf{\Psi}} \in C^{n\times n}$ is a matrix formed by the eigenvectors stacked per columns. The realization $\left\{\hat{\mathbf{A}}\,,\hat{\mathbf{B}}\,,\hat{\mathbf{C}}\right\}$ can be transformed in the realization $\left\{\hat{\mathbf{\Lambda}}, \hat{\mathbf{\Psi}}^{-1}\,\hat{\mathbf{B}}\,,\hat{\mathbf{C}}\,\hat{\mathbf{\Psi}}\right\}$ by using spectral decomposition. The diagonal matrix $\hat{\mathbf{\Lambda}}$ contains the informations of modal damping rates and damped natural frequencies. The matrix $\hat{\mathbf{\Psi}}^{-1}\,\hat{\mathbf{B}}$ defines the initial modal amplitudes and the matrix $\hat{\mathbf{C}}\,\hat{\mathbf{\Psi}}$ the mode shapes at the sensor points. All the modal parameters of a dynamic system can thus be identified by the unique triplet $\left\{\hat{\mathbf{\Lambda}}, \hat{\mathbf{\Psi}}^{-1}\,\hat{\mathbf{B}}\,,\hat{\mathbf{C}}\,\hat{\mathbf{\Psi}}\right\}$. This discrete-time realization can be transformed to its continuous-time counterpart $\left\{\hat{\mathbf{\Lambda}}_c, \hat{\mathbf{\Psi}}^{-1}\,\hat{\mathbf{B}}_c\,,\hat{\mathbf{C}}\,\hat{\mathbf{\Psi}}\right\}$ by using the zero-order-hold assumption. Finally, assuming that all the identified system modes are underdamped, modal damping rates and damped natural frequencies can be computed from the diagonal matrix $\hat{\mathbf{\Lambda}}_c \in C^{n\times n}$ as follows:

$$\begin{cases} \hat{\omega}_{n,i} = \sqrt{\hat{\varepsilon}_i^2 + \hat{\omega}_{d,i}^2} \quad , \quad i = 1, 2, \ldots, n_2 \\ \hat{\xi}_i = \frac{-\hat{\varepsilon}_i}{\sqrt{\hat{\varepsilon}_i^2 + \hat{\omega}_{d,i}^2}} \quad , \quad i = 1, 2, \ldots, n_2 \end{cases} \tag{15}$$

where $\hat{\varepsilon}_i \ , \ i = 1, 2, \ldots, n_2$ and $\hat{\omega}_{d,i} \ , \ i = 1, 2, \ldots, n_2$ are respectively the real and imaginary part of the system eigenvalues $\hat{\lambda}_{c,j} \ , \ j = 1, 2, \ldots, n$.

In many practical applications the hypothesis of proportional damping can be assumed as satisfied, especially in the case of structural systems in which damping is small and no a priori informations about its nature are available. Proportional damping assumption is the following:

$$\mathbf{R} = \alpha \, \mathbf{M} + \beta \, \mathbf{K} \tag{16}$$

where $\mathbf{M}$ and $\mathbf{K}$ are the mass and stiffness matrices, respectively, whereas α and β are proportional coefficients. If the system is lightly damped, authors propose a simple and efficient method to identify damping matrix starting from identified state space representation [8, 9]. The proportional damping assumption implies that the identified modal damping are related to the identified natural frequencies according to the following equations:

$$\hat{\xi}_i = \frac{\hat{\alpha}}{2\hat{\omega}_{n,i}} + \frac{\hat{\beta}\,\hat{\omega}_{n,i}}{2} \quad , \quad i = 1, 2, \ldots, n_2 \tag{17}$$

where $\omega_{n,i} \ , \ \ i = 1, 2, \ldots, n_2$ are the identified natural frequencies. These equations can be grouped in a matrix from to yield:

$$\begin{bmatrix} \frac{1}{2\hat{\omega}_{n,1}} & \frac{\hat{\omega}_{n,1}}{2} \\ \frac{1}{2\hat{\omega}_{n,2}} & \frac{\hat{\omega}_{n,2}}{2} \\ \vdots & \vdots \\ \frac{1}{2\hat{\omega}_{n,n_2}} & \frac{\hat{\omega}_{n,n_2}}{2} \end{bmatrix} \begin{bmatrix} \hat{\alpha} \\ \hat{\beta} \end{bmatrix} = \begin{bmatrix} \hat{\xi}_1 \\ \hat{\xi}_2 \\ \vdots \\ \hat{\xi}_{n_2} \end{bmatrix} \tag{18}$$

At this point the proportional coefficients α and β that optimal fits the identified natural frequencies $\omega_{n,i} \ , \ \ i = 1, 2, \ldots, n_2$ in the least-square sense can be computed taking the pseudo-inverse matrix:

$$\begin{bmatrix} \hat{\alpha} \\ \hat{\beta} \end{bmatrix} = \begin{bmatrix} \frac{1}{2\hat{\omega}_{n,1}} & \frac{\hat{\omega}_{n,1}}{2} \\ \frac{1}{2\hat{\omega}_{n,2}} & \frac{\hat{\omega}_{n,2}}{2} \\ \vdots & \vdots \\ \frac{1}{2\hat{\omega}_{n,n_2}} & \frac{\hat{\omega}_{n,n_2}}{2} \end{bmatrix}^{\dagger} \begin{bmatrix} \hat{\xi}_1 \\ \hat{\xi}_2 \\ \vdots \\ \hat{\xi}_{n_2} \end{bmatrix} \tag{19}$$

This approximation represents a simple and useful mathematical tool to deals with real experimental data.

3 CONSTRUCTION OF SECOND ORDER MODEL FROM IDENTIFIED STATE-SPACE REPRESENTATION

Consider the following matrices:

$$\mathbf{V}_c = \begin{bmatrix} \mathbf{R} & \mathbf{M} \\ \mathbf{M} & \mathbf{O} \end{bmatrix} \tag{20}$$

$$\mathbf{S}_c = \begin{bmatrix} -\mathbf{K} & \mathbf{O} \\ \mathbf{O} & \mathbf{M} \end{bmatrix} \tag{21}$$

$$\mathbf{B}_3 = \begin{bmatrix} \mathbf{B}_2 \\ \mathbf{O} \end{bmatrix} \tag{22}$$

Using these definitions, a symmetric formulation of system continuous-time state-space model can be developed:

$$\mathbf{V}_c\,\dot{\mathbf{z}}(t) = \mathbf{S}_c\,\mathbf{z}(t) + \mathbf{B}_3\,\mathbf{u}(t) \tag{23}$$

$$\mathbf{y}(t) = \mathbf{C}\,\mathbf{z}(t) + \mathbf{D}\,\mathbf{u}(t) \tag{24}$$

where the matrices $\mathbf{V}_c \in R^{n\times n}$, $\mathbf{S}_c \in R^{n\times n}$ and $\mathbf{B}_3 \in R^{n\times r}$ are all symmetric matrices. The symmetric formulation of system state-space model can be easily reconnected to the typical one (5) noting that the output equations are unchanged and that system transition matrix and state influence matrix can be computed in this way:

$$\mathbf{A}_c = \mathbf{V}_c^{-1}\,\mathbf{S}_c \tag{25}$$

$$\mathbf{B}_c = \mathbf{V}_c^{-1}\,\mathbf{B}_3 \tag{26}$$

The advantages of reformulating system state-space model in this way is that now the associated eigenvalues problem is kept symmetric. Indeed:

$$\mathbf{S}_c\,\boldsymbol{\Psi} = \mathbf{V}_c\,\boldsymbol{\Psi}\,\boldsymbol{\Lambda}_c \tag{27}$$

In general, these eigenvectors can be arbitrarily scaled but if the scaling is chosen such that:

$$\boldsymbol{\Psi}^T\,\mathbf{V}_c\,\boldsymbol{\Psi} = \mathbf{I} \tag{28}$$

$$\boldsymbol{\Psi}^T\,\mathbf{S}_c\,\boldsymbol{\Psi} = \boldsymbol{\Lambda}_c \tag{29}$$

then, for a proportionally damped system, the real and imaginary parts of the components of these complex eigenvectors are equal in magnitude. Once that the symmetric eigenvalues problem has been solved, it can be proved [5, 6, 7] that a transformation matrix can be computed in order to extract multibody model eigenvectors matrix $\hat{\mathbf{W}}$ from state-space realization $\left\{\hat{\mathbf{A}}\,,\hat{\mathbf{B}}\,,\hat{\mathbf{C}}\right\}$. Finally, using this method it is possible to construct a second-order model of the mechanical system by using the following formulae:

$$\left\{\begin{array}{l} \hat{\mathbf{M}} = (\hat{\mathbf{W}}\,\hat{\boldsymbol{\Lambda}}_c\,\hat{\mathbf{W}}^T)^{-1} \\ \hat{\mathbf{K}} = -(\hat{\mathbf{W}}\,\hat{\boldsymbol{\Lambda}}_c^{-1}\,\hat{\mathbf{W}}^T)^{-1} \\ \hat{\mathbf{R}} = -\hat{\mathbf{M}}\,\hat{\mathbf{W}}\,\hat{\boldsymbol{\Lambda}}_c^2\,\hat{\mathbf{W}}^T\,\hat{\mathbf{M}} \end{array}\right. \tag{30}$$

This numerical procedure is referred as MKR algorithm [5, 6, 7].

4 SYSTEM IDENTIFICATION OF A TWO-STORY BUILDING MODEL

We have set up a two-story building model composed of four steel pillars and two aluminum beams as showed in figure (**??**). The first floor pillars have a section $1mm$ x $35mm$ and are $300mm$ long while the second floor pillars have a section $1mm$ x $35mm$ and are $350mm$ long. The two beams are $200mm$ long with a square section $45mm$ x $45mm$. On the first and on the second floor there are two piezoelectric accelerometers as showed in figure (1). The 4507 Bruel & Kjaer accelerometers are connected to 6160 Bruel & Kjaer Pulse spectrum analyzer. The excitation signal is produced by the 8202 Bruel & Kjaer impact hammer, which is connected to the spectrum analyzer too.

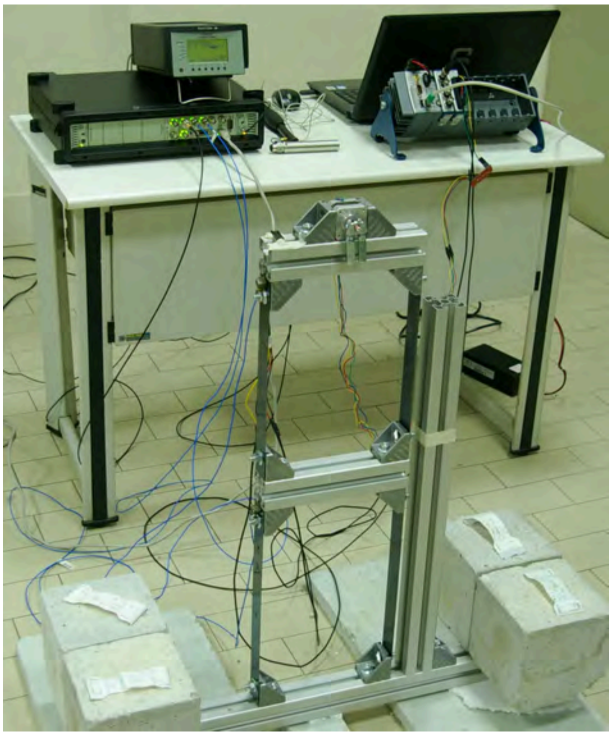

Figure 1: Experimental Apparatus

4.1 CASE-STUDY 1

We have studied two experimental configuration. In the first case, we analyzed the two-story building frame. In the second case, we placed an additional mass on the first floor. In figure (2) is showed the force measurement applied on the first floor and in figure (3) there is the system response corresponding to the input. In order to get statistically meaningful results, we repeated the experimental acquisition ten times but in the figures (2), (3) is showed only the first test.

Once the acquisition has been performed, we used ERA/DC OKID to get a state-space representation of the system. The following matrices represent the realization corresponding to the input and output measurements, figures (2), (3):

$$\hat{\mathbf{A}} = \begin{bmatrix} 0.6220 & -0.7789 & -0.0003 & -0.0021 \\ 0.7839 & 0.6191 & 0.0031 & -0.0012 \\ -0.0036 & 0.0061 & 0.9623 & 0.2616 \\ 0.0041 & 0.0044 & -0.2676 & 0.9634 \end{bmatrix} \tag{31}$$

$$\hat{\mathbf{B}} = \begin{bmatrix} 0.0541 \\ -0.0268 \\ 0.0412 \\ 0.0363 \end{bmatrix} \tag{32}$$

$$\hat{\mathbf{C}} = \begin{bmatrix} -37.8710 & -5.0124 & -5.8513 & 1.8479 \\ 26.5700 & 3.2700 & -7.2966 & 2.2001 \end{bmatrix} \tag{33}$$

$$\hat{\mathbf{D}} = \begin{bmatrix} 3.6387 \\ 0.0739 \end{bmatrix} \tag{34}$$

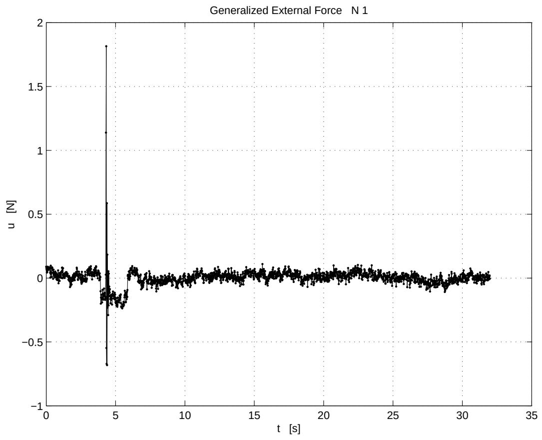

Figure 2: CASE 1 - Force Measurement

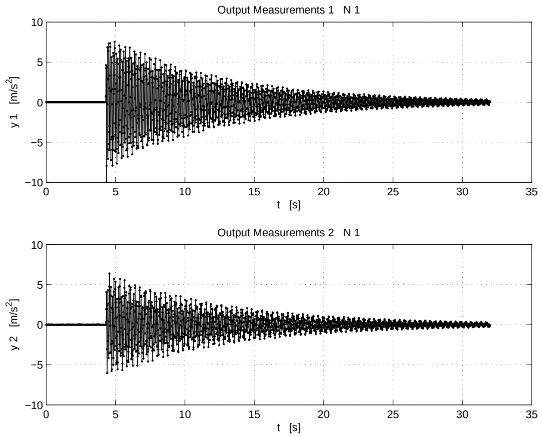

Figure 3: CASE 1 - Acceleration Measurements

Examining the singular value $\bar{\Sigma}_n$ of the Hankel matrix $\bar{H}(0)$ showed in figure (4) it is possible to determine the order of the system. Indeed, there are only 4 singular values whose magnitude is not negligible: it means that the system state has dimension $\hat{n} = 4$. Obviously, the same system has an infinite set of realizations which will predict the identical response for any particular input. Minimum realization means a model of the smallest state space dimensions among all realizable systems that have the same input-output relation. All minimum realizations have the same set of eigenvalues and eigenvectors, which are the modal parameters of the system itself:

$$\hat{\mathbf{\Lambda}} = diag(0.6205 + 0.7814\mathbf{i},\, 0.6205 - 0.7814\mathbf{i},\, 0.9629 + 0.2646\mathbf{i},\, 0.9629 - 0.2646\mathbf{i}) \tag{35}$$

$$\hat{\mathbf{\Psi}} = \begin{bmatrix} 0.0013 + 0.7059\mathbf{i} & 0.0013 - 0.7059\mathbf{i} & -0.0007 - 0.0019\mathbf{i} & -0.0007 + 0.0019\mathbf{i} \\ 0.7082 & 0.7082 & 0.0016 + 0.0008\mathbf{i} & 0.0016 - 0.0008\mathbf{i} \\ -0.0069 - 0.0030\mathbf{i} & -0.0069 + 0.0030\mathbf{i} & -0.0015 + 0.7031\mathbf{i} & -0.0015 - 0.7031\mathbf{i} \\ 0.0016 - 0.0071\mathbf{i} & 0.0016 + 0.0071\mathbf{i} & -0.7111 & -0.7111 \end{bmatrix} \tag{36}$$

System eigenvectors are graphically showed in figure (5). The discrete-time realization can

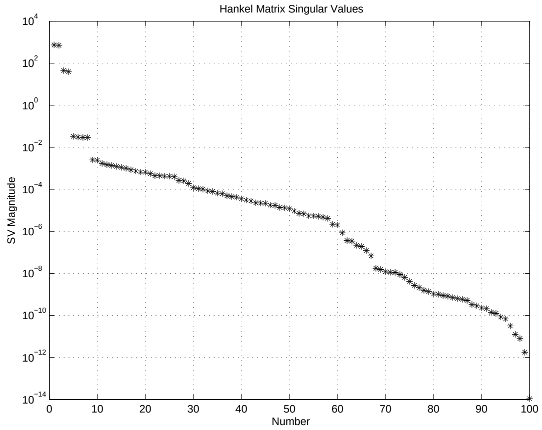

Figure 4: CASE 1 - Hankel Matrix Singular Values

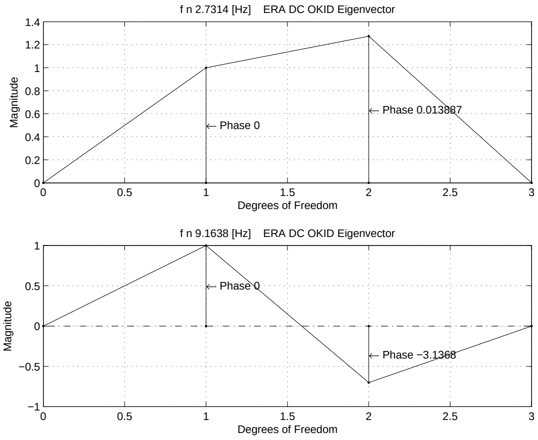

Figure 5: CASE 1 - System Eigenvalues and Eigenvectors

be transformed to its continuous-time counterpart by using the zero order hold assumption and subsequently modal damping rates and natural frequencies can be computed from the diagonal matrix $\hat{\mathbf{\Lambda}}_c \in C^{n \times n}$ to yield:

$$\hat{f}_{n,1} = 2.7314 \quad [Hz] \tag{37}$$

$$\hat{f}_{n,2} = 9.1638 \quad [Hz] \tag{38}$$

$$\hat{\xi}_1 = 0.0054 \quad [\backslash] \tag{39}$$

$$\hat{\xi}_2 = 0.0025 \quad [\backslash] \tag{40}$$

The optimally damping coefficients $\hat{\alpha}$ and $\hat{\beta}$ that fit identified natural frequencies in the least-square sense can be computed according to equations (19) to yield:

$$\hat{\alpha} = 0.1755 \tag{41}$$

$$\hat{\beta} = 3.2283 \cdot 10^{-5} \tag{42}$$

Finally, using the MKR algorithm a mechanical model of system mass, stiffness and damping matrices can be computed:

$$\hat{\mathbf{\Phi}} = \begin{bmatrix} -0.1317 + 0.0758\mathbf{i} & 0.1582 - 0.1057\mathbf{i} \\ 0.0927 - 0.0527\mathbf{i} & 0.2034 - 0.1319\mathbf{i} \end{bmatrix} \tag{43}$$

$$\hat{\mathbf{M}} = \begin{bmatrix} 0.2913 & 0.0153 \\ 0.0153 & 0.3387 \end{bmatrix} \quad [kg] \tag{44}$$

$$\hat{\mathbf{K}} = \begin{bmatrix} 630.44 & -425.83 \\ -425.83 & 439.01 \end{bmatrix} \quad [kg/s^2] \tag{45}$$

$$\hat{\mathbf{R}} = \begin{bmatrix} 6.9208 & -3.6833 \\ -3.6833 & 5.6759 \end{bmatrix} \quad [kg/s] \tag{46}$$

where $\hat{\mathbf{\Phi}}$ is system eigenvectors matrix scaled according to equations (28), (29). While in the case of mass $\hat{M}$ and stiffness $\hat{K}$ matrices the experimental results of the MKR algorithm are acceptable, the identified damping matrix $\hat{R}$ appears to be incongruous. Authors propose a different estimation of damping matrix (**??**optimal damping)) based on the identified proportional coefficients $\hat{\alpha}$ and $\hat{\beta}$. The resulting $\hat{R}$ matrix is the following:

$$\hat{\mathbf{R}} = \begin{bmatrix} 0.0715 & -0.0111 \\ -0.0111 & 0.0736 \end{bmatrix} \quad [kg/s] \tag{47}$$

this damping matrix is a better estimation of actual system damping.

4.2 CASE-STUDY 2

In the second case, we placed an additional mass on the first floor. In figure (6) is showed the force measurement applied on the first floor and in figure (7) there is the system response corresponding to the input. Even in this case, in order to get statistically meaningful results, we repeated the experimental acquisition ten times but in the figures (6), (7) is showed only the first test.

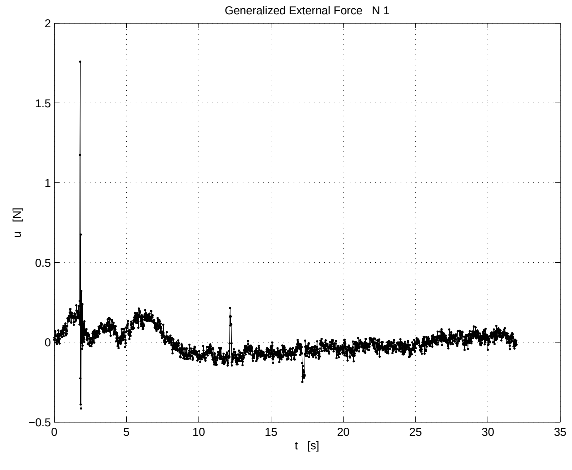

Figure 6: CASE 2 - Force Measurement

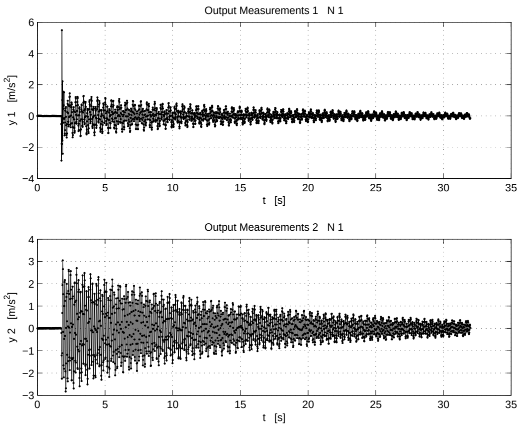

Figure 7: CASE 2 - Acceleration Measurements

Once the acquisition has been performed, we used ERA/DC OKID to get a state-space representation of the system. The following is the realizations corresponding to the input and output measurements, figures (6), (7):

$$\hat{\mathbf{A}} = \begin{bmatrix} 0.7776 & -0.6220 & 0.0041 & -0.0044 \\ 0.6205 & 0.7848 & 0.0014 & -0.0011 \\ -0.0116 & 0.0064 & 0.9799 & 0.1867 \\ 0.0072 & -0.0023 & -0.1848 & 0.9824 \end{bmatrix} \tag{48}$$

$$\hat{\mathbf{B}} = \begin{bmatrix} -0.0524 \\ -0.0317 \\ -0.0561 \\ 0.0124 \end{bmatrix} \tag{49}$$

$$\hat{\mathbf{C}} = \begin{bmatrix} -5.4178 & -3.7972 & -1.9582 & 1.7973 \\ 12.0353 & 8.4148 & -1.8316 & 1.9635 \end{bmatrix} \tag{50}$$

$$\hat{\mathbf{D}} = \begin{bmatrix} -2.7906 \\ -0.0621 \end{bmatrix} \tag{51}$$

Indeed, examining the singular value $\bar{\Sigma}_n$ of the Hankel matrix $\bar{H}(0)$ showed in figure (8) it is possible to determine the order of the system. In fact, there are only 4 singular values whose magnitude is not negligible: it means that the system state has dimension $\hat{n} = 4$. Now system modal parameters can be computed to yield:

$$\hat{\mathbf{\Lambda}} = diag(0.7812 + 0.6213\mathbf{i}, 0.7812 - 0.6213\mathbf{i}, 0.9812 + 0.1857\mathbf{i}, 0.9812 - 0.1857\mathbf{i}) \tag{52}$$

$$\hat{\mathbf{\Psi}} = \begin{bmatrix} 0.7075 & 0.7075 & 0.0015 + 0.0008\mathbf{i} & 0.0015 - 0.0008\mathbf{i} \\ -0.0041 - 0.7065\mathbf{i} & -0.0041 + 0.7065\mathbf{i} & 0.0044 - 0.0057\mathbf{i} & 0.0044 + 0.0057\mathbf{i} \\ -0.0046 + 0.0161\mathbf{i} & -0.0046 - 0.0161\mathbf{i} & 0.7089 & 0.7089 \\ -0.0047 - 0.0081\mathbf{i} & -0.0047 + 0.0081\mathbf{i} & 0.0049 + 0.7053\mathbf{i} & 0.0049 - 0.7053\mathbf{i} \end{bmatrix} \tag{53}$$

System eigenvectors are graphically showed in figure (9). The discrete-time realization can be transformed to its continuous-time counterpart by using the zero order hold assumption and

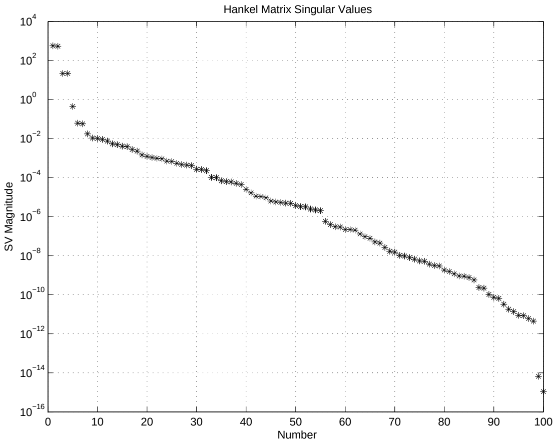

Figure 8: CASE 2 - Hankel Matrix Singular Values

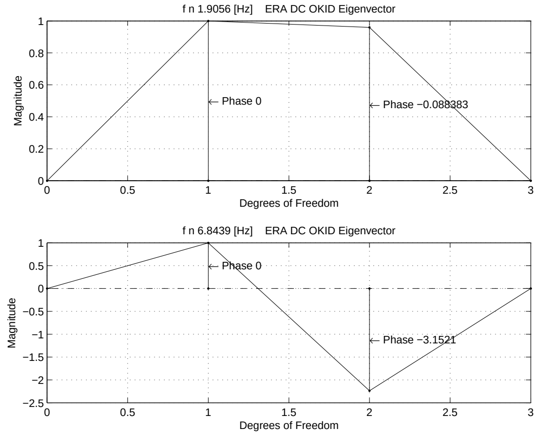

Figure 9: CASE 2 - System Eigenvalues and Eigenvectors

subsequently modal damping rates and natural frequencies can be computed from the diagonal matrix $\hat{\mathbf{\Lambda}}_c \in C^{n\times n}$ to yield:

$$\hat{f}_{n,1} = 1.9056 \quad [Hz] \tag{54}$$

$$\hat{f}_{n,2} = 6.8439 \quad [Hz] \tag{55}$$

$$\hat{\xi}_1 = 0.0075 \quad [\backslash] \tag{56}$$

$$\hat{\xi}_2 = 0.0028 \quad [\backslash] \tag{57}$$

Now it is straightforward to note that the effect of the additional mass is the reduction of system natural frequencies whereas the damping ratios are roughly unaffected. At this point the optimal damping coefficients $\hat{\alpha}$ and $\hat{\beta}$ that fits in the least-square sense the identified natural frequencies can be computed according to equations (19) to yield:

$$\hat{\alpha} = 0.1752 \tag{58}$$

$$\hat{\beta} = 3.4355 \cdot 10^{-5} \tag{59}$$

This parameters have almost the same magnitude compared to the preceding case. Finally, using the MKR algorithm a mechanical model of system mass, stiffness and damping matrices can be computed to yield:

$$\hat{\mathbf{\Phi}} = \begin{bmatrix} 0.0168 + 0.0824\mathbf{i} & -0.0579 - 0.1785\mathbf{i} \\ -0.0395 - 0.1840\mathbf{i} & -0.0705 - 0.1657\mathbf{i} \end{bmatrix} \tag{60}$$

$$\hat{\mathbf{M}} = \begin{bmatrix} 1.3771 & 0.0119 \\ 0.0119 & 0.5566 \end{bmatrix} \quad [kg] \tag{61}$$

$$\hat{\mathbf{K}} = \begin{bmatrix} 630.44 & -425.83 \\ -425.83 & 439.01 \end{bmatrix} \quad [kg/s^2] \tag{62}$$

$$\hat{\mathbf{R}} = \begin{bmatrix} 59.9062 & -34.1418 \\ -34.1418 & 38.4897 \end{bmatrix} \quad [kg/s] \tag{63}$$

where $\hat{\mathbf{\Phi}}$ is system eigenvectors matrix scaled according to equations (28), (29). Even in this case, while the identified mass $\hat{\mathbf{M}}$ and stiffness $\hat{\mathbf{K}}$ matrices are satisfactory acceptable, the identified damping matrix $\hat{\mathbf{R}}$ appears to be in some way incongruous. On the other hand, by using the proposed formulae (19), the result is the following:

$$\hat{\mathbf{R}} = \begin{bmatrix} 0.2739 & -0.0223 \\ -0.0223 & 0.1231 \end{bmatrix} \quad [kg/s] \tag{64}$$

this damping matrix is a better estimation of actual system damping. Note that there is a marked difference between results of case-study 1 and case-study 2. Indeed, the introduction of the additional mass on the first floor increases the magnitude of the first element of identified mass matrix $\hat{\mathbf{M}}$.

5 CONCLUSIONS

In this paper we performed an experimental investigation on a two-story frame in order to identify a second-order mechanical model, that is to derive system mass, stiffness and damping matrices. First, we identified system modal parameters through Eigensystem Realization Algorithm with Data Correlation using Observer/Kalman Filter Identification (ERA/DC OKID) [4]. Then we obtained mass, stiffness and damping matrices using a numerical method (MKR) proposed by [5, 6, 7]. Authors also proposed a new method to identify damping matrix from modal parameters [8, 9]. The structure was excited by an impulse yielded by 8202 Bruel & Kjaer impact hammer and the response was recorded by 4507 Bruel & Kjaer accelerometers connected to 6160 Bruel & Kjaer Pulse spectrum analyzer. The identification procedure was carried out several times, changing system mass and stiffness, and the results obtained are in good agreement with our FEM simulations. This work is the first step of our research project aimed at setting up a new virtual passive controller in order to regulate structural vibrations.

REFERENCES

[1] J. N. Juang, R. S. Pappa, *An Eigensystem Realization Algorithm for Modal Parameter Identification and Model Reduction*. J. Guid. Control Dyn., **8**(5), pp. 620627, 1985.

[2] J. N. Juang, J. E. Cooper, J. R. Wright, *An Eigensystem Realization Algorithm Using Data Correlation (ERA/DC) for Modal Parameter Identification*. Cont. Theor. Adv. Technol., **4**(1), pp. 514, 1988.

[3] J. N. Juang, M. Phan, L. G. Horta, R. W. Longman, *Identification of Observer/Kalman Filter Markov Parameters: Theory and Experiments*. J. Guid. Control Dyn., **16**(2), pp. 320329, 1993.

[4] J. N. Juang, *Applied System Identification*. Prentice Hall PTR, 1994.

[5] M. De Angelis, H. Lus, R. Betti, R. W. Longman, *Extracting Physical Parameters of Mechanical Models from Identified State-Space Representations*. J. App. Mech., **69**, pp. 617-625, 2002.

[6] H. Lus, M. De Angelis, R. Betti, R. W. Longman, *Constructing Second-Order Models of Mechanical Systems from Identified State Space Realizations. Part I: Theoretical Discussions*. J. Eng. Mech., **129**(5), pp. 477-488, 2003.

[7] H. Lus, M. De Angelis, R. Betti, R. W. Longman, *Constructing Second-Order Models of Mechanical Systems from Identified State Space Realizations. Part II: Numerical Investigations*. J. Eng. Mech., **129**(5), pp. 489-501, 2003.

[8] D. Guida, F. Nilvetti, C. M. Pappalardo, *Parameter Identification of a Two Degrees of Freedom Mechanical System*. WSEAS transaction on International Journal of Mechanics (NAUN), **2**(3), pp. 23-30, 2009.

[9] D. Guida, F. Nilvetti, C. M. Pappalardo, *Parameter Identification of a Full-Car Model for Active Suspension*. Worldwide Journal of Achievements in Materials and Manufacturing Engineering, **2**(40), pp. 138-148, 2010.

COMPDYN 2011
III ECCOMAS Thematic Conference on
Computational Methods in Structural Dynamics and Earthquake Engineering
M. Papadrakakis, M. Fragiadakis, V. Plevris (eds.)
Corfu, Greece, 25–28 May 2011

FINITE ELEMENT MODEL VALIDATION AND PREDICTIONS USING DYNAMIC REDUCTION TECHNIQUES

Dimitra-Christina Papadioti[1], **and Costas Papadimitriou**[1]

[1]University of Thessaly
Department of Mechanical Engineering, Volos 38334, Greece
e-mail: {dxpapadioti,costasp}@uth.gr

Keywords: Model Updating, Structural Identification, Multi-Objective Optimization, Component Mode Synthesis.

Abstract. *Finite element (FE) model updating and validation techniques are formulated as single and multi-objective optimization problems. A multi-objective optimization framework results in multiple Pareto optimal models that are consistent with the measured data and the residuals used to measure the discrepancies between the measured and the FE model predicted characteristics. The uncertainty in the Pareto optimal models can then be propagated to predict the uncertainty in the response predictions. Gradient-based optimization algorithms, such as the Normal Boundary Intersection algorithm, are used to compute the Pareto optimal solutions. These iterative algorithms require repeated solutions of the FE model for various values of the model parameters, as well as repeated computation of the gradients of the response characteristics involved in the residuals. For FE models with very high number of degrees of freedom, of the order of millions, repeated solutions of the FE models can be computationally very demanding. Component mode synthesis (CMS) methods are integrated into the updating method in order to reduce the computational effort required for performing the single- and multi-objective optimization problems. Exploiting certain schemes often encountered in FE model parameterization, it is shown that CMS allows the repeated computations to be carried out efficiently in a significantly reduced space of generalized coordinates, avoiding the solution of the fixed-interface/constrained modes and the assembling of reduced system matrices at each iteration. The final computational cost is associated with that of estimating the response characteristics of the reduced system at each iteration.*

1 INTRODUCTION

Structural model updating methods (e.g. [1]) have been proposed in the past to reconcile mathematical models, usually discretized finite element models, with experimental data. The estimate of the optimal model from a parameterized class of models is sensitive to uncertainties that are due to limitations of the mathematical models used to represent the behavior of the real structure, the presence of measurement and processing error in the data, the number and type of measured modal or response time history data used in the reconciling process, as well as the norms used to measure the fit between measured and model predicted characteristics. The optimal structural models resulting from such methods can be used for improving the model response and reliability predictions [2], structural health monitoring applications [3-6] and structural control [7].

Structural model parameter estimation problems based on measured data, such as modal characteristics (e.g. [3-6]) or response time history characteristics [8], are often formulated as weighted least-squares problems in which metrics, measuring the residuals between measured and model predicted characteristics, are build up into a single weighted residuals metric formed as a weighted average of the multiple individual metrics using weighting factors. Standard optimization techniques are then used to find the optimal values of the structural parameters that minimize the single weighted residuals metric representing an overall measure of fit between measured and model predicted characteristics. Due to model error and measurement noise, the results of the optimization are affected by the values assumed for the weighting factors.

The model updating problem has also been formulated in a multi-objective context [9,10] that allows the simultaneous minimization of the multiple metrics, eliminating the need for using arbitrary weighting factors for weighting the relative importance of each metric in the overall measure of fit. The multi-objective parameter estimation methodology provides multiple Pareto optimal structural models consistent with the measured data and the residuals used to measure the discrepancies between the measured and the finite element model predicted characteristics, in the sense that the fit each Pareto optimal model provides in a group of measured modal properties cannot be improved without deteriorating the fit in at least one other modal group. The Normal Boundary Intersection algorithm [11] is used to compute the Pareto optimal solutions.

Optimization algorithms used in the model updating methodology require repeated computations of the finite element model for various values of the model parameters. In addition, gradient-based algorithms require the estimation of the gradients of the residuals. For finite element models with a very high number of degrees of freedom, of the order of a few millions, the model updating methods require very high computational effort. Dynamic reduction techniques can be incorporated in the finite element model updating formulation to alleviate the computational burden.

In this work, a framework is presented for integrating component mode synthesis (CMS) [12,13] methods into existing finite element model updating methods in order to reduce the time consuming operations involved. The CMS allows the repeated computations to be carried out in a significantly reduced space of generalized coordinates. CMS techniques divide the structure into sub-structural components with mass and stiffness matrices that are reduced using fixed-interface and constrained modes. For structural components behaving linearly, an efficient model updating technique arises for component mass and stiffness matrices that depend linearly on only one of the free model parameters to be updated. In this case the reduced mass and stiffness matrices of a component also depends linearly on the free model parameter, allowing significant computational savings to be achieved during optimization by avoiding the repeated computation of the fixed-interface and constrained modes of each component during the iterative process. Using the resulting linear representation of the assembled mass and stiffness matrices of the reduced system in terms of the model parameters, computationally efficient algorithms [14] can be used to further reduce the computational cost involved in estimating the gradients and Hessians of the objective functions representing the modal residuals.

2 FINITE ELEMENT MODEL UPDATING FORMULATION

2.1 Modal residuals

Let $D=\{\hat{\omega}_r^{(k)}, \hat{\underline{\phi}}_r^{(k)} \in R^{N_0},\ r=1,\cdots,m,\ k=1,\cdots,N_D\}$ be the measured modal data from a structure, consisting of modal frequencies $\hat{\omega}_r^{(k)}$ and mode shape components at N_0 measured DOFs, where m is the number of observed modes and N_D is the number of modal data sets available. Consider a parameterized class of linear structural models used to model the dynamic behavior of the structure and let $\underline{\theta} \in R^{N_\theta}$ be the set of free structural model parameters to be identified using the measured modal data. The objective in a modal-based structural identification methodology is to estimate the values of the parameter set $\underline{\theta}$ so that the modal data $\{\omega_r(\underline{\theta}),\ \underline{\phi}_r(\underline{\theta}) \in R^{N_d}, r=1,\cdots,m\}$, where N_d is the number of model degrees of freedom (DOF), predicted by the linear class of models best matches, in some sense, the experimentally obtained modal data in D. For this, let

$$\varepsilon_{\omega_r}(\underline{\theta}) = \frac{\omega_r^2(\underline{\theta}) - \hat{\omega}_r^2}{\hat{\omega}_r^2} \tag{1}$$

and

$$\varepsilon_{\underline{\phi}_r}(\underline{\theta}) = \frac{\left\| L\Phi(\underline{\theta})\underline{\beta}_r(\underline{\theta}) - \hat{\underline{\phi}}_r \right\|}{\left\| \hat{\underline{\phi}}_r \right\|} \tag{2}$$

$r=1,\cdots,m$, be the measures of fit or residuals between the measured modal data and the model predicted modal data for the r-th modal frequency and modeshape components, respectively, where $\| \underline{z} \|^2 = \underline{z}^{\mathrm{T}} \underline{z}$ is the usual Euclidian norm, the matrix $L \in R^{N_0 \times N_d}$ is an observation matrix comprised of zeros and ones that maps the N_d model DOFs to the N_0 observed DOFs, $\Phi(\underline{\theta}) \in R^{N_d \times m}$ is the matrix of the modeshapes predicted by the model, and $\underline{\beta}_r(\underline{\theta}) = [\Phi^T(\underline{\theta}) L^T L \Phi(\underline{\theta})]^{-1} [L\Phi(\underline{\theta})]^T \hat{\underline{\phi}}_r$ is a normalization vector that guaranties that the distance of the measured modeshape $\hat{\underline{\phi}}_r$ from the space spanned by the model predicted modeshapes in $L\Phi(\underline{\theta}) \in R^{N_d \times m}$ is minimal.

It should be noted that for modes that are not closely spaced, the elements $\beta_{jr}(\underline{\theta})$ of the normalization vector $\underline{\beta}_r(\underline{\theta})$ are expected to have values close to zero for $j \neq r$ and so the measure of fit $\varepsilon_{\underline{\phi}_r}(\underline{\theta})$ is approximately the same as $\varepsilon_{\underline{\phi}_r}(\underline{\theta}) = \left\| L\underline{\phi}_r(\underline{\theta})\beta_{rr}(\underline{\theta}) - \hat{\underline{\phi}}_r \right\| / \left\| \hat{\underline{\phi}}_r \right\|$. However, for closely spaced modes, the measure of fit $\varepsilon_{\underline{\phi}_r}(\underline{\theta})$ in (2) is used to express the fact that any vector in the subspace spanned by the identified modeshapes for these closely spaced modes is also a modeshape. Thus, any of the identified closely spaced modeshapes should be expected to be a linear combination of the model predicted modeshapes for the closely spaced modes. This fact is reflected in the use of the measure of fit $\varepsilon_{\underline{\phi}_r}(\underline{\theta})$ in (2).

In order to proceed with the model updating formulation, the measured modal properties are grouped into n groups. Each group contains one or more modal properties. The modal properties assigned in the ith group are identified by the set $g_i(k)$, $i = 1, \cdots, n$ and $k = 1, 2$, with any element in the set $g_i(k)$ is an integer from 1 to m. An element in the set $g_i(k)$ with $k = 1$ refer to the number of the measured modal frequency assigned in the group i, while the elements of the set $g_i(k)$ with $k = 2$ refer to the number of the measured modeshape assigned in the group i. For the ith group, a norm $J_i(\underline{\theta})$ is introduced to measure the residuals of the difference between the measured values of the modal properties involved in the group and the corresponding modal values predicted from the model class for a particular value of the parameter set $\underline{\theta}$. The measure of fit in a modal group is the sum of the individual square errors in (1) for the corresponding modal properties involved in the modal group. Specifically, the measure of fit is given by

$$J_i(\underline{\theta}) = \sum_{r \in g_i(1)} \varepsilon^2_{\omega_r}(\underline{\theta}) + \sum_{r \in g_i(2)} \varepsilon^2_{\underline{\phi}_r}(\underline{\theta}) \tag{3}$$

The grouping of the modal properties $\{\omega_r(\underline{\theta}), \ \underline{\phi}_r(\underline{\theta}), r = 1, \cdots, m\}$ into n groups and the selection of the measures of fit (residuals) $J_1(\underline{\theta}), \cdots, J_n(\underline{\theta})$ are usually based on user preference. The modal properties assigned to each group are selected by the user according to their type and the purpose of the analysis.

2.2 Multi-objective identification

The problem of identifying the model parameter values $\underline{\theta}$ that minimize the modal or response time history residuals can be formulated as a multi-objective optimization problem stated as follows [10]. Find the values of the structural parameter set $\underline{\theta}$ that simultaneously minimizes the objectives

$$\underline{y} = \underline{J}(\underline{\theta}) = (J_1(\underline{\theta}), \cdots, J_n(\underline{\theta})) \tag{4}$$

subject to inequality constrains $\underline{c}(\underline{\theta}) \le \underline{0}$ and parameter constrains $\underline{\theta}_{low} \le \underline{\theta} \le \underline{\theta}_{upper}$, where $\underline{\theta} = (\theta_1, \cdots, \theta_{N_\theta}) \in \Theta$ is the parameter vector, Θ is the parameter space, $\underline{y} = (y_1, \cdots, y_n) \in Y$ is the objective vector, Y is the objective space, $\underline{c}(\underline{\theta})$ is the vector function of constrains, and $\underline{\theta}_{low}$ and $\underline{\theta}_{upper}$ are respectively the lower and upper bounds of the parameter vector . For conflicting objectives $J_1(\underline{\theta}), \cdots, J_n(\underline{\theta})$, there is no single optimal solution, but rather a set of alternative solutions, known as Pareto optimal solutions, that are optimal in the sense that no other solutions in the parameter space are superior to them when all objectives are considered.

Using multi-objective terminology, the Pareto optimal solutions are the non-dominating vectors in the parameter space Θ, defined mathematically as follows. A vector $\underline{\theta} \in \Theta$ is said to be non-dominated regarding the set Θ if and only if there is no vector in Θ which dominates $\underline{\theta}$. A vector $\underline{\theta}$ is said to dominate a vector $\underline{\theta}'$ if and only if

$$J_i(\underline{\theta}) \le J_i(\underline{\theta}') \quad \forall i \in \{1, \cdots, n\} \quad \text{and} \quad \exists \ j \in \{1, \cdots, n\} \ : \ J_j(\underline{\theta}) < J_j(\underline{\theta}') \tag{5}$$

The set of objective vectors $\underline{y} = \underline{J}(\underline{\theta})$ corresponding to the set of Pareto optimal solutions $\underline{\theta}$ is called Pareto optimal front. The characteristics of the Pareto solutions are that the residuals cannot be improved in any group without deteriorating the residuals in at least one other group. The multiple Pareto optimal solutions are due to modelling and measurement errors. The level of modelling and measurement errors affect the size and the distance from the origin of the Pareto front in the objective space, as well as the variability of the Pareto optimal solutions in the parameter space.

2.3 Weighted modal residuals identification

The parameter estimation problem is traditionally solved by minimizing the single objective

$$J(\underline{\theta};\underline{w}) = \sum_{i=1}^{n} w_i J_i(\underline{\theta}) \tag{6}$$

formed from the multiple objectives $J_i(\underline{\theta})$ using the weighting factors $w_i \geq 0$, $i = 1,\cdots,n$, with $\sum_{i=1}^{n} w_i = 1$. The objective function $J(\underline{\theta};\underline{w})$ represents an overall measure of fit between the measured and the model predicted characteristics. The relative importance of the residual errors in the selection of the optimal model is reflected in the choice of the weights. The results of the identification depend on the weight values used. Conventional weighted least squares methods assume equal weight values, $w_1 = \cdots = w_n = 1/n$.

2.4 Computational issues

The proposed single and multi-objective identification problems are solved using available single- and multi-objective optimization algorithms. The optimization of $J(\underline{\theta};\underline{w})$ in (6) with respect to $\underline{\theta}$ for given $\underline{w}$ can readily be carried out numerically using any available gradient-based algorithm for optimizing a nonlinear function of several variables. The set of Pareto optimal solutions can be obtained using available multi-objective optimization algorithms. A very efficient algorithm for solving the multi-objective optimization problem is the Normal-Boundary Intersection (NBI) method [11]. Each Pareto optimal solutions is obtained by solving a single-objective optimization problem using gradient based optimization algorithms. Thus, the computational time is of the order of the number of points used to represent the Pareto front multiplied by the computational time required to solve a single-objective problem for computing each point on the front.

It is obvious that the search for the Pareto optimal models require repeated computations of the finite element model for various values of the model parameters. In addition, gradient-based algorithms require the estimation of the gradients of the residuals. For finite element models with a very high number of degrees of freedom, of the order of a few millions, the computational time involved for repeatedly solving the large-scale eigen-problems may be excessive, especially if the number of iterations is high. The objective of this work is to examine the conditions under which substantial reductions in the computational effort can be achieved using dynamic reduction techniques such as component mode synthesis methods. Dividing the structure into components and reducing the number of physical coordinates to a much smaller number of generalized coordinates certainly alleviates part of the computational effort. However, at each iteration one needs to re-computed the eigen-problem for each component which can be a very time consuming operation. It is shown that for certain parameterization schemes, often encountered in finite element model updating formulations, the repeated solutions of the component eigen-problems are avoided, reducing substantially the computational demands in finite element model updating formulations.

3 COMPONENT MODE SYNTHESIS

In component mode synthesis [12,13] a structure is divided into several components. Reduction techniques are applied on a number of these components, while the rest are the non-reduced parts of the structure which could be left un-altered. For each component, the unconstrained DOFs are divided into the boundary DOFs, denoted by the subscript b and the internal DOFs, denoted by the subscript i. The boundary DOFs of a component are common with the DOFs of adjacent components, while the internal DOFs of a component are not shared with any adjacent component.

The stiffness and mass matrices $K^{(s)}$ and $M^{(s)}$ of a component s are partitioned to blocks related to the internal and boundary DOFs, with the undamped equation of motion of a component given by

$$\begin{bmatrix} M_{ii}^{(s)} & M_{ib}^{(s)} \\ M_{bi}^{(s)} & M_{bb}^{(s)} \end{bmatrix} \begin{Bmatrix} \underline{\ddot{u}}_i^{(s)} \\ \underline{\ddot{u}}_b^{(s)} \end{Bmatrix} + \begin{bmatrix} K_{ii}^{(s)} & K_{ib}^{(s)} \\ K_{bi}^{(s)} & K_{bb}^{(s)} \end{bmatrix} \begin{Bmatrix} \underline{u}_i^{(s)} \\ \underline{u}_b^{(s)} \end{Bmatrix} = \begin{Bmatrix} \underline{f}_i^{(s)} \\ \underline{f}_b^{(s)} + \underline{r}_b^{(s)} \end{Bmatrix} \tag{7}$$

where $\underline{f}_i^{(s)}$ and $\underline{f}_b^{(s)}$ are the external forces, while $\underline{r}_b^{(s)}$ are the reaction forces on the component from the adjacent components at the boundary DOFs. The indices i and b are sets containing the internal and boundary DOFs of the component s.

In component mode synthesis, the physical displacement coordinates $\underline{u}^{(s)}$ of a component are represented in terms of the generalized coordinates $\underline{p}^{(s)}$ of the component by the Ritz coordinate transformation

$$\underline{u}^{(s)} = \Psi^{(s)} \underline{p}^{(s)} \tag{8}$$

According to the Craig-Bampton fixed-interface-mode method, the physical coordinates of the component are related to the generalized coordinates using the fixed-interface normal modes and the interface constrained modes as follows

$$\underline{u}^{(s)} = \begin{Bmatrix} \underline{u}_i^{(s)} \\ \underline{u}_b^{(s)} \end{Bmatrix} = \Psi^{(s)} \underline{p}^{(s)} = \begin{bmatrix} \Phi_{ik}^{(s)} & \Psi_{ib}^{(s)} \\ 0_{bk}^{(s)} & I_{bb}^{(s)} \end{bmatrix} \begin{Bmatrix} \underline{p}_k^{(s)} \\ \underline{p}_b^{(s)} \end{Bmatrix} \tag{9}$$

where $\Phi_{ik}^{(s)}$ is the interior partition matrix of kept fixed-interface modes satisfying the eigen-problem

$$K_{ii}^{(s)} \Phi_{ik}^{(s)} = M_{ii}^{(s)} \Phi_{ik}^{(s)} \Lambda_{kk}^{(s)} \tag{10}$$

with all boundary DOFs for the considered component restrained, and the $\Psi_{ib}^{(s)}$ is the interior partition matrix of the constrained-modes given by $\Psi_{ib}^{(s)} = -[K_{ii}^{(s)}]^{-1} K_{ib}^{(s)}$. The matrix $\Lambda_{kk}^{(s)} = diag(\omega_j^{2(s)})$ is diagonal containing the eigenvalues $\omega_j^{2(s)}$ of the kept fixed-interface normal modes. The fixed-interface modes $\Phi_{ik}^{(s)}$ are considered mass normalized, satisfying

$$\Phi_{ik}^{(s)T} M_{ii}^{(s)} \Phi_{ik}^{(s)} = I_{kk}^{(s)}, \qquad \Phi_{ik}^{(s)T} K_{ii}^{(s)} \Phi_{ik}^{(s)} = \Lambda_{kk}^{(s)} \tag{11}$$

The reduced set of component equations of motion in generalized coordinates is

$$\hat{M}^{(s)}\ddot{\underline{p}}^{(s)} + \hat{K}^{(s)}\underline{p}^{(s)} = \underline{\hat{f}}^{(s)} + \underline{\hat{r}}^{(s)} \tag{12}$$

where the reduced mass, stiffness matrix and force vectors for the component are given in terms of the original matrices and force vectors in the form

$$\hat{M}^{(s)} = \Psi_{ik}^{(s)T} M^{(s)} \Psi_{ik}^{(s)}, \quad \hat{K}^{(s)} = \Psi_{ik}^{(s)T} K^{(s)} \Psi_{ik}^{(s)}, \quad \underline{\hat{f}}^{(s)} = \Psi_{ik}^{(s)T} \underline{f}^{(s)} \quad \text{and} \quad \underline{\hat{r}}^{(s)} = \Psi_{ik}^{(s)T} \underline{r}^{(s)} \tag{13}$$

with the partitions for the mass and stiffness matrices given respectively by

$$\begin{aligned} \hat{M}_{kk}^{(s)} &= I_{kk}^{(s)} \\ \hat{M}_{kb}^{(s)} &= \hat{M}_{bk}^{(s)T} = \Phi_{ik}^{(s)T} M_{ii}^{(s)} \Psi_{b}^{(s)} + \Phi_{ik}^{(s)T} M_{ib}^{(s)} \\ \hat{M}_{bb}^{(s)} &= (\Psi_{b}^{(s)T} M_{ii}^{(s)} + M_{bi}^{(s)}) \Psi_{b}^{(s)} + \Psi_{b}^{(s)T} M_{ib}^{(s)} + M_{bb}^{(s)} \end{aligned} \tag{14}$$

and

$$\begin{aligned} \hat{K}_{kk}^{(s)} &= \Lambda_{kk}^{(s)} \\ \hat{K}_{kb}^{(s)} &= \hat{K}_{bk}^{(s)T} = 0_{kb}^{(s)} \\ \hat{K}_{bb}^{(s)} &= K_{bb}^{(s)} - K_{bi}^{(s)} [K_{ii}^{(s)}]^{-1} K_{ib}^{(s)} = K_{bb}^{(s)} + \Psi_{b}^{(s)T} K_{ib}^{(s)} \end{aligned} \tag{15}$$

In the substructure assembly process, the vector $\underline{p} = [\underline{p}^{(1)T}, \cdots, \underline{p}^{(S)T}]^T$ of all generalized coordinates for each components is introduced. Letting $\underline{q} = [\underline{p}_k^{(1)T}, \cdots, \underline{p}_k^{(S)T}, \underline{u}_b^T]^T$ be the vector of independent generalized coordinates formed from the generalized coordinates (fixed-interface modal and boundary coordinates) of all components, the following transformation holds

$$\underline{p} = S\underline{q} \tag{16}$$

where the component coupling matrix S couples the independent generalized coordinates with the generalized coordinates of each component. Using the continuity of displacement/rotations and the equilibrium of forces along the shared boundaries of the components, the equations of motion in the reduced space of independent generalized coordinates takes the final form

$$\hat{M}^{CB}\ddot{\underline{q}} + \hat{K}^{CB}\underline{q} = S^T \underline{\hat{f}} \tag{17}$$

where the assembled mass and stiffness matrices for the reduced system are given by

$$\hat{M}^{CB} = S^T \begin{bmatrix} \hat{M}^{(1)} & 0 & 0 \\ 0 & \ddots & 0 \\ 0 & 0 & \hat{M}^{(S)} \end{bmatrix} S \qquad \text{and} \qquad \hat{K}^{CB} = S^T \begin{bmatrix} \hat{K}^{(1)} & 0 & 0 \\ 0 & \ddots & 0 \\ 0 & 0 & \hat{K}^{(S)} \end{bmatrix} S \tag{18}$$

Solving the eigen-problem

$$\hat{K}^{CB} Q = \hat{M}^{CB} Q \, \Lambda \tag{19}$$

associated with the reduced mass and stiffness matrices $\hat{M}^{CB}$ and $\hat{K}^{CB}$, respectively, one obtains the modal frequencies in $\Lambda = diag(\omega_i^2)$ and the mode shapes Q of the reduced system. The mode shapes of the original structure are assembled from the reduced ones. Specifically, using (8) and (16), the physical mode shapes are recovered as follows

$$\Phi = \begin{bmatrix} \Psi^{(1)} & 0 & 0 \\ 0 & \ddots & 0 \\ 0 & 0 & \Psi^{(s)} \end{bmatrix} SQ \tag{20}$$

4 MODEL UPDATING USING COMPONENT MODE SYNTHESIS

Next, the component mode synthesis procedure is integrated into the finite element formulation. We limit the presentation for the case for which the stiffness and mass matrices depend linearly on the model parameters to be estimated using the measured data. Specifically, it is assumed that the mass and stiffness matrix takes the form

$$\begin{aligned} K &= K_0 + \sum_{i=1}^{N_\theta} K_{,j}\theta_j \\ M &= M_0 + \sum_{j=1}^{N_\theta} M_{,j}\theta_j \end{aligned} \tag{21}$$

This implies that the component mass and stiffness matrix as well as their partitions admit a similar representation. Specifically, the following is true for a component stiffness and mass matrix

$$\begin{aligned} K^{(s)} &= K_0^{(s)} + \sum_{i=1}^{N_\theta} K_{,j}^{(s)}\theta_j \\ M^{(s)} &= M_0^{(s)} + \sum_{j=1}^{N_\theta} M_{,j}^{(s)}\theta_j \end{aligned} \tag{22}$$

Let $J = \{j_1, \cdots, j_s\}$ be a set of index values with $j_1 \cup \cdots \cup j_s = \{1, \cdots, N_\theta\}$, where j_s is a subset of the set J, with integer elements, denoting the parameters in the set $\underline{\theta}$ on which the structural component s depends on. Note that more than one components are allowed to depend on a parameter in the set $\underline{\theta}$.

Consider the following three special cases of structural component parameterization. In the first case, the mass and stiffness matrix of a component s do not depend on the model parameters $\underline{\theta}$. In this case the set j_s is empty. The component fixed-interface and constrained modes are independent of the parameter values. Only a single analysis is required to estimate the fixed-interface and constrained modes. Within the model updating iteration scheme, these component modes are computed once and are then used in the iterations involved, thus reducing the computational effort for assembling the reduced system from these components at each iteration.

In the second case, the mass or stiffness matrix of a structural component s depends only on one model parameter in the set $\underline{\theta}$. In this case the subset j_s contains only one element and the stiffness or mass matrices take the form

$$K^{(s)} = \bar{K}_{,j_s}^{(s)}\theta_{j_s} \qquad \text{or} \qquad \mathrm{M}^{(s)} = \bar{M}_{,j_s}^{(s)}\theta_{j_s} \tag{23}$$

Equivalently, the partitions of the component mass and stiffness matrices take the form

$$K_{ii}^{(s)} = \bar{K}_{ii,j_s}^{(s)}\theta_{j_s}, \qquad K_{ib}^{(s)} = \bar{K}_{ib,j_s}^{(s)}\theta_{j_s}, \qquad K_{bb}^{(s)} = \bar{K}_{bb,j_s}^{(s)}\theta_{j_s} \tag{24}$$

or

$$\mathrm{M}_{ii}^{(s)} = \bar{M}_{ii,j_s}^{(s)}\theta_{j_s}, \qquad \mathrm{M}_{ib}^{(s)} = \bar{M}_{ib,j_s}^{(s)}\theta_{j_s}, \qquad \mathrm{M}_{bb}^{(s)} = \bar{M}_{bb,j_s}^{(s)}\theta_{j_s} \tag{25}$$

In the case of stiffness dependence of the parameter θ_{j_s}, it can be readily shown that the matrix of the kept eigenvalues and eigenvectors of the component fixed-interface modes are given with respect to the parameter θ_{j_s} in the form

$$\Lambda^{(s)} = \bar{\Lambda}_{,j_s}^{(s)}\theta_{j_s}, \qquad \omega_j^{2(s)} = \bar{\omega}_j^{2(s)}\theta_{j_s} \qquad \text{and} \qquad \Phi_{ik} = \bar{\Phi}_{ik,j_s} \tag{26}$$

where the matrices $\bar{\Lambda}^{(s)}$ and $\bar{\Phi}_{ik}$ are solutions of the following eigen-problem

$$\bar{K}_{ii,j_s}^{(s)}\bar{\Phi}_{ik,j_s}^{(s)} = \bar{M}_{ii,j_s}^{(s)}\bar{\Phi}_{ik,j_s}^{(s)}\bar{\Lambda}_{kk,j_s}^{(s)} \tag{27}$$

which is independent of the values of θ_{j_s}. Also the constrained modes, given by $\Psi_{ib}^{(s)} = -[K_{ii}^{(s)}]^{-1}K_{ib}^{(s)} = -[\bar{K}_{ii,j_s}^{(s)}]^{-1}\bar{K}_{ib,j_s}^{(s)}$, are constant independent of the values of the parameter θ_{j_s}. It should be noted that even in this case only a single component analysis is required to estimate the fixed-interface and constrained modes, independent of the values of θ_{j_s}.
Substituting the stiffness matrices (24) and the eigenproperties (26) of a component into the reduced stiffness matrix (15), one obtains

$$\hat{K}^{(s)} = \hat{\bar{K}}_{,j_s}^{(s)}\theta_{j_s} \tag{28}$$

where $\hat{\bar{K}}_{,j_s}^{(s)}$ is given by

$$\begin{aligned} \hat{\bar{K}}_{kk,j_s}^{(s)} &= \bar{\Lambda}_{kk,j_s}^{(s)} \\ \hat{\bar{K}}_{kb,j_s}^{(s)} &= \hat{\bar{K}}_{bk,j_s}^{(s)T} = 0_{kb}^{(s)} \\ \hat{\bar{K}}_{bb,j_s}^{(s)} &= \bar{K}_{bb,j_s}^{(s)} - [\bar{K}_{ii,j_s}^{(s)}]^{-1}\bar{K}_{ib,j_s}^{(s)}\bar{K}_{ib,j_s}^{(s)} \end{aligned} \tag{29}$$

and it is independent on values of the the model parameters. Finally, substituting (28) into (18), the stiffness matrix of the reduced system admits the representation

$$\begin{aligned} K^{CB} &= K_0^{CB} + \sum_{i=1}^{N_\theta} K_{,j}^{CB}\theta_j \\ M^{CB} &= M_0^{CB} + \sum_{j=1}^{N_\theta} M_{,j}^{CB}\theta_j \end{aligned} \tag{30}$$

where the matrices K_0^{CB} and $K_{,j}^{CB}$ are given by

$$\hat{K}_0^{CB} = S^T \begin{bmatrix} \ddots & 0 & 0 \\ 0 & \hat{\bar{K}}^{(0)} & 0 \\ 0 & 0 & \ddots \end{bmatrix} S \qquad \text{and} \qquad \hat{K}_{,j}^{CB} = S^T \begin{bmatrix} \ddots & 0 & 0 \\ 0 & \hat{\bar{K}}^{(s)} & 0 \\ 0 & 0 & \ddots \end{bmatrix} S \tag{31}$$

It is important to note that the matrices $\hat{K}_0^{CB}$ and $\hat{K}_{,j}^{CB}$ are independent of $\underline{\theta}$. In order to save computational time, these constant matrices are computed and assembled once and, therefore, there is no need this computation to be repeated during the iterations involved in optimization algorithms for model updating. This aforementioned procedure saves significant computational time since it avoids (a) re-computing the fixed-interface and constrained modes and (b) assembling the reduced matrices from these components, at each iteration step involved in model updating.

In the third case, the mass and stiffness matrices of a component depend on more than one model parameters. In this case the subset j_s contains more than one element. The stiffness and mass matrices are given by

$$\begin{aligned} K^{(s)} &= K_0^{(s)} + \sum_{j \in j_s} K_{,j}^{(s)} \theta_j \\ M^{(s)} &= M_0^{(s)} + \sum_{j \in j_s} M_{,j}^{(s)} \theta_j \end{aligned} \tag{32}$$

The fixed-interface and constrained modes have to be recomputed in each iteration involved in the model updating procedure and used to form the reduced stiffness and mass matrices of the components. This iterative computation, however, is usually confined a small number of components with sets j_s involving more than one elements.

5 CONCLUSIONS

Component mode synthesis methods were presented to substantially reduce the computational effort required in the iterative optimization algorithms used for finite element model updating. Exploiting certain schemes often encountered in finite element model parameterization, the mass and stiffness matrices of the reduced system are shown to depend linearly on the model parameters with the mass and stiffness sensitivity matrices to be assembled once and to remain constant during the iteration process. The only time consuming operation left is associated with the solution of the eigen-problem of the reduced system, avoiding the expensive estimation of the component eigen-problems at each iteration. In the proposed model updating formulation, the division of the structure into components is controlled by the parameterization scheme. The methodology is particularly efficient for large-scale finite element models where the solution of the component eigen-problem may be a computationally demanding operation. The methodology described in this work is also applicable to damage detection methods based on finite element model updating methods. According to available damage detection methods [6], the structure is subdivided into one components with properties that remain unchanged during the search for the damaged sub-structure and components with mass and stiffness properties that depend linearly on the parameter indicative of damage.

ACKNOWLEDGEMENTS

This research was co-funded by the Greek Ministry of National Education and Religious Affairs and the European Union (European Social Fund) in the context of ESPA 2007-2013 under a Hrakleitos II grant. This support is gratefully acknowledged.

REFERENCES

[1] J.E. Mottershead, M.I. Friswell, Model updating in structural dynamics: A survey. *Jounal of Sound and Vibration*, **167**, 347-375, 1993.

[2] C. Papadimitriou, J.L. Beck, L.S. Katafygiotis, Updating robust reliability using structural test data. *Probabilistic Engineering Mechanics*, **16**, 103-113, 2001.

[3] C.P. Fritzen, D. Jennewein, T. Kiefer, Damage detection based on model updating methods. *Mechanical Systems and Signal Processing*, **12** (1), 163-186, 1998.

[4] A. Teughels, G. De Roeck, Damage detection and parameter identification by finite element model updating. *Archives of Computational Methods in Engineering*, **12** (2), 123-164, 2005.

[5] M.W. Vanik, J.L. Beck, S.K. Au, Bayesian probabilistic approach to structural health monitoring. *Journal of Engineering Mechanics (ASCE)*, **126**, 738-745, 2000.

[6] E. Ntotsios, C. Papadimitriou, P. Panetsos, G. Karaiskos, K. Perros, Ph. Perdikaris, Bridge health monitoring system based on vibration measurements. *Bulletin of Earthquake Engineering*, **7**(2), 469-483, 2009.

[7] K.V. Yuen, J.L. Beck, Reliability-based robust control for uncertain dynamical systems using feedback of incomplete noisy response measurements. *Earthquake Engineering and Structural Dynamics*, **32 (**5), 751-770, 2003.

[8] J.L. Beck, L.S. Katafygiotis, Updating models and their uncertainties- I: Bayesian statistical framework. *Journal of Engineering Mechanics (ASCE)*, **124 (**4), 455-461, 1998.

[9] Y. Haralampidis, C. Papadimitriou, M. Pavlidou, Multi-objective framework for structural model identification. *Earthquake Engineering and Structural Dynamics*, **34** (6), 665-685, 2005.

[10] K. Christodoulou, E. Ntotsios, C. Papadimitriou, P. Panetsos, Structural model updating and prediction variability using Pareto optimal models. *Computer Methods in Applied Mechanics and Engineering*, **198** (1), 138-149, 2008.

[11] I. Das, J.E. Jr. Dennis, Normal-boundary intersection: A new method for generating the Pareto surface in nonlinear multi-criteria optimization problems. *SIAM Journal of Optimization*, **8**, 631-657, 1998.

[12] R.R. Craig, *Structural Dynamics*, John Wiley & Sons, New York, 1981.

[13] R.R. Craig Jr., M.C.C. Bampton, Coupling of substructures for dynamic analysis. *AIAA Journal*, **6** (7), 678–685, 1965.

[14] E. Ntotsios, C. Papadimitriou, Multi-objective optimization algorithms for finite element model updating", ISMA2008 International Conference on Noise and Vibration Engineering, Leuven, 1895-1909, 2008.

COMPDYN 2011
ECCOMAS Thematic Conference on
Computational Methods in Structural Dynamics and Earthquake Engineering
M. Papadrakakis, M. Fragiadakis, V. Plevris (eds.)
Corfu, Greece, 25-28 May 2011

EXTENSIONS OF THE GENERALIZED-α METHOD TO MULTI-TIME-STEP INTEGRATION IN STRUCTURAL DYNAMICS

Leqia He[1] **and Guido De Roeck**[1]

[1]Department of Civil Engineering, K.U.Leuven
Kasteelpark Arenberg 40, B-3001 Leuven, Belgium
e-mail: {Leqia.He, Guido.DeRoeck}@bwk.kuleuven.be

Keywords: Multi-time-step Method, Implicit-explicit Integration, Generalized-α Method, Numerical Dissipation.

Abstract. *We present an implicit-explicit multi-time-step method for structural dynamics using the family of Generalized-α methods. With the proposed partitioned method, one can divide a complex structural domain into several subdomains and solve the individual subdomains separately. The solution of the original global problem is retrieved by enforcing the prescribed velocity continuity at subdomain interfaces like the method of Gravouil and Combescure (GC method). For large-scale simulations, e.g., to solve a global-local Finite Element model with a coarse global model of the whole structure and several refined local models of parts of the structure, the proposed scheme can be effective. In order to implement the Generalized-α method to the multi-time-step integration, first we derive a new predictor-corrector form of the implicit Generalized-α method from the implicit method previously introduced by Arnold and Brüls. Secondly, we propose a new predictor-corrector form of the explicit Generalized-α method. Both the implicit method and the explicit method are the one-step four-stage variants of the Generalized-α methods. Finally, we built our partitioned scheme with the extended Generalized-α methods. The multi-time-step method is obtained based on the Prakash and Hjelmstad's method (PH method). We study the convergence of the current multi-time-step method by examining a single degree of freedom model problem. It is found that the current multi-time-step method maintains second-order accuracy, both with a unique time scale and with different time scales in each subdomain. Moreover, the current multi-time-step method is not dissipative at subdomain interfaces. Its numerical dissipation is solely introduced by the Generalized-α methods in each subdomain.*

1 INTRODUCTION

In transient structural dynamics, partitioned time integration schemes are appealing for simulation of complex engineering systems with large-scale Finite Element (FE) models [8, 7]. By dividing a structural domain into several subdomains, partitioned time integration methods use different time steps and/or different integration methods to different subdomains, according to their individual physical and computational considerations [12, 4, 9, 10, 11]. For example, a steel railway bridge can be modelled with a coarse model of the whole structure including several refined models of the fatigue-critical connections [17, 16]. Classical monolithic algorithms use a uniform time step for all elements. Refined local models ask for a relatively small time step because of numerical accuracy and/or stability requirements. It creates a heavy computational task for the global simulation. On the contrary, partitioned integration schemes use a big time step for the global model and a small time step for the refined local models. As a result, the computational cost of the global problem is reduced while the accuracy of the solution for the refined local models is maintained [20].

Fatigue assessment of existing steel railway bridges becomes more and more important in Europe and North America, because of the aging of the structures [21, 18]. For fatigue life estimation, one needs to calculate the bridge responses under and after the train passages by transient analysis. For calibration of the Finite Element model, operational modal analysis is often performed [13]. To improve the computational efficiency and accuracy for the transient analysis, the competitive advantages of the multi-time-step methods over the monolithic methods are exploited.

Among the monolithic methods, the Generalized-α method is well known by its optimal numerical dissipation for both linear and non-linear dynamic problems [3, 15, 6]. In this paper, we extend the Generalized-α method to implicit-explicit integration with different time steps in different subdomains. The proposed partitioned scheme is built on the method previously introduced by Prakash and Hjelmstad (PH method) [20]. The PH method enables implicit/explicit Newmark methods to be coupled with different time steps in each subdomain. Their method is energy preserving and unconditionally stable as long as the stability requirement of individual subdomains is satisfied. Moreover, the PH method solves the subdomain interface problem only at each coarse time step instead of at each small time step. Therefore, it is computationally more efficient in comparison to other methods [19].

The paper is organized as follows. In Section 2, we give the formulas of the extended Generalized-α methods. In Section 3, we study the properties of the proposed monolithic methods. In Section 4, we build the multi-time-step method with the extended Generalized-α methods and examine its properties by a numerical test in Section 5. In Section 6, the conclusions are presented.

2 EXTENSIONS OF THE GENERALIZED-α METHOD

We consider here the implicit Generalized-α method as introduced by Arnold and Brüls[1]. The predictor-corrector form of their method can be written as:
Equilibrium equation:

$$\mathbf{M}\ddot{\mathbf{u}}_{n+1} + \mathbf{C}\dot{\mathbf{u}}_{n+1} + \mathbf{K}\mathbf{u}_{n+1} = \mathbf{F}_{n+1} \tag{1}$$

Predictors:

$$\widetilde{\mathbf{u}}_{n+1} = \mathbf{u}_n + \Delta t\dot{\mathbf{u}}_n + \Delta t^2(\frac{1}{2} - \frac{\beta}{1-\alpha_m})\mathbf{a}_n + \Delta t^2\beta\frac{\alpha_f}{1-\alpha_m}\ddot{\mathbf{u}}_n \tag{2}$$

$$\widetilde{\dot{\mathbf{u}}}_{n+1} = \dot{\mathbf{u}}_n + \Delta t(1 - \frac{\gamma}{1-\alpha_m})\mathbf{a}_n + \Delta t\gamma\frac{\alpha_f}{1-\alpha_m}\ddot{\mathbf{u}}_n \tag{3}$$

Correctors:

$$\mathbf{u}_{n+1} = \widetilde{\mathbf{u}}_{n+1} + \Delta t^2\beta\frac{1-\alpha_f}{1-\alpha_m}\ddot{\mathbf{u}}_{n+1} \tag{4}$$

$$\dot{\mathbf{u}}_{n+1} = \widetilde{\dot{\mathbf{u}}}_{n+1} + \Delta t\gamma\frac{1-\alpha_f}{1-\alpha_m}\ddot{\mathbf{u}}_{n+1} \tag{5}$$

Recurrence relation:

$$(1-\alpha_m)\mathbf{a}_{n+1} + \alpha_m\mathbf{a}_n = (1-\alpha_f)\ddot{\mathbf{u}}_{n+1} + \alpha_f\ddot{\mathbf{u}}_n \ , \ \mathbf{a}_0 = \ddot{\mathbf{u}}_0 \tag{6}$$

The recurrence equation (6) defines $\mathbf{a}$ in function of $\ddot{\mathbf{u}}$. $\mathbf{a}$ is considered as the acceleration-like auxiliary variable, whereas $\ddot{\mathbf{u}}$ is known as the true acceleration [1].

A consistent explicit form of the Generalized-α method is defined by replacing (1) with the following equilibrium equation:

$$\mathbf{M}\ddot{\mathbf{u}}_{n+1} + \mathbf{C}\dot{\mathbf{u}}_{n+1} + \mathbf{K}\widetilde{\mathbf{u}}_{n+1} = \mathbf{F}_{n+1} \tag{7}$$

We implement the extended Generalized-α methods by the following $\ddot{\mathbf{u}}$-form:

$$\widetilde{\mathbf{M}}\ddot{\mathbf{u}}_{n+1} = \mathbf{F}_{n+1} - \mathbf{C}\widetilde{\dot{\mathbf{u}}}_{n+1} - \mathbf{K}\widetilde{\mathbf{u}}_{n+1} \tag{8}$$

where $\widetilde{\mathbf{M}}$ is defined by

$$\widetilde{\mathbf{M}} = \widetilde{\mathbf{M}}^I = \mathbf{M} + \Delta t\gamma\frac{1-\alpha_f}{1-\alpha_m}\mathbf{C} + \Delta t^2\beta\frac{1-\alpha_f}{1-\alpha_m}\mathbf{K}, \tag{9}$$

$$\widetilde{\mathbf{M}} = \widetilde{\mathbf{M}}^E = \mathbf{M} + \Delta t\gamma\frac{1-\alpha_f}{1-\alpha_m}\mathbf{C}. \tag{10}$$

$\widetilde{\mathbf{M}}^I$ and $\widetilde{\mathbf{M}}^E$ are the effective mass matrices for the implicit method and the explicit method, respectively. At each time step, the acceleration $\ddot{\mathbf{u}}_{n+1}$ is solved by Equation (8) and then $\mathbf{u}_{n+1}$, $\dot{\mathbf{u}}_{n+1}$ and $\mathbf{a}_{n+1}$ are updated by Equations (4)-(6).

Both the extended implicit and explicit Generalized-α methods use the integration parameters defined by the following formulas:

$$\alpha_m = \frac{2\rho-1}{\rho+1} \ , \ \alpha_f = \frac{\rho}{\rho+1} \ , \ \beta = \frac{1}{4}(\frac{1}{2}+\gamma)^2 \text{ and } \gamma = \frac{1}{2} - \alpha_m + \alpha_f \tag{11}$$

where $\rho = \rho_\infty$ is the spectral radius of the implicit method at the infinite frequency limit and $\rho = \rho_b$ is the spectral radius of the explicit method at the bifurcation point. Note that Equation (11) adopts the same formulas as the implicit Generalized-α method of Chung and Hulbert [3], but it is different from the explicit Generalized-α method of Hulbert and Chung [15]. We will justify these parameters in Section 3.

Moreover, the extended Generalized-α methods can be written in the following form:

$$\overline{\mathbf{M}}\,\overline{\mathbf{U}}_{n+1} = \overline{\mathbf{F}}_{n+1} - \overline{\mathbf{N}}\,\overline{\mathbf{U}}_n \tag{12}$$

where

$$\overline{\mathbf{M}} = \overline{\mathbf{M}}^I = \begin{bmatrix} \mathbf{M} & \mathbf{0} & \mathbf{K} & \mathbf{0} \\ -\Delta t\gamma\frac{1-\alpha_f}{1-\alpha_m}\mathbf{I} & \mathbf{I} & \mathbf{0} & \mathbf{0} \\ -\Delta t^2\beta\frac{1-\alpha_f}{1-\alpha_m}\mathbf{I} & \mathbf{0} & \mathbf{I} & \mathbf{0} \\ -(1-\alpha_f)\mathbf{I} & \mathbf{0} & \mathbf{0} & (1-\alpha_m)\mathbf{I} \end{bmatrix}, \tag{13}$$

$$\overline{\mathbf{M}} = \overline{\mathbf{M}}^E = \begin{bmatrix} \mathbf{M}-\Delta t^2\beta\frac{1-\alpha_f}{1-\alpha_m}\mathbf{K} & \mathbf{0} & \mathbf{K} & \mathbf{0} \\ -\Delta t\gamma\frac{1-\alpha_f}{1-\alpha_m}\mathbf{I} & \mathbf{I} & \mathbf{0} & \mathbf{0} \\ -\Delta t^2\beta\frac{1-\alpha_f}{1-\alpha_m}\mathbf{I} & \mathbf{0} & \mathbf{I} & \mathbf{0} \\ -(1-\alpha_f)\mathbf{I} & \mathbf{0} & \mathbf{0} & (1-\alpha_m)\mathbf{I} \end{bmatrix}, \tag{14}$$

for the implicit method and the explicit method, respectively, and

$$\overline{\mathbf{N}} = \begin{bmatrix} \mathbf{0} & \mathbf{0} & \mathbf{0} & \mathbf{0} \\ -\Delta t\gamma\frac{\alpha_f}{1-\alpha_m}\mathbf{I} & -\mathbf{I} & \mathbf{0} & -\Delta t(1-\frac{\gamma}{1-\alpha_m})\mathbf{I} \\ -\Delta t^2\beta\frac{\alpha_f}{1-\alpha_m}\mathbf{I} & -\Delta t\mathbf{I} & -\mathbf{I} & -\Delta t^2(\frac{1}{2}-\frac{\beta}{1-\alpha_m})\mathbf{I} \\ -\alpha_f\mathbf{I} & \mathbf{0} & \mathbf{0} & \alpha_m\mathbf{I} \end{bmatrix} \tag{15}$$

$$\overline{\mathbf{U}}_n = \begin{Bmatrix} \ddot{\mathbf{u}}_n \\ \dot{\mathbf{u}}_n \\ \mathbf{u}_n \\ \mathbf{a}_n \end{Bmatrix}, \overline{\mathbf{F}}_{n+1} = \begin{Bmatrix} \mathbf{F}_{n+1} \\ \mathbf{0} \\ \mathbf{0} \\ \mathbf{0} \end{Bmatrix} \tag{16}$$

The damping terms are omitted for simplicity of the expression.

3 ANALYSIS OF THE EXTENDED GENERALIZED-α METHOD

3.1 Relation of the extended implicit method to the method of Chung and Hulbert

In this subsection, we show the relation between the extended implicit method in Section 2 and the method of Chung and Hulbert [3].

The Chung and Hulbert's method [3] includes only three numerical variables $\mathbf{a}$, $\dot{\mathbf{u}}$, $\mathbf{u}$ and therefore it is a one-step three-stage method [22]. In contrast, the extended implicit Generalized-α method includes four numerical variables $\mathbf{a}$, $\ddot{\mathbf{u}}$, $\dot{\mathbf{u}}$, $\mathbf{u}$ and therefore it is a one-step four-stage method. By joining the recurrence equation (6) with the basic formulas of the Chung and Hulbert's method [3], we obtain the following one-step four-stage variant of their method:

$$\hat{\mathbf{M}}\,\hat{\mathbf{U}}_{n+1} = \hat{\mathbf{F}}_{n+1} - \hat{\mathbf{N}}\,\hat{\mathbf{U}}_n \tag{17}$$

where

$$\hat{\mathbf{M}} = \begin{bmatrix} \mathbf{0} & \mathbf{0} & (1-\alpha_f)\mathbf{K} & (1-\alpha_m)\mathbf{M} \\ \mathbf{0} & \mathbf{I} & \mathbf{0} & -\Delta t\gamma\mathbf{I} \\ \mathbf{0} & \mathbf{0} & \mathbf{I} & -\Delta t^2\beta\mathbf{I} \\ -(1-\alpha_f)\mathbf{I} & \mathbf{0} & \mathbf{0} & (1-\alpha_m)\mathbf{I} \end{bmatrix}, \tag{18}$$

$$\hat{\mathbf{N}} = \begin{bmatrix} \mathbf{0} & \mathbf{0} & \alpha_f\mathbf{K} & \alpha_m\mathbf{M} \\ \mathbf{0} & -\mathbf{I} & \mathbf{0} & -\Delta t(1-\gamma)\mathbf{I} \\ \mathbf{0} & -\Delta t\mathbf{I} & -\mathbf{I} & -\Delta t^2(\frac{1}{2}-\beta)\mathbf{I} \\ -\alpha_f\mathbf{I} & \mathbf{0} & \mathbf{0} & \alpha_m\mathbf{I} \end{bmatrix} \tag{19}$$

$$\hat{\mathbf{U}}_n = \left\{ \begin{array}{c} \ddot{\mathbf{u}}_n \\ \dot{\mathbf{u}}_n \\ \mathbf{u}_n \\ \mathbf{a}_n \end{array} \right\}, \hat{\mathbf{F}}_{n+1} = \left\{ \begin{array}{c} \mathbf{F}(t_{n+1-\alpha_f}) \\ \mathbf{0} \\ \mathbf{0} \\ \mathbf{0} \end{array} \right\} \tag{20}$$

with $t_{n+1-\alpha_f} = (1-\alpha_f)t_{n+1}+\alpha_f t_n$. We omit the damping terms for simplicity of the expression like in Equation (12). Note that the stage number is equal to the row dimension of $\hat{\mathbf{U}}_n$ in Equation (20). The recurrence equation (6), which defines the relation between $\mathbf{a}$ and $\ddot{\mathbf{u}}$, is consistent with the Chung and Hulbert's method [6]. For this reason, the convergence properties of the one-step four-stage variant method defined by Equation (17) are inherited from those of the Chung and Hulbert's method [3].

In the following, we show that the extended implicit method is equivalent to the above one-step four-stage variant of the Chung and Hulbert's method.

First, we write the equilibrium equation (1) of the extended implicit method at t_n:

$$\mathbf{M}\ddot{\mathbf{u}}_n + \mathbf{C}\dot{\mathbf{u}}_n + \mathbf{K}\mathbf{u}_n = \mathbf{F}_n \tag{21}$$

We multiply Equation (1) by $(1-\alpha_f)$ and Equation (21) by α_f. By summing them, we obtain

$$\begin{aligned} \mathbf{M}[(1-\alpha_f)\ddot{\mathbf{u}}_{n+1} + \alpha_f\ddot{\mathbf{u}}_n] + \mathbf{C}[(1-\alpha_f)\dot{\mathbf{u}}_{n+1} + \alpha_f\dot{\mathbf{u}}_n] + \mathbf{K}[(1-\alpha_f)\mathbf{u}_{n+1} + \alpha_f\mathbf{u}_n] \\ = (1-\alpha_f)\mathbf{F}_{n+1} + \alpha_f\mathbf{F}_n \end{aligned} \tag{22}$$

Substituting Equation (6) into Equation (22), we get:

$$\mathbf{M}\mathbf{a}_{n+1-\alpha_m} + \mathbf{C}\dot{\mathbf{u}}_{n+1-\alpha_f} + \mathbf{K}\mathbf{u}_{n+1-\alpha_f} = \mathbf{F}_{n+1-\alpha_f} \tag{23}$$

where

$$\begin{aligned} \mathbf{a}_{n+1-\alpha_m} &= (1-\alpha_m)\mathbf{a}_{n+1} + \alpha_m\mathbf{a}_n && (24) \\ \dot{\mathbf{u}}_{n+1-\alpha_f} &= (1-\alpha_f)\dot{\mathbf{u}}_{n+1} + \alpha_f\dot{\mathbf{u}}_n && (25) \\ \mathbf{u}_{n+1-\alpha_f} &= (1-\alpha_f)\mathbf{u}_{n+1} + \alpha_f\mathbf{u}_n && (26) \\ \mathbf{F}_{n+1-\alpha_f} &= (1-\alpha_f)\mathbf{F}_{n+1} + \alpha_f\mathbf{F}_n && (27) \end{aligned}$$

Equation (23) is given by Chung and Hulbert as the equilibrium equation for their implicit method [3]. With the damping terms omitted, it is equivalent to the first row in the equation system defined by (17).

Secondly, by substituting Equations (2), (3) and (6) into both (4) and (5), we obtain the Newmark time approximation:

$$\begin{aligned} \mathbf{u}_{n+1} &= \mathbf{u}_n + \Delta t\dot{\mathbf{u}}_n + \Delta t^2(\frac{1}{2}-\beta)\mathbf{a}_n^2 + \Delta t^2\mathbf{a}_{n+1}^2 && (28) \\ \dot{\mathbf{u}}_{n+1} &= \dot{\mathbf{u}}_n + \Delta t(1-\gamma)\mathbf{a}_n + \gamma\mathbf{a}_{n+1} && (29) \end{aligned}$$

Equations (28) and (29) are respectively equivalent to the second and the third rows in the equation system defined by (17).

Finally, the implicit Generalized-α method of Chung and Hulbert [3] is defined by Equations (23)-(29). With the damping terms omitted, they are equivalent to the first three rows in the equation system defined by (17). And the recurrence equation (6) is equivalent to the last row in the equation system defined by (17). As a result, the extended implicit method in Section 2 is equivalent to the one-step four-stage variant of the Chung and Hulbert's method [3]. Moreover, the convergence properties of the extended implicit method are inherited from those of the Chung and Hulbert's method [3].

3.2 Relation of the extended explicit method to the method of Daniel

Daniel introduced an explicit form of the Generalized-α method [5], which uses the same integration parameters as the implicit method of Chung and Hulbert [3]. In this subsection, we show the relation between the extended explicit method in Section 2 and the Daniel's method.

The Daniel's method [5] includes only three numerical variables $\mathbf{a}$, $\dot{\mathbf{u}}$, $\mathbf{u}$ and therefore it is a one-step three-stage method [22]. In contrast, the extended explicit Generalized-α method includes four numerical variables $\mathbf{a}$, $\ddot{\mathbf{u}}$, $\dot{\mathbf{u}}$, $\mathbf{u}$ and therefore it is a one-step four-stage method. By joining the recurrence equation (6) with the basic formulas of the Daniel's method [5], we obtain the following one-step four-stage variant of his method:

$$\check{\mathbf{M}}\,\check{\mathbf{U}}_{n+1} = \check{\mathbf{F}}_{n+1} - \check{\mathbf{N}}\,\check{\mathbf{U}}_n \tag{30}$$

where

$$\check{\mathbf{M}} = \begin{bmatrix} \mathbf{0} & \mathbf{0} & \mathbf{0} & (1-\alpha_m)\mathbf{M} \\ \mathbf{0} & \mathbf{I} & \mathbf{0} & -\Delta t\gamma\mathbf{I} \\ \mathbf{0} & \mathbf{0} & \mathbf{I} & -\Delta t^2\beta\mathbf{I} \\ -(1-\alpha_f)\mathbf{I} & \mathbf{0} & \mathbf{0} & (1-\alpha_m)\mathbf{I} \end{bmatrix}, \tag{31}$$

$$\check{\mathbf{N}} = \begin{bmatrix} \mathbf{0} & \Delta t(1-\alpha_f)\mathbf{K} & \mathbf{K} & \Delta t^2(1-\alpha_f)(\frac{1}{2}-\frac{\beta}{1-\alpha_m})\mathbf{K}+\alpha_m\mathbf{M} \\ \mathbf{0} & -\mathbf{I} & \mathbf{0} & -\Delta t(1-\gamma)\mathbf{I} \\ \mathbf{0} & -\Delta t\mathbf{I} & -\mathbf{I} & -\Delta t^2(\frac{1}{2}-\beta)\mathbf{I} \\ -\alpha_f\mathbf{I} & \mathbf{0} & \mathbf{0} & \alpha_m\mathbf{I} \end{bmatrix} \tag{32}$$

$$\check{\mathbf{U}}_n = \begin{Bmatrix} \ddot{\mathbf{u}}_n \\ \dot{\mathbf{u}}_n \\ \mathbf{u}_n \\ \mathbf{a}_n \end{Bmatrix}, \check{\mathbf{F}}_{n+1} = \begin{Bmatrix} \mathbf{F}(t_{n+1-\alpha_f}) \\ \mathbf{0} \\ \mathbf{0} \\ \mathbf{0} \end{Bmatrix} \tag{33}$$

with $t_{n+1-\alpha_f} = (1-\alpha_f)t_{n+1} + \alpha_f t_n$. We omit the damping terms for simplicity of the expression like in Equation (12). Note that the stage number is equal to the row dimension of $\check{\mathbf{U}}_n$ in Equation (33). The recurrence equation (6), which defines the relation between $\mathbf{a}$ and $\ddot{\mathbf{u}}$, is consistent with the Hulbert and Chung's explicit method [15, 6]. Therefore, it is also consistent with the Daniel's method, because the Daniel's method is the result of a similarity transformation on the amplification matrix of the Hulbert and Chung's explicit method [15, 5]. As a result, the convergence properties of the one-step four-stage variant method defined by Equation (30) are inherited from those of the Daniel's method [5].

In the following, we show that the extended explicit method is equivalent to the above one-step four-stage variant of the Daniel's method.

First, we write the equilibrium equation (7) of the extended explicit method at t_n:

$$\mathbf{M}\ddot{\mathbf{u}}_n + \mathbf{C}\dot{\mathbf{u}}_n + \mathbf{K}\widetilde{\mathbf{u}}_n = \mathbf{F}_n \tag{34}$$

We multiply Equation (7) by $(1-\alpha_f)$ and Equation (34) by α_f. By summing them, we obtain:

$$\begin{aligned} &\mathbf{M}[(1-\alpha_f)\ddot{\mathbf{u}}_{n+1} + \alpha_f\ddot{\mathbf{u}}_n] + \mathbf{C}[(1-\alpha_f)\dot{\mathbf{u}}_{n+1} + \alpha_f\dot{\mathbf{u}}_n] + \mathbf{K}[(1-\alpha_f)\widetilde{\mathbf{u}}_{n+1} + \alpha_f\widetilde{\mathbf{u}}_n] \\ &= (1-\alpha_f)\mathbf{F}_{n+1} + \alpha_f\mathbf{F}_n \end{aligned} \tag{35}$$

We write Equation (4) at t_n and then obtain:

$$\widetilde{\mathbf{u}}_n = \mathbf{u}_n - \Delta t^2\beta\frac{1-\alpha_f}{1-\alpha_m}\ddot{\mathbf{u}}_n \tag{36}$$

We multiply Equation (2) by $(1-\alpha_f)$ and Equation (36) by α_f. By summing them, we obtain:

$$(1-\alpha_f)\widetilde{\mathbf{u}}_{n+1} + \alpha_f \widetilde{\mathbf{u}}_n = \mathbf{u}^P_{n+1-\alpha_f} \tag{37}$$

where,

$$\begin{aligned} \mathbf{u}^P_{n+1-\alpha_f} &= (1-\alpha_f)\mathbf{u}^P_{n+1} + \alpha_f \mathbf{u}_n, & (38)\\ \mathbf{u}^P_{n+1} &= \mathbf{u}_n + \Delta t \dot{\mathbf{u}}_n + \Delta t^2 (1/2 - \frac{\beta}{1-\alpha_m})\mathbf{a}_n & (39) \end{aligned}$$

We multiply Equation (5) by $(1-\alpha_f)$ and add $\alpha_f \dot{\mathbf{u}}_n$ on both sides. By substituting both Equations (3) and (6) into the resulting equation, we obtain:

$$(1-\alpha_f)\dot{\mathbf{u}}_{n+1} + \alpha_f \dot{\mathbf{u}}_n = \dot{\mathbf{u}}^P_{n+1-\alpha_f} + \Delta t \gamma \frac{1-\alpha_f}{1-\alpha_m}\mathbf{a}_{\alpha m} \tag{40}$$

where,

$$\begin{aligned} \dot{\mathbf{u}}^P_{n+1-\alpha_f} &= (1-\alpha_f)\dot{\mathbf{u}}^P_{n+1} + \alpha_f \dot{\mathbf{u}}_n & (41)\\ \dot{\mathbf{u}}^P_{n+1} &= \dot{\mathbf{u}}_n + \Delta t (1 - \frac{\gamma}{1-\alpha_m})\mathbf{a}_n & (42)\\ \mathbf{a}_{\alpha m} &= (1-\alpha_m)\mathbf{a}_{n+1} + \alpha_m \mathbf{a}_n & (43) \end{aligned}$$

Substituting Equations (6), (37) and (40) into (35), we obtain:

$$\mathbf{M}\mathbf{a}_{\alpha m} - \mathbf{C}(\dot{\mathbf{u}}^P_{n+1-\alpha_f} + \Delta t \gamma \frac{1-\alpha_f}{1-\alpha_m}\mathbf{a}_{\alpha m}) - \mathbf{K}\mathbf{u}^P_{n+1-\alpha_f} = \mathbf{F}_{n+1-\alpha_f}, \tag{44}$$

or,

$$\mathbf{M}_T \mathbf{a}_{\alpha m} = \mathbf{F}_{n+1-\alpha_f} - \mathbf{C}\dot{\mathbf{u}}^P_{n+1-\alpha_f} - \mathbf{K}\mathbf{u}^P_{n+1-\alpha_f} \tag{45}$$

where

$$\mathbf{M}_T = \mathbf{M} + \Delta t \gamma \frac{1-\alpha_f}{1-\alpha_m}\mathbf{C} \tag{46}$$

Equation (45) is given by Daniel for his explicit method to solve $\mathbf{a}_{\alpha m}$ [5]. With the damping terms omitted, it is equivalent to the first row in the equation system defined by (30).

Secondly, by substituting Equations (2), (3) and (6) into both (4) and (5), we obtain the Newmark time approximation: Equations (28) and (29). They are respectively equivalent to the second and the third rows in the equation system defined by (30).

Finally, the explicit Generalized-α method of Daniel is defined by Equations (28), (29) and (45) [5]. With the damping terms omitted, they are equivalent to the first three rows in the equation system defined by (30). And the recurrence equation (6) is equivalent to the last row in the equation system defined by (30). As a result, the extended explicit method in Section 2 is equivalent to the one-step four-stage variant of the Daniel's method [3]. Moreover, the convergence properties of the extended explicit method are inherited from those of the Daniel's method [3].

We provide some convergence results of the extended explicit Generalized-α method. To reach second-order accuracy, the algorithmic parameters of the extended explicit method are

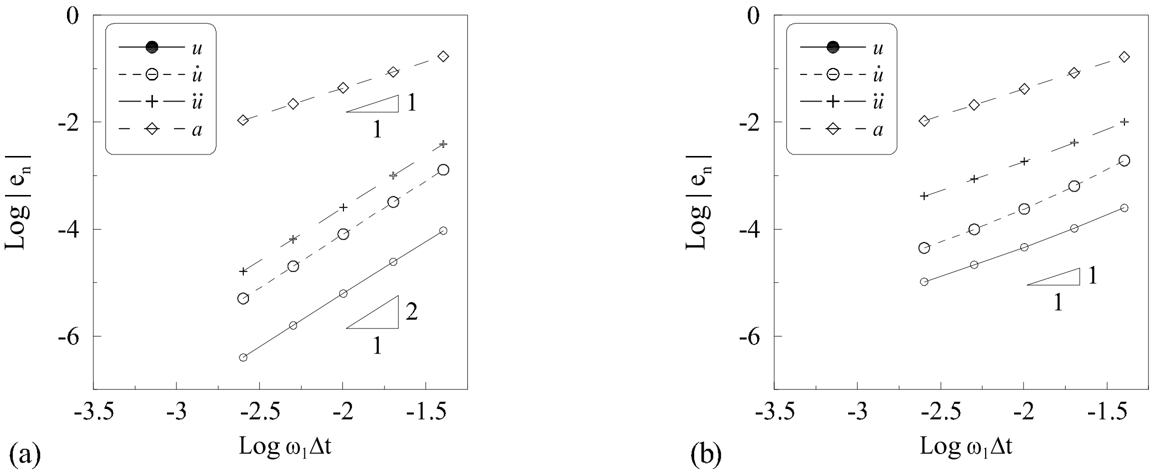

Figure 1: Convergence rate for the extended explicit method with $\rho_b = 0.8$ ($\omega_1 = \sqrt{k_1/m_1}$): (a) with the implicit treatment of the physical damping by Equation (7); (b) with the explicit treatment of the physical damping by Equation (47).

defined by Equation (11), as the Daniel's method [5]. Specifically, the method reduces to first-order accurate, if the physical damping is explicitly treated in the equilibrium equation, i.e.,

$$\mathbf{M}\ddot{\mathbf{u}}_{n+1} + \mathbf{C}\widetilde{\dot{\mathbf{u}}}_{n+1} + \mathbf{K}\widetilde{\mathbf{u}}_{n+1} = \mathbf{F}_{n+1} \tag{47}$$

Figure 1 plots the numerical error versus the time step for a single degree of freedom mass-spring system: $m_1\ddot{u} + c_1\dot{u} + k_1 u = 0$, with $m_1 = 1$, $k_1 = 4\pi^2$, $c_1 = 2m_1\xi_1\sqrt{k_1/m_1}$ and $\xi_1 = 0.005$. The convergence rate of $\mathbf{u}$, $\dot{\mathbf{u}}$ and $\ddot{\mathbf{u}}$ reduces from two to one with the explicit treatment of the physical damping (Equation (47)). Note that with the implicit treatment of the physical damping $\mathbf{u}$, $\dot{\mathbf{u}}$ and $\ddot{\mathbf{u}}$ are second-order accurate while $\mathbf{a}$ is only first-order accurate, as shown in Figure 1(a).

The Daniel's method [5] is spectrally identical to the explicit Generalized-α method of Hulbert and Chung [15]. For this reason, the extended explicit method is also spectrally identical to the explicit Generalized-α method of Hulbert and Chung [15]. For example, the bifurcation limit Ω_b and the stability limit Ω_s, when $\mathbf{C} = \mathbf{0}$, are:

$$\Omega_b = (1+\rho_b)\sqrt{2-\rho_b} \tag{48}$$

$$\Omega_s = \sqrt{\frac{12(1+\rho_b)^3(2-\rho_b)}{10+15\rho_b-\rho_b^2+\rho_b^3-\rho_b^4}}, \tag{49}$$

respectively. Here, $\Omega = \omega\Delta t$ denotes the non-dimensional angular frequency, being ω the natural angular frequency.

4 APPLICATION TO THE MULTI-TIME-STEP INTEGRATION

4.1 Coupled equations of motion

In this subsection, we briefly state the coupled equations of motion to be solved by the multi-time-step integration scheme. We consider a structural domain Ω, which is partitioned into *sd* subdomains. By enforcing the velocity continuity at the subdomain interfaces [12], we obtain

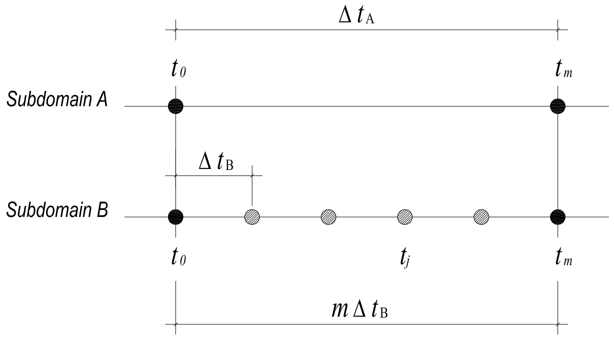

Figure 2: Time discretization of the multi-time-step scheme for two subdomains A and B.

the following semi-discrete coupled equations of motion:

$$\mathbf{M}^i\ddot{\mathbf{u}}^i(t) + \mathbf{K}^i\mathbf{u}^i(t) = \mathbf{F}^i(t) + \mathbf{L}^{i^T}\boldsymbol{\Lambda}(t) \qquad (i = 1, \ldots, sd) \tag{50}$$

$$\sum_{i=1}^{sd}\mathbf{L}^i\dot{\mathbf{u}}^i(t) = \mathbf{0} \tag{51}$$

where $\mathbf{M}^i$ and $\mathbf{K}^i$ are the *i*-th subdomain mass and stiffness matrices, respectively; $\mathbf{F}^i(t)$ is the *i*-th subdomain load vector; $\mathbf{u}^i(t)$ is the *i*-th subdomain displacement vector; $\mathbf{L}^i$ are the constraint matrices which express linear relationships at the *i*-th subdomain interfaces and $\boldsymbol{\Lambda}(t)$ is the vector of Lagrange multipliers. The associated initial value problem consists in determining the function $\mathbf{u}^i = \mathbf{u}^i(t)$ fulfilling Equations (50) and (51) for all $t \in [0, t_f]$, $t_f > 0$, for given initial conditions $\mathbf{u}^i(0) = \mathbf{d}_0^i$ and $\dot{\mathbf{u}}(0) = \mathbf{v}_0^i$.

4.2 The multi-time-step integration scheme

For simplicity, we consider a problem with two subdomains A and B. They are integrated with time steps Δt_A and Δt_B, respectively, with

$$\Delta t_A = m\,\Delta t_B \tag{52}$$

where m is an integer and defines the number of substeps. As an illustration of the multi-time-step scheme, we advance the solution from t_0 to $t_m = t_0 + \Delta t_A$ by Δt_A in Figure 2.

Hereinafter, we apply the extended Generalized-α methods defined by Equation (12) to solve the coupled equations (50) and (51). The fully discretized equations can be written as:

$$\overline{\mathbf{M}}^A\overline{\mathbf{U}}_m^A = \overline{\mathbf{F}}_m^A + \overline{\mathbf{L}}^A\boldsymbol{\Lambda}_m - \overline{\mathbf{N}}^A\overline{\mathbf{U}}_0^A \tag{53}$$

$$\overline{\mathbf{M}}^B\overline{\mathbf{U}}_j^B = \overline{\mathbf{F}}_j^B + \overline{\mathbf{L}}^B\boldsymbol{\Lambda}_j - \overline{\mathbf{N}}^B\overline{\mathbf{U}}_{j-1}^B, \forall j \in [1, 2, ..., m] \tag{54}$$

$$\mathbf{L}^A\dot{\mathbf{u}}_m^A + \mathbf{L}^B\dot{\mathbf{u}}_m^B = \mathbf{0}, \tag{55}$$

where

$$\overline{\mathbf{L}}^i = \left\{ \begin{array}{c} \mathbf{L}^{i^T} \\ \mathbf{0} \\ \mathbf{0} \\ \mathbf{0} \end{array} \right\} \tag{56}$$

and $\overline{\mathbf{M}}$, $\overline{\mathbf{N}}$, $\overline{\mathbf{U}}$ and $\overline{\mathbf{F}}$ are given by Equations (13)-(16). Note that in Equation (55) the velocity continuity at the subdomain interfaces is enforced only at t_m of the coarse time scale [20].

In order to solve the coupled problem (53)-(55), we split the kinematic quantities $\overline{\mathbf{U}}_m$ into two parts:

$$\overline{\mathbf{U}} = \overline{\mathbf{V}} + \overline{\mathbf{W}} \tag{57}$$

where $\overline{\mathbf{V}} = [\ddot{\mathbf{v}},\ \dot{\mathbf{v}},\ \mathbf{v},\ \mathbf{a}_f]^T$ and $\overline{\mathbf{W}} = [\ddot{\mathbf{w}},\ \dot{\mathbf{w}},\ \mathbf{w},\ \mathbf{a}_l]^T$. First, $\overline{\mathbf{V}}_m^A$ and $\overline{\mathbf{W}}_m^A$ of subdomain A at t_m are defined by the following equations:

$$\overline{\mathbf{M}}^A \overline{\mathbf{V}}_m^A = \overline{\mathbf{F}}_m^A - \overline{\mathbf{N}}^A \overline{\mathbf{U}}_0^A \tag{58}$$

$$\overline{\mathbf{M}}^A \overline{\mathbf{W}}_m^A = \overline{\mathbf{L}}^A \mathbf{\Lambda}_m \tag{59}$$

The above equations (58) and (59) define the free problem and the link problem of subdomain A, respectively [12].

Secondly, $\overline{\mathbf{V}}_j^B$ and $\overline{\mathbf{W}}_j^B$ of subdomain B are defined by the following equations:

$$\overline{\mathbf{M}}^B \overline{\mathbf{V}}_j^B = \overline{\mathbf{F}}_j^B - \overline{\mathbf{N}}^B \overline{\mathbf{V}}_{j-1}^B,\ \forall j \in [1, 2, ..., m]\ \text{(if } j = 1, \overline{\mathbf{V}}_0^B = \overline{\mathbf{U}}_0^B\text{)} \tag{60}$$

$$\overline{\mathbf{M}}^B \overline{\mathbf{W}}_j^B = \overline{\mathbf{L}}^B \mathbf{\Lambda}_j - \overline{\mathbf{N}}^B \overline{\mathbf{W}}_{j-1}^B,\ \forall j \in [1, 2, ..., m]\ \text{(if } j = 1, \overline{\mathbf{W}}_0^B = \mathbf{0}\text{)} \tag{61}$$

The above equations (60) and (61) define the free problem and the link problem of subdomain B, respectively [12].

Thirdly, from Equation (55) we have:

$$\mathbf{L}^A \dot{\mathbf{w}}_m^A + \mathbf{L}^B \dot{\mathbf{w}}_m^B = -(\mathbf{L}^A \dot{\mathbf{v}}_m^A + \mathbf{L}^B \dot{\mathbf{v}}_m^B) \tag{62}$$

We need to define transitional operators in order to connect the kinematic quantities of two subdomains at the intermediate time steps t_j. Note that in (58) and (59) the kinematic quantities of A are only defined at t_m of the coarse time scale. In order to solve this problem, we use the following equation [20]:

$$\mathbf{\Lambda}_j = -\mathbf{S}_j + \frac{j}{m}\mathbf{\Lambda}_m, \forall j \in [1, 2, ..., m] \tag{63}$$

with $\mathbf{S}_j = \mathbf{L}^A(\mathbf{F}_j - \mathbf{M}^A \ddot{\mathbf{v}}_j^A - \mathbf{K}^A \mathbf{v}_j^A)$.

Below we give a brief derivation of Equation (63), though it is similar to the derivation of the similar equation in [20]. We write the equilibrium equation of subdomain A at the intermediate time step t_j as

$$\mathbf{F}_j^A - \mathbf{M}^A \ddot{\mathbf{u}}_j^A - \mathbf{K}^A \mathbf{u}_j^A + \mathbf{L}^{A^T} \mathbf{\Lambda}_j = 0 \tag{64}$$

From Equation (64), by considering Equation (57) we have:

$$\mathbf{S}_j = \mathbf{L}^A(\mathbf{F}_j^A - \mathbf{M}^A \ddot{\mathbf{v}}_j^A - \mathbf{K}^A \mathbf{v}_j^A) \tag{65}$$

$$\mathbf{T}_j = \mathbf{L}^A(-\mathbf{M}^A \ddot{\mathbf{w}}_j - \mathbf{K}^A \mathbf{w}_j^A + \mathbf{L}^{A^T} \mathbf{\Lambda}_j) \tag{66}$$

We consider $\mathbf{S}_j$ as the unbalanced interface reaction for the subdomain A free problem. And we consider $\mathbf{T}_j$ as the unbalanced interface reaction for the subdomain A link problem. To derive

(63) we also need to interpolate $\overline{\mathbf{V}}_j^A$ and $\overline{\mathbf{W}}_j^A$ at the intermediate time step t_j, $\forall j \in [1, 2, ..., m]$ [20]:

$$\overline{\mathbf{V}}_j^A = (1 - \frac{j}{m})\overline{\mathbf{U}}_0^A + \frac{j}{m}\overline{\mathbf{V}}_m^A \tag{67}$$

$$\overline{\mathbf{W}}_j^A = \frac{j}{m}\overline{\mathbf{W}}_m^A \tag{68}$$

Substituting (68) into (66), we obtain:

$$\mathbf{T}_j \;\; = \;\; -\frac{j}{m}\mathbf{L}^A(\mathbf{M}^A\ddot{\mathbf{w}}_m^A + \mathbf{K}^A\mathbf{w}_m^A) + \mathbf{\Lambda}_j \tag{69}$$

From (59), we have:

$$\mathbf{M}^A\ddot{\mathbf{w}}_j^A + \mathbf{K}^A\mathbf{w}_m^A = \mathbf{L}^{A^T}\mathbf{\Lambda}_m \tag{70}$$

Substituting (70) into (69), we have:

$$\mathbf{T}_j = -\frac{j}{m}\mathbf{\Lambda}_m + \mathbf{\Lambda}_j \tag{71}$$

From (64) for the equilibrium, we have:

$$\mathbf{S}_j + \mathbf{T}_j = 0 \tag{72}$$

Substituting (71) into (72), we have:

$$\mathbf{S}_j - \frac{j}{m}\mathbf{\Lambda}_m + \mathbf{\Lambda}_j = 0 \tag{73}$$

From (73), we get Equation (63).

After substituting (63) into (61), we rearrange Equations (60) and (61). The reason for the rearrangement is to have $\mathbf{S}_j$ in (60) instead of (61) and therefore the link quantity $\overline{\mathbf{W}}_j^B$ is only dependent on the interface tractions $\mathbf{\Lambda}_m$.

$$\overline{\mathbf{M}}^B\overline{\mathbf{V}}_j^B = \overline{\mathbf{F}}_j^B - \overline{\mathbf{N}}^B\overline{\mathbf{V}}_{j-1}^B - \overline{\mathbf{L}}^B\mathbf{S}_j,\ \forall j \in [1, 2, ..., m]\ \text{(if } j = 1,\ \overline{\mathbf{V}}_0^B = \overline{\mathbf{U}}_0^B\text{)} \tag{74}$$

$$\overline{\mathbf{M}}^B\overline{\mathbf{W}}_j^B = \frac{j}{m}\overline{\mathbf{L}}^B\mathbf{\Lambda}_m - \overline{\mathbf{N}}^B\overline{\mathbf{W}}_{j-1}^B,\ \forall j \in [1, 2, ..., m]\ \text{(if } j = 1,\ \overline{\mathbf{W}}_0^B = 0\text{)} \tag{75}$$

Note that by summing (74) and (75) the original equation (59) of subdomain B will be recovered. To summarize, we define by Equations (58), (59), (74), (75) and (62) the new multi-time-step scheme.

4.3 Solution procedure

We propose to use the same solution procedure as the PH method [20]. The solution procedure can be represented in the following four stages.

4.3.1 The preliminary stage

In the preliminary stage, first we solve the subdomain A scaled link problem as:

$$\overline{\mathbf{M}}^A \overline{\mathbf{Y}}^A_m = \overline{\mathbf{L}}^A \tag{76}$$

with $\overline{\mathbf{Y}}^A_m = [\ddot{\mathbf{y}}^A_m,\ \dot{\mathbf{y}}^A_m,\ \mathbf{y}^A_m,\ \tilde{\mathbf{a}}^A_{ml}]^T$. Equation (76) is obtained from Equation (59) by assuming $\boldsymbol{\Lambda}_m = \mathbf{I}$. Secondly, we solve the subdomain B scaled link problem as:

$$\begin{bmatrix} \overline{\mathbf{M}}^B & & & \\ \overline{\mathbf{N}}^B & \overline{\mathbf{M}}^B & & \\ & \ddots & \ddots & \\ & & \overline{\mathbf{N}}^B & \overline{\mathbf{M}}^B \end{bmatrix} \begin{Bmatrix} \overline{\mathbf{Y}}^B_1 \\ \overline{\mathbf{Y}}^B_2 \\ \vdots \\ \overline{\mathbf{Y}}^B_m \end{Bmatrix} = \begin{Bmatrix} \frac{1}{m}\overline{\mathbf{L}}^B \\ \frac{2}{m}\overline{\mathbf{L}}^B \\ \vdots \\ \overline{\mathbf{L}}^B \end{Bmatrix} \tag{77}$$

with $\overline{\mathbf{Y}}^B_j = [\ddot{\mathbf{y}}^B_j,\ \dot{\mathbf{y}}^B_j,\ \mathbf{y}^B_j,\ \tilde{\mathbf{a}}^B_{jl}]^T$, $j \in [1, 2, ..., m]$. Equation (77) is obtained from Equation (75) by assuming $\boldsymbol{\Lambda}_m = \mathbf{I}$. Note that from (59) and (75), we have:

$$\overline{\mathbf{W}}^A_m = \overline{\mathbf{Y}}^A_m \boldsymbol{\Lambda}_m \tag{78}$$

$$\overline{\mathbf{W}}^B_j = \overline{\mathbf{Y}}^B_j \boldsymbol{\Lambda}_m,\ j \in [1, 2, ..., m] \tag{79}$$

4.3.2 The predictor stage

In the predictor stage, we solve the free problem (58) of subdomain A and the free problem (74) of subdomain B. Specifically, the free problem of B can be written as the following form:

$$\begin{bmatrix} \overline{\mathbf{M}}^B & & & \\ \overline{\mathbf{N}}^B & \overline{\mathbf{M}}^B & & \\ & \ddots & \ddots & \\ & & \overline{\mathbf{N}}^B & \overline{\mathbf{M}}^B \end{bmatrix} \begin{Bmatrix} \overline{\mathbf{V}}^B_1 \\ \overline{\mathbf{V}}^B_2 \\ \vdots \\ \overline{\mathbf{V}}^B_m \end{Bmatrix} = \begin{Bmatrix} \overline{\mathbf{F}}^B_1 - \overline{\mathbf{N}}^B \mathbf{U}^B_0 - \overline{\mathbf{L}}^B \mathbf{S}_1 \\ \overline{\mathbf{F}}^B_2 - \overline{\mathbf{L}}^B \mathbf{S}_2 \\ \vdots \\ \overline{\mathbf{F}}^B_m - \overline{\mathbf{L}}^B \mathbf{S}_m \end{Bmatrix} \tag{80}$$

4.3.3 The solution of the interface problem

The condensed global interface problem is obtained by substitution of Equations (78) and (79) ($j = m$) into (62).

$$\mathbf{H}\boldsymbol{\Lambda}_m = -(\mathbf{L}^A \dot{\mathbf{v}}^A_m + \mathbf{L}^B \dot{\mathbf{v}}^B_m) \tag{81}$$

with $\mathbf{H} = \mathbf{L}^A \dot{\mathbf{y}}^A_m + \mathbf{L}^B \dot{\mathbf{y}}^B_m$. We solve Equation (81) for $\boldsymbol{\Lambda}_m$.

4.3.4 The corrector stage

In the corrector stage, we compute the link quantities $\overline{\mathbf{W}}^A_m$ and $\overline{\mathbf{W}}^B_j$ by Equations (78) and (79). Then, we sum the free quantity $\overline{\mathbf{V}}$ and the link quantity $\overline{\mathbf{W}}$ to obtain $\overline{\mathbf{U}}$ according to Equation (57). Note that the above procedure can be generalized from t_n to t_{n+m}.

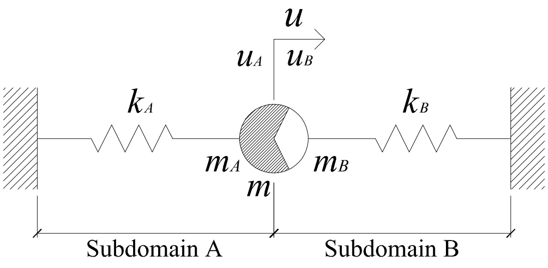

Figure 3: A split SDOF mass and spring system

5 A NUMERICAL TEST

Convergence of the proposed partitioned method can't be analysed by a modal approach, because the modal decomposition is no more valid for multi-time-step implicit-explicit schemes [14]. There are two ways for the convergence analysis of the multi-time-step methods: the first is the energy approach [12, 20] and the second is to examine some linear problems using symbolic and numerical computation [2]. Because an appropriate energy norm of the Generalized-α method is difficult to define, we choose to examine the convergence properties of the current method on a linear model problem.

The model problem to be examined is a split single degree of freedom (SDOF) mass-spring system. The SDOF system is split into two subdomains A and B, as shown in Figure 3. We choose to integrate subdomain A with the extended implicit Generalized-α method and subdomain B with the extended explicit Generalized-α method. The system parameters are chosen as follows: $m_A + m_B = 1$, $k_A + k_B = 4\pi^2$ and $r = \frac{m_A}{m_B} = \frac{k_B}{k_A}$. We use the parameter r to adjust the ratio between the angular frequencies of the two subdomains.

Numerical results for the free vibration with a unity initial displacement are given in Figures (4) and (5). The substep number $m = 2$. By choosing $r = \omega_B/\omega_A = 2$, we have $\omega_A \Delta t_A = \omega_B \Delta t_B = 0.5$, being ω_A and ω_A the subdomain angular frequencies. In Figure (4), we see a significant amplitude decay when $\rho = \rho_\infty = \rho_b = 0$. Note that ρ_∞ is for the implicit subdomain A and ρ_b is for the explicit subdomain B. The amplitude decay is much less when $\rho = \rho_\infty = \rho_b = 0.5$. When $\rho = \rho_\infty = \rho_b = 1$, we don't see an amplitude decay by comparing the numerical results to the exact solution. Moreover, the results of the current method with $\rho = \rho_\infty = \rho_b = 1$ are compared to the results of the PH method. As shown in Figure (5), they are almost overlapping each other. Similar numerical results are given in Figure (6) and (7) for $m = 100$. By choosing $r = \omega_B/\omega_A = 5$, we have $\omega_A \Delta t_A = 0.25$ and $\omega_B \Delta t_B = 0.0125$. We see again the different amplitude decay rate of the current method with $\rho = \rho_\infty = \rho_b = 0$, $\rho = \rho_\infty = \rho_b = 0.5$ and $\rho = \rho_\infty = \rho_b = 1$, respectively. Note that with the smaller Δt_A the numerical results for $\rho = \rho_\infty = \rho_b = 1$ are more accurate in comparison to Figure 4. And again the results of the current method with $\rho = \rho_\infty = \rho_b = 1$ almost overlap the results of the PH method, as shown in Figure (7). Because the PH method is energy preserving, the current method is not dissipative at the subdomain interfaces and its numerical dissipation is solely decided by the Generalized-α methods of each subdomain.

We study the convergence rate for the multi-time-step method by plotting the numerical error versus the time step. As shown in Figure 8, the current method is second-order accurate both for the single time scale ($m = 1$) and for the multiple time scales ($m > 1$). We present the results for the current method with $\rho = \rho_\infty = \rho_b = 0.8$ and $r = 10$.

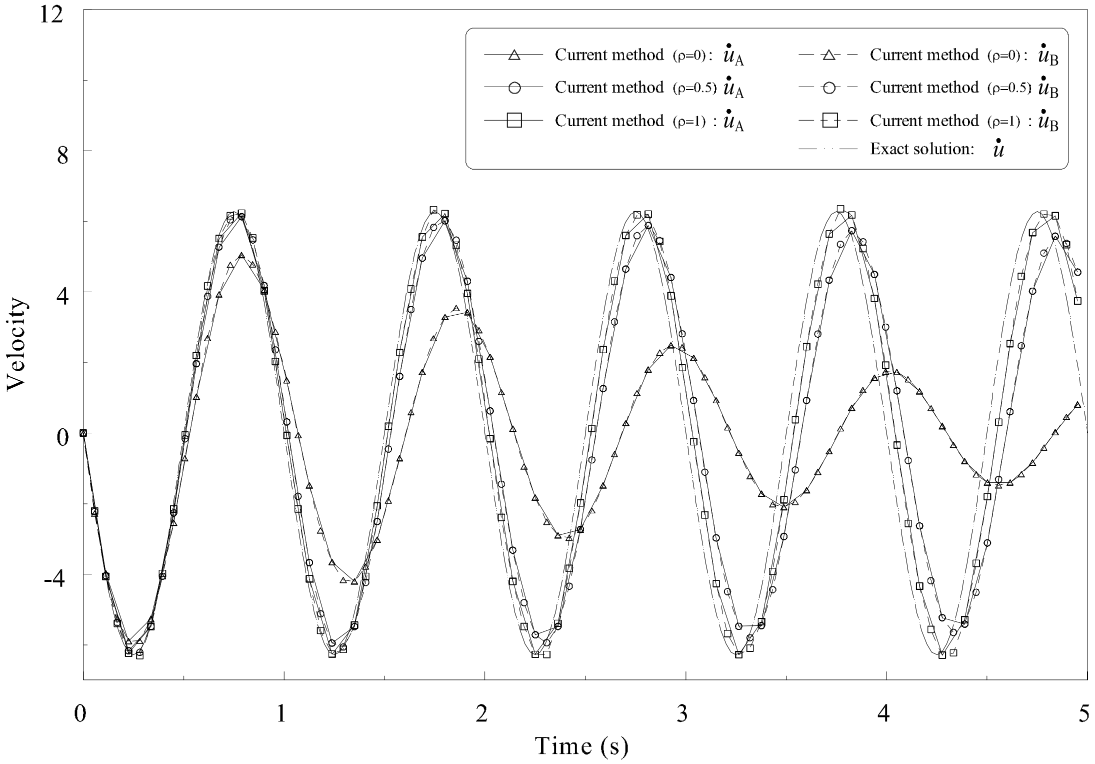

Figure 4: Velocity responses for the current method with $m = 2$ and $\omega_A \Delta t_A = \omega_B \Delta t_B = 0.5$.

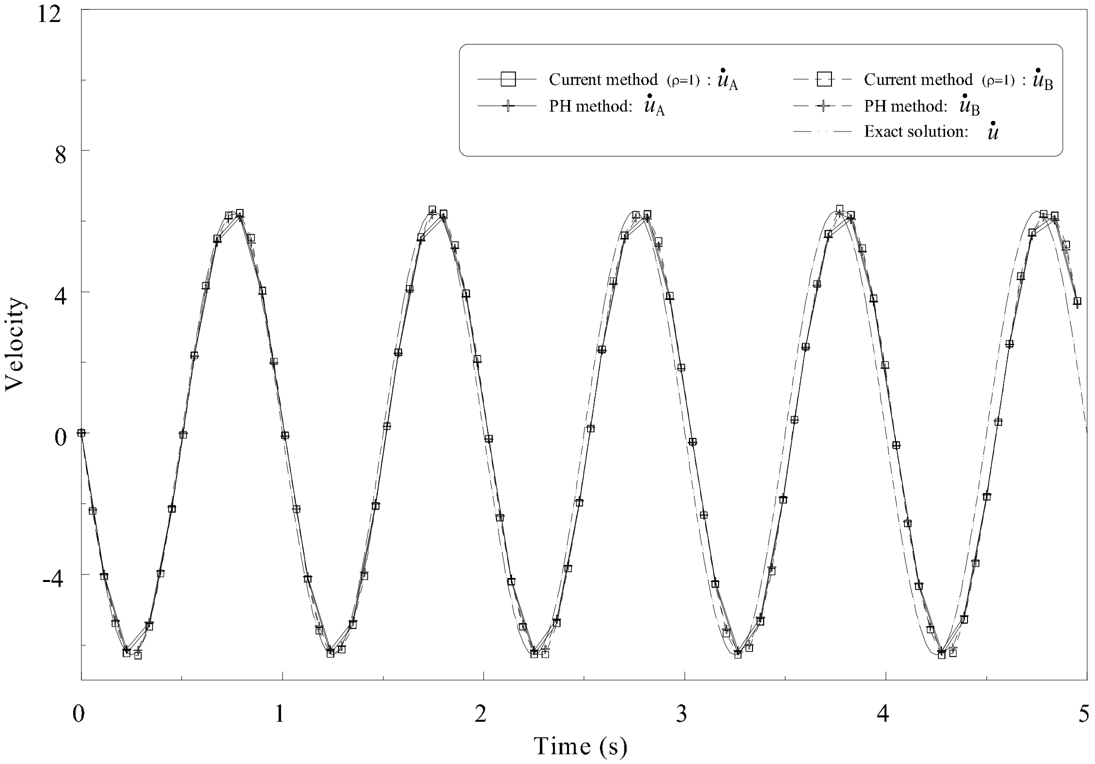

Figure 5: Velocity responses: comparison between the current method with $\rho = \rho_\infty = \rho_b = 1$ and the PH method for $m = 2$.

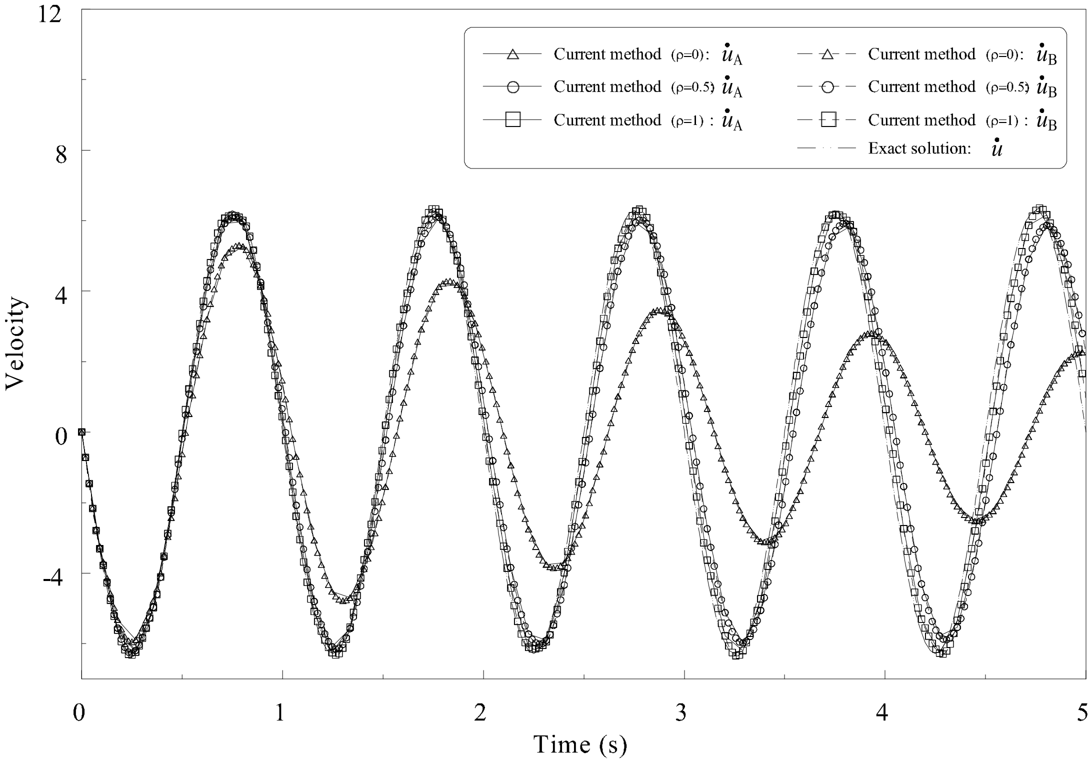

Figure 6: Velocity responses for the current method with $m = 100$, $\omega_A \Delta t_A = 0.25$ and $\omega_B \Delta t_B = 0.0125$.

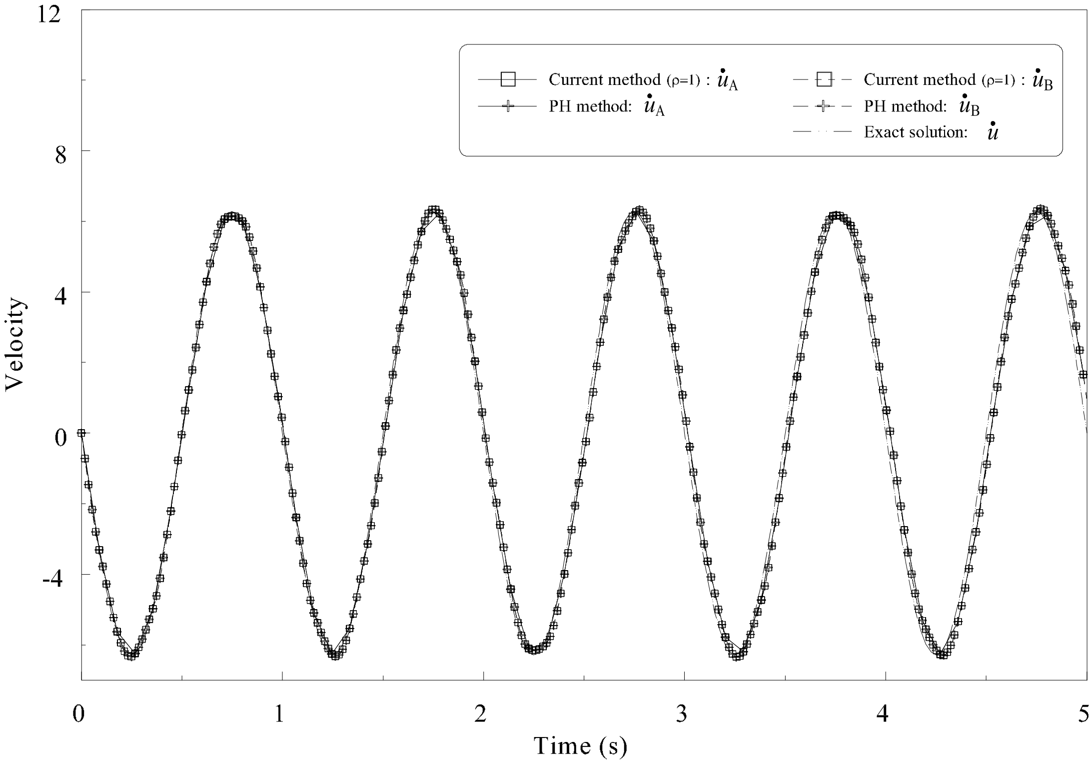

Figure 7: Velocity responses: comparison between the current method with $\rho = \rho_\infty = \rho_b = 1$ and the PH method for $m = 100$.

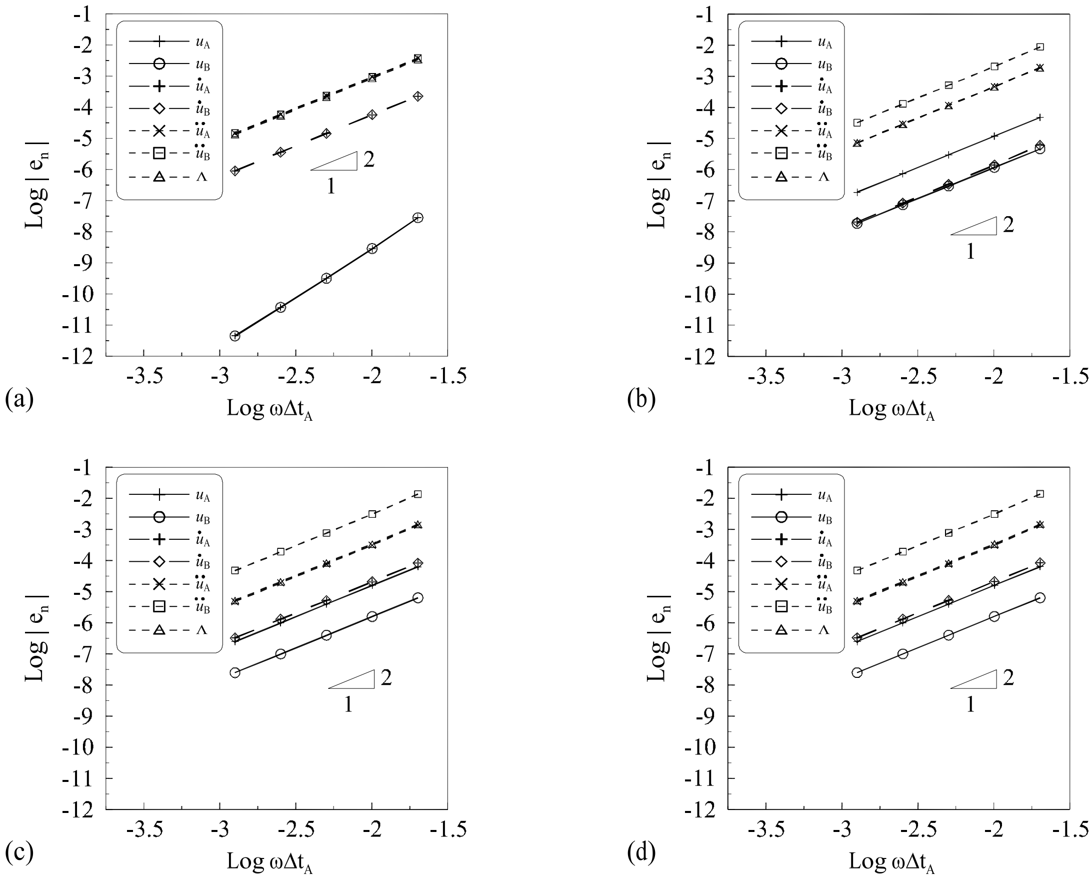

Figure 8: Convergence rate of the current multi-time-step scheme with: (a) $m = 1$; (b) $m = 2$; (c) $m = 20$; and (d) $m = 200$ ($\omega = \sqrt{(k_A + k_B)/(m_A + m_B)}$).

6 CONCLUSIONS

The proposed multi-time-step scheme enables to couple arbitrary Generalized-α methods with different time scales in each subdomain. The Generalized-α methods can either be the extended implicit method or the extended explicit method. Both of them are the variants of the implicit and the explicit Generalized-α methods. The uniform formulas can be used to decide upon their algorithmic parameters. The numerical dissipation of the partitioned method is found to be solely decided by the Generalized-α methods in each subdomain. Moreover, the multi-time-step method is still second-order accurate as the monolithic algorithms in each subdomain. Work is in progress to study the stability of the partitioned method by spectral analysis, though we find in the numerical simulations that the method is still stable when the explicit subdomain satisfies its own stability condition.

REFERENCES

[1] M. Arnold and O. Brüls. Convergence of the Generalized-α scheme for constrained mechanical systems. *Multibody System Dynamics*, 18:185–202, 2007.

[2] A. Bonelli, O. S. Bursi, L. He, P. Pegon, and G. Magonette. Convergence analysis of a parallel interfield method for heterogeneous simulations with dynamic substructuring. *International Journal for Numerical Methods in Engineering*, 75:800–825, 2008.

[3] J. Chung and G. Hulbert. A time integration algorithm for structural dynamics with improved numerical dissipation: the Generalized-α method. *Journal of Applied Mechanics*, 60:371–375, 1993.

[4] A. Combescure and A. Gravouil. A numerical scheme to couple subdomains with different time-steps for predominantly linear transient analysis. *Computer Methods in Applied Mechanics and Engineering*, 191:1129–1157, 2002.

[5] W. J. T. Daniel. Explicit/implicit partitioning and a new explicit form of the generalized alpha method. *Communications in Numerical Methods in Engineering*, 19:909–920, 2003.

[6] S. Erlicher, L. Bonaventura, and O. S. Bursi. The analysis of the Generalized-alpha method for non-linear dynamic problems. *Computational Mechanics*, 28(2):83–104, 2002.

[7] C. Farhat, L. Crivelli, and M. Géradin. Implicit time integration of a class of constrained hybrid formulations - part I: Spectral stability theory. *Computer Methods in Applied Mechanics and Engineering*, 125(1):71–107, 1995.

[8] C. Farhat, L. Crivelli, and F. X. Roux. A transient FETI methodology for large-scale implicit computations in structural mechanics. *International Journal for Numerical Methods in Engineering*, 37:1945–1975, 1994.

[9] V. Faucher and A. Combescure. A time an space mortar method for coupling linear modal subdomains and non-linear subdomains in explicit structural dynamics. *Computer Methods in Applied Mechanics and Engineering*, 192:509–533, 2003.

[10] V. Faucher and A. Combescure. Local modal reduction in explicit dynamics with domain decomposition. Part 1 : extension to subdomains undergoing finite rigid rotations. *International Journal for Numerical Methods in Engineering*, 60:2531C2560, 2004.

[11] V. Faucher and A. Combescure. Local modal reduction in explicit dynamics with domain decomposition. Part 2: specific interface treatment when modal subdomains are involved. *International Journal for Numerical Methods in Engineering*, 61:69C95, 2004.

[12] A. Gravouil and A. Combescure. Multi-time-step explicit-implicit method for non-linear structural dynamics. *International Journal for Numerical Methods in Engineering*, 50:199–225, 2001.

[13] Leqia He, Edwin Reynders, Guido De Roeck, Volkmar Zabel, Maik Brehm, and Sofyan Ahmad. Case study Saaletalbrücke bridge Großheringen, Germany: Report of the modal tests on 27th and 28th May 2010. Technical Report BWM-2010-19, Institute of Structural Mechanics, Bauhaus-University Weimar and Department of Civil Engineering, K.U.Leuven, September 2010. RFCS project FADLESS.

[14] T. J. R. Hughes. *The Finite Element Method, Linear Static and Dynamic Finite Element Analysis*. Prentice-Hall, Englewood Cliffs, NJ, 1987.

[15] G. M. Hulbert and J. Chung. Explicit time integration algorithms for structural dynamics with optimal numerical dissipation. *Computer Methods in Applied Mechanics and Engineering*, 137:175–188, 1996.

[16] B.M. Imam and M.K. Chryssanthopoulos. Numerical modelling of riveted railway bridge connections for fatigue evaluation. *Engineering Structures*, 29(11):3071–3081, 2007.

[17] B.M. Imam and T.D. Righiniotis. Fatigue evaluation of riveted railway bridges through global and local analysis. *Journal of Constructional Steel Research*, 66:1411–1421, 2010.

[18] J. Leander, A. Andersson, and R. Karoumi. Monitoring and enhanced fatigue evaluation of a steel railway bridge. *Engineering Structures*, 32(3):854–863, 2010.

[19] N. Mahjoubi, A. Gravouil, and A. Combescure. Coupling subdomains with heterogeneous time integrators and incompatible time steps. *Computational Mechanics*, 44(6):825–843, 2009.

[20] A. Prakash and K. D. Hjelmstad. A FETI-based multi-time-step coupling method for Newmark schemes in structural dynamics. *International Journal for numerical methods in engineering*, 61:2183–2204, 2004.

[21] T.D. Righiniotis, B.M. Imam, and M.K. Chryssanthopoulos. Fatigue analysis of riveted railway bridge connections using the theory of critical distances. *Engineering Structures*, 30(10):2707–2715, 2008.

[22] W.L. Wood. *Practical Time-Stepping Schemes*. Clarendon Press, Oxford, 1990.

COMPDYN 2011
III ECCOMAS Thematic Conference on
Computational Methods in Structural Dynamics and Earthquake Engineering
M. Papadrakakis, M. Fragiadakis, V. Plevris (eds.)
Corfu, Greece, 25–28 May 2011

STRONG AND WEAK FORMS OF A FULLY NON-CONFORMING FSI ALGORITHM IN FAST TRANSIENT DYNAMICS FOR BLAST LOADING OF STRUCTURES

F. Casadei[1], **M. Larcher**[2], **and N. Leconte**[3]

[1] Joint Research Center, European Laboratory for Structural Assessment
T.P. 480, 21027 Ispra, Italy
e-mail: folco.casadei@jrc.ec.europa.eu

[2] Universität der Bundeswehr München, Institut für Mechanik und Statik
Werner-Heisenberg-Weg 39, 85577 Neubiberg, Germany
martin.larcher@unibw.de

[3] Université de Valenciennes, LAMIH FRE CNRS-UVHC 3304
Le Mont-Houy, Bât. Jonas – 59313 Valenciennes Cedex 9, France
nicolas.leconte@univ-valenciennes.fr

Keywords: Fluid-Structure Interaction, Transient Dynamics, Blast Loading.

Abstract. *The simulation of blast loading effects on structures undergoing very large deformations, possibly up to complete failure and fragmentation, requires robust and specific Fluid-Structure Interaction (FSI) algorithms. The FLSR algorithm uses fully non-conforming fluid and structure meshes (the structure is "embedded" within the fluid), that are "strongly" coupled by suitable constraints on velocities near the F-S interface, enforced by Lagrange multipliers. This technique allows using a regular (or even a structured, typically Eulerian) fluid mesh, while the structure is Lagrangian and can undergo failure and fragmentation without the mesh entanglement difficulties that would arise with more traditional (conforming) FSI algorithms. However, the localization of coupled F-S nodes is more expensive than in the conforming case and must be continuously updated, by means of fast search algorithms, as the structure moves and deforms. The strong form of the algorithm (FLSR) is suitable for a Finite Element (FE) description of the fluid domain and has been used with success in large realistic simulations. Application to Node-Centered Finite Volumes (NCFV) requires an additional treatment of numerical fluxes, presented in the paper. Recently a "weak" variant of the algorithm (FLSW) has been developed for use with Cell-Centered Finite Volumes (CCFV) in the fluid domain. Suitable pressure (interaction) forces are used for the coupling, rather than strong conditions on velocities. Like for NCFV, appropriate treatment of numerical fluxes is required. The rationale and implications of this choice are discussed in the paper.*

1 INTRODUCTION

Fluid-structure interaction (FSI) phenomena play an important role in many areas, ranging from aeronautical and space applications, to civil and marine/offshore engineering and to the transport industry, to name just a few. The JRC has been involved for many years in the development of numerical methods for FSI modeling applied to safety studies—initially for the nuclear industry and more recently for conventional power plants (electrical machinery)—to civil engineering (vulnerability of buildings and other critical infrastructures to terrorist attacks) and to land mass transports (blast effects in railway stations, metro lines, rolling stock).

All these studies are characterized by the violent blast loading, resulting either from an accident or from an intentional attack, and by the very short time scale (fast transient dynamics). Strong pressure waves propagate in the fluid and load the surrounding structures, which typically undergo large deformations and in some cases reach complete failure and fragmentation. For this class of problems, an explicit time marching algorithm is usually adopted, where the fluid is modelled as compressible and inviscid (Euler equations). An Arbitrary Lagrangian Eulerian (ALE) formulation is adopted for the fluid sub-domain, while the structure is Lagrangian. These models are implemented in the EUROPLEXUS code [1], developed jointly by the JRC and by the French CEA.

Three different discretization approaches are available in the code for the fluid sub-domain, see Fig. 1: finite elements (FE), node-centred finite volumes (NCFV) and cell-centred finite volumes (CCFV). In the FE case, kinematic variables (such as the velocity $\mathbf{v}$) are discretized at the element nodes, while state variables (such as the fluid pressure p) are discretized at Gauss points, typically located at the element (shaded area in Fig. 1a) centroid. In the NCFV case, a virtual FV (dual) mesh centred on fluid nodes (shaded area in Fig. 1b) is automatically built up starting from the FE-like (primal) mesh provided in input, and all variables are discretized at the nodes. In the CCFV case, the FV mesh (shaded area in Fig. 1c) looks similar to the FE case, but all variables are discretized at the volume centres. Note that in this case the ―nodes” carry no relevant information other than their position, used to compute the volume.

The coupling between the fluid (ALE) and the structure (Lagrangian) is realized by suitable FSI algorithms. Two broad classes of algorithms are considered here. The first class uses a ―*strong*” approach, based on constraints imposed on the (velocity of) fluid and structure nodes at the F-S interface. The second class uses a ―*weak*” approach, based on direct application of fluid pressure forces to the structure. This terminology (strong/weak) is tentatively adopted here in an attempt to characterize the different nature of the two approaches, but it should not be confused with other uses of the same terms in the literature, in particular with weak (i.e. integral) forms in continuum mechanics. Traditionally, strong FSI algorithms are mainly used in FE, while weak FSI algorithms are mainly used in FV.

Yet another classification of FSI algorithms concerns the degree of deformation/damage that the structure can undergo (and thus the type of application). One class of ―*basic*” algorithms is suitable for large motion and large deformation of structures, but only provided these do not fail. Another class of algorithms can go up to complete *failure*, and *fragmentation*, of the loaded structures.

Finally, FSI algorithms can be classified in three types according to spatial discretization: (nodally) *conforming*, *non-conforming*, and *embedded* (or immersed). The first two types are mostly used in applications without structural failure (but there are exceptions, see Section 3.3), while embedded algorithms are the only ones capable of dealing with extreme loading cases where the structure fails and breaks up in pieces.

Examples of all such different algorithms are shortly presented, by highlighting their characteristics. The paper is organized as follows. Section 2 reviews some algorithms of the basic type (no structure failure), either conforming or non-conforming, which use the strong approach in a FE or NCFV context. Section 3 presents algorithms of the weak type, in a CCFV context. Section 4 shows embedded algorithms with strong and weak formulations. Some numerical examples are presented in Section 5. Finally, Section 6 contains some conclusions and perspectives for future work.

2 BASIC FSI ALGORITHMS OF THE STRONG TYPE

The basic FSI algorithms—valid for largely deforming (but *not failing*) structures and using a strong approach—are briefly summarized, first in a FE and then in a NCFV context. Readers interested in full details should consult references [2-7]. A sample FSI problem is assumed as a reference, see Fig. 2a (continuous domain). A shell-like structure S is considered, in 2D for simplicity, but a junction (J) completely surrounded by fluid is included for generality. As indicated by colors, the nature of the fluid(s) may be different from one side to the other of the structure (F_1, F_2, F_3). Since by assumption the structure cannot fail, these fluids never come into contact and do not mix up with one another.

2.1 Conforming FE discretization

A spatial discretization must be chosen for the two sub-domains. The simplest case is that of a (nodally) conforming mesh, see Fig. 2b. In this case, to each node S of the structure there corresponds one node F of the fluid, and reciprocally (in case of more than one fluid sub-domain, this holds for each sub-domain). The nodes S and F are superposed, i.e. they have the same coordinates, but they are distinct (not merged). At a junction such as J there can be several fluid nodes (one for each fluid sub-domain) matching the same structure node.

The strong approach (*FSA algorithm* [2]) is illustrated in Fig. 3. Assuming an ALE formulation, there are *two* velocity vectors at each node, one for the particles ($\mathbf{v}$) and one for the mesh ($\mathbf{w}$). At each couple of matching F-S nodes the constraint on particle velocities reads:

$$\mathbf{v}_F \cdot \mathbf{n} = \mathbf{v}_S \cdot \mathbf{n}, \tag{1}$$

where subscript F indicates the fluid, subscript S indicates the structure and $\mathbf{n}$ is the unit normal to the *discrete* F-S interface at the concerned (fluid) node, see Fig. 3a. This condition on normal velocity components ensures that the fluid can neither traverse the structure wall, nor detach from it. The tangential components of the fluid and structure particle velocities are independent, so that the fluid (assumed inviscid) can freely slide along the structural walls. This is one of the arguments in favor of keeping the fluid and structure nodes distinct (though superposed) in the FSA algorithm: one single node would not provide enough degrees of freedom (dofs) for two distinct tangential velocity components. Computing the discrete normal(s) is not a trivial task in general, see [2-3] for a detailed discussion. In fact, the only (relatively) complex part of the algorithm is the automatic determination of the normal(s) in geometrically complex 3D cases, such as in the presence of junctions, free edges etc. especially when shell elements are used for the structure.

Relations of the form (1) are exactly enforced by Lagrange multipliers; see [2-3]. Thanks to implicit solution of the system of constraints, FSI conditions are automatically coupled with any other (compatible) essential conditions imposed by the user, e.g. blockages, symmetries, contact between solid bodies, etc. This is the only implicit part of the transient dynamic algorithm, which is otherwise completely explicit.

As concerns mesh velocity, which is arbitrary in ALE, the following compatibility condition is (trivially) imposed, see Fig. 3b:

$$\mathbf{w}_F = \mathbf{w}_S = \mathbf{v}_S, \tag{2}$$

ensuring that the fluid and the structure nodes at the F-S interface remain constantly superposed in the motion and deformation process. The second equality in (2) holds because a Lagrangian description is normally adopted for the structure. Then, the first equality provides the value of the fluid mesh velocity $\mathbf{w}_F$ along the F-S interface, necessary to complete the ALE description.

2.2 Non-conforming FE discretization

The FSA algorithm is easily generalized to the case of a nodally non-conforming F-S interface, see [4] and Fig. 4. This generalization is important in practical applications, because typically a finer mesh is needed in the fluid than in the structure—especially if the latter is meshed by shells—in order to obtain an accurate pressure field. The so-called *hierarchic* approach is usually convenient, see Fig. 4b, whereby to each structure node along the F-S interface there always corresponds a fluid node (*matching* nodes), but the inverse is not true in general (*non-matching* nodes) since F-S fluid nodes are more numerous than structure nodes.

For each couple of matching nodes, expressions (1) and (2) continue to hold. At a non-matching fluid node F (see Fig. 5) similar expressions can be written, involving the fluid node itself and the corresponding *point* S^* of the structure (note that this is *not* a node). For the particle velocity, in analogy with (1):

$$\mathbf{v}_F \cdot \mathbf{n}_F = \mathbf{v}_{S^*} \cdot \mathbf{n}_F, \tag{3}$$

where the local normal is now $\mathbf{n}_F$, perpendicular to the fluid domain. This normal is easily computed because the fluid domain is flat at non-conforming nodes. The constraint is then expressed in terms of nodal dofs (of the structure) by means of suitable shape functions N_I. For example, in the case of Fig. 5a the constraint (3) becomes:

$$\mathbf{v}_F \cdot \mathbf{n}_F = (N_1 \mathbf{v}_{S_1} + N_2 \mathbf{v}_{S_2}) \cdot \mathbf{n}_F. \tag{4}$$

Similarly, for the mesh velocity at non-matching nodes, see Fig. 5b, one has instead of (2):

$$\mathbf{w}_F = \mathbf{w}_{S^*} = \mathbf{v}_{S^*} = (N_1 \mathbf{w}_{S_1} + N_2 \mathbf{w}_{S_2}). \tag{5}$$

2.3 Application to NCFV

The strong FSI algorithms presented so far fit particularly well in a FE discretization of the fluid sub-domain, because the corresponding constraints are imposed at fluid nodes, which coincide (spatially) with structure nodes (in the conforming case) or with other points of the structure (in the non-conforming case). The constraint (1) is quite ~~"n~~atural" in this case, because it expresses the physically intuitive condition that the fluid cannot traverse the solid wall, but is allowed to slide along it.

Exactly the same algorithms can be applied in the NCFV context [5-7], because also in that case fluid velocities are discretized at the ~~"n~~odes" of the (primal) fluid mesh, which coincide with the FV centroids of the dual mesh, see Fig. 1b. Like in the FE case, enforcement of constraints is obtained via Lagrange multipliers, see [5-7] for details. Note, however, that in this case the constraint (1) is ~~"s~~tronger" than in the FE case, because $\mathbf{v}_F$ represents the velocity of the whole NCFV to which the fluid node belongs, while in FE it is the local value at the node. In fact, in FE the velocity is linearly interpolated over the element, while in NCFV (and also in CCFV) the velocity is uniform (just one value) over the entire finite volume.

3 FSI ALGORITHMS OF THE WEAK TYPE

The weak FSI algorithms considered here do not use constraints, but consist in applying directly to the structure the pressure forces generated by the fluid. These forces are interpreted as ―external" forces in computing the equilibrium (in a dynamic sense) of the structure, and are assembled together with any other (user-imposed) external forces and with the internal forces resulting from the stress state in the structure.

The (ALE) fluid nodes at the F-S interface are tied to continuously follow the motion of the structure, and this provides a (weak) feed-back mechanism, influencing the physical state of the fluid. Like in the strong case, eqs. (2) or (5) are used to compute the mesh velocity at conforming or non-conforming fluid nodes at the F-S interface, respectively.

3.1 Conforming CCFV discretization

The weak FSI formulation seems particularly well suited for use with CCFV [8]. In the conforming case, illustrated in Fig. 6, the simplest technique is to merge together each couple of fluid and structure nodes along the F-S interface, rather than keeping them distinct. In this way, the pressure forces computed in the FV act directly on the structure thanks to the standard force assembly procedure. If p is the fluid pressure in the FV, L the length (area in 3D) of its face on the F-S interface, and $\mathbf{n}_S$ the unit normal to the structure (coincident with the normal to the fluid face), see Fig. 6a, the pressure force contribution for this volume is:

$$\mathbf{f}_p = pL\mathbf{n}_S\,. \tag{6}$$

This force is equally distributed on the nodes of the corresponding face, which belong both to the fluid and to the structure, and therefore contributes to the motion of the structure.

3.2 Non-conforming CCFV discretization

The weak FSI algorithm for a non-conforming (hierarchic) CCFV mesh is shown in Fig. 7. In this case, some fluid nodes on the F-S interface match a corresponding structure node, some don't. Each couple of matching nodes can be merged together, like in the conforming case, but this is not possible for the non-matching fluid nodes. Therefore, the algorithm is set up in such a way that the merging or not of the (matching) nodes has no effect on the solution. In Fig. 7a the matching nodes are kept distinct, for example.

Apart from this, the only difference with respect to the conforming case is the distribution of fluid pressure forces to the structure nodes, see Fig. 7b. Let p_i be the fluid pressure in the i-th FV, L_i the length of its face (area in 3D) on the F-S interface, and $\mathbf{n}_S$ the unit normal to the structure (coincident with the normal to the fluid face), see Fig. 7a. Then, the pressure force contribution for this volume is again given by (6), which becomes in this case:

$$\mathbf{f}_{p,i} = p_i L_i \mathbf{n}_S\,. \tag{7}$$

This force is supposed to act at the point C_i of the structure coinciding with the centroid of the fluid face (Fig. 7b). Therefore, in the 2D case, if $L_S = L_{Ai} + L_{Bi}$ is the length of the structure face, the force contributions at the two nodes A and B of the structure are:

$$\mathbf{f}_{p,Ai} = (L_{Bi}/L_S)\mathbf{f}_{p,i} \qquad ; \qquad \mathbf{f}_{p,Bi} = (L_{Ai}/L_S)\mathbf{f}_{p,i}\,. \tag{8}$$

3.3 Structural failure with CCFV

The CCFV formulation, in conjunction with the present weak FSI algorithm, lends itself to the treatment of structural failure even in the basic cases of conforming or non-conforming meshes (which is *not* the case for FE or CCFV, see Section 4).

Consider a structure separating two fluid sub-domains occupied by the *same type of fluid*, see Fig. 6b for the conforming and Fig. 7a for the non-conforming case. The key observation is that, since in CCFV the velocities are discretized at volume centers (not at nodes), the fluid meshes on either part of the structure can be set up as a *continuous mesh*. That is, assuming that fluid nodes occupy the same positions on either side of the structure, these nodes can be merged together two by two—and this independently from whether they are also merged with structure nodes and from whether the structure mesh is conforming or not with the fluid mesh—as shown in the Figures.

As long as the structure resists, each fluid FV transmits its pressure force to the structure and the corresponding volume face is considered as a boundary face (solid wall). Therefore, no mass or energy numerical fluxes (typical of FV technology) are computed across such faces, and the result is that the fluid cannot traverse the wall.

When the structure fails, the structural element is eroded and no longer takes part in the computation. To let the fluid freely flow across the (failed) wall, it is then sufficient to change the status of the corresponding FV face from solid wall (i.e. no neighbor FV) to internal fluid face. That is, the two FV on either part of the structure suddenly become neighbors.

This technique has been applied with success in some realistic simulations. It does extend the range of application of basic algorithms to the case of structural failure but, if the structure undergoes too large motions (in particular rotation) before failing, it suffers from the same limitations (fluid mesh entanglement) as the basic algorithms.

The condition that the same type of fluid be present in both sub-domains is necessary to let the two fluids mix up after structure failure, assuming that a single-material model is used in the formulation, i.e. a volume (or element) can only contain one type of material. This is often the case in real applications, think e.g. of explosions in buildings where the explosive gas products can often be modeled by the same constitutive equation as the gas (air) which fills and surrounds the building. When this is not the case, e.g. in under-water explosions, one can resort to using a multi-material model (but usually with an associated loss of precision).

3.4 Weak boundary condition algorithm for NCFV

A weak boundary condition algorithm has been implemented for the NCFV fluid model; see [5-7]. It consists of the following evaluation of numerical fluxes. Assume that a NCFV i, currently at pressure p_i, is adjacent to a ―solid wall" (either fixed or moving at velocity $\mathbf{v}_S$) along a facet (portion of the FV boundary) of area F and of unit normal $\mathbf{n}$. Note that in such a case the node i representing the FV is located on the wall, see Fig. 1. Then the mass flux across the facet is set to zero, the momentum flux is given by $p_i F\mathbf{n}$ and the energy flux is given by $p_i F(\mathbf{v}_i \cdot \mathbf{n})$, where $\mathbf{v}_i$ is the fluid velocity in volume i.

This technique has been used with success in purely Eulerian calculations, where the (solid) wall is fixed ($\mathbf{v}_S = 0$) by definition and no real FSI takes place (the structure is not even modeled). Note that even in such a case using the above expression for the momentum flux does *not* guarantee, in general, that the normal component of the fluid velocity is exactly zero (i.e. that $\mathbf{v}_i \cdot \mathbf{n} = 0$). This is characteristic of a weak formulation and is in line with the fact that $\mathbf{v}_i$ represents the (average) velocity over the entire volume i, not the value at point i (i.e. at the wall).

3.5 Comparison of strong and weak FSI formulations

As shown in the previous Sections, the strong FSI approach is the most natural with a FE discretization of the fluid, because velocities are discretized at fluid nodes and they represent the local value. Exact enforcement of strong constraints by Lagrange multipliers guarantees high precision and consistency of numerical results. In the coupling process, the two sub-domains are treated at the same level (there is no “master” and no “slave”) and the constraints ensure that both the internal forces and the masses of each sub-domain are taken into account in the (coupled) equilibrium equation.

The weak FSI approach is the most natural with a CCFV discretization of the fluid. In this case velocities are discretized at volume centers (and represent the average value for the entire volume), so that imposing strong constraints would be less appropriate than in the FE case. The coupling is qualified as weak because the fluid transmits a pressure force to the structure, but the feedback (structure action on the fluid) only occurs via the motion of the structure, which drives the numerical flux in the fluid at the F-S interface. In a certain sense, the structure acts as a “master”, and the fluid as a “slave”. Furthermore, the fluid mass is typically not taken into account in computing the structure motion (at least not in the non-conforming case). The effect can be negligible with low-density fluids (gases), but not so much with liquids.

The case of NCFV fluid discretization lies somewhat in between. Fluid velocities are discretized at nodes, like in FE, but represent the average value for the entire volume, like in CCFV. Both strong and weak FSI formulations can appear as natural in this case (and have been implemented), each one with its advantages and drawbacks.

4 EMBEDDED FSI ALGORITHMS

The basic FSI algorithms presented so far are built on the ALE formulation for the fluid sub-domain, which allows the fluid mesh to *constantly follow* the structure mesh at the F-S interface. Fluid nodes in the interior of the fluid sub-domain are typically moved (arbitrarily) by a suitable automatic mesh rezoning algorithm, whose primary goal is to prevent the fluid mesh from entangling. The technique is quite elegant and, as long as it can be applied, it provides highly accurate results with a comparably low computational effort (CPU time). However, it suffers from two limitations:

- If the structure motion, especially *rotation*, is too large, then the mesh rezoning algorithm is unable to keep the fluid mesh reasonably regular, and the calculation must stop.
- If the structure *fails* and is either simply eroded or replaced by a set of flying debris (e.g. a cloud of particles), then it is difficult to “sew” the two fluid sub-domains which were previously separated by the structure in order to let the fluid flow through.

The second limitation stems from the fact that in the basic algorithms the fluid nodes at the interface are kept distinct from structure nodes (because fluid velocities are discretized at nodes), and thus the two fluid sub-domains on either part of the structure are not merged together. A notable exception is the weak algorithm for CCFV, see Section 3.3, for which this second limitation does not hold. However, note that the first limitation applies also in the case of Section 3.3, and this considerably reduces the range of applicability of that algorithm.

To overcome these limitations (at the expense of lower accuracy, however), a basically different approach to FSI is taken, see Fig. 8: the structure sub-domain and the fluid sub-domain are discretized in a completely independent manner, and then the structure mesh is *embedded* (or immersed) within the fluid mesh, i.e. the two meshes are simply superposed. With this technique, it is no longer necessary to use an unstructured (conforming or non-conforming) fluid mesh. The fluid mesh can be structured, and even regular, see Fig. 8b. Furthermore, it is no longer necessary to use an ALE formulation in the fluid sub-domain. This sub-domain can be simply Eulerian (fixed mesh), so that the (background) fluid mesh will never entangle.

In order to prescribe suitable FSI conditions (either in a strong or in a weak manner) between the two sub-domains, it is necessary to find the nodes (or points) of the fluid mesh to be coupled with the structure, i.e. which are sufficiently “close” to the structure. Note that this search is not trivial and must be repeated during the transient calculation as the structure moves and deforms. This must be done with an efficient fast search algorithm, otherwise the computational cost of the search becomes preponderant in realistic applications. For example, a bucket sort algorithm is used in the current implementation.

The *coupled fluid nodes* are defined as all fluid nodes located within the *influence domain* of the structure, the shaded area in Fig. 9a. This influence domain is built up at each time step in the following manner: first, a sphere (circle in 2D) is generated, centered on each node of the structure. The radius of these spheres can either be prescribed by the user, or be computed automatically based on the local size of the fluid mesh. Spheres should be big enough so that at least some fluid nodes fall within them, but not too big. Then, the spheres are connected by quadrangles in 2D (or by cones, prisms and hexahedra in 3D) in the way shown in Fig. 9a. The union of nodal spheres and of all other mentioned geometric entities is the influence domain, used to find the coupled fluid nodes (marked by circles in Fig. 9a). Note that, on one hand, too thin a domain (too small sphere radius) produces some fluid leakage (spurious fluid passage) across the structure. But, on the other hand, too thick a domain (too big sphere radius) ties too much fluid to the motion of the structure (too large “added mass”). Therefore, a good compromise must be found for the sphere radii.

4.1 Embedded FSI algorithm of the strong type

The strong form of the embedded FSI algorithm, called the *FLSR algorithm*, is suitable for use either with FE [10-11] or with NCFV [9]. In both cases the fluid velocities are discretized at nodes. Let F be a coupled fluid node, see Fig. 9b. Then, the closest point of the structure S^* (not a node, in general) is found and then a suitable constraint is imposed on particle velocities. Two alternatives have been tested. The first one is similar to eq. (4) and reads in this case:

$$\mathbf{v}_F \cdot \mathbf{n}_S = \mathbf{v}_{S^*} \cdot \mathbf{n}_S = (N_1 \mathbf{v}_{S_1} + N_2 \mathbf{v}_{S_2}) \cdot \mathbf{n}_S \,. \tag{9}$$

Note that in the present case the normal to the fluid domain $\mathbf{n}_F$ cannot be defined, so we use the normal to the structure $\mathbf{n}_S$ instead (assuming that it can be computed). This form of the constraint aims at leaving the fluid free to slide along the structure, like in the basic algorithms. However, numerical examples have shown that sometimes this may produce fluid leakage, i.e. spurious (non-physical) passage of fluid across the structure.

The second alternative form of the constraint reads simply:

$$\mathbf{v}_F = \mathbf{v}_{S^*} = N_1 \mathbf{v}_{S_1} + N_2 \mathbf{v}_{S_2} \,, \tag{10}$$

i.e. the fluid is tied to the structure in all directions (both along the normal and along the tangent). This condition is “stronger” than (9) and may lead to some non-physical loading of the structure along the tangent direction, but it has the advantage that it avoids fluid leakage.

4.2 Application to NCFV

The FLSR algorithm of Section 4.1 works very well with FE fluids [10-11], but when used as such with NCFV it tends to produce spurious fluid leakage, and this irrespective of the width of the chosen structure influence domain (radius of the spheres).

This behavior is due to the way in which transport terms, in particular the transport of density (mass) and of energy, are computed in the different fluid formulations. In FE, transport terms in the governing Euler equations (for conservation of mass and energy) depend (are proportional to) the relative velocity $\mathbf{u}=\mathbf{w}-\mathbf{v}$ between the grid (mesh) and the fluid particles at the fluid nodes (i.e. at the interface between two neighboring elements). Consider for a moment a rigidly blocked structure wall embedded in an Eulerian fluid domain. The grid velocity $\mathbf{w}$ is zero because of the Eulerian description, and the structure velocity $\mathbf{v}_S$ is also zero because the structure is blocked. The FLSR algorithm enforces condition (10) strongly, so that $\mathbf{v}_F$ is zero as well. The result is that the relative velocity $\mathbf{u}$ vanishes at the fluid node, thus no mass and energy are transported across the node (and across the blocked structure).

In NCFV (and more generally in FV) technology, transport terms are represented by so-called *numerical fluxes*. The calculation of such fluxes is more complex in FV than in FE formulations, since it depends on the space order of the chosen algorithm (first or second order) and on the chosen Riemann solver (e.g. Roe's solver or others). The result is that a vanishing relative velocity at a node (i.e. in the corresponding NCFV) does *not* ensure zero local mass and energy fluxes. This is due, *in primis*, to the fact that fluxes are computed not at nodes, but at inter-volume faces, using an interpolated value $\mathbf{u}_{ij}$ of the velocity. Thus, if two volumes i and j are neighbors and $\mathbf{u}_i$ is zero but $\mathbf{u}_j$ is not, then $\mathbf{u}_{ij}\neq 0$ and some mass and energy are exchanged between the two volumes. It would then seem that blocking *two* (or more) consecutive fluid nodes rather than just one (i.e. using a larger sphere radius in the FLSR algorithm) should avoid fluid leakage, because in this case the relative velocity $\mathbf{u}_{ij}$ is strictly zero. However, numerical tests show that unfortunately this is *not* the case (at least when Roe's solver is used): spurious fluid leakage is reduced but not eliminated.

The solution to the above problem consists in explicitly setting to zero the mass and energy numerical fluxes at locations ―close" to the structure. Two alternatives have been tested. The first one consists in blocking fluxes between two NC volumes when *both* volumes (i.e. both fluid nodes F_1, F_2) are coupled with the structure, see Fig. 10a. The second one consists in blocking fluxes between two NC volumes when *at least one* of them is coupled with the structure, see Fig. 10b. The second condition is ―stronger" than the first one (it blocks more fluxes).

4.3 Embedded FSI algorithm of the weak type

The weak form of the embedded FSI algorithm, called the *FLSW algorithm*, is best suited for use with CCFV. The structure influence domain is built up exactly like for the strong algorithm (FLSR). However, instead of searching for fluid nodes, it is convenient to search directly for the element-to-element interfaces—indicated simply as *faces* in following for brevity—located within the influence domain (*coupled faces*), see Fig. 11a. Recall in fact that in the CCFV case the fluid velocities are discretized at the volume centers, not at the nodes. The numerical fluxes, already introduced above for the NCFV case, are evaluated in this case at face centers, marked by small squares in Figs. 11 and 12.

According to the weak approach, the forces generated by fluid pressure have to be computed and transmitted to the structure. With reference to Fig. 11b, for each coupled face f located between two volumes V_1, V_2 currently at pressures p_1, p_2, the pressure drop force $\mathbf{f}_{\Delta p}$ is evaluated according to:

$$\mathbf{f}_{\Delta p} = (p_1 - p_2) L \mathbf{n}_f \,, \tag{11}$$

where L is the length (area, in 3D) of the face and $\mathbf{n}_f$ is the unit normal to the face. Then, as shown in Fig. 12a, the point S^* of the structure closest to the face center is computed. The force (11) is supposed to act at this point S^* and is distributed on the structure nodes A, B according to an expression (in 2D) similar to (8), where $L_S = L_A + L_B$:

$$\mathbf{f}_{\Delta p,A} = (L_B / L_S)\mathbf{f}_{\Delta p} \qquad ; \qquad \mathbf{f}_{\Delta p,B} = (L_A / L_S)\mathbf{f}_{\Delta p} \,. \tag{12}$$

Then, exactly as in the NCFV case discussed in Section 4.2, in order to avoid spurious fluid leakage across the structure it is necessary to inhibit the mass and energy numerical fluxes at each coupled face, as illustrated in Fig. 12b (thick shaded line).

Note that expression (11) is the weak equivalent of (10), i.e. the fluid and the structure are coupled in all directions. Alternatively, one may project the pressure drop force along the normal to the structure $\mathbf{n}_S$ (assuming that this can be computed), obtaining the weak equivalent of (9). However, like in the strong case, such an expression risks to produce fluid leakage.

5 NUMERICAL EXAMPLES

Three numerical examples are presented. The first one is an academic problem comparing all the FSI algorithms presented in a relatively simple case: an internal explosion in a 2D rectangular box, with relatively small structural deformations and without structural failure. The second and third examples are realistic applications: blast effects on a railway station with a glass roof (which completely fails), and on a metallic container placed in a long tunnel.

5.1 Explosion in a metallic box

An elasto-plastic deformable box in 2D (plane strain) geometry, see Fig. 13a, contains a 0.4 m long deformable internal wall. The box measures 2 m width by 1 m height, and is filled by air at atmospheric pressure (1 bar). The left compartment contains an explosive bubble of 0.4 m by 0.4 m, represented by air at a higher initial pressure (10 bar). Externally to the box acts a constant atmospheric pressure (1 bar). The structure is uniformly meshed by 64 thin shell elements each 0.1 m long and with a thickness of 0.01 m. The fluid mesh within the box is a uniform grid of 3,200 (i.e. 80×40) four-node quadrilaterals of size 0.025 m, i.e. $1/4$ of the shell element length, so that non-conforming (hierarchic) FSI is used.

This test problem is taken from [9], where FE, NCFV and CCFV solutions were presented, obtained with the basic (non-conforming) strong and weak FSI algorithms, respectively. Here three solutions are added and compared, obtained with FE, NCFV and CCFV using the strong and weak embedded FSI algorithms, respectively. In the embedded case the fluid mesh extends all around the box for an additional 0.2 m. The total number of fluid elements is therefore 5,376 (96×56). A layer of absorbing elements is placed along the external boundary of the fluid mesh in order to simulate an infinite atmosphere and to prevent spurious pressure wave reflections.

All FV solutions shown are second-order in space and time. Calculations are performed up to 5 ms. This is sufficient to see propagation of the pressure waves to the top and to the right part of the box and several reflections. The structural displacements computed at points P9S, P10S and P12S of Fig. 13a are compared in Figs 13b, 13c and 13d, showing very good agreement of all six solutions.

Then, Figs. 14, 15, 16 and 17 compare the fluid velocity field (not shown in the explosive bubble region) and the fluid pressure field, at an intermediate time and at the final time. The agreement is very good for the first three solutions, which use the basic non-conforming FSI algorithms. The other three solutions, which use the (new) embedded FSI algorithms, show a larger variability, but this has to be expected, given the lower accuracy of such algorithms (for the same fluid mesh). The shown embedded techniques are just a first implementation and can certainly be ameliorated, but already now one can say that results are consistent with the basic algorithms (see the comparison of box displacements in Fig. 13), so that the embedded algorithms can be used to predict structural behavior in applications with failing structures.

5.2 Blast effects in a railway station

Blast effects in railway stations, metro stations and rolling stock have been recently studied at JRC within the RailProtect project; see e.g. [12-14]. In Fig. 18a an historical railway station with a glass roof supported by metallic trusses is shown. A big explosion at the center of the main hall is simulated. Most roof glass panels completely fail and are replaced by clouds of flying debris particles in the simulation.

The numerical model uses about 4.5 million elements, of which more than 90% are fluid FE. The simulation up to 250 ms takes about 2 weeks on a PC (single-processor code version). The FLSR algorithm is used for FSI because of structure failure and fragmentation and of very large rotations of the (macroscopic) flying debris. Figs. 18b and 18e show the model before blast, while Figs 18c and 18f show blast effects at 100 ms. Fig. 18d shows the map of death risk [12-13] for the occupants of the station, automatically computed from blast overpressure and impulse time histories in the fluid sub-domain.

5.3 Blast effects on an ISO container

Standard 20 ft ISO containers are sometimes used as first shelters in peacekeeping, rescue and reconstruction operations. The resistance of such containers to blast loading is studied at the Norwegian University of Science and Technology (NTNU) in Trondheim, Norway [15-16]. Blast tests were carried out in the Large Blast Simulator (LBS) at the Bundeswehr Technical Center for Protective and Special Technologies (WTD 52) in Oberjettenberg, Germany.

Fig. 19a shows one of the experiments in the LBS. The container is placed at one end of a 100 m long tunnel. A blast wave is generated at the other end, propagates along the tunnel and hits the container. Large motions and plastic deformation occur in the container, but failure is much localized and no fragmentation occurs. Fig. 19b shows the FE model of the container (~50 thousand FE), and Fig 19c shows the container within the tunnel. The air in the tunnel is meshed by about 0.6 million fluid FE or FV.

Simulation of the container alone by applying the pressure recorded in the test (no fluid in the model) reproduces well the experiment, see Fig. 19d. However, in order to make predictive simulations the fluid must be modeled as well. Figs. 19e and 19f show two such simulations, for different load cases. The first one uses a FE model of the fluid, and the FLSR algorithm. The second one uses a CCFV model of the fluid—more accurate and less diffusive than FE in modeling the very long propagation of the blast wave in the tunnel—and the FLSW algorithm. These (purely demonstrative) simulations take from 3 to 9 weeks on a PC (single-processor code version) up to 280 or 700 ms of physical time, respectively.

6 CONCLUSIONS AND PERSPECTIVES

The strong and weak approaches to fluid-structure interaction in fast transient dynamics have been shortly reviewed. Examples of basic (either conforming or non-conforming) and of embedded FSI algorithms have been presented and their application with FE, NCFV or CCFV fluid discretization has been discussed.

The embedded FSI algorithms are the latest ones developed and have not yet reached full maturity and validation, at least not at the same level as the basic algorithms. However, numerical results are encouraging and, in any case, these are the only algorithms applicable in extreme loading cases with complete structure failure and fragmentation, typical of blast effect studies.

These algorithms are more general than the basic ones but, as a counterpart, they are less accurate for the same size of the fluid cells (elements or volumes). Therefore, along with improvement of the embedded algorithms by thorough numerical testing, future work will concentrate on implementing mesh adaptivity in the fluid sub-domain, i.e. automatic mesh refinement in fluid zones near an embedded structure wall.

REFERENCES

[1] The EUROPLEXUS manual: http://europlexus.jrc.ec.europa.eu/.

[2] F. Casadei, J. P. Halleux, An algorithm for permanent fluid-structure interaction in explicit transient dynamics. *Computer Methods in Applied Mechanics and Engineering*, **128**/3-4, 231-289, 1995.

[3] F. Casadei, J.P. Halleux, A. Sala, F. Chillè, Transient fluid-structure interaction algorithms for large industrial applications. *Computer Methods in Applied Mechanics and Engineering*, **190**/24-25, 3081-3110, 2001.

[4] F. Casadei, S. Potapov, Permanent fluid-structure interaction with non-conforming interfaces in fast transient dynamics. *Computer Methods in Applied Mechanics and Engineering*, **193**/39-41, 4157-4194, 2004.

[5] A. Soria, F. Casadei, Arbitrary Lagrangian-Eulerian multicomponent compressible flow with fluid-structure interaction. *International Journal for Numerical Methods in Fluids*, **25**, 1263-1284, 1997.

[6] A. Sala, F. Casadei, A. Soria, A 3D finite volume numerical model of compressible multicomponent flow for fluid-structure interaction applications. *4th Congreso de Métodos Numéricos en Ingenieria*, Sevilla, Spain, June 7–10, 1999.

[7] F. Casadei, A. Sala, Finite element and finite volume simulation of industrial fast transient fluid-structure interactions. *European Conference on Computational Mechanics – Solids, Structures and Coupled Problems in Engineering (ECCM '99)*, Munich, Germany, August 31 – September 3, 1999.

[8] P. Galon, V. Faucher, F. Casadei, S. Potapov, Modeling complex fluid-structure interaction problems with EUROPLEXUS. *8th World Congress on Computational Mechanics* (*WCCM8)*, Venice, Italy, June 30 – July 5, 2008.

[9] F. Casadei, N. Leconte, Coupling finite elements and finite volumes by Lagrange multipliers for explicit dynamic fluid-structure interaction. *International Journal for Numerical Methods in Engineering*, DOI: 10.1002/nme.3042 (in publication).

[10] F. Casadei, Fast transient fluid-structure interaction with failure and fragmentation. *8th World Congress on Computational Mechanics* (*WCCM8)*, Venice, Italy, June 30 – July 5, 2008.

[11] F. Casadei, M. Larcher, On some computational methods for the simulation of structures subjected to blast loading and fragmentation. *4th European Conference on Computational Mechanics (ECCM2010)*, Paris, France, May 16–21, 2010.

[12] G. Giannopoulos, M. Larcher, F. Casadei and G. Solomos, Risk analysis of the fatality in land mass transport infrastructure by fast transient dynamic analysis. *Journal of Hazardous Materials*, **173**, 401-408, 2010.

[13] M. Larcher, F. Casadei and G. Solomos, Risk analysis of explosions in trains by fluid-structure calculations. *Journal of Transportation Security*, **3**, 57-71, 2010.

[14] M. Larcher, F. Casadei and G. Solomos, Influence of venting areas on the air blast pressure inside tubular structures like railway carriages. *Journal of Hazardous Materials*, **183**, 839-846, 2010.

[15] T. Børvik, A. Burbach, H. Langberg, M. Langseth, On the ballistic and blast load response of a 20 ft. ISO container protected with aluminum panels filled with local mass – Phase II: Validation of protective system. *Engineering Structures*, **30**/6, 1621-1631, 2008.

[16] T. Børvik, A.G. Hanssen, M. Langseth, L. Olovsson, Response of structures to planar blast loads – A finite element engineering approach. *Computers and Structures*, **87**, 507-520, 2009.

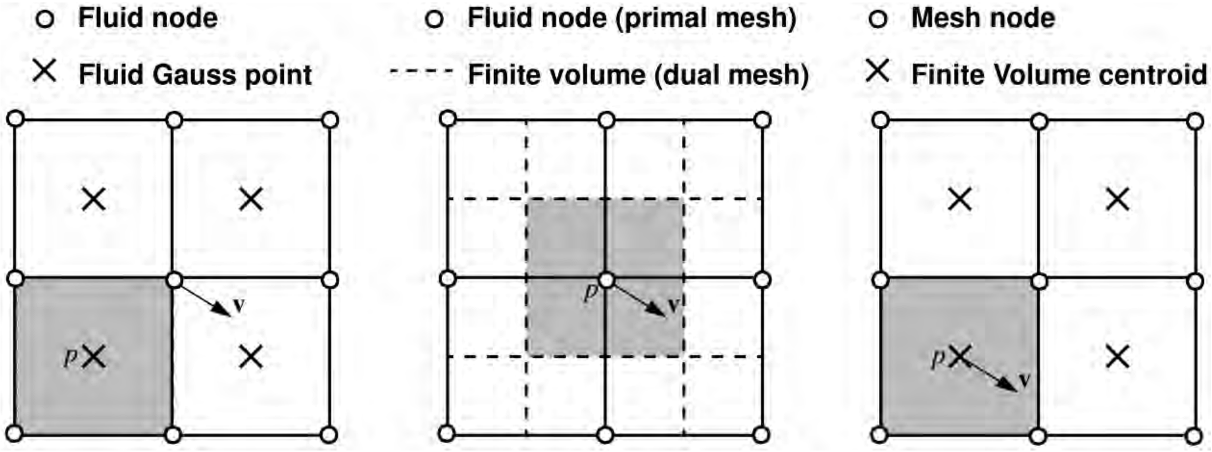

a) FE mesh. b) NCFV mesh. c) CCFV mesh.

Fig. 1 – Finite-element, node-centred finite volume and cell-centred finite volume meshes.

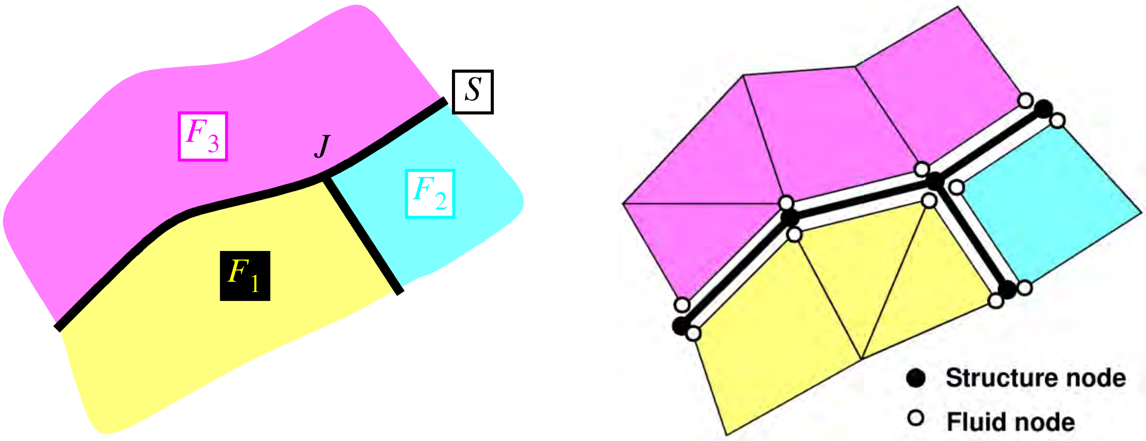

a) Continuous F-S domain. b) Nodally conforming discretization.

Fig. 2 – Sample FSI problem and its conforming discretization.

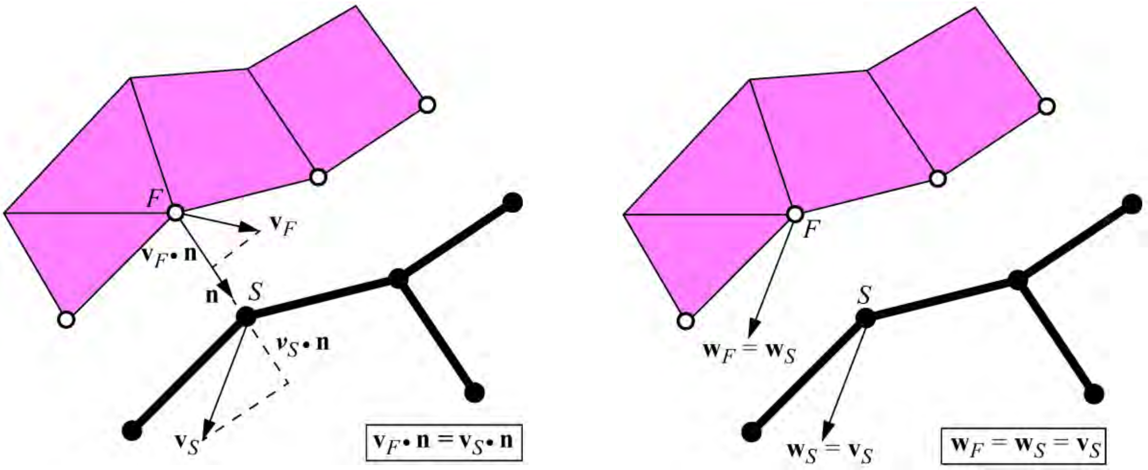

a) Constraints on particle velocities. b) Compatibility of mesh velocities.

Fig. 3 – FSA algorithm (strong approach) for a conforming F-S mesh.

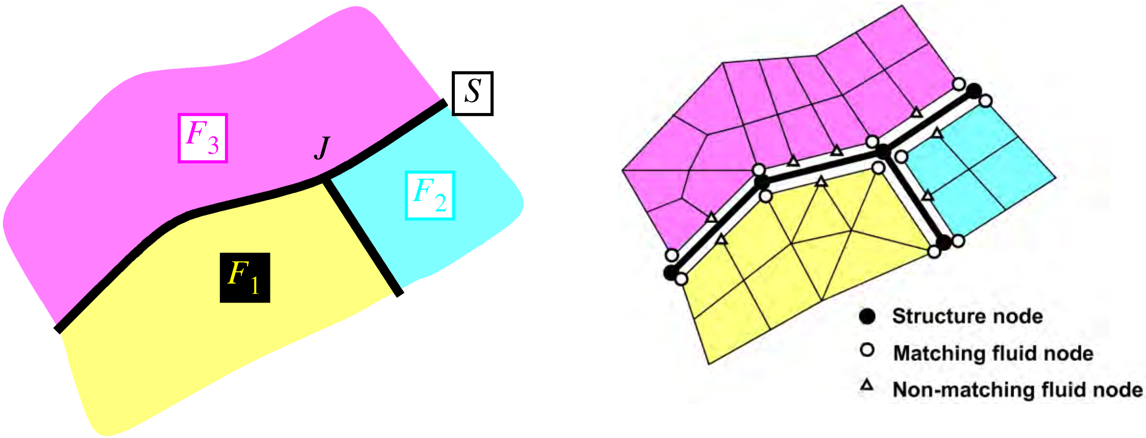

a) Continuous F-S domain. b) Non-conforming (hierarchic) discretization.

Fig. 4 – Sample FSI problem and its non-conforming discretization.

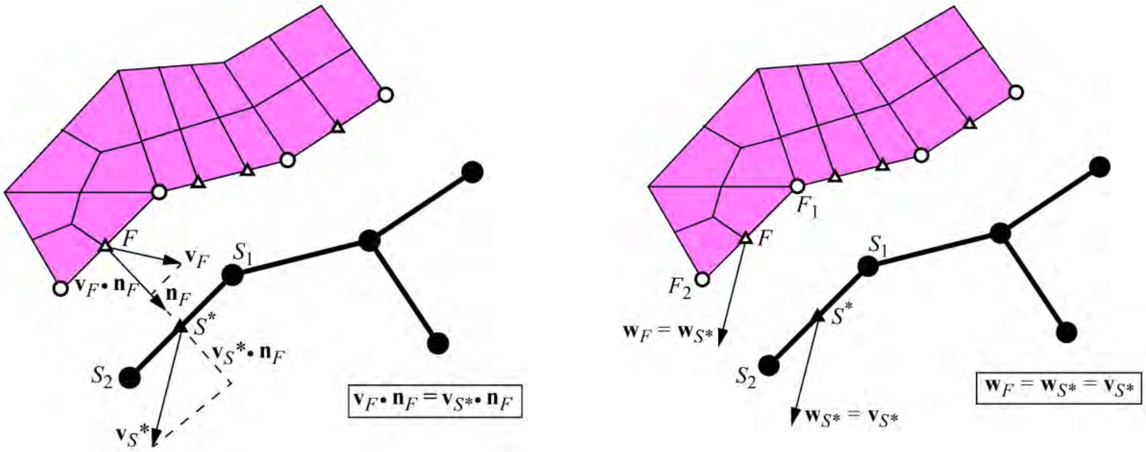

a) Constraints on particle velocities. b) Compatibility of mesh velocities.

Fig. 5 – FSA algorithm (strong approach) for a non-conforming F-S mesh.

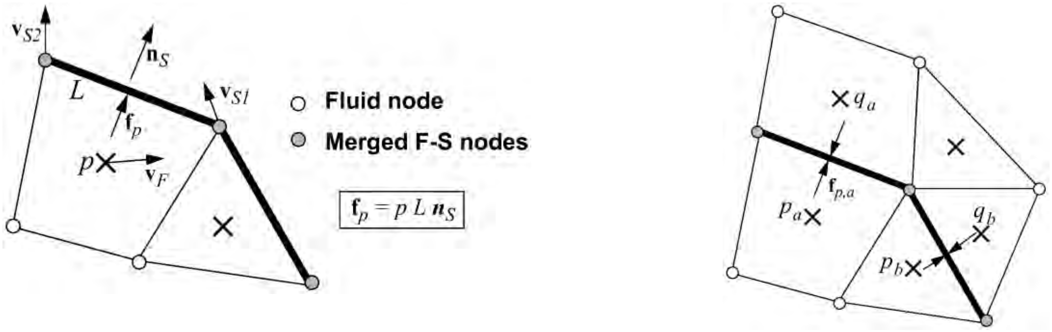

a) One fluid. b) Two fluids.

Fig. 6 – Weak algorithm for a conforming F-S mesh (with merged nodes).

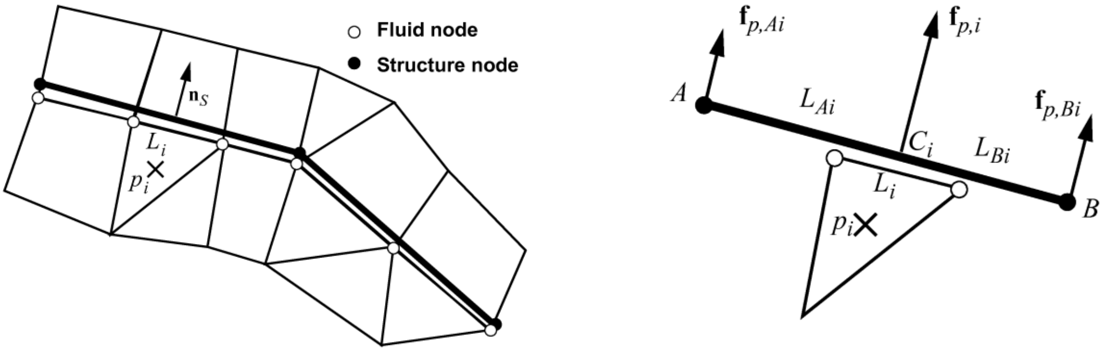

a) Hierarchic mesh, two fluids (continuous mesh). b) Distribution of pressure force.

Fig. 7 – Weak algorithm for a non-conforming F-S mesh.

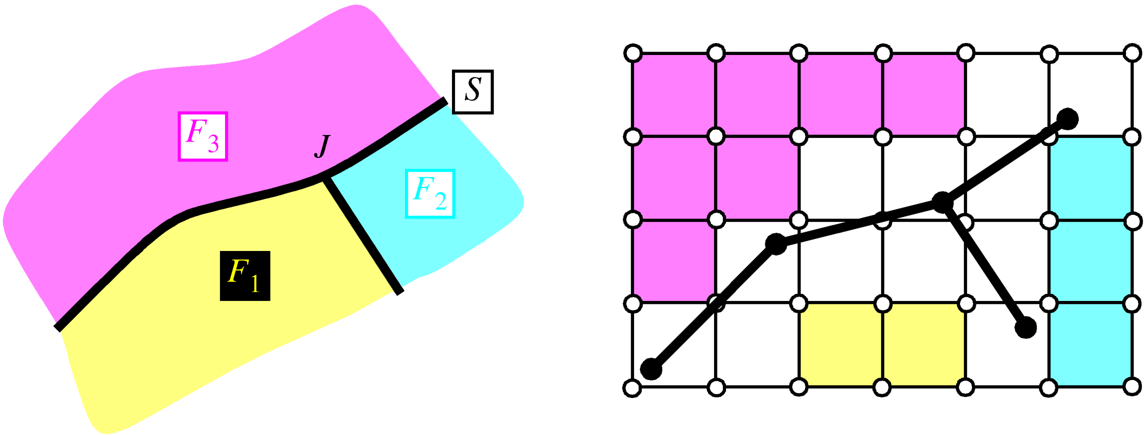

a) Continuous F-S domain. b) Structure mesh embedded in the fluid.

Fig. 8 – Sample FSI problem and its embedded discretization.

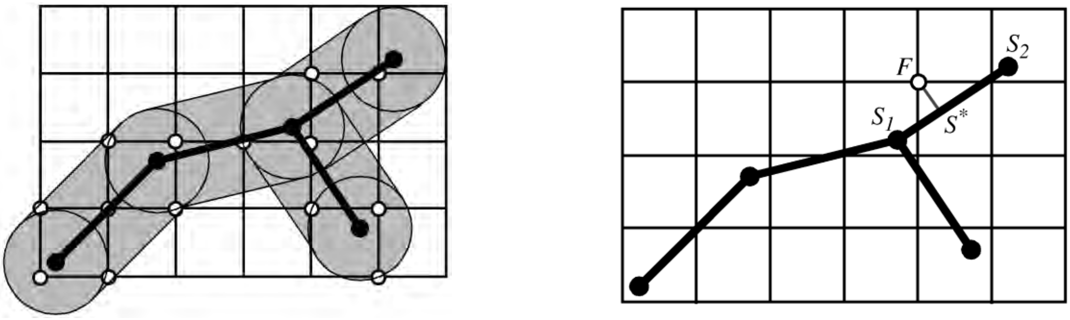

a) Influence domain (shaded) of the structure. b) F-S coupling.

Fig. 9 – Embedded FSI algorithm (strong approach).

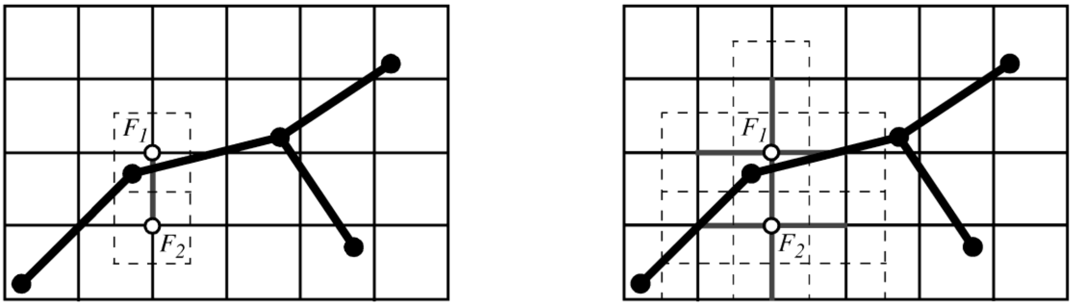

a) NCFV flux blockage (thick shaded line). b) More restrictive flux blockage.

Fig. 10 – Embedded FSI algorithm (strong approach) with NCFV.

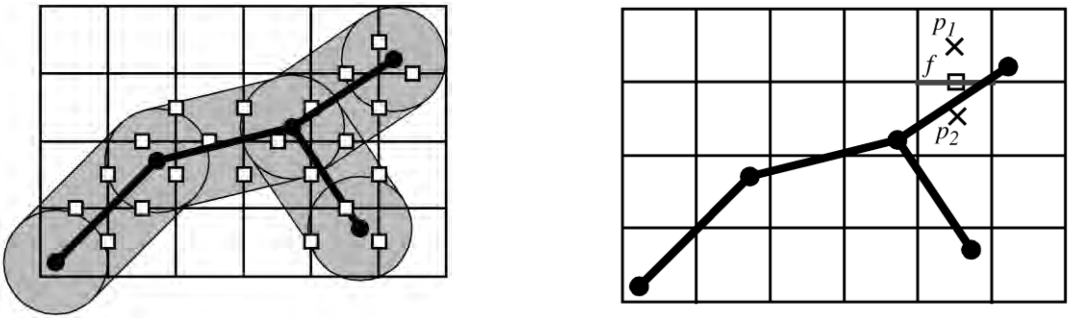

a) CCFV faces in the influence domain.

b) Pressure drop force calculation.

Fig. 11 – Embedded FSI algorithm (weak approach) with CCFV.

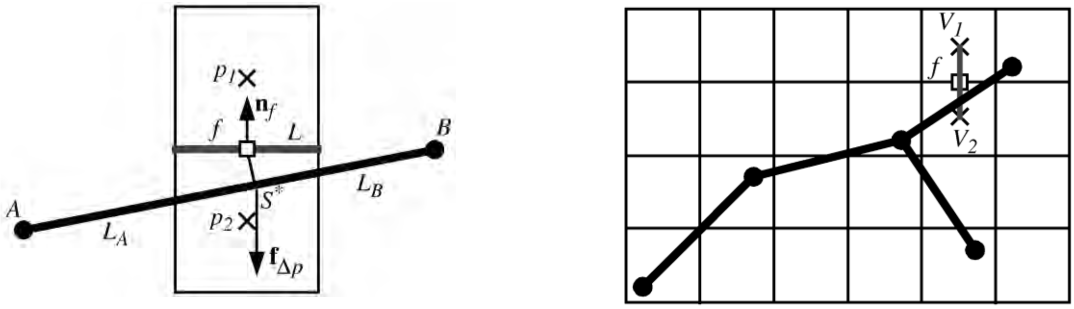

a) F-S coupling force.

b) CCFV flux blockage (thick shaded line).

Fig. 12 – Embedded FSI algorithm (weak approach) with CCFV.

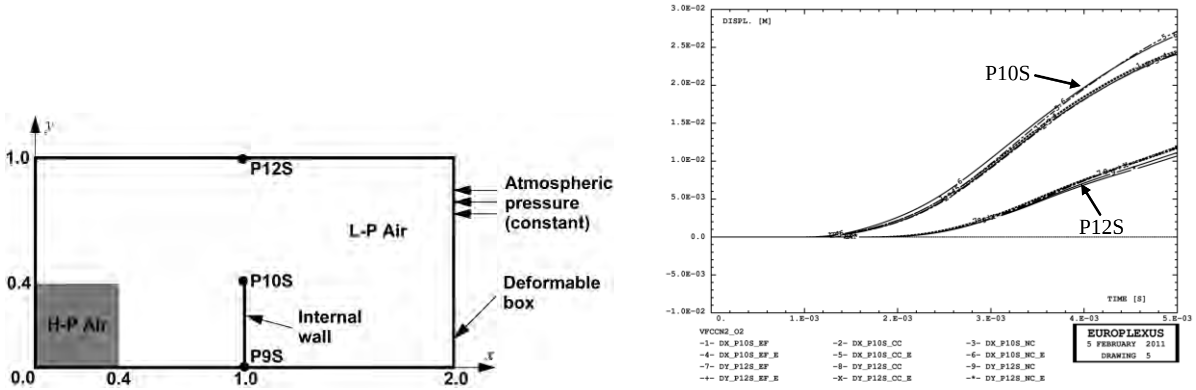

a) Geometry.

b) Structure displacements at P10S (in *x*) and at P12S (in *y*).

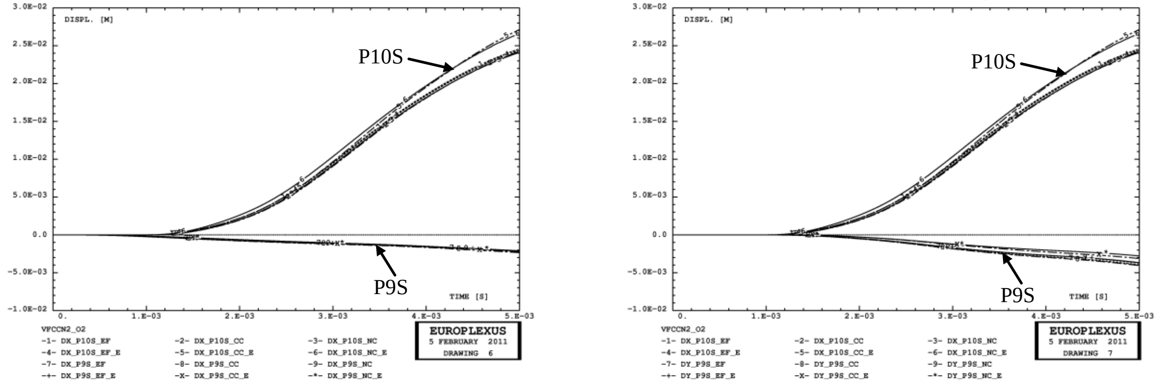

c) Structure displacements at P10S (in *x*) and at P9S (in *x*).

d) Structure displacements at P10S (in *x*) and at P9S (in *y*).

Fig. 13 – Explosion in a metallic box.

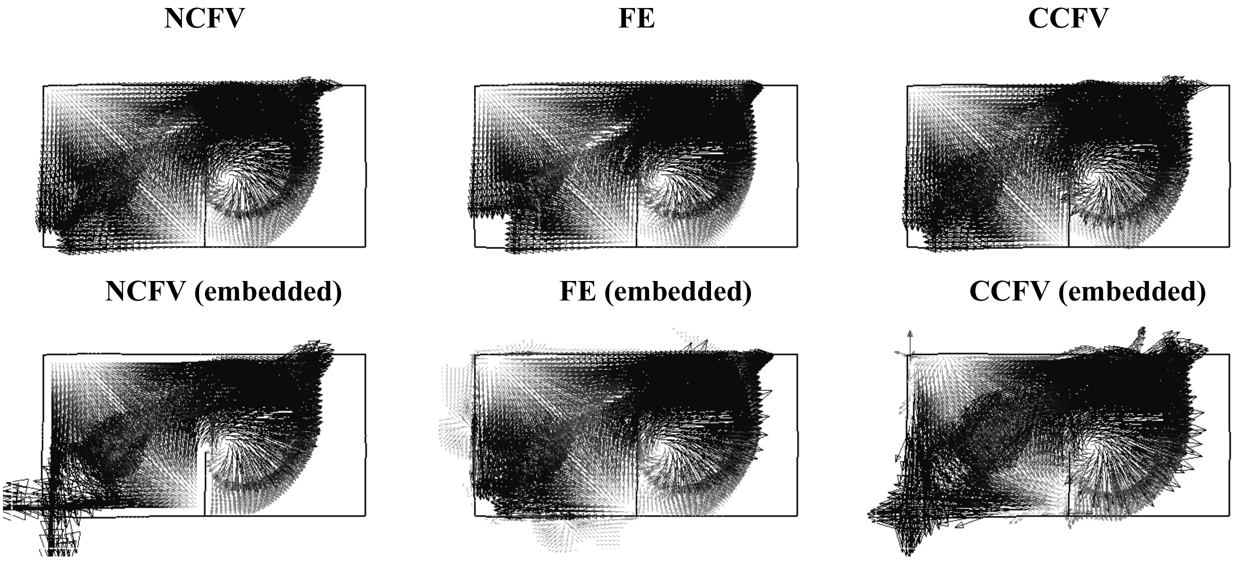

Fig. 14 – Explosion in a metallic box: fluid velocity at 2.5 ms.

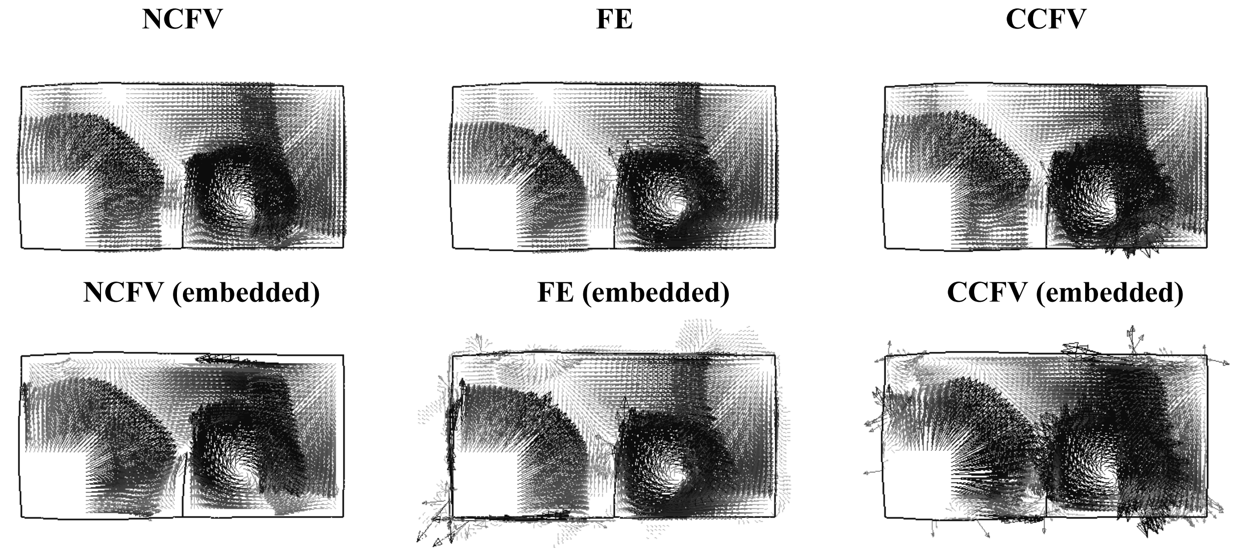

Fig. 15 – Explosion in a metallic box: fluid velocity at 5.0 ms.

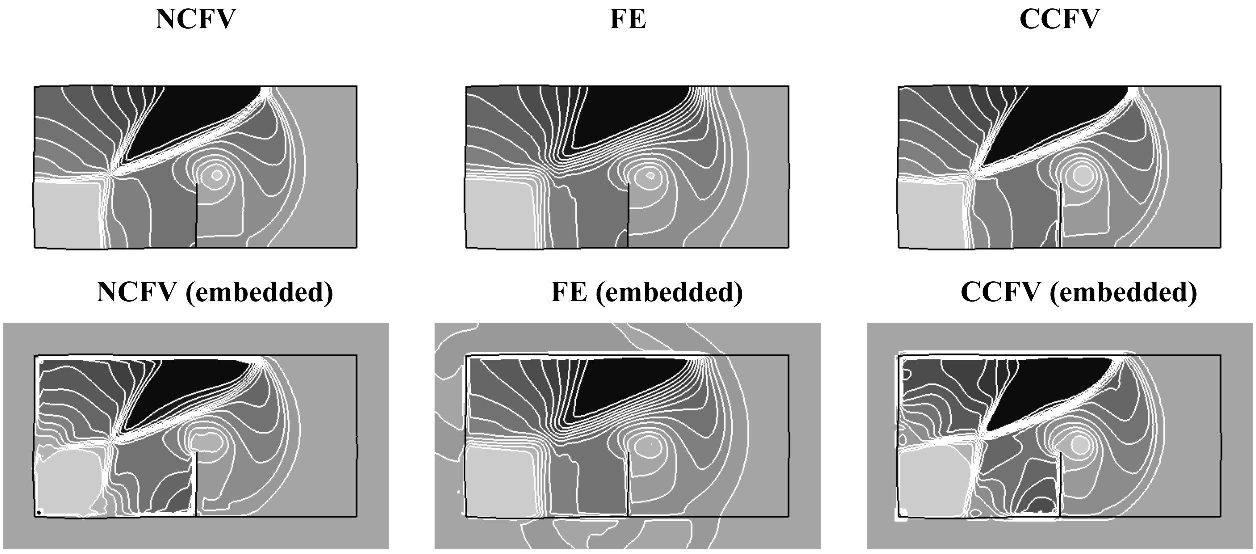

Fig. 16 – Explosion in a metallic box: fluid pressure at 2.5 ms.

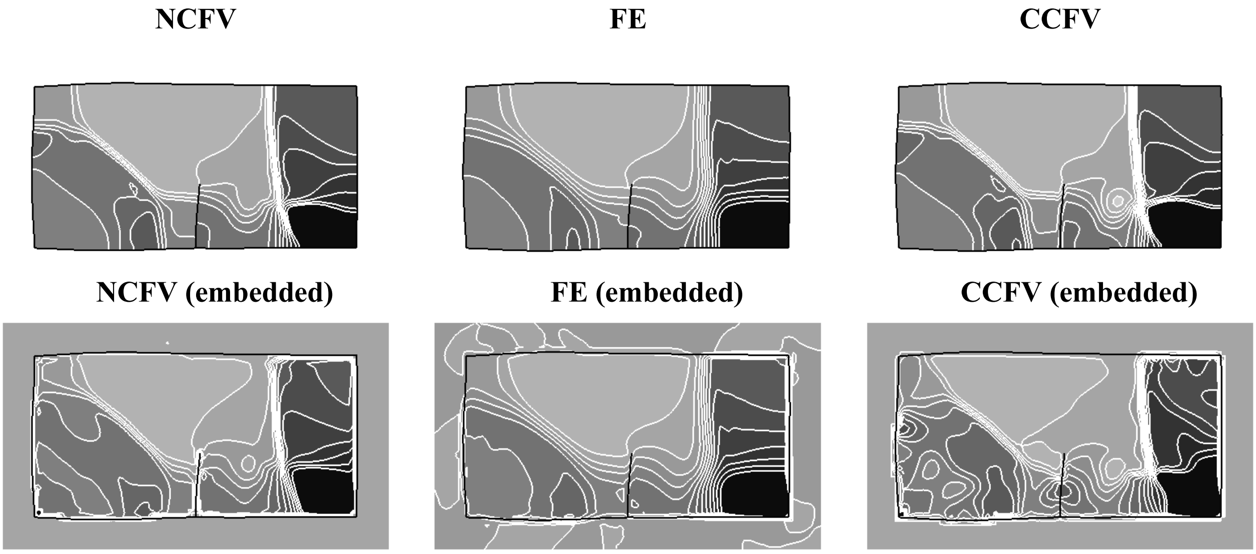

Fig. 17 – Explosion in a metallic box: fluid pressure at 5.0 ms.

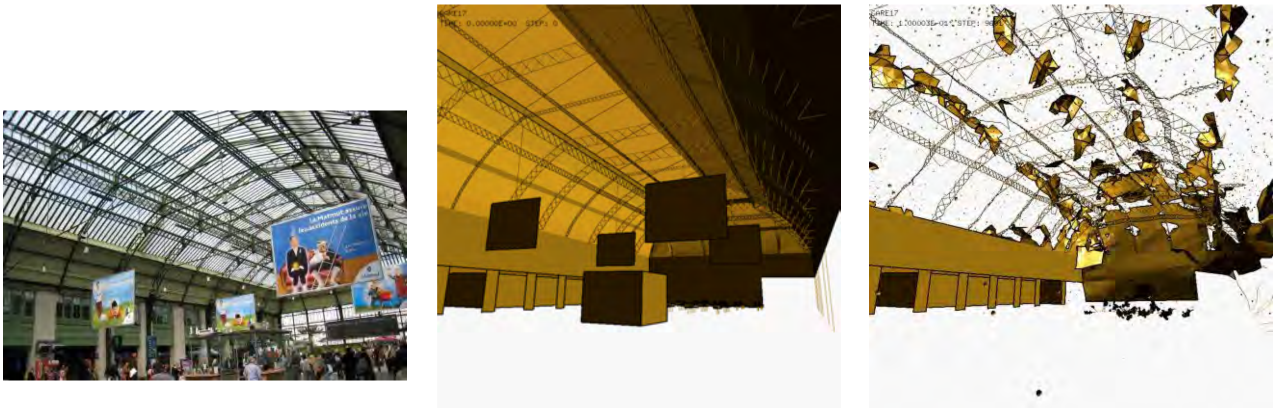

a) Glass roof. b) Internal view of the model. c) Blast effects (internal view).

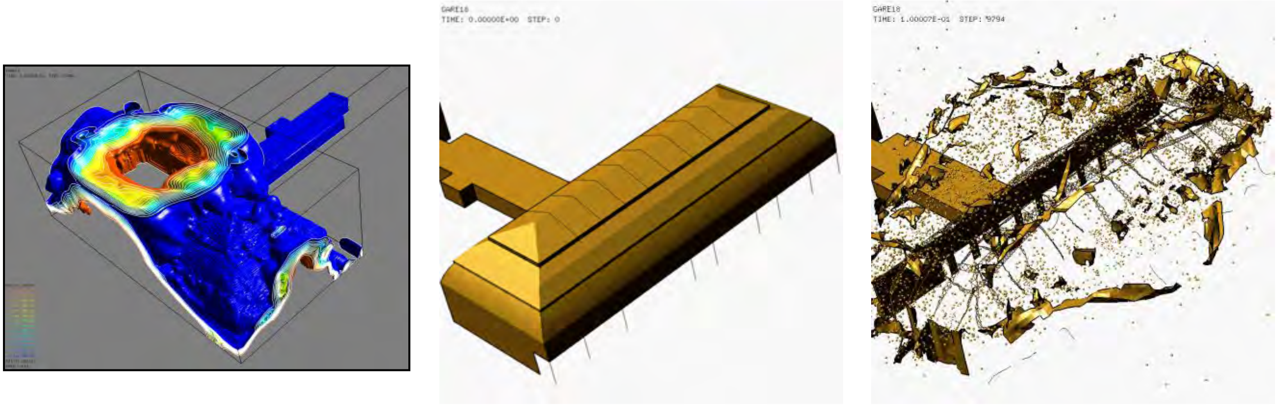

d) Risk map. e) External view of the model. f) Blast effects (external view).

Fig. 18 – Blast effects in a railway station.

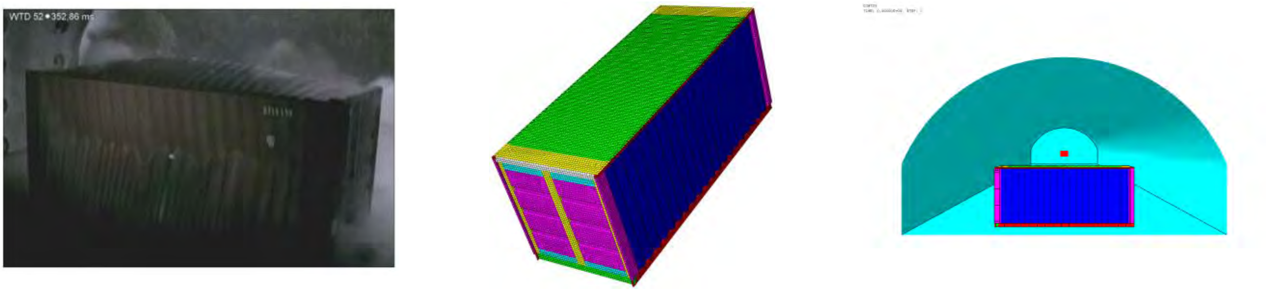

a) Experiment (case 1). b) Container model. c) Container in the tunnel.

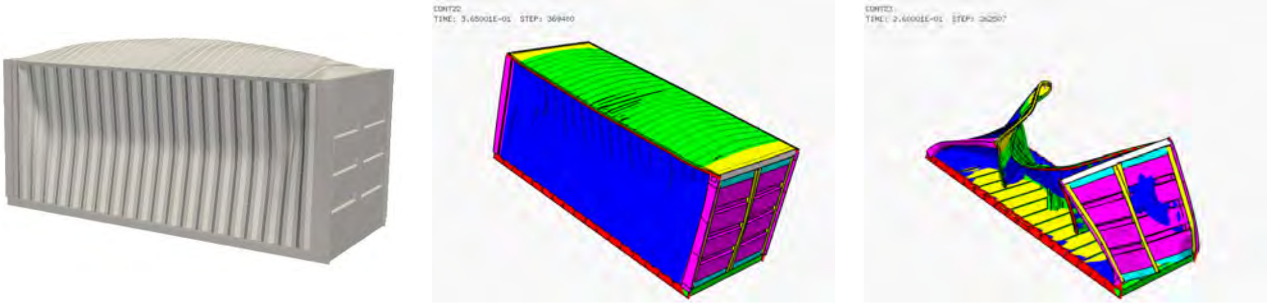

d) Blast effects (applied pressure). e) Blast effects (case 1). f) Blast effects (case 2).

Fig. 19 – Blast effects on an ISO container.

COMPDYN 2011
ECCOMAS Thematic Conference on
Computational Methods in Structural Dynamics and Earthquake Engineering
M. Papadrakakis, M. Fragiadakis, V. Plevris (eds.)
Corfu, Greece, 25-28 May 2011

A MESHLESS METHOD FOR FLUID-STRUCTURE INTERACTIONS: APPLICATION TO THE FAILURE PREDICTION OF A TANK UNDER IMPACT

Fabien Caleyron[1,2], **Alain Combescure**[1], **Vincent Fauher**[2] **and Serguei Potapov**[2]

[1]Université de Lyon, CNRS, INSA-Lyon, LaMCoS UMR 5259
e-mail: {fabien.caleyron, alain.combescure}@insa-lyon.fr,

[2] LaMSID UMR EDF-CNRS-CEA 2832
e-mail: vincent.faucher@cea.fr, serguei.potapov@edf.fr

Keywords: meshless, SPH, shell, fluid, impact, failure.

Abstract. *The development of numerical methods for the simulation of thin structures in interaction with a fluid is an industrial issue. In particular, such simulations should be able to predict a possible failure of the shell and the resulting leakage rate in situations involving impacts. This kind of simulations involves three key components: a thin structural model that includes highly nonlinear behaviors leading to failure, a fluid model able to handle sloshing and spatters phenomena, and finally, fluid-structure interactions whose topology can change drastically during calculations. This paper presents a solution based on a meshless method called Smoothed Particles Hydrodynamics (SPH) which is used to model both the fluid and the shell. The fluid-structure interaction is handled via a unilateral contact algorithm adapted to the SPH context. The capabilities of the method are illustrated on several problems involving fracturing shells and by simulating an experiment involving fluid leakage of a tank impacted by a bullet.*

1 INTRODUCTION

The purpose of meshless methods is to discretize a domain with a set of nodes rather than elements for which the connectivity is fixed. The neighbourhood of each node can vary during the calculation which simplifies the treatment of large deformations, cracks and fractures. Meshless methods can be distinguished depending on the approximation functions they use as well as the formulation they rely on (strong or weak form). A detailed overview of meshless methods is presented in [1]. Methods based on the weak form of the equilibrium equations are generally more accurate and stable but the need to perform numerical integrations complicates the treatment of fractures. As a consequence, methods based on the strong form of the equilibrium equations are sometimes preferred to perform simulations involving impacts and fragmentations.

A full SPH fluid-shell interaction model is described in this paper. The SPH method relies on the strong form of the equilibrium equations and was one of the first proposed meshless method [2]. It is traditionally used in fluid dynamics, especially for the simulation of free surface flows. The method has recently been extended to structural dynamics and more specifically to shells theory [3]. This paper is the extension of [3] to the modeling of damage, fracture and failure.

The fundamentals of the SPH method and the corresponding fluid model are presented in the first section of the paper. Then, we explain the application of the SPH method to the Mindlin-Reissner's thick shells theory and its extension to fracture modeling in the second section. The Pinballs method [4] which is used to handle fluid-structure interactions is described in the third section. Finally, the simulation of a water filled tank impacted by a projectile is presented.

2 SPH METHOD AND SPH FLUID MODEL

2.1 SPH method

The SPH method discretizes the domain of interest Ω with a set of N nodes whose neighbourhood can vary in time. Each node represents a material amount m_i chosen so that the total mass of the structure is described correctly $m = \sum m_i$. Nodes interact one with each other through the use of functions for the approximation of a physical field or the approximation of its gradient. These functions have a compact support which means they are non-zero within a domain Ω_{V_i} (i.e. Ω_{V_i} is the neighbourhood of node i) and null elsewhere. The size of the neighbourhood Ω_{V_i} is a fundamental parameter of the method and is often denoted $2h$ in the SPH method. The B3 spline function is often used in the SPH method:

$$w_i(\overrightarrow{x_j}) = w_{ij} = C \left\{ \begin{array}{l} \frac{3}{2}\left[\frac{2}{3} - \left(\frac{r_{ij}}{h}\right)^2 + \frac{1}{2}\left(\frac{r_{ij}}{h}\right)^3\right] \text{ if } 0 \leq \frac{r_{ij}}{h} \leq 1 \\ \frac{1}{4}\left[2 - \frac{r_{ij}}{h}\right]^3 \text{ if } 1 < \frac{r_{ij}}{h} < 2 \\ 0 \text{ otherwise} \end{array} \right. \tag{1}$$

where $r_{ij} = \|\overrightarrow{x_i} - \overrightarrow{x_j}\|$ and $C = 10/7\pi h^2$ in dimension 2. It is a normalization factor that is chosen to ensure the partition of unity property. The approximation of a field $\{f_j\}$, $j = \{1, ..., N\}$ and its gradient can be written:

$$f(\overrightarrow{x_i}) \approx \sum_{j \in \Omega_{V_i}} f_j w_{ij} V_j \tag{2}$$

$$\overrightarrow{\nabla} f(\overrightarrow{x_i}) \approx \sum_{j \in \Omega_{V_i}} f_j \overrightarrow{\nabla} w_{ij} V_j \tag{3}$$

where V_j is the material volume represented by node j.

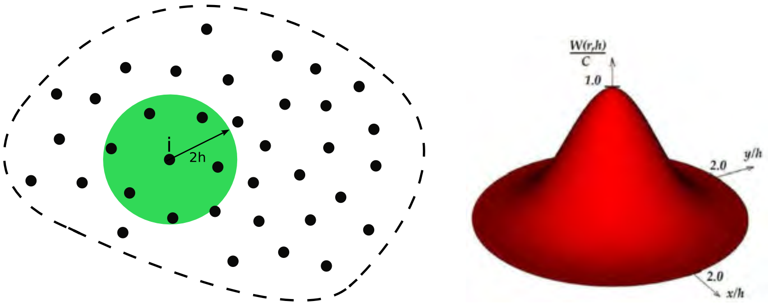

(a) Neighbourhood of an SPH node (b) Spline B3

Figure 1: Definition of the neighbourhood Ω_{V_i} through the B3 spline.

2.2 SPH fluid model

The fluid is assumed to be perfect, weakly compressible and acoustic. The governing equations, once discretized in the updated Lagrangian framework, can be written:

- equilibrium equation:

$$\left(\frac{\partial \overrightarrow{v}}{\partial t}\right)_i = -\sum_{j\in\Omega_{V_i}} m_j \left(\frac{p_i}{{\rho_i}^2} + \frac{p_j}{{\rho_j}^2}\right) \overrightarrow{\nabla} w_{ij} \tag{4}$$

  where p is the pressure, ρ density and $\overrightarrow{v}$ the velocity vector. We can notice that equation (4) is symmetric so it respects Newton's third law of motion.

- continuity equation:

$$\left(\frac{\partial \rho}{\partial t}\right)_i = \rho_i \sum_{j\in\Omega_{V_i}} \frac{m_j}{\rho_j} \left(\overrightarrow{v_i} - \overrightarrow{v_j}\right) \overrightarrow{\nabla} w_{ij} \tag{5}$$

  This equation was chosen because it cancels the density variations when the fluid flow is uniform.

- equation of state:

$$\Delta p_i = c^2 \Delta \rho_i \tag{6}$$

  where c is the speed of sound in the fluid.

Artificial linear and quadratic viscosity terms are used to stabilize calculations in presence of shocks.

3 FRACTURING SPH SHELL MODEL

This section presents the application of the SPH method to structural dynamics and more specifically to Mindlin-Reissner's thick shells theory. The model described in [3] is extended in this article for the modeling of shells damage and fracture.

3.1 SPH shell formulation (SPHS)

The SPH method presents three major drawbacks when it is applied to structural dynamics. They are well known and widely discussed in the literature where solutions are found:

- the method has bad consistency properties, especially near the boundary of the SPH domain where nodes have incomplete neighbourhoods. This drawback prevents the method from having good mesh convergence properties. The solution proposed in [5] consists in using Moving Least Square (MLS) approximation functions. These functions are constructed from a polynomial basis of degree n and, as a consequence, exhibit a n order consistency. The approximation in $\overrightarrow{x}$, built around $\overrightarrow{x}^*$, of a data field $\{u_i\}$, $i = \{1, ..., N\}$, is:
$$u(\overrightarrow{x}, \overrightarrow{x}^*) = \overrightarrow{p}^T(\overrightarrow{x})\overrightarrow{a}(\overrightarrow{x}^*) \tag{7}$$
$\overrightarrow{p}$ is the polynomial basis and $\overrightarrow{a}$ is a vector of coefficients obtained by minimizing the following weighted L_2 norm:
$$J = \sum_{j=1}^{N} \left[\overrightarrow{p}^T(\overrightarrow{x_j})\overrightarrow{a}(\overrightarrow{x}^*) - u_j\right]^2 w_j(\overrightarrow{x}^*) \tag{8}$$
The weighting function is often the standard SPH B3 spline.

- the SPH method applied to structural mechanics suffers from numerical instabilities. In [6], authors have shown that the Eulerian form of the SPH kernel w_{ij} exhibits a numerical instability in presence of tension stresses. The solution given in [7] consists in using a total Lagrangian formulation for which the kernel is stable.

- finally, most of the meshless methods suffers from the presence of zero energy modes due to the use of the collocation technique (strong form) or the nodal integration technique (weak form). This problem is extensively studied in [7]. Authors show that the use of a total Lagrangian formulation can reduce significantly the development of such zero energy modes. However, it is not sufficient in the case of a shell model because the field of the normals to the mean surface is very sensitive to instabilities that can occur in the curvature of the shell. [7] shows that the problem comes from the fact the kinematic variables and the strains and stresses are carried by the same nodes. The solution from [7] consists in introducing a second set a points denominated Stress Points (SP). These points a similar to Gauss points in the finite elements method (FEM) since they are only used to compute strains and stresses.

The SPH shell formulation is defined according to Mindlin-Reissner's thick shells theory. It relies on the assumption that the thickness e of the structure is small compared to its other dimensions, so the position vector $\overrightarrow{x}$ of any point located at a distance ξ from the mean plane can be expressed as:
$$\overrightarrow{x}(t) = \overrightarrow{x}_m(t) + \xi\overrightarrow{n}(t) \quad \xi \in \left[-\frac{e}{2}; +\frac{e}{2}\right] \tag{9}$$
$\overrightarrow{x}_m$ is the position of a point in the mean surface of the shell and $\overrightarrow{n}$ is the pseudo-normal vector that represents the orientation of the material. Mindlin-Reissner's shells theory takes

into account the influence of transverse shear on the model so that the pseudo-normal vector $\overrightarrow{n}$ does not remain normal to the mean plane. The displacement vector in the global coordinate system $R(x, y, z)$ is given as a function of the initial coordinates in the local coordinate system $R_{L0}(x_{L0}, y_{L0}, z_{L0})$ whose direction z_{L0} is normal to the shell:

$$\overrightarrow{u}\,(\overrightarrow{x}_{L0}, t) = \overrightarrow{u}_m(x_{L0}, y_{L0}, t) + z_{L0}\left[\overrightarrow{n}(x_{L0}, y_{L0}, t) - \overrightarrow{n}_0(x_{L0}, y_{L0})\right] \tag{10}$$

where $\overrightarrow{x}_{L0} = \mathbf{G}_{L0}\overrightarrow{x}_0$ and $\overrightarrow{n}_0$ is the initial pseudo-normal.

Green-Lagrange strain tensor in R_{L0} is given by:

$$(\mathbf{E})_{R_{L0}} = \frac{1}{2}\left[\frac{\partial \overrightarrow{u}_{L0}}{\partial \overrightarrow{x}_{L0}} + \frac{\partial \overrightarrow{u}_{L0}}{\partial \overrightarrow{x}_{L0}}^T + \frac{\partial \overrightarrow{u}_{L0}}{\partial \overrightarrow{x}_{L0}}^T \frac{\partial \overrightarrow{u}_{L0}}{\partial \overrightarrow{x}_{L0}}\right] = (\mathbf{E}^m)_{R_{L0}} + z_{L0}\left(\mathbf{E}^f\right)_{R_{L0}} \tag{11}$$

Tensor $\mathbf{E}^m$ contains membrane and transverse shear terms which are constant through thickness and $\mathbf{E}^f$ contains bending terms which vary linearly through thickness. Non-linear terms are taken into account.

Plane stresses assumption requires the application of the constitutive law in the mean plane of the shell in its current configuration. As a consequence, a local coordinate system $R_L(x_L, y_L, z_L)$ whose direction z_L is normal to the mean plane at the current point, is defined. Euler-Almansi strains corresponding to membrane and bending effects $(\overrightarrow{\varepsilon_{mf}})_{R_L}$ and transverse shear $(\overrightarrow{\varepsilon_c})_{R_L}$ are computed in R_L. Corresponding Cauchy stresses vectors $(\overrightarrow{\sigma_{mf}})_{R_L}$ and $(\overrightarrow{\sigma_c})_{R_L}$ are calculated through the use of a plane stresses constitutive law. Membrane and transverse shear resultants N_{ij} and T_i as well as bending moments m_{ij} are then obtained by integration of Cauchy stresses through thickness:

$$\begin{aligned} N_{ij} &= \int_{-e/2}^{e/2} \sigma_{ij}^m d\xi = e\sigma_{ij}^m \\ T_i &= \int_{-e/2}^{e/2} \sigma_{iz}^c d\xi = e\sigma_{iz}^c \\ m_{ij} &= \int_{-e/2}^{e/2} \xi\sigma_{ij}^f(\xi) d\xi = \frac{e^3}{12}\sigma_{ij}^f \end{aligned} \tag{12}$$

Because of the total Lagrangian formulation, the equilibrium equations are finally written in the global coordinate system R by means of Piola-Kirchoff 1 stresses.

3.2 Damage and fracture

Phenomena at the microscopic scale (microvoids and microcracks growth) leading to the failure of the shell are homogenized at the macroscopic scale through the use of continuum damage mechanics. A macroscopic crack appears in a reference volume element (RVE) once its damage variable reaches a critical damage value. The crack propagates at the structure scale when additional RVEs reach the critical damage value. Macroscopic cracks are treated as strong discontinuities in the SPH shell model.

3.2.1 Damage

For metals, damage comes from shear phenomena that favour the apparition of plasticity and from volumetric deformation that favours microvoids and microcracks growth. Damage criterion beyond which damage occurs is classical for this class of material and can be written [8]:

$$\left[\frac{2}{3}(1+\nu)+3(1-2\nu)\left(\frac{\sigma_H}{\sigma_{eq}}\right)^2\right]p-\epsilon_p^s\leq 0 \tag{13}$$

σ_H is the hydrostatic stress, σ_{eq} the equivalent Von-Mises stress, σ_H/σ_{eq} the triaxiality factor, ϵ_p^s an equivalent critical plastic strain, p the accumulated plastic strain and ν the Poisson's ratio. The damage evolution law is then given by [8]:

$$\dot{D}=\frac{D_c}{\epsilon_p^c-\epsilon_p^s}\left[\frac{2}{3}(1+\nu)+3(1-2\nu)\left(\frac{\sigma_H}{\sigma_{eq}}\right)^2\right]\dot{p} \tag{14}$$

ϵ_p^c is an equivalent critical plastic strain beyond which the material fails and D_c is the corresponding critical damage which is representative of the fraction of defaults (voids and cracks) in the RVE at failure. The damage evolution law must be coupled with a plasticity model (Von-Mises or Johnson-Cook plasticity for instance).

Numerical simulations performed with a material whose stress-strain curve presents a negative slope (softening or damaging material) are not satisfying since strains and damage are artificially localized in a single element when the failure is imminent. As a consequence, the energy dissipated in the fracture process and the failure time tend to zero as the mesh size decreases to zero. It means that microvoids and microcracks growth rate would be infinite, which is not physically acceptable. This problem is widely discussed in the literature [9] and is known as the numerical localization problem. Authors of [10] show that the problem comes from the transformation of the initial hyperbolic equations of the problems into elliptic equations when material softening occurs. As a consequence, the velocity of the waves in the material becomes complex which means they are trapped in the first element where softening occurs. Solutions proposed in the literature consists in preserving the initial hyperbolic form of the equation by introducing a characteristic length or time in model. This characteristic length or time is representative of the interaction of one element of the mesh with its neighbours. A characteristic time τ_c can be introduced in the model through the use of the following standard delayed damage model [11]:

$$\begin{array}{l}\text{if } D\leq D_c\\ \quad \dot{D}_r=\dfrac{1}{\tau_c}\left[1-e^{-a\langle D-D_r\rangle}\right]\\ \text{otherwise}\\ \quad \dot{D}_r=0\end{array} \tag{15}$$

D is the damage given by the damage evolution law, D_r is the regularized or delayed damage and $\langle . \rangle$ is the positive part operator. a is a second material parameter.

3.2.2 Damage-fracture transition

In the model presented in this paper, a crack is defined as the continuous set of fractured REV, see figure 2. This method is attractive since it does not require the explicit representation of the cracks, which simplifies the treatment of crack branching process for example.

Fully damaged REV are handled by introducing strong discontinuities into the model. As a consequence, interactions between SPH points (nodes or SP) through the cracked zone have to be deleted. Thus, the cracked zone is considered to be opaque such that points that are on

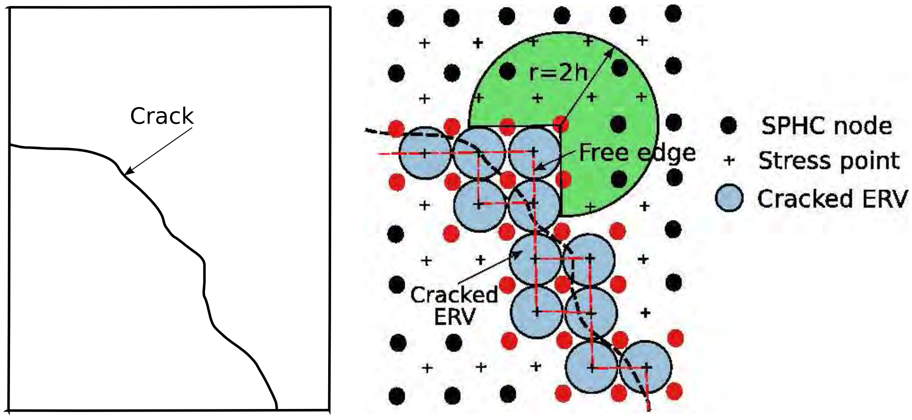

(a) Crack (b) SPHS Model

Figure 2: Modeling of a crack with SPHS model.

Remark: the method is illustrated with a regular quadrilateral mesh but it is applicable to any mesh constructed through a Vorono diagram.

the opposite side of the crack are excluded in the approximation of the displacement field. The shape of the support of the weighting functions is then represented in figure 2. This method is known as the visibility method [12]. In figure 2, it is obvious that some SPH points can come to the point where they do not have anymore neighbours. In this situation, if the point is a SP, it is chosen to eliminate it from the calculation by setting $D = D_c$. If the point is a node, it is kept in the calculation without interacting with the other points: its motion depends only on the kinetic energy he had at the time step he became a fragment and eventually on the contacts with other parts of the model. As a consequence, we keep two major advantages of meshless methods:

- fractures are simulated without mass and energy loss,
- fragments (i.e. SPH nodes without neighbourhood) can eventually interact with other parts of the model.

Finally, it is necessary to recompute MLS shape functions when fracture occurs since the neighbourhood of the nodes changes. The order of the polynomial basis used to compute MLS shape functions might be lowered when the number of neighbours decreases.

3.3 Numerical examples

3.3.1 Perforation of a plate

This test case is based on a work presented in [13] concerning the experimental and numerical analysis of the failure process of a mild steel sheet subjected to normal impact by hemispherical projectiles. A plug ejection was observed during experiments followed by a petalling process. The number of petals appearing during this process depends essentially on the velocity impact.

Figures 3(a) and 3(b) show the final state of the plate simulated with the SPHS method and compared with the calculations performed in [13] for an impact velocity $V_{imp} = 300 m.s^{-1}$. The model used in [13] is a FEM model with erosion of the element whose accumulated plastic strain exceeds a critical value. Failure time as a function of the impact velocity is ploted in figure 3(c) for SPHS model and calculations from [13]. The agreement between the various results is good.

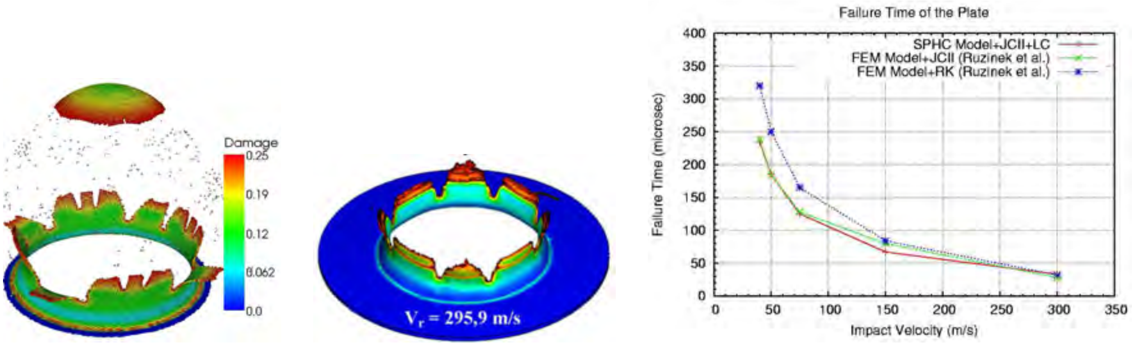

(a) SPHS Model (b) FEM Model [13] (c) Failure time

Figure 3: Perforation of a plate by an hemispherical projectile.

3.3.2 Fragmentation of explosively driven cylinders

This test case is based on an experimental work presented in [14] concerning the fragmentation of cylinders filled with a high explosive called LX-17. The cylinder is modeled with the SPHS method. The high explosive is modeled with FEM by using Jones-Wilkins-Lee equation of state which is characteristic of explosive materials. Figure 4(a) compares the fragments distribution obtained with the SPHS method with experimental data. Figure 4(b) represents the simulated fragments on the undeformed configuration of the cylinder.

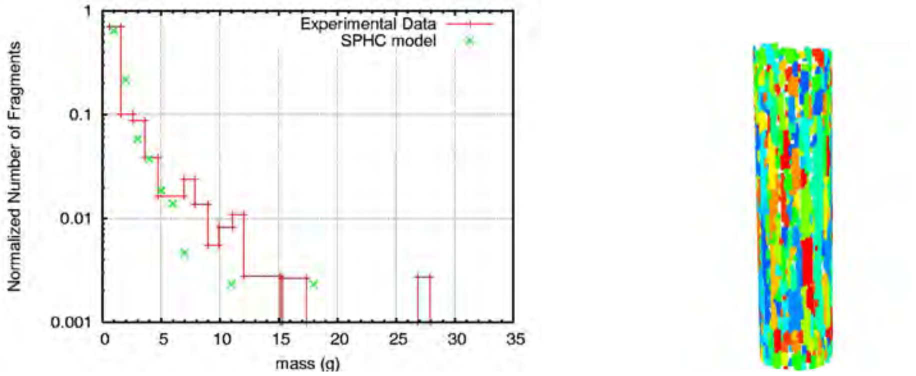

(a) Fragments distribution (b) Fragments identification

Figure 4: Fragmentation of explosively driven cylinders.

4 FLUID-STRUCTURE INTERACTIONS

Simulations of the failure of thin structures filled with fluid are complex problems for which the fluid-structure interface can change drastically during the transient. The Pinballs method [4] has already demonstrated its capability to handle this kind of problems in the FEM framework.

The method has been extended for the modeling of full SPH fluid-shell interactions in [15]. The main ingredients of the method are recalled in this section.

Each SPH node is filled with a so-called Pinball of spherical shape for fluid nodes and cylindrical shape for shell nodes. The detection of the contact then reduces to a simple geometrical interpenetration check between the Pinballs of the distinct contacting bodies. Once the contact is detected, contact forces are computed by enforcing impenetrability between the two impacting bodies. Contact forces should ensure that for a non viscous fluid:

$$(\overrightarrow{v_1} - \overrightarrow{v_2}).\overrightarrow{n} = 0 \tag{16}$$

where $\overrightarrow{v}_1$, $\overrightarrow{v}_2$ are the Pinballs velocities and $\overrightarrow{n}$ is a suitable normal direction to the contact surface. Much of the effectiveness and performance of the Pinballs algorithm depends on the choice made for the expression of $\overrightarrow{n}$. The method is primarily intended for impacts problems where sliding and friction are not crucial: the oscillations of the normal $\overrightarrow{n}$ to the interface (in the case of large radius Pinballs for example) can cause troubles in the case of two plane bodies sliding. In the particular case of the interaction between a SPH fluid and an SPH shell, the normal $\overrightarrow{n}$ is chosen to be the normal of the shell pinballs. The problem is solved through the use of Lagrange multipliers rather than penalty method which requires the introduction of a user-tuned parameter. This method is attractive since the contact detection requires simple geometrical checks. Moreover, the procedure is symmetric since both solids play the same role and no distinction is needed between a master and a slave.

5 APPLICATION: FAILURE PREDICTION OF A TANK UNDER IMPACT

The full SPH model presented in this paper is used to simulate the impact of a bullet onto a steel cylinder, according to the experimental conditions described in [16]. First, the cylinder is empty and the impact produces a simple perforation of the shell as can been seen in figure 5(a). The same was observed in the case of a cylinder filled with water for low velocity impacts. For high velocity impacts, for example $V_{imp} = 730 m.s^{-1}$ in figure 5(c), the impact leads to a longitudinal crack and a fluid leakage.

Both the fluid and the cylinder are modeled with the SPH method described previously. The projectile is assumed to behave like a rigid body. In the case of an empty cylinder, the simulation predicts a simple perforation of the shell, see figure 5(b), which is in agreement with the experimental results. In the case of a water filled cylinder, the simulation predicts a longitudinal crack similar to the one observed in the experiment, see figure 5(d).

6 CONCLUSION

A full SPH method for the simulation of fluid-shell interactions until failure was presented in this paper. The fluid model is very classical in the SPH framework. The method has been extended to the simulation of fracturing shells by using the continuum damage mechanics and introducing strong discontinuities in the model once cracks appeared. The method is attractive since it does not require the explicit representation of the cracks, which simplifies the treatment of crack branching and fragmentation for example. Finally, the method is easily extended to fluid-structure interactions simulations through the Pinballs method. The model was developed in the fast dynamic software EUROPLEXUS.

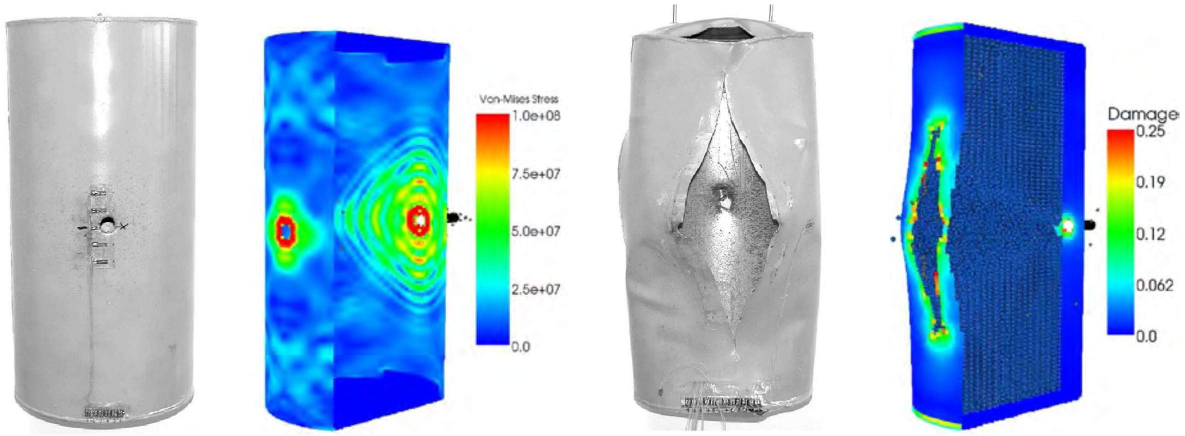

(a) Empty tank [16] (b) Empty tank SPH (c) Full tank [16] (d) Full tank SPH

Figure 5: Failure prediction of a tank under impact.

ACKNOWLEDGMENTS

The authors thank the French Atomic Energy Commission (CEA) and the French Electricity Company (EDF) for their support on the EUROPLEXUS software.

REFERENCES

[1] V.P. Nguyen, T. Rabczuk, S. Bordas, M. Duflot, Meshless methods: A review and computer implementation aspects. *Mathematics and Computers in Simulation*, **79**, 763-813, 2008.

[2] R.A. Gingold, J.J. Monaghan, Smoothed particle hydrodynamics: theory and application to non-spherical stars. *Monthly Notices of the Royal Astronomical Society*, **181**, 375-389, 1977.

[3] B. Maurel, A. Combescure, An SPH shell formulation for plasticity and fracture analysis in explicit dynamic. *International Journal for Numerical Methods in Engineering*, **76**, 949-971, 2008.

[4] T. Belytschko, MO. Neal, Contact-impact by the pinball method with penalty and Lagrangian methods. *International Journal for Numerical Methods in Engineering*, **31**, 547-572, 1991.

[5] G. A. Dilts, Moving least squares particle hydrodynamics - I : consistency and stability. *International Journal for Numerical Methods in Engineering*, **44**, 1115-1155, 1999.

[6] J.W. Swegle, D.L. Hicks, Y. Chen, Stabilizing SPH with conservative smoothing. SANDIA, *Report NSAN94-1932*, 1994.

[7] T. Belytschko, Y. Guo, W.K. Liu, S.P. Xiao, A unified stability analysis of meshless particle methods. *International Journal for Numerical Methods in Engineering*,**40**, 1359-1400, 2000.

[8] J. Lemaitre, J.-L Chaboche, *Mécanique des matériaux solides.* Dunod, 2004.

[9] Z.P. Bazant, Instability, ductility and size effect in strain softening concrete. *Mechanics and Journal of the Engineering Mechanics Division*, **102**, 331-344, 1976.

[10] Z.P. Bazant, T. Belytschko, Wave propagation in strain-softening bar: exact solution. *Journal of the Engineering Mechanics Division*, **111**, 381-389, 1985.

[11] O. Allix, J.-F. Deü, Delayed-damage modelling for fracture prediction of laminated composites under dynamic loading. *Engineering Transactions*, **45**, 29-46, 1997.

[12] T. Belytschko, L. Gu, Y.Y. Lu, Fracture and crack growth by element-free Galerkin methods. *Modelling and Simulation in Materials Science and Engineering*, **2**, 519-534, 1994.

[13] A. Ruzinek et al., Experimental and numerical study on the perforation process of mild steel sheets subjected to perpendicular impact by hemispherical projectiles. *International Journal of Impact Engineering*, **36**, 565-587, 2009.

[14] D.M. Goto et al, Investigation of the fracture and fragmentation of explosively driven rings and cylinders. *International Journal of Impact Engineering*, **35**, 1547-1556, 2008.

[15] B. Maurel, S. Potapov, S. Fabis, A. Combescure, Full SPH fluid-shell interaction for leakage simulation in explicit dynamics. *International Journal for Numerical Methods in Engineering*, **80**, 210-234, 2009.

[16] T. Timm, Beschuss von flssigkeitsgefllten Behltern. *PhD Thesis*, Karlsruhe University, Germany, 2003.

COMPDYN 2011
III ECCOMAS Thematic Conference on
Computational Methods in Structural Dynamics and Earthquake Engineering
M. Papadrakakis, M. Fragiadakis, V. Plevris (eds.)
Corfu, Greece, 25–28 May 2011

COMPARISON BETWEEN A NEW EXTERNAL CODE COUPLER GC+ EXTENDED IN NON-LINEAR DYNAMICS AND ABAQUS/CO-SIMULATION

A. Batti[1], M. Brun[2], A. Gravouil[1], and A. Combescure[1]

[1]Laboratoire de Mécanique des Contacts et des Structures, UMR CNRS 5259, INSA-Lyon,
20, Avenue Albert Einstein, 69621 Villeurbanne, France
{anis.batti, anthony.gravouil, alain.combescure}@insa-lyon.fr

[2] Laboratoire de Génie Civil et d'Ingénierie Environnementale, EA 4126, INSA-Lyon,
20, Avenue Albert Einstein, 69621 Villeurbanne, France
michael.brun@insa-lyon.fr

Keywords: External Code Coupling, Finite Elements, Non-Linear Dynamics, Abaqus/Co-Simulation, Sub-domain Decomposition.

Abstract. *The aim of this work is to propose a comparison between our new GC+ external code coupler extended to non-linear cases with the new capability Abaqus/co-simulation which is able to couple Abaqus/Explicit with a Finite Element code Abaqus/Standard (Implicit scheme). The external code coupler available in Abaqus version 6.9 called Abaqus/co-simulation is based on the sub-domain decomposition method named GC method. This method has been proposed by Gravouil and Combescure for Newmark time schemes in linear dynamics and, then, extended to non linear dynamics. First, the GC sub-domain decomposition method and the GC+ method issued from a reformulation of the GC method are presented. Then, the use-case called "Airbus plane panel" which will be used to compare our non-linear GC+ code coupler with the co-simulation method of Abaqus 6.9 is described. Finally, obtained results in non-linear cases are presented and discussed. This work is funded by the European project MAAXIMUS.*

1 INTRODUCTION

The main difficulties of the non-linear transient structural computations lie in the computation costs and the memory requirements for storing the data.

The objective of this paper is to propose a method extended to non-linear cases, which permits reduction of time costs as well as memory necessary to solve the problem. All the paper is based on the use of Newmark time integration schemes with different parameters.

A relevant way in order to considerably reduce computational costs is to use sub-domain decomposition methods. In order to accurately represent impacts phenomena, preserve the stability of the time integration scheme and optimize the finite element structural analysis, it is very efficient to decompose the complete structure into several sub-domains associated with appropriate time step and appropriate mesh element size depending on sub-domains.

Several families of decomposition methods can be identified depending on the way of enforcing the continuity of quantities across the interface. The GC method imposing the continuity of velocities at the interface has been proposed by Gravouil and Combescure for Newmark time schemes in linear dynamics [1] and, then, extended to non linear dynamics [2], explicit non linear dynamics [3], coupling of modal sub-domains [4] and space-time automatic refinement techniques [5]. It has been proved that the GC method can produce some numerical dissipation at the interface between sub-domains. Prakash and Hjelmstad [6] have proposed a more complex algorithm for linear transient dynamics (PH method) without dissipation at the interface and which also enforces velocity continuity at the interface. The velocity constraint is applied on the macro time step, contrary to the GC method applying the velocity constraint on the micro time step. Then, Mahjoubi, Gravouil and Combescure [8] proposed a general method in the case of linear transient dynamics, labelled as MGC method, which ensures that the interface energy remains equal to zero for any time integrator. This method is able to couple Simo, Krenk, Verlet, HHT and Newmark time schemes with different time steps. The MGC method imposes on the macro time step the continuity of the velocities at the interface in a weak sense. The GC method has been recently improved by Batti et al. [12] labeled as GC+ method which is energy conserving as PH and MGC methods. In addition, the formulation of the new algorithm appears much simpler than PH and MGC methods.

In the first section of this article, the algorithm of the GC & GC+ sub-domain decomposition methods will be presented in the case of homogeneous time scale and then, in the case of heterogeneous time scales. Then, we will explain how the GC+ method can be extended to non-linear cases. Furthermore, we will present how to set up an external code coupler based on the modified GC+ method. Finally, an industrial example subjected to crash loads will permit us to compare our coupler with Abaqus/co-simulation (an external code coupler developed in Abaqus v6.9 which is using the GC sub-domain decomposition method).

2 THE GC & GC+ METHODS AND THE GC & GC+ COUPLERS IN LINEAR CASES

First, in the case of an identical time step used for each sub-domain of the global structure, the GC and GC+ sub-domain decomposition methods are the same. The difference between these two methods appears in the case of multi time scale.

2.1 A sub-domain decomposition method with mono time step scale (GC=GC+)

The following explanations aim at highlighting the key points of the method. The main idea of the method is to decompose the solution into two parts (free solution and link solution).

Decomposition into a free part and a link part of the complete solution:

The Finite Element Method used for the numerical simulation of a global structure gives the semi-discrete equilibrium equation in space:

$$M\,a + F_{\text{int}}(u) = F_{ext} \tag{1}$$

where M is the symmetric, definite, positive mass matrix, F_{ext} the external forces and $F_{\text{int}}(u)$ the internal forces, a the acceleration. The whole structure is decomposed into several sub-domains, denoted by the superscript $k = 1,...,s$. In each separated sub-domain k, the equilibrium equation can be rewritten as:

$$M^k a^k + F_{\text{int}}^k = F_{ext}^k + F_{link}^k \quad \forall\{1,...,s\} \tag{2}$$

with F_{link}^k representing the interface loads applied on the sub-domain k under consideration (interface loads), which can be linked to the kinematic constraints on interfaces of the k sub-domain. The kinematic constraint connecting all sub-domains together is written in a global form, for the whole domain:

$$\sum_{k=1}^{s} L^k v^k = 0 \tag{3}$$

where L^k is the constraint matrix for a given k sub-domain. The link force is then obtained by introducing Lagrange multipliers Λ for the whole domain:

$$F_{link}^k = L^{kT}\Lambda \tag{4}$$

2.2 Sub-domain decomposition methods with multi time step scale (GC$\neq$GC+)

The GC and GC+ sub-domain decomposition methods become different in the case of multi time step scale. The free problem, the condensed problem at the interface and the link problem are not solved in the same order for the two GC & GC+ methods in the case of sub-domains with different time steps. The difference between these methods is schematically presented in Figure 1 in the case of two sub-domains (a sub-domain A with a large time step and a sub-domain B with a small time step).

These sub-domain decomposition methods are used to build up respective external code couplers. A sub-domain is modeled by a separated FE code whereas the mechanical behavior of another sub-domain of the structure is simulated by another FE code. An external code coupler is used to communicate with the separated FE codes simulating each one a sub-domain of the structure. A coupled FE code solves the free and the link problems of a sub-domain whereas the external code coupler manages the computation of the problem of condensation at the interface. Data exchanges between the external code coupler and the coupled FE codes are ensured by pipes.

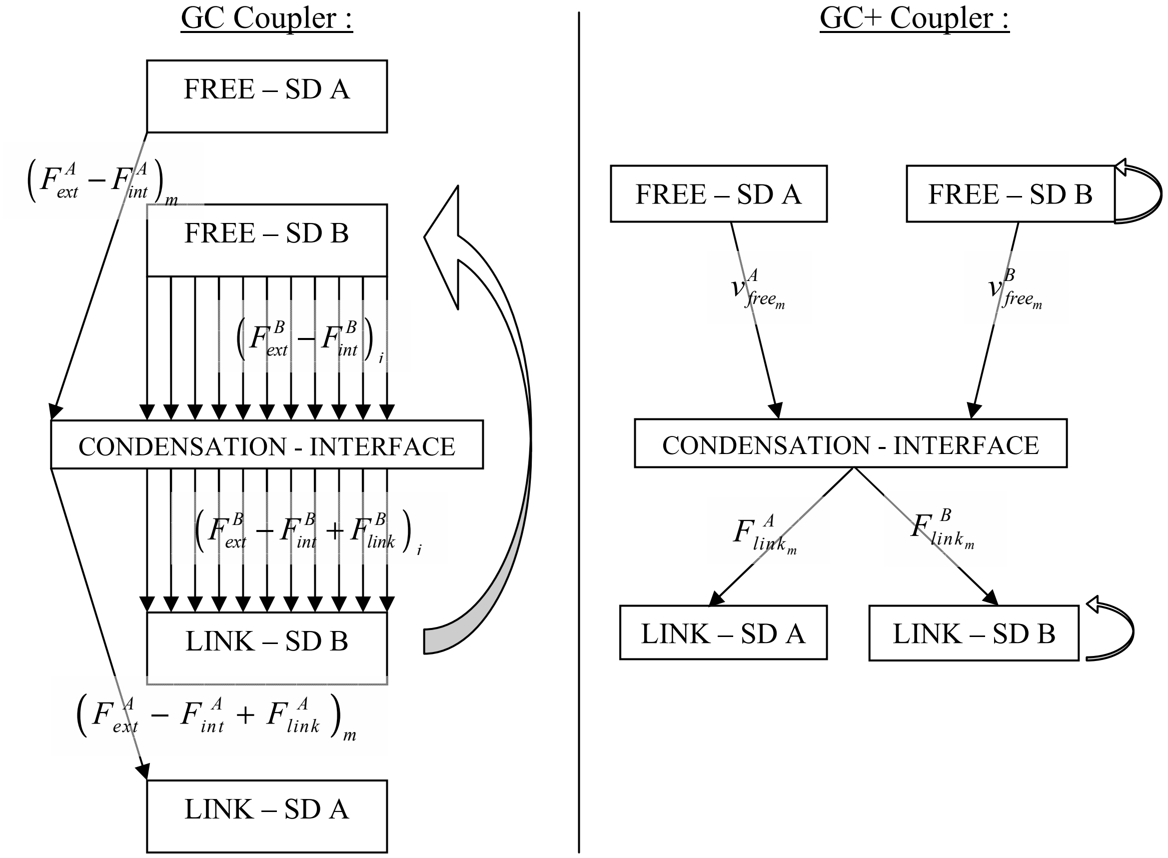

Figure 1: The GC & GC+ couplers.

3 THE GC & GC+ METHODS AND THE GC & GC+ COUPLERS IN NON-LINEAR CASES

First, the GC sub-domain decomposition method presented above already works in the case of non-linearity. So, it is not needed to modify the GC sub-domain decomposition method in non-linear cases.

In this section, we will present the modifications imposed to the previously presented GC+ method in order to be able to extend it to the case of material non-linearities. The case of a coupling of a macro-time step non-linear implicit sub-domain A with a micro-time step non-linear explicit sub-domain B is studied here.

First, a modification of the part of the algorithm corresponding to the non-linear micro explicit sub-domain B is necessary in non-linear cases. This improvement is schematically presented in Figure 2.

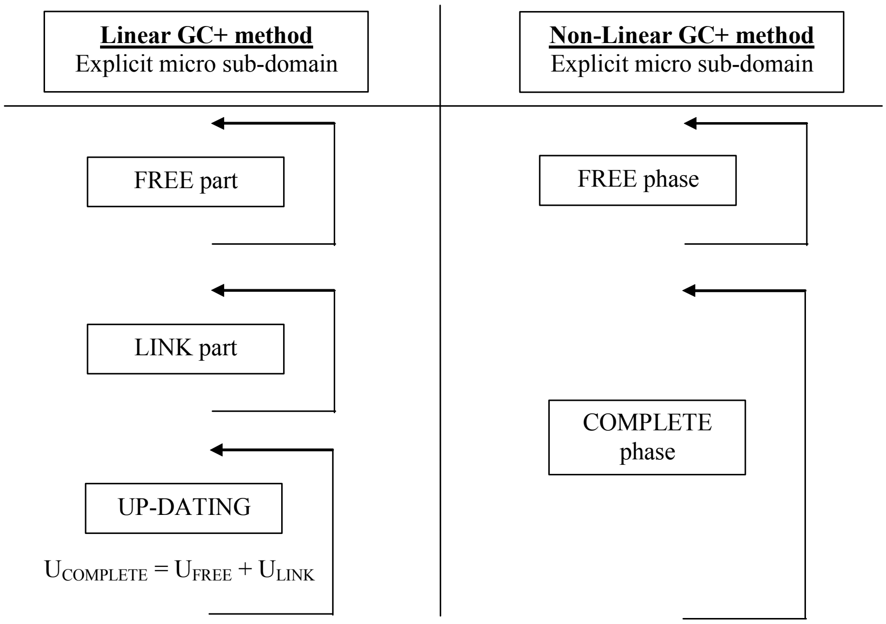

Figure 2: New strategy with GC+ method for coupling a non-linear micro explicit sub-domain.

A complete phase used in the new method permits to avoid the addition of the free and the link parts which is valid only for linear cases and not for non-linear cases.

Secondly, the modification of the part of the algorithm corresponding to the non-linear macro implicit sub-domain A is now presented. The difficulty for an implicit scheme in order to compute non-linearities is to implement an iterative scheme such as Newton algorithm in order to ensure the balance at the end of the implicit time step. At the end of a macro implicit time step, the complete solution has to satisfy a stopping criterion and if it is not the case, a new computation of the macro sub-domain A is done. So, data exchanges between the coupled codes and the external code coupler for a non-linear GC+ external code coupling must be adapted with the stopping criterion of the Newton algorithm.

4 COMPARISON BETWEEN THE EXTERNAL CODE COUPLER GC+ EXTENDED IN NON-LINEAR DYNAMICS AND ABAQUS/CO-SIMULATION

A comparison for a transient non-linear dynamics problem is proposed between the new GC+ non-linear external code coupler and the code coupler available in Abaqus v6.9 named “Abaqus/Co-Simulation” which is built by using the GC sub-domain decomposition method. In this section, a non-linear dynamics application is considered. It is the Airbus plane panel used as Maaximus use-case with an open interface with compatible mesh at the interface between the two chosen (non-linear macro implicit & non-linear micro explicit) sub-domains.

Our GC+ coupler extended in non-linear cases couple here the code CASTEM 2009 developed at the Commissariat à l’énergie atomique (CEA).

A simplified Airbus plane panel is a case of interest for engineering application in the aeronautic field. A panel is a part of a plane‘s barrel. The panel is composed by a skin, frames and stiffeners. The panel is pinned along the two small sides of the contour. Charge is applied on the very small zone at the centre of the panel. The mechanical behaviour is assumed to be perfectly plastic for each component of the panel. The application example computed with external code coupling using two (Macro-implicit & micro-explicit) sub-domains is presented in Figure 3.

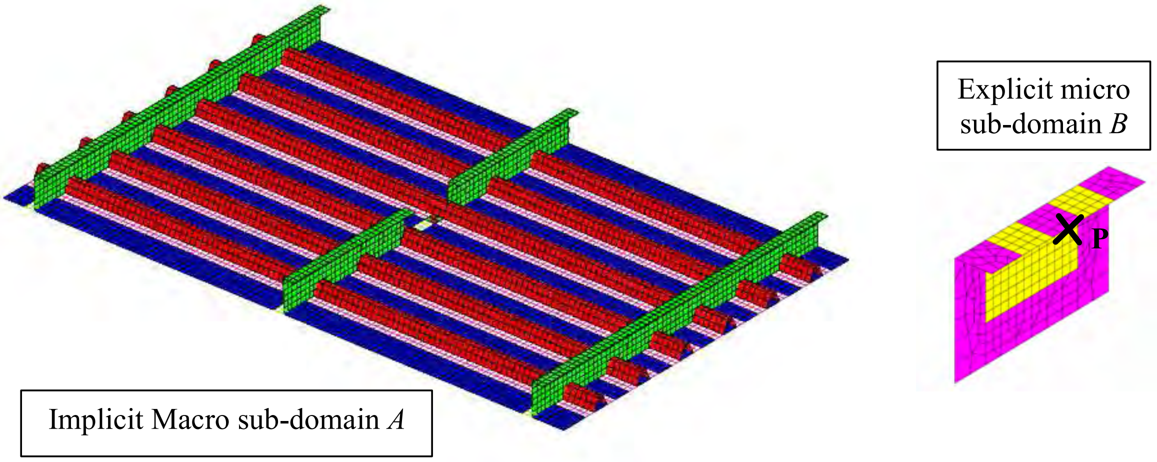

Figure 3: Definition of the two sub-domains composing the Airbus panel structure.

The displacements at point P (see Figure 3) obtained by our GC+ external code coupler extended in non-linear cases and obtained by a classical mono-domain explicit code are compared in Figure 4.

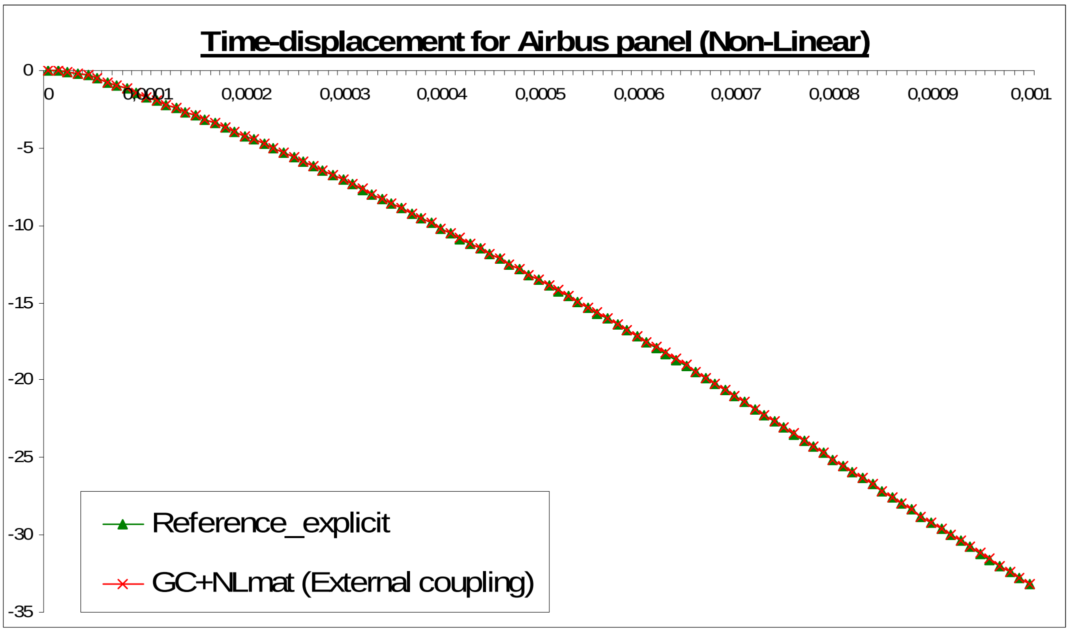

Figure 4: Comparison between the GC+ code coupler and the explicit mono-domain computation responses in terms of displacements.

As shown in Figure 4, the prediction ensured by computation done by our non-linear GC+ external code coupler compared to a classical solving using a unique micro explicit FE code used as Reference is very good in terms of maximal vertical displacement response.

The results in terms of displacement at point P given by a classical unique solving Abaqus/Explicit and by the new capability Abaqus/co-simulation (Abaqus/Standard coupled with Abaqus/Explicit) for the Airbus plane panel numerical simulation are compared in non-linear case in Figure 5.

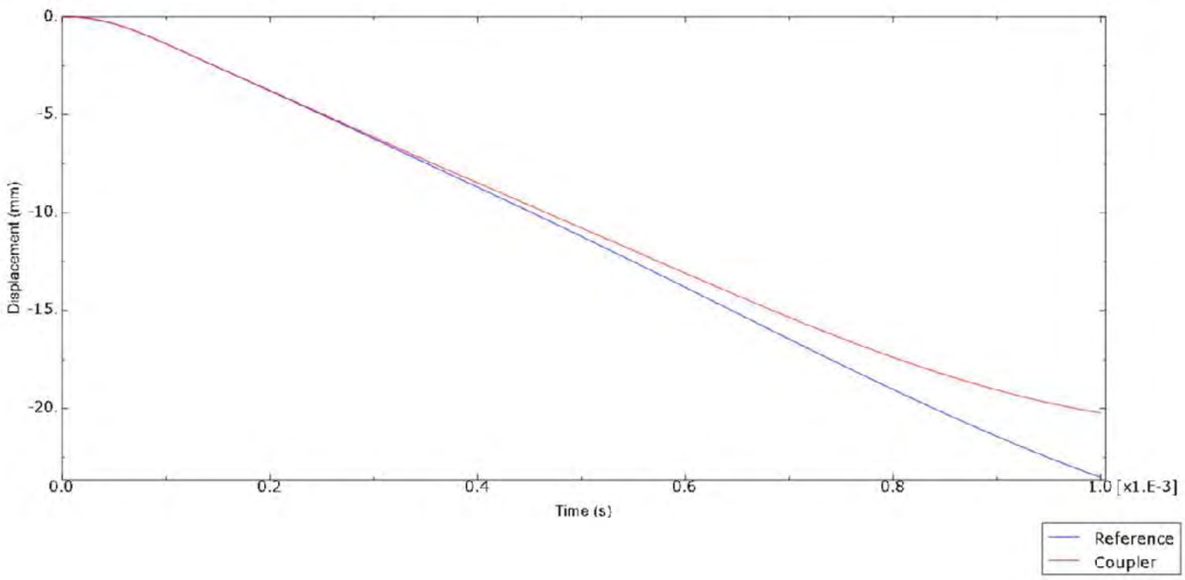

Figure 5: Comparison of results in terms of displacement obtained by the coupler called Abaqus/co-simulation and by a classical explicit computation (Non-linear case).

Contrary to the GC+ code coupler, we can observe in Figure 5, that the prediction in terms of displacements given by Abaqus/co-simulation compared to the reference is not good. At the beginning of simulations, the two obtained time-displacement curves are very close but as long as time passes, we can see that the difference between the two curves increases regularly.

5 CONCLUSION

In this article, we have presented the key equations of the GC &GC+ sub-domain decomposition methods in the case of a same time step used for all the sub-domains composing the structure. Moreover, we have described a linear external code coupler using the GC+ sub-domain method in the case of multi time scales. Then, the extensions of the GC+ sub-domain decomposition method and of the GC+ external code coupling to the non-linear cases have been proposed. The non-linear GC+ external code coupler manages to couple a macro non-linear implicit FE code with a micro non-linear explicit FE code. Finally, a comparison of this GC+ code coupler with Abaqus/Co-simulation which is able to couple Abaqus/Explicit with Abaqus/Standard and based on the GC sub-domain decomposition method.

It seems that Abaqus/Co-simulation available in Abaqus 6.9 should be used with care for displacement responses in material nonlinear case. The proposed GC+ code coupler is already able to couple Castem2009 and Europlexus finite element codes and a possible perspective to this work can be to generalize it for other existing commercial finite element codes (Abaqus, Aster …).

6 ACKNOWLEDGEMENTS

The authors wish to acknowledge the FP7 European program MAAXIMUS (Grant 213371) piloted by Airbus for its financial support.

REFERENCES

[1] A. Combescure, A. Gravouil, A numerical scheme to couple subdomains with different time-steps for predominantly linear transient analysis. *Computer methods in applied mechanics and engineering,* **191**, 1129-1157, 2002.

[2] A. Gravouil, A. Combescure A multi-time-step explicit-implicit method for non-linear structural dynamics. *International Journal for Numerical Methods in Engineering,* **50**, 199-225, 2001.

[3] B. Herry, L. Di Valentin, A. Combescure, An approach to the connection between subdomains with non-matching meshes for transient mechanical analysis. *International Journal for Numerical Methods in Engineering*, **55**, 973-1003, 2002.

[4] V. Faucher, A. Combescure, Local modal reduction in explicit dynamics with domain decomposition. Part 1: extension to sub-domains undergoing finite rigid rotations. *International Journal for Numerical Methods in Engineering,* **60**, 2531-2560, 2004.

[5] P. Cavin, A. Gravouil, A.A. Lubrecht, A. Combescure, Automatic energy conserving space-time refinement for linear dynamic structural problems. *International Journal for Numerical Methods in Engineering,* **64**, 304-321, 2005.

[6] A. Prakash, K.D. Hjelmstad, A FETI-based multi-time-step coupling method for Newmark schemes in structural dynamics. *International Journal for Numerical Methods in Engineering,* **61**, 2183-2204, 2004.

[7] N. Mahjoubi, A. Gravouil, A. Combescure, Coupling subdomains with heterogeneous time integrators and incompatible time steps. *Computational mechanics* 2009; DOI 10.1007/s00466-009-0413-4.

[8] N. Mahjoubi, A. Gravouil, A. Combescure, N. Greffet, A general energy conserving method to couple heterogeneous time integrators with incompatible time steps in structural dynamics. *Computational Methods in Applied Mechanics and Engineering,* 2009: submitted.

[9] P. Verpeaux, T. Charras, A. Millard, CASTEM 2000 une approche moderne du calcul de structures. *Calcul de structure et intelligence artificielle*. Pluralis, Fouet JM, Ladeveze P., Ohayon R. (ed.), 261-271, 1988.

[10] EuroPlexus, A computer program for the finite element simulation of fluid-structure systems under dynamic loading, User’s manual, CEA Saclay, CEA/DEN/SEMT/DYN, 2002.

[11] T. J. R. Hughes, A note on the stability of newmark’s algorithm in nonlinear structural dynamics. *International Journal for Numerical Methods in Engineering*, **11**, 383–386, 1977.

[12] A. Batti, M. Brun, A. Gravouil, A. Combescure, An external code coupler based on an improved sub-domain decomposition method, *Computers & Structures*, 2010: submitted.

[13] A. Batti, M. Brun, N. Mahjoubi, A. Gravouil, A. Combescure, Comparison of external code couplers based on four monolithic sub-domain decomposition methods. *Advances in engineering software,* 2010: submitted.

COMPDYN 2011
III ECCOMAS Thematic Conference on
Computational Methods in Structural Dynamics and Earthquake Engineering
M. Papadrakakis, M. Fragiadakis, V. Plevris (eds.)
Corfu, Greece, 25–28 May 2011

ADVANCED PARALLEL COMPUTING FOR EXPLOSIVE FLUID-STRUCTURE INTERACTION

V. Faucher[1]

[1] CEA, DEN, DANS, DM2S, SEMT, DYN
CEA/Saclay, 91 191 Gif sur Yvette Cedex, France
e-mail: vincent.faucher@cea.fr

Keywords: Fast transient dynamics, fluide structure interaction, kinematic links.

Abstract. *Present contribution exposes current R&D issues in the framework of parallel computing for fast transient dynamics involving fluid-structure interaction and coupled models. In particular, simulation of accidental explosive situations often requires simultaneous representation of both fluids with multiple components and structures that may undergo large deformation down to complete ruin. Is especially considered the generic treatment of kinematic links by means of Lagrange Multipliers , and the parallel concurrency it implies amoung solving algorithms throughout the simulation. Current research and investigated solutions are illustrated with industrial examples performed with EUROPLEXUS software.*

1 INTRODUCTION

Simulation of fast transient phenomena arising from accidental situations often requires simultaneous modeling of fluids, both liquids and gases, interacting with surrounding structures that may undergo large deformations down to complete ruin. This yields couplings between various kinds of models, such as Finite Elements, Finite Volumes or SPH particles for the fluids, and Finite Elements, SPH particles or Discrete Elements for the structures (cf. figure 1). Examples of such simulations in explosive fluid-structure interaction are given in [1][2].

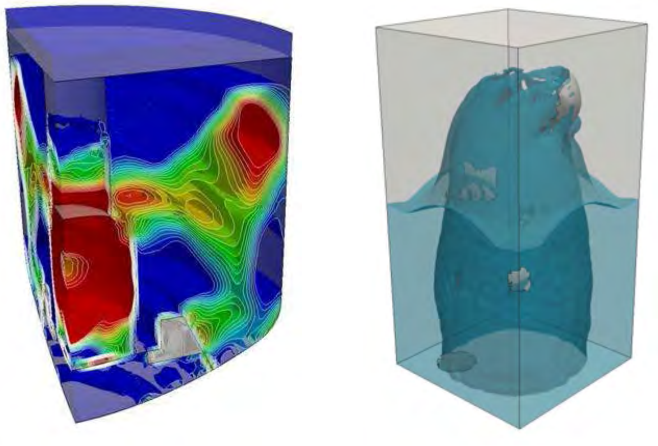

(a) Explosion in a vessel with internal structures

(b) Explosion et fragmentation d’un bidon immergé dans un liquide

Figure 1: Examples of explosive FSI simulations.

Kinematic links between various models is thus a fundamental issue and the choice is made in EUROPLEXUS to verify the link equations exactly by means of Lagrange Multipliers, avoiding the use of user defined penalty parameters to simplify the input process and prevent any dependency of the solution on non-physical parameters. From the algorithmic point of view, this introduces a strong specificity for the temporal solver: time integration scheme is classically central differences explicit scheme, but solving a linear system at each step is necessary to compute link forces, leading to a partially implicit solving procedure.

Parallel handle of both building and solving the system giving Lagrange Multipliers for all the kinematic connections available in the program competes with classical parallel algorithms used in fast transient dynamics software and is addressed by current paper.

2 GENERAL ALGORITHM

2.1 Dynamic equilibrium for fluid-structure interaction with explicit time integration

Conservation of momentum at time t^{n+1} of the time integration process, all quantities assumed to be known at times t^n (displacements, for structure only) and $t^{n+1/2}$ (velocities), takes general form:

$$\begin{aligned}&\mathbf{M}^{n+1}\ddot{\mathbf{U}}^{n+1}+\mathbf{F}_i\left(\mathbf{U}^n,\dot{\mathbf{U}}^{n+1/2}\right)+\mathbf{C}^{{n+1}^T}\mathbf{\Lambda}^{n+1}=\mathbf{F}_{ext}^{n+1}\\&\mathbf{C}^{n+1}\dot{\mathbf{U}}^{n+3/2}=\mathbf{B}^{n+1}\\&\dot{\mathbf{U}}^{n+3/2}=\dot{\mathbf{U}}^{n+1/2}+\Delta t\cdot\ddot{\mathbf{U}}^{n+1}\end{aligned}\tag{1}$$

Forces $\mathbf{F}_i$ represent internal forces for the structure or transport forces for the fluid. The system is completed for the fluid by conservation of mass and energy equations, written in EUROPLEXUS using a Finite Volume formalism, i.e. computing fluxes of quantities through faces of the fluid mesh cells. $\mathbf{M}^{n+1}$ is a diagonal matrix.

Matrix $\mathbf{C}^{n+1}$ is the kinematic connections matrix, linking velocities of both fluid and structural nodes, whose construction is presented in next paragraph. Its dimension, profile and coefficients are all variable with time.

Before computing nodal accelerations allowing advancing to next time-step in the simulation, Lagrange Multipliers are obtained by a condensation procedure, yielding a system of the form:

$$\mathbf{C}^{n+1}\mathbf{M}^{n+1^{-1}}\mathbf{C}^{n+1^{T}}\mathbf{\Lambda}^{n+1}=\mathbf{H}^{n+1}\mathbf{\Lambda}^{n+1}=\mathbf{S}^{n+1} \tag{2}$$

2.2 Writing fluid-structure interaction links

Two types of fluid-structure links are considered in classical transient explosive simulations [1][3]. First is conform node-to-node links, when the structure coincides with fluid domain's envelop. Second is diffuse links for immersed structures, for which enforcing a conform mesh between fluid and structure generates large extra work for data sets creation and lack of robustness for ALE rezoning of the fluid grid. Figure 2 illustrates both types of links.

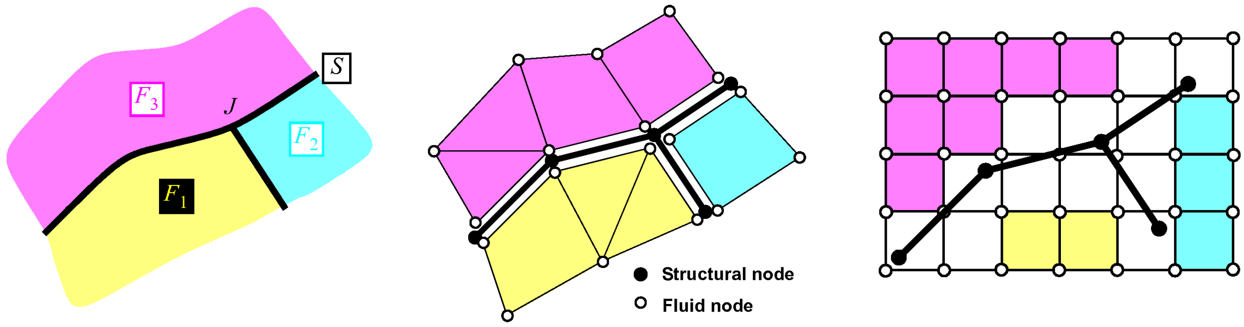

(a) Interface F/S continue (situation de reference)

(b) Interface discrétisée avec maillages conformes

(c) Interface discrétisée avec liaison diffuse

Figure 2: Fluid-structure interaction links.

Interaction with conform meshes produces permanent links, whose coefficients are variable along with direction normal to the structure. Diffuse interaction with topologically uncoupled meshes generates links whose support and coefficients are variable with time.

Second type of link is mandatory to deal with problems where structural fragmentation occurs, to simulate fluid flow through created openings, as shown on figure 1-b or on figure 3.

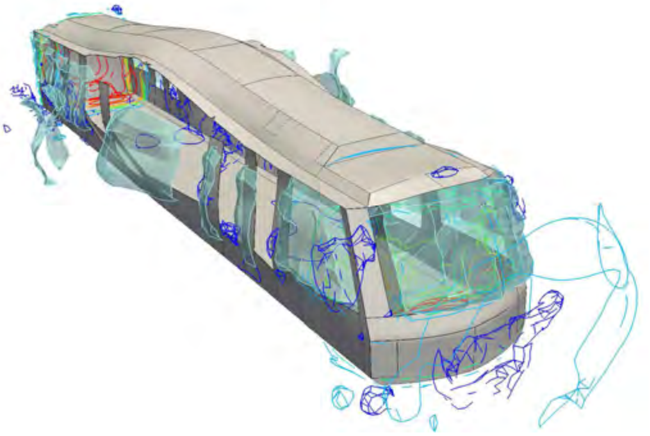

Figure 3: Simulation of an explosion in a metro carriage.

3 PARALLEL SOLUTION WITH DISTRIBUTED MEMORY

3.1 Principle and problematic of *remote* links

Parallel solution in EUROPLEXUS relies on domain decomposition, splitting elements upon available processing units with minimum interface size between subdomains. Formally, system (1) becomes, for example in the case of 3 subdomains:

$$\begin{aligned}
&(a)\quad \begin{bmatrix} \mathbf{M}_1 & & \\ & \mathbf{M}_2 & \\ & & \mathbf{M}_3 \end{bmatrix}\begin{bmatrix} \ddot{\mathbf{U}}_1 \\ \ddot{\mathbf{U}}_2 \\ \ddot{\mathbf{U}}_3 \end{bmatrix} + \begin{bmatrix} \mathbf{F}_{i1} \\ \mathbf{F}_{i2} \\ \mathbf{F}_{i3} \end{bmatrix} + \mathbf{C}^T \begin{bmatrix} \mathbf{\Lambda}_1 \\ \mathbf{\Lambda}_2 \\ \mathbf{\Lambda}_3 \end{bmatrix} = \begin{bmatrix} \mathbf{F}_{ext1} \\ \mathbf{F}_{ext2} \\ \mathbf{F}_{ext3} \end{bmatrix} \\
&(b)\quad \mathbf{C}\begin{bmatrix} \ddot{\mathbf{U}}_1 \\ \ddot{\mathbf{U}}_2 \\ \ddot{\mathbf{U}}_3 \end{bmatrix} = \mathbf{B}
\end{aligned} \tag{3}$$

Parallel acceleration is first achieved by distribution of the work for both internal forces vector computation and fluid-structure links building.

However, connections matrix **C** must be considered at global level for the multi-domain system, since links may couple nodes belonging to different subdomains, for example with large displacements of structural fragments through fluid domain. Such links are called *remote* links, to emphasize the fact that they concerns non-local quantities on subdomains.

The problematic associated to these *remote* links is the global treatment they require.

In the rare situation where no link couples degrees of freedom belonging to different subdomains (i. e. no *remote* links in the model), system (3) can be uncoupled and parallelism is straightforward. On the contrary, if couplings exist, a solution procedure implying all subdomains must be provided to compute Lagrange Multipliers.

Existing approach consists in identifying in condensation operator **H** blocks that can be solved inside one subdomain, i. e. corresponding to groups of fully local links with only local nodes involved. Figure 4 illustrates the process in the elementary case of 2 subdomains. On each subdomain, dofs are partitioned between those concerned by any *remote* link (or a link coupled to a *remote* link, the two having to be treated simultaneously) and the others.

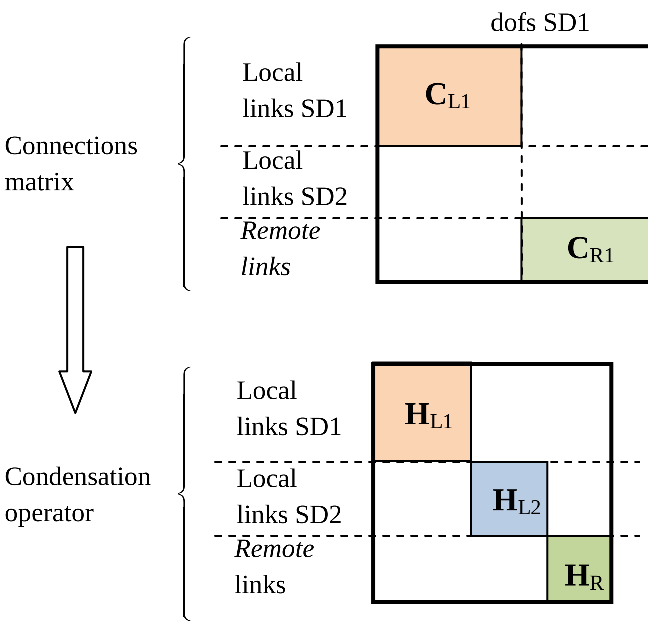

$$\mathbf{H}_{\mathrm{L}1} = \mathbf{C}_{\mathrm{L}1}\mathbf{M}_1^{-1}\mathbf{C}_{\mathrm{L}1}^{T}$$

$$\mathbf{H}_{\mathrm{L}2} = \mathbf{C}_{\mathrm{L}2}\mathbf{M}_2^{-1}\mathbf{C}_{\mathrm{L}2}^{T}$$

$$\mathbf{H}_{\mathrm{R}} = \begin{bmatrix}\mathbf{C}_{\mathrm{R}1} & \mathbf{C}_{\mathrm{R}2}\end{bmatrix}\begin{bmatrix}\mathbf{M}_1^{-1} & \\ & \mathbf{M}_2^{-1}\end{bmatrix}\begin{bmatrix}\mathbf{C}_{\mathrm{R}1}^{T} \\ \mathbf{C}_{\mathrm{R}2}^{T}\end{bmatrix}$$

Figure 3: Identification of diagonal blocks in condensation operator.

Global block $\mathbf{H}_{\mathrm{R}}$ is then solved on a single processor, resulting in a loss of parallelism all the more important that kinematic couplings between subdomains are numerous. This can severely harm scalability, again for example when large displacements of structural fragments occur, these fragments interacting with initially distant fluid elements.

Let us also notice that building global block $\mathbf{H}_{\mathrm{R}}$ requires centralizing all concerned *remote* links data on the processor dedicated to the solution. These communications done, a distributed linear solver is useless to compute Multipliers, since time necessary for data redistribution prior to solution easily compensate parallel acceleration provided by the solver.

3.2 Algorithmic solutions

Keeping the same distributed memory parallel structure for the program, two alternative parallel algorithms can be proposed to deal with the problematic exposed above. They are being developed and tested in the framework of French ANR REPDYN project [4]. In both cases, the point is to increase parallelism for the solution of the problem involving *remote* links.

3.2.1 Correct use of a distributed linear solver

As noticed earlier, this option is worthless if data have to be centralized on one unique processor to build to system to be solved. Instead, to achieve efficiency, a distributed linear solver must start from a matrix whose terms (either its lines or its terms individually) are already equally split upon available resources.

One way to provide such a distribution is to share among all processors data concerning *remote* links (and links coupled to them), yielding block $\mathbf{H}_{\mathrm{R}}$ to be solved at global level. This represents a reduced extra-cost in communications, compared to existing transfer from all processors to one unique destination.

Each processor is then able to compute terms of $\mathbf{H}_{\mathrm{R}}$. Its building becomes a parallel task and matrix distribution is controlled in order to benefit from a parallel solver, such as

MUMPS [5][6] for example.

3.2.2 Iterative solution with no operator building

Even if building global block becomes parallel and produces a distributed matrix, linear solver are known to suffer from limited scalability, especially in the present situation where the matrix size is small, the number of linked nodes being far lower than the total number of nodes.

An alternative strategy is to avoid building the operator within an iterative solution of the link problem, using Conjugate Gradient for example. Starting from system (3) with value of Lagrange Multipliers at iteration *k*, corresponding accelerations are obtained from (3-a):

$$\begin{bmatrix} \ddot{\mathbf{U}}_1^k \\ \ddot{\mathbf{U}}_2^k \\ \ddot{\mathbf{U}}_1^k \end{bmatrix} = \begin{bmatrix} \mathbf{M}_1 & & \\ & \mathbf{M}_2 & \\ & & \mathbf{M}_3 \end{bmatrix}^{-1} \left(\begin{bmatrix} \mathbf{F}_{ext1} \\ \mathbf{F}_{ext2} \\ \mathbf{F}_{ext3} \end{bmatrix} - \begin{bmatrix} \mathbf{F}_{i1} \\ \mathbf{F}_{i2} \\ \mathbf{F}_{i3} \end{bmatrix} \text{-}\mathbf{C}^T \begin{bmatrix} \mathbf{\Lambda}_1^k \\ \mathbf{\Lambda}_1^k \\ \mathbf{\Lambda}_1^k \end{bmatrix} \right) \tag{4}$$

Residual on kinematic links is then computed by:

$$\mathbf{S}^k = \mathbf{C} \begin{bmatrix} \ddot{\mathbf{U}}_1^k \\ \ddot{\mathbf{U}}_2^k \\ \ddot{\mathbf{U}}_3^k \end{bmatrix} \text{-}\mathbf{B} \tag{5}$$

These two evaluations are parallel steps using operators local to subdomains. For residual computation, vector is obtained by blocks, each block corresponding to links written on a given subdomain.

Preconditioning the algorithm is necessary to speed-up convergence. One preconditioner of interest consists in solving links written on a subdomain, potentially involving dofs it does not own, as if they were not coupled to any other links on another subdomain, which the global link operator classically handles.

Considering again simplified case (4), this first means isolating in *remote* links block of connections matrix the links written locally:

$$\begin{bmatrix} \mathbf{C}_{\mathrm{R}1} & \mathbf{C}_{\mathrm{R}2} \end{bmatrix} = \begin{bmatrix} \mathbf{C}_{\mathrm{R}1}^1 & \mathbf{C}_{\mathrm{R}2}^1 \\ \mathbf{C}_{\mathrm{R}1}^2 & \mathbf{C}_{\mathrm{R}2}^2 \end{bmatrix} \tag{6}$$

Global condensation operator then writes:

$$\mathbf{H}_{\mathrm{R}} = \begin{bmatrix} \mathbf{C}_{\mathrm{R}1}^1 & \mathbf{C}_{\mathrm{R}2}^1 \\ \mathbf{C}_{\mathrm{R}1}^2 & \mathbf{C}_{\mathrm{R}2}^2 \end{bmatrix} \begin{bmatrix} \mathbf{M}_1^{-1} & \\ & \mathbf{M}_2^{-1} \end{bmatrix} \begin{bmatrix} \mathbf{C}_{\mathrm{R}1}^{1\ T} & \mathbf{C}_{\mathrm{R}1}^{2\ T} \\ \mathbf{C}_{\mathrm{R}2}^{1\ T} & \mathbf{C}_{\mathrm{R}2}^{2\ T} \end{bmatrix} = \begin{bmatrix} \mathbf{H}_{\mathrm{R}}^1 & \mathbf{H}_{\mathrm{RC}} \\ \mathbf{H}_{\mathrm{RC}}^{\ T} & \mathbf{H}_{\mathrm{R}}^2 \end{bmatrix} \tag{6}$$

with
$$\mathbf{H}_{\mathrm{R}}^1 = \mathbf{C}_{\mathrm{R}1}^1 \mathbf{M}_1^{-1} \mathbf{C}_{\mathrm{R}1}^{1\ T} + \mathbf{C}_{\mathrm{R}2}^1 \mathbf{M}_2^{-1} \mathbf{C}_{\mathrm{R}2}^{1\ T}$$

$$\mathbf{H}_{\mathrm{R}}^2 = \mathbf{C}_{\mathrm{R}1}^2 \mathbf{M}_1^{-1} \mathbf{C}_{\mathrm{R}1}^{2\ T} + \mathbf{C}_{\mathrm{R}2}^2 \mathbf{M}_2^{-1} \mathbf{C}_{\mathrm{R}2}^{2\ T}$$

$$\mathbf{H}_{\mathrm{RC}} = \mathbf{C}_{\mathrm{R}1}^1 \mathbf{M}_1^{-1} \mathbf{C}_{\mathrm{R}1}^{2\ T} + \mathbf{C}_{\mathrm{R}2}^1 \mathbf{M}_2^{-1} \mathbf{C}_{\mathrm{R}2}^{2\ T}$$

Blocks $\mathbf{H}_R^1$ and $\mathbf{H}_R^2$ can be assembled locally on subdomains 1 and 2 respectively, knowing only locally written links and masses of all involved dofs, potentially belonging to another subdomain, which implies small communications.

Ignoring couplings in the preconditioner then consists in neglecting block $\mathbf{H}_{\mathrm{RC}}$ in the solution procedure. A diagonal per block operator is thus obtained, each block locally solved on a subdomain. Extension to any number of subdomains is straightforward.

4 TOWARDS HYBRID PARALLELISM

In addition to scalability improvement for solving kinematic links with domain decomposition, recent hardware evolution suggests an alternative parallelism: a distributed memory approch with domain decomposition between nodes interconnected by a high-performance network, coupled to a shared memory parallel acceleration using local cores inside a node, with optional additional acceleration obtained from GPU(s).

From a theoretical point of view, this allows to lighten concurrency between domain decomposition and kinematic links enforcement for a given number of processing units, provided an efficient multi-CPU/GPU shared memory parallelism.

Again, research in this area is carried out for EUROPLEXUS software in the framework of REPDYN project, in collaboration with MOAIS team from INRIA/LIG laboratory. Dynamic load balancing is handled through KAAPI library [7][8], implementing graph partitioning methods and work stealing between SMP threads.

A strict goal is to achieve a cooperative hybrid parallelism among all available resources efficient for all EUROPLEXUS functionalities. Originality is thus to propose different simulaneous parallel solutions adapting to multiple algorithms occurring together in a coupled simulation, instead of parallel efficiency demonstrations based on restricted model applications, which are classically hard to extend to industrial level.

REFERENCES

[1] F. Casadei, Fast Transient Fluid-Structure Interaction with Failure and Fragmentation, *8th World Congress on Computational Mechanics*, June 30-July 5, 2008.

[2] V. Faucher, S. Kokh. Explosive Fluid-Structure Interaction using Multi-Component Flows with Anti-Dissipation, *IV European Conference on Computational Mechanics*, May 16-21, 2010.

[3] F. Casadei, J.P. Halleux, A. Saha, F. Chille, Transient Fluid-Structure Interaction Algorithm for Large Industrial Applications, *Comp. Meth. in Appl. Mech. and Engrg.*, 2001.

[4] http://www.repdyn.fr

[5] P.R. Amestoy, I.S. Duff & J.-Y. L'Excellent, Multifrontal parallel distributed symmetric and unsymmetric solvers, *ENSEEIHT-IRIT Technical Report, 1998. Revised version appeared in Comp. Meth. in Appl. Mech. Eng.*, **184**, 501-520 (2000).

[6] http://graal.ens-lyon.fr/MUMPS/

[7] T. Gautier, X. Besseron & L. Pigeon, KAAPI : a thread scheduling runtime system for data flow computations on cluster of multi-processors. *In Parallel Symbolic Computation'07 (PASCO'07)*, number 15-23, London, Ontario, Canada, 2007.

[8] http://kaapi.gforge.inria.fr/

COMPDYN 2011
3rd ECCOMAS Thematic Conference on
Computational Methods in Structural Dynamics and Earthquake Engineering
M. Papadrakakis, M. Fragiadakis, V. Plevris (eds.)
Corfu, Greece, 25-28 May 2011

A NEW POST-PROCESSING PROCEDURE FOR THE INCREASE IN THE ORDER OF ACCURACY OF THE TRAPEZOIDAL RULE AT TIME INTEGRATION OF LINEAR ELASTODYNAMICS PROBLEMS

A. Idesman

Texas Tech University
Box 41021, Lubbock, TX 79409, USA
e-mail: alexander.idesman@coe.ttu.edu

Keywords: elastodynamics; trapezoidal rule; time integration; error estimator; finite elements

Abstract. *In the current presentation, we suggest a very simple and effective post-processing procedure to increase the order of accuracy in time for numerical results obtained at time integration of linear elastodynamics problems by the trapezoidal rule. This technique is based on a new exact, closed-form, a-priori error estimator for time integration of linear elastodynamics equations by the trapezoidal rule with non-uniform time increments. Based on this error estimator, we suggest a new post-processing procedure (containing additional time integration of elastodynamics equations by the trapezoidal rule with few time increments) that systematically improves the order of accuracy of numerical results, with the increase in the number of additional time increments used for post-processing. For example, the use of just one additional time increment for post-processing after time integration with any number of uniform time increments, renders the order of accuracy of numerical results equal to 10/3 = 3.3333. Numerical examples of the application of the new techniques to a system with a single degree of freedom and to a multi-degree system confirm the corresponding increase in the order of convergence of numerical results after post-processing. Because the same trapezoidal rule is used for basic computations and post-processing, the new technique retains all of the properties of the trapezoidal rule, requires no writing of a new computer program for its implementation, and can be easily used with any current commercial and research codes for elastodynamics.*

1 INTRODUCTION

The application of finite elements in space to linear elastodynamics problems leads to a system of ordinary differential equations in time

$$\boldsymbol{M}\ddot{\boldsymbol{U}} + \boldsymbol{C}\dot{\boldsymbol{U}} + \boldsymbol{K}\boldsymbol{U} = \boldsymbol{R}, \tag{1}$$

where $\boldsymbol{M}$, $\boldsymbol{C}$, $\boldsymbol{K}$ are the mass, damping, and stiffness matrices, respectively, $\boldsymbol{U}$ is the vector of the nodal displacement, $\boldsymbol{R}$ is the vector of the nodal load. Eq. (1) can be also obtained by the application of other discretization methods in space such as the spectral element method, the boundary element method, the smoothed particle hydrodynamics (SPH) method and others. For long-term time integration of semi-discrete elastodynamics equations (1), higher-order accurate methods in time are more computationally effective compared with second order methods. For example, high accuracy in time can be obtained from the unified set of a single step method [1] by the use of higher-order interpolation polynomials in time. However, these methods are not unconditionally stable for elastodynamics. Recently, new high-order accurate methods with a step-by-step time integration scheme have been developed for elastodynamics (see [2, 3, 4, 5, 6, 7, 8, 9, 10] and many others). Most of them are based on semi-discrete equations (1) with the polynomial time approximations of unknown functions. The polynomial coefficients are derived with the use of different approaches such as time-continuous Galerkin (TCG) and time-discontinuous Galerkin (TDG) methods, weighted residual methods, collocation methods and others. The ultimate goal in the development of high-order accurate implicit methods is to construct an unconditionally stable method with controllable numerical dissipation that is much more computationally effective than known second-order methods. Because many high-order accurate methods require the solution of a large system of equations (much larger than a system of equations for second-order methods), the development of effective iterative predictor/multi-corrector solvers is an important component of a high-order method. For example, the predictor/multi-corrector solver suggested in [10] for modified Nørsett methods requires one additional iteration at each time step in order to improve the order of accuracy by one. Many different iterative solvers were developed for the TDG method with linear time approximations of displacements and velocities that correspond to the third order of accuracy (see [2, 3, 8, 9] and others). By the use of three different time increments for each time step, a very effective formulation of fourth-order time-integration methods is obtained from second-order methods in [11]. However, the authors of [11] could not extend their approach to higher orders of accuracy.

To summarize, the development of a computationally effective high-order accurate time-integration method for elastodynamics is still a challenging problem in computational mechanics.

In this paper, we will use a new post-processing procedure (containing additional time integration of elastodynamics equations by the trapezoidal rule with few time increments) that systematically improves the order of accuracy of numerical results, with the increase in the number of additional time increments used for post-processing (see our paper [12]). We should mention that the trapezoidal rule does not include numerical dissipation. However, as was shown in our papers [13, 14, 15, 16], numerical dissipation is not required for long-term integration with the new solution strategy suggested in [13, 14, 16]. It was also shown in [13, 14, 16] that the trapezoidal rule is the best time-integration method (the fastest and most accurate method) for long-term integration of elastodynamics problems (including wave propagation and impact problems) among all implicit second-order time-integration methods.

2 SUMMARY OF THE NUMERICAL TECHNIQUE

In our paper [12], we have developed a new numerical time-integration technique for the increase in the order of accuracy at the integration by the trapezoidal rule. This technique is based on a new exact, closed-form, a-priori error estimator for time integration of linear elastodynamics equations by the trapezoidal rule with non-uniform time increments. Based on this error estimator, we developed a new post-processing procedure that systematically improves the order of accuracy of numerical results, with the increase in the number of additional time increments used for post-processing. The suggested procedure includes time integration at basic computations by the trapezoidal rule with uniform time increments and time integration at post-processing by the trapezoidal rule with few time increments. The sizes of time increments at post-processing (positive and negative time increments are used) are calculated from the new a-priori error estimator and depend on the size and the total number of time increments used at basic computations. For example, the use of just one, three or five additional time increments for post-processing after time integration with any number of uniform time increments at basic computations, renders the order of accuracy of numerical results equal to 10/3, 14/3 and 6, respectively. The sizes of time increments for post-processing should be calculated as follows: $\Delta t = -\sqrt[3]{m}\Delta\bar{t}$ for one time increment; $\Delta t = \alpha_1\Delta\bar{t}$, $\Delta t = \alpha_1\Delta\bar{t}$ and $\Delta t = \alpha_2\Delta\bar{t}$ for three time increments (α_1 and α_2 should be taken from Table 1); $\Delta t = \alpha_1\Delta\bar{t}$, $\Delta t = \alpha_1\Delta\bar{t}$, $\Delta t = \alpha_2\Delta\bar{t}$, $\Delta t = \alpha_2\Delta\bar{t}$ and $\Delta t = \alpha_3\Delta\bar{t}$ for five time increments (α_1, α_2 and α_3 should be taken from Table 2) where m and $\Delta\bar{t}$ are the number of uniform time increments and the size of time increments at basic computations by the trapezoidal rule.

Table 1. Coefficients α_1 and α_2 for post-processing with three time increments for different numbers m.

m	2	10	50	100	500	1000	10000	100000	1000000
α_1	-1.48091	-2.68405	-4.65819	-5.8846	-10.092	-12.7221	-27.4292	-59.1037	-127.339
α_2	1.65042	3.0607	5.3386	6.75003	11.5871	14.6095	31.5058	67.8914	146.274

Table 2. Coefficients α_1, α_2 and α_3 for post-processing with five time increments for different numbers m.

m	2	10	50	100	500	1000	10000	100000	1000000
α_1	1.93940	3.68743	6.46987	8.18896	14.0732	17.748	38.2851	82.505	177.762
α_2	-1.57145	-2.89162	-5.03795	-6.3688	-10.9307	-13.7815	-29.7189	-64.0403	-137.977
α_3	-2.06674	-3.9562	-6.95145	-8.80069	-15.1286	-19.0799	-41.161	-88.704	-191.119

3 NUMERICAL EXAMPLES

3.1 A single degree of freedom system

First let's consider the increase in the order of accuracy by post-processing for time integration of the following elastodynamics equation for a single degree of freedom system:

$$\ddot{u}(t) + 2\xi\dot{u}(t) + \omega^2 u(t) = f(t)\,, \tag{2}$$

with the natural frequency $\omega = \pi = 3.1416$ and the following initial conditions $u(0) = 1$ and $v(0)/\pi = \dot{u}(0)/\pi = 1$. Zero damping ($\xi = 0$) for the observation time $T = 50$, nonzero damping ($\xi = 0.1, 0.2$) for the observation time $T = 5$, zero ($f(t) = 0$) and non-zero load

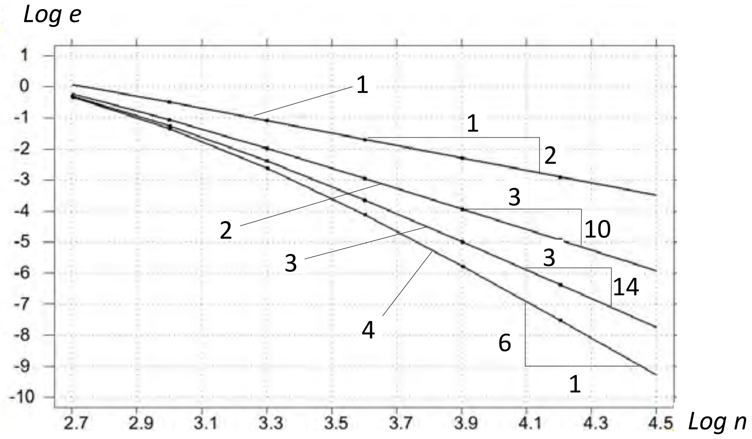

Figure 1: The relative error in displacements and velocities e at the observation time $T = 50$ versus the total number of time increments n in the logarithmic scale at integration of a single degree of freedom system (no damping $\xi = 0$ and zero load $f(t) = 0$) without post-processing (curve 1) and the subsequent post-processing with one (curve 2), three (curve 3) and five (curve 4) time increments.

($f(t) = 2 + 2t$), and post-processing with one, three and five time increments as described in Section 2 are considered. Different total numbers n ($n = m$ plus the number of time increments used at post-processing) of time increments are used in calculations (the corresponding time increments in basic computations can be calculated as $\Delta\bar{t} = \frac{T}{n}$ for the case of basic computations without post-processing, $\Delta\bar{t} = \frac{T}{((n-1)-\sqrt[3]{n-1})}$ for the case of basic computations and the subsequent post-processing with one time increment, $\Delta\bar{t} = \frac{T}{(n-3+2\alpha_1+\alpha_2)}$ for the case of basic computations and the subsequent post-processing with three time increments, and $\Delta\bar{t} = \frac{T}{(n-5+2\alpha_1+2\alpha_2+\alpha_3)}$ for the case of basic computations and the subsequent post-processing with five time increments.

Figs. 1 - 2 show the relative numerical error $e = \frac{e_{uv}}{\sqrt{u^2(0)+(\frac{v(0)}{w})^2}}$ (with $e_{uv} = \sqrt{[u(t_n) - u_{num}(t_n)]^2 + [\frac{v(t_n)-v_{num}(t_n)}{w}]^2}$ where $u(t_n)$, $v(t_n)$ and $u_{num}(t_n)$, $v_{num}(t_n)$ are the exact and numerical solutions of Eq. (2) for the displacement and velocity at time t_n) versus the number of time increments in the logarithmic scale. At the fixed observation time T and a large number of time increments, the number of time increments n is inversely proportional to a time increment Δt ($n \approx m \approx \frac{T}{\Delta t}$ or $Log\, n \approx Log\, T - Log\, \Delta t$. Therefore, the slope of the curves in Figs. 1 - 2 (which are plotted in the logarithmic scale) describes the order of convergence (order of accuracy) of numerical results at large numbers n of time increments.

As can been seen from Fig. 1, at a large number of time increments n, the order of convergence (order of accuracy) of numerical results after post-processing with one, three and five time increments is in agreement with the analytical estimations reported in Section 2 (see the slope of curves 2, 3 and 4). For example, it also follows from Fig. 1 that at the error of 1% (or $Log\, e = -2$) for the observation time $T = 50$, post-processing with one, three and five time increments reduces the total number of time increments by factors of $2.8, 3.8, 4$, respectively (compared with the results with no post-processing, curve 1). Post-processing is even more effective if we are interested in more accurate results (for multi-dimensional problems a general solution is the superposition of the solutions for separate modes and requires more accurate results for individual modes). For example, at the error of 0.01% (or $Log\, e = -4$) for the ob-

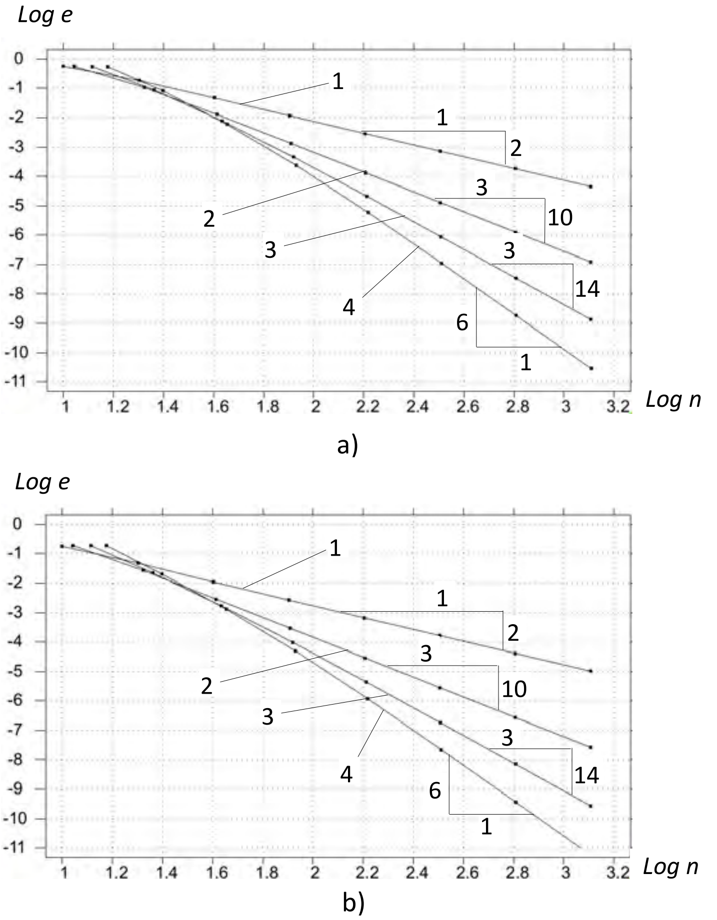

Figure 2: The relative error in displacements and velocities e at the observation time $T = 5$ versus the total number of time increments n in the logarithmic scale at integration of a single degree of freedom system (with zero load $f(t) = 0$ and damping $\xi = 0.1$ (a) and $\xi = 0.2$ (b)) without post-processing (curve 1) and the subsequent post-processing with one (curve 2), three (curve 3) and five (curve 4) time increments.

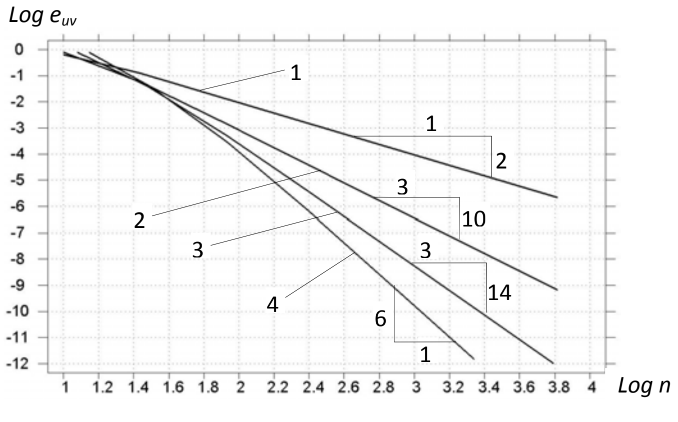

Figure 3: The numerical error in displacements and velocities $\tilde{e}_{uv}$ at the observation time $T = 5$ versus the total number of time increments n in the logarithmic scale at integration of a single degree of freedom system with damping $\xi = 0.1$ and non-zero loading $f(t) = 2 + 2t$ without post-processing (curve 1) and the subsequent post-processing with one (curve 2), three (curve 3) and five (curve 4) time increments.

servation time $T = 50$, post-processing with one, three and five time increments reduces the total number of time increments by factors of $6, 10, 12$, respectively. However, we should also remember that post-processing with one, three and five time increments requires the additional factorization of one, two and three stiffness matrices, respectively. Therefore, the reduction in computation time at the application of the post-processing procedure can be easily calculated if the computation times for the factorization of a stiffness matrix and the back-substitution stage of the solution of a system of linear equations are known for the selected computer code at the given numbers of degrees of freedom.

As can been seen from Figs. 2 and 3, for linear elastic problems with non-zero damping, the order of convergence (order of accuracy) of numerical results after post-processing with one, three and five time increments is in agreement with the analytical estimations described in Section 2. It also follows from Fig. 2 that if after basic computations with the trapezoidal rule the error is smaller than 10% for $\xi = 0.1$ or 5% for $\xi = 0.2$ (for the frequency and observation time used), the suggested post-processing procedure improves the numerical results. For multi-degree problems, numerically solving single degree of freedom problems for the maximum and leading (i.e., those with large amplitudes) modes is recommended in order to roughly estimate the range of time increments at which the suggested post-processing procedure improves the results.

3.2 Harmonic response of an elastic rod

Next we show the application of the post-processing technique described in Section 2 to time integration of the 1-D elastodynamics problem related to harmonic response of an elastic rod. An elastic rod of the length $L = 1$ is considered. Both ends of the rod are fixed, no external loads are applied, the initial velocity is zero, and the initial displacement is proportional to the first harmonic $u_0(x, 0) = sin(\pi x)$; see Fig. 4a. The observation time is assumed to be $T = 50$, Young's modulus to be $E = 1$, and the density to be $\rho = 1$. A uniform mesh with 100 linear finite elements along the bar is used. The elastodynamics problem was integrated in time by the trapezoidal rule with different numbers m of uniform time increments and the subsequent post-processing with one and three time increments as described in Section 2 (a time increment Δt is calculated similar to that described above for a single degree of freedom system). Numerical results show that a numerical solution can be approximated as $u_n(x, t) = sin(\pi x) g_1(t)$, where $g_1(t)$ is a function of time only. This means that only frequencies close to π are excited in the numerical solution. For comparison of the accuracy of the numerical results, the following errors in displacements ($\tilde{e}_u$), velocities ($\tilde{e}_v$) and the combined error in displacements and velocities ($\tilde{e}_{uv}$) at time t were calculated: $\tilde{e}_u(t) = \max_{0 \le x \le L}[u_a(x, t) - u_n(x, t)] = u_a(L/2, t) - u_n(L/2, t)$, $\tilde{e}_v(t) = \max_{0 \le x \le L} \frac{[v_a(x,t) - v_n(x,t)]}{\pi} = \frac{[v_a(L/2,t) - v_n(L/2,t)]}{\pi}$ and $\tilde{e}_{uv}(t) = \frac{\sqrt{\tilde{e}_u^2 + \tilde{e}_v^2}}{u^0_{max}}$, where $u_n(x, t)$ and $v_n(x, t)$ are numerical solutions for displacements and velocities at current time t, and $u_a(x, t) = sin(\pi x) cos(\pi t)$, $v_a(x, t) = -\pi sin(\pi x) sin(\pi t)$ are the analytical solutions for displacements and velocities at current time t, and the maximum numerical errors in displacements and velocities occur at $x = L/2$, $u^0_{max} = 1$ is the maximum initial displacement. For this problem, we selected a relatively fine mesh which yields a very small error in space. Therefore, for relatively large time increments, the combined error in displacements and velocities $\tilde{e}_{uv}$ should relate to the global error in time with a scaling factor. Fig. 4b shows the numerical error in displacements and velocities $\tilde{e}_{uv}$ versus the number of time increments n in the logarithmic scale. As can be seen from Fig. 4b, at a large number of time increments, the order of convergence (order of accuracy) of numerical results after post-

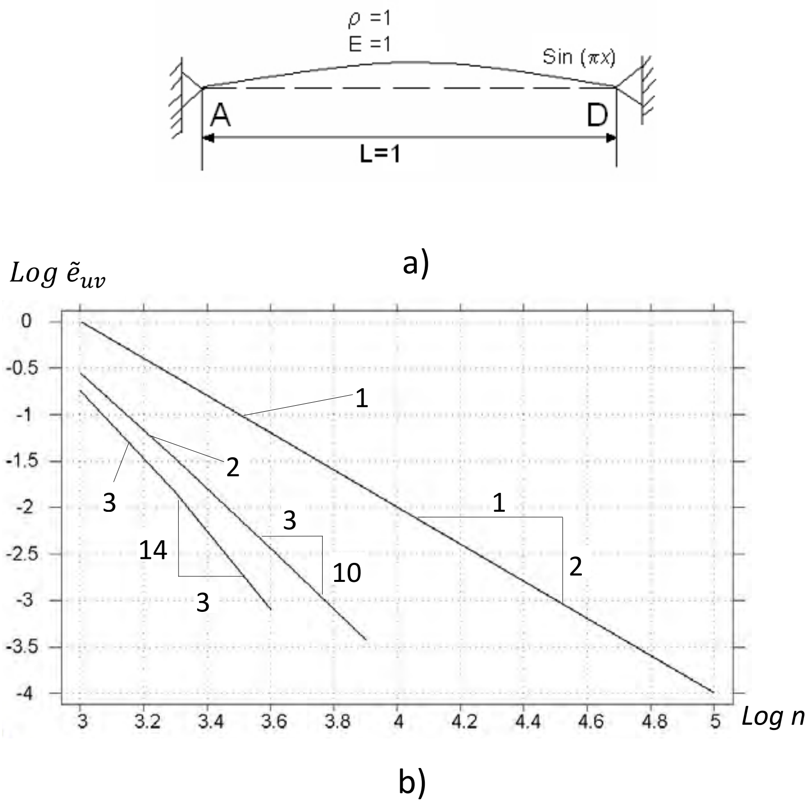

Figure 4: Modeling of harmonic response of an elastic rod (a). The numerical error in displacements and velocities $\tilde{e}_{uv}$ at the observation time $T = 50$ versus the total number of time increments n in the logarithmic scale (b) at time integration by the trapezoidal rule (curve 1) and the subsequent post-processing with one (curve 2) and three (curve 3) time increments.

processing with one (curve 2) and three (curve 3) time increments is in agreement with the analytical estimations reported in Section 2. It also follows from Fig. 4b that at the error of 1% (or $Log\, \tilde{e}_{uv} = -2$) for the observation time $T = 50$, post-processing with one and three time increments reduces the total number of time increments n by factors of 3.5 and 4.6, respectively (compared with the results with no post-processing, curve 1). For more accurate results with the error of 0.1% (or $Log\, \tilde{e}_{uv} = -3$) at the observation time $T = 50$, post-processing with one and three time increments reduces the total number of time increments n by factors of 5.5 and 8.5, respectively. However, we should also remember that post-processing with one and three time increments requires the additional factorization of one and two stiffness matrices, respectively.

3.3 Impact of an elastic bar against a rigid wall

Here we show the application of the post-processing technique described in Section 2 to time integration of a 1-D impact elastodynamics problem for which all frequencies of the semi-discrete system, Eq. (1), are excited. An elastic rod of the length $L = 4$ is considered. The following boundary conditions are applied: the displacement $u(0,t) = t$ (it corresponds to the velocity $v(0,t) = v_0 = 1$) and $u(4,t) = 0$ (it corresponds to $v(4,t) = 0$). Initial displacements and velocities are zero; i.e., $u(x,0) = v(x,0) = 0$. The observation time is assumed to be $T = 2$, Young's modulus to be $E = 1$, and the density to be $\rho = 1$. Zero damping $\boldsymbol{C} = \boldsymbol{0}$ and two cases of non-zero Rayleigh damping $\boldsymbol{C} = b_1\boldsymbol{M} + b_2\boldsymbol{K}$ with the coefficients $b_1 = 0.005$, $b_2 = 0.01$ and with the coefficients $b_1 = 0.05$, $b_2 = 0.1$ are considered. A uniform mesh with

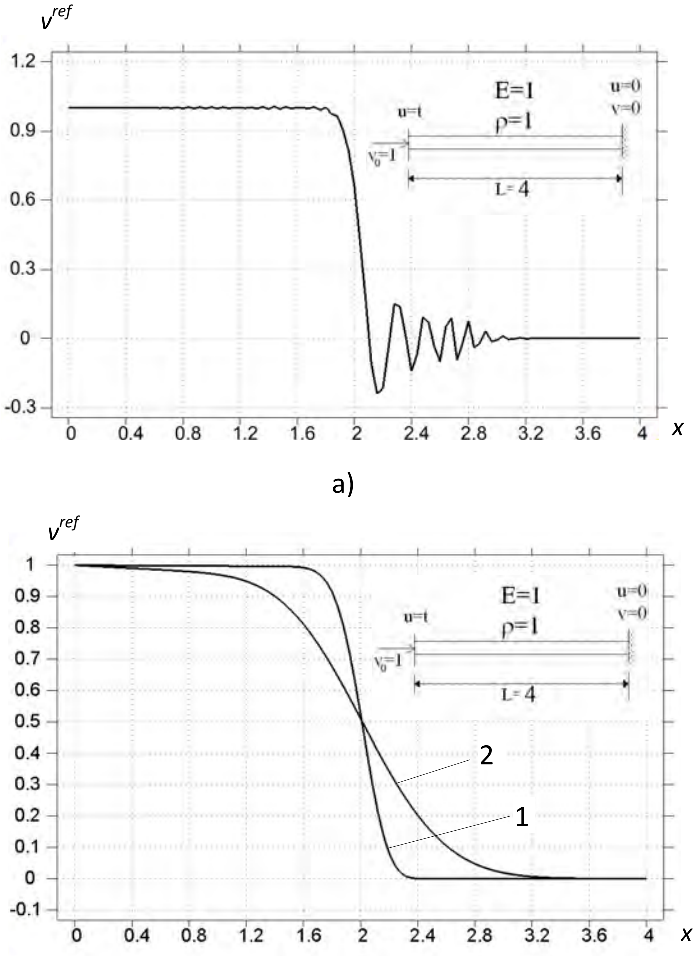

a)

b)

Figure 5: Velocity distribution v^{ref} along the bar at time $T = 2$ for the impact problem with zero (a) and non-zero Rayleigh damping (b). Curves 1 and 2 in b) correspond to the damping coefficients $b_1 = 0.005$, $b_2 = 0.01$ and $b_1 = 0.05$, $b_2 = 0.1$, respectively. The solutions are obtained by the trapezoidal rule with 400000 uniform time increments.

100 linear finite elements along the bar is used. In this paper we will consider the convergence in time of numerical results to a solution of the semidiscrete problem, Eq. (1), which differs from the analytical solution of the continuous impact problem. Because the semidiscrete problem includes 100 degrees of freedom, the simplest way to find the solution of the semidiscrete system is to use accurate time integration of Eq. (1) with very small time increments. This solution, called the reference solution, is obtained by the trapezoidal rule with 400000 time increments and is shown for the velocity v^{ref} in Fig. 5. An accurate numerical solution of the original continuous impact problem with non-zero damping is considered in our papers [14, 16]. To study convergence of the trapezoidal rule after post-processing, the following measure for the velocity error of the semi-discrete system at time $T = 2$ is introduced:

$$e_v(T=2) = \sqrt{\sum_{i=1}^{100} (v_i^{ref}(T=2) - v_i^{num}(T=2))^2}\,, \tag{3}$$

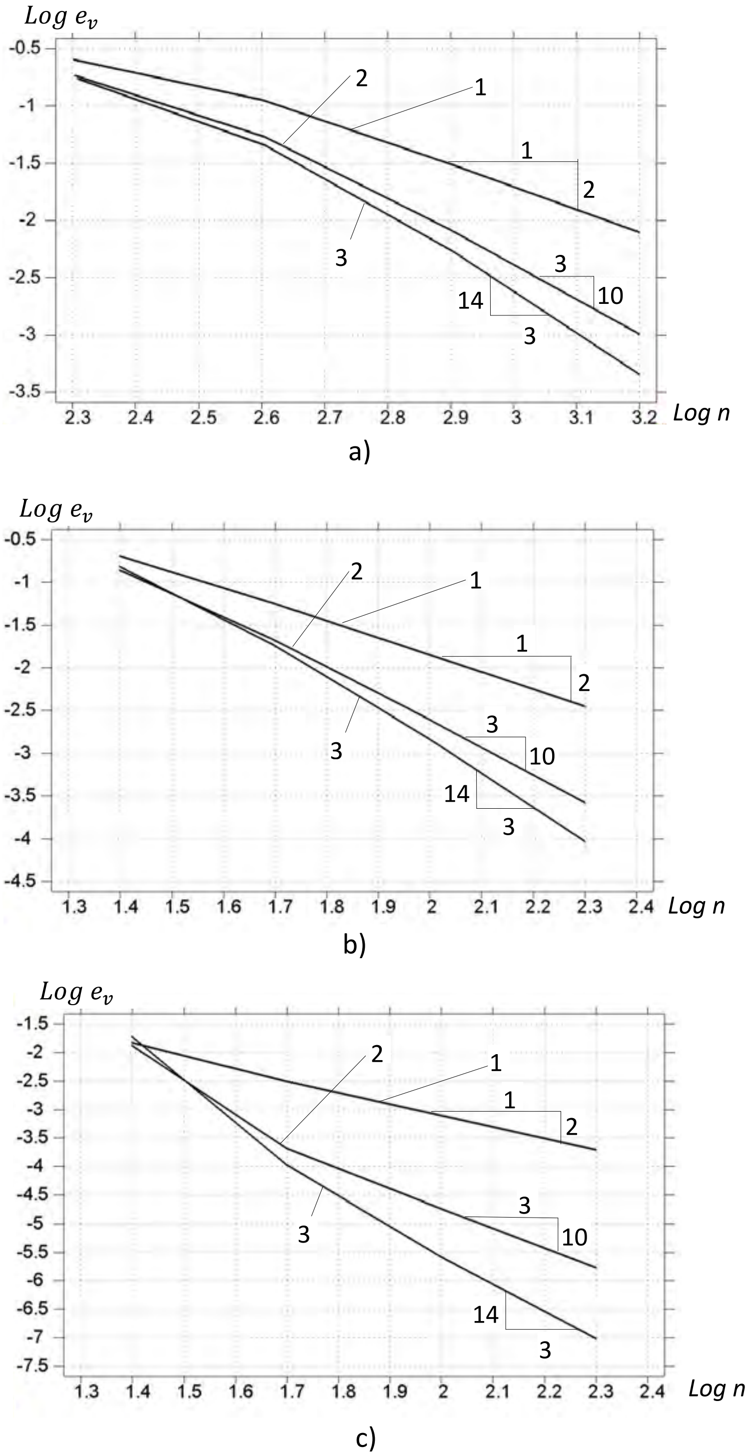

Figure 6: The numerical error in velocity e_v at the observation time $T = 2$ versus the total number of time increments n for the impact problem in the logarithmic scale at time integration by the trapezoidal rule (curve 1) and the subsequent post-processing with one (curve 2) and three (curve 3) time increments. a), b) and c) correspond to non-zero damping and to Rayleigh damping with the damping coefficients $b_1 = 0.005$, $b_2 = 0.01$ and with the damping coefficients $b_1 = 0.05$, $b_2 = 0.1$, respectively.

where $v_i^{ref}(T = 2)$ and $v_i^{num}(T = 2)$ $(i = 1, 2, ..., 100)$ are the nodal velocities of the reference and numerical solutions at time $T = 2$, respectively.

Fig. 6 shows the numerical error e_v at time $T = 2$ versus the number of time increments in the logarithmic scale. At a large number of time increments, the number of time increments n is inversely proportional to a time increment Δt. Therefore, the slope of the curves at large numbers n of time increments in Fig. 6 (which are plotted in the logarithmic scale) describes the order of convergence (order of accuracy) of numerical results. As can been seen from Fig. 6, the order of convergence (order of accuracy) of numerical results after post-processing with one and three time increments is in agreement with the analytical estimations reported in Section 2 (see the slopes of curves 2 and 3).

4 CONCLUSIONS

In our previous papers, we suggested a new solution strategy for elastodynamics problems and showed that for long-term time integration, a time-integration method at basic computations does not need numerical dissipation even for wave propagation and impact problems. In the current paper, we suggest a very simple and effective post-processing procedure to increase the order of accuracy in time for numerical results obtained by the trapezoidal rule. Because the same trapezoidal rule is used for basic computations and for post-processing, the new technique retains all of the properties of the trapezoidal rule. For example, at zero physical damping C = 0, the trapezoidal rule conserves the total energy and the linear and angular momentum of a mechanical system during time integration. We should also mention that the new technique requires no writing of a new computer program for its implementation and can be easily used with any current commercial and research codes for elastodynamics. Of course, post-processing with a time increment, the size of which differs from that used in basic computations, requires the factorization of a tangent matrix and leads to additional computational costs. However, these additional costs are small compared with those for long-term integration by the trapezoidal rule in basic computations.

REFERENCES

[1] O. C. Zienkiewicz and R. L. Taylor. *The Finite Element Method.* Butterworth-Heinemann, Oxford, UK, 2000.

[2] A. Bonelli and O. S. Bursi. Explicit predictor-multicorrector time discontinuous galerkin methods for linear dynamics. *Journal of Sound and Vibration*, 246(4):625–652, 2001.

[3] C. C. Chien and T. Y. Wu. Improved predictor/multi-corrector algorithm for a time-discontinuous galerkin finite element method in structural dynamics. *Computational Mechanics*, 25(5):430–437, 2000.

[4] T. C. Fung. Construction of higher-order accurate time-step integration algorithms by equal-order polynomial projection. *Journal of Vibration and Control*, 11(1):19–49, 2005.

[5] G. M. Hulbert. Time finite element methods for structural dynamics. *International Journal for Numerical Methods in Engineering*, 33(2):307–331, 1992.

[6] G. M. Hulbert and T. J. R. Hughes. Space-time finite element methods for second-order hyperbolic equations. *Computer Methods in Applied Mechanics and Engineering*, 84(3):327–348, 1990.

[7] S. J. Kim, J. Y. Cho, and W. D. Kim. From the trapezoidal rule to higher-order accurate and unconditionally stable time-integration method for structural dynamics. *Computer Methods in Applied Mechanics and Engineering*, 149(1-4):73–88, 1997.

[8] X. D. Li and N. E. Wiberg. Structural dynamic analysis by a time-discontinuous galerkin finite element method. *International Journal for Numerical Methods in Engineering*, 39(12):2131–2152, 1996.

[9] M. Mancuso and F. Ubertini. An efficient integration procedure for linear dynamics based on a time discontinuous galerkin formulation. *Computational Mechanics*, 32(3):154–168, 2003.

[10] M. Mancuso and F. Ubertini. A methodology for the generation of low-cost higher-order methods for linear dynamics. *International Journal for Numerical Methods in Engineering*, 56(13):1883–1912, 2003.

[11] N. Tarnow and J.C. Simo. How to render second order accurate time-stepping algorithms fourth order accurate while retaining the stability and conservation properties. *Computer Methods in Applied Mechanics and Engineering*, 115(3-4):233–252, 1994.

[12] A. V. Idesman. Use of post-processing to increase the order of accuracy of the trapezoidal rule at time integration of linear elastodynamics problems. *International Journal for Numerical Methods in Engineering*, pages 1–34, 2011 (submitted).

[13] A. V. Idesman. A new high-order accurate continuous galerkin method for linear elastodynamics problems. *Computational Mechanics*, 40:261–279, 2007.

[14] A. V. Idesman, H. Samajder, E. Aulisa, and P. Seshaiyer. Benchmark problems for wave propagation in elastic materials. *Computational Mechanics*, 43(6):797–814, 2009.

[15] A. Idesman, K. Subramanian, M. Schmidt, J. R. Foley, Y. Tu, and R. L. Sierakowski. Finite element simulation of wave propagation in an axisymmetric bar. *Journal of Sound and Vibration*, 329:2851–2872, 2010.

[16] A. V. Idesman. Accurate time integration of linear elastodynamics problems. *Computer Modeling in Engineering and Sciences*, pages 1–38, 2011 (accepted).

COMPDYN 2011
3rd ECCOMAS Thematic Conference on
Computational Methods in Structural Dynamics and Earthquake Engineering
M. Papadrakakis, M. Fragiadakis, V. Plevris (eds.)
Corfu, Greece, 25–28 May 2011

SPEED ENHANCEMENT OF DYNAMIC BEM ON INEXPENSIVE HARDWARE WITH PARALLEL FORTRAN 2008

A. A. Stamos

National Technical University of Athens
Iroon Polytechniou 9, 15780 Athens, Greece
e-mail: stamthan@central.ntua.gr

Keywords: BEM, dynamic steady-state problems, transient problems, parallel, Fortran 2008.

Abstract. *The Boundary Element Method (BEM) has been extensively used in dynamic problems in structural engineering. The method is computationally intensive and traditionally depends on raw computer processing power to solve larger structures. However, advances on processor speed have stagnated due to physical limits. Instead, processing power is now based on parallel computing. The BEM can benefit from parallel computing, in dynamic problems in the Laplace transform domain, as the computation for each (complex) frequency is independent to each other, and can be executed concurrently by a different core or processor. The volume, in bytes, of the outcome of each frequency computation is small, so that it can be sent through a network with negligible overhead. Thus, the method does not need special hardware and it can be executed equally well by an ordinary, off-the-shelf, multi-core and/or multiprocessor computer, as well as by a typical computer cluster of low bandwidth. The method is implemented using coarrays as described in the upcoming Fortran 2008 standard. The biggest advantage of Fortran 2008 is that remote memory is referred to directly, like an array with the instance identity as index, instead of having to call a subroutine for loading and storing data. A small but sufficient set of easily learned statements and constructs are defined, which make the program much clearer. The method is tested with typical dynamic problems and shows promising results.*

INTRODUCTION

After the invention of the Boundary Element Method (BEM) more than three decades ago, BEM has been used extensively for structural analysis and especially for dynamic problems. BEM is computationally intensive and despite the tremendous advancement of computer systems since its invention, it can still saturate the resources of the typical contemporary computer. BEM software, typically written in FORTRAN, traditionally depends on the raw processing power of single processors, the faster the better. However, advances on processor speed have stagnated due to physical limits. Recent advances on processors now focus on the proliferation of the number of cores per processor. A processing core works almost independently to other cores, and it is inexpensive enough to make parallel computing possible for the individual researcher, and indeed for the casual user. Parallel computing is a form of computation in which many computations are carried out simultaneously operating on the principle that large problems can be divided into smaller independent segments. Each segment is then computed by a different processing core concurrently. Parallel computing may also use different processors on the same physical computer (symmetric multiprocessing), or even processors on different physical computers (distributed computing). Parallel computing is much harder than traditional sequential computing, since the segments are rarely fully independent. Some form of communication and synchronization must happen between the cores, which may lead to race conditions [1]. Various primitives have been developed to aid parallel computing, such as semaphores, condition variables, message passing and RPCs [2], but it is easy to use them inappropriately and produce race conditions, deadlocks and other forms of unpredictable and irreproducible behavior [2]. To make parallel computing easier special libraries and frameworks such as lapack and OPENMP [3] have been developed to hide the underlying use of the parallel primitives. For example [4] used OPENMP to parallelize the integration of the static BEM kernels for each node. The framework, while better than using the raw synchronization primitives, is still awkward to use, it works only with shared memory and it requires to link the appropriate libraries for the specific processor, architecture and Operating System (platform), if they exist. A better solution is to let the compiler handle the primitives and present the user with a few robust high level constructs, conveniently integrated to the syntax of the computer language. This concept, developed in the last century [5], is introduced to the upcoming standard of the FORTRAN language, FORTRAN2008 [6]. FORTRAN2008 introduces a small number parallel statements/constructs which are integrated smoothly with the rest of the language, and accomplish an elegant, platform independent way to develop parallel software for both shared-memory processors and computer clusters (computers linked by not necessarily high-speed network).The present paper exploits FORTRAN2008 to develop a portable, platform independent method for parallelizing dynamic BEM suited for inexpensive networks of existing computers, and inexpensive, run of the mill contemporary multi-core computers, or combination of them. To the knowledge of the author, no previous research on parallelizing BEM with FORTRAN2008 exists, although it is an active field of research in other disciplines [7].

1 PARALLEL COMPUTING

1.1 The emergence of parallel computing

During the last decade the rate of making faster microprocessors has almost halted due to fundamental physical limits such as the speed of light and uncontrolled induction in high frequencies. However the size of the electronic circuits is still becoming smaller and smaller, following the Moore's law [8], which states that the number of transistor in a processor doubles every 18 months. The consequence was to cram many processing units, or cores, in the same die or microprocessor, as substitute to raw processing power. This essentially moved the burden of making faster programs from the processors to the programmers. In theory, the more processing cores the faster a computation will be done. Ideally, if a program needed time t to complete in a single core, and N_{pr} cores were available, then the expected time would be t/N_{pr}. In theory, it would be possible to split the work of the program in separate segments and to run each segment on a different processor at the same time, in parallel. In practice, parallel computing has proved to be very difficult [1]. Computer time t/N_{pr} is very seldom true in practical problems. Some programs simply can not be "parallelized", either because they do a single computation such as a simple word processor, or the computations they do are strictly sequential, like the time steps in a transient dynamic analysis software, which means that a time step must be completed in order to compute the next one.

If P is the proportion (with respect to time of execution) of the program which can be parallelized, the improved execution time of the program is given by Amdahl's law [9]:

$$t_{MP}=t\cdot\left[(1-P)+\frac{P}{N_{pr}}\right]$$

where (1-P) is the proportion of the program that remains sequential. Again, in practice P is not independent to N_{pr}, as P is in the form of discrete packets, and there is delay due to synchronization and communication which is proportional to the number of cores. Thus, experimental results are necessary to evaluate the utilization of the parallel process. Amdahl's law limits the speed enhancement that a program can achieve through parallel-computing, even with infinite processors. Worse, as the number of processors grows to very high values the speed enhancement dwindles to imperceptibility (Figure 1).

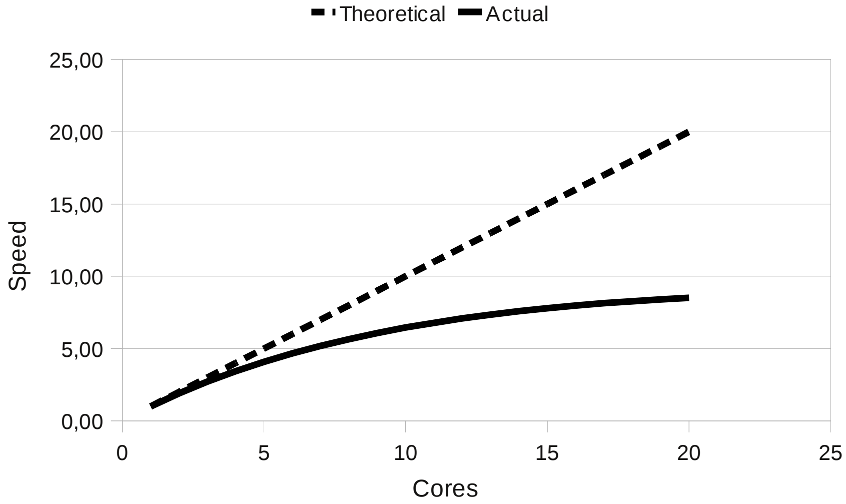

Figure 1. Theoretical and actual relative speed due to P=0.05 and synchronization delays.

1.2 Realization of parallel computing

Many attempts with various degrees of success have been used to produce parallel architectures. Usually they depend to Symmetric Multiprocessing, or SMP, which is a multiprocessor computer architecture where two or more identical processors are connected to a single shared main memory. Most common multiprocessor systems today use an SMP architecture. In case of multi-core processors, the SMP architecture applies to the cores, treating them as separate processors. The advantage of this approach is that the various program segments, called threads [2], which run in parallel, can communicate rapidly via the shared memory, and they can synchronize themselves. The disadvantage is that it does not scale well as a processor locks the memory when it updates it. In contrast Non Uniform Memory Architecture (NUMA) multiprocessors and computer networks, or clusters, do not share the same memory and they are linked via a comparatively much slower network. This means that the traffic between the processes must be minimized in order to achieve speed. There are 2 more or less practical ways to achieve parallelizing [1]. One is to instruct each processor core to execute the same operation but to different data (single instruction multiple data – SIMD). Example of this is the WHERE and FORALL constructs in FORTRAN95 [3]. The other is to instruct each processor to execute independent to another, the same or other code (multiple instruction multiple data – MIMD), on the different data. Examples of this are frameworks like OPENMP and PVM [3], and parallel FORTRAN2008 [10]. In order to develop new parallel software, very careful analysis and design must precede the coding and the method [11], and very often compromises must be made.

1.3 Parallel Computing with FORTRAN

FORTRAN95 and FORTRAN2003 has support for Single Instruction Multiple Data (SIMD) [1] through the WHERE and FORALL constructs [3] which are useful for array operations. These are very important as they provide for a platform independent way to implement parallelization with almost no effort, and they are useful in many numerical cases. But they are not suitable for computer clusters and they can not provide for different execution on each processor.

The upcoming FOTRAN2008 [10] standard provides for Multiple Instruction Multiple Data (MIMD) [1], or rather for a special case of it, Single Program Multiple Data, as the instructions are executed from a single FORTRAN program [12]. Many instances (or images) of the same program are run by different processors either in the same computer or in different computers connected to a, not necessarily high-speed, network. Each image is aware of its identity (an integer count) and can follow different execution path according to its identity.In most but the simplest cases, there has to be some means of communications or synchronization among the images, which typically involves calling subroutines of special, often platform dependent, libraries. FORTRAN2008 uses the concept of coarrays [6] which are a solution along these lines, with the difference being much tighter integration with the Fortran language itself, and therefore platform independence. The biggest advantage is that remote memory is referred to directly like an array with the instance identity as index, instead of having to call a subroutine for loading and storing data. These subroutines are still called “under the hood”, but coarrays are designed with legibility in mind. A small but sufficient set of easily learned statements and constructs are defined, which make the program much clearer. A program that runs over several processors is inherently more complicated than a single-threaded program so that clear and well understood statements are extremely important. Apart from the coarray references, the statement SYNC ALL prevents any image for executing any further statements until all instances reach this statement, thus making sure that all the previous computations have been done by all images. The function NUM_IMAGES() returns the number of parallel instances which run simultaneously, and the function THIS_IMAGE() returns the identity of the current instance, an integer between 1 and NUM_IMAGES(). The construct CRITICAL … END CRITICAL achieves mutual exclusion of images. It is guaranteed that only one image at a time executes the statements between CRITICAL and END CRITICAL. All images are created at the start of the program and they begin execution at the same time. An image can not be created dynamically at the middle of the program, though it can exit without affecting the remaining images.

Coarrays are part of the upcoming FORTRAN2008 standard. The original proposal of Numrich and Reid [6] was recently scaled back in the draft. A forward implementation of the core features, which were left in the draft, has been introduced in the G95 Fortran compiler [13], available for the x86/Linux, IA64/Linux and x86-64/Linux platforms.

2 STRATEGY OF PARALLEL COMPUTING IN BEM

As stated above, the transient BEM dynamic analysis is inherently a sequential process. The displacements and tractions of the boundary nodes must be known in a previous time step in order to compute the displacements and tractions at the next time step. However, if the governing equations are transformed with the Laplace transform, they do not depend on time, but on the complex frequency s of the Laplace transform [14]:

$$c_{ij}\bar{u}_{ij}(x)=\int \bar{t}_{(n)i}(y)\bar{U}ij(y,x,s)\,dS-\int \bar{u}_{i}(y)\bar{T}ij(y,x,s)\,dS$$

It turns out that for a given complex frequency s, the equations do not depend on any other complex frequency. Thus the computation of each frequency step is completely independent to one another, and can be done in parallel, by different processing cores, or by different processors in different computers.

In theory, any of the loops of the typical dynamic Boundary Element Method program may be made parallel. The typical process of the computations is given in Figure 2. If the inner loops were made parallel, then intermediate results should be sent via the network to an accumulator process, which would probably be more time consuming than the computations. The second outer loop, for each node, could be made parallel, in shared-memory computers but it would probably be time consuming in a network. Furthermore, the solution of the system of equations should also be run in shared-memory computer. This leaves the outer loop which can be parallelized without affecting the bulk of the code of the BEM program. Furthermore, the results of each frequency step (transformed displacements and tractions) are far smaller in gigabytes than the whole matrices. In fact they are so small that they can be transferred through the network with little delay, and thus it is suitable for both shared memory multicore computers and computer clusters.

A typical transient dynamic BEM program computes 50 frequency steps, which means that up to 50 processors may be used. This exceeds by far the number of cores (typically 4-16) in contemporary processors of inexpensive modern computers. Also, it is enough to keep busy the Local Area Network (LAN) of a standard department in a university or a corporation, when it is used as cluster. The method certainly does not scale well in supercomputers with thousands of processors. However the high cost of supercomputers as well as Amdahl's law

(Figure 1) justify the development of relatively easy parallel method suitable for inexpensive hardware. It must be noted that if the parallelizing is done on multi-core shared memory computer, substantial memory, enough to hold the matrices [A] and [B] of the system of equations for each parallel process, is needed. It is fortunate that huge memory (4GB) is available in modern computers, and that the number of cores is still too small to exhaust it.

```
START
Read data.
For each complex frequency step S:
    Zero matrices [A] and [B].
    For each node J:                          (* Create equation for the node *)
        For each element E:                   (* Integrate over all the boundary *)
            For each integration parameter xi1:  (* Numerically integrate over element *)
                For each integration parameter xi2:
                    Evaluate kernels.
                    Multiply by weights and add to sums.
                End For.
            End For.
        End For.
        Add the equation coefficients to matrices [A] and [B].
    End For.
    Solve the system of equations [A] [x] = [B].
End For.
Invert Laplace transform for the results.
Print results.
END.
```

Figure 2. Typical algorithm of a dynamic BEM program.

3 IMPLEMENTATION OF PARALLEL COMPUTING IN BEM

In order to maximize the parallelization gain the following rules must hold:

1 The volume of data transferred between images, or coarrays references, creates (relatively slow) network traffic and it must be as little as possible.

2 The process synchronization delay the images and the synchronization signals between images creates network traffic. The number of synchronization statements must be as little as possible.

3 Each process must do as much computational work as possible, unless this breaks the first or second rule. In this case a trade off between the competing rules must be reached through experimentation.

Applying the rules to the case of BEM parallelization, the following steps of the algorithm were concluded:

1. *The first image reads the data.*
2. *Each image except 1 copies the data from image 1.*
3. *Each image pre-processes the data.*
4. *Process 1 keeps a counter of all the frequencies.*
5. *Each image except 1 increments the counter, computes the relevant frequency, and stores the result to co-arrays of image 1.*
6. *Each image except 1 repeats step 5 until all frequencies have been computed and then dies.*
7. *Image 1 does numerical inversion of the Laplace transform.*
8. *Image 1 prints the results.*

There are many points to note in this algorithm:

1 In steps 2, 3 and 5 computations are done in parallel.

2 In step 2 a lot of distinct variables are transferred which cause noticeable delay in computer clusters but not in shared-memory SMP.

3 In step 5 all the results are transferred through an array which cause little delay.

4 In step 2 each image performs exactly the same computations. The alternative would let image 1 do the computations (which would gain nothing since the other images would be idle waiting for image 1) and then copy them to the other images, which would be more time consuming.

5 Step 5 implies that a soon as an image finishes a frequency step, it gets another one to compute. This means that fast processors in a computer cluster, compute more frequency steps than slow processors. In effect, the requirement to distribute the computing load evenly to the computers according to their relative speed, is automatically satisfied.

4 APLLICATION

The method was tested with a 3D transient dynamic problem; the response of the infinite elastic medium containing a spherical cavity under suddenly applied internal pressure was considered [15]. The problem was solved with a multi-dimensional BEM FORTRAN program [16], which was modified to enable FORTRAN2008 parallel computing. The discretization of the problem led to 1131 degrees of freedom and 1131x1131 full non-symmetric matrices. The Laplace transform was used with 20 complex frequency steps. The following two test runs were performed.

Cores	Time (sec)	Relative speed		Utilization
		Theoretical	Actual	
1	369,0	1,0	1,0	100%
2	223,4	2,0	1,7	83%
3	187,7	3,0	2,0	66%
4	140,0	4,0	2,6	66%

Table 1. Speed enhancement in a 4 core computer.

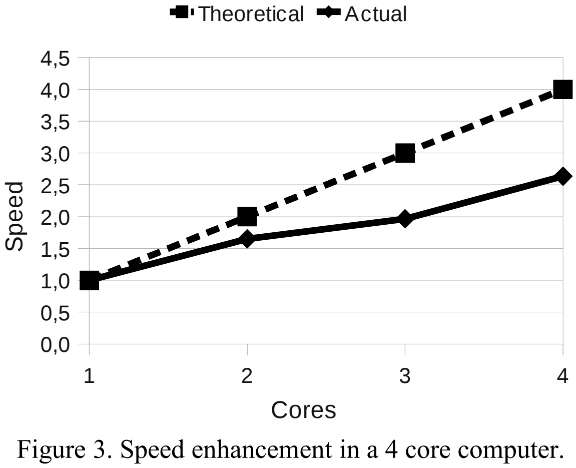

Figure 3. Speed enhancement in a 4 core computer.

4.1 Symmetric multi-core processing

The program was run in an inexpensive computer with the Intel Core i7 processor which contains 4 cores running at 1.60GHz. The program was run with 1, 2, 3 and 4 cores under the SuSE Linux 11.4 SMP64 Operating System. The results are shown in Table 1.The low utilization is probably due to conflicting access to the common memory. Each core processes data that is much greater than the memory cache provided to each core. Thus each core locks the main memory for writing, delaying the remaining cores. The results are also shown in Figure 3.

4.2 Distributed computing in cluster

The program was run in a cluster of 4 ordinary computers linked by 100Mbits/sec ethernet Local Area Network. The program was run independently in each computer. The specifications of each computer and its relative speed is shown in Table 2. Note that the computers differ.

Computer	Processor	Frequency (Mhz)	Cores	Memory (GB)	Operating System	Time (sec)	Relative Speed
1	AMD Athlon64 3400+	2,4	1	3	SuSE LINUX 11.3 SMP64	698	1,0
2	AMD Athlon64 3800+	2,4	1	4	SuSE LINUX 11.3 SMP64	673	1,0
3	Intel(R) Pentium(R) Dual CPU T3200	3	2	1	SuSE LINUX 11.4 SMP32	520	1,3
4	Intel core i7	1,6	4	4	SuSE LINUX 11.4 SMP64	369	1,9

Table 2. Computer cluster specifications.

The program was also run in the cluster using 1, 2, 3 and 4 computers. Computers 3 and 4 used only 1 of their cores for the computation. In order to calculate the utilization of different computers running in a cluster, their combined theoretical relative speed is the sum of their relative speeds. The results are shown in Table 3.

Computers	Time (sec)	Relative speed		Utilization
		Theoretical	Actual	
1	698,0	1,0	1,0	100%
1+2	351,3	2,0	2,0	98%
1+2+4	205,7	3,9	3,4	86%
1+2+3+4	150,0	5,3	4,7	88%

Table 3. Speed enhancement in a computer cluster.

The utilization is perfect for 2 computers. In the case of computers 1+2+4, one of them computes 1 frequency step more than the others (20 is not divided by 3), and this can be more than 5% of the total time, which explains the sudden drop in utilization. In the case of 1+2+3+4 computers this is also partially true, as the computers have different relative speeds, which explains the slight increase in the utilization. The results are also shown in Figure 4.

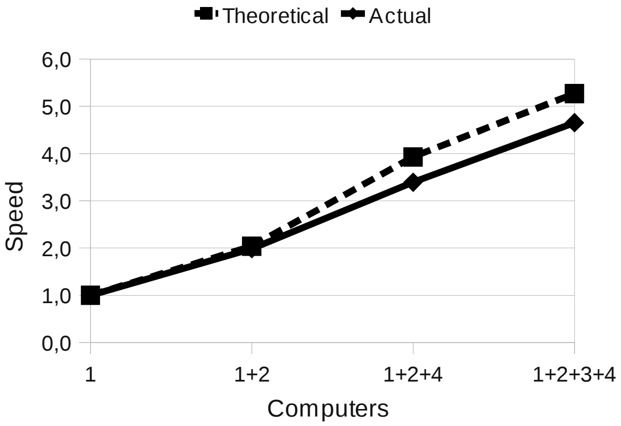

Figure 4. Speed enhancement in a computer cluster.

5 CONCLUSIONS

The elegant parallel framework of FORTRAN2008 was used to speed up the BEM. The parallelization of the computation of frequency steps in the Laplace transform domain was implemented. The method scales well and fully exploits a computer cluster. The method exploits the parallel capabilities of modern multi-core computers, but the utilization is lower than that of a computer cluster, probably due to mutual exclusion when two or more cores try to write the shared memory.

The method can also be applied to the dynamic Finite Element Method, in the Laplace transform domain.

REFERENCES

[1] S.A. Tanenbaum, *Modern Operating Systems*. Prentice-Hall, 1992.

[2] S.A. Tanenbaum, S.A. Woodhull, *Operating Systems Design and Implementation, 2nd Edition.* Prentice-Hall, 1997.

[3] I. Chivers, J. Sleightholme, *FORTRAN 95*. Springer–Verlag, 2000.

[4] M. T. F Cunha, J. C. F. Telles, A. L. G. A. Coutinho, J. Panetta, On the parallelization of boundary element codes using standard and portable libraries. *Engineering Analysis with Boundary Elements*, **28(7)**, 893-902, 2004.

[5] C.A.R., Hoare, Monitors, An Operating System Structuring Concept. *Commun. Of the ACM*, **17**, 549-557, 1974.

[6] J. Reid, Coarrays in the next Fortran Standard. *UK ISO/IEC JTC1/SC22/WG5 document N1747*, 2008.

[7] A.A Stamos, D.I. Vassilaki, C.C. Ioannidis, Speed Enhancement of Free-form Curve Matching with Parallel Fortran 2008. *Proceedings of the First International Conference on Parallel, Distributed and Grid Computing for Engineering*, Civil-Comp Press, Stirlingshire, 2009.

[8] E. Moore, G. Gordon, Cramming more components onto integrated circuits. *Electronics*, **38(8)**, 1965.

[9] G.M. Amdahl, Validity of the single-processor approach to achieving large scale computing capabilities. *Proceedings of AFIPS Conference Atlantic City, N.J., 18-20 April,* **30**, 483-485, 1967.

[10] US Fortran Committee (NCITS/J3), Fortran 2008 Working Draft, document J3/07-007r3, 2007.

[11] B. Blaise, *Introduction to Parallel Computin*g. http://computing.llnl.gov/tutorials/parallel_comp/, 2007.

[12] A. Vaught, Coarray Compendium. www.g95.org/compendium, 2008.

[13] A. Vaught, G95: a production Fortran 95 compiler. www.g95.org, 2010.

[14] G.D. Manolis, D.E. Beskos, *Boundary Element Methods in Elastodynamics.* Unwin-Hyman, 1988.

[15] P.K. Banerjee, S. Ahmad, G.D. Manolis, Advanced Elastodynamic Analysis, Boundary Element Methods in Mechanics, D.E. Beskos (ed.), pp. 257--284, North-Holland, Amsterdam, 1987.

[16] A.A. Stamos, (1994), *Dynamic Response of Underground Structure*s. Phd Thesis, Department of Civil Engineering, University of Patras, Greece, 1994.

COMPDYN 2011
III ECCOMAS Thematic Conference on
Computational Methods in Structural Dynamics and Earthquake Engineering
M. Papadrakakis, M. Fragiadakis, V. Plevris (eds.)
Corfu, Greece, 25–28 May 2011

RETROFITTING BY BASE ISOLATION OF EXISTING BUILDINGS IN ARMENIA AND IN ROMANIA AND COMPARATIVE ANALYSIS OF INNOVATIVE VS. CONVENTIONAL RETROFITTING

Mikayel Melkumyan[1*], Valentin Mihul[2], Emma Gevorgyan[3]

[1] Armenian Association for Earthquake Engineering (AAEE)
1st lane of Nansen str. 6, 0056, Yerevan, Armenia
e-mail: mmelkumi@yahoo.com

[2] MIHUL S.R.L.
Stroici str. 8B, 700373 Iasi, Iasi county, Romania
e-mail: mihulsrl@gmail.com

[3] Armenian Association for Earthquake Engineering (AAEE)
1st lane of Nansen str. 6, 0056, Yerevan, Armenia
e-mail: emgevorgyan@yandex.ru

Keywords: Base Isolation, Innovative Retrofitting, Existing Building, Conventional Retrofitting, Comparative Analysis, Cost Effectiveness

Abstract. *In recent years seismic isolation technologies in Armenia were extensively applied in construction of new buildings, as well as in retrofitting of existing buildings. Three remarkable projects on retrofitting by base isolation are described in the paper. One of them is retrofitting of a 5-story stone apartment building. The operation was made without resettlement of the occupants. World practice provides no similar precedent in retrofitting of apartment buildings. The other project is retrofitting of the 60 years old non-engineered 3-story stone school building. This building has historical and architectural value. Unique operations which were carried out in order to install the isolation system within the basement of this building and to preserve its architectural appearance are described. Accumulated experience created a good basis for participation in the international competition announced by the Government of Romania for development of the design on retrofitting by base isolation of the 178 years old historical building of the Iasi City Hall. The structural concept, including the new approach on installation of seismic isolation rubber bearings in this building, is described and detailed results of the earthquake response analysis for two cases, i.e. when the building is base isolated and when it has a fixed base, are given. For all three buildings comparative analyses of innovative vs. conventional retrofitting are carried out. Different methods of conventional retrofitting are considered and their costs are compared with the cost of innovative retrofitting by base isolation.*

1 APPLICATION OF BASE ISOLATION FOR RETROFITTING OF BUILDINGS WITH STONE BEARING WALLS

Isolation of structures from horizontal ground motions is gradually becoming a more common method of providing protection from earthquake damage. By reducing the seismic forces transmitted, isolation protects the contents and secondary structural features as well as the main structure; the safety of occupants and passers-by is thus also enhanced. Moreover, it is practicable to design the isolation system so that the structure responds elastically to the design level earthquake. Thus repair coast should be greatly reduced and continued serviceability of the structure assured [1]. The rehabilitation of existing structures by the insertion of isolators at foundation level has been carried out on historic buildings in California such as the Oakland City Hall, San Francisco City Hall [2, 3], Salt Lake City and County Building [4, 5]. For these, isolation may provide the only viable means that is not unduly intrusive and damaging for the appearance of the building. Together with that the retrofitting technique using base isolation has great potential for rehabilitation of ordinary civil structures such as apartment blocks. The first retrofit of stone apartment building of series 1A-450 has been carried out in Armenia [6, 7].

1.1 Retrofitting of the Existing Fife-Story Stone Apartment Building

Buildings on typical design of series 1A-450 have been erected in all regions of Armenia. They have the plan dimensions 52x15 m, symmetrical about the center of the long side and the bearing walls with 45-50 cm of thickness located mainly in transverse direction. The horizontal stiffness in the longitudinal direction is provided partly by the R/C frames with strong beams and columns, made inside the body of walls, and by longitudinal walls at the edge parts of the buildings. The analysis of consequences of the 1988 Spitak earthquake has shown that the most vulnerable zones in these buildings are the edge parts where the direction of bearing walls had been changed. It is in these very zones that intensive plastic deformations resulting in failure of the buildings have been developed due to the weak connections between longitudinal and transverse walls.

The developed structural concept aims at retrofitting an existing building by means of seismic isolators using simple working technology [8]. This is a unique pioneering seismic isolation project introduced for an existing 5-story stone building (Fig.1).

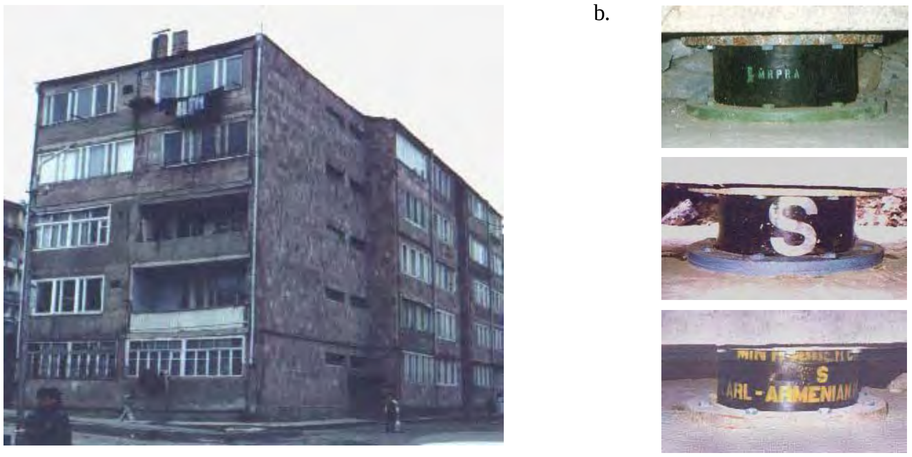
a.
b.

Figure 1: General view of the retrofitted by base isolation existing 5-story stone apartment building (a) and a fragments of its isolation system (b)

The idea is to supply this building with seismic isolation in the foundation by gradually cutting the isolators into the walls at the level of foundation upper edge by means of a two-stage system of R/C beams. Base isolation method for existing buildings with bearing walls that envisions placing of seismic isolators at the level of the foundation or the basement solves the problem as shown on Figure 2. According to the innovative technology developed by the first author of this paper (Patent of the Republic of Armenia #579), in the basement bearing walls openings with certain spacing are made to accommodate reinforcement frames of lower and upper pedestals with seismic isolators. Then reinforcement frames are placed between pedestals thus forming lower and upper continuous beams along all bearing walls of the building. The parts of existing walls between seismic isolators are removed creating gaps and the building appears separated from its foundation and linked to it only by seismic isolators. It is very important that openings in walls are made so that two adjacent openings are not made simultaneously; parts of walls existing between seismic isolators should be cut off beginning from the middle of building plan.

The above described operation was made without re-settlement of the dwellers. The world practice has had no similar precedent in retrofitting of apartment buildings. The project was implemented in 1995-1996, was financed by the World Bank and co financed by UNIDO. The high damping rubber bearings (HDRB) for this retrofit project were designed with significant help and support of the UK based Malaysian Rubber Producers' Research Association (MRPRA), particularly of Dr. K.N.G. Fuller. To implement the project 60 HDRBs were used, 28 bearings have been manufactured in MRPRA and 32 in Malaysia by Min Rubber Products Sdn. Bhd. and Sime Engineering Rubber Products Sdn. Bhd.

1.1.1 Design of Isolation System

High damping rubber bearings are a simple economical means of providing isolation. They have the low horizontal stiffness required to give a long vibration period (typically 2 s) to the structure when mounted on the bearings. Their vertical stiffness is high, thus minimizing any rocking of the structure during an earthquake. The damping needed to limit the displacement of the structure and reduce the response at the isolation frequency is incorporated into the rubber compound so that there are generally no needed auxiliary dissipation devices. The bearings can be designed to withstand safely the large horizontal displacements imposed during an earthquake. The service life of the bearings is expected to be several decades [9], and they should require no maintenance. There has been much emphasis on the suitability of base isolation for critically important structures such as hospitals and emergency centers. The protection of both structure and contents, however, would be advantageous for civil structures such as apartment blocks.

The isolators are located by upper and lower recesses provided by annular steel rings bolted to outer steel plates which are connected to the reinforcement in the upper continuous and lower foundation beams; the isolators themselves are not bolted to the structure. This method of connection helps to minimize the cost of the isolators themselves and simplifies their installation on site. Because the bearing is simply located in a recess, no tapped holes for bolted connections are needed in the end-plate. The side, top and bottom rubber cover layers ensure the steel plates are protected from corrosion. In the considered existing building the bearings were not be located in an enclosed, heated basement, but would be exposed to the outside environment. The severe winter weather at the site meant that particular attention had to be paid to the low temperature crystallization resistance of the rubber compound.

The plan of foundation is given in Figure 3, along with the location of the HDRBs and the total static load on each. The range of the vertical loads on bearings is quite high so it was decided to have two types of bearing, but differing only in the shear modulus of the rubber.

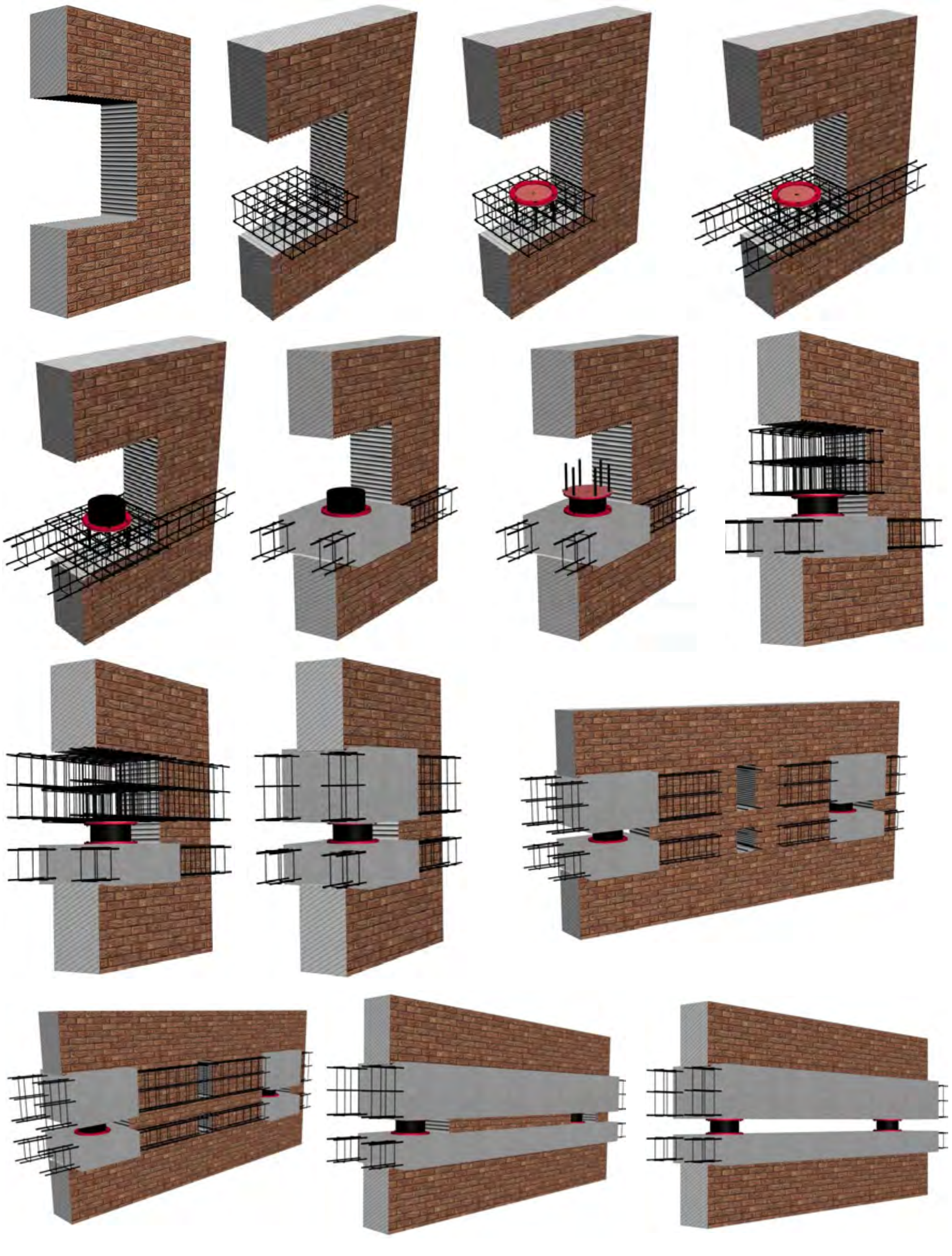

Figure 2: Stages of installation of seismic isolation system in the existing building with stone bearing walls

One type (designated Hard) would support loads in the range 740-900 kN and the other (Soft) loads in the range 500-680 kN. This strategy would lead to a somewhat more uniform distribution of the horizontal seismic forces, and help ensure that the centre of stiffness of the isolation system is close to the projection of the centre of mass of the building on to the ground plan. The latter minimizes the excitation of torsional vibration of the building on the isolators during an earthquake.

An isolation frequency of 0.5 Hz was chosen. For the design earthquake input and a damping in the isolation system of 10%, this implies a design horizontal displacement of 130 mm. The bearings were to operate safely up to 1.5 times of the design displacement. The design parameters including the horizontal stiffness needed for the two types of bearing are summarized in Table 1.

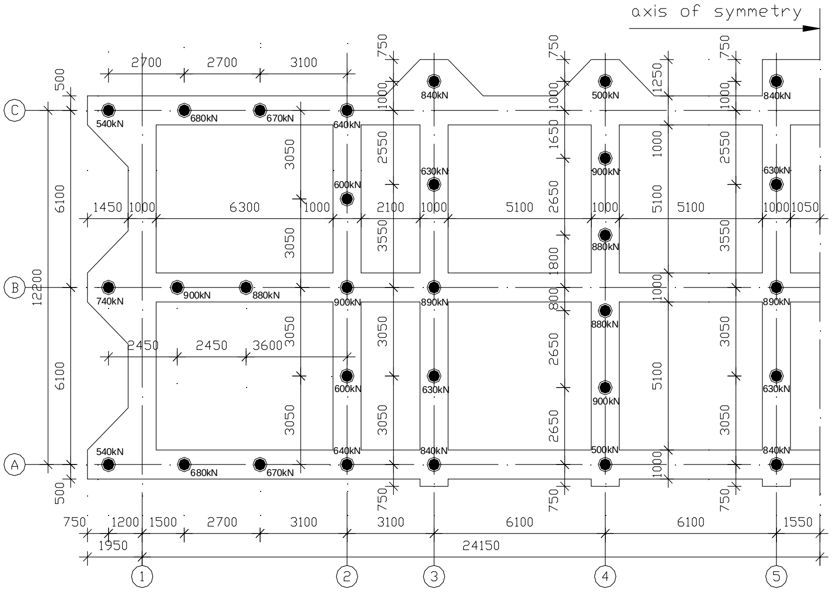

Figure 3: Plan of foundation of the existing 5-story stone apartment building with location of high damping rubber bearings

Bearing type	Hard	Soft
Horizontal stiffness, kN/mm	0.81	0.58
Design vertical load, kN	820	590
Design horizontal displacement, mm	130	130
Max. horizontal displacement, mm	195	195
Max. static vertical load, kN	900	680
Vertical loads (kN) at max horizontal displacement: Max.	1240	980
Min.	440	140

Table 1: Design parameters of isolation bearings

1.1.2 Design of Bearings

Design details and geometrical dimensions of the laminated rubber-steel bearings meeting the requirements listed in Table 1 are given in Table 2 and Figure 4. The rubber shear strain at the design displacement is chosen to be 100%. As it mentioned above the simple recess connection detail was chosen. Such an option necessitates a check that the bearings are safe against roll-out at the maximum horizontal displacement; the check has take account of the reduction in vertical load on some of the bearings due to the overturning of the building at large displacements.

Type	Hard	Soft
Rubber shear modulus*, MPa	0.97	0.69
Static compressive stress (max), MPa	8.7	6.5
Critical load (kN)	3260	2360
Load for internal plate yield (kN)	4800	4800
Horizontal displacement at onset of roll-out, mm		
for design vertical load	300	300
for min. vertical load	260	196
Nominal vertical stiffness**, kN/mm	400	310

* At 100% strain, 0.5Hz

** Estimated using shear rubber modulus in this Table and a bulk modulus of 2500 MPa

Table 2: Design details of bearings

Because the bearings are located in a recess the side cover is reduced from 10 mm to 3 mm layer over the end-plates. The 2 mm thick rubber end cover layers afford corrosion protection to end-plates (Fig. 4).

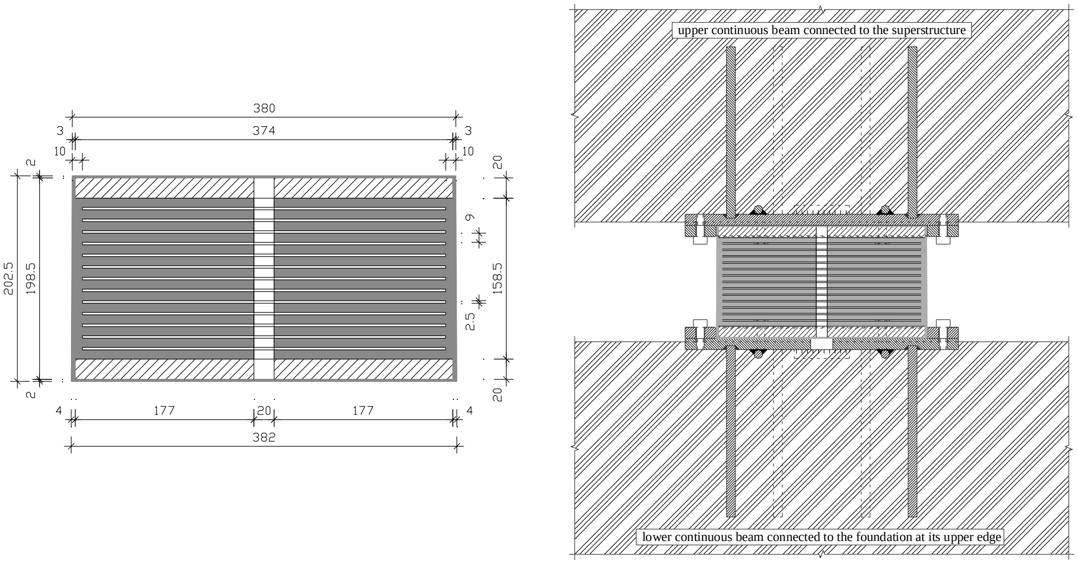

Figure 4: Geometrical dimensions of the designed HDRB for existing 5-story stone apartment building and location of HDRB by upper and lower recesses provided by annular steel rings bolted to the outer steel plates connected to reinforcement in the upper continuous and lower foundation beams

1.2 Retrofitting of the Existing Three-Story Stone School Building

The considered in this section building (school #4 in the city of Vanadzor) has historical and architectural value for the city. Taking this into account the financing organization - “Caritas Switzerland” - has agreed with the proposal to retrofit this building by base isolation. Below the unique operations, which were carried out in order to install seismic isolation bearings in the considered building are described in detail. The project on retrofitting the school #4 building was initiated by “Caritas Switzerland” in 2001. At that time the donor had carried out the feasibility study and was supposed to start the project using conventional design. The reason for making such a decision was in wide application of conventional retrofitting in the country and also in the unawareness of the donor about retrofitting by base isolation that has been already implemented with high efficiency in the same city.

The school is a 3-story 60 years old building with thick bearing walls constructed using tuff stones. Actually this building is a non-engineered structure with wooden floors. The design for conventional retrofitting of this school envisaged strengthening of bearing walls by reinforced concrete jackets and by construction of R/C frames in addition to the existing walls in order to decrease the distance between the existing walls. Also it was envisaged to replace the wooden floors by the R/C slabs. However, “Caritas Switzerland” being approached with a new proposal to use base isolation for retrofitting of the school instead of conventional retrofitting had changed its initial decision. The following advantages were taken into account: high reliability, lower cost and reduced duration of construction in comparison with conventional retrofitting as well as preservation of the architectural view of the building.

1.2.1 Bearing Structure of the School Building

School building (Fig. 5) has mainly a Π-shape plan and has load-bearing walls located in transverse and longitudinal directions. The thickness of bearing walls in the basement is varying from 600 mm to 1150 mm and in the floors above ground is varying from 600 mm to 700 mm. There is a school sport hall located between the axes “A”-“C” and “5”-“6”. The height of the sport hall is equal to the height of the basement plus the height of the first floor. This, as well as the Π-shape plan, causes significant asymmetry to the building relative to the longitudinal axis “D”. Actually the plan of the building in the limits of the basement and the first floor is almost rectangular while the plans of the second and third floors are of Π-shape.

.

Figure 5: General view of the retrofitted by base isolation 3-story school building

The school building had survived the 1988 Spitak Earthquake and fortunately the effect of this earthquake on the building was not very damaging. The building received inclined cracks mainly in the walls located around the staircases with the evaluated damage extent between 2 and 3. Therefore, it was decided to strengthen parts of the existing damaged walls by cement injection and/or by reinforced concrete jackets and also to replace the wooden floors by the R/C slabs. These operations were made simultaneously with installation of the base isolation system on the level of the school basement.

1.2.2 Structural Concept of Retrofitting by Base Isolation and Technique of Installation of Rubber Bearings

Seismic isolation interface for the school building was created in the middle part along the height of the school basement [10]. This approach has conditioned some differences in retrofitting of the school building in comparison with the described in the Section 1.1 retrofitting of the apartment building. In the case of the school building the lower continuous beams were structurally connected to the bearing walls of the basement. This has given the possibility to strengthen the bearing walls by means of the lower continuous beams before cutting the building and passing its weight through the seismic isolators to the bearing walls of the basement. Such structural solution permits to reliably carry the concentrated vertical loads by the bearing walls of the basement.

For the given project the medium damping rubber bearings from neoprene have been designed and tested locally. An isolation frequency again was chosen equal to 0.5 Hz. For the design level earthquake and damping in the isolation system of 8-9% the calculated horizontal displacement was equal to 140 mm. The maximal horizontal displacement was equal to 210 mm. Geometrical dimensions are the same as given in Figure 4. The other main parameters of the designed MDRBs are as follows: horizontal stiffness - 0.81±0.1 kN/mm; vertical stiffness - ≥300 kN/mm; rubber shear modulus - 0.97±0.15 MPa; critical vertical load - 4500 kN; vertical load at max horizontal displacement - 1500 kN.

The isolators in the school building were also located by the upper and lower recesses, however, the annular steel rings in this case were bolted directly to the anchors. The outer steel plates were also modified and instead of 20 mm thick plates the 6 mm plates were envisaged (Fig. 6). The given modifications in the design of the isolators' sockets have brought to significant reduction of steel consumption. Figure 6 also shows the cross-sections of the basement bearing wall in the place where isolator is installed between the lower and upper pedestals and where there is no isolator but the lower and upper continuous beams are seen from both sides of the bearing wall. All together 41 MDRBs had been manufactured by the Yerevan Factory of Rubber Technical Articles (YFRTA) for retrofitting of school building. The plan of location of seismic isolators on the lower continuous beams is shown on Figure 7.

For the considered building, which has historical and architectural value the technique of installation of seismic isolators has especially important meaning. First of all an infringement of the external view of the building should not take place under any circumstances. Secondly, no one stone of the façade should fall down during making openings in the bearing walls.

There are three different cases of making openings in the existing walls of the basement, which were mainly used at the retrofitting of the building [11]. The relatively simple case is the one, when the opening has the part of existing wall above it (Fig. 8). In this case there is no need to put any additional supports, as the strength of the wall is sufficient in order to avoid falling. When the opening is made, the lower reinforcement frame of the lower pedestal with the isolator socket can be placed and after that binding reinforcement lower frames are passed along both sides of bearing wall through the frame of the lower pedestal (Fig. 9).

At the next step the concrete of the lower pedestal is casted, the isolator is installed (Fig. 10) and above it the upper socket and the reinforcement frame of the upper pedestal are placed. Then the binding reinforcement upper frames are passed through the reinforcement frame of the upper pedestal along both sides of existing bearing wall (Fig.10). After casting the concrete of the upper pedestal all lower and upper pedestals should be connected to each other forming a two-stage system of R/C continuous beams (Fig. 11).

More complicated case of making openings is when any of existing beams or girders is crossing the space of the opening. In this case one of the ends of the existing beam loses its support (Fig. 12) and it is necessary to create temporary supports in order to carry dead load of the existing building.

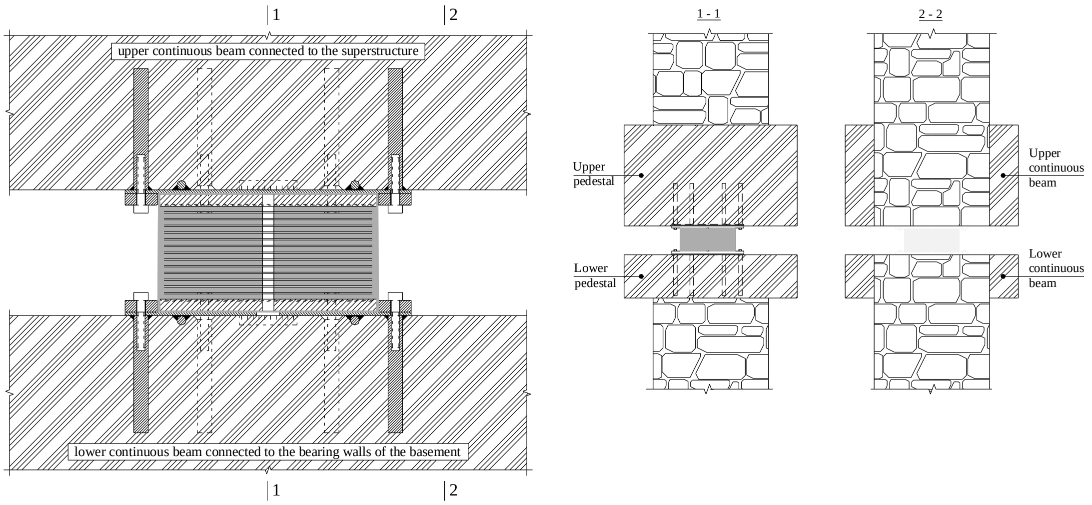

Figure 6: Location of MDRB by upper and lower recesses provided by annular steel rings bolted to the anchors connected to the upper and lower continuous beams in school building

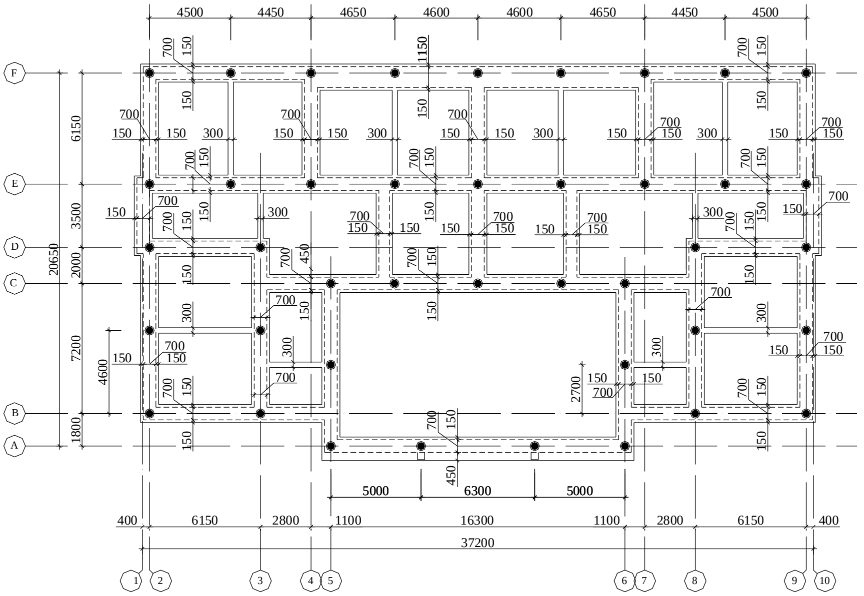

Figure 7: Plan of MDRBs' location on the lower continuous beams in the basement of the school building

The operation should be made very carefully in order to avoid any damages in the superstructure after making openings in the existing walls. It is important to make all operations described above as quickly as possible. Therefore, for such cases everything should be prepared in advance and after casting the concrete the temporary supports should be taken out only when concrete gets about 70% of its strength.

Figure 8: Retrofitting of existing 3-story stone school building: the case when the opening has the part of the existing wall above it

Figure 9: The views of the lower reinforcement frames of the lower pedestal installed in the opening together with the isolator socket

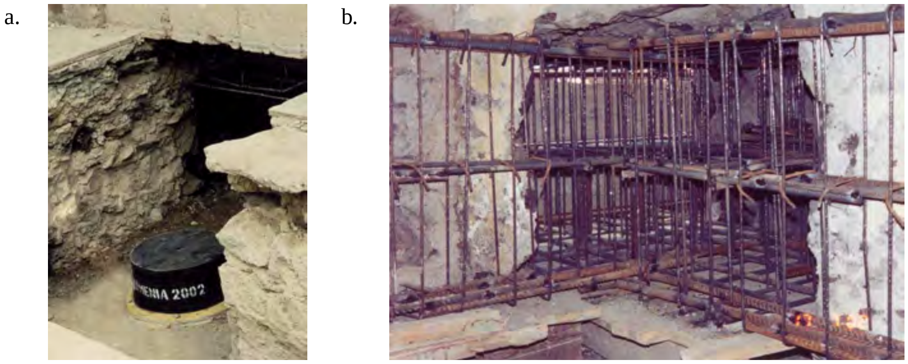

Figure 10: The view of the isolator installed in the socket after casting the concrete of the lower pedestal (a), and of the upper reinforcement frame installed in the opening together with the upper socket and with the binding reinforcement upper frames (b)

Figure 11: The views of a two-stage system of R/C continuous beams, which separate the building from its foundation and create the seismic isolation system

Figure 12: Existing beam is crossing the space of the opening and supported by temporary columns

Sometimes it is necessary to install temporary supports inside the opening in the plane of existing walls. In this case the supports should be prepared from steel, as after casting the concrete they will remain in the lower and upper pedestals. Later the parts of such supports between pedestals should be cut.

Most complicated case is the one when the opening does not have any part of existing wall above it. For school building such cases happened at the entrance when openings should be made just beneath the columns and the arches. Before starting to make openings the arches must be temporarily supported (Fig.13a). Then gradually the opening under the column should be made. With this purpose, at the beginning the part of the foundation only under the one quarter of the column section should be taken out (Fig. 13b). This will allow installing under the column a mechanical jack. After that the other part of foundation under another quarter of the column section can be demolished.

When this work is finished a temporary support under the one half of the column section should be installed and the mechanical jack can be taken out (Fig. 14a). Then again gradually the foundation under the other half of the column section should be demolished and this part of the column section also should be temporarily supported. In cases like this the reinforcement frames of the lower and upper pedestals cannot be prepared in advance and should be made in situ (Fig. 14b).

The following operations are similar to those described above. However, during every step of implementation of such complicated cases of retrofitting it is necessary to take care of the condition of the existing structures not permitting development of any damages as these structures are part of the valuable architectural appearance of the building.

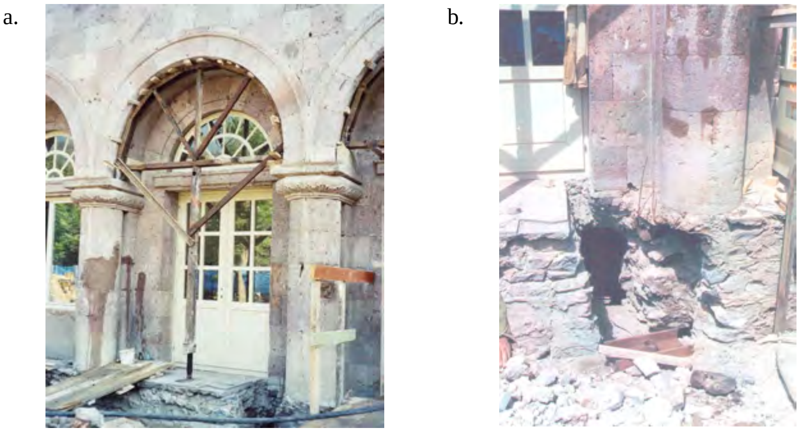

Figure 13: Temporary support under the existing arches (a) and the part of the foundation under the one quarter of the column section is taken out (b)

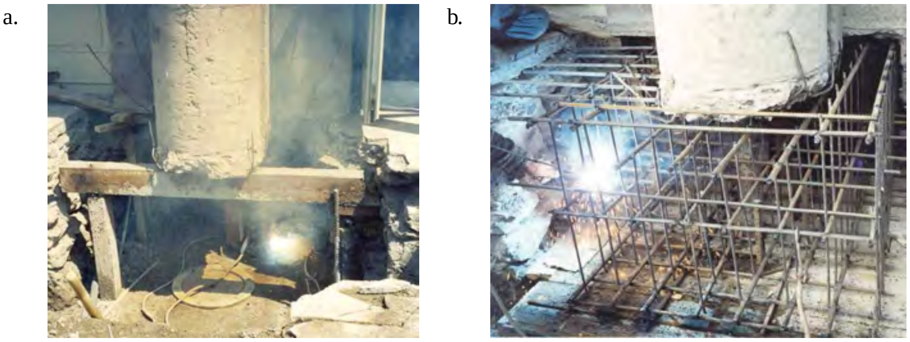

Figure 14: Temporary support under the one half of the existing column section (a), and existing column and the wall behind it are supported temporarily and the reinforcement frame of the upper pedestal is installed (b)

1.3 Retrofitting Design of the Existing Cultural Heritage Iasi City Hall Building (Iasi County, Romania) by Means of Base Isolation

Experience accumulated in Armenia in retrofitting of existing buildings including those of historical and architectural value created a good basis for participation in the international competition announced by the Government of Romania for development of the design on retrofitting by base isolation of the 178 years old historical building of the Iasi City Hall (Fig. 15). Design was developed in cooperation with Romanian company MIHUL S.R.L. It was approved by the Technical Committee for Seismic Rick Reduction (TCSRR, a body especially created by the Government of Romania) on June 1, 2009.

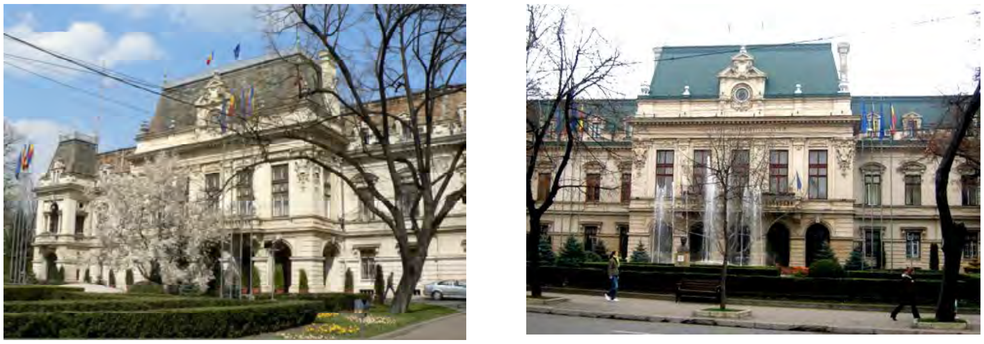

Figure 15: Views of the Iasi City Hall building

The structural system consists of un-reinforced masonry walls with primarily wood horizontal diaphragms. The thicknesses of the interior and exterior walls vary between 40 to 60 cm and up to 100 cm respectively. Stone foundations have been provided under the masonry bearing walls. The building suffered repairable damage after the 1977 Vrancea earthquake. Thus, the bearing walls were repaired by grout injection, reinforced concrete slabs replaced damaged floors, and the tall chimneys were anchored in place using steel ties. The Iasi City Hall is located in the seismic zone C, and based on Romanian Building Code P100-92, the expected peak ground acceleration for that zone is 0.2 g. The soil in the vicinity of the building is classified as stiff clay sensitive to moisture; the ground water table is approximately 6 m below surface [12]. However, the TCSRR has requested to accept the peak ground acceleration (PGA) for retrofitting design of the Iasi City Hall building equal to 0.28 g. TCSRR had justified its request mentioning that either for the 100 years mean recurrence interval

0.2 g PGA shall be multiplied by the importance factor 1.4 according to the Romanian seismic code in force P100-1/2006 or for the 475 years mean recurrence interval PGA at Iasi City, estimated by Probabilistic Seismic Hazard Assessment for Vrancea earthquakes is also equal to 0.28 g.

The key objective of the given work was elaboration of structural concept and the design of retrofitting by base isolation of the Iasi City Hall building, which will ensure cost-effectiveness of the construction works, high reliability of the structure and preservation of the historical and architectural value of this building.

1.3.1 Structural Concept of Retrofitting by Base Isolation of the Iasi City Hall Historical Building

Base isolation method for an existing building with bearing walls that envisions placing of seismic isolators at the level of basement solves the problem according to the innovative technology described in Sections 1.1 and 1.2. It is known that the City Hall building does not have a basement under its whole area. Only a partial basement exists under a part of the building between the axes “3”-“5” and “K”-“P”, as well as the axes “5”-“8” and “M′”-“N”. It was proposed based on the accumulated experience [8, 11, 13] on retrofitting of the similar buildings by base isolation to extend the basement throughout the whole building built surface.

This will require to excavate the soil from the inside of the building and to bare the existing foundation walls. Obviously, that these walls before creation of the isolation system must be thoroughly cleaned and washed from the remainders of soil and then adequately strengthened. The suggested structural solution provides for jacketing of the natural stone walls of foundations. The typical thickness of concrete utilized for the jacketing of masonry walls is 5 cm. There is no need for increasing of the thickness of jacketing as in base isolated structures significant reduction of the shear forces takes place. For the same reason there is also no need for cementitious injection of the basement walls. By implementing the shotcrete 5 cm thickness of jacketing could be achieved easily. However, TCSRR was insisting on increasing of the thickness of R/C jacket and on increasing of the diameter of reinforcing bars in the jacket. Therefore, finally the thickness of the basement walls jackets was increased from 5 cm to 8 cm and the diameter of reinforcing bars of the jackets steel meshes of 150x150 mm was increased from 5 mm to 8 mm. Also at the level of the basement floor a R/C slab with the thickness of 10 cm was additionally designed. Nevertheless, it was mentioned by the designers that the need in such a slab and in increasing of the jacket’s thickness is questionable and not justified.

The new approach on installation of clusters of seismic isolators which was successfully implemented in many buildings in Armenia was also proposed for retrofitting of the Iasi City Hall building (Fig. 16). Immediately above the seismic isolation plane a 150 mm thick reinforced concrete slab, which will cover the basement, was also proposed. This approach will significantly increase the reliability of the whole structure (building plus the isolation system), will bring to increased rigidity of the superstructure (the part of the building above the isolation plane) and will bring to more uniform distribution of seismic forces on isolators.

By implementing the suggested base isolation method a new basement will be created. The height of that basement under the slab is 1.85 m, however under the upper beam of isolation system the height is 1.3 m (Fig. 17). The height of the basement is limited because of the deepness of the foundation walls. This deepness was discovered in-situ through excavation of soil along one of the exterior walls of the building and was equal to 2.4 m approximately. According to the Romanian Codes at least 0.4 m of the foundation walls should remain in the soil. Therefore, the basement could be designed with the mentioned height only. Of course, such a basement can not be considered as a luxury premise, but it can be successfully used for many purposes. At the same time the height of the existing basement will not be changed/reduced.

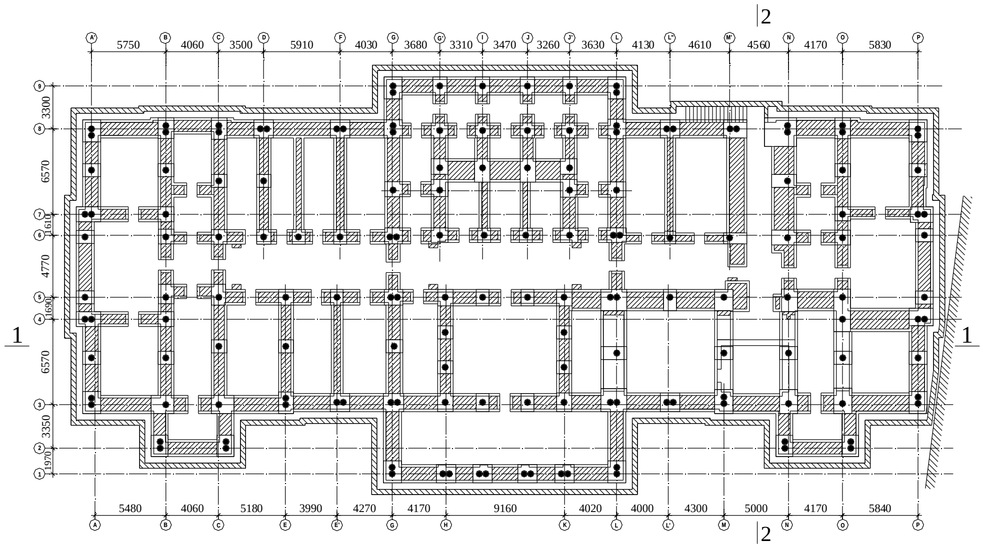

Figure 16: Plan of location of seismic isolators on the level of the newly created basement highlighting the lower pedestals under the isolators and the lower continuous beams along the whole perimeter of the bearing walls

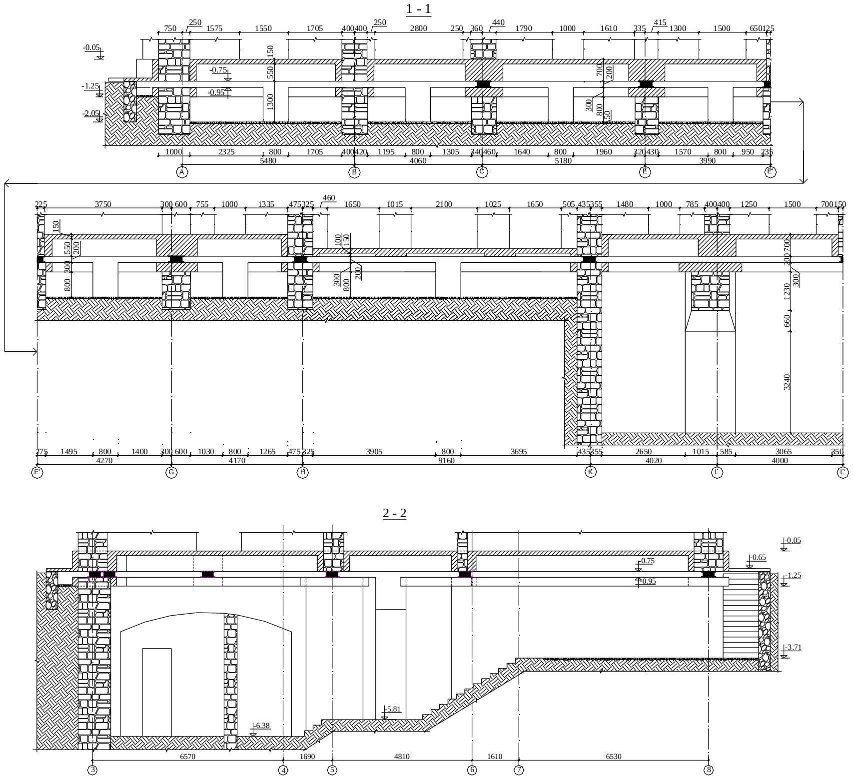

Figure 17: Longitudinal (1-1) and transverse (2-2) vertical elevations of the basement and isolation system of the building according to the developed structural solution

Regarding the bearing walls above the isolation interface it is suggested to execute local strengthening of walls where local cracks exist by cement injection in the cracks and by fixing here of 6 mm steel clamps and plastering those parts. This is just a constructive measure, which is actually not required by carried out calculations. Despite this TCSRR has requested to change the mentioned clamps by the steel meshes of 100x100 mm with the reinforcing bars of diameter 8 mm.

1.3.2 Seismic Isolation Laminated Rubber Steel Bearings (SILRSB) to be Applied for Retrofitting of the Iasi City Hall and Some Results of its Earthquake Response Analysis

In order to develop the retrofitting design the Iasi City Hall building was analyzed under the seismic impacts with PGA equal to 0.28g following the request of TCSRR. This committee has also mentioned that according to the Code P100-1/2006 the demand spectral displacement at the period of vibrations of base isolated building equal to 2.0 sec and the damping ratio of 5% for Iasi is 27 cm. Therefore, it was suggested by designers to accept the value of the actual damping ratio for seismic isolators equal to 15%. In this case according to the Annex A of P100-1/2006 the mentioned displacement demand shall be recomputed and reduced by a factor of 0.707 (27x0.707=19.09 cm). Period of vibrations of the base isolated Iasi City Hall building, as it is given in [15], is the same in longitudinal (X) and in transverse (Y) directions and is equal to 2.13 sec. This means that the calculated displacement demand will actually be equal to 2:2.13x19.09=17.92 cm. TCSRR has also mentioned that “Good practice and the international codes request a total displacement for design increased by 50% with respect to displacement demand”. Satisfying this requirement the final value of a total displacement D=17.92x1.5=26.88 cm was accepted for retrofitting design of the Iasi City Hall building.

However, the statement given by TCSRR about a total displacement seems weak and not justified. In Science and Engineering such statements are not acceptable as they are not clear and are made without any references. Also when it is stated as “Good practice …” shall some one understand that there is a “Better practice…” or “Best practice…” and what has to be done in these cases? Most probably the absence of the extensive experience on base isolation in Romania is forcing the members of TCSRR to require an over designed isolation system, which will bring to artificial increase of the cost of retrofitting of the Iasi City Hall building. Is there a need for that? Those countries, which are currently extensively using seismic isolation technologies for retrofitting or for new construction like Japan [16], Russia [17], China [18], Italy [19], Armenia [13], and others are constantly reporting on reliability and cost effectiveness of these technologies.

If it is so then why seismic isolation should be expensive in Romania? There is a risk that in case of artificial increase of retrofitting cost the Iasi City Hall, being over designed, will become the first and the last building retrofitted by base isolation following the sad experience of USA where because of similar extremely high conservatism seismic isolation is actually dying. But TCSRR was arbitrarily requesting to significantly increase the values of PGA and of design displacement of isolation system. This was forcedly done in the design with the understanding that it will raise the cost of retrofitting works unnecessarily.

Based on the above for creation of seismic isolation system under the Iasi City Hall building the SILRSBs made from neoprene were accepted similar to those used for retrofitting of the apartment and school buildings with the damping factor equal to 15% [14]. Earthquake response analysis of the building was carried out by SAP2000 non-linear program. The design model was developed using different types of finite elements for walls, floor slabs and seismic isolators.

The non-linearity was considered only for seismic isolators because for cases like Iasi City Hall building there is no need to apply non-linearity to superstructure. For the linear model the isolators are given the effective stiffness equal to 0.81 kN/mm. For non-linear model the isolators have initial stiffness equal to 3 kN/mm and post yield stiffness equal to 0.81 kN/mm.

For the analysis TCSRR has requested to select only those acceleration time histories which "… characterized by a corner period of response spectra T_c close to the value of 0.7 sec. The design accelerograms might be also compatable with local soil condition in Iasi, as those conditions have been experienced during the Vrancea 1986 and 1990 earthquakes". Finally 9 accelerograms were selected and scaled to acceleration 0.28g: 4.03.1977 Vrancea Earthquake, EW direction at Buc-INCERC station ($T_c = 0.78$); 30.05.1990 Vrancea Earthquake, EW direction at Buc-Magurele station ($T_c = 0.64$); 30.08.1986 Vrancea Earthquake, NS direction at Iasi station ($T_c = 0.44$); 30.08.1986 Vrancea Earthquake, EW direction at Iasi station ($T_c = 0.36$); 31.05.1990 Vrancea Earthquake, EW direction at Iasi station ($T_c = 0.40$); 30.08.1986 Vrancea Earthquake, NS direction at Istrita station ($T_c = 0.62$); 31.05.1990 Vrancea Earthquake, EW direction at Istrita station ($T_c = 0.64$); 30.08.1986 Vrancea Earthquake, NS direction at Muntele Rosu station ($T_c = 0.70$); 30.05.1990 Vrancea Earthquake, EW direction at Muntele Rosu station ($T_c = 0.72$).

The following results of calculations were obtained: periods of vibrations in X and Y directions are equal to each other and equal to 2.13 sec; floor accelerations along the height of superstructure in both directions are the same and are equal to 0.085g in average, which means that thanks to application of base isolation the input PGA of 0.28g decreases by about 3.3 times; in none of the isolators the vertical force exceeds 1500 kN; superstructure is moving in horizontal direction as an absolutely rigid body without any overturning and this as well as the above results underline the high effectiveness of the implemented base isolation system.

Also it should be mentioned that at small deformations, which correspond to the wind impact, the initial stiffness of rubber bearings is much higher than their effective stiffness and, thus, the ability of the system to provide an intrinsic restraint against wind loading is confirmed. Structural elements above and below the isolation interface are working only in elastic stage. In comparison with the linear analysis non-linear analysis brings to increase (27%) of average displacement of isolation system and to decrease (35%) of average floor accelerations above it. Other average results of calculations by linear and non-linear versions are given below in the Table 3. Figure 18 visually illustrates the reduction of input acceleration in the superstructure of the base isolated Iasi City Hall in longitudinal direction under the impact of the 30.08.1986 Vrancea Earthquake acceleration time history, NS direction recorded at Muntele Rosu station.

To the best demonstration of the effectiveness of the proposed retrofitting by base isolation the Iasi City Hall building was also analyzed as a fixed base structure using the same selected acceleration time histories. The obtained average results are given in Table 4.

It is easy to notice that in base isolated building the maximum average story drift of superstructure is equal to 1.67 mm while in fixed base building this value reaches to 6.23 mm, which is about 3.7 time bigger. The checked stress-strain states show that the fixed base building must be totally strengthened. Otherwise the fixed base building will not resist the earthquake with PGA of 0.28g and even 0.2g. In the same time the retrofitting of this building by base isolation excludes the necessity of strengthening of superstructure. As an example, Figure 19 presents the distribution of in-plane direct stresses and of in-plane shear stresses over the surface of the wall along the axis "G" for fixed base and base isolated buildings and Figure 20 visually illustrates amplification of the input acceleration along the height of the fixed base building in longitudinal direction under the impact of the 30.08.1986 Vrancea Earthquake acceleration time history, NS direction recorded at Muntele Rosu station.

Level	Longitudinal (X) direction			Transverse (Y) direction		
	Displacement, mm	Acceleration, g	Shear force, kN	Displacement, mm	Acceleration, g	Shear force, kN
Linear analysis						
First floor slab	118.50	0.13		118.01	0.13	
Ground floor slab	117.43	0.13		116.80	0.13	
Top of isolators	116.40	0.13		116.42	0.13	
Bottom of isolators	0.12	0.28		0.11	0.28	
Foundation	0.00	0.28	15031	0.00	0.28	15025
Non-linear analysis						
First floor slab	151.35	0.09		151.48	0.09	
Ground floor slab	150.72	0.08		148.77	0.09	
Top of isolators	148.54	0.08		147.61	0.08	
Bottom of isolators	0.55	0.28		0.52	0.28	
Foundation	0.00	0.28	19132	0.00	0.28	19000

Table 3: The average results of the linear and non-linear earthquake response analyses of the base isolated Iasi City Hall building using 9 acceleration time histories scaled to 0.28g

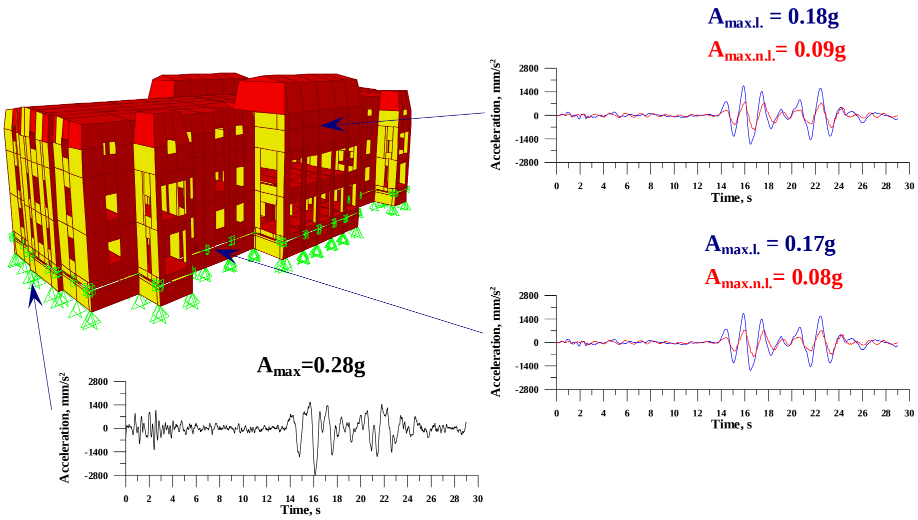

Figure 18. Comparison of the response accelerations on the levels of the top of isolators and of the slab of conference hall by the linear and non linear analyses in longitudinal direction using 30.08.1986, NS Muntele Rosu accelerogram with T_c=0.7 sec

Level	Longitudinal (X) direction			Transverse (Y) direction		
	Displacement, mm	Acceleration, g	Shear force, kN	Displacement, mm	Acceleration, g	Shear force, kN
First floor slab	13.26	1.04		12.81	1.18	
Ground floor slab	7.16	0.66		6.82	0.63	
Basement slab	0.55	0.28		0.62	0.28	
Foundation	0.00	0.28	58583	0.00	0.28	62605

Table 4: The average results of earthquake response analyses of the fixed base Iasi City Hall building using 9 acceleration time histories scaled to 0.28g

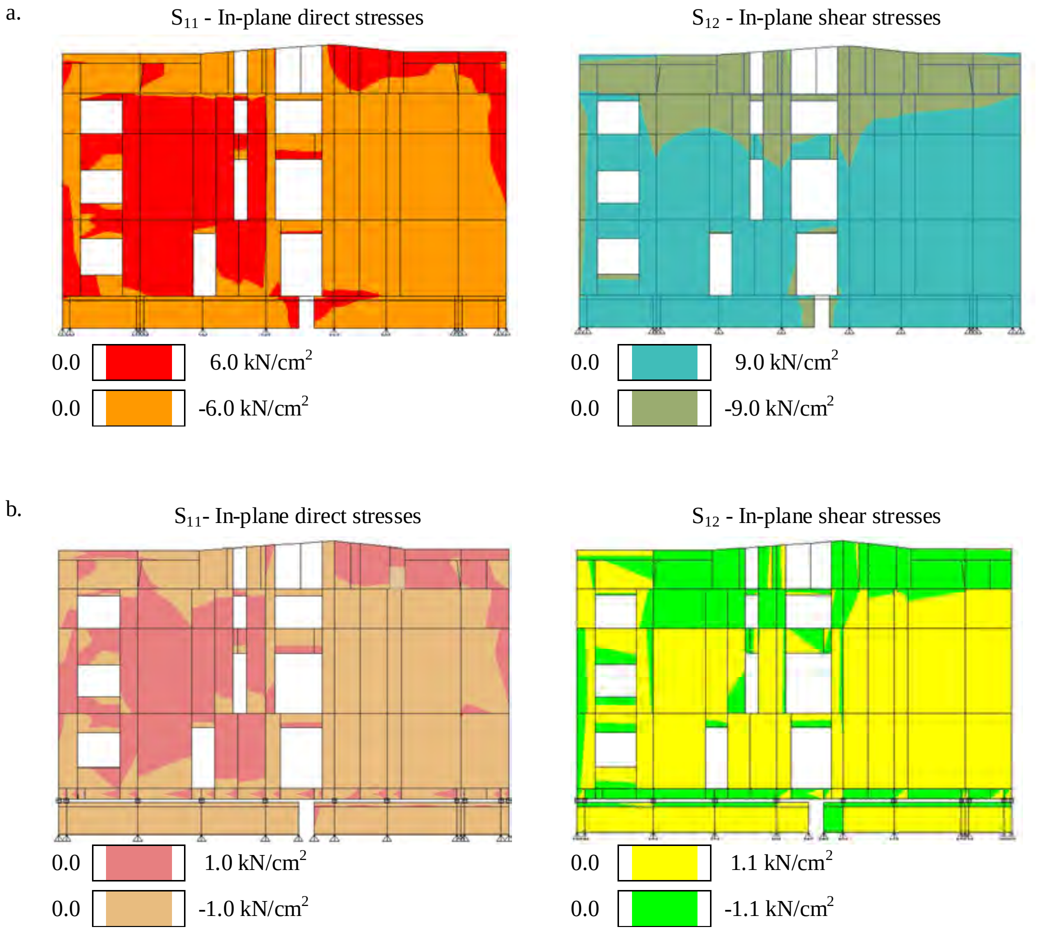

Figure 19: Stress distribution over the wall along the axis "G" for fixed base (a) and for base isolated buildings (b)

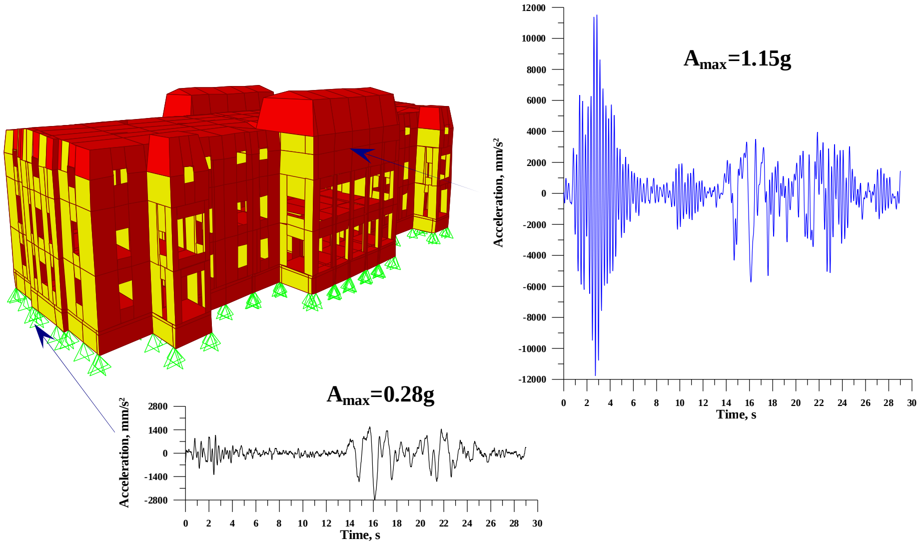

Figure 20: Response acceleration at the top (the slab of conference hall) of fixed base building in longitudinal direction using 30.08.1986, NS Muntele Rosu accelerogram with T_c=0.7 sec

2 RETROFITTING BY BASE ISOLATION VS. CONVENTIONAL RETROFITTING

Conventional retrofitting techniques to be applied for existing buildings most probably are not acceptable in Armenia and generally in developing low income countries as such techniques require huge investments including those related to the re-settlement of residents. However, still conventional retrofitting is used much more widely and frequently than innovative retrofitting which is conditioned by the lack of knowledge and by conservatism of engineers/designers, developers and building owners. Nevertheless, their vision of the philosophy of retrofitting/strengthening of existing buildings should be and will be changed in the course of time as little by little with more and more applications of innovative retrofitting technologies it become obvious that such technologies are incomparably more effective and reliable structurally and more cost efficient.

2.1 Comparison of Retrofitting Technologies in Armenia

Conventional strengthening/retrofitting techniques are including: stiffening existing wooden floors and roofs by covering them with a layer of reinforced concrete; insertion of reinforced concrete ring-beams into the inner face of external walls at floor and eaves level to tie vertical and horizontal elements together; strengthening of walls (mainly when cracked) by cement injection or by adding a thin layer of cement render reinforced with steel mesh on either side of the wall, etc.

In [20] it is mentioned that in rare instances, base isolation has been used to protect the structure from the ground shaking, but this is very expensive. This statement is not always true and is not reflecting real situation in every country where seismic (base or roof) isolation is widely implementing. For example in Armenia due to seismic isolation the cost of retrofitting is about 2.0 times less in comparison with the cost of conventional retrofitting. In this regard an interesting analysis was carried out by one of the Armenian design company “Project-6” LLC (Director G. Gulanyan). With participation of the first author of this paper the company has analyzed and compared the cost of strengthening of existing stone apartment buildings of series 1A-450 by different methods (Tab. 5). It was assumed that the cost of the most expensive method of traditional strengthening comprises 100%.

Method of strengthening	Cost in %	Needed action
Traditional method with application of reinforced concrete jackets, frames and floor slabs. This method is applicable for buildings with damage extent from 2 to 3*	100	Evacuation of tenants, move out furniture
Traditional method with application of only reinforced concrete frames. This method is applicable for buildings with damage extent from 1 to 2	43	Evacuation of tenants
Innovative method with application of base isolation and local strengthening of walls only by reinforced concrete jackets. This method is applicable for buildings with damage extent from 2 to 3*	37	Without evacuation of tenants, partial move of furniture
Innovative method with application of base isolation and total strengthening of walls by cement injection. This method is applicable for buildings with damage extent from 2 to 3	31	Without evacuation of tenants, partial move of furniture
The same as previous but with local strengthening of wall by cement injection for buildings with damage extent from 1 to 2	27	Without evacuation of tenants, partial move of furniture
The same as previous without touching the superstructure for buildings with damage extent from 0 to 1	21	Without evacuation of tenants

* This method can also be applied for buildings with damage extent 4, however, with due regard of economic and social factors

Table 5: Comparison of the cost of strengthening of existing stone apartment buildings of series 1A-450 by different methods

From Table 5 it follows that in Armenia the cost of innovative method of strengthening/retrofitting of stone apartment buildings with application of base isolation is 2.5 times less in average in comparison with the cost of traditional methods of retrofitting. And this is of course with consideration of the cost of seismic isolation rubber bearings but without consideration of the cost of evacuation of tenants. It is easy to understand that evacuation of tenants requires huge additional investments in order to provide evacuated tenants with temporary shelters, water, sewer, electricity and relevant infrastructure. Consideration of these additional investments makes in absolutely clear and obvious that at least in those earthquake prone countries where progressive thinking of designers/engineers, developers, building owners and decision-makers, as well as progressive codes are exist and also where it is possible manufacturing or importing low-cost seismic isolators the preference should be given to the innovative methods of retrofitting with application of base isolation. In the result of its analysis “Project-6” had concluded that the most cost effective technique for strengthening of existing buildings is base isolation in combination with cement injection or with polymer-cement slurry injection for total or local strengthening of the damaged bearing walls.

Above several remarkable projects on retrofitting by base isolation are described. One of them is retrofitting of the existing stone apartment building of series 1A-450 in the city of Vanadzor. This project is an actual example of cost effectiveness of retrofitting by base isolation vs. conventional retrofitting. The cost of retrofitting of this building defined in the result of competitive bidding is equal to 165.600 USD including the cost of rubber bearings. Other two similar buildings in the same city were retrofitted conventionally. One was retrofitted with application of reinforced concrete jackets and frames and it cost is equal to 340.000 USD. The other one was retrofitted by insertion only of reinforced concrete horizontal ring-beams and vertical columns into the external and internal bearing walls and it cost is equal to 294.200 USD. These actual examples prove ones again that substantial saving (about 2.0 times) could be achieved thanks to application of base isolation. Also this innovative technology allows avoiding infringement of the external and internal views of the buildings which is extremely important especially at seismic protection of historic buildings and structures of cultural heritage like, for example, the above described building of Iasi City Hall.

2.2 Comparison of Retrofitting Technologies in Romania

Special analysis was carried out by the second author of this paper in order to reveal cost effectiveness of retrofitting by base isolation of the buildings that represent an architectural monument. Four buildings were considered which were strengthened conventionally (Fig. 21, 22, 23 and 24) and the results were compared with those obtained in retrofitting design of Iasi City Hall by application of base isolation.

Structural systems of these buildings as well as of the Iasi City Hall building are similar. They have bearing walls made of brick on the continuous stone masonry foundation. Their floors are made of wooden beams but above the basements (if there are) the floors are made of small brick arches. The shaped limestone of foundations is walled up with dirty sand and lime mortar. The compressive strength of brick corresponds to the grade of 25-50 and of mortar – to the grade of 4-10.

In the considered buildings there were inclined cracks observed along the height of the bearing walls with the opening of 1-3 mm. Most of them occurred around the windows and doors as a possible result of the earthquake impact. Also cracks are usually increase in their number, length and openings by the uneven settlements of the ground under the foundation because of wetting or exceeding its local bearing capacity.

Fig. 21: View of “Georghe Pirvan “ Museum, Bârlad constructed in 1880

Fig. 22: View of Palace of “Alexandru Ioan Cuza” University of Iasi which was constructed in two stages: first in 1894 and then in 1928-1934

Fig. 23: "Alexandru Ioan Cuza" University of Iasi building "D" constructed in 1880 and improved in 1938

Fig. 24: School Inspectorate of Iasi building "A" constructed at the beginning of the 20th century

Conventional strengthening of these buildings included reinforced concrete jacketing of foundations with the thickness of 8-20 cm and the execution of reinforced concrete belts at the bottom and at the top of foundations. Sometimes the belts were designed larger at the bottom to increase the width of foundations. Above the foundations the strengthening included:

- injection of all the cracks with additive cement;
- reinforced concrete jacketing of the bearing walls by shotcrete in 2-3 layers;
- introduction of a system of reinforced concrete elements (additional shear walls, columns, belts);
- reinforced concrete framing of the door and window openings connected to the walls' jackets;
- execution of a continuous belts at the top of the walls;
- replacing the wooden floors by the reinforced concrete slabs, etc.

The major inconvenience of these strengthening systems is the need to remove and restore all the architectural elements inside and outside the building and replacing the original fresco plaster of the monument. In many cases these original elements cannot be removed, and these will require restoration after the next severe earthquake that will affect the building.

Actually the cost of retrofitting of the considered buildings of cultural heritage consist of the cost of structural strengthening and of total architectural restoration, which is not the case in retrofitting by base isolation. During the retrofitting by base isolation the original architectural elements, frescos, etc. are preserved in high proportion and they may need only local intervention with incomparably lower costs. At the conventional retrofitting a very difficult task is restoration of the original finishes that requires high qualified manpower to execute the plasterwork of architectural elements, mosaics, shaping the stones, etc. Table 6 gives the information on retrofitting costs for all considered buildings.

Comparison of the values given in Table 6 shows significant difference in the costs of innovative retrofitting vs. conventional retrofitting. The average cost of structural strengthening by conventional methods is equal to 233 €/sqm which is higher than the cost of retrofitting by base isolation (including the cost of seismic isolators) by 1.14 times. For architectural restoration these figures are 248 €/sqm and 2.16 times, respectively. Thus, finally retrofitting by base isolation costs 1.5 times less then conventional retrofitting. However, above in Section 1.3 was mentioned that in the retrofitting design for Iasi City Hall many additional strengthening measures were envisaged by the requests of TCSRR which actually have artificially increased the cost of retrofitting by base isolation. If to take this into account one can definitely say that cost savings would be much more and the figure of 1.5 may be closer to 2.0 what was obtained for ordinary buildings.

Name of the building	Type of retrofitting	Cost of structural strengthening €/sqm	Cost of architectural restoration €/sqm	Total cost of retrofitting €/sqm
“Georghe Pirvan “ Museum, Bârlad	conventional	230	260	490
Palace of “Alexandru Ioan Cuza” University of Iasi	conventional	240	250	490
“Alexandru Ioan Cuza” University of Iasi building “D”	conventional	230	240	470
School Inspectorate of Iasi building “A”	conventional	230	240	470
Iasi City hall	base isolation	204	115	319

Table 6: Retrofitting costs for different buildings of cultural heritage/architectural monuments in Romania

REFERENCES

[1] K. Fuller, C. Lim, S. Loo, M. Melkumyan, K. Muniandy, Design and Testing of High Damping Rubber Earthquake Bearings for Retrofit Project in Armenia. Earthquake Hazard and Seismic Risk Reduction. Editors – Serguei Balassanian, Armando Cisternas and Mikayel Melkumyan. *Kluwer Academic Publishers.* The Netherlands, 379-385, 2000.

[2] M. Walters, B. Honeck, E. Elsesser, Use of Seismic Isolation in New and Retrofit Construction. *Proceedings of the Joint ASME/JSME Pressure Vessels and Piping Conference, Seismic, Shock and Vibration Isolation,* Honolulu, HI, Vol. PVP319, 31-38,1995.

[3] S. Naaseh, Seismic Retrofit of San Francisco City Hall: The Role of Masonry and Concrete. *Proceedings of the 3rd National Concrete Masonry Engineering Conference,.* San Francisco CA, Vol.2, 769-795, 1995.

[4] R. Skinner, W. Robinson, G. McVerry, An Introduction to Seismic Isolation. *John Willey & Sons, Ltd.*, 1993.

[5] Report by the Ehrenkrants Group, Burtch Beall, E.W. Allen and Associates, Forell/Elsesser Engineers and SSD, Inc., Base Isolation Study for the Renovation of the City and County Building, Salt Lake City, Utah, 1986.

[6] M. Melkumyan, Base Isolation Retrofit Project In Armenia. *Proceedings of the UNIDO Workshop on Use of Natural Rubber Based Bearings for Earthquake Protection of Small Buildings,* Jakarta, Indonesia, 1994.

[7] M. Melkumyan, Seismic Isolation of Civil Buildings in Armenia. *Journal “Progress in Structural Engineering and Materials”*, Vol.4, No. 4, 344-352, 2002.

[8] M. Melkumyan, The Use of High Damping Rubber Isolators to Upgrade Earthquake Resistance of Existing Buildings in Armenia. *Proceedings of the International Post-SMiRT Conference Seminar on Seismic Isolation, Passive Energy Dissipation and Active Control of Seismic Vibrations of Structures*, Taormina. Sicily, Italy, 861-867, 1997.

[9] K. Fuller, A. Roberts, Longevity of Natural Rubber Structural Bearings. *Proceedings IRC 97*, Kuala Lumpur, 777-87, 1997.

[10] M. Melkumyan, G. Käppeli, R. Khalatyan, H. Hovivyan, Application of Seismic Isolation for Retrofitting of Existing 3-story Stone Building of the School #4 in the City of Vanadzor, Armenia. *Proceedings of the 8th World Seminar on Seismic Isolation, Energy Dissipation and Active Vibration Control of Structures,* Yerevan, Armenia, 557-565, 2003.

[11] M. Melkumyan, H. Hovivyan, L. Movsessyan, S. Terjanyan, Technique of Installation of Seismic Isolation Bearings in an Existing Building with Historical and Architectural Value. *Proceedings of the 8th World Seminar on Seismic Isolation, Energy Dissipation and Active Vibration Control of Structures,* Yerevan, Armenia, 629-641, 2003.

[12] K. Miyamoto, A. Gilani, Base Isolation for Seismic Retrofit of Structures, Application to a Historic Building in Romania. *Seismic Risk Reduction, Proceedings of the International Symposium.* Bucharest, Romania, 585-592, 2007.

[13] M. Melkumyan, Base and Roof Isolation for Earthquake Retrofitting and Protection of Existing Buildings in Armenia. *Proceedings of the International Symposium on Seismic Risk Reduction (the JICA Cooperation Project in Romania),* Bucharest, Romanian, 593-600, 2007.

[14] M. Melkumyan, A. Hakobyan, Testing of Seismic Isolation Rubber Bearings for Different Structures in Armenia. *Proceedings of the 9th World Seminar on Seismic Isolation, Energy Dissipation and Active Vibration Control of Structures,* Kobe, Japan, , Vol.2, 439-446, 2005

[15] M. Melkumyan, E. Gevorgyan, Structural Concept on Retrofitting by Base Isolation and Analysis of the Iasi City Hall Historical Building in Romania. *Proceedings of the International Conference on Protection of Historical Buildings by Reversible Mixed Technologies,* Rome, Italy, 2009.

[16] T. Fujita, Demonstration of Effectiveness of Seismic Isolation in the Hanshin-Awaji Earthquake and Progress of Applications of Base-Isolated Buildings. *Report on 1995 Kobe Earthquake by INCEDE, ERC and KOBEnet. IIS, University of Tokyo-Voluntary Information Network for Earthquake Disaster Mitigation,* Serial No. 15, 197-216, 1999.

[17] V. Smirnov, J. Eisenberg, F. Zhou, Y. Chung, A. Nikitin, Seismoisolation for Upgrading of an Existing Historical Building in Irkutsk-City, Siberia-Russia. *Proceedings of the 12th World Conference on Earthquake Engineering,* Auckland, New Zealand, Paper No. 0962, 2000.

[18] F. Zhou, W. Liu, Z. Xu, State of the Art on Application, R & D and Design Rules for Seismic Isolation and Energy Dissipation in China. *Proceedings of the 8th World Seminar on Seismic Isolation, Energy Dissipation and Active Vibration Control of Structures,* Yerevan, Armenia, 174-186, 2004.

[19] **A.** Martelli, M. Forni, S. Rizzo, Seismic Isolation: Present Application and Perspectives. *Proceedings of the International Workshop on Base Isolated High-Rise Buildings,* Yerevan, Armenia, 1-26, 2008.

[20] A. Coburn, R. Spence, Earthquake Protection. *Second Edition. - John Willey & Sons, Ltd.,* 2002.

COMPDYN 2011
III ECCOMAS Thematic Conference on
Computational Methods in Structural Dynamics and Earthquake Engineering
M. Papadrakakis, M. Fragiadakis, V. Plevris (eds.)
Corfu, Greece, 25–28 May 2011

SEISMOISOLATION FOR UPGRADING OF EXISTING HISTORICAL BUILDINGS AND CHURCHES

Jacob M. Eisenberg[1], Vladimir I. Smirnov[2], Alexander A. Bubis[2]

[1] Research Center for Earthquake Engineering, TsNIISK
2th Institutsky Str. 6, Moscow, 109428, Russia
eisenberg@raee.su

[2] Research Center for Earthquake Engineering, TsNIISK
2th Institutsky Str. 6, Moscow, 109428, Russia
smirnov@raee.su

Keywords: seismoisolation, historical buildings, steel-rubber supports, horizontal permissible displacements.

Abstract. *In the beginning of the 70-th a program of analytical and experimental investigations of structure seismoisolation was carried out in Earthquake Engineering Research Center, TsNIISK, Russian Construction State Committee.*

As a result of the research program different structural systems of seismoisolation are designed. Different seismoisolated structures were constructed taking into account the investigation results. More than 500 buildings and historical monuments are seismoisolated in Siberia, Far East, Crimea, Caucasus, Middle Asia and other earthquake hazardous areas of Russian Federation.

Some examples of seismoisolation for upgrading of existing historical buildings, including a bahk building and churches in Irkutsk-city (Siberia) are presented. All steps of installment of the steel-rubber supports in the bank building and church foundations are given.

Seismoisolation was used in the designs of two churches in Irkutsk-city as well: Kharlampiyevskaya (Mikhailo-Arkhangelskaya) and Spasskaya churches which are historical and cultural monuments built in 1779-1790 and 1706-1713 accordingly.

The structural concept includes an asymmetric in plan, columnless brick masonry structure. The building consists of several parts with different design, connected by walls in one unit, except for the porch. Its walls do not have bonding with main building walls.

Also two cultural centers have been strengthened in seismic high earthquake hazardous areas using steel-rubber seismic isolation. One is the Chechen Republic Cultural Center Building Complex, which was damaged during the war. The other building was the Gorno-Altaysk National Drama Theater. Both complexes are situated at sites with design seismic intensity MSK 9 degree.

INTRODUCTION

A program of analytical and experimental investigations of structural seismoisolation was carried out Earthquake Engineering Research Center, TsNIISK, Russian Construction State Committee, Eisenberg [1].

The strong motion accelerograms up to the present time demonstrated very different predominant periods of earthquake ground motions not only during different earthquakes but sometimes even during the same earthquake at distant and the close distances, for example, during Loma-Prieta, 1989, earthquake. The mathematical semi-probabilistic models of earthquake inputs were developed which take in consideration the uncertainty of the predicted spectra and other motion parameters of the future earthquakes and artificial design accelerograms were computer generated, Eisenberg [1], in the early 70-th of XX century.

Experimental part of the investigation program included:

1. Shaking table model and fragment tests;
2. Full scale building dynamic tests using large exciters. The maximum dynamic loading of the structure by means of an exciter corresponded to the design load of 9 MM – intensity and more;
3. Static and dynamic tests of the elements of seismoisolation system (flexible supports, dampers, dry friction elements a.a.).

As a result of the research program different structural system of seismoisolation are designed and buildings are constructed recently in Siberia, Far East, Crimea, Caucasus, Middle Asia and others earthquakes dangerous areas. Specific for these systems is that they are simple in construction and are not expensive. Different structures using seismoisolation were constructed taking into account the investigation results. More than 500 buildings and bridges are seismoisolated in Russia and in former USSR countries.

The prevailing amount of constructed seismoisolation systems in Russia is non-rubber seismoisolation. The seismoisolation effect is achieved by using two and sometimes more than two elements. The two elements are 1 – flexibility elements and 2 – dampers. The flexibility elements are flexible columns in the ground storey of the building, or rocking supports (rocking columns, rocking converted mushroom type supports, other configuration rocking supports). The dampers are mild steel hysteretic elements or RC damaged during earthquake diaphragms, or dry friction elements.

The main design demands are large enough critical horizontal displacements of the flexible columns or rocking supports. Several dozens building are constructed on sliding supports and sliding belts of controlled damping. Usually the steel-teflon pairs were the controlled friction elements. Additional elements of seismoisolation used in Russia are horizontal displacement rigid limiters (stops) and reserve disengaging elements for energy dissipation and for frequency spectra adaptation.

Recent years steel-rubber supports were used in some seismoisolated buildings constructed in Russia, Smirnov, at al [6]. Now some buildings with steel rubber seismoisolation supports are in design process. One of these buildings will be constructed at Alexandrov-city, Sakhalin (a 4 storey school building). The steel-rubber supports for this building are produced in China, Shantou, “Vibro-Tech” Company.

As a result of studies in Moscow EERC the seismic safety of buildings with soft ground stories was exonerated. The reason of many buildings with soft ground stories collapses during recent earthquakes was reinforced concrete as material of bearing ground story columns, not the flexibility of the ground story itself. Design of soft ground story buildings with steel columns as seismoisolation elements combined with dampers and fuse elements is presented.

SEISMOISOLATION FOR UPGRADING OF AN EXISTING HISTORICAL BUILDING IN IRKUTSK-CITY, SIBERIA-RUSSIA

A historical building of an Irkutsk Bank needed retrofitting and upgrading as observation and analysis have brought to conclusions that the seismic reliability of the building doesn't meet the current Seismic Building Code requirements. The bank building was retrofitted using seismic isolation to prevent the damage by earthquakes expected in the future (Figure 1).

The building consists of three blocks. The external bearing system is: brick wall, thickness is 64 cm. The internal system is reinforced concrete columns and brick masonry. The building height is 3 to 4 stories, where walls and columns lower storey were cut at their mid height and LRB's (lead rubber bearings) were installed.

The decision to install seismic lead rubber bearings in the mid level of the ground floor was taken to provide maximum seismic isolation of the existing walls and building columns. The total number of seismic bearings to be installed is 108. Every bearing is designed for 2500 kN load. All the bearings have equal dimensions: diameter – 510 mm, height – 216 mm.

The high-damping steel-rubber supports were produced at the Shantou-city (Southern China) "Vibro-Tech Industrial and Development Co Ltd". The dynamic tests of supports were carried out in South China Construction University in Guangzhou with participation of Russian experts. Due to the reduction of seismic force by isolation, strengthening of the structure above isolators has come to be unnecessary. The part of structure below isolators has been strengthened. A specific construction technology of supports installation in the existing building without its exploitation interruption was developed. The site dynamic tests of the full scale building to investigate the dynamic properties of the seismoisolated building and the correlation between the actual and design values were carried out.

Figure 1: General view of an Irkutsk Bank
a –before reconstruction; b – after reconstruction

The numerical analysis of earthquake response of this Building was carried out in EERC, Moscow by J. Eisenberg and V. Smirnov. The results of the investigation are that in case of the seismoisolation high damping (27% of critical damping) supports both response acceleration and response displacements are sufficiently lower comparing to non-isolated existing building.

The maximum response displacements of the seismoisolated building do not exceed 2.5 cm, maximum response acceleration are in the limits of 550 gals. These values are not hazardous for from point of view of the building safety.

The method of seismic isolation of the existing bank building has revealed the advantages of this method comparing to the conventional methods of retrofitting and strengthening of the buildings located in highly hazardous seismic zones.

1. Seismic isolation of the ground floor part of the building enabled to preserve the building exterior look and to avoid architectural features violation.
2. The result of comparative nonlinear analysis of isolated and non-isolated buildings is that both displacement and acceleration in isolated buildings are significantly lower than in non-isolated ones.
3. The method of gradual isolation of lead rubber bearings in the building blocks enables normal work of the bank.

DESIGN OF A CHURCH BUILDING SEISMOISOLATION

The design of church building in Irkutsk-city seismoisolation in now carried out (Figure 2). Kharlampiyevskaya (Mikhailo-Arkhangelskaya) church is a historical and cultural monument built in 1779-1790.

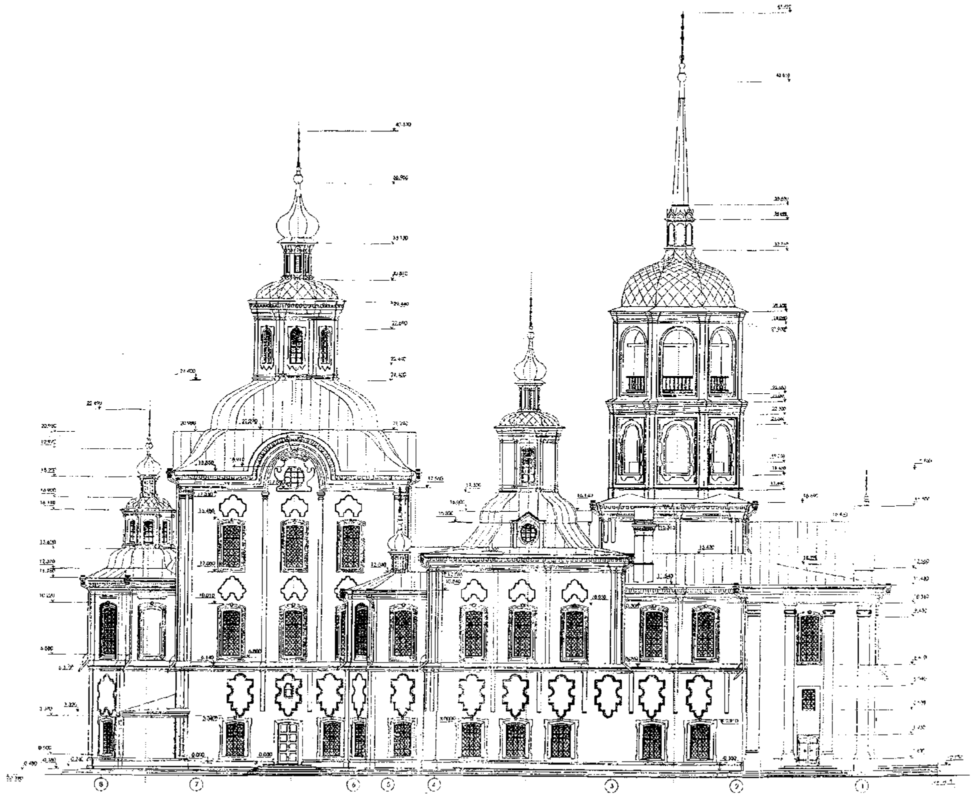

Figure 2: Church buildings

The structural concept includes an asymmetric in plan, columnless brick masonry structure. The building consists of several parts with different design, connected by walls in one unit, except for the porch. Its walls do not have bonding with main building walls. The northern and southern side-chapels have similar structural concept in the form of two-storey parallel bays of different length. On the east side, the bays are completed with the multifaceted apses.

Side-chapels' ground floor is spanned with cylindrical brick vaults, including strippings in the wall vaulted bay. In the first floor, the northern side-chapel narthex and the southern side-chapel refectory are spanned with cylindrical brick vaults. The northern and southern side-chapel churches and the southern side-chapel altar are spanned with octagonal tent brick vaults. The altar apses in the ground and the first floor are spanned with multifaceted closed brick vaults.

The foundations are of shallow, strip, stone masonry type with the artificial subgrade, consisting of pebble and fine sandy loam mixture poured with mortar. The masonry is made of loam Flemish bricks on mortar. Wall thickness is 1.26–2.35 meters. To provide building earthquake stability seismoisolation system, including metal-rubber supports is used in Mikhailo-Arkhangelskaya church foundations.

In order to reduce lateral seismic loads, metal-rubber isolators are installed on the church building superstructures. It is enabled by pliable bracing between building superstructures and foundation. It also provides seismoisolating support dampening quality. These measures are used to increase building natural period of vibrations and to decrease transmission of earthquake power and ground motion to the building superstructures. Estimated building weight is 158060 кN. Total number of rubber-metal seismoisolating supports are 92.

The following sequence of works was offered for supports installation in the existing church building (Figure 3). Foundation replacement and exterior wall seismoisolation installation are carried out in the following sequence:

1. The mortar is injected via injectors (1), to reinforce the upper zone (4) of ground pad (5) (Figure 3a).
2. The antiseismic belt (8) is provided (Figure 3c, d):

- 3 meter long trenches (24) are dug with some intervals;
- Trench bottom is smoothed and covered with two layers of polyethylene film (7);
- Formwork panels (6) are installed;
- Support antiseismic belt (8) with embedded parts (26) for seismic supports fixing (Figure 3c).

3. After the support antiseismic belt is arranged in the whole building, each second hole is open in places where seismic supports are to be installed (25), the walls must be fastened (10), pillar formwork (11, 12) is provided, and support columns (14) for seismic supports are cast in situ (Figure 3e).
4. Wells in ground-and-concrete mass (4) are drilled via holes (27), left in support seismic belt, and coupling bolt studs (9) are passed through them. Bolts are tightened, wells pressure grouting via special channels (18) is carried out, and additional strengthening of ground-and-concrete is provided (4).
5. Each second foundation column along the perimeter is dug out (after reaching 70 percent concrete strength), hole bracing is dismantled, and formwork is removed. Then foundation slabs (19) are installed and foundations are connected (31) (Figure 3f, g).
6. The rest foundations are erected with separate foundation slabs connected into a continuous belt.
7. The foundations for the interior walls are laid down in a similar way.
8. After all foundations are ready and the support antiseismic belt is underpinned, the trench under the whole building is to be open for ground floor arranging. Basement solid-cast reinforced-concrete walls (20) and solid-cast reinforced-concrete ceiling over the basement (22), resting on support antiseismic belt and rigidly connected with it are erected (Figure 3g).
9. Cantilevered solid-cast reinforced-concrete plate (21), rigidly built in the outside branch of support antiseismic belt, which has to overlap the distance between the belt and basement wall is installed along exterior walls contour. A horizontal antiseismic joint, 50 mm high, separating the building overground part from the underground part is provided between the upper basement wall batter and cantilevered plate (21). The joint is stuffed with mineral wool plate, wrapped in polyethylene case, and is sealed with thiokol sealant.
10. After complete basement closing seismic supports are erected.
11. Seismic supports underpinning is to be provided in the following succession:

– Seismic supports (16) are hung in the recesses which were left when concreting support columns (Figure 3f, g) to the top embedded parts (27) with four bolts (29);

– Lower embedded parts (similar to 27) with foundation bolts (15) are hung with the help of four bolts on the lower connecting plates of seismic supports;

– Reinforced concrete support pads (17) (Figure 3f, g) are concreted under embedded parts, 50 mm gap is to be left between a support pad and an embedded part which must be carefully caulked with firm fine concrete, grade V20.

12. After all seismic supports are installed, they are loaded by filing off and removing support columns (30) from under antiseismic support belt.

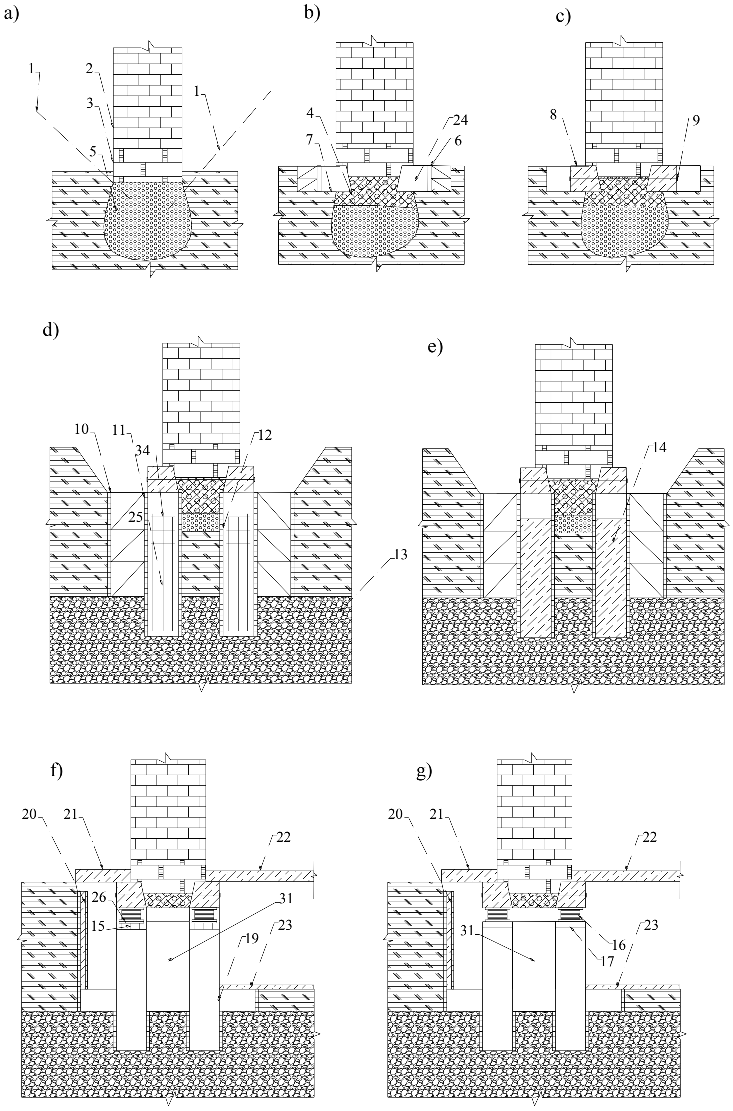

Figure 3: The sequence support installation

CONCLUSIONS

Some new Projects of historical seismoisolated structures used in Russia recently are presented.

Among them are newly constructed buildings and existing buildings, which are strengthened.

Rubber and non-rubber seismoisolation supports were used.

Provisions for seismoisolated buildings of different seismoisolation types were prepared.

Mild steel columns or frames as base isolation elements are presented. Two aspects of their seismoisolation ability are taken into account in design. The one is the building flexibility achieved using these columns. The other aspect is energy dissipation and large enough permissible (safe) horizontal displacement.

REFERENCES

[1]. J.M. Eisenberg, *Adaptive Seismoisolation with Reserve Elements Structures for Earthquake Hazardous Areas*, Moscow, Stroyizdat, 1976.

[2]. J.M. Eisenberg, V.I. Smirnov, M.A. Dashevsky, *Seismic Isolation of Buildings. New Applications and Design Rules in Russia.* International Post-SMIRT Conference Seminar on Seismic Isolation, Santiago, Chile, 457-463, 1995.

[3]. J.M. Eisenberg, *Energy Dissipation and Control of Vibrations of Structures. Low-Cost Seismoisolation In View Of Recent Strong Earthquakes.* International Post-SMIRT Conference Seminar on Seismic Isolation, Capri (Napoli), Italy. 1993.

[4]. J.M. Eisenberg, V.I. Smirnov, A.M. Uzdin, *Progress in Applications and Development Rules for Base Isolation and Passive energy Dissipation of Civil Buildings, Bridges and Nuclear Reactors in the Russia Federation.* International Post-Smirt Conference Seminar on Seismic Isolation, Passive Energy Dissipation and Active Control of Seismic Vibration of Structures, Taormina, Sicily, Italy, 97-112, 1997.

[5]. M.G. Melkumian, *The Use of High Damping Rubber Isolators to Upgrade Earthquakes Resistance of Exiting Building in Armenia.* International Post-Smirt Conference Seminar on Seismic Isolation, Passive Energy Dissipation and Active Control of Seismic Vibration of Structures, Taormina, Sicily, Italy, 861-868, 1997.

[6]. V.I. Smirnov, J.M. Eisenberg, F.L. Zhou, Y. Chung, A.N. Nikitin, *Seismoisolation for Upgrading of an Existing Historical Building in Irkutsk-city, Siberia-Russia.* XI WCEE, New Zealand, 2000.

COMPDYN 2011
III ECCOMAS Thematic Conference on
Computational Methods in Structural Dynamics and Earthquake Engineering
M. Papadrakakis, M. Fragiadakis, V. Plevris (eds.)
Corfu, Greece, 25–28 May 2011

INNOVATIVE MULTIFUNCTIONAL REINFORCEMENT TECHNOLOGY FOR MASONRY BUILDINGS: NUMERICAL VALIDATION AND DAMAGE DETECTION INVESTIGATION

C. Fuggini[1*], E. Chatzi[2], D. Zangani[3], T. B. Messervey[3]

[1]Industrial Innovation Division, D'Appolonia S.p.A.
Via San Nazaro 19, 16145 Genova (Italy)
clemente.fuggini@dappolonia.it

[2] Institute of Structural Engineering, ETH Zürich
Wolfgang-Pauli-Strasse 15, CH-8093 Zürich
chatzi@ibk.baug.ethz.ch

[3] Industrial Innovation Division, D'Appolonia S.p.A
Via San Nazaro 19, 16145 Genova (Italy)
donato.zangani@dappolonia.it, thomas.messervey@dappolonia.it

Keywords: Damage Detection, Masonry Buildings, Numerical Simulations, Multifunctional textiles, Genetic Algorithm.

Abstract. *This paper reports the outcomes of an experimental test campaign for the validation of the performance of a seismic reinforcing strategy of masonry buildings based on the full covering of the building by means of an innovative multifunctional technical textile. This innovative solution, the "Composite Seismic Wallpaper" is made of glass and polymeric fibres in a multiaxial textile structure featuring embedded fiber optics sensors which is connected to the substrate using a special cementitius matrix. The composite obtained is multifunctional in the sense that on one side it reinforces the structure, increasing its capacity to resist to seismic events, and on the other side, it provides localized and distributed static and dynamic measurements before, during and after a seismic event, by means of the integrated sensors. Recently "Seismic Wallpaper" has been full-scale tested as reinforcement of a two-story stone building. The reinforced building has been tested in shaking table tests campaign to prove the feasibility of the distributed and passive reinforcing solution and to investigate the reliability, in detecting the building dynamics, of Fiber Bragg Grating (FBG) sensors embedded in the textile fabric. Sensors measurements recorded during hammer shock tests and shaking tables have been analyzed towards a modal identification of the building modal parameters. This paper first presents the building modelling by means of finite elements analyses, then describes the buildings dynamics as characterized from experimental tests, finally proposes a methodology for damage detection by means of an inverse problem approach that combines an evolutionary method (Genetic Algorithms) and a plain FEM simulation based model for the localization of damage.*

1 INTRODUCTION

Masonry structures are complex structures, as they are constituted by non-homogeneous materials (i.e., bricks, stones, mortar), they exhibit in-plane and out-of-plane failure mechanism which are prevalently sliding, flexural and shear type and they are prone to damages and fragile collapses when excited by dynamic loads. In particular when excited by seismic loads, masonry structures are subjected to cracks propagations which progressive lead the structure to collapse. In which way the structural collapse due to a seismic action may be avoided or move away it is an open point of discussion in the scientific community as many and different techniques may be considered and may be reliable, depending on the characteristics of the input dynamic load and on the different parameters which may be involved.

Most of masonry buildings are old buildings which have not been designed against earthquakes but only to resist to gravity loads and the effect of seismic loads were. During earthquake, seismic loads introduce severe in-plane and out-of-plane forces to unreinforced masonry buildings, many of them, collapse in out-of-plane bending due to lack of reinforcement.

When dealing with the reinforcement of masonry building against natural hazards such as earthquakes, all the aforementioned considerations should be taken into account.

To this aim, the techniques investigated and adopted for the reinforcement of masonry building aimed at providing more flexibility and ductility to the masonry walls and at preventing out-of-plane and/or in-plane failing mechanism by means of guaranteeing a stronger and reliable confinement and connection of the masonry walls. In general the objective of the retrofitting should be to enhance the earthquake resistance of masonry structures in order to avoid its failure in brittle manner.

Following a short review of the historic developments of masonry reinforcement solutions, as they are reported in the more important codes, guidelines and handbooks, they can be divided in traditional (i.e. conventional) techniques and innovative techniques.

Traditional methods of strengthening are intervention techniques to remedy structural deficiency by means of local or overall modification of damaged or undamaged elements (repair, strengthening or full replacement). The conventional methods are:

- Addition of new structural elements (bracings system; steel, timber or reinforced concrete belts);
- Injection of cement or epoxy grout into cracks to fill cracks and voids;
- Local replacement of damaged masonry bricks and reassembling them with improved mortar and proper reinforcement (reinforcing bars);
- Improving the connection between intersecting walls through construction of a reinforced concrete belt, addition of steel plates in the bed-joints, or insertion of inclined steel bars in drilled holes;
- Strengthening and stiffening of horizontal diaphragms;
- Addition of steel ties (along or transversely to the walls, external or within holes drilled in the walls) to connect walls and to improve the overall behaviour of a masonry building;
- Strengthening of rubble core masonry walls by cement grouting;
- Strengthening of walls by confinement with reinforced concrete jackets or steel profiles.

Among the innovative techniques, three main areas can be identified:

- Seismic Isolation (i.e., base isolation);

- Fiber Reinforced Polymers materials;
- Energy Dissipation Devices (as example passive control devices based on Shape Memory Alloy (SMA).

Furthermore seismic retrofitting of most of masonry structures requires compliance with restrictive constraints related to the preservation of the original structural features. Any conceived intervention must achieve structural performance yet still respect the appearance and structural mechanism of the original and be as minimally invasive as possible. Therefore, traditional retrofit strategies may not be suitable for such purposes, and structural engineers need to develop specific techniques. Innovative materials, such as textile composites may be helpful with respect to these issues. In fact composites provide a non-intrusive technique to provide reinforcing strength to a structure and are feasible for applications which include localized crack repair, the reinforcement of critical walls, or the wrapping of existing columns.

In addition, conventional methods add significant mass to the structure, encroach upon the available working space, and adversely affect the aesthetics of the repaired portions. The extra mass added to the structure during strengthening increases the earthquake induced inertia forces and may necessitate the strengthening of the footings. Also from this point of view solution based on innovative composites materials should be adopted. In particular Fiber Reinforced Polymer (FRP) composites offer a viable alternative to the conventional strengthening methods as they offer: high strength to weight ratio, resistance to electro-chemical corrosion, larger creep strain, good fatigue strength, potential for decreased installation costs and repairs, non-magnetic properties.

In the field of strengthening, textiles composite materials combined with mortars were used recently as a means of increasing the strength of masonry, either in diagonal compression [5] or in uniaxial compression through confinement [6, 7]. Studies have dealt with strengthening of: walls, through external prestressing [8]; columns, through confinement [9]; walls subjected to in-plane or out-of-plane loading, through externally bonded strips or overlays [10]; walls through near-surface mounted reinforcement [11].

In general solutions of this type are based on narrow fabric/sheets strips of FRP composite materials (carbon or glass fibers based) glued by means of a resin on masonry walls in localized position. Strips reinforcement solutions based textile materials represent an efficient reinforcement strategy. However, striped reinforcements of masonry walls they may excessively increasing the walls stiffness and may create stress concentrations, which may change the way the structure is responding to actions such as earthquakes and may transfer to weak zones the capacity of the wall to resist.

A step further should be on one side to investigate innovative materials and on the other side to adopt new strategy for the reinforcement solution. An answer to the first need could be to adopt multi-axial composite textiles, while to address the second issue one strategy is to move from localized (i.e. striped) reinforced solutions to global full-cover solutions.

Both issues have been addressed within the EU funded project Polytect (“Polyfunctional Technical Textiles for Protection against Natural Hazard”) which developed an innovative concept for the reinforcement and protection of masonry buildings against earthquakes by means of a multi-axial composite based skin for the full-covering of masonry walls. This solution, in the following “Composite Seismic Wallpaper”, was awarded at the JEC2010, as innovative product in the Building and Construction Category.

The Composite Seismic Wallpaper is an innovative solution, as it not only provides reinforcement capability by means of a multi-axial FRP, but also because it provides monitoring capability by means of fiber optics sensors embedded into the textile since the manufacturing stage. The wallpaper represents a progress beyond the state of the art of masonry building reinforcement solutions using textile materials because:

- It reinforces the building by increasing the structural strength;
- It increases the building's ductility, without stiffness increase;
- It monitors the building structural health by means of strain measurements;
- It detects the damage in the building walls.

Furthermore, the aforementioned characteristics of the wallpaper make it suitable for reinforcing application in compliance with Italian and EU codes referring to this topic. In particular it can be stated that the integration of a monitoring system into a reinforcing solution is needed since there is a lack of information on long-term behaviour of reinforcing applications with textiles materials [12]. In fact from paragraph 5.8.5 "Monitoring of the strengthening system" of [12] it can be extracted what follows: "Due to the poor availability of data regarding long term behavior of FRP systems… it is recommended to perform appropriate monitoring …. to keep the following parameters under control: Temperature… humidity…. displacements and deformations… Potential damage of fibers…. Extensions of defects and delamination…". The seismic wallpaper is an effective and reliable answer to this need.

2 THE COMPOSITE SEISMIC WALLPAPER

From a components point of view, the wallpaper consists of:

- Multi-axial, warp-knitted, AR-glass and Polypropylene (PP) fibres, which constitute the composite fibers (Figure 1);
- Nanoparticle enhanced coatings for the textile fabric;
- Nanoparticle enhanced mortar (the matrix of the composite) to bond the textile to the structure;
- Fibre optic sensors (Figure 2);
- An interrogation system to acquire data from the sensor-embedded textile-mortar composite.

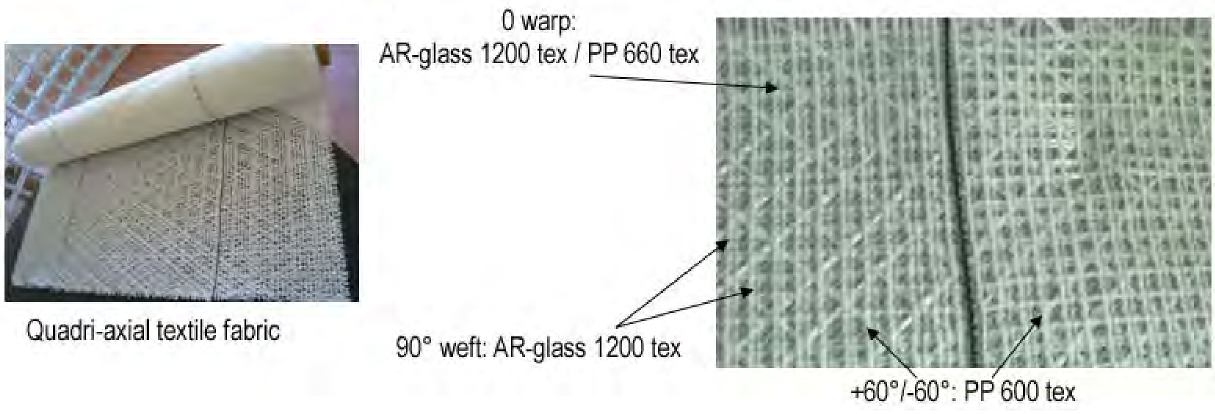

Figure 1: Quadric-axial technical textile

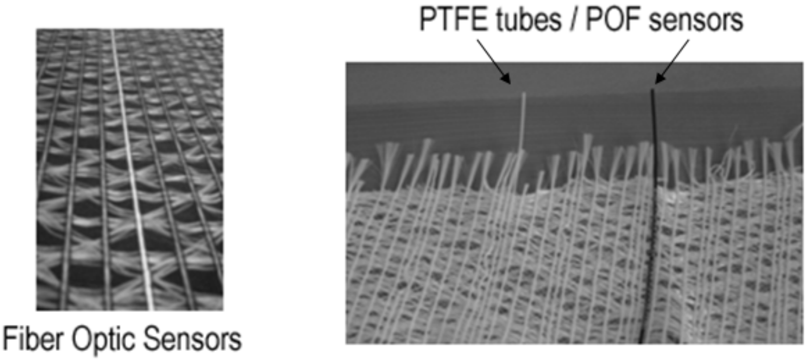

Figure 2: Fiber optic sensors embedded textile

The realization of these components, their processing, and application onto real structures has been investigated within the Polytect project and tested in full-scale seismic tests at the European Centre for Training and Research in Earthquake Engineering (Eucentre) under the "Seismic Engineering Research Infrastructures for European Synergies" (Series) initiative.

An un-reinforced two stories stone building (Figure 3) has been identified to be suitable for the full-scale application of the seismic wallpaper reinforcing solution.

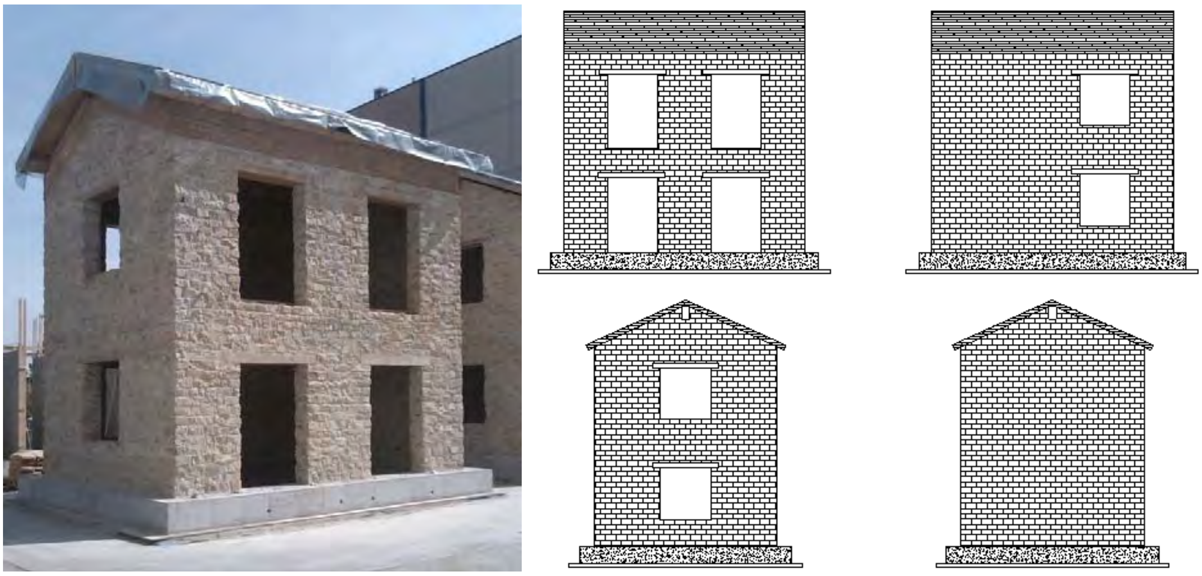

Figure 3: 3D View of the un-reinforced stone building (left); N-S-W-E fronts (right)

The building is made of natural stones which mechanical properties. The roof is wood made and is simply supported to the walls. Its structure is made of longitudinal and transversal beams. The building is 5.80m long (X direction), 4.40m width (Y direction) and 5.80m high (Z direction). The foundation (40cm tall) is made of concrete, while a wood slab is realized in between the first and the second story (Figure 4). The mechanical properties of the materials constituting the building are reported in Table 1 below.

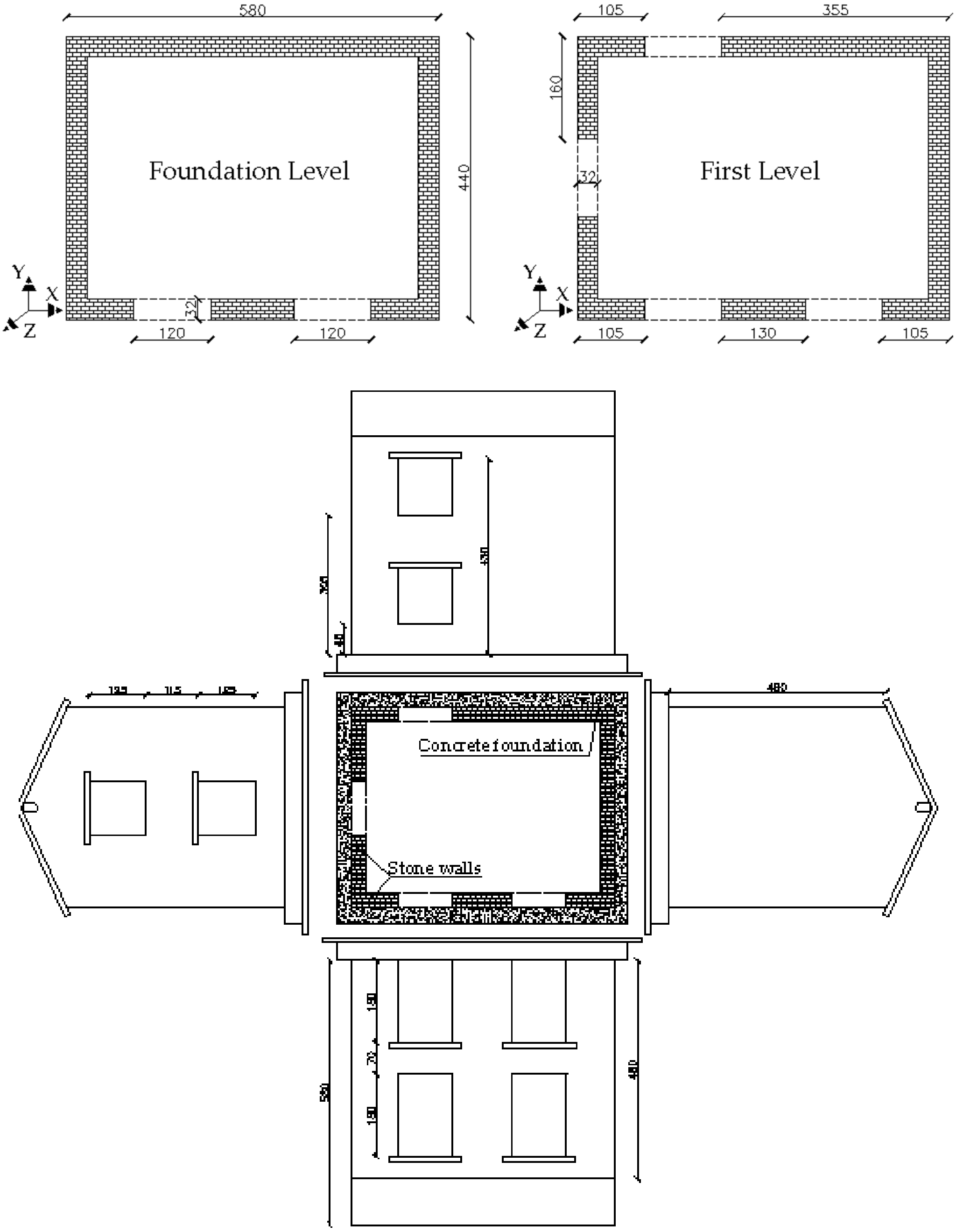

Figure 4: The un-reinforced stone building: plan view (top); sectional view (bottom)

Density	2579 kg/m3
Young Modulus $E_{x,y}$	2550 MPa
Young Modulus E_z	2550 MPa
Poisson Coefficient ν	0.4
Shear Modulus G_{xy}=G_{xz}	840 MPa
Shear Modulus G_{yz}	840 MPa
Maximum compression stress σ_c	3.28 MPa
Maximum tensile stress σ_t	0.137 MPa
Density	750 kg/m3

Young Modulus E	11000 MPa
Poisson Coefficient ν	0.2
Density	2400 kg/m3
Young Modulus E	30000 MPa
Poisson Coefficient ν	0.2

Table 1: Mechanical properties of material adopted in the un-reinforced building: natural stone (top); wood (middle); concrete (bottom)

Afterwards the stone building has been reinforced by means of the seismic wallpaper, which has been applied to the stone walls using a mortar compound, constituted of an epoxy-cementitious matrix combined with nanoacrylic polymers. The cohesion of the masonry part of the structure is achieved by using this matrix of ductile type, which benefit is a damping effect through load distribution. The matrix also protects the glass fibres against the alkaline environment of the plaster. In detail (Figure 5), the reinforcement has been realized by means of further steps:

- first the matrix has been applied fresh to the walls external surface, making the surface as smoothed as possible;
- then the textile was rolled out from the roof, applied to the fresh mortar, pushed against it till a mortar penetration into the textile fabric structure was reached,
- finally a second layer of matrix was applied to externally cover the textile.

This procedure guarantees that a perfect bonding between masonry, matrix and textile is reached.

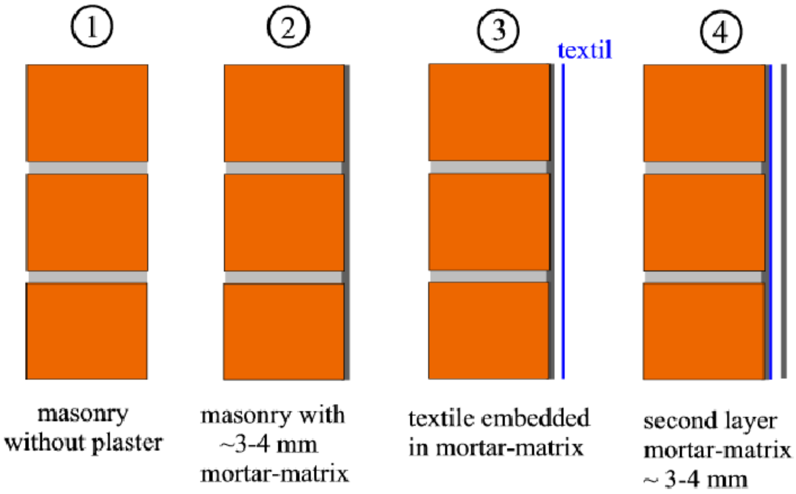

Figure 5: Seismic Wallpaper application procedure

The result is the reinforced building depicted in Figure 6, the grey colour is given by the outer cementitious matrix layer, covering the quadric-axial textile, which mechanical properties are reported in Table 2 below.

Figure 6: View of the reinforced building

Density	2000 kg/m3
Young Modulus E_x	40000 MPa
Young Modulus $E_{y,z}$	32000 MPa
Poisson Coefficient ν_{xy}	0.14
Poisson Coefficient $\nu_{xz,\ yz}$	0.2
Shear Modulus G_{xy}=G_{xz}= G_{xz}	4500 MPa
Maximum tensile stress σ_t	40 MPa
Maximum shear stress σ_s	10 MPa

Table 2: Mechanical properties of the quadric-axial textile

Before and in parallel with the experimental tests carried on at the Eucentre by means of subsequent seismic events of increasing intensity applied to the base of the reinforced building mounted on an uni-axis shaking table, numerical simulation were mandatory to assess the effectiveness of the reinforcing solution, to predict the building behavior and to achieve knowledge of the textile response to dynamic loads.

This process has been developed and is presented within this paper by means of subsequent steps/analysis which from preliminary finite element model (FEM) and numerical investigations of the un-reinforced building, the building as damaged and the reinforced building, is aimed at describing a proper method for the simulation of the inelastic behavior of this innovative technical textile concept.

3 PRELIMINARY FE ANALYSIS AND COMPARISON WITH EXPERIMENTAL RESULTS

Preliminary numerical simulations have been carried out with the aim of understanding the structural behavior of the un-reinforced building (URB) as a mean of comparison with the reinforced building (REB) behavior. It is worth noting that these simulations did not account for any micro-scale modeling of the seismic wallpaper (i.e. of the quadric-axial textile) since this optimization has been performed in a further step of the study, as reported in chapter4. Here modal as well as non-linear static and non-linear dynamic analyses have been conceived towards the prediction of the building dynamics in terms of modal parameters (frequencies, damping and mode shapes) for both the URR and the REB. The simulations aimed at understanding the benefits of a full-cover solution with respect to traditional strips reinforcing solution in terms of stress distribution, in ductility capability and in dissipation of energy capacity.

The Ansys software has been identified as suitable for the numerical analyses. The classical implicit formulation has been adopted; the Newton-Raphson iteration algorithm has been implemented. A solid model has been conceived for modeling the stone walls, while shell elements have been used for meshing the wood slab and the wood roof. According to the requirements of the analysis performed the Solid45 and/or the Solid65 element have been used for the stone walls, in particular: the Solid45 element (3-D Structural Solid) has been used when simulating a modal analysis, while the Solid65 element has been judged more suitable, due to its nonlinear capability, to be adopted when performing a non-linear analysis. The seismic wallpaper has been modeled as an equivalent homogeneous lamina by means of shell elements, accounting for both the quadri-axial textile (with fiber oriented at 0°, 90° and ±60°) and the epoxy-cementitious matrix. A perfect contact in between the solid elements (representing the wall stones) and the shell elements for the wallpaper has been simulated. Shell43 4node non-linear element has been chosen, with both bending and membrane capability.

The FEM of the URB as well as of the REB are shown in Figure 7 below.

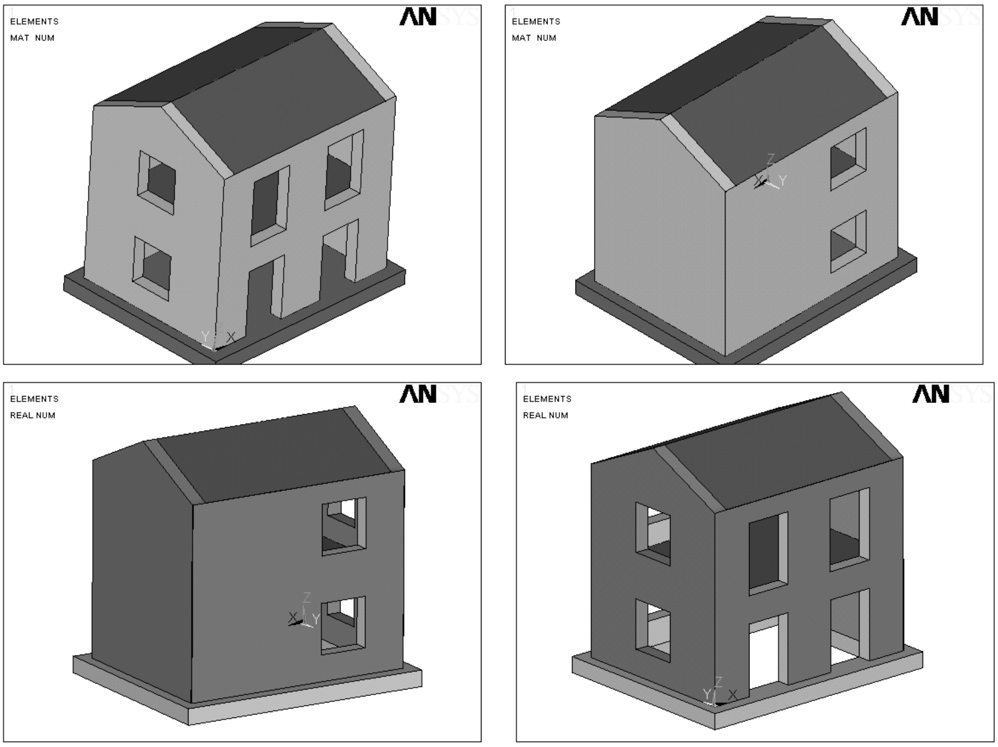

Figure 7: FEM of the un-reinforced building (top) and of the reinforced building (bottom)

3.1 Modal Analysis

The modal analysis aims at predicting the building natural frequencies and modes shapes to be compared with the same parameters identified from experimental tests. In addition a comparison between the un-reinforced and the reinforced building natural frequencies, as calculated from numerical simulations, is also realized.

Figures 8 reports the displacements field mode shapes for the 1st, the 2nd and the 3rd mode, for the URB and the REB respectively. Table 3 summarizes the results for both configurations in terms of calculated natural frequencies.

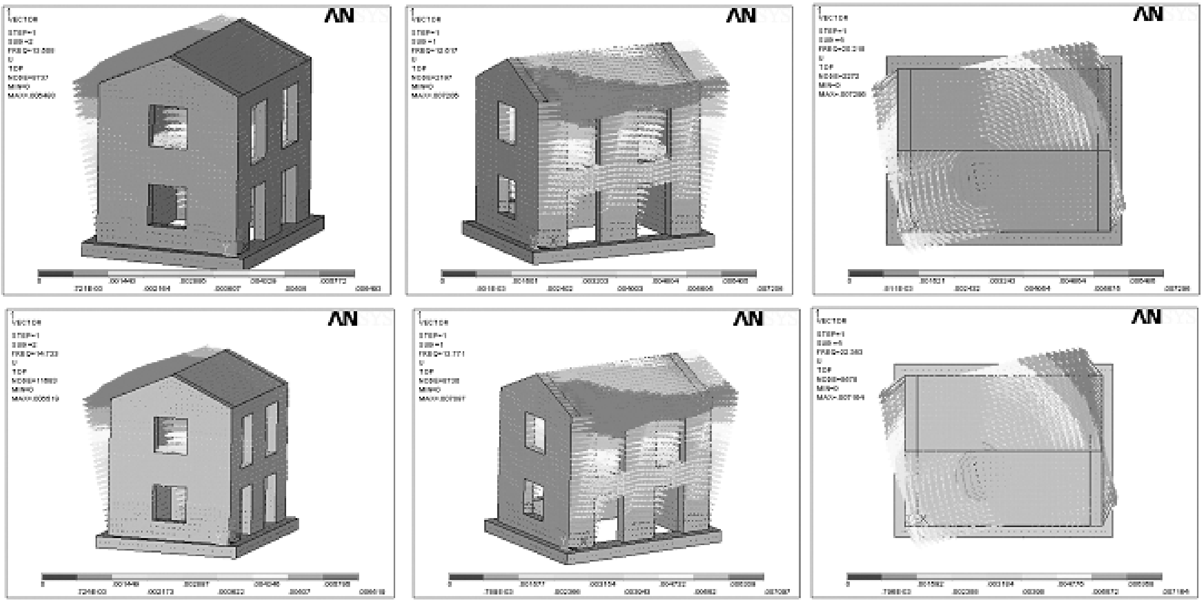

Figure 8: Modal analysis results of the URB (top) and the REB (bottom). Displacements field of the 1st (left plot), 2nd (middle plot) and 3rd (right plot) mode shape

Mode	URB Frequency [Hz]	REB Frequency [Hz]
1st (translation in Y)	13.51	14.73
2nd (translation in X)	12.62	13.77
3rd (torsional)	20.22	22.35

Table 3: Modal analysis results

The results calculated from numerical simulations have been then compared with those coming from experimental ambient vibrations tests carried on for both the URB and the REB. The aim here is to calibrate the numerical model and to give an estimate of the changes the reinforcement is given in terms of the building dynamics.

Four three-axis Geophones have been located on the parapet of the building windows according to the set-up configuration showed of Figure 9. Two sets of ambient vibrations have been recorded at a sampling rate of 265Hz for around half an hour. Two minutes of measurements have been extracted from the global records for both ambient vibration sets. The Operational Modal Analysis (OMA) has been carried on by processing with suitable algorithms (Natural Excitation Technique combined with the Eigensystem Realization Algorithm: Next-ERA) the two minutes records.

Far from the scope of this study, the experimental process is not described in detail. The results are reported in terms of identified natural frequencies for comparison with the numerical calculations (Table 4). The correlation between experimental and numerical natural frequencies is also highlighted in Figure 10, with reference to the URB.

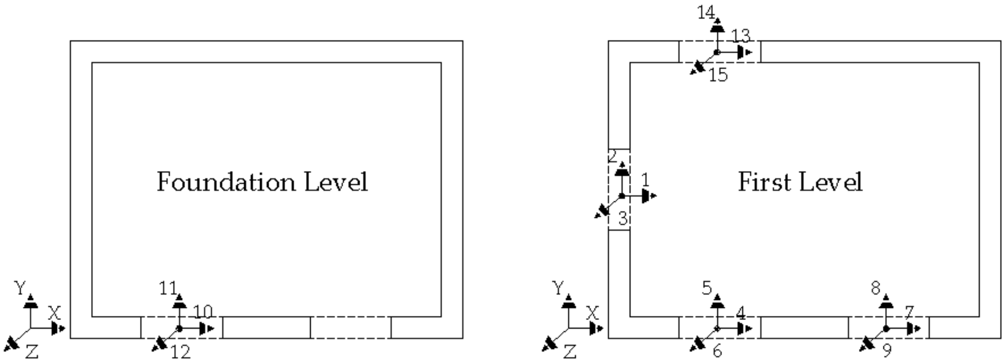

Figure 9: Experimental Ambient Vibration tests sensor set-up

Mode	URB Frequency [Hz]		REB Frequency [Hz]	
	Experimental	Numerical	Experimental	Numerical
1st (translation in Y)	12.07	13.51	10.30	14.73
2nd (translation in X)	11.55	12.62	7.41	13.77
3rd (torsional)	16.27	20.22	18.25	22.35

Table 4: Correlation between experimental and numerical results

With reference to the URB the correlation between numerical and experimental results is good enough (variations in the order of the 10%) to dictate the validity of the FE model. On the contrary for the REB building the difference is quite significant (variation up to 85% on the 2nd natural frequency). The reason comes from the fact that the stone building before being reinforced has been damaged and this damage has not been quantitatively identified while also the crack patters was not defined. The uncertainties in modeling the existing damage probably caused the not perfect fit between the numerical and the experimental results for the REB. This suggests that a quantification of the damage can be achieved by only micro-scale simulations of the reinforcement as will be presented in chapter 4 of this paper. The preliminary model, with reference to modal analysis, can be considered suitable in defining a reference framework where optimized models can be conceived.

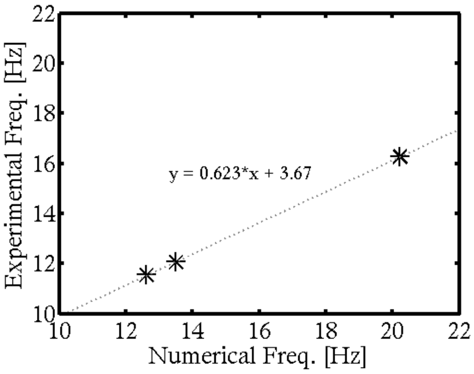

Figure 10: Correlation between experimental and numerical natural frequencies for the URB

3.2 Non-Linear Static Analysis

A non-linear static analysis (pushover) has been carried out to identify the crack patterns and to predict the damage propagation of both the URB and the REB. A distribution of forces proportional to the mass of the building is applied in the longitudinal direction at the level of the first slab and of the wood roof. The force is incrementally increased till the failure level of the stone material is reached. The Solid65 element has been adopted to model the walls stones as it provides the capability to identify the propagation of cracks during the application of the load, as it is suitable for treatment of nonlinear material properties. The element allows cracking in three orthogonal directions, crushing, plastic deformation, and creep. Bilinear stress-strain tension-compression behavior is adopted to simulate the mechanical behavior of the stone elements.

The aim of the analysis for the URB is to show the crack patterns at failure in order to provide a reference case for the simulation of the reinforced building. This allows understanding the benefit in terms of cracks propagation due to the adoption of full-cover reinforcement. In fact, as done for the URB, a pushover analysis has been carried on for the REB. The forces herein applied account for the textile mass.

Figure 11 below reports the results of the simulation for both the URB (top plots) and the REB (bottom plots). In detail the results are depicted in terms of crack patterns (left plots); and plastic strain distribution (right plots).

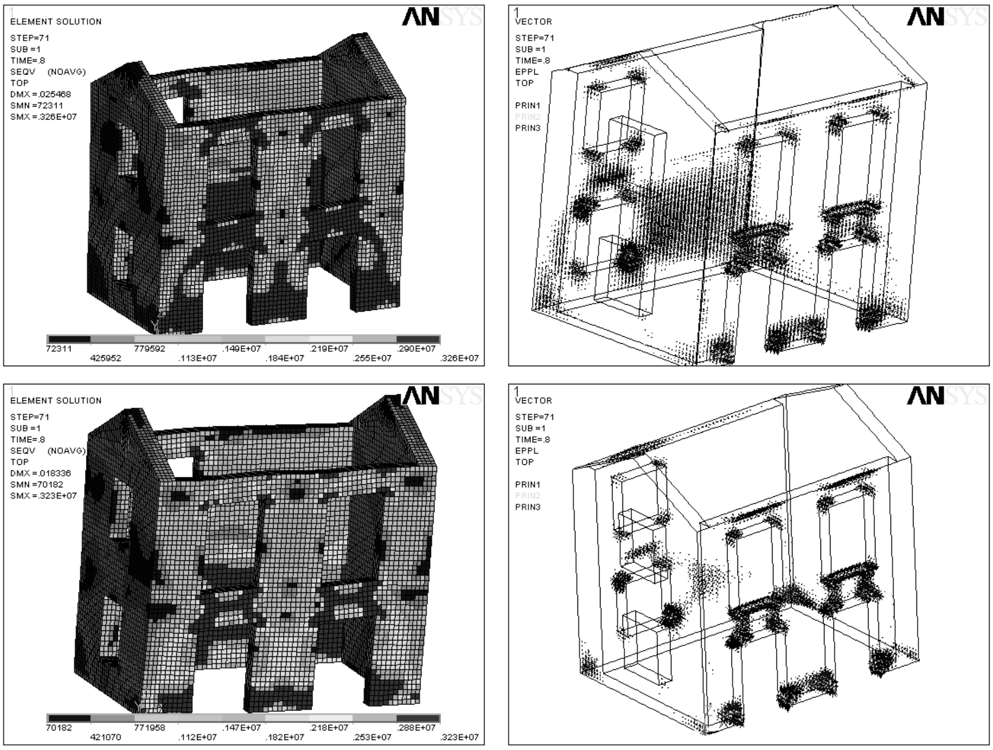

Figure 11: Pushover analysis results of the URB (top) and the REB (bottom): crack patterns at failure (left plots), plastic strain distribution (right plots)

From Figure 11 it is clear that in terms of plastic strain, a reduction in terms of their amplitude could be reached by the REB with respect to the URB.

To better understand how the reinforcement is modifying the buildings mechanics, a comparison in terms of stress-strain diagram of a control node (located at the top of the frontal wall façade) is given in Figure 12. This allow for quantifying the increase in ductility the REB has been claimed within this paper to give.

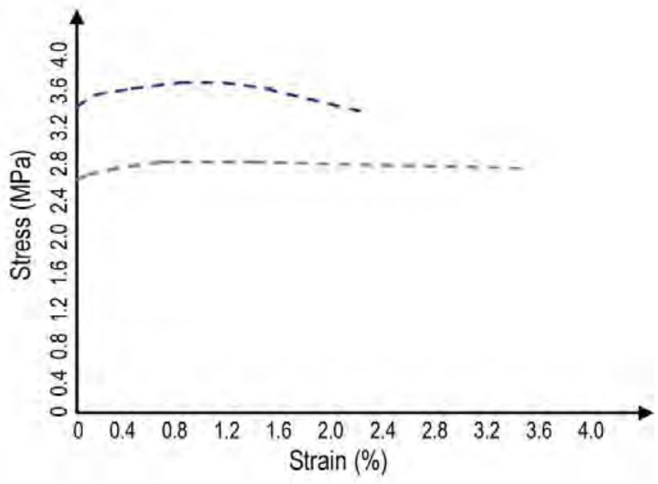

Figure 12: Stress and strain diagram of the control node for the URB (blue line) and the REB (grey line)

The REB building exhibits an elastic-plastic behavior with an increase in ductility which is evident by looking at the stress-strain plot in the post-yield field: a decreasing slope corresponding to a brittle material behavior is shown on the top right plot, while a linear horizontal trend (i.e. ductile behavior) is shown by looking at the diagram of Figure 12.

From the pushover analysis it is shown that the full-cover reinforcement allow for accounting a reduction of plasticity and an increase in ultimate strength and ductility of the stone building.

3.3 Non-Linear Dynamic Analysis

Dynamic analyses have been carried out to simulate the building response in its two configurations (URB and REB) under dynamic loads, as those of seismic events. The aim here is to assess in terms of stress-strain distribution the effects of the reinforcement solution.

A series of accelerogram, of increasing intensity, have been simulated. The Montenegro accelerogram scaled at different value of Peak Ground Acceleration (PGA) has been used. It refers to the Montenegro Earthquake happened the 19th of April 1979, with a Magnitude (Ms) of 7.0 and a PGA of 0.22g.

For simplifying the numerical simulations and in accordance to the implicit FE approach (as developed within the Ansys software) instead of a base acceleration, a base displacement is applied to the base nodes of the model. An example of the base displacement time history (referring to the Montenegro accelerogram scaled at 0.1g of PGA) is given in Figure 13 below.

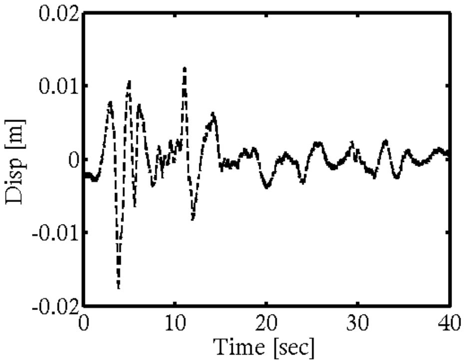

Figure 13: FE dynamic analysis: input displacement time histories referring to the Montenegro accelerogram with PGA scaled to 0.1g

The field vector of the principal stress distribution and the plastic stress distribution at critical time (12.1sec) are chosen as output parameters to be used as a source of comparison in between the URB and the REB results. They allow quantifying the benefits in terms of reduction of the limit stress amplitude and of redistribution (i.e. a more uniform configuration) of the stress field vector due to the full-cover reinforcement. Figure 14 reports these outputs for both the URB (top plots) and the REB (bottom plots).

From Figure 14, it arises that a significant reduction of the plastic strain amplitude is achieved by means of the reinforcement. This is particularly true for the front transversal walls. The beneficial effect of this reduction is obtained thanks to the confinement effect of the full-cover textile reinforcement and to its ability of increasing the building resistance to dynamic loads.

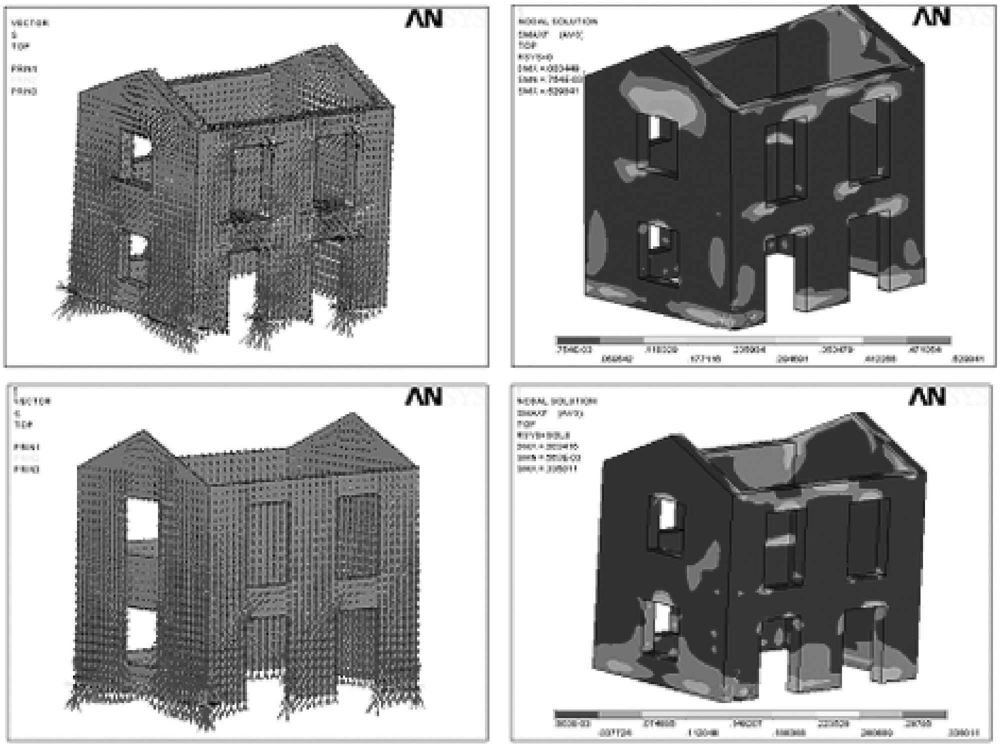

Figure 14: FE dynamic analysis: stress field vector distribution (left) and plastic stress distribution (right) at critical time

4 HEURISTIC TOOL FOR THE SIMULATION OF THE TEXTILE BEHAVIOUR

For the proper simulation of the inelastic behavior of this innovative textile an evolutionary approach will be implemented. This process utilizes Genetic Algorithms (GAs) as the optimizing tool for the identification of the parameters that govern the multiaxial polymer material behavior. This heuristic tool has been chosen for this problem since in contrast to gradient based approaches GAs do not require a straightforward analytical relationship connecting the function to be optimized to the design parameters of the problem. Instead, they can handle even loosely defined problems. A meso-scale approach will be followed, where a finite element algorithm (ANSYS) is used for the simulation of the model structure. The parameters to be identified involve both the setup of the finite element characteristic volume chosen to simulate the polymer textile, i.e. number of layers, thickness, layout, as well as the polymer and masonry material properties, i.e. Elasticity modulus, ultimate strength, etc. This constitutes the setup of the forward problem (Figure 15) which will have to be iteratively solved as part of the evolutionary cycle until convergence is achieved to a minimal error between the experimentally observed and the numerically computed behavior.

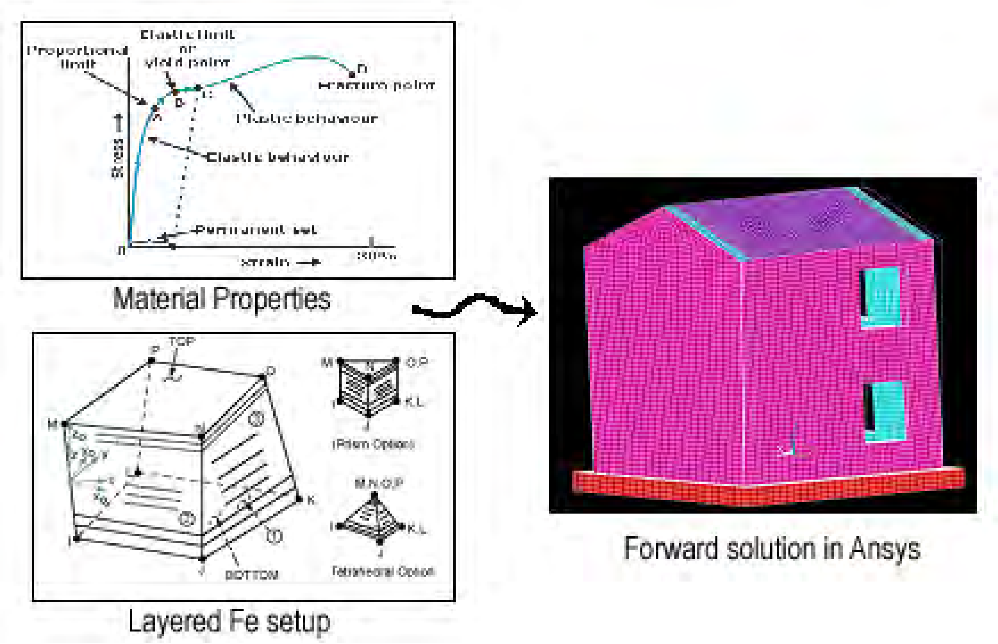

Figure 15: Forward Run

All genetic algorithms are based on the following scheme:

4.1 Representation

Depending on the application the parameters of the problem can be either integer or real numbers. Usually, the set of parameters can be appropriately encoded into a finite length binary string. Once a representation is decided a number of different chromosomes is randomly generated to form the initial population.

4.2 Fitness evaluation/selection

The evaluation of the fitness for each member of the population is carried out through the use of an objective function associated with each problem. The suitability of each chromosome is the criterion based on which this individual will be selected for reproduction. Selection can be performed through various schemes like “roulette wheel” selection or “tournament” selection. The roulette wheel selection is solely dependent upon the performance (fitness) of each individual. In the case of the second method, the probability of a string selection is also dependent upon the fitness of the “competitive” strings chosen to participate in a tournament round. The latter contributes toward the preservation of the diversity of the population.

4.3 Crossover

This operator is applied with a certain probability, to the pairs of the previously selected individuals (parents). In general the crossover procedure randomly selects a position in the binary string and mutually exchanges the parts of the chromosome before and after this location in order to produce two offsprings.

4.4 Mutation

The use of the crossover procedure as the only means for generating new individuals could result in the loss of the diversity of the population. This problem can be overcome using the mutation operator which involves the random flip of the binary genes of the chromosome for the case of jump mutation, or the alteration of the phenotypic (real) representation of the design parameters by a small increment or decrement for the case of creep mutation. More information on the basic (classic) GA scheme can be found in [10]-[14]. The following figure illustrates the basic workings of the GA-FE optimization scheme.

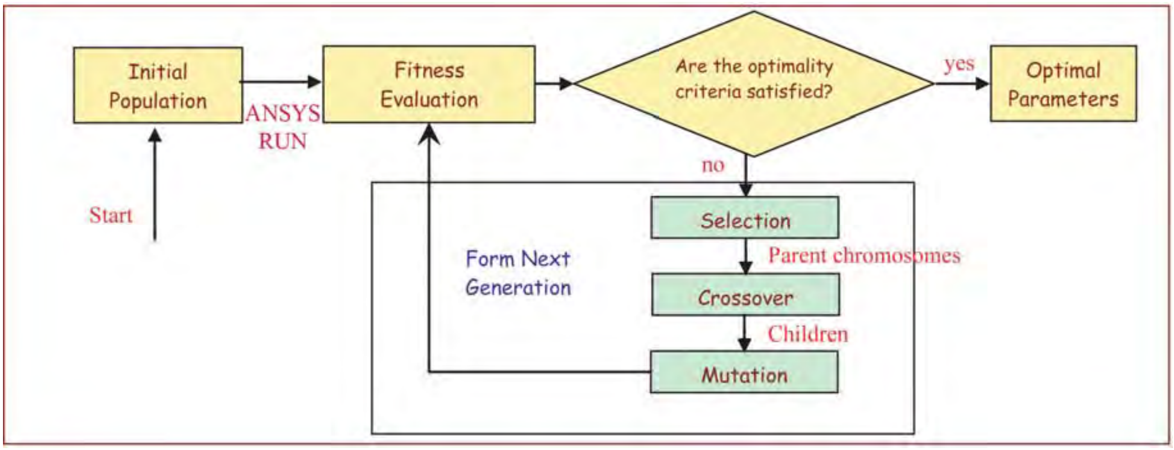

Figure 16: GA-FE Scheme

On a first level, the experimental modal analysis results listed in Table 4 for the Unreinforced Structure will serve as a reference for the calibration of the masonry material properties. On a second level the experimental modal frequencies of the Retrofitted Structure will serve as a reference for the calibration of the polymer elastic properties as well as the representative volume configuration. The error function used to evaluate the fitness of each potential set of parameters in both cases is expressed as the L_2 relative error norm:

$$r = \frac{\|\lambda_e - \lambda_m\|}{\|\lambda_m\|} \tag{1}$$

Where λ_e is the GA estimated eigenvalue vector and λ_m is the experimentally determined one. Finally, the acceleration and strain history results from the shake table test number 3, after which failure was originally noted will serve as the basis for the proper configuration of the masonry and polymer textile ultimate strength properties.

A full transient time history analysis is generally computationally expensive; therefore a response spectrum analysis will serve as the tool for the forward problem solution in this final stage, cutting down significantly on the computational cost. The fitness function in this case will be defined as the L_2 relative error norm of the maximum displacements and trains obtained from the FE Response Spectrum analysis as compared to the experimentally observed ones during the shake table test.

The finally identified parameters will ultimately be validated using a full on transient time history analysis the results of which will be compared to the actually recorded acceleration and train records at the available sensor locations.

5 DAMAGE DETECTION BY MEANS OF STRAIN MEASUREMENTS

An experimental tests campaign has been carried on aimed at detecting the REB dynamics by means of FBG sensors embedded textile. Hammer tests were performed after each simulated seismic event as reported in Table 5.

Test	Description
1	Modal identification after the 1st seismic test (Montenegro accelerogram scaled to 0.1g of PGA)
2	Modal identification after the 2nd seismic test (Montenegro accelerogram scaled to 0.3g of PGA)
3	Modal identification after the 3rd seismic test (Montenegro accelerogram scaled to 0.4g of PGA)
4	Modal identification after the 5th seismic test (Montenegro accelerogram scaled to 0.6g of PGA)

Table 5: Experimental modal identification tests chronology

The sensor topology was chosen as shown in Figure 17: a total of 8 FBG sensors (active length of 2m) have been installed on Wall1, 2, 3 and 4. The excitation point is also depicted with a red arrow in Figure 17.

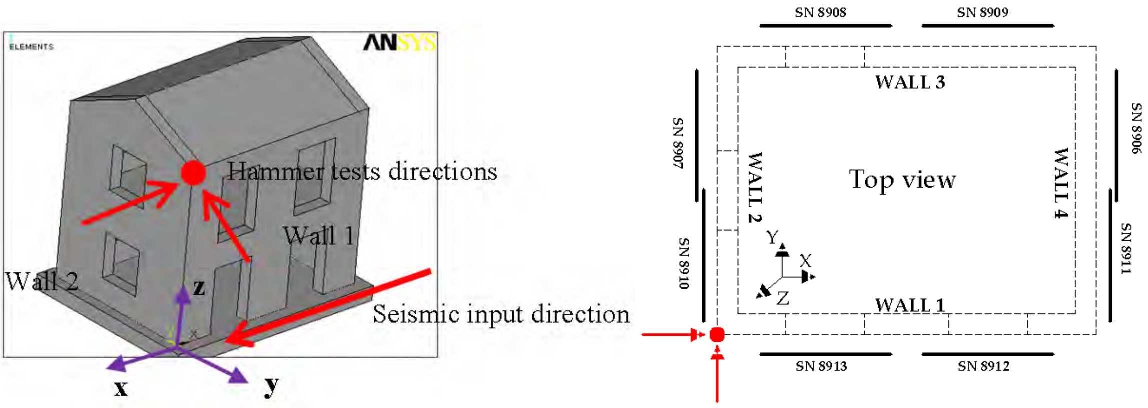

Figure 17: Experimental modal identification tests set-up: 3D view (left); plane view (right)

For each test, two hammer trials along X-direction and two along Y-direction have been conducted. From the data recorded by FBG sensors an Operational Modal Analysis (OMA) has been carried by adopting the ERA algorithm.

For seek of brevity in what follows only the most significant results (for test1 and test4) are depicted in the time (strain Time History) and frequency (Power Spectral Density function – PSD) domain. Singular Values Decomposition (SVD) plots are also showed. Table 6 summarizes the results in terms of identified natural frequencies.

Each sensor records the structural response in terms of axial strain, sampling at 1000Hz, manually down-sampled at 100Hz. Such sampling frequency defines a frequency range 0-50Hz (according to the Nyquist theorem) which is good enough to detect the building natural frequencies, as dictated by the FE modal simulations.

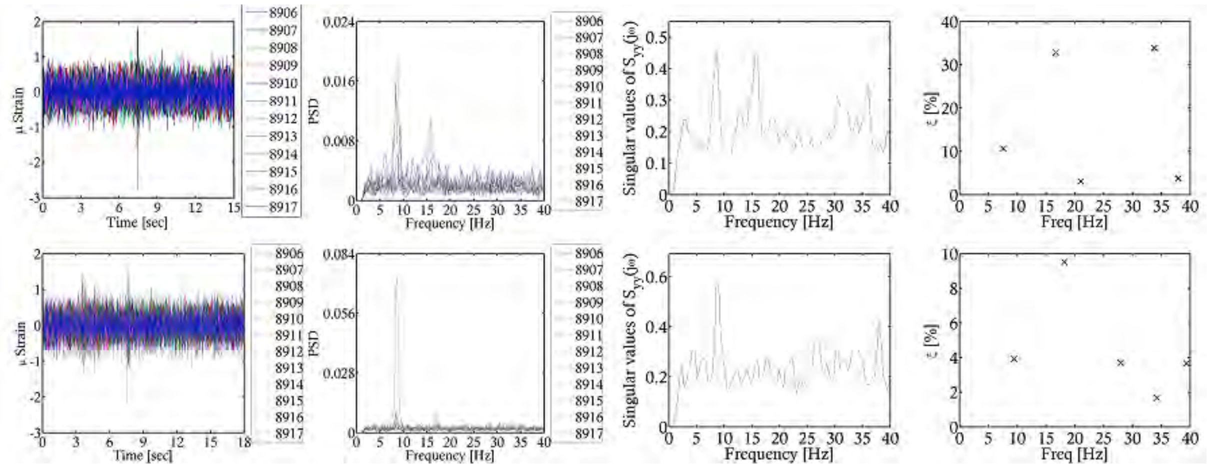

Figure 18: Test1 results for the hammer tests along X (top) and hammer tests along Y (bottom). Calculated displacements Time History (left plot), Power Spectral Density function (middle left plot); Singular Values as obtained by the SVD of the PSD matrix (middle right plot); Identified frequency vs. identified damping from Next-ERA algorithm (right plot)

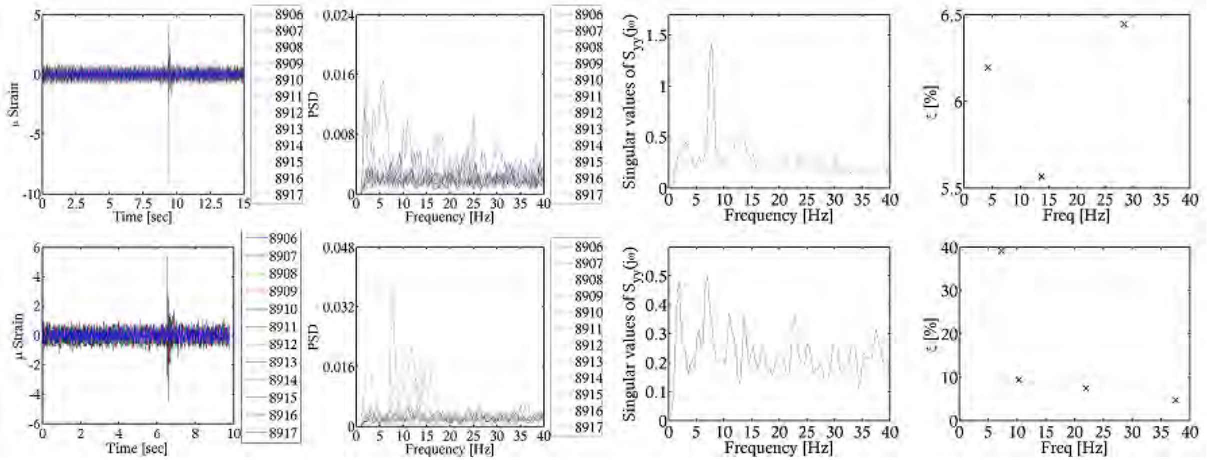

Figure 19: Test4 results for the hammer tests along X (top) and hammer tests along Y (bottom). Calculated displacements Time History (left plot), Power Spectral Density function (middle left plot); Singular Values as obtained by the SVD of the PSD matrix (middle right plot); Identified frequency vs. identified damping from Next-ERA algorithm (right plot)

Mode	Test1 (1st seismic test) Freq. [Hz]	Test2 (2nd seismic test) Freq. [Hz]	Test3 (3rd seismic test) Freq. [Hz]	Test4 (5th seismic test) Freq. [Hz]
First mode (Y)	8.98	8.88	12.42	8.98
Second mode (X)	7.60	8.07	7.86	7.78
Third mode (tors)	15.39	15.49	13.92	13.86

Table 6: Identified natural frequencies

To define the evolution/variations of the building natural frequencies from Test1 to Test4, Figure 20 depicts the SVDs as calculated for the hammer tests in the X and Y direction respectively. This graph gives an idea of how, at least for the 1st and the 2nd mode, the natural frequencies associated to translational modes of the building (1st in Y direction, 2nd in X direction) varies according to the different structural configuration of the building after each seismic test.

It is worth noting, as not mentioned previously that some considerations may be done, based on the measurements recorded during the seismic tests, on the structural changes of the stones building and on the development of a progressive failure condition. These following considerations are strongly related to what it is expended to extract from the hammer tests data in terms of frequencies and then of damage detection. In other words if a failure is locally and/or globally identified after a seismic event, this has to corresponds to changes in the building dynamics (i.e. variation of natural frequencies). To understand if a correlation is possible the following considerations should be preliminary highlighted:

- After the 1st seismic test (PGA 0.1g) the #REB was not affected by any damage, the structure resists to the dynamic force easily and not visual damage was detected. From the data processing, no plastic (i.e. permanent) deformation was measured;
- After the 2nd seismic test (PGA 0.3g) the #REB was not affected by any evident damage and no plastic deformations were detected;
- After the 3rd seismic test (PGA 0.4g) the #REB was affected by structural damage which mainly occurred at the top of the windows of wall2, where sensors SN8912 and SN8913 were installed. From the data processing of the measurements recorded during the seismic test, plastic strains were detected;
- After the 4th seismic test (PGA 0.5g) the #REB, localized damage by the 3rd test, was able to respond with no apparent further cracks. No additional plastic deformation was recorded;
- After the 5th seismic test (PGA 0.6g) the #REB was able to resist to the strong seismic shake with evident damages which were globally located on the building walls (above all on Wall1). Additional and significant plastic deformations were recorded during the seismic test. A damaged configuration seems to be the more appropriate to describe the #REB after the 5th test.

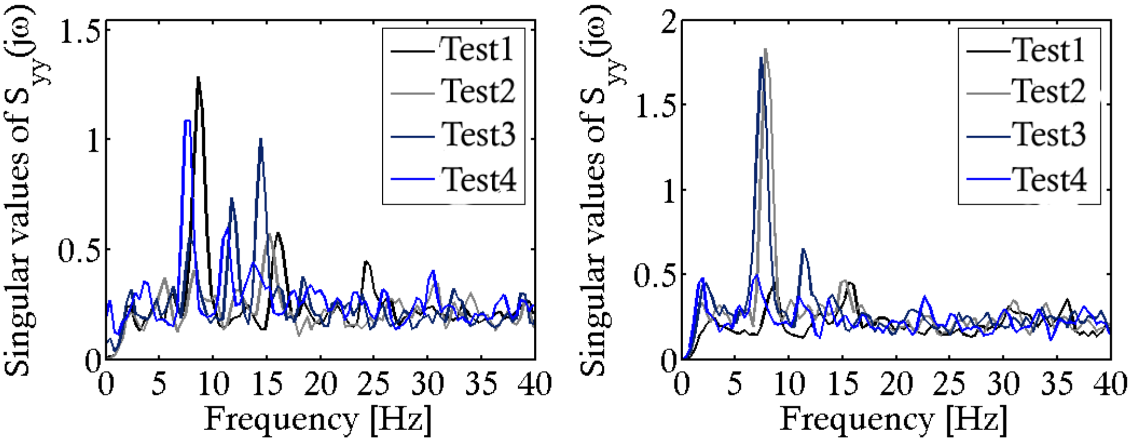

Figure 20: Tests 1-4 system identification results: Singular Values as obtained by the SVD of the PSD matrix for the hammer tests in X direction (left), in Y direction (right)

From Figure 20 some trends may be evidenced in terms of 1st in X and 1st in Y (see blue and black lines at the first peak) natural frequencies variations from test1 to test4. Figure 21 highlights them by separating the SVD graphs obtained for Test1 to those of Test4. The values of the natural frequencies depicted in Figure 21 are reported in Table 7 below.

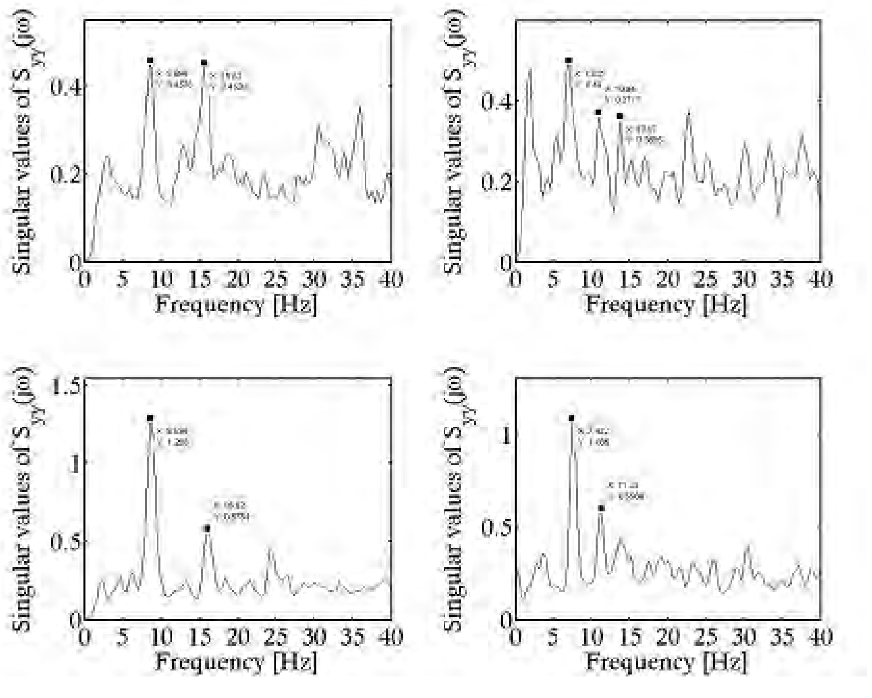

Figure 21: Tests 1-4 system identification results: Singular Values as obtained by the SVD of the PSD matrix for the hammer tests in X direction (top) and in Y direction (bottom): Test1 results (left), Test4 results (right)

From Figure 21 it can be noted that:

- the 1st first mode natural frequency decreases from 8.59Hz to 7.81Hz, which means a reduction of the 9.1%. This indicates also for the building natural movements along the transversal direction (Y axis) that the building stiffness decreased from the 1st to the 5th seismic test, due to cracks opening into Wall2;

- the 2nd mode natural frequency decreases from 8.59Hz to 7.03Hz, which means a reduction of the 18.2% X. This indicates that the REB was either less stiff or its weight was increased after the last seismic test than after the 1st seismic test. As no mass was added, the building after five subsequent seismic tests was less stiff due to cracks openings in localized positions. In addition this was also due to an out-of-plane mechanism of Wall1 along the longitudinal direction (X-axis).

	Test1 (after the 1st seismic test) Freq. [Hz]		Test4 (after the 5th seismic test) Freq. [Hz]	
	First mode (Y)	Second mode (X)	First mode (Y)	Second mode (X)
FBG sensors	8.59	8.59	7.81	7.03

Table 7: Identified natural frequencies for test1 and test4 from SVD

6 CONCLUSIONS

Sensor-embedded reinforcing textiles offer the engineer a new tool for the retrofit of masonry structures. These multifunctional materials reinforce and monitor in one product. As such, they strengthen, reduce seismic risk, and provide the engineer with data that can be utilized to assess a structure in all phases of its life cycle.

The “Composite Seismic Wallpaper”, described along this paper, is an innovative example of such type of multifunctional materials. The main outcomes from an experimental tests campaign, as well as the main results of numerical investigations have been here detailed. The objective was to furnish elements for the validation of the performance of the wallpaper as seismic reinforcement of masonry buildings.

The characterization of the wallpaper behavior is highlighted in Chapter 4, while its ability to be used as a tool for damage detection of cracks in the reinforced structure is reported in Chapter 5.

REFERENCES

[1] T. B. Messervey, D. Zangani, C. Fuggini, Sensor-embedded textiles for the reinforcement, dynamic characterisation, and structural health monitoring of masonry structuress, *Proceedings of the 5th EWSHM 2010*, June 28–July 2, 2010, Sorrento, Italy, pp. 1075-1282.

[2] Faella C, Martinelli E, Nigro E, Paciello S, Tuff masonry walls strengthened with a new kind of C-FRP sheet: experimental tests and analysis. *Proceedings of the 13th world conference on earthquake engineering*, paper no. 923, 2004.

[3] Krevaikas T, Strengthening of unreinforced masonry structures with advanced composites. *PhD Dissertation*, University of Patras, Greece, 2005.

[4] Nurchi A, Valdes M, Strengthening of stone masonry columns by means of cement-based composite wrapping. *Hamelin P (ed) CCC 2005: 3rd international conference on composites in construction*. Lyon, France, July 2005, pp 1189–1196

[5] Triantafillou TC, Fardis MN, Strengthening of historic masonry structures with composite materials, *Material Structure*, 30, 486–486, 1997.

[6] Krevaikas T, Triantafillou TC, Masonry confinement with fiber reinforced polymers. *J Compos Constr*, 9(2), 128–135, 2005.

[7] Krevaikas TD, Triantafillou TC, Computer aided strengthening of masonry walls using fibrereinforced polymer strips. *Mater Struct* 38, 93–98, 2005.

[8] Li T, Galati N, Tumialan JG, Nanni A, Analysis of unreinforced masonry concrete walls strengthened with glass fiber-reinforced polymer bars, *ACI Struct J*, 102(4), 569–577, 2005.

[9] CNR-DT 200/2004: Guide for the Design and Construction of Externally Bonded FRP Systems for Strengthening Existing Structures

[10] D. Whitley, A genetic algorithm tutorial, Stat Comput **4** (1994), p. 6585.

[11] B.L. Miller, B.L. Miller and D.E. Goldberg, Genetic algorithms, tournament selection, and the effects of noise, Complex Syst **9** (1995), pp. 193–212.

[12] Goldberg DE. Sizing populations for serial and parallel genetic algorithms, In: Proceedings of the 3rd International conference on genetic algorithms, Morgan Kaufman; 1989. p. 70–9.

[13] M. Mitchell, An introduction to genetic algorithms, MIT Press, Cambridge, MA (1998).

[14] T. Back, D.B. Fogel and Z. Michalewicz, Handbook of evolutionary computation, IOP Publishing Ltd, Bristol, UK (1997).

COMPDYN 2011
3rd ECCOMAS Thematic Conference on
Computational Methods in Structural Dynamics and Earthquake Engineering
M. Papadrakakis, M. Fragiadakis, V. Plevris (eds.)
Corfu, Greece, 25–28 May 2011

SEISMIC RETROFIT OF EXISTING BUILDINGS BY MEANS OF SEISMIC ISOLATION: SOME REMARKS ON THE ITALIAN EXPERIENCE AND NEW PROJECTS

A. Martelli[1] and M. Forni[2]

[1] Director, Bologna Research Centre of ENEA,
President, GLIS, Past President, *ASSISi*, and Coordinator, EAEE-TG5
Via Martiri di Monte Sole, 4, I-40129 Bologna, Italy
e-mail: alessandro.martelli@enea.it

[2] Head, Technical Unit on Seismic Engineering, and Secretary General, GLIS and *ASSISi*
Via Martiri di Monte Sole, 4, I-40129 Bologna, Italy
e-mail: massimo.forni@enea.it

Keywords: Seismic Isolation, Buildings, Bridges, Plants, Cultural Heritage, Retrofit.

Abstract. *Seismic isolation (SI) has been used in Italy for several applications, which include important retrofits of civil structures and cultural heritage. Some new hospitals, all new civil defence centres and most new schools have already been (or are being) isolated, together with a significant number of dwelling buildings and other constructions. The 2009 Abruzzo earthquake caused an increase of the number of the Italian isolated buildings from about 70 to over 300. Prior to the aforesaid event, the Italian SI systems consisted in High Damping Rubber Bearings (HDRBs) or Lead Rubber Bearings, to which plane surfaces steel-PTFE Sliding Devices (SDs) were added in the last years. Now, Curved Surface Slider devices are also in use. The first Italian building to be retrofitted with SI was a reinforced concrete (r.c.) civic centre in Naples in 2004. Its foundation pillars and walls were cut, approximately 600 HDRBs were installed and a steel beams floor was added above the isolators to stiffen the superstructure base as necessary. In the same year, two 4-storey r.c. dwelling buildings were retrofitted, each with 12 HDRBs and 13 SDs, in Solarino, near Syracuse. In 2005 the first European retrofit with SI in a sub-foundation was completed: it concerned a 3-storey r.c. house in Fabriano that had suffered severe but non-structural damage in the 1997-98 Marche & Umbria quake. For this intervention 56 HDRBs were used. Further retrofits with SI were also performed for churches, schools, further dwelling buildings, tanks, single masterpieces, etc. The significant extension of the use of SI after the Abruzzo quake concerns this and other Italian regions. The new applications include numerous retrofits: at L'Aquila they mainly concern civil and monumental buildings damaged by the quake. In the latter, the SI system will be inserted in a sub-foundation, not to cut the structural elements or existing foundations, and a new method patented by ENEA and Polytechnic of Torino in 2010 will also be used.*

1 INTRODUCTION

Over 16,000 structures in the world have been protected by anti-seismic (AS) systems and devices, mainly by the seismic isolation (SI) or energy dissipation (ED) ones [1-11]. They are located in over 30 countries (Figure 1) and concern both new constructions and retrofits of existing structures of all kinds: bridges and viaducts, civil and industrial buildings, cultural heritage and industrial components and installations, including some high risk nuclear and chemical plants. The use of the AS systems in a civil context already includes not only the strategic structures (civil defence centres, hospitals) and the public ones (schools, churches, commercial centres, hotels, airports), but also residential buildings and even many small private houses. Everywhere, the number of such applications is increasing more and more, although it is strongly influenced by earthquake experience and the availability and features of the design rules used [9].

Most SI systems rely on the use of rubber bearings (RBs), namely High Damping Rubber Bearings (HDRBs), or Lead Rubber Bearings (LRBs) or (mainly in Japan) Low Damping Rubber Bearings (LDRBs) in parallel with dampers of various kinds; in buildings, some plane surfaces steel-teflon (PTFE) Sliding Devices (SDs) are frequently added to the RBs to support their light parts and/or minimize the torsion effect if they are significantly asymmetric in the horizontal plane [9].

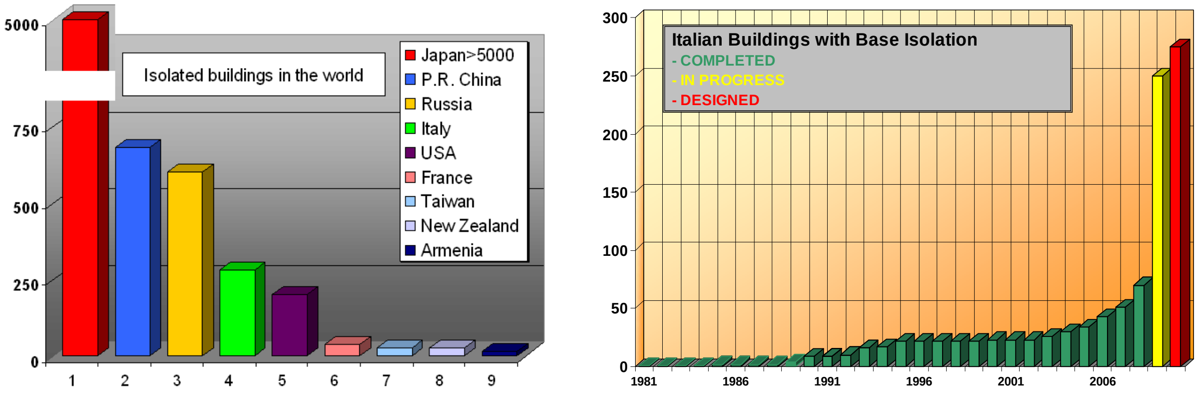

Figure 1: Overall number of building applications of seismic isolation in the most active countries (left); overall number of building applications of SI in Italy during years (right). Data refer to the end of 2009.

2 WORLDWIDE APPLICATION OF THE ANTI-SEISMIC SYSTEMS & DEVICES

Japan is largely the worldwide leader for the number of applications of the AS systems (Figure 1). This occurs also thanks to an adequate code and the excellent behaviour of numerous buildings protected by SI during an already significant number of earthquakes (starting from the 1995 *Hyogo-ken Nanbu* event, of magnitude M = 7.3). More precisely, in Japan there are now over 6,000 isolated buildings or houses [11, 12], besides several isolated bridges & viaducts and (at the end of 2009) about 3,000 constructions protected by dampers [9, 10]. There the trend is to isolate, on the one hand, even high-rise buildings and sets of buildings supported by common "artificial ground" slabs and, on the other hand, even small private houses. Moreover, recent projects concern three-directional (3D) SI of civil buildings, retrofit of cultural heritage, protection of industrial factories (e.g. for semi-conductors), etc.

The USA are second, with "only" 100÷200 large, new and retrofitted, civil and historical, isolated buildings, but over 650 isolated bridges or viaducts and approximately 1,000 applications of dampers at the end of 2009 [9, 10]. Building application of SI is relatively limited (in spite of the excellent behaviour of some isolated ones during the 1994 *Northridge* earthquake), due to a very penalizing code [9, 10].

The Peoples' Republic (P.R.) of China is third, with about 690 isolated buildings and over 100 ones with ED or other systems (at the end of 2009), besides numerous isolated bridges & viaducts [9, 10]. There too application is rapidly increasing. It includes several reinforced concrete (r.c.) and also masonry dwelling buildings, as well as SI of some Liquefied Natural Gas (LNG) tanks. Like in Japan, the use of 3D SI and "artificial grounds" started, together with retrofit of cultural heritage and roof SI of large span structures. The excellent behaviour of some isolated r.c. and masonry buildings during the 2008 *Wenchuan* earthquake (of magnitude M close to 8.0), although this had been largely underestimated [7, 9, 10], is further accelerating the use of AS systems in China.

Forth is the Russian Federation, with about 600 isolated buildings (including retrofits of some important historical constructions) and several new ongoing projects, concerning even high-rise buildings (one, the 27-storey *Sea Plaza* Hotel in Sochi, is protected by Italian HDRBs) [9, 10].

Italy remains fifth and first in Western Europe for the overall number of applications of the AS systems (Section 3) [5, 9, 10, 11]. It is followed by South Korea, Taiwan, Armenia, New Zealand, France, Mexico, Canada and Chile [9, 10]. In Taiwan the present significant use of the AS systems is due to the 1999 *Chi Chi* earthquake and the subsequently enforced new seismic code, which promotes the use of the AS systems. In Armenia the adoption of SI began after the 1988 *Spitak* event and the number of applications per inhabitants is the largest in the world after that in Japan, although this country is still developing [6]. In New Zealand, one of the motherlands of AS devices (in particular of those based on the use of lead) and third for the number of their applications per inhabitants, the isolated structures had an excellent behaviour in the 2010 *Canterbury* earthquake of M = 7.1 [10, 11]. In France SI has been used to protect the *Jules Horowitz Reactor* and has been planned for the *ITER* plant for the controlled nuclear fusion in the mainland, while it is obligatory for schools and other public buildings in its Martinique island. Finally, similar to New Zealand, the isolated structures in Santiago had an excellent behaviour in Chile too, during the 2010 *Maule* earthquake of M = 8.8 [10, 11].

Important applications of the AS systems also began in Turkey (after the 1999 *Kocaeli* and *Duzce* earthquakes) and other European countries [8-11]: many of them make use of Italian AS devices (in Turkey, Greece, Portugal, Spain) or Italian designs too (in Cyprus, Romania). Italian devices have also been installed in Taiwan, South Korea, Venezuela, Indonesia, the USA, Canada, Iran (where a huge project is in progress for isolating the whole new town of Parand, near Tehran), etc. Finally, Macedonia shall be cited, because it hosts the first modern application of SI worldwide, that to the *Pestolazzi* school in Skopje, erected after the destructive 1963 earthquake: its original poorly laminated and very deteriorated rubber isolators were replaced by HDRBs in 2007 [9-11].

3 APPLICATION OF THE ANTI-SEISMIC SYSTEMS & DEVICES IN ITALY

As mentioned above, Italy is fifth at worldwide level and first in Western Europe for the overall number of applications of the AS systems (Figure 1). There, the use of such systems began in 1975 for bridges and viaducts (*Somplago* viaduct of the *Udine-Tarvisio* freeway, which survived intact the second shock of the 1976 *Friuli* earthquake) and in 1981, namely 4 years before Japan and the USA, for buildings (main building of the new *Fire Command Centre* of Naples, the design of which was "retrofitted" with isolators, dampers and other AS devices as a consequence of the seismic classification of the Naples area in seismic category 3 after the 1980 *Campano-Lucano* earthquake) [1, 2].

In 2009, Italy passed the USA for the number of isolated buildings [5, 8, 9]: those in use were about 70 before the *Abruzzo* earthquake of April 6 of that year (M = 6.3), with further

20÷30 under construction or design, and are now approximately 300 (Figure 1). In fact, in Italy, after many years of a rather limited use of the AS systems (due to the lack of design rules to the end of 1998, then to their inadequacy and very complicated and time-consuming approval process to May 2003 [1, 2]), there has been a large increase of the number of new projects in the last years [3, 8-11].

Figure 2: Collapse of the *Francesco Jovine* primary school of San Giuliano di Puglia (Campobasso) during the 2002 *Molise & Puglia* earthquake and search of survivors amid the debris. Prior to the aforesaid earthquake the San Giuliano di Puglia area was not seismically classified (now it is classified in seismic zone 2).

Figure 3: The *Prefettura* building (provincial headquarters of the national government) of L’Aquila, a symbol of lack of prevention of the seismic risk in Italy until 2009 (left), and the *Santa Maria Paganica Church* (right), collapsed after the 2009 *Abruzzo* earthquake.

This occurred first thanks to the new Italian seismic code, enforced in May 2003, which freed and simplified the adoption of the AS systems [1, 2, 5, 8, 9]. This code, which became of obligatory use after the 2009 *Abruzzo* earthquake, was mostly a consequence of the collapse of the *Francesco Jovine* school in San Giuliano di Puglia (due to its bad construction and even worse raising) during the 2002 *Molise & Puglia* event (Figure 2).

An even larger use of the AS systems is now in progress, as a consequence of the heavy damage caused by the 2009 *Abruzzo* earthquake to the conventionally founded civil structures and cultural heritage (Figure 3 and 4) [5, 10, 11]: in particular, 184 pre-fabricated houses were erected in L’Aquila, each on a large isolated large r.c. slab to provisionally host 17,000 homeless persons (at least in the first years). These have been isolated using Italian Curved Surface Slider (CSS) devices, but the use of the traditional HDRBs or LRBs, in conjunction with some SDs, is also going on, for both new constructions and retrofits (Section 4). In particular, the new *Francesco Jovine*, protected by a SI system designed with the collaboration of ENEA and formed by HDRBs and SDs (Figure 5), which has been first Italian isolated school, has been followed by several further projects of this kind: seismic protection of schools by means of SI, besides that of hospitals and other strategic structures, is now a “priority 1” objective in Italy (see Section 5) [9-11].

Figure 4: Collapse of statues in the L’Aquila Museum after the 2009 *Abruzzo* earthquake. Such a disaster should make the opponents of the development and installation of an adequate seismic protection system for the marble statue of *David of Michelangelo* think it over (this worldwide known masterpiece, exhibited in the *Galleria dell’Accademia* in Florence, is severely fissured at its ankles, which makes it very vulnerable to both seismic and even environmental vibrations [1-4]).

Figure 5: The new *Francesco Jovine* primary school and the *“Tre Torri”* multifunctional complex in San Giuliano di Puglia (now seismic zone 2), supported by a common isolated artificial ground slab, which was certified as safe by A. Martelli in September 2008 (left); their SI system, formed by 61 HDRBs and 12 SDs donated by the Italian manufacturers, during construction (right). These buildings will be seismically monitored [10, 11].

Moreover, the use of the AS systems is going on for bridges and viaducts (those with such systems were already at least 250 in 2009 [4]) and cultural heritage [9-11]: new retrofit techniques using SI, applicable to monumental buildings, will be applied for the reconstruction of L’Aquila (Sect. 4).

It is noted that the application of the AS systems in Italy has greatly benefitted from the collaborations in progress in the framework of the national association GLIS (“GLIS – Isolamento ed altre Strategie di Progettazione Antisismica”, namely “GLIS – Isolation and other Anti-Seismic Design Strategies”) since 1989 at national level and in that of *ASSISi* (*A*nti-*S*eismic *S*ystems *I*nternational *S*oc*i*ety) since 2002 at international level.

4 ITALIAN RETROFITS WITH SEISMIC ISOLATION

As previously stressed, the *Abruzzo* earthquake of April 6, 2009 caused an increase of the number of the Italian seismically isolated buildings from about 70 to over 300. Several new Italian hospitals, all new civil defence centres and most new schools have already been (or are already being) seismically isolated, together with a significant number of dwelling buildings and other constructions [9-11]. SI has also been used for some important retrofits of civil structures and precious masterpieces. Prior to the aforesaid event, in almost all applications, the Italian SI systems consisted in HDRBs or LRBs, to which some SDs were added in the last years. Now, as mentioned in Sect. 3, CSS devices are also in use (mainly at L'Aquila).

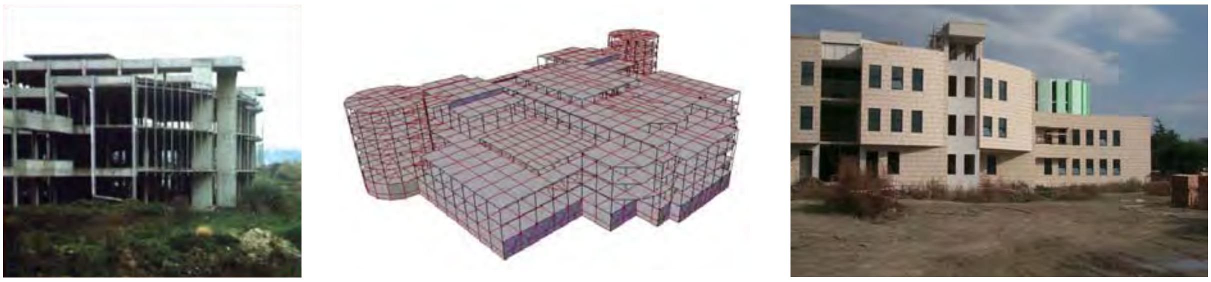

Figure 6: The *Rione Traiano Polyfunctional Centre* in Soccavo (Naples) before being retrofitted (left); its finite-element model, which stresses its large asymmetries (at the centre); completion of its external parts, which was carried out in parallel to the insertion of the SI system (right).

Figure 7: Phases of the retrofit of the building of Figure 6, with installation of 4 hydraulic jacks to provisionally support the weight after removal of the pillar part to be replaced by an isolator and to locally lift the building, so as to allow for the subsequent insertion of the isolator (left), and cut of the pillar with a linear saw (at the centre); view of the isolator after its installation and its mechanical fixing to the upper and lower pillar parts (right).

Figure 8: Installation of the steel beams floor in the building of Figure 6 just above the isolators and reinforcement of the pillars (left); the lower floor after cut of the building supporting pillars and walls (at the centre); the building after retrofit completion (right).

4.1 Rione Traiano Polyfunctional Centre in Naples

The first Italian building to be retrofitted with SI was the *Rione Traiano Polyfunctional Centre* in Naples in 2004. It is a large (100,000 m^3 volume, 33,000 m^2 living area), very asymmetric, 4-storey r.c. building with piled foundations, erected in the years '70s, when the Naples area was not yet considered as seismic, then left incomplete, due to lack of funds (Figure 6) [1, 2]. The intervention was designed by the GLIS members Prof. R. Sparacio of the University of Naples "Federico II", his collaborator F. Cavuoto, Prof. P. Pinto of the University of Rome "La Sapienza" and A. Dusi of NUMERIA (Cremona).

Retrofit with SI was found by the designers to be the only way to avoid demolition and reconstruction. Thus, the foundation pillars and walls were cut (Figure 7), approximately 600 HDRBs were installed, the pillars were reinforced and a steel beams floor was added just above the isolators to provide the stiffness necessary to allow for the correct transmission of the horizontal forces to the isolators themselves and to the superstructure (Figure 8). The retrofit method was similar to that used in 1991 for the Rockwell International Building in Seal Bach, near Los Angeles (California, USA).

This retrofit was designed and performed according to the seismic code applicable before the enforcement of the new one in 2003. As required at that time for the isolated buildings, the design was submitted to the approval of the High Council of Public Works ("Consiglio Superiore dei Lavori Pubblici" or CSLLPP) of the Italian Ministry of Constructions. The overall cost of the intervention was 2.5 M€, namely 80 €/m^2. Of the total costs, 1.3 M€ concerned the isolators and their insertion, 0.6 € the steel slab, 0.5 € the ground retaining walls and the structural gaps and 0.1 € accessories. In normal conditions 20 HDRBs per week were installed by each workers team (with up to 3 teams, in the most busy period).

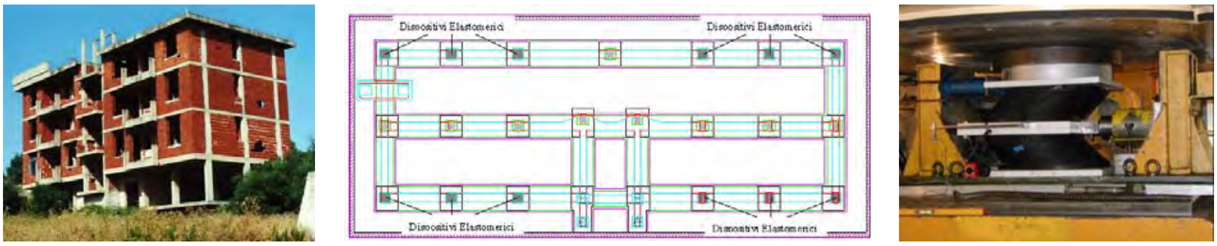

Figure 9: The two dwelling buildings in Solarino before being retrofitted (left); horizontal section of one of the buildings, with location of the isolators (at the centre); two superposed HDRBs during their acceptance tests concerning the application of transverse deformations under the design vertical load (right).

Figure 10: A HDRB during its installation in one of the buildings of Figure 9 (left); this building after retrofit completion (at the centre); an isolator laterally deformed during the on-site tests (right).

4.2 Solarino dwelling buildings

The second Italian building retrofit with SI was performed again in 2004. It concerned two 4-storey r.c. dwelling buildings in Solarino (Syracuse), which had also been left incomplete for some years due to lack of funds (Figures 9 and 10) [1, 2]. Each of them was retrofitted by means of 12 HDRBs and 13 SDs. This retrofit too was performed (by Prof. G. Oliveto of Catania University and others) according to the seismic code applicable before the enforcement of the new one in 2003.

After completion of the intervention, one of the buildings was subjected to free vibration pull-back on-site tests (similar to those previously performed in 1990 for one of the 5 isolated buildings, 25 m high, of the *Telecom Italia Regional Centre* in Ancona and, later, for one of the isolated buildings of the *University of Basilicata* in Potenza and an isolated house in Rapolla, near the same town [1, 2]).

4.3 Fabriano house

In 2005 the first European retrofit with SI in a sub-foundation was completed: it concerned a rather asymmetric 3-storey r.c. dwelling house (11 apartments), which had suffered severe but non-structural damage during the 1997-98 *Marche & Umbria* quake (Figures 11-12).

Figure 11: Vertical and horizontal sections of the original and the retrofitted dwelling house in Fabriano (from left to right).

Figure 12: External and internal non structural damage suffered by the house of Figure 11 in the 1997-98 *Marche & Umbria* earthquake.

Figure 13: Creation of the structural gap around the house of Figure 11 (left); view from the top of the original lower floor and the new underground one after excavation of the latter and construction of new curbs (at the centre); view from the bottom of the new underground floor, the original foundation piles and the new foundations under constructions (right).

This type of intervention (Figure 13-20), which made use of 56 HDRBs of two sizes (400 mm and 450 mm diameters – see Figure 16), was selected by the designer (the GLIS and *ASSISi* member G. Mancinelli of Fabriano) and funded by the government for economic reasons: in fact, its cost was demonstrated to be 20% lower than that of a conventional intervention (which would have required the demolition of all non-structural elements, reinforcement of pillars and beam-pillar nodes and not easy insertion of shear walls); it also enabled to considerably improve the foundations (which consisted of couples of piles) and to obtain a new underground floor. For this building too, the design was completed before the enforcement of the 2003 new seismic code, thus it was submitted for approval to the CSLLPP (it was necessary to wait more than 2 years before obtaining such an approval, although this was given based on the documentation that had been provided to CSLLPP since the beginning!).

Figure 14: Newly built foundation piles, in the part of the house of Figure 11 where the original ones were failing (left and at the centre); pillar eccentric with respect to the original foundation piles (right).

Figure 15: Setting up of the reinforcement of the lower stump of the new pillar (by means of a dummy isolator) and of the lower plate for connecting the isolator in the new underground floor of the house of Figure 11.

The planned construction phases consisted in:

- realization of the ground retaining wall around the house (Figure 13);
- reinforcement or reconstruction of curbs at the existing basement level (Figure 13);
- excavation under the existing basement level at the side of the original foundation piles (Figure 13);
- injection of the new foundations piles around the base of the original ones and realization of the basement of the new underground floor (Figures 13 and 14);
- construction of the r.c. upper stumps of the pillars in the new underground floor, by encompassing the upper part of the original foundation piles, with the upper connection plates for the isolators attached through shanks (Figure 15);
- setting up of the steel reinforcement of the lower stumps of the pillars in the new underground floor, with the lower connection plate for the isolators attached through shanks, using a dummy isolator to correctly fix the distance between the two stumps (Figure 15);

- subsequent construction of the lower stumps of the pillars in the new underground floor;
- construction of the first r.c. slab above the new underground floor (Figure 16);
- insertion of the isolators (Figure 16), superposed to flat jacks (Figure 17), and injection of epoxy resins inside the latter to release the original foundation piles and let the vertical load be carried by the isolators;
- cut of the original foundation columns at the side of the isolators, by leaving the two resulting stumps in place to create a vertical fail-safe system (separated by a few centimetres, in order to avoid contact when the isolated superstructure lowers due to its transverse motion) and completion of the lateral structural gap around the house (Figure 17);

Figure 16: New r.c. slab of the ground level floor of the house of Figure 11 (left); the HDRBs before their installation in the new underground floor (at the centre and right).

Figure 17: Lateral structural gap of the house of Figure 11 before the installation of its protection plates (left); the new underground floor after installation of the HDRBs, but before demolition of the parts of the original foundation piles which were not encompassed by the new pillars (at the centre); an installed HDRB superposed to an epoxy flat jack (right).

Figure 18: HDRBs installed between two original (left) and two newly built (at the centre) foundation piles of the house of Figure 11, before demolition of their parts which were not encompassed by the new pillars; the underground floor after demolition of the aforesaid parts (right).

- installation of the various pipe lines, provided with suitable fixing systems and adequate joints for the interface ones, to let them remain undamaged during the isolated superstructure motion (Figure 19) and of the protection plates of the structural gap (such as not to hinder both the lateral and the small vertical motions of the isolated superstructure during an earthquake).

However, some unexpected problems were detected during the works, which considerably complicated them and delayed the retrofit completion, e.g.:

- the absence of about 50% of the foundation piles in one of the house two halves (evidently due to the presence of large water quantities in the ground during the initial construction), which may at least partly explain the damages caused by the earthquake and made it necessary to build these piles before going on with the retrofit intervention (Figures 14 and 18);
- eccentricities between the foundation piles and the house original pillars, in some positions (Figure 14), which made it impossible to set up the aforesaid planned fail-safe systems through the simple cut of the old foundation piles at the side of the isolators and forced, on the contrary, to fully demolish the parts of such piles that were not encompassed in the new upper and lower pillar stumps (Figure 18 and 19).

Furthermore, some "classical" construction errors were found, for instance holes in the beams to realize passages for pipes (Figure 20).

Figure 19: A HDBR installed, after demolition of the parts of the original foundation piles which were not encompassed by the new pillars (left); the new underground floor in the aforesaid conditions and after the installation of the pipe lines (at the centre and right).

Figure 20: Holes and breaks in the beams of the house of Figure 11, made during the initial construction to create passages for the pipe lines (left and at the centre); the house after retrofit completion (right).

The building safety was certified by A. Martelli, after the full construction completion (i.e. including the installation of the protection plates of the structural gaps and that of all pipilines). It is noted that, according to the construction permissions obtained, the use of the new underground floor is not permitted (it is considered as a “technical volume”), although its spaces would allow for its utilization as garage and/or cellars. Should this change of use be permitted in the future, protections of the HDRBs from fire shall be inserted.

4.4 Further retrofits performed or designed before the 2009 *Abruzzo* earthquake

Further retrofits with SI have also concerned other types of buildings, like churches (starting from that of the dome of the *Sanctuary of Madonna delle Lacrime* of Syracuse in 2006, see Figure 21), r.c. and masonry dwelling buildings (starting from that of one at Rocca di Castell’Ottieri, Grosseto, in 2007), schools (starting from that of the *Quasimodo* school at Riposto, Catania, in 2009), hotels (Figure 22), etc. [5].

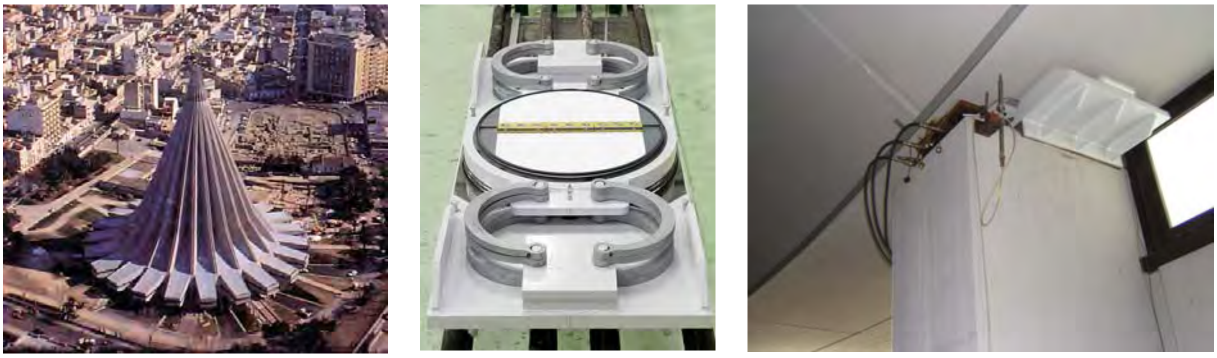

Figure 21: Seismic retrofit of the *Madonna delle Lacrime Santuary* at Syracuse (containing up to 11·000 people), performed in 2007 by uplifting the 22,000 t dome (left) and by inserting isolators with elastic-plastic damping elements (at the centre and right).

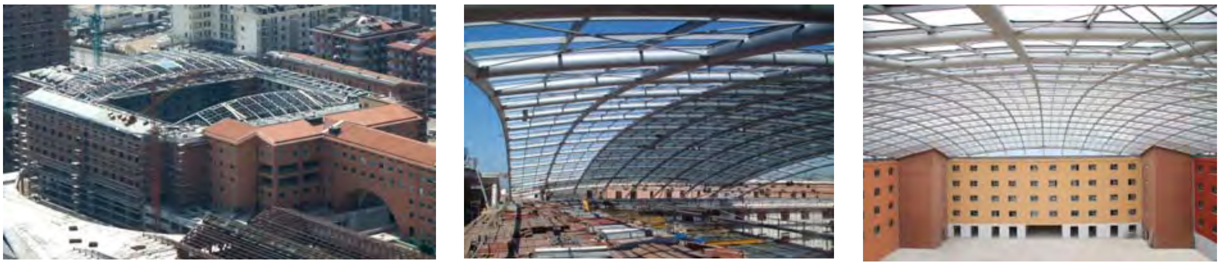

Figure 22: New ceiling of the *Crowne Plaza Hotel* in Caserta, set up by the GLIS board member and *ASSISi* member G.C. Giuliani of Milan in 2006 by constraining it by means of SDs to 3 of the 4 buildings to which it is connected.

Figure 23: One of the 3 tanks of *Polimeri Europa* located in Priolo Gargallo (Augusta, Syracuse, seismic zone 2*), which were seismically retrofitted using U.S. FPS devices in the years 2005-2008 and one of the isolators during and after its installation.

In the years 2005-2008, three chemical tanks of the company *Polimeri Europa* of the Italian ENI Group were also retrofitted in Sicily by means of U.S. CSS devices, namely by the so called Friction Pendulum System (FPS), after cutting the supporting columns (Figure 23) [11, 13]. This is the only application of SI to chemical plants and components so far existing in Italy. Prior to the 2009 *Abruzzo* earthquake, it was also the only application of Curved Surface Slider (CSS) isolators to Italian structures (a similar intervention, using 3 HDRBs and 8 SDs, had been designed by ENEA, APAT – now ISPRA – and the University of Rome “La Sapienza” for a sphere tank of Enichem, located in the same site [1, 2], but was never performed, although it had been demonstrated to be very effective).

Figure 24: External and internal damages suffered by the *San Giovanni Battista Church* in Apagni (Perugia) during the 1997-98 *Marche & Umbria* earthquake.

Figure 25: The *Santa Croce della Ficarella Church* in Case Basse (Perugia) put in safe conditions after the 1997-98 *Marche & Umbria* earthquake (left) and subsequent conventional restoration works (at the centre and right), which should have been followed by the construction of a sub-foundation and insertion there of a SI system formed by 8 HDRBs with 600 mm diameters and 294 mm height (maximum design displacement = 256 mm).

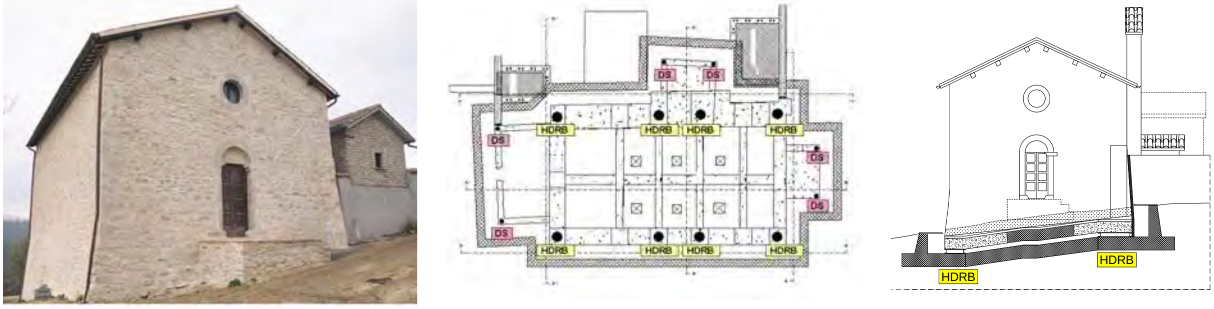

Figure 26: The *San Giovanni Battista Church* of Figure 24 after the new conventional restoration (left); horizontal section of the church with location of the 8 HDRBs and 6 SDs foreseen by the retrofit design with SI (at the centre); vertical section, where the sub-foundation curb is shown.

In addition, the use of SI in a sub-foundation was planned by ENEA and others for two small old churches, decorated by valuable paintings (of Giotto school) which had been severely damaged by the 1997-98 *Marche & Umbria* earthquake: the *San Giovanni Battista Church* in Apagni, near Sellano (Figure 24), and the *Santa Croce della Ficarella Church* in Case Basse, near Nocera Umbra (Figure 25), which are both located in the Umbrian Perugia Province [1, 2, 14, 15]. They had already suffered similar damages during the 1979 *Valnerina* earthquake, after which they had been conventionally restored: this stresses the limits of the conventional restoration. Both churches were conventionally retrofitted again and the SI design was developed by the partners of the PROSEESM National Project, which included ENEA (see Figures 26 and 27 for the *San Giovanni Battista Church*) [1, 2]. Such designs were approved by the Regional Technical-Scientific Committee which was entrusted for the examination of the reconstruction designs, but were never funded later!

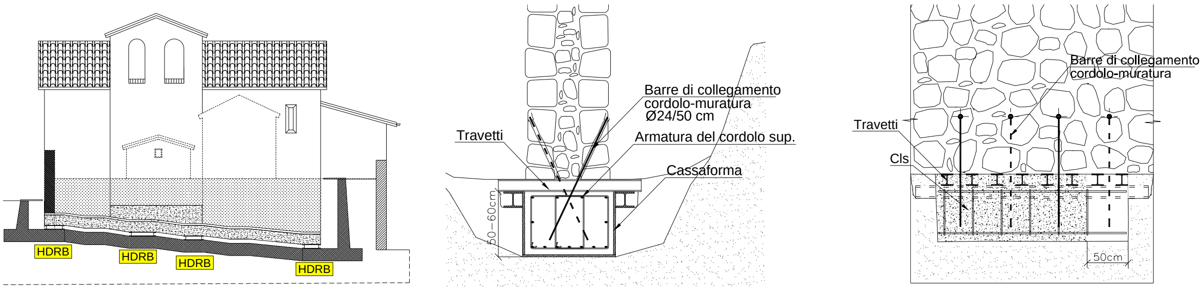

Figure 27: Details of the retrofit with SI in a sub-foundation designed by ENEA for the *San Giovanni Battista Church* of Figures 24 and 26.

Figure 28: Mevale di Visso as reconstructed with conventional techniques after the damages suffered during the 1979 *Valnerina* earthquake (left) and again heavily damaged after the 1997-98 *Marche & Umbria* event (at the centre and right)

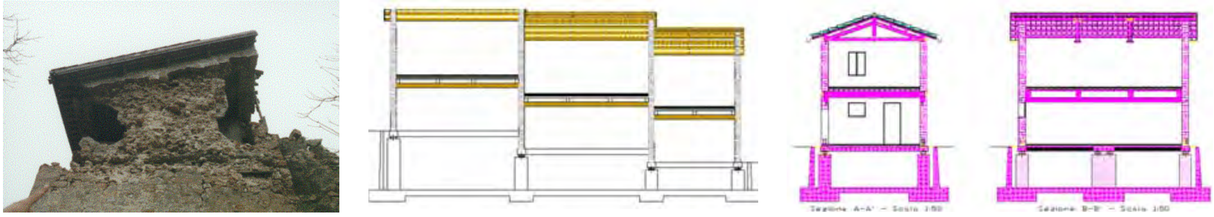

Figure 29: Damage suffered by a house in Mevale di Visso during the 1997-98 *Marche & Umbria* event (left) and vertical sections of isolated houses proposed in the reconstruction designs of ENEA and other partners (at the centre and right).

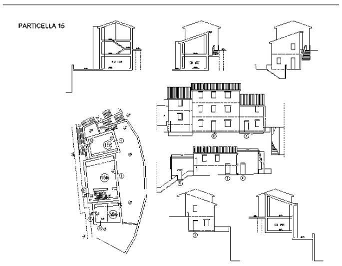

	TT	IS	CA
	361.881,35	**394.962,59**	**357.675,70**
TT	_	33.081,24	-4.205,65
	_	**9,14%**	**-1,16%**
IS	-33.081,24	_	-37.286,89
	-8,38%	_	**-9,44%**
CA	4.205,65	37.286,89	_
	1,18%	**10,42%**	_

Figure 30: Design selected for the first application of SI in the reconstruction of portions of Mevale di Visso and related cost differences among the various retrofit methods (TT = fixed-base masonry; IS = seismically isolated masonry buildings; CA = fixed base r.c. structure).

Another project that was developed by ENEA and other partners and was technically approved by the Marche Technical-Scientific Committee for a first application after the 1997-98 *Marche & Umbria* earthquake (but, again, never funded until now) concerned the reconstruction of portions of the ancient village of Mevale di Visso (on the Apennines in the Marche Macerata Province), with the original materials and construction methods, but on seismically isolated r.c. slabs [1, 2, 14, 15]. This village (Figures 28 and 29) was severely damaged by several earthquakes during its history, including the aforesaid *Valnerina* and *Marche & Umbria* events. The latter caused the partial collapse of several buildings. The reconstruction designs of ENEA and other partners (Figures 29 and 30) showed that the use of SI requires an additional cost of only 5-9% with respect to the case of simple reconstruction of the masonry buildings without any reinforcement and of 3-11% with respect to that of reconstruction using r.c., namely with respect to two solutions that, in any case, are inappropriate or not permitted in Italy: in the first case due to insufficient seismic protection, in the second because it would be in contrast with the conservation requirements which apply for cultural heritage in Italy.

Figure 31: *Bronzes of Riace*, which were isolated in the Reggio Calabria Museum (seismic zone 1) in the years ‘90s (left); its present 3-stage HDRBs system (at the centre), which should be soon replaced by an improved SI system; *Dancing Satyr* in the Mazara del Vallo Museum, again protected by a 3-stage HDRBs system (right).

Figure 32: The original statue of *Scylla,* in the Museum of Messina, in seismic zone 1 (left); monument including copies of the statues of *Scylla and Neptune* in Messina (at the centre); the SI system developed for protecting the originals of both aforesaid statues in the Museum of Messina (right).

Finally, it is worthwhile citing that SI has also already been used in Italy to protect some unique masterpieces. In particular [1, 2, 14, 15]:

- the *Bronzes of Riace* in the Museum of Reggio Calabria, the bronze statue of *Germanicus Emperor* at the National Museum of Perugia and that of the *Dancing Satyr* of Mazara del Vallo (Figure 31) have been seismically isolated by means of 3-stage HDRBs systems (an unique isolators stage would cause geometrical instability of the isolators, because their diameter shall be small for such light bronze statues);

- the original marble statues of *Scylla* and *Neptune* in the Museum of Messina have been supported by a SI system formed by SDs and Shape Memory Alloy Devices (SMADs), the latter acting both as dampers and as re-centring elements (Figure 32);
- steel sphere isolators were used to protect display cases in the Assisi Museum;
- four 3D isolators, developed in the framework of the SPACE Project, funded by the European Commission, were installed in the Ercolano Museum to protect a wooden Roman ship, very vulnerable to seismic vibrations even in the vertical direction, which was excavated in that area, after having been buried by materials erupted by Vesuvius in 79 AD for a long time (each of these isolators is formed by 3 steel spheres rolling between steel plane surfaces with a re-centring rubber cylinder for the horizontal excitations and by a spring and a viscous damper for the vertical one, see Figure 33).

Figure 33: Roman ship excavated near Ercolano (Naples) and exhibited in the local museum, which is located in seismic zone 2 (left); one of the four 3D isolators manufactured to protect it (at the centre); shake table tests of its SI system (right).

Figure 34: The dwelling building of Via Borgo dei Tigli 6-8-10 in L'Aquila (Pianola area), before the 2009 *Abruzzo* earthquake (its construction had been just completed before this event).

4.5 Further retrofits planned after the 2009 *Abruzzo* earthquake

As mentioned, the very significant extension of the applications of SI begun after the 2009 *Abruzzo* earthquake concerns this and other Italian regions. Such applications include numerous retrofits. With regard to those in L'Aquila, to be stressed are those:

- beginning for numerous dwelling buildings damaged by the earthquake, partly based on the experience achieved for the retrofit of the previously mentioned Fabri-

ano house, damaged by the 1997-98 *Marche & Umbria* quake (Figures 34 and 35);
- which should soon begin for some public buildings (e.g. for the town court, the upper storeys of which will be demolished, then reconstructed after the insertion of a SI system at the top of the first floor);
- planned for some monumental buildings, to be partly performed within a collaboration agreement signed between ENEA and L'Aquila municipality in 2010.

Figure 35: Damage caused by the 2009 *Abruzzo* earthquake to the building of Figure 34; its retrofit by means of HDRBs and SDs has been planned, based on a design of the already mentioned GLIS and *ASSISi* member G. Mancinelli of Fabriano, with safety certification of A. Martelli.

Figure 36: The monumental building *Palazzo Margherita* in L'Aquila before the 2009 *Abruzzo* earthquake (left) and put in safe conditions because of the damages suffered during this event (at the centre); its internal courtyard after the earthquake (right).

The latter will concern *Palazzo Margherita* (Figure 36), the historical *De Amicis* primary school (Figure 37) and other buildings. For these the SI system will be inserted in a sub-foundation, in order not to cut any structural elements, including the existing foundations (according to the conservation requirements to be respected in Italy for cultural heritage). Among others, a new method patented by ENEA and the Polytechnic of Torino will be used (Figure 37): it consists in inserting large tubes below the building, laterally to it, and placing the isolators between the upper and the lower semi-spherical halves of such tubes (the upper ones will be the base of the superstructure, the lower ones will form the surface of the new foundation).

Retrofits of existing buildings, even not damaged by the 2009 *Abruzzo* earthquake or other seismic events, have already been planned in other Abruzzo towns or other Italian regions, as well. With regard to Abruzzo, to be cited are some monumental buildings (including at least one school) to be retrofitted in Sulmona, which is also an earthquake prone town, not distant from L'Aquila: where possible, SI in a sub-foundation will be used. To select the intervention types and to control their adequate execution, a collaboration agreement between ENEA and the Sulmona municipality is under preparation. The support of GLIS experts to ENEA is also being considered in this agreement.

Figure 37: The *De Amicis* primary school in L'Aquila, damaged by the 2009 *Abruzzo* earthquake (left); sketch of the new sub-foundation technique patented by ENEA and the Polytechnic of Torino in 2010 (right).

Figure 38: Front view of the *Romita High School* for scientific studies in Campobasso, when it was still in use, namely before the 2009 *Abruzzo* earthquake (left); block "C" of the school (at the centre); horizontal section of the school, showing the different blocks (right).

Figure 39: The *Romita High School* in July 2010, after the demolition of blocks "A" and "B" (left); two HDRBs and a SD installed in the underground technical floor of the new block "B" of the school, during its reconstruction (at the centre); state of the reconstruction of the new block "B" in October 2010, before casting of the upper deck, at the side of the original block "C" (right).

With regard to building retrofits with SI planned in other Italian regions, an interesting case to be cited is that of the *Romita High School* for scientific studies in Campobasso (Figure 38), which hosted about 1,300 students, when it was in use [1, 2, 9, 10]. It consists of various blocks, erected in different years. When it was built, Campobasso was not seismically classified (while now it belongs to seismic zone 2), thus, no seismic design was performed for the school. In addition, the results of investigations performed by a team of experts (including ENEA ones) after the 2002 *Molise & Puglia* earthquake showed that blocks “A” and “B” (Figure 38) were particularly unsafe, even statically, due to very bad quality of the construction materials, and that block “C” was in better but not fully satisfactory conditions.

Based on these results, ENEA immediately advised the school owner (Campobasso Province) to demolish and reconstruct, with SI, at least blocks “A” and “B”. In spite of this, the fear that demolition would have given rise to questions of the population, very difficult to answer, on the static and seismic safety of the other schools of the town, led the owner to decide to first reinforce the unsafe blocks (to make them statically safe) and only later, when possible, to retrofit them with SI or ED. However, such retrofits had not been performed, yet, when the 2009 *Abruzzo* earthquake occurred.

This affair, commented by the first author of this paper during a conversation with a journalist, was reported by his newspaper a few days after the latter event: this led to bitter controversies in Campabasso (with a general strike of the students of the town). Thus, at the end of April 2009, at last, the Campobasso Province accepted the ENEA suggestion to demolish block “A” and “B”, immediately reconstruct block “B” with SI and do the same for block “A”, with the same technique, as soon as the necessary funding would have become available.

As shown by Figure 39, blocks “A” and “B” were both demolished (in July 2010) and reconstruction of block “B” (for which safety will be certified by the first author of this paper) is now in advanced progress (the upper deck was completed in 2010). On the contrary, no funds were found, yet, to reconstruct block “A” too (however, reinforcement rods have been placed in block “A” so as to easily connect them to those of block “B” when it will be built). With regard to block “C”, it is noted that it has been suggested not to demolish it (due to the better construction materials), but to retrofit it by inserting RBs at the top of the pillars of the first floor (Figure 38).

Finally, with regard to the seismic protection of single Italian masterpieces, it is noted that Japanese steel sphere recirculation devices have been used in Italy to isolated the *Worrier of Capestrano* during the 2009 G8 meeting in L’Aquila and that U.S. rolling devices will go on supporting statues that will be returned by the *J. Paul Getty Museum* of Santa Monica (California, USA) to Sicily (Figure 40) [10, 15].

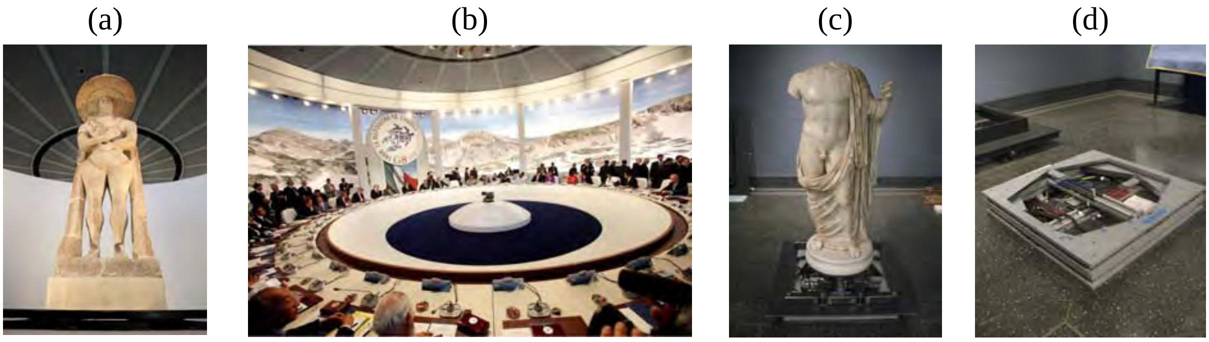
(a) (b) (c) (d)

Figure 40: The statue of the *Worrier of Capestrano* (a) exhibited during the G8 Summit of L’Aquila in 2009 (b), protected by a Japanese SI table, which makes use of steel sphere recirculation isolators; one of the 9 statues which have already been isolated at the *J. Paul Getty House* in Santa Monica (California, USA) and their “wheel” rolling SI system (c & d).

5 LEGISLATIVE MEASURES ALREADY ADOPTED BY THE ITALIAN GOVERNMENT TO PROMOTE THE USE OF ANTI-SEISMIC SYSTEMS

The Italian Government, besides making the use of the new seismic code at last obligatory (during Summer 2009, in the framework of the law for the reconstruction in Abruzzo), already decided some legislative measures to favour the extension of the adoption of the anti-seismic systems and devices (especially of SI), for both erecting new buildings and retrofitting existing ones [9]. These measures were largely based on proposals of GLIS and, in particular, of the first author of this paper. For instance, economic incentives for those adopting such technologies were decided by the Regional Government of Sicily in 2010 and are under discussion at national level and in other regions.

With regard to the seismic protection of schools, it is worthwhile reporting a translation of the whole text of an "agenda" (consistent with a "declaration" of UNESCO-IPRED-ITU [16] and based on a proposal of the first author of this paper [17]) which was submitted by the President of the 8th Commission on Environment, Territory and Public Works of the Italian Chamber of Deputies [18] in the framework of the vote of the 2009 Financial Law and was immediately accepted by the Italian Government [19]:

"The Chamber of Deputies, considering that:

- paragraph 229 of article 2 of the bill under examination contains measures aimed at guaranteeing the safety of schools and, in this framework, in order to ensure the maximum quickness for the completion of the interventions necessary to put the school buildings in safe conditions and to seismically retrofit them, prescribes, in particular, that, within thirty days from the date of enforcement of the financial law itself, the interventions which can be immediately undertaken shall be the first to be identified;
- it shall be stressed in such a framework that, among all construction types, the school buildings, together with hospitals, should be the most protected from earthquakes, which are the events characterized by the highest risk in Italy;
- for such buildings the objective shall be the full safety of the students and the other occupants;
- to this aim, besides preventing the collapse of school buildings in the case of earthquakes (which is the requirement foreseen by the seismic codes, including the new Technical Norms for Constructions), it is also indispensable to guarantee their full integrity, with no damage even to the non-structural elements and the objects contained;
- furthermore, the level of the seismic vibrations transmitted by the ground to the buildings shall be minimized, to prevent panic;
- the aforesaid objectives cannot be achieved by the conventional anti-seismic design, which is based on the «robustness» of structures, while they can be fully achieved thanks to base seismic isolation and can be achieved to a large extent by inserting energy dissipation systems inside the structures themselves;
- more than half of the school buildings existing in our country result to be inadequate to withstand the earthquakes to which they may be subjected;
- for many of such buildings retrofits able to guarantee a sufficient seismic safety are very difficult or too costly, either because they are monumental buildings (thus also subjected to the conservation requirements), or because they are rather old;
- in the first case it would be desirable to assign the buildings to a different use and move the school functions to other structures, possibly of new construction; in the second the best solution would be demolition and subsequent *ex novo* reconstruction;
- for the new school buildings there are no obstacles of technical nature against their construction with seismic base isolation (in Italy 5 new isolated schools have already been completed and further 12 are under construction); in favour of this tech-

nological solution there are, besides the largely higher safety level with respect to a conventionally founded construction, the overall economic balance too (which takes into account not only the construction costs, but also those of demolition and repair, removal and storage of the debris, displacement of the school activities) and the evident environmental and energetic benefits;

- with regard to the sole construction costs, it is worthwhile noting that, in Italy, the school buildings have a limited number of storeys and usually do not need for an underground storey; thus, although the new Italian seismic code allows for lightening the superstructure and foundations of seismically isolated buildings, for school buildings with base isolation some additional construction costs due to the use of such a protection (isolators, an additional storey above them, etc.) have to be foreseen sometimes;
- for interventions on existing school buildings, seismic isolation may be used only if the room necessary for the «rigid body» motion which characterizes the building part supported by the isolators exists or can be created around the building; the related costs may be even significantly lower than those characterizing a conventional retrofit, because it is possible to avoid stripping the structure, strengthening pillars and beam-pillar nodes and inserting shear walls;
- when seismic isolation is not applicable, it is usually possible to seismically improve the buildings by inserting dampers inside them; in this case the cost of dampers is usually largely balanced by the possibility of avoiding stiffening of the structure;
- in Italy the most famous seismically isolated building is the new Francesco Jovine or «Angels of San Giuliano», school; such a school was the first, among those protected by seismic isolation, to be completed in Italy, in September 2008; the isolation system was designed by a team of experts co-ordinated by ENEA and the structure was subjected to inspections during construction and safety certification of an expert of the Agency; ENEA also contributed to the design of the seismic isolation system and/or certified or will certify the safety of further new schools, in Marzabotto (Bologna), Campobasso, Vado (Bologna) e Mulazzo (Massa); to be cited are also the design and safety certification of 4 further new seismically isolated schools in Tuscany, performed in the framework of the Collaboration Agreement on «Applications of seismic isolation and other modern anti-seismic technologies to constructions and buildings, in particular for educational use» signed by Tuscany Region, ENEA and GLIS in 2004;
- previously other existing schools had been seismically improved by means of energy dissipation systems, first of all at Potenza and its province, then in the Marche Region too: among the latter it is worth citing the Gentile Fermi school in Fabriano, of rationalist architecture, which, due to the damages suffered during the 1997-98 Marche and Umbria earthquake, was seismically improved by means of visco-elastic dampers developed in the framework of the EU-funded project REEDS promoted by ENEA;
- ENEA, in the framework of school building, may profitably contribute in its specific competence fields, among which:
  - the development of new anti-seismic devices and, by means of its experimental equipment, tests on such devices and mock-ups of structures protected by them;
  - the definition of seismic input, also by means of on-site seismic tests, and

analysis of local seismic response and seismic micro-zoning, with definition of site-specific spectra and/or acceleration time-histories;
- the evaluation of the seismic vulnerability of existing buildings, also by means of experimental tests on the materials and structures, with the identification of the most suitable techniques for the seismic retrofit of the structures;
- specialist consultancy in support to the structural design, with particular reference to the sizing and verification of the modern seismic protection systems, for both new buildings and retrofits of existing buildings;
- specialist consultancy in support to the installation of the anti-seismic devices;
- inspections during construction and final safety certification of the buildings;
- seismic monitoring of the structures,

commits the Government,

in the framework of the realization of the provisions of paragraph 229 of article 2 of the bill under examination, to evaluate the opportunity of involving ENEA and, in the affirmative, to draw up specific agreements, as to define interventions for the seismic safety of schools which are not only highly effective, but are also both the most advanced with regard to the construction technologies to be adopted and as advantageous as possible as far as costs, safety and functionality are concerned."

6 CONCLUSIONS AND REMARKS ON THE CORRECT USE OF SEISMIC ISOLATION

The overview reported in Sections 2 and 3 of this paper has stressed the large effects of earthquake experience and seismic design code features on the extent of the use of the AS systems, in particular of the SI technique, in the various countries [9-11]. With regards to the code features, it is noted that, in countries like, for instance, Japan, the USA and Chile, SI is considered as a safety measure additional to the conventional design; consequently, the use of SI obviously always introduces additional construction costs. In spite of this, this technique is being widely adopted by the Japanese, because of their high level of perception of the seismic risk and due to the fact that violent earthquakes are very frequent in Japan.

The aforesaid level of perception is much lower in other countries: this is the reason why, in order to limit or even balance the additional construction cost entailed by the use of SI (and, thus, promote a significant application of such a technique), the seismic codes of other countries (including Italy, the P.R. China, Armenia, etc.) allow for somewhat lowering the seismic forces acting on the superstructure and (consequently) foundations when SI is used.

It is worthwhile stressing, however, that, in the latter countries, a real safety will be ensured to the isolated structures <u>if and only if</u> great care is paid to [10, 11]:

- the selection of the SI devices (taking into account the amplitude of vertical and low frequency vibrations), their qualification, production quality, installation, protection, maintenance and verification that their design features remain unchanged during the entire useful life of the structure;
- some further construction details (structural gaps, their protections, interface elements – like gas and other safety-related pipes, cables, stairs and lifts –, etc.).

Otherwise, the isolators, instead of largely enhancing the seismic protection (as they do, if the aforesaid conditions are satisfied), will make the structure <u>less earthquake resistant</u> with respect to a conventionally founded one and, thus, will expose both human life and the entire SI technology to a great risk [10, 11].

Finally [6], a common key requirement for the optimal performance of all the AS systems and devices (but especially of the isolators) is the realistic and reliable definition of seismic input, which cannot rely upon the oversimplified routine probabilistic methods, mainly when dealing with displacements definition (on which the design of isolated structures is based): thus, because of the ongoing rapid extension of the use of the AS systems and devices, the need for a considerable improvement of the *Probabilistic Seismic Hazard Assessment* (PSHA) approach, which is at present that in use in several countries (including Italy), is very urgent now, by complementing it through the development and application of deterministic models [20]. This particularly applies to the P.R. China and Italy, to ensure safe reconstruction after the 2008 *Wenchuan* and 2009 *Abruzzo* earthquakes, because in the areas struck by both events a wide use of SI is in progress.

All the aforesaid items were discussed at the already mentioned 8th Commission on Environment, Territory and Public Works of the Italian Chamber of Deputies in February 2011, by also interviewing some experts (including the first author of this paper, as ENEA representative). The aim of the Commission is to agree on a resolution which shall stress again the benefits of SI, clarify the conditions for its correct use and recommend modifications of the current national and European design rules applicable to the seismically isolated buildings, based on the presently available knowledge and technological developments. This resolution should integrate those proposed by the president of the commission, who belongs to a governmental party [21], and by an expert member of an opposition party [21] (these two texts, written with the collaboration of the first author of this paper, have very similar contents and contain the same recommendations). The aforesaid recommendations (where particular attention is given to building retrofits) should be drafted by CSLLPP with the collaboration of ENEA (a specific agreement to this purpose should be soon signed between the two institutions).

REFERENCES

[1] M. Dolce, A. Martelli, G. Panza, *Proteggersi dal terremoto: le moderne tecnologie e metodologie e la nuova normativa sismica, 2nd edition, ISBN 88-87731-28-4*. 21mo Secolo, Milan, Italy, 2005.

[2] M. Dolce, A. Martelli, G. Panza, *Moderni metodi di protezione dagli effetti dei terremoti, Special edition for the Italian Civil Defence Department, A. Martelli ed., ISBN 88-87731-30-6*. 21mo Secolo, Milan, Italy, 2006.

[3] A. Martelli, U. Sannino, A. Parducci, F. Braga, *Moderni sistemi e tecnologie antisismici. Una guida per il progettista, ISBN 978-88-87731-37-8*. 21mo Secolo, Milan, Italy, 2008.

[4] U. Sannino, H. Sandi, A. Martelli, I. Vlad, *Modern systems for mitigation of seismic action – Proceedings of the symposium held at Bucharest, Romania, on October 31, 2008, ISBN 978-973-720-223-9*. AGIR Publishing House, Bucharest, Romania, 2009.

[5] A. Martelli, M. Forni, Recenti applicazioni dei sistemi di isolamento sismico in Italia. *Ingegneria Sismica*, Anno XXVII, **1**, 63-73, 2010.

[6] A. Martelli, On the need for a reliable seismic input assessment for optimized design and retrofit of seismically isolated civil and industrial structures, equipment and cultural heritage. *Pure and Applied Geophysics*, DOI 10.1007/s00024-010-0120-2, 2010.

[7] A. Martelli, Protezione degli edifici dal terremoto mediante moderne tecnologie – Parte 2. *L'Edilizia – Structural*, **162**, 60-70, 2010 (in Italian).

[8] A. Martelli, M. Forni, Recent progress of application of seismic isolation in Italy. Invited lecture, *Engineering Mechanics Institute (EMI) 2010*, Los Angeles, California,

USA, August 8-11, 2010; *Technical Program and Book of Abstracts*, USC Viterbi School of Engineering, 142, 2010.

[9] A. Martelli, M. Forni, Seismic isolation and other anti-seismic systems: recent applications in Italy and worldwide. *Seismic Isolation And Protection Systems (SIAPS), **1**, N. 1*, 75-123, DOI 10.2140/siaps.2010.1.75, Mathematical Sciences Publishers (MSP), Berkeley, California, USA, 2010.

[10] A. Martelli, M. Forni, Recent worldwide application of seismic isolation and energy dissipation and conditions for their correct use. Invited lecture, *Structural Engineering World Congress (SEWC)*, Cernobbio, Como, Italy, April 4-6, 2011.

[11] A. Martelli, M. Forni, Seismic isolation and other passive anti-seismic systems: worldwide application and conditions for their correct use. Invited lecture, *Minisymposium MS09 on Active, Semi-Active and Passive Vibration Control, EURODYN2011 – 8th International Conference on Structural Dynamics*, Leuven, Belgium, July 4-6, 2011.

[12] N. Kani, *Recent trends of seismically isolated structures in Japan*. Japan Society for Seismic Isolation (JSSI), Tokyo, Japan, 2011.

[13] N. Scibilia, Tecniche di riduzione del rischio sismico – Isolamento di serbatoi. *Meeting on Moderne Tecniche di Protezione Sismica*, Palermo, Italy, October 16, 2010.

[14] A. Martelli, Development and application of innovative anti-seismic systems for the seismic protection of cultural heritage. Key-note lecture, F.M. Mazzolani ed. *Protection of Historical Buildings – PROHITECH 2009, ISBN 13:978-0-415-55803-7,* **1**, 43-52, CRC Press – Taylor and Francis Group, Leiden, The Netherlands, 2009.

[15] A. Martelli, Development and application of innovative anti-seismic systems for the seismic protection of cultural heritage. Invited lecture, *Proceedings of the International Conference on the Protection of Cultural Heritage from Earthquake Damage*, Palermo, Italy, October 13-15, 2010.

[16] UNESCO-IPRED-ITU, *Declaration of participants in the UNESCO-IPRED-ITU Workshop, Istanbul, 7 July 2009*. UNESCO, Paris, France, 2009.

[17] A. Martelli, Sicurezza sismica delle scuole: possibili contributi dell'ENEA. *Il Portale dell'Ingegneria Sismica*, www.ingegneriasismica.net/Tematiche/5CS/5CStecnologieM/5CStecnologieM_martelli06/5CStecnologieM_martelli06.htm.

[18] A. Alessandri, L. Rainieri, M. Lanzarin, Ordine del giorno n. 9/2936-A/50. *Atti parlamentari, XVI Legislatura – Allegato A ai Resoconti – Seduta N. 259*, 51-53, Rome, Italy, December 16, 2009

[19] Camera dei Deputati, *Atti Parlamentari, XVI Legislatura – Allegato A ai Resoconti – Seduta del 16 Dicembre 2009 – N. 259*. VII-VIII, Rome, Italy, December 16, 2009.

[20] G. Panza *et al.*, eds., Advanced seismic hazard assessment. *Pageoph Topical Volume, ISBN 978-3-0348-0039-6 & ISBN 978-3-0348-0091-4*, 2011.

[21] A. Alessandri, G. Dussin, M. Lanzarin, R. Togni, Risoluzione in commissione n. 7/00409 in materia di isolamento sismico delle costruzioni civili e industriali. *Atti Camera dei Deputati*, Rome, Italy, October 14, 2010.

[22] G. Benamati, T. Ginoble, Risoluzione in commissione n. 7/00414 in materia di isolamento sismico delle costruzioni civili e industriali. *Atti Camera dei Deputati*, Rome, Italy, October 14, 2010.

COMPDYN 2011
III ECCOMAS Thematic Conference on
Computational Methods in Structural Dynamics and Earthquake Engineering
M. Papadrakakis, M. Fragiadakis, V. Plevris (eds.)
Corfu, Greece, 25–28 May 2011

NUMERICAL SIMULATION OF THE DYNAMIC AND EARTHQUAKE BEHAVIOUR OF GREEK POST-BYZANTINE CHURCHES WITH AND WITHOUT BASE ISOLATION

G.C. Manos[1], N. Karamitsios[1]

[1] Department of Civil Engineering, Aristotle University, Thessaloniki 54006, Greece

emaill: gcmanos@civil.auth.gr

Keywords: Byzantine Churches, Masonry Structures, Dynamic Response, Earthquake Performance, Base Isolation

Abstract. *The dynamic and earthquake response of Post-Byzantine stone masonry churches, which were subjected to a damaging earthquake sequence in the region of Western Macedonia in Greece, is studied. Two structural systems of the "basilica" form are first examined. Apart from these two "basilica" churches, the behavior of another much older church, which represents a much simpler orthogonal structural formation, is also examined. This is a two-story church with a simple orthogonal vault and a wooden roof that belongs to an 11th century monastic-complex. Two of these churches are also studied together with the introduction of a base isolation system. The performance of each of these three distinct structures is studied under the combination of the gravitational and seismic forces. The predicted performance of the various structural elements, located at the peripheral masonry walls is then checked by applying an assumed Mohr-Coulomb failure envelope that is believed to represent the limit-state stone-masonry behavior. The seismic damage, due to a relatively recent strong earthquake sequence, is utilized to validate the realism of the numerical predictions. The numerical introduction of a base-isolation system was quite effective in lowering the demands and thus resulting for most structural elements in Capacity/Demand ratio values larger than one (Capacity/Demand > 1), which is assumed to indicate acceptable structural performance. However, the introduction of base isolation under an existing old stone-masonry structure is also faced with considerable difficulties, despite the advantages that are shown by the results of numerical investigation. In the particular case of "The Church of The Virgin Mary of Tourniki" these difficulties must be faced because this old church has to be moved in a different location due to flooding. Thus, the placement of a base isolation scheme under this structure in its new location is a feasible solution for this particular case with no significant extra cost. Obviously, thus base isolation scheme should be considered in addition to all other traditional repair and strengthening measures for this church.*

1 INTRODUCTION

During the last thirty years various parts of Greece have been subjected to a number of damaging earthquakes ranging from Ms=5.2 to Ms=7.2 on the Richter scale. One of the most demanding tasks for counteracting the consequences of all these seismic events was the effort to ensure the structural integrity of old churches, that were built in periods ranging from 400 A.D. up to today; in many cases they sustained considerable damage (ref. 1., Manos et.al. 2008). In what follows, selected results and summary observations are presented of the dynamic and seismic behavior of two specific types of structural systems that are utilized in a considerable number of churches belonging to the so-called Post-Byzantine period (16th to 19th century A.D.). The first is the structural system of the "Basilica" that takes a number of variations in plan and height whereas the second type is a simple box-type structural formation. The present study examines the seismic behavior of two churches belonging to the 1st structural system ("Typical Post-Byzantine Basilica" and "Taxiarhes") and a church belonging to the 2nd structural system (Virgin Mary at Tourniki). All these churches are located in the region of Western Macedonia – Greece and they were all subjected to the damaging strong Kozani earthquake sequence of May, 1995. The numerical results presented here are part of an attempt to numerically explain the observed behavior. The numerical investigation includes modal analysis results; no attempt was made to compare these results with in-situ measurements for dynamic identification. Next, for all examined structures the numerical analysis predicts the demands imposed on the masonry structural elements by critical load combinations which include earthquake loading as specified by the Greek Seismic Code (ref. 2). Finally, the performance of the various masonry structural elements is evaluated in section 3 by examining the ratio values of the Capacity / Demand. The demands are obtained by assumed strength values, without the incorporation of any safety factors. Space limitations allow only very limited presentation of the observed actual damage. In general, the predicted damage regions agree well with observed damage.

It is obvious that an important next step is the rehabilitation of the damaged masonry. The structural repairs of the stone-masonry churches examined here are inhibited by restrictions arising from retaining the visible stone-masonry architectural formations at the exterior and the frescos at the interior of the masonry walls. An acceptable type of repair is the application of low-pressure lime-mortar injections enriched with ceramic powder, resulting in a modest increase in the capacities of the various structural elements. The application of techniques used for the repair of reinforced concrete structural elements (jacketing or use of fiber reinforcing plastics), utilizing the resultant considerable capacity increase, is not acceptable for the stone masonry of such heritage structures. An alternative solution is lowering the demands by the use of base-isolation as the one investigated here. However, the introduction of base isolation under an existing old stone-masonry structure is also faced with considerable difficulties, despite the advantages that are shown by the results of numerical investigations as the one performed here.

1.1 The "Typical Post Byzantine Basilica"

The first case is a three-nave Post Byzantine "Basilica" structural formation which, in the overall geometry, is typical of a number of churches with similar geometry which were damaged by a strong earthquake sequence in the region of Western Macedonia, Greece during the Kozani Earthquake of 1995. The overall dimensions of this "typical" case are 19m length, 11m width and 6.8m height of the central nave (the level at the top of the roof). The internal colonnades are made of wood (figures 1a, 1b and 1c).

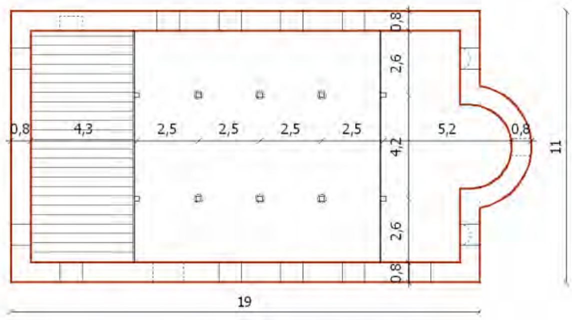

Figure 1a plan

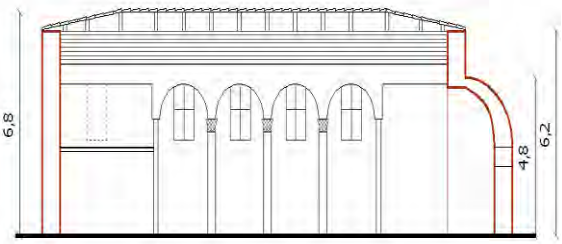

Figure 1b Cross section.

Figure 1c. East wall and Apse.

Figure 1. Typical Post-Byzantine “Basilica”

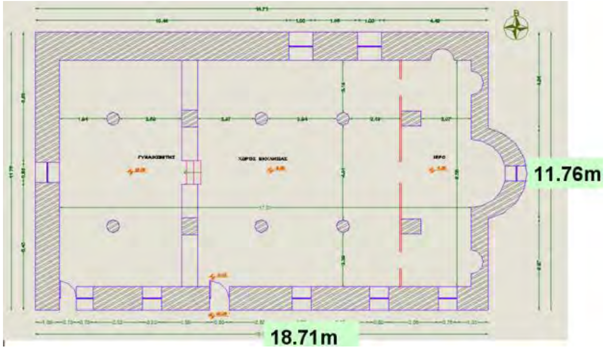

Figure 2a plan

Figure 2 “ The church of Taxiarhes”

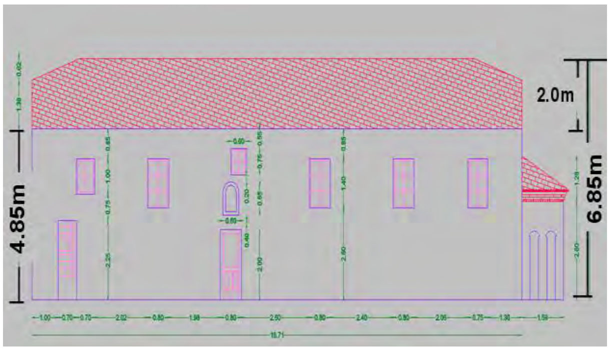

Figure 2b South Elevation

1.2 The “Post Byzantine Basilica church of Taxiarhes”

This structural formation is also a 19th century Post Byzantine church of Taxiarhes at the village of Rodiani in the prefectures of Kozani, Greece; it was also damaged by the Kozani Earthquake of 1995. The length of the longitudinal walls is 18.7m whereas that of the transverse walls 11.75m, almost similar to the plan dimensions of the 1st church. However, the height of the peripheral walls is 4.85m, lower than that of the 1st case. Moreover, an additional distinct difference from the 1st case is a system of masonry cylindrical vaults, spherical domes and arches which are utilized to support the wooden roof that rises another 2.0m from the top of the peripheral masonry walls (Figures 2a and 2b). The thickness of the masonry walls varies from 700mm to 1200mm.

1.3. The “church of The Virgin Mary of Tourniki”

This is a simple box-type structural system of rectangular shape, formed by the peripheral walls; a semi-cylindrical apse is part of the East wall, whereas the interior is usually divided into a number of naves by longitudinal colonnades of various dimensions and shapes. The simplest formation of a “Basilica” is that of a single-space rectangular structure without interior separations. Such a structure is also examined in this paper; this is a two-story Basilica, which is devoted to the Virgin Mary and belongs to the Monastic complex of Tourniki.

Such a two-story Basilica (Figure 3) is a rather rare structural system that can be found in the monastic complexes of Mt. Athos. The behavior of this two-story Basilica is numerically simulated by focusing on the super-structure and in particular on the influence of the cylindrical vaulting system that exists at the 1st story level as well as at the roof. The numerical investigation for this 2nd church is extended to study the introduction of a base isolation system.

Fig. 3a.

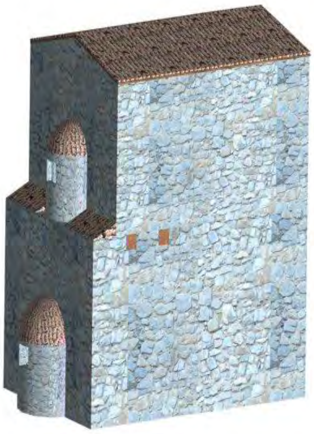

Fig 3b.

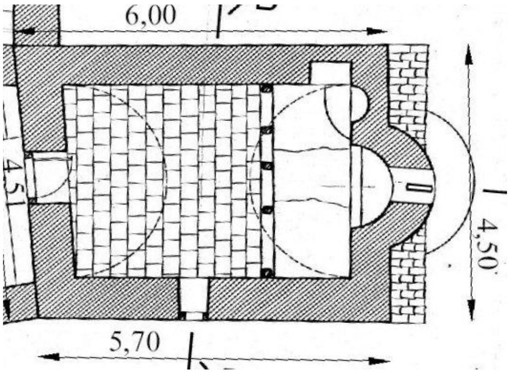

Fig. 3c. Plan

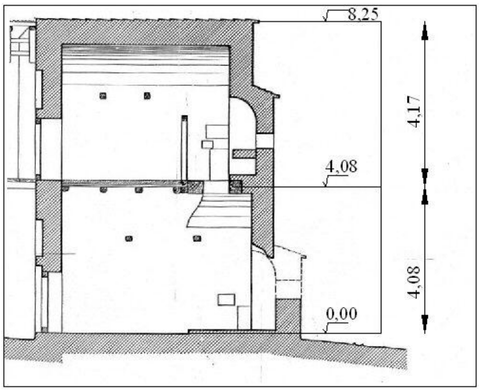

Figure 3d. Cross section

Figure 3. of Virgin Mary of the Monastic complex of Tourniki

1.3.1. Main Features of The church of The Virgin Mary of Tourniki

The establishment of the monastic complex and the building of this church is set at the 11th century A.D. This church is a two-story box-type “Basilica” structural system formed by two longitudinal walls (North and South) and two transverse walls (East and West) with a thickness of 700mm. The East transverse wall is dominated by two apses (one for each story) with a thickness of 700mm (Figs 3a and 3b). A relatively complex system is constructed at the East transverse wall with the two Apses in order to transfer the gravitational forces of the top East wall and Apse, which are offset by 700mm towards the interior of the church, when compared with the East wall and Apse of the bottom story (Figures 3a to 3d). The top story ceiling is formed by a longitudinal semi-cylindrical vault with a thickness of 350mm which supports the wooden roof together with the peripheral walls that extend appropriately for this purpose. Despite some small differences in the length of the North and South longitudinal walls, the structural system as a whole can be assumed to retain a mid-axis of symmetry with respect to the East-West longitudinal direction. Apart from the difference in the length of the longitudinal walls the exact location of the window openings deviates from this symmetry; however, these deviations are not believed to be very significant. This church was also subjected to the same 1995 strong earthquake when the monastic complex was not in use; damage visible at the cylindrical vaults cannot be linked directly to the event.

2. RESULTS FROM THE MODAL ANALYSIS OF THE POST-BYZANTINE AND THE BYZANTINE BASILICAS

A linear-elastic modal analysis was conducted assuming a value for the Young's Modulus for the masonry walls equal to 2500Mpa. The mass of these stone masonry walls was assumed to be equal to 2.70t/m3. All the walls were numerically simulated by shell F.E. The arches on top of the internal colonnades as well as the wooden roof was also numerically simulated; the Young's Modulus of all the wooden parts was taken equal to 8400Mpa with the corresponding mass equal to 0.66t/m3.

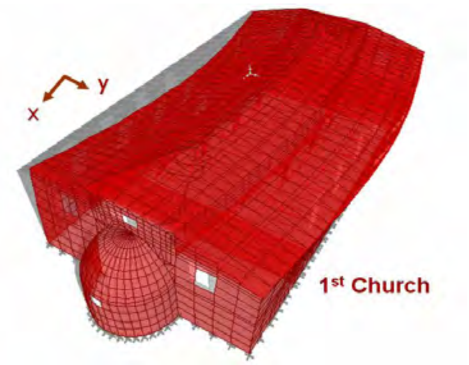

Translational y-y
Ty = 0.102 sec., uy = 51.38%
(Non-Isolated)
Figure 4a

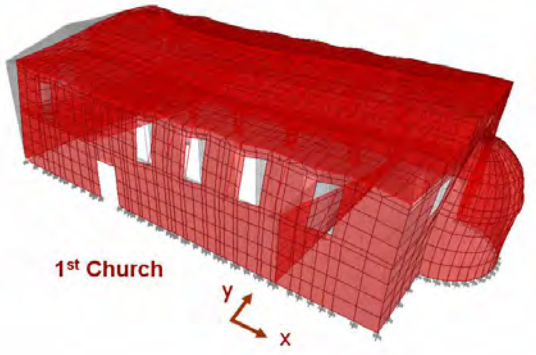

Translational x-x
Tx = 0.069 sec., ux = 49,63%
(Non-Isolated)
Figure 4b

Figure 4. Dynamic characteristics "*Typical Basilica*"

2.1 The "Typical Post Byzantine Basilica"

Figures 4a and 4b depict the mainly horizontal translational eigen-modes for the 1st structure. The translational eigen-mode in the transverse North-South (y-y) direction is the one with the longest eigen-period (Figure 4a T = 0.102seconds). The structural response in this mode displaces the longitudinal peripheral walls mainly out-of-plane; this is done with the transverse peripheral walls resisting mainly in-plane. The translational eigen-mode in the longitudinal East-West (x-x) direction is the next longest eigen-period (Figure 4b T = 0.069 seconds). The structural response in this mode displaces the longitudinal peripheral walls mainly in-plane; this is done with the transverse peripheral walls resisting mainly out-of-plane. Each one of these modes mobilizes approximately 50% of the total mass of the structure. These two modes are next followed by higher modes; however; these latter modes mobilize relatively small portions of the total mass.

2.2 The "Post Byzantine Basilica church of Taxiarhes"

In comparison, figures 5a and 5b depict the mainly horizontal translational modes for the 2nd structure. It can be seen that the eigen-periods in both the longitudinal and the transverse directions for the 2nd church are somewhat longer than those of the 1st structure. However, this time the modal mass ratios, that are mobilized by these two translational modes, are noticeably larger than those of the 1st structure. Both these effects must be attributed to the mass of the system of masonry cylindrical vaults, spherical domes and arches.

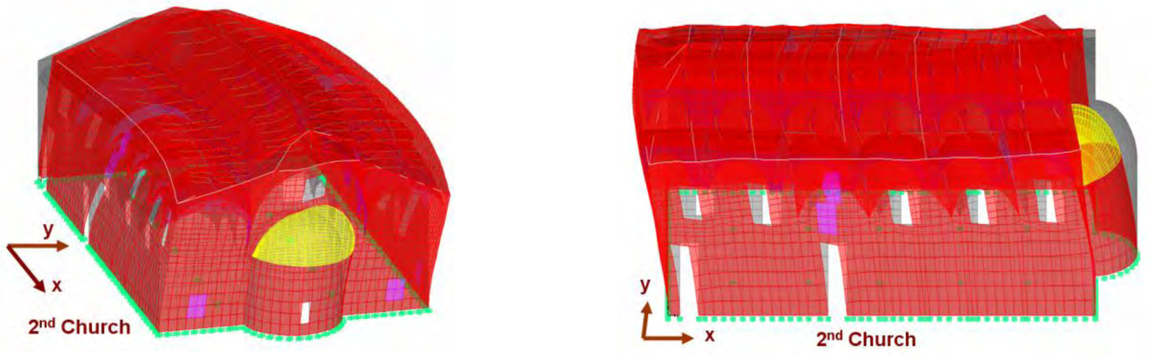

Translational y-y
Ty = 0.1053 sec., uy = 61.8%
(Non-Isolated)
Figure 5a

Translational x-x
Tx = 0.0724 sec., ux = 63,966%
(Non-Isolated)
Figure 5b

Figure 5. Dynamic characteristics *"Church of Taxiarhes"*

2.3. The "church of The Virgin Mary of Tourniki"

For this structural system the first two horizontal translational mode shapes and eigen-periods are shown in figures 6a and 6b. As can be seen, due to the two-story formation, these two eigen-periods are relatively longer than the corresponding values of the previously examined Post-Byzantine Basilicas. Moreover, these two eigen-modes also mobilize much larger modal mass ratios than the corresponding values of the previously examined Post-Byzantine Basilicas, a fact that must be attributed to the box-type form of this structure; moreover, the peripheral masonry walls have relatively small dimensions to excite them in an out-of-plane manner.

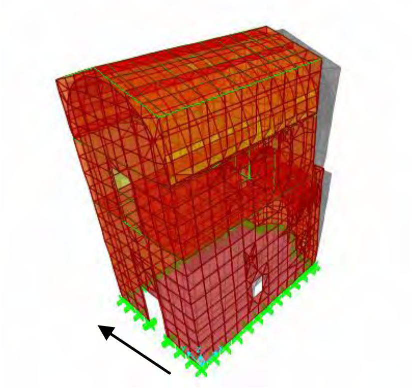

Figure 6a. 1st y-y
T=0.1375sec., Uy =73.94 %
Non -Isolated

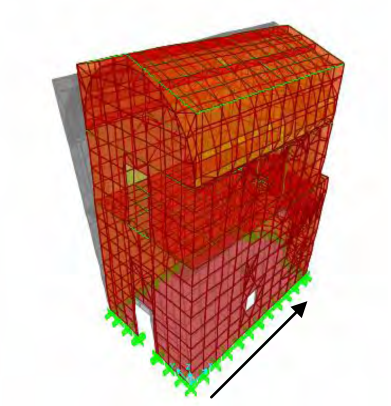

Figure 6b 1st x-x
T= 0.0942 sec Ux = 68.02 %
Non –Isolated

Figure 6. Dynamic characteristics Virgin Mary of Tourniki"

3. THE DEMANDS ON THE STRUCTURE FROM THE GRAVITATIONAL AND EARTHQUAKE LOADING

The behavior of all three structures was examined next when they were subjected to three distinct loading conditions. The forces in all these three loading conditions were applied in a static manner. The structures were assumed to have all three translational degrees of freedom (ux, uy, uz) restrained for all masonry at the foundation level. The first loading case included the dead (G) loads of all parts plus the live (Q) loads (mainly snow at the roof level plus the live load at the level used as women's quarters). During the second and third loading conditions the earthquake forces Ex and Ey were applied along the x-x and the y-y axis, respectively. This was done in a simple way assuming unit acceleration for all the parts of the structure equal to 1g (where g is the acceleration of gravity). The dynamic nature of the seismic forces was taken into account in a separate series of simulations presented in the next section.

3.1 The "Typical Post Byzantine Basilica" and the "church of Taxiarhes"

The results for the 1st and 2nd Post-Byzantine Basilicas are depicted in figures 7 and 8, respectively. As can be seen in these figures, the structural system of both churches is more flexible in the transverse than in the longitudinal direction. The resistance of the internal colonnades to either the x-x or the y-y seismic forces is very small as these structural elements are quite flexible. The maximum horizontal displacement at the roof level is equal to 1.94mm for the 1st church (0.16mm for the 2nd church) for the loading case Ex whereas it attains the value of 4.447mm for the 1st church (3.86mm for the 2nd church) for the loading case Ey, more than double.

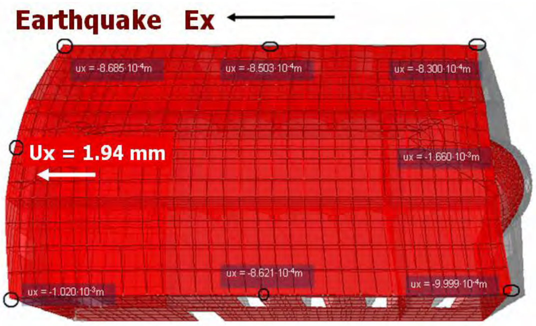

Figure 7a. Deformations for seismic forces Ex

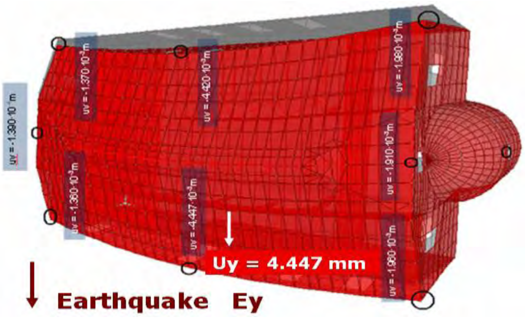

Figure 7b. Deformations for seismic forces Ey

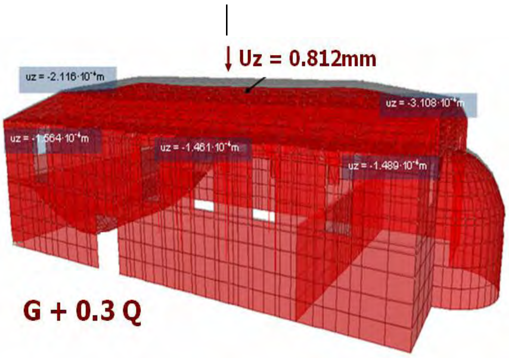

Figure 7c. Deformations for gravity forces

Figure 7 Deformations of *"Typical Post Byzantine Basilica"*

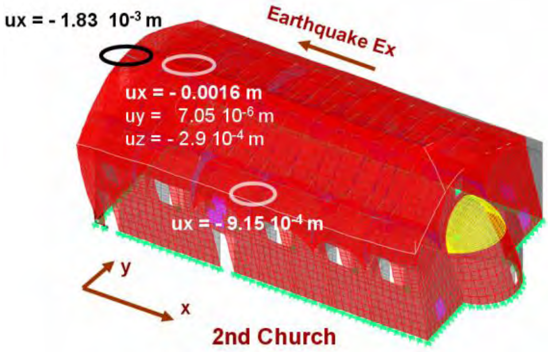

Figure 8a. Deformations for seismic forces Ex

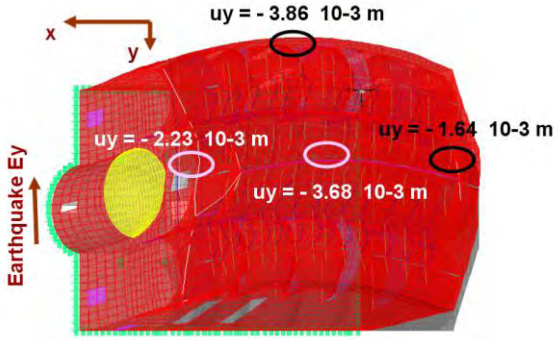

Figure 8b. Deformations for seismic forces Ey

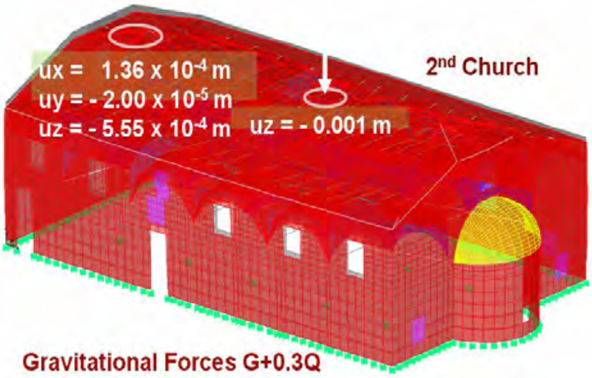

Figure 8c. Deformations for gravity forces

Figure 8. Deformations *"Church of Taxiarhes"*

The seismic forces are mainly resisted by the in-plane action of the peripheral walls parallel to the direction of these forces as well as by the out-of-plane action of the peripheral walls normal to the direction of these forces. The maximum value of deformations from the gravitational forces is equal to 0.812mm for the 1st church (1.0mm for the 2nd church); this occurs along the vertical direction at mid-span of the top of the roof. The vertical deformations at the top of the peripheral walls are of the order of 0.1mm to 0.2mm; moreover, the out-of-plane flexibility of the longitudinal walls results, at their top, in out-of-plane deformations of the order of 0.15mm when the structure is subjected to the gravitational forces.

3.2. The "church of The Virgin Mary of Tourniki"

The small size in plan for this church and the box-type form results in relatively small horizontal displacement amplitudes at the roof level for the combination of gravity loads and seismic forces along the x-x and the y-y direction as depicted in figures 9a and 9b, respectively. The maximum value of the horizontal displacements at this level is approximately 3.1mm and develops, as expected, along the direction with the relatively smaller stiffness (North-South, y-y). This structural formation is designated in these figures as non-isolated to differentiate it with the same structure being isolated, as will be presented in section 5.

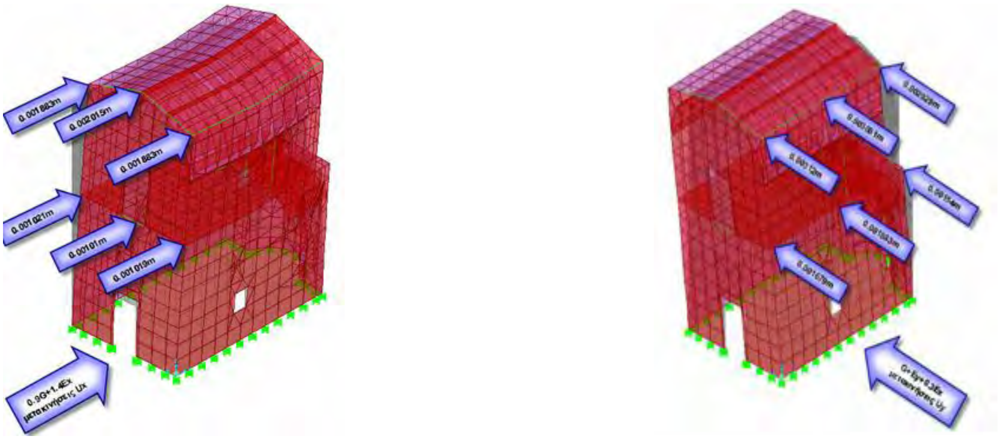

Figure 9a.
Non-Isolated, 0.9G + 1.4Ex
δmax = 2.015mm

Figure 9b
Non-Isolated, 0.9G + 1.4Ey
δmax = 3.081mm

Figure 9. Displacements of The Virgin Mary of Tourniki"

4. EVALUATION OF THE STRESS RESULTS FOR THE THREE BASILICAS SUBJECTED TO EARTHQUAKE LOADING.

This time the design spectrum of the Greek Seismic Code (Greek Seismic Code 2000, ref. 2) was utilized for seismic zone I (ground design acceleration 0.16g), soil category B, response modification factor q = 1.5 and importance factor 1.3. In the spectral dynamic analyses that were conducted, the resultant seismic forces were obtained from the Greek Seismic Code response spectrum and the following loading combinations (G the dead loads, Ex and Ey the earthquake action in the x and y directions). 0.9G+1.4Ey / 0.9G+1.4Ex / G+Ey+0.3Ex / G+Ex+0.3Ey.

From all the load combinations, the most critical in-plane demand values, either in normal or shear stresses, can be identified for all four peripheral walls. This can also be done for the most critical out-of-plane normal stress demand values for all four peripheral walls. For the 2nd church this study was also extended to the masonry vaults and domes of the superstructure. Next, certain commonly used masonry failure criteria were adopted for either in-plane tension-compression or shear or out-of-plane tension. Table 1 lists values which were assumed to be valid for the critical mechanical properties for the masonry segments (refs. [1] and [3]).

Table 1. Assumed Mechanical Characteristics of the Stone Masonry

	Stone Masonry Compressive Strength (N/mm2)	Stone Masonry Tensile Strength (N/mm^2)	shear strength f_{vko} (N/mm^2)
Upper limit	3.846	0.250	0.192
Lower limit	1.00	0.192	0.192

Moreover, a Mohr-Coulomb failure envelope was adopted for the in-plane shear limit state of the stone masonry, when a σ_n normal stress is acting simultaneously, that is defined through the relationship

$$f_{vk} = f_{vko} + 0.4\,\sigma_n \qquad (1)$$

where: f_{vko} is the shear strength of the stone masonry when the normal stress is zero; f_{vko} was assumed to be equal to 0.192 N/mm2.

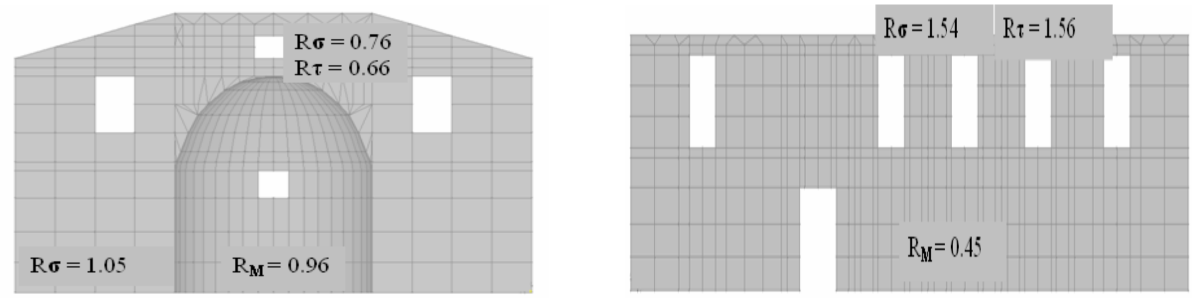

East wall – Ratio values of strength over demands
South wall – Ratio values of strength over demands

Figure 10. "Typical Post Byzantine Basilica"

All the masonry parts of the three studied structures were examined in terms of in-plane and out-of-plane stress demands posed by the considered load combinations against the corresponding capacities, as these capacities were obtained by applying the Mohr-Coulomb criterion of equation (1) or the upper stone masonry compressive and tensile strength limits listed in Table 1.

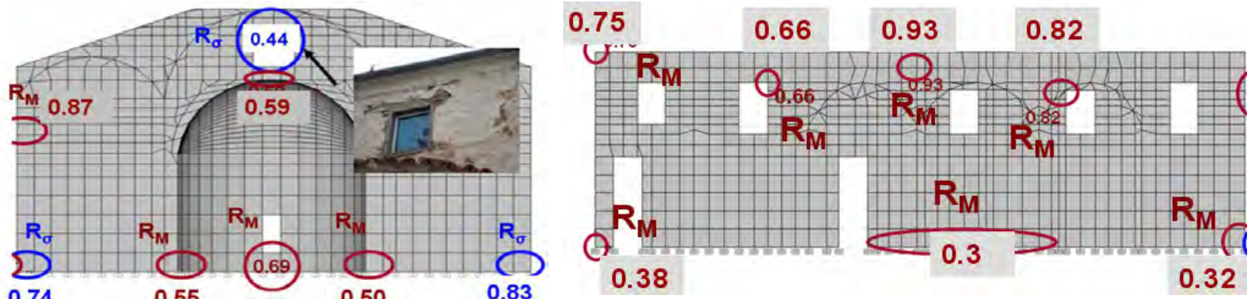

East Wall
South Wall

Figure 11. *"Post Byzantine Basilica church of Taxiarhes"*

Due to space limitations such results are not shown in detail here. Selective results obtained from this evaluation process are shown in figures 10, 11 and 12, for the three studies churches, respectively. With $R\sigma$ or with $R\tau$ the ratio of the in-plane tensile or shear strength value over the corresponding demand is signified whereas with RM the ratio of the out-of-plane tensile strength value over the corresponding demand is denoted. Ratio values smaller than 1.0 predict a corresponding limit state condition.

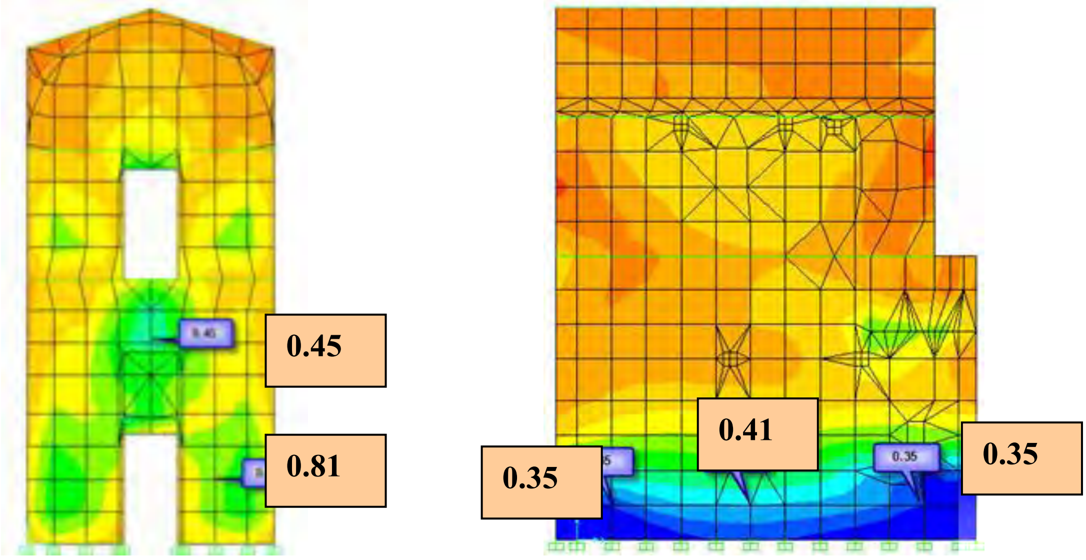
Ratio Values
Shear stress Capacity / demand $R\tau$

Ratio Values
Normal stress Capacity / demand $R\sigma$

Non-Isolated 0.9G + 1.4Ey

Non-Isolated 0.9G + 1.4Ex

Figure 12. *The "church of The Virgin Mary of Tourniki"*

As can be seen from the capacity over demand ratio values presented in figures 10, 11 and 12 there are regions on the masonry walls that these ratio values are well below 1, indicating damage. All these predicted zones of potential failure are credible, as can be deduced from such damage patterns observed in the three studied structural systems after the 1995 strong earthquake event.

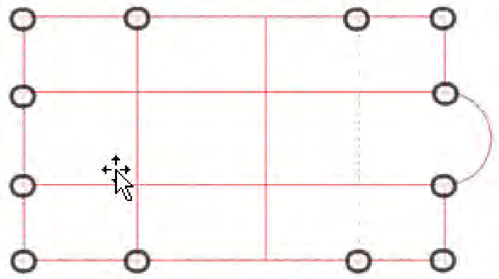
Fig. 13a. *Typical Basilica*

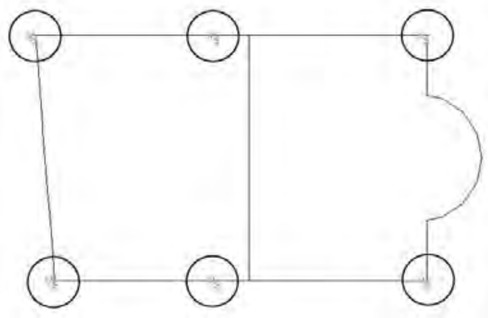
Fig. 13b. *Church at Tourniki*

Figure 13. Arrangement of the base isolation scheme

5. THE PREDICTED PERFORMANCE OF THE EXAMINED STRUCTURAL SYSTEMS BY INTRODUCING A BASE ISOLATION

This investigation is next extended to include a base isolation system which was introduced in the structural system representing the "Typical Post Byzantine Basilica" , as it is schematically indicated in figure 13a as well as the one representing the "church of The Virgin Mary of Tourniki” as it is schematically indicated in figure 13b. In figure14 the design spectrum considered for the non-isolated (fixed) and the isolated structural systems is shown together with the corresponding fundamental eigen-periods of the non-isolated (fixed) and the isolated structural systems. As can be seen in this figure, the dynamic amplification for the non-isolated and the isolated structures is approximately of the same order. This is due to the fact that for seismic isolated structures the response modification factor is given the value of q=1 instead of q=1.5 that was used for un-reinforced masonry structures. The possibility to use more flexible isolation base isolation schemes is currently investigated.

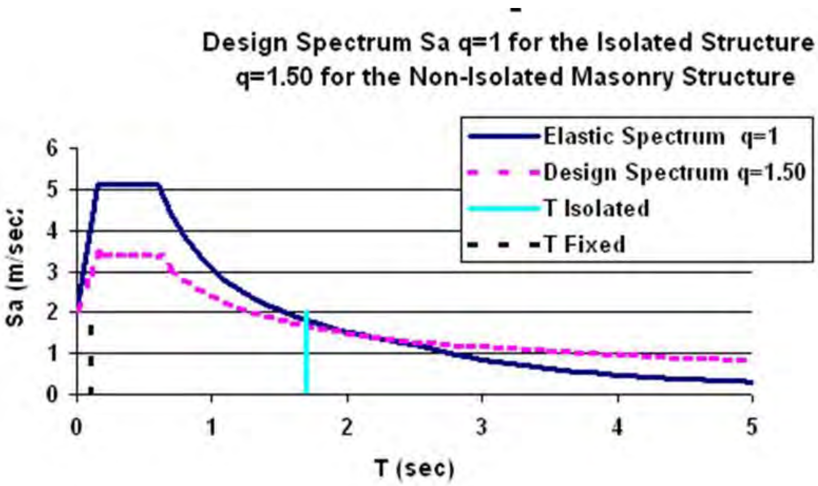

Figure 14. Design spectrum

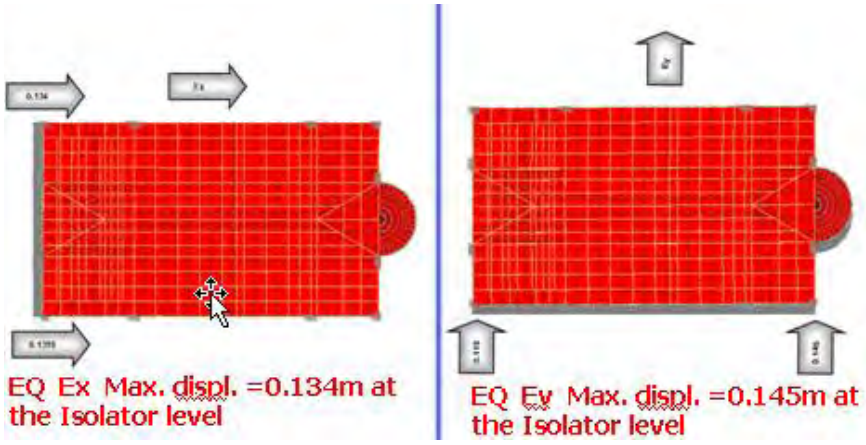

Figure 15. Horizontal displacement of base isolated *“Typical Post Byzantine Basilica”*.

In figures 15 and 16 the deformation demands at the isolation level are depicted for the “Typical Post Byzantine Basilica” and the “church of The Virgin Mary of Tourniki”, respectively. As can be seen they are of the order of 145mm maximum for the first structural system and only 163mm for the second structural system.

What is of the outmost interest, apart from the deformation demands of the base isolation devices, is the effect the introduced base isolation scheme had on the values of the capacity / demand ratio, which were used in the section 4 before to predict numerically the observed earthquake structural damage for these churches (figure 17). This is presented in the following section by comparing these ratio values for the non-isolated structure with the corresponding values of the isolated structure.

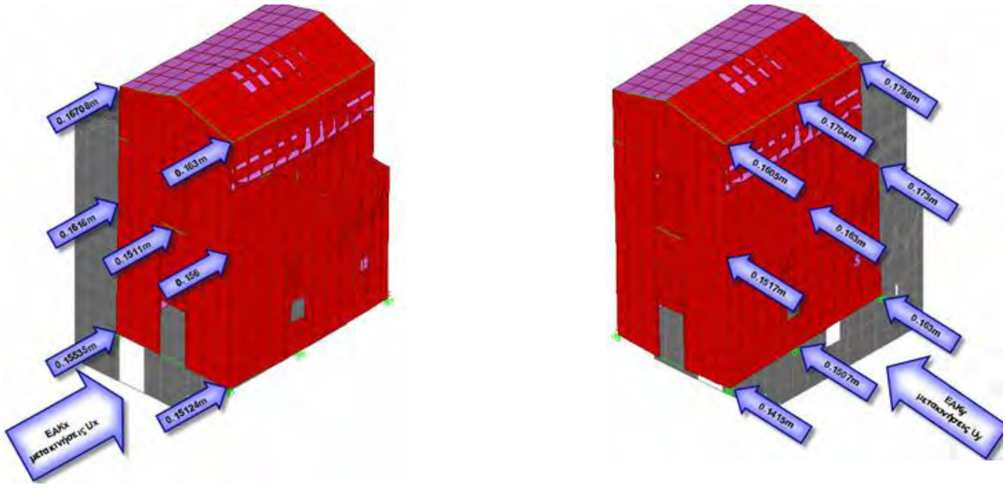

0.9G + 1.4Ex
Top δmax = 167.08mm Base δmax = 156.35mm

0.9G + 1.4Ey
Top δmax = 179.8mm Base δmax = 163.0mm

Figure 16. Horizontal displacement of base isolated Base "church of The Virgin Mary of Tourniki"

Figure 17. Representative damage patterns of the "Typical Basilica"

5.1. The predicted capacity/demand performance of the isolated structures.

In this section, the results that were obtained for the isolated structures are processed in the same way as presented in section 4 by applying the same failure criteria that were employed for the non-isolated structures. The results of this evaluation must be viewed with the consideration that there is no reduction in the earthquake loads of the isolated structures, due to the moderate flexibility of the used isolation schemes and the employed design spectrum of figure 14 combined with the response modification factor value q=1.0 for the isolated structure, as already mentioned. Such a reduction of the earthquake loads will result from the use of a more flexible base isolation scheme than the one employed here.

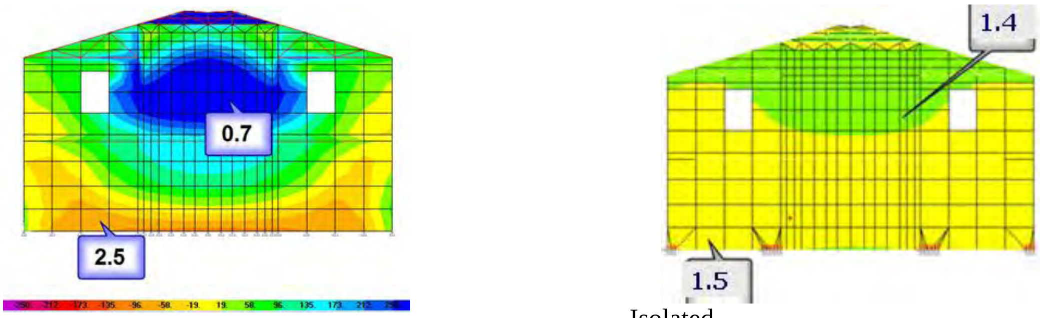

Non-Isolated

Isolated

Fig. 18a. West Wall (Outside Face), 0.9G + 1.4 Ex , Out-of-plane S22 , strength / demand ratio

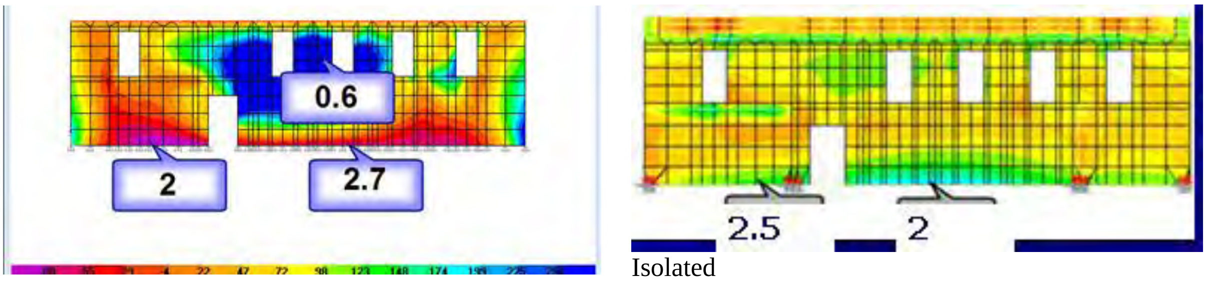

Non-Isolated

Isolated

Fig. 18b. South Wall (Outside Face) 0.9G + 1.4 Ey , Out-of-plane S22 strength / demand ratio

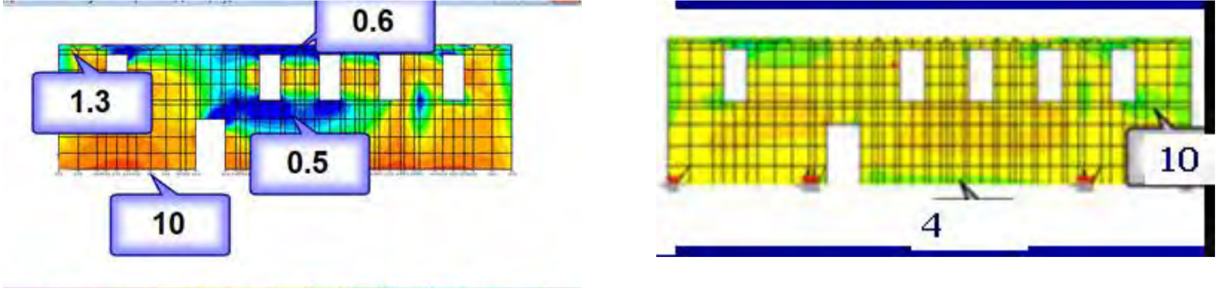

Non-Isolated

Isolated

Fig. 18c. South Wall (Inside Face), 0.9G + 1.4 Ey , Out-of-plane S11 strength / demand ratio
Figure 18. Strength over demand ratio values

5.1.1. The "Typical Post Byzantine Basilica"

In figure 18 the strength over demand ratio values for the "Typical Post Byzantine Basilica" structural system are shown for both the non-isolated as well as the isolated case. These selected results for the non-isolated structure correspond to ratio values well smaller than 1, which as explained in section 4 represents structural damage. As can be seen, for the case of the isolated structure the corresponding strength over demand ratio values at the same locations are well above 1, which indicates that with the introduction of the base isolation scheme structural damage from earthquake loads should be minimized.

Non-Isolated

Isolated

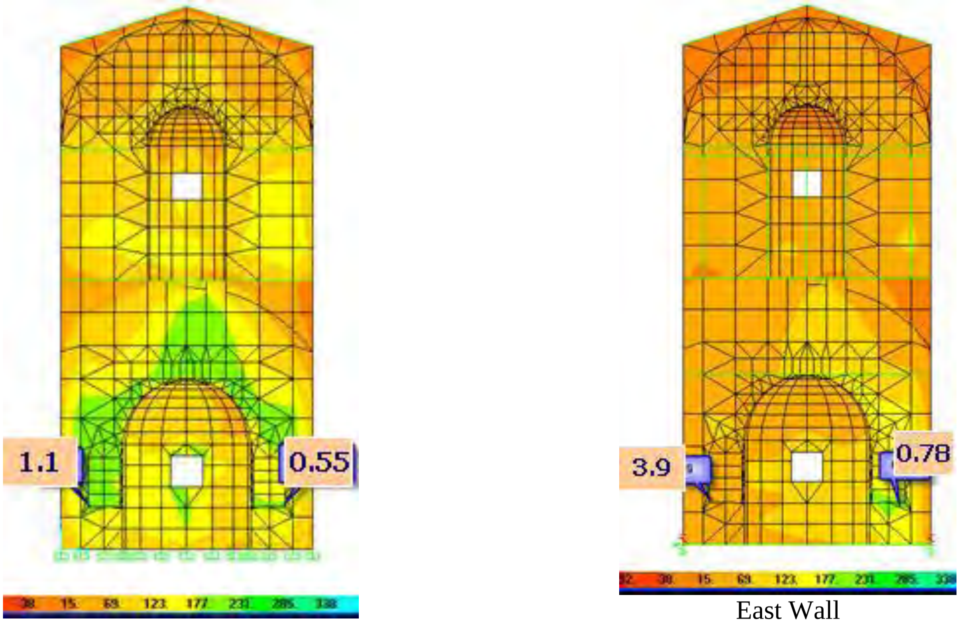

East Wall

East Wall

Figure 19. Shear Strength / Demand ratio Rτ, Loading G+Ey

5.1.2 "The Church of The Virgin Mary of Tourniki"

In figures 19 and 20 the strength over demand ratio values for the "Virgin Mary of Tourniki" are shown for both the non-isolated and the isolated case. The selected results for the non-isolated structure correspond to ratio values well smaller than 1, which, as explained in section 4, represents structural damage. As was the case before, the corresponding strength over demand ratio values at the same locations are well above 1 in almost all cases for the isolated structure. Thus, as expected, structural damage from earthquake loads should be minimized with a base isolation scheme. This improvement in the expected earthquake performance of the studied structural systems will become even better if a more flexible isolation scheme than the one employed here is used.

Obviously, the increased flexibility of the base isolation scheme will result in larger deformation demands of the base isolation devices than the ones predicted here (figures 15 and 16); the selected devices must then pass such relevant checks.

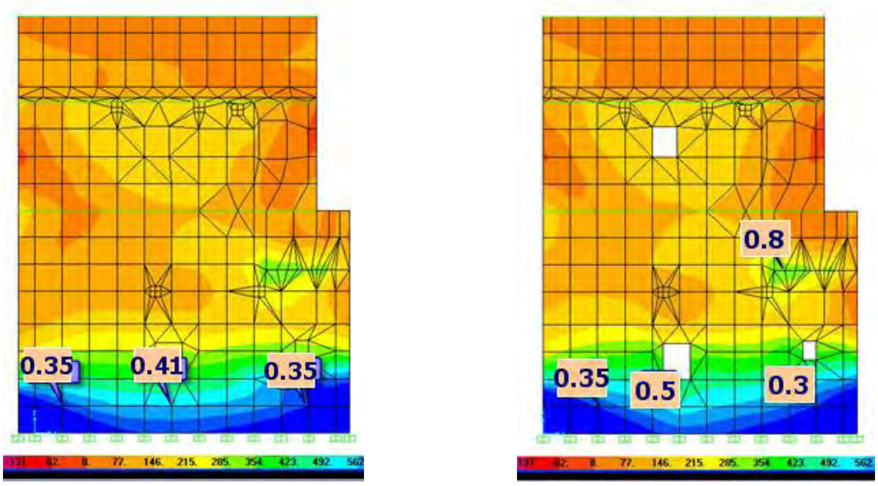

Non-Isolated Non-Isolated

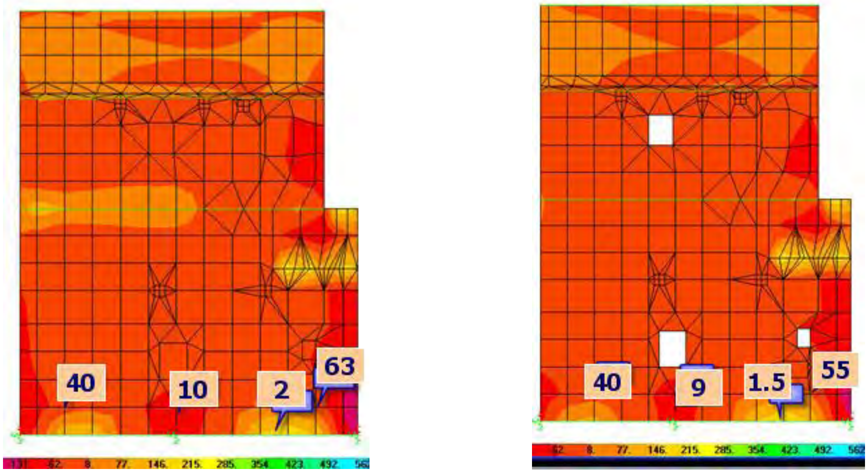

Figure 20. Normal stress Strength / Demand ratio Rσ , Loading G+Ey

At this point it is important to stress the following difficulties in applying a base isolation scheme on an existing structural system especially in the case that the structural system is unreinforced masonry, as is the case of both structural systems that were investigated here. In order to place the base isolation devices under the existing structure a system of additional foundation must be constructed under the masonry walls that will enable such an operation. Such systems have been tried in the past; however, apart from the difficulty in construction this additional foundation one should also consider the extra cost. Another difficulty is the fact that many times below the existing churches lie older structures; thus the excavation for constructing the additional foundation will unveil such old remains. This is not the case for the structures that were investigated here. On the contrary, "The Church of The Virgin Mary of Tourniki" has to be moved in a different location due to the flooding of the current location, where it was constructed almost eight hundred (800) years ago, from the construction of a dam that already starts filling the valley. In this case, the operation of construction an additional foundation for lifting and sliding this church cannot be avoided. The authors of this paper argue in favor of the placement of a base isolation scheme under this structure in its new location is a feasible solution for this particular case with no significant extra cost. Obviously, thus base isolation scheme should be considered in addition to all other traditional repair and strengthening measures for this church.

6. CONCLUSIONS

1. The numerical results presented here are part of an attempt to numerically explain the observed seismic behavior of Post-Byzantine stone masonry churches. The relatively simplified linear analysis approach together with the adopted failure criteria seems to verify the development of the actual damage in all three examined structural formations. Both predicted and actual damage is mainly concentrated at the keys and supports of the arches and vaults, at the supports of the roofing system as well as at the door and window openings and the bases of the peripheral walls. Further extensive verification is needed for the assumed strength values utilized by the failure criteria. A number of tests are currently under way.
2. The numerical introduction of a base-isolation system for the third structural formation, was quite effective in lowering the demands and thus resulting for most structural elements in Capacity/Demand ratio values larger than one (Capacity/Demand > 1), which is assumed to indicate acceptable structural performance. However, the introduction of base isolation under an existing old stone-masonry structure is also faced with considerable difficulties, despite the advantages that are shown by the results of numerical investigation.
3. In the particular case of "The Church of The Virgin Mary of Tourniki" these difficulties must be faced because this old church has to be moved in a different location due to flooding. Thus, the placement of a base isolation scheme under this structure in its new location is a feasible solution for this particular case with no significant extra cost. Obviously, thus base isolation scheme should be considered in addition to all other traditional repair and strengthening measures for this church.

REFERENCES

[1]. Manos G.C., Soulis V., Diagouma A. (2008) "Numerical Investigation of the behavior of the church of Agia Triada, Drakotrypa, Greece", Journal in Advances in Engineering Software 39 (2008) 284-300.
[2]. Provisions of Greek Seismic Code 2000 , OASP, Athens, December 1999.
[3]. European Committee for Standardization, Euro code 6; "Design of Masonry Structures, Part 1-1:General Rules for Building. Rules for Reinforced and Un-reinforced Masonry", EN 1996-1-1:2005

COMPDYN 2011
III ECCOMAS Thematic Conference on
Computational Methods in Structural Dynamics and Earthquake Engineering
M. Papadrakakis, M. Fragiadakis, V. Plevris (eds.)
Corfu, Greece, 25–28 May 2011

REINFORCEMENT AND MEASUREMENT METHOD FOR EARTHQUAKE DAMAGED MASONRY BUILDINGS TESTED ON A SHAKING TABLE

M. Urban[1], **L. Stempniewski**[2]

[1] Karlsruhe Institute of Technology
e-mail: moritz.urban@kit.edu

[2] Karlsruhe Institute of Technology
e-mail: lothar.stempniewski@kit.edu

Keywords: Earthquake, masonry reinforcement, multiaxial textile, fibre reinforced cement, glass fibre, polypropylene fibre.

Abstract: *Experimental investigations about the behavior of Unreinforced Masonry (URM) structures in comparison with masonry structures reinforced with Fibre Reinforced Cement (FRC) is carried out on the large shaking table at the EU Centre in Pavia. The tests were part of the EU project Polyfunctional Technical Textiles against natural Hazards POLYTECT and POLYMAST. Intention of both projects within the 6th and 7th EU Framework Program is the development of multifunctional textiles with embedded sensors.*

For the purpose of the project a 5.8 m tall 2-storey test structure was built. Archetype of the structure was a typical historical building made of natural stones from the earthquake region "Abruzzo" in Central Italy. A 6.3 magnitude earthquake struck this region in 2009 (L'Aquila earthquake) and caused 260 losses, 1,000 injured and 28,000 homeless.

In an optimization process different new developed textile and special mortar combinations were tested with small in-plane shear walls under cyclic horizontal displacements to find the optimal strengthening solution for masonry structures.

In the first test, the unreinforced structure (URM) was analyzed under seismic impact. The ground acceleration was increased till nearly before collapse of the building. This damaged building was the basis for further investigation. For the second test the specimen was repaired and reinforced with a new developed FRC in a full covering solution on the surface outside the structure. The used fabric is a woven glass/polypropylene fibre combination in four directions.

1 INTRODUCTION

Masonry is a material with a high compression strength compared with his low tensile strength. Under horizontal load cases like wind or earthquake seven decisive failure modes are observable in the bricks and the mortar joints caused by low shear and/or tensile strength. In figure 1 these modes are presented. The idea to upgrade the mechanical material properties is in the first instance to add thin fibre materials with a high tensile strength like carbon fibers, glass fibers or others. To design and manufacture technical textiles in an optimal way for seismic retrofit, the real fracture mechanism in masonry structures is very important. Generally there are:

By applying fibre reinforcement on the wall surface one can observe a failure in the fibers, in the fibre matrix, the brick surface or in the interaction areas. Due to the fact that masonry has high compressive strength, but low tensile strength, diagonal cracks form due to a compression strut under lateral gas pass [5]. Not often the cracks are crossing the bricks. The reason for failure [6] and [7] is the different material behavior from bricks and mortar. The soft mortar has a low Young's modulus, but in comparison the bricks are very stiff. As a result the mortar carries more lateral strain than the brick and with the interconnection, the adverse three dimensional load case compression-tension-tension and the low tension strength occurs vertical or diagonal cracks [6], [7]. In most cases gaping cracks are developed if the tension forces are higher than the adhesive tensile strength between mortar and brick.

If fibers are oriented in such a way that they cross existing or potential crack locations, they provide resistance against tensile forces which can prevent or stop crack growth. Especially in sliding joints [2] diagonal fibers prevent the decrement of shear resistance in the wall. This is the main factor for in-plane loading and for the bracing system of a building in earthquake areas. The shear failure occurs by exceeding the adhesive shear strength of the mortar or uncommonly in the stones. Similar to the function of rebar in reinforced concrete the fibers more "bridge over" the cracks by providing tensile strength. However, the fibers do not improve the compressive strength. Different to reinforced concrete is the size of the crack width. Instead of millimeters the fiber reinforcement has to work in the centimeter region. Due to this reason the ductility of the fiber system has a high impact.

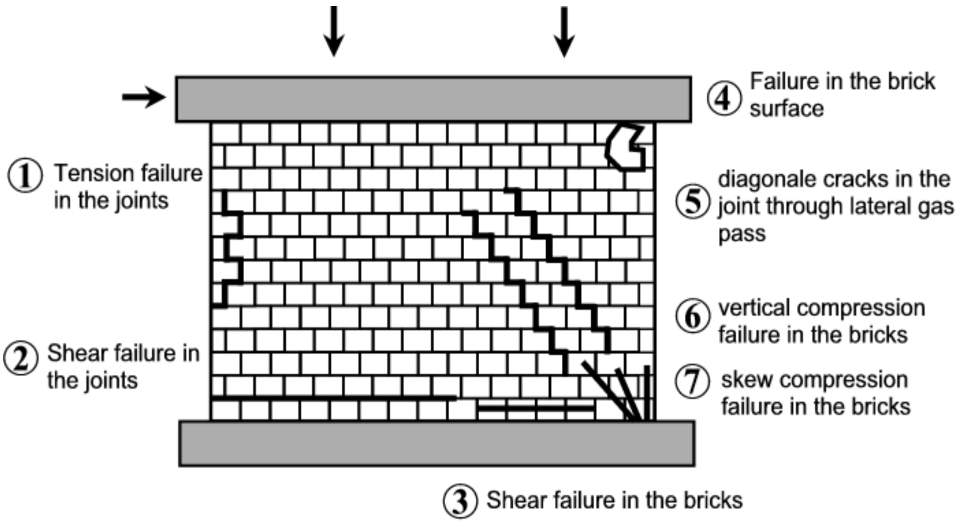

Figure 1: Common failure modes in masonry structures

2 THE TEXTILE

With four main characteristics it is possible to construct a special textile for masonry: (a) Amount of fibre directions, (b) respective inclination angle between the fibers, (c) single or different material types and (d) amount of fibers. For the last point the common way is to calculate with the (fibre-)weight per m² the required tensile strength. Fiber selection is a design problem with polymer, glass, and carbon fibers being the primary material types. Generally, strip reinforcement calls for uniaxial stiff fibers with epoxy adhesive, in opposite to wide area coverage systems calling for more ductile fibers in a multiaxial weave or warp knit pattern. A matrix compound adhesive in combination with carbon fibers with its low strain capacity is an unfavorable option, while the high tensile strength is advantageous. A better solution is a combination with polypropylene fibers (PPF) and AR-glass fibers (ARGF). The PPF performs a high strain rate capacity till the full force is activated. The AR-glass fibers with high stiffness and tensile strength can overtake the first load until the strains reach the ultimate strain value and break. After breaking the PPF will be activated. Through the weight ratio of PPF and ARGF the ductility from the masonry and the textile is adjustable.

The special weaving technique enables the production of multiaxial textiles with different fibre directions with user defined orientation angles. For different small shear and wall tests 2-axial, 3-axial and 4-axial textiles with integrated optical fibers sensors were produced and tested. The range of the weights per square meter was between 290 g/m² and 590 g/m². The weight from the optimized textile was around 425 g/m² and had 4 fibre directions. Especially for failure mode [2] fibers in 45° angel over the cracks can stabilize the shear resistance and this effect is very important for the ductile behavior of the structure.

The textile-stone-mortar composite acts like a laminar ductile tensile reinforcement. The optimal functionality is affected through the high adhesive tensile strength between the mortar brick interface, a lot of small cracks in the matrix without bonding decline, the stiff ARGF at the beginning and the ductile PPF after greater cracks in the masonry.

3 THE MORTAR

The mortar is the link between textile and the structure. The fabric is embedded in two 4 mm thick mortar layers not only to get the best possible bonding but also for the protection of the fragile fibers. The different components of the matrix and the textile fibers are the main elements of this reinforcement method. Both have to be designed to ensure maximum ductility. High adhesive tension strength on the stone surface and a high bonding with the fibers are required for any potential matrix. Different matrixes with different properties were tested at the Institute of Reinforced Concrete Structures (KIT-IMB) to determine their performance characteristics when used for the textile masonry composite system. The matrixes tested were: a) one “soft” mortar with high ductility from BG Polymers, b) a high “stiff” epoxy resin system (“Sika 331 W”) and c) an epoxy surfacer with 3 components (“Sikagard 720 Epo-Cem”). The first two compounds are an epoxy-dispersion and the last is a hard mineral granulation. The compression strength is approximately 40 N/mm² and the adhesive tensile strength is around 3-4 N/mm².

Small shear tests in size 363 mm x 240 mm x 175 mm with three sand lime bricks and between 2 mortar joints were produced to simulate the shear failure [2] in masonry walls. The two outer stones were hold and loaded with a compression force in the horizontal direction in such a way that the mortar bed joints are under normal compressive stresses. The mid brick was pushed using a displacement controlled piston. The force and the corresponding vertical displacement were measured. These tests indicated that the best material solution is between the extreme cases high stiffness (epoxy system) and the high strain rate (BG Polymers). The reason why the cement based epoxy surfacer (“Sikagard 720EpoCem”) represented the best solution was a micro cracking and sliding crack direct over the bed joint. For a ductile behavior very stiff or a soft material is able to reach the same deformation for this effect like a “singularity line”. While the Sikagard has a consistent load decline the BGP is on a lower strength level more volatile. Further developments will prefer cement based mortars like Sikagard 720 EpoCem, because they are working not like epoxy or other glues as an air barrier for the building which causes fungi and other water based damages.

4 EXPERIMENTS

4.1 Scaled wall tests

Scaled wall tests were conducted with different test specimens to select the best materials for the matrix-fibre-system. Small initial shear test specimens with three stones (363 mm x 240 mm x 175 mm) first simulated the failure mode [2] for walls with textile. Maintain tense consistency scaled wall test (1.25 m x 1.25 m) and full-size wall tests (2.5 m x 2.5 m) were conducted. In these tests the different parameters were the mortar matrix, the textiles and the vertical load value. The shear loading in-plane was in the strong inertia force direction with a vertical load between 0.2 and 1.0 MN/m². For the horizontal cyclic displaced head beam the displacement and the horizontal force were measured. Integrated optical sensors were fixed on the edges of the walls and measured continuously the strains in the mortar and textile (see figure 2).

Figure 2: Wall 1.25 m x 1.25 m

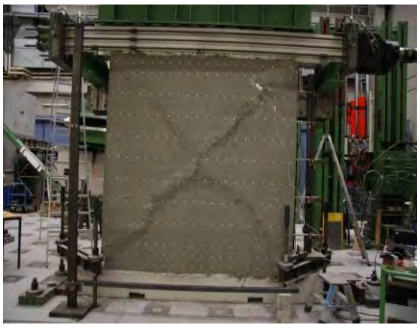

Figure 3: Wall 2.5 m x 2.5 m

Representative results of unreinforced masonry (URM) and reinforced masonry (RM) tests (1.25 m x 1.25 m) are shown below in figure 4 and 5. For the RM wall an optimized hybrid multiaxial textile and Sikagard 720 EpoCem was used. The maximum resistance force of the URM wall was 98 kN and the maximum load of the RM structure was 232 kN. This is an increase of 136%. But the more important effect is the increase of ductility of more than 200%.

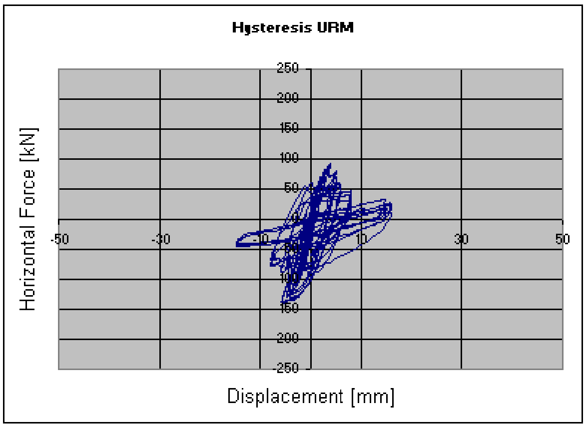

Figure 4: Hysteresis for the URM wall

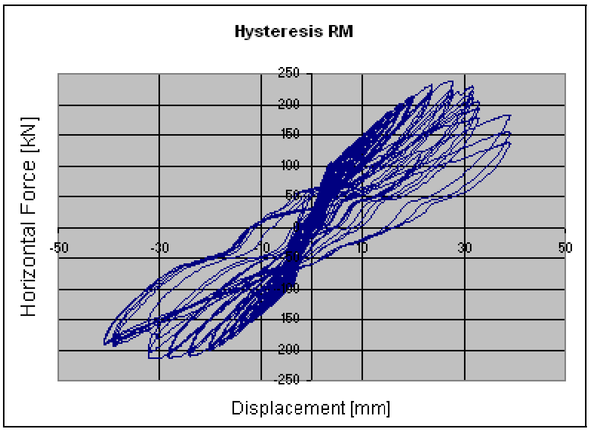

Figure 5: Hysteresis for the RM wall

4.2 Shaking table test with an full-scaled unreinforced masonry building

Motivated by like buildings damaged in the L'Aquila earthquake (2009) the EUCENTRE located in Pavia (Italy) emulated a building with the typical archetype with natural stones and a size from 5.8 m high, 5.8 m long and 4.4 m width. A uniaxial shaking table simulated the L'Aquila earthquake with different increasing amplification factors. After 0.4 g PGA the building was nearby destroyed.

Test number	Peak ground acceleration (PGA)
1	0.05 g
2	0.1 g
3	0.2 g
4	0.3 g
5	0.4 g
6	0.4 g with additional steel anchors

Table 1: Test program

The test of the URM structure exhibited common failure modes. The very soft wooden slab at the ground level led to out of plane bending failures in the front side (failure [1] and [2] in figure 6). Diagonal bending/tension cracks trough the mortar joints [5] over the window parts were the most important failures, due to the fact that the front corner in figure 6 was shortly before collapse. Only the wooden beam held this part together with friction and the roof load. A joint sliding [3], for the "in-plane" walls occurred in the cross between windows and doors and on the bottom between the doors [6]. After the shear cracks in the "beam"-parts [5] the front corner was the most moving part in the building and was the reason for the high deformation in this corner. An existing eccentricity though the asymmetrical arrangement of the wall stiffness led to an additional torsion moment which was increased after cracks in the front side and shear point shift toward the walls without openings (figure 7). This led to very high accelerations in the point A (figure 6). High local deformations in this area caused different orientated cracks in this corner region [4] (see figure 8).

Six tests were conducted until the building was damaged that a collapse was imminent. In the last step the peak ground acceleration was the same, but additional installed steel rods (see figure 6) were used to hold the building like a box together.

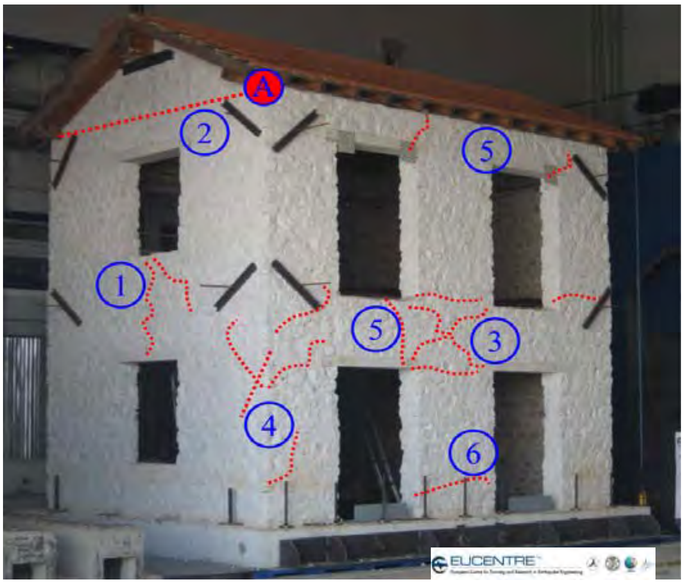

Figure 6: Crack pattern of the URM building

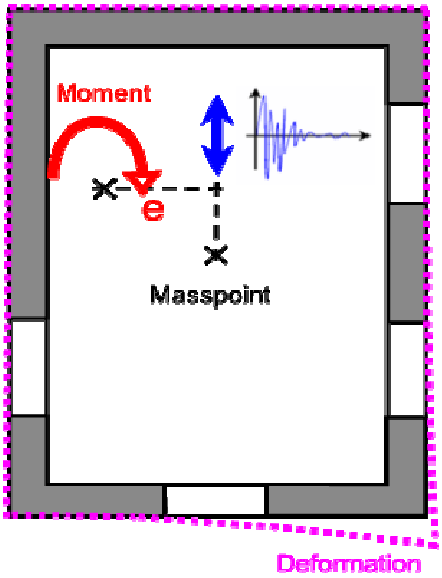

Figure 7: Deformation of the URM building

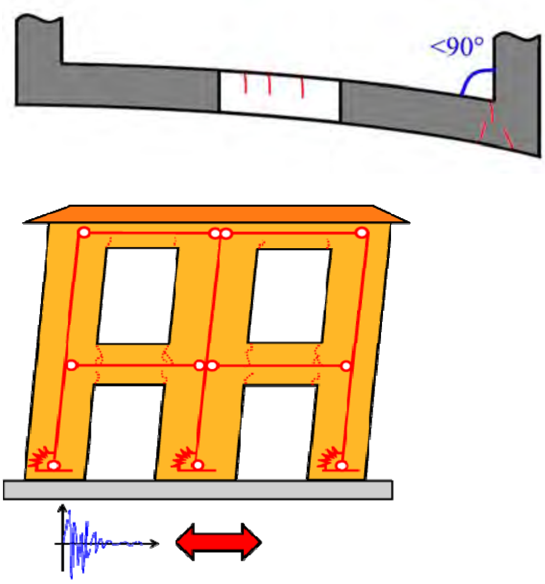

Figure 8: Crack patterns

4.3 Shaking table test with an reinforced masonry building

The idea behind the reinforcement method is to stabilize a building after huge cracks with ductile polypropylene fibers, to add more tensile strength with AR-glass fibers and to increase the global displacement ductility for horizontal force diminishing. The strengthening system is so flexible that it can be used as a repairing tool of nearly damaged masonry structures.

The base for the shaking table test with the reinforced building was the structure described in the chapter before. The pre damage structure was repaired and retrofitted with the mortar-textile system through full coverage application in a sandwich practice mortar - fabric - mortar (figure 9).

Figure 9: Masonry building with textile application

The same earthquake load time history was used. The corresponding response spectrum is shown in figure 11. The applied dynamic load was different between the original and the pre-damage sample due to the damages and cracks. During the test the main frequency of the URM building dropped down from 11.55 Hz (0.107 sec.) to 9.31 Hz (0.086 sec.). This caused a slight increase in the horizontal load.

Figure 10: Crack pattern: a) delamination, b) broken glass fibers

Regardless to the higher accelerations, the building reached with marginal cracks under the window location in the front side (figure 10) a maximum peak ground acceleration of 0.6 g without any tendency of stability failure. This was an increase of 50 % compared the unstrengthened URM structure. After inspection of the applied textile only the projected cracks in the stiff glass fibers were visible while the soft polypropylene fibers hold the crack together and worked like a damping spring in the system. Further frequency and system analysis will be presented in the presentation in the workshop.

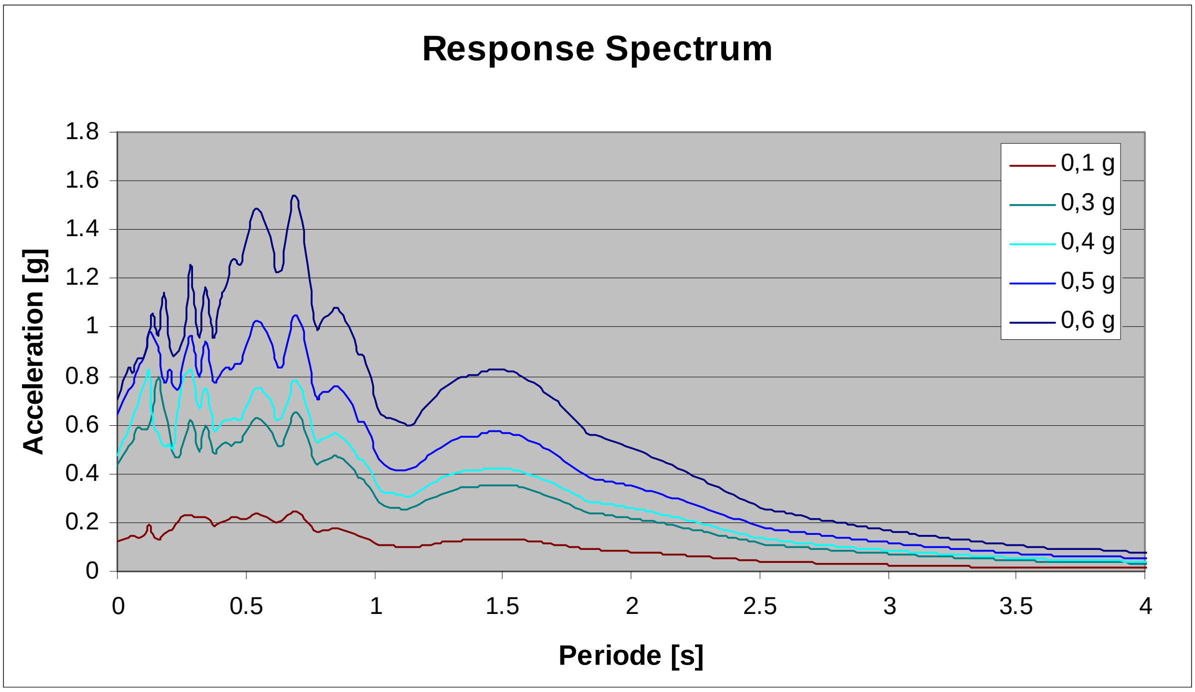

Figure 11: Response Spectrum of the Montenegro earthquake (1979)

5 CONCLUSIONS

Multi axial fiber reinforcing provides the engineer with a new tool for the seismic retrofit of unreinforced masonry structures. This special mortar/textile system adds strength, improves ductility and provides the opportunity to conduct structural health monitoring. Special optical fibers were used to measure strains online within the textile. The design, manufacturing, and testing of these textiles have occurred and are underway in the EU research project POLYTECT. The testing at the EUCENTRE showed the possibilities of such a system.

REFERENCES

[1] P. Corvaglia, J. C. Münich, S. Liehr, R. Base: Test results on small scale and full-scale retrofitted masonry structures (progress report), Karlsruhe 2008.

[2] C. Wallner: Erdbebengerechtes Verstärken von Mauerwerk durch Faserverbundwerkstoffe, Dissertation, Karlsruhe 2008.

[3] J. C. Münich: Hybrid Textile Reinforcement in a cement-based matrix for Retrofitting of Masonry, Karlsruhe 2008.

[4] C. Waller, L. Stempniewski: Experiments on seismic retrofitting of In-plane loaded masonry walls with fibre composites, in: Brebbia, C. A. et al: Fifth world conference on earthquake resistant engineering structures, Wessex Institute of Technology, UK, p. 601-610, 2006.

[5] D. C. Schermer: Verhalten von unbewehrtem Mauerwerk unter Erdbebenbeanspruchung, Dissertation, München, 2004.

Acknowledgements

The partial funding support of European Grant NMP2-CT-2006-026789 in support of the POLYTECT project and SERIES - Seismic Engineering Research Infrastructures for European Synergies - FP7 Grant agreement no.: 277887 is gratefully acknowledged. In addition, the contribution of the companies and research institutions performing the work mentioned in this paper is acknowledged which include D'Appolonia and KIT.

COMPDYN 2011
III ECCOMAS Thematic Conference on
Computational Methods in Structural Dynamics and Earthquake Engineering
M. Papadrakakis, M. Fragiadakis, V. Plevris (eds.)
Corfu, Greece, 26–28 May 2011

A CASE STUDY OF STRENGTHENING OF DEFICIENT RC BUILDING WITH INTERNAL STEEL FRAME

R. Ozcelik[1], **B. Binici**[2]

[1] Middle East Technical University
Middle East Technical University, Department of Civil Engineering, Turkey
rozcelik@metu.edu.tr

[2]Middle East Technical University
Middle East Technical University, Department of Civil Engineering, Turkey
binici@metu.edu.tr

Keywords: Internal Steel Frame, Seismic Retrofit, RC Frames.

Abstract. *This study examines the strengthening of existing deficient reinforced concrete (RC) building by using internal steel frame (ISF). Test results indicated that ISF increased the lateral strength, ductility and energy dissipation capacity of the deficient RC building significantly. The test results were compared with simulations to observe performance levels. A case study building was analyzed to demonstrate the performance of an ISF retrofitted deficient RC building by using an analytical model calibrated with test results. The analyzed building was located at Marmara region in Turkey where the region most susceptible to severe earthquakes. The performance based evaluation with respect to Turkish Earthquake Code indicated that this building should be strengthened under Duzce ground motion demand. After strengthening by using ISF, the building was within the life safety performance level which is the performance level that needs to be satisfied for residential buildings. The modeling strategy and construction details of the ISF are also presented in this study.*

1 INTRODUCTION

Poor performance of reinforced concrete (RC) buildings was demonstrated dramatically in recent earthquakes (Northridge 1994, Kobe 1994, Kocaeli 1999, Taiwan 2003, India 2001) due to insufficient lateral load resisting system. Common deficiencies of RC buildings in many of the developing countries owe either to lack of knowledge about seismic risk or to malpractice and insufficient quality control during construction. The poor quality control results in low strength concrete (in the range of 8 to 15 MPa), insufficient spacing of transverse confining reinforcement in beams, columns and joints, and insufficient splice length at column critical regions that may result in excessive bond slip of plain longitudinal reinforcement. To reduce the effect of these deficiencies on existing structures, seismic retrofitting techniques should be developed. Furthermore, application of the seismic retrofitting techniques should be encouraged to be used by the authority and people live in high seismic regions.

There are many strengthened techniques namely adding structural walls [1-4], steel braces [5-13], FRP diagonal braces integrated in the infill walls [14-16], precast-shear walls that fit perfectly into the existing frame [17], steel frames attached externally to the perimeter of the existing frame [17], and steel frames attached within the frame without using anchors [18]. Although the most commonly used strengthened technique is adding structural wall, this technique requires interrupting building use for a substantial period of time and may conflict with architectural requirements.

The literature review indicated that there is urgent need to develop a rapid, safe and practical strengthening technique. The internal steel frames (ISFs) which are one of the candidate retrofitting techniques are installed within bays of the deficient RC frames. The ISF is intended to easily accommodate wall openings for architectural requirements. In this study, firstly an experimental test frame with and without ISF was examined and then the analytical study was conducted to calibrate test frame with ISF. By using analytical results, the performance level of the frame with ISF was performed with respect to Turkish Earthquake Code (TEC 2007) [19]. Based on calibration of the test frame with ISF, an existing five story residential building was strengthened with ISF and the performance of such building was evaluated by using procedure suggested by TEC 2007 [19]. Duzce earthquake record was utilized in the nonlinear time history analysis to determine the performance points of the building before and after retrofitting. This study also explains the installation procedure of the ISF to the RC frame.

2 TEST FRAME AND ISF INSTALLATION PRODECURE

Two, one bay-by-one story, portal RC frames were examined to determine cyclic performance of the ISF. First test specimen SP1 was reference frame tested without any retrofitting while second specimen SP2 was tested after implementing ISF in the RC frame. Although comprehensive information about the test frames is available in elsewhere [20], a summary was introduced in this study. As shown in Figure 1, the center-to-center span length was 1400 mm and the column height was 1000 mm. The dimensions of the columns were 100 mm × 150 mm with four 8-mm diameter longitudinal reinforcement plain bars resulting in about 1.33 % longitudinal reinforcement ratio. 4 mm diameter plain bars were used for stirrups. TEC 2007 requires stirrups to be anchor using 135 degree hooks however 90 degree hooks were used for all columns and beam to simulate the detailing deficiency of the Turkish construction practice before the establishment of the modern seismic codes. To simulate the insufficient confinement details of the columns, the stirrup spacing of the columns was equal to the smaller dimension of the column section (100 mm). The 100 mm × 150 mm beam was cast with a 450-mm wide, 55-mm thick slab. A 70-mm transverse reinforcement spacing was used for the beams. The RC beam-column joint had only one column stirrup extending into the joint. The yield strength of the 4-mm and 8-mm diameter reinforcement bars was determined as 270 and 330 MPa, respectively. The target 28-day cylinder compression strength was 8 MPa to simulate the existing deficient structures with low concrete strength determined in field investigations [21-23].

A constant gravity load of 62 kN was applied by placing steel blocks on the RC frame (see Figure 1(c)). This gravity resulted in the axial load ratio (i.e. ratio of gravity load to axial load carrying capacity) for the RC column was roughly 20% for all specimens. Cyclic lateral loading was introduced by controlling the drift ratio (DR) as in Figure 1 (d).

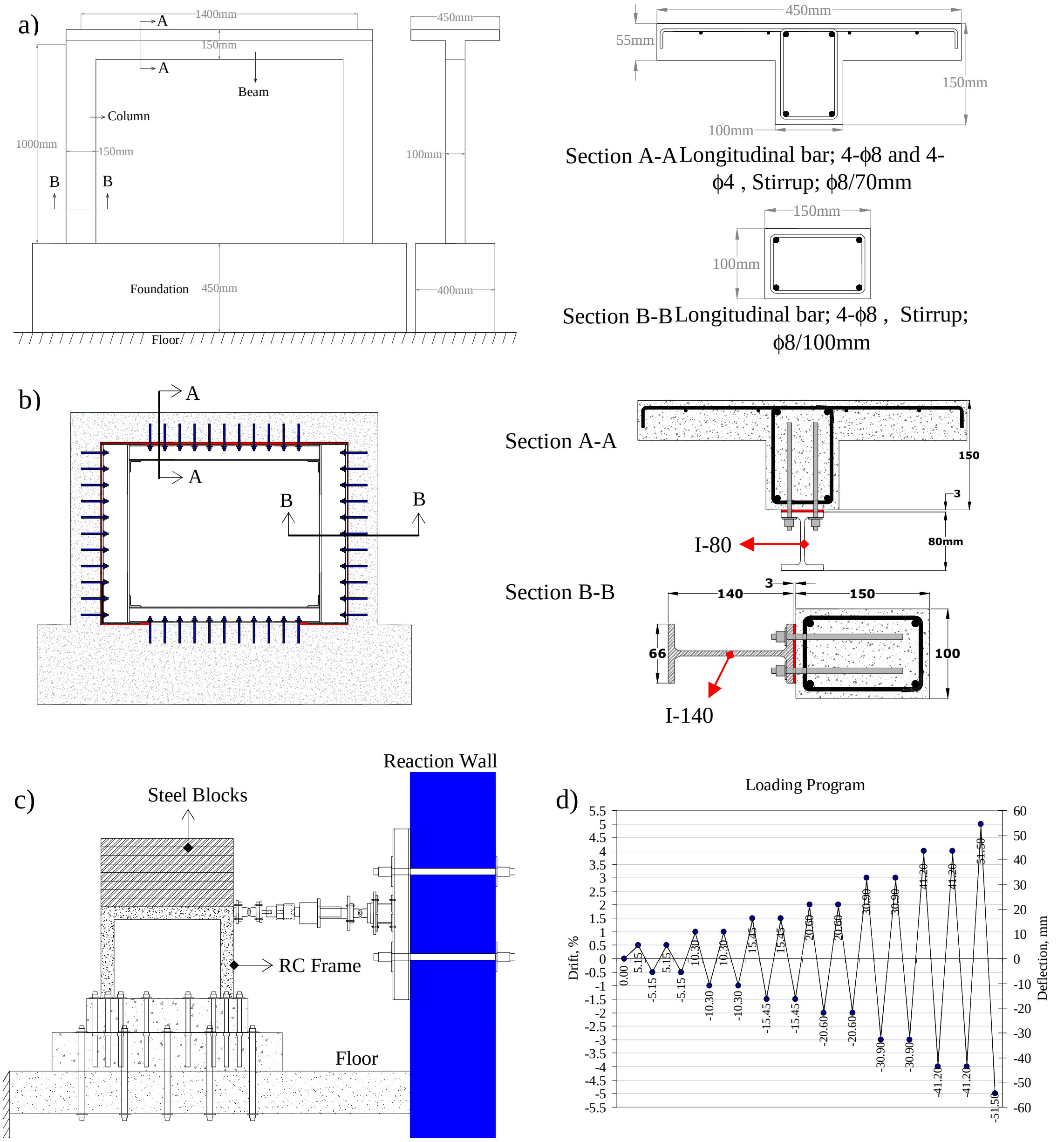

Figure 1: a) Analyzed building floor view, b) Analyzed 4-story frame, c) Beam and column section.

The ISF was composed of rigidly connected beams and columns. The ISFs were implemented after constant gravity load was applied on the RC frame to simulate actual retrofit conditions. The application procedure was as flows; firstly, anchor holes were drilled into the column face and bottom side of the RC beams. Than, these wholes were cleaned up by air blowing, brushing and air blowing (Figure 1 (b)). Next, epoxy primer was injected into these holes and the anchor rods were inserted and left for curing. In the second stage, a thin layer (about 3 mm) repair putty was applied on the RC member on all surfaces that contact the ISF (Figure 1). Before the epoxy cured, the anchor rods were tightened to fasten the individual steel members to the RC frame. Finally, the steel beams were welded to the steel column. The diameter of the anchor rods and holes were 6 mm and 8 mm, respectively. The anchors were embedded 120 mm into the RC beam and columns.

2.1 TEST RESULTS

Figure 2 shows the hysteretic response obtained from both specimens [20]. Specimens SP1 and SP2 developed a lateral stiffness (the peak positive and negative loading points during the first cycle (± 0.5% DR)) of 2.48 and 12.68 kN/mm, respectively. The lateral strength of the specimens SP1 and SP2 were 13.7 and 118.9 kN.

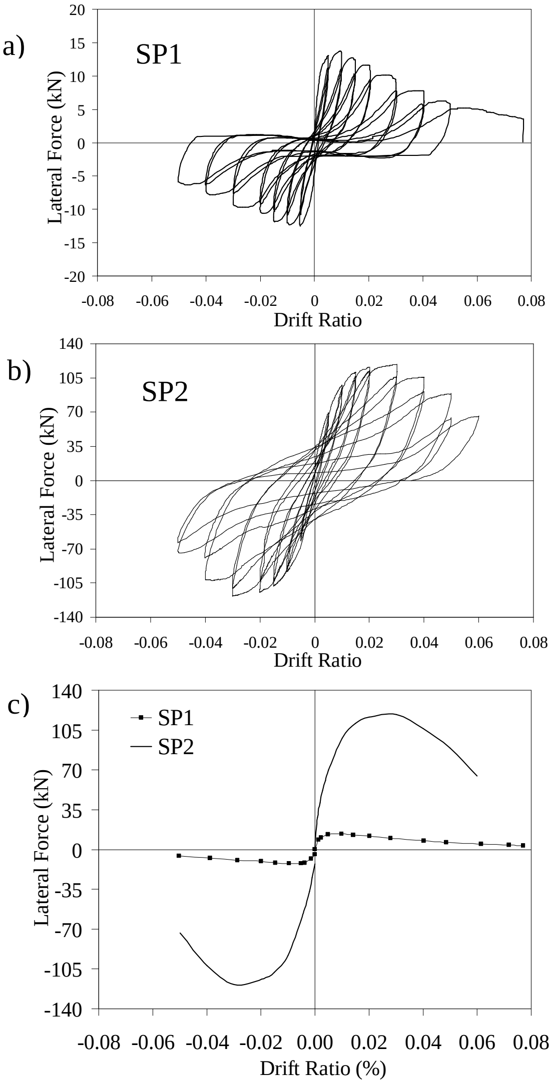

Figure 2: a) Cyclic response of the reference frame, b) Cyclic response of the strengthened frame, c) Envelope response of the frames.

Plastic hinges were first observed at the bases for the reference frame (specimen SP1). A plastic mechanism was formed at a drift ratio DR slightly higher than ± 2%. Upon further lateral displacements, pinching behavior and severe stiffness degradation was observed. Specimen SP2 was designed to develop composite action in the beam and two columns. Cracks in the concrete widened during each loading excursion that produced tension in the concrete portion of the composite section. The specimen SP2 failed due to fracture of the welded beam-to-column connection that initiated at ± 3 % DR. These test results indicated that the ISF retrofitting increased the lateral strength, stiffness and energy dissipation capacity of the deficient RC frame significantly.

2.2 ANALYTICAL STUDY OF THE TEST FRAME

The test frame, specimen SP2, was analyzed by using nonlinear static pushover procedure in order to determine plastic rotations at the ends of the beam and columns. Firstly, moment rotation relations were derived from sections indicated in Figure 1(b). The composite column and beam members had two moment curvature relation whether bending directions is positive or negative. When the composite section was under positive bending, the steel member (I-80 for beam and I140 for column) was under tension but the concrete was under compression. At the negative bending direction, this case was vise verse. Hence, two different moment curvature relations were developed for both composite column and beam. The moment curvature relation was converted into moment rotation relation. The plastic hinge length was assumed as half of the section height (TEC 2007).

Mander confined concrete model was used for columns and beam [24]. Longitudinal bar buckling was modeled by employing the backbone curve of Dhakal and Maekawa [25]. P-Δ effect was incorporated into the analytical model. SAP2000 [26] was used for the nonlinear static analysis. The analytical model was designed by using exact section dimensions and material properties (Figure 3).

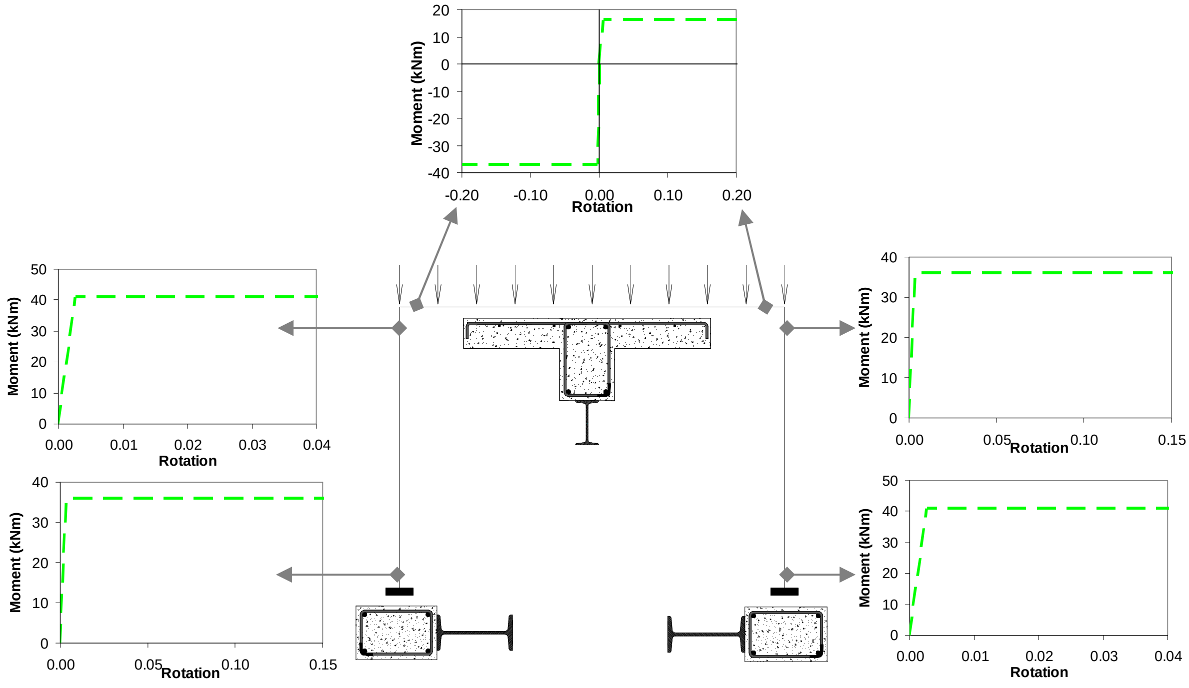

Figure 3: Analytical model of the specimen SP2.

In the TEC-2007, the moment rotation relation can be designed as elastic perfectly plastic behavior. Hence, after yielding, no hardening was used to model the moment rotation behavior (Figure 3). The performance of the member in the procedure suggested in TEC 2007 depends on the reinforcement bar and concrete strain (Figure 4). The following equations were defined for three performance levels in TEC-2007; immediate occupancy (IO), life safety (LS) and collapse prevention (CP) performance levels.

IO performance level;

$$(\varepsilon_{cu})_{IO} = 0.0035$$

$$(\varepsilon_s)_{IO} = 0.010$$

LS performance level;

$$(\varepsilon_{cg})_{LS} = 0.0035 + 0.01(\rho_s/\rho_{sm}) \leq 0.0135$$

$$(\varepsilon_s)_{IO} = 0.040$$

CP performance level;

$$(\varepsilon_{cg})_{CP} = 0.004 + 0.014(\rho_s/\rho_{sm}) \leq 0.018$$

$$(\varepsilon_s)_{CP} = 0.060$$

Where,

εcu; concrete strain at the top fiber

εcg; concrete strain at the top fiber of the confined concrete

εs; Reinforcement bar strain

ρs; available volumetric ratio of the stirrup of the member

ρsm; volumetric ratio of the stirrup of the member calculated by utilizing the TEC-2007

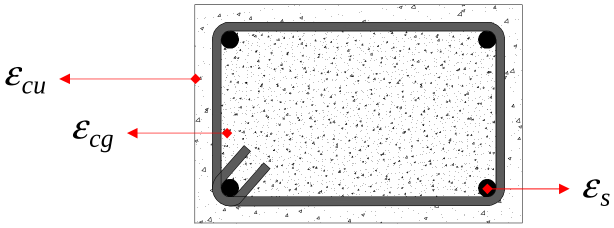

Figure 4: Strain at the cross section of the RC member.

Figure 5 indicates the static pushover curve of the test frame (specimen SP2). This figure also indicated the performance of the columns and beam in term of drift ratio. IO, LS and CP were determined by the method suggested in TEC 2007. Each performance levels indicated in Figure 5 exceeded the suggested strain limits at the bottom and top of the columns. Furthermore, at the end of each performance levels, the damage observed during the test are also seen in Figure 5. The interstory drift ratio (IDR) limits suggested in TEC 2007 are marked on this figure at 1, 3 and 4% DR. The average DR of the each three performance levels are about 1.0, 2.5 and 3.5 %, respectively.

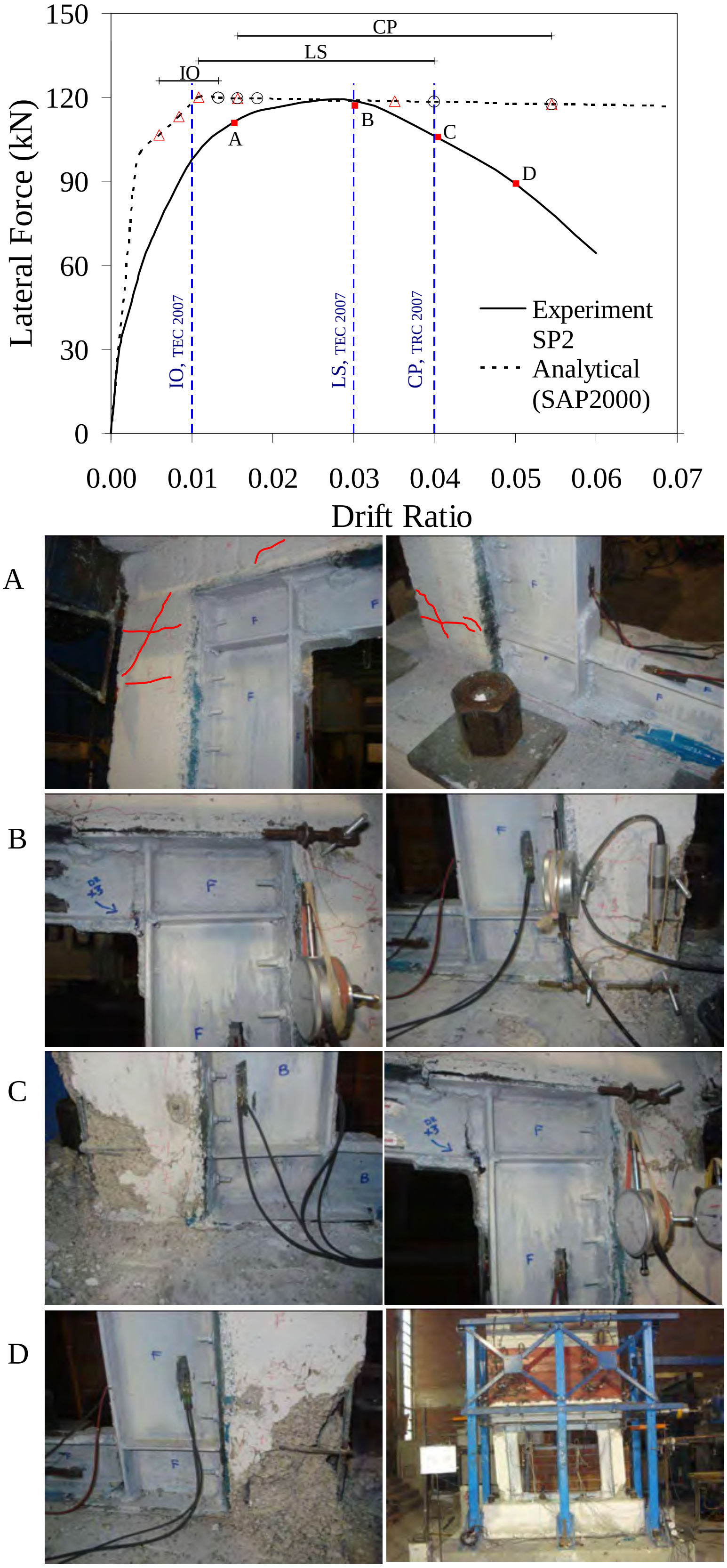

A; Crack iniation, B; Fracture initiation of the steel beam, C; Concrete spalling at the bottom of the column, D; Base hinge mechanism and lateral displacement at 5% DR.

Figure 5: Analytical result of the test frame (specimen SP2).

3 CASE STUDY

In this section, the performance based design of existing five story RC building located in the Istanbul is presented. The building is a reinforced concrete frame structure with rigid shear wall surrounding the basement (Figure 6). Within this study, a performance

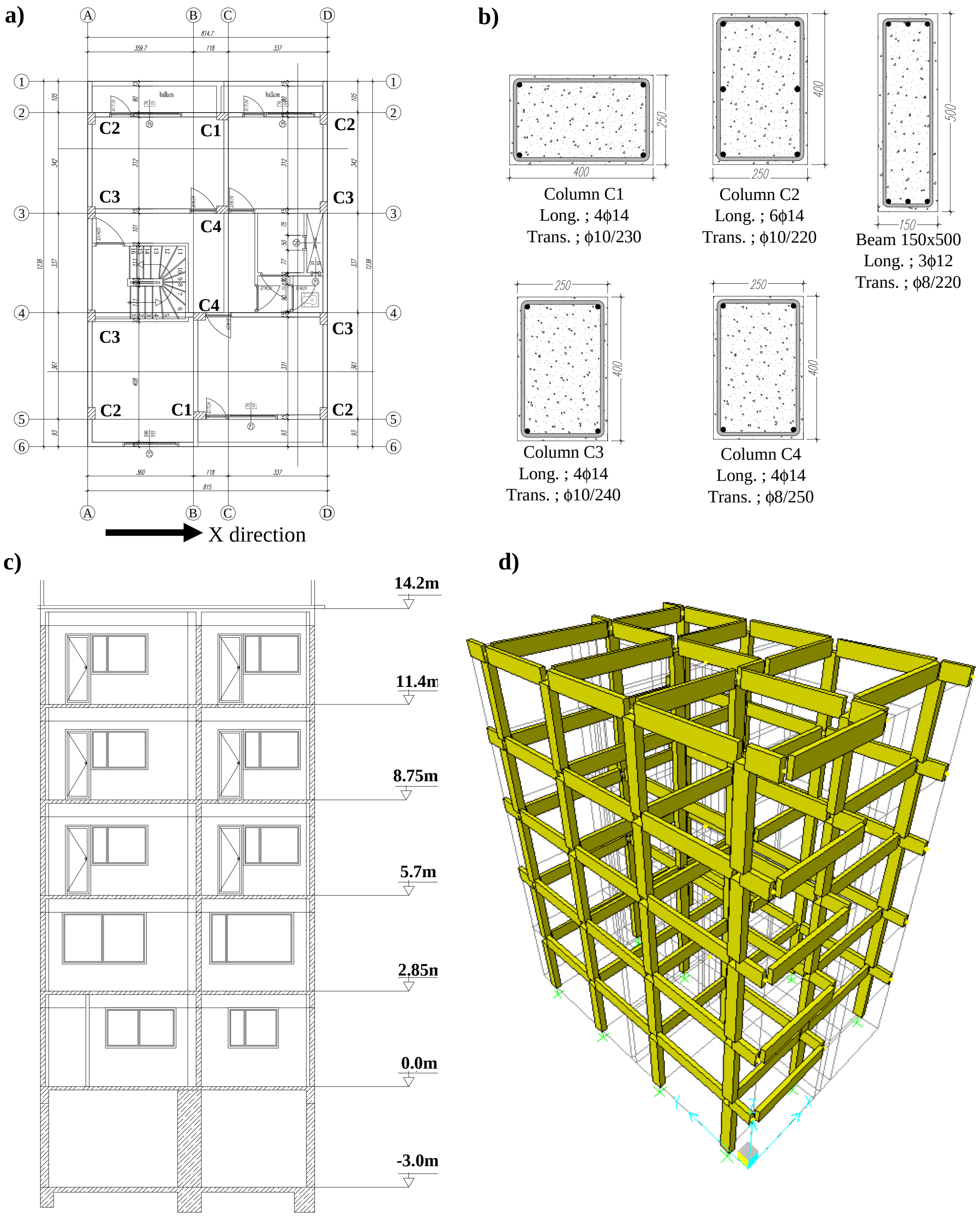

Figure 6: Five story building a) Plan view, b) column and beam dimensions, c) front view of the building, e) analytical model of the building (SAP2000).

evaluation method based on nonlinear pushover analysis is carried out using structural data. The strengthening of the building based on the methodology described previously from the test data is performed. Figure 6 indicates the plan view of the building. Uniaxial compressive strength and modulus of elasticity (calculated from [27]) are 8 MPa (close to test frame) and 13435 MPa, respectively. The yield strength of reinforcing steel was found as 220 MPa. The dimensions of the building in the x and y direction are 8.75 m and 12.23 m, respectively. The columns and beam dimensions are 250x400 and 150x500 mm, respectively. The orientation and also size of the beams and columns are shown in Figure 6. The stirrups spacing of the columns and beam are about 220 mm with a clear cover of 20 mm. It is important to mention that the stirrup spacing of columns and beams does not satisfy the current code TEC-2007 [19]. Furthermore, the in-situ concrete strength is lower than the code specified minimum. The steel grade of the longitudinal and transverse reinforcement is S220 whose yield strength is 220 MPa.

3.1 STRENGHENED BUILDING WITH ISF

The strengthened technique was applied to enhance the lateral load resisting capacity of the direction only. Figure 7 indicates the strengthened bays of the building. There were two strengthened cases namely ISF 1 and ISF 2. The difference between them is; the ISF2 had additional strengthened bays, axis 3-3 and axis 4-4, at the first and second story. The steel members to build composite columns and beams are I-400 and 13mm-thick-steel plate (Figure 7). The yield strength of the both steel members was taken as 235 MPa.

3.2 PERFORMANCE OF THE BUILDING WITH AND WITOUT ISF

Nonlinear static pushover analyses were conducted in order to estimate displacement capacity of the building for the required evaluation techniques. The 3D computer model of the building was generated using SAP2000 [26] from the original drawings of the building (Figure 6). All the joints on each floor were constrained in order to model the diaphragm effect. Moment–rotation properties derived from sectional analyses with the plastic hinge length (taken equal to half the member depth in the direction of loading as suggested by TEC 2007) idealization were assigned to the beam and column ends (similar to given moment rotation as seen in Figure 3). Axial force-moment yield surfaces obtained from interaction diagrams were used for column plastic hinge regions. Load distributions proportion to story mass and first mode amplitude were used for pushover analysis for x direction. Prior to conducting the pushover analyses, gravity loads and 30% of the live load on the structure were applied. The displacement-controlled pushover analysis was then performed to obtain performance point of the building and plastic deformations (rotations) of the members. After performing the pushover analysis and obtaining the capacity curve, the performance points of the building in x direction was calculated using method namely single degree of freedom (SDOF) approach employing the Duzce ground motion (DGM) (Figure 7). Pushover curve was converted into the acceleration displacement response spectrum (ADRS), Figure 8, by using Equation 1:

$$S_a = \frac{V_b}{\alpha_1 W} \text{ and } S_d = \frac{\Delta r}{\Gamma_1 \varphi_{r,1}} \tag{1}$$

where W is the total weight of the MDOF structure, Vb is the base shear, Δr is the roof displacement of the MDOF structure, α1 is the modal mass coefficient for the first mode (first fundamental mode), and Γ1 is the modal participation factor for the first fundamental mode.

ϕr,1 is the amplitude of the first fundamental mode at the roof, Sa is spectral acceleration, and Sd is the spectral displacement.

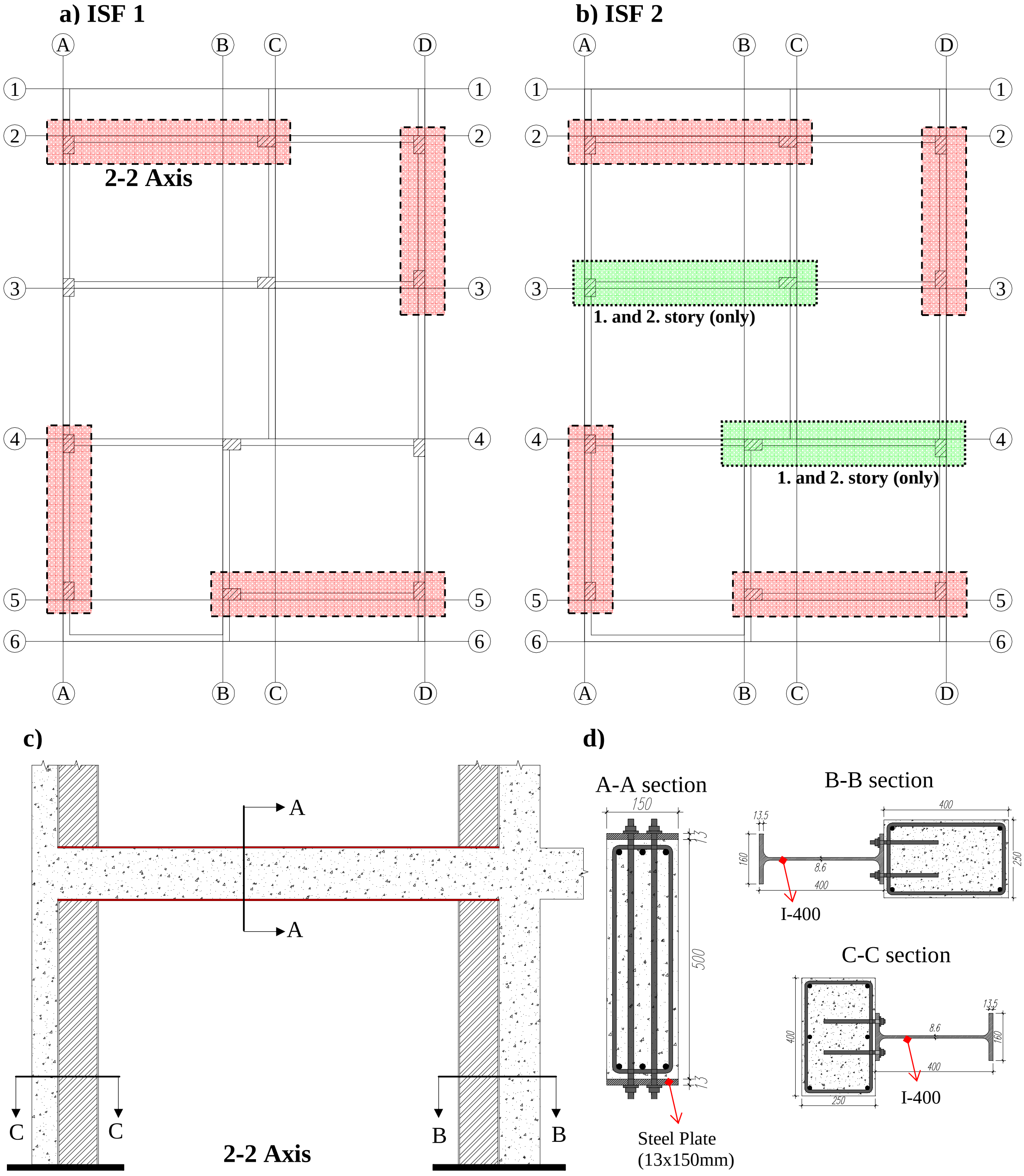

Figure 7: a) and b) Strengthened building with ISF1 and ISF2, c) frame view of the axis 2-2, d) Section of the composite members.

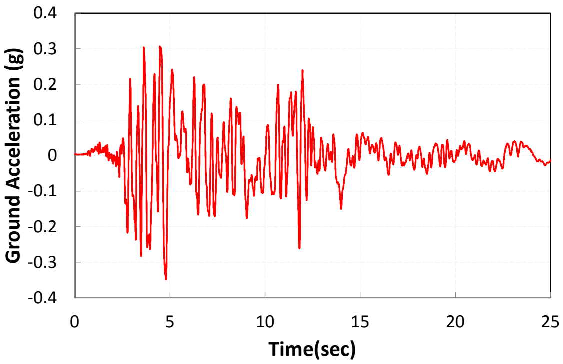

Figure 7: Duzce ground motion

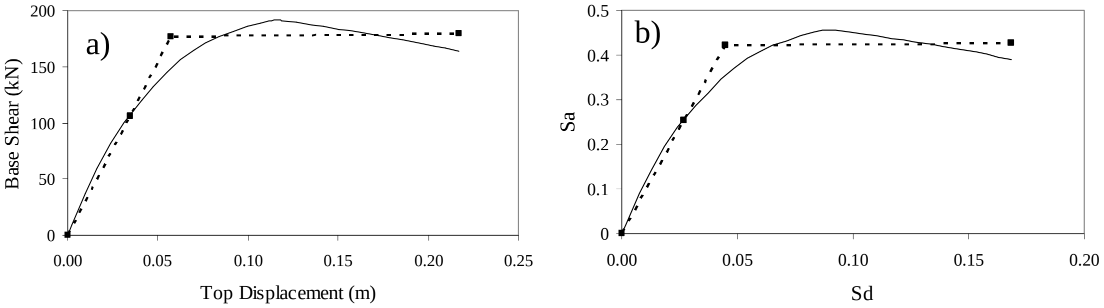

Figure 8: a) Pushover curve of the building, b) ADRS of the building.

For the SDOF approach, the linearization was performed based on the procedure given in FEMA 353 [29] (Figure 8). The mass of the building is taken as the mass corresponding to the governing x modes and 5% critical damping is assumed. Using the bilinear idealization with elastic unloading a SDOF analysis is conducted using the DGM to obtain the top displacement (performance point).

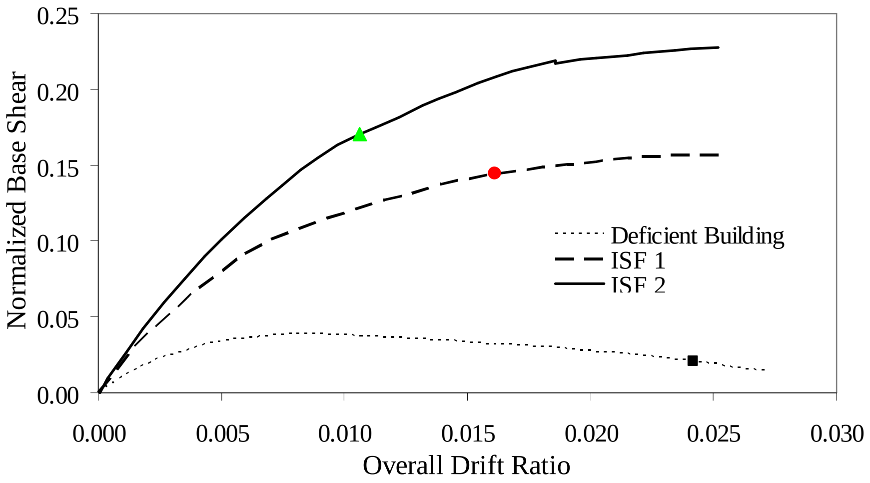

Figure 9: Pushover curve of the buildings, building with ISF1 and ISF2.

The performance points according to DGM are shown on the pushover curves in Figure 9. It can be observed that the building experiences an overall drift ratio of about 2.4 % in the x direction prior to retrofit.

A member by member evaluation is then performed to determine the damage level of the members. The number of columns and beams at different performance levels are presented in Table 1. This evaluation indicated that 100% and 36% of the first story columns and beams of the deficient building with any ISFs were at the total collapse (TC) performance level for x directions, respectively. This results indicates that this deficient building needs to be retrofitted.

Upon retrofitting, the number of the columns which were in the TC performance level decreased. Although 33% of the first story columns of the building implemented ISF 1 was within the TC performance level, this condition did not satisfy the performance level of the residential building suggested in TEC 2007. Finally, the desired performance level of the deficient building retrofitted with ISF2 was obtained by increasing numbers of retrofitted bays.

Column Performance Levels	1. story			2. story			3. story			4. story			5. story		
	Deficient	ISF 1	ISF 2	Deficient	ISF 1	ISF 2	Deficient	ISF 1	ISF 2	Deficient	ISF 1	ISF 2	Deficient	ISF 1	ISF 2
IO	0	4	10	1	11	12	5	12	12	12	12	12	12	12	11
LS	0	3	2	4	0	0	6	0	0	0	0	0	0	0	1
CP	0	1	0	3	0	0	1	0	0	0	0	0	0	0	0
Total Collapse	12	4	0	4	1	0	0	0	0	0	0	0	0	0	0

Beam Performance Levels	1. story			2. story			3. story			4. story			5. story		
	Deficient	ISF 1	ISF 2	Deficient	ISF 1	ISF 2	Deficient	ISF 1	ISF 2	Deficient	ISF 1	ISF 2	Deficient	ISF 1	ISF 2
IO	12	16	18	16	19	21	17	19	18	23	19	19	24	22	24
LS	2	5	4	1	4	3	7	5	6	1	5	5	0	2	0
CP	0	1	0	5	1	0	0	0	0	0	0	0	0	0	0
Total Collapse	8	0	0	2	0	0	0	0	0	0	0	0	0	0	0

Table 1: Performance levels of the members.

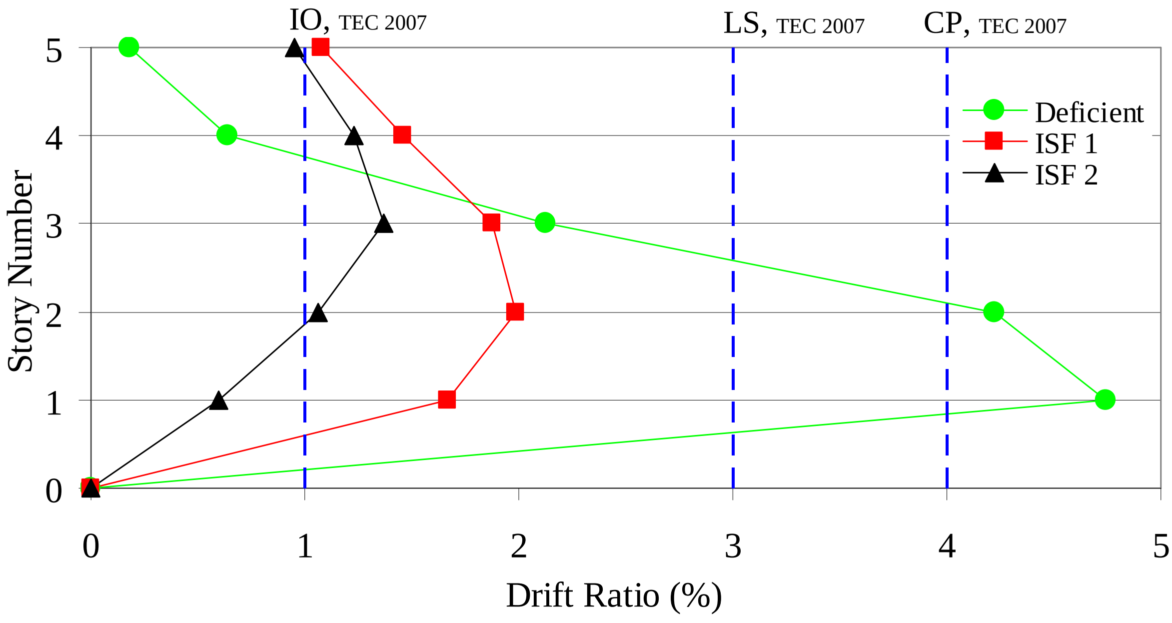

Figure 10: IDR of the building at the performance points.

The IDR profiles for x directions obtained from pushover analysis at performance points of DGM are shown in Figure 10. It can be observed that highest IDR, which was about 4.7 % in the x direction, occurred in the first story level of the building without any ISF retrofit. Upon retrofit the IDR reduced to about 1.4% for the x directions. It should be noted that the observed drift ratio is in good agreement with those limits proposed in the TEC 2007 (Figure 10). This result shows that the ISF retrofit scheme was successful in controlling drift deformations and reducing the demands in the columns. As a results, the ISF retrofit design presented above was found to be successful in LS performance level of the building by reducing the deformation demands on the RC columns and controlling the drift deformations. In addition, above results clearly indicates that a retrofit technique needs to increase lateral stiffness and strength aside from increasing global ductility capacity (if any member base retrofitting technique is not used) when ductility capacity of the existing columns and beams are insufficient.

4 CONCLUSION

The test results indicated that the ISF increased the lateral strength, stiffness and energy dissipation capacity of the deficient RC frames. The analytical study of the test frame simulated the behavior of the test frame successfully. The test frame load-deformation and damage observed during the test was correlated by the proposed performance levels suggested in TEC 2007. It was observed that the performance levels defined in TEC 2007 can be utilized conservatively to evaluate the frame retrofitted with ISF. Based on the data gained from the test and analytical results of the test frame, a case study consisted of a real existing residential building before and after ISF retrofit was evaluated by utilizing procedures suggested by the TEC 2007 under imposed DGM demand. It was observed that although seismically deficient five story RC building did not satisfy the performance levels of a residential building acceptance criterion with respect to TEC 20007, it was adequate after retrofitting with ISF. As a result, the ISF can be considered as a rapid, safe and practical retrofitting technique.

5 AKNOWLWEDGE

The research discussed in this paper was conducted at Middle East Technical University (METU)-Structural Mechanics Laboratory. Funding provided by TÜBİTAK (project no: 106M493) is greatly appreciated.

REFERENCES

[1] E. Canbay, U. Ersoy, G. Ozcebe. Contribution of reinforced concrete infills to seismic behavior of structural systems. Structural Journal, ACI, 100(5):637-643, 2003.

[2] M.O. Sonuvar, G. Ozcebe, U. Ersoy. Rehabilitation of reinforced concrete frames with reinforced concrete infills. Structural Journal, ACI, 101(4):494-500, 2004.

[3] S. Altin, U. Ersoy, T. Tankut. Hysteretic response of reinforced-concrete infilled frames. J Struct Engrg ASCE, 118(8):2133-2150, 1992.

[4] M.B.D Hueste, JW Bia. Seismic retrofit of a reinforced concrete flat-slab structure: Part I —seismic performance evaluation. Eng Struct, 29(6):1165–1177, 2006.

[5] M. Badoux, JO Jirsa. Steel bracing of RC frames for seismic retrofitting. J Struct. Engrg ASCE, 116(1):55-74, 1990.

[6] A. Ghobarah, H. Abou-Elfath, Rehabilitation of a reinforced concrete frame using eccentric steel bracing. Eng Struct, 23(7):745-755, 2001.

[7] M.R. Raheri, A. Sahebi, Use of steel bracing in reinforced concrete frames. Eng Struct, 19(12):1018-1024, 1997.

[8] R. Ozcelik, B. Binici, Application of steel retrofit schemes for deficient buildings in Turkey. In: Proceedings of the First European Conference on Earthquake Engineering and Seismology 2006 Geneva, Switzerland. ID 1030.

[9] F.J. Molina, S. Sorace, G. Terenzi, G. Magonette, B. Viaccoz, Seismic tests on reinforced concrete and steel frames retrofitted with dissipative braces. Earthquake Engng Struct. Dyn, 33(15):1373–1394, 2004.

[10] R. Ozcelik, B. Binici, Use of internal V braces for strengthening deficient reinforced concrete frames. In: 8th International Conference on Advances in Civil Engineering, Eastern Mediterranean University, Famagusta, North Cyprus, 2008 CD Rom Proceedings ID 246.

[11] T.D. Bush, E.A. Jones, J.O. Jirsa, Behavior of the RC frames strengthened using structural steel bracing. Proc ASCE, J Struct Engrg, 117(4):1115-26, 1991.

[12] J.A. Pincheira, J.O. Jirsa, Seismic response of RC frames retrofitted with steel braces or walls. J Struct Engrg ASCE, 121(8):1225-1235, 1995.

[13] A.C. Masri, S.C. Goel, Seismic design and testing of an RC slab-column frame strengthened by steel bracing. Earthquake Spectra, 12(4):645-666, 1996.

[14] S. Ozden, U. Akguzel, CFRP overlays in strengthening of frames with column rebar lap splice problem. Advances in Earthquake Engineering for Urban Risk Reduction NATO Science Series, Earth and Environmental Sciences, 66:455-471, 2006.

[15] B. Binici, G. Ozcebe, R. Ozcelik, Analysis and design of FRP composites for seismic retrofit of infill walls in reinforced concrete frames. Composites Part B: Engineering, 38(5):575-583, 2007.

[16] I. Erdem, U. Akyuz, U. Ersoy, G. Ozcebe, An experimental study on two different strengthening techniques for RC frames. Eng Struct, 28(13):1843-1851, 2006.

[17] I. Kazunori, H, Norimitsu, H. Kiyoshi, H. Kei, Development of seismic strengthening technology using the fitting shear wall construction method and the external frame method. Kumagai Technical Research Report, 58(1):61-67, 1999. (in Japanese)

[18] K. Takahiro, M. Yasuyoshi, Study on retrofitting adhered steel brace. Journal of Structural and Construction Engineering (Transactions of AIJ), 539:103-109, 2005. (in Japanese).

[19] Turkish Ministry of Public Works and Settlement. Turkish code for buildings in seismic zones (TEC). Ankara, Turkey; 2007. (in Turkish).

[20] R. Ozcelik, B. Binici, U, Akpınar, Seismic Retrofit of Deficient RC Structures with Internal Steel Frames, Advances in Structural Engineering, 2011 (accepted).

[21] I.H. Çağatay, Experimental evaluation of buildings damaged in recent earthquakes in Turkey. Engineering Failure Analysis, 12(3): 440-452, 2005.

[22] S.S. Tezcan, M.A. Ipek, A reconnaissance report: 1995 Dinar, Turkey, earthquake. Eng Struct, 18(12):906-916, 1996.

[23] A. Doğangün, Performance of reinforced concrete buildings during the May 1, 2003 Bingöl Earthquake in Turkey. Eng Struct, 26(6):841-856, 2004.

[24] J.B. Mander, M.J.N. Priestley, R. Park, Theoretical Stress□Strain Model for Confined Concrete. J. Struct. Engrg. 114(8), 1804- 1826, 1988.

[25] R.P. Dhakal, K. Maekawa, Modeling for Postyield Buckling of Reinforcement, *Journal of Structural Engineering*, Vol. 128, No.9, 1139-1147, 2002.

[26] SAP2000, version 8.1., SAP2000 integrated finite element analysis and design of structures. Computers and Structures, Inc., Univ. Avenue. Berkeley, CA. 2001

[27] Building Code Requirements for Structural Concrete and Commentary. American Concrete Institute (ACI 318-08), Farmington Hills, MI, 2008.

[28] American Society of Civil Engineers, Prestandard and Commentary for the Seismic Rehabilitation of Buildings, Report No. FEMA 356. Reston, Virginia, 2000.

COMPDYN 2011
III ECCOMAS Thematic Conference on
Computational Methods in Structural Dynamics and Earthquake Engineering
M. Papadrakakis, M. Fragiadakis, V. Plevris (eds.)
Corfu, Greece, 25–28 May 2011

INVESTIGATION OF THE SLIDING RESPONSE OF A RIGID BODY SYSTEM SUBJECTED TO UNI-DIRECTION HORIZONTAL DYNAMIC AND EARTHQUAKE EXCITATIONS

George C. Manos[1], **George Koidis**[1], **and Milton Demosthenous**[2]

[1] Laboratory of Experimental Strength of Materials and Structures, Dept. of Civil Engineering, Aristotle University, Thessaloniki, Greece.
e-mail: gcmanos@civil.auth.gr

[2] Institute of Engineering Seismology and Earthquake Engineering, Thessaloniki, Greece.
demilton@itsak.gr

Keywords: Sliding, Rigid Body, Friction, Seismic Isolation.

Abstract. *An experimental and numerical investigation is presented that studies the sliding response of a rigid body when subjected to horizontal dynamic and earthquake excitations. For this purpose, a steel block mock-up of a rigid body has been constructed and tested at the shaking table of Aristotle University. The dynamic excitations were based on either sinusoidal motions of various amplitudes and frequencies or simulated earthquake excitations based on actual recordings of prototype earthquake ground motions. The experimental results have shown that when sliding of this rigid block is permitted then its peak acceleration response is moderately amplified, provided that the excitation frequency is not close to the resonant frequency range of the block-spring dynamic system. This is particularly true for earthquake excitations and for relatively flexible spring-links thus achieving in this way a type of seismic isolation for the rigid block. A computer software was developed in order to numerically simulated this dynamic sliding response. The numerical results obtained through this specially developed computer software are next compared with the corresponding experimental measurements. The numerically predicted rigid block acceleration response is in good agreement, in all examined cases, with the measured values. The numerically predicted rigid body sliding displacement response also exhibits innumerous cases good agreement with the measured values. However, significant deviation between predicted and measured rigid body sliding displacement amplitudes were also observed. Despite these limitations of the predicted results it is believed that the developed software, although it deals with a complex problem in a relatively simple way, it can be useful in the preliminary design of structural systems with sliding capability at their support.*

1 INTRODUCTION

This paper presents results from an experimental and numerical investigation that deals with the sliding response of a rigid body when subjected to horizontal dynamic and earthquake excitations. The layout of this problem is shown in figure 1, where a rigid body (figure 1, designated with light color) is initially resting on a platform (figure 1, designated with dark color) that can move in a prescribed way in one horizontal direction, thus subjecting the rigid body to horizontal dynamic and earthquake excitations. The contact area between the rigid body and the moving platform is a horizontal plane having a friction coefficient μ (μ_{st}, the static coefficient of friction and μ_d, the dynamic coefficient of friction). Moreover, the rigid body of mass m is connected with the moving platform with an elastic spring having stiffness K and with a damper having a damping coefficient C. The motion of the moving platform is defined by the displacement vector U(t) with respect to an motionless coordinate system x, y whereas the corresponding displacement vector of the rigid body is X(t). The velocity and acceleration vectors of the rigid body and the moving platform are $\dot{X}(t)$ $\ddot{X}(t)$ and $\dot{U}(t)$ $\ddot{U}(t)$, respectively. The sliding displacement between the rigid body and the supporting moving platform is U(t)-X(t). The following are the forces (figure 1) that arise in this rigid body – moving platform dynamic system [1].

F_{ine} = The inertia force, F_{spr} = The spring force , F_{damp} = The damping force
F_{fr} = μ_d m g = The friction force during sliding
F_{fr} = μ_{st} m g = The friction force when no sliding occurs

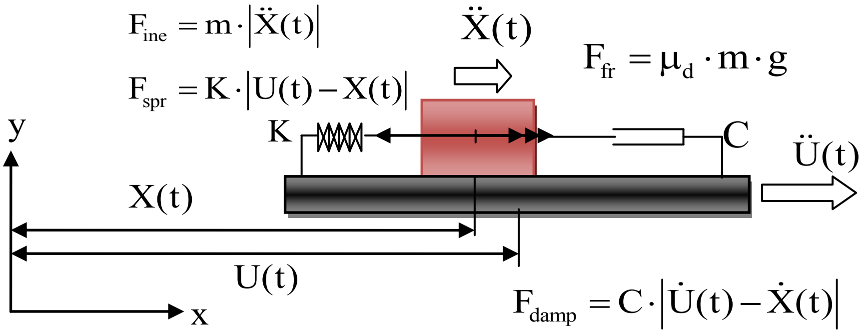

Figure 1. Layout of the problem

This particular problem appears to be of interest either in predicting the dynamic and earthquake response of relatively very stiff objects (rigid) that simple rest on horizontal floors or the behavior of stiff structures that incorporate a sliding surface as means of protection against dynamic or earthquake excitations.

2 EXPERIMENTAL INVESTIGATION

For this purpose, a special mock-up has been constructed that represents physically the previously stated problem (figure 1). It consisted of a steel rigid block rectangular in shape with dimensions 430mm x 430mm in plan and a height either 205mm or 410mm (upper part of figure 2); This block was simply resting on a steel moving platform (lower part of figure 2) and it was restrained to all other directions so that in could move only in the longitudinal horizontal direction. The mass of this sliding rigid block was either 124kg or 248kg. The various important physical parameters for this block sliding response are measured [6], [7], such as the coefficient of friction at the contact surface between the block and the moving platform and the stiffness of the elastic spring as will be shown in the following sections 2.1. and 2.2. No viscous damper was introduced at this part of the experimental investigation.

Figure 2. Experimental set-up

2.1 Measuring the coefficient of friction

A special series of tests were performed in order to define the coefficient of friction of the contact surface between the sliding block and the moving platform. This surface was machined in a special way so that full contact conditions could be ensured between the sliding block and the moving platform. Moreover, this contact surface has been lubricated throughout all the experimental sequences [6], [8], [9]. Figure 3 depicts the friction force versus sliding displacement diagram when the mass of the sliding block was equal to 284kg (by placing 36kg extra mass on top of the rigid block). The frequency of the cycling displacements during these tests was varied from 0.1Hz to 1.0Hz. The values for the coefficient of friction found from these tests are listed below. A total number of 10 tests were performed.

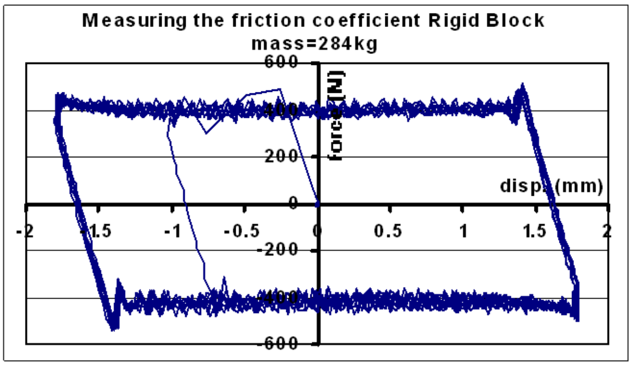

Figure 3. Test for measuring the friction coefficient

When the rigid block mass was equal to 124kg the values of the friction coefficient were:

$\mu_{st} = 0.165$ $\mu_d = 0.153$

When the rigid block mass was equal to 284kg the values of the friction coefficient were:

$\mu_{st} = 0.158$ $\mu_d = 0.136$

2.2 Measuring the stiffness of the spring

Another series of tests were conducted in order to accurately measure the stiffness K of the spring that was employed to link the rigid block to the moving platform, as indicated in figure 1. Two types of springs were tested; the first was a spring that was certified for its properties whereas the second one was not certified. The loading arrangement which is depicted in figure 4 was employed during these tests whereby the force applied on the spring was measured together with the resulting spring displacement. Figure 5a shows the resulting certified spring response during such a test whereby no pre-stressing force was applied at the spring. In figures 5b and 5c the resulting response is depicted when a pre-stressing force is applied through a special for this purpose system attached to either the certified or the non-certified spring, respectively. As was done for measuring the coefficient of friction, during the tests for measuring the spring stiffness the frequency of the cycling displacement was varied from 0.1Hz to 1.0Hz.

Figure 4. Test for measuring the spring stiffness

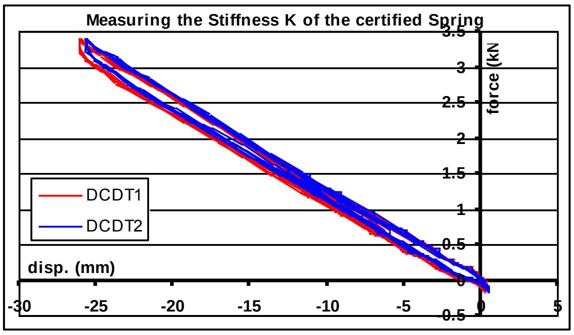

Figure 5a. The certified spring load-displacement response with no pre-stress

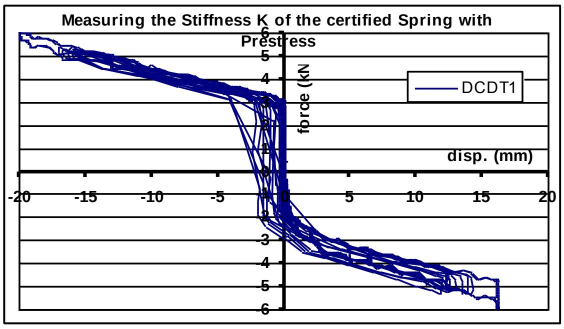

Figure 5b. The certified spring load-displacement response with pre-stress

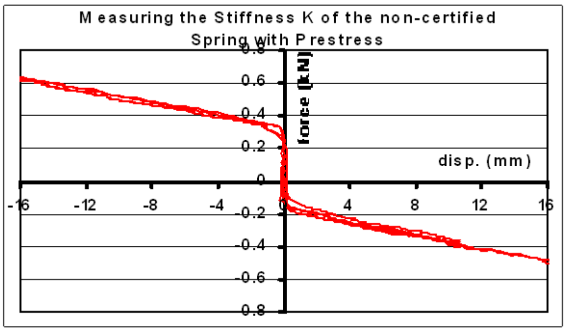

Figure 5c. The non-certified spring load-displacement response with pre-stress

The stiffness of the certified spring with no pres-stress, as was estimated from the load-displacement response of these tests (figure 5a), had an average value K= 128.6 KN/m.

The stiffness of the certified spring with pre-stress, as was estimated from the load-displacement response of these tests (figure 5b), had an average value K= 143 KN/m.

The stiffness of the non-certified spring with pre-stress, as was estimated from the load-displacement response of these tests (figure 5b), had an average value K= 19.4 KN/m.

2.3 Measuring the sliding response of the rigid block

Figure 6 depicts the experimental arrangement, whereby a number of displacement and acceleration sensors were used to monitor the sliding response of the rigid block and the actual motion of the moving platform [6], [7], [8], [9]. The force of the spring link was also monitored. The dynamic excitations of the moving platform were based on sinusoidal motions of various amplitudes and frequencies. The earthquake excitations of the moving platform were laboratory simulations based on actual recordings of prototype earthquake ground motions. The non-certified as well as the certified spring was used in a number of tests with sinusoidal or simulated earthquake excitations. In addition, a number of tests were also conducted whereby there was no spring link between the rigid block and the moving platform.

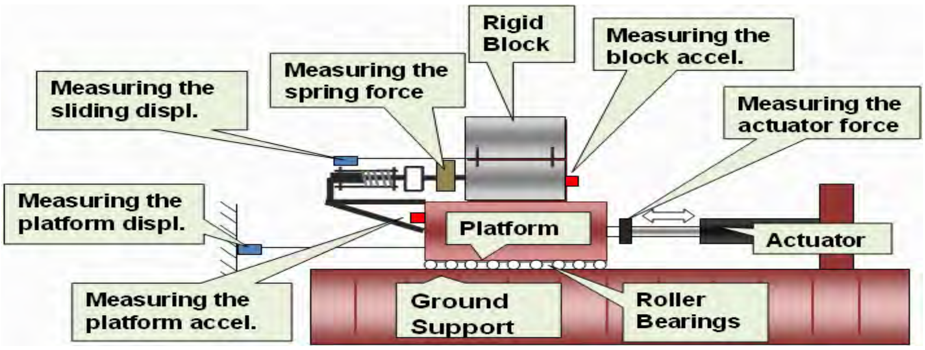

Figure 6. Experimental arrangement for measuring the sliding response of the rigid block.

3 EXPERIMENTAL RESULTS

Selective experimental results are presented in the next sections whereby the rigid block is linked to the moving platform either with the non-certified or with the certified spring or with no spring at all. The moving platform is subjected to either sinusoidal motions, in the frequency range from 0.5Hz to 4Hz, or to simulated earthquake excitations based on the prototype Kern Country 1953 prototype earthquake horizontal acceleration recording (HTaft0407.int). The non-certified spring with a pre-stressing force is used in section 3.1. The results that are presented in this section are for a test that used a sinusoidal motion of 1.5Hz for the moving platform. The certified spring with no pre-stressing force is used in section 3.2. The results that are presented in this section are for a test that used a sinusoidal motion of 3.0Hz for the moving platform whereas in section 3.3. the certified spring with no pre-stress is again employed but this time the above named simulated earthquake motion is utilized. Finally, in sections 3.4. and 3.5. there is no spring linking the rigid block with the moving platform; a sinusoidal motion of 1.5Hz is employed in section 3.4. whereas the above named simulated earthquake motion is utilized in section 3.5.

3.1 Sinusoidal excitation 1.5Hz with non-certified spring (with pre-stress)

The presented results include the acceleration response (m/sec^2) of the moving platform and of the sliding rigid block (figure 7a) whereas the displacement (mm) of the moving platform and the spring is depicted in figures 7b and 7d respectively. Figures 7c and 7e depict the force that develops at the spring (KN) as well as the force-displacement response of this spring. Finally figure 7f depicts the sliding displacement of the rigid block relatively to the moving platform. Obviously, this sliding displacement must be theoretically equal to the spring displacement; this practically materializes in the used experimental set-up as can be seen by comparing the displacement response of figures 7f and 7d. Moreover, it can be seen that the non-certified spring force-displacement response with pre-stress measured individually (figure 5c) is in good agreement with that measured during the sliding response of the rigid body that mobilizes the response of the spring (figure 7e)

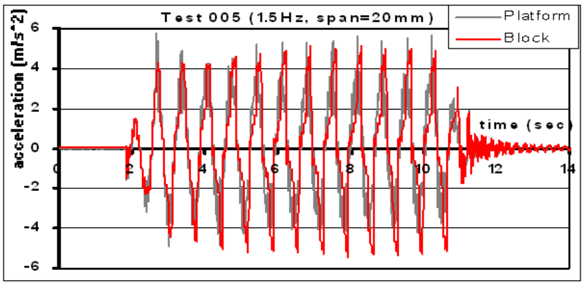

Fig. 7a. Acceleration response of moving platform (ground) and of the sliding rigid block .

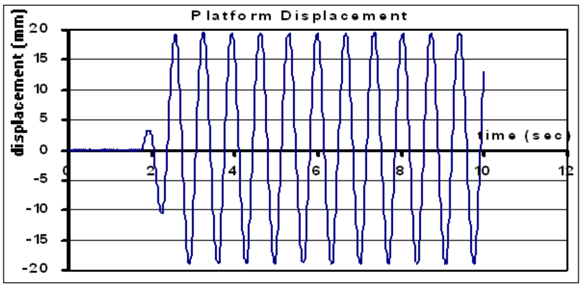

Fig. 7b. Displacement of the moving platform, (Test 005 29-11-2007)

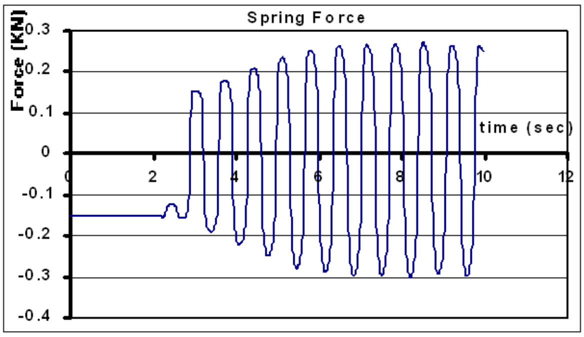

Fig. 7c. Force that was measured at the spring

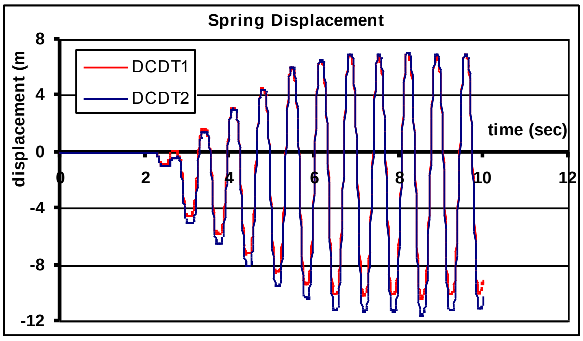

Fig. 7d. Displacement of the spring

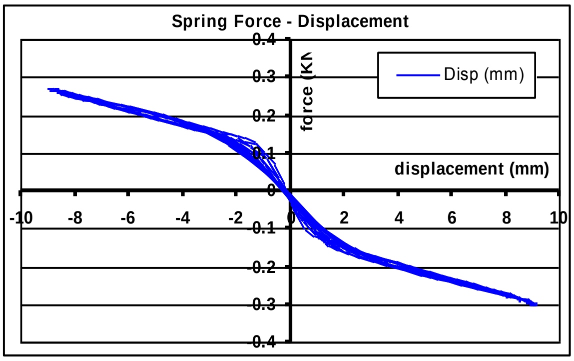

Fig. 7e. Force-displacement response of the spring

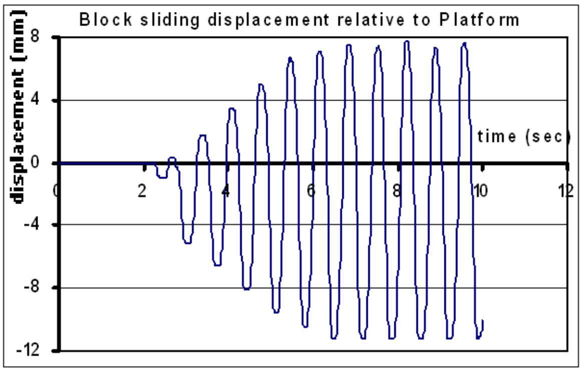

Fig. 7f. Sliding displacement of the rigid block relative to the moving platform

3.2 Sinusoidal excitation 3.5Hz with certified spring (no pre-stress)

Again, the presented results include the acceleration response (m/sec^2) of the moving platform and of the sliding rigid block in figure 8a whereas the displacement (mm) of the moving platform and the spring is depicted in figures 8b and 8d respectively. Figures 8c and 8e depict the force that develops at the spring (KN) as well as the force-displacement response of this spring. Moreover, it can be seen that the certified spring response with no pre-stress measured during the sliding response of the rigid body that mobilizes the response of the spring (figure 8e) is in good agreement with that measured individually (figure 5a).

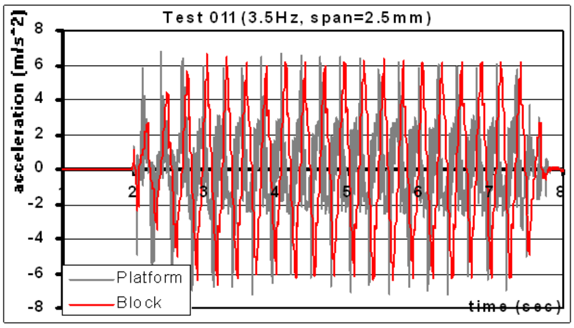

Fig. 8a. Acceleration response of the moving platform and of the sliding block

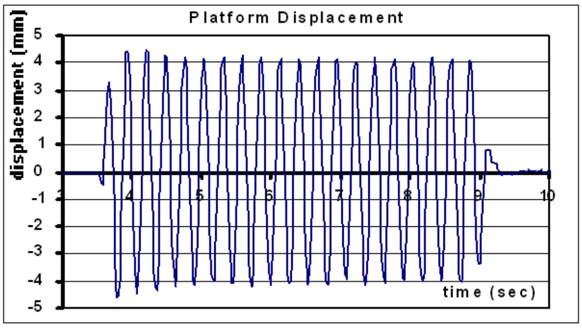

Fig. 8b. Displacement of the moving platform, Test 011, 19-12-2007

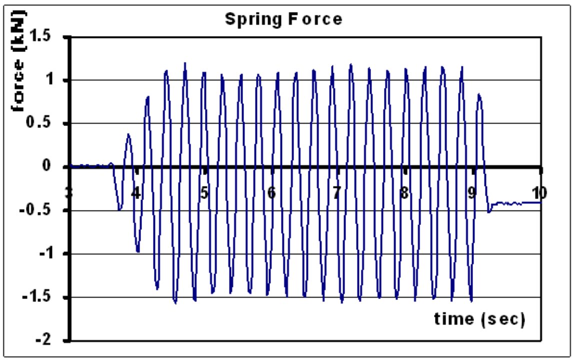

Fig. 8c. Force that was measured at the spring

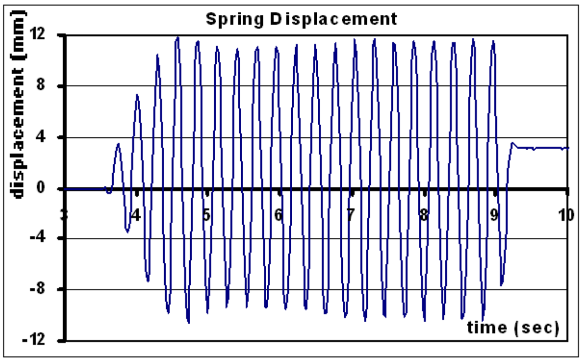

Fig. 8d. Displacement of the spring and sliding displacement of the rigid block

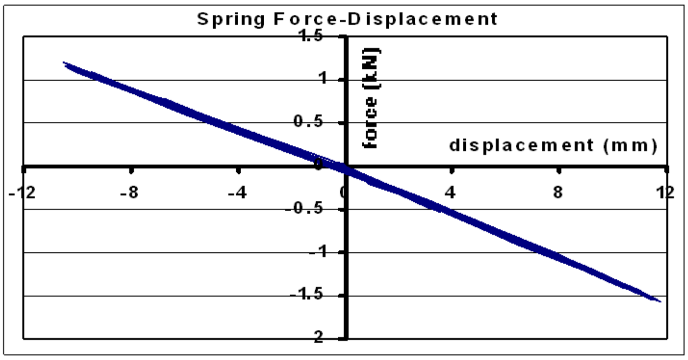

Fig. 8e. Force-displacement response of the spring

3.3 Simulated earthquake excitation with certified spring.

The results of two tests are presented here, both conducted with the certified spring; they are Test 002 (with small pre-stress, figures 9a to 9e) and Test 004 (with no pre-stress, figures 10a to 10e). Again, the presented results include the acceleration response of the moving platform and of the sliding rigid block in figures 9a (small pre-stress) or in figure 10a (no pre-stress). The displacement of the moving platform is depicted in figures and the spring is depicted in figures 9b (small pre-stress) or in figure 10b (no pre-stress). Figures 9d and 10d depict the displacement of the spring, which coincides with the sliding displacement of the rigid block, whereas figures 9c and 10c depict the corresponding spring force. The force-displacement response of this certified spring is depicted in figures 9e and 10e, for either the small pre-stress or the no-pre-stress case, respectively. These force displacement response curves can be compared again with figures 5b and 5a, whereby a relatively good agreement can again be observed. Moreover, it can be seen that due to sliding the maximum acceleration response that develops at the rigid block is much smaller than the maximum acceleration response of the moving platform (figures 9a and 10a). However, this reduction in the acceleration response of the rigid block is accompanied with considerable sliding displacement response of the rigid block that attains a maximum value equal to 3.65mm for Test 002 and to 14mm for Test 004.

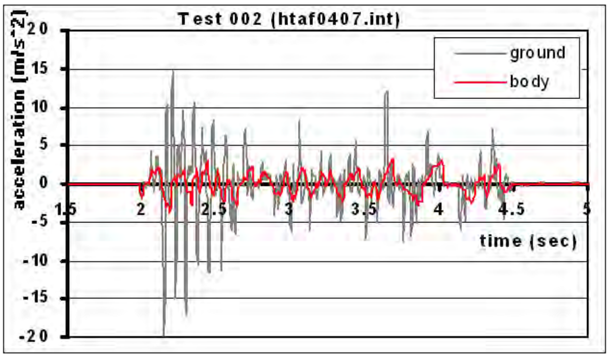

Fig. 9a. Acceleration response of the moving platform and of the sliding block

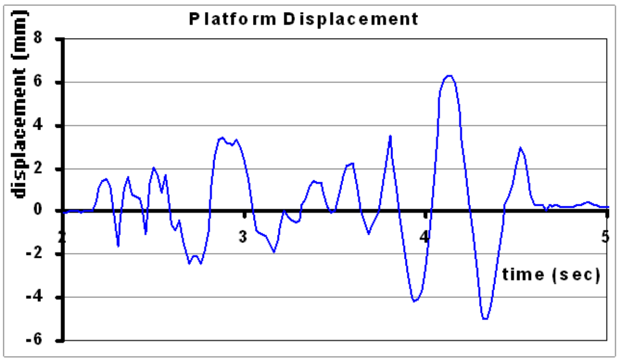

Fig. 9b. Displacement of the moving platform, Test 002, 21-12-2007

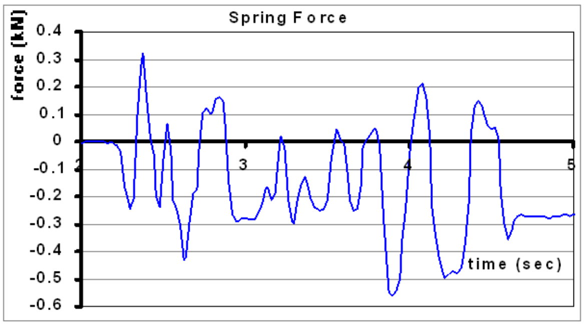

Fig. 9c. Force that was measured at the spring

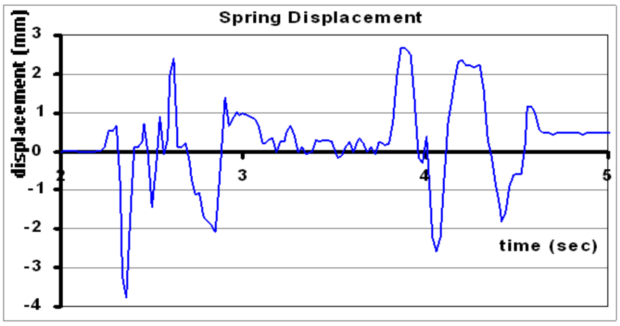

Fig. 9d. Displacement of the spring – rigid block sliding displacement

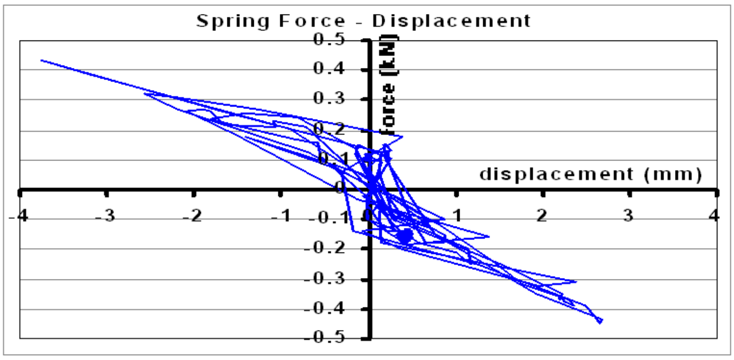

Fig. 9e. Force-displacement response of the spring

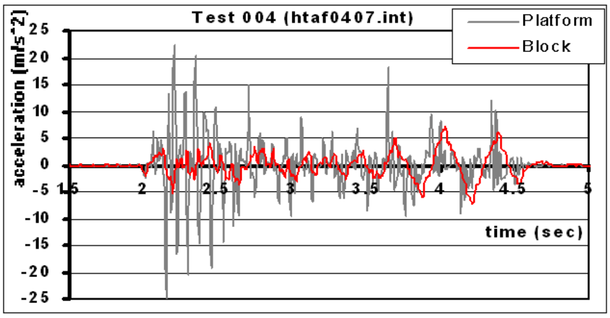

Fig. 10a. Acceleration response of the moving platform and of the sliding block

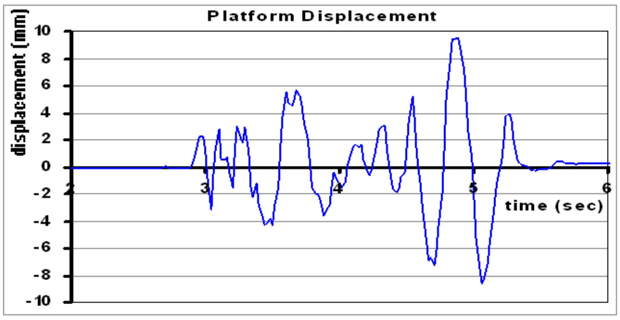

Fig. 10b. Displacement of the moving platform, Test 004, 21-12-2007

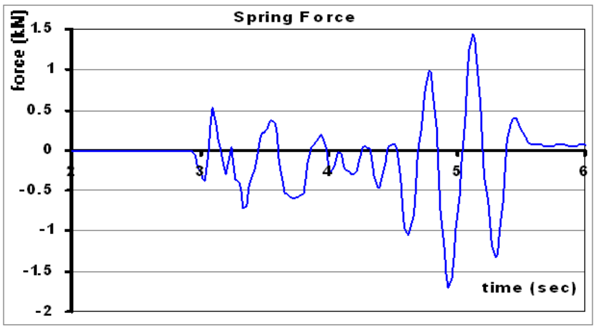

Fig. 10c. Force that was measured at the spring

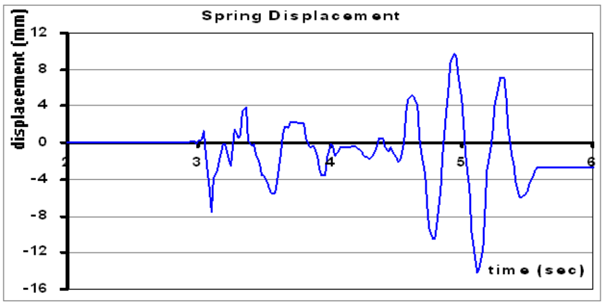

Fig. 10d. Displacement of the spring – rigid block sliding displacement

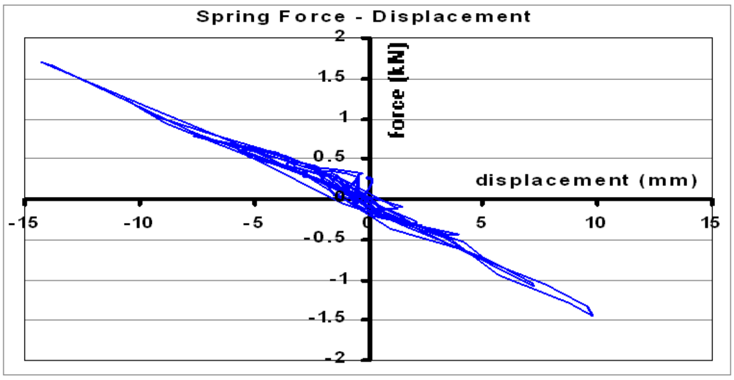

Fig. 10e. Force-displacement response of the spring

3.4 Sinusoidal excitation 1.5Hz without spring link.

In this section as well as in the next section 3.5 the rigid block is simply resting on the moving platform having removed the spring that linked during the previous experiments the rigid block with the moving platform. In the present section the platform is moving in a horizontal sinusoidal motion of 1.5Hz.

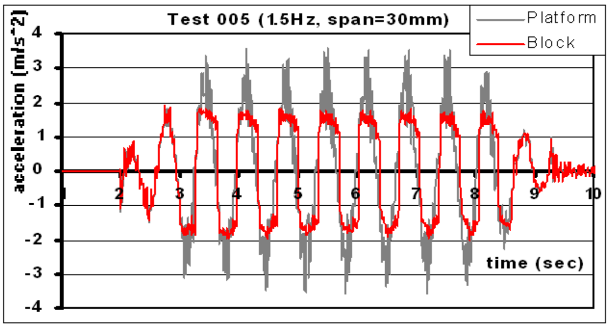

Fig. 11a. Acceleration response of the moving platform and of the sliding block

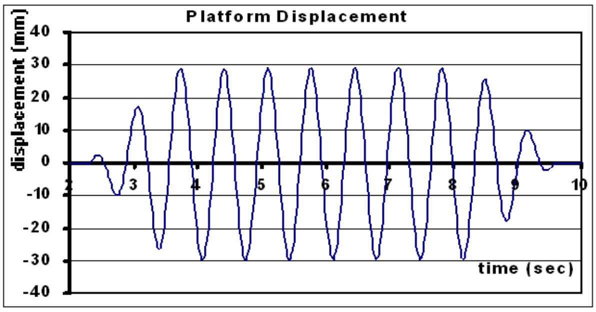

Fig. 11b. Displacement of the moving platform, Test 005, 14-1-2008

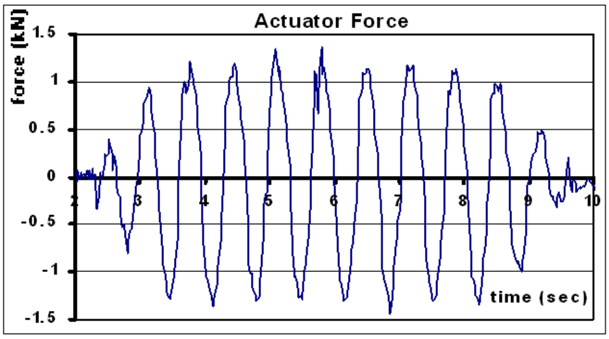

Fig. 11c. Force that was measured at the actuator

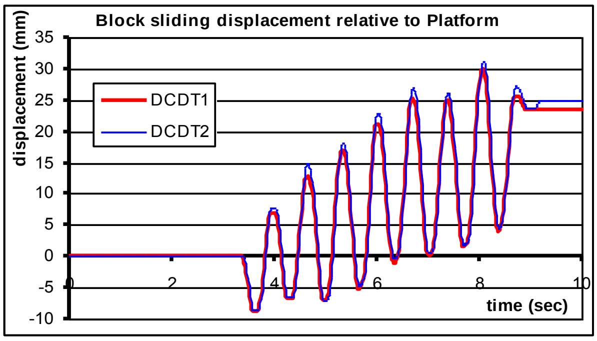

Fig. 11d. Sliding displacement of the rigid block

The acceleration response of the moving platform and of the sliding rigid block is depicted in figure 11a whereas the displacement of the moving platform and the sliding displacement of the rigid block is depicted in figures 11b and 11d respectively. Figure 11c depicts the force that develops at the actuator during this experiment. In this case of free sliding, the maximum rigid block acceleration response is theoretically equal to $\mu_d \cdot g$, which is approximately confirmed by the measured response (if it processed with the proper low-pass filter). It is interesting to note that, in the absence of the spring link, the sliding displacement response of the rigid block develops relatively large values (30mm); moreover, there is a cumulative sliding displacement that appears as an offset from the initial zero displacement condition. This may be attributed to manufacturing tolerances whereby the contact surface between the rigid block and the moving platform deviates from the ideal horizontal plane. This deviation, which was beyond the means of our laboratory checking capabilities, may be also present in actual in-situ applications. The presence of the spring during the previous sinusoidal tests (section 3.1. and 3.2.) has as a result the reduction of the maximum sliding displacement values and the symmetric sliding with respect to the initial zero displacement condition (no cumulative sliding, see figures 7f and 8d). As was observed in all the previously depicted experiments the acceleration response of the rigid block is smaller than that of the moving platform.

3.5 Simulated earthquake excitation without spring link.

Again, the rigid block is simply resting on the moving platform having removed the spring-link. This time, the moving platform is subjected to a simulated earthquake excitation based on the prototype Kern Country 1953 prototype earthquake horizontal acceleration recording (HTaft0407.int).

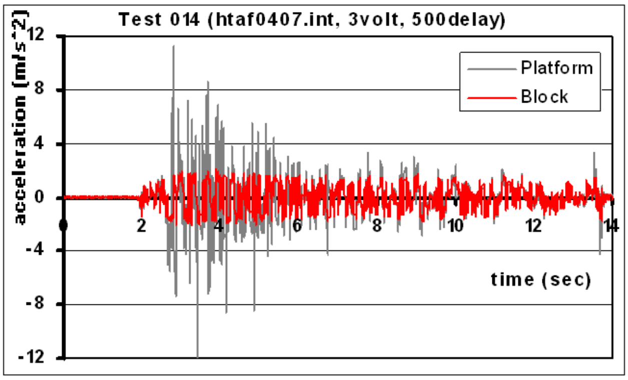

Fig. 12a. Acceleration response of the moving platform and of the sliding block

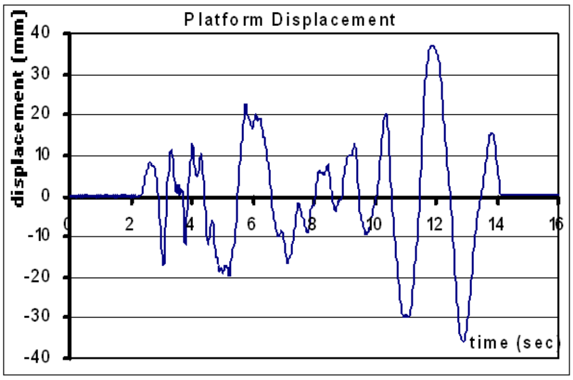

Fig. 12b. Displacement of the moving platform, Test 014, 14-1-2008

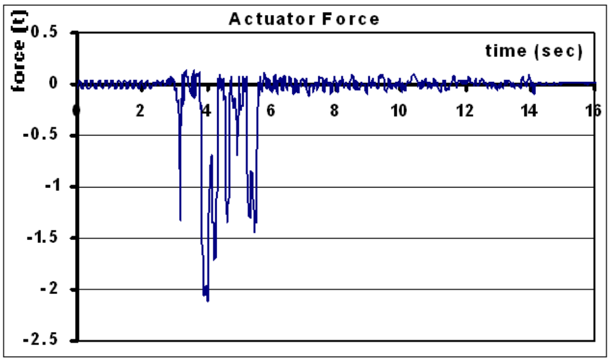

Fig. 12c. Force that was measured at the actuator

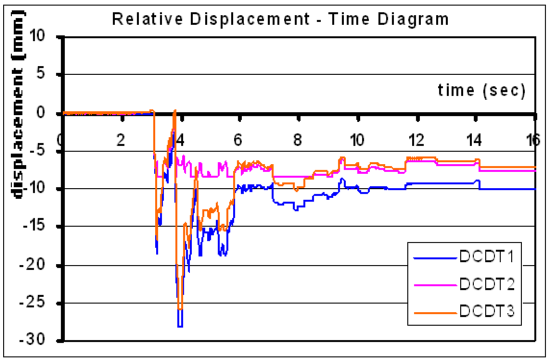

Fig. 12d. Sliding displacement of the rigid block relative to the moving platform

As before, the presented results include the acceleration response of the moving platform and of the sliding rigid block in figure 12a whereas the displacement of the moving platform and the spring is depicted in figures 12b and 12d, respectively. It can be seen that, due to sliding of the block without the spring link, the maximum rigid block acceleration response is much smaller than the maximum moving platform acceleration response (figure 12a). It is again interesting to note that in the absence of the spring link, the sliding displacement response of the rigid block develops relatively large values (30mm), as was also observed in section 3.4; moreover, there is again a cumulative sliding displacement that appears as an offset from the initial zero displacement condition. As mentioned in the previous section, this may be attributed to manufacturing tolerances whereby the contact surface between the rigid block and the moving platform deviates from the ideal horizontal plane. The sliding displacement response of the rigid block without the spring develops maximum sliding almost 30mm (figure 12d) which is twice as much as the sliding response of the rigid block linked to the moving platform with the certified spring and subjected to the simulated earthquake motion of HTaft0407.int (15mm, figure 10d, section 3.3).

4 NUMERICAL INVESTIGATION

The basic conditions, which are given below, are governing the sliding of the rigid body that is linked with a spring (K) and a damper (C) to a moving platform when it is subjected to horizontal $\ddot{U}(t)$ and vertical $\ddot{V}(t)$ acceleration. This represents the most general two dimensional rigid body sliding set-up [1], [2], [3], [4], [5].

Starting from an initial condition of no motion, in order for the rigid body to start sliding the platform acceleration $\ddot{U}(t)$ must exceed the value given by the following inequality (1)

$$\left|\ddot{U}(t)\right| > \mu_{st} \cdot g \cdot \left(1 + \frac{\ddot{V}(t)}{g}\right) \quad (1)$$

In this case, the rigid body acceleration will be given by the following relationship (2):

$$\ddot{X}(t) = \mu_d \cdot g \cdot \left(1 + \frac{\ddot{V}(t)}{g}\right) \cdot \left[\mathrm{sign}\left(\dot{U}(t) - \dot{X}(t)\right)\right] + \frac{K}{m} \cdot \left(U(t) - X(t)\right) + \frac{C}{m} \cdot \left(\dot{U}(t) - \dot{X}(t)\right) \quad (2)$$

When the rigid body is sliding it will be checked for reattachment to the moving platform by examining the absolute value of its relative velocity $\left|\dot{U}(t) - \dot{X}(t)\right|$, e.g. the relative velocity of the rigid body to the moving platform. If the value of the relative velocity becomes equal to zero and inequality (3) holds the rigid body will keep sliding.

$$\text{If } \left|\dot{U}(t) - \dot{X}(t)\right| = 0 \text{ and } \left|\ddot{U}(t) - \frac{K}{m} \cdot \left(U(t) - X(t)\right)\right| > \mu_{st} \cdot g \cdot \left(1 + \frac{\ddot{V}(t)}{g}\right) \quad (3)$$

If the value of the relative velocity becomes equal to zero and inequality (4) holds the rigid body is reattached to the moving platform

$$\text{If } \left|\dot{U}(t) - \dot{X}(t)\right| = 0 \text{ and } \left|\ddot{U}(t) - \frac{K}{m} \cdot \left(U(t) - X(t)\right)\right| \le \mu_{st} \cdot g \cdot \left(1 + \frac{\ddot{V}(t)}{g}\right) \quad (4)$$

The above conditions were included in a computer software (namely *block* and *blockr*) that used a time step-by-step integration procedure incorporating an iteration scheme to reach acceptable limits of convergence. In this step-by-step integration procedure the following simple relationships (5) and (6) were used for defining the velocity and displacement at a time t_i for the rigid body.

$$\dot{X}(t_i)=\dot{X}(t_{i-1})+\left(\ddot{X}(t_{i-1})+\ddot{X}(t_i)\right)\cdot\frac{\Delta t}{2} \tag{5}$$

$$X(t_i)=X(t_{i-1})+\left(\dot{X}(t_{i-1})+\dot{X}(t_i)\right)\cdot\frac{\Delta t}{2} \tag{6}$$

This computer software was next validated by numerically simulating the dynamic sliding response of the tested rigid block and by comparing the measured in the laboratory response, as briefly presented and discussed in sections 3.1. to 3.5 with the corresponding numerical predictions. In this numerical simulation all the important physical parameters of the problem at hand, such as the friction coefficients, the spring stiffness, the rigid body mass and the moving platform motion, were given as input to this computer software with values that were found from the laboratory measurements. The numerical results that describe the sliding response of the rigid block, obtained through this software, are next compared with the corresponding test results in the following sections 4.1. to 4.5.

4.1 Comparison of numerical predictions with the response measured during the test employing sinusoidal excitation 1.5Hz with non-certified spring (with pre-stress)

Figure 13a,b depicts a comparison of the predicted by the block software acceleration response of the rigid block with the corresponding measured response during this test when the moving platform is subjected to a sinusoidal motion of 1.5Hz. Apart from the platform motion that is input to the software the rest of the input parameters, are listed in figures 13a,b such as the static (μst) and dynamic coefficient (μd) of friction, the mass of the rigid block (M) and the stiffness of the spring.

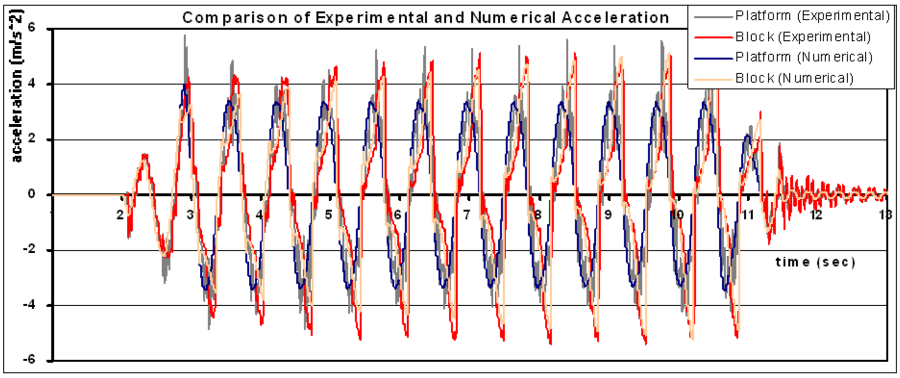

block (no-prestress)

Input parameters
μst= .32 , μd= .27
K (N/m)= 20500
M (kg)= 248
DtF (sec)= .005
Dt (sec)= .001
TIME (sec)= 14.995

Fig. 13a.

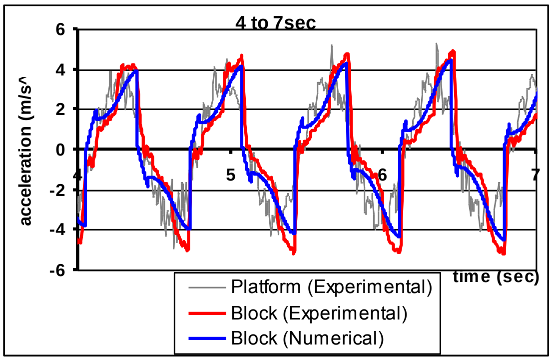

Fig. 13b block (no-prestress) K (N/m)= 20500

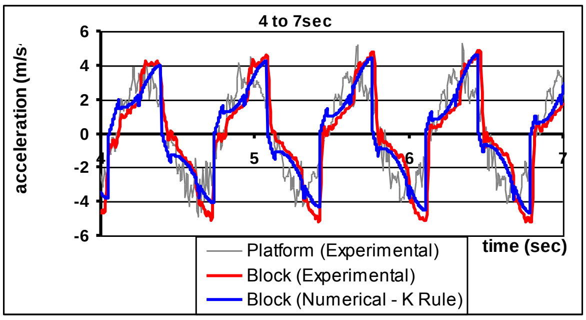

Fig. 13c blockr (pre-stress) K1 (N/m) = 58000
K2 (N/m) = 21500

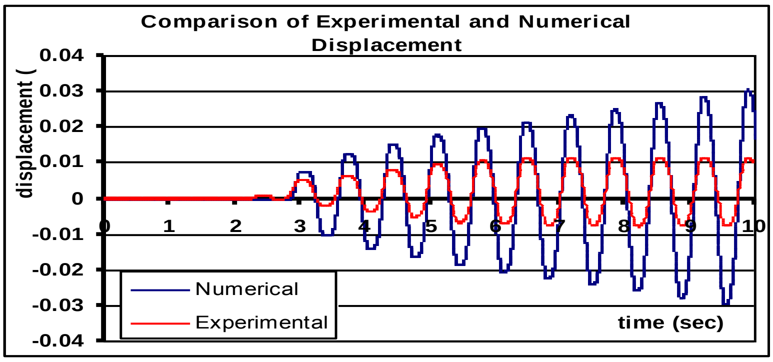

Figure 13d. Block sliding displacement response (Test 005 29-11-2007)

The stiffness of the spring is denoted as K when no pre-stress is present and K1/K2 when the spring is pre-stress and this is taken into account in the software (blockr). Figure 13a represents this measured and predicted rigid block acceleration response for the whole duration of the performed experiment whereas figure 13b and 13c represent time windows of this response between 4 and 7seconds of the total time history. For predicting the rigid block acceleration response the spring pre-stress was initially ignored (figure 13b) and then it was taken into account (figure 13c). In the same figure the measured acceleration of the moving platform is also plotted together with the input platform acceleration used by the software.

As can be seen in figure 13b a relatively good agreement is obtained between predicted and measured rigid block acceleration response which is further improved when the spring pre-stress is included in the software (figure 13c). In figure 13d, the predicted sliding displacement response of the rigid block is compared with the corresponding measured response for the same test. As can be seen, the predicted sliding displacement response is significantly larger than the one measured in the laboratory.

4.2 Comparison of numerical predictions with the response measured during the test employing sinusoidal excitation 3.5Hz with certified spring (no pre-stress)

The comparison between predicted and measured rigid block acceleration response is presented in figures 14a,b as was done in the previous section whereas the predicted rigid block sliding response is presented in figure 14c.

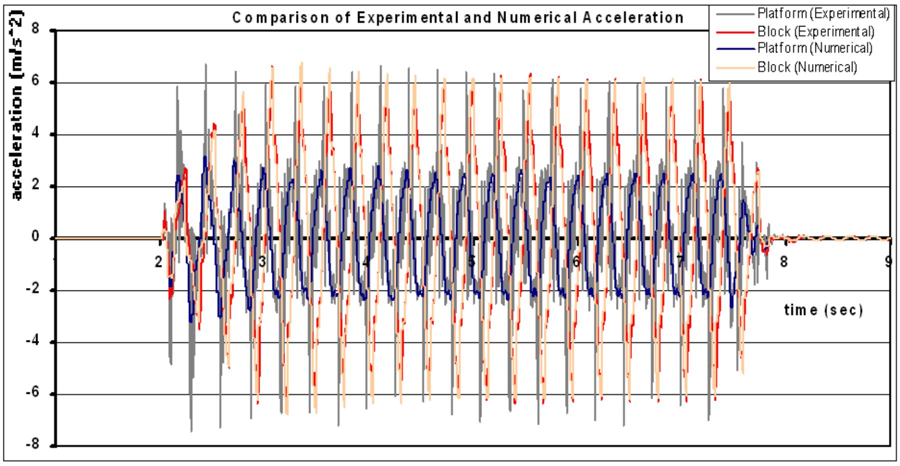

block (no-prestress)

Input parameters

μst= .15
μd= .145
K (N/m)= 100000
M (kg)= 248
DtF (sec)= .005
Dt (sec)= .0005
TIME (sec)= 10.005

Fig.14a. Acceleration response of moving platform and of the sliding rigid block (Test 011, 19-12-2007)

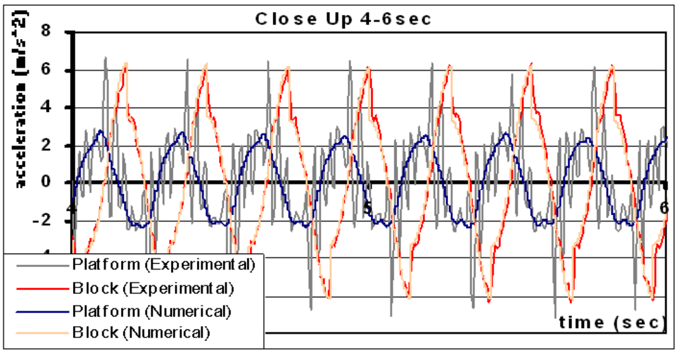

Fig. 14b Acceleration response of moving platform and of the sliding rigid block (Test 011, 19-12-2007)

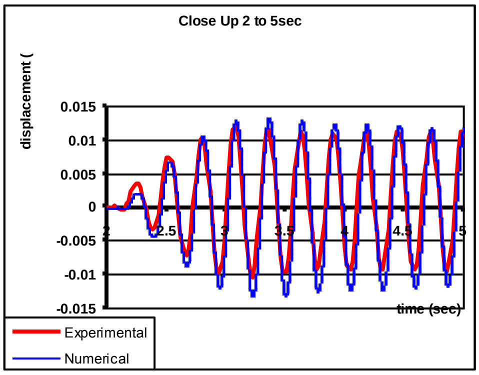

Figure 14c. Rigid block sliding displacement response (Test 011, 19-12-2007)

As can be seen in figures 14a,b good agreement is obtained between predicted and measured rigid block acceleration response. In figure 14c, the predicted sliding displacement response of the rigid block is compared with the corresponding measured response for the same test. As can be seen, this time very good agreement is obtained between the predicted rigid block sliding displacement response and the one measured in the laboratory.

4.3 Comparison of numerical predictions with the response measured during the test employing simulated earthquake excitation with non-certified spring (with pre-stress)

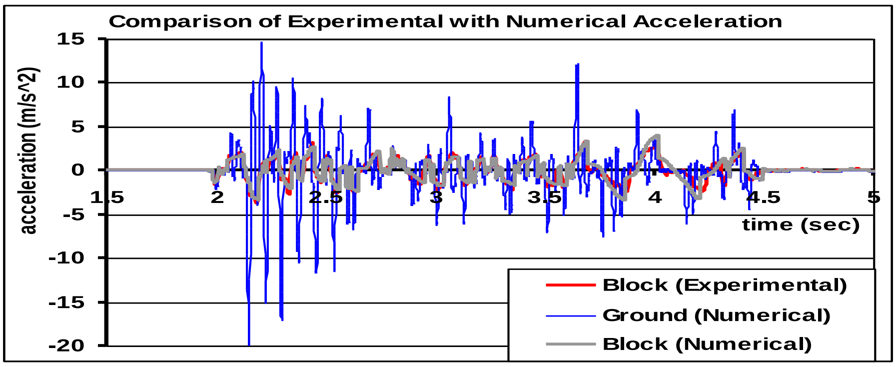

Input parameters

μst= .15

μd= .13

K (N/m)= 123000

M (kg)= 248

DtF (sec)= .005

Dt (sec)= .001

TIME (sec)= 5.495

Fig. 15a. Acceleration response of moving platform and of the sliding rigid block (Test 002, 21-12-2007)

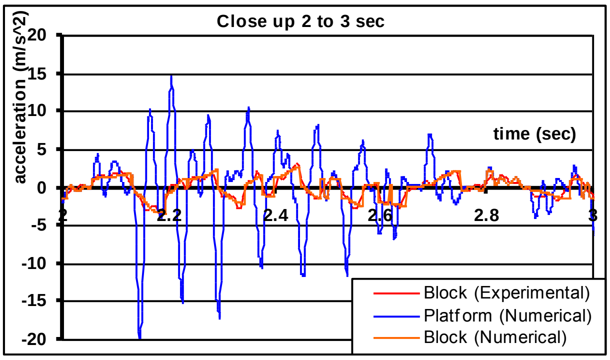

Fig. 15b. Acceleration response of moving platform and of the sliding rigid block (Test 002, 21-12-2007)

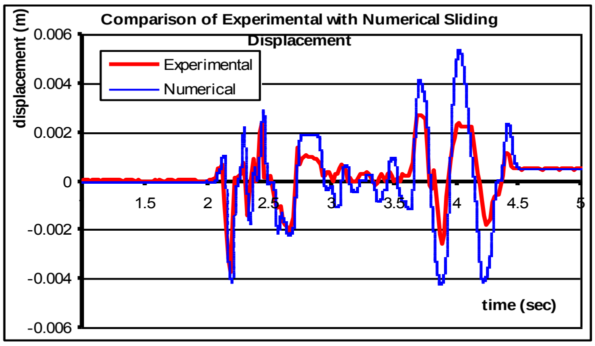

Fig. 15c. Sliding displacement response of rigid block (Test 002, 21-12-2007)

The comparison between predicted and measured rigid block acceleration response is presented in figures 15a,b as was done in the previous sections, whereas the predicted rigid block sliding displacement response is presented in figure 15c. The rigid block is linked to the moving platform with the non-certified spring (with pre-stress). This time the excitation is a simulated earthquake motion (see section 3.3). As can be seen, good agreement is obtained between predicted and measured rigid block acceleration response. The predicted rigid block sliding displacement response correlates reasonably well with the one measured in the laboratory in the time domain. However, the predicted sliding displacement response, in terms of amplitude, is significantly larger than the one measured in the laboratory.

The measured response is again compared with the one predicted by the software in figures 16a,b,c for a simulated earthquake test (Test 004, 21-12-2007), which is more intense than the one used before (Test 002, 21-12-2007). This time, the good agreement between observed and predicted rigid block response can be seen for both the acceleration (figures16a,b) as well as the sliding displacement response (figure 16c)

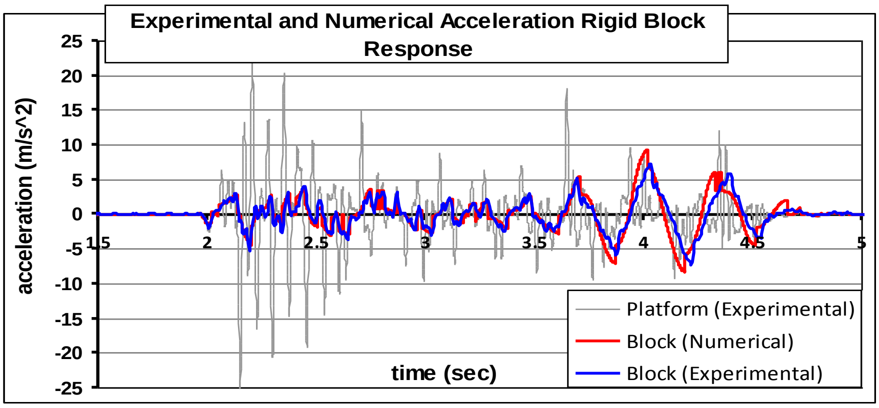

Input parameters
μst= .15
μd= .13
K (N/m)= 120000
M (kg)= 248
DtF (sec)= .005
Dt (sec)= .001
TIME (sec)= 5.995

Fig. 16a. Acceleration response of moving platform and of the sliding rigid block (Test 004, 21-12-2007

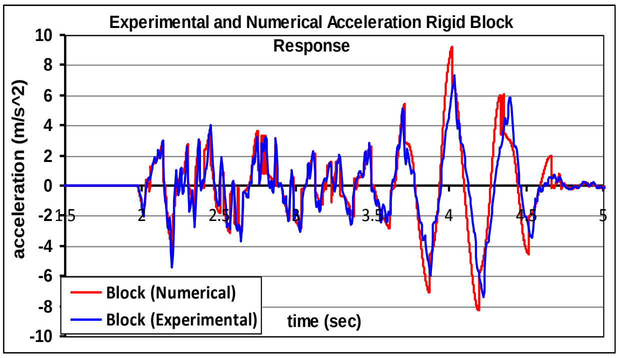

Fig. 16b. Acceleration response of moving platform and of the sliding rigid block (Test 004, 21-12-2007)

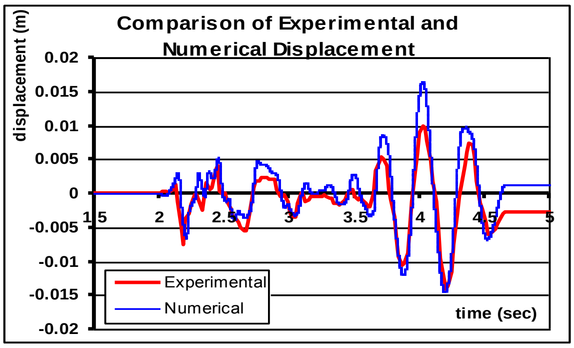

Fig. 16c. Sliding displacement response of rigid block (Test 004, 21-12-2007)

4.4 Comparison of numerical and measured response during the test employing Sinusoidal excitation 1.5Hz without spring

The comparison between predicted and measured rigid block acceleration response is presented in figures 17a,b as was done in the previous sections whereas the predicted rigid block sliding response is presented in figure 17c. The rigid block is resting this time to the moving platform without any spring link attachment, which was used in the previous sections (4.1 to 4.3). The excitation of the moving platform is initially sinusoidal 1.5Hz. As can be seen, good agreement is obtained between predicted and measured rigid block acceleration response. The predicted rigid block sliding displacement response correlates reasonably well with the one measured in the laboratory in the time domain. However, the predicted sliding displacement response, in terms of amplitude, is significantly larger than the one measured in the laboratory. It is interesting to note that the cumulative sliding displacement, which appears as an offset from the initial zero displacement condition in the measurements, is not predicted by the software. This partly confirms the explanation given in section 3.4. that this measured cumulative (offset) sliding displacement response may be attributed to manufacturing tolerances whereby the contact surface between the rigid block and the moving platform deviates from the ideal horizontal plane.

.

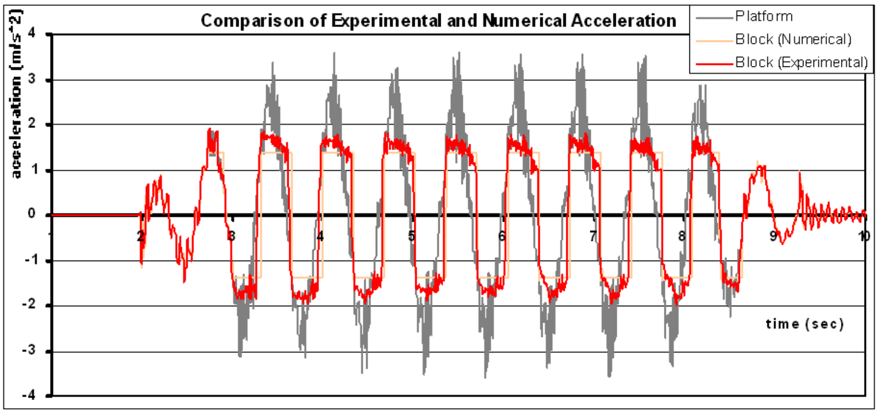

Input parameters
μst= .15
μd= .14
K (N/m)= 0
M (kg)= 248
DtF (sec)= .005
Dt (sec)= .001
TIME (sec)= 10.845

Fig. 17a. Acceleration response of moving platform and of the sliding rigid block (Test 005, 14-1-2008)

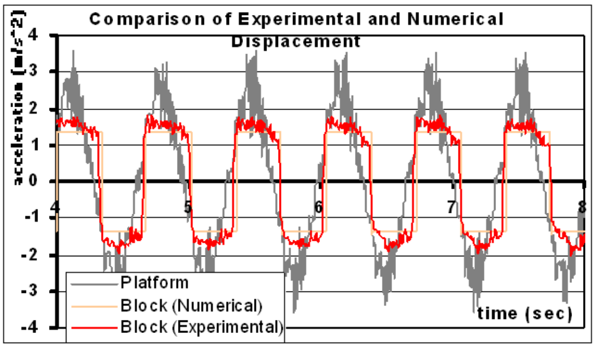

Fig. 17b. Acceleration response of moving platform and of the sliding rigid block (Test 005, 14-1-2008)

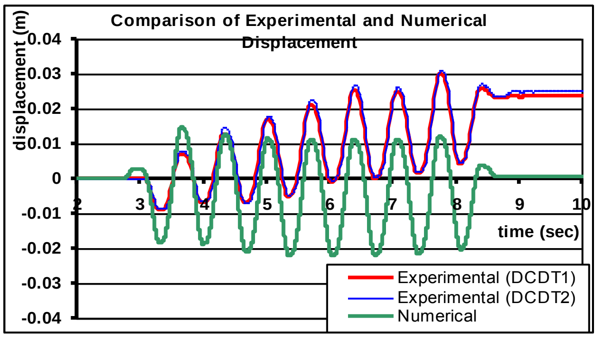

Fig. 17c. Sliding displacement response of rigid block (Test 005, 14-1-2008)

4.5 Comparison of numerical predictions with the response measured during the test employing simulated earthquake excitation without spring

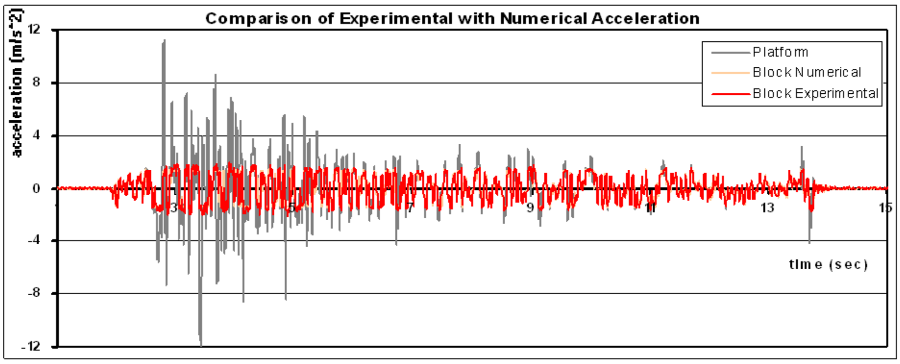

Input parameters
μst= .15
μd= .14
K (N/m)= 0
M (kg)= 248
DtF (sec)= .005
Dt (sec)= .001
TIME (sec)= 15.725

Fig. 18a. Acceleration response of moving platform and of the sliding rigid block (Test 014, 14-1-2008

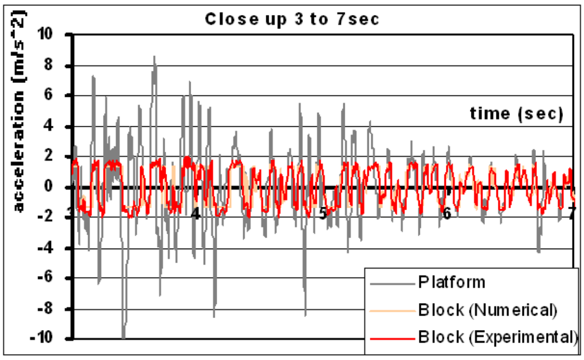

Fig. 18b. Acceleration response of moving platform and of the sliding rigid block (Test 014, 14-1-2008)

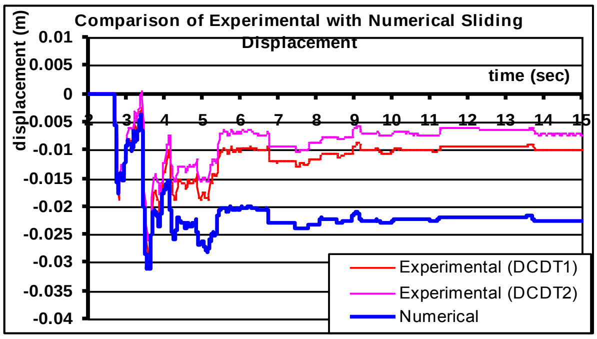

Fig. 18c. Sliding displacement response of rigid block (Test 014, 14-1-2008)

The comparison between predicted and measured rigid block acceleration response is presented in figures 18a,b as was done in the previous sections whereas the predicted rigid block sliding response is presented in figure 18c. The rigid block is resting, as in section 4.4., to the moving platform without any link employing any spring attachment; however, this time a simulated earthquake excitation is used. As can be seen, good agreement is obtained between predicted and measured rigid block acceleration response. The predicted rigid block sliding displacement response correlates reasonably well with the one measured in the laboratory in the time domain as well as in terms of maximum amplitude. It is again interesting to note that, there is a cumulative sliding displacement that appears as an offset from the initial zero displacement condition in the predicted response that is much larger than the one observed during the experiment. This observation contradicts the explanation, which was given before in section 4.4., that this measured cumulative (offset) sliding displacement response may be attributed to manufacturing tolerances whereby the contact surface between the rigid block and the moving platform deviates from the ideal horizontal plane. As an alternative explanation, these differences between predicted and measured rigid block cumulative (offset) sliding displacements may also be attributed to the integration scheme which was used by the computer software. This alternative explanation needs verification.

In figure 19, the ratio of the acceleration response spectral values based on the rigid block acceleration response over the corresponding acceleration spectral values based on the platform acceleration is plotted in the period range from 0 to 2 seconds. This is done for test 14 (14-1-2008) whereby the rigid block was subjected to a simulated earthquake motion, as is shown in figures 19a,b,c. The relevant spectral ratio values are for 5% damping and correspond to both the predicted and the observed block acceleration response.

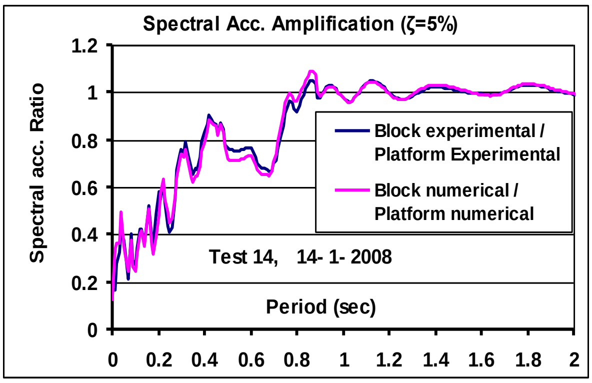

Figure 19. Ratio of response spectral values

As can be seen in this figure, these response spectral ratio values are, as expected, smaller than 1, which indicates the influence of sliding in reducing the rigid block acceleration response, as means of seismic isolation.

4.6 Comparison of numerical predictions with the response measured during a sweep test in the frequency domain.

In this section, a final comparison is performed between measured and predicted rigid block acceleration response. The developed software is utilized to perform a series of numerical solutions whereby the same rigid block with the same mass, spring stiffness and friction coefficients is used by subjecting it to a series of distinct sinusoidal excitations of the moving platform keeping the peak acceleration amplitude constant but varying the frequency of the excitation (numerical sweep test). The ratio of the maximum rigid block acceleration response over the peak acceleration of the moving platform from each numerical solution is plotted in figure 20 against the frequency of the corresponding excitation. This is done simulating three distinct physical problems representing the following:

- The tested during the experimental sequence rigid block with the certified spring (μst= 0.15 μd=0.14, M=248kg, K=100000N/m no pre-stress) , presented in sections 3.1. to 3.5.
- The tested during the experimental sequence rigid block with the certified spring (μst= 0.15 μd=0.14, K=20000N/m no pre-stress), presented in sections 3.1. to 3.5.
- The tested during the experimental sequence rigid block with the certified spring (μst= 0.15 μd=0.14, K=2000N/m no pre-stress) , presented in sections 3.1. to 3.5. This simulates a case whereby the spring link between the rigid block and the moving platform is very flexible, towards approximating a case whereby there is no spring link.

The resulting numerical values are plotted in figure 20 with solid lines whereas the corresponding experimental values are also plotted in the same figure with the dotted lines that connect the measured values (squares) at distinct frequencies during specific experiments. The following observations can be made based on the results presented in this figure.

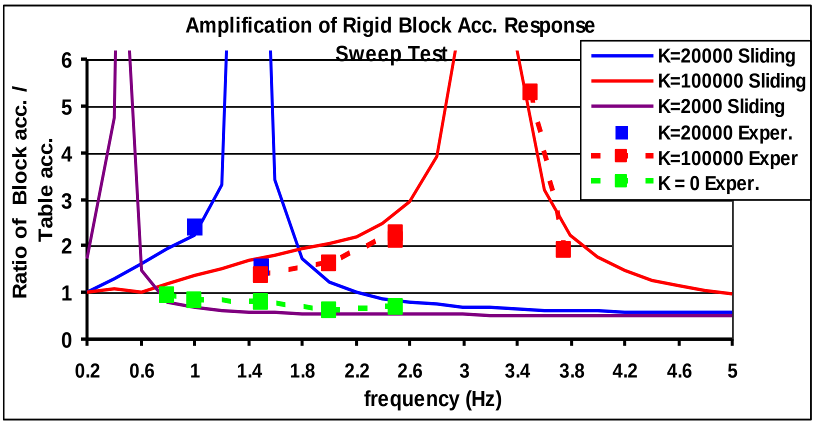

Figure 20. Comparison of measured and predicted rigid body acceleration response

a. As expected, the presence of the spring introduces an amplification in the rigid block acceleration response with amplification ratio values less than two (2), except when the frequency of the excitation is close to the resonant frequency of the spring-block dynamic system. It must be pointed out that in the examined cases apart from the friction there is absence of any other damping mechanism; moreover, the friction coefficients were measured to have relatively small values (section 2.1). The absence of any other damping mechanism apart from the friction, with small values of the coefficients of friction, can also explain the large amplification values when the excitation frequency becomes close to the resonant frequency [1].

b. When, the value of the spring stiffness is relatively small, the amplification of the rigid body acceleration response is smaller than one (<1) in the frequency range of many practical applications in the seismic design.(for frequencies larger than 0.5Hz, or for periods smaller than 2 seconds), thus introducing in this way the well known seismic isolation of such a rigid block, which is obtained by many such sliding devices.

c. The comparison between the measured results and the predicted values in this plot exhibit relatively good agreement, especially when this comparison is done in frequencies that are not close to the resonant frequency range.

d. In the tested case whereby there is no spring between the rigid block and the moving platform the response amplification value is smaller than one (<1) in a more extended frequency range.

5 CONCLUSIONS

1. An extensive experimental sequence has been performed studying the sliding response of a rigid block linked with a spring, having a wide variety of stiffness values, to a moving platform and being subjected to sinusoidal and simulated earthquake excitations. There was no other damping mechanism apart from the friction between sliding block and moving platform with relatively low values of the coefficient of friction. The experimental results have shown that when sliding of this rigid block is permitted then its peak acceleration response is moderately amplified, provided that the excitation frequency is not close to the resonant frequency range of the block-spring dynamic system. This is particularly true for earthquake excitations and for relatively flexible spring-links thus achieving in this way a type of seismic isolation for the rigid block.

2. This sliding response of the rigid block is accompanied by sliding displacements that can be of relatively large amplitude, when the stiffness of the spring that links the rigid block with the moving platform is relatively low. This sliding displacement response is accompanied by a cumulative sliding displacement, which may result in a permanent sliding displacement of considerable amplitude at the end of the excitation. The amplitude of the sliding displacement response decreases with the increase of the spring stiffness, when the excitation is not close to the resonant frequency of the spring-block dynamic system.

3. A computer software was developed in order to predict this rigid block sliding response. The numerical predictions were validated by comparing them to a large number of experimental measurements. As can be seen from this comparison, the numerical predictions confirm all the behavioral observations of the studied phenomenon, as they were recorded during this extensive experimental sequence.

4. The numerically predicted rigid block acceleration response is in good agreement with the measured values for all examined cases of spring stiffness and for both the sinusoidal as well as the simulated earthquake excitation of the moving platform.

5. The numerically predicted rigid block sliding displacement response exhibited in some cases good agreement with the measured values. However, in some other cases the deviation between predicted and measured rigid body sliding displacement response values were significant (of the order of 100%). It is interesting to note the cumulative sliding displacements that appear as an offset from the initial zero displacement condition; this is successfully reproduced by the predicted response only in some cases. Possible explanations that are given for this are manufacturing tolerances, whereby the contact surface between the rigid block and

the moving platform deviates from the ideal horizontal plane, as well as the integration scheme that is included in the computer software.

6. Despite the limitations of the predicted results it is believed that the developed software, although it deals with a complex problem in a relatively simple way, it can be useful in the preliminary design stages of structural systems with the sliding capability at their support.

REFERENCES

[1] Anil K. Chopra, "Dynamics of Structures: Theory and Applications to Earthquake Engineering", 2006

[2] M. Aslam et al. (1975), Sliding response of rigid bodies to earthquake motions, Rep. No. LBL-368, Lawrence Berkeley Laboratory, University of California.

[3] B. Westermo and F. Udwadia, (1983), Periodic response of sliding oscillator system to harmonic excitation, Earth. Engin. and Str. Dyn., 11, pp.135-146.

[4] C.J. Younis and I.G. Tadjbakhsh, (1984), Response of sliding rigid structure to base excitation, J. of eng. Mech., ASCE 110, pp. 417-432.

[5] H. W. Shenton and N. P. Jones (1991), Base excitation of rigid bodies, I: Formulation, J. of Eng. Mechanics, ASCE, 117(10), pp. 2286-2306.

[6] M. Demosthenous, (1994), Experimental and numerical study of the dynamic response of solid or sliced rigid bodies, Ph. D. Thesis, Dept. of Civil Engineering, Aristotle University of Thessaloniki, Greece.

[7] G.C. Manos and M. Demosthenous, (1990), The behavior of solid or sliced rigid bodies when subjected to horizontal base motions, Proc. of 4th U.S. National Confer. on Earthquake Engineering, Vol. 3, pp41-50.

[8] G.C. Manos and M. Demosthenous, (1993), Dynamic Response of Sliced Rigid Bodies Subjected to Harmonic Base Excitations, SMIRT-12, Vol. K1, K11/3, pp. 313-318.

[9] G. C. Manos et al. (2000), Study of the dynamic and earthquake behavior of models of ancient columns and colonnades with and without the inclusion of wires with energy dissipation characteristics", presented at the 12th WCEE, Auckland, New Zealand.

COMPDYN 2011
III ECCOMAS Thematic Conference on
Computational Methods in Structural Dynamics and Earthquake Engineering
M. Papadrakakis, M. Fragiadakis, V. Plevris (eds.)
Corfu, Greece, 25–28 May 2011

THE EFFECT OF INFILL WALL ON SEISMIC PERFORMANCE OF DEFICIENT RC STRUCTURES

U. Akpınar[1], R. Ozcelik[2], B. Binici[3]

[1] Middle East Technical University
Middle East Technical University, Department of Civil Engineering, Turkey
augur@metu.edu.tr

[2] Middle East Technical University
Middle East Technical University, Department of Civil Engineering, Turkey
rozcelik@metu.edu.tr

[3] Middle East Technical University
Middle East Technical University, Department of Civil Engineering, Turkey
binici@metu.edu.tr

Keywords: Infill Walls, RC Frames, Nonlinear Time History Analyses.

Abstract. *This study investigates the possible adverse effects of the infill walls on the seismic response of the deficient reinforced concrete structures. It is shown herein that neglecting the presence of infill walls may not always a safe design approach. First the modeling approach is verified against available pseudo dynamic test results. Afterwards, the response of a 4-story 3-bay RC frame was examined with and without infill wall schemes. 7.14 magnitudes 1999 Duzce Earthquake was applied as the ground motion record in the nonlinear time history analyses. In order to simulate failure of infill walls accurately, element removal algorithm was employed in the middle bay of RC frame with strut and tie model. Analysis results indicated that, including infill walls with element removal algorithm led unsafe results in terms of inter-story drift ratio in first story and rotations at the critical plastic hinge location. As a result, neglecting infill wall contribution to the lateral stiffness and strength is not always a conservative design approach.*

1 INTRODUCTION

Numerical simulations have been playing an important role on both design and assessment processes of the building structures. Infill walls are usually neglected in numerical approaches due to their limited effects on the lateral strength and stiffness of the system. Including infill walls also increases the complexity of the nonlinear numerical models which is not desired for time history analyses. There are several studies that investigate the lateral load resisting systems consisting unreinforced infill members. Behavior of masonry-infilled non-ductile reinforced concrete frames was studied in several studies [1]. [2] developed a three-strut model for concrete masonry-infilled steel frames. [3] performed one-story and five story structural systems that have deficient columns and infill walls with unreinforced masonry. An analytical formulation that implements automated removal of collapsed elements during an on-going simulation was proposed [3].

This study deals with numerical simulation of RC frames with infill walls by employing strut and tie model and element removal algorithm. First, validation of the proposed algorithm is presented by comparing simulation results with pseudo dynamic test results. Afterwards, a case study is presented to demonstrate the expected effects of including infill walls and their failure.

2 NUMERICAL VALIDATION

2.1 TEST FRAME

In order to gain confidence on the applied simulation algorithm simulation technique that will be described later in the paper, results were validated against recently obtained pseudo dynamic test data. A two story-three bay RC frame was constructed and tested in that study. Figure 1 indicates the frame dimensions and test setup. This RC frame was tested by utilizing pseudo dynamic test procedures. The details of the test frame and test results are available in elsewhere [4].

The north-south component of the 1999 Duzce earthquake as seen in Figure 2 was used for the pseudo dynamic test. This figure also shows the spectral acceleration vs. time plot of the Duzce earthquake and spectrum defined in Turkish Earthquake Code (TEC 2007) [5] and the fundamental period the analyzed frames. It can be observed that spectrum of the Duzce ground motion is expected to cause more demand in the constant acceleration region while being relatively close to the code specified spectrum.

2.2 NUMERICAL MODELING

Nonlinear time history analysis (NTHS) of test structure were performed by utilizing Opensees Simulation Platform [6] to observe the ability of estimating the dynamic response of a analyzed frame. Although general modeling approach of the test frame was mentioned in this study, compressive data about test frame and test data are available in elsewhere [4].

In order to compare the effect of infill walls on analyzed frame two NTHAs were conducted; frame with and without infill walls. Bare frame analysis was conducted without adding any new structural component to the system. On the other hand, frame with infill wall was analyzed with the diagonal strut model with the element removal algorithm. It was assumed that infill wall had a width of 150 mm (110 mm brick, 40 mm mortar). Compressive strength of the mortar was taken as 14 MPa.

Force based fiber frame elements were used to model beams and columns. The material model used for concrete (Concrete01) follows the rules of the confined and unconfined concrete models proposed by [7] with plastic offset rules [8]. Due to welding of longitudinal reinforcements to the foundation in the column ends, bond-slip was not observed at test frame. Hence, reinforcing steel was modeled using a bilinear elasto-plastic model (Steel 02) with a kinematic hardening slope of 1%. The infill walls were modeled using compression only truss elements connected to the diagonal nodes of the boundary frame.

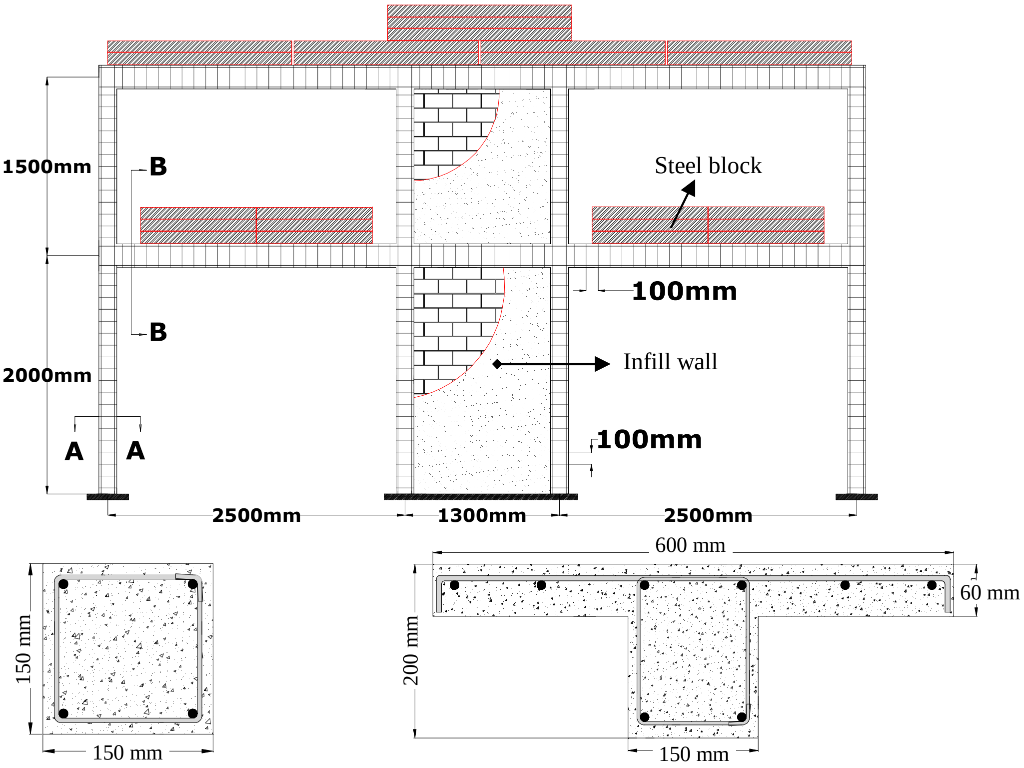

A-A Section
Longitudinal Reinforcement; 4ϕ8
Transverse Reinforcement; ϕ4/100 mm

B-B Section
Longitudinal Reinforcement; 4ϕ8
Transverse Reinforcement; ϕ4/100 mm

Figure 1: Test frame and setup (adopted by [4])

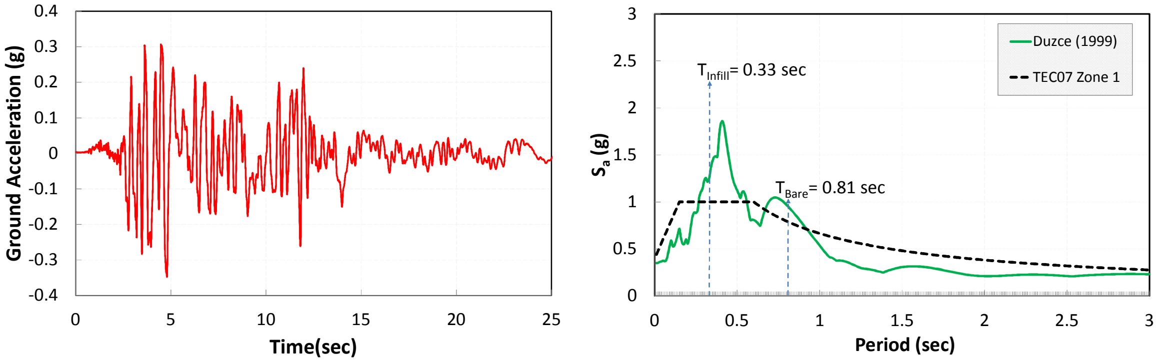

Figure 2: Duzce ground motion and spectrum

Frame	Concrete Compressive Strength (Mpa)	Longitudinal Reinforcement Yield Strength (MPa)	Transverse Reinforcement Yield Strength (MPa)
Analized Frame	9.0	220	220
Test Frame	7.4	330	290

Table 1: Mechanical properties of the materials.

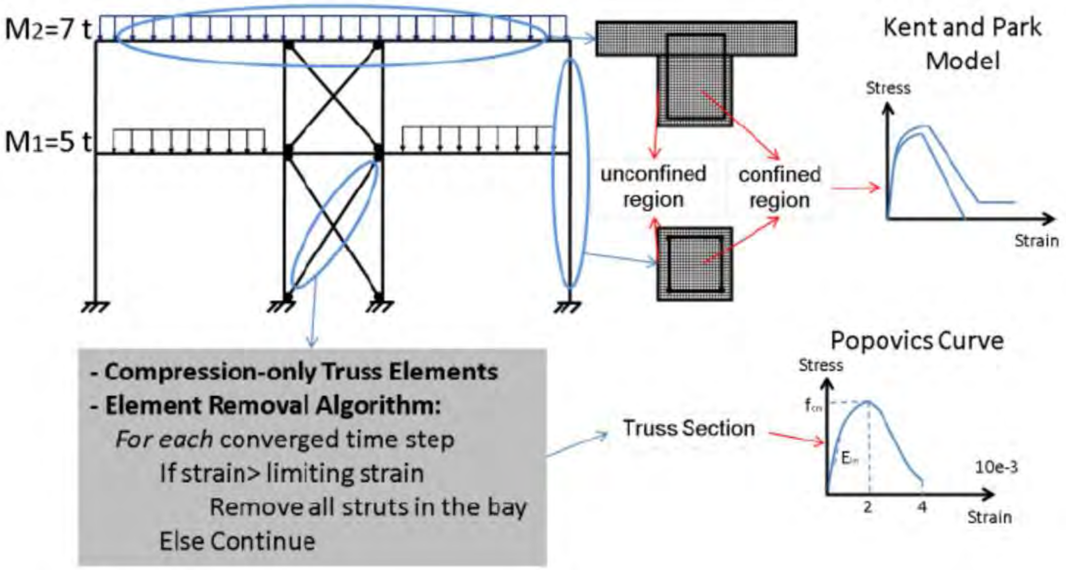

Figure 3: Infill wall layout and analytical model of the test frame.

The material properties and relevant equations from ASCE/SEI-41 guidelines [9] were employed. In this way it was possible to observe the success of estimating the natural period of the test structure with these stiffness values. Effective strut area for the infill walls was calculated according to ASCE/SEI-41 guidelines and found as 0.025 and 0.021 m^2 for the first and second stories using the following equations:

$$a = 0.175(\lambda_1 \times h_{col})^{-0.4} r_{\inf} \tag{1}$$

$$\lambda_1 = \left[\frac{E_{ms}(t_{in} + t_p)\sin 2\theta}{4E_c I_c h_{in}} \right]^{1/4} \tag{2}$$

Above, h_{col} is the column height, r_{inf} is the diagonal length of infill panel, θ is the angle whose tangent is the infill height to length ratio, E_c and E_{ms} are the modulus of elasticity of concrete and the plaster-infill composite and t_{in} and t_p are the thicknesses of brick units and the plaster. The modulus of elasticity of the plaster-brick composite, E_{sm}, was computed as 10000 MPa from Binici and Ozcebe 2006 [10]:

$$E_{ms} = \frac{E_{in}t_{in} + E_m t_p}{t_{st}} \tag{3}$$

where E_{in} and E_m are the modulus of elasticity of the infill wall and mortar/plaster, and t_{in} and t_m are the thickness of the infill wall and mortar. Accordingly, E_{in} was taken as 7700MPa ($550F_m$) based on ASCE/SEI-41 recommendations and t_u was calculated as 16200 MPa ($4700\sqrt{F_c}$) using ACI 318-05 [11] equation.

The observations made during the test showed that diagonal cracks formed in the central region of the infill in both directions. Later these cracks extended in a step pattern indicating the failure of bed joints along the diagonal. Consequently, compressive strength of the strut (F_{cm}) was computed from ASCE/SEI-41 assuming that bed-joint shear strength governs the strength of the diagonal strut either in the form of a diagonal crack or a single horizontal bed joint by using equations:

$$V_{ss} = f_{mv}L\left(t_{in} + t_p\right) \tag{4}$$

$$f_{cm} = V_{ss}/\left(a\cos\theta\right) \tag{5}$$

in which V_{ss} is the total shear resistance along the wall length, L is the length of the infill wall, f_{mv} is the shear strength of bed mortar/plaster mix which was taken from ASCE/SEI-41 as 0.25 MPa for masonry in good condition. Popovics equation [12] was employed for the compressive stress-strain behavior of the infill struts (Concrete 04) as suggested by [13]. The strain at peak compressive strength and diagonal strut failure were taken as 0.002 and 0.004, respectively.

Although the infill diagonal strut fails in one direction in the numerical simulations, the strut in the opposite direction at the first story had still significant capacity and stiffness. Hence the frame could not deform in the opposite direction upon failure of only one diagonal strut. In order to overcome this modeling error, element removal algorithm as suggested by [3] was adopted. When the failure strain of the diagonal strut is exceeded in one direction, the struts in both directions are removed from the model. Upon element removal, internal forces were redistributed to achieve an equilibrium state at failure time. In this way, failure of the strut in one direction results in complete failure of the infill wall.

Nodes were constrained to act as rigid diaphragms for all stories. Lumped mass approach with a Rayleigh critical damping of 5% was utilized during the analyses by also incorporating the second order nonlinear geometric effects. The details of modeling and the properties of effective truss model are given in Figure 3. The NTHA results of the test frame indicate that the proposed model of the infill wall was able to capture the load deformation behavior (Figure 4) in a fairly accurate manner. It can be observed that inclusion of the element removal algorithm is necessary in order to capture the damage state of the test frame at the verge of collapse.

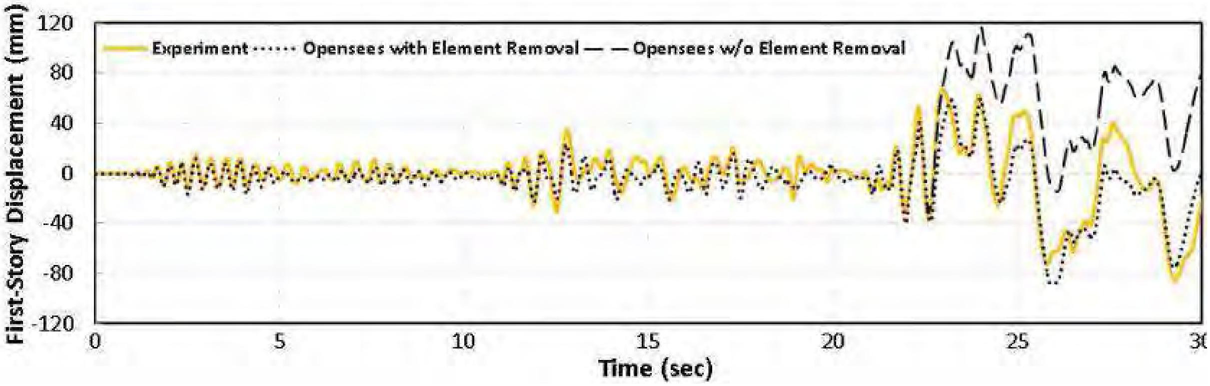

Figure 4: NTHA results of the test frame

3 CASE STUDY

3.1 FOUR STORY-THREE BAY RC FRAME

An exterior frame of a deficient existing 4-story RC building was analyzed with and without infill strut model to reflect the importance of infill modeling and element removal algorithm. The first floor plan view of this building is indicated in Figure 5. The evaluated 4-story 3-bay frame is given in Figure 5 where the complete details of the analyzed building are available elsewhere [14]. The frame had 250x400 mm columns which were oriented in their strong axis for B-axis and their weak axis for A, C and D-axes. All the beam dimensions were 150x500 mm. Interior bay of the frame (B-C axes) were used for installing infill walls as truss members. Table 1 indicates the mechanical properties of the materials. Accordingly, uniaxial compressive strength of the concrete was 9 MPa and the yield strength of reinforcing steel was 220 MPa. Stirrup spacing was 260 mm for beams and 280 mm for columns with a clear cover of 25 mm. Beams, columns and further structural details are given in Figure 5.

3.2 NUMERICAL MODEL OF FOUR STORY-THREE BAY RC FRAME

The modeling approach of the case study was similar to that of test frame. It was assumed that infill wall had a width of 150 mm (110 mm brick, 40 mm mortar) which is same as width of beams in analyzed structure. Effective strut area for the infill walls was calculated according to ASCE/SEI-41 guidelines and found as 0.042 m^2. Compressive strength of the mortar and the elastic section modulus of the infill wall were taken as 14 MPa and 10000 MPa, respectively. The analytical model is shown in Figure 6.

3.3 ANALYSIS RESULTS OF THE FOUR STORY-THREE BAY FRAME

The NTHA results of the frames with and without infill walls are presented in Figure 7. For the analysis of the test frame with infill walls, the element removal algorithm was incorporated. The structure excluding the presence of infill walls exhibited a peak first-story drift ratio (DR) of about 3.6%. However, the structure with infill walls experienced more than 8% DR upon automatically removing the wall struts from the system. Structure with infill walls suffered higher DRs than the structure without infill walls and finally it collapsed under the extreme first-story DR demands. Effect of soft-story formation could be seen more clearly in Figure 8.

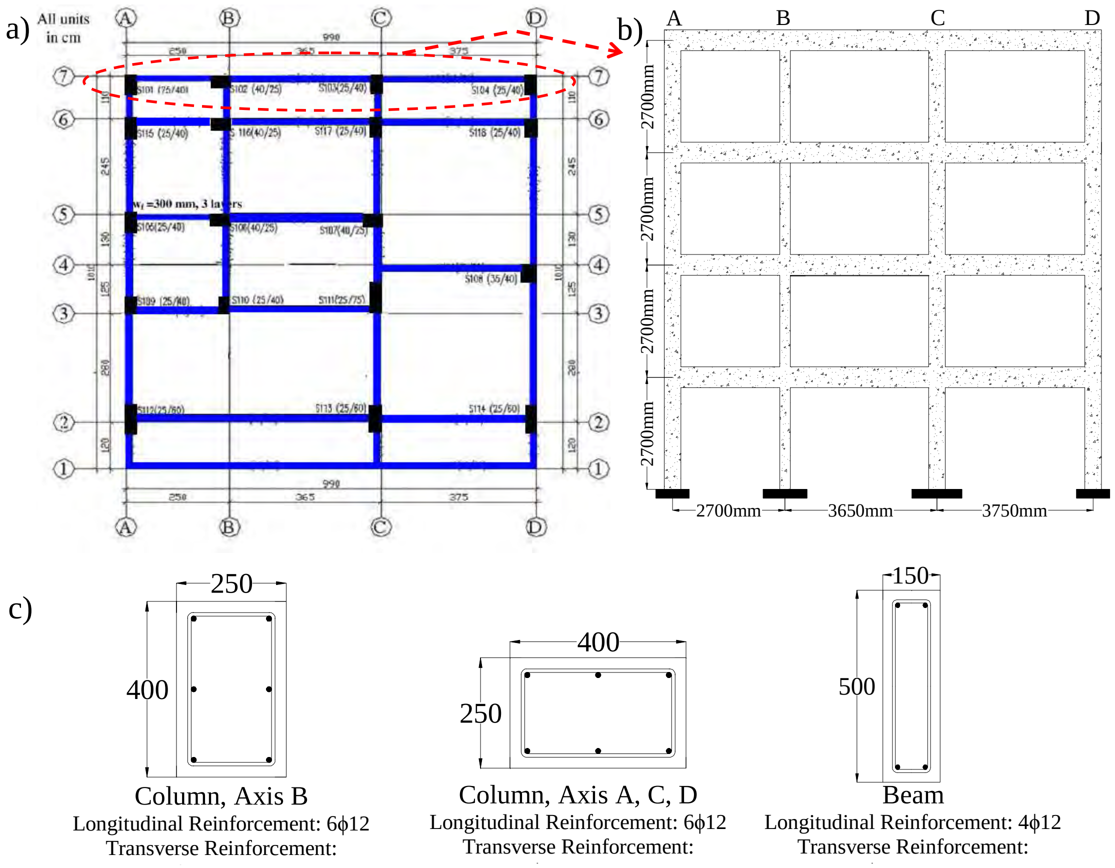

Column, Axis B
Longitudinal Reinforcement: 6ϕ12
Transverse Reinforcement:

Column, Axis A, C, D
Longitudinal Reinforcement: 6ϕ12
Transverse Reinforcement:

Beam
Longitudinal Reinforcement: 4ϕ12
Transverse Reinforcement:

Figure 5: a) Analyzed building floor view, b) Analyzed 4-story frame, c) Beam and column section.

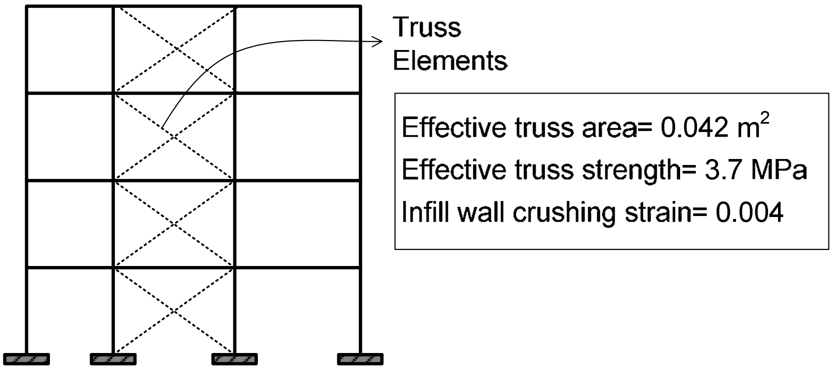

Figure 6: Infill wall layout and analytical model of the test and 4 story-3story frames.

According to results structure without infill walls satisfied inter story drift ratio (IDR) limits of TEC 2007 for the collapse prevention (CP) limit state and remained in the high damage region. Results reveal that neglecting infill walls for design purposes may not ensure designer to stay on the safe side for all the cases. The main difference between the results of two frames is the sudden collapse of the infill wall and change of dynamic properties of the test frame during the ground motion. The infill walls, although beneficial and control inter story drift deformations at low deformation demands, provide significant amplification of deformations (1st story in this example) when sudden collapse of the infill wall occurs. The estimation of deformations when infill walls are neglected may not necessarily be on the safe side for design purposes.

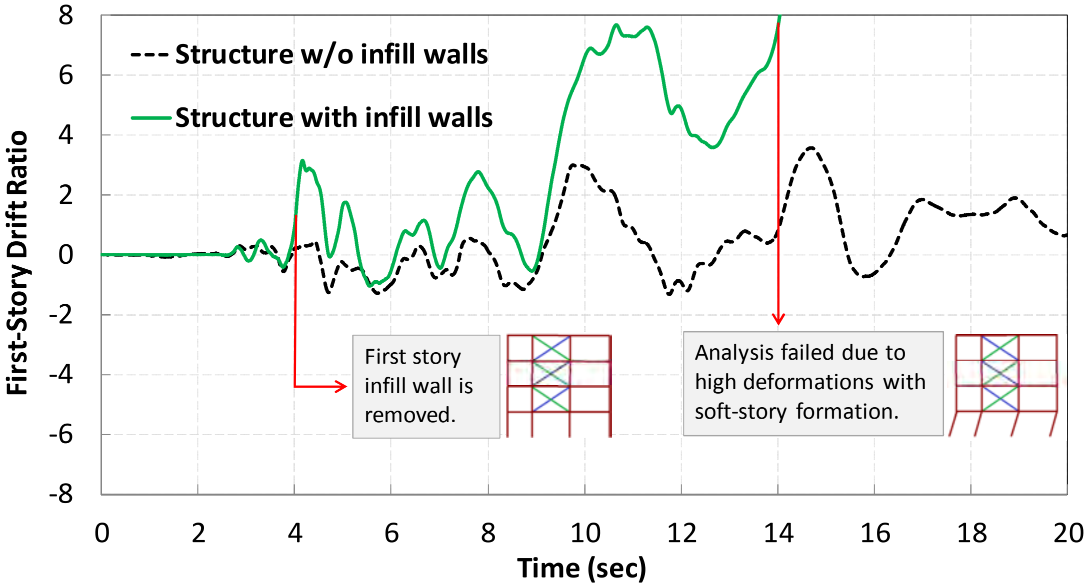

Figure 7: Comparison of simulation results with and w/o infill walls.

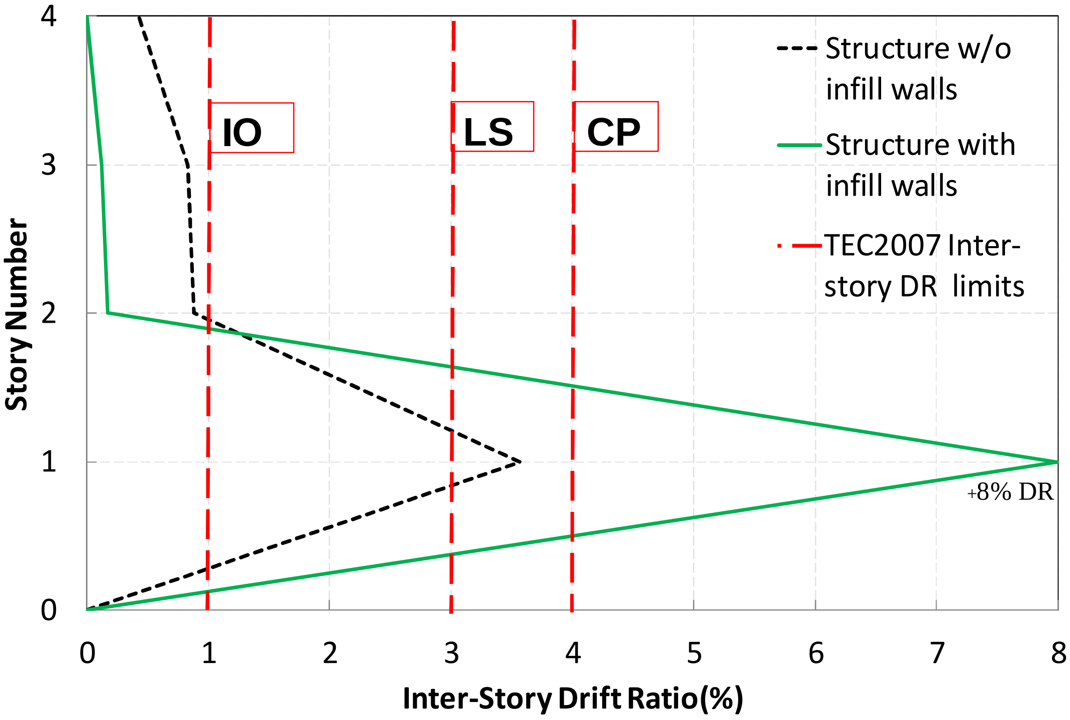

Figure 8: Comparison of inter-story DR with and w/o infill walls.

Base shear versus top story DR responses are given in Figure 9. Results show that incorporating infill walls to the system increased both the stiffness and the lateral load capacity of the frame significantly. However, after crushing of first story infill wall, this capacity dropped to the same level that was observed on the results of the bare frame. Therefore, capacity enhancement of infill walls to the system is not accountable at large deformation demands. The presence of an element removal algorithm clearly imposes more demand on the RC members than the case without the infill walls.

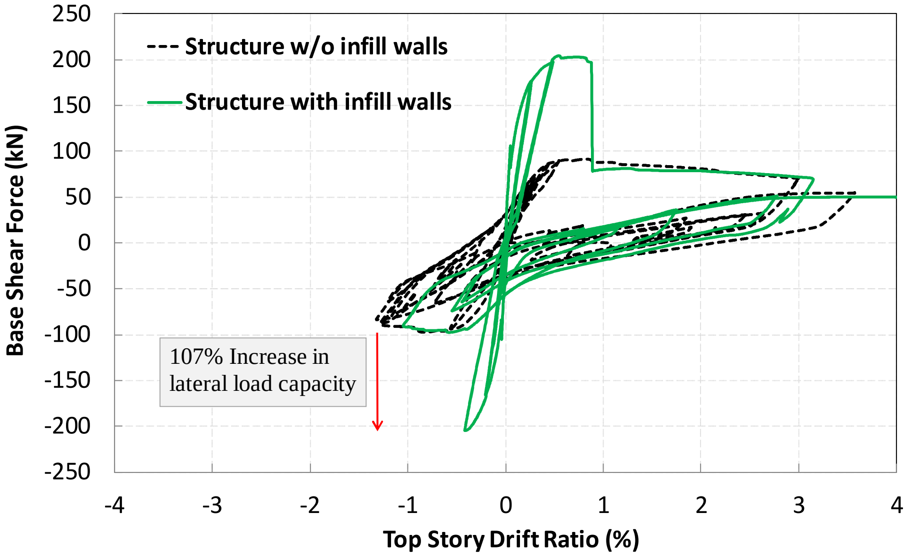

107% Increase in lateral load capacity

Figure 9: Base shear versus top-story DR with and w/o infill walls.

Performance evaluation of the both frames led to similar results for the first story (Figure 10). For the case without infill walls 75% of the columns passed beyond CP performance limit at first story. However, for the case with infill walls, all the first story columns of the test frame passed beyond CP performance limit as expected. Incorporating infill walls in the NTHA also changed the response on the upper stories. Frame without infill wall mainly experienced damage at the interior columns of first and second stories and exterior beams of first story. Violation of CP performance limit was observed for these beams. For the case with infill walls, formation of soft story oriented the distribution of damage to first story and prevented upper stories experiencing any significant damage. Both of the systems did not satisfy the overall performance criteria of TEC 2007 and found to be in collapse region.

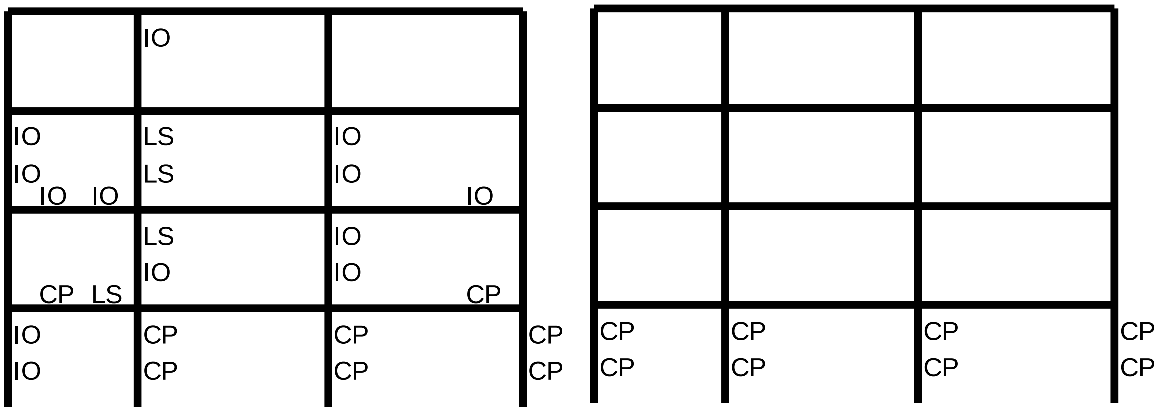

a) Without infill walls

b) With infill walls

Figure 10: Performance evaluation of RC frame members with and w/o infill walls.

4 CONCULUSIONS

For assessment purposes, contribution of infill walls may be included to have a better estimation of displacement demands. Results showed that ASCE-SEI-41 recommendations for strut modeling may lead to satisfactory estimation along with the use of element removal algorithm. The formation of a soft story mechanism was found to be better simulated with the use of such a removal algorithm. Performance evaluation of the 4 story-3 bay frame showed that after failure of the infill wall, all the first story columns passed the CP limit state and sustained heavy damage due to excessive IDR levels. As a result, for design purposes neglecting infill walls may not always lead to safe design or assessment results.

5 AKNOWLWEDGE

The research discussed in this paper was conducted at Middle East Technical University (METU)-Structural Mechanics Laboratory. Funding provided by TÜBİTAK (project no: 106M493) is greatly appreciated.

REFERENCES

[1] G. Al-Chaar, M. Issa, S. Sweeney, Behavior of Masonry-Infilled Nonductile Reinforced Concrete Frames,. Journal of Structural Engineering, 128, No. 8, 2002.

[2] W. El-Dakhakhni, F. M. Elgaaly and A. A. Hamid, Three-Strut Model for Concrete Masonry-Infilled Steel Frames. Journal of Structural Engineering, **129**, No. 2, 2003.

[3] K. Talaat, K.M. Mosalam, Modeling Progressive Collapse in Reinforced Concrete Buildings Using Direct Element Removal. Earthquake Engineering & Structural Dynamics, **38**(5), 609-634, 2009.

[4] E.G. Kurt, B. Binici, O. Kurc, E. Canbay, U. Akpinar and G. Ozcebe, Seismic Performance of a Reinforced Concrete Test Frame with Infill Walls, Earthquake Spectra, article in press, 2010.

[5] Turkish Code for Buildings in Seismic Zones (TEC 2007). Ministry of Public Works and Settlement Ankara, Turkey, (In Turkish), 2007.

[6] S. Mazzoni, H. McKenna, M.H. Scott, G.L. Fenves, OpenSees Manual. Pacific Earthquake Engineering Research Canter, http://opensees.berkeley.edu, 01/09/2010.

[7] D.C. Kent, R. Park, Flexural Members with Confined Concrete. Journal of Structures Division, ASCE, ST7, 97, 1969–1990, 1971

[8] I.D. Karsan, J.O. Jirsa, Behavior of Concrete under Compressive Loading. Journal of Structural Division, ASCE, ST12, 95, 2543-2563, 1969.

[9] American Society of Civil Engineers, “Seismic Rehabilitation of Existing Buildings, Report”, No. ASCE/SEI 41-06, Reston, Virginia, 428, 2007.

[10] Binici, B. Ozcebe, G, Analysis of infilled reinforced concrete frames strengthened with FRPs, Advances in Earthquake Engineering for Urban Risk Reduction, Editors Wasti, S.T. and Ozcebe, G. NATO Science Series, Earth and Env. Sciences, **66**, 455-471.

[11] American Concrete Institute (ACI 318-05), “Building Code Requirements for Structural Concrete and Commentary”, ACI Committee 318, 430 pp, 2005.

[12] S. Popovics, A Review of Stress–Strain Relationships for Concrete. American Concrete Institute Journal, 67(3) pp. 243–248, 1975.

[13] A. Madan, A.M. Reinhorn, J.B. Mandar, R.E. Valles, Modeling of Masonry Infill Panels for Structural Analysis. Journal of Structural Engineering, ASCE, **123** (10):1295-1302, 1997.

[14] Binici, B., Ozcebe, G. and Ozcelik, R, Analysis and design of FRP composites for seismic retrofit of infill walls in reinforced concrete frames. Composites Part B: Engineering, **38**(5), pp. 575-583.

COMPDYN 2011
III ECCOMAS Thematic Conference on
Computational Methods in Structural Dynamics and Earthquake Engineering
M. Papadrakakis, M. Fragiadakis, V. Plevris (eds.)
Corfu, Greece, 25–28 May 2011

1D SEISMIC RESPONSE OF SOIL: CONTINUOUSLY INHOMOGENEOUS VS EQUIVALENT HOMOGENEOUS SOIL

George E. Mylonakis[1], **Emmanouil Rovithis**[2], **Haralambos Parashakis**[3]

[1]Department of Civil Engineering, University of Patras
Rio, Greece, 26500
e-mail: mylo@upatras.gr

[2] Institute of Engineering Seismology and Earthquake Engineering (ITSAK)
Thessaloniki, Greece, 55102
rovithis@itsak.gr

[3] Department of Civil Works, Technological Educational Institute of Crete
Heraclion, Greece
parashaki_m@hotmail.com

Keywords: Seismic response, wave propagation, inhomogeneous soil, transfer function, equivalent homogeneous soil

Abstract. *Equivalent homogeneous soils are investigated as simplified approximations of continuously inhomogeneous soils. The examined system comprises of an inhomogeneous surface layer over a homogeneous one of higher stiffness. Five alternative definitions are adopted for the representative shear wave velocity (V_{hom}) in the inhomogeneous layer: (i) V_{hom1} at the base of the inhomogeneous layer (ii) V_{hom2} in the middle of the inhomogeneous layer (iii) V_{hom3} equal to the mean shear wave velocity within the inhomogeneous layer (iv) V_{hom4} providing equal travel time from base to surface between homogeneous and inhomogeneous soil and (v) V_{hom5} corresponding to an equivalent homogeneous soil having the same fundamental frequency as the inhomogeneous profile. Seismic response between inhomogeneous and equivalent homogeneous soils is compared by means of exact analytical solutions for single- and two-layer inhomogeneous soils. Fundamental frequencies and resonant peak amplitudes are examined, as affected by salient model parameters such as inhomogeneity factor, surface-to-base shear wave velocity ratio in the inhomogeneous layer, shear wave velocity contrast between the inhomogeneous and the homogeneous layer and relative layer thickness. It is observed that resonant frequencies of a smoothly-to-moderately inhomogeneous soil may be adequately captured by an equivalent homogeneous soil of either equal shear wave propagation velocity at the mid depth of the inhomogeneous layer, or of equal mean shear wave velocity within the whole layer. On the contrary, resonant amplitudes of a moderately-to-strongly inhomogeneous soil may be significantly underestimated or overestimated when an equivalent homogeneous soil is adopted, especially at higher resonances. The response of inhomogeneous soils with vanishing shear wave velocity near soil surface is explored.*

1 INTRODUCTION

Based on a detailed in-situ investigation of dynamic properties of soft deposits, Towhata [1] demonstrated analytically that shear wave propagation velocity may vary continuously with depth even for complex stratifications involving different soil materials. Utilizing a one-dimensional model of inhomogeneous soils with zero or finite stiffness at the surface, the above author showed analytically the possibility of higher amounts of seismic energy reaching the ground surface with respect to soils with discontinuous variation in shear modulus. Continuously inhomogeneous soils have been studied for different types of soil inhomogeneity or of seismic waves in multiple directions providing closed-form solutions for natural frequencies, modal shapes and amplification functions. Following the early work of Ambrasseys [2] and Seed and Idriss [3], Dobry et al.[4] studied the dynamic response of inhomogeneous soils with shear wave propagation velocity of the form $V_s=c\,z^{\,n}$, z being depth and n a positive inhomogeneity coefficient, corresponding to zero shear modulus at ground surface. A special case of the above equation, corresponding to $n = 2/3$, was adopted by Travasarou and Gazetas [5] as part of an investigation of seismic response of soft marine clay sediments verifying analytically that exceedingly large amplification of seismic motion may occur on the free surface. The effect of rate and type of heterogeneity on the seismic response of heterogeneous soils with shear wave velocity increasing from a non-zero value at the free surface has been examined by Ambraseys [2], Toki & Cherri [6], Schreyer [7] and Gazetas [8]. More recently, Parashakis [9] and Semblat and Pecker [10] extended the aforementioned models to obtain analytical solutions of the wave equation for a heterogeneous soil with shear wave velocity increasing with depth according to a generalized power law.

On the other hand, according to most modern seismic codes [11-13], site classification is based on the average shear wave propagation velocity within the top 30 metres (i.e. $V_{s,30}$) of the soil profile. The above regulations essentially refer to a homogeneous or inhomogeneous profile without strong gradients in shear wave propagation velocity with depth. However, in case of a moderately-to-strongly inhomogeneous soil, the choice of a pertinent, “representative” shear wave velocity is not straightforward especially when thick and soft soil deposits are encountered. In this case, conventional analyses based on discretizing soil in a multi-layer system with constant properties within each layer, may underestimate soil amplification with respect to the actual response of a continuously inhomogeneous medium, depending primarily on frequency content of input motion [1].

In light of the above considerations, “equivalent” homogenous soils are investigated as simplified approximations of continuously inhomogeneous soils. The investigation focuses on layered inhomogeneous soils as an extension of a previous research effort by the authors referring to single-layer systems [14]. The examined system comprises of a surficial inhomogeneous zone followed by a homogeneous layer on rigid base. A generalized parabolic function is adopted to describe the shear wave propagation velocity in the inhomogeneous layer, allowing modeling of inhomogeneous soils having vanishing values of shear modulus at ground surface. The problem is treated analytically by implementing closed-form solutions derived both for single- and two-layer inhomogeneous soil deposits in terms of base-to-surface transfer functions [9, 15, 16]. Seismic response between inhomogeneous and equivalent homogeneous soils is compared by means of fundamental frequencies and resonant amplitudes ratios, as affected by governing model parameters such as layer thickness, surface-to-base shear wave velocity ratio in the inhomogeneous layer, impedance contrast between surface and base layer and rate of inhomogeneity. The dependence of near-surface shear strains for inhomogeneous soils with very small surface-to-base shear wave velocity ratios is investigated by means of asymptotic analyses.

2 PROBLEM DEFINITION

A continuously inhomogeneous viscoelastic soil zone of thickness H over a rigid base (Fig.1a) is considered as a basis of the layered inhomogeneous soil examined. Soil mass density, ρ, and hysteretic damping ratio, ξ, are considered constant with depth. Shear wave propagation velocity is assumed to increase with depth according to the generalized power law function:

$$V_s(z) = V_H \left[b + (1-b)\frac{z}{H} \right]^n \tag{1}$$

where b is defined as a function of the shear wave velocity at the surface (V_o) and base (V_H) of the inhomogeneous soil layer [i.e. $b=(V_o/V_H)^{1/n}$], n is a dimensionless inhomogeneity factor varying in the common range of 0 to 1 ([9], [17], [18]) and z stands for the vertical coordinate (depth) measured from ground surface. For small values of the inhomogeneity factor n, Eq.1 simplifies to a uniform distribution while values of n close to unity correspond to linear increase in shear wave velocity with depth.

The single-layer system is extended to account for the presence of an underlying homogeneous layer of thickness (h_b) and shear wave propagation velocity (V_b) forming a generalized two-layer inhomogeneous soil with bounded shear wave velocity at large depths (Fig.1b). In this manner, a wide set of soil types can be modeled encompassing different soil properties between the inhomogeneous and the homogeneous layer.

Seismic response of layered inhomogeneous soils is compared to different equivalent homogenous cases. The latter are defined through a representative shear wave velocity V_{hom} in the inhomogeneous layer using the following definitions [14]:

- V_{hom1}, equal to the shear wave propagation velocity V_H at the base of the inhomogeneous layer:

$$V_{\mathrm{hom1}} = V_H \tag{2}$$

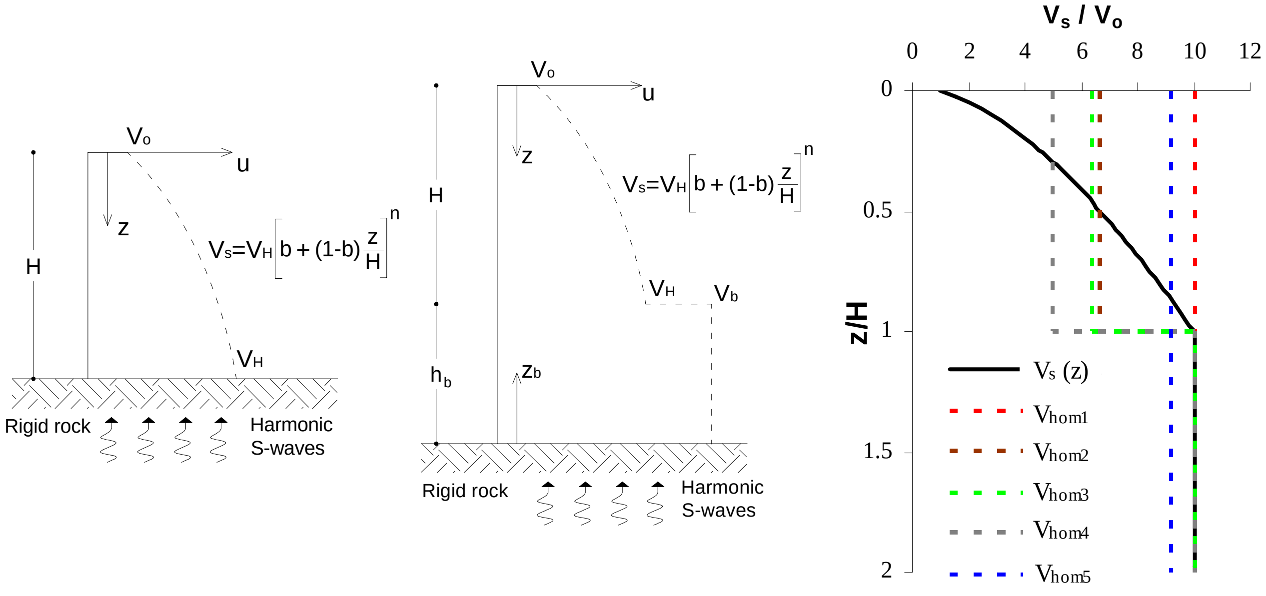

(a) (b) (c)

Figure 1. (a) Single inhomogeneous layer over rigid rock (b) Inhomogeneous surface layer over a homogeneous layer (c) Comparison of a two-layer inhomogeneous soil to the shear wave velocities of five equivalent homogeneous profiles ($V_o/V_H = 0.1$, $V_b/V_H=1$, $h_b/H=1$, $n=0.6$)

representing an always-stiffer soil with respect to the actual one

- V_{hom2}, equal to the shear wave propagation velocity at the mid depth of the inhomogeneous layer [8]:

$$V_{\mathrm{hom}2} = V_s(H/2) \tag{3}$$

pertaining to an elementary yet potentially useful solution.

- V_{hom3}, equal to the mean shear wave propagation velocity within the inhomogeneous layer:

$$V_{\mathrm{hom}3} = \frac{1}{H}\int_O^H V_s(z)dz \tag{4}$$

where $V_s(z)$ is given by Eq.1.

- V_{hom4}, providing equal base to surface travel times between homogeneous and inhomogeneous soil [19]

$$V_{\mathrm{hom}4} = H\left[\int_O^H \frac{1}{V_s(z)}dz\right]^{-1} \tag{5}$$

- V_{hom5}, corresponding to an equivalent homogeneous soil having the same fundamental frequency as the inhomogeneous profile

$$V_{\mathrm{hom}5} = f_{1In\,\mathrm{hom}} 4H \tag{6}$$

Alternatively, V_{hom5} may be viewed as the shear wave propagation velocity in the inhomogeneous soil corresponding to the "equivalent" depth (z_{eq}) proposed by Dobry et al. [20]. The two-layer equivalent homogeneous soils are compared to the inhomogeneous case in Fig. 1c based on the above V_{hom} profiles and the generalized parabola $V_s(z)$ in Eq.1. In this graph, the model parameters n, V_o/V_H, V_b/V_H and h_b/H were selected at 0.6, 0.1, 1 and 1 respectively. The deviation observed among the shear wave velocity profiles of the equivalent homogeneous soils is due to the small surface-to-base shear wave velocity ratio (V_o/V_H). Naturally, larger V_o/V_H ratios correspond to a smoother variation of $V_s(z)$ leading to comparable V_{hom} profiles.

The input motion is imposed at the base of the system in the form of a harmonic horizontal displacement, $u=u_o exp(i\omega t)$, ω being the cyclic excitation frequency, generating vertically propagating S waves.

3 ANALYTICAL SOLUTION

Starting from the following ordinary differential equation:

$$\frac{d}{dz}\left[G(z)\frac{du}{dz}\right] + \rho\omega^2 u = 0 \tag{7}$$

which describes one-dimensional shear waves under harmonic oscillations in a soil layer with constant mass density ρ and variable shear modulus $G(z)$, it can be shown [14-16] that the displacement field of an inhomogeneous layer such as that described in Eq.1 is given by:

$$u(z) = \frac{C_1\left(b + q\frac{z}{z_r}\right)^{\mu}}{N_{\nu+1}\left(\lambda b^{\ell/2}\right)}\left\{J_\nu\left[\lambda\left(b+q\frac{z}{z_r}\right)^{\ell/2}\right]N_{\nu+1}\left[\lambda b^{\ell/2}\right] - J_{\nu+1}\left[\lambda b^{\ell/2}\right]N_\nu\left[\lambda\left(b+q\frac{z}{z_r}\right)^{\ell/2}\right]\right\} \tag{8}$$

where $q=1-b$, C_1 is an integration constant determined from the boundary conditions, $J_v(\,)$ and $N_v(\,)$ denote the Bessel functions of the first and second kind and order v, respectively, and $\ell = 2(1-n)$ is a dimensionless parameter representing the step of the associated power series solutions [21]. Parameters μ and v are obtained from the asymptotic convergence of the solution close to zero, as $\mu=(1-2n)/2$ and $v=(2n-1)/2(1-n)$, while the asymptotic behavior of the solution at infinity requires $\lambda = 2k_r z_r / \ell q$, k_r and z_r being a reference wave number ($=\omega/V_r$) and a reference depth.

By definition, the base-to-surface transfer function is expressed as [22, 23]:

$$F(\omega) \equiv \frac{u(0)}{u(H)} \tag{9}$$

where $u(0)$ and $u(H)$ stand for the horizontal soil displacement at the free surface and the base of the single-layer system, computed from Eq.8 by setting $z=0$ and $z=H$, respectively. After some algebra, Eq.9 yields:

$$F(\omega) = \frac{2b^{\mu-\ell/2}}{\pi\lambda}\left[J_{v+1}\left(\lambda b^{\ell/2}\right)N_v\left(\lambda\right) - J_v\left(\lambda\right)N_{v+1}\left(\lambda b^{\ell/2}\right)\right]^{-1} \tag{10}$$

Referring to the two-layer inhomogeneous soil, the base-to-surface transfer function is defined in the same spirit as in Eq. 9:

$$F(\omega) \equiv \frac{u(0)}{u_b(0)} \tag{11}$$

where $u_b(0)$ denotes the soil displacement at base level ($z_b=0$). The response of the underlying homogeneous layer is given by the function [22, 23]:

$$u_b(z_b) = A_1 \sin(k_b z_b) + A_2 \cos(k_b z_b) \tag{12}$$

where A_1 and A_2 represent the amplitudes of the waves travelling upward and downward in the layer, respectively, and k_b ($=\omega / V_b$) is the corresponding wave number. Upon enforcing the continuity of shear stresses and displacements at the base of the system and the interface of the surface and the base layer:

$$\begin{aligned} u_b(0) &= u_o \\ u_b(h_b) &= u(H) \\ \tau_b(h_b) &= -\tau(H) \end{aligned} \tag{13}$$

by means of Eqs. 8 and 12 yield the following solution for the base-to-surface transfer function in Eq.11:

$$\begin{aligned} F(\omega) = \left[\frac{2(1-n)(1-b)\rho_b}{\pi b^{1/2} H}\right] & \Big\{k_H \rho_b \left[J_v\left(\theta_H\right)N_{v+1}\left(\theta_O\right) - J_{v+1}\left(\theta_O\right)N_v\left(\theta_H\right)\right]\cos(k_b h_b) - \\ & - k_b \rho_H \left[J_{v+1}\left(\theta_H\right)N_{v+1}\left(\theta_O\right) - J_{v+1}\left(\theta_O\right)N_{v+1}\left(\theta_H\right)\right]\sin(k_b h_b)\Big\}^{-1} \end{aligned} \tag{14}$$

where $\theta_O = \lambda b^{\ell/2}, \theta_H = \lambda\left(b + qH / z_r\right)^{\ell/2}$; ρ_H and ρ_b stand for soil mass density of the inhomogeneous and the homogeneous layer, respectively, and k_H ($=\omega/V_H$), k_b ($=\omega/V_b$) the corresponding wave numbers. Material damping can be accounted for in the above solutions by replacing the real wave numbers with the complex counterparts $k_H^*\left(=\omega / V_H^*\right)$ and $k_b^*\left(=\omega / V_b^*\right)$, respectively. Further details on the analytical derivations of Eqs.10 and 14 can be found in references [9] and [14].

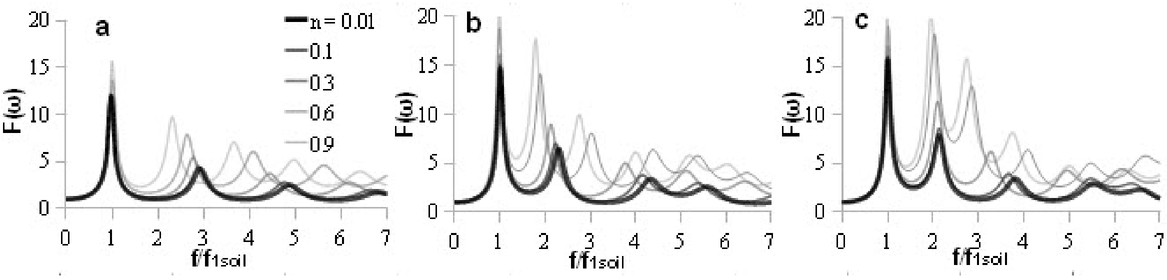

Figure 2. Base-to-surface transfer functions of two-layer inhomogeneous soil for (a) V_b/V_H=1 (b) V_b/V_H=2 (c) V_b/V_H=3. In all graphs V_o/V_H=0.1, h_b/H=2, ρ_b/ρ_H=1, ξ=0.05

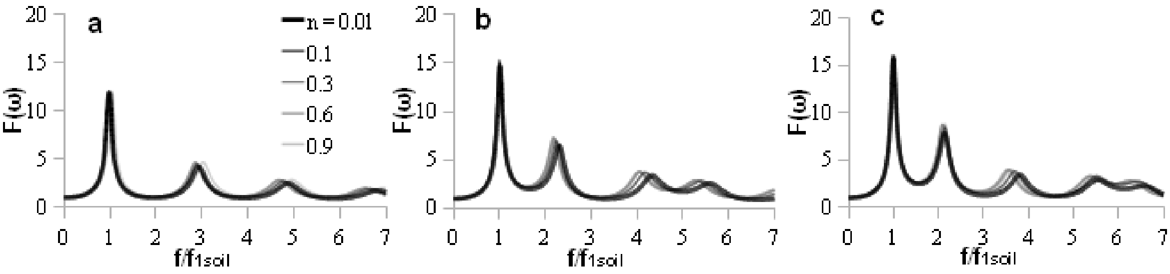

Figure 3. Base-to-surface transfer functions of two-layer inhomogeneous soil for (a) V_b/V_H=1 (b) V_b/V_H=2 (c) V_b/V_H=3. In all graphs V_o/V_H=0.75, h_b/H=2, ρ_b/ρ_H=1, ξ=0.05

4 HARMONIC RESPONSE OF THE TWO-LAYER INHOMOGENEOUS SOIL

Analytical base-to-surface transfer functions obtained for the two-layer inhomogeneous soil by means of Eq.14 are plotted in Fig.2 referring to the combined effect of inhomogeneity factor n and shear wave velocity ratio (V_b/V_H) at the interface of the inhomogeneous and the homogeneous layer, with the abscissa normalized by the fundamental frequency of the soil, f_{1soil}. Shear wave velocity ratio V_o/V_H at the surface and the base of the inhomogeneous layer was set at 0.1 corresponding to strong gradients in shear wave velocity with depth. For this range of soil inhomogeneity, increasing the inhomogeneity factor n amplifies response and shifts higher mode resonances to lower frequencies [15, 16], especially for large shear wave velocity contrast (i.e large V_b/V_H ratios) between the surface and the base layer (Fig.2c). Of particular interest is the strong amplification observed at higher modes, indicating reduced soil damping effects, contrary to the response of a piece-wise homogeneous two-layer soil, where the role of higher soil modes progressively diminishes.

On the contrary, for higher surface-to-base wave velocity ratio (V_o/V_H) corresponding to a mild variation of shear wave propagation velocity within the surface inhomogeneous layer, the harmonic response of the two-layer inhomogeneous soil resembles that of the homogeneous case (n=0.01). This is clearly demonstrated in Fig.3 where Eq.14 is computed for a V_o/V_H ratio of 0.75 providing comparable base-to-surface transfer functions. Note that the only difference between the results shown in Fig.2 and Fig.3 is the value of V_o/V_H ratio. The above behavior was found to exist regardless of thickness (h_b) of the underlying homogeneous layer. The effect of the latter is explored in Fig. 4 for a two-layer inhomogeneous soil described by three layer thickness values (h_b/H) and a V_o/V_H ratio of 0.1. It is observed that as the inhomogeneity factor n approaches 1, deeper soil deposits tend to respond at lower frequencies with larger peak amplitudes (Figs. 4b-4c). However, the effect of both relative layer thickness and inhomogeneity factor is minimized with increasing V_o/V_H ratio, as shown in Figure 5 where base-to-surface transfer functions are computed for a higher V_o/V_H ratio (0.75).

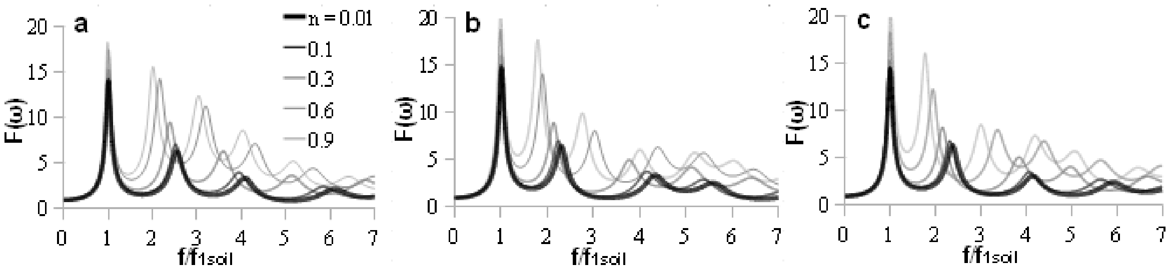

Figure 4. Base-to-surface transfer functions of two-layer inhomogeneous soil for (a) $h_b/H=1$ (b) $h_b/H=2$ (c) $h_b/H=3$. In all graphs $V_o/V_H=0.1$, $V_b/V_H=2$, $\rho_b/\rho_H=1$, $\xi=0.05$

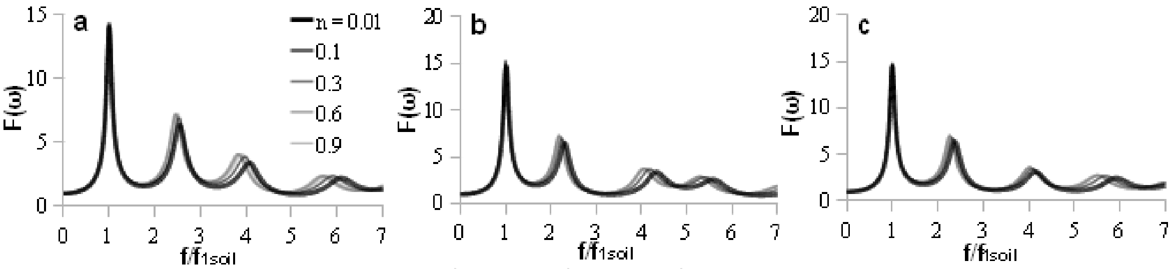

Figure 5. Base-to-surface transfer functions of two-layer inhomogeneous soil for (a) $h_b/H=1$ (b) $h_b/H=2$ (c) $h_b/H=3$. In all graphs $V_o/V_H=0.75$, $V_b/V_H=2$, $\rho_b/\rho_H=1$, $\xi=0.05$

Conclusively, the harmonic response of the generalized two-layer inhomogeneous system under investigation is primarily controlled by V_o/V_H ratio corresponding to a critical measure of soil inhomogeneity. Similar observations have been reported by Rovithis et al [14] referring to the single-layer system (Fig.1a) based on Eq.10.

5 COMPARISON WITH “EQUIVALENT” HOMOGENEOUS SOIL

The response of the inhomogeneous two-layer system was compared to the equivalent homogeneous soils in terms of natural frequencies and resonant peak amplitudes. Recall in this regard that for a homogeneous viscoelastic two-layer soil, base-to-surface transfer function is given by the expression [22]:

$$F(\omega)=\left[\cos\left(q_{\mathrm{hom}}H\right)\cos\left(q_b h_b\right)-I_R\sin\left(q_{\mathrm{hom}}H\right)\sin\left(q_b h_b\right)\right]^{-1} \tag{15}$$

where $q_{hom}(=\omega/V_{hom})$ and $q_b(=\omega/V_b)$ stand for the wave numbers of the surface and the base layer, respectively, and I_R $(=\rho_b V_b/\rho_H V_{hom})$ is the impedance contrast between the two layers.

Resonant frequencies and peak amplitudes ratios between equivalent homogeneous and inhomogeneous soils were obtained by means of Eqs.14 and 15 for each representative shear wave propagation velocity V_{hom} according to Eqs 2-6. For the purpose of this parametric investigation both (V_b/V_H) and (h_b/H) ratios were consecutively set at 1, 2 and 3.

Ratio of the fundamental frequency of the equivalent homogeneous profile to the first natural frequency of the inhomogeneous soil (f_{1hom}/f_{1Inhom}) is plotted in Fig.6 against the inhomogeneity factor n for the examined V_o/V_H ratios. In all graphs, V_{hom} is defined by Eq.2 (i.e $V_{hom}=V_H$) and V_b/V_H is equal to 3. Each plot corresponds to a different h_b/H ratio; 1, 2 and 3 respectively. Naturally, the use of V_H as the equivalent shear wave propagation velocity of the inhomogeneous layer results in a stiffer soil, leading to frequency ratios above unity especially for moderately-to-strongly inhomogeneous soils (small V_o/V_H ratios and large inhomogeneity factors n). However, larger h_b/H values referring to deeper soil deposits lead to lower f_{1hom}/f_{1Inhom} ratios (Fig. 6b-6c), indicating a prevailing contribution of the underlain homogeneous layer to the overall response.

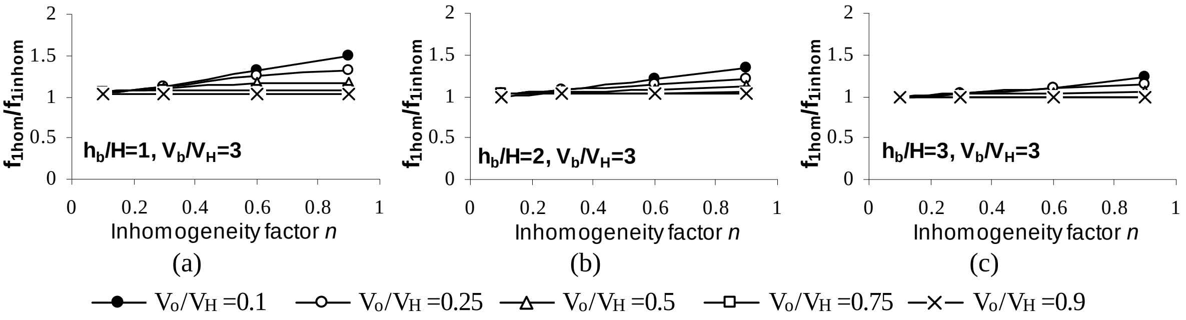

Figure 6. Ratio of fundamental frequency of the equivalent homogeneous soil (f_{1hom}) to first natural frequency of the inhomogeneous soil (f_{1Inhom}) as function of inhomogeneity factor *n*: (a) $h_b/H=1$ (b) $h_b/H=2$ (c) $h_b/H=3$. In all plots, $\boldsymbol{V_{hom}=V_{hom1}}$, $V_b/V_H=3$, $\rho_b/\rho_H=1$, $\xi=0.05$

Resonant frequencies of a smoothly-to-moderately inhomogeneous soil (i.e $V_o/V_H > 0.25$) are well-predicted by an equivalent homogeneous soil with a surface layer of either equal shear wave propagation velocity at the mid depth of the inhomogeneous layer (Eq.3), or of equal mean wave propagation velocity within the whole layer (Eq.4). Figures 7a-7c show f_{1hom}/f_{1Inhom} ratios computed by means of Eq.3 for various h_b/H and V_b/V_H ratios. Similar results obtained from Eq.4 are plotted in Figs. 7d-7f referring to the second natural frequency of the deposit (i.e. f_{2hom}/f_{2Inhom}). In all cases, frequency ratios are close to unity indicating a good approximation of the resonant frequencies of the inhomogeneous soil. The latter should be correlated with the continuous nature of the generalized parabola adopted to describe the wave propagation velocity in the inhomogeneous layer. Insignificant deviations from the exact solution are observed for low V_o/V_H ratios ($V_o/V_H=0.1$) leading to slightly overestimated frequencies with increasing inhomogeneity factor *n,* especially at high resonances (Figs. 7d-7f).

On the contrary, when the equivalent homogeneous soil is defined through Eq.5 ($V_{hom}=V_{hom4}$) the actual fundamental frequency of the inhomogeneous deposit is underestimated. Fig.8 shows the corresponding $f_{1hom}/f_{11inhom}$ ratios for three values of shear wave velocity contrast at the interface of the inhomogeneous and the homogeneous layer. It is observed

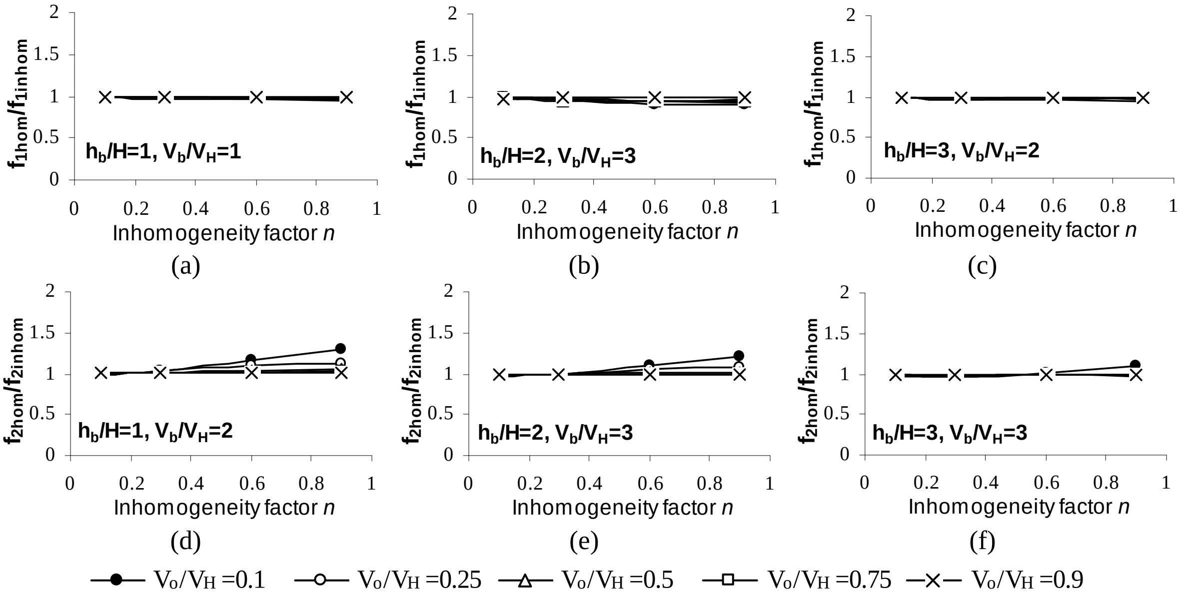

Figure 7. (a-c) f_{1hom}/f_{1Inhom} ratios as function of inhomogeneity factor *n*: $\boldsymbol{V_{hom}=V_{hom2}}$ (d-f) f_{2hom}/f_{2Inhom} ratios as function of inhomogeneity factor *n*: $\boldsymbol{V_{hom}=V_{hom3}}$. In all plots $\rho_b/\rho_H=1$, $\xi=0.05$

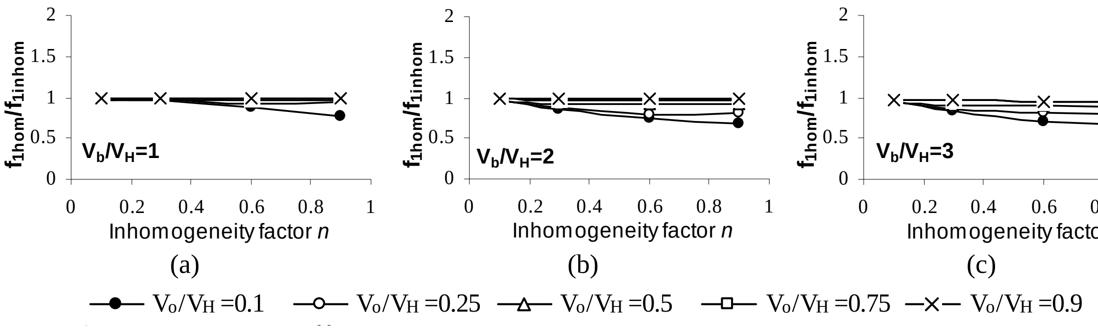

Figure 8. f_{1hom}/f_{1Inhom} ratios as function of inhomogeneity factor n: (a) $V_b/V_H=1$ (b) $V_b/V_H=2$ (c) $V_b/V_H=3$. In all plots, $\boldsymbol{V_{hom}=V_{hom4}}$, $h_b/H=1$, $\rho_b/\rho_H=1$, $\xi = 0.05$

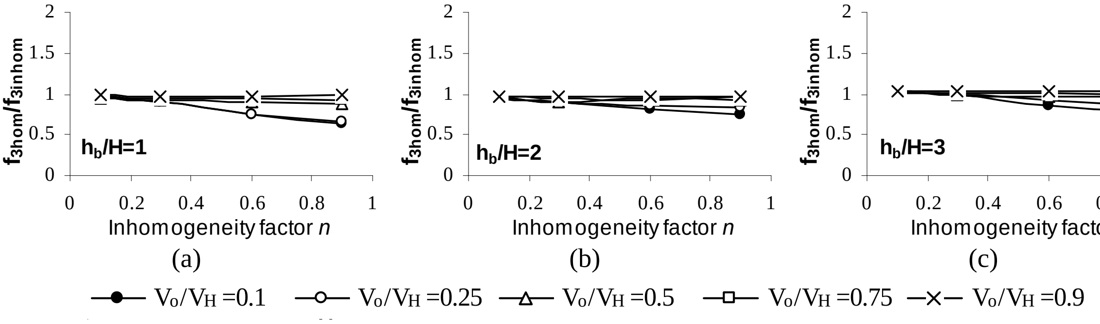

Figure 9. f_{3hom}/f_{3nhom} ratios as function of inhomogeneity factor n: (a) $V_b/V_H=1$ (b) $V_b/V_H=2$ (c) $V_b/V_H=3$. In all plots, $\boldsymbol{V_{hom}=V_{hom5}}$, $h_b/H=2$, $\rho_b/\rho_H=1$, $\xi = 0.05$

that indeed the fundamental frequency ratio is lower than 1 especially for large V_b/V_H ratios (Fig.8b-8c). Similar trends can be seen in Fig. 9 where f_{3hom}/f_{3Inhom} ratios referring to the third natural frequency of a two-layer homogeneous soil having the same fundamental frequency as the inhomogeneous one are plotted by means of Eq.6 ($V_{hom}=V_{hom5}$).

Further comparisons between continuously inhomogeneous and equivalent homogeneous soils were performed, relating peak resonant amplitudes of base-to-surface transfer functions. Resonant amplitude ratios (A_{hom}/A_{inhom}) defined in the same spirit as the resonant frequency ratios are plotted in Fig. 10 corresponding to the first natural frequency (i.e. A_{1hom}/A_{1Inhom}) of a two-layer system with (V_b/V_H) and (h_b/H) ratio of 3 and 2, respectively. Each plot in Fig.10 corresponds to a different equivalent homogeneous soil based on Eqs 2-6. Linear hysteretic damping was taken at 0.05 for both inhomogeneous and equivalent homogeneous cases. The same results are shown in Fig.11 for the second natural frequency of the deposit (A_{2hom}/A_{2Inhom}). It is observed that the replacement of a continuously inhomogeneous soil with an equivalent homogeneous may lead to substantial overestimated or underestimated resonant amplitudes depending on the value of V_{hom}. Note, for example, that for a strongly inhomogeneous soil (i.e. $V_o/V_H = 0.1$, $n = 0.9$), A_{1hom}/A_{1inhom} ratio based on Eq.5 can be about 0.6 (Fig.10d), which suggests an underestimation of the actual resonant amplitude while Eq.6 yields a value of 1.7 (Fig.10e) overestimating strongly the amplitude of the fundamental resonance. The above deviation becomes larger at higher resonances. For example, A_{2hom}/A_{2Inhom} ratios may vary in the range 0.4 (Fig.11a) to 4.5 (Fig.11e) depending on the approach followed to define V_{hom}. Thereby, the replacement of a continuously inhomogeneous soil layer with an equivalent homogeneous one in terms of peak resonant amplitudes may be valid only for a sufficiently smooth variation of shear wave velocity with depth. The latter was observed independently of V_b/V_H ratio, h_b/H ratio and V_{hom}.

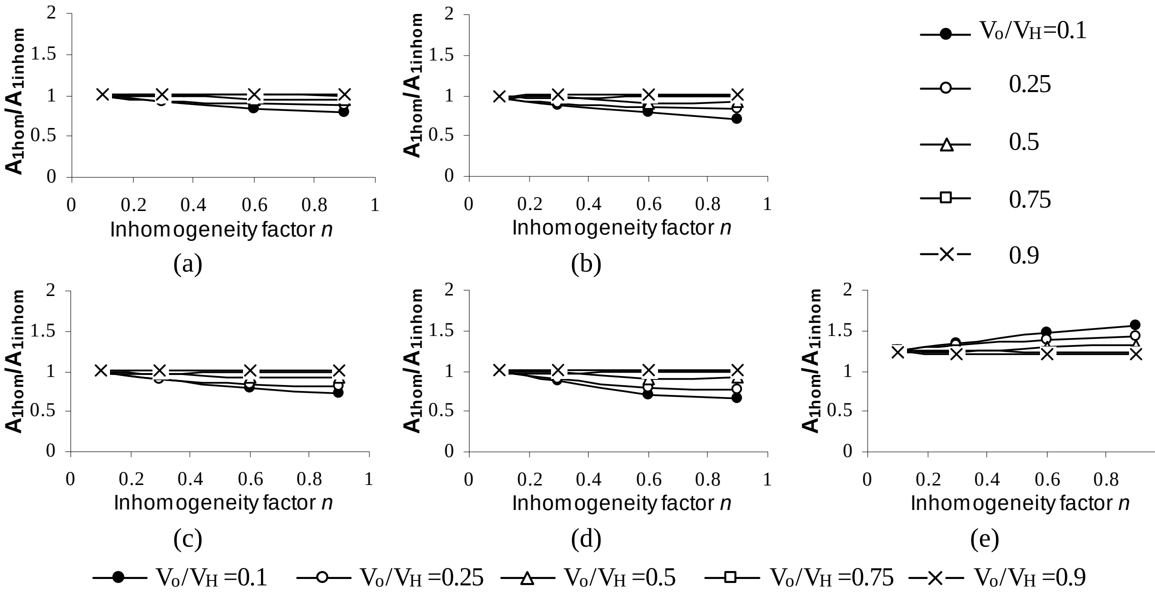

(a) (b) (c) (d) (e)

Figure 10. Resonant amplitude ratios (A_{1hom}/A_{11nhom}) corresponding to the first natural frequency of the system as function of inhomogeneity factor n: (a) $V_{hom}=V_{hom1}$ (b) $V_{hom}=V_{hom2}$ (c) $V_{hom}=V_{hom3}$ (d) $V_{hom}=V_{hom4}$ (e) $V_{hom}=V_{hom5}$. In all plots, $V_b/V_H=3$, $h_b/H=2$, $\rho_b/\rho_H=1$, $\xi = 0.05$

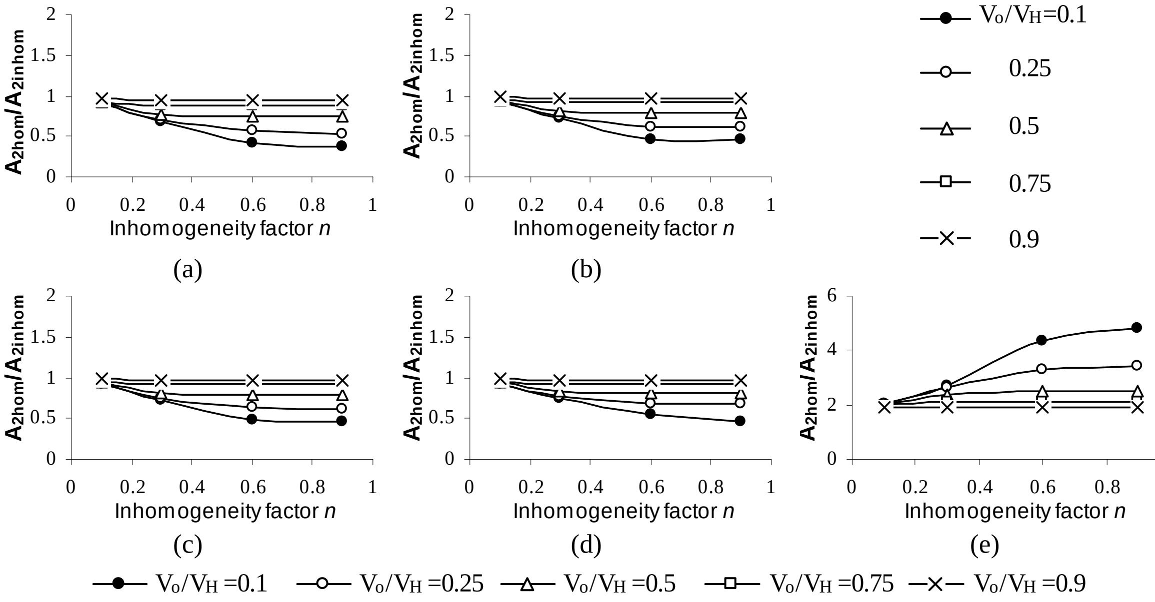

(a) (b) (c) (d) (e)

Figure 11. Resonant amplitude ratios (A_{2hom}/A_{21nhom}) corresponding to the second natural frequency of the system as function of inhomogeneity factor n: (a) $V_{hom}=V_{hom1}$ (b) $V_{hom}=V_{hom2}$ (c) $V_{hom}=V_{hom3}$ (d) $V_{hom}=V_{hom4}$ (e) $V_{hom}=V_{hom5}$. In all plots, $V_b/V_H=3$, $h_b/H=2$, $\rho_b/\rho_H=1$, $\xi = 0.05$

6 INHOMOGENEOUS SOIL WITH VANISHING STIFFNESS AT SOIL SURFACE

For an inhomogeneous soil layer having zero stiffness at the free surface (b=0), it can be shown [14-16] that shear strain γ(z) in the soil is given by:

$$\gamma(z) = -\frac{\omega^2 H}{V_H^2}\left(\frac{z}{H}\right)^{-2n} C_1 z^{1/2} J_\nu\left(\lambda b^{\ell/2}\right) \tag{16}$$

where $\nu=1/2(1-n)$, $\ell = 2(1-n)$ and $\mu=1/2$.

For values of z close to zero the term $z^{1/2} J_{\nu}\left(\lambda b^{\ell/2}\right)$ becomes asymptotically equal to [24]:

$$z^{1/2} J_{\nu}\left(\lambda b^{\ell/2}\right) \sim z^{1/2} \frac{1}{\Gamma(1+\nu)} \left(\frac{\lambda z^{\ell/2}}{2}\right)^{\nu} \tag{17}$$

where Γ( ) is the Gamma function. Accordingly the solution in Eq.16 takes the form:

$$\gamma(z) = -\frac{\omega^2 H}{V_H^2} \left(\frac{z}{H}\right)^{-2n} C_1 z^{1/2} \frac{1}{\Gamma(1+\nu)} \left(\frac{\lambda z^{\ell/2}}{2}\right)^{\nu} \tag{18}$$

which for small z's yields the expression (recall that $\nu\ell = 2(1-n)/2(1-n) = 1$ in this solution):

$$z^{-2n+1/2+\nu\ell/2} = z^{-2n+1/2+1/2} = z^{1-2n} \tag{19}$$

indicating that for *n*>1/2 the exponent (1-2*n*) becomes negative and, thereby, the magnitude of shear strain becomes infinite, regardless of frequency and excitation amplitude and despite the fact that the corresponding shear stress is zero. On the contrary, for *n*<1/2 the exponent is positive and shear strain is zero at the ground surface. Therefore, strain amplitude at the surface can be either zero or infinite, depending on the value of the inhomogeneity factor, but never finite. These findings are in agreement with those obtained in [5] for *n*=2/3.

However, as real soils inherently possess a finite amount of stiffness at the surface, the behavior of the solution at very small V_o/V_H ratios is investigated in Fig.12, for a single inhomogeneous layer described by four inhomogeneity factors. Damping ratio, ξ, was set at 0.05 in this graph. Strong amplification is evident at higher mode resonances, as V_o/V_H and *n* tend to 0 and 1, respectively. This suggests that strong amplification will develop even for finite surface stiffness (under zero shear strain), which will merely get maximized at the theoretical

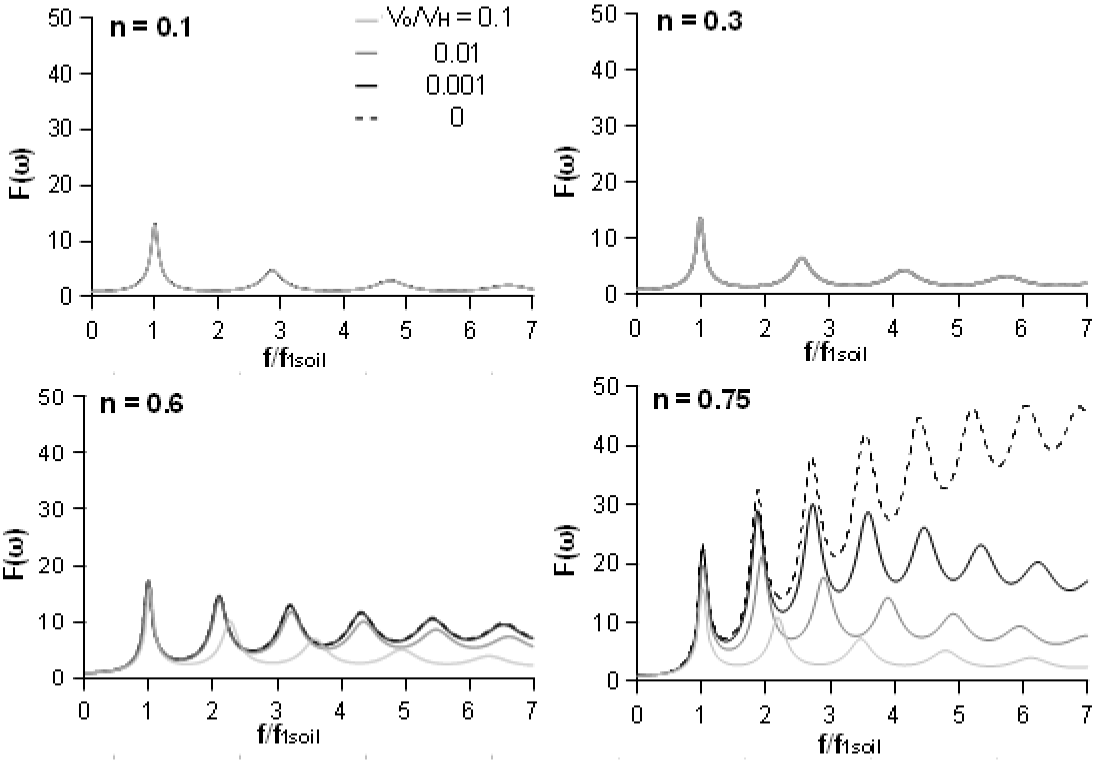

Figure 12. Effect of inhomogeneity factor n on base-to-surface transfer functions for a single inhomogeneous layer having V_o/V_H ratio of 0.1, 0.01, 0.001 and 0. In all plots, ξ = 0.05

limit V_o/V_H=0. An explanation is that the strong amplification is associated with transition phenomena (i.e., accumulation of wave energy in areas of progressively smaller elastic modulus near the surface leading to an increase in wave amplitude) as opposed to reflection phenomena associated with development of resonance in the layer.

7 CONCLUSIONS

Equivalent homogeneous soils were examined as simplified approximations of layered continuously inhomogeneous soils implementing alternative definitions for the representative shear wave propagation velocity. The investigation focused on resonant frequencies and peak resonant amplitudes, as affected by salient model parameters. The special case of an inhomogeneous soil having zero stiffness at the surface was explored as to the variation of shear strain with depth.

The harmonic response of a two-layer strongly inhomogeneous soil (V_o/V_H = 0.1) is amplified with increasing inhomogeneity factor n shifting higher mode resonance to lower frequencies. The above effect is more pronounced for deeper soil deposits with large shear wave velocity contrast between the surface and the base layer. Comparison of resonant frequencies and amplitudes between two-layer inhomogeneous and equivalent homogeneous soils revealed that the response of a smoothly-to-moderately inhomogeneous soil in terms of resonant frequencies may be adequately captured by an equivalent homogeneous soil with a surface layer of either equal shear wave propagation velocity at the mid depth of the inhomogeneous deposit, or of equal mean wave propagation velocity within the whole layer. For moderately-to-strongly inhomogeneous soil (V_o/V_H<0.5 and inhomogeneity factor n>0.3) the above equivalent homogeneous approximations remain a promising solution given that deep soil deposits (h_b/H>2) are encountered. On the contrary, resonant amplitudes of a moderately-to-strongly inhomogeneous soil may be significantly overestimated or underestimated when an equivalent homogeneous soil approach is adopted, especially at higher resonances. For the special case of inhomogeneous soils with vanishing shear wave velocity at the free surface (V_o/V_H = 0), near-surface shear strain may be either zero (for n < 0.5) or infinite (for n >0.5) but never finite. Strong amplification will develop even for finite surface stiffness (under zero shear strain) which will get maximized at the theoretical limit V_o/V_H = 0. From a practical viewpoint, a V_o/V_H ratio of less than 0.1 combined with an inhomogeneity factor n of over 0.5 will suffice to trigger this effect.

REFERENCES

[1] I. Towhata, Seismic wave propagation in elastic soil with continuous variation of shear modulus in the vertical direction. *Soils and Foundations*, **36**(1), 61-72, 1996.

[2] N.N. Ambraseys, A note on the response of an elastic overburden of varying rigidity to an arbitrary ground motion. *Bulletin of the Seismological Society of America*, **49**(3), 211-220, 1959.

[3] H.B. Seed and I.M. Idriss, The influence of ground conditions on ground motions during earthquakes. *Journal of Soil Mechanics and Foundations Division, ASCE* **94**: 93-137, 1969.

[4] R. Dobry, R. Whitman and J.M. Roesset, Soil properties and the one-dimensional theory of earthquake amplification. M.I.T., Department of Civil Engineering, 1971, Research Report, R71-18.

[5] T. Travasarou and G. Gazetas, On the linear response of soils with modulus varying as a power of depth-The Maliakos marine clay. *Soils and Foundations*, **44**(5), 85-93, 2004.

[6] K. Toki and S. Cherry, Inference of subsurface accelerations and strain from accelerograms recorded at ground surface. *4th European Symposium on Earthquake Engineering, London, 1972.*

[7] H. Schreyer, One-dimensional elastic waves in inhomogeneous media. *Journal of the Engineering Mechanics Division*, **103**(5), 979-990, 1977.

[8] G. Gazetas, Vibrational characteristics of soil deposits with variable wave velocity. *International Journal for Numerical and Analytical Methods in Geomechanics*, **6**, 1-20, 1982.

[9] H. Parashakis, 1D seismic wave propagation in a class of inhomogeneous soil deposits, Master Thesis, Hellenic Open University, 2009 (in Greek).

[10] Semblat JF. and Pecker A. *Waves and Vibrations in Soils: Earthquakes, Traffic, Shocks, Construction Works*, IUSS Press, 2009.

[11] Building Seismic Safety Council (BSSC). NEHRP, recommended provisions for seismic regulations for new buildings, Part 1-Provisions, 1997, FEMA Federal emergency Management Agency 302, 290 p.

[12] National Building Code of Canada (NBCC), 2005, National Research Council Canada

[13] CEN, European Committee for Standardization. EN 1998–1:2004 Eurocode 8: design of structures for earthquake resistance, Part 1: General rules, seismic actions and rules for buildings. 2004, Brussels, Belgium.

[14] E.N. Rovithis, H. Parashakis, G.R. Mylonakis, 1D Seismic response of layered inhomogeneous soil: analytical investigation, *Soil Dynamics and Earthquake Engineering* (in press)

[15] K. Schulze, Vibrational characteristics and seismic response of inhomogeneous soils. MSc Thesis, Department of Civil Engineering, City University of New York, 2005.

[16] V. Miha, Seismic response of inhomogeneous soil deposits. MSc Thesis, Department of Civil Engineering, University of Patras, 2007 (In Greek with English Abstract)

[17] D. Muir Wood, *Geotechnical modelling*. E & FN Spon (488pp) ISBN 0-419-23730-5

[18] P. Dakoulas and G. Gazetas, A class of inhomogeneous shear models for seismic response of dams and embankments. *Soil Dynamics and Earthquake Engineering*, **4**(4), 166-182, 1985.

[19] J.X. Zhao, Modal analysis of soft-soil sites including radiation damping. *Earthquake Engineering and Structural Dynamics*, **26**(1), 93-113, 1997.

[20] R. Dobry, I. Oweis and A. Urzua, Simplified procedures for estimating the fundamental period of a soil profile. *Bulletin of the Seismological Society of America*, **66**(4), 1293-1321, 1976.

[21] C. R. Wylie and L.C. Barrett, *Advanced engineering mathematics*. NewYork: McGraw-Hill Higher Education, 1995.

[22] J.M Roesset, Soil amplification of earthquakes. Numerical Methods in Geotechnical Engineering (C.S. Desai and J.T. Christian eds), McGraw-Hill, New York, 1976.

[23] Kramer L.S. *Geotechnical Earthquake Engineering*. Prentice Hall International Series, 1996.

[24] Hildebrand FB. *Advanced Calculus for Applications*, Prentice-Hall, Inc. Englewood Cliffs, 1962.

COMPDYN 2011
3rd ECCOMAS Thematic Conference on
Computational Methods in Structural Dynamics and Earthquake Engineering
M. Papadrakakis, M. Fragiadakis, V. Plevris (eds.)
Corfu, Greece, 25–28 May 2011

EXPERIMENTAL INVESTIGATION ABOUT THE INFLUENCE OF THE USE OF GLUE IN JOINTS IN LIGHTWEIGHT STRUCTURES

J. Negreira Montero[1], A. Sjöström[2], and D. Bard[1]

[1] Lunds Tekniska Högskola – Division of Engineering Acoustics
BOX 118, 221 00 Lund, Sweden
Juan.Negreira_Montero@construction.lth.se
Delphine.Bard@construction.lth.se

[2] Lunds Tekniska Högskola – Division of Structural Mechanics
BOX 118, 221 00 Lund, Sweden
Anders.Sjostrom@construction.lth.se

Keywords: Lightweight, Joints, Glue.

Abstract. *Lightweight timber structures have many advantages, but high-demand acoustic quality is hard to achieve due to the relatively poor insulation through the junctions, especially in the low frequency range (20 Hz-200 Hz) where the weight (mass per unit of area) of a construction is an important parameter for the air-borne insulation properties [1]. Increasing the mass would improve the insulation but this would go against the main advantage of lightweight constructions. Impact sound from a walking person is the most common sound insulation problem for these kinds of structures, where the footsteps produce a high-degree of noise disturbance. Similar investigations of junctions have been done before [2]. The aim of this particular investigation, however, is to show how glue modifies the sound transmission through the joints in a wooden floor. Theory shows that coupling occurs in a joint either along a line or at individual points depending on the distance between the screws or nails with regard to the bending wavelength [3], [4]. When a viscous elastic material as glue is inserted in between the parts of the joint, the behavior will change and it is therefore important to be studied. To achieve this aim, two structures were built. The first one constituted of two squared plates of dimension 0.6 m x 0.6 m, each one of them fixed onto one beam 4.5 m wide and 22 cm high, by means of equidistant screws. A second set-up was built too, but this time only a single 1.2 m x 0.6 m plate was fixed onto the beam. The same structures were built again a second time, but this time glue was applied around the screws on the contact surfaces.*

1 INTRODUCTION

Lightweight timber structures have many advantages, but high-demand acoustic quality is hard to achieve due to the relatively poor insulation through the junctions, especially in the low frequency range (20 Hz-200 Hz) where the weight (mass per unit of area) of a construction is an important parameter for the air-borne insulation properties [1]. Increasing the mass would improve the insulation but this would go against the main advantage of lightweight constructions. Impact sound from a walking person is the most common sound insulation problem for these kinds of structures, where the footsteps produce a high-degree of noise disturbance. Similar investigations of junctions have been done before [2]. The aim of this particular investigation, however, is to show how glue modifies the sound transmission through the joints in a wooden floor. Theory shows that coupling occurs in a joint either along a line or at individual points depending on the distance between the screws or nails with regard to the bending wavelength [3], [4]. When a viscous elastic material as glue is inserted in between the parts of the joint, the behavior will change and it is therefore important to study this latter. To achieve this aim, two structures were built. The first one constituted of two squared plates of dimension 0.6 m x 0.6 m, each one of them fixed onto one beam 4.5 m wide and 22 cm high, by means of equidistant screws. A second set-up was built but this time only a single 1.2 m x 0.6 m plate was fixed onto the beam. The same structures were built a second time, but this time glue was applied around the screws on the contact surfaces**.**

2 TEST MODELS

2.1 Geometry

A total number of four mockups were built. The first one was constituted of two squared plates of dimension 0.6 m x 0.6 m, each one of them fixed onto one beam, 4.5 cm wide and 22 cm high, by means of equidistant screws. A second set-up was built this time consisting only of a single 1.2 m x 0.6 m plate fixed onto an identical beam. The same structures were built a second time, but this time glue was applied around the screws on the contact surfaces.

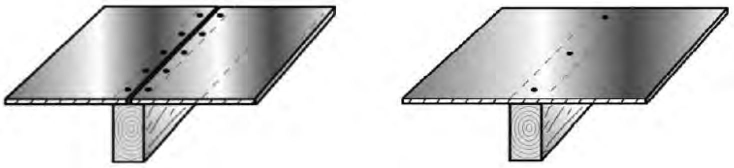

Figure 1: Set-ups.

The distance between the screws connecting the chipboard plates to the bearing beam, following the recommendations of manufacturers, was set to 25 cm in the case of a single plate and 12.5 cm in the case of two plates. The last screws were placed with a distance of 5 cm from the edges in both cases. Both types of connections are realistic and can therefore be found in real timber lightweight structures.

2.2 Materials

The properties of the materials used are listed in Table 1, where E is the Modulus of Elasticity, v the Poisson´s ratio, d the damping coefficient, ρ the mass density and G is the shear modulus.

Spruce Beam		Chipboard		Screws	
E_1	$8.5 \cdot 10^9$ Pa	E_t	$3 \cdot 10^9$ Pa	E	$2.1 \cdot 10^{11}$ Pa
E_2=E_3	$3.5 \cdot 10^8$ Pa	v	0.3	v	0.3
v_{12}=v_{13}	0.25	ρ	767 kg/m^3	ρ	7800 kg/m^3
v_{13}	0.3	d	0.055	d	0.02
G_{12}=G_{13}	$7 \cdot 10^8$ Pa				
G_{23}	$5 \cdot 10^7$ Pa				
ρ	432 kg/m^3				
d	0.025				

Table 1: Properties of the different materials used.

Those properties were obtained from the manufacturers who provided the materials. The glue used was ordinary commercial PVAc glue commonly used in real constructions.

3 WAVE PROPAGATION

3.1 Bending Waves

Bending waves are likely to be excited in bodies or structures where one or two dimensions are becoming small compared to the wavelength at an actual frequency, i.e. it is the dominant type of wave in construction elements (beams, plates…). If the plates of the floor structure are sufficiently thin, the shear wave propagation can be ignored and the acoustic wave propagation that leads to sound radiation are only the bending waves [5].

According to [7], the wave equation for a bending wave propagating along the x-axis has the following expression for the displacement η in the z-direction (orthogonal to the surface):

$$\eta(x,t) = [\eta_{+} e^{(-ik_B x)} + \eta_{-} e^{(ik_B x)} + \eta_{\eta -} e^{(-k_B x)} + \eta_{\eta +} e^{(k_B x)}] e^{i\omega t} \qquad (1)$$

where η_{+}, η_{-}, $\eta_{\eta -}$ and $\eta_{\eta +}$ are constants. While the first two terms within the brackets correspond to travelling waves (sinusoidal harmonic waves), the third and forth terms define the so-called evanescent waves (near field vibration waves which decrease exponentially in both the positive and negative directions of the x-axis). Since our excitation consists on short impacts, only evanescent waves will be considered.

4 MEASUREMENT PROCEDURE

In order to measure the vibrations as accurately as possible, the set-ups were hung from the ceiling, suspended to soft rubber springs. The resonance frequency of those springs was calculated beforehand assuring that it is sufficiently low and lower than the lowest eigenfrequency for the structure so that no effect from them is caught in the measurements.

The structure was excited with a hammer producing a sound impact. Nine different excitation points were considered. Dual-axis accelerometers *(iMEMS ADXL203* and *ADXL202E)* were fixed on the structure to record the vibrations. The acquisition software used was *Spectrum SBench 6.1*. The measurement disposition can be seen in Figure 2.

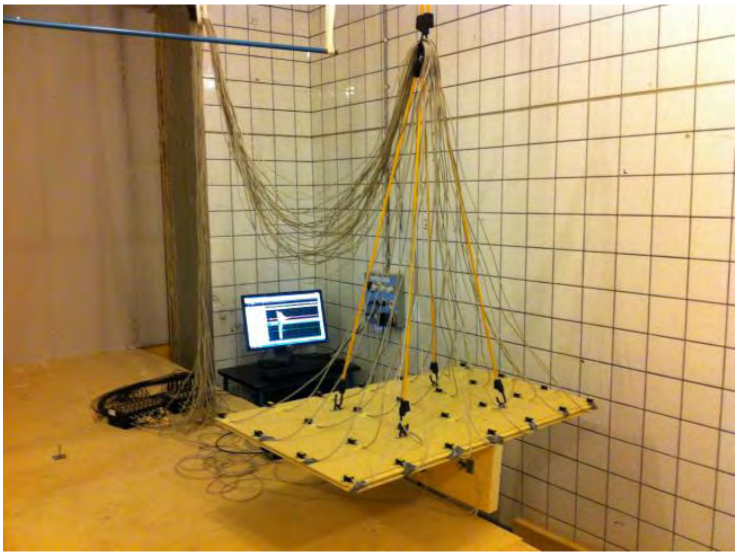

Figure 2: Measurement disposition.

The overall transmission rate in the floor structure depends on discontinuities present in the structure in addition to other factors such as the location of the internal stiffness, the dimension of the standard chipboard plates used in the construction, the thickness of the beam and the distance between the screws [5].

5 RESULTS

In order to present the results in a general fashion, the data acquired by the accelerometers was scaled with the force applied. As previously mentioned, the structure was excited at nine different locations. As a modal analysis is to be performed, it is not desired that the results are influenced by the excitation point. Thus, an average was carried out over all the excitation points according to [6].

In order to compare the behavior of both set-ups, the modal analysis previously mentioned was used to investigate the influence of the use of glue in the junctions.

5.1 Single-plate Set-up

In Figure 3, the normalized relative acceleration plots corresponding to different eigenmodes are presented. In the left column, the non-glue case is shown while the right column corresponds to the glued case.

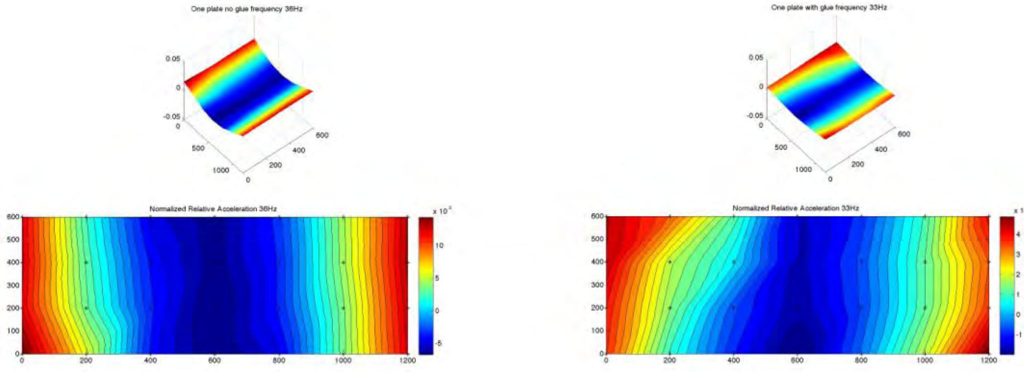

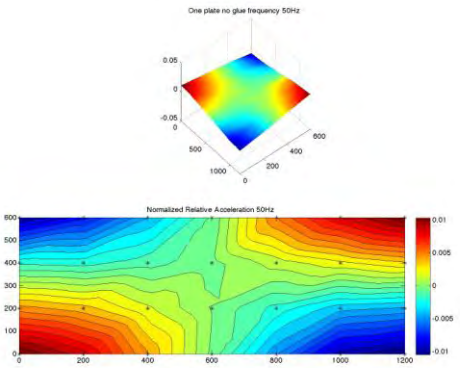
One plate no glue frequency 50Hz
0.05
0
-0.05
500
1000
200
400
600
Normalized Relative Acceleration 50Hz
0.01
0.005
0
-0.005
-0.01

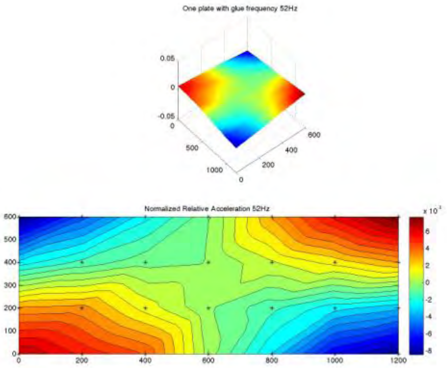
One plate with glue frequency 52Hz
0.05
0
-0.05
Normalized Relative Acceleration 52Hz
x 10^-3
6
4
2
0
-2
-4
-6
-8

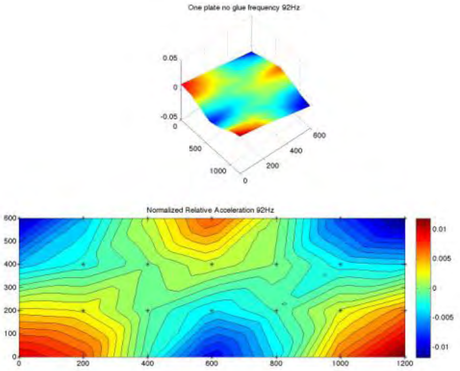
One plate no glue frequency 92Hz
Normalized Relative Acceleration 92Hz
0.01
0.005
0
-0.005
-0.01

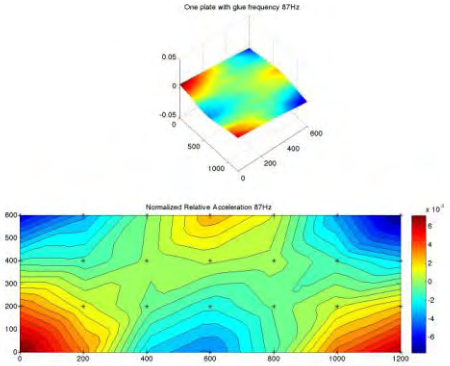
One plate with glue frequency 87Hz
Normalized Relative Acceleration 87Hz
x 10^-3
6
4
2
0
-2
-4
-6

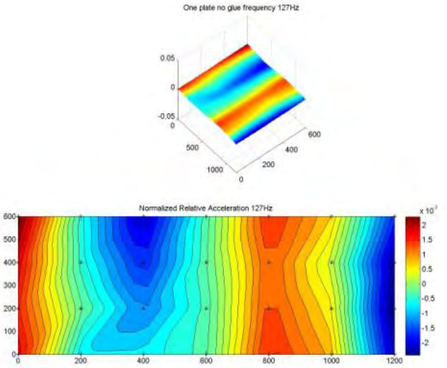
One plate no glue frequency 127Hz
Normalized Relative Acceleration 127Hz
x 10^-3
2
1.5
1
0.5
0
-0.5
-1
-1.5
-2

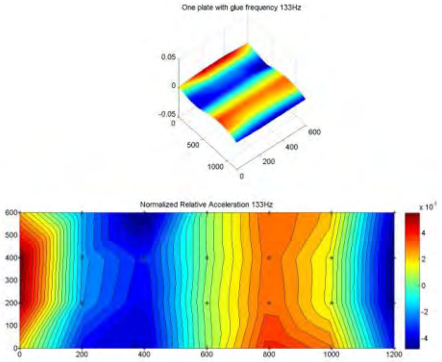
One plate with glue frequency 133Hz
Normalized Relative Acceleration 133Hz
x 10^-3
4
2
0
-2
-4

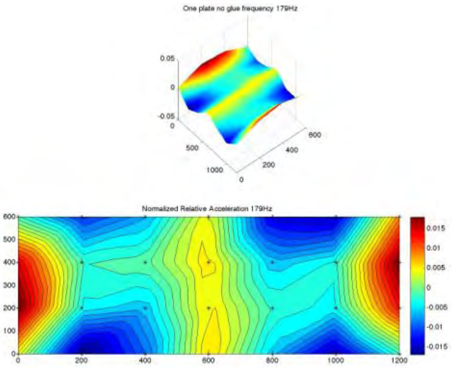
One plate no glue frequency 179Hz
Normalized Relative Acceleration 179Hz
0.015
0.01
0.005
0
-0.005
-0.01
-0.015

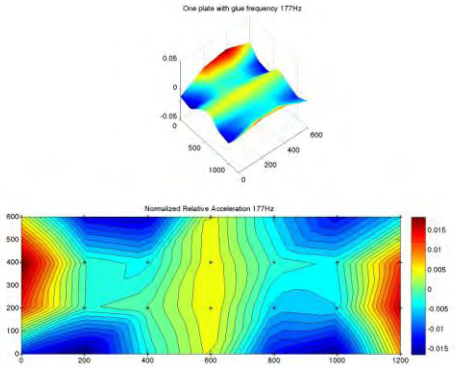
One plate with glue frequency 177Hz
Normalized Relative Acceleration 177Hz
0.015
0.01
0.005
0
-0.005
-0.01
-0.015

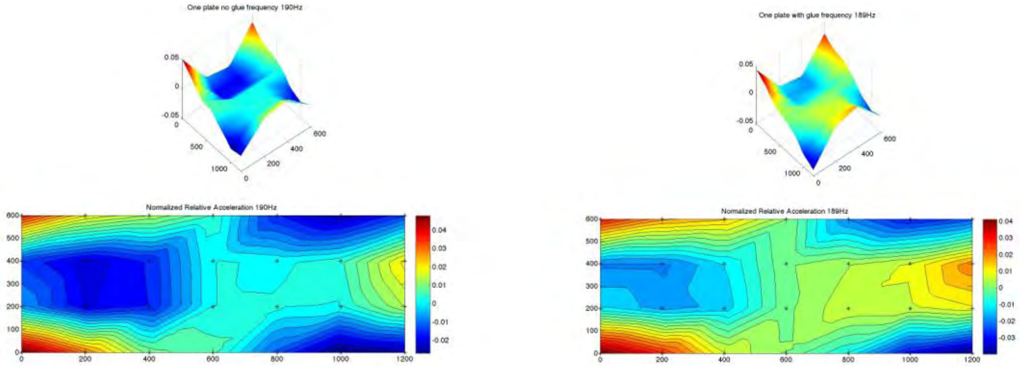

Figure 3: Comparison of modes of vibration. In the left hand side, six modes for the single non-glued plate are presented while the correspondent modes for the plate with glue are listed in the right column.

It can be observed that the glue does not have that much of an influence in the modal shapes or the frequencies they occur at, since their values are quite similar in both cases. Just a slight damping effect can be observed.

All the modes can be easily identified. The influence of the glue is visible in a reduction of the frequencies for the eigenmodes, especially for the frequencies within the higher part of the observed frequency range, particularly for the torsional modes (f_3, and f_6). Note that the magnitudes of the accelerations are quite low due to the scaling with the force and the fact that the hammer blows were quite soft. Table 2 summarizes the eigenfrequencies.

One plate no glue		One plate with glue	
f_1	36 Hz	f_1	33 Hz
f_2	50 Hz	f_2	52 Hz
f_3	92 Hz	f_3	87 Hz
f_4	127 Hz	f_4	133 Hz
f_5	179 Hz	f_5	177 Hz
f_6	190 Hz	f_6	189 Hz

Table 2: Eigenfrequencies for the single plate case.

5.2 Two plates Set-up

In Figure 4, the normalized relative acceleration plots corresponding to different eigenmodes are presented. In the left column, the non-glue case is shown while the right column corresponds to the glued case.

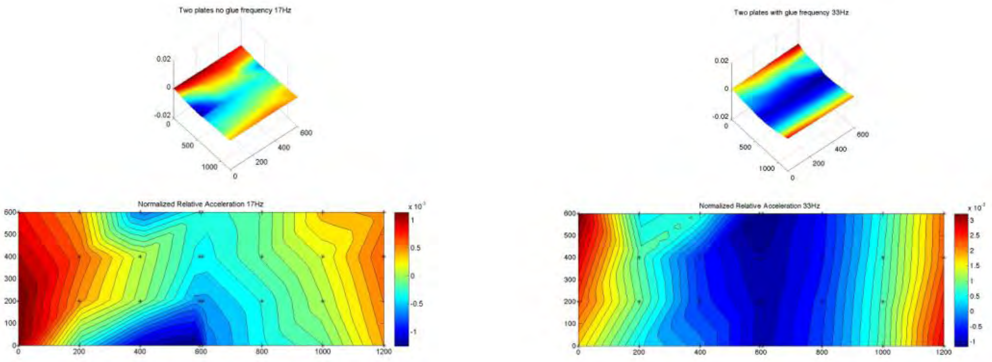

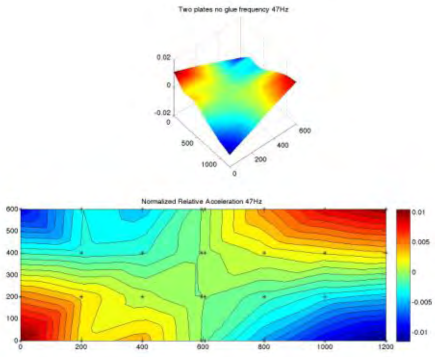
Two plates no glue frequency 47Hz

Normalized Relative Acceleration 47Hz

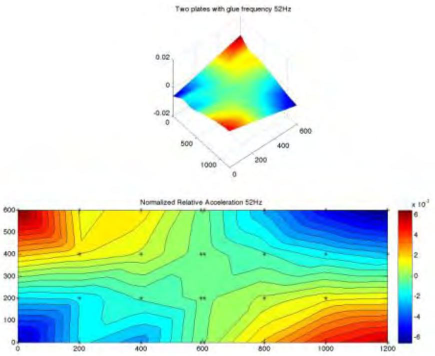
Two plates with glue frequency 52Hz

Normalized Relative Acceleration 52Hz

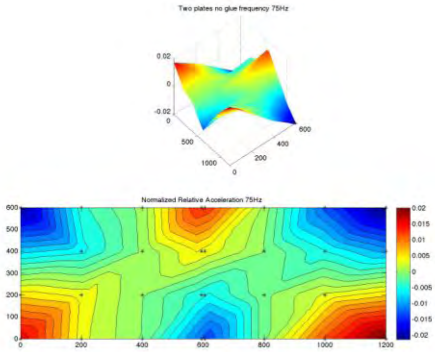
Two plates no glue frequency 75Hz

Normalized Relative Acceleration 75Hz

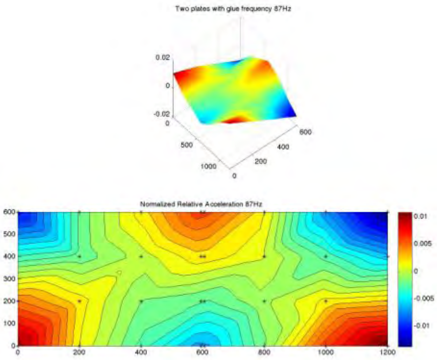
Two plates with glue frequency 87Hz

Normalized Relative Acceleration 87Hz

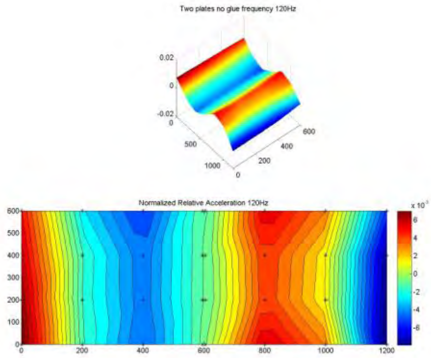
Two plates no glue frequency 120Hz

Normalized Relative Acceleration 120Hz

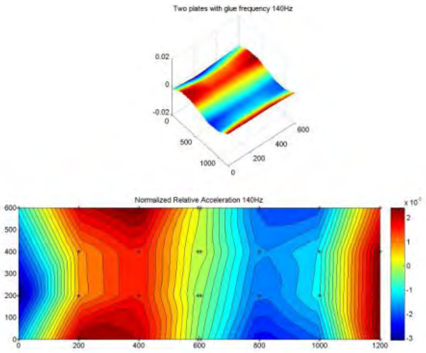
Two plates with glue frequency 140Hz

Normalized Relative Acceleration 140Hz

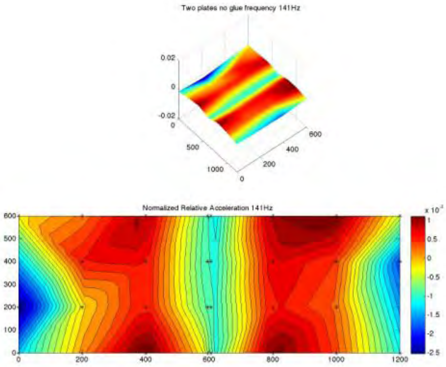
Two plates no glue frequency 141Hz

Normalized Relative Acceleration 141Hz

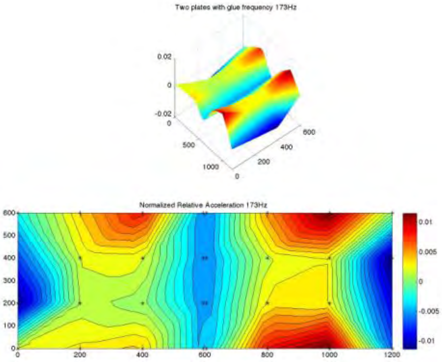
Two plates with glue frequency 173Hz

Normalized Relative Acceleration 173Hz

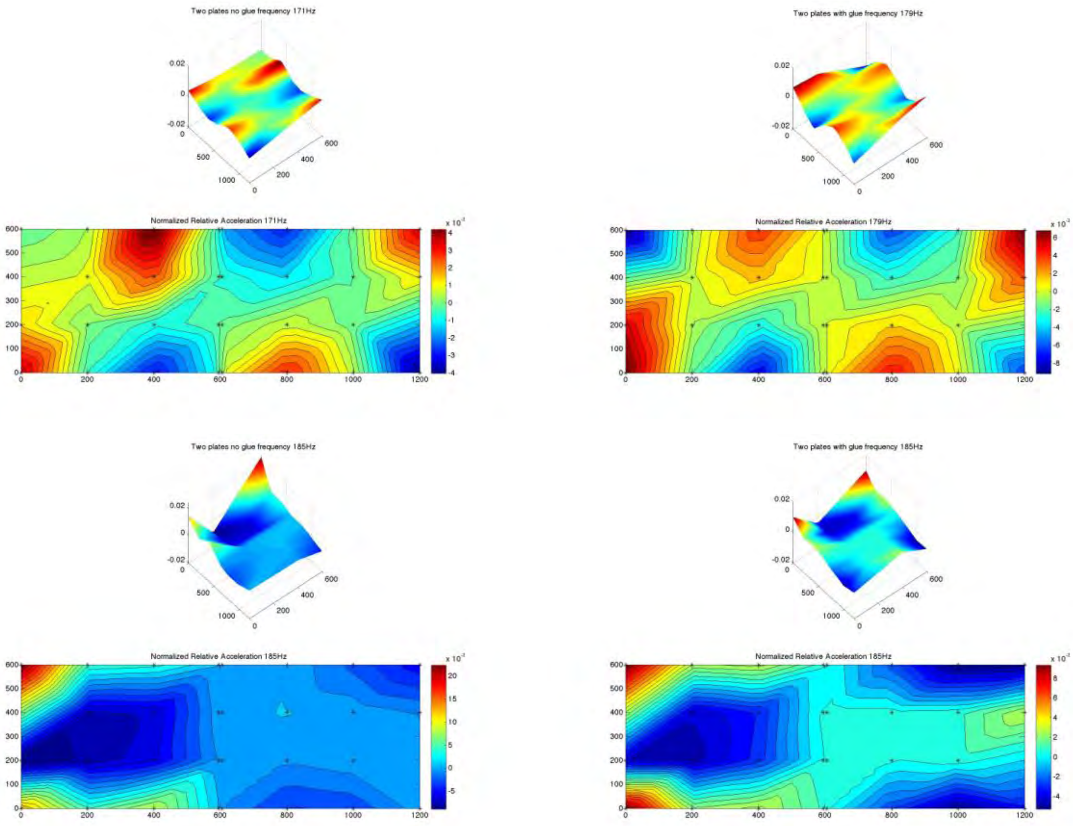

Figure 4: Comparison of modes of vibration. In the left hand side, seven modes for the single non-glued plate are presented while the modes for the plate with glue are listed in the right column.

The non-glued case is, as expected in advance, softer and thus the eigenfrequencies are lower than in the glued case for the correspondent mode (see Table 3). Again, the magnitudes of the accelerations are quite low due to the scaling with the force and the fact that the hammer blows were quite soft. Likewise, the modal shapes can be also easily identified. Table 3 summarizes the eigenfrequencies for each case.

Two plates no glue		Two plates with glue	
f_1	17 Hz	f_1	33 Hz
f_2	47 Hz	f_2	52 Hz
f_3	75 Hz	f_3	87 Hz
f_4	120 Hz	f_4	140 Hz
f_5	141 Hz	f_5	173 Hz
f_6	171 Hz	f_6	179 Hz
f_7	185 Hz	f_7	185 Hz

Table 3: Eigenfrequencies for the two-plate case.

Table 4 compares both glued cases. Note the similarity between them due to the use of glue, which seems to force the two plates to behave as a single plate.

One plate with glue		Two plates with glue	
f_1	33 Hz	f_1	33 Hz
f_2	52 Hz	f_2	52 Hz
f_3	87 Hz	f_3	87 Hz
f_4	133 Hz	f_4	140 Hz
f_5	177 Hz	f_5	173 Hz
	Not found	f_6	179 Hz
f_6	189 Hz	f_7	185 Hz

Table 4: Eigenfrequencies for the glued cases.

6 CONCLUSIONS

In this study, the influence of the use of glue in lightweight junctions has been investigated through measurements on set-ups. The conclusions that can be made are:

- It can be observed that in the single plate case, the glue did not have much of an influence. The slight differences observed may be due to the anisotropy of the spruce beam and its different properties in the different set-ups. This can be the result of, for instance, knots or also because of the damping properties of the glue.
- In the two-plate case it was noticed that the glue plays an important role since it stiffens the junction by pulling both plates together. Due to that, the non-glued case is, as expected, much softer and its eigenfrequencies therefore lower.
- It has been shown that the glue plays a double role within the joints. In the vertical layer when keeping together both plates it acts as a stiffener while in the horizontal layer (on top of the beam) it acts as a dampener. Further work is needed to study both behaviors of the glue.
- The previous conclusion can be validated comparing both cases with glue (Table 4). Note the similarities between both of them. The glue in the vertical layer (two-plate case) stiffens the junction letting them behave almost as a single plate glued onto a beam (the eigenfrequencies in both cases are almost identical).
- Further investigations about the double role of the glue are needed in order to obtain a better understanding of its behavior. Moreover, accurate models for simulation may be developed as a prediction tool for comparison. Likewise, the types of junctions studied could also be identified within a larger real structure and compared with the set-ups studied by similar measurement techniques.

REFERENCES

[1] L. Cremer, M. Heckl, B. A. T. Petersson. *Structure borne-sound*. 3rd Edition. Springer-Verlag. Berlin. ISBN 3-540-22696-6.

[2] D. Bard, L.G. Sjökvist. Sound Transmission through a complete wood cross junction in a light-weight building. *Internoise, 37th International Congress and Exposition on Noise Control Engineering*, Shanghai, China, October 26-28, 2008.

[3] R. J. M. Craik, R. S. Smith. Sound transmission through light-weight parallel plates, part II: structure borne sound. *Applied Acoustics*. 2000; 61(2):247-69.

[4] L. Galbrun, Vibration transmission through plate/beam structures typical of light-weight buildings: Applicability and limitations of fundamental theories, *Applied Acoustics*. 2010; 71:587-596.

[5] D. Bard, J. Sonnerup, G. Sandberg. A finite element solution of structure-borne sound attenuation for a light-weight timber floor. *Building Acoustics*. 2008. 15(2):137-151.

[6] SIS (1997). SS-ISO 2631-1. *Vibration and shock – Evaluation of human exposure to whole-body vibration – Part 1: General requirements.* Swedish Standards Institution.

[7] C. Hopkins, *Sound Insulation*, Elsevier, ISBN 978-0-7506-6526-1 (2007).

COMPDYN 2011
III ECCOMAS Thematic Conference on
Computational Methods in Structural Dynamics and Earthquake Engineering
M. Papadrakakis, M. Fragiadakis, V. Plevris (eds.)
Corfu, Greece, 25–28 May 2011

DISTRIBUTION OF SEISMIC EARTH PRESSURES ON RIGID RETAINING Walls

Mahmoud Ghazavi[1], **Massoud Moshfegh Yeganeh**[2]
[1] Faculty of Civil Engineering, K. N. T. University of Technology, Tehran, Iran
ghazavi_ma@kntu.ac.ir
[2] Faculty of Civil Engineering, K. N. T. University of Technology, Tehran, Iran
mmyeganeh@sina.kntu.ac.ir

Keyword: Retaining wall, lateral earth pressure, pseudo dynamic, limit equilibrium approach

Abstract. *The distribution of seismic earth pressures on rigid retaining walls is an important task in design. On the basis of the limit equilibrium approach and limit state analysis, this paper presents a solution to compute the seismic earth pressure on the back of a retaining wall. For this purpose, the equilibrium of forces acting on an element of the failed wedge is considered and the earth pressure on the wall is obtained using a mathematical procedure. In this study, the effects of both horizontal and vertical components of earthquake are taken into account using a pseudo-dynamic approach. The effect of phase differences in both shear and primary waves travelling through the backfill due to seismic excitation are also considered by entering the finite shear and primary wave velocities in the analysis. The results are provided in tabular and graphical non-dimensional forms and compared with pseudo-static method to highlight the realistic non-linearity of the seismic pressure distribution.*

1 INTRODUCTION

Estimation of the seismic earth pressure is an important topic of research for safe design of retainings wall in the seismic areas. It is common in practice that the seismic accelerations in both horizontal and vertical directions are considered in terms of equivalent static forces, the so called pseudo-static accelerations. Using the pseudo-static approach, several researchers have developed various methods to determine the seismic earth pressure on rigid retaining walls. These have been started from pioneering work performed by Okabe (1926) and Mononobe & Matsuo (1929), commonly known as Mononobe-Okabe (MO) method. The MO method was modified and simplified by Seed and Whitman. The MO method is attractive due to its simplicity since engineers are familiar with the Coulomb method. The MO method basically employs only force equilibrium and thus is not capable of determining other information such as the location of the resultant force or variation of earth pressure distribution along the wall. Moreover, the pseudo static approaches, do not, in essence, incorporate time dependent effect of applied earthquake load and effect of shear and primary waves.

Steedman and Zeng (1990) considered a harmonic sinusoidal term for horizontal seismic acceleration and studied the effect of phase change and finite shear wave velocity in analysis of retaining walls. They found that the finite shear wave velocity does not have significant influence on the magnitude of the total thrust on the wall. However, it has significant effect on the pressure distribution.

Choudhury and Nimbalkar (2006) have incorporated the effect of vertical seismic acceleration due to vertically propagating primary waves through the backfill soil. They have studied the effect of various parameters such as wall friction angle (δ) and soil friction angle (φ) on lateral earth pressures.

In earlier pseudo dynamic approaches, the seismic earth pressure distribution was obtained by differentiating the total active thrust. The static earth pressure and the dynamic earth pressure acting on the retaining wall could be obtained separately. In this manner, the static earth pressure distribution becomes a linear function of depth. However many experimental results show that the distribution of static active earth pressure on the face of a rough wall depends on the mode of wall movement and the distribution of active earth pressure on a rigid wall is nonlinear (Tsagareli, 1965; Sherif and Fang, 1984). Therefore, assuming linear earth pressure distribution on walls in static condition in these methods is questionable.

Recently, two methods were developed to present mathematical solutions for computing the distribution of lateral earth pressures in static (Wang, 2000) and seismic (Ghazavi and Safarzadeh, 2003) conditions. However, these solutions are crude and need further improvement.

The present study develops a new method for determination of magnitude, distribution and the height of point of application of total active thrust on rigid retaining walls in seismic condition. It also incorporates the effects of both horizontal and vertical seismic excitations. Moreover, the effects of seismic load on lateral earth pressure are investigated using pseudo-dynamic approach.

2 BASIC EQUATION OF ANALYTICAL METHOD:

There are some assumptions required to determine the seismic active earth pressure. As shown in Fig. 1, a fixed base vertical rigid retaining wall with H height is considered. The backfill is assumed to be homogenous, dry, and cohesionless. The failure surface is also assumed to be planar (Fig. 2). Considering analytical model for propagating waves through the backfill soil in the horizontal and vertical directions, the effect of horizontal and vertical seismic acceleration are investigated.

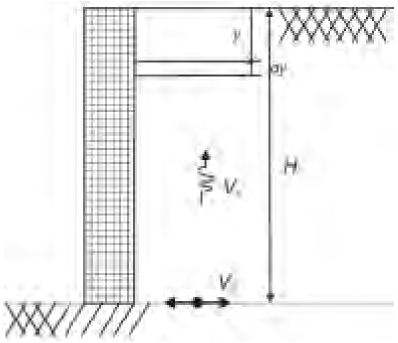

Figure 1. Model for Wave Propagation in Backfill Soil

Fig. 2 shows a failure plane inclined at an angle α with respect to the horizontal direction. An element with a thickness of dy at depth y from the ground surface is considered.

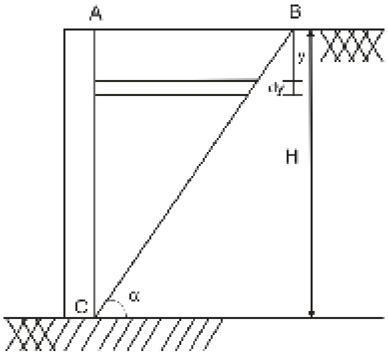

Figure 2. Soil Failed Wedge and Element of Soil Backfill

If the base of the wall is subjected to harmonic horizontal seismic acceleration ($a_h = k_h . g$) and harmonic vertical seismic acceleration ($a_v = k_v . g$), the accelerations at any depth z and time t from the wall top can be expressed as:

$$a_h(z,t) = a_h \, sin(\omega(t - \frac{H-y}{V_s}) \tag{1}$$

$$a_v(z,t) = a_v \, sin(\omega(t - \frac{H-y}{V_p}) \tag{2}$$

where H = height of the wall, V_P , V_s = wave velocities in the horizontal and vertical directions, respectively, and a_h , a_v = amplitude of acceleration in the horizontal and vertical directions, respectively. The horizontal and vertical seismic accelerations acting on the soil wedge as described in Eqs. (1) and (2) are not constants but dependent on time and phase difference in shear and primary waves propagating vertically through the backfill. This is normally proposed in pseudo-dynamic analysis of retaining walls.

3 DETERMINATION OF LATERAL EARTH PRESSURE

In the following sections the lateral static and seismic earth pressure determine separately then the total active earth pressure is obtained by add these two separate parts.

3.1 Determination of static lateral earth pressure

Consider as element of soil wedge with a thickness of **dy** at depth y from the ground surface (Fig.2). The forces exerted on this element are due to the vertical pressure $\boldsymbol{\sigma_y}$ on the top of the element, the vertical reaction $\boldsymbol{\sigma_y} + \boldsymbol{d\sigma_y}$ on the bottom of the element, the normal reaction $\boldsymbol{\sigma_x}$ of the retaining wall, the shear $\boldsymbol{\tau_x}$ between the backfill and the back of the retaining wall, the normal reaction $\boldsymbol{\sigma_r}$ of the rest of the soil, the shear stress $\boldsymbol{\tau_r}$ between the sliding wedge and the rest of the backfill. Fig. 3 shows the stresses and forces exerted on an arbitrary element of the backfill soil.

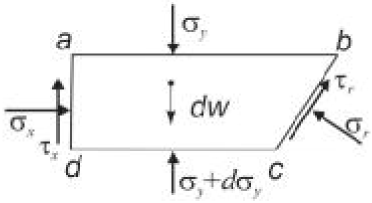

Figure 3. Forces and Stresses on an Element of Backfill

The equilibrium of horizontal forces on the element (Fig. 3) results in:

$$\sigma_x + \tau_r \cot \alpha - \sigma_r = 0 \tag{3}$$

Considering cohesionless backfill and assuming a full mobilization of shear forces along the failure plane gives:

$$\tau_x = \sigma_x \tan \delta \tag{4}$$

$$\tau_r = \sigma_r \tan \varphi \tag{5}$$

The horizontal earth pressure acting on the wall (σ_x)is equal to:

$$\sigma_x = K\sigma_y \tag{6}$$

where K is the lateral pressure coefficient.

Applying equilibrium condition to the vertical forces on the element (Fig. 3) results in:

$$\sigma_y(H-y)\cot \alpha + dW - (\sigma_y + d\sigma_y)(H-y-dy) \times \cot \alpha - \tau_x\, dy - \tau_r \frac{r}{\sin \alpha} \sin \alpha - \sigma_r \times \frac{dy}{\sin \alpha} \cos \alpha = 0 \tag{7}$$

With more simplifications, Eq. (7) may be converted to:

$$\frac{\sigma_y}{dy} = \gamma + \frac{1}{(H-y)}\left[\sigma_y - \sigma_r - (\tau_r + \tau_x) \tan \alpha\right] \tag{8}$$

$$\frac{\sigma_y}{dy} = [1 - ak]\frac{\sigma_y}{H-y} + \gamma \tag{9}$$

where:

$$a = \frac{\cos(\alpha - \varphi - \delta)}{\sin(\alpha - \varphi)} \frac{\tan \alpha}{\cos \delta}$$

Eq. (9) is basic for computing the seismic lateral earth pressure on the wall and its solution is expressed as:

$$\sigma_y = \frac{A}{k}[H-y]^{aK-1} + \gamma \frac{H-y}{ak-2} \tag{10}$$

where:

$$A = \left(\frac{\gamma K H^{2-aK}}{2-aK}\right) \tag{11}$$

From Fig. 2, it is seen that the boundary condition is ($\sigma_{y=0} = 0$). Thus the following solution for the lateral earth pressure on the wall is obtained:

$$\sigma_{asx} = K \times H \left[\frac{1-\frac{y}{H}-\left(1-\frac{y}{H}\right)^{aK-1}\gamma}{ak-2}\right] \tag{12}$$

The lateral active earth pressure is obtained from:

$$\sigma_{as} = \sqrt{{\sigma_x}^2 + {\tau_x}^2} = \sqrt{{\sigma_x}^2 + {\sigma_x}^2\, tan^2\,\delta} = \frac{\sigma_{asx}}{cos\,\delta} \tag{13}$$

3.1.1 Determination of lateral earth pressure coefficient (K)

The lateral earth pressure coefficient, K, has a significant influence on the pressure distribution in seismic condition. Evaluation of this is a very important issue, which must be treated carefully. This paper proposed a method to determination of the lateral earth pressure coefficient, K. By using of moment equilibrium of each element of soil an attempt to determination of lateral earth pressure coefficient is made. The moment equilibrium of forces about point b in Fig. 3 gives:

$$\tau_x \times l \times dy - dW \times \frac{l}{2} + d\sigma_y \times \frac{l^2}{2} = 0 \tag{14}$$

where l is the length of upper side of element and given by:

$$l = \gamma \times l \times dy = cot\,\alpha\,(H-y) \tag{15}$$

Substituting Eq. (4) and (5) into Eq. (14) and omitting the differential terms of the second order gives:

$$\frac{d\sigma_y}{dy} = \gamma - \frac{2\,tan\,\varphi}{l} K\sigma_y \tag{16}$$

Equating Eq. (16) and Eq. (9) gives:

$$[1-ak]\frac{\sigma_y}{H-y} + \gamma = \gamma - \frac{2\,tan\,\varphi}{l} K\sigma_y \tag{17}$$

More simplification gives:

$$[1-ak] = -2\,tan\,\varphi \cot\alpha\, K \tag{18}$$

The lateral earth pressure coefficient is given by:

$$K = \frac{1}{(a - 2tan\,\varphi \tan\alpha)} \tag{19}$$

3.2 Determination of seismic lateral earth pressure

Similar to the pseudo-dynamic approach which considers finite shear wave velocity within the backfill material (Steedman and Zeng, 1990), it is also assumed that the backfill shear modulus (G) is constant with the depth. Only the phase and not the magnitude of accelerations are varying along the depth of the wall within backfill.

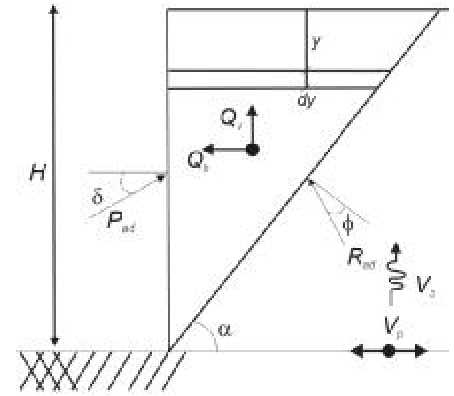

Figure 4. Analytical Model Considered for Computation of Seismic Part of Active Earth Pressure.

The mass of an element of wedge at depth z is

$$m = \frac{dW}{g} = \frac{\gamma}{g} \times l \times dz \tag{20}$$

The inertial force acting on a soil element is:

$$q_h = m.a_h(z,t) \tag{21}$$

Consider the shear wave velocity, $Vs = (\frac{G}{\rho})^{\frac{1}{2}}$, where, ρ is the density of the backfill material and primary wave velocity, $Vp = [\frac{G(2-2v)}{\rho(1-2v)}]^{1/2}$, where ν is the Poisson's ratio of the backfill are assumed to act within the soil media due to earthquake loading. For most geological materials, $\frac{Vp}{Vs}$ = 1.87 (Das, 1993).

The period of lateral shaking, $T = \frac{2\pi}{\omega} = \frac{4H}{V_s}$, where ω is the angular frequency is considered in the analysis.

By substituting Eq. (1) into Eq. (22), the total horizontal inertial force acting within the failure zone can be expressed as:

$$Q_h(t) = \int_0^H m(z).a_h(z,t)dz = \frac{\lambda\gamma a_h}{4\pi^2 \mathrm{g} \tan\alpha}(2\pi H\cos\omega\xi + \lambda(sin\omega\xi - sin\omega t)) \tag{22}$$

where

$$\xi = t - \frac{H}{V_s}$$
$$\lambda = TV_s$$

By substituting Eq. (2) into Eq. (23), the total vertical inertial force acting within the failure zone can be expressed as:

$$Q_v(t) = \int_0^H m(z).\, a_v(z,t)dz = \frac{\eta\gamma a_v}{4\pi^2 g\, tan\, \alpha}(2\pi H\, cos\, \omega\psi + \eta(sin\omega\psi - sin\omega t)) \tag{23}$$

where

$$\psi = t - \frac{H}{V_p}$$

$$\eta = TV_p$$

The total seismic active thrust $\mathrm{P_{ad}}(\mathrm{t})$ can be obtained by resolving the forces on the wedge and considering the equilibrium of the forces. Hence $\mathrm{P_{ad}}(\mathrm{t})$ can be expressed as:

$$P_{ad} = \frac{Q_h \cos(\alpha - \varphi) - Q_v sin\,(\alpha - \varphi)}{\cos(\alpha - \alpha + \varphi)} \tag{24}$$

The seismic portion of active earth pressure distribution can be obtained from:

$$\sigma_{ad} = \frac{\partial P_{ad}(z)}{\partial z} = \frac{cos(\alpha - \varphi)k_h\gamma z}{cos(\delta - \alpha + \varphi)\, tan\, \alpha} sin\, \omega(t - \frac{z}{V_s}) - \frac{cos(\alpha - \varphi)k_v\gamma z}{cos(\delta - \alpha + \varphi)\, tan\, \alpha} sin\, \omega(t - \frac{z}{V_p}) \tag{25}$$

4 DETERMINATION OF TOTAL LATERAL EARTH PRESSURE AND RESULTANT THRUST

The total lateral earth pressure is obtained by adding static and seismic portions of active earth pressure. Thus, the total earth pressure can be express as:

$$\sigma_{ae} = \sigma_s + \sigma_d \tag{26}$$

where

$$\sigma_s = \frac{\gamma H}{(a - 2tan\, \varphi \tan \alpha)\, cos\, \delta}\left[\frac{1 - \frac{y}{H} - \left(1 - \frac{y}{H}\right)^{\frac{a}{(a - 2tan\, \varphi \tan \alpha)} - 1}}{\frac{a}{(a - 2tan\, \varphi \tan \alpha)} - 2}\right] \tag{27}$$

$$\sigma_d = \frac{cos(\alpha - \varphi)\gamma y}{cos(\delta - \alpha + \varphi)\, tan\, \alpha}(k_h sin\, \omega(t - \frac{y}{V_s}) - k_v sin\, \omega(t - \frac{y}{V_p})) \tag{28}$$

The total lateral active thrust is obtained by integrating static and seismic earth pressures. This gives:

$$P_{ae} = P_{as} + P_{ad} = \int_0^H \sigma_{ae} dy + \int_0^H \sigma_{ad} dy \tag{29}$$

Substituting static and seismic thrust in Eq. (29) gives:

$$P_{ae} = \frac{1}{2}\gamma H^2 \frac{\sin(\alpha-\varphi)\cot\alpha}{\cos(\alpha-\varphi-\delta)} + (\frac{T}{2H\pi^2\tan\alpha}) \times \frac{(k_h V_s \cos(\alpha-\varphi) m_1 - k_v V_p\, sin(\alpha-\varphi)\, m_2)}{\cos(\delta+\varphi-\alpha)} \tag{30}$$

where

$$m_1 = 2\pi\cos 2\pi\left(\frac{t}{T}-\frac{H}{TV_s}\right) + \frac{TV_s}{H}[\sin 2\pi\left(\frac{t}{T}-\frac{H}{TV_s}\right) - \sin 2\pi\frac{t}{T}]$$

$$m_2 = 2\pi\cos 2\pi\left(\frac{t}{T}-\frac{H}{TV_P}\right) + \frac{TV_P}{H}[\sin 2\pi\left(\frac{t}{T}-\frac{H}{TV_P}\right) - \sin 2\pi\frac{t}{T}]$$

The maximum value of P_{ae} is obtained by maximizing P_{ae} with respect to t and α

5 HEIGHT OF APPLICATION OF RESULTANT EARTH PRESSURE

The locations of the resultant of earth pressures on retaining wall in static and seismic conditions are determined using the Coulomb and MO methods for static and seismic conditions, respectively. In both methods, a linear distribution of earth pressures on the wall is assumed and thus the location of the total thrust is exact. In the MO method, Eq. (31) is normally used to obtain H_{ae} (Seed and Withman, 1970):

$$H_{ae} = \frac{P_a\left(\frac{H}{3}\right) + \Delta P_{ae}(0.6H)}{P_{ae}} \tag{31}$$

where $\Delta P_{ae} = P_{ae} - P_a$

For curvilinear distribution earth pressure presented in this paper, the height of the application of the resultant earth pressure can be determined using the following procedure. The resultant moment of the pressure about the wall bottom can be obtained from:

$$M_{ae} = \int_0^L (H-y)\sigma_{ae} dl \tag{32}$$

The height H_{ae} of application of the resultant pressure is:

$$H_{ae} = \frac{M_{ae}}{P_{ae} \cos \delta} \tag{33}$$

6 RESULTS AND DISCUSSION:

In this section, an example for a rigid retaining wall with a height of 5 m is considered. All necessary parameters are given in Fig. 5. As seen, the earth pressure distribution is non-linear and its maximum does not occur at the wall bottom.

Moreover the earth pressure decrease to zero at the bottom of wall in static condition but zero earth pressure does not occur at the bottom of wall in seismic condition.

For better comparison of result the distribution of earth pressure by assuming linear distribution of earth pressure in static condition is shown in Fig. 5. As observed, by making this assumption, the maximum earth pressure occurs at the wall bottom.

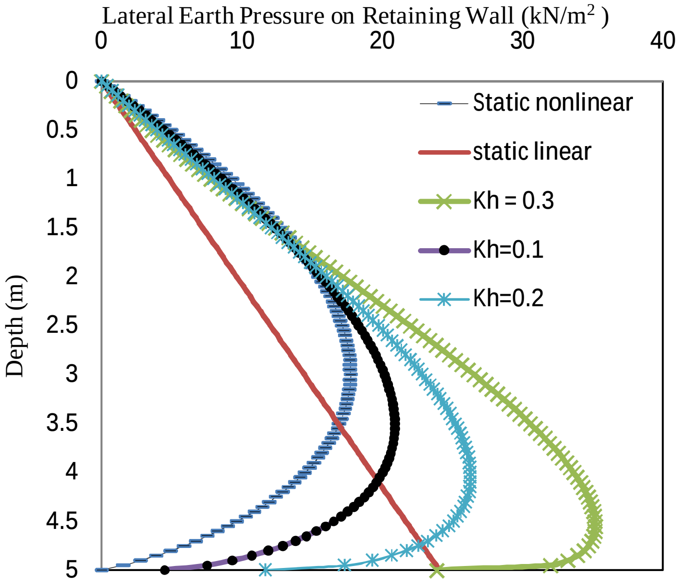

Figure 5. Distribution of Horizontal Earth Pressure on Retaining Wall for
$\varphi = 33^{\circ}, \delta = 16^{\circ} k_v = 0\,, V_s = 100\ \frac{m}{s}, H = 5\ m, T = 0.2s, \frac{H}{\lambda} = 0.167, \frac{H}{\eta} = 0.09,\ \beta = 90^{\circ}, \gamma = 18\ \frac{kN}{m^3}$

As shown in Fig. 5, due to changes of lateral earth pressure with time and angle of slip surface (α), the distribution shown makes the total lateral thrust maximum. Hence the distribution of lateral earth pressure nonlinearly comes close to triangular. However, if the maximum overturning is taken into consideration, the distribution of earth pressure becomes close to parabolic variation (Fig. 6). Therefore, in the design of retaining wall, both distributions of lateral earth pressure should be taken into account.

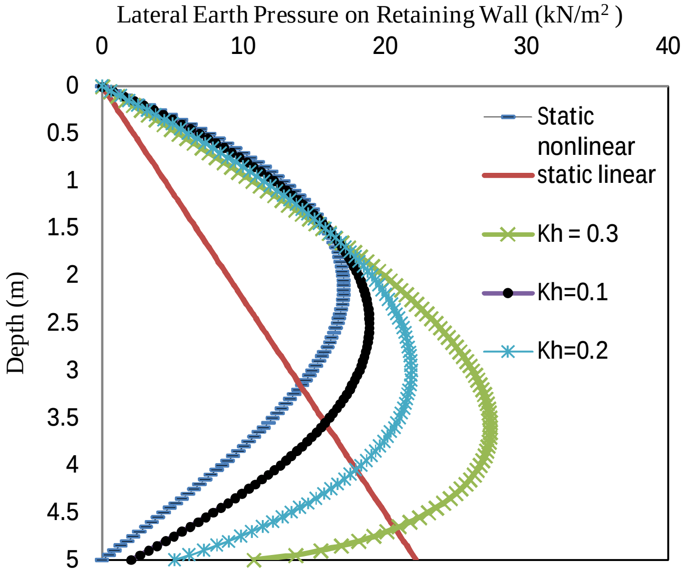

Figure 6. Distribution of Horizontal Earth Pressure on Retaining Wall for $\varphi = 33^{\circ}, \delta = 16^{\circ} k_v = 0\,, V_s = 100\ \frac{m}{s}\,, H = 5\ m, T = 0.2s, \frac{H}{\lambda} = 0.167, \frac{H}{\eta} = 0.09,\ \beta = 90^{\circ}, \gamma = 18\ \frac{kN}{m^3}$

7 CONCLUSIONS:

This paper has proposed a pseudo-dynamic method by considering the time effect and phase change in shear and primary waves propagating in the backfill behind the rigid retaining wall. The seismic and static total thrust, the location of the thrust and distribution of lateral earth pressures due to static and seismic loading on rigid retaining walls have been presented using a closed form solution. The differential equation governing an arbitrary element at a given depth along the wall height has been derived and solved explicitly using appropriate boundary conditions. The seismic earth pressure distributions, the total thrust on the wall, and the location of the thrust have then been determined. The present study considers both static and seismic earth pressure distributions in a nonlinear manner. Parametric studies were performed to show how the earth pressure is distributed on a rigid retaining wall. The general superiority of the current solution is that the value of lateral earth pressure coefficient, K, is more accurate and lacks any simplifying assumptions. It has also been demonstrated that K is the most important parameter which influences the non-linear pressure distribution. It has also been found that due to changes of the lateral earth pressure with time and angle of slip surface (α), a certain distribution gives the maximum total lateral thrust. If the wall overturning is critical, a parabolic distribution of earth pressures offer the maximum moment. In general, in the design of retaining walls, both distributions of lateral earth pressures should be taken into account.

REFERENCES

[1] Choudhury, D, Nimbalkar, S.S, Pseudo-dynamic approach of seismic active earth pressure behind retaining wall, Geotechnical and Geological Engineering, Springer, The Netherlands, 24(5), 1103-1113, 2006.

[2] Das, B.M, Theoretical foundation engineering, Ross Publication Edition, 2007.

[3] Ghazavi, M. , Safarzadeh, Z, Distribution of seismic active earth pressure on rigid retaining walls, Forth International Conference on Earthquake Engineering and Seismology (SEE4), IIEES, Tehran, Iran, Vol. I, Paper No. SF15, 563-570, 2003.

[4] Seed, H. B. and Whitman, R.V, Design of earth retaining structure for dynamic loads, proc. of the ASCE Specialty Conf. on Lateral Stress in the Ground and Design of Earth Retaining Structures, ASCE, 103-147, 1970.

[5] Sherif, M. A., I. Ishibashi, and C. D. Lee, Earth pressure against rigid retaining walls. Journal of Geotechnical Engineering, ASCE, Vol. 108(GT5), 679-693,1982.

[6] Steedman, R.S. and Zeng, X, The influence of phase on the calculation of pseudo-static earth pressure on a retaining wall, Geotechnique, 40(1), 103–112, 1990.

[7] Tsagareli, Z. V. (1965): Experimental investigation of the pressure of a loose medium on retaining walls with a vertical back face and horizontal backfill surface. J. Soil Mech. Found. Eng, ASCE 91, No. 4, 197–200.

[8] Wang, Y.Z. (2000): Distribution of earth pressure on a retaining wall, Ge´otechnique, Vol. 50, No. 1, pp. 83–88,1943.

COMPDYN 2011
ECCOMAS Thematic Conference on
Computational Methods in Structural Dynamics and Earthquake Engineering
M. Papadrakakis, M. Fragiadakis , V. Plevris (eds.)
Corfu, Greece, 25-28 May 2011

MODELLING MOVING ONE-DIMENSIONAL WAVEGUIDES USING WAVES AND FINITE ELEMENT ANALYSIS

E. Manconi[1], **R. Garziera**[1]

[1]Department of Industrial Engineering, University of Parma
Viale G.P. Usberti 181/A, 43124 Parma, Italy
e-mail: elisabetta.manconi@unipr.it

Keywords: Waves, Wave Basis, Finite Elements, Dispersion Equation, Axially Moving Beam.

Abstract. *One approach to the numerical analysis of complex waveguides is the Wave Finite Element (WFE) method. In this method conventional Finite Elements (FEs) are used to discretise a small segment of a waveguide. The FE model of just this small part of the structure is post-processed using periodicity conditions, and an eigenproblem is then solved to predict dispersion characteristics and wavemodes. Once the wave characteristics are predicted, free vibration and response of the structure as a whole can be modelled in terms of these waves. This paper presents an extension of the method to moving one-dimensional waveguides. In particular an axially moving beam is considered. The FE formulation of a moving beam element is developed and the WFE method is applied to find the wave properties of such a beam. Natural frequency are obtained using the Phase Closure Principle and the Dynamic Stiffness Matrix, both formulated in terms of wavemodes and dispersion relation obtained from the WFE eigenproblem. The analytical equation of transverse motion of the travelling beam is also solved in terms of propagating and decaying waves, and the frequency equation is obtained using the phase closure principle. Numerical results are shown.*

1 INTRODUCTION

The research on the dynamics of moving media has had a renewed interest in the last few decade giving rise to large scientific production. There are a number of applications which involve moving structures and fluids, and the necessity to improve their performance has motivated the development of numerical and analytical methods to investigate the dynamics of mechanical models involving transport of mass. Studies on the dynamics of axially moving structures have been made by several authors, and many original and interesting studies have been produced. To cite just a few, the works [1, 2, 3, 4] can be listed.

In this paper the dynamics of a travelling one-dimensional waveguides is investigated using a Wave Finite Element method [5, 6]. The method is an FE post-processing technique for obtaining numerical prediction of wave characteristics. The method involves conventional FE analysis of a small segment of the structure. Typically this consists of just a single finite element, or a stack of elements meshed through the cross-section. The FE matrices of this segment are then post-processed using periodicity conditions, resulting in an eigenproblem, whose solutions yield the dispersion curves, frequency evolution of the wavenumber, and wavemodes. Once the dispersion characteristics are known, existing wave propagation methods can be applied to take into account boundary conditions, calculate natural frequencies, forced response or determine the systems stability [7].

An axially moving beam, modelled using the classical linear theory, is studied in the present paper. The FE element formulation of a linear moving beam element is derived following [8], and application of the WFE method is briefly described. Free vibrations of the moving beam are predicted using the Phase Closure Principle [9] and the Dynamic Stiffness Matrix [10] formulated in terms of wavemodes. These are applied once the wave characteristics are known from the WFE model. An analytical wave approach is also presented to show some characteristics of the elastic waves propagating in such a beam. Numerical results are shown and the accuracy of the proposed approach is discussed. The theory used in this paper is linear, therefore results are consistent with ‘low’ axial velocity and small deformation. However, this linear model well approximates the behaviour of many real cases, and it can be helpful for predicting instability region, where nonlinear terms become significant [11]. It must be pointed out that wave propagation in a travelling beam were also investigated by Chakraborty and Mallik in [12], and a Dynamic Stiffness Formulation of a moving beam was given by Banerjee and Gunawardana [13]. Both these works involve an analytical formulation of the equation of motion, while the present work concerns the application of a numerical technique based on FE analysis.

Although for the case of a moving beam there are no practical advantages in calculating dispersion curves and natural frequencies using the proposed method, this work shows that the WFE method can provide results for moving waveguides. This is of particular interest in more complicated cases where analytical formulation of the problem can be difficult and computational cost using standard numerical approaches can be very large.

2 EQUATION OF MOTION AND FE FORMULATION OF A MOVING BEAM ELEMENT

A prismatic axially moving beam is considered. The beam is modelled using an Eulero–Bernoulli beam with constant mass per unit length ρ and constant flexural rigidity EI. The beam moves with axial speed $v(t)$, and its transverse displacement, measured by a stationary observer, is denoted by $y(x,t)$, figure 1. External excitation are not taken into account.

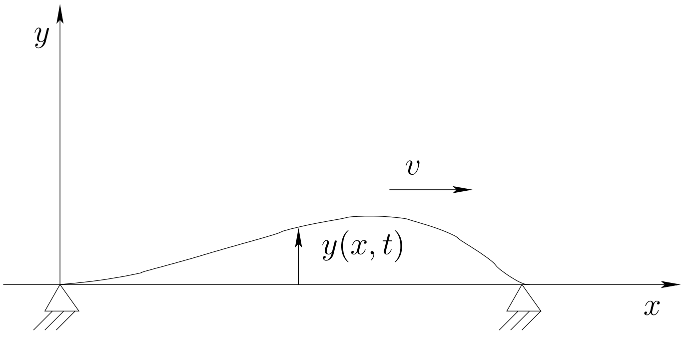

Figure 1: Schematic model of an axially moving beam.

Time differentiation of the displacement yields

$$\begin{aligned} \frac{\mathrm{d}y}{\mathrm{d}t} &= \frac{\partial y}{\partial t} + v\frac{\partial y}{\partial x}; \\ \frac{\mathrm{d}^2y}{\mathrm{d}t^2} &= \frac{\partial^2 y}{\partial t^2} + 2v\frac{\partial^2 y}{\partial x\partial t} + v^2\frac{\partial^2 y}{\partial x^2} + \frac{\partial v}{\partial t}\frac{\partial y}{\partial x}. \end{aligned} \tag{1}$$

Accordingly, the analytical equation of transverse motion is

$$EI\frac{\partial^4 y}{\partial x^4} + \rho\left(\frac{\partial^2 y}{\partial t^2} + 2v\frac{\partial^2 y}{\partial x\partial t} + v^2\frac{\partial^2 y}{\partial x^2} + \frac{\partial v}{\partial t}\frac{\partial y}{\partial x}\right) = 0. \tag{2}$$

In order to apply the WFE approach, a small segment of length L is taken and discretised using FE elements. Therefore a moving beam FE element is developed. The kinetic and potential energy of the element are

$$\begin{aligned} T &= \tfrac{1}{2}\rho\int_0^L\left(\frac{\partial^2 y}{\partial t^2} + 2v\frac{\partial^2 y}{\partial x\partial t} + v^2\frac{\partial^2 y}{\partial x^2}\right)\mathrm{d}x; \\ V &= \tfrac{1}{2}EI\int_0^L\left(\frac{\partial^2 y}{\partial x^2}\right)^2\mathrm{d}x. \end{aligned} \tag{3}$$

The transverse displacement of the beam element is modelled by standard cubic shape function $N(x)$ [14] and nodal displacements $\mathbf{q}$, that is

$$y = N(x)\mathbf{q}. \tag{4}$$

Substituting this equation in (3), the Lagrangian of the moving element is given by [8]

$$L = \frac{1}{2}\dot{\mathbf{q}}^T\mathbf{M}\dot{\mathbf{q}} + \mathbf{\frac{1}{2}q^TK_1q} - \mathbf{\frac{1}{2}q^TK_2q} + \mathbf{\frac{1}{2}q^TC_1}\dot{\mathbf{q}} + \mathbf{\frac{1}{2}}\dot{\mathbf{q}}^\mathbf{T}\mathbf{C_2q}, \tag{5}$$

with

$$\begin{aligned} &\mathbf{M} = \rho\int_\mathbf{0}^\mathbf{L}\mathbf{N^TN}\,\mathrm{d}\mathbf{x}; \quad \mathbf{K_1} = \rho\mathbf{v^2}\int_\mathbf{0}^\mathbf{L}\mathbf{N'^TN'}\,\mathrm{d}\mathbf{x}; \quad \mathbf{K_2} = \mathbf{EI}\int_\mathbf{0}^\mathbf{L}\mathbf{N''^TN''}\,\mathrm{d}\mathbf{x}; \\ &\mathbf{C_1} = \rho\mathbf{v}\int_\mathbf{0}^\mathbf{L}\mathbf{N'^TN}\,\mathrm{d}\mathbf{x}; \quad \mathbf{C_2} = \rho\mathbf{v}\int_\mathbf{0}^\mathbf{L}\mathbf{N^TN'}\,\mathrm{d}\mathbf{x}, \end{aligned} \tag{6}$$

where $'$ denotes differentiation with respect to x. The FE equation of motion can be obtained using Euler–Lagrangian equations. Therefore the FE equations of motion of a moving beam element are

$$\mathbf{M}\ddot{\mathbf{q}} + \left(\mathbf{C_2} - \mathbf{C_2^T}\right)\dot{\mathbf{q}} + \left(\dot{\mathbf{C}}_\mathbf{2} - \mathbf{K_2} + \mathbf{K_1}\right)\mathbf{q} = \mathbf{f}, \tag{7}$$

where **f** are nodal forces.

Although in this section a general formulation considering time dependent velocity is given, in the following sections a constant axial velocity is assumed, that is $\frac{\partial v}{\partial t} = 0$ in equation (2) and $\dot{\mathbf{C}}_2 = \mathbf{0}$ in equation (7).

3 WAVE MOTION AND FREE VIBRATION

In this section the dynamics of the travelling beam is described using a wave approach. Solution of equation (2) are written in terms of harmonic waves $y(x,t) = Ae^{i(\omega t - kx)}$ which, substituted into (2), gives the dispersion relation between wavenumbers and frequencies:

$$a^2k^4 - v^2k^2 + 2vwk - w^2 = 0, \tag{8}$$

where $a = \sqrt{\frac{EI}{\rho}}$. The roots of this equation are

$$\begin{aligned} k_d &= -\frac{1}{2}\frac{v}{a} + \frac{1}{2}\sqrt{\frac{v^2}{a^2} + 4\frac{w}{a}}; \qquad k_u = \frac{1}{2}\frac{v}{a} + \frac{1}{2}\sqrt{\frac{v^2}{a^2} + 4\frac{w}{a}}; \\ k_{de} &= \frac{1}{2}\sqrt{4\frac{w}{a} - \frac{v^2}{a^2}} + i\frac{1}{2}\frac{v}{a}; \qquad k_{ue} = \frac{1}{2}\sqrt{4\frac{w}{a} - \frac{v^2}{a^2}} - i\frac{1}{2}\frac{v}{a}, \end{aligned} \tag{9}$$

and the solution of the homogeneous equation (2) can be written as a linear combination of these four flexural waves

$$y(x,t) = A_d e^{-ik_d x}e^{iwt} + A_u e^{ik_u x}e^{iwt} + A_{de}e^{-k_{de}x}e^{iwt} + A_{ue}e^{k_{ue}x}e^{iwt}. \tag{10}$$

For $0 < v < 2\sqrt{\omega a}$ solutions k_{de} and k_{ue} represent attenuating waves, therefore equations (9) represent one positive-going and one negative-going propagating waves, k_d and k_u respectively, and one positive-going and one negative-going decaying waves, k_{de} and k_{ue} respectively. On the other side, for $v > 2\sqrt{\omega a}$ solutions k_{de} and k_{ue} are real numbers representing two positive-going propagating waves. Hence, when $v > 2\sqrt{\omega a}$ there are four propagating waves, three positive-going waves, k_d, k_{de} and k_{ue}, and one negative-going wave, k_u. However, $v_g = 2\sqrt{\omega a}$ is the group velocity of a disturbance propagating in the beam, and it is expected that instability occurs when the axial velocity is faster than the energy velocity in the medium considered. Moreover, the axial speed is often much smaller than the speed of any travelling disturbance in the beam. Therefore the inequality $0 < v < 2\sqrt{\omega a}$ is assumed in the present paper.

Using the same formalism proposed in [9], the wave amplitude of the positive and negative going waves is given by $\mathbf{A}^+ = [A_d, A_{de}]^T$ and $\mathbf{A}^- = [A_u, A_{ue}]^T$, while the transfer matrices $\mathbf{F}^+$ and $\mathbf{F}^-$ describe the propagation from one point to another through appropriate wavenumber

$$\mathbf{F}^+(x) = \begin{bmatrix} e^{-ik_d x} & 0 \\ 0 & e^{-k_{de}x} \end{bmatrix}, \qquad \mathbf{F}^-(x) = \begin{bmatrix} e^{ik_u x} & 0 \\ 0 & e^{k_{ue}x} \end{bmatrix}. \tag{11}$$

To evaluate the free vibration, the interaction of both propagating and decaying waves with discontinuities is considered, and wave amplitudes and phases after reflection and transmission are arranged in reflection and transmission matrices. The elements of these matrices are obtained imposing equilibrium conditions [9]. In this paper we consider boundary conditions at the ends of the beam $A(x=0)$ and $B(x=L_{tot})$, where L_{tot} is the total length of the beam, and the reflection matrices at the boundaries are denoted by $\mathbf{R}_A$ and $\mathbf{R}_B$.

The wave amplitudes at each ends of the beam are denoted by $\mathbf{A}^+$, $\mathbf{A}^-$, $\mathbf{B}^+$ and $\mathbf{B}^-$. If the incident waves impinging upon the right end at $A(x=0)$ are the negative-going waves $\mathbf{A}^-$, then reflected waves have amplitude $\mathbf{A}^+ = \mathbf{R}_A\ \mathbf{A}^-$. Similarly if the incident waves impinging upon the left end are the positive-going waves of amplitude $\mathbf{B}^+$, reflected waves are $\mathbf{B}^- = \mathbf{R}_B\ \mathbf{B}^+$. Considering the wave reflection matrices and using the transfer matrices, the following relations can be written

$$\mathbf{A}^+ = \mathbf{R}_A\ \mathbf{A}^-;\ \ \mathbf{B}^- = \mathbf{R}_B\ \mathbf{B}^+;\ \ \mathbf{B}^+ = \mathbf{F}^+(L_{tot})\ \mathbf{A}^+;\ \ \mathbf{A}^- = \mathbf{F}^-(-L_{tot})\ \mathbf{B}^-. \tag{12}$$

Combing equations in (12), the characteristic equation is obtained

$$\left[\mathbf{R}_A\ \mathbf{F}^-(-L)\ \mathbf{R}_A\ \mathbf{F}^+(L) - \mathbf{I}\right]\ \mathbf{A}^+ = 0. \tag{13}$$

For non trivial solution, the determinant of the coefficients $\mathbf{A}^+$ must be zero, that is

$$\left|det\left(\mathbf{R}_A\ \mathbf{F}^-(-L_{tot})\ \mathbf{R}_A\ \mathbf{F}^+(L_{tot}) - \mathbf{I}\right)\right| = 0. \tag{14}$$

Solutions of equations (14) and (13) give the natural frequencies and natural modes.

4 WAVE FINITE ELEMENT MODEL

In this section the WFE approach is briefly described. The FE equation of motion (7) of the moving beam element is considered with $\dot{\mathbf{C}}_2 = \mathbf{0}$. Assuming time harmonic behaviour, the equation of motion is

$$\left(-\omega^2\mathbf{M} + i\omega\mathbf{C}_{eq} + \mathbf{K}_{eq}\right)\mathbf{q} = \mathbf{f}, \tag{15}$$

where $\mathbf{C_{eq}} = \mathbf{C_2} - \mathbf{C_2^T}$ and $\mathbf{K_{eq}} = \mathbf{K_2} - \mathbf{K_1}$.

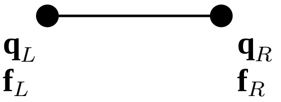

Figure 2: WFE model and node numbering.

The nodal degrees of freedom (DOFs) $\mathbf{q}$ and the nodal forces $\mathbf{f}$ are partitioned into left and right, figure 2, that is

$$\mathbf{q} = [\mathbf{q}_L^T\ \ \mathbf{q}_R^T]^T; \tag{16}$$

T denoting the transpose, with a similar expression for the nodal forces $\mathbf{f}$. Under the passage of a wave the nodal DOFs are related by periodicity conditions [15]

$$\mathbf{q}_R = \lambda\mathbf{q}_L, \tag{17}$$

where $\lambda = e^{-ikL}$ and k is the wavenumber, while equilibrium at left side of the segment implies

$$[\mathbf{I}\quad \lambda^{-1}\mathbf{I}]\mathbf{f} = \mathbf{0}. \tag{18}$$

By substituting equation (17) in equation (15), and premultiplying both sides of equation (15) by the matrix in equation (18), the equation of free wave motion takes the form

$$[\overline{\mathbf{K}_{eq}}(kL) - \omega^2\overline{\mathbf{M}}(kL) + i\omega\overline{\mathbf{C}_{eq}}(kL)]\mathbf{q}_L = \mathbf{0}. \tag{19}$$

Solutions of equation (19) yield the dispersion curves and the wavemode shapes. This involves solving a quadratic polynomial eigenvalue problem, which is recast as the standard linear eigenvalue problem [5, 6]. Associated with eigenvalues, viz. wavenumbers, are eigenvectors Φ_{qj}, which represent wavemodes, and vectors

$$\Phi_{fj} = \left[\overline{\mathbf{K}_{eq}}(kL) - \omega^2\overline{\mathbf{M}}(kL) + i\omega\overline{\mathbf{C}_{eq}}(kL)\right]\Phi_{qj}. \tag{20}$$

These can be partitioned into positive-going and negative-going waves, which are denoted by $(\lambda_j^+, \Phi_{qj}^+, \Phi_{fj}^+)$ and $(\lambda_j^-, \Phi_{qj}^-, \Phi_{fj}^-)$ respectively. Positive going waves are typically characterised by [7]

$$|\lambda_j^+| <= 1; \quad Real[i\omega \mathbf{f}_L \mathbf{q}_L] < 0 \;\text{ if }\; |\lambda_j^+| = 1. \tag{21}$$

Note that if there are n degrees of freedom for node L and R, then there are $2n$ eigenvalues and the eigenvectors matrix Φ_q and Φ_f are $n \times 2n$.

5 FREE VIBRATION USING WFE DISPERSION RELATION AND WAVEMODES

Free vibration and dynamic response can be obtained using wave-based methods, in particular when the analysis focus on disturbance propagation [7]. In this section natural frequencies are predicted using wavemodes and dispersion curves obtained from the WFE eigenproblem (19). In the following it is assumed that nodal forces and displacements are described in terms of wave amplitudes $\mathbf{A}$ using wavemodes as a basis, that is

$$\mathbf{q}_L = \Phi_q\mathbf{A}; \quad \mathbf{f}_L = \Phi_f\mathbf{A}. \tag{22}$$

In practise displacements are often expanded onto a reduced basis and only $m < 2n$ pairs of waves - positive and negative going waves - are retained, so that Φ_q and Φ_f are $n \times m$ matrices and λ is an array of size m [7]. Although there is not a rigorous criterium, this reduced basis is supposed to include all the wavemodes which mostly contributes to the structure response. Typically all the propagating waves are retained together with the attenuating and evanescent waves which either decay not very rapidly with distance or are becoming propagating in the frequency band of interest.

5.1 Dynamic Stiffness Formulation

The dynamic stiffness matrix [10] of the beam is developed using wavemodes and dispersion curves, and subsequently used to investigate free vibration characteristics. If $N = L_{tot}/L$, where L_{tot} is the total length of the beam and N is typically an entire number, the total displacement at $A(x = 0)$ and $B(x = NL)$ can be expanded as

$$\mathbf{Q} = \begin{bmatrix} \mathbf{q}(0) \\ \mathbf{q}(NL) \end{bmatrix} = \begin{bmatrix} \Phi_q \\ \Phi_q\wedge^N \end{bmatrix}\mathbf{A} = \mathbf{D}_q\mathbf{A}. \tag{23}$$

In equation (23) the diagonal matrix $\wedge = diag(\lambda_1, \ldots, \lambda_m)$ contains the WFE eigenvalues, and the matrix $\mathbf{D}_q$ is a rectangular $2n \times m$ matrix. A similar expression is given for nodal forces

$$\mathbf{F} = \begin{bmatrix} \mathbf{f}(0) \\ \mathbf{f}(NL) \end{bmatrix} = \begin{bmatrix} \Phi_f \\ \Phi_f\wedge^N \end{bmatrix}\mathbf{A} = \mathbf{D}_f\mathbf{A}. \tag{24}$$

Since wavemodes are assumed to be linearly independent, the matrix $\mathbf{D}_q$ is a full column rank matrix, i.e. $rank(\mathbf{D}_q) = m$, and the left pseudoinverse $\mathbf{D}_q^\dagger$ can be calculated. Hence the wave amplitude can be obtained from

$$\mathbf{A} = \mathbf{D}_q^\dagger\mathbf{Q}. \tag{25}$$

Substituting equation (25) in equation (24) yields

$$\mathbf{F} = \mathbf{D}_f \mathbf{D}_q^{\dagger} \mathbf{Q} = \overline{\mathbf{D}} \mathbf{Q}, \tag{26}$$

where $\overline{\mathbf{D}}$ is the dynamic stiffness matrix. Once the dynamic stiffness matrix is obtained, free vibration are calculated in the usual way as it is done in the FE method. In particular resonances occur when $|det(\overline{\mathbf{D}}')| = 0$, where $\overline{\mathbf{D}}'$ is obtained from $\overline{\mathbf{D}}$ after applying boundary conditions. A numerical procedure is used in the present work. Therefore the determinant is evaluated numerically for each frequency, and resonances occur when $|det(\overline{\mathbf{D}}')|$ shows stationary values. It is of worth to point out that the present formulation can also be used to evaluated the forced response of the structure.

5.2 Phase Closure Principle

Following section 3, consider a beam with some boundary conditions at the end $A(x = 0)$ and $B(x = L_{tot})$. Again wave amplitudes at each end are denoted by $\mathbf{A}^+$, $\mathbf{A}^-$, $\mathbf{B}^+$ and $\mathbf{B}^-$ and the boundary conditions have reflection matrices $\mathbf{R}_A$ and $\mathbf{R}_B$. According to [7], the boundary conditions can be written as $\mathbf{Eq} + \mathbf{Gf} = \mathbf{0}$. Complicated boundary conditions can be easily introduced using this formulation. Since displacements and forces can be expanded as $\mathbf{q} = \Phi_q^+ \mathbf{A}^+ + \Phi_q^- \mathbf{A}^-$ and $\mathbf{f} = \Phi_f^+ \mathbf{A}^+ + \Phi_f^- \mathbf{A}^-$, reflection matrices are

$$\begin{aligned} \mathbf{R}_B &= -(\mathbf{E}_B \Phi_f^- + \mathbf{G}_B \Phi_q^-)^{\dagger} (\mathbf{E}_B \Phi_f^+ + \mathbf{G}_B \Phi_q^+); \\ \mathbf{R}_A &= -(\mathbf{E}_A \Phi_f^+ + \mathbf{G}_A \Phi_q^+)^{\dagger} (\mathbf{E}_A \Phi_f^- + \mathbf{G}_A \Phi_q^-). \end{aligned} \tag{27}$$

Equation (12) can be rewritten as $\mathbf{B}^+ = [\wedge^+]^N \mathbf{A}^+$, $\mathbf{A}^- = [\wedge^-]^N \mathbf{B}^-$, $\mathbf{B}^- = \mathbf{R}_B \mathbf{B}^+$ and $\mathbf{A}^+ = \mathbf{R}_A \mathbf{A}^-$, which solved give

$$[\mathbf{R}_A \left[\wedge^-\right]^N \mathbf{R}_B \left[\wedge^+\right]^N - \mathbf{I}]\mathbf{A}^+ = \mathbf{0}, \tag{28}$$

where $[\wedge^+] = diag(\lambda_1^+, \ldots, \lambda_m^+)$ and $[\wedge^-] = diag(\lambda_1^-, \ldots, \lambda_m^-)$ correspond to positive-going and negative-going waves. Therefore natural frequencies occur when

$$|det(\mathbf{R}_A \left[\wedge^-\right]^N \mathbf{R}_B \left[\wedge^+\right]^N - \mathbf{I})| \tag{29}$$

shows stationary values.

6 NUMERICAL EXAMPLE

In this section a numerical example is presented and WFE results are compared with those obtained using the wave approach described in section 3. The beam considered is an aluminum beam with cross section $h = 0.002$m. The element length for the WFE formulation is $L = 0.001$m. Figure 3 shows the complex dispersion curves obtained from equations (9) and (19), where $\Omega = L^2\omega/a$ is the non-dimensional frequency. It can be noticed that results agree very well. Table 1–3 show natural frequencies of the beam predicted for different values of the axial velocity. The beam is simply supported, and its total length is $L_{tot} = 0.4$m. Results obtained from equations (14), (26), and (28) are compared. It can be noticed that equation (28) gives more accurate results with respect to equation (26). Hence the Phase Closure Principle seems to be preferable for WFE application. Accuracy of the numerical WFE results increases with frequency. This is perhaps due to the short length of the FE element. It can also be noticed that natural frequencies decrease when the axial velocity increases. Divergence instability in

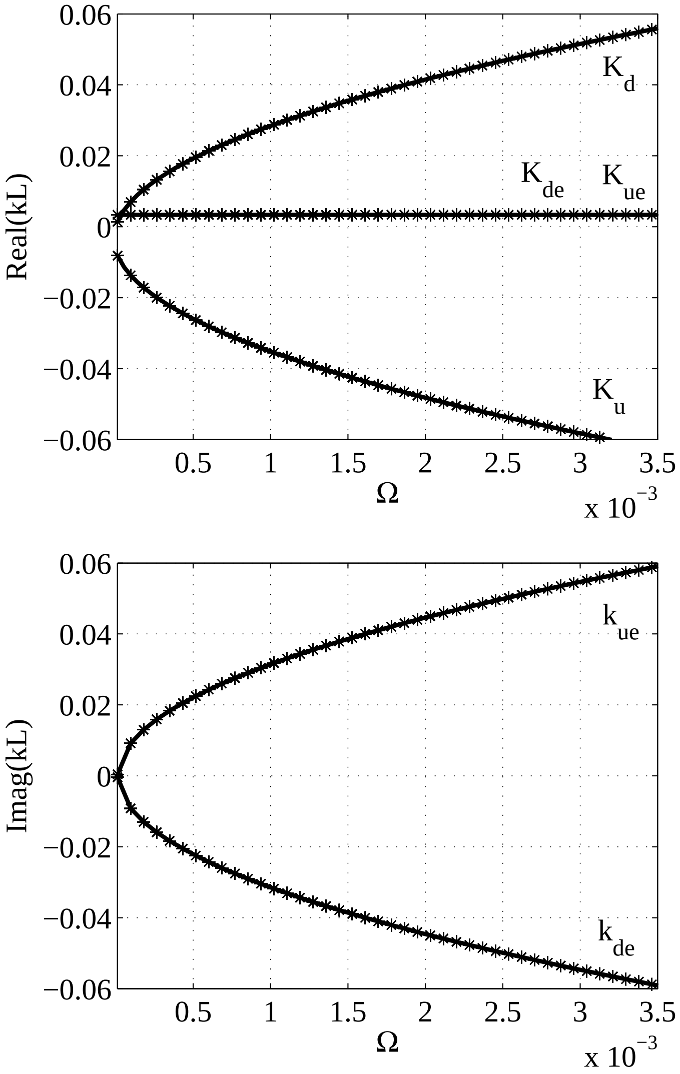

Figure 3: Complex valued dispersion curves, $v = 20$m/s. Analytical results from (9): ——- ; WFE results from (19): * * * *.

Natural frequency [Hz]						
Analytical solutions, Eq. (14)	28.9	116.8	263.3	468.4	732.1	1054.4
WFE Dynamic Stiffness Matrix Eq. (26)	28.5	116.6	263.2	468.3	732.0	1054.3
WFE Phase Closure Principle Eq. (28)	28.9	116.8	263.3	468.4	732.1	1054.4

Table 1: Simply supported beam, $v = 5$m/s.

Natural frequency [Hz]						
Analytical solutions, Eq. (14)	23.96	111.9	258.4	463.4	727.1	1049.4
WFE Dynamic Stiffness Matrix Eq. (26)	-	108.2	256.0	461.7	725.7	1048.3
WFE Phase Closure Principle Eq. (28)	-	112	258.4	463.4	727.1	1049.4

Table 2: Simply supported beam, $v = 20$m/s.

Natural frequency [Hz]						
Analytical solutions, Eq. (14)	17.3	105.2	251.7	456.7	720.5	1042.7
WFE Dynamic Stiffness Matrix Eq. (26)	-	96.0	246.2	452.8	717.3	1040.1
WFE Phase Closure Principle Eq. (28)	-	106.0	252.0	456.9	720.5	1042.8

Table 3: Simply supported beam, $v = 30$m/s.

fact occurs at a critical moving speed [11], where the linear theory breaks down. However, far from the critical speed, which for the present case is quite high, the method proposed offers a powerful alternative to analytical approaches, in particular for more complicated cases, such as pipe conveying fluid, which will be the subject of further analysis. Moreover, the linear theory can be the first step in the analsysis to provides useful information for a more refined nonlinear investigation.

It is of worth noting that, for a simply supported beam, a closed form approximate frequency neglecting evanescent waves in (14) is

$$\omega = \frac{n^2\pi^2}{L^2}a - \frac{v^2}{4a}. \tag{30}$$

Accuracy of equation (30) is related to the rate of decay of evanescent waves k_{de} and k_{ue}, thus it is expected that equation (30) is more accurate for higher frequency and low axial speed.

7 CONCLUSIONS

In the present paper the dynamics of a travelling one-dimensional waveguide was studied using a Wave Finite Element method. In particular an axially moving beam, modelled using the classical linear theory, was considered. The FE formulation of a moving beam element was developed, and a brief description of the WFE method was given. Natural frequencies were then calculated using the Dynamic Stiffness Matrix and the Phase Closure Principle, both formulated in terms of wave characteristics obtained from the WFE eigenproblem. An analytical wave approach was also presented to show some characteristics of the elastic waves propagating in such a beam. Numerical examples were shown. Results were compared with those obtained using the analytical approach, showing the accuracy of the proposed technique, in particular at higher frequency.

Acknowledgements

Part of this work was carried out while the first author was a visiting fellow at the Institute of Sound and Vibration Research, University of Southampton.

REFERENCES

[1] B. Tabarrok, C. M. Leech, Y. I. Kim, On the dynamics of an axially moving beam, *Journal of the Franklin Institute*, **297**, 201–220, 1974.

[2] J. A. Wickert and C. D. Jr Mote, Classical vibration analysis of axially moving continua. *American Society of Mechanical Engineers, Journal of Applied Mechanics*, **57**, 738–744, 1990.

[3] R. J. Theodore, J. H. Arakeri, A. Ghosal, The Modelling of Axially Translating Flexible Beams. *Journal of Sound and Vibration*, **191**, 363–376, 1996.

[4] L. Q. Chen, Analysis and control of transverse vibrations of axially moving strings. *Applied Mechanics Reviews*, **58**, 91–116, 2005

[5] E. Manconi and B. R. Mace, Modelling wave propagation in two-dimensional structures using finite element analysis. *Journal of Sound and Vibration*, **318**, 884–902, 2008.

[6] E. Manconi and B. R. Mace, Wave characterization of cylindrical and curved panels using a finite element method. *Journal of the Acoustical Society of America*, **125**, 154-163, 2009.

[7] J.M. Renno and B.R. Mace, On the forced response of waveguides using the wave finite element method. *Journal of Sound and Vibration*, **329**, 5474–5488, 2010.

[8] K. Rogers, N. S. Ferguson, A. A. Perryman, B. R. Mace, Modelling axially moving beams of varying length using the finite element method. *7th EUROMECH Solid Menchanics Conference*, Lisbon, Portugal, September 7–11, 2009.

[9] B.R. Mace, Wave reflection and transmission in beams. *Journal of Sound and Vibration*, **97**, 237-246, 1984.

[10] J. R. Banerjee, Dynamic stiffness formulation for structural elements: a general approach. *Journal of Computers and Structures*, **63**, 101-103, 1997.

[11] J. A. Wickert, Non-linear vibration of a traveling tensioned beam. *International Journal of Non-Linear Mechanics*, **27**, 503–517, 1992.

[12] G. Chakraborty, A. K. Mallik, Wave propagation in and vibration of a traveling beam with and without non-linear effects, Part I: free vibration. *Journal of Sound and Vibration*, **236**, 277-305, 2000.

[13] J. R. Banerjee, W. D. Gunawardana, Dynamic stiffness matrix development and free vibration analysis of a moving beam. *Journal of Sound and Vibration*, **303**, 135–143, 2007.

[14] M. Petyt, *Introduction to finite element vibration analysis*. Cambridge University Press, 1990.

[15] L. Brillouin, *Wave propagation in periodic structures*. Dover Publications Inc., New York, 1953.

COMPDYN 2011
3^{rd} ECCOMAS Thematic Conference on
Computational Methods in Structural Dynamics and Earthquake Engineering
M. Papadrakakis, M. Fragiadakis, V. Plevris (eds.)
Corfu, Greece, 25–28 May 2011

NON-STATIONARY PROBLEMS OF ELASTIC WAVEGUIDES WITH INCLUSIONS

Dmitry A. Indeitsev, Andrey K. Abramyan, Yulia A. Mochalova, and Boris N. Semenov

Institute of Problems in Mechanical Engineering Russian Academy of Sciences
199178, V.O., Bolshoy pr., 61 Saint-Petersburg, Russia
e-mail: dmitry.indeitsev@gmail.com, andabr33@yahoo.co.uk,
yumochalova@yandex.ru, bsemenov@rambler.ru

Keywords: Elastic waveguide, Localizing oscillations, Trapped modes, Film delamination.

Abstract. *In modern constructions, thin-layer coats are often used as protecting or strengthening elements. Deformations of such constructions may cause significant stresses on the interface between the base and the coat because of the difference in their physical-mechanical properties, which leads to the destruction or delamination of the cover. Of special interest is strength analysis under dynamical or vibrational impacts because of the possibility of localizing oscillations in a neighborhood of the initial inhomogeneities (such as inclusions, defects, construction elements, etc.). In this paper, on the example of the delamination of a string from an elastic substrate, the possibility of localizing oscillations on a delamination defect is demonstrated and the effect of this localization on the growth of the delamination zone is analyzed. A simplified setting of the problem is considered. The possibility of localizing oscillations on a delamination defect is demonstrated and an approximate analytical solution is constructed, which takes into account only the first symmetric form of oscillations describing the development of the initial delamination. A numerical modeling of the problem is performed, and the results of modeling are compared with the approximate analytical solution.*

1 INTRODUCTION

In modern constructions, thin-layer coats are often used as protecting or strengthening elements. Deformations of such constructions may cause significant stresses on the interface between the base and the coat because of the difference in their physical-mechanical properties, which leads to the destruction or delamination of the cover. Delamination of multilayer constructions under static and dynamic (shock) loads have an extensive bibliography. We mention the fundamental works [1-8]. The impact of static or shock loads on the emergence and development of delamination in multilayer constructions has been studied fairly well, but much less is known about destructions of this type under nonstationary (vibrational) loads. The interest in the latter is caused by the fact that even small variable actions may cause the localization of oscillations in a neighborhood of inhomogeneities (such as inclusions, defects, construction elements, etc.) [9] and lead to the emergence and growth of defects, which strongly affects the reliability and functionality of the whole construction.

An example of such coated constructions in which delamination destructions are observed is the blades of a wind turbine, which are becoming increasingly popular because of the interest in alternative energy sources. In recent years, the increase in the power of wind turbines has enhanced requirements to rotor blades.

During the operation of the rotor, the top coat of a blade, which is a thin film, may detach on some part of its length. To estimate the functionality of the construction, it is important to know the further scenario of the behavior of such a film with a detached fragment. Such defects may appear and grow for several reasons, which include wind loads and stationary oscillations arising in blades during their operation.

This paper studies the possibility of oscillation localization near delaminations from cracks and the impact of localization on the growth of the defects. We suggest a model for analyzing conditions under which a delamination zone grows or ceases to grow.

2 STATEMENT OF THE PROBLEM

Taking into account the fact that the thickness of a thin-layer coat is usually much less than the characteristic size of the substrate, in the first approximation, we replace a coat attached to a substrate by a film on an elastic substrate.

The main purpose of this paper is to show that, if an elastic substrate has an inhomogeneity (the coefficient of the elastic substrate vanishes for some part of the film length), then, under a non-stationary harmonic load, some part of the propagating wave energy is localized near the inhomogeneity. Depending on the parameters of the film and the elastic substrate, various scenarios of the film behavior are possible: the length delamination zone may increase unlimitedly, or it may cease to grow at some time.

Note that if there are only propagating waves in the film, then the wave processes only insignificantly affect the behavior of the delamination zone, because the excited wave process rapidly fades out. The situation changes if the waves in the film-waveguide localize near the defect. As is known, in the absence of dissipation, localized oscillations of certain frequencies may not attenuate for an infinitely long time [9], thereby substantially affecting the behavior of the delamination zone. The existence of standing waves localized near the delamination zone means that the corresponding spectral problem has not only continuous but also discrete spectrum of eigenfrequencies.

This paper considers the simplest mathematical model for the behavior of such a film under the action of a transverse non-stationary harmonic load. The film is attached to an elastic Win-

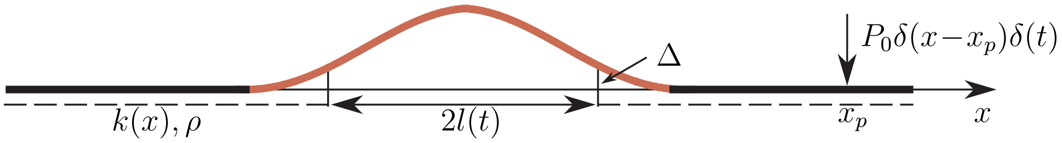

Figure 1: A scheme of film delamination

kler foundation, which models an element of a blade. In the framework of this model, the birth of a delamination is not studied; it is assumed that, at initial moment of time, a film fragment of length $2l_0$ is torn away from the elastic substrate.

We assume that the delamination emerges not near the blade boundaries, which is confirmed by in-situ observations. The tension of the detached part of the film differs from the tension of the film on the elastic substrate, and when the detached part oscillates, the interaction between the film and the elastic substrate has the character of a one-sided contact, and the interaction of the film with the substrate has a relay characteristic. These two factors significantly complicate constructing a solution; for this reason, at the present stage of modeling, we assume that tension is constant over the entire film and the detached part does not interact with the elastic substrate. Vibro-impact loads in the delamination zone and a variable tension of the film will be taken into account at the next modeling stage.

As the simplest model we consider the following case, in which the problem under consideration reduces to a one-dimensional problem: the delamination zone is contained in the domain $-l_0 < x < l_0$, $-\infty < y < \infty$, and the force is applied along the line $x = x_p$, $-\infty < y < \infty$. In this case, the problem reduces to the problem about oscillations of a string on an elastic substrate with variable stiffness $k[x, l(t)]$: namely, stiffness vanishes on the detached part of the string, and on remaining part of the string, it equals k_0. The equation describing the displacement of a string on an elastic substrate under a load applied at a point $x = x_p$ has the form

$$\begin{aligned} &\rho u_{tt} - T u_{xx} + k[x, l(t)]u = -P(x,t), \quad -\infty < x < \infty, \\ &u,\ u_x \to 0 \qquad |x| \to \infty \end{aligned} \tag{1}$$

Here, ρ is the specific density of the string, u is the vertical displacement of the string, T is the tension of the unperturbed string, and $P(t)\delta(x - x_p)$ is the exciting force. We assume that, at the initial moment of time $t = 0$, there is a film fragment of length $2l_0$ detached from the elastic substrate. For the delamination criterion we take the following deformation criterion: when the displacement of at least one end of the detached part attains a critical value Δ, the delamination zone grows with rate β (see Fig. 1). The equation describing the growth of the delamination zone has the form [8]

$$\frac{\mathrm{d}l}{\mathrm{d}t} = \beta\Big\{H\Big[u(x,t)|_{x=l_-(t)} - \Delta\Big] + H\Big[u(x,t)|_{x=l+(t)} - \Delta\Big]\Big\} \tag{2}$$

Here, $l_-(t)$ is the coordinate of the left end of the detached fragment, $l_+(t)$ is the coordinate of the right end of the detached fragment, $2l(t) = l_- + l_+$ is the length of the detached fragment, $u(x,t)$ is the displacement of the string point with coordinate x at a moment t, H is the Heaviside function, β is the coefficient determining the growth rate of the delamination, and Δ is the critical displacement, under which the film separates from the elastic substrate.

Under certain conditions, oscillations may localize on the initial delamination fragment of length $2l_0$ (see [9]), and the amplitude of oscillations at the endpoints of the delamination zone may surpass the critical displacement value Δ at some moment of time, which leads to the growth of the delamination zone. The increase in the length of the detached film fragment, in turn, affects the localization of oscillations near the defect, so that the passage to other forms of localized oscillations may occur. Therefore, we must solve the system of equations (1) and (2) under the initial conditions

$$l|_{t=0} = l_0; \quad u, u_t|_{t=0} = 0 \tag{3}$$

and the following boundary conditions for any fixed t:

$$u,\ u_x \to 0 \qquad |x| \to \infty \tag{4}$$

Thus, we have obtained a connected problem about non-stationary oscillations of a string on an elastic substrate and the growth of the zone of the delamination of a part of this string from an elastic substrate, which is described by the system of equations (1)-(4).

3 STEADY-STATE OSCILLATIONS OF A STRING. LOCALIZED MODES

First, consider the case where the length of the delamination domain is constant: $2l = 2l_0$. The corresponding spectral problem $u(x,t) = v(x)\mathrm{e}^{\mathrm{i}\omega t}$ takes the form

$$\begin{aligned} &Tv_{xx} - [k(x) - \rho\omega^2]v = 0, \quad -\infty < x < \infty, \\ &v,\ v_x \to 0 \qquad |x| \to \infty \end{aligned} \tag{5}$$

Here, ω is the frequency and $k = k0[H(x+l_0) - H(x-l_0)]$. The specific density of the string is assumed to be constant. We denote the sound speed in the string by $c = \sqrt{T/\rho}$ and the cut-off frequency by $\omega_b = \sqrt{k_0/\rho}$.

This spectral problem is a special case of the problem about oscillations of a string with a distributed elastic-mass inclusion, which was considered in detail in [9]. It was shown that problem (5) has not only continuous spectrum of oscillation eigenfrequencies, which begins with the cut-off frequency ω_b, but also discrete spectrum, which goes before the cut-off frequency consists of finitely many eigenfrequencies. The eigenforms of oscillations corresponding to the discrete spectrum, known as localized (trapped) modes, are localized near the inclusion and do not carry energy away to infinity.

The symmetric localized modes corresponding to the eigenfrequencies ω_{sn}, which are determined by the dispersion relation

$$\tan\frac{l_0}{c}\omega = \frac{\sqrt{\omega_b^2 - \omega^2}}{\omega}, \tag{6}$$

have the form

$$v_i^s = \begin{cases} \cos\gamma_1 x, \ |x| < l_0, \\ \\ \cos\gamma_1 l_0\, \mathrm{e}^{-\gamma_0|x-l_0|}, \ |x| > l_0 \end{cases} \tag{7}$$

where $\gamma_1 = \omega/c$ and $\gamma_0 = \sqrt{\omega_b^2 - \omega^2}/c$.

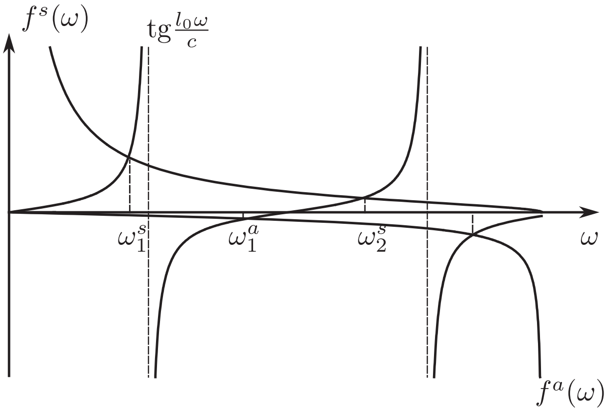

Figure 2: The eigenfrequencies.

The antisymmetric localized modes are determined by the spectrum of frequencies determined from the dispersion relation

$$\tan\frac{l_0}{c}\omega = -\frac{\omega}{\sqrt{\omega_b^2-\omega^2}} \tag{8}$$

and have the form

$$v_i^a = \begin{cases} \sin\gamma_1 l_0\, \mathrm{e}^{-\gamma_0|x-l_0|},\ x > l_0 \\ \sin\gamma_1 x,\ |x| < l_0, \\ -\sin\gamma_1 l_0\, \mathrm{e}^{\gamma_0|x+l_0|},\ x < -l_0. \end{cases} \tag{9}$$

The scheme of the determination of the roots of the frequency equations (6) and (8) is shown in Fig.2. The abscissas of the intersection points of the curves determining the right- and left-hand sides of the frequency equations give the required eigenfrequencies, provided that the parameter values ω_b, c, and l_0 are known. Note that the first eigenfrequency corresponds to a symmetric localized mode, the second corresponds to an antisymmetric mode, etc. The number of eigenfrequencies before the cut-off frequency is determined by the parameters of the waveguide and the length of the delamination zone.

The eigenfunctions corresponding to frequencies $\omega > \omega_b$ from the continuous spectrum (we call them traveling modes) are determined in [9].

It can be shown that the localized modes (7)-(9) and traveling modes are orthogonal in the sense of generalized functions [10].

4 THE NON-STATIONARY PROBLEM: EXPANSION IN EIGENFORMS

As above, we assume that the length of the delamination zone is constant and equals $2l_0$. Let $v_i(x)$ denote the localized modes (eigenfunctions) corresponding to the discrete eigenfrequencies ω_i $(i = 1, 2, ..., N)$, and let $v_\omega(x)$ be the traveling modes (eigenfunctions) corresponding to frequencies from the continuous spectrum.

Then we seek a solution of (1) in the form of an expansion in the eigenfunctions of the spectral problem (5) [10]

$$u(x,t) = \sum_{i=1}^{N} v_i(x) q_i(t) + \int_{\omega_b}^{\infty} v_\omega(x) q_\omega(t) \mathrm{d}\omega. \tag{10}$$

where $q_i(t)$ and $q_\omega(t)$ are unknown functions so-called generalized coordinates.

Substituting (10) into (1), multiplying by eigenfunctions, integrating with respect to x, and applying the dispersion relations (6) and (8), we obtain

$$\ddot{q}_i + \omega_i^2 q_i = \frac{Q_i(t)}{M_i}, \quad q_i, \dot{q}_i|_{t=0} = 0, \quad i = 1, 2, ..., N \tag{11}$$

$$\ddot{q}_\omega + \omega^2 q_\omega = \frac{Q_\omega(t)}{M_\omega}, \quad q_\omega, \dot{q}_\omega|_{t=0} = 0. \tag{12}$$

Here, Q_i are generalized forces acting on the forms from the discrete spectrum, the Q_ω are generalized forces acting on the forms from the continuous spectrum, and the M_i and M_ω are generalized masses, which are determined as follows:

$$Q_i = \int_{-\infty}^{-\infty} v_i(x) P(x,t) \mathrm{d}x, \quad M_i = \frac{1}{c^2} \int_{-\infty}^{-\infty} v_i^2(x) \mathrm{d}x$$

$$Q_\omega = \int_{-\infty}^{-\infty} v_\omega(x) P(x,t) \mathrm{d}x, \quad M_\omega = \frac{1}{c^2} \int_{-\infty}^{-\infty} v_\omega^2(x) \mathrm{d}x$$

Solving the system of equations (11)-(12), we obtain the following expression for the string deflection:

$$u(x,t) = \sum_{i=1}^{N} \frac{v_i(x)}{M_i \, \omega_i} \int_0^t \sin \omega_i (t-\tau) Q_i(\tau) \mathrm{d}\tau + \int_{\omega_b}^{\infty} \frac{v_\omega(x)}{M_\omega \, \omega} \int_0^t \sin \omega (t-\tau) Q_\omega(\tau) \mathrm{d}\tau \mathrm{d}\omega. \tag{13}$$

Thus, we have obtained a solution of Eq.(1) in the form of an expansion in localized and traveling modes for the string with a distributed inclusion. Using the Riemann-Lebesgue lemma, we can show that the integral determining the expansion in the continuous spectrum in formula (13) tends to zero as $t \to \infty$, and for large t, the solution of problem (1) is determined only by localized forms of oscillations:

$$u(x,t) \to \sum_{i=1}^{N} \frac{v_i(x)}{M_i \, \omega_i} \int_0^t \sin \omega_i (t-\tau) Q_i(\tau) \mathrm{d}\tau \quad \text{for} \quad t \to \infty. \tag{14}$$

Thus, an external action leads to the localization of waves in the film delamination zone, and in the absence of dissipation in the system, these localized waves may exist infinitely long.

5 FILM DELAMINATION

After the localization of oscillations on a defect of fixed length is analyzed, we proceed to study the initial problem (1)-(4) on film delamination, that is, on the growth of the initial delamination zone.

Suppose that, at the initial moment of time, the length of the zone of film delamination from the substrate equals $2l_0$. We assume that the value l_0 is such that there exists a unique eigenfrequency $\omega_0 < \omega_b$, which determines a symmetric eigenform according to (7). Then we seek a solution of the initial problem (1)-(4) in the form

$$u(x,t) = v_0(x) q_0(t). \tag{15}$$

Remark. In expansion (10) only the first term corresponding to a localized mode is retained; thus, the transition processes related to the propagation of traveling waves are not taken into account.

Thanks to the existence of the first symmetric form of oscillations, we can assume that $l_+ = l_-$ and write Eq.(2), which describes the growth of the delamination zone, in the form

$$\frac{\mathrm{d}l}{\mathrm{d}t} = \beta\, H\Big[u(x,t)|_{x=l(t)} - \Delta\Big]. \tag{16}$$

The length of the delamination zone varies in time, and now the symmetric form $v_0(x,l)$ depends on time and is defined on a variable interval, namely,

$$v_0(x,l) = \cos\lambda x\, H(l-x) + \cos\lambda l\, \mathrm{e}^{-\gamma(x-l)} H(x-l), \quad 0 < x < \infty,$$

where $\lambda = \omega_0/c$. Substituting (15) into the equation (1) for string oscillations, multiplying the obtained equation by $v_0(x,l)$, and integrating the result with respect to x, we arrive at a fairly complicated nonlinear equation with respect to $q_0(t)$ and $l(t)$. Discarding nonlinear terms, we obtain the following equation for the generalized coordinate $q_0(t)$:

$$\ddot{q}_0 + \omega^2(l) q_0 = \frac{Q_0(t)}{M_0}, \quad q_0, \dot{q}_0|_{t=0} = 0,$$

where

$$\omega^2(l) = \left[2\omega_b^2 \int_l^{+\infty} v_0^2\, \mathrm{d}x + c^2 \int_{-\infty}^{+\infty} v_{0x}^2\, \mathrm{d}x\right] / \int_{-\infty}^{+\infty} v_0^2\, \mathrm{d}x.$$

We assume that $\lambda\tilde{l} = \omega_0[l(t) - l_0]/c \ll 1$. It is easy to show that, in this case, we have

$$\omega^2(l) = \omega_0^2 + o[(\lambda\tilde{l})^2], \quad \tilde{l} = l(t) - l_0.$$

Replacing $\omega(l)$ by ω_0 in the last equation, we reduce the initial problem to the system of equations

$$\ddot{q}_0 + \omega_0^2 q_0 = \frac{Q_0(t)}{M_0}, \quad q_0, \dot{q}_0|_{t=0} = 0, \tag{17}$$

$$\frac{\mathrm{d}l}{\mathrm{d}t} = \beta H\Big[v_0(l,\omega_0) q_0(t) - \Delta\Big], \quad l(t))|_{t=0} = l_0. \tag{18}$$

First, consider the simplest example of an external action, namely, the oscillations initiated by an impulse exciting force $P(t) = P_0\delta(t)$. In this case, the generalized force is

$$Q_0(t) = P_0 \cos\lambda l\, \mathrm{e}^{-\gamma_0(x_p - l)}\delta(t).$$

The generalized mass does not depend on the exciting force and has the form

$$M_0(t) = \rho[l + \sin 2\lambda l/2\lambda + \cos\lambda l/\gamma_0].$$

Thus, Eq. (17) can be rewritten in the form

$$q_0(t) = \frac{P_0 \mathrm{e}^{-\gamma_0(x_p - l)}}{M_0\omega_0} \cos\lambda l\, \sin\omega_0 t \tag{19}$$

Substituting (19) into (18), we obtain

$$\frac{\mathrm{d}l}{\mathrm{d}t} = \beta H\Big[\frac{P_0\varepsilon\,\cos^2\lambda l}{M_0(l)\,\omega_0}\,\sin\omega_0 t - \Delta\Big],\quad l(t)|_{t=0} = l_0 \tag{20}$$

where $\varepsilon = \mathrm{e}^{-\gamma_0(x_p-l)}$. We assume that the force is applied so that $\varepsilon < 1$. We seek an approximate solution to Eq.(20). Since $|\sin\omega_0 t| \le 1$, it follows from (20) that a necessary condition for the growth of the delamination zone has the form

$$\frac{P_0\varepsilon\,\cos^2\lambda l}{M_0(l)\,\omega_0} > \Delta. \tag{21}$$

If l_0 is such that condition (21) is violated (the amplitude of string oscillations does not attain the critical value), then the delamination zone cannot grow. If the initial conditions are such that inequality (21) holds, then the delamination zone begins to linearly grow at rate β at the moment $t = t_1$, which can be approximately determined from the expression

$$\sin\omega_0 t = \frac{\Delta\,\omega_0 M_0(l_0)}{P_0\varepsilon\cos^2\lambda l_0}$$

and

$$l(t) = l_0 + \beta\, t\, H(t - t_1).$$

The length of the delamination zone increases until time $t = t_2$, at which the argument of the Heaviside function (20) vanishes. The growth of the delamination zone resumes at time $t = t_3$, which can be found from the expression

$$\sin\omega_0 t = \frac{\Delta\,\omega_0 M_0(l_2)}{P_0\varepsilon\cos^2\lambda l_2}.$$

Such a step growth of the delamination zone continues until $l(t)$ reaches a certain critical value. Indeed, as the length of the delamination zone decreases, the amplitude of string oscillations decreases; thus, there exists a moment of time t_k and the corresponding length $l = l_k$ for which condition (20) ceases to hold, and the growth of the delamination zone stops.

A similar picture is observed in the case where the exciting force is harmonic, in which this force has the form $P(t) = P_0\sin\nu t$, where ν denotes frequency. In this case, Eq. (17) has the approximate solution

$$q_0(t) = P_0\varepsilon\int_0^t \frac{\cos\lambda l(\tau)}{M_0(\tau)}\,\sin\nu(t-\tau)\sin\omega_0\tau\mathrm{d}\tau. \tag{22}$$

As well as in the case of impulse load, it can be proved that the moments of time ti determining the growth periods of the delamination zone, can be found from the equation

$$q_0(t)\cos\lambda l = \Delta$$

Thus, the approximate analytic solution of the problem constructed on the basis of only the symmetric eigenform (7) describes the step growth of the delamination zone, and the growth rate is determined by the value of the parameter β. An analysis of Eq.(18), which describes the

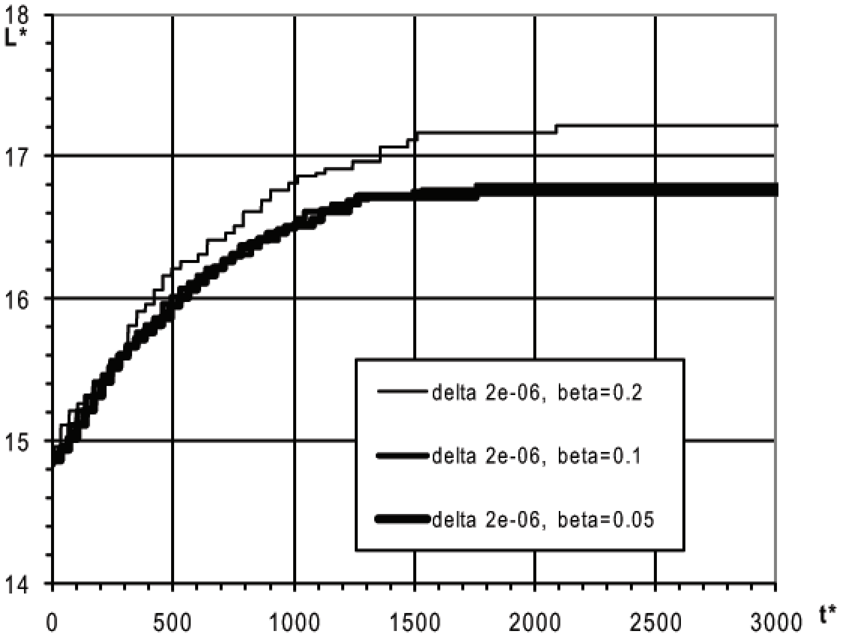

Figure 3: The behavior of the boundary of the delamination zone.

growth of the delamination zone, shows that various modes of growth are possible, which are determined by the behavior of the argument of the Heaviside function in (18).

A numerical modeling of the initial problem (1)-(4) was performed. Motion was excited by a harmonic force. Results of the numerical modeling of the growth of the delamination zone for the parameter values $\beta = 0.2, 0.1, 0.05$ and $\Delta = 2 \cdot 10^{-6}$ are shown in Fig.3.

An analysis of numerical results demonstrates the possibility of the localization of oscillations near a delamination defect under certain loads and problem parameter values and of the following three cases of the delamination development: (i) the absence of growth of the delamination zone for large values of the critical displacement Δ, provided that the amplitude of the displacements does not attain the critical value; (ii) the growth of the delamination zone up to a certain size, after which the growth stops (see Fig.3); (iii) for very small Δ, the growth of the delamination zone is virtually unbounded. Thus, the numerical solution of the system of equations (1)-(4) well agrees qualitatively with the approximate analytic solution.

6 CONCLUSIONS

The delamination of thin-layer elements caused by dynamic or vibrational loads, which is observed during the exploitation of real-life constructions, leads to the destruction of these constructions. Therefore, problems related to determining reasons for such destructions are of great practical interest. In this paper, for the example of the delamination of a string from an elastic substrate, the possibility of the localization of oscillations near a delamination defect was demonstrated and the impact of this localization on the growth of the delamination zone was analyzed. The problem considered here is only the first approximation of a fairly complicated problem. A simplified setting of the problem under consideration was suggested. In constructing an approximated analytic solution, only the first symmetric form of oscillations was taken into account. In the future, non-symmetric forms and the transformation of oscillations as the delamination zone grows must be taken into account. The simplest criterion for the growth of the delamination zone was chosen, which does not take into account the real rheology near the boundaries of the delamination zone. It is quite natural to consider the generalization of the obtained results to the case of the delamination of a two-dimensional film, a bar, and a thin plate.

However, even the simplified model makes it possible to explain the destructions observed in constructions with thin-layer coats under comparatively mild loads, which are caused by the localization of oscillations near various defects.

REFERENCES

[1] G. P. Cherepanov, *Mechanics of Destruction of Composite Materials*. Nauka, Moscow, 1983 (in Russian).

[2] G. P. Cherepanov, *Prikl. Mat. Mekh.* **47**, 832–845, 1983.

[3] V. V. Bolotin, *Prikl. Mat. Mekh.* **56**, 150–162, 1992.

[4] V. V. Bolotin, *Mekh. Kompozit. Mater.*, **2**, 239–255, 1984.

[5] V. V. Bolotin, *Mekh. Kompozit. Mater.*, **3**, 410-418 (1988).

[6] S. S. Pos, W. Illg, and D. R. Sarber, Hidden impact damage in thick composites *in Review of Progress in Quantitative Nondestructive Evaluation, Plenum, New York*, **5**, 1986

[7] S. P. Joshi and C. T. Sun, Impact induced fracture in a laminated composite *J. Composite Mater.* **19**, 51–66, 1985.

[8] M. G. Andrews, R. Massabo, A. Cavicchi, and B. N. Cox, Dynamic interaction effects of multiple delaminations in plates subject to cylindrical bending, *Int. J. Solids Struct*, **46**, 1815–1833, 2009.

[9] D. A. Indeitsev, N. G. Kuznetsov, O. V. Motygin, and Yu. A. Mochalova, *Localization of Linear Waves*. Izd. S.Peterb. Univ., 2007 (in Russian).

[10] V. M. Babich and N. S. Grigor'eva, *Orthogonal Expansions and the Fourier*. Izd. S.Peterb. Univ., 1983 (in Russian).

COMPDYN 2011
ECCOMAS Thematic Conference on
Computational Methods in Structural Dynamics and Earthquake Engineering
M. Papadrakakis, M. Fragiadakis, V. Plevris (eds.)
Corfu, Greece, 25-28 May 2011

TRANSMISSION OF SOUND THROUGH DOUBLE-PLATE PANEL STRUCTURES – A NUMERICAL STUDY OF COUPLING PARAMETERS IN LIGHTWEIGHT PANEL STRUCTURES

Kristoffer A. Dickow[1], **Parthkumar D. Gandalal**[2],
Lars Andersen[2] **and Poul Henning Kirkegaard**[2]

Aalborg University, Department of Civil Engineering
Sohngaardsholmsvej 57, DK-9000 Aalborg, Denmark
e-mail: [1]kad@civil.aau.dk, [2]{pdg,la,phk}@civil.aau.dk

Keywords: Acoustics, Sound Transmission, Finite Element Method, Structure-Borne Sound

Abstract. *In the present paper, a finite-element model of a double-plate panel is implemented to investigate the transmission of sound through a simple lightweight structure. A numerical study is performed of the following three coupling configurations: 1) Structure-borne sound via plate-stud-plate structures without air inclusions; 2) transmission via the plate-stud-plate structure including the internal acoustic medium; 3) transmission via plate-air-plate connections in a double-leaf panel with no structural coupling between the two plates. A fully coupled analysis is performed in which solid finite elements are adopted for the structure, whereas the acoustic medium is discretized into fluid continuum elements. The computations are carried out in frequency domain in the low frequency range and the load acts as a diffuse sound field on one side of the panel.*

1 INTRODUCTION

Lightweight building techniques are currently progressing faster than the development of prediction tools for the acoustic behavior of such structures. In order to ensure that the increasing demands to sound insulation between dwellings are being accommodated, reliable prediction tools are needed at an early stage of the building design. For a variety of simple structures, analytical solutions have been established [9], and for heavy structures, statistical energy analysis (SEA) [15, 7, 6, 13] has in general been found to provide a reliable prediction of noise transmission. However, SEA has limited validity for lightweight structures such as wooden floor and wall panels.

Fahy and Gardonio [13] describe the transmission of sound through bounded partitions from a wave point-of-view, but when it comes to bounded double-leaf partitions the transmission behavior becomes too complicated for analytical approaches. Therefore, the wave propagation problems have to be numerically analyzed using a method depending of the frequency region considered. The conventional finite element method (FEM) [2] can be used, especially for low-frequency problems where the considered elements can be considered short compared with the wavelength. However, the frequency range of interest for wave propagation problems is often such that FEM analysis seems to be quite difficult due to the requirement of small element sizes to match the wavelength which implies huge unmanageable data sets. Therefore, instead of FEM for high-frequency analysis, where the elements are long compared to a wavelength, the so-called energy methods such as SEA and energy finite element method (EFEM) [3, 17, 4, 18] are well established methods. Another energy based method is the European standard EN 12354 [1], which is widely used to predict sound transmission in buildings. However, as with SEA, EN 12354 is based on assumptions which are typically not fulfilled by lightweight building structures. Therefore, predictions of sound transmission in such structures using EN 12354 may be imprecise [16].

Currently there is an increasing focus on the transmission of low frequency noise, as sources like road and air traffic or even home theater subwoofers become part of everyday life for many people. Recently, research has been presented where sound transmission in the low frequency range through lightweight structures has been predicted with numerical methods [5, 12, 10]. The results from these papers indicates that FEM tools can give reliable results for prediction of sound transmission loss, however more investigations have to be performed in this field where the influence of different modeling strategies will be considered. The construction of a lightweight structure is fairly complex and many variables belonging to material models, junction types and coupling phenomenons between structure and acoustic medium have to be modeled in a proper way. Although basic theories are well established, modeling transmission through simple structural elements is not straightforward as numerous of the mentioned variables need to be considered. Some of the modeling difficulties are well known, but only a limited number of applications have been evaluated. Ongoing research is concerned with the loss factors in the different types of couplings that occur in lightweight structures including both different types of beams [8, 14] as well as line coupling versus point coupling [13, 8, 14]. The goal of the present paper is to obtain a greater knowledge on the coupling between fluid and structure using FEM tools for the prediction of sound transmission in lightweight building structures. The method of investigations will primarily be based on a numerical investigation using available elements in the commercial FEM software package ABAQUS [11]. The following Section 2 presents the double panel lightweight wall element and different modeling scenarios and finally results are given and discussed in Section 3 and 4.

Flanking noise in a similar panel structure is analysed in a companion paper by Gandalal, Dickow, Andersen and Sorokin.

2 PROBLEM DESCRIPTION

Lightweight wall and floor constructions are often made from panel structures with plates on stud (or joist) frames. In such a panel, the frames may be either single or double-stud frames with or without different porous and elastic layers included to reduce the transmission of sound and vibration through the panel. In the case of single-stud frames there is direct structural coupling from one side of the panel to the other. In the present study the subject of investigation is a single-stud double-plate panel without porous or elastic layers, see Figure 1. The goal of this preliminary study is to investigate the effect of the air inclusions in the model while at the same time gaining experience regarding how to model such structures for future investigations.

2.1 Numerical model

The panel consists of two plates mounted on a frame structure with a total of six cavities, see Figure 1. The stud dimensions are 50 mm by 60 mm and the plate thickness is 20 mm. The total wall dimension is 3350 mm (w) by 2600 mm (h) by 100 mm (d). The studs are placed 550 mm part (center-to-center). Homogeneous and isotropic materials are assumed. The material properties are:

- Timber (plate and studs): Young's modulus 14 GPa, Poisson Ratio 0.35, density 500 kg/m^3. Damping is set to 1% of the stiffness.
- Air: Bulk modulus 141360 Pa, density 1.2 kg/m^3.

The damping is applied as structural damping, i.e. the damping forces are assumed proportional to the forces caused by stressing of the structure. This simulates the effects of friction in the timber.

The panel is modeled in the commercial FEM package ABAQUS using solid continuum finite elements for the structure and fluid continuum elements for the air inclusions in the fi-

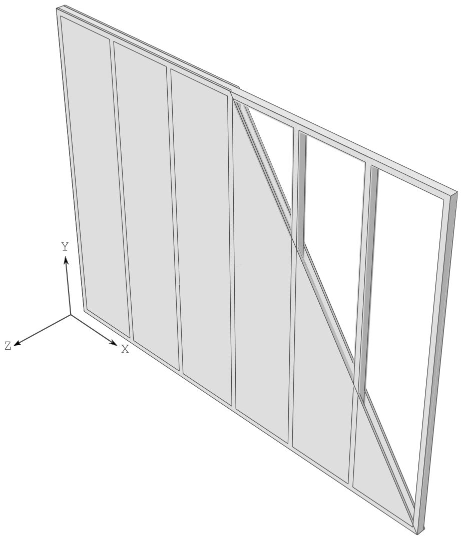

Figure 1: Overall geometry of the double-plate wall panel. The structure consists of two plates tied to a stud frame. A specification of the panel is given in Section 2.1

nite cavities. 20-node brick elements with quadratic spatial interpolation of the displacement are adopted with a mesh size of 5 cm. The mesh is designed such that the nodes constituting the plate mesh align with the nodes on the frame structure. All structural contact points are connected using tie constraints in x, y, and z-directions. As three-dimensional solid continuum elements have no rotational degrees of freedom, only displacements are considered. The coupling between the structure and the acoustic medium in the cavities is handled by tie constraints as well. The boundaries are clamped, i.e. all nodes on the top, bottom and side surfaces of the structure are rigid. Three different scenarios are investigated:

1. Structure-borne sound via plate-stud-plate structures without air inclusions,
2. transmission via the plate-stud-plate structure including the internal acoustic medium,
3. plate-air-plate transmission when there is no structural connection between the two plates.

In the latter case, half of the studs are tied to one plate, while the other half are tied to the other. Thus, the total mass of the panel is unchanged while the stiffness is of course reduced significantly. Furthermore the size of the cavities is unchanged compared with cases 1 and 2. When calculating the eigenfrequencies of the panel, a fourth case is investigated; similar to case 3 but without the structural-acoustical coupling. This is done to see how the coupling affects the modes related to the finite air-filled cavities inside the panel.

2.2 Excitation

If a concentrated load (point force) is applied directly to the panel, the position of the excitation is likely to be located in a nodal line of one or more of the structural modes of the panel. Therefore, as the present paper is dealing with transmission of sound through the entire panel, a diffuse field excitation model has been utilized. In ABAQUS, a diffuse field loading condition may be approximated by a number of deterministic incident plane waves coming from angles distributed over a hemisphere encapsulating the loaded surface. The number of incident plane waves used for the approximation is given by N^2, where N is called the number of seeds.

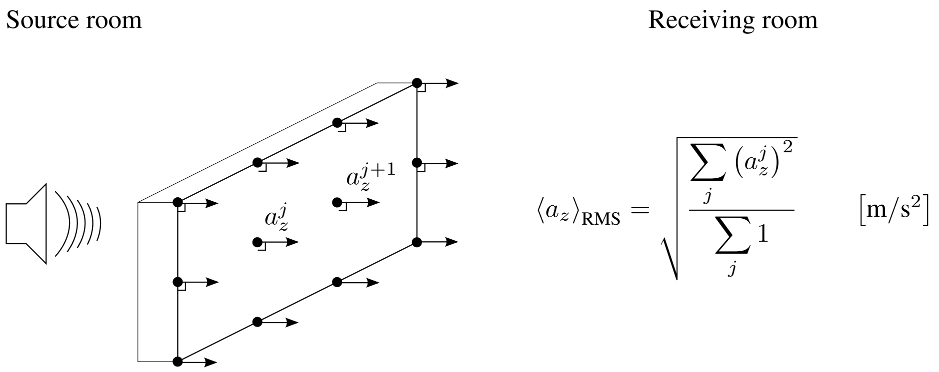

$$\langle a_z \rangle_{\text{RMS}} = \sqrt{\frac{\sum_j \left(a_z^j\right)^2}{\sum_j 1}} \qquad [\text{m/s}^2]$$

Figure 2: The structure is excited by a diffuse field in the source room. The investigated output quantity in the receiving room is the translational surface acceleration, normal to the plane of the plate, expressed as the root-mean-square (spatial average) acceleration. Here a_z^j is the magnitude of the acceleration (z-direction) of the jth node on the plate surface.

2.3 Response

Preferably, the model should include an acoustic medium inside the receiving room such that the sound pressure could be used to find the transmission loss of the structure. However, due to the computational complexity associated with such a model, this is not included yet. Instead, the investigated output quantity in the receiving room, $\langle a_z \rangle_{\text{RMS}}$, is the translational surface acceleration, normal to the plane of the plate, expressed as the spatial root-mean-square acceleration. This is depicted in Figure 2.

3 RESULTS

3.1 Modal analysis

Eigenfrequencies of the four different configurations, i.e. 1) without air inclusions, 2) with air inclusions, 3) without structural coupling and 4) without any coupling, have been found using the Lanczos algorithm implemented in ABAQUS. In the cases without structural coupling between sending and receiving room, half of the ribs are connected to one plate, while the other half are connected to the other plate. The results are shown in Figure 3. A comparison of calculated eigenfrequencies in the case of using shell elements for the plates instead of solid continuum elements is shown in Figure 4.

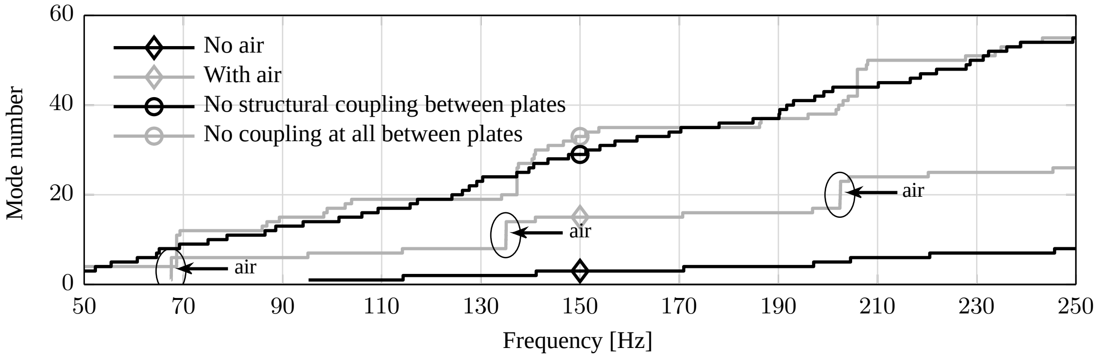

Figure 3: Eigenfrequencies of the four different configurations: 1) without air inclusions, 2) with air inclusions, 3) without structural coupling and 4) without any coupling between the two plates. Groups of air-modes in the fully coupled case are indicated by arrows.

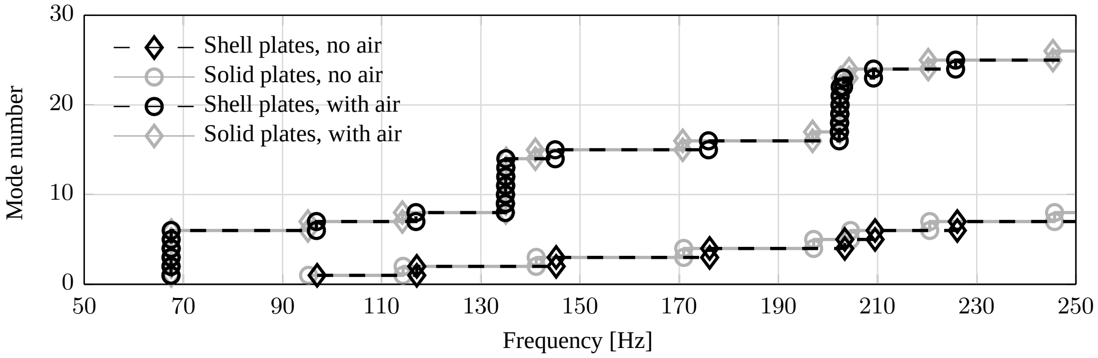

Figure 4: Eigenfrequencies with and without air when the plates are modeled using shell elements and solid continuum elements respectively.

By inspecting curves for cases 1) and 2) in Figure 3 it is clearly seen that the air inclusions provide a number of modes occurring in groups of six. Such a group is found between the 2nd and 3rd structural modes and the modeshapes of these are shown in Figure 6. Figure 5 shows the modeshape of the 2nd and 3rd structural modes.

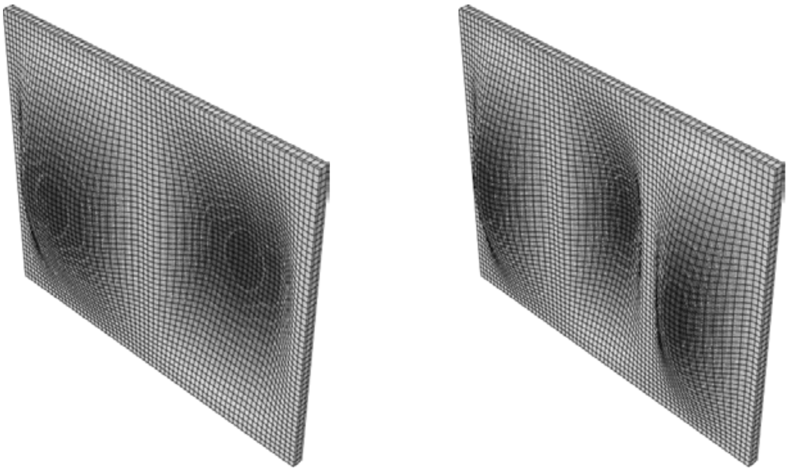

(a) Mode at 114 Hz (b) Mode at 141 Hz

Figure 5: Modeshapes showing the second and third structural modes.

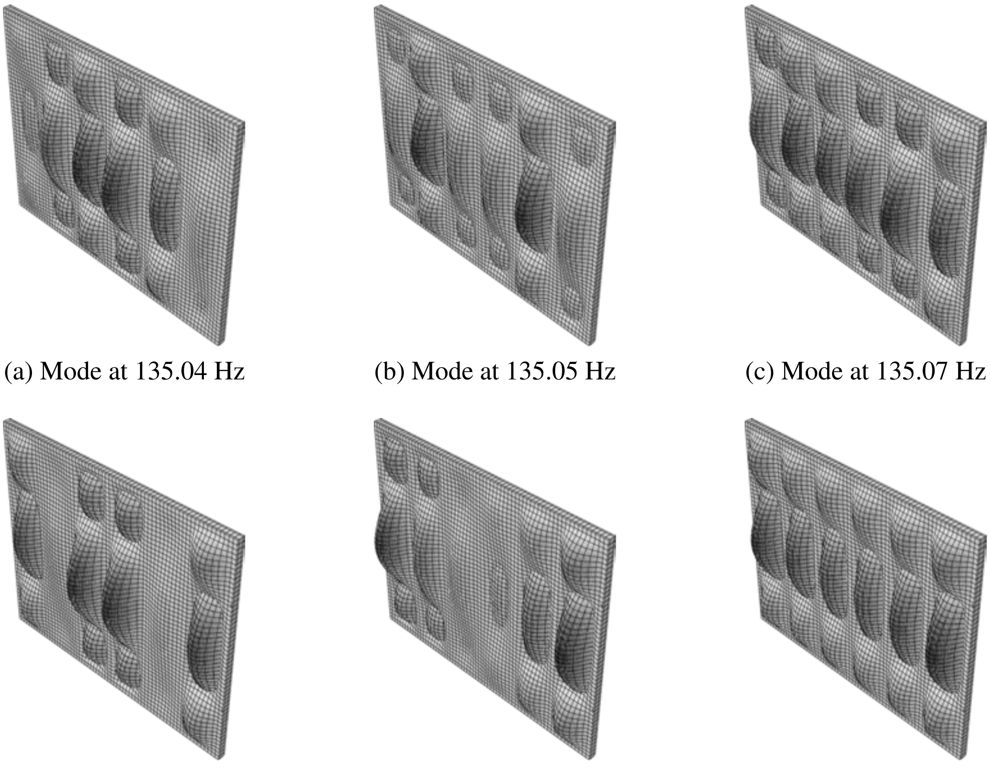

(a) Mode at 135.04 Hz (b) Mode at 135.05 Hz (c) Mode at 135.07 Hz

(d) Mode at 135.09 Hz (e) Mode at 135.11 Hz (f) Mode at 135.11 Hz

Figure 6: A group of modes provided by the air inclusions.

3.2 Frequency response

The frequency response of the panel has been investigated in the range 50-250 Hz with a 1 Hz resolution. The panel is excited by a diffuse field on one side and the response is considered on the opposite side. First, a comparison between responses of the structure (without air inclusions) when using respectively 10, 30 and 40 seeds is performed. The result is shown in Figure 7.

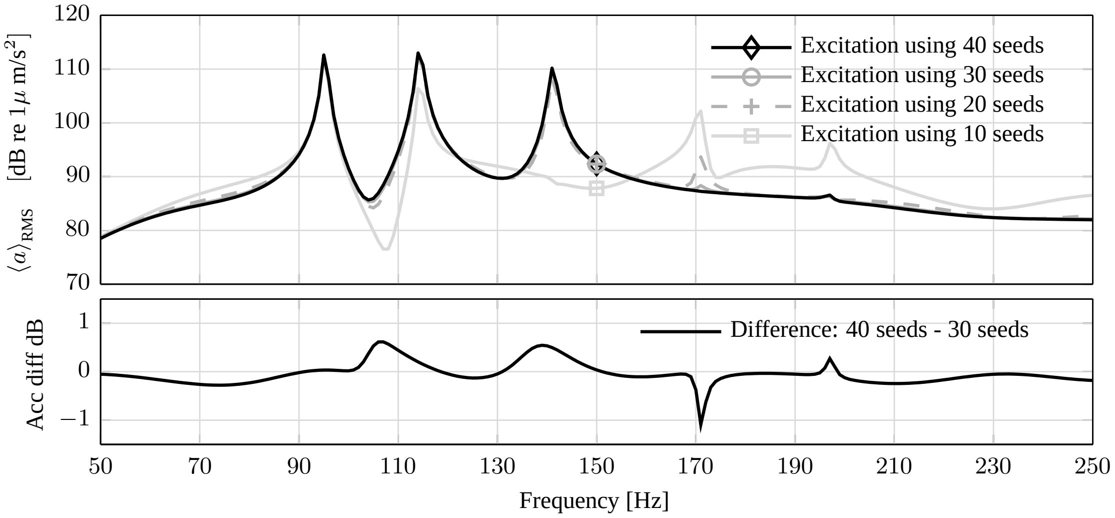

Figure 7: Spatial RMS acceleration of the receiving room plate surface as a function of frequency. The excitation of the sending room is a diffuse field simulated using 10, 30 and 40 seeds, i.e. using respectively 100, 900 and 1600 incident plane waves in ABAQUS. The calculations are performed without air inclusions in the model.

Next, using 30 seeds for diffuse field simulation in ABAQUS, the frequency responses with and without air inclusions are compared in Figure 8. The bottom part of the figure shows the difference between the two curves in the upper part. Finally, Figure 9 shows the response in the case of no structural coupling between the two plates in the panel structure.

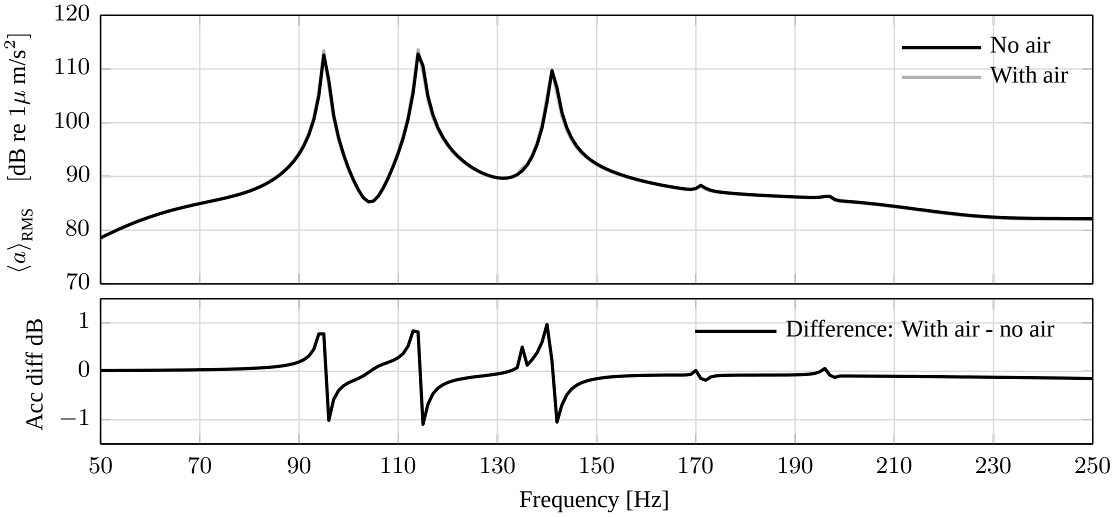

Figure 8: The effect of including the air inside the structure. The structure is excited by simulating a diffuse field using 30 seeds in ABAQUS. The bottom figure shows the difference between the two curves in the top figure.

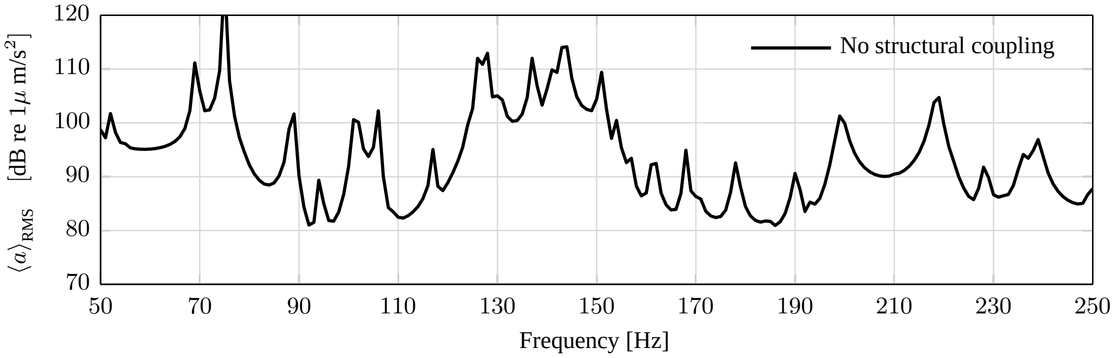

Figure 9: Spatial RMS acceleration of the receiving room plate surface as a function of frequency when there is no structural coupling in the model. The structure is excited by simulating a diffuse field using 30 seeds in ABAQUS.

4 DISCUSSION

As the presented results only represent the preliminary steps of a larger research project on sound transmission through lightweight building structures, focus has been on the basic details of how such structures are modeled for research purposes. Here, solid continuum elements have been adopted for the structure rather than elements based on simplified theory like that of shells and beams. For the considered frequency range, however, shell elements are expected to yield similar results as the wavelengths are large compared with the thickness of the panel. For the eigenfrequencies this is confirmed by looking at Figure 4, where it is seen that the difference is a slight frequency shift in the structural modes due to the shell elements having fewer degrees of freedom.

4.1 Modal analysis

By looking at Figure 3 and comparing the two curves with and without air inclusions in the cavities, it is seen that more modes appear within the considered frequency region when the air is included. Furthermore, the (structural) modes of the calculation without air appear in the calculation with air (the curves take a step up at the same frequencies). What is interesting, is the observation that the extra modes in the calculation with air inclusions are grouped together very closely in bunches of six. Based on this observation the actual modeshapes of such a group have been investigated. Figure 5 shows the second and third structural modes while Figure 6 shows the (air-related) modes in between the two. These modes (one for each cavity) differ slightly from each other in frequency due to the different positions of the air inclusions in the structure to which they are coupled.

Next, the eigenfrequencies in the case of no structural coupling between the two sides of the panel are considered. The curve (Figure 3) does not show the same groups of air related modes, which is rather unexpected as the air inclusions are identical to the other cases. This result may be explained by the fact that the coupling between the structure and the air becomes relatively stronger). Thus, movement of the air will be affected much more by the two structurally independent plates coupled to either side of the air cavities and vice versa. In order to verify this hypothesis, a fourth case have been considered, in which there is still no structural coupling between the plates, but furthermore the air is not coupled to the structural parts either. It is seen that the air related modes now appear in groups as expected.

4.2 Diffuse field excitation

A convergence study of the number of seeds needed in ABAQUS to adequately approximate a diffuse field has been done. The results show (see Figure 7) that for the given structure convergence seems to be fairly good when using 30 seeds for the approximation. Similar results are seen when examining the model including air inside the cavities.

4.3 Frequency response

The frequency response for the panel with air inclusions is compared to the panel without air inclusions in Figure 8. It is seen that the two configurations yield nearly identical results for the given frequency region. The peaks located at the first three structural modes of the panel are slightly lower in frequency when the air is included. This is due to the added mass of the air. Aside from this, only a very small difference is seen around 135 Hz where a group of air-related modes occurs. From an overall perspective the air inclusions do not show significant behavior in this frequency range.

When examining the response of the uncoupled case (see Figure 9), more peaks are seen as more modes are present. The overall acceleration level is quite similar to the coupled case. This does not quite match the expectations as the main transmission path is now broken. However, the calculations are for a constructed case where the enclosed volumes of air are still rather small having relatively (to the properties of air) rigid boundaries. Because of this, the air inclusions show a spring like behavior. At low frequencies the displacement is relatively large, meaning that the stiffness of the air enclosures becomes significant, resulting in the observed behavior.

5 CONCLUSION

Using a finite element approach, the effect of including an acoustic medium in the cavities of a double-plate single-stud lightweight wall/floor panel has been examined in the low frequency range. It is seen, that the air inclusions contribute to the mode count of the panel as they provide groups of modes related to the pressure field in the cavities. These modes, however, have very little effect on the frequency response when exciting the panel using an approximated diffuse sound field. The significance of the air-to-structure couplings depends strongly on the stiffness of the structure and it is expected, that the effect of the air-inclusions will be more pronounced for a limp structure. In the case of no structural coupling the sound transmission surely depends on the air-inclusions, as these constitute the only transmission path between the two plates.

Furthermore, it has been shown, that when shell elements are used rather than solid continuum elements for modeling the plates, the panel becomes slightly stiffer due to the reduced degrees of freedom. However, the same modes occur – only shifted slightly in frequency.

It has been demonstrated that for the model at hand a diffuse field approximation in ABAQUS converges and that using 30 seeds gives reasonably good results.

The present paper merely presents the introductory steps in a larger research project on sound transmission in lightweight building structures. Along the line of the model presented here, future work includes adding a sound field in the receiving room in order to predict the transmission loss, making a more efficient diffuse field excitation, investigate elastic couplings between plate/stud, investigating screw connections and other coupling properties. The greater goal being a better understanding of the different parameters affecting the sound transmission of such structures. This understanding is needed in order to develop a simplified prediction tool like [1] to be used with lightweight building structures.

5.1 Acknowledgements

The present research is part of the InterReg project ”Silent Spaces”, funded by the European Union. The authors highly appreciate the financial support.

REFERENCES

[1] *EN 12354-1:2000 Building Acoustics. Estimation of Acoustic Performance in Buildings from the Performance of Elements. Airborne Sound Insulation between Rooms*. European Committee for Standardization, 3rd edition, 2000.

[2] K. J. Bathe. *Finite Element Procedures*. Prentice Hall, 1 edition, 1995.

[3] F. Bitsie. *The Structural-Acoustic Energy Finite Element Method and Energy Boundary Method*. Ph.D. thesis, Purdue University, 1995.

[4] O. M. Bouthier and R. J. Bernhard. Simple models of the energetics of transversely vibrating plates. *Journal of Sound and Vibration*, 182(1):148–164, 1995.

[5] J. Brunskog and P. Davidsson. Sound Transmission of Structures. A Finite Element Approach with Simplified Room Description. *Acta Acustica united with Acustica*, 90:847–857, 2004.

[6] C. B. Burroughs, R. W. Fischer, and F. R. Kern. An introduction to statistical energy analysis. *The Journal of the Acoustical Society of America*, 101(4):1779–1789, 1997.

[7] R. J. M. Craik. *Sound Transmission Through Buildings using Statistical Energy Analysis*. Gower, 1996.

[8] R.J.M. Craik and R.S. Smith. Sound transmission through lightweight parallel plates. Part II: structure-borne sound. *Applied Acoustics*, 61:247–269, 2000.

[9] L. Cremer, M. Heckl, and B.A.T. Petersson. *Structure-Borne Sound*. Springer-Verlag, 3rd edition, 2005.

[10] J. Sonnerup D. Bard and G. Sandberg. Prediction model of the flanking transmission through a light-weight building construction utilizing fluid-structure interaction procedures. In *Proceedings of Internoise 2008*, 2008.

[11] Dassault Systèmes Simulia Corp., Providence, RI, USA. *ABAQUS Anaysis. User's Manual Version 6.10.*

[12] P. Davidsson. *Structure-acoustic analysis, finite element modelling and reduction methods,*. PhD thesis, Lund University, Department of Structural Mechanics, 2004.

[13] F. Fahy and P. Gardonio. *Sound and Structural Vibration*. Elsevier, 2nd edition, 2007.

[14] L. Galbrun. Vibration transmission through plate/beam structures typical of lightweight buildings: Applicability and limitations of fundamental theories. *Applied Acoustics*, 71:587–596, 2010.

[15] R.H. Lyon and R.G. DeJong. *Theory and Application of Statistical Energy Analysis*. Butterworth-Heinemann, 2nd edition, 1996.

[16] J. Mahn. Prediction of Flanking Noise Transmission in Lightweight Building Constructions: A Theoretical and Experimental Evaluation of the Application of EN12354-1. Technical report, University of Canterbury, Acoustics Research Group, 2007.

[17] D. J. Nefske and Sung S. H. Power flow finite element analysis of dynamic systems: Basic theory and application to beams. *Journal of Vibration, Acoustics, Stress, and Reliability in Design*, 111:94–100, 1989.

[18] N. Vlahopoulos, X. Zhao, and T Allen. An approach for evaluating power transfer coefficients for spot-welded joints in an energy finite element formulation. *Journal of Sound and Vibration*, 220:135–154, 1999.

COMPDYN 2011
III ECCOMAS Thematic Conference on
Computational Methods in Structural Dynamics and Earthquake Engineering
M. Papadrakakis, M. Fragiadakis, V. Plevris (eds.)
Corfu, Greece, 25–28 May 2011

MITIGATION OF FLANKING NOISE IN DOUBLE-PLATE PANEL STRUCTURES BY PERIODIC STIFFENING—FINITE ELEMENT ANALYSIS IN THE LOW-FREQUENCY RANGE

Parthkumar G. Domadiya[1*], Kristoffer A. Dickow[1],
Lars Andersen[1], and Sergey V. Sorokin[2]

[1] Aalborg University, Department of Civil Engineering
Sohngaardsholmsvej 57, DK-9000 Aalborg, Denmark
{pdg,kad,la}@civil.aau.dk

[2] Aalborg University, Department of Mechanical and Manufacturing Engineering
Fibigerstræde 16, DK-9220 Aalborg East, Denmark
svs@m-tech.aau.dk

Keywords: Lightweight panel structure, flanking noise, periodic stiffening, finite element method.

Abstract: *The present analysis focuses on flanking noise transmission within a two-wall structure of finite size. The walls are lightweight panel structures, each consisting of two plates with internal ribs. A finite-element model is utilized, assuming that the studs are fully fixed to the plates. Further, the air enclosed in the cavities within the structure is taken into consideration, whereas the external air has been disregarded. A fully coupled analysis is performed in which solid finite elements are adopted for the structure, whereas the acoustic medium within the panel is discretized into fluid continuum elements. The computations are carried out in frequency domain in the range below 500 Hz and the load acts as a concentrated force on one side of one of the panels. The responses of the same panel as well as the adjacent wall are studied.*

The position of the load relative to the stiffeners is important. Hence, analyses are carried out for different positions of the load. It has been found that the ribs have a significant impact, not only on the flanking noise but also on the direct radiation of sound from the wall on which the external force has been placed. Furthermore, the response changes when the air inside the wall panels is disregarded.

1 INTRODUCTION

Noise transmission within building structures is one of the main concerns in current time. For heavy structures, e.g. concrete buildings, statistical energy analysis (SEA) has been found to provide a reliable framework for prediction on noise transmission [1]. For example, Nightingale [5] found that a full wave SEA model of the junction produced useful results regarding the transmission of vibrational energy via flanking junctions from the point of excitation on a finite periodic rib-stiffened plates using SEA. However, SEA has limited validity for lightweight structures such as wooden floors with joists spanning in one direction or double-plate panel walls with vertical ribs [2, 12]. The periodic nature of the stiffening provides a nonhomogeneous modal density due to the formation of stop bands. Thus the vibrations are not diffuse and the number of modes in certain frequency bands may be limited. Hence, other methods of analysis must be employed.

As an alternative to SEA, the finite-element method (FEM) can be used [17] to describe flanking transmission in dwellings. Numerical simulations can reduce the cost of experiments and may also improve the design of sound insulation. However, modelling of lightweight structures is complicated, since such structures contain various materials and junctions as well as a relatively strong coupling to the acoustic medium compared to heavier structures such as concrete walls and decks. Furthermore, the FEM has limitations when it comes to the high-frequency range. Small elements must be employed in order to obtain an adequate discretization of the waves propagating in the structure and the acoustic medium. This results in a huge number of degrees of freedom, leading to long computation times.

Some research has been done in which sound transmission in the low-frequency range through lightweight structures has been predicted with numerical methods [6, 7, 14]. For example, Motoki [9] investigated sound radiation from a double-leaf structure under point force excitation, applying the load on a lightweight interior leaf connected to a massive exterior leaf. It was deduced that redesigning the interior leaf does not provide a significant reduction of the radiated sound power. In order to reduce the sound radiation, it is required to take damping mechanisms into account, e.g. acoustical damping.

Currently, there is also an increasing interest in periodic structures for better sound insulation. By a theoretical study, Takahashi [3] found that the spacing between ribs and the stiffness of the connector as well as the use of thick rigid materials all have a significant importance regarding the minimization of sound radiation from periodically connected infinite double-plate structures.

The current paper focuses on flanking noise transmission between two adjacent walls forming an L-shape with a rigid connection at the joint. The analyses concern the dynamic response to point-force excitation with the load applied at different positions on the source wall. The walls are identical, and with reference to the work by Hongisto [16] it is expected that flanking noise transmission can be very strong. Hence, a study is made of the energy transmission at various frequencies within the low-frequency range below 500 Hz. The findings of the paper indicate that the FEM can be applied to predict flanking noise in lightweight building structures with periodic stiffening.

Since flanking noise is the main consideration, the acoustic medium in the adjacent room is not modelled. However, the influence of including the air enclosed within the cavities inside the panel has been examined. The distribution of energy between the structure and the air has been analysed. The commercial code ABAQUS has been employed to model the double-plate panel structure using elements available in the ABAQUS/Standard library [19]. Material damping was introduced in the structure, whereas no damping was assumed in the air. For comparison, an analysis was performed in which the structural damping has been disregarded.

The aim of the paper is to get a better understanding of flanking-noise behaviour within two adjacent panels having couplings between the internal acoustic medium and the structure. Section 2 represents the model of the double-panel lightweight wall structures, whereas the results are discussed in Section 3 and concluding remarks are given in Section 4. Direct transmission of noise through a similar panel structure is analysed in a companion paper by Dickow, Domadiya, Andersen and Kirkegaard.

2 PROBLEM DESCRIPTION

Lightweight structures are usually constructed in panels with plates on stud or joist frames. To reduce the transmission of sound, frames are usually designed with single or double studs or constructed with layers of foam or another viscoelastic material. In the present case, single-stud double-plate panels have been considered. The structure consists of two identical panels forming an L-shape such that there is a direct structural coupling between the two panels. Furthermore, the plates are directly attached to the frame with no inclusion of elastic or viscoelastic layers. The aim of the study is to investigate the flanking noise transmission between the two walls under different circumstances. Thus, analyses are carried out with and without inclusion of the acoustic medium enclosed in the cavities within the panels. Further, different positions of a point force on one of the panels have been considered (see Figure 1), and the influence of structural damping is investigated.

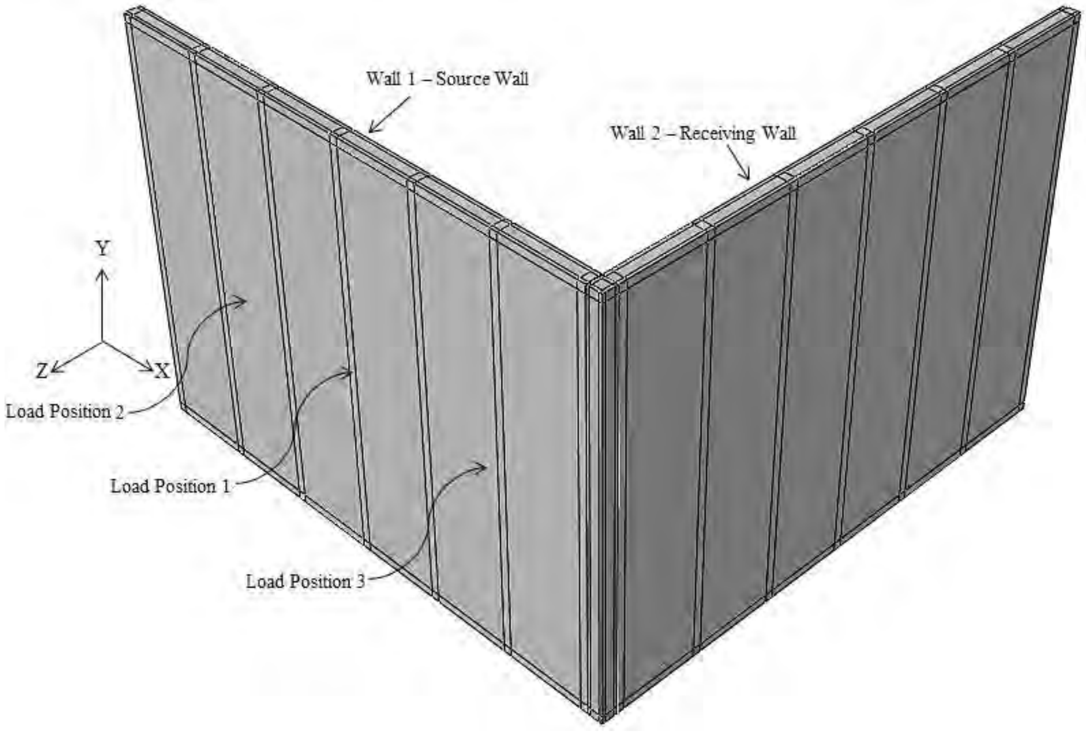

Figure 1: Complete geometry of two-wall structure.

2.1 Geometry and materials

The structure consists of two panels which are identical in sense of materials and geometry. Each panel consists of two plates mounted on a frame structure with six acoustic cavities (see Figure 1). The stud dimensions are 50 mm by 60 mm and the plate thickness is 20 mm. The total wall dimensions are 3350 mm (width) by 2600 mm (height) by 100 mm (thickness). The studs are placed with a distance of 550 mm (centre-to-centre). Homogeneous and isotropic materials are assumed. The material properties are:

- Timber (plates and frame): Young's modulus 14 GPa, Poisson ratio 0.35, mass density 550 kg/m^3. Damping is set to 1% of the stiffness (frequency-independent structural damping).
- Air (acoustic cavities): Bulk modulus 141,360 Pa, mass density 1.2 kg/m^3. No damping is introduced in the air inclusions.

It should be noted that the external air has not been included into the computational model, i.e. the acoustic medium surrounding the walls has been disregarded. Introduction of the surrounding air has an anticipated effect of reducing the Eigen frequencies of the structure due to the added-mass effect, and at the same time damping will occur due to radiation of sound.

2.2 Computational model

The panel is modelled in the commercial FEM package ABAQUS using solid continuum finite elements for the structure and fluid continuum elements for the air inclusions in the finite cavities. 20-node brick elements with quadratic spatial interpolation of the displacement (structure) and pressure (acoustic medium) are adopted with a mesh size of 50 mm. The mesh size has been chosen based on the wavelengths of waves propagating in the model at the higher frequency of interest—in this case 500 Hz.

The mesh is generated in such a way that nodes constituting the plate mesh align with the nodes on the frame structure. All structural contact points are connected using tie constraints in the x, y and z directions. Three-dimensional solid continuum elements have no rotational degrees of freedom, i.e. only displacements are considered. However, due to the local piecewise second-order interpolation of the displacements, the model adequately describes bending in the plates with a single element over the thickness direction.

The fluid–structure coupling is generated by using tie constraints within ABAQUS [19]. The two walls are connected by a column with cross-sectional dimensions of 100 mm by 100 mm and consisting of the same material as the remaining structure. Finally, the panels are fixed along the entire outer edge, i.e. at the top and bottom of the walls as well as the ends of the two adjacent panels.

2.3 Method of analysis

Two analyses have been performed on the present lightweight structure: 1) Modal analysis; 2) analysis of the steady state response to point excitation. In the modal analysis, the real Eigen frequencies were determined with and without air inclusions inside the panel structure. The Lanczos solver implemented in ABAQUS was applied in order to account for the structure–fluid coupling. In case of the steady state response to point excitation, direct steady state analysis was performed. Currently, mode-based analysis in ABAQUS does not support simultaneous modelling of fluid–structure coupling and structural damping. The steady state response analysis has been done under five different specifications of the model and load:

1. Transmission from wall 1 to wall 2 with air inclusions (load position 1),
2. Transmission from wall 1 to wall 2 without air inclusions (load position 1),
3. Transmission from wall 1 to wall 2 with air inclusions (load position 2),
4. Transmission from wall 1 to wall 2 with air inclusions (load position 3),
5. Energy deviation on receiving wall with and without damping (load position 1).

The three different load positions are considered in order to quantify the influence of the load position on the transmission to the adjacent wall, i.e. the flanking noise transmission. Material damping is introduced within the two panels, but as indicated by item 5 above, a comparison is made with an alternative model without structural damping. In addition to the total transmitted energy, the relative distribution of energy between the structure and the enclosed acoustic medium is also investigated at wall 2 for the three different loading positions.

3 RESULTS AND DISCUSSION

3.1 Eigen modes and Eigen frequencies

The undamped Eigen modes and corresponding Eigen frequencies of two panel structures with and without air inclusions were extracted using ABAQUS. Figure 2 shows the accumulated number of modes occurring below a given frequency in the interval 0 to 500 Hz. In the case with no internal air inclusions, only structural modes are present, and below approximately 420 Hz the modal density is low with the first mode occurring at approximately 95 Hz (see Figure 3). Beyond 420 Hz, the modal density increases significantly due to local modes of resonance in the plate fields between the studs.

When the air inclusions inside the panel are introduced into the computational model, Figure 2 shows that the number of modes increases dramatically. The first modes occur at about 67 Hz. However, these are not structural modes but modes related to resonance of the air in the cavities inside the panel. These “bubble modes” appear in bunches of 12 since there are 12 cavities in the structure. Due to the coupling between the structure and the acoustic medium, some spreading is present in the Eigen frequencies related to a bunch of “bubble modes”. However, since the coupling is weak in the present case at low frequencies, the frequencies are closely spaced as indicated by Figure 2 and the first two subfigures of Figure 4. With the inclusion of the air, the first structural mode in the panel structure is reduced from 95 Hz to about 80 Hz as an effect of the added mass (see Figure 2). A similar observation can be made for the subsequent structural modes up to about 340 Hz. At higher frequencies, there is a rapid increase in the number of modes, i.e. a higher modal density, within the panel. Further, a clear distinction between structural modes and “bubble modes” cannot be made, thus indicating a higher degree of structure–fluid coupling at higher frequencies.

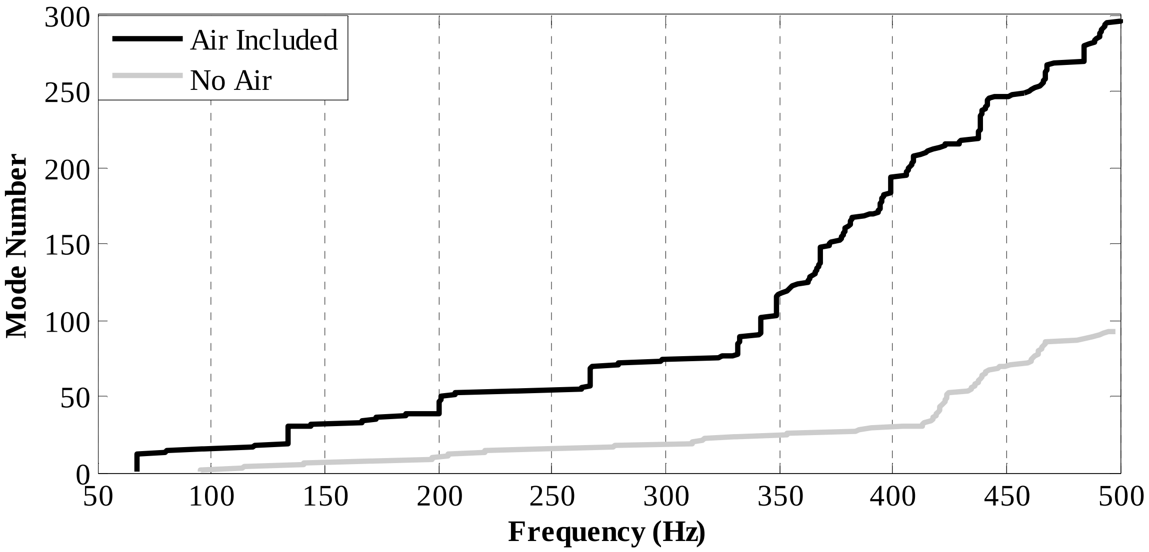

Figure 2: Eigen frequencies within whole panel with and without air inclusions.

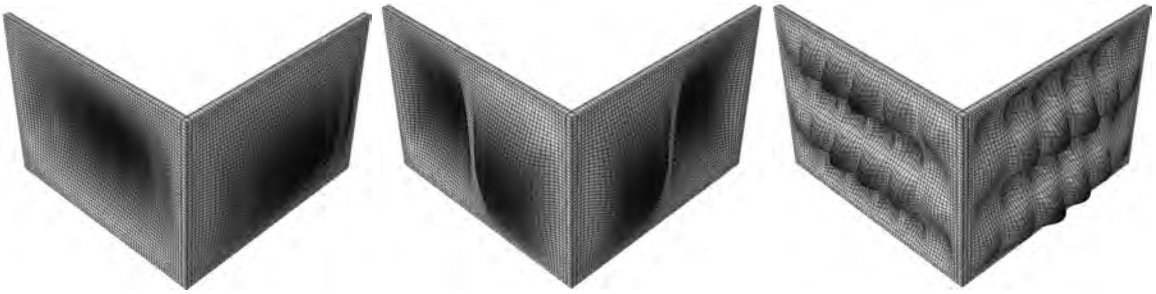

Mode at 94.94 Hz Mode at 114.92 Hz Mode at 413.13 Hz

Figure 3: Structural modes at different frequencies in the model without air inclusions.

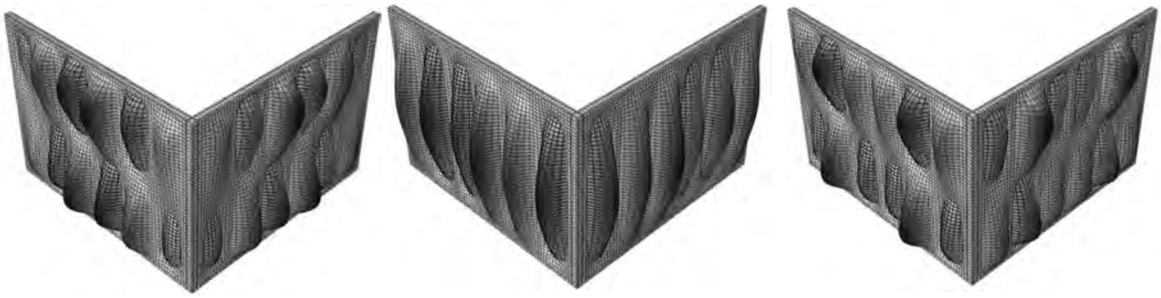

Mode at 67.11 Hz Mode at 67.12 Hz Mode at 364.73 Hz

Figure 4: “Bubble modes” generated due to resonance in the air inclusions.

3.2 Steady state response to point excitation

The steady state response of the panel structure to point excitation on one of the walls (the *source wall*) has been analysed for three different positions of the load (see Figure 1). The focus of the analyses has been put on the *receiver wall* in order to study the flanking noise transmission. Furthermore, for load position 1 (at the centre of the source wall), the energy transferred to the receiver wall was determined with and without the air inclusions in the two panels, and computations were made with and without structural damping.

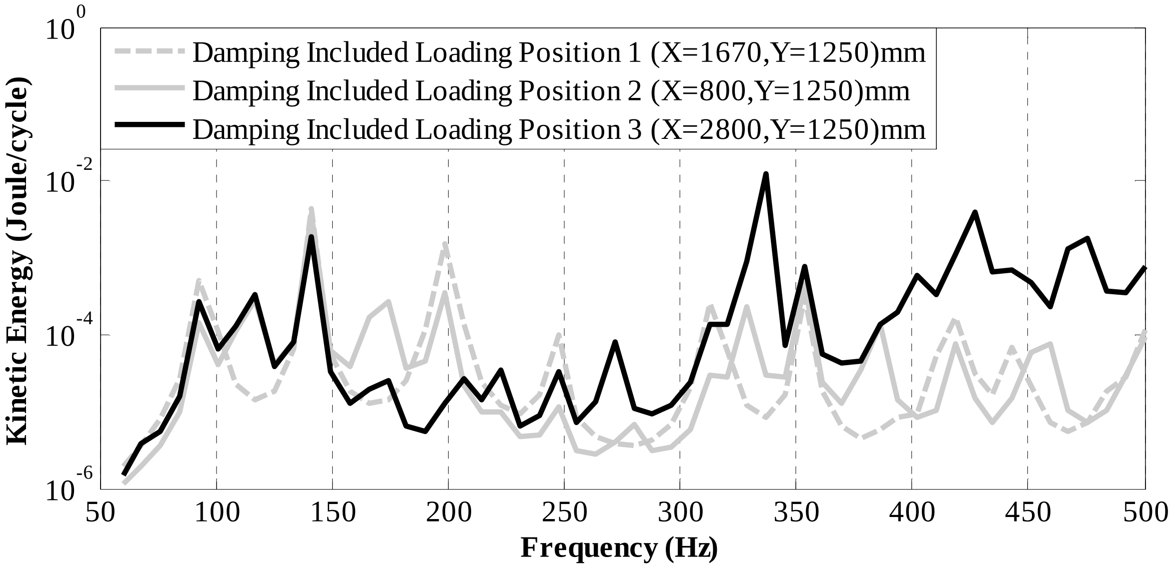

Figure 5: Kinetic energy per load cycle in whole model for the three different load positions.

Figure 5 shows a comparison of the kinetic energy per load cycle (absolute values) in the whole model for load positions 1, 2 and 3 and at 55 frequencies in the interval from 60 Hz to 500 Hz. It is noted that the models include the air inside the cavities as well as structural damping corresponding to 1% of the stiffness. At lower frequencies, peaks occur in the response near the structural Eigen frequencies. The point forces placed at load positions 1 and 2 provide nearly the same magnitude of response. With reference to Figures 1 and 3 this can be explained by the fact that the two loads act at positions leading to a similar strength of the excitation of the source panel within the first few structural modes of vibration. The analyses show that the peaks near 80 Hz and 200 Hz are slightly more pronounced for load position 1 compared to the two other load positions. This can be explained by the fact that a load applied to the centre of the source wall provides a stronger excitation of the first and third structural mode than a load applied near one of the ends of the panel. By contrast, the load applied at the centre of the source wall (i.e. at load position 1) acts near a node of the second mode, leading to a smaller response than observed for load positions 2 and 3.

For an excitation near 67 Hz it is expected that the load will induce strong vibrations in the “bubble modes”. This is not visible in Figure 5, which can be explained by the coarse frequency spacing combined with the fact that the “bubble modes” are weakly damped and almost uncoupled from the structural modes at lower frequencies. Hence, unless the “bubble modes” are excited very close to their resonance frequencies, they are not excited at all.

At higher frequencies, load positions 1 and 2 provide a significantly lower energy level than observed for load position 3—especially beyond 360 Hz. This can be explained by the longer distance from the load to the main part of the structure leading to a longer transmission path. Hence, the effect of structural damping is stronger. Moreover, the periodicity introduced by the ribs has an influence at the higher frequencies.

The kinetic energy transferred to the receiver wall with and without structural damping is presented in Figure 6 for load position 1. The structural behaviour with and without damping is almost identical in the low frequency range, but there is a reduction in the level of energy for frequencies beyond 260 Hz when damping is included, in particular near the resonance frequencies. If a higher frequency resolution is adopted, the peaks will go to infinity in the case without damping. At the higher frequencies, i.e. 400 to 500 Hz, the modal density is relatively higher than observed at lower frequencies. Hence, the influence of the structural damping is visible for all frequencies in the range.

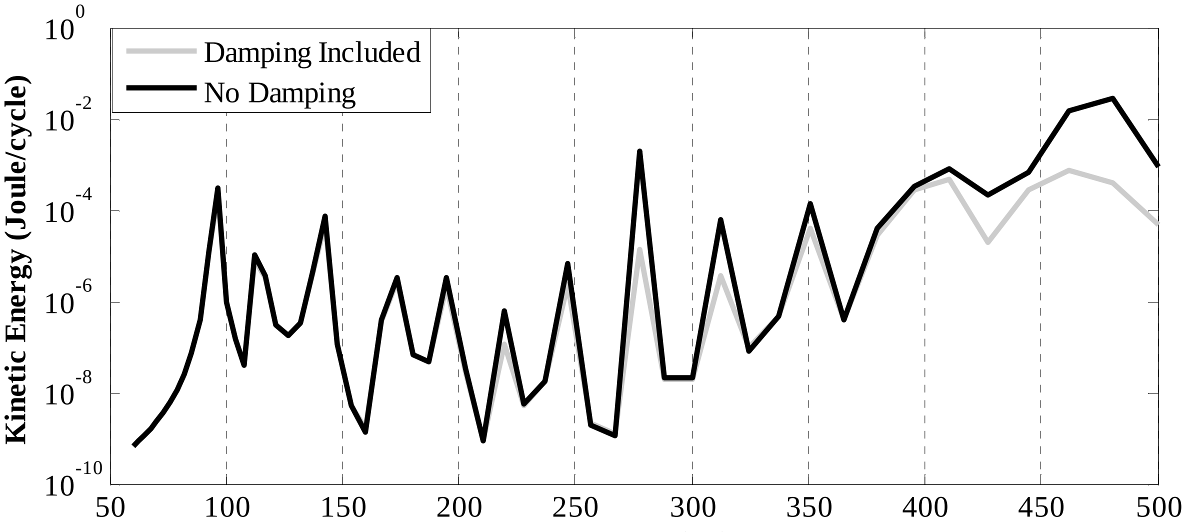

Figure 6: Energy transferred to the receiving wall with and without structural damping for load position 1.

Another interesting observation can be made regarding the response at frequencies above 350 Hz, where the modal density becomes higher. Thus, the total amount of kinetic energy transferred to the receiving panel may be similar for a number of frequencies in this interval. However, the local distribution of the energy over the receiving panel can be very different. This is illustrated in Figure 8 which shows the distribution of the kinetic energy at three different frequencies for the panel without air and with the point force placed at load position 1. At the frequency 394 Hz the main part of the energy is contaminated in the half of the receiver wall that is closer to the joint with the source wall. However, as the frequency is gradually increased to 410 Hz, the energy is transferred to the other end of the receiver wall.

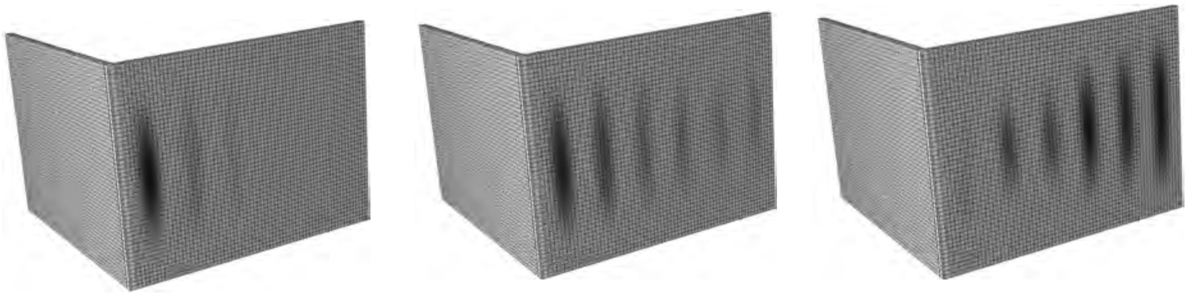

Response at 394.1 Hz

Response at 402.2 Hz

Response at 410.4 Hz

Figure 7: Response at three different frequencies for the panel without air and load position 1. The shades of grey indicate the magnitude of kinetic energy per unit volume (darker shades correspond to more energy).

Figure 8 shows the kinetic energy transferred to the receiver wall with and without air inclusions for load position 1. An increase of the energy due to the inclusion of the air within the cavities is seen at almost all frequencies. Finally, Figure 9 shows the relative distribution of energy between the air and the structure in the receiver wall for all three different load positions. It is observed that the structure generally carries the main part of the energy in all three cases. The energy contained in the air is 1–3 orders of magnitude smaller, which corresponds well to the fact that the mass of the air is less than 1% of the structural mass. However, a strong fluid–structure coupling is seen for load positions1, 2 and 3, respectively, at the frequencies 200 Hz, 140 Hz and 340 Hz. Here, some of the “bubble modes” are excited.

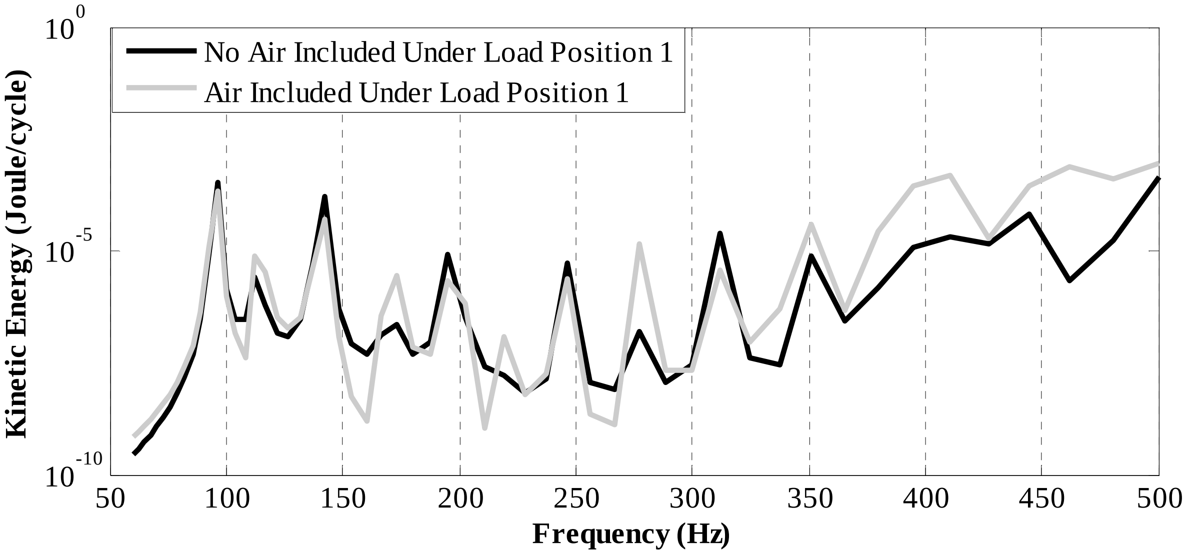

Figure 8: Energy transferred to the receiving wall with and without air inclusions for load position 1.

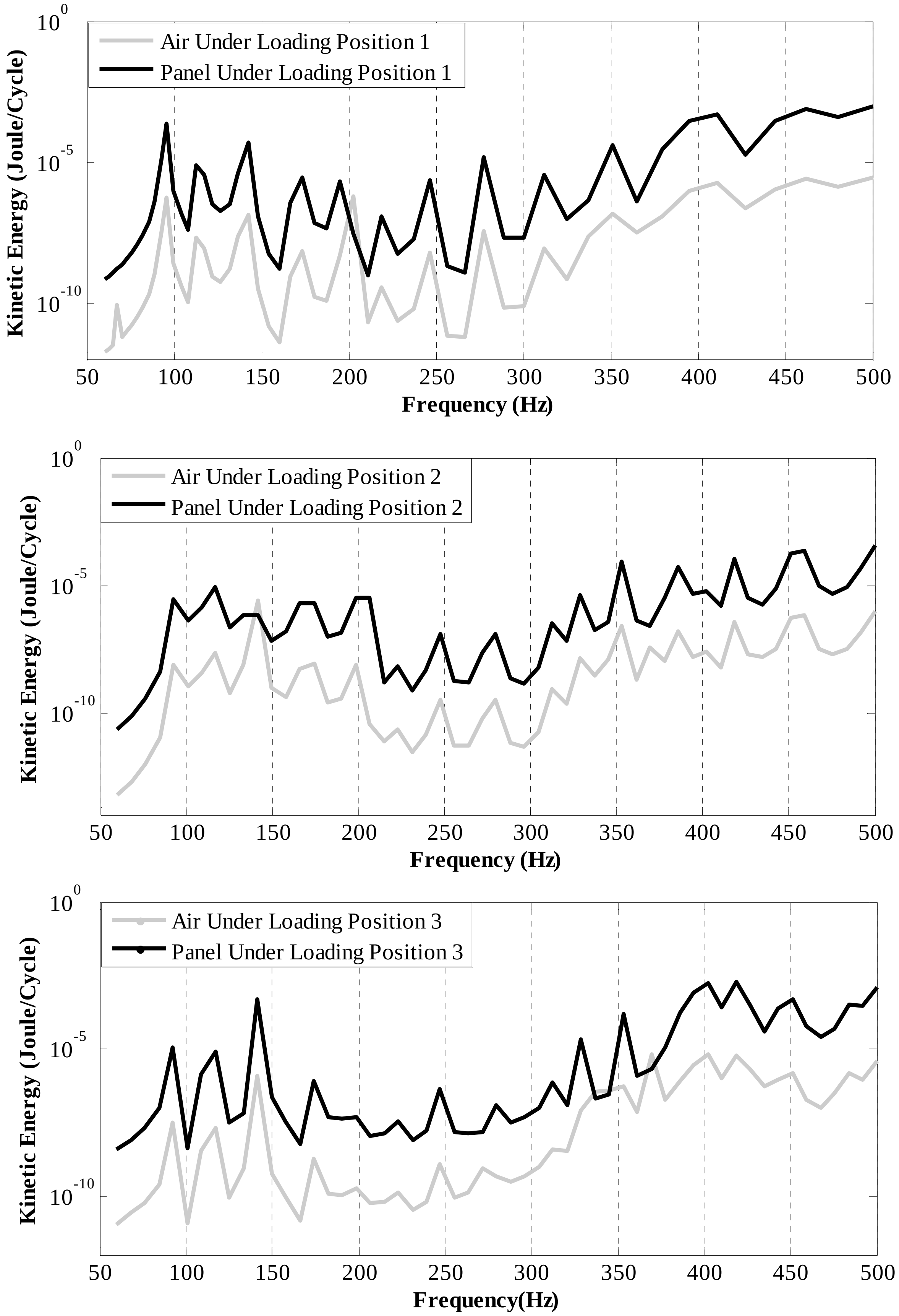

Figure 9: Distribution of energy between air and panel at receiver wall for three different load positions.

4 CONCLUDING REMARKS

Flanking transmission between two double-plate single-stud lightweight panels has been analysed under different conditions in the frequency range below 500 Hz. Slight differences have been observed in the Eigen frequencies depending on whether the air inside the cavities within the panels has been included or not. For example, the first structural mode with and without air inclusions occurs at 80 Hz and 95 Hz, respectively. The kinetic energy per load cycle within the whole structure was extracted for three different positions of a point force acting on one of the panels. It was observed that the energy level is highly influenced by the load position, especially at higher frequencies. Material damping as well as periodic stiffening may contribute to a decrease of the transmission when the load is applied on the source panel at a greater distance away from the receiver panel.

It is also seen that the energy present in the receiver wall is slightly increased when air is included within the panel structure. The structure still carries the main part of the energy and in most situations the coupling between the structure and the fluid is weak. Due to resonance of the air inside the cavities, “bubble modes” exist, but due to the weak coupling with the structure at lower frequencies, excitation of these modes will not lead to a significant excitation of the structure and vice versa. However, for certain combinations of the load position and the excitation frequency, a significant part of the energy is transferred to the air inside the receiver panel. At frequencies beyond 350 Hz the modal density becomes much higher than observed at lower frequencies and the structural and acoustic modes become mixed, indicating a stronger fluid–structure coupling with increasing frequency.

The present paper is a result of preliminary research in a larger research project on mitigation of flanking transmission in lightweight building structures. Future work involves a closer investigation of the influence of periodicity in the stiffening of lightweight structures. Further, the energy dissipation at junctions will be examined, and a sound field will be introduced in the adjacent room in order to predict the flanking noise behaviour of the structure. Comparisons will be made between panels with unidirectional ribs and with two sets of orthogonal stiffeners. The aim is to predict flanking noise behaviour via joints or as direct transmission between adjacent rooms.

Acknowledgement

The present research is part of the InterReg Project “Silent Space”, funded by the European Union. The authors highly appreciate the financial support.

REFERENCES

[1] R.H. Lyon, R.G. DeJong, Theory and application of statistical energy analysis, 2nd edition. Butterworth-Heinemann, 1996.

[2] L. Galbrun, Vibration transmission through plate/beam structures typical of lightweight buildings: Applicability and limitations of fundamental theories. *Applied Acoustics*, **71**, 587–596, 2010.

[3] D. Takahashi, Sound radiation from periodically connected double-plate structures. *Journal of Sound and Vibration*, **90**(4), 541–557, 1983.

[4] B.R. Mace, Sound Radiation from a plate reinforced by two sets of parallel stiffeners. *Journal of Sound and Vibration*, **71**(3), 435–441, 1980.

[5] T.R.T. Nightingale, On the distribution of transverse vibration in a periodic rib stiffened plate. *Forum Acusticum*, 2005.

[6] J. Brunskog, The influence of finite cavities in sound insulation of double-plate structures. Div. Engineering Acoustics, Lund University, TVBA-3119, 2002

[7] J. Brunskog, Near-periodicity in acoustically excited stiffened plates and its influence on vibration, radiation and sound insulation. *Div. Engineering Acoustics, Lund University*, TVBA-3120, 2002

[8] D.J. Mead, Wave propagation in continuous periodic structures: research contributions from Southampton, *Journal of Sound and Vibration*, **190**(3), 495–524, 1996

[9] Y. Motoki, S. Kimihiro, E. Sakagami, M. Masayuki, A. Minemura, K. Andow, Sound radiation from a double leaf elastic plate with a point force excitation: effect of an interior panel on the structure borne sound radiation. *Applied Acoustics*, **63**, 737–757, 2002

[10] C.T. Yeh, Damping sources in wood structures. *Journal of Sound and Vibration*, **19**(4), 411–419, 1971.

[11] F.Fahy and P. Gardonio. *Sound and Structural Vibration*. Elseveir,2nd edition, 2007

[12] J. Mahn. Prediction of flanking noise transmission in lightweight building constructions: A theoretical and experimental evaluation of the application of en12345-1. Technical report, University of Canterbury, Acoustics Research Group, 2007.

[13] R.J.M. Craik. Sound Transmission Through Buildings using Statistical Energy Analysis. Gower, 1996.

[14] J.Sonnerup, D.Bard, G. Sandberg. Prediction model of the flanking transmission through a lightweight building construction utilizing fluid-structure interaction procedures. In *Proceedings of Internoise*, 2008.

[15] E.Gerretsen, Calculation of the sound transmission between dwellings by partitions and flanking structures. *Applied Acoustics*, 0003-682X/79, 1979

[16] V. Hongisto, A case study of flanking transmission through double structures, *Applied Acoustics*, **62**, 589–599, 2001.

[17] D. Clasen, S. Langer, Finite element approach for flanking transmission in building acoustics. *Building Acoustics*, **14**(1), 1–14, 2007.

[18] R.J.M. Craik, R.S. Smith. Sound transmission through lightweight parallel plates. Part-II: Structure-borne sound. *Applied Acoustics*, **61** (2000), 247-269.

[19] “ABAQUS Analysis, User’s Manual, Version 6.10”. *Dassault Systèmes Simulia corp.*, Providence, RI, USA, 2010.

COMPDYN 2011
III ECCOMAS Thematic Conference on
Computational Methods in Structural Dynamics and Earthquake Engineering
M. Papadrakakis, M. Fragiadakis, V. Plevris (eds.)
Corfu, Greece, 25–28 May 2011

A HIERARCHY OF TIMOSHENKO BEAM THEORIES

S. V. Sorokin[1], **C. J. Chapman**[2]

[1] Department of Mechanical and Manufacturing Engineering, Aalborg University
Pontoppidanstraede 101, DK 9220 Aalborg, Denmark
e-mail: svs@m-tech.aau.dk

[2] Department of Mathematics, University of Keele
Keele, Staffordshire, ST5 5BG, United Kingdom
c.j.chapman@maths.keele.ac.uk

Keywords: Bending Wave, Dispersion Relation, Finite Products, Beam, Timoshenko Theory.

Abstract. *This paper shows that conventional Timoshenko theory for bending waves is a member of a two-parameter family (m; n) of approximations to the exact equations of linear elasticity. Higher members of the family are shown to represent the exact dispersion relation with extraordinary accuracy; in particular, an arbitrary number of branches can be captured accurately over their entire length, i.e. up to arbitrarily high frequencies and wavenumbers. The theory admits a rational accuracy analysis, and resolves certain controversies about the validity of higher-branch approximations. The paper demonstrates conclusively that Timoshenko theory is a completely rational theory, thus ending decades of doubt on the matter. The standard Euler-Bernoulli theory is a lower member of the two-parameter family. Especially useful is Timoshenko (1; 2) theory, which extends conventional Timoshenko (0; 1) theory by capturing the first four branches of the exact dispersion relation rather than merely the first two.*

1 INTRODUCTION

In the hierarchy of bending-wave theories for plates and beams, the first and simplest theory is Euler-Bernoulli theory, valid at the lowest frequencies and wave numbers; next comes Timoshenko theory, with or without various correction factors, valid to higher frequencies and wavenumbers; and finally comes exact linear theory, based on the full equations of linear elasticity, valid to any frequency and wavenumber for which linear theory still holds. The aim of this paper is to fill the very large gap between these last two theories, but use only polynomials. The gap is worth filling, because the dispersion relations obtained from exact linear theory are transcendental (when they can be obtained analytically at all), i.e. do not have the simple polynomial form of the earlier two theories, and engineers concerned with bending waves have overwhelmingly preferred the simplicity of polynomial theories

We shall fill the gap by means of a hierarchy of Timoshenko-type theories, in which the simplicity and accuracy of Timoshenko-type polynomial dispersion relations are maintained at very high frequencies and wavenumbers. At first sight, the quest for such dispersion relations would appear to be a hopeless undertaking. One reason is that the conventional Timoshenko dispersion relation is invariably derived from a kinematic hypothesis about the shape of frequencies. Another reason is that any truncated Taylor-series expansion of an exact dispersion relation must likewise fail at higher frequencies, because of the known finite radius of convergence of such an expansion. Thus strategies based on more elaborate kinematic hypotheses, or on ever-longer Taylor-series truncations, can at best succeed in a limited range of frequency and wavenumber.

The fundamental idea of this paper is to separate completely the derivation of a Timoshenko-type dispersion relation from any dependence on a kinematic hypothesis or a Taylor-series approximation. Instead, we use two families of finite-product polynomials, namely ‘sine-based’ polynomials S_m of degree m, and ‘cosine-based’ polynomials C_n of degree n. These polynomials are products of factors corresponding to a specified finite number of roots of a sine or cosine function. The roots correspond to the cut-on frequencies of different types of modes. The result is a two-parameter family (m, n) of polynomial approximations to the exact dispersion relation, of which the member (m, n)= (0, 1) is a conventional Timoshenko approximation.

If an analytical expression is available for the exact dispersion relation, the method is trivial to implement: for any (m, n), the corresponding finite-product approximation may be written down; and numerical computation of all of its roots, real or complex, is instantaneous on any computer, because of the universal availability and reliability of software for calculating the roots of polynomials. If, instead of an analytical expression, a numerical code is available for calculating the dispersion relation, the method may be implemented by first computing the cut-on frequencies of the low-order modes; these frequencies are then used to determine the appropriate finite-product polynomials.

In this paper, we implement the method in complete detail for the canonical problem of the subject, namely bending waves in a planar elastic layer, for which exact linear theory leads to the Rayleigh-Lamb dispersion relation. The numerical accuracy of the approximations obtained can be displayed explicitly in plots comparing the exact and approximate dispersion relations. It reveals the almost incredible accuracy of the above polynomials in representing the exact dispersion relation for small values of (m, n). Particularly accurate approximations are obtained when n = m+1. Hence a sequence of approximations is obtained which may be referred to as the Timoshenko (0, 1) dispersion relation, the Timoshenko (1, 2) dispersion relation, etc. This family of approximations approaches the exact Rayleigh-Lamb dispersion relation arbitrarily closely at arbitrarily high frequencies and wave numbers. The structure of these approximations, together with a detailed account of their numerical accuracy, is fully presented. The fact that such approximations can exist at all is far from obvious, but was demonstrated by Chapman & Sorokin [1]. Especially useful is the Timoshenko (1, 2) dispersion relation, which offers a massive extension of the range of validity of conventional Timoshenko (0, 1) dispersion relation, and provides ample accuracy for practically all anti-symmetric plate waves and vibrations of engineering interest.

2 TERMINOLOGY

We use the term Timoshenko-type theory for any theory or approach which leads to a polynomial dispersion relation of a certain type (specified explicitly) which generalises the conventional Timoshenko dispersion relation to a higher order polynomial. It must be emphasized that the type of theory refers only to how the dispersion relation is derived from physical principles and approximations, not to the final form of the dispersion relation itself. In every case, the dispersion relation is of the same form, namely a member of a specific two-parameter family of dispersion relations labelled by the parameters (m, n). This codified scheme brings unity to what would otherwise be a ‘zoo’ of approximate methods. Two main aspects of the paper are, first, the demonstration that established approximations fit within the scheme, and second, that, when applied to slightly higher (m, n) than hitherto, the scheme gives new approximations displaying an extraordinary increase in accuracy and scope at almost no cost. Our use of the terms Timoshenko theory and Timoshenko dispersion relation is an extension of their familiar use, but is entirely logical in describing the results obtained in the paper.

One might wonder why such a simple method as ours has not been exploited already. The answer lies in Runge’s phenomenon, namely the fact that the polynomials S_m and C_n do not represent the underlying sine and cosines accurately on account of the high-amplitude oscillations which the polynomials display away from the centre of their range. Such oscillations are known to anyone who has tried polynomial interpolation with an equally spaced set of grid points. The crucial fact underlying this paper is that, in a homogeneous linear combination of products of sines and cosines, Runge’s phenomenon cancels out almost exactly if an appropriate choice is made of the number of factors in the sine-based and cosine-based polynomials. With such a choice, inaccuracy in the individual representations of the sines and cosines does not lead to inaccuracy in the resulting approximation to the dispersion relation. In this context the term homogeneous means that in every term of the exact dispersion relation the number of sines or cosines multiplied together is the same; for the Rayleigh-Lamb dispersion relation, this number is two.

The cancelling out of Runge’s phenomenon answers a long-standing objection to Timoshenko theory from devotees of ‘rational mechanics’. It has repeatedly been claimed that Timoshenko theory is ‘just an engineering approximation’, and in particular that the excellent performance of the Timoshenko dispersion relation in capturing the first thickness-shear branch near cut-on is spurious. Indeed, it has been stated that Timoshenko theory is a ‘low-frequency theory trying to be a high-frequency theory’. The key point, emphasized in this paper, is that the Timoshenko dispersion relation can be derived by a method independent of a kinematic hypothesis or a Taylor-series truncation. This method shows that the Timoshenko dispersion relation is an early member of a sequence of approximations which, because of the cancelling-out of Runge’s phenomenon, approaches the exact dispersion relation at high frequencies and wavenumbers with extraordinary rapidity. Accordingly, Timoshenko theory is completely rational. A mathematically rigorous justification of the above assertions is given in [1] for waves in a planar layer.

3 FINITE-PRODUCT TIMOSHENKO THEORY

The key idea in finite-product Timoshenko theory for a planar layer is to start with the exact dispersion relation of Rayleigh-Lamb theory, and immediately replace the sine and cosine terms by finite-product polynomials, chosen to have the same roots as the original sines and cosines in a finite region. After this step has been taken, all calculations are performed with polynomials, and the original transcendental dispersion relation is not used again, unless accuracy analysis is required. The lengths of the finite regions are at the choice of the investigator: the longer the regions, the higher is the polynomial order of the finite-product dispersion relation, and the greater is its region of accuracy in the frequency-wavenumber plane. This region of accuracy increases rapidly with polynomial order, and may be made arbitrarily large. In this sense, finite-product Timoshenko theory fills completely the gap between conventional Timoshenko theory and Rayleigh-Lamb theory, referred to in the Introduction.

The exact Rayleigh-Lamb dispersion relation for this problem is (see [2]):

$$L_3^4 S_1 C_2 + K^2 L_2^2 C_1 S_2 = 0 . \tag{1}$$

Here $S_i \equiv S\left(L_i^2/4\right)$, $C_i \equiv C\left(L_i^2/4\right)$, $L_i^2 = \Omega_i^2 - K^2$, $i = 1,2$ and $L_3^2 = \frac{1}{2}\Omega_2^2 - K^2$. Furthermore, $\left(K, \Omega_1, \Omega_2\right) = \left(kh, \frac{\omega h}{c_1}, \frac{\omega h}{c_2}\right)$ with conventional notations for velocities of P- and S-waves.

The functions S and C are defined by $S\left(s^2\right) = s^{-1}\sin(s)$ and $C\left(s^2\right) = \cos(s)$. The use of S and C, rather than sine and cosine, helps avoid square roots in equations, where the square roots ultimately cancel out in pairs, and so maintains polynomial form. We define the finite products as follows:

$$S_{mi} = \prod_{m'=1}^{m}\left(1 - \frac{L_i^2}{4\left(m'\pi\right)^2}\right),\ C_{ni} = \prod_{n'=1}^{n}\left(1 - \frac{L_i^2}{\left(2n'-1\right)^2\pi^2}\right),\ i = 1,2 \tag{2}$$

If $m = 0$ or $n = 0$, the value of the corresponding finite product is defined as 1. Then the equation (1) is approximated by:

$$L_3^4 S_{m1} C_{n2} + K^2 L_2^2 C_{n1} S_{m2} = 0 \tag{3}$$

Although equation (3) is of simple form, it is divisible by $L_1^2 - L_2^2$. We introduce

$$I_{mn} = 4\frac{S_{m1}C_{n2} - C_{n1}S_{m2}}{L_1^2 - L_2^2} \tag{4}$$

Then equation (3) becomes ($\Omega_B = \frac{\omega h}{c_B}$, $c_B^2 = \frac{c_2^2\left(c_1^2 - c_2^2\right)}{3c_1^2}$)

$$-\frac{1}{3}\Omega_B^2 S_{m1} C_{n2} = K^2 L_2^2 I_{mn} \tag{5}$$

Equations (3) and (5) give the cut-on frequencies of the first m thickness-stretch modes and the first n thickness-shear modes. The reason is that these equations are satisfied if $K = 0$ and either $S_{m1} = 0$ or $C_{n2} = 0$. This is the motivation for using the finite-product method, since the exact Rayleigh-Lamb dispersion relation (1) is satisfied if $K = 0$ and either $S\left(L_1^2/4\right) = 0$ or $C\left(L_2^2/4\right) = 0$. The finite-product approximations (3) and (5) agree with the exact dispersion relation on a grid of points in the (K, Ω) plane, for which the above cut-on points form the boundary; details of the grid are given in [1].

The simplest way to introduce correction factors is to replace the term L_2^2 on the right-hand side of equation (5) by the quantity $L_{2\gamma\delta}^2$ defined by $L_2^2 = \gamma\Omega_2^2 - \delta K^2$:

$$-\frac{1}{3}\Omega_B^2 S_{m1} C_{n2} = K^2 L_{2\gamma\delta}^2 I_{mn} \tag{6}$$

At this stage, the values of γ and δ are arbitrary. The replacement of L_2^2 by $L_{2\gamma\delta}^2$ is not made in any other term, thus C_{n2} and I_{mn} contain L_2^2 not $L_{2\gamma\delta}^2$. Hence, the grid is preserved.

4 TIMOSHENKO (0,1) THEORY

The finite product theory, presented above for arbitrary m and n, will now be analyzed in detail for $(m,n) = (0,1)$. In this case, the reduced equation (6) becomes:

$$\Omega_B^2 = \frac{1}{\pi^2}\Omega_B^2\Omega_2^2 - \frac{1}{\pi^2}\left(12\gamma + \frac{c_2^2}{c_B^2}\right)\Omega_2^2 K^2 + \frac{12\delta}{\pi^2}K^4 \tag{7}$$

For equation (7), to recover the Bernoulli-Euler limit $\Omega_B^2 = K^4$, we must take $\delta = \frac{\pi^2}{12}$. Further analysis shows that γ is a re-parametrization of the standard stiffness correction factor κ via the relation

$$\gamma = \frac{\pi^2}{12\kappa} - \frac{c_2^2}{12c_B^2}(1-\kappa) \tag{8}$$

For the conventional Timoshenko dispersion relation with $\kappa = \frac{\pi^2}{12}$, this formula gives

$$\gamma = 1 - \frac{c_2^2}{12c_B^2}\left(1 - \frac{\pi^2}{12}\right) \tag{9}$$

In all these formulas, $\frac{c_2^2}{3c_B^2} = \frac{c_1^2}{c_1^2 - c_2^2}$ for both plane strain and plane stress.

5 TIMOSHENKO (1,2) THEORY

Then $(m,n) = (1,2)$, the definitions give: $S_{mi} = 1 - \frac{L_i^2}{4\pi^2}$, $C_{mi} = \left(1 - \frac{L_i^2}{\pi^2}\right)\left(1 - \frac{L_i^2}{9\pi^2}\right)$, $i = 1,2$.

Hence $I_{mn} = \frac{31}{9\pi^2}\left[1 - \frac{4}{31\pi^2}\left(L_1^2 + L_2^2\right) + \frac{4}{31\pi^2}L_1^2L_2^2\right]$. In the reduced equation (7), we must take $\delta = \frac{3\pi^2}{31}$ to recover the Bernoulli-Euler limit $\Omega_B^2 = K^4$. Then the reduced equation becomes

$$\Omega_B^2\left(1 - \frac{L_1^2}{4\pi^2}\right)\left(1 - \frac{L_2^2}{\pi^2}\right)\left(1 - \frac{L_2^2}{9\pi^2}\right) = -K^2\left(\frac{31\gamma}{\pi^2}\Omega_2^2 - K^2\right)\left[1 - \frac{4}{31\pi^2}\left(L_1^2 + L_2^2\right) + \frac{4}{31\pi^2}L_1^2L_2^2\right] \tag{10}$$

This simple equation has a truly extraordinary range of numerical accuracy.

6 TIMOSHENKO (M, N) THEORY

We have seen that for the finite-product equation (7) or (10) to recover the Bernoulli-Euler limit $\Omega_B^2 = K^4$, the correction factor $\delta = \frac{3\pi^2}{31}$ must take value $\frac{\pi^2}{12}$ when $(m,n)=(0,1)$ and the value $\frac{3\pi^2}{31}$ when $(m,n)=(1,2)$. These are examples of the general result that, for arbitrary (m,n), the value of the correction factor is $\delta = \frac{1}{3(c_{n1}-s_{m1})}$, where $s_{m1} = \frac{1}{\pi^2}\sum_{m'=1}^{m}\frac{1}{m'^2}$ and $c_{n1} = \frac{4}{\pi^2}\sum_{n'=1}^{n}\frac{1}{(2n'-1)^2}$. Thus δ is always a rational multiple of π^2. For example, the next value in the sequence above is $\delta = \frac{300\pi^2}{3019}$ for $(m,n)=(2,3)$. Since $s_{m1} \to \frac{1}{6}$ as $m \to \infty$, and $c_{n1} \to \frac{1}{2}$ as $n \to \infty$, it follows that $\delta \to 1$ as m and n increase. The above results are consequences of series expansions

$$S_m = \prod_{m'=1}^{m}\left(1-\frac{s}{(m'\pi)^2}\right) = 1 - s_{m1}s + s_{m2}s^2 - s_{m3}s^3 + \ldots \tag{11}$$

$$C_{ni} = \prod_{n'=1}^{n}\left(1-\frac{4c}{(2n'-1)^2\pi^2}\right) = 1 - c_{n1}c + c_{n2}c^2 - c_{n3}c^3 + \ldots \tag{12}$$

$$I_{mn} = c_{n1} - s_{m1} - (c_{n2}-s_{m2})(s+c) + (c_{n3}-s_{m3})(s^2+cs+c^2) + (s_{m1}c_{n2} - s_{m2}c_{n1})sc + \ldots \tag{13}$$

Expansion of the products in equations (11-12) gives $s_{m1} = \frac{1}{\pi^2}\sum_{m'=1}^{m}\frac{1}{m'^2}$ and $c_{n1} = \frac{4}{\pi^2}\sum_{n'=1}^{n}\frac{1}{(2n'-1)^2}$ (see above). Then substitution of equations (11-13), with appropriate arguments, into the finite-product equation (6) determines the correction factor as $\delta = \frac{1}{3(c_{n1}-s_{m1})}$.

7 BOUNDARY CONDITIONS

We have considered the planar elastic layer as a waveguide, i.e. as having indefinite length. For more general problems, boundary conditions at the ends must be included. The question then arises of solving a complete boundary-value problem if the Timoshenko (m, n) dispersion relation is to be used. Within the approach of this paper, this would be tackled by first formulating the problem with the exact equations of linear elasticity (either directly or using Hamilton’s principle with the exact Lagrangian), and then using the Timoshenko (m, n) field structure to reduce the problem to finite-dimensional modal form. This is an important direction for further work.

8 CONCLUSIONS

The method just described provides an incentive to re-examine certain classical problems for which analytical dispersion relations have been derived, but for which reasonable polynomial approximations have not been found. For example, the exact dispersion relation for elastic waves in a cylindrical shell contains many combinations of Bessel functions, quite beyond the range of analysis ‘by hand’. Yet the finite-product method can be applied, yielding a family of polynomial approximations readily obtained with a symbolic mathematical software package. A theoretical task would be to relate the families of approximations arising in such problems to the wave-hierarchy theories of Whitham [3].

REFERENCES

[1] C.J. Chapman, S.V. Sorokin, The finite-product method in the theory of waves and stability. *Proceedings of the Royal Society of London* **A** 466, 471-491, 2010

[2] J.D. Achenbach, *Wave propagation in elastic solids*. Amsterdam: North-Holland, 1973.

[3] G.B. Whitham, *Linear and nonlinear waves.* New York: Wiley, 1974.

COMPDYN 2011
3rd ECCOMAS Thematic Conference on
Computational Methods in Structural Dynamics and Earthquake Engineering
M. Papadrakakis, M. Fragiadakis, V. Plevris (eds.)
Corfu, Greece, 25-28 May 2011

ON THE POTENTIAL OF LOCAL RESONATORS TO OBTAIN LOW-FREQUENCY BAND GAPS IN PERIODIC LIGHTWEIGHT STRUCTURES

Claus C. Claeys, Paul Sas and Wim Desmet

Department of Mechanical Engineering,
Katholieke Universiteit Leuven
Celestijnenlaan 300B, B-3001 Heverlee (Leuven), Belgium
e-mail: claus.claeys@mech.kuleuven.be

Keywords: local resonators, band gap, vibro-acoustic insulation, lightweight structures

Abstract. *Periodic structures, such as honeycomb core panels, combine excellent mechanical properties with a low mass, making them attractive for application in transport and machine design. However, the high stiffness to mass ratio of these lightweight panels may result in unsatisfactory dynamic behavior in that it may impair the panels' ability to reduce noise and vibration levels. Their noise and vibration properties can be improved by the application of band gaps, i.e. zones with no free wave propagation. As indicated by Brillouin, periodic structures can exhibit band gap behavior, which in the case of sandwich panels could lead to frequency zones of reduced sound radiation or improved sound transmission loss. Band gaps are commonly the result of interference of traveling waves on the unit cell level, which implies that the lower limit of band gap zones is set by the length scale of the unit cell. However, band gaps can also be obtained by the addition of local resonators. These local resonance band gaps can be freely tuned in a low-frequency zone, independent of the unit cell scale length, making them an appealing engineering tool to improve the dynamic behavior of periodic lightweight structures. By means of numerical models the potential of local resonance band gaps for lightweight periodic panels is shown and compared with interference based band gaps.*

1 INTRODUCTION

For the improvement of vibro-acoustic attenuation a variety of methods exists. Conventional methods rely on the acoustic mass law or the addition of an absorptive layer. The first method results in heavy materials. The second method leads to thick materials, since to be efficient, the thickness of the absorptive layer should be in the same order of magnitude as the acoustic wave length. Often both methods are unsatisfactory to improve the low-frequency vibro-acoustic response of lightweight applications.

The noise and vibration properties of periodic structures can be improved by the application of band gaps, i.e. zones with no free wave propagation. As indicated by Brillouin [1], periodic structures can exhibit such band gap behavior. These gaps result in frequency zones of attenuated structural response. The question arises whether the band gap behavior can be exploited to produce sandwich panels with reduced sound radiation or improved sound transmission loss.

The understanding of periodicity in material crystals and the resulting energy band gaps has led to a high number of applications in solid state physics, such as ‘photonic crystals’. Recently quite some research has been performed to transfer these concepts to elastodynamics. Often these band gaps are obtained by incorporating a periodic distribution of wave scatters distributed in a matrix material. These ‘phononic crystals’ show attenuation of elastic waves in certain frequency bands, although often outside the audible frequency range. Recently, band gaps are actively pursued in order to obtain better structural dynamic behavior in periodic engineering systems such as truss core structures, stiffened plates and cylindrical shells [2, 3, 4].

In solid state physics, there are two theoretical approaches to the understanding of band gaps [5]. The first approach is based on Bragg scattering: zones with destructive interference between reflected and transmitted waves and hence high reflection and low transmission [6]. A second approach utilizes the tight-binding approach, starting from individual atoms/molecules, consisting of well-defined discrete electronic states. Where the first approach is dependent on the wavelength and relies strongly on periodicity, the second approach has as key element the discrete electronic states in individual atoms/molecules and the existence of local modes or local resonances.

The main physical principle behind the band gaps in aforementioned applications is the interference of traveling waves on the unit cell level. This implies that the frequency zone of the band gap is linked to the length scale of the unit cell which is a major drawback to obtain low frequency band gaps. Examples of applications based on the second approach are more scarce, although this method is equally well applicable to elastodynamics problems. In recent literature, examples of this second approach show a huge potential for vibro-acoustic problems [7, 8]. The decoupling of band gap frequency and unit cell length scale opens up the possibility of low frequency vibro-acoustic attenuation, beating the mass law.

This paper compares both methods of band gap creation with respect to vibro-acoustic attenuation. Mainly two characteristics are investigated: strength of vibro-acoustic attenuation and ease of manipulation of the band gap frequencies. Since band gaps show up as zones with no free wave propagation in infinite structures, only infinite structures are investigated. The first section elaborates on the modeling techniques used. The second section provides a one dimensional example to illustrates the difference in attenuation factors. In a third section, a two dimensional example is used to compare band gap frequencies.

2 MODEL OF PERIODIC STRUCTURES

2.1 Bloch's theorem

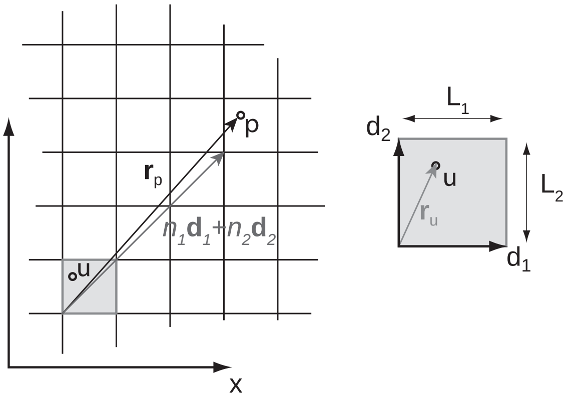

Figure 1: Schematic presentation of an infinite periodic structure (left). The shaded rectangle (right) represents a unit cell of the structure. Each point *p* in the structure can be expressed with respect to a corresponding point *u* in the unit cell.

Figure 1 represents a schematic view of a two-dimensional periodic structure. The structure is built as a repetition of the unit cell in two directions ($\mathbf{d}_1$ and $\mathbf{d}_2$), with $\mathbf{d}_1$ and $\mathbf{d}_2$ basis-vectors of the unit cell with length L_1 and L_2, respectively. Since the structure is periodic, each point *p* in the structure can be expressed with respect to a corresponding point *u* in the unit cell, translated n_1 cells along $\mathbf{d}_1$ and n_2 times along $\mathbf{d}_2$ (Fig. 1):

$$\mathbf{r}_p = \mathbf{r}_u + n_1\mathbf{d}_1 + n_2\mathbf{d}_2 \tag{1}$$

The theorem of Bloch (eq. 4) states that the response of a two-dimensional periodic system can be expressed in terms of the response of a reference unit cell, and an exponential term defining amplitude and phase change as the wave propagates from one cell to the next [1, 9]. The proportionate change in wave amplitude occurring when transitioning from one cell to the next, is independent of the cell location within the periodic system.

$$u(\mathbf{r}_p,\omega) = u_{ref}[\mathbf{r}_u,\omega].e^{\mathbf{k}.(n_1\mathbf{d}_1+n_2\mathbf{d}_2)} \tag{2}$$

The amplitude and phase change is determined by the wave vector $\mathbf{k}$, which is a general term expressing the amplitude decay and phase change of a wave per meter. In practice the wave vectors are expressed in terms of the length of the unit cell:

$$\boldsymbol{\mu} = \mathbf{k}.\mathbf{d} \tag{3}$$

The propagation vector $\boldsymbol{\mu}$ (eq. 3) expresses the complex phase shift when moving across a cell in the $\mathbf{d}_1$ $\mathbf{d}_2$-direction. With this notation the Bloch theorem is rewritten as:

$$u(\mathbf{r}_p,\omega) = u_{ref}[\mathbf{r}_u,\omega].e^{\boldsymbol{\mu}.\mathbf{n}} \tag{4}$$

Where $\mathbf{n}$ is a vector indicating the amount of cells moved in the $\mathbf{d}_1$- and $\mathbf{d}_2$-direction with respect to the unit cell.

2.2 Modelling the unit cell

Since the response of the entire structure is characterized by the response of the unit cell, a model of the unit cell suffices to investigate the wave propagation in the entire structure.

The finite element approach is chosen to model the unit cell [10, 11]. The equation of motion for harmonic motion is written in the usual matrix form:

$$(\mathbf{K} - \omega^2\mathbf{M})\mathbf{q} = \mathbf{f} \tag{5}$$

with **K** the stiffness matrix, **M** the mass matrix, **q** the generalized displacements, **f** the generalized forces and ω the angular frequency.

The equation of motion (Eq. 5) can be reduced by taking the boundary condition of the unit cell into account. The Bloch theorem states that the displacements and the forces are scaled with a factor e^{μ_1} and e^{μ_2} when moving from one cell to the next in the $\mathbf{d}_1$- resp. $\mathbf{d}_2$-direction. Demanding compatible displacements and force balance at the boundaries of the unit cell, a reduction matrix $\boldsymbol{R}$ in terms of the wave vector $\boldsymbol{\mu}$ can be derived [12].

$$\begin{aligned}(\mathbf{K} - \omega^2\mathbf{M})\mathbf{q} &= \mathbf{f}\\ \mathbf{R}^{*^T}(\mathbf{K} - \omega^2\mathbf{M})\mathbf{R}\mathbf{q}^{(red)} &= \mathbf{R}^{*^T}\mathbf{f}\end{aligned} \tag{6}$$

Under the assumption of no internal forces, the reduced force vector ($\mathbf{R}^{*^T}\mathbf{f}$) equals the zero vector and the equation of motion (eq. 5) reduces to an eigenvalue problem (eq. 7) in terms of the reduced stiffness and mass matrices $\mathbf{K}^{(red)} = \mathbf{R}^{*^T}\mathbf{K}\mathbf{R}$ and $\mathbf{M}^{(red)} = \mathbf{R}^{*^T}\mathbf{M}\mathbf{R}$.

$$(\mathbf{K}^{(red)} - \omega^2\mathbf{M}^{(red)})\mathbf{q}^{(red)} = \mathbf{0} \tag{7}$$

In this paper two approaches are used to solve this eigenvalue problem.

Direct approach In one-dimensional problems only propagation in one direction exists: the propagation vector $\boldsymbol{\mu}$ reduces to a complex scalar μ. For each frequency the eigenvalue problem can be rewritten in a polynomial form in terms of e^{μ} which can be solved for [13]. Stop bands are frequency zones where free wave propagation is inhibited and thus the propagation constant has a real part. Inspection of the propagation constant results therefore in the identification of stop bands.

Inverse approach Assuming free wave propagation, the propagation vector is strictly imaginary $\boldsymbol{\mu} = i\boldsymbol{\epsilon}$. Solving Eq. 7 for the frequency ω as a function of imaginary propagation vector $\boldsymbol{\epsilon}$, the frequencies of free wave propagation are found. In the case of imaginary propagation constants, the matrix $(\mathbf{K}^{(red)} - \omega^2\mathbf{M}^{(red)})$ is Hermitian and the solutions for ω are always real [12].

Considering the advantage of obtaining complex propagation constants, the first method will be applied to gain insight in the difference in attenuation factors between interference based and local resonance based band gaps. The second method will be used to investigate the manipulation of band gap frequencies for structures with two-dimensional periodicity.

2.3 Irreducible Brillouin contour

To obtain the pass and stop bands with the inverse approach, eq. 7 needs to be solved for every possible combination of purely imaginary propagation constants $\mu_1 = i\epsilon_1$ and $\mu_2 = i\epsilon_2$. The solved frequencies make up a surface in the wave domain (ϵ_1, ϵ_2), the so called dispersion surface $\omega = f(\epsilon_1, \epsilon_2)$. This dispersion surface yields the frequencies for which wave propagation without attenuation is possible. The frequencies which are not a solution of the eigenvalue problem, are frequencies where only attenuated wave propagation is possible and thus these frequencies belong to stop bands.

Since the analyzed structure is periodic, also the dispersion surface will be periodic and hence not the entire wave domain must be investigated. A periodic zone in the wave domain is called a Brillouin zone, and only the first Brillouin zone needs to be examined [1, 6]. Exploiting the symmetry of the unit cell, the first Brillouin zone can be further reduced to an irreducible Brillouin zone which is the smallest zone in the wave space that comprehends all information [2, 14].

A further reduction in computational cost can be achieved by limiting the variation of the wave vector along the contour of the irreducible Brillouin zone. The maxima and minima of each dispersion surface can be found on this boundary. The resulting dispersion curves contain sufficient information for the calculation of band gaps. Although this procedure is widely accepted in literature, according to the authors, no rigorous proof of this is available, but also no counterexamples can be found.

In this paper, the unit cell will be limited to a symmetric rectangular unit cell. As a result in the (ϵ_1, ϵ_2) domain only the contour with corner points $(0,0), (0,\pi), (\pi,\pi), (0,0)$ needs to be investigated [2].

3 ATTENUATION FACTOR

To drastically improve the vibro-acoustic behavior, a strong vibro-acoustic attenuation is required. The propagation vector $\boldsymbol{\mu}$ is a measure of vibro-acoustic attenuation: a larger real part, yields stronger attenuation. To compare attenuation factors for both interference and local resonance band gaps, the direct approach of solving eq. 5 is followed.

An infinite Euler-Bernoulli beam serves as a test case: this example is easy to grasp while computationally non demanding. Periodicity is introduced by the addition of a point mass or a spring-mass system. Table 1 summarizes the material characteristics and cross section dimensions of the infinite beam.

Name	Symbol	Value
Young's modulus	E	210 GPa
Density	ρ	7800 $\frac{kg}{m^3}$
Poisson's ratio	ν	0.3
Cross sectional area	A	$1 * 10^{-4} m^2$
Second moment of inertia (bending)	I	$8.33 * 10^{-10} m^4$

Table 1: Material characteristics and dimensions of the infinite beam used in the examples.

3.1 Interference band gap

Interference results from the combination of reflected and transmitted waves. A point mass without rotational inertia is added repeatedly every distance L to the infinite beam to introduce scatterers for reflection. Figure 2 shows the unit cell of the infinite beam. The added mass is 20% of the mass of the unit cell.

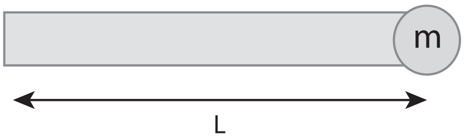

Figure 2: Unit cell of an infinite Euler-Bernoulli beam with a periodic point mass.

Since the band gap is due to interference, the frequency of the band gap is linked to standing wave behavior. The first standing waves will occur for a frequency where the unit cell length (L) equals half a structural wavelength. This condition is mathematically equivalent to claiming that the phase shift across the unit cell ϵ equals π. For an infinite Euler-Bernoulli beam, this frequency for bending equals to:

$$f_{\frac{\lambda}{2}} = \frac{\pi}{2L^2}\sqrt{\frac{EI}{\rho A}}. \tag{8}$$

This frequency $f_{\frac{\lambda}{2}}$ is used to make the frequency in the results dimensionless and independent of the periodicity length.

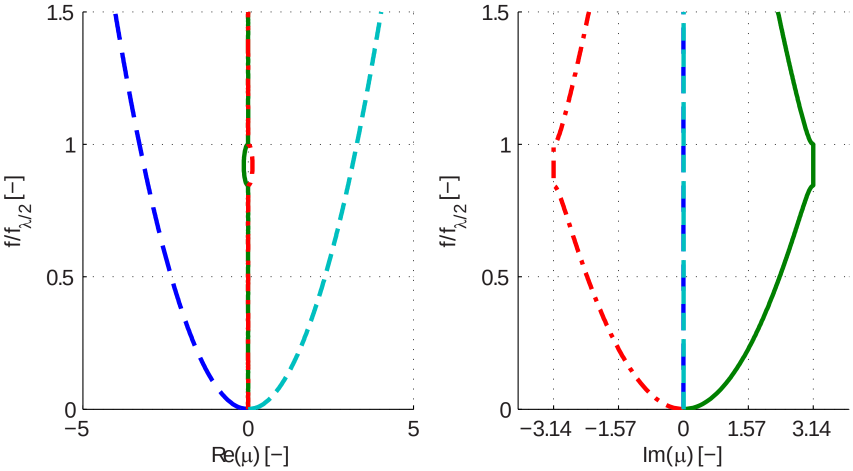

Figure 3: Dispersion curves for an infinite Euler-Bernoulli beam with a periodic point mass. The frequency zone without strictly imaginary wave propagation constant μ indicates a band gap.

Figure 3 shows the calculated propagation constants for a frequency range 0 to $1.5 f_{\frac{\lambda}{2}}$. The solutions for both the right and left running waves are shown. Two different wave types are found. The first wave type (dashed lines) has a purely real wavenumber, expressing a damped exponential decay. The second wave type (full and dash-dotted line) starts as a free propagating wave with increasing phase shift for increasing frequency. This trend stops as the phase shift ϵ across the unit cell becomes π (dimensionless frequency 0.85). Between dimensionless frequency 0.85 and 1 the imaginary part of the propagation constant μ remains constant and the real part differs from zero. In this frequency zone, no free wave propagation is possible and a band gap is found. For higher frequencies the wave transitions again to a free propagating wave.

3.2 Local resonance band gap

The existence of a local resonance in the unit cell can also lead to a band gap. A periodic repetition of a spring-mass system is added to the infinite Euler Bernoulli beam to simulate this behavior. Figure 4 shows the unit cell. The added mass is 20% of the mass of the unit cell, the stiffness is chosen such that the resonance of the spring-mass system equals $0.5 f_{\frac{\lambda}{2}}$.

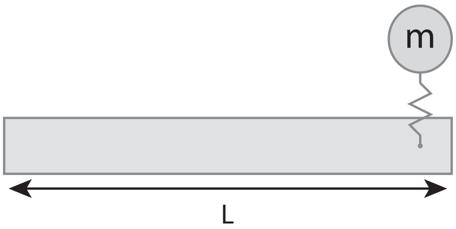

Figure 4: Unit cell of an infinite Euler-Bernoulli beam with a periodically attached spring-mass.

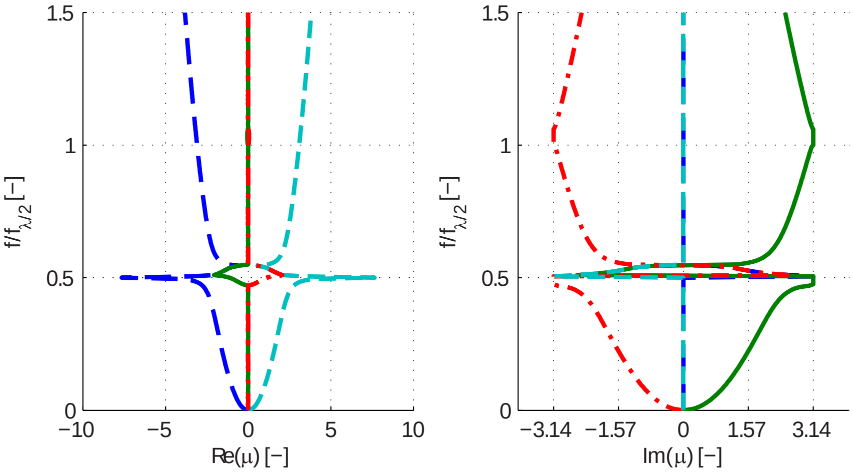

Figure 5: Dispersion curves for an infinite Euler-Bernoulli beam with a periodic spring-mass system. The resonance frequency of the spring-mass system is $0.5 f_{\frac{\lambda}{2}}$. The frequency zone without strictly imaginary wave propagation constant μ indicates a band gap.

The propagation constants for a frequency range 0 to $1.5 f_{\frac{\lambda}{2}}$ are shown in Fig. 5. For frequencies lower than the resonance frequency, the system is very similar to the beam with periodic masses: a free propagating wave (full and dash-dotted line) and a damped wave (dashed lines) are found. In the zone close to the resonance frequency the behavior changes drastically: both wave types have complex propagating constants and a band gap opens up from dimensionless frequency 0.47 to 0.55.

The local resonance band gap is smaller than the interference band gap (Fig.3), but shows very strong attenuation. For higher frequencies the wave types correspond again with the previous example.

It can be noticed that from dimensionless frequency 1 up to 1.065 a second band gaps opens up, although this band gap has a very low attenuation. This band gap is linked to standing wave behavior and can be explained as scattering due to the impedance of the resonator.

3.3 Comparison

For the same mass addition, the local resonance band gap shows a stronger attenuation, while the interference band gap opens up a larger band gap. The position of the band gap due to interference is linked to the standing wave behavior of the unit cell, whereas for the local resonance the band gap frequencies depend on the resonance frequency of the mass-spring system. The manipulation of band gap frequencies will be investigated in more detail in the next section.

4 BAND GAP FREQUENCIES

To improve vibro-acoustic behavior, it is crucial to be able to control the band gap frequencies. Attenuation in a certain frequency region often suffices to improve the vibro-acoustic behavior of a system drastically.

An infinite steel plate serves as a test case. Periodicity is again introduced by the addition of a point mass or a spring-mass system. Table 2 summarizes the material characteristics and dimensions.

Name	Symbol	Value
Young's modulus	E	210 GPa
Density	ρ	7800 $\frac{kg}{m^3}$
Poisson's ratio	ν	0.3
Thickness	t	$1mm$

Table 2: Material characteristics and dimensions of the infinite plate used in the examples.

Only the dispersion curves linked to out-of-plate motion of the plate will be examined. The in-plane modes of the plate are decoupled from the out-of-plane modes for flat plates and can be omitted from a vibro-acoustic point of view.

4.1 Interference band gap

To investigate interference band gaps, a point mass without rotational inertia is added periodically in two dimensions. The length of repetition in x and y direction is the same, so that the unit cell (Fig. 6) is symmetrical and square. The mass of the point mass is 20$\%$ of the mass of the unit cell.

The interference band gap will be linked to the standing wave behavior of the plate, however, now standing waves in different directions are possible. The first standing wave in y direction occurs when the wave length in y direction equals double the length of the unit cell (L). For the

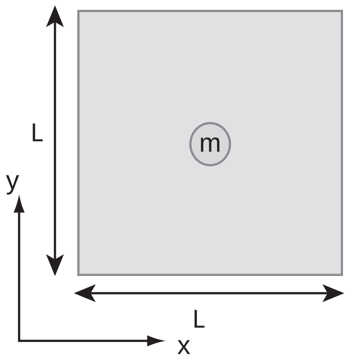

Figure 6: Square unit cell of an infinite plate with a periodic point mass.

x direction the same frequency is found due to symmetry. The first standing wave in diagonal direction occurs when the projected wavelength in both x and y direction equal double the unit cell length, hence when the diagonal wavelength equals $\sqrt{2}L$. These conditions are mathematically equivalent to claiming that the phase shift across the unit cell (ϵ_x, ϵ_y) is equal to $(0, \pi)$ for a wave in y direction and equal to (π, π) for the diagonal wave. It is worth pointing out that these are two of the three corner points of the irreducible Brillouin contour.

For an infinite plate with plane stress assumption the relationship between frequency and wavelength for bending waves is given by:

$$f = \frac{2\pi}{\lambda^2}\sqrt{\frac{t^2 E}{12(1-\nu^2)\rho}}. \tag{9}$$

The frequency for which the wavelength λ equals two times the unit cell length is used to make the frequency in the results dimensionless. Hence for the first standing wave in y direction the dimensionless frequency will by 1, for the first diagonal standing wave the dimensionless frequency will be 2.

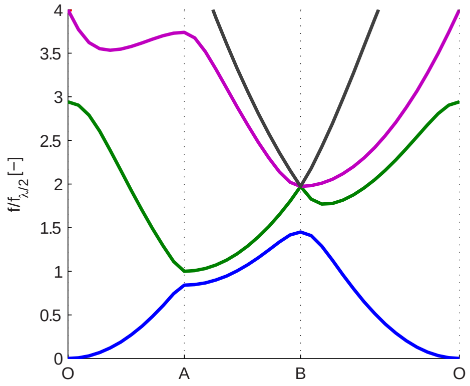

Figure 7: Dispersion curves for an infinite plate with a point mass repeated periodically in two dimensions. The dispersion curves are calculated along the contour of the irreducible Brillouin Contour: O,A,B,O $\mapsto (0,0), (0,\pi), (\pi,\pi), (0,0)$. The added mass is 20% of the unit cell mass.

Figure 7 shows the dispersion curves obtained with the inverse approach. For each frequency there is a corresponding point in the wave domain, and thus direction, for which free wave propagation is possible. Point A corresponds with propagation constants $(0, \pi)$ and a partial band gap from dimensionless frequency 0.84 to 1 is noticeable. For point B, corresponding with propagation constants (π, π) a partial band gap from dimensionless frequency 1.45 to 2 is found. Interference causes band gaps for waves in a certain direction in the frequency region corresponding to the standing wave in that direction, but these band gaps are not large enough to create a band gap across the entire wave domain.

Figure 8 shows the dispersion curves for an added periodic point mass of 80% of the unit cell. The partial band gap clearly comprises a broader frequency range and the partial band gaps are large enough to result in a complete band gap of $0.07 f_{\frac{\lambda}{2}}$.

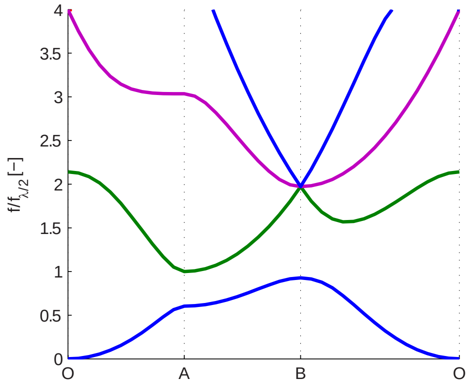

Figure 8: Dispersion curves for an infinite plate with a point mass repeated periodically in two dimensions. The dispersion curves are calculated along the contour of the irreducible Brillouin Contour. The added mass is 80% of the unit cell mass.

4.2 Local resonance band gap

Local resonance band gaps are achieved by the addition of a mass-spring system in the same manner as the point mass in the previous example. Figure 9 shows the unit cell. The mass is 20% of the mass of the unit cell, the stiffness is chosen so that the resonance of the unit cell is at a dimensioless frequency of 0.5.

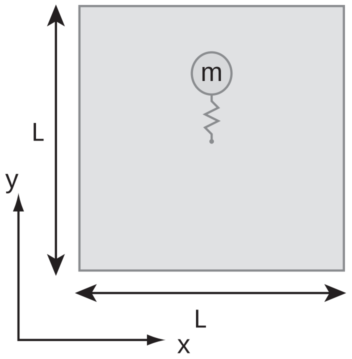

Figure 9: Unit cell of an infinite plate with a spring-mass system periodically attached.

The dispersion diagram (Fig. 10) shows a band gap from a dimensionless frequency of 0.48 up to 0.54. In a frequency region around the resonance frequency of the spring-mass system, no free wave propagation is possible. The original dispersion curve is pulled down to frequencies below the resonance of the spring-mass system. Above the resonance frequency a new dispersion curve appears. The pulled down dispersion curve relates to in phase movement of plate and resonator; the new dispersion curve contains modes where resonator and plate move out-of-phase.

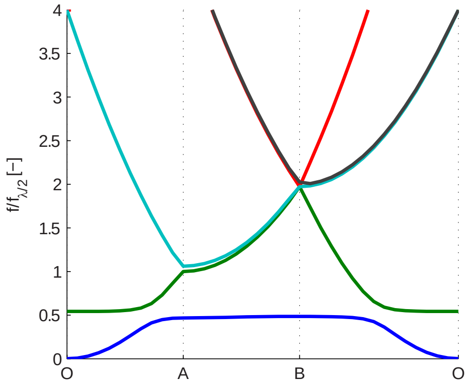

Figure 10: Dispersion curves for an infinite plate with a spring-mass system added periodically in two dimensions. The dispersion curves are calculated along the contour of the irreducible Brillouin Contour: O,A,B,O $\mapsto$ $(0,0),(0,\pi),(\pi,\pi),(0,0)$. The added mass is 20% of the unit cell mass. The resonance frequency of the spring-system is $0.5f_{\frac{\lambda}{2}}$.

Figure 11 shows the link between band gap width and added mass of the local resonator. The stiffness of spring-mass system is changed in function of the mass addition so that the dimensionless resonance frequency is kept at 0.5. Increasing the mass of the local resonator leads to a larger band gap. Although the lower limit of the band gap is pushed down a little, the higher limit of the band gap is affected the most. This agrees with the statement that the lower limit of the band gap is strongly linked to the local resonator resonance, while the upper limit is more influenced by the interaction of the resonator and the plate [15].

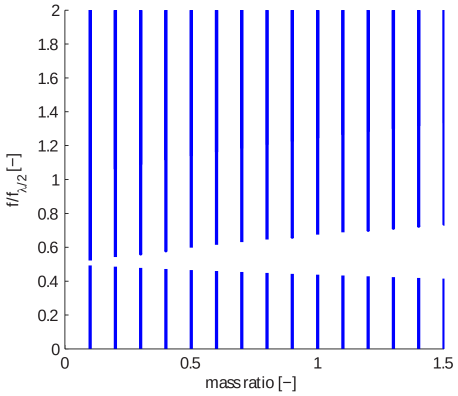

Figure 11: Relationship between frequencies of free wave propagation for an infinite plate with a spring-mass system added periodically in two dimensions and the mass the of spring-mass system. The spring stiffness is adjusted as function of the added mass to keep the resonance frequency fixed at a $0.5f_{\frac{\lambda}{2}}$.

Figure 12 shows the link between band gap and resonance frequency of the local resonator. The mass of the local resonator is kept at 20% of the plate mass and the stiffness is changed to change the resonance frequency. For the different resonance frequencies band gaps are calculated, which are represented as white gaps in Fig. 12. Up to a dimensionless frequency of 1, the resulting band gap is always centered at the resonance frequency of the local resonator. For higher frequencies no band gap is found.

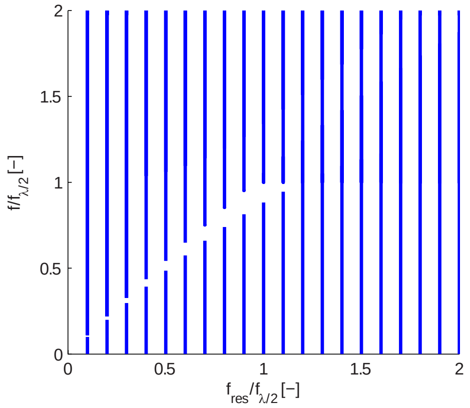

Figure 12: Relationship between frequencies of free wave propagation for an infinite plate with a spring-mass system added periodically in two dimensions and the resonance frequency of spring-mass system. The added mass of the local resonator is 20% of the plate mass.

The upper frequency of the highest band gap obtained is linked to standing wave behavior. Figure 13 shows the dispersion diagram for a spring-mass system with a dimensionless resonance frequency of 1.5. A free propagation wave at a dimensional frequency of 1.5 is found for the point with imaginary propagation constants $(0.72\pi, \pi)$, indicated with a black circle in Fig. 13. This correlates with a standing wave in y-direction and traveling wave in x-direction. In the corresponding wave motion all the spring-mass systems are in nodal points and hence not excited. For frequencies higher than the first standing wave frequency, it will always be possible to have traveling waves for which the mass-spring systems are in nodal positions: the dimensionless frequency of 1 is thus the upper-limit for local resonance band-gaps.

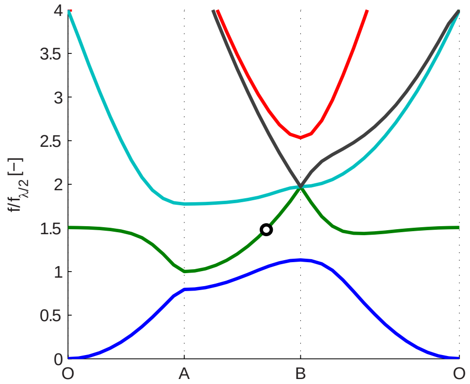

Figure 13: Dispersion curve for an infinite plate with a spring-mass system added periodically in two dimensions. The dispersion curves are calculated along the contour of the irreducible Brillouin Contour: O,A,B,O $\mapsto$ $(0,0),(0,\pi),(\pi,\pi),(0,0)$. The added mass is 20% of the unit cell mass. The resonance frequency of the spring-mass system is $1.5f_{\frac{\lambda}{2}}$. The black circle indicates the point $(0.72\pi, \pi)$ and dimensionless frequency 1.5.

Figures 14 is the result of a comparable analysis as Fig. 12 but with an added relative mass of 80%. It is clear that once again no band gaps show up for frequencies higher than a dimensionless frequency 1. Although, this time spring-mass-systems with a dimensionless resonance frequency higher than 1 still result in band gaps. For these resonance frequencies however, the link between resonance frequency and band gap frequency is lost. The resulting band gap is not a purely local resonance band gap: due to the relative large added mass and the resonance frequency in the vicinity of the standing wave frequency, the large impedance of the spring-mass-system at the standing wave frequency will lead to an interference based band gap.

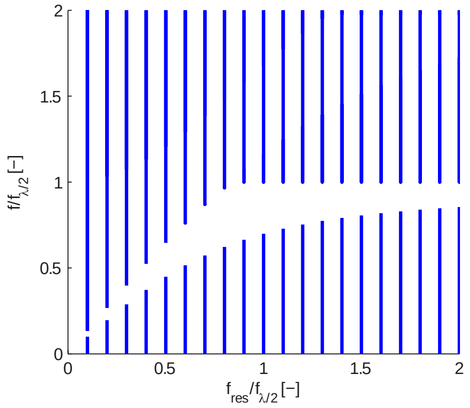

Figure 14: Relationship between frequencies of free wave propagation for an infinite plate with a spring-mass system added periodically in two dimensions and the resonance frequency of spring-mass system. The added mass of the local resonator is 80% of the plate mass.

4.3 Comparison

Although interference is a method of creating band gaps, these band gaps are not guaranteed for two dimensional topologies and can only be formed at frequencies corresponding with standing waves across the unit cell. Local resonance based resonators create a band gap at the frequency of the local resonator although this band gap is only guaranteed for frequencies lower than the first standing wave frequency of the unit cell.

For spring-mass-systems with a high impedance at the standing wave frequency, a combination of local resonance based band gaps and interference band gaps is possible.

5 CONCLUSIONS

This paper shows the potential of band gaps to suppress wave motion in certain frequency ranges. Band gaps can be created due to interference or by the addition of a local resonators in each unit cell.

Interference band gaps are linked to standing wave behavior and are not guaranteed. This explains why, although a lot of panels are periodic, band gaps are not often encountered: either the band gap frequency is too high or a complete band gap is not found.

The periodic introduction of a local resonator introduces a band gap at the resonance frequency of the local resonator. This is the case as long as the resonance frequency of the local resonator is below the first standing wave frequency in the unit cell.

In general the local resonance band gap shows stronger vibro-acoustic attenuation and the frequencies of the band gap are easier to manipulate. In conclusion, local resonance band gaps seem to have a high potential to improve the vibro-acoustic behavior of periodic lightweight structures in the low-frequency region.

6 ACKNOWLEDGEMENTS

The research of Claus Claeys is funded by a Ph.D. grant of the Institute for the Promotion of Innovation through Science and Technology in Flanders (IWT-Vlaanderen).

REFERENCES

[1] L. Brillouin, *Wave Propagation in Periodic Structures*. Dover, 1946.

[2] A. R. Diaz, A. G. Haddow, L. Ma, Design of band-gap grid structures. *Structural and Multidisciplinary Optimization*, **29**, 418–431, 2005.

[3] S. Lee, N. Vlahopoulis, A.M. Waas, Analysis of wave propagation in a thin composite cylinder with periodic axial and ring stiffeners using periodic structure theory. *Journal of Sound and Vibration*, **329**, 3304–3318, 2010.

[4] S. V. Sorokin, O.A. Ershova, Plane wave propagation and frequency band gaps in periodic plates and cylindrical shells with and without heavy fluid loading. *Journal of Sound and Vibration*, **278**, 501–526, 2004.

[5] P. Sheng, C. Chan, Classic wave localization and spectral gap materials. *International Journal for structural, physical and chemical aspects of crystalline material*, **220**, 757–764, 2005.

[6] C. Kittel, *Introduction to Solid State Physics*. Wiley, 2005.

[7] Z. Liu, X. Zhang, Y. Mao, Y.Y. Zhu, Z. Yang, C.T. Chan, P. Sheng, Locally resonant sonic materials. *Science*, **289**, 1734–1736, 2000.

[8] G. Wang, X. Wen, J. Wen, L. Shao, Y. Liu, Two-dimensional locally resonant phononic crystals with binary structures. *Physical review letters*, **93**, 154302, 2004.

[9] F. Bloch, Über die Quantenmechanik der Elektronen in Kristallgittern. *Zeitschrift fr Physik A Hadrons and Nuclei*, **52**, 555-600, 1929.

[10] J.D. Mead, A general theory of harmonic wave propagation in linear periodic systems with multiple coupling. *Journal of Sound and Vibration*, **27**, 235–260, 1972.

[11] J.D. Mead, Wave Propagation In Continuous Periodic Structures: Research Contributions From Southampton: 1964-1995. *Journal of Sound and Vibration*, **190**, 495–524, 1996.

[12] R. Langley, A note on the force boundary conditions for two-dimensional periodic structures with corner freedoms. *Journal of Sound and Vibration*, **167**, 377–381, 1993.

[13] B.R. Mace, D. Duhamel, M.J. Brennan, L. and Hinke, Finite element prediction of wave motion in structural waveguides. *The Journal of the Acoustical Society of America*, **117**, 2835–2843, 2005.

[14] S.J. Cox, D.C. Dobson, Maximizing band gaps in two-dimensional photonic crystals. *SIAM Journal on Applied Mathematics*, **55**, 2108–2120, 1999.

[15] C. Goffaux, J. Sánchez-Dehesa Two-dimensional phononic crystals studied using a variational method: Application to lattices of locally resonant materials *Physical Review B*, **67**, 144301, 2003.

COMPDYN 2011
III ECCOMAS Thematic Conference on
Computational Methods in Structural Dynamics and Earthquake Engineering
M. Papadrakakis, M. Fragiadakis, V. Plevris (eds.)
Corfu, Greece, 25–28 May 2011

DESIGN OPTIMIZATION OF FOUNDATION FOR ROTATING MACHINERY AGAINST STANDING-WAVE VIBRATION IN A BUILDING

Bin Niu, Niels Olhoff

Department of Mechanical and Manufacturing Engineering, Aalborg University
Fibigerstraede 16, DK-9220 Aalborg East, Denmark
e-mail: {bni, no}@m-tech.aau.dk

Keywords: Machinery Foundation, Design Optimization, Forced Vibration, Vibration Isolation.

Abstract. *This paper deals with the problem of optimum design of a foundation for rotating machinery on a storey of a building with a view to minimize the level of standing-wave vibration in the building. The foundation is usually designed as a base plate for the machinery, with some resilient mounts fixed to the bottom of the base plate and supported by the floor of the storey in order to provide a suitable level of vibration isolation of the building. Due to variable service speeds and the existence of non-balanced masses, the rotating machinery may be considered a source that within a given range of excitation frequencies excites forced vibration of the foundation, and thereby the floors and walls, etc., of the building. The transmission of such vibrations through the building may result in undesirable sound emission and unsatisfactory comfort conditions for the people in dwellings and offices of the building. To remedy this, the objective of this work is to develop and implement a method of design optimization to determine optimum stiffness values of resilient mounts subject to constraints on availability of physical properties of material to be used. The design objective is chosen as minimization of the power transmitted from the machine to the floor of the building where the foundation for the rotating machinery is mounted. At the current stage of our project, this problem is only carried out for a given, quite simplified model of a building. However, for this building model, the design and performance of the optimized machinery foundation will be illustrated and discussed using several numerical examples. In the next stage of our work, a multi-material, parameterized building model will be developed with detailed dimensions and connections of components, and the current problem will be extended to encompass simultaneous design optimization of both the building and the foundation for the rotating machinery in order to minimize the level of standing-wave vibration in the building.*

1 INTRODUCTION

Rotating machinery in buildings is usually applied in central heating and ventilation systems, and larger machinery of this type including a pump is normally mounted on a foundation, which is usually designed as a base plate for the machinery with some resilient mounts fixed to the bottom of the base plate and supported by the floor of the storey. Due to variable service speeds and the existence of non-balanced masses, the rotating machinery may be considered a source that within a given range of excitation frequencies excites forced vibration of the foundation, and thereby the floors and walls, etc., of the building. The transmission of such vibrations through the building may result in undesirable sound emission and unsatisfactory comfort conditions for the people in dwellings and offices of the building. Aside from that, vibrations increase safety hazards in machinery, buildings and installations. The primary goals of vibration insulation are to restrict the detrimental effects of vibrations on people to within reasonable limits, and to protect sensitive apparatus and safety systems from excessive stresses from vibrations.

Problems of design optimization of machinery foundations against vibration have been mainly studied from two aspects:

1. Free vibration design, also termed as frequency design. This aims at keeping the operating frequency as far away as possible from the eigenfrequencies of the machinery mounting system by adjusting the mounting system in order to avoid resonance. It is usually realized by maximization of the fundamental eigenfrequency or frequency gaps between two consecutive eigenfrequencies of the machinery mounting system.
2. Forced vibration design. The machinery mounting system is assumed to be subjected to a time-varying unbalanced mechanical loading, and this system will be designed by minimizing a chosen cost function describing the level of vibration response or transmission.

The problem of forced vibration design optimization of the installation systems of machinery in buildings has been extensively researched under the assumption of a rigid supporting structure [1-3]. The design based on a rigid supporting structure model is reasonable for the installation of machinery in many real engineering situations. However, this rigid support based model may not be appropriate for the problem studied in the present paper where the machinery is to be installed on a relatively flexible floor of the storey in a lightweight building. Based on a flexible support model, Ashrafiuon [4] studied design optimization of aircraft engine-mount systems for vibration isolation, and Xie et al [5] considered optimization of the mounting system for microelectronics manufacturing equipment using the receptance matrix method. In these works, minimization of the transmitted force from the vibrating machine to the receiver is chosen as the design objective. In the work [6] it was suggested to choose the power flow as the cost function because it combines both forces and velocities in a single concept. Furthermore, the transmitted power from the unbalanced machine to the floor is closely related to the structural noise emission from the floor. Power flow is considered to be a more reasonable measure of the vibratory state in vibro-acoustic modeling. The power flow from a vibrating machine to different flexible receivers through resilient mounts is presented in the works [6-9].

When rotating machinery is to be mounted on building floors rather than directly on a soil foundation, suitable resilient mounts should be provided as vibration isolation elements under the machine with a view to reduce the transmission of vibration.

The design optimization of machinery mounting systems is studied in this paper. The system consists of a rotating, unbalanced machine as vibration source, a mounting system as isolator, and a flexible floor as receiver. By assuming a simple time harmonic excitation generated within the machine by its operating mechanisms, it is convenient to characterize the individual sub-structures by their complex mobilities evaluated at the interfaces of contiguous sub-structures. The mobility is defined as the ratio of the complex amplitudes of the velocities and forces at any interface for a given frequency [10]. The physical quantities, such as velocities, forces and moments at the interfaces, are solved in terms of the mobility matrices of sub-structures.

A generalized mathematical model of mobility power flow is developed in this paper for evaluation of the response of the total system subjected to a given external excitation. In this model, the machine is modeled as a rigid mass subjected to a harmonically time-varying force. The base plate is assumed to be rigidly connected with the machine, and included in the modeling of the machine. The mounting system of the machine is designed as some resilient supports fixed to the bottom of the machine and supported by the floor of the storey in order to provide a suitable level of vibration isolation of the floor. The flexible floor is modeled as an elastic uniform plate, and the driving point and transfer mobilities of the plate are adopted in the model. The degrees of freedom associated with flexural vibration of the supporting structure are of main interest because the flexural wave motion is usually dominating the sound radiation compared with the in-plane wave motion.

The objective of minimizing vibration transmission is realized by sizing optimization of the stiffness coefficients of the resilient mounts. The design objective is chosen as minimization of the power flow transmitted to the building floor through the resilient mounts at the excitation frequency of the machinery. The design and performance of the optimized machinery foundation will be illustrated and discussed using several numerical examples.

The rest of this paper is organized as follows. First, a generalized mathematical model of mobility power flow is developed in this paper. The formulation of minimization of transmitted power flow is presented in Section 3. Section 4 presents a simplified parametric example only considering the vertical flexural motion, and a generalized optimization example with more degrees of freedom. In Section 5, a shape optimization problem of a pad that is placed on a flexible floor to support a resilient mount, is presented. Finally, observations and conclusions are drawn based on the optimization results.

2 A GENERAL MOBILITY FORMULATION OF THE MACHINERY MOUNTING SYSTEM

A general model with a rotating, unbalanced machine as vibration source, a mounting system as isolator, and a flexible floor as receiver, is developed for analysis and optimization of vibration transmission, see the model in Figure 1. The machine is modeled as a rigid body subjected to a harmonically time-varying force. The mounting system of the machine is designed as some resilient supports fixed to the bottom of the machine and supported by the floor of the storey in order to provide a suitable level of vibration isolation of the floor. The flexible floor is modeled as an elastic uniform plate, and the driving point and transfer mobilities [11] of the plate are adopted in the model. Figure 1 gives a representation of a vibratory rigid body resiliently mounted on a four-edge simply supported plate via multiple resilient mounts. The forces and velocities at the interface of the contiguous sub-systems are shown in Figure 2, where the arrows define the positive directions of the forces and velocities.

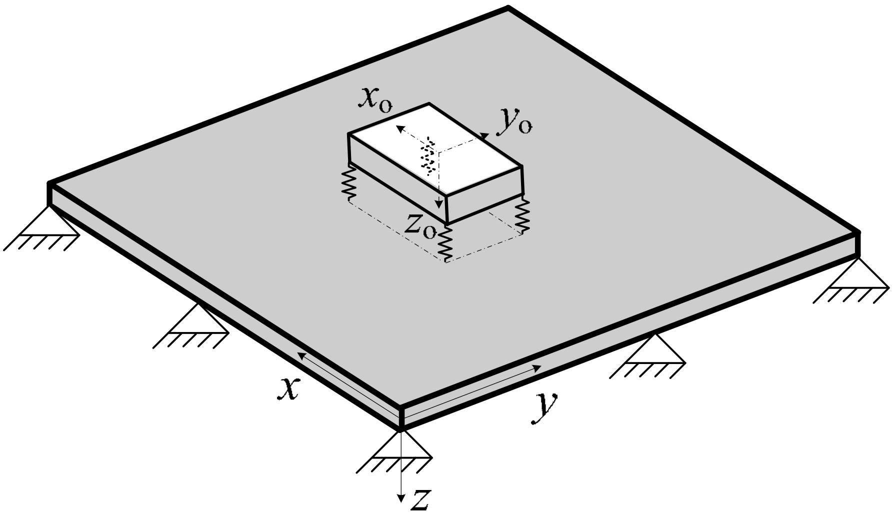

Figure 1: A machine mounted to a flexible floor via multiple resilient mounts

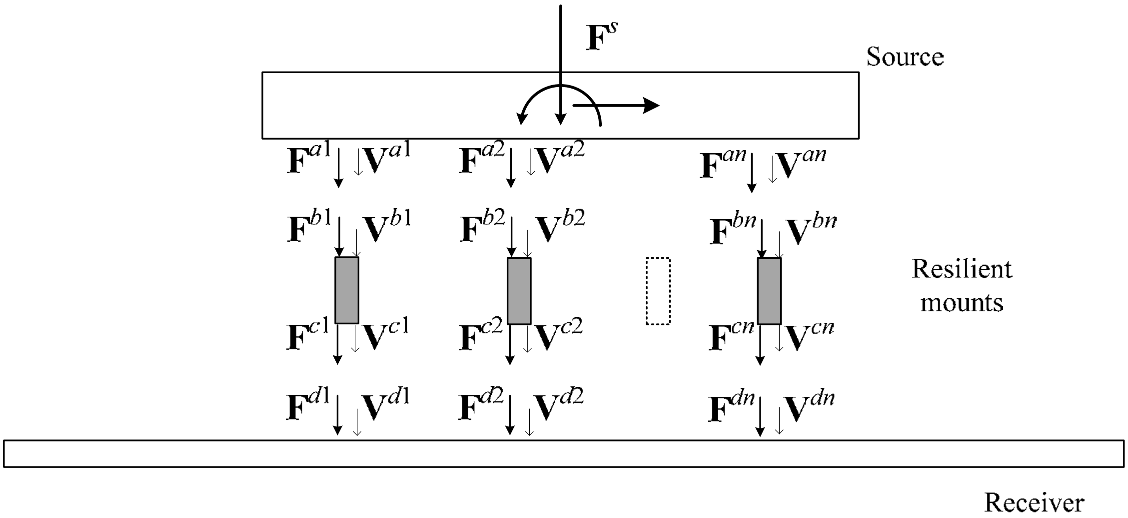

Figure 2: Description of forces and velocities between three sub-systems: source, resilient mounts and receiver

2.1 Rigid body

A local coordinate system $x_o y_o z_o$, cf. Figure 1, is adopted with origin in the center of gravity of the machine. It is assumed that the machine is excited by a generalized concentrated force vector $\mathbf{F}^s$ with three force and three moment components acting at the center of gravity. The corresponding generalized velocity vector at the center of gravity is denoted as $\mathbf{V}^s$.

$$\mathbf{F}^s = \left\{F_1^s, F_2^s, F_3^s, F_4^s, F_5^s, F_6^s\right\}^T \tag{1}$$

$$\mathbf{V}^s = \left\{V_1^s, V_2^s, V_3^s, V_4^s, V_5^s, V_6^s\right\}^T \tag{2}$$

where the superscript T represents the transpose of a matrix or vector.

A number of resilient mounts are assumed to be attached to the bottom of the machine, and the generalized output force and velocity vectors from the rigid body to the resilient mounts at the n junctions are assembled in the vectors

$$\mathbf{F}^a = \left\{ \mathbf{F}^{a1} \quad \mathbf{F}^{a2} \quad \dots \quad \mathbf{F}^{an} \right\}^T, \ \mathbf{V}^a = \left\{ \mathbf{V}^{a1} \quad \mathbf{V}^{a2} \quad \dots \quad \mathbf{V}^{an} \right\}^T \tag{3}$$

Correspondingly, the generalized force and velocity vectors acting at the *j*-th resilient mount by the machine are $\mathbf{F}^{bj}$ and $\mathbf{V}^{bj}$, and each of them includes six components, respectively.

The dynamics governing equation of the rigid body [12] can be written in terms of the mobility matrices,

$$\begin{Bmatrix} \mathbf{V}^s \\ \mathbf{V}^a \end{Bmatrix} = \begin{bmatrix} \mathbf{M}_{11}^s & \mathbf{M}_{12}^s \\ \mathbf{M}_{21}^s & \mathbf{M}_{22}^s \end{bmatrix} \begin{Bmatrix} \mathbf{F}^s \\ \mathbf{F}^a \end{Bmatrix} \tag{4}$$

where $\mathbf{M}_{11}^s = \frac{1}{i\omega}\mathbf{J}^{-1}$, $\mathbf{M}_{12}^s = \frac{1}{i\omega}\mathbf{J}^{-1}\mathbf{R}$, $\mathbf{M}_{21}^s = \frac{1}{i\omega}\mathbf{R}^T\mathbf{J}^{-1}$, $\mathbf{M}_{22}^s = \frac{1}{i\omega}\mathbf{R}^T\mathbf{J}^{-1}\mathbf{R}$. The symbol ω is the excitation frequency, i represents the imaginary unit, $i = \sqrt{-1}$, $\mathbf{R}$ represents the location matrix of the resilient mounting junctions with respect to the center of gravity of the machine, and $\mathbf{J}$ is the general mass matrix. The time dependent term $\exp(i\omega t)$ is omitted in the remainder.

2.2 Resilient mounts

The resilient mounts are used as vibration isolators for minimizing vibration transmission from the machine to the building floor. At the mounting junctions on the plate, the generalized force and velocity vectors at the bottom ends of the resilient mounts, see Figure 2, are assembled in the vectors

$$\mathbf{F}^c = \left\{ \mathbf{F}^{c1} \quad \mathbf{F}^{c2} \quad \dots \quad \mathbf{F}^{cn} \right\}^T, \ \mathbf{V}^c = \left\{ \mathbf{V}^{c1} \quad \mathbf{V}^{c2} \quad \dots \quad \mathbf{V}^{cn} \right\}^T \tag{5}$$

The relation between the velocity vectors and force vectors at the two ends of the *j*-th resilient mount is given by using the four-pole equation [13, 14],

$$\begin{Bmatrix} \mathbf{F}^{bj} \\ \mathbf{V}^{bj} \end{Bmatrix} = \begin{bmatrix} \mathbf{diag}\left(\mathbf{T}_{11}^j\right) & \mathbf{diag}\left(\mathbf{T}_{12}^j\right) \\ \mathbf{diag}\left(\mathbf{T}_{21}^j\right) & \mathbf{diag}\left(\mathbf{T}_{22}^j\right) \end{bmatrix} \begin{Bmatrix} \mathbf{F}^{cj} \\ \mathbf{V}^{cj} \end{Bmatrix} \tag{6}$$

where $\mathbf{diag}\left(\mathbf{T}_{pq}^j\right)$, $p, q = 1, 2$, means the diagonal transmission sub-matrix of the *j*-th resilient mount.

For generality, in this study, each resilient mount is modelled as six lumped stiffness components with negligible mass, where three components with translational stiffness and three with rotational stiffness are assumed without coupling between the different stiffness components. For example, the *p*-th component of the *j*-th resilient mount is described by the following four-pole equation

$$\begin{Bmatrix} F_p^{bj} \\ V_p^{bj} \end{Bmatrix} = \begin{bmatrix} -1 & 0 \\ -\dfrac{i\omega}{\mu_p^j} & 1 \end{bmatrix} \begin{Bmatrix} F_p^{cj} \\ V_p^{cj} \end{Bmatrix} \tag{7}$$

where F_p^{bj} denotes the *p*-th (p = 1, …, 6) component of the generalized force at the *j*-th resilient mount, and μ_p^j denotes the stiffness coefficient of the *p*-th stiffness component in the *j*-th resilient mount.

For all resilient mounts, the transmission matrix equation is obtained as

$$\begin{Bmatrix} \mathbf{F}^b \\ \mathbf{V}^b \end{Bmatrix} = \begin{bmatrix} \mathbf{T}^{11} & \mathbf{T}^{12} \\ \mathbf{T}^{21} & \mathbf{T}^{22} \end{bmatrix} \begin{Bmatrix} \mathbf{F}^c \\ \mathbf{V}^c \end{Bmatrix} \tag{8}$$

The conditions for force equilibrium and motion compatibility at the junctions can be written as

$$\mathbf{F}^a = -\mathbf{F}^b,\ \mathbf{V}^a = \mathbf{V}^b,\ \mathbf{F}^c = -\mathbf{F}^d,\ \mathbf{V}^c = \mathbf{V}^d \tag{9}$$

2.3 The supporting floor

The supporting floor is modeled as a thin, elastic uniform plate. When there are no significant reflections from the boundaries or from discontinuities within the receiver, an infinite, uniform plate model may be assumed. Otherwise, a finite plate with suitable boundary conditions should be considered. The supporting plate floor is excited by the force and moment components at the bottom of each resilient mount. The force and velocity vectors at the plate mounting points, see Figure 2, are assembled in the vectors

$$\mathbf{F}^d = \left\{\mathbf{F}^{d1} \quad \mathbf{F}^{d2} \quad \dots \quad \mathbf{F}^{dn}\right\}^T,\ \mathbf{V}^d = \left\{\mathbf{V}^{d1} \quad \mathbf{V}^{d2} \quad \dots \quad \mathbf{V}^{dn}\right\}^T \tag{10}$$

The force vector at each resilient mount junction j = 1, …, n includes six components,

$$\mathbf{F}^{dj} = \left\{F_1^{dj}, F_2^{dj}, F_3^{dj}, F_4^{dj}, F_5^{dj}, F_6^{dj}\right\}^T \tag{11}$$

Accordingly, the velocity vector at each resilient mount junction j = 1, …, n includes three translation components and three rotational components, i.e.,

$$\mathbf{V}^{dj} = \left\{V_1^{dj}, V_2^{dj}, V_3^{dj}, V_4^{dj}, V_5^{dj}, V_6^{dj}\right\}^T \tag{12}$$

The mobility equation of the plate can be now written as follows [11, 15-18], where $[\mathbf{Y}]$ is the mobility matrix,

$$\begin{Bmatrix} \mathbf{V}^{d1} \\ \mathbf{V}^{d2} \\ \vdots \\ \mathbf{V}^{dn} \end{Bmatrix} = \begin{bmatrix} \mathbf{y}^{d11} & \mathbf{y}^{d12} & \dots & \mathbf{y}^{d1n} \\ \mathbf{y}^{d21} & \mathbf{y}^{d22} & \dots & \mathbf{y}^{d2n} \\ \dots & & & \vdots \\ \mathbf{y}^{dn1} & \mathbf{y}^{dn2} & \dots & \mathbf{y}^{dnn} \end{bmatrix} \begin{Bmatrix} \mathbf{F}^{d1} \\ \mathbf{F}^{d2} \\ \vdots \\ \mathbf{F}^{dn} \end{Bmatrix} = [\mathbf{Y}] \begin{Bmatrix} \mathbf{F}^{d1} \\ \mathbf{F}^{d2} \\ \vdots \\ \mathbf{F}^{dn} \end{Bmatrix} \tag{13}$$

Since the flexural vibration dominates the noise emission of the building floor, only the out-of-plane flexural wave will be taken into account. Thus, the in-plane shear and longitudinal motions induced by in-plane forces, and drilling motion of the plate induced by twisting moment are neglected. The out-of-plane flexural waves are induced by the out-of-plane force and the in-plane moment components. For example, the mobility sub-matrix $\mathbf{y}^{d21}$ can be written as

$$\mathbf{y}^{d21} = \begin{bmatrix} 0 & 0 & 0 & 0 & 0 & 0 \\ 0 & 0 & 0 & 0 & 0 & 0 \\ 0 & 0 & y^{21}_{wF_z} & y^{21}_{wM_x} & y^{21}_{wM_y} & 0 \\ 0 & 0 & y^{21}_{\theta_x F_z} & y^{21}_{\theta_x M_x} & y^{21}_{\theta_x M_y} & 0 \\ 0 & 0 & y^{21}_{\theta_y F_z} & y^{21}_{\theta_y M_x} & y^{21}_{\theta_y M_y} & 0 \\ 0 & 0 & 0 & 0 & 0 & 0 \end{bmatrix} \tag{14}$$

where the mobility term $y^{21}_{wF_z}$ relates an out-of-plane translational velocity V_z^{d2} at the junction no.2 to an out-of-plane force excitation F_z^{d1} at junction no.1, where the latter junction is the excitation point, and the former junction is the response point.

The mobility representation is a useful tool to describe the dynamic properties of the supporting floor. For a realistic complicated floor, force and moment mobilities at the mounting junctions can be measured by experiments. For some simple infinite and finite structures, the mobility matrices can be derived analytically. The mobility formulations for an elastic uniform plate with simply supported edges and an infinite plate can be found in, e.g., Refs. [10, 11, 15].

2.4 Power flow

The time averaged power flow transmitted from the machine to the building floor can be expressed as

$$\Pi = \frac{1}{2}\mathrm{Re}\left[\left(\mathbf{F}^d\right)^* \mathbf{V}^d\right] = \frac{1}{2}\mathrm{Re}\left[\left(\mathbf{F}^d\right)^* \mathbf{Y}\mathbf{F}^d\right] \tag{15}$$

where the symbol $(\ )^*$ represents conjugate transpose of a matrix or vector.

The transmitted force $\mathbf{F}^d$ can be solved from Eqs. (4), (8) and (13) by applying the conditions of force equilibrium and motion compatibility in Eq. (9). For brevity, the somewhat lengthy derivation is omitted here, as the same result can be found in Ref. [14]. Thus one gets the following expression for the transmitted force $\mathbf{F}^d$,

$$\mathbf{F}^d = \left(-\mathbf{T}^{21} - \mathbf{M}^s_{22}\mathbf{T}^{11} + \mathbf{T}^{22}\mathbf{Y} + \mathbf{M}^s_{22}\mathbf{T}^{12}\mathbf{Y}\right)^{-1} \mathbf{M}^s_{21}\mathbf{F}^s \tag{16}$$

In order to avoid excessive vibration of the machine, a suitable constraint on the velocity $\mathbf{V}^s$ of the rigid body may be applied. Thus, the velocity $\mathbf{V}^s$ is sometimes of interest in design optimization of machinery mounting system. The expression for the velocity $\mathbf{V}^s$ given in Eq. (17) is obtained by solving Eqs. (4), (8) and (13) with the conditions of force equilibrium and motion compatibility in Eq. (9),

$$\mathbf{V}^s = \mathbf{M}^s_{11}\mathbf{F}^s + \mathbf{M}^s_{12}\left(\mathbf{T}^{11} - \mathbf{T}^{12}\mathbf{Y}\right)\mathbf{F}^d \tag{17}$$

3 OPTIMIZATION FORMULATION FOR MINIMIZATION OF POWER TRANSMISSION

3.1 Optimization formulation

The problem of design optimization of the rotating machinery mounting system with the objective of minimizing the total power flow transmitted from the machine to the building floor via several resilient mounts, can be formulated as

$$\begin{aligned} &\min_{\mu}\left\{\Pi=\frac{1}{2}\left(\mathbf{F}^{d}\right)^{*}\operatorname{Re}\left\{\mathbf{Y}\right\}\mathbf{F}^{d}\right\} \\ &\text{s.t. Given constraints} \qquad (18) \\ &\mu_{\min}\leq\mu_{i}\leq\mu_{\max},\, i=1,\ldots,n^{dv} \end{aligned}$$

The present work aims to realize this objective by optimizing stiffness coefficients μ_i of resilient mounts in a given range between $\mu_{\min}$ and $\mu_{\max}$. The lower and upper limits of the stiffness coefficients are usually determined by physical properties of the resilient mounts. A reasonable lower limit is important for satisfying requirements on the static displacement of the machine, or the motion during starting and stopping stages. It is well-known that the stiffness of resilient mounts is normally frequency dependent. However, for simplicity the stiffness will be assumed to be independent of frequency in the following.

In the expression for the total transmitted power Π in (18), $\mathbf{F}^d$ denotes the vector of amplitudes of the loading vector acting on the plate with the excitation frequency ω. The given constraints are specified by physical and geometrical requirements on mounting systems. The symbol n^{dv} denotes the number of design variables.

3.2 Design sensitivity analysis

The sensitivity of the objective function Π in Eq. (18) with respect to the design variable μ_k can be derived as

$$\frac{\partial\Pi}{\partial\mu_k}=\frac{1}{2}\frac{\partial\left(\operatorname{Re}\left\{\left[\mathbf{F}^{d}\right]^{*}\left[\mathbf{Y}\right]\left[\mathbf{F}^{d}\right]\right\}\right)}{\partial\mu_k}=\operatorname{Re}\left\{\left[\mathbf{F}^{d}\right]^{*}\left[\mathbf{Y}\right]\frac{\partial\left[\mathbf{F}^{d}\right]}{\partial\mu_k}\right\},\; k=1,\ldots,\; n^{dv} \qquad (19)$$

where the symmetric characteristics of the mobility matrix $\left[\mathbf{Y}\right]$ have been used.

In order to derive the sensitivity of the transmitted force $\frac{\partial\mathbf{F}^d}{\partial\mu_k}$ with respect to the design variables, Eq. (16) is rewritten as

$$\left(-\mathbf{T}^{21}-\mathbf{M}^{s}_{22}\mathbf{T}^{11}+\mathbf{T}^{22}\mathbf{Y}+\mathbf{M}^{s}_{22}\mathbf{T}^{12}\mathbf{Y}\right)\mathbf{F}^{d}=\mathbf{M}^{s}_{21}\mathbf{F}^{s} \qquad (20)$$

By differentiating both sides of Eq. (20) with respect to the design variable μ_k, considering the condition that only $\mathbf{T}^{21}$ is dependent on design variables among the mobility matrices of the machine, resilient mounts and the floor plate, and assuming that the generalized excitation force $\mathbf{F}^s$ generated by the rotating unbalanced machine is design independent, $\frac{\partial\mathbf{F}^d}{\partial\mu_k}$ can be obtained as

$$\frac{\partial\mathbf{F}^{d}}{\partial\mu_k}=\left(-\mathbf{T}^{21}-\mathbf{M}^{s}_{22}\mathbf{T}^{11}+\mathbf{T}^{22}\mathbf{Y}+\mathbf{M}^{s}_{22}\mathbf{T}^{12}\mathbf{Y}\right)^{-1}\frac{\partial\mathbf{T}^{21}}{\partial\mu_k}\mathbf{F}^{d},\; k=1,\ldots,\; n^{dv} \qquad (21)$$

The accuracy of analytical sensitivities has been validated by overall finite difference sensitivity calculations. With these sensitivity results, the design problem (18) may be solved by a mathematical programming method, e.g., MMA by Svanberg [19].

4 NUMERICAL EXAMPLES

4.1 A simplified parametric example

First, a simple special case of the vibratory system shown in Figure 1 is considered. Here, four identical resilient mounts are placed symmetrically with respect to the machine, and mounted on a flexible floor, which is assumed to be an infinite elastic plate of constant thickness. This simplification leads to an equivalent system of the resilient mounts as shown in Figure 3, which consists of four separate sets of a spring of stiffness μ and a mass m^s equal to $m/4$, where the symbol *m* represents the total mass of the machine. The dynamic governing equation is simplified correspondingly, i.e., the forces acting on all four mounting points are assumed to be the same, that is, $F^0/4$, where F^0 denotes the vertical excitation force acting on the machine. A similar simplified model using a finite four-edge simply supported plate as the receiver is studied in [20].

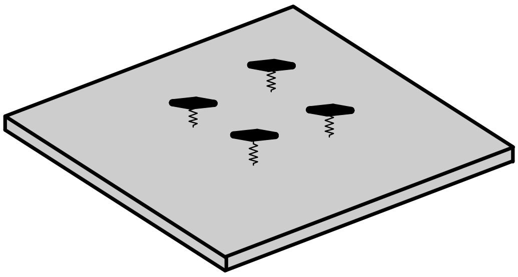

Figure 3: A simplified modeling for the machine connected to a flexible floor via four symmetrically placed mounts

From the vibration equation of a system with a single degree of freedom, see, e.g. [21], the force F_j transmitted from the mass m^s to the floor via the *j*-th spring is obtained from [11, 20]

$$F_j = \frac{F_0}{4} \frac{1}{1 - \dfrac{m\omega^2}{4\mu} + i\omega \dfrac{m}{4} Y_j} \tag{22}$$

where μ is the stiffness of the spring.

Since only the out-of-plane force excitation on the plate is considered, the mobility matrix of the plate in Eq. (13) can be simplified. By the concept of effective point mobility Y_j as a space averaged effective mobility over all excitation points [22], Y_j can be expressed as $Y_j = Y_{j1} + Y_{j2} + Y_{j3} + Y_{j4}$ for *j*=1, 2, 3, and 4. The symbol Y_{jk} is the general mobility element from the excitation point *k* to the response point *j*, where Y_{jk} with $k = j$ is the driving point mobility, while Y_{jk} with $k \neq j$ denotes the transfer mobility. The effective mobility represents the ratio of the total velocity due to all applied forces to the force acting at the point *j*. It can be calculated that the effective point mobility of an infinite plate Y_j (*j*=1, 2, 3, 4) are same, i.e., $Y_1 = Y_2 = Y_3 = Y_4$. The driving point and transfer mobilities of an infinite plate can be found in, e.g., [11, 15].

The velocity V_0 of the machine is calculated based on the same assumption

$$V_0 = \frac{F_0}{4} \frac{\frac{\mu}{i\omega} + \frac{1}{Y_1}}{\left(\frac{\mu}{i\omega} + \frac{1}{Y_1}\right)\left(\frac{\mu}{i\omega} + i\omega\frac{m}{4}\right) - \left(\frac{\mu}{i\omega}\right)^2} \tag{23}$$

Thus, from Eq. (15) the time averaged power $P = \Pi$ transmitted from the machine to the floor can be rewritten as

$$P = 2\operatorname{Re}\left(Y_1\right)\left|\frac{F_0}{4}\right|^2 \left|\frac{1}{1 - \frac{m\omega^2}{4\mu} + i\omega\frac{m}{4}Y_1}\right|^2 \tag{24}$$

As a reference to evaluate the effect of the spring isolator, the power flow P^{ws} from the machine to the building floor without spring isolators is given in Eq. (25) below. The modeling without isolation is obtained by removing the spring isolators from Figure 3, and we find that the power P^{ws} transmitted from the machine to the floor without spring isolators is given by

$$P^{ws} = 2\operatorname{Re}\left(Y_1\right)\left|\frac{F_0}{4}\right|^2 \left|\frac{1}{1 + i\omega\frac{m}{4}Y_1}\right|^2 \tag{25}$$

The velocity V_0^{ws} of the machine without spring isolators is calculated as

$$V_0^{ws} = \frac{F_0}{4} \frac{Y_1}{i\frac{m}{4}\omega Y_1 + 1} \tag{26}$$

Assuming four springs with the same stiffness coefficient, the dependence of transmitted power P in Eq. (24) on the stiffness coefficient μ will be studied for different excitation frequency and mass values of the machine. In this section, no damping is assumed for the springs and the plate.

For a rigid building floor, the velocity at the mounting junction on the plate is zero, $V_1 = 0$, thus the transmitted power $P = 0$. If the stiffness of the spring is reasonably selected to make the resonance frequency $\omega_0 = \sqrt{\frac{\mu}{m/4}}$ of the mass-spring system to be located far from the excitation frequency ω, the transmitted force $\left|F_i\right|$ on the floor is relatively small.

When a flexible floor is considered, the mobility of the plate must be taken in account, and the velocity of the mounting point on the plate $V_1 \neq 0$. Thus we should pay attention to the transmitted power P, the velocity V_1 and force F_1.

When the bending stiffness of the plate is quite large, the corresponding mobility Y_1 is very small. The conclusion is similar to the case of a rigid floor above. The transmitted power P, shown in Figure 4 (a), and force F_1 are very large only in the vicinity of resonance, and in other cases both of them are generally small. In this example, the given circular excitation frequency ω is 50 rad/s.

A suitably flexible plate of thickness 0.2 made of a material with Young's modulus 2×10^9, Poisson's ratio 0.3 and mass density 840, is studied here. SI units are assumed. Transmitted powers for different mass values of machine and excitation frequencies are presented in Figure 4 (b). For a specified excitation frequency and a given stiffness coefficient, it is seen that when the mass of the machine increases, then the transmitted power decreases. Actually, an inertia concrete block is sometimes placed at the bottom of machine to increase the mass of the vibrating rigid body. The extra inertia block can be deemed beneficial for reduction of transmitted power when an infinite plate is the receiver, in which case no resonant behavior can occur. Though infinite structures do not exist in reality, the assumption of infinite structures is applicable in many circumstances where there are no significant reflections from discontinuities or boundaries within the receiver [6].

The only peak of each curve in Figure 4 (b) comes from the resonance of the spring-rigid body system. Obviously, the peak will move to the right when the mass of the machine is increased, and the maximum value at the peak also decreases significantly. If the mass of the machine is the same, then the value of the transmitted power at the peak point is reduced for a higher value of the excitation frequency. This can be explained from Eq. (24) where the term $\omega m^s Y_1$ in the denominator increases with increasing excitation frequency, which can be approximately considered as increasing the effect of damping.

Compared with the power flow P^{ws} from the machine to the building floor without spring isolators, it is found that if a very soft spring is provided under the machine, the transmitted power to the floor will be considerably reduced, but it may cause significant vibration velocity of the machine, see Figure 5. If a machine is rigidly bolted to the floor in the infinite plate case, then the vibratory movement of the machine may be reduced, but the transmitted power to the floor will be relatively large. Thus, some compromise must be made between the two requirements, and motivates optimization.

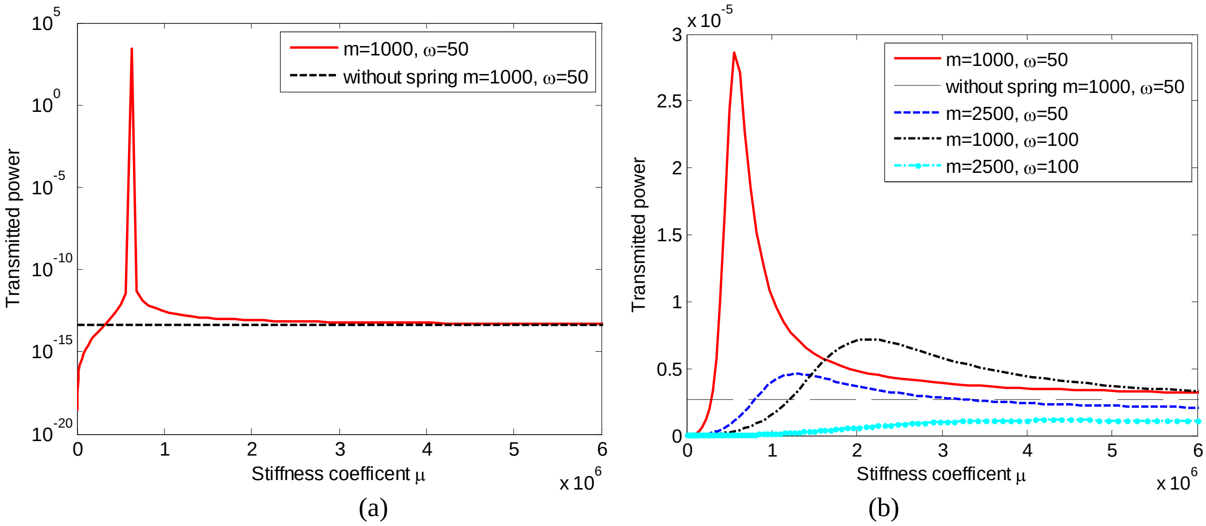

(a) (b)

Figure 4: Transmitted power for different masses of machine and excitation frequencies: (a) very stiff floor plate, (b) relatively flexible floor plate

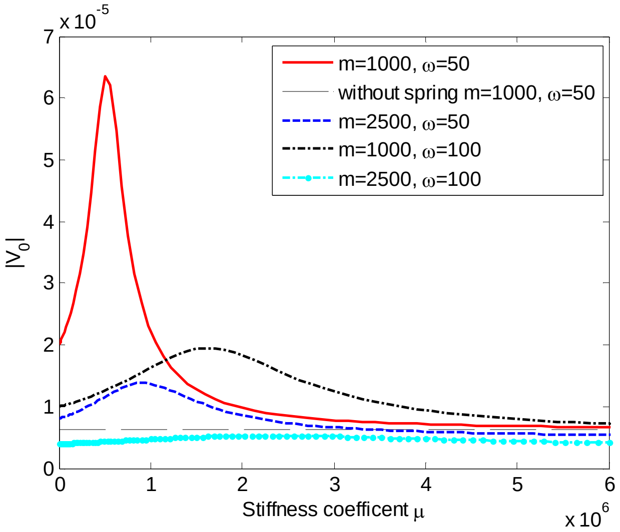

Figure 5: Velocity of machine for different masses of machine and excitation frequencies

4.2 Optimization of the mounting system of a machine with six degrees of freedom subjected to generalized excitation forces

The model shown in Figure 1 is considered for minimizing the power flow. It is now assumed that a machine with six degrees of freedom is excited by a concentrated force vector $\mathbf{F}^s$ acting at its center of gravity. The receiver is modeled as a four-edge simply supported finite plate of uniform thickness 0.1, which is made of the same material as in the previous example. A loss factor $\eta = 0.005$ is introduced for the material.

The stiffness coefficients of four resilient mounts are chosen as design variables, i.e. we have $n^{dv} = 24$ when considering the stiffness components in every direction to be design variables.

The lower and upper limits $\mu_{\min}$ and $\mu_{\max}$ of the stiffness coefficients are given as 10^2 and 10^5, respectively. The units of stiffness coefficients of translational and rotational stiffness components are N/m and Nm/rad. First, a vertical excitation force $\mathbf{F}^s = \{0, 0, 1000, 0, 0, 0\}^T$ is considered. The initial values of all design variables are taken to be 5×10^4, which provides a convenient reference for evaluation and discussion of the vibration reduction by optimization. At the same time, the power flow without resilient mounts is calculated as a reference to evaluate the effect of the isolator. When considering vertical force excitation, the design objective is independent on the stiffness components in the directions of the in-plane and twisting motions. However, the rotational stiffness with respect to the *x* and *y* directions and the vertical translational stiffness will influence the transmitted power.

Excitation frequency ω	Power flow		
	Initial design	Optimized design	Design without resilient mounts
10	1.2134	0.0997	1.3508
20	0.0712	0.0075	0.0776
50	0.2660	5.1457e-005	0.8417
100	0.0312	5.6883e-005	0.0617

Table 1: Optimized result for the case with an excitation force in the *z* direction, only

As stated in Table 1, it is found that, in comparison with the initial design and design without resilient mounts, the optimization has reduced the power flow significantly for four different excitation frequencies, ω = 10, 20, 50, 100.

Next, an excitation force $\mathbf{F}^s = 1/\sqrt{2}\left\{1000, 0, 1000, 0, 0, 0\right\}^T$ with a different direction but the same magnitude as above, is considered. When simultaneously considering the vertical and horizontal (in the *x* direction) force excitations, the design objective depends on the vertical translational stiffness, the rotational stiffnesses with respect to the *x* and *y* directions, and the horizontal stiffness with respect to the *x* direction. The same initial design is used.

Excitation frequency ω	Power flow		
	Initial design	Optimized design	Design without resilient mounts
10	0.8528	0.0499	0.7780
20	3.7194	0.0038	2.1498
50	0.1334	2.5622e-05	0.4561
100	0.0157	2.8445e-05	0.0353

Table 2: Optimized result for case with excitation forces in both the *x* and *z* directions

The results shown in Table 2 for this case also illustrate that substantial reduction of the power flow can be achieved for the excitation frequencies considered. When the excitation frequency ω is taken to be 10 or 20, the design without resilient mounts gives relatively lower values of the power flow compared with those of the initial design. This implies that an inappropriately chosen isolator may increase the vibration transmission. The important conclusion that can be drawn from the results reported in Tables 1 and 2 is that design optimization is extremely useful for the best possible selection of an isolator.

5 SHAPE OPTIMIZATION OF A SUPPORTING PAD PLACED ON A FLEXIBLE FLOOR FOR A RESILIENT MOUNT

This section deals with the shape optimization of a rotationally symmetric pad (see Figure 6) which, as illustrated in Figure 7, transfers a vertical force F from a resilient mount to a distributed pressure loading $-f(x)$ on a flexible wooden floor. One- and two-parameter analytical expressions for the distributed pressure loading are derived in Brunskog and Hammer [23] for the problem of pressing a rigid, plane indenter a small uniform distance into the plane surface of an elastic body. For simplicity and in order to apply the result from [23], we shall model the wooden floor as an infinite, isotropic, elastic plate as considered in Section 4.1. Moreover, we assume that the Young's modulus of the pad is large relative to that of the plate, and that the radius r_b of the pad is sufficiently small such that the introduction of the pad does not change the force equilibrium condition $\mathbf{F}^c = -\mathbf{F}^d$ and the motion compatibility condition $\mathbf{V}^c = \mathbf{V}^d$ in Eq. (9).

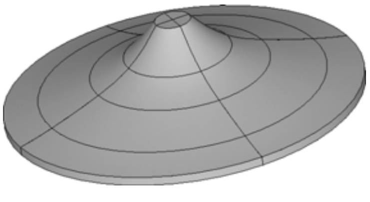

Figure 6: Schematic figure of a rotationally symmetric supporting pad for a resilient mount

The pad is assumed to be a circular truncated cone with a slant boundary subject to design. Due to rotational symmetry of the pad, the design problem can be formulated as a shape optimization problem of the curved part of the plane radial section of the pad shown in Figure 7, where the *y* axis is oriented along the center line, and *x* indicates the radial direction. The design boundary is defined by Spline curves evaluated in terms of the positions of the given points a and b and three master nodes, i.e., node 1, 2 and 3 shown in Figure 7. The coordinates of the master nodes are chosen as design variables. The design domain is meshed by a number of 4-node axisymmetric finite elements.

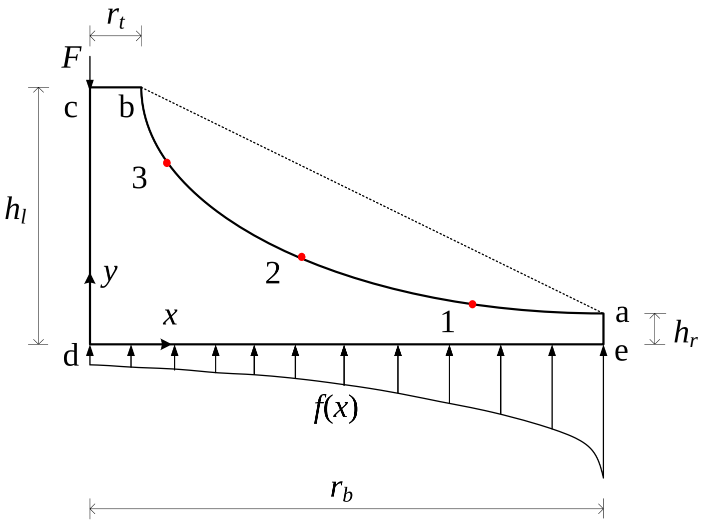

Figure 7: The axisymmetric planar design domain with three master nodes on the design boundary

All dimensions of the design domain are normalized by the radius r_b of the plane bottom surface, i.e., $r_t = \lambda_t r_b$, $h_l = \lambda_l r_b$, $h_r = \lambda_r r_b$.

The shape optimization problem is formulated as

$$\begin{aligned} &\min_{\mathbf{x}} C = \mathbf{P}^T \mathbf{U} \\ &\text{s.t. } V \le \overline{V} \\ &\quad \mathbf{x}_L \le \mathbf{x} \le \mathbf{x}_U \end{aligned} \tag{27}$$

where C is the static compliance of the structure. Assuming the point *c* of action of the force *F* to be fixed, the compliance C is defined as the scalar product of the nodal force vector $\mathbf{P}$ and the vector $\mathbf{U}$ of nodal displacements in the *y* direction at the bottom surface of the pad. Moreover, V denotes the volume of the axisymmetric structure, $\overline{V}$ is the given upper limit on the volume, and $\mathbf{x}_L$ and $\mathbf{x}_U$ denote allowable lower and upper limits of the design variables which are the coordinates of three master nodes on the design boundary. The upper limit of the volume is prescribed as $\overline{V}$ =0.51 which corresponds to 75% of the volume of the circular truncated cone formed by 360^{o} rotation of the area a-b-c-d-e along the *y* axis when $r_b = 1$.

The design variable vector $\mathbf{x}$ is expressed as

$$\mathbf{x} = \{ x_1 \quad x_2 \quad x_3 \quad y_1 \quad y_2 \quad y_3 \}^T \tag{28}$$

where subscripts 1, 2 and 3 represent node numbers of master nodes on the design boundary.

A numerical example is presented here with the dimensions of design domain taken to be $r_b = 1$, $r_t = 0.1r_b$, $h_l = 0.5r_b$, $h_r = 0.05r_b$. The pressure function is adopted from the paper [23] in the form

$$f(x) = \frac{c}{\sqrt{1 - x^2 + \varepsilon}}, \; c = 1.59 \times 10^4 \tag{29}$$

where a small value $\varepsilon = 10^{-6}$ is introduced for avoiding singularity when x equals r_b at the outer edge, and the integral of pressure over the circular bottom surface is obtained as

$$F = 2\pi \int_0^{r_b=1} f(x) x dx = 10^5 \tag{30}$$

The lower and upper limits of design variables are chosen as $0.7 \le x_1 \le 1.0$, $0.4 \le x_2 \le 0.7$, $0 \le x_3 \le 0.4$, $h_b = 0.05 \le y_1 \le 0.2$, $0.2 \le y_2 \le 0.35$, and $0.35 \le y_3 \le 0.5 = h_l$. The initial and final designs are compared in Figure 8. The values of the design variables, volume and compliance of initial and optimized designs are given in Table 3. As a result of the shape optimization, the compliance is reduced from 51.73 to 49.16.

	Initial design	Optimized design
x_1	0.80	0.80
x_2	0.50	0.51
x_3	0.20	0.17
y_1	0.10	0.10
y_2	0.20	0.22
y_3	0.40	0.38
C	51.73	49.16
V	0.50	0.51

Table 3: Comparison of initial and final designs ($\bar{V}$ =0.51)

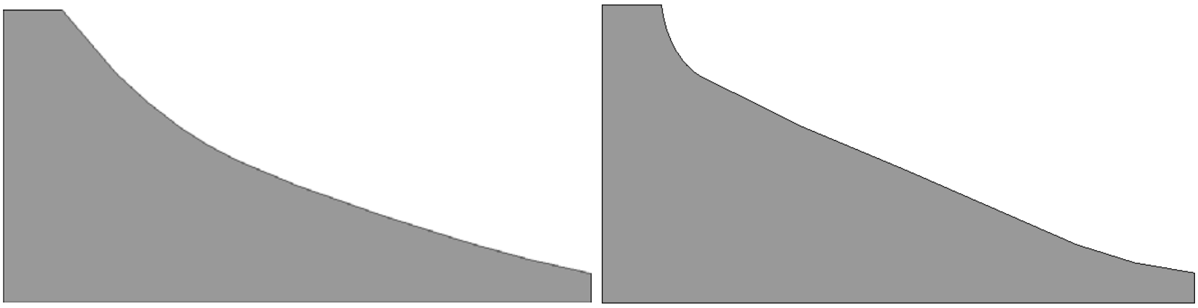

(a) Initial design (b) Optimized design

Figure 8: Radial sections of initial and optimized pad designs

6 CONCLUSIONS

The problem of optimization of the machinery mounting system in a lightweight building is studied in this paper. A general mobility equation is developed for the system consisting of source, isolator and receiver of vibration by assembling the mobility matrices of each subsystem. The objective of minimizing vibration transmission is realized by sizing optimization of stiffness coefficients of resilient mounts. In comparison with designs without resilient mounts, designs with optimized isolators can provide significant reduction of the power flow.

Shape optimization of a supporting pad for a resilient mount is also studied. Such a pad may be used for transferring a vertical force from a resilient mount to a distributed pressure loading on a flexible floor. Artificial modeling of the resilient mounts and the floor of the building is adopted in this study. Work on more practical modeling of resilient mounts and building structures is in progress.

REFERENCES

[1] P. Srinivasulu, C.V. Vaidyanathan, *Handbook of machine foundations*. Tata Mcgraw Hill, 1976.

[2] J.A. Snyman, P.S. Heyns, P.J. Vermeulen, Vibration isolation of a mounted engine through optimization. *Mechanism and Machine Theory*, **30**, 109-118, 1995.

[3] R. Alkhatib, G.N. Jazar, M.F. Golnaraghi, Optimal design of passive linear suspension using genetic algorithm. *Journal of Sound and Vibration*, **275**, 665-691, 2004.

[4] H. Ashrafiuon, Design optimization of aircraft engine-mount systems. *Journal of Vibration and Acoustics-Transactions of the Asme*, **115**, 463-467, 1993.

[5] S. Xie, S.W. Or, H.L.W. Chan, P.K. Choy, P.C.K. Liu, Design optimization of machinery mounting systems with an elastic support structure. *Engineering Optimization*, **39**, 229-244, 2007.

[6] H.G.D. Goyder, R.G. White, Vibrational power flow from machines into built-up structures Part 1: Introduction and approximate analyses of beam and plate-like foundations. *Journal of Sound and Vibration*, **68**, 59-75, 1980.

[7] H.G.D. Goyder, R.G. White, Vibrational power flow from machines into built-up structures Part 3: Power flow through isolation systems. *Journal of Sound and Vibration*, **68**, 97-117, 1980.

[8] J. Pan, J.Q. Pan, C.H. Hansen, Total power flow from a vibrating rigid body to a thin panel through multiple elastic mounts. *Journal of the Acoustical Society of America*, **92**, 895-907, 1992.

[9] L. Sun, A.Y.T. Leung, Y.Y. Lee, K. Song, Vibrational power-flow analysis of a mimo system using the transmission matrix approach. *Mechanical Systems and Signal Processing*, **21**, 365-388, 2007.

[10] F. Fahy, P. Gardonio, *Sound and structural vibration, 2nd Edition*. Elsevier, 2007.

[11] L. Cremer, M. Heckl, B.A.T. Petersson, *Structure-borne sound: Structural vibrations and sound radiation at audio frequencies*. Springer, 2005.

[12] C.M. Harris, A.G. Piersol (eds.), *Shock and vibration handbook*. McGraw-Hill, London, 2002.

[13] C.T. Molloy, Use of four-pole parameters in vibration calculations. *The Journal of the Acoustical Society of America*, **29**, 842-853, 1957.

[14] J.I. Soliman, M.G. Hallam, Vibration isolation between non-rigid machines and non-rigid foundations. *Journal of Sound and Vibration*, **8**, 329-351, 1968.

[15] P. Gardonio, S.J. Elliott, Driving point and transfer mobility matrices for thin plates excited in flexure. *Technical report no 277,* ISVR, University of Southampton, 1998.

[16] S. Ljunggren, Generation of waves in an elastic plate by a vertical force and by a moment in the vertical plane. *Journal of Sound and Vibration*, **90**, 559-584, 1983.

[17] S. Ljunggren, Generation of waves in an elastic plate by a torsional moment and a horizontal force. *Journal of Sound and Vibration*, **93**, 161-187, 1984.

[18] F. Fahy, J. Walker (eds.), *Advanced applications in acoustics, noise and vibration*. Spon Press, New York, 2004.

[19] K. Svanberg, The method of moving asymptotes - a new method for structural optimization. *International Journal for Numerical Methods in Engineering*, **24**, 359-373, 1987.

[20] C.M. Mak, J.X. Su, A power transmissibility method for assessing the performance of vibration isolation of building services equipment. *Applied Acoustics*, **63**, 1281-1299, 2002.

[21] S.S. Rao, *Mechanical vibrations*, *4th edition*. Prentice Hall, 2003.

[22] B. Petersson, J. Plunt, On effective mobilities in the prediction of structure-borne sound-transmission between a source structure and a receiving structure, Part 1: Theoretical background and basic experimental studies. *Journal of Sound and Vibration*, **82**, 517-529, 1982.

[23] J. Brunskog, P. Hammer, Rigid indenter excitation of plates. *Acta Acustica United with Acustica*, **89**, 460-470, 2003.

COMPDYN 2011
ECCOMAS Thematic Conference on
Computational Methods in Structural Dynamics and Earthquake Engineering
M. Papadrakakis, M. Fragiadakis, V. Plevris (eds.)
Corfu, Greece, 25-28 May 2011

IDENTIFICATION AND SIZING OF DEFECTS IN PIPELINES BY THE WAVE FINITE ELEMENT METHOD USING TORSIONAL GUIDED WAVES

M. Kharrat, W. Zhou, O. Bareille, M. Ichchou

Laboratoire de Tribologie et Dynamique des Systèmes, Ecole Centrale de Lyon,
36 Avenue Guy de Collongue 69134 Ecully Cedex, France
E-mails: mohamed.kharrat@ec-lyon.fr, zhou.wenjin@ec-lyon.fr, olivier.bareille@ec-lyon.fr,
mohamed.ichchou@ec-lyon.fr

Keywords: Guided waves, Reflection coefficient, Damage identification, Defect sizing, Wave finite element method, Torsional wave.

Abstract. *Structural health monitoring of pipelines by guided waves is a technique under continuous development. It proved a relevant efficiency in defects detection in pipes. The analysis of reflections from cracks provides guidance to defects sizing. A guided wave technique capable of screening long lengths of pipes has been developed in our laboratory. The wave finite element method, adapted for the case of hollow cylinders as waveguide, was used to calculate reflection coefficients from different rectangular notches sizes and some singularities located in industrial pipeline. The numerical simulations were established while varying the excitation frequency. The aim of this work is to create a database for the identification and approximation of defects sizes detected in an industrial installation subject of experimental tests. The results were compared to usual finite element simulations in order to validate the technique. Good agreement was found between the results. Thus, the database can be used to size approximately the founded defects.*

1 INTRODUCTION

The technique of defect detection by guided-waves is the solution that becomes more and more widespread in the non-destructive testing field. This technique allows the scanning of long-distance pipeline from a single position through the use of guided-waves propagation along the tested pipes and facilitates the defect detection. Torsional mode has shown relevant advantages in defect detection in pipes [1, 2]. These found damages need to be dimensioned in order to be classified depending on its severity. The reflection and transmission of the wave through defects gives good information about its sizes. Indeed, guided wave reflection and transmission depends on the defect size and shape, as well as the incident wave type and frequency. Since the near field is complex due to the presence of defects, analytical model can not readily be used to describe the near field effect that accounts for the energy redistribution of the scattered wave modes. Structural waveguides usually consist of many local features, such as welding, ribs, curved members, supports and others. They could also largely destroy the original wave form and evoke spurious echoes.

Wave propagation in waveguides has been studied for a long time as far as the question of propagation through periodic structures was addressed [3, 4]. The Wave Finite Element Method (WFEM) was employed for the low and midfrequency description of coupled structures and the analysis of wave propagation through a notch was studied [5]. Other studies consider the applicability of the WFEM and study the guided elastic wave propagation in cylindrical pipes with local inhomogeneities [6]. The intact and damaged curved structures was also treated to determine their response to incident waves [7].

In this paper, we present firstly the basis of the WFEM. This latter was then used to construct a database of reflection coefficients from a rectangular notch in pipe with three dimensions : depth, axial and circumferential extents. The chosen mode was the torsion and calculations was made in the frequency range $[5-15]kHz$.

2 WAFE FINITE ELEMENT METHOD

In this section, we present the basis of the WFEM that was used to construct a database of reflection coefficients from defects and features in the pipe. A hybrid WFE/FE method was employed for the scattered field calculation [6].

By using axisymmetric elements, WFE method for the 1-D wave propagation problem is employed to extract the wave numbers and mode shapes for axisymmetric modes (longitudinal modes L(0, m) and torsional modes T(0, m)). Those eigenmodes are then superposed to form a scattering equation by connecting with FE formulation of the pipe segment with inhomogeneities. The dynamic reduction technique, component modal synthesis (CMS) is combined to formulate a numerically efficient scattering equation when dealing with the complex substructure models. This reduction technique fully takes into account the fact that the pipelines usually have some standard local features, and also allows various types of 3-D defects to be considered with ease.

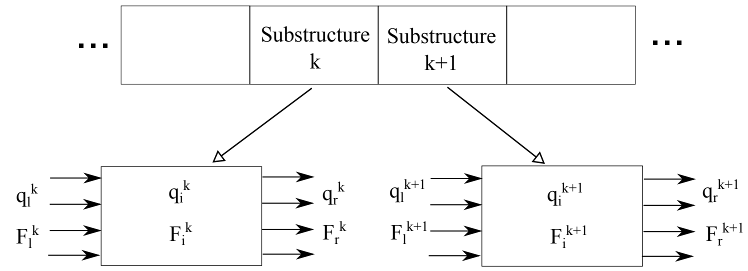

Figure 1: Structure discretized to identical cells

2.1 Finite element description

The structure can be discretized to identical cells as is shown in figure 1. The general FE formulation of a typical cell for the 1-D wave propagation in the pipe can be written as

$$\begin{bmatrix} \mathbf{D}_{ll} & \mathbf{D}_{li} & \mathbf{D}_{lr} \\ \mathbf{D}_{il} & \mathbf{D}_{ii} & \mathbf{D}_{ir} \\ \mathbf{D}_{rl} & \mathbf{D}_{ri} & \mathbf{D}_{rr} \end{bmatrix} \begin{Bmatrix} \mathbf{q}_l \\ \mathbf{q}_i \\ \mathbf{q}_r \end{Bmatrix} = \begin{Bmatrix} \mathbf{F}_l \\ \mathbf{F}_i \\ \mathbf{F}_r \end{Bmatrix}, \tag{1}$$

where [D] is the structure dynamic stiffness matrix, subscripts *l*, *r* and *i* denote the left, right and interior components, respectively. Assume that no external force be applied at interior dofs, eq.1 is condensed as

$$\begin{bmatrix} \mathbf{S}_{ll} & \mathbf{S}_{lr} \\ \mathbf{S}_{rl} & \mathbf{S}_{rr} \end{bmatrix} \begin{Bmatrix} \mathbf{q}_l \\ \mathbf{q}_r \end{Bmatrix} = \begin{Bmatrix} \mathbf{F}_l \\ \mathbf{F}_r \end{Bmatrix}, \tag{2}$$

where

$$\mathbf{S}_{ll} = \mathbf{D}_{ll} - \mathbf{D}_{li}\mathbf{D}_{ii}{}^{-1}\mathbf{D}_{il}\ ; \quad \mathbf{S}_{lr} = \mathbf{D}_{lr} - \mathbf{D}_{li}\mathbf{D}_{ii}{}^{-1}\mathbf{D}_{ir}\ ;$$
$$\mathbf{S}_{rl} = \mathbf{D}_{rl} - \mathbf{D}_{ri}\mathbf{D}_{ii}{}^{-1}\mathbf{D}_{il}\ ; \quad \mathbf{S}_{rr} = \mathbf{D}_{ri} - \mathbf{D}_{ri}\mathbf{D}_{ii}{}^{-1}\mathbf{D}_{ir}.$$

To describe the wave motion, eigensolution need to be decomposed to positive and negative going wave modes for the computational purpose. These modes include both the propagating and non-propagating modes. Through the eigensolutions, the non-reflecting boundaries are described by the incident wave mode bases

$$\mathbf{q}_r = [\mathbf{q}^+]\mathbf{A}^+, \quad \mathbf{F}_r = -[\mathbf{F}^+]\mathbf{A}^+. \tag{3}$$

Substitution into Equation 2 yields

$$\left\{(\mathbf{S}_{rl}\mathbf{S}_{ll}^{-1}\mathbf{S}_{lr} - \mathbf{S}_{rr})[\mathbf{q}^+] - [\mathbf{F}^+]\right\}\mathbf{A}^+ = \mathbf{S}_{rl}\mathbf{S}_{ll}^{-1}\mathbf{F}_l. \tag{4}$$

From Equation 4, the excited wave modes can be calculated for a given excitation. The wave field is thus represented fully by the incident wave modes.

The eigenmodes in the structural waveguide that come from the spectral solutions of WFE method can be superposed to describe the wave field. Those eigenmodes travel independently and do not interfere with one another. A set of wave modes can be traveling at the same time in the waveguides, thus the motion at any point therein is simply regarded as the sum of the motion of various modes. The incident, reflected and transmission waves can be expressed as

$$\mathbf{q}^{inc} = [\mathbf{q}^+]\Lambda^+\mathbf{A}^{inc}, \quad \mathbf{q}^{ref} = [\mathbf{q}^-]\Lambda^-\mathbf{A}^{ref}, \quad \mathbf{q}^{tra} = [\mathbf{q}^+]\Lambda^+\mathbf{A}^{tra}, \tag{5}$$

where $\mathbf{q}^{inc}$ and $\mathbf{q}^{tra}$ are formed of the same bases, $[\mathbf{q}^{+}]$ and $[\mathbf{q}^{-}]$ are normalized N by N_r matrices, $\mathbf{A}^{inc}$, $\mathbf{A}^{ref}$ and $\mathbf{A}^{tra}$ denote the amplitudes of the corresponding waves, Λ^{+} and Λ^{-} are diagonal matrices relating respectively to the positive and negative going waves, which are given as

$$\Lambda^{\pm} = diag\left\{e^{\pm jk_i x}\right\}, (i = 1, 2, ...N_r). \tag{6}$$

Analogically, we can obtain the expressions of $\mathbf{F}^{inc}$, $\mathbf{F}^{ref}$ and $\mathbf{F}^{tra}$:

$$\mathbf{F}^{inc} = [\mathbf{F}^{+}]\Lambda^{+}\mathbf{A}^{inc}, \quad \mathbf{F}^{ref} = [\mathbf{F}^{-}]\Lambda^{-}\mathbf{A}^{ref}, \quad \mathbf{F}^{tra} = [\mathbf{F}^{+}]\Lambda^{+}\mathbf{A}^{tra}, \tag{7}$$

where the force vectors are also eigenvectors or obtained from the displacement vectors.

2.2 Wave propagation in an infinite structural waveguide with a local defect

Consider an infinitely long structure with the local inhomogeneities which are due to the geometry or material variation. A monochromatic incident wave, which comprises a single or multiple wave modes, is assumed to be generated at $x - \infty$ and travel in the positive $x - \infty$ direction. Scattering phenomenon emerges when the incident wave impinges on those inhomogeneities as is shown in figure 2.

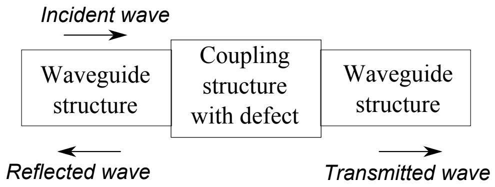

Figure 2: Waves propagation through damaged coupling structure.

The resultant wave field consists of the incident and scattered components (both reflection and transmission).The modeling of damaged cell is similar to that of typical one for modes extraction except that additional interior dofs might be included. The coupling condition is governed by the dynamics equation of coupling structures that can be condensed as

$$\begin{bmatrix} \mathbf{S}^{c}_{ll} & \mathbf{S}^{c}_{lr} \\ \mathbf{S}^{c}_{rl} & \mathbf{S}^{c}_{rr} \end{bmatrix} \begin{Bmatrix} \mathbf{q}^{c}_{l} \\ \mathbf{q}^{c}_{r} \end{Bmatrix} = \begin{Bmatrix} \mathbf{F}^{c}_{l} \\ \mathbf{F}^{c}_{r} \end{Bmatrix}. \tag{8}$$

Considering the couple conditions

$$\mathbf{q}^{c}_{l} = \left[\mathbf{q}^{+}\right]\mathbf{A}^{inc} + \left[\mathbf{q}^{-}\right]\mathbf{A}^{ref}, \quad \mathbf{q}^{c}_{r} = \left[\mathbf{q}^{+}\right]\mathbf{A}^{tra}, \tag{9}$$

and

$$\mathbf{F}^{c}_{l} = \left[\mathbf{F}^{+}\right]\mathbf{A}^{inc} + \left[\mathbf{F}^{-}\right]\mathbf{A}^{ref}, \quad \mathbf{F}^{c}_{r} = \left[\mathbf{F}^{+}\right]\mathbf{A}^{tra}, \tag{10}$$

the governing equations for the scattering problem can be obtained from eq. 7 :

$$\begin{bmatrix} \mathbf{S}^{c}_{ll}\left[\mathbf{q}^{-}\right] - \left[\mathbf{F}^{-}\right] & \mathbf{S}^{c}_{lr}\left[\mathbf{q}^{+}\right] \\ \mathbf{S}^{c}_{rl}\left[\mathbf{q}^{-}\right] & \mathbf{S}^{c}_{rr}\left[\mathbf{q}^{+}\right] + \left[\mathbf{F}^{+}\right] \end{bmatrix} \begin{Bmatrix} \mathbf{A}^{ref} \\ \mathbf{A}^{tra} \end{Bmatrix} = \begin{bmatrix} \left[\mathbf{F}^{+}\right] - \mathbf{S}^{c}_{ll}\left[\mathbf{q}^{+}\right] \\ -\mathbf{S}^{c}_{rl}\left[\mathbf{q}^{+}\right] \end{bmatrix} \left\{\mathbf{A}^{inc}\right\}, \tag{11}$$

Given a single or a set of incident modes as the input in Equation 10, scattered modes (reflection and transmission) acting as the output can be obtained. Numerically, the base number Nr is suggested to be frequency dependent, which can be implemented by a routine to include those slightly evanescent wave modes into the bases.

To numerically describe the wave mode scattering, the reflection and transmission coefficients are defined by the solution of response from Equation 11:

$$\mathbf{R}_i = \frac{\mathbf{A}_i^{ref}}{\mathbf{A}_i^{inc}}, \quad \mathbf{T}_i = \frac{\mathbf{A}_i^{tra}}{\mathbf{A}_i^{inc}} \tag{12}$$

where $i = 1, 2, ..., Nr$. It should be mentioned that the coefficients depend not only on the defects, but also on the normalization method of eigenmodes and the size of intact part of waveguide that included for the reduction of high order near-field modes. The change of the phase of the coefficient with the frequency is partially owing to the size of intact part of waveguide in coupling structure model.

3 NUMERICAL IMPLEMENTATIONS

Guided wave techniques have two main objectives: defect localization and defect sizing. The location of the defect can be easily evaluated from the reflection of a well tuned wave packet. Practically, the time frequency analysis or denoise processing of the obtained testing signal is necessary. The sizing of the defects is much more difficult, because the reflection or transmission signal depends not only the defect size or shape, but also the mode type and frequency, potential mode conversion, and the attenuation due to dissipation, leakage or geometry. However, the wave-defect interaction analysis will help to find out which type of modes are sensitive to a given type of defects. Generally, the numerical wave-defect interaction analysis will provide a reference of the sizing in the practical test, at least to some extent.

3.1 Methodology

To construct the database of reflection coefficients, a numerical finite element model of a pipe-damaged section was created. The defect is a rectangular notch with three-dimensional variables: depth, axial and circumferential extents (figure 3). These parameters can describe most of defects types that can be encountred such as (notchs, corrosion, metal loss ...). The pipe is steel with a density $\rho = 7800 kg.m^{-3}$, a Young modulus $E = 2.10^{11} Pa$ and a Poisson‘s ratio $\nu = 0.3$. The outer diameter is $168mm$ and the thickness of the pipe wall is $11mm$. Reflection coefficients calculation was made depending on the frequency in the range $[5 - 15] kHz$. This latter corresponds practically to the signal frequency by wich the pipe under test was excited. The torsion mode was considered in the calculation process. In fact, the inspection system use this mode to generate guided waves for the defect detection.

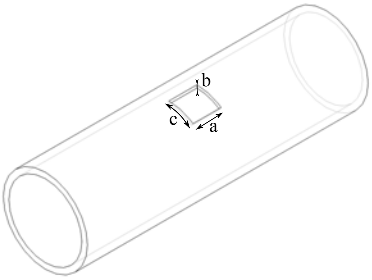

Figure 3: Damaged pipe with defect dimensions.

The waveguide 1 is a pipe section connected to the waveguide 2 wich is a coupling structure with defect and it is in turn connected to waveguide 3 similar to the 1^{st} one (see figure 4). Several iterations conduct us to obtain a database that contain reflection coefficients as a function of four variables : a, b, c and f, respectively, axial, depth, circumferential extents and frequency.

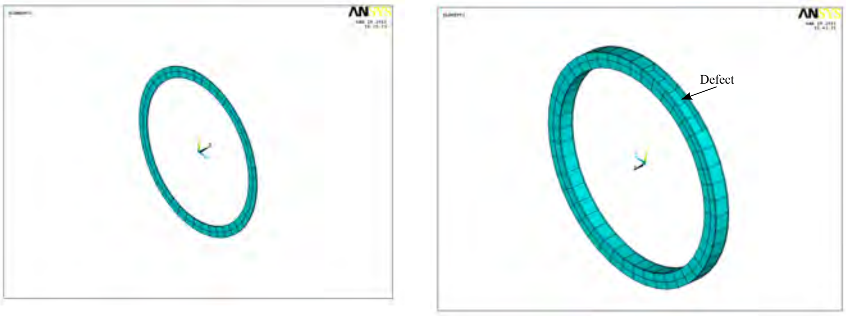

(a) (b)

Figure 4: Finite element models of waveguides : (a) Waveguide 1 and 3, (b) Waveguide 2

3.2 Numerical results and interpretations

Figure 5 shows the reflection coefficients variation with frequency for different defect sizes. These curves prove the dependence of reflection coefficients with the excitation frequency. Generally speaking, these coefficients increase with the frequency. Figure 6 shows the reflection coefficients variation with axial, circumferential and depth defect extents at 10kHz for different sizes. These curves demonstrate the increase of the reflection coefficients with the defect sizes. The database constructed by a large diversity of defect sizes let us to plot the 3-D curves showing the evolution of reflection coefficients with two chosen variables from the defect dimensions (a, b or c) at a given frequency. In figure 7 we can see 3-D graphs of the reflection coefficients variation with defect sizes at $10kHz$. It is clear that the reflection monotonically increases with axial extent at constant depth and vice versa, it also increases with circumferential extent at constant axial extent and vice versa.

Figure 8 shows color maps of the 3-D reflection plot in figure 7. The lines are isolines of constant reflection coefficient as described by the color bar. From these isolines we can observe that the reflection coefficient obtained for example at a certain depth and axial extent is also obtained at smaller depth and larger axial extent.

4 CONCLUSIONS

In this study, the Wave Finite Element Method was used to calculate the reflection coefficients from a rectangular notch, with varying dimensions, located in a pipe excited by torsional mode. The database created will serve for the sizing of defects detected by an experimental inspection system. Results show the increase of the reflection coefficients with the defect sizes and its dependence on the frequency. The reflection coefficients generally have nonlinear relationship with defects size of transverse size except at some frequencies. This means the choice of central frequency is crucial for the accurate estimation of the damage severity.

REFERENCES

[1] A Demma. The reflection of guided waves from notches in pipes: a guide for interpreting corrosion measurements. *NDT & E International*, 37(3):167–180, 2004.

[2] J. Ma, F. Simonetti, and M. J. S. Lowe. Scattering of the fundamental torsional mode by an axisymmetric layer inside a pipe. *The Journal of the Acoustical Society of America*, 120(4):1871–1880, October 2006.

[3] Lon Brillouin. *Wave Propagation in Periodic Structures*. Courier Dover Publications, December 2003.

[4] W. X. Zhong and F. W. Williams. On the direct solution of wave propagation for repetitive structures. *Journal of Sound and Vibration*, 181(3):485–501, March 1995.

[5] M.N. Ichchou, J.-M. Mencik, and W. Zhou. Wave finite elements for low and mid-frequency description of coupled structures with damage. *Computer Methods in Applied Mechanics and Engineering*, 198(15-16):1311–1326, 2009.

[6] W Zhou, M Ichchou, and J Mencik. Analysis of wave propagation in cylindrical pipes with local inhomogeneities. *Journal of Sound and Vibration*, 319(1-2):335–354, 2009.

[7] W.J. Zhou and M.N. Ichchou. Wave propagation in mechanical waveguide with curved members using wave finite element solution. *Computer Methods in Applied Mechanics and Engineering*, 199(33-36):2099–2109, 2010.

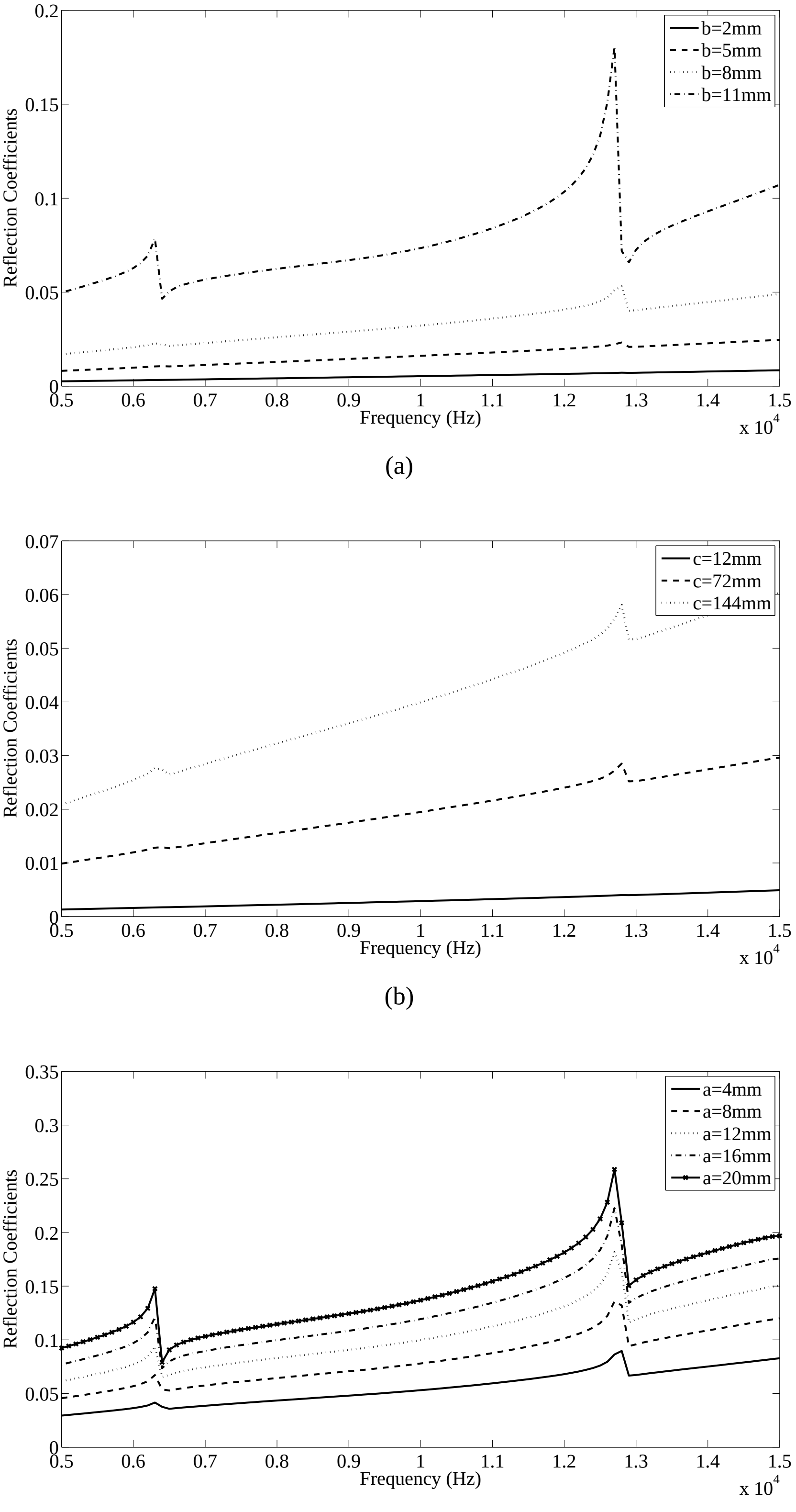

(a)

(b)

(c)

Figure 5: Reflection coefficients variation with frequency for : (a) different defect depth with $a = 8mm$, $c = 60mm$; (b) different defect circumferential-extents with $a = 8mm$, $b = 5mm$; and (c) different defect axial-extents with $c = 132mm$, $b = 8mm$

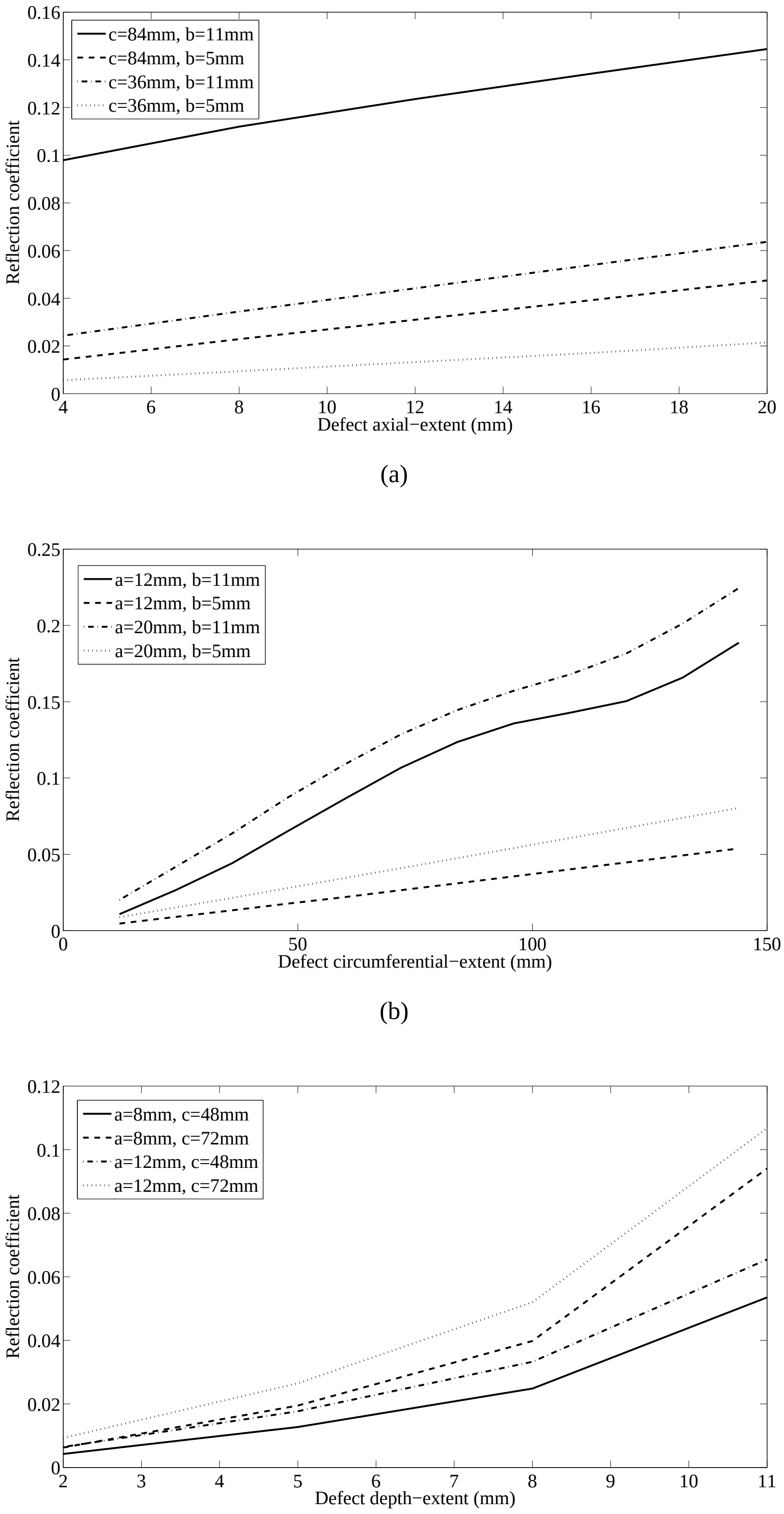

(a)

(b)

(c)

Figure 6: Reflection coefficients variation with : (a) defect axial-extents for different circumferential and depth sizes; (b) defect circumferential-extents for different axial and depth sizes; and (c) defect depth for different circumferential and axial sizes; at $10kHz$

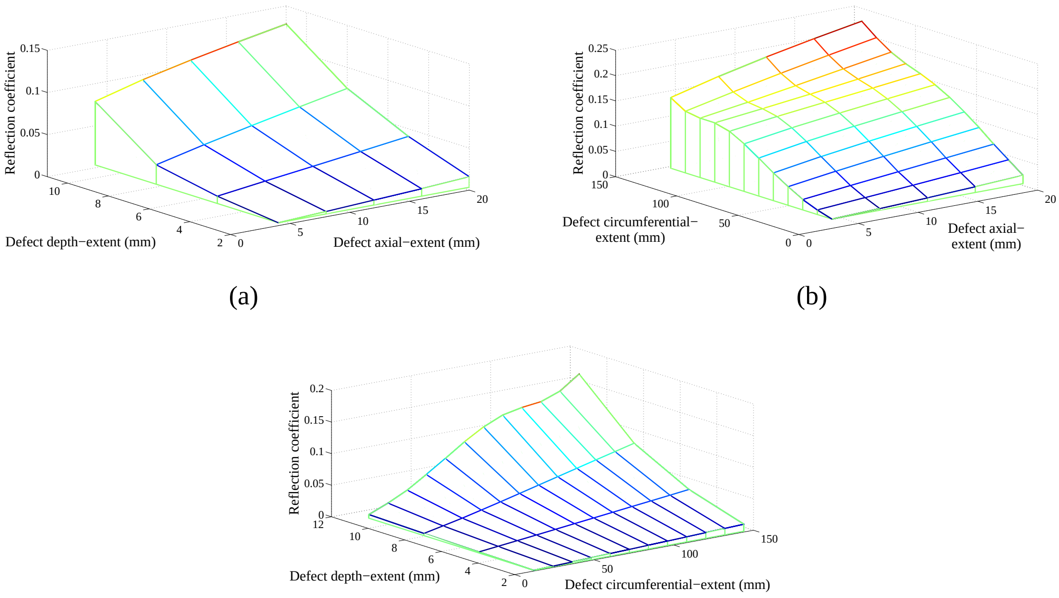

(a)

(b)

(c)

Figure 7: 3D graph of reflection coefficients at $10kHz$ with : (a) varying depth and axial extent $(c = 72mm)$, (b) varying circumferential and axial extents (through thickness defect) and, (c) varying depth and circumferential extent $(a = 8mm)$.

.

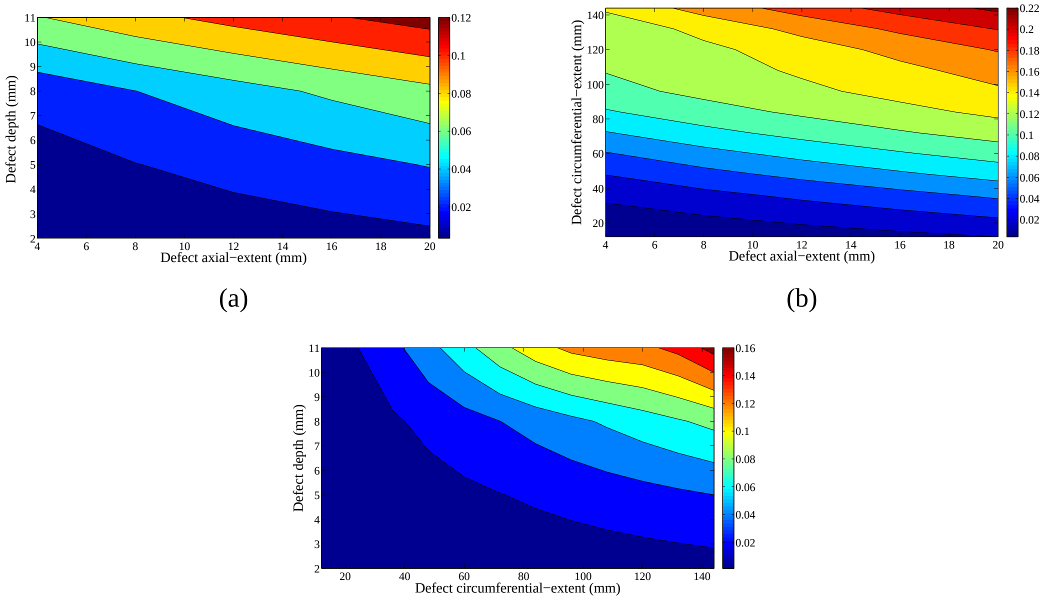

(a)

(b)

(c)

Figure 8: Color map of reflection coefficients at $10kHz$ with : (a) varying depth and axial extent $(c = 72mm)$, (b) varying circumferential and axial extents (through thickness defect) and, (c) varying depth and circumferential extent $(a = 8mm)$.

.

COMPDYN 2011
ECCOMAS Thematic Conference on
Computational Methods in Structural Dynamics and Earthquake Engineering
M. Papadrakakis, M. Fragiadakis, V. Plevris (eds.)
Corfu, Greece, 25-28 May 2011

SEISMIC WAVE PROPAGATION AND PERFECTLY MATCHED LAYERS USING GFDM

F. Ureña[1], J.J. Benito[2], E. Salete[2] and L. Gavete[3]

[1]Universidad de Castilla-La Mancha
Avda. Camilo José Cela s/n, 13071, Ciudad Real, Spain
francisco.urena@uclm.es

[2]Universidad Nacional de Eduacación a Distancia
Apdo. de correos 60149, 28080 Madrid, Spain
jbenito@ind.uned.es, esalete@ind.uned.es

[3]Universidad Politécnica de Madrid
C/ Alenza 4, 28003 Madrid, Spain
lu.gavete@upm.es

Keywords: meshless methods, generalized finite difference method, moving least squares, seismic waves, perfectly matched layer.

Abstract. *The interior of the Earth is heterogeneous with different material and may have complex geometry. The free surface can also be uneven. Therefore, the use of a meshless method with the possibility of using and irregular grid-point distribution can be interest for modelling this kind of problem.*

This paper shows the application of Generalized Finite Difference Method (GFDM) to the problem of seismic wave propagation in 2-D. To use this method in unbounded domains one must truncate the computational grid-point avoiding reflection from the edges. Perfectly Matched Layers (PML) absorbing boundary condition has then been included in the numerical model proposed in this work.

1 Introduction

During recent years, meshless methods have emerged as a class of effective numerical methods which are capable of avoiding the difficulties encountered in conventional computational mesh based methods. Considerable research in computational mechanics has been devoted to the development of meshless methods. In these methods, the domain of interest is discretized by a scattered set of points.

An important path in the evolution of meshless methods has been the development of the Generalized Finite Difference Method (GFDM), also called Meshless Finite Difference Method (MFDM). The bases of the GFD were published in the early seventies. The idea of using an eight node star and weighting functions to obtain finite difference formulae for irregular meshes, was first put forward by [9] using moving least squares (MLS) interpolation and an advanced version of the GFDM was given by [12]. [1] reported that the solution of the generalized finite difference method depends on the number of nodes in the cloud, the relative coordinates of the nodes with respect to the star node, and on the weight function employed.

An h-adaptive method in GFDM is described in [2], [4] and [5].

In this paper, this meshless method is applied to seismic wave propagation. The GFDM is a robust numerical method applicable to structurally complex media. Due to its relative accuracy and computational efficiency it is the dominant method in modeling earthquake motion [10] and [11]. The perfectly matched layer (PML) absorbing boundary performs more efficiently and more accurately than most traditional or differential equation-based absorbing boundaries ([6], [7], [13] and [8]).

The paper is organized as follows. Section 1 is an introduction. Section 2 describes the GFDM obtaining the explicit generalized differences schemes for the seismic waves propagation. In Section 3 a stability condition is obtained. In Section 4 the grid dispersion relations is derived. In Section 5 are analyzed the relations between irregularity of cloud of nodes, the step of time and star-dispersion. In Section 6 an PML is defined in 2-D. In Section 7 some numerical results are included. Finally, in Section 8 some conclusions are given.

2 Explicit Generalized Differences Schemes for the seismic waves propagation problem for a perfectly elastic, homogeneous and isotropic medium

2.1 Equation of motion

The equations of motion for a perfectly elastic, homogeneous, isotropic medium in 2-D are

$$\left\{\begin{array}{l} \dfrac{\partial^2 U_x(x,y,t)}{\partial t^2} = \alpha^2 \dfrac{\partial^2 U_x(x,y,t)}{\partial x^2} + \beta^2 \dfrac{\partial^2 U_x(x,y,t)}{\partial y^2} + (\alpha^2-\beta^2)\dfrac{\partial^2 U_y(x,y,t)}{\partial x \partial y} \\ \dfrac{\partial^2 U_y(x,y,t)}{\partial t^2} = \beta^2 \dfrac{\partial^2 U_y(x,y,t)}{\partial x^2} + \alpha^2 \dfrac{\partial^2 U_y(x,y,t)}{\partial y^2} + (\alpha^2-\beta^2)\dfrac{\partial^2 U_x(x,y,t)}{\partial x \partial y} \end{array}\right. \quad (1)$$

with the initial conditions

$$U_x(x,y,0) = f_1(x,y); U_y(x,y,0) = f_2(x,y)$$
$$\frac{\partial U_x(x,y,0)}{\partial t} = f_3(x,y); \frac{\partial U_y(x,y,0)}{\partial t} = f_4(x,y) \quad (2)$$

and the boundary condition

$$\left\{\begin{array}{l} a_1 U_x(x_0,y_0,t) + b_1 \frac{\partial U_x(x_0,y_0,t)}{\partial n} = g_1(t) \\ a_2 U_y(x_0,y_0,t) + b_2 \frac{\partial U_y(x_0,y_0,t)}{\partial n} = g_2(t) \end{array}\right. \qquad en \quad \Gamma \quad (3)$$

where $f_1(x,y)$, $f_2(x,y)$, $f_3(x,y)$, $f_4(x,y)$, $g_1(t)$ y $g_2(t)$ are showed functions,

$$\alpha = \sqrt{\frac{\lambda + 2\mu}{\rho}}, \quad \beta = \sqrt{\frac{\mu}{\rho}}$$

ρ is the density, λ and μ are Lamé elastic coefficients and Γ is the boundary of Ω.

2.2 A GFDM Explicit Scheme

The aim is to obtain explicit linear expressions for the approximation of partial derivatives in the points of the domain. First of all, an irregular grid or cloud of points is generated in the domain $\Omega \cup \Gamma$. On defining the central node with a set of nodes surrounding that node, the star then refers to a group of established nodes in relation to a central node. Every node in the domain has an associated star assigned to it.

This scheme uses the central-difference form for the time derivative

$$\frac{\partial^2 U_x(x_0,y_0,n\triangle t)}{\partial t^2} = \frac{u_{x,0}^{n+1} - 2u_{x,0}^{n} + u_{x,0}^{n-1}}{(\triangle t)^2}; \qquad \frac{\partial^2 U_y(x_0,y_0,n\triangle t)}{\partial t^2} = \frac{u_{y,0}^{n+1} - 2u_{y,0}^{n} + u_{y,0}^{n-1}}{(\triangle t)^2} \tag{4}$$

Following [1], [2] and [4], the explicit difference formulae for the spatial derivatives are obtained,

$$\begin{aligned}
\frac{\partial^2 U_x(x_0,y_0,n\triangle t)}{\partial x^2} &= -m_0 u_{x,0}^n + \sum_{j=1}^{N} m_j u_{x,j}^n; & \frac{\partial^2 U_y(x_0,y_0,n\triangle t)}{\partial x^2} &= -m_0 u_{y,0}^n + \sum_{j=1}^{N} m_j u_{y,j}^n \\
\frac{\partial^2 U_x(x_0,y_0,n\triangle t)}{\partial y^2} &= -\eta_0 u_{x,0}^n + \sum_{j=1}^{N} \eta_j u_{x,j}^n; & \frac{\partial^2 U_y(x_0,y_0,n\triangle t)}{\partial y^2} &= -\eta_0 u_{y,0}^n + \sum_{j=1}^{N} \eta_j u_{y,j}^n \\
\frac{\partial^2 U_x(x_0,y_0,n\triangle t)}{\partial x \partial y} &= -\zeta_0 u_{x,0}^n + \sum_{j=1}^{N} \zeta_j u_{x,j}^n; & \frac{\partial^2 U_y(x_0,y_0,n\triangle t)}{\partial x \partial y} &= -\zeta_0 u_{y,0}^n + \sum_{j=1}^{N} \zeta_j u_{y,j}^n
\end{aligned} \tag{5}$$

where N is the number of nodes in the star whose central node has the coordinates (x_0, y_0) (in this work $N = 8$ and the are selected by using the four quadrants criteria ([**?**])).

m_0, η_0, ζ_0 are the coefficients that multiply the approximate values of the functions U and V at the central node for the time $n\triangle t$ (u_0^n and v_0^n respectively) in the generalized finite difference explicit expressions for the space derivatives.

m_j, η_j, ζ_j are the coefficients that multiply the approximate values of the functions U and V at the rest of the star nodes for the time $n\triangle t$ (u_j^n and v_j^n respectively) in the generalized finite difference explicit expressions for the space derivatives.

The replacement in Eq. 1 of the explicit expressions obtained for the partial derivatives leads to

$$\left\{\begin{aligned} u_{x,0}^{n+1} &= 2u_{x,0}^{n} - u_{x,0}^{n-1} + (\triangle t)^2[\alpha^2(-m_0 u_{x,0}^n + \sum_1^N m_j u_{x,j}^n) + \beta^2(-\eta_0 u_{x,0}^n + \sum_1^N \eta_j u_{x,j}^n) \\ &\qquad + (\alpha^2-\beta^2)(-\zeta_0 u_{y,0}^n + \sum_1^N \zeta_j u_{y,j}^n)] \\ u_{y,0}^{n+1} &= 2u_{y,0}^{n} - u_{y,0}^{n-1} + (\triangle t)^2[\beta^2(-m_0 u_{y,0}^n + \sum_1^N m_j u_{y,j}^n) + \alpha^2(-\eta_0 u_{y,0}^n + \sum_1^N \eta_j u_{y,j}^n) \\ &\qquad + (\alpha^2-\beta^2)(-\zeta_0 u_{x,0}^n + \sum_1^N \zeta_j u_{x,j}^n)] \end{aligned}\right. \tag{6}$$

3 Stability Criterion

For the stability analysis the first idea is to make a harmonic decomposition of the approximated solution at grid points and at a given time level (n). Then we can write the finite difference approximation in the nodes of the star at time n, as

$$u_0^n = A\xi^n e^{\boldsymbol{i}\boldsymbol{k}^T\boldsymbol{x_0}}; \quad u_j^n = A\xi^n e^{\boldsymbol{i}\boldsymbol{k}^T\boldsymbol{x_j}}; \quad v_0^n = B\xi^n e^{\boldsymbol{i}\boldsymbol{k}^T\boldsymbol{x_0}}; \quad v_j^n = B\xi^n e^{\boldsymbol{i}\boldsymbol{k}^T\boldsymbol{x_j}} \tag{7}$$

where $\boldsymbol{x_0}$ is the position vector of the central node of the star, $\boldsymbol{x_j}, j = 1, \cdots, N$ are the position vectors of the rest of the nodes in the star and $\boldsymbol{h_j}$ are the relative position vectors of the nodes in the star in respect to the central node whose coordinates are $h_{jx} = x_j - x_0, h_{jy} = y_j - y_0$. ξ is the amplification factor whose value will determine the stability condition, w is the angular frequency in the grid.

$$\boldsymbol{x_j} = \boldsymbol{x_0} + \boldsymbol{h_j}; \qquad \xi = e^{-iw\triangle t}$$

$\boldsymbol{k}$ (fig. 1) is the column vector of the wave numbers

$$\boldsymbol{k} = \left\{ \begin{array}{c} k_x \\ k_y \end{array} \right\} = k \left\{ \begin{array}{c} \cos\varphi \\ \sin\varphi \end{array} \right\}$$

Then we can write the stability condition as: $\|\xi\| \leq 1$.

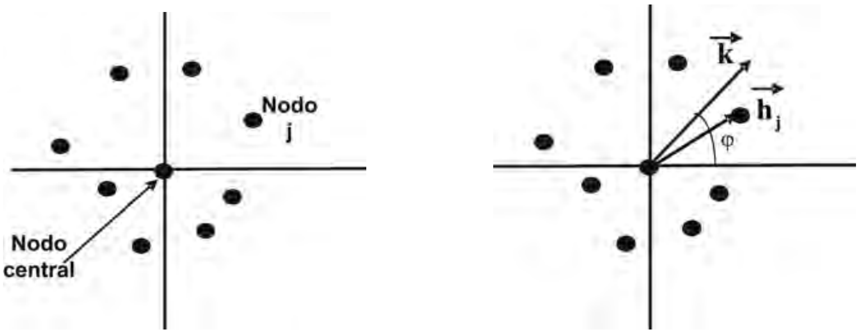

Figure 1: Irregular star (9 nodes) The wavenumber $\vec{\boldsymbol{k}}$

Including 7 into 6, cancelation of $\xi^n e^{i\boldsymbol{\nu}^T \boldsymbol{x_0}}$, leads to

$$\begin{aligned}
A\xi = 2A - \frac{A}{\xi} + (\triangle t)^2[\alpha^2(-Am_0 + A\sum_1^N m_j e^{i\boldsymbol{k}^T\boldsymbol{h_j}}) + \beta^2(-A\eta_0 + A\sum_1^N \eta_j e^{i\boldsymbol{k}^T\boldsymbol{h_j}}) + \\
(\alpha^2 - \beta^2)(-B\zeta_0 + B\sum_1^N \zeta_j e^{i\boldsymbol{k}^T\boldsymbol{h_j}})] \\
B\xi = 2B - \frac{B}{\xi} + (\triangle t)^2[\beta^2(-Bm_0 + B\sum_1^N m_j e^{i\boldsymbol{k}^T\boldsymbol{h_j}}) + \alpha^2(-B\eta_0 + B\sum_1^N \eta_j e^{i\boldsymbol{k}^T\boldsymbol{h_j}}) + \\
(\alpha^2 - \beta^2)(-A\zeta_0 + A\sum_1^N \zeta_j e^{i\boldsymbol{k}^T\boldsymbol{h_j}})]
\end{aligned} \tag{8}$$

where

$$m_0 = \sum_1^N m_j; \quad \eta_0 = \sum_1^N \eta_j; \quad \zeta_0 = \sum_1^N \zeta_j \tag{9}$$

Including 9 into 8, the system of equations is obtained

$$\begin{aligned}
A[\xi - 2 + \frac{1}{\xi} + (\triangle t)^2\alpha^2\sum_1^N m_j(1 - e^{i\boldsymbol{k}^T\boldsymbol{h_j}}) + (\triangle t)^2\beta^2\sum_1^N \eta_j(1 - e^{i\boldsymbol{k}^T\boldsymbol{h_j}})] \\
+ B(\triangle t)^2(\alpha^2 - \beta^2)\sum_1^N \zeta_j(1 - e^{i\boldsymbol{k}^T\boldsymbol{h_j}}) = 0 \\
A(\triangle t)^2(\alpha^2 - \beta^2)\sum_1^N \zeta_j(1 - e^{i\boldsymbol{k}^T\boldsymbol{h_j}}) + B[\xi - 2 + \frac{1}{\xi} + (\triangle t)^2\beta^2\sum_1^N m_j(1 - e^{i\boldsymbol{k}^T\boldsymbol{h_j}}) \\
+ (\triangle t)^2\alpha^2\sum_1^N \eta_j(1 - e^{i\boldsymbol{k}^T\boldsymbol{h_j}})] = 0
\end{aligned} \tag{10}$$

B can be obtained from the second equation and included into the first, then operating with the real and imaginary parts of conditions obtained, and canceling with conservative criteria, the condition for stability of star is obtained.

$$\triangle t < \sqrt{\frac{4}{(\alpha^2 + \beta^2)[(|m_0| + |\eta_0|) + \sqrt{(m_0 + \eta_0)^2 + \zeta_0^2}]}} \tag{11}$$

4 Star dispersion

4.1 Star-dispersion relations for the P and S waves

The real part of the condition obtained from Eq. 10 leads to

$$\omega = \frac{1}{\triangle t}\arccos\Phi \tag{12}$$

where

$$\Phi = 1 - \frac{(\triangle t)^2}{4}((\alpha^2+\beta^2)(a_1+a_3) + ((\alpha^2+\beta^2)^2(a_1+a_3)^2 + \\ 4[(\alpha^2-\beta^2)^2(a_5^2-a_6^2) + (\alpha^2 a_2+\beta^2 a_4)(\beta^2 a_2+\alpha^2 a_4) - (\alpha^2 a_1+\beta^2 a_3)(\beta^2 a_1+\alpha^2 a_3)])^{\frac{1}{2}}) \tag{13}$$

with

$$\begin{gathered}
a_1 = \sum_1^N m_j(1-\cos \boldsymbol{k}^T\boldsymbol{h_j}) \Rightarrow \frac{\partial a_1}{\partial k} = a_{1,k} = \sum_1^N m_j d \sin kd \\
a_2 = \sum_1^N m_j \sin \boldsymbol{k}^T\boldsymbol{h_j} \Rightarrow \frac{\partial a_2}{\partial k} = a_{2,k} = \sum_1^N m_j d \cos kd \\
a_3 = \sum_1^N \eta_j(1-\cos \boldsymbol{k}^T\boldsymbol{h_j}) \Rightarrow \frac{\partial a_3}{\partial k} = a_{3,k} = \sum_1^N \eta_j d \sin kd \\
a_4 = \sum_1^N \eta_j \sin \boldsymbol{k}^T\boldsymbol{h_j} \Rightarrow \frac{\partial a_4}{\partial k} = a_{4,k} = \sum_1^N \eta_j d \cos kd \\
a_5 = \sum_1^N \zeta_j(1-\cos \boldsymbol{k}^T\boldsymbol{h_j}) \Rightarrow \frac{\partial a_5}{\partial k} = a_{5,k} = \sum_1^N \zeta_j d \sin kd \\
a_6 = \sum_1^N \zeta_j \sin \boldsymbol{k}^T\boldsymbol{h_j} \Rightarrow \frac{\partial a_6}{\partial k} = a_{6,k} = \sum_1^N \zeta_j d \cos kd
\end{gathered} \tag{14}$$

and

$$\boldsymbol{k}^T\boldsymbol{h_j} = k(h_{jx}\cos\varphi + h_{jy}\sin\varphi) = kd$$

Is known that

$$\omega = 2\pi \frac{c^{grid}}{\lambda^{grid}} \tag{15}$$

where c^{grid} and λ^{grid} are the phase velocity (α^{grid} or β^{grid}) and the wavelength (λ_P^{grid} or λ_S^{grid}) in the star respectively.
Defining the relations:

$$s = \frac{2}{\lambda_S^{grid}\sqrt{(r^2+1)[(|m_0|+|\eta_0|)+\sqrt{(m_0+\eta_0)^2+\zeta_0^2}]}} \tag{16}$$

$$s_P = \frac{2}{\lambda_P^{grid}\sqrt{(r^2+1)[(|m_0|+|\eta_0|)+\sqrt{(m_0+\eta_0)^2+\zeta_0^2}]}} \tag{17}$$

$$p = \frac{\beta\triangle t\sqrt{(r^2+1)[(|m_0|+|\eta_0|)+\sqrt{(m_0+\eta_0)^2+\zeta_0^2}]}}{2} \tag{18}$$

$$r = \frac{\alpha}{\beta} \tag{19}$$

$$s_P = \frac{s}{r} \tag{20}$$

Substituting Eqs. 12, 17, 18 and 20 into Eq. 15, the star-dispersion relations for P and S waves are obtained:

$$\frac{\alpha^{grid}}{\alpha} = \frac{\arccos \Phi}{2\pi sp} \tag{21}$$

$$\frac{\beta^{grid}}{\beta} = \frac{\arccos \Phi}{2\pi sp} \tag{22}$$

4.2 Star-dispersion for group velocity

By definition the group velocity is the derivative of w (see Eq.12) with respect to k, thus

$$\alpha^{grid}_{group} = \frac{\partial w}{\partial k} = \frac{\triangle t}{4}\frac{\beta^2 \Upsilon}{\sqrt{1-\Phi^2}} \tag{23}$$

where

$$\begin{aligned}\Upsilon = {} & (r^2+1)(a_{1,k}+a_{3,k}) + \frac{1}{2}[2(r^2+1)^2(a_1+a_3)(a_{1,k}+a_{3,k})+ \\ & 4[2(r^2-1)^2(a_5 a_{5,k} - a_6 a_{6,k}) + (r^2 a_{2,k} + a_{4,k})(a_2 + r^2 a_4)+ \\ & (r^2 a_2 + a_4)(a_{2,k} + r^2 a_{4,k}) - (r^2 a_{1,k} + a_{3,k})(a_1 + r^2 a_3)- \\ & (r^2 a_1 + a_3)(a_{1,k} + r^2 a_{3,k})]] \times [(r^2+1)^2(a_1+a_3)^2+ \\ & 4[(r^2-1)^2(a_5^2 - a_6^2) + (r^2 a_2 + a_4)(a_2 + r^2 a_4) - (r^2 a_1 + a_3)(a_1 + r^2 a_3)]]^{-\frac{1}{2}}\end{aligned} \tag{24}$$

Defining

$$\begin{aligned}F = {} & (r^2+1)(a_1+a_3) + [(r^2+1)^2(a_1+a_3)^2+ \\ & 4[(r^2-1)^2(a_5^2 - a_6^2) + (r^2 a_2 + a_4)(a_2 + r^2 a_4) - (r^2 a_1 + a_3)(a_1 + r^2 a_3)]]^{\frac{1}{2}}]\end{aligned} \tag{25}$$

and substituting Eqs. 18 and 25 into Eq. 23, the star-dispersion for waves P and S are

$$\frac{\alpha^{grid}_{group}}{\alpha} = \frac{1}{2\sqrt{2}r}\frac{\Upsilon}{\sqrt{F - \left(\frac{pF}{\sqrt{(r^2+1)[(|m_0|+|\eta_0|) + \sqrt{(m_0+\eta_0)^2+\zeta_0^2}]}\sqrt{2}}\right)^2}} \tag{26}$$

$$\frac{\beta^{grid}_{group}}{\beta} = \frac{1}{2\sqrt{2}}\frac{\Upsilon}{\sqrt{F - \left(\frac{pF}{\sqrt{(r^2+1)[(|m_0|+|\eta_0|) + \sqrt{(m_0+\eta_0)^2+\zeta_0^2}]}\sqrt{2}}\right)^2}} \tag{27}$$

5 Irregularity of the star (IIS) and dispersion

In this section we are going to define the index of irregularity of a star (IIS) and also the index of irregularity of a cloud of nodes (IIC).
The coefficients m_0, η_0, ζ_0 are functions of: a) the number of nodes in the star, b) the coordinates of each star node referred to the central node of the star and c) the weighting function (see references $[1, 4]$). If the number of nodes by star is fixed, in this case 9 ($N = 8$), and the weighting function

$$w(h_{jx}, h_{jy}) = \frac{1}{(\sqrt{h_{jx}^2 + h_{jy}^2})^3} \tag{28}$$

the expression

$$\frac{1}{\sqrt{(r^2+1)[(|m_0| + |\eta_0|) + \sqrt{(m_0+\eta_0)^2 + \zeta_0^2}]}} \tag{29}$$

is function of the coordinates of each node of star referred to its central node.
The coefficients m_0, η_0, ζ_0, are functions of $\frac{1}{h_{jx}^2 + h_{jy}^2}$.
Denoting τ_l a the average of the distances between of the nodes of the star l and its central node and denoting τ the average of the τ_l values in the stars of the mesh, then

$$\boldsymbol{h_j} = \tau \left\{ \begin{array}{c} \overline{h_{jx}} \\ \overline{h_{jy}} \end{array} \right\} \tag{30}$$

$$\overline{m_0} = m_0\tau^2; \quad \overline{\eta_0} = \eta_0\tau^2; \quad \overline{\zeta_0} = \zeta_0\tau^2 \tag{31}$$

The stability criterion can be rewritten

$$\triangle t < \frac{2\tau}{\beta\sqrt{(r^2+1)}\sqrt{(|\overline{m_0}| + |\overline{\eta_0}|) + \sqrt{(\overline{m_0} + \overline{\eta_0})^2 + \overline{\zeta_0}^2}}} \tag{32}$$

For the regular mesh case, the inequality 32 is

$$\triangle t < \frac{\tau}{\beta\sqrt{r^2+1}} \frac{2(\sqrt{2}-1)\sqrt{3}}{\sqrt{5}} \tag{33}$$

Multiplying the right-hand side of inequality 35 by the factor

$$\frac{\sqrt{5}(\sqrt{2}+1)}{\sqrt{3(|\overline{m_0}| + |\overline{\eta_0}| + \sqrt{(\overline{m_0} + \overline{\eta_0})^2 + \overline{\zeta_0}^2})}} \tag{34}$$

the inequality 32 is obtained.
For each one of the stars of the cloud of nodes, we define the IIS for a star with central node in (x_0, y_0) as Eq. 34

$$IIS_{(x_0,y_0)} = \frac{\sqrt{5}(\sqrt{2}+1)}{\sqrt{3(|\overline{m_0}| + |\overline{\eta_0}| + \sqrt{(\overline{m_0} + \overline{\eta_0})^2 + \overline{\zeta_0}^2})}} \tag{35}$$

that takes the value of one in the case of a regular mesh and $0 < IIS \leq 1$
If the index IIS decreases, then absolute values of $\overline{m_0}, \overline{\eta_0}, \overline{\zeta_0}$ increases and then according with 33, $\triangle t$ decreases and star dispersion increases (see 21, 22, 26 and 27).
The irregularity index of a cloud of nodes (IIC) is defined as the minimum of all the IIS of the stars of a cloud of nodes

$$IIC = min\{IIS_{(x_z,y_z)}/z = 1, \cdots, NT\} \tag{36}$$

where NT is the total number of nodes of the domain.

6 Recursive Equations

6.1 Recursive equations with PML in x-direction.

For computational convenience, we split the second order equations of motion (1) into five coupled first order equations by introducing the new field variables $\gamma_{xx}, \gamma_{xy}, \gamma_{yy}$

$$\begin{cases} \rho\dfrac{\partial U_x(x,y,t)}{\partial t} = \dfrac{\partial \gamma_{xx}(x,y,t)}{\partial x} + \dfrac{\partial \gamma_{xy}(x,y,t)}{\partial y} \\[2ex] \rho\dfrac{\partial U_y(x,y,t)}{\partial t} = \dfrac{\partial \gamma_{xy}(x,y,t)}{\partial x} + \dfrac{\partial \gamma_{yy}(x,y,t)}{\partial y} \\[2ex] \dfrac{\partial \gamma_{xx}(x,y,t)}{\partial t} = (\lambda + 2\mu)\dfrac{\partial U_x(x,y,t)}{\partial x} + \lambda\dfrac{\partial U_y(x,y,t)}{\partial y} \\[2ex] \dfrac{\partial \gamma_{xy}(x,y,t)}{\partial t} = \mu\dfrac{\partial U_x(x,y,t)}{\partial y} + \mu\dfrac{\partial U_y(x,y,t)}{\partial x} \\[2ex] \dfrac{\partial \gamma_{yy}(x,y,t)}{\partial t} = \lambda\dfrac{\partial U_x(x,y,t)}{\partial x} + (\lambda + 2\mu)\dfrac{\partial U_y(x,y,t)}{\partial y} \end{cases} \tag{37}$$

We shall make two simplifications, we shall assume that the space far from the region of interest is homogeneous, linear and time invariant.Then, under these assumptions, the radiating solution in infinite space must be (superposition of plane waves):

$$\boldsymbol{\omega}(\boldsymbol{x},t) = \boldsymbol{W}(\boldsymbol{x},t)e^{i(\boldsymbol{\kappa}\cdot\boldsymbol{x} - wt)} \tag{38}$$

As w is an analytic function of $\boldsymbol{x}$,then we can analytically continue it, evaluating the solution at complex values of $\boldsymbol{x}$. Then, the solution is not changed in the region of interest and the reflections are avoided.

$$\begin{cases} U_x(x,y,t) = u_x(x,y)e^{-iwt} \Rightarrow \dot{U}_x(x,y,t) = -iwu_x(x,y)e^{-iwt} = -iwU_x(x,y,t) \\ U_y(x,y,t) = u_y(x,y)e^{-iwt} \Rightarrow \dot{U}_y(x,y,t) = -iwu_y(x,y)e^{-iwt} = -iwU_y(x,y,t) \\ \gamma_{xx}(x,y,t) = \Gamma_{xx}(x,y)e^{-iwt} \Rightarrow \dot{\gamma}_{xx}(x,y,t) = -iw\Gamma_{xx}(x,y)e^{-iwt} = -iw\gamma_{xx}(x,y,t) \\ \gamma_{xy}(x,y,t) = \Gamma_{xy}(x,y)e^{-iwt} \Rightarrow \dot{\gamma}_{xy}(x,y,t) = -iw\Gamma_{xy}(x,y)e^{-iwt} = -iw\gamma_{xy}(x,y,t) \\ \gamma_{yy}(x,y,t) = \Gamma_{yy}(x,y)e^{-iwt} \Rightarrow \dot{\gamma}_{yy}(x,y,t) = -iw\Gamma_{yy}(x,y)e^{-iwt} = -iw\gamma_{yy}(x,y,t) \end{cases} \tag{39}$$

Thus, we have a complex coordinate

$$\tilde{x} = x + if \tag{40}$$

As this complex coordinate is inconvenient, we have a change variables in this region (PML)

$$\partial\tilde{x} = (1 + i\frac{df}{dx})\partial x \tag{41}$$

In order to have an attenuation rate in the PML independent of frequency (ω), we have

$$\frac{df}{dx} = \frac{\delta_x(x)}{\omega} \tag{42}$$

where ω is the angular frequency and δ_x is some function of x.
PML x-dir can be conceptually assumed up by a single transformation of the original equation. Then wherever an x derivative appears in the wave equations, it is replaced in the form

$$\frac{\partial}{\partial x} \rightarrow \frac{1}{1 + i\frac{\delta_x(x)}{w}}\frac{\partial}{\partial x} \tag{43}$$

The equations are fecuency-dependent, and to advoid it a solution is to use an auxiliary differential equation (ADE) approach in the implementation of PML. The following equations are obtained

$$\begin{cases} \dfrac{\partial U_x(x,y,t)}{\partial t} = \dfrac{1}{\rho}[\dfrac{\partial \gamma_{xx}(x,y,t)}{\partial x} + \dfrac{\partial \gamma_{xy}(x,y,t)}{\partial y}] + \psi_1(x,y,t) - \delta_x U_x(x,y,t) \\ \dfrac{\partial U_y(x,y,t)}{\partial t} = \dfrac{1}{\rho}[\dfrac{\partial \gamma_{xy}(x,y,t)}{\partial x} + \dfrac{\partial \gamma_{yy}(x,y,t)}{\partial y}] + \psi_2(x,y,t) - \delta_x U_y(x,y,t) \\ \dfrac{\partial \gamma_{xx}(x,y,t)}{\partial t} = (\lambda + 2\mu)\dfrac{\partial U_x(x,y,t)}{\partial x} + \lambda\dfrac{\partial U_y(x,y,t)}{\partial y} + \psi_3(x,y,t) - \delta_x \gamma_{xx}(x,y,t) \\ \dfrac{\partial \gamma_{xy}(x,y,t)}{\partial t} = \mu\dfrac{\partial U_x(x,y,t)}{\partial y} + \mu\dfrac{\partial U_y(x,y,t)}{\partial x} + \psi_4(x,y,t) - \delta_x \gamma_{xy}(x,y,t) \\ \dfrac{\partial \gamma_{yy}(x,y,t)}{\partial t} = \lambda\dfrac{\partial U_x(x,y,t)}{\partial x} + (\lambda + 2\mu)\dfrac{\partial U_y(x,y,t)}{\partial y} + \psi_5(x,y,t) - \delta_x \gamma_{yy}(x,y,t) \\ \dfrac{\partial \psi_1(x,y,t)}{\partial t} = \dfrac{\delta_x}{\rho}\dfrac{\partial \gamma_{xy}(x,y,t)}{\partial y} \\ \dfrac{\partial \psi_2(x,y,t)}{\partial t} = \dfrac{\delta_x}{\rho}\dfrac{\partial \gamma_{yy}(x,y,t)}{\partial y} \\ \dfrac{\partial \psi_3(x,y,t)}{\partial t} = \lambda\delta_x\dfrac{\partial U_y(x,y,t)}{\partial y} \\ \dfrac{\partial \psi_4(x,y,t)}{\partial t} = \mu\delta_x\dfrac{\partial U_x(x,y,t)}{\partial y} \\ \dfrac{\partial \psi_5(x,y,t)}{\partial t} = (\lambda + 2\mu)\delta_x\dfrac{\partial U_y(x,y,t)}{\partial y} \end{cases} \tag{44}$$

Where the five last equations 46 are ADE approach and the new field variables

$$\begin{cases} \psi_1(x,y,t) = \dfrac{1}{\rho}i\dfrac{\delta_x}{\omega}\dfrac{\partial \gamma_{xy}(x,y,t)}{\partial y} \\ \psi_2(x,y,t) = \dfrac{1}{\rho}i\dfrac{\delta_x}{\omega}\dfrac{\partial \gamma_{yy}(x,y,t)}{\partial y} \\ \psi_3(x,y,t) = i\lambda\dfrac{\delta_x}{\omega}\dfrac{\partial U_y(x,y,t)}{\partial y} \\ \psi_4(x,y,t) = i\mu\dfrac{\delta_x}{\omega}\dfrac{\partial U_x(x,y,t)}{\partial y} \\ \psi_5(x,y,t) = i(\lambda + 2\mu)\dfrac{\delta_x}{\omega}\dfrac{\partial U_y(x,y,t)}{\partial y} \end{cases} \tag{45}$$

6.1.1 An scheme in GDFM for elastic part

Following [1], [2] and [4], the explicit difference formulae for the spatial derivatives of a function are obtained,

$$\frac{\partial U_x(x_0,y_0,n\triangle t)}{\partial x} = -m_{1,0}u^n_{x,0}+\sum_{j=1}^{N} m_{1,j}u^n_{x,j}; \quad \frac{\partial U_x(x_0,y_0,n\triangle t)}{\partial y} = -m_{2,0}u^n_{x,0}+\sum_{j=1}^{N} m_{2,j}u^n_{x,j} \tag{46}$$

and similarly for first spatial derivatives of the functions: $U_y, \gamma_{xx}, \gamma_{xy}, \gamma_{yy}, \psi_1, \psi_2, \psi_3, \psi_4, \psi_5$ Substituting Eq. 46 into Eq. 37 the an scheme in GFDM for elastic part are obtained

$$\left\{ \begin{array}{l}
u^{n+1}_{x,0} = u^n_{x,0} + \dfrac{\triangle t}{\rho}[-m_{1,0}\gamma^n_{xx,0} + \displaystyle\sum_{j=1}^{N} m_{1,j}\gamma^n_{xx,j} - m_{2,0}\gamma^n_{xy,0} + \displaystyle\sum_{j=1}^{N} m_{2,j}\gamma^n_{xy,j}] \\
u^{n+1}_{y,0} = u^n_{y,0} + \dfrac{\triangle t}{\rho}[-m_{1,0}\gamma^n_{xy,0} + \displaystyle\sum_{j=1}^{N} m_{1,j}\gamma^n_{xy,j} - m_{2,0}\gamma^n_{yy,0} + \displaystyle\sum_{j=1}^{N} m_{2,j}\gamma^n_{yy,j}] \\
\gamma^{n+1}_{xx,0} = \gamma^n_{xx,0} + \triangle t[(\lambda+2\mu)(-m_{1,0}u^n_{x,0} + \displaystyle\sum_{j=1}^{N} m_{1,j}u^n_{x,j}) \\
+\lambda(-m_{2,0}u^n_{y,0} + \displaystyle\sum_{j=1}^{N} m_{y,j}u^n_{2,j})] \\
\gamma^{n+1}_{xy,0} = \gamma^n_{xy,0} + \triangle t[\mu(-m_{2,0}u^n_{x,0} + \displaystyle\sum_{j=1}^{N} m_{2,j}u^n_{x,j}) \\
+\mu(-m_{1,0}u^n_{y,0} + \displaystyle\sum_{j=1}^{N} m_{1,j}u^n_{y,j})] \\
\gamma^{n+1}_{yy,0} = \gamma^n_{yy,0} + \triangle t[\lambda(-m_{1,0}u^n_{x,0} + \displaystyle\sum_{j=1}^{N} m_{1,j}u^n_{x,j}) \\
+(\lambda+2\mu)(-m_{2,0}u^n_{y,0} + \displaystyle\sum_{j=1}^{N} m_{2,j}u^n_{y,j})]
\end{array} \right. \tag{47}$$

6.1.2 An scheme in GDFM for PML part

Substituting Eq. 46 into Eq. 44 the an scheme in GFDM for PML part are obtained

$$
\left\{
\begin{array}{l}
u_{x,0}^{n+1} = u_{x,0}^{n} + \dfrac{\triangle t}{\rho}[-m_{1,0}\gamma_{xx,0}^{n} + \displaystyle\sum_{j=1}^{N} m_{1,j}\gamma_{xx,j}^{n} - \\
m_{2,0}\gamma_{xy,0}^{n} + \displaystyle\sum_{j=1}^{N} m_{2,j}\gamma_{xy,j}^{n}] + \triangle t[\psi_{1,0}^{n} - \delta_x u_{x,0}^{n}] \\
u_{y,0}^{n+1} = u_{y,0}^{n} + \dfrac{\triangle t}{\rho}[-m_{1,0}\gamma_{xy,0}^{n} + \displaystyle\sum_{j=1}^{N} m_{1,j}\gamma_{xy,j}^{n} - \\
m_{2,0}\gamma_{yy,0}^{n} + \displaystyle\sum_{j=1}^{N} m_{2,j}\gamma_{yy,j}^{n}] + \triangle t[\psi_{2,0}^{n} - \delta_x u_{y,0}^{n}] \\
\gamma_{xx,0}^{n+1} = \gamma_{xx,0}^{n} + \triangle t[(\lambda + 2\mu)(-m_{1,0}u_{x,0}^{n} + \displaystyle\sum_{j=1}^{N} m_{1,j}u_{x,j}^{n}) + \\
\lambda(-m_{2,0}u_{y,0}^{n} + \displaystyle\sum_{j=1}^{N} m_{2,j}u_{y,j}^{n})] + \triangle t[\psi_{3,0}^{n} - \delta_x \gamma_{xx,0}^{n}] \\
\gamma_{xy,0}^{n+1} = \gamma_{xy,0}^{n} + \triangle t[\mu(-m_{2,0}u_{x,0}^{n} + \displaystyle\sum_{j=1}^{N} m_{2,j}u_{x,j}^{n}) + \\
\mu(-m_{1,0}u_{y,0}^{n} + \displaystyle\sum_{j=1}^{N} m_{1,j}u_{y,j}^{n})] + \triangle t[\psi_{4,0}^{n} - \delta_x \gamma_{xy,0}^{n}] \\
\gamma_{yy,0}^{n+1} = \gamma_{yy,0}^{n} + \triangle t[\lambda(-m_{1,0}u_{x,0}^{n} + \displaystyle\sum_{j=1}^{N} m_{1,j}u_{x,j}^{n}) + \\
(\lambda + 2\mu)(-m_{2,0}u_{y,0}^{n} + \displaystyle\sum_{j=1}^{N} m_{2,j}u_{y,j}^{n})] + \triangle t[\psi_{5,0}^{n} - \delta_x \gamma_{yy,0}^{n}] \\
\psi_{1,0}^{n+1} = \psi_{1,0}^{n} + \dfrac{\triangle t}{\rho}\delta_x[-m_{2,0}\gamma_{xy,0}^{n} + \displaystyle\sum_{j=1}^{N} m_{2,j}\gamma_{xy,j}^{n}] \\
\psi_{2,0}^{n+1} = \psi_{2,0}^{n} + \dfrac{\triangle t}{\rho}\delta_x[-m_{2,0}\gamma_{yy,0}^{n} + \displaystyle\sum_{j=1}^{N} m_{2,j}\gamma_{yy,j}^{n}] \\
\psi_{3,0}^{n+1} = \psi_{3,0}^{n} + \lambda\triangle t\delta_x[-m_{2,0}u_{y,0}^{n} + \displaystyle\sum_{j=1}^{N} m_{2,j}u_{y,j}^{n}] \\
\psi_{4,0}^{n+1} = \psi_{4,0}^{n} + \mu\triangle t\delta_x[-m_{2,0}u_{x,0}^{n} + \displaystyle\sum_{j=1}^{N} m_{2,j}u_{x,j}^{n}] \\
\psi_{5,0}^{n+1} = \psi_{5,0}^{n} + (\lambda + 2\mu)\triangle t\delta_x[-m_{2,0}u_{y,0}^{n} + \displaystyle\sum_{j=1}^{N} m_{2,j}u_{y,j}^{n}]
\end{array}
\right. \tag{48}
$$

6.2 Recursive equations with PML in x-direction and y-direction.

In this case

$$\begin{cases} \dfrac{\partial}{\partial x} \rightarrow \dfrac{\partial}{\partial x}(1+i\dfrac{\delta}{\omega})^{-1} \\ \dfrac{\partial}{\partial y} \rightarrow \dfrac{\partial}{\partial y}(1+i\dfrac{\delta}{\omega})^{-1} \end{cases} \tag{49}$$

We obtain

$$\begin{cases} \dfrac{\partial U_x(x,y,t)}{\partial t} = \dfrac{1}{\rho}[\dfrac{\partial \gamma_{xx}(x,y,t)}{\partial x} + \dfrac{\partial \gamma_{xy}(x,y,t)}{\partial y}] - \delta U_x(x,y,t) \\ \dfrac{\partial U_y(x,y,t)}{\partial t} = \dfrac{1}{\rho}[\dfrac{\partial \gamma_{xy}(x,y,t)}{\partial x} + \dfrac{\partial \gamma_{yy}(x,y,t)}{\partial y}]) - \delta U_y(x,y,t) \\ \dfrac{\partial \gamma_{xx}(x,y,t)}{\partial t} = (\lambda+2\mu)\dfrac{\partial U_x(x,y,t)}{\partial x} + \lambda\dfrac{\partial U_y(x,y,t)}{\partial y} - \delta\gamma_{xx}(x,y,t) \\ \dfrac{\partial \tau_{xy}(x,y,t)}{\partial t} = \mu\dfrac{\partial U_x(x,y,t)}{\partial y} + \mu\dfrac{\partial U_y(x,y,t)}{\partial x} - \delta\gamma_{xy}(x,y,t) \\ \dfrac{\partial \gamma_{yy}(x,y,t)}{\partial t} = \lambda\dfrac{\partial U_x(x,y,t)}{\partial x} + (\lambda+2\mu)\dfrac{\partial U_y(x,y,t)}{\partial y} - \delta\gamma_{yy}(x,y,t) \end{cases} \tag{50}$$

6.2.1 An scheme in GDFM for elastic part

The equations of the elastic part is given by Eq. 47

6.2.2 An scheme in GDFM for PML part

Substituting Eq. 46 into Eq. 50 the an scheme in GFDM for PML part are obtained

$$\begin{cases} u_{x,0}^{n+1} = u_{x,0}^{n} + \dfrac{\triangle t}{\rho}[-m_{1,0}\gamma_{xx,0}^{n} + \sum_{j=1}^{N} m_{1,j}\gamma_{xx,j}^{n} - \\ m_{2,0}\gamma_{xy,0}^{n} + \sum_{j=1}^{N} m_{2,j}\gamma_{xy,j}^{n}] - \triangle t\delta u_{x,0}^{n} \\ u_{y,0}^{n+1} = u_{y,0}^{n} + \dfrac{\triangle t}{\rho}[-m_{1,0}\gamma_{xy,0}^{n} + \sum_{j=1}^{N} m_{1,j}\gamma_{xy,j}^{n} - \\ m_{2,0}\gamma_{yy,0}^{n} + \sum_{j=1}^{N} m_{2,j}\gamma_{yy,j}^{n}] - \triangle t\delta u_{y,0}^{n} \\ \gamma_{xx,0}^{n+1} = \gamma_{xx,0}^{n} + \triangle t[(\lambda+2\mu)(-m_{1,0}u_{x,0}^{n} + \sum_{j=1}^{N} m_{1,j}u_{x,j}^{n}) + \\ \lambda(-m_{2,0}u_{y,0}^{n} + \sum_{j=1}^{N} m_{y,j}u_{y,j}^{n})] - \triangle t\delta\gamma_{xx,0}^{n} \\ \gamma_{xy,0}^{n+1} = \gamma_{xy,0}^{n} + \triangle t[\mu(-m_{2,0}u_{x,0}^{n} + \sum_{j=1}^{N} m_{2,j}u_{x,j}^{n}) + \\ \mu(-m_{1,0}u_{y,0}^{n} + \sum_{j=1}^{N} m_{1,j}u_{y,j}^{n})] - \triangle t\delta\gamma_{xy,0}^{n} \\ \gamma_{yy,0}^{n+1} = \gamma_{yy,0}^{n} + \triangle t[\lambda(-m_{1,0}u_{x,0}^{n} + \sum_{j=1}^{N} m_{1,j}u_{x,j}^{n}) + \\ (\lambda+2\mu)(-m_{2,0}u_{y,0}^{n} + \sum_{j=1}^{N} m_{2,j}u_{y,j}^{n})] - \triangle t\delta\gamma_{yy,0}^{n} \end{cases} \tag{51}$$

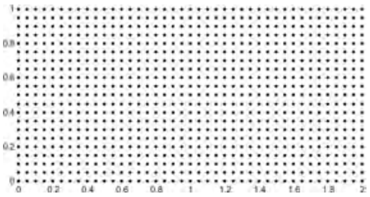

Figure 3 Regular mesh (861 nodes)

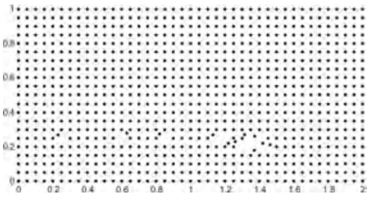

Figure 4 Irregular mesh($IIC = 0.9072$)

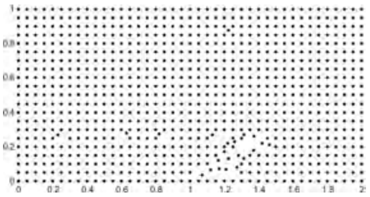

Figure 5 Irregular mesh($IIC = 0.8312$)

7 Numerical Results

7.1 GFDM with known boundary conditions

Let us solve the Eq. 1, in $\Omega = [0,2] \times [0,1] \subset \mathbf{R}^2$, with Dirichlet boundary conditions

$$\begin{cases} U_x(0,y,t) = 0 & \forall y \in [0,1] \\ U_x(1,y,t) = \sin 2 \sin y \cos(\sqrt{2}\beta t) & \forall y \in [0,1] \\ U_x(x,0,t) = 0 & \forall x \in [0,1] \\ U_x(x,1,t) = \sin x \sin 2 \cos(\sqrt{2}\beta t) & \forall x \in [0,1] \end{cases}$$

$$\begin{cases} U_y(0,y,t) = 0 & \forall y \in [0,1] \\ U_y(1,y,t) = \cos 2 \cos y \cos(\sqrt{2}\beta t) & \forall y \in [0,1] \\ U_y(x,0,t) = 0 & \forall x \in [0,1] \\ U_y(x,1,t) = \cos x \cos 2 \cos(\sqrt{2}\beta t) & \forall x \in [0,1] \end{cases} \tag{52}$$

and initial conditions

$$U_x(x,y,0) = \sin x \sin y; U_y(x,y,0) = \cos x \cos y; \quad \frac{\partial U_x(x,y,0)}{\partial t} = 0; \frac{\partial U_y(x,y,0)}{\partial t} = 0 \tag{53}$$

using a regular mesh (see Fig. 3 with 861 nodes) and irregular meshes (see Figs. 4 and 5) with 861 nodes. The analytical solutions (see Fig. 6) is

$$U_x(x,y,t) = \cos(\sqrt{2}\beta t) \sin x \sin y; \quad U_y(x,y,t) = \cos(\sqrt{2}\beta t) \cos x \cos y \tag{54}$$

The weighting function is given by Eq. 29 and the criterion for the selection of star nodes is the quadrant criterion (see references $[1,4,5]$). The global error is evaluated for each time increment, in the last time step considered, using the following formula

$$Global \quad error = \frac{\sqrt{\frac{\sum_{j=1}^{NT}(sol(j)-exac(j))^2}{NT}}}{|exac_{max}|} \times 100 \tag{55}$$

where $sol(j)$ is the GFDM solution at the node j $exac(j)$ is the exact value of the solution at the node j, $exac_{max}$ is the maximum value of the exact solution in the cloud of nodes considered and NT is the total number of nodes of the domain.

Table 1 shows the global error, with $\triangle t = 0.0005$, for value of $\alpha = 1$ and $\beta = 0.5$, in the regular mesh (see Fig. 3) with $n = 500$.

Table 2 shows the values of the global error for several values of $\triangle t$, using the irregular mesh with 861 nodes (see Fig. 4), with $n = 500$ and $IIC = 0.9072$.

Table 3 shows the values of the global error for several values of $\triangle t$, using the irregular mesh with 861 nodes (see Fig. 5), with $n = 500$ and $IIC = 0.8312$.

Table 1: The global errors with $\alpha = 1; \beta = 0.5$

N of Nodes	Global Error U_x	Global ErrorU_y
861	0.0004222	0.0004712

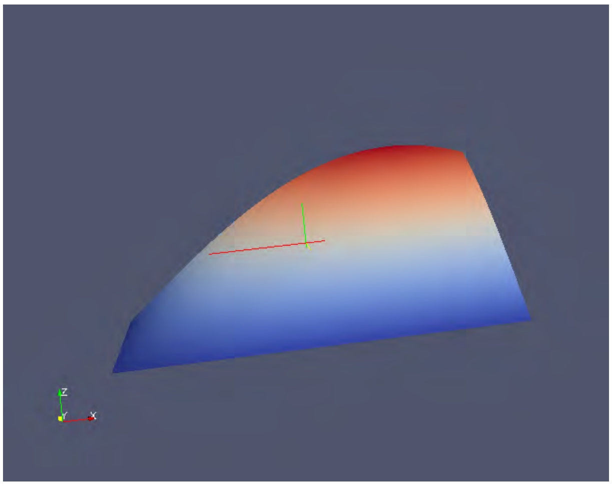

Figure 6: Exact solution U_x without PML.

Table 2: Influence of the $\triangle t$ in the global error with $\alpha = 1; \beta = 0.5; n = 500; IIC = 0.9072$

$\triangle t$	Global Error U_x	Global Error U_y
0.005	0.004105	0.004326
0.001	0.0017170	0.001374
0.0005	0.000662	0.000669

Table 3: Influence of the $\triangle t$ in the global error with $\alpha = 1; \beta = 0.5; n = 500; IIC = 0.8312$

$\triangle t$	Global Error U_x	Global Error U_y
0.005	0.005234	0.005321
0.001	0.001983	0.002110
0.0005	0.000821	0.000840

7.2 GFDM with PML

Let us solve the Eq. 1, in $\Omega = [0,2] \times [0,1] \subset \mathbf{R}^2$, with homogeneous the Dirichlet boundary conditions and the initial conditions are given by Eq. 53, using the regular mesh with 861 nodes (see Fig. 6) used in subsection 7.1, the analytical solutions is given by Eq. 54. The weighting function is given by Eq. 28 and the criterion for the selection of star nodes is the quadrant criterion.
Figure 8 shows the graphic the approximated solution of u_x, after 100 time steps, with PML in x-direction and y-direction for $1.4 \leq x \leq 2$ and $0.6 \leq y \leq 1$ (see Fig. 7).
Figure 10 shows the graphic the approximated solution of u_x, after 100 time steps, with PML in x-direction and y-direction for $\leq x \leq 0.6$ and $0 \leq y \leq 0.2,\ 0.8 \leq y \leq 1$ (see Fig. 9).

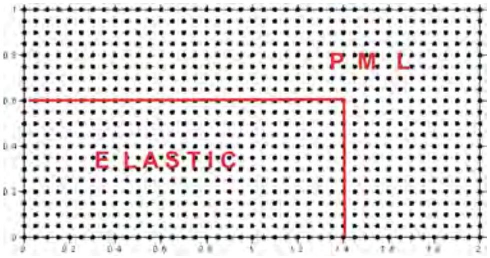

Figure 7: Regular mesh with PML region.

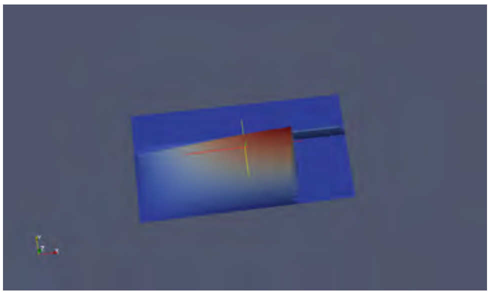
Figure 8: Approximated solution U_x with PML.

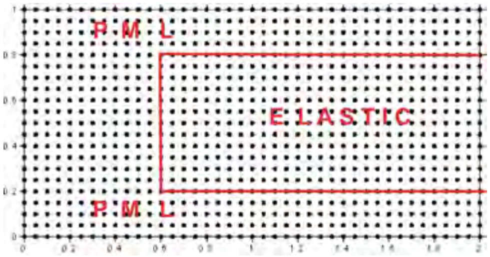

Figure 9: Regular mesh with PML region.

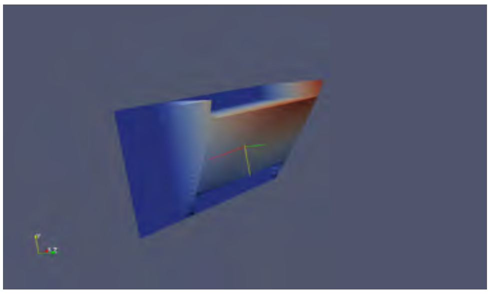
Figure 10: Approximated solution U_x with PML.

8 Conclusions

This paper shows a scheme in generalized finite differences, for seismic wave propagation in 2-D. The von Neumann stability criterion has been expressed as a function of the coefficients of the star equation and the velocity ratio.
The investigated star dispersion has been related with the irregularity of the star using the irregularity indicator of the mesh. The use of irregular meshes, adjusted to the geometry of the problem, may create high dispersion in certain stars which is related to high values of the irregularity index of the mesh (IIC). In this case the mesh can be redefined by an adaptive process ([2]) until a mesh whit suitable dispersion and irregularity index values is obtained.
The formulation of the PML is compatible with GFDM and numerical results confirm that PML has an extraordinary performance in absorbing outgoing waves.

ACKNOWLEGMENTS.

The authors acknowledge the support from Ministerio de Ciencia e Innovación of Spain, project CGL$2008-01757$/CLI.

REFERENCES

[1] J.J. Benito, F. Ureña, L. Gavete, *Influence several factors in the generalized finite difference method*. Applied Mathematical Modeling 25, 1039–1053 (2001).

[2] J.J. Benito, F. Ureña, L. Gavete, R. Alvarez, *An h-adaptive method in the generalized finite difference*. Comput. Methods Appl. Mech. Eng. 192, 735–759 (2003).

[3] J.J. Benito, F. Ureña, L. Gavete, B. Alonso, *Solving parabolic and hyperbolic equations by Generalized Finite Difference Method*. Journal of Computational and Applied Mathematics 209 Issue 2, 208–233 (2007).

[4] J.J. Benito, F. Ureña, L. Gavete, *Leading-Edge Applied Mathematical Modelling Research (chapter 7)*. Nova Science Publishers, New York, (2008).

[5] J.J. Benito, F. Ureña, L. Gavete, B. Alonso, *Application of the Generalized Finite Difference Method to improve the approximated solution of pdes*. Computer Modelling in Engineering & Sciences. 38, 39–58 (2009).

[6] J.P. Berenger, *A perfectly matched layer for the absortion of electromagnetic*. J. Comput. Physics, 114, 185–200, (1994).

[7] W.C. Chew, Q.H. Liu, *Perfectly matched layer for elastodinamycs, a new absorbing boundary condition.* J. Comput. Acoustics, 4, 341–359, (1996).

[8] S.G. Johnson, *Notes on Perfectly Matched Layers (PMLs)*. Courses 18.369 and 18.336 at MIT. July (2008).

[9] T. Liszka, J. Orkisz, *The finite difference method at arbitrary irregular grids and its application in applied mechanics*. Computer & Structures, 83–95, (1980).

[10] P. Moczo, J. Kristek , L. Halada, *The Finite-Difference method for seismologists. An introduction.*. Comenius University Bratislava, 158 pgs.(1994).

[11] P. Moczo, J. Kristek , M. Galis, P. Pazak , M. Balazovjech, *The Finite-Difference and Finite-Element modelling of seismic wave propagation and earthquake motion*. Acta Physica Slovaca, vol. 57 No. 2, 177-406 (2007).

[12] J. Orkisz, *Finite Difference Method. (Part.III) in Handbook of Computational Solid Mechanics*. M. Kleiber (eds.), Springer-Verlag, Berlin, (1998)

[13] E.A. Skelton, S.D.M. Adams, R.V Craster, *Guided elastic waves and perfectly matched layers*. Wave Motion, Elsevier, 44, 573-592 (2007).

COMPDYN 2011
ECCOMAS Thematic Conference on
Computational Methods in Structural Dynamics and Earthquake Engineering
M. Papadrakakis, M. Fragiadakis, V. Plevris (eds.)
Corfu, Greece, 25-28 May 2011

DYNAMIC ANALYSIS OF PLATES AND BEAMS BY GFDM

F. Ureña[1], L. Gavete[2], J.J. Benito[3], and E. Salete[3]

[1]Universidad de Castilla-La Mancha
Avda. Camilo José Cela s/n, 13071, Ciudad Real, Spain
francisco.urena@uclm.es

[2]Universidad Politécnica de Madrid
C/ Alenza 4, 28003 Madrid, Spain
lu.gavete@upm.es

[3]Universidad Nacional de Eduacación a Distancia
Apdo. de correos 60149, 28080 Madrid, Spain
jbenito@ind.uned.es, esalete@ind.uned.es

Keywords: meshless methods, generalized finite difference method, moving least squares, beams, plates, stability.

Abstract. *This paper shows the application of Generalized Finite Difference Method (GFDM) to dynamic analysis of beams and plates. The use of a meshless method with the possibility of using an irregular grid-point distribution can be of interest for modeling this problem.*

1 INTRODUCTION

The Generalized finite difference method (GFDM) is evolved from classical finite difference method (FDM). GFDM can be applied over general or irregular clouds of points [7]. The basic idea is to use moving least squares (MLS) approximation to obtain explicit difference formulae which can be included in the partial differential equations [9]. Benito, Ureña and Gavete have made interesting contributions to the development of this method [1, 2, 6, 4, 5, 12]. The paper [3] shows the application of the GFDM in solving parabolic and hyperbolic equations.

This paper decribes how the GFDM can be applied for solving dynamic analysis problems of plates [10, 11, 13].

The paper is organized as follows. Section 1 is the introduction. Section 2 describes the explicit generalized finite difference schemes. In section 3 is studied the von Neumann stability. In Section 4 is analyzed the relation between stability and irregularity of a cloud of nodes. In Section 5 some applications of the GFDM for solving problems of dynamic analysis are included. Finally, in Section 6 some conclusions are given.

2 EXPLICIT GENERALIZED FINITE DIFFERENCE SCHEMES

2.1 Vibrations of simple beam

Let us consider the problem governed by the following partial differential equation (pde)

$$\frac{\partial^2 U(x,t)}{\partial t^2} + A_1^2 \frac{\partial^4 U(x,t)}{\partial x^4} = F_1(x,t) \quad x \in (0,L), \quad t > 0 \tag{1}$$

with boundary conditions at the ends of the beam of length L for each particular case and initial conditions

$$U(x,0) = 0; \quad \frac{\partial U(x,t)}{\partial t}|_{(x,0)} = F_2(x) \tag{2}$$

where F_1 and F_2 are two known smooth functions, the constant A_1 depends of the material and geometry of the beam.

Firstly, we use the explicit difference formulae for the values of partial derivatives in the space variable. The intention is to obtain explicit linear expressions for the approximation of partial derivatives in the points of the domain.

First of all, an irregular grid or cloud of points is generated in the domain. On defining the composition central node with a set of N points surrounding it (henceforth referred as nodes), the star then refers to the group of established nodes in relation to a central node. Each node in the domain have an associated star assigned [1, 5, 7, 9].

If u_0 is an approximation of fourth-order for the value of the function at the central node (U_0) of the star, with coordinate x_0 and u_j is an approximation of fourth-order for the value of the function at the rest of nodes, of coordinates x_j with $j = 1, \cdots, N$, then, according to the Taylor series expansion

$$U_j = U_0 + h_j \frac{\partial U_0}{\partial x} + \frac{h_j^2}{2} \frac{\partial^2 U_0}{\partial x^2} + \frac{h_j^3}{6} \frac{\partial^3 U_0}{\partial x^3} + \frac{h_j^4}{24} \frac{\partial^4 U_0}{\partial x^4} + \cdots \tag{3}$$

where $h_j = x_j - x_0$.

If in equation 3 the terms over fourth order are ignored. It is then possible to define the function $B_4(u)$ as in [1, 3, 4, 5, 7, 9]

$$B_4(u) = \sum_{j=1}^{N} [(u_0 - u_j + h_j \frac{\partial u_0}{\partial x} + \frac{h_j^2}{2} \frac{\partial^2 u_0}{\partial x^2} + \frac{h_j^3}{6} \frac{\partial^3 u_0}{\partial x^3} + \frac{h_j^4}{24} \frac{\partial^4 u_0}{\partial x^4}) w(h_j)]^2 \tag{4}$$

where $w(h_j)$ is the denominated weighting function.
If the norm 4 is minimized with respect to the partial derivatives the linear equations system is obtained

$$\boldsymbol{A_4 D_{u_4}} = \boldsymbol{b_4} \tag{5}$$

where

$$\boldsymbol{A_4} = \begin{pmatrix} \sum_{j=1}^{N} h_j^2 w^2 & \sum_{j=1}^{N} \frac{h_j^3}{2} w^2 & \sum_{j=1}^{N} \frac{h_i^4}{6} w^2 & \sum_{j=1}^{N} \frac{h_j^5}{24} w^2 \\ & \sum_{j=1}^{N} \frac{h_j^4}{4} w^2 & \sum_{j=1}^{N} \frac{h_j^5}{12} w^2 & \sum_{j=1}^{N} \frac{h_j^6}{48} w^2 \\ & & \sum_{j=1}^{N} \frac{h_j^6}{36} w^2 & \sum_{j=1}^{N} \frac{h_j^7}{144} w^2 \\ & SYM & & \sum_{j=1}^{N} \frac{h_j^8}{576} w^2 \end{pmatrix} \tag{6}$$

and

$$\boldsymbol{D_{u_4}} = \left\{ \begin{array}{cccc} \frac{\partial u_0}{\partial x} & \frac{\partial^2 u_0}{\partial x^2} & \frac{\partial^3 u_0}{\partial x^3} & \frac{\partial^4 u_0}{\partial x^4} \end{array} \right\}^T \tag{7}$$

$$\boldsymbol{b_4} = \left\{ \begin{array}{c} \sum_{j=1}^{N} (-u_0 + u_j) h_j w^2 \\ \sum_{j=1}^{N} (-u_0 + u_j) \frac{h_j^2}{2} w^2 \\ \sum_{j=1}^{N} (-u_0 + u_j) \frac{h_j^3}{6} w^2 \\ \sum_{j=1}^{N} (-u_0 + u_j) \frac{h_j^4}{24} w^2 \end{array} \right\} \tag{8}$$

and solving system 5 the explicit difference formulae are obtained as in [2]. On including the explicit expressions for the values of the partial derivatives the star equation is obtained

$$\frac{\partial^4 U(x,t)}{\partial x^4}|_{(x_0,n)} = \eta_0 u_0 + \sum_{j=1}^{N} \eta_j u_j \tag{9}$$

with

$$\eta_0 + \sum_{j=1}^{N} \eta_j = 0 \tag{10}$$

Secondly, we shall use an explicit formula for the part of the equation 1 that depends on time. This explicit formula can be used to solve the Cauchy initial value problem. This method involves only one grid point at the advanced time level. The second derivative with respect to time is approached by

$$\frac{\partial^2 U}{\partial t^2}|_{(x_0,y_0,n)} = \frac{u_0^{n+1} - 2u_0^n + u_0^{n-1}}{(\triangle t)^2} \tag{11}$$

If the equations 9 and 11 are substituted in equation 1 the following recursive relationship is obtained

$$u_0^{n+1} = 2u_0^n - u_0^{n-1} - A_1^2(\triangle t)^2[\eta_0 u_0^n + \sum_{j=1}^{N} \eta_j u_j^n] + F_1(x_0, n) \tag{12}$$

The first derivative with respect to the time is approached by the central difference formula

$$\frac{\partial U}{\partial t}|_{x,0} = \frac{u_0^1 - u_0^{-1}}{2\triangle t} = F_2(x_0) \Rightarrow u_0^{-1} = u_0^1 - 2\triangle t F_2(x_0) \tag{13}$$

If equation 13 is substituted in equation 12 and taking into account initials conditions (2), the following equation is obtained

$$u_0^1 = \triangle t F_2(x_0) + \frac{F_1(x_0, 0)}{2} \tag{14}$$

The equation 14 relates the value of the function at the central node of the star, at time $n = 1$, with the values $F_1(x_0, 0)$ and the initial conditions $F_{(}x_0)$.

2.2 Vibrations of plates

Let us to consider the problem governed by

$$\begin{aligned} \frac{\partial^2 U(x,y,t)}{\partial t^2} + A_2^2[\frac{\partial^4 U(x,y,t)}{\partial x^4} + 2\frac{\partial^4 U(x,y,t)}{\partial x^2 \partial^2} + \frac{\partial^4 U(x,y,t)}{\partial y^4}] = G_1(x,y,t) \\ (x,y) \in (0,L) \times (0,L), \quad t > 0 \end{aligned} \tag{15}$$

with boundary conditions at the edges of the plate $[0, L] \times [0, L]$ for each particular case and initial conditions

$$U(x,y,0) = 0; \qquad \frac{\partial U(x,y,t)}{\partial t}|_{(x,y,0)} = G_2(x,y) \tag{16}$$

where G_1 and G_2 are two known smooth functions, the constant A_2 depends of the material and geometry of the plate.

In a similar way that the one used in the subsection previous. If u_0 is an approximation of fourth-order for the value of the function at the central node (U_0) of the star, with coordinates (x_0, y_0) and u_j is an approximation of fourth-order for the value of the function at the rest of nodes, of coordinates (x_j, y_j) with $j = 1, \cdots, N$, then, according to the Taylor series expansion

$$\begin{aligned} U_j = U_0 + h_j \frac{\partial U_0}{\partial x} + k_j \frac{\partial U_0}{\partial y} + \frac{h_j^2}{2}\frac{\partial^2 U_0}{\partial x^2} + \frac{k_j^2}{2}\frac{\partial^2 U_0}{\partial y^2} + h_j k_j \frac{\partial^2 U_0}{\partial x \partial y} + \\ + \frac{h_j^3}{6}\frac{\partial^3 U_0}{\partial x^3} + \frac{k_j^3}{6}\frac{\partial^3 U_0}{\partial y^3} + \frac{h_j^2 k_j}{2}\frac{\partial^3 U_0}{\partial x^2 \partial y} + \frac{h_j k_j^2}{2}\frac{\partial^3 U_0}{\partial x \partial y^2} + \frac{h_j^4}{24}\frac{\partial^4 U_0}{\partial x^4} + \frac{k_j^4}{24}\frac{\partial^4 U_0}{\partial y^4} + \\ + \frac{h_j^3 k_j}{6}\frac{\partial^4 U_0}{\partial x^3 \partial y} + \frac{h_j^2 k_j^2}{4}\frac{\partial^4 U_0}{\partial x^2 \partial y^2} + \frac{h_j k_j^3}{6}\frac{\partial^4 U_0}{\partial x \partial y^3} + \cdots \end{aligned} \tag{17}$$

where $h_j = x_j - x_0; k_j = y_j - y_0$.
If in equation 17 the terms over fourth order are ignored. It is then possible to define the function

$$B_{14}(u) = \sum_{j=1}^{N}[(u_0 - u_j + h_j\frac{\partial u_0}{\partial x} + k_j\frac{\partial u_0}{\partial y} + \frac{h_j^2}{2}\frac{\partial^2 u_0}{\partial x^2} + \frac{k_j^2}{2}\frac{\partial^2 u_0}{\partial y^2} + h_j k_j\frac{\partial^2 u_0}{\partial x\partial y} + \\ + \frac{h_j^3}{6}\frac{\partial^3 u_0}{\partial x^3} + \frac{k_j^3}{6}\frac{\partial^3 u_0}{\partial y^3} + \frac{h_j^2 k_j}{2}\frac{\partial^3 u_0}{\partial x^2\partial y} + \frac{h_j k_j^2}{2}\frac{\partial^3 u_0}{\partial x\partial y^2} + \frac{h_j^4}{24}\frac{\partial^4 u_0}{\partial x^4} + \frac{k_j^4}{24}\frac{\partial^4 u_0}{\partial y^4} + \\ + \frac{h_j^3 k_j}{6}\frac{\partial^4 u_0}{\partial x^3\partial y} + \frac{h_j^2 k_j^2}{4}\frac{\partial^4 u_0}{\partial x^2\partial y^2} + \frac{h_j k_j^3}{6}\frac{\partial^4 u_0}{\partial x\partial y^3})w(h_j, k_j)]^2 \quad (18)$$

where $w(h_j, k_j)$ is the denominated weighting function.
If the norm 18 is minimized with respect to the partial derivatives the linear equation system is obtained

$$\boldsymbol{A_{14}D_{u_{14}}} = \boldsymbol{b_{14}} \quad (19)$$

where $\boldsymbol{A_{14}}$, $\boldsymbol{D_{u_{14}}}$ and $\boldsymbol{b_{14}}$ can be obtained in a similar way that the one used in the expressions 6, 7 and 8, and solving system the explicit difference formulae are obtained. On including the explicit expressions for the values of the partial derivatives the star equation is obtained

$$[\frac{\partial^4 U(x,y,t)}{\partial x^4} + 2\frac{\partial^4 U(x,y,t)}{\partial x^2\partial^2} + \frac{\partial^4 U(x,y,t)}{\partial y^4}]_{(x_0,y_0,n)} = \mu_0 u_0 + \sum_{j=1}^{N}\mu_j u_j \quad (20)$$

with

$$\mu_0 + \sum_{j=1}^{N}\mu_j = 0 \quad (21)$$

If the equations 9 and 20 are substituted in equation 15 the following recursive relationship is obtained

$$u_0^{n+1} = 2u_0^n - u_0^{n-1} - A_2^2(\triangle t)^2[\mu_0 u_0^n + \sum_{j=1}^{N}\mu_j u_j^n] + G_1(x_0, y_0, n) \quad (22)$$

Using a similar process for to obtain the equation 14 the following equation is obtained

$$u_0^1 = \triangle t G_2(x_0, y_0) + \frac{G_1(x_0, y_0, 0)}{2} \quad (23)$$

The expressions 12 and 22 relates the value of the function at the central node of star, at time step $n+1$, with the values of the functions in the nodes of the star at time step n.

3 CONVERGENCE

According to Lax's equivalence theorem, if the consistency condition is satisfied, stability is the necessary and sufficient condition for convergence. In this section we study firstly the truncation error of the equations 1 and 14, and secondly consistency and stability.

3.1 Truncation error

As it is well known, the truncation errors for second order time derivative (TEt) is given as follows:

$$\frac{\partial^2 U(\boldsymbol{x},t)}{\partial t^2} = \frac{u_0^{t+\triangle t} - 2u_0^t + u_0^{t-\triangle t}}{(\triangle t)^2} - \frac{(\triangle t)^2}{12}\frac{\partial^4 U(\boldsymbol{x},t_1)}{\partial t^4} + \Theta((\triangle t)^4), t < t_1 < t + \triangle t \quad (24)$$

$$(TE_t) = -\frac{(\triangle t)^2}{12}\frac{\partial^4 U(\boldsymbol{x},t_1)}{\partial t^4} + \Theta((\triangle t)^4), t < t_1 < t + \triangle t \quad (25)$$

In order to obtain the truncation error for space derivatives, Taylor's series expansion including higher order derivatives is used and then higher order functions $B_p^*[u]$, $p = 4, 14$ are obtained. The expressions of $B_p[u]$, $p = 4, 14$ are similar to the ones given in 4 and 18, but incorporating now higher order derivatives. If the new norms $B_p^*[u]$, $p = 4, 14$ are minimized with respect to the partial derivatives until the fourth order, the following linear equation systems are obtained:

$$\boldsymbol{A_p D_{u_p}} = \boldsymbol{b_p^*} \quad (26)$$

where $\boldsymbol{A_p}$, $\boldsymbol{D_{u_p}}$ and $\boldsymbol{b_p}$ with $(p = 4, 14)$ are as previously calculated in 6, 7, 8 for $p = 4$ and similarly for $p = 14$, and $\boldsymbol{b_p^*}$ can be split in two parts as follows

$$\boldsymbol{b_p^*} = \boldsymbol{b_p} + \boldsymbol{b_p^{**}} \quad (27)$$

where the news terms $\boldsymbol{b_p^{**}}$ correspond to the new higher order derivatives incorporated in the Taylor's series expansion to extend the functions from $B_p[u]$, $p = 4, 14$ to $B_p^*[u]$, $p = 4, 14$. Then a better approximation of the partial derivatives can be obtained using the inverse matrix $\boldsymbol{A_p^{-1}}$

$$\boldsymbol{D_{u_p}} = \boldsymbol{A_p^{-1} b_p} + \boldsymbol{A_p^{-1} b_p^{**}} \quad (28)$$

In the equation 28 the expression $\boldsymbol{A_p^{-1} b_p}$ is the approximation used in the GFDM (see [3] and [12]) and then the truncation errors for spatial derivatives are given by

$$TE_{x_p} = \boldsymbol{A_p^{-1} b_p^{**}} \quad (29)$$

We develop only the truncation error corresponding to $p = 4$ case. The other truncation error for $p = 14$ case can be obtained in a similar way that the one used in $p = 4$ case.

$$B_4^*(u) = \sum_{j=1}^{N} [(U_0 - U_j + h_j \frac{\partial U_0}{\partial x} + \frac{h_j^2}{2!}\frac{\partial^2 U_0}{\partial x^2} + \frac{h_j^3}{3!}\frac{\partial^3 U_0}{\partial x^3} + \frac{h_j^4}{4!}\frac{\partial^4 U_0}{\partial x^4} + \frac{h_j^5}{5!}\frac{\partial^5 U_0}{\partial x^5} + \frac{h_j^6}{6!}\frac{\partial^6 U_0}{\partial x^6} + \cdots)w(h_j)]^2 \quad (30)$$

If the function 29 is minimized with respect partial derivatives up to the fourth order, the following linear equations system is defined

$$\boldsymbol{A_4 D_{u_4}} = \left(\sum_{j=1}^{N} \Xi h_j \quad \sum_{j=1}^{N} \Xi \frac{h_j^2}{2!} \quad \sum_{j=1}^{N} \Xi \frac{h_j^3}{3!} \quad \sum_{j=1}^{N} \Xi \frac{h_j^4}{4!} \right)^T \quad (31)$$

where

$$\Xi = [-U_0 + U_j - \frac{h_j^5}{5!}\frac{\partial^5 U_0}{\partial x^5} - \frac{h_j^6}{6!}\frac{\partial^6 U_0}{\partial x^6} - \cdots)]w(h_j)^2 \tag{32}$$

with $N \geq 4$, and then

$$TE_{x_4} = -\frac{1}{A_1^2}\boldsymbol{A_4^{-1}} \times \left(\sum_{j=1}^{N} \Upsilon h_j \quad \sum_{j=1}^{N} \Upsilon \frac{h_j^2}{2!} \quad \sum_{j=1}^{N} \Upsilon \frac{h_j^3}{3!} \quad \sum_{j=1}^{N} \Upsilon \frac{h_j^4}{4!} \right)^T \tag{33}$$

where

$$\Upsilon = -[\frac{h_j^5}{5!}\frac{\partial^5 U_0}{\partial x^5} + \frac{h_j^6}{6!}\frac{\partial^6 U_0}{\partial x^6} + \cdots)]w(h_j)^2 \tag{34}$$

and operating

$$TE_{x_4} = \frac{1}{A_1^2}[\sum_{j=1}^{N} \Psi_{1,j}\frac{\partial^5 U}{\partial x^5} + \Psi_{2,j}\frac{\partial^6 U}{\partial x^6} + ...] + \Theta(h_j) \tag{35}$$

where $\Psi_{1,j}(h_j)$ and $\Psi_{2,j}(h_j)$ are homogeneous rational functions of order two and $\Theta(h_j)$ is a series of third- and higher-order functions.
The expression 35 is the truncation error for spatial derivatives.
Taking into account that the total truncation errors (TTE) is given by

$$TTE = TE_t + TE_{x_4} \tag{36}$$

where TE_t and TE_{x_4} are given by 25 and 35 respectively.

3.2 Consistency

By considering bounded derivatives in 36

$$\lim_{(\triangle t, h_j)\to(0,0)} TTE \to 0 \tag{37}$$

Then, the truncation error condition given in 37 shows the consistency of the approximation.

3.3 Stability criterion

For the difference schemes, the von Neumann condition is sufficient as well as necessary for stability [8]. ”Boundary conditions are neglected by the von Neumann method which applies in theory only to pure initial value problems with periodic initial data. It does however provide necessary conditions for stability of constant coefficient problems regardless of the type of boundary condition”.
For the stability analysis the first idea is to make a harmonic decomposition of the approximated solution at grid points and at a given time level n. Then we can write the finite difference approximation in the nodes of the star at time n, as

$$u_0^n = \xi^n e^{i\boldsymbol{\nu}^T \boldsymbol{x_0}}; \quad u_j^n = \xi^n e^{i\boldsymbol{\nu}^T \boldsymbol{x_j}} \tag{38}$$

where ξ is the amplification factor,

$$\boldsymbol{x_j} = \boldsymbol{x_0} + \boldsymbol{h_j}; \qquad \xi = e^{-iw\triangle t}$$

$\boldsymbol{\nu}$ is the column vector of the wave numbers

$$\boldsymbol{\nu} = \left\{ \begin{array}{c} \nu_x \\ \nu_y \end{array} \right\}$$

then we can write the stability condition as: $\|\xi\| \leq 1$.
Including the equation 38 into the equation 12 or 22, cancelation of $\xi^n e^{i\boldsymbol{\nu}^T \boldsymbol{x_0}}$, leads to

$$\xi = 2 + \frac{1}{\xi} - (\triangle t)^2 A^2 (m_0 + \sum_1^N m_j e^{i\boldsymbol{\nu}^T \boldsymbol{h_j}}) \tag{39}$$

where A is the constant A_1 or A_2 respectively and m_0, m_j are the coefficients η_0, η_j or μ_0, μ_j.
Using the equations 10 or 21 and after some calculus we obtain the quadratic equation

$$\xi^2 - \xi[2 + A^2(\triangle t)^2 (\sum_1^N m_j (1 - \cos \boldsymbol{\nu}^T \boldsymbol{h_j}) - i \sum_1^N m_j \sin \boldsymbol{\nu}^T \boldsymbol{h_j})] + 1 = 0 \tag{40}$$

Hence the values of ξ are

$$\xi = b \pm \sqrt{b^2 - 1} \tag{41}$$

where

$$b = 1 + \frac{A^2(\triangle t)^2}{2} \sum_1^N m_j (1 - \cos \boldsymbol{\nu}^T \boldsymbol{h_j}) - i \frac{A^2(\triangle t)^2}{2} \sum_1^N m_j \sin \boldsymbol{\nu}^T \boldsymbol{h_j} \tag{42}$$

If we consider now the condition for stability, we obtain

$$\|b \pm \sqrt{b^2 - 1}\| \leq 1 \tag{43}$$

Operating with the equations 42 and 43, canceling with conservative criteria, the condition for stability of star is obtained as

$$\triangle t \leq \frac{1}{4A\sqrt{|m_0|}} \tag{44}$$

4 IRREGULARITY OF THE STAR (IIS) AND STABILITY

In this section we are going to define the index of irregularity of a star (IIS) and also the index of irregularity of a cloud of nodes (IIC).
The coefficient m_0 is function of:

- The number of nodes in the star
- The coordinates of each star node referred to the central node of the star
- The weighting function (see references $[1, 4]$)

If the number of nodes by star and the weighting function are fixed, then the equation 44 is function of the coordinates of each node of star referred to its central node.
Denoting τ_0 as the average of the distances between of the nodes of the star and its central node with coordinates (x_0, y_0) and denoting τ the average of the τ_0 values in the stars of the cloud of nodes, then

$$\overline{m_0} = m_0 \tau^4 \tag{45}$$

The stability criterion can be rewritten as

$$\triangle t < \frac{\tau^2}{4A\sqrt{|\overline{m_0}|}} \tag{46}$$

For the regular mesh case, the inequality 44 is for the cases of one and two dimensions as follows

$$\begin{cases} \triangle t < \dfrac{\sqrt{2}\tau^2}{18A\sqrt{3}} & if \quad N=4 \\ \triangle t < \dfrac{9\tau^2}{A\sqrt{13}[3(1+\sqrt{2})+2\sqrt{5}]^2} & if \quad N=24 \end{cases} \tag{47}$$

Multiplying the right-hand side of inequalities 47, respectively, by the factors

$$\begin{cases} \dfrac{9\sqrt{3}}{2\sqrt{2|\overline{m_0}|}} & if \quad N=4 \\ \dfrac{\sqrt{13}[3(1+\sqrt{2})+2\sqrt{5}]^2}{36\sqrt{|\overline{m_0}|}} & if \quad N=24 \end{cases} \tag{48}$$

the inequality 46 is obtained.
For each one of the stars of the cloud of nodes, we define the IIS for a star with central node in (x_0, y_0) as Eq. 48

$$\begin{cases} IIS_{x_0} = \dfrac{9\sqrt{3}}{2\sqrt{2|\overline{m_0}|}} & if \quad N=4 \\ IIS_{(x_0,y_0)} = \dfrac{\sqrt{13}[3(1+\sqrt{2})+2\sqrt{5}]^2}{36\sqrt{|\overline{m_0}|}} & if \quad N=24 \end{cases} \tag{49}$$

that takes the value of one in the case of a regular mesh and $0 < IIS \leq 1$
If the index IIS decreases, then absolute values of $\overline{m_0}$ increases and then according with 43, $\triangle t$ decreases.
The irregularity index of a cloud of nodes (IIC) is defined as the minimum of all the IIS of the stars of a cloud of nodes.

5 NUMERICAL RESULTS

In this section we present different numerical results.

5.1 Transverse vibrations of a simply supported beam

In this section, the weighting function used is

$$\Omega(h_j) = \frac{1}{(\sqrt{h_j^2})^3} \tag{50}$$

The global exact error can be calculated as

$$Global \quad exact \quad error = \sqrt{\frac{\sum_{i=1}^{NT} e_i^2}{NT}} \tag{51}$$

Figure 1: regular and irregular mesh

Figure 2: irregular meshes

where NT is the number of nodes in the domain and e_i is the exact error in the node i.

Let us solve the pde

$$\frac{\partial^2 U(x,t)}{\partial t^2} + \frac{1}{\pi^4}\frac{\partial^4 U(x,t)}{\partial x^4} = 0 \quad x \in (0,1), \quad t > 0 \tag{52}$$

with boundary conditions

$$\begin{cases} U(0,t) = U(1,t) = 0 \\ \frac{\partial^2 U(x,t)}{\partial x^2}|_{(0,t)} = \frac{\partial^2 U(x,t)}{\partial x^2}|_{(1,t)} = 0, \end{cases} \tag{53}$$

and initial conditions

$$U(x,0) = 0; \quad \frac{\partial U(x,t)}{\partial t}|_{(x,0)} = \sin(\pi x) \tag{54}$$

The exact solution is

$$U(x,t) = \sin(\pi x)\sin t \tag{55}$$

Table 1 shows the results of the global error, using a regular mesh of 21 nodes (figure 1), for several values of $\triangle t$.

$\triangle t$	Global error
0.005	0.00276
0.002	0.00109
0.001	0.00017
0.0005	0.00002

Table 1: Influence of $\triangle t$ in the global error.

IIC	Global error
0.96	0.00107
0.78	0.00295
0.62	0.00534
0.46	0.00903

Table 2: Influence of irregularity of mesh in the global error

Table 2 shows the results of global error with $\triangle t = 0.001$ for several irregular meshes of 21 nodes (figures 1 and 2). We have established a measure of the irregularity of the nodes distribution in the domain. For this purpose we have assigned to every node in the domain a value that corresponds with the average of the distances from it to the rest of its star nodes. Then, the index of irregularity (IIC) is defined as the standard deviation of these values.

Figure 3 shows the approximated solution of the equations 52, 53 and 54 in the last time step $(n = 1000)$ with $\triangle t = 0.005$.

As new initial conditions let us assume that due to impact an initial velocity is given to a point of the beam at the distance $x = 0.5$ from the left-hand support, which give the initial conditions

$$U(x,0) = 0; \quad \begin{cases} \frac{\partial U(x,t)}{\partial t}|_{(x,0)} = 1 \quad if \quad x = 0.5 \\ \frac{\partial U(x,t)}{\partial t}|_{(x,0)} = 0 \quad if \quad x \neq 0.5 \end{cases} \tag{56}$$

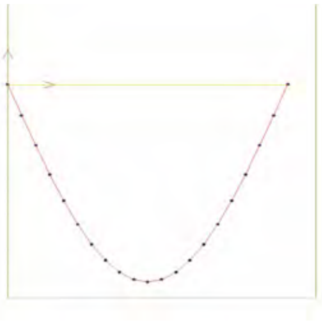

Figure 3: Approximated solution in the last time step ($\triangle t = 0.005$)

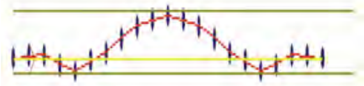

Figure 4: Approximated solution with n=100

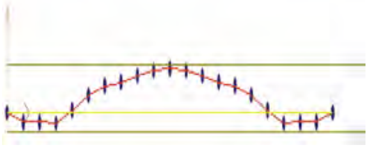

Approximated solution with n=200

The exact solution in this case is given by

$$U(x,t) = 2(\sin(\pi x)\sin(t) - \frac{1}{9}\sin(3\pi x)\sin(9t) + \frac{1}{25}\sin(5\pi x)\sin(25t) - \cdots) \tag{57}$$

Table 3 shows the results of the global error, using a regular mesh of 21 nodes (figure 1) and $\triangle t = 0.001$, when we increases the number of time steps (n).

Figures 4 and 5 shows the approximated solution of the equation 52 with the initial conditions 56 in the last time step for $n = 100$, $n = 200$, $n = 500$ and $n = 1000$ respectively.

n	Global error
100	0.001628
200	0.001700
500	0.001816
1000	0.002252

Table 3: Variation of global error versus the number of time steps.

5.2 Forced vibrations of a simply supported beam

In this section, the weighting function used is 50 and the global error is calculated by 51 The pde is given by

$$\frac{\partial^2 U(x,t)}{\partial t^2} + \frac{1}{\pi^4}\frac{\partial^4 U(x,t)}{\partial x^4} = 15\sin(2\pi x)\sin t \quad x \in (0,1), \quad t > 0 \tag{58}$$

with boundary conditions

$$\begin{cases} U(0,t) = U(1,t) = 0 \\ \frac{\partial^2 U(x,t)}{\partial x^2}|_{(0,t)} = \frac{\partial^2 U(x,t)}{\partial x^2}|_{(1,t)} = 0, \end{cases} \tag{59}$$

Figure 5: Approximated solution withn=500 Approximated solution with n=1000

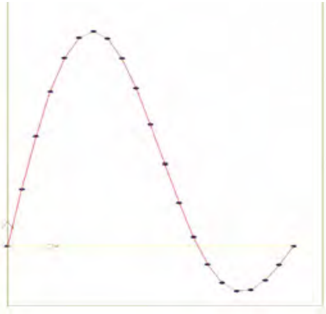

Figure 6: Approximated solution in the last step ($\triangle t = 0.005$)

and initial conditions

$$U(x,0) = 0; \quad \frac{\partial U(x,t)}{\partial t}|_{(x,0)} = \sin(\pi x) + \sin(2\pi x) \tag{60}$$

The exact solution for this case is given by

$$U(x,t) = (\sin(\pi x) + \sin(2\pi x)) \sin t \tag{61}$$

Table 4 shows the results of the global error, using a regular mesh of 21 nodes (figure 1) for several values of $\triangle t$.
Table 5 shows the results of global error with $\triangle t = 0.001$ for several irregular meshes of 21 nodes (figures 1 and 2).
Figure 6 shows the approximated solution of the equation 57 in the last time step $(n = 1000)$ with $\triangle t = 0.005$.

$\triangle t$	Global error
0.005	0.01025
0.002	0.00987
0.001	0.00625
0.0005	0.00126

Table 4: Influence of $\triangle t$ in the global error.

IIC	Global error
0.96	0.00744
0.78	0.00751
0.62	0.01960
0.46	0.04496

Table 5: Influence of irregularity of mesh in the global error.

5.3 Natural vibrations of a simply supported plate

In this section, the weighting function used is

$$\Omega(h_j, k_j) = \frac{1}{(\sqrt{h_j^2 + k_j^2})^3} \tag{62}$$

and the global exact error can be calculated by 51
The pde is

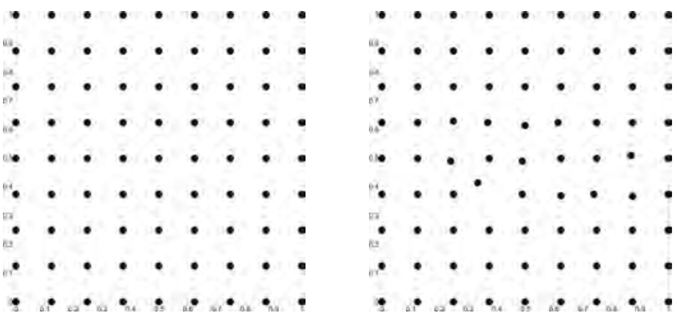

Figure 7: Regular and irregular mesh

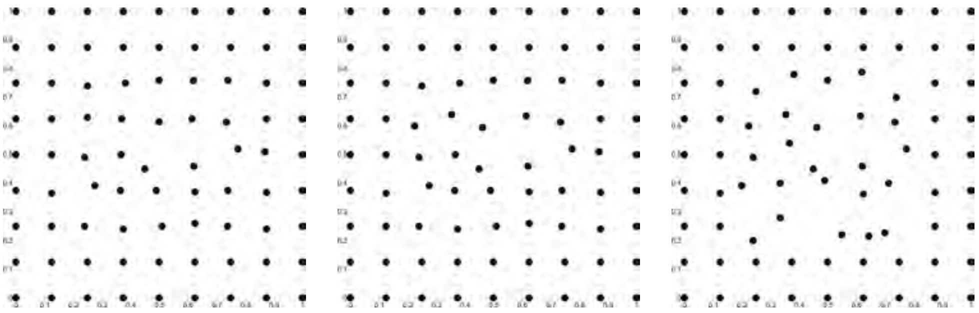

Figure 8: Three irregular meshes

$$\frac{\partial^2 U(x,y,t)}{\partial t^2}+\frac{1}{4\pi^4}[\frac{\partial^4 U(x,y,t)}{\partial x^4}+2\frac{\partial^4 U(x,y,t)}{\partial x^2\partial^2}+\frac{\partial^4 U(x,y,t)}{\partial y^4}]= \\ 15\sin t\sin(2\pi x)\sin(2\pi y)\quad (x,y)\in(0,1)\times(0,1),\quad t>0 \tag{63}$$

with boundary conditions

$$\begin{cases} U(x,y,t)|_\Gamma = 0 \\ \frac{\partial^2 U(x,y,t)}{\partial y^2}|_{(0,y,t)} = \frac{\partial^2 U(x,y,t)}{\partial y^2}|_{(1,y,t)} = 0, \forall y\in[0,1] \\ \frac{\partial^2 U(x,y,t)}{\partial x^2}|_{(x,0,t)} = \frac{\partial^2 U(x,y,t)}{\partial x^2}|_{(x,1,t)} = 0, \forall x\in[0,1] \end{cases} \tag{64}$$

where Γ is the boundary of the domain $[0,1]\times[0,1]$, and initial conditions

$$U(x,y,0)=0;\qquad \frac{\partial U(x,y,t)}{\partial t}|_{(x,y,0)}=\sin(\pi x)\sin(\pi y) \tag{65}$$

The exact solution is given by

$$U(x,y,t)=\sin(\pi x)\sin(\pi y)\sin t \tag{66}$$

Table 6 shows the results of the global error, using a regular mesh of 81 nodes (figure 7), for several values of $\triangle t$.

Table 7 shows the results of global error with $\triangle t = 0.001$ for several irregular meshes of 81 nodes (figures 7 and 8).

Figure 9 shows the approximated solution of the equation 63 in the last time step $(n = 1000)$.

As new initial conditions let us assume that due to impact an initial velocity is given to a point $(x = y = 0.5)$ of the plate, which give the conditions

$$U(x,y,0)=0;\qquad \begin{cases} \frac{\partial U(x,y,t)}{\partial t}|_{(x,y,0)} = 1 \quad if \qquad x=y=0.5 \\ \frac{\partial U(x,y,t)}{\partial t}|_{(x,y,0)} = 0 \quad if \quad (x,y)\neq(0.5,0.5) \end{cases} \tag{67}$$

$\triangle t$	Global error
0.01	0.08254
0.005	0.03513
0.002	0.01339
0.001	0.00212

Table 6: Influence of $\triangle t$ in the global error.

IIC	Global error
0.92	0.00224
0.83	0.00224
0.76	0.00231
0.58	0.00251

Table 7: Influence of irregularity of mesh in the global error.

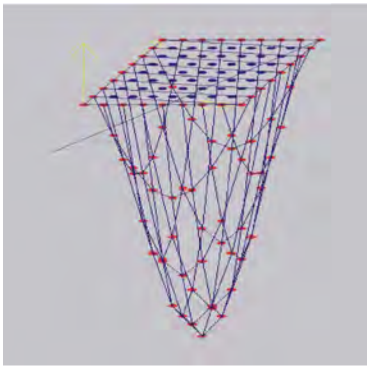

Figure 9: Approximated solution in the last time step

The exact solution is given by

$$U(x,y,t) = 2[\sin(\pi x)\sin(\pi y)\sin(t) - \frac{1}{9}\sin(3\pi x)\sin(3\pi y)\sin(9t) + \frac{1}{25}\sin(5\pi x)\sin(5\pi y)\sin(25t) - \cdots] \quad (68)$$

Table 8 shows the results of the global error, using a regular mesh of 81 nodes (figure 7) and $\triangle t = 0.001$, versus the number of time steps (n).

n	Global error
100	0.01122
200	0.01858
600	0.02690
1200	0.03363

Table 8: Variation of global error versus the number of time steps

Figures 10 and 11 show the approximated solution of the equation 63 with the initial conditions 67 in the last time steps for the cases $n = 100$, $n = 200$, $n = 600$ and $n = 1200$ time steps respectively.

5.4 Forced vibrations of a simply supported plate

In this section, the weighting function used is 62 and the global error is calculated by 51
The pde is

$$\frac{\partial^2 U(x,y,t)}{\partial t^2} + \frac{1}{4\pi^4}[\frac{\partial^4 U(x,y,t)}{\partial x^4} + 2\frac{\partial^4 U(x,y,t)}{\partial x^2 \partial^2} + \frac{\partial^4 U(x,y,t)}{\partial y^4}] = 15\sin t\sin(2\pi x)\sin(2\pi y)) \quad (x,y) \in (0,1)\times(0,1), \quad t > 0 \quad (69)$$

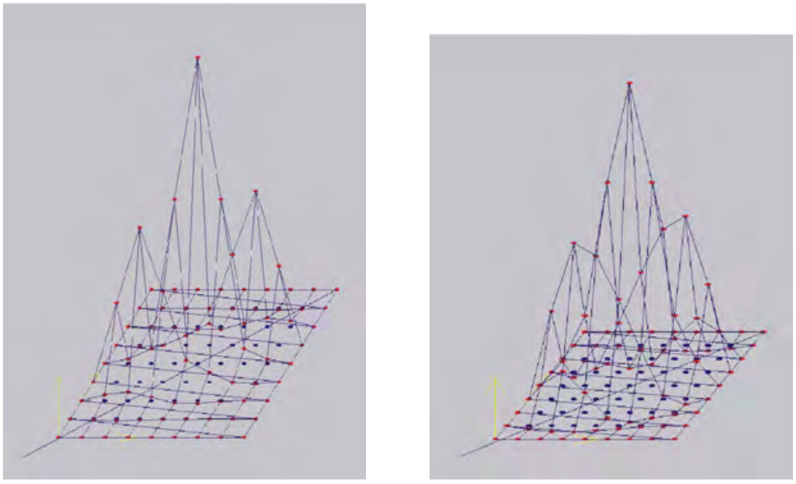

Figure 10: Approximated solution with n=100 Approximated solution with n=200

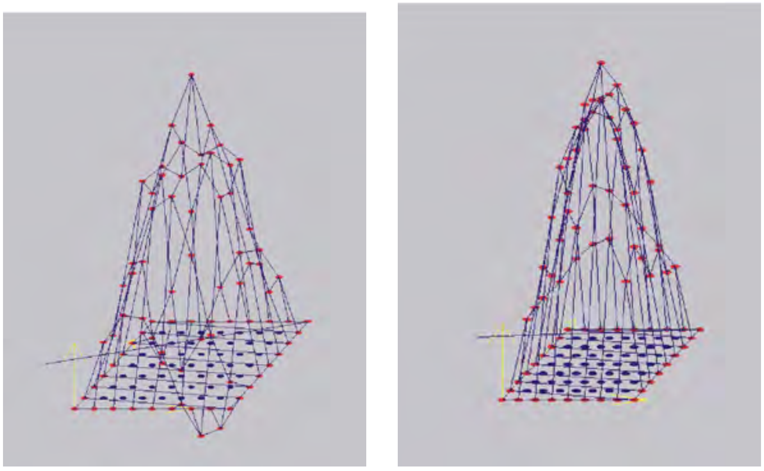

Figure 11: Approximated solution with n=600 Approximated solution with n=1200

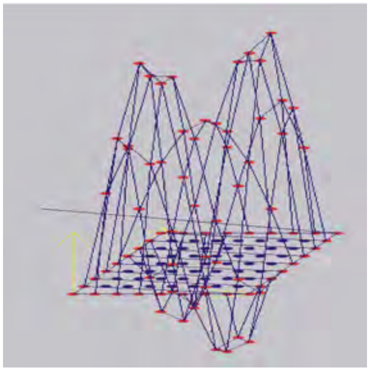

Figure 12: Approximated solution in the last time step

with boundary conditions

$$\begin{cases} U(x,y,t)|_{\Gamma} = 0 \\ \frac{\partial^2 U(x,y,t)}{\partial y^2}|_{(0,y,t)} = \frac{\partial^2 U(x,y,t)}{\partial y^2}|_{(1,y,t)} = 0, \forall y \in [0,1] \\ \frac{\partial^2 U(x,y,t)}{\partial x^2}|_{(x,0,t)} = \frac{\partial^2 U(x,y,t)}{\partial x^2}|_{(x,1,t)} = 0, \forall x \in [0,1] \end{cases} \tag{70}$$

and initial conditions

$$U(x,y,0) = 0; \quad \frac{\partial U(x,y,t)}{\partial t}|_{(x,y,0)} = \sin(\pi x)\sin(\pi y) + \sin(2\pi x)\sin(2\pi y) \tag{71}$$

The exact solution is given by

$$U(x,y,t) = (\sin(\pi x)\sin(\pi y) + \sin(2\pi x)\sin(2\pi y))\sin t \tag{72}$$

Table 9 shows the results of the global error, using regular mesh of 81 nodes (figure 7), for several values of $\triangle t$. Table 10 shows the results of global error with $\triangle t = 0.001$ for several irregular meshes of 81 nodes (figures 7 and 8).

$\triangle t$	Global error
0.01	0.53070
0.005	0.14640
0.002	0.07837
0.001	0.01444

Table 9: Influence of $\triangle t$ in the global error.

IIC	Global error
0.92	0.01412
0.83	0.01437
0.76	0.01442
0.58	0.01447

Table 10: Influence of irregularity of mesh in the global error.

Figure 12 shows the approximated solution of the equation 68 in the last time step ($n = 1000$).

5.5 Transverse vibrations of a beam with fixed ends

In this section, the weighting function used is 50 and the global exact error can be calculated as 51.

The pde is

$$\frac{\partial^2 U(x,t)}{\partial t^2} + \frac{1}{4.73^4}\frac{\partial^4 U(x,t)}{\partial x^4} = 0 \quad x \in (0,1), \quad t > 0 \tag{73}$$

Figure 13: Approximated solution in last time step

with boundary conditions

$$\begin{cases} U(0,t) = U(1,t) = 0 \\ \frac{\partial U(x,t)}{\partial x}|_{(0,t)} = \frac{\partial U(x,t)}{\partial x}|_{(1,t)} = 0, \end{cases} \tag{74}$$

and initial conditions

$$U(x,0) = 0; \quad \frac{\partial U(x,t)}{\partial t}|_{(x,0)} = \cos(4.73x) - \cosh(4.73x) - 0.982501[\sin(4.73x) - \sinh(4.73x)] \tag{75}$$

The exact solution is given by

$$U(x,t) = (\cos(4.73x) - \cosh(4.73x) - 0.982501[\sin(4.73x) - \sinh(4.73x)])\sin t \tag{76}$$

Table 11 shows the results of the global error, using a regular mesh of 21 nodes (figure 1), for several values of $\triangle t$.

$\triangle t$	Global error
0.01	0.04649
0.005	0.01960
0.002	0.00798
0.001	0.00216

Table 11: Influence of $\triangle t$ in the global error.

IIC	Global error
0.96	0.00419
0.78	0.00423
0.62	0.00763
0.46	0.00781

Table 12: Influence of irregularity of mesh in the global error.

Table 12 shows the results of global error with $\triangle t = 0.001$ for several irregular meshes of 21 nodes (figures 1 and 2).

Figure 13 shows the approximated solution of the equation 73, 74 and 75 in the last time step $(n = 1000)$ with $\triangle t = 0.001$.

5.6 Natural vibrations of a fixed plate

In this section, the weighting function used is 62 and the global exact error can be calculated by 51.

The pde is

$$\frac{\partial^2 U(x,y,t)}{\partial t^2} + \frac{1}{4(4.73)^4}[\frac{\partial^4 U(x,y,t)}{\partial x^4} + 2\frac{\partial^4 U(x,y,t)}{\partial x^2 \partial^2} + \frac{\partial^4 U(x,y,t)}{\partial y^4}] =$$
$$15\sin t \sin(2\pi x)\sin(2\pi y) \quad (x,y) \in (0,1)\times(0,1), \quad t > 0 \tag{77}$$

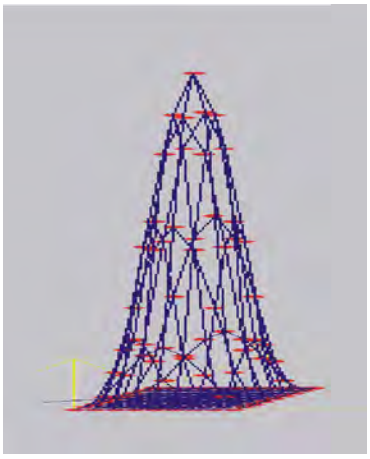

Figure 14: Approximated solution in the last time step

with boundary conditions 64, and initial conditions

$$\begin{cases} U(x,y,0)=0 \\ \frac{\partial U(x,y,t)}{\partial t}|_{(x,y,0)} = (\cos(4.73x)-\cosh(4.73x)-0.982501[\sin(4.73x)- \\ \sinh(4.73x)])(\cos(4.73y)-\cosh(4.73y)-0.982501[\sin(4.73y)-\sinh(4.73y)]) \end{cases} \quad (78)$$

The exact solution is given by

$$U(x,y,t)=(\cos(4.73x)-\cosh(4.73x)-0.982501[\sin(4.73x)-\sinh(4.73x)])(\cos(4.73y) \\ -\cosh(4.73y)-0.982501[\sin(4.73y)-\sinh(4.73y)])\sin t \quad (79)$$

Table 13 shows the results of the global error, using a regular mesh of 81 nodes (figure 7), for several values of $\triangle t$.

Table 14 shows the results of global error with $\triangle t = 0.001$ for several irregular meshes of 81 nodes (figures 7 and 8).

$\triangle t$	Global error
0.005	0.36490
0.002	0.03519
0.001	0.00492
0.0005	0.00064

Table 13: Influence of $\triangle t$ in the global error.

IIC	Global error
0.92	0.00492
0.83	0.00494
0.76	0.00496
0.58	0.00504

Table 14: Influence of irregularity of mesh in the global error.

Figure 14 shows the approximated solution of the equation 77, 78 and 79 in the last time step $(n = 500)$.

6 CONCLUSIONS

The use of the generalized finite difference method using irregular clouds of points is an interesting way of solving partial differential equations. The extension of the generalized finite difference to the explicit solution of some dynamic analysis problems has been developed.

The von Neumann stability criterion has been expressed in function of the coefficients of the

star equation for irregular cloud of nodes.
The index of irregularity of a clouds of nodes (IIC) is given and, also, its relation with the stability. As it is shown in the numerical results, a decrease in the value of the time step, always below the stability limits, leads to a decrease of the global error.

ACKNOWLEGMENTS.

The authors acknowledge the support from Ministerio de Ciencia e Innovación of Spain, project CGL2008 − 01757/CLI.

REFERENCES

[1] J.J. Benito, F. Ureña, L. Gavete, *Influence several factors in the generalized finite difference method.* Applied Mathematical Modeling 25, 1039–1053 (2001).

[2] J.J. Benito, F. Ureña, L. Gavete, R. Alvarez, *An h-adaptive method in the generalized finite difference*. Comput. Methods Appl. Mech. Eng. 192, 735–759 (2003).

[3] J.J. Benito, F. Ureña, L. Gavete, B. Alonso, *Solving parabolic and hyperbolic equations by Generalized Finite Difference Method.* Journal of Computational and Applied Mathematics 209 Issue 2, 208–233 (2007).

[4] J.J. Benito, F. Ureña, L. Gavete, *Leading-Edge Applied Mathematical Modelling Research (chapter 7).* Nova Science Publishers, New York, (2008).

[5] J.J. Benito, F. Ureña, L. Gavete, B. Alonso, *Application of the Generalized Finite Difference Method to improve the approximated solution of pdes*. Computer Modelling in Engineering & Sciences. 38, 39–58 (2009).

[6] L. Gavete, M.L. Gavete, J.J. Benito, *Improvements of generalized finite difference method and comparison other meshless method.* Applied Mathematical Modelling. 27, 831–847 (2003).

[7] T. Liszka, J. Orkisz, *The Finite Difference Method at Arbitrary Irregular Grids and its Application in Applied Mechanics*.Computer & Structures. 11, 83–95 (1980).

[8] A.R. Mitchell, D.F. Griffiths, *The Finite Difference Method in Partial Differential Equations*. Jhon Wiley & Sons, New York, 1980.

[9] J. Orkisz, *Finite Difference Method (Part, III) in handbook of Computational Solid Mechanics*. M. Kleiber (Ed.), Spriger-Verlag, Berlin (1998).

[10] W.T. Thomson, *Vibration Theory and Applications*. Prentice Hall Publishers, (1965)

[11] S.P. Timoshenko, D.H. Young, *Teoría de Estructuras*. Urmo S.A. de Ediciones, Spain.

[12] F. Ureña, J.J. Benito, L. Gavete, *Application of the generalized finite difference method to solve the advection-diffusion equation*. Journal of Computational and Applied Mathematics. 235(2011) pp: 1849–1855.

[13] J.R. Vinson, *The Behavoir or Thin Walled Structures: Beams, Plates ans Shells*. Kluwer Academic Publishers, Boston.

COMPDYN 2011
III ECCOMAS Thematic Conference on
Computational Methods in Structural Dynamics and Earthquake Engineering
M. Papadrakakis, M. Fragiadakis, V. Plevris (eds.)
Corfu, Greece, 25–28 May 2011

SPH MODELING OF RAPID MULTIPHASE FLOWS AND SHOCK WAVE PROPAGATION

Sauro Manenti[1], Stefano Sibilla[1], Mario Gallati[1], Giordano Agate[2], Roberto Guandalini[2]

[1] University of Pavia, Dept. Of Hydraulic and Environmental Eng.
via Ferrata, 1 27100 Pavia (Italy)
e-mail: {sauro.manenti, stefano.sibilla, gallati}@unipv.it

[2] Environment and Sustainable Development Dept., RSE s.p.a.
Via Rubattino, 54 – 20134 Milan, Italy
{giordano.agate, roberto.guandalini}@rse-web.it

Keywords: Smoothed Particle Hydrodynamics, non-cohesive sediment, reservoir flushing, underwater explosion, experimental validation.

Abstract. *This work shows an application of the Smoothed Particle Hydrodynamics (SPH) for the numerical modeling of engineering problems involving rapid evolution over time, high strain and gradients, heterogeneity, deformable contours and the presence of mobile material interfaces.*

Following a Lagrangian approach the continuum is discretized by means of a finite number of material particles carrying physical properties and moving according to Newton's equations of the classical physics. Spatial derivatives of a variable at a point are approximated by using the information on the neighboring particles based on the kernel approximation.

This paper recalls the basics of the method along with some numerical aspects concerning boundaries treatment, time integration scheme etc.; furthermore some details are provided about the recent improvements carried out for SPH simulations of: a) non-cohesive sediment flushing by rapid water discharge in an hydropower reservoir, b) underwater explosion for bottom sediment resuspension in an artificial reservoir.

Numerical examples are illustrated and discussed concerning 2D and 3D test cases carried out with the aim of investigating the basic features of both sediment dynamics and gas explosion: obtained results shows that the SPH method can be applied to model the relevant engineering aspects of the considered problems and can be a helpful tool for future design applications in the field of hydropower reservoir management.

1 INTRODUCTION

The key idea at the base of a meshfree method is to obtain a discretization of the continuum through a set of arbitrarily distributed nodes (or particles) that lack of a connective mesh and can adapt to possible topological and geometrical changes.

With respect to traditional grid-based approaches, a meshless method allows tracing the deformation undergone by the material without excessive degradation of numerical results (owing to conflicts between mesh and physical compatibility) and high computational effort (e.g. adaptive mesh refinement).

When the nodes assumes a physical meaning (i.e. they represent material particles carrying physical properties such as mass, momentum etc.) is said a meshfree particle method and follows, in general, a Lagrangian approach.

Among the different meshfree particle methods the Smoothed Particle Hydrodynamics (SPH) was originally developed as a probabilistic model for simulating astrophysical problems [1, 2]. It was later modified as a deterministic meshfree particle method and applied to continuum solid and fluid mechanics [3, 4] because the kinematics and dynamics of the liquid particles, responding to Newton's Equations of the classical physics, could be described in analogy with the simulation of the collective movement of astrophysical particles at large scale.

According to standard SPH, a continuous physical quantity $A(\mathbf{x})$, defined on the domain Ω as a function of the position vector $\mathbf{x}$, and its spatial derivatives at the i–th material point are approximated by using the information on the neighboring particles based on the kernel estimate.

This procedure adopts a kernel function $W(r, h)$, which is continuous, non-zero and depends on the modulus of the relative position $r = |\mathbf{x}_i - \mathbf{x}_j|$ of the neighboring j–th particle falling within a circular space (spherical in 3D problems) with radius $2h$, where h is generally referred to as the smoothing length (Fig.1).

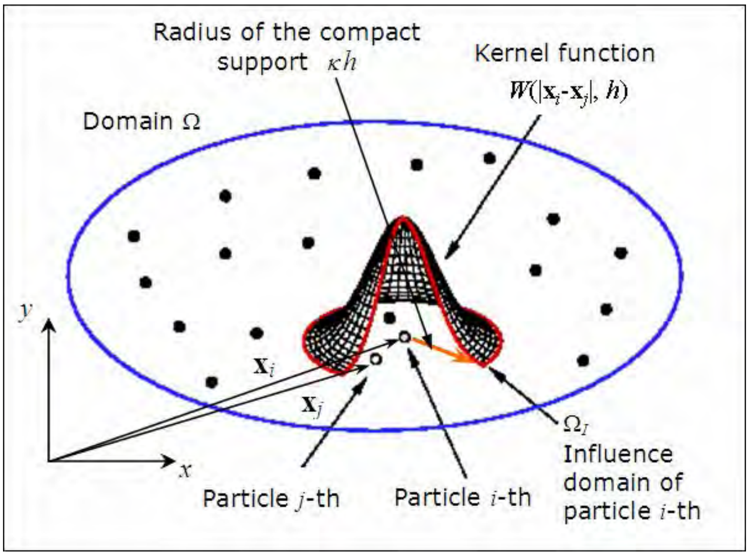

Figure 1: Typical representation of particle discretization and kernel function.

The SPH approximation of the field function $A(\mathbf{x})$ originates from the concept of integral representation:

$$A(\mathbf{x}) = \int_{\Omega} \delta(\mathbf{x} - \mathbf{x}')\, A(\mathbf{x}')\, d\Omega_{\mathbf{x}'} \tag{1}$$

In Eq.1 the Dirac delta function δ is replaced by the kernel function leading to the kernel approximation:

$$\langle A(\mathbf{x})\rangle = \int_{\Omega} W(r,h)\,A(\mathbf{x}')\,d\Omega_{\mathbf{x}'} \tag{2}$$

The discrete form of the Eq.2, for the set of material particles representing the discretized continuum, can be obtained by the so called particle approximation:

$$\langle A(\mathbf{x}_i)\rangle = \sum_{j=1}^{N} \frac{m_j}{\rho_j} A(\mathbf{x}_j)\,W(r_{ij},h) \tag{3}$$

The summation in Eq.3 is extended over the N–neighboring particles, having volume $\Delta V_j = m_j / \rho_j$, falling within the compact support (or influence domain) Ω_I of the i–th particle.

In a similar fashion it can be demonstrated that the particle approximation of the function derivative can be obtained by shifting the differential operation on the kernel; two alternative expressions are commonly adopted in fluid mechanics [5, 6]:

$$\begin{aligned} \langle \nabla\cdot A(\mathbf{x}_i)\rangle &= \frac{1}{\rho_i}\sum_{j=1}^{N} m_j \left[A(\mathbf{x}_j) - A(\mathbf{x}_i)\right]\cdot\nabla W(r_{ij},h) \\ \langle \nabla\cdot A(\mathbf{x}_i)\rangle &= \rho_i \sum_{j=1}^{N} m_j \left[\frac{A(\mathbf{x}_j)}{\rho_j^2} + \frac{A(\mathbf{x}_i)}{\rho_i^2}\right]\cdot\nabla W(r_{ij},h) \end{aligned} \tag{4}$$

Applying the SPH interpolation, the Lagrangian form of the Navier-Stokes equations for a weakly compressible viscous fluid can be transformed into a system of ordinary differential equations that, by adopting the equations (4) and replacing $W(r_{ij}, h)$ with W_{ij}, are written as:

$$\begin{aligned} \left\langle \frac{D\rho}{Dt}\right\rangle_i &= -\sum_{j=1}^{N} m_j (\mathbf{u}_j - \mathbf{u}_i)\cdot\nabla W_{ij} \\ \left\langle \frac{D\mathbf{u}}{Dt}\right\rangle_i &= -\sum_{j=1}^{N} m_j \left(\frac{p_i}{\rho_i^2} + \frac{p_j}{\rho_j^2} + \Pi_{ij}\right)\nabla W_{ij} + \mathbf{g} \\ &\quad + \sum_{j=1}^{Ni} \frac{m_j}{\rho_i\,\rho_j}\,\frac{4\mu_i\,\mu_j}{\mu_i + \mu_j}\,\frac{\mathbf{x}_{ij}\cdot\nabla W_{ij}}{\mathbf{x}_{ij}^2 + 0.01h^2}\,\mathbf{u}_{ij} \end{aligned} \tag{5}$$

The additional term Π_{ij} in Eq.5 is the so called Monaghan artificial viscosity [4] introduced for numeric stability:

$$\Pi_{ij} = \begin{cases} \dfrac{-\alpha_M\,(c_{s\,i} + c_{s\,j})}{\rho_i + \rho_j}\phi_{ij} + \dfrac{2\beta_M}{\rho_i + \rho_j}\phi_{ij}^2 & \text{if } \mathbf{u}_{ij}\cdot\mathbf{x}_{ij} < 0 \\ 0 & \text{if } \mathbf{u}_{ij}\cdot\mathbf{x}_{ij} > 0 \end{cases} \qquad \phi_{ij} = \frac{h\mathbf{u}_{ij}\cdot\mathbf{x}_{ij}}{\mathbf{x}_{ij}^2 + (0.1h)^2} \tag{6}$$

The are several advantages that can be obtained from such an approach: representation of the evolution of both free-surfaces, moving-interfaces and breaking becomes more simple to face with [7]; treatment of large deformation and shock problems becomes a relatively easier task [8]; the particle tracking along with the relevant field variables can be obtained by numerical solution of the discretized set of governing equations in Lagrangian form [9].

2 NUMERICAL ASPECTS

The solution strategy of a meshfree particle method follows a pattern similar to a grid-based method.

The computational domain is divided into a finite number of particles, followed by the numerical discretization of the system of partial differential equations according to the procedure described in the previous section; the resulting ordinary differential equations are solved through any stable time-stepping algorithm [10]: here a first order explicit numerical scheme is used and a cubic spline function is adopted for kernel representation [8].

The obtained velocity field allows one to update the particle position **x** and to compute the density field by means of the continuity equation (1); the pressure p_i at each point is then calculated through the equation of state for a weakly compressible fluid and then smoothed out:

$$\begin{aligned} p_i &= p_{0i} + \frac{\varepsilon}{\rho}\left(\rho_i - \rho_{0i}\right) \\ p_i^{smth} &= p_i + \vartheta_p \frac{\sum_{j=1}^{N}\left(p_j - p_i\right)\Delta V_j\, W_{ij}}{\sum_{j=1}^{N}\Delta V_j\, W_{ij}} \end{aligned} \tag{7}$$

Solid boundaries are treated by means of the semi-analytic technique [8]. Each portion of the solid contour contributing to the mass and momentum equations of the generic i-th particle is replaced by a fluid region extending beyond the boundary and treated as a material continuum with uniform velocity ($\mathbf{u}_b = \mathbf{u}_i$), and hydrostatic pressure distribution (Fig.2).

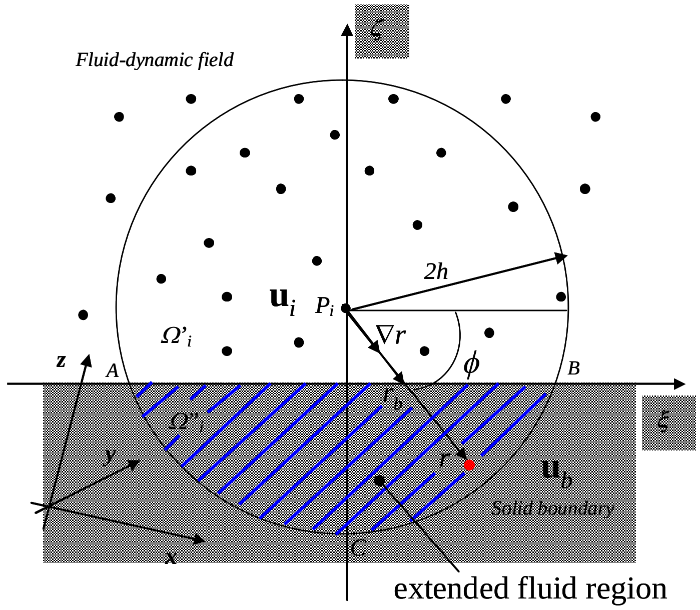

Figure 2: Scheck of boundary treatment (2D case).

A typical term for boundary contribution in the balance equations is:

$$C_1 \int_{\alpha} C_2 \; J_n(\vartheta,\varphi)\, d\alpha$$
$$\text{with}: \quad C_1 = f(\rho_i, \mathbf{u}_i, \mathbf{u}_b, \nu) \quad C_2 = f(\nabla r) \quad J_n(\vartheta,\varphi) = \int_{r_b(\vartheta,\varphi)}^{2h} \frac{dW}{dr} r^n dr \tag{8}$$

In Eq.8 $\alpha = f(\vartheta, \varphi)$ denotes the solid angle under which the *i*-th particle sees the portion of the solid boundary intersected by its sphere of influence and the integrals J_n (n=1, 2, 3) depends on the boundary's geometry and can be computed analytically.

3 MODELING NON-COHESIVE SEDIMENT FLUSHING

This Section illustrates some details concerning the SPH modeling of fluid-sediment coupled dynamics in flushing problems induced by rapidly varied water flows.

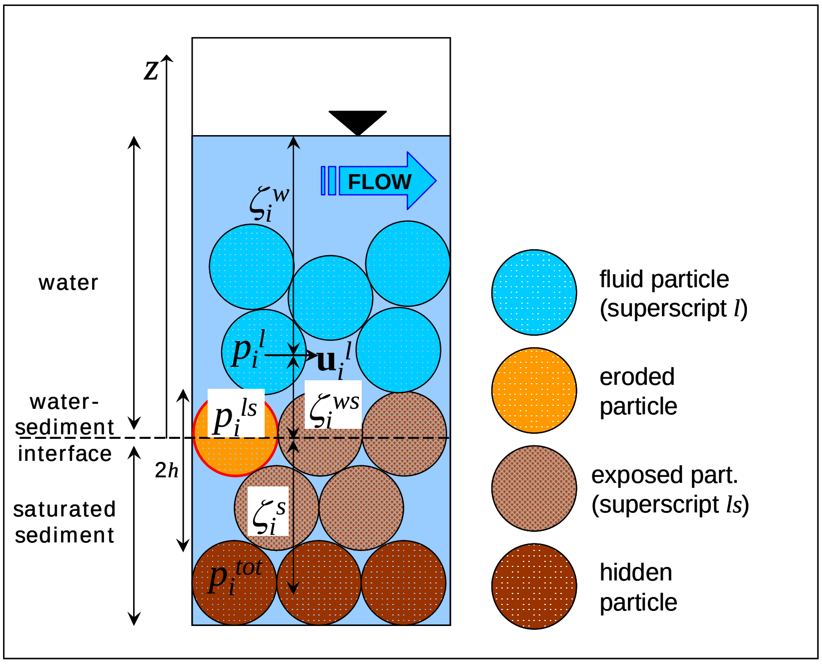

Figure 3: Sketch of the bottom sediment.

In a typical situation schematized by Fig.3, the solid grains can be: *a*) at or very close to the fluid-sediment interface and thus exposed to the hydrodynamic bottom shear or *b*) hidden by the overlaying solid particles.

3.1 Exposed grains

In the first condition the erosion of a single grain is evaluated by means of a failure criterion which is based on the Shields theory and defines a critical threshold that triggers the motion of the solid particle.

The critical bottom shear for an horizontal bed $\tau_{b\,cr,0}$ is evaluated through the Shields parameter ϑ_{cr} which can be computed as a function of the grain Reynolds number Re_*:

$$\vartheta_{cr} \equiv \frac{\tau_{b\,cr,0}}{(\rho^s - \rho)\, g\, d} = f\left(\mathrm{Re}_* \equiv u_* \, d_{50} / \nu\right) \tag{9}$$

The erosion of the grain occurs only if the critical bottom shear is exceeded by the hydrodynamic bottom shear:

$$\tau_b = \rho\, u_*^2 \tag{10}$$

From equations (9) and (10) follows that the friction velocity u_* should be evaluated for determining particle erosion: this is obtained from the computed fluid velocity u^l at a given position z close to the water-sediment interface and assuming a logarithmic velocity profile:

$$u^l(z) = \frac{u_*}{\kappa} \ln\left(\frac{z}{z_0}\right) \tag{11}$$

An iterative procedure should be applied since the characteristic bed roughness z_0 is a function of the friction velocity in turn.

Additional corrective coefficients should be introduced in order to account for a reduction of $\tau_{b\,cr,0}$ owing to both longitudinal and transverse bed slope [11].

If a solid particle is eroded it is considered as a viscous fluid whose kinematics and dynamics responds to the governing equations (5); elsewhere is treated as explained in the following point.

3.2 Hidden grains

In the second condition granular particles are treated as part of the boundary and excluded from the computation of the velocity and density fields; their total pressure (p_i^{tot}) is imposed according to the lithostatic condition and then included in the pressure smoothing of the fluid particles:

$$\begin{aligned} p_i^{ls} &= \zeta_i^{ws}\, g\, \rho + p_i^l + \frac{(u_i^l)^2}{2}\rho \\ p_i^{tot} &= p_i^{ls} + \zeta_i^s\, g\, \rho^s \end{aligned} \tag{13}$$

Equations (13) imply that the total pressure at the i-th particle inside the solid matrix can be evaluated only if ζ_i^s and ζ_i^{ws} are known: this means that the local fluid-sediment interface needs to be identified at each time step. Such task is accomplished, with a relatively reduced effort, within the algorithm for the neighboring particle search: the spatial domain is divided into squared columns with base length of $2h$ and, for each column, the highest solid and the lowest fluid particles are stored and adopted for imposing the total lithostatic pressure at every time step.

4 MODELING GAS EXPLOSION

The explosion process of a high explosive (HE) material is characterized by a violent oxidation involving a chemical compound and an oxidizer; since the internal energy of the products is lower then the one of the reactants, a great amount of heat (say reaction heat) is quickly released [12].

Even if such a phenomenon develops at very high speed of reaction, in the early phase it is characterized by two distinct inhomogeneous zones: a detonation-produced explosive gas and a non-oxidized explosive; between them a very thin layer exists which represents the front of a reacting shock wave (detonation wave) advancing with a characteristic velocity U.

Anyway in several applications the detonation speed can be assumed indefinitely high and the HE charge completely transformed into gaseous products; their expansion can be analyzed by considering the Euler equation for an inviscid fluid and assuming adiabatic process [6, 13].

As a result the viscous contribution at the right hand side of the linear momentum Eq.5 is neglected, and a balance equation for the gas internal energy is introduced:

$$\left\langle \frac{De}{Dt} \right\rangle_i = \frac{1}{2}\sum_{j=1}^{N} m_j \left(\frac{p_i}{\rho_i^2} + \frac{p_j}{\rho_j^2} + \Pi_{ij} \right) \left(\mathbf{u}_i - \mathbf{u}_j\right)\cdot \nabla W_{ij} \tag{14}$$

The state equation given by eq.15 is used for adiabatic transformation.

$$p_i = (\gamma - 1)\rho_i\, e_i \tag{15}$$

The kernel function adopted in subsequent analyses is a quintic spline [14], while the time integration is carried out through an explicit numerical scheme deriving from the symplectic algorithm [15].

5 NUMERICAL EXAMPLES

This section provides some numerical results concerning basic SPH simulations of both sediment flushing and gas explosion; the models previously described are adopted.

5.1 Sediment flushing

In the following are illustrated 2D and 3D numerical simulations of non-cohesive sediment flushing by a rapid water flow.

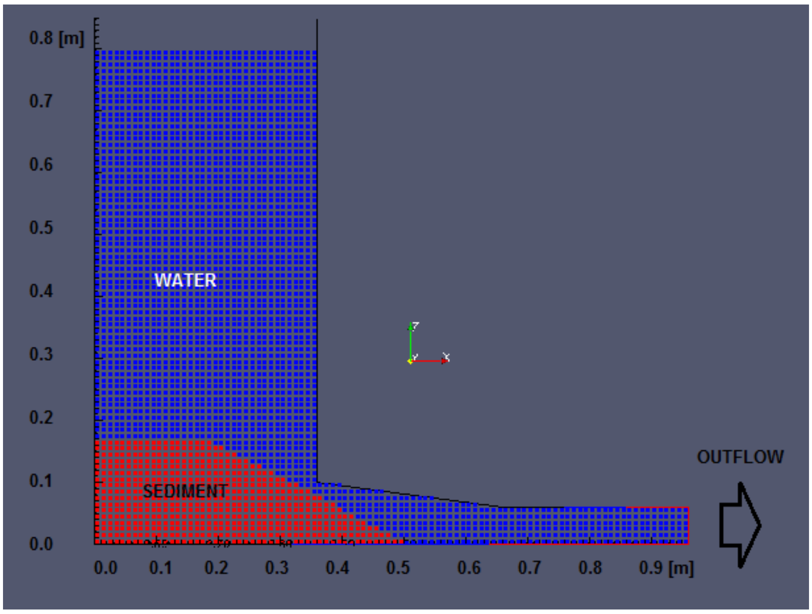

Figure 4: Longitudinal cross-section of the sediment flushing model.

The problem set up is schematized in Fig.4: it simplifies a more refined laboratory test [16] for the analysis of sediment erosion at the midsection of a long-narrow artificial reservoir induced by the opening of the bottom outlet for siltation control.

In order to moderate the computational time, the volume of both sediment and stored water has been lowered by reducing the longitudinal length of the tank toward its left-hand boundary; at the initial time the same water level as in the abovementioned experiment has been assumed, thus keeping the hydraulic head invariant.

The horizontal deposit of non-cohesive sediment is composed of uniform sand with median diameter d_{50}=0.1 mm, bed porosity n=0.53 and saturated unit volume density ρ^s=1750 kg/m^3.

The longitudinal measures of the SPH model are shown in Fig.4; the transverse thickness of the 3D model is equal to 0.03m; the resulting total particles number (water plus sediment) is 3300 and 9900 respectively in the 2D and 3D geometry (transverse thickness equal to 0.03 m); other relevant physical and numerical model parameters are summarized in Tab.1.

MODEL PARAMETERS		
h_0	interpart. distance	0.01 m
h	smoothing length	1.25 h_0
ρ_0	water ref. density	1000 kg/m^3
ρ^s	sediment ref. density	1750 kg/m^3
μ	water viscosity	1.0E-3 Pa/s
μ^s	sediment viscosity	750 Pa/s
ε	water comp. modulus	1.0E-6 kg/(m s^2)
ε^s	sediment comp. mod.	1.75E-6 kg/(m s^2)
α_M	artificial viscosity	0.2
β_M	artificial viscosity	0.0
ϑ_p	pressure smoothing	0.2
d_{50}	median grain diameter	1.0E-4 m
k_s	char. grain roughness	3.0 d_{50}

Table 1: Principal model parameters adopted for flushing computations.

At the initial time the sediment bed has a vertical thickness of 0.165 m; the water height is 0.8 m and it is discharged from the lower right-hand side of the tank at a constant flow rate of q_0 = 7.9E-3 m^3/s producing the scouring of the bottom sediment.

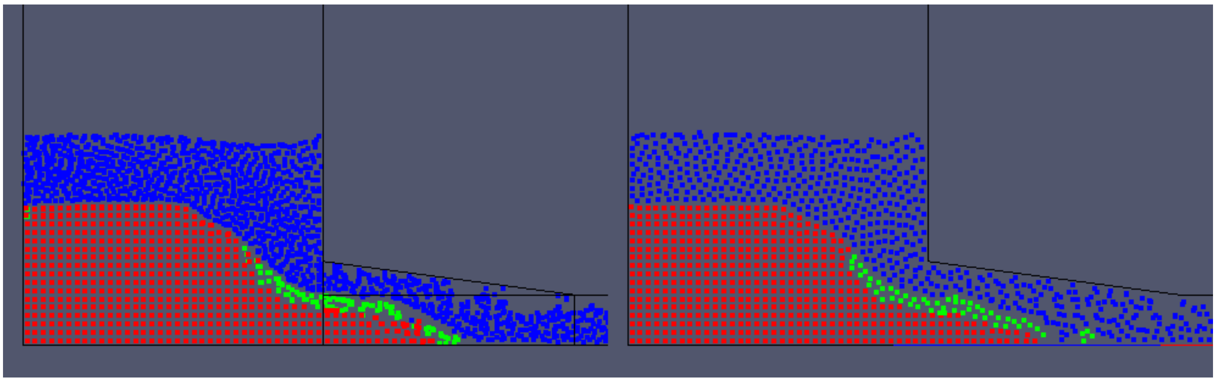

Figure 5: Comparison of eroded profile in 3D (left-hand) and 2D geometry at t = 11.0 s.

Fig.5 shows a comparison of the eroded sediment profiles at time 11s; water particles are depicted in blue while the color of solid grains depends on their status: the red indicates fixed particles (both hidden and exposed) that are treated as a solid boundary and excluded from the computation, while the green color denotes eroded sediment transported as bed load; the latter are located in that zone where the velocity reaches the highest values (see Fig.6) and are confined within a distance of 2h from the water-sediment interface.

From Fig.5 can be seen a good qualitative agreement between 3D and 2D model: similar water free surface and eroded profile are obtained; in both cases the sediment slope is characterized by the presence of a sub-horizontal berm past the intake: this is consistent with the velocity profile along the flow path during the transient phase and is confirmed by the experimental test during the early phase.

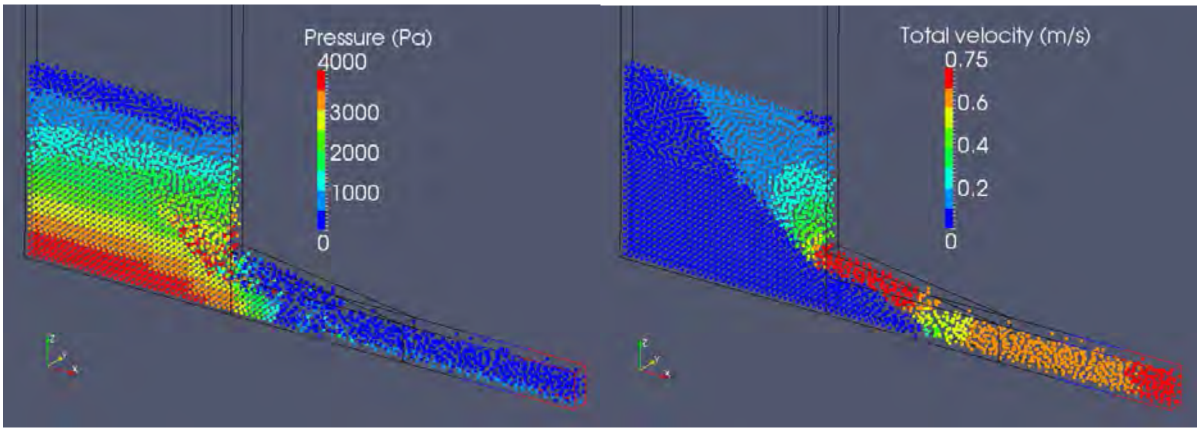

Figure 6: Pressure (left-hand) and velocity profile in 3D model.

Figure 6 displays pressure and velocity profiles obtained with the 3D geometry at t = 9.00 s: lithostatic pressure distribution in the fixed solid particles is visible; the velocity modulus is maximum around the intake.

5.2 Gas explosion

In the following are shown some numerical simulations of the expansion process of a HE gas; both the underwater and vacuum expansion of a circular-shaped charge are considered. As previously specified the detonation velocity U is assumed to be indefinitely high with respect to the gas kinematic: thus the explosive charge is assumed completely detonated.

Table 2 summarizes the relevant model parameters adopted in subsequent computations.

MODEL PARAMETERS		
h_0	interpart. distance	0.005 m
h	smoothing length	1.3 h_0
ρ_0	water ref. density	1000 kg/m^3
$\rho^g{}_0$	gas ref. density	1630 kg/m^3
e_0	spec. detonation energy	4.29E+06 J/kg
c_s	speed of sound	5.0E+4 m/s
α_M	artificial viscosity	0.2
β_M	artificial viscosity	10.0
ϑ_v	velocity smoothing	0.2
γ_W	water state equation	1.4 – 7.0
γ_G	gas state equation	1.4

Table 2: Principal model parameters adopted for gas explosion computations.

When considering the vacuum gas expansion, at the initial time 20 particles are placed in the radial direction while 60 particles are positioned along the tangential direction resulting in a total number of 1200. The particle position, velocity and pressure are depicted in Fig.7 at time intervals of 10μs; axes labels are in meters.

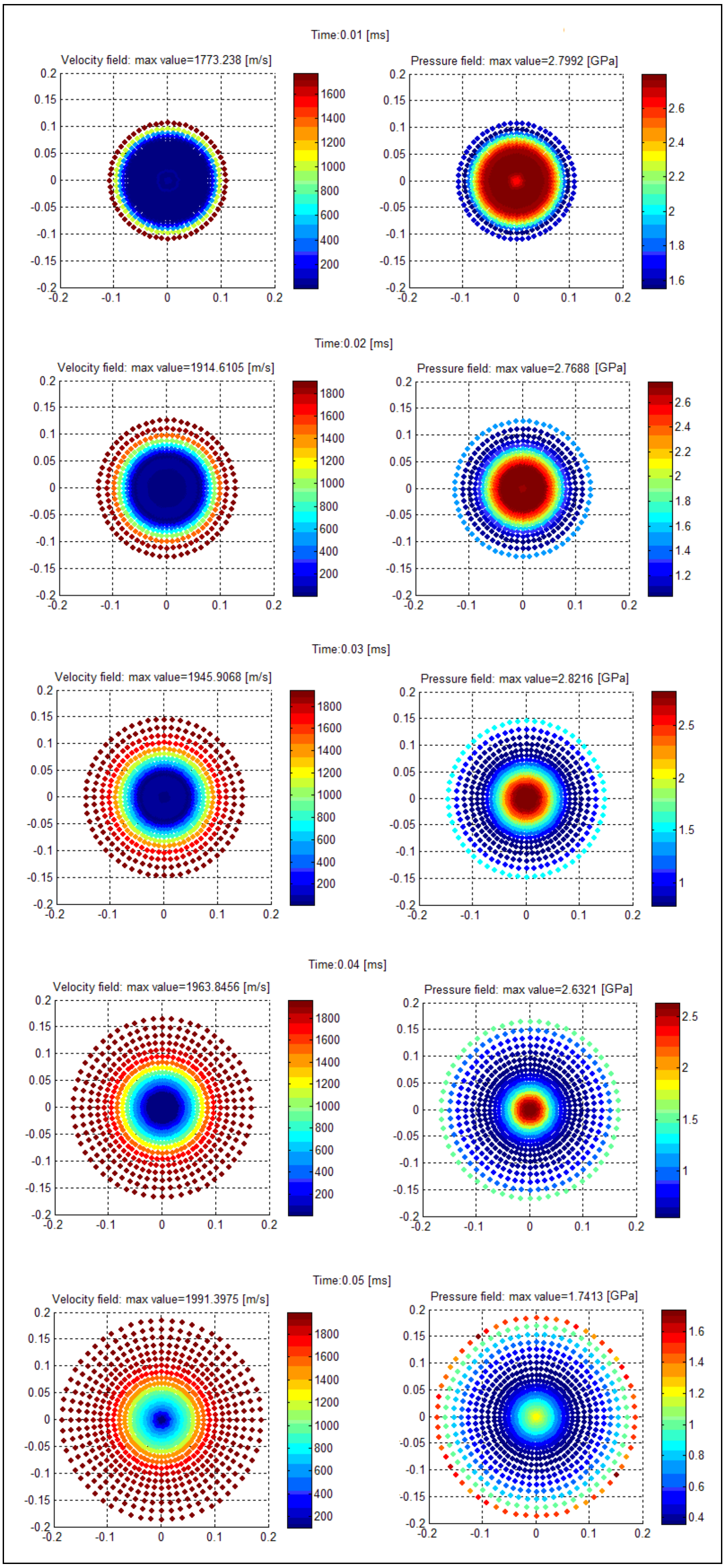

Figure 7: Expansion of detonated gas in vacuum; axes scale in meters.

The charge centre represents a singular point since no particle is placed on it and this explains the lower pressure.

The expansion process reflects theoretical expectation until t=40μs: past that time some irregularities in the pressure distribution at the outer boundary of the gaseous mass appear; such a fact should be connected with the lack of information owing to the low number of neighbors in the interaction domain of external particles.

Such non-physical behavior is however avoided if a surrounding medium is considered for confinement of the explosive charge.

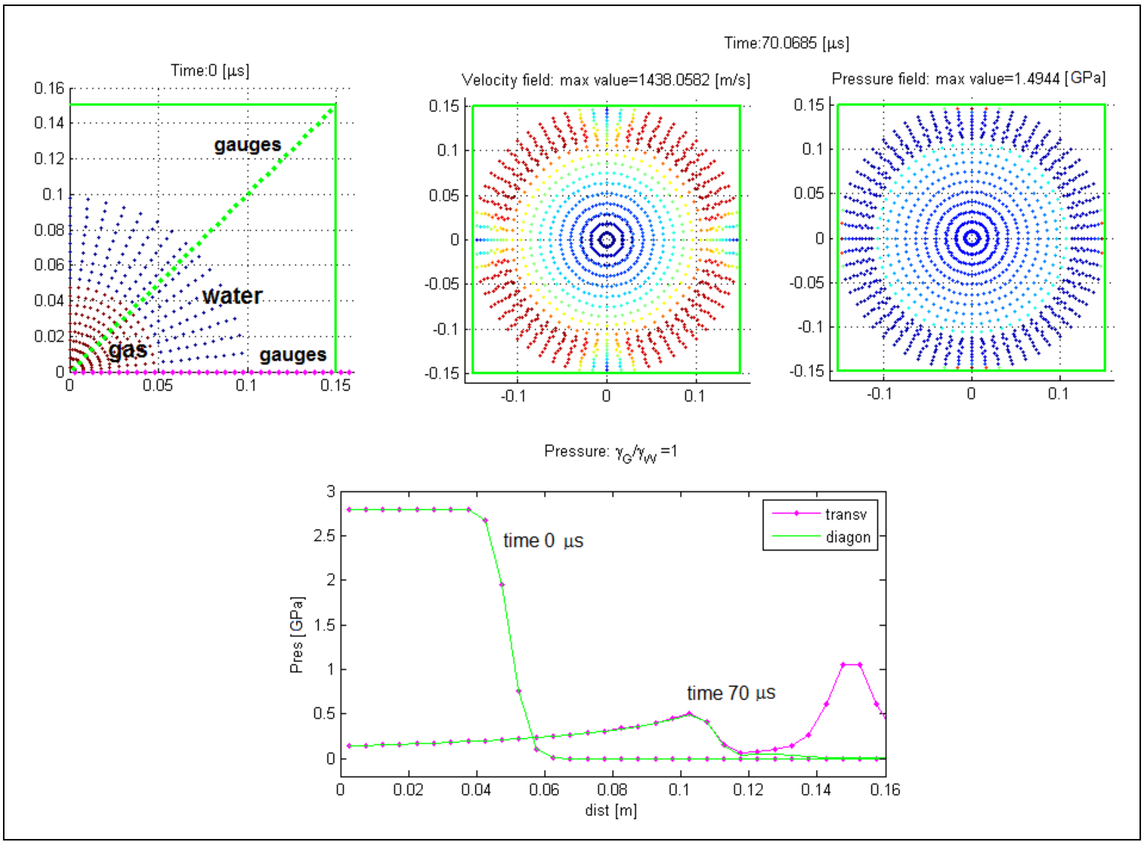

Figure 8: Expansion of detonated gas surrounded by a water crown into a rigid box; axes scale in meters.

Fig.8 shows the expansion of a circular charge surrounded by a water crown and confined in a rigid squared box with length of 0.30 m; the simulation is carried out considering the same compressibility modulus for both gas and water (i.e. $\gamma_G/\gamma_W = 1$).

The upper left-hand panel displays the initial configuration and the position of the gauges for pressure detection on the transversal and diagonal directions; continuous green line denotes the rigid box contour.

The central and right-hand upper panels show particles position, velocity modulus and pressure at time t = 0.07 ms when the water impacts with the box walls.

The lower panel shows pressure distribution at initial time (t = 0.0 ms) and at the impact time (t = 0.07 ms): in the latter a pressure wave is reflected by the box wall and propagates backward along the transversal direction with a peak of about 1 GPa.

The simulation ends at 0.2 ms: after the gas and water particles have completely expand occupying the whole box internal volume, symmetrical jets originates from both transversal and diagonal directions thus pumping the gas toward the box center and producing a contraction of its volume.

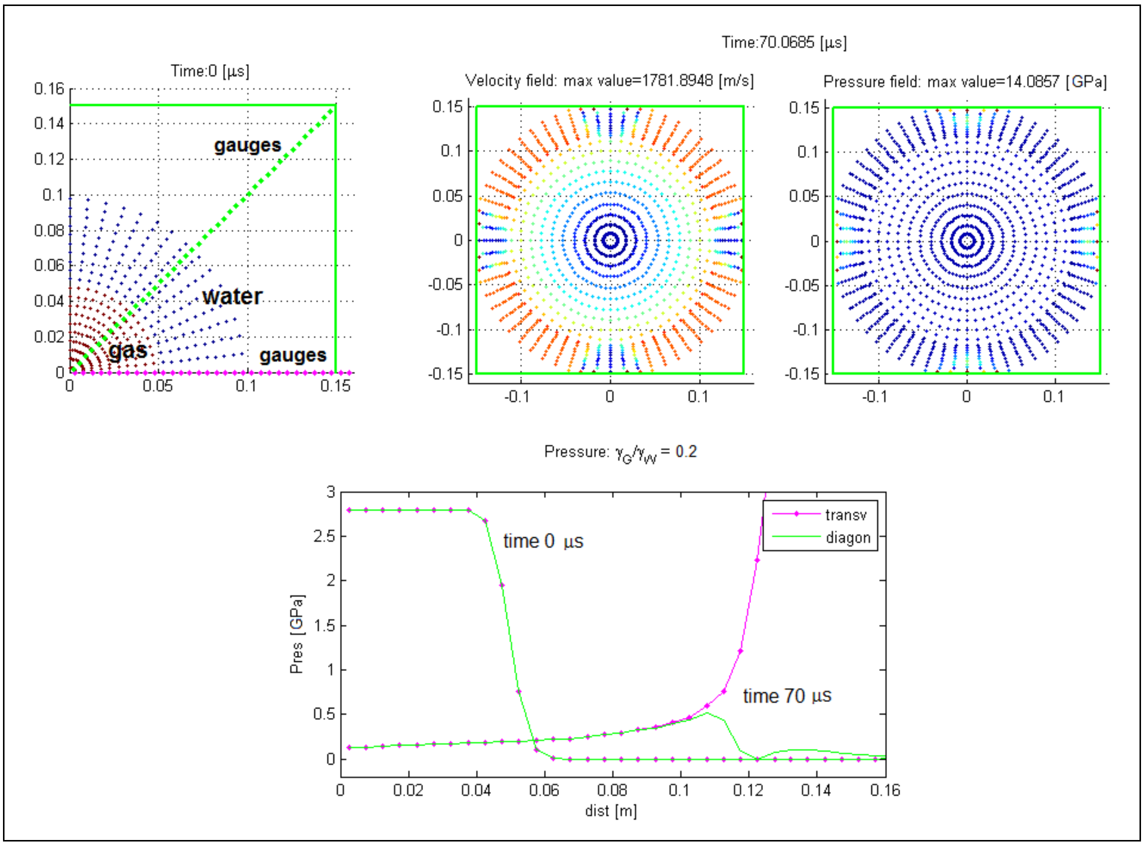

Figure 9: Expansion of detonated gas surrounded by a water crown into a rigid box; axes scale in meters.

Fig.9 shows the results obtained when increasing to 7.0 the value of the gamma water constant in the state equation (i.e. $\gamma_G/\gamma_W = 0.2$).

The particles dynamics is rather similar to that one described in the case $\gamma_G/\gamma_W = 1$: anyway now the water compressibility modulus is greater than the gas and this produces reflected pressure waves with higher peaks and celerity; the pulsation frequency of the gas expansion and contraction described in the previous analysis is also increased.

6 CONCLUSIONS

An advanced application of the Smoothed Particle Hydrodynamics method for the numerical modeling of rapid multiphase flow and underwater explosion problems have been illustrated in this paper.

The basic features of the numerical model adopted for simulating both non-cohesive sediment flushing and underwater expansion of a HE gas have been illustrated.

The proposed results have shown that the physics of the investigated problems can be simulated with an adequate degree of accuracy for engineering applications.

7 ACKNOWLEDGMENTS

This work has been financed by the Research Fund for the Italian Electrical System under the Contract Agreement between RSE (formerly known as ERSE) and the Ministry of Economic Development - General Directorate for Nuclear Energy, Renewable Energy and Energy Efficiency stipulated on July 29, 2009 in compliance with the Decree of March 19, 2009.

8 LIST OF SYMBOLS

A	physical field function (scalar or vector)
C_n	normalization factor for kernel functions
c_s	speed of sound
d_{50}	median sediment diameter
D/Dt	material derivative
e	internal energy
k_s	characteristic grain roughness height
h	smoothing length
h_0	initial interparticle distance
ΔV	particle volume
m	mass
n	dimension of the physical space
N	neighboring particles
p	pressure
p_0	reference pressure
$r_{ij}=\lvert\mathbf{x}_i-\mathbf{x}_j\rvert$	modulus of the relative distance vector
u_*	friction velocity
U	detonation wave characteristic velocity
∇r	radial unit vector
$\mathbf{g}$	gravitational acceleration vector
$\mathbf{u}$	velocity vector
$\mathbf{u}_{ij}$	relative velocity vector
$\mathbf{u}_b$	velocity vector of the solid boundary
$\mathbf{x}$	position vector
$\mathbf{x}_{ij}$	relative position vector
dV	elementary volume
α_M, β_M	constants of Monaghan artificial viscosity
δ	*Dirac* delta function
γ	state equation parameter
ε	fluid compressibility modulus
κ	Von Kàrmàn constant
φ, ϑ, r	spherical coordinates
μ	dynamic viscosity
ν	cinematic viscosity
Π	Monaghan artificial viscosity
ρ	density
ρ^s	sediment density
ρ^g	gas density
ρ_0	reference density
ϑ_{cr}	Shields parameter
θ_p	pressure smoothing coefficient
$\tau_{b\,cr,0}$	critical bottom shear stress (horizontal bed)
τ_b	hydrodynamic bottom shear
ζ^s	solid particle distance from the water-sediment interface
ζ^w	local draught of the water-sediment interface
ζ^{ws}	fluid particle distance from the water-sediment interface

W	kernel smoothing function
$d\Omega$	elementary volume of the continuum
Ω	spatial domain
Ω_I	compact support (or influence domain) of the *i*-th particle

REFERENCES

[1] Lucy L. A numerical approach to the fission hypothesis, *Astron J.*, 82-1013, 1977.

[2] Gingold R.A., Monaghan J.J. Smoothed particle hydrodynamics: theory and application to non-spherical stars, *Mon Not Roy Astron Soc*, 181-375,1977.

[3] Monaghan J.J. Simulating free surface flows with SPH, *J. Comput. Phys.* Vol. 110, 399-406, 1992.

[4] Monaghan J.J. Smoothed particle hydrodynamics, *Ann. Rev. Astronomy and Astrophysics*, Vol. 30, 543-574, 1992.

[5] Li S., Liu W.K. *Meshfree Particle Methods*, Springer Ed. 2004.

[6] Liu G.R., Liu M.B. *Smoothed Particle Hydrodynamics - a Meshfree Particle Method*, World Scientific Publ. 2007.

[7] Manenti S., Ruol P., Fluid-Structure Interaction in Design of Offshore Wind Turbines: SPH Modeling of Basic Aspects, *Proc. Int. Workshop Handling Exception in Structural Engineering*, Nov. 13–14 2008, Sapienza University (Italy) DOI: 10.3267/HE2008.

[8] Di Monaco A., Manenti S., Gallati M., Sibilla S., Agate G., Guandalini R., SPH modeling of solid boundaries through a semi-analytic approach. *J. Eng Appl. Comp. Fluid Mech.* Vol. 5, No. 1, pp. 1–15 (2011).

[9] Manenti S., Agate G., Di Monaco A., Gallati M., Maffio A., Guandalini R., Sibilla S., SPH Modeling of Rapid Sediment Scour Induced by Water Flow. *33rd IAHR Cong.* August 9–14 2009 Vancouver, British Columbia (Canada).

[10] Monaghan, JJ. Smoothed particle hydrodynamics, *Rep. Prog. Phys.* 68 1703–1759, (2005) doi:10.1088/0034-4885/68/8/R01.

[11] Van Rijn L.C. Principles of sediment transport in rivers, estuaries, and coastal seas. *Aqua Publications* 1993 .

[12] Cooper P.W. *Explosives Engineering*. Wiley-VCH, 1937.

[13] Kedrinskii V.K. *Hydrodynamics of explosion – Experiments and models*. Springer, 2005.

[14] Morris J.P., Fox P.J., Zhu Y. Modeling Low Reynolds Number Incompressible Flows Using SPH. *J. Comput. Phys.* 136, 214–226 (1997).

[15] Kajtar J.B., Monaghan J.J. SPH simulations of swimming linked bodies. *J. Comput. Phys.* 227 (2008) 8568–8587.

[16] Manenti S., Sibilla S., Gallati M., Agate G., Guandalini R. Prediction of Sediment Scouring through SPH. *Proc. 5th SPHERIC Int. Workshop* June 23-25 Manchester, Uk, pp. 56-60 2010.

COMPDYN 2011
III ECCOMAS Thematic Conference on
Computational Methods in Structural Dynamics and Earthquake Engineering
M. Papadrakakis, M. Fragiadakis, V. Plevris (eds.)
Corfu, Greece, 26–28 May 2011

NUMERICAL AND EXPERIMENTAL ASSESSMENT OF VARIOUS NON-CLASSICAL METHODS FOR PARAMETRIC IDENTIFICATION OF NONLINEAR VISCOUS DAMPERS

Jennifer Avakian[1], **Giuseppe Carlo Marano**[1], **Giorgio Monti**[2] , **Giuseppe Quaranta**[2] **and F. Trentadue**[1]

[1] Dept. of Environmental Engineering and Sustainable Development, Technical University of Bari
viale del Turismo 10, 74100, Taranto, Italy {jeneva,g.marano}@poliba.it

[2] Dept. of Structural Engineering and Geotechnics, Sapienza University of Rome
via A. Gramsci 53, 00197, Roma, Italy {giorgio.monti,giuseppe.quaranta}@uniroma1.it

Keywords: Differential Evolution, Genetic Algorithm, Parametric Identification, Particle Swarm Optimization, Viscous Damper.

Abstract. *Passive strategies based on the introduction of energy dissipating devices into the structures have received considerable attention in recent years. Within this framework, as reliable and cheap energy-dissipation devices, viscous fluid dampers have been largely used in seismic protection of industrial machines, technical equipments, buildings and bridges. Since the versatility of this passive protection system satisfactorily meets a wide range of requirements, a reliable identification of their nonlinear mechanical behavior is of outstanding importance. This paper focuses on the parametric identification of fractional derivative based models for nonlinear viscous dampers by means of non-classical methods, which are unconventional algorithms whose inner work is based on socially, physically and/or biologically inspired paradigms. Non-classical strategies are potentially powerful tools for solving complex identification problems because of their start-point independence, noise robustness and the capability in looking for the best solution in a global way. In contrast, it is important to highlight that they typically possess weak forms of convergence. For better assessing the correctness of some non-classical methods in parametric identification of viscous dampers, we perform a large comparative analysis which involve the following soft computing based techniques: a multi-species genetic algorithm, six standard differential evolution algorithms and four swarm intelligence based algorithms (including a chaotic particle swarm optimization algorithm). A numerical study is initially conducted in order to investigate the general reliability of these methods. Moreover, the paper also provides some results about the parametric identification of nonlinear viscous dampers by using experimental data. A critical review of the obtained evidences is given in order to provide useful guidelines for similar engineering applications.*

1 INTRODUCTION

Existing strategies for enhancing structural performances and safety against natural and manmade hazards can be grouped into three broad areas: base isolation, passive energy dissipation and active control. Passive energy dissipation systems can be realized by using a very wide range of materials and devices for enhancing damping, stiffness and strength. They can be used both for seismic hazard mitigation and for rehabilitation of aging or deficient structures. These devices generally operate on principles such as frictional sliding, yielding of metals, phase transformation in metals, deformation of viscoelastic solids or fluids and fluid orificing [1]. In this paper, the attention is focused on viscous damper devices whose most interesting features are: (*i*) low maintenance costs; (*ii*) usability for several severe earthquakes without damage; and (*iii*) forces exerted by the damper devices do not increase the stress in the structural system, being out of phase with the elastic forces. A viscous fluid damper typically consists of a piston within a damper housing filled with a compound of silicone or similar type of oil. Through a number of small orifices, the fluid pass from one side of the piston to the other: therefore, this device is able to dissipate energy through the movement of a piston in a highly viscous fluid based on the concept of fluid orificing [1]. Nowadays, a large number of civil engineering structures (buildings as well as bridges) is equipped with viscous fluid dampers in order to control seismic or wind induced motions and thermal expansions.

Since the applications of viscous dampers is growing very fast, their characteristics must be carefully investigated in order to provide a reliable support for designing an efficient protection strategy. Because of their inherent nonlinear behavior, condition assessment techniques require appropriate identification techniques. For instance, several identification approaches, both parametric and nonparametric, are compared in [2] by using real data carried out from full-scale nonlinear viscous dampers commonly used with large flexible bridges. About the parametric techniques, in [2] are explored the capability of the Adaptive Random Search: to this end, the authors solved an optimization problem in which the numerical values of the unknown model parameters were estimated by minimizing an objective function based on the normalized mean square error between the measured and identified damper responses. Since its weak form of convergence, the Adaptive Random Search belongs to the class of non-classical identification techniques [3], which are unconventional numerical identification methods mostly based on socially, physically and/or biologically inspired paradigms (i.e., ant colony based algorithms, artificial neural networks, differential evolution algorithms, genetic algorithms, genetic programming, particle swarm optimization algorithms, etc.).

This paper provides a comprehensive investigation about the parametric identification of viscous dampers via non-classical methods. To this end, we perform a large comparative analysis in which the following soft computing based techniques are examined: a special multi-species genetic algorithm, six standard differential evolution algorithms and four swarm intelligence based algorithms (including a chaotic particle swarm optimization algorithm). A numerical study is initially conducted in order to investigate the general reliability of these methods. Moreover, the paper also provides some results about the parametric identification of a full-scale nonlinear viscous damper by using experimental data. A critical review of the obtained evidences is given in order to provide useful guidelines for similar engineering applications.

2 PARAMETRIC IDENTIFICATION OF VISCOUS DAMPERS

The application of non-classical methods for the parametric identification of viscous dampers requires (i) the definition of an appropriate single-degree-of-freedom mechanical model and (ii) the formalization of the objective (or cost) function to be minimized.

2.1 Dynamic models

The damper effect is an output resistive force, therefore it acts in the opposite direction to that of the relative velocity between the ends of the damper device itself. The typical damping force ψ_d is:

$$\psi_d = C_\alpha \mathrm{sgn}\left[\dot{y}\right]\left|\dot{y}\right|^\alpha \tag{1}$$

where y is the displacement time-history (the time variable t is omitted for the sake of conciseness, the upper dots indicate the time-derivative). Moreover, sgn[·] is the signum function, C_α is the damping coefficient and α is the damping law exponent. The value of α for seismic applications ranges between 0.10 and 0.50 (in this way the force rises very fast for small velocity values and becomes almost constant for large velocity values). Regarding the elastic force ψ_e, both linear and parabolic models were investigated in [4]:

$$\psi_e = K_1 y \tag{2}$$

$$\psi_e = K_2 y^2 + K_1 y + K_0 \tag{3}$$

in which K_1 is the elastic stiffness, K_2 and K_0 are two constants. In [4] is stated that the parabolic function reproduces the shape of the test cycles more precisely, but the linear one may be preferred because it is more simple and yields a comparable energy balance. By combining Eq. (1) and Eq. (2), the equation of motion of a fractional viscous damper system subjected to a time-varying force p is [4]:

$$M\ddot{y} + C_\alpha \mathrm{sgn}\left[\dot{y}\right]\left|\dot{y}\right|^\alpha + K_1 y = p \tag{4}$$

where M is the effective mass. If the parabolic model given by Eq. (3) is taken into account, then the equation of motion becomes [4]:

$$M\ddot{y} + C_\alpha \mathrm{sgn}\left[\dot{y}\right]\left|\dot{y}\right|^\alpha + \left(K_2 y^2 + K_1 y + K_0\right) = p \tag{5}$$

In [5] are considered a fraction viscous model and a linear one as follows:

$$M\ddot{y} + C_1\dot{y} + C_\alpha \mathrm{sgn}\left[\dot{y}\right]\left|\dot{y}\right|^\alpha + K_1 y = p \tag{6}$$

where C_1 is the internal damping coefficient.

The system response can be determined as solution of the considered equation of the motion by using standard numerical time-marching techniques if the initial conditions and the values of the system parameters are known.

2.2 Parametric identification

The model parameters $\mathbf{x}$ of the viscous damper are identified by solving the following single-objective optimization problem :

$$\begin{gathered} \min_{\mathbf{x}} \left\{ f\left(\mathbf{x}\right) \right\} \\ \text{s.t. } \mathbf{x}^l \le \mathbf{x} \le \mathbf{x}^u \end{gathered} \tag{7}$$

in which $\mathbf{x}^l$ and $\mathbf{x}^u$ are the lower and upper bounds of the system parameters, respectively.

The objective or cost function $f(\mathbf{x})$ is:

$$f\left(\mathbf{x}\right) = \frac{100}{S\sigma_y^2}\sum_{s=1}^{S}\left(y_s - y_s^*\left(\mathbf{x}\right)\right) \tag{8}$$

where y_s is the measured displacement, y_s^* is the computed displacement, S is the number of data points (s is a generic sample index) and σ_s^2. The cost function in Eq. (8) coincides with that in [2] as the weight for the velocity-based addend is equal to zero. In fact, although the information regarding the velocity response may help the parametric identification, it introduces some additional complications. First, the velocity response is not typically measured, so that it needs to be calculated from the displacement response. Second, the weights of a mixed displacement-velocity cost function should be tuned for better matching the experimental data, and thus it requires preliminary user-supervised runs. On the other hand, the objective function in Eq. (8) can be directly used with experimental data without preliminary runs.

The Adaptive Random Search was used in [2] to solve a single-objective optimization problem as in Eq. (7) in order to identify the system parameter **x**. In this paper, we perform comparative analyses involving differential evolution, particle swarm optimization and genetic algorithm.

3 IDENTIFICATION VIA DIFFERENTIAL EVOLUTION

Differential evolution algorithm (DEA) is a relatively recent stochastic, population-based global optimization method whose positive features are attracting the interest of several researches in the field of the applied sciences. Different from traditional evolutionary algorithms, this optimizer is completely self-organizing and requires few lines of code in most of the existing programming languages. Moreover, its functionality requires a small set of embedded control parameters, which makes it easy to use for non-experts.

3.1 Mutation operators

The standard version of the DEA [1] uses the differences between randomly selected individuals as the source of random variations for a third individual referred to as the target vector. Trial solutions are generated by adding weighted difference vectors to the target vector. This process is dubbed mutation operator: its main goal is to enable diversity in the current population as well as "to move" the individuals in such a way a better result is expected. By computing the differences between two individuals randomly chosen from the population, the algorithm estimates the gradient in that zone rather than in a single point of the search space. Let us consider ${}^k\mathbf{x}_i=\{{}^kx_{i1},\ldots,{}^kx_{ij},\ldots,{}^kx_{in}\}$ the ith individual (with i=1,…,N) at iteration k. The initial population ${}^0\mathbf{x}_i$ for i=1,…,N is defined by generating randomly the collection of N solutions within the specified search space. During the iteration k+1, for each individual ${}^k\mathbf{x}_i$ a mutation vector ${}^{(k+1)}\mathbf{z}_i$ is computed by using one of the following alternatives:

$$ {}^{(k+1)}\mathbf{z}_i = {}^k\mathbf{x}_{r1} + F^1\left({}^k\mathbf{x}_{r2} - {}^k\mathbf{x}_{r3}\right) \tag{9} $$

$$ {}^{(k+1)}\mathbf{z}_i = {}^k\mathbf{x}_{best} + F^1\left({}^k\mathbf{x}_{r1} - {}^k\mathbf{x}_{r2}\right) \tag{10} $$

$$ {}^{(k+1)}\mathbf{z}_i = {}^k\mathbf{x}_i + F^2\left({}^k\mathbf{x}_{best} - {}^k\mathbf{x}_i\right) + F^1\left({}^k\mathbf{x}_{r1} - {}^k\mathbf{x}_{r2}\right) \tag{11} $$

$$ {}^{(k+1)}\mathbf{z}_i = {}^k\mathbf{x}_{best} + F^2\left({}^k\mathbf{x}_{r1} - {}^k\mathbf{x}_{r2}\right) + F^1\left({}^k\mathbf{x}_{r3} - {}^k\mathbf{x}_{r4}\right) \tag{12} $$

$$ {}^{(k+1)}\mathbf{z}_i = {}^k\mathbf{x}_{r1} + F^2\left({}^k\mathbf{x}_{r2} - {}^k\mathbf{x}_{r3}\right) + F^1\left({}^k\mathbf{x}_{r4} - {}^k\mathbf{x}_{r5}\right) \tag{13} $$

where $r1$, $r2$, $r3$ and $r4$ denote integers randomly selected within the set $\{1,\ldots,i\text{-}1,i+1,\ldots,N\}$ such that $r1\neq r2\neq r3\neq r4$. The individual ${}^k\mathbf{x}_{best}$ is the best performer in the population at iteration k. The coefficients F^1 and F^2 are the so-called mutation coefficients and they are real positive constants whose typical values are in the range [0.40,1.00], 0.50 in our numerical applications.

These parameters control the amplification level of the mutation (for this reason they are also dubbed “scale factors”).

3.2 Crossover operator

The crossover follows the mutation phase. For each mutated vector ${}^{(k+1)}\mathbf{z}_i$ a trial vector ${}^{(k+1)}\mathbf{u}_i$ (offspring) is generated by using the following so-called binomial crossover:

$$ {}^{(k+1)}u_{ij} = \begin{cases} {}^{(k+1)}z_{ij} & \mathit{if}\ q \le p^c\ \mathit{or}\ j = \mathit{randint}(1,n) \\ {}^{k}x_{ij} & \mathit{otherwise} \end{cases} \tag{14} $$

where q is a random number generated by using the uniform probability density function in the range [0,1]. The parameter p^c is the probability of crossover and it takes values between 0 and 1 (usually, 0.50). Moreover, *randint*(1,*n*) is an integer randomly selected within the set $\{1,\ldots,n\}$ and it is adopted to ensure that at least one parameter is taken into account for constructing the vector ${}^{(k+1)}\mathbf{u}_i$.

3.3 Selection operator

An opportune strategy is needed to ensure the feasibility of the obtained solutions in Eq. (14), that means the fulfillment of both lower and upper bounds of the search space: in this paper, if a vector out-of-range is obtained, then its projection on the prescribed interval is considered (so-called projection scheme). Subsequently, the selection operator is performed by means of a very simple one-to-one competition scheme between ${}^{(k+1)}\mathbf{u}_i$ and ${}^{(k+1)}\mathbf{x}_i$ as follows:

$$ {}^{(k+1)}\mathbf{x}_i = \begin{cases} {}^{(k+1)}\mathbf{u}_i & \mathit{if}\ f\left({}^{(k+1)}\mathbf{u}_i\right) < f\left({}^{(k+1)}\mathbf{x}_i\right) \\ {}^{k}\mathbf{x}_i & \mathit{otherwise} \end{cases} \tag{15} $$

Therefore the winner ${}^{(k+1)}\mathbf{x}_i$ in the selection stage is the best performer between the parent individual ${}^{k}\mathbf{x}_i$ and its trial one ${}^{(k+1)}\mathbf{u}_i$. The output of this operator is a new population for the next generation, unless a stopping criteria has not been fulfilled. In this study, we will stop the evolutionary search once a maximum number of iterations L is achieved.

3.4 An adaptive mutation operator

In [7] is presented a mutation operator in which only one control parameter is required and the mutation coefficients are adaptive. The mutation operator proposed in [7] deals with the following revised version of Eq. (11):

$$ {}^{(k+1)}\mathbf{z}_i = {}^{k}\mathbf{x}_i + {}^{k}F_{r3,i}\left({}^{k}\mathbf{x}_{r3} - {}^{k}\mathbf{x}_i\right) + {}^{k}F_{r1,r2}\left({}^{k}\mathbf{x}_{r1} - {}^{k}\mathbf{x}_{r2}\right)\ \mathit{if}\ k \le \kappa L \tag{16} $$

and

$$ {}^{(k+1)}\mathbf{z}_i = {}^{k}\mathbf{x}_{r1} + {}^{k}F_{best,i}\left({}^{k}\mathbf{x}_{best} - {}^{k}\mathbf{x}_i\right) + {}^{k}F_{r1,r2}\left({}^{k}\mathbf{x}_{r1} - {}^{k}\mathbf{x}_{r2}\right)\ \mathit{if}\ k > \kappa L \tag{17} $$

where κ is the only one control parameter. The adaptive mutation coefficients in Eq. (16) and in Eq. (17) are calculated as follows:

$$ {}^{k}F_{r3,i} = \max\left\{\left|\frac{f\left({}^{k}\mathbf{x}_{r3}\right) - f\left({}^{k}\mathbf{x}_i\right)}{{}^{k}f_{\max} - {}^{k}f_{\min}}\right|, 0.5\right\} \tag{18} $$

$$
{}^{k}F_{r1,r2} = \begin{cases} \max\left\{\left|\dfrac{f\left({}^{k}\mathbf{x}_{r1}\right)-f\left({}^{k}\mathbf{x}_{r2}\right)}{{}^{k}f_{\max}-{}^{k}f_{\min}}\right|, 0.5\right\} & if\ k \le \kappa L \\ \left|\dfrac{f\left({}^{k}\mathbf{x}_{r1}\right)-f\left({}^{k}\mathbf{x}_{r2}\right)}{{}^{k}f_{\max}-{}^{k}f_{\min}}\right| & if\ k > \kappa L \end{cases} \tag{19}
$$

$$
{}^{k}F_{best,i} = \left|\frac{{}^{k}f_{\min}-f\left({}^{k}\mathbf{x}_{i}\right)}{{}^{k}f_{\max}-{}^{k}f_{\min}}\right| \tag{20}
$$

in which:

$$
\begin{aligned} {}^{k}f_{\min} &= \min_{i=1,\ldots,N}\left\{f\left({}^{k}\mathbf{x}_{i}\right)\right\} \\ {}^{k}f_{\max} &= \max_{i=1,\ldots,N}\left\{f\left({}^{k}\mathbf{x}_{i}\right)\right\} \end{aligned} \tag{21}
$$

Taking into account this operator, the mutation occurs in two distinct ways. The first one takes place when $k \le \kappa L$ and its goal is to help the exploration of the search space. In this effort, the weighted difference vectors in Eq. (16) only involves randomly selected individuals and the mutation coefficients are forced to be greater than 0.5, see Eq. (18) and the first equality in Eq. (19). Once $k > \kappa L$, the mutation scheme proposed in Eq. (19) is performed. In this case, the current best individual ${}^{k}\mathbf{x}_{best}$ is taken into account. Substantially, the goal of this alternative scheme is to keep track of the current best performer within the population. Moreover, an improved exploitation can be achieved by removing the lower bounds for the adopted mutation coefficients (therefore numerical values less than 0.50 are accepted at this time). However, there is not rigid separation between exploration and exploitation because the numerical values of the scale factors are dynamically adjusted during the evolutionary search (adaptive property): for instance, if the exploration of the search space is not concluded for $k \le \kappa L$ then the numerical values of the mutation remain sensibly large and the global recognition is not penalized. Our numerical analyses – on both mathematical and engineering problems – demonstrate that a good value for κ (the only parameter of the proposed mutation operator) should be selected within 0.40 and 0.60, κ=0.50 in this paper.

3.5 A free-parameter crossover operator

The binomial scheme in Eq. (14) was replaced in [7] with the following one:

$$
{}^{(k+1)}\mathbf{u}_{i} = {}^{(k+1)}\mathbf{q}_{i} \times {}^{k}\mathbf{x}_{i} - \left(\mathbf{1} - {}^{(k+1)}\mathbf{q}_{i}\right) \times {}^{(k+1)}\mathbf{z}_{i} \tag{22}
$$

where ${}^{(k+1)}\mathbf{q}_i$ is a vector whose n components are random numbers generated by using the uniform probability density functions in the range [0,1]. Moreover, $\mathbf{1}=\{1_1,\ldots,1_j,\ldots,1_n\}$. The results of the binomial crossover in Eq. (14) are vertex points of the hypercube defined by ${}^{(k+1)}\mathbf{z}_i$ and ${}^{(k+1)}\mathbf{x}_i$. Similarly, these vertex points are possible solutions of the crossover operator presented in Eq. (22) when ${}^{(k+1)}q_{ij}\rightarrow 0$ or ${}^{(k+1)}q_{ij}\rightarrow 1$ for each $j=1,\ldots,n$. Additionally, this crossover operator allows the exploration of the inner space bounded by this hypercube. It is evident that the probability of reproduction is not required for performing the proposed crossover, and thus Eq. (22) is a free-parameter operator.

4 IDENTIFICATION VIA PARTICLE SWARM OPTIMZIATION

Based on the swarm intelligence theory, two different categories of optimizers can be formulated:

- Particle swarm optimization algorithms (PSOAs) in which is assumed that a Newtonian dynamic regulates the movement of the particles. Therefore, position and velocity can be determined simultaneously.
- Quantum-behaved particle swarm optimization algorithms (Q-PSOAs) in which the Newtonian hypothesis is rejected. In this case, the classical mechanic is replaced with the quantum mechanics in which the term "trajectory" is meaningless [8].

The first class of PSOAs is the object of investigation in this paper.

4.1 General model

The *i*th particle (with $i=1,\dots,N$) at iteration k has two attributes, that are its velocity ${}^{k}\mathbf{v}_i=\{{}^{k}\mathbf{v}_{i1},\dots,{}^{k}\mathbf{v}_{ij},\dots,{}^{k}\mathbf{v}_{in}\}$ and position ${}^{k}\mathbf{x}_i=\{{}^{k}\mathbf{x}_{i1},\dots,{}^{k}\mathbf{x}_{ij},\dots,{}^{k}\mathbf{x}_{in}\}$. To protect the cohesion of the swarm the velocity ${}^{k}\mathbf{v}_{ij}$ is forced to be (in absolute value) less than a maximum velocity $v_j^{\max}$ with $\mathbf{v}^{\max}=\{v_1^{\max},\dots,v_j^{\max},\dots,v_n^{\max}\}$. Typically, it is assumed $\mathbf{v}^{\max}=\gamma(\mathbf{x}^u-\mathbf{x}^l)/\tau$ (the time factor $\tau = 1$ is introduced to assign a physical meaning to the formula) but there is not sufficient degree of uniformity about γ whose numerical value can vary in a large interval (usually its value is 0.50). The initial positions ${}^{0}\mathbf{x}_i$ for $i=1,\dots,N$ are defined by generating randomly the collection of N solutions within the assigned search space. Moreover, ${}^{0}v_{ij}$ is randomly generated using an uniform distribution between $-v_j^{\max}$ and $+v_j^{\max}$. At iteration $k+1$ the velocity ${}^{(k+1)}\mathbf{v}_i$ and the position ${}^{(k+1)}\mathbf{x}_i$ are evaluated as follows [9]:

$$ {}^{(k+1)}\mathbf{v}_i = w\,{}^{k}\mathbf{v}_i + c_1\,{}^{(k+1)}\mathbf{r}_{i1}\times\left({}^{k}\mathbf{x}_i^{Pb}-{}^{k}\mathbf{x}_i\right)+c_2\,{}^{(k+1)}\mathbf{r}_{i2}\times\left({}^{k}\mathbf{x}^{Gb}-{}^{k}\mathbf{x}_i\right) \tag{23} $$

$$ {}^{(k+1)}\mathbf{x}_i = {}^{k}\mathbf{x}_i + \tau\,{}^{(k+1)}\mathbf{v}_i \quad (\tau=1) \tag{24} $$

in which w is the inertia weight whereas c_1 and c_2 are the so-called acceleration factors (they are called cognitive and social parameter, respectively). In Eq. (23), ${}^{(k+1)}\mathbf{r}_{1i}$ and ${}^{(k+1)}\mathbf{r}_{2i}$ are vectors whose n terms are random numbers uniformly distributed between zero and one, the symbol × denotes the term-by-term multiplication. The superscripts on the left and the subscripts on the right denote that a different couple of random vectors is needed for each particle at any iteration. The symbol ${}^{k}\mathbf{x}_i^{Pb}$ denotes the best previous position of the *i*th particle (also known as *pbest*):

$$ {}^{k}\mathbf{x}_i^{Pb} = \begin{cases} {}^{(k-1)}\mathbf{x}_i^{Pb} & if\ f\left({}^{k}\mathbf{x}_i\right) > f\left({}^{(k-1)}\mathbf{x}_i^{Pb}\right) \\ {}^{k}\mathbf{x}_i & otherwise \end{cases} \tag{25} $$

given that ${}^{0}\mathbf{x}_i^{Pb}={}^{0}\mathbf{x}_i$. According to the adopted definition for ${}^{k}\mathbf{x}^{Gb}$, there are two versions of PSOAs. If ${}^{k}\mathbf{x}^{Gb}$ is the best position among all the particles in the swarm (also known as *gbest*) such a version is called global PSOA (and the swarm is said to be fully informed or fully connected). On the other hand, if ${}^{k}\mathbf{x}^{Gb}$ is evaluated on a smaller number of adjacent particles (also known as *lbest*, ${}^{k}\mathbf{x}^{Lb}$) we have a local PSOA. In this paper, we will consider that all particles share information with each other about the best performer of the swarm, so that

$$ {}^{k}\mathbf{x}^{Gb} = \arg\min_{i=1,\dots,N}\left\{f\left({}^{k}\mathbf{x}_i^{Pb}\right)\right\} \tag{26} $$

The check on the maximum admissible velocity for each particle *i* is performed at iteration *k* in the following manner:

$$ {}^{k}v_{ij} = \begin{cases} \operatorname{sgn}\left[{}^{k}v_{ij}\right] v_j^{\max} & if\ \left|{}^{k}v_{ij}\right| > \left|v_j^{\max}\right| \\ {}^{k}v_{ij} & otherwise \end{cases} \quad \forall j = 1,\dots n \tag{27} $$

Another check is needed to verify that the particle is within the feasible search space:

$$ \left({}^{k}x_{ij}, {}^{k}v_{ij}\right) = \begin{cases} \left({}^{k}x_{ij}, {}^{k}v_{ij}\right) & if\ x_j^l \le {}^{k}x_j \le x_j^u \\ \left({}^{k}x_{ij} = x_j^l, {}^{k}v_{ij} = 0\right) & if \quad {}^{k}x_j < x_j^l \quad \forall j = 1,\dots n \\ \left({}^{k}x_{ij} = x_j^u, {}^{k}v_{ij} = 0\right) & otherwise \end{cases} \tag{28} $$

In Eq. (28), the unfeasible particle's velocity is fixed to zero for the next iteration to avoid considering any points outside the search space.

A typical operator (called “craziness operator”) is performed to increase the direction diversity in the swarm. Specifically, the adopted version for the craziness operator works on the particle's velocity only. Assigned a probability of craziness P_{cr}, the particle's velocity in Eq. (27) is replaced as follows:

$$ if\ r \le P_{cr} \rightarrow {}^{(k+1)}v_{ij} \sim U\left(-v_j^{\max}, v_j^{\max}\right)\ \forall j = 1,\dots n \tag{29} $$

in which r is a uniform random number between 0 and 1, $U(\cdot)$ is the uniform probability density function. Once the particle's velocity is assigned by means of Eq. (29), a new position ${}^{(k+1)}\mathbf{x}_i$ is calculated for the particle by including this result in Eq. (24). A high value for P_{cr} results in (ineffective) pure random search, therefore its value should be less than 0.1 (0.05 in this study). Following iteratively this simple set of instructions, the swarm is expected to “fly” toward the global optimum of the problem. In our studies, the routine is stopped once a maximum number of iterations L is achieved.

4.2 Inertia weight and acceleration factors

The constriction factor χ is alternative to the use of the static inertia weight, initially proposed by [10] to replace the $\mathbf{v}^{\max}$ clamping. The constriction model describes the way of choosing w, c_1 and c_2 as follows:

$$ \begin{aligned} {}^{(k+1)}\mathbf{v}_i &= \chi\left[{}^{k}\mathbf{v}_i + c_1\, {}^{(k+1)}\mathbf{r}_{i1} \times \left({}^{k}\mathbf{x}_i^{Pb} - {}^{k}\mathbf{x}_i\right) + c_2\, {}^{(k+1)}\mathbf{r}_{i2} \times \left({}^{k}\mathbf{x}^{Gb} - {}^{k}\mathbf{x}_i\right)\right] \\ \chi &= \frac{2}{\left|2 - \varphi - \sqrt{\varphi^2 - 4\varphi}\right|} \\ \varphi &= c_1 + c_2 \ge 4 \end{aligned} \tag{30} $$

The new particle's position is computed as indicated in Eq. (24). Very typical values for this model are c_1=c_2=2.05, that is χ=0.73.

The model given by Eq. (23) can be modified by assuming both inertia weight and acceleration factors as dynamic parameters, that is: $w={}^{k}w$, $c_1={}^{k}c_1$, $c_2={}^{k}c_2$. In [11] is proposed a linearly decreasing inertia weight:

$$ {}^{k}w = \left({}^{0}w - {}^{L}w\right)\frac{L-k}{L} + {}^{L}w \tag{31} $$

where ${}^{0}w$ and ${}^{L}w$ are the initial and final values of the inertia weight (typically 0.9 and 0.4 respectively). Similarly, in [12] are proposed linearly iteration-dependent models for the acceleration factors:

$$\begin{aligned} {}^{k}c_1 &= \left({}^{0}c_1 - {}^{L}c_1\right)\frac{L-k}{L} + {}^{L}c_1 \\ {}^{k}c_2 &= \left({}^{0}c_2 - {}^{L}c_2\right)\frac{L-k}{L} + {}^{L}c_2 \end{aligned} \tag{32}$$

In several papers, ${}^{k}c_1$ changes from 2.5 to 0.5 and ${}^{k}c_2$ from 0.5 to 2.5.

4.3 Chaotic particle swarm optimization

One of the major drawbacks of the PSOA is its premature convergence, especially for search spaces with several local optima. In order to overcome this problem, some researchers proposed to introduce chaotic maps with certainty, ergodicity and pseudo-randomness property into PSOA so as to improve the global convergence [13]. Moreover, in [8] and [14] is stated that – due to the non-repetition of chaos – chaos-based optimization algorithms can carry out overall searches at higher speeds than stochastic ergodic searches that depend on probabilities. The ways in which the chaos entries into PSOAs are different but in this study we consider the most diffused one: in detail, we assume that chaotic maps are adopted to select the numerical values for the parameters of the particle's velocity in Eq. (23). Different numerical studies have been conducted for choosing the better chaotic maps. Looking for a synthesis of the documented results, we assume that the inertia weight is updated by adopting the logistic map [13]:

$${}^{(k+1)}\tilde{w} = \lambda\, {}^{k}\tilde{w}\left(1 - {}^{k}\tilde{w}\right) \quad with \ {}^{k}\tilde{w} \in (0,1) \tag{33}$$

where λ is assumed equal to 4 to obtain ergodicity in (0,1). The upper symbol ~ indicates that the corresponding quantity is evaluated by means of an opportune chaotic map. In our applications, the adopted value of the chaotic inertia weight are scaled within the interval [0.40,0.90]. About the acceleration factors, in [14] is proposed the use of the Zaslavskii map:

$${}^{(k+1)}\zeta_1 = \mathrm{mod}\left[{}^{k}\zeta_1 + \nu + \delta\, {}^{(k+1)}\zeta_2, 1\right] \tag{34}$$

$${}^{(k+1)}\zeta_2 = \cos\left(2\pi\, {}^{k}\zeta_1\right) + e^{-\rho}\, {}^{k}\zeta_2 \tag{35}$$

in which mod[·] is the modulus (signed remainder after division). The use of Zaslavskii map has been theoretically justified in [14] for virtue of its ergodicity and unpredictability, since a strange attractor with large Lyapunov exponent can be found for ν=400, ρ=3 and δ=12.6695 (in this case, ${}^{k}\zeta_2 \in$[-1.0512,1.0512]). Therefore, in [14] is stated that a Zaslavskii map-based chaotic PSOA should be more capable of escaping from local optima than random search. In our applications, both chaotic acceleration factors are functions based on the results of Eq. (35), but final values are scaled within the interval [0.50,2.50].

4.4 Passive congregation

The dynamic of natural swarms can be modeled by taking into account two grouping forms [15]:

- Aggregation, that is a grouping by environmental forces. Two types of aggregation forms can be identified. The passive aggregation is a passive grouping due to physical phenomena (i.e., transport caused by water currents) whereas the active aggregation is a grouping by attractive resources (i.e., food or space within the environment);

- Congregation, that is a grouping by social forces (it depends on the group itself and not on the environment). Also in this case two different forms of congregation can be analyzed. The passive congregation is the attraction between members of the group without the existence of observable social behaviors and therefore it looks as a random phenomenon. On the other hand, the social congregation happens under active information transfer, so that the behavior of the group depends on the relations among the members of the group.

It has been pointed out in [15] that the third addend of the standard PSOA in Eq. (23) models an active aggregation rather than a passive congregation because ${}^{k}\mathbf{x}_{Gb}$ can be regarded (using a biologic metaphor) as “the place with most food”. Therefore, the standard model in Eq. (23) does not incorporate a congregation form. Starting from this consideration, in [15] is proposed a new rule for updating the particle’s velocity: by including a passive congregation term the information sharing within the swarm may be improved and the recognition of the search space as well. Accounting for the passive congregation, the particle’s velocity is updated as follows [15]:

$$ {}^{(k+1)}\mathbf{v}_i = w^k\,\mathbf{v}_i + c_1\,{}^{(k+1)}\mathbf{r}_{i1} \times \left({}^{k}\mathbf{x}_i^{Pb} - {}^{k}\mathbf{x}_i \right) + c_2\,{}^{(k+1)}\mathbf{r}_{i2} \times \left({}^{k}\mathbf{x}^{Gb} - {}^{k}\mathbf{x}_i \right) + c_3\,{}^{(k+1)}\mathbf{r}_{i3} \times \left({}^{k}\mathbf{x}_{rand} - {}^{k}\mathbf{x}_i \right) \quad (36) $$

in which ${}^{k}\mathbf{x}_{rand}$ is a particle selected randomly from the swarm, ${}^{(k+1)}\mathbf{r}_{3i}$ is a vector whose terms are random numbers uniformly distributed between zero and one and c_3 is another acceleration factor (called passive congregation coefficient, a constant positive real value). The adopted (constant) numerical values for the control parameters in Eq. (36) are taken from [15].

5 IDENTIFICATION VIA GENETIC ALGORITHM

Genetic algorithms are well known non-classical techniques for parametric identification: during a succession of generations, these methods generate new points in the admissible search space by applying operators on the current solutions set and “statistically” moving toward more optimal places in virtue of the Darwinian strife for survival. A detailed state-of-the-art review about genetic algorithm based mechanical system identification can be found in [16].

A modified real-coded genetic algorithm [17] for parametric identification of mechanical system is considered in this paper. The algorithm – whose acronym is MGAR – utilizes several subpopulations and a migration operator with a ring topology is periodically performed to allow the interaction between them. For each subpopulation, a specialized medley of recent genetic operators (crossover and mutation) has been adopted and is briefly discussed. The final algorithm includes an operator based on the auto-adaptive asexual reproduction of the best individual in the current subpopulation. This latter was introduced to avoid a long stagnation at the start of the evolutionary process due to insufficient exploration as well as to attempt an improved local exploration around the current best solution at the end of the search. The original algorithm included a search space reduction technique, but it is not considered in this paper because of the small number of unknown parameters to be identified. This algorithm was successfully adopted for nonlinear [17] and large linear system identification [18]. The interested reader can refer to [17] and [18] for more information about it and the adopted numerical values for the embedded control parameters.

6 NUMERICAL RESULTS

A large numerical investigation is conducted to assess the performances of the above presented non-classical identification techniques for parametric identification of a nonlinear viscous damper subject to various dynamic loads (harmonic and earthquake loading). The effect of the noise contamination in the reference response is also studied.

6.1 Problem data and non-classical identification methods under investigation

A list of the considered non-classical identification methods is given in Tab. 1.

Algorithm	Short description
DEA01	A DEA whose mutation operator is given by Eq. (9) and with binomial crossover as in Eq. (14)
DEA02	A DEA whose mutation operator is given by Eq. (10) and with binomial crossover as in Eq. (14)
DEA03	A DEA whose mutation operator is given by Eq. (11) and with binomial crossover as in Eq. (14)
DEA04	A DEA whose mutation operator is given by Eq. (12) and with binomial crossover as in Eq. (14)
DEA05	A DEA whose mutation operator is given by Eq. (13) and with binomial crossover as in Eq. (14)
DEA06	A DEA with adaptive mutation – as in Eq. (16) and Eq. (17) – and a free-parameter crossover given by Eq. (22), see [7]
PSOA01	A PSOA whose velocity model is Eq. (23), with inertia weight as in Eq. (31), social and cognitive factors as in Eq. (32)
PSOA02	A PSOA in which the velocity updating rule (based on the use of the constriction factor) is given by Eq. (30)
PSOA03	A PSOA based on the use of chaotic maps (so-called chaotic PSOA) for both inertia weight and acceleration factors
PSOA04	A PSOA with passive congregation in which the velocity updating rule is given by Eq. (36)
MGAR	A modified multi-species real-coded genetic algorithm with specialized operators for each subpopulation, see [17] and [18]

Table 1: List of non-classical identification methods under investigation.

The parametric identification of the viscous damper is performed by solving the optimization problem in Eq. (7) whose cost function is given in Eq. (8). For this numerical investigation, the adopted mechanical model is that in Eq. (6) and the numerical values of the involved parameters are taken from [5]: M=1000, C_1=100, C_α=400, K_1=1000 and α=0.20. The set of parameters to be identified is $\mathbf{x}=\{M, C_1, K_1, C_\alpha, \alpha\}$ and $\mathbf{x}^*$ is its true real value. Lower and upper bounds are, $\mathbf{x}^l=0.10\mathbf{x}^*$ and $\mathbf{x}^u=2.00\mathbf{x}^*$, respectively. The population size and the maximum number of iterations are N=50 and L=400, respectively.

6.2 Nonlinear viscous damper subject to harmonic base motion

The viscous damper is subject to harmonic base motion:

$$p(t) = -Ma_g^{\max}\sin(\Omega t) \tag{37}$$

in which a_g^{max}=0.25g (g is the gravity acceleration) and Ω is given in Tab. 2 as function of the natural frequency of the system, that is $\omega = \sqrt{(K_1/M)}$.

Initial velocity and initial displacement are both equal to zero. The total number of samples is $S = 2000$. Unit of measures are arbitrary but consistent.

Load case	Ω/ω
L1	1.00
L2	0.50
L3	2.00

Table 2: Load cases.

Mean results over thirty distinct runs (that is, with different initial populations) are presented in Fig. 1 (for M), Fig. 2 (for C_1), Fig. 3 (for K_1), Fig. 4 (for C_α) and Fig. 5 (for α). The black horizontal solid line denotes the true parameter value.

A general overview of the obtained results leads to the following considerations:

- Non-classical identification methods provide an effective way for the parametric identification of nonlinear viscous dampers subject to harmonic-type dynamic loading, because the final errors are acceptable for practical applications.
- The load case L1 causes the most critical situation for the parametric identification of nonlinear viscous dampers. This is may be imputable to the use of harmonic excitation whose frequency coincides with that of the viscous damper.
- The DEA06 and MGAR are the best competitor for this numerical application because the identified parametric values are very close to the exact solution. Their performance in the parametric identification are strongly better than the others for the load case L1.

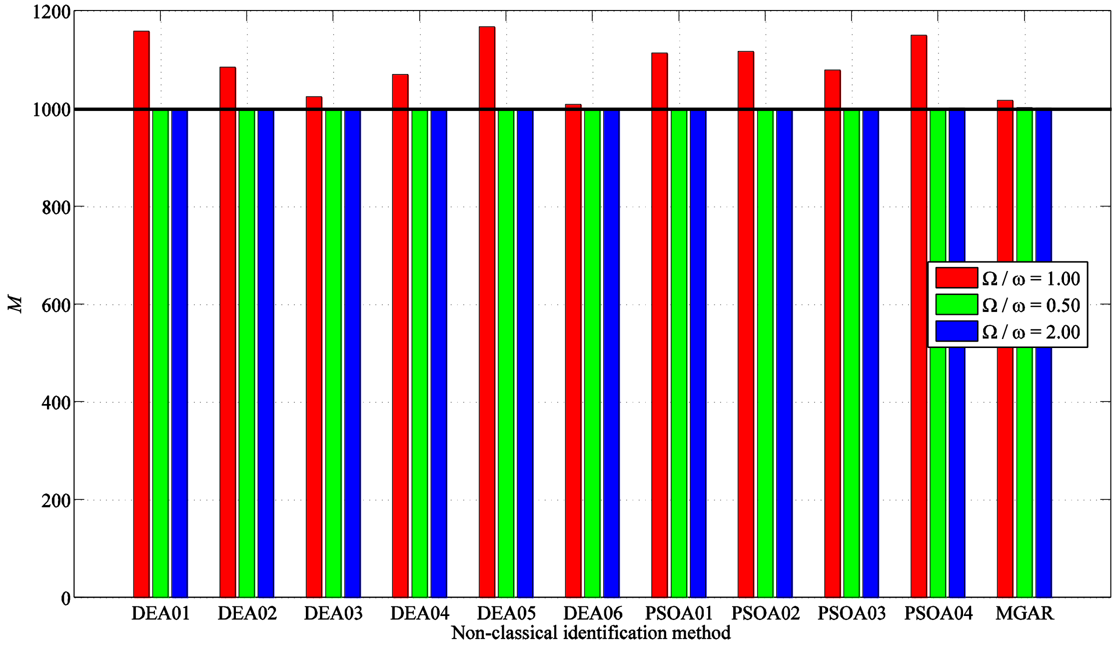

Figure 1: Identification results for M.

However, it was observed that all non-classical methods can achieve the exact solution of the identification problem by increasing the number of objective function evaluations. In this perspective, DEA06 and MGAR are more competitive than the others from a computational standpoint.

A more detailed inspection of the plotted results may provide further practical information. For instance, it appears that DEAs and PSOAs lead to comparable final results. There are no significant differences within the standard DEAs. On the other hand, the chaotic PSOA (labeled as PSOA03 in Tab. 01) is slightly better than the others.

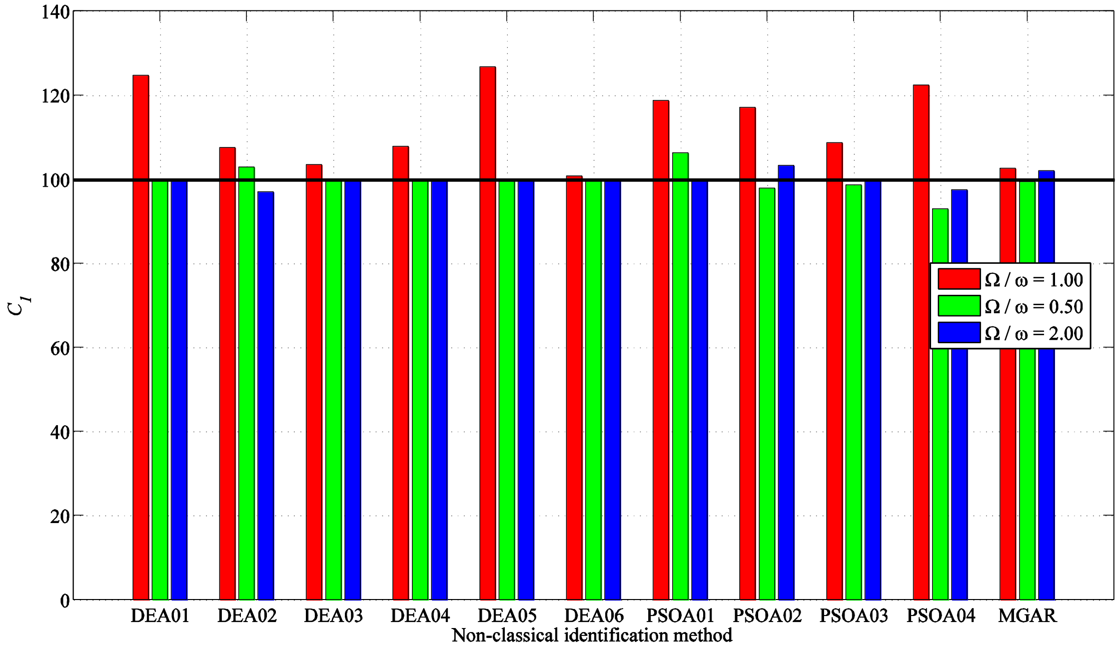

Figure 2: Identification results for C_1.

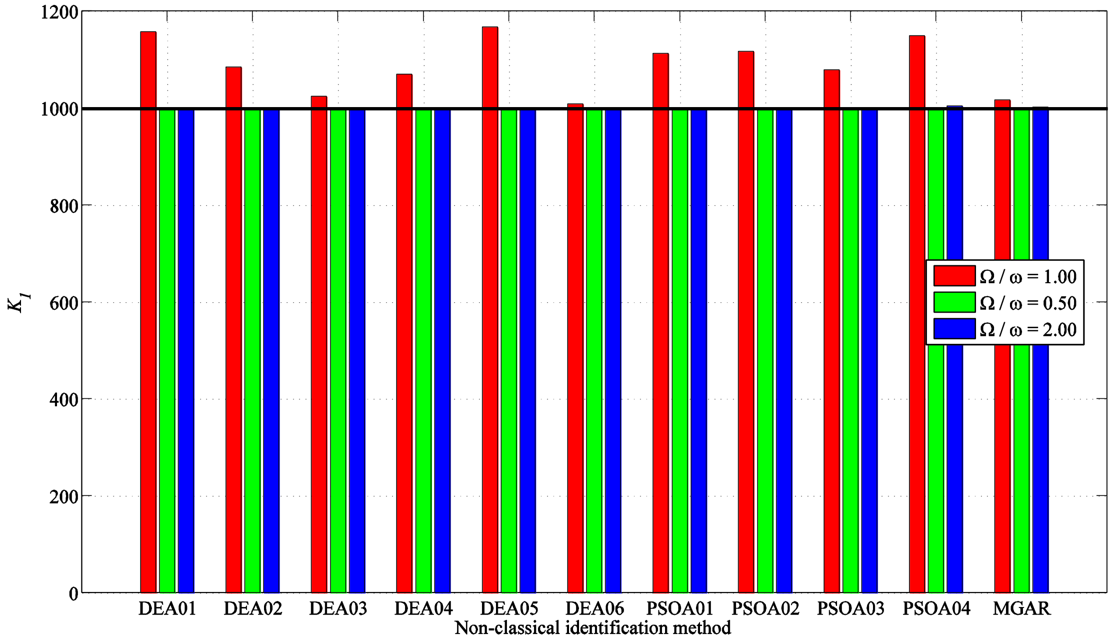

Figure 3: Identification results for K_1.

The most critical parameters to be identified is C_α: as it can be seen in Fig. 4, its numerical value for the load case L1 is approximately identified by the most of the investigated techniques (not so good results are obtained by using DEA01, DEA05, PSOA01, PSOA02 and PSOA04). For the most critical loading condition (L1), it is observed that (*i*) the identified values of M, C_1 and K_1 (mean values over thirty runs) are greater than the exact ones whereas (*ii*) the identified values of C_α (mean values over thirty runs) are lower than the exact ones.

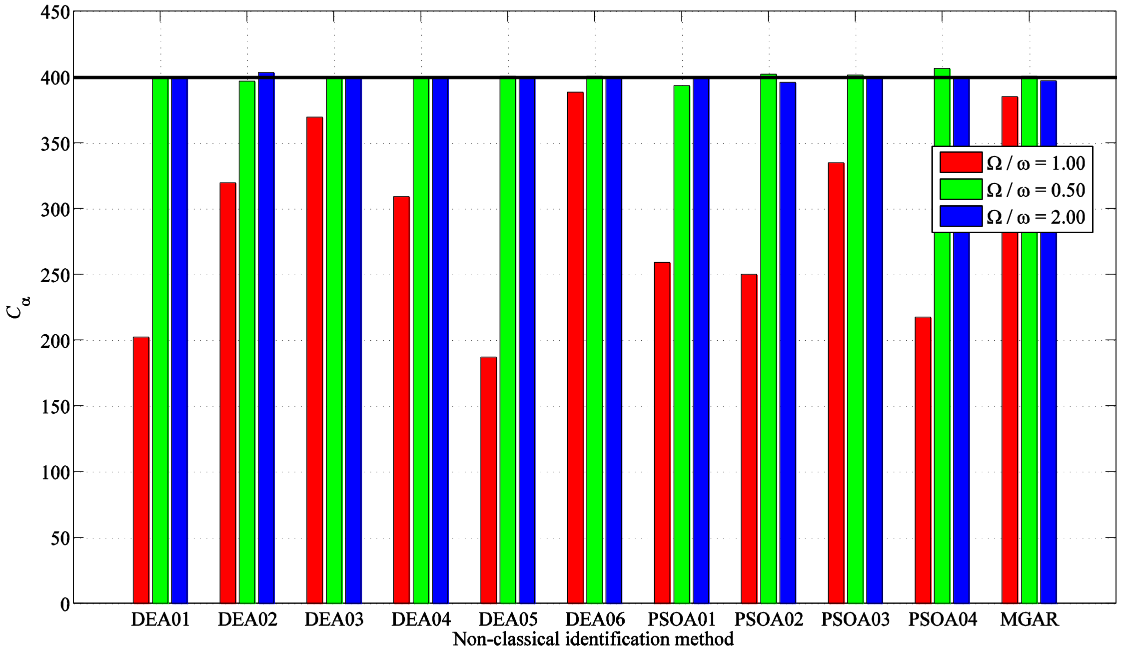

Figure 4: Identification results for C_α.

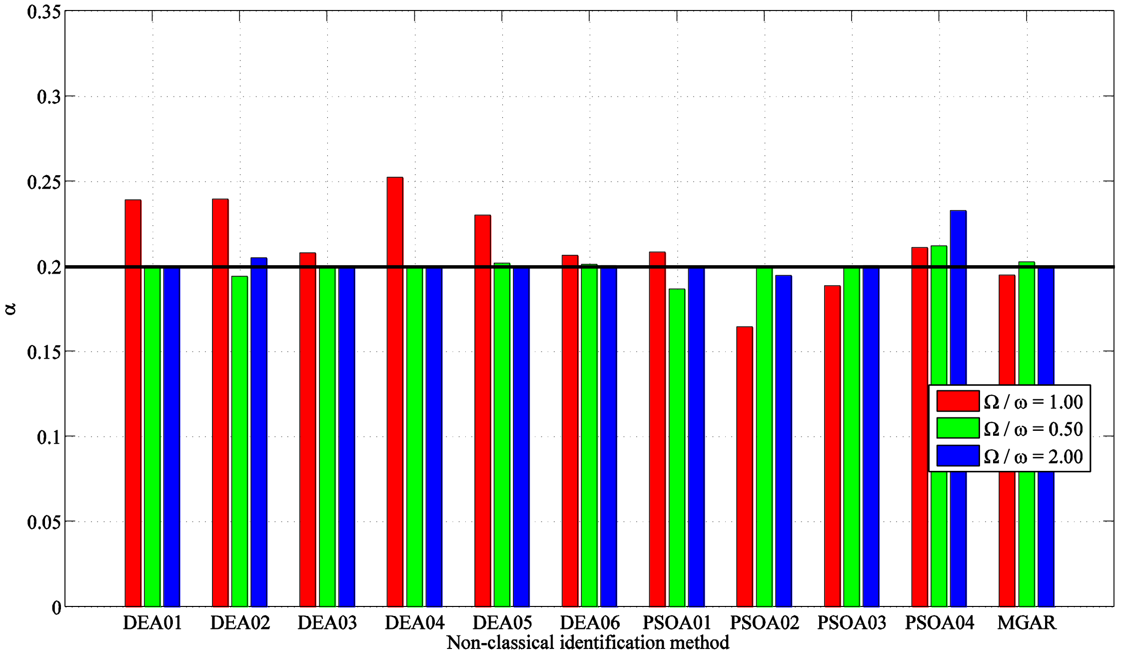

Figure 5: Identification results for α.

Some samples of the convergence histories for DEA06 are shown in Fig. 6 (for load case L1), Fig. 7 (for load case L2) and Fig. 8 (for load case L3). As above, the black horizontal solid line denotes the true parameter value. The objective function shows a small number of stagnations (number of iterations without improvements). This means that the exploration phase of the evolutionary search for DEA06 is very efficient.

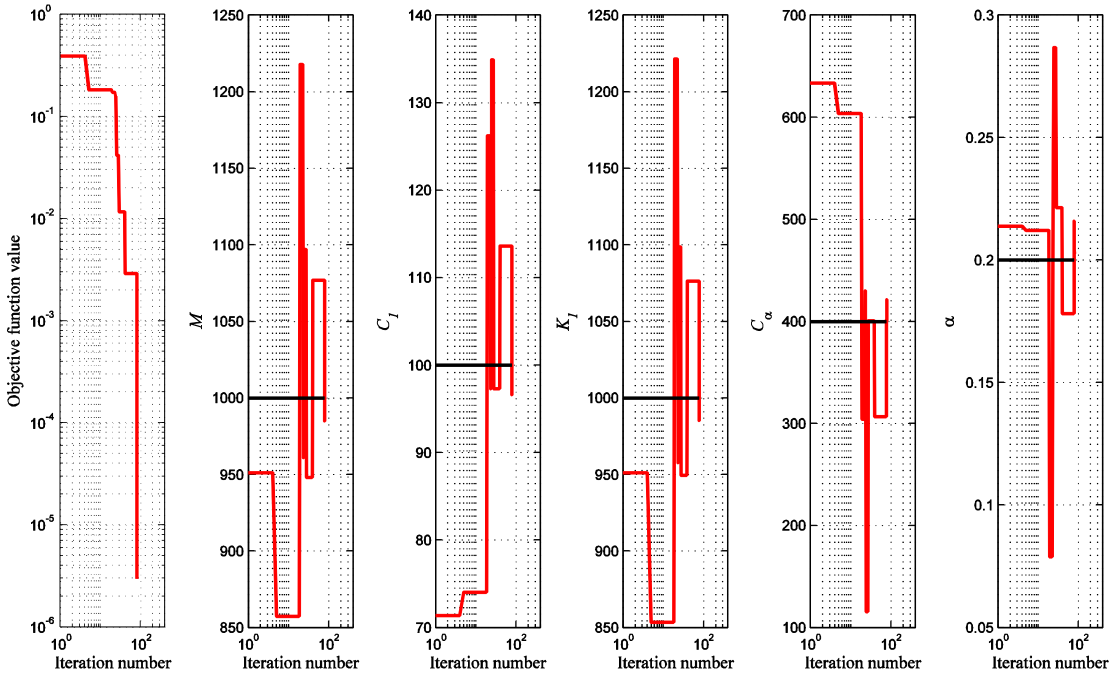

Figure 6: A sample of the convergence histories for DEA06 (load case L1).

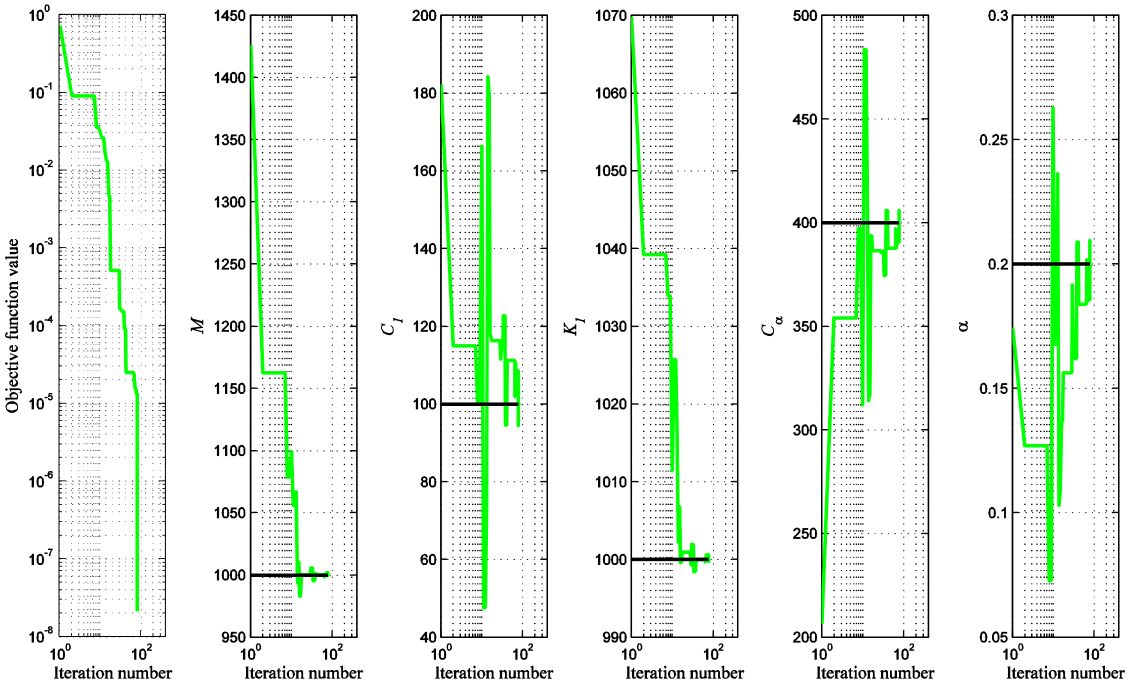

Figure 7: A sample of the convergence histories for DEA06 (load case L2).

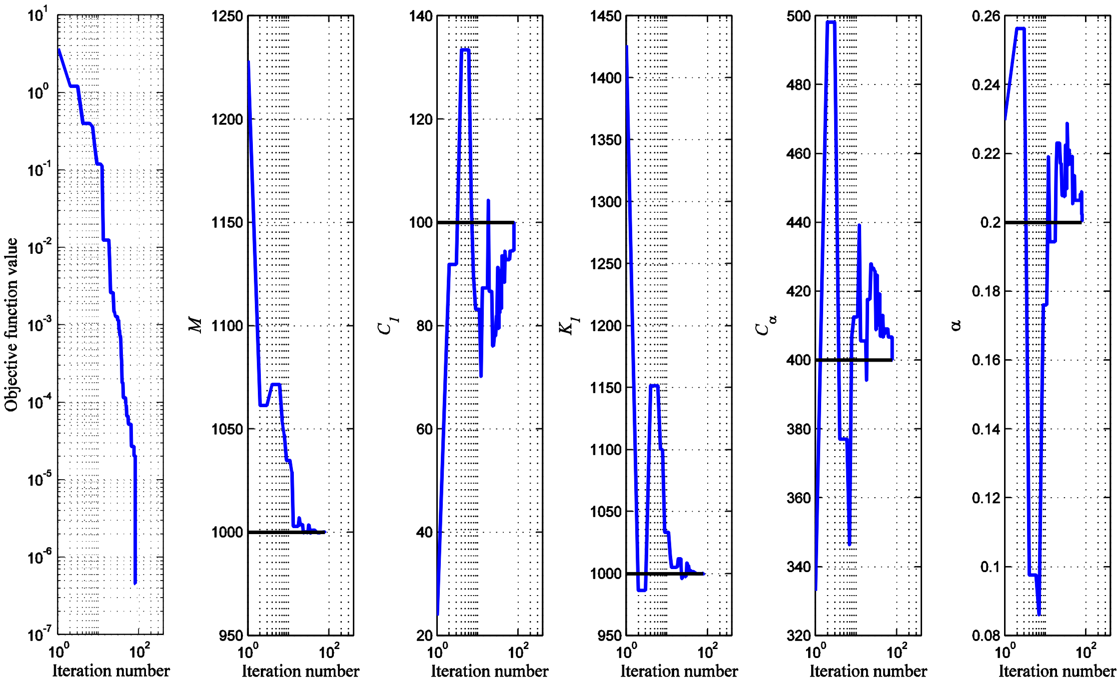

Figure 8: A sample of the convergence histories for DEA06 (load case L3).

Convergence histories of the model parameters confirm the effectiveness of DEA06 in parametric identification of the nonlinear viscous damper because a quasi exact results is achieved once 200÷300 iterations are completed. As a consequence, the total elaboration time can be reduced without jeopardizing the correctness of the identification process.

6.3 Nonlinear viscous damper subject to earthquake motion

The same nonlinear viscous dampers was identified under, both, white random noise and earthquake excitation. Using the non-classical methods under investigation (as they are listed in Tab. 1), all the model parameters were exactly identified (i.e., to four decimal digits). It has been observed that the final accuracy is slightly better than the obtained one for harmonic loading. It is an expected results, because the efficiency of the identification depends on the information contained in the input-output data: in this sense, harmonic loads with a low frequencies content are a limited excitation source. Herein, only results for a viscous damper subject to a real earthquake record are shown. Thus, the dynamic load is:

$$p(t) = -Ma_g(t) \tag{38}$$

in which a_g is the adopted earthquake record (for this numerical application, the El Centro earthquake is considered). Moreover, in order to study the detrimental effect of the noise contamination, a noisy reference system response is taken into account. A uniform-type noise was considered whit a noise-to-signal-ration (NSR) equal to 15%. The obtained noisy signal has not been subject to de-noising.

The results – summarized in Fig. 9 – demonstrate that DEA06 is relatively insensitive to moderate noise levels. The noise robustness of non-classical identification methods is well known in the current literature and it depends on the implicit parallelism in such numerical techniques [7][17]. Comparing the identification results by using a noise-free (solid lines in Fig. 9) and a noisy reference response, it is observed that:

- Because of the noise contamination, the minimum value of the objective function in Eq. (8) is not equal to zero. The final minimum value of the objective function under noisy signals may be very far from the ideal one (that is, equal to zero).
- The role of the exploration phase increases as the NSR value grows. In fact, the convergence histories toward the optimal solutions using noise-free data are faster than those for a NSR=15%. It is observed that the initial parts of the evolutionary search are more irregular when using a noisy system response, thus highlighting the importance of the exploration stage.

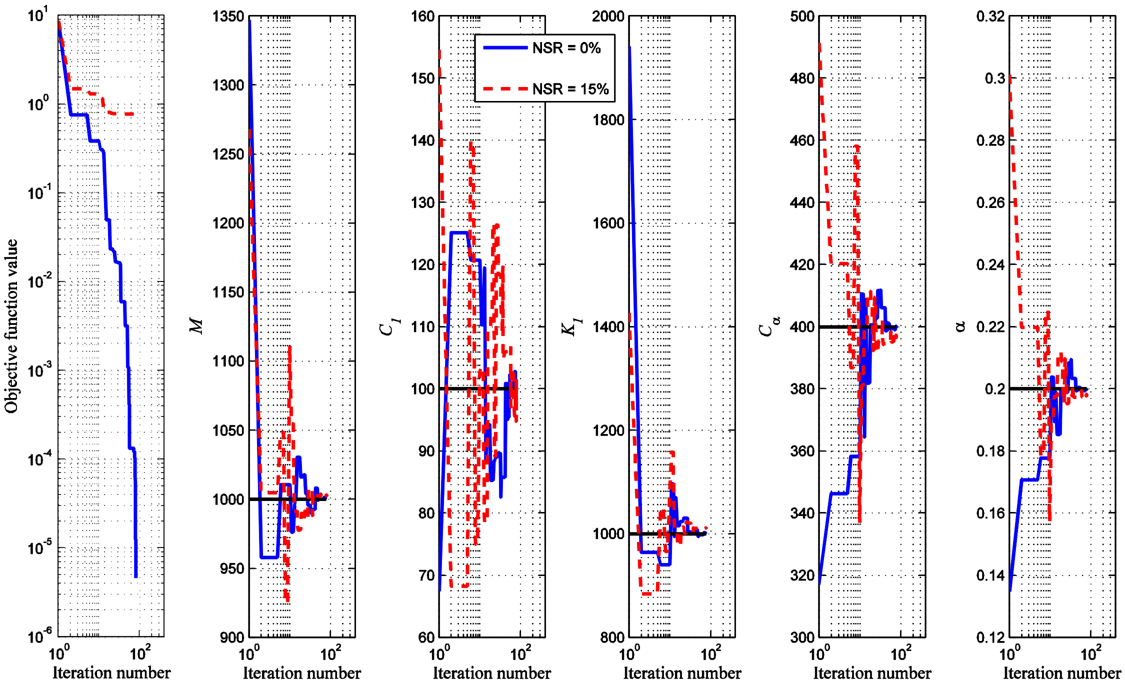

Figure 9: Convergence histories for DEA06 using free-noise and noisy reference response.

7 EXPERIMENTAL RESULTS

The synthesis of the conducted numerical studies provide positive evidences about the reliability of the investigated non-classical identification techniques for parametric identification of nonlinear viscous dampers. Moreover, useful aspects regarding the computational efficiency and the robustness against the instrumental noise were addressed. Nonetheless, the real viscous damper response may be more complicated and neglected nonlinearities can be relevant. Therefore it is essential to assess the applicability of these methods by using experimental data. To this end, some experimental tests were performed on a full-scale nonlinear viscous damper.

7.1 Experimental tests

?? [19]

7.2 Results of the identification based on experimental data

??

8 CONCLUSIONS

??

9 ACKNOLEDGMENTS

??

REFERENCES

[1] T.T. Soong, B.F. Spencer Jr, Supplemental energy dissipation: state-of-the-art and state-of-the practice. *Engineering Structures*, **24**, 243-259, 2002.

[2] H.B. Yun, F. Tasbighoo, S.F. Masri, J.P. Caffrey, R.W. Wolfe, N. Makris, C. Black, Comparison of Modeling Approaches for Full-scale Nonlinear Viscous Dampers. *Journal of Vibration and Control*, **14**, 51-76, 2008.

[3] C.G. Koh, Y.F. Chen, C.Y. Liaw, A hybrid computational strategy for identification of structural parameters. *Computers and Structures*, **81**, 107-117, 2003.

[4] G. Terenzi, Dynamics of SDOF Systems with Nonlinear Viscous Damping. *Journal of Engineering Mechanics*, 125, 956-963, 1999.

[5] A. Della Valle, Sulla progettazione in zona sismica di strutture dotate di dissipatori fluido-viscosi. Ph. D. Thesis, 2008 (in Italian).

[6] R. Storn, K. Price, Differential evolution – A simple and efficient heuristic for global optimization over continuous space. *Journal of Global Optimization*, **4**, 359-431, 1997.

[7] G. Quaranta, G. Monti, G.C. Marano, Parameters identification of Van der Pol-Duffing oscillators via particle swarm optimization and differential evolution. *Mechanical Systems and Signal Processing*, **24**, 2076-2095, 2010.

[8] L.S. Coelho, A quantum particle swarm optimizer with chaotic mutation operator. *Chaos, Solitons and Fractals*, **37**, 1409-1418, 2008.

[9] Y. Shi, R. Eberhart, A modified particle swarm optimizer. *IEEE World Congress on Computational Intelligence*, Anchorage, AK, USA, May 4-9, 1998.

[10] M. Clerc, The swarm and the queen: towards a deterministic and adaptive particle swarm optimization. *Proceedings of the congress on evolutionary computation (CEC 1999)*, Washington DC, USA, July 6-9, 1999.

[11] Y. Shi, R. Eberhart, Empirical study of particle swarm optimization, *Congress on evolutionary computation (CEC 1999)*, Washington DC, USA, July 6-9, 1999.

[12] A. Ratnaweera, S.K. Halgamuge, H.C. Watson, Self-Organizing Hierarchical Particle Swarm Optimizer With Time-Varying Acceleration Coefficients. *IEEE Transactions on Evolutionary Computation*, **8**, 240-255, 2004.

[13] J. Chuanwen, E. Bompard, A hybrid method of chaotic particle swarm optimization and linear interior for reactive power optimisation. *Mathematics and Computers in Simulation*, **68**, 57-65, 2005.

[14] L.S. Coelho, B.M. Herrera, Fuzzy Identification Based on a Chaotic Particle Swarm Optimization Approach Applied to a Nonlinear Yo-yo Motion System. *IEEE Transactions on Industrial Electronics*, **54**, 3234-3245, 2007.

[15] S. He, Q.H. Wu, J.Y. Wen, J.R. Saunders, R.C. Paton, A particle swarm optimizer with passive congregation. *Biosystems*, **78**, 135-47, 2004.

[16] G.C. Marano, G. Quaranta, G. Monti, Genetic Algorithms in Mechanical Systems Identification: State-of-the-art Review, in *Soft Computing in Civil and Structural Engineering* (Chapter 2), B.H.V. Topping and Y. Tsompanakis, Eds., Stirlingshire (Scotland): Saxe-Coburg Publications, 2009.

[17] G. Monti, G. Quaranta, G.C. Marano, Genetic-algorithm-based strategies for dynamic identification of nonlinear systems with noise corrupted response, *Journal of Computing in Civil Engineering*, **24**, 173-187, 2010.

[18] G.C. Marano, G. Quaranta, G. Monti, Modified Genetic Algorithm for the Dynamic Identification of Structural Systems Using Incomplete Measurements. *Computer Aided Civil and Infrastructure Engineering*, article in press, 2010.

[19] Norme Tecniche per le Costruzioni, D.M. 14 gennaio 2008, G.U. n. 29, 4 febbraio, n. 30, 2008.

COMPDYN 2011
III ECCOMAS Thematic Conference on
Computational Methods in Structural Dynamics and Earthquake Engineering
M. Papadrakakis, M. Fragiadakis, V. Plevris (eds.)
Corfu, Greece, 25–28 May 2011

OPTIMAL WHOLE-LIFE-CYCLE SEISMIC DESIGN OF CONCRETE FRAMES

Bora Gencturk[1] **and Amr S. Elnashai**[2]

[1] University of Illinois at Urbana-Champaign
Department of Civil and Environmental Engineering, 1240 Newmark Lab, 205 N Mathews Ave, Urbana, IL, 61801
e-mail: bgenctu2@illinois.edu

[2] University of Illinois at Urbana-Champaign
Department of Civil and Environmental Engineering, 1114 Newmark Lab, 205 N Mathews Ave, Urbana, IL, 61801
email: aelnash@illinois.edu

Keywords: Reinforced concrete, ECC, dynamic analysis, structural optimization, Pareto-front, Life-cycle cost analysis.

Abstract. *In this study multi-objective optimization of structural frames is investigated. Two different materials, reinforced concrete and reinforced engineered cementitious composites (ECC), with different response characteristics are used to model the frames. ECC is characterized by high tensile strength and ductility, high energy absorption and reduced crack widths when compared to conventional concrete. However, the material is more expensive than conventional concrete. Therefore, in order to quantify the potential benefits that could be obtained by replacing concrete with ECC, the structural performance is evaluated for the whole-life-cycle of the structure. The results of the optimization problem are presented in Pareto-optimal form which is preferred by decision makers due to the provided flexibility in selecting the solution alternatives. The option of replacing the conventional material, concrete, with a high performance alternative, ECC, is investigated in an optimization framework with the ultimate goal of higher safety, increased sustainability and improved performance.*

1 INTRODUCTION

Optimal and sustainable design of structures has become an important issue in the recent years. Through the use of optimization techniques, it is possible to reduce the material usage, hence environmental impacts, and concurrently prevent failures by better understanding the structural behavior at different limit states. This paper investigates the use of a high-performance material, engineered cementitious composites (ECC), to reduce the life-cycle cost (LCC) of concrete frames and improve the structural performance at different limit states.

ECC is a fiber-reinforced high-performance material introduced as a replacement for concrete by Li and co-workers [1-4]. ECC differs from other types of high-performance cementitious materials in that the microstructures are optimized using micromechanical models to achieve ultra-high ductility, with crack widths limited to below 100µm and ultimate tensile strain capacity as high as 5 percent [5]. The improved performance of ECC comes with an increased cost and reduced greenness. The ECC mixtures are less environmental friendly and cost 1.5-3.3 times more than concrete. However, the seismic structural performance of ECC evaluated in terms of stiffness, strength, ductility and energy absorption capacity is significantly higher [6]. Therefore, the material has to be utilized in the most efficient way to reduce the LCC, increase sustainability through less material usage and extended lifetime, and improve safety through higher performance. This is best investigated by defining an optimization problem that includes structural response in addition to initial and whole-life-cycle costs as the primary objectives.

In the following, a multi-objective optimization problem is formulated taking into account the structural performance, and the initial and whole life-cycle costs. In order to utilize the ECC material in the most efficient way, the critical (potential plastic hinge) locations of the structural frames, i.e. beam-column connections and bases of the columns are deployed with ECC and for the rest of the structure conventional concrete is used. Here, these are referred as multi-material (MM) frames. To assess the performance of this intervention strategy, the results are compared to those of the frames made of concrete only and ECC only.

The ground motions that are used for inelastic dynamic time history analysis of the structural frames are derived by probabilistic seismic hazard analysis (PSHA) at a selected site. This computationally intensive inelastic dynamic time history analysis is employed so as to accurately obtain the earthquake demand and to distinguish the response of reinforced concrete (RC) and ECC frames from that of MM frames. The structural capacity is evaluated by pushover analysis and local response measures, strains in longitudinal reinforcement and matrix (concrete or ECC), are used to define the limit states. The optimal solutions in the search space are found by a Taboo search algorithm which is shown to be very efficient in solving combinatorial problems. The results are presented in Pareto-optimal form to provide flexibility in selecting the alternative solutions and to compare the performance of different frames in the objective function space.

2 SEISMIC HAZARD AND EARTHQUAKE GROUND MOTIONS

2.1 Definition of the seismic hazard

In this study uniform hazard spectra (UHS) obtained from PSHA are used to characterize the seismic hazard for a selected site. The UHS used here are based on the developments by U.S. Geological Survey (USGS) on 2008 national seismic hazard mapping [7].

A site at the intersection of 2nd and Market Streets in San Francisco, CA (with coordinates 37° 47′ 21.58′′ N, 122° 24′ 04.77′′ W) is selected and the seismic hazard is consistently derived. The sources of seismicity contributing to the hazard at the selected site are shown in Figure 1(a). The governing faults for the selected site are the San Andreas, the San Gregorio and the Hayward faults. The source-to-site distance varies between 11 km to 25 km depending on the fault. The soil conditions might significantly alter the characteristics of the ground motions at a site, therefore, the soil conditions are also taken into account in the development of UHS. The soil at the selected site is determined as D on the NEHRP [8] scale with a shear wave velocity in the range from 180 m/sec to 360 m/sec.

Site specific hazard curve for peak ground acceleration (PGA), and UHS for three different return periods (i.e. 75, 475, and 2475 years) are calculated as shown in Figure 3(a) and (b), respectively. These return periods correspond to three structural limit states: immediate occupancy (IO), life safety (LS) and collapse prevention (CP), respectively.

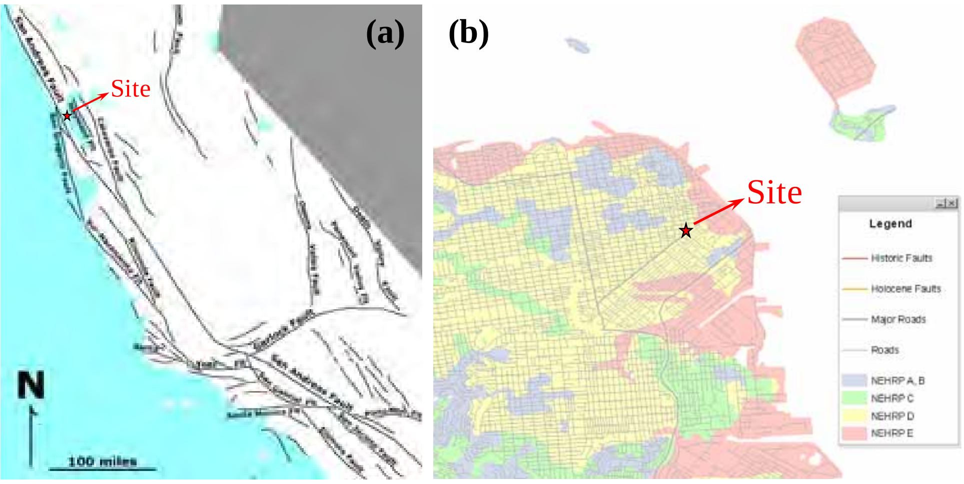

Figure 1: (a) Sources of seismicity [9], and (b) soil profile at the selected site [10].

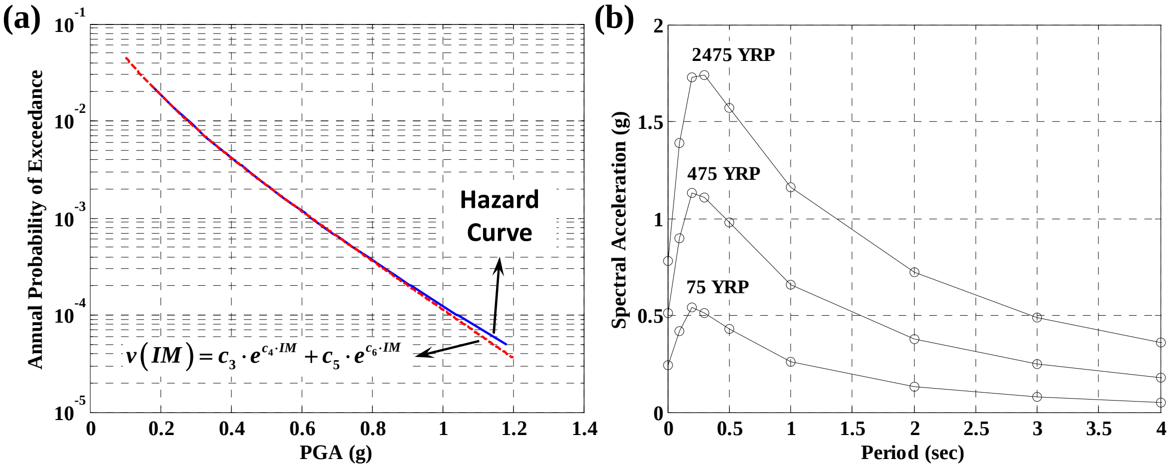

Figure 2: (a) PGA hazard curve, and (b) UHS at different return periods (YRP stands for years return period).

2.2 Selection and spectrum matching of the earthquake ground motions

The disaggregation is performed in order to determine the relative contribution of seismic sources to hazard at a particular location. As a result of the disaggregation calculations the significant parameters, i.e. magnitude, distance, and PGA that characterize the seismic hazard are determined. These values together with the soil conditions and UHS control the selection of earthquake time histories that are used for seismic design and assessment purposes.

The PEER NGA database [11] is utilized to select seven earthquake recordings are for each of the three return periods. The following criteria are used for selecting the records: (1) earthquakes having similar mechanisms to those which are pertinent to the faults affecting the site, (2) magnitudes within ±1 with the governing magnitude for the considered return period, (3) shear wave velocity of the recording station within the range from 180 m/sec to 360 m/sec, and (4) the acceleration spectrum of the earthquake time history matching as closely as possible the UHS associated with the considered return period.

Spectrum matching is utilized to make the selected ground motions compatible with the UHS at different return periods. For this purpose the RSPMatch software [12] is utilized. The relevant period range for the structural frames considered in this study is from 0-1 sec (see Section 3.1). Therefore, in order not to introduce unrealistic low frequency oscillations in the spectrum compatible ground motions, when target spectra are defined the original spectra of the records are retained for periods longer than 1 sec, and UHS are used for periods shorter than 1 sec. The response spectra, and the acceleration time history before and after spectrum matching of an example record for 475 years return period are shown in Figure 3(a) and (b), respectively.

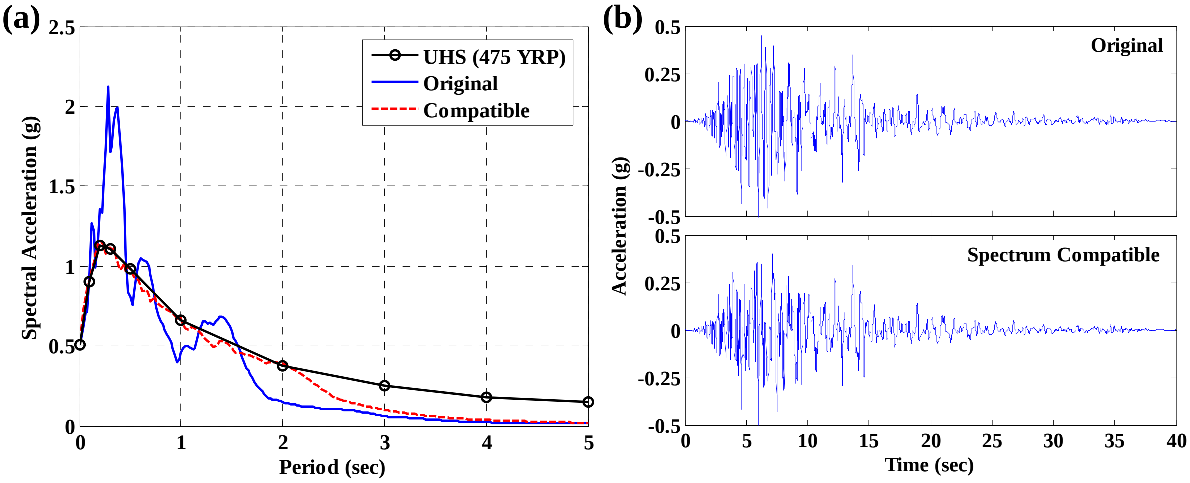

Figure 3: (a) UHS, and response spectrum, and (b) acceleration time history of the selected record, before and after spectrum matching for the 475 years return period.

3 DESCRIPTION OF THE MULTI-OBJECTIVE OPTIMIZATION PROBLEM

3.1 Structural frames

The frame considered for structural optimization is illustrated in Figure 4. The critical locations, i.e. beam-column connections and the column bases are made of ECC, while the rest of the frame is concrete. One tenth of the members' length on each side is assumed to be the critical regions. As mentioned earlier RC only and ECC only frames are also considered for comparison purposes. Seven design variables are defined for the optimization problem as given in Table 1, alongside the minimum and maximum values and increments. The combination of these design variables results in 30,000 cases which constitute the search space for each frame type.

The initial cost of the frames considers only the material costs. The unit prices for concrete and steel are assumed to $0.13/liters and $0.66/kg, respectively. It is assumed that the structural members are properly designed to prevent shear failure and the amount shear reinforcement is calculated following a capacity design approach. First, the moment capacity of the sections are calculated and increased by 20 percent to account for overstrength. Then, the shear force that produces the moment capacity is evaluated and the required shear reinforcement is calculated according to ACI-318 [13]. The cost of shear reinforcement is also included in the initial cost of the frames. It is demonstrated through experimental studies that the shear reinforcement can be eliminated for flexural ECC members [6]. Therefore, no shear reinforcement is added to sections where ECC is used. Labor costs are not considered in this study.

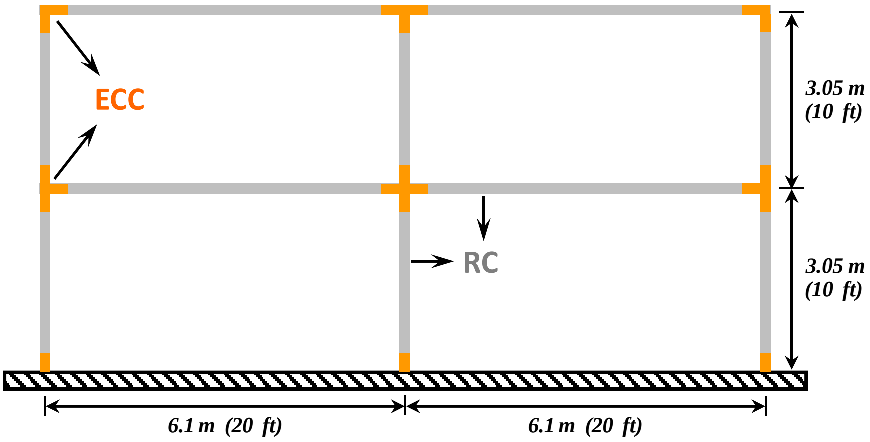

Figure 4: The considered structural frame for optimization.

	Minimum	Maximum	Increment
Column Reinforcement Ratio	1.0%	2.5%	0.50%
Beam Reinforcement Ratio	0.5%	2.0%	0.50%
Width of Exterior Columns (mm)	660.4	863.9	50.8
Width of Interior Columns (mm)	711.2	914.4	50.8
Width of Columns (mm)	457.2	660.4	50.8
Depth of Beams (mm)	508	711.2	50.8
Depth of Beams (mm)	406.4	508	50.8

Table 1: Design variables and ranges for the considered structural frames.

3.2 Evaluation of structural capacity and earthquake demand

Structural capacity is evaluated by pushover analysis. The frames described in Section 3.1 are modeled using fiber-based finite element analysis software ZEUS NL [14] which includes a validated constitutive model for ECC [6]. The three structural limit states, IO, LS and CP that correspond to the three return periods, 75, 475 and 2475 years are determined from the pushover analysis using local response measures, i.e. strains in concrete and longitudinal reinforcement. Based on previous research on testing of steel reinforcement and concrete [15], the occurrence of IO and LS limit states are defined as the reaching or exceeding 0.5 and 5 percent strain, respectively, in the reinforcing steel of any of the columns or beams. The occurrence CP limit state is defined as reaching or exceeding 10 percent strain in reinforcing steel or 1 percent compressive strain in core concrete in any of the columns or beams.

In order to establish the mean values for the limit states to be used in the LCC model, 50 cases are selected randomly from the 30,000 combinations. Pushover analyses of the RC, MM and ECC frames are conducted and the limit states are found in terms of interstory drift.

The selected cases are also utilized to quantify the dispersion in earthquake demand due to variability in the ground motion which is a critical parameter for LCC calculation. Each of the previously mentioned 50 cases is subjected seven ground motions (using inelastic dynamic time history analysis) for each return period. A lognormal distribution is fitted to the earthquake demand at each return period and for each frame type to obtain the dispersion values (β_D in Section 3.3). It is seen that the dispersion in earthquake demand increases for increasing hazard level (return period). 0.25, 0.35 and 0.45 are used as to describe the dispersion in earthquake demand at return periods of 75, 475 and 2475 years, respectively.

3.3 Derivation of the life-cycle cost model

The LCC of a structure (due to post earthquake repair) is a critical parameter for structural engineers and decision makers such as owners. Therefore, it is important to include the LCC as one of the objectives in optimal seismic design of structures. The expected LCC of a structure is calculated as [16]

$$E\left[C_{LC}\left(t\right)\right]=C_0+\frac{\left(1-e^{-\lambda t}\right)}{\lambda}\sum_{i=1}^{N}C_iP_i \tag{1}$$

where C_0 is the initial construction cost, t is the service life of the structure (here taken as 75 years), λ is the constant discount rate per year that converts costs due to hazard that occurs in the future into present value (taken as 1 percent), N is the total number of limit-states considered (here equal to 3), P_i is the probability that the structure will be in the i$^{\text{th}}$ damage state given the earthquake occurrence, and C_i is the corresponding cost as a fraction of the initial cost of the structure. P_i is given by

$$P_i=P\left(\Delta_D>\Delta_{C,i}\right)-P\left(\Delta_D>\Delta_{C,i+1}\right) \tag{2}$$

where Δ_D is the earthquake demand and $\Delta_{C,i}$ is the structural capacity, in terms of drift ratio, defining the i$^{\text{th}}$ damage state as described in Section 3.2. The probability of demand being greater than capacity is evaluated as

$$P\left(\Delta_D>\Delta_{C,i}\right)=\int_0^{\infty}P\left(\Delta_D>\Delta_{C,i}\,|\,IM=im\right)\left|\frac{dv\left(IM\right)}{dIM}\right|dIM \tag{3}$$

where the first term inside the integral is the conditional probability of demand being greater than the capacity given the ground motion intensity, *IM*. This term is also known as the fragility function. The second term is the slope of the mean annual rate of exceedance of the ground motion intensity. The hazard curve defined as *v(IM)* in Eqn. (3), where *IM* is PGA for this study, is shown in Figure 2(a). The conditional probability of demand being greater than the capacity is

$$P\left(\Delta_D>\Delta_{C,i}\,|\,IM=im\right)=\int_0^{\infty}P\left(\Delta_D>\delta\,|\,IM=im\right)f_C\left(\delta\right)d\delta \tag{4}$$

where δ is the variable of integration and f_C is the probability density function for structural capacity. This formulation assumes that the demand and the capacity are independent of each other. Structural capacity is assumed to be lognormally distributed with $\Delta_{C,i}$ and β_C that are, respectively, the mean and the standard deviation of the corresponding normal distribution. $\Delta_{C,i}$ is evaluated as described in Section 3.2 for RC, MM and ECC frames. The structural demand is also assumed to follow a lognormal distribution and the probability of demand exceeding a certain value, δ, is given by

$$P\left(\Delta_D > \delta \mid IM = im\right) = 1 - \Phi\left[\frac{\ln\left(\delta\right) - \lambda_{D|IM=im}}{\beta_D}\right] \tag{5}$$

where $\Phi[\cdot]$ is the standard normal cumulative distribution, λ_D is the natural logarithm of the mean of the earthquake demand as a function of the ground motion intensity, and β_D is the standard deviation of the corresponding normal distribution of the earthquake demand. Although, β_C and β_D are dependent on ground motion intensity, in most studies they are taken as constants due to lack of information. The uncertainty in capacity (here represented with β_C) due to sources such as modelling error, lack of knowledge and variation in material properties was investigated in several studies [17]. In this study it is assumed to be equal to 0.35 taking previous research as a reference [17]. The dispersion in earthquake demand (here represented with β_D) due to variability in ground motions is evaluated here as described in Section 3.2. The mean of earthquake demand, μ_D, as a continuous function of the ground motion intensity is described using

$$\mu_D\left(IM\right) = c_1 \cdot IM^2 \tag{6}$$

where the constant c_1 is determined by curve fitting to the three data points that match the PGA of the ground motions records at return periods 75, 475 and 2475 years with the earthquake demand evaluated using inelastic dynamic analysis.

The hazard curve shown in Figure 2(a) is also described in the mathematical form

$$v\left(IM\right) = c_3 \cdot e^{c_4 \cdot IM} + c_5 \cdot e^{c_6 \cdot IM} \tag{7}$$

where c_3 through c_6 are constant to be determined from curve fitting. The results of the curve fitting using the functional form described by Eqn. (7) to the PGA hazard curve at the selected site is shown in Figure 2(a).

With the above described formulation each term in Eqn. (3) is represented as an analytical function of the ground motion intensity, *IM*. Thus, using numerical integration the desired probabilities of Eqn. (2) can easily be calculated. The LCC is evaluated through Eqn. (1).

4 TABOO SEARCH ALGORITHM

As described earlier the optimization problem is reduced to a combinatorial one due to discrete nature of the design variables. Taboo search (TS) algorithm which is known to be very efficient in solving combinatorial problems is used here.

To describe the modified TS algorithm used here, first, it is required to make the following definitions. The taboo list includes points in the design space for which the objective functions are evaluated for. Since inelastic dynamic time history analysis is computationally costly, this list is used to avoid multiple runs with the same combination of design variables. That is, a point in the taboo list is not evaluated again. The Pareto list includes the points that are not dominated by other points within the set for which the evaluation of objective functions is performed (i.e. the taboo list). The seed list includes the points around which optimal solutions are looked for. The latter are called as the neighboring points and they are basically the adjacent elements of the multidimensional array, that defines the decision (or design) variables, around the given seed point. The modified TS algorithm works as follows:

a. Start with the minimum cost combination evaluate the objective function and add this point into taboo, seed and Pareto lists. Use this point as the initial seed point.
b. Find the neighboring points around the current seed. Here the number of neighboring points is chosen equal to the number of design variables and selected randomly amongst all the adjacent elements of the multidimensional array that defines the design variables.
c. Evaluate the objective function for all the neighboring points and add these into taboo list.
d. Find the Pareto-front using the set of points for which the objective function is evaluated and update the Pareto list as the current Pareto-front.
e. Amongst the neighboring points for the current iteration choose the one that is on the Pareto-front and minimizes the cost function as the next seed point and add this point into the seed list. If there is no point which satisfies these conditions choose randomly one of the points from the Pareto list amongst the ones that are not already in the seed list.
f. Check if the predetermined maximum number of objective function evaluations is exceeded; if yes stop, if not go to Step b.

5 RESULTS AND DISCUSSION

As an example of how the TS algorithm conducts the search within the search space, in Figure 5(a), the results for initial cost vs. maximum interstory drift for the MM frame at 2475 years return period is shown. It is seen that the TS algorithm is very efficient in narrowing down the search space to the points that are close to the Pareto-front, which is shown with solid line with circle marks. In Figure 5(b), the Pareto-fronts at the three hazard levels are compared for the MM frame. These results are very useful for decision makers. It allows the decision maker, whether it is the owner or the engineer, to choose among the set of optimal solutions depending on the requirements of the project. As an example, if the requirement of the project is that the maximum interstory drift under the 2475 years return period earthquake is less than four percent, one can easily find the least cost solution. Later on, if the requirement of the project changes and it becomes necessary to limit the maximum interstory drift to three percent, no additional analysis will be required to find the optimal solution.

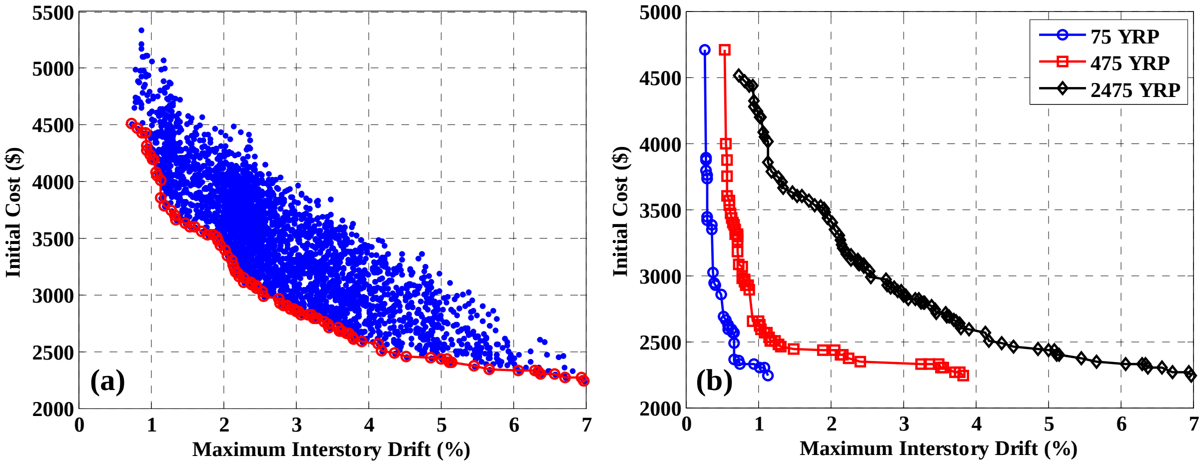

Figure 5: (a) Initial cost vs. maximum interstory drift for the MM frame at 2475 years return period, (b) Pareto-fronts for different return periods – MM frame.

As shown in Figure 6(a), in terms of total cost, the MM frame performs slightly better than RC frame due to reduced repair cost resulting from the increase in structural capacity as described in Section 3.2. However, as mentioned in Section 3.1, for simplicity in calculation of the initial cost, the workmanship costs are not included, and the initial cost is solely based on the material cost. In other words, the reduction in workmanship costs due to reduction in reinforcement detailing and prevention of congestion problems that result from the elimination of shear reinforcement is not taken into account. Furthermore ECC material is proven to be more durable than conventional concrete due to reduced crack widths with a distributed cracking pattern which increases the lifetime of the buildings [18, 19]. MM frame performs better when this additional information is taken into account. It is seen in Figure 6(a) that with the ECC frame the maximum interstory drift could be lowered to levels which cannot be achieved with the RC or MM frames. The Pareto-fronts for repair vs. initial cost for the three frames are compared in Figure 6(b). It is seen that the repair cost of the ECC frame is significantly less compared to RC frame for similar initial costs. The repair cost of the ECC frame is higher as it is based on the higher initial material cost.

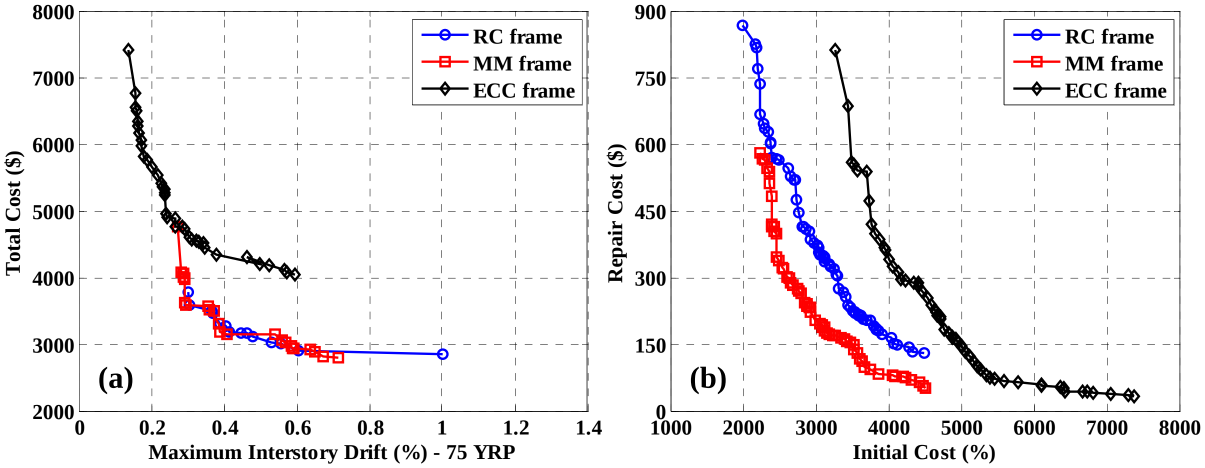

Figure 6: Pareto fronts for the three frames (a) total (life-cycle) cost vs. maximum interstory drift at 75 years return period, (b) repair cost vs. initial cost.

The seismic LCC analysis poses significant challenges to researchers. There are various parameters that have direct effect on the LCC results. Most importantly, for the formulation provided in this paper, the constants C_i in Eqn. (1) which define the cost of repair for the i^{th} damage state as a fraction of the initial cost have strong influence on the LCC. It is not straightforward to determine damage states for structures and the associated cost for repair. Furthermore, based on the adopted definitions, the limit state threshold values may vary significantly which affects the failure probabilities. Eqn. (4) assumes that the structural capacity is independent of earthquake demand which is another simplification that is usually adopted. Finally, the evaluation of workmanship cost is difficult as it is dependent on various parameters, above all the cost of labor at the location of construction. These are the most important assumptions of this study that warrant further investigation in the future studies.

6 CONCLUSIONS

The use of engineered cementitious composite (ECC) materials for improving the seismic design of buildings in terms of safety, economy and sustainability, is investigated through a multi-objective optimization problem. The objectives are selected as the structural performance, initial and the life-cycle cost (LCC). Three types of structural frames are considered:

made from reinforced concrete (RC) and reinforced ECC only, and a multi-material (MM) frame where the ECC is only used at the beam-column connections and at the bases of the columns. It is observed that, although the earthquake demand is significantly reduced in the case of ECC frame, the gain is not justified due to increased initial cost. On the other hand, the structural capacity of the MM frame is significantly higher which results in reduced repair hence LCC. If the additional benefits such as the reduction in workmanships costs and increased in life-time with enhanced ECC material durability are taken into account, the MM frame come forward as the most optimal solution to achieve the multiple objectives of the problem.

REFERENCES

[1] Li, V.C., *Postcrack Scaling Relations for Fiber Reinforced Cementitious Composites.* Journal of Materials in Civil Engineering, 1992. **4**(1): p. 41-57.

[2] Li, V.C. *Performance Driven Design of Fiber Reinforced Cementitious Composites*. in *4th International Symposium on Fiber Reinforced Concrete*. 1992: Chapman and Hall.

[3] Li, V.C. and C.K.Y. Leung, *Steady-State and Multiple Cracking of Short Random Fiber Composites.* Journal of Engineering Mechanics, 1992. **118**(11): p. 2246-2264.

[4] Li, V.C. and H.C. Wu, *Conditions for Pseudo Strain-Hardening in Fiber Reinforced Brittle Matrix Composites.* Journal of Applied Mechanics Review, 1992. **45**(8): p. 390-398.

[5] Li, V.C., S. Wang, and C. Wu, *Tensile Strain-Hardening Behavior of Polyvinyl Alcohol Engineered Cementitious Composite (PVA-ECC).* ACI Materials Journal, 2001. **98**(6): p. 483-492.

[6] Gencturk, B., *Multi-Objective Optimal Seismic Design of Building Using Advanced Engineering Materials*, in *Department of Civil and Environmental Engineering*. 2011, University of Illinois at Urbana-Champaign: Urbana, IL.

[7] USGS. *Documentation for the 2008 Update of the United States National Seismic Hazard Maps*, Open-File Report 2008-1128, 2008, United States Geological Survey, Reston, Virginia, USA.

[8] FEMA. *NEHRP Recommended Provisions for Seismic Regulations for New Buildings and Other Structures, FEMA 450, Part 1: Provisions*, 2003, Federal Emergency Management Agency, Washington, District of Columbia.

[9] U.S. Geological Survey. *Major Faults of California*. 2009, Accessed on May 13, 2009. Available from: http://education.usgs.gov/california/maps/faults_names3.htm.

[10] U.S. Geological Survey. *Soil Type and Shaking Hazard in the San Francisco Bay Area.* 2009, Accessed on February 1, 2011. Available from: http://earthquake.usgs.gov/regional/nca/soiltype/.

[11] PEER. *Pacific Earthquake Engineering Research (PEER) Center: NGA Database.* 2005, Accessed on January 1, 2009. Available from: http://peer.berkeley.edu/nga/.

[12] Abrahamson, N., *Non-Stationary Spectral Matching.* Seismological Research Letters, 1992. **63**(1): p. 30.

[13] ACI, *Building Code Requirements for Structural Concrete (ACI 318-08) and Commentary*. 2008, American Concrete Institute, Farmington Hills, MI, USA.

[14] Elnashai, A.S., V.K. Papanikolaou, and D. Lee. *ZEUS NL - A System for Inelastic Analysis of Structures*, User's Manual, 2010, Mid-America Earthquake (MAE) Center, Department of Civil and Environmental Engineeering, University of Illinois at Urbana-Champaign, Urbana, IL.

[15] Goodfellow, R.G.C., *Ductility of Reinforced Concrete Flexural Members Constructed from High Performance Steel and Concrete*, in *Civil Engineering Department*. 1999, Imperial College of Science, Technology and Medicine: London.

[16] Wen, Y.K. and Y.J. Kang, *Minimum Building Life-Cycle Cost Design Criteria. I: Methodology*. Journal of Structural Engineering, 2001. **127**(3): p. 330-337.

[17] Wen, Y.K., B.R. Ellingwood, and J.M. Bracci. *Vulnerability Function Framework for Consequence-Based Engineering*, Project DS-4 Report, 2004, Mid-America Earthquake (MAE) Center, Urbana, IL.

[18] Lepech, M.D. and V.C. Li. *Durability and Long Term Performance of Engineered Cementitious Composites*. in *International RILEM Workshop on High Performance Fiber Reinforced Cementitious Composites in Structural Applications*. 2006: RILEM Publications SARL.

[19] Li, V.C., T. Horikoshi, A. Ogawa, S. Torigoe, and T. Saito, *Micromechanics-Based Durability Study of Polyvinyl Alcohol-Engineered Cementitious Composite.* ACI Materials Journal, 2004. **101**: p. 242-248.

COMPDYN 2011
III ECCOMAS Thematic Conference on
Computational Methods in Structural Dynamics and Earthquake Engineering
M. Papadrakakis, M. Fragiadakis, V. Plevris (eds.)
Corfu, Greece, 25–28 May 2011

OPTIMIZATION OF STRUCTURES EQUIPPED WITH VISCOELASTIC DAMPERS MODELED USING THE FRACTIONAL ORDER DERIVATIVES

Zdzislaw Pawlak[1], **Roman Lewandowski**[2]

[1] Institute of Structural Engineering, Poznan University of Technology
ul. Piotrowo 5, 60-965 Poznan, Poland
e-mail: zdzislaw.pawlak@put.poznan.pl

[2] Institute of Structural Engineering, Poznan University of Technology
ul. Piotrowo 5, 60-965 Poznan, Poland
e-mail: roman.lewandowski@put.poznan.pl

Keywords: viscoelastic dampers, rheological models, fractional derivative, particle swarm optimization.

Abstract. *Viscoelastic (VE) dampers are now among preferable energy dissipation devices used for passive seismic response control. It is the aim of this paper to find the optimal damper placement and to determine the optimal parameters of dampers. The dynamic behavior of VE dampers, as described by the fractional Maxwell rheological model, is written in the form of a fractional differential equation. Fractional models have an ability to correctly describe the behavior of VE materials and dampers using a small number of model parameters. The equation of motion for the structure considered is expressed in the state space. The structure is subjected to a base acceleration. For the harmonic external forces the displacement response of the structure is determined. Solving the equation of motion yields an input-output relationship with the matrix frequency response function. The objective function, which we minimize, is the weighted sum of amplitudes of the transfer functions of interstorey drifts, evaluated at the fundamental, natural frequency of the frame with the dampers. The solution is obtained using the sequential optimization method and the particle swarm optimization method (PSO). The results obtained by both methods are compared.*

1 INTRODUCTION

Viscoelastic dampers are successfully applied to reduce excessive vibrations of buildings caused by winds and earthquakes. Incorporation of the VE dampers into a structure leads to a significant reduction of undesirable vibrations, see Soong [1]. A number of applications of VE dampers in civil engineering are listed in [2]. The dampers' behavior depends mainly on the rheological properties of the VE material the dampers are made of and their geometric parameters. In the past, several rheological models were proposed to describe the dynamic behavior of VE materials and dampers. Both the classic and the so-called fractional-derivative models of dampers are available. In the classic approach, mechanical models consisting of springs and dashpots are used to describe the rheological properties of VE dampers [3]. A good description of the VE dampers requires mechanical models consisting of a set of appropriately connected springs and dashpots. In this approach, the rheological properties of VE dampers are described using the fractional calculus and the fractional mechanical models. The fractional calculus has received considerable attention and has been used in modeling the rheological behavior of VE materials [4] and dampers [5]. The fractional models have an ability to correctly describe the behavior of VE materials and dampers using a small number of model parameters. A single equation is enough to describe the VE damper dynamics, which is an important advantage of the discussed model. However, in this case, the VE damper equation of motion is the fractional differential equation. The dynamic analysis of frame or building structures with dampers is presented in many papers [6, 7], where the fractional-derivative rheological model is used to model the dampers' behavior.

In this paper, planar frame structures with VE dampers mounted on them are considered. The VE dampers are modeled using the three-parameter fractional rheological Maxwell model. The structures are treated as linear elastic systems. The equations of motion of the whole system (structure with dampers) are written in terms of both physical and state-space variables. The proposed approach to the state space formulation is new. This is the main advantage of the proposed formulation, which does not require matrices with huge dimensions. However, the resulting matrix equation of motion is a fractional differential equation.

It is aim of the present paper to find the optimal placements of the dampers and to determine their optimal parameters. The objective function, which we minimize, is the weighted sum of amplitudes of the transfer functions of interstorey drifts, evaluated at the fundamental, natural frequency of a frame with dampers. The optimality criterion is expressed by the vector consisting of the values of the above mentioned transfer functions of the interstorey drifts.

The solution to the considered optimization problem is arrived at using the sequential optimization method and the particle swarm optimization method (PSO), which is based on the study of social behavior in a self–organized population system [8, 9]. Numerical tests carried out for a multi-storey building structure modeled as a shear plane frame with VE dampers mounted on it show that the presented methods are simple and efficient.

2 THE RHEOLOGICAL MODEL OF DAMPER

In this paper, the fractional Maxwell model is used to represent the rheological properties of VE dampers. The considered model consists of a fractional dashpot with the constants: c_i, α_i ($0 < \alpha_i \leq 1$) and a spring of the stiffness k_i. The equations of motion for the Maxwell model could be written using the so-called relative internal variable v_i (see Figure 1). The above-mentioned equations of motion for the damper are as follows:

$$\begin{aligned} u_i &= c_i D_t^{\alpha_i}(x_i - v_i) \\ u_i &= k_i v_i \end{aligned} \tag{1}$$

where u_i is the damper force and x_i is the relative damper displacement. Moreover, $D_t^{\alpha_i}(\bullet)$ denotes the Riemann-Liouville fractional derivative of the order α_i with respect to time, *t*.

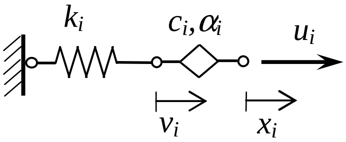

Figure 1: Rheological model of fractional Maxwell damper

The equation of motion of the classical Maxwell models could be obtained after substituting $\alpha_i = 1$ into Equations (1).

3 EQUATIONS OF MOTION

The frame with VE dampers is treated as the elastic linear system, which could be modeled as the shear frame. The mass of the system is lumped at the level of storeys.

3.1 The equations of motion expressed in physical coordinates

The equation of motion of the whole system (structure with dampers) can be written as follows:

$$\mathbf{M}_s \ddot{\mathbf{q}}_s(t) + \mathbf{C}_s \dot{\mathbf{q}}_s(t) + \mathbf{K}_s \mathbf{q}_s(t) = \mathbf{s}(t) + \mathbf{p}(t) \tag{2}$$

where the symbols $\mathbf{M}_s$, $\mathbf{C}_s$ and $\mathbf{K}_s$ denote the mass, the damping, and the stiffness $(n \times n)$ matrices, respectively. Moreover, $\mathbf{q}_s(t) = col(q_{s,1},...,q_{s,j},...,q_{s,n})$ and $\mathbf{p}(t) = col(p_1,...,p_j,...,p_n)$ denote the vector of displacements of the structure and the vector of excitation forces, respectively. The $\mathbf{s}(t) = col(s_1, s_2,...,s_n)$ vector is the $(n \times 1)$ vector of interaction forces between the frame and the dampers [10].

For the Maxwell model of dampers, the vector of interactive forces $\mathbf{s}(t)$ is treated as a sum of two vectors, i.e., $\mathbf{s}(t) = \mathbf{s}_1(t) + \mathbf{s}_2(t)$. The vector $\mathbf{s}_1(t)$ contains interactive forces which are reactions of the elastic part of the Maxwell dampers to the frame, while the vector $\mathbf{s}_2(t)$ contains interactive forces which are reactions of the dashpot part of the dampers. It is assumed that the dashpot part of the Maxwell model is joined with the upper storey while the elastic part is joined with the lower storey. Moreover, the brace stiffness could be taken into account in the stiffness parameter of the Maxwell model. If a structure with only one damper, denoted as the damper number *i*, mounted between two successive storeys, *j* and *j+1*, is considered then the vectors $\mathbf{s}_1(t)$ and $\mathbf{s}_2(t)$ could be written in the following form:

$$\begin{aligned} \mathbf{s}_1(t) \equiv \mathbf{s}_{1i}(t) = col(0,...,s_j = u_i,.....,0) = \tilde{\mathbf{e}}_i u_i(t) \\ \mathbf{s}_2(t) \equiv \mathbf{s}_{2i}(t) = col(0,...,s_{j+1} = -u_i,.....,0) = \hat{\mathbf{e}}_i u_i(t) \end{aligned} \tag{3}$$

where $\tilde{\mathbf{e}}_i = col(0,...,\tilde{e}_j = 1, \tilde{e}_{j+1} = 0,...,0)$, $\hat{\mathbf{e}}_i = col(0,...,\hat{e}_j = 0, \hat{e}_{j+1} = -1,...,0)$.

Taking into account that $q_{s,j}(t)) = \tilde{\mathbf{e}}_i^T \mathbf{q}_s(t)$ and $q_{s,j+1}(t) = -\hat{\mathbf{e}}_i^T \mathbf{q}_s(t)$, the damping force $u_i(t)$ of the Maxwell damper could be shown in two equivalent forms:

$$\begin{aligned} u_i(t) &= k_i(v_i(t) - q_{s,j}(t)) = k_i v_i(t) - k_i \tilde{\mathbf{e}}_i^T \mathbf{q}_s(t) \\ u_i(t) &= c_i(D_t^{\alpha_i} q_{s,j+1}(t) - D_t^{\alpha_i} v_i(t)) = -c_i D_t^{\alpha_i} v_i(t) - c_i \hat{\mathbf{e}}_i^T D_t^{\alpha_i} \mathbf{q}_s(t) \end{aligned} \tag{4}$$

and the interaction force vectors $\mathbf{s}_{1,i}(t)$ and $\mathbf{s}_{2,i}(t)$ are given by:

$$\begin{aligned} \mathbf{s}_1^{(i)}(t) &= \tilde{\mathbf{e}}_i k_i v_i(t) - \tilde{\mathbf{e}}_i k_i \tilde{\mathbf{e}}_i^T \mathbf{q}_s(t) = \tilde{\mathbf{e}}_i k_i \mathbf{h}_i^T \mathbf{q}_r(t) - \tilde{\mathbf{e}}_i k_i \tilde{\mathbf{e}}_i^T \mathbf{q}_s(t) \\ \mathbf{s}_2^{(i)}(t) &= -\hat{\mathbf{e}}_i c_i D_t^{\alpha_i} v_i(t) - \hat{\mathbf{e}}_i c_i \hat{\mathbf{e}}_i^T D_t^{\alpha_i} \mathbf{q}_s(t) = -\hat{\mathbf{e}}_i c_i \mathbf{h}_i^T D_t^{\alpha_i} \mathbf{q}_r(t) - \hat{\mathbf{e}}_i c_i \hat{\mathbf{e}}_i^T D_t^{\alpha_i} \mathbf{q}_s(t) \end{aligned} \tag{5}$$

where the vector of internal variables $\mathbf{q}_r(t) = col(v_1(t), ..., v_i(t), ..., v_m(t))$ and the vector $\mathbf{h}_i = col(0, ..., h_i = 1, ..., 0)$ have the dimension ($m \times 1$). Moreover, from the equilibrium condition of the internal node of the Maxwell model of damper we obtain:

$$-c_i D_t^{\alpha_i} q_{s,j+1}(t) + c_i D_t^{\alpha_i} v_i(t) - k_i q_{s,j}(t) + k_i v_i(t) = 0 \tag{6}$$

In the matrix notation, Equation (6) for $i = 1,2,...m$, may be rewritten in the form:

$$c_i \hat{\mathbf{e}}_i^T D_t^{\alpha_i} \mathbf{q}_s(t) + c_i \mathbf{h}_i^T D_t^{\alpha_i} \mathbf{q}_r(t) - k_i \tilde{\mathbf{e}}_i^T \mathbf{q}_s(t) + k_i \mathbf{h}_i^T \mathbf{q}_r(t) = 0 \tag{7}$$

When m dampers are present in the frame, and all the fractional parameters are equal, (i.e., $\alpha_i = \alpha = const.$) then the interaction force vectors are:

$$\begin{aligned} \mathbf{s}_1(t) &= \sum_{i=1}^{m} \tilde{\mathbf{e}}_i k_i \mathbf{h}_i^T \mathbf{q}_r(t) - \sum_{i=1}^{m} \tilde{\mathbf{e}}_i k_i \tilde{\mathbf{e}}_i^T \mathbf{q}_s(t) \\ \mathbf{s}_2(\mathrm{t}) &= -\sum_{i=1}^{m} \hat{\mathbf{e}}_i c_i \mathbf{h}_i^T D_t^{\alpha} \mathbf{q}_r(t) - \sum_{i=1}^{m} \hat{\mathbf{e}}_i c_i \hat{\mathbf{e}}_i^T D_t^{\alpha} \mathbf{q}_s(t) \end{aligned} \tag{8}$$

After pre-multiplying Equation (7) by $\mathbf{h}_i$ and summing up all equations with respect to *i*, we have:

$$\sum_{i=1}^{m} \mathbf{h}_i c_i \hat{\mathbf{e}}_i^T D_t^{\alpha} \mathbf{q}_s(t) + \sum_{i=1}^{m} \mathbf{h}_i c_i \mathbf{h}_i^T D_t^{\alpha} \mathbf{q}_r(t) - \sum_{i=1}^{m} \mathbf{h}_i k_i \tilde{\mathbf{e}}_i^T \mathbf{q}_s(t) + \sum_{i=1}^{m} \mathbf{h}_i k_i \mathbf{h}_i^T \mathbf{q}_r(t) = \mathbf{0} \tag{9}$$

Taking into account that $\mathbf{s}(t) = \mathbf{s}_1(t) + \mathbf{s}_2(t)$ and substituting Equations (8) into (2) we obtain the following equation of motion for the frame with the Maxwell dampers:

$$\begin{aligned} &\mathbf{M}_s D_t^2 \mathbf{q}_s(t) + \mathbf{C}_s D_t^1 \mathbf{q}_s(t) + \mathbf{C}_{ss}^d D_t^{\alpha} \mathbf{q}_s(t) + (\mathbf{K}_s + \mathbf{K}_{ss}^d)\, \mathbf{q}_s(t) + \\ &\qquad + \mathbf{C}_{sr}^d D_t^{\alpha} \mathbf{q}_r(t) - \mathbf{K}_{sr}^d \mathbf{q}_r(t) = \mathbf{p}(t) \end{aligned} \tag{10}$$

Equation (9) could be rewritten in the form:

$$\mathbf{C}_{rs}^d D_t^{\alpha} \mathbf{q}_s(t) + \mathbf{C}_{rr}^d D_t^{\alpha} \mathbf{q}_r(t) - \mathbf{K}_{rs}^d \mathbf{q}_s(t) + \mathbf{K}_{rr}^d \mathbf{q}_r(t) = \mathbf{0} \tag{11}$$

The following symbols

$$\mathbf{C}_{ss}^d = \sum_{i=1}^{m} \hat{\mathbf{e}}_i c_i \hat{\mathbf{e}}_i^T,\ \mathbf{C}_{sr}^d = \sum_{i=1}^{m} \hat{\mathbf{e}}_i c_i \mathbf{h}_i^T,\ \mathbf{C}_{rs}^d = \sum_{i=1}^{m} \mathbf{h}_i c_i \hat{\mathbf{e}}_i^T = (\mathbf{C}_{sr}^d)^T,\ \mathbf{C}_{rr}^d = \sum_{i=1}^{m} \mathbf{h}_i c_i \mathbf{h}_i^T,$$

$$\mathbf{K}_{rs}^{d}=\sum_{i=1}^{m}\mathbf{h}_i k_i \tilde{\mathbf{e}}_i^T=(\mathbf{K}_{sr}^{d})^T\,,\ \mathbf{K}_{rr}^{d}=\sum_{i=1}^{m}\mathbf{h}_i k_i \mathbf{h}_i^T\,,\ \mathbf{K}_{sr}^{d}=\sum_{i=1}^{m}\tilde{\mathbf{e}}_i k_i \mathbf{h}_i^T\,,\ \mathbf{K}_{ss}^{d}=\sum_{i=1}^{m}\tilde{\mathbf{e}}_i k_i \tilde{\mathbf{e}}_i^T\,,$$

were introduced in Equations (10) and (11). The system of fractional differential Equations (10) and (11) constitute a set of equations from which the dynamic response of the structure with the Maxwell dampers can be determined.

3.2 The equations of motion expressed in the state space

In many cases it is very convenient to use the equation of motion expressed in the state space. In the case of frames with the Maxwell dampers the vector of state variables and the vectors of state variables' derivatives are defined as:

$$\begin{aligned}&\mathbf{z}(t)=col(\mathbf{q}_r(t),\ \mathbf{q}_s(t),\ D_t^1\mathbf{q}_s(t))\\&D_t^1\mathbf{z}(t)=col(D_t^1\mathbf{q}_r(t),\ D_t^1\mathbf{q}_s(t),\ D_t^2\mathbf{q}_s(t))\\&D_t^{\alpha}\mathbf{z}(t)=col(D_t^{\alpha}\mathbf{q}_r(t),\ D_t^{\alpha}\mathbf{q}_s(t),\ D_t^{\alpha+1}\mathbf{q}_s(t))\end{aligned}\tag{12}$$

Moreover, when the following additional matrix equation:

$$\mathbf{M}_s D_t^1\mathbf{q}_s(t)-\mathbf{M}_s D_t^1\mathbf{q}_s(t)=\mathbf{0}\tag{13}$$

is appended to the Equation (10) and (11) a set of equations is obtained which could be rewritten using the state variables defined above. The resulting matrix equation is in the form:

$$\mathbf{A}\,D_t^1\mathbf{z}(t)+\mathbf{A}_1 D_t^{\alpha}\mathbf{z}(t)+\mathbf{B}\mathbf{z}(t)=\tilde{\mathbf{p}}(t)\tag{14}$$

where

$$\mathbf{A}=\begin{bmatrix}\mathbf{0}&\mathbf{0}&\mathbf{0}\\\mathbf{0}&\mathbf{C}_s&\mathbf{M}_s\\\mathbf{0}&\mathbf{M}_s&\mathbf{0}\end{bmatrix},\ \mathbf{A}_1=\begin{bmatrix}\mathbf{C}_{rr}^{d}&\mathbf{C}_{rs}^{d}&\mathbf{0}\\\mathbf{C}_{sr}^{d}&\mathbf{C}_{ss}^{d}&\mathbf{0}\\\mathbf{0}&\mathbf{0}&\mathbf{0}\end{bmatrix},\ \mathbf{B}=\begin{bmatrix}\mathbf{K}_{rr}^{d}&-\mathbf{K}_{rs}^{d}&\mathbf{0}\\-\mathbf{K}_{sr}^{d}&\mathbf{K}_s+\mathbf{K}_{ss}^{d}&\mathbf{0}\\\mathbf{0}&\mathbf{0}&-\mathbf{M}_s\end{bmatrix},\ \tilde{\mathbf{p}}(t)=\begin{Bmatrix}\mathbf{0}\\\mathbf{p}(t)\\\mathbf{0}\end{Bmatrix}$$

The above approach to the state space formulation is new. In comparison with previous ones, such as those given in [11, 12], matrices with huge dimensions were not required which is the main advantage of the proposed formula. Moreover, all of the matrices appearing in Equation (14) are symmetrical.

4 DYNAMIC ANALYSIS

4.1 Dynamic characteristics of structures

Applying the Laplace transform, taking into account that $\tilde{\mathbf{p}}(t)=\mathbf{0}$:

$$\mathcal{L}[\mathbf{z}(t)]=\mathbf{Z}\,,\ \mathcal{L}\left[D_t^{\alpha}\,\mathbf{z}(t)\right]=s^{\alpha}\,\mathbf{Z}\,,\ \mathcal{L}\left[D_t^1\mathbf{z}(t)\right]=s\mathbf{Z}\,,\tag{15}$$

the equation of motion (14) can be written as

$$\left(s\mathbf{A}+s^{\alpha}\mathbf{A}_1+\mathbf{B}\right)\mathbf{Z}=\mathbf{0}\,,\tag{16}$$

Equation (16) constitutes a non-linear eigenproblem which can be solved using the continuation method. The solution to the considered non-linear equation could be shown as a curve in the configuration space, i.e., the s, $\mathbf{Z}$ space. The first point in this curve is obtained for $\alpha=1$, in this case Equation (16) expresses the linear eigenvalue problem. Next, the solution to the eigenproblem (16) for the chosen value of $\alpha \in (0,1)$ is investigated. The incremental-iteration method, presented in detail in [10], is used. Usually, one incremental step and three or four iterations are enough to reach the solution for the final value of the fractional parameter. The continuation method enables the eigenvalues s_i to be determined.

The dynamic behavior of a frame with viscoelastic dampers is characterized by the natural frequency ω_i and the non-dimensional damping parameter γ_i. Similarly to viscous damping, the above-mentioned properties are defined as follows:

$$\omega_i^2 = \mu_i^2 + \eta_i^2 , \; \gamma_i = -\mu_i / \omega_i , \tag{17}$$

where $\mu_i = \mathrm{Re}(s_i)$, $\eta_i = \mathrm{Im}(s_i)$.

4.2 Frequency response functions

In this section we investigate the steady state harmonic responses of structures governed by Equations (14). For the harmonic external forces described by:

$$\mathbf{p}(t) = \mathbf{P} \exp(i\lambda t) , \tag{18}$$

where $i = \sqrt{-1}$, λ is the frequency of excitation, the displacement response of the structure can be expressed as:

$$\mathbf{q}_s(t) = \mathbf{Q}_s(\lambda) \exp(i\lambda t) . \tag{19}$$

If relationships (18) and (19) are substituted into the equation of motion (14), written in the state space, the following equation is obtained:

$$\mathbf{Q}_s(\lambda) = \tilde{\mathbf{H}}(\lambda) \tilde{\mathbf{P}} , \tag{20}$$

where:

$$\tilde{\mathbf{H}}(\lambda) = \left[i\lambda\, \mathbf{A} + (i\lambda)^{\alpha} \mathbf{A}_1 + \mathbf{B} \right]^{-1} . \tag{21}$$

When the structure is subjected to a base acceleration $\ddot{u}_g(t)$, the excitation vector is written as $\mathbf{p}(t) = -\mathbf{M}\, \mathbf{r}\, \ddot{u}_g(t)$, where $\mathbf{r} = col\{1,1,.....,1\}$. For the harmonic external forces, $\ddot{u}_g(t) = \ddot{U}_g \exp(i\lambda t)$. The displacement response of the structure is given by relationship (19) and $\mathbf{Q}_s(\lambda)$ is determined from:

$$\mathbf{Q}_s(\lambda) = \mathbf{H}(\lambda) \ddot{U}_g . \tag{22}$$

where the vector $\mathbf{H}(\lambda) = -\tilde{\mathbf{H}}(\lambda)\mathbf{Mr}$ will be called the vector of frequency transfer functions of displacements.

5 OPTIMIZATION PROBLEM

It is the aim of this paper to find the optimal dampers' placements and to determine the optimal parameters of the dampers k_{di} and c_{di}. The objective function, which is minimized, is the weighted sum of amplitudes of the transfer functions of interstorey drifts, $h_i(\lambda)$, evaluated at the fundamental, natural frequency ($\lambda = \omega_1$) of the frame with the dampers. The optimality criteria may by described as follows:

$$F = \mathbf{w}^T \mathbf{h}(\omega_1) . \tag{23}$$

where the vector $\mathbf{h}(\omega_1) = col(h_1(\omega_1), h_2(\omega_1), ..., h_n(\omega_1))$ consists of the values of the above mentioned amplitudes of transfer functions of interstorey drifts, $\mathbf{w} = col(w_1, w_2, ..., w_n)$ is the vector of weight coefficients, and n stands for the number of the structure's degrees of freedom.
The considered optimization problem is subjected to some constraints. We assume that the sum of damping coefficients and the sum of stiffness parameters are known and constant. Moreover, the values of the parameters of damping, $c_{d,i}$, and stiffness, $k_{d,i}$, for every damper must be non-negative. The above constraints are written as:

$$\sum_{i=1}^{m} c_{d,i} = C_d , \quad \sum_{i=1}^{m} k_{d,i} = K_d , \quad c_{d,i} \geq c_{\min} , \quad k_{d,i} \geq k_{\min} . \tag{24}$$

where $c_{\min}, k_{\min}$ represent the assumed low-value positive numbers ($c_{\min} = 1.0 N \sec^{\alpha} / m$ was chosen in our example).

The vector $\mathbf{H}_d(\lambda)$ of the frequency transfer functions of interstorey drifts can be calculated from the following formula:

$$\mathbf{H}_d(\lambda) = \mathbf{T}\mathbf{H}(\lambda) , \tag{25}$$

where the transformation matrix is:

$$\mathbf{T} = \begin{bmatrix} 1\ 0\ 0 ... 0 \ \ 0\ \ 0 \\ -1\ 1\ 0 ... 0\ \ 0\ \ 0 \\ .... \\ 0\ \ 0\ \ 0 ... 0 -1\ \ 1 \end{bmatrix} . \tag{26}$$

The solution is obtained using the sequential optimization method and the particle swarm optimization method (PSO). In the first case, for every possible location of one damper the values of the objective function are calculated. The right fixed location of the damper is the position for which the minimum value of the objective function is obtained. When the first damper's location is determined the procedure is repeated until all locations are found for the dampers. However, there is no proof for the solution's convergence although many examples show that this method is simple and efficient in many engineering applications (for instance [13]).

The PSO algorithm which is based on the study of social behavior in a self-organized population system (i.e., ant colonies, fish schools), searches a space by adjusting the trajectories of so-called particles. In the considered optimization problem, the vector of the *i*-th particle's position $\mathbf{p}_i$ consists of damping coefficients of dampers currently mounted on the structure, i.e., $\mathbf{p}_i = col(c_{d,1}^{(i)}, c_{d,2}^{(i)}, ..., c_{d,n}^{(i)})$. The dimension of the vector $\mathbf{p}_i$ is equal to the number of building storeys. Moreover, to reduce the number of elements of the particle position vector and because of technological requirements for the damper, the stiffness parameter of the damper is calculated assuming that the ratio $c_{d,i} / k_{d,i}$ is given and will not change during iteration.

A population of particles is initialized with random positions and velocities [9]. Taking into account the best positions of the particles at subsequent iteration *k*+1, the algorithm adjusts the behavior of the particles by the following rules:

$$\begin{aligned} &\mathbf{v}_i(k+1) = w(k)\mathbf{v}_i(k) + \frac{c_1}{\Delta t}\mathbf{R}_1(k)\big(\mathbf{b}_i(k) - \mathbf{p}_i(k)\big) + \frac{c_2}{\Delta t}\mathbf{R}_2(k)\big(\mathbf{g}_i(k) - \mathbf{p}_i(k)\big) \\ &\mathbf{p}_i(k+1) = \mathbf{p}_i(k) + \mathbf{v}_i(k+1)\Delta t \end{aligned} \tag{27}$$

where $\Delta t = 1$, $\mathbf{p}_i(k)$ is the position of *i*-th particle at *k*-th iteration, $\mathbf{v}_i(k)$ is the corresponding velocity vector; $\mathbf{b}_i(k)$ and $\mathbf{g}_i(k)$ stand for the best position found by the particle *i* and the best position in the particle's neighbourhood achieved so far, respectively; $\mathbf{R}_1(k)$, $\mathbf{R}_2(k)$ are the diagonal matrices of independent random numbers uniformly distributed in the range $(0,\ 1)$; $w(k)$ is the inertia factor providing balance between exploration and exploitation, c_1 is the individuality constant, and c_2 is the sociality constant. To speed up convergence, the inertia weight could be linearly reduced. A new velocity, which moves the particle in the direction of a potentially better solution, is calculated based on its previous value, and the particle location at which the best fitness so far has been achieved.

The initial values of the elements $v_{i,j}(0)$ of the velocity vector $\mathbf{v}_i(0)$ are calculated from the following formula:

$$v_{i,j} = r_3\, C_d\, \varepsilon_0\,, \tag{28}$$

where r_3 is the random number taken from the range (0, 1) and ε_0 is a constant ($\varepsilon_0 = 0.05$ is assumed). The initial values of the elements of the vector $\mathbf{p}_i(0)$ are determined from the following relationship:

$$c_{d,i}(0) = \frac{\tilde{r}_i C_d}{\sum_{j=1}^{m} \tilde{r}_j}\,, \tag{29}$$

where $\tilde{r}_i$ is a random number taken from the range (0, 1). The above choices assure that all assumed initial approximations of dampers parameters, i.e., vectors $\mathbf{p}_i(0)$ and $\mathbf{v}_i(0)$ fulfill the optimization constraints (24).

An important part of the PSO algorithm is the way of handling the constraints introduced in the optimization problem. Here, the following very simple procedure is used to fulfill the constraints (24):

- if non-admissible values $c_{d,i}(k+1) < 0$ result from the relationship (27) then $c_{d,i}(k+1) = c_{\min}$ is artificially introduced,
- in order to fulfill the constraint (27.1), elements of the vector $\mathbf{p}_i(k+1)$ are normalized in such a way that:

$$\tilde{c}_{d,i} = \frac{c_{d,i}}{\sum_{j=1}^{m} c_{d,j}} C_d \tag{30}$$

The PSO procedure is ceased if the change of the objective function is sufficiently small, i.e., when:

$$\left| F(k+1) - F(k) \right| \le \varepsilon_1 F(k+1) \tag{31}$$

where ε_1 is an assumed low-value number.

6 NUMERICAL TEST

In the numerical example, a ten-storey building structure modeled as a shear plane frame with VE dampers mounted on it is investigated. The bending rigidity of columns varies in sequence, for every two storeys: $k_1 = k_2 = 68710.0\ kN/m$, $k_3 = k_4 = 54010.0\ kN/m$, $k_5 = k_6 = 42170.0\ kN/m$, $k_7 = k_8 = 28660.0\ kN/m$, $k_9 = k_{10} = 16450.0\ kN/m$, but the mass value is the same for every floor: $m_s = 2.07 Mg$. The structure's damping ratios corresponding to the stiffness of the storeys are: $c_1 = c_2 = 4.76\ kN\sec/m$, $c_3 = c_4 = 3.73\ kN\sec/m$, $c_5 = c_6 = 2.91\ kN\sec/m$, $c_7 = c_8 = 1.98\ kN\sec/m$, $c_9 = c_{10} = 1.44\ kN\sec/m$ (data taken from [13]).

Firstly, the calculations were carried out for a frame without dampers (see Figure 2a), only the damping properties of structure were taken into account.

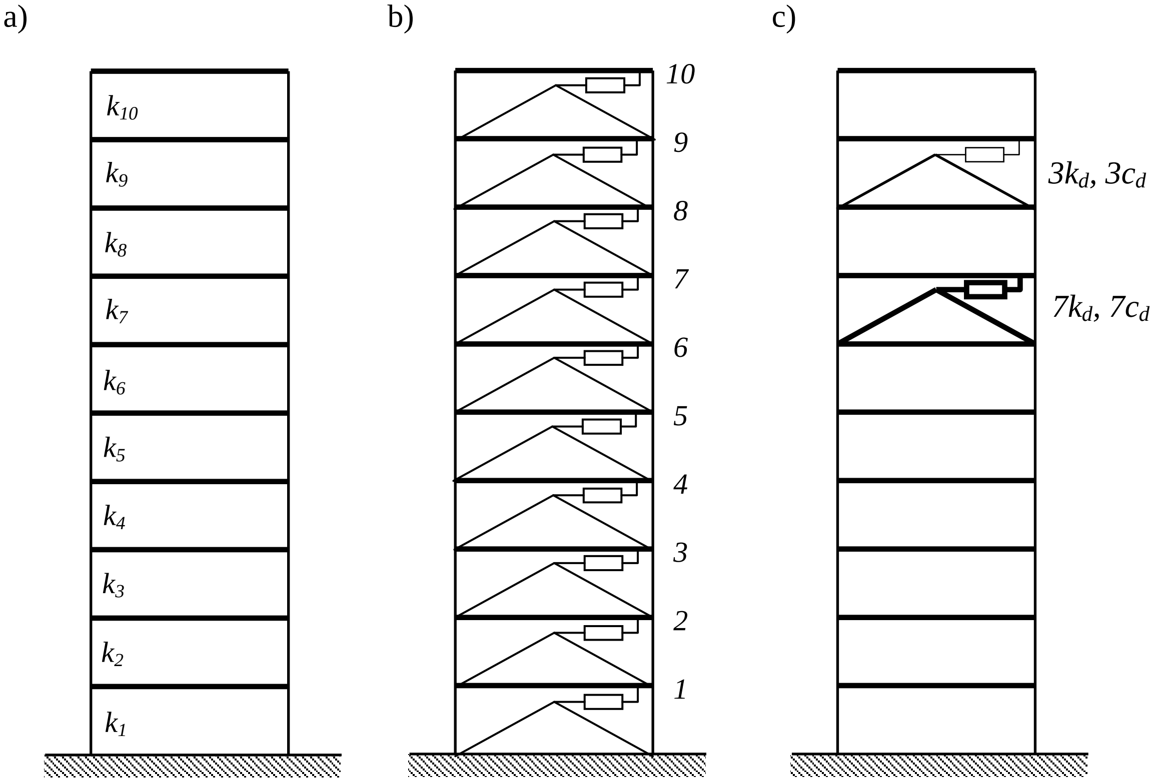

Figure 2: Diagram of a 10-storey frame with different distributions of dampers

The solution to Equation (16), where $\mathbf{A}_1 = \mathbf{0}$ and $\mathbf{K}_{rr}^d = \mathbf{K}_{sr}^d = \mathbf{K}_{rs}^d = \mathbf{K}_{ss}^d = 0$, leads to the eigenvalues s_i which enable determination of the dynamic properties of the structure described by Equation (17). The results, the natural frequencies of the structure and the values of non-dimensional damping factor are presented in Table 1.

Next, the authors investigated a structure with one damper mounted on every storey (see Figure 2b). The assumed value of the sum of the damping coefficients and the sum of the stiffness parameters are: $C_d = 500\ kN\sec^{\alpha}/m$, and $K_d = 25000\ kNm^2$, respectively. If dampers are uniformly distributed within a structure, the data for every single damper are: $k_d = 2500\ kNm^2$, $c_d = 50\ kN\sec^{\alpha}/m$, $\tau_d = c_d / k_d = 0.02$. The values of fractional parameters for all dampers are identical, i.e., $\alpha = 0.6$. Using the suggested procedure, the dynamic properties of the considered system were computed (see Table 1).

A first solution to the optimization problem is obtained using the sequential optimization method. For every possible location of one damper, the values of fundamental frequency are calculated (see Figure 3).

Modal number	No dampers		Dampers's distribution			
			uniform		optimal	
	ω_i	γ_i	ω_i	γ_i	ω_i	γ_i
1	22.690	0.0008	22.816	0.0126	22.934	0.0162
2	56.534	0.0022	58.114	0.0246	59.421	0.0338
3	91.909	0.0035	95.255	0.0212	96.309	0.0182
4	127.472	0.0047	132.284	0.0177	129.866	0.0094
5	151.769	0.0061	159.807	0.0209	163.766	0.0204
6	182.399	0.0066	188.678	0.0151	190.317	0.0213
7	208.638	0.0073	216.278	0.0152	220.389	0.0146
8	245.147	0.0085	252.143	0.0136	261.260	0.0210
9	281.524	0.0097	288.274	0.0135	283.755	0.0122
10	324.052	0.0112	330.492	0.0139	324.065	0.0112

Table 1: Natural frequencies ω_i and non-dimensional damping factors γ_i

Next, the objective function is evaluated for the frame, taking into account every possible position of the damper. The results are presented in Figure 4. It was assumed that the values of the weight coefficients w_i in Equation (23) are equal to one.

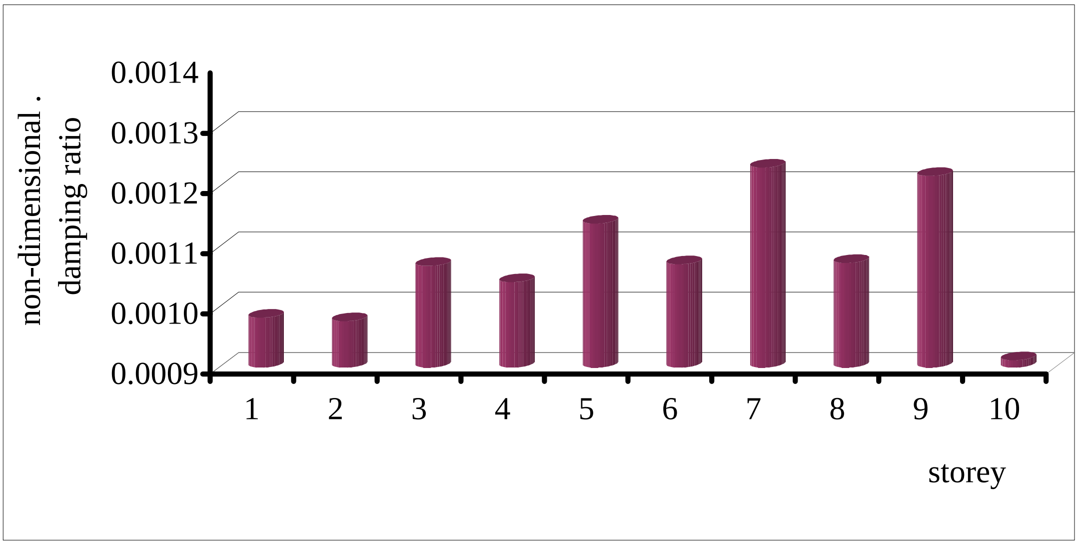

Figure 3: Non-dimensional damping factors versus first damper's position

The correct fixed location of the first damper is at the seventh storey, for which the minimum value of the objective function is obtained. When the first damper's location is determined the procedure is repeated until all locations for the dampers are found. The optimal locations of ten successive dampers are found to be: seven at the seventh storey and three at the ninth storey (see also Figure 2c). The dynamic properties of structures with optimally distributed dampers are shown in Table 1.

It can be noted that the non-dimensional damping ratio of the first mode of vibration is greater (by about 28%), compared with the same ratio for the structure with uniformly distributed dampers. Moreover, the damping ratios of the third, fourth, fifth, seventh, ninth, and tenth modes of vibration are smaller.

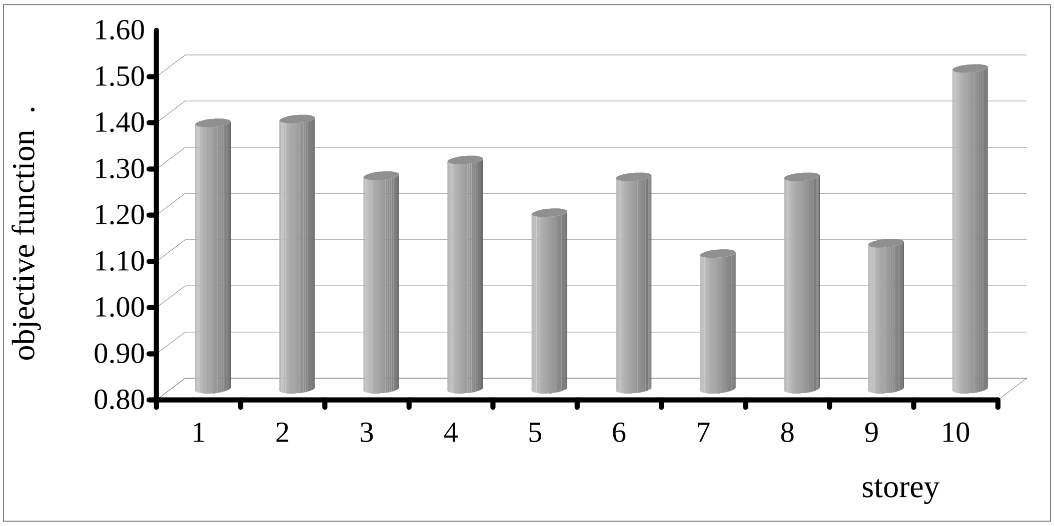

Figure 4: Objective function versus first damper's position

In the second approach, the PSO method is applied. In Equation (27), we define the values of coefficients $c_1 = c_2 = 2$ and the declining value of the inertia factor; starting with $w = 0.9$, it decreased by 0.005 at every step of iteration. A population of ten particles was initialized with random positions. The coordinates of every particle position describe the current distribution of damping properties on the frame. On every storey, the value of the damping coefficient must be non-negative and smaller than the assumed constant value $C_d = 500\, kN \sec^{\alpha} / m$ (i.e., $c_{\min} \le c_{d,i} \le C_d$). The stiffness parameters of the dampers are calculated from the value of the ratio $c_{d,i} / k_{d,i}$ which is equal to 0.02 and constant for every damper.

Changes of the best value of the objective function during the iteration process are presented in Figure 5. The solution to the optimization problem, i.e., the optimal distribution of VE dampers obtained with the help of both optimization methods is shown in Table 2.

The objective function, the weighted sum of amplitudes of the transfer functions of interstorey drifts is: $F_0 = 1.7053$, $F_U = 0.3739$, $F_S = 0.2759$ for the frame without dampers, for uniformly distributed dampers, and for the optimal solution obtained by the sequential and PSO methods, respectively.

It can be concluded that results obtained by both methods yield similar dampers' distributions on the frame. Differences between the optimal values of damping coefficients obtained as the result of optimization procedures are partially affected by an incremental way of distribution of damping coefficients in the sequential optimization method. Moreover, in the PSO method the values of the damping $c_{d,i}$ parameters of every damper must be non-negative.

Number of storey	Damping coefficient	
	Sequential method	PSO method
1	0	0.78
2	0	0.78
3	0	0.78
4	0	0.78
5	0	0.78
6	0	0.78
7	350	347.23
8	0	0.78
9	150	146.48
10	0	0.78
Total	500	499.95

Table 2: Optimal distribution of VE dampers

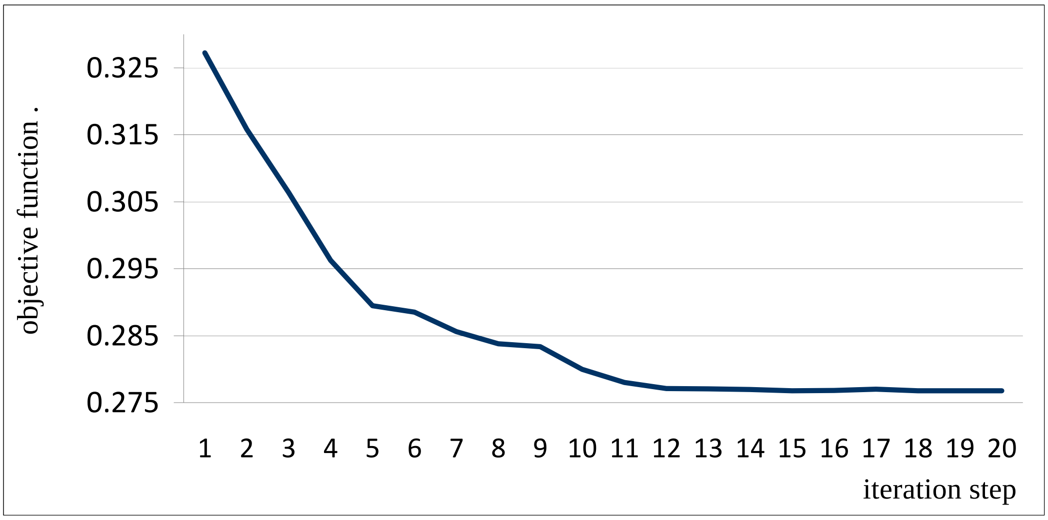

Figure 5: Convergence of objective function at PSO iteration

7 CONCLUDING REMARKS

In this paper, frame structures with viscoelastic dampers mounted on them are considered. Viscoelastic dampers are modeled using a three-parameter, fractional rheological Maxwell model which more precisely describes the VE damper's properties, compared with the classical one. The resulting matrix equation of motion is the fractional differential equation. The problem of optimal distribution of VE dampers modeled by the fractional rheological Maxwell model is solved for the first time. The considered optimization problem is solved by minimization of the objective function which is the weighted sum of amplitudes of the transfer functions of interstorey drifts. The sequential optimization method and the particle swarm optimization method are used to successfully solve the optimization problem. Examples of numerical calculations were shown. The presented results demonstrate the effectiveness and applicability of the proposed approach.

REFERENCES

[1] T.T. Soong, B.F. Spencer, *Supplemental energy dissipation: state-of-the-art and state-of-the-practice*, Engineering Structures, 24, 243-259, 2002.

[2] C. Christopoulos, A. Filiatrault, *Principles of passive supplemental damping and seismic isolation*, IUSS Press, Pavia, Italy, 2006.

[3] S.W. Park, *Analytical modelling of viscoelastic dampers for structural and vibration control*, International Journal of Solids and Structures, 38, 8065 – 8092, 2001.

[4] R.L. Bagley, P.J. Torvik, *Fractional calculus – a different approach to the analysis of viscoelastically damped structures*, AIAA J, 27, 1412–1417, 1989.

[5] Yu.A. Rossikhin, M.V. Shitikova, *A new method for solving dynamic problems of fractional derivative viscoelasticity*, International Journal of Engineering Sciences, 39(2), 200a, 149-176.

[6] T. Chang, M.P. Singh, *Seismic analysis of structures with a fractional derivative model of viscoelastic dampers*, Earthquake Engineering and Engineering Vibration, 1: 251-260, 2002.

[7] M.H. Tsai, K.C. Chang, *Higher-mode effect on the seismic responses of buildings with viscoelastic dampers*, Earthquake Engineering and Engineering Vibration, 1: 119-129, 2002.

[8] R.E. Perez, K. Behdinan, *Particle swarm approach for structural design optimization*, Computer & Structures, 85, 1579-1588, 2007.

[9] J. Kennedy, R. C. Eberhart, *Particle Swarm Optimization*, Proc. IEEE Int. Conf. On Neural Networks, Piscataway, 1942-1948, NJ 1995.

[10] R. Lewandowski, Z. Pawlak, *Dynamic Analysis of Frames with Viscoelastic Dampers Modelled by Rheological Models with Fractional Derivatives.* Journal of Sound and Vibration, 2011, 330: 923-936.

[11] T. Chang and M.P. Singh, *Seismic analysis of structures with a fractional derivative model of viscoelastic dampers*, Earthquake Engineering and Engineering Vibration, 2002, 1: 251-260.

[12] L.E. Suarez, A. Shokooh, *An Eigenvector Expansion Method for the Solution of Motion Containing Fractional Derivatives*, Journal of Applied Mechanics, 1997, 64: 629-635.

[13] R.H. Zhang, T. T. Soong, *Seismic design of viscoelastic dampers for structural applications,* J. Structural Engineering, Vol. 118, 1375 – 1392, 1992.

COMPDYN 2011
3rd ECCOMAS Thematic Conference on
Computational Methods in Structural Dynamics and Earthquake Engineering
M. Papadrakakis, M. Fragiadakis, V. Plevris (eds.)
Corfu, Greece, 25–28 May 2011

Normalized domination selection criteria for differential evolution algorithms in constrained optimization for seismic engineering

J. Avakian[1], A. Fiore[2], D. Serio[1], R. Greco[2] G.C. Marano[1]

1Department of Environmental Engineering and Sustainable Development, Technical University of Bari, viale del Turismo 10, 74100 Taranto, Italy
[2]Department of Civil and Architectural Engineering, Technical University of Bari, viale del Turismo 10, 74100 Taranto, Italy

Keywords: Structural optimization, constrained optimization, evolution algorithms, selection criteria

Abstract. *Optimization is a central aspect of structural engineering, but its practical application hasn't been supported by mathematical and numerical tools because of inner strong non-linear aspects involved. Moreover during last few decades Evolutionary Algorithms (EAs) gives new interest and horizons in this specific topic, thanks to their strong capacity in treatment of these problems more efficiently than standard methods. But a common criticism to EAs is lack of efficiency and robustness in handling constraints, mainly because they were originally developed for unconstraint problems only. For this reason during past decade hybrid algorithms combining evolutionary computation and constraint-handling techniques have shown to be effective in this specific area. Moreover still now this is a crucial point for practical applications in structural optimization. In this paper a Normalized Domination Selection-based (NDS) rule is proposed to solve constrained-handling optimization problems using a modified version of proposed Differential Evolution algorithm (NDS - DEa). The strategy developed doesn't requires any additional parameter, increasing the appeal for a simple implementation in many real problems by structural designer without a specific knowledge in the field. Mainly it is based on a domination criteria in selection phase. Actually a common way for constrained handling is introducing a specific role for selection step, so that all other phase of EA aren't modified; in this way DE flow chart scheme doesn't present any modification from a standard unconstrained one. Anyway the specific constrained selection scheme plays an important role in solution search efficiency, certainly more than in unconstrained cases. Unconstrained selection is based only on comparing individuals OF values, but in constrained one it seemed somewhat different and complicated. The more simple, common and intuitive way for approaching this phase is the penalty function, where OF values are reduced for those individuals don't satisfying constraints disqualifies (unfeasible individuals). It is immediate (and well known in literature) that depending on penalty low adopted, a more drastic or permissive surviving of unfeasible solutions happened. But this is a central point in this problems, because of in many cases indeed real optimal solutions lies*

just on one constraints, so that its correct evaluation needs of specific research around the boundary, not only in the feasible space. to develop this strategy the domination concept is related to the specific selection that has to be implemented. If in a unconstrained contest it means simply that the domination coincide with the OF ranking, in the constrained contest the question has to be properly treated. In fact there are three possible scenarios:

- *both two individuals are feasible -> selection based on rank*
- *both two individuals are unfeasible -> selection of the feasible one*
- *one is feasible and the other is unfeasible -> selection of less unfeasible*

Moreover the last case presents same some ambiguity because in general there are many constraints with different scales, so that it is impossible to rank correctly to different unfeasible individuals. For this reason a normalized criteria is here proposed and analyzed with different cross over methodology. A comparative analysis using different test cases is performed.

1 INTRODUCTION

Optimization techniques play an important role in many scientific, economical, social and many other problems, the very purpose of which is to find the best way to do something or alternatively to help decision makers to derive the maximum benefit from limited available resources. A common way in many cases has been using past experiences in similar conditions or extending indications from comparable situations. These approaches will not lead in general to the best solution, but the shortcomings of indirect design can be overcame by adopting a direct or optimal design procedure.

An optimization problem or an optimal design procedure consists in finding a maximum or a minimum function problem under some constraint conditions. To deal with this class of problems many different approaches are possible in theory and many heuristic intelligent algorithms have been developed for different classes of optimization problems.

Within the framework of the soft computing methodologies, an incredible number of non-conventional paradigms has been explored in order to create efficient and user-friendly optimizers. Nowadays, a wide variety of biological, social and physical metaphors has been analyzed and tested. Evolutionary Algorithms EAs are stochastic search methods that mimic the metaphor of natural biological evolution and/or the social behavior of species. EAs are ubiquitous nowadays, having been effectively applied to several problems from different domains, including optimization, automatic programming, machine learning, operations research, bioinformatics, and social systems. Usually grouped under the term Evolutionary Computation or Evolutionary Algorithms, one can find the domains of Genetic Algorithms, Evolution Strategies, Evolutionary Programming and Genetic Programming.

These are stochastic search and optimization heuristics derived from the classic evolution theory, which are implemented on computers in the majority of cases. The basic idea is that if only those individuals of a population reproduce, which meet a certain selection criteria, and the other individuals of the population die, the population will converge to those individuals that best meet the selection criteria. If imperfect reproduction is added, the population can begin to explore the search space and will move to individuals that have an increased selection probability and that inherit this property to their descendants. These population dynamics follow the basic rule of the Darwinist evolution theory, which can be described in short as the ―survival of the fittest" . To solve optimization problems with an evolutionary heuristic the individuals of a population have to represent a possible solution of a given problem and the selection probability is set proportional to the quality of the represented solution.

The interest toward this class of optimizers is continuously attracting consensus, substantially because the objective function and constraints are not required to be differentiable, continuous or even explicit. In effect, no preliminary assumptions or *a priori* information are needed for solving constrained optimization problems by means of EAs.

In these author knowledge, at the moment, there isn't a unique accepted classification of different EAs proposed in literature, so that a possible non exhaustive one is proposed in the following, where similar techniques differ in the implementation details and in the nature of the particular applied problem.

- **Genetic algorithm**: *This is the most popular (and older) type of EA. One seeks the solution of a problem in the form of strings of numbers (traditionally binary, although the best representations are usually those that reflect something about the problem being solved), by applying operators such as recombination and mutation (sometimes one, sometimes both). This type of EA is often used in optimization problems;*
- **Genetic programming**: *Here the solutions are in the form of computer programs, and their fitness is determined by their ability to solve a computational problem.*

- ***Evolutionary programming**: Like genetic programming, only the structure of the program is fixed and its numerical parameters are allowed to evolve;*
- ***Evolution strategy** - This works with vectors of real numbers as representations of solutions, and typically uses self-adaptive mutation rates;*
- ***Differential evolution**: It is based on vector differences and it is therefore primarily suited for numerical optimization problems.*
- ***Particle swarm optimization**: This is based on the ideas of animal flocking behavior and it is also primarily suited for numerical optimization problems.*
- ***Ant colony optimization**: This is based on the ideas of ant foraging by pheromone communication to form paths. It is primarily suited for combinatorial optimization problems.*
- ***Invasive weed optimization algorithm**: It is based on the ideas of weed colony behavior in searching and finding a suitable place for growth and reproduction.*
- ***Harmony search**: Based on the ideas of musicians' behavior in searching for better harmonies. This algorithm is suitable for combinatorial optimization as well as parameter optimization.*
- ***Gaussian adaptation**: This is based on information theory. Used for maximization of manufacturing yield, mean fitness or average information. See for instance Entropy in thermodynamics and information theory.*

Among these approaches one of the more promising one is the Differential Evolution algorithm (DEa): this can be defined a recent stochastic, population-based global optimization method and was proposed about a decade ago [10][11]. The algorithm is based on the use of a special crossover-mutation operator, based on the linear combination of three different individuals and one subject-to-replacement parent. The selection process is performed via deterministic tournament selection between the parent and the child created by it. It is immediate noting that the general structure of the DEa shares similar features with other evolutionary algorithms like GAs. For instance, both optimizers adopt the same terminology to define the key elements of the algorithm (i.e. a collection of solutions is called ―population", each solution is called ―individual" and each iteration is called ―generation") and incorporate operators (like mutation, crossover and selection scheme) that work in similar manners. Nonetheless, it is different in handling distance and direction information to move from the population at the current generation toward the next one because it has constructive cooperation between individuals: in this sense, it behaves like Particle Swarm Optimization algorithms (PSOs). Another interesting feature of DEa deals with the selection operator that performs very well and sometimes it is more efficient and faster than other population based algorithms, because of the one-to-one competition scheme. In more general terms, its fashion can be imputable to two positive features; firstly, the DEs provides more simple operators in comparison to the most advanced GAs. Moreover, it requires only few embedded control parameters (typically the total number of control parameters is less than the adopted ones for GAs and PSOAs), so that the parameter tuning stage is less time consuming and maybe more practical for non-experts in the field of soft computing techniques.

All attractive features of EAs are in opposition to some criticisms. For instance, EAs suffer the lack of well posed theories about their convergence and a larger computational time is typically required. Moreover, in their original formulation they was limited to unconstrained problems and do not include a method to incorporate feasibility information into the fitness function. In effect, many real-world optimization problems in science and engineering involve a number of constraints which the optimal solution must satisfy. Actually, due to constraints, the feasible space might be reduced to some portion, sometimes very narrow if compared with the overall search space. Sometimes simply finding feasible solutions itself could be a daunting challenge for some specific practical problems.

As it is know, the ultimate goal of constrained optimization problem is to find the feasible optimal solution. To achieve this goal in EAs, it is required that more feasible individuals are involved in the evolution process. However, on the other hand, some infeasible individuals may carry some information, sometime important, for the final solution than their feasible counterparts in some generations. Hence, these two aspects lead to a contradiction in constrained evolutionary optimization. To address this contradiction, the main challenge is to handle the constraints and to optimize the objective function simultaneously. One possible way is to determinate the tradeoff between the constraint violations and the objective function.

This has trigger a considerable amount of researches and a wide variety of approaches have been suggested in the last few years to incorporate constraints into the fitness function of an evolutionary algorithm. The most popular approach is the use of (mainly exterior) penalty function [12] where the aim is to decrease the fitness of infeasible solutions in order to favor the selection of feasible solutions. Several alternative constraint-handling techniques have been proposed [9].

Actually it is generally accepted that performance of an algorithm largely depends on the underlying mechanism of constraint handling. Motivated by this fact, a number of constraint-handling techniques have been proposed for evolutionary algorithms, and over last few years several methods have been proposed.

These methods have been grouped by different authors into the following categories [1][2][4]:

- *Methods based on preserving the feasibility of solutions. The idea behind the method is based on specialized operators which transform feasible parents into feasible offspring. The method assumes linear constraints only and a feasible starting point or feasible initial population.*
- *Methods based on penalty functions. Many evolutionary algorithms incorporate a constraint-handling method based on the concept of exterior penalty functions which penalize infeasible solutions. These methods differ in important details, such as how the penalty function is designed and applied to infeasible solutions.*
- *Methods which make a clear distinction between feasible and infeasible solutions. There are a few methods which emphasize the distinction between feasible and infeasible solutions in the search space. One of those methods distinguishes between feasible and infeasible individuals: for any feasible individual* $\mathbf{x}$ *and any infeasible individual* $\mathbf{y}: f(\mathbf{x}) \lhd f(\mathbf{y})$*, i.e. any feasible solution is better than any infeasible one.*
- *Other hybrid methods. These methods combine evolutionary computation techniques with deterministic procedures for numerical optimization problems. Most constrained problems can be handled by the penalty function method. A measure of the constraint violation is often useful when handling constraints.*

According to the no free lunch theorem, it is impossible for a single constraint handling technique to outperform all other techniques on every problem. In other words, depending on several factors such as the ratio between feasible search space and the whole search space, multimodality of the problem, the chosen EA and global exploration/local exploitation stages of the search process, different constraint handling techniques can be effective on different problems and during different stages of the search process.

The most used techniques incorporate constraints into the fitness function, such as in penalty functions approach, but they usually eliminate all unfeasible individuals. On the other hand it is particularly important to maintain diversity in the population and to be able to keep solutions both inside and outside the feasible region. In fact, several studies have shown that, despite their popularity, traditional (external) penalty functions, even when used with dynamic penalty factors, tend to have difficulties to deal with highly constrained search spaces and with problems in which the constraints are active in the optimum. In these situations infeasible individuals may carry more important information for the final solution than their feasible counterparts in some generations. Hence, these two aspects lead to a contradiction in constrained evolutionary optimization. The use of (exterior) penalty functions is one of the most popular methods to deal with constrained search spaces when using Constrained optimization Evolution Algorithms (COEAs).

For these reasons an efficient and adequate constraint-handling technique is a key element in the design of competitive COEAs to solve complex optimization problems. In this way, this subject deserves special research efforts, with the main aim of proposing approaches able to prevent a too fast convergence without an adequate global (feasible and unfeasible space) research process. Some recent proposes in this way investigated modification of what is generally known as the *Constraint Domination Selection (CDS) rule*.

This methodology was initially proposed by Deb [3] as a modification of Powell and Skolnick method which gives a dynamic penalty to each element so that at each generation the best unfeasible element has a rank that is better than the worst unfeasible one. The Deb's method uses a tournament selection operator, where two solutions are compared. In this method, any feasible solution is preferred to any infeasible solution; among two feasible solutions, the one having a better objective function value is preferred and among two infeasible solutions, the one having smaller constraint violation is preferred. Moreover all these method are static application of a *Constraint Domination Selection* (CDS) rule, that practically prefers feasible solutions to unfeasible ones. Finally this was implemented on different types of Evolution Strategies in which the results were very promising [7][6]

The main motivation of this work was to increase this selection criteria to better perform constrained optimization by correctly using selection criteria with specific crossover operators.

Standard differential evolution algorithms in unconstrained Optimum Design

The feature of the optimal design is that it consists of only logical decisions in a mathematical way, setting out constraints, and minimizes or maximizes an objective function, that is generally either cost, benefit or a generic merit function. Many of the methods give rise to local minimum/maximum. This, however, depends on the mathematical nature of the optimization problem, that generally can be described as follows:

Find the best vector $\mathbf{x} \in \mathbf{\Omega}$ *that minimizes* $f(\mathbf{x})$ (1)

Satisfying the following constraints

$$g_i(\mathbf{x}) \leq 0 \quad \mathrm{i} = 1, 2, .., n_g \tag{2}$$

$$h_j(\mathbf{x}) = 0 \quad j = 1, 2, .., n_h \tag{3}$$

in which $\mathbf{x} = \{x_1, \ldots, x_j, \ldots, x_n\}$ is a vector whose components are real numbers, $f(\mathbf{x})$ is the objective function (OF) to be minimized and $\mathbf{\Omega}$ is a box-type search space. For instance, if $[x^l_j, x^u_j]$ is the admissible interval for the j^{th} variable (x^l_j and x^u_j are its lower and the upper bounds, respectively), then:

$$\mathbf{\Omega} = \left[x_1^l, x_1^u\right] \otimes \left[x_2^l, x_2^u\right] \ldots \otimes \left[x_j^l, x_j^u\right] \otimes \ldots \left[x_n^l, x_n^u\right] \subseteq \mathbb{R} \tag{4}$$

where the symbol $\otimes$ denotes the Cartesian product between intervals.

The constraints of the optimization problems can be both inequalities $g_i(\mathbf{x})$ or equalities $h_j(\mathbf{x})$. Without loss of generality, all equalities can be converted into inequalities using the transformation $\left|h_j\left(\mathbf{x}\right)\right|-\varepsilon\leq 0, \quad j=1,2,..,n_h$, where ε is a tolerance parameter.

Therefore, in the following we will refer only to inequalities-based constraints, *e.g.* $g_p(\mathbf{x}) \leq 0$ with $p = 1,\ldots,n_g, n_g+1,\ldots,n_g+n_h$.
A solution $\mathbf{x}$ is regarded as *feasible if*:

$$\sum_{k=1}^{n_p}\max\left(0,g_k\left(\mathbf{x}\right)\right)\leq 0 \tag{5}$$

otherwise it is called as *unfeasible*.

A general optimization problem can be formulated as a typical minimization problem in the form

$$\begin{aligned}&\min_{\mathbf{x}}\left\{f\left(\mathbf{x}\right)\right\}\\&\text{s.t.}\quad \mathbf{x}^l\leq\mathbf{x}\leq\mathbf{x}^u\end{aligned} \tag{6}$$

in which $\mathbf{x} = \{x_1,\ldots, x_j,\ldots,x_n\}$ is the design vector (for example the collection of n system parameters to be identified), $\mathbf{x}^l = \{x_1^l,\ldots, x_j^l,\ldots,x_n^l\}$ and $\mathbf{x}^u = \{x_1^u,\ldots, x_j^u,\ldots,x_n^u\}$are its lower and upper bounds, respectively. The shape of the objective function may have many local optima and high complex topology, therefore, when preliminary information are not available it may not always be convex. In these circumstances special optimizers have to be used.
In the following it is illustrated the state of the art of DEa for problems in form (6).
Differential evolution is a simple but powerful population-based stochastic search technique for solving global optimization problem which is characterized by simplicity, effectiveness and robustness. Its main idea is to construct at each generation, for each element of the population a mutant vector. This mutant vector is constructed trough a specific mutation operation based on adding differences between randomly selected elements of the population to another element. The original DE algorithm is described in the following briefly. The main variation introduced for constrained problems is in selection process, where use of CDS gives to algorithms for unconstrained problem a natural extension for constrained ones. Moreover the CDS is also applied to evaluation of –best” individual over the entire population. This because some proposed DE algorithm present a mutation that take into account information about the –best” individual over the entire population. In this case a –direction” to escape from constrained space is available at each iteration.
The general structure of a DE is typically for evolutionary algorithms, the particularity of the algorithm being related with the mutation and crossover operators. By combining different mutation and crossover operators various schemes have been developed. In literature different DE schemes are denoted using the convention DE/a/b/c where a denotes the way of constructing the mutant vector, b denoted the number of differences in the construction of the mutant vector and, finally, c denotes the crossover type.
The working of DEa depends on the manipulation and the efficiency of three main operators: mutation, crossover and selection.

2 MUTATION

The main idea of DEa is to construct at each generation for each element of the population a mutation vector. The mutant vector is constructed through a specific mutation operation based on adding differences between randomly selected element of the population to another element.

DEa uses the differences betiween two randomly selected individuals as the source of random variations for a third indivdual referred to as the *target vector*. *Trial solutions* are generated by adding weighted difference vectors to the target vector. This process is referred to as the mutation operator: its main goal is to enable diversity in the current population as well as to direct the individuals in such a way a better result is expected. By computing the differences between two individuals randomly chosen from the population, the algorithm estimates the gradient in that zone rather than in a point. Let consider ${}^{k}\mathbf{x}_i = \{{}^{k}x_{i1},\ldots,{}^{k}x_{ij},\ldots,{}^{k}x_{in}\}$ the i^{th} individual (for $i = 1,\ldots,N$) at iteration k. The initial population ${}^{0}\mathbf{x}_i$ for $i = 1,\ldots, N$ is defined by generating pseudo-randomly the collection of N solutions within the specified search space. In this study the Latin Hypercube Sampling (LHS) technique has been iteratively used to generate the best initial population with minimum correlation between samples [8]. At iteration k+1, for each individual ${}^{k}\mathbf{x}_i$ a mutation vector ${}^{(k+1)}\mathbf{v}_i$ is computed by means of one of the following alternatives:

rand /1/bin

$${}^{(k+1)}\mathbf{v}_i = {}^{k}\mathbf{x}_{r1} + F^{1}\left({}^{k}\mathbf{x}_{r2} - {}^{k}\mathbf{x}_{r3}\right) \tag{7}$$

best /1/bin

$${}^{(k+1)}\mathbf{v}_i = {}^{k}\mathbf{x}_{best} + F^{1}\left({}^{k}\mathbf{x}_{r1} - {}^{k}\mathbf{x}_{r2}\right) \tag{8}$$

current-to-best /1/bin

$${}^{(k+1)}\mathbf{v}_i = {}^{k}\mathbf{x}_{i} + F^{2}\left({}^{k}\mathbf{x}_{best} - {}^{k}\mathbf{x}_{i}\right) + F^{1}\left({}^{k}\mathbf{x}_{r1} - {}^{k}\mathbf{x}_{r2}\right) \tag{9}$$

best /2/bin

$${}^{(k+1)}\mathbf{v}_i = {}^{k}\mathbf{x}_{best} + F^{2}\left({}^{k}\mathbf{x}_{r1} - {}^{k}\mathbf{x}_{r2}\right) + F^{1}\left({}^{k}\mathbf{x}_{r3} - {}^{k}\mathbf{x}_{r4}\right) \tag{10}$$

rand /2/bin

$${}^{(k+1)}\mathbf{v}_i = {}^{k}\mathbf{x}_{r1} + F^{2}\left({}^{k}\mathbf{x}_{r2} - {}^{k}\mathbf{x}_{r3}\right) + F^{1}\left({}^{k}\mathbf{x}_{r4} - {}^{k}\mathbf{x}_{r5}\right) \tag{11}$$

Two new possible mutation strategy candidates are thus here reported to evaluate their effectiveness in

rand /1/bin (based on tournament selection

$$\begin{gathered}{}^{(k+1)}\mathbf{v}_i = {}^{k}\mathbf{x}_{i} + {}^{k}F_{r3,i}\left({}^{k}\mathbf{x}_{r3} - {}^{k}\mathbf{x}_{i}\right) + {}^{k}F_{r1,r2}\left({}^{k}\mathbf{x}_{r1} - {}^{k}\mathbf{x}_{r2}\right)\\ if\ k \le 0.5L\end{gathered} \tag{12}$$

rand/1/bin (based on attraction-repulsion paradigm)

$$\begin{gathered}{}^{(k+1)}\mathbf{v}_i = {}^{k}\mathbf{x}_{r1} + {}^{k}F_{best,i}\left({}^{k}\mathbf{x}_{best} - {}^{k}\mathbf{x}_{i}\right) + {}^{k}F_{r1,r2}\left({}^{k}\mathbf{x}_{r1} - {}^{k}\mathbf{x}_{r2}\right)\\ if\ k > 0.5L\end{gathered} \tag{13}$$

The mutation coefficients in (12) and in (13) are calculated as follows:

$${}^{k}F_{r3,i} = \max\left\{\left|\frac{f\left({}^{k}\mathbf{x}_{r3}\right) - f\left({}^{k}\mathbf{x}_{i}\right)}{{}^{k}f_{\max} - {}^{k}f_{\min}}\right|, 0.5\right\} \tag{14}$$

$${}^{k}F_{r1,r2} = \begin{cases}\max\left\{\left|\dfrac{f\left({}^{k}\mathbf{x}_{r1}\right) - f\left({}^{k}\mathbf{x}_{r2}\right)}{{}^{k}f_{\max} - {}^{k}f_{\min}}\right|, 0.5\right\} & if\ k \le 0.5L\\ \left|\dfrac{f\left({}^{k}\mathbf{x}_{r1}\right) - f\left({}^{k}\mathbf{x}_{r2}\right)}{{}^{k}f_{\max} - {}^{k}f_{\min}}\right| & if\ k > 0.5L\end{cases} \tag{15}$$

$$ {}^{k}F_{best,i} = \left| \frac{{}^{k}f_{\min} - f\left({}^{k}\mathbf{x}_i\right)}{{}^{k}f_{\max} - {}^{k}f_{\min}} \right| \tag{16} $$

in which

$$ {}^{k}f_{\min} = \min_{i=1,\dots,N}\left\{f\left({}^{k}\mathbf{x}_i\right)\right\} \quad {}^{k}f_{\max} = \max_{i=1,\dots,N}\left\{f\left({}^{k}\mathbf{x}_i\right)\right\} \tag{17} $$

From Equation (7) to Equation (11) $r1$, $r2$, $r3$ and $r4$ denote integers randomly selected within the set $\{1,\dots,i-1,i+1,\dots,N\}$ and $r1 \neq r2 \neq r3 \neq r4$. The individual ${}^{k}\mathbf{x}_{best}$ is the best performer in the population at the iteration k. The coefficients F^1 and F^2 are the so-called mutation coefficients and they are real positive constants. These parameters control the amplification level due to the mutation operator (for this reason they are also dubbed scale factors). Any alternative mutation operator leads to different versions of DEAs [10]: rand/1/bin, best/1/bin, current-to-best/1/bin, best/2/bin, rand/2/bin, respectively. Storn and Price shown that the usage of two difference vectors may improve the diversity of the population, especially when the population size is high enough.

As before stated, only mutation in (8), (9) and (10) are used in the following for constrained handling problems. This because they are specifically implemented with a ~~–b~~est" selection based on a CDS rule.

3 CROSSOVER

The perturbed individual ${}^{(k+1)}\mathbf{v}_i$ and the current population ${}^{k}\mathbf{x}_i$ are then subject to crossover operation. The crossover follows the mutation phase and for each mutated vector ${}^{(k+1)}\mathbf{v}_i$ a trial vector ${}^{(k+1)}\mathbf{u}_i$ (offspring) is generated by using the binomial crossover formalized in Equation (18).

$$ {}^{(k+1)}u_{ij} = \begin{cases} {}^{(k+1)}v_{ij} & if\ u \leq p^c \ \text{for}\ j = randint(0,n) \\ {}^{k}x_{ij} & otherwise \end{cases} \tag{18} $$

In Equation (18) u is a pseudo-random number generated by using the uniform probability density functions in the range [0,1]. The parameter p^c is the probability of crossover (or crossover ratio or probability of reproduction) and it takes values between 0 and 1 and it is set by the user. Moreover, $randint(0,n)$ is a pseudo-randomly integer selected within the set $\{1,\dots,j,\dots,n\}$: based on its realization, an additional condition is introduced to ensure that at least one parameter is taken into account for constructing the vector ${}^{(k+1)}\mathbf{u}_i$.

4 SELECTION

The selection operator in case of unconstrained problems employs a very simple one-to-one competition scheme between ${}^{(k+1)}\mathbf{u}_i$ and ${}^{(k+1)}\mathbf{x}_i$ as follows

$$ {}^{(k+1)}\mathbf{x}_i = \begin{cases} {}^{(k+1)}\mathbf{u}_i & if\ f\left({}^{(k+1)}\mathbf{u}_i\right) < f\left({}^{(k+1)}\mathbf{x}_i\right) \\ {}^{k}\mathbf{x}_i & otherwise \end{cases} \tag{19} $$

Therefore, the winner in the selection stage is the best performer between the parent individual and its trial one. The output of this operator is a new population for the next generation, if a stopping criteria has not been satisfied. Likely to the evolutionary algorithms, the required number of iterations L is not known a priori and therefore a stopping criterion is needed. In more general terms, the stopping criteria can be the same typically adopted for GAs, see for instance[8] and its references. In this study, we stop the search once a maximum number of iterations L is achieved.

A general way the most used way to deals with constraint handling problems consists in replacing standard selection criteria with one that considers not only performance (OF) of solution but feasibility too. In this sense, this selection criteria is obtained by operating a solutions ranking by a generalized domination concept between different individuals: given two solutions, namely ${}^{(k+1)}\mathbf{u}_i$ and ${}^{(k+1)}\mathbf{x}_i$ the concept of dominance can be introduced:

$$ {}^{(k+1)}\mathbf{x}_i \succ {}^{(k+1)}\mathbf{u}_i \tag{20}$$

that denotes that ${}^{(k+1)}\mathbf{u}_i$ is dominated by ${}^{(k+1)}\mathbf{x}_i$

In a constrained based selection the concept of domination must be expressed in a wider sense than those obtained considering simply the OF. Taking into account individuals feasibility, violation function for the i^{th} individual is evaluated by the violation function:

$$\Phi\left({}^{k}\mathbf{x}_i\right) = \sum_{p=1}^{n_q+n_h} \max\left\{0, g_p\left({}^{k}\mathbf{x}_i\right)\right\} \geq 0 \tag{21}$$

so that its value is zero if and only if all constrains are satisfied (the i^{th} individual lies in the feasible design variable space); differently (the i^{th} individual lies in the unfeasible design variable space) the violation function is a positive scalar number.

The selection method able to consider properly feasibility in dominance should be formulated in the following way:

$$ {}^{(k+1)}\mathbf{x}_i \succ {}^{(k+1)}\mathbf{u}_i \Leftrightarrow \begin{cases} \left(f\left({}^{(k+1)}\mathbf{x}_i\right) < f\left({}^{(k+1)}\mathbf{u}_i\right)\right) \mathit{and} \left(\Phi\left({}^{(k+1)}\mathbf{x}_i\right) = 0\right) \wedge \left(\Phi\left({}^{(k+1)}\mathbf{u}_i\right) = 0\right) \\ \mathit{or} \\ \left(\Phi\left({}^{(k+1)}\mathbf{x}_i\right) = 0\right) \mathit{and} \left(\Phi\left({}^{(k+1)}\mathbf{u}_i\right) > 0\right) \\ \mathit{or} \\ \Phi\left({}^{(k+1)}\mathbf{x}_i\right) < \Phi\left({}^{(k+1)}\mathbf{u}_i\right) \end{cases} \tag{22}$$

These should be summarized in simply words by the following rule:

${}^{(k+1)}\mathbf{x}_i$ dominates ${}^{(k+1)}\mathbf{u}_i$ if :

- ${}^{(k+1)}\mathbf{x}_i$ *and* ${}^{(k+1)}\mathbf{u}_i$ *are both feasible solutions, and* ${}^{(k+1)}\mathbf{x}_i$ *has the minimum value of OF*
- ${}^{(k+1)}x_i$ *is feasible and* ${}^{(k+1)}\mathbf{u}_i$ *is unfeasible*
- ${}^{(k+1)}\mathbf{x}_i$ *and* ${}^{(k+1)}\mathbf{u}_i$ *are both unfeasible solutions, and* ${}^{(k+1)}\mathbf{x}_i$ *has the minimum value of violation.*

This domination criterion should be simply expressed in words as the rule that *"feasible solutions survive to the infeasible in any cases"*.

Moreover, selection scheme (20) based on (22) is well defined in cases 1 and 2. The first is nothing else than standard selection (both two individuals are feasible, so that the selection can't deal with constraints. The second simply defines that when are compared two individuals that are one feasible and the other unfeasible, the feasible survives.

The third case presents some drawbacks because it is not so well defined as the first two. Actually, because of number of constraints involved in a optimization problem (usually greater than one) it is impossible to correctly ranking violation levels of unfeasible individuals by using directly the violation function presented in (21). To properly clarify this point, in a generic search space selecting between two unfeasible individuals, we have to prefer those more closer to the feasible space; unfortunately the violation function, as it has been obtained in (21) is not able to evaluate this distance, so that it isn't able to ranking solutions according their distance to the feasible space because it is obtained simply adding violation levels of different constraints that are not homogeneous according their effective distance from the feasible space. In simply words it means that, once two solutions are both unfeasible, it isn't possible evaluating correctly which of them is the *"less far"* from the feasible space boundary. This piece of information is needed in evolutionary search algorithms to properly select the best solution among a group of unfeasible ones. So that, the dominance based selection criterion for two unfeasible individuals is still an open question and there isn't a metric measure to evaluate what is the ―less worst".

In order to overcome this limitation, modified versions of the standard rule are here proposed, to evaluate if and how they increase algorithm performance in convergence to a feasible space. This aspect is extremely important especially in engineering optimizations, where the necessity of a feasible solution is priority respect to those of a performance ones.

A first variation of standard Deb's Dominance Selection rule consists in using a normalization of violation function in (21). In this way, one scraps from the effective numerical value of the violated constraint, whose value should be very different regardless of the effective distance of individual from the admissible domain. The final goal in this manner is to obtain a ranking in which individuals nearest

to the admissible domain work better.

For this aim, each constraint violation is normalized according to:

$$^{k}\chi_{r}^{i}=\frac{\max\left(0,{}^{k}g_{r}^{i}\right)}{g_{r}^{\max}} \tag{23}$$

where:

$$g_{r}^{\max}=\max_{j=1,n_p}\left({}^{k}g_{r}^{j}\right) \tag{24}$$

being n_p the number of the population.

It is clear that $^{k}\chi_{r}^{i}\in\left[0,1\right]$ for all k considered, so that having a normalized weight for all constraints considered.

The violation function is thus defined as

$$^{k}\Phi^{i}=\sum_{r=1}^{n_v}{}^{k}\chi_{r}^{i} \tag{25}$$

5 NUMERICAL ANALYSIS

The proposed domination-based selection schemes have been applied to eleven mathematical and three engineering benchmark optimization problems.

A complete presentation of these benchmark problems is given in Appendix. The optimization problems are solved fifty times by using the NDS_DE and the final results are recorded. The initial population is different for each run. The best, the worst, the mean value of the OF at hand as well as its standard deviation are calculated over the fifty simulated runs. For better understanding the inner work of the proposed selection schemes, the behaviors of an additional indicator is also analyzed.

With this aim, a measure of the difficulty of solving each test problem, a metric measure ρ (as suggested by Koziel and Michalewicz [4]) was introduced as the ratio of the feasible and total population number at each generation, so that considering the following set:

$$^{k}S=\left\{{}^{k}\mathbf{x}_{i}\in\mathbf{\Omega}\middle|\,g_{p}\left({}^{k}\mathbf{x}_{i}\right)\leq 0\ \forall p=1,\ldots,n_{q}+n_{r}\right\} \tag{26}$$

whose cardinality is denoted $\#(^{k}S)\leq N$, the ratio $^{k}\rho$ is:

$$^{k}\rho = \frac{\#\left({}^{k}S\right)}{N} \in [0,1] \tag{27}$$

whose value is 0 when no individual lies in feasible space, and is 1 when all of them are feasible. To properly measure the ratio between feasible and infeasible space dimension, in table 1 it is reported the value of ρ for the mathematical test functions here analyzed, using 10^6 individuals randomly generated [7].

Problem	N	Type of function	ρ	LI	NI	LE	NE
g01	13	*quadratic*	**0,0003%**	9	0	0	0
g02	20	*nonlinear*	**99,9973%**	2	0	0	0
g03	10	*nonlinear*	**0,0026%**	0	0	0	1
g04	5	*quadratic*	**27,0079%**	4	2	0	0
g05	4	*nonlinear*	**0,0000%**	2	0	0	3
g06	2	*nonlinear*	**0,0057%**	0	2	0	0
g07	10	*quadratic*	**0,0000%**	3	5	0	0
g08	2	*nonlinear*	**0,8581%**	0	2	0	0
g09	7	*nonlinear*	**0,5199%**	0	4	0	0
g10	8	*linear*	**0,0020%**	6	0	0	0
g11	2	*quadratic*	**0,0973%**	0	0	0	1

Table 1: Values of ρ (evaluated in a pure random way) for the 11 mathematical test problems chosen

The different values of ρ for each of the functions chosen are shown in Table 1, where n is the number of decision variables, LI is the number of linear inequalities, NI the number of nonlinear inequalities, LE is the number of linear equalities and NE is the number of nonlinear equalities.

A standard and a normalized domination-based selection scheme have been adopted and they are indicated in Table 2.

6 RESULTS ANALYSIS

This study takes into consideration designers basic rule that is to prefer a feasible but not economuc solution to a more economic but unfeasible ones. This is an important point in structural and seismic design, where constraints violations usually are associated to an unaceptable low safety level. So that, differently from standard analysis to constrained optimization problems, in this research is analysed firstly the ability of alghoritms to produce feasible solutions and only after is analised their performances. In this research are analyzed 12 test functions from literatures [3].

Tree main efficience indicators are used to evaluate performances, with references to differ selection criteria and cross over alghoritms; the performane indives are :

- *Objective Function*
- *Stagnation*
- *ratio between Unfeasible individuals and total population size* ρ

Due to random nature of DE, performanes are evaluatred as statistically over 100 indepenedent runs, and in particolar as:

- Best
- Worst

- Mean
- Standard Deviation

The first analysis is performer over a population of 50 individuals and a number of 300 generations. As first analyzed index the ration between unfeasible and total population size ρ.

This ratio ρ is evaluated with reference to how many iterations are necessary to reach two different goals: the first is to have at least one feasible individual over all independent runs (figure 1) and the second is to have at least one feasible individuals over all independent runs. From a pragmatic point of view the first indication concerns performance while the second concerns robustness of algorithms with reference to ability to reach feasible solutions.

Smaller is number of generations needs to reach both to indicators, and greater is effectiveness of algorithms in reaching feasible solutions. If finally generations number is 300, than any feasible solution is reached at all.

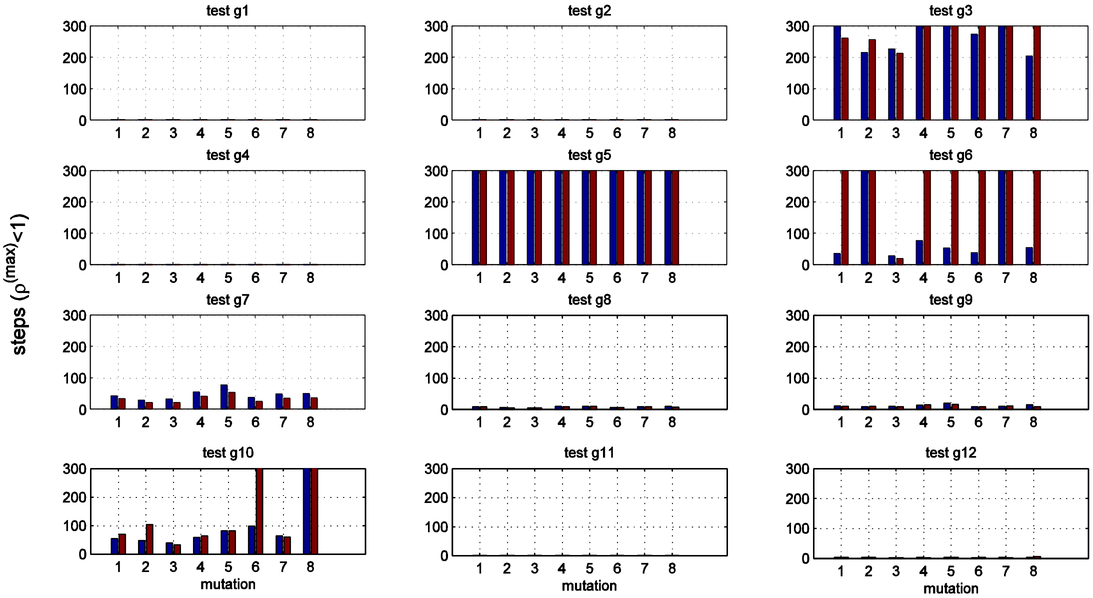

Figura 1: number of steps necessary to have that all runs gives at least one feasible solution. Mutation are those reported in table XX, while blu bars are for normalised approach, while red ones are for standard approach

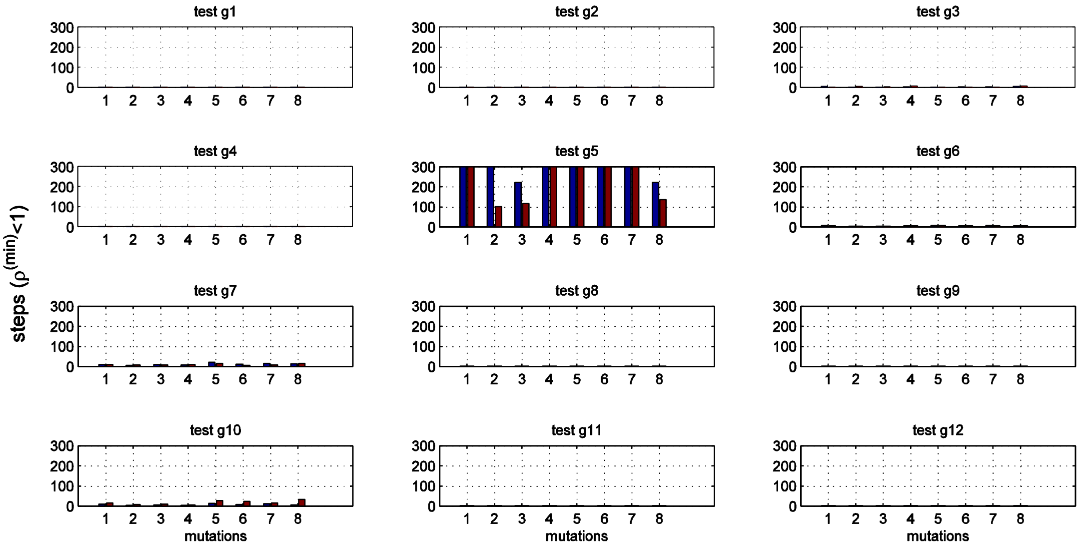

Figura 2: number of steps necessary to have that at least one runs presents a single feasible solution. Mutation are those reported in table XX, while blu bars are for normalised approach, while red ones are for standard approach

Mutation type	denomination	Equation reference
1	rand/1/bin	(7)
2	best/1/bin	(8)
3	current-to-best/1/bin	(9)
4	best/2/bin	(10)
5	rand/2/bin	(11)
6	Proposed 1	(12)
7	Proposed 2	(13)
8	Random (1-7)	(7) - (13)

Table 2: mutation type used in the analysis.

It is immediate that the function g5 is the more difficult to deal with. From figure 2 it appears that without any combination of cross over and selection criteria we have all independent runs with at all a single feasible solution. That means that the worst case is that after 300 generations we are not able to reach any feasible individual.

To better understand performances for ratios ρ are reported for each test function, for all considered combinations of cross over and selection criteria, that are Normalized (on the left) and Standard (on the right). Results are reported after 100, 200 and 300 generations (to evaluate efficiency under different number of generations) in best case (minimum value) in table 3 and worst case (maximum value) in table 4. When rho is equal to one means that no feasible solution are present, and when is equal to 0 means that all solutions are feasible.

generations	test functior	mutation															
		rand/1/bin		best/1/bin		rrent-to-best/1/		best/2/bin		rand/2/bin		rand/1/bin		rand/1/bin		random	
		N	S	N	S	N	S	N	S	N	S	N	S	N	S	N	S
100	1	0	0	0	0	0,02	0	0	0	0	0	0	0	0	0	0,02	0
	2	0	0	0	0	0	0	0	0	0	0	0	0	0	0	0	0
	3	0,92	0,9	0,88	0,86	0,22	0,84	0,2	0,18	0,9	0,9	0,9	0,9	0,92	0,94	0,86	0,92
	4	0	0	0	0	0	0	0	0	0	0	0	0	0	0	0	0
	5	1	1	1	1	1	1	1	1	1	1	1	1	1	1	1	1
	6	0	0	0	0	0,06	0	0,34	0	0,42	0	0	0,84	0	0,98	0,46	0,98
	7	0	0	0	0	0	0	0,12	0	0,36	0	0	0	0	0	0	0
	8	0	0	0	0	0	0	0	0	0	0	0	0	0	0	0	0
	9	0	0	0	0	0	0	0	0	0	0	0	0	0	0	0	0
	10	0	0	0	0	0,02	0	0	0	0,1	0,2	0	0,06	0	0	0	0
	11	0	0	0	0	0	0	0	0	0	0	0	0	0	0	0	0
	12	0	0	0	0	0	0	0	0	0	0	0	0	0	0	0	0
200	1	0	0	0	0	0,02	0	0	0	0	0	0	0	0	0	0,02	0
	2	0	0	0	0	0	0	0	0	0	0	0	0	0	0	0	0
	3	0,88	0,88	0,82	0,74	0,08	0,74	0,06	0,04	0,86	0,86	0,86	0,84	0,88	0,9	0,78	0,84
	4	0	0	0	0	0	0	0	0	0	0	0	0	0	0	0	0
	5	1	1	1	0	1	0,04	1	1	1	1	1	1	1	1	1	0,48
	6	0	0	0	0	0,04	0	0	0	0	0	0	0	0	0,98	0	0,98
	7	0	0	0	0	0	0	0	0	0	0	0	0	0	0	0	0
	8	0	0	0	0	0	0	0	0	0	0	0	0	0	0	0	0
	9	0	0	0	0	0	0	0	0	0	0	0	0	0	0	0	0
	10	0	0	0	0	0,02	0	0	0	0	0	0	0	0	0	0	0
	11	0	0	0	0	0	0	0	0	0	0	0	0	0	0	0	0
	12	0	0	0	0	0	0	0	0	0	0	0	0	0	0	0	0
300	1	0	0	0	0	0,02	0	0	0	0	0	0	0	0	0	0,02	0
	2	0	0	0	0	0	0	0	0	0	0	0	0	0	0	0	0
	3	0,84	0,84	0,7	0,64	0,06	0,6	0,04	0	0,8	0,78	0,78	0,76	0,86	0,86	0,74	0,8
	4	0	0	0	0	0	0	0	0	0	0	0	0	0	0	0	0
	5	1	1	1	0	0,22	0	1	1	1	1	1	1	1	1	0,08	0
	6	0	0	0	0	0,02	0	0	0	0	0	0	0	0	0,98	0	0,98
	7	0	0	0	0	0	0	0	0	0	0	0	0	0	0	0	0
	8	0	0	0	0	0	0	0	0	0	0	0	0	0	0	0	0
	9	0	0	0	0	0	0	0	0	0	0	0	0	0	0	0	0
	10	0	0	0	0	0,02	0	0	0	0	0	0	0	0	0	0	0
	11	0	0	0	0	0	0	0	0	0	0	0	0	0	0	0	0
	12	0	0	0	0	0	0	0	0	0	0	0	0	0	0	0	0

table 3: ratio ρ, best solutions over 100 independent runs

generations	test function	mutation															
		rand/1/bin		best/1/bin		rent-to-best/1/		best/2/bin		rand/2/bin		rand/1/bin		rand/1/bin		random	
		N	S	N	S	N	S	N	S	N	S	N	S	N	S	N	S
100	1	0	0	0	0	0,08	0	0,02	0	0	0	0,04	0	0	0	0,08	0
	2	0,02	0,02	0,04	0,04	0,04	0,04	0,04	0,04	0,04	0,04	0	0	0,02	0,02	0,04	0,02
	3	1	1	1	1	1	1	1	1	1	1	1	1	1	1	1	1
	4	0	0	0	0	0	0	0	0	0	0	0	0	0	0	0	0
	5	1	1	1	1	1	1	1	1	1	1	1	1	1	1	1	1
	6	0,56	1	1	1	0,54	0,3	0,86	1	0,88	1	0,86	1	1	1	0,92	1
	7	0,18	0	0,08	0	0,1	0,02	0,64	0,16	0,82	0,26	0,06	0	0,22	0	0,24	0
	8	0	0	0	0	0	0	0	0	0	0	0	0	0	0	0	0
	9	0,02	0	0,02	0	0,02	0	0,02	0	0,02	0	0	0	0	0	0,02	0
	10	0,42	0,44	0,12	1	0,4	0,08	0,66	0,36	0,86	0,9	0,98	1	0,44	0,48	1	1
	11	0	0	0,54	0	0,1	0,12	0	0	0	0	0	0	0,02	0,02	0,12	0
	12	0	0	0	0	0,02	0	0	0	0	0	0	0	0	0	0,04	0
200	1	0	0	0	0	0,06	0	0,02	0	0	0	0,02	0	0	0	0,08	0
	2	0	0	0,02	0,02	0,02	0,02	0,04	0,04	0,04	0,04	0	0	0	0,02	0,02	0
	3	1	1	1	1	1	1	1	1	1	1	1	1	1	1	1	1
	4	0	0	0	0	0	0	0	0	0	0	0	0	0	0	0	0
	5	1	1	1	1	1	1	1	1	1	1	1	1	1	1	1	1
	6	0	1	1	1	0,44	0,12	0,54	1	0,66	1	0,32	1	1	1	0,62	1
	7	0,02	0	0,02	0	0,04	0	0,1	0	0,16	0	0,02	0	0,02	0	0,04	0
	8	0	0	0	0	0	0	0	0	0	0	0	0	0	0	0	0
	9	0	0	0	0	0	0	0	0	0,02	0	0	0	0	0	0	0
	10	0,02	0	0,04	0,08	0,16	0,04	0,08	0,02	0,04	0,04	0,04	1	0,02	0,02	1	1
	11	0	0	0,06	0	0,06	0,1	0	0	0	0	0	0	0,02	0	0,08	0
	12	0	0	0	0	0,02	0	0	0	0	0	0	0	0	0	0,04	0
300	1	0	0	0	0	0,06	0	0,02	0	0	0	0,02	0	0	0	0,06	0
	2	0	0	0	0,02	0,02	0	0,04	0,04	0,04	0,04	0	0	0	0	0	0
	3	1	0,98	0,96	0,96	0,98	0,96	1	1	1	1	0,98	1	1	1	0,98	1
	4	0	0	0	0	0	0	0	0	0	0	0	0	0	0	0	0
	5	1	1	1	1	1	1	1	1	1	1	1	1	1	1	1	1
	6	0	1	1	1	0,42	0,08	0,42	1	0,4	1	0	1	1	1	0,48	1
	7	0,02	0	0,02	0	0,02	0	0,02	0	0,04	0	0,02	0	0,02	0	0,02	0
	8	0	0	0	0	0	0	0	0	0	0	0	0	0	0	0	0
	9	0	0	0	0	0	0	0	0	0	0	0	0	0	0	0	0
	10	0	0	0,02	0	0,16	0,04	0,04	0,02	0	0	0,02	1	0	0	1	1
	11	0	0	0	0	0,04	0,06	0	0	0	0	0	0	0	0	0,06	0
	12	0	0	0	0	0,02	0	0	0	0	0	0	0	0	0	0,02	0

table 4: ratio ρ, worst solutions over 100 independent runs

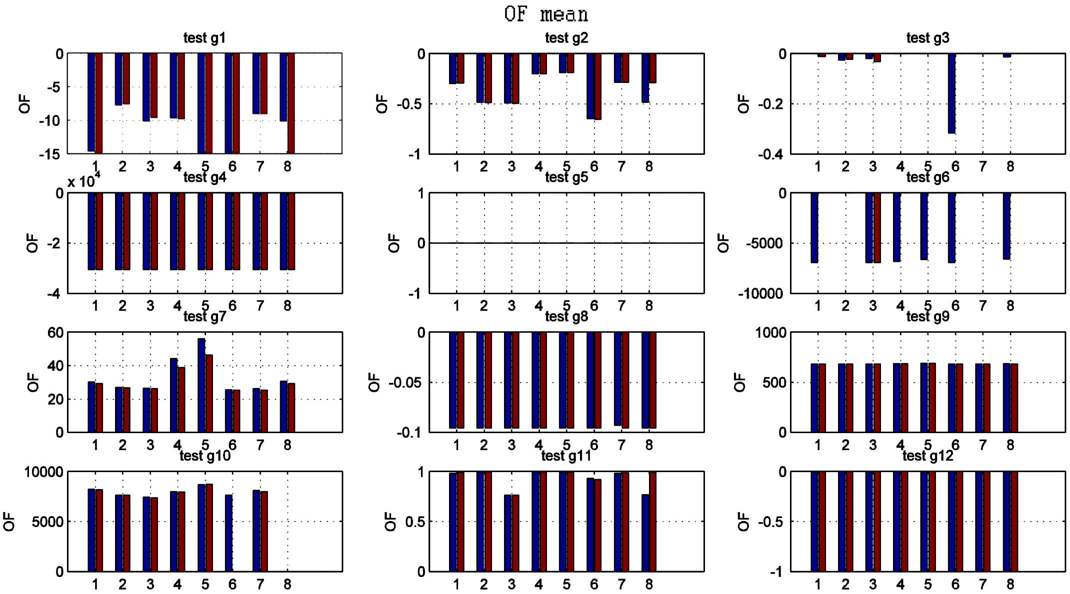

Figure 3: mean values of OF

Finally an aveluation of OF is reported in figure 3, where are reported

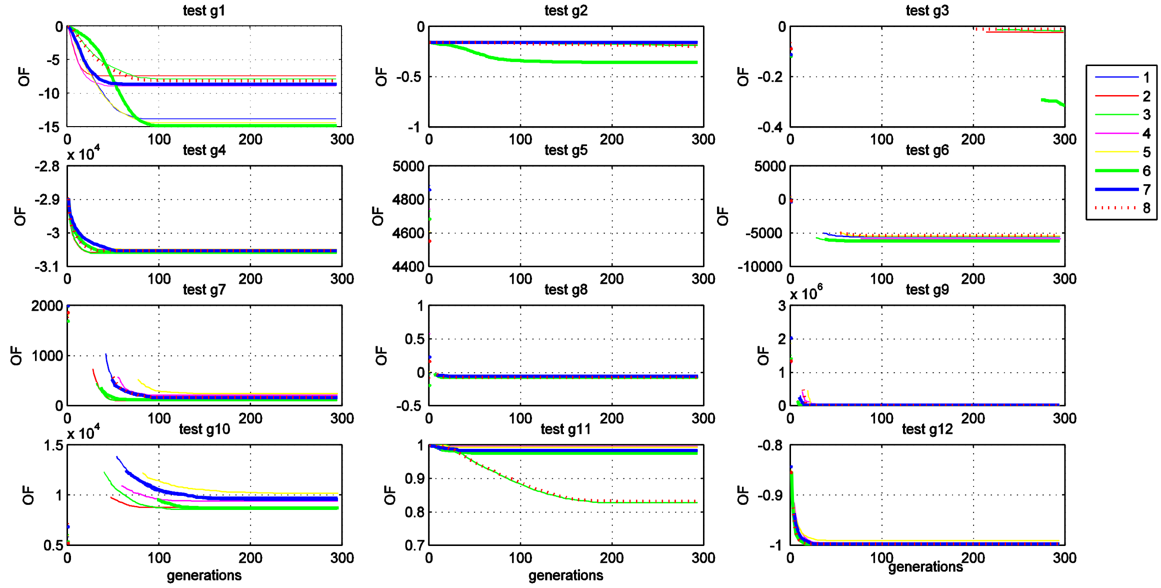

Figura 4: mean values of OF using a normalised selection criteria

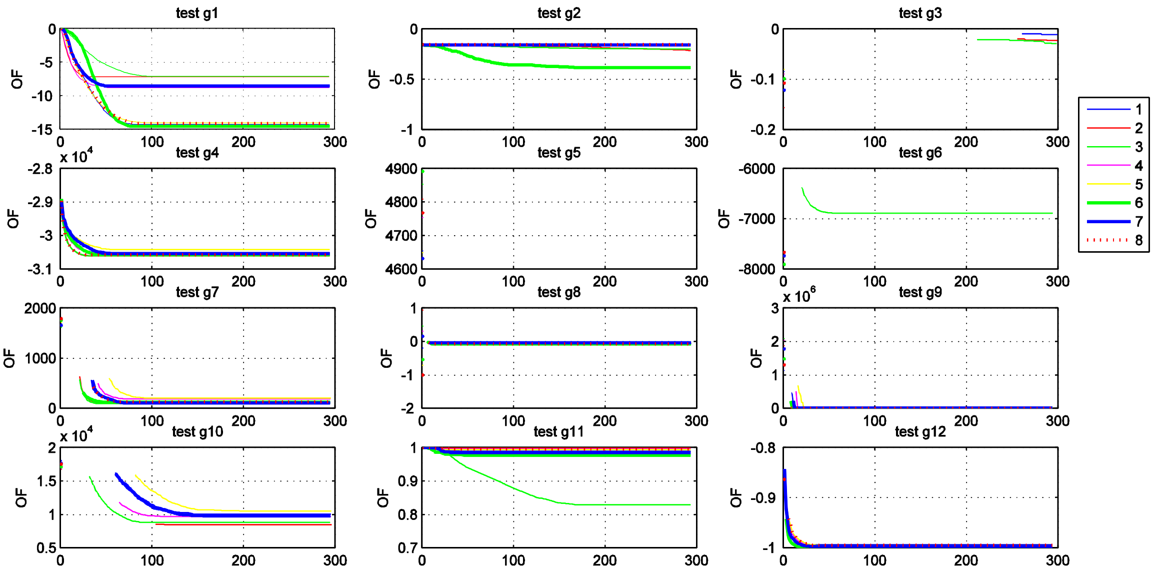

Figure 5: mean values of OF using a standard selection criteria

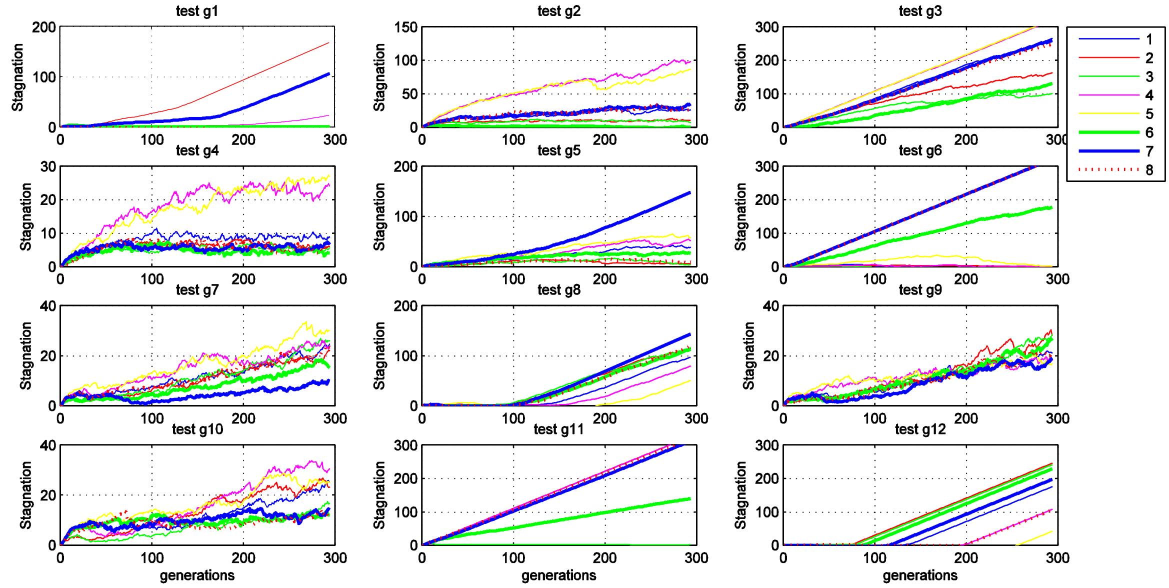

Figure 6: mean values of stagnations using a standard selection criteria

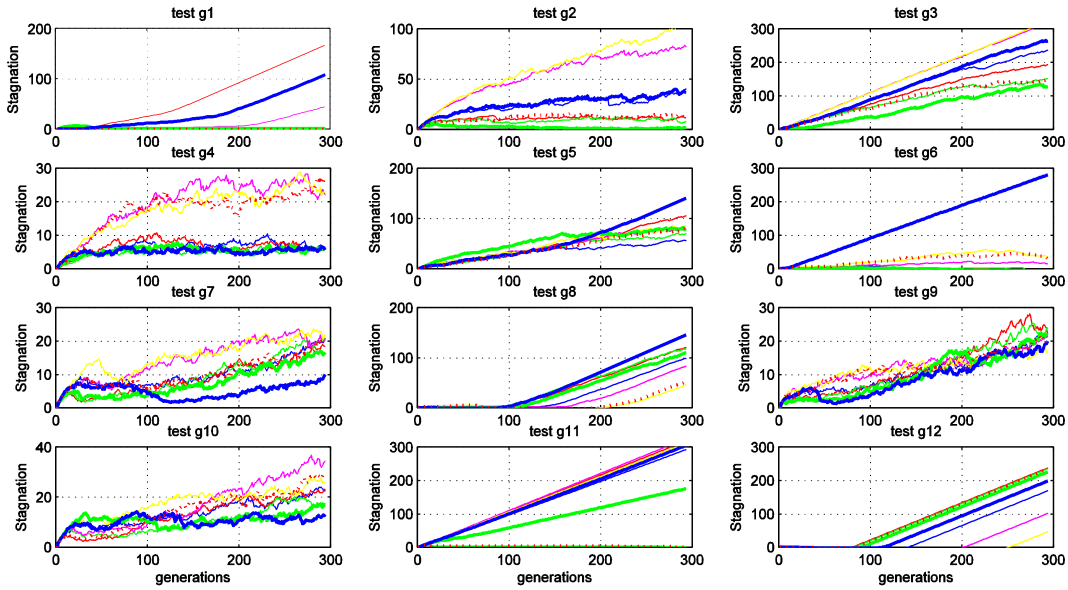

Figura 7 mean values of stagnations using a Normalized selection criteria

A deeper analysis of the two more difficult functions to be optimized - from the feasibility point of view - is thus developed. In details two more selection criteria have been used, in addition to the Standard - eq. (21) - and Normalized - eq. (25) - before considered.
In details the first one is a Normalized modified to take into consideration number of active violations in each selection, that means violation table search

$$ {}^{k}\Phi_{m}{}^{i} = n_a \left(1 + \sum_{r=1}^{n_v} {}^{k}\chi_r^i \right) \tag{28} $$

where n_a is the number of active constraints. Finally a complete different criteria is considered, based on the Kreisselmeier–Steinhsauser (KS) function that was first presented by G. Kreisselmeierand R. Steinhauser in [5], that is in the following form:

$$ {}^{k}\Phi_{KS}{}^{i} = \ln \left(\sum_{r=1}^{n_v} e^{{}^{k}\chi_r^i} \right) \tag{29} $$

The selection used for a deep analysis og functions g3 and g5 are thus reported in table

Violation type	Denomination	Equation reference
Standard	A	(25)
Normalized	B	(21)
Normalized modified	C	(28)
Kreisselmeier–Steinhsauser	D	(29)

Table 5: mutation type used in the analysis.

In table 6 and 7 are reported results obtained for the four selection criteria. Are reported the results in terms of best, worst, mean and standard deviation of the OF, evaluated over 2000 generations using 100 independent runs. Results in terms of mean and standard deviation are reported only if all 100 independent runs produce at least a single feasible solution. As reprted results of g5 presents only few positive results. In details considering this function's results (table 5) only mutation *current-to-best/1/bin* type - eq (9) - gives positive results (all indepen-

dent runs produce at least one feasible solution) associated with selection C and D. Moreover in tables 4 and 5 are reported the better four combinations in green, and the worsted four in red. The best one is thus underlined to be well recognizable from the others.
An interesting observation is done in terms of the worst results, that deals directly with robustness of the algorithms. In this since we should notice that the here proposed mutation criteria (eq 12) presents in all analyzed cases the best results, independently from the specific selection criteria used.

	mutation type	violation type			
		A	**B**	**C**	**D**
best	**1**	-0.590085	-0.5166404	-0.5104957	-0.4439761
	2	-0.8749872	-0.8037016	-0.7836352	-0.8001065
	3	-0.8250566	-0.7726869	-0.9282868	-0.8733928
	4	-0.141305	-0.1859609	-0.1059074	-0.1886541
	5	-0.3008128	-0.1389607	-0.0194375	-0.0587828
	6	-0.8889512	-0.9072688	-0.90685	-0.9351505
	7	***-0.945052***	-0.2654813	-0.0521805	-0.9321886
mean	**1**	-0.0878921	-0.0981476	-0.1108218	-0.1014194
	2	-0.2492862	-0.2529975	-0.2851858	-0.2946302
	3	-0.3248937	-0.3045726	-0.3084063	-0.3298275
	4	-0.0047889	-0.0080551	-0.0023269	-0.0028046
	5	-0.0049531	-0.0019552	-0.0005526	-0.0017174
	6	-0.7156717	-0.7066208	-0.7563377	***-0.773117***
	7	-0.7230272	-0.0065023	-0.0016844	-0.7615129
worst	**1**	-6.731E-05	-0.0001251	-0.0004741	-1.921E-05
	2	-0.0003809	0	0	-0.0034442
	3	-0.0056007	-0.007803	-0.0073629	-0.0138165
	4	0	0	0	0
	5	0	0	0	0
	6	-0.5242883	-0.4700976	-0.5002015	***-0.536492***
	7	-0.4452317	0	0	-0.425281
std	**1**	0.0872463	0.1027619	0.1094379	0.0962279
	2	0.2139432	0.1894743	0.2145767	0.2263379
	3	0.215557	0.2118199	0.2321309	0.2112057
	4	0.0182519	0.0306952	0.0113859	0.0191684
	5	0.0313684	0.0141752	***0.0027731***	0.0070985
	6	0.0863034	0.0845136	0.0843159	0.0901844
	7	0.0983988	0.02907	0.0081292	0.0931918

Table 4: Objective Functions results evaluated using 2000 generations for test function g3

	mutation type	violation type			
		A	**B**	**C**	**D**
best	**1**	5167.1009	5134.2465	5126.4989	5126.4971
	2	5126.4967	5126.4967	***5126.4967***	***5126.4967***
	3	5126.4967	***5126.4967***	***5126.4967***	***5126.4967***
	4				
	5				
	6	5126.4967	5126.4967	5126.4967	5126.4967
	7				
mean	**1**				
	2				
	3			5484.539	***5422.7768***
	4				
	5				
	6				
	7				
worst	**1**	5716.0382	5853.421	5696.6796	5560.2758
	2	6112.2237	6112.2238	6112.2237	6112.2237
	3	6111.1807	6076.805	6041.9826	6055.8937
	4				
	5				
	6	5127.7672	5126.5732	5155.8446	***5126.4988***
	7				
std	**1**				
	2				
	3			357.31161	***345.25123***
	4				
	5				
	6				
	7				

Table 5: Objective Functions results evaluated using 2000 generations for test function g3

7 CONCLUSIONS

With the aim of better explore possibilities of Differential Evolutionary (DE) algorithms in solving structural and seismic optimization problems, a numerical analysis has been conducted over standard test functions with the aim of compare different DE strategies using combinations of selection criteria and cross over. The constrained nature of the problem has been approached by using a number of selection criteria able to take into consideration elements feasibility starting from the original Deb's proposal in this way. Main advantages of this technique is inner simplicity due to absence of additional parameters to be opportunely regulated by tray and error initial procedure. Tree variations of original Deb's one are proposed, using each of them with different cross over criteria. Five are just proposed in literature, while 2 are here proposed to evaluate their performances in accordance with selection criteria. A first numerical analysis has been carried on a reduced number of generations (300) and using a small population size over 12 standard test functions. Algorithms performances in reaching feasible solutions has been evaluated over a set of 100 independent runs,; best mean and worst conditions have been analyzed. Finally a deeper analysis has been evaluate over the two more problematic functions , using a more wide number of possible cross over - selection criteria . Using a greater number of generations (2000), results have been carried on using four selections and seven cross over different criteria (for 28 different DE). Results have indicated that results are strongly influenced by proper selection of those two DE elements, and that a modified Deb's selection criteria shows a general higher performance instead of the original one.

REFERENCES

[1] C.A. Coello Coello, Theoretical and numerical constraint handling techniques used with evolutionary algorithms: a survey of the state of the art, Computer Methods in Applied Mechanics and Engineering, 2002, N. 191 (11–12), pp.1245–1287.

[2] N. Cruz-Cortés, Handling constraints in global optimization using artificial immune systems, E. Mezura-Montes (Ed.), Constraint-Handling in Evolutionary Optimization, Studies in Computational Intelligence Series, 2009, N. 198, Springer-Verlag, ISBN 978-3-642-00618-0, pp. 237–262.

[3] K. Deb, An efficient constraint handling method for genetic algorithms, Computer Methods in Applied Mechanics and Engineering, 2000, N. 186 (2–4), pp. 311–338.

[4] Koziel S., Michalewicz Z., Evolutionary Algorithms, Homomorphous Mappings, and Constrained Parameter Optimization, Evolutionary Computation, 1999, N. 7(1), pp. 19–44.

[5] G.KreisselmeierandR.Steinhauser.Systematiccontroldesignbyoptimizingavectorperformance index.In International Federation of Active Controls Syposium on Computer Aided Design of Control Systems, Zurich, Switzerland, 1979.

[6] E. Mezura-Montes (Ed.), Constraint-Handling in Evolutionary Optimization, Studies in Computational Intelligence, 2009, N. 198, Springer-Verlag.

[7] E. Mezura-Montes, C.A. Coello Coello, Constrained optimization via multiobjective evolutionary algorithms, J. Knowles, D. Corne, K. Deb (Eds.), Multiobjective Problems Solving from Nature: From Concepts to Applications, Natural Computing Series, Springer-Verlag, 2008, ISBN 978-3-540- 72963-1, pp. 53–76.

[8] Monti G, Quaranta G, Marano GC, Genetic-algorithm-based strategies for dynamic identification of nonlinear systems with noise-corrupted response, Journal of Computing in Civil Engineering ASCE, 2009

[9] A. Oyama, K. Shimoyama, K. Fujii, New constraint-handling method for multi-objective and multi-constraint evolutionary optimization, Transactions of the Japan Society for Aeronautical and Space Sciences, 2007, N. 50 (167), pp. 56–62.

[10] Storn R, Price K, Differential evolution – A simple and efficient heuristic for global optimization over continuous spaces, Journal of Global Optimization, 1997, N. 11(4), pp. 359–431.

[11] K. Price, R. Storn, J. Lampinen, Differential Evolution: A Practical Approach to Global Optimization, Natural Computing Series, Springer-Verlag, 2005.

[12] A.E. Smith, D.W. Coit, Constraint handling techniques—penalty functions, T. Bäck, D.B. Fogel, Z. Michalewicz (Eds.), Handbook of Evolutionary Computation, Oxford University Press, Institute of Physics Publishing, 1997. pp. C 5.2:1–C 5.2:6.

COMPDYN 2011
III ECCOMAS Thematic Conference on
Computational Methods in Structural Dynamics and Earthquake Engineering
M. Papadrakakis, M. Fragiadakis, V. Plevris (eds.)
Corfu, Greece, 25–28 May 2011

AN ANALYTICAL APPROACH FOR THE VULNERABILITY ASSESSMENT OF RC BUILDINGS SUBJECTED TO EARTHQUAKE INDUCED GROUND DISPLACEMENTS

Stavroula D. Fotopoulou[1] **and Kyriazis D. Pitilakis**[2]

[1] Aristotle University of Thessaloniki

Department of Civil Engineering
e-mail: sfotopou@civil.auth.gr

[2] Aristotle University of Thessaloniki

Department of Civil Engineering
e-mail: kpitilak@civil.auth.gr

Keywords: fragility curves, seismically induced landslide displacements, RC buildings, foundation system, structural damage index, corrosion of reinforcement

Abstract. *The present study aims at the development of an efficient analytical methodology for the vulnerability assessment of RC buildings subjected to earthquake triggered slope movements. The vulnerability is defined through specific probabilistic fragility functions for specified limit states. The fragility curves are numerically estimated in terms of peak ground acceleration at the "seismic bedrock", versus the probability of exceedance of each limit state, for the considered structure types. A two -step, uncoupled approach is performed. In the first step, the differential permanent displacements at the building's foundation level are estimated using an adequate finite difference dynamic slope model. Properly selected and corrected acceleration time histories are applied at the base of the model to assess the building's foundation response and the associated ground and foundation displacements are computed accordingly. Then, the calculated differential displacements are imposed to the fiber-based building model at the foundation level to assess the building's response for different ground landslide displacements induced by the earthquake. Limit states are defined in terms of a threshold value of building's material strain. Various sources of uncertainty concerning the capacity of the building, the deformation demand and the definition of limit states are considered in the analysis. The developed methodology is applied to both "low code" and "high code" RC frame buildings resting on shallow foundations with varying strength and stiffness characteristics (isolated footings, continuous foundation), standing near the crest of a relative slow moving soil slide. In case of the "low code" (usually old) RC buildings, the effect of corrosion of the reinforcement on the vulnerability estimation is also considered. The final goal of this research is to propose efficient fragility functions for a variety of RC building typologies.*

1 INTRODUCTION

Major landslide events occurred in Taiwan, California, Japan, Italy, China and elsewhere represent some of the most pronounced collateral hazards associated with earthquakes in terms of human losses and direct and indirect damage to the built environment. Seismically induced permanent ground deformation occurring as a result of landslides can adversely affect the likely performance of vulnerable engineering structures as it may account for a significant proportion of the total earthquake damage. Thus, predicting the expected performance of precarious slopes and affected facilities within the unstable area during or after an earthquake event, is of primary importance for design, urban planning, and for seismic hazard and risk studies.

Various methods of different complexity have been proposed to assess earthquake induced landslide hazards including the estimation of the probability of occurrence of a landslide and the slope permanent co-seismic displacement along a slip surface using Newmark-type displacement methods or advanced numerical approaches. However little work has been done on the quantification of the physical vulnerability of structures affected by earthquake triggered landslides. A major constraint to this may be considered the scarcity of accurate and reliable information on seismically induced landslide damage. HAZUS [1] multi-hazard loss estimation methodology may be considered an exception. Separate fragility curves, distinguishing between ground failure due to lateral spreading and ground failure due to ground settlement, and between shallow and deep foundations, were generated considering one combined Extensive/Complete damage state. However, the aforementioned methodology, exclusively based on expert judgment, involves a high degree of subjectivity and simplification as it does not account for the various landslide types and mechanisms, the soil type, the building typology, the stiffness of the foundation and the different damage states.

The present study, recognizing the need to improve the available background, aims at the proposition and quantification of an analytical procedure to assess the vulnerability of RC structures as a consequence of earthquake induced landslide displacements. The final goal of this research is to propose adequate fragility functions for a variety of RC building typologies.

2 METHODOLOGY

The proposed methodology [2], largely inspired from the seismic risk analysis, may be applied for the vulnerability assessment of RC buildings subjected to earthquake triggered relative slow moving soil slides. The proposed approach is principally based on a comprehensive set of numerical computations and statistical analysis. In terms of numerical simulation, a two-step uncoupled analysis is conducted. In the first step, the differential permanent displacements at the building's foundation level are estimated using the FLAC2D [3] finite difference dynamic slope model. The effect of ground shaking to the structure's response and the associated damages is not considered in the vulnerability of the building itself, which is assessed only for the differential movements due to slow moving seismically triggered landslides. Then, the computed differential displacements are applied as input to the building model at the foundation level, to assess the building's response for different differential ground landslide displacements induced by earthquake with progressively increased intensities. The numerical analysis of the building's response is performed through the fiber-based finite element code SEISMOSTRUCT [4]. Limit states are defined in terms of a threshold value of building's material strain.

The fragility curves are numerically estimated in terms of peak ground acceleration at the "seismic bedrock", (PGA) versus the probability of exceedance of each limit state considering various sources of uncertainty. The selection of the PGA against the differential displacements value is a key point of the present method and it is explicitly related to the main parameter of any seismic hazard assessment.

Figure 1 illustrates a schematic representation of the proposed framework. Building classification (foundation type, superstructure) constitute the capacity of the building. The earthquake demand, the landslide type and the relative location of the building to the potential unstable slope, constitute the deformation demand of the building. These two components (building capacity, deformation demand) can be considered as inputs to the simulation engine which is the third major component, i.e. the methodology for structural assessment. Structural response data obtained by analyzing the building capacity under the deformation demand is processed by the methodology for fragility curve generation to yield the results. Limit states, which are determined with respect to the building classification, properly selected empirical criteria and expert judgment, are required at this step. The final step of the methodology will result to the construction of the fragility relationships.

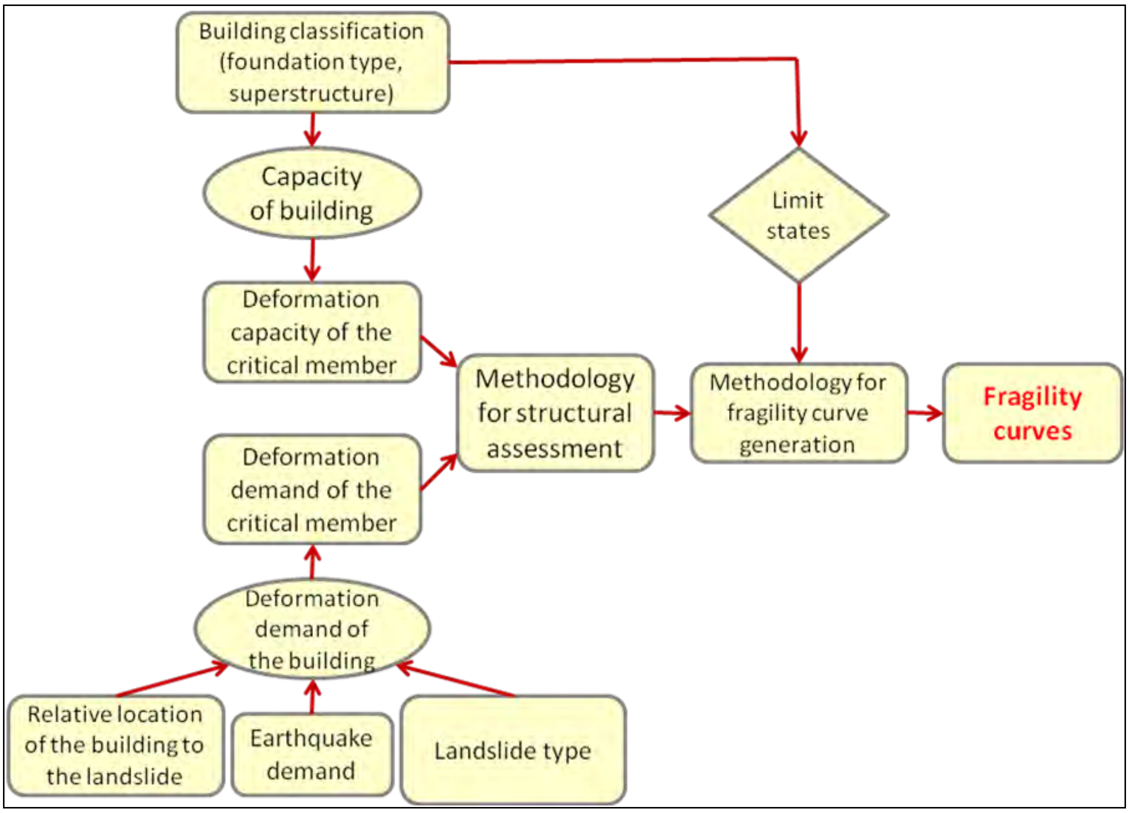

Figure 1: Flowchart for the proposed framework of fragility analysis of RC buildings.

The description of the methodological framework together with a simplified case study has already presented in [2]. In the present study an improved version of the methodology and the corresponding application is attempted, emphasizing at the variability on the earthquake ground motion and on the associated differential displacements, yielding a more descriptive characterization of the structural damage and considering buildings with different strength and stiffness characteristics and code design level. Some key points of the proposed framework are highlighted in the following paragraphs:

The landslide type is a crucial parameter of the proposed methodology as landslides of different types and sizes usually require different and complementary methods to estimate vulnerability. While damage to the built environment resulting from the occurrence of rapid landslides such as debris flows and rock falls is generally the highest and most severe, as it may lead to the complete destruction of any structure within their path, slow-moving slides also have adverse effects on affected facilities [5]. The damage caused by a slow moving landslide on a building is mainly attributed to the cumulative permanent (absolute or differential) displacement and it is concentrated within the unstable area. A relative slow moving soil slide that will produce tension cracks due to differential displacement to a RC building, exposed to the landslide hazard, is considered in this study.

The characteristics (amplitude, frequency content and duration) of the earthquake ground motion in relation to the soil dynamic properties and stratigraphy can significantly influence the derived deformation demand for the building. Material damping, the impedance contrast between sediments and the underlying bedrock, and the characteristics of incident wavefield are considered to represent the governing factors for site amplification/attenuation [6,7]. A fundamental period of the earthquake close to the natural period of the site can lead to resonance phenomena and, consequently, to an amplified energy content of the ground motion. Combining a low-frequency seismic input motion together with a resonance phenomenon in the low-frequency range, the slope failure potential assumes its highest values [8].

The position of the building with respect to the landslide area is a very important contributing factor in estimating vulnerability. Landslides triggered by earthquakes tend to be clustered near ridge crests and hill slope toes. Peng et al. [9] attributed this ridge- crest clustering to topographic effects, and the clustering at hill slope toes to dynamic pore-pressure changes in the water-saturated material of lower hill slopes. In this study, a building standing near the crest where the seismic ground motion due to topographic effects is generally amplified is considered [10,11].

For a landslide of given type, mechanism and intensity, the typology of the exposed structure is also a key factor in the vulnerability assessment methodology. Geometry, material properties, state of maintenance, code design level, soil conditions, foundation and structure details, number of floors etc. are among typical typological parameters which determine the capacity of the building to withstand the specified co-seismic landslide displacement. The response to permanent total and differential ground deformation depends primarily on the foundation type. A structure on a deep foundation (e.g. piles) compared to shallow foundations often experiences higher resistance ability and hence a lower vulnerability. For shallow foundations, the distinction is between rigid or flexible/unrestrained foundation systems. When the foundation system is rigid (e.g. continuous raft foundation), the building is expected rather to rotate as a rigid body and a failure mainly attributed to the loss of functionality of the structure is anticipated. In this case, the damage states are defined empirically, as there is limited structural demand to the members of the building (apart from possible P-Δ effects at larger rotations). On the contrary, when the foundation system is flexible (e.g. isolated footings), the various modes of differential deformation produce structural damage (e.g. cracks) to the building members [12,13] that can be estimated using an analytical procedure analogous to that of the response due to seismic ground motion.

When building response to ground failure comprises structural damage, damage states can be classified using the same schemes used for structural damage caused by ground shaking. Limit states are defined in terms of limit value of a component’s strain based on damage observation from previous earthquake events, the existing knowledge related to earthquake damage levels, and published tolerances for non-earthquake related foundation deformations [14,12].

In the probabilistic approach proposed herein, the uncertainties related to the capacity of the building, the definition of the limit states and the deformation demand (differential permanent displacement) should be considered. The uncertainty in the displacement capacity is a function of the material properties, geometric properties, and the yield strain of steel and post-yield strain capacities of the steel and concrete. The uncertainty in the demand includes all of the variability associated with the ground motion estimation plus the additional uncertainties associated with the landslide type and size, the relative position of the building to the landslide area, the variability in soil parameters and stratigraphy and the uncertainty within the assessment of ground deformations.

3 APPLICATION

3.1 Deformation demand- Numerical analysis

An application of the proposed methodology to an idealized case study is presented herein. To estimate the input differential displacements at the building's foundation level, we applied FLAC 2D finite difference dynamic model [3] (fig. 2) using an elastoplastic constitutive model with Mohr-Coulomb failure criterion and non associated plastic flow rule, able to simulate large deformations for slope stability assessments. A small amount of Rayleigh damping (1 to 3%) is assigned to account for the energy dissipation in the elastic range. The center frequency of the installed Rayleigh damping is selected to lie between the fundamental frequencies of the input acceleration time histories and the natural modes of the system. In the slope area, a fine grid discretization is adopted, whereas towards the lateral boundaries of the model, where the accuracy requirements loosen, the mesh is coarser. The slope height and inclination are 20m and 30^o respectively. Free field absorbing boundaries are applied along the lateral boundaries while quiet (viscous) boundaries are applied along the bottom of the dynamic model to minimize the affect of reflected waves. In order to apply quiet boundary conditions along the same boundary as the dynamic input, the seismic motions must be input as stress loads combining with the quiet (absorbing) boundary condition. The soil type is selected to represent a homogenous dry sand corresponding to soil category C of EC8 [15]; its material, physical and dynamic properties are provided in Table 1.

A building is assumed to be located 3m from the slope crest. The building is modeled only by its foundation with a width of 6m (uncoupled approach). Two different foundation systems are considered (Table 2): isolated footings and a uniform loaded continuous slab foundation. In the first case, the foundation is simulated with concentrated loads at the footings' links. In the second case, the foundation system is modeled as a deformable elastic beam connected to the grid through appropriate frictional interface elements that can approximate the potential Coulomb sliding and/or tensile separation of the beam. The static factor of safety of the slope is calculated through a limit equilibrium method as Fs=1.45.

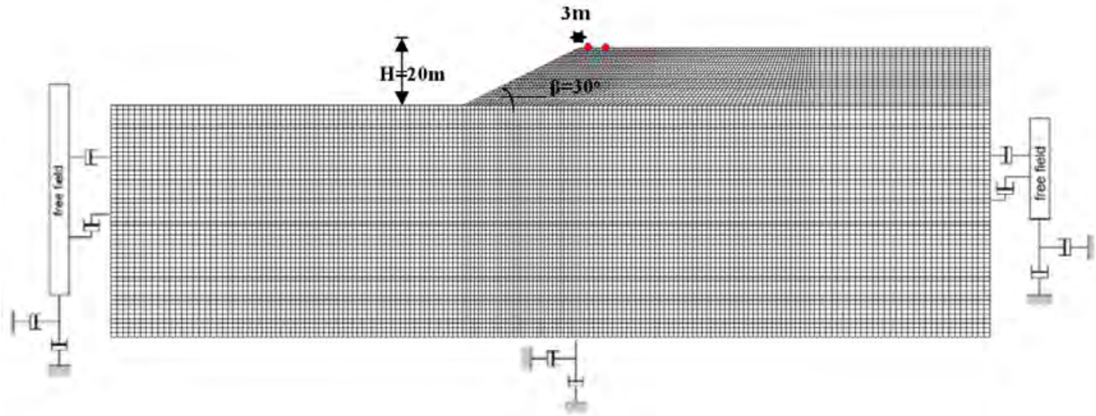

Figure 2: FLAC dynamic model

Properties	Soil C
Constitutive model	Mohr Coulomb
Dry density (KN/m^3)	18
Vs (m/sec)	250
Poisson's ratio	0.3
Cohesion (KPa)	0
Friction angle (degrees)	36
Dilation angle (degrees)	0
$N_{1(60)}$	21
Dr(%)	60

Table 1: Soil properties

Properties	Foundation system	
	Stiff foundation	Flexible foundation
Element	beam	
Length (m)	6	
Density (KN/m^3)	24	
Young's modulus (KPa)	2.90E+7	
Moment of inertia I (m^3)	0.0053	
Area (A) (m^2)	0.4	
Load (KN/m)	Uniform distributed q=25KN/m2	Concentrated load P=50KN/m

Table 2: Foundation properties

Prior to the dynamic simulations, a static analysis is carried out to establish the initial effective stress field throughout the model. The dynamic input motion consists of SV waves vertically propagating from the base. Six different earthquake records are used as excitation for the dynamic analysis: (i) Valnerina (Cascia-L), Italy, Ms=5.8 , 1979, (ii) Athens (Kypseli-L), Greece, Mw=5.9, 1999, (iii) Montenegro-[TRA (EW)], former Yugoslavia, Mw=6.9, 1979 and (iv) Northridge (Pacoima Dam -L), USA, Ms=6.7, 1994, (v) Campano Lucano (Sturno-L), Italy, Mw=6.9 , 1980 and (vi) Duzce (L), Turkey, Mw=7.2, 1999. They all refer to outcrop conditions. The selected records cover a wide range of seismic motions in terms of the seismotectonic environment, amplitude, frequency content and significant duration. Before applied along the base of the model, they are subjected to appropriate correction (baseline correction, filtering and tapering) to assure an accurate representation of wave transmission through the model. Figure 3 presents the normalized elastic response spectra of the input motions together with the proposed elastic design spectrum of EC8 [15] for soil type A (rock).

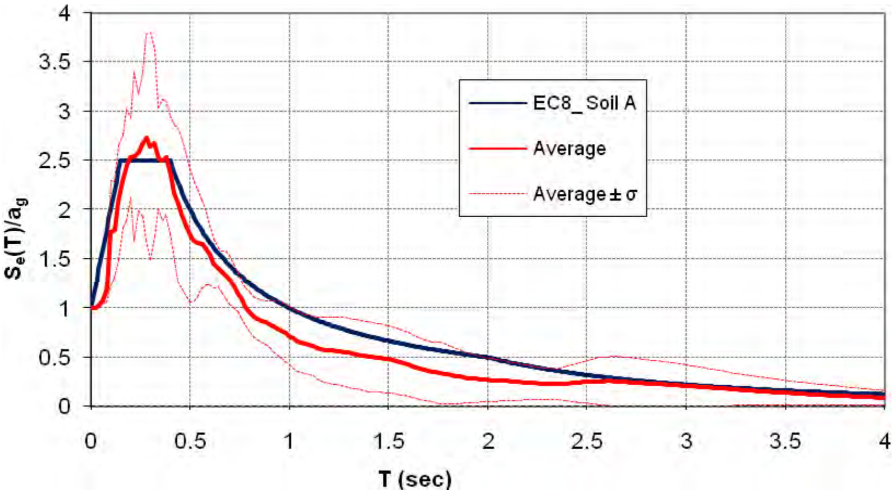

Figure 3: Normalized average elastic response spectrum of the input motions in comparison with the corresponding elastic design spectrum for soil type A (rock) according to EC8.

The input accelerograms are scaled to five levels of peak ground acceleration (PGA=0.1, 0.3, 0.5, 0.7 and 0.9g) so as to assess the building response for different displacement magnitudes. This procedure will allow resulting in different damage states for the building and finally to be able to construct the corresponding vulnerability curves. Figure 4 presents the maximum values of differential displacements for the building with flexible and stiff foundation system derived from the dynamic analysis by applying the different scaled accelerograms. It is observed that the specific characteristics (frequency content and duration) of the seismic ground motions can significantly influence the magnitude of the computed differential displacement at the foundation level. Moreover, it is worth noticing that when the soil structure interaction is considered, the differential horizontal displacements at the beam foundation are practically zero and the total differential displacement vector for the building is generally decreased.

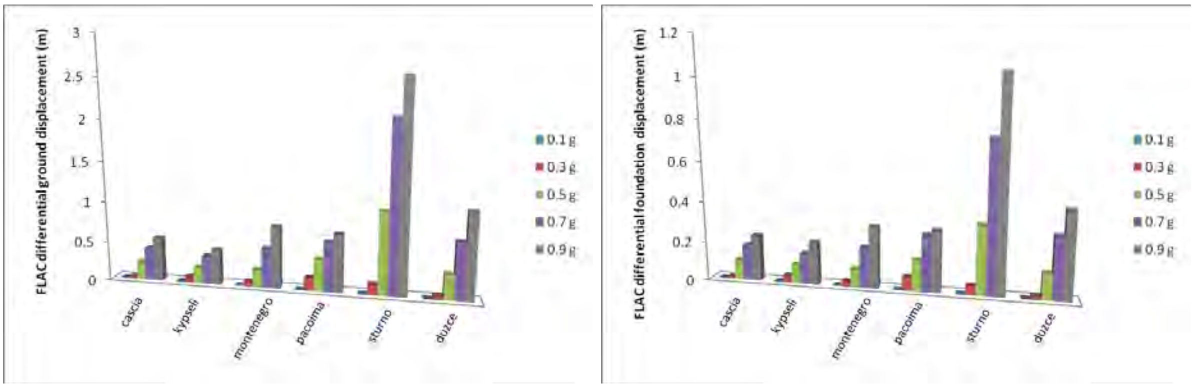

Figure 4: Maximum values of differential displacement vector for buildings with flexible and stiff foundation system

3.2 Comparison with simplified displacement methods

To validate the numerical results, they are compared, in terms of maximum permanent horizontal displacement, with the simplified Newmark-type displacement methods. The conventional Newmark rigid block model [16,17], as well as a recent improved version to account for the soil deformability using a coupled stick-slip deformable sliding block model [18], are used to calculate permanent displacements of the slide mass.

Bray and Travasarou [18] displacement model captures the primary influence of the system's yield coefficient (k_y), its initial fundamental period (Ts), and the ground motion's spectral acceleration at a degraded period equal to 1.5Ts. The input accelerograms applied to both methods are the scaled acceleration time histories recorded on rock multiplied by the site amplification factor S=1.15 (as proposed in EC8 for subsoil class C), in an effort to conservatively approximate the equivalent acceleration time histories acting on the potentially sliding mass. The yield coefficient, k_y, is computed by applying the following relationship, as proposed in [19]:

$$k_y=\tan(\varphi-\beta)+\ c/(\gamma\cdot H\cdot \cos 2\beta\cdot (1+\tan\varphi\cdot\tan\beta)) \tag{1}$$

where φ= friction angle, c= cohesion, H= height of the critical sliding surface and β= slope angle.

The results of the above methods are summarized in figure 5 (a) and (b) respectively in comparison with the co-seismic numerical displacements calculated herein. The direct application of Newmark rigid block approach is found to underestimate the computed displacements. This can be regarded as relevant considering that Newmark's method treats the potential landslide block as a rigid mass (no internal deformation) that slides in a perfectly plastic manner on an inclined plane, which is not realistic in our case. The results of fully coupled stick-slip deformable sliding block model introduced by Bray and Travasarou [18] are generally in good agreement with that of the dynamic analysis. In both cases, however, a large scatter on the predicted residual displacements is detected recognizing the need to adopt a fully probabilistic framework, as proposed in Bray and Travasarou [18].

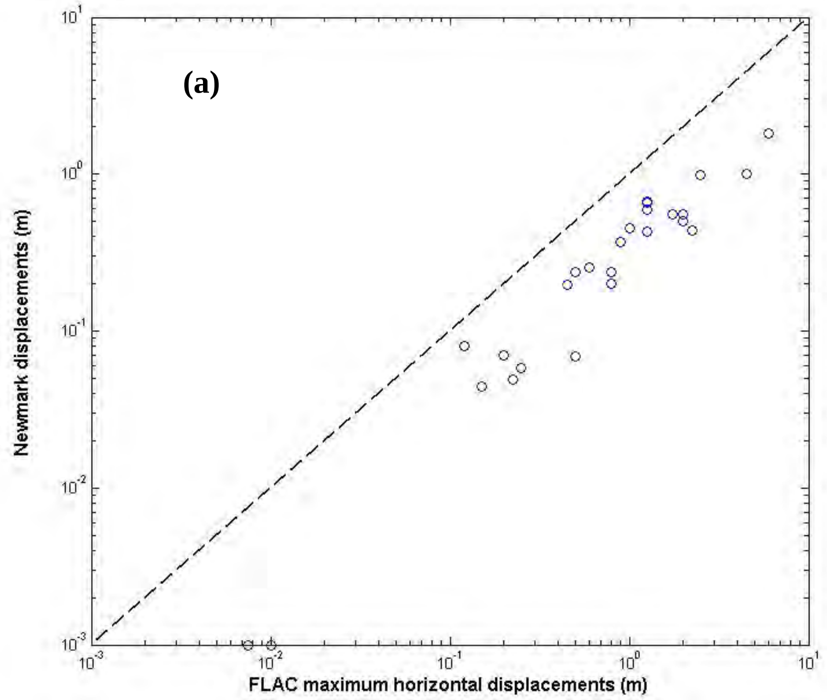

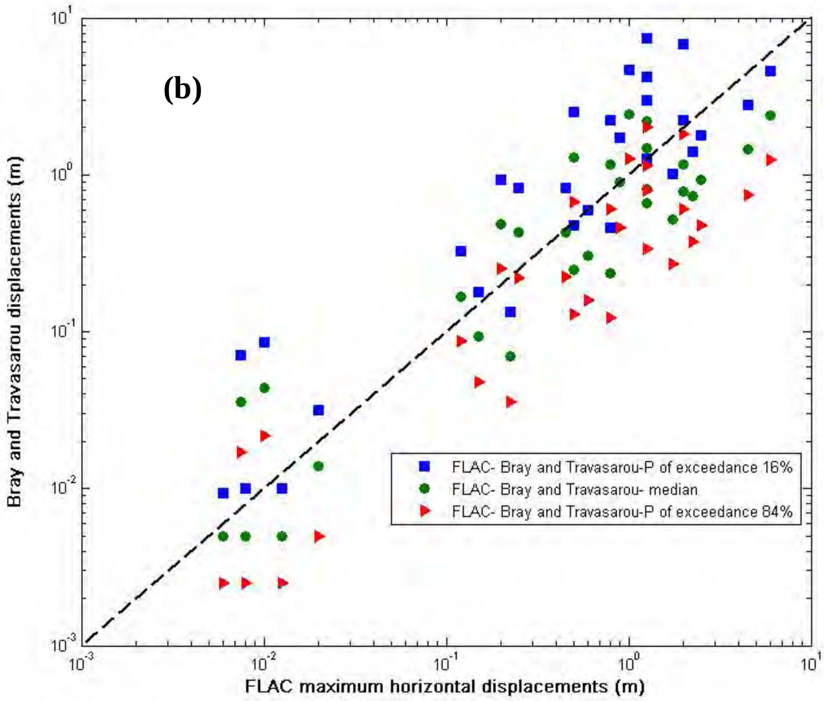

Figure 5: Comparison of Newmark [16] (a) and Bray and Travasarou [18] (b) displacements with maximum horizontal displacement from 2D dynamic analyses.

3.3 Analysis of the building's response

The analyses of the buildings is conducted using the finite element code SeismoStruct [4], which is capable of calculating the large displacement behavior of space frames under static or dynamic loading, taking into account both geometric nonlinearities and material inelasticity. Both local (beam-column effect) and global (large displacements/rotations effects) sources of geometric nonlinearity are automatically taken into account. The spread of material inelasticity along the member length and across the section area is represented through the employment of a fiber-based modeling approach, implicit in the formulation of SeismoStruct's inelastic beam-column frame elements. Nonlinear static time-history analyses are performed for all numerical simulations. In particular, the differential permanent (ground or beam) displacement (versus time) curves, directly extracted from the FLAC dynamic analysis, are statically imposed at one of the RC frame supports.

The studied buildings are single bay-single storey RC bare frame structures that vary in their foundation system and design code level. Regarding the foundation system, buildings with flexible foundation system (isolated footings) and buildings with stiff but not completely rigid foundation system (continuous uniform loaded foundation of finite stiffness characteristics) are considered. Both "low code" and "high code" design buildings that differ in the strength and stiffness characteristics and the corresponding assigned limit strain levels are examined. The reference building's height and length are 3m and 6m respectively. All columns and beams have rectangular cross sections (0.40x 0.40m). The longitudinal reinforcement used is 8Φ14 ($A=0.00123m^2$) for all the cross sections considered.

The use of such simple structures is justified from the observation that the number of storeys and bays do not seem to comprise crucial parameters in the determination of the building's performance subjected to permanent ground displacements. The latter is also confirmed in [12] for the vulnerability assessment of RC buildings due to liquefaction induced ground deformations. Hence, one bay-one storey RC structures despite their simplicity are found to be adequately representative of the performance of real low rise RC frame buildings.

The material properties assumed for the members of the reference RC buildings are described below. A uni-axial nonlinear constant confinement model (fig. 6 (a)) is used for the concrete material (fc=20MPa, ft=2.1MPa, strain at peak stress 0.002mm/mm, confinement factor 1.2), assuming a constant confining pressure throughout the entire stress-strain range [20]. For the reinforcement, a uni-axial bilinear stress-strain model with kinematic strain hardening (fig. 6(b)) is utilized (fy=400MPa, E=200GPa, strain hardening parameter μ =0.005). This simple model is characterized by easily identifiable calibrating parameters and by its computational efficiency.

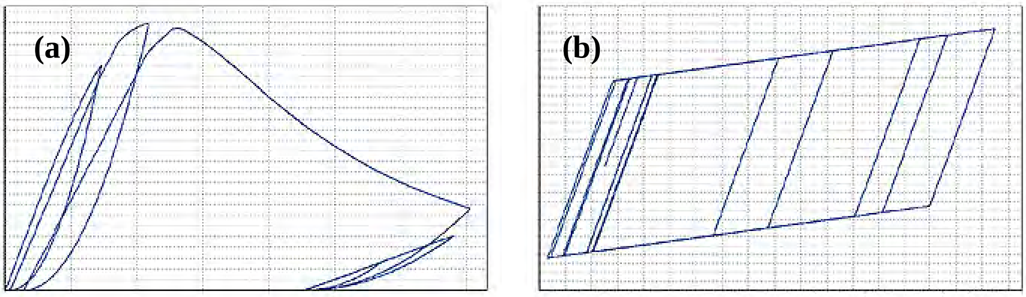

Figure 6: Stress-strain models for concrete (a) and steel (b).

A sensitivity analysis is performed for the reference building cases which allows for indentifying the influence of different parameters on the structural response and proposing a preliminary probabilistic framework of the damage estimation. The parameters selected to vary are: the yield strength of steel (fy=210, 400 MPa for "low code" and 400,500 MPa for "high code"), the compressive (fc=16, 20 MPa for "low code" and 20, 30 MPa for "high code") and tensile (ft=2.0, 2.1 MPa for "low code" and 2.1, 3.0 MPa for "high code") strength of concrete, the reinforcement bar size (Φ12, Φ14 for "low code" and Φ14, Φ16 for "high code") and the confinement factor (1.0, 1.2 for "low code" and 1.2, 1.3 for "high code") for progressively increasing levels of differential displacements extracted from the previous dynamic stress strain analysis for increasing level of input acceleration time histories. In case of the "low code" (usually old) RC buildings, the effect of corrosion of the reinforcement on the vulnerability estimation is also considered. The loss of area of steel due to corrosion of the RC elements is modeled as a reduction in longitudinal reinforcing bar cross sectional area compared to the elements in the initial nondegraded state. In this study, a 50% reduction of the area of reinforcing steel is assumed.

The deformed shapes of buildings with flexible foundation system are essentially the same irrespective of the variability in the strength parameters and the level of demand, observation that is in accordance with that of [12]. The same trend is observed to the buildings with stiff foundation (Fig. 7). In both building typologies, a column failure mechanism is detected (see also [21]). The reason is that the axial stiffness of the beams is generally much higher compared to the flexural stiffness of the columns. Moreover, in the case of buildings with flexible foundations, the applied differential displacement vector is mainly governed by the horizontal component that determines the deformation mode (fig. 7(a)). On the contrary, in buildings with stiff foundation system the applied displacements are practically vertical. Hence, it is concluded that the inclination of the applied differential permanent displacement constitutes a fundamental parameter in determining the deformed shape of the building when subjected to a permanent displacement at the foundation level. It is worth noting that the deformed shape of building with flexible and stiff foundations and the associated computed displacements at the critical column are found to closely approximate the idealized response of a RC frame building subjected to liquefaction induced lateral movement (with an associated vertical component) and to vertical settlements respectively, as proposed in [12].

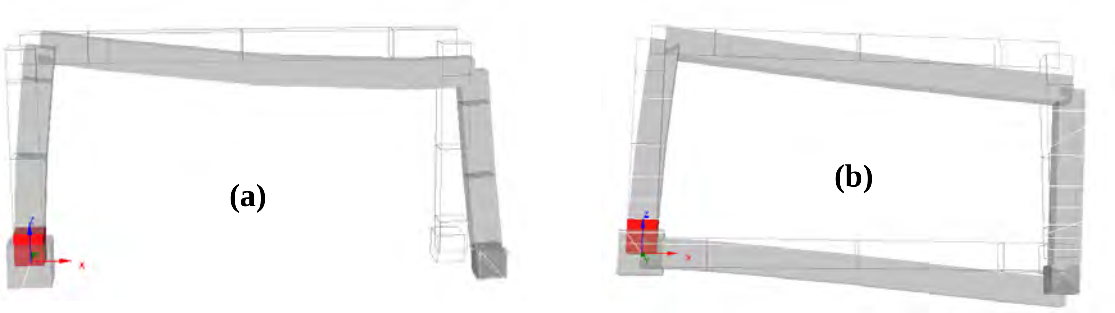

Figure 7: Deformed shapes for buildings with flexible (a) and stiff (b) foundations. The failure mechanism at the critical column is also shown.

3.4 Analytical fragility curves

We derived in this stage different sets of analytical fragility curves for low rise (single bay-single storey) RC buildings with varying stiffness of the foundation system and different code design level. Fragility curves for "low code" corroded RC buildings are also constructed. Each curve provides the conditional probability of exceeding a certain limit or damage state under a range of seismic induced landslide events of given type and intensity. The landslide intensity is expressed in this work in terms of peak ground acceleration at the seismic bedrock that is the initial trigger of the slow moving slide. This will result to permanent differential displacements at the foundation level.

The probabilistic nature of the problem is treated by accounting for the variability associated with the building capacity (yield strength of steel, compressive and tensile strength of concrete, reinforcement bar size, confining factor), as well as the variability in the demand, assuming different progressively increasing acceleration time histories that result in different permanent differential displacement magnitudes at the building's foundation links. In order to identify the building performance (damage) state and to construct the corresponding fragility curves, a damage index (DI) is introduced describing the steel and concrete material strains. Within the context of a fibre-based modelling approach, such as that implemented in SeismoStruct, material strains do usually constitute the best parameter for identification of the performance state of a given structure [4]. In all cases analyzed (600 in total), the steel material strain (ε_s) yields more critical results. Thus, it was decided to adopt only this parameter as a damage index hereafter for simplicity reasons. In this way, it is possible to establish a relationship between the damage index (ε_s) and the input motion intensity in terms of the PGA values at the assumed seismic bedrock, for the different building typologies and consequently to assign a median value of PGA to each limit state. Figure 8 presents representative PGA - damage index curves for low rise, "high code" design RC frame buildings with stiff and flexible foundation system.

The next step is the definition of the damage or limit states. Based on the work of Crowley et al. [14], Bird et al. [12,13] and engineering judgment, 4 limit states (LS_1, LS_2, LS_3, LS_4) are defined. Considering that low code RC buildings are poorly constructed structures characterized by a low level of confinement, the limit steel strains needed to exceed post yield limit states should have lower values compared to high code, properly constructed RC buildings. As a consequence, it was decided to adopt different limit state values for excedance of extensive and complete damage for low and high code frame RC buildings. A qualitative description of each damage band for reinforced concrete frames is given in Table 3 while the limit state values finally adopted in quantitative terms are presented in Table 4. These concern exceedance of minor, moderate, extensive and complete damage of the building. The first limit state is specified as steel yielding that is the ratio between yield strength and modulus of elasticity of the steel material.

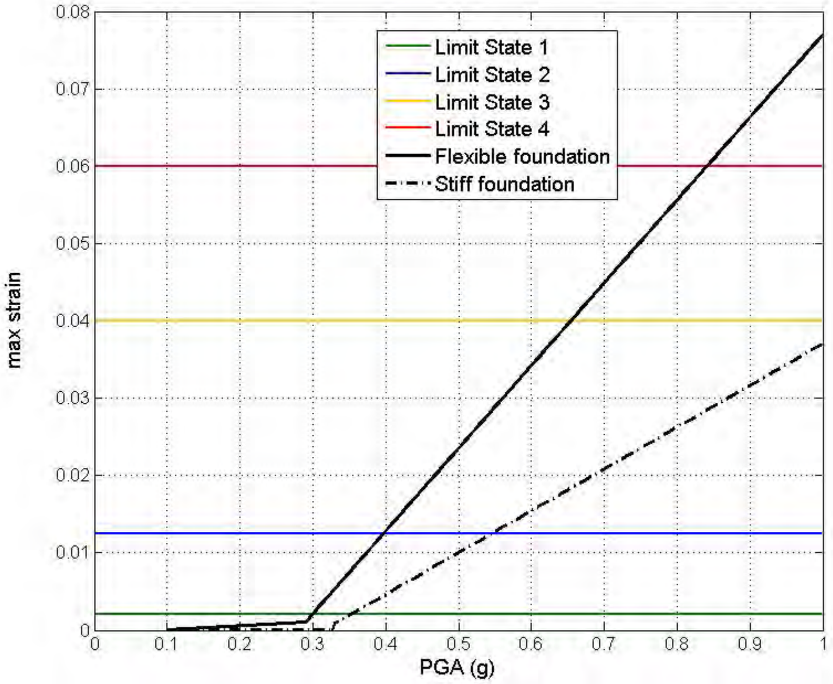

Figure 8: PGA–damage index relationships for 1story-1story "high code" RC frame buildings with stiff and flexible foundation system

Structural damage band	Description
None to slight	Linear elastic response, flexural or shear type hairline cracks (<1.0 mm) in some members, no yielding in any critical section
Moderate	Member flexural strengths achieved, limited ductility developed, crack widths reach 1.0 mm, initiation of concrete spalling
Extensive	Significant repair required to building, wide flexural or shear cracks, buckling of longitudinal reinforcement may occur
Complete	Repair of building not feasible either physically or economically, demolition after earthquake required, could be due to shear failure of vertical elements or excessive displacement

Table 3: Structural damage state descriptions for RC frame buildings (after [14])

Limit state	Steel strain (ε_s) –low code	Steel strain (ε_s) – high code
LS1	Steel bar yielding	Steel bar yielding
LS2	0.0125	0.0125
LS3	0.025	0.04
LS4	0.045	0.06

Table.4. Definition of Limit states for “low” and “high” code design RC buildings

In order to construct the fragility relationships, appropriate cumulative distribution functions, as the ones proposed in HAZUS [1], that describe the fragility relationships have been generated. For structural damage, given peak ground acceleration PGA, the probability of exceeding a given limit state, SLi, is modeled as:

$$f(PGA) = \Phi\left[\frac{1}{\beta_i} In\left(\frac{PGA}{\overline{PGA_i}}\right)\right] \tag{2}$$

Where:

- Φ is the standard normal cumulative distribution function,
- $\overline{PGA_i}$ is the median value of peak ground acceleration at which the building reaches the limit state, i,

βi is the standard deviation of the natural logarithm of peak ground acceleration for limit state, i.

The median values of peak ground acceleration that correspond to each limit state can be defined for the threshold values of the aforementioned damage indexes as the values that corresponds to the 50% probability of exceeding each limit state. The standard deviation values [β] describe the total variability associated with each fragility curve. Three primary sources contribute to the total variability for any given damage state [1], namely the variability associated with the definition of the limit state value, the capacity of each structural type and the demand (seismic demand, landslide type, relative position of the structure to the landslide). Based on the work of Crowley et al [14], Bird et al [13] and HAZUS [1] prescriptions, the uncertainty in the definition of limit states, for all building types and limit states, is assumed to be equal to 0.4 while the variability of the capacity is assumed to be $\beta = 0.3$ for “low code” and $\beta = 0.25$ for “high code” buildings. The last source of uncertainty associated with the demand, is taken into consideration by calculating the variability in the results of numerical simulation carried out in FLAC 2D for the different input motions at each level of PGA applied at the base of the dynamic model. It should be mentioned that this variability is different for the two different building types. In particular, it is higher in the case of the buildings with flexible foundation system. The total uncertainty is estimated as the root of the sum of the squares of the component dispersions. The median (expressed in terms of peak ground acceleration PGA) and beta values of each limit state for the building with flexible and stiff foundation system are shown in Table 5.

Figures 9-11 illustrate the derived sets of fragility curves for the different building typologies, design code level and considering the effect of rebar corrosion for an assumed deterioration scenario in case of “low code” buildings. As expected, the building with stiff foundation system sustain less damage due to earthquake induced slow moving slides compared to the building with the flexible foundation system. More specifically, only minor and moderate damages are possible for the “high code” stiff buildings while minor, moderate and extensive damage are expected for “low code” stiff buildings for the specified levels of landslide intensity. Low code, poorly designed and constructed buildings are associated with a rapid transition from low levels of damage to collapse. This can be seen from the closeness of the four limit state curves and the steepness of their slopes. In contrast, well-designed buildings generally present a more ductile behavior, allowing for larger distinction between the curves. The consideration of corroded structural members in case of low code RC buildings reveals a significant increase in the system’s vulnerability. This is more evident for buildings with flexible foundations and low levels of damage.

Foundation type	Design level	Median PGA (g)				β_i
		LS_1 (g)	LS_2 (g)	LS_3 (g)	LS_4 (g)	
Flexible	High	0.3	0.4	0.67	0.85	0.8
	Low	0.3	0.395	0.51	0.69	0.81
	Low_corroded	0.2	0.365	0.455	0.59	0.81
Stiff	High	0.36	0.55	>0.9		0.74
	Low	0.345	0.525	0.74	>0.9	0.76
	Low_corroded	0.25	0.5	0.71		0.76

Table 5: Parameters of fragility functions

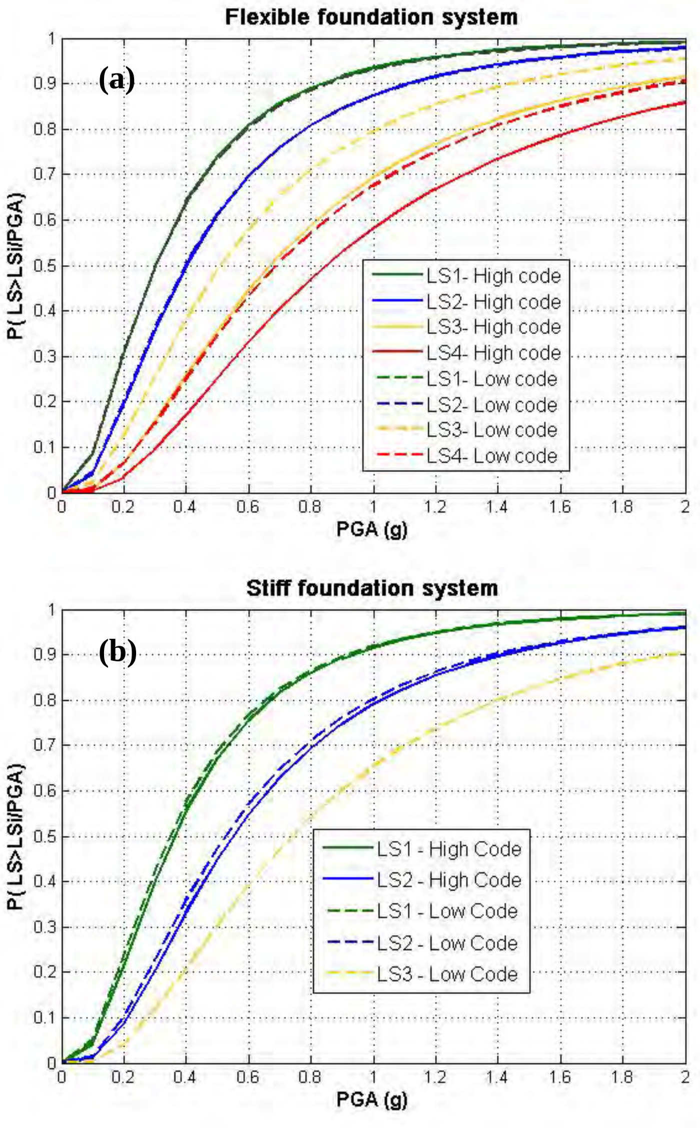

Figure 9: Fragility curves for low rise RC buildings with flexible (a) and stiff (b) foundation system

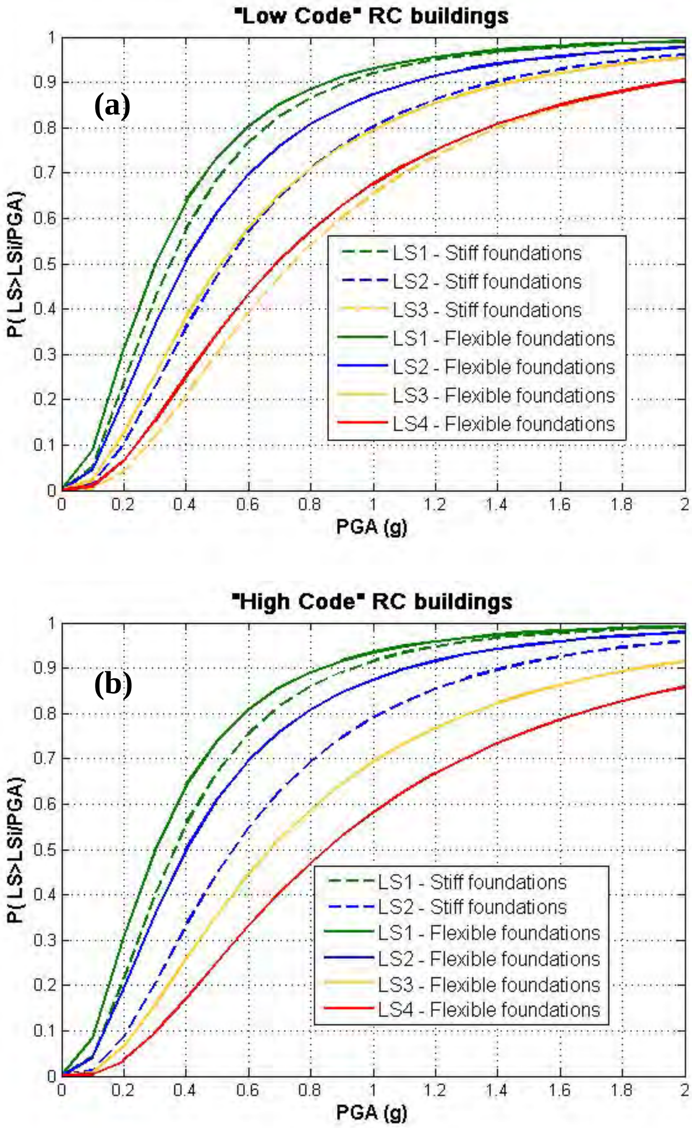

Figure 10: Fragility curves for low rise RC buildings, “low code” (a) and “high code” (b) design

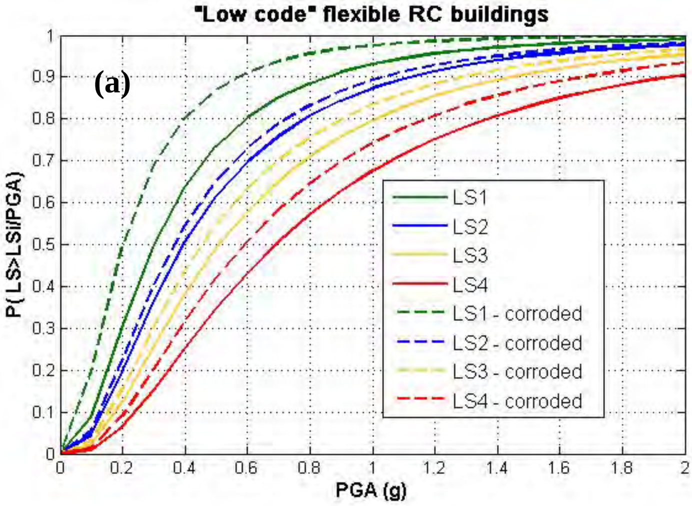

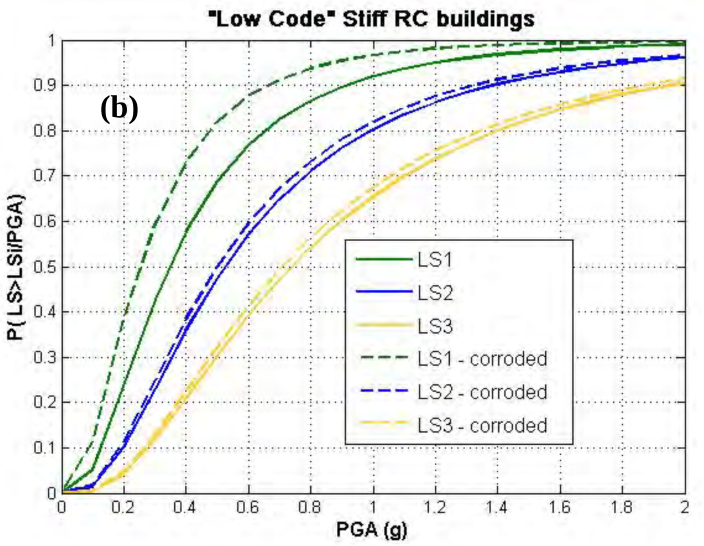

Figure 11: Fragility curves for low rise "low code" flexible (a) and stiff (b) RC buildings

It should be noticed that only the structural damage of the building members is considered in this study. The total damage (structural and non-structural) will be quite different (certainly larger) in case of the building with the stiff foundation as a considerable amount of damage may be attributed to the rotation of the whole building as a rigid body. In the latter, the damage can only be defined using empirical criteria and expert opinion [12]. Furthermore, it is worth pointing out that the complex issue of combined ground shaking and ground failure due to landslide is not taken into account in the evaluation of the building 's vulnerability. The authors are planning to include this in a future work. Finally, although the results are limited by some of the idealizations and assumptions of the analysis, they should provide a useful starting point in the vulnerability assessment of affected buildings standing near the crest of precarious slopes, providing the basis for more sophisticated numerical analysis for the particular governing conditions in selected real case studies.

4 CONCLUSIONS

An analytical-numerical methodology to estimate physical vulnerability of RC buildings subjected to co-seismic landslide displacements has been presented. The analysis results to the construction of fragility relationships for single bay-single story RC buildings that differ in the foundation system (isolated footing and continuous foundation) and code design level. For low code, usually old, structures the effect of corrosion of the reinforcement on the vulnerability estimation is also investigated. Various uncertainties, related to the capacity of the building, the deformation demand and the definition of limit states are considered in the analysis. It is observed that "high code" buildings with stiff foundation system are expected to suffer less structural damage compared to the other building typologies examined. The performance of "low code" RC structures is found to be degraded due to the consideration of corroded structural members, revealing a substantial increase in the vulnerability of buildings resting on flexible foundations. Finally the proposed fragility curves can be used to estimate the seismic risk and to design appropriate mitigation measures at building or aggregate scale.

AKNOWLEDGEMENTS

The work described in this paper was supported by the project SafeLand "Living with landslide risk in Europe: Assessment, effects of global change, and risk management strategies" under Grant Agreement No. 226479 in the 7th Framework Programme of the European Commission. This support is gratefully acknowledged.

REFERENCES

[1] National Institute of Building Sciences, Direct Physical Damage - General Building Stock. *HAZUS-MH Technical manual, Chapter 5*, Federal Emergency Management Agency, Washington, D.C, 2004.

[2] S. Fotopoulou, K. Pitilakis K., C. Anagnostopoulos, Vulnerability Assessment of RC buildings due to earthquake induced slow moving slides. *5th International Conference on Earthquake Geotechnical Engineering*, Santiago, Chile, 2011.

[3] Itasca Consulting Group, Inc. *FLAC (Fast Lagrangian Analysis of Continua), ver. 5.0.* Itasca Consulting Group, Inc., Minneapolis, 2005.

[4] SeismoSoft, SeismoStruct – *A computer program for static and dynamic nonlinear analysis of framed structures,* 2007, (online): Available from URL: www.seismosoft.com

[5] M.F. Mansour, N. I. Morgenstern, C. D. Martin, Expected damage from displacement of slow-moving slides. *Landslides*, 1-15, June 16, 2010.

[6] K.D. Pitilakis, *Geotechnical Earthquake Engineering*. Ziti Publications, 2010. (in Greek)

[7] Kramer S.L., Stewart J.P. (2004). Geotechnical Aspects of Seismic Hazards. In: Earthquake Engineering: from Engineering Seismology to Performance-Based Engineering, Y. Bozorgnia, V. Bertero (Eds.), CRC Press, **4**, 85 pp.

[8] C. Bourdeau, H.B. Havenith H.B. J.A. Fleurisson J.A., A.G. Grandjean, Numerical Modelling of Seismic Slope Stability. *Engineering Geology for Infrastructure Planning in Europe*, Springer Berlin / Heidelberg, **104**, 671-684, 2004.

[9] W.F. Peng, C.L.Wang, S.T. Chen, S.T. Lee, Incorporating the effects of topographic amplification and sliding areas in the modeling of earthquake-induced landslide hazards, using the cumulative displacement method. *Computers and Geosciences*, **35**(5), 946-966, 2009.

[10] G.D. Bouckovalas, A.G. Papadimitriou, Numerical evaluation of slope topography effects on seismic ground motion. *Soil Dynamics and Earthquake Engineering*, 25, 547-558, 2005.

[11] O.-J Ktenidou, *Theoretical and instrumental study of site and topographic effects on strong ground motion in Aegion*. Ph.D. thesis, Aristotle University Thessaloniki, Greece, 2010.

[12] J.F. Bird, H. Crowley, R. Pinho, J.J. Bommer, Assessment of building response to liquefaction induced differential ground deformation. *Bulletin of the New Zealand Society for Earthquake Engineering*, **38**(4), 215-234, 2005.

[13] J.F. Bird, J.J. Bommer, , H. Crowley, R. Pinho, Modelling liquefaction-induced building damage in earthquake loss estimation. *Soil Dynamics and Earthquake Engineering* **26**(1), 15-30, 2006.

[14] H. Crowley, R. Pinho, J.J. Bommer, A probabilistic displacement-based vulnerability assessment procedure for earthquake loss estimation. *Bulletin of Earthquake* Engineering, **2**(2),173-219, 2004.

[15] Eurocode 8, *Design provisions for earthquake resistance of structures - Part 1-1: General rules - Seismic actions and general requirements for structures*, European Prestandard, ENV 1998-1-1, Oct.1994, CEN-European Committee for Standardization.

[16] N.M. Newmark, Effects of earthquakes on dams and embankments. *Geotechnique*, **15**, 139–160, 1965.

[17] R.W. Jibson, M.W. Jibson, *Java programs for using Newmark's method and simplified decoupled analysis to model slope performance during earthquakes*. US Geological Survey Open File Report: 03-005, 2003.

[18] J.D. Bray, T. Travasarou, Simplified Procedure for Estimating Earthquake-Induced Deviatoric Slope Displacements. *Journal of Geotechnical and Geoenvironmental Engineering*, **133**(4), 381-392, 2007.

[19] J.D. Bray, *Simplified seismic slope displacement procedures*. Earthquake Geotechnical Engineering. Ed. K. D. Pitilakis, Springer, 2007.

[20] J.B. Mander, M.J.N. Priestley, R. Park, Theoretical stress-strain model for confined concrete", Journal of Structural Engineering, **114**(8), 1804-1826, 1988.

[21] C. Negulescu, E. Foerster, Parametric studies and quantitative assessment of the vulnerability of a RC frame building exposed to differential settlements. *Natural Hazards and Earth System Sciences*, **10**, 1781–1792, 2010.

COMPDYN 2011
III ECCOMAS Thematic Conference on
Computational Methods in Structural Dynamics and Earthquake Engineering
M. Papadrakakis, M. Fragiadakis, V. Plevris (eds.)
Corfu, Greece, 25–28 May 2011

INTRODUCING A NEW SCALING METHOD FOR NEAR-FAULT GROUND MOTIONS BASED ON THE ROOT-MEAN-SQUARE OF SPECTRAL RESPONSES

A. Yahyaabadi[1], **M. Tehranizadeh**[1]

[1]Department of Civil and Environmental Engineering, Amirkabir University of Technology
424 Hafez Ave, Tehran, Iran, 15875-4413
A.Yahyaabadi@aut.ac.ir, Dtehz@yahoo.com

Keywords: Nonlinear Dynamic Analysis, Near-Fault Ground Motions, Scaling Method, Seismic Demand, Collapse Capacity, Variability.

Abstract. *Assessment of the seismic performance of a structure often requires conducting nonlinear dynamic analyses under a set of ground motion records scaled to a specific level of intensity. Recent researches have demonstrated that pseudo spectral acceleration at the first mode period of vibration,* $S_a(T_1)$*,which is commonly used as the seismic intensity scaling index, may introduce a large scatter in the estimated seismic demands under near-fault pulse-like ground motions. Considering the need to provide more accurate estimation of seismic demands by using a smaller number of records, development of an improved scaling method that can reduce the variability in seismic demands becomes inevitable.*

In this paper, an improved intensity measure is developed based on the Root-Mean-Square (RMS) value of spectral responses, which is calculated over an appropriate period range. For this purpose, Incremental Dynamic Analyses (IDAs) are carried out for five generic frames of short to relatively long periods under 40 pulse-like earthquake records rotated to the fault-normal direction. Statistical study of the IDAs results is performed to determine the type of the response spectrum (i.e. pseudo acceleration, velocity or displacement) and the optimal period range for calculating the RMS value as the improved scaling method.

Statistical evaluation reveals that the RMS of pseudo spectral accelerations,$(S_a)_{rms}$*, provides much superior results than RMS of spectral displacements,* $(S_d)_{rms}$*, and RMS of spectral velocities,* $(S_v)_{rms}$*. It is concluded that the optimal period range varies with the fundamental period of a structure, and that* $(S_a)_{rms}$*, if calculated over the optimal period range, can predict the seismic demands with the overall dispersions that are generally reduced by the relative amount of 14 percent with respect to those of* $S_a(T_1)$*. The newly proposed parameter can also reduce the dispersion in predicted collapse capacities of the frames by the relative amount of 24 percent compared to* $S_a(T_1)$ *on average.*

1 INTRODUCTION

Performance Based Earthquake Engineering (PBEE) has received much attention in recent years as the new proficient method that can provide a quantitative basis in assessment of the seismic performance of structures. PBEE is a desirable concept and its implementation depends strongly on the ability to confidently estimate the probability that Engineering Demand Parameter (EDP), such as maximum storey drift, plastic hinge rotation and member force, exceeds a specific value. The probability that the EDP exceeds a specific value is a function of seismological random variables (such as magnitude and distance) and structural random variables (such as stiffness, strength, ductility and mass), and it is typically estimated through combining the results of Incremental Dynamic Analyses (IDAs) of a structure and seismic hazard analysis. In IDA, the intensity of each record is incremented after each inelastic dynamic analysis by using an intermediate quantity as the seismic intensity scaling index which is usually referred to as Intensity Measure (IM) [1].

The IM, as the seismic intensity scaling index, should represent those parameters of earthquake ground motions that strongly influence the structural responses, and it is required to introduce a small variability in EDP at any given IM level ($\sigma_{EDP|IM}$). A small variability is desirable because the standard error of sample mean of $\ln(EDP)$ for any specified IM level is equal to the ratio of the $\sigma_{EDP|IM}$ to the square root of n, where n is the number of earthquake records that have been sampled, and the sample mean of $\ln(EDP)$ is typically the first-order information used in quantifying the probabilistic seismic demand analysis [2].

Selecting the appropriate intensity measure for near-fault ground motions requires more accurate attention for special characteristics of this type of motions. In near-fault records influenced by forward directivity or fling step phenomena, most of the seismic energy from the rupture appears as a single coherent pulse-type motion. Ground motions having such a distinct pulse-like character generally arise at the beginning of the seismogram, and their effects tend to increase the long-period portion of the acceleration response spectrum. Studies have shown that for this type of motions, the maximum demand is a function of the ratio of the ground motion's pulse period, T_P, to the fundamental period of the structure [3]. With respect to this issue, the pseudo spectral acceleration measured at the first mode period of vibration, $S_a(T_1)$, which is commonly used as the IM in the performance-based earthquake engineering, cannot adequately predict the seismic demands imposed on structures by near-fault pulse-like ground motions [3], because it is not good representative for those parameters of near-fault earthquakes, such as pulse period, that affect the response of the structures.

The major shortcoming of $S_a(T_1)$, as the IM, is its inability in describing the effective frequency content of earthquakes at $T \neq T_1$. This weakness is more pronounced when pulse motions dominate the structural responses. The efficiency of $S_a(T_1)$ can be approximately improved by incorporating ε, shown to capture the average local spectral shape at T_1, via a vector IM for ordinary earthquakes [4]. Nevertheless, pulse-like motions cannot be adequately characterized by the vector of $S_a(T_1)$ and ε, because their response spectra usually exhibit a sharp change, making it difficult to simply estimate spectral shape using $S_a(T_1)$ and local spectral shape at T_1 via epsilon [5, 6].

For near-fault earthquakes, Yang and Coworker have proposed intensity measures of Improved Effective Peak Acceleration (IEPA) for rigid systems, and Improved Effective Peak Velocity (IEPV) for medium to long period systems [7]. IEPA and IEPV have been respectively defined based on the average value of spectral accelerations and spectral velocities around their predominant peak. Whereas IEPA and IEPV have been developed based on the frequency characteristics of near-fault earthquakes, since these IMs are calculated over individual period ranges of records, and these period ranges are only defined based on the predominant period of each response spectrum without any consideration of modal periods of a structure, they may introduce a large record to record variability [8]. It has been shown that the frequency content of earthquakes at a period range around the first mode period of a structure can describe the damaging effects of ground motions on the structure in a much better manner [8].

In this paper, an improved intensity measure is developed based on the Root-Mean-Square (RMS) value of spectral responses, calculated over an optimal period range, in order to reduce the variability in seismic demands under near-fault pulse-like ground motions. Based on the Incremental Dynamic Analyses (IDAs) of five frames of various heights under 40 near-fault pulse-like ground motions, it is shown that RMS of pseudo spectral accelerations, $(S_a)_{\mathrm{rms}}$, provides much superior results than RMS of spectral velocities, $(S_v)_{\mathrm{rms}}$, and RMS of spectral displacements, $(S_d)_{\mathrm{rms}}$. All possible period ranges for calculating the RMS value are considered, and the optimal period range that can significantly reduce the overall variability in seismic demands obtained from IDAs is proposed. It is shown that the optimal period range is a function of the fundamental period of the structure, and that RMS of pseudo spectral accelerations, $(S_a)_{\mathrm{rms}}$, calculated over the proposed period range, can considerably increase the accuracy of the seismic demand prediction with respect to $S_a(T_1)$.

2 STRUCTURAL SYSTEMS

Incremental dynamic analyses results of two-dimensional generic one-bay frames were used to develop the newly improved IM. The advantage of using the generic frames is that they do not represent a specific structure and thereby the results from analyses are not a function of a particular system. They are adequate to capture the global behavior of multi-bay frames and to evaluate the sensitivity of the results to various structural heights [9].

The generic frames used in this study consist of frames with number of stories, N, equal to 3, 6, 9, 12, 15 and the fundamental periods, T_1, of 0.1N. Seismic demands of these frames under near-fault ground motions were obtained using the Open System for Earthquake Engineering Simulation (OpenSees) [10]. The main characteristics of these models can be found in references 8 and 9. Non-linear behavior of the frames was modeled by using rotational springs at the beam ends and at the bottom of the first-storey columns. Peak oriented hysteretic model and the energy based deterioration model was used to represent the non-linear load-deformation behavior of abovementioned rotational springs [11].

3 NEAR-FAULT PULSE-LIKE GROUND MOTIONS DATABASE

Increasing number of recorded near-fault ground motions, with seismologists and engineers efforts, may do recognizing those characteristics of this type of motions that strongly affect the dynamic responses of structures [12-14]. These researches have been generally focused on the pulse motions contained in near-fault records due to forward directivity and the fling step effects.

Considering that the pulse motions in near-fault records strongly affect the dynamic responses of structures [15], a large variability in the seismic demands of structures under scaled pulse-type motions may be observed, unless an appropriate method is used to scale this type of ground motions. Therefore, this study focused on a database of 40 near-fault earthquake records compiled from records that exhibit intense velocity pulses. The database includes the acceleration time-histories of the 2003 Bam (Bam station), the 1998 Golbaft (Sirch station), the 1990 Rudbar (Abbar station), the 1978 Tabas (Tabas station) and the 1977 Naghan (Naghan station) Iranian near-fault pulse-like earthquakes that were taken from Iran strong motion network data bank [16]. Moreover, 35 near-fault records, having distinct velocity pulses, were taken from PEER strong motion database and added to this database [17]. All ground motions have been recorded on stiff soil, very dense soil and rock based on the ASCE7-10 [18] site classification for all faulting styles. The earthquake magnitude, M_w, ranges from 6.2 to 7.2, and the closest distance to fault rupture ranges from 0.07 to 18.2 km.

Near-fault ground motions have orientation that is controlled by the geometry of the fault, and thereby it is necessary to treat them as a vector rather than scalar quantities [19]. In this paper, 40 near-fault ground motion records were rotated to the fault-normal and fault-parallel components using the transformations proposed by Somerville [19]. Owing to more severity of the fault-normal components relative to the fault-parallel components [14], the normal components of the records were used as the seismic input in this study. It is worth noting that the pulse period and the peak spectral velocity of the used fault-normal components respectively range from 0.45 to 8.93 (*sec*), and from 84 to 500 (*cm/sec*).

4 DEVELOPMENT OF AN IMROVED SCALING METHOD

Intensity measures (IM) are intermediate quantities which describe earthquake strength in terms of parameters that can be strongly related to seismic demands of structures. The pseudo spectral acceleration at the first period of a structure, $S_a(T_1)$, which is commonly used as the IM, may not show satisfactory correlation with the seismic demands distribution, particularly under near-fault pulse-like ground motions [5, 6]. This brought about as a result of two flaws of $S_a(T_1)$; one flaw is that this parameter does not describe the frequency content of ground motions at higher modes of vibration; and the other one is that it does not account for inelastic lengthening of modal periods as a structure softens under stiffness degradation. When the input time history is a near-fault pulse, these shortcomings are accentuated due to the sharp change in spectral ordinates around the pulse period [5].

In this study, in an attempt to compensate for the shortcomings of $S_a(T_1)$, a new improved scaling parameter was developed on the basis of the root-mean-square (RMS) value of spectral responses over the period range of $[T_a , T_b]$ in accordance with the following equation:

$$(S_{res})_{rms} = \left[\frac{1}{n}\sum_{i=1}^{n} S_{res}^2(T_i)\right]^{0.5}, \quad T_a \le T_i \le T_b \qquad (1)$$

$$T_{i+1} = T_i + \Delta T$$

In Equation 1, $S_{res}(T_i)$ is the spectral response at T_i, and ΔT is equal to 0.025 (*sec*) for the 3-strorey frame and 0.05 (*sec*) for other frames.

In developing this new improved IM according to Equation 1, there are two important key issues that should be carefully accounted in order to achieve the minimum amount of variability in seismic demands; firstly, which type of response spectrum (i.e. pseudo acceleration, velocity or displacement) is more capable to be used for calculating the root-mean-square value. In other words, which one of the parameters of $(S_a)_{\text{rms}}$, $(S_v)_{\text{rms}}$ and $(S_d)_{\text{rms}}$ is more efficient; secondly, with respect to the first mode period of a structure, which period range is more appropriate to be used for calculating the RMS value as improved IM.

4.1 Evaluation of the efficiency of the $(S_a)_{rms}$, $(S_v)_{rms}$ and $(S_d)_{rms}$ as the IM

Incremental dynamic analyses (IDAs) of the genetic frames under the near-fault ground motions were employed to determine the type of the response spectrum and the period range that can be reliably used to calculate the RMS value according to Equation 1. IDAs for the peak maximum interstory drift ratio, IDR_{max}, of the 6-storey and 12-storey frames in terms of $S_a(T_1)$ as the IM, are shown in Figure 1. Each point in these figures corresponds to the IDR_{max}

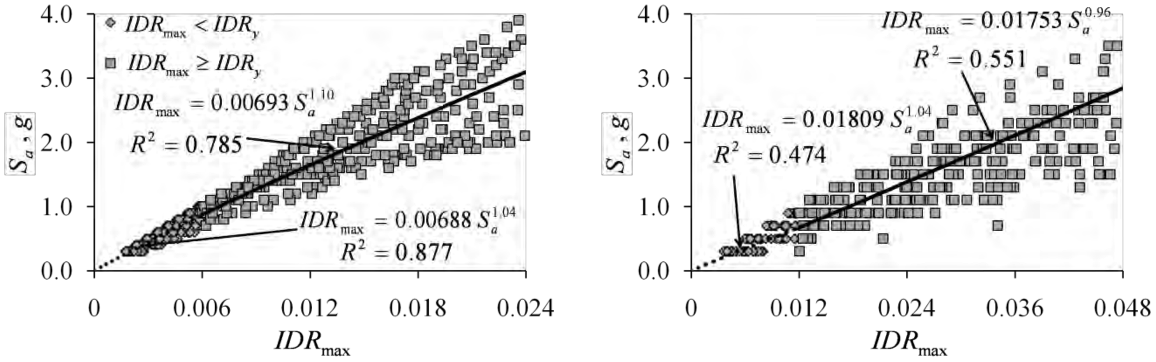

(a) IDAs results of the 6-storey frame (b) IDAs results of the 12-storey frame

Figure 1: IDAs results of the 6 and 12-storey frames in terms of $S_a(T_1)$

of the frame obtained from a nonlinear dynamic analysis under a record scaled to a specific level of intensity.

The variability in IDAs can be quantified in terms of Coefficient Of Variation (COV) of IM values corresponding to a specific level of response (conditioned on a specific value of IDR_{max}) which was characterized by $COV_{\langle IM|IDR_{max}\rangle}$. The average value of $COV_{\langle IM|IDR_{max}\rangle}$ on the interval [0 , IDR_c] was calculated as the mean COV of the IM values, where IDR_c is the individual drift ratio capacities of the frames.

To select the best type of response spectrum for development of the improve IM, all possible period ranges of $[T_a\ ,\ T_b]$ were used to calculate each of the parameters of $(S_a)_{\mathrm{rms}}$, $(S_d)_{\mathrm{rms}}$ and $(S_v)_{\mathrm{rms}}$ as the alternative for IM. For each one of these alternatives, and based on the IDAs of the frames, the mean COV was calculated. The minimum amount of mean COV that can be achieved by using each of the parameters of $(S_a)_{\mathrm{rms}}$, $(S_d)_{\mathrm{rms}}$ and $(S_v)_{\mathrm{rms}}$ was determined, which is provided in Figure 2.

Figure 2 indicates that the efficiency of $(S_a)_{\mathrm{rms}}$, $(S_v)_{\mathrm{rms}}$ and $(S_d)_{\mathrm{rms}}$ is approximately similar for the 9 and 12-storey frames; however, $(S_a)_{\mathrm{rms}}$ becomes more capable as the number of stories decreases to 3 and 6 or as it increases to 15. Based on these observations, velocity-based improved intensity measures are only appropriate for the 9, 12 and 15- storey frames included in the relatively low to moderate frequency systems. Therefore, with respect to the efficiency of $(S_a)_{\mathrm{rms}}$ for all ranges of structural height, the parameter of $(S_a)_{\mathrm{rms}}$ is chosen as the best estimation of an earthquake strength.

4.2 Selection of the optimal period range in order to reduce the overall variability

Relation of the mean COV to the period range of $[T_a\ ,\ T_b]$ over which the parameter of $(S_a)_{\mathrm{rms}}$ has been calculated according to Equation 1, is respectively shown in Figures 3a and 3b for the 6 and 12- storey frames, for instance. In these figures, the abscissa represents the ratio of T_a to T_1 and the ordinate represents the ratio of T_b to T_1, where T_a and T_b are the lower and upper limits of the period range of $[T_a\ ,\ T_b]$, and T_1 is the individual fundamental periods of the frames. The optimal period range, leading to the minimum mean COV, can be found from these figures, which strongly depends on the fundamental period of the frames as follows:

Optimal period range for short-period frames: Studying the relation of the mean COV to the period range for the 3 and 6-storey frames, which is presented in Figure 3a for the 6-stroey frame as an example, reveals that the minimum scatter in the IDAs of short-period frames can be obtained by using the optimal period range of $[0.9T_1\ ,\ 1.3T_1]$, among all period ranges. This implies that the period elongation effects in the seismic demand prediction of short-period

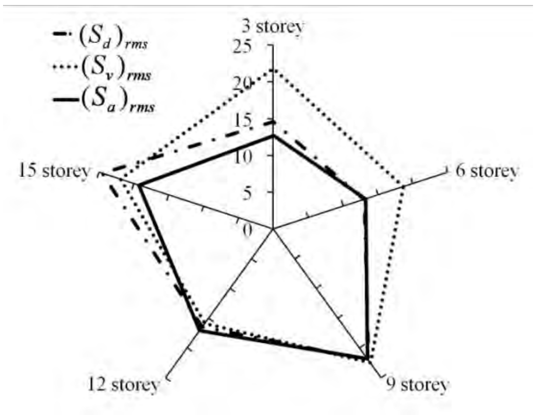

Figure 2: Minimum value of mean COV% in IDAs using $(S_a)_{\text{rms}}$, $(S_d)_{\text{rms}}$ and $(S_v)_{\text{rms}}$, calculated over the respective optimal period range

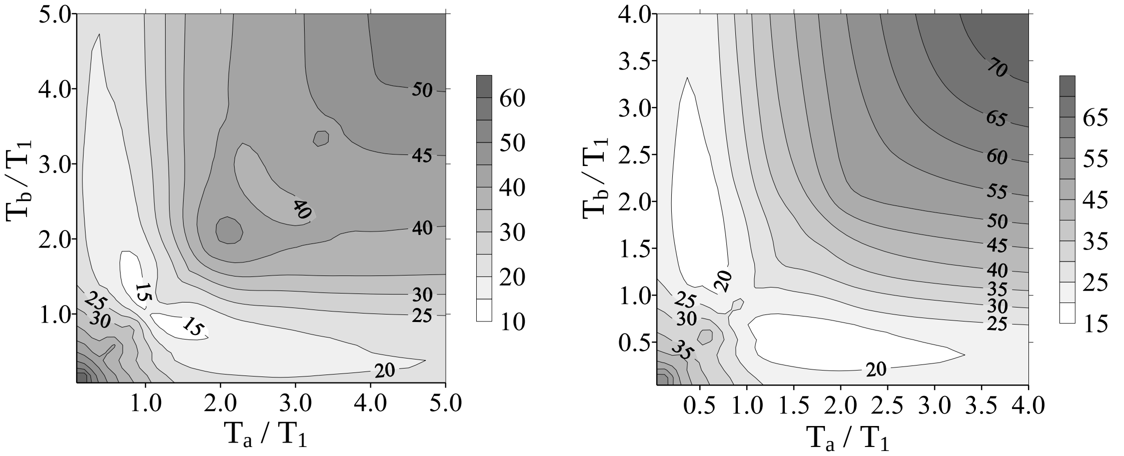

(b) Mean COV% of the 6-storey frame (d) Mean COV% of the 12-storey frame

Figure 3: Mean COV% in IDAs results for $(S_a)_{rms}$ calculated over various period ranges of $[T_a, T_b]$

frames are significant, whereas the higher modes effects are insignificant.

Optimal period range for moderated to relatively long-period frames: Studying the results of the statistical evaluation shows that in addition to the effects of period elongation on the seismic demands of the 9, 12 and 15-storey frames, the effects of higher modes are also significant in these frames. Therefore, both higher modes effects and period elongation effects emerge in the optimal period range for these frames. Based on the mean COV values for the 9, 12 and 15-storey frames, which is presented in Figure 3b for 12-storey frame as an example, the minimum scatter in the IDAs of moderate to relatively long-period frames can be obtained by using the optimal period range of $[0.3T_1, 1.9T_1]$. It is worth nothing that considering the modal periods of the 9, 12 and 15-storey frames shows that the lower limit of the optimal period range (i.e. $0.3T_1$) is approximately equal to the average value of the T_2 and T_3, where T_2 and T_3 are respectively the second and the third mode periods of the frame.

5 COMPARING THE EFFICIENCY OF $(S_A)_{RMS}$ AND $S_A(T_1)$

When performing IDAs of a structure under an ensemble of ground motions, a fraction of Ground Motions (GMs) will result in collapse of the structure at any given intensity level. Therefore, seismic demand prediction requires statistical response evaluation of the non collapse data (denoted NC) as well as the collapse data (denoted C) in accordance with the following equation [5]:

$$P[IDR_{max} > x|IM = im] = P[IDR_{max} > x|IM = im, NC].\left(1 - P_{C|IM=im}\right) + P_{C|IM=im} \qquad)2($$

where $P[IDR_{max} > x|IM = im, NC]$ is the probability of IDR_{max} exceeding a given level x at a given intensity level of $im,$ for non-collapse data; and $P_{C|IM=im}$ is the probability of collapse at each im level. It should be mentioned that the collapse data (denoted C) was indicated by either non-convergence of dynamic analysis or excessive IDR_{max} demand in this study.

To improve the accuracy of seismic demand prediction in accordance with Equation 2, the improved IM should be able to reduce the variability in the non-collapse data as well as the collapse data, which will be discussed in the following for $S_a(T_1)$ and $(S_a)_{\mathrm{rms}}$.

***IDAs of short-period frames*:** Incremental dynamic analyses results of the 3 and 6-strorey frames were adapted for the new improved IM of $(S_a)_{\mathrm{rms}}$, calculated over the optimal period range of $[0.9T_1\,,\ 1.3T_1]$, in order to compare the efficiency of this new parameter with the commonly used parameter of $S_a(T_1)$. Non-collapse IDAs results of the 6-storey frame, presented in terms of $S_a(T_1)$ in Figure 1a, are provided in terms of $(S_a)_{\mathrm{rms}}$ in Figure 4a as the example for IDAs of short-period frames. From comparing these figures, following observations can be made; for low levels of intensity at which the response is elastic the parameter of $(S_a)_{\mathrm{rms}}$ results in more variability than $S_a(T_1)$. This follows the fact that linear responses of the short-period frames are dominated by the first mode of vibration. As the intensity of GMs is increased, period elongation effects become significant, and $(S_a)_{\mathrm{rms}}$ provides more accurate estimation of responses. Using the optimal period range for calculating $(S_a)_{\mathrm{rms}}$ made possible to significantly reduce the dispersions at large intensities so as not to substantially increase the scatter at low levels of intensity, and consequently the overall variability can be reduced.

Based on the non-collapse IDAs results (as shown in Figures 1a and 4a for the 6-storey frame), the overall variability was quantified in terms of dispersion of drift response conditioned on the ground motion intensity measure. For this purpose, dispersion was calculated according to the following equation as the standard deviation of the drift data from an average response curve obtained from regression analysis between drift and the seismic intensity:

$$\sigma_{IDR_{max}} = \left[\sum_{i=1}^{n} \left(IDR_{max\,,i} - I\widehat{D}R_{max\,,i}\right)^2 / (n-1)\right]^{1/2} \qquad)3($$

In Equation 3, $IDR_{max,i}$ is the ith response obtained from a nonlinear dynamic analysis under a record scaled to a specific level of intensity, $I\widehat{D}R_{max\,,i}$ is the average response obtained from regression curve at the same intensity for which $IDR_{max,i}$ was calculated, and n is the sample size of the non-collapse data at all levels of intensity (as an example for the 6-storey frame, n is the number of points in Figures 1a or 4a).

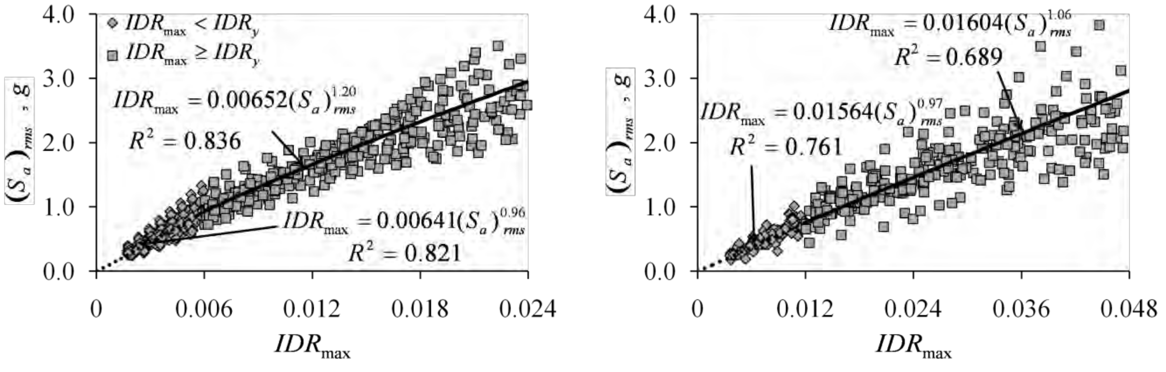

(a) IDAs results of the 6-storey frame

(b) IDAs results of the 12-storey frame

Figure 4: IDAs results of the 6 and 12-storey frames in terms of $(S_a)_{rms}$

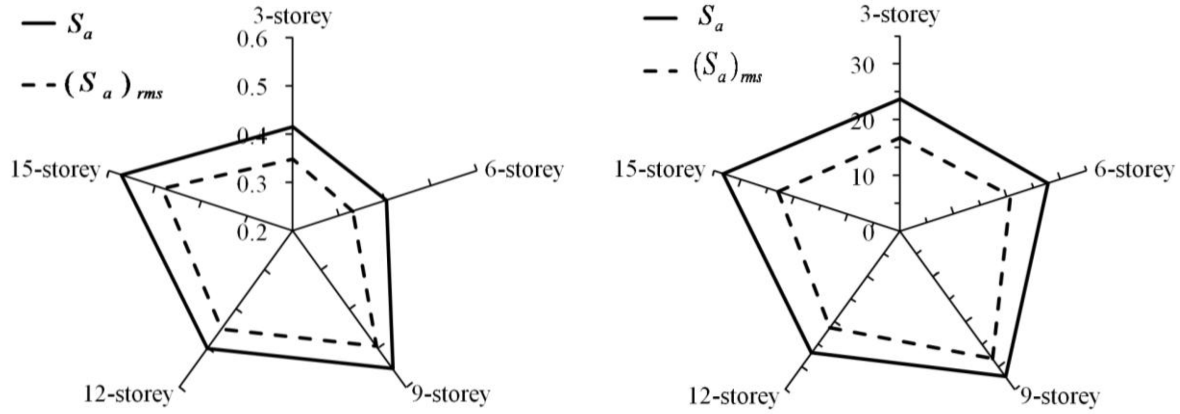

(a) (b)

Figure 5: (a) The ratio of the standard deviation to IDR_y for IDAs results of the frames based on $S_a(T_1)$ and $(S_a)_{rms}$, (b) COV% in the IM values leading to collapse for $S_a(T_1)$ and $(S_a)_{rms}$

Figure 5a provides the ratio of the standard deviation, which was calculated in accordance with Equation 3, to the individual yield drift ratios of frames (i.e. $\sigma_{IDR_{max}}/IDR_y$), for all frames and for $S_a(T_1)$ and $(S_a)_{rms}$. It can be seen that $(S_a)_{rms}$ can respectively reduce the $\sigma_{IDR_{max}}/IDR_y$ of the 3 and 6-storey frames from 0.42 and 0.40 for $S_a(T_1)$ to 0.35 and 0.33, and in so doing can improve the accuracy of the non-collapse seismic demand prediction (i.e. $P[IDR_{max} > x|IM = im, NC]$ in Equation 2).

While $(S_a)_{rms}$ reduces the overall dispersion, this reduction is most apparent at larger drifts, where the structure behaves nonlinearity. This implies that in addition to improvement of the accuracy in predicting the non-collapse seismic demand, $(S_a)_{rms}$ can increase the accuracy of collapse capacity prediction. The intensity (IM value) at which structural collapse is occurred under an earthquake record, is referred to as collapse capacity of the structure under the earthquake record. The considerable difference between the efficiency of $S_a(T_1)$ and $(S_a)_{rms}$ in collapse capacity prediction of the 3 and 6-storey frames, can be clearly observed in Figure 5b. From this figure, it can be observed that the COV in the IM values leading to collapse of the 3 and 6-storey frames were respectively reduced from 23.7 and 27.8 percent for $S_a(T_1)$ to 16.8 and 20.8 percent for $(S_a)_{rms}$. Therefore, the parameter of $(S_a)_{rms}$ can considerably improve the accuracy of the collapse prediction of the short-period frames (i.e. $P_{C|IM=im}$ in Equation 2).

IDAs of moderate to relatively long-period frames: Non-collapse IDA results of the 12-storey frame, presented in terms of $S_a(T_1)$ in Figure 1b, are provided in terms of $(S_a)_{rms}$ in Figure 4b as the example for the IDAs of moderate to relatively long-period frames. It should be mentioned that for these frames, $(S_a)_{rms}$ was calculated over the optimal period range of $[0.3T_1, 1.9T_1]$. From Figures 1b and 4b, it can be observed that R^2 factor, an indicator of how well the equation resulting from the regression analysis, is significantly increased from 0.474 for $S_a(T_1)$ to 0.761 for $(S_a)_{rms}$ at low levels of response ($IDR_{max}<IDR_y$), and from 0.551 for $S_a(T_1)$ to 0.689 for $(S_a)_{rms}$ at high levels of response ($IDR_{max}>IDR_y$), where IDR_y is the yield interstorey drift ratio of the frame.

The ratio of $\sigma_{IDR_{max}}/IDR_y$ was calculated according to Equation 3 for non-collapse IDAs results of the 9, 12 and 15-storey frames for $S_a(T_1)$ and $(S_a)_{rms}$, which is shown in Figure 5a. This figure demonstrates that $(S_a)_{rms}$ can considerably reduce the $\sigma_{IDR_{max}}/IDR_y$, and thereby can enhance the accuracy of the non-collapse seismic demand prediction. In addition to the ability in non- collapse seismic demand prediction, $(S_a)_{rms}$ can be efficiently employed in predicting the probability of collapse. The COV in collapse capacities of the 9, 12 and 15-storey frames for $S_a(T_1)$ and $(S_a)_{rms}$ are presented in Figure 5b. This figure implies that using $(S_a)_{rms}$

can respectively reduce the COV in collapse prediction of the 9, 12 and 15-storey frames from 32.1, 26.9 and 33.3 percent for $S_a(T_1)$ to 28.2, 21.4 and 23.0 percent. Reduction in the dispersion of non-collapse data as well as the collapse data in this way helps reducing the number of records necessary to predict the probability that seismic demand exceeds a given value, in accordance with Equation 2, within a specified confidence interval.

6 CONCLUSION

With the goal of developing an improved intensity measure (IM) for scaling near-fault pulse-like ground motions, the ability of root-mean-square (RMS) of spectral responses, calculated over the optimal period range, was considered in this study. The evaluation of RMS of spectral responses has led to the following conclusions:

1. It was concluded that root-mean-square of pseudo spectral accelerations, $(S_a)_{\mathrm{rms}}$ generally provides much superior results with respect to those of spectral displacements, $(S_d)_{\mathrm{rms}}$, and spectral velocities, $(S_v)_{\mathrm{rms}}$.
2. Statistical evaluations of IDAs results of the 3 and 6-storey frames, short-period frames, revealed that calculating the $(S_a)_{\mathrm{rms}}$ over the optimal period range of $[0.9T_1, 1.3T_1]$, compared to all possible period ranges, was led to the minimum overall variability in the predicted seismic demands. This illustrates the significance of period elongation effects in seismic demand prediction of short-period frames through incremental dynamic analyses.
3. Based on the statistical evaluation of IDAs results of the 9, 12 and 15-storey frames, moderated to relatively long-period frames, it was concluded that the minimum overall scatter in the IDAs results can be obtained by using the optimal period range of $[0.3T_1, 1.9T_1]$, among all possible period ranges. This indicated that both higher modes effects and period elongation effects are significantly important in seismic demand prediction of these frames in terms of $(S_a)_{\mathrm{rms}}$.
4. The seismic intensity scaling index of $(S_a)_{\mathrm{rms}}$, calculated over the optimal period, compared to $S_a(T_1)$ can considerably reduce the $\sigma_{IDR_{max}}/IDR_y$, the ratio of the standard deviation of non-collapse IDR_{max} demands to the individual yield IDR of the frames. By using $(S_a)_{\mathrm{rms}}$, the ratio of $\sigma_{IDR_{max}}/IDR_y$ for the 3, 6, 9, 12 and 15-storey frames was respectively reduced by the relative amount of 16, 18, 10, 10 and 15 percent compared to those of $S_a(T_1)$.
5. The newly proposed IM can also reduce the dispersion in predicted collapse capacities of the frames by the relative amount of 24 percent compared to $S_a(T_1)$ on average.

REFERENCES

[1] D. Vamvatsikos, C.A. Cornell, Incremental dynamic analysis. *Earthq. Eng. Struct. Dynam.*, **31**(3), 491-514, 2002a.

[2] J.R. Benjamin, C.A. Cornell, *Probability, Statistics, and Decision for Civil Engineers*, McGraw Hill, 1970.

[3] E. Kalkan, S.E. Kunnath, Effects of fling step and forward directivity on seismic response of buildings. *Earthq. Spectra*, **22** (2), 360-390, 2006.

[4] J.W. Baker, C.A. Cornell, A vector-valued ground motion intensity measure consisting of spectral acceleration and epsilon. *Earthq. Eng. Struct. Dynam.*, **34**(10), 1193-1217, 2005.

[5] P. Tothong, C.A. Cornell, Probabilistic seismic demand analysis using advanced ground motions intensity measures, attenuation relationships, and near-fault effects, Report 2006/11, Pacific Earthquake Engineering Research Center, Berkeley, CA, 2007.

[6] J.W. Baker, C.A. Cornell, A vector-valued ground motion intensity measures for pulse-like near-fault ground motions. *Eng. Struct.*, **30**(4), 1048-1057, 2008.

[7] D. Yang, J. Pan, G. Li, Non-structure-specific intensity measures parameters and characteristics of near-fault ground motions. *Earthq. Eng. Struct. Dynam.*, **38**(11), 1257 – 1280, 2009.

[8] A. Yahyaabadi, M. Tehranizadeh, Nonlinear dynamic analysis of structures under near-fault ground motions using an improved scaling method. *Asian Journal of Civil Engineering*, **11**(5), 627-643, 2010.

[9] R. Medina, H. Krawinkler, Seismic Demands for Nondeteriorating Frame Structures and Their Dependence on Ground Motions, Report No. PEER 2003/15, Pacific Earthquake Engineering Research Center, Berkeley, CA, 2004.

[10] OpenSees, Open System for Earthquake Engineering Simulation, Pacific Earthquake Engineering Research Center, Berkeley, CA, 2009.

[11] L.F. Ibarra, R.A. Medina, H. Krawinkler, Hysteretic models that incorporate strength and stiffness deterioration. *Earthq. Eng. Struct. Dynam*, **34**(12), 1489-1511, 2005.

[12] P.G. Somerville, R. Graves, Conditions that give rise to unusually large long period ground motions. *Struct. Des. Tall Spec.,* **2**(3), 211-232, 1993.

[13] J.D. Bray, A. Rodriguez-Marek, Characterization of forward-directivity ground motions in the near-fault region. *Soil Dyn. Earthq. Eng.*, **24**(11), 815-828, 2004.

[14] E. Chioccarelli, I. Iervolino, Near-source seismic demand and pulse-like records: A discussion for L Aquila earthquake. *Earthq. Eng. Struct. Dynam.,* **39**(9), 1039-1062, 2010.

[15] H. Krawinkler, B. Alavi, F. Zareian, Impact of near-fault pulses on engineering design. *Direction in Strong Motion Instrumentation,* **58**(2), 83-106, 2005.

[16] Iran Strong Motion Network Data Bank, http://www.bhrc.ac.ir

[17] PEER Strong Ground Motion Database, http://peer.berkeley.edu/smcat/

[18] American Society of Civil Engineering, ASCE7-10: Minimum Design loads for buildings and other structures. Reston, Virginia, 2010.

[19] P.G. Somerville, Characterizing near fault ground motion for the design and evaluation of bridges. *Third National Seismic Conference and Workshop on Bridges and Highways,* Portland, Oregon, 2002.

COMPDYN 2011
ECCOMAS Thematic Conference on
Computational Methods in Structural Dynamics and Earthquake Engineering
M. Papadrakakis, M. Fragiadakis, V. Plevris (eds.)
Corfu, Greece, 25-28 May 2011

MODELING ENERGY DISSIPATION: A PARADIGM FOR PERFORMANCE-BASED ENGINEERING OF RC MOMENT-RESISTING FRAME IN SEISMIC LOADING

Pierre Jehel[1], **Pierre Léger**[2], **and Adnan Ibrahimbegovic**[3]

[1] École Centrale Paris, Laboratory of Soil, Structures and Materials Mechanics
Grande Voie des Vignes, 92295 Châtenay-Malabry Cedex, France
pierre.jehel[at]ecp.fr

[2] École Polytechnique of Montreal, Department of Civil Engineering
University of Montreal Campus, P.O. Box 6079, Station CV Montreal, PQ, Canada H3C 3A7
pierre.leger[at]polymtl.ca

[3] LMT-Cachan (ENS Cachan/CNRS/UPMC/PRES UniverSud Paris)
61 av. du Président Wilson, 94235 Cachan Cedex, France
ai[at]lmt.ens-cachan.fr

Keywords: Earthquake Engineering, Damping, Energy Dissipation, Performance-based Engineering, Moment-resisting Frame, Reinforced concrete.

Abstract. *Inelastic structural models used for performance-based design intrinsically dissipate a part of the total amount of the seismic energy imparted to the structure. To take into account the energy dissipation sources not considered in the structural model but that nevertheless exist, damping generally is added. Given an inelastic structural model, state-of-the-practice documents thus advocate to add a portion of damping that is consistent with the inelastic structural model used. The main purpose of this contribution is to investigate whether it is* a priori *straightforward for practitioners to consistently add damping or not. There is indeed no clear theoretical framework for adding damping. This investigation is based on a reinforced concrete moment-resisting frame tested on the shaking table of the École Polytechnique of Montreal. Numerical analyses were carried out with ten different combinations of inelastic structural models and added viscous damping models. The main conclusion of this investigation is that it is a complex task to add viscous damping in a way that is consistent with the capacity of the inelastic structural model to dissipate imparted seismic energy. In the context of RC moment-resisting frame structures in seismic loading, without considering any interaction with the surrounding environment, computing energy dissipation quantities can serve as an indicator for assessing the consistency looked for and appears as a paradigm for performance-based engineering.*

1 INTRODUCTION

The theoretical formalism we use to derive the set of equilibrium equations that governs the motion of a civil engineering structure in dynamic loading is inherited from the mathematical works achieved at the end of the 17th century and during the 18th. Mechanics was at that time a branch of mathematics and the development of infinitesimal calculus and variational calculus has been motivated by the need to rationally describe the world as human beings can perceive it. The world was in particular assumed to be perfect in the sense that it was conservative: no energy dissipation source was considered.

The first introduction of a source of energy dissipation in the formulation of a mechanical problem is attributed to Sir John William Strutt, better known as Lord Rayleigh. His analytical method, along with modal damping, is nowadays still widely used to model the damping phenomenon observed in the response of elastic mechanical systems. It is also common practice, *e.g.* in earthquake engineering, to introduce Rayleigh's damping in the simulation of inelastic systems. Although Lord Rayleigh himself mentioned that his theory lacks physical insight, it is suitable for correctly representing the behavior of a structure as far as i) it remains in its elastic range and ii) there is no need for a microscopic description of the internal mechanisms that generate damping.

When the assumption of elasticity is discarded, *e.g.* for performance-based engineering, there are two main reasons why an explicit description of internal mechanisms becomes necessary. First, internal mechanisms cause irreversible modifications in the structure that have to be accurately described to assess its performance level. For instance, strength and stiffness degradations of structural elements are key indicators to assess residual structural capacity. Second, they dissipate part of the imparted seismic energy and thus participate to the global damping characteristics observed in the structural response. It is however not realistic to explicitly model each internal energy dissipative mechanism, but the most important should be modeled.

Combining explicitly modeled energy dissipation sources with added viscous damping, such as Rayleigh's damping, is common practice in performance-based earthquake engineering [1]. This will be shown in the next section where we will first present the definitions we adopted for damping and finally introduce the concept of *consistent added damping*. As mentioned in recent building rules [2], the portion of added damping should be consistent with the inelastic structural model. As far as performance-based engineering is concerned, the main purpose of this contribution is to investigate whether it is *a priori* straightforward to consistently add damping or not. To this end, the third section is dedicated to the numerical modeling of a reinforced concrete moment-resisting frame tested on the shaking table of the École Polytechnique of Montreal [3]. Ten numerical simulations are carried out according to different combinations of inelastic structural models and Rayleigh's damping models. An analyses of the results is provided an its main conclusion, expressed in the context of RC moment-resisting frame in seismic loading, is that the proportion of seismic energy that is dissipated by the added viscous damping model E_D, even when associated to small critical damping ratios, can become preponderant with respect to the proportion of seismic energy that is dissipated by the inelastic structural model E_H. This sounds not physical. Modeling a portion of added damping that is consistent with a given inelastic structural model thus appears as a complex task. According to this conclusion, in this particular context of RC moment-resisting frame structure in seismic loading and without considering any interaction between the structure and its surrounding environment, computing the E_D/E_H ratio could *a posteriori* be used as an indicator of consistency.

2 CONSISTENT ADDED DAMPING

2.1 Definitions for damping

The definition of damping might somehow be ambiguous. The definition we adopted in this paper needs thus to be clarified. First, in [2], the following definitions are proposed:

- Inherent damping: damping due to inherent dissipation of energy by elements of the structure.
- Additional viscous damping: damping added in the simulation to take into account inherent energy dissipation sources not explicitly considered in the inelastic structural model.

In the numerical simulations, there are thus two sources of damping: damping that comes from the inelastic structural model and additional viscous damping.

Then, in [4], in the context of inelastic structural analysis, damping is defined as ”*the portion of energy dissipation that is not captured in the hysteretic response of components that have been included in the model*”. According to this definition, it is also suggested in [4] to use ”*un-modeled energy dissipation*” as a more appropriate terminology for damping.

In this contribution, we adopt the following definitions:

- Hysteretic damping: energy dissipation due to the inelastic response of the structural elements included in the model.
- Added damping: damping added in the simulation, for instance Rayleigh’s damping, to take into account energy dissipation sources not explicitly modeled in the inelastic structural model.

On the contrary to what is suggested in [4], we decided to also qualify the hysteretic energy dissipation as damping. Indeed, in experimental investigations, measured damping is due to all the energy dissipative phenomena; then, in the numerical simulations, hysteretic energy dissipation sources also participate to the damping characteristics of the structure. In what follows, all the energy dissipation sources, that is total damping, is thus split into an explicitly modeled part (hysteretic damping) and an additional part (added damping). This latter part is introduced in the simulations to take into account the energy dissipation sources not explicitly modeled in the inelastic structural model.

2.2 Some words on the state of the practice

Section 2.4 in [4] is a very useful and detailed presentation of damping in the buildings in the context of nonlinear structural analysis. We provide here a very short summary of it.

Experimental evidence concerning $1/3$ to $1/2$ scale reinforced concrete frame systems are presented. The critical damping ratios in the first mode versus level of damage measured from 7 shaking table tests are shown and it is concluded that:

- In the initial or undamaged condition, the critical damping ratio ranges from 1% to 3%.
- In structures that have undergone modest levels of shaking (less than 1% drift) and sustained slight damage (*i.e.* hairline cracking, minor spalling), damping values increase to about 4%.
- Following significant damage, damping increases beyond 5% up to a maximum measured value of 11% of critical.

Inelastic structural models cannot represent all the energy dissipation mechanisms involved in the measured damping. It is mentioned in [2] section 6.4.4 that "*most of the structural damping [should] be modeled directly in the analysis through hysteretic response of the structural components*". And then, "*depending on the type and characteristics of the nonlinear model, additional viscous damping may be used to simulate the portion of energy dissipation arising from both structural and nonstructural components (*e.g. *cladding, partitions) that is not otherwise incorporated in the model*".

Concerning now the choice of the critical damping ratios to be considered for adding viscous damping, the general principle to be appealed for is expressed in the following terms in [2] section 6.4.4: "*When used, viscous damping should be consistent with the inherent damping in the structure that is not already captured by the nonlinear hysteretic response that is directly simulated in the model*". It is stated in [4] that "*many of the currently available guidelines on damping are intended for use with elastic dynamic analysis*". Nevertheless, the value of 5% of critical damping is presented as common practice for nonlinear studies of low to mid-rise buildings. In [5], the dynamic behavior of steel-concrete composite structures is modeled and the authors conclude that the two critical damping ratios of 1% and 5% "*can be viewed as reasonable lower and upper bounds when energy dissipation due to material hysteretic behavior is already modeled explicitly*". In works developed with the finite element computer program *Vector* [6], it is advocated not to add damping and thus to use the inelastic structural model as the sole source of seismic energy dissipation.

2.3 Adding viscous damping

The inelastic earthquake response of RC structures is computed according to the following discrete equations of motion:

$$\mathbf{M}\ddot{\mathbf{U}}(t) + \mathbf{C}(t)\dot{\mathbf{U}}(t) + \mathbf{R}(t) = \mathbf{F}^{sta} - \mathbf{M}\boldsymbol{\Delta}\ddot{\mathbf{U}}_g(t) \tag{1}$$

where $\mathbf{M}$, $\mathbf{C}(t)$ are the mass and damping matrices and $\mathbf{R}(t)$ is the nonlinear restoring forces vector; $\mathbf{F}^{sta}$ is the applied static forces, and $-\mathbf{M}\boldsymbol{\Delta}\ddot{\mathbf{U}}_g(t)$ represents the applied seismic forces with $\boldsymbol{\Delta}$ the matrix indicating the active dynamic degrees of freedom for directional mass and $\ddot{\mathbf{U}}_g(t)$ the applied ground acceleration.

There are several methods for introducing added viscous damping ($\mathbf{C}(t)\dot{\mathbf{U}}(t)$) in numerical simulations: the so-called Rayleigh's or Caughey's methods or modal damping. We only present here Rayleigh's methods that will be used for the numerical simulations presented in the next section:

$$\mathbf{C}_{[i]}(t) = (a_M\mathbf{M} + b_K\mathbf{K}_0)_{[1]} \ , \ (a_M\mathbf{M} + b_K\mathbf{K}_{tan}(t))_{[2]} \text{ or } (a_M(t)\mathbf{M} + b_K(t)\mathbf{K}_{tan}(t))_{[3]} \tag{2}$$

where $\mathbf{K}_0$ and $\mathbf{K}_{tan}(t)$ are the initial and tangent stiffness matrices. The coefficients a_M and b_K determine the critical damping ratio for two chosen structural frequencies.

Although all of these methods have clear significance and computational benefits in elastic simulations, they might be inappropriate in inelastic analyses and thus have to be handled with care. Several researchers presented seismic analyses of nonlinear structural systems using different damping models from Eqs. (2) [7, 8, 9, 10]. It was concluded that $\mathbf{C}_{[3]}(t)$ was the best model to maintain a constant value of added viscous damping throughout the analysis and avoid spurious internal damping forces. However, the update of parameters $a_M(t)$ and $b_K(t)$ with the progress of the solution is not practical from a computational aspect and damping models $\mathbf{C}_{[1]}$ or $\mathbf{C}_{[2]}(t)$ are generally preferred. The coefficients a_M and b_K are most often computed from the initial dynamic properties of the structures, but pushover analysis (or other approximations) could also be used to predict the secant stiffness at the target ductility to estimate an elongated natural period of vibration in the computation of a_M and b_K.

The purpose of the following section is to investigate how far such commonly used added viscous Rayleigh's damping models can be considered as consistent with the hysteretic damping coming from the inelastic structural model. Then, to *a posteriori* quantify this consistency, an indicator based on energy quantities is suggested.

3 ENERGY AS AN INDICATOR OF CONSISTENCY FOR ADDED DAMPING

In this section, numerical inelastic seismic analyses of a RC moment-resisting frame tested on a shaking table are compared. Different computer programs available to practitioners and researchers are used to combine different RC inelastic and added viscous damping models, and to compare their relative amount of energy dissipated during the seismic time-history.

3.1 Description of the RC frame structure and ground motions

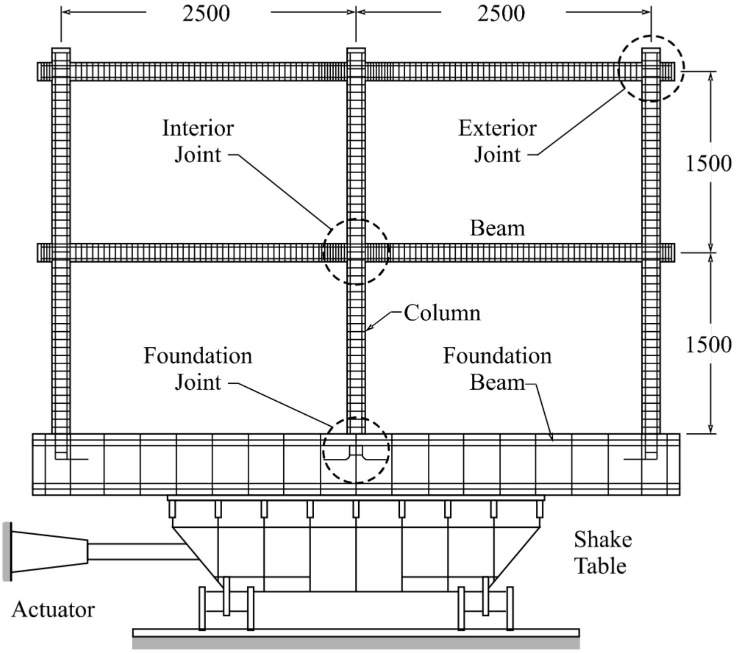

Figure 1: RC frame tested on a shaking table.

Fig. 1 shows the geometry and reinforcing steel of the half scale RC moment-resisting frame that was tested on a shaking table some years ago by Filiatrault *et al.* [3] at École Polytechnique of Montreal. The structure was designed according to the Canadian National Building Codes CNBC 1995 for a global displacement ductility demand $R = 2$. A detailed description of the frame is given in [3]. The two bays, two stories frame is 5 m wide, 3 m high with rectangular cross-sections of 15x16 cm and 14x15 cm for the 1st and 2nd floor beams, 17x13 cm and 18x13 cm for the external and internal columns. Resulting properties of RC are as follows: concrete Young's modulus 25,200 MPa, compressive strength 31 MPa and Poisson's ratio 0.17; the longitudinal steel Young's modulus 224,600 MPa with a yield strength 438 MPa and the ultimate strength 601 MPa. Four inverted U shape concrete blocks attached in each span of the beams were used to simulate concentrated gravity loads from framing joints. The centers of gravity of the added masses were computed such that they coincide with the center of gravity of the beams. Service cracks were induced by the added masses. The total weight of the frame was 95 kN. The fundamental period was measured at 0.36 s in a free-vibration test with a first modal damping ratio of 3.3%. Mode 1 is preponderant.

The ground motion record that was selected for the test program corresponds to the N04W component of the accelerogram recorded in Olympia, Washington (April 13, 1949). Fig. 2 presents the feedback record measured on the shaking table during the test initially scaled to a peak ground acceleration PGA = 0.21 g, as well as the corresponding response spectrum.

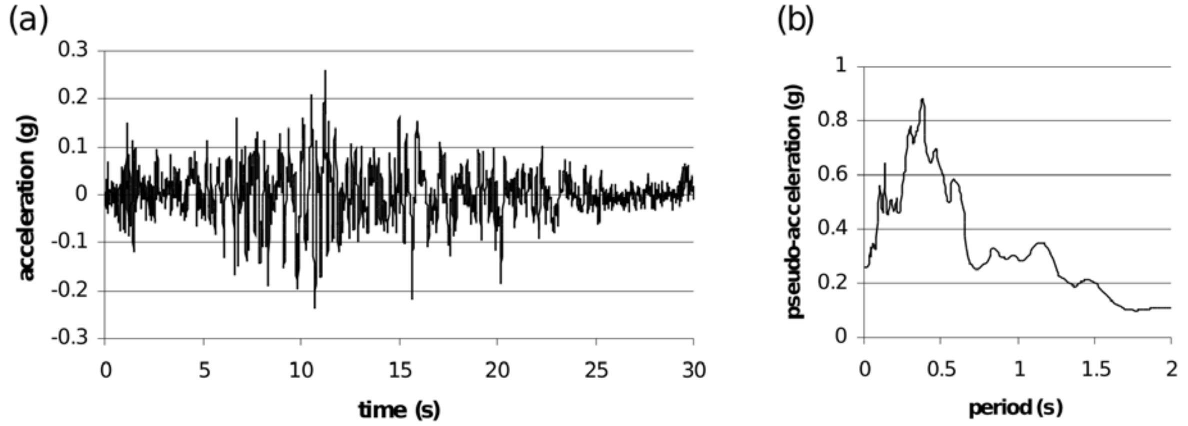

Figure 2: Seismic input motion: (a) shaking table acceleration, (b) response spectrum (5% critical damping ratio).

The frame structure was designed according to the CNBC 1995. The structural response observed during the shaking table test, expressed in terms of displacements, shear forces and plastic hinges positions, is in accordance with the building code.

3.2 Structural models

It is well known that all the inelastic analyses do not provide identical results and it is not realistic to aim at modeling all the energy dissipative phenomena that can occur during seismic time-history. However, as mentioned in [11], there are ”*phenomena that affect the behavior at or near collapse and that cannot be detected and evaluated by means of conventional elastic analysis techniques*”; among others, the author focuses on i) structure P-delta effects, ii) deterioration in strength and stiffness and, for moment-resisting frame structures, iii) the capacity design strong column–weak girder concept for which excessive plastic hinging in columns should be avoided. The inelastic structural models used thus have to be at least capable of reproducing these key issues.

The model developed with the computer program *Ruaumoko* [12] (Fig. 3a) is based on beam-column elements with plastic hinges lumped at the member ends. The Q-HYST degrading rule version of the modified Takeda model (Fig. 3b) was used to represent the inelastic moment-rotation behavior in plastic hinges. The backbone of the hysteretic curve was obtained from a plane section analysis program. At each node the connection was modeled using rigid end beam and column offsets (infinitely stiff zones whose length is equal to the depth of the adjacent beam or column) and plastic hinges whose lengths are equal to half the height inside the stirrups. *Ruaumoko* allows using the damping models $\mathbf{C}_{[1]}$ or $\mathbf{C}_{[2]}(t)$ defined in Eqs. 2.

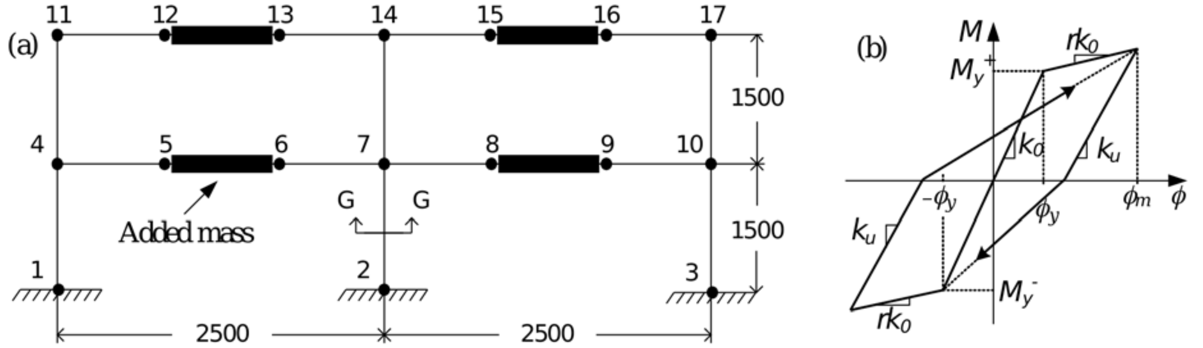

Figure 3: Ruaumoko lumped plasticity model: (a) geometry; (b) modified Takeda hysteretic model.

We also used the computer program *Perform3D* [13] allowing for the discretisation of the various frame cross-sections into fibers. A division of the sections into 6 concrete and steel layers for the columns and 8 layers for the beams was used. A 1D behavior law was associated to each material; Fig. 4a shows the stress-strain behavior of the concrete material models. The mesh is the same as in Fig. 3a. For the structural model referred to as Perform3D_1, unconfined concrete material was assigned to each concrete fiber and 5 numerical integration points (NIPs) per element were considered. For the structural model Perform3D_2, the concrete material was defined as confined concrete inside the stirrup and as unconfined outside (Fig. 4b), and only 2 NIPs per element were considered. Connections at each node were modeled by using rigid end beam and column offsets, that is, for *Perform3D* program, zones whose length is equal to the depth of the adjacent beam or column and whose stiffness is 10 times those of the element. In *Perform3D*, Rayleigh's damping models are not exactly defined as in Eqs. 2. We consequently define both $\mathbf{C}_{[F1]}$ as a Rayleigh's damping model computed according to the initial stiffness, as for model $\mathbf{C}_{[1]}$, and $\mathbf{C}_{[F2]}$ as a Rayleigh's damping model computed according to the reduced stiffness associated to a global displacement ductility $R = 2$, in the spirit of model $\mathbf{C}_{[2]}$. To this, the methodology is described in [13].

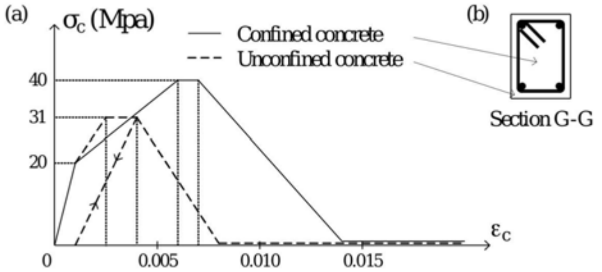

Figure 4: Perform3D fiber element model: (a) concrete model, (b) confined and unconfined fibers. Stiffness degradation is modeled and there is no strength in tension.

Degradations, and thus energy dissipation phenomena, were observed in the beam-column joints during the test. For more detailed structural models, rigid end zones should thus be replaced by inelastic connections.

3.3 Results analysis

The total weight of the structure P and the fundamental elastic period T^{ela} are first indicated in Tab. 1. *A posteriori*, with the experimental results at hand, the values obtained for T^{ela} can be validated as follows. Because of the dead load, there is significant initial damage in the structure and the experimental fundamental period that is initially measured ($T_{FV}^{ini,exp} = 0.36$ s) is longer than the elastic one. The elastic dynamic properties of the mock-up are thus not known. For *Perform3D*, we evaluate the initial fundamental period by weakly exciting the structure after the dead load has been applied, letting it return to rest in free vibrations and measuring T_{FV}^{ini} (mode 1 is predominant). Then, the maximum top-displacement d_{max} is indicated. The quantities E_T, E_D and E_H correspond to the total seismic energy dissipated by the numerical model, the energy dissipated by the added viscous damping model and by the inelastic structural model. Finally, the fundamental period T_{FV}^{fin} is computed when the structure returns to rest at the end of the seismic motion.

	Exp.	Ruaumoko					Perform3D_1			Perform3D_2	
Damping model	/	/ (1)	$[C]_{[1]}$	$[C]_{[2]}$	$[C]_{[1]}$	$[C]_{[2]}$	$[C]_{[F1]}$	$[C]_{[F1]}$	$[C]_{[F2]}$	$[C]_{[F1]}$	$[C]_{[F2]}$
$\xi_{1,2}$ (%)	/	0.0	1.5	1.5	3.3	3.3	0.1	1.5	1.5	1.5	1.5
P (kN)	95	93.8					94.8				
T^{ela} (s)	NA(2)	0.28					0.26				
T_{FV}^{ini} (s)(3)	0.36	0.44					0.38				
d_{max} (mm)	48.9	47.1	44.1	45.8	42.2	42.2	46.4	45.5	46.1	43.6	43.8
E_T (N.m)	/	3735	3307	3442	2861	3089	2782	3534	3557	2698	2620
E_D/E_T (%)	/	0.0	23.7	22.2	46.2	43.3	8.2	60.2	55.9	83.0	81.7
E_H/E_T (%)	/	100.0	76.3	77.8	53.8	56.7	89.8	38.2	42.4	20.4	18.3
T_{FV}^{fin} (s)	0.55	0.46	0.45	0.45	0.46	0.45	0.51	0.49	0.50	0.40	0.40

(1) No added damping introduced in the model.
(2) NA: Not Available.
(3) FV: Free Vibrations.

Table 1: Earthquake response analyses of a RC moment-resisting frame using different inelastic structural and added viscous damping models (excerpt of the results).

Our purpose here is to show that it is somehow difficult to *a priori* assess that an added damping model is consistent with the inelastic structural model. Indeed, even for Rayleigh's damping models defined with small critical damping ratios, E_D can become very larger than E_H. This sounds not acceptable for most of the performance-based analyses. One can hope that this non-realistic behavior would be avoided with a ”good” inelastic structural model. However, there is *a priori* no reason not to check whether added damping is consistently modeled or not and the computation of the amounts of energy dissipated all along the seismic time-history seems to provide a pertinent indicator for this.

The following tendencies can be observed from Tab. 1:

- The $E_{H/D}/E_T$ ratio is affected by the choice of a structural model. 1) For the lumped plasticity models (*Ruaumoko*), hysteretic energy is preponderant, which is no more the case for the *Perform3D* fiber element models; this is illustrated in Fig. 5. 2) For *Perform3D* models, the assumptions made on the concrete behavior law also significantly affect the energy ratios.

- For a given computer program, the larger the E_H/E_T ratio is, the larger and closer to the experimental response is the maximum top-displacement. This observation supports some researchers' opinion, who advocate not to introduce added damping in inelastic simulations [6].

- For both *Ruaumoko* and *Perform3D* models, the energy repartition is not significantly affected by the choice of a Rayleigh's damping model of the $\mathbf{C}_{[(F)1]}$ or $\mathbf{C}_{[(F)2]}$ kind. Defining added viscous damping according to a reduced stiffness matrix with respect to the initial one nevertheless leads to a slight reduction of the E_D/E_T ratio.

- For both *Ruaumoko* and *Perform3D* models, the energy ratios are sensitive to $\xi_{1,2}$, the critical damping ratio attributed to modes 1 and 2.

- For all *Ruaumoko* models, the final fundamental structural frequency is roughly $T_{FV}^{fin} = 0.45$ s. This indicates that the global structural stiffness degradation is independent from the E_H/E_T ratio. On the contrary, for *Perform3D* models, there is a clear correlation between the amount of energy dissipated by the model and the degradation of the global stiffness. Considering *Perform3D* models only, the best approximation is obtained when there is almost no added damping.

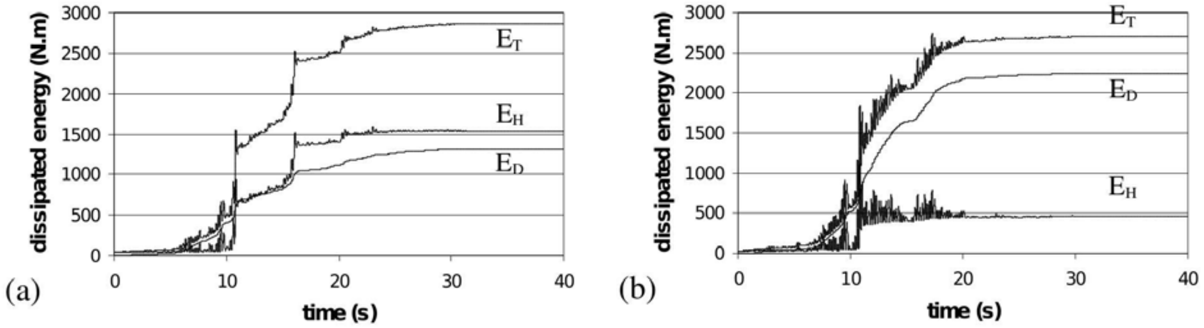

Figure 5: Energy dissipation sources: (a) Ruaumoko $\mathbf{C}_{[1]}$-3.3%, (b) Perform3D_2 $\mathbf{C}_{[F2]}$-1.5%.

Besides, computing energy quantities allows to compare the relative importance of the inelastic mechanisms accounted for in the structural model. For instance, for detailed material constitutive models developed in the theoretical frameworks of continuum mechanics and thermodynamics with interval variables, it is often difficult, in the context of seismic inelastic time-history analysis, to assess whether enriching the model with new local mechanism is meaningful or not. However, for this kind of models, it is often straightforward to compute the energy dissipated by each local phenomenon such as plasticity or damage [14], and it is thus possible to quantify the relative importance of each local phenomena.

4 CONCLUSIONS

In the particular context of RC moment-resisting frame structure in seismic loading, and without considering any interaction between the structure and its surrounding environment:

- **Facts.** The seismic energy imparted to a structure is dissipated consequently to inelastic mechanisms, that are irreversible modifications, in the structure.

- **Issue.** Performance-based methods ideally require that the irreversible modifications in the structure are predicted. One of the main issues related to performance-based engineering thus is: how to model the energy dissipation mechanisms in the structure?

- **Methodological aspects.** The need for modeling internal energy dissipation provides methodological indications for the development of inelastic analyses. Energy dissipation in a structural numerical model should be mostly hysteretic to predict the internal modifications. However, it is not always satisfied for inelastic numerical simulations, even when added viscous damping is associated to a small critical damping ratio. Therefore, developments should be oriented towards both increasing the capacity of inelastic structural models to reproduce the physical mechanisms that dissipate the imparted energy and reducing the portion of added damping.

- **Results interpretation.** Results of inelastic time-history analyses can be better interpreted according to energetic quantities, which indicate whether the energy dissipation is, as expected, mostly hysteretic or not. In the case most of the energy is dissipated by added damping, it can be inferred that the numerical simulation failed to predict the internal modifications in the structure (strength and stiffness loss, drift, etc.). Elastic simulations are an extreme case: all the seismic energy is dissipated by added damping and, consequently, the structure after the earthquake is the same as before. Computing the portion of the total energy dissipated by a particular nonlinear mechanism during the seismic time-history would also allow to decide whether it is worth modeling this mechanism or not.

For these reasons, expressed in the context of RC frame structures in seismic loading, and without considering any interaction between the structure and its surrounding environment, modeling energy dissipation is a paradigm [15] for performance-based engineering.

REFERENCES

[1] M.J.N. Priestley, G.M. Calvi, M.J. Kowalsky, *Displacement-based seismic design of structures*. IUSS Press, Pavia, Italy, 2007.

[2] FEMA P695, *Quantification of Building Seismic Performance Factors*. FEMA, Washington DC, June 2009.

[3] A. Filiatrault, E. Lachapelle, P. Lamontagne, Seismic performance of ductile and normally ductile concrete moment resisting frames - Part I: Experimental study. *Canadian Journal of Civil Engineering*, **25**, 331–352, 1998.

[4] PEER-2010/111 or PEER/ATC-72-1, *Modeling and Acceptance Criteria for Seismic Design and Analysis of Tall Buildings*. PEER, Richmond (CA), October 2010.

[5] A. Zona, M. Barbato, J.P. Conte, Nonlinear Seismic Response Analysis of Steel–Concrete Composite Frames. *ASCE Journal of Structural Engineering*, **134**(6), 986–997, 2008.

[6] S. Saatci, *Behavior and modeling of reinforced concrete structures subjected to impact loads*. PhD Thesis, University of Toronto, Department of Civil Engineering, Canada, 2007. `http : //www.civ.utoronto.ca/vector/`

[7] J. Wang, Intrinsic damping: Modeling techniques for engineering systems. *ASCE Journal of Structural Engineering*, **135**(3), 282–291, 2009.

[8] F.A. Charney, Unintended consequences of modeling damping in structures. *ASCE Journal of Structural Engineering*, **134**(4), 581–592, 2008.

[9] J.F. Hall, Problems encountered from the use (or misuse) of Rayleigh damping. *Earthquake Engineering and Structural Dynamics*, **35**, 525–545, 2006.

[10] P. Léger, S. Dussault, Seismic-Energy Dissipation in MDOF Structures. *ASCE Journal of Structural Engineering*, **118**(6), 1251–1267, 1992.

[11] H. Krawinkler, Importance of good nonlinear analysis. *The Structural Design of Tall and Special Buildings*, **15**, 515–531, 2006.

[12] A.J. Carr, *Ruaumoko manual, theory and user's guide to associated programs*, University of Cantabury, Christhurch, New Zealand, 2004.

[13] CSI, *Perform3D user's manual*, California, 2007.

[14] P. Jehel P, A. Ibrahimbegovic, P. Léger, L. Davenne, Towards robust viscoelastic-plastic-damage material model with different hardenings / softenings capable of representing salient phenomena in seismic loading applications. *Computers and Concrete*, **7**(4), 365–386, 2010.

[15] T.S. Kuhn, *The Structure of Scientific Revolutions, 2^{nd} edition*. In *International Encyclopedia of Unified Science*. The University of Chicago Press, Chicago, 1970.

COMPDYN 2011
III ECCOMAS Thematic Conference on
Computational Methods in Structural Dynamics and Earthquake Engineering
M. Papadrakakis, M. Fragiadakis, V. Plevris (eds.)
Corfu, Greece, 25–28 May 2011

A SINGLE MODE ENERGY-BASED PUSHOVER PROCEDURE

Grigorios E. Manoukas[1], **Asimina M. Athanatopoulou**[2], **and Ioannis E. Avramidis**[2]

[1] Aristotle University of Thessaloniki
University Campus, 54124, Thessaloniki, Greece
e-mail: grman7@otenet.gr

[2] Aristotle University of Thessaloniki
University Campus, 54124, Thessaloniki, Greece
{minak, avram}@civil.auth.gr

Keywords: Pushover Analysis, Displacement Modification Method, Strain Energy, Equivalent Single Degree of Freedom System, Nonlinear Response History Analysis.

Abstract. *In this paper a new energy-based pushover procedure is presented in order to achieve an approximate estimation of structural performance under strong earthquakes. The steps of the proposed methodology are quite similar to those of the well-known displacement modification method. However, the determination of the characteristics of the equivalent single degree of freedom (E-SDOF) system is based on a different concept. Its main idea is to determine the E-SDOF system by equating the external work of the lateral loads acting on the multi degree of freedom (MDOF) system under consideration to the strain energy of the E-SDOF system. After a brief outline of the theoretical background, the sequence of the steps needed for the implementation of the proposed methodology along with the necessary equations are systematically presented. Finally, the accuracy of the proposed method is evaluated by an extensive parametric study which shows that, in general, it provides better results compared to those produced by other similar procedures.*

1 INTRODUCTION

In the last decades many research efforts have focused on developing simplified procedures for the approximate estimation of the inelastic performance of buildings under seismic excitation, in order to avoid the significant computational cost and the various inherent disadvantages of an accurate inelastic dynamic analysis. As a result of these efforts the idea of pushover analysis has been born. In the last decade a variety of more or less similar inelastic static pushover procedures have been developed, some of which have been already adopted by several seismic codes ([1], [2], [3], etc.).

Static Pushover Analysis, or Nonlinear Static Procedure (NSP) as it is denoted in seismic codes, seems to be a useful tool for engineering practice. Nevertheless, as it has already been stressed by many researchers (e.g., [4]), this procedure involves many shortcomings and can provide reasonable results only for low and medium rise planar systems. This is due to the fact that the determination of the structure's response is based on the assumption that the dynamic behavior depends only on a single elastic vibration mode. In addition, this elastic mode is supposed to remain constant despite the successive formation of plastic hinges during the seismic excitation. Also, the choice of roof displacement - as characteristic response quantity for the construction of the capacity curve - instead of any other displacement is arbitrary and it is doubtful whether the base shear-roof displacement curve is the most meaningful index of the nonlinear response of a structure, especially for irregular in height and asymmetric in plan systems. To overcome these shortcomings various modified pushover procedures have been proposed in the recent past (e.g., [5], [6], [7], [8]). Some of them [6], [7], [8] are based on the energy equivalence between the multi degree of freedom (MDOF) and the equivalent single degree of freedom (E-SDOF) systems (energy-based procedures). According to energy-based procedures, the strain energy of the structure or, equivalently, the work done by the external loads is considered to be the most representative index of its nonlinear response.

Hernadez-Montes et al. [6] suggested an energy-based formulation of pushover analysis which was motivated by the reversals in the higher mode capacity curves that were observed when applying Modal Pushover Analysis [5]. This method uses an energy-based displacement derived from the work done by the lateral loads to establish the capacity curve, instead of using the roof displacement. In each step of the pushover procedure, the work done by lateral loads associated with each mode is computed using an incremental formulation. The corresponding increment in the energy-based displacement is calculated by dividing the increment of work at each step by the base shear at that step. The incremental displacements are accumulated to obtain the energy-based displacement of the E-SDOF system. Thus, a modified capacity curve is plotted for each mode, which is used in lieu of the conventional pushover curve. These modified curves resemble traditional first mode pushover curves and do not exhibit the anomalies observed in higher mode curves.

Parducci et al. [7] proposed the determination of an equivalent energy-based displacement of the E-SDOF system. This displacement does not correspond to any actual point of the structural model, but it is a virtual value equalizing the work done by the lateral loads to the strain energy of the E-SDOF system. Then, the strain energy versus equivalent displacement diagram is plotted and - in combination with a pseudo-energy response spectrum - the performance point is determined. This point is used to estimate the response of the structure.

Earlier, Oliveto et al. [8] determined a displacement parameter based on power equivalence (which in finite terms translates into energy equivalence) between MDOF and E-SDOF systems. The properties of the E-SDOF system are then calculated as function of this energy-based displacement. Recently, this procedure was extended to include Modal Pushover Analysis [9].

The objective of the present paper is the formulation and preliminary evaluation of a new energy-based Nonlinear Static Procedure (NSP) for the approximate estimation of the seismic response of structures. The proposed procedure uses the strain energy which is considered as a more reliable index of the structural response than the base shear. This is due to the fact that the strain energy depends on the values of all forces acting to the structure as well as on the values of the displacements of all the system's degrees of freedom. The steps of the proposed methodology are quite similar to those of the well-known displacement modification method [1], [3]. However, the determination of the characteristics of the E-SDOF system is based on a different concept. Specifically, the definition of the E-SDOF system is based on the equalization of the external work of the lateral loads acting on the MDOF system under consideration to the strain energy of the E-SDOF system. In contrast to other energy-based procedures, the energy equivalence is used to derive a modified resisting force of the E-SDOF system, instead of an energy-based displacement. Thus, a modified capacity curve is plotted. As a first step, the procedure is formulated in a manner that takes into account only the predominant vibration mode and in its current form it can be rigorously applied to low and medium rise planar systems.

Firstly, the theoretical background and the assumptions of the proposed methodology are presented and briefly discussed. Secondly, both the sequence of the steps needed for the implementation of the proposed methodology along with the necessary equations are systematically presented. Finally, the accuracy of the proposed methodology is evaluated by an extensive parametric study. The paper closes with comments on results and conclusions. The whole investigation proved that the here proposed methodology gives, in general, better results as compared to other similar procedures.

2 THEORETICAL BACKGROUND

It is well known that the linear elastic response of a MDOF system can be decomposed to responses of SDOF systems, one for each elastic vibration mode (modal analysis). Although this concept lacks a theoretical basis in the inelastic range of behavior, it has been widely used by many researchers (e.g., [5]) in order to develop approximate, simplified nonlinear static procedures. It is obvious that this approach includes some fundamental assumptions. A major assumption is that the response of a MDOF system can be expressed as superposition of the responses of appropriate SDOF systems just like in the linear range. Of course, such an assumption violates the very logic of nonlinearity, as the superposition principle is not valid to nonlinear systems. However, it must be thought as a fundamental postulate, which constitutes the basis on which many simplified pushover procedures are built. Thus, each SDOF system corresponds to a vibration "mode" i with "modal" vector $\boldsymbol{\varphi}_i$ (the quotation marks indicate that the application of the superposition principle is not strictly valid). The displacements $\mathbf{u}_i$ and the inelastic resisting forces $\mathbf{F}_{si}$ are supposed to be proportional to $\boldsymbol{\varphi}_i$ and $\mathbf{M}\boldsymbol{\varphi}_i$, respectively (where $\mathbf{M}$ is the mass matrix of the system). Furthermore, "modal" vectors $\boldsymbol{\varphi}_i$ are supposed to be constant, despite the successive development of plastic hinges.

Taking into account the aforementioned assumptions and applying well-known principles of structural dynamics the following conclusion is derived [10]: the nonlinear response of a MDOF system with N degrees of freedom subjected to an horizontal earthquake ground motion $\ddot{u}_g(t)$ can be expressed as superposition of the responses of N E-SDOF systems, each one corresponding to a vibration "mode" having mass equal to the effective modal mass M_i^*, displacement D_i which depends on the roof displacement u_{Ni} and inelastic resisting force equal to the "modal" base shear parallel to the direction of excitation V_i. Furthermore, the external work of "modal" forces $\mathbf{F}_{si}$ on the differential displacements $d\mathbf{u}_i = \nu_i \, \boldsymbol{\varphi}_i \, dD_i$ (where ν_i is the modal participation factor of mode i) is equal to the work of the resisting force (or the strain energy) of the corresponding E-SDOF system for the differential displacement dD_i.

Some basic equations correlating the properties of the “modal” E-SDOF systems to the properties of the MDOF system are derived and summarized in Table 1. However, these equations are derived on the basis of the aforementioned assumptions and cannot be valid all together at the same time when a pushover analysis is conducted. Thus, Modal Pushover Analysis [5] leaves out the 3rd equation and uses the two others to establish the “modal” E-SDOF systems. The conventional procedures adopted by codes follow a similar approach with some additional assumptions. More specifically, they take into account only the predominant vibration mode and permit modifications to the corresponding mode shape vector. The existing energy-based single or multimodal procedures keep the last two equations and determine the E-SDOF systems’ displacements on the basis of the energy equivalence between E-SDOF and MDOF system. On the contrary, the proposed method keeps the 1st and the 3rd equation and uses the energy equivalence to determine a modified resisting force of the E-SDOF systems.

MDOF system		E-SDOF systems
“modal” displacements $\mathbf{u}_i^T = \boldsymbol{\varphi}_i^T \nu_i D_i$ (roof displacement u_{Ni})	⇒	displacement $D_i = u_{Ni} / \nu_i \varphi_{Ni}$ (1st)
“modal” base shear V_i	⇒	resisting force $V_{SDOFi} = V_i$ (2nd)
work of “modal” forces on the differential “modal” displacements $d\mathbf{u}_i^T = \boldsymbol{\varphi}_i^T \nu_i dD_i$ $E(d\mathbf{u}_i)$	⇒	work of resisting force on the differential displacement dD_i $E(dD_i) = E(d\mathbf{u}_i)$ (3rd)

Table 1: Definition of the E-SDOF systems.

3 THE PROPOSED METHODOLOGY

As a first step, the proposed methodology is formulated in a manner that takes into account only the predominant vibration mode in the excitation direction. Thus, in its current form, it is suitable for structural systems with small contributions of higher modes, such as low and medium rise planar frames. The steps needed for its implementation are as follows [10]:

- Step 1: Create the structural model.
- Step 2: Apply to the model a set of lateral incremental forces proportional to the vector $\mathbf{M}\boldsymbol{\varphi}_1$ of the fundamental elastic vibration mode 1 and determine the (strain energy)-(roof displacement) curve E_1-u_{N1}. E_1 is equal to the work of the external forces and moments.
- Step 3: Divide the abscissas of the E_1-u_{N1} diagram by the quantity $\nu_1\varphi_{N1} = u_{N1}/D_1$ and determine the (strain energy)-(displacement) diagram E_1-D_1 of the E-SDOF system (Figure 1).
- Step 4: Calculate the work $\Delta E_{1,\lambda}$ (Figure 1) of the external forces in each of λ discrete intervals between the successive formation of plastic hinges. $dE_{1,\lambda}$, as part of $\Delta E_{1,\lambda}$ (Equation (1)), is considered to derive from Equation (2).

$$dE_{1,\lambda} = \Delta E_{1,\lambda} - V_{1,\lambda-1} (D_{1,\lambda} - D_{1,\lambda-1}) = \Delta E_{1,\lambda} - V_{1,\lambda-1}\, dD_{1,\lambda} \tag{1}$$

$$dE_{1,\lambda} = \frac{1}{2} k_{1,\lambda}\, dD_{1,\lambda}{}^{2} \Rightarrow k_{1,\lambda} = 2\, dE_{1,\lambda} / dD_{1,\lambda}{}^{2} \tag{2}$$

where $k_{1,\lambda}$ is the stiffness of the E-SDOF system corresponding to mode 1 in the interval λ. The resisting force $V_{1,\lambda}$ is given by Equation (3):

$$V_{1,\lambda} = V_{1,\lambda-1} + k_{1,\lambda}\, dD_{1,\lambda} \tag{3}$$

For $\lambda = 1$ (i.e., when the first plastic hinge is created) the force $V_{1,1}$ is equal to the base shear parallel to the direction of excitation. By utilizing Equations (1), (2) and (3) for each interval, determine the (resisting force)-(displacement) diagram V_1-D_1 of mode 1 (Figure 2).

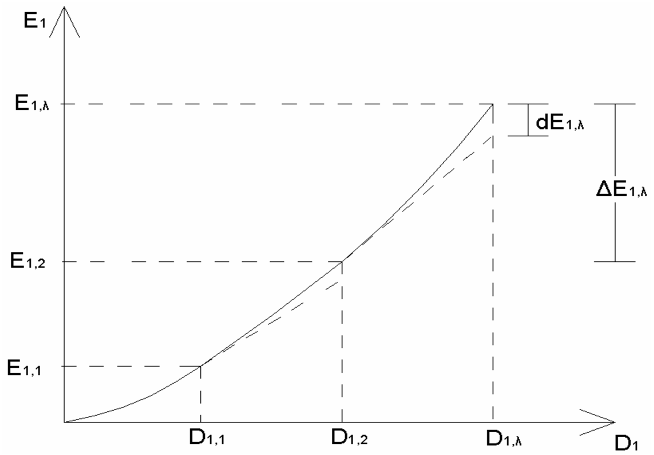

Figure 1: (Strain energy)-(displacement) diagram E_1-D_1 of the E-SDOF system.

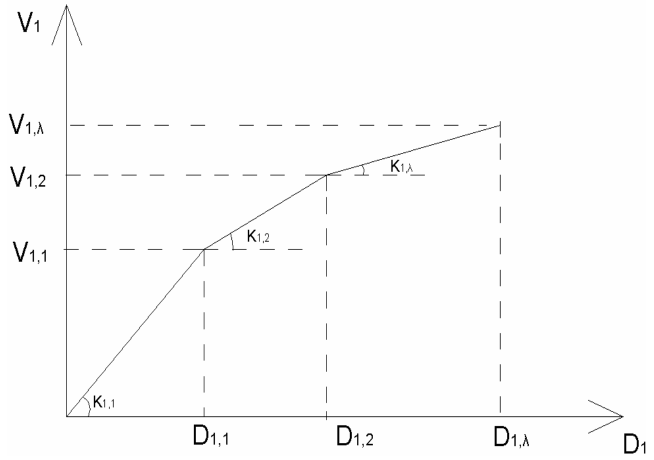

Figure 2: (Resisting force)-(displacement) diagram V_1-D_1 of the E-SDOF system.

- Step 5: Idealize V_1-D_1 to a bilinear curve using one of the well known graphic procedures (e.g., [1], Section 3.3.3.2.5) and calculate the period T and the yield strength reduction factor R of the E-SDOF system corresponding to mode 1.

- Step 6: Calculate the target displacement and other response quantities of interest (drifts, plastic rotations, etc.) of mode 1, using one of the well known procedures of displacement modification (e.g., [1], Section 3.3.3.3.2 / [11], Section 10.4). If the procedure is applied for research purposes using recorded earthquake ground motions, it is recommended to estimate the inelastic displacement of the E-SDOF system by means of nonlinear dynamic analysis, instead of using the relevant coefficients (e.g., C_1 in ASCE 41-06 and FEMA 440). This is due to the fact that the coefficient values given by codes are based on statistical processing of data with excessive deviations and, therefore, large inaccuracies might result [12].

- Step 7: Repeat steps 2 to 6 applying the incremental forces in the opposite direction. It is obvious that this step is necessary to apply only for asymmetric structures.

4 EVALUATION OF THE PROPOSED METHODOLOGY

In order to evaluate the accuracy of the proposed methodology an extensive parametric study is carried out. In particular, the methodology is applied to a series of 3-, 6-, 9- and 12-storey R/C planar frames (Figures 3 to11). Each frame is characterized by a string symbol comprising one or two letter(s) and a number which indicates the number of its storeys. The meaning of the letter(s) is as follows:

- R – Regular frames.
- M – frames with irregular distribution of Mass along the height. (Odd and even storeys have different masses).
- S – frames with irregular distribution of Stiffness along the height. (Odd storeys have greater height).
- SS – frames with Soft Storey. (1st storey has greater height).

For each frame three sets of pushover analyses are performed: i) one based on the proposed methodology (PM), ii) a second based on a procedure similar to the existing energy-based methods, i.e. according to it the energy equivalence between MDOF and E-SDOF systems is achieved by modifying the displacements (EB) and iii) a third based on the conventional displacement modification procedure (CP). The only difference between the three applied pushover procedures is the determination of the V_1-D_1 diagram (step 4), while the rest of the steps and assumptions are identical. V_1-D_1 diagram affects the characteristics of the E-SDOF system (T and R) and as a consequence the estimation of the target displacement. Each set of analyses comprises 12 different accelerograms corresponding to strong earthquake motions recorded in Greece. The maximum response of the E-SDOF system is calculated by means of nonlinear dynamic analysis for each excitation. Then, the target roof displacement is either estimated by multiplication of the resulting response by the quantity $\nu_1\varphi_{N1}$ (PM, CP) or obtained by the roof displacement – energy-based displacement correspondence (EB) [6].

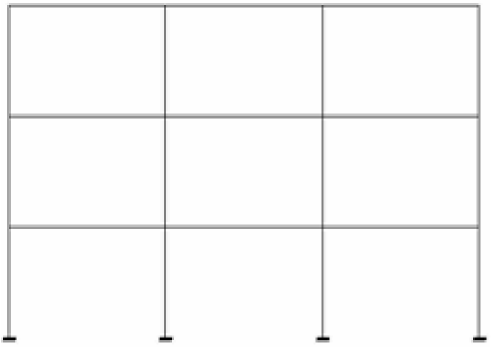

Storey height: 3m - Bay width: 5m
Restraints: columns fixed at base
Constraints: diaphragm at each level
Seismic mass: 30t per level (90t total)
Gravity loads: not considered
Column cross-sections: 40/40 cm
Column reinforcement: 8Φ16
Beam cross-sections: 25/40 cm
Beam reinforcement: 2Φ14 (over and under)
Concrete: C16/20 (f_{ck}=16 MPa)
Reinforcement bars: S400 (f_{yk}=400 MPa)

Figure 3: Frame R3.

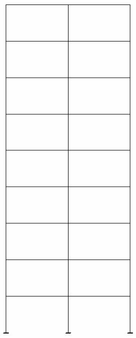

Storey height: 3m - Bay width: 5m
Restraints: columns fixed at base
Constraints: diaphragm at each level
Seismic mass: 30t per level (270t total)
Gravity loads: not considered
Column cross-sections: 60/60 cm
Column reinforcement: 8Φ20
Beam cross-sections: 25/50 cm
Beam reinforcement: 2Φ14 (over and under)
Concrete: C16/20 (f_{ck}=16 MPa)
Reinforcement bars: S400 (f_{yk}=400 MPa)

Figure 4: Frame R9.

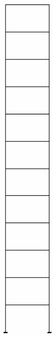

Storey height: 3m - Bay width: 5m
Restraints: columns fixed at base
Constraints: diaphragm at each level
Seismic mass: 15t per level (180t total)
Gravity loads: not considered
Column cross-sections: 60/60 cm
Column reinforcement: 8Φ20
Beam cross-sections: 25/50 cm
Beam reinforcement: 2Φ14 (over and under)
Concrete: C16/20 (f_{ck}=16 MPa)
Reinforcement bars: S400 (f_{yk}=400 MPa)

Figure 5: Frame R12.

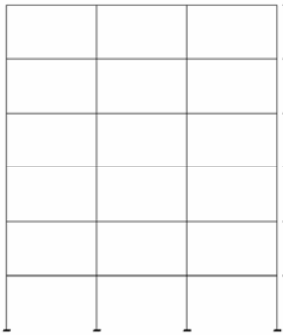

Storey height: 3m - Bay width: 5m
Restraints: columns fixed at base
Constraints: diaphragm at each level
Seismic mass: 20t (odd storeys) or 40t (even storeys) (180t total)
Gravity loads: not considered
Column cross-sections: 50/50 cm
Column reinforcement: 8Φ20
Beam cross-sections: 25/40 cm
Beam reinforcement: 2Φ12 (over and under)
Concrete: C16/20 (f_{ck}=16 MPa)
Reinforcement bars: S400 (f_{yk}=400 MPa)

Figure 6: Frame M6.

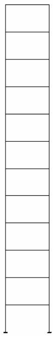

Storey height: 3m - Bay width: 5m
Restraints: columns fixed at base
Constraints: diaphragm at each level
Seismic mass: 9t (odd storeys) or 16t (even storeys) (150t total)
Gravity loads: not considered
Column cross-sections: 60/60 cm
Column reinforcement: 8Φ25
Beam cross-sections: 25/50 cm
Beam reinforcement: 2Φ14 (over and under)
Concrete: C16/20 (f_{ck}=16 MPa)
Reinforcement bars: S400 (f_{yk}=400 MPa)

Figure 7: Frame M12.

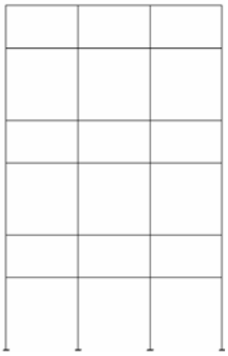

Storey height: 5m (odd storeys) or 3m (even storeys) - Bay width: 5m
Restraints: columns fixed at base
Constraints: diaphragm at each level
Seismic mass: 25t per level (150t total)
Gravity loads: not considered
Column cross-sections: 50/50 cm
Column reinforcement: 8Φ20
Beam cross-sections: 25/40 cm
Beam reinforcement: 2Φ12 (over and under)
Concrete: C16/20 (f_{ck}=16 MPa)
Reinforcement bars: S400 (f_{yk}=400 MPa)

Figure 8: Frame S6.

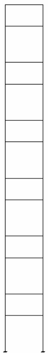

Storey height: 5m (odd storeys) or 3m (even storeys) - Bay width: 5m
Restraints: columns fixed at base
Constraints: diaphragm at each level
Seismic mass: 10t per level (120t total)
Gravity loads: not considered
Column cross-sections: 60/60 cm
Column reinforcement: 8Φ25
Beam cross-sections: 25/50 cm
Beam reinforcement: 2Φ14 (over and under)
Concrete: C16/20 (f_{ck}=16 MPa)
Reinforcement bars: S400 (f_{yk}=400 MPa)

Figure 9: Frame S12.

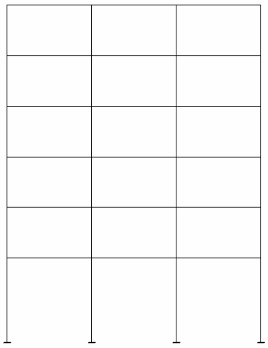

Storey height: 5m (1^{st} storey) or 3m (rest storeys) - Bay width: 5m
Restraints: columns fixed at base
Constraints: diaphragm at each level
Seismic mass: 30t per level (180t total)
Gravity loads: not considered
Column cross-sections: 50/50 cm
Column reinforcement: 8Φ20
Beam cross-sections: 25/40 cm
Beam reinforcement: 2Φ12 (over and under)
Concrete: C16/20 (f_{ck}=16 MPa)
Reinforcement bars: S400 (f_{yk}=400 MPa)

Figure 10: Frame SS6.

Storey height: 5m (1^{st} storey) or 3m (rest storeys) - Bay width: 5m
Restraints: columns fixed at base
Constraints: diaphragm at each level
Seismic mass: 13t per level (156t total)
Gravity loads: not considered
Column cross-sections: 60/60 cm
Column reinforcement: 8Φ25
Beam cross-sections: 25/50 cm
Beam reinforcement: 2Φ14 (over and under)
Concrete: C16/20 (f_{ck}=16 MPa)
Reinforcement bars: S400 (f_{yk}=400 MPa)

Figure 11: Frame SS12.

The storey displacements and drifts of the frames under consideration are compared to those obtained by nonlinear response history analysis (NL-RHA), which is considered as the reference solution. In Figures 12 to 20 the mean errors for the 12 excitations (in relevance to the NL-RHA results) of storey displacements and drifts are shown. Notice that the positive sign (+) means that the response parameters obtained by NSPs are greater than those obtained by NL-RHA. Conversely, the negative sign (-) means that the response parameters are underestimated by NSPs. From Figures 12 to 20 becomes clear that the proposed concept for the determination of the E-SDOF system leads to more accurate estimation of the target roof displacement (only in the case of frame R12 EB gives a little lower mean error). Mean errors range from -1% to 17% for PM, from 1% to 45% for EB and from 5% to 52% for CP. Concerning the rest response quantities, the mean errors resulting from the PM are sufficiently smaller in most cases (80% and 73% of cases in relevance to CP and EB, respectively). All the three applied procedures fail to provide a reasonable estimation for drifts at the upper storeys of taller frames. Such failures have been observed in many similar investigations due to the higher mode effects (e.g., [12]).

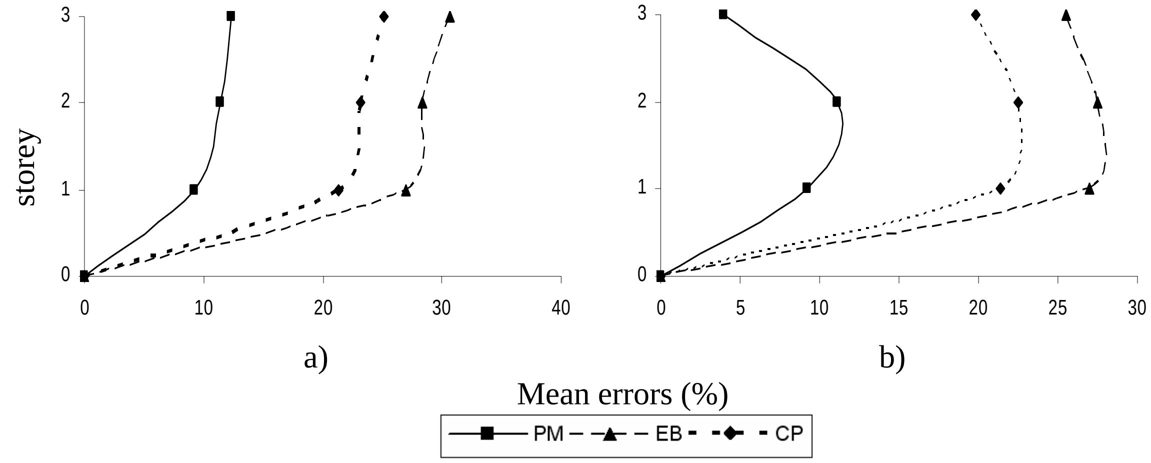

Figure 12: Mean errors (%) of storey displacements (a) and drifts (b) - Frame R3.

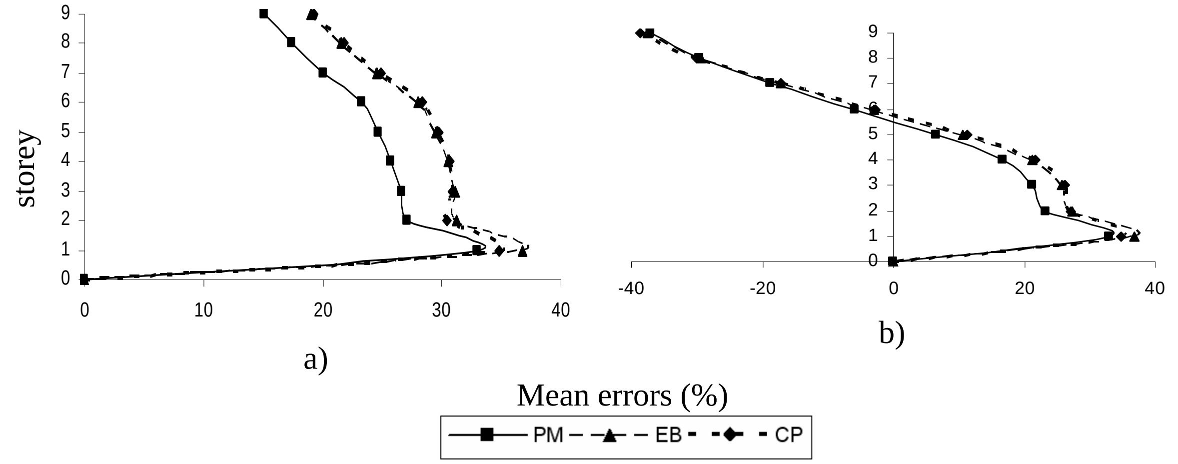

Figure 13: Mean errors (%) of storey displacements (a) and drifts (b) - Frame R9.

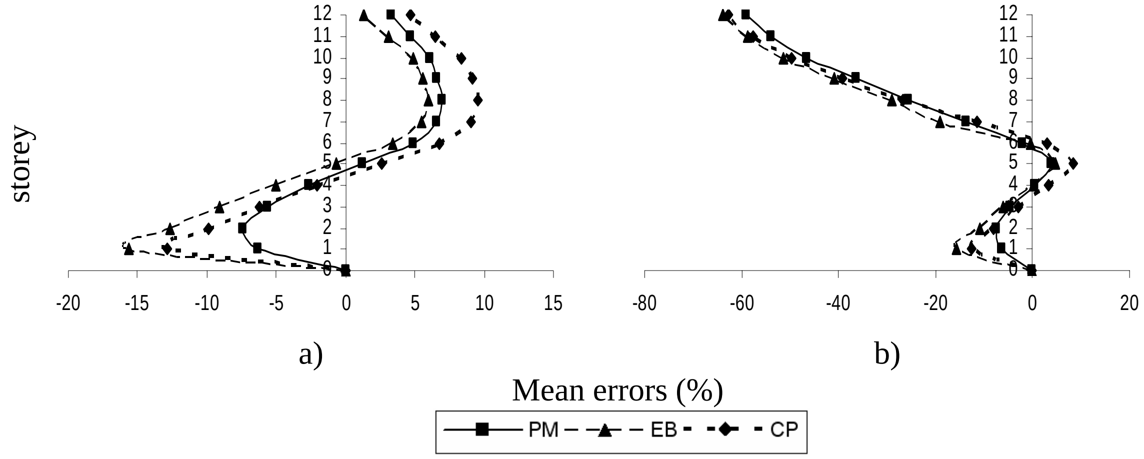

Figure 14: Mean errors (%) of storey displacements (a) and drifts (b) - Frame R12.

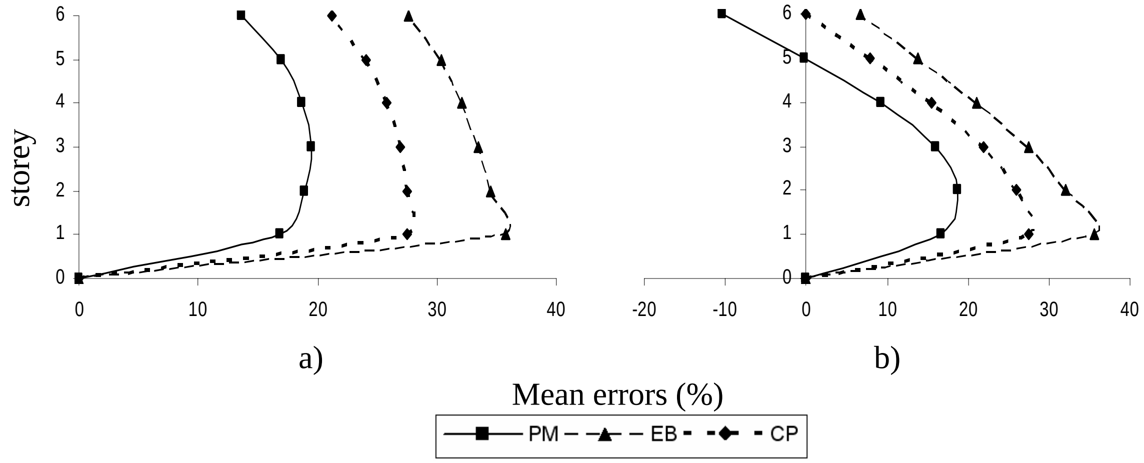

Figure 15: Mean errors (%) of storey displacements (a) and drifts (b) - Frame M6.

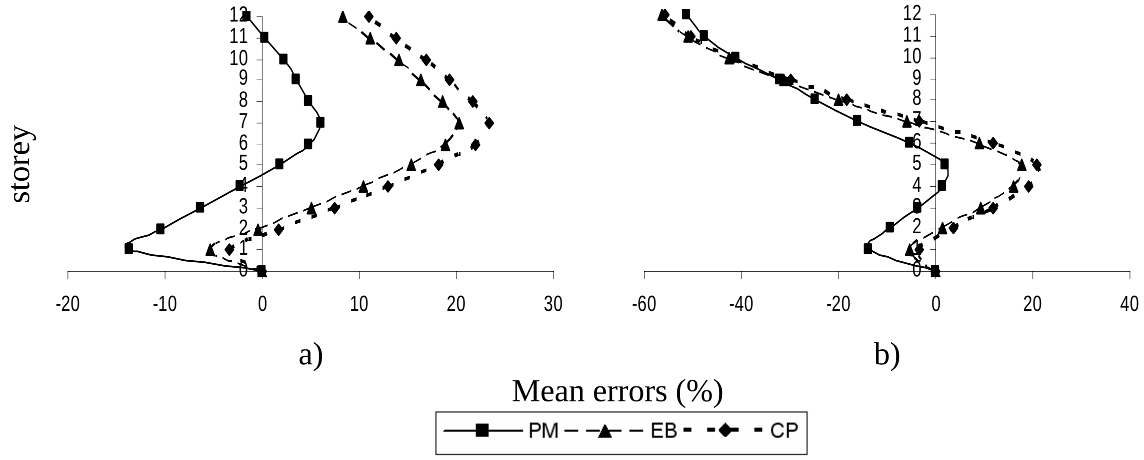

Figure 16: Mean errors (%) of storey displacements (a) and drifts (b) - Frame M12.

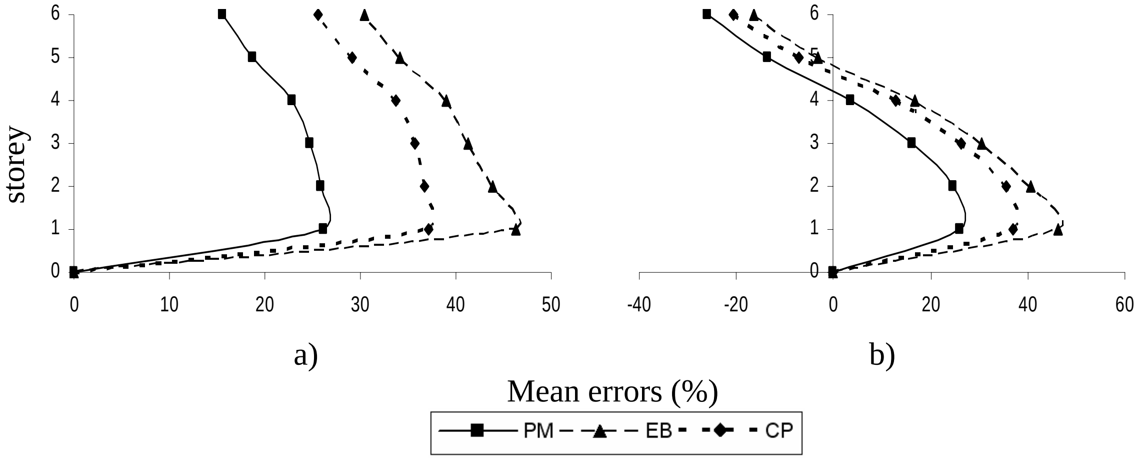
a)

b)

Figure 17: Mean errors (%) of storey displacements (a) and drifts (b) - Frame S6.

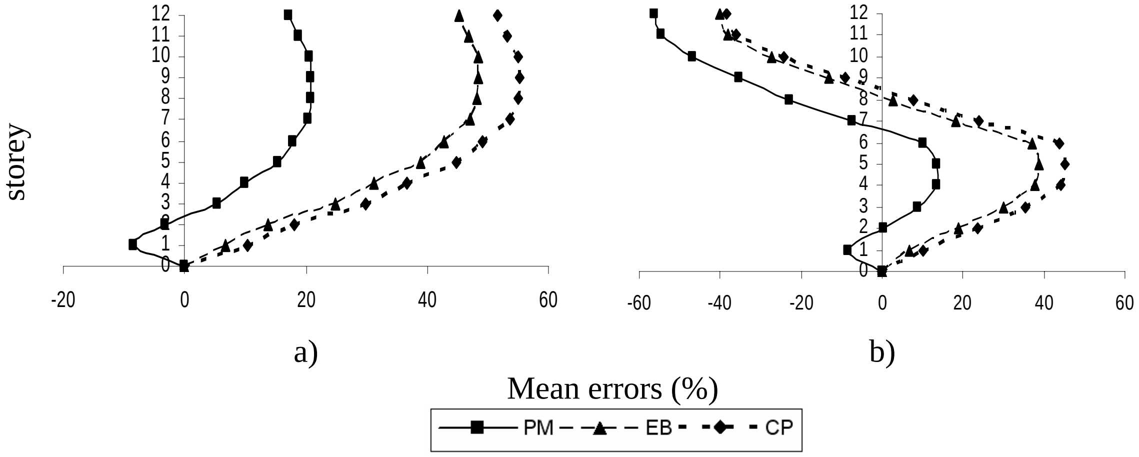
a)

b)

Figure 18: Mean errors (%) of storey displacements (a) and drifts (b) - Frame S12.

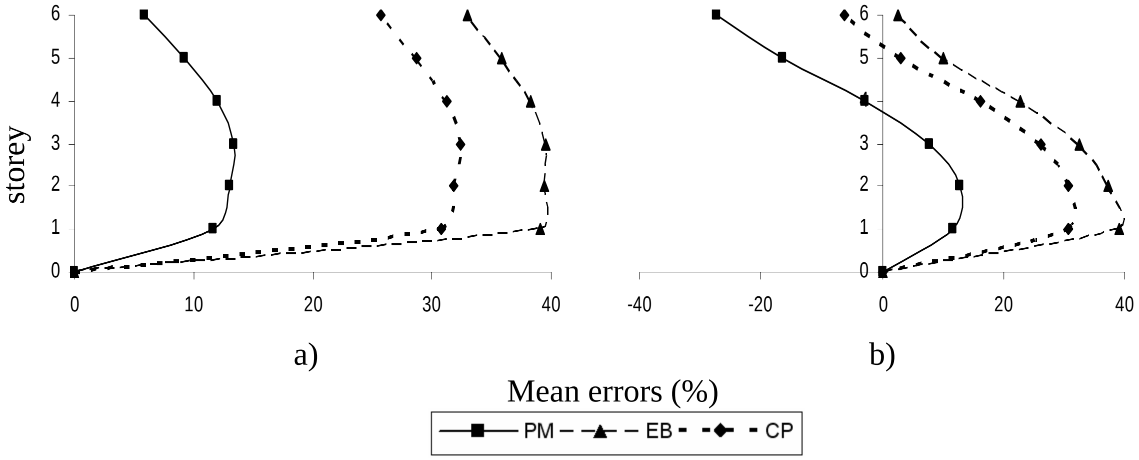
a)

b)

Figure 19: Mean errors (%) of storey displacements (a) and drifts (b) - Frame SS6.

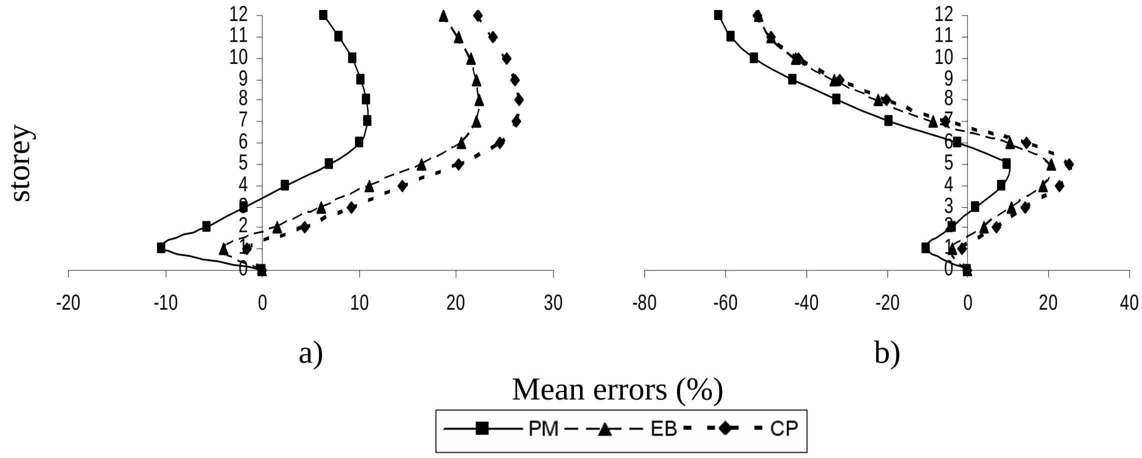

a) b)

Figure 20: Mean errors (%) of storey displacements (a) and drifts (b) - Frame SS12.

5 CONCLUSIONS

A new energy-based Nonlinear Static Procedure (NSP) is formulated and evaluated in this paper. According to this procedure

- The properties of the E-SDOF system are determined by equating the external work of the lateral loads acting on the MDOF system under consideration to the strain energy of the E-SDOF system, and
- In contrast to other energy-based procedures, this energy equivalence is used to derive a modified resisting force of the E-SDOF system, instead of an energy-based displacement.

According to the results of an extensive parametric study the following conclusions can be drawn:

- The proposed method leads to a more accurate estimation of the target roof displacement.
- In most cases the values of other significant response parameters (e.g., displacements and drifts) are more accurate too.
- None of the three compared pushover procedures can provide reasonable estimations of drifts at upper storeys of tall buildings due to higher modes effects.

For the present, the proposed methodology can be rigorously applied to low and medium rise planar frame structures with rather small contributions of higher mode effects. However, it can be easily extended in a manner that allows its application to high rise planar frames with significant contributions of higher modes as well as to multi-storey asymmetric 3D-buildings.

Finally, it is worth noticing that the implementation of the proposed procedure in existing analysis software can be accomplished without particular difficulty.

REFERENCES

[1] American Society of Civil Engineers, *Seismic Rehabilitation of Existing Buildings.* ASCE/SEI 41-06 Standard, 2008.

[2] Applied Technology Council (ATC), *Seismic Evaluation and Retrofit of Concrete Buildings, Vol. 1.* Report No. ATC-40, Redwood City, CA, 1996.

[3] European Committee for Standardization, *Eurocode 8: Design of Structures for Earthquake Resistance.* B-1050 Brussels, 2004.

[4] H. Krawinkler, G.D.P.K. Seneviratna, Prons and cons of a pushover analysis of seismic performance evaluation. *Engineering Structures*, **20**, 452–464, 1998.

[5] A.K. Chopra, R.K. Goel, *A Modal Pushover Analysis Procedure to estimating seismic demands of buildings: theory and preliminary evaluation, PEER Report 2001/03*. Pacific Earthquake Engineering Research Center, University of California, Berkeley, 2001.

[6] E.Hernadez-Montes, O.S. Kwon, M.A. Aschheim, An energy-based formulation for first- and multiple-mode nonlinear static (pushover) analysis. *Journal of Earthquake Engineering*, Vol. **8**, No. **1**, 69-88, 2004.

[7] A. Parducci, F. Comodini, M. Lucarelli, M. Mezzi, E. Tomassoli, Energy-based non linear static analysis. *1st European Conference on Earthquake Engineering and Seismology*, Geneva, Switzerland, September 3-8, 2006.

[8] G. Oliveto, I. Calio, M. Marleta, Seismic Resistance and Vulnerability of Reinforced Concrete Buildings not Designed for Earthquake Action. *Innovative Approaches to Earthquake Engineering*, WIT Press, UK, 119-201, 2001.

[9] B. Biondi, G. Oliveto, Energy Based Modal Pushover Analysis for the Estimate of the Seismic Response of Irregular Buildings. *5th European Workshop on the Seismic Behaviour of Irregular and Complex Structures*, *5EWICS*, Catania, Italy, September 16-17, 2008.

[10] G.E. Manoukas, A.M. Athanatopoulou, I.E. Avramidis, Static Pushover Analysis Based on an Energy-Equivalent SDOF System. *Earthquake Spectra*, Vol. **27**, No. **1**, 1-16, 2011.

[11] Federal Emergency Management Agency - Applied Technology Council (ATC), *Improvement of Nonlinear Static Seismic Analysis Procedures.* Report No. ATC-55 (FEMA 440), 2004.

[12] G.E. Manoukas, A.M. Athanatopoulou, I.E. Avramidis, Comparative evaluation of static pushover analysis' variations according to modern codes (in Greek). *15th Hellenic Conference on R/C structures,* Alexandroupoli, Greece, October 25-27, 2006.

COMPDYN 2011
3rd ECCOMAS Thematic Conference on
Computational Methods in Structural Dynamics and Earthquake Engineering
M. Papadrakakis, M. Fragiadakis, V. Plevris (eds.)
Corfu, Greece, 25–28 May 2011

RELIABILITY-BASED ASSESSMENT OF SEISMIC POUNDING RISK BETWEEN ADJACENT BUILDINGS

E. Tubaldi[1], **M. Barbato**[2]

[1] Dipartimento di Architettura Costruzione e Strutture, Marche Polytechnic University,
Via Brecce Bianche, 60131, Ancona (AN), Italy
e-mail: etubaldi@libero.it

[2] Department of Civil & Environmental Engineering, Louisiana State University and A&M College,
3531 Patrick F. Taylor Hall, Nicholson Extension, Baton Rouge, Louisiana 70803, USA
mbarbato@lsu.edu

Keywords: Pounding, performance based earthquake engineering, non stationary random process, spectral characteristics.

Abstract. *Earthquake ground motion excitation can induce pounding in adjacent buildings with inadequate separation distance. This hazard is particularly relevant in densely inhabited metropolitan areas, due to the very limited space among buildings.*

Existing procedures for minimum separation distance are based on approximations of the peak relative horizontal displacement between adjacent buildings, and are characterized by unknown safety levels. The present study proposes a reliability-based procedure for assessing the level of safety corresponding to a given value of the separation distance between adjacent buildings exhibiting linear elastic behavior. The seismic input is modeled as a nonstationary random process, and the first-passage reliability problem corresponding to the pounding event is solved employing analytical techniques involving the determination of some specific statistics of the response processes. Comparison of computed analytical results with numerical simulation results are also shown, in order to validate the proposed methodology.

The proposed procedure is employed for evaluating the reliability of simplified design code formulae used to determine building separation distances. Furthermore, the capability of the proposed method to deal with complex systems is demonstrated by assessing the effectiveness of the use of viscous dampers, according to different retrofit schemes, in reducing the pounding probability of adjacent buildings modeled as multi-degree-of-freedom systems.

1 INTRODUCTION

Earthquake ground motion excitation can induce pounding in adjacent buildings with inadequate separation distance. The corresponding risk is particularly relevant in densely inhabited metropolitan areas, due to the need of maximizing the land use and the consequent limited separation distance between adjacent buildings.

The problem of seismic pounding has been investigated by several researchers in the last two decades. A significant number of early studies focused on the definition of simplified rules, such as the Double Difference Combination (DDC) rule, for determining the peak relative displacement response of adjacent buildings at the potential pounding locations [1],[2],[3]. A critical separation distance (CSD) was defined and set equal to the mean peak relative displacement between adjacent buildings, by neglecting the associated probability of pounding. In the same context, considerable research effort was devoted to the assessment of the accuracy of code rules (e.g., the absolute sum (ABS) and square-root-of-the-sums-squared (SRSS) rule) [4] in determining the mean peak relative displacement response (i.e., the CSD) of adjacent buildings [5].

More recent studies have adopted a probabilistic approach for the assessment of the seismic pounding risk. In Lin [6], a method was proposed to estimate the first two statistical moments of the random variables describing the peak relative displacement response between linear elastic structures subjected to stationary base excitation. In Lin and Weng [7], a numerical simulation approach was suggested to evaluate the pounding probability, over a 50-year design lifetime, of adjacent buildings separated by the code-specified CSD. The latter study considered both the uncertainty affecting the seismic input intensity (by using a proper hazard model) and the record-to-record variability (by using artificially generated spectrum-compatible ground acceleration time histories as input loading). The buildings were modeled as multi-degree of freedom systems with inelastic behavior and deterministic properties. In Hong et al. [8], a procedure was developed to assess the fractiles of the CSD between linear elastic systems with deterministic and uncertain structural properties subjected to stationary base excitation. The previous study was later extended by Wang and Hong [9] to include nonstationary seismic input.

Despite the numerous studies available in the literature on seismic pounding, to the best of the authors' knowledge, a reliability-based methodology for the evaluation of the safety levels associated with specified CSDs is still needed. In addition, the gradual progress of seismic design codes from a prescriptive to a performance-based design philosophy generates a significant need for new advanced, accurate, and computationally efficient reliability-based methodologies for the assessment and mitigation of seismic pounding risk.

This paper presents a fully probabilistic methodology for assessing the seismic pounding risk between adjacent buildings with linear behavior. This methodology is consistent with and can be easily incorporated into a performance-based earthquake engineering (PBEE) approach such as the Pacific Earthquake Engineering Research center (PEER) framework [10],[11]. The presented methodology considers the uncertainty affecting both the seismic input (i.e., site hazard and record-to-record variability) and the parameters used to describe the structural systems of interest (i.e., material properties, geometry, and damping properties). The seismic input is modeled as a nonstationary random process. The seismic pounding risk is computed from the solution of a first-passage reliability problem. While the approach proposed is general, the methodology presented here is specialized to linear elastic systems subjected to Gaussian loading. Under these assumptions, approximate analytical solutions and efficient simulation techniques can be used to solve the relevant first-passage reliability problem. Thus, this methodology is appropriate for structural systems that remain in their linear elastic behavior range before pounding (which is a very common condition for low values of the CSDs and, thus, high seismic pounding risk), although it can be extended to account for nonlinear behavior of the considered structural systems.

2 PBEE FRAMEWORK FOR SEISMIC POUNDING RISK ASSESSMENT

The PEER PBEE framework is a general probabilistic methodology, based on the total probability theorem, for risk assessment and design of structures subjected to seismic hazard [10],[11]. The PEER PBEE methodology involves four probabilistic analysis components: (1) probabilistic seismic hazard analysis (PSHA), (2) probabilistic seismic demand analysis (PSDA), (3) probabilistic seismic capacity analysis (PSCA), and (4) probabilistic seismic loss analysis (PSLA). PSHA provides the probabilistic description of an appropriate ground motion intensity measure (*IM*), usually expressed as mean annual frequency (MAF) $\nu_{IM}(im)$ of exceedance of a specific value *im*. PSDA provides the statistical description of structural response parameters of interest, usually referred to as engineering demand parameters (*EDP*s), conditional to the value of the seismic intensity *IM*. PSCA consists in computing the probability of exceeding a specified physical limit-state, defined by structure-specific damage measures (*DM*s), and conditional to the values of the *EDP*s. Finally, PSLA provides the probabilistic description of a decision variable (*DV*), which is a measurable attribute of a specific structural performance and can be defined in terms of cost/benefit for the users and/or the society.

The reliability-based procedure developed in this paper consists in computing the mean annual frequency (MAF) of pounding, ν_p, between two adjacent buildings. This procedure is a specialization for the seismic pounding problem of the first three steps of the general PEER PBEE framework (i.e., PSLA is out of the scope of this paper). It is noteworthy that the proposed approach is conceptually very different from the computation of the CSD, which does not explicitly provide the probability of pounding associated with a given separation distance. The computation of the MAF of pounding can be expressed as

$$\nu_p = \int_{edp} \int_{im} G_{DM|EDP}\left(dm|edp\right) \cdot \mathrm{d}G_{EDP|IM}\left(edp|im\right) \cdot \left|\mathrm{d}\nu_{IM}\left(im\right)\right| \tag{1}$$

in which, $G_{DM|EDP}\left(dm|edp\right)$ = cumulative probability function of variable *DM* conditional to *EDP* = *edp*, and $G_{EDP|IM}\left(edp|im\right)$ = cumulative probability function of variable *EDP* conditional to *IM* = *im*, where upper case symbols indicate random variables and lower case symbols denote specific values assumed by the corresponding random variable. The *IM* must be selected so that it can be readily related to the stochastic description of an appropriate random process model for the input ground motion. This selection must also account for sufficiency and efficiency of the *IM* in describing the effects of the ground motion excitation on the structural response [12]. However, an exhaustive selection of appropriate *IM*s for different types of structures and structural performances is outside the scope of this paper.

The maximum value $U_{rel,\max}$ of the relative distance $U_{rel}(t)$ between the adjacent buildings observed during the seismic event (i.e., for $t \in \left[0, t_{\max}\right]$, with t = time and $t_{\max}$ = duration of the seismic event) is assumed here as *EDP*. The probabilistic distribution of $U_{rel,\max}$ reflects the record-to-record variability of the ground motions expected to occur at the site for a given intensity, as well as the effects of the uncertainty in the parameters used to describe the structural model. Finally, the pounding event is assumed as the controlling limit-state in PSCA, by using the following limit-state function, g:

$$g = \Xi - U_{rel,\max} \tag{2}$$

in which Ξ = random variable describing the building separation distance, and the pounding event corresponds to $g \le 0$. Thus, $G_{EDP|IM}\left(epd\middle|im\right) = P\left[U_{rel,\max} \ge u\middle|IM = im\right]$ and $G_{DM|EDP}\left(dm\middle|edp\right) = P\left[g < 0\middle|U_{rel,\max} = u\right]$. An important intermediate result of the procedure is the convolution of PSCA and PSDA, also called fragility analysis, which yields a fragility curve. Fragility curves describe the probability $P_{p|IM}$ of pounding conditional on the seismic intensity, i.e.,

$$P_{p|IM} = \int_{edp} G_{DM|EDP}\left(dm\middle|edp\right) \cdot \mathrm{d}G_{EDP|IM}\left(edp\middle|im\right) \tag{3}$$

The MAF of pounding, ν_p , can be used to compute the MAF of exceeding a specified value of *DV*, e.g., the MAF of repair cost due to pounding damage. The computation of the latter quantity requires the definition of a realistic loss model, based on appropriate structural response models (e.g., dynamic impact between adjacent systems) and damage models (e.g., damage produced by floor-to-floor and floor-to-column pounding). Structural response and damage models involve the definition of other *EDP*s and *DM*s, respectively, in addition to those already employed in this paper for assessing the pounding risk. Several structural response and damage models available in the literature could be employed to define an appropriate loss model [13],[14],[15],[16].

In addition, ν_P can be directly used to determine the pounding risk, $P_p(t_L)$, for a given structure over its design life (t_L = design lifetime, e.g., 50 years). Assuming that the occurrence of a pounding event can be described by a Poisson process and that the buildings are immediately restored to their original condition after pounding occurs, $P_p(t_L)$ can be easily computed as

$$P_p\left(t_L\right) = 1 - e^{-\nu_p \cdot t_L} \tag{4}$$

3 SEISMIC POUNDING RISK ASSESSMENT METHODOLOGY

Fragility analysis is the most computationally challenging component of the probabilistic PBEE framework. A simple and general approach for fragility analysis in seismic pounding assessment is provided by Monte Carlo simulation (MCS) [5],[7]. For any given value of *IM*, MCS-based fragility analysis requires (1) the definition of a set of ground motions that are selected from an appropriate database of real records or generated from an appropriate random process, (2) the sampling of the structural parameters that define the structural systems and of their separation distances, (3) the numerical simulation of the structural response for each ground motion time history and each set of structural parameters and separation distances, and (4) the evaluation of $P_{p|IM}$ as the ratio between the number of failures and the number of samples. However, the computational cost associated with MCS can be very high and even prohibitive when small failure probabilities need to be estimated by numerically simulating the time history response of complex multi-degree-of-freedom (MDOF) systems.

In this paper, an efficient combination of analytical and simulation techniques is proposed for the calculation of $P_{p|IM}$ under the assumptions of linear elastic behavior for the buildings and of Gaussian input ground motion. The methodology is described first for linear elastic systems with deterministic structural properties and separation distance, and then generalized to stochastic linear systems.

It is noteworthy that, for low values of the building separation distance ξ, the buildings are expected to behave elastically before pounding occurs, while the assumption of linear behavior of the buildings before pounding becomes less realistic for larger values of ξ. If the buildings are expected to enter their nonlinear behavior before pounding, the methodology described in the remainder of this paper needs to be extended to nonlinear systems, e.g., by using statistical linearization techniques [17] or subset simulation [18]. This extension is out of the scope of this paper.

3.1 Linear systems with deterministic structural properties

The computation of the conditional failure probability $P_{p|IM}$ can be expressed in the form of a single-barrier first-passage reliability problem as [5],[9]

$$P_{p|IM} = P\left\{ \max_{0 \le t \le t_{\max}} \left[U_{rel}\left(t\right) \right] \ge \xi \middle| IM = im \right\} \tag{5}$$

in which $U_{rel}\left(t\right) = U_{\mathrm{A}}\left(t\right) - U_{\mathrm{B}}\left(t\right)$, $U_{\mathrm{A}}(t)$ and $U_{\mathrm{B}}(t)$ = displacement response of the adjacent buildings A and B at the (most likely) pounding location, and ξ = deterministic value of the building separation distance (Fig. 1).

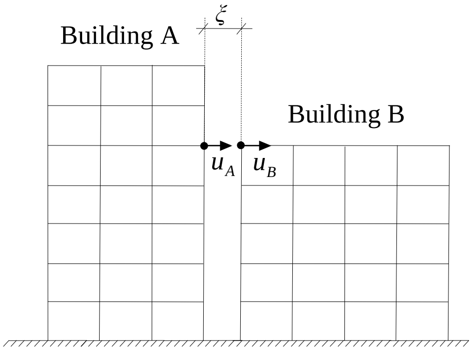

Fig. 1. Geometric description of the pounding problem between adjacent buildings.

Under the hypotheses of deterministic linear elastic systems subjected to Gaussian loading processes and deterministic threshold, several analytical approximations of $P_{p|IM}$ exist in the literature [19],[20],[21],[22]. These analytical approximations require computing the following statistics of the relative displacement process $U_{rel}\left(t\right)$ for a given $IM = im$: $\sigma^2_{U_{rel}}\left(t\right)$ = variance of $U_{rel}\left(t\right)$, $\sigma^2_{\dot{U}_{rel}}\left(t\right)$ = variance of the relative velocity process $\dot{U}_{rel}\left(t\right)$, $\rho_{U_{rel}\dot{U}_{rel}}\left(t\right)$ = correlation coefficient between $U_{rel}\left(t\right)$ and $\dot{U}_{rel}\left(t\right)$, $\omega_{c,U_{rel}}\left(t\right)$ = time-variant central frequency of $U_{rel}\left(t\right)$, and $q_{U_{rel}}\left(t\right)$ = bandwidth parameter of $U_{rel}\left(t\right)$.These statistics can be obtained from the spectral characteristics of order zero to two of process $U_{rel}\left(t\right)$ [23],[24],[25].

Following the methodology described in Barbato and Conte [24], a state-space formulation of the equations of motion for the two buildings is employed to compute exactly and in closed-form the required spectral characteristics. The seismic input is modeled as a time-modulated Gaussian colored noise process. For this specific input ground motion process, the spectral characteristics of the displacement processes (and of any response process obtained as a linear combination of the displacement processes) are available in exact closed-form for SDOF systems and both classically and non-classically damped MDOF systems [25].

The equations of motion for the linear system constituted by two non-connected adjacent buildings can be expressed as follows:

$$\mathbf{m}\cdot\ddot{\mathbf{U}}(t)+\mathbf{c}\cdot\dot{\mathbf{U}}(t)+\mathbf{k}\cdot\mathbf{U}(t)=\mathbf{p}\cdot F(t) \tag{6}$$

in which $\mathbf{m}=\begin{pmatrix}\mathbf{m}_\mathrm{A} & \mathbf{0}\\ \mathbf{0} & \mathbf{m}_\mathrm{B}\end{pmatrix}$, $\mathbf{c}=\begin{pmatrix}\mathbf{c}_\mathrm{A} & \mathbf{0}\\ \mathbf{0} & \mathbf{c}_\mathrm{B}\end{pmatrix}$, $\mathbf{k}=\begin{pmatrix}\mathbf{k}_\mathrm{A} & \mathbf{0}\\ \mathbf{0} & \mathbf{k}_\mathrm{B}\end{pmatrix}$, $\mathbf{U}=\begin{pmatrix}\mathbf{U}_\mathrm{A}\\ \mathbf{U}_\mathrm{B}\end{pmatrix}$, $\mathbf{m}_i$, $\mathbf{k}_i$, $\mathbf{c}_i$ and $\mathbf{U}_i$ = mass matrix, damping matrix, stiffness matrix, and vector of nodal displacements of building *i*, respectively (*i* = A, B), $\mathbf{p}$ = load distribution vector, $F(t)$ = scalar function describing the time-history of the external loading (input random process), and a superposed dot denotes differentiation with respect to time. It is noteworthy that connections between the two buildings (e.g., damping devices interposed between the building to mitigate seismic pounding risk) can be easily modeled by introducing the appropriate terms in matrix $\mathbf{c}$. The response process of interest $U_{rel}(t)$ can be related to the displacement response vector $\mathbf{U}(t)$ by means of a linear operator $\mathbf{b}$ as $U_{rel}(t)=\mathbf{b}\cdot\mathbf{U}(t)$.

The probability of pounding conditional on $IM = im$ is given by

$$P_{p|IM}=1-P\left[U_{rel}(t=0)<\xi\middle|IM=im\right]\cdot\exp\left\{-\int_0^{t_{\max}} h_{U_{rel}|im}(\xi,\tau)\,d\tau\right\} \tag{7}$$

in which $P\left[U_{rel}(t=0)<\xi\middle|IM=im\right]$ = probability that the random process $U_{rel}(t)$ is below the threshold ξ at time $t=0$, and $h_{u_{rel}|im}(\xi,\tau)$ = time-variant hazard function (i.e., up-crossing rate of threshold ξ conditioned on zero up-crossing before time *t*) conditional on $IM = im$. For systems with at rest initial conditions, $P\left[U_{rel}(t=0)<\xi\middle|IM=im\right]=1$.

To date, no exact closed-form expressions exist for the time-variant hazard function $h_{U_{rel}|im}(\xi,t)$. However, several approximate solutions are available in the literature, e.g., Poisson's (P), $h^{(\mathrm{P})}_{U_{rel}|im}(\xi,t)=\nu_{U_{rel}|im}(\xi,t)$, classical Vanmarcke's (cVM), $h^{(\mathrm{cVM})}_{U_{rel}|im}(\xi,t)$, and modified Vanmarcke's (mVM), $h^{(\mathrm{mVM})}_{U_{rel}|im}(\xi,t)$, approximations [22],[26]. These analytical approximations can be readily computed based on the closed-form expressions of the spectral characteristics of process $U_{rel}(t)$, as shown in Barbato and Vasta [25]. In addition, for linear elastic systems subjected to Gaussian loading, $P_{p|IM}$ can be efficiently and accurately estimated by using the Importance Sampling using Elementary Events (ISEE) method [27].

3.2 Linear systems with uncertain structural properties and separation distance

In addition to the uncertainty in the seismic input, significant uncertainty can be found in geometrical, mechanical, and material properties characterizing the structural systems and their models. Hereinafter, the uncertainty in geometrical, mechanical, and material properties of the structural models, as well as in their separation distance, Ξ, is referred to as model parameter uncertainty (MPU). MPU can significantly modify the structural performance and, thus, must be considered in the assessment of seismic pounding risk.

In order to include the effects of MPU, the total probability theorem is employed to compute the conditional probability of pounding as follows:

$$P_{p|IM} = \int_{\mathbf{X}} P_{p|IM,\mathbf{X}}\left(\mathbf{x}\right)\cdot f\left(\mathbf{x}\right)\cdot \mathrm{d}\mathbf{x} = E_{\mathbf{X}}\left[P_{p|IM,\mathbf{X}}\right] \tag{8}$$

in which $\mathbf{X}$ = vector of uncertain model parameters (including the uncertain separation distance Ξ) with joint probability density function $f_{\mathbf{X}}\left(\mathbf{x}\right)$, and $P_{p|IM,\mathbf{X}}\left(\mathbf{x}\right)$ = probability of pounding conditional on $\mathbf{X}$ and *IM*.

MCS, or any variance reduction technique such as stratified sampling, can be employed to evaluate $P_{p|IM}$ in Eq. (8). For example, Latin hypercube sampling (LHS) can be employed for its computational efficiency [28]. The samples of $\mathbf{X}$ generated by using LHS can be used to define a set of deterministic linear elastic models with deterministic separation distance, for which the conditional probability of pounding can be computed as in Eq.(7).

4 APPLICATION EXAMPLES

In this section, the proposed methodology is applied to: (1) compute the pounding risk for SDOF systems with deterministic model parameters, (2) evaluate the reliability of simplified design code formulae used to determine building separation distance, and (3) to evaluate the effectiveness of different retrofit solutions using viscous dampers in reducing the pounding risk for deterministic MDOF models of multistory buildings. In all the application examples considered here, the input ground acceleration is modeled by a time-modulated Gaussian process. The time-modulating function, $I(t)$, is represented by the Shinozuka-Sato's function [29], i.e.,

$$I\left(t\right) = c\cdot\left(e^{-b_1\cdot t} - e^{-b_2\cdot t}\right)\cdot H\left(t\right) \tag{9}$$

in which $b_1 = 0.045\pi\ \mathrm{s}^{-1}$, $b_2 = 0.050\pi\ \mathrm{s}^{-1}$, $c = 25.812$, and $H(t)$ = unit step function. A duration $t_{\max} = 30\mathrm{s}$ is considered for the seismic excitation.

The power spectral density (PSD) of the embedded stationary process is described by the widely-used Kanai-Tajimi model, as modified by Clough and Penzien [30], i.e.,

$$S_{CP}\left(\omega\right) = S_0 \frac{\omega_g^4 + 4\xi_g^2\omega^2\omega_g^2}{\left[\omega_g^2 - \omega^2\right]^2 + 4\xi_g^2\omega^2\omega_g^2}\cdot\frac{\omega^4}{\left[\omega_f^2 - \omega^2\right]^2 + 4\xi_f^2\omega^2\omega_f^2} \tag{10}$$

in which S_0 = amplitude of the bedrock excitation spectrum, considered to be a white process, ω_g and ξ_g = fundamental circular frequency and damping factor of the soil, respectively, and ω_f and ξ_f = parameters describing the Clough-Penzien filter. The values of the parameters employed for all the applications are $\omega_g = 12.5\mathrm{rad/s}$, $\xi_g = 0.6$, $\omega_f = 2\mathrm{rad/s}$, and $\xi_f = 0.7$. The PSD function in Eq. (10) is shown in Fig. 2(a) for $S_0 = 1$.

The peak ground acceleration, *PGA*, is assumed as *IM*. In order to derive the fragility curves in terms of the selected *IM*, the relationship between the parameter S_0 of the Kanai-Tajimi spectrum and the *PGA* at the site is assessed empirically. A set of 500 synthetic stationary ground motion records are generated using the spectral representation method [31] based on the PSD function given in Eq. (10) with $S_0 = 1$. Each ground motion realization is then modulated in time using the function defined in Eq. (9). The peak ground acceleration corresponding to $S_0 = 1$, $PGA_{S_0=1}$, is estimated as the mean of the PGAs of the sampled ground motion time histories. The values of S_0 corresponding to different values of PGA are obtained as follows:

$$S_0 = \left(\frac{PGA}{PGA_{S_0=1}} \right)^2 \tag{11}$$

In this study, the site hazard curve is expressed in the approximate form used in Cornell et al. [32], i.e.,

$$\nu_{IM}(im) = P\left[IM \geq im \middle| 1yr \right] = k_0 \cdot im^{-k_1} \tag{12}$$

in which k_0 and k_1 = parameters obtained by fitting a straight line through two known points of the site hazard curve in logarithmic scale. The site hazard curve is taken from Eurocode 8-Part 2 [33], assuming that, for the site of interest, PGA = 0.3g corresponds to a return period of 475 years. Using $k_1 = 2.857$ [34], the site hazard curve becomes (see Fig. 2(b))

$$\nu_{PGA}(pga) = 6.734 \cdot 10^{-5} \cdot pga^{-2.857} \tag{13}$$

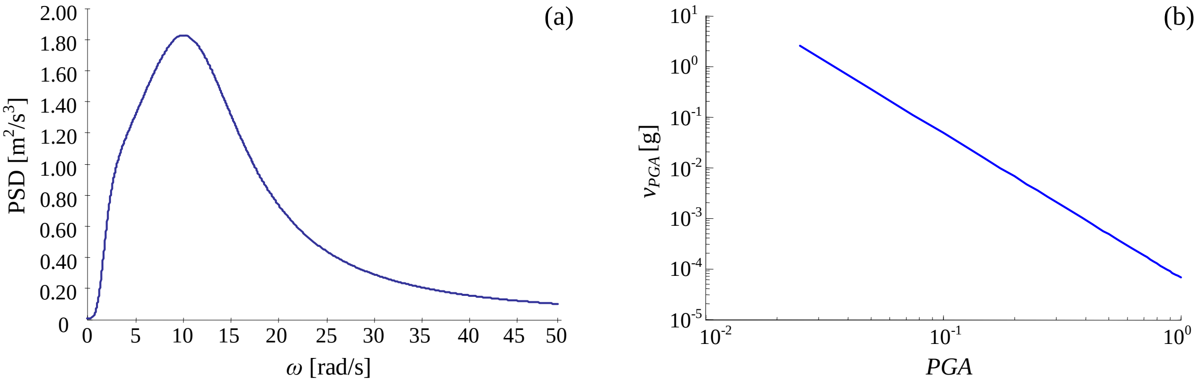

Fig. 2. Input ground motion: (a) PSD function of the embedded stationary process, and (b) site hazard curve.

4.1 Pounding risk for linear SDOF systems with deterministic model parameters

The first application example consists in the assessment of the pounding risk between two adjacent buildings modeled as deterministic linear elastic SDOF systems with periods t_A and t_B, and damping ratios $\zeta_A = \zeta_B$ = 5%. The conditional probability of pounding $P_{p|IM}$ is calculated using the approximate analytical hazard functions $h^{(\mathrm{P})}_{U_{rel}|im}(\xi,t)$, $h^{(\mathrm{cVM})}_{U_{rel}|im}(\xi,t)$, and $h^{(\mathrm{mVM})}_{U_{rel}|im}(\xi,t)$, for a deterministic distance between the buildings $\xi = 0.1$m and for two different combinations of natural periods of the two systems, i.e., (1) t_A = 0.5s and t_B = 1.0s, referred to as well separated natural periods (Fig. 3(a)), and (2) t_A = 0.9s and t_B = 1.0s, referred to as close natural periods (Fig. 3(b)). The obtained conditional probabilities are presented in Fig. 3 as fragility curves and compared with the corresponding results obtained using ISEE method [27], which are assumed as reference solution.

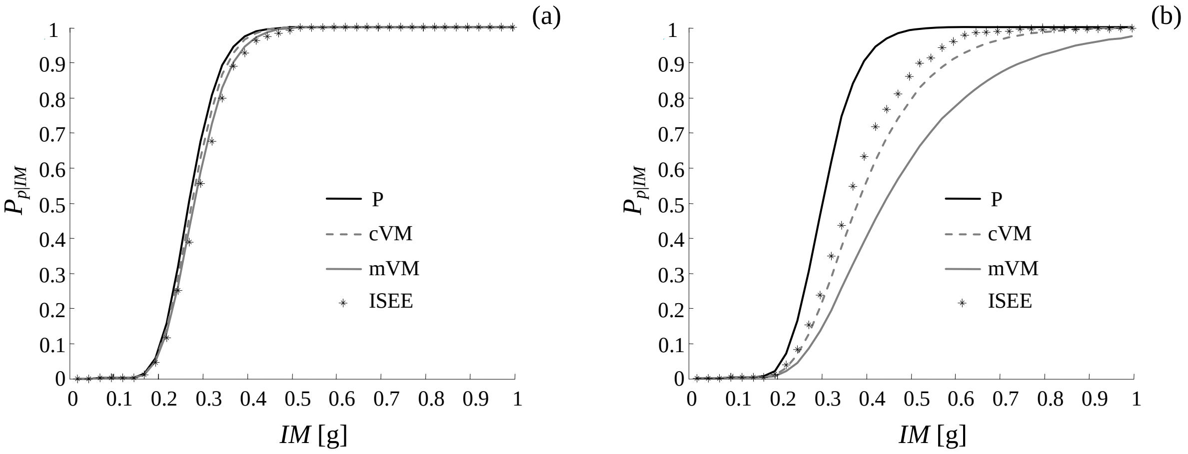

Fig. 3. Fragility curves for $\xi = 0.1$m: (a) $t_A = 0.5$s and $t_B = 1.0$s, and (b) $t_A = 0.9$s and $t_B = 1.0$s.

In the case of well separated natural periods for the structures (Fig. 3(a)), the fragility curves estimated using the P, cVM, and mVM approximations are very similar and close to the fragility curves obtained using the ISEE method. In the case of close natural periods (Fig. 3(b)), the fragility curves estimated with the approximate analytical methods show significant differences, and only the cVM approximation provides results that are close to the fragility curves estimated using the ISEE method. The observed result can be explained by recognizing that the relative displacement process $U_{rel}(t)$ can be interpreted as a response process of a two-degree-of-freedom system. This multi-modal characteristic of $U_{rel}(t)$ can significantly affect the accuracy of the different approximations of the time-variant hazard function $h_{U_{rel}|im}(\xi,t)$ [35]. In the case of well separated natural periods, the contribution of the higher period vibration mode to $U_{rel}(t)$ is significantly larger than the contribution of the lower period vibration mode. By contrast, in the case of close natural periods, both vibration modes provide a significant contribution to the response process.

Fig. 4 shows the MAF of pounding, v_p, as a function of the building separation distance ξ (in semi-logarithmic scale) for the cases of well separated natural periods (Fig. 4 (a)) and of close natural periods (Fig. 4(b)), respectively. The estimates of the MAF of pounding obtained using the analytical approximations (P, cVM, and mVM) of the hazard function are compared to the corresponding estimate obtained using the ISEE method. Fig. 5 plots (in semi-logarithmic scale) the pounding risk for a design lifetime of 50 years, evaluated according to Eq. (4), for the same two cases of well separated and close natural periods. Considerations similar to the ones made for the fragility curves can be made also for the MAF of pounding and the 50-year pounding risk, i.e., the analytical approximations provide very accurate results for the case of well separated natural periods and less accurate results for the case of close natural periods, with the exception of the cVM approximation, which is accurate in both cases.

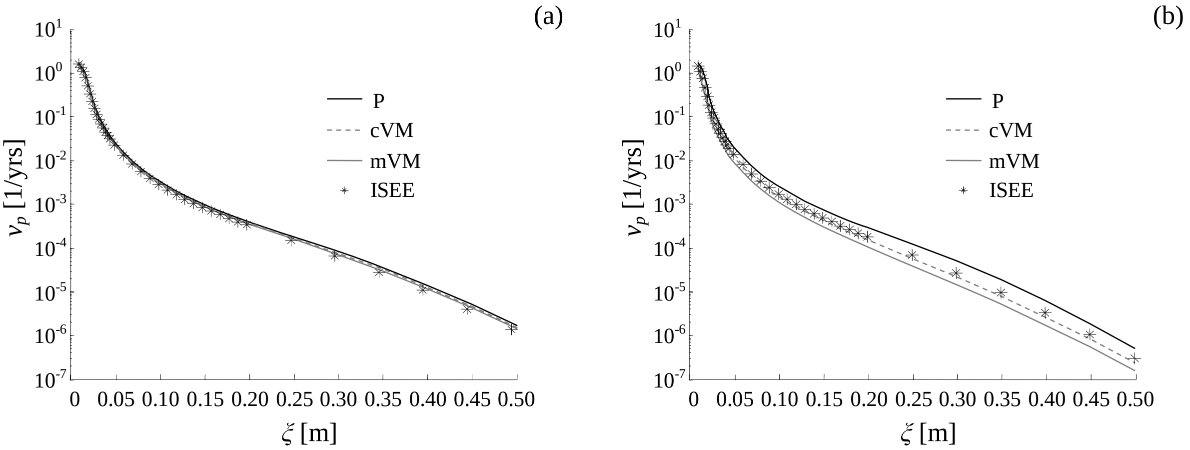

Fig. 4. MAF of pounding for varying separation distance: (a) t_A = 0.5s and t_B = 1.0s, and (b) t_A = 0.9s and t_B = 1.0s.

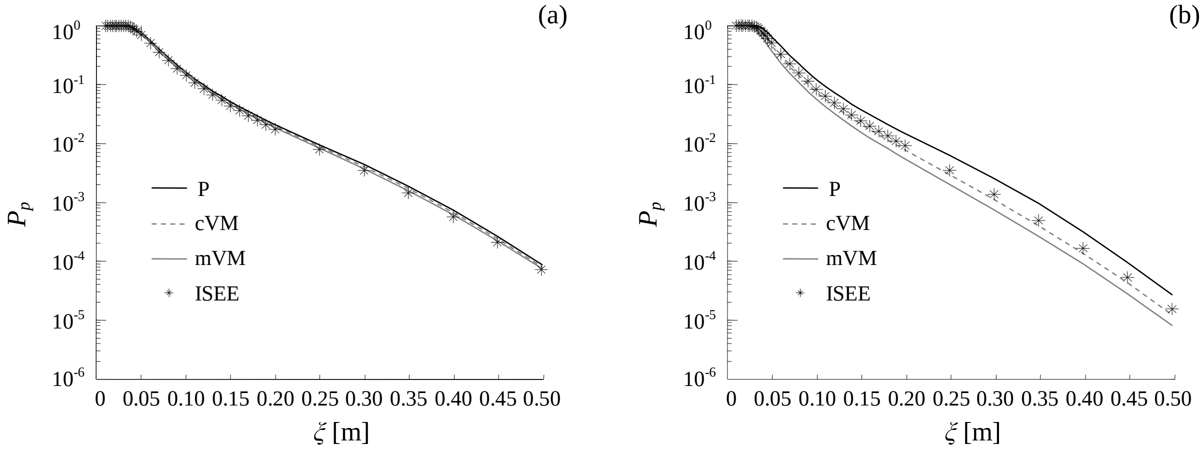

Fig. 5. 50-year pounding risk for varying separation distance: (a) t_A = 0.5s and t_B = 1.0s, and (b) t_A = 0.9s and t_B = 1.0s.

It is observed that the Poisson’s approximation of the time-variant hazard function always yields conservative results, while the mVM approximation underestimates the risk computed using the ISEE method for the case of close natural periods. Similar results have been documented for the first-passage reliability problem of SDOF and MDOF systems subjected to time-modulated white and colored noise excitations [26].

4.2 Reliability of code formulae

The proposed methodology is applied here to evaluate the pounding risk corresponding to the separation distance prescribed by anti-seismic design codes. In order to avoid pounding between new adjacent buildings, current seismic design codes (e.g., [4],[33]) prescribe a minimum clearance to be provided between the structures. This minimum clearance between two adjacent buildings is assumed equal to the expected valued of the peak relative displacement (or CSD), for a given site-specific earthquake action and a given value of the seismic intensity (hazard level). Given the seismic input, the peak relative displacement is obtained by combining (using simplified combination rules) the values of the peak displacements of the two adjacent structural systems, which are computed using (deterministic) structural analysis. The most commonly employed rules are the ABS method or the slightly more accurate SRSS method. The major limit of these approximate rules is that they neglect the response phase differences between the adjacent structures. In order to overcome this drawback, the use of the Double Difference Combination rule for determining the CSD has been proposed and investigated by several researchers [1], [2],[3].

In the application presented here, the values of the CSD according to the ABS, SRSS, and DDC rules are calculated following the procedure described in [5]. This procedure involves (1) generating a set of 500 samples of input ground motion time histories for the reference value of the peak ground acceleration, (2) computing the corresponding 500 peak displacement responses of systems A and B ($U_{\mathrm{A,max}}$ and $U_{\mathrm{B,max}}$), (3) computing the sample means $\bar{U}_{\mathrm{A,max}}$ and $\bar{U}_{\mathrm{B,max}}$ of $U_{\mathrm{A,max}}$ and $U_{\mathrm{B,max}}$, respectively, and (4) combining $\bar{U}_{\mathrm{A,max}}$ and $\bar{U}_{\mathrm{B,max}}$ using the ABS, the SRSS, and the DDC rule to derive estimate of the peak relative displacement $\bar{U}_{rel,\max}$.

Table 1 shows the values of the separation distance computed according to different combination rules and the corresponding 50-year probability of failure, computed based on the cVM approximation of the time-variant hazard function.

t_{A} = 0.5s and t_{B} = 1s				t_{A} = 0.9s and t_{B} = 1s			
	ABS	SRSS	DDC		ABS	SRSS	DDC
ξ [m]	0.1379	0.1049	0.1042	ξ [m]	0.1832	0.1298	0.0946
Pp	0.0620	0.1351	0.1376	Pp	0.0106	0.0334	0.0857

Table 1: Critical separation distance and corresponding 50-year pounding risk using different combination rules.

It is observed that the CSDs obtained using simplified combination rules yield inconsistent values of the failure probability, which are also strongly dependent on the natural periods of the two adjacent buildings. It is concluded that a methodology is still needed to determine the CSD between adjacent buildings corresponding to consistent safety levels for different combinations of the buildings' natural periods and location's seismic hazard.

4.3 MDOF models of multistory buildings retrofitted by means of viscous dampers

As a third application, the proposed methodology is employed to assess the risk of pounding between two adjacent multistory buildings modeled as linear MDOF systems, before and after retrofit with viscous dampers (Fig. 6). Different retrofit solutions are considered and their effectiveness in reducing the seismic pounding risk is compared (Fig. 6(b)). The considered buildings are steel moment-resisting frames with shear-type behavior. The properties of the buildings are taken from Lin [36]. Building A is a six-story building with story stiffness k_A = 548,183kN/m (equal for every story) and floor mass m_A = 454.545tons (equal for each floor), building B is a four-story building with story stiffness k_B = 470,840kN/m and floor mass m_B = 454.545tons. A Rayleigh-type damping matrix $\mathbf{c_R}$ is used to model the inherent buildings' damping and is built by considering a damping ratio ζ_R = 2% for the first two vibration modes of each system. MPU is not considered in this application. The fundamental vibration periods of building A and B are t_A = 0.751s and t_B = 0.562s, respectively.

The following six different retrofit solutions, based on the use of braces with purely viscous behavior [37], are considered: (1) braces located at each story of both buildings (retrofit scheme 1), (2) braces located at all stories of the tall building only (retrofit scheme 2), (3) braces located at all stories of the short building only (retrofit scheme 3), (4) braces located at the lower four stories of the tall building only (retrofit scheme 4), (5) braces located at the lower four stories of both buildings, and (6) a single brace located at the first story of the tall building only. The two buildings before retrofit are shown in Fig. 6(a), while the six retrofit schemes are shown in Fig. 6(b). The viscous braces provide an additional source of damping, modeled by means of a damping matrix $\mathbf{c_V}$. The total damping matrix for the two buildings' systems becomes $\mathbf{c} = \mathbf{c_R} + \mathbf{c_V}$. The damping coefficient corresponding to the dampers at each floor of buildings A and B is c_d = 10,000kN·s/m. The systems corresponding to retrofit schemes 4, 5, and 6 are non-classically damped and their analysis requires the use of the complex modal analysis technique [25].

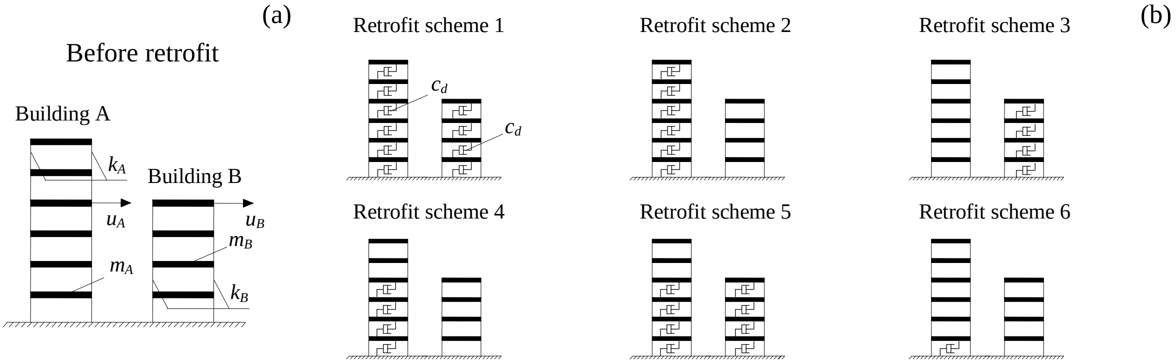

Fig. 6. Pounding between adjacent multistory buildings: (a) building A and B before retrofit, and (b) different retrofit schemes considered in this study.

Fig. 7(a) shows three different analytical estimates (P, cVM, and mVM approximations) of the 50-year probability of pounding between the two un-retrofitted buildings, for different values of the separation distance. Fig. also reports the 50-year probability of pounding obtained using the ISEE method, which is considered as reference solution. The analytical estimates provide a very good estimate of the pounding risk for a wide range of separation distances. In this particular case, the results obtained using the cVM hazard function give the best approximation of the ISEE results.

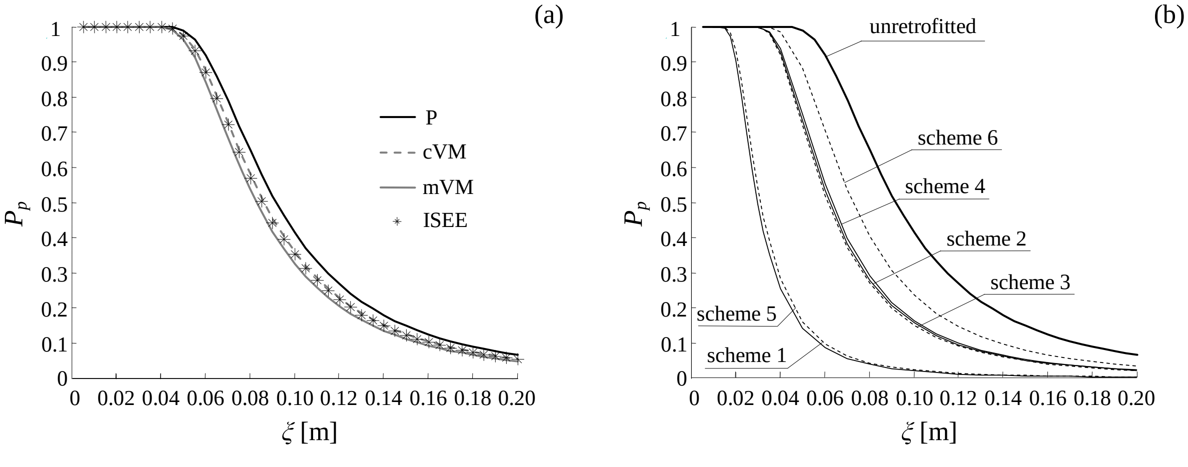

Fig. 7. Pounding risk between multistory buildings A and B: (a) comparison of different analytical solution and ISEE results, and (b) comparison of different retrofit schemes.

Fig. 7(b) shows compares the 50-year probability of pounding of the un-retrofitted buildings and of the buildings retrofitted following the six different retrofit solutions considered in this application example. The results presented in Fig. 7(b) are obtained using the cVM approximation of the hazard function.

It is observed that the use of viscous dampers can be very effective in reducing the risk of pounding between the two buildings. It is also found that the introduction of viscous braces according to scheme 3, scheme 5, and scheme 6 (corresponding to the dotted lines in Fig. 7(b)) is a very efficient retrofit solution, since it obtains a significant reduction of the pounding risk at a significantly lower retrofit cost when compared with other retrofit schemes. In particular, retrofit scheme 3 appears to achieve a very good compromise between retrofit cost and reduction of pounding risk.

CONCLUSIONS

This paper presents a fully probabilistic performance-based methodology for assessment of the seismic pounding risk between adjacent buildings. This methodology, which is consistent with the PEER PBEE framework, is able to account for all pertinent sources of uncertainty that can affect the pounding risk, e.g., uncertainty in the seismic input (i.e., site hazard and record-to-record variability) and in the parameters used to describe the structural systems of interest (i.e., material properties, geometry, damping properties, separation distance).

An efficient combination of analytical and simulation techniques is proposed for the calculation of the pounding risk under the assumptions of linear elastic behavior for the buildings and of non-stationary Gaussian input ground motion. The pounding problem is recast as a first-passage reliability problem, which is solved analytically by using the spectral characteristics (up to the second order) of the non-stationary stochastic process representing the relative displacement between the buildings. Three different analytical approximations of the time-variant hazard function are used: (1) the Poisson's approximation, (2) the classical Vanmarcke's approximation, and (3) the modified Vanmarcke's approximation. Results obtained by employing the importance sampling using elementary events method are assumed as reference solutions to evaluate the absolute and relative accuracy of the three analytical approximations considered here. The proposed formulation is very convenient in the case of linear elastic MDOF systems with both proportional and non-proportional damping, since the spectral characteristics of the relative displacement processes can be computed in exact closed form. The effects of uncertainty in the model parameters are efficiently included by means of the total probability theorem and the Latin hypercube sampling technique.

The proposed methodology is applied to investigate the risk of pounding between SDOF systems, both with deterministic and uncertain properties. With reference to this specific application example, the following observations are made. (1) The proposed combination of analytical and simulation techniques provides sufficiently accurate estimates of the pounding risk when the classical Vanmarcke's approximation is used to estimate the time-variant hazard function. (2) The accuracy of the analytical approximations of the time-variant hazard function depends on the ratio between the natural periods of the adjacent buildings. Higher accuracy is reached when the natural periods of the two buildings are well separated. (3) The Poisson's approximation of the time-variant hazard function yields always conservative estimates of the risk. (4) The design codes' simplified combination rules for calculating the critical separation distance yield inconsistent values of the pounding probability, which are also strongly dependent on the natural periods of the adjacent buildings.

In addition, the capabilities of the proposed method are demonstrated by assessing the effectiveness of the use of viscous dampers, according to different retrofit schemes, in reducing the pounding probability of adjacent multi-story buildings modeled as linear elastic multi-degree-of-freedom systems. Based on the results presented, the following considerations are made. (1) The analytical approximations provide very accurate estimates of the pounding risk, due to the fact that the fundamental periods of the two buildings are well separated. (2) The use of viscous dampers can dramatically reduce the risk of pounding between the two systems for any given separation distance. (3) The use of viscous braces in the lower levels of the taller building is a very efficient and cost-effective technique for minimizing the pounding risk.

Based on the results presented in this paper, it is concluded that the proposed methodology can be efficiently employed (1) for the assessment of pounding risk of adjacent buildings exhibiting linear elastic behavior before pounding, (2) for the computation of the mean annual frequency of pounding between adjacent buildings in the context of performance-based earthquake engineering, and (3) for the rational evaluation of the absolute and relative effectiveness of different retrofit solutions for adjacent building with high risk of seismic pounding.

REFERENCES

[1] V. Jeng, K. Kasai, B.F. Maison, A spectral difference method to estimate building separations to avoid pounding. *Earthquake Spectra*, **8**, 201-223, 1992.

[2] K. Kasai, R.A. Jagiasi, V. Jeng, Inelastic vibration phase theory for seismic pounding. *Journal of Structural Engineering* **122**, 1136-1146, 1996.

[3] J. Penzien, Evaluation of building separation distance required to prevent pounding during strong earthquake. *Earthquake Engineering and Structural Dynamics*, **26**, 849-858, 1997.

[4] International conference of building officials (ICBO), *Uniform Building Code*, Whittier, California, 1997.

[5] D. Lopez-Garcia, T.T. Soong, Assessment of the separation necessary to prevent seismic pounding between linear structural systems. *Probabilistic Engineering Mechanics*, **24**, 210-223, 2009.

[6] J.H. Lin, Separation distance to avoid seismic pounding of adjacent buildings. Earthquake Engineering and Structural Dynamics, **26**, 395-403, 1997.

[7] J.H. Lin, C.C. Weng, Probability analysis of seismic pounding of adjacent buildings. *Earthquake Engineering and Structural Dynamics*, **30**,1539-1557, 2001.

[8] H.P. Hong, S.S. Wang, P. Hong, Critical building separation distance in reducing pounding risk under earthquake excitation. *Structural Safety*, **25**, 287-303, 2003.

[9] S.S. Wang, H.P. Hong, Quantiles of critical separation distance for nonstationary seismic excitations. *Engineering Structures*, **28**, 985-991, 2006.

[10] K.A. Porter, An overview of PEER’s performance-based earthquake engineering methodology. *9th International Conference on Application of Statistics and Probability in Civil Engineering (ICASP9)*, San Francisco, California, 2003.

[11] Y. Zhang, G. Acero, J. Conte, Z. Yang, A. Elgamal, Seismic Reliability Assessment of a Bridge Ground System. *13th World Conference on Earthquake Engineering*, Vancouver, Canada, 2004.

[12] N. Luco, C.A. Cornell, Structure-specific scalar intensity measures for near-source and ordinary earthquake ground motions. *Earthquake Spectra*, **23**, 357-392, 2007.

[13] C.G. Karayannis, M.J. Favvata, Earthquake-induced interaction between adjacent reinforced concrete structures with non-equal heights. *Earthquake Engineering & Structural Dynamics*, **34**, 1-20, 2005.

[14] R. Jankowski. Non-linear viscoelastic modelling of earthquake-induced structural pounding, *Earthquake Engineering and Structural Dynamics*, **34**, 595-611, 2005.

[15] S. Muthukumar, R. DesRoches, A Hertz contact model with nonlinear damping for pounding simulation. *Earthquake Engineering and Structural Dynamics*, **35**, 811-828, 2006.

[16] G. Cole, R. Dhakal, A. Carr, D. Bull, An investigation of the effects of mass distribution on pounding structures. *Earthquake Engineering and Structural Dynamics*; in press, 2010.

[17] J.B. Roberts, P.D. Spanos, *Random vibrations and statistical linearization*. New York, Dover, 1993.

[18] S. Au, J.L. Beck, Estimation of small failure probabilities in high dimensions by subset simulation. *Probabilistic Engineering Mechanics*, **16**, 263-277, 2001.

[19] S.H. Crandall, First-crossing probabilities of the linear oscillator. *Journal of Sounds and Vibrations*, **12**, 285-299, 1970.

[20] Y.K. Wen, Approximate methods for nonlinear time-variant reliability analysis. *Journal of Engineering Mechanics*, **113**, 1826-1839, 1987.

[21] E.H. Vanmarcke, On the distribution of the first-passage time for normal stationary random processes. *Journal of Applied Mechanics*, 42, 215-220, 1975.

[22] M. Barbato, Use of time-variant spectral characteristics of nonstationary random processes in structural reliability and earthquake engineering applications. Accepted, to be published in *Computational Methods in Stochastic Dynamics*. M. Papadrakakis, G. Stefanou, V. Papadopoulos Editors, Springer, 2010.

[23] G. Michaelov, S. Sarkani, L.D. Lutes, Spectral characteristics of nonstationary random processes - A critical review. *Structural Safety*, **21**, 223-44, 1999.

[24] M. Barbato, J.P. Conte, Spectral characteristics of non-stationary random processes: Theory and applications to linear structural models. *Probabilistic Engineering Mechanics*, **23**, 416-26, 2008.

[25] M. Barbato, M. Vasta, Closed-form solutions for the time-variant spectral characteristics of non-stationary random processes. *Probabilistic Engineering Mechanics*, **25**, 9-17, 2010.

[26] M. Barbato, J.P. Conte, Structural Reliability Applications of Spectral Characteristics of Non-Stationary Random Processes. *ASCE Journal of Engineering Mechanics*, in print, 2011.

[27] S.K. Au, J.L. Beck, First excursion probabilities for linear systems by very efficient importance sampling. *Probabilistic Engineering Mechanics*, **16**, 193-207, 2001.

[28] Iman RL, Conover WJ, Small sample sensitivity analysis techniques for computer models, with an application to risk assessment. *Communications in statistics*, **A9**, 1749-1842, 1980.

[29] M. Shinozuka, Y. Sato, Simulation of nonstationary random processes. *Journal of the Engineering Mechanics Division*, **93**(EM1), 11-40, 1967.

[30] R.W. Clough, J. Penzien, *Dynamics of Structures*. New York, McGraw-Hill, 1993.

[31] M. Shinozuka, G. Deodatis, Simulation of stochastic processes by spectral representation. *Applied Mechanics Reviews*, **44**, 191-203, 1991.

[32] A.C. Cornell, F. Jalayer, R.O, Hamburger. Probabilistic basis for 2000 SAC federal emergency management agency steel moment frame guidelines. *Journal of Structural Engineering*, **128**, 526-532, 2002.

[33] European Committee for Standardization (ECS), *Eurocode 8 - Design of structures for earthquake resistance*. EN1998, Brussels, 2005.

[34] Z.A. Lubkowski, Deriving the seismic action for alternative return periods according to Eurocode 8. *14th European conference on Earthquake engineering*, Ohrid, Macedonia, 2010.

[35] G.R. Toro, C.A. Cornell, Extremes of Gaussian processes with bimodal spectra, *Journal of Engineering Mechanics*, **112**, 465-484, 1986.

[36] J.H. Lin, Evaluation of seismic pounding risk of buildings in Taiwan. Journal of the Chinese Institute of Engineers, **28**, 867-872, 2005.

[37] A. Occhiuzzi, Additional Viscous Dampers for Civil Structures: Analysis of Design Methods Based on Effective Evaluation of Modal Damping Ratios. *Engineering Structures*, **31**, 1093-1101, 2009.

COMPDYN 2011
III ECCOMAS Thematic Conference on
Computational Methods in Structural Dynamics and Earthquake Engineering
M. Papadrakakis, M. Fragiadakis, V. Plevris (eds.)
Corfu, Greece, 25–28 May 2011

AN OVERVIEW OF THE E.C.S.S. HANDBOOK FOR SPACECRAFT LOADS ANALYSIS

Adriano Calvi[1]

[1] European Space Agency
Keplerlaan 1, Noordwijk, The Netherlands
e-mail: Adriano.Calvi@esa.int

Keywords: Loads Analysis, Spacecraft Structure, Structural Dynamics, Standardization, ECSS, Handbook.

Abstract. *The handbook of the European Cooperation for Space Standardization (ECSS) E-HB-32-26 titled "Guidelines for Loads Analysis of Spacecraft and Payloads" is developed with the goal to harmonize methodologies, procedures and practices currently applied for the conduct of spacecraft and payloads loads analysis. The handbook will make available to the European Space Community a set of well proved methods and procedures for the calculation and assessment of structural design loads and for the evaluation of the test loads.*

The handbook is presently drafted by the "Loads Analysis Handbook Working Group" and contains a number of topics strictly related to computational structural dynamics. An overview of the proposed handbook, with a synopsis of some chapters, has been developed and it is here presented. It is planned that the handbook be published in the year 2012. Comments on the proposed handbook are solicited from the scientific community and industry.

1 INTRODUCTION

European Cooperation for Space Standardization (ECSS) [1] is an initiative established to develop a single set of consistent space documents for use by the entire European space community. The objective is to increase the effectiveness of all space programs in Europe through the application of the ECSS documents recognized by all potential European customers and equally accepted by industry. The ECSS documents have evolved from the previous 30 years of experience in the management and implementation of European space projects. ECSS is supported by several agencies and companies. The actual members of ECSS are the European Space Agency (ESA), the National Space Agencies of Canada, France, Germany, Italy, Norway, the Netherlands, the United Kingdom, and the European space industry represented by Eurospace.

The ECSS handbooks are nonnormative documents providing background information, orientation, advice or recommendations. A handbook therefore contains advice about how to properly do something important and useful information about a subject.

The ECSS E-HB-32-26 “Loads Analysis Handbook” [2] is developed with the goal to harmonize methodologies, procedures and practices currently applied for the conduct of spacecraft and payloads loads analysis. It will make available to the European Space Community a set of well proved methods and procedures for the calculation and assessment of structural design loads and for the evaluation of the test loads.

The handbook is presently drafted by the “Loads Analysis Handbook Working Group” and contains a number of topics related to computational structural dynamics. In particular, recent advances in the area of structural dynamics and vibrations, in both methodology and capability, have the potential to make spacecraft system analysis and testing more effective from technical, cost, and hardware safety points of view. However, application of advanced analysis methods varies among the Space Agencies and their contractors. Identification and refinement of the best of these methodologies and implementation approaches is an objective the Working Group. An overview of the proposed handbook, with a synopsis of some chapters, has been developed and it is here presented.

2 GENERAL CONTENT OF THE HANDBOOK

The handbook is organized in a number of chapters which cover the following topics:

1. Terms and definitions
2. General aspects of the loads verification
3. Loads combination
4. Launcher/spacecraft coupled loads analysis (CLA)
5. Static loads
6. Sine vibration environment
7. Random vibration and vibro-acoustic environments
8. Shock environment
9. Structural stability
10. Dimensional stability
11. Fatigue and fracture control
12. Microgravity and micro-vibration environment
13. Mathematical models

Some topics are briefly illustrated in the following sections.

3 SPACECRAFT FLIGHT ENVIRONMENTS AND DYNAMIC LOADS

There are three basic types of flight environments that generate dynamic loads on payload components [7]:

a) The low-frequency dynamic response, typically from 0 to 100 Hz, of the launch vehicle/payload system to transient flight events.
b) The high-frequency random vibration environment, which typically has significant energy in the frequency range from 20 Hz to 2000 Hz, transmitted from the launch vehicle to the payload at the launch vehicle/payload interfaces.
c) The high frequency acoustic pressure environment, typically from 20 Hz to 8000 Hz, inside the payload compartment. The payload compartment acoustic pressure environment generates dynamic loads on components in two ways: (1) by direct impingement on the surfaces of exposed components, and (2) by the acoustic pressure impingement upon the component mounting structures, which induces random vibrations that are mechanically transmitted to the components.

Combinations of these loads may occur at different times in flight.

4 SPACECRAFT-LAUNCHER COUPLED LOADS ANALYSIS

The structural response of the spacecraft to transient flight events (low frequency mechanical environment) is simulated by spacecraft-launcher coupled dynamic analysis [3]. This is normally a transient analysis performed by using the finite element models (FEM) of the satellite and launcher, merged together, and by applying the forcing functions for the different launch events (figure 1).

The main objective of the CLA is to calculate the loads on the spacecraft, where the term “loads” refers to the set of internal forces, displacements and accelerations that characterise the structural response to the applied forces. The loads of the spacecraft derived from the analysis are taken as a basis to verify the dimensioning of the spacecraft itself. Spacecraft programs typically perform a number of analysis loops (called ‘‘loads cycles’’), for example one each for preliminary design, final design, and final verification. The latter is done with “test verified” mathematical models.

The low frequency domain typically ranges from 0 to up 100 Hz and corresponds to the frequency content of the forcing functions used in the CLA. The excitation may be of aerodynamic origin (wind, gust, buffeting at transonic velocity) or may be induced by the propulsion system (thrust build up or tail-off transient, acoustic loads in the combustion chambers, etc.). Of primary interest are the spacecraft interface accelerations and interface forces. The interface accelerations can be used to derive an equivalent sine spectrum at the spacecraft interface. The interface forces can be employed to calculate the “equivalent accelerations” at the spacecraft centre of gravity. Of large interest is also the recovery of the internal responses which are used to verify the structural integrity of the spacecraft and its components. The computed responses and their deduced minimum and maximum levels can be employed within the design, verification and test phases of the spacecraft. For example, secondary structures and flexible components such as solar arrays, booms, instruments and propellant tanks must also be designed (and test verified) to withstand the dynamic environment induced at the base of the spacecraft. The dynamic loads (accelerations, forces, stresses, etc.) on these components can be verified directly by means of the CLA (apart from acoustic loads under the fairing which are analysed separately).

In the test verification phase of the spacecraft, the equivalent sine spectrum computed by means of CLA is used to locally reduce the prescribed spectrum from the launcher user’s manual at specific resonant frequencies. This might be required to avoid possible damage to the spacecraft structure itself or its components (solar arrays, booms, etc.).

The chapter on launcher/spacecraft coupled loads analysis includes:

- Description of load cases
- Methodology
- Static and dynamic contributions
- Generation of reduced mathematical models and output transformation matrices
- Damping modelling
- Uncertainty factors
- Output and results evaluation
- Sensitivity analysis
- Non-linearity

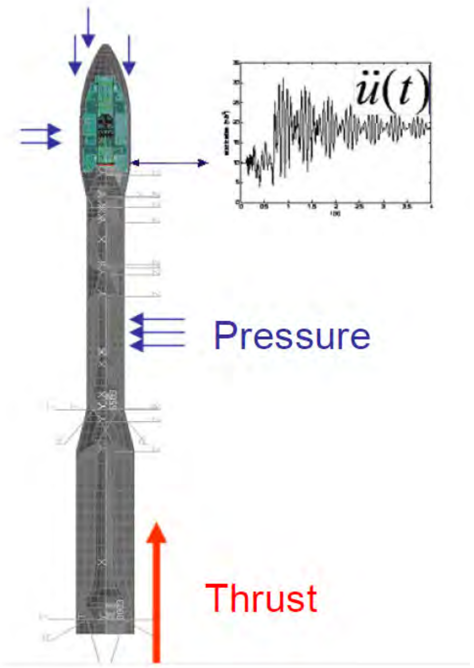

Figure 1: GOCE satellite FEM merged with VEGA launcher FEM for CLA (source [6]).

5 SINE VIBRATION ENVIRONMENT

In a number of situations sine-wave excitations are used for qualification and protoflight testing of space vehicle hardware, even though the “mission” dynamic excitation being simulated is not periodic [4]. In particular the low frequency transient is often simulated at the subsystem and system assembly level using a swept-sine vibration test over a frequency range up to about 100 Hz. The magnitude and sweep rate for the resulting vibration are selected supposedly to cause the hardware response to be similar to the response predicted for the transient. Some common procedures to derive such a test are reported in [2, 4].

The use of a swept-sine excitation to simulate a transient excitation can result in the unique situation of causing a simultaneous undertest and overtest of the hardware. The undertest is due to exciting only one hardware resonance at a time during the sweep-sine test, as opposed to the simultaneous excitation of multiple resonances of the hardware, as would be induced by the transient excitation. The potential overtest is due to applying a larger number of stress cycles to the hardware during the swept-sine test than occurs during the transient excitation. Of course, the amount of overtesting can be reduced by increasing the sweep rate.

However the main cause of potential overtesting is the difference in structure boundary conditions between test and flight configurations. During a vibration test, the test article is usually attached to a very rigid fixture and it is excited or driven along a single linear direction, with the structure being completely restrained along the other five degrees-of-freedom (DOF). This generates a response of the spacecraft in its “clamped natural modes” and not in the coupled launcher-spacecraft modes as exhibited during the flight [5, 6].

In the flight configuration the satellite is attached to a mounting structure (i.e. adapter and launcher) that normally exhibits some flexibilities in all six DOF in the frequency range of interest. The flexibility difference in the direction of excitation is the main contributor to the overtesting phenomenon. In the flight configuration, the acceleration at the interface between the mounting structure and the test article drops at certain frequencies, resulting in valleys in the acceleration spectra. These frequencies correspond to the resonance frequencies of the test article when attached to a rigid support (such as a shaker). This phenomenon is known as the vibration absorber effect. In other words, during a vibration test, the structure is excited with a specified input acceleration that is the envelope of the flight interface acceleration, despite the amplitude at certain frequencies drops in the flight configuration. This results in exaggerated amplification of input forces, and internal stresses, at the resonance frequencies of the test article. In practice, because the input spectrum does not consider the actual flight behaviour and excites the spacecraft modes, the structural response of the spacecraft would exceed the spacecraft design capability and the values encountered during the launch simulations.

To avoid such effects, the sine test input spectrum needs to be notched. However, it should be clear that the criteria used for notching do not have to generate an input spectrum that can jeopardize the flightworthiness of the spacecraft. For example this can happen if the testing levels are not coherent with the levels required by the CLA. As a general rule, the notching should be kept to a minimum and the input spectrum to be applied to the spacecraft as much as possible similar to the one requested by the launcher authority. The reason is that this spectrum provides robustness to the spacecraft design compliant with it since it covers a wide range of responses found in past spacecraft-launcher CLA and in addition it provides a sweep over the frequency band of interest, therefore covering possible deviations of local modes.

It should be noted that the dynamic environments for space vehicle hardware are typically multiple-axis, i.e., the excitations occur simultaneously along all three orthogonal axes of the hardware. Acoustic tests naturally simulate a multiple-axis excitation, but shock and vibration test facilities are commonly uniaxial (figure 2). Multiple axis test facilities designed to simulate low frequency shock and vibration environments (generally below 100 Hz) are available (figure 3). For space vehicle hardware, however, it is more common to perform shock and vibration tests using machines that apply the excitation sequentially along one axis at a time. The potential error caused by simulating a multiple-axis shock and/or vibration excitation with sequentially applied single-axis excitations is widely debated.

The chapter on sine vibration environment includes:

- Source of the sine environment
- Response analysis
- Environment and test specifications for instruments and components
- Methods and procedures for notching of the input spectrum in sine vibration test

Figure 2: GOCE satellite on large slip table at ESTEC (courtesy of ESA).

Figure 3: Herschel satellite on Hydra at ESTEC (courtesy of ESA).

6 RANDOM VIBRATION AND VIBRO-ACOUSTIC ENVIRONMENTS

Some load environments must be treated as random phenomena, when the forces involved are controlled by non-deterministic parameters [7]. Examples include high frequency engine thrust oscillation, aerodynamic buffeting of fairing, and sound pressure on the surfaces of the payload.

Random vibration analysis describes the forcing functions and the corresponding structural response statistically. It is generally assumed the phasing of vibration at different frequencies is statistically uncorrelated. The amplitude of motion at each frequency is described by a power spectral density function. In contrast to transient analysis which predicts time histories of response quantities, random vibration analysis generates the power spectral densities of these response quantities. From the power spectral density, the root mean square (rms) amplitude of the response quantity is calculated. The root-mean-square (rms) acceleration is the square root of the integral of the acceleration PSD over frequency. Random vibration limit loads are typically taken as the 3- sigma load (obtained by multiplying the rms load by 3).

The most appropriate measure of the severity of a random vibration environment is the maximum PSD value or the PSD value at the frequency of the resonances of the structural item. It is a common mistake to use the rms value of the input as a measure of its severity. The problem with the rms value is that it depends strongly on the values of the PSD at very high frequencies and on the upper frequency limit, which are often irrelevant.

The chapter on random vibration and vibro-acoustic environments includes:

- Source of the environment
- Response analysis
- Environment and test specifications for instruments and components
- Notching of the input spectrum in random vibration test
- Methodology and procedures for vibro-acoustic analysis

7 MICRO-GRAVITY AND MICRO-VIBRATION ENVIRONMENT

One of the major goals for the future space utilization projects is conducting activities, experiments and processes in a very low gravity environment, the so-called micro-gravity environment [2]. This micro-gravity environment is usually made available in low-earth-orbiting spacecraft systems and pressurized module compartments over long period of days and months without interruptions. Consequently the spacecraft systems should be designed and should be operated such that limit acceleration levels are not exceeded during the performance of experiments and processes.

The chapter on microgravity and micro-vibration environment includes:

- General aspects related to the micro-gravity environment
- Identification of the microgravity disturbance sources
- Derivation of microgravity specifications
- Verification of the microgravity requirements

8 MATHEMATICAL MODELS

This chapter addresses the mathematical models of space structures with a special emphasis on the finite element models used for loads analysis. In particular it provides some guidelines for ensuring finite element analysis quality, i.e. the correct use of this specific technology, – the finite element method - and the acceptance of the results. The handbook promotes the verification and validation (V&V) guidance proposed in the ASME Guide for V&V [8].

The chapter includes the following topics:

- Requirements for structure mathematical models (e.g. [9, 10])
- Introduction to verification and validation in computational mechanics [8]
- Uncertainty quantification during design and verification loads cycles
- Model verification and quality assurance for spacecraft finite element analysis
- Mathematical model validation

9 CONCLUSIONS

Recent advances in the area of structural dynamics and vibrations, in both methodology and capability, have the potential to make spacecraft system analysis and testing more effective from technical, cost, and hardware safety points of view. However, application of advanced analysis methods varies among the Space Agencies and their contractors.

The ECSS Handbook for spacecraft loads analysis [2] is presently in the drafting phase and is developed with the goal to harmonize methodologies, procedures and practices currently applied for the conduct of spacecraft and payloads loads analysis. The handbook will make available to the European Space Community a set of well proved methods and procedures for the calculation and assessment of structural design loads and for the evaluation of the test loads. It is planned that the handbook be published in the year 2012. Comments on the proposed handbook are solicited from the scientific community and industry.

Acknowledgments

The work described in this paper was carried out by the members of the E-HB-32-26 Loads Analysis Handbook Working Group. Their contributions are gratefully acknowledged. The handbook is funded by the European Cooperation for Space Standardization.

REFERENCES

[1] European Cooperation for Space Standardization, www.ecss.nl

[2] Guidelines for loads analysis of spacecraft and payloads, *ECSS Handbook E-HB-32-26*, Draft Issue (To Be Published), Noordwijk, The Netherlands

[3] S. Fransen, *Methodologies for launcher-payload coupled dynamic analysis* – PhD Thesis, Technical University of Delft, The Netherlands, 2005, ISBN 90-9020293-5.

[4] Dynamic Environmental Criteria, *NASA-HDBK-7005*, March 2001

[5] Y. Soucy, A. Coté – Reduction of Overtesting during Vibration Tests of Space Hardware – *Canadian Aeronautics and Space Journal*, Vol. 48, No 1, March 2002

[6] Calvi A., Nali P. – Some Remarks on the Reduction of Overtesting during Base-Drive Sine Vibration Tests of Spacecraft – *Proc. of the ECCOMAS Conf. on Computational Methods in Structural Dynamics and Earthquake Engineering* - Rethymno, Crete, Greece, June 2007

[7] Load Analyses of Spacecraft and Payloads, *NASA-STD-5002*, June 1996

[8] Guide for Verification and Validation in Computational Solid Mechanics, *ASME V&V 10-2006*, New York, NY, USA, 2006

[9] Space engineering, Structural finite element models, *ECSS-E-ST-32-03C*, Noordwijk, The Netherlands, July 2008

[10] Space engineering, Modal survey assessment, *ECSS-E-ST-32-11C*, Noordwijk, The Netherlands, July 2008

COMPDYN 2011
3rd ECCOMAS Thematic Conference on
Computational Methods in Structural Dynamics and Earthquake Engineering
M. Papadrakakis, M. Fragiadakis, V. Plevris (eds.)
Corfu, Greece, 25–28 May 2011

NONLINEAR MODAL ANALYSIS OF AEROSPACE STRUCTURES

M. Peeters[1], G. Kerschen[1], J.C. Golinval[1], C. Stephan[2], and P. Lubrina[2]

[1]Aerospace and Mechanical Engineering Department
University of Lige, Lige, Belgium
e-mail: g.kerschen@ulg.ac.be

[2] Office National dEtudes et de Recherches Aerospatiales (ONERA), DADS-ADSE
Chatillon, France

Keywords: Modal Analysis, Nonlinearity, Aerospace.

Abstract. *The dynamic systems theory is well-established for linear systems and can rely on mature tools such as the theories of linear operators and linear integral transforms. This is why theoretical and experimental modal analysis, i.e., the computation of vibration modes from a mathematical model and from experimental data, respectively, is really quite sophisticated and advanced. Even though linear modal analysis served, and is still serving, the structural dynamics community for applications ranging from bridges to satellites, it is commonly accepted that nonlinearity is a frequent occurrence in engineering structures.*

Because linear modal analysis fails in the presence of nonlinear dynamical phenomena, the development of a practical nonlinear analog of modal analysis would be an extremely timely contribution; it is clearly missing in the structural dynamics literature. A new framework for nonlinear modal analysis of real-world structures, which includes the computation of nonlinear modes from finite element models, is introduced in this paper. This framework will permit a rigorous, yet understandable by the practicing engineer, analysis of nonlinear dynamical phenomena. It will also provide solid theoretical foundations for extending finite element model validation to nonlinear aerospace structures.

1 INTRODUCTION

Nonlinear normal modes (NNMs) offer a solid theoretical and mathematical tool for interpreting a wide class of nonlinear dynamical phenomena, yet they have a clear and simple conceptual relation to the LNMs [1, 2, 3]. However, most structural engineers still view NNMs as a concept that is foreign to them, and they do not yet consider NNMs as a useful concept for structural dynamics. One reason supporting this statement is that most existing constructive techniques for computing NNMs are based on asymptotic approaches and rely on fairly involved mathematical developments.

There have been very few attempts to compute NNMs using numerical methods [4, 5, 6, 7]. Algorithms for the continuation of periodic solutions are really quite sophisticated and advanced (see, e.g., [8, 9, 10]), and they have been extensively used for computing the forced response and limit cycles of nonlinear dynamical systems (see, e.g., [11]). Interestingly, they have not been fully exploited for the computation of nonlinear modes.

In this paper, we support that these numerical algorithms pave the way for an effective and practical computation of NNMs. The proposed algorithm, implemented in MATLAB, relies on two main techniques, namely a shooting procedure and a method for the continuation of NNM motions. The objective is to demonstrate that the numerical computation of the NNMs of complex real-world structures is then within reach. The application considered in this study is the airframe of the Morane-Saulnier Paris aircraft, whose ground vibration tests have exhibited some nonlinear structural behaviors.

2 Nonlinear Normal Modes (NNMs)

A detailed description of NNMs and their fundamental properties (e.g., frequency-energy dependence, bifurcations and stability) is given in [1, 2, 3]. For completeness, the two main definitions of an NNM are briefly reviewed in this section.

The free response of discrete conservative mechanical systems with n degrees of freedom (DOFs) is considered, assuming that continuous systems (e.g., beams, shells or plates) have been spatially discretized using the finite element method. The equations of motion are

$$\mathbf{M}\,\ddot{\mathbf{x}}(t) + \mathbf{K}\,\mathbf{x}(t) + \mathbf{f}_{\text{nl}}\left\{\mathbf{x}(t), \dot{\mathbf{x}}(t)\right\} = 0 \tag{1}$$

where $\mathbf{M}$ is the mass matrix; $\mathbf{K}$ is the stiffness matrix; $\mathbf{x}$, $\dot{\mathbf{x}}$ and $\ddot{\mathbf{x}}$ are the displacement, velocity and acceleration vectors, respectively; $\mathbf{f}_{\text{nl}}$ is the nonlinear restoring force vector.

There exist two main definitions of an NNM in the literature due to Rosenberg and Shaw and Pierre:

1. Targeting a straightforward nonlinear extension of the linear normal mode (LNM) concept, Rosenberg defined an NNM motion as a *vibration in unison* of the system (i.e., a synchronous periodic oscillation).

2. To provide an extension of the NNM concept to damped systems, Shaw and Pierre defined an NNM as a two-dimensional invariant manifold in phase space. Such a manifold is invariant under the flow (i.e., orbits that start out in the manifold remain in it for all time), which generalizes the invariance property of LNMs to nonlinear systems.

At first glance, Rosenberg's definition may appear restrictive in two cases. Firstly, it cannot be easily extended to nonconservative systems. However, the damped dynamics can often be interpreted based on the topological structure of the NNMs of the underlying conservative system [3]. Secondly, in the presence of internal resonances, the NNM motion is no longer synchronous, but it is still periodic.

In the present study, an NNM motion is therefore defined as a *(non-necessarily synchronous) periodic motion* of the conservative mechanical system (1). As we will show, this extended definition is particularly attractive when targeting a numerical computation of the NNMs. It enables the nonlinear modes to be effectively computed using algorithms for the continuation of periodic solutions.

3 Numerical Computation of NNMs

The numerical method proposed here for the NNM computation relies on two main techniques, namely a shooting technique and the pseudo-arclength continuation method. A detailed description of the algorithm is given in [12].

3.1 Shooting Method

The equations of motion of system (1) can be recast into state space form

$$\dot{\mathbf{z}} = \mathbf{g}(\mathbf{z}) \tag{2}$$

where $\mathbf{z} = [\mathbf{x}^* \quad \dot{\mathbf{x}}^*]^*$ is the $2n$-dimensional state vector, and star denotes the transpose operation, and

$$\mathbf{g}(\mathbf{z}) = \begin{pmatrix} \dot{\mathbf{x}} \\ -\mathbf{M}^{-1}\left[\mathbf{K}\mathbf{x} + \mathbf{f}_{\text{nl}}(\mathbf{x}, \dot{\mathbf{x}})\right] \end{pmatrix} \tag{3}$$

is the vector field. The solution of this dynamical system for initial conditions $\mathbf{z}(0) = \mathbf{z}_0 = [\mathbf{x}_0^* \quad \dot{\mathbf{x}}_0^*]^*$ is written as $\mathbf{z}(t) = \mathbf{z}\,(t, \mathbf{z}_0)$ in order to exhibit the dependence on the initial conditions, $\mathbf{z}\,(0, \mathbf{z}_0) = \mathbf{z}_0$. A solution $\mathbf{z}_p(t, \mathbf{z}_{p0})$ is a periodic solution of the autonomous system (2) if $\mathbf{z}_p(t, \mathbf{z}_{p0}) = \mathbf{z}_p(t + T, \mathbf{z}_{p0})$, where T is the minimal period.

The NNM computation is carried out by finding the periodic solutions of the governing nonlinear equations of motion (2). In this context, the *shooting method* is probably the most popular numerical technique. It solves numerically the two-point boundary-value problem defined by the periodicity condition

$$\mathbf{H}(\mathbf{z}_{p0}, T) \equiv \mathbf{z}_p(T, \mathbf{z}_{p0}) - \mathbf{z}_{p0} = \mathbf{0} \tag{4}$$

$\mathbf{H}(\mathbf{z}_0, T) = \mathbf{z}(T, \mathbf{z}_0) - \mathbf{z}_0$ is called the *shooting function* and represents the difference between the initial conditions and the system response at time T. Unlike forced motion, the period T of the free response is not known a priori.

The shooting method consists in finding, in an iterative way, the initial conditions $\mathbf{z}_{p0}$ and the period T that realize a periodic motion. To this end, the method relies on direct numerical time integration and on the Newton-Raphson algorithm.

Starting from some assumed initial conditions $\mathbf{z}_{p0}^{(0)}$, the motion $\mathbf{z}_p^{(0)}(t, \mathbf{z}_{p0}^{(0)})$ at the assumed period $T^{(0)}$ can be obtained by numerical time integration methods (e.g., Runge-Kutta or Newmark schemes). In general, the initial guess $(\mathbf{z}_{p0}^{(0)}, T^{(0)})$ does not satisfy the periodicity condition (4). A Newton-Raphson iteration scheme is therefore to be used to correct an initial guess and to converge to the actual solution. The corrections $\Delta\mathbf{z}_{p0}^{(k)}$ and $\Delta T^{(k)}$ at iteration k are found by expanding the nonlinear function

$$\mathbf{H}\left(\mathbf{z}_{p0}^{(k)} + \Delta\mathbf{z}_{p0}^{(k)}, T^{(k)} + \Delta T^{(k)}\right) = 0 \tag{5}$$

in Taylor series and neglecting higher-order terms (H.O.T.).

The phase of the periodic solutions is not fixed. If $\mathbf{z}(t)$ is a solution of the autonomous system (2), then $\mathbf{z}(t+\Delta t)$ is geometrically the same solution in state space for any Δt. Hence, an additional condition, termed the *phase condition*, has to be specified in order to remove the arbitrariness of the initial conditions. This is discussed in detail in [12].

In summary, an isolated NNM is computed by solving the augmented two-point boundary-value problem defined by

$$\mathbf{F}(\mathbf{z}_{p0},T) \equiv \left\{ \begin{array}{rcl} \mathbf{H}(\mathbf{z}_{p0},T) & = & 0 \\ h(\mathbf{z}_{p0}) & = & 0 \end{array} \right. \tag{6}$$

where $h(\mathbf{z}_{p0}) = 0$ is the phase condition.

3.2 Continuation of Periodic Solutions

Due to the frequency-energy dependence, the modal parameters of an NNM vary with the total energy. An NNM family, governed by equations (6), therefore traces a curve, termed an NNM branch, in the $(2n+1)$-dimensional space of initial conditions and period $(\mathbf{z}_{p0},T)$. Starting from the corresponding LNM at low energy, the computation is carried out by finding successive points $(\mathbf{z}_{p0},T)$ of the NNM branch using methods for the *numerical continuation* of periodic motions (also called *path-following methods*) [8, 9]. The space $(\mathbf{z}_{p0},T)$ is termed the continuation space.

Different methods for numerical continuation have been proposed in the literature. The so-called pseudo-arclength continuation method is used herein.

Starting from a known solution $(\mathbf{z}_{p0,(j)},T_{(j)})$, the next periodic solution $(\mathbf{z}_{p0,(j+1)},T_{(j+1)})$ on the branch is computed using a *predictor step* and a *corrector step*.

Predictor step

At step j, a prediction $(\tilde{\mathbf{z}}_{p0,(j+1)},\tilde{T}_{(j+1)})$ of the next solution $(\mathbf{z}_{p0,(j+1)},T_{(j+1)})$ is generated along the tangent vector to the branch at the current point $\mathbf{z}_{p0,(j)}$

$$\left[\begin{array}{c} \tilde{\mathbf{z}}_{p0,(j+1)} \\ \tilde{T}_{(j+1)} \end{array} \right] = \left[\begin{array}{c} \mathbf{z}_{p0,(j)} \\ T_{(j)} \end{array} \right] + s_{(j)} \left[\begin{array}{c} \mathbf{p}_{z,(j)} \\ p_{T,(j)} \end{array} \right] \tag{7}$$

where $s_{(j)}$ is the predictor stepsize. The tangent vector $\mathbf{p}_{(j)} = [\mathbf{p}_{z,(j)}^{*} \; p_{T,(j)}]^{*}$ to the branch defined by (6) is solution of the system

$$\left[\begin{array}{cc} \left.\dfrac{\partial \mathbf{H}}{\partial \mathbf{z}_{p0}}\right|_{(\mathbf{z}_{p0,(j)},T_{(j)})} & \left.\dfrac{\partial \mathbf{H}}{\partial T}\right|_{(\mathbf{z}_{p0,(j)},T_{(j)})} \\ \left.\dfrac{\partial h}{\partial \mathbf{z}_{p0}}^{*}\right|_{(\mathbf{z}_{p0,(j)})} & 0 \end{array} \right] \left[\begin{array}{c} \mathbf{p}_{z,(j)} \\ p_{T,(j)} \end{array} \right] = \left[\begin{array}{c} \mathbf{0} \\ 0 \end{array} \right] \tag{8}$$

with the condition $\left\| \mathbf{p}_{(j)} \right\| = 1$. The star denotes the transpose operator. This normalization can be taken into account by fixing one component of the tangent vector and solving the resulting overdetermined system using the Moore-Penrose matrix inverse; the tangent vector is then normalized to 1.

Corrector step

The prediction is corrected by a shooting procedure in order to solve (6) in which the variations of the initial conditions and the period are forced to be orthogonal to the predictor step. At iteration k, the corrections

$$\begin{aligned} \mathbf{z}_{p0,(j+1)}^{(k+1)} &= \mathbf{z}_{p0,(j+1)}^{(k)} + \Delta\mathbf{z}_{p0,(j+1)}^{(k)} \\ T_{(j+1)}^{(k+1)} &= T_{(j+1)}^{(k)} + \Delta T_{(j+1)}^{(k)} \end{aligned} \tag{9}$$

are computed by solving the overdetermined linear system using the Moore-Penrose matrix inverse

$$\begin{bmatrix} \left.\frac{\partial \mathbf{H}}{\partial \mathbf{z}_{p0}}\right|_{\left(\mathbf{z}_{p0,(j+1)}^{(k)},T_{(j+1)}^{(k)}\right)} & \left.\frac{\partial \mathbf{H}}{\partial T}\right|_{\left(\mathbf{z}_{p0,(j+1)}^{(k)},T_{(j+1)}^{(k)}\right)} \\ \left.\frac{\partial h}{\partial \mathbf{z}_{p0}}^{*}\right|_{\left(\mathbf{z}_{p0,(j+1)}^{(k)}\right)} & 0 \\ \mathbf{p}_{z,(j)}^{*} & p_{T,(j)} \end{bmatrix} \begin{bmatrix} \Delta\mathbf{z}_{p0,(j+1)}^{(k)} \\ \Delta T_{(j+1)}^{(k)} \end{bmatrix} = \begin{bmatrix} -\mathbf{H}(\mathbf{z}_{p0,(j+1)}^{(k)},T_{(j+1)}^{(k)}) \\ -h(\mathbf{z}_{p0,(j+1)}^{(k)}) \\ 0 \end{bmatrix} \tag{10}$$

where the prediction is used as initial guess, i.e, $\mathbf{z}_{p0,(j+1)}^{(0)} = \tilde{\mathbf{z}}_{p0,(j+1)}$ and $T_{(j+1)}^{(0)} = \tilde{T}_{(j+1)}$. The last equation in (10) corresponds to the orthogonality condition for the corrector step.

This iterative process is carried out until convergence is achieved. The convergence test is based on the relative error of the periodicity condition:

$$\frac{\|\mathbf{H}(\mathbf{z}_{p0},T)\|}{\|\mathbf{z}_{p0}\|} = \frac{\|\mathbf{z}_p(T,\mathbf{z}_{p0}) - \mathbf{z}_{p0}\|}{\|\mathbf{z}_{p0}\|} < \epsilon \tag{11}$$

where ϵ is the prescribed relative precision.

3.3 Sensitivity Analysis

Each shooting iteration involves the time integration of the equations of motion to evaluate the current shooting residue $\mathbf{H}\left(\mathbf{z}_{p0}^{(k)},T^{(k)}\right) = \mathbf{z}_p^{(k)}(T^{(k)},\mathbf{z}_{p0}^{(k)}) - \mathbf{z}_{p0}^{(k)}$. As evidenced by equation (10), the method also requires the evaluation of the $2n \times 2n$ Jacobian matrix

$$\frac{\partial \mathbf{H}}{\partial \mathbf{z}_0}(\mathbf{z}_0,T) = \left.\frac{\partial \mathbf{z}(t,\mathbf{z}_0)}{\partial \mathbf{z}_0}\right|_{t=T} - \mathbf{I} \tag{12}$$

where $\mathbf{I}$ is the $2n \times 2n$ identity matrix.

The classical finite-difference approach requires to perturb successively each of the $2n$ initial conditions and integrate the *nonlinear* governing equations of motion. This approximate method therefore relies on extensive numerical simulations and may be computationally intensive for large-scale finite element models.

Targeting a reduction of the computational cost, a significant improvement is to use sensitivity analysis for determining $\partial\mathbf{z}(t,\mathbf{z}_0)/\partial\mathbf{z}_0$ instead of a numerical finite-difference procedure. The sensitivity analysis consists in differentiating the equations of motion (2) with respect to the initial conditions $\mathbf{z}_0$ which leads to

$$\frac{d}{dt}\left[\frac{\partial \mathbf{z}\left(t,\mathbf{z}_0\right)}{\partial \mathbf{z}_0}\right] = \left.\frac{\partial \mathbf{g}(\mathbf{z})}{\partial \mathbf{z}}\right|_{\mathbf{z}(t,\mathbf{z}_0)} \left[\frac{\partial \mathbf{z}(t,\mathbf{z}_0)}{\partial \mathbf{z}_0}\right] \tag{13}$$

with

$$\frac{\partial \mathbf{z}(0,\mathbf{z}_0)}{\partial \mathbf{z}_0} = \mathbf{I} \tag{14}$$

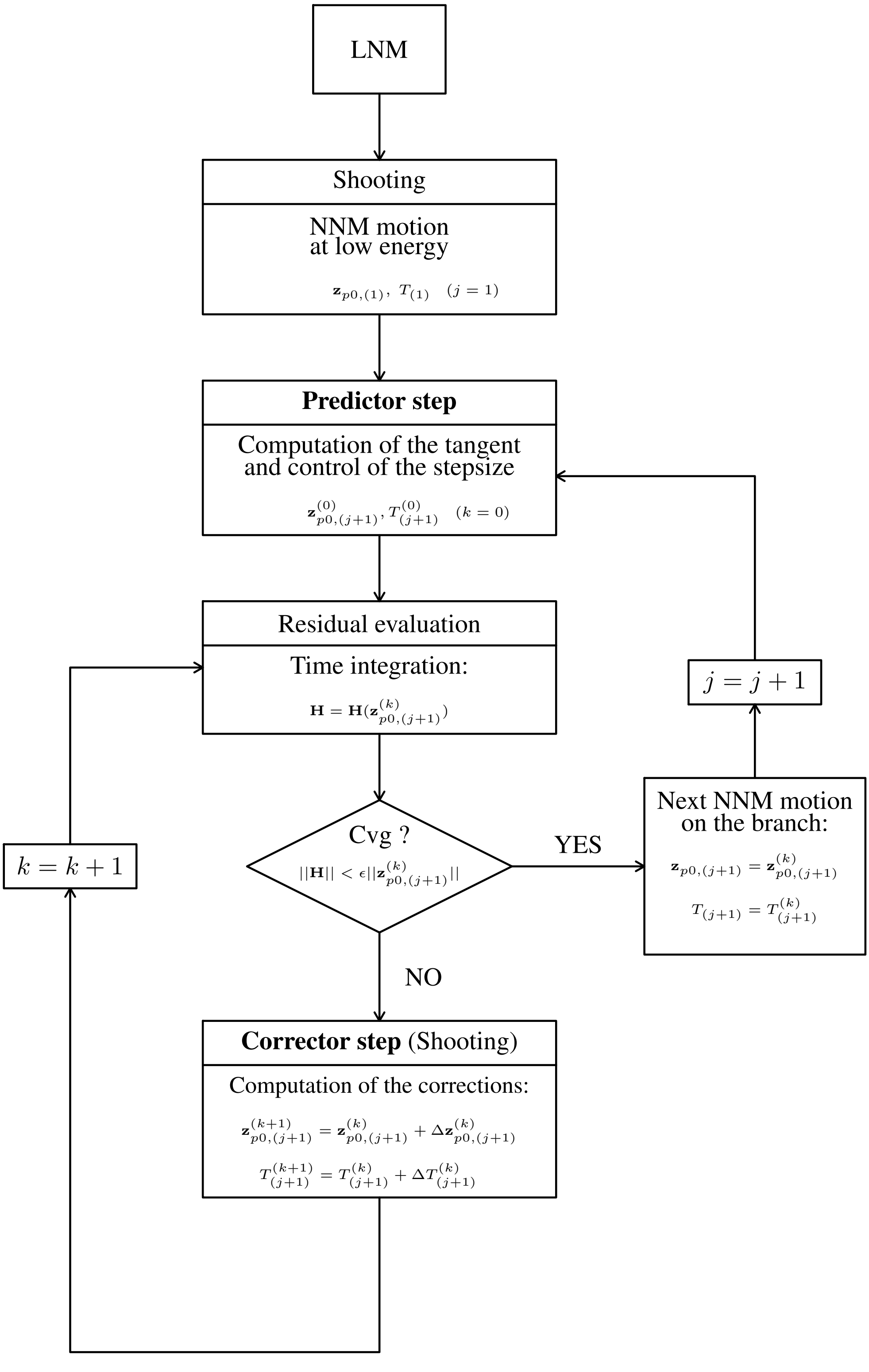

Figure 1: Algorithm for NNM computation.

since $\mathbf{z}(0, \mathbf{z}_0) = \mathbf{z}_0$. Hence, the matrix $\partial \mathbf{z}(t, \mathbf{z}_0)/\partial \mathbf{z}_0$ at $t = T$ can be obtained by numerically integrating over T the initial-value problem defined by the *linear* ordinary differential equations (ODEs) (13) with the initial conditions (14).

In addition to the integration of the current solution $\mathbf{z}(t, \mathbf{x}_0)$ of (2), these two methods for computing $\partial \mathbf{z}(t, \mathbf{z}_0)/\partial \mathbf{z}_0$ require $2n$ numerical integrations of $2n$-dimensional dynamical systems, which may be computationally intensive for large systems. However, equations (13) are linear ODEs and their numerical integration is thus less expensive. The numerical cost can be further reduced if the solution of equations (13) is computed together with the solution of the nonlinear equations of motion in a single numerical simulation [13].

The sensitivity analysis requires only one additional iteration at each time step of the numerical time integration of the current motion to provide the Jacobian matrix. The reduction of the computational cost is therefore significant for large-scale finite element models. In addition, the Jacobian computation by means of the sensitivity analysis is exact. The convergence troubles regarding the chosen perturbations of the finite-difference method are then avoided. Hence, the use of sensitivity analysis to perform the shooting procedure represents a meaningful improvement from a computational point of view.

As the monodromy matrix $\partial \mathbf{z}_p(T, \mathbf{z}_{p0})/\partial \mathbf{z}_{p0}$ is computed, its eigenvalues, the Floquet multipliers, are obtained as a by-product, and the stability analysis of the NNM motions can be performed in a straightforward manner.

3.4 Algorithm for NNM Computation

The algorithm proposed for the computation of NNM motions is a combination of shooting and pseudo-arclength continuation methods, as shown in Figure 1. It has been implemented in the MATLAB environment. Other features of the algorithm such as the step control, the reduction of the computational burden and the method used for numerical integration of the equations of motion are discussed in [12].

So far, the NNMs have been considered as branches in the continuation space $(\mathbf{z}_{p0}, T)$. An appropriate graphical depiction of the NNMs is to represent them in a frequency-energy plot (FEP). This FEP can be computed in a straightforward manner: (i) the conserved total energy is computed from the initial conditions realizing the NNM motion; and (ii) the frequency of the NNM motion is calculated directly from the period.

4 Numerical Experiment - Full-Scale Aircraft

The numerical computation of the NNMs of a complex real-world structure is addressed. This structure is the airframe of the Morane-Saulnier Paris aircraft, which is represented in Figure 2. This French jet aircraft was built during the 1950s and was used as a trainer and liaison aircraft. The structural configuration under consideration corresponds to the aircraft without its jet engines and standing on the ground through its three landing gears with deflated tires. For information, general characteristics are listed in Table 1. A specimen of this plane is present in ONERA's laboratory, and ground vibration tests have exhibited nonlinear behavior in the connection between the wings and external fuel tanks located at the wing tip. As illustrated in Figure 3, this connection consists of bolted attachments.

Figure 2: Morane-Saulnier Paris aircraft.

Table 1: Properties of the Morane-Saulnier Paris aircraft

Length (m)	Wingspan (m)	Height (m)	Wing area (m^2)	Weight (kg)
10.4	10.1	2.6	18	1945

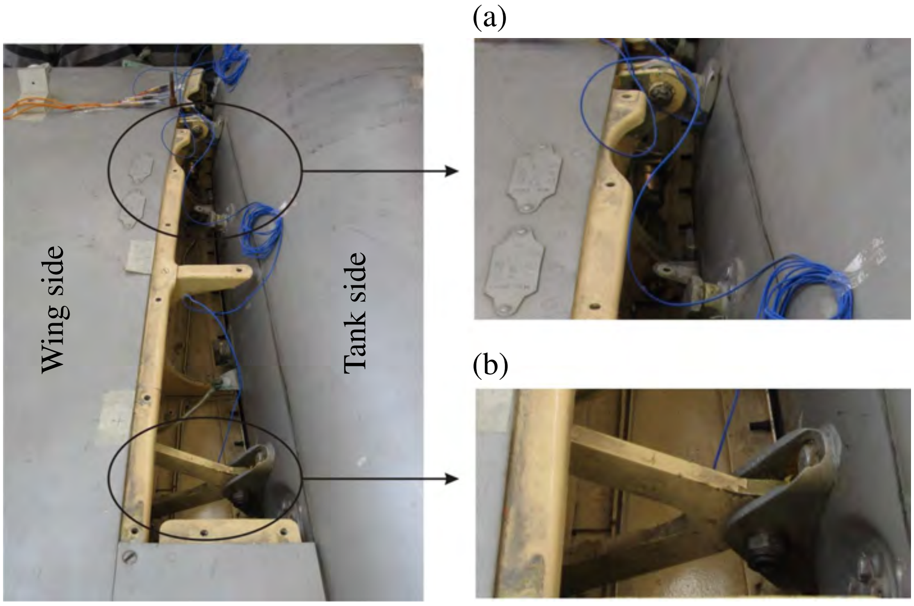

Figure 3: Connection between external fuel tank and wing tip (top view). Close-up of (a) front and (b) rear bolted attachments.

4.1 Structural Model of the Paris Aircraft

4.1.1 Finite Element Model of the Underlying Linear Structure

The linear finite element model of the full-scale aircraft, illustrated in Figure 4, was elaborated from drawings by ONERA [14]. The wings, vertical stabilizer, horizontal tail and fuselage are modeled by means of 2-dimensional elements such as beams and shells. The complete finite element model has more than 80000 DOFs. Three-dimensional spring elements, which take into account the structural flexibility of the tires and landing gears, are used as boundary conditions of the aircraft. At each wing tip, the external fuel tank is connected with front and rear attachments (see Figure 3). In this linear model, these connections between the wings and the fuel tanks are modeled using beam elements. The linear model, originally created in the Nastran software, was converted and exploited in the Samcef finite element environment for this study.

The natural frequencies of the underlying linear system in the [0-50Hz] frequency range are given in Table 2. The first nine modes correspond to aircraft rigid-body modes: six modes are modes of suspensions of the landing gear while the three others are associated to rigid-body motions of the control surfaces (i.e., the ailerons, elevator and rudder). The frequency range of the rigid-body modes is comprised between 0.09 and 3.57 Hz, i.e., noticeably lower than the first flexible mode located at 8.19 Hz. The modal shapes of different elastic normal modes of vibrations are depicted in Figure 5. Figure 5(a) represents the first wing bending mode. The first and second wing torsional modes are depicted in Figures 5(b) and 5(c). These two torsional modes correspond to symmetric and anti-symmetric wing motions, respectively. As shown thereafter, these modes are of particular interest in nonlinear regime since there is a significant deformation of the connections between the wings and fuel tanks. Indeed, the other modes mainly concern the aircraft tail and are consequently almost unaffected by these nonlinear connections.

4.1.2 Reduced-Order Model

The proposed algorithm for the numerical computation of NNMs is computationally intensive for the large-scale original model possessing more than 80000 DOFs. Since the nonlinearities are spatially localized, condensation of the linear components of the model is an appealing approach for a computationally tractable and efficient calculation.

A reduced-order model of the linear finite element system is constructed using the Craig-Bampton (also called component mode) reduction technique [15]. This method consists in describing the system in terms of some retained DOFs and internal vibration modes. By partitioning the complete system in terms of n_R remaining $\mathbf{x}_R$ and $n_C = n - n_R$ condensed $\mathbf{x}_C$ DOFs, the n governing equations of motion of the global finite element model are written as

$$\begin{bmatrix} \mathbf{M}_{RR} & \mathbf{M}_{RC} \\ \mathbf{M}_{CR} & \mathbf{M}_{CC} \end{bmatrix} \begin{bmatrix} \ddot{\mathbf{x}}_R \\ \ddot{\mathbf{x}}_C \end{bmatrix} + \begin{bmatrix} \mathbf{K}_{RR} & \mathbf{K}_{RC} \\ \mathbf{K}_{CR} & \mathbf{K}_{CC} \end{bmatrix} \begin{bmatrix} \mathbf{x}_R \\ \mathbf{x}_C \end{bmatrix} = \begin{bmatrix} \mathbf{g}_R \\ \mathbf{0} \end{bmatrix} \tag{15}$$

The Craig-Bampton method expresses the complete set of initial DOFs in terms of: (i) the remaining DOFs through the static modes (resulting from unit displacements on the remaining DOFs) and (ii) a certain number $m < n_C$ of internal vibration modes (relating to the primary structure fixed on the remaining nodes). Mathematically, the reduction is described by relation

$$\begin{bmatrix} \mathbf{x}_R \\ \mathbf{x}_C \end{bmatrix} = \begin{bmatrix} \mathbf{I} & \mathbf{0} \\ -\mathbf{K}_{CC}^{-1}\mathbf{K}_{CR} & \mathbf{\Phi}_m \end{bmatrix} \begin{bmatrix} \mathbf{x}_R \\ \mathbf{y} \end{bmatrix} = \mathbf{R} \begin{bmatrix} \mathbf{x}_R \\ \mathbf{y} \end{bmatrix} \tag{16}$$

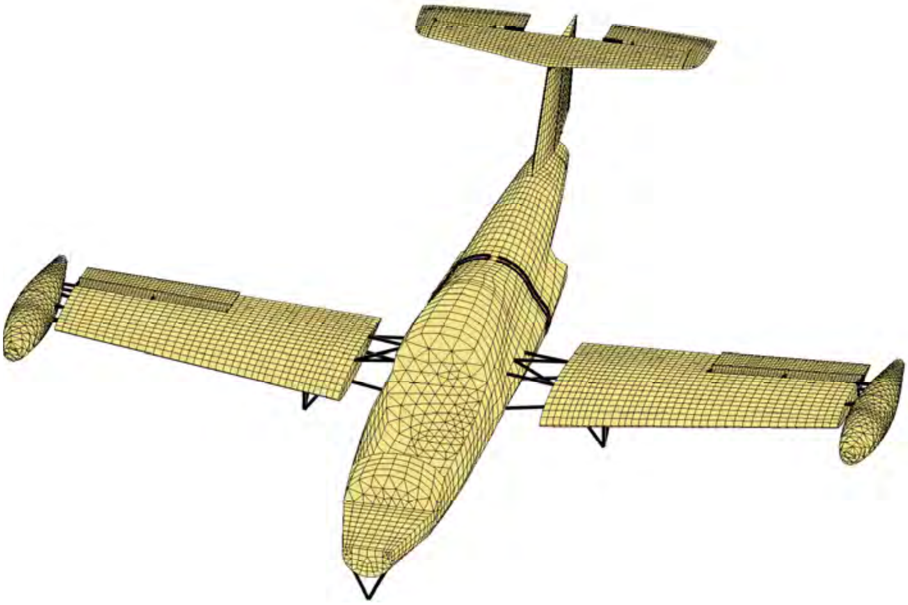

Figure 4: Finite element model of the Morane-Saulnier Paris aircraft.

Mode	Freq. (Hz)	Mode	Freq. (Hz)
1	0.0936	13	21.2193
2	0.7260	14	22.7619
3	0.9606	15	23.6525
4	1.2118	16	25.8667
5	1.2153	17	28.2679
6	1.7951	18	29.3309
7	2.1072	19	31.0847
8	2.5157	20	34.9151
9	3.5736	21	39.5169
10	8.1913	22	40.8516
11	9.8644	23	47.3547
12	16.1790	24	52.1404

Table 2: Natural frequencies of the linear finite element model of the Paris aircraft.

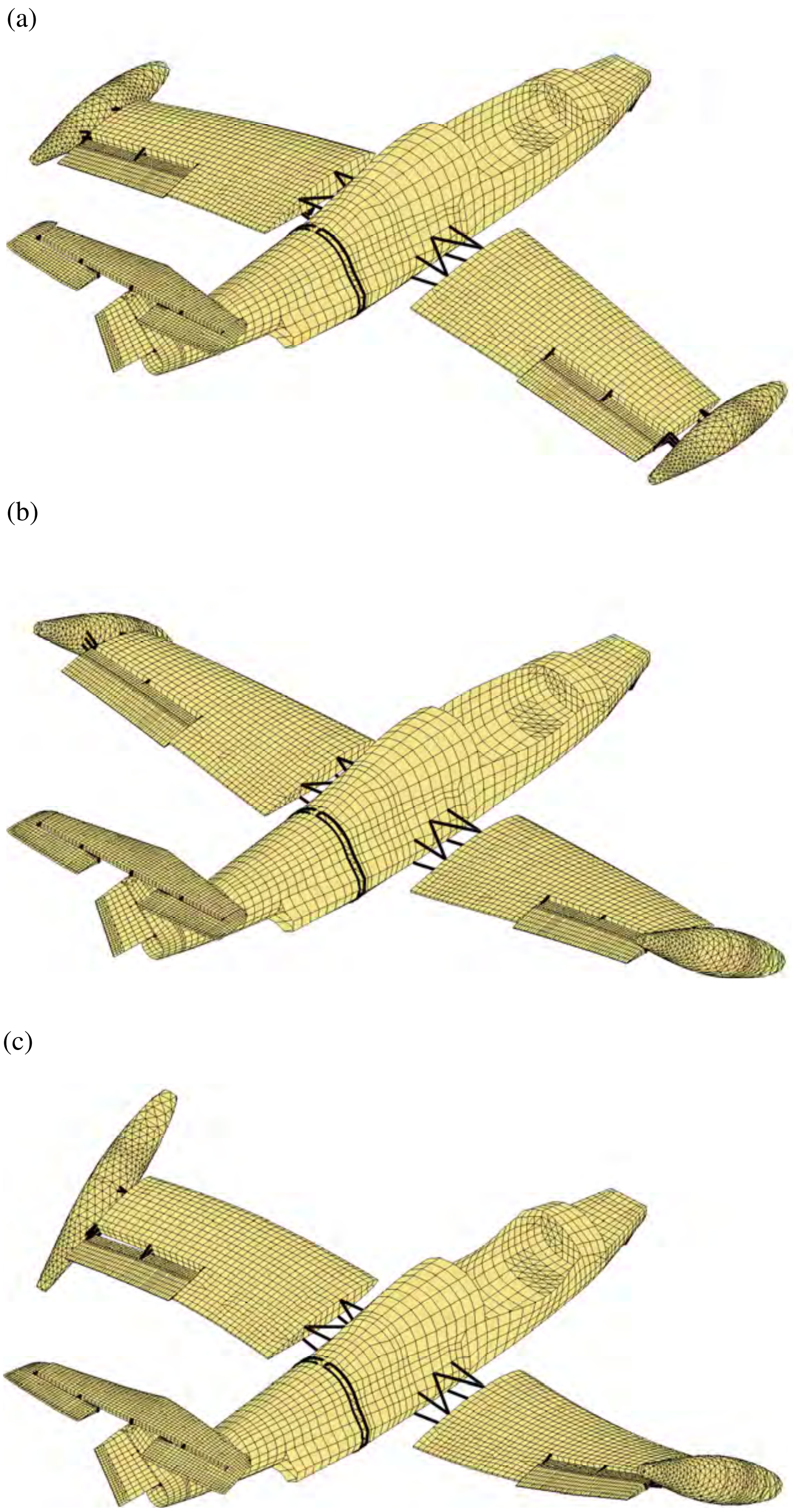

Figure 5: Normal modes of the linear finite element model of the Morane-Saulnier Paris aircraft. (a) First wing bending mode (8.19 Hz), (b) first (symmetric) wing torsional mode (31.08 Hz) and (b) second (anti-symmetric) wing torsional mode (34.92 Hz).

which defines the $n \times (n_R + m)$ reduction matrix $\mathbf{R}$. $\mathbf{y}$ are the modal coordinates of the m internal linear normal modes collected in the $n_C \times m$ matrix $\mathbf{\Phi}_m = [\phi_{(1)} \dots \phi_{(m)}]$. These modes are solutions of the linear eigenvalue problem corresponding to the system fixed on the remaining nodes

$$\left(\mathbf{K}_{CC} - \omega_{(j)}^2 \mathbf{M}_{CC}\right) \phi_{(j)} = \mathbf{0} \tag{17}$$

The reduced model is thus defined by the $(n_R + m) \times (n_R + m)$ reduced stiffness and mass matrices given by

$$\begin{aligned} \overline{\mathbf{M}} &= \mathbf{R}^* \mathbf{M} \mathbf{R} \\ \overline{\mathbf{K}} &= \mathbf{R}^* \mathbf{K} \mathbf{R} \end{aligned} \tag{18}$$

where star denotes the transpose operation. After reduction, the system configuration is expressed in terms of the reduced coordinates (i.e., the remaining DOFs and the modal coordinates). The initial DOFs of the complete model are then determined by means of the reduction matrix using relation 16.

In order to introduce the nonlinear behavior of the connections between the wings and the tanks, the reduced-order linear model of the aircraft is constructed by keeping one node on both sides of the attachments. For each wing, four nodes are retained: two nodes for the front attachment and two nodes for the rear attachment. In total, only eight nodes of the finite element model are kept to build the reduced model. It is completed by holding the first 500 internal modes of vibrations. Finally, the model is thus reduced to 548 DOFs: 6 DOFs per node (3 translations and 3 rotations) and 1 DOF per internal mode. The reduction is performed using the Samcef software. The generated reduced-order model is next exported in the MATLAB environment.

Before proceeding to nonlinear analysis, the accuracy of the reduced-order linear model is assessed. To this end, the linear normal modes of the initial complete finite element model are compared to those predicted by the reduced model. The deviation between the mode shapes of the original model $\mathbf{x}_{(o)}$ and of the reduced model $\mathbf{x}_{(r)}$ is determined using the Modal Assurance Criterion (MAC)

$$\text{MAC} = \frac{\left|\mathbf{x}_{(o)}^* \mathbf{x}_{(r)}\right|^2}{\left|\mathbf{x}_{(o)}^* \mathbf{x}_{(o)}\right| \left|\mathbf{x}_{(r)}^* \mathbf{x}_{(r)}\right|} \tag{19}$$

MAC values range from 0 in case of no correlation to 1 for a complete coincidence. In the [0-100Hz] range, MAC values between modes shapes are all greater than 0.999 and the maximum relative error on the natural frequencies is 0.2%. It therefore validates the excellent accuracy of the reduced linear model in this frequency range. It is worth noticing that less internal modes are sufficient to ensure such as a correlation in the [0-100Hz] frequency range, which is typically the range of interest for aircrafts. However, a larger number of modes was deliberately chosen for two main reasons. On the one side, it serves to illustrate the ability of the numerical algorithm to deal with the NNM computation of higher-dimensional systems. On the other hand, due to nonlinearity, modes of higher frequencies may interact with lower modes of interest. In nonlinear regimes, higher internal modes should then be necessary to guarantee the accuracy of the model.

Figure 6: Instrumentation of the rear attachment of the right wing.

4.1.3 Nonlinear Model

The existence of a softening nonlinear behavior was evidenced during different vibration tests conducted by ONERA. In particular, FRF measurements reveal the decrease of resonant frequencies with the level of excitation. The connections between the wings and fuel tanks are assumed to cause this observed nonlinear effect.

To confirm this hypothesis, both (front and rear) connections of each wing were instrumented and experimental measurements were carried out. Specifically, accelerometers were positioned on both (wing and tank) sides of the connections and two shakers were located at the tanks. This is illustrated in Figure 6 for rear connection.

The dynamic behavior of these connections in the vertical direction is investigated using the restoring force surface (RFS) method [16]. By writing Newton's second law at the wing side of each connection, it follows

$$m_c \ddot{x}_c(t) + f_{r,c} = 0 \tag{20}$$

where $f_{r,c}$ is the restoring force applied to this point. The index c is related to the connection under consideration (i.e., either the rear or front attachment of the left or right wing). From Equation (20), the restoring force is obtained by

$$f_{r,c} = -m_c \ddot{x}_c(t) \tag{21}$$

Except the multiplicative mass factor m_c, the restoring force is then given by the acceleration $\ddot{x}_c(t)$. Nevertheless, this total restoring force does not consist only of the internal force related to the connection of interest, but also includes contributions from the linking forces associated to the wing elastic deformation. Provided that these latter do not play a prominent role, the measurement of the acceleration signal may still provide a qualitative insight into the nonlinear part of the restoring force in the connection between the tank and the wing.

The aircraft is excited close to the second torsional mode (see Figure 5(c)) using a band-limited swept sine excitation in the vicinity of its corresponding resonant frequency. In Figure 7, the measured acceleration at the wing side is represented in terms of the relative displacement x_{rel} and velocity $\dot{x}_{rel}$ of the connection obtained by integrating the accelerations on both sides of the attachment. It is given for the rear connections of the right and left wings. A nonlinear softening elastic effect is observed from the evolution of these estimated restoring force surfaces. In particular, the detected behavior has a piecewise characteristic. This is more clearly

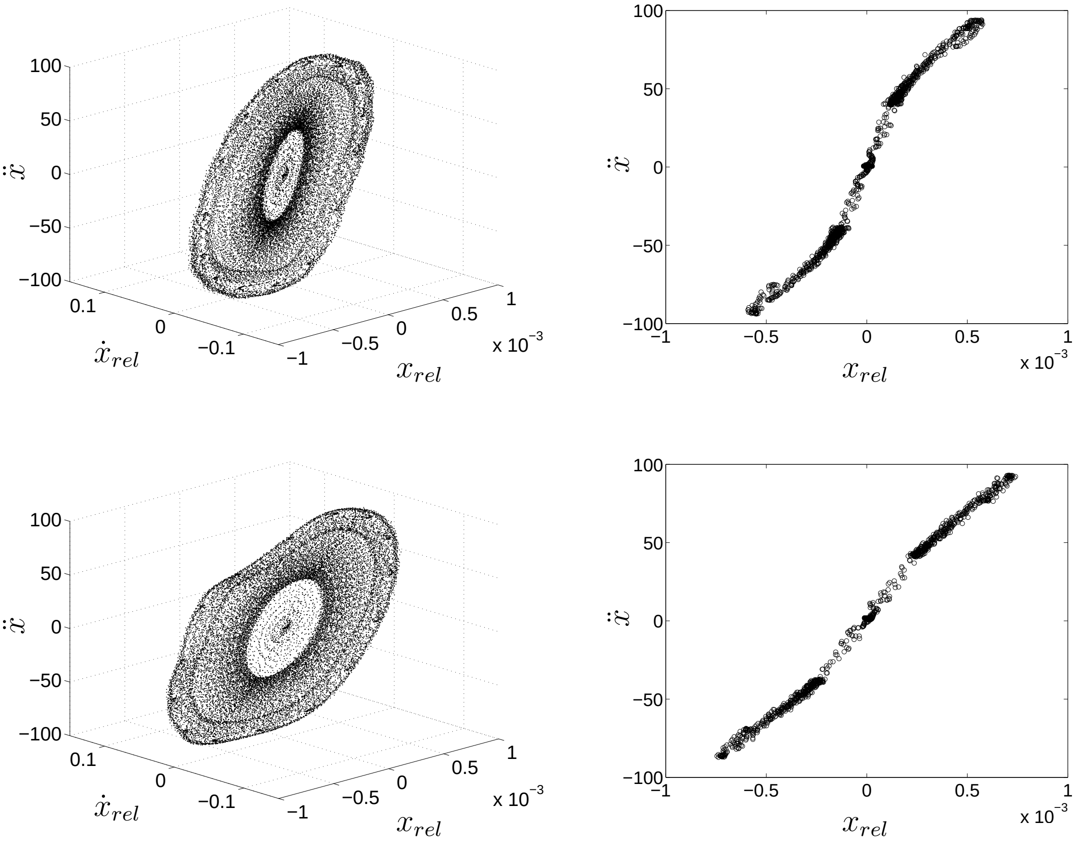

Figure 7: Estimated restoring force in the connections between tanks and wings. Left plots: measured acceleration in terms of the relative displacement (m) and velocity (m/s). Right plots: stiffness curve given by the measured acceleration for zero velocity. Top plots: rear tank connection of the left wing. Bottom plots: rear tank connection of the right wing.

evidenced by the corresponding stiffness curves also depicted in Figure 7. Softening nonlinearity is typical of bolted connections [17, 18]. Similar nonlinear effect occurs for the front connections, but they participate much less in the considered response. Finally, the deviation between the right and left connections seems to show asymmetry of the connections.

Although purely qualitative, the RFS results therefore indicate that the tank connections present a softening stiffness in the vertical direction. As previously mentioned, a model with piecewise characteristic might be consistent with the experimental observations. However, the NNM algorithm, in its present form, cannot handle nonsmooth nonlinearities. Alternatively, linear and negative cubic stiffness terms are one possible manner of describing the observed nonlinear behavior. Indeed, the reconstructed stiffness curve obtained by fitting to the data the mathematical model

$$f_{r,c} = kx_{rel} + k_{nl}^{-}x_{rel}^{3} \qquad (k_{nl}^{-} < 0) \tag{22}$$

is in relatively good agreement.

In view of the qualitative value of this approach, we note that the objective followed here is to derive a simplified realistic model in order to illustrate the numerical computation procedure of NNMs. Accordingly, in the present study, the nonlinear behavior is modeled by adding negative cubic stiffness nonlinearities into the linear part of the connections. An indicative value of -10^{13}N/m^{3} is adopted for each connection. Finally, the nonlinear system is then constructed from the reduced-order model by means of cubic springs positioned vertically between both corresponding nodes retained on either side of connections.

4.2 Nonlinear Normal Modes

From the nonlinear reduced-order model, the numerical computation of NNMs is realized in the MATLAB environment using the previously developed algorithm. The goal followed here is to show that the proposed method can deal with complex structures such as this real-aircraft model. In this context, this section focuses on some specific modes.

4.2.1 Fundamental NNMs

The modes of the aircraft can be classified into two categories, depending on whether they correspond to wing motions or not. The modes localized mainly on other structural parts (such as the vertical stabilizer, the horizontal tail or the fuselage) are almost unaffected by the nonlinear connections located at the wing tips. Only the modes involving wing deformations are perceptibly affected by nonlinearity. According to the relative motion of the fuel tanks, these modes are more or less altered for increasing energy levels.

An unaffected mode is first examined in Figure 8. It corresponds to the nonlinear extension of the first tail bending LNM (mode 13 in Table 2). In this figure, the computed backbone and related NNM motions are depicted in the FEP. The modal shapes are given in terms of the initial displacements (with zero initial velocities assumed) that realize the NNM motion. It clearly confirms that the modal shape and the oscillation frequency remain practically unchanged with the energy in the system.

Modes involving wing deformations are now investigated. The first wing bending mode (i.e., the nonlinear extension of mode 10 in Table 2) is illustrated in Figure 9. The FEP reveals that this mode is weakly affected by the nonlinearities. The frequency of the NNM motions on the backbone slightly decreases with increasing energy levels, which results from the softening characteristic of the nonlinearity. Regarding the modal shapes, they are almost similar over the energy range and resemble the corresponding LNM. MAC value between the NNM shapes at low and high energy levels (see (a) and (b) in Figure 9) is 0.99.

Figure 10 represents the FEP of the first (symmetric) wing torsional mode (i.e., mode 19 in Table 2). For this mode, the relative motion of the fuel tanks is more important, which enhances the nonlinear effect of the connections. As a result, the oscillation frequency have a more marked energy dependence along the backbone branch. On the other hand, the modal shapes are still weakly altered. MAC value between the NNM shapes on the backbone at low and high energy levels (see (a) and (b) in Figure 10) is equal to 0.98. In addition, the FEP highlights the presence of three tongues, revealing the existence of internal resonances between this symmetric torsional mode and other modes. These observed modal interactions are discussed in the next section.

Finally, the second (anti-symmetric) wing torsional mode (i.e., mode 20 in Table 2) is plotted in the FEP of Figure 11. While the oscillation frequency is noticeably altered by nonlinearity, modal shapes are again slightly changed. Over the energy range of interest, the decrease in frequency is around 5% along the backbone branch. MAC value between the modal shapes at low and high energy levels (see (a) and (b) in Figure 11) is 0.97. It shows that the nonlinearities spatially localized between the wing tips and the tanks weakly influence the NNM spatial shapes. Besides the NNM backbone, one tongue is present at higher energy. For information, the computation of the backbone branch up to the tongue needs 20 min with 100 time steps over the half period (using Intel i7 920 2.67GHz processor). Due to the presence of turning points, the computation of the tongue is more expensive and demands about one hour.

Similar dynamics were observed for the higher modes and are not further described herein.

4.2.2 Internally Resonant NNMs

Besides the backbone branches, the previous FEPs show the presence of tongues of internally resonant NNMs. Following a resonance scenario similar to that described in [3], theses additional branches emanate from the backbone of a specific NNM and coalesce into the backbone branch of another NNM, thereby realizing an internal resonance between the two modes.

This is briefly illustrated in Figure 12 regarding the 3:1 tongue emanating from the backbone of the first wing torsional mode (see Figure 10). Modal shapes are given at three different locations on the tongue (see (a), (b) and (c) in Figure 12). When the energy gradually increases along the tongue, a smooth transition from the first wing torsional mode to a higher tail torsional mode clearly occurs. Interestingly, Figure 12(b) shows an inherently nonlinear mode with no counterpart in the underlying linear system. It corresponds to a 3:1 internal resonance as evidenced by the evolution of the time series and the frequency content, also represented in Figure 12, of the periodic motions along the tongue. A third harmonic progressively appears, and the structure vibrates according to a subharmonic motion characterized by two dominant frequency components. The relative importance of the third harmonic grows along the tongue, until the mode transition is realized.

Similarly, two other tongues corresponding to a 5:1 and a 9:1 internal resonance between this first wing torsional mode and higher modes are observed in the FEP of Figure 10. Moreover, the FEP of Figure 11 reveals the presence of a 9:1 internal resonance between the second wing torsional mode and another higher mode of the aircraft. We note that the practical realization of these internal resonances is questionable in view of the low frequency changes.

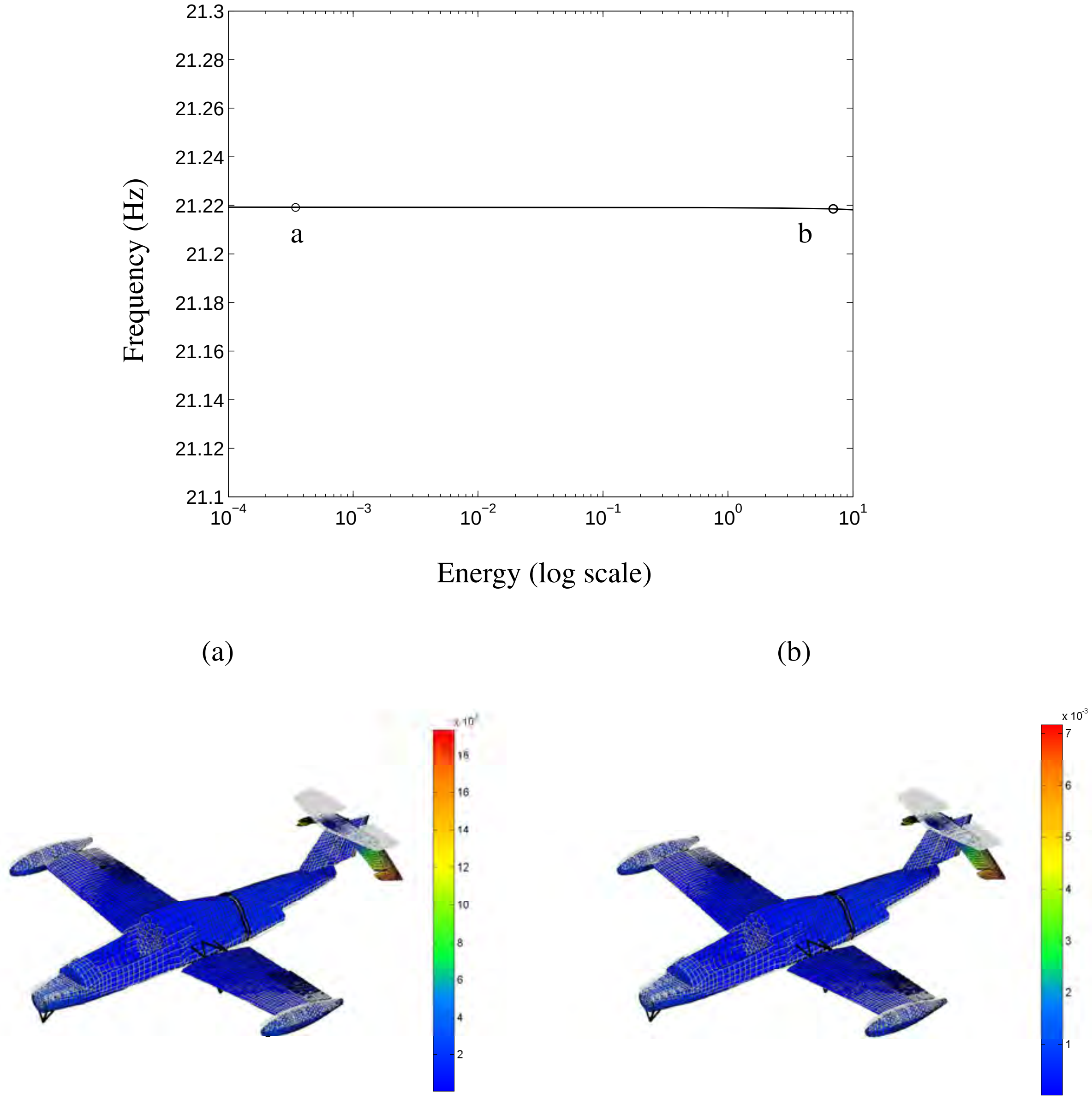

(a)

(b)

Figure 8: FEP of the first tail bending NNM of the Paris aircaft. NNM shapes at energy levels marked in the FEP are inset; they are given in terms of the initial displacements (m) that realize the periodic motion (with zero initial velocities assumed).

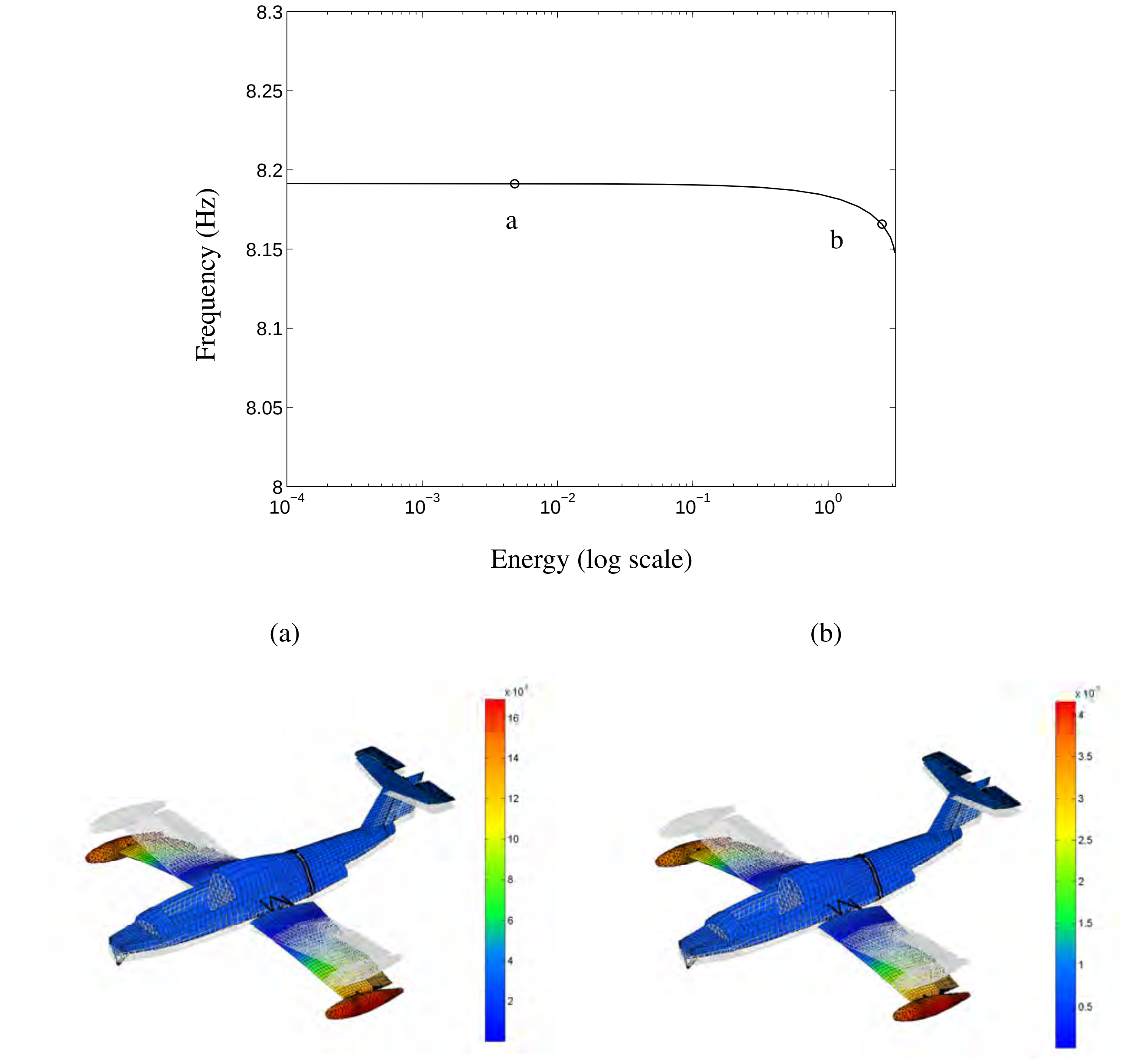

(a) (b)

Figure 9: FEP of the first wing bending NNM of the Paris aircraft. NNM shapes at energy levels marked in the FEP are inset; they are given in terms of the initial displacements (m) that realize the periodic motion (with zero initial velocities assumed).

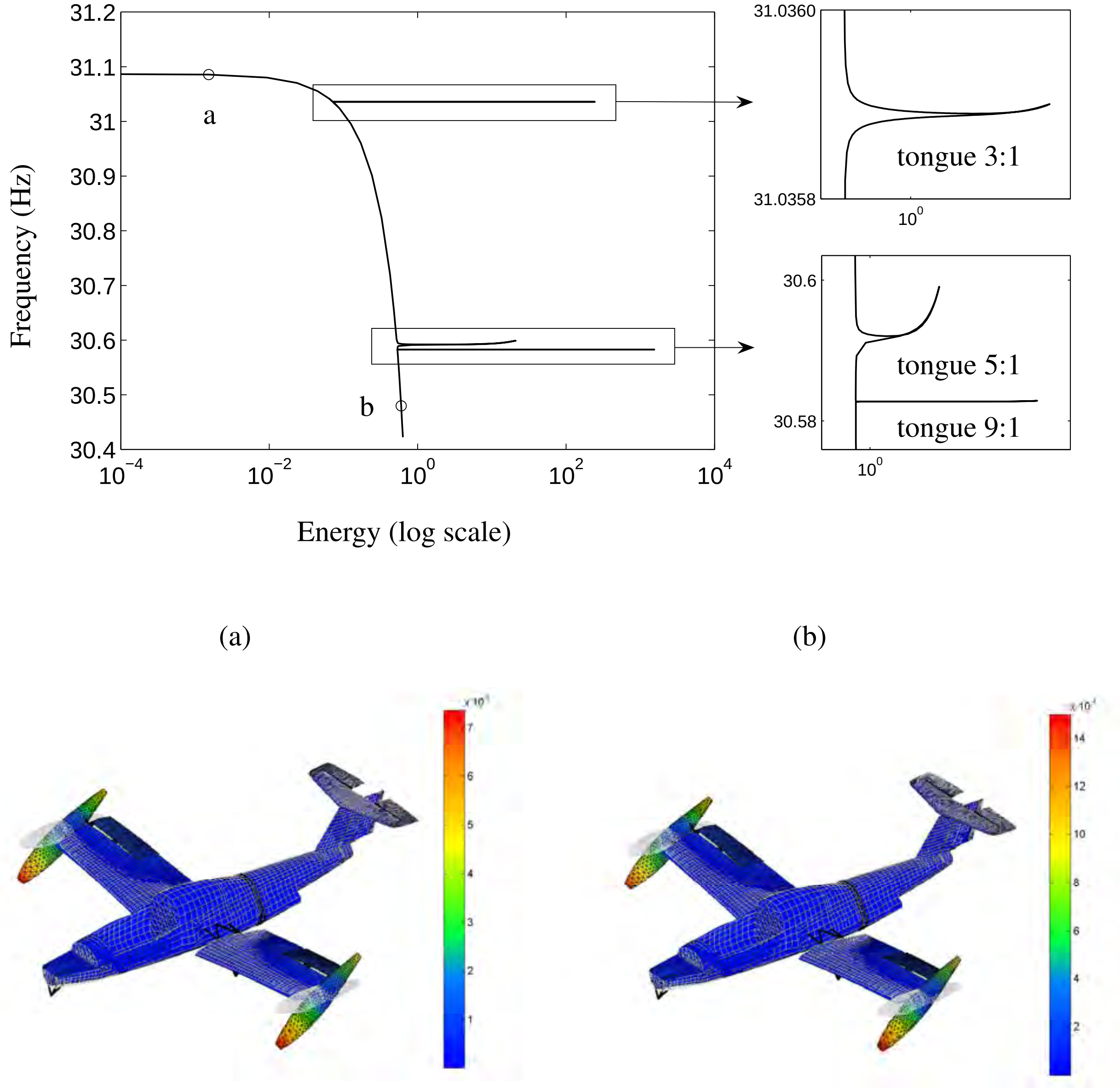

(a)

(b)

Figure 10: FEP of the first (symmetric) wing torsional NNM of the Paris aircraft. NNM shapes at energy levels marked in the FEP are inset; they are given in terms of the initial displacements (m) that realize the periodic motion (with zero initial velocities assumed).

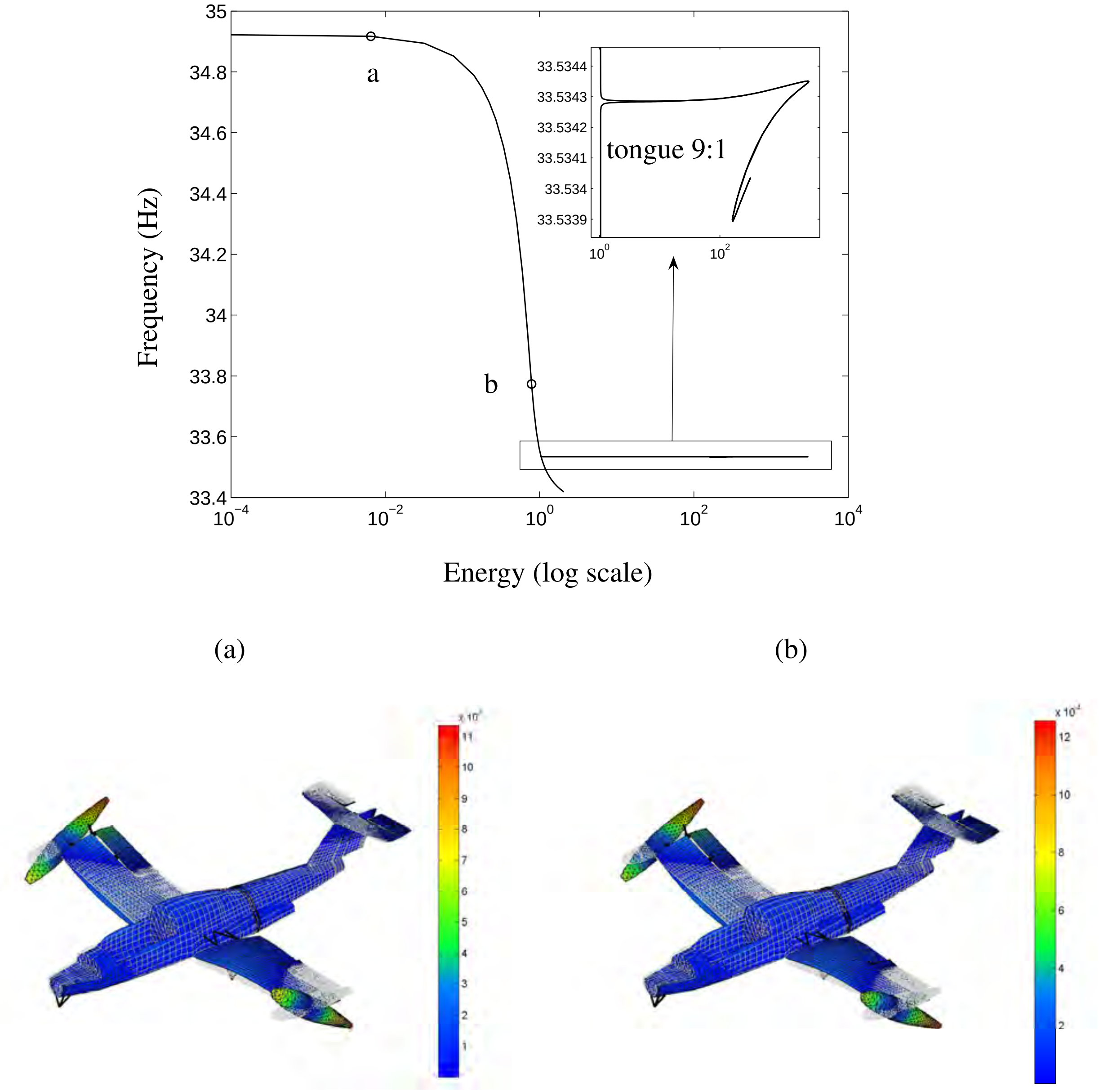

(a) (b)

Figure 11: FEP of the second (anti-symmetric) wing torsional NNM of the Paris aircraft. NNM shapes at energy levels marked in the FEP are inset; they are given in terms of the initial displacements (m) that realize the periodic motion (with zero initial velocities assumed).

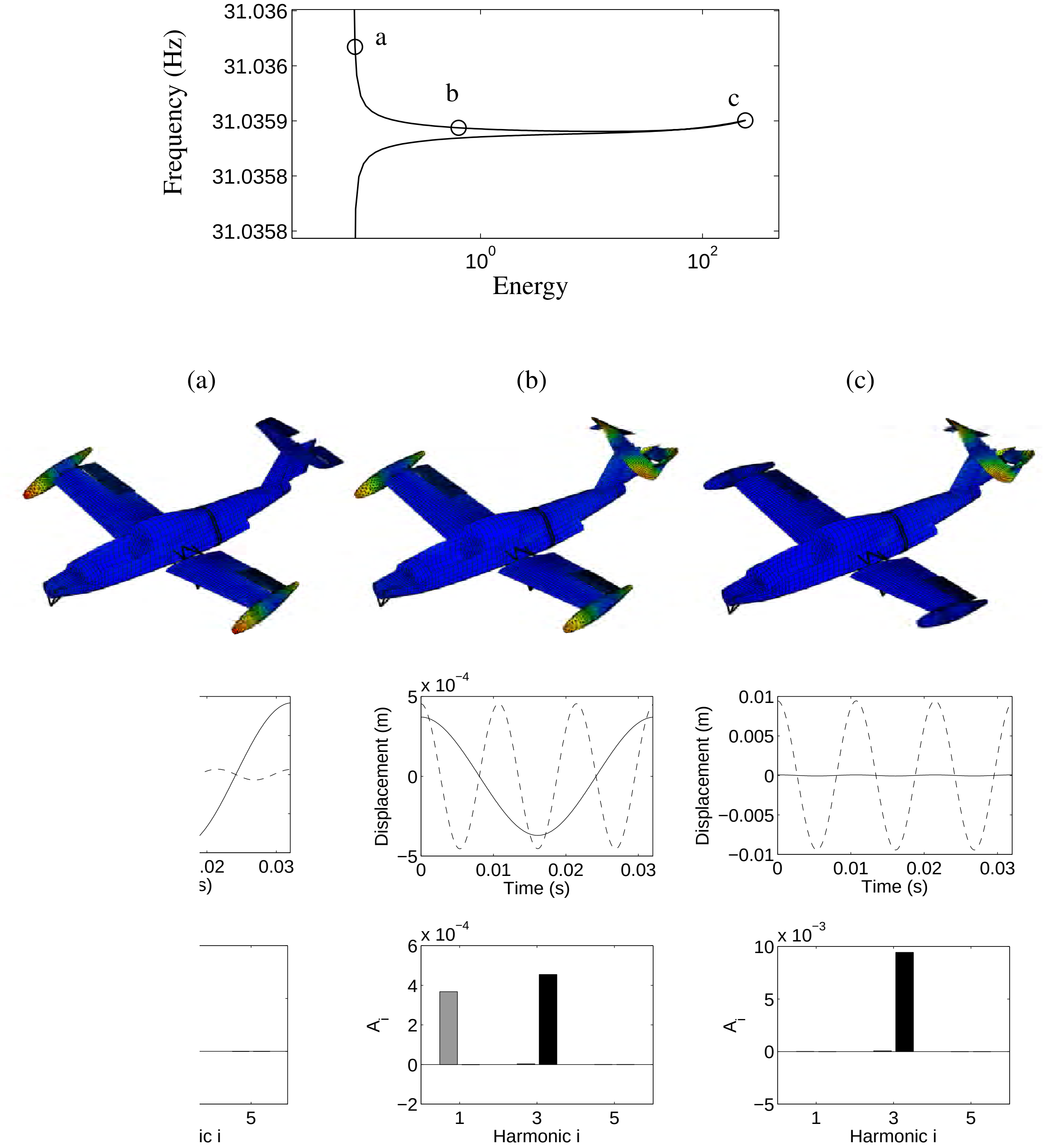

Figure 12: 3:1 internal resonance between the first wing torsional mode and a higher tail mode of the Paris aircraft. Top plot: close-up in the FEP of the 3:1 tongue of Figure 10. Bottom plots: NNM motions at (a) beginning of the tongue (in the vicinity of the backbone of the the first wing torsional mode); (b) middle of the tongue; and (c) extremity of the tongue. From top to bottom: NNM shapes; time series of the vertical displacements at the rear tip of the right tank (——) and at the right side of the horizontal tail (– – –); Fourier coefficients of both displacements (in grey and black, respectively).

5 Conclusion

In this paper, a numerical method for the computation of NNMs of mechanical structures was introduced. The approach targets the computation of the undamped modes of structures discretized by finite elements and relies on the continuation of periodic solutions.

This computational approach turns out to be capable of dealing with complex real-world structures, such as the full-scale aircraft studied herein. Through a reduced-order model accurate in the [0-100Hz] range, the NNMs were indeed computed accurately even in strongly nonlinear regimes and with a reasonable computational burden. Internal resonances were also computed by the algorithm and were briefly discussed.

REFERENCES

[1] A.F. Vakakis, L.I. Manevitch, Y.V. Mikhlin, V.N. Pilipchuk, A.A. Zevin, *Normal Modes and Localization in Nonlinear Systems*, John Wiley & Sons, New York (1996).

[2] A.F. Vakakis, *Non-linear normal modes (NNMs) and their applications in vibration theory: An overview*, Mechanical Systems and Signal Processing, Vol. 11, No. 1 (1997), pp. 3-22.

[3] G. Kerschen, M. Peeters, J.C. Golinval, A.F. Vakakis, *Nonlinear normal modes, Part I: A useful framework for the structural dynamicist*, Mechanical Systems and Signal Processing, Vol. 23, No. 1 (2009), pp. 170-194.

[4] J.C. Slater, *A numerical method for determining nonlinear normal modes*, Nonlinear Dynamics, Vol. 10, No. 1 (1996), pp. 19-30.

[5] E. Pesheck, *Reduced-order modeling of nonlinear structural systems using nonlinear normal modes and invariant manifolds*, PhD Thesis, University of Michigan, Ann Arbor (2000).

[6] Y.S. Lee, G. Kerschen, A.F. Vakakis, P.N. Panagopoulos, L.A. Bergman, D.M. McFarland, *Complicated dynamics of a linear oscillator with a light, essentially nonlinear attachment*, Physica D-Nonlinear Phenomena, Vol. 204, No. 1-2 (2005), pp. 41-69.

[7] R. Arquier, S. Bellizzi, R. Bouc, B. Cochelin, *Two methods for the computation of nonlinear modes of vibrating systems at large amplitudes*, Computers & Structures, Vol. 84, No. 24-25 (2006), pp. 1565-1576.

[8] R. Seydel, *Practical Bifurcation and Stability Analysis, from Equilibirum to Chaos*, Springer-Verlag, 2nd Edition (1994).

[9] A.H. Nayfeh, B. Balachandran, *Applied Nonlinear Dynamics: Analytical, Computational, and Experimental Methods*, Wiley-Interscience, New York (1995).

[10] E. Doedel, *AUTO, Software for Continuation and Bifurcation Problems in Ordinary Differential Equations*, (2007).

[11] C. Touz, A. Amabili, O. Thomas, *Reduced-order models for large-amplitude vibrations of shells including in-plane inertia*, In *Proceedings of the EUROMECH Colloquium on Geometrically Nonlinear Vibrations, Porto, Portugal, July 2007*, Porto (2007).

[12] M. Peeters, R. Vigui, G. Srandour, G. Kerschen, J.C. Golinval, *Nonlinear normal modes, Part II: Toward a practical computation using numerical continuation techniques*, Mechanical Systems and Signal Processing, Vol. 23, No. 1 (2009), pp. 195-216.

[13] O. Brüls, P. Eberhard, *Sensitivity analysis for dynamic mechanical systems with finite rotations*, International Journal for Numerical Methods in Engineering, Vol. 1 (2006), pp. 1-29.

[14] A. Remy, *Updating of the finite element model of the MS 760 Paris aircraft*, Training period report at ONERA (2006).

[15] R. Craig, M. Bampton, *Coupling of substructures for dynamic analysis*, AIAA Journal, Vol. 6 (1968), pp. 1313–1319.

[16] S.F. Masri, T.K. Caughey, *A nonparametric identification technique for nonlinear dynamic problems*, Journal of Applied Mechanics, Vol. 46 (1979), pp. 433-447.

[17] L. Gaul, J. Lenz, *Nonlinear dynamics of structures assembled by bolted joints*, Acta Mechanica, Vol. 125 (1997), pp. 169-181.

[18] C.J. Hartwigsen, Y. Song, D.M. McFarland, L.A. Bergman, A.F. Vakakis, *Experimental study of non-linear effects in a typical shear lap joint configuration*, Journal of Sound and Vibration, Vol. 277 (2004), pp. 327-351.

COMPDYN 2011
3rd ECCOMAS Thematic Conference on
Computational Methods in Structural Dynamics and Earthquake Engineering
M. Papadrakakis, M. Fragiadakis, V. Plevris (eds.)
Corfu, Greece, 25-28 May 2011

FILTER FAILURE ANALYSIS FOR THE SWAP INSTRUMENT ON BOARD OF PROBA2

Stijn Jonckheere[1], Bart Bergen[1], Bert Pluymers[1], Jean-Philippe Halain[2], Pierre Rochus[2], Wim Desmet[1], Dirk Vandepitte[1]

[1]Department of Mechanical Engineering, K.U. Leuven
Celestijnenlaan 300B – box 2420, B-3001, Heverlee (Leuven), Belgium.
Tel: +32 16 322480; fax: +32 16 322987
e-mail: Stijn.Jonckheere@mech.kuleuven.be

[2] Centre Spatiale de Liège
Avenue Pré Aily, B-4031 Angleur (Liège), Belgium

Keywords: SWAP, PROBA2, optical membranes, vibro-acoustics.

Abstract. *During its intensive testing campaign, SWAP (Sun Watcher using Active Pixel System detector and image Processing), an optical instrument developed by Centre Spatiale de Liège (CSL) and mounted onto the Belgian satellite PROBA2, was subjected to a multitude of load cases to verify the integrity of the instrument during and after the launch and during the operational phase.*

The front and rear filters of SWAP, 200 nm thin films, survived intensive vibration tests on the qualification model and acceptance tests on the flight model, both at an instrument level. During the acoustic test on the spacecraft, the front filter exploded while the rear one was undamaged. A new, strengthened filter, coated with a very fine metal mesh was mounted in the instrument. However, this new filter has less good optical properties due to optical diffraction. Therefore a profound analysis of the filter failure is necessary to provide the best possible optical accuracy for future missions with similar equipment.

Three load cases are further studied in this paper: the acceleration of the rocket, the instrument depressurisation and the vibro-acoustic behaviour under the large sound and vibration levels. The acceleration and depressurisation are studied together in a two-level computational fluid dynamics (CFD) analysis to assess the effect of the venting of the instrument on the differential pressure over the filter. The main focus of this paper is on a numerical vibro-acoustic analysis, following the procedures used by CSL and ESTEC (European Space Research and Technology Centre). This analysis needs special attention because of the presence of a stochastic excitation (diffuse field) and the very nonlinear behaviour of the filter itself due to its small thickness. Also, an additional postprocessing step based on filter displacements, rather than differential pressure, as done in the ESTEC procedure, is discussed.

1 INTRODUCTION

On November 2^{nd} 2009 PROBA2[1], the second completely Belgian mini-satellite, produced by the company Verhaert (now QinetiQ), was launched from the ESA-base in Plesetsk, Russia. The goals of the mission were dual: providing a proving ground for new technologies to test their flightworthiness and studying the interaction between the Earth and the Sun and the impact on the so called space weather. One of the scientific instruments on board was the SWAP[2]-instrument, an optical instrument designed by Centre Spatiale de Liège (CSL) to study the solar corona. For this purpose, it is equipped with two optical filters that retain only the frequencies of the solar spectrum relevant to the spaceweather (eUV-frequencies).

The instrument (roughly 50 cm x 15 cm x 10 cm in size) is constructed as is illustrated in Figure 1(a). The instrument cavity is closed, a.o. for cleanliness of the instrument, by a heavy door maintained by a launch lock mechanism with a dedicated labyrinth for depressurisation. Behind that door, which is designed to protect the instrument from acoustic overload, lies a first (small) cavity. Between this small cavity and the large instrument cavity lies the front optical filter, an aluminum membrane with a thickness of 200 nm, which can withstand an ultimate differential pressure of 200 Pa.

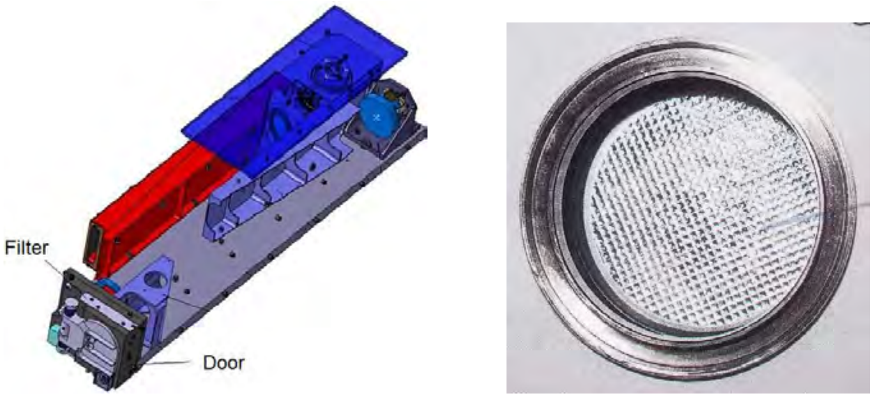

(a) SWAP architecture [1]. (b) Strengthened filter [2].

Figure 1: General SWAP architecture and strengthened filter.

The front and rear filters of SWAP survived intensive vibration tests on the qualification model and acceptance tests on the flight model, both at an instrument level. During the acoustic tests of the spacecraft, as in-flight images indicate, the front filter exploded, while the rear one was undamaged. Because of the tight schedule for further testing and launch, the problem had to be dealt with very quickly. Therefore, a new, strengthened filter, coated with a very fine (20 lpi) nickel mesh was mounted (figure 1(b)). This however degrades the optical properties of the filter due to optical diffraction and is therefore not the optimal solution. To learn lessons for future missions, a profound analysis is necessary to assess the true cause of failure for the original filter. A preliminary vibro-acoustic analysis, as performed at ESTEC[3], raised quite some questions. Therefore, CSL proposed to K.U.Leuven to further explore the problem in the context of the master's thesis study [3] of the first author of this paper.

This paper discusses three load cases that can cause filter failure. Apart from the apparent (acoustic) cause of failure in the tests, which was first studied at ESTEC and then at K.U.Leuven

---

[1] Project for Onboard Autonomy 2

[2] Sun Watcher using Active Pixel System Detector and Image Processing

[3] European Space Research and Technology Centre

adopting the ESTEC procedures, the more or less steady-state acceleration of the rocket and the instrument depressurisation, which were tackled by GDTech [4] in a preliminary design study commissioned by CSL, is also discussed.

This acceleration and depressurisation will be studied together in a two-level computational fluid dynamics (CFD) analysis to assess the effect of the venting of the instrument on the differential pressure over the filter.

The main focus of this paper, however, lies on a numerical vibro-acoustic analysis. The analysis needs special attention because of the presence of a stochastic excitation (diffuse sound field), the very nonlinear nature of the filter itself due to its small thickness and the imprecise impact behaviour of the door, which can start flapping and whose acoustic effect is unclear. The procedure followed the same lines as the analysis procedures used by CSL and ESTEC. An additional postprocessing step based on the filter displacements, rather than pressure differences in arbitrary points was added. This approach leads to better, but nevertheless inconclusive results.

The application of these procedures for this type of vibro-acoustic analysis shows that it may in some cases be very hard, or even impossible, to make accurate predictions of the system behaviour when strong nonlinearities are present. Despite the fact that some predictions on the system behaviour can be made in an approximative manner, these predictions have to be used with great care.

2 FLUID DYNAMICS: DEPRESSURISATION AND ACCELERATION

A first important loading on the filter arises from the air escaping the instrument. This so called venting is caused by two effects: the cavity depressurisation and the inertia of the air while the rocket accelerates. These effects are elaborated in the following subsections.

To allow this air to escape smoothly, ventilation labyrinths are put at five distinct locations (see Figure 2(a)). Of these vents, the two utter left on the figure (near the door and just behind the filter) are the most interesting from a filter loading point of view. Since no light is allowed to enter or leave through these ventilation holes (otherwise the instrument would not be able to exclusively study the eUV-spectrum), these vents are engineered as labyrinths (Figure 2(b)). This way, unwanted light is attenuated by means of multiple reflections.

The analyses presented in this section were performed by GDTech [4] in a preliminary study commissioned by CSL. In the analysis, the air was considered to be an ideal gas at 20°C. A preliminary study showed laminar flow in all of the vents.

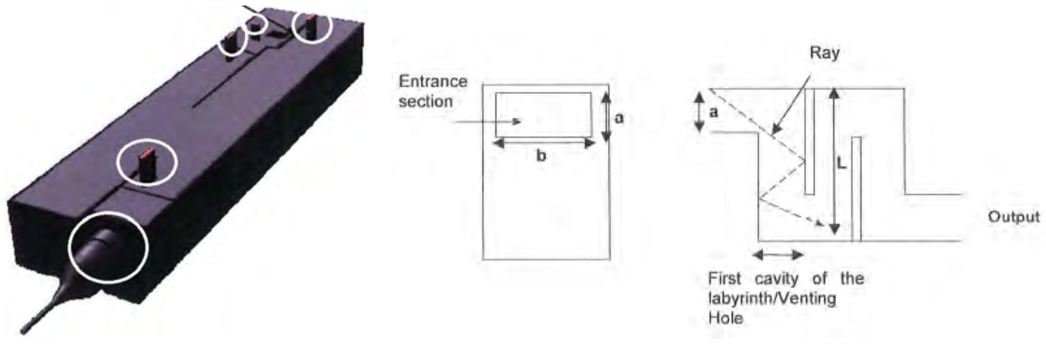

(a) Location of the venting labyrinths [4].

(b) Conceptual drawing of the venting labyrinths [4].

Figure 2: Instrument venting system.

2.1 Depressurisation

Due to the rocket gaining height, the pressure of the instrument environment decreases in time (Figure 3(a)). This causes a pressure difference between the inside and the outside. This creates a flow which is governed by Cauchy's momentum equation.

$$\rho \frac{D\vec{v}}{Dt} = \nabla \cdot (-p\mathbb{I} + \mathbb{T}) \tag{1}$$

with ρ being the fluid density, v the fluid velocity, t the time, p the pressure, $\mathbb{I}$ the identity tensor, $\mathbb{T}$ the fluid stress tensor.

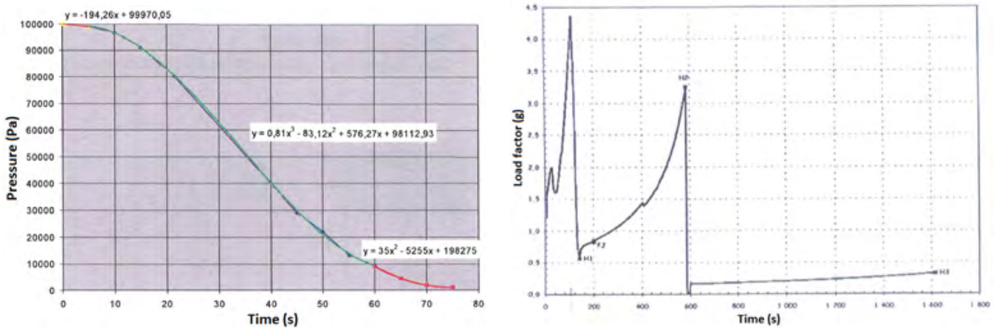

(a) Surrounding pressure variation.

(b) Rocket acceleration.

Figure 3: Variation of the imposed loading conditions in time [4].

2.2 Acceleration

The acceleration of the rocket produces a loading on the filter because of the inertia of the air surrounding it. This section will not discuss acceleration effects on the filter itself, which will be quite small because of the very low mass.

The acceleration profile can be found in Figure 3(b). The most penalising situation[4], being a loading perpendicular to the filter, is considered here, for the first eighty seconds.

This inertial loading is introduced into the governing momentum equation (Equation 1) by means of a source term $\rho\vec{a}$, with $\vec{a}$ the rocket acceleration, resulting in:

$$\rho \frac{D\vec{v}}{Dt} = \nabla \cdot (-p\mathbb{I} + \mathbb{T}) + \rho\vec{a} \tag{2}$$

2.3 Analysis

The analysis of the flow effects was performed on two levels: a lower, very detailed level, and a higher, more general one, using approximated results from the lower level.

On the low level we consider the flow inside the venting labyrinths in a detailed 2D CFD analysis (Figures 4(a) and 4(b)).

$$dP_i = aV_{ref} + b\frac{1}{2}\rho_i V_{ref}^2 \tag{3}$$

where a is related to a friction pressure loss (via e.g. the Hagen-Poiseuille equation) and b to a singular pressure drop. This approach was inspired by [5].

---

[4] This is not the true situation.

By carrying out CFD calculations for several fluid densities ρ_i, the unknown coefficients a and b can be easily determined.

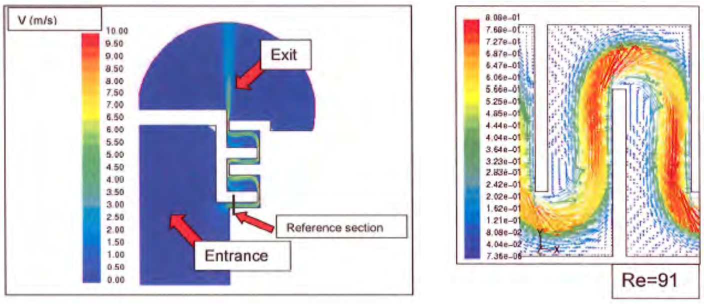

(a) Velocity distribution in the vents. (b) Detailed view of the velocity distribution.

Figure 4: Detailed 2D velocity distribution in the venting labyrinths [4].

These pressure laws for the different labyrinths are then plugged in a higher-level calculation. This makes it possible to evaluate the pressure difference over the filter caused by the dynamics of the fluid. These results, for the first 80 seconds, are represented in Figure 5.

From this graph it becomes clear that neither the acceleration, nor the depressurisation could be the cause for the failure of the filter. The maximal value for the differential pressure never even comes close to the allowed value of 200 Pa. Other possibilities for the filter failure thus have to be considered.

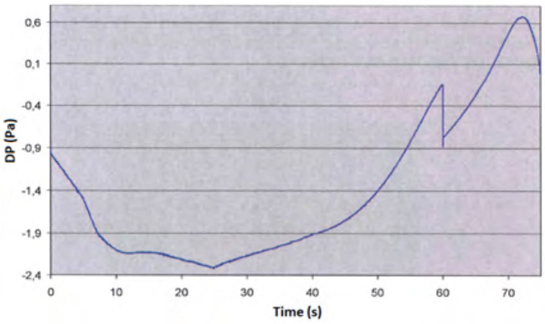

Figure 5: Pressure difference over the filter caused by depressurisation and acceleration effects [4].

3 (VIBRO-)ACOUSTIC ANALYSIS

This section describes the numerical vibro-acoustic analysis that was performed upon the instrument. The focus lies on the acoustic part of the vibro-acoustics, studying the instrument response under the acoustic load caused by the rocket engine. The structural loading was tested extensively by CSL in all types of shaker tests [6]. However, no measurement data of the filter is available for these tests. Visual inspections showed that vibrations alone could not have damaged the filter.

Before discussing this numerical analysis itself, the paper treats the implementation that was used, which differs from standard deterministic vibro-acoustic analyses and the numerical model. Then the (preliminary) results of the analysis itself will be covered. The analysis is concluded with the postprocessing of the acquired results.

3.1 Model

From an initial model, used by CSL for a static structural analysis, the vibro-acoustic system is built by coupling two derived models: a structural model (Figure 6(a)) and an acoustic model (Figure 6(b)).

The structure is modelled using the Finite Element Method (FEM [7]). This procedure discretises the problem domain into nodes and elements. The exact solution within these elements is approximated using simple polynomial shape functions. The application of a weighted residual formulation of the governing differential equation and boundary conditions leads to a system of equations which can be solved for the unknowns, in this case the nodal structural displacements. In a postprocessing step, strains and stresses can then be calculated.

The acoustics are modelled using the Indirect Boundary Element Method (iBEM [8],[9]). This method uses a boundary integral formulation of the governing differential equations. The boundary is discretised into nodes and elements similarly to the FEM. The resulting system of equations is then solved for the unknowns, here acoustic potentials related to pressure and velocity differences across the considered surface. In a next step, the results can be postprocessed to obtain acoustic pressures and velocities anywhere in the field.

Finally, both models are coupled to each other to account for the interaction between structural vibrations and acoustics: structural vibrations impose acoustic normal velocity fields, thus generating pressure waves, while acoustic pressures produce a dynamic loading on the structure. This leads to a vibro-acoustic model in which the structural model (50,000 degrees of freedom) is fully coupled to the acoustic model (20,000 degrees of freedom).

The frequency band for which the models are valid, is determined by the size of the elements. One of the core concepts of the element based methods (FEM and BEM), namely the representation of the dynamic behaviour by polynomial shape functions, limits the frequency range in which these methods are valid. The application of polynomial shape functions introduces two types of numerical errors: interpolation errors, since the dynamic behaviour cannot be exactly covered using polynomials, and pollution errors, caused by a difference between the physical wavelength and the calculated wavelength for the discretised problem. Using the rules of thumb presented in [10],[11], the limiting frequency can be found to be in the structural mesh at 800 Hz. The main acoustic and structural resonances, as well as the highest excitation levels (reaching up to 500 Hz) are located below this frequency. Therefore the mesh is valid in the studied frequency band from 26 to 700 Hz.

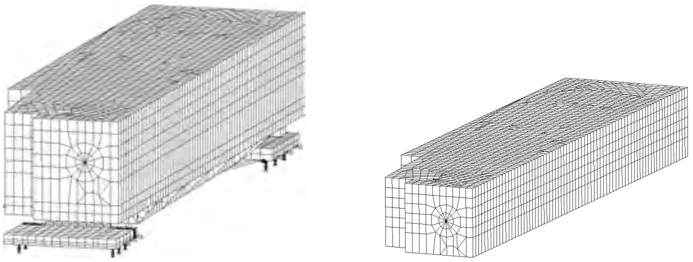
(a) Structural FEM-model.
(b) Acoustic BEM-model.

Figure 6: Models for the vibro-acoustic analysis.

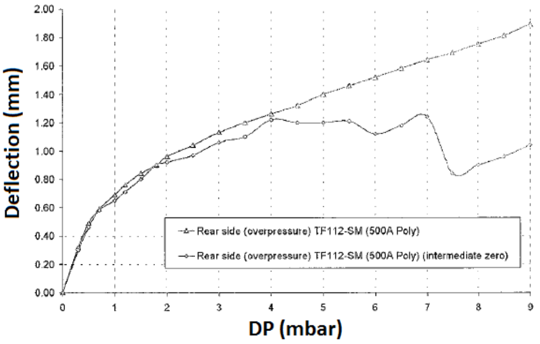

Figure 7: Deflection curve of the filter's central point as a function of differential pressure [2].

3.1.1 Sensitivity parameters

A straightforward analysis is impeded by two pronounced nonlinearities in the problem. Firstly there is the complex behaviour of the door. Secondly the nonlinear filter behaviour is discussed.

The complexity of both effects requires the behaviour to be divided into 'extreme' cases. The door will be modelled in a sealed (no more door behaviour as such) and a completely open way (door removed) and the filter in a very flexible and a very rigid way.

Modelling the door A numerical structural analysis shows that the door might not always perfectly close the cavity. This would introduce acoustic leakage and partially expose the filter to the large sound pressure levels. Also, when the door starts 'flapping', repeated impact of the door introduces an additional nonlinearity. Creating an accurate structural model that captures these effects is very difficult. One could create a model based on plate elements that have the kinematic freedom to rotate around a hinge line. The door lock would then be provided by a nodal relationship.

This way of modelling, however, poses serious problems for the acoustics. It is very difficult to impose the correct acoustic boundary conditions since they depend on the degree of structural deformation, which in turn depends on the acoustic behaviour and thus on the acoustic boundary conditions themselves. To account for a possible vibration of the door, two cases are considered. The true situation lies somewhere in between.

1. Door closed: A model with the door completely sealed, thus protecting the filter from any direct exposure to the diffuse sound field.

2. Door open: A model in which the door is completely removed, thus exposing the filter directly to the diffuse sound field.

It is impossible to account for the repeated impact of the door in a steady-state vibro-acoustic analysis. Filter failure caused by this phenomenon will therefore not be detected in the following analysis. This poses an important limitation on the validity of the results and the possible conclusions that can be drawn from it.

Modelling the filter From static deflection tests performed by CSL upon several filter types with and without different protective measures (see.g. Figure 7), it becomes clear that all filters exhibit a very nonlinear behaviour, caused by high membrane forces.

With the software that is commercially available, which is aimed at linear vibro-acoustics, it is impossible to create an accurate model that accounts for these membrane forces and that can be plugged into a fully coupled vibro-acoustic analysis. One can however attempt to incorporate these membrane forces into the flexural behaviour by means of a linearisation of the deflection curve, using the well-known analytical expressions for the deflection of a simply supported, circular plate under a uniform differential pressure (Equation 4).

$$\begin{aligned} w(0) &= \Delta p \frac{r_0^4(5+\nu)}{64D(1+\nu)} \\ D &= \frac{Et^3}{12(1-\nu^2)} \end{aligned} \tag{4}$$

In this equation $w(0)$ stands for the deflection of the central point, Δp for the differential pressure, r_0 for the radius of the filter, D for the flexural rigidity, ν for Poisson's ratio, E for the Young's modulus, t for the thickness of the filter.

It is clear from Equation 4 that the flexural rigidity D mainly depends on two parameters: the Young's modulus E and the thickness t. Adjusting the thickness t, however, would not only change the stiffness of the filter, but would also alter the mass. Therefore only the Young's modulus will be varied since this only affects the filter stiffness and not the filter mass.

As a reference, the deflection under a differential pressure of 200 Pa is used. This point is chosen because here the results for a cyclic increase of the differential pressure with intermediate zero difference ($\circ$ on Figure 7) and the results for a continuous increase of the differential pressure (Δ on Figure 7) start to diverge. This divergence indicates irreversible behaviour and thus filter damage. A calculation based on Equation 4 leads to an equivalent value of the Young's modulus $E_{eq} = 2.30 \cdot 10^9$ GPa. The high value shows the large impact of the membrane forces on the flexural behaviour. The reader should however bear in mind that this is a linearisation around a working point and is thus only exact in that single working point. Also, this altered Young's modulus will lead to a less accurate acoustic behaviour of the filter because by using E_{eq}, the filter is modelled too stiff for small deflections.

For the reasons listed above, two values for the Young's modulus will be studied, one acoustically more correct and the other one more correct from a structural side. The actual situation will again lie somewhere in between.

1. The acoustically more correct $E_{mat} = 70$ GPa, which is standard value for aluminum.
2. The structurally more correct $E_{eq} = 2.30 \cdot 10^9$ GPa (= 2.30 ExaPascal).

3.1.2 Boundary conditions and excitation

Apart from the coupling conditions between the structural and the acoustic model two additional boundary conditions are imposed.

Structural Both 'feet' of the structural model are clamped at six points (see the arrows on Figure 6(a)). This clamping represents the bolting of the instrument onto the base plate on PROBA2.

Acoustic For the case of the filter with E_{eq}, the large cavity is locally opened near the filter to retain the acoustic open-closed behaviour. By doing so, a clear image of the deformations and stresses can be created, unlike when using the acoustically more correct E_{mat}, where there are problems due to a very high modal density in the filter (see page 14). The acoustic impact of the ventilation labyrinths, intended to protect the filter from depressurisation effects (see page 3), is neglected in this analysis. Even though low-frequent noise will easily diffract through the labyrinth, and some noise will thus penetrate into the instrument, there will be a lot of reflection in the ducts. Further analyses could incorporate a better estimate for the acoustic admittance of these labyrinths.

The model is acoustically loaded by a diffuse sound field that has the same third octave spectral content and amplitude as the noise generated by the rocket engines.

3.2 Analysis

The following section treats the conducted vibro-acoustic analysis itself and the specific details of the followed implementation.

3.2.1 Implementation

The stochastic nature of the excitation, a diffuse sound field, requires an approach that differs from (standard) deterministic vibro-acoustic analyses. There are different approaches to deal with the stochasticity, like Statistical Energy Analysis (SEA [12]). We are however interested in filter deformations and thus (quasi) deterministic results that indicate whether or not the filter will fail. We therefore need to incorporate the stochastic diffuse field excitation into a deterministic framework. Figure 8 shows the practical implementation of the analysis, which is the way it is implemented in LMS Sysnoise® [13].

From the structural model a modal basis is calculated which contains the mode shapes and modal stresses at the structural resonance frequencies. This modal basis is then imposed on the elements that couple to the acoustic model.

The diffuse field input $X(\omega)$ is decomposed into uncorrelated deterministic excitations $\widetilde{X_i}(\omega)$, in this case plane waves, and their participation factors $q_i(\omega)$ using a Principal Component Analysis [14].

$$X(\omega) = \sum_{i=1}^{n} \widetilde{X_i}(\omega) q_i(\omega) \tag{5}$$

Next, a vibro-acoustic analysis is performed upon the fully coupled structural and acoustic model. A first postprocessing step provides the acoustic power spectral density of the pressure, and the structural power spectral density of the displacements. In the performed analysis a structural modal basis from 0 to 1400 Hz is used, following the rule of thumb to take into account modes with eigenfrequencies up to twice the studied frequency. The diffuse field input is decomposed into 24 uncorrelated plane wave sources.

3.2.2 Analysis

In the vibro-acoustic analysis, as was mentioned earlier (section 3.1.1), four cases are studied: door closed and door open, both for E_{mat} and E_{eq}, based on the procedures followed by CSL and ESTEC.

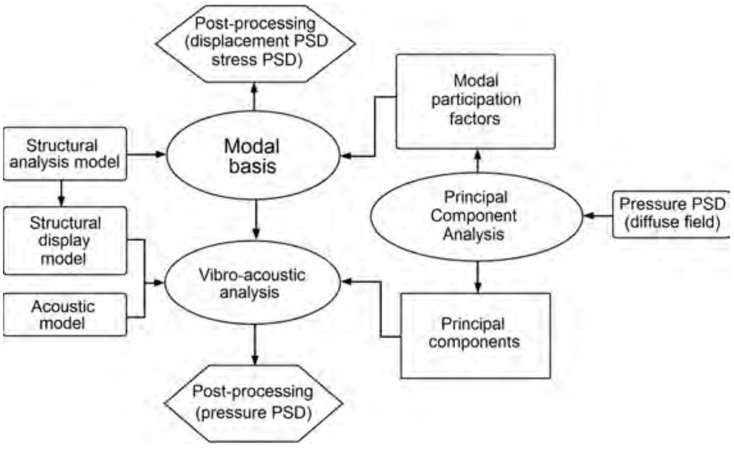

Figure 8: Flow chart of the analysis implementation (based on [15]).

The response is studied in terms of power spectral density of the pressure, in three arbitrary points as defined in Table 1, and the power spectral density of the out-of-plane filter displacements.

Position	Code
1 m outside	□
1 mm in front of filter	×
1 mm behind filter	+

Table 1: Points for Pressure Power Spectral Density.

Door closed A first set of subcases is based on the assumption that the door perfectly seals the instrument cavity and protects the filter from the harmful sound pressure levels outside. Firstly the purely acoustic behaviour is studied for the cavity as such. Subsequently the vibro-acoustic response is calculated for both E_{mat} and E_{eq}.

Acoustic behaviour Figure 9(a) shows the frequency response function of pressure in the instrument. The pressure distributions corresponding to the resonances are shown in Figure 9(b). The first (332 Hz) and third resonance (674 Hz) can be related to the analytical case of an acoustically rigid closed box with similar dimensions.

Vibro-acoustic behaviour (E_{mat}) The case with E_{mat} is, as indicated earlier, acoustically closer to reality because of the (usually small) deflections caused by an acoustic field.

Figure 10(a) shows that the presence of the sealed door gives adequate protection to the filter; the sound levels inside the instrument are much lower than outside. At the higher frequencies, acoustically driven resonances appear, but these don't appear to cause problems.

Vibro-acoustic behaviour (E_{eq}) The case with the equivalent Young's modulus gives a more accurate structural model for high deflections because it attempts to incorporate the effect of the membrane forces into the bending behaviour.

The (too) rigid filter will however seal the large cavity so that it becomes a closed-closed cavity on its own. This results in the frequency shift of the resonances that is observed when

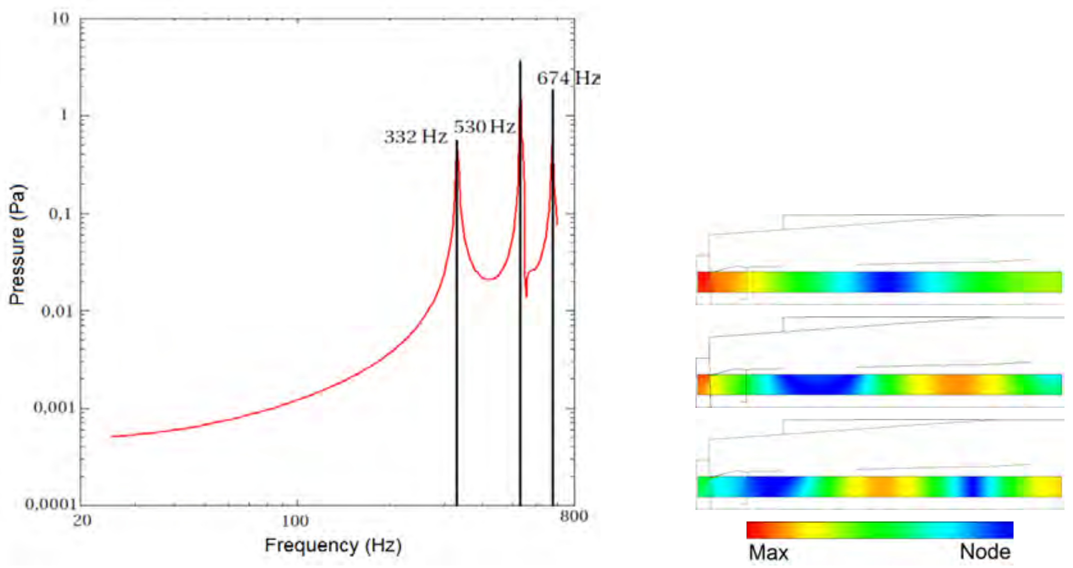

(a) Frequency response function.

(b) Pressure distribution at selected resonances (from top to bottom: 332-530-674 Hz).

Figure 9: Acoustic behaviour of the cavity with a closed door.

comparing Figure 10(b) to Figure 10(a). The differential pressure appears to stay well below the 200 Pa mentioned on page 8. Following sections (page 12) will however show the relativity of using pressure power spectral data.

Door open When the door is open, the front of the filter is directly exposed to the diffuse sound field, leading to a large sound level in the small cavity. This produces a large loading on the filter. Similar to the cases with the door closed, firstly the purely acoustic behaviour will be studied and secondly the vibro-acoustic behaviour for both E_{mat} and E_{eq}.

Acoustic behaviour Figure 11(a) shows the acoustic frequency response function of the instrument. The pressure distributions corresponding to the peaks are shown in figure 11(b). The three resonances (135-398-667 Hz) can all be related to the acoustic modes of an acoustic open-closed box with similar dimensions.

Vibro-acoustic behaviour (E_{mat}) Figure 12(a) shows that for low frequencies the power spectral density of the pressure in front of the filter, as well as behind the filter, follows the sound pressure level outside of the instrument. This is caused by the very low flexural rigidity of the filter which allows the high sound pressure levels in the small cavity in front of the filter to penetrate into the large cavity behind the filter.

Especially at the first two acoustic resonances (135-398 Hz), a considerable differential pressure over the filter may arise.

The location of the resonances corresponds again very well to the purely acoustic case. The resonances are again acoustically driven.

Vibro-acoustic behaviour (E_{eq}) Figure 12(b) shows results that are counterintuitive since we would expect the very rigid filter to practically seal off the instrument cavity.

The differences can be explained by the extra boundary condition that locally opens up the

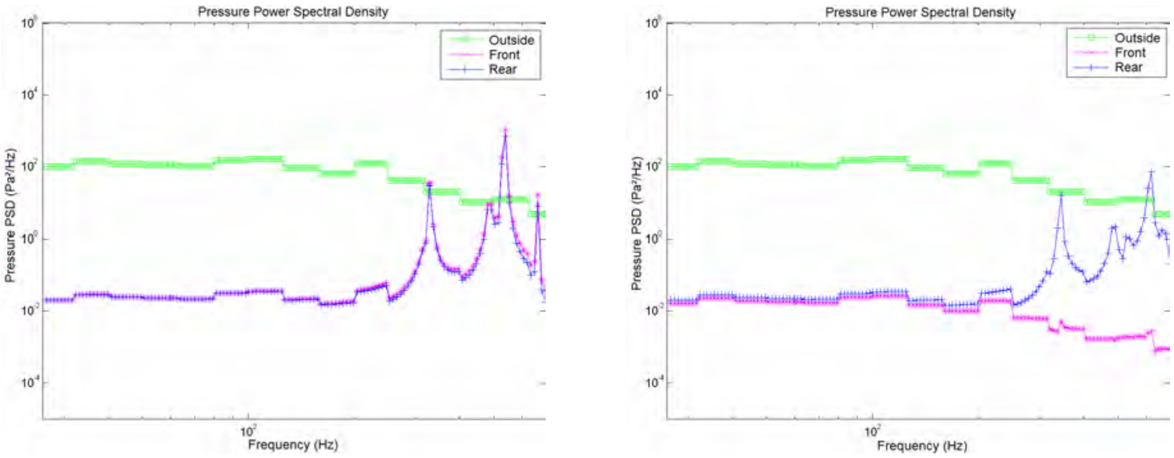

(a) E_{mat}

(b) E_{eq}

Figure 10: Power spectral density of the pressure (door closed).

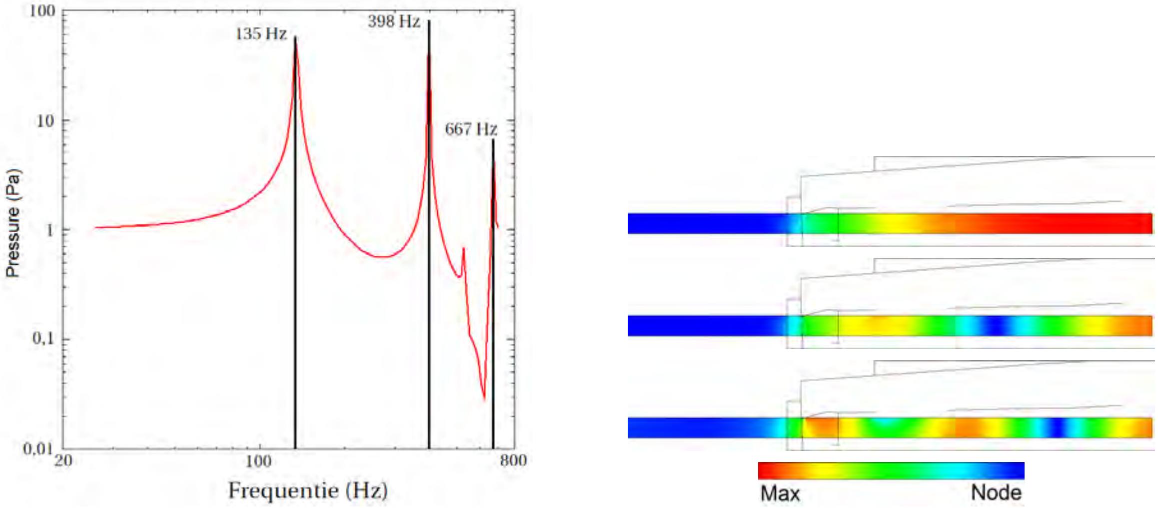

(a) Frequency response function.

(b) Pressure distribution at selected resonances (from top to bottom: 135-398-667 Hz).

Figure 11: Acoustic behaviour of the cavity with the door open.

large cavity, as was discussed on page 8. Without this boundary condition, the results for the point in the rear (+) would be practically indistinguishable from the results on Figure 12(a) since the larger cavity is closed by the very stiff filter, rather than by the door.

3.3 Postprocessing

The power spectral data obtained in the vibro-acoustic analysis can now be used to further assess filter failure and filter failure mechanisms. The practical use of both pressure and displacement data is studied in more detail. Firstly the method using the pressure difference in two arbitrarily chosen points as an estimate of the differential pressure over the filter, as done in the ESTEC procedure, is discussed. Then a more profound approach based on the filter deformation is elaborated.

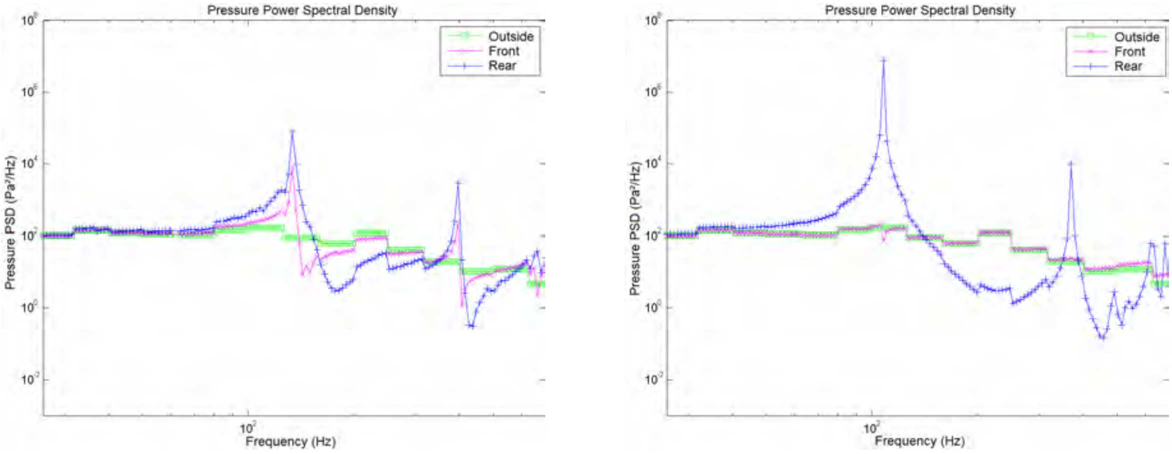

(a) E_{mat} (b) E_{eq}

Figure 12: Power spectral density of the pressure (door open).

3.3.1 Differential pressure

A first way to assess the loading on the filter is to estimate the differential pressure across the filter. At first sight this differential pressure can be derived, based on the pressure difference between two points, one in front of the filter and one in the rear, as was done earlier (page 9). Moreover, there is experimental data available about the maximal differential pressure the filter can withstand without irreversible deformation or failure (Figure 7), so this variable seems very appealing.

The method has however a major disadvantage that jeopardises its applicability. The results are very sensitive to the estimation for the filter rigidity and the location of the evaluation points. When this rigidity is very low, the main effect that causes a difference between two evaluation points near the filter, is the distance between these points and the mode shapes that govern the response at the given frequencies, rather than the differential pressure over the filter itself. When the rigidity is very high, the filter is acoustically too stiff, and the pressure difference is largely overestimated.

These problems make the interpretation of the results based on the power spectral density of the pressure extremely difficult and even dangerous since it can easily lead to wrong conclusions when the observation points, or the (approximated) filter rigidity are chosen badly. Furthermore this method is not able to show failure mechanisms, it can only (at most) determine whether failure occurs.

3.3.2 Deformations and stresses

A more fundamental way to assess the state of the filter is to look at the deformation of the filter itself by evaluating the displacement of the filter nodes.

Since we model the filter as a plate because no membrane model was available in the software for the vibro-acoustic analysis, and thus not take the membrane behaviour into account, the modal bases for the filter (displacements and stresses) are only partially correct. As a result, it will be impossible to get accurate information on the actual displacements and stresses.

An attempt to ease the problems in a postprocessing step can however be made. By applying (more) appropriate displacement-strain relationships, the distribution of the stresses in the filter elements can be calculated. This will make it possible to identify possible causes for the filter failure, but it will remain impossible to assess whether or not failure itself will occur.

Constitutive relationships For a membrane, which exhibits large deflections compared to its thickness, the linearisations made in the plate theory are no longer valid. Higher-order (quadratic) terms also have to be taken into account. Considering these higher-order terms, the displacement-strain relations can, with $\bullet_{i,j} = \frac{\partial \bullet_i}{\partial j}$, be written as [16]

$$\epsilon_{\alpha\beta} = \frac{1}{2}(u_{\alpha,\beta} + u_{\beta,\alpha} + w_{,\alpha}w_{,\beta}) \tag{6}$$

From these equations, the in-plane membrane dispacements u and v can be deleted since all calculations were made with a plate assumption, which has no in-plane deformation, only out-of-plane deformation w. The calculated values do not account in any way for in-plane rigidity. This means no failure mechanisms corresponding to membrane behaviour can be identified. Equation 6 can be rewritten for the different strain components as

$$\epsilon_{xx} = \frac{1}{2}w_{,x}^2 \qquad \epsilon_{yy} = \frac{1}{2}w_{,y}^2 \qquad \gamma_{xy} = w_{,x}w_{,y} \tag{7}$$

Using a proper constitutive relationship, stresses can be calculated from the strains. We assume, because of the small thickness of the membrane, a plane stress situation.

Secondly, an isotropic, linear elastic material is chosen. This is another simplification since failure of the filter is linked with irreversible deformations and thus with plastic behaviour of the material.

These assumptions result in following relationship.

$$\sigma_{ij} = \frac{Et}{(1-\nu^2)} \begin{bmatrix} 1 & \nu & 0 \\ \nu & 1 & 0 \\ 0 & 0 & \frac{1-\nu}{2} \end{bmatrix} \begin{bmatrix} \epsilon_{xx} \\ \epsilon_{yy} \\ \gamma_{xy} \end{bmatrix} \tag{8}$$

For the numerical implementation of this deformation-based postprocessing step, a FEM-procedure was used.

Results E_{mat} In absence of membrane forces, the filter will have a low flexural rigidity and thus a low flexural eigenfrequency. The filter will exhibit unrealistically large deflections and, in the considered frequency range, a high modal density (Figures 13(a) and 13(b) for the door opened and Figure 14 for the door closed). Because of this high modal density, it is impossible to assess filter stresses. The mesh would need to be drastically refined to be able to calculate the deformations accurately. This is, however, impossible since the calculation time would very strongly increase. But even if this would be feasable, the added value of this refinement is doubtful since the membrane behaviour would still not be incorporated.

When we compare Figure 14 to Figure 13(a), the effect of the closed door on the filter is very clear. The deflection of the filter, and thus its loading, is reduced significantly because of the shielding effect of the door.

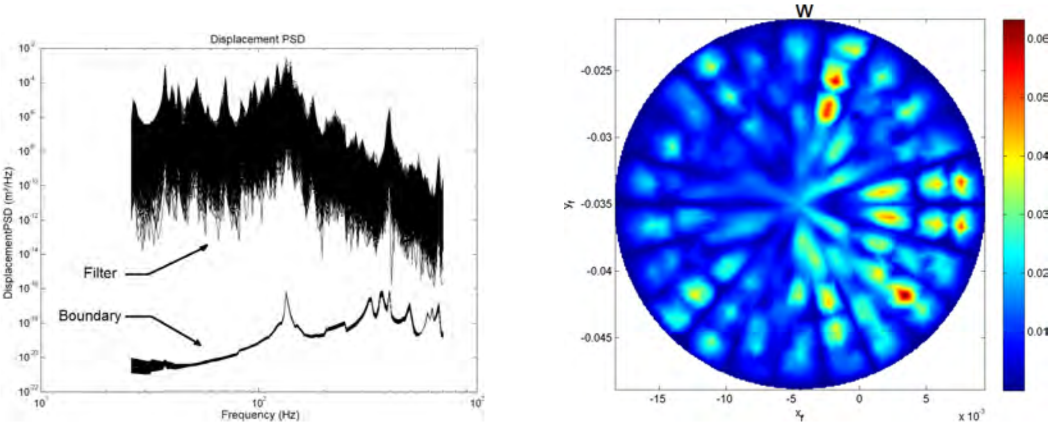

(a) Power spectral density.
(b) Displacements at 135 Hz.

Figure 13: Out-of-plane displacements of the filter (door open - E_{mat}).

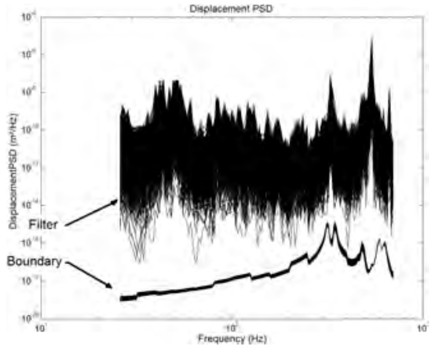

Figure 14: Power spectral density of the out-of-plane displacements of the filter (door closed - E_{mat}).

Results E_{eq} When the equivalent Young's modulus is used to incorporate the membrane behaviour, the deflections will be a lot smaller and the high modal density disappears (Figure 15(a) and 15(b)). Therefore the mesh is fine enough to create an accurate image of the deflection and the stresses.

Door open Because of the extra boundary condition that locally opens the cavity (see page 8), the case with E_{eq} and the door opened, exhibits acoustic open-closed behaviour. In that way, it is possible to look at the deformations in the filter for the acoustically open instrument (Figure 15(b)). This image shows an asymmetric deflection of the filter, caused by the excentric position of the filter with respect to the door opening (thick line in Figure 15(b)). This creates large gradients in the deformations, leading to very local stress peaks (see Figure 16 for von Mises-stresses).

Filter failure may thus be caused by an asymmetry of the door with respect to the filter.

Door closed The deformation pattern for the case with a closed door (Figure 17(a)) is very different. Because the sound pressure level in the cavity is a lot smaller since the cavity is acoustically closed, the differential pressure over the filter is lower. Also, the filter is modelled very stiff, thus giving low deformations. The global instrument deformations under the diffuse field however, remain relatively unchanged. Therefore Figure 17(b) shows a structural mode of the instrument as a whole, rather than the deflection of the filter. These deformations are thus of no relevance to the filter loading by cavity acoustics.

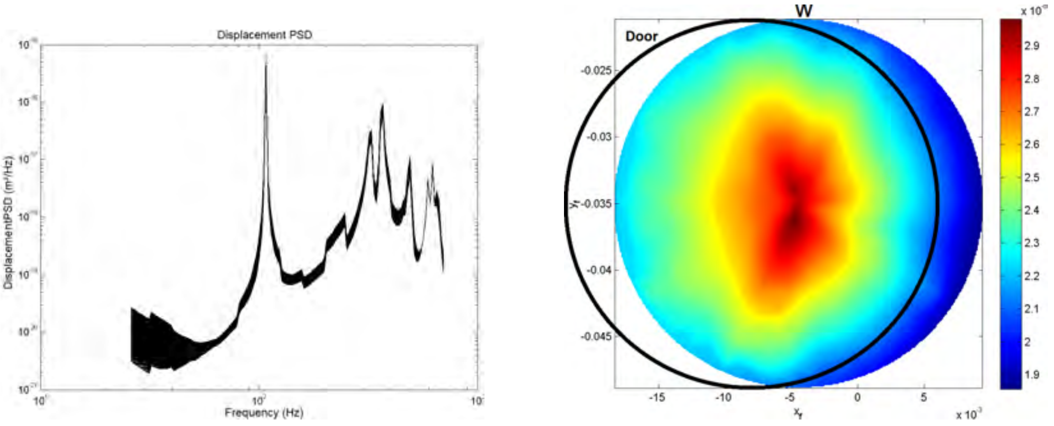

(a) Power spectral density.

(b) Displacements at 135 Hz.

Figure 15: Out-of-plane displacements of the filter (door open - E_{eq}).

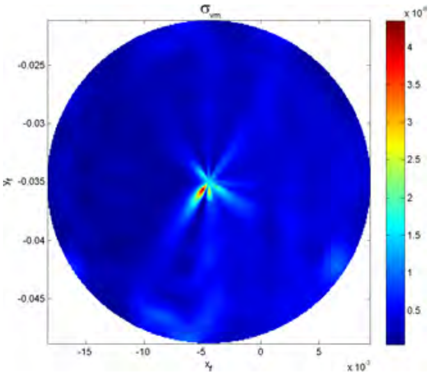

Figure 16: von Mises stresses in the filter at 135 Hz (door open - E_{eq}).

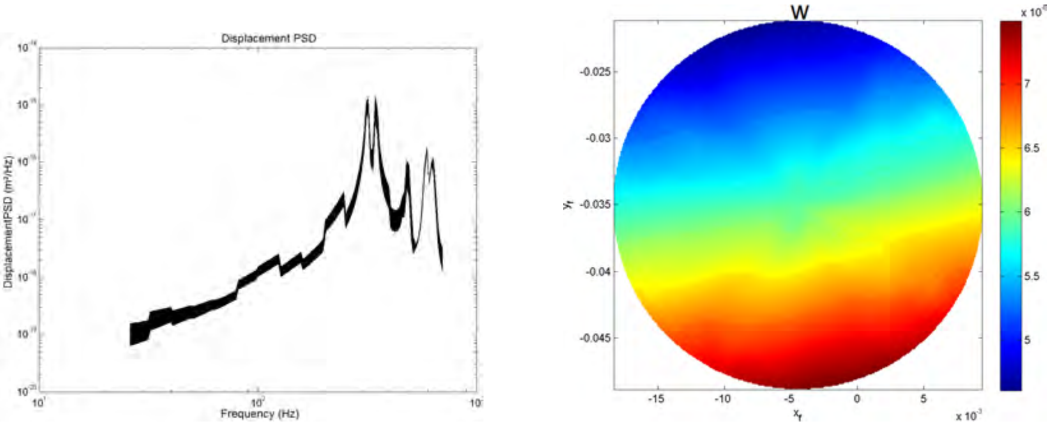

(a) Power spectral density.

(b) Displacements at 332 Hz.

Figure 17: Out-of-plane displacements of the filter (door closed - E_{eq}).

3.4 Summary

To conclude the discussion of the vibro-acoustic analysis, this section provides a small summary. The reader should however bear in mind the simplifications (Table 2) that were introduced to make a linear vibro-acoustic analysis possible.

Assumption	Cases	Simplification
Door behaviour	Closed and Open	No impact loading Both cases are extremes
Filter model	E_{mat} and E_{eq}	Overestimation stiffness for acoustics E_{eq} is a linearisation
Ventilation labyrinths	–	Vents have no acoustic impact

Table 2: Simplifications and assumptions made.

Door closed When the door is completely sealed, we have a closed acoustic cavity which is almost completely isolated from the diffuse field loading. The pressures in front and behind the filter (Figure 10) practically coincide and stay at a level well below the level of the diffuse sound field outside. The deformations in the filter are also very low, as Figures 14 and 17 indicate. Although the analysis cannot prove undeniably that the door provides enough protection, because it is difficult to estimate the filter rigidity, it does however show that an acoustically sealing door is a very effective protective measure.

Door open When the door is removed, the situation changes. The cavity becomes acoustically halfopen and the diffuse field loading can penetrate into the instrument. A substantial pressure difference arises over the filter (Figure 12). It is however difficult to draw conclusions based on this pressure data because of the strong dependency of the results on the studied points. When looking at the more fundamental deformations (Figures 13 and 15), we see that the filter exhibits a substantial deformation. The precise magnitude of this deformation is very hard to predict due to the assumptions (Table 2) made about the filter rigidity, but the (partially) opened door might cause irreversible filter deformation, e.g. by the asymmetric deformation mechanism which was indicated in Figure 15(b).

4 CONCLUSIONS

Several analyses were performed at very different stages of development; in the design stage (CFD analysis), after the testing campaign and even (partially) after the launch of the instrument itself (vibro-acoustic analysis), to check what was the problem that caused a front filter failure, which occured during pre-launch testing.

A CFD analysis was performed by GDTech to assess the effect of the depressurisation and acceleration and the impact of the venting system on the differential pressure over the filter. This analysis was performed on two different levels. Firstly a detailed CFD calculation of the flow through the labyrinths was made and translated to a relation between the entrance velocity and the pressure drop over the labyrinth. These pressure laws were then used in a larger scale analysis to assess the depressurisation of the instrument as a whole. The resulting differential pressure over the filter is very small and never comes near the allowed value. Filter failure caused by depressurisation is therefore not very likely.

The eventually most probable cause for filter failure was linked with the (vibro-)acoustic behaviour of the instrument cavity, which was studied at ESTEC and later on at K.U.Leuven, following the ESTEC procedures. Though a door was foreseen, a first numerical analysis indicated that this door could start flapping, thus partially opening the acoustic cavity and exposing the filter front to large sound pressure levels. In this way a larger than allowed differential pressure may arise over the front filter. The analysis was, nevertheless, very difficult to do with the currently available commercial software since the optical membrane has a pronounced nonlinear behaviour which cannot be retained entirely in a fully coupled linear vibro-acoustic analysis. Therefore, there is no firm proof that the filter fails indeed due to a mere acoustic overload. Anyhow, the analysis has raised out a plausible cause of this failure (if to be acoustically driven), namely an eccentricity between the door and the filter.

ACKNOWLEDGEMENT

The authors would like to thank the Institute for the Promotion of Innovation through Science and Technology in Flanders (IWT-Vlaanderen) for their support of the doctoral research of Stijn Jonckheere and Bart Bergen.

REFERENCES

[1] PROBA2 Science Center, *About SWAP*. `http://proba2.sidc.be/index.html/swap/article/swap-description`, 2010.

[2] J.P. Halain, *Filter Mechanical Characterisation*. Internal CSL report, 2008.

[3] S. Jonckheere, *Vibro-akoestische analyse van het SWAP-instrument aan boord van de PROBA2*, K.U.Leuven, division PMA, Master's thesis, 2010.

[4] Global Design Technology, *SWAP Filter protection study*. Study commissioned by CSL, 2004.

[5] S. Dushman, J.M. Laferty, *Scientific foundations of vacuum technique*. John Wiley & Sons, 1962.

[6] J.S. Servaye, *Vibration test report (SWAP STM)*. Internal CSL report, 2006.

[7] O.C. Zienkiewicz, R.L. Taylor, *The finite element method - The three volume set (6th ed.)*. Butterworth-Heinemann, 2005

[8] C.A. Brebbia, J.C.F. Telles, L.C. Wrobel, *Boundary Element Techniques*. Springer Verlag, 1984.

[9] O. von Estorff, *Boundary elements in acoustics: advances and applications*. WIT, 2000.

[10] S. Marburg, Six elements per wavelength. Is that enough?. *Journal of Computational Acoustics*, **10**, 25–51, 2002.

[11] F. Ihlenburg, I. Babuska, Finite element solution of the Helmholtz equation with high wave number part II: The h-p version of the FEM. *SIAM Journal on Numerical Analysis*, **34(1)**, 315–358, 1997.

[12] R.H. Lyon, R.G. DeJong, *Theory and application of statistical energy analysis (2nd ed.)*. Butterworth-Heinemann, 1995.

[13] LMS International, *Sysnoise User manual, Rev. 5.6*.

[14] G.H. Dunteman, *Principal component analysis*. Sage publications, Inc., 1989.

[15] P. Segaert, *Efficient simulation technology for the evaluation of the dynamic response of payloads to diffuse sound field excitation*. `www.aero.org/conferences/sclv/pdfs/segaert_simulation_05.pdf`, 2005.

[16] G.C. Tsiatas, J.T. Katsikadelis, Large deflection analysis of elastic space membranes. *International journal for numerical methods in engineering*, **65**, 264–294, 2006.

COMPDYN 2011
III ECCOMAS Thematic Conference on
Computational Methods in Structural Dynamics and Earthquake Engineering
M. Papadrakakis, M. Fragiadakis, V. Plevris (eds.)
Corfu, Greece, 25–28 May 2011

DISTURBANCE SOURCES MODELING FOR ANALYSIS OF STRUCTURE-BORNE MICRO-VIBRATION

G.S Aglietti[1], Z. Zhang[1], G Richardson[2], B. Le Page[2], A Haslehurstl[2]

[1]School of Engineering Science, University of Southampton,
Highfield, Southampton, SO17 1BJ, UK
gsa@soton.ac.uk

[2] Surrey Satellite Technology Limited,
Guildford, Surrey, UK

Keywords:.

Abstract. *Micro-vibration is a low level disturbance, which cannot be controlled or reduced by the Attitude and Orbit Control System of a spacecraft. It can emanate from various sources on a typical spacecraft, notably subsystems with moving parts such as reaction wheels or cooler mechanisms. Micro-vibration can also result from thermo-elastic effects due to stick-slip from differential expansion of parts. It causes problems for sensitive payloads especially high resolution cameras where the demand for higher resolution (which drives stability requirements), has made analysis and control of microvibrations relevant for a larger number of satellites. The availability of mathematical models to represent the disturbance sources in a format that can themselves be coupled to the mathematical model of the structure to perform end-to-end analysis to obtain predictions of the stability level at the receiver is crucial.*

In the simplest form the sources can be represented with forces and moments of appropriate characteristics, adding also some inertia at the source location. But even for this simplistic implementation it is necessary to have available the details of the forces and moment produced by a source, and these can be either calculated from schematic models of the functioning of the device, or experimentally determined, or a mixture of the two. Typical test techniques applied to micro-vibration measurement /characterization will be described, highlighting advantages and drawbacks of the various methods. A simple experimental apparatus for the measurement of the micro-vibrations emitted by a reaction wheel is presented. A mathematical model of the reaction wheel disturbances is also presented together with its coupling to a typical spacecraft structural model.

1 INTRODUCTION

Since the early 1990’s, the resolution and pointing stability required for Earth and deep space astronomical observation spacecraft instruments have continuously increased. Current high resolution military reconnaissance satellites have achieved centimeter-level ground resolution. For example, the KH-13 surveillance satellite recently launched has reached a ground resolution of 0.05 m. Space telescopes for astronomical observations usually have a resolution one to two orders of magnitude higher than Earth observation satellites [1], and looking at the future, the James Webb Space Telescope (JWST) planned to launch in 2014 or 2015 should reach a pointing stability 0.004 arcsec [2].

On board satellites there is often equipment (e.g. Reaction & Momentum Wheel Assemblies, Cryocoolers, pointing mechanisms, switches etc) in this context called sources, which during their functioning produce dynamic disturbances, micro-vibrations that are transmitted through the platform affecting the performance of sensitive payloads receivers also mounted on the platform. The micro-vibration produced by the sources can also be amplified by structural resonances thus making micro-vibration prediction complicated.

In this context, the term micro-vibration refers to low-level mechanical disturbances in the range of micro-g’s (μg), typically occurring at frequencies from a few Hz up to 1000 Hz [3]. In some extreme cases of high precision spacecraft [4-6] even disturbances at frequencies down to 10-2 Hz are relevant. Micro-vibration can be considered as excitations resulting from impulsive phenomena (device release); translating parts (cryocoolers); or rotating parts (RWAs/MWAs), for example, which are sinusoidal (or multi-tone) or broad band frequency in nature.

Generally speaking, micro-vibration sources exist on most spacecraft; however, due to their small amplitudes and often high frequencies they do not have serious impacts (e.g. typical satellites for telecommunication) and thus are ignored. Spacecraft with optical instruments and cameras are generally those most affected by micro-vibration issues. Micro-vibration generally cannot be controlled or reduced by the Attitude and Orbit Control System (AOCS) because they usually involve the flexible modes of the spacecraft structure (rather than its rigid body motion, which is controlled by the AOCS) and because the frequency range of the spacecraft AOCS usually has an upper limit of controllable frequency of a few Hz, whereas micro-vibration generally occurs at higher frequencies.

Micro-vibration can be managed passively and/or actively at the source, along the transmission path and at the receiver location. For example, in order to reduce disturbances, RWAs can be placed on a vibration isolation mount [7] or bracket [8] which is connected to the primary structure, micro-vibration isolators can be incorporated in to primary structure components [9], and/or active optics such as an image stabilization system used within optical payloads [10]. Passive or active isolation may also be used between the receiver and the spacecraft structure.

2 MICRO-VIBRATION NOISE SOURCES

Micro-vibration disturbances mainly arise from fast moving (rotating and translating) mechanisms installed onboard such as RWAs, cryocoolers and pointing systems, etc. [11]. They may also arise from non-moving systems such as electronics and sensors [12], the release of strain energy at structural interfaces (joints, latches, hinges) during "thermal snap" events [13, 14] and the bending of solar arrays, antennas, etc. due to sudden temperature change [15].

The mechanical disturbances produce by the noise sources are usually characterized by forces and torques that appear at the interface between the equipment and spacecraft. These forces/torques propagate through the primary structure to the sensitive instruments. Since the spacecraft is an isolated system, the mechanical energy produced by these excitations must be dissipated into this system.

Generally micro-vibration sources can be divided into two broad groups:

- Single disturbance event
- Continuous disturbances.

The single disturbance event, also known as transient loads, are clanks and intermittent disturbances, which may occur randomly (sudden stress release due to slippage between parts with differential temperatures and/or thermal expansion of their materials; micro-cracking in laminates and sandwiches; and buckling of foils due to thermal expansion/contraction) or at specified commands (for example firing a thruster). These disturbances are low level shock type forces with small dynamic amplitudes.

The continuous disturbances, also known as vibratory loads, are accelerations which are sinusoidal (or multi-tone) or broad band frequency in nature. The continuous disturbance can be further broken down based on the speed, magnitude and noise source type. For example, based on the first criteria high speed moving mechanisms include RWAs/MWAs, gyros, etc.; medium ones include liquid flowing and sloshing, cryocoolers, etc and low speed ones include antennas, solar arrays, etc. Based on the second criteria, mechanical mechanism induced disturbances include those mentioned above except those induced from liquid flowing and sloshing, which are regarded as non-mechanical mechanisms. Either way, these sources produce permanent disturbances in spacecraft, and are usually considered as “internal noise” [1, 12]. Other possible disturbances include inductive electromagnetic forces between wires and heaters; electrical noise, etc.

2.1 Physical causes of micro-vibrations

Within the noise sources micro-vibration arises from common mechanical components or phenomenon. These are summarized below

- Rotor imbalance: Rotating devices such as RWA, MWA, gyroscope, etc. can pro-duce large disturbances in spacecraft, especially when spin speed is very high. At nominal high speed, rotor imbalance is considered as the major disturbance source in these devices. It cannot be totally avoided because of manufacturing tolerances. Usually rotor imbalance is considered as the sum of static and dynamic imbalance, both of which produce disturbance forces and torques. These forces and torques are proportional to spin speed squared with a fundamental frequency equal to spin speed.

- Mechanical bearing irregularity: Disturbances caused by mechanical bearing irregularity are mainly due to ball irregularities; internal race irregularities; external race irregularities and cage disturbances. These are also due to manufacturing tolerances. For high speed continuous rotation devices such as brushless DC motor and stepper motor, interactions between them, e.g. abnormal contacts between balls and raceway, balls and cage, cage and raceways, create non-linear disturbance force and torque, they appear as sub- and super-harmonics in the device disturbance signature.

- Bearing friction: Bearing friction occurs in all rotating devices through their entire operational range, but it is particularly important at low speed. If a device needs to reverse directions (crossing zero speed), e.g. an RWA, there are two disturbance possibilities either the device will stop rotating briefly (there will be a dead band) or there will be a discontinuity in acceleration (due to the change in the relative signs of the friction and motor torque).

- lubrication degradation: In rotating devices, such as RWA and SADM, lubrication degradation over life can lead to increased noise or as is with some systems using a sacrificial liberation system can change the noise performance during life as the cages wears or can lead to periodic high torque (noise).

- Motor cogging, Motor ripple: For a permanent magnet brushless DC motor, motor disturbances include cogging and torque ripple. These disturbances generally only be-come significant when wheel speed is low or the motor reverses spin direction. Motor cogging torque originates from the magnetic interaction between stator slots and rotor permanent magnets, and it is an undesirable effect that prevents the smooth rotation of the flywheel and results in noise. Motor ripple torque is defined as the change in mo-tor torque with respect to the angular position, or simply by the profile of the Back-Electro Motive Force (B-EMF) and current waveform, which is not exactly sinusoidal.

- Stepper motors, gear meshing and contact: For APMs, usually two or three phase stepper motor actuators are used to drive antenna in two axes (azimuth and elevation), respectively. Each actuator step imparts a small disturbance torque into the spacecraft. Also gear meshing and contacts are also sources of vibration.

- Axial motion of inertias, such as the compressor and other moving parts in a cryocooler can become sources of vibration [16]. The linearly reciprocating motion of the elements gives rise to a momentum imbalance. Particularly for cryocoolers the piston is typically driven with a sinusoidal signal, it oscillates against a non-linear gas spring formed by the compression space, resulting in a non-sinusoidal piston motion. A disturbance of this type manifests itself in the vibration signature as the presence of harmonics of the moving inertia's drive frequency [17].

As rotor imbalance is one of the main causes of microvibrations this article focuses on the modeling of this phenomena and its integration with a structural model of the satellite.

3 MATHEMATICAL MODEL

The wheel imbalance typically consists of the flywheel static imbalance (offset of the center of mass (CoM) of the flywheel with respect to its spin axis) and dynamic imbalance (misalignment of the flywheel's principal axis and the rotation axis). The wheel-induced vibrations are mostly sinusoidal (often multi-tone) in nature, and below the first resonant frequency, the imbalance causes a disturbance force and moment respectively at the flywheel's spin rate (the fundamental harmonic) with amplitude proportional to the rotational speed squared.

Common flywheel configurations of a WA are either symmetrical (flywheel at mid-span of the shaft) or cantilevered (flywheel at one end of the shaft), see Fig. 1. Flywheel imbalance analytical models of such configurations have been studied in the literature.

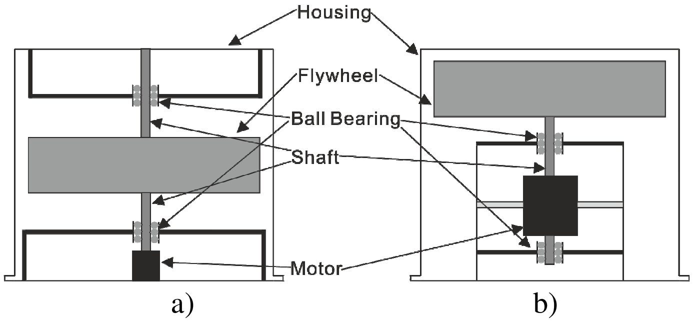

Fig. 1 Two typical RWA configurations a) symmetrical b) cantilever

In this article, the WA studied has a cantilevered flywheel supported by a soft suspension system, which provides both rotational and translational support (see Fig. 2). The soft suspension system is designed as a passive system that filters the vibrations produced by the motor (e.g. its bearings), thus minimizing the mechanical disturbances emitted by the WA when spinning. Also the WA is designed to have a speed range beyond 10000 rpm, making it suitable for use as either a RWA or MWA.

Based on the energy method (i.e. the Lagrange's approach), the flywheel imbalance analytical model of the wheel is coupled with an arbitrary supporting structure (in this case, an aluminum ”cube” acting as a seismic mass), see Fig. 2. The analytical model representing the flywheel imbalance can then be integrated with disturbance empirical models (i.e. the semi-empirical models) and linked to a complete satellite numerical model to predict its performance at the receivers’ location (e.g. the effect on the line of sight of an optical instrument).

The whole system (WA and seismic mass, which also includes the wheel base) is suspended using elastic cords on each side of the seismic mass, thus simulating a “free-free” condition. The elastic cords were chosen such that the system resonant frequency is less than 1 Hz (verified with a “tap” test), and not in the frequency range interested in this article.

The seismic mass has coordinate $x_c y_c z_c$ with origin C at its CoM; θ_c, φ_c and ψ_c are the corresponding rotations around each axis. Note that, in the shaft pointing direction, the kinetic energy of the wheel is much larger than that of the seismic mass, thus the perturbation of the seismic mass about this axis, ψ_c is ignored. M_c is the mass of the seismic mass; I_{c_xx} and I_{c_yy} are moment of inertias of the seismic mass about x_c and y_c axis respectively. The vertical distance from the soft suspension system-wheel base interface to the CoM of the seismic mass is l.

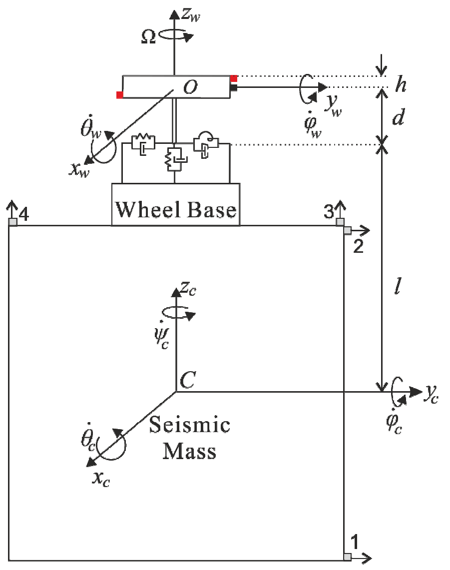

Fig. 2 Simplified model of reaction Wheel coupled with seismic mass

The seismic mass can be considered as a rigid body connected with a flywheel (another rigid body) by the soft suspension system. With small displacement assumption, the kinetic energy of the seismic mass T_c is obtained as:

$$T_c \approx \frac{1}{2}\left[M_c\left(\dot{x}_c^2+\dot{y}_c^2+\dot{z}_c^2\right)+I_{c\_xx}\dot{\theta}_c^2+I_{c\_yy}\dot{\varphi}_c^2\right] \tag{1}$$

The potential energy U_s of the system can be obtained (using the small displacement assumption) through the relative motion at the soft suspension system/flywheel base interface:

$$U_s=\frac{1}{2}\left[k_z\left(z_w-z_c\right)^2+k_r\left(\theta_w-\theta_c\right)^2+k_t\left[(y_w-y_c)+(d\theta_w+l\theta_c)\right]^2+k_r(\varphi_w-\varphi_c)^2+k_t\left[(x_w-x_c)-(d\varphi_w+l\varphi_c)\right]^2\right] \tag{2}$$

The fully linearized EoMs of the system with respect to each of the ten DoFs (the axial rotation of flywheel and seismic mass are not included) are obtained. They are written in matrix form as:

$$\boldsymbol{M}_s\ddot{\boldsymbol{q}}_s+\boldsymbol{G}_s\dot{\boldsymbol{q}}_s+\boldsymbol{K}_s\boldsymbol{q}_s=\boldsymbol{F}_s \tag{3}$$

The mathematical model was validated against test results, and various tests were carried out to validate the effect of the stiffness of the mechanism supporting the rotor.

In particular Figure 3 shows a comparison of waterfall plot for the in-plane force emitted by the wheel for tow cases a soft suspension system, and a rigid one. It is possible to notice that the rigid assembly emits considerable more vibration in the frequency range between 200Hz and 400Hz.

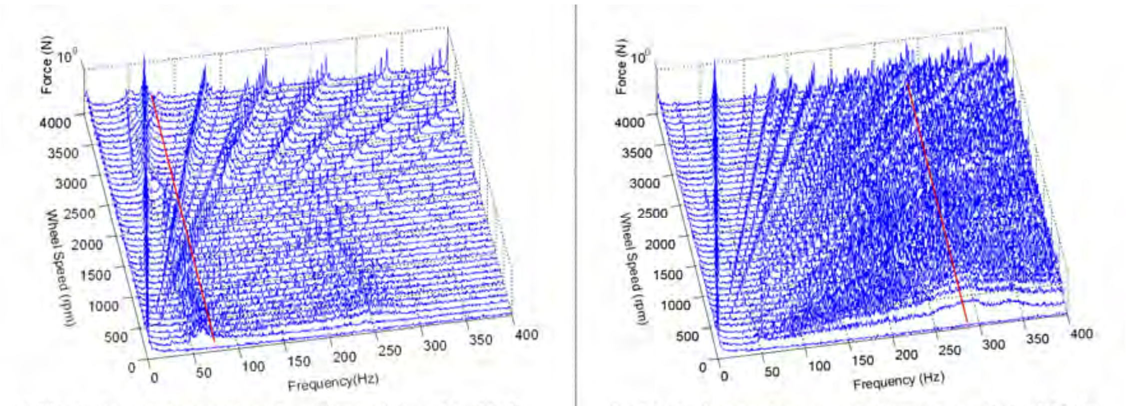

a) Disturbance force in y direction of flexible WA b) Disturbance force in y direction of rigid WA

Fig.3 Waterfall plots for flexible and rigid WA

4 SOURCE-STRCUTRE INTEGRATION

Measured interface disturbance force and torque generated by mechanisms need to be integrated with the spacecraft model in order to assess performance at receivers. Methods of disturbance source implementation vary depending on the source and spacecraft model type, i.e. sources could be analytical, empirical or semi-analytical, the spacecraft model could be FE model or Matlab/Simulink model. The most common method is to implement semi-analytical source models and integrate them in typical spacecraft FE model (whose behavior is described using its transfer functions). Typically, this can be described mathematically as:

$$\boldsymbol{Z} = \boldsymbol{GW} \tag{4}$$

where $\boldsymbol{Z}$ is the performance metrics at some point, such as displacement or acceleration at the receivers. $\boldsymbol{G}$ is the transfer function matrix between the receivers and sources, usually obtained from the spacecraft FE model. W is the disturbance sources. Eq. (4) is most often written into spectral density form:

$$\boldsymbol{\Phi}_{ZZ} = \boldsymbol{G}\boldsymbol{\Phi}_{FF}\boldsymbol{G}^{H} \tag{5}$$

where $\boldsymbol{\Phi}_{FF}$ is the measured disturbance in spectral density matrix form - usually a 6×6 matrix in the form:

$$\boldsymbol{\Phi}_{FF} = \begin{bmatrix} \Phi_{F_x} & \Phi_{F_xF_y} & \Phi_{F_xF_z} & \Phi_{F_xM_x} & \Phi_{F_xM_y} & \Phi_{F_xM_z} \\ \Phi_{F_yF_x} & \Phi_{F_y} & \Phi_{F_yF_z} & \Phi_{F_yM_x} & \Phi_{F_yM_y} & \Phi_{F_yM_z} \\ \Phi_{F_zF_x} & \Phi_{F_zF_y} & \Phi_{F_z} & \Phi_{F_zM_x} & \Phi_{F_zM_y} & \Phi_{F_zM_z} \\ \Phi_{M_xF_x} & \Phi_{M_xF_y} & \Phi_{M_xF_z} & \Phi_{M_x} & \Phi_{M_xM_y} & \Phi_{M_xM_z} \\ \Phi_{M_yF_x} & \Phi_{M_yF_y} & \Phi_{M_yF_z} & \Phi_{M_yM_x} & \Phi_{M_y} & \Phi_{M_yM_z} \\ \Phi_{M_zF_x} & \Phi_{M_zF_y} & \Phi_{M_zF_z} & \Phi_{M_zM_x} & \Phi_{M_zM_y} & \Phi_{M_z} \end{bmatrix} \tag{6}$$

where diagonal Φ_{ii} are the PSD, Φ_{ij} are the CSD. The spectral matrix $\mathbf{\Phi}_{FF}$ is the input in the spacecraft FE model.

Methods to obtain the $\mathbf{\Phi}_{FF}$ are usually empirical test results or a semi-analytical model.

For the first method, for every speed, disturbance force and moment **F**(ω) in frequency domain at the mechanism interface is obtained through load cell or Kistler table, i.e. a 6×1 vector.

$$\boldsymbol{F}(\omega) = \begin{Bmatrix} F_x \\ F_y \\ F_z \\ M_x \\ M_y \\ M_z \end{Bmatrix} \tag{7}$$

This vector is then converted into spectral density matrix (Eq. (6)) utilizing signal processing technique, which can then be used in Eq. (5).

The second methods involves semi-analytical model of disturbance. In general, wheel imbalance induced disturbance has the analytical form of:

$$F(t) = \sum_{i=1}^{n} C_i f_{rwa}^2 \sin(2\pi h_i f_{rwa} t + \phi_i) + W(t) \tag{8}$$

where $F(t)$ is the disturbance force or torque in time domain; n is the number of harmonics; C_i is the amplitude of the i_{th} harmonic; f_{rwa} is the flywheel speed rate in Hz; h_i is the i^{th} harmonic number and ϕ_i is a random phase; $W(t)$ is the random noise disturbance.

Note Eq. (8) is an alternative form of the excitation, i.e. right hand side, of the Eq. (3). From Eq. (8), parameters for each harmonic and the number of harmonics need to be mapped from experimental data (i.e. empirical results) for each speed (the choice of these values depends on the accuracy of the model want to obtained). And high frequency random (white) noise has to be generated and incorporated with the model. Once the disturbance force and moment in time domain obtained, they can processed into frequency domain to obtain **F**(ω), the following analysis becomes the same as the first method.

5 CONCLUSIONS

In this article, the importance of microvibrations modeling has been briefly discussed to highlight its importance in the design of high stability satellite platforms. The various physical mechanisms that produce microvibrations on board a typical satellite have been reviewed and a mathematical model of a typical source, i.e. a reaction wheel, has been described. Finally the article describes a possible method to introduce the loads produced by the source(s) in a model describing the structure transfer functions, which could be obtained using any modeling technique such as the Finite Element Method.

REFERENCES

[1]. Zhang, Z., Yang, L., and Pang, S. "Jitter Environment Analysis for Micro-precision Spacecraft," *Spacecraft Enviroment Engineering* Vol. 26, No. 6, 2009, pp. 528-534.

[2]. Meza, L., Tung, F., Anandakrishnan, S., Spector, V., and Hyde, T. "Line of Sight Stabilization of James Webb Space Telescope," *27th Annual AAS Guidance and Control Conference*. AAS 05-002, Breckenridge, CO, 2005.

[3]. Bely, P. Y., Lupie, O. L., and Hershey, J. L. "The Line-of-sight Jitter of the Hubble Space Telescope," *Space Astronomical Telescopes and Instruments II.* 1 ed. Vol. 1945, SPIE, Orlando, FL, USA, 1993, pp. 55-61.

[4]. Aglietti, G., Langley, R., Rogers, E., and Gabriel, S. "Model Building and Verification for Active Control of Microvibrations with Probabilistic Assessment of the Effects of Uncertainties," *Proceedings of the Institution of Mechanical Engineers, Part C: Journal of Mechanical Engineering Science* Vol. 218, No. 4, 2004, pp. 389-399.

[5]. Katsukawa, Y., Masada, Y., Shimizu, T., Sakai, S., and Ichimoto, K. "Pointing Stability of Hinode and Requirements for the Next Solar Mission Solar-C," *International Conference on Space Optics*. Rhodes, Greece, 2010.

[6]. Pierrart, C., Clerc, C., Eaton, D. G., and Lefevre, Y. M. "Microvibration Transmission in Space Structures at Medium High Frequencies," *Spacecraft Structures and Mechanical Testing Conference*. Paris, France, 1994.

[7]. Kamesh, D., Pandiyan, R., and Ghosal, A. "Modeling, Design and Analysis of Low Frequency Platform for Attenuating Micro-vibration in Spacecraft," *Journal of Sound and Vibration* Vol. 329, No. 17, 2010, pp. 3431-3450.

[8]. Shankar Narayan, S., Nair, P. S., and Ghosal, A. "Dynamic Interaction of Rotating Momentum Wheels with Spacecraft Elements," *Journal of Sound and Vibration* Vol. 315, No. 4-5, 2008, pp. 970-984.

[9]. Vaillon, L., and Philippe, C. "Passive and Active Microvibration Control for Very High Pointing Accuracy Space systems," *Smart Materials and Structures* Vol. 8, No. 6, 1999, p. 719.

[10]. Sakurai, T. *The Hinode Mission*: Springer, 2008.

[11]. Laskin, R. A., and Martin, M. S. "Control/Structure System Design of a Spaceborne Optical Interferometer," *Proceedings of AAS/AIAA Astrodynamics Specialist Conference*. AAS 89-424, 1989, pp. 369-395.

[12]. Wacker, T., Weimer, L., and Eckert, K. "GOCE Platform Micro-vibration Verification by Test and Analysis," *Proceedings of the European Conference on Spacecraft Structures, Materials and Mechanical Testing*. Noordwijk, The Netherlands, 2005.

[13]. Ingham, M. D. "Microdynamics and Thermal Snap Response of Deployable Space Structures," *Department of Aeronautics and Astronautics*. Vol. M.Sc., Massachusetts Institute of Technology Cambridge, MA, 1995, p. 187.

[14]. Ingham, M., Kim, Y., Crawley, E., McManus, H., and Miller, D. "Experimental Characterization of Thermal Creak Response of Deployable Structures," *Journal of Spacecraft and Rockets* Vol. 37, No. 3, 2000.

[15]. Foster, C. L., Tinker, M. L., Nurre, G. S., and Till, W. A. "The Solar-array-induced Disturbance of the Hubble Space Telescope Pointing System," *Journal of Spacecraft and Rockets* Vol. 32, No. 4, 1995, pp. 634-644.

[16]. Jedrich, N., Zimbelman, D., Turczyn, M., Sills, J., Voorhees, C., and Clapp, B. "Cryo Cooler Induced Micro-Vibration Disturbances to the Hubble Space Telescope," *The 5th Cranfield Dynamics and Control of Systems and Structures in Space Conference*. Cambridge, UK, 2002.

[17]. Collins, S. A. "Multi-axis Analog Adaptive Feedforward Cancellation of Cryocooler Vibration," *Department of Aeronautics and Astronautics*. Vol. Ph.D, Massachusetts Institute of Technology, Cambridge, MA, 1994, p. 222.

COMPDYN 2011
III ECCOMAS Thematic Conference on
Computational Methods in Structural Dynamics and Earthquake Engineering
M. Papadrakakis, M. Fragiadakis, V. Plevris (eds.)
Corfu, Greece, 25–28 May 2011

DIMENSIONAL STABILITY LOSS IN STRUCTURES SUBJECT TO RANDOM VIBRATION

Ruben L. Edeson[1], Guglielmo S. Aglietti[2], Adrian R. Tatnall[2]

[1] RAL Space
STFC Rutherford Appleton Laboratory, Harwell Oxford, Didcot, OX11 0QX, UK
e-mail: ruben.edeson@stfc.ac.uk

[2] School of Engineering Science, University of Southampton
Highfield, Southampton, SO17 1BJ
email: gsa@soton.ac.uk; art4@soton.ac.uk

Keywords: Dimensional Stability, Random Vibration, Cyclic Plasticity.

Abstract. *Highly stable structures that are destined for space use are vulnerable to dimensional stability loss due to random vibration loads experienced during launch and ground testing. Small movements at structural interfaces and non-recoverable strains induced in metering elements can have negative implications for optical performance on-orbit.*

Often the dimensional stability aspects of optical bench structures are verified by environmental tests on Engineering or Protoflight Model instruments. It is proposed that a better understanding of vibration-induced structural dimensional stability loss could enable the assessment of stability loss through analysis at an early stage.

To this end, several tests have been developed at RAL to assess dimensional stability loss in materials and joints in a controlled manner under random vibration. One test has been used to assess Al alloy and CFRP material samples in a 4-point bending configuration, and another has been used to assess micron-level slipping at a bolted interface.

The aim of these tests was to provide useful material data, and also to assess the feasibility of predicting stability loss caused by random vibration events. It was found that the classical frequency domain random vibration Finite Element Analysis commonly performed to assess safety margins against structural failure on space structures is probably insufficient to predict instability. This is because the results are highly dependent on non-symmetry in the stress response (ie, due to gravity, pre-stress, or non-linear response). However a good correlation with test results was achieved with a time domain FEA model which incorporates nonlinear kinematic hardening rules in the materials.

This paper will outline the Al alloy sample test and results, as well as propose a way to estimate random vibration-induced dimensional stability loss using static microyield test results.

1 INTRODUCTION

Optical instruments used in space typically require that vital components are maintained in alignment within certain tolerances throughout their operational lifetime in order to guarantee adequate system performance. This is particularly true for low-cost Earth observation missions which seek to package large optics in small lightweight instruments with minimal or no need for on-orbit readjustment mechanisms.

For a camera structure which is aligned in a ground based cleanroom, a number of potential sources of instability exist during the ground test, launch and operational phases. Thermal expansion is possibly the most significant, driving the use of low expansivity materials such as CFRP. Moisture desorption is another issue, as are gravity release, creep, erosion by atomic oxygen, and dynamic loads during launch. This paper deals with the last of these effects.

Payload structures are subject to a period of dynamic loading during launch. These loads originate from aeroacoustic noise and stage separation events. During the design and development of such structures, there is often some uncertainty over the exact vibration levels that will be witnessed during launch. This leads to potentially high qualification test specifications. These test specifications can be used to dimension a structure in the early part of the design process, and validate it against gross structural failure using Finite Element Analysis (FEA). Dimensional stability failures due to random vibration can be harder to assess however, and this aspect of the design is usually verified by test at a later stage.

This paper seeks to introduce methods of reducing the risk to structural dimensional stability earlier in the development process, using FEA methods. It draws on the test results of some dimensional stability tests recently performed at RAL, and demonstrates that these can be replicated with a simple FEA model using cyclic plasticity material properties.

2 TEST DESCRIPTION

The aim of the test was to investigate the dimensional stability response of various material samples to random vibration. The material described here is aluminium alloy 2024 T3.

The test setup made use of a simply supported material test sample in strip form. There were a pair of masses attached inboard of the support positions (see Figure 1). The sample was then subject to random vibration in the direction that induces bending in the strip. The masses were selected such that the first modeshape of the sample approximates a standard four-point bending test, at a frequency of 41 Hz. Three identical samples were tested simultaneously, using an LDS V8-440 SPA56K shaker.

The simple support was achieved by clamping the samples between a pair of stainless steel rods at each support point (see Figure 2). The clamping force was achieved using extension springs. The spring force was determined to be enough to just prevent unloading under the highest loads possible from the shaker.

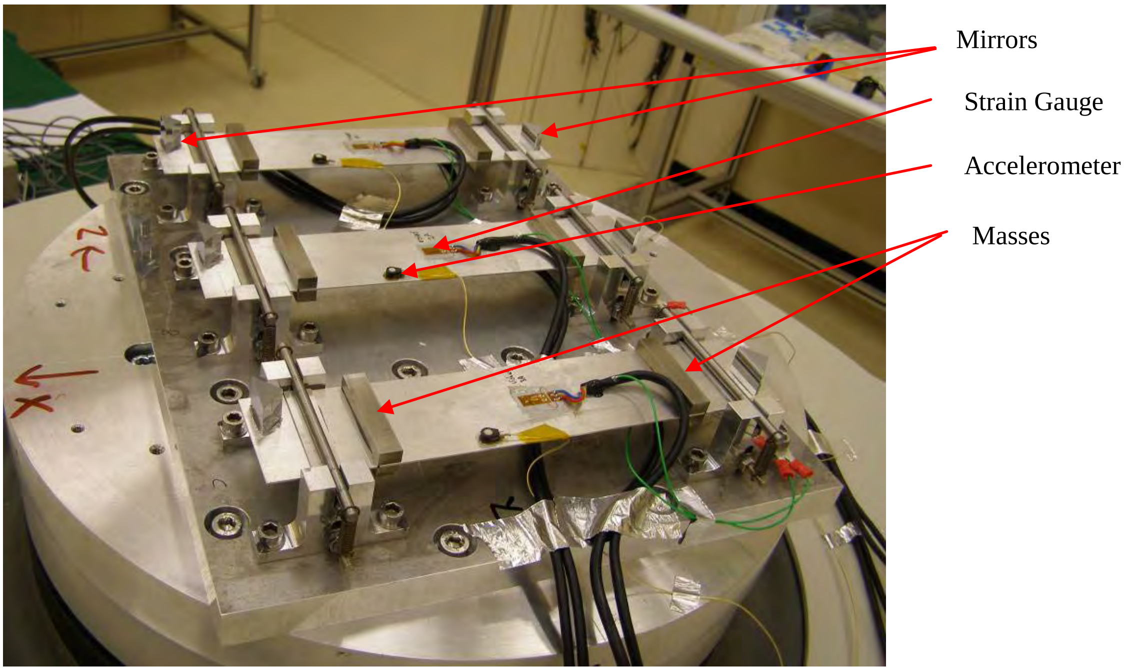

Figure 1 : Test setup.

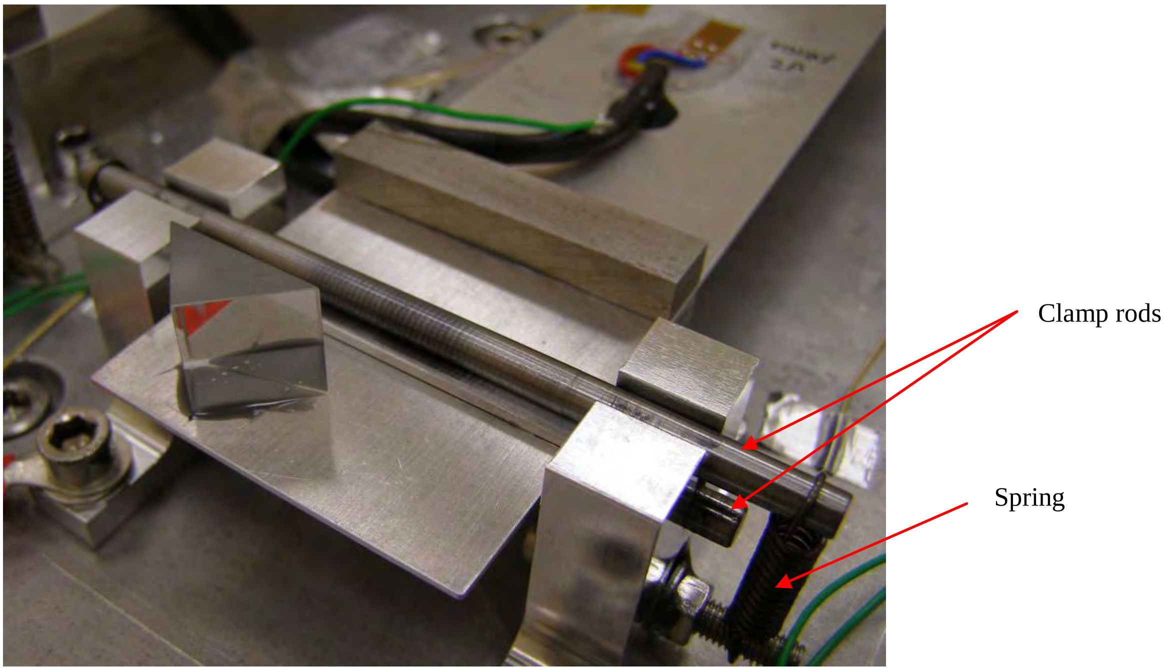

Figure 2 : Support clamp.

The random vibration loads were provided by the shaker. They started with very low level shakes, increasing in severity from 0.8 to 36 gRMS in increments of 3 or 6dB. The test spectra were based on the baseline shown in Table 1. This is similar to a typical verification test spectrum [1], though with the plateau starting at a fairly low frequency to ensure that it fully covers the first mode. Test durations were 60 s each.

Frequency	Level
20-30 Hz	+3dB/oct
30-200 Hz	0.1 g^2/Hz
200-2000Hz	-5dB/oct

Table 1 : Baseline test spectrum (6.44 gRMS).

Between each shake, metrology data were recorded to assess residual plastic strains in the samples as a result of the prior shake. This was accomplished with two separate methods – strain gauges and optical autocollimation. A pair of strain gauges was mounted on each test sample, one on the upper surface and one on the lower surface in the beam centre. Strain gauge resolution was quoted by the manufacturer to be ±0.25 μstrain. The optical method made use of a pair of mirrors at either end of the samples. The angle between these mirrors was measured very accurately with an autocollimator to derive an average bending strain along the samples. The resolution of this method was ±0.17 μstrain. Experimental errors due to the test setup were about +/-10 μstrain.

A fourth sample was subjected to static testing on a Testometric tensile test rig. The setup for this test was a four-point configuration, equivalent to the dynamic tests. The purpose of this test was to compare static and dynamic test data, and assess whether static test results in the microyield region could be used to predict dynamic results.

3 TEST RESULTS

The test results are summarized in Figure 3. There are several clear conclusions. Firstly, the low-level shakes (up to 13 gRMS) produce little discernable effect outside the error range. Secondly, at high levels, a definite trend in residual strains is observed – all samples start to show an increase in positive (tensile) residual strain for both top and bottom strain gauges. Effectively the samples are growing in length.

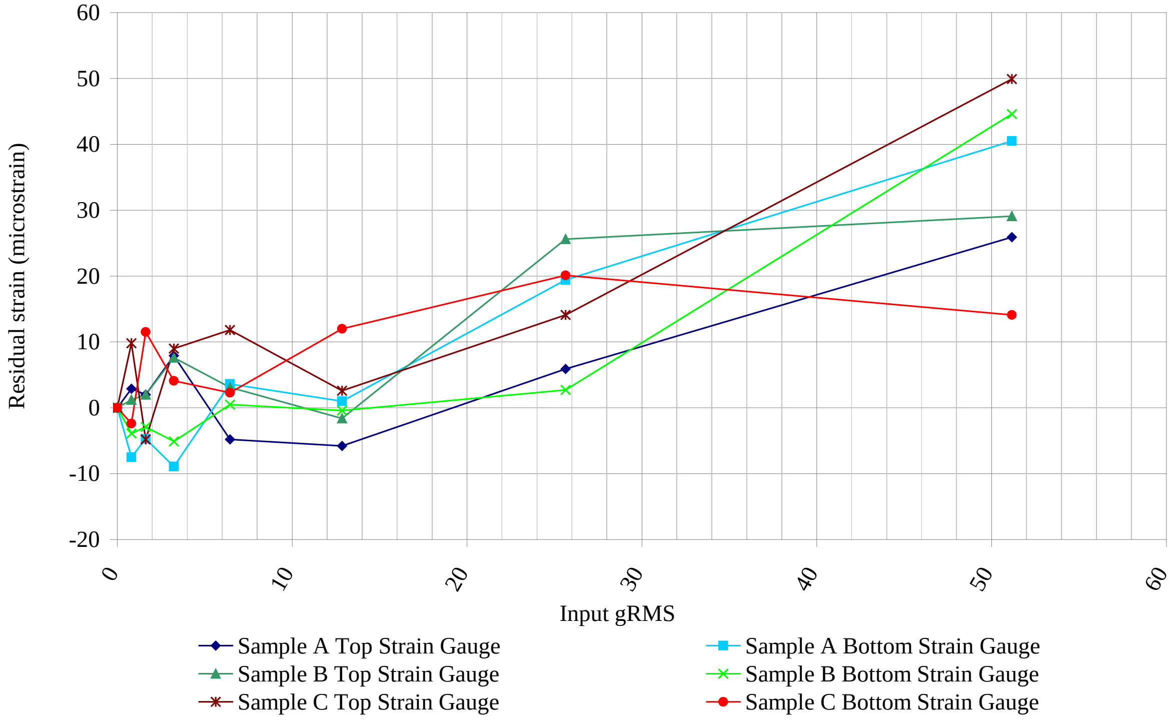

Figure 3 : Test results summary.

This result was somewhat unexpected – it was thought that the residual strains would be dominated by bending strains, which would be manifested in top and bottom strain gauges giving roughly equal and opposite responses. To better visualize the residual strain response, it was divided into a residual axial strain (from the average of the top and bottom strain gauges) and a residual bending strain (from the difference between them). These are shown in Figure 4 and Figure 5, in a traditional stress versus strain format. The RMS stress was obtained from the strain spectral density response of the strain gauges during the test.

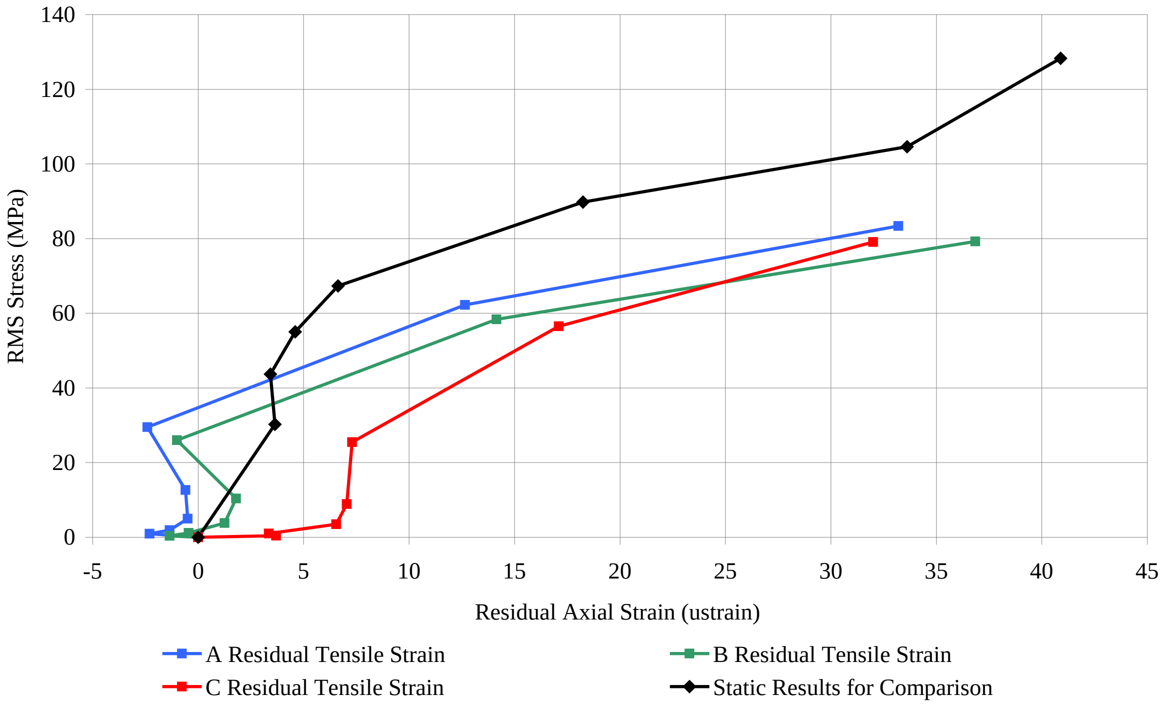

Figure 4 : Residual axial strain.

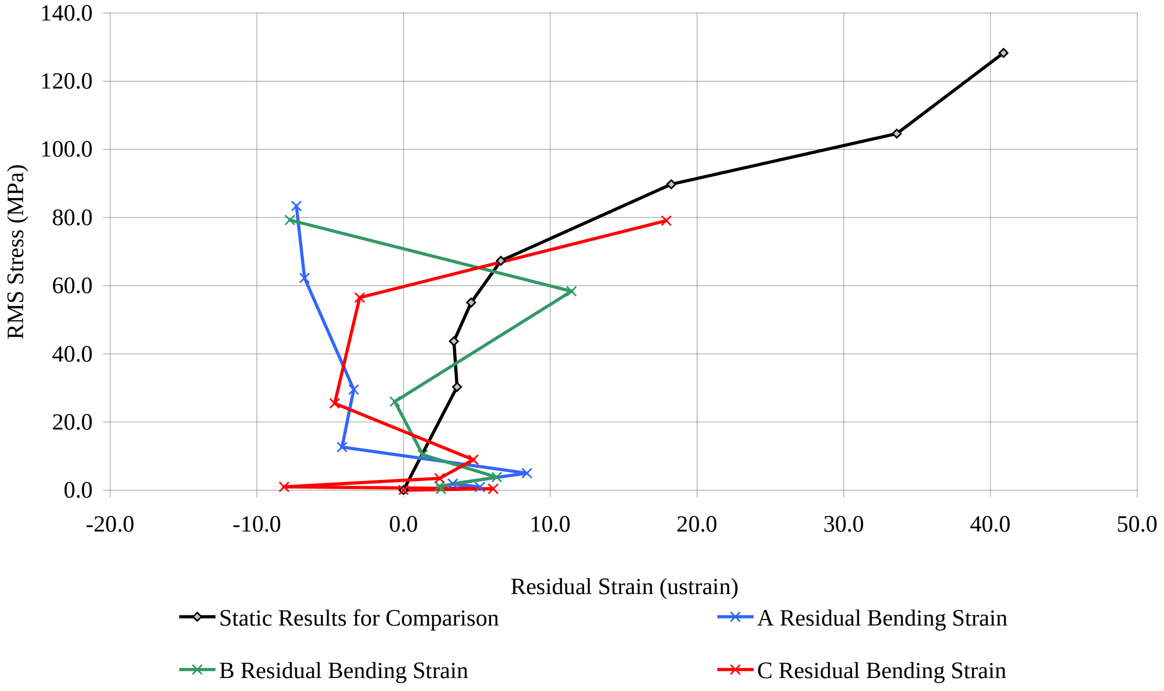

Figure 5 : Residual bending strain.

The axial strain results follow the same trend as the static test results, albeit at a lower stress level. The bending strain results generally increase in magnitude with increasing dynamic stress, but do not generally increase in the same direction.

As the test items are simply supported, the dynamic stresses are almost purely due to bending, with tensile stresses on one surface being equal and opposite to compressive stresses on the other. At the mounting positions, there is a small axial force due to friction between the test sample and the clamp rods. This force is very small by comparison though – for the penultimate dynamic test (25.6 gRMS), the RMS bending stress was 56 MPa, while the friction-induced axial component was only 0.5 MPa.

4 ANALYSIS

It was decided to investigate these results further using Finite Element Analysis, with cyclic plasticity material behaviour. It was assumed that the residual strain response was due to the first vibration mode, and that the contribution of higher modes to residual strain was negligible. ANSYS Version 12.1 was used, and the model was two-dimensional with large deformations and nonlinear material properties. The 25.6 gRMS test run was chosen for analysis, as this was the first run where a significant plastic strain response was seen. The results of Sample “B” were used.

There were two parts to the analysis. The first part was to correlate the model with the test results in order to validate the model and boundary condition assumptions. The second part was a time-domain analysis, with a large number of quasi-static load reversals applied to the model to simulate the time history of the stresses within the sample. The responses of the correlated model at the centre of the sample (where the accelerometer was located) and the FEA model are shown in Figure 6. The responses are well correlated for the first two modes, but not after this (the difference in high frequency behaviour is probably due to the FEA model being only two-dimensional).

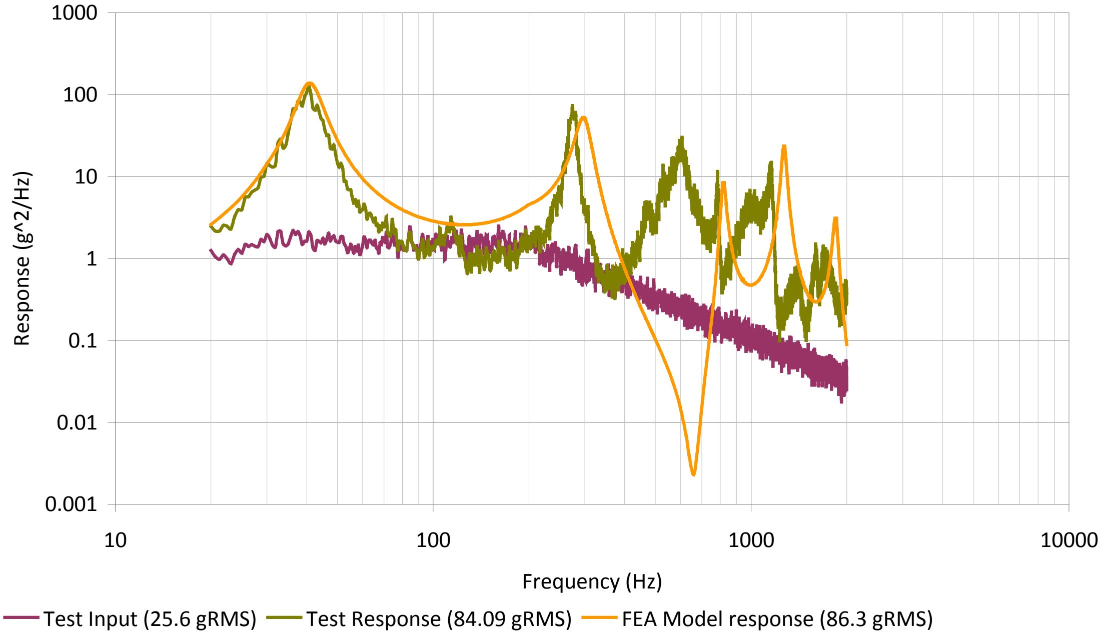

Figure 6 : Comparison between FEA model and test PSD responses.

The PSD response was then truncated between the first and second modes (at a factor of $\sqrt{2}$ from the first natural frequency). The RMS value of this truncated response was obtained, and assumed to be the quasi-static acceleration load applied to simulate the first modeshape for the static analysis (39.1 g). The FEA model with quasi-static loads applied is shown in Figure 7 and Figure 8. It contained 232 elements and 1658 degrees of freedom. It was constructed in two dimensions to minimize the solution time for a large number of sequential nonlinear solutions.

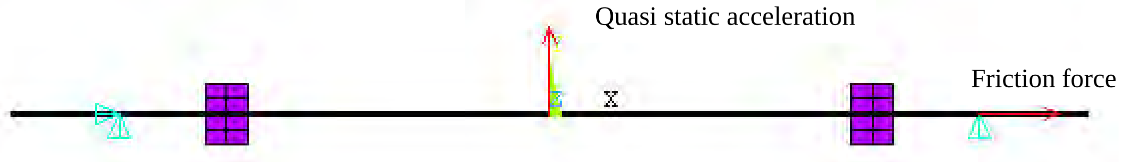

Figure 7 : FEA model showing quasi-static acceleration upwards

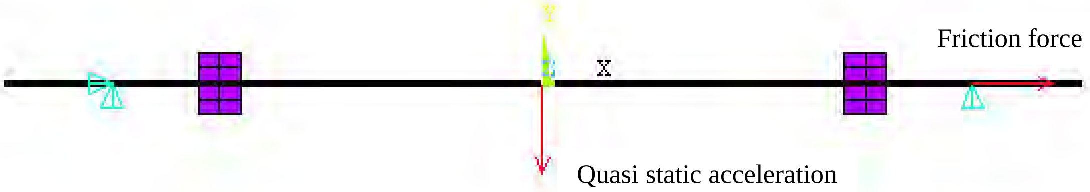

Figure 8 : FEA model showing quasi-static acceleration downwards

The X-direction stress response is shown in Figure 9, and enlarged in Figure 10. The stresses on the upper and lower surfaces (56.7 and 55.7 MPa) compare well with the RMS stress recorded by the strain gauges, of 58.9 and 57.9 MPa.

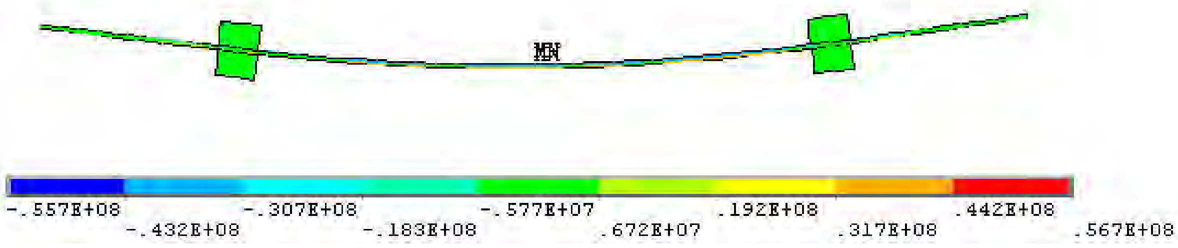

Figure 9 : Stress response to quasi-static acceleration

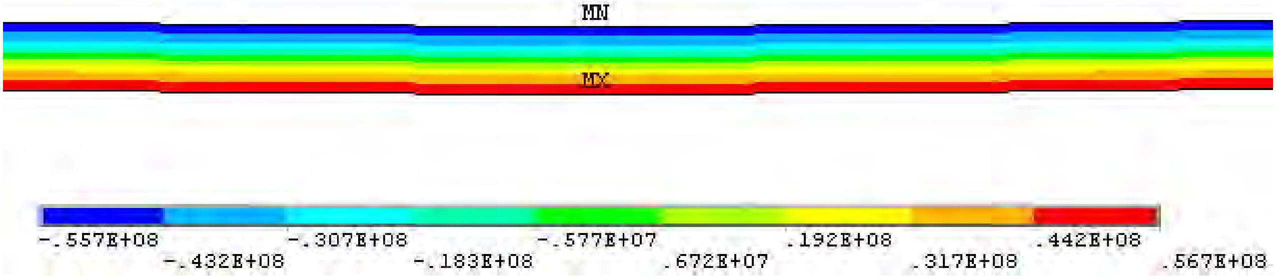

Figure 10 : Stress response enlarged at sample centre

To simulate the time history of the loads, an approach similar to Miner’s rule [2] was taken. Load cycles of 1-σ, 2-σ and 3-σ (ie, 39.1, 78.2 and 117.3 g) were applied. The number of cycles of each were determined from the probability of exceedance multiplied by the total number of first mode cycles witnessed during the test (the natural frequency multiplied by the test duration). The number of fully reversed cycles was 779, 112 and 7 for the 1-σ, 2-σ and 3-σ cases respectively.

To model material cyclic plasticity, it was decided to use the nonlinear kinematic hardening model of material behaviour [3]. This model was chosen for several reasons – it was a supported material model in the FEA code used; it can effectively model plastic strain evolution effects such as ratchetting and shakedown; some material data can be found in the literature for materials similar to the one tested here.

The model requires three basic parameters to be defined: k, C_i and γ_i. Here, k is the elastic limit or yield stress, C_i is the initial hardening modulus, and γ_i is a parameter that controls the rate at which the hardening modulus decreases with increasing strain. All three parameters are best determined from cyclic stress tests where a stable hysteresis cycle is obtained for several levels of plastic strain of interest. Additional values of C_i and γ_i (representing additional kinematic models) can be superimposed to better represent additional strain ranges. In this case, two superimposed kinematic models were used - C_1 and γ_1 were obtained from the static test data using a "goal-seek" spreadsheet function (representing a very low range of plastic strain, 10^{-6} – 10^{-5}) and C_2 and γ_2 were obtained from [4] for alloy 2024 T4 (for a much higher strain range, above about 10^{-3}). It should be noted that the static test data used to determine C_1 and γ_1 was monotonic – ideally this would have been cyclic. The superimposed model is shown in Figure 11, along with test data and the model from [4]. As the first kinematic model is based on test data only up to about 40 µstrain (plastic), and the second is intended for a much higher strain range, there is effectively a gap in the validity of this model after about 40 µstrain. Fortunately, most of the dynamic stress effects observed in this test are covered in the lower strain range. The material constants used are summarized in Table 2.

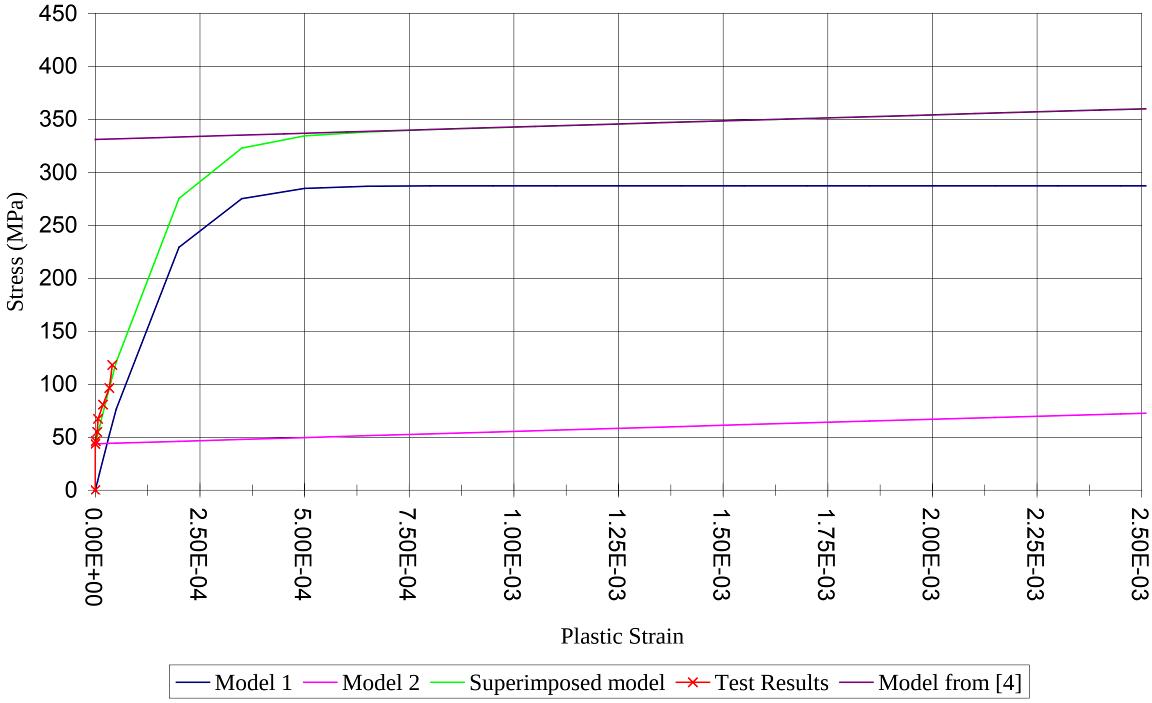

Figure 11 : Determination of material constants

Constant	Value	Units
k	4.37e7	Pa
C_1	6.57e12	Pa
γ_1	2.29e4	-
C_2	1.18e10	Pa
γ_2	1.03e2	-

Table 2 : Material constants

For ease of load application, the cycles were applied in groups of the same level – ie, the 3-σ cycles were applied first, followed by the 2-σ and 1-σ cycles. The results are shown in Figure 12 for a node in the same location as the strain gauge on the upper surface.

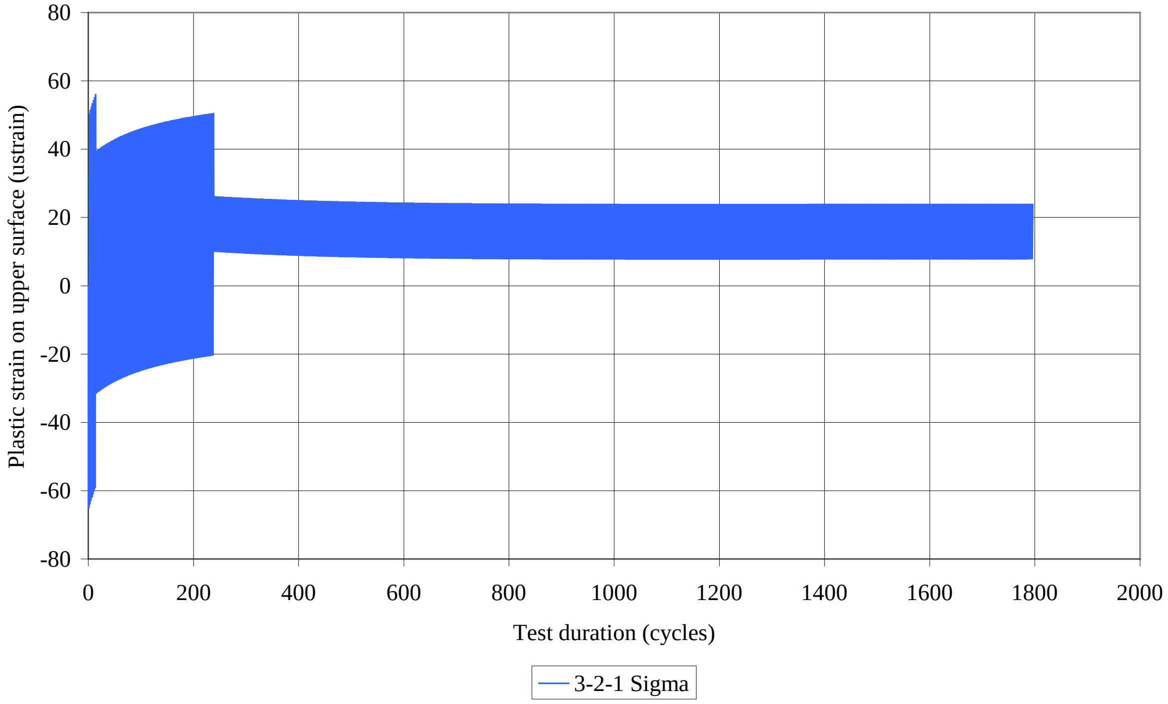

Figure 12 : Plastic strain results

There are several points to note about this curve. Firstly, the plastic strain amplitudes are high (as expected) for the 3-σ case, in the region of ±57 μstrain. This reduces to about ±8 μstrain for the 1-σ case. Secondly, shakedown is apparent. This is mostly complete following the 2-σ case, and results in a mean plastic strain of around 16 μstrain. As this mean plastic strain is positive, the trend is for a growth in length of the sample, as witnessed during testing. The mean value from testing, effectively the average of residual strain on the upper and lower surfaces, is 14 μstrain (from Figure 4). Thus there is also a good agreement with the level of residual axial strain.

The difference between upper and lower surface residual strain was 23 μstrain under testing. From results in Figure 12, it is clear that the equivalent FEA results are somewhat dependent on the level of the final stress cycle, in this case 1-σ. Here, the difference is 16 μstrain, suggesting that a level slightly higher than 1-σ would have been appropriate for this last cycle.

5 MORE COMPLEX STRUCTURES

It is proposed that the method applied here could be used for more complex structures, such as a mirror mounted on flexures that requires very high levels of dimensional stability following random vibration exposure. For such structures, a fully kinematic mounting design may mean that structural pre-stresses are low. However the results of this test have shown that even a low level of stress asymmetry in cases where peak stresses exceed the material's elastic limit can lead to significant residual strain. Also, gravity and static launch accelerations may be important.

For a complex structure, the first modeshape must firstly be determined with some accuracy. Next, acceleration loads must be determined that generate a deformed shape that approximates this modeshape. This will necessarily be an approximation – even for the simple geometry described in this paper, the first modeshape is not identical to the deformed shape under static acceleration. Next, the magnitude of the acceleration loads should be adjusted so that the deflections are equivalent to 1-σ deflections from a random vibration run. These accelerations can finally be applied in reversed cycles at several levels (ie 1-σ, 2-σ etc) with the commensurate number of cycles. For areas where microyield is expected, the material properties must include nonlinear kinematic hardening. This will probably mean a bespoke material test, as there appears to be a paucity of data in the literature for these levels of plastic strain. A single kinematic model would probably suffice unless a very large range of stresses above the elastic limit is expected. A final issue to tackle will be determining the number of cycles to apply for each load level. Nonlinear kinematic hardening makes use of the von Mises ductile failure criterion. It is a well known problem in random vibration analysis that von Mises equivalent stresses are do not observe a Gaussian probability density function, even if the component x, y and z stresses do. However there are methods to determine or estimate the correct von Mises probability density function [5], [6] that could be applicable.

6 CONCLUSION

Aluminium strip samples in a four-point bending configuration were subject to random vibration in order to assess their dimensional stability. At moderate levels of dynamic stress, the samples exhibited significant residual strain along the length of the strip. A finite element model using nonlinear kinematic hardening material properties was produced to investigate this behaviour. This model was solved in the time domain with a number of reversed load cycles superimposed on a small frictional force. The results of this analysis exhibited a shakedown effect which agreed well with the test observations. This method of analysis has been proposed for more complex structures with high dimensional stability requirements.

REFERENCES

[1] "Space Engineering—Testing," ESA, European Space Research and Technology Centre, Rept. ECSS-E-10-03A, Noordwijk, The Netherlands, 2002.

[2] J.E. Shigley, "Mechanical Engineering Design", McGraw-Hill, 1986.

[3] J. Lemaitre, J-L. Chaboche, "Mechanics of Solid Materials", Cambridge University Press, 1990.

[4] M.L.M. Francois, "A Pasticity Model with Yield Surface Distortion for Non Proportional Loading", International Journal of Plasticity, Vol. 17, No. 5, pp. 703 - 718, 2001.

[5] D. Segalman, G. Reese, R. Field Jr., C. Fulcher, "Estimating the Probability Distribution of von Mises Stress for Structures Undergoing Random Excitation", Transactions of the ASME, Vol. 122, 2000.

[6] De la Fuente, "Von Mises Stresses in Random Vibration of Linear Structures", Computers and Structures, Vol. 87, Iss. 21-22, 2009.

COMPDYN 2011
III ECCOMAS Thematic Conference on
Computational Methods in Structural Dynamics and Earthquake Engineering
M. Papadrakakis, M. Fragiadakis, V. Plevris (eds.)
Corfu, Greece, 25–28 May 2011

DYNAMIC SHAPE RECONSTRUCTION OF THREE-DIMENSIONAL FRAME STRUCTURES USING THE INVERSE FINITE ELEMENT METHOD

Marco Gherlone[1], Priscilla Cerracchio[1], Massimiliano Mattone[1], Marco Di Sciuva[1] and Alexander Tessler[2]

[1] Department of Aeronautics and Space Engineering – Politecnico di Torino,
Corso Duca degli Abruzzi 24, 10129 Torino, Italy
{marco.gherlone, priscilla.cerracchio, massimiliano.mattone, marco.disciuva}@polito.it

[2] Structural Mechanics and Concepts Branch – NASA Langley Research Center,
Mail Stop 190, Hampton, Virginia, 23681-2199, U.S.A.
a.tessler@larc.nasa.gov

Keywords: Shape sensing, Frame structures, Inverse Finite Element Method, Strain gauge.

Abstract. *A robust and efficient computational method for reconstructing the three-dimensional displacement field of truss, beam, and frame structures, using measured surface-strain data, is presented. Known as "shape sensing", this inverse problem has important implications for real-time actuation and control of smart structures, and for monitoring of structural integrity. The present formulation, based on the inverse Finite Element Method (iFEM), uses a least-squares variational principle involving strain measures of Timoshenko theory for stretching, torsion, bending, and transverse shear. Two inverse-frame finite elements are derived using the interdependent interpolations whose interior degrees-of-freedom are condensed out exactly at the element level. In addition, relationships between the order of kinematic-element interpolations and the number of required strain gauges are established. As an example problem, a thin-walled, circular cross-section cantilevered beam subjected to harmonic excitations in the presence of structural damping is modeled using iFEM; where, to simulate strain-gauge values and to provide reference displacements, a high-fidelity MSC/NASTRAN shell finite element model is used. Examples of low and high-frequency dynamic motion are analyzed and the solution accuracy examined with respect to the increased fidelity of the iFEM's discretization and the number of strain gauges.*

1 INTRODUCTION

Real-time reconstruction of structural deformations, using measured strain data, is a key technology for actuation and control of smart structures, as well as for Structural Health Monitoring (SHM) [1]. Known as "shape sensing", this inverse problem is commonly formulated with the assumption that multiple strain sensors at various structural locations provide real-time strain measurements. Most inverse algorithms use some type of Tikhonov's regularization, which is manifested by constraint (regularity) terms that ensure a certain degree of solution smoothness (refer to [2-5] and references therein.)

Most of the shape sensing efforts focused exclusively on beam-bending problems. Davis et al. [6] used optimized trial functions and weights to reconstruct a simple static-beam response from discrete strain measurements. To model more complex deformations, their approach requires a large number of trial functions and strain sensors. Kang et al. [7] used vibration mode shapes to reconstruct the beam response due to dynamic excitation. In their approach, modal coordinates are computed using strain-displacement relationship and measured surface strain measurements; the method requires the same number of mode shapes and strain sensors. Kim et al. [8] and Ko et al. [9] used classical beam equations to integrate the discretely measured strains to determine the deflection of a beam. By regression of experimental strain data and by accounting for the applied loading, Kim et al. [8] obtained a continuous curvature function, leading to the evaluation of the beam deflection. Ko et al. [9] developed a load-independent method by approximating the beam curvature using piece-wise polynomials; the authors demonstrated the validity of this one-dimensional scheme by evaluating the deflection and cross-section twist of an aircraft wing.

To enable shape-sensing analyses of plates undergoing bending deformations, Bogert et al. [10] examined a modal transformation method that allows the development of suitable strain-displacement transformations. The approach makes use of a large number of natural vibration modes. When applied to high-fidelity finite element models, however, the method requires a computationally intensive eigenvalue analysis and a detailed description of the elastic and inertial material properties. Jones et al. [11] employed a least-squares formulation for shape sensing of a cantilever plate, where the axial strain was fitted with a cubic polynomial. The strain field was then integrated with the use of approximate boundary conditions at the clamped end to obtain plate deflections according to classical bending assumptions. Shkarayev et al. [12,13] used a two-step solution procedure: the first step involves the structural analysis of a plate/shell finite element model, and the second, a least-squares algorithm. The methodology reconstructs the applied loading first, which then leads to the displacements. In a series of four papers, Mainçon and co-authors [14-17] developed a finite element formulation that seeks the solution for the displacements and loads simultaneously, requiring a priori knowledge of a subset of applied loading and the material properties. The solution procedure minimizes a cost function consisting of unknown loads and differences between the measured and estimated quantities (displacements or strains); the cost function is regularized by way of equilibrium constraints. The number of unknowns is three times the number of the degrees-of-freedom in the finite element discretization. Importantly, the accuracy of the solution strongly depends on the choice of suitable weights; these are computed from a complex procedure involving the probability distributions of the unknown loads and measured data. In [16,17], sensitivity analyses were carried out for truss structures, investigating variations in the input data as well as the modeling errors. Nishio et al. [18] employed a weighted-least-squares formulation to reconstruct, on the basis of measured strain data, the deflection of a composite cantilever plate. The weighting coefficients in the least-square terms were adjusted in order to account for the inherent errors in the measured strain data. The weights were computed for the given data-acquisition apparatus, load case, and test article, with the consequent difficulties in generalizing the procedure.

Many of the aforementioned inverse methods either lack generality with respect to structural topology and boundary conditions, or require sufficiently accurate loading and/or elastic-inertial material information – the kind of data that are either unavailable or difficult to obtain outside the laboratory environment; for these reasons, such approaches are generally unsuited for use in on-board SHM algorithms. An algorithm that is well-suited for SHM should be: (1) able to model general structural topologies and boundary conditions (e.g., built-up aircraft structures), (2) robust, stable, and accurate under a wide range of loadings, material systems, inertial/damping characteristics, and inherent errors in the strain measurements, and (3) sufficiently fast for real-time applications.

An algorithm that appears to fulfill the aforementioned requirements, labeled the inverse Finite Element Method (iFEM), was recently developed by Tessler and Spangler [1,19]. The methodology employs a weighted-least-square variational principle which is discretized by C^0-continuous finite elements that accommodate arbitrarily positioned and oriented strain-sensor data. The iFEM framework, providing accurate and stable solutions of the displacement and strain fields for the discretized structural domain, is amenable to any type of structural modeling including frame (truss and beam), plate, shell, and solid idealizations. Because only strain-displacement relations are used in the formulation, both static and dynamic regimes can be modeled without any a priori knowledge of the material, inertial, loading, or damping structural properties. To model arbitrary plate and shell structures, Tessler [20] developed, using the first-order shear-deformation theory, a three-node *inverse shell element* formulation. The numerically generated [20] and experimentally measured-strain data [21,22] were used to assess the formulation's robustness and accuracy.

This paper consolidates the authors' recent efforts in [23-25], presenting the development and assessment of simple and efficient inverse-frame finite elements. The methodology permits effective and computationally efficient shape-sensing analyses to be performed on truss, beam, and frame structures instrumented with strain gauges. The kinematic assumptions are those of Timoshenko shear-deformation theory [26]; they incorporate stretching, torsion, bending, and transverse shear deformation modes in three dimensions. The formulation uses a least-squares variational principle that is specialized from [19] for three-dimensional frame analysis. The variational framework, in conjunction with suitable finite element discretizations involving inverse finite elements, yields a system of linear algebraic equations; the equations are efficiently solved for the unknown displacement degrees-of-freedom (dof's), thus providing the deformed structural-shape predictions.

In the remainder of the paper, the kinematic assumptions for a three-dimensional frame are discussed, followed by the description of the least-squares variational principle suitable for three-dimensional deformations of frame structures. This is followed by a discussion of two C^0-continuous, inverse-frame elements that use the well-established interdependent interpolations that resolve the shear locking effect. Finally, to examine the predictive capabilities of the inverse elements for a given set of distributed strain gauges, shape-sensing studies are carried for a cantilevered beam undergoing harmonic excitations in the presence of structural damping.

2 GOVERNING EQUATIONS

Consider a straight frame member of constant cross-section positioned in the three-dimensional Cartesian coordinates (x,y,z) as depicted in Figure 1; the coordinate origin, O, is located at the cross-section's center of mass, which is also coincident with the shear center. The longitudinal, elastic x-axis is normal to the cross-sectional plane (y, z), where y and z are the cross-section's principal inertial axes. The frame member has length L and its cross section has area A, area moments of inertia with respect to the y- and z-axis I_y and I_z, respectively, and polar moment of inertia $I_P = I_y + I_z$ (Figure 1). The frame member is made of an isotropic material, represented by the elastic constants: E (Young's modulus), G (shear modulus), and ν (Poisson ratio).

Neglecting the effect of axial warping due to torsion, and assuming the kinematics of Timoshenko theory [26] in three dimensions, i.e., each cross-section remains flat and rigid with respect to thickness-stretch deformations along the y and z axes, gives rise to the three Cartesian components of the displacement vector of the form

$$\begin{aligned} u_x(x,y,z) &= u(x) + z\theta_y(x) - y\theta_z(x) \\ u_y(x,y,z) &= v(x) - z\theta_x(x) \\ u_z(x,y,z) &= w(x) + y\theta_x(x) \end{aligned} \tag{1}$$

where u_x, u_y, and u_z are the displacements along the x, y, and z axes, respectively, with u, v, and w denoting the displacements at $y = z = 0$; θ_x, θ_y, and θ_z are the rotations about the three coordinate axes. The positive orientations for the six *kinematic variables*, $\mathbf{u} \equiv \left[u, \quad v, \quad w, \quad \theta_x, \quad \theta_y, \quad \theta_z\right]^T$, are depicted in Figure 1.

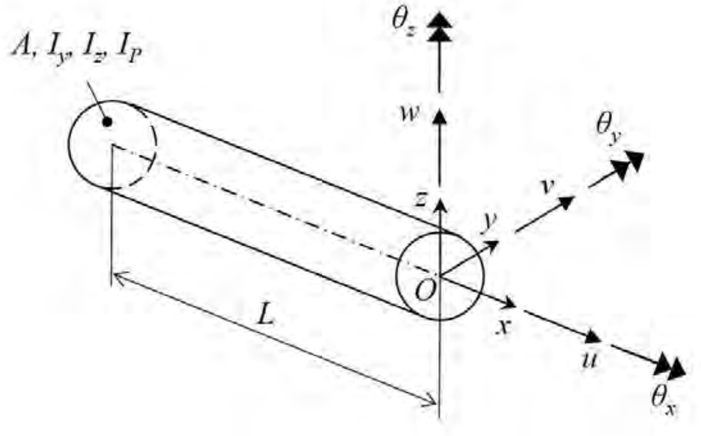

Figure 1: Beam geometry and kinematic variables.

Adhering to the small-strain hypothesis, the non-vanishing strain components have the form

$$\begin{aligned} \varepsilon_x(x,y,z) &= e_1(x) + z\,e_2(x) + y\,e_3(x) \\ \gamma_{xz}(x,y) &= e_4(x) + y\,e_6(x) \\ \gamma_{xy}(x,z) &= e_5(x) - z\,e_6(x) \end{aligned} \tag{2}$$

where $\mathbf{e}(\mathbf{u}) \equiv [e_1, \quad e_2, \quad e_3, \quad e_4, \quad e_5, \quad e_6]^T$ denote the strain measures of the theory, related to the kinematic variables by first-order partial differentiation

$$\begin{array}{ll} e_1(x) \equiv u_{,x}(x) & e_4(x) \equiv w_{,x}(x) + \theta_y(x) \\ e_2(x) \equiv \theta_{y,x}(x) & e_5(x) \equiv v_{,x}(x) - \theta_z(x) \\ e_3(x) \equiv -\theta_{z,x}(x) & e_6(x) \equiv \theta_{x,x}(x) \end{array} \tag{3}$$

The forces {N, Q_y, and Q_z} and moments {M_x, M_y, and M_z} are related to the strain measures, e_i, by way of the constitutive equations (refer to Figure 2)

$$\begin{array}{ll} \mathrm{N} = A_x e_1 & \mathrm{M}_x = J_x e_6 \\ \mathrm{Q}_y = G_y e_5 & \mathrm{M}_y = D_y e_2 \\ \mathrm{Q}_z = G_z e_4 & \mathrm{M}_z = D_z e_3 \end{array} \tag{4}$$

where $A_x \equiv EA$ is the axial stiffness, $G_y \equiv k_y^2 GA$ and $G_z \equiv k_z^2 GA$ are the shear stiffnesses (with k_y^2 and k_z^2 shear correction factors), $J_x \equiv GI_P$ is the torsional stiffness, and $D_y \equiv EI_y$ and $D_z \equiv EI_z$ are the bending stiffnesses.

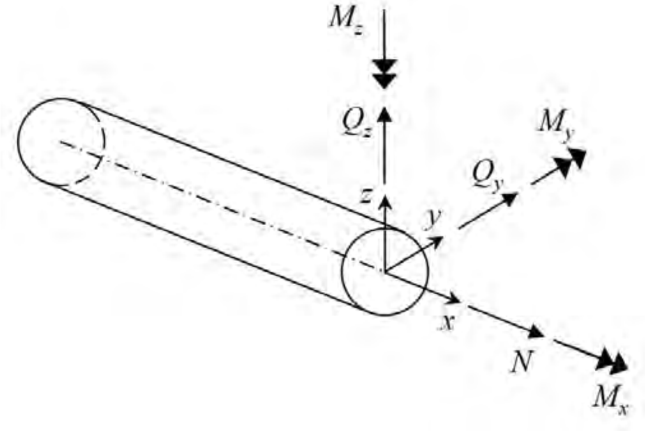

Figure 2: Beam resultant forces and moments.

If $q_x(x)$, $q_y(x)$, and $q_z(x)$ are the distributed loads applied along the x, y and z directions, respectively, the frame-member equilibrium equations become

$$\begin{array}{ll} \dfrac{\mathrm{dN}}{\mathrm{d}x} = -q_x & \dfrac{\mathrm{dM}_x}{\mathrm{d}x} = 0 \\ \dfrac{\mathrm{dQ}_y}{\mathrm{d}x} = -q_y & \dfrac{\mathrm{dM}_y}{\mathrm{d}x} = \mathrm{Q}_z \\ \dfrac{\mathrm{dQ}_z}{\mathrm{d}x} = -q_z & \dfrac{\mathrm{dM}_z}{\mathrm{d}x} = \mathrm{Q}_y \end{array} \tag{5}$$

To reconstruct the deformed shape of a frame structure for which certain in-situ strain measurements are known, a functional $\Phi(\mathbf{u})$ that matches, in a least-square sense, the complete set of the analytic strain measures, $\mathbf{e}(\mathbf{u})$, to those corresponding to the strain measurements, $\mathbf{e}^{\varepsilon}$, is minimized with respect to the kinematic variables, $\mathbf{u}$; where the superscript ε denotes those quantities that are computed from the in situ strain measurements. Thus, the $\Phi(\mathbf{u})$ functional can be written in compact notation as

$$\Phi(\mathbf{u}) = \left\| \mathbf{e}(\mathbf{u}) - \mathbf{e}^{\varepsilon} \right\|^2 \tag{6}$$

$\Phi(\mathbf{u})$ is then discretized by the piecewise-continuous displacements, $\mathbf{u}^h$, i.e.,

$$\mathbf{u}(x) \simeq \mathbf{u}^h = \mathbf{N}(x)\mathbf{u}^e \tag{7}$$

where $\mathbf{N}(x)$ denotes C^0-continuous shape functions and $\mathbf{u}^e$ the nodal dof's. Consequently, the total least-squares functional is a sum of the individual element contributions, $\Phi^e(\mathbf{u}^h)$, i.e., $\Phi = \sum_{e=1}^{N} \Phi^e$, with N denoting the total number of elements. Accounting for the axial stretching, bending, twisting, and transverse shearing, the element functional is given by

$$\Phi^e(\mathbf{u}^h) \equiv \sum_{k=1}^{6} \lambda_k \, \Phi_k^e \tag{8}$$

where

$$\boldsymbol{\lambda} \equiv \left[\lambda_1^0 \quad \lambda_2^0 A^e \quad \lambda_3^0 A^e \quad \lambda_4^0 \quad \lambda_5^0 \quad \lambda_6^0 A^e \right] \tag{9}$$

with λ_k^0 $(k = 1,...,6)$ denoting the dimensionless weight coefficients, and A^e the cross-sectional area of the element. The six components of the element functional are given as the Euclidean norms

$$\Phi_k^e \equiv \frac{L^e}{n} \sum_{i=1}^{n} \left[e_k(x_i) - e_k^{\varepsilon i} \right]^2 \quad (k = 1,...,6) \tag{10}$$

where L^e denotes the element length, n is the number of strain sensors, x_i $(0 \le x_i \le L^e)$ are the positions at which the strain sensors are located, and the superscript εi is used to denote the strain measures that are computed from the strain-sensor values (experimental values) at the location x_i.

Substituting Eq. (7) into Eq. (3) gives the strain measures in terms of the nodal dof's as

$$\mathbf{e}(\mathbf{u}) = \mathbf{B}(x)\mathbf{u}^e \tag{11}$$

where the matrix $\mathbf{B}(x)$ contains the derivatives of the shape functions $\mathbf{N}(x)$. Substituting Eq. (11) into Eq. (8) results in the following quadratic form

$$\Phi^e = \frac{1}{2}\left(\mathbf{u}^e\right)^T \mathbf{k}^e\mathbf{u}^e - \left(\mathbf{u}^e\right)^T \mathbf{f}^e + \mathbf{c}^e \tag{12}$$

where $\mathbf{k}^e$ and $\mathbf{f}^e$ are defined in terms of $\mathbf{B}(x)$ and $\mathbf{c}^e$ is a constant. Note that $\mathbf{k}^e$ depends only on the measurement locations, x_i, whereas $\mathbf{f}^e$ depends on the experimentally measured strain values. Minimization of the functional Φ^e with respect to $\mathbf{u}^e$ leads to the inverse element matrix equation

$$\mathbf{k}^e\mathbf{u}^e = \mathbf{f}^e \tag{13}$$

The assembly of the finite element contributions, while accounting for the appropriate coordinate transformations and by specifying problem-dependent displacement boundary conditions, results in a non singular system of algebraic equations of the form

$$\mathbf{KU} = \mathbf{F} \tag{14}$$

The solution of these equations for the unknown dof's is efficient: the **K** matrix is inverted only once, since it is independent of the values of the measured strains. The **F** vector, however**,** is dependent on the measured strain values that change during deformation. Thus, at any strain-measurement update during deformation, the matrix-vector multiplication provides the solution for the unknown nodal displacement dof's, **U** = **K**$^{-1}$ **F**, where **K**$^{-1}$ remains unchanged for a given distribution of strain sensors[1].

The remaining part of the element formulation involves the selection of suitable shape functions, symbolically defined by Eq. (7), and the computation of the experimental strain measures, $e_k^{\varepsilon i}$, appearing in Eq. (10). In Section 3, the shape functions for two alternative inverse-frame elements, each having two nodes and twelve dof's, are derived. In Section 4, a procedure for computing $e_k^{\varepsilon i}$ is described; it relates the number of strain gauges to the interpolation order of the shape functions.

---

[1] Depending on the selected shape functions (refer to Section 3), interior dof's may be present. These are condensed out at the element level by straightforward partitioning of the element equations, $\mathbf{k}^e\mathbf{u}^e = \mathbf{f}^e$, and then by solving exactly for the condensed dof's in terms of the end-node dof's. This process results in the reduced element equations (without the interior dof's), $\mathbf{k}_R^e\mathbf{u}_R^e = \mathbf{f}_R^e$, where $\mathbf{k}_R^e$ is a function of the partitioned parts of the original $\mathbf{k}^e$ matrix, and $\mathbf{u}_R^e$ contains the end-node dof's. Since the unreduced $\mathbf{k}^e$ matrix is independent of the strain values, so is the $\mathbf{k}_R^e$ matrix. This implies that even for the elements with the condensed-out interior dof's, the corresponding system matrix, $\mathbf{K}$, is also strain-value independent.

3 ELEMENT SHAPE FUNCTIONS

In this section, inverse frame elements of 0th and 1st order are formulated. The elements use the interdependent interpolations that enable excellent predictions even for very slender frame members, without incurring any form of excessive stiffening due to shear locking [27]. The 0th-order shape functions are guided by Timoshenko equilibrium equations, Eq. (5), that correspond to the forces and moments applied exclusively at the end nodes, resulting in constant distributions of the transverse-shear strain measures. The 1st-order shape functions accommodate Eq. (5) for uniformly distributed transverse loads, giving rise to linear distributions of the transverse-shear strain measures.

A frame element is referred to a local axial coordinate $x \in \left[0, L^e\right]$, where L^e denotes the element length. Furthermore, a non-dimensional coordinate $\xi \equiv (2x / L^e - 1) \in \left[-1, 1\right]$ is used to define the element shape functions (Figure 3). The initial nodal configurations are defined by the two end nodes, 1 (at $\xi = -1$) and 2 (at $\xi = +1$) and one or three interior nodes. Thus, the initial configuration for the 0th-order element has the interior node, r (at the midspan, $\xi = 0$); whereas the interior nodes of the 1st-order element are q (at $\xi = -1/2$), r (at $\xi = 0$), and s (at $\xi = +1/2$).

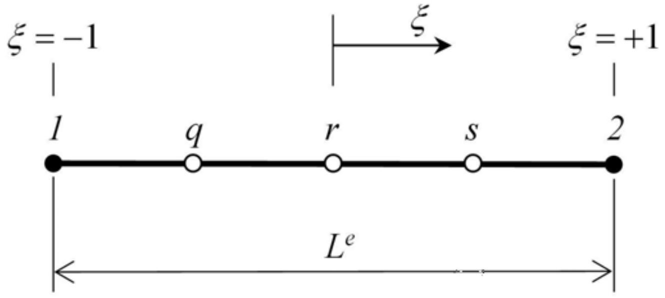

Figure 3: Inverse finite element geometry and nodal topology.

The initial nodal configurations of the 0th- and 1st-order elements are readily reduced to two nodes and twelve dof by condensing out the interior dof's at the element level, Eq. (13), in a manner analogous to static condensation. The resulting elements have three-displacement and three-rotation dof's at each end node (Figure 4)

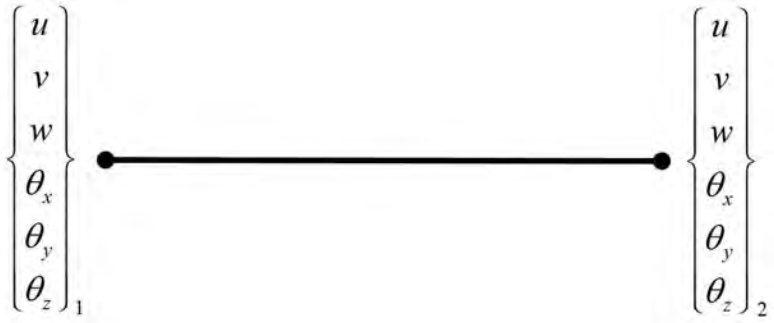

Figure 4: Two-node inverse finite element.

3.1 0th-order element

The formulation of the 0th-order element is guided by Eq. (5) for the loading case of end-node forces and moments. For this case, the axial force, twisting moment, and shear forces are constant along the element; whereas the bending moments are linear. Equations (5) in terms of the strain measures (after Eq. (4) have been introduced) indicate that the strain measures e_i (i=1, 4-6) are constant, and e_i (i=2,3) are linear. From Eq. (3), it is deduced that u and θ_x are linear, θ_y and θ_z parabolic, v and w cubic.

Thus, u and θ_x are interpolated using the linear Lagrange polynomials $L_i^{(1)}(\xi)$ $(i=1,2)$

$$\begin{aligned} u(\xi) &= \sum_{i=1,2} L_i^{(1)}(\xi) u_i \\ \theta_x(\xi) &= \sum_{i=1,2} L_i^{(1)}(\xi) \theta_{xi} \end{aligned} \tag{15}$$

The polynomial degrees for the deflection, v and w, and bending rotation, θ_y and θ_z, variables are interrelated: if v and w are defined by cubic polynomials, then θ_y and θ_z need to be represented by quadratic polynomials to form consistent, free of locking, transverse shear-strain measures e_4, e_5 (This is a key requirement of the interdependent interpolation strategy, IIS.) Thus, the remaining kinematic variables, which enable both bending and shear deformation along the *x* and *y* orthogonal directions, are interpolated as

$$\begin{aligned} v(\xi) &= \sum_{i=1,2} L_i^{(1)}(\xi) v_i - \sum_{j=1,r,2} N_j^{(3)}(\xi) \theta_{zj} \\ w(\xi) &= \sum_{i=1,2} L_i^{(1)}(\xi) w_i + \sum_{j=1,r,2} N_j^{(3)}(\xi) \theta_{yj} \\ \theta_y(\xi) &= \sum_{j=1,r,2} L_j^{(2)}(\xi) \theta_{yj} \\ \theta_z(\xi) &= \sum_{j=1,r,2} L_j^{(2)}(\xi) \theta_{zj} \end{aligned} \tag{16}$$

where $L_j^{(2)}(\xi)$ are standard quadratic Lagrange polynomials, and $N_j^{(3)}(\xi)$ $(j=1,r,2)$ are special-form cubic polynomials; these functions are obtained from standard cubic Lagrange polynomials by enforcing the transverse shear-strain measures to be constant along the element, i.e.,

$$\begin{aligned} e_4 &= \left(w_{,x} + \theta_y\right) = const. \\ e_5 &= \left(v_{,x} - \theta_z\right) = const. \end{aligned} \tag{17}$$

The expression for $L_i^{(1)}(\xi)$, $L_j^{(2)}(\xi)$, and $N_j^{(3)}(\xi)$ $(i=1,2;\ \ j=1,r,2)$ are summarized in the Appendix. The element has fourteen dof's, six at each element end, plus the rotations θ_{yr} and θ_{zr} at the element's midspan

$$\mathbf{u}^e \equiv \left\{u_1,\ v_1,\ w_1,\ \theta_{x1},\ \theta_{y1},\ \theta_{z1},\ \theta_{yr},\ \theta_{zr},\ u_2,\ v_2,\ w_2,\ \theta_{x2},\ \theta_{y2},\ \theta_{z2}\right\}^T \tag{18}$$

Thus, in order to achieve a two-node element with twelve dof's (Figure 4), the internal dof's, θ_{yr}, θ_{zr}, are condensed out statically.

3.2 1st-order element

Consider a frame element loaded by uniformly distributed transverse loads, $q_y(x)$ and $q_z(x)$. From Eqs. (5), after the substitution of Eqs. (4), it is readily deduced that (e_4, e_5) need to be linear and (e_2, e_3) parabolic. The u and θ_x variables remain linear and interpolated by Eq. (15). Moreover, (v, w) and (θ_y, θ_z) are respectively quartic and cubic, and are interpolated as

$$\begin{aligned}
v(\xi) &= \sum_{k=1,q,r,s,2} L_k^{(4)}(\xi)\, v_k \\
w(\xi) &= \sum_{k=1,q,r,s,2} L_k^{(4)}(\xi)\, w_k \\
\theta_y(\xi) &= \sum_{i=1,2} L_i^{(1)}(\xi)\,\theta_{yi} + \sum_{k=1,q,r,s,2} \overline{N}_k^{(3)}(\xi)\, w_k \\
\theta_z(\xi) &= \sum_{i=1,2} L_i^{(1)}(\xi)\,\theta_{zi} - \sum_{k=1,q,r,s,2} \overline{N}_k^{(3)}(\xi)\, v_k
\end{aligned} \tag{19}$$

where $\overline{N}_k^{(3)}(\xi)$ $(k = 1, q, r, s, 2)$ are cubic polynomials that satisfy the conditions (for the detailed expressions, refer to the Appendix)

$$\begin{aligned}
e_4 &= \left(w_{,x} + \theta_y\right) = linear \\
e_5 &= \left(v_{,x} - \theta_z\right) = linear
\end{aligned} \tag{20}$$

Interpolation described by Eqs. (15) and (19) leads to a formulation with eighteen dof's

$$\mathbf{u}^e \equiv \left\{u_1,\ v_1,\ w_1,\ \theta_{x1},\ \theta_{y1},\ \theta_{z1},\ v_q,\ w_q,\ v_r,\ w_r,\ v_s,\ w_s,\ u_2,\ v_2,\ w_2,\ \theta_{x2},\ \theta_{y2},\ \theta_{z2}\right\}^T \tag{21}$$

The interior dof's are condensed out at the element level, leading again to a twelve dof's inverse element (Figure 4).

4 INPUT DATA FROM SURFACE STRAIN MEASUREMENTS

A key step in the iFEM formulation is to compute the strain measures due to experimentally measured surface strains. Herein, the relationships between the measured surface strains and the six strain measures, e_i, are established. Also discussed are strain-gauge positions along the frame axis and their angular orientations that enable the complete description of the experimental strain measures. The present analysis is restricted to frame members with circular cross sections; the cylindrical coordinate system (θ, x, r) is shown in Figure 5.

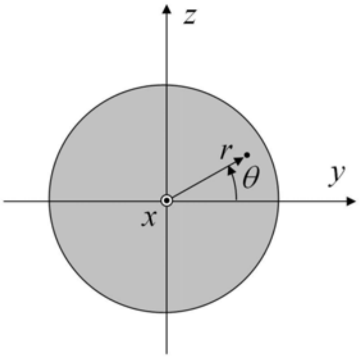

Figure 5: Orthogonal and cylindrical coordinate systems.

4.1 Strain measures from linear strain gauge measurements

Taking the usual assumption of negligible σ_y and σ_z, σ_x and $\tau_{x\theta}$ are the only non-zero stress components acting on the external surface $r = R_{ext}$ (Figure 6(a)). The corresponding strain state is (Figure 6(b))

$$\varepsilon_x = \frac{\sigma_x}{E}, \quad \varepsilon_\theta = -\frac{\nu}{E}\sigma_x = -\nu\varepsilon_x, \quad \gamma_{x\theta} = \frac{\tau_{x\theta}}{G} \tag{22}$$

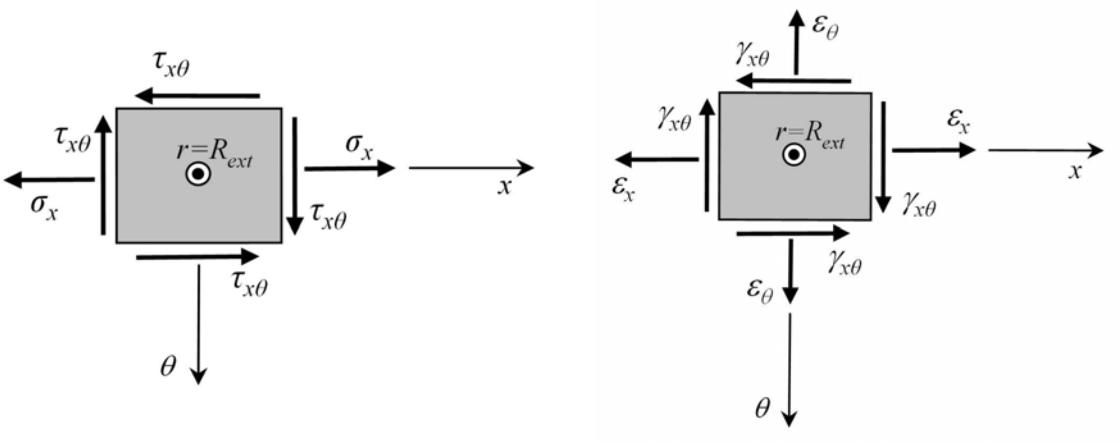

(a) Stress state.

(b) Strain state.

Figure 6: Stress and strain states on the frame external surface (r=R_{ext}) in the cylindrical coordinate system.

Consider a linear strain gauge placed on the external surface at $x = x_i$, at a particular θ and with an angle β with respect to the beam axis (Figure 7); (x_1, x_2, x_3) is a local Cartesian coordinate system having x_2-axis along the strain gauge measurement axis, x_1-axis on the frame surface and x_3-axis normal to the frame surface and coincident with *r*-axis.

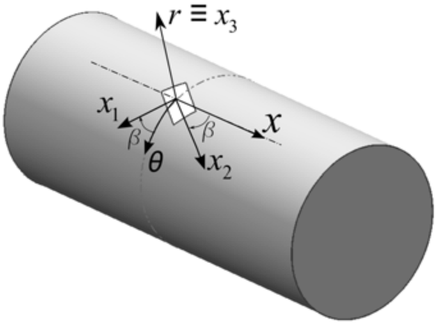

Figure 7: Location and coordinate system of a linear strain gauge placed on the frame external surface.

Using the appropriate strain-tensor transformations, from the (θ, x, r) to (x_1, x_2, x_3) coordinates [28], the relationship between the measured strain ε_2 and the strain tensor in Eq. (22) becomes

$$\varepsilon_2 = \varepsilon_x \cos^2\beta + \varepsilon_\theta \sin^2\beta + \gamma_{x\theta}\cos\beta\sin\beta \tag{23}$$

or, using the second of Eqs. (22),

$$\varepsilon_2 = \varepsilon_x\left(\cos^2\beta - \nu\sin^2\beta\right) + \gamma_{x\theta}\cos\beta\sin\beta \tag{24}$$

Expressing Eq. (2) for $r = R_{ext}$, yields [23-25]

$$\begin{aligned} \varepsilon_x &= e_1 + e_2 R_{ext}\sin\theta + e_3 R_{ext}\cos\theta \\ \gamma_{x\theta} &= e_4\cos\theta - e_5\sin\theta + e_6 R_{ext} \end{aligned} \tag{25}$$

Substituting Eq. (25) into Eq. (24) results in the relation between the measured strain ε_2 and the six strain measures at $x = x_i$

$$\begin{aligned} \varepsilon_2(x_i,\theta,\beta) = e_1(x_i)&\left(c_\beta^2 - \nu s_\beta^2\right) \\ &+ e_2(x_i)\left(c_\beta^2 - \nu s_\beta^2\right)s_\theta R_{ext} \\ &- e_3(x_i)\left(c_\beta^2 - \nu s_\beta^2\right)c_\theta R_{ext} \\ &+ e_4(x_i)c_\beta s_\beta c_\theta \\ &- e_5(x_i)c_\beta s_\beta s_\theta \\ &+ e_6(x_i)c_\beta s_\beta R_{ext} \end{aligned} \tag{26}$$

where the following notation has been used: $c_\theta \equiv \cos\theta$, $s_\theta \equiv \sin\theta$, $c_\beta \equiv \cos\beta$, $s_\beta \equiv \sin\beta$.

4.2 Strain gauge distributions

The 0th-order element, having constant e_1, e_4, e_5, and e_6 and linear e_2 and e_3, requires eight strain measurements. This number may be reduced to six by invoking the moment-shear equilibrium equations, Eq. (5). Substituting Eq. (4) into Eq. (5) results in

$$D_y e_{2,x} = G_z e_4, \quad D_z e_{3,x} = G_y e_5 \tag{27}$$

The 1st-order element has constant e_1 and e_6, linear e_4 and e_5, and parabolic e_2 and e_3 , thus requiring twelve strain measurements. For this element, each of the equations in Eqs. (27) is linear in *x*, thus four constraint equations are obtained; the number of the strain-gauge measurements is thus reduced from twelve to eight. This procedure should be viewed as a convenient means of reducing the required number of strain gauges by solving for e_4 and e_5 analytically rather than measuring these quantities experimentally. Since the magnitudes of e_4 and e_5 are generally much smaller compared to the bending strain measures, this treatment should be quite adequate for both static and dynamic applications. In Section 5, the validity of this constraint strategy for dynamically loaded beams is examined quantitatively.

Since the strain gauges can be placed anywhere along the beam surface, the distributions summarized in Table 1 are considered in this study (also refer to Figures 8 and 9); additional strain-gauge locations have been examined in [24]. To refer to a specific combination of the element type and strain-gauge configuration, a compact notation, #-#E, is used; where the first position, #, refers to the element order (0 or 1), the second position, #, indicates the number of strain gauges per element (6 or 8), and the letter “E” indicates that Eqs. (27) have been used in the formulation. The strain gauges are placed at different positions $x = (L^e/3, L^e/2, 2L^e/3)$ along the element. The strain-gauge angular orientations (θ, β) are also allowed to be different; for example, (θ, β) = (-2π/3, π/4) indicates that the strain gauge is placed at the circumferential angle θ=-2π/3 and is oriented with an angle β=π/4 with respect to the frame *x*-axis (Figure 7).

Element-strain gauge notation	Orientation (θ, β) of strain gauges at $x=L^e/3$	Orientation (θ, β) of strain gauges at $x=L^e/2$	Orientation (θ, β) of strain gauges at $x=2L^e/3$
0-6E	-	(-2π/3,0), (-2π/3,π/4), (0,0), (0,π/4), (2π/3,0), (2π/3,π/4)	-
1-8E	(-2π/3,π/4)	(-2π/3,0), (-2π/3,π/4), (0,0), (0,π/4), (2π/3,0), (2π/3,π/4)	(2π/3,π/4)

Table 1: Strain-gauge distributions x, (θ, β) corresponding to the 0th- and 1st –order elements.

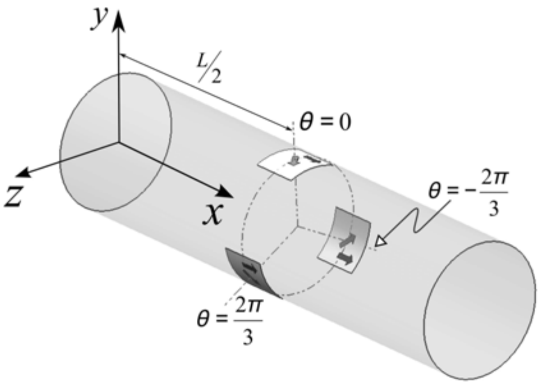

Figure 8: 0-6E strain gauge distribution.

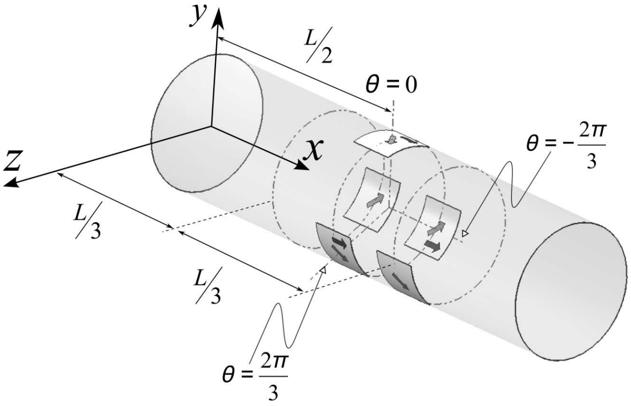

Figure 9: 1-8E strain gauge distribution.

5 NUMERICAL RESULTS

A simple cantilevered beam subjected to dynamic loading is analyzed to assess the accuracy of the inverse finite element method. The beam is made of an aluminum alloy (E=73,000 MPa, ν=0.3, and ρ=2557 Kg/m^3) and has a thin-walled circular cross-section with the average radius R=39 mm, wall thickness s=2 mm, and length L=800 mm. The beam is fully clamped on one end and subjected at the other end to a harmonic vertical force $F_z(t)$ (where t denotes time) acting in the z-direction at frequency f_0, i.e.,

$$F_z(t) = F_{z0}\sin\left(2\pi f_0 t\right) \tag{28}$$

where F_{z0} is the force amplitude (F_{z0}=10^3 N.) To simulate the experimental-strain measurements and to assess the accuracy of the inverse method, high-fidelity forward FE analyses are performed using QUAD4 shell elements in MSC/NASTRAN. The model consists of 114 elements along the cross-sectional circumference and 360 elements along the beam axis, for a total of 41,040 elements and 41,156 nodes. The tip force is applied at the cross-sectional center at a node which is connected to all other nodes within the cross-section by means of multipoint constraints (or MPC’s) [29].

The dynamic response of the beam is calculated via a modal transient analysis keeping the modes up to 5,000 Hz, with the inclusion of viscous damping of magnitude 5% with respect to the critical value at each frequency. In the frequency range from 0 to 5,000 Hz, 51 modes are present: these include the first lowest flexural beam modes, 1F-5F, appearing twice due to the cross-section symmetry, and the first membrane mode (1M). Table 2 summarizes the order of the global modes, their type, and corresponding frequency value f ; the first three flexural mode shapes are shown in Figures 10-12. The other modes in the same frequency range are associated with the shell modes describing the cross-sectional distortion.

Mode order	1st and 2nd modes	3rd and 4th modes	12th mode	13th and 14th modes	30th and 31st modes	40th and 41st modes
Mode type	1F	2F	1M	3F	4F	5F
f frequency [Hz]	126.8	729.5	1,670	1,835	3,187	4,671

Table 2: Global modes of the cantilevered beam in the frequency range of 0-5,000 Hz. (F-type modes are flexural; M-type modes are membrane.)

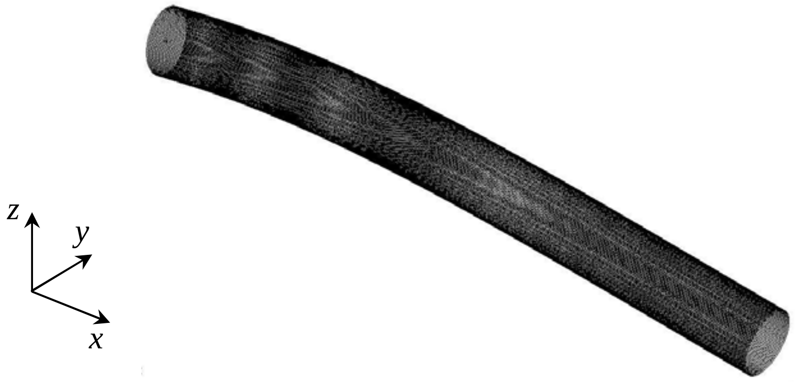

Figure 10: 1st flexural mode (1F, f = 126.8 Hz).

Figure 11: 2nd flexural mode (2F, f =729.5 Hz).

Figure 12: 3rd flexural mode (3F, f =1,835 Hz).

To investigate the accuracy of the iFEM modeling for dynamic applications in both low- and high-frequency regimes, three different values of the applied-force frequency f_0 have been considered, namely: f_0=60 Hz (about half of the fundamental frequency), f_0=450 Hz (halfway between 1F and 2F modes), and f_0=1,400 Hz (halfway between 2F and 3F). Figures 13-15 compare the tip-deflection time histories, $w_{max}(t)$, calculated by means of a high-fidelity FEM shell model using MSC/NASTRAN and the corresponding iFEM frame-element models. The tip deflection of the NASTRAN model corresponds to the cross-sectional center, and is computed at a node which is connected to all other nodes within the cross-section by means of MPC's. The present iFEM models used the strain-gauge distributions in Table 1 and the uniform weight coefficients $\lambda_k^0 = 1 \quad (k = 1,...,6)$ in Eq. (9); the strain values were taken from the nodes (at the specific locations in Table 1) of the NASTRAN model. It is noted that slightly more accurate strain values reside at the element Gauss points. However, considering the high fidelity of the reference FEM model, the "measured" strains taken at the nodes are quite satisfactory.

For the low-frequency loading of f_0=60 Hz, a single 0th-order inverse element gives accurate results, with a maximum error in the tip deflection of 2.3% (Figure 13). At this excitation frequency, when $t \geq 0.1$, viscous damping has reduced the structural vibrations to a steady state response, proceeding at a constant amplitude and the same frequency as the forcing function. When the excitation frequency of the forcing function is increased, the response has a longer transient region, which is manifested by interactions between the natural modes of vibration and those due to the applied dynamic loading. To model the transient response at higher frequencies, finer discretizations are required. Thus, for f_0 = 450 Hz, a two-element, 1st-order model yields a 1.1% error in the maximum deflection (Figure 14). At the f_0=1,400 Hz frequency, a three-element iFEM discretization using the 1st- order element results in the maximum deflection error of 1.3% (Figure 15). These results clearly demonstrate that the methodology is highly efficient, requiring only few inverse elements and strain-gauge measurements, and is applicable not only for the steady state portion of the response but also for the transient regime at high frequencies.

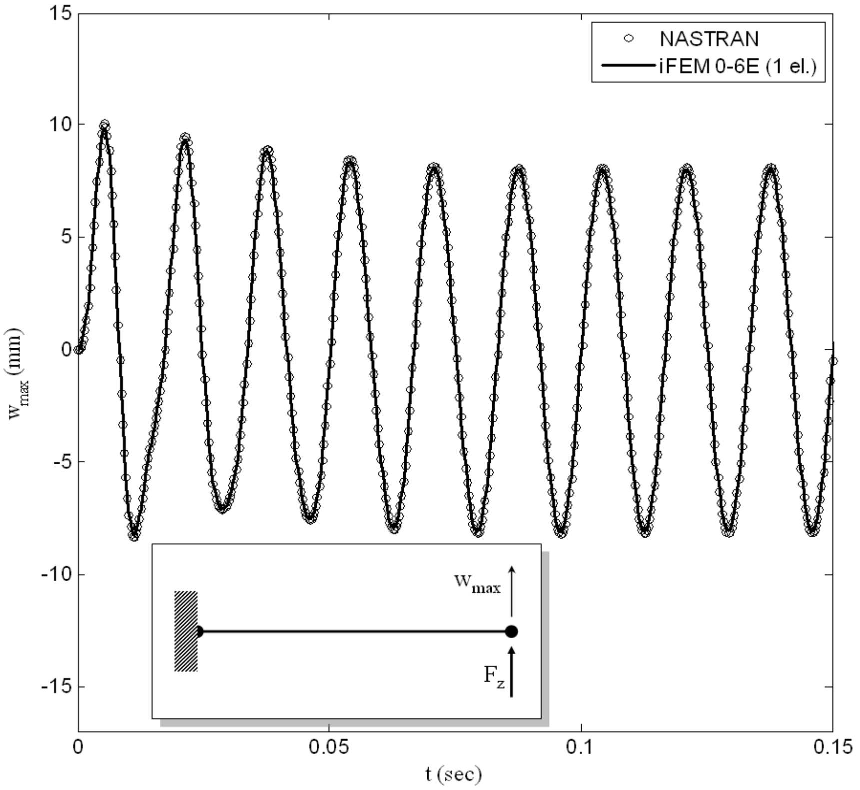

Figure 13: Tip deflection w_{max} of the beam loaded by a transverse concentrated force F_z at f_0=60 Hz.

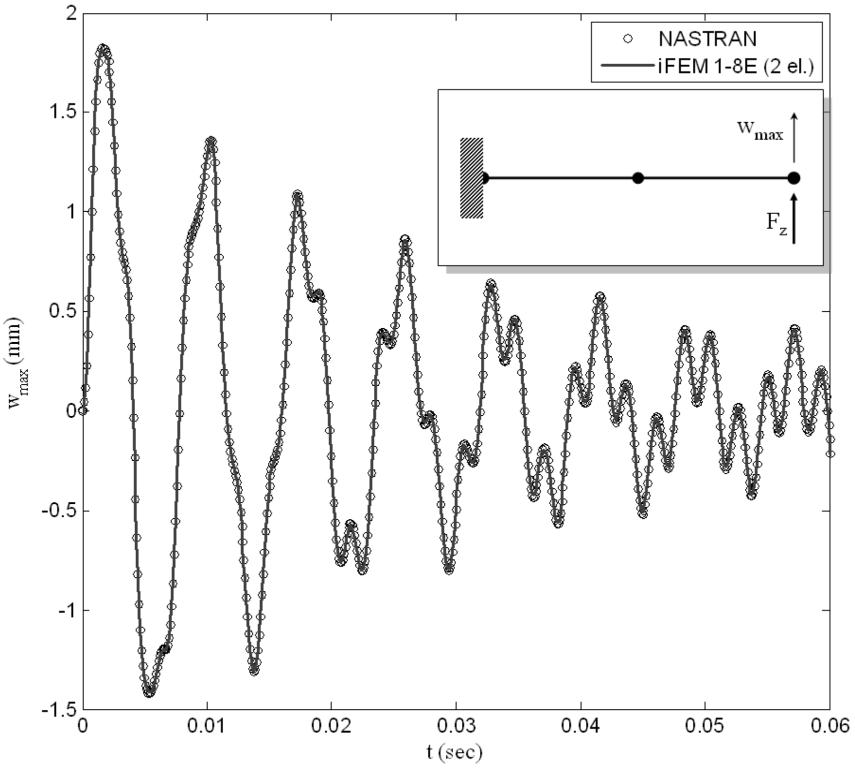

Figure 14: Tip deflection w_{max} of the beam loaded by a transverse concentrated force F_z at f_0=450 Hz.

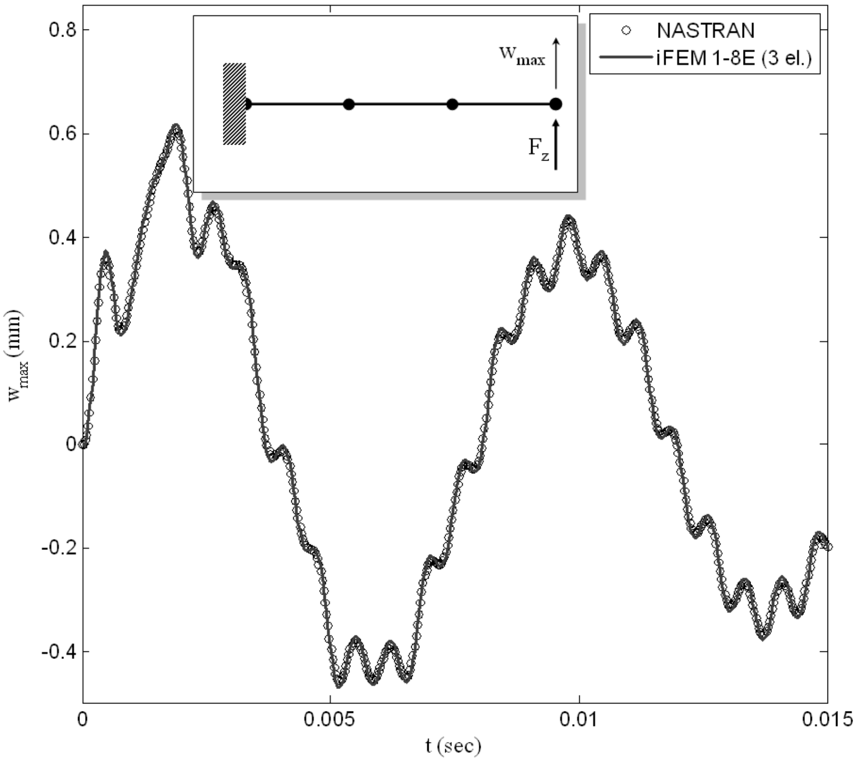

Figure 15: Tip deflection w_{max} of the beam loaded by a transverse concentrated force F_z at f_0=1,400 Hz.

6 CONCLUSIONS

In search of a suitable computational method for use in Structural Health Monitoring (SHM) systems, an inverse Finite Element Method (iFEM) has been formulated to perform the displacement-field reconstruction analysis (shape-sensing) of three-dimensional frame structures undergoing dynamic motion. The methodology uses a least-squares variational principle, which is discretized by C^0-continuous displacement-based *inverse* frame elements. Linear strain-displacement relations and their components, known as strain measures, are based on the Timoshenko (first-order) shear deformation theory that includes the deformations due to stretching, torsion, bending, and transverse shear. The variational statement enforces experimentally measured strains to be least-square compatible with those interpolated within the inverse frame elements. The implementation of this least-square compatibility is accomplished using the individual strain measures.

Two inverse frame elements, each having two nodes and twelve dof’s, have been developed. The 0th-order element has a shear-strain measure which is constant along the element length; whereas the 1st-order element has a linear shear-strain measure. The element shape functions are based on interdependent interpolations that ensure free-of-shear-locking bending of slender frame members. The element interpolation order is linked to the definition of the number and orientation of the uniaxial strain gauges that are necessary for the analysis. Two simple and effective strain-gauge distributions have been selected and used in the numerical examples.

The present shape-sensing capability has been demonstrated on a thin-walled, circular cross-section cantilevered beam subjected to harmonic excitations in the presence of structural damping. To provide the *simulated* strain-gauge measurements, as well as the reference displacements, a high-fidelity shell finite element model was developed using the MSC/NASTRAN commercial code. Low- and high-frequency dynamic beam motions were analyzed and time history of the tip deflection examined, comparing several iFEM discretizations and strain-gauge schemes. The iFEM shape-sensing analysis, which is based only on the strain-displacement relations and the measured strain data (without any reliance on the material, inertial, or damping properties of the structure), has been shown to be highly effective and efficient in predicting the dynamic structural response of a damped beam. Accurate predictions of both the steady-state and transient response required only few elements and strain-gauge measurements, where the higher-frequency excitations necessitated somewhat higher fidelity of the iFEM models.

Although beyond the scope of the present effort, additional studies need to be performed, including: (a) shape-sensing analysis of spatial frame structures using the strains measured in a laboratory, and (b) studies of the strain-gauge distributions that provide optimal (or nearly optimal) solutions.

ACKNOWLEDGEMENTS

The first author acknowledges the support of Politecnico di Torino within the *Young Researchers Program 2010.*

REFERENCES

[1] A. Tessler, J.L. Spangler, A least-squares variational method for full-field reconstruction of elastic deformations in shear-deformable plates and shells, *Computer Methods in Applied Mechanics and Engineering,* **94**, 327–339, 2005.

[2] D.S. Schnur, N. Zabaras, Finite element solution of two-dimensional inverse elastic problems using spatial smoothing, *International Journal for Numerical Methods in Engineering,* **30**, 57–75, 1990.

[3] A.M. Maniatty, N.J. Zabaras, K. Stelson, Finite element analysis of some inverse elasticity problems, *Journal of Engineering Mechanics*, **115**, 1303–1317, 1989.

[4] A.M. Maniatty, N.J. Zabaras, Investigation of regularization parameters and error estimating in inverse elasticity problems, *International Journal for Numerical Methods in Engineering,* **37**, 1039–1052, 1994.

[5] P.L. Liu, H.T. Lin, Direct identification of non-uniform beams using static strains, *International Journal of Solids and Structures*, **33**, 2775–2787, 1996.

[6] M.A. Davis, A.D. Kersey, J. Sirkis, E.J. Friebele, Shape and vibration mode sensing using a fiber optic Bragg grating array, *Smart Materials and Structures*, **5**, 759–765, 1996.

[7] L.H. Kang, D.K. Kim, J.H. Han, Estimation of dynamic structural displacements using fiber Bragg grating strain sensors, *Journal of Sound and Vibration*, **305**, 534–542, 2007.

[8] N.S. Kim, N.S. Cho, Estimating deflection of a simple beam model using fiber optic Bragg-grating sensors, *Experimental Mechanics*, **44**, 433–439, 2004.

[9] W.L. Ko, W.L. Richards, V.T. Fleischer, Applications of the Ko displacement theory to the deformed shape predictions of the doubly-tapered Ikhana wing, *NASA/TP-2009-214652*, October 2009.

[10] P.B. Bogert, E.D. Haugse, R.E. Gehrki, Structural shape identification from experimental strains using a modal transformation technique, *44th AIAA/ASME/ASCE/AHS Structures, Structural Dynamics and Materials Conference*, Norfolk, Virginia, 2003.

[11] R.T. Jones, D.G. Bellemore, T.A. Berkoff, J.S. Sirkis, M.A. Davis, M.A. Putnam, E.J. Friebele, A.D. Kersey, Determination of cantilever plate shapes using wavelength division multiplexed fiber Bragg grating sensors and a least-squares strain-fitting algorithm, *Smart Materials and Structures*, **7**, 178–188, 1998.

[12] S. Shkarayev, R. Krashantisa, A. Tessler, An inverse interpolation method utilizing in-flight strain measurements for determining loads and structural response of aerospace vehicles, *3rd International Workshop on Structural Health Monitoring*, Stanford, California, 2001.

[13] S. Shkarayev, A. Raman, A. Tessler, Computational and experimental validation enabling a viable in-flight structural health monitoring technology, *1st European Workshop on Structural Health Monitoring*, Cachan, Paris, France, 2002.

[14] P. Mainçon, Inverse FEM I: Load and response estimates from measurements, *2nd International Conference on Structural Engineering, Mechanics and Computation*, Cape Town, South Africa, 2004.

[15] P. Mainçon, Inverse FEM II: Dynamic and non-linear problems, *2nd International Conference on Structural Engineering, Mechanics and Computation*, Cape Town, South Africa, 2004.

[16] A.J. Maree, P. Mainçon, Inverse FEM III: Influence of measurement data availability, *2nd International Conference on Structural Engineering, Mechanics and Computation*, Cape Town, South Africa, 2004.

[17] Barnardo, P. Mainçon, Inverse FEM IV: Influence of modelling error, *2nd International Conference on Structural Engineering, Mechanics and Computation*, Cape Town, South Africa, 2004.

[18] M. Nishio, T. Mizutani, N. Takeda, Structural shape reconstruction with consideration of the reliability of distributed strain data from a Brillouin-scattering-based optical fiber sensor, *Smart Materials and Structures*, **19**, 1-14, 2010.

[19] A. Tessler, J.L. Spangler, A variational principal for reconstruction of elastic deformation of shear deformable plates and shells, *NASA TM-2003-212445*, August 2003.

[20] A. Tessler, J.L. Spangler, Inverse FEM for full-field reconstruction of elastic deformations in shear deformable plates and shells, *2nd European Workshop on Structural Health Monitoring*, Munich, Germany, 2004.

[21] S.L. Vazquez, A. Tessler, C.C. Quach, E.G. Cooper, J. Parks, J.L. Spangler, Structural health monitoring using high-density fiber optic strain sensor and inverse finite element methods, *NASA TM-2005-213761*, May 2005.

[22] C.C. Quach, S.L. Vazquez, A. Tessler, J.P. Moore, E.G. Cooper, J.L. Spangler, Structural anomaly detection using fiber optic sensors and inverse finite element method, *AIAA Guidance, Navigation, and Control Conference and Exhibit*, San Francisco, California, 2005.

[23] M. Gherlone, Beam inverse finite element formulation, *LAQ Report Politecnico di Torino 1*, October 2008.

[24] P. Cerracchio, M. Gherlone, M. Mattone, M. Di Sciuva, A. Tessler, Inverse finite element method for three-dimensional frame structures, *DIASP Report Politecnico di Torino 285*, January 2010.

[25] P. Cerracchio, M. Gherlone, M. Mattone, M. Di Sciuva, A. Tessler, Shape sensing of three-dimensional frame structures using the inverse finite element method, *5th European Workshop on Structural Health Monitoring, Sorrento*, Italy, 2010.

[26] S.P. Timoshenko, On the correction for shear of differential equations for transverse vibrations of prismatic bars, *Philosophical Magazine*, **41**, 744–746, 1921.

[27] A. Tessler, S.B. Dong, On a hierarchy of conforming Timoshenko beam elements, *Computers & Structures*, **14**, 335–344, 1981.

[28] A.I. Lurie, *Theory of Elasticity*, Springer-Verlag Berlin Heidelberg, New York, 2005.

[29] MSC/MD-NASTRAN, *Reference Guide*, Version 2006.0, MSC Software Corporation, Santa Ana, CA.

[30] Bazoune, Y.A. Kulief, Shape functions of three-dimensional Timoshenko beam element, *Journal of Sound and Vibration*, **259-2**, 473–480, 2003.

APPENDIX

The 1st, 2nd, and 4th-degree Lagrange shape functions are given as

- 1st degree

$$\left[L_1^{(1)},\, L_2^{(1)}\right] \equiv \frac{1}{2}\left[\left(1-\xi\right),\left(1+\xi\right)\right] \tag{A1}$$

- 2nd degree

$$\left[L_1^{(2)}, L_r^{(2)}, L_2^{(2)}\right] \equiv \frac{1}{2}\left[\xi\left(\xi-1\right), 2\left(1-\xi^2\right), \xi\left(\xi+1\right)\right] \tag{A2}$$

- 4th degree

$$\begin{aligned} \left[L_1^{(4)}, L_2^{(4)}\right] &\equiv \frac{1}{6}\xi\left(4\xi^2-1\right)\left[\left(\xi-1\right),\left(\xi+1\right)\right] \\ \left[L_q^{(4)}, L_r^{(4)}, L_s^{(4)}\right] &\equiv \frac{1}{3}\left(1-\xi^2\right)\left[4\xi\left(2\xi-1\right), 3\left(1-4\xi^2\right), 4\xi\left(2\xi+1\right)\right] \end{aligned} \tag{A3}$$

where $\xi \equiv 2x/L^e - 1 \in \left[-1,1\right]$ is a non-dimensional axial coordinate; $x \in \left[0, L^e\right]$ and L^e denotes the element length. The subscripts 1 and 2 represent the end nodes, whereas *q*, *r*, and *s* denote the uniformly spaced interior nodes.

The 3rd –degree shape functions, $N_j^{(3)}\left(\xi\right)$, of the 0th-order element have the form

$$\left[N_1^{(3)}, N_r^{(3)}, N_2^{(3)}\right] \equiv \frac{L^e}{24}\left(1-\xi^2\right)\left[\left(2\xi-3\right), -4\xi, \left(2\xi+3\right)\right] \tag{A4}$$

whereas the $\overline{N}_k^{(3)}\left(\xi\right)$ shape functions of the 1st-order element are

$$\left[\overline{N}_1^{(3)}, \overline{N}_q^{(3)}, \overline{N}_r^{(3)}, \overline{N}_s^{(3)}, \overline{N}_2^{(3)}\right] \equiv \frac{4}{3L^e}\left(1-\xi^2\right)\left[\left(4\xi-3\right), -2\left(8\xi-3\right), 24\xi, -2\left(8\xi+3\right), \left(4\xi+3\right)\right] \tag{A5}$$

COMPDYN 2011
3rd ECCOMAS Thematic Conference on
Computational Methods in Structural Dynamics and Earthquake Engineering
M. Papadrakakis, M. Fragiadakis, V. Plevris (eds.)
Corfu, Greece, 25–28 May 2011

EFFICIENT MODEL UPDATING OF THE GOCE SATELLITE BASED ON EXPERIMENTAL MODAL DATA

B. Goller[1], **M.Broggi**[1], **A. Calvi**[2] **and G.I. Schuëller**[1]

[1]Institute of Engineering Mechanics, University of Innsbruck
Technikerstr. 13, 6020 Innsbruck, Austria, EU
e-mail: mechanik@uibk.ac.at

[2] Structures Section TEC-MSS, European Space Agency / ESTEC
P.O. Box 299, 2200 AG Noordwijk, The Netherlands, EU
e-mail: adriano.calvi@esa.int

Keywords: Model updating, model validation, uncertainty quantification, model reduction

Abstract. *The accurate prediction of the structural response of spacecraft systems during launch and ascent phase is a crucial aspect in design and verification stages which requires accurate numerical models. The enhancement of numerical models based on experimental data is denoted model updating and focuses on the improvement of the correlation between finite element (FE) model and test structure. In aerospace industry the judgment of the agreement between model and real structure involves the comparison of the modal properties of the structure. Model updating techniques have to handle several difficulties, like incomplete experimental data, measurement errors, non-unique solutions and modeling uncertainties. To cope with the computational challenges associated with the large-scale FE-models involving up to over one million degrees of freedom (DOFs), enhanced strategies are required. A large-scale numerical example, namely a satellite model, will be used for demonstrating the applicability of the employed updating procedure to complex aerospace structures.*

1 INTRODUCTION

The dynamic loads acting on a spacecraft during the launch and ascent phase are modeled by the spacecraft-launcher coupled dynamic analysis. The accuracy of the structural response in this low-frequency mechanical environment depends on the quality of the underlying mechanical model of the spacecraft. Therefore, it is mandatory to ensure that the FE-model represents the real structure accurately enough. This level of accuracy to be reached for aerospace structures is defined in [1] and is based on the agreement of experimentally and computationally determined modal properties, respectively. Possible sources for discrepancies between test data and respective computed values are e.g. uncertainties in the modeling process arising from inadequate theory for some system behaviors, simplifying assumptions made in order to reduce the complexity of the model and uncertainties about model parameter values. Hence, the need for improving the mechanical model based on experimental data arises which is referred to as model updating and the consecutive corroboration of the model by means of modal properties is denoted by validation [2, 3, 4].

The use of deterministic updating procedures does not allow for a quantification of the involved uncertainties in the design and verification processes which will subsequently affect the accuracy of the predictive structural response. Probabilistic methods for model updating provide a means for tackling these problems and for avoiding a wrong conclusion about the fit of the experimental data and analytical results [5]. A significant obstacle in the consideration of uncertainties when performing model updating of complex structures is posed by the associated computational efforts. Therefore, the most frequently used approaches for model updating performed by industry are deterministic approaches (see e.g. [6, 7, 8, 9]). While stochastic methods have been developing successfully in this research field, applications in industry are relatively limited (see e.g. [10]). Hence, in this work it is aimed at a computationally efficient application of a stochastic model updating procedure to complex aerospace models.

The thereby adopted updating process is the Bayesian approach which is based on updating the initial engineering knowledge about the ranges of the adjustable parameters using experimental data [11, 12, 13]. In this way, a revised information about the parameters is obtained, which is expressed by posterior probability density functions. Probability is therefore not interpreted in the usual frequentist sense, where it refers to the relative frequency of occurrence in case of many events, but it is based on the idea of reasonable expectation, i.e. probability is interpreted as a measure of plausibility of the hypothesis. This interpretation makes it possible to extend the application of probability theory to fields where the frequentist interpretation may not be directly intuitive, as it is the case for one-of-a-kind structures, where no ensemble exists, and also in the case of limited data, where classical statistics is of limited applicability. Therefore, Bayesian statistics makes it possible to deal with the usual situation in aerospace industry, where a large amount of experimental data is infeasible due to the enormous costs associated with test campaigns, and it provides a means for making decisions based on limited, incomplete information.

The computational tools for the Bayesian updating procedure are sampling-based algorithms, where a multi-level Markov chain Monte Carlo algorithm is adopted in this approach [14]. As a remedy for the large computational efforts associated with the Bayesian updating procedure, the application of a surrogate model (a so-called “meta-model”) is proposed. This meta-model is formulated with respect to the repeated analysis tasks, which are the eigensolutions in case of model updating based on modal data. Hence, a simple relation between the input data and output quantity of interest has to be established in order to replace the computationally intensive evaluation of a full finite element analysis by a function evaluation at low computational costs. Several techniques, e.g. linear or polynomial regression, kriging and the radial basis functions have been developed in this context (see e.g. [15]), where in this work neural networks [16] will be adopted in order to approximate the modal properties of the structure.

This manuscript will demonstrate the feasibility of the application of Bayesian model updating procedures on spacecraft structures using eigenfrequencies and mode shape vectors. Sec. 2 is devoted to the presentation of the basic steps of Bayesian model updating, and in Sec. 3 the algorithm for the generation of samples in the solution space is summarized. Computational aspects will be addressed in the following (Sec. 4), where the basic concepts of neural networks are discussed. In order to apply these outlined concepts to an FE-model of a spacecraft structure, the use of a surrogate model within the updating process is adopted for the FE-model of the GOCE satellite (Sec. 5).

2 BAYESIAN MODEL UPDATING

2.1 Introduction

The fundamental rule that governs the Bayesian updating procedure is Bayes' Theorem, which is formulated in general terms as [17]

$$P(H|\mathcal{D},I)=\frac{P(\mathcal{D}|H,I)P(H|I)}{P(\mathcal{D}|I)}, \tag{1}$$

where H is any hypothesis to be tested, $\mathcal{D}$ denotes the data and I is the available background information. Bayes' Theorem provides a means to update the prior probability density function (PDF) of H, $P(H|I)$, by using the data in the likelihood function $P(\mathcal{D}|H,I)$ in order to obtain the posterior distribution of H, $P(H|\mathcal{D},I)$. The denominator $P(\mathcal{D}|I)$ is a normalizing constant and does not affect the shape of the posterior PDF. All probabilities in Eq. (1) are conditional on I, which means that the outcome of the updating procedure depends on the available information.

2.2 Bayesian updating using modal data

If applying Bayes' Theorem for structural model updating [11, 12], the hypothesis H is interpreted as the vector of unknown (i.e. adjustable) parameters, which will be referred to as θ in the following, and $\mathcal{D}$ denotes the experimental data, which consist of the measured modal properties of the investigated structure. The available information I is interpreted as the experience and knowledge of the engineer which is reflected by the established model itself and is therefore denoted as $\mathcal{M}$. This leads to the following form of Eq. (1):

$$p(\theta|\mathcal{D},\mathcal{M})=\frac{p(\mathcal{D}|\theta,\mathcal{M})p(\theta|\mathcal{M})}{p(\mathcal{D}|\mathcal{M})}. \tag{2}$$

The prior distribution $p(\theta|\mathcal{M})$ expresses the initial knowledge about the adjustable parameters. The choice of the distribution can be based on the principle of maximum entropy [18]. In this case, the PDF used for describing the initial uncertainty maximizes the uncertainty subject to the prescribed constraints, which can be given by e.g. imposing moment constraints. The likelihood function $p(\mathcal{D}|\theta, \mathcal{M})$ gives a measure of the agreement between the system data and the corresponding structural model output. This measure of the data fit of each model defined by the parameters vector θ, is given by the probability model established for the system output. The derivation of the likelihood function for modal data will be summarized in Sec. 2.3. The posterior distribution $p(\theta|\mathcal{D}, \mathcal{M})$ expresses the revised knowledge about the parameters θ conditional on the initial knowledge and the experimental data.

2.3 Formulation of the likelihood function for modal data

In general terms, the connection between the model output $q(\theta)$ and the corresponding system output y is given by the prediction error e in the form of

$$y = q(\theta) + e. \tag{3}$$

The choice for the probability model of the prediction error e, which is the difference between the model output for a certain value of θ and the corresponding system output, is based on the maximum entropy principle [18] which yields a multi-dimensional Gaussian distribution with zero mean and covariance matrix Σ. The Gaussian PDF arises because it gives the largest amount of uncertainty among all probability distributions for a real variable whose first two moments are specified. Hence, the predictive PDF for the system output conditional on the parameter vector θ is given by

$$p(y|\theta, \mathcal{M}) = \frac{1}{(2\pi)^{N/2}|\Sigma|^{1/2}} \exp\left[-\frac{1}{2}(y - q(\theta))^T \Sigma^{-1} (y - q(\theta))\right], \tag{4}$$

where N_0 N denotes the length of the vector y, i.e. the number of observed points. If a set of measured output $\mathcal{D} = \{y_j : j = 1, \ldots, N_s\}$ is available, then the likelihood function can be constructed as $p(\mathcal{D}|\theta, \mathcal{M}) = \prod_{j=1}^{N_s} p(y_j|\theta, \mathcal{M})$ if the prediction errors are modeled as statistically independent.

The formulation of the likelihood function using modal data is derived in [19] and is summarized in the following. The experimental data $\mathcal{D}$ from the structure is assumed to consist of N_s sets of modal data, $\mathcal{D} = \{\hat{\omega}_{1,j} \ldots \hat{\omega}_{N_m,j}, \hat{\Psi}_{1,j} \ldots \hat{\Psi}_{N_m,j}\}_{j=1}^{N_s}$ comprised of N_m modal frequencies $\hat{\omega}_r$ and N_m incomplete mode shape vectors $\hat{\Psi}_r \in \mathbb{R}^{N_0}$, where N_0 is the number of observed DOFs. The model output $q(\theta)$ is the set of corresponding modal properties of the structural model, i.e. eigenfrequencies $\omega_r(\theta)$ and partial eigenvectors $\psi_r(\theta)$, $r = 1, \ldots, N_m$, defined by the parameter vector $\theta \in \Theta \in \mathbb{R}^{N_p}$.
The probability model conditional on the parameter vector θ is chosen to have statistical independence between the mode shape vectors and modal frequencies, between the different modes, and between one data set to another. Therefore, the likelihood function can be written as the product of the probability density functions for the modal frequencies and mode shape components:

$$p(\mathcal{D}|\theta, \mathcal{M}) = \prod_{j=1}^{N_s} \prod_{r=1}^{N_m} p(\hat{\omega}_{r,j}^2|\theta, \mathcal{M}) p(\hat{\psi}_{r,j}|\theta, \mathcal{M}), \tag{5}$$

where $p(\hat{\omega}_{r,j}^2|\theta, \mathcal{M})$ and $p(\hat{\psi}_{r,j}|\theta, \mathcal{M})$, $r = 1, \ldots, N_m$ and $j = 1, \ldots, N_s$, are, respectively, the PDFs for the squared modal frequency and the mode shape vector of the rth mode in the jth data set.

In the first step, the likelihood function for the mode shape vectors is formulated by rewriting Eq. (3) as

$$\hat{\psi}_{r,j} = a_r \psi_r(\theta) + e_{\psi_r}, \tag{6}$$

where a_r is an optimal scaling factor to relate the scaling of the model mode shape vector $\psi_r(\theta)$ to that of the experimental mode shape vector $\hat{\psi}_{r,j}$, which is assumed to be normalized so that its Euclidean norm $\|\hat{\psi}_{r,j}\| = 1$. Since the latter is usually constituted by an incomplete set of observed DOFs N_0, the corresponding model mode shape vector is given by $\psi_r = \Gamma\phi_r$, where the matrix Γ picks the observed degrees of freedom from the complete model eigenvector ϕ_r. Using a Gaussian distribution for the probabilistic characterization of the prediction error for the mode shape vector, the likelihood function for the mode shape vector, after some algebraic manipulation, may be written as:

$$\begin{aligned} p(\hat{\psi}_{r,j}|\theta,\mathcal{M}) &= c_1 \exp\left(\frac{\psi_r^T(I-\hat{\psi}_{r,j}\hat{\psi}_{r,j}^T)\psi_r}{2\delta_r^2\|\psi_r\|^2}\right) & (7)\\ &= c_1 \exp\left(\frac{1}{2\delta_r^2}\left[1-\frac{|\psi_r^T\hat{\psi}_{r,j}|^2}{(\psi_r^T\psi_r)^2}\right]\right) & (8)\end{aligned}$$

where I is the identity matrix of dimension N_m and $\delta_r^2 I$ denotes the mode shape prediction error covariance matrix for the rth mode. The equality in Eq. (8) shows that the probability density function for $\hat{\psi}_{r,j}$ involves the MAC (Modal Assurance Criterion) between $\hat{\psi}_{r,j}$ and $\psi_r(\theta)$, the experimental and model partial mode shapes of the rth mode, respectively.

Secondly, Eq. (3) is formulated for the squared modal frequencies, which yields

$$\hat{\omega}_{r,j}^2 = \omega_r^2(\theta) + e_{\omega_r^2}. \tag{9}$$

Using again a Gaussian probability model for the prediction error of the modal frequencies, the likelihood function for the modal frequencies is given by

$$p(\hat{\omega}_{r,j}^2|\theta,\mathcal{M}) = c_2 \exp\left[-\frac{1}{2}\left(\frac{1-\hat{\omega}_{r,j}^2/\omega_r^2}{\varepsilon_r}\right)^2\right], \tag{10}$$

where ε_r^2 denotes the variance of the prediction error of the squared r-th eigenfrequency, i.e. of $e_{\omega_r^2}$. Using the probability distributions for the mode shape vectors and modal frequencies given in Eqs. (8) and (10), the likelihood function in Eq. (5) can be written as

$$p(\mathcal{D}|\theta,\mathcal{M}) = c_3 \exp\left(-\frac{1}{2}\sum_{r=1}^{N_m} J_r(\theta)\right), \tag{11}$$

where the modal measure of fit $J_r(\theta)$ is defined by

$$J_r(\theta) = \sum_{j=1}^{N_s}\left[\left(\frac{1-\hat{\omega}_{r,j}^2/\omega_r^2}{\varepsilon_r}\right)^2 + \left(1-\frac{|\psi_r^T\hat{\psi}_{r,j}|^2}{(\psi_r^T\psi_r)^2}\right)/\delta_r^2\right] \tag{12}$$

3 TRANSITIONAL MARKOV CHAIN MONTE CARLO ALGORITHM

The evaluation of Eq. (2) requires the computation of high-dimensional integrals for the determination of the normalizing constant of the posterior PDF, which cannot be tackled analytically or numerically. Recently, efficient stochastic simulation algorithms have been proposed which generate samples of the posterior distribution and which hence identify the parameter regions with the highest posterior probability mass. In this work, the so-called Transitional Markov Chain Monte Carlo (TMCMC) algorithm [14] is applied whose basic steps are discussed in the following.

The main idea of this algorithm is to iteratively proceed from the prior to the posterior distribution. It starts with the generation of samples from the prior PDF in order to populate the space in which also the most probable regions of the posterior distribution lie. Then, some intermediate PDFs are defined, where the shape does not change remarkably from the intermediate PDF $p[j]$ to the next $p[j+1]$. The small change of the shape makes it possible to efficiently sample according to $p[j+1]$ if samples according to $p[j]$ have been generated. The intermediate distributions are defined by

$$p[j+1] \propto p(\mathcal{D}|\theta, \mathcal{M})^{\beta_j} p(\theta|\mathcal{M}), \tag{13}$$

with $j = 0, \ldots m$ as the step index and $0 = \beta_0 < \beta_1 < \ldots < \beta_m = 1$. Hence, the exponent β_j can be interpreted as the percentage of the total information provided by the experimental data which is incorporated in the jth iteration of the updating procedure: $\beta_0 = 0$ corresponds to the prior distribution and for $\beta_m = 1$ the samples are generated from the posterior distribution.

Samples of the subsequent intermediate distribution $p[j+1]$ are obtained by generating Markov chains where the lead samples are selected from the distribution $p[j]$ by computing their probability weights with respect to $p[j+1]$, which are given by

$$w(\theta_j^{(l)}) = \frac{p(\mathcal{D}|\theta, \mathcal{M})^{\beta_{j+1}} p(\theta|\mathcal{M})}{p(\mathcal{D}|\theta, \mathcal{M})^{\beta_j} p(\theta|\mathcal{M})} = p(\mathcal{D}|\theta, \mathcal{M})^{\beta_{j+1}-\beta_j}, \tag{14}$$

where the upper index $l = 1, \ldots, N_j$ denotes the sample number in the jth iteration step. Each sample of the current step is generated using the Metropolis-Hastings algorithm [20, 21]: the starting point of a Markov chain is a sample from the previous step that is selected according to the probability equal to its normalized weight

$$\overline{w}(\theta_j^{(l)}) = \frac{w(\theta_j^{(l)})}{\sum_{l=1}^{N_j} w(\theta_j^{(l)})} \tag{15}$$

and the proposal density for the Metropolis-Hastings algorithm is a Gaussian distribution centered at the preceding sample of the chain and with a covariance matrix Σ_0 which is equal to the scaled version of the estimated covariance matrix of the current intermediate PDF:

$$\Sigma_0 = c^2 \sum_{l=1}^{N_j} \overline{w}(\theta_j^{(l)})(\theta_j^{(l)} - \overline{\theta}_j)^T(\theta_j^{(l)} - \overline{\theta}_j), \tag{16}$$

where

$$\overline{\theta}_j = \sum_{l=1}^{N_j} \overline{w}(\theta_j^{(l)})\theta_j^{(l)}. \tag{17}$$

The parameter c is a scaling parameter that is used to control the rejection rate of the Metropolis-Hastings algorithm at each step. These steps are repeated until $\beta_j = 1$ is reached, i.e. until the samples are generated from the posterior distribution.

4 COMPUTATIONAL ASPECTS

4.1 General remarks

Due to the repeated execution of the normal mode analysis of the FE-model, the computational effort of the Bayesian updating method might become infeasible for large FE-models. Hence, in order to reduce the wall clock time, i.e. the time between submitting the updating analysis and its completion, a strategy based on the reduction of the computational efforts associated with the normal mode analysis of the full FE-model is applied in this manuscript. This strategy is based on the use of neural networks for the modal parameters, which will be addressed in the following.

4.2 Neural networks

An Artificial Neural Network (ANN) is a machine-learning algorithm that tries to simulate the structure and functional aspects of biological networks of neurons in order to approximate a relation $f : \theta \rightarrow q$ by a simple mathematical model at low computational efforts. It consists of an interconnected group of computational units, called neurons or nodes, and processes information using consecutively connected layers of neurons. In the following, the most widely used neural network, namely the so-called feed-forward neural network, is discussed (see e.g. [22, 23]). It is composed of a multi-layered structure, with a first layer of nodes, called input layer, one or more intermediate layers, called hidden, and a final output layer. For simplicity, but without loss of generality, the scheme is discussed when using one single hidden layer.

Each layer is characterized by a different number of neurons, indicated by N_{inp}, N_{hid} and N_{out} for the input, hidden and output layers, respectively. Each node of the hidden layer receives as input a linear combination $\sum_{i=1}^{N_{inp}} w_{i,j}\theta_i$ of the input values θ_i of all the nodes of the input layer, scaled by a so-called connection weight $w_{i,j}$, where j denotes the number of the hidden node. Then, the node proceeds this function value through a non-linear function K, which is called activation function and which is of the form $g_j = K(\sum_{i=1}^{N_{inp}} w_{i,j}\theta_i)$. This collection of function values $(g_1, \ldots, g_{N_{hid}})$ is then sent to all the nodes of the subsequent, i.e. output, layer, where the approximated model output $\hat{q}_k(\theta) = K(\sum_{j=1}^{N_{hid}} w_{j,k}y_j))$, $k = 1, \ldots N_{out}$ is evaluated. A schematic representation of this algorithm is shown in Fig. 1.

Hence, the connection weights act as parameters of the meta-model which have to be adapted through a calibration procedure of supervised learning, called also training, by means of e.g. the error back-propagation algorithm. In this calibration phase, the network, which is initialized with random weights, is fed with a set of input/output values which is called calibration set and which is obtained from the target physical model. The network processes the inputs and produces then an estimation of the outputs; such outputs are compared with the real outputs through a predefined error measurement (typically, a sum of the squared errors of each output). The training consists thus of an optimization problem which aims to minimize the error of the network in the output prediction. Such optimization is carried out by computing the gradient of the error with respect to the connection weights, and it is interrupted when a target error is reached or when a certain number of input/output pairs have been processed.

An important indicator of the goodness of the network after training is the coefficient of

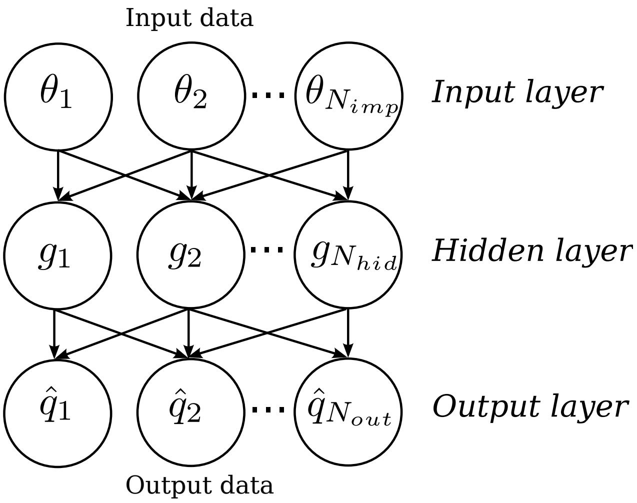

Figure 1: Schematic representation of the concept of neural networks

determination R^2, defined as

$$R^2 = 1 - \frac{\sum\limits_{i=1}^{N_{data}} (q_i - \hat{q}_i)^2}{\sum\limits_{i=1}^{N_{data}} (q_i - \overline{q}_i)^2} \tag{18}$$

where q_i are the real outputs of the physical model, $\overline{q}_i = \frac{1}{N_{data}} \sum_{i=1}^{N_{data}} q_i$ and $\hat{q}_i$ are the output values predicted by the meta-model. The accuracy of the output prediction of the neural network can be judged by the closeness of the value R^2 to the target value of 1.0, which expresses an exact match of the network prediction and the output of the full model. This quantity is computed both using the calibration set and a new set of input/output values, called validation or verification set. In the latter case, a qualitative indication of the generalization capabilities of the network is obtained.

The freely available Fast Artificial Neural Network (FANN) library [24], which is an implementation of the here discussed Neural Network and learning algorithm, has been used for the approximation of the modal properties in the following numerical example.

5 NUMERICAL EXAMPLE: GOCE SATELLITE

5.1 Problem statement

The use of a meta-model within the Bayesian updating procedure is illustrated using the Gravity Field and Steady-State Ocean Circulation Explorer (GOCE) satellite. The mission of the GOCE satellite is to determine the geoid and to measure the gravitational field of Earth with a very high degree of accuracy in a low Earth orbit. The particularities of the GOCE are its arrow-shape with winglets and its ion propulsion engine, used to compensate the air-drag induced orbit-decay. The total length of the satellite is 5.3 m, and the mass amounts to approximately 1,000 kg including the fuel of the propulsion system.

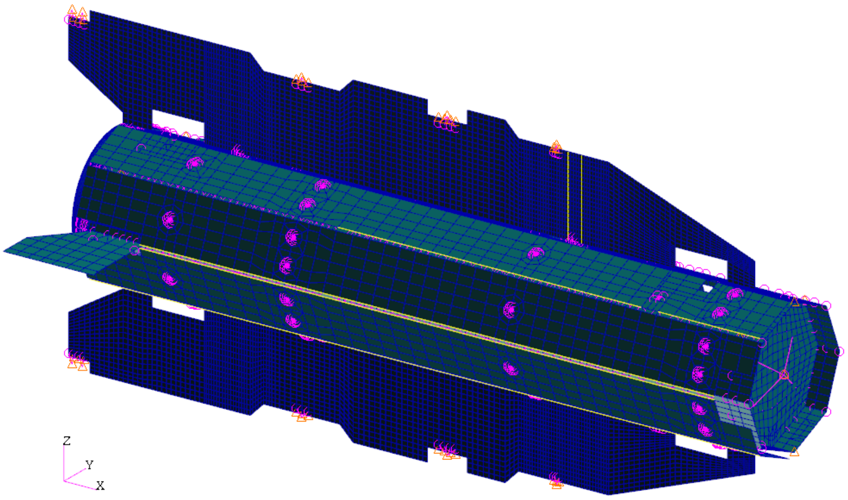

Figure 2: FE model of the GOCE satellite (courtesy of Thales Alenia Space Italy)

Fig. 2 shows the FE model of the satellite, provided by Thales Alenia Space (Italy) for use within the commercial FE code MSC.Nastran [25]. Approximately 360,000 DOFs and 74,000 elements compose the FE model, with half of the elements used in the main satellite platform and half in the gravitational gradiometer.
In the main GOCE platform, quadrilateral (QUAD4) and triangular (TRIA3) shell elements are used to model the body panels, the wings and the winglets, the internal floors and the solar panels. Beam elements (BAR, ROD and BEAM) constitute the connections of the wings to the main structure and of the instrumentation to the floors. Solid elements (HEXA and PENTA) are used in the Launch Vehicle Adapter (LVA) ring, and scalar spring elements (CELAS2) represent the connection between the solar panels and the structure, as well as the fixing of the wing to the main octagonal body.

A total number of 18 groups combining 3047 structural parameters are defined according to the type and location of the respective materials or geometric specifications (see Tab. 1). This grouping is carried out with the purpose of remarkably reducing the number of parameters to be used within the Bayesian updating procedure since an independent processing of all involved parameters might become infeasible. Hence, the updating procedure is carried out with the goal of identifying as to which changes have to be performed to the single parameter groups in order to obtain a better agreement of the numerical model with the real satellite structure.

5.2 Experimental modal data

The experimental data used for model updating consists of $N_s = 1$ set of 7 modal frequencies and partial mode shapes vectors (83 components) which have been determined from the vibration responses during the GOCE structural model qualification test. The dynamic qualification test was performed on the multi-axis vibration test facility of ESA/ESTEC in Noordwijk (The Netherlands). The correlation of the experimental and computed eigenvectors of the initial model is shown by means of the MAC matrix in Fig. 3 and the initial comparison of the eigenfrequencies can be found in Tab. 2. The large discrepancies, especially for the first two modes,

Group no.	Parameters
1	Young's modulus of isotropic materials
2	Poisson's ratio of isotropic materials
3	Young's modulus in the principal direction of orthotropic materials
4	Young's modulus in the secondary direction of orthotropic materials
5	Poisson's ratio of orthotropic materials
6	In-plane shear modulus of orthotropic materials
7	First out-of-plane shear modulus of orthotropic materials
8	Second out-of-plane shear modulus of orthotropic materials
9	Densities of the materials
10	Thicknesses of the shells
11	Linear elastic connections of panels to the main satellite structure
12	Linear elastic connections of panels to the satellite wings
13-18	Linear elastic connections of the wings to the main satellite structure

Table 1: Definition of the groups of parameters of the GOCE satellite

arise the need for model updating which will be discussed in the following.

Mode no.	f_a [Hz]	f_e [Hz]	Δ [%]
1	18.43	15.98	13.29
2	18.37	16.40	10.69
3	28.84	29.59	-2.60
4	34.96	33.33	4.66
5	46.90	48.91	-4.28
6	49.13	51.61	-5.04
7	65.81	61.35	6.77

Table 2: Comparison of the analytical eigenfrequencies f_a and the experimental data f_e

5.3 Accuracy analysis of the neural network

A set of $N_{data} = 2,000$ finite element simulations have been performed using Gaussian distributions with the mean values equal to the nominal values and coefficients of variation of 10%. Out of these samples, 1,900 have been dedicated to calibrate the neural networks, and 100 have been kept to verify the generalization capabilities of the networks after training. Each of the 14 neural networks, constituted by $N_{inp} = 18$ inputs and $N_{out} = 1$ output, predicts either one of the eigenfrequencies or one of the diagonal terms of the MAC matrix.
An automated training procedure has been implemented such that various network topologies are tested and the best networks, characterized by the highest R^2 value (see Eq. (18)) obtained with the verification data, are kept. As an indication of the accuracy of the network, Fig. 4 shows the regression plots for the neural network of the first eigenfrequency, using the calibration and verification data, respectively. Moreover, the values of R^2 of all the networks obtained with the verification data are listed in Tab. 3.

5.4 Bayesian model updating

The prior distributions assigned to the 18 groups of parameters to be updated are all Gaussian with the moments as specified for the calibration of the neural networks. For these ranges, the

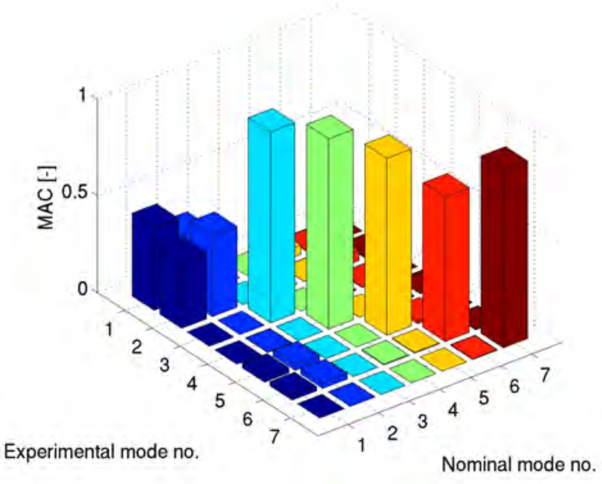

Figure 3: Initial MAC values obtained with the nominal model and the experimental data $\hat{\psi}$

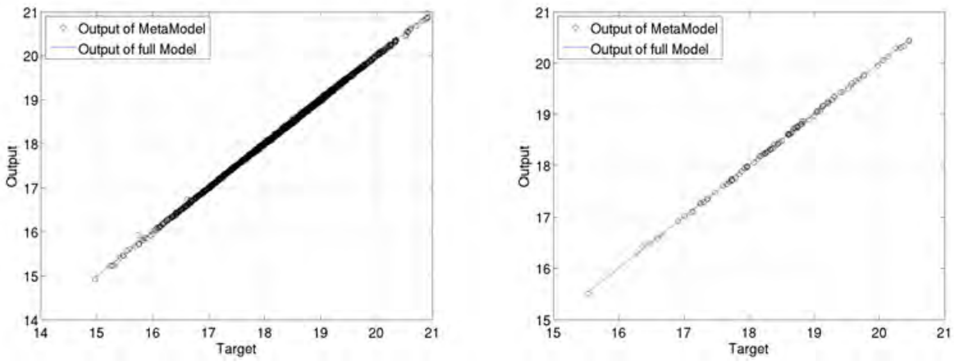

(a)

(b)

Figure 4: Regression plot of the output of the neural network of the first eigenfrequency for (a) calibration data and (b) verification data.

Neural network output	R^2 of verification data
Frequency 1	0.99960
Frequency 2	0.99966
Frequency 3	0.99968
Frequency 4	0.99957
Frequency 5	0.88299
Frequency 6	0.97804
Frequency 7	0.95822
$\mathrm{MAC}_{1,1}$	0.99886
$\mathrm{MAC}_{2,2}$	0.99782
$\mathrm{MAC}_{3,3}$	0.99577
$\mathrm{MAC}_{4,4}$	0.99861
$\mathrm{MAC}_{5,5}$	0.94947
$\mathrm{MAC}_{6,6}$	0.97623
$\mathrm{MAC}_{7,7}$	0.82779

Table 3: R^2 values of the 14 neural networks

neural networks of the considered modal properties show high accuracy as discussed in the previous section and are therefore applied for substituting the full FE-analysis when evaluating the likelihood function within the updating process.

The results of the updating procedure are shown exemplarily for three parameter groups, namely the thickness, the Young's moduli of the orthotropic materials and the group of stiffnesses of joints between the wings and the main structure (groups no. 10, 3 and 14 in Tab. 1). The prior and posterior histograms of these parameters, which are all transformed in standard normal space, are depicted in Figs. 5-7. This representation in standard normal space is advantageous due to the fact that these figures do not show one single parameter each but a parameter group, where the members of each group may have different initial values. Hence, in order to obtain the posterior values in physical space, a back-transformation has to be performed for each parameter of a group, which is achieved by

$$\theta_i = \theta_i^* \sigma_i + \theta_{i,\mathrm{nom}}, \tag{19}$$

where θ_i denotes the i-th parameter in the physical space, θ_i^* the value in the standard normal space, σ_i the prior standard deviation and $\theta_{i,\mathrm{nom}}$ the prior (nominal) mean of this parameter.

In Fig. 5, the prior and posterior histograms of the thickness of shell elements are depicted. This figure leads to the conclusion that the information contained in the experimental data suggests a decrease of these values. A reduction of approximately 10% of the mean value of the prior distribution leads to a better fit with the experimental modal properties. Also for the Young's modulus of the orthotropic material in the longitudinal direction (material card MAT8 in the MCS.Nastran input file), the updating process suggests a decrease of the mean values (see Fig. 6). As opposed to these two parameter groups, all other 16 out of 18 parameter groups used in the updating process show small changes if compared to the prior distribution. As an example, the stiffness values of the joints of the main structure to the wings (used for the specification of the CELAS2 elements in the MCS.Nastran input file) is shown in Fig. 7. Due to the information extracted from the experimental values, the prior uncertainty about these parameters could be reduced which is visible through the smaller variation of the posterior distribution.

The effect of the choice of the prior on the posterior distribution has not been investigated in this example, however a few remarks will be added in this context: in general, the influence

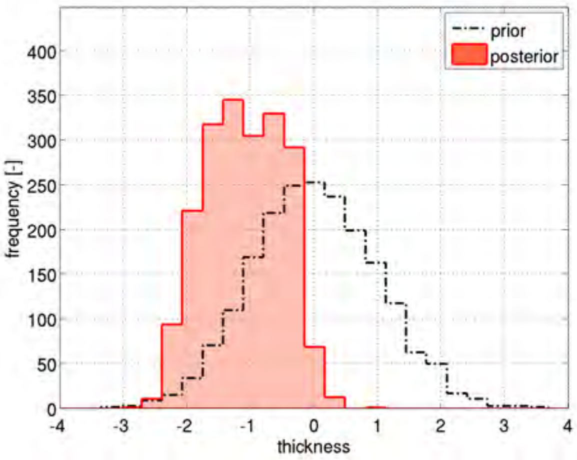

Figure 5: Histograms of the prior and posterior samples of the group of thicknesses (group no. 10 in Tab. 1)

of the prior distribution on the results decreases with increasing amount of experimental data. This is due to the fact that the likelihood function becomes the dominant term in comparison to the prior distribution in Eq. (2). In this case, also values in the tails of the prior distribution can be identified and only values with zero probability (e.g. values out of the interval of uniform distributions) cannot be reached since they are excluded from the possible solution space due to the prior knowledge. In case of limited data the selection of the prior distribution clearly has an influence on the results. The prior distribution can therefore be seen as a means to incorporate initial knowledge about parameter ranges into the identification process and it is subjective in the sense that people with different experience may use different priors leading to broader ranges of the solution in case smaller amount of prior information is available. The selection can therefore be seen as part of the modeling process since also the model itself is affected by a certain amount of subjectivity of the designer. However, the probability content of the prior PDF is updated by the data and if one felt uncomfortable with the choice of the prior distribution the effect of different prior PDFs on the posterior PDF can be studied.

5.5 Effect on the correlation of modal data

The effect of the updating procedure on the correlation of the experimental and computed modal properties is shown exemplarily for the two lowest and highest considered modes. Figs. 8-11 are devoted to the eigenfrequencies and Fig. 12 to the corresponding diagonal MAC-values. The figures show that a successful shift of the PDFs towards the experimental values could be achieved, as it can be seen for modes 1, 2 and 7, where it shall be annotated that the correlation of the eigenvector no. 7 with respect to the corresponding experimental data reveals to be high already for the initial model (initial $\mathrm{MAC}_{7,7}$=0.92).

However, for the 6th eigenfrequency and eigenvector no improvement could be achieved. The reasons might lie in the fact that there is no parameter combination possible which affects an improvement of the fit with respect to all 14 target values defined by the first 7 modal frequencies and mode shape vectors. Only a revision of the model itself might lead to the situation where the

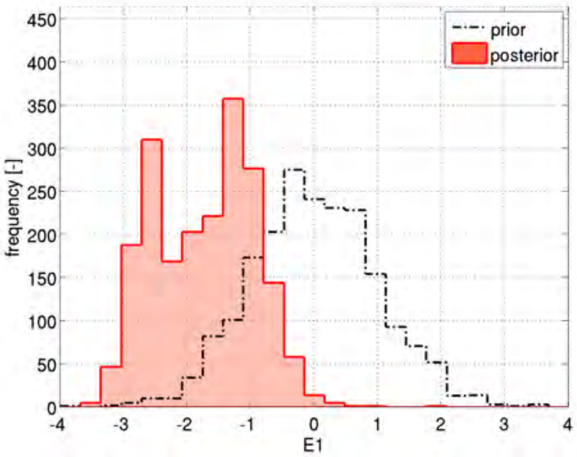

Figure 6: Histograms of the prior and posterior samples of the group of Young's moduli of the orthotropic materials (group no. 3 in Tab. 1)

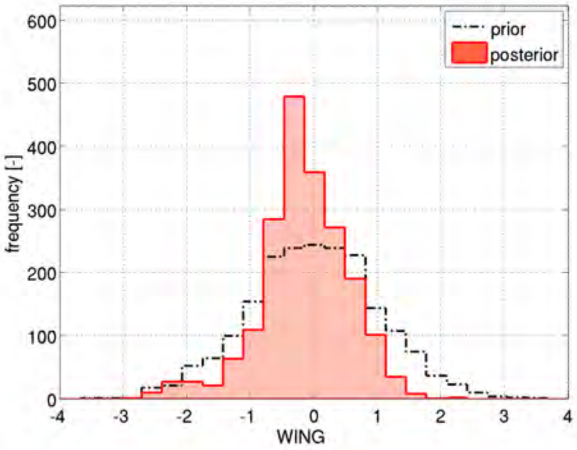

Figure 7: Histograms of the prior and posterior samples of the group of stiffnesses of the joints between wings and main structure (group no. 14 in Tab. 1)

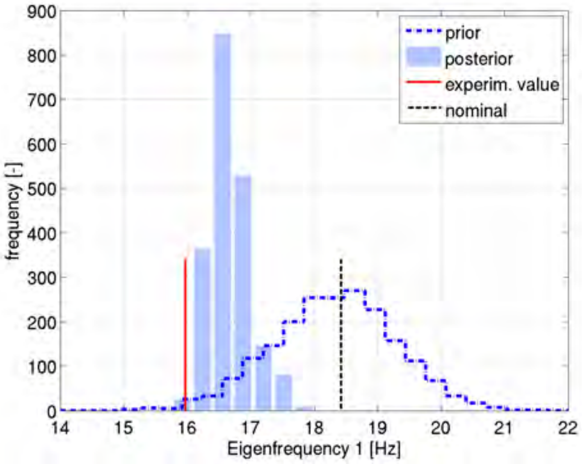

Figure 8: Prior (dashed-dotted line) and posterior (shaded bars) histograms of the 1st eigenfrequency with experimental value (solid line) and nominal value (dashed line)

prior distributions span the full solution space, meaning that posterior samples provoke a high correlation with all targets. As opposed to the first numerical example, where a perturbed model is used for the generation of the target modal data, the present example uses real experimental data and hence a fit with respect to all targets might not be possible without revising the FE-model itself.

5.6 Computational aspects

In the first example, the most time-consuming task of the updating algorithm, namely the parts involving eigensolutions, have been parallelized. In the present example, the eigensolution of the full FE-model is replaced by an approximate relation at low computational costs which is given by a neural network for each modal property. If considering that on the above described dual quad-core Xeon server *i)* the replacement of the nominal parameter values θ_{nom} by the current value θ in the FE-input file, the normal mode analysis of the full model performed with MSC.Nastran and the import of the modal quantities into Matlab [26] requires 220 sec (see Appendix A for details on the interaction of Matlab with MSC.Nastran), *ii)* the updating process of the present model involves approximately 32 iterations × 2,000 eigensolutions and *iii)* the remaining part of the updating process lasts for about 96 min, then the total time amounts up to a theoretical value of

$$t_{\text{full}} = 64,000 \cdot 220\,\text{sec} + 96 \cdot 60\,\text{sec} \approx 160\,\text{days}.$$

In the present example, the computational time of 220 sec of a normal mode analysis of the full FE-model is replaced by the evaluation of the neural networks which takes 0.0014 sec. Hence, in this way the analysis time can be remarkably reduced to

$$t_{\text{NN}} = 64,000 \cdot 0.0014\,\text{sec} + 96 \cdot 60\,\text{sec} \approx 100\,\text{min}.$$

However, it shall be noted that in addition 2,000 calibration samples have been generated (see Sec. 5.3), which require evaluations of the full FE-model lasting for a total time of approx-

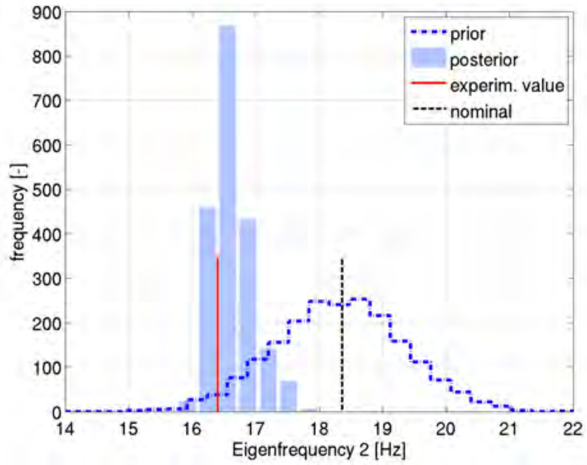

Figure 9: Prior (dashed-dotted line) and posterior (shaded bars) histograms of the 2nd eigenfrequency with experimental value (solid line) and nominal value (dashed line)

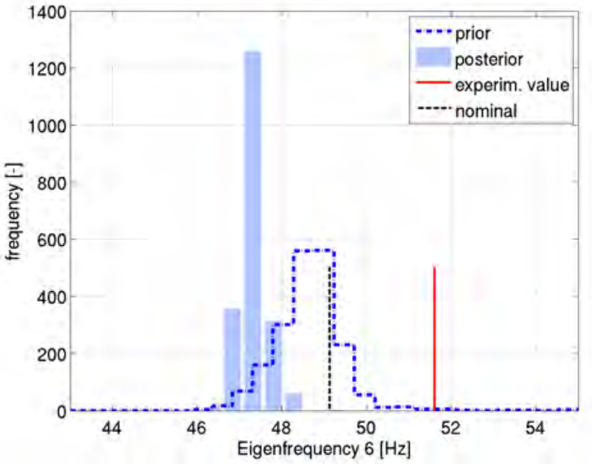

Figure 10: Prior (dashed-dotted line) and posterior (shaded bars) histograms of the 6th eigenfrequency with experimental value (solid line) and nominal value (dashed line)

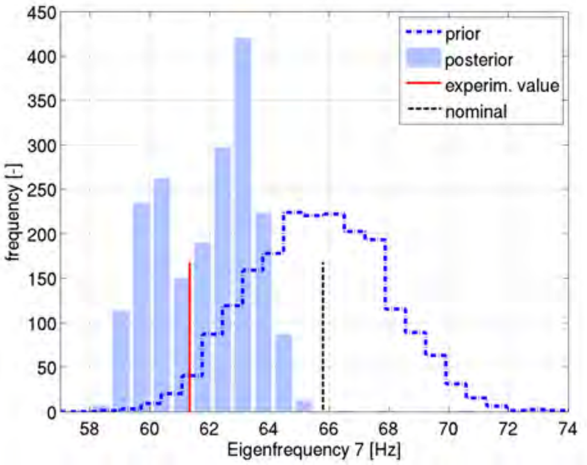

Figure 11: Prior (dashed-dotted line) and posterior (shaded bars) histograms of the 7th eigenfrequency with experimental value (solid line) and nominal value (dashed line)

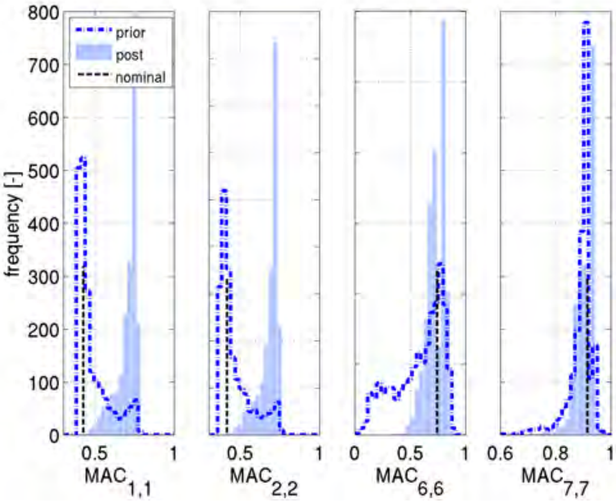

Figure 12: Prior (dashed-dotted line) and posterior (shaded bars) histograms of the diagonal terms of the MAC matrix corresponding to modes no. 1, 2, 6 and 7 and nominal values (dashed lines)

imately 5 days if performed sequentially (see Appendix A for the interaction with 3rd party software).

6 CONCLUSIONS

In this manuscript, the basic steps of model updating within the Bayesian framework using modal data have been summarized and strategies for reducing the analysis time are proposed. The numerical example shows the applicability of the Bayesian updating procedure on complex aerospace structures. It demonstrates that ill-conditioned inverse problems in the high-dimensional parameter space can be tackled and that the limited, incomplete data can be used for reducing the initial uncertainty about the adjustable parameters. As a remedy for the large computational efforts of model updating the establishment of a surrogate model has been proposed which approximates the modal properties at a low computational cost. In this way, model updating of a finite element model of a full satellite structure of a size of approximately 360,000 DOFs becomes feasible as shown in the numerical example.

ACKNOWLEDGEMENTS

This research was partially supported by the European Space Agency (ESA) under Contract No. 20829/07/NL/EM, which is gratefully acknowledged by the authors. The authors thank Thales Alenia Space Italy for the FE-model of the GOCE satellite and the experimental modal data. The first author is a recipient of a DOC-fForte-fellowship of the Austrian Academy of Science at the Institute of Engineering Mechanics (University of Innsbruck).

REFERENCES

[1] European Cooperation for Space Standardization. Space engineering: Modal survey assessment, *ECSS-E-ST-32-11C*, 2008.

[2] The American Institute of Aeronautics and Astronautics. Guide for the verification and validation of computational fluid dynamics simulations, *AIAA Standards Series (G-077)*, 1998.

[3] The American Society of Mechanical Engineers. Guide for verification and validation in computational solid mechanics, *ASME V&V* (10), 2006.

[4] D. Göge, M. Link, Assessment of computational model updating procedures with regard to model validation, *Aerospace Science and Technology* 7 (2003) 47–61.

[5] A. Calvi, S. Garcia de Paredes, N. Roy, Y. Lefevre, On the development of a stochastic approach for the validation of spacecraft structural dynamic models, in: *Proceedings of the European Conference on Spacecraft Structures, Materials and Mechanical Testing* (CD-ROM), Toulouse, France, 2002.

[6] M. Friswell, J. Mottershead, *Finite Element Model Updating in Structural Dynamics*, Kluwer Academic Publishers, 1995.

[7] A. Girard, N. Roy, *Structural dynamics in industry*, John Wiley & Sons, 2008.

[8] F. Buffe, Application of updating methods on the finite element model of Picard, in: *European Conference on Spacecraft Structures, Materials and Mechanical Testing* (ECSS-MMT 2009; CD-ROM), Toulouse, France, 2009.

[9] D. Göge, M. Link, Results obtained by minimizing natural frequencies and mode shape errors of a beam model, *Mechanical Systems and Signal Processing* 17 (1) (2003) 21–27.

[10] A. Calvi, Uncertainty-based loads analysis for spacecraft: finite element model validation and dynamic responses, *Computers & Structures* 83 (14) (2005) 1103–1112.

[11] J. Beck, L. Katafygiotis, Updating models and their uncertainties. I: Bayesian statistical framework, *Journal of Engineering Mechanics* 124 (4) (1998) 455.

[12] L. Katafygiotis, J. Beck, Updating models and their uncertainties. II: Model identifiability, *Journal of Engineering Mechanics* 124 (4) (1998) 463.

[13] K.-V. Yuen, *Bayesian methods for structural dynamics and civil engineering*, John Wiley & Sons, 2010.

[14] J. Ching, Y.-C. Chen, Transitional Markov Chain Monte Carlo method for Bayesian updating, model class selection, and model averaging, *Journal of Engineering Mechanics* 133 (2007) 816–832.

[15] J. Kleijnen, R. Sargent, A methodology for fitting and validating metamodels in simulation, *European Journal of Operational Research* 124 (1) (2000) 14–29.

[16] D. Rumelhart, J. McClelland, *Parallel Distributed Processing, Exploration in the Microstructure of cognition, Vol. 1 and 2*, MIT Press, Cambridge, MA, 1986.

[17] T. Bayes, An essay towards solving a problem in the doctrine of chances, *Philosophical Transactions of the Royal Society of London* 53 (1763) 370–418.

[18] E. Jaynes, *Probability Theory: The Logic of Science*, Cambridge University Press, 2003.

[19] M. Vanik, J. Beck, S.-K. Au, Bayesian probabilistic approach to structural health monitoring, *Journal of Engineering Mechanics* 126 (2000) 738–745.

[20] N. Metropolis, A. Rosenbluth, M. Rosenbluth, A. Teller, E. Teller, Equations of state calculations by fast computing machines, *Journal of Chemical Physics* 21 (6) (1953) 1087–1092.

[21] W. Hastings, Monte Carlo sampling methods using Markov chains and their applications, *Biometrika* 57 (1) (1970) 97–109.

[22] J. Anderson, *Introduction to Neural Network*, MIT Press, Cambridge, MA, 1995.

[23] C. Bishop, *Neural Networks for Pattern Recognition*, Oxford Univ. Pres, 1995.

[24] S. Nissen, *Implementation of a fast artificial neural network library (fann)*, Tech. rep., Department of Computer Science University of Copenhagen (DIKU) (2003).

[25] MSC.Software Corporation, Santa Ana (CA), USA, MSC.NASTRAN, Version 2007.1.0 (2007).

[26] The MathWork, Natick (MA), USA, Matlab R2009b (2009).

[27] COSSAN-X, COmputational Stochastic Structural ANalysis, Chair of Engineering Mechanics, University of Innsbruck, Innsbruck, Austria, EU (2010).

A INTERACTION WITH 3RD PARTY SOFTWARE

FE models are defined uniquely by one or more ASCII input files. These files contain the definition of the nodes and elements constituting the model, as well as the structural parameters and boundary and loading conditions in form of fixed numerical values. However, in a stochastic analysis some of these values change, since they are samples from a given probability distribution function. Thus, it is envisioned to automatically manipulate the input files such that in each simulation the respective sample values are inserted into the FE-input file. For this purpose, XML-like tags, called identifiers, are inserted into the master input files in order to define the parameters which have to be changed in each simulation, as shown in Fig. 13. An identifier defines the name of the random variable used within the stochastic analysis, the format in which the number is written into the file as well as the original value of the parameter.

```
MAT1, 1, <cossan name="E" format="%8.2e" original="7.e+10"/>,,

<cossan name="nu" format="%8.2e" original="0.33"/>,

<cossan name="rho" format="%8.2e" original="2000."/>,

2.40E-5, 20.0000
```

Figure 13: Excerpt of a master input file with identifiers

The code used to drive the simulation is COSSAN-X, a software for computational stochastic structural analysis [27]. This code parses the master input files in order to identify the positions and the insertion formats of all variables. In each analysis, these identifiers are replaced by sampled numerical values, obtaining a valid input file which is then used for the finite element analyis (see Fig. 14). It shall be noted that this software is not restricted to a particulare FE-code, but it is applicable to any FE-solver which uses ASCII input files.

```
MAT1, 1, 6.13e+10,, 3.98e-01, 2.22e+03, 2.40E-5, 20.0000
```

Figure 14: Excerpt of a stochastic analysis input file with sampled values.

COMPDYN 2011
III ECCOMAS Thematic Conference on
Computational Methods in Structural Dynamics and Earthquake Engineering
M. Papadrakakis, M. Fragiadakis, V. Plevris (eds.)
Corfu, Greece, 25–28 May 2011

NON-LINEAR EXPERIMENTAL MODAL ANALYSIS AND APPLICATION TO SATELLITE VIBRATION TEST DATA

M. Link[1], M. Boeswald[2], S. Laborde[3], M. Weiland[1], A. Calvi[4]

[1]University of Kassel
34109 Kassel, Germany
link@uni-kassel.de

[2]DLR, Institute of Aeroelasticity
37073 Göttingen, Germany
marc.boeswald@dlr.de

[3]ASTRIUM Satellites
31402 Toulouse Cedex 4, France
sebastien.laborde@astrium.eads.net

[4]European Space Agency, ESTEC
2200 AG Noordwijk, The Netherlands
adriano.calvi@esa.int

Keywords: Structural Dynamics, Experimental Modal Analysis, Structural Non-Linearity

Abstract. *The DYNAMITED project realised by a European space industry and university team associated around EADS ASTRIUM and funded by the European Space Agency (ESA) aimed to assess and improve dynamic test data. In the field of post test activities, the detection, characterisation, identification and prediction of the non-linear behaviour of space structures during tests is of prime importance. The paper therefore starts with a short overview of such methods. Present evaluation methods for spacecraft vibration tests are based on the assumption of linear structural behaviour. The resonance shifts and frequency response (FRF) peak variations observed in the case of non-linear structural behaviour are generally not reflected in practice by non-linear evaluation procedures. In order to avoid overloading of the structure during the qualification test on a shaking table the dynamic response is generally controlled at specified levels and locations by input notching. This approach generates an effectively quasi linear structural behaviour at the different input levels which enables the utilization of classical linear modal extraction tools to be applied separately at each level. However, the measured dynamic responses (transmissibilities) reveal peak shifts and amplitude changes depending on the input level of the base excitation. In the paper an approach is presented where three different input levels are used with the response levels controlled to be constant within a narrow frequency band around the dominant resonances. The premises of a technique will be described and how its aim of predicting the responses to not measured input* *levels is achieved by applying interpolation and extrapolation techniques to the modal data extracted by conventional modal analysis from the transmissibilities measured at three different input levels. Results are presented from an application of the technique to the vibration test data measured during a typical qualification test campaign of a satellite structure.*

1 INTRODUCTION

In space industry present experimental vibration test evaluation methods are generally based on the assumption of linear structural behaviour. Test procedures to check the linearity assumption are described in the European Space Agency (ESA) standard on modal survey assessment (ECSS-E-ST-32-11C see www.ecss.nl for details) and are applied for base driven tests on the shaking table (an application is shown in Figure 1) as well as in modal survey testing. The resonance shifts and FRF peak variations observed in the case of non-linear structural behaviour are generally not reflected in practice by non-linear analytical modelling. Instead, equivalent linear modelling adapted to a specified load level is used.

This approach can be tolerated since experience shows that in many practical cases the non-linear structural behaviour is not too strong so that the experimental modal data still lie within the natural scatter generated by other sources of test data variability like fabrication tolerances, multiple assembly or test reproducibility.

When evaluating test data obtained from spacecraft (S/C) qualification testing on a shaking table it is an important goal to characterise the non-linear behaviour of the structure with respect to its magnitude (weak or strong) to enable a decision if equivalent linear modelling is applicable or not. Examples of techniques for detection, characterisation and identification of structural non- linearities are described in this paper.

Since existing codes for experimental modal analysis (EMA) rely on the linearity assumption, the scatter of the modal identification results when applying such codes to non-linear vibration test data will be particularly high. It was therefore one of the goals of a research project realized by a consortium of European space industry and universities associated around EADS ASTRIUM and funded by the European Space Agency (ESA) to identify non-linear modal parameters in addition to the traditional modal parameters related to the underlying linear system. The method that was developed and presented in this paper is fully based on experimental data and does not need an analytical model of the structure. In addition, the method was required to be compatible with the test procedures typically applied in vibration testing of spacecraft structures. This means, it is based on transmissibilities of at least three different input levels. Other test data is not required for the method.

2 DETECTION OF NON-LINEAR RESPONSE PROPERTIES

A large number of methods are described in the literature directed towards detection and quantification of structural non-linearities (e.g. refs. [1] – [6]). Examples of the most promising and practically relevant methods will be presented here. A first classification of the available methods is based on the type of data to be used by these methods. Methods for characterizing non-linear structural behaviour may be based on:

- combined analytical/experimental data
- experimental frequency-domain response data
- experimental time-domain response data
- dedicated excitation signals

Figure 1: Aeolus Structural Model (STM) on the ESA/ESTEC Multishaker being prepared for vibration testing (source: ESA/Estec)

2.1 Methods based on Combined Analytical/Experimental Data

The methods described in this subchapter are based on the idea to compare measured characteristic non-linear response features with a catalogue of basic analytical formulations. The response features to be used can either be frequency domain response data measured at different excitation force levels, such as frequency response functions and transmissibilities, or modal features measured at different excitation force levels, such as eigenfrequencies and damping ratios.

(a) Distortions of frequency response functions calculated by harmonic balancing

A simple approach for the detection and characterization of non-linearities is the comparison of FRFs measured at different levels of constant harmonic excitation force with analytical solutions. The different FRF distortion characteristics shall be discussed in the following on a single degree of freedom oscillator with a non-linear equation of motion in the frequency domain:

$$\left(-\Omega^2 m + j\Omega c_{eq}(\hat{u}) + k_{eq}(\hat{u})\right)\hat{u} = \hat{f} \tag{1}$$

where m denotes the mass, c_{eq} and k_{eq} the equivalent damping and stiffness which depends on the vibration amplitude $\hat{u}$. Ω is the excitation frequency and $\hat{f}$ the excitation force.

Analytical representations for c_{eq} and k_{eq} are typically calculated by the harmonic balance method and have been derived for many types of non-linearities (see e.g. refs. [1] and [7]) such as

- pre-loaded bilinear spring (e.g. gapping of bolted flanges),
- clearance type non-linearity and piecewise linear springs, (e.g. structures assembled with joints that have freeplay),
- cubic spring and other polynomial type stiffness non-linearities, (e.g. non-linear elastomer springs and geometric non-linearities due to large displacements),
- quadratic damper (e.g. polynomial type damping non-linearity such as vibration absorbers with elastomer material),

- elasto-slip friction non-linearity such as the 3-parameter Masing model (e.g. structures with loosely assembled bolted joints and rivet joints) or
- combined stiffness and damping non-linearities (e.g. combinations of the aforementioned types of non-linearities).

The equivalent non-linear stiffness of a pre-loaded bilinear spring is characterised by the stiffness parameters k_1 and k_2 and the transition parameter u_c shown in Figure 2(a). These parameters can be calculated by the harmonic balance method (e.g. [7]) resulting in

$$k_{eq}(\hat{u}) = \begin{cases} k_1, & \forall\, \hat{u} \le u_c \\ k_1 + \dfrac{k_2 - k_1}{2\pi}\left(\pi - 2\alpha + \sin\left(2\alpha - \dfrac{4u_c}{\hat{u}}\cos\alpha\right)\right), & \forall\, \hat{u} > u_c \end{cases} \tag{2}$$

with $\sin\alpha = \dfrac{u_c}{\hat{u}}$.

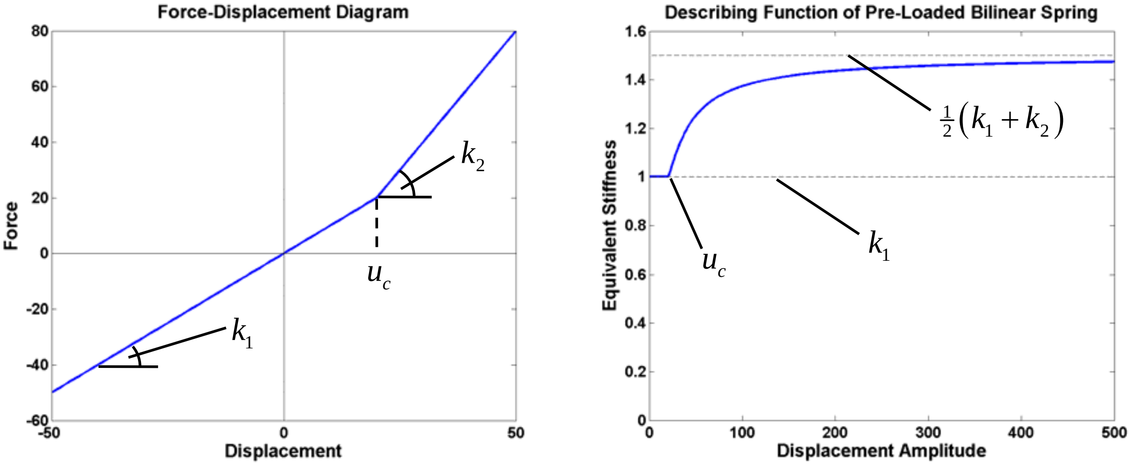

(a) (b)

Figure 2: Force-displacement diagram and equivalent stiffness of a pre-loaded bilinear spring

The evolution of the equivalent stiffness k_{eq} according to equation (2) is shown in Figure 2(b) for a particular single- DOF example. It can be observed that k_{eq} equals the underlying linear stiffness k_1 until the displacement amplitude $\hat{u}$ exceeds the stiffness transition point u_c. After exceeding the stiffness transition point the equivalent non-linear stiffness changes dramatically from its underlying linear value and finally converges towards the average stiffness $\frac{1}{2}(k_1 + k_2)$ for very large displacement amplitudes. The complex response calculated by iteratively solving equation (1) with the amplitude dependent equivalent non-linear spring according to equation (2) exhibits characteristic distortions of the frequency response function (FRF), $h = \hat{u} / \hat{f}$. Analytical FRFs of the non-linear single-DOF oscillator with pre-loaded bilinear spring simulated by using different constant excitation force levels are shown in Figure 3. It can be seen that for low excitation force levels (and hence low vibration amplitudes) the non-linear FRF does not deviate much from the linear one. In fact, the system remains linear as long as the vibration amplitudes remain smaller than the stiffness transition point. The FRF distortions increase with increasing vibration amplitudes. The resonance frequency shift decreases at large vibration levels which can be explained by the convergence behaviour of the equivalent non-linear stiffness:

$$\omega_{eq}(\hat{u}) = \sqrt{\frac{k_{eq}(\hat{u})}{m}} \tag{3}$$

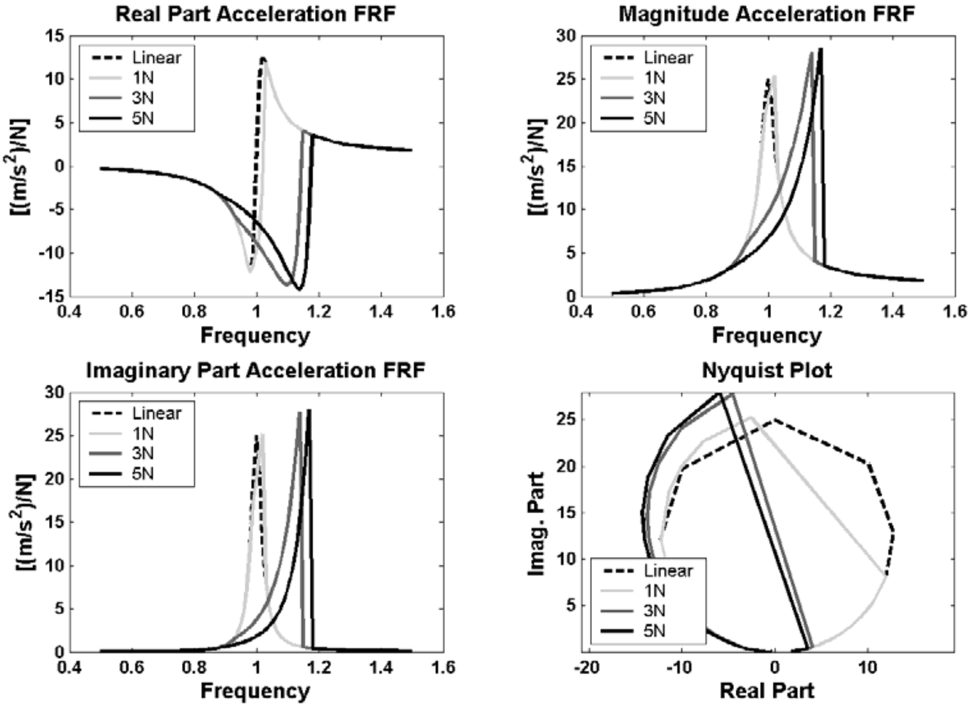

Figure 3: FRF distortion caused by pre-loaded bilinear spring
(upper stable response branch only)

It should be noted that the equivalent non-linear stiffness of the bilinear spring without pre-load is independent from the response amplitude and equals the average stiffness $\frac{1}{2}(k_1 + k_2)$. Even though the force-displacement curve of the pure bilinear spring is definitely non-linear, it would not cause distortions to the fundamental harmonic FRF. Thus, the bilinear spring without pre-load cannot be analyzed with the (single-) harmonic balance method.

The comparison of analytical non-linear FRFs like those of Figure 3 with experimental FRFs represents a useful tool for characterizing the type of non- linearity, especially when analytical non-linear FRFs are available for a set of oscillators with practical types of non-linearities. For the computation of non-linear FRFs, the response amplitude dependent equivalent stiffness and damping formulations for many different types of non-linearities like those mentioned above can be found in textbooks, e.g. refs. [1] and [8] and other publications, e.g. [7], and [9] – [12].

(b) Industrial Example: Aero engine at large response amplitudes

Within the EU research project CERES (refs. [6], [13]), a subassembly of an aircraft engine has been tested at different constant harmonic excitation force levels using stepped sine excitation. The force levels were sufficiently high to drive the structure into the non-linear regime. Figure 4 shows the experimental set-up. The Finite Element model is shown in Figure 5 together with the global bending mode exhibiting the strongest non-linear behaviour. In this case, the bolted flange joint between the component IMC and the component CCOC was assumed to be the source of non-linear behaviour. This bolted flange joint interface is highly loaded when the global bending mode contributes to high response levels. Other bolted flange joints were loaded much less and are therefore not assumed to cause significant non-linear behaviour.

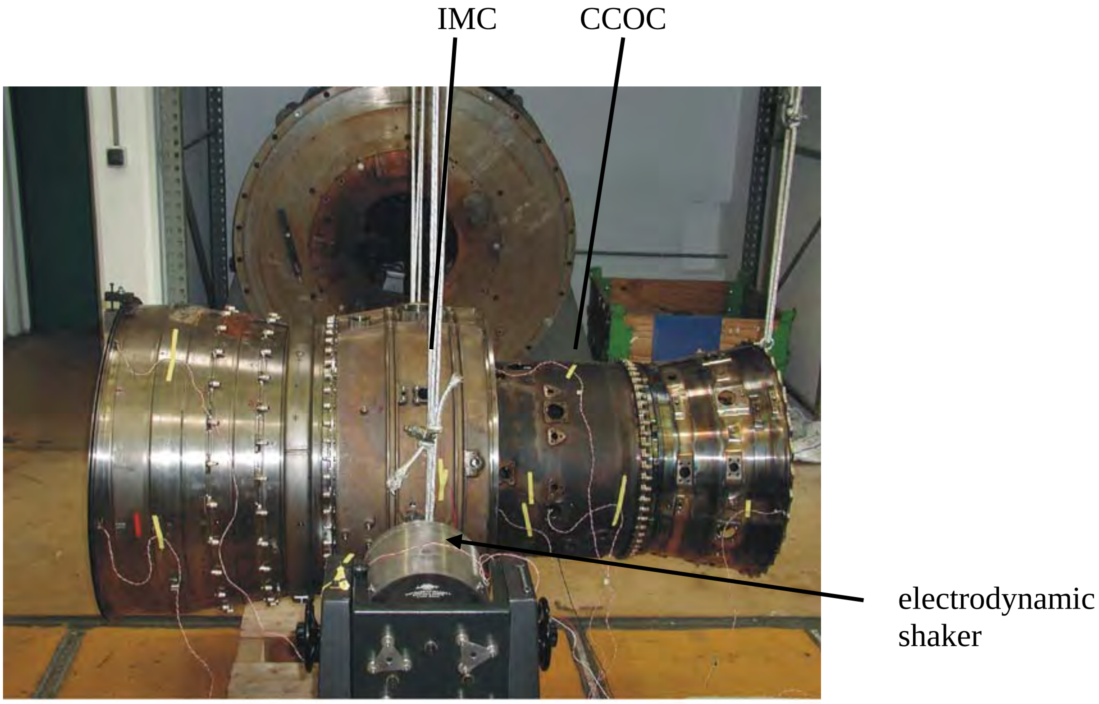

Figure 4: Aero-engine subassembly supported by bungee cords with a shaker attached[1]

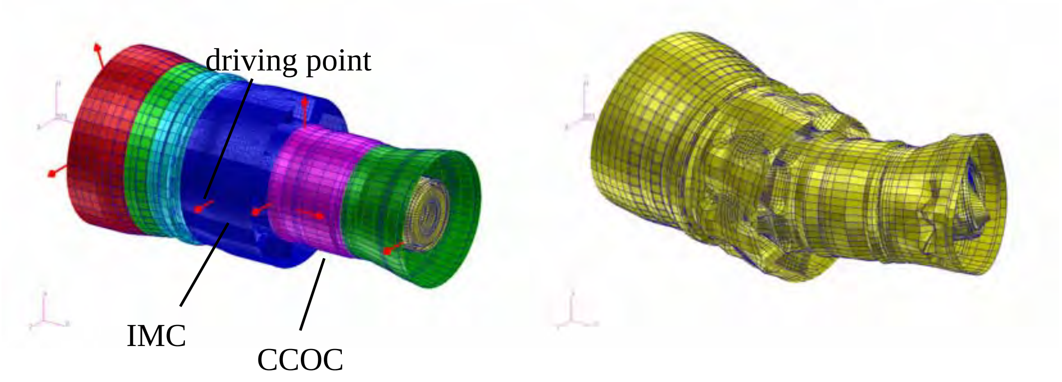

(a) **(b)**

Figure 5: FE model, Pick-up locations (a) and bending mode (b) of an aero-engine subassembly

From the measured non-linear driving point FRFs in Figure 6(a) it can be observed that the resonance shifts towards lower frequencies with increasing excitation force level. In addition, the peak response is increasing indicating a reduction of damping with respect to the load level. When comparing the measured non-linear FRFs with analytical FRFs of different types of non-linearity one could conclude that the most appropriate type would be the assumption of a pre-loaded (softening) bilinear spring and a quadratic damper, see restoring force diagrams

---

[1] Photo of test set up at MTU, Munich, and Imperial College, London, UK

in Figure 7. A number of such non-linear elements were introduced into the FE model between the components IMC and CCOC.

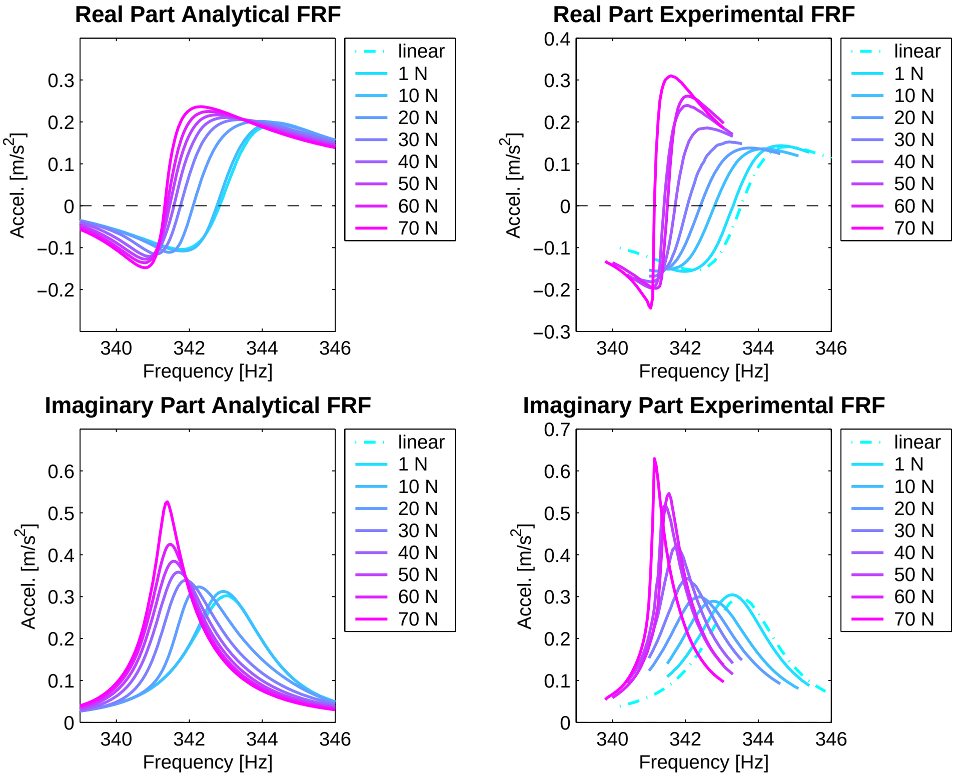

(a) (b)

Figure 6: Comparison of analytical (a) and experimental (b) non-linear FRFs

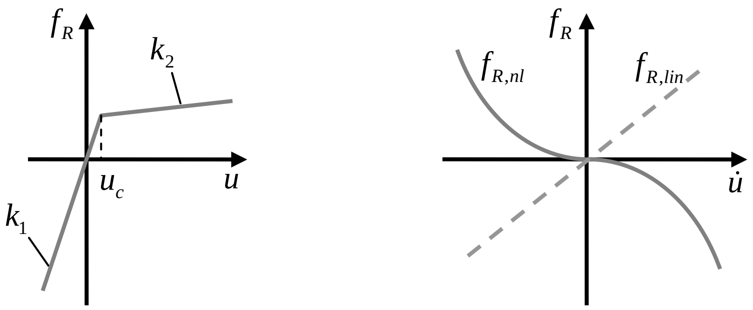

$$f_R = \begin{cases} k_1 u, & u \le u_c \\ k_2\left(u - u_c\right) + k_1 u_c, & u > u_c \end{cases}$$

$$f_R = f_{R,nl} + f_{R,lin}$$
$$f_{R,lin} = c_{lin}\dot{u}, \quad c_{lin} > 0$$
$$f_{R,nl} = c_{nl}\left|\dot{u}\right|\dot{u}, \quad c_{nl} < 0$$

Figure 7: Restoring force functions of non-linear elements used to model the joint non-linearity

From the comparison of the analytical results in Figure 6(b) obtained from computational updating of the non-linear flange joint parameters k_1 , k_2 , u_c and c_{nl} with the experimental results in Figure 6(a) one may conclude that the characteristics and the magnitude of the analytical response is well reflected. See ref. [6] for details of the procedure for numerical parameter updating.

2.2 Methods Based on Experimental Frequency-Domain Response Data

One way to characterise the non-linear behaviour of a structure is the application of different kinds of signal processing and visualisation tools to the measured frequency response functions. The comparison of the processed data to a certain reference indicates possible deviations from linear behaviour. Most of the techniques, however, only provide the possibility for detection but not for quantification of non-linear behaviour.

The following methods are widely used for non- linearity detection

- Overlay of FRF plots
- Frequency isochrones in Nyquist plots
- Hilbert transformation of measured FRFs
- Inverse FRF plots
- Carpet plots of modal damping
- Analysis of coherence functions

Many examples are reported in the literature for the application of these techniques, e.g. refs. [2], [4] and [14]. The most simple and most appropriate for practical industrial applications is the analysis of experimental FRF plots measured under different load levels. Such plots are shown in Figures 15 and 19 for the transmissibility test data[2] obtained from shaking table testing of the SWARM satellite. The non- linear behaviour is clearly detected from the peak shifts and the amplitude variations depending on the magnitude of load levels.

In a Nyquist plot the imaginary parts of the FRF are plotted versus the real parts at each measured frequency point. Linear responses appear as (almost) circular curves in the Nyquist plot, whereas non-linearities cause distortions from the circular shape.

When the frequency responses (forced response, not FRF) obtained at different levels of excitation are overlaid in a single Nyquist plot, then the deviation of the frequency isochrones (lines connecting points of equal frequency among a set of different response curves) from straight lines indicate the presence of non-linearity, ref.[11]. This can be observed in Figure 8 where the Nyquist plots with frequency isochrones of a linear and a non-linear system are shown. Examples for the other methods mentioned above are described in refs. [1], [2] and [14].

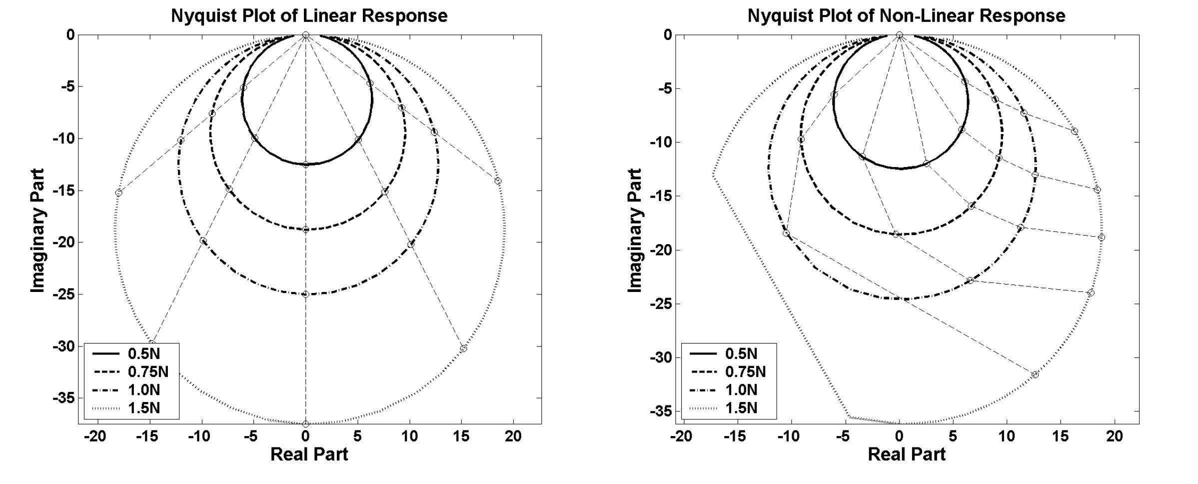

Figure 8: Nyquist plots with frequency isochrones of linear and non-linear system

---

[2] the transmissibility is calculated from the response divided by the table acceleration which is equivalent to the FRF where the response is divided by the excitation force

2.3 Methods Based on Experimental Time-Domain Response Data

Time domain methods for the detection and characterization of non-linearities have significant advantages over frequency-domain methods. The most obvious point is the typical low sampling rate when acquiring frequency domain data. Usually, Shannon's Theorem is applied, which states that at least two data samples per period of vibration must be acquired to avoid error in subsequent Fourier transformation. It is known, however, that non-linear effects can cause higher harmonic responses. These higher harmonic responses can easily be measured in the time domain by using a sampling rate which can be set 5 or even 10 times higher than for typical FRF measurements. Thus, more information is available from high frequency responses and this can be used to characterize or even identify the non-linearities.

An accepted time-domain approach for the characterization of non-linearities is the *restoring force surface method* according to [15], which has later been published as force-state mapping according to [16].

The restoring force methods are based on the non-linear equation of motion of a single degree of freedom system:

$$m\ddot{u}(t) + \underbrace{d(\dot{u})\dot{u}(t) + k(u)u(t)}_{f_R(u,\dot{u},t)} = f(t) \quad \rightarrow \quad m\ddot{u}(t) + f_R(u,\dot{u},t) = f(t) \tag{4}$$

$$\rightarrow \quad f_R(u,\dot{u},t) = f(t) - m\ddot{u}(t) \tag{5}$$

Here, m is the mass of the system, $\ddot{u}(t)$ is the acceleration response, $f(t)$ is the time history of the excitation force. If these quantities are known by measurements, the restoring force $f_R(u,\dot{u},t)$ can be calculated as a function of time. It is obvious from the above equations, that in case of a linear system, the restoring force is a linear function of displacement $u(t)$ and also a linear function of velocity $\dot{u}(t)$:

$$f_R(u,\dot{u},t) = k\,u(t) + d\,\dot{u}(t) \tag{6}$$

If displacement and velocity response are also available, e.g. from measurements or from numerical integration of the measured acceleration response, the restoring force can be plotted as a 3D surface over displacement and velocity. In case of a linear system, the restoring force surface is a planar flat surface. The slope of the surface in the displacement direction (i.e. sections of constant velocity but variable displacement) equals the stiffness k. On the other hand, the damping d is the slope of the restoring force surface in the direction of velocity (i.e. sections of constant displacement but variable velocity).

If velocity and displacement response are not available from measurements, they can be derived numerically by integrating the measured acceleration response. Digital filtering and/or offset removal is necessary in this case because otherwise numerical integration can lead to unsatisfactory results.

The utilization of dedicated excitation signals can also be applied for experimental analysis of non-linear structures. For example, when using sinusoidal excitation, the acceleration response of a non-linear system will be periodic (fundamental harmonic plus a number of higher harmonics). It would be possible to curve-fit the response and to integrate each harmonic individually. This can be done most effectively in the frequency domain.

The three-dimensional restoring force surface produced by the restoring force surface method can be used not only to characterize the type of stiffness and damping non-linearity. By curve-fitting of the 3D surface using a reasonable model for the type of non-linearity, it is possible to identify the coefficients of the non-linear model used. By proceeding this way, a mathematical description for the observed non-linearity can be obtained which is a valuable feedback information for finite element modelling. Based on the identified mathematical model of the non-linearity, it can be assessed up to which response levels an equivalent linear model is sufficient, or respectively, if the non-linearity must be included in the FE model to improve the prediction capabilities in the large response amplitude regime.

As can be seen from equation (6), the restoring force is indeed only a function of the status of the system defined by displacement and velocity. Individual response points of velocity and displacement at each time step will form a repeatable surface provided that the damping non-linearity is not too severe with strong hysteresis character. If this is not the case, the nature and shape of the surface will be independent of the time history of the applied force. This, however, requires that a sufficiently large number of independent states are included in the test data for the generation of the restoring force surface. For example, if a pure sinusoidal signal of constant amplitude is used for excitation, only one ellipse in the displacement/velocity plane is generated. This is obviously not enough to generate the complete restoring force surface. In [16] a pure sine excitation with continuously increasing amplitude is used to generate the restoring force surface. In [15], Chebyshev polynomials are used to extrapolate the restoring force surface to unmeasured state points.

If the non-linear restoring force is not only a function of the status of the system, i.e. if hysteresis effects are present in the dynamics of the system under consideration (e.g. systems with elasto-slip type friction non-linearities), the interpretation of the restoring force surface might not be obvious and the method may even fail to produce a repeatable 3D surface.

The simulated response signals of a non-linear single degree of freedom system with a cubic hardening spring were analyzed as an example. Due to the relatively low number of independent states (i.e. independent combinations of displacement and velocity response) in case of sinusoidal excitation, the restoring force surface is not well populated (see Figure 10) even though the harmonic amplitude has been increased linearly. In contrast to sinusoidal excitation, random excitation provides a huge number of independent displacement/velocity combinations. Consequently, a well populated restoring force surface can be generated (see Figure 9). It must be stated, however, that this is a rather academic statement, because in case of random excitation, the excitation energy is distributed over a broad frequency range so that very high force RMS values would be required to reach the same response levels compared to harmonic excitation. This can be difficult to achieve with standard laboratory equipment.

In the case of multi- DOF systems selected single modes have to be excited by appropriated exciter configurations since the restoring force method is a single- DOF technique. This allows for applying the restoring force method on a single non-linear modal equation of motion. It should be noted that broadband random excitation is not suited for force appropriation. Extensions of the restoring force method to multi DOF systems were developed by Dimitriadis [17], Wright [18] and Göge [19].

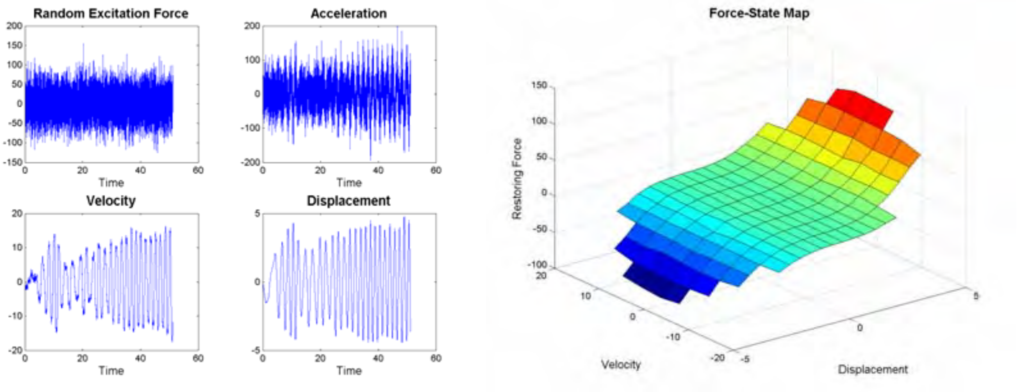

Figure 9: Restoring force surface generated from high level random excitation

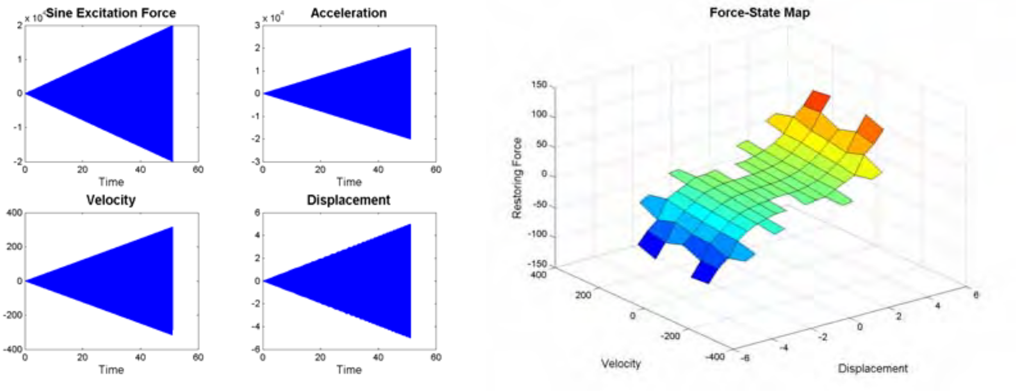

Figure 10: Restoring force surface generated from sinusoidal excitation
with increasing force amplitude

2.4 Methods Based on Dedicated Excitation Signals

One of the best ways of dealing with non-linearities in practical structures is to control the vibration levels during the measurements. For example, Figure 11(a) shows the frequency response functions (i.e. upper branch of non-linear FRF) of an analytical single-DOF system with a cubic stiffness non-linearity calculated under harmonic excitation force with different constant excitation force amplitudes. It can be seen that the distortion of the FRFs is increasing with increasing force level. As a result, problems can be expected when applying classical (linear) experimental modal analysis to such deformed FRFs. The modal parameters extracted this way will suffer from inaccuracy, especially for the damping and the modal mass due to the distortion of the response curve. Non-linear distortion characteristics of FRFs may lead to additional (artificial) eigenvalues that are difficult to distinguish from true eigenvalues of the system analyzed, see ref. [22]. However, the analysis of FRF distortions can be used for the characterization of the non-linearity, e.g. by comparison with analytical non-linear FRFs of different types of non-linearities as discussed before. Keeping the excitation force level constant would mean to increase the level of the drive signal of the electro-dynamic shaker when approaching resonance. This involves an unavoidable risk of damaging the structure in the test, especially in case of lightly damped structures and powerful shakers.

Figure 11(b) shows the calculated FRFs of the same non-linear system now keeping the response amplitude constant. The legend in Figure 11(b) shows the levels of the constant displacement responses of the different simulations. In contrast to Figure 11(a) it can be seen that the excitation force was changed in order to maintain constant response level. By proceeding this way the non-linearity was also kept constant and thus each FRF in Figure 11(b) reflects a linear characteristics (not distorted) with slightly different underlying linear stiffness (in contrast to Figure 11(a) where all FRFs exhibit non-linear distortions).This approach generates an effectively quasi linear structural behaviour around the main resonances at the different input levels which enables the utilization of classical linear modal extraction tools to be applied separately at each response level. However, the measured dynamic responses (transmissibilities) reveal peak shifts and amplitude changes depending on the input level of the base excitation which can be utilized to describe the non-linear behaviour.

Another advantage of constant response level testing is that the structure under test can be prevented from being damaged. This requires that the response levels to be investigated have to be defined carefully. It should be mentioned that constant response amplitude levels can only be realized in a narrow frequency band around the resonance of an isolated non-linear mode that is investigated in detail. If broad frequency ranges are considered, many modes may contribute to the response of a structure so that constant response amplitudes can only be realized at a single response DOF. In industrial qualification procedures for spacecraft testing it is common practice to apply input notching in order to avoid overloading of the structure during the qualification test on a shaking table which requires the control of the dynamic response at specified levels and locations. In this case the table acceleration levels are reduced in the range of the main resonances such that the response of the structure at selected locations does not exceed a specified limit. It could therefore be expected that the responses and load levels around the notching ranges would exhibit similar characteristics like that of Figure 11(b).

This behaviour has been investigated at a typical example taken from a STM satellite structure (Structural Test Model) test campaign. The measured sinusoidal shaking table accelerations (input) for three different load levels are shown in Figure 13. The absolute response amplitudes of the 17 largest DOFs around resonance shown in Figure 14 confirm that the goal of constant output control was fulfilled satisfactorily. The corresponding transmissibilities obtained from dividing the responses by the table accelerations are shown in Figure 15. The similarity of the curves in Figures 13 and 15 with the curves in Figures 11(b) for the analytical example is obvious. It can be observed that like in Figure 11(b) the transmissibilities in Figure 15 do not exhibit significant distortions so that the utilization of classical linear modal extraction tools may be applied separately for each input level.

3 INTERPOLATION METHOD

In the following a technique is described that is aimed at predicting the responses to ***other than the measured*** input levels which is achieved by applying interpolation and extrapolation techniques to the modal data extracted from the transmissibilities measured at three measured input levels, i.e. the experimental data base is formed by ***three sets*** of natural frequencies, mode shapes, modal damping values and modal masses related to each load level. The response prediction at unmeasured load levels is subsequently performed by standard modal synthesis using the inter- or extrapolated modal data.

At least three load levels have to be used for identifying equivalent linear modal data with classical EMA (Experimental Modal Analysis) techniques. This interpolation forms the basis of the ISSPA_NL code which is described in the following. The interpolation starts from classical linear modal analysis data extracted by any existing EMA code (the in-house code ISSPA has been used, ref. [20]) from experimental frequency response functions (FRF) measured at three load levels. Figure 12 shows the principle of the interpolation and extrapolation scheme.

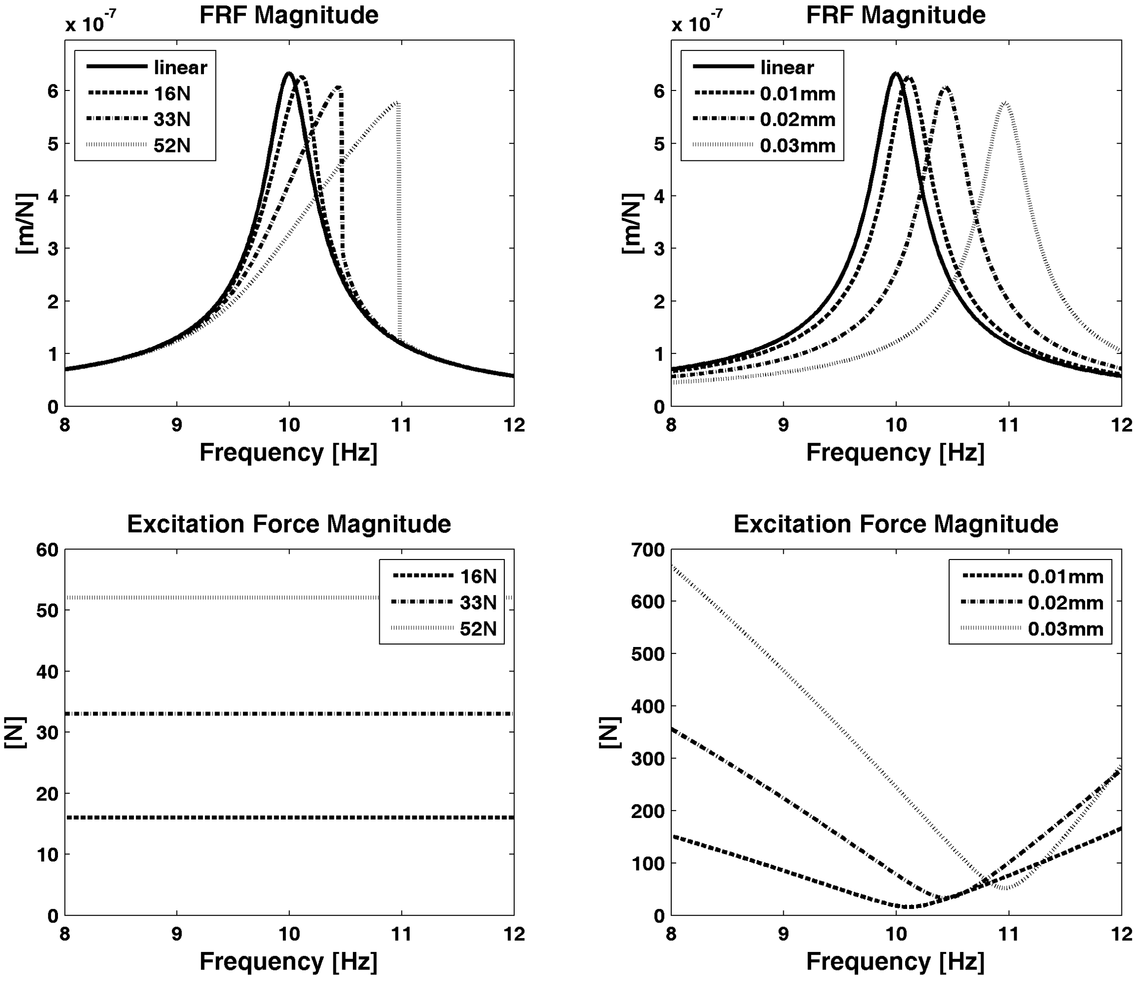

(a) constant excitation

(b) constant response

Figure 11: FRFs obtained with constant excitation force levels (a) and constant response levels (b)

The three data points for the variable Z on the vertical axis stand for any of the extracted natural frequencies, modal displacements, modal damping values or modal masses. The variable A stands for the load level used during the test (e.g. the g-level used on the shaking table). A distinction is made for input levels that lie within the input level range covered by test data (i.e. $A_{int,i}$ with i=1,2,…) and input levels that lie outside the range covered by test data (i.e. $A_{low,i}$ and $A_{up,i}$). Polynomial interpolation is performed inside the input level range covered by test data, whereas linear extrapolation is applied for input levels that lie outside the range covered by test data. In principle, any suitable polynomial interpolation can be used. However, in the qualification test campaigns of spacecraft structures, three different input levels are typically used, that is a low level, an intermediate level, and the final qualification level. Due to this, the polynomial interpolation cannot go higher than quadratic (parabolic) interpolation in order to maintain compatibility with the spacecraft structures test procedures.

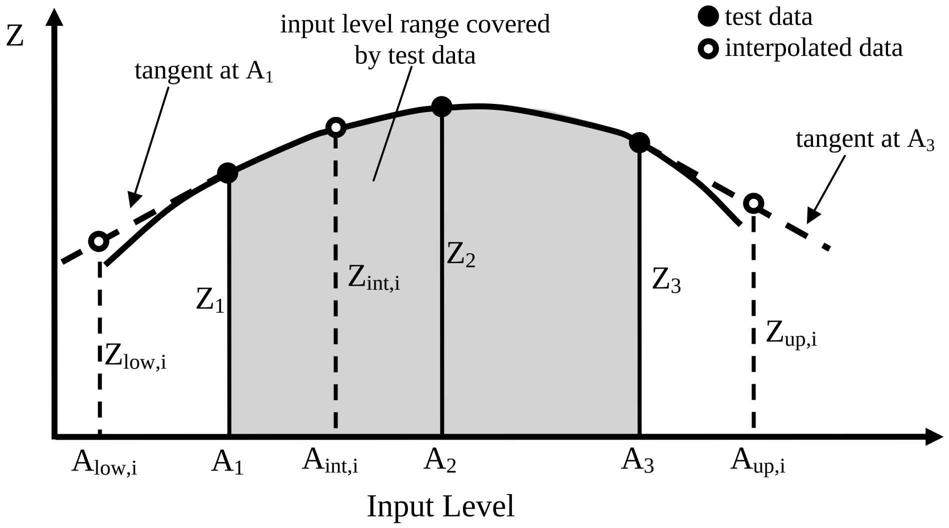

Figure 12: Interpolation and extrapolation scheme

It must be stated that the parabolic interpolation of modal parameters lacks physical significance. Nonetheless, it is a suitable interpolation between test data points observed at different input levels. Therefore, it is clear that the linear extrapolation to input levels outside the input level range covered by test data must be bounded by meaningful limits. In general, the validity bounds of the extrapolation are dependent on the character and strongness of the nonlinearity. The validity range of the linear extrapolation are given by $A_{low} \leq A_{low,i} \leq A_1$ and $A_3 \leq A_{up,i} \leq A_{up}$ where the bounds A_{low} and A_{up} have to be specified by the user. Practical limits can be, for example, $A_{low} = 0.9A_1$ and $A_{up} = 1.1A_3$.

The parabolic interpolation scheme between levels A_1 and A_3 is described by

$$Z_{int,i} = a_1 + a_2 A_{int,i} + a_3 A_{int,i}^2 = \left[A_{int}\right]_i^T \{a\} \tag{7}$$

Since this equation must also be valid at the measured load levels A_1 to A_3 one gets three equations for determining the interpolation constants $a_1 - a_3$:

$$\begin{Bmatrix} Z_1 \\ Z_2 \\ Z_3 \end{Bmatrix} = \begin{bmatrix} 1 & A_1 & A_1^2 \\ 1 & A_2 & A_2^2 \\ 1 & A_3 & A_3^2 \end{bmatrix} \begin{Bmatrix} a_1 \\ a_2 \\ a_3 \end{Bmatrix} = [A]\{a\} \tag{8}$$

The vector $\{z\}$ holds the measured variables at the three load levels. This equation can easily be solved for the interpolation constants:

$$\{a\} = [A]^{-1}\{Z\} \tag{9}$$

Any interior variable $Z_{int,i}$ at any interior load level $A_{int,i}$ (i=1,2…n) is calculated from

$$\begin{Bmatrix} Z_{int,1} \\ \vdots \\ Z_{int,n} \end{Bmatrix} = \{Z\}_{int} = [A]_{int}^T [A]^{-1} \{Z\} \tag{10a}$$

where the matrix $[\mathrm{A}]_{int}^{T}$ holds the n interior load levels in the form

$$[\mathrm{A}_{int}]^{T} = \begin{bmatrix} 1 & \mathrm{A}_{int,1} & \mathrm{A}_{int,1}^{2} \\ \vdots & \vdots & \vdots \\ 1 & \mathrm{A}_{int,n} & \mathrm{A}_{int,n}^{2} \end{bmatrix} \tag{10b}$$

For the linear extrapolation scheme the tangents of the parabola at load levels A_1 and A_3 as shown in figure 12 are used which results in the interpolation formula for the lower and the upper range

$$\mathrm{Z}_{low,i} = \mathrm{Z}_{1} + tan(\mathrm{Z}(\mathrm{A}_{1}))(\mathrm{A}_{low,i} - \mathrm{A}_{1}) \tag{11a}$$

$$\mathrm{Z}_{up,i} = \mathrm{Z}_{3} + tan(\mathrm{Z}(\mathrm{A}_{3}))(\mathrm{A}_{up,i} - \mathrm{A}_{3}) \tag{11b}$$

with $tan(\mathrm{Z}(\mathrm{A}_{1})) = a_{2} + 2a_{3}\mathrm{A}_{1}$ and $tan(\mathrm{Z}(\mathrm{A}_{3})) = a_{2} + 2a_{3}\mathrm{A}_{3}$ where a_2 and a_3 denote the interpolation coefficients of eq.(9).

As stated above, this interpolation and extrapolation scheme can be applied to any modal parameter. In detail, the eigenfrequencies, the damping ratio, the generalized mass, and the elements of the mode shape vectors are interpolated. The new modal parameters interpolated or extrapolated to a new (unmeasured) input level can be used for response synthesis.

4 INDUSTRIAL APPLICATIONS

Test data for the first application were measured during a vibration test campaign of a typical STM satellite structure (Structural Test Model). The shaking table was driven in lateral direction at low, intermediate and qualification g – levels as shown in Figure 13. The data shown in Figure 15 represent the transmissibilities (transfer functions) calculated by division of the sensor responses (at altogether 164 DOFs) by the pilot response which was chosen as the maximum of the four pilot sensors located on the shaking table.

The test data evaluation procedure consisted of the following steps:

(a) Analysis of the transmissibilities over the whole frequency range in order to identify the most significant response areas.

(b) Selection of a frequency range which is considered to be representative for non-linear behaviour. The frequency range around the fundamental resonance in lateral x-direction is presented here which exhibited the most significant peak shifts and large deviations of amplitudes.

(c) Identification of natural frequencies, mode shapes and modal damping values for each load level within the frequency range selected under (b) using ISSPA, ref. [20], classical modal extraction technique.

(d) Extraction of input levels at resonance from pilot response spectra.

(e) Application of ISSPA_NL for prediction of modal data and responses at not measured input levels.

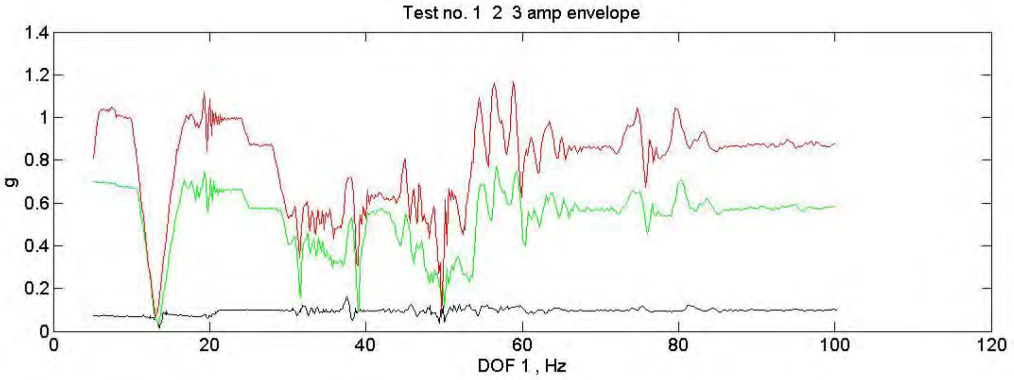

(a) Table acceleration (input) notched around resonances

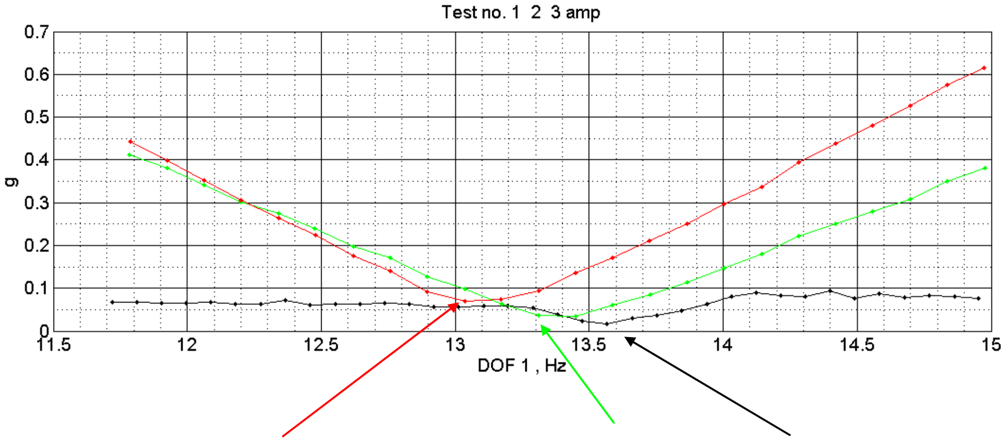

f_{qual}= 13.10 Hz (qualification level), f_{inter}= 13.38 Hz (intermediate level), f_{low}= 13.56 Hz (low level)
L_{qual} = 0.0715 g L_{inter}= 0.0350 g L_{low}= 0.0162 g

(b) Table acceleration (pilot sensor) zoomed around first resonances

Figure 13: Sinusoidal shaking table accelerations (input)
low level (black), intermediate (green), qualification level (red)

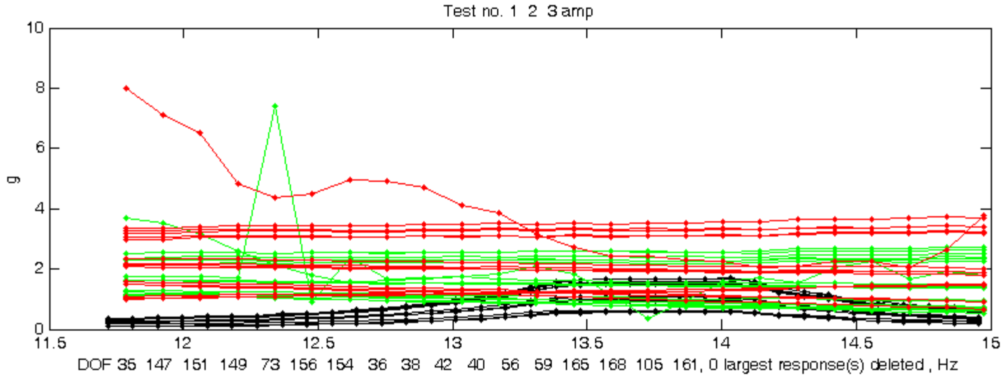

Figure 14: Nearly constant absolute response amplitudes of the 17 largest DOFs around resonance

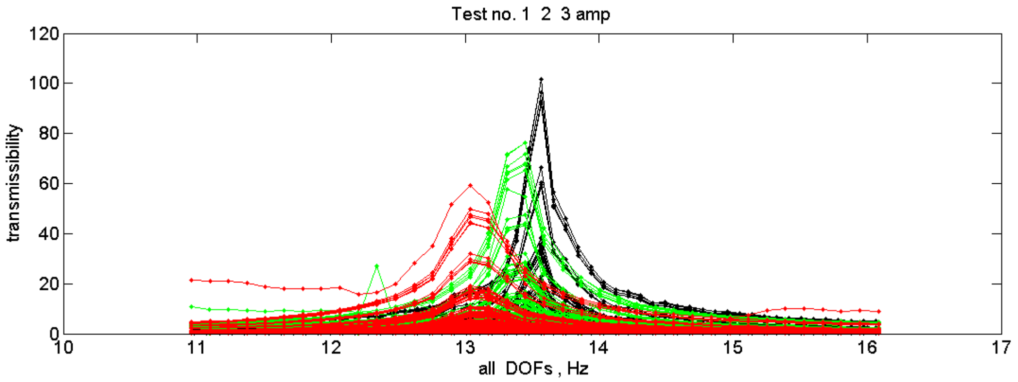

Figure 15: Amplitudes of the 17 largest transmissibilities
Low level (black), intermediate level (green), qualification level (red)

4.1 Identification of Modal Parameters

The characteristics of the transmissibilities in Figure 15 permitted the extraction the modal data separately for each load level using classical curve fitting procedure (ISSPA) which is based on the linearity assumption. The results of experimental modal analysis are summarized in Table 1:

Table 1: Results of linear modal analysis of three different input levels

Description	Input Level [g]	Eigen-freq. [Hz]	Damping Ratio [%]
Low	0.0162	13.56	0.8
Intermediate	0.0350	13.38	1.3
Qualification	0.0715	13.10	1.7

The following MAC-values compare the mode shapes extracted from the three load levels (100% would mean perfect agreement):

- MAC (low/ intermediate) 93.2 %,
- MAC (low/ qualification) 93.0 %,
- MAC (intermediate/qualification) 96.9 %.

These numbers and the plot in Figure 17 show

- a small variation of the resonance frequency,
- a significant increase of the damping values with the load level,
- a small influence of the load level on the mode shapes.

In Figure 16 the good correlation between test and modal synthesis is shown for one representative measurement DOF on top of the structure (the correlation for other DOFs was similar). This confirmes the assumption that due to controlled output levels the response of the structure exhibited linear behaviour and that the identified modal parameters are meaningful. Figure 16(a) compares the indicator functions which indicate the quality of modal excitation. In the ideal case when just one single mode contributes to the response the indicator value equals zero. This figure shows that the mode around 13.4 Hz was very well excited. The shift of the resonance frequencies and the variation of the response peaks in Figure 16(b) show the load level dependent nonlinear behaviour equivalent to the analytical system shown in Figure 11(b).

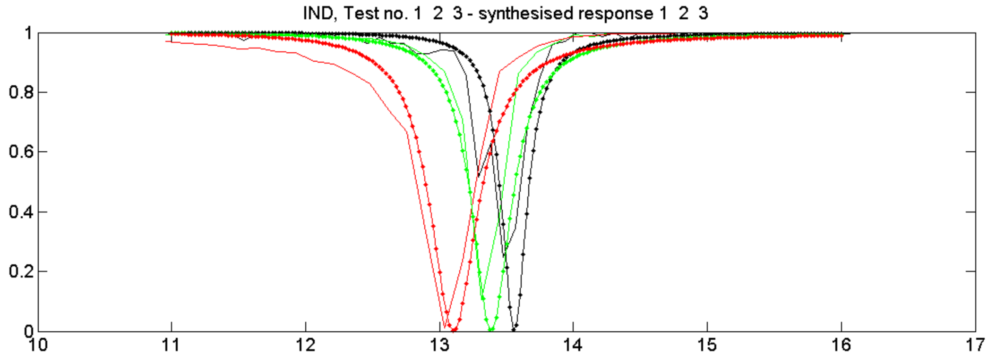

(a) Indicator functions

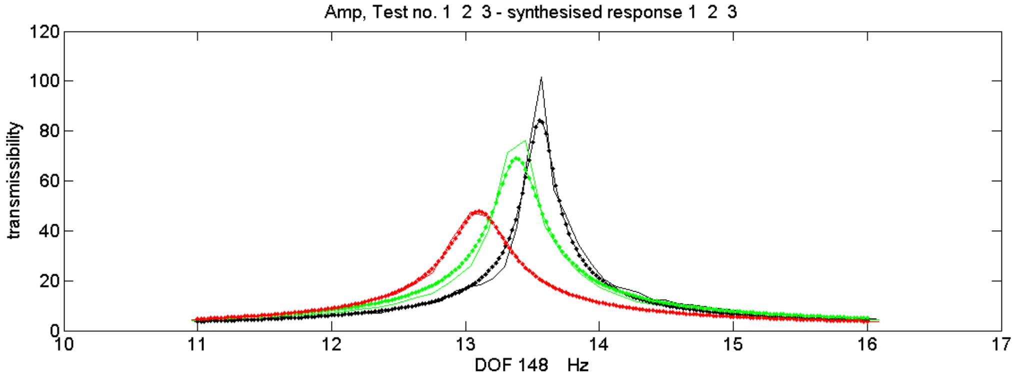

(b) Transmissibilities

Figure 16: Measured (——) and synthesised (• • •) indicator functions (a) and transmissibility amplitudes (b) low level (black), intermediate level (green), qualification level (red)

4.2 Application of the Interpolation Method

The application of the interpolation method seeks to predict the modal data and the responses at any other than the measured load levels. In the present application two additional load levels were chosen, one at $X1_{add}=(L_{low}+L_{inter})/2$ = 0.0256 g and the other at $X2_{add}$ = $(L_{inter}+L_{qual})/2$ = 0.0532 g, L_{low} = 0.0162 g, L_{inter} = 0.0350 g and L_{qual} = 0.0715 g denote the load levels taken at f_{low} = 13.56 Hz, f_{inter} = 13.38 Hz and f_{qual} = 13.10 Hz (see Figure 13b).

The basic modal data extracted by the classical (linear) modal extraction technique ISSPA, ref. [20], using the transmissibilities of each load level are used as data points for the interpolation functions as described before.

The results of interpolating the modal data between the load levels L_{low} = 0.0162 g at 13.56 Hz and L_{qual} = 0.0715 g at 13.10 Hz are shown in Figure 17 (the modal displacements are not shown because of their low variability).

A considerable variation of the modal damping was observed whereas the maximum variation of the resonance frequency is restricted to not more than about 0.5 Hz. Using the modal data at the additional load levels $X1_{add}$ = 0.0256 g and $X2_{add}$ = 0.0532 g together with the modal data from the measured load levels yields the indicator functions and the transmissibilities shown in Figure 18.

It may be noted that the indicator functions and the transmissibilities at the additional load levels exhibit a physically meaningful interpolation between the measured levels and thus seems to confirm the achievement of the goals of the interpolation technique implemented in ISSPA_NL. It should also be noted that the calculation of the load level dependent modal data was based on experimental modal data only, i.e. there was no mathematical model involved.

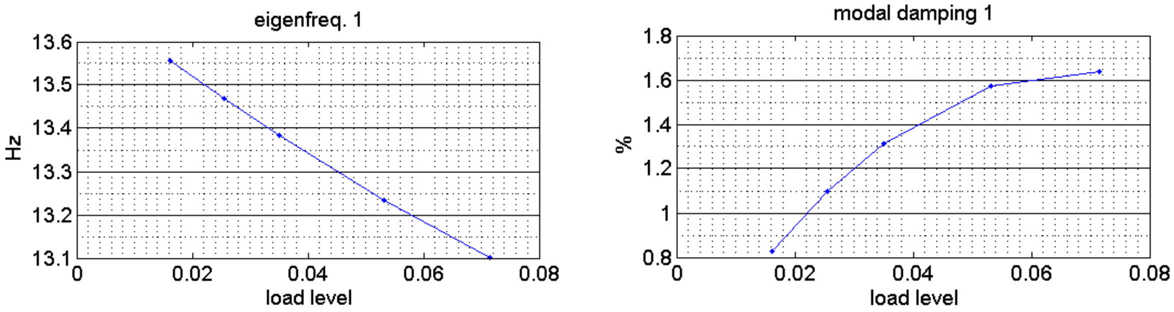

Figure 17: Resonance frequency and modal damping vs. load level [g]

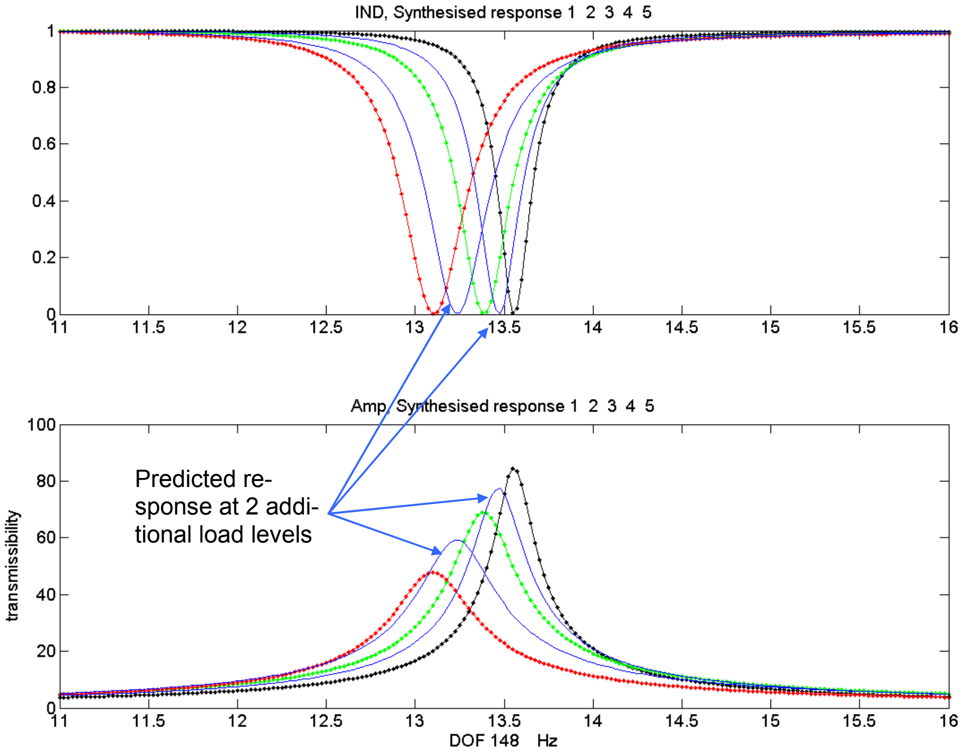

Figure 18: Indicator functions and transmissibilities using the modal data at two additional load levels (blue) together with the modal data from the measured load levels
(qualification level red, intermediate level green, low level black)

From the viewpoint of verifying the predictions it was a disadvantage that the additional load level were not measured during the test campaign. Therefore, the technique was applied to the data available from the SWARM [21] qualification test campaign where **one additional** intermediate load level was measured. Figure 19 shows the measured transmissibilities at all

181 test DOFs which exhibit the peak shifts and the amplitude variations depending on the magnitude of load levels.

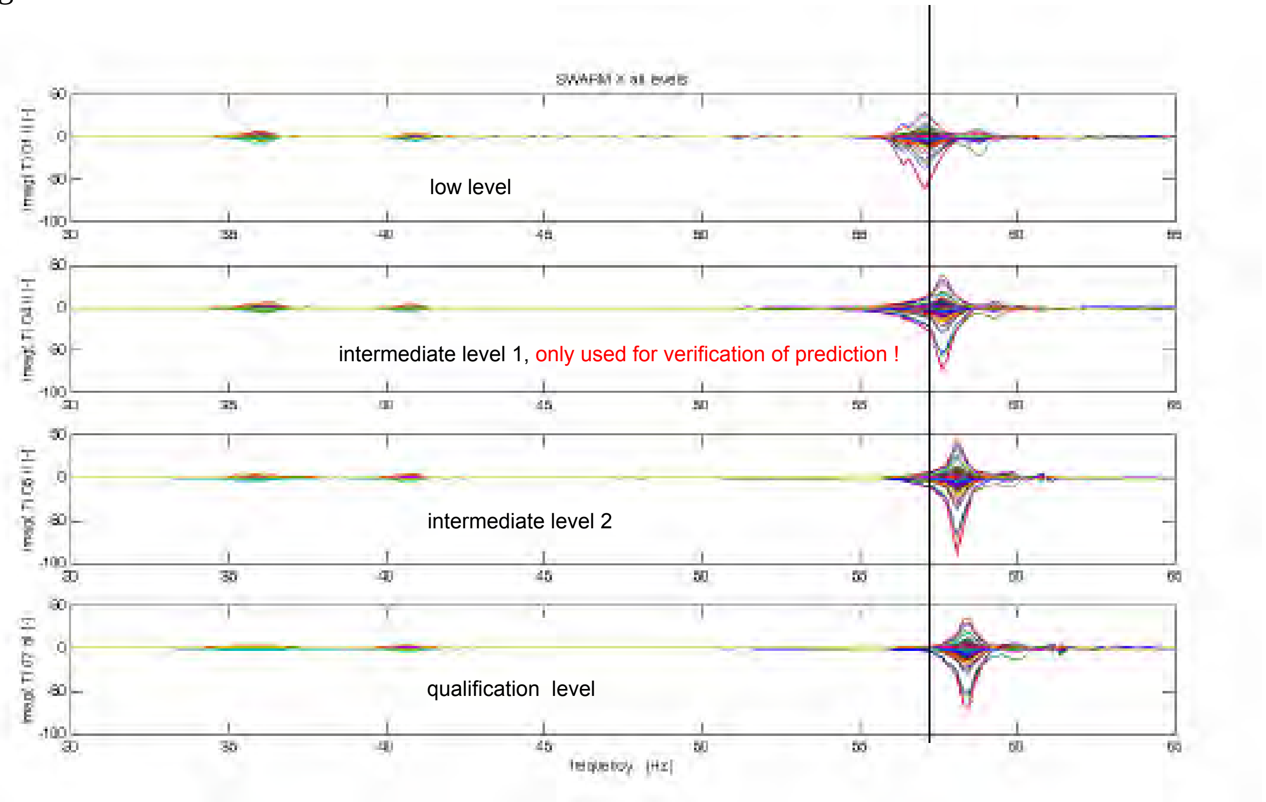

Figure 19: Measured transmissibilities at all 181 test DOFs

The success of constant output control can again be assessed from the 15 largest responses plotted in Figure 20. This plot shows that the requirement of constant responses within the notch range was not fulfilled as good as with the data of the previous application in Figure 14. Nonetheless, the described procedure was applied.

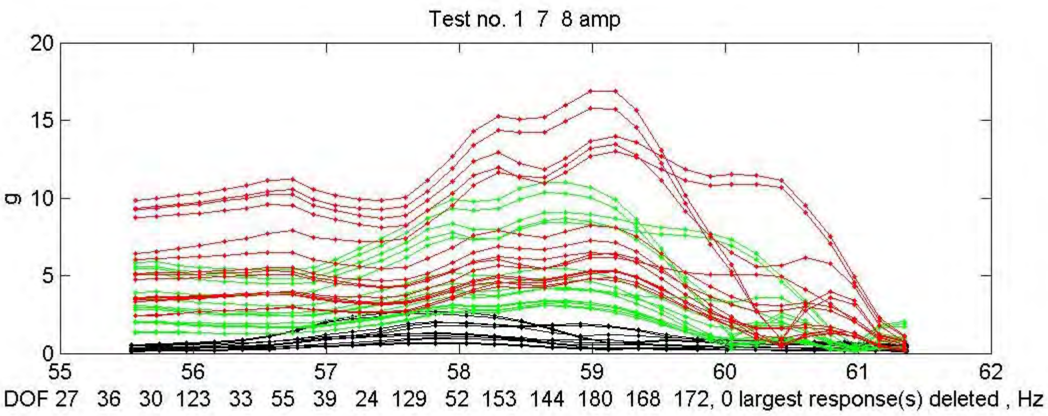

Figure 20: Absolute response amplitudes of the 15 largest DOFs around resonances at 58 Hz low level (black), intermediate level (green), qualification level (red)

At first the modal data in the narrow frequency range around the resonance at about 58 Hz were extracted by linear experimental modal analysis techniques which subsequently were used for interpolation. The results from linear identification of modal parameters from three sets of transmissibilities with x-excitation is summarized in Table 2 and displayed in Figure 21 together with the interpolated data at the additional level. The results of the SWARM linear modal identification shows:

- variation of the resonance frequency between 57 Hz and 58.4 Hz,
- significant change of the damping values with the load level,
- small influence of the load level on the mode shapes (not shown here).

Table 2: Results of SWARM linear modal analysis of three different input levels

Description	Input Level [g]	Eigen-freq. [Hz]	Damping Ratio [%]
Low	0.06	57.00	0.7
Intermediate	0.12	58.14	1.3
Qualification	0.21	58.38	0.5

Using the modal data at the additional load level together with the modal data from the three measured load levels which were used to derive the fix points for the modal data interpolation yields the synthesized transmissibilities shown in Figure 22.

From the results in Figure 22 a very good correlation of the synthesized and experimental response can be observed, not only at those three measured load levels which were used to derive the fix points for modal data interpolation but in particular at the **one additional load level.** The results thus seem to confirm the achievement of the research goal.

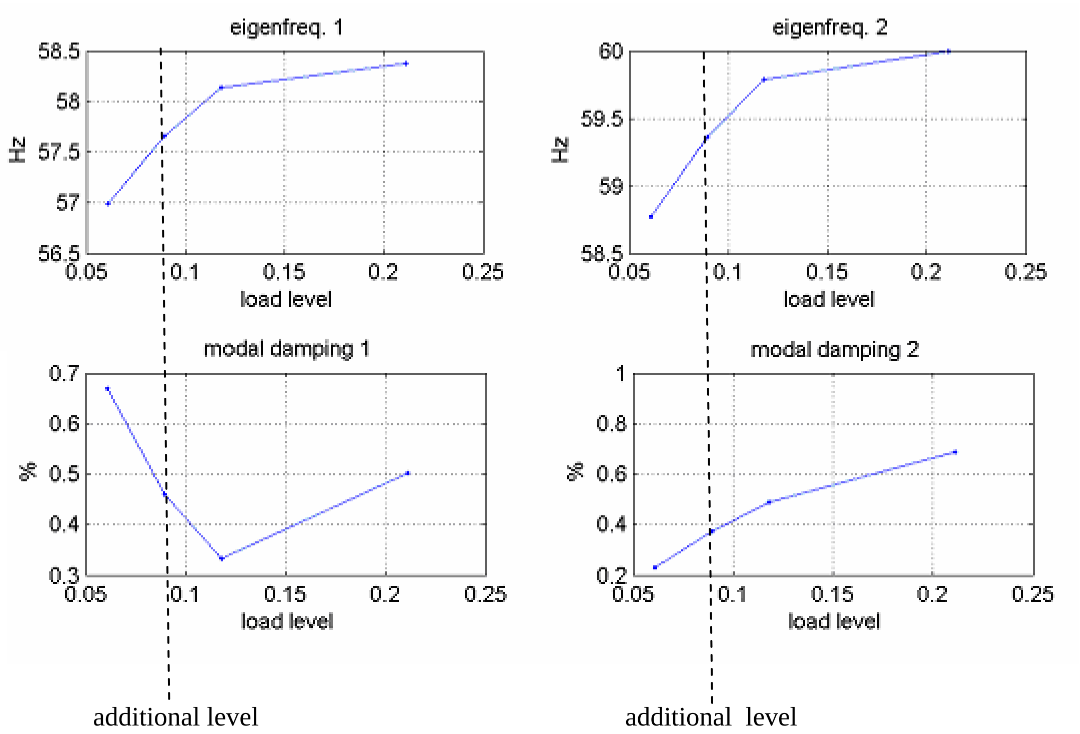

Figure 21: Modal data interpolated at one additional load level

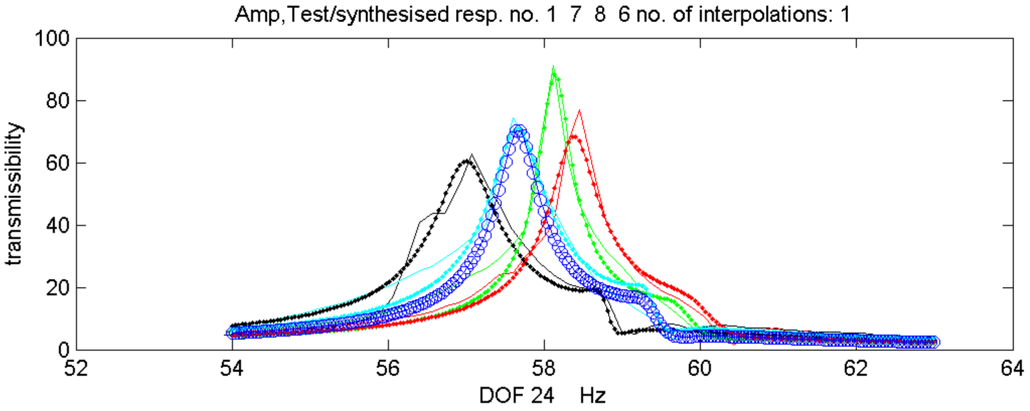

Figure 22: Measured (—) and synthesised (…) transmissibilities for three load levels: low level (black), intermediate level (green), qualification level (red) and ***one additional level*** (sythesized ○-○-○ , measured ——)

5 CONCLUSIONS

Many different tools and methods have been described in the literature for characterization of non-linearities from vibration test data, e.g. in ref. [23]. This paper does not claim to present a comprehensive list of such methods. Instead, selected methods have been presented which either utilize combined analytical/experimental data or experimental frequency domain response data obtained with controlled input levels or controlled output levels. According to the experience of the authors, application of methods for characterization of non-linear systems is largely dependent on the compatibility with standard test processes and the respective results that these processes can provide. It was therefore one of the objectives of the DYNAMITED project to summarize available tools and finally to set up a process for identification of non-linear systems.

Due to response control at selected sensor locations during a vibration test on a shaking table it can be observed that the transmissibilities do not exhibit significant non-linear distortions so that the utilization of classical linear modal extraction tools may be applied separately for each input level. However, the measured dynamic responses (transmissibilities) reveal peak shifts and amplitude changes depending on the notched input level of the base excitation which can be utilized to describe the non-linear behaviour.

The technique described in the paper utilizes this well established industrial test procedure to analyze the non-linearity based on controlled response at three different table acceleration levels all of them assumed to be constant within the notching frequency ranges. The technique (implemented in the ISSPA_NL code) aimed at predicting the responses to ***other than the measured*** input levels which is achieved by applying interpolation and extrapolation techniques to the modal data extracted by classical (linear) experimental modal analysis from the transmissibilities measured at three measured input levels.

The procedure was applied using the test data from a STM satellite structure (Structural Test Model) and also from the SWARM satellite test campaign. For each application one characteristic frequency range was selected exhibiting non-linear behaviour around a dominant resonance. Subsequently, natural frequencies, mode shapes and modal damping values were extracted for each load level within the selected frequency ranges which subsequently were used for inter- or extrapolation and used for predicting the responses at one ore more unmeasured load levels.

It was found that for the first application the predicted indicator functions and the transmissibilities at the two additional (not measured) load levels exhibit a physically meaningful interpolation between the measured levels. In particular this holds for the response prediction for the second application (SWARM satellite), where an additional second intermediate load level was measured but was only used for verification purposes. The good results from both applications thus seem to confirm the achievement of the research goals.

It could be of interest for future research to investigate how the load dependent modal data could be utilized for the parameter identification of a physical non-linear Finite Element model.

REFERENCES

[1] K. Worden, G. Tomlinson: “Nonlinearity in Structural Dynamics – Detection, Identification and Modelling”, Institute of Physics Publishing, Bristol, 2001

[2] K. Vanhoenacker, J. Schoukens, J. Swevers, D. Vaes: “Summary and Comparing Overview of Techniques for the Detection of Non-Linearities”, Proc. of the International Conference on Noise and Vibration Engineering ISMA 2002, Leuven, Belgium, 2002

[3] J. Wong, J.E. Cooper, J.R. Wright: “Detection and Quantification of Structural Non-Linearities”, Proc. of the International Conference on Noise and Vibration Engineering ISMA 2002, Leuven, Belgium, 2002

[4] Göge D., Sinapius M., Füllekrug U. and Link M.: “Detection and Description of Non-linear Phenomena in Experimental Modal Analysis via Linearity Plots”. Int. Journal of Non-linear Mechanics 40, 2005

[5] Ewins D.J.: “Modal Testing: Theory, Practice and Application”, 2nd Ed.. Research Studies Press, Baldock, UK , 2000

[6] Böswald M. and Link M.: “Identification of Non-linear Joint Parameters by Using Frequency Response Residuals”. Int. Modal Analysis Conf. IMAC XXIII, 2005

[7] Gelb A. and Van der Velde W.E.: “Multiple-Input Describing Functions and Nonlinear System Design”, McGraw Hill, 1968

[8] Ehrich F. And Abramson H.N.: “Nonlinear Vibration” in “Shock and Vibration Handbook”, 4th Edition, edited by Harris C.M. McGraw-Hill, New York, 1995

[9] Budak E., Özgüven H.N.: “Iterative receptance Method for Determining Harmonic Response of Structures with Symmetrical Non-Linearities”, Mechanical Systems and Signal processing (MSSP), 7(1), 1993

[10] Gaul L. And Nitsche R.: “Dynamics of Structures with Joint Connections” in “Structural Dynamics 2000 – Current Status and Further Directions”, Ewins D.J. and Inman D. Eds., Research Studies Press, England, 2001

[11] Tomlinson G.R. and Lam J.: “Frequency Response Characteristics of Structures with Single and Multiple Clearance –Type Non-Linerity”, J. Of Sound and Vibration, 96(1), 1984

[12] Meyer S. And Link M.: Local Non-linear Softening Behavior: “Modelling Approach and Updating of Linear and Non-Linear Parameters Using Frequency Response Residuals”. Proc. Of the 21st IMAC, Kissimmee,USA, 2003

[13] Link M., Staples B., Böswald M., Boettcher Th. and Göge D.: “Linking Analysis to Test – Parameter Identification and Validation”. Proc. of the Int. Conference on Noise and Vibration Engineering (ISMA2004), University of Leuven, Belgium, 2004

[14] Maia N.M.M. and Silva J.M.M. Eds., “Theoretical and Experimental Modal Analysis”, Research Studies Press, England, 2000

[15] Masri S.F. and Caughey T.K.: “A Nonparametric Identification Technique for Nonlinear Dynamic Problems”, Journal of Applied Mechanics, Vol. 46, pp. 433-447, 1979

[16] Crawley E.F. and Aubert A.C.: “Identification of Nonlinear Structural Elements by Force-State Mapping”, AIAA Journal, Vol. 24(1), pp. 155-162, 1986

[17] Dimitriadis G.: “Experimental Validation of the Constant Level Method for Identification of Nonlinear Multi Degree of Freedom Systems”, Proc. of the 14th International Congress on Condition Monitoring and Diagnostic Engineering Management, Manchester, UK, 2001

[18] Wright J.R., Platten M.F., Cooper J.E. and M. Sarmast M.: “Identification of Multi-Degree of Freedom Weakly Non-Linear Systems using a Model based in Modal Space”, Proc. of the International Conference on Structural System Identification, Kassel, Germany, 2001

[19] Göge D., Sinapius M., Füllekrug U. and M. Link M.: “Detection and Description of Non-Linear Phenomena in Experimental Modal Analysis Via Linearity Plots”, International Journal of Non-Linear Mechanics, No. 40, pp. 27-48, 2005

[20] ISSPA User’s Manual: http://www.uni-kassel.de/fb14/leichtbau/downloads/

[21] http://www.esa.int/esaMI/Operations/SEM27Z8L6VE_0.html

[22] Böswald M., Göge D., Füllekrug U., Govers Y.: “A Review of Experimental Modal Analysis Methods with respect to their Applicability to Test Data of Large Aircraft Structures”, Proc. of the International Conference on Noise and Vibration Engineering ISMA 2006, Leuven, Belgium, 2006

[23] Kerschen G., Worden K., Vakakis A., Golinval JC.:“Past, Present and Future of Nonlinear System Identification in Structural Dynamics“, Mechanical Systems and Signal Processing, Vol. 20, Issue 3, April 2006, pp. 505-592

COMPDYN 2011
III ECCOMAS Thematic Conference on
Computational Methods in Structural Dynamics and Earthquake Engineering
M. Papadrakakis, M. Fragiadakis, V. Plevris (eds.)
Corfu, Greece, 25–28 May 2011

IN-PLANE DESIGN LOADS FOR SEISMIC ASSESSMENT AND RETROFIT OF WALLS IN UNREINFORCED MASONRY BUILDINGS

Jason M. Ingham[1], Charlotte L. Knox[2], Aaron W. Wilson[3], and Kenneth J. Elwood[4]

[1] Department of Civil and Environmental Engineering, The University of Auckland
Private Bag 92019, Auckland, New Zealand
e-mail: j.ingham@auckland.ac.nz

[2] Department of Civil and Environmental Engineering, The University of Auckland
Private Bag 92019, Auckland, New Zealand
Ckno015@aucklanduni.ac.nz

[3] Department of Civil and Environmental Engineering, The University of Auckland
Private Bag 92019, Auckland, New Zealand
Awil222@aucklanduni.ac.nz

[4] Department of Civil Engineering, University of British Columbia
6250 Applied Science Lane, Vancouver, BC, V6T 1Z4, Canada
elwood@civil.ubc.ca

Keywords: Unreinforced masonry, Flexible diaphragms, Seismic Loads, Design guide.

Abstract. *It is well established and routinely observed that unreinforced masonry buildings perform poorly in large earthquakes. This knowledge directly points to the need for a detailed procedure for the seismic assessment and retrofit of unreinforced masonry buildings. Pivotal to the entire assessment and retrofit process is the accurate treatment of the dynamic characteristics of flexible timber floor diaphragms, and the development of a straightforward and accurate method for determining the in-plane seismic loads on walls when accounting for both excitation due to self weight, and seismic demand transmitted via wall-diaphragm connections.*

Pertinent details of the M7.1 2010 Darfield (Canterbury) earthquake are presented, followed by a review of results from a large scale experimental program that investigated the strength and stiffness characteristics of timber diaphragms. Next, details are provided of a procedure for determining diaphragm dynamic characteristics recognizing that diaphragm deformations are primarily associated with shear rather than flexure. Finally, details are summarised of a methodology now adopted in New Zealand for determining the in-plane seismic demand on unreinforced masonry walls.

1 INTRODUCTION

Unreinforced masonry (URM) buildings represent the predominant architectural heritage of many nations, and outside of Europe were typically constructed with solid clay brick perimeter walls and comparatively flexible timber floor diaphragms. Unfortunately the preservation of these buildings in seismically active regions is threatened due to their well established inadequacy to withstand earthquakes, as recently demonstrated again in the 2010 Darfield earthquake, which was the largest natural disaster to occur in New Zealand since the 1931 Hawke's Bay earthquake. Observed damage in the earthquake included toppled chimneys and parapets, failure of gables and poorly secured face-loaded walls, and in-plane damage to masonry frames.

Timber floor diaphragms are widely recognized to have significant impact on the overall seismic response of URM structures, and the accurate assessment of diaphragms is therefore crucial during the seismic assessment and retrofit of URM buildings. A series of full-scale diaphragm tests that were performed to generate data to aid in understanding the dynamic characteristic of flexible timber diaphragms is presented.

When compared to the URM buildings of most countries worldwide, the URM building stock in New Zealand is comparatively homogeneous in terms of age, material properties, and architectural form. This observation presents an opportunity to develop a detailed seismic assessment guideline for these buildings that has the dual goals of providing clarification on the appropriate method for deploying existing recommendations, plus incorporating new research results to arrive at the most accurate assessment of seismic capacity currently possible. Such an exercise allows the seismic strength of the URM building to then be expressed in terms of the „percentage of New Building Strength' (%NBS) and to establish whether seismic improvement of the building is necessary.

2 OVERVIEW OF THE 2010 DARFIELD EARTHQUAKE

2.1 Introduction

At 4.35 am on the morning of Saturday the 4th of September 2010 a magnitude 7.1 earthquake occurred approximately 40 km west of the city of Christchurch NZ at a depth of about 10 km [1], having an epicentre located near the town of Darfield. The ground motion had a peak ground acceleration of about 0.25g and a spectral acceleration in the plateau region of about 0.75g, which corresponds well with the design spectra for a site class D soil site in Christchurch for spectral periods greater than 0.2 seconds. In general, the earthquake represented 67-100% of the design level event, depending upon the spectral period being considered (see Figure 1), with most of Canterbury reporting damage consistent with MM8 on the Modified Mercalli intensity scale. The single most striking statistic was that there were no fatalities directly associated with the earthquake (although there was one heart attack fatality and one person hospitalised due to a falling chimney [2], and the overall impression is that damage in the central business district (CBD) was reasonably contained, restricted primarily to URM buildings and damage to windows in taller steel and concrete structures. The absence of fatalities and more extensive damage was attributed to the comparatively high level of seismic design capability in New Zealand, and the fact that the CBD, which is the region containing the highest density of URM buildings, was almost completely unoccupied at 4.35 am [3].

The soil conditions in Christchurch have three separate material types: river outwash gravels, sands, and marshy ground in former swamp areas, with the central city built mainly on gravels, although there are pockets of sand and soft soil in former marsh deposits. The earthquake ground motion characteristics shown in Figure 1 reflect the underlying soil condition, with the long period nature of the motion resulting from the soft soils upon which Christchurch is founded. These soft soils effectively act as a filter and remove high frequency ground motion (leading to smaller PGA values than on rock sites) but amplify long period motion, resulting in significantly larger longer period motion at about 2.5 second. As most URM buildings have a fundamental period of 0.2-0.3 seconds, the underlying ground conditions appear to have assisted in reducing the seismic demand in this period range to approximately 70% of the design level loading stipulated in the current New Zealand Loadings Standard. As can be seen in Figure 1(b), strong ground shaking in the CBD had a duration of approximately 30 seconds with similar amplitudes in the two orthogonal recording directions. This lack of distinct directionality probably explains why parapet failures were observed in streets running in both the North-South and East-West directions.

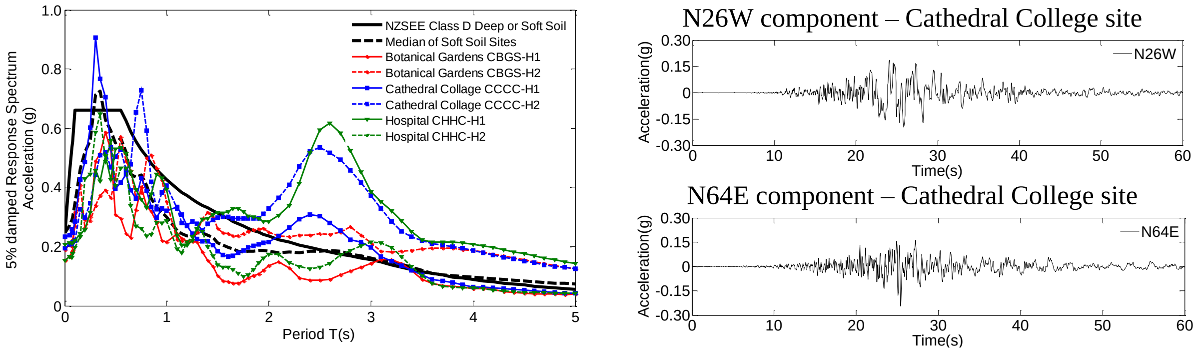

(a) Acceleration spectra

(b) Acceleration time-history record

Figure 1: Details of earthquake ground motion [2]

2.2 Building Damage Statistics

In general, the observed damage to URM buildings in the 2010 Darfield Earthquake was consistent with the expected seismic performance of this building form [4]. As part of the emergency response to this earthquake, building were tagging with either a green, yellow or red placard depending, respectively, upon whether a building was safe for public use, had limited accessibility for tenants/occupants, or was not accessible. Many examples of earthquake damage were observed during this exercise, as well as many examples of seismic retrofits to URM buildings that had performed well [5].

2.3 Parapet failures

Numerous parapet failures were observed along both the building frontage and along their side walls, and for several URM buildings located on the corners of intersections, the parapets collapsed on both perpendicular walls (refer Figure 2). Restraint of URM parapets against lateral loads has routinely been implemented since the 1940s, so whilst it is difficult to see these restraints unless roof access is available, it is believed that the majority of parapets that exhibited no damage in the earthquake were provided with suitable lateral restraint. In several cases, it appears that parapets were braced back to the perpendicular parapet, which proved unsuccessful.

2.4 Anchorage failures

Falling parapets typically landed on awnings, resulting in an overloading of the braces that supported these awnings and leading to collapse. Most awning supports in Christchurch involved a tension rod tied back into the building through the front wall of the building. Many of these connections appear to consist of a long, roughly 25 mm diameter rod, with a rectangular steel plate (about 5 mm thick) at the wall end that is about 50 mm wide x 450 mm long and fastened to the rod and positioned either inside the brick wall or in the centre of a masonry pier or wall. In most cases the force on the rod exceeded the capacity of the masonry wall anchorage, causing a punching shear failure in the masonry wall identified by a crater in the masonry (refer Figure 3).

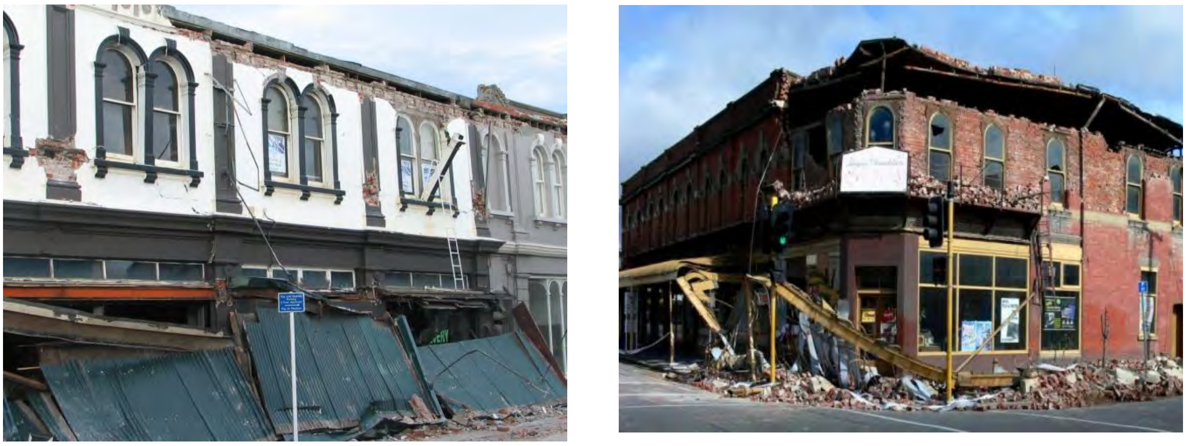

(a) Multiple front wall parapet failures

(b) Corner of Sandyford and Colombo Street

(c) Side wall parapet collapse onto roof.

(d) Corner Columbo and Tuam Street

Figure 2: Examples of typical parapet failures.

2.5 Wall failures

Out-of-plane wall failures were the first images to appear on television directly after the earthquake. Inspection of this damage typically indicated poor or no anchorage of the wall to its supporting timber diaphragm. Several examples of wall failure are shown below. Figure 4(a) shows a corner building that had walls fail in the out-of-plane direction along both directions. Figure 4(b) shows a 3-storey building where walls in the upper two stories suffered out-of-plane failures and Figure 4(c) shows similar damage for a 2-storey building. In all three of these instances, it appears that the walls were not carrying significant vertical gravity loads, other than their self weight, due to the fact that the remaining roof structures appear to be primarily undamaged. In contrast, Figure 4(d) shows an out-of-plane failure of a side wall which was supporting the roof trusses prior to failure.

3 FLEXIBLE TIMBER DIAPHRAGMS

While URM buildings outside of Europe are typically comprised of rigid clay brick perimeter walls, the floors are usually constructed of comparatively light timber framing. These floors are generally made up of either straight-edge or tongue & groove floorboards nailed perpendicular to joists that span between the URM walls. When perimeter walls are close enough (approximately less than 6 m) joists often span continuously between these elements. For larger spans, joists are typically lapped or butted over intermediate steel or timber cross-beams supported on columns. Diaphragm blocking and chord elements are almost never present, and timber cross-bracing is typically fitted intermittently between joists to prevent out-of-plane buckling. Joist ends are typically either simply supported on a brick ledge resulting from the perimeter walls reducing in width at each storey height, or pocketed into the wall to a depth equal to one brick width. Examples of timber floor configurations are given in Figure 5.


(a) Anchorage failure (b) Close-up of failed anchorage detail

Figure 3: Anchorage failure of awning brace due to parapet collapse.

Timber floors in URM buildings act as diaphragms that have routinely demonstrated significant influence on the seismic performance of the complete URM structure due to their flexible nature and often inadequate connection to the perimeter URM walls [6] (Bruneau 1994). The in-plane strength and stiffness of these diaphragms is therefore crucial to the overall performance of the URM building and accurate assessment of their performance is essential for the design of appropriate retrofitting techniques when seismic strengthening is required. Due to a complete lack of experimental data and appropriate analysis [7-9], the validity of diaphragm assessment procedures offered in current state-of-the-art assessment documents [10-11] are questionable. Furthermore, communication from engineering practitioners suggests that such documents are difficult to understand and to follow with confidence. Given these shortcomings, significant motivation currently exists to investigate the performance of timber floor diaphragms and the accuracy of assessment procedures. Before non-destructive testing techniques are considered as a viable assessment tool, it is necessary to generate in-plane performance data for timber diaphragms with which to appropriately update and improve current seismic assessment desktop procedures.

Results of a series of full-scale diaphragm tests are summarized and are used to review the validity of the current desktop assessment procedures published in [10] and [11]. Performance predictions using the assessment techniques are compared against experimental results and where possible, recommendations to improve their accuracy are suggested.

3.1 As-built diaphragm testing

A total of four diaphragm specimens labeled FS1a to FS4a, constructed with new pine timber, were tested. Each specimen measured 10.4 m x 5.535 m and was comprised of 135 mm x 18 mm straight edge floorboards nailed perpendicular to 45 mm x 290 mm joists spaced at 400 mm centers. Joists were orientated in the 5.535 m dimension. Cross-bracing was fitted between the joists at 1/3 joist length locations using 45 mm x 75 mm framing. Every floorboard-joist connection was fastened using two 75 mm x 3.15 mm bright power driven nails spaced at approximately 95 mm.

(a) Corner Worcester and Manchester streets

(b) 118 Manchester Street

(c) 179 Victoria Street

(d)

Figure 4: Examples of out-of-plane failures in solid masonry walls.

Diaphragms FS1a and FS2a were tested in the direction parallel to joists so that the diaphragm span to depth ratio was 1.88 to 1. In this direction the two side joists were bolted to steel frames that were fastened to the warehouse concrete slab which replicated in-situ boundary conditions where the edge joists would simply be bolted intermittently to the perimeter URM walls (see Figure 6(a)). Lateral loading was introduced into the diaphragm using a hinged steel frame „whiffle tree’ on castors that distributed the hydraulic actuator point load into four equal point loads. It can be observed in Figure 6(b) that the loading frame was comprised of a main truss and two secondary beams that were capable of rotating with the deforming diaphragm. Reversed cyclic loading was achieved by positioning loaders on both ends of the loaded joists, and post-tensioning these loaders together using M16 threaded rods that spanned the depth of the diaphragm (Figure 6(b)). The diaphragm was supported vertically by Teflon pads that allowed the diaphragm to deform laterally without measurable friction. Diaphragm FS1a shown in Figure 6(a) was a homogenous diaphragm while diaphragm FS2a shown in Figure 6(c) included a corner penetration measuring 3.2 m x 1.08 m that represented a typical stairwell present in many timber diaphragms.

Diaphragms FS3a and FS4a were tested in the direction perpendicular to joists so that the diaphragm span to depth ratio was 1 to 1.88. Realistic conditions were created for this set-up by constructing URM walls on each side of the diaphragm for the joists to pocket into, similar to that illustrated in Figure 5(b). Sliding of the brick walls was prevented by post-tensioning the walls with M16 rods epoxied into the warehouse concrete slab (measurement of wall position during testing showed that no wall displacement was observed). Loading was introduced into the diaphragm using the same hinged steel frame as for the previous set-up but with only two points of loading. Diaphragms FS3a and FS4a were equivalent in construction except that diaphragm FS3a had continuous joists spanning between the brick walls while diaphragm FS4a had discontinuous joists with a two-bolt lapped central connection.

(a) Underside showing joists, sheathing and cross-bracing

(b) Joists pocketed into URM perimeter wall

Figure 5: Typical timber diaphragm configuration

3.2 Test Results

Overall the diaphragms displayed flexible and highly nonlinear characteristics with low levels of hysteretic pinching, as illustrated in the force versus midspan displacement plots in Figure 7. The open hysteretic loops demonstrate that these diaphragms are capable of dissipating considerable amounts of energy when subject to lateral loading. No splitting of timber, nail tear-out or other failure mechanisms were observed during testing, even at displacements in excess of 150 mm, and all diaphragms appeared to remain completely serviceable at the conclusion of each test.

A comparison of the force-displacement responses of specimens FS2a and FS1a suggests that a small diaphragm opening such as a stairwell does not significantly affect the diaphragm’s performance, with these responses being largely indistinguishable. It is appreciated that larger penetrations may worsen this effect however. Another interesting observation is that diaphragms FS3a and FS4a behaved analogously despite the presence of a central discontinuity in the joists in diaphragm FS4a. This could be explained by the deformation profile of the diaphragms displaying little amounts of relative displacement between the two point-load locations. With the majority of deformation occurring in the outer regions of the diaphragm, the curvature near the centralized joist connection was low and therefore considerably reduced its effect on diaphragm response.

(a) Diaphragm FS1a

(b) Loading frame set-up

(c) Penetration in Diaphragm FS2a

(d) Diaphragm FS3a/4a

Figure 6: Experimental program

It is difficult to directly compare force-displacement response between the two principal loading directions due to the influence of diaphragm geometry. Diaphragms FS3a and FS4a demonstrated greater stiffness and strength than FS1a and FS2a, but this is clearly due to a considerably lower span to depth ratio. As a general observation, the hysteretic loops are larger in the direction parallel to joists which could result from greater engagement of the yielding nail couples in this direction as opposed to loading in the direction perpendicular to joists, where the nail couples are less engaged and the out-of-plane bending of the joists has greater influence on response.

Figure 8 shows the bilinear curves produced for diaphragm tests FS1a to FS4a. The bilinear curves defined the yield force (F_y), yield displacement (Δ_y), maximum force at $\Delta = 150$ mm (F_{max}), and initial and secondary stiffness (K_1 and K_2) values presented in Table 2 that were used to calculate the desired diaphragm performance parameters. Diaphragm stiffness K_d was defined as initial stiffness K_1 while shear strength R_n was calculated by simply dividing yield force by two times the diaphragm depth. Ductility was determined using the conventional assumption of elastic-perfectly plastic response and calculating the ratio between maximum displacement and yield displacement. These values are presented in Table 1 for comparison.

	Shear strength, R_n [kN/m]				***Stiffness K_d*** [kN/m]			***Shear stiffness, G_d*** [kN/m]			***Ductility, μ***		
	NZSEE (i)	NZSEE (ii)	ASCE	Exp	NZSEE	ASCE	Exp	NZSEE	ASCE	Exp	NZSEE	ASCE	Exp
FS1a	1.4	6.0	1.75	1.6	207	745	647	97	350	304	-	2.0	5.6
FS2a	1.4	6.0	1.75	1.6	207	745	606	97	350	284	-	2.0	5.2
FS3a	1.4	6.0	1.75	1.2	730	2630	1297	97	350	173	-	2.0	7.7
FS4a	1.4	6.0	1.75	1.2	730	2630	1842	97	350	245	-	2.0	10.8

Table 1: Diaphragm performance parameters

	F_y [kN]	Δ_y [mm]	F_{max} [kN]	Δ_{max} [mm]	K_1 [kN/m]	K_2 [kN/m]
FS1a	17.2	26.6	36.8	150	647	159
FS2a	17.6	29.1	35.9	150	606	151
FS3a	25.4	19.6	110.0	150	1297	649
FS4a	25.7	13.9	104.3	150	1842	578

Table 2: Experimental bilinear values

3.3 Discussion

Overall, the guidelines offered in both assessment documents poorly predict diaphragm performance. The values listed in Table 1 illustrate that diaphragm shear strength, stiffness, shear stiffness and ductility are either under predicted or over predicted using the NZSEE [10] and ASCE 41-06 [11] assessment procedures. Shear strength is the most accurately predicted parameter with approximately 10% discrepancy from experimentally determined values, with the exception of the alternative default value offered by NZSEE that grossly over estimates strength. The reason for this large discrepancy remains unknown. Diaphragm stiffness and shear stiffness is considerably under predicted using the methodology in NZSEE, while is over predicted using ASCE 41-06 guidelines. NZSEE offers no explicit guidance for diaphragm ductility while ASCE 41-06 provisions where shown to under estimate diaphragm ductility by up to five times.

An important observation from the experimental performance parameters listed in Table 1 is the highly orthotropic behavior demonstrated by the timber diaphragms. The shear strength and shear stiffness values, which are independent of diaphragm geometry, are significantly different in each principal direction of the diaphragm, yet the current assessment documents offer no provisions to address this behavior. In order to improve the transparency and accuracy of the assessment procedures, diaphragm performance parameters should be explicitly provided for in each principal direction.

It is recognized that heritage diaphragm performance may differ from the experimental performance values presented in Table 1 due to out-dated construction materials and the effects of age and decay. A component of the current research program involves testing extracted floor sections and nail connections from ~100 year old timber floor diaphragms. It is hoped that the data generated from testing will provide the necessary information to appropriately modify the performance parameters to ensure they are representative for heritage construction. For the interim, the considerable difference observed between predicted and measured diaphragm performance suggests that the current procedures offered in NZSEE and ASCE 41-06 require updating. In addition, it is believed that these documents should be harmonized so that international assessment procedures are consistent with one another.

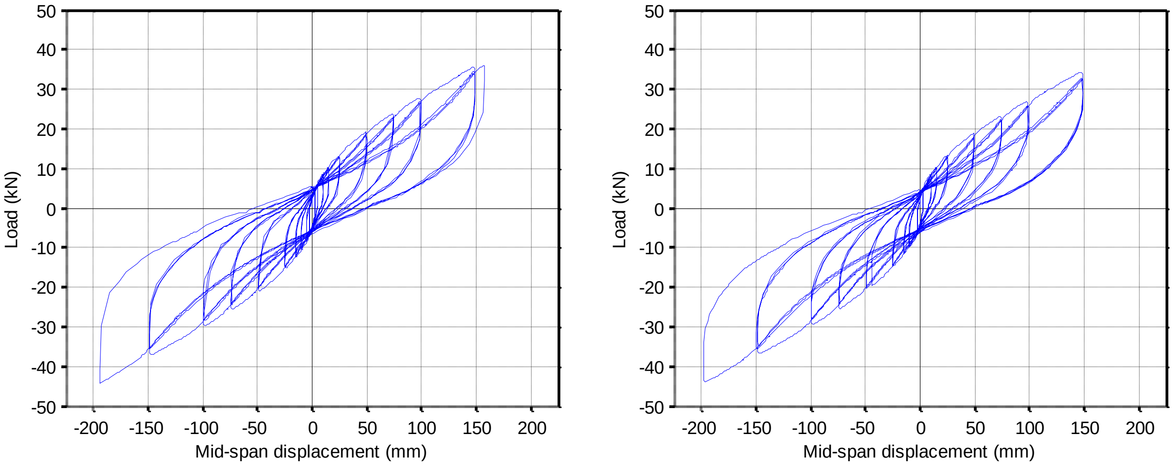

(a) Diaphragm FS1a

(b) Diaphragm FS2a

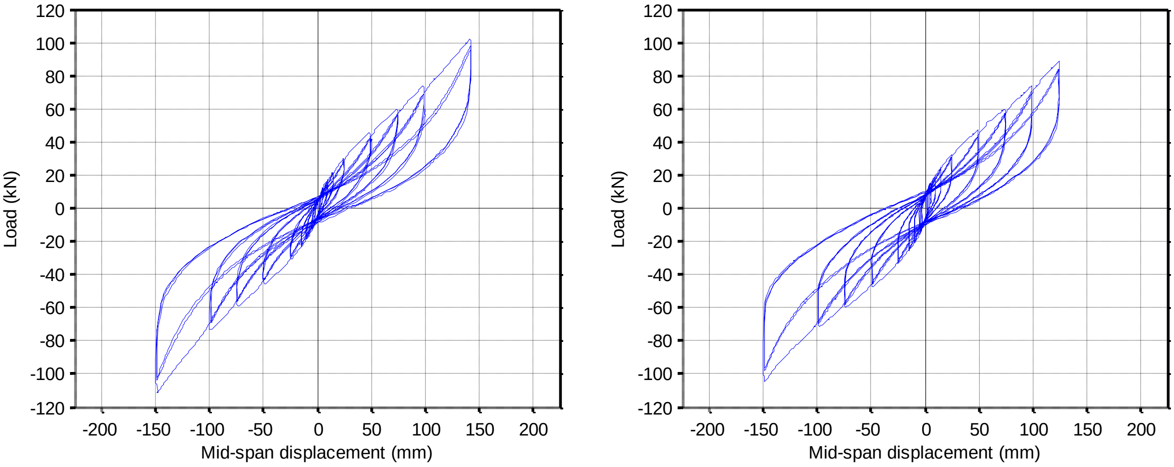

(c) Diaphragm FS3a

(d) Diaphragm FS4a

Figure 7: Full-scale diaphragm testing results

4 PERIOD OF FLEXIBLE DIAPHRAGM

Common assessment guides [10, 11] stipulate a diaphragm fundamental period that is calculated as:

$$T = \sqrt{3.07\Delta_d} \tag{1}$$

However neither document clarifies the source of this equation, and as period values derived using Equation 1 can appear somewhat questionable, it is useful to outline the derivation of this equation. If we consider a fixed-ended flexural beam with distributed mass, then the deformed shape and mid-span deflection are as shown in column 1 of Table 3. Note that the period calculation is independent of the magnitude of applied acceleration, but that for convenience it is useful to evaluate deflections when subjected to gravity acceleration, g, even though horizontal deformations are being considered in the plane of the diaphragm, rather than vertical deflections due to sagging. As outlined in [12], a shape function can be used to describe the beam deformations, which can then be used to develop a generalised mass $m^* = \int_0^L \bar{m}\varphi(x)^2 dx$ and generalised stiffness $k^* = \int EI\varphi''(x)^2\, dx$ (for flexural) or $k^* = \int_0^L \frac{GA}{\kappa}\varphi'(x)^2\, dx$ (for shear). This information can then be introduced to the generalised period equation to obtain a specific expression for the period.

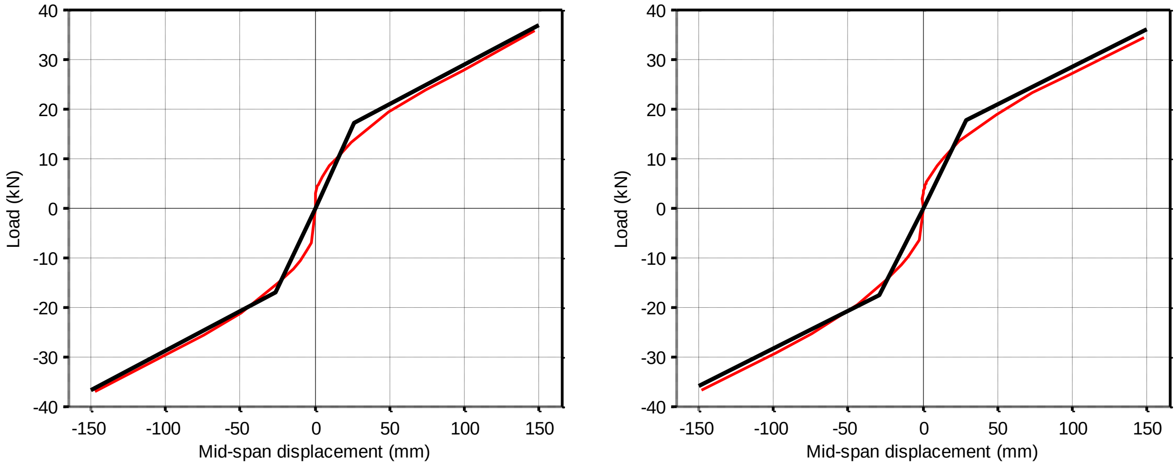

(a) Diaphragm FS1a

(b) Diaphragm FS2a

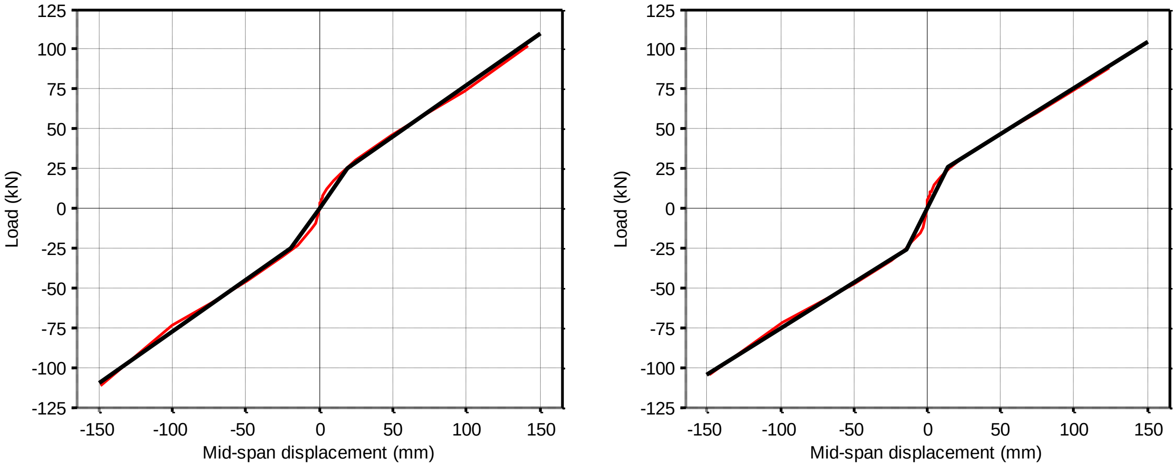

(c) Diaphragm FS3a

(d) Diaphragm FS4a

Figure 8: Bilinear curves for tested as-built diaphragms

Whilst the above discussion satisfactorily explains the origin of the equation in [10-11], there are several further issues to consider. Firstly, the assumption of the diaphragm having a fixed boundary condition when connected to the in-plane walls is inconsistent with the nature of most diaphragm connection details, and the corresponding period calculations for a pin-ended flexural beam would appear to be more realistic. This information is provided in column 2 of Table 1, illustrating that the boundary effects had an inconsequential influence on the equation coefficient, but a 230% change on the calculated period. More importantly, as flexible diaphragm deformations are governed by shear deformations rather than flexural deformations. Hence the corresponding process is presented in column 3 of Table 3, showing that again this modification has had only a small impact on the coefficient used in the period

	Fixed end flexural beam	**Pin ended flexural beam**	**Shear beam**
Deflected geometry, δ(x)	$\delta(x)=\frac{\bar{m}gx^2}{24EI}(L-x)^2$	$\delta(x)=\frac{\bar{m}gx}{24EI}(x^3-2Lx^2+L^3)$	$\delta(x)=\frac{\bar{m}g\kappa}{GA}\left(\frac{L}{2}x-\frac{x^2}{2}\right)$
Maximum deflection	$\Delta_{ff}=\frac{\bar{m}gL^4}{384EI}$	$\Delta_{pf}=\frac{5\bar{m}gL^4}{384EI}=5\Delta_{ff}$	$\Delta_{sb}=\frac{\bar{m}g\kappa L^2}{8GA}$
Shape function	$\varphi(x)=\frac{16x^2}{L^4}(L-x)^2$	$\varphi(x)=\frac{16x}{5L^4}(x^3-2Lx^2+L^3)$	$\varphi(x)=\frac{8}{L^2}\left(\frac{Lx}{2}-\frac{x^2}{2}\right)$
Generalised mass	$m^*=\frac{256}{630}m$	$m^*=\frac{23808}{47250}m$	$m^*=\frac{8}{15}m$
Generalised stiffness	$k^*=\frac{1024}{5}\frac{EI}{L^3}$	$k^*=\frac{36864}{750}\frac{EI}{L^3}$	$k^*=\frac{16}{3}\frac{GA}{L\kappa}$
General period expression	$T=2\pi\sqrt{\frac{m^*}{k^*}}$	$T=2\pi\sqrt{\frac{m^*}{k^*}}$	$T=2\pi\sqrt{\frac{m^*}{k^*}}$
Specific period expression	$T=\sqrt{3.07\Delta_{ff}}$ $=1.75\sqrt{\Delta_{ff}}$ $=1.75\sqrt{\frac{\omega L^4}{384EI}}$ $=0.0894\sqrt{\frac{\omega L^4}{EI}}$	$T=\sqrt{3.17\Delta_{pf}}$ $=\sqrt{15.85\Delta_{ff}}$ $=1.78\sqrt{\frac{5\omega L^4}{384EI}}$ $=0.2032\sqrt{\frac{\omega L^4}{EI}}$	$T=\sqrt{3.21\Delta_{sb}}$ $=1.79\sqrt{\Delta_{sb}}$ $=1.79\sqrt{\frac{\omega L^2}{4G_d b}}$ $=0.8958\sqrt{\frac{\omega L^2}{G_d b}}$

Table 3: Period of flexible diaphragm accounting for boundary effects and deformation modes

calculation. The deflection used in column 3 is consistent with calculated diaphragm deflections according to [11]:

$$\Delta_d=\frac{\bar{m}gL^2}{4G_d b}=\frac{\omega L^2}{4G_d b} \tag{2}$$

In Equation 2 it is important to appreciate that G_d refers to a shear stiffness (having units of kN/m), whereas in the derivation in Table 1, G refers to the Shear Modulus (having units of MPa or kN/m^2). By equating the resulting mid-span deflections and recognising that the shape factor κ = 1.2 for rectangular sections, we arrive at the relationship:

$$G_d=\frac{2Gt}{\kappa}=\frac{5Gt}{3}=1.667Gt \tag{3}$$

where t is the diaphragm thickness.

5 IN-PLANE LOADS ON SHEAR WALLS

The in-plane loads on shear walls are calculated from two components, one based on the diaphragm response, and the other based on the wall in-plane response. The dynamic response of a multi-storey unreinforced masonry building with flexible diaphragms is concentrated in the diaphragms. The equivalent static method assumes that the in-plane wall is rigid in comparison to the flexible diaphragm for the purpose of calculating the inertial force induced in the diaphragm. Adequate connections between the diaphragm and the in-plane loaded walls are required in order to transfer the inertial force induced in the diaphragms and the out-of-plane loaded walls into the in-plane loaded walls. The wall in-plane response component is based on the shear wall behaving in its fundamental mode. For solid shear walls, calculation of the elastic stiffness and therefore period is relatively simple, but for the case of perforated walls this calculation is much more complicated and hence the recommendation that the in-plane loaded wall period is assumed to lie in the constant acceleration region of the response spectra.

5.1 Damping

Unreinforced masonry does not respond is a classical elastic-plastic manner, exhibiting more of a nonlinear elastic response with pinched hysteretic loops. From analysis of full scale pseudo-static tests on in-plane loaded flanged walls and spandrel/pier sub-structures, a range of 5-15% equivalent hysteretic damping was found. The past recommendation of 15% of critical was formed from a combination of approximately 5% inherent viscous damping associated with elastic structures, 5% hysteretic damping and 5% damping from dynamic impact [10]. The hysteretic damping includes Coulomb (or “dry”) damping associated with sliding shear, radiation damping, pinched hysteretic damping associated with flexural/diagonal shear softening and equivalent damping due to impact on rocking. The current recommendation of 5% is supported by the increase in displacement ductility recommended for use in finding demand on in-plane loaded URM shear walls which allows for a reduction in loads based on nonlinear behaviour. The recommendation of 5% of critical is based on the understanding that the increase in ductility to 2, and the reduction due to the structural performance factor, allows for the reduction in load due to nonlinear response and therefore the reduction would be two-fold if damping was also increased.

5.2 Ductility

Unreinforced masonry is generally considered a brittle material and therefore it has been justified in the past to use a displacement ductility factor of 1. The notion of URM as a brittle material is inaccurate and conservative. Ductility is present not from conventional yielding of steel reinforcing bars, but from inelastic response and energy dissipation due to shear sliding along mortar joints and rocking of masonry block elements. When URM walls respond in-plane, particularly with a rocking mechanism, there is significant inelastic displacement capacity and a strongly nonlinear behaviour. A typical shear response is shown in Figure 9(a), and shows no rapid and severe strength loss as associated with a typical brittle failure. The force-displacement plot associated with pier and pier/spandrel sub-structure testing indicates that a flexural failure mechanism, or a flexural/shear combined failure mechanism, is capable of ultimate displacements that greatly exceed the yield displacement, as shown in Figure 9(b). URM buildings have multiple sources of ductility that develop from energy dissipation drawn from shear mechanisms in the in-plane loaded walls, rocking of in-plane loaded URM elements, and energy dissipation from deformations of the timber diaphragms. The recommendation for using a displacement ductility of 2 recognises the nonlinear response of URM walls to in-plane loading and the energy dissipation that occurs during loading cycles beyond the elastic state.

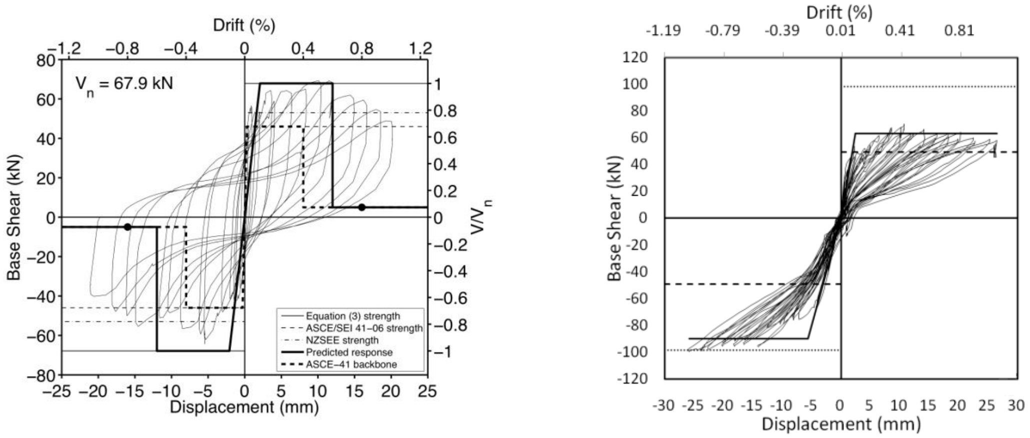

(a) URM pier

(b) URM spandrel substructure

Figure 9: Plots of Force-displacement response of URM assemblages

5.3 Vertical Distribution of Inertial Shear Load

A rectangular distribution of the inertial shear load vertically up the height of the building reflects the assumption of effectively rigid wall response in comparison to the flexible diaphragm response. A rectangular distribution implies no modification of the ground accelerations up the height of the wall. Storey shear load is the addition of the diaphragm shear load and the component of in-plane inertial shear load distributed to that level using the Square Root of Sum of Squares rule. Summation of the inertial storey shear load and the individual diaphragm shear loads using a CQC or SRSS method allows for the individual elements to respond at different periods and therefore not necessarily in phase.

6 CONCLUSIONS AND RECOMMENDATIONS

- The significant number of URM buildings damaged in the 2010 Darfield earthquake was consistent with the level of damage that can be expected for an earthquake of this scale.
- The types of failure modes to URM buildings that were observed in the 2010 Darfield earthquake are consistent with those routinely observed in previous last earthquakes.
- Timber floor diaphragms have proven to significantly influence the overall seismic performance of URM buildings.
- Stiffness sand strength data generated from a series of full-scale diaphragm tests will lead to improved accuracy of dynamic modeling of URM buildings.
- Diaphragm deformations are governed by shear deformations rather than flexure deformations.
- In-plane loads on URM walls are comprised of inertial loads and diaphragm transfer loads.

ACKNOWLEDGMENTS

The authors would like to gratefully acknowledge Stuart Oliver of Holmes Consulting Group for his continued guidance, and David Moore of Grayson Engineering and Warwick

Banks of Carter Holt Harvey Woodproducts for their generous support that ensured the successful completion of the flexible diaphragm experimental program reported herein.

REFERENCES

[1] GNS, Darfield earthquake damages Canterbury, http://www.geonet.org.nz/news/article-sep-4-2010-christchurch-earthquake.html, 16 Sept 2010; Retrieved Sept 16, 2010.

[2] NZ Herald, Christchurch earthquake victim: 'I was pinned to the ground', *New Zealand Herald*, http://www.nzherald.co.nz/nz/news/article.cfm?c_id=1&objectid=10673369; Sept 14 2010; Retrieved Sept 20, 2010.

[3] J.M. Ingham, M.C. Griffith, Performance of unreinforced masonry buildings during the 2010 Darfield (Christchurch, NZ) earthquake. *Australian Journal of Structural Engineering*, **In Press**, 2011.

[4] A.P. Russell, J.M. Ingham, Prevalence of New Zealand's Unreinforced Masonry Buildings. *Bulletin of the New Zealand Society for Earthquake Engineering,* **43**(3), 182-201, 2010.

[5] D. Dizhur, N. Ismail, C.L. Knox, R. Lumantarna, J.M. Ingham, Performance of Unreinforced and Retrofitted Masonry Buildings during the 2010 Darfield Earthquake. *Bulletin of the New Zealand Society for Earthquake Engineering,* **43**(4), 321-339, 2010.

[6] M. Bruneau, State-of-the-art report on seismic performance of unreinforced masonry buildings. *Journal of Structural Engineering*, **120**(1), 230-251, 1994.

[7] ABK, *Methodology for mitigation of seismic hazards in existing unreinforced masonry buildings: Diaphragm testing ABK-TR-03*. National Science Foundation, El Segundo, California, 1981.

[8] D.F. Peralta, *Seismic Performance of Rehabilitated Wood Diaphragms*, PhD Dissertation, Texas A&M University, College Station, Texas, 2003.

[9] M. Piazza, *The Role of In-Plane Floor Stiffness in the Seismic Behaviour of Traditional Buildings*. 14th World Conference on Earthquake Engineering, Beijing, China, October 12-17, 2008.

[10] NZSEE, *Assessment and improvement of the structural performance of buildings in earthquakes : prioritisation, initial evaluation, detailed assessment, improvement measures : recommendations of a NZSEE study group on earthquake risk buildings*, New Zealand Society for Earthquake Engineering, Wellington, New Zealand, 2006.

[11] ASCE. *Seismic Rehabilitation of Existing Buildings, ASCE/SEI 41-06*. American Society of Civil Engineers, Reston, VA, 2007.

[12] A.K. Chopra, *Dynamics of Structures (2nd Ed)*, Prentice Hall, Upper Saddle River, NJ, 2001.

COMPDYN 2011
III ECCOMAS Thematic Conference on
Computational Methods in Structural Dynamics and Earthquake Engineering
M. Papadrakakis, M. Fragiadakis, V. Plevris (eds.)
Corfu, Greece, 25–28 May 2011

SEISMIC REHABILITATION OF TRADITIONAL UN-REINFORCED MASONRY BUILDINGS IN IRAN

Alireza Azarbakht[1]

[1] Assistant Professor, Department of Civil Engineering, Faculty of Engineering, Arak University, Arak, 38156-8-8849, Iran.
e-mail: a-azarbakht@araku.ac.ir

Keywords: Seismic rehabilitation, ASCE 41-06 standard, Un-reinforced masonry building, Steel I-beam jack arch slab, Iran.

Abstract. *Un-reinforced masonry buildings are a major population of residential and school buildings in Iran which have been shown severe damages during past earthquakes e.g. Bam earthquake in 2003 with at least 26000 fatalities. The most important weaknesses of this sort of buildings are coming form the in-adequate lateral load resisting system and the weakness in the element connections. This kind of construction is not (or rarely) used anymore in urban regions. However, any effort for the seismic rehabilitation of the current buildings can save a reasonable amount of life in a future earthquake. That is, a detailed seismic rehabilitation for a typical un-reinforced masonry building in Iran has been described in this paper. The rehabilitation methodology is based on the ASCE 41-06 standard recommendations but adopted in details for the Iranian traditional masonry construction type. The rehabilitation cost is around thirty percent of the re-construction procedure which is quite promising.*

1 INTRODUCTION

Most of the un-reinforced masonry (URM) buildings in Iran have not been engineered whereas constructed based on experiences. Moreover, the construction of URM buildings varies from country to country in many aspects including material properties, layering methods, floor systems, connections and etc. Therefore, despite a considerable amount of research in the behaviour of masonry buildings subjected to the seismic actions carried out in many countries during last decades [1, 2 and 3], it seems difficult to extrapolate the previous research results in order to predict the seismic behaviour of URM buildings in Iran. It is worth to emphasis that most of the researches have been focused on the behaviour of a single URM wall and the corresponding results cannot be extrapolated to the behaviour of a URM structure.

Most URM buildings, which are more than fifty percent of the buildings population in Iran, are characterized by un-reinforced masonry walls and many openings on exterior walls and either a one-way concrete joist slab or a steel I-beam jack arch slab. The traditional URM buildings usually are limited to the two stories with or without a basement. The steel I-beam jack-arch flooring system was, as shown typically in Figure 1, developed in early Victorian Britain and was used to cover large floor areas at warehouses. By the middle of the twentieth century it became a popular flooring system in many Middle Eastern countries. The popularity of this flooring system stems from its relatively low cost and easy construction process. This old system of flooring has shown robustness under normal gravity loading but serious lacks of criteria for an earthquake resistant slab as shown in Figure 2. An example of bam earthquake, from several cases that this kind of flooring system has been collapsed during sever earthquakes, is shown in Figure 2. As a number of advantages, the traditional jack-arch slabs are still very popular in the Middle East, particularly in Iran where even many medium rise steel framed buildings are still floored by this method. Some of these advantages include; simple construction technique, speed in construction, low cost of construction, availability of materials and workmanship and the possibility of altering the slab after construction. The floor slabs, constructed using the steel I-beam jack arch system, are stable under normal static conditions as the brick arches transfer the gravity loads mainly in compression along the arch to the supporting beams. The load is then transferred along the unconnected parallel steel beams to the supporting walls or beams. The geometric form of the steel I-beam jack-arch system and the load path through the steel beams make the slab act as a one-way system. For the purpose of simplicity the total dead load is usually assumed to be used for the design of the steel beams whereas the brick arches are not taken into the design procedure. The large stresses which usually develop in the brick arches due to the gravity loads and the earthquake out-of-plane dynamic loads are ignored by this assumption. The disadvantages of the traditional steel I-beam jack arch floor system make it inconsistence for the seismic loads. The inconsistency of the floor prevents it to act as a semi-rigid diaphragm in which significant damages including the floor collapse were observed during past earthquakes (Figure 2). The most deficiencies of the traditional un-reinforced masonry buildings are discussed in Section 2 and the detailed seismic rehabilitation procedure is then illustrated in Section 3.

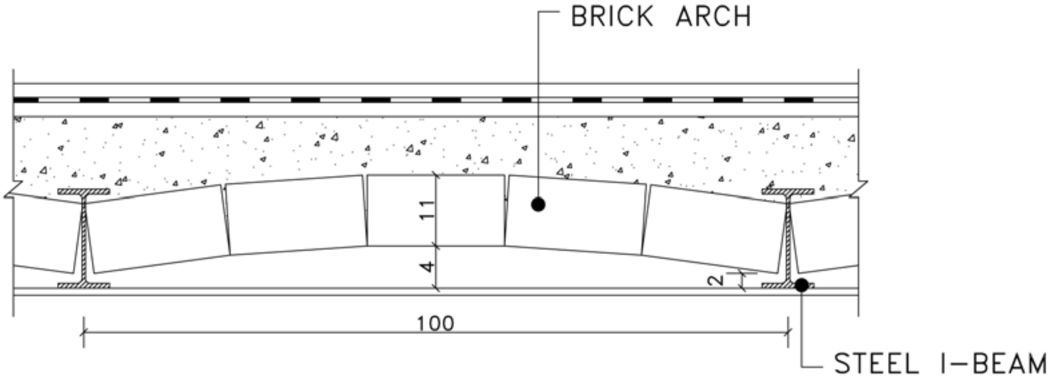

Figure 1. A typical section of steel I-beam jack-arch flooring system (length dimension is cm).

Figure 2. Damage to a traditional jack arch slab during Bam earthquake, 2003 [4].

2 SEISMIC VULNERABILITY ASSESSMENT

The third chapter of the 'Iranian code of practice for the seismic resistant design of buildings, 3rd Edition of Standard No. 2800-05' contains some criteria for designing the URM buildings which are based on engineering judgments and past earthquake experiences [5]. The seismic vulnerability assessment of any URM building can be obtained based on the following criteria.

- Limitations for the number and height of stories and opening dimensions
- Plan's shape and aspect ratio limitations
- Symmetry
- Minimum structural walls
- Complete 3D tie system
- Floor integrity
- Floor to wall connection adequacy

By satisfaction of the above criteria, it is expected that the building can resist against the design (475 years return period) earthquake. It is equivalent to satisfy at least the "Basic Safety Rehabilitation Objective" on the basis of [6]. On the other hand, the main typical deficiencies of URM buildings in Iran can be summarized as Table I. By considering the mentioned deficiencies, in the most cases, the traditional masonry buildings are vulnerable.

Table I. The common deficiency sources in URM buildings in Iran.

Deficiency Source	Description
Floors	Inadequate connection between floor and walls
	No connection between floor components
	Floor is without integrity and diaphragm action performance
Masonry Bearing Walls	Low values for mortar shear strength
	Insufficient shear area in each storey
	Weakness of slender bearing walls due to out of plane force
3D Tie System	Large distance (more than 500 cm in most cases) between vertical tie beams
	Lack of horizontal tie beams in some axes
	Insufficient connection between tie joints
Openings	The short distance between window and the edge of wall
	The long width of window
	The large area of window
Non-Structural Masonry Walls	Weakness of non-structural walls due to out of plane earthquake force
	Insufficient connection with bearing walls (in some cases)

3 SEISMIC REHABILITATION METHODOLOGY

The ASCE 41-06 guidelines [6] introduce eight general strategies for the seismic rehabilitation of buildings which are (1) local modification of components; (2) removal or lessening of existing irregularities; (3) global structural stiffening; (4) global structural strengthening; (5) mass reduction; (6) seismic isolation; (7) supplemental energy dissipation and (8) occupancy changing. A combination of the three mentioned strategies (No. 1, 3 and 4) has been used for the seismic rehabilitation of the Iranian traditional URM buildings. For this purpose the floor integrity has been improved, the wall to wall connection was enhanced and the floor to wall connection was improved. These modifications increase the stiffness and the integrity of the floor as well as changing the boundary condition of bearing walls, load distribution and failure modes. On the other hand, the strengthening of the weak bearing walls and the opening modification has been applied. In this step the strength of the local elements were increased. All the rehabilitation procedures are summarized in this section.

3.1 Openings modification

The openings height or width in the masonry walls has been changed in order to reduce the opening dimensions as well as increasing the coupling beams dimensions. The new part of the masonry wall, as seen in Figure 3, should be connected to the existing part of the masonry wall by enough number of U shape rebars to be able to transfer the shear forces.

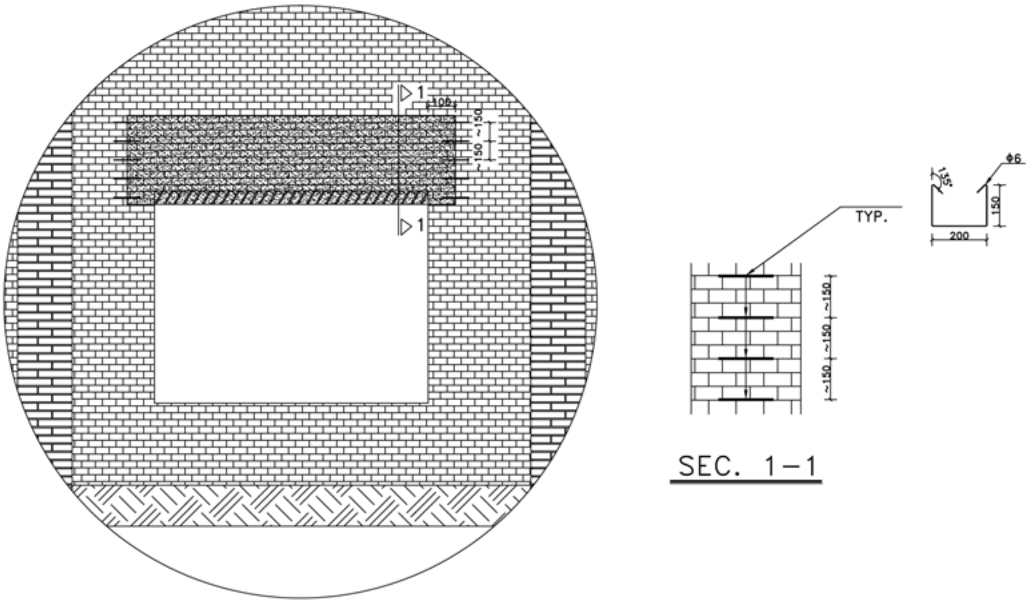

Figure 3. Decreasing of the opening dimensions.

3.2 Floor integrity

The traditional jack arch floor slab, as described in Section 3, can not act as an integrate slab. Hence, $50\times 5mm$ flat bar was welded to the bottom flange of all steel I beams of the floor as shown in Figure 4. The added bar was welded, at the end, to the steel angle which is in the wall and floor intersection. The last steel I beam joist, which usually has the brick floor in only one side, should be connected to the adjacent I beam steel joist by steel flat bars at each 2 m.

Figure 4. Adding $50\times 5mm$ steel plates in order to integrate the traditional jack arch slab joists.

3.3 Floor to wall connection

The floor to wall connection, as described in Section 3, is usually without enough strength. That is, a steel angle $60 \times 60 \times 6mm$ was added to all intersections between floor and walls. The function of the new angle can be summarized as (1) to connect the floor to the wall; (2) acts as a horizontal tie beam; (3) prevents relative movement of the steel joists in earthquake movements and (4) increases the steel joist support length. The details of the added angel are shown in Figure 5 and Figure 6, respectively, in the case of the floor slab joists are perpendicular or parallel to the wall.

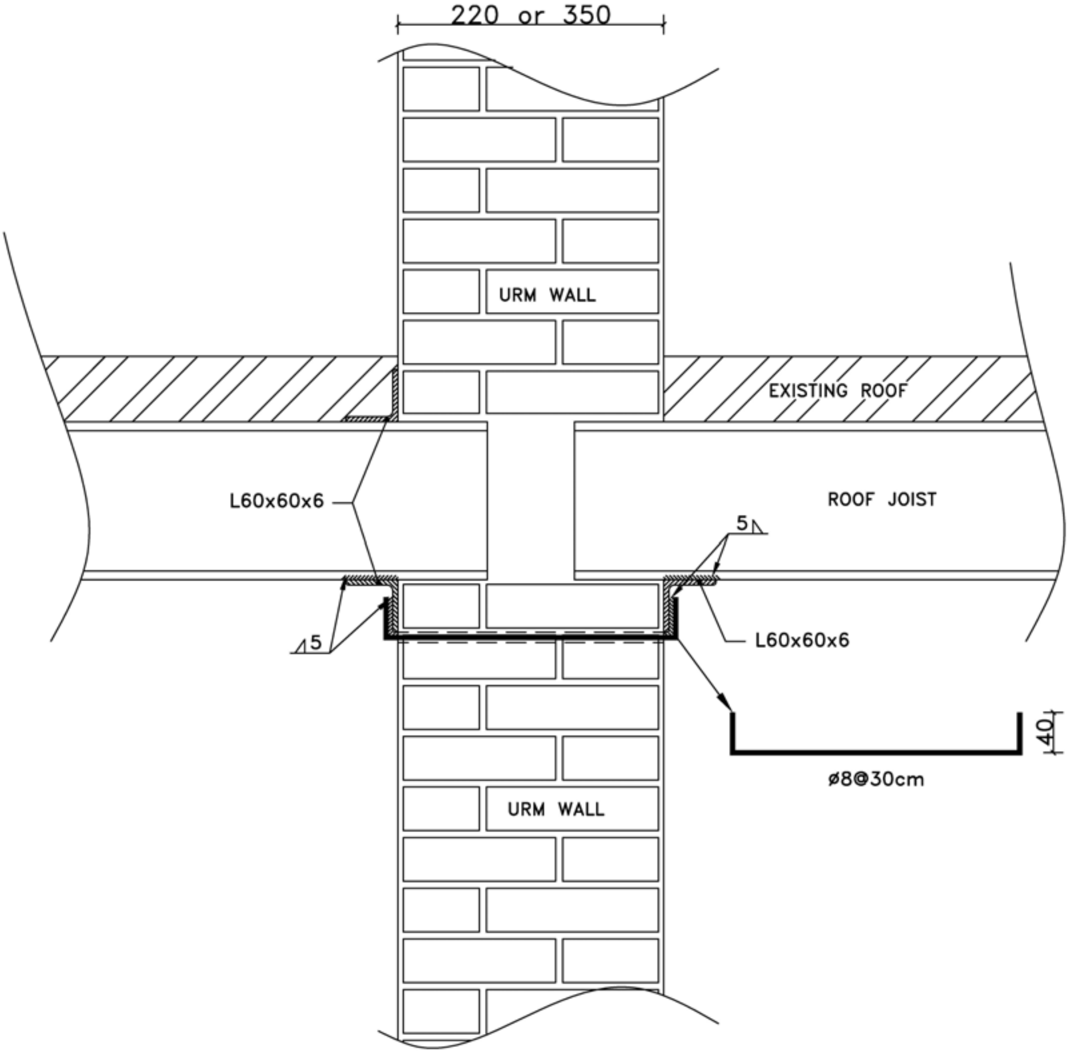

Figure 5. Adding an $60 \times 60 \times 6mm$ angle to connect the wall to the floor where the floor slab joists are perpendicular to the wall.

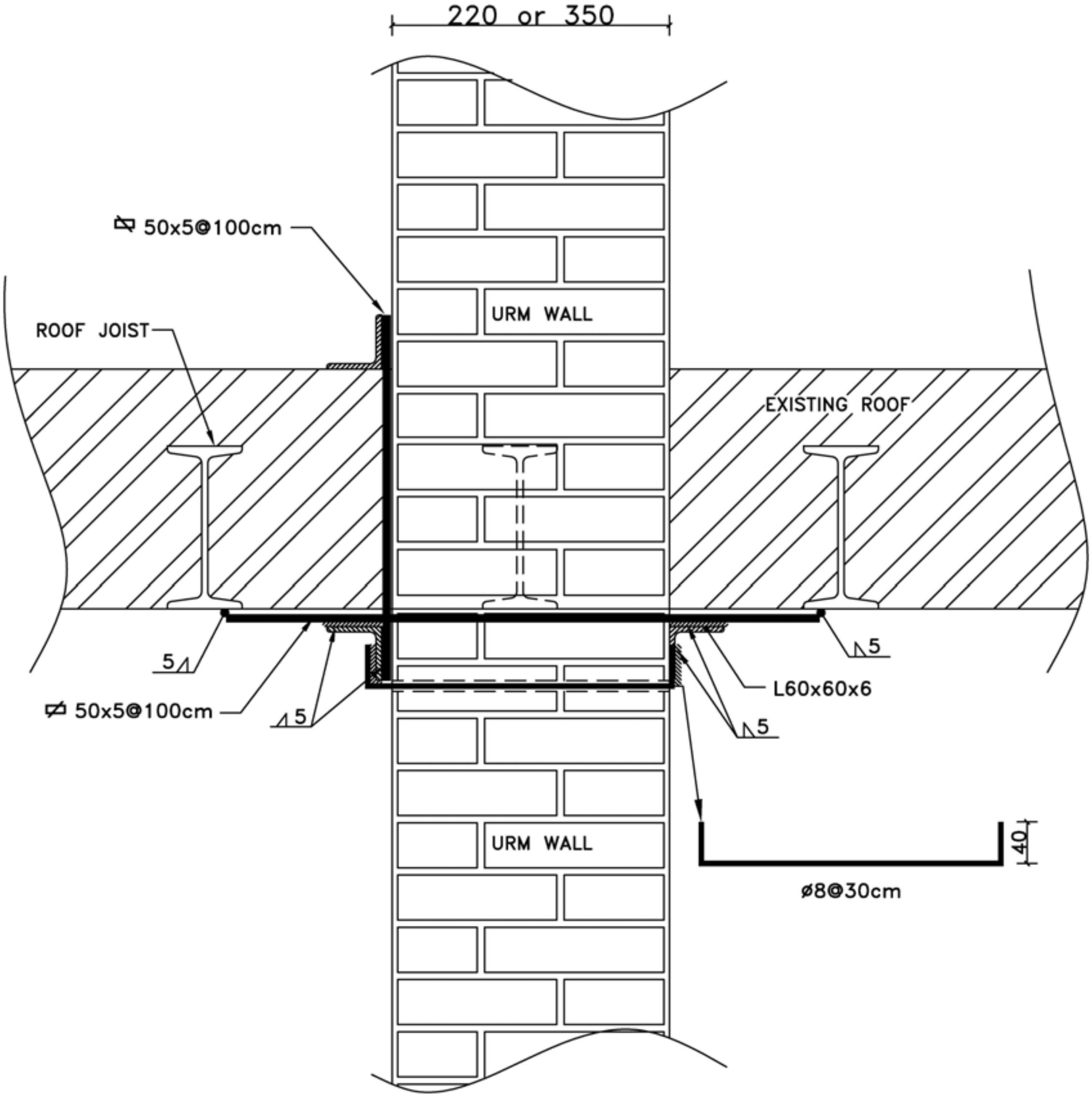

Figure 6. Adding an $60 \times 60 \times 6mm$ angle to connect the wall to the floor where the floor slab joists are parallel to the wall.

3.4 Ties enhancement

There is not any complete 3D tie system in the majority of the URM buildings, as discussed in Section 3. For construction of the 3D tie system, where necessary, a new vertical tie should be executed. Vertical rebars should be implanted in horizontal ties in the top and bottom of the walls. An alternative is the construction of masonry vertical tie beam as seen in Figure 7.

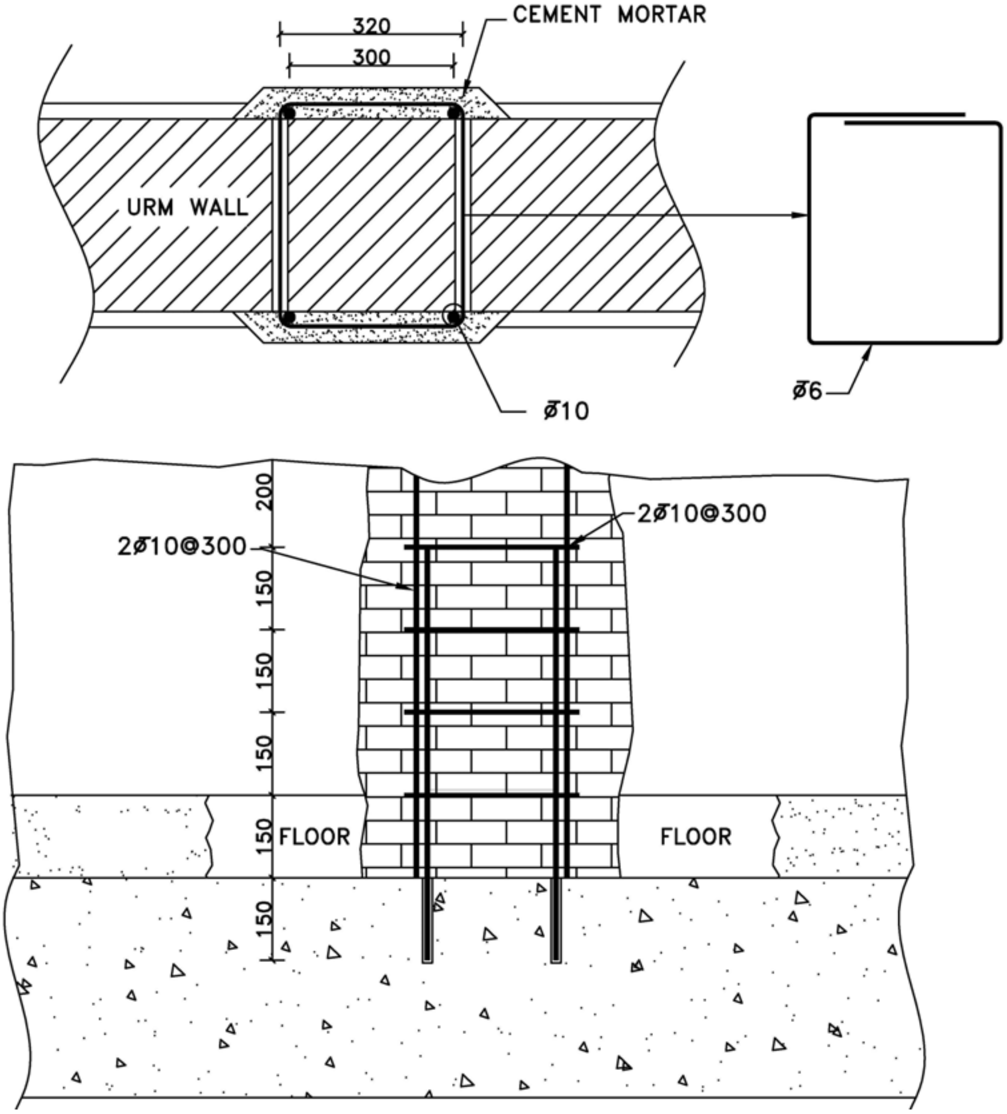

Figure 7. A typical view of the ties enhancement.

3.5 Enhancement of the shear capacity of bearing walls

The masonry wall is enhanced by jacketing with the wire mesh and cement plaster where the capacity of the bearing wall is less than the induced earthquake forces. The details of this method, which is one of the URM wall enhancing methods, can be seen in Figure 8. The enhancement layer should be connected properly to the surrounded ties to be able to transfer the load through stories and deliver it to the foundation. Approximately nine bricks are pulled out from the existing masonry wall, as shown in Figure 9, to make the shear keys between the new layer and the existing masonry wall. The added steel mesh connects to the existing masonry wall by enough number of steel nails. The steel mesh is welded to the corner steel angels, as seen in Figure 10, to make a robust connection between the bearing wall and the floor slab. However the bearing wall is not always without openings. Hence, as shown in Figure 11, the bars should be placed around the openings and the 45° added bars should be placed around the electrical equipment boxes.

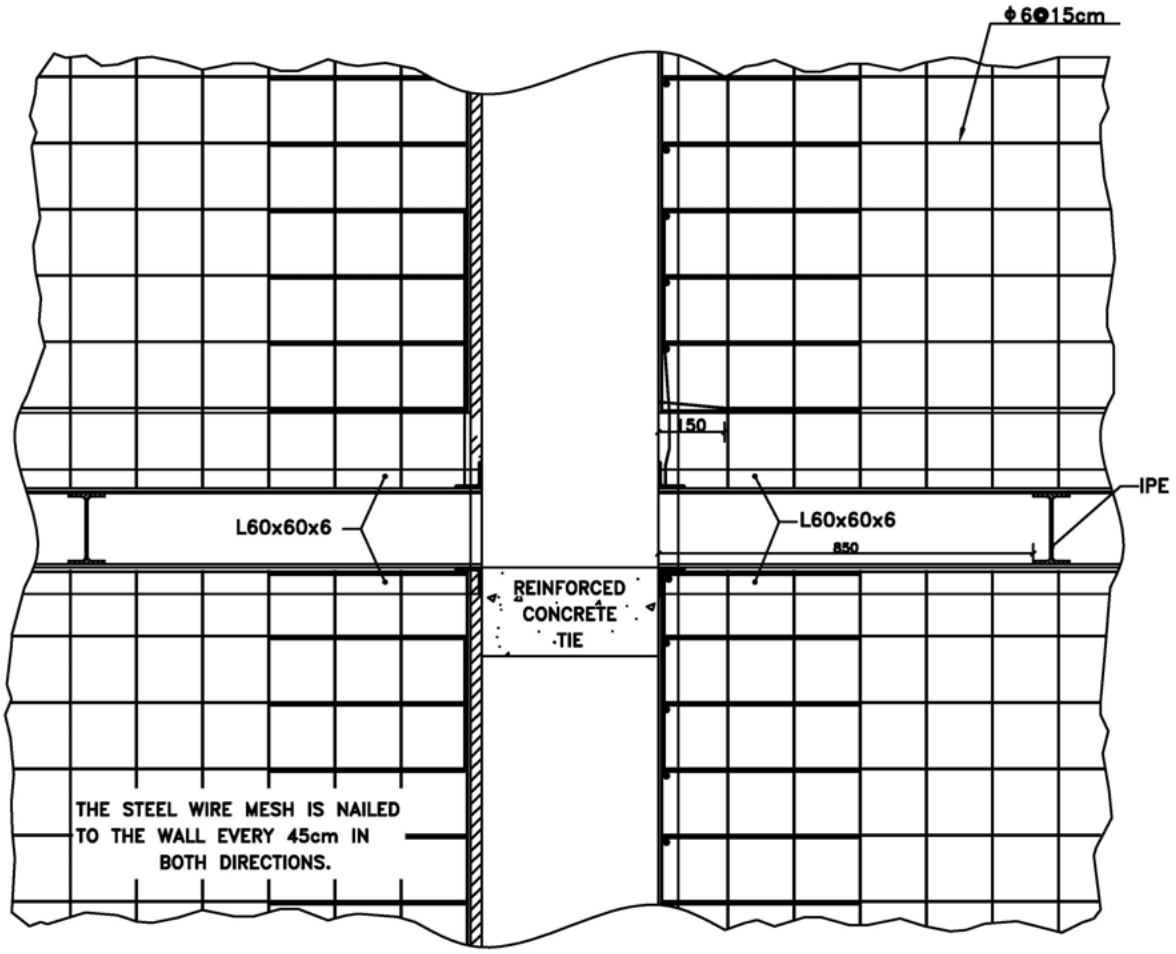

THE STEEL WIRE MESH IS NAILED TO THE WALL EVERY 45cm IN BOTH DIRECTIONS.

Figure 8. A typical view of the bearing wall enhancement through stories.

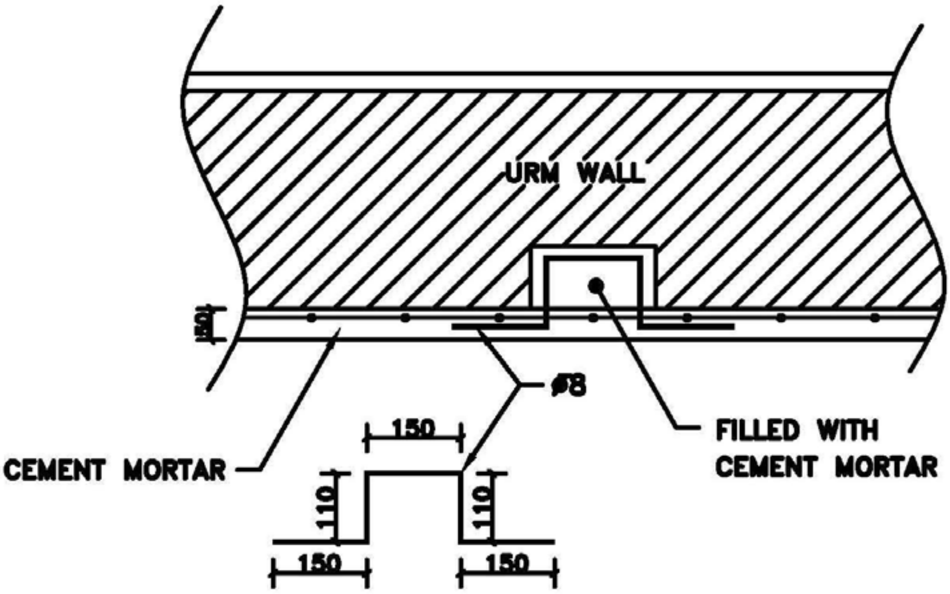

Figure 9. Increasing the strength of the URM wall.

Figure 10. A typical view of the intersection between enhanced bearing walls and floor slab.

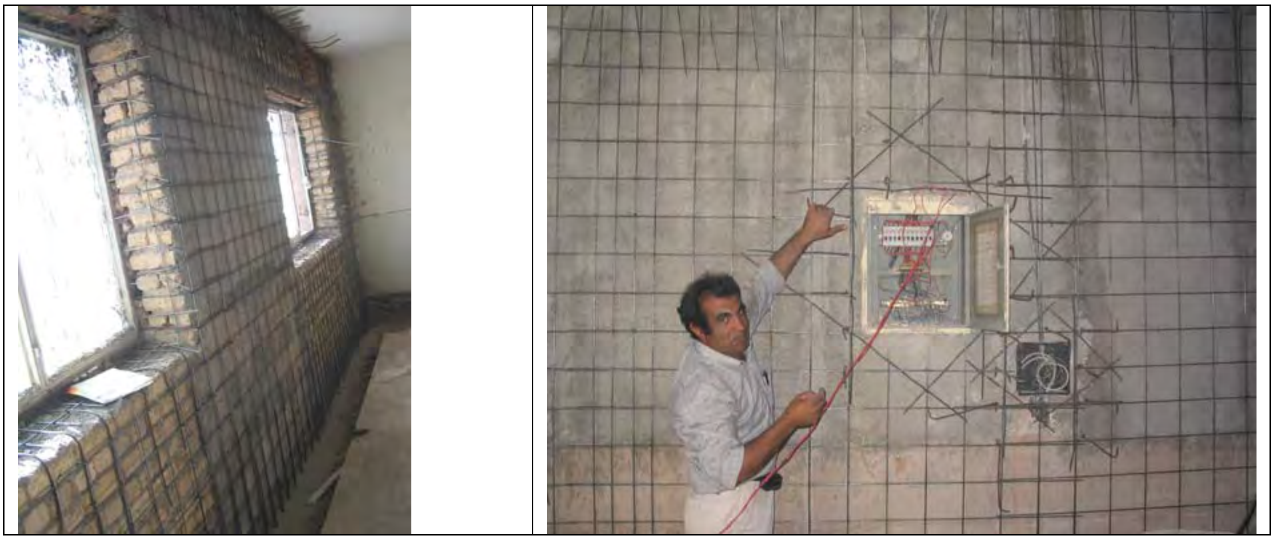

Figure 11. (left) A typical view of the enhanced bearing wall around the openings, (right) A typical view of the enhanced bearing wall around the electrical equipments box.

4 CONCLUSION

A detailed seismic rehabilitation program for a traditional un-reinforced masonry building in Iran has been described in this paper. The walls, floors, openings, and connections were enhanced in order to comply with the code requirements.

The rehabilitation program has been applied to the building under consideration in 50 days. The expense of the project was around 30% of the reconstruction cost which is quite reasonable. The minor architectural modifications were happened mainly in the size of large openings and the overall view has not been changed. This issue is important if it belongs to the client's interest or the building has any historical value.

REFERENCES

[1] D.P. Abrams, N. Shah, *Cyclic load testing of un-reinforced masonry walls*. ACTC No.92-26-10, U.S. Army Research Office Triangle Park, NC, 1992.

[2] G.M. Calvi, G. Magenes, Experimental research on response of URM building systems. *Proceedings of the U.S.-Italy Workshop on Guideleines for Seismic Evaluation and Rehabilitation of Un-reinforced Masonry Buildings*, Section III, 41-57, 1994.

[3] A.C. Costley, D.P. Abrams, Dynamic response of un-reinforced masonry buildings with flexible diaphragms. *Report No. NCEER-96-0001*, National Center for Earthquake Engineering Research, State University of New York at Buffalo, Buffalo, New York, USA, 1996.

[4] M.R. Maheri, Seismic evaluation and design of jack arch slabs. *13th world conference on earthquake engineering*, Vancouver, Canada, 2004.

[5] BHRC. Iranian code of practice for seismic resistant design of buildings, standard No. 2800-05 (3rd Edition). *Building and Housing Research Centre*, Tehran, Iran, 2005.

[6] ASCE. Seismic Rehabilitation of Existing Buildings. Report No. ASCE/SEI 41-06, *American Society of Civil Engineers*, 1801 Alexander Bell Drive Reston, Virginia 20191, 2006.

COMPDYN 2011
III ECCOMAS Thematic Conference on
Computational Methods in Structural Dynamics and Earthquake Engineering
M. Papadrakakis, M. Fragiadakis, V. Plevris (eds.)
Corfu, Greece, 25–28 May 2011

HIGH CONTINUITY SECOND-ORDER HOMOGENIZATION OF IN-PLANE LOADED PERIODIC MASONRY

A. Bacigalupo[1] and L. Gambarotta[2]

[1] Department of Civil, Environmental and Architectural Engineering
via Montallegro, 1 – 16145 Genova, Italy
e-mail: andrea.bacigalupo@unige.it

[2] Department of Civil, Environmental and Architectural Engineering
via Montallegro, 1 – 16145 Genova, Italy
gambarotta@dicat.unige.it

Keywords: Masonry, Second-order homogenization, Boundary layer effects, Dispersive waves, Material characteristic length.

Abstract. *In this paper the second-order homogenization of periodic masonry based on a computational analysis of the unit cell representative of the masonry wall is derived. The multi-scale approach is based on an appropriate representation of the micro-displacement field as the superposition of a local macroscopic displacement field, represented in a polynomial form related to the macro-displacement field, and an unknown micro-fluctuation field accounting for the effects of the heterogeneities. By this approach a continuous micro-displacement field is obtained, i.e. in each unit cell and across the interfaces between adjacent unit cells. The computational procedure is applied in two steps: the first one corresponds to the standard homogenization, while the second step is a second-order homogenization based on the results of the first step. Two numerical examples are presented concerning running bond and English bond masonry. For both the masonry patterns the overall elastic moduli of the second-order model and the corresponding characteristic lengths are obtained; the effects on the characteristic lengths of the stiffness mismatch between the brick phase and the mortar phase are considered. Moreover, the wave propagation in the homogenized medium is considered and dispersive waves are obtained. It is shown that remarkable differences in the phase and group velocities between the first-order and the second-order homogenized models are obtained for wavelengths shorter than ten times the average brick unit size.*

1 INTRODUCTION

The non-local homogenization of periodic masonry is a subject of some interest because in many cases the brick size is not negligible if compared with the structural size, the characteristic length of applied forces or, finally, the wavelength of waves propagating in the wall.

Cosserat constitutive models of periodic masonry have been proposed by several Authors [1-4] as result of homogenization procedures based on an idealization of the masonry as an assemblage of rigid blocks interacting through linear elastic interfaces represented as a Lagrangian system. To overcome the limits deriving from the assumption of rigid blocks Casolo [5] proposed a Cosserat homogenization based on a heuristic evaluation of the mean local rotation of the brick units. The Cosserat homogenization technique proposed by Forest and Sab [6] for continuously deformable heterogeneous media has been extended to periodic masonry by Bacigalupo and Gambarotta [7,8] and by Addessi *et al.* [9], the last contribution to include elasto-damage constitutive equations at the microscale. In Bacigalupo and Gambarotta [8] an evaluation of the reliability of Cosserat homogenization has been carried out by analysing a boundary shear layer problem concerning a masonry wall. The extension of this analysis to second-order homogenization has shown this last one to be more suitable with respect to the micropolar models (Cosserat and Couple-stresses models).

Although second-order homogenization techniques have been proposed through an extension of the classical asymptotic homogenization theory [10-13], they have not been applied in the past to the homogenization of periodic masonry because, as observed by Peerlings and Fleck [14], they result to be computationally burdensome.

The second-order computational procedure here considered is obtained by the analysis of the unit cell representative of the heterogeneous periodic material and is based on an enhanced representation of the micro-displacement field as the superposition of a local macroscopic displacement field, expressed in a polynomial form related to the macro-displacement field, and an unknown micro-fluctuation field accounting for the effects of the heterogeneities [15]. This assumption guarantees the resulting micro-fluctuation field to be continuous on the masonry domain, i.e. in each unit cell and across the interfaces between adjacent unit cells.

Running bond masonry and English bond masonry are analyzed through the second-order homogenization procedure here considered and the elastic moduli and the characteristic lengths of the equivalent continuous are obtained. Moreover, the wave propagation along the symmetry lines of the equivalent orthotropic continuum is analysed. Dispersive waves are obtained and the resulting phase and group velocity are evaluated at different wavelengths.

2 MULTI-SCALE IN-PLANE MODELLING OF PERIODIC MASONRY

Let us consider a masonry wall with periodic arrangement of the bricks in its own plane as shown in Figure 1.a. If only in-plane loads are envisaged and body forces are neglected, the masonry wall may be represented as a plane domain under the simplifying assumption of plane stress condition. The obtained heterogeneous model is analysed as a Cauchy continuum undergoing small strains and the phases are assumed to behave elastically. The position vector $\mathbf{x}$ of a material point is denoted by its components (x_1, x_2) with respect to the reference $(0, \mathbf{e}_1, \mathbf{e}_2)$. The periodic continuum is fully characterized by the unit cell $\mathscr{A} = [0, d_1] \times [0, d_2]$ shown in figure 1.b (width d_1 and height d_2), i.e. the smallest plane portion that contains all the essential information about the masonry pattern. This unit cell is spanned by the two independent orthogonal vectors $\mathbf{v}_1 = d_1 \mathbf{e}_1$, $\mathbf{v}_2 = d_2 \mathbf{e}_2$, so that the boundary C of the unit cell is made up of two pairs of opposite sides corresponding to each other by means of a translation along $\mathbf{v}_1$ or $\mathbf{v}_2$. According to this representation, a variable is periodic in the unit cell $\mathscr{A}$, or $\mathscr{A}$-periodic, if it takes identical values at two points on the boundary of the unit cell whose difference is a vector of periodicity. In this sense, the elasticity tensor $\mathbb{C}^m(\mathbf{x})$ is $\mathscr{A}$-periodic, i.e. $\mathbb{C}^m(\mathbf{x}+\mathbf{v}_i)=\mathbb{C}^m(\mathbf{x})$, i=1,2.

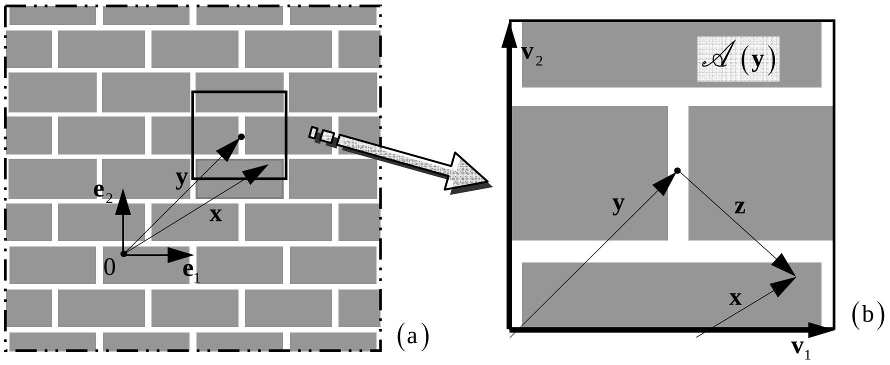

Fig. 1 (a) Periodic masonry; (b) Unit cell and periodicity vectors.

At the material point $\mathbf{x}$ of the heterogeneous elastic medium the micro-displacement $\mathbf{u}(\mathbf{x},t)$ is considered together with the corresponding micro-strain tensor $\varepsilon(\mathbf{x},t)=sym\nabla_{\mathbf{x}}\mathbf{u}(\mathbf{x},t)$ and the micro-stress tensor $\sigma(\mathbf{x},t)=\mathbb{C}^m(\mathbf{x})\varepsilon(\mathbf{x},t)$ which has to satisfy the local equation of motion $div_{\mathbf{x}}\sigma(\mathbf{x},t)=\rho\ddot{\mathbf{u}}(\mathbf{x},t)$. The resulting set of partial differential equations

$$div_{\mathbf{x}}\left(\mathbb{C}^m(\mathbf{x})\nabla_{\mathbf{x}}\mathbf{u}(\mathbf{x},t)\right)=\rho\ddot{\mathbf{u}}(\mathbf{x},t) \tag{1}$$

has to be solved in terms of the micro-displacement components on the whole masonry wall domain with a remarkable computational burden.

Being the solution of this fine-scale computational approach out of reach, it is convenient to replace the heterogeneous model of masonry wall by an equivalent homogeneous one so obtaining equations whose coefficients are not rapidly oscillating while their solutions are close to those of the original equations. In general, an equivalent standard (Cauchy) continuum is considered, but in cases for which the unit cell size is non vanishing if compared to the wall size or to the wavelength it is convenient to introduce an equivalent second-order continuum model [16]. This continuum model is defined at the macroscale where the slow varying macroscopic position vector $\mathbf{y}$ is considered and the displacement field $\mathbf{U}(\mathbf{y},t)$ is defined (with component U_i in the assumed reference). The displacement gradient is denoted by $\mathbf{H}(\mathbf{y},t)=\nabla_{\mathbf{y}}\mathbf{U}(\mathbf{y},t)$ and, according to Germain [17], the strain field in the second gradient continuum is represented by the symmetric first-order strain tensor and by the second-order strain tensor, respectively,

$$\mathbf{E}(\mathbf{y},t)=sym\nabla_{\mathbf{y}}\mathbf{U}(\mathbf{y},t), \qquad \boldsymbol{\kappa}(\mathbf{y},t)=\nabla_{\mathbf{y}}\otimes\nabla_{\mathbf{y}}\mathbf{U}(\mathbf{y},t), \tag{2}$$

the latter being a third-order tensor having components $\kappa_{ijk}=\kappa_{ikj}$ symmetric with respect to j and k.

The stress field is described by the symmetric first-order stress tensor $\mathbf{\Sigma}(\mathbf{y},t)$ ($\Sigma_{ij}=\Sigma_{ji}$) and by second-order stress tensor $\boldsymbol{\mu}(\mathbf{y},t)$ (third-order tensor having components $\mu_{ijk}=\mu_{ikj}$ symmetric with respect to j and k). From these stress tensors the real stress at the macro-scale is defined as $\mathbf{T}(\mathbf{y},t)=\mathbf{\Sigma}(\mathbf{y},t)-Div_{\mathrm{y}}\boldsymbol{\mu}(\mathbf{y},t)$ so that, in general, $\mathbf{T}(\mathbf{y},t)$ is not symmetric. In case of vanishing body forces, the equation of motion is expressed according to Mindlin [16] in the form

$$Div_{\mathrm{y}}\left(\mathbf{\Sigma}(\mathbf{y},t)-Div_{\mathrm{y}}\boldsymbol{\mu}(\mathbf{y},t)\right)=\rho_M\left[\ddot{\mathbf{U}}(\mathbf{y},t)-\left(\nabla_{\mathrm{y}}\otimes\nabla_{\mathrm{y}}\ddot{\mathbf{U}}(\mathbf{y},t)\right)\mathbf{J}\right], \tag{3}$$

being the inertia properties defined by the mass density at the macro-scale ρ_M and the inertia tensor $\mathbf{J}=\int_{\mathscr{A}}\rho\mathbf{y}\otimes\mathbf{y}da\Big/\int_{\mathscr{A}}\rho da$, where ρ is the mass density at the micro-scale. The first-order and second-order stress tensors are energetically conjugate to the corresponding strain tensors by the virtual power theorem; therefore, the constitutive equations in case of linear elasticity take the form

$$\mathbf{\Sigma}=\mathbb{C}\mathbf{E}+\mathbb{Y}\boldsymbol{\kappa},\qquad \boldsymbol{\mu}=\mathbb{Y}\mathbf{E}+\mathbb{S}\boldsymbol{\kappa}, \tag{4}$$

$\mathbb{C}$ being the (standard) fourth-order elasticity tensor, $\mathbb{S}$ the sixth order tensor related to second-order stress and strain tensors and $\mathbb{Y}$ a fifth order tensor taking into account the coupling between the first and second-order stress and strain tensors. The equation of motion of the second order continuum is obtained for centro-symmetric unit cells, namely with vanishing tensor $\mathbb{Y}$, from the field equations (2), (3) and (4) and takes the form

$$Div_{\mathrm{y}}\left(\mathbb{C}\nabla_{\mathrm{y}}\mathbf{U}(\mathbf{y},t)-Div_{\mathrm{y}}\mathbb{S}\nabla_{\mathrm{y}}\otimes\nabla_{\mathrm{y}}\mathbf{U}(\mathbf{y},t)\right)=\rho_M\left[\ddot{\mathbf{U}}(\mathbf{y},t)-\left(\nabla_{\mathrm{y}}\otimes\nabla_{\mathrm{y}}\ddot{\mathbf{U}}(\mathbf{y},t)\right)\mathbf{J}\right], \tag{5}$$

or in components

$$C_{ijhk}U_{h,kj}-S_{ijkrpq}U_{r,pqjk}=\rho_M\left(\ddot{U}_i-J_{kk}\ddot{U}_{i,kk}\right),\qquad i=1,2,3. \tag{6}$$

In order to replace the first-order heterogeneous model, where the micro-fields are defined, with the second-order homogeneous equivalent medium, the variables defined at the corresponding scales have to be properly coupled by means of transition strategies for the strains and strains gradients from the macroscale to the discribed microstructure. In the following, a kinematic multi-scale model proposed by the Authors [15] is considered.

3 SECOND ORDER HOMOGENIZATION OF PERIODIC MATERIALS

In order to couple the kinematics of the classical continuum at the micro-scale to the kinematics of the second-order continuum at the macro-scale, the micro-displacement field in the unit cell is represented in the form $\mathbf{u}(\mathbf{x},t)=\mathbf{u}(\mathbf{y},\mathbf{z},t)$. Here, $\mathbf{y}$ denotes the position vector of the unit cell in which $\mathbf{x}$ is located and vector $\mathbf{z}=\mathbf{x}-\mathbf{y}$ its relative position. This representation highlights the dependence of the displacement field on both the unit cell position $\mathbf{y}$, called the macro-position, and the local position $\mathbf{z}$ at a point of interest. The effective micro-displacement field $\mathbf{u}(\mathbf{y},\mathbf{z},t)$ is approximated by the vector field

$$\mathbf{u}(\mathbf{y},\mathbf{z},t)\approx\mathbf{u}^{\alpha}(\mathbf{y},\mathbf{z},t)=\mathbf{U}(\mathbf{y},t)+\mathbf{H}(\mathbf{y},t)\mathbf{z}+\frac{1}{2}\boldsymbol{\kappa}(\mathbf{y},t):(\mathbf{z}\otimes\mathbf{z})+\tilde{\mathbf{u}}(\mathbf{y},\mathbf{z},t), \tag{7}$$

superposition of a polynomial function depending on both the macro-displacement and the macro-strain fields and a complementary displacement field $\tilde{\mathbf{u}}(\mathbf{y},\mathbf{z},t)$ that represents the microstructural displacement fluctuation field at the microscale due to the inhomogeneities. To obtain continuous micro-displacement fields across the unit cell interfaces, the complementary displacement field is assumed according to [15], in the form

$$\tilde{\mathbf{u}}(\mathbf{y},\mathbf{z},t)=\mathbf{r}^1(\mathbf{y},\mathbf{z},t)+\mathbf{r}^2(\mathbf{y},\mathbf{z},t), \tag{8}$$

each of them having the following representation in components

$$r_i^1(\mathbf{y},\mathbf{z},t)=\theta^1_{ikl}(\mathbf{z})\left[H_{kl}(\mathbf{y},t)+\kappa_{klp}(\mathbf{y},t)\,z_p\right],\quad r_i^2(\mathbf{y},\mathbf{z},t)=\theta^2_{iklp}(\mathbf{z})\,\kappa_{klp}(\mathbf{y},t), \tag{9}$$

where the functions $\theta^1_{ikl}(\mathbf{z})$ and $\theta^2_{iklp}(\mathbf{z})$ have to satisfy the condition of $\mathscr{A}$-periodicity, namely $\theta^1_{ikl}(\mathbf{z}_0^i+\mathbf{v}_i)=\theta^1_{ikl}(\mathbf{z}_0^i)$ and $\theta^2_{iklp}(\mathbf{z}_0^i+\mathbf{v}_i)=\theta^2_{iklp}(\mathbf{z}_0^i)$, $\forall\mathbf{z}_0^i\in C_i$, $i=1,2$.

The representation of the micro-displacement fluctuation field (9) in the unit cell $\mathscr{A}(\mathbf{y})$ is the key point on which the following two-step computational homogenization is based. The first step is the standard first-order homogenization in which the unknown functions $\theta^1_{ikl}(\mathbf{z})$ have to be evaluated. Here the function $\theta^1_{ikl}(\mathbf{z})$ represents the fluctuation displacement along direction $\mathbf{e}_i$ associated to the homogeneous component $H_{kl}=1$ of the macro-displacement gradient; it is obtained by the computational analysis of the unit cell $\mathscr{A}(\mathbf{y})$ with prescribed classic periodic boundary conditions on the micro-displacement field

$$\mathbf{u}^I(\mathbf{z}_b+\mathbf{v}_i)-\mathbf{u}^I(\mathbf{z}_b)=\mathbf{H}\mathbf{v}_i,\qquad \forall\mathbf{z}_b\in C_i,\quad i=1,2, \tag{10}$$

where $\mathbf{z}_b$ is the local position vector at a point on the boundary C_i, $i=1,2$ (see figure 2.b). Once the micro-displacement $\mathbf{u}^I(\mathbf{z})$ in the unit cell $\mathscr{A}(\mathbf{y})$ is obtained for $H_{kl}=1$ prescribed, the 2^3 unknown functions $\theta^1_{ikl}(\mathbf{z})$ are evaluated $\theta^1_{ijk}(\mathbf{z})=u^I_{ijk}(\mathbf{z})-\delta_{ij}z_k$. Following this procedure for all the components of tensor $\mathbf{H}$ the overall (Cauchy) elasticity tensor $\mathbb{C}$ is evaluated through an application of the Hill-Mandel condition.

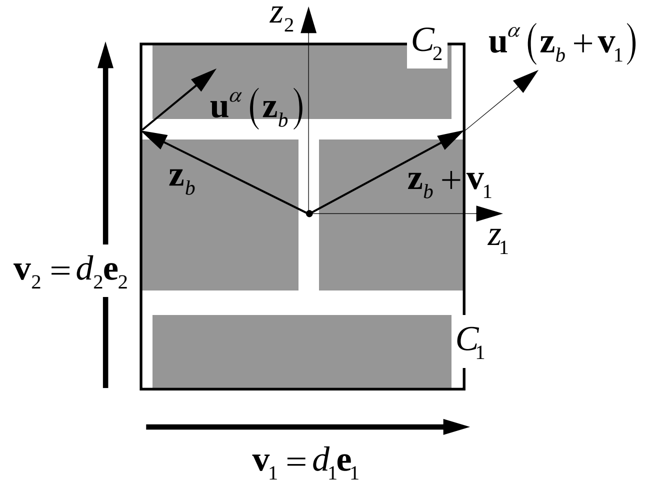

Fig. 2 Displacement vectors of points at the boundary of the unit cell.

The second step is carried out by considering a homogeneous second-order strain field and vanishing macro-strain $\mathbf{E} = \mathbf{0}$. The 2^4 unknown functions $\theta^2_{ijkl}(\mathbf{z})$ are obtained by analysing the unit cell $\mathscr{A}(\mathbf{y})$ with prescribed boundary conditions on the micro-displacement field derived from the $\mathscr{A}$-periodicity condition (9.2). For an arbitrary prescribed homogeneous second-order strain tensor $\boldsymbol{\kappa}$, the micro-displacement $\mathbf{u}^{II}(\mathbf{z})$ is written at corresponding points on the boundary $\mathbf{z}_b$ and $\mathbf{z}_b + \mathbf{v}_i$ (see figure 2) according to representation (7), (8), (9) and including the condition of $\mathscr{A}$-periodicity on the functions $\theta^2_{ijkl}(\mathbf{z})$

$$\mathbf{u}^{II}(\mathbf{z}_b + \mathbf{v}_i) - \mathbf{u}^{II}(\mathbf{z}_b) = \mathbf{u}^{*}(\mathbf{z}_b + \mathbf{v}_i) - \mathbf{u}^{*}(\mathbf{z}_b) + \boldsymbol{\Theta}^1(\mathbf{z}_b) : \boldsymbol{\kappa}\mathbf{v}_i, \qquad \mathbf{z}_b \in C_i, \quad i=1,2, \qquad (11)$$

$\boldsymbol{\Theta}^1$ being the third order tensor having components $\theta^1_{ikl}(\mathbf{z})$.

The boundary conditions referred to the vertical side C_1 and horizontal side C_2 are written in components in the following form, respectively:

$$\begin{aligned} u^{II}_i(z_1^+) - u^{II}_i(z_1^-) &= u^*_i(z_1^+) - u^*_i(z_1^-) + \theta^{1+}_{i11} d_1 \kappa_{111} + \theta^{1+}_{i12} d_1 \kappa_{112} + \theta^{1+}_{i21} d_1 \kappa_{211} + \theta^{1+}_{i22} d_1 \kappa_{221}, \\ u^{II}_i(z_2^+) - u^{II}_i(z_2^-) &= u^*_i(z_2^+) - u^*_i(z_2^-) + \theta^{1+}_{i11} d_2 \kappa_{112} + \theta^{1+}_{i12} d_2 \kappa_{122} + \theta^{1+}_{i21} d_2 \kappa_{212} + \theta^{1+}_{i22} d_2 \kappa_{222}, \end{aligned} \qquad (12)$$

where the notation $z_i^{\pm} = \pm d_i/2, \quad i = 1,2$ and $\theta^{1+}_{hkl} = \theta^1_{hkl}(z_i^+)$ is assumed.

The corresponding micro-displacement field $\mathbf{u}^{II}(\mathbf{z})$ is obtained by a FE analysis of the unit cell under the assumption $\mathbf{E} = \mathbf{0}$ and $\boldsymbol{\kappa}$ homogeneous in the unit cell. Each displacement functions $\theta^2_{iklp}(\mathbf{z})$ is obtained from the displacement field $u^{II}_{iklp}(\mathbf{z})$ resulting by the FE analysis of the unit cell with prescribed non-zero component $\kappa_{klp} = 1$, as follows

$$\theta^2_{iklp}(\mathbf{z}) = u^{II}_{iklp}(\mathbf{z}) - \frac{1}{2}\left(\delta_{ik} z_l z_p + \theta^1_{ikl}(\mathbf{z}) z_p + \theta^1_{ikp}(\mathbf{z}) z_l\right), \qquad (13)$$

being the fluctuation $\theta^1_{ijk}(\mathbf{z})$ known from the first-order homogenization.

The elastic moduli of the second-order continuum are evaluated in the unit cell with reference to the macro-strain vectors $\underline{E} = \{H_{11} \quad H_{22} \quad H_{12} + H_{21}\}^{\mathrm{T}}$ and $\underline{\kappa} = \{\kappa_{111} \quad \kappa_{222} \quad \kappa_{122} \quad \kappa_{211} \quad \kappa_{121} \quad \kappa_{212} \quad \kappa_{112} \quad \kappa_{221}\}^{\mathrm{T}}$. The Hill-Mandel macro-homogeneity condition is applied $\mathscr{E}_M = \mathscr{E}_m$, where $\mathscr{E}_M$ is the macro-strain energy at a point $\mathbf{y}$ of the homogenized continuum written in the following quadratic form

$$\mathscr{E}_M(\underline{E}, \underline{\kappa}) = \frac{1}{2}\left\{\underline{E}^{\mathrm{T}} \quad \underline{\kappa}^{\mathrm{T}}\right\} \begin{bmatrix} \underline{\underline{C}} & \underline{\underline{Y}} \\ \underline{\underline{Y}}^{\mathrm{T}} & \underline{\underline{S}} \end{bmatrix} \begin{Bmatrix} \underline{E} \\ \underline{\kappa} \end{Bmatrix}. \qquad (14)$$

In equation (14) $\underline{\underline{C}}$, $\underline{\underline{Y}}$ and $\underline{\underline{S}}$ are the sub-matrices of the second-order elastic stiffness matrix written according to the constitutive equations (4); $\mathscr{E}_m = \dfrac{1}{2A}\displaystyle\int_A \underline{\varepsilon}^{\mathrm{T}} \underline{\underline{C}}^m \underline{\varepsilon}\, \mathrm{d}a$ is the mean value of the micro-strain energy over the unit cell. According to the multi-scale kinematics here considered the micro-strain field $\underline{\varepsilon} = \{\varepsilon_{11} \quad \varepsilon_{22} \quad 2\varepsilon_{12}\}^{\mathrm{T}}$ in the heterogeneous cell may be written in the following linear form $\underline{\varepsilon} = \underline{\underline{B}}^E(\mathbf{z})\underline{E} + \underline{\underline{B}}^{\kappa}(\mathbf{z})\underline{\kappa}$, $\underline{\underline{B}}^E(\mathbf{z})$ and $\underline{\underline{B}}^{\kappa}(\mathbf{z})$ being matrices depending on the functions $\theta^1_{ikl}\left(\mathbf{z}\right)$ and $\theta^2_{iklp}\left(\mathbf{z}\right)$, i.e. on the microstructure of the unit cell. As a consequence the mean value of the micro-strain energy turns out to be a quadratic form in the variables $\underline{E}$, $\underline{\kappa}$ and may be compared with the macro-strain energy (14) in order to obtain the sub-matrices

$$\underline{\underline{C}} = \frac{1}{A}\int_A \underline{\underline{B}}^{E\mathrm{T}}\underline{\underline{C}}^m\underline{\underline{B}}^E \mathrm{d}a, \quad \underline{\underline{Y}} = \frac{1}{A}\int_A \underline{\underline{B}}^{E\mathrm{T}}\underline{\underline{C}}^m\underline{\underline{B}}^\kappa \mathrm{d}a, \quad \underline{\underline{S}} = \frac{1}{A}\int_A \underline{\underline{B}}^{\kappa\mathrm{T}}\underline{\underline{C}}^m\underline{\underline{B}}^\kappa \mathrm{d}a\,. \tag{15}$$

The matrices $\underline{\underline{C}}$ and $\underline{\underline{S}}$ are symmetric and because of the symmetry of the second-gradient strain $\kappa_{ijk} = \kappa_{ikj}$ the additional symmetries are obtained: $S_{i5} = S_{i7}$, $S_{i6} = S_{i8}$, $Y_{i5} = Y_{i7}$ and $Y_{i6} = Y_{i8}$, $i = 1,...,8$. In general, the stiffness matrix of the second-order elastic plane model is characterised by 45 elasticities (matrix $\underline{\underline{C}}$ - 6 elasticities, matrix $\underline{\underline{S}}$ - 21 elasticities, matrix $\underline{\underline{Y}}$ - 18 elasticities). In the case of centro-symmetric unit cell one obtains $\underline{\underline{Y}} = \underline{\underline{0}}$ and the first order-strain and the second-order strain are uncoupled.

Finally, the constitutive equations are written in the matrix form $\underline{\Sigma} = \partial\mathscr{E}_M / \partial\underline{E} = \underline{\underline{C}}\,\underline{E} + \underline{\underline{Y}}\,\underline{\kappa}$, $\underline{\mu} = \partial\mathscr{E}_M / \partial\underline{\kappa} = \underline{\underline{Y}}^{\mathrm{T}}\underline{E} + \underline{\underline{S}}\,\underline{\kappa}$, being the stress vectors written in the form $\underline{\Sigma} = \left\{\Sigma_{11} \quad \Sigma_{22} \quad \Sigma_{12}\right\}^{\mathrm{T}}$ and $\underline{\mu} = \left\{\mu_{111} \quad \mu_{222} \quad \mu_{122} \quad \mu_{211} \quad \mu_{121} \quad \mu_{212} \quad \mu_{112} \quad \mu_{221}\right\}^{\mathrm{T}}$, respectively.

4 IN-PLANE DISPERSIVE WAVES IN PERIODIC MASONRY

The homogenization technique presented in the previous Section allows to analyse the in-plane wave propagation in a masonry wall. Let us consider the wave propagation along the orthotropy direction $\mathbf{e}_\beta$, with $\beta = 1, 2$, represented at the macro-scale by the component of the displacement vector $U_\alpha\left(y_\beta, t\right)$ with $U_\gamma \equiv 0$ where $\alpha, \beta, \gamma = 1, 2$ and $\alpha \neq \gamma$ (see figure 3). The equation of motion of a second-order continuum is specialized to the case of an orthotropic material that is equivalent to a heterogeneous periodic material characterized by centro-symmetric unit cells and from equation (6) is written in the form

$$C_{\beta\alpha\beta\alpha}U_{\alpha,\beta\beta} - S_{\alpha\beta\beta\alpha\beta\beta}U_{\alpha,\beta\beta\beta\beta} = \rho_M\left(\ddot{U}_\alpha - J_{\beta\beta}\ddot{U}_{\alpha,\beta\beta}\right). \tag{16}$$

By noting that $\hat{c}^\alpha_\beta = \sqrt{C_{\beta\alpha\beta\alpha}/\rho_M}$ denotes the velocity of the longitudinal $\left(\alpha = \beta\right)$ and transverse $\left(\alpha \neq \beta\right)$ waves along direction $\mathbf{e}_\beta$ in a corresponding Cauchy continuum ($S_{\alpha\beta\beta\alpha\beta\beta} = J_{\beta\beta} = 0$ in equation (16)), $\lambda^\alpha_\beta = \sqrt{S_{\alpha\beta\beta\alpha\beta\beta}/C_{\beta\alpha\beta\alpha}}$ denotes the extensional $\left(\alpha = \beta\right)$ and shearing $\left(\alpha \neq \beta\right)$ characteristic length of the masonry bond as shown in [15], and $J_{\beta\beta} = \eta d^2$, being d the cell size and η a parameter that depends on the geometrical and mechanical properties of the cell, the displacement equation of motion may be written in the form

$$\left(\lambda^\alpha_\beta \hat{c}^\alpha_\beta\right)^2 U_{\alpha,\beta\beta\beta\beta} - \hat{c}^{\alpha 2}_\beta U_{\alpha,\beta\beta} = \ddot{U}_\alpha - \eta d^2 \ddot{U}_{\alpha,\beta\beta}\,. \tag{17}$$

To evaluate the dispersion functions, the solution of equation (17) is considered having the form $U_\alpha\left(y_\beta, t\right) = A\exp\left[i\left(ky_\beta - \omega t\right)\right]$, where $i^2 = -1$, k is the wave number and ω is the angular frequency. The wavelength and the phase velocity of the in-plane waves along direction $\mathbf{e}_\beta$ are $\lambda = 2\pi/k$ and $c^{\alpha}_{\beta} = \omega/k$, respectively. The dispersion function corresponding to the longitudinal $(\alpha = \beta)$ transverse $(\alpha \neq \beta)$ oscillatory motion of the derived equivalent continuum takes the following form

$$\omega = k\hat{c}^{\alpha}_{\beta}\sqrt{\frac{1+\lambda^{\alpha 2}_{\beta}k^{2}}{1+\eta d^{2}k^{2}}} = k\hat{c}^{\alpha}_{\beta}\sqrt{\frac{1+4\pi^{2}\left(\lambda^{\alpha}_{\beta}/\lambda\right)^{2}}{1+4\pi^{2}\eta\left(d/\lambda\right)^{2}}}\,, \tag{18}$$

that depends on the wave number *k*. From equation (18) it results that for large wavelengths $(\lambda \to \infty)$ the angular frequency tends to the value related to the standard continuum, i.e $\omega \to k\hat{c}^{\alpha}_{\beta}$.

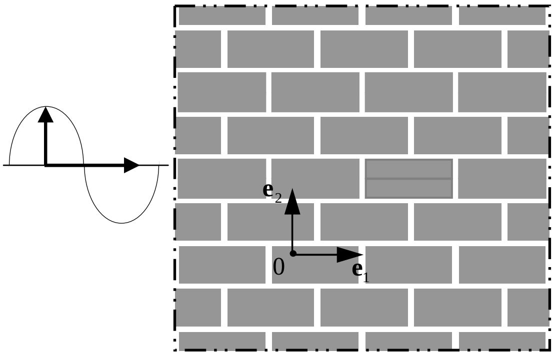

Fig. 3 Shear wave propagation along the orthotropy direction $\mathbf{e}_1$.

5 NUMERICAL EXAMPLES

The computational homogenization procedure described in the previous Sections has been applied to the in-plane analysis of both running bond and English bond masonry. In both cases the bricks and the mortar are assumed elastic and isotropic in order to assess the reliability of the procedure and to analyze the propagation of elastic waves. The two steps of the homogenization procedure are carried out by a FE analysis of the unit cell and the overall elastic moduli of the second-order equivalent continuum model are obtained for different stiffness ratios E_b/E_m, being E_b and E_m the Young's modulus of the brick and the mortar, respectively. Moreover, the unit cells analysed for the two considered masonry patterns are characterized by orthogonal axes of symmetry z_1 and z_2, so that the constitutive equations of the equivalent second-order continuum are orthotropic. The propagation of shear waves along the two axes of orthotropy z_1 and z_2 of the considered masonry bonds is analysed assuming the ratio $E_b/E_m = 10$ between the brick and the mortar Young modulus, respectively.

5.1 Running bond masonry

The considered running bond masonry having the unit square cell shown in figure 1.b is analysed. The brick dimensions are 120mm x 60mm and the mortar thickness is 10mm; the unit cell size is $d = 130\text{mm}$. The constituents are assumed isotropic, perfectly bonded and in plane stress condition. The Young's modulus $E_m = 500\text{MPa}$ of the mortar is assumed and for both the constituents equal Poisson ratios are assumed $\nu_m = \nu_b = 0.1$. The elastic moduli of the homogeneous equivalent continuum have been evaluated for increasing values of the Young modulus of the bricks ($E_b = 10 \div 10^3 E_m$) in order to appreciate the effect of mismatch in the elastic moduli of the constituents. The mass density for bricks and mortar are $\rho_b = 1600\ \mathrm{kg/m^3}$ and $\rho_m = 1500\ \mathrm{kg/m^3}$ respectively. The mass density at the macro-scale ρ_M and the inertia tensor components J_{11}, J_{22} take the following values: $\rho_M = 1585\ \mathrm{kg/m^3}$, $J_{11} = 1406\ \mathrm{mm^2}$, $J_{22} = 1410\ \mathrm{mm^2}$. The elastic moduli $\mathbb{C}$ obtained by the standard first-order (Cauchy) homogenization (first step of the homogenization) are given in Table 1. The elastic moduli $\mathbb{S}$, obtained in the second step of the homogenization for the second order continuum are given in Table 2.

Tab.1 Elastic moduli - first order (Cauchy) homogenization C_{ijhk} (MPa).

E_b	C_{1111}	C_{2222}	C_{1122}	C_{1212}
$10E_m$	2.763E+03	2.013E+03	1.794E+02	8.186E+02
$10^2 E_m$	6.194E+03	2.997E+03	1.587E+02	1.169E+03
$10^3 E_m$	7.136E+03	3.155E+03	1.287E+02	1.227E+03

Tab.2 Elastic moduli - second order homogenization S_{ijhkpq} (N).

E_b	S_{111111}	S_{222222}	S_{122122}	S_{211211}	S_{121121}	S_{212212}
$10E_m$	3.326E+04	1.912E+02	9.304E+04	3.778E+05	1.089E+06	5.682E+05
$10^2 E_m$	8.978E+04	6.827E+01	2.662E+05	1.959E+06	2.495E+06	7.483E+05
$10^3 E_m$	1.127E+05	1.077E+01	3.139E+05	2.687E+06	2.942E+06	7.847E+05

E_b	S_{111122}	S_{111212}	S_{222211}	S_{222121}	S_{122212}	S_{211121}
$10E_m$	2.707E+04	1.669E+04	-5.686E+01	9.817E+01	-9.506E+04	1.922E+05
$10^2 E_m$	5.992E+04	3.478E+04	-4.069E+02	-1.401E+02	-2.165E+05	6.907E+05
$10^3 E_m$	5.720E+04	4.707E+04	-1.249E+02	6.976E+01	-2.377E+05	8.376E+05

The characteristic lengths associated to the shear and to extensional strain along directions z_1 and z_2 take the form

$$\begin{aligned} \lambda_{Sh-1} = \lambda_1^2 = \sqrt{\frac{S_{211211}}{C_{1212}}}, \quad \lambda_{Sh-2} = \lambda_2^1 = \sqrt{\frac{S_{122122}}{C_{1212}}}, \\ \lambda_{Ext-1} = \lambda_1^1 = \sqrt{\frac{S_{111111}}{C_{1111}}}, \quad \lambda_{Ext-2} = \lambda_2^2 = \sqrt{\frac{S_{222222}}{C_{2222}}}, \end{aligned} \tag{19}$$

respectively, and the numerical values for the considered unit cell are given in Table 3. In Table 3 it is observed that when decreasing the stiffness mismatch between the brick and mortar E_b/E_m , the characteristic lengths associated with one-dimensional shear and extensional problems tend to zero.

Tab.3 Characteristic lengths (mm) of the homogeneous second-order model.

E_b	λ_{Sh-1}	λ_{Sh-2}	λ_{Ext-1}	λ_{Ext-2}
$10E_m$	21.5	10.7	3.5	0.31
$10^2 E_m$	40.9	15.1	3.8	0.15
$10^3 E_m$	46.8	16.0	4.0	0.06

The shear dispersive waves along directions $\mathbf{e}_\beta$, $\beta = 1,2$, for $E_b/E_m = 10$ are described in terms of the dispersion functions. The diagrams representing the dimensionless dispersion $\omega d/\hat{c}_1^2$ as a function of the dimensionless wavenumber kd are shown in figure 4 (red line $\mathbf{e}_1$ propagation, blue line $\mathbf{e}_2$ propagation) and compared with the corresponding one referred to the first-order continuum (black straight line). The group velocity $c_{g-\beta}^\alpha/\hat{c}_1^2$ and the phase velocity $c_\beta^\alpha/\hat{c}_1^2$ as functions of the wavelength are shown in figure 5, respectively. Unlike the first order continuum (Cauchy), where the frequency is proportional to the wave number, dispersive waves propagate in the second-order equivalent continuum with phase velocity c_β^α and group velocity $c_{g-\beta}^\alpha = \dfrac{\mathrm{d}\omega}{\mathrm{d}k}$ which differ at different wave numbers. In the Running bond pattern an appreciable difference between the results provided by the equivalent second-order continuum and the corresponding ones by the standard Cauchy continuum are observed in the diagrams of figures 4 and 5. For wavelength $\lambda = 5d$ from the diagrams in figure 5 one obtains $c_{g-1}^2 \approx 0.85\hat{c}_1^2$ and $c_1^2 \approx 0.94\hat{c}_1^2$.

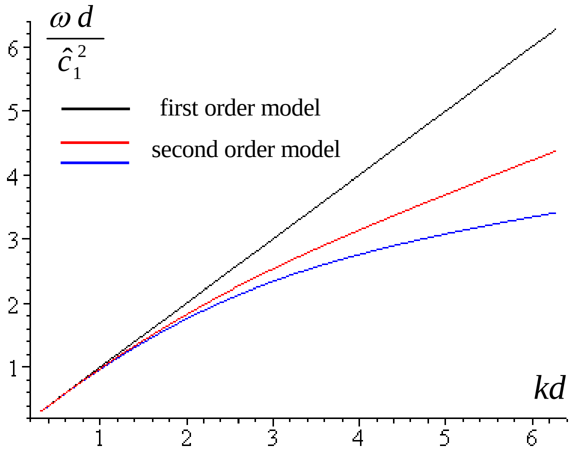

Fig. 4 Dimensionless dispersion functions. Red line $\mathbf{e}_1$ propagation, blue line $\mathbf{e}_2$ propagation; black line: first-order continuum.

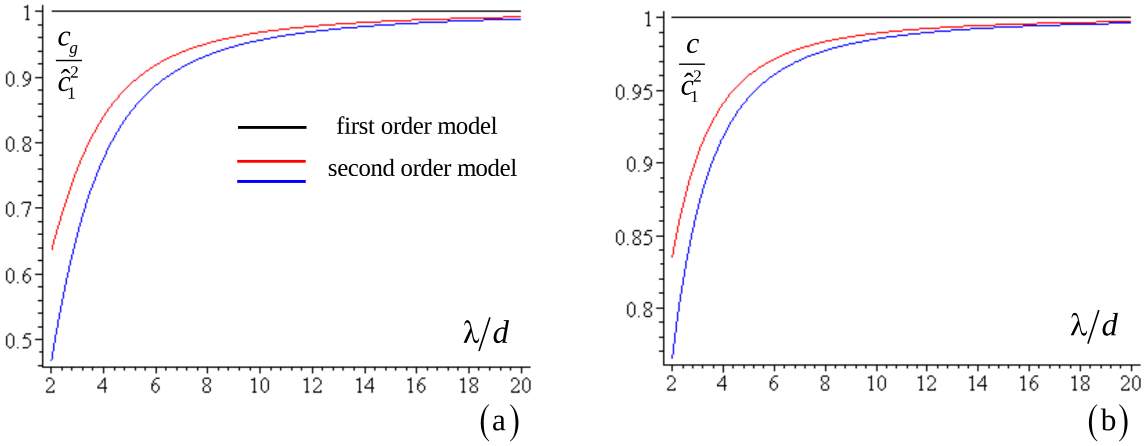

Fig. 5 Group and phase velocities. Red line $\mathbf{e}_1$ propagation, blue line $\mathbf{e}_2$ propagation; black line: first-order continuum.

5.2 English bond masonry

The English bond masonry having the rectangular unit cell shown in figure 6, with sides $d_1 = 260\mathrm{mm}$, $d_2 = 140\mathrm{mm}$, is considered. The brick dimensions are 250mm x 120mm x 60mm and the mortar thickness is 10mm. The constituents are assumed isotropic, perfectly bonded and in plane stress condition; the Young modulus $E_m = 500\mathrm{MPa}$ is assumed for the mortar and equal Poisson ratio is assumed $\nu_m = \nu_b = 0.1$ for both the constituents. The elastic moduli of the homogeneous equivalent continuum have been evaluated for increasing values of the Young modulus of the bricks ($E_b = 10 \div 10^3 E_m$). The mass density for bricks and mortar are $\rho_b = 1600\ \mathrm{kg/m^3}$ and $\rho_m = 1500\ \mathrm{kg/m^3}$ respectively. The mass density at the macro-scale ρ_M and the inertia tensor components J_{11}, J_{22} take the following values: $\rho_M = 1581\ \mathrm{kg/m^3}$, $J_{11} = 5625\ \mathrm{mm^2}$, $J_{22} = 1638\ \mathrm{mm^2}$. The elastic moduli $\mathbb{C}$ obtained by the standard first-order (Cauchy) homogenization (first step of the homogenization) are given in Table 4. The elastic moduli $\mathbb{S}$, obtained in the second step of the homogenization for the second order continuum are given in Table 5. Moreover, the characteristic lengths associated to the shear and to extensional strain along directions z_1 and z_2 (see relation (19)) for the considered unit cell are given in Table 6.

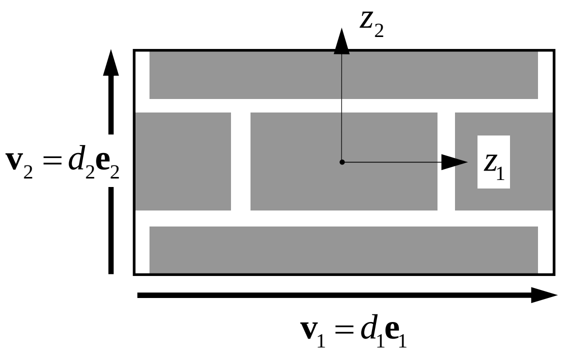

Fig. 6 Unit cell for English bond patterns.

Tab.4 Elastic moduli first order (Cauchy) homogenization C_{ijhk} (MPa).

E_b	C_{1111}	C_{2222}	C_{1122}	C_{1212}
$10E_m$	3.101E+03	2.125E+03	1.911E+02	8.756E+02
$10^2 E_m$	8.799E+03	3.239E+03	1.757E+02	1.279E+03
$10^3 E_m$	1.112E+04	3.422E+03	1.345E+02	1.346E+03

Tab.5 Elastic moduli second order homogenization S_{ijhkpq} (N).

E_b	S_{111111}	S_{222222}	S_{122122}	S_{211211}	S_{121121}	S_{212212}
$10E_m$	1.022E+05	1.905E+02	7.147E+04	8.394E+05	1.641E+06	2.647E+06
$10^2 E_m$	5.177E+05	3.001E+02	2.041E+05	4.486E+06	5.373E+06	3.821E+06
$10^3 E_m$	7.782E+05	4.287E+01	2.436E+05	6.179E+06	7.385E+06	3.999E+06

E_b	S_{111122}	S_{111212}	S_{222211}	S_{222121}	S_{122212}	S_{211121}
$10E_m$	3.760E+04	2.795E+04	-1.831E+01	-1.216E+02	-2.495E+05	4.454E+05
$10^2 E_m$	1.083E+05	7.246E+04	-4.107E+03	-1.832E+03	-6.113E+05	1.947E+06
$10^3 E_m$	1.096E+05	1.125E+05	-1.497E+03	1.977E+01	-7.059E+05	2.396E+06

Tab.6 Characteristic lengths (mm) of the homogeneous second-order model.

E_b	λ_{Sh-1}	λ_{Sh-2}	λ_{Ext-1}	λ_{Ext-2}
$10E_m$	31.0	9.0	5.7	0.30
$10^2 E_m$	59.2	12.6	7.7	0.30
$10^3 E_m$	67.7	13.5	8.4	0.11

The diagrams representing the dimensionless dispersion $\omega d_2 / \hat{c}_1^2$ as a function of the dimensionless wavenumber kd_2 are shown in figure 7 for $E_b / E_m = 10$; the group velocity $c^{\alpha}_{g-\beta} / \hat{c}_1^2$ and the phase velocity $c^{\alpha}_{\beta} / \hat{c}_1^2$ as functions of the wavelength are shown in the diagrams of figure 8. From these diagrams a remarkable difference between the results provided by equivalent second-order continuum and the corresponding ones from the standard Cauchy continuum are observed. For wavelength $\lambda = 5d_2$ one obtains $c^2_{g-1} \approx 0.65\hat{c}_1^2$ and $c_1^2 \approx 0.85\hat{c}_1^2$.

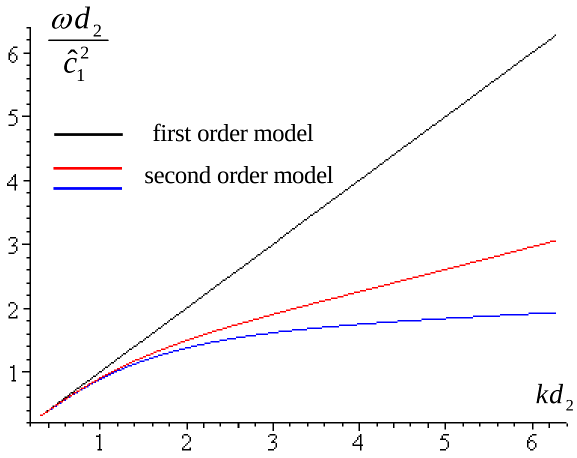

Fig. 7 Dimensionless dispersion functions. Red line $\mathbf{e}_1$ propagation, blue line $\mathbf{e}_2$ propagation; black line: first-order continuum.

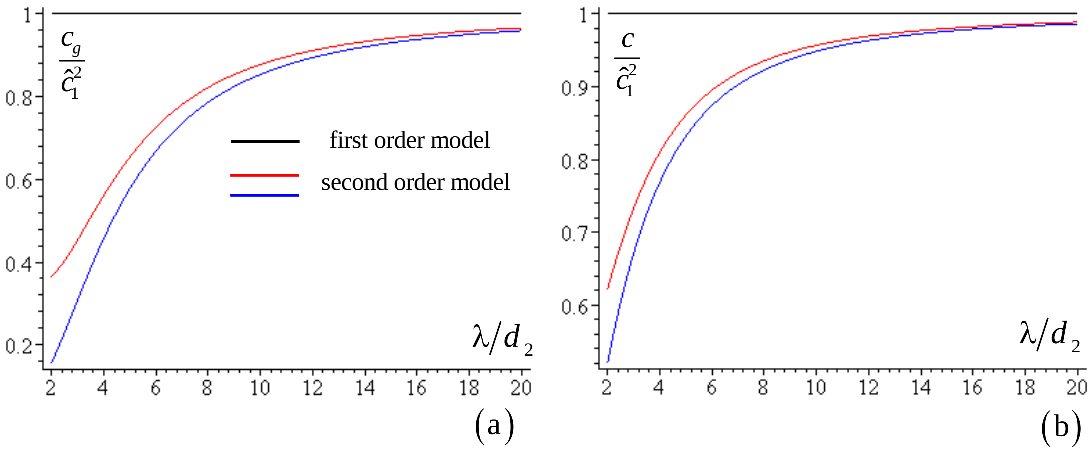

Fig. 8 Group and phase velocities. Red line $\mathbf{e}_1$ propagation, blue line $\mathbf{e}_2$ propagation; black line: first-order continuum.

6 CONCLUSIONS

The in-plane static and dynamic response of elastic periodic masonry is analyzed on the basis of a second order homogenization technique that is developed by considering an enhanced representation of the micro-displacement field at the brick scale in terms of the macro-kinematics at the structural scale. This kinematical micro-macro framework guarantees the continuity of the micro-displacement field in the representative unit cell and across the interfaces between adjacent unit cells. A computationally efficient procedure is developed which is applied in two steps: the first step corresponds to the standard homogenization, while the second step, that is based on the results of the first step, completes the second-order homogenization. Moreover, it is shown that in the equivalent second-order model dispersive waves propagate.

Running bond and English bond masonry are analysed in the examples to illustrate the capabilities of the homogenization techniques. The overall elastic moduli and the characteristic lengths of the second-order equivalent continuum are obtained by the computational homogenization carried out by the FE analysis of the unit cell and the effects of the stiffness mismatch between the brick phase and the mortar phase are considered.

Finally, it is shown that for wavelengths shorter than ten times the average brick unit size the propagation of elastic waves in the second-order homogenized model takes place with appreciable differences in the phase and group velocities with respect to the standard Cauchy model.

7 ACKNOWLEDGMENT

The authors acknowledge financial support of the (MURST) Italian Department for University and Scientific and Technological Research in the framework of the research MIUR Prin07 project 2007YZ3B24, *Multi-scale problems with complex interactions in Structural Engineering*, coordinated by prof. A. Corigliano.

REFERENCES

[1] R. Masiani, N. Rizzi, P. Trovalusci, Masonry as structured continuum, *Meccanica*, **30**, 673-683, 1995.

[2] J. Sulem, H.B. Mühlhaus, A continuum model for periodic two-dimensional block structures, *Mech. Cohesive-frictional Materials*, **2**, 31-46, 1997.

[3] G. Salerno, G. de Felice, Continuum modeling of periodic brickwork, *Int. J. Solids and Structures*, **46** ,1251-1267, 2009.

[4] Stefanou I., Sulem J., Vardoulakis I., Three-dimensional Cosserat homogenization of masonry structures: elasticity, *Acta Geotecnica*, **3**, (1), 71-83, 2008.

[5] S. Casolo, Macroscopic modelling of structured materials: Relationship between orthotropic Cosserat continuum and rigid elements, *Int. J. Solids and Structures*, **43** ,475-496, 2006.

[6] S. Forest, K. Sab, Cosserat overall modeling of heterogeneous materials, *Mechanics Research Communications*, **25**, 449-454, 1998.

[7] Bacigalupo A., Gambarotta L., Cosserat homogenization of elastic periodic blocky masonry, *8th World Congress on Computational Mechanics* (Venice), Schrefler B. Perego U. Eds., 2 pagg, ISBN 9788496736559, CIMNE, 2008.

[8] A. Bacigalupo, L. Gambarotta, Non-Local Computational Homogenization of Periodic Masonry, *Int. J. for Multiscale Computational Engineering*, to appear, 2011.

[9] D. Addessi, E. Sacco, A. Paolone, Cosserat model for periodic masonry deduced by nonlinear homogenization, *European Journal of Mechanics A/Solids*, **29**, 724-737, 2010.

[10] N.S. Bakhvalov, G.P. Panasenko, *Homogenization: Averaging Processes in Periodic Media*. Nauka, Moscow (in Russian). English translation in: Mathematics and its Applications (Soviet Series) 36, Kluwer Academic Publishers, Dordrecht-Boston-London, 1984.

[11] C. Boutin, Microstructural effects in elastic composites, *Int. J. Solids and Structures,* **33** ,1023-1051, 1996.

[12] N. Triantafyllidis, S. Bardenhagen, The influence od scale size on the stability of periodic solids and the role of associated higher order gradient continuum models, *J. Mechanics and Physics of Solids*, **11**, 1891-1928, 1996.

[13] V.P. Smyshlyaev, K.D. Cherednichenko, On rigorous derivation of strain gradient effects in the overall behaviour of periodic heterogeneous media, *J. Mechanics and Physics of Solids*, **48**, 1325-1357, 2000.

[14] R.H.J. Peerlings, Fleck N.A., Computational Evaluation of Strain Gradient Elasticity Constants, Int. J. for Multiscale Computational Engineering, 2, 599-619, 2004.

[15] A. Bacigalupo, L. Gambarotta, Second-order computational homogenization of heterogeneous materials with periodic microstructure, *ZAMM Z. Angew. Math. Mech.*, **90**, No. 10–11, 796 – 811, 2010.

[16] R.D. Mindlin, Micro-structure in linear elasticity, *Arch. Ration. Mech. Anal.*, **16**, 51–78, 1965.

[17] P. Germain, The method of virtual power in continuum mechanics. Part 2: microstructure, *SIAM J. Appl. Math.* , **25** (3), 556–575, 1973.

COMPDYN 2011
III ECCOMAS Thematic Conference on
Computational Methods in Structural Dynamics and Earthquake Engineering
M. Papadrakakis, M. Fragiadakis, V. Plevris (eds.)
Corfu, Greece, 25-28 May 2011

MASONRY INFILLED REINFORCED CONCRETE FRAMES WITH OPENINGS

Panagiotis G. Asteris[1], Christis Z. Chrysostomou[2], Ioannis P. Giannopoulos [1], and Eleni Smyrou[3]

[1] Computational Mechanics Laboratory, School of Pedagogical & Technological Education
141 24 Heraklion, Athens, Greece
e-mail: asteris@aspete.gr

[2] Department of Civil Engineering & Geomatics, Cyprus University of Technology
3603 Lemesos, Cyprus
c.chrysostomou@cut.ac.cy

[3] Laboratory for Earthquake Engineering, National Technical University of Athens
15700 Athens, Greece
smiroulena@gmail.com

Keywords: Finite Element Method, Infilled Frames, Masonry, Seismic Response, Stiffness.

Abstract. *This work presents an assessment of the behavior of infilled frames. The feasibility of possible immediate implementation of some recent developments both in analysis and design of infilled frames for practical design is investigated. It is now widely recognised that masonry infill panels, used in reinforced concrete (R/C) frame structures, significantly enhance both the stiffness and the strength of the surrounding frame. However, their contribution is often not taken into account because of the lack of knowledge of the composite behaviour of the surrounding frame and the infill panel.*

Currently, Seismic Design Guidelines (EC8 – Part 3, FEMA – 440, ASCE 41-06) contain provisions for the calculation of the stiffness of solid infilled frames mainly by modeling infill walls as "diagonal struts." However, such provisions are not provided for infilled frames with openings. The present study, based on available finite element results, proposes analytical equations for obtaining the reduction factor, which is the ratio of the effective width of a diagonal strut representing a wall with an opening over that of the solid RC infilled frame. That will allow the calculation of the initial lateral stiffness of infills when an opening is present. The validity of the proposed equations is demonstrated by comparing our results, against work done by various researchers.

1 INTRODUCTION

It has been known for long that masonry infill walls affect the strength and stiffness of infilled frame structures. In seismic areas, ignoring the frame-infill panel interaction is not always on the safe side, since, under lateral loads, the infill walls dramatically increase the stiffness by acting as a compressed diagonal ‘strut/area’, resulting, thus, in a possible change of the seismic demand due to significant reduction in the natural period of the composite structural system [1, 2].

The rationale behind neglecting infill walls in the design process is partly attributed to incomplete knowledge of the behaviour of quasi-brittle materials such as unreinforced masonry (URM), of the composite behaviour of the frame and the infill, as well as due to the lack of conclusive experimental and analytical results to substantiate a reliable design procedure for this type of structures, despite the extensive experimental efforts [3-9], and analytical investigations [10-19] over the past decades. Moreover, due to the large number of interacting parameters, if the infill wall is to be considered in the analysis and design stages, a modelling problem arises because of the many possible failure modes that need to be evaluated with a high degree of uncertainty. Therefore, it is not surprising that no consensus has emerged leading to a unified approach for the design of infilled frame systems in spite of more than five decades of research. However, it is generally accepted that under lateral loads an infill wall acts as a diagonal strut connecting the two loaded corners, an approach that is only applicable to the case of infill walls without openings on the diagonal of the infill panel. The reader is referred to Moghaddam and Dowling [20] and Asteris et al. [21] for an extensive review of research on testing and modeling of masonry infilled frames up to 2010.

In this paper the macro-modeling of infilled frames is briefly presented along with a reduction parameter for the representation of infills with openings. Then some analytical studies are presented which are calibrated on experimental results, to show the effect of the openings on the period of vibration of structures and on interstorey drifts using nonlinear dynamic analysis.

2 MACRO-MODELLING OF MASONRY INFILL

Since the first attempts to model the response of the composite infilled-frame structures, experimental and conceptual observations have indicated that a diagonal strut with appropriate geometrical and mechanical characteristics could possibly provide a solution to the problem (Fig. 1).

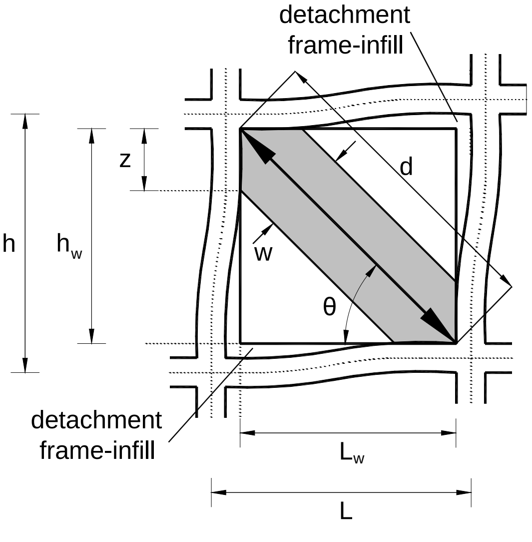

Figure 1: Masonry infill frame sub-assemblage.

Early research on the in-plane behavior of infilled frame structures undertaken at the Building Research Station, Watford (later renamed Building Research Establishment, and now simply BRE) in the 1950s served as an early insight into this behavior and confirmed its highly indeterminate nature in terms solely of the normal parameters of design [22-24]. On the basis of these few tests a purely empirical interaction formula was later tentatively suggested by Wood [25] for use in the design of tall framed buildings. By expressing the composite strength of an infilled frame directly in terms of the separate strengths of the frame and infill, he short-circuited a mass of confusing detail and he recognized the desirability of a higher load factor where strengths were most dependent on the infills.

2.1 Single-strut models

In the early sixties, Polyakov [26] suggested the possibility of considering the effect of the infilling in each panel as equivalent to diagonal bracing, and this suggestion was later adopted by Holmes [27], who replaced the infill by an equivalent pin-jointed diagonal strut made of the same material and having the same thickness as the infill panel and a width defined by

$$\frac{w}{d}=\frac{1}{3} \tag{1}$$

where d is the diagonal length of the masonry panel. The “one-third” rule was suggested as being applicable irrespective of the relative stiffness of the frame and the infill. One year later, Stafford Smith [28], based on experimental data from a large series of tests using masonry infilled steel frames, found that the ratio w/d varied from 0.10 to 0.25. On the second half of sixties Stafford Smith and his associates using additional experimental data [3][4][29] related the width of the equivalent diagonal strut to the infill/frame contact lengths using an analytical equation, which has been adapted from the equation of the length of contact of a free beam on an elastic foundation subjected to a concentrated load [30]. They proposed the evaluation of the equivalent width λ_h as a function of the relative panel-to-frame-stiffness parameter, in terms of

$$\lambda_h = h\sqrt[4]{\frac{E_w t_w \sin 2\theta}{4EIh_w}} \tag{2}$$

where E_w is the modulus of elasticity of the masonry panel, EI is the flexural rigidity of the columns, t_w the thickness of the infill panel and equivalent strut, h the column height between centerlines of beams, h_w the height of infill panel, and θ the angle, whose tangent is the infill height-to-length aspect ratio, being equal to

$$\theta=\tan^{-1}\left(\frac{h_w}{L_w}\right) \tag{3}$$

in which L_w is the length of infill panel (all the above parameters are explained in Fig. 1).

Based on experimental and analytical data Mainstone [31] proposed an empirical equation for the calculation of the equivalent strut width, given by

$$\frac{w}{d}=0.16\lambda_h^{-0.3} \tag{4}$$

Mainstone and Weeks [32] and Mainstone [33], also based on experimental and analytical data, proposed an empirical equation for the calculation of the equivalent strut width:

$$\frac{w}{d} = 0.175\lambda_h^{-0.4} \qquad (5)$$

This formula was included in FEMA-274 (Federal Emergency Management Agency 1997) [34] for the analysis and rehabilitation of buildings as well as in FEMA-306 (Federal Emergency Management Agency 1998) [35], as it has been proven to be the most popular over the years. This equation was accepted from the majority of researchers dealing with the analysis of infilled frames.

2.2 Multiple struts models

Crisafulli (1997) [36] in his PhD thesis investigated the influence of different multi-strut models on the structural response of reinforced concrete infilled frames, focusing on the stiffness of the structure and the actions induced in the surrounding frame. Numerical results, obtained from the single, two and three strut models, were compared with those corresponding to a refined finite element. The lateral stiffness of the structure was similar in all the cases considered, with smaller values for two- and three-strut models. It must be noted that, for the multi-strut models, the stiffness may significantly change depending on the separation between struts. The single strut model underestimates the bending moment because the lateral forces are primarily resisted by a truss mechanism. On the other hand, the two-strut model leads to larger values than those corresponding to the finite element model. A better approximation is obtained from the three-strut model, although some differences arise at the ends of both columns. Although the single-strut model constitutes a sufficient tool for the prediction of the overall response and the triple-strut model is superior in precision, Crisafulli adopted the double-strut model approach, accurate enough and less complicated compared to the other models.

More recently, Crisafulli and Carr (2007) [37] proposed a new macro-model in order to represent, in a rational but simple way, the effect of masonry infill panels. The model is implemented as a four-node panel element which is connected to the frame at the beam-column joints. Internally, the panel element accounts separately for the compressive and shear behavior of the masonry panel using two parallel struts and a shear spring in each direction as shown in Fig. 2.

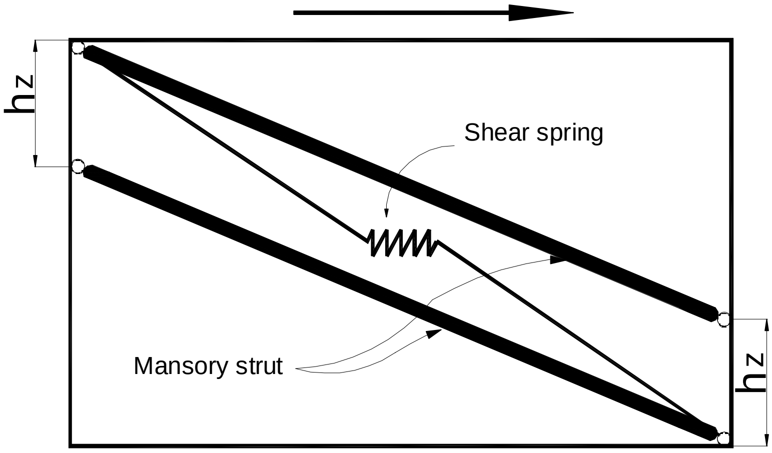

Figure 2: Multi-strut model proposed by Crisafulli and Carr [37] for masonry infill panel (only the struts and the shear spring active in one direction are represented.

This configuration allows an adequate consideration of the lateral stiffness of the panel and of the strength of masonry panel, particularly when a shear failure along mortar joints or diagonal tension failure is expected. Furthermore, the model is easy to apply in the analysis of large infilled frame structures. The main limitation of the model results from its simplicity, since the panel is connected to the beam-column joints of the frame, being thus not able to properly predict the bending moment and shear forces in the surrounding frame.

The proposed model for masonry infill panels was implemented in RUAUMOKO [38], a computer-based analytical tool able to accurately model three dimensional structures whilst providing ancillary design data such as earthquake spectra. The proposed model has been also implemented in the program SeismoStruct [39] and numerical results were compared to experimental data by Smyrou [40] and Smyrou et al. [41], showing the accuracy of the model to evaluate the nonlinear response of the structure. Furthermore, they conducted an interesting sensitivity analysis to evaluate the relative importance of the parameters used in the model to represent the cyclic response of masonry.

2.3 Effect of openings in the lateral stiffness of infill walls

Although infill walls usually have oversized openings, recent research has mainly focused on the simple case of infill wall without openings. Research on infill walls with openings is mostly analytical, restricted to special cases, and as such cannot provide rigorous comparison to actual cases because of its focus on specific materials used and specific types of openings. It is worth noting that the contribution of the infill wall to the frame lateral stiffness is much reduced when the structure is subjected to reversed cyclic loading, as in real structures under earthquake conditions.

In order to investigate the effect of openings in the lateral stiffness of masonry infill walls a finite element technique proposed by Asteris [15][18] has been used in this paper. The basic characteristic of this analysis is that the infill/frame contact lengths and the contact stresses are estimated as an integral part of the solution, and are not assumed in an ad-hoc way.

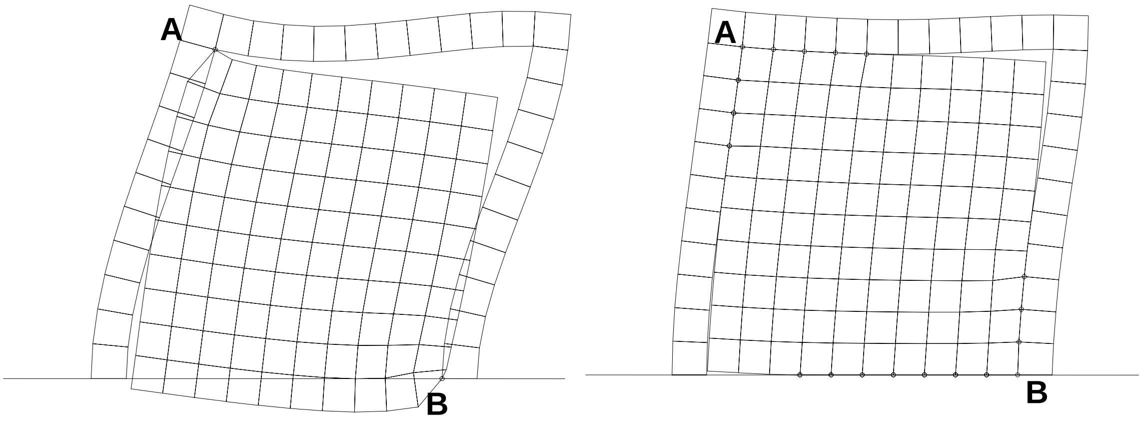

(a) 1st derived mesh (b) 8th-final derived mesh

Figure 3: Deformed meshes of an one-storey one-bay infilled frame using the finite element technique proposed by Asteris [15][18] (Method of Contact Points).

In brief, according to this technique, the infill finite element models are considered to be linked to the surrounding frame finite element models at two corner points (only), at the ends of the compressed diagonal of the infill (points A and B in Fig. 3a). Then, the nodal displacements are computed and checked whether the infill model points overlap the surrounding frame finite elements. If the answer is positive, the neighboring points (to the previous linked) are also linked and the procedure is repeated. If the answer is negative, the procedure is stopped and the derived deformed mesh is the determined one (Fig. 3b).

Using this technique, analytical results are presented on the influence of the opening size on the seismic response of masonry infilled frames. Fig. 4 shows the variation of the λ factor as a function of the opening percentage (opening area/infill wall area), for the case of an opening on the compressed diagonal of the infill wall (with aspect ratio of the opening the same as that of the infill). As expected, the increase in the opening percentage leads to a decrease in the frame's stiffness. Specifically, for an opening percentage greater than 50% the stiffness reduction factor tends to zero.

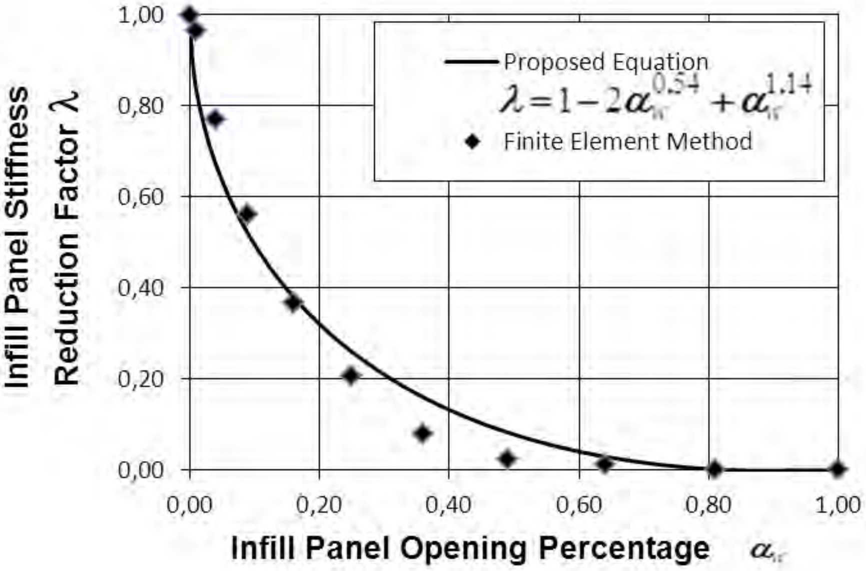

Figure 4: Infill panel stiffness reduction factor in relation to the opening percentage.

The findings of the present parametric study using the finite-element method, lead to the following relationship for the infill wall stiffness reduction factor λ:

$$\lambda = 1 - 2\alpha_w^{0.54} + \alpha_w^{1.14} \tag{6}$$

in which α_w is the infill wall opening percentage (area of opening to the area of infill wall).

The above coefficient could be used to find the equivalent width of a strut for the case of an infill with opening by multiplying the results of Eqns 1, 4 and 5 above. It can also be used to modify the equations of the Crisafulli model, which is described below.

3 NUMERICAL EXAMPLE

In order to illustrate the inadequacy of the single strut models to represent the structural response of infill walls with openings in frame structures, a case-study was carried out, employing a reinforced concrete frame, whereby the infill walls are modeled with each of the two approaches. For the multi-strut case the Crisafulli double-strut model has been chosen, since it is satisfactorily precise to represent accurately the local effect between the infill and the frame and less complicated than a triple-strut model. The single-strut model used is a rather 'gross' model that can be employed in commercial packages. It consists of a pair of diagonal elastic struts that are active at all times, each of which has a stiffness of 50% of the calculated infill-wall stiffness.

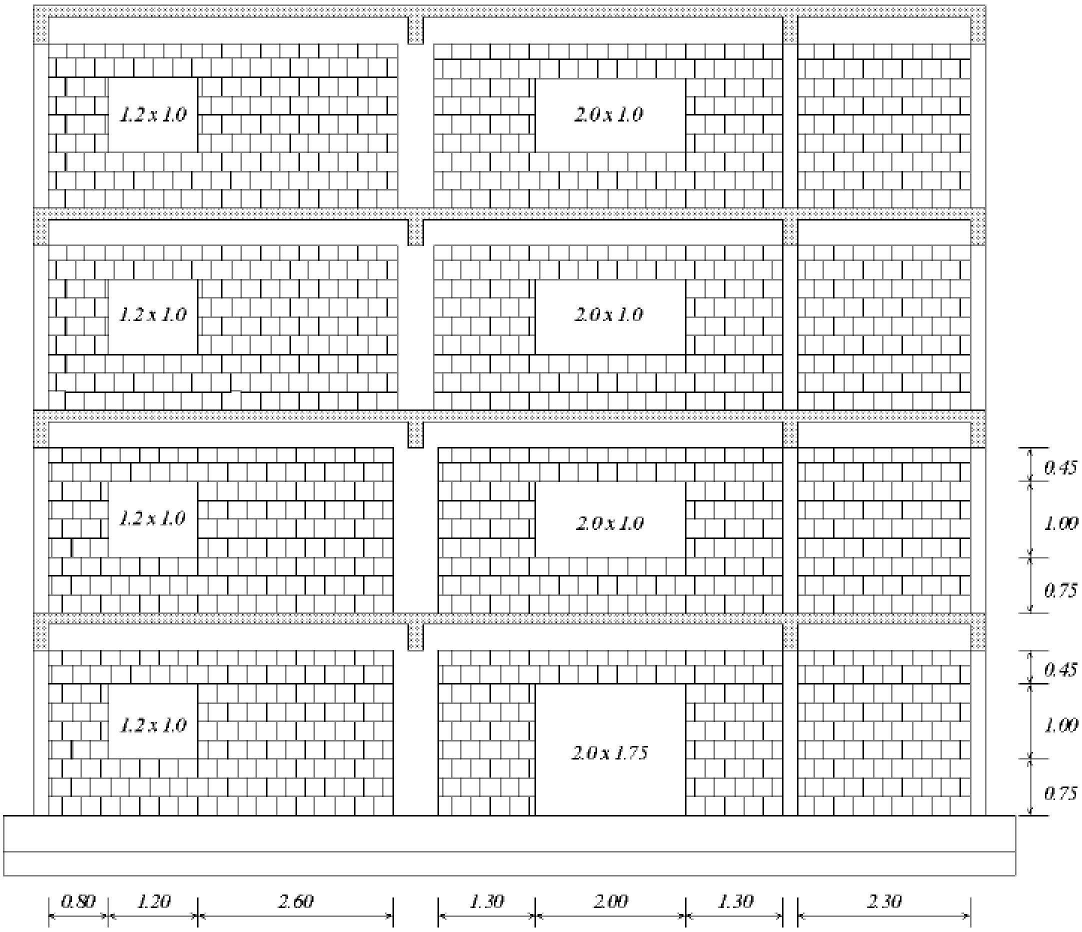

Figure 5: Elevation view of the infilled frame-Location and dimensions of openings [42].

The relative accuracy of the models is assessed through comparison with experimental results obtained from pseudo-dynamic tests of a full-scale four-storey, three-bay reinforced concrete frame, which was tested at the ELSA reaction-wall laboratory within the framework of the ICONS research programme [42]. The frame was infilled with brick walls that included openings of different dimensions (Fig. 5). It can be regarded as representative of the design and construction practice of the 60’s in Southern Europe, designed to withstand only vertical loads, without satisfying the modern seismic-code design-requirements.

The experimental seismic response was obtained with pseudo-dynamic testing, i.e. a step by step integration technique to compute the displacement response of the frame that was subjected to three different, numerically specified seismic records, utilizing the non-linear restoring forces actually developed during the test. The input seismic motions were chosen to be representative of a moderate-high European hazard scenario. The acceleration time-histories were artificially generated [43] and three of increasing return periods of 475, 975 and 2000 years were used for the experiment (only the first two were employed in the present study).

The non-linear structural analysis program SeismoStruct [39] was employed for the analyses. SeismoStruct is an internet-downloadable fiber-based Finite Element package capable of predicting the large displacement behavior of space frames under static or dynamic loading, considering both geometric nonlinearities and material inelasticity and fully accounting for the spread of inelasticity along the member length and across the section depth.

In section 3.1, a comparison is made between the analysis results for the above structure using a single strut and a multi-strut model. This is done to calibrate the model based on experimental data. Then, the same frame is used but having infills with the same percentage of openings in all the panels at all floors. The analyses are used to examine the influence of openings on the period of the structure and the inter-story drift. The effectiveness of the proposed model to represent the effects of soft-stories ('pilotis') is also examined.

3.1 Single strut model vs multiple struts model

Representative numerical results obtained from the single and multi-strut models are depicted in Figure 6. It can be easily concluded that the multi-strut model provides a very good fit to the experimental results and better approximation with the use of finite elements is hardly justified. However it should be stressed that the correct modeling of the infill required the selection of the value of a significant number of parameters, a difficult and intricate task, which is not always appropriate in everyday practice.

On the contrary, the single-strut model lacks a similar ability to represent adequately the experimental behavior, providing significantly less accurate results. This is entirely attributed to the inability of such over-simplified models to reproduce all the complex aspects of the infill walls' behavior. Similar to the above conclusions have been drawn regarding the displacement and the shear-force profiles along the height of the building.

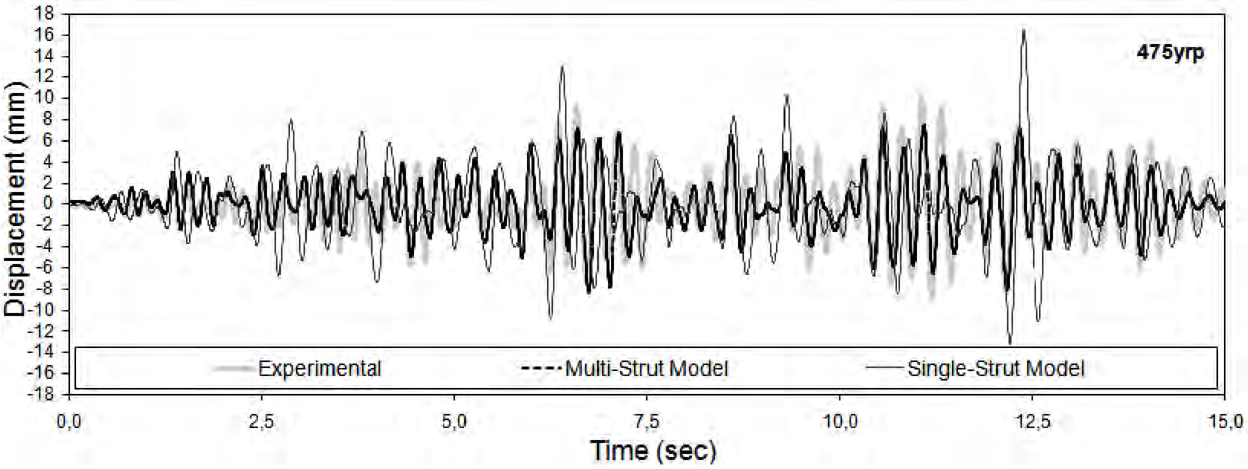

Figure 6: Comparison of the top displacement of the infill frame and the two structural models (475yrp record.

3.2 Effect of openings on fundamental periods

The infill wall enhances the lateral stiffness of the framed structures, however, the presence of openings within the infill wall will reduce the lateral stiffness. Fig. 7 shows the variation of the fundamental period with the opening percentage. All values are also presented in a tabular form (Table 1), where the mass contribution for the fundamental period is given as well. The fundamental period increases as the opening size increases, as expected, due to reduction in stiffness of the model. Such variation of periods cannot be considered using the formulas proposed by design codes. There is no clear relationship between the opening size and the fundamental period, but the opening size does have an influence on the fundamental period of the structure.

By comparing the fundamental periods of a fully infilled (FI) and a bare frame (BF), a difference of magnitude of roughly 9 is observed, which is in agreement with the literature.

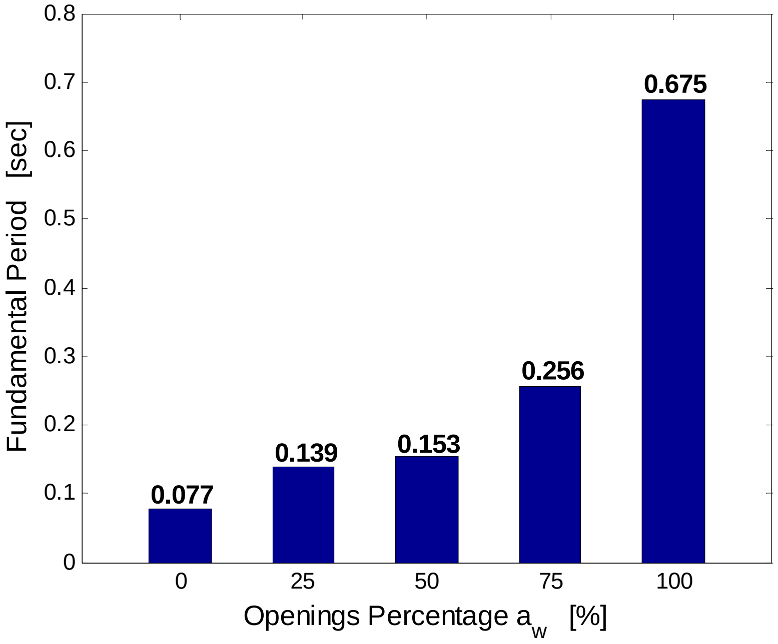

Figure 7: Variation of fundamental period with opening size

Openings a_w [%]	Period [sec]	Mass contribution [%]
0	0.077	59.48
25	0.139	85.76
50	0.153	88.33
75	0.256	87.26
100	0.675	83.17

Table 1: Fundamental periods and mass contributions of various percentage openings

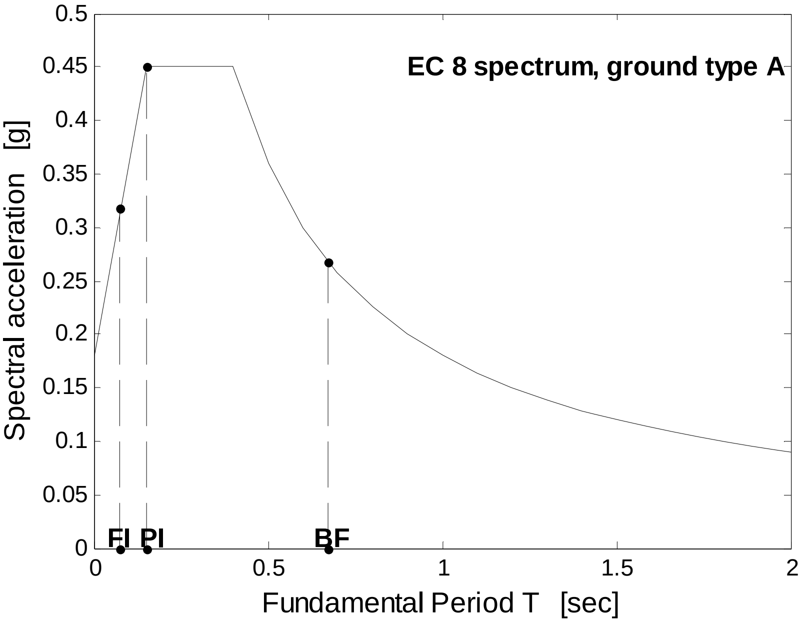

Figure 8: Elastic acceleration spectra for a 475 yrp and the fundamental periods of a fully infilled frame (FI), a partially infilled frame (PI) and a bare frame (BF)

An elastic spectrum according to the standard EC 8 [44] for ground type A was chosen, as can be seen in Fig. 8. In this figure, the periods of the idealized systems representing the fully infilled frame (T=0.077 s), a partially infilled frame (with 50% of openings) (T=0.153 s) and a bare frame (T=0.675 s) are indicated. It can be observed that the spectral acceleration, which corresponds to the bare frame (BF), is only about half of the spectral acceleration, which corresponds to the partially infilled frame (PI) and a bit lower than the corresponding value for a fully infilled frame (FI). It is clear that such a variation of the period of vibration will have a considerable effect on the dimensioning of the infilled-frame members.

3.3 Effect of openings on inter-storey drift ratios

The displacement variation along the building height is a typical way of illustrating the behaviour of a building in each storey. A better representation of the above is the use of the interstorey drift curve given in Fig. 9.

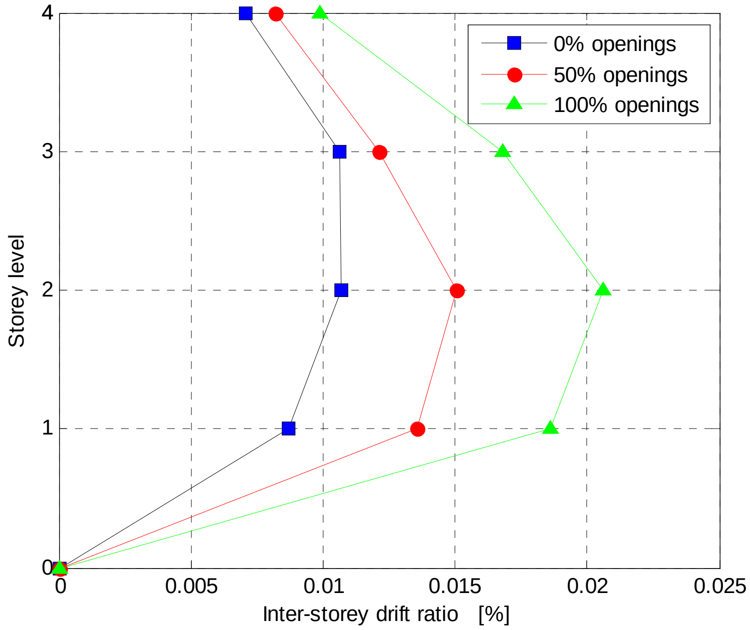

Figure 9: Inter-storey drift after 15 load-cycles (475 yrp)

This figure shows the inter-storey drift ratio after 15 complete load cycles. The ‘weakeness’ of the second floor is more pronounced when larger openings in the infill panels are present. Three different cases of openings are illustrated and the resulting inter- storey drift ratio confirms the previous statement. The same conclusion was reached by Dorji et al. [45], who presented the inter-storey drifts ratios for three different opening percentages.

Fig. 10 shows the response-history of the infilled frame for the same percentages of openings as those of Fig. 9. When there are no infill walls (a_w = 100%) the interstory drifts are considerably larger compared to the ones for the other two cases, when the structure is considerably stiffer. Even in the case when there are 50% openings the interstory drifts are considerably smaller that those of the bare frame. Another observation is that there is clear distinction in the periods of vibration of the three structures with the bare structure having the larger and the fully infilled the smaller of the three.

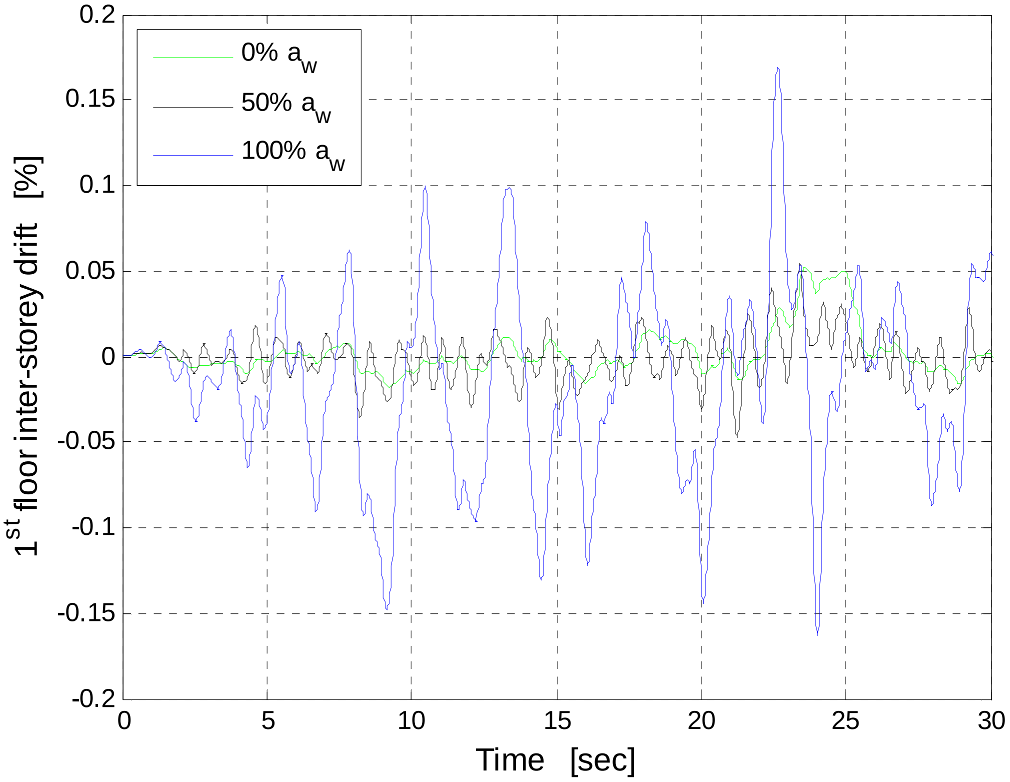

Figure 10: Response-history of inter-storey drift of the 1st floor for 0%, 50% & 100% openings (475 yrs)

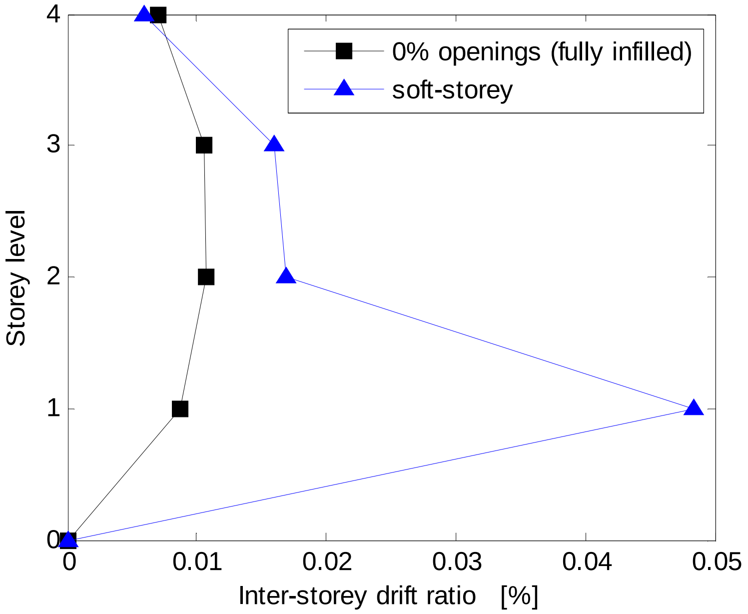

Figure 11: Inter-storey drift showing the soft-storey effect after 15 load cycles (475 yrs)

The applicability of the proposed procedure for representing the openings in the walls was examined by introducing a ‘pilotis’, which may cause the soft-storey phenomenon during dynamic earthquake loads. This study investigated this problem by comparing two models;

(a) A structure with fully infilled frames throughout the height of the building.
(b) A structure which does not have any infill at the first floor but has fully infilled frames in the rest of the floors, representing the presence of a ‘pilotis’.

From Fig. 11, which shows the results at the 15th cycle of the analysis, it can be concluded that there is a strong soft-storey effect, which is captured by the proposed modeling. The drift ratio value at the ground floor for case (b) is increased almost 5 times when compared to case (a).

4 CONCLUSIONS

In this paper the attempts of researchers through many decades to model infill walls are summarized and the most commonly used macromodels are presented. One of the main difficulties to introduce infill walls, which are universally accepted as having a significant influence in the response of frames in the modeling of structures is the absence of a way to represent openings in the infills. In this work, a reduction factor, λ, is proposed that can be used as a multiplication factor on well know equations to calculate the reduced equivalent equivalent width of compression struts, so as to be able to model infill walls with openings. The same reduction factor can be use in models of multiple-struts so as to be able to idealize the nonlinear behaviour of infill walls with openings.

Using this approach, a two-strut model, which was calibrated on experimental results, was used to examine the effects of openings on the period of vibration of infilled structures with openings and on interstorey drifts.

It was shown that, as expected, the period of vibration of the structures is largely affected by the presences of openings, which in turn has an effect on the earthquake load that such structures will be subjected to during an earthquake. The period of vibration of the infilled frame was found to be 9 times smaller than that of the bare frame, with the periods of vibration of the frames with openings to be in-between, but without a clear trend.

Regarding the interstory drifts, it is shown that at the beginning of the analysis, when the infill and the structure are still in linear behaviour, the bare frame has interstory drifts of the order of 2 times larger than those of the fully infilled frame (Fig. 9). When the structure moves into more cycles, this difference goes as high as 3 times larger (Fig. 10).

The proposed procedure was also used to study the behaviour of a structure with a soft-story, and as it is shown in Fig. 11, the interstory drift at the 1st storey has increased dramatically, while a small increase was also introduced in the higher stories.

It can be therefore concluded, that the proposed reduction factor can be used to model infill frames with openings with satisfactory results. Further work needs to be done, using a larger number of ground motions and frame configurations , so as to fully validate this methodology.

REFERENCES

[1] W.W. El-Dakhakhni, M. Elgaaly, A.A. Hamid, Three-Strut model for concrete masonry-infilled frames, *J. Struct. Eng.*, ASCE, **129**(2), 177-185, 2003.

[2] M.M. Kose, Parameters affecting the fundamental period of RC buildings with infill walls, *Engineering Structures*, **31**, 93-102, 2009.

[3] B.S. Smith, Behavior of square infilled frames, *J. Struct. Div.*, ASCE, ST1, 381-403, 1966.

[4] B.S. Smith, C. Carter, A method of analysis for infilled frames, *Proc., Instn. Civ. Engrs.*, 44, 31-48, 1969.

[5] A.W. Page, P.W. Kleeman, M. Dhanasekar, An In-Plane Finite Element Analysis Model for Brick Masonry, *Proc. of a session held in conjunction with Structures Congress'85*, Chicago, Ill, 1-18, 1985.

[6] A.B. Mehrabi, P.B. Shing, M. Schuller, J. Noland, Experimental evaluation of masonry-infilled RC frames, *J. Struct. Engrg*., ASCE, **122**(3), 228-237, 1966.

[7] S.G. Buonopane, R.N. White, Pseudodynamic Testing of Masonry Infilled Reinforced Concrete Frame, *J. Struct. Eng.*, ASCE, **125**(6), 578-589, 1999.

[8] M.H. Santhi, G.M.S. Knight, K. Muthumani, Evaluation of seismic response of soft-storey infilled frames, *Computers and Concrete*, **2** (6), 423-437, 2005.

[9] M.H. Santhi, G.M.S. Knight, K. Muthumani, Evaluation of Seismic Performance of Gravity Load Designed Reinforced Concrete Frames, *Journal of Performance of Constructed Facilities*, **19**(4), 277-282, 2005.

[10] T.C. Liauw, K.H. Kwan, Nonlinear behaviour of non-integral infilled frames, *Comp. and Struct.*, **18**, 551-560, 1984.

[11] M. Dhanasekar, A.W. Page, Influence of brick masonry infill properties on the behaviour of infilled frames, *Proc., Instn. Civ. Engrs.*, London, Part 2, 81, 593-605, 1986.

[12] C.Z. Chrysostomou, *Effects of degrading infill walls on the nonlinear seismic response of two-dimensional steel frames*, PhD thesis, Cornell University, Ithaca, N.Y, 1991.

[13] A. Saneinejad, B. Hobbs, Inelastic design of infilled frames, *J. Struct. Engrg.*, ASCE, **121**(4), 634-650, 1995.

[14] C.Z. Chrysostomou, P. Gergely, J.F. Abel, A six-strut model for nonlinear dynamic analysis of steel infilled frames, *International Journal of Structural Stability and Dynamics*, **2**(3), 335-353, 2002.

[15] P.G. Asteris, Lateral stiffness of brick masonry infilled plane frames, *J. Struct. Eng.*, ASCE, **129**(8), 1071-1079, 2003.

[16] H.A. Moghaddam, Lateral Load Behavior of Masonry Infilled Steel Frames with Repair and Retrofit, *J. Struct. Engrg*., ASCE, **130**(1), 56-63, 2004.

[17] P.G. Asteris, Closure to Lateral Stiffness of Brick Masonry Infilled Plane Frames by P. G. Asteris, *J. Struct. Engrg. ASCE*, **131**(3), 523-524, 2005.

[18] P.G. Asteris, Finite Element Micro-Modeling of Infilled Frames, *Electronic Journal of Structural Engineering*, **8**, 1-11, 2008.

[19] D.J. Kakaletsis, C.G. Karayannis, Experimental Investigation of Infilled Reinforced Concrete Frames with Openings, *ACI Structural Journal*, **106**(2), 132-141, 2009.

[20] H.A. Moghaddam, P.J. Dowling, *The State of the Art in Infilled Frames*, ESEE Research Report No. *87-2*, Imperial College of Science and Technology, Civil Eng. Department, London, U.K, 1987.

[21] P.G. Asteris, S.T. Antoniou, D.S. Sophianopoulos, C.Z. Chrysostomou, Mathematical Macro-Modeling of Infilled Frames: State-of-the-Art, *J. Struct. Engrg.*, ASCE, (http://dx.doi.org/10.1061/(ASCE)ST.1943-541X.0000384).

[22] F.G. Thomas, The strength of brickwork, *Struct. Engrg.*, **31**(2), 44-46, 1953.

[23] R.H. Wood, The stability of tall buildings, *Proc., Instn. Civ. Engrs.*, 11, 69-102, 1958.

[24] R.J. Mainstone, Discussion on steel frames with brickwork and concrete infilling, *Proc., Instn. Civ. Engrs.*, 23, 94-99, 1962.

[25] R.H. Wood, Discussion on the stability of tall buildings, *Proc., Instn. Civ. Engrs.*, 12, 517-518, 1959.

[26] S.V. Polyakov, On the interaction between masonry filler walls and enclosing frame when loading in the plane of the wall, *Translation in earthquake engineering, Earthquake Engineering Research Institute*, San Francisco, 36-42, 1960.

[27] M. Holmes, Steel frames with brickwork and concrete infilling, *Proc., Instn. Civ. Engrs.*, London, Part 2, 19, 473-478, 1961.

[28] B.S. Smith, Lateral Stiffness of Infilled Frames, *J. Struct. Div.*, ASCE, Vol. 88, No. ST6, 183-199, 1962.

[29] B.S. Smith, Methods for Predicting the Lateral Stiffness and Strength of Multi-Storey Infilled Frames, *Building Science*, Vol. 2, 247-257, 1967.

[30] M. Hetenyi, *Beams on elastic foundations*, University of Michigan Press, Ann Arbor, 1946.

[31] R.J. Mainstone, On the stiffnesses and strengths of infilled frames, *Proc., Instn. Civ. Engrs.*, Supp. (iv), 57-90, 1971.

[32] R.J. Mainstone, G.A. Weeks, The influence of Bounding Frame on the Racking Stiffness and Strength of Brick Walls, *Proceedings of the 2nd International Brick Masonry Conference,* Building Research Establishment, Watford, England, pp. 165-171, 1970.

[33] R.J. Mainstone, Supplementary note on the stiffness and strengths of infilled frames, *Current Paper CP 13/74*, Building Research Station, Garston, Watford, U.K, 1974.

[34] Federal Emergency Management Agency (1997). “NEHRP Commentary on the Guidelines for the Seismic Rehabilitation of Buildings.” FEMA-274,Applied Technology Council, Washington, DC.

[35] Federal Emergency Management Agency (1998). “Evaluation of earthquake damaged concrete and masonry wall buildings: basic procedures manual.” FEMA-306, Applied Technology Council, Washington, DC.

[36] F.J. Crisafulli, Seismic Behaviour of Reinforced Concrete Structures with Masonry Infills, *Ph.D. Thesis*, University of Canterbury, Christchurch, New Zealand, 1997.

[37] F.J. Crisafulli, A.J. Carr, Proposed macro-model for the analysis of infilled frame structures. *Bulletin of the New Zealand Society for Earthquake Engineering,* **40**(2), 69-77, 2007.

[38] A,J. Carr, RUAUMOKO: Inelastic Dynamic Analysis, Department of Civil Engineering, University of Canterbury, <http://www.ruaumoko.co.nz>.

[39] SeismoSoft (2009), SeismoStruct – A Computer Program for the Static and Dynamic Analysis of Framed Structures, http://www.seismosoft.com.

[40] E. Smyrou, Implementation and verification of a masonry panel model for nonlinear dynamic analysis of infilled rc frames, Dissertation for the MSc in Earthquake Engineering, European School for Advanced Studies in Reduction of Seismic Risk (ROSE SCHOOL), Universita degli Studi di Pavia, Italy, 2006.

[41] E. Smyrou, C. Blandon-Uribe, S. Antoniou, R. Pinho, H. Crowley, Implementation and Verification of a Masonry Panel Model for Nonlinear Pseudo-Dynamic Analysis of Infilled RC Frames, *Proceedings of the First European Conference on Earthquake Engineering and Seismology*, Geneva, Switzerland, 2006.

[42] A. Pinto, G. Verzeletti, J. Molina, H. Varum, R. Pinho, E. Coelho, Pseudo-Dynamic Tests on Non-Seismic Resisting RC Frames (Bare and Selective Retrofit Frames), Joint Research Centre, Ispra, 1999.

[43] A. Campos-Costa, A.V. Pinto, A.V. (1999), European Seismic Hazard Scenarios – An Approach to the Definition of Input Motions for Testing and Reliability Assessment of Civil Engineering Structures , JRC Special Publication, no X.99.XX, ELSA, JRC – Ispra, Italy, 1999.

[44] CEN. Eurocode 8: Design of structures for earthquake resistance. Part I: General rules, seismic action and rules for buildings. Brussels; 2004.

[45] J. Dorji and D.P. Thambiratnam, Modelling and Analysis of Infilled Frame Structures Under Seismic Loads, *The Open Construction and Building Technology Journal*, **3**, 119-126, 2009.

COMPDYN 2011
III ECCOMAS Thematic Conference on
Computational Methods in Structural Dynamics and Earthquake Engineering
M. Papadrakakis, M. Fragiadakis, V. Plevris (eds.)
Corfu, Greece, 25–28 May 2011

RISK ASSESSMENT OF HISTORIC RESIDENTIAL BRICK-MASONRY BUILDINGS IN VIENNA BY RAPID-VISUAL-SCREENING

Günther Achs[1], **and Christoph Adam**[2]

[1] VCE-Holding GmbH
Hadikgasse 60, 1140 Vienna, Austria
achs@vce.at

[2] University of Innsbruck, Department of Civil Engineering Sciences
Technikerstr. 13, 6020 Innsbruck, Austria
christoph.adam@uibk.ac.at

Keywords: Rapid-Visual-Screening, Damage scenario, Inspection form, Vulnerability estimation.

Abstract. *In recent years the evaluation of risk levels of existing buildings by Rapid-Visual-Screening (RVS) has become a common tool for seismic hazard assessment. If RVS is applied to buildings of similar type located in a well-defined urban area, it is useful to specify and to adapt existing screening rules and forms to the needs of these buildings. In a research effort presented in this paper the RVS procedure is adapted for the seismic assessment of historic residential brick-masonry buildings located in the City of Vienna, Austria. Considering the consistent building typology the proposed RVS methodology enhances the validity and quality of the seismic hazard assessment of this type of buildings. The evaluation and assessment methodology is based on two parameters, i.e. the damage relevance DR, and the structural parameter SP. Limiting conditions of the damage relevance DR are generated for risk classification to consider human and economic influence of damages on a certain building. The structural parameter SP consists of several indicators to describe the condition of certain structural parts of the building itself. In a large-scale in situ investigation a set of 375 buildings within the 20th district of Vienna has been evaluated by the proposed methodology. The results of this visual investigation are integrated into a local seismic building hazard map.*

1 INTRODUCTION

1.1 Objective

Reliability of existing buildings against seismic collapse is a major issue of a comprehensive seismic hazard assessment. Particularly in urban areas with a huge amount of historic buildings the evaluation and assessment of those buildings is essential. In the city center of Vienna so-called *Gründerzeithäuser*, historic residential brick-masonry structures erected within the building phase between 1840 and 1918, represent the predominant type of building. Mostly, these structures have been retained unchanged without considerable structural improvement for decades, but nevertheless are typically still used as residential buildings. Especially the lack of information and scientific investigations about the material properties, the detailed construction, and the dynamic behavior of those buildings has led to many discussions about their vulnerability under seismic loading.

The main intent of the investigations proposed in this paper is to carry out a comprehensive assessment and evaluation methodology based on visual inspections for historic brick-masory buildings in Vienna in order to obtain a realistic estimation of the damage potential under seismic loading of this particular building type [1].

1.2 Prevalent Risk Assessment Methodologies

Several different methodologies for the assessment and classification of existing buildings were developed in the last few years [2]. Many of them, so called Rapid-Visual-Screening (RVS) techniques, are based on visual inspection of the buildings using predefined forms. Their main advantage is the fast and elementary implementation, which allows the user to evaluate a huge amount of buildings in a relatively short time period.

Particularly in areas with high seismicity the application of RVS techniques is widespread. One of the basic documents, developed and used in the United States of America, is the RVS technique described in the handbook for seismic evaluation of existing buildings by the Applied Technology Council [3]. This method has already been used for years and is an important foundation for various international techniques. In particular the method is based on a scoring system, whereby different building parameters are classified and benchmarked.

Apart from the RVS procedures in the United States of America several other techniques have been developed in different countries. The Japanese technique [4] is based on the so-called Seismic Index (I_S), which describes the resisting earthquake capacity of a story and is estimated from the strength and ductility of the building, the regularity of the building and a certain time index. In contrast, the RVS procedure in Canada accounts for structural parameters, such as the stiffness and the regularity of the building, as well as for nonstructural parameters including the foundation of the building, building occupancy, importance of the building, and falling hazards. Compared to other countries, India has a very large amount of existing buildings of different types, which led to the development of different RVS procedures in the last few years [5, 6].

Most of the European RVS procedures were developed in Greece [7, 8] and in Turkey [9, 10, 11], whereby the investigated masonry buildings of the high seismicity area of Istanbul [12, 13] are of primary interest for the proposed RVS procedure developed for historic residential brick-masonry buildings in Vienna.

The fundamentals of the procedure described in this paper were developed for historic masonry buildings in Italy [14] and Portugal [15]. On the one hand, the assessment of brick-masonry facades can be directly applied by quantifying the building geometries [1, 14]. On the other hand the connection of the damage relevance *DR* with damage grades from EMS-98 [16] according to *Ferreira* [15] gives a reliable estimation of the possible extent of losses.

Among the numerous other RVS procedures methods developed in Germany [17, 18] are of particular interest for the proposed RVS technique in Vienna, as they were applied on similar historic buildings in areas with comparable seismicity.

2 APPLICATION TO HISTORIC RESIDENTAL BUILDINGS IN VIENNA

2.1 Basic Data

It was necessary to consider historic documents, such as building codes from the 19th century [19, 21, 22, 29] and findings from actual investigations [23, 24, 25], in order to develop a suitable RVS procedure for the historic residential brick-masonry buildings in Vienna. Particularly in the last few years a guideline for the in-situ assessment for existing buildings was developed, mainly focused on the evaluation of the state of preservation of the structural system [24].

2.2 Inspection Form and Rating Methodology

As most of the international RVS procedures are focused on typical construction types, an adopted method with specific parameters for the historic residential buildings in Vienna had to be developed. The fundamentals for the evaluation and assessment methodology are based on two types of parameters to describe

- the damage relevance *DR* and
- the structural parameter *SP* of the inspected building,

as shown in [26]. The damage relevance *DR* includes parameters to evaluate the social and economic influence of damages on a certain building. One of the main parameters of the damage relevance is the number of exposed persons within the inspected object. An overview on the content of the damage relevance *DR* and the description and quantification of several parameters is presented in Table 1. The structural parameter SP mainly consists of single indicators to describe certain structural parts of the building itself. The most important parameters, which can be directly related to earthquake induced damage, are the regularity of the building in elevation and the state of preservation. The description of the structural parameter *SP* is given in Table 2.

To categorize and prioritize the buildings the combination of damage relevance *DR* and structural parameter *SP* is used to define hazard classes:

Hazard Class *I:* $SP < 50$ and $DR < 50$

Hazard Class *II:* $80 > SP \geq 50$ and $DR < 100$
or $100 > DR \geq 50$ and $SP < 80$

Hazard Class *III:* $140 > SP \geq 80$ and $DR < 150$
or $150 > DR \geq 100$ and $SP < 140$

Hazard Class *IV:* $SP \geq 140$ or $DR \geq 150$

The visualization of the conditions to define the hazard classes is illustrated in Figure 1.

Parameter	Description	Benchmarks
D_{01} Human exposure	Number of endangered individuals within the inspected object (estimation accepted in case of limited accessibility of the inspected object).	$D_{01} = No.\ of\ Individuals$
D_{02} Importance	Importance of the inspected object according to [27], ranging from importance class I to IV.	$D_{02} = 1.0 - 50.0$
D_{03} Economic importance	Useable living area ULA multiplied by the potential price per m² and consideration of the remaining life time RLT of the inspected object.	$D_{03} = \frac{ULA \cdot Price}{100000} \cdot \frac{RLT}{25}$
D_{04} Material assets	Consideration of buildings with special purposes ranging from residential use (I), to archives and libraries (II) and museums or churches (III).	$D_{04} = 1.0 - 10.0$
D_{05} Neighboring effects	Assessment of possible effects due to collapsed buildings or building parts, ranging from low exposure (I), to medium exposure (II) and high exposure (III).	$D_{05} = 1.0 - 10.0$
	Damage Relevance	$DR = \sum_{i=1}^{5} D_i$

Table 1: Set of parameters describing the damage relevance *DR*.

Parameter	Description	Benchmarks
S_{01} Seismicity	Evaluation of the seismic zone according to [28].	$S_{01} = 1.0 - 1.5$
S_{02} Regularity in plan	Classification of the regularity in plan according to [27] and a defined regularity in plan [1].	$S_{02} = 1.0 - 10.0$
S_{03} Regularity in elevation	Consideration of vertical irregularities with special attention on soft stories.	$S_{03} = 1.0 - 100.0$
S_{04} Type of construction	Evaluation of steel ties, masonry ceilings, etc. [1].	$S_{04} = 1.0 - 25.0$
S_{05} Local failure	Potential local failure mechanism of the facades of the inspected buildings [1] according to [14].	$S_{05} = 1.0 - 20.0$
S_{06} Secondary structures	Evaluation of exposed secondary structures [1] (chimneys, sculptures and statues of the façade, etc.).	$S_{06} = 0.0 - 20.0$
S_{07} Soil conditions	Assessment of the local soil conditions classified according to [27].	$S_{07} = 1.0 - 10.0$
S_{08} Foundation	Classification of the foundation of the inspected building [1].	$S_{08} = 1.0 - 10.0$
S_{09} State of preservation	Evaluation of the state of preservation of the structure [1] (ceilings, columns, brick-masonry, etc.).	$S_{09} = 0.0 - 30.0$
	Structural Parameter	$SP = \sum_{i=1}^{9} S_i$

Table 2: Set of parameters describing the structural parameter *SP*.

To simplify the visual screening of the building on-site a short inspection form was generated [1]. The form should give the surveyor a step-by-step concept and support the inspection. After digitalization of the data several parameters were generated automatically.

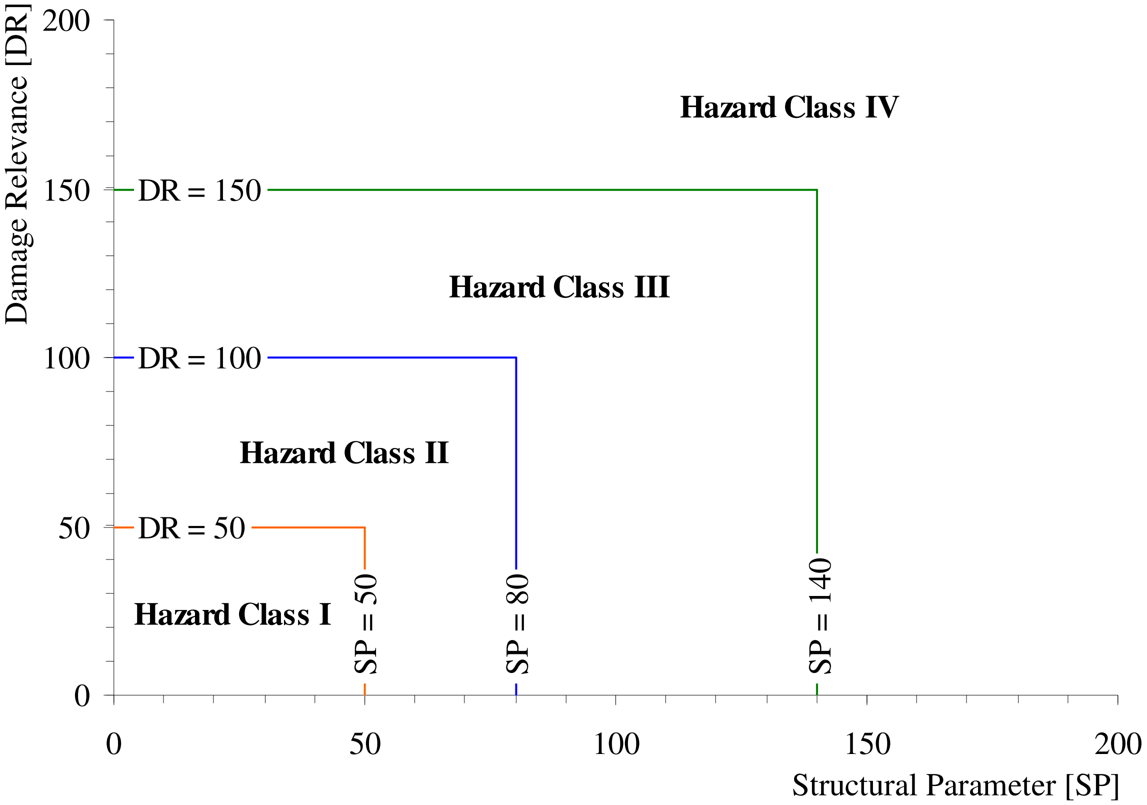

Figure 1: Visualization of the conditions to define the hazard classes.

2.3 Damage Estimation

The outcome of post-earthquake assessment reports was used to correlate the evaluated results from the proposed RVS technique for historic residential brick-masonry buildings in Vienna with a possible damage behavior under seismic action. This method can be used if no particular vulnerability curves of the inspected buildings are available [15].

In a first step an earthquake event with similar characteristics like it is predicted for the Vienna basin area [29] related to magnitude, focal depth and site properties as well as adequate building stock was selected. From the past earthquakes the 2009 Earthquake, which hit the city of L'Aquila in the Abruzzo region in Italy, was chosen [30]. The description of damages occurred to historic residential masonry buildings after this event can be found in [30, 31]. The main outcome of the post-earthquake reports was that some of the proposed structural parameters for historic residential brick-masonry buildings in Vienna can be directly related to seismic damage. The most important ones apparently are the regularity in elevation, soft stories and the detailed design of connections between timber ceilings and bearing walls and of course the state of preservation of the affected building structure.

The comparison between damages occurred in L'Aquila [30, 31], the damage description of the EMS-98 Scale [16], which are given in Table 3, and the outcome of the RVS technique for historic residential brick-masonry buildings in Vienna led to the relations listed in Table 4.

Grade	Description of Damage	Visualization
1	**Negligible to slight damage** ***(no structural damage, slight non-structural damage)*** - Hair-line cracks in very few walls - Fall of small pieces of plaster only - Fall of loose stones from upper parts of buildings in very few cases.	
2	**Moderate damage** ***(slight structural damage, moderate non-structural damage)*** - Cracks in many walls - Fall of fairly large pieces of plaster - Partial collapse of chimneys	
3	**Substantial to heavy damage** ***(moderate structural damage, heavy non-structural damage)*** - Large and extensive cracks in most walls - Roof tiles detach - Chimneys fracture at the roof line - Failure of individual non-structural elements (partitions, gable walls).	
4	**Very heavy damage** ***(heavy structural damage, very heavy non-structural damage)*** - Serious failure of walls - Partial structural failure of roofs and floors	
5	**Destruction** ***(very heavy structural damage)*** - Total or near total collapse	

Table 3: Classification of masonry buildings according to EMS-98 [16].

Therein several values of the assessment results, which were interpreted as boundary conditions for the proposed hazard classes, were related to predicted damage grades according to EMS-98 [16] and relevant structural conditions, which have to be fulfilled by the inspected object. It is obvious that buildings with high regularity in plan and elevation and a very good state of preservation, which were classified in hazard class *I*, should resist an earthquake similar to the one occurred in L'Aquila [30] with moderate damages. On the other hand building structures with high irregularity in elevation and potential soft stories, which are generally in a poor state of preservation and therefore were classified in hazard class *IV*, might be predicted to show very heavy damages up to total destruction of the building under the exposure of the proposed earthquake. In between the buildings with slight or moderate irregularity in plan and elevation and moderate up to good state of preservation, which were classified into hazard classes *II* or *III* respectively, were predicted to show different grades of damage according to EMS-98 [16], ranging from moderate to very heavy damage.

Hazard Class	Assessment requirements Structural Parameter *SP* Damage Relevance *DR*	Predicted Damage Grade based on EMS-98	Relevant Structural Conditions
I	$SP < 50$ and $DR < 50$	2	High regularity in plan and elevation; excellent state of preservation
II	$80 > SP \geq 50$ and $DR < 100$ or $100 > DR \geq 50$ and $SP < 80$	2-3	Slight irregularity in plan and elevation; good state of preservation
III	$140 > SP \geq 80$ and $DR < 150$ or $150 > DR \geq 100$ and $SP < 140$	3-4	Moderate irregularity in elevation; subsequently removed bearing elements; moderate state of preservation
IV	$SP \geq 140$ or $DR \geq 150$	4-5	High irregularity in elevation; soft-story; in general poor state of preservation

Table 4: Set of parameters describing the structural parameter *SP*.

3 APPLICATION

The developed RVS technique for historic residential brick-masonry buildings in Vienna has been calibrated by application to a set of buildings with very well known construction type, material behavior, and socio-economic parameters. These 18 buildings distributed across the historic city center of Vienna should represent a wide range of evaluation parameter possibilities. A comprehensive description of those buildings, the results of the RVS technique application and outcome of the calibration are shown in [1].

After the calibration of the technique a large scale experimental investigation was performed. Therefore an adequate test area was chosen in the 20th district of Vienna with a set of 375 historic residential brick-masonry buildings. A site plan of the test area is shown in Figure 2 with the inspected objects highlighted in red. It can be seen that the historic residential brick-masonry buildings are the predominant building type within the test area. In particular, whole blocks of buildings remained homogeneous since their erection in the 19th century.

3.1 Results

According to the developed RVS technique an engineer was trained on the characteristics of the methodology. The inspection of the buildings was performed continuously within a time period of three months. Besides the in-situ completed inspection forms where digitalized and analyzed. The comprehensive results of each inspected building and any evaluated parameter can be found in [1]. In Figure 3 the results of the damage relevance *DR* plotted against the structural parameter *SP* of the large scale application is shown.

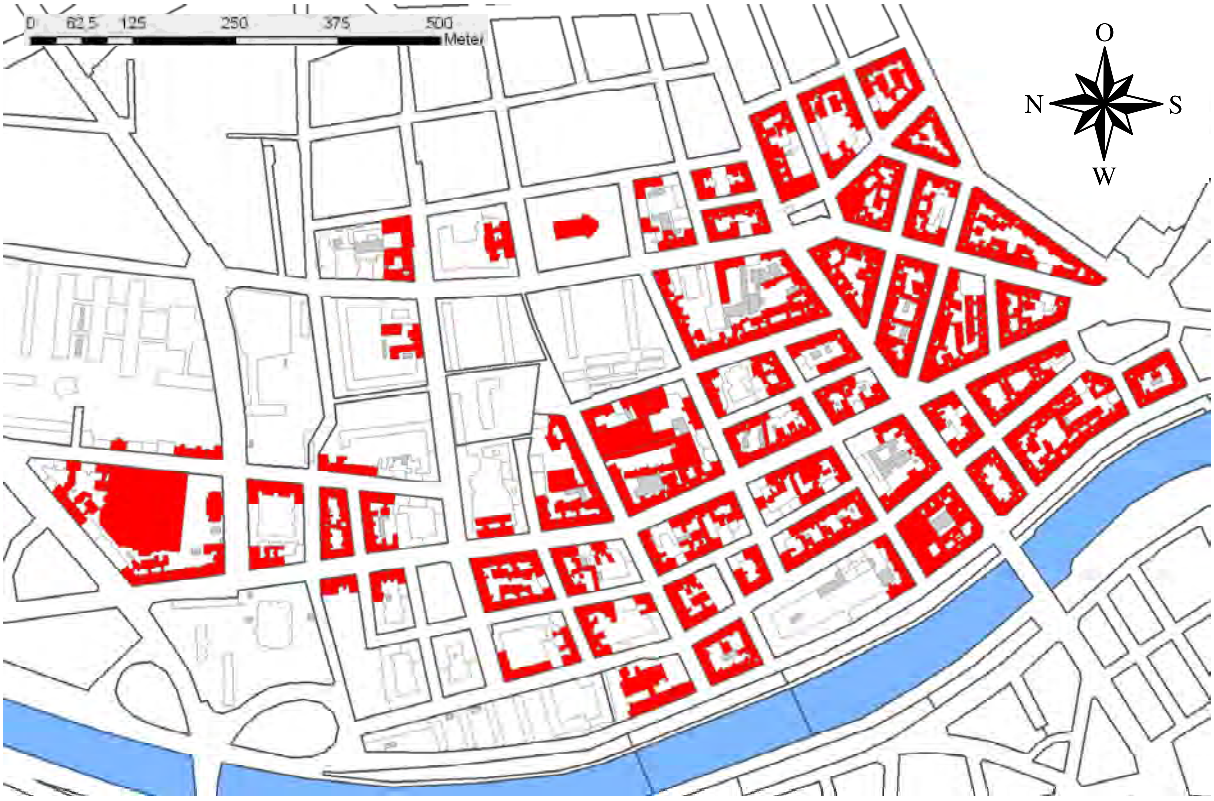

Figure 2: Map of the test area in Vienna; inspected historic residential buildings (highlighted in red).

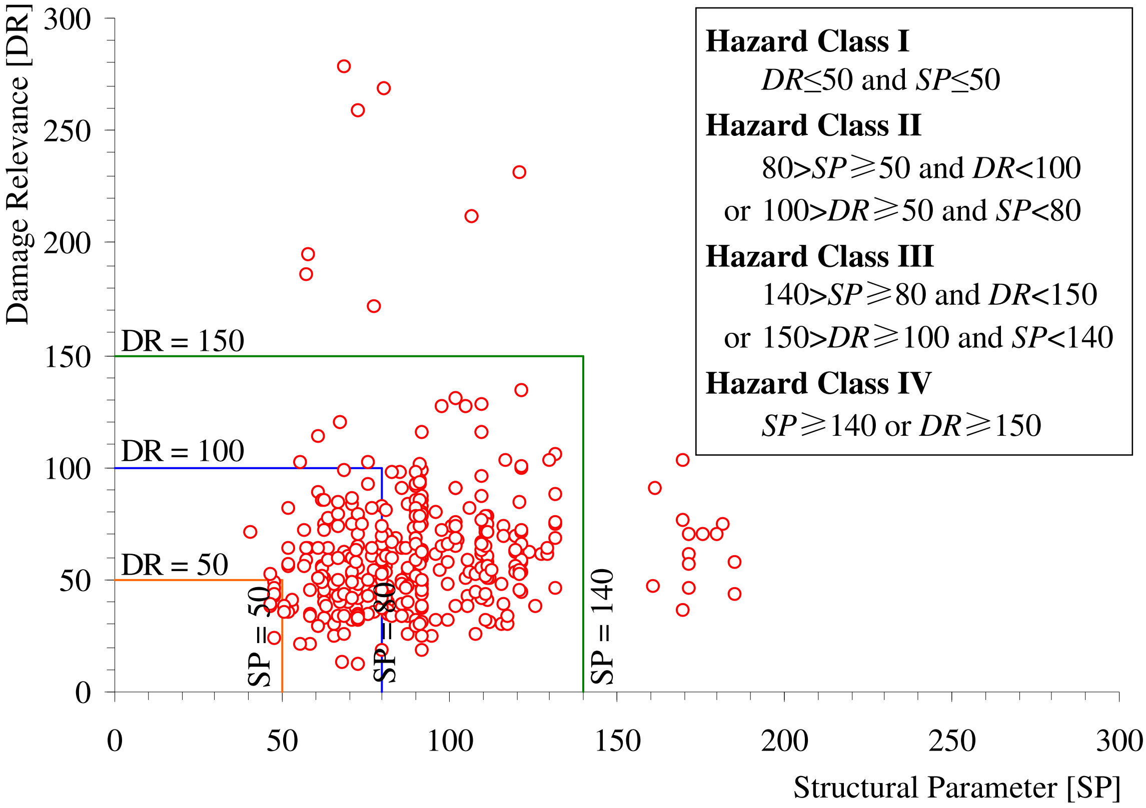

Figure 3: Results of the damage relevance *DR* plotted against the structural parameter *SP* of the large scale application.

It can be seen from Figure 3 that the results of the large scale experiment show a precise separation of hazard classes *III* and *IV* either in terms of the damage relevance *DR* or the structural parameter *SP*. Hence inspected objects classified in hazard class *IV* either have a comparatively high damage relevance *DR*, predominantly caused by the high number of exposed persons within the building, or have a very high structural parameter *SP*, which can be only generated by an irregularity in elevation.

According to Figure 3 most of the inspected objects were classified in hazard classes *II* or *III*, whereby no precise separation between those classes can be observed. The main reason for that is the high number of different parameters and hence the benchmarks of a single parameter at a specific building may vary a lot.

The previously proposed methodology was used to correlate the results of the RVS assessment with predicted building damage, see section 2.3. In a first step the inspected objects were classified according to their structural parameter *SP*. Hence the damage grades according to EMS-98 [16] were correlated with the inspected buildings considering the scheme from Table 4, see Figure 4. It can be seen that the separation between damage grades 3 and 4 according to EMS-98 does not exactly correspond to the classification of the hazard classes *II* and *III* from Table 4. The reason therefore is that the frequency distribution of the structural parameter *SP* of the inspected buildings gives a better separation at *SP* = 100, instead of *SP* = 80 from Table 4. In general the direct correlation between hazard classes and damage grades according to EMS-98 seems to be problematic, as the damage distribution of different buildings within a certain hazard class may vary, as already shown in Table 4. Nevertheless the correlation of the results from the RVS technique with EMS-98 damage grades offers a comprehensive and fast prediction of the possible consequences of a certain earthquake. An illustrative presentation of the results from the investigated test area is shown in Figure 5.

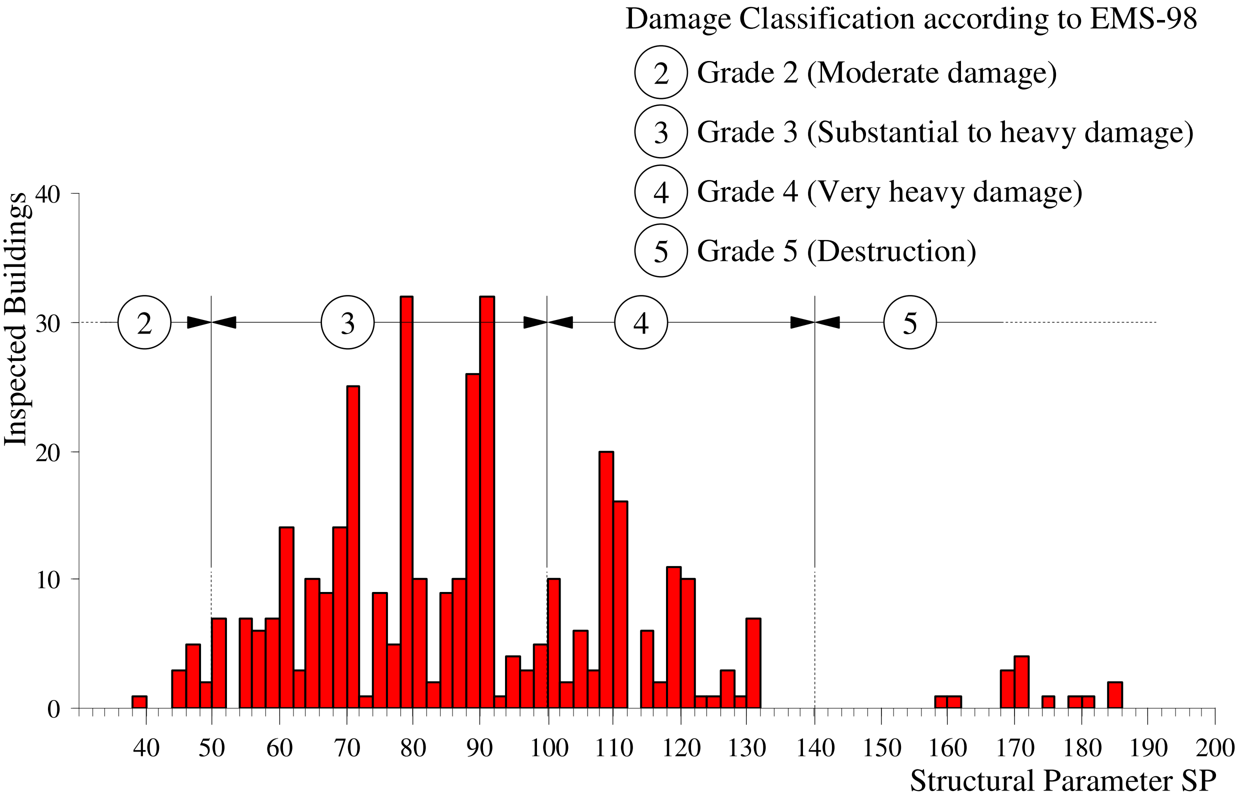

Figure 4: Correlation between damage grades according to EMS-98 [16] and the structural parameter of the inspected buildings.

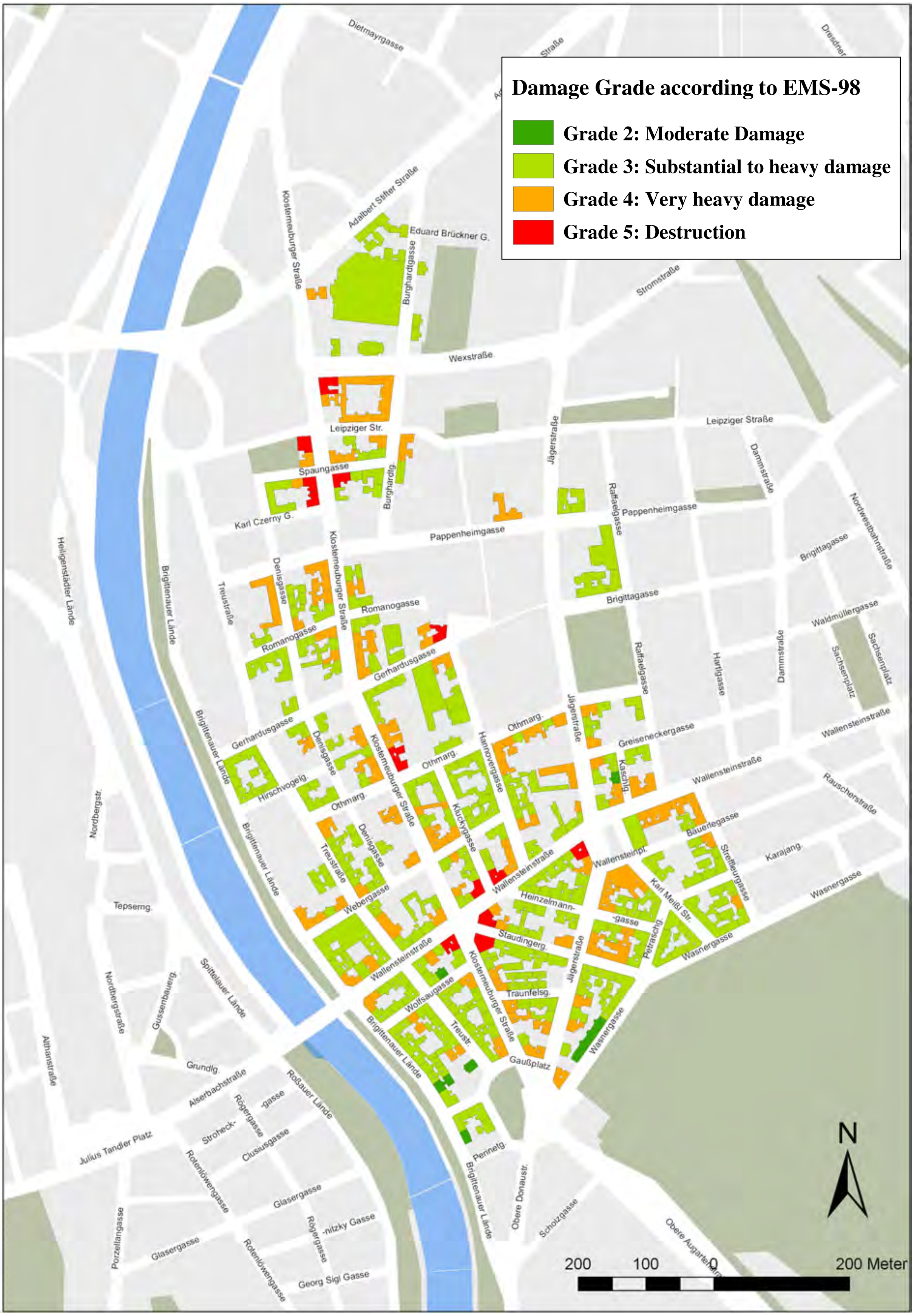

Figure 5: Map of the test area in Vienna; results of the assessment of historic residential buildings and their correlation with damage grades according to EMS-98 [16].

4 CONCLUSIONS

The Rapid-Visual-Screening (RVS) technique is a fast and widespread method for seismic hazard assessment of existing buildings. During the last few years a RVS technique for historic residential brick-masonry buildings in Vienna was adopted, due to the fact that those buildings represent the predominant type of constructions in the city center of Vienna and so far there was no information about their resistance against seismic actions.

The developed methodology to assess historic brick-masonry buildings consists of a visual inspection form and the subsequent evaluation of several parameters to capture the effects of possible damages to the environment and to describe and rate the structural behavior of the building. Furthermore the buildings were classified into certain hazard classes to prioritize the building stock by using the evaluated parameters.

Post-earthquake assessments from adequate past earthquake events have been used to correlate the results of the RVS technique with realistic seismic damages and hence EMS-98 damage grades were predicted.

In a large-scale investigation a set of 375 historic brick-masonry buildings were evaluated by the proposed methodology. The results of these tests could be integrated into a local seismic building hazard map.

The outcome of the proposed methodology supplies a good prediction of the damage distribution within the test area. The evaluated hazard maps give useful information for emergency and evacuation planning as well as for identification of critical objects and further investigations.

ACKNWOLEDGEMENT

The investigations described were performed within the Austrian research project SEISMID [32], which aims among others to develop a methodology to assess the actual seismic bearing capacity of historic buildings. SEISMID is funded by the ZIT Center for Innovation and Technology, which is a subsidiary of the Vienna Business Agency (WWFF). This support is gratefully acknowledged.

REFERENCES

[1] G. Achs, Seismic hazard of historic residential buildings. Evaluation, classification, and experimental investigations. (Erdbebengefährdung von Gründerzeithäusern. Berurteilung, Klassifierung und experimentelle Untersuchungen.) Doctoral Thesis (in German), Vienna University of Technology, to appear 2011.

[2] G.M. Calvi,R. Pinho, G. Magenes, J.J. Bommer, L.F. Restrepo-Vélez, H. Crowley, Development of seismic vulnerability assessment methodologies over the past 30 years. *ISET Journal of Earthquake Technology*, **43**, 75-104, 2006.

[3] Applied Technology Council ATC-21-1, Rapid visual screening of buildings for potential seismic hazards: Supporting documentation. Applied Technology Council, 1988.

[4] JBDPA - Japan Building Disaster Prevention Association, Seismic Evaluation and Retrofit, Tokyo, Japan, 2001.

[5] S.K. Jain, K. Mitra, M. Kumar, M. Shah, A Proposed Rapid Visual Screening Procedure for Seismic Evaluation of RC-Frame Buildings in India. *Earthquake Spectra*, **26**, 709–729, 2010.

[6] I. Gogoi, Rapid Visual Screening of Buildings in Assam. MAEE (Macedonian Association for Earthquake Engineering), *14th European Conference on Earthquake Engineering (14th ECEE)*, Ohrid, Macedonia, August 30 - September 03, 2010.

[7] OASP - Greek Earthquake Planning and Protection Organization, Provisions for Pre-Earthquake Vulnerability Assessment of Public Buildings (Part A), Athen, Greece, 2000.

[8] K. Demartinos, S. Dristos, First-level pre-earthquake assessment of buildings using fuzzy logic, *Earthquake Spectra*, **22,** 865–885, 2006.

[9] Z. Sen, Rapid visual earthquake hazard evaluation of existing buildings by fuzzy logic modeling. *Expert Systems with Applications*, **37**, 5653-5660, 2010.

[10] A.F. Hassan, M.A. Sozen, Seismic vulnerability assessment of low-rise buildings in regions with infrequent earthquakes. *ACI Structural Journal*, **94**, 31-39, 1997.

[11] R. Ozdemir, B. Taskin, Seismic safety screening method for Istanbul Metropolitan City. *10th East Asia Pacific Conference on Structural Engineering and Construction (EASEC 10)*, Bangkok, Thailand, August 3-5, 2006,

[12] M. Vatan, G. Arun, A method for assessing the risk level of monumental historical structures by visual inspections. MAEE (Macedonian Association for Earthquake Engineering), *14th European Conference on Earthquake Engineering (14th ECEE)*, Ohrid, Macedonia, August 30 - September 03, 2010.

[13] M.A. Erberik, Seismic risk assessment of masonry buildings in Istanbul for effective risk mitigation. *Earthquake Spectra*, **26**, 967-982, 2010.

[14] D. D'Ayala, E. Speranza, An integrated procedure for the assessment of seismic vulnerability of historic buildings. ICE (Institution of Civil Engineers), *12th European Conference on Earthquake Engineering (12th ECEE)*. London, England, September 9-13, 2002.

[15] T. Ferreira, R. Vicente, H. Varum, Seismic vulnerability assessment of masonry facade walls. MAEE (Macedonian Association for Earthquake Engineering), *14th European*

Conference on Earthquake Engineering (14th ECEE), Ohrid, Macedonia, August 30 - September 03, 2010.

[16] G. Grünthal, R. Mußon, J. Schwarz, M. Stucchi, European Macroseismic Scale 1998. *Cahiers du Centre Européen de Geodynamique et de Séismologie*, **15**, 1998.

[17] K.H. Meskouris, H. Sadegh-Azar, H. Bérézowsky, R. Dümling, Fast assessment of seismic hazard of buildings (in German). (Schnellbewertung der Erdbebengefährdung von Gebäuden.) *Der Bauingenieur*, **7/8**, 370 – 376, 2001.

[18] H. Sadegh-Azar, Fast assessment of seismic hazard of buildings (in German). (Schnellbewertung der Erdbebengefährdung von Gebäuden.) Doctoral Thesis (in German), RWTH Aachen University, 2002.

[19] Technical Building Code for Vienna, 1859, Regulation of the Ministry of the Interior, September 23, 1859, to enact a technical building code for the imperial capital and residence city of Vienna, Journal of the provincial government of the Archduchy Austria below the river of Enns, Volume 1859, first division, part 52. Released and dispatched on October 15, 1859, Imperial-royal national press, Vienna (in German). (Bauordnung Wien, 1859. Verordnung des Ministeriums des Innern vom 23. September 1859, womit eine Bauordnung für die k.k. Reichshaupt- und Residenzstadt Wien erlassen wird, Landes-Regierungsblatt für das Erzherzogthum Oesterreich unter der Enns, Jahrgang 1859. Erste Abtheilung. LII. Stück. Ausgegeben und versendet am 15. Oktober 1859. Wien: Kaiserlich-Königliche Hof und Staatsdruckerei.)

[20] Technical Building Code for Vienna, 1869, Regulation of the Ministry of the Interior, December 2, 1868, to enact a technical building code for the imperial capital and residence city of Vienna, Journal of the provincial government of the Archduchy Austria below the river of Enns, Imperial-royal national press, Vienna (in German). (Bauordnung Wien, 1868. Landesgesetz vom 2. Dezember 1868, womit eine Bauordnung für die k.k. Reichshaupt- und Residenzstadt Wien erlassen wird. Landes-Gesetz- und Verordnungsblatt für das Erzherzogthum Oesterreich unter der Enns. Wien: Kaiserlich-Königliche Hof und Staatsdruckerei.)

[21] Technical Building Code for Vienna, 1883, Regulation of the Ministry of the Interior, January 17, 1883, to enact a technical building code for the imperial capital and residence city of Vienna, Journal of the provincial government of the Archduchy Austria below the river of Enns, Part 12, Regulation 35, Imperial-royal national press, Vienna (in German). (Bauordnung Wien, 1883. Bauordnung für die k.k. Reichshaupt- und Residenzstadt Wien. Gesetz vom 17. Jänner 1883, Nr. 35. Landes-Gesetz- und Verordnungsblatt für das Erzherzogthum Oesterreich unter der Enns, XII. Stück. 35. Gesetz. Wien: Kaiserlich-Königliche Hof und Staatsdruckerei.)

[22] Municipality of Vienna, Technical building code for the imperial capital and residence city of Vienna, January 17, 1883, Journal of the provincial government of the Archduchy Austria below the river of Enns, Regulation 35, and Regulation of December 26, 1890, Journal of the provincial government of the Archduchy Austria below the river of Enns, Regulation 48, including instructions for officials of the urban building authority for the execution of the technical building code for Vienna, released on January 17, 1883. Private publishing venture, Vienna (in German). (Magistrat Wien, 1892: Bau-Ordnung für die k.k. Reichshaupt- und Residenzstadt Wien; Gesetz vom 17. Jänner 1883, L.-G.-Bl. Nr. 35 und Gesetz vom 26. December 1890, L.-G. u. V.-Bl. Nr. 48; inkl. Instructionen für die Beamten des Stadtbauamtes bei Handhabung des Baugesetzes für

Wien vom 17. Jänner 1883. Im Verlage des Magistrates, Druck von Johann R. Bernah der Stadt Wien.)

[23] R. Flesch, W. Lenhardt, R. Geier, Earthquake induced damages in Austria - Assessment of existing buildings (in German). (Schadensbeben in Österreich - Beurteilung bestehender Bauwerke.) *Bautechnik*, **82**, 533-538, 2005.

[24] ÖIBI, Special seminar "Engineer Diagnostics" (in German). (Spezialseminar Ingenieurbefund.) Course Material, Ingenieurbefund (in German), Vienna University of Technology, 2009.

[25] B. Rusnov, Analysis of buildings vulnerable to earthquakes with empahsis on old and historic buildings. (Analyse von erdbebengefährdeten Bauwerken mit dem Schwerpunkt auf alten und historischen Gebäuden.) Doctoral Thesis (in German), Vienna University of Technology, 2006.

[26] SIA, Assessment of existing buildings with respect to earthquakes. (in German). (Überprüfung bestehender Gebäude bezüglich Erdbeben.) Technical Note 2018, Swiss Society of Civil Engineers and Architects, Zurich, Switzerland, 2004.

[27] European Committee for Standardization - Eurocode 8, Design of structures for earthquake resistance - Part 1: General rules, seismic actions and rules for buildings, Technical Building Code ÖN EN 1998-1 (in German), Austrian Standards plus inc., 2005.

[28] European Committee for Standardization - Eurocode 8, Design of structures for earthquake resistance - Part 1: General rules, seismic actions and rules for buildings, National specifications concerning ÖNORM EN 1998-1 and national comments, Technical Building Code ÖN B 1998-1 (in German), Austrian Standards plus inc., 2006.

[29] R. Hinsch, K. Decker, Do seismic slip deficits indicate an underestimated earthquake potential along the Vienna Basin Transfer Fault System? *Terra Nova*, **15**, 343–349, 2003.

[30] O.C. Celik, H. Sesigur, Performance of historic masonry buildings during the April 6, 2009 L'Aquila Earthquake. MAEE (Macedonian Association for Earthquake Engineering), *14th European Conference on Earthquake Engineering (14th ECEE)*, Ohrid, Macedonia, August 30 - September 03, 2010.

[31] J.E. Alarcon, G. Franco, P. Bazzurro, M. Simic, The L'Aquila (Abruzzo) earthquake of 6th April 2009 - Field survey and loss estimation. MAEE (Macedonian Association for Earthquake Engineering), *14th European Conference on Earthquake Engineering (14th ECEE)*, Ohrid, Macedonia, August 30 - September 03, 2010.

[32] SEISMID, Seismic System Identification, Austrian research project, funded by the ZIT Center for Innovation and Technology, Vienna.

COMPDYN 2011
III ECCOMAS Thematic Conference on
Computational Methods in Structural Dynamics and Earthquake Engineering
M. Papadrakakis, M. Fragiadakis, V. Plevris (eds.)
Corfu, Greece, 25–28 May 2011

A STUDY ON THE EFFECT OF TIE ELEMENTS' PROPERTIES ON THE SEISMIC BEHAVIOR OF CONFINED MASONRY WALLS BY USING NONLINEAR FINITE ELEMENT ANALYSES

Fariman Ranjbaran[1] and Mahmood Hosseini[2]

[1] Islamic Azad University (IAU), Islamshahr Branch,
Islamshahr, Iran
E-mail: ranjbaran_far@iiau.ac.ir

[2] Int'l Institute of Earthquake Engineering and Seismology (IIEES)
Tehran, Iran
Email: hosseini@iiees.ac.ir

Keywords: Confined masonry wall, DIANA, Pushover, Tie elements, Confinement.

Abstract. *In this study the nonlinear finite element analysis has been employed to find out how the properties of ties, either vertical or horizontal, affect the seismic behavior of confined masonry walls. For this purpose the DIANA software (Version 9.3), which is powerful tool for numerical modeling of such structures, has been used. Among the parameters, which are believed to be effective in the confined wall seismic behavior, four ones relate to the ties. These include compressive strength of concrete used in tie elements, cross sectional area of ties, the amount of longitudinal reinforcement in vertical ties, and finally the rigidity of connections between horizontal and vertical ties. With regard to the amounts of the four mentioned parameters, the values recommended by the National Iranian Code of Practice for Seismic Design of Buildings (Iranian Standard No. 2800) were used as the bench mark values. The type of analysis conducted for the wall numerical samples was Push-Over Analysis (POA) and in all cases some reasonable value was considered for the amount of surcharge imposing on the confined wall due to the dead load of the corresponding floor. The results of POA were obtained by assigning various values, from very low to very high, to the four mentioned parameters, and the lateral force – displacement curves were plotted for each set of values. Numerical results show that with variations of the four parameters, considered for the ties' properties, between some limits the global behavior of wall changes slightly, however, if some of these four parameters get values beyond some limits the wall behavior changes drastically from one state to another.*

1 INTRODUCTION

It is more than 100 years that confined masonry structures are used in construction. This type of structure is consisted of masonry walls and confining elements (horizontal and vertical ties), located at four sides of the wall panel. The confining elements are usually made of reinforced concrete (R/C), steel profile, or timbers. Therefore, the features of the confined walls are a combination of those of un-reinforced masonry walls and reinforced concrete or other used frames. It should be noted that the performance of confining elements is not similar to the performance of common R/C beams and columns, and is basically for creating the following features in the confined wall [1]:

a) Increasing the stability and integrity of the wall against seismic in-plane and out-of-plane forces,
b) Increasing the strength of the wall,
c) Decreasing the brittleness of the wall.

These features all together lead to better seismic performance of the wall. The major difference between these walls and the R/C frame with infill walls is that the infill walls do not act as the load bearing elements, while the Confined Masonry Wall (CMW) is basically a load bearing element. The purpose of this research is studying the effect of confining elements on the behavior of confined masonry walls. These effects consists of compressive strength of concrete used in tie elements, cross sectional area of ties, the amount of longitudinal reinforcement in vertical ties, and finally the rigidity of connections between horizontal and vertical ties. For the four mentioned parameters the values recommended by the National Iranian Code of Practice for Seismic Design of Buildings (Iranian Standard No. 2800) were used as the bench mark values and then the change of these values was studied on the behavior of CMW's in the form of capacity curve and fracture mechanism. Non-homogeneity and anisotropy of the wall materials has made its modeling very difficult, particularly when post-cracking analysis is concerned. Lourenco has presented a constitutive behavior model for the unreinforced masonry walls [2]. In that method, masonry wall is modeled as a continuous homogenous and anisotropic medium, and Rankine-type's criterion is used as the yielding criteria in tension and Hill-type's criterion in compression. In the detailed analyses, performed by DIANA (version 9.3) computer program in this study, Lourenco model [2] was used for the nonlinear behavior of wall. It takes into account the different strengths in directions parallel and perpendicular to bricks interfaces with mortar. In the detailed models, considered for analyses, cracking in ties concrete, interaction between ties and wall, and interaction between walls and its foundation, reinforcing steel bars in ties and orthotropic behavior in masonry wall were considered. The type of analysis was nonlinear static analysis (pushover) based on displacement control and in all of the analysis the weight of components and surcharge were considered.

2 STATING THE PROBLEM

The purpose of this research is to evaluate the effect of properties of the tie columns and beams on the behavior of CMW. In the codes and guidelines of confined masonry structures the properties of confinement elements are prescribed and nominal. For example, in the National Iranian Code of Practice for Seismic Design of Buildings (Iranian Standard No. 2800) horizontal and vertical ties are in the form of reinforced concrete with dimensions of 20×20 cm for vertical ties, and 20×20 and 20×35 cm for horizontal ties, corresponding to 22 and 35 cm wall thickness respectively. Reinforcement inside ties was assumed to be consisted of 4 steel bars of 10mm diameter with yielding strength 300MPa and Compression strength of concrete was also assumed to be 15MPa. In this research these values were considered as the bench mark values and the effect of change of these parameters was evaluated on the behavior of CMW. In modeling the properties of masonry wall was fixed and the geometrical and mechanical properties were assumed to be the same for all cases. The thickness of wall was assumed 22 cm, the length and height of wall was considered as 3 meters and the surcharge was 23.2 N/mm. The tensional and compressional strengths of masonry unit were equal to 0.25 and 6.23 MPa, respectively. In addition to benchmark values for tie elements the compression strength of concrete was assumed as 10 and 20 MPa, cross sectional area of ties 10×10, 15×15, and 25×25 cm, assuming that the width of horizontal tie as 20 cm for all cases. The amount of longitudinal reinforcement in vertical ties was 4ϕ6, 8, 14. For studying the effect of connection's rigidity between horizontal and vertical tie elements the type of tie elements was changed, such that in case of rigid connection the beam elements was used for ties, and in case of hinge connection the truss element was used. Using the aforementioned quantities and taking into account the wall weight in loading process, and assuming the boundary conditions of wall as a cantilever, the pushover analysis in displacement control state were performed with a target displacement of 30 mm (0.01h) [3], and the capacity curves for all of the numerical models were developed.

3 MODELING

For modeling the masonry walls in DIANA (version 9.3) software, the Continuum Finite Element method (macro-model method) was used, which has relatively high precision and is also more appropriate for studying the general behavior of walls, and enormous analysis cases [2]. In this method, masonry wall is simulated in the form of a continuous homogenized environment and Rankin-type's criterion and Hill-type's criterion are used for expressing the inelastic behavior in tension and compression respectively. These models also take into account the orthotropic behavior. The value of fracture energy in compression and tension were considered as common values in clay brick materials, which are in the vertical direction, respectively, 0.018N/mm in tension and 15N/mm in compression. Furthermore, the combined crack-shear-crush interaction model is believed to be suitable for the simulating fracture caused by tension, fractional slide caused by shear and crush resulted from compression [4]. Regarding the existence of friction between the wall and its foundation after cracking, this model was also considered to be suitable for simulating wall-foundation interaction [5].

For wall-ties-interaction the discrete crack model was used [6]. Normal and shear stresses are functions of total relative displacement, i.e. width and slide of crack. Tension and shear strengths and stiffness after crack between tie and wall were neglected and the behavior of element was considered in brittle type without softening. To avoid the penetration of wall and tie elements into each other, a large value was considered for the axial stiffness in compression. For the numerical stability of interaction element, sliding, with initial shear stiffness, is likely. Beam elements with moment resisting connections were used in order to model the confining elements in the software. For modeling the concrete material of ties the Total Strain Rotating Crack was used [6]. In this model, stresses were defined based on the strain-stress relation, and the average principal strain rate was calculated and transferred to the global system of coordinates of the element [7]. Stress-strain relation defined in modeling for the tensile stress was the Maekawa model [8], and for the compression stress was the perfect elasto-plastic considering 28-day compression strength of concrete. Finally, for modeling the reinforcement of ties the longitudinal bars were assumed to have full bond with concrete around them and follow von Mises Criteria with perfect elastoplastic flow criteria [6].

4 VERIFICATION OF NUMERICAL MODELING

For verifying the numerical modeling, those developed based on the behaviors explained in the previous section were compared with some experimental models. These models include a double-storey concrete frame without infill walls for verifying the ties modeling [9], one masonry wall without confinement for verifying masonry wall modeling [10], and also one confined masonry walls for verifying the modeling of the compound system of masonry wall and ties [11]. Lateral loading was monolithically applied to the numerical models, and at first the vertical loading and after that the lateral loading was applied. Figures 1 to 3 shows comparisons between the experimental results and those obtained by the developed numerical models in this study.

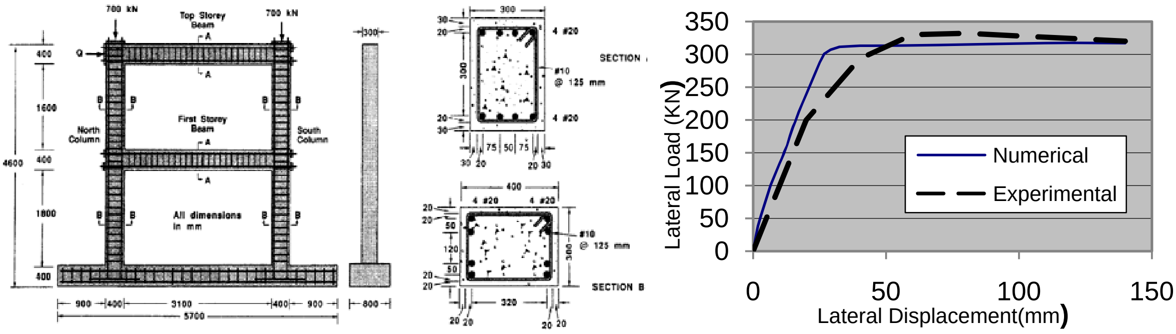

a) b)

Figure1.Comparison between experimental and numerical models related to the 2-storey concrete frame [9]: a) the 2-story frame and its features, b) the capacity curves

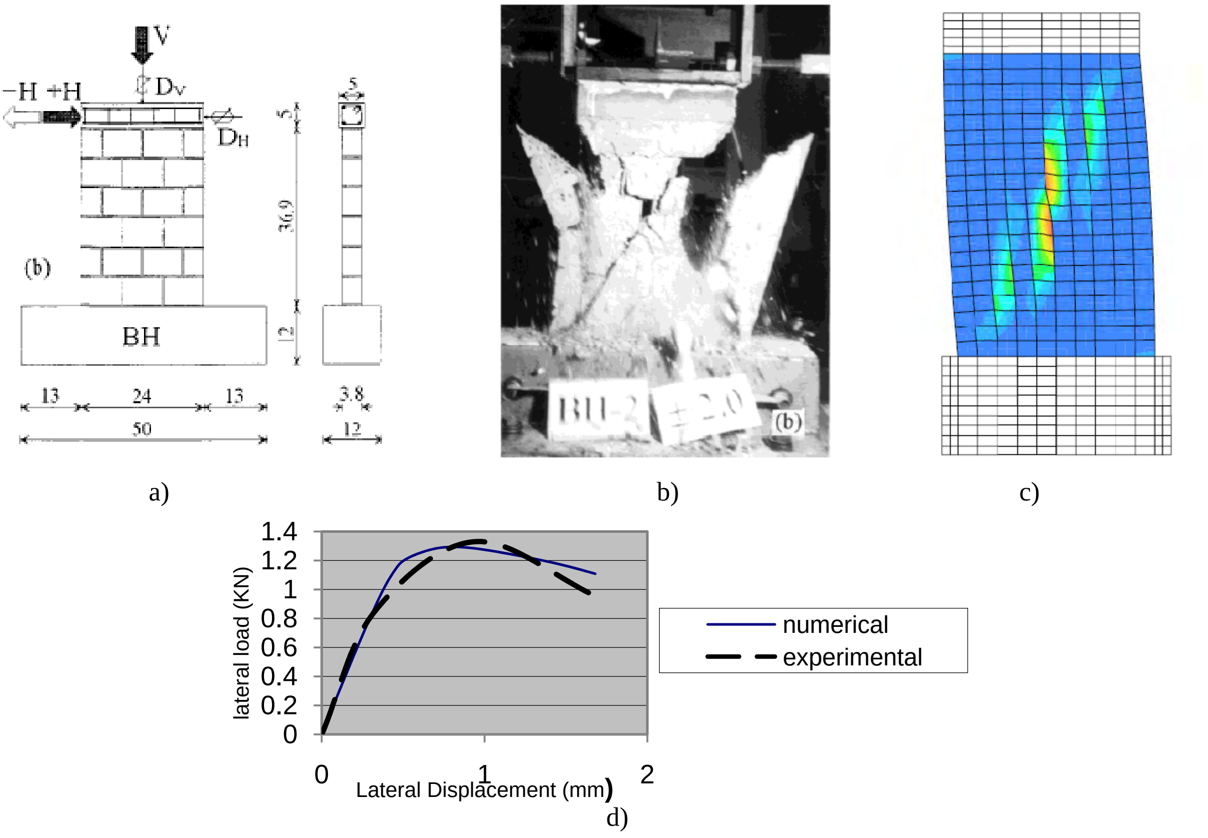

a) b) c)

d)

Figure 2: Comparison between experimental and numerical models related to the masonry wall without Confinement [10]: a) the experimental model, b) the experimental fracture mechanism, c) the fracture mechanism obtained by DIANA, d) the capacity curves

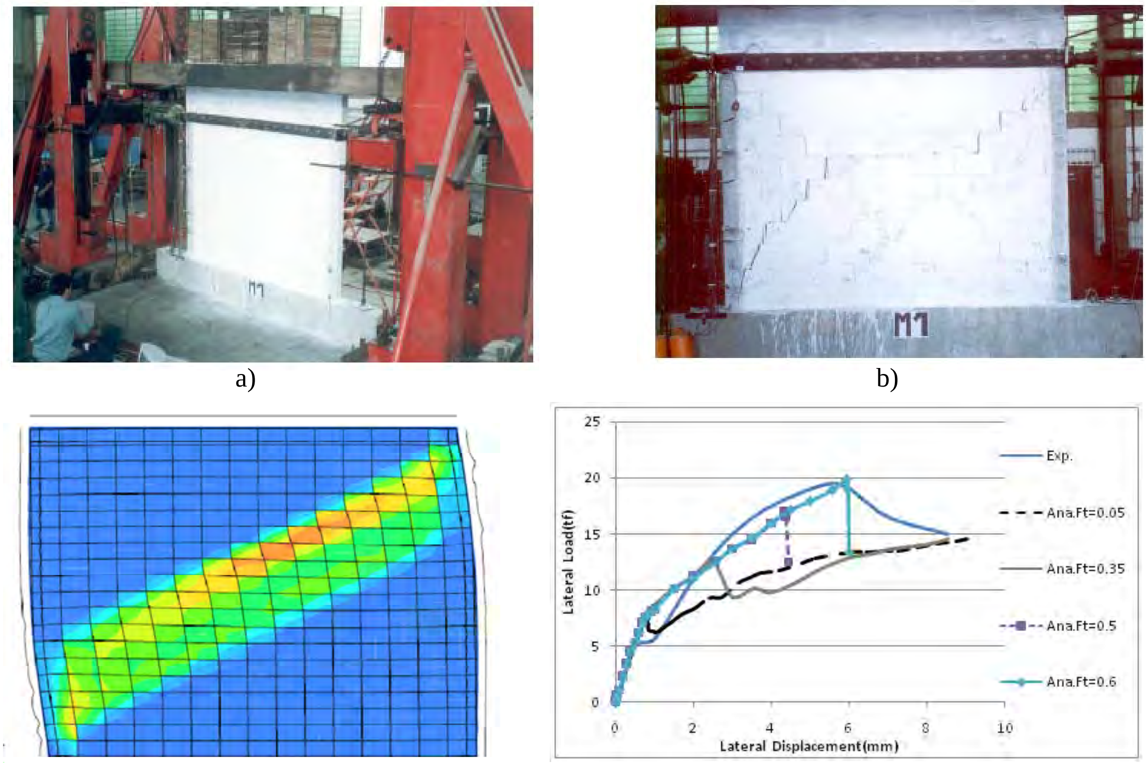

a) b)

c) d)

Figure 3: Comparison between experimental and numerical models related to the masonry wall with confinement [11]: a) the experimental model, b) the experimental fracture mechanism, c) the fracture mechanism obtained by DIANA, d) the experimental and numerical capacity curves

It is seen that in cases of the 2-storey concrete frame without infill walls and the masonry wall without confinement there are good agreement between the numerical and experimental results. For the cases of confined masonry walls, since the tensile strength of the masonry (f_t) was not reported, various values between 0.3 to 0.9 MPa were tried, based on Tomazevic recommendation. Figure 3 shows that with a value of 0.6 MPa a good agreement between the numerical and experimental results is achieved.

5 THE EFFECT OF COMPRESSIVE STRENGTH OF THE CONCRETE

In order to study of the effect of compressive strength of the concrete 3 levels of 100, 150, and 200 kgf/cm^2 were considered for it. Accordingly, with change of compressive strength of the concrete its tensile strength and modules of elasticity were also changed (see Figure 4).

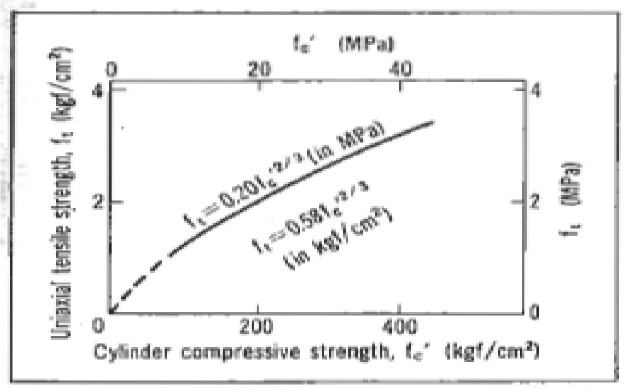

Figure 4: Variation of the tensile strength of concrete based on its compressive strength [8]

All three levels of strength were employed in DIANA software, and the results of analyses are presented in Figure 5.

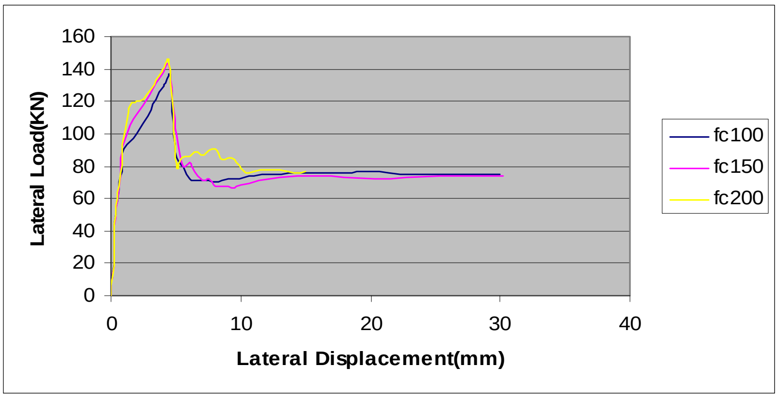

Figure 5: The CMW capacity curves based on the change of compressive strength of the concrete

It is seen in Figure 5 that increase of the concrete compressive strength has minor effect on the wall's capacity curve. Just a little increase in elastic limit strength and also maximum strength is observed. It is also worth mentioning that the fracture mechanism is the same for the three models, and is of the form of shear fracture with diagonal cracks.

6 THE EFFECT OF CROSS SECTIONAL AREA OF TIES

In order to study of the effect of cross sectional are of ties 4 sections of 10×10, 15×15, 20×20, and 25×25 cm^2 were considered for the vertical tie elements, but the width of the horizontal tie element was considered to be 20cm in all cases to match with the thickness of masonry wall. The corresponding results are presented in Figure 6.

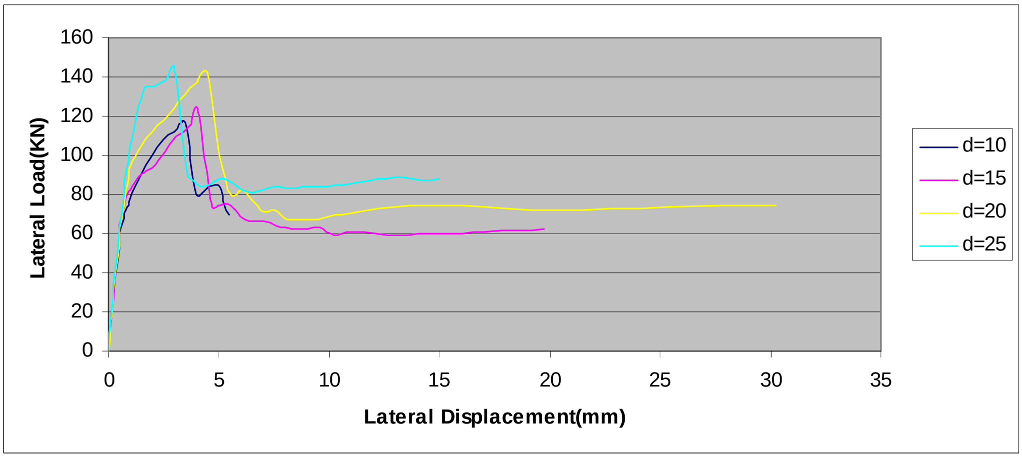

Figure 6: The CMW capacity curves based on cross sectional area of ties

It is observed from Figure 6 that with cross sectional area of 10×10 cm^2 for tie elements, elastic limit, ultimate, as well as residual strength, and also the ductility of the wall are all very low. These values increase as the cross sectional area of tie elements increases. In other words, with decreasing the cross sectional area of tie elements, the behavior of confined masonry wall tends to unconfined masonry wall, in both aspects of resistance and ductility. However, the wall initial stiffness does not change with the tie cross sectional area. The increased resistance and ultimate ductility is due to increased effect of confinement resulted from tie elements on the masonry wall and its increased frame action. In the level of 25×25 cm^2 it is seen that the elastic limit strength increases but ductility corresponding to maximum strength decreases and maximum strength does not change considerably. The decrease of ductility could be due to increase of pressure resulted from interaction between ties and wall because of increased stiffness and frame action in tie elements, which results to brittle behavior in confined masonry wall. It should be mentioned the fracture mechanism is again the same for all models, as is of the form of shear fracture with diagonal cracks.

7 THE EFFECT OF LONGITUDINAL REINFORCEMENT IN VERTICAL TIES

In order to study of the effect of the amount of longitudinal reinforcement in vertical ties on the CMW's behavior four levels of reinforcement in vertical ties were considered, including 4 bars with diameter of 6, 8, 10, and 14 mm. The results of numerical model are presented in Figure 7.

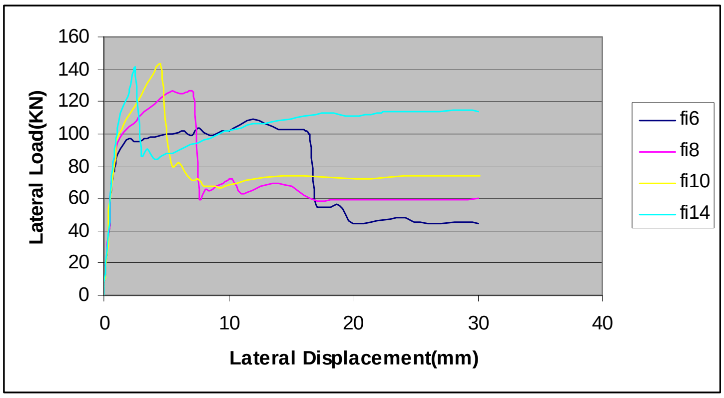

Figure 7: The CMW capacity curves based on the amount of longitudinal reinforcement in vertical ties

It is seen in Figure 7 that with increasing the amount of longitudinal reinforcement in vertical ties, the elastic limit, and maximum and residual strengths increase, but ductility corresponding to maximum strength decreases. With increasing reinforcement from 4Φ10 to 4Φ14 the maximum strength does not change but elastic limit and residual strength increases, but the wall ductility decreases, which can be due to increasing of frame action of tie elements. With decreasing reinforcement from 4Φ8 to 4Φ6, the fracture mechanism changes from shear to flexural fracture.

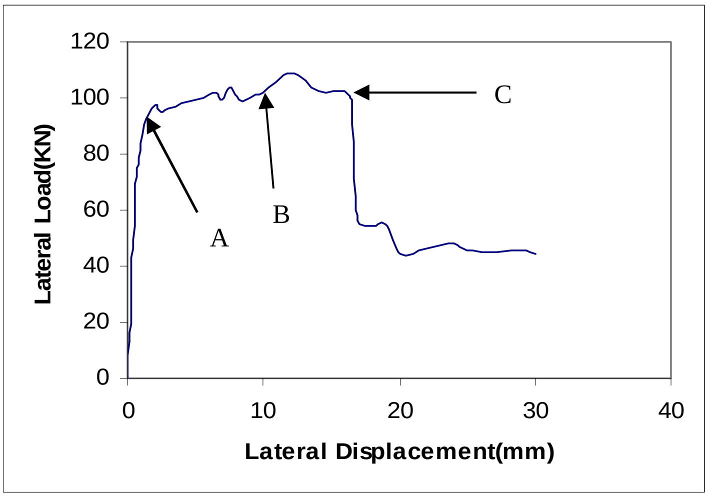

Figure 8: Capacity curve for model with 4Φ6 reinforcement

It is useful to pay attention to the correspondence of the CMW fracture mechanism to the variations of its capacity curve. For this purpose the capacity curve of the model with 4Φ6 reinforcement in vertical ties on which various stages of the wall fracture are indicated by point A to C is presented in Figures 8. As shown in this figure, point "A" on the curve is corresponding to the first observable stiffness degradation, and the start of transverse cracking at the upper end of vertical tie, as shown in Figure 9.

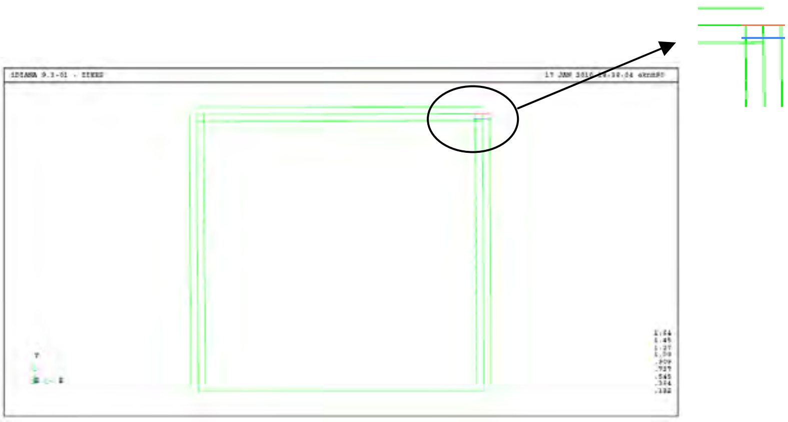

Figure 9: The start of transverse cracking at the upper end of vertical tie

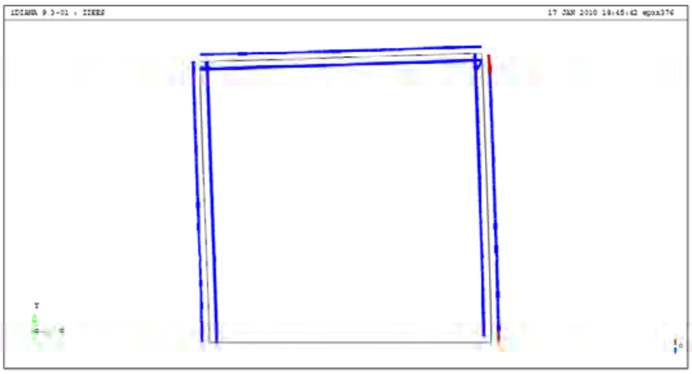

Figure 10: The yielding of reinforcement in lower and upper ends of tensile vertical tie

By increasing the top displacement of the wall and reaching 10 mm, corresponding to the point "B" on the curve, reinforcement in the connection zones of the vertical tie yields in tension, as shown in Figure 10. After this stage the CMW gradually reaches its maximum strength and diagonal cracks appear in the wall. This stage corresponds to point "C" on the curve. After this stage the wall's strength drops to its residual strength.

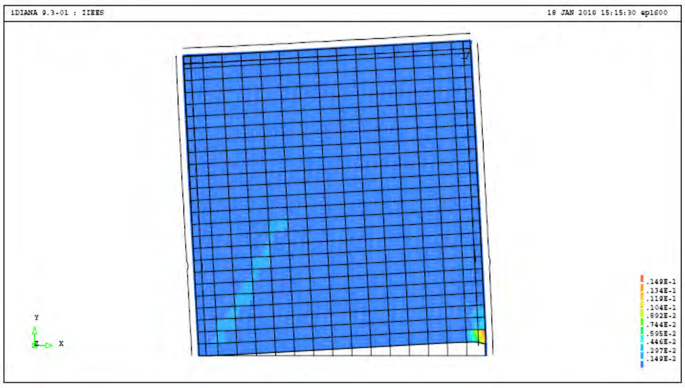

Figure 11: The start of diagonal cracking in masonry wall

It should be mentioned in models with 4Φ8 to 4Φ14 the fracture mechanism is shear fracture, since the reinforcement does not yield before maximum strength.

8 THE EFFECT OF RIGIDITY OF CONNECTIONS BETWEEN HORIZONTAL AND VERTICAL TIES

One of effective parameters in the behavior of CMW is the detailing and the amount of rigidity in the ties' connections. Past earthquakes (Indonesia earthquake, 2007) [1], have shown that inadequacy of connection in ties could resulted in vulnerability of the CMW. With decreasing the rigidity of connections in the tie elements and change of its rigidity from fully rigid to hinge, the behavior of CMW is changed to a truss, as shown in Figure 12.

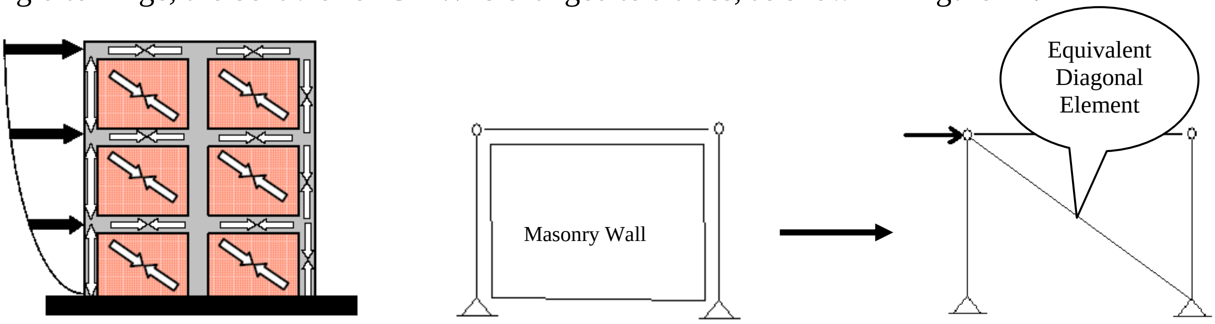

Figure 12: Replacement of CMW by a truss due to lack of rigidity in its tie connections

In order to study the effect of the rigidity of connections between horizontal and vertical ties, the experimental model of Marinilli [11], shown in Figure 4, was modeled as a vertical truss, by replacing the beam elements of ties by truss elements. Analysis results show that the initial stiffness and the ultimate resistance of the truss model is almost the same as that of the beam model, however, the ductility of truss model increases to some extent, in comparison of unconfined masonry wall, with ties modeled as beam elements. On the contrary, with increasing the rigidity of ties connections and reaching the fully rigid state, both resistance and ductility of the CMW increase in comparison with those of the unconfined masonry wall. This is due to the creation of frame behavior in tie elements. The capacity curve for confined masonry wall with truss confining elements (CMWT) along with its fracture mechanism corresponding to different state in capacity curve are presented in Figures 13 to 19. Also for comparison, the capacity curve of the confined masonry wall with beam confining elements (CMWB) along with its fracture mechanism corresponding to different state in capacity curve are presented in Figures 20 to 23.

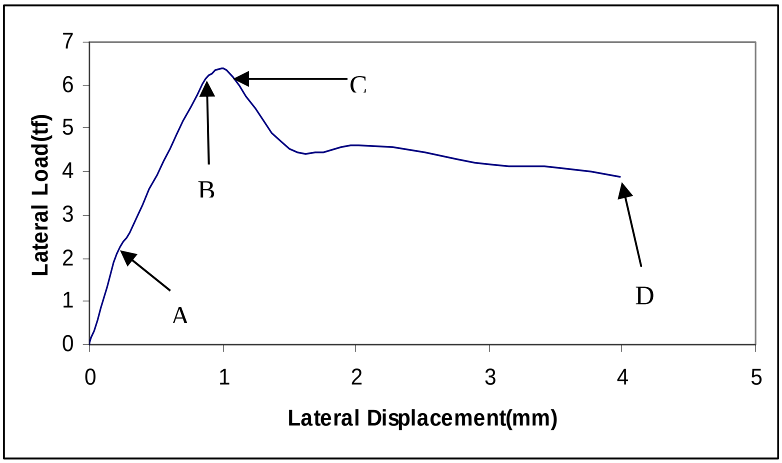

Figure 13: The capacity curve of the modeled CMWT

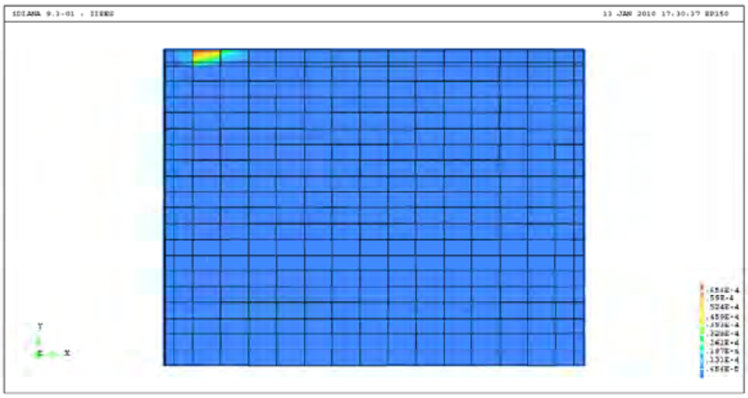

Figure 14: The start of cracking in the region between masonry and horizontal tie (corresponding to point A)

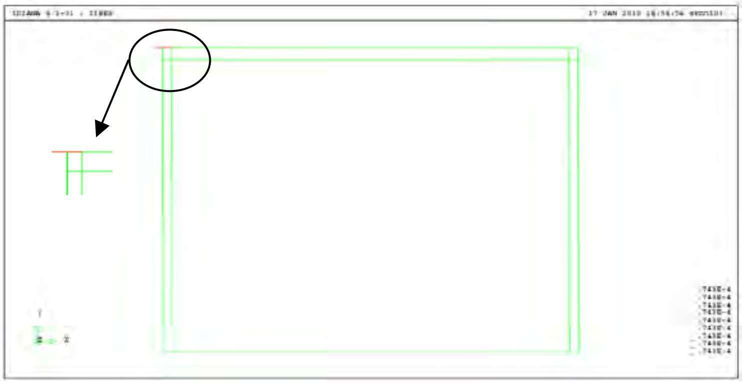

Figure15: The start of cracking in the vertical tie (corresponding to point B)

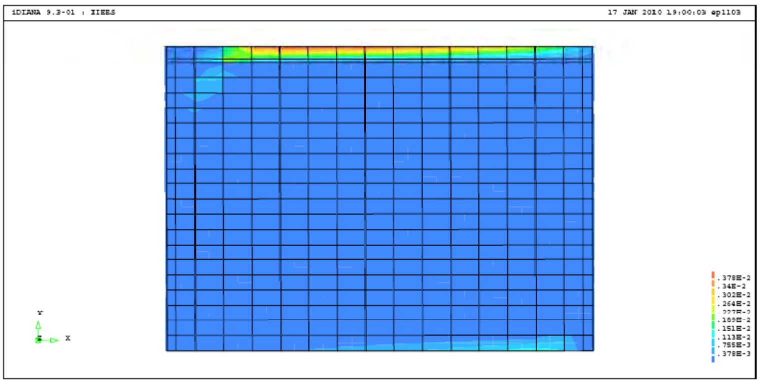

Figure 16: Development of cracks in the region between masonry wall and horizontal tie (corresponding to the part of capacity curve between points B and C)

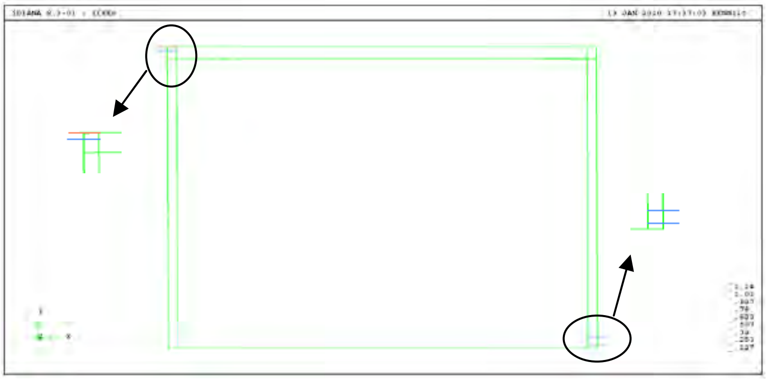

Figure 17: Development of cracks in the vertical ties (corresponding to point C)

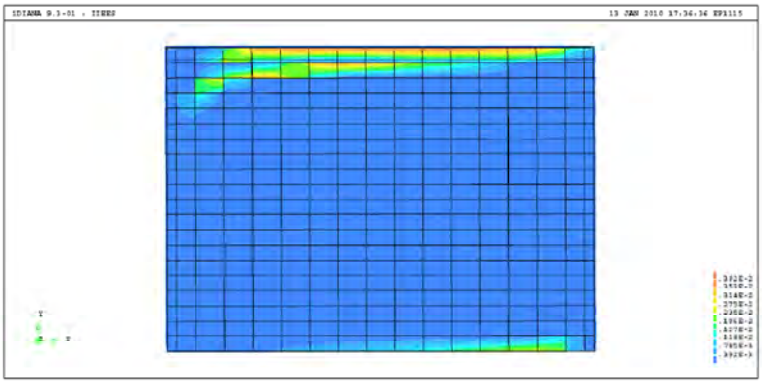

Figure 18: Development of cracks in masonry wall (corresponding to point C)

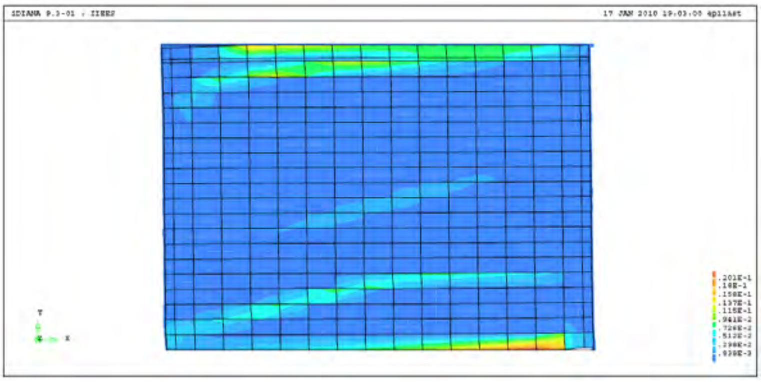

Figure 19: Development of widespread cracks in masonry wall (corresponding to point D)

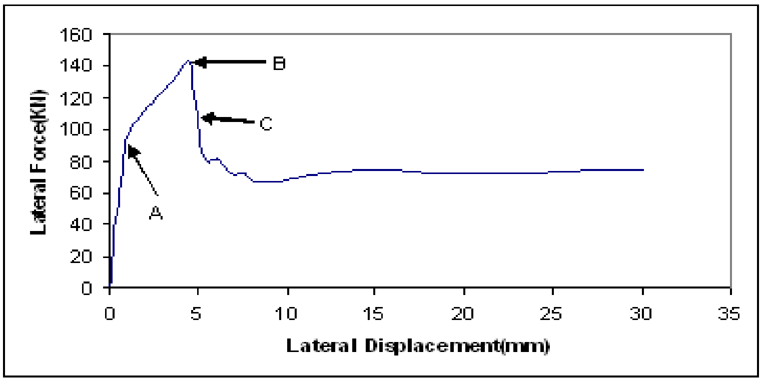

Figure 20: The capacity curve of the modeled CMWB

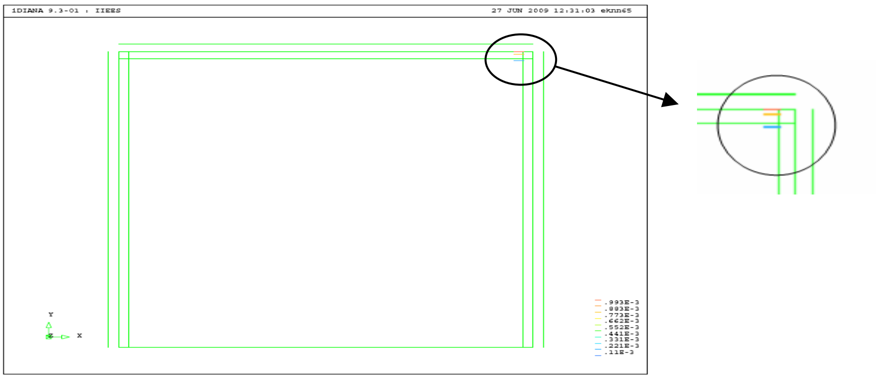

Figure 21: The start of cracking in the tie-column (corresponding to point A)

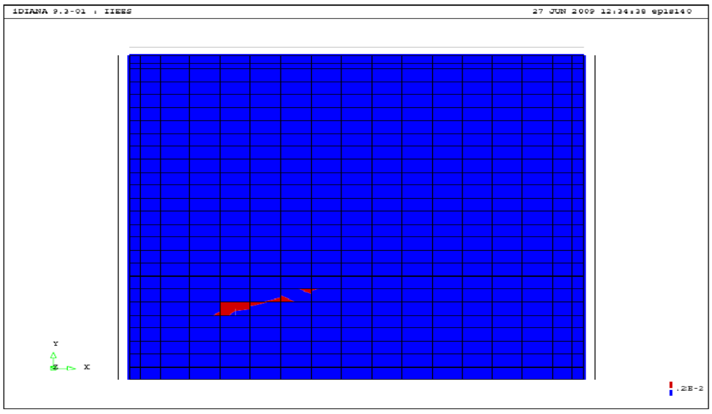

Figure 22: Diagonal cracks in masonry wall (corresponding to point B)

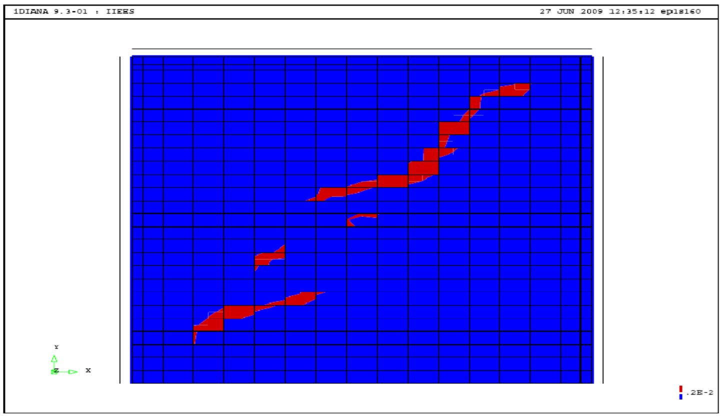

Figure 23: Development of diagonal cracks in masonry wall (corresponding to point C)

In the CMWB ties are of 22 cm thickness, 3.0 m height, and 0.25 MPa tensile strength, and the amount of surcharge on the wall is 23.2 N/mm. It should be mentioned the load was applied from right to left. It can be observed from Figures 13 to 23 that the fracture mechanism in the CMWB is different from the CMWT. As it is shown in Figures 13 to 19 in case of CMWT the onset of cracking is in the masonry wall, while in case of CMWB cracking starts in the horizontal tie. This difference is believed to be due to the fact that in CMWT, initially the masonry wall panel resists the lateral load, and the confining elements do not play any significant role in load bearing, while in the CMWB initially the ties resists against the lateral loads but because of their frame action. Also the values of initial stiffness, maximum and residual strength, as well as ductility are quite different in CMWT and CMWB. The initial stiffness of the CMWB is less than 1.5 times of that of the CMWT, while its maximum and residual strength is more than two time of the CMWT. The failure mechanism of the CMWB is also different from that of the CMWT. It can be said that the CMWT behaves similar to the unconfined masonry wall, as expected, while the CMWB behaves similar to the infilled frame.

9 CONCLUSIONS

In this study based on the nonlinear finite element analysis (by using DIANA software), the effect of ties' specifications, including compressive strength of concrete used in tie elements, cross sectional area of ties, the amount of longitudinal reinforcement in vertical ties, and finally the rigidity of connections between horizontal and vertical ties, in the seismic behavior of confined masonry walls were studied. With regard to the amounts of the four mentioned parameters, the values recommended by the National Iranian Code of Practice for Seismic

Design of Buildings (Iranian Standard No. 2800) were used as the bench mark values. Then some changes were applied to those bench mark values to find out the effects of the aforementioned parameters. The results of analyses are as follow:

- The changes of the mentioned parameters do not affect so much the initial stiffness of confined masonry wall, and it was shown that basically the masonry wall provides the initial stiffness in the confined masonry wall.
- With little changes in compressive strength of concrete in tie elements related to bench mark value (15 MPa), due to decrease or increase of tensile strength of concrete, only elastic limit strength decreases or increases respectively and other indices in capacity curve do not change considerably, also fracture mechanism does not change.
- It is believed that the 20×20 cm^2 (bench mark) for cross sectional area in tie elements, is an optimal case, so that with decrease of mentioned value, the behavior of confined masonry wall tends to unconfined masonry wall, and on the other hand, with increase in that some considerable change in the behavior was observed. However, the fracture mechanism is almost the same for all models.
- It is believed that the 4Φ10 (bench mark) for vertical reinforcement in tie-columns, is an optimal value, so that with decrease in that the ductility corresponding to the maximum strength increases and maximum strength itself decreases. It should be mentioned with 4Φ6 in tie columns the fracture mechanism changes from shear to flexural failure. On the other hand, it was observed that by using 4Φ14 in tie-columns, not only the maximum strength does not increase, but the ductility corresponding to the maximum strength decreases.
- It is believed that, with decreasing rigidity in the connections of ties elements, the surcharge resulted from confinement decreases, and the behavior of the confined wall approaches that of the unconfined wall.

REFERENCES

[1] S. Brzev, *Earthquake-resistant confined masonry construction*, National information center of earthquake engineering (NICEE), 2007.

[2] P. Lourenco, G. Rots, and J. Blaauvendraad, Continuum model for masonry: parameter estimation and validation, *Journal of structural engineering*, Vol. 124, No. 6, 1998.

[3] M.O. Moroni, M. Astroza, and S. Tavonatti, Nonlinear models for shear failure in confined masonry walls, *TMS Journal*, pp 72-78, 1994.

[4] P. Lourenco, *Computational strategies for masonry structures*, Delft University, 1996.

[5] A. Mohebkhah, A.A. Tasnimi, and H.A. Moghadam, Nonlinear analysis of masonry–infilled steel frames with openings using discrete element method, *Journal of constructional steel research*, pp 1463-1472, 2008.

[6] A. Hashemi and K. Mosalam, *Seismic evaluation of reinforced concrete buildings including effects of masonry infill walls*, PEER Technical Report, 255 pages, 2007.

[7] H. Mostafaei, F.J. Vecchio, and T. Kabeyasawa, Nonlinear displacement based response prediction of reinforced concrete columns, *Journal of engineering structures*, pp 2436-2447, 2008.

[8] K. Maekawa and H. Okamura, *Nonlinear analysis and constructive models of reinforced concrete*, University of Tokyo, 1990.

[9] F. Vecchio and M. Basil Emara, Shear deformations in reinforced concrete frames, *ACI Structural Journal*, January-February 1992.

[10] M. Tomazevic and I. Klemenc, Seismic behavior of confined masonry walls, *Earthquake engineering and structural dynamics*, Vol. 26, pp 1059-1071, 1998.

[11] A. Marinilli and E. Castilla, Experimental evaluation of confined masonry walls with several confining-columns, *Proceedings of the 13th World Conference on Earthquake Engineering*, Canada, Paper No. 2129, 2004.

COMPDYN 2011
3rd ECCOMAS Thematic Conference on
Computational Methods in Structural Dynamics and Earthquake Engineering
M. Papadrakakis, M. Fragiadakis, V. Plevris (eds.)
Corfu, Greece, 25–28 May 2011

Composite Materials Technologies in Constructions Structural Retrofitting: New Developments and Applications in Historical Buildings and Applications in Seismic Zone

Lino Credali [1*], **Gianluca Ussia**[2],

[1-2] Ardea Progetti e Sistemi s.r.l.
Via Cristoni 58 - 40033 Casalecchio Di Reno (Bologna - Italy)
ardea.credali@betontex.it; tecnico@betontex.it

Keywords: FRP, Composite Materials, Carbon Fibres, Structural Reinforces, Retrofitting, Structural Retrofitting.

Abstract. *Application of composite materials to construction started in Italy at beginning of the „90's and was generally accepted as one of the most important technologies for retrofitting and structural recovery of buildings. In 2004 the Italian National Research Council (CNR) issued the guideline for design and applications of composite materials in constructions and in 2009 it has been officially adopted for reconstruction at " L'Aquila" after the earthquake of April 6, 2009.*

The big advantage offered by Composites, mainly based on carbon fibres, is attributed to the special properties of the reinforcing fibres. Applications of composites range from concrete structures to masonry, bricks, steel and wood structures and more specifically reinforcement of beams, columns, vaults, arches, walls, concrete slabs, floors and total building belting.

Since 1993 many important original solutions and know how on materials, design and applications have been developed: reinforcing fabrics produced by an original patented process of thermo welding; connection systems based on Ardfix innovative technology, to prevent delamination; technology for wood beams reinforcements; cables technology and anchoring systems, new water base matrix systems with high fire resistance and good permeability to humidity and water.

A large experience in new solutions, and an important know how in applications has been developed.

New thermo welded mashes produced with alkali resistant zircon glass fibres, have been developed for direct application in concrete or calcium based mortar matrices. This special mesh grade is produced avoiding traditional induction process with plastic coating, leaving the surface of the fibre free from polymer and preserving the good capacity of adhesion to cement or calcium.

Many applications example of the above concept are reported, mainly related to retrofitting historical building.

1-INTRODUCTION

Application of composite materials in construction started in Italy in 1993 with laboratory tests at University of Bologna , and in just ten years reached a very large diffusion and was generally accepted as one of the most important technologies for retrofitting and structural recovery of buildings [1]. The important role of this technology has been generally recognized. In 2004 the Italian National Research Council (CNR) issued the guideline for design and applications of composite materials in construction [2-4] and in 2009 it was officially adopted as one important technology for rehabilitation and recovery of buildings damaged by earthquakes and largely used in seismic situation like in " L'Aquila" after the earthquake of April 6, 2009.

It is well known that the great advantage offered by composites , mainly based on carbon fibres is attributed to the special properties of the reinforcing fibres: very high mechanical properties, high chemical resistance, low weight, low thickness and low invasiveness.

Properties of Composites

- **High mechanical properties:** Carbon fibers are five time more resistent compared to steel.
- **Lightness:** Carbon fiber density is 1,8g/cm3, steel density is 8 g/cm3.
- **No invasive:** Reinforcements are generally applied externally, in very low thickness , easily covered by plaster in final coating.
- **No corrosion and high environmental resistance:** no maintenance in the time.
- **High fatigue resistance**: Vibration dumping.
- **Reversibility of the application:** External applications are easily removed.
- **Easy application**: Very simple application technology without need of important equipments

Tab. 1- Main Properties of Composites Applications in Constructions

Reinforcement effect is obtained without addition of mass and rigidity, that means a big advantage in seismic zone applications.(Tab.1)

Technology Solutions of Composite Materials

- **Fibers:** ***Carbon, Aramid, LCP, Glass, AR-Glass.***
- **Reinforcement Grade:**
  - Textile : Unidirectional , Biax-fabrics, Multiax, Net - fabrics.
  -Preimpregnated reinforcements : Pultruded lamina, Bars and Rods or Special shapes, properly designed.
- **Application Technologies :** ***External Lamination of dry textile, External Adhesion of pultruded lamina, Internal reinforces by Pultruded Bars, Lamina and Cables***
- **Delamination and failure mode control -** ***Connectors***

Tab.2 - FRP- Technical Possible Solutions

Applications of composites range from concrete, masonry, brick, steel and wood and more specifically reinforcement of : beams, columns, vaults, arches, walls, concrete slabs, floors and total building belting.

The large development of technology leads to many different solutions in terms of fibre type and variety of applications. Engineering and architectural criteria to select the appropriate technology among different possibilities should be considered. Products, material and technology optimization is also an important consideration for designers, applicators and end users (Tab.2).

2-FRP: MATERIALS AND TECHNOLOGY DESIGN

In our work, taking advantage of a large experience in composite applications on construction, starting in 1993, many important innovative solutions and „know how' on materials, design and applications have been developed. In the following paragraphs several criteria for structural reinforcement design and solution selection, among the different opportunities offered by the market are presented [5-9].

2.1 - Fibre Selection

Carbon Fibres: They are the most important fibres used in construction. The high level of crystallinity, over 99 %, and the high packed crystal structure of graphite makes this fibre very stable in respect to corrosion, even in high alkaline conditions, chemically stable at pH variations and with high thermal resistance, even over 1000° C. (Fig. 1). Besides the high mechanical properties, the special structure and morphology of this fibre make carbon fibres the most stable and safe with respect to environmental durability and for applications under severe conditions. Creep is also an important property when the reinforced structure is subjected to permanent loads. It is well known that carbon fibres show no significant creep under permanent loads.

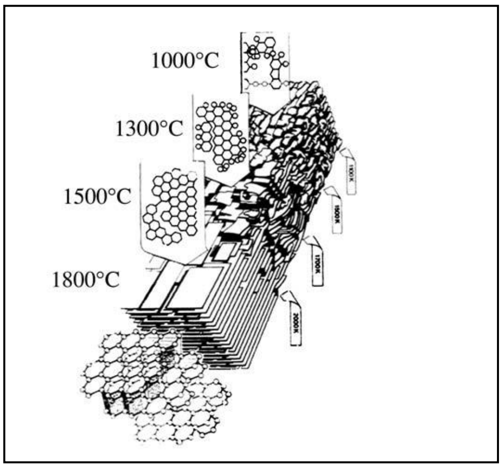

Fig. 1- The packed crystal structure of carbon fiber under thermal treatment process, in production [10].

Aramid Fibres: aramid fibres, are based on organic polymers, characterized by high mechanical properties, thermal resistance , and unusual capacity of vibration energy absorption

However this fibre lacks in resistance to humidity, to pH variation and UV radiation. Creep resistance of the fibre may be a property that designers should take in consideration with attention.

The high capacity of vibration dumping of Aramid fibre make this material very attractive to apply to earthquake rehabilitation construction, or application to constructions near high traffic roads, in order to prevent vibrations. A combination of aramid fibres as vibration energy dumping elements and carbon fibres as perfectly elastic elements can be a very good solution with excellent synergistic effects.

In practice, when aramid fibres are used, a good protection of the fibre, to humidity, environmental corrosion and UV radiation, should be warranted by the impregnation of resins.

Glass Fibres: glass fibres, largely used in traditional composites applications for a long time, are very cheap products, but they lack in terms of mechanical properties and weight (fibre density is 2,5g/cm3). For this reason the use of this fibre is usually limited to large surface applications when the role of the mechanical properties are not very important.

AR- Glass Fibres: AR- glass fibres nets are easily found in the market and used directly in combination with mortar, mainly for masonry or brick walls reinforcement. This special glass grade is based on composition containing a minimum amount (16%) of zirconium oxide, that provides superior performance under alkaline conditions.
Commercial glass nets based on A.R. fibres, are obtained by traditional waving process which includes an induction process with plastic coating to fix the fibre. So any adhesion between the fibre and the mortar is prevented, adhesion is extremely poor and generated only by mechanical bonds.

2.2- Reinforcements alternatives

The **market** of fibre reinforcements offer a variety of solutions that can be selected by designers. Several alternatives are listed in Table 3.

Fibre Reinforcement

- **Woven fabrics : Unidirectional tape , Biax and Multiax Fabrics and Biax-Nets for in situ lamination :** very simple application , may be easily adapted to the shape of support, it is the only solution for columns wrapping.
- **Pultruded Lamina :** important fibre sections may be applied in only one shot . Lamina cannot permit bending and wrapping.
- **Pultruded Rods and Connectors:** for inside concrete reinforce and connections.
- **Cables :** building belting, connections and walls reinforcement.

Tab.3- Different reinforcement solutions are available

Fabrics and woven tapes can permit an easy application by direct lamination. Woven fabrics are characterized by very good draping properties and reinforcement may take any shape and perfectly follow the substrate profile, for example when the reinforcement should be applied to columns by wrapping to increase confinement

Betontex reinforcing fabrics (Fig.2) are produced by an original patented process of thermo-welding, with high efficiency in reinforcement effects [5]. This special process has been developed by Ardea technology and comprise the use of a special thermo welding of the warp and the weft by means of a thin glass fibre coated by a hot melted adhesive [5, 6].

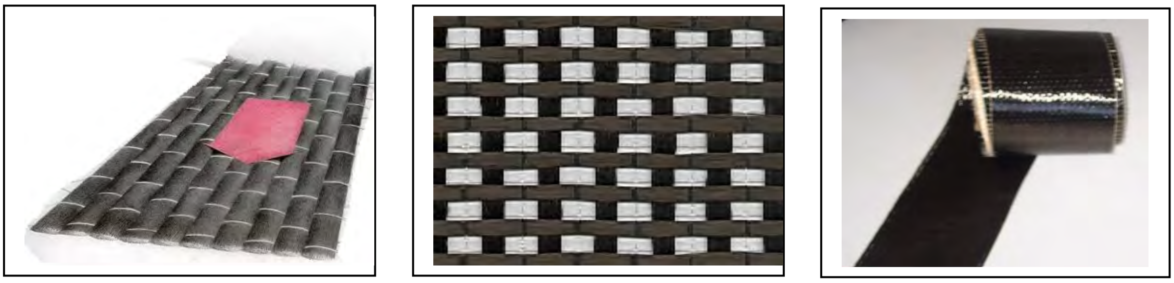

a-Unidirectional Thermo Welded Tape

b-Thermo Welded Net

c-Unidirectional Fabric Roll

Fig.2- Thermo welded carbon reinforces based on Betontex® technology.

Industrial production comprise unidirectional tapes , thermo welded biax- fabrics and nets, using different fibres, and weights and different fibre orientation. Reinforcements produced with this technology present very good handling properties, very good impregnation capability and perfect linearity of the fibre. Betontex reinforcements are easily applicable using optimized epoxy resins systems in all different conditions.

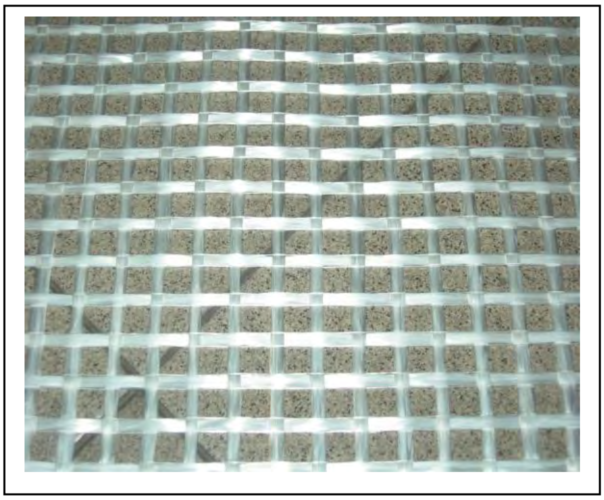

Fig.3.Betontex Thermo welded Net produced with AR- glass. Without plastic coating over the fiber.

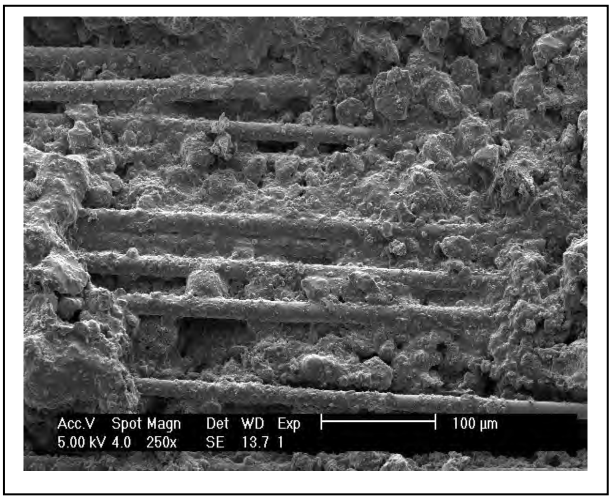

Fig.4.SEM view of interface between AR- .glass fiber surface and concrete, adhesion of the fiber is improved by Betontex IPN promoter.

New thermo welded nets produced with high zircon A.R. glass fibres, have been developed for direct application in concrete or in calcium based mortar matrices.

This special net grade is produced avoiding traditional induction plastic process , leaving the surface of the fibre free from polymer coating and preserving the good capacity of the fibre surface of adhesion to cement or calcium matrices. The free surface of the fibre can develop a good interaction with the concrete by direct physicochemical bonds formation (Fig.3-4).

In order to improve adhesion properties a special adhesion promoter has also been developed. This special adhesive system is based on a new concept of matrices with an IPN (Interpenetrated Polymer Network) structure, derived by a combination of two water based resins , one of which is supported over an active inorganic matrix. In fig.4 a view of the interaction between the fibre and the concrete is clearly shown.

Lamina may be used mainly in beam reinforcements whena significant amount of fibre sections should be applied, instead of using many layers of woven fabrics . Banding is a limitation in lamina applications thus, they are generally used only as beam reinforcements for straight on linear shape.

Pultruded rods**,** generally based on E-glass fibres and vinyl ester resins are very low prices materials, traditionally used for internal reinforcement of concrete.

Pultruded rods made of carbon fibres are primarily used to enhance mechanical properties in many cases and when there is a need to improve adhesion of carbon fibre reinforcements to the structure.

.

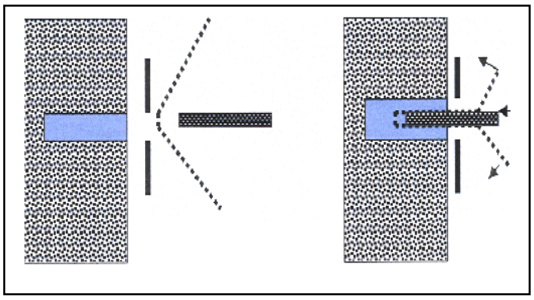

Fig.5. Schematic drawing of Ardfix connection system: a carbon bar push inside the wall a strip of unidirectional carbon fabric.

Connectors are very important for the general technology of composite materials applications in construction. The use of connectors made of carbon rods is extending and many alternative solutions have been proposed. In our research we have developed a very effective and easy to apply connection system that combine the application of carbon rods and unidirectional carbon strips.

.

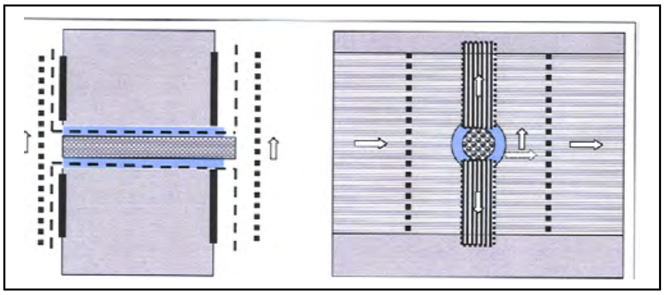

Fig. 6. Ardfix connecting the two faces of a wall. Loads are transferred through a net work structure.

Connectors should be used to improve adhesion of reinforcement to substrate, and are recommended when the quality of concrete or substrate is very poor.

Connectors may be very useful to prevent delamination, to transfer the tension from the reinforcement to the substrate and, also, to create a connection between the two sides of a structure, as in slabs or walls.
The use of high performance connectors, removes uncertainties related to substrate quality in terms of delamination resistance and allow designers to use the complete strength properties of the reinforcement without limitations induced by delamination phenomena.
The connection system, optimized in our work and described in reference `[7],` combines the application of a carbon fibre rod with a strip of tape and is represented in Fig.5 and 6. This system, after its introduction in the market with the name of Ardfix®, has been widely applied in many diverse applications.

.

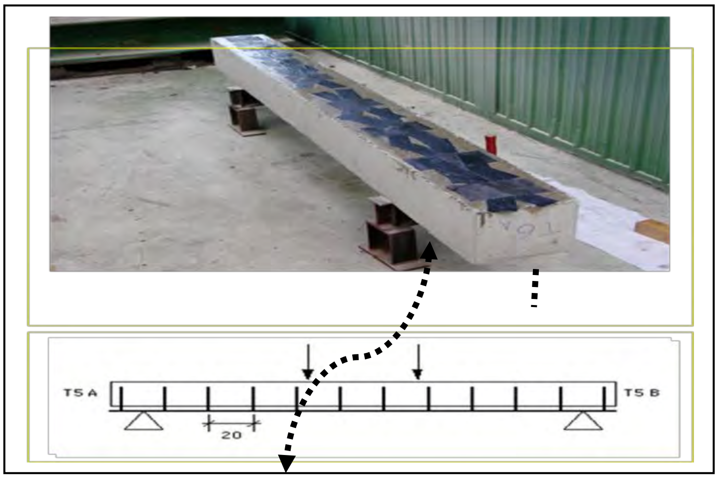

Fig.7.Application of Ardfix connectors on the intrados side of a concrete beam .After application of unidirectional reinforcing tapes, the beam is subjected to a flexural four points test.

A large number of laboratory tests have been carried on concrete beams reinforced with unidirectional carbon fibre, using Ardfix connectors. In fig.7 a beam reinforced with Ardfix connectors and unidirectional reinforcements is shown.

Fig.8a.Four point Flexion test on a concrete beam reinforced with n°3 layer of 300g/m^2 of high modulus (E=390 GPa) carbon fibre. No delamination has been detected during test.

Regarding the application, connectors are applied first, then, over connectors terminations, a unidirectional carbon tape is applied to reinforce the intrados of the beam.

With the Ardfix in all four-point flexural tests (Fig. 8a), no delamination of the reinforcement was observed and, at the ultimate load, the beam collapsed following the breaking of the carbon fibre at the centre of the beam, at the maximum moment (Fig.8b). Under such conditions, the ultimate bending resistance of the beam is governed by the ultimate tensile strength of the fiber.

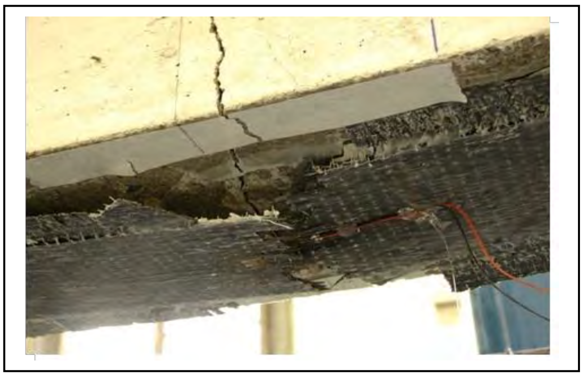

Fig.8b.Breaking of carbon fibre at the centre of the beam at the ultimate strength, without delamination. Calculated tension on the fibre at break was equal to 3500 MPa.

The calculated values of strength for the carbon fibre, detected at the ultimate braking load of the beam, was equal to 3500 MPa, compared to the nominal tensile strength of 4200 MPa of the original fibre, Tenax HM grade.

Cables made of high modulus fibres, can be successfully used to many construction rehabilitation applications. Cables, based on a combination of aramid, glass and carbon fibres are new products developed by Ardea research, and can be used in connections, as ties, walls reinforcement, building belting and pre-stressing.

Fig.9. Application of Betontex Aramid Tie 85 HM on the tambour of " *Anime Sante* " Cathedral , L'Aquila, damaged by earthquake of 2009. The Tambour was put in security to proceed with further works.

An interesting application of aramid-carbon cable was the securing of the tambour of the Cathedral of "Anime Sante" -L'Aquila, damaged by earthquake of April 2009.

Cables made on aramid fibre, with a weight of 85 g per linear meter and a tensile resistance over 12 tons, were applied by specialized technicians, lowered by an helicopter around the damaged tambour (Fig.9). An important task was the connection at the ends of the cable in order to apply the desired tension. In order to do that, a special ring coated with Dynema fibres was prepared at the ends of each cable. The 38 m long cables were pre-stressed by standard jacks.
A new and challenging application of cables is the reinforcement of historical walls or façades made of either stones or bricks, when the external old appearance should be preserved. Cables may be introduced in very thin slits applied in courses of breaks or stones, avoiding any modification of the external surface.

Fig.10. Historical City Walls in stones (Bassano- Italy), reinforced with hybrid aramid – carbon fibres cable, prestressed and impregnated with epoxy resins. Courses among stones will be filled by traditional mortar.

Fig.11. Bricks walls reinforced with carbon fibres cable coated with aramid fibres, prestressed and impregnated with epoxy resins. Courses among bricks will be closed by traditional plaster.

Figures 10 and 11 show the cable application on stones and bricks walls. The examples refers to the City Walls of Bassano (Italy) and to a facade wall of an historical Cathedral in Bologna. In both cases cables have been pre-stressed and impregnated with special high fluidity epoxy resins and filled with traditional mortar.

2.3- Wood rehabilitation.

Wood-beam retrofitting is an important task that may be easily resolved by using FRP. Many different solutions have been proposed and described in literature [4] using: lamina , rods and unidirectional fabrics. However, all these solutions lack of a good reinforcing effect.
The low external surface compression resistance of wood, compared to the high tensile force of composites at internal surface, is a strong limitation on the strengthening effect.

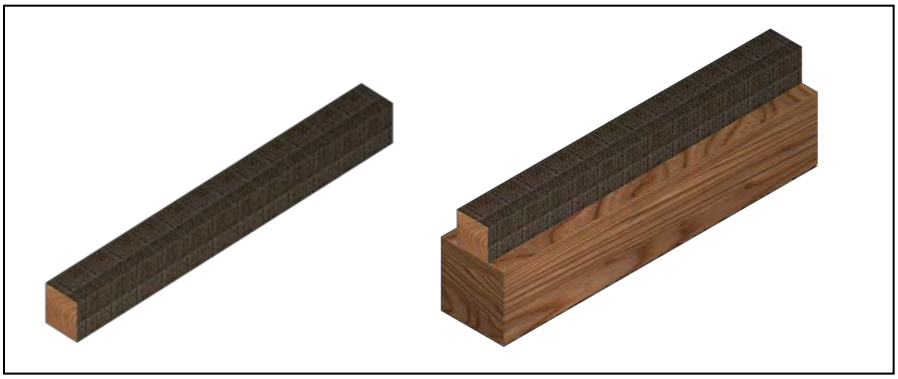

Fig.12-a. Ardwood, a wood element confined by carbon fibre net. Application of confined element to the extrados of wood beam.

This problem was resolved by applying a parallelepipedon of wood of square section, confined by a carbon fibre net, on the upper part (external surface) of the beam. This phase is followed by the application of carbon unidirectional fabrics or a lamina at the internal surface side of the beam.

Fig.12-b. Ardwood application on a beam, lateral view and section. Connection between Ardwood element and beam is made with Ardfix connectors. The intrados of the beam is reinforced with a carbon fibre lamina or a fabric.

The confined wood at the external surface of the beam be subjected to compression forces, equilibrating the high tensile force of the carbon fibre at internal surface side.
The system has been used for many years with the trade name Ardwood [8]. The schematic drawing of the Ardwood system for the rehabilitation of wood beams is shown in Fig 12(a-b).

3-MATRICES

Matrices are the second components of composite systems, the first being fibres. Matrices play a very important role in composite applications: impregnate the fibres, give shape to the reinforcement element, create a good adhesion to the building structure and transfer stresses from the structural element to the fibres

3.1 – Epoxy Matrices

Many types of matrices can be used in composite technology ranging from polymeric to ceramic and metal matrices.

Resin Grade	RC01	RC02	RC02/3 Tixo	RC30	RC30/3 Tixo
Functionality	Primer, surface preparation	Tixotropic Impregnating and adhesive	High tixotropic Impregnating and adhesive.	Tixotropic epoxy mortar	High tixotropic epoxy mortar
Resin A / Catalyst B ratio	2:1	2:1	2:1	4:1	4:1
Mixing ratio by weight	100:50	100:50	100:50	100:25	100:25
Gel Time at 20°C	50-60 (min.)	50-60 (min.)	50-60 (min.)	40-45 (min.)	40-45 (min.)
Hardening Time at 20°C	180-240 (min)	180-240 (min)	180-240 (min)	120-180 (min)	120-180 (min)
Total Hardening Time at 20 °C	14-16 (hrs)	14-16 (hrs)	14-16 (hrs)	12-14 (hrs)	12-14 (hrs)
Application Temperature range (°C)	From +5°C to 30°C	From +5°C to 30°C	From +5°C to 30°C	From +5°C to 30°C	From +5°C to 30°C

Tab. 4- Betontex Two Components Epoxy Resins Systems

Properties	methods	RC01	RC02	RC02/3 Tixo	RC30	RC30/3 Tixo
Adhesion to concrete	ACI 440.3R-04	≥ 3,00 MPa (*)	≥ 3,00 MPa (*)	≥ 3,00 MPa (*)	≥ 3,00 MPa (*)	≥ 3,00 MPa (*)
Tensile Strength	ASTM D 638	≥ 35,00 MPa	≥ 35,00 MPa	≥ 35,00 MPa	≥ 45,00 MPa	≥ 45,00 MPa
Tensile Modulus	ASTM D 638	≥2,50 GPa	≥2,50GPa	≥2,50 GPa	≥3,00	≥3,00
Tensile Elongation	ASTM D 638	≥ 2,80 %	≥ 3,00 %	≥ 3,00 %	≥ 2,0 %	≥ 1,50
Shear Resistance	ASTM D 2344	≥ 25,00 MPa	≥ 25,00 MPa	≥ 25,00 MPa	n.d.	n.d.
Density 25 °C	ASTM D 792	1,10 g/cm^3	1,10 g/cm^3	1,12 g/cm^3	1,50 g/cm^3	1,60 g/cm^3
HDT	ASTM D 648 A	≥ 70,0 °C	90-100 °C	90-100 °C	90-100 °C	90-100 °C

(*) with concrete delamination

Tab. 5- Betontex Two Components Epoxy Resins Systems : Mechanical Properties.

In most structural applications a two component epoxy resin system is used, they are formulated at different viscosity grades: *primer resin:* a low viscosity resins for surface preparation, *impregnation and adhesion resin:* a medium viscosity resin to impregnate fibres, *epoxy resins mortar:* a high viscosity resin, for surface adjustment, and for lamina and Ardfix bar application (tab.4)

Epoxy resins show the best properties (Tab.5) for application of composites to constructions in terms of mechanical properties, aging resistance, and durability in every condition. In construction epoxy resins have been introduced many years for applications of steel bars and plates, as *" beton plaque",* and engineers are familiar and confident with their use. Nevertheless some caution should be taken regarding: the distortion temperature (HDT) (Tab.5) , a property strictly related to the second order transition temperatures *Tg*, which is in the range between 90-100 °C. In general applications the usual coating with traditional plasters or protective paints may be sufficient to protect FRP. In case of high temperature applications or when fire resistance is required, a protective coating should be applied, as for steel structures.

3.2 – Concrete matrices,

Some applications of carbon fibre fabrics reinforcements, directly dipped in special cement mortar, have been reported in the market. These systems may have the advantage to partially overcome some lack of properties of epoxy resins, but also exhibit some other problems that should be considered.

Carbon yarn, used in waving, is generally composed by a number of basic fibre ranging from 3.000 to 24.000. Polymeric matrices have the capacity to impregnate the single basic fibres, that is to enter inside the yarn, between the single fibres, generating a real "*composite material"*. Cement particles do not have the capability to impregnate the single fibres, but can only coat the yarn externally, leaving the single basic fibres unbounded. For this reason the carbon fibre, in terms of strength, develop very low results, ranging between 25-40 % of the strength of composites impregnated with epoxy resins.

Furthermore there is no bond formation between carbon fibre, surface and cement, so the incorporation of carbon fibres in cement matrices do not generate a *"composite material"* but only a mechanical blend with poor mechanical properties.

3.3- New water based resin system.

Considering the above described problems related to matrices, both of epoxy type or cement mortar based matrices, we have investigated and optimized new resins system based on the IPN (Interpenetrated Polymer Network) concept, commercialized with the trade name of Betontex IPN Resins (Fig.13).

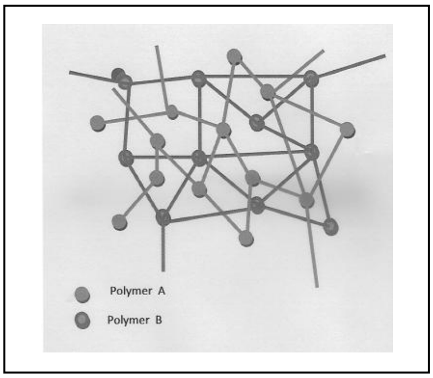

Fig.13 –IPN resins concept

This type of matrices is based on a new formulated resin in water solution or dispersion, supported over special micronized mineral filler. After mixing and hardening the two components, an IPN structure is obtained.
Similar to epoxy resins, this new type of resins is used in different grades as: IPN primer of low viscosity, IPN impregnation resins of medium viscosity, or IPN mortar of high viscosity.

.

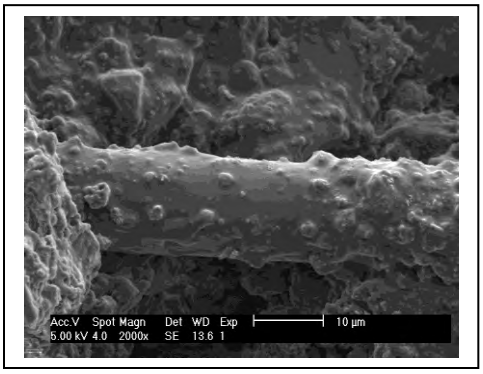

Fig. 14- Interface between IPN matrix and the reinforcing fibre, SEM x 2000 view ..

Betontex IPN resins may be used to applications with carbon fibres nets or AR Zirconglass nets, over concrete or over bricks or stone masonry structures.

The resins show very good adhesion capacity and very good mechanical properties; in tensile tests with carbon fibres 70-80% of epoxy resin properties are reached.

Temperature resistance is very good, no thermodynamic transition is observed until 180 °C, and degradation temperature may be observed over 300 °C, without melting.
Betontex IPN resins show a good burning resistance (class 1; following UNI 9176 D), can permit water vapour transmission, may be used over humid surfaces without any problem, and demonstrate very good aging properties even under also in severe conditions.
Many applications have been successfully carried out for reinforcement of walls and vaults and new tests are in progress for beam and plate reinforcement with unidirectional fabrics

4-APPLICATIONS EXAMPLES AND CONCLUSIONS.

Many application examples of the described technology are reported.
The most important are related to historical building retrofitting, among them we will refer to:
a) “Venaria Reale”, a Royal Palace in Venaria near Turin.

In Venaria the large arcades were reinforced with unidirectional hybrid carbon-aramid fibres, partially overlapped in the central area of the arcades to increase the fibre section.

b) Basilica of S.Antonio in Padua where the Vaults of convent were reinforced with aramid and carbon unidirectional strips. The walls of the tympanum of Library, were reinforced with unidirectional carbon and hybrid carbon-aramid fibres in both sides of the walls and connected by Ardfix connectors in order to create a tridimensional network structure.


Fig. 15- Venaria Royal Palace –Turin.


Fig. 16- Intrados reinforcement of arcades - Venaria Royal Palace –Turin. (1999)


Fig.17 – The Basilica f S. Antonio in Padova- Italy (2001-2004).

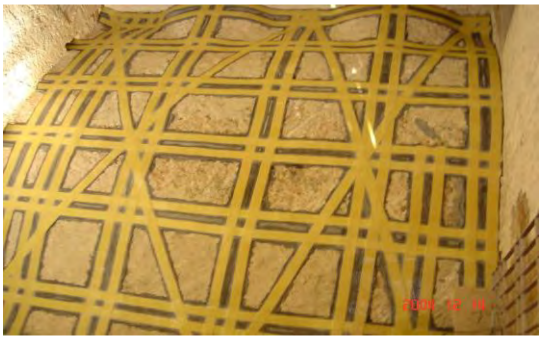
Fig.18 – The Basilica f S. Antonio in Padova- Italy . Vaults reinforcement of monastry cells.


Fig. 19 -Outside walls reinforcement of Tympanum of Library .


Fig. 20 -Inside walls reinforcement of Tympanum of Library.

We can also mention many other important churches and basilicas such as: Basilica of Vicoforte and Alba near Cuneo, Basilica of S. Petronio and S. Pietro in Bologna that have been subjected to rehabilitation works by using carbon fibres strips with the design and technology concepts described in this paper.

Fig.21- Example of extrados vaults reinforcement by carbon fibres tapes,
(S. Giorgio Church, near Bologna-Italy)

Fig.22- Example of walls reinforcement using Ardfix connectors, at Alba Cathedral in Cuneo- Italy.

A representative example of carbon fibre application with unidirectional strips, at the exterior of church vaults, is shown in figure 21. This reinforcement configuration presented is generally applied to many retrofitting works of old historical buildings and churches in Italy.

Application of connectors on the sides walls of the Alba Cathedral (Cuneo-Italy) is presented in photo 22. Over the connector ends two strips of unidirectional carbon fibre reinforcement is applied in orthogonal direction to the fibres (shown in the picture) and over them, a unidirectional reinforcement strip is placed. All laminations are made using, fresh resins at the same time. In such a way a connection of superior behavior is obtained.
Applications on old concrete buildings, retrofitting of bridges and old industrial building have been performed from many years and are now widely applied.

Fig.23- Example of old concrete rehabilitation using thermo welded Betontex unidirectional carbon reinforces.

Picture 23 shows the rehabilitation of an old concrete structure. The Beams are reinforced toincrease shear and flexure, while columns are reinforced for bending, compression by confinement and shear. Connectors are used to avoid debonding.
New solutions have been developed for seismic zones. In picture 24 an example of internal belting of an old Villa, damaged by earthquake of 1996 in Reggio Emilia, is shown. A similar reinforcement was applied at the external side of the wall. The strengthening is applied to avoid both out of plane and in plane failure of the masonry walls. Both sides have been connected with Ardfix.

Fig.24- Example of building complete belting (inside and outside) , at Villa Bertani- Reggio Emilia damaged by earth quake of 1996 , using thermo welded Betontex unidirectional carbon reinforces.

Fig.25a-25b- Concrete rehabilitation in a civil building at L'Aquila- Italy, damaged by earthquake of April 2009. Joint Column-Beam reinforcement. and Columns confinement.

Recent reinforced concrete industrial constructions damaged by the "L'Aquila-Italy" earthquake in April 2009 have been rehabilitated using Betontex carbon fibre reinforcements (Fig.25a-b). Reinforcement of old traditional bricks and masonry buildings, damaged by the same earthquake, are in progress, following the technical solutions and using the design concepts and materials reported in this paper.

REFERENCES

[1] L.Credali, A. Santini, –" *Building and Construction for Engineers : "Il rinforzo di strutture con FTS Betontex*$^{®}$*"*, L'EDILIZIA, 7/8 , pag. 78, 1999

[2] Italian National Research Council, Advisory Committee on Technical Recommendations for Constructions: "*Guide for the Design and Construction of Externally Bonded FRP Systems for Strengthening Existing Structures*" , CNR DT 200/2004

[3] Italian National Research Council, Advisory Committee on Technical Recommendations for Constructions: "*Guide for the Design and Construction of Externally Bonded FRP Systems for wood structures*" , CNR DT 201/2005

[4] Italian National Research Council, Advisory Committee on Technical Recommendations for Constructions: "*Guide for the Design and Construction of Externally Bonded FRP Systems for steel structures"* , CNR DT 202/2005

[5] L.Credali, EP 0994223 "*Fabric suitable to the application as reinforcement of building works"*, priority October 13, 1998

[6] L.Credali, EP 1788164 *"Reinforcement method for stone materials and reinforced slab"*, priority May 23, 2007

[7] L.Credali, IT Patent 1338380 *"Metodo per il rinforzo di strutture edilizie e strutture edilizie rinforzate"* January 22, 2002

[8] L.Credali, IT Patent 1365358*,"Struttura di trave rinforzata e relative metodo di realizzazione"* , priority April 7, 2005

[9] L.Credali, *"Selection criteria for design and application of composites materials in constructions*" INARCOS, 676 ,1-10, 2007

[10] E.Fitzer, M.Heine,-*" Fibre reinforcements for composite materials" ,*Elseviar, A.R.Bunsell Editor, pag. 120, 1988

COMPDYN 2011
3rd ECCOMAS Thematic Conference on
Computational Methods in Structural Dynamics and Earthquake Engineering
M. Papadrakakis, M. Fragiadakis, V. Plevris (eds.)
Corfu, Greece, 25–28 May 2011

RELIABILITY SENSITIVITY OF LINEAR DYNAMICAL SYSTEMS SUBJECT TO GAUSSIAN EXCITATION

Marcos A. Valdebenito[1], **Héctor A. Jensen**[1], **Gerhart I. Schuëller**[2] **and Fernando E. Caro**[1]

[1]Department of Civil Engineering, Santa Maria University
Casilla 110-V, Valparaiso, Chile
e-mail: {marcos.valdebenito,hector.jensen}@usm.cl

[2] Chair of Engineering Mechanics, University of Innsbruck
Technikerstraße 13, A-6020, Innsbruck, Austria, EU
e-mail: Mechanik@uibk.ac.at

Keywords: Reliability, Sensitivity Analysis, Gaussian Stochastic Process, First Excursion Probability.

Abstract. *Probability theory offers an appropriate framework for quantifying the level of safety of a structural system. Thus, it is possible to evaluate the chances that a structure fulfills prescribed performance criteria during its lifetime due to uncertainties in loadings, deterioration processes, etc. The aforementioned chances are usually termed as the reliability associated with a structure. Although reliability constitutes a fundamental metric of safety, knowledge on the sensitivity of the reliability with respect to variables such as material properties, cross section of structural members, etc. is also of paramount importance. The information on reliability sensitivity is most valuable as it allows, for example, taking decisions on the final design of a structure such that its level of safety is relatively invariant in case unexpected changes occur. Within the aforementioned framework, this contribution presents a novel approach for estimating the reliability sensitivity of a particular type of structures, namely linear structural systems subject to dynamic loading modeled as a Gaussian stochastic process. The sensitivity is computed with respect to deterministic variables that affect the structural performance (such as stiffness, cross section of structural members, etc.). The proposed approach is based on an efficient simulation technique and local approximations of the functions used to model the structural performance. The reliability measure is expressed in terms of the first excursion probability, which is a criterion widely used in stochastic structural dynamics. In addition, the error associated with the estimator of the reliability sensitivity is computed by means of the Bootstrap method.*

1 INTRODUCTION

One of the key issues for the analysis and design of civil engineering systems is the appropriate identification of the actions (such as water wave loading, wind loading, ground acceleration, etc.) that affect the structural performance during the life time. In most cases, such actions cannot be characterized deterministically due to inherent uncertainties [14]. Probability theory offers an appropriate framework for accounting for these uncertainties by means of, e.g. stochastic processes [28]. In this way, it is possible to generate a metric of the level of safety of a structural system. This metric refers to the reliability, i.e. the probability that a structure fulfills certain performance requirements during its lifetime. The complement of the reliability is the probability of failure (P_F), i.e. the probability that a structure violates prescribed performance criteria.

Besides determining the level of safety associated with a particular structural system, it is also of interest analyzing the sensitivity of the reliability with respect to variations in the properties of the structure [1, 6, 9, 21]. For example, the determination of the variation in the reliability due to a change in the size of a structural member can provide useful information to increase the safety level or to identify the most influential design parameters.

In cases of practical interest, the quantification of the reliability of a structure is an extremely challenging task, as it requires evaluating integrals in high dimensional spaces involving implicit domains [25]. In consequence, the evaluation of the sensitivity of the reliability with respect to system parameters will be usually even more involved than the reliability assessment. In view of this issue, this contribution proposes a novel approach for estimating reliability sensitivity for a particular class of structural systems, namely linear structures subject to dynamic loading modeled as a Gaussian stochastic process. The sensitivity is computed with respect to deterministic variables that affect the structural performance (such as mass, stiffness, cross section of structural members, etc.). The proposed approach is based on an efficient simulation technique and local approximations of the functions used to model the structural performance. The reliability measure is expressed in terms of the first excursion probability, which is a criterion widely used in stochastic structural dynamics. In addition, the error associated with the reliability sensitivity estimator (computed using simulation) is evaluated efficiently applying the Bootstrap method [10, 11].

The subject of efficient reliability sensitivity analysis has been considered several times in the literature. For example, sensitivity analysis of reliability estimates generated using approximate methods such as the First- and Second-Order Reliability Methods (FORM and SORM, respectively; see, e.g. [9]) has been thoroughly studied in the literature for problems involving component or system reliability, see e.g. [6, 12, 13, 18]. These approaches take advantage of the so-called design point associated with a particular reliability problem and eventual correlations between different individual failure modes in order to estimate the sought sensitivity efficiently. Reliability sensitivity analysis has also been studied within the framework of simulation methods. For example, in [22], a method combining Monte Carlo Simulation (MCS) with a linear approximation scheme allows estimating the sought sensitivity. In [30], an estimator for the sensitivity based on Importance Sampling (IS) is proposed. A common aspect of the two aforementioned approaches based on simulation is that they are applicable whenever sensitivity is estimated with respect to a parameter characterizing the random variables of the reliability problem, such as the mean or standard deviation. However, these approaches are not directly applicable in case one seeks to estimate the sensitivity with respect to a deterministic variable. Thus, alternative approaches have been developed to address this case. For example, in [24], an algorithm for estimating the gradient of the failure probability using either MCS or IS is presented. This algorithm requires solving equations characterizing the structural performance either analytically or numerically; however, this can be an involved task. An alternative approach for reliability sensitivity analysis was introduced in [1]. The key issues of this approach are the association of an *instrumental variability* with the deterministic design variables involved in the sensitivity analysis and the application of the Bayes' theorem. Nonetheless, the range of applicability of this approach is limited as no more than 3 or 4 design variables can be considered simultaneously when performing sensitivity analysis [19]. A different strategy for estimating reliability sensitivity within the context of non linear structural dynamics was introduced in [16, 29]. The main aspect of this strategy is the introduction of a series of approximation concepts both at the level of reliability estimation and the functions modeling the structural performance. This approach has been tested successfully in problems involving up to 10 design variables.

In this contribution, the strategy developed in [16, 29] is applied in order to estimate the reliability sensitivity of linear systems subject to dynamic Gaussian excitation. Novel aspects explored herein are the integration of the aforementioned strategy with an efficient IS scheme developed in [3] and an efficient means for generating approximations of functions related with the structural performance based on the sensitivity analysis of the spectral properties of the linear system under study, following the method proposed in [23]. These two novel aspects lead to a considerable reduction in the numerical costs associated with reliability sensitivity estimation when compared with the case of non linear structural systems. Finally, the error associated with the reliability sensitivity estimator is estimated most efficiently by applying the Bootstrap method introduced in [10].

The structure of this paper is as follows. Section 2 presents the details on the problem studied in this contribution. The approach for evaluating the structural response considering uncertainties in the excitation is discussed in Section 3. Then, Section 4 addresses an efficient simulation technique introduced in [3] for reliability evaluation of linear systems subject to Gaussian excitation. The proposed approach for reliability sensitivity estimation is discussed in Sections 5 and 6. Section 7 addresses the issue of quantifying the error of the estimator for reliability sensitivity developed in the two previous Sections by applying the Bootstrap method. A numerical example demonstrating the properties of the proposed approach is presented in Section 8. Finally, the paper closes with some final remarks and outlook.

2 GENERAL FORMULATION OF THE PROBLEM

Consider a structural system subject to a stochastic excitation of duration T. Let this excitation be represented by a random variable vector $\boldsymbol{z} \in \Omega_z \subset \mathbb{R}^{n_z}$ of dimension n_z characterized by a probability density function $p(\boldsymbol{z})$. Moreover, consider a set of responses of interest $r_i,\ i = 1, \ldots, n_r$ of the system modeling the structural performance due to the stochastic excitation such as, e.g. displacements. As the excitation acting over the structure is uncertain, the responses of interest will be uncertain as well. In addition, suppose there is a set of design variables grouped in a vector $\boldsymbol{y}$ of dimension n_y modeling properties of the system (such as cross section of structural members, material properties, etc.) that can be changed in order to alter the responses of interest. Clearly, the aforementioned responses of interest will be a function of both the design variable vector $\boldsymbol{y}$ and the random variable vector $\boldsymbol{z}$ characterizing the excitation. As this last vector also depends on time t, the responses will be also a function of time, i.e. $r_i = r_i(t, \boldsymbol{y}, \boldsymbol{z}),\ i = 1, \ldots, n_r,\ t \in [0, T]$.

For design purposes, the responses of interest $r_i,\ i = 1, \ldots, n_r$ are compared against acceptable threshold levels $r_i^*,\ i = 1, \ldots, n_r$. Within a deterministic framework, the objective would be ensuring that these responses do not exceed their prescribed thresholds. However, when uncertainties are considered, the aforementioned condition can be fulfilled only in a fraction of the possible cases, i.e. there is a probability that the responses do exceed their prescribed thresholds. Thus, reliability offers the means for quantifying the level of safety associated with a structural system. A criterion widely used to characterize the level of safety of a structure is the first excursion probability (see, e.g. [28]). This probability measures the chances that the uncertain responses exceed in magnitude the prescribed thresholds within a specified time interval. In other words, this probability measures the chances of occurrence of the following *failure event* F.

$$F = \left\{ \boldsymbol{z} \in \Omega_z : \max_{i=1,\ldots,n_r} \left(\max_{t \in [0,T]} \left(\frac{|r_i(t, \boldsymbol{y}, \boldsymbol{z})|}{r_i^*} \right) \right) \geq 1 \right\} \tag{1}$$

It is important to remark that *failure* does not necessarily imply collapse. In fact, the criterion proposed in eq. (1) may refer to, e.g. partial damage states or unacceptable system performance. Alternatively, the failure event defined in eq. (1) can be expressed in terms of the so-called *normalized demand* $D_N(\boldsymbol{y}, \boldsymbol{z})$ [2]:

$$F = \{ \boldsymbol{z} \subset \mathbb{R}^{n_z} : D_N(\boldsymbol{y}, \boldsymbol{z}) \geq 1 \} \tag{2}$$

where:

$$D_N(\boldsymbol{y}, \boldsymbol{z}) = \max_{i=1,\ldots,n_r} \left(\max_{t \in [0,T]} \left(\frac{|r_i(t, \boldsymbol{y}, \boldsymbol{z})|}{r_i^*} \right) \right) \tag{3}$$

Once the failure event has been defined, it is possible to express its probability of occurrence by means of the following classical probability integral.

$$P_F(\boldsymbol{y}) = \int_{D_N(\boldsymbol{y},\boldsymbol{z}) \geq 1} p(\boldsymbol{z}) d\boldsymbol{z} = \int_{\boldsymbol{z} \in \Omega_z} I_F(\boldsymbol{y}, \boldsymbol{z}) p(\boldsymbol{z}) d\boldsymbol{z} \tag{4}$$

In the last equation, $P_F(\boldsymbol{y})$ denotes the probability of failure (i.e. probability of occurrence of the event F) and $I_F(\boldsymbol{y}, \boldsymbol{z})$ is the indicator function which is equal to 1 in case the normalized demand is equal or larger than 1 and 0 otherwise.

As indicated in eq. (4), the probability of failure depends on the design variable vector $\boldsymbol{y}$. This has a clear physical interpretation: modifications on this vector (such as an increase in mass or stiffness) will certainly alter the response of the structure and also the probability of exceeding the prescribed thresholds. Thus, for design purposes, it is important to know not only the probability of failure $P_F(\boldsymbol{y})$ but also the change that this probability experiments due to changes in the design vector, as this allows determining the most influential design variables. This is denoted as the reliability sensitivity. A classical measure for sensitivity is calculating the gradient of the quantity of interest. However, within the context of linear dynamics, the estimation of the gradient of a probability may not be feasible as the gradient may not exist due to the non smooth normalized demand (see, e.g. [17]). Therefore, in this contribution, an approximate representation of the failure probabilities that is differentiable is constructed and then, the gradient of this approximation is estimated. Details on this strategy are described in Sections 5 and 6.

3 STRUCTURAL RESPONSE EVALUATION

3.1 Mechanical Model

The first step for assessing reliability and its sensitivity is characterizing the structural response. The differential equation describing the motion of a linear structure of n degrees of freedom excited by a dynamical excitation is given by (see, e.g. [7]):

$$\boldsymbol{M}\ddot{\boldsymbol{x}}(t) + \boldsymbol{C}\dot{\boldsymbol{x}}(t) + \boldsymbol{K}\boldsymbol{x}(t) = \boldsymbol{G}\boldsymbol{f}(t) \tag{5}$$

where $\boldsymbol{x}(t)$ is the displacement response vector of dimension n; $\boldsymbol{M}$, $\boldsymbol{C}$ and $\boldsymbol{K}$ are the mass, damping and stiffness matrices of dimension $n \times n$; $\boldsymbol{f}(t)$ is a vector of dimension n_f modeling the excitations acting over the structure; and $\boldsymbol{G}$ is a $n \times n_f$ dimensional matrix that couples the excitation components of the vector $\boldsymbol{f}(t)$ with the degrees of freedom of the structure. Note that the excitation vector $\boldsymbol{f}(t)$ depends on the vector of random variables $\boldsymbol{z}$ described in Section 2; the detailed relation between these vectors is discussed in Section 3.2. The responses of interest $r_i,\ i = 1, \ldots, n_r$ associated with a particular set of values of $\boldsymbol{y}$ can be evaluated using a convolution integral including the so-called impulse response functions $h_{i,j}(t, \boldsymbol{y}),\ i = 1, \ldots, n_r,\ j = 1, \ldots, n_f$, as indicated below.

$$r_i(t, \boldsymbol{y}, \boldsymbol{z}) = \sum_{j=1}^{n_f} \int_0^t h_{i,j}(t - \tau, \boldsymbol{y}) f_j(\tau) d\tau \tag{6}$$

In the last equation, $f_j(t)$ is the j-th component of the excitation vector and $h_{i,j}(t, \boldsymbol{y})$ is the impulse response function for the response function r_i at time t due to a unit impulse applied at the j-th input at time 0, where zero initial conditions have been assumed without loss of generality. It is noted that the dependence of the response function r_i on the vector of random variables $\boldsymbol{z}$ is due to the characterization of the stochastic excitation $\boldsymbol{f}(t)$. In case the response function of interest is given, for example, as a linear combination of the components of the displacement vector, that is, $r_i = \boldsymbol{\gamma}_i^T \boldsymbol{x}(t)$ and if the system possesses classical damping, the corresponding impulse response function is given by:

$$h_{i,j}(t, \boldsymbol{y}, \boldsymbol{z}) = \sum_{r=1}^{n} \alpha_r^{i,j} \frac{1}{\omega_{d,r}} e^{-\zeta_r \omega_r t} \sin(\omega_{d,r} t), \quad \alpha_r^{i,j} = \frac{\boldsymbol{\gamma}_i^T \boldsymbol{\phi}_r \boldsymbol{\phi}_r^T \boldsymbol{g}_j}{\boldsymbol{\phi}_r^T \boldsymbol{M} \boldsymbol{\phi}_r} \tag{7}$$

where $\alpha_r^{i,j},\ r = 1, \ldots, n,\ i = 1, \ldots, n_r,\ j = 1, \ldots, n_f$ are mode factors, $\boldsymbol{\phi}_r,\ r = 1, \ldots, n$ are the eigenvectors associated with the eigenproblem of the undamped equation of motion, $\omega_r,\ r = 1, \ldots, n$ are the natural frequencies of the system, $\zeta_r,\ r = 1, \ldots, n$ are the corresponding damping ratios, $\omega_{d,r} = \omega_r \sqrt{(1 - \zeta_r^2)},\ r = 1, \ldots, n$ are the damped frequencies and $\boldsymbol{g}_j$ is the j-th column of the $\boldsymbol{G}$ matrix. The last equation can be interpreted as the modal superposition formula for the impulse response functions. One advantage of this representation is that in general only a relatively small number of modes m will be required for performing dynamic analysis, i.e. $m \ll n$. Eventually, the contribution of the remaining modes can also be considered in the formulation by using the static solution of the structural modes of higher order [4].

3.2 Stochastic Excitation

Stochastic processes offer an adequate means for describing quantities fluctuating randomly in time such as earthquake ground motion, water wave loading, etc. In particular, a Gaussian process $X_t,\ t \in [0, T]$ is such that for every finite set $\{t_1, t_2, \ldots, t_{n_T}\} \in [0, T]$, the random variables $X_{t_1},\ X_{t_2}, \ldots, X_{t_{n_T}}$ are jointly normally distributed (see, e.g. [28]). A quite general means for representing Gaussian processes is by applying the Karhunen-Loève (K-L) expansion of the corresponding covariance function (see, e.g. [20]). This representation is applicable to stationary as well as to non stationary stochastic processes. In order to apply this representation for the excitation vector $\boldsymbol{f}(t)$ acting over a particular structural system (see eq. (5)), consider a discrete representation of time such that $\Delta t = T/(n_T - 1)$ where T is the duration of the excitation and n_T the number of time points so that the time instants of analysis are $t_k = (k-1)\Delta t,\ k = 1, \ldots, n_T$. Thus, the discrete K-L representation of the j-th component of $\boldsymbol{f}(t)$ is the following.

$$f_j(t_k) \approx f_j^0(t_k) + \sum_{s=1}^{n_{KL}} f_j^s(t_k) z_s^j,\ k = 1, \ldots, n_T,\ j = 1, \ldots, n_f \tag{8}$$

In the equation above, $z_s^j,\ s = 1, \ldots, n_{KL}$ are independent, identically distributed standard Gaussian random variables, $f_j^0(t_k)$ and $f_j^s(t_k)$ denote the mean function and the s-th K-L component of $f_j(t_k)$, respectively, and n_{KL} is the order of truncation of the series expansion. The K-L vectors are determined by solving an eigenproblem of the corresponding covariance matrix of the discrete process. In the remaining part of this contribution, it is assumed – without loss of generality – that the excitation is a zero-mean process, i.e. $f_j^0(t_l) = 0,\ l = 1, \ldots, n_T$.
Considering the characterization of the components of the excitation vector described above and considering the convolution integral in eq. (6), the dynamic response of interest evaluated at time t_k can be written as:

$$r_i(t_k, \boldsymbol{y}, \boldsymbol{z}) = \Delta t \sum_{j=1}^{n_f} \sum_{s=1}^{n_{KL}} \left(\sum_{l=1}^{k} \epsilon_l h_{i,j}(t_k - t_l, \boldsymbol{y}) f_j^s(t_l) \right) z_s^j \tag{9}$$

where ϵ_l is a coefficient depending on the numerical integration scheme used in the evaluation of the convolution integral.

4 RELIABILITY ANALYSIS

4.1 Characterization of Elementary Failure Events

According to the definition in eq. (1), failure takes place whenever the absolute value of any of the responses exceeds the prescribed thresholds at any time within the duration of the stochastic excitation. Considering the discretization scheme proposed above, the occurrence of the failure event reduces to comparing the value of the n_r responses during the n_T discrete time steps against the prescribed thresholds. Thus, the failure event F can be expressed as the union of *elementary failure events* $F_{i,k},\ i = 1, \ldots, n_r,\ j = 1, \ldots, n_T$, i.e.:

$$F = \bigcup_{i=1}^{n_r} \bigcup_{k=1}^{n_T} F_{i,k} \tag{10}$$

where:

$$F_{i,k} = \left\{ \boldsymbol{z} \in \Omega_z : \frac{|r_i(t_k, \boldsymbol{y}, \boldsymbol{z})|}{r_i^*} \geq 1 \right\} \tag{11}$$

Based on eq. (10), it is clear that the probability of failure is actually the probability of the union of a number of elementary failure elements. According to eq. (11), the elementary failure regions are defined as the region in the random variables space which cause a barrier crossing at instant t_k due to the i-th response function. Then, it is seen that the evaluation of $P_F(\boldsymbol{y})$ corresponds to a reliability problem of a series system of $n_r \times n_T$ failure elements. Using the linear

relations between input and response in terms of the Gaussian random variables $\boldsymbol{z}$ (see eq. (9)), the so-called design points can be established in a straightforward manner defining uniquely the elementary failure regions $F_{i,k},\ i = 1, \dots, n_r,\ j = 1, \dots, n_T$, see e.g. [8, 9]. It is reminded that the design point associated with the (i, k)-th elementary failure domain – which is denoted as $\boldsymbol{z}^*_{i,k}$ – can be defined using two equivalent criteria [14]. According to the geometrical criterion, the design point is the realization in the standard normal space that belongs to $F_{i,k}$ with the minimum Euclidean norm with respect to the origin. According to the probabilistic interpretation, the design point is the point belonging to $F_{i,k}$ with highest probability density $p(\boldsymbol{z})$.
Once the design point $\boldsymbol{z}^*_{i,k}$ has been established, the calculation of the probability of occurrence of the elementary failure events is straightforward. In particular, this probability is equal to $2\Phi(-\beta_{i,k}(\boldsymbol{y}))$, where $\Phi(\cdot)$ is the cumulative distribution function of the standard Gaussian distribution, and $\beta_{i,k}(\boldsymbol{y})$ is the so-called reliability index. Note that this reliability index is the norm of the corresponding design point, i.e. $\beta_{i,k}(\boldsymbol{y}) = ||\boldsymbol{z}^*_{i,k}||$. For the particular case under study, the expression for calculating the reliability index associated with the i-th response and k-th discrete time is the following (see, e.g. [8]).

$$\beta_{i,k}(\boldsymbol{y}) = ||\boldsymbol{z}^*_{i,k}|| = \frac{r^*_i}{\Delta t \sqrt{\sum_{j=1}^{n_f} \sum_{s=1}^{n_{KL}} \left(\sum_{l=1}^{k} \epsilon_l h_{i,j}(t_k - t_l, \boldsymbol{y}) f^s_j(t_l) \right)^2}} \tag{12}$$

Additionally, the (s, j)-th component of the vector $\boldsymbol{z}^*_{i,k}$ is equal to:

$$\left(\boldsymbol{z}^*_{i,k}\right)^s_j = \frac{r^*_i \left(\sum_{l=1}^{k} \epsilon_l h_{i,j}(t_k - t_l, \boldsymbol{y}) f^s_j(t_l) \right)}{\Delta t \sum_{j=1}^{n_f} \sum_{s=1}^{n_{KL}} \left(\sum_{l=1}^{k} \epsilon_l h_{i,j}(t_k - t_l, \boldsymbol{y}) f^s_j(t_l) \right)^2},\ s = 1, \dots, n_{KL},\ j = 1, \dots, n_f \tag{13}$$

4.2 Simulation Strategy

As the elementary failure regions are fully described by the design points, Importance Sampling (IS) arises as an option for evaluating the probability of occurrence (see, e.g. [26]). Thus, the probability integral in eq. (4) is estimated as:

$$P_F(\boldsymbol{y}) = \int_{z \in \Omega_z} I_F(\boldsymbol{y}, \boldsymbol{z}) \frac{p(\boldsymbol{z})}{p_{IS}(\boldsymbol{z})} p_{IS}(\boldsymbol{z}) d\boldsymbol{z} \approx \frac{1}{N} \sum_{v=1}^{N} I_F(\boldsymbol{y}, \boldsymbol{z}^{(v)}) \frac{p(\boldsymbol{z}^{(v)})}{p_{IS}(\boldsymbol{z}^{(v)})} \tag{14}$$

where $p_{IS}(\boldsymbol{z})$ is the Importance Sampling density (ISD) function and $\boldsymbol{z}^{(v)},\ v = 1, \dots, N$ are samples of the vector of uncertain parameters simulated according to $p_{IS}(\boldsymbol{z})$. The key issue for the application of the IS scheme described in eq. (14) is the design of an appropriate ISD function ensuring a low variability of the estimator of the probability. In particular,the ISD function proposed in [3] is applied here. This importance sampling density is defined as a weighted sum of probability density functions conditioned on the elementary failure events described previously, that is:

$$p_{IS}(\boldsymbol{z}) = \sum_{i=1}^{n_r} \sum_{k=1}^{n_T} \omega_{i,k}(\boldsymbol{y}) p_{IS}(\boldsymbol{z}/F_{i,k}) \tag{15}$$

where $\omega_{i,k} \geq 0$ is the weight associated with the elementary failure domain $F_{i,k}$ and it is defined such that:

$$\omega_{i,k}(\boldsymbol{y}) = \frac{\Phi(-\beta_{i,k}(\boldsymbol{y}))}{\sum_{l=1}^{n_r} \sum_{s=1}^{n_T} \Phi(-\beta_{l,s}(\boldsymbol{y}))} \tag{16}$$

Additionally, the distribution of $\boldsymbol{z}$ conditioned on the elementary failure domain $F_{i,k}$ is defined as (according to Bayes' theorem):

$$p_{IS}(\boldsymbol{z}/F_{i,k}) = \frac{p(\boldsymbol{z}) I_{F_{i,k}}(\boldsymbol{y}, \boldsymbol{z})}{2\Phi(-\beta_{i,k}(\boldsymbol{y}))} \tag{17}$$

where $I_{F_{i,k}}(\boldsymbol{y}, \boldsymbol{z})$ is an indicator function equal to one in case the (i,k)-th failure event takes place and zero, otherwise. Replacing the expressions in eqs. (15), (16) and (17) into eq. (14) yields the following estimator for the failure probability:

$$P_F(\boldsymbol{y}) \approx \hat{P}_F(\boldsymbol{y}) = \frac{2}{N} \left(\sum_{i=1}^{n_r} \sum_{k=1}^{n_T} \Phi(-\beta_{i,k}(\boldsymbol{y})) \right) \sum_{v=1}^{N} \frac{1}{\sum_{i=1}^{n_r} \sum_{k=1}^{n_T} I_{F_{i,k}}(\boldsymbol{y}, \boldsymbol{z}^{(v)})} \tag{18}$$

where $\hat{P}_F(\boldsymbol{y})$ denotes an estimator of the failure probability. It should be noted that in the estimator in eq. (18), the indicator function $I_F(\boldsymbol{y})$ is set equal to one, as the generation of samples of $\boldsymbol{z}$ conditioned on an elementary failure event ensures that the failure events occurs. In summary, the estimation of the failure probability using the estimator in eq. (18) requires the characterization of the elementary failure domains through the design points and reliability indexes. Samples of the vector $\boldsymbol{z}$ conditioned on the elementary failure events are required as well. These samples can be generated according to the technique proposed in [3]. Finally, the structural response associated with each of the samples of $\boldsymbol{z}$ must be evaluated and compared with the threshold levels in order to compute the indicator function $I_{F_{i,k}}(\boldsymbol{y}, \boldsymbol{z})$.

5 FRAMEWORK FOR ESTIMATING RELIABILITY SENSITIVITY

As already mentioned above, the sought sensitivity of the probability of failure is expressed as the gradient of an approximate representation of the probability. This approximation is continuous and smooth, ensuring differentiability. In particular, consider the following approximate representation of the normalized demand function:

$$D_N(\boldsymbol{y} + \Delta\boldsymbol{y}, \boldsymbol{z}) \approx \tilde{D}_N(\boldsymbol{y} + \Delta\boldsymbol{y}, \boldsymbol{z}) = D_N(\boldsymbol{y}, \boldsymbol{z}) + \sum_{q=1}^{n_y} a_q \Delta y_q \tag{19}$$

where $\Delta\boldsymbol{y}$ is a certain perturbation of the design variable vector and $a_q,\ q = 1, \ldots, n_y$ are real coefficients (the issue on how to compute these coefficients is discussed in Section 6). Now, consider the following limit, expressing the derivative of the approximate failure probability $\tilde{P}_F(\boldsymbol{y})$ with respect to $y_q,\ q = 1, \ldots, n_y$.

$$\frac{\partial \tilde{P}_F(\boldsymbol{y})}{\partial y_q} = \lim_{\Delta y_q \to 0} \frac{\tilde{P}_F(\boldsymbol{y} + \boldsymbol{v}(q)\Delta y_q) - \tilde{P}_F(\boldsymbol{y})}{\Delta y_q} \tag{20}$$

$$= \lim_{\Delta y_q \to 0} \frac{P\left[\tilde{D}_N(\boldsymbol{y} + \boldsymbol{v}(q)\Delta y_q, \boldsymbol{z}) \geq 1\right] - P\left[\tilde{D}_N(\boldsymbol{y}, \boldsymbol{z}) \geq 1\right]}{\Delta y_q} \tag{21}$$

where $P[\cdot]$ denotes the probability of occurrence of the event between brackets and where $\boldsymbol{v}(q)$ is a vector of length n_y with zero entries, except by the q-th entry, which is equal to one. Introducing the approximation of the normalized demand function of eq. (19) in eq. (21) yields the following result.

$$\frac{\partial \tilde{P}_F(\boldsymbol{y})}{\partial y_q} = \lim_{\Delta y_q \to 0} \frac{P\left[D_N(\boldsymbol{y}, \boldsymbol{z}) \geq 1 - a_q \Delta y_q\right] - P\left[D_N(\boldsymbol{y}, \boldsymbol{z}) \geq 1\right]}{\Delta y_q} \tag{22}$$

To evaluate the limit in eq. (22), it is necessary to estimate the probability that the normalized demand (for a given design $\boldsymbol{y}$) exceeds two different threshold levels. That is, it is necessary to estimate $P[D_N(\boldsymbol{y}, \boldsymbol{z}) \geq b]$ for the values $b = 1$ and $b = 1 - a_q \Delta_{y_q}$. Numerical experience has shown that this relation can be approximated by means of an exponential function [15], i.e.:

$$P\left[D_N(\boldsymbol{y}, \boldsymbol{z}) \geq b\right] \approx e^{\psi_0 + \psi_1 (b-1)}, \quad b \in [1-\epsilon, 1+\epsilon] \tag{23}$$

where ϵ is a small constant, e.g. $\epsilon = 0.02$ and where $\psi_0,\ \psi_1$ are real coefficients (the details on the calculation of these coefficients are discussed in Section 6). After introducing eq. (23) in (22), an expression for computing the probability sensitivity can be obtained, as shown below.

$$\frac{\partial \tilde{P}_F(\boldsymbol{y})}{\partial y_q} = \lim_{\Delta y_q \to 0} \frac{e^{\psi_0 - \psi_1 a_q \Delta y_q} - e^{\psi_0}}{\Delta y_q} = -\psi_1 a_q e^{\psi_0} = -\psi_1 a_q \hat{P}_F(\boldsymbol{y}) \tag{24}$$

It is most interesting to note that the expression for estimating the derivative of the failure probability in eq. (24) depends on the estimate of the failure probability $\hat{P}_F(\boldsymbol{y})$, the coefficient ψ_1 and on $a_q,\ q = 1, \ldots, n_y$. While the estimate of the failure probability can be computed with the procedure outlined in Section 4, the remaining coefficients are obtained using the procedure outlined in the following Section.

6 IMPLEMENTATION OF RELIABILITY SENSITIVITY ANALYSIS

6.1 Exponential Approximation of Probability

As discussed in the previous Section, the implementation of the proposed strategy for reliability sensitivity requires the generation of an exponential approximation of the probability that the normalized demand exceeds a threshold b. The procedure for reliability estimation described in Section 4 allows estimating the probability that the normalized demand exceeds 1. However, this procedure can be easily extended for estimating the required relation. As this required relation must be estimated for a range $b \in [1-\epsilon, 1+\epsilon]$, the definition of the elementary failure domains is slightly altered. In particular, the reliability indexes and design points defined in eqs. (12) and (13) are modified as follows: the term that denotes the threshold level r_i^* is replaced by $r_i^*(1-\epsilon)$. This change ensures that the samples of $\boldsymbol{z}$ are such that the values of the associated normalized demands are equal or larger than $(1-\epsilon)$. In the second place, an indicator function $I_{F,b}(\boldsymbol{y}, \boldsymbol{z})$ is introduced in the estimator of eq. (18). This indicator function is defined such that:

$$I_{F,b}(\boldsymbol{y}, \boldsymbol{z}) = \begin{cases} 1 & \text{if } D_N(\boldsymbol{y}, \boldsymbol{z}) \geq b \\ 0 & \text{if } D_N(\boldsymbol{y}, \boldsymbol{z}) < b \end{cases} \tag{25}$$

The indicator function in the equation above is dependent on the threshold level b. This function is then included in the probability estimator of eq. (18) as shown below.

$$\hat{P}\left[D_N(\boldsymbol{y}, \boldsymbol{z}) \geq b\right] = \frac{2}{N} \left(\sum_{i=1}^{n_r} \sum_{k=1}^{n_T} \Phi(-\beta_{i,k}(\boldsymbol{y})) \right) \sum_{v=1}^{N} \frac{I_{F,b}(\boldsymbol{y}, \boldsymbol{z}^{(v)})}{\sum_{i=1}^{n_r} \sum_{k=1}^{n_T} I_{F_{i,k}}(\boldsymbol{y}, \boldsymbol{z}^{(v)})} \tag{26}$$

The estimator above can be used directly to estimate the probability that the normalized demand exceeds a certain threshold level . Thus, the estimator is applied as follows. Firstly, samples of the vector $\boldsymbol{z}$ conditioned on the modified elementary failure events are generated. Then, response and normalized demand associated with each of these samples is computed. In the next step, the probability that the normalized demand exceeds a threshold level is computed over a suitable grid $b \in [1-\epsilon, 1+\epsilon]$. This allows generating pairs $(b, \hat{P}\left[D_N(\boldsymbol{y}, \boldsymbol{z}) \geq b\right])$. Finally, the coefficients $\psi_0,\ \psi_1$ of the exponential approximation proposed in eq. (23) are calculated on a least square sense using the aforementioned pairs.

An important feature of the approach proposed above for calculating the coefficients $\psi_0,\ \psi_1$ is that it requires a single run of the simulation algorithm. Moreover, it should be noted that only minor modifications are introduced to the original approach for estimation the probability of failure presented in [3] and described in Section 4 of this contribution.

6.2 Linear Approximation of Normalized Demand Function

The expression in eq. (19) is as a *linear* expansion of the normalized demand function with respect to a perturbation in the design variable vector. In most cases, this expansion will not be exact, as changes in the normalized demand function due to perturbations in the design variables are non linear, implicit functions. Nonetheless, as long as the coefficients $a_q,\ q = 1, \ldots, n_y$ are calibrated appropriately, it could be expected that $\tilde{D}_N(\boldsymbol{y} + \Delta\boldsymbol{y}, \boldsymbol{z})$ can approximate $D_N(\boldsymbol{y} + \Delta\boldsymbol{y}, \boldsymbol{z})$ reasonably well. For a better understanding of the last point, consider the definition of normalized demand function in eq. (3). As this function includes the $\max(\cdot)$ operator, several elementary failure domains may be relevant in the calculation of $P_F(\boldsymbol{y})$. The sensitivity of each these elementary domains with respect to the design variables will be – in general – different. Thus, the linear expansion shown in eq. (19) will not capture those individual sensitivities. However, the coefficients a_q represent an *average sensitivity*, i.e. they are an approximate representation of the sensitivity of the individual elementary failure domains.

In view of the issues discussed above, the proposed approach for calibrating the coefficients a_q consists in two steps. In the first one, samples of the vector modeling the uncertain excitation $\boldsymbol{z}$ are generated such that they lie precisely in the boundary of the failure event. The second step consists in calculating the sensitivity of the normalized demand function with respect to the design variables at the samples generated at the previous step. Thus, the sought coefficients can be calculated as the average of the sensitivities calculated for each sample.

From the two steps described above, the first one can be easily achieved by scaling the samples of $\boldsymbol{z}$ generated at the reliability analysis step. Suppose that for a particular sample $\boldsymbol{z}^\star$, the associated normalized demand function is equal to $D_N(\boldsymbol{y}, \boldsymbol{z}^\star) = b^\star$. Then, the required sample is equal to the original sample multiplied by the reciprocal of $b^\star$, i.e. $D_N(\boldsymbol{y}, (1/b^\star)\boldsymbol{z}^\star) = 1$. This property holds due to the linearity of the equation of motion with respect to the excitation (see eq. (5)).

The second step of the proposed approach for calibrating the coefficients a_q consists in estimating the sensitivity of the normalized demand function with respect to the design variables at the sample point $\boldsymbol{z}^\star$. Suppose that the sample $\boldsymbol{z}^\star$ lies in the boundary of the $(i^\star, k^\star)$-th elementary failure domain. That means that the failure event is reached because the $i^\star$-th response achieved the threshold value $r^*_{i^\star}$ at the $k^\star$-th discrete time step. Thus, the sensitivity of the associated normalized demand function can be approximated by considering the derivatives of corresponding response at that particular time, i.e.:

$$\frac{\Delta D_N(\boldsymbol{y}, (1/b^\star)\boldsymbol{z}^\star)}{\Delta y_q} \approx \frac{1}{r^*_i} \mathrm{sgn}\left(r_i(t_k, \boldsymbol{y}, (1/b^\star)\boldsymbol{z}^\star)\right) \frac{\partial r_i(t_k, \boldsymbol{y}, (1/b^\star)\boldsymbol{z}^\star)}{\partial y_q},\ q = 1, \ldots, n_y \quad (27)$$

In the last equation, $\mathrm{sgn}(\cdot)$ is the sign function. The derivative of the response function r_i at the k-th time can be computed by calculating the derivative of the impulse response function with respect to the design variables. Thus, considering the expression for calculating the response of interest in eq. (9), the expression for estimating the sensitivity of the response is as follows.

$$\frac{\partial r_i(t_k, \boldsymbol{y}, \boldsymbol{z})}{\partial y_q} = \Delta t \sum_{j=1}^{n_f} \sum_{s=1}^{n_{KL}} \left(\sum_{l=1}^{k} \epsilon_l \frac{\partial h_{i,j}(t_k - t_l, \boldsymbol{y})}{\partial y_q} f_j^s(t_l) \right) z_s^j \tag{28}$$

In the equation above, $\partial h_{i,j}(t_l, \boldsymbol{y})/\partial y_q$ represents the derivative of the impulse response function with respect to the q-th design variable. Moreover, it is assumed that the coefficients of the K-L expansion of the stochastic excitation do not depend on the design variable $y_q,\ q = 1, \ldots, n_y$.

The calculation of the derivative of the impulse response function implies calculating the derivative of the spectral properties (frequencies and eigenvectors associated with the eigenproblem of the undamped equation of motion). In this contribution, an efficient procedure for determining eigenvector derivatives developed in [23] is used. In that procedure the calculation of the derivatives of a given eigenvector requires only eigendata associated with that eigenvector. The simplified procedure is much more efficient than standard methods in which eigenvector derivatives are expressed in terms of all eigenvectors.

Once the sensitivities of the responses are calculated according to eq. (28), the sought coefficients a_q are calculated taking the average of the sensitivities calculated for all the samples generated.

$$a_q = \frac{1}{N} \sum_{v=1}^{N} \frac{\Delta D_N(\boldsymbol{y}, (1/b^{\star,(v)})\boldsymbol{z}^{\star,(v)})}{\Delta y_q} \tag{29}$$

An interesting feature of the approach proposed above is that it requires a single sensitivity analysis of the spectral properties. The numerical costs associated with this analysis can be considerably lower than solving the eigenproblem for perturbed values of the design variables.

7 VARIABILITY OF RELIABILITY SENSITIVITY ESTIMATOR

The approach for evaluating the sensitivity of a reliability metric with respect to design variables described in Sections 5 and 6 is based on the information provided by N samples of the uncertain parameters generated through IS. More specifically, some local approximations involving these samples and the sensitivity of the normalized demand associated with them is used to compute an approximate measure of the sought quantity, as shown in eq. (24). In mathematical terms, this dependence of the estimator on the samples is represented as shown below.

$$\frac{\partial \tilde{P}_F(\boldsymbol{y})}{\partial y_q} = m_S(\boldsymbol{y}, q, \boldsymbol{z}_1, \boldsymbol{z}_2, \ldots, \boldsymbol{z}_N) \tag{30}$$

In the equation above, $m_S(\cdot)$ denotes the (nonlinear) function that allows estimating the sensitivity based on N samples of the uncertain parameters, q is the index associated with the q-th design variable and $\boldsymbol{z}_v,\ v = 1, \ldots, N$ represents a random variable vector distributed according to the prescribed probability density function associated with the simulation method being used to estimate reliability; in this case, $\boldsymbol{z}_v \sim p_{IS}(\boldsymbol{z}),\ v = 1, \ldots, N$. From eq. (30), it is clear that the estimator of the sensitivity is subject to variability, as it is a function of a finite sample N. Therefore, besides assessing the estimator of the sensitivity considering the aforementioned approach, it is also important to assess the variability of this estimator, as this allows gaining insight on its error. This error can be quantified by means of the standard deviation of the estimator:

$$\sigma_{\partial \tilde{P}_F/\partial y_q} = \sqrt{V\left[m_S(\boldsymbol{y}, q, \boldsymbol{z}_1, \boldsymbol{z}_2, \ldots, \boldsymbol{z}_N)\right]} \tag{31}$$

where $\sigma_{\partial \tilde{P}_F/\partial y_q}$ is the standard deviation of the sensitivity of probability w.r.t. the q-th design variable and $V[\cdot]$ represents the variance. It should be noted that assessing the standard deviation $\sigma_{\partial \tilde{P}_F/\partial y_q}$ analytically can be a challenging task, as $m_S(\cdot)$ is an involved nonlinear function. Thus, some alternative approach must be applied in order to assess the sought standard deviation.

A simple means for assessing $\sigma_{\partial \tilde{P}_F/\partial y_q}$ would be simply generating N_R estimates of the probability sensitivity and then calculating the sample standard deviation, i.e.:

$$\sigma_{\partial \tilde{P}_F/\partial y_q} \approx \hat{\sigma}_{\partial \tilde{P}_F/\partial y_q} = \sqrt{\frac{1}{N_R - 1} \sum_{w=1}^{N_R} \left(\frac{\partial \tilde{P}_F^{(w)}(\boldsymbol{y})}{\partial y_q} - \frac{\partial \bar{\tilde{P}}_F(\boldsymbol{y})}{\partial y_q} \right)^2} \tag{32}$$

where

$$\frac{\partial \bar{\tilde{P}}_F(\boldsymbol{y})}{\partial y_q} = \frac{1}{N_R} \sum_{w=1}^{N_R} \frac{\partial \tilde{P}_F^{(w)}(\boldsymbol{y})}{\partial y_q} \tag{33}$$

and $\partial \tilde{P}_F^{(w)}(\boldsymbol{y})/\partial y_q,\ w = 1, \ldots, N_R$ is the w-th estimate of the sensitivity. Although this approach can be implemented, it is highly inefficient from a numerical point of view, as for generating one estimate of the sensitivity (out of the N_R required) it is necessary to compute the dynamical response of the structural system N times. An alternative approach that allows calculating the sought standard deviation and that avoids the repeated simulation of the dynamical response is the so-called Bootstrap method [10]. Bootstrap consists in estimating a particular property of an estimator (such as the standard deviation) based on samples distributed according to an empirical probability distribution. This empirical distribution is constructed based on the very same sample pool used for calculating the estimator. Thus, applying resampling over this pool it is possible to generate a sample set of the estimator and then, calculate the sought property directly from the latter sample set. Algorithmically, this procedure is implemented as described below. For further details on the implementation of the Bootstrap method and its convergence it is referred to, e.g. [5, 10, 11, 27]

1. Generate N samples of the uncertain parameter vector (ground acceleration) and group them in a set C, i.e. $C = \left\{ \boldsymbol{z}^{(1)}, \boldsymbol{z}^{(2)}, \ldots, \boldsymbol{z}^{(N)} \right\}$. Note that the samples generated at this step are the same samples generated for estimating the probability of failure and its sensitivity.

2. Draw a bootstrap sample $C^* = \left\{ \boldsymbol{z}^{*,(1)}, \boldsymbol{z}^{*,(2)}, \ldots, \boldsymbol{z}^{*,(N)} \right\}$ by making independent random sampling from C. Note that this sampling considers replacement and the relative weight of each member of set C is equal to $1/N$. Estimate the reliability sensitivity for the sample set C^* considering the nonlinear mapping function $m_S(\cdot)$, i.e.:

$$\frac{\partial \tilde{P}_F^*(\boldsymbol{y})}{\partial y_q} = m_S(\boldsymbol{y}, q, \boldsymbol{z}^{*,(1)}, \boldsymbol{z}^{*,(2)}, \ldots, \boldsymbol{z}^{*,(N)}) \tag{34}$$

3. Repeat step 2 a total of N_R times in order to obtain bootstrap replications $\partial \tilde{P}_F^{*,(1)}(\boldsymbol{y})/\partial y_q$, $\partial \tilde{P}_F^{*,(2)}(\boldsymbol{y})/\partial y_q$, …, $\partial \tilde{P}_F^{*,(N_R)}(\boldsymbol{y})/\partial y_q$. Estimate $\sigma_{\partial \tilde{P}_F/\partial y_q}$ based on the sample standard deviation of the bootstrap replications.

Provided that N_R is chosen sufficiently large, the procedure described above can produce accurate estimates of the sought standard deviation. For the particular case of this contribution, it

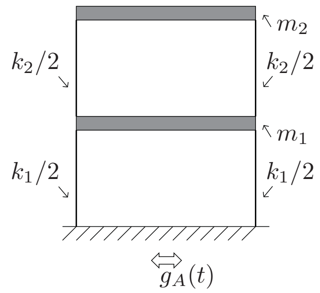

Figure 1: Example - 2-DOF shear beam model

has been found that the Bootstrap method is a very convenient approach for estimating the error of the reliability sensitivity estimator, as no additional computations of the dynamical response are required once the estimator has been calculated. This is a crucial point, as the assessment of the dynamical response can be numerically demanding due to the duration of the stochastic excitation and also due to the size of the matrices associated with the structural model.

8 NUMERICAL EXAMPLE

8.1 Description

A 2-DOF linear shear beam model is considered in the example. The model is depicted in fig. (1). The system is excited by a horizontal ground acceleration $g_A(t)$ of 15 [s] duration, which is modeled as a discrete white noise. The responses of the system to be controlled involve the displacements of each floor due to the ground acceleration. These responses are compared with prescribed thresholds in order to define whether or not failure occurs. The objective is estimating the sensitivity of the probability of failure with respect to the stiffnesses of each of floor.

As shown in fig. (1), each floor of the model is supported by two columns. It is assumed that the columns are perfectly clamped and axially very stiff. Thus, each column can be described by its lateral stiffness $k_i/2 = 9 \times 10^6$ [N/m], $i = 1, 2$. The mass of each floor of the model is equal to $m_1 = m_2 = 30 \times 10^3$ [kg]. It is assumed that the damping associated with the structure is classical with modal damping ratios equal to 4% for each vibration mode. The external force vector is defined as $\boldsymbol{f}(t) = -\boldsymbol{M} g_A(t)$, where $\boldsymbol{M}$ is the mass matrix and $g_A(t)$ is a horizontal ground acceleration, which is modeled as a discrete white noise of 15 [s] duration. A time discretization step equal to $\Delta t = 0.01$ [s] is used to model the ground acceleration. The discrete representation of the white noise signal is such that the coefficients of the K-L expansion of the ground acceleration g_A are equal to:

$$f^s(t_k) = \begin{cases} \sqrt{\frac{2\pi S}{\Delta t}} & \text{if } s = k \\ 0 & \text{if } s \neq k \end{cases}, \; k = 1, \ldots, 1501 \tag{35}$$

In the above equation, $S = 10^{-4}$ [m^2/s^3] is the power spectral density of the white noise. Note that a total of 1501 random variables are involved in the characterization of the excitation.

The failure event is formulated as a first passage problem during the time of analysis. The structural responses to be controlled are the 2 interstorey drift displacements and the roof displacement. The threshold values are chosen equal to 6×10^{-3} [m] for each of these three responses. In addition, the design variable vector $\boldsymbol{y}$ groups the stiffnesses of the columns of each floor, i.e. $\boldsymbol{y} = \langle k_1, k_2 \rangle^T$. Thus, the reliability problem is formally defined as:

$$P_F(\boldsymbol{y}) = \int_{D_N(\boldsymbol{y},\boldsymbol{z}) \geq 1} p(\boldsymbol{z}) d\boldsymbol{z} \tag{36}$$

where:

$$D_N(\boldsymbol{y}, \boldsymbol{z}) = \max_{i=1,2,3} \left(\max_{k=1,\ldots,1501} \left(\frac{|r_i(\Delta t(k-1), \boldsymbol{y}, \boldsymbol{z})|}{r_i^*} \right) \right) \tag{37}$$

8.2 Results

Before reporting on the results of reliability sensitivity, the results of reliability are presented for the sake of completeness. Applying the simulation strategy described in Section 4 considering a total of 200 samples of the stochastic ground acceleration, it is determined that the probability of failure related with the system described above is equal to $P_F = 4 \times 10^{-4}$. Moreover, the associated coefficient of variation (CoV) of this estimator is equal to 6.5%. Recall that the coefficient of variation is defined as the ratio between the standard deviation of the estimator and the mean value of the estimator. It should be noted that the probability of failure of the system is quite low, thus precluding the possibility of using direct Monte Carlo Simulation for its estimation because of high numerical costs associated.

Next, in order to estimate the reliability sensitivity of the failure probability in eq. (36) with respect to the stiffnesses, two different approaches are considered, namely:

- **Approach 1**: the sensitivity is estimated by performing finite differences, i.e.:

$$\frac{\Delta \hat{P}_F(\boldsymbol{y})}{\Delta y_q} = \frac{\hat{P}_F(\boldsymbol{y} + \boldsymbol{v}(q)\Delta y_q) - \hat{P}_F(\boldsymbol{y} - \boldsymbol{v}(q)\Delta y_q)}{2\Delta y_q}, \quad q = 1, 2 \tag{38}$$

  In the estimator of the equation above, the perturbation introduced is such that $\Delta y_q / y_q = 0.1\%$. As it can be noted from the formula, two reliability analyses are required for estimating the sensitivity with respect to one design variable. For each of these reliability analyses, a total of 200 samples of the vector modeling the excitation are generated. As the sensitivity metric in eq. (38) may be affected by the variability of the probability estimator $\hat{P}_F(\boldsymbol{y})$, a total of 200 independent estimations of the sensitivity are performed and then, an average result is considered. Thus, the estimate of the sensitivity generated using this procedure is considered as a reference.

- **Approach 2**: the sensitivities are estimated using the approach proposed in Sections 5 and 6. A total of 200 independent runs of this approach are performed, in order to assess the variability of the estimates. Each individual simulation involves generating 200 samples of the vector modeling the stochastic excitation.

The results obtained are shown in figs. (2) and (3), respectively. Figure (2) shows the estimates of probability sensitivity in the form of arrows indicating the magnitude of the sensitivity; the results obtained with the proposed approach are presented with gray, thin line (only ten simulations were plotted for the sake of clarity) and the reference result with black, thick line. It can be observed that the estimates generated with the proposed approach present very little dispersion. Moreover, on the average, they tend to converge to the reference result. Figure (3) also shows the probability sensitivity estimates for the two approaches described above. Note that this figure includes the results for the proposed approach in terms of the mean plus/minus one

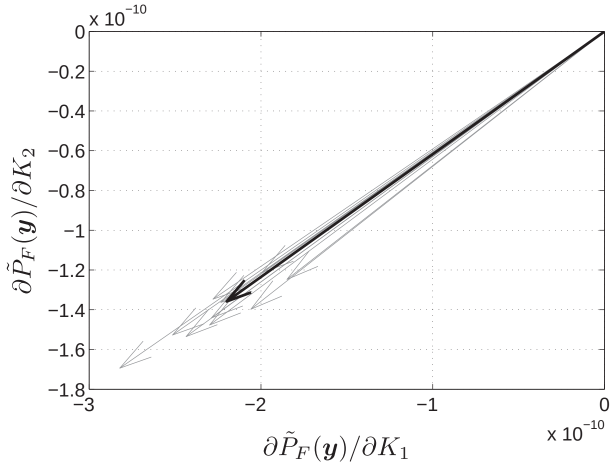

Figure 2: Sensitivity Analysis - 10 independent estimations using proposed approach (gray, thin line) compared to reference solution (black, thick line)

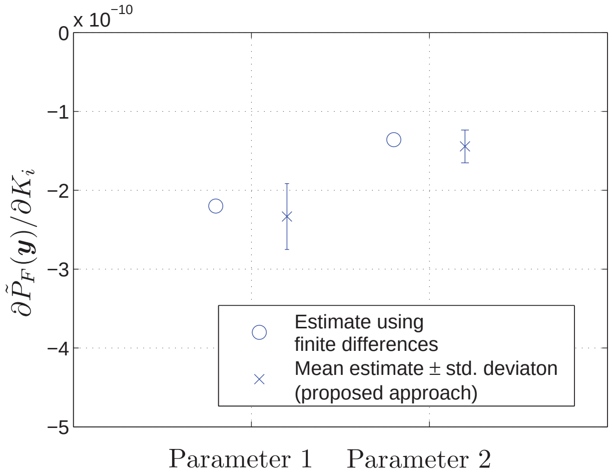

Figure 3: Sensitivity Analysis - mean ± std. deviation using results of proposed approach compared to reference solution

standard deviation. As it can be observed, the variability of the proposed approach is quite low, producing accurate estimates of the probability sensitivity. Finally, in order to assess the error associated with the reliability sensitivity estimators, the Bootstrap method described in Section 7 is applied. In particular, the number bootstrap replications of the sensitivity metric that are generated is selected such that $N_R = 1000$. It is found that this number ensures sufficient accuracy for estimating the standard deviation of the reliability sensitivity estimator. Recall that the numerical cost associated with the generation of bootstrap replications is negligible, as no additional dynamic analysis are required. The results obtained are presented in Table 1. In this table, the standard deviations of the estimators of reliability sensitivity calculated with the Bootstrap method are compared with the results obtained through approach 2 described above. Note that the latter approach for calculating the aforementioned standard deviations is numerically demanding; however, these results are included here as they constitute a reference. In addition, Table 1 also summarizes the coefficients of variation of each estimator (indicated in parenthesis). It can be seen that the results obtained with Bootstrap are in excellent agreement with the reference results.

Method	$\sigma_{\partial \tilde{P}_F/\partial K_1}$ $\left(\text{CoV}_{\partial \tilde{P}_F/\partial K_1}\right)$	$\sigma_{\partial \tilde{P}_F/\partial K_2}$ $\left(\text{CoV}_{\partial \tilde{P}_F/\partial K_2}\right)$	Number of Dynamic Analyses
Bootstrap	4.1×10^{-11} (0.18)	2.1×10^{-11} (0.14)	200
Direct Simulation (Approach 2)	4.2×10^{-11} (0.18)	2.1×10^{-11} (0.14)	$200 \times 200 = 4 \times 10^4$

Table 1: Standard deviation of reliability sensitivity estimator

9 CONCLUSIONS AND OUTLOOK

This contribution has presented an approach for estimating reliability sensitivity of linear structures subject to Gaussian stochastic excitation. The approach is based on a general framework that was proposed for non linear systems. Taking advantage of the linearity of the problem studied here, this general framework was modified appropriately.

The key issue of the proposed approach is replacing the original reliability problem by one that is differentiable. Thus, the sought sensitivities are calculated by combining an efficient simulation technique with two approximation concepts. The first of these approximations involves the construction of an exponential function modeling the probability that the normalized demand exceeds a prescribed threshold. This approximation can be constructed using the information generated by the simulation technique when estimating reliability. The second approximation involves the sensitivity analysis of the responses of interest of the structural system with respect to design variables. This sensitivity analysis can be performed most efficiently by applying a specific procedure for computing the sensitivity of spectral properties.

A salient feature of the proposed approach for reliability sensitivity is that it can be very efficient from a numerical point of view. The same samples generated for reliability sensitivity can be employed for constructing the aforementioned exponential approximation. In addition, the second approximation mentioned above requires a sensitivity analysis of the spectral properties, which is a problem that is numerically inexpensive when compared to solving a full eigenproblem for perturbed values of the design variable vector. Besides these two approximations, the application of the Bootstrap method allows estimating the error of the estimator most efficiently, as no additional dynamic analyses are required.

Future research efforts aim at testing the proposed approach in examples involving a larger number of design variables, subject not only to white noise but also to other types of Gaussian processes.

10 ACKNOWLEDGMENTS

This research is partially supported by CONICYT (National Commission for Scientific and Technological Research) grants number 1070903 and 1110061 and the Austrian Research Council (FWF) under Project No. P20251-N13. This support is gratefully acknowledged by the authors.

REFERENCES

[1] S.K. Au. Reliability-based design sensitivity by efficient simulation. *Computers & Structures*, 83(14):1048–1061, 2005.

[2] S.K. Au and J.L. Beck. Estimation of small failure probabilities in high dimensions by subset simulation. *Probabilistic Engineering Mechanics*, 16(4):263–277, 2001.

[3] S.K. Au and J.L. Beck. First excursion probabilities for linear systems by very efficient importance sampling. *Probabilistic Engineering Mechanics*, 16(3):193–207, 2001.

[4] K.J. Bathe. *Finite Element Procedures*. Prentice Hall, New Jersey, 1996.

[5] P.J. Bickel and D.A. Freedman. Some asymptotic theory for the Bootstrap. *The Annals of Statistics*, 9(6):1196–1217, 1981.

[6] P. Bjerager and S. Krenk. Parametric sensitivity in first order reliability theory. *Journal of Engineering Mechanics*, 115(7):1577–1582, 1989.

[7] A.K. Chopra. *Dynamics of structures: theory and applications to earthquake engineering*. Prentice Hall, 1995.

[8] A. Der Kiureghian. The geometry of random vibrations and solutions by FORM and SORM. *Probabilistic Engineering Mechanics*, 15(1):81–90, 2000.

[9] O. Ditlevsen and H.O. Madsen. *Structural Reliability Methods*. John Wiley and Sons, 1996.

[10] B. Efron. Bootstrap methods: Another look at the Jackknife. *The Annals of Statistics*, 7(1):1–26, 1979.

[11] B. Efron and R. Tibshirani. *An Introduction to the Bootstrap*. Chapman & Hall, 1993.

[12] I. Enevoldsen and J.D. Sørensen. Reliability-based optimization of series systems of parallel systems. *Journal of Structural Engineering*, 119(4):1069–1084, 1993.

[13] I. Enevoldsen and J.D. Sørensen. Reliability-based optimization in structural engineering. *Structural Safety*, 15(3):169–196, 1994.

[14] A.M. Freudenthal. Safety and the probability of structural failure. *ASCE Transactions*, 121:1337–1397, 1956.

[15] M. Gasser and G.I. Schuëller. Reliability-based optimization of structural systems. *Mathematical Methods of Operations Research*, 46(3):287–307, 1997.

[16] H.A. Jensen, M.A. Valdebenito, G.I. Schuëller, and D.S. Kusanovic. Reliability-based optimization of stochastic systems using line search. *Computer Methods in Applied Mechanics and Engineering*, 198(49-52):3915–3924, 2009.

[17] B.-S. Kang, G.-J. Park, and J.S. Arora. A review of optimization of structures subjected to transient loads. *Structural and Multidisciplinary Optimization*, 31(2):81–95, 2006.

[18] A. Karamchandani and C. A. Cornell. Sensitivity estimation within first and second order reliability methods. *Structural Safety*, 11(2):95–107, 1992.

[19] P.S. Koutsourelakis. Design of complex systems in the presence of large uncertainties: A statistical approach. *Computer Methods in Applied Mechanics and Engineering*, 197(49-50):4092–4103, 2008.

[20] M. Loève. *Probability theory*. D. Van Nostrand Company, Inc., Princeton, New Jersey, third edition, 1963.

[21] K. Marti. Differentiation of probability functions: The transformation method. *Computers & Mathematics with Applications*, 30(3-6):361–382, 1995.

[22] R.E. Melchers and M. Ahammed. A fast approximate method for parameter sensitivity estimation in Monte Carlo structural reliability. *Computers & Structures*, 82(1):55–61, 2004.

[23] R.B. Nelson. Simplified calculation of eigenvector derivatives. *AIAA Journal*, 14(9):1201–1205, 1976.

[24] J.O. Royset and E. Polak. Reliability-based optimal design using sample average approximations. *Probabilistic Engineering Mechanics*, 19(4):331–343, 2004.

[25] G.I. Schuëller, H.J. Pradlwarter, and P.S. Koutsourelakis. A critical appraisal of reliability estimation procedures for high dimensions. *Probabilistic Engineering Mechanics*, 19(4):463–474, 2004.

[26] G.I. Schuëller and R. Stix. A critical appraisal of methods to determine failure probabilities. *Structural Safety*, 4(4):293–309, 1987.

[27] K. Singh. On the asymptotic accuracy of Efron's Bootstrap. *The Annals of Statistics*, 9(6):1187–1195, 1981.

[28] T.T. Soong and M. Grigoriu. *Random Vibration of Mechanical and Structural Systems*. Prentice Hall, Englewood Cliffs, New Jersey, 1993.

[29] M.A. Valdebenito and G.I. Schuëller. Efficient strategies for reliability-based optimization involving non linear, dynamical structures. *Computers & Structures*, 2011, available online.

[30] Y.T. Wu. Computational methods for efficient structural reliability and reliability sensitivity analysis. *AIAA Journal*, 32(8):1717–1723, 1994.

COMPDYN 2011
3rd ECCOMAS Thematic Conference on
Computational Methods in Structural Dynamics and Earthquake Engineering
M. Papadrakakis, M. Fragiadakis, V. Plevris (eds.)
Corfu, Greece, 25–28 May 2011

OPTIMAL DESIGN OF BASE-ISOLATED SYSTEMS UNDER STOCHASTIC EARTHQUAKE EXCITATION

Hector A. Jensen[1], **Marcos A. Valdebenito**[2], **Juan A. Sepulveda**[2]

[1] Santa Maria University
Av. España 1680, Valparaiso, Chile
hector.jensen@usm.cl

[2] Santa Maria University
Av. España 1680, Valparaiso, Chile

Keywords: Approximation strategies, Base-isolated systems, Simulation, Reliability-based design.

Abstract. *The development of a general framework for reliability-based design of base-isolated structural systems under uncertain conditions is presented. The uncertainties about the structural parameters as well as the variability of future excitations are characterized in a probabilistic manner. Nonlinear elements composed by hysteretic devices are used for the isolation system. The optimal design problem is formulated as a constrained minimization problem which is solved by a sequential approximate optimization scheme. First excursion probabilities that account for the uncertainties in the system parameters as well as in the excitation are used to characterize the system reliability. The approach explicitly takes into account all non-linear characteristics of the combined structural system (superstructure-isolation system) during the design process. Numerical results highlight the beneficial effects of isolation systems in reducing the superstructure response.*

1 INTRODUCTION

There has been a growing interest during the last years in the application of base isolation techniques in order to improve the earthquake resistant performance of civil structures such as buildings, bridges, nuclear reactors, etc. [8, 10, 23, 34]. In fact, the potential advantages of seismic isolation and the recent advancements in isolation-system products have lead to the design and construction of an increasing number of seismically isolated structural systems. Also, seismic isolation is extensively used for seismic retrofitting of existing structures [11, 27]. One of the difficulties in the design of base-isolated structural systems is the explicit consideration of the nonlinear behavior of the isolators during the design process. Similarly, the consideration of uncertainty about the structural model and the potential variability of future ground motions is a major challenge in the analysis and design of these systems. The goal of this work is the development of a general framework for reliability based design of base-isolated systems under uncertain conditions. In particular, base-isolated building structures subject to earthquake excitation are considered in this study. A probabilistic approach is adopted for addressing the uncertainties about the structural model as well as the variability of future excitations. The uncertain earthquake excitation is modeled as a non-stationary stochastic process with uncertain model parameters. Specifically, a point-source model characterized by the moment magnitude and epicentral distance is adopted in this formulation [6]. Isolation elements composed by hysteretic devices are used for the isolation system and they are characterized by the Bouc-Wen type model [5]. The model provides general parametric hysteresis rules that gives a smooth transition of the change of stiffness as the deformation of the nonlinear elements changes. The reliability-based optimization problem is formulated as the minimization of an objective function subject to multiple design requirements including reliability constraints. First excursion probabilities are used as measures of system reliability. Such probabilities are estimated by an adaptive Markov Chain Monte Carlo procedure [4]. A sequential optimization approach based on global conservative, convex and separable approximations is implemented for solving the optimization problem [14, 18, 21]. The approach explicitly takes into account all non-linear characteristics of the structural response in the design process and it allows for a complex characterization of structural systems and excitation models. The solution of the equation of motion of the combined system (superstructure-isolation system) required during the simulation process is computed by a modified Runge-Kutta scheme of fourth-order. A numerical example is presented in order to illustrate the applicability and effectiveness of the proposed framework for reliability-based design of a base-isolated building.

2 RELIABILITY-BASED DESIGN PROBLEM

The optimal design problem is defined as the identification of a vector $\{\phi\}$ of design variables that minimizes an objective function , that is

$$\text{Minimize } f(\{\phi\}) \tag{1}$$

subject to design constraints

$$h_j(\{\phi\}) \leq 0 \ \ , \ \ j = 1, ..., n_c \tag{2}$$

and side constraints

$$\phi_i^l \leq \phi_i \leq \phi_i^u \ ; , \ \ i = 1, ..., n_d \tag{3}$$

The objective function is defined in terms of quantities such as initial, construction, repair, or downtime costs. On the other hand, the design constraints are given in terms of reliability constraints and/or constrains related to deterministic design requirements. In a stochastic setting the reliability constraints are usually defined in terms of failure probabilities. These probabilities provide a measure of the plausibility of the occurrence of unacceptable behavior (failure) of the system, based on the available information. The probability of failure $P_{F_j}(\{\phi\})$ corresponding to a failure event F_j evaluated at the design $\{\phi\}$ can be expressed in terms of the multidimensional probability integral [13, 15]

$$P_{F_j}(\{\phi\}) = \int_{\Theta} I_{F_j}(\{\phi\},\{\theta\})\, q(\{\theta\})\, d\{\theta\} \tag{4}$$

where $I_{F_j}(\{\phi\},\{\theta\})$ is the indicator function for failure, which is equal to one if the system fail and zero otherwise, and $\{\theta\}, \theta_i, i = 1, ..., n_u$ is the vector that represents the uncertain system parameters involved in the problem (structural parameters and excitation). The uncertain system parameters $\{\theta\}$ are modeled using a prescribed probability density function $q(\{\theta\})$ which incorporates available knowledge about the system. Note, that the failure probability function $P_{F_j}(\{\phi\})$ accounts for the uncertainty in the system parameters as well as the uncertainties in the excitation. A model prediction error, that is, the error between the response of the actual system and the response of the model, can also be considered in the formulation [12, 31]. In this case the prediction error may be modeled probabilistically by augmenting the vector $\{\theta\}$ to form an uncertain parameter vector composed of both the structural and excitation model parameters as well as the model prediction-error. The failure domain $\Omega_{F_j}(\{\phi\})$ corresponding to the failure event F_j evaluated at the design $\{\phi\}$ is typically described in terms of a performance function g_j as

$$\Omega_{F_j}(\{\phi\}) = \{\{\theta\} \mid g_j(\{\phi\},\{\theta\}) \geq 0\} \tag{5}$$

Then, the probability of failure can also be expressed in terms of the failure domain in the form

$$P_{F_j}(\{\phi\}) = \int_{\Omega_{F_j}(\{\phi\})} q(\{\theta\}) d\{\theta\} \tag{6}$$

With the previous notation, a reliability constraint can be written as $h_j(\{\phi\}) = P_{F_j}(\{\phi\}) - P^*_{F_j} \leq 0$, where $P^*_{F_j}$ is the target failure probability. The last inequality expresses the requirement that the probability of system failure must be smaller than an appropriate tolerance. It is noted that in the context of stochastic design a system that corresponds to a feasible design can not be certified with complete certainty, but with a tolerance $P^*_{F_j}$. In other worlds, the system will operate safely within the pre-specified probability of failure tolerance.

3 STRUCTURAL MODEL

In general, base-isolated buildings are designed such that the superstructure remains elastic. Hence, the structure is modeled as a linear elastic system in the present formulation. The base and the floors are assumed to be infinitely rigid in plane. The superstructure and the base are modeled using three degrees of freedom per floor at the center of mass. Each nonlinear isolation element is modeled explicitly using the Buoc-Wen model. Let $\{x_s(t)\}$ be the n-th dimensional vector of absolute displacements for the superstructure with respect to the base, and $[M_s]$, $[C_s]$, and $[K_s]$ be the corresponding mass, damping and stiffness matrices. Also, let $\{x_b(t)\}$ be the vector of base displacements with three components and $[G_s]$ be the matrix of earthquake influence coefficients of dimension $n \times 3$, that is, the matrix that couples the excitation components of the vector $\{\ddot{x}_g(t)\}$ to the degrees of freedom of the superstructure. The schematic representation of the base-isolated structural system as well as the displacement coordinates are shown in Figure (1). The equation of motion of the elastic superstructure is then expressed in the form

$$[M_s]\{\ddot{x}_s(t)\} + [C_s]\{\dot{x}_s(t)\} + [K_s]\{x_s(t)\} = -[M_s][G_s](\{\ddot{x}_b(t)\} + \{\ddot{x}_g(t)\}) \tag{7}$$

where $\{\ddot{x}_b(t)\}$ is the vector of base accelerations relative to the ground. On the other hand, the equation of motion of the base can be written as

$$([G_s]^T[M_s][G_s] + [M_b])(\{\ddot{x}_b(t)\} + \{\ddot{x}_g(t)\}) + [G_s]^T[M_s]\{\ddot{x}_s(t)\} + \{f_{is}\} = \{0\} \tag{8}$$

where $[M_b]$ is the diagonal mass matrix of the rigid base, and $\{f_{is}\}$ is the vector containing the nonlinear isolation elements forces (three components). The characterization of such forces is treated in a subsequent Section. Rewriting the previous equations, the combined equation of motion of the base-isolated structure system can be formulated in the form

$$\begin{bmatrix} [M_s] & [M_s][G_s] \\ [G_s]^T[M_s] & [M_b] + [G_s]^T[M_s][G_s] \end{bmatrix} \begin{Bmatrix} \{\ddot{x}_s(t)\} \\ \{\ddot{x}_b(t)\} \end{Bmatrix} + \begin{bmatrix} [C_s] & [0] \\ [0]^T & [0] \end{bmatrix} \begin{Bmatrix} \{\dot{x}_s(t)\} \\ \{\dot{x}_b(t)\} \end{Bmatrix} +$$

$$\begin{bmatrix} [K_s] & [0] \\ [0]^T & [0] \end{bmatrix} \begin{Bmatrix} \{x_s(t)\} \\ \{x_b(t)\} \end{Bmatrix} = -\begin{Bmatrix} [M_s][G_s] \\ [M_b] + [G_s]^T[M_s][G_s] \end{Bmatrix} \{\ddot{x}_g(t)\} - \begin{Bmatrix} \{0\} \\ \{f_{is}(t)\} \end{Bmatrix} \tag{9}$$

It is noted that elastic and viscous isolation elements can also be incorporated in the isolation model. Also, the above formulation can be directly extended to more complex cases, for example to nonlinear models for the superstructure.

4 EARTHQUAKE EXCITATION MODEL

The ground acceleration is modeled as a non-stationary stochastic process. In particular, a point-source model characterized by the moment magnitude M and epicentral distance r is considered here [3, 6]. The model is a simple, yet powerful means for simulating ground motions and it has been successfully applied in the context of earthquake engineering. The time-history of the ground acceleration for a given magnitude M and epicentral distance r is obtained by modulating a white noise sequence by an envelope function and subsequently by a ground motion spectrum through the following steps: 1) generate a discrete-time Gaussian white noise sequence $\omega(t_j) = \sqrt{I/\Delta t}\,\theta_j$, $j = 1, ..., n_T$, where $\theta_j, j = 1, ..., n_T$, are independent, identically distributed standard Gaussian random variables, I is the white noise intensity, Δt is the sampling interval, and n_T is the number of time instants equal to the duration of the excitation T divided by the sampling interval; 2) the white noise sequence is modulated by an envelope function $h(t, M, r)$ at the discrete time instants; 3) the modulated white noise sequence is transformed to the frequency domain; 4) the resulting spectrum is normalized by the square root of the average square amplitude spectrum; 5) the normalized spectrum is multiplied by a ground motion spectrum (or radiation spectrum) $S(f, M, r)$ at discrete frequencies $f_l = l/T, l = 1, ..., n_T/2$; 6) the modified spectrum is transformed back to the time domain to yield the desired ground acceleration time history. Details of the characterization of the

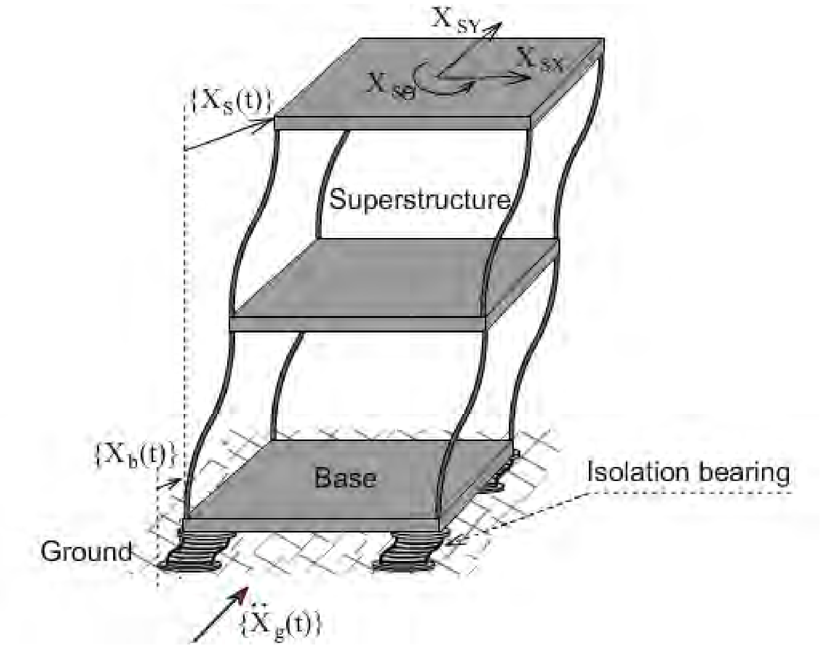

Figure 1: Schematic representation of the base-isolated structural model

envelope function $h(t,M,r)$ and the ground acceleration spectrum $S(f,M,r)$ are provided in the subsequent sections. The probabilistic model for the seismic hazard at the emplacement is complemented by considering that the moment magnitude M and epicentral distance r are also uncertain. The uncertainty in moment magnitude is modeled by the Gutenberg-Richter relationship truncated on the interval $[6.0, 8.0]$, which leads to the probability density function [25]

$$p(M) = \frac{b\ e^{-bM}}{e^{-6.0b} - e^{-8.0b}}\ ,\ \ 6.0 \leq M \leq 8.0 \tag{10}$$

where b is a regional seismicity factor. For the uncertainty in the epicentral distance r, a log-normal distribution with mean value $\bar{r}$ (km) and standard deviation σ_r (km) is used. The point source stochastic model previously described is well suited for generating the high-frequency components of the ground motion (greater than 0.1 Hz). Low-frequency components can also be introduced in the analysis by combining the above methodology with near-fault ground motion models [26].

4.1 Envelope function

The envelope function for the ground acceleration is represented by [29, 6]

$$h(t,M,r) = a_1 \left(\frac{t}{t_n}\right)^{a_2} e^{-a_3\left(\frac{t}{t_n}\right)} \tag{11}$$

where

$$a_2 = \frac{-0.2\ln(0.05)}{1 + 0.2(\ln(0.2) - 1)}\ ,\ a_3 = \frac{a_2}{0.2}\ ,\ a_1 = \left(\frac{e^1}{0.2}\right)^{a_2} \tag{12}$$

The envelope function has a peak equal to unity when $t = 0.2\ t_n$, and $h(t,M,r) = 0.05$ when $t = t_n$, with $t_n = 2.0\ T_{gm}$, where T_{gm} is the duration of ground motion, expressed as a sum of a path dependent and source dependent component $T_{gm} = 0.05\sqrt{r^2 + h^2} + 0.5/f_a$, where r is the epicentral distance, and the parameters h and f_a (corner frequency) are moment dependent given by $\log(h) = 0.15M - 0.05$ and $\log(f_a) = 2.181 - 0.496M$ [3]. As an example Figure (2) shows the envelope function for $r = 20$ km, and $M = 5$ and $M = 7$. Note that increasing the moment magnitude increases the duration of the envelope function, as expected.

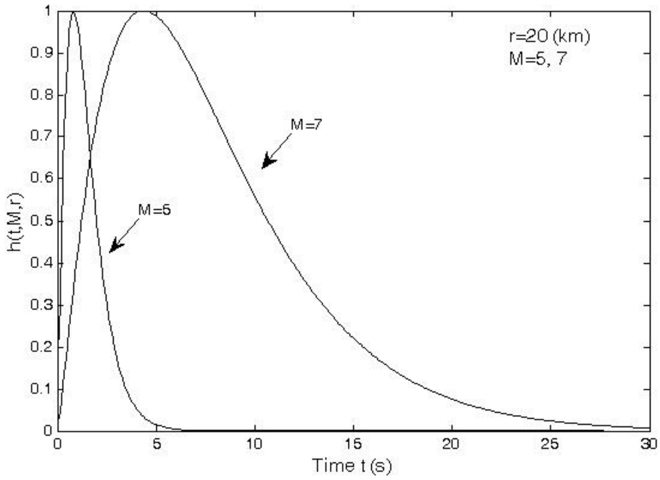

Figure 2: Envelope function for epicentral distance $r = 20$ km and moment magnitudes $M = 5$ and $M = 7$

4.2 Ground motion spectrum

The total spectrum of the motion at a site $S(f, M, r)$ is expressed as the product of the contribution from the earthquake source $E(f, M)$, path $P(f, r)$, site $G(f)$ and type of motion $I(f)$, i.e.

$$S(f, M, r) = E(f, M)\ P(f, r)\ G(f)\ I(f) \tag{13}$$

The source component is given by

$$E(f, M) = C\ M_0(M)\, S_a(f, M) \tag{14}$$

where C is a constant, $M_0(M) = 10^{1.5M+10.7}$ is the seismic moment, and the factor S_a is the displacement source spectrum given by [3]

$$S_a(f, M) = \frac{1-\varepsilon}{1 + \left(\frac{f}{f_a}\right)^2} + \frac{\varepsilon}{1 + \left(\frac{f}{f_b}\right)^2} \tag{15}$$

where the corner frequencies f_a and f_b, and the weighting parameter ε are defined, respectively, as $\log(f_a) = 2.181 - 0.496M$, $\log(f_b) = 2.41 - 0.408M$, and $\log(\varepsilon) = 0.605 - 0.255M$. The constant C is given by $C = UR_\Phi VF/4\pi\rho_s\beta_s^3 R_0$, where U is a units dependent factor, R_Φ is the radiation pattern, V represents the partition of total shear-wave energy into horizontal components, F is the effect of the free surface amplification, ρ_s and β_s are the density and shear-wave velocity in the vicinity of the source, and R_0 is a reference distance.

Next, the path effect $P(f,r)$ which is another component of the process that affect the spectrum of motion at a particular site it is represented by functions that account for geometrical spreading and attenuation

$$P(f,r) = Z(R(r))\, e^{-\pi f R(r)/Q(f)\beta_s} \tag{16}$$

where $R(r)$ is the radial distance from the hypocenter to the site given by $R(r) = \sqrt{r^2 + h^2}$. The attenuation quantity $Q(f)$ is taken as $Q(f) = 180 f^{0.45}$ and the geometrical spreading function is selected as $Z(R(r)) = 1/R(r)$ if $R(r) < 70.0$ km and $Z(R(r)) = 1/70.0$ otherwise [3]. The modification of seismic waves by local conditions, site effect $G(f)$, is expressed by the multiplication of a diminution function $D(f)$ and an amplification function $A(f)$. The diminution function accounts for the path-independent loss of high frequency in the ground motions and can be accounted for a simple filter of the form $D(f) = e^{-0.03\pi f}$ [2]. The amplification function $A(f)$ is based on empirical curves given in [7] for generic rock sites. An average constant value equal to 2.0 is considered. Finally, the filter that control the type of ground motion $I(f)$ is chosen as $I(f) = (2\pi f)^2$ for ground acceleration. The particular values of the different parameters of the stochastic ground acceleration model are given in Table (1) (see Application Problem Section). For illustration purposes Figure (3) shows the ground acceleration spectrum for a nominal distance $r = 20$ km, moment magnitudes $M = 5$ and $M = 7$, and model parameters given in Table (1). As the moment magnitude increases, the spectral amplitude increases at all frequencies, with a shift of dominant frequency content towards the lower frequency regime, as anticipated.

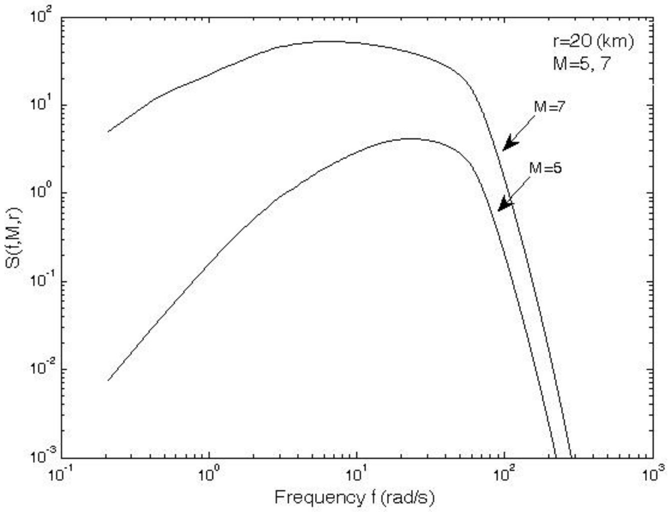

Figure 3: Ground acceleration spectrum for epicentral distance $r = 20$ km and moment magnitudes $M = 5$ and $M = 7$

5 ISOLATION MODEL

Several isolation elements can be used to model isolation systems. They include elastic, viscous, nonlinear fluid dampers, hysteretic (uniaxial or biaxial) elements for bilinear elastomeric bearings, hysteretic (uniaxial or biaxial) elements for sliding bearings, etc. Uniaxial bilinear elastomeric bearings with hysteretic behavior, such as lead rubber bearings, are used in the present implementation. They are modeled using the Buoc-Wen model as [5]

$$U^y\ \dot{z}(t) = \begin{cases} \dot{x}_b(t)[\alpha - z^n(t)(\gamma\ \text{sgn}(\dot{x}_b(t)z(t)) + \beta)] & \text{if n is even} \\ \dot{x}_b(t)[\alpha - z^n(t)(\gamma\ \text{sgn}(\dot{x}_b(t)) + \beta\ \text{sgn}(z(t)))] & \text{if n is odd} \end{cases} \tag{17}$$

where $z(t)$ is a dimensionless hysteretic variable, α, β, and γ are dimensionless quantities, U^y is the yield displacement, $x_b(t)$ and $\dot{x}_b(t)$ represent the base displacement and velocity, respectively, and sgn$(\cdot)$ is the sign function. The forces activated in the elastomeric isolation bearing are modeled by an elastic-viscoplastic model with strain hardening

$$f_{is}(t) = k_p\ x_b(t)\ +\ c_v\ \dot{x}_b(t)\ +\ (k_e - k_p)\ U^y\ z(t) \tag{18}$$

where k_e is the pre-yield stiffness, k_p is the post-yield stiffness, c_v is the viscous damping coefficient of the elastomeric bearing, and U^y is the yield displacement. If the post-yield stiffness is written as $k_p = \alpha_L k_e$, where α_L is a factor which defines the extent to which the force is linear, the isolator forces can be expressed as

$$f_{is}(t) = \alpha_L k_e\ x_b(t)\ +\ c_v\ \dot{x}_b(t)\ +\ (1 - \alpha_L)k_e\ \ U^y\ z(t) \tag{19}$$

6 SEQUENTIAL APPROXIMATE OPTIMIZATION

The solution of the reliability-based optimization problem given by Eqs. (1-3) is obtained by transforming it into a sequence of sub-optimization problems having a simple explicit algebraic structure. Thus, the strategy is to construct successive approximate analytical sub-problems. To this end, the objective and the constraint functions are represented by using approximate functions dependent on the design variables. In particular, a hybrid form of linear, reciprocal and quadratic approximations is considered in the present formulation [28, 14, 20]. The approximate discrete sub-optimization problems takes the form

$$\text{Minimize}\ \ \tilde{f}_k(\{\phi\}) \tag{20}$$

subject to

$$\tilde{h}_{jk}(\{\phi\}) \leq 0\ \ ,\ \ j = 1, ..., n_c \tag{21}$$

with side constraints

$$\phi_i^l \leq \phi_i \leq \phi_i^u\ ;\ ,\ \ i = 1, ..., n_d \tag{22}$$

where $\tilde{f}_k$ and $\tilde{h}_{jk}, j = 1, ...n_c$ represent the approximate objective and constraint functions at the current point $\{\phi^k\}$ in the design space, respectively. The approximate objective function is obtained as

$$\tilde{f}_k(\{\phi\}) = f_{1k}(\{\phi\}) + f_{2k}(\{\phi\}) + f_{3k}(\{\phi\}) \tag{23}$$

where $f_{1k}(\{\phi\})$ is a linear function in terms of the design variables, $f_{2k}(\{\phi\})$ is a linear function with respect to the inverse of the design variables, and $f_{3k}(\{\phi\})$ is a quadratic function of the design variables. They are given by

$$f_{1k}(\{\phi\}) = \sum_{(i^+)} \frac{\partial f(\{\phi^k\})}{\partial \phi_i}\phi_i \ \ , \ \ f_{2k}(\{\phi\}) = -\sum_{(i^-)} \frac{\partial f(\{\phi^k\})}{\partial \phi_i}\frac{(\phi_i^k)^2}{\phi_i} \tag{24}$$

$$f_{3k}(\{\phi\}) = -2\chi^f \sum_{(i^-)} \frac{\partial f(\{\phi^k\})}{\partial \phi_i}\phi_i(\frac{\phi_i}{\phi_i^k} - 2) \tag{25}$$

where (i^+) is the group that contains the variables for which the partial derivative of the objective function is positive, (i^-) is the group that includes the remaining variables, and χ^f is a user-defined positive scalar that control the conservatism of the approximation [17, 18]. On the other hand, the constraint functions involving reliability measures (reliability constraints) are first transformed as $h_j^t(\{\phi\}) = \ln[P_{F_j}(\{\phi\})]$. Then the transformed constraint functions are approximated in the form

$$\tilde{h}_{jk}^t(\{\phi\}) \ = h_{j1k}^t(\{\phi\}) + h_{j2k}^t(\{\phi\}) + h_{j3k}^t(\{\phi\}) + \bar{h}_{jk}^t(\{\phi^k\}) \tag{26}$$

where

$$h_{j1k}^t(\{\phi\}) = \sum_{(i_j^+)} \frac{\partial h_j^t(\{\phi^k\})}{\partial \phi_i}\phi_i \ \ , \ \ h_{j2k}^t(\{\phi\}) = -\sum_{(i_j^-)} \frac{\partial h_j^t(\{\phi^k\})}{\partial \phi_i}\frac{(\phi_i^k)^2}{\phi_i} \tag{27}$$

$$h_{j3k}^t(\{\phi\}) = 2\chi^{h_j^t} \sum_{(i_j^-)} \frac{\partial h_j^t(\{\phi^k\})}{\partial \phi_i}\phi_i(\frac{\phi_i}{\phi_i^k} - 2) \tag{28}$$

$$\begin{aligned}\bar{h}_{jk}^t(\{\phi^k\}) = h_j^t(\{\phi^k\}) &- \sum_{(i_j^+)} \frac{\partial h_j^t(\{\phi^k\})}{\partial \phi_i}\phi_i^k \\ &-(2\chi^{h_j^t} - 1)\sum_{(i_j^-)} \frac{\partial h_j^t(\{\phi^k\})}{\partial \phi_i}\phi_i^k\end{aligned} \tag{29}$$

where $\sum_{(i_j^+)}$ and $\sum_{(i_j^-)}$ mean summation over the variables belonging to group (i_j^+) and (i_j^-), respectively, and $\chi^{h_j^t}$ is as before a user-defined positive scalar that control the conservatism of the approximations. Group (i_j^+) contains the variables for which $\partial h_j^t(\{\phi^k\})/\partial\phi_i$ is positive, and group (i_j^-) includes the remaining variables. The same type of approximations can be applied to the deterministic constraint functions. The explicit discrete sub-optimization problems (20-22) are solved by standard methods that treat the problem directly in the primal design variable space such as branch and bound techniques, combinatorial methods, evolution-based optimization techniques, etc. [16, 24, 32]. The level of effectiveness of the above sequential optimization scheme depends on the degree of convexity of the functions involved in the optimization problem. For example, if the curvatures are not too large and relatively uniform throughout the design space the proposed algorithm converges within few iterations [9, 21, 30]. For more general cases methods based on trust regions and line search methodologies are more appropriate [1, 19, 22].

7 RELIABILITY AND SENSITIVITY ASSESSMENT

The characterization of the sub-optimization problems (20-22) requires the estimation of first excursion probabilities and their sensitivities. In order to estimate the excursion probabilities at a given design high-dimensional integrals need to be evaluated. This difficulty favors the application of Monte Carlo Simulation as fundamental approach to cope with the probability integrals. However, in most engineering applications the probability that a particular system fails is expected to be small, e.g. between $10^{-4} - 10^{-6}$. Direct Monte Carlo is robust to the type and dimension of the problem, but it is not suitable for finding small probabilities. Therefore, advanced Monte Carlo strategies are needed to reduce the computational efforts. In particular a generally applicable method, called subset simulation, is implemented in this work [4]. On the other hand, the sensitivity of the failure probability functions with respect to the design variables is estimated by an approach recently introduced in [33]. The approach is based on the approximate local representation of two different quantities. The first approximation involves the performance functions that define the failure domains while the second includes the probability of failure in terms of the maximum response levels for safe system operation. For a detailed discussion of the approach the reader is referred to [22, 33].

8 APPLICATION PROBLEM

8.1 Description

A four-story building with a base-isolation system under earthquake motion is considered as an application problem. The plan view, as well as the dimensions for each floor are shown in Fig. (4), and the elevation of one resistant element (A-axis) is illustrated in Fig. (5). Each of the four floors is supported by 80 columns of square cross section. The first floor has a height equal to 3.5 m while the other floors have a constant height equal to 3.0 m, leading to a total height of 12.5 m.

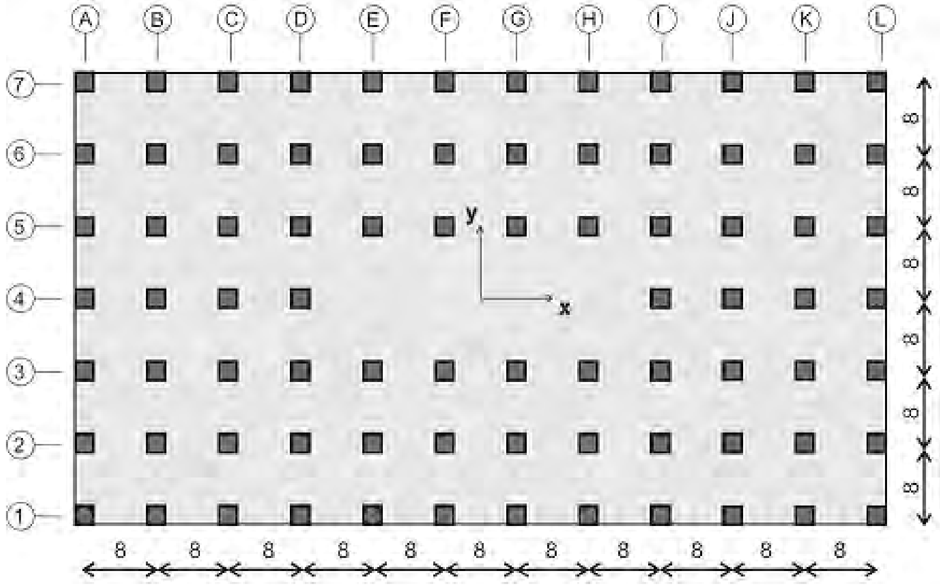

Figure 4: Plan view of the structural model

As previously pointed out (see Structural Model Section) each floor is represented by three degrees of freedom, i.e. two translational displacements in the direction of the x axis and y axis,

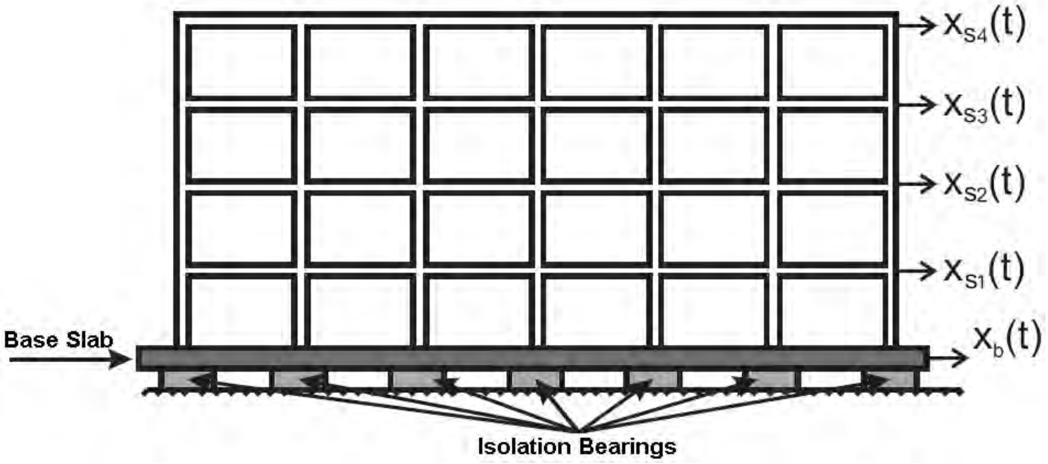

Figure 5: Elevation view of axis A

and a rotational displacement. The associated active masses in the x and y direction are taken constant for the first three floors and equal to 2.50×10^6 kg and 1.50×10^6 kg for the last floor. The corresponding mass moments of inertia are taken as 2.10×10^9 kg-m^2 and 1.20×10^9 kg-m^2, respectively. On the other hand, the mass of the base is equal to 6.0×10^6 kg, and its mass moment of inertia 5.00×10^9 kg-m^2. The Young's modulus and the modal damping ratios are treated as uncertain system parameters. The Young's modulus is modeled by a truncated normal random variable with most probable value $\bar{E} = 2.50 \times 10^{10}$ N/m^2 and coefficient of variation of 20%. Moreover, the damping ratios are modeled by independent Log-normal random variables with mean value $\bar{\zeta} = 0.03$ and coefficient of variation of 40%. The base isolation system is composed of 80 uniaxial bilinear lead rubber bearings with hysteretic behavior. The nonlinear behavior of these devices is modeled using the equations described in Section 5 with model parameters $n = 1$, $\alpha = 1.0$, $\beta = -0.65$, $\gamma = 0.5$, $U^y = 0.5$ cm, $\varepsilon = 0.1$, $k_e = 3 \times 10^6$ N/m, and $c_v = 0.0$. Figures (6) and (7) show a schematic representation of a lead rubber bearing and a typical displacement-restoring force curve of the isolation element, respectively. The structural system is excited horizontally by a ground acceleration applied in the y direction. The induced ground acceleration is characterized as in Section 4, with model parameters listed in Table 1.

Parameter	Numerical Value	Parameter	Numerical Value
$\bar{r}$ (km)	20.0	σ_r (km)	9.0
b	1.8	U	10^{-20}
ρ_s (gm/cc)	2.8	β_s (km/s)	3.5
V	$1/\sqrt{2}$	R_Φ	0.55
F	2.0	R_0 (km)	1.0
T (s)	20.0	Δt (s)	0.01

Table 1: Parameters for the stochastic ground acceleration model.

8.2 Optimal design problem

The objective function f is defined as the volume of the column elements of the structural system. The design variables $\{\phi\}$ are chosen as the dimensions of the columns throughout

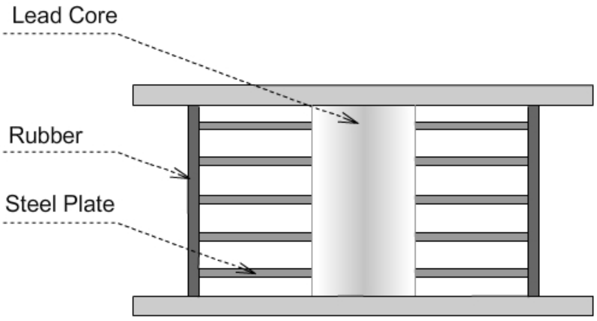

Figure 6: Lead rubber bearing

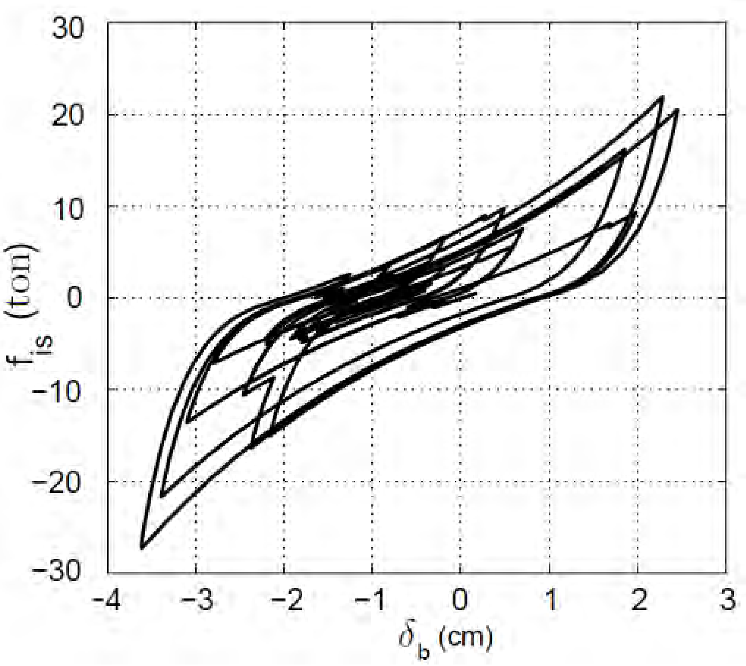

Figure 7: Typical displacement-restoring force curve of the isolation element (lead rubber bearing)

the height, grouped in four design variables, i.e. the dimensions of the columns of each floor constitute each of the design groups. The failure event is formulated as a first passage problem during the duration of the ground acceleration. The structural responses to be controlled are the 4 interstorey drift displacements. The threshold value is chosen equal to 0.2% of the floor height for the interstorey drift displacements. Thus, the failure domains evaluated at the design $\{\phi\}$ are given by

$$\Omega_{F_j}(\{\phi\}) = \{\{\theta\} \mid \max_{t_k, k=1,..,2001} |\delta_j(t_k, \{\phi\}, \{\theta\})| - \delta^* \geq 0\} \ \ , \ \ j = 1, ..., 4 \tag{30}$$

where $\delta_j(t_k, \{\phi\}, \{\theta\})$ is the relative displacement between the $(j-1, j)$-th floor evaluated at the design $\{\phi\}$, t_k are the discrete time instants, δ^* is the critical threshold level and equal to 0.006 m, and $\{\theta\}$ is the vector that represents the uncertain system parameters (structural parameters and excitation). Note that more than two thousand random variables are involved in the characterization of the uncertain model parameters. The reliability-based optimization problem is defined as

$$\text{Min } f(\{\phi\})$$

subject to

$$\begin{aligned} &P_{F_j}(\{\phi\}) \leq P_F^*; \ , j = 1, 2, 3, 4 \\ &0.30 \leq \phi_i \leq 1.10, \ i = 1, \ldots, 4 \end{aligned} \tag{31}$$

Two target failure probabilities are considered: $P_F^* = 10^{-2}$ and $P_F^* = 10^{-4}$. The first case can be interpreted as a design problem with a moderate level of reliability while the second case corresponds to a high level of reliability. In what follows the first case will be referred as Problem 1 while the second case as Problem 2.

8.3 Results

The initial and final designs of Problems 1 and 2 are given in Table (2). The results of the optimization process are presented in Figs.(8), (9) and (10) in terms of the evolution of the objective function and failure probabilities, respectively.

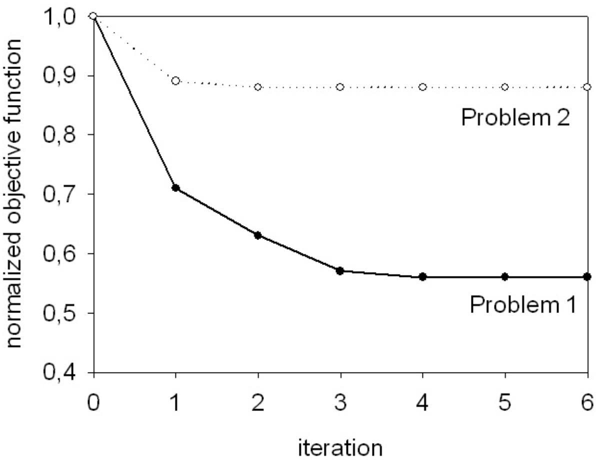

Figure 8: Iteration history in terms of the objective function. Problem 1: moderate level of reliability . Problem 2: high level of reliability

The objective function is normalized by its value at the initial design. It is observed that only a few optimization cycles are required for obtaining convergence. Moreover, most of the improvement of the objective function takes place in the first 3 iterations. It is also seen that the method generates a series of steadily improved feasible designs that move toward the optimum. The results indicate that the value of the objective function at the final design of Problem 2 is greater than the corresponding value of Problem 1. This is turn implies that the structural components (columns) at the final design of Problem 2 are bigger than the corresponding components of Problem 1, as expected. The beneficial effects of the base isolation system are shown

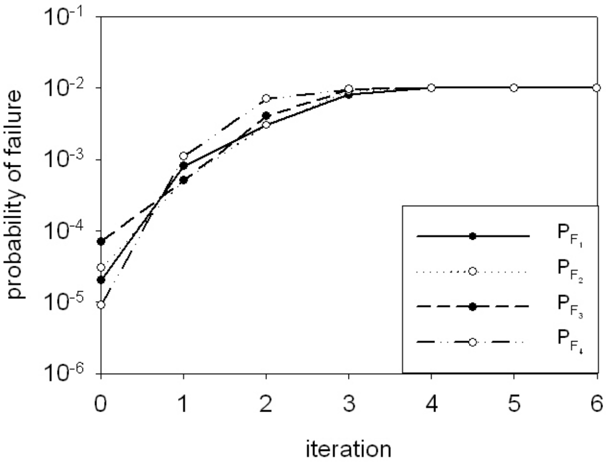

Figure 9: Iteration history in terms of the reliability constraints. Problem 1

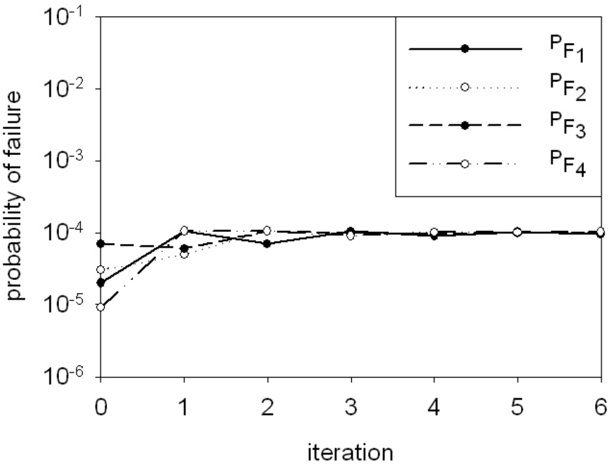

Figure 10: Iteration history in terms of the reliability constraints. Problem 2

in Table (3). This table shows the value of the objective function at the final design of Problems 1 and 2 for models with and without the isolation system. The effect of the isolation system is clear from these results. The difference between the values of the objective functions is almost 40% in both Problems.

Finally, the effect of the base isolation system can also be observed from a constraint violation viewpoint. Table (4) shows the probability of occurrence of the failure events associated with the final design of Problem 2 (see Table (2)) for the case where no base isolation is considered. The probability is normalized by the target failure probability $P_F^* = 10^{-4}$. It is seen for example that the probability of occurrence of failure event F_1 is more than 100 times greater than the target failure probability. Once again, the effect of the isolation system is evident from these results.

Design variable	Initial design	Final design	
		Problem 1	Problem 2
ϕ_1 (m)	0.90	0.68	0.85
ϕ_2 (m)	0.80	0.59	0.75
ϕ_3 (m)	0.75	0.57	0.72
ϕ_4 (m)	0.70	0.51	0.64
Normalized objective function	1.00	0.56	0.88

Table 2: Initial and final designs.

Model	Normalized objective function	
	Problem 1	Problem 2
With base isolation system	0.56	0.88
Without base isolation system	0.78	1.21
Difference	39 %	38 %

Table 3: Objective function value of models with and without the base isolation system.

	Problem 2
P_{F_1}/P_F^*	103
P_{F_2}/P_F^*	55
P_{F_3}/P_F^*	20
P_{F_4}/P_F^*	2
$P_F^* = 10^{-4}$	

Table 4: Constraint violations.

9 CONCLUSIONS

A general framework for reliability-based design of base-isolated buildings under uncertain conditions has been presented. The reliability-based design problem is formulated as an optimization problem with a single objective function subject to multiple reliability constraints. First excursion probabilities that account for the uncertainties in the system parameters as well as in the excitation are used to characterize the system reliability. The high computational cost associated with the solution of the optimization problem is addressed by the use of approximate reliability analyses during portions of the optimization process. The proposed approach takes into account all nonlinear characteristics of the structural response in the design process and it allows for a complex characterization of structural systems and excitation models. At the same time, uncertainty in structural and excitation model parameters are considered explicitly during the design process. The numerical results and additional validation calculations highlight the beneficial effects of base-isolation systems in reducing the superstructure response. This in turn implies more robust and safer designs.

10 ACKNOWLEDGMENTS

This research was partially supported by CONICYT (National Commission for Scientific and Technological Research) under grants number 1070903 and 1110061. This support is gratefully

acknowledged by the authors.

REFERENCES

[1] N.M. Alexandrov, J.E. Dennis Jr., R.M. Lewis, and V. Torczon. A trust-region framework for managing the use of approximation models in optimization. *Structural Optimization*, 15(1):16–23, 1998.

[2] J.G. Anderson and S.E. Hough. A model for the shape of fhe Fourier amplitude spectrum of acceleration at high frequencies. *Bulletin of the Seismological Society of America*, 74(5):1969–1993, 1984.

[3] G.M. Atkinson and W. Silva. Stochastic modeling of California ground motions. *Bulletin of the Seismological Society of America*, 90(2):255–274, 2000.

[4] S.K. Au and J.L. Beck. Estimation of small failure probabilities in high dimensions by subset simulation. *Probabilistic Engineering Mechanics*, 16(4):263–277, 2001.

[5] T.T. Baber and Y. Wen. Random vibration hysteretic, degrading systems. *Journal of the Engineering Mechanics Division*, 107(6):1069–1087, 1981.

[6] D.M. Boore. Simulation of ground motion using the stochastic method. *Pure and Applied Geophysics*, 160(3-4):635–676, 2003.

[7] D.M. Boore, W.B. Joyner, and T.E. Fumal. Equations for estimating horizontal response spectra and peak acceleration from western north american earthquakes: A summary of recent work. *Seismological Research Letters*, 68(1):128153, 1997.

[8] C. Ceccoli, C. Mazzotti, and M. Savoia. Non-linear seismic analysis of base-isolated rc frame structures. *Earthquake Engineering & Structural Dynamics*, 28(6):633653, 1999.

[9] H. Chickermane and H.C. Gea. Structural optimization using a new local approximation method. *International Journal for Numerical Methods in Engineering*, 39:829–846, 1996.

[10] A.K. Chopra. *Dynamics of structures: theory and applications to earthquake engineering*. Prentice Hall, 1995.

[11] A. De Luca, E. Mele, J. Molina, G. Verzeletti, and A.V. Pinto. Base isolation for retrofitting historic buildings: Evaluation of seismic performance through experimental investigation. *Earthquake Engineering & Structural Dynamics*, 30(8):1125–1145, 2001.

[12] A. Der Kiureghian. Analysis of structural reliability under parameter uncertainties. *Probabilistic Engineering Mechanics*, 23(4):351–358, 2008.

[13] O. Ditlevsen and H.O. Madsen. *Structural Reliability Methods*. John Wiley and Sons, 1996.

[14] C. Fleury and V. Braibant. Structural optimization: A new dual method using mixed variables. *International Journal for Numerical Methods in Engineering*, 23(3):409–428, 1986.

[15] A.M. Freudenthal. Safety and the probability of structural failure. *ASCE Transactions*, 121:1337–1397, 1956.

[16] D. Goldberg. *Genetic Algorithms in Search, Optimization, and Machine Learning*. Addison Wesley, Reading, MA, 1989.

[17] A.A. Groenwold, L.F.P. Etman, J.A. Snyman, and J.E. Rooda. Incomplete series expansion for function approximation. *Structural and Multidisciplinary Optimization*, 34(1):21–40, 2007.

[18] A.A. Groenwold, D.W. Wood, L.F.P. Etman, and S. Tosserams. Globally convergent optimization algorithm using conservative convex separable diagonal quadratic approximations. *AIAA Journal*, 47(11):2649–2657, 2009.

[19] R.T. Haftka and Z. Gürdal. *Elements of Structural Optimization*. Kluwer, 3^{rd} edition, 1992.

[20] H.A. Jensen. Structural optimization of non-linear systems under stochastic excitation. *Probabilistic Engineering Mechanics*, 21(4):397–409, 2006.

[21] H.A. Jensen and J.G. Sepulveda. Structural optimization of uncertain dynamical systems considering mixed-design variables. *Probabilistic Engineering Mechanics*, 2010, available online.

[22] H.A. Jensen, M.A. Valdebenito, G.I. Schuëller, and D.S. Kusanovic. Reliability-based optimization of stochastic systems using line search. *Computer Methods in Applied Mechanics and Engineering*, 198(49-52):3915–3924, 2009.

[23] J.M. Kelly. Aseismic base isolation: review and bibliography. *Soil Dynamics and Earthquake Engineering*, 5(4):202–216, 1986.

[24] L.B. Kovács. *Combinatorial methods of discrete programming*, volume 2 of *Mathematical methods of operation research*. Akadémiai Kiadó, Budapest, 1980.

[25] S.L. Kramer. *Geotechnical earthquake engineering*. Prentince Hall, 2003.

[26] G.P. Mavroeidis and A.S. Papageorgiou. A mathematical representation of near-fault ground motions. *Bulletin of the Seismological Society of America*, 93(3):A Mathematical Representation of Near–Fault Ground Motions, 2003.

[27] A.S. Mokha, N. Amin, M.C. Constantinou, and V. Zayas. Seismic isolation retrofit of large historic building. *Journal of Structural Engineering*, 122(3):298–308, 1996.

[28] B. Prasad. Approximation, adaptation and automation concepts for large scale structural optimization. *Engineering Optimization*, 6(3):129–140, 1983.

[29] G.R. Saragoni and G.C. Hart. Simulation of artificial earthquakes. *Earthquake Engineering & Structural Dynamics*, 2(3):249267, 1974.

[30] K. Schittkowski, C. Zillober, and R. Zotemantel. Numerical comparison of nonlinear programming algorithms for structural optimization. *Structural Optimization*, 7(1-2):1–19, 1994.

[31] A.A. Taflanidis and J.L. Beck. Stochastic subset optimization for optimal reliability problems. *Probabilistic Engineering Mechanics*, 23(2-3):324–338, 2008.

[32] J.A Tomlin. *lnteger and non-linear programming*, chapter Branch and bound methods for integer and non-convex programming, pages 437–450. North Holland, Amsterdam, 1970.

[33] M.A. Valdebenito and G.I. Schuëller. Efficient strategies for reliability-based optimization involving non linear, dynamical structures. *Computers & Structures*, 2011, available online.

[34] X.-K. Zou, Q. Wang, G. Li, and C.-M. Chan. Integrated reliability-based seismic drift design optimization of base-isolated concrete buildings. *Journal of Structural Engineering*, 136(10):1282–1295, 2010.

COMPDYN 2011
3rd ECCOMAS Thematic Conference on
Computational Methods in Structural Dynamics and Earthquake Engineering
M. Papadrakakis, M. Fragiadakis, V. Plevris (eds.)
Corfu, Greece, 25–28 May 2011

COMPUTATIONAL STOCHASTIC DYNAMICS BASED ON ORTHOGONAL EXPANSION OF RANDOM EXCITATIONS

X. Frank Xu[1], George Stefanou[2]

[1] Department of Civil, Environmental and Ocean Engineering
Stevens Institute of Technology, Hoboken, NJ 07030, USA
e-mail: xxu1@stevens.edu

[2] Institute of Structural Analysis & Antiseismic Research
National Technical University of Athens, 15780 Athens, Greece
e-mail: stegesa@mail.ntua.gr

Keywords: Orthogonal Expansion, Nonlinear, Random Vibration.

Abstract. *A major challenge in stochastic dynamics is to model nonlinear systems subject to general non-Gaussian excitations which are prevalent in realistic engineering problems. In this work, an n-th order convolved orthogonal expansion (COE) method is proposed. For linear vibration systems, the statistics of the output can be directly obtained as the first-order COE about the underlying Gaussian process. The COE method is next verified by its application on a weakly nonlinear oscillator. In dealing with strongly nonlinear dynamics problems, a variational method is presented by formulating a convolution-type Lagrangian and using the COE representation as trial functions.*

1 INTRODUCTION

To evaluate probabilistic response of a structural dynamic system subject to parametric and external excitations, there are generally two approaches. The first approach uses Fokker-Planck-Kolmogorov (FPK) equation to directly find probability density function (pdf) by assuming a white noise excitation. To solve FPK equation especially for nonlinear systems, various techniques have been proposed, including weighted residual, path integral, etc, which however are all limited to systems of low dimension (up to 4). The second approach includes perturbation method, moment closure method, and statistical equivalent techniques. While the perturbation method is limited to weak nonlinearity, the accuracy of moment closure method and statistical equivalent techniques on highly nonlinear problems remains an open question.

A major deficiency of the existing approaches is their incapability in dealing with general non-Gaussian excitations which are prevalent in realistic engineering problems [5]. The marginal pdf and power spectral density of a loading process play a major role in determining the response of systems, e.g. seismic wave in earthquake engineering. Therefore, a new approach to model dynamic systems subject to non-Gaussian excitations is highly desired.

A novel stochastic computation method based on orthogonal expansion of random fields is recently proposed [6]. In this study, the idea of orthogonal expansion is extended to the so-called *n*-th order convolved orthogonal expansions (COE) especially in dealing with nonlinear dynamics. For linear vibration systems, the statistics of the output can be directly obtained as the first-order COE about the underlying Gaussian process. The COE is next verified by its application on a weakly nonlinear oscillator. In dealing with strongly nonlinear dynamics problems, a variational method is presented by formulating the convolution-type Lagrangian and using the COE representation as trial functions [7]. Theoretically, substitution of the trial response function into the Lagrangian will lead to the optimal solution. The effect of using different trial functions (COE of different orders) on the accuracy and efficiency of the proposed approach will be examined in a forthcoming paper.

2 CONVOLVED ORTHOGONAL EXPANSIONS

2.1 The zero-th order convolved orthogonal expansion

An underlying stationary Gaussian excitation $h_1(t,\vartheta)$ is characterized with the autocorrelation function $\rho(t)$ and unit variance, where $\vartheta \in \Theta$ indicates a sample point in random space. Based on the so-called diagonal class of random processes [1], the zero-th order convolved (or memoryless) orthogonal expansion of $h_1(t,\vartheta)$ is proposed as [6]

$$u(t,\vartheta) = \sum_{i=0} u_i(t) h_i(t,\vartheta) \tag{1}$$

where the random basis function h_i corresponds to the i-th degree Hermite polynomial with $h_0 = 1$. According to the generalized Mehler's formula [4] the correlations among the random basis functions are given as

$$\begin{aligned} R_{s_1 s_2 \cdots s_n}(t_1,t_2,\cdots,t_n) &= \overline{h_{s_1}(t_1,\vartheta)\cdots h_{s_n}(t_n,\vartheta)} \\ &= \sum_{\nu_{12}=0}^{\infty}\cdots\sum_{\nu_{n-1,n}=0}^{\infty} \delta_{s_1 r_1}\cdots\delta_{s_n r_n}\prod_{j<k}\frac{\rho^{\nu_{jk}}(t_j-t_k)}{\nu_{jk}!} s_1!\cdots s_n! \end{aligned} \tag{2}$$

where $r_k = \sum_{j \neq k} \nu_{jk}$, $\nu_{jk} = \nu_{kj}$, $\delta_{s_k r_k} = \begin{cases} 1 & s_k = r_k \\ 0 & s_k \neq r_k \end{cases}$, and the overbar denotes ensemble average. Following Eq. (2), the two-point and three-point correlation functions are specifically obtained as

$$R_{ij}(t_1 - t_2) = \overline{h_i(t_1, \vartheta) h_j(t_2, \vartheta)} = \delta_{ij} i! \rho^i (t_1 - t_2) \tag{3}$$

$$\begin{aligned} R_{ijk}(t_1 - t_2, t_1 - t_3, t_2 - t_3) &= \overline{h_i(t_1, \vartheta) h_j(t_2, \vartheta) h_k(t_3, \vartheta)} \\ &= \frac{i! j! k!}{i'! j'! k'!} \rho^{k'}(t_1 - t_2) \rho^{j'}(t_1 - t_3) \rho^{i'}(t_2 - t_3) \\ i' = \frac{j+k-i}{2}, j' &= \frac{i+k-j}{2}, k' = \frac{i+j-k}{2} \end{aligned} \tag{4}$$

where i', j', k' must be non-negative integers, otherwise $R_{ijk} = 0$.

The correlation relations can be extended to the derivatives of the random basis functions, e.g.

$$\begin{aligned} R_{ij,pq}(t_1 - t_2) &= \overline{h_{i,p}^{(0)}(t_1, \vartheta) h_{j,q}^{(0)}(t_2, \vartheta)} = \delta_{ij} i! \frac{\partial^{p+q}}{\partial t_1^p \partial t_2^q} \rho^i (t_1 - t_2) \\ &= \delta_{ij} (-1)^q i! \frac{\partial^{p+q}}{\partial \tau^{p+q}} \rho^i(\tau) \end{aligned}$$

where $\tau = t_1 - t_2$, and the subscripts p, q denote p-th and q-th derivatives. Similarly, the derivations can be made for the convolution of the random basis functions, e.g.

$$\begin{aligned} C_{ij} &= \overline{h_i(t_1, \vartheta) * h_j(t_2, \vartheta)} = \delta_{ij} i! \int_{-\infty}^{\infty} \rho^i (t_1 - 2t_2) dt_2 = \delta_{ij} i! \tau_i \\ C_{ij,11} &= \overline{h_{i,1}(t_1, \vartheta) * h_{j,1}(t_2, \vartheta)} = \delta_{ij} i! \int_{-\infty}^{\infty} \frac{\partial^2}{\partial t_1 \partial t_2} \rho^i (t_1 - 2t_2) dt_2 = 0 \end{aligned} \tag{5}$$

where $\tau_i = \int_{-\infty}^{\infty} \rho^i(t) dt$ is the correlation time.

2.2 *n*-th order convolved orthogonal expansion

The idea of the memoryless orthogonal expansion presented above can be generalized to an n-th order convolved orthogonal expansion (COE) for representation of nonlinear output processes

$$u(t, \vartheta) = \sum_{n=0} \sum_{i=0} u_i^{(n)}(t) h_i^{(n)}(t, \vartheta) \tag{6}$$

$$h_i^{(n)}(t, \vartheta) = \overbrace{g * g * \cdots * g}^{n} * h_i = g^{*n} * h_i \tag{7}$$

where g is a given kernel, and the symbol * denotes the convolution operator. For notational simplicity, the superscript (0) of the zero-th order COE is usually dropped throughout the paper. The memoryless orthogonal expansion thus corresponds to the zero-th order COE with n=0 in (6). The correlation functions of the n-th order basis functions are therefore obtained as

$$\begin{aligned} R^{m_1\cdots m_n}_{s_1\cdots s_n}(t_1,t_2,\cdots,t_n) &= \overline{h^{(m_1)}_{s_1}(t_1,\vartheta)\cdots h^{(m_n)}_{s_n}(t_n,\vartheta)} \\ &= \sum_{\nu_{12}=0}^{\infty}\cdots\sum_{\nu_{n-1,n}=0}^{\infty}\delta_{s_1r_1}\cdots\delta_{s_nr_n}\int_{-\infty}^{\infty}\cdots\int_{-\infty}^{\infty} g^{*m_1}(t_1,\tau_1)\cdots \\ & g^{*m_n}(t_n,\tau_n)\prod_{j<k}\frac{\rho^{\nu_{jk}}(t_j-t_k)}{\nu_{jk}!}s_1!\cdots s_n!\,d\tau_1\cdots d\tau_n \end{aligned} \tag{8}$$

with the two-point correlations

$$\begin{aligned} R^{mn}_{ij}(t_1-t_2) &= \overline{h^{(m)}_i(t_1,\vartheta)h^{(n)}_j(t_2,\vartheta)} \\ &= \delta_{ij}i!\int_{-\infty}^{\infty}\int_{-\infty}^{\infty} g^{*m}(t_1,\tau_1)g^{*n}(t_2,\tau_2)\rho^i(\tau_1-\tau_2)\,d\tau_1d\tau_2 \end{aligned} \tag{9}$$

The derivatives of the n-th order basis functions can be similarly obtained, e.g.

$$\begin{aligned} R^{mn}_{ij,pq}(t_1-t_2) &= \overline{h^{(m)}_{i,p}(t_1,\vartheta)h^{(n)}_{j,q}(t_2,\vartheta)} \\ &= \delta_{ij}i!\int_{-\infty}^{\infty}\int_{-\infty}^{\infty} g^{*m}(t_1,\tau_1)g^{*n}(t_2,\tau_2)\frac{\partial^{p+q}}{\partial\tau_1^p\partial\tau_2^q}\rho^i(\tau_1-\tau_2)\,d\tau_1d\tau_2 \end{aligned} \tag{10}$$

By letting $U=\Phi(u)$, $H=\Phi(h)$, $S=\Phi(R)$, $G^n=\Phi(g^{*n})$ and $S^{*i}=\Phi(\rho^i)$, with Φ being the Fourier transform operator, we specially rewrite the two-point correlation functions of the COE basis functions in frequency domain

$$S^{mn}_{ij}(\omega) = \overline{H^{(m)}_i(\omega,\vartheta)\tilde{H}^{(n)}_j(\omega,\vartheta)} = \delta_{ij}i!G^m(\omega)\tilde{G}^n(\omega)S^{*i}(\omega) \tag{11}$$

$$\begin{aligned} S^{mn}_{ij,pq}(\omega) &= \left(\omega\sqrt{-1}\right)^{p+q}\overline{H^{(m)}_i(\omega,\vartheta)\tilde{H}^{(n)}_j(\omega,\vartheta)} \\ &= \delta_{ij}i!\left(\omega\sqrt{-1}\right)^{p+q}G^m(\omega)\tilde{G}^n(\omega)S^{*i}(\omega) \end{aligned} \tag{12}$$

where the tilde denotes complex conjugate. Note that in the cases of stationary correlation functions, it specially follows

$$\begin{aligned} &\overline{H^{(m)}_{i,p}(\omega_k,\vartheta)\tilde{H}^{(n)}_{j,q}(\omega_l,\vartheta)} = \delta_{kl}S^{mn}_{ij,pq}(\omega) \\ \\ &\overline{H^{(m)}_{i,p}(\omega_k,\vartheta)H^{(n)}_{j,q}(\omega_l,\vartheta)} \\ &= \delta_{kl}\delta_{ij}i!\left(\omega\sqrt{-1}\right)^{p+q}G^m(\omega)\tilde{G}^n(\omega)\tau_i \end{aligned} \tag{13}$$

Remark: The advantage of the n-th order COE (6) can be demonstrated by comparing it with the classical Volterra series expansion

$$u(t,\vartheta)=\sum_{n=0}\frac{1}{n!}\int_{-\infty}^{\infty}\cdots\int_{-\infty}^{\infty}k^{(n)}(t_1,t_2\cdots t_n)h(t-t_1,\vartheta)$$
$$h(t-t_2,\vartheta)\cdots h(t-t_n,\vartheta)dt_1dt_2\cdots dt_n \tag{14}$$

The Volterra representation typically suffers from severe difficulties in solving for the unknown kernels $k^{(n)}$. In the COE representation, the kernels are all explicitly given, and the problem is significantly reduced to solving of the unknown coefficients $u_i^{(n)}$.

3 THE COE METHOD ON RANDOM VIBRATION

3.1 Linear oscillators

Suppose the linear oscillator

$$\begin{aligned}&\ddot{u}+2\zeta\omega_n\dot{u}+\omega_n^2u=f\\&u(0)=\dot{u}(0)=0\end{aligned} \tag{15}$$

is subjected to a non-stationary non-Gaussian translation input, i.e.

$$f(t,\vartheta)=\sum_{i=0}f_i(t)h_i(t,\vartheta) \tag{16}$$

By using the Green function

$$\begin{aligned}&g(t)=\frac{1}{\omega_d}e^{-\zeta\omega_n t}\sin(\omega_d t)\\&\omega_d=\omega_n\sqrt{1-\zeta^2}\\&G(\omega)=\frac{1}{\omega_n^2-\omega^2+\sqrt{-1}2\zeta\omega\omega_n}\end{aligned} \tag{17}$$

the first three correlations of the non-stationary output u can be directly calculated from

$$\bar{u}(t)=\int_0^t g(t-\tau)f_0(\tau)d\tau \tag{18}$$

$$R_{uu}(t_1,t_2)=\int_0^{t_2}\int_0^{t_1}g(t_1-\tau_1)g(t_2-\tau_2)\sum_{i=0}i!$$
$$\rho^i(\tau_1-\tau_2)f_i(\tau_1)f_i(\tau_2)d\tau_1d\tau_2 \tag{19}$$

$$R_{uuu}(t_1,t_2,t_3)=\int_0^{t_3}\int_0^{t_2}\int_0^{t_1}g(t_1-\tau_1)g(t_2-\tau_2)g(t_3-\tau_3)$$
$$\sum_{i,j,k=0}R_{ijk}(\tau_1-\tau_2,\tau_1-\tau_3,\tau_2-\tau_3)d\tau_1d\tau_2d\tau_3 \tag{20}$$

where R_{ijk} is given in Eq. (4).

When the excitation in Eq. (15) is stationary, the output can be directly given as

$$u(t,\vartheta)=\sum_{i=0} f_i\, h_i^{(1)}(t,\vartheta) \tag{21}$$

which is a special case of the COE representation (6). Note that, with the Green function g and the underlying Gaussian process being given, the stationary probability density function (pdf) of the output in Eq. (21) can be rapidly estimated by using Monte Carlo method in the frequency domain.

A numerical example for application of the COE on linear oscillator is given in [6]. With regard to the multi-degree-of-freedom linear systems, the oscillator equations given above can be directly applied by using the modal decomposition as shown in [8].

3.2 Weakly nonlinear oscillators

A Duffing oscillator subjected to a Gaussian white noise excitation with intensity D is considered

$$\ddot{u}+2\zeta\omega_n\dot{u}+\omega_n^2(u+\alpha u^3)=W \tag{22}$$

The Gaussian response of the linear filter can be given as $u_0=\sigma_0 h_1$, and h_1 is characterized by unit variance and power spectral density (PSD)

$$S=\frac{D}{\sigma_0^2}\left|G(\omega)\right|^2 \tag{23}$$

$$\sigma_0^2=D\int_{-\infty}^{\infty}\left|\frac{1}{\omega_n^2-\omega^2+\sqrt{-1}2\zeta\omega\omega_n}\right|^2 d\omega=\frac{D\pi}{2\zeta\omega_n^3} \tag{24}$$

For small α, the nonlinear output of Eq. (22) can be approximated as

$$u=\sigma_0 h_1-\alpha\omega_n^2\sigma_0^3 g*h_1^3+3\alpha^2\omega_n^4\sigma_0^5 g*\left(h_1^2 g*h_1^3\right)+O(\alpha^3) \tag{25}$$

By noting $h_1^3=h_3+3h_1$ and $h_1^2=h_2+1$, Eq. (25) can be rewritten in terms of the random basis functions

$$\begin{aligned}u=\sigma_0 h_1-\alpha\omega_n^2\sigma_0^3 g*\left(h_3+3h_1\right)+\\ 3\alpha^2\omega_n^4\sigma_0^5 g*\left[(h_2+1)g*(h_3+3h_1)\right]+O(\alpha^3)\end{aligned} \tag{26}$$

$$\begin{aligned}U=\sigma_0 H_1-\alpha\omega_n^2\sigma_0^3 G\left(H_3+3H_1\right)+\\ 3\alpha^2\omega_n^4\sigma_0^5 G\left[(H_2+\delta(0))*G(H_3+3H_1)\right]+O(\alpha^3)\end{aligned} \tag{27}$$

By using the correlations of Eqs. (3)-(4) and (11), it follows that the stationary mean

$$\overline{u}=O(\alpha^3) \tag{28}$$

and the stationary PSD

$$\begin{aligned}S_{UU}=\overline{U\tilde{U}}=\sigma_0^2 S-3\alpha\omega_n^2\sigma_0^4(G+\tilde{G})S+\alpha^2\omega_n^4\sigma_0^6[9S(\left|G\right|^2+G^2\\ +\tilde{G}^2)+6\left|G\right|^2 S^{*3}]+O(\alpha^3)\end{aligned} \tag{29}$$

Since

$$\int_{-\infty}^{\infty} \frac{2(\omega_n^2-\omega^2)}{(\omega_n^2-\omega^2)^2+(2\zeta\omega\omega_n)^2}\left|\frac{1}{\omega_n^2-\omega^2+\sqrt{-1}2\zeta\omega\omega_n}\right|^2 d\omega = \frac{\pi}{2\zeta\omega_n^5} \tag{30}$$

the variance calculated from the first two terms of Eq. (29) is simply obtained as

$$\sigma^2 = \sigma_0^2(1-3\alpha\sigma_0^2) \tag{31}$$

which is identical to the result obtained using other approaches, e.g. [2,3]. In addition to serving as verification to the COE method, this example shows simplicity and efficiency of the orthogonal expansions in nonlinear problems.

3.3 Strongly nonlinear oscillators

For strongly nonlinear systems, the perturbation method is inapplicable. In this part, a variational method will be presented following the variational principles formulated for random media elastodynamics [7]. The variational functional, or Lagrangian, of a nonlinear oscillator

$$\ddot{u} + 2\zeta\omega_n\dot{u} + \omega_n^2\big(u + g(u,\dot{u})\big) = f \tag{32}$$

can be formulated by using the convolution form

$$\delta\ell = \delta u * [\ddot{u} + 2\zeta\omega_n\dot{u} + \omega_n^2\big(u + g(u,\dot{u})\big) - f] = 0 \tag{33}$$

For a Duffing oscillator $g(u,\dot{u}) = \alpha u^3$, the Lagrangian is derived from Eq. (33) as

$$\begin{aligned}\ell(u) &= \frac{1}{2}\dot{u}*\dot{u} + \zeta u*\dot{u} + \frac{1}{2}\omega_n^2 u*u \\ &+ \alpha\omega_n^2\Big(u^3*u - \frac{3}{4}u^2*u^2\Big) - f*u + \dot{u}(0)u\end{aligned} \tag{34}$$

where any trial function u satisfies the specified initial condition $u(0)$. To the authors' knowledge, the convolution Lagrangian (34) is the first variational form formulated for nonlinear dissipative systems. It is especially noted that the classical point-wise Lagrangian form does not work on the dissipative term.

For nonlinear random vibrations, the stochastic Lagrangian is directly obtained by taking ensemble average of Eq. (34), i.e.

$$\delta\bar{\ell} = 0 \tag{35}$$

with the trial function u based on the COE representation (6).

For stationary solutions, Eq. (35) can be rewritten in frequency domain as

$$\begin{aligned}&\delta\overline{L}(U) = 0 \\ &\overline{L}(U) = \left(-\frac{1}{2}\omega^2 + \sqrt{-1}\omega\zeta + \frac{1}{2}\omega_n^2\right)\overline{U^2} + \\ &\alpha\omega_n^2\left[\overline{(U*U*U)U - \frac{3}{4}(U*U)^2}\right] - \overline{FU}\end{aligned} \tag{36}$$

Suppose the excitation is stationary

$$f(t,\vartheta) = \sum_{i=0} f_i h_i(t,\vartheta) \tag{37}$$

and choose the zeroth-order COE

$$u(t,\vartheta) = \sum_{i=0} u_i h_i(t,\vartheta) \tag{38}$$

as the trial function for the stationary solution. By substituting Eq. (38) into Eqs. (34)-(35) and taking derivative with respect to u_i, it leads to a series of equations to solve for u_i

$$\frac{\partial \overline{\ell}}{\partial u_i} = 0 \tag{39}$$

Similarly the first- or higher-order COE can be chosen as the trial function. The detail of numerical examples and investigation of accuracy and computational efficiency of the different trial functions will be provided in a forthcoming paper.

4 CONCLUDING REMARK

By developing a diagonal class of random fields/stochastic processes to represent high-dimensional uncertainty, the proposed convolved orthogonal expansion method opens a new direction to deal with nonlinear stochastic dynamics. The advantage is especially noted for its efficiency in computing of large and nonlinear dynamical systems, in comparison with the classical Volterra series representation and the recently developed random variable based polynomial chaos expansions.

REFERENCES

[1] J.F. Barrett, D.G. Lampard, An expansion for some second-order probability distributions and its application to noise problems, *IRE Trans. Inform. Theory*, vol. IT-I, 10-15, 1955.

[2] Y.K. Lin, *Probabilistic Theory of Structural Dynamics,* Krieger Pub., Florida, 1976.

[3] G.D. Manolis, P.K. Koliopoulos, *Stochastic Structural Dynamics in Earthquake Engineering*, WIT Press, UK, 2001.

[4] D. Slepian, On the symmetrized Kronecker power of a matrix and extensions of Mehler's formula for Hermite polynomials, *SIAM J. on Mathematical Analysis*, **3**, 606–616, 1972.

[5] G. Stefanou, The stochastic finite element method: past, present and future, *Computer Methods in Applied Mechanics and Engineering,* **198**, 1031-1051, 2009.

[6] X.F. Xu, Stochastic computation based on orthogonal expansion of random fields, *Computer Methods in Applied Mechanics and Engineering,* to appear.

[7] X.F. Xu, Variational principles of random media elastodynamics, submitted for publication.

[8] X.F. Xu, Quasi-weak and weak formulations of stochastic finite element methods, *Probabilistic Engineering Mechanics* (Special issue on CSM 6), to appear.

COMPDYN 2011
ECCOMAS Thematic Conference on
Computational Methods in Structural Dynamics and Earthquake Engineering
M. Papadrakakis, M. Fragiadakis, V. Plevris (eds.)
Corfu, Greece, 25-28 May 2011

ENHANCED MONTE CARLO FOR RELIABILITY-BASED DESIGN AND CALIBRATION

Arvid Naess[1], **Marc Maes**[2] **and Markus R. Dann**[2]

[1]Centre for Ships and Ocean Structures & Dept of Mathematical Sciences
NTNU, NO-7491 Trondheim, Norway
e-mail: arvidn@math.ntnu.no

[2]University of Calgary
T2N 1N4 Calgary, Canada
e-mail: mamaes@ucalgary.ca, markusdann@gmx.de

Keywords: Reliability; Calibration; Enhanced Monte Carlo; System failure probability.

Abstract. *This paper extends the recently developed enhanced Monte Carlo approach to the problem of reliability-based design. The objective is to optimize a design parameter(s) so that the system, represented by a set of failure modes or limit states, achieves a target reliability. In a large majority of design and/or calibration contexts, the design parameter* α *itself can be used to parameterize the system safety margin* $M(\alpha)$*. The lower tail of this random variable behaves in a regular way and is therefore amenable to straightforward parametric analysis. In contrast to the original Naess et al. method [1], the intention is to estimate the value* α_T *that corresponds to a (very) small target system failure probability* p_{fT}*. Monte Carlo sampling occurs at a range of values for* α *that result in larger failure probabilities, and so the design problem essentially amounts to a statistical estimation of a high quantile. Bounds for* α_T *can easily be constructed. Several examples of the approach are given in the paper.*

1 INTRODUCTION

A new Monte Carlo (MC) based method for estimating system reliability was recently developed in [1]. The aim of this method is to reduce computational cost while maintaining the advantages of crude MC simulation, specifically, its ease in dealing with complex systems. The key idea is to exploit the regularity of tail probabilities to enable an approximate prediction of far tail failure probabilities based on small Monte-Carlo sample results obtained for much more moderate levels of reliability. The motivation behind this approach is that systems with multiple and complex failure modes or limit states are often exceedingly difficult to analyze using traditional methods of structural reliability. While direct MC does not suffer from this problem, it is computationally burdensome for small probabilities. Hence originates the idea of sampling in a different less reliable range and performing a statistical extrapolation unto the tail. A similar but somewhat different idea is presented in [2].

The fundamentals of the method proposed in [1] are as follows. A safety margin $M = G(X_1, \ldots, X_n)$ expressed in terms of n basic variables, is extended to a parameterized class of safety margins using a scaling parameter λ ($0 \leq \lambda \leq 1$):

$$M(\lambda) = M - (1 - \lambda)\mu_M \, . \tag{1}$$

The failure probability is then assumed to behave as follows:

$$p_f(\lambda) = \text{Prob}\big(M(\lambda) \leq 0\big) \underset{\lambda \to 1}{\approx} q(\lambda) \exp\big\{ - a(\lambda - b)^c \big\} \, , \tag{2}$$

where the function $q(\lambda)$ is slowly varying compared with the exponential function $\exp\{-a(\lambda - b)^c\}$. It may be pointed out that the assumed behaviour of the failure probability applies to any safety margin for which FORM or SORM approximations can be used, but actually its range of applicability is much wider than that.

Clearly, the target failure probability $p_f = p_f(1)$ can be obtained from values of $p_f(\lambda)$ for $\lambda < 1$. It is now far easier to estimate the (larger) failure probabilities $p_f(\lambda)$ for $\lambda < 1$ accurately than the target value itself, since they are larger and hence require less simulations. Fitting the parametric function given by Eq. (2) for $p_f(\lambda)$ to the estimated values would then allow us to provide an estimate of the target value by extrapolation. The viability of this approach is demonstrated by both analytical and numerical examples in [1] and [3].

In the next sections, the Naess et al. [1] approach is extended to reliability-based design and calibration.

2 USING ENHANCED MONTE CARLO TO OPTIMIZE A DESIGN PARAMETER

First consider a typical component design, the reliability of which is governed by the safety margin:

$$M(\alpha) = G(X_1, \ldots, X_n; \alpha) \tag{3}$$

with

$$p_f(\alpha) = \text{Prob}(M(\alpha) \leq 0) \, , \tag{4}$$

where α acts as a design factor which ”controls” the reliability of the component. The objective is now to determine the (assumed to be unique) value of $\alpha = \alpha_T$ that corresponds to a specified (target) component failure probability p_{fT}, i.e.:

$$\alpha_T : \text{Prob}(M(\alpha_T) \leq 0) = p_{fT} \, , \tag{5}$$

This assumes that the function $p_f(\alpha)$ is a monotonic function, that is, that the safety of the system either strictly increases or strictly decreases as the design factor α increases and approaches α_T. In practical design situations, α may represent a safety factor, a partial load or resistance factor, or some exceedance level and, the condition of monotonicity is generally speaking satisfied, unless the problem relates to a poor or an unfeasible design.

A more general situation, typical in the context of calibration of design specifications, consists of having the safety margin controlled by a design check function $c(\alpha) = c(x_{1c}, \ldots, x_{nc}; \alpha)$ involving characteristic values x_{ic} of each basic variable X_i. Admissible design are such that $c(\alpha) \leq 0$. Minimal acceptable designs are marked by $c(\alpha) = 0$, an assumption which is made throughout this paper. Often the design check function $c(\alpha)$ is selected to be the same mathematical function as G but this is not required - all that matters is that the resulting safety margin $M(\alpha) = G\big(X_1, \ldots, X_n | c(x_{1c}, \ldots, x_{nc}; \alpha) = 0\big)$ is monotonic with respect to α in its approach to the target α_T. Hence the objective is to determine α_T as follows:

$$\alpha_T : \text{ Prob}\Big(G\big(X_1, \ldots, X_n | c(x_{1c}, \ldots, x_{nc}; \alpha_T) = 0\big) \leq 0\Big) = p_{fT} \,. \tag{6}$$

Typically, p_{fT} is a very small target probability and hence the behavior of p_f as a function of of α is similar to a deep tail estimation problem so that it is reasonable to assume that:

$$p_f(\alpha) \underset{\alpha \to 1}{\approx} q(\alpha) \exp\big\{ - a(\alpha - b)^c \big\} \,, \tag{7}$$

where $q(\alpha)$ is slowly varying compared to the exponential expression.

To illustrate this premise, consider a basic load and resistance safety margin $M(\alpha) = R(\alpha) - S$ controlled by a design check function $c(\alpha) = (r_c(\alpha)/\alpha) - s_c$, where r_c and s_c are characteristic values of a resistance R and a load S, and α acts as a partial resistance factor ($\alpha > 1$). Assume the load S is Weibull distributed with exponent d and scale parameter s_0, then the characteristic load s_c at its $(1-\theta)$ quantile, is equal to $s_c = (-\ln\theta)^{1/d} s_0 = k s_0$ where k is a known positive constant > 1. First consider the limiting case where the variance of R is zero, $\sigma_R^2 = 0$, hence $r_c(\alpha) = \alpha s_c$ such that $p_f(\alpha) = \text{Prob}(M(\alpha) \leq 0) = \exp\big(- (\alpha k)^d \big)$ which is fully consistent with Eq. (7) above. If the variance of $R(\alpha)$ now increases, then the mean resistance will shift even further down the tail since $r_c(\alpha)$ is a small quantile of R. But, the function $p_f(\alpha)$ will only be slightly "contaminated" by a much slower varying function of α; however, and this is certainly valid in the tail area as $\alpha \to \alpha_T$, the general form in Eq. (7) will persist and it is amenable to be fitted to data pairs $(p_f(\alpha), \alpha)$ obtained for (much) higher failure probabilities.

Once a satisfactory fit is achieved, the target value α_T corresponding to p_{fT} needs to be estimated, a problem which is similar to a high quantile estimation.

3 EXTENSION TO SYSTEM RELIABILITY

Using Monte Carlo methods for system reliability analysis has several attractive features, the most important being that the failure criterion is relatively easy to check almost irrespective of the complexity of the system. In order to limit the amount of computational effort that may be involved, it is useful to extend the above approach to systems.

Let $M_j(\alpha) = G_j(X_1, \ldots, X_n, \alpha)$, $j = 1, \ldots, m$ be a set of m given safety margins expressed in terms of n basic variables and a single design parameter α. The series system reliability expressed in terms of the failure probability can then be written as,

$$p_f(\alpha) = \text{Prob}\big(\bigcup_{j=1}^{m} \{M_j(\alpha) \leq 0\} \big) \,, \tag{8}$$

while for the parallel system,

$$p_f(\alpha) = \text{Prob}\big(\bigcap_{j=1}^{m}\{M_j(\alpha) \leq 0\}\big)\,. \tag{9}$$

In general, any system can be written as a series system of parallel subsystems. The failure probability would then be given as,

$$p_f(\alpha) = \text{Prob}\big(\bigcup_{j=1}^{l}\bigcap_{i\in C_j}\{M_i(\alpha) \leq 0\}\big)\,, \tag{10}$$

Here each C_j is a subset of $1,\ldots,m$, for $j = 1,\ldots,l$. The C_js denote the index sets defining the parallel subsystems.

We then make the assumption that $p_f(\alpha)$ can also be represented as in Eq. (7) for the system reliability problems. Again, the objective is to determine the value α_T that achieves a stated overall system reliability.

4 IMPLEMENTATION

The method to be described in this section is based on the assumption expressed by Eq. (7). For practical applications it is implemented in the following form:

$$p_f(\alpha) \approx q(\alpha)\exp\big\{-a(\alpha-b)^c\big\}\,,\text{for }\ \alpha_0 \leq \alpha \leq \alpha_T\,, \tag{11}$$

for a suitable value of α_0. An important part of the method is therefore to identify a suitable range for α so that the right hand side of Eq. (7) represents a good approximation of $p_f(\alpha)$ for $\alpha \in [\alpha_0, \alpha_T]$.

For a sample of size N of the vector of basic random variables $\mathbf{X} = (X_1,\ldots,X_n)$, let $N_f(\alpha)$ denote the number of outcomes of the random vector in the failure domain of $M(\alpha)$. The estimate of the failure probability is then

$$\hat{p}_f(\alpha) = \frac{N_f(\alpha)}{N}\,. \tag{12}$$

The coefficient of variation C_v of this estimator is

$$C_v(\hat{p}_f(\alpha)) = \sqrt{\frac{1-\hat{p}_f(\alpha)}{\hat{p}_f(\alpha)N}}\,. \tag{13}$$

A fair approximation of the 95% confidence interval for the value $\hat{p}_f(\alpha)$ can be obtained as $\text{CI}_{0.95} = (C^-(\alpha),\, C^+(\alpha))$, where

$$C^{\pm}(\alpha) = \hat{p}_f(\alpha)(1 \pm 1.96C_v(\hat{p}_f(\alpha)))\,. \tag{14}$$

Assuming now that we have obtained empirical Monte Carlo estimates of the failure probability, the problem then becomes one of optimal use of the information available. By plotting $\log|\log\hat{p}_f(\alpha)/q(\alpha)|$ versus $\log(\alpha-b)$, it is expected that an almost perfectly linear tail behavior will be obtained according to Eq. (11). Recalling that the function $q(\alpha)$ was assumed to be slowly varying compared with the exponential function $\exp\{-a(\alpha-b)^c\}$ for values of α close to α_T, it is now tentatively proposed to replace $q(\alpha)$ by a suitable constant value, q say, for tail values of α, say $\alpha > \alpha_1 (\geq \alpha_0)$. Hence, we will investigate the viability of the following simpler version of Eq. (11):

$$p_f(\alpha) \approx q \exp\big\{ -a(\alpha - b)^c \big\}\,, \text{for } \alpha_1 \leq \alpha \leq \alpha_T\,, \tag{15}$$

for a suitable choice of α_1.

The problem of finding the optimal values of the parameters a, b, c, q is carried out by optimizing the fit on the log level by minimizing the following mean square error function with respect to all four arguments [4],

$$F(a, b, c, q) = \sum_{j=1}^{M} w_j \big(\log \hat{p}_f(\alpha_j) - \log q + a(\alpha_j - b)^c \big)^2\,, \tag{16}$$

where $\alpha_1 < \ldots < \alpha_M$ denotes the set of α values where the failure probability is empirically estimated. The w_j denote weight factors that put more emphasis on the more reliable data points, alleviating the heteroscedasticity of the estimation problem at hand. The choice of weight factor is to some extent arbitrary. In this paper, we use $w_j = \big(\log C^+(\alpha_j) - \log C^-(\alpha_j)\big)^{-\theta}$ with the values θ = 1 and 2, combined with a Levenberg-Marquardt least squares optimization method [5]. Note that the form of w_j puts some restriction on the use of the data. Usually, there is a level α_j beyond which w_j is no longer defined. Hence, the summation in Eq. (16) has to stop before that happens. Also, the data should be preconditioned by establishing the tail marker α_1 in a sensible way.

Although the Levenberg-Marquardt method as described above generally works well, it may be simplified by exploiting the structure of F. It is realized by scrutinizing Eq. (16) that if b and c are fixed, the optimization problem reduces to a standard weighted linear regression problem. That is, with both b and c fixed, the optimal values of a and $\log q$ are found using closed form weighted linear regression formulas in terms of w_j, $y_j = \log \hat{p}_f(\alpha_j)$ and $x_j = (\alpha_j - b)^c$.

It is obtained that the optimal values of a and q are given by the relations,

$$a^*(b, c) = -\frac{\sum_{j=1}^{M} w_j (x_j - \overline{x})(y_j - \overline{y})}{\sum_{j=1}^{M} w_j (x_j - \overline{x})^2}\,, \tag{17}$$

and

$$\log q^*(b, c) = \overline{y} + a^*(b, c)\overline{x}\,, \tag{18}$$

where $\overline{x} = \sum_{j=1}^{M} w_j x_j / \sum_{j=1}^{M} w_j$, with a similar definition of $\overline{y}$.

The Levenberg-Marquardt method may now be used on the function $\tilde{F}(b, c) = F(a^*(b, c), b, c, q^*(b, c))$ to find the optimal values b^* and c^*, and then the corresponding a^* and q^* can be calculated from Eq. (17) and (18).

For estimation of the confidence interval for the predicted target quantile α_T provided by the optimal curve, the empirical confidence band is reanchored to the optimal curve. The range of fitted curves that stay within the reanchored confidence band will determine an optimized confidence interval of the predicted value.

5 NUMERICAL EXAMPLES

The examples in the following two sections all have simple explicit limit state functions in terms of the basic random variables. The computational issue is therefore minor and no effort has been made to investigate the possibility of implementing more effective sampling strategies.

If the proposed method were to be used in combination with computationally demanding procedures involving e.g. a FE method for calculating the sample, it would be necessary in general to use more effective sampling strategies than the brute force procedure used here.

5.1 Component load factor calibration

In this first example, the 10-bar truss structure shown in Fig. 1 is studied. An enhanced Monte-Carlo reliability analysis of this truss is given in [1]. Here a load factor for a transversal load P is calibrated in order to achieve a target reliability of (10^{-6}) with respect to the horizontal sway of the truss. The ten truss members are cut from three different aluminum rods with cross-sectional areas A_1, A_2 and A_3, as shown in Fig. 1. The structure is subjected to external loads P as shown in Fig. 1. The horizontal displacement D at the upper right hand corner of the truss structure can be written as [6]:

$$\begin{aligned} D = & \frac{BPL}{A_1A_3E}\Big\{\frac{4\sqrt{2}A_1^3(24A_2^2+A_3^2)+A_3^3(7A_1^2+26A_2^2)}{D_T} \\ & + 4A_1A_2A_3\frac{20A_1^2+76A_1A_2+10A_3^2}{D_T} \\ & + 4\sqrt{2}A_1A_2A_3^2\frac{25A_1+29A_2}{D_T}\Big\} \end{aligned} \tag{19}$$

where $D_T = 4A_2^2(8A_1^2+A_3^2)+4\sqrt{2}A_1A_2A_3(3A_1+4A_2)+A_1A_3^2(A_1+6A_2)$ and E is Young's modulus. The random variable B accounts for model uncertainties. It is assumed that A_1, A_2, A_3, B, P, E are independent basic random variables. Their properties are summarized in Table 1. Also shown are the characteristic values used in the design check Eq. (21).

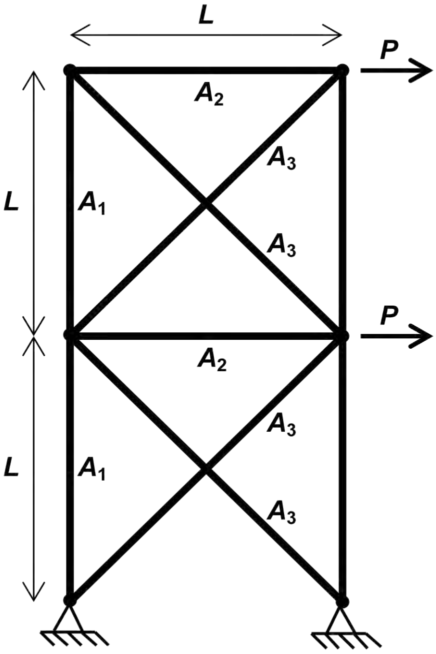

Figure 1: Ten-bar truss structure

The safety margin

$$M(\alpha) = d_0 - D\big(A_1, A_2, A_3, B, E, P(\alpha)\big)\,, \tag{20}$$

	Mean value	Coef. of var.	Prob. distr.	Char. value in (20)
A_1	10^{-2} m^2	0.05	Normal	1% quantile
A_2	$1.5 \cdot 10^{-3}$ m^2	0.05	Normal	1% quantile
A_3	$6.0 \cdot 10^{-3}$ m^2	0.05	Normal	1% quantile
B	1.0	0.10	Normal	mean
E	$6.9 \cdot 10^4$ MPa	0.05	Lognormal	1% quantile
P	based on Eq. (21)	0.10	Gumbel	95% quantile
d_0	0.1 m	-	-	-
L	9.0 m	-	-	-

Table 1: Basic variables.

and the design check constraint is

$$c(\alpha) = d_0 - D\big(A_{1c}, A_{2c}, A_{3c}, B_c, E_c, \alpha P_c(\alpha)\big) \, , \tag{21}$$

where α represents the transversal load factor.

Figs. 2 and 3 show the optimized fitted parametric curve to the empirical data in a log plot for sample size 10^5 and for weighted regression coefficients θ = 2 and θ = 1, respectively. The difference between the two tail extrapolations is minimal. Applying the proposed procedure with a sample of size 10^5 gives the estimated value for α_T with the 95% confidence interval shown in Table 2 for both θ = 2 and 1. Note that a crude Monte Carlo simulation verification of $(\alpha_T = 1.46, p_{fT} = 10^{-6})$ using $3 \cdot 10^9$ samples to within 2.5% at 95% confidence requires a computation time of about 24h on a laptop computer. The CPU time for the results shown in Table 2 was only about 40 seconds on a standard laptop.

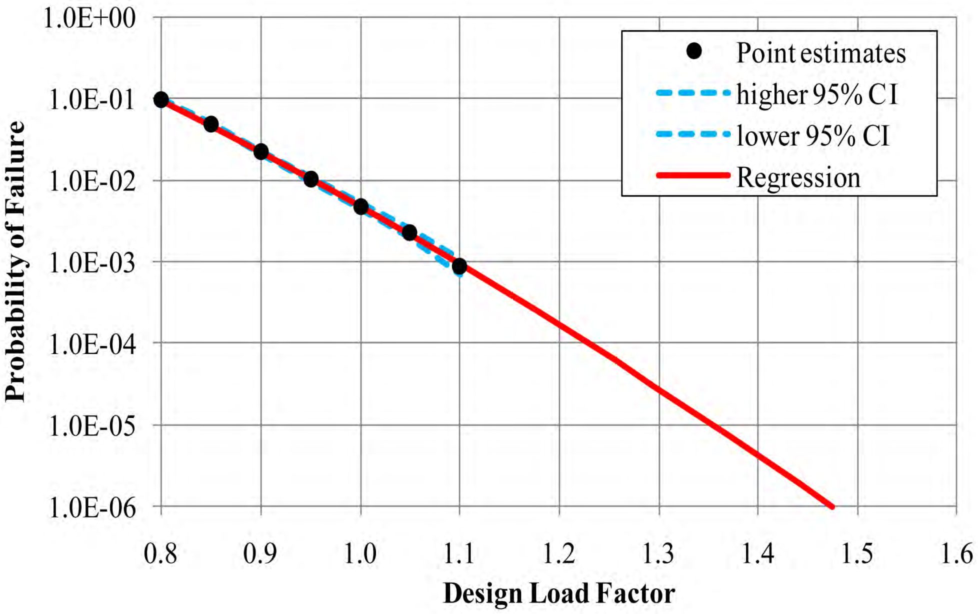

Figure 2: Sample size 10^5 — weighted regression θ = 2.

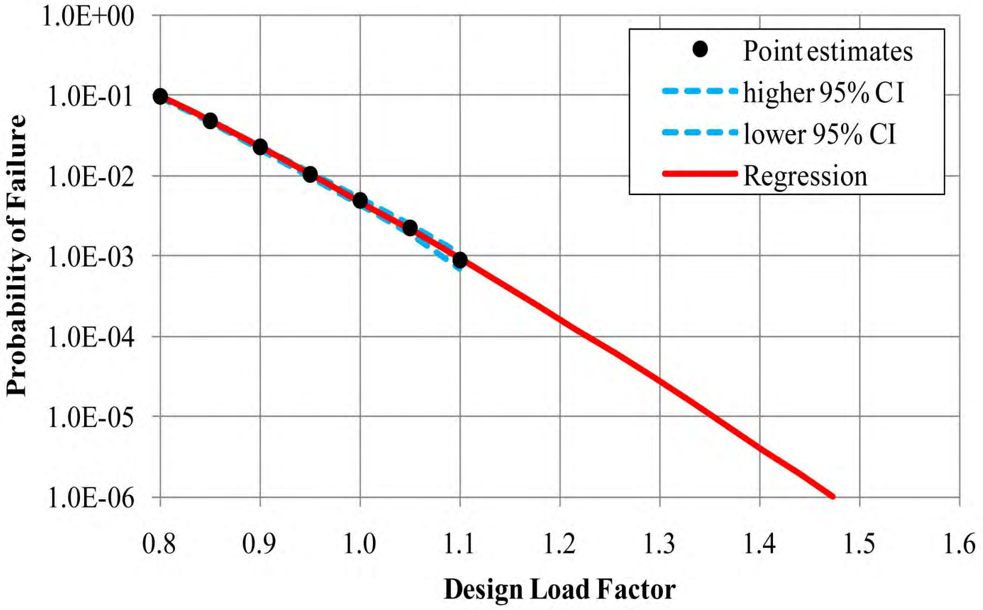

Figure 3: Sample size 10^5 — weighted regression θ = 1.

	$\theta = 2$	$\theta = 1$
higher 95% CI	1.48	1.48
α_T	1.47	1.47
lower 95% CI	1.46	1.46

Table 2: Optimal load factor α_T corresponding to $p_{fT} = 10^{-6}$ using sample size 10^5.

5.2 Design resistance safety factor in a series system

This example concerns the maximum internal forces in the members of a statically determinate 13-member truss structure subjected to external loading. The structure is shown in Fig. 4, which also displays the numbering of the truss elements from 1 to 13. The external loads P_1, P_2, P_3 which are acting on the structure as shown in Fig. 4, are modelled as independent Gaussian variables. The capacity for axial stress of truss element number j is expressed as $R_j = \sigma_{yj} A_j$ where σ_{yj} = the yield stress (MPa) and A_j = the cross-sectional area of this element (cm^2), and α is a resistance safety factor > 1 used as a division factor in the design check equation below. It is assumed that $A_1 = A_7 = 18.7$, $A_2 = A_8 = 13.1$, $A_3 = A_9 = A_{12} = A_{13} = 11.7$, $A_4 = A_{10} = 11.3$, $A_5 = A_{11} = 3.3$, $A_6 = 8.0$. The 13 yield stresses are assumed to be independent Gaussian variables. The 16 basic random variables in this problem are listed in Table 3.

	Mean Value	Coef. of Var.	Prob. distr.	Char. value in Eq. (22)
P_j , $j = 1, 2, 3$	89 kN	0.15	Normal	99% quantile
σ_{yj} , $j = 1, \ldots, 13$	based on Eq. (23)	0.15	Normal	5% quantile
L	2.54 m	-	-	-

Table 3: The 16 basic variables.

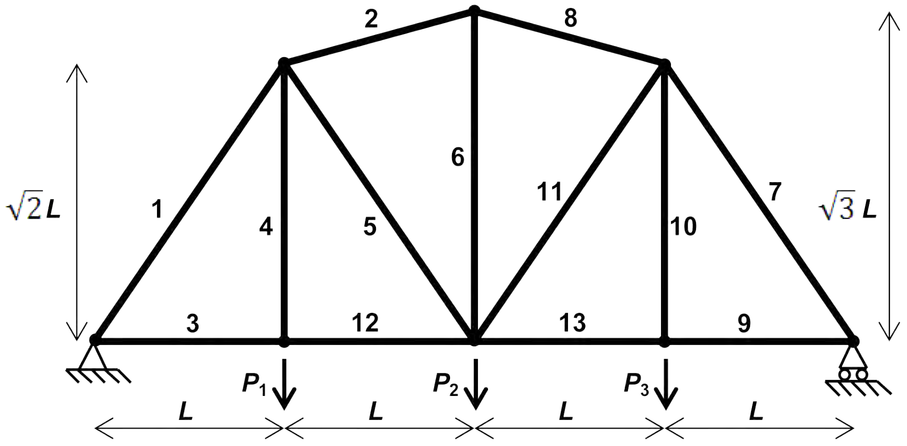

Figure 4: Truss bridge example.

$$\begin{aligned}
M_1 &= R_1 - 0.9186P_1 - 0.6124P_2 - 0.3062P_3 \\
M_2 &= R_2 - 0.3029P_1 - 0.6058P_2 - 0.3029P_3 \\
M_3 &= R_3 - 0.5303P_1 - 0.3535P_2 - 0.1768P_3 \\
M_4 &= R_4 - P_1 \\
M_5 &= R_5 + 0.4186P_1 - 0.3876P_2 - 0.1938P_3 \\
M_6 &= R_6 - 0.1835P_1 - 0.3670P_2 - 0.1835P_3 \\
M_7 &= R_7 - 0.3062P_1 - 0.6124P_2 - 0.9186P_3 \\
M_8 &= R_8 - 0.3029P_1 - 0.6058P_2 - 0.3029P_3 \\
M_9 &= R_9 - 0.1768P_1 - 0.3535P_2 - 0.5303P_3 \\
M_{10} &= R_{10} - P_1 \\
M_{11} &= R_{11} - 0.1938P_1 - 0.3876P_2 + 0.4186P_3 \\
M_{12} &= R_{12} - 0.5303P_1 - 0.3536P_2 - 0.1768P_3 \\
M_{13} &= R_{13} - 0.1768P_1 - 0.3536P_2 - 0.5303P_3
\end{aligned} \tag{22}$$

The 13 design check equations have the same mathematical set of 13 equations except that the deterministic characteristic values of Table 3 are used and a resistance safety factor is involved. The most severe constraint is the compressive stress in members 1 and 7 which therefore governs the design of the system as a whole:

$$\frac{\sigma_{yc}(\alpha)A_1}{\alpha} - 1.8372P_c = 0\,, \tag{23}$$

The objective is to find the value α_T such that the series system failure probability given by Eq. (8) is equal to a target $p_{fT} = 10^{-5}$. The log plot of $p_f(\alpha)$ versus α is shown in Figures 5 and 6 for θ = 1 and for samples of size 10^4 and 10^5, respectively. The estimated α_T corresponding to $p_f = 10^{-5}$ together with their CIs are shown in Table 4. A Winbugs script runs the entire analysis in under 1min for 10^5 samples. As a contrast, crude Monte Carlo simulation with $5\cdot10^9$ samples confirms $(\alpha_T = 1.89, p_f = 10^{-5})$ for the series system accurate to within about 0.5% with 95% confidence, but requires a computation time of about 24h on a laptop computer.

	$N = 10^4$	$N = 10^5$
higher 95% CI	1.95	1.92
α_T	1.85	1.88
lower 95% CI	1.69	1.80

Table 4: Optimal resistance safety factor α_T corresponding to a system $p_{fT} = 10^{-5}$ using sample size 10^4 and 10^5 with θ = 1.

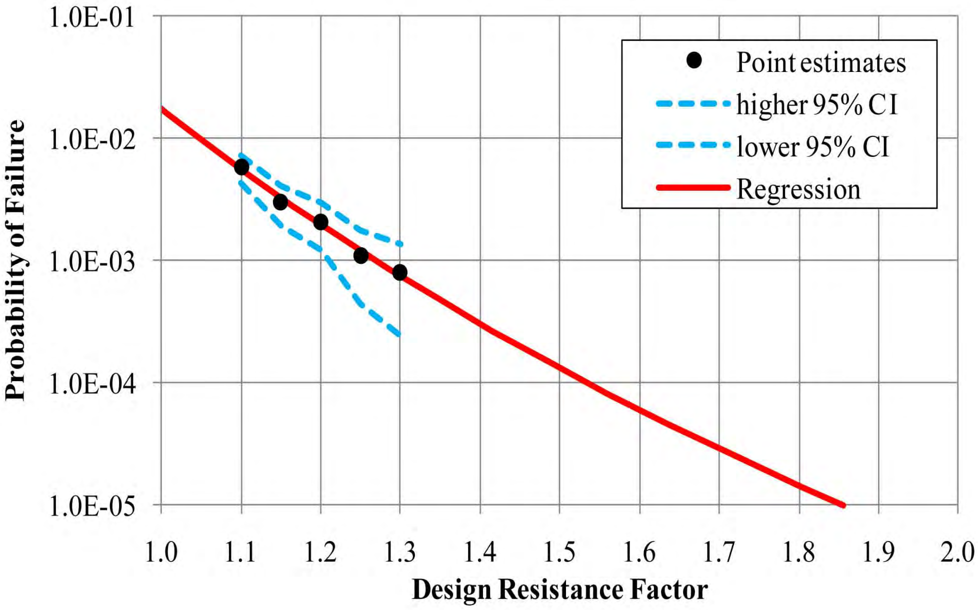

Figure 5: Sample size 10^4 — weighted regression with θ = 1.

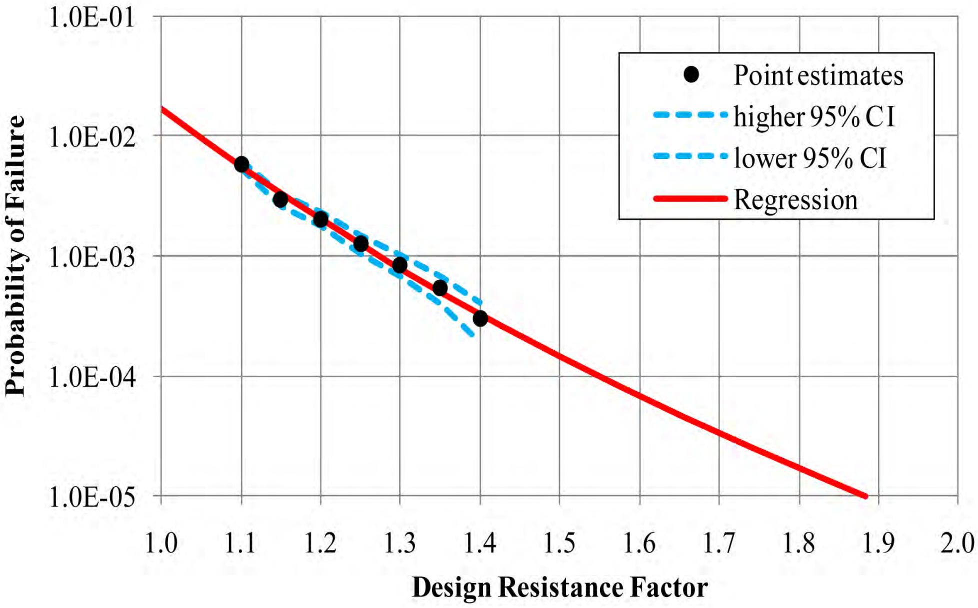

Figure 6: Sample size 10^5 — weighted regression with θ = 1.

6 CONCLUSIONS

In this paper, we have described a Monte Carlo based method for a reliability-based calibration of design parameters such as load/resistance factors, safety factors or specification levels of structural systems. It has been shown that the method may provide good estimates of design factors for structural systems with a moderate computational effort. It has been pointed out that the use of Monte Carlo methods for system reliability analysis has several very attractive features, the most important being that the failure criterion is usually relatively easy to check almost irrespective of the complexity of the system and the number of basic random variables.

7 ACKNOWLEDGEMENTS

The first author is grateful for the financial support from the Research Council of Norway (NFR) through the Centre for Ships and Ocean Structures (CeSOS) at the Norwegian University of Science and Technology. The second and third authors gratefully acknowledge financial support from NSERC Canada.

REFERENCES

[1] A. Naess, B. J. Leira, and O. Batsevych. System reliability analysis by enhanced Monte Carlo simulation. *Structural Safety*, 31:349–355, 2009.

[2] C. Bucher. Asymptotic sampling for high-dimensional reliability analysis. *Probabilistic Engineering Mechanics*, 24:504–510, 2009.

[3] A. Naess, B. J. Leira, and O. Batsevych. Efficient reliability analysis of structural systems with a high number of limit states. In *Proceedings 29th International Conference on Offshore Mechanics and Arctic Engineering*, pages OMAE–2010–21179. New York, ASME, 2010.

[4] A. Naess and O. Gaidai. Estimation of extreme values from sampled time series. *Structural Safety*, 31:325–334, 2009.

[5] P. Gill, W. Murray, and M. H. Wright. *Practical Optimization*. Academic Press, London, 1981.

[6] S.-K. Choi, R. V. Grandhi, and R. A. Canfield. *Reliability-based Structural Design*. Springer-Verlag, London, 2007.

COMPDYN 2011
III ECCOMAS Thematic Conference on
Computational Methods in Structural Dynamics and Earthquake Engineering
M. Papadrakakis, M. Fragiadakis, V. Plevris (eds.)
Corfu, Greece, 26–28 May 2011

THE EFFECT OF NON-SYNCHRONOUS SENSING IN WIRELESS SENSORS ON STRUCTURAL MODAL IDENTIFICATION

Zhouquan Feng[1], Lambros S. Katafygiotis[2]

[1] The Hong Kong University of Science and Technology
Clear Water Bay, Hong Kong, China
e-mail: simonce@ust.hk

[2] The Hong Kong University of Science and Technology
Clear Water Bay, Hong Kong, China
lambros@ust.hk

Keywords: non-synchronous sensing, wireless sensor network, modal identification.

Abstract. *Structural health monitoring (SHM) employing wireless sensor networks (WSN) is becoming increasingly popular in recent years. Accurate synchronized sensing amongst wireless sensors is a key issue enabling the implementation of such smart systems for SHM based on vibration measurements. However, perfect synchronized sensing is unachievable in WSN. The effect of non-synchronous sensing when using wireless sensors on structural modal identification is addressed and a methodology for correcting such errors is proposed herein. This paper first discusses the potential sources causing non-synchronous sensing and estimates their extents based on data samples collected from Imote2 sensors, and then investigates the impact of synchronization errors in the measured output response on modal identification using numerical simulations. The simulation results show that even small synchronization errors in the output response can distort the identified mode shapes. A new methodology is proposed herein for eliminating such errors. This methodology estimates the power spectral densities (PSDs) of output responses using non-synchronous samples directly based on a modified FFT. As long as the corrected PSDs are obtained, the correlation functions can also be easily obtained by IFFT. Then these corrected PSDs or correlation functions can be fed into various output-only modal identification algorithms. The proposed methodology is validated using numerical simulations. It is found that the simulation results closely match the identified parameters based on synchronous data.*

1 INTRODUCTION

In recent years, the emerging wireless sensor networks (WSN) for structural health monitoring (SHM) have attracted a lot of attention from both the academic and industrial communities [1].A wireless sensor network consists of a group of sensors using wireless links to perform distributed sensing and processing tasks. Compared with traditional wired sensor monitoring systems, there is no extensive wiring between sensors and data acquisition system involved, resulting in fast and flexible deployment, easier maintenance and cost reduction. In addition, wireless sensing technology allows sensor data to be processed locally at each sensor node, which can reduce the amount of data that needs to be transmitted and distribute the computing burden across the network. Inspired by these advantages, WSN are becoming even more popular in structural health monitoring applications.

Though WSN have the potential to improve SHM dramatically, a number of issues need to be addressed before wireless sensors can be utilized in SHM [2]. Time synchronization in WSN has been an important concern that has restricted the application of these networks since vibration-based SHM needs synchronous measured data. However, each wireless sensor in the network has its own intrinsic clock, and these clocks on the sensors have to be frequently synchronized with each other to maintain a consistent global time. For clock synchronization, several methods have been developed and tested [3]. The flooding time synchronization protocol (FTSP) [4] is adopted in our network, which is capable of clock synchronization with errors estimated to be about 10μs [5]. The clock synchronization is periodically performed to eliminate the clock offsets and skews. Thus, accurate clock synchronization among sensor nodes has been shown to be achievable.

However, even when the clocks on all sensor nodes are precisely synchronized, the measured signals may not be synchronized with each other due to the decentralized nature of WSN and resource limitations in each wireless sensor. In the following sections the potential sources causing non-synchronous sensing are first discussed and their extents are estimated using data collected from Imote2 sensors [6]. Then, the impact of non-synchronous sensing on modal identification is investigated by numerical simulations. A new methodology for eliminating such errors is proposed. Finally, the proposed methodology is validated by an illustrative example using simulated data.

2 SOURCES CAUSING NON-SYNCHRONOUS SENSING

Sensing on Imote2 sensors is performed in the following way. Prior to sensing, clock synchronization is conducted to convert the local clock times to global clock time using the estimated offsets and skews between local clocks and reference clock. Next the base station node sends sensing parameters such as sampling frequency and number of data points to remote nodes. When the prescribed start-sensing time arrives, sensing tasks are posted on the remote nodes. Once the sensing driver is ready, sensing starts. The sensing tasks continue running until the predetermined amount of data is acquired. During sensing, the acquired data points are first stored in a buffer. Every data point or every several data points can be marked with a local time stamp. When the buffer is filled, the data is passed to the sensing application for possible processing and/or transmission, and the emptied buffer becomes available for the next block of data. By examining the above sensing procedures, potential sources causing non-synchronous sensing are summarized below. A schematic diagram depicting these errors is shown in Figure 1.

(a). Clock synchronization error: for FTSP in Imote2 platform, this error is less than 10μs most of the time, with the maximum observed value being 80μs [5]. This error is comparatively small for SHM applications.

(b). Non-simultaneity in sensing start-up: starting sensing on all imote2 nodes simultaneously is challenging. Even if the time of start of sensing is set to be the same global time, the real execution time may have different delays in each node, and thus sensing may not start simultaneously.

(c). Differences in sampling frequency among sensor nodes: the actual sampling frequency may differ from the nominal value by at most 10 percent for the Imote2 Basic Sensor Board [7].

(d). Non-uniform sampling interval over time: a non-uniform sampling interval is observed in the Imote2 sensor boards. The coefficient of variation (COV) of the sampling interval is about 0.01~0.02%, which is relative small.

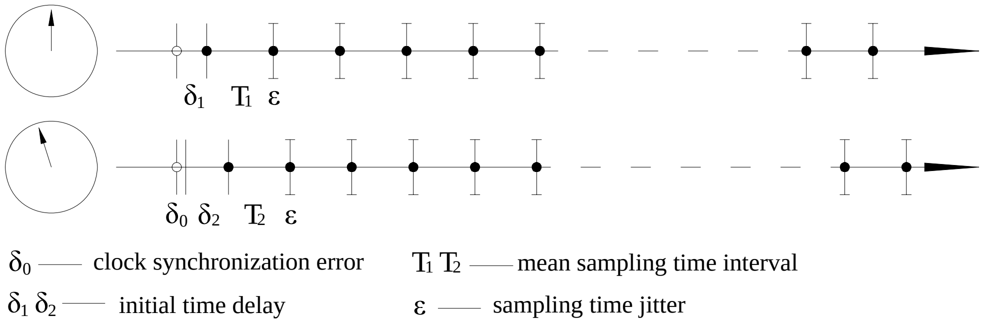

Figure 1: Illustration of non-synchronous sensing.

Ideally, the signal is sampled uniformly (with a constant sampling interval T_s) and synchronously (all the sensors start sensing at the same global time). The time at $(k+1)^{th}$ sampling instant is:

$$t_k = kT_s \tag{1}$$

Due to the reasons mentioned above, the $(k+1)^{th}$ data point is actually sampled at a different time instant:

$$t_k' = kT_s + \delta + ck + \varepsilon(k) \tag{2}$$

where, δ is a constant time shift, coming from sources (a) and (b); because the clock synchronization error is relatively small, only sensing start-up time delay is considered here; ck is a linear time shift, coming from source (c); the coefficient c is the difference between real sampling interval and nominal sampling interval; $\varepsilon(k)$ is a random time shift, coming from source (d), and these time jitters result in non-uniform sampling.

3 ERROR ESTIMATION

3.1 Test of non-synchronous sensing when using Imote2's

The extent of non-synchronous sensing when using Imote2's is evaluated using time stamps marked with data points when sampling. To evaluate these non-synchronous sensing errors, a group of ten Imote2 sensors were programmed with a sensing application. The sensing application was modified slightly from Illinois SHM Project (ISHMP) Services Toolsuite [8]. The sensor boards used are Imote2 basic sensor board ITS400B [6]. One sensor serves as base station node, the other nine sensors serve as remote nodes. After the base station node sends sensing parameters to these nine remote nodes, they start to sample at the same set time and also record the time stamps of every data point. Processing these time stamps, we can estimate the non-synchronous sensing effect on Imote2 sensors. The statistical properties of the sampling times are listed in Table 1, and the differences of the start-sensing time among sensors are listed in Table 2.

node ID	mean sampling frequency (Hz)	mean sampling interval (μs)	% error $(\overline{\Delta t_i} - \Delta t_i) / \Delta t_i$	standard deviation of sampling interval	COV of sampling interval
3	38.64	25878	3.51%	3.0	0.01%
32	39.09	25584	2.33%	3.8	0.01%
98	38.20	26179	4.71%	3.7	0.01%
99	39.84	25099	0.40%	2.5	0.01%
101	40.50	24690	-1.24%	2.9	0.01%
102	40.47	24711	-1.16%	4.1	0.02%
104	39.22	25499	1.99%	4.6	0.02%
105	39.98	25011	0.04%	3.0	0.01%
113	38.77	25791	3.16%	5.2	0.02%

Notes: $\overline{\Delta t_i}, \Delta t_i$ are the actual mean sampling interval and the nominal sampling interval, respectively

Table 1: Statistics of sampling time (40Hz, 1000 points)

Node ID	3	32	98	99	101	102	104	105	113
relative time delay δ_i (μs)	14942	14160	16582	16582	8601	910	17908	10484	0
fractional time delay $\delta_i / \Delta t_i$	0.60	0.57	0.66	0.66	0.34	0.04	0.72	0.42	0

Table 2: Differences of the start-up time (Node 113 as reference)

From Table 1, we can see that the sampling frequencies of the accelerometers on the Imote2 sensor boards have various non-negligible deviations from the nominal value (40Hz), with a maximum of 4.71% error in Node #98. Differences in the sampling frequencies among the sensor nodes will result in inaccurate estimation of modal parameters unless appropriate post-processing is performed. From the last column in Table 1 we can see that the time intervals fluctuate about 0.01~0.02%, which is quite small, thus the non-uniform sampling effect (random shift term $\varepsilon(k)$) can be neglected. From Table 2 we can see that sensing start-up at all Imote2 sensor nodes is not simultaneous. Some of them start earlier and some later. Node #113 is the first one to start sensing, while Node #104 is the last one. Another observation is that these differences are all less than one sampling time interval. The maximum difference is 0.72 time step observed in Node #104. Although the commands to start sensing are set at exactly the same time, the execution times of the commands are different in different sensor nodes.

3.2 Effect of non-synchronous sensing on modal identification

The effect of time synchronization error on modal identification has been studied by Krishnamurthy et al. [12] and it was found that these errors affect the identified mode shape results. However, Krishnamurthy considered that these errors only come from clock synchronization errors and these errors have been overestimated. In reality, clock synchronization errors are comparatively small compared with other errors in Imote2 sensors.

To study the impact of synchronization errors on modal identification, we simulate a 2-DOF shear structural model subjected to white noise excitation. The 2-storey shear building model and the theoretical modal parameters (natural frequencies, modal shapes) are shown in Figure 2. In order to study the non-synchronous sensing effect, three cases of output response are considered: no time shift, constant time shift and linear time shift. According to the extent of synchronization errors showed in section 3.1, the simulations of non-synchronous sensing are done using three scenarios: 1) Baseline (no time shift): both of the sampling frequencies are 40Hz; 2) Case1 (constant time shift): both of sampling frequencies are 40Hz, but channel #2 has 20000μs time delay; 3) Case2 (linear time shift): The sampling frequencies of channel #1 & #2 are 39.8406Hz & 40.4858Hz, respectively.

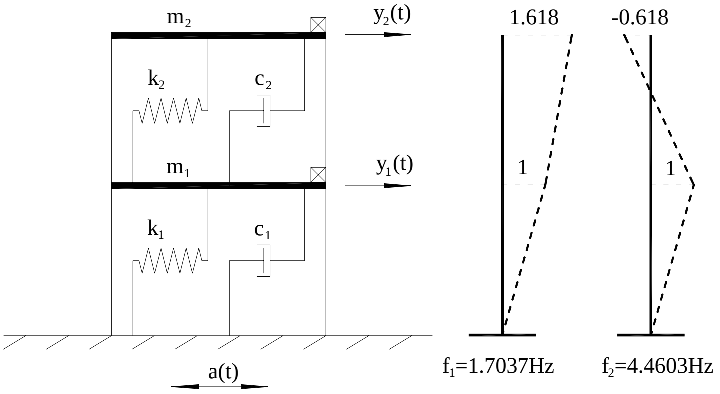

Figure 2: Two-storey shear structure

	Baseline: no shift		Case 1: constant shift		Case 2: linear shift	
	mode 1	mode 2	mode 1	mode 2	mode 1	mode 2
frequency (Hz)	1.7090	4.4824	1.7090	4.4824	1.7090	4.5020
%error	-	-	0.00%	0.00%	0.00%	0.44%
mode shape magnitude	1	1	1	1	1	1
	1.617	0.697	1.617	0.695	1.582	0.495
%error	-	-	0.00%	-0.29%	-2.16%	-28.98%
phase angle (^{o})	0	127	-12	94	-144	-105

Table 3: Comparison of identified modal parameters using PP method

	Baseline: no shift		Case 1: constant shift		Case 2: linear shift	
	mode 1	mode 2	mode 1	mode 2	mode 1	mode 2
frequency (Hz)	1.6992	4.4727	1.6992	4.4727	1.6797	4.5801
%error	-	-	0.00%	0.00%	-1.15%	2.40%
mode shape magnitude	1	1	1	1	1	1
	1.617	0.696	1.617	0.694	13.579	0.008
%error	-	-	0.00%	-0.29%	739.76%	-98.85%
phase angle (^{o})	0	127	-12	94	129	-115

Table 4: Comparison of identified modal parameters using FDD method

	Baseline: no shift		Case 1: constant shift		Case 2: linear shift	
	mode 1	mode 2	mode 1	mode 2	mode 1	mode 2
frequency (Hz)	1.7062	4.4593	1.7058	4.4832	1.7111	4.5032
%error	-	-	-0.02%	0.54%	0.29%	0.98%
mode shape magnitude	1	1	1	1	1	1
	1.615	0.526	1.600	0.589	0.257	0.006
%error	-	-	-0.93%	11.98%	-84.09%	-98.86%
phase angle (^{o})	0	-176	13	-155	108	53

Table 5: Comparison of identified modal parameters using NExT/ERA method

After obtaining the output response data of the structure, various modal identification algorithms can be applied to identify the modal parameters. In this study three popular output-only modal identification algorithms are utilized: Peak-Picking (PP) [9], Frequency Domain Decomposition (FDD) [10] and Natural Excitation Technique in conjunction with Eigensystem Realization Algorithm (NExT/ERA) [11]. The identified results are summarized and compared in Table 3, 4 & 5. It can be seen that all these three algorithms suffer from errors when using the non-synchronous samples directly. These errors affect only slightly the identified frequencies but affect the mode shapes considerably. The constant time shift error almost only affects the phase information of the mode shape. The linear time shift error has more influence on the modal parameters, especially the mode shapes, of which both the magnitude and phase suffer big errors. For these three output-only modal identification algorithms, FDD and NExT/ERA are more susceptible to synchronization errors, especially for linear time shift errors.

4 ERROR ELIMINATION

4.1 Proposed algorithm

In order to eliminate the synchronization errors, direct intuition suggests reconstructing the synchronous samples from measured non-synchronous ones. This is so called signal reconstruction, and some work has been done for this purpose such as interpolation based approach [13] and resampling based approach [5]. Nevertheless, such approaches can be computationally extensive. Rather than reconstructing the signal in the time domain, we develop a correction approach to recover the true spectral density using non-synchronous samples in the frequency domain. This approach is based on the spectral relationship of synchronous data and non-synchronous data. Because only spectral densities or correlation functions are needed for most of modal identification algorithms and raw synchronous time histories are not needed, reconstruction of the signal in the time domain is unnecessary. As long as we are able to obtain the corrected spectral densities, the correlation functions can also be easily obtained by IFFT.

4.1.1 Constant time shift

Consider two time histories $\{x_\alpha(0), x_\alpha(\Delta t),\ldots x_\alpha((N\text{-}1)\Delta t)\}^T$ and $\{x'_\beta(\delta), x'_\beta(\Delta t+\delta),\ldots x'_\beta((N\text{-}1)\Delta t+\delta)\}^T$, i.e., $\mathbf{x}'_\beta$ has a constant time shift δ. The discrete Fourier transform (DFT) for $\mathbf{x}_\alpha$ is given by

$$X_\alpha(\omega_k) = \sum_{n=0}^{n=N-1} x_\alpha(n\Delta t)e^{-j\omega_k n\Delta t} \tag{3}$$

where $\omega_k = k\Delta\omega$, $\Delta\omega = \dfrac{2\pi}{N\Delta t}$, $k = 0,1,\ldots,\mathrm{int}(N/2)$. The DFT for the shifted signal $\mathbf{x}'_\beta$ is given by

$$X'_\beta(\omega_k) = e^{j\omega_k\delta}\cdot X_\beta(\omega_k) \tag{4}$$

where $X_\beta(\omega_k)$ is the DFT of the original signal. Therefore,

$$X_\beta(\omega_k) = X'_\beta(\omega_k)\cdot e^{-j\omega_k\delta} = X'_\beta(\omega_k)\cdot\left(e^{-j\frac{2\pi}{N}\frac{\delta}{\Delta t}}\right)^k \tag{5}$$

Then, the true cross spectral density estimate can be obtained by

$$S_{x_\alpha x_\beta}(\omega_k)=\frac{\Delta t}{N}E[X_\alpha(\omega_k)X^*{}_\beta(\omega_k)] \tag{6}$$

where $(\cdot)^*$ denotes the complex conjugate operation.

4.1.2 Linear time shift

Consider two time histories $\{x_\alpha(0), x_\alpha(\Delta t_\alpha),\ldots x_\alpha((N_\alpha-1)\Delta t_\alpha)\}^T$ and $\{x_\beta(0), x_\beta(\Delta t_\beta),\ldots x_\beta((N_\beta-1)\Delta t_\beta)\}^T$, having different sampling frequencies, i.e. $\Delta t_\alpha \neq \Delta t_\beta$, with corresponding sampling time lengths $T_\alpha = N_\alpha \Delta t_\alpha$ and $T_\beta = N_\beta \Delta t_\beta$, respectively. In discrete Fourier transform, we know that $\omega_k = k\Delta\omega$ and $\Delta\omega = 2\pi/T = 2\pi/N\Delta t$. In order to ensure that $X_\alpha(\omega_k)$ and $X_\beta(\omega_k)$ correspond to the same discrete frequency when calculating the cross spectral density, their frequency resolutions should be identical, i.e., $\Delta\omega_\alpha \equiv \Delta\omega_\beta$, thus their duration time should be the same, i.e.,

$$N_\alpha \Delta t_\alpha = N_\beta \Delta t_\beta,\ \frac{N_\alpha}{N_\beta}=\frac{\Delta t_\beta}{\Delta t_\alpha} \tag{7}$$

Based on this relationship, the cross spectral density can be estimated by

$$S_{x_\alpha x_\beta}(\omega_k)=\frac{\Delta t_\beta}{N_\alpha}E[X_\alpha(\omega_k)X^*{}_\beta(\omega_k)]=\frac{\Delta t_\alpha}{N_\beta}E[X_\alpha(\omega_k)X^*{}_\beta(\omega_k)],\ \text{when}\ N_\alpha, N_\beta \to \infty \tag{8}$$

where $\omega_k = k\Delta\omega, \Delta\omega=\dfrac{2\pi}{N_\alpha \Delta t_\alpha}=\dfrac{2\pi}{N_\beta \Delta t_\beta},\ k=0,1,\ldots,\min\{\mathrm{int}(N_\alpha/2),\mathrm{int}(N_\beta/2)\}$.

4.1.3 Summary of proposed procedure

In reality, the time shifts of non-synchronous data are a combination of constant time shifts and linear time shifts. The most popular FFT-based method for power spectral density estimation is Welch's refined periodogram approach [14]. The procedures for computing the true power spectral density estimate from non-synchronous data in WSN are as follows:

(1) Calibrate the sampling frequencies of each sensor board before sensing experiment.

(2) Perform sensing experiment, and make sure the time stamps are also recorded when sampling.

(3) Set one sensor as reference and partition the data into several segments. Each segment has a length of N_r data points.

(4) Partition the data in other sensors into several segments as well. The first data point of each segment is chosen as close as possible to the first data point of the corresponding segment in the reference sensor data by comparing their time stamps. The length N_i of each segment is chosen such that the Eq. (7) holds approximately.

(5) Calculate the Fourier transform of each segment and correct it using Eq. (5).

(6) Calculate the cross spectral density using Eq. (8).

4.2 Numerical example

The structural system used is the same as before in section 3.2. The i^{th} sampling instant is chosen as follows: $t_1(i)$ =0.0250×(i-1), $t_2(i)$ =0.0247×(i-1)+0.0200, i.e. sensor #1 has a sampling frequency 1/0.0250 (40) Hz, while sensor #2 has a slightly different sampling frequency 1/0.0247 (40.4858) Hz and a time delay 0.02 sec. The measurement noise for the response is taken to be 10 percent, i.e. the RMS of the measurement noise for a particular channel is equal to 10 percent of the RMS of the noise-free response at the corresponding channel.

The identified modal parameters using PP, FDD and NExT/ERA methods are summarized and compared in Table 6, 7 & 8. It can be seen that the modified methods using the proposed corrected spectral densities or correlation functions can achieve better accuracy than the original methods.

	Baseline (Synchronous Data)		Non-synchronous Data			
			Direct PP		Modified PP	
	mode 1	mode 2	mode 1	mode 2	mode 1	mode 2
frequency (Hz)	1.7090	4.4824	1.7090	4.4824	1.7090	4.4824
%error	-	-	0.00%	0.00%	0.00%	0.00%
mode shape magnitude	1	1	1	1	1	1
	1.617	0.703	1.498	0.553	1.625	0.684
%error	-	-	-7.36%	-21.34%	0.49%	-2.70%
phase angle (^{o})	0	131	174	-179	6	141

Table 6: Identified modal parameters (PP)

	Baseline (Synchronous Data)		Non-synchronous Data			
			Direct FDD		Modified FDD	
	mode 1	mode 2	mode 1	mode 2	mode 1	mode 2
frequency (Hz)	1.6992	4.4727	1.6797	4.5117	1.6992	4.4727
%error	-	-	-1.15%	0.87%	0.00%	0.00%
mode shape magnitude	1	1	1	1	1	1
	1.617	0.700	24.786	0.046	1.619	0.688
%error	-	-	1432.90%	-93.41%	0.14%	-1.79%
phase angle (^{o})	0	127	63	50	6	142

Table 7: Identified modal parameters (FDD)

	Baseline (Synchronous Data)		Non-synchronous Data			
			Direct NExT/ERA		Modified NExT/ERA	
	mode 1	mode 2	mode 1	mode 2	mode 1	mode 2
frequency (Hz)	1.7030	4.4660	1.7032	4.4770	1.7032	4.4509
%error	-	-	0.01%	0.25%	0.01%	-0.34%
mode shape magnitude	1	1	1	1	1	1
	1.614	0.545	0.062	0.007	1.629	0.451
%error	-	-	-96.14%	-98.80%	0.91%	-17.32%
phase angle (^{o})	0	-174	-78	-114	-6	-180

Table 8: Identified modal parameters (NExT/ERA)

5 CONCLUSIONS

The purpose of this paper is to address the problem of non-synchronous sensing on modal identification when using wireless sensor networks. The potential sources causing non-synchronous sensing are first discussed and their extents are estimated based on data collection from Imote2 sensors. Among these error sources the dominant ones are non-simultaneity in sensing start-up and differences in sampling frequency among sensor nodes. According to numerical simulations, these errors can distort the identified results of the mode shapes. A new methodology is proposed for eliminating such errors. This methodology estimates the power spectral density (PSD) of output responses using non-synchronous samples based on a modified FFT. As long as we obtain the corrected spectral density, the correlation functions can also be easily obtained by IFFT. Then, these corrected PSDs or correlation functions can be fed into various output-only modal identification algorithms. Comparing with other existing methods of raw synchronous time history reconstruction, this methodology is simple and computationally efficient. The proposed methodology is validated using numerical simulations. The simulation results closely match the identified parameters based on synchronous data.

6 ACKNOWLEDGEMENTS

This research has been supported by the Hong Kong Research Grants Council under grant 614406. This support is gratefully acknowledged.

7 APPENDIX A – DERIVATION OF EQ(4)

The discrete Fourier transform for shifted $\mathbf{x}'_\beta$ is given by

$$\begin{aligned} X'_\beta(\omega_k) &= \sum_{n=0}^{n=N-1} x'_\beta(n\Delta t+\delta)e^{-j\omega_k n\Delta t} = \sum_{n=0}^{n=N-1} x'_\beta(n\Delta t+\delta)e^{-j\omega_k(n\Delta t+\delta)}\cdot e^{j\omega_k\delta} \\ &= e^{j\omega_k\delta}\cdot\sum_{n=0}^{n=N-1} x'_\beta(n\Delta t+\delta)e^{-j\omega_k(n\Delta t+\delta)} = e^{j\omega_k\delta}\cdot X_\beta(\omega_k) \end{aligned} \tag{9}$$

8 APPENDIX B – DERIVATION OF EQ(8)

The cross spectral density function between $\mathbf{x}_\alpha$ and $\mathbf{x}_\beta$ is defined by [15]

$$\begin{aligned} S_{x_\alpha x_\beta}(\omega_k) &= \lim_{T\to\infty}\frac{1}{T}E\left[X_\alpha(\omega_k,T)\cdot X^*{}_\beta(\omega_k,T)\right] \\ &= \lim_{T\to\infty}\frac{1}{T}E\left[\int_0^T x_\alpha(t)e^{-j\omega_k t}dt\cdot\left(\int_0^T x_\beta(t)e^{-j\omega_k t}dt\right)^*\right] \\ &= \lim_{T\to\infty}\frac{1}{T}E\left[\int_0^T x_\alpha(t)e^{-j\omega_k t}dt\cdot\int_0^T x_\beta(t)e^{j\omega_k t}dt\right] \\ &= \lim_{N_\alpha\to\infty}\frac{1}{N_\alpha\Delta t_\alpha}E\left[\Delta t_\alpha\sum_{n_1=0}^{N_\alpha-1}x_\alpha(n_1\Delta t_\alpha)e^{-j\omega_k n_1\Delta t_\alpha}\cdot\Delta t_\beta\sum_{n_2=0}^{N_\beta-1}x_\beta(n_2\Delta t_\beta)e^{j\omega_k n_2\Delta t_\beta}\right] \\ &= \lim_{N_\alpha\to\infty}\frac{\Delta t_\beta}{N_\alpha}E\left[\sum_{n_1=0}^{N_\alpha-1}x_\alpha(n_1\Delta t_\alpha)e^{-j\omega_k n_1\Delta t_\alpha}\cdot\sum_{n_2=0}^{N_\beta-1}x_\beta(n_2\Delta t_\beta)e^{j\omega_k n_2\Delta t_\beta}\right] \\ &= \lim_{N_\alpha\to\infty}\frac{\Delta t_\beta}{N_\alpha}E\left[X_\alpha(\omega_k)X^*_\beta(\omega_k)\right] \end{aligned} \tag{10}$$

REFERENCES

[1] J.P. Lynch, K.J. Loh, A Summary Review of Wireless Sensors and Sensor Networks for Structural Health Monitoring. *The Shock and Vibration Digest*, 38(2), 91-128, 2006.

[2] T. Nagayama, S.-H. Sim, Y. Miyamori, and B.F. Spencer Jr., Issues in Structural Health Monitoring Employing Smart Sensors. *Smart Structures and Systems*, 3(3), 299-320, 2007.

[3] B. Sundararaman, U. Buy, A.D. Kshemkalyani, Clock synchronization for wireless sensor networks: a survey. *Ad Hoc Networks*, 3(3), 281-323, 2005.

[4] M. Maróti, B. Kusy, G. Simon, Á. Lédeczi, The flooding time synchronization protocol. *Proceedings of the 2nd international conference on Embedded networked sensor systems*, Baltimore, MD, USA, November 3-5, 2004.

[5] T. Nagayama, B.F. Spencer Jr., *Structural Health Monitoring Using Smart Sensors*. Newmark Structural Engineering Laboratory Report Series 001, Available on: <https://www.ideals.illinois.edu/handle/2142/3521>, 2007.

[6] Crossbow Technology, Inc. Available on: < http://www.xbow.com/>.

[7] ST Microelectronics. Available on: < http://www.st.com/stonline/>.

[8] Illinois SHM Project (ISHMP) Services Toolsuite, Available on: < http://shm.cs.uiuc.edu/index.html>.

[9] A.J. Felber, *Development of a hybrid bridge evaluation system*. PhD Thesis, University of British Columbia (UBC), Vancouver, Canada, 1993.

[10] R. Brincker, L. Zhang, P. Andersen, Modal identification of output-only systems using frequency domain decomposition. *Smart Materials and Structures*, 10(3), 441-445, 2001.

[11] J.M. Caicedo, S.J. Dyke, E.A. Johnson, Natural Excitation Technique and Eigensystem Realization Algorithm for Phase I of the IASC-ASCE Benchmark Problem: Simulated Data. *Journal of Engineering Mechanics*, 130(1), 49-60, 2004.

[12] V. Krishnamurthy, K. Fowler and E. Sazonov, The effect of time synchronization of wireless sensors on the modal analysis of structures. *Smart Materials and Structures*, 17, 1-13, 2008.

[13] V. Divi, G. Wornell, Bandlimited signal reconstruction from noisy periodic nonuniform samples in time-interleaved ADCS. *Proceedings of IEEE International Conference on Acoustics, Speech and Signal Processing*, Las Vegas, NV, USA, March 30-April 4, 2008.

[14] P.D. Welch, The use of fast Fourier transform for the Estimation of Power Spectra: A Method Based on Time Aver- aging Over Short, Modified Periodograms. *IEEE Transactions on Audios and Electroacoustics*, AU-15, 70-76, 1967.

[15] J.S. Bendat, A.G. Piersol, *Engineering Applications of Correlation and Spectral Analysis*. John Wiley & Song, Inc. 1993.

COMPDYN 2011
3rd ECCOMAS Thematic Conference on
Computational Methods in Structural Dynamics and Earthquake Engineering
M. Papadrakakis, M. Fragiadakis, V. Plevris (eds.)
Corfu, Greece, 25–28 May 2011

A NEW METHOD FOR PROBABILISTIC AFTERSHOCK RISK EVALUATION OF DAMAGED BRIDGE

S.Alessandri, R. Giannini, and F. Paolacci,

Department of Structures, University of Roma Tre
via C.Segre 4/6, 00146 Rome, Italy
e-mail: giannini@uniroma3.it

Keywords: Time-varying risk, aftershock hazard, fragility curves, damaged structure, bridges.

Abstract. *A critical issue in the emergency management after the earthquake is the functionality of the main infrastructure (hospitals, road network, etc.) and the decision on their usability just after the main shock. At present, a decision is taken on the basis of a structure in-situ inspection; an analytical assessment is in contrast with the lack of time and data. For this reason in this paper a method that rationally combines information from the analytical approach and the in situ inspection is proposed. In particular an effective tool to speed-up the decision making phase concerning the evaluation of the seismic risk of mainshock-damaged structures due to aftershocks has been proposed. The risk is calculated combining the aftershock hazard using the Omori law and the fragility curves of the structure calculated using IDA technique and updated using in-situ inspection data. The procedure has been applied to a highway r.c. bridge. The results have highlighted a high sensitivity to the Bayesian updating especially when the damage predicted by the numerical analysis does not correspond to the real damage. The mean annual rates of collapse provided by the method has shown that the risk structure change dramatically when an aftershock sequence strike the bridge and this risk decreases with time allowing the authorities to decide if and when re-open the bridge to traffic.*

1 INTRODUCTION

The earthquakes, as well known, are cluster phenomena: thus the sequence of a seismic event is non-poissonian. In order to simplify the model, the phenomenon is usually represented by a superposition of two different phenomena: the mainshock, considered as stationary, that is the major intense event of each cluster; the second one (aftershock), strongly non-stationary, follows the mainshock event. Although the mainshock may be preceded by precursor events (foreshocks), usually these latter are low-intensity shocks, whereas, the sequence of the aftershocks due to a high magnitude event is made of numerous earthquakes, some of which may be have an intensity similar to the mainshock one.

For a long time, the evaluation of the seismic risk was based on mainshocks. This is justified by the fact that a mainshock is usually the most violent event, capable to induce relevant damages to the building and to catch the people inside the buildings, and in case of collapse, to provoke the most number of victims. Aftershocks, although as much violent, act on empty buildings, and their potentiality in terms of victims is much lower. Nevertheless, the aftershock risk is relevant for two aspects: a) in the estimation of the risk based not only on the human life preservation, but also on the direct and indirect economic consequences of an earthquake, the damages induced by aftershocks may increase highly the cost of a seismic event; b) in assuming decisions about the feasibility of buildings and transitability of the streets, the aftershock risk represents the main parameter.

Usually, these decisions are taken in the field, on the basis of simple vision inspections and on a synthetic evaluation of the situation, based on the experience of the inspector, often not so wide given that the seismic events are likely rare events.

The decision about the feasibility of a construction, in a post-earthquake scenario, has relevant consequences, because if an imprudent choice can produce further victims, a conservative choice may produce a social inconvenience and useless costs for the housing of the displaced persons or for the interruption of the productive activities.

For some years some researcher and institutions [1, 2, 3, 4, 5, 6, 7] have suggested a more rational and analytical approach to the problem of the feasibility of the seismically damaged constructions, in particular in the period immediately after the mainshock.

The application of analytical methods, for a rapid estimation of the feasibility of buildings, introduces so many difficulties that the final decision cannot ignore the judgment of the detector; in fact, the buildings are numerous and complex structure for which is difficult to define general damage levels that account for the behavior of non-structural elements (partitions, ceilings, etc..), as well as the risk related to the surrounding situation (e.g. collapse of adjacent buildings). More affordable seems to be a rational and analytical procedure to manage the decisions about the transitability of bridges; in fact, bridges are more simple structures and less numerous, for which appears more plausible to organize a customized procedure to use in emergency situations.

The bridges are strategic structures because their unavailability can cause the interruption of the road ways, prevent the ordinary means to reach the zone struck by the seismic event. This condition becomes particularly penalizing during the post-earthquake emergency, when high amount of transportation means have to be employed for the rescue operations. The decision to close to the traffic a bridge of an important roadway, which connect the most struck zones, is therefore very delicate, and it should be taken on the basis of the most possible rational and objective criteria. In a recent paper [8] some authors have studied the problem to correlate the intensity of the event with the vertical load carrying capacity (traffic) of the bridge. The results are given in terms of fragility curves for different percentages of traffic reduction. Nevertheless the correlation of the residual vertical load carrying capacity with the seismic damage is very difficult and uncertain, both for the limits of the current models and because the live loads often represent a limited fraction of the bridge weight.

More promising seems to be the way proposed by [9, 10] to relate the decision of the usability of a bridge to the risk due to aftershocks. For this purpose, is necessary to perform an Afterschock Probabilistic Seismic Hazard Analysis (APSHA) [3]; as soon as the magnitude and position of the main event is known, this analysis, as similar as the ordinary Probabilistic Seismic Hazard Analysis (PSHA), provides the probability that, in the unit time, an earthquake occurs with an intensity greater than a given one.

The analysis is completed with a convolution between the hazard and the vulnerability of the structure; in the post-earthquake the structures will be probably damaged, therefore fragility curves depending on the damage induced by the mainshock have necessary to build.

A relevant difficulty consists in the evaluation of the damage level suffered by the structure. In fact, an inspection will allow to detect only some visible effects due to the seismic action (e.g. cracks, spalling of concrete cover, buckling of reinforcement, etc..). These observations are certainly correlated with the damage suffered the structure but with a high dispersion.

Alternatively, it is possible to proceed analytically; being known position and magnitude of the event, the seismic intensity of the site is determined (e.g. the median spectrum) using an attenuation law; however, also in this case the dispersion of the intensity, of the shape of the spectra and the reliability of the model render the estimation of the suffered damage very uncertain; furthermore, the result of a predictive model based on the analysis cannot to conflict with the observation.

In a recent work [10], the authors use both the methods synergically. The predicted damage, on the basis of the attenuation curves and the fragility curves of the undamaged structure, is used as prior estimation of the probability, which are updated on the basis of the observed damage, using as likelihood function the probability function conditioned to the observed one; this function can be built using numerous experimental tests [11].

Another difficulty regards the use of the results in the decision process about the usability of the structure (e.g. the functionality of the bridge). In fact, differently from the mainshock, the aftershock process is strongly non-stationary, therefore, the hazard (and then the risk) vary day by day, decreasing rapidly with the time, measured starting from the mainshock event.

The risk threshold under which is possible to use the construction has been highly discussed. A reasonable criteria is based on the comparison between the prior risk of the undamaged structure, due to the mainshock, with the aftershock risk, but the non-stationarity of the aftershock process renders very problematic the comparison.

Different proposals have been done to make comparable the above two quantities. Yeo and Cornell [12] compare the cost (discounted) required to save a human life with respect to the mainshock risk (in an infinite time) with the same cost associated with the aftershock; with some approximations the conversion factor is the social discount factor (3-5%). More simply, Pinto and Franchin [9] compare the average risk (annualized) in the residual time between the data of the decision and the end of the aftershock sequence. Both the criteria will be applied and compared.

2 DESCRIPTION OF THE METHOD

In this section a rational method for probabilistic aftershock risk evaluation of damaged bridges is presented. Basically, the procedure consists of the following four steps:

- Evaluation of the fragility curves of damaged and undamaged bridge
- Damage evaluation phase

- Aftershock hazard analysis
- Evaluation of the aftershock risk

The main goal of the method is to provide the mean annual rate of collapse for aftershocks of a mainshock-damaged bridge. The method, already proposed by the authors [10], is here improved introducing a new technique for the evaluation of the fragility curves, which is based on the Latin Hypercube Sampling technique. All the relevant aspects of the proposed procedure is illustrated in the following sections.

2.1 Evaluation of the fragility curves

The first phase of the procedure, to be carried out before the earthquake occurs, consists of evaluating the fragility curves of undamaged and damaged structure. A parameter of damage measure has to be adopted (in the following the maximum drift will be adopted) and a series of dynamic analysis on a proper structural model has to be executed in order to calculate the probabilities functions $\bar{F}_{\phi,Y}(\phi_i, y)$ of the damage ϕ_i, versus the local intensity y_i of the earthquake. The IDA procedure [13] is the most used method for the evaluation of the fragility curves.

Following this method a series of increasing damage levels is established (ϕ_1, ϕ_2,..) and a wide sample of accelerograms are chosen together with the representative parameter of the local intensity (e.g. PGA or spectral ordinate).

Nonlinear dynamic time-history analysis are performed using the selected set of ground motions, scaling each record, in an iterative procedure, until the intensity that causes precisely the damage level ϕ_i is found.

It is now possible, for each accelerogram, to induce in the structure the damage level j^{th}, and then, starting from that point, to apply another series of accelerograms with increasing intensity, in order to simulate the effects of the aftershocks. It is necessary to repeat the IDA procedure for a number of times equal to the product between the number of damage levels and the number of the accelerograms selected for simulate the mainshock. Altogether, the required number of analysis is rather large and significantly increase when the probability $\bar{F}_D(\phi_i \mid \phi_j, y)$ that the structure, with an initial damage level ϕ_j, reaches or exceeds the damage level ϕ_i caused by an aftershock, has to be evaluated; the latter is given by $n_{\mathtt{an}} = n_{\mathtt{dl}} \times n_{\mathtt{am}} \times n_{\mathtt{aa}} \times n_{\mathtt{il}}$, in which $n_{\mathtt{dl}}$ is the number of the considered damage levels, $n_{\mathtt{am}}$ is the number of the accelerograms used for the mainshock, $n_{\mathtt{aa}}$ is the number of the accelerograms used for the aftershocks and $n_{\mathtt{il}}$ is the number of the intensity levels considered in the IDA procedure.

Therefore the IDA technique can only be applied to simple structural schemes for which the time of calculation remains acceptable; the extension to more complex structures will require a more efficient procedure.

With the aim of extending the procedure to more complex structures, the regression analysis is here used to evaluate the fragility curves, significantly reducing the number of analysis and, consequently, the computation time. A set of accelerograms is selected together to a range of variation of the PGA and the Latin Hypercube Sampling technique (LHS) is applied to select the sample used for the structural analysis.

This technique uses a stratified sampling scheme that generates a sample containing n values on each of p variables; these are obtained by dividing the range of variation of each variable into n equiprobable and non-overlapping intervals; the values are randomly distributed with one from each interval (0,1/*n*), (1/n,2/*n*), ..., (1-1/*n*,1), and then they are randomly permuted.

The LHS technique is used to extract a significant sample of variables on which to perform the analysis and then the regressions. In particular, in order to determine the fragility curves of the undamaged structure, n_m couples of variables (accelerogram, intensity y_i) are extracted and the damage level ϕ_i, obtained in the analysis, is used to build n_m couples (y_i, ϕ_i).

To obtain the "fragility surface" of the damaged structure, n_a, quadruples of variables (A_{mi}, y_{mi}, A_{ai}, y_{ai}) are extracted, where A_{mi} and A_{ai} indicate the i^{th} mainshock and the i^{th} aftershock accelerogram respectively, whereas y_{mi} and y_{ai} are the corresponding intensities. From the analysis of the structure subjected to this couple of accelerograms, the corresponding two levels of damage ϕ_{mi} and ϕ_{ai} are recorded, on condition that $\phi_{ai} \geq \phi_{mi}$. Consequently the following n_a triples (y_a, ϕ_{mi}, ϕ_{ai}) are obtained. The objective is to find the distribution function of the damage ϕ_i,$|y_i$ caused to the undamaged structure by the mainshock and then the distribution function of the damage ϕ_{ai},$|$ ϕ_{mi}, y_{ai} caused by the aftershock to the structure with a pre-existing damage level ϕ_{mi},.

For both the analyses the following polynomial regression model is used:

$$\log\phi = \mathbf{X\beta} + \varepsilon \tag{1}$$

where $\mathbf{X} = \begin{bmatrix} 1 & x_1 & x_2 & ... & x_1^2 & x_1x_2 & ... \end{bmatrix}$ is the vector (1 × *m*) of the polynomial variables, whereas β is the coefficient vector and ε is a random variable.

The use of the logarithms of ϕ depends on hypothesis that this quantity (non-negative) is better described by a lognormal random variable. The random variable ε is instead Gaussian.

In the examined case the variables in **X** are the intensity y_m in the first analysis and the pairs (y_a, ϕ_m) of the intensity of the aftershock and the initial damage.

If $\hat{\mathbf{\Phi}}$ is a vector (n_a × 1) built using the logarithms of the calculated damages and $\hat{\mathbf{X}}$ is the matrix (n_a × *m*) of the polynomial variables calculated in the sample points, it found, by the regression analysis, that log ϕ is a random variable with mean:

$$E[\log\phi] = \hat{\mathbf{X}}\mathbf{\beta} \tag{2}$$

with

$$\mathbf{\beta} = \left(\hat{\mathbf{X}}^T\hat{\mathbf{X}}\right)^{-1}\hat{\mathbf{X}}^T\hat{\mathbf{\Phi}} \tag{3}$$

and variance

$$\sigma^2_{\log\phi} = s^2\frac{\left\|\hat{\mathbf{X}}^T\hat{\mathbf{X}} + \mathbf{X}^T\mathbf{X}\right\|}{\left\|\hat{\mathbf{X}}^T\hat{\mathbf{X}}\right\|} \tag{4}$$

where

$$s^2 = \frac{\left(\hat{\mathbf{\Phi}} - \hat{\mathbf{X}}\hat{\mathbf{\beta}}\right)^T\left(\hat{\mathbf{\Phi}} - \hat{\mathbf{X}}\hat{\mathbf{\beta}}\right)}{\nu - 2} \tag{5}$$

The term $\log\phi$ follows the t-Student distribution with ν = *n*–*m* degrees of freedom. It is observed that if the dimensions *m* of the sample are high, the t-student distribution approximates the Gauss distribution, so ϕ becomes lognormal.

2.2 Damage evaluation

After a seismic event, the magnitude m_0 and the position r of the epicenter are quickly available; with such a data and using a proper attenuation law [14], 15, 16] it is possible to find the average value and the standard deviation of the selected parameter of local intensity as function of the magnitude and the epicentral distance (or minimum distance from the fault). Assuming for y a log-normal distribution, the conditional probability density of the intensity y is:

$$f_{Y|M,R}\left(y\,|\,m_0,r_0\right)=\frac{1}{\sqrt{2\pi}\zeta_0 y}\exp\left[-\frac{\left(\ln y-\mu_0\right)^2}{2\zeta_0^2}\right] \tag{6}$$

in which $\zeta_0=\sqrt{\ln\left(1+\left(\sigma_y/\bar{y}\right)^2\right)}$ and $\mu_0=\ln\bar{y}-\zeta_0^2/2$.

Consequently the probability of exceeding the damage level ϕ_i conditioned to the occurrence of an event of magnitude m_0 and distance r_0 can be calculated by integrating the product between seismic hazard and fragility:

$$\bar{F}_\Phi\left(\phi_i\,|\,m_0,r_0\right)=\int_0^\infty \bar{F}_{\Phi|Y}\left(\phi_i\,|\,y\right)f_{Y|M,R}\left(y\,|\,m_0,r_0\right)dy \tag{7}$$

This (probabilistic) damage estimation does not account for what is really occurred in the structure. As stressed above, the post-earthquake observation of the damage does not allow, at least for moderate intensity events, to evaluate the damage index ϕ_i used in the analytical model without a permanent instrumentation placed on the structure.

To evaluate the CDF of the damage index ϕ conditioned to the observed damage θ_k, $F_\phi\left(\phi|\theta_k\right)$, a relationship between the two variables must be known; on the basis of laboratory tests, Berry and Eberhard [11] have developed relationships that provides, as function of the characteristics of the reinforced concrete element (normal force, sectional area, length, percentage of reinforcement, etc..), the average value and the coefficient of variation of the damage index ϕ_i (drift) corresponding to the observed damage θ_k, ($k=1,2,3$), where θ_1 = spalling, θ_2 = buckling of the steel bars, θ_3 = failure of the steel bars.

Assuming that the probability of ϕ conditioned to the damage θ_k can be expressed as lognormal, the previous data permit to determine the CDF of the drift ϕ conditioned to θ_k, $F_\phi\left(\varphi|\theta_k\right)$. The probability $p\left(\theta_k\,|\,\varphi\right)$ can be obtained observing that, if ϕ_k is the drift for the damage level θ_k, then $\phi<\min_k\left(\phi_k\right)$ = no damage, $\phi_1\le\phi<\min\left(\phi_2,\phi_3\right)$ = damage θ_1, $\max\left(\phi_1,\phi_2\right)\le\phi<\phi_3$ = damage θ_2, and finally $\max_k\left(\phi_k\right)\le\phi$ = damage θ_3. Consequently, if θ_0 stands for no damage condition, we can assume:

$$\begin{aligned}
p\left(\theta_0\,|\,\phi\right)&=\Pr\left[\min_k\left(\phi_k\right)>\phi\right]=\prod_{k=1}^{3}\left[1-F_{\phi_k}\left(\phi\,|\,\theta_k\right)\right]\\
p\left(\theta_i\,|\,\phi\right)&=\prod_{j=1}^{i}F_{\phi_1}\left(\phi\,|\,\theta_j\right)\prod_{k=i+1}^{3}\left[1-F_{\phi_k}\left(\phi\,|\,\theta_k\right)\right]\quad(i=1,2)\\
p\left(\theta_3\,|\,\phi\right)&=\Pr\left[\max_k\left(\phi_k\right)\le\phi\right]=\prod_{k=1}^{3}F_{\phi_k}\left(\phi\,|\,\theta_k\right)
\end{aligned} \tag{8}$$

where $p(\theta_k \mid \phi)$ is the probability of the observed damage θ_k conditioned to the drift ϕ. If we consider $p_0(\phi) = f_\Phi(\phi \mid m_{0,} r_0)$ a prior probability distribution, estimated before the direct observation of the damage, and θ_k is the level of the real observed damage, applying the Bayes theorem using $p(\theta_k \mid \phi)$ as likelihood function, the updated estimation of the probability can be obtained as:

$$p(\phi \mid \theta_k) = \frac{p(\theta_k \mid \phi)\, p_0(\phi)}{\int p(\theta_k \mid \phi)\, p_0(\phi)\, d\phi} \tag{9}$$

This probability function of the damage index ϕ combines the results of a predictive analysis carried out on the numerical model of the structure with the information gathered from the visual observation of the residual damage of the structure.

2.3 Aftershock hazard analysis

Since it is supposed that the main event has occurred and then magnitude, epicentral distance and (possibly) fault line and position are known, it is possible to carry out an Aftershock Probabilistic Hazard Analysis (APSHA), similarly to the procedure illustrated in [2].

In this paper we will suppose that the length of the rupture zone (L_R), if not directly known, can be estimated as function of the magnitude as indicated in [17]:

$$L_R = 10^{(a+bm_0)} \tag{10}$$

where a and b are parameters depending on the fault rupture type and L_R is expressed in Km.

Unlike the standard hazard analysis (PSHA), in which the seismic events is assumed Poissonian and stationary, the aftershocks process is highly non-stationary; the mean instantaneous daily rate of events at time t with magnitude greater or equal to m following a mainshock of magnitude m_m, is given by the “modified Omori Law” [18] .

$$\gamma(t, m, m_{\mathrm{m}}) = \frac{10^{a+b(m_{\mathrm{m}}-m)}}{(t+c)^p} \tag{11}$$

where a,b,c, and p are regional parameters that can be estimated on the basis of the past seismic events [19] .

Moreover, by introducing a truncation of the magnitude m such that $m_l<m<m_m$, the average number of daily events with intensity greater than m is given by [2]:

$$\gamma(t, m, m_{\mathrm{m}}) = \gamma_0(t, m_1, m_{\mathrm{m}}) \frac{e^{-\beta m} - e^{-\beta m_{\mathrm{m}}}}{e^{-\beta m_1} - e^{-\beta m_{\mathrm{m}}}} = \gamma_0(t, m_1, m_{\mathrm{m}}) \left[1 - F_M(m)\right] \tag{12}$$

where $\beta = b \ln 10$ and $\gamma_0(t, m_1, m_{\mathrm{m}})$ is the average number of the daily events at time t with magnitude $m_l<m<m_m$ and

$$\gamma_0(t, m_1, m_{\mathrm{m}}) = \frac{10^{a+b(m_{\mathrm{m}}-m_1)} - 10^a}{(t+c)^p} \tag{13}$$

The mean number of aftershocks with magnitudes m such that $m_l<m<m_m$ in the time interval [t; $t + T$] following a mainshock of magnitude m_m is given by:

$$\gamma(t,T;m_m)=\int_t^{t+T}\gamma_0(\tau,m_1,m_m)\,d\tau=\frac{10^{a+b(m_m-m_1)}-10^a}{p-1}\left[(c+t)^{1-p}-(c+t+T)^{1-p}\right] \tag{14}$$

For an aftershock of magnitude *m* and epicenter *P*, the local intensity at the site is deduced by the attenuation law: $\log y=\psi(r,m)+\varepsilon$, in which ψ is a function of the magnitude *m* and of the distance *r* between the structure and the epicenter (or the minimum distance from the fault), whilst ε is a zero-mean Gaussian variable with standard deviation σ_ε. The probability density of *Y* for a given event conditioned to *m* and *r* is then:

$$f_{Y|R}(y\,|\,r,m)=\frac{1}{y}\varphi\left(\frac{\ln y-\psi(r,m)}{\sigma_\varepsilon}\right) \tag{15}$$

where $\varphi(.)$ is the standard normal PDF.

In order to obtain the probability of *Y* unconditioned with respect to the magnitude, the equation (15) must be multiplied by the PDF of the magnitude of the aftershocks, $f_M(m)=dF_M(m)/dm=\beta e^{-\beta m}/\left(e^{-\beta m_1}-e^{-\beta m_m}\right)$ and integrated over *m*:

$$f_{Y|R}(y\,|\,r)=\frac{1}{y}\int_{m_1}^{m_m}\varphi\left(\frac{\ln y-\psi(r,m)}{\sigma_\varepsilon}\right)f_M(m)\,dm \tag{16}$$

As frequently occurs, when the attenuation law is a linear function of *m*, $\log y=\psi(r)+qm+\varepsilon$, the integral (16) can be developed in closed form [25]:

$$\begin{aligned}f_{Y|R}(y\,|\,r)&=\frac{1}{\sqrt{2\pi}\sigma_\varepsilon y}\int_{m_1}^{m_m}\exp\left(-\frac{\left(\ln y-\psi(r)-qm\right)^2}{2\sigma_\varepsilon^2}\right)\frac{\beta e^{-\beta m}}{e^{-\beta m_l}-e^{-\beta m_m}}\,dm=\\&=\frac{e^{\beta\left(m_l+m_m+\psi(r)/q+\sigma_\varepsilon^2\beta/q^2\right)}}{2\left(e^{-\beta m_l}-e^{-\beta m_m}\right)y^{\beta/q+1}q\beta}\left[\operatorname{erf}\left(\frac{-\beta\sigma_\varepsilon^2-q\left[qm_l-\ln(y)+\psi(r)\right]}{\sqrt{2}\sigma_\varepsilon q}\right)+\right.\\&\left.-\operatorname{erf}\left(\frac{-\beta\sigma_\varepsilon^2-q\left[qm_m-\ln(y)+\psi(r)\right]}{\sqrt{2}\sigma_\varepsilon q}\right)\right]\end{aligned} \tag{17}$$

If *R* denotes the region where the aftershocks may occur (in the following it will be assumed that coincides with the length of mainshock fault, similarly to [2]), and $f_R(r)$ is the probability density function of the distances *r* from the site, the probability density of an event with intensity *y*, conditioned to the occurring of the event, is:

$$f_Y(y)=\int_R f_{Y|R}(y\,|\,r)\,f_R(r)\,dr \tag{18}$$

2.4 Evaluation of the aftershock risk

The functions $\overline{F}_D(\phi_i\,|\,\phi_j,y)$ and $p(\phi_j\,|\,\theta_k)$ previously defined have the following meaning; the first one provides the probability that the structure, stricken by the mainshock with a damage level ϕ_j, could exceeds the damage level $\phi_i\geq\phi_j$ because of an aftershock, while the second one is the probability that the structure, stricken by the mainshock, has suffered the damage ϕ_j.

Therefore, if an aftershock occurred, the probability that a damage $\phi\geq\phi_i$ is:

$$Pr\left(\phi \geq \phi_i\right) = \int_0^{\phi_i}\int_0^{\infty} \overline{F}_D(\phi_i \mid \phi_j, y) f_Y\left(y\right) p\left(\phi_j \mid \theta_k\right) dy d\phi_j \tag{19}$$

At time *t,* the daily mean number of the shaking that induce in the structure a level of damage greater or equal to ϕ_i is therefore $\gamma(\phi_i \mid t) = \gamma_0(t, m_1, m_{\mathfrak{m}})\Pr(\phi \geq \phi_i)$. If an aftershock cluster is represented by a Poisson process, the probability (risk) that the damage is exceeded in the time $[t, t+T]$ is:

$$\Pr\left(\phi \geq \phi_i \mid t, T\right) = 1 - e^{-N_{\mathrm{a}}(\phi_i, t, T)} \tag{20}$$

where:

$$\begin{aligned} N_{\mathrm{a}}\left(\phi_i, t, T\right) &= \int_t^{t+T} \gamma\left(\phi_i \mid \tau\right) d\tau = \\ &= \int_t^{t+T} \gamma_0\left(\tau, m_1, m_{\mathfrak{m}}\right) \Pr\left(\phi \geq \phi_i\right) d\tau = \Pr\left(\phi \geq \phi_i\right) \int_t^{t+T} \gamma_0\left(\tau, m_1, m_{\mathfrak{m}}\right) d\tau = \\ &= \Pr\left(\phi \geq \phi_i\right) \frac{10^{a+b(m_{\mathfrak{m}} - m_1)} - 10^a}{p-1} \left[\left(c+t\right)^{1-p} - \left(c+t+T\right)^{1-p}\right] \end{aligned} \tag{21}$$

is the mean number of the events that produce the damage φ_i in the time interval [*t*, *t*+ *T*].

3 DECISION-MAKING ANALYSIS

The probability evaluated with equation (20) represents the risk, due to an aftershock, that a damage level ϕ_i in the structure is exceeded during the time interval *T*, starting from the time *t*; in the following, ϕ_i will be assumed as collapse condition. This data is useful to assume a rational decision on the usability of the construction (e.g. the functionality of a bridge). A reasonable criterion to orient such a decision consists of comparing the risk due to the aftershocks (provided by eq. (17)) with the risk due to the mainshock. Nevertheless, this comparison introduces considerable conceptual difficulties.

In fact, in the Probabilistic Seismic Risk Analysis (PSRA), the process of the events is assumed to be stationary, therefore the mean number of the events that produce the damage ϕ_i in the time *T* is simply, $\gamma_{\mathfrak{m}}(\phi_i)T$, where $\gamma_{\mathfrak{m}}(\phi_i)$ is the mean number of events in the unit time (generally one year). The comparison among these two risks can simply be done comparing the frequencies, independently from the used time unit, because of the simple proportionality with the time *T*. In case of aftershocks, the Omori law shows that the process is strongly non-stationary, and the average frequency decades as *~1/t*; for instance, using the values of the coefficients of the Omori law obtained by [20] for the Italian earthquakes, after 7 days the activity is reduced to less than the 17% of that of the first day, while after one month it is a little bit more than 4%. Similar results, but even more pronounced, are found using the values of Reasemberg and Jones for the southern California.

The dependency of the aftershocks risk from the initial time *t* can be employed for establishing a date over which the risk decrease up to a level comparable with the mainshock risk and therefore considered as acceptable; for this purpose the problem of establishing for what time *T* the risk has to be measured, must be overcome. For instance, it may be assumed *T*=1 year in order to make N_a directly comparable with the annual frequency of collapses due to mainshocks. But if a lower value of *T* is assumed (e.g. 6 months), N_a is reduced, at least in the first ten days, less than 20% (Lolli and Gasparini data [20]), while the expected mean number of the mainshocks halves. The choice of T=1 year appears therefore arbitrary and related only to common criteria.

More realistic appears the approach proposed by [9] consisting in using the maximum duration of the aftershocks sequence expressed as $t_u = 60 + 60(m_{\mathrm{m}} - 4)\text{days}$ [20]. In this way however the duration of the time period $T = t_u - t$ varies with t. For a direct comparison between this quantity and the annual stationary frequency, an "equivalent" annual frequency expressed as: $[365/(t_u - t)]N_{\mathrm{a}}(\varphi_i, t, t_u - t)$ has to calculated. Another interesting approach is that carried out from Yeo and Cornell [12]; in this work the authors assume as equivalence criteria the condition that the expected investment into life-safety technologies for saving an arbitrary building occupant in the future is the same for both cases. As result, an equivalent, time-independent collapse rate is obtained multiplying the total number of collapses in the interval $(t - \infty)$ by the “inflation-adjusted discount rate”.

4 INCREMENTAL DYNAMIC ANALYSIS AND REGRESSION METHODS FOR THE EVALUATION OF FRAGILITY CURVES

To validate the application of the regression method for fragility curves evaluation the results obtained on a case study have been compared with those obtained by the IDA procedure.

In a previous author's work [9] the developed procedure with IDA has been applied to a simply supported highway viaduct (Vallone del Duca) of the A16 Napoli-Canosa highway, composed by two independent roadways, each one composed by three simply supported reinforced concrete beams with a span of 32 m.

For the fragility calculation, a set of 10 ground motion records has been selected from the *PEER* database; the same set of records has been used to represent the mainshocks and aftershocks.

A first cycle of analysis (*IDA*), representing the mainshock event, has been carried out to evaluate the fragility curves for the undamaged structure and the PGA leading to predefined damage levels; 350 analysis have been executed: 10 accelerograms × 35 intensity levels.

A second cycle of analysis (*IDA*) has been performed to evaluate the fragility curves of the damaged structure due to the aftershocks leading to collapse; in this cycle 56000 analysis have been executed combining 16 mainshock damage level for each of the 10 accelerograms with 35 intensity levels for each of the 10 aftershock records. The regression significantly reduces the analysis number; in this case 160 analysis have been performed for the mainshock fragility evaluation and 1600 for the aftershock ones.

Figure 1 and Figure 2 show the comparison between the mainshock and aftershock fragility curves obtained by IDA and those obtained by the regression method; it can be noticed that the IDA curves presents some differences with respect to approximate curves obtained with a small size sample; therefore IDA curves can be well approximated using the regression.

Figure 3 shows the comparison between the mean annual frequency of collapse due to mainshocks and to aftershocks evaluated by the two methods; for the aftershocks the risk has been evaluated as mean daily rate, calculated using equation (21) and assuming T = 1 day. Then, it is transformed in annual rate multiplying by 365. The comparison show a good agreement from the results of two methods, with the clear advantage, for regression method, of a substantial reduction of the computational time.

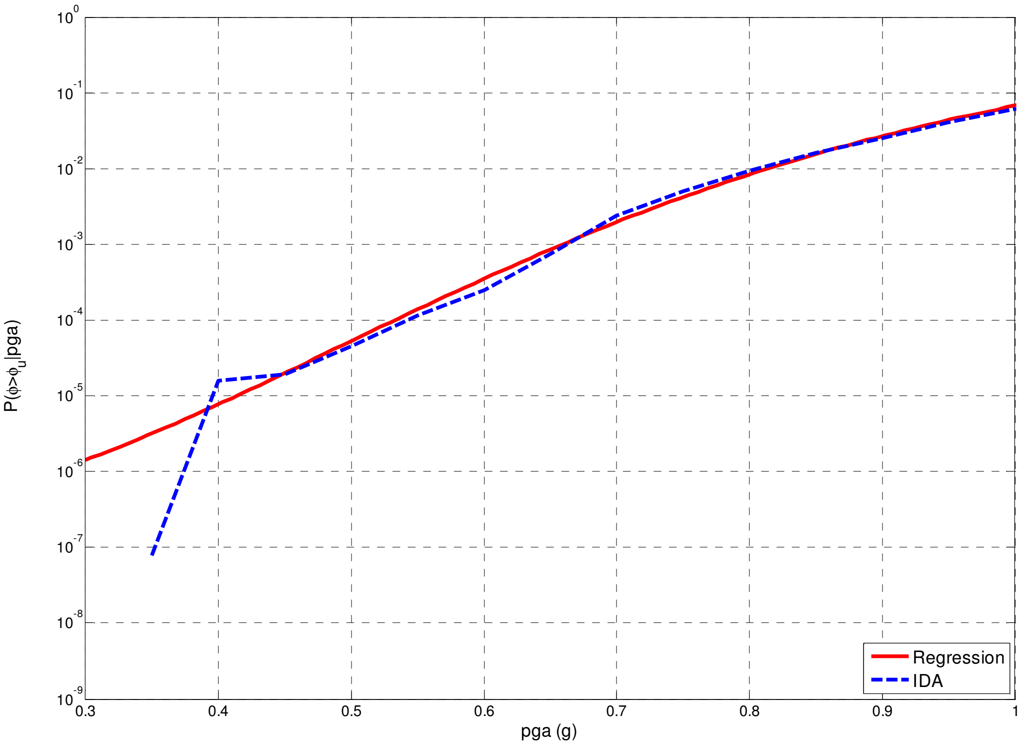

Figure 1: Comparison between the mainshock fragility curves obtained using IDA and the regression method

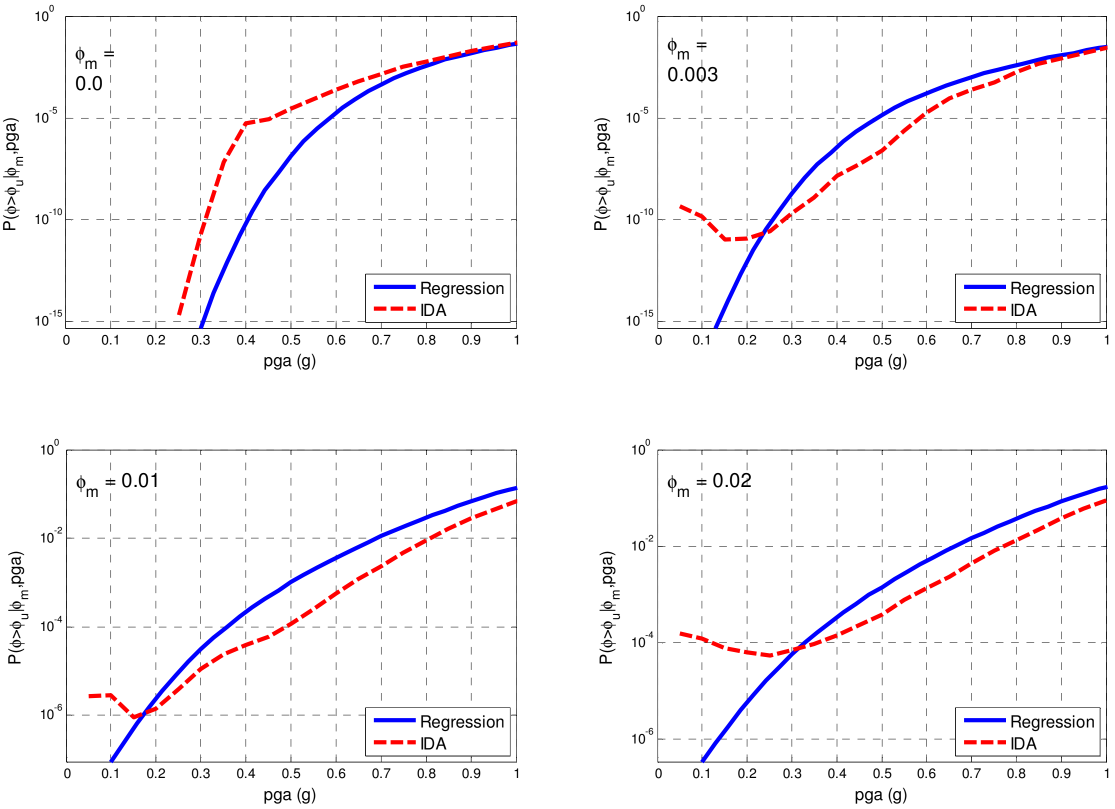

Figure 2: Comparison between the aftershock fragility curves obtained using IDA and the regression method

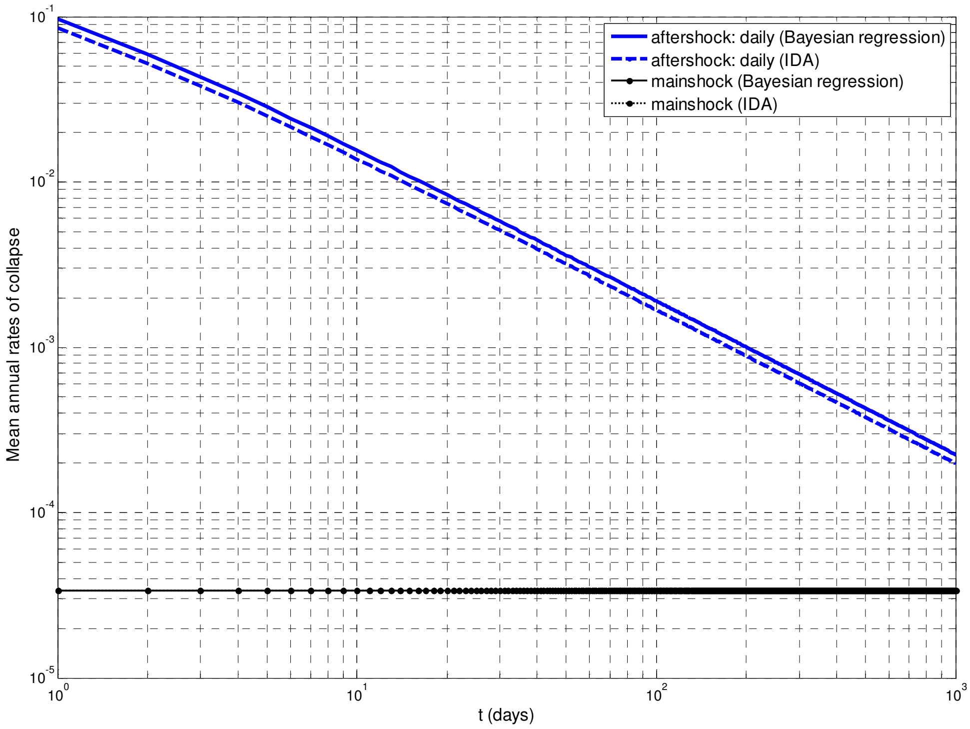

Figure 3: Comparison between the mean annual frequency of collapse evaluated with fragility with IDA and the regression method

5 APPLICATION

The bridge object of this study is an old reinforced concrete viaduct consisting of a thirteen-span bay deck with two independent roadways sustained by 12 couples of portal frame piers (Figure 4), each composed of two solid or hollow circular columns of variable diameter (120-160 cm), connected at the top by a cap-beam and at various heights by one or more transverse beams of rectangular section.

The height of the piers varies between 13.8m, near the abutments, to 41 m, at the center of the bridge. The deck is realized by two Π reinforced concrete beams 2.75m high, which are interrupted by some Gerber saddles placed at the second, seventh and twelfth bay respectively. The deck is connected to the piers by two steel bars inserted in the concrete.

The linear distributed weight of the deck is approximately 200 kN/m for each road-way. This means that to each pier receives a vertical load varying between 6600 kN and 8400 kN, while the length of the bays varies between 33 and 42 m.

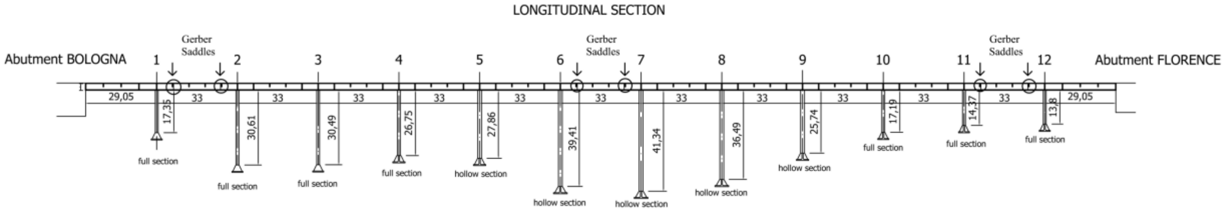

Figure 4: The Rio Torto highway viaduct

The examined pier (Figure 5) has a total height of 25.14 m and it is composed by two columns with hollow section of external and internal diameter equal to 160 cm and 120 cm respectively. The longitudinal and transverse reinforcement consists respectively of 16 steel bars ϕ20 mm and spiral stirrups ϕ 6 mm with spacing s=14cm. The transverse beam has a rectangular section 40 × 130 cm with a symmetrical longitudinal reinforcement realized with ϕ24 and ϕ20 mm and stirrups ϕ 8 mm with variable spacing (s=10cm at nodes and s=14 cm in the meddle). The cap-beam presents a U-shaped section with longitudinal reinforcement 4ϕ24+8ϕ20 mm and stirrups ϕ8 mm with variable step.

The average strengths of the material, specified in original design drawings and report, are: concrete compressive strength f_c=26 MPa and steel yield strength f_y =360 MPa. The deck weight of 200kN/m correspond to a frame load of 6600kN divided over the two columns.

The dynamic analysis have been performed using Opensees software [21]. The pier have been modeled as 2D-frame composed of nonlinear beam column elements, including uniaxial bending and axial force modeled by a fiber-discretized section; the P-delta effect is also included.

The axial/flexural response of transverse beams have been coupled at each integration point, by the section aggregator command, with the shear response modeled by an uniaxial hysteretic law. The shear force-deformation law is represented in Figure 7. The envelope is multilinear with characteristic points at cracking, peak and residual strength given evaluated according to [22].

The typical cyclic response, for a given axial force, here assumed as constant, is shown in Figure 6; Figure 7 shows the cyclic shear response of the end section of a transverse beam.

The viaduct here analyzed has been realized in a zone with moderate-to-high seismic activity. The seismogenic zone (913) in which the bridge is placed is indicated in Figure 8. The return period for the life safety condition is about 2000 years. The associated shaking map (from INGV) shows (Figure 9) that the expected PGA ranges between 0.23g and 0.25g, whereas considering the collapse prevention condition (probability of 2% in 50 years) PGA ranges between 0.30g and 0.35g.

In order to evaluate the aftershock hazard of the site, two mainshocks have been here considered, with epicenter placed at a distance R = 10 km from the site and magnitude M = 6.5 and M = 6. These latter have been adopted taking into account that the maximum value of the magnitude associated with an event within 20 km from the site in the parametric catalogue of damaging earthquakes in the Italian area [23] is M = 6.0; this value is compatible with a value of the *pga* corresponding to an average return period equal to 2475 (0.34g), resulting from a conventional PSHA analysis [23] and evaluated using the most recent data for seismogenic zones for the Italian territory [24].

For the evaluation of the aftershock rate (eq.(10)), the parameters suggested by Lolli and Gasperini [20] are here adopted: $a = -1.676$, $b = 0.96$, $c = 0.0295$, $p = 0.93$ and $m_1 = 4.5$; moreover, the fault length has been calculated as function of the magnitude m using eq. (10) as suggested in [17].

A Montecarlo simulation, using 1000 samples, has also been used for the integration over the distance R.

For the evaluation of the fragility curves, a set of 10 ground motion records has been selected from the *PEER* database, with the following parameters: 6 ≤ Magnitude ≤ 7, Source-Site distance ≤ 25km; the records have been normalized to the peak ground acceleration and scaled according to target spectrum provided by the Italian Code for an average return period of 2475 years. In this work the same set of records used to represent the mainshocks has also been used for the aftershocks.

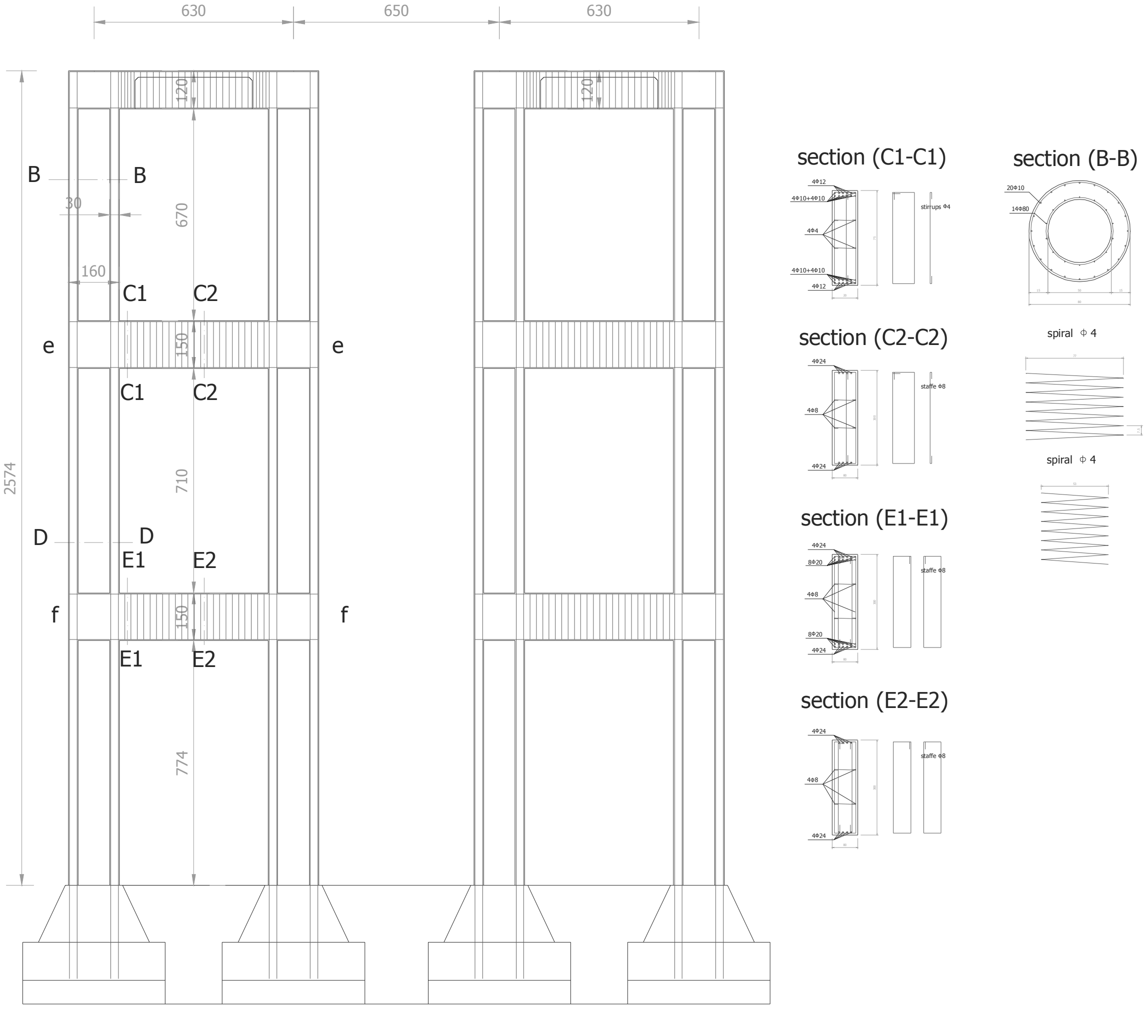

Figure 5: Geometry and reinforcement details of pier n. 9

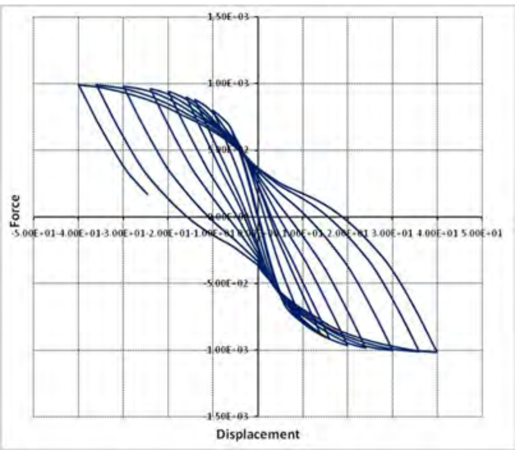

Figure 6: Cyclic behaviour of the pier

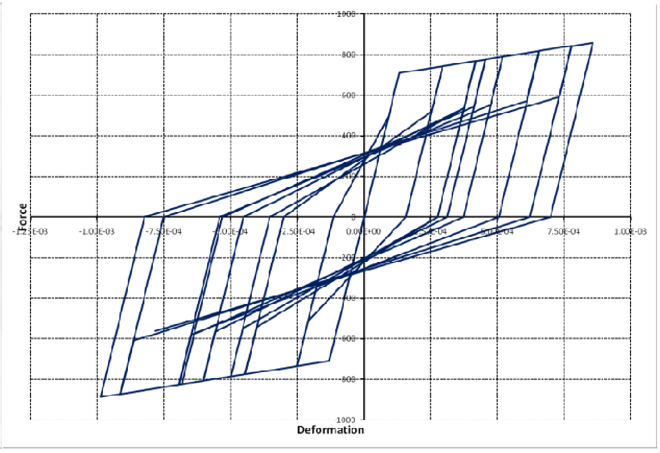

Figure 7: Cyclic shear force-deformation of a transverse

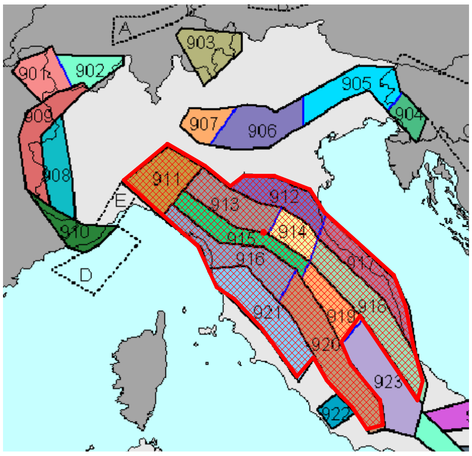

Figure 8: ZS9, Seismogenetic area for Italian territory.

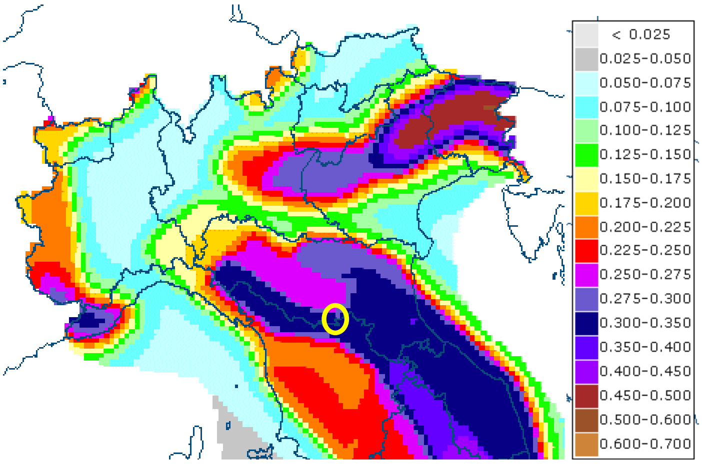

Figure 9: Seismic hazard for the probability of exceedance of the 2% in 50 years (mean return period 2475 years) [26].

In Figure 10 the daily rate of exceeding site PGA of the aftershocks is illustrated for different level of PGA as a function of the elapsed time from the initial rupture *t* (1, 5, 10 ,15 days from the mainshock).

To calculate the fragility curve of the intact structure subjected to a mainshock, 160 non-linear time history analysis have been carried out, by selecting, with the LHS technique, the records and the relevant PGA in the range 0.5g ÷ 1.5g. The lower limit of 0.5g on the PGA has been adopted taking into account that only the drifts that cause structural damage are considered.

To calculate the fragility curve of the mainshock-damaged structure, subjected to an aftershock that causes collapse (corresponding to a drift ϕ_u =0.025), a second cycle of 1600 analysis has been performed by selecting, with the LHS technique, the records of the mainshock and the aftershock and the relevant PGA in the range 0.1g ÷ 1.5g.

Figure 11 shows the fragility curves of the undamaged structure due to the mainshock $p_0(\phi) = f_\Phi(\phi \,|\, m_{0,} r_0)$, estimated before the direct observation of the damage, in comparison with fragility curves due to aftershocks $\overline{F}_D(\phi_i \,|\, \phi_j, y)$, for three levels of damage caused by mainshock (ϕ_1 =0.003, ϕ_3 =0.01, ϕ_3 =0.02). The effect of the initial damage on the probability of failure due to an aftershock generally increases the probability of failure for each value of PGA.

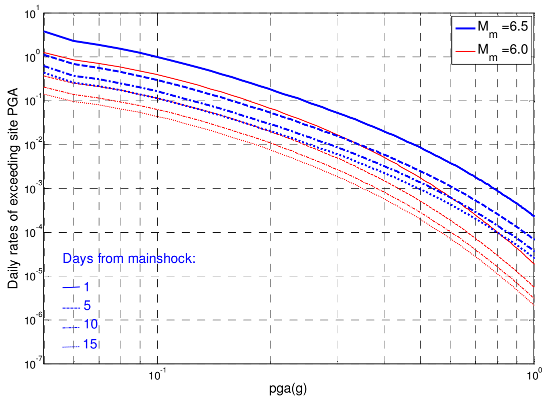

Figure 10: Daily rates of exceeding site PGA

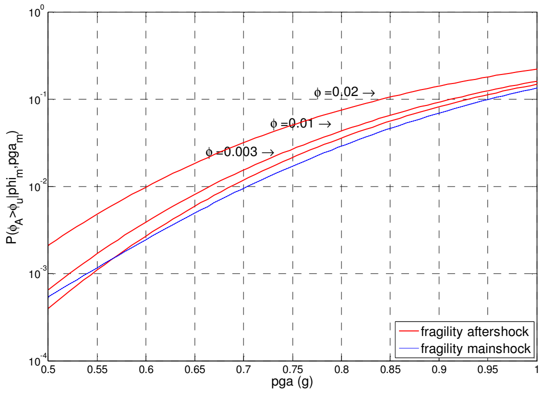

Figure 11: Fragility curves of the pier undamaged and for three levels of damage

The three level of damage considered in this work have been evaluated by experimental tests performed by some of the authors [27] in the laboratory of the Department of Structures of the University of Roma Tre. The tests consist of cyclically imposed displacement to a 1:4 scale of one of the piers; they have shown that the shear behaviour of the pier is extremely relevant; in particular, the shear failure of the transverse beam has a strong influence on global cyclic behaviour of the specimen, with a pronounced pinching effect that reduces the dissipation capability of the pier. The assumed drift values (ϕ_1 =0.003, ϕ_3 =0.01, ϕ_3 =0.02) correspond to the shear cracking of the transverse beam and flexural cracking at the base of the column.

In 12 the effect of the Bayesian updating on the probability function of the damage (drift) produced by the mainshock is shown; the continuous curve is the CDF of the drift due to the seismic event, evaluated using the attenuation law and the fragility curve of the undamaged structure (eq. (7)). The dashed curves represent the updated function [eq. (9)] assuming two different observed damages θ_1 and θ_2 with the relevant drift mean value from tests and assuming a lognormal distribution. A high sensitivity to the Bayesian updating, considering the limited level of damage here adopted, can be noticed. In particular, an event with magnitude M = 6.0 causes a calculated median drift of 0.52% that undergoes a small variation if a damage θ_1 is observed, but moves to 0.97% if a damage θ_2 is observed; an event with magnitude M = 6.5 causes drift with a median value of 0.65% that undergoes reduces to 0.6% or moves to 1.1% if a damage θ_1 or θ_2, respectively, are observed. This result shows as the Bayesian updating can strongly modify the damage curve, when the damage predicted by the numerical analysis does not correspond to the in-situ one, although the high dispersion of the observed damages.

Observed damage	θ1	θ1	θ1
Drift mean value	0.003	0.01	0.02
Correlation coefficient	0.35	0.25	0.2
Physical description	Hairline cracks	Onset of concrete spalling - development of shear cracks	Wide-cracks widths - longitudinal bars buckling
	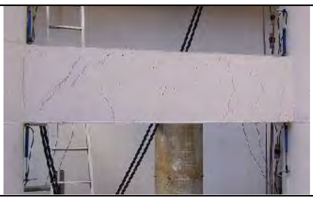		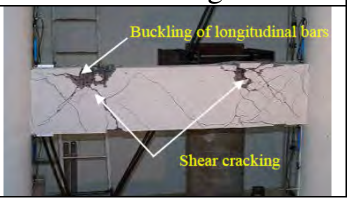

Table 4.1. Mean value and correlation coefficient of the drift

Figure 3 shows the results of the analysis in terms of risk for the two assumed values of the mainshock magnitude. The continuous lines represent the mean daily rate of collapse, calculated using equation (20) assuming $T = 1$ day, transformed in annual rate multiplying by 365; the dashed lines represent the equivalent mean annual rate of collapse, computed using the variable observation time $T = t_u - t$ (in this equation t_u is the time duration of the aftershocks [20]). In the same graph the lines with markers represent the equivalent rates of collapse evaluated applying a discount rates of 2.5% .

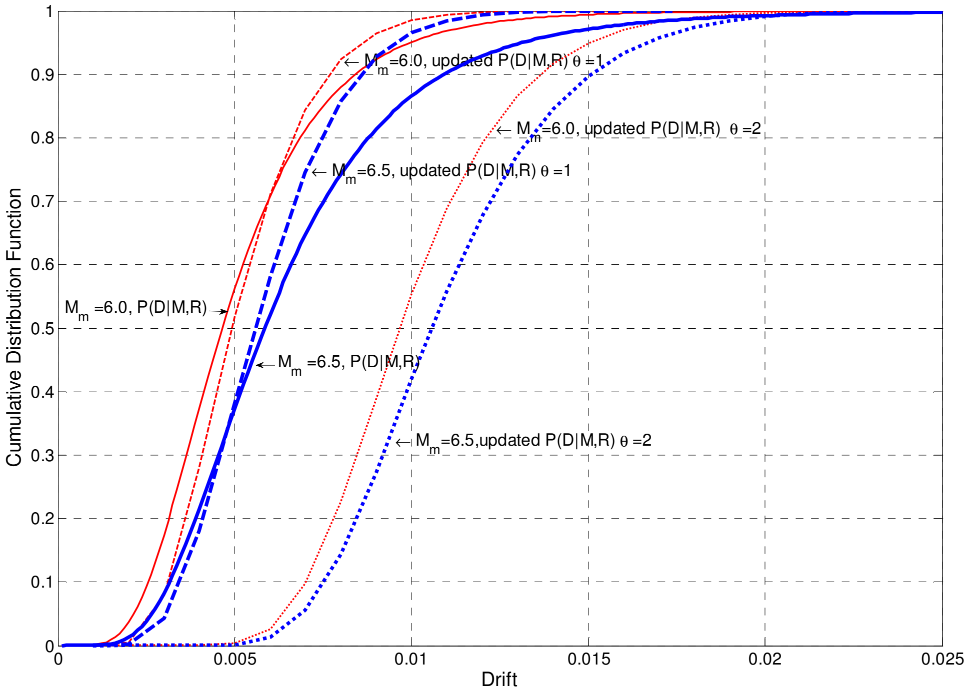

Figure 12: CDF of the drift for different observed damages θ_k

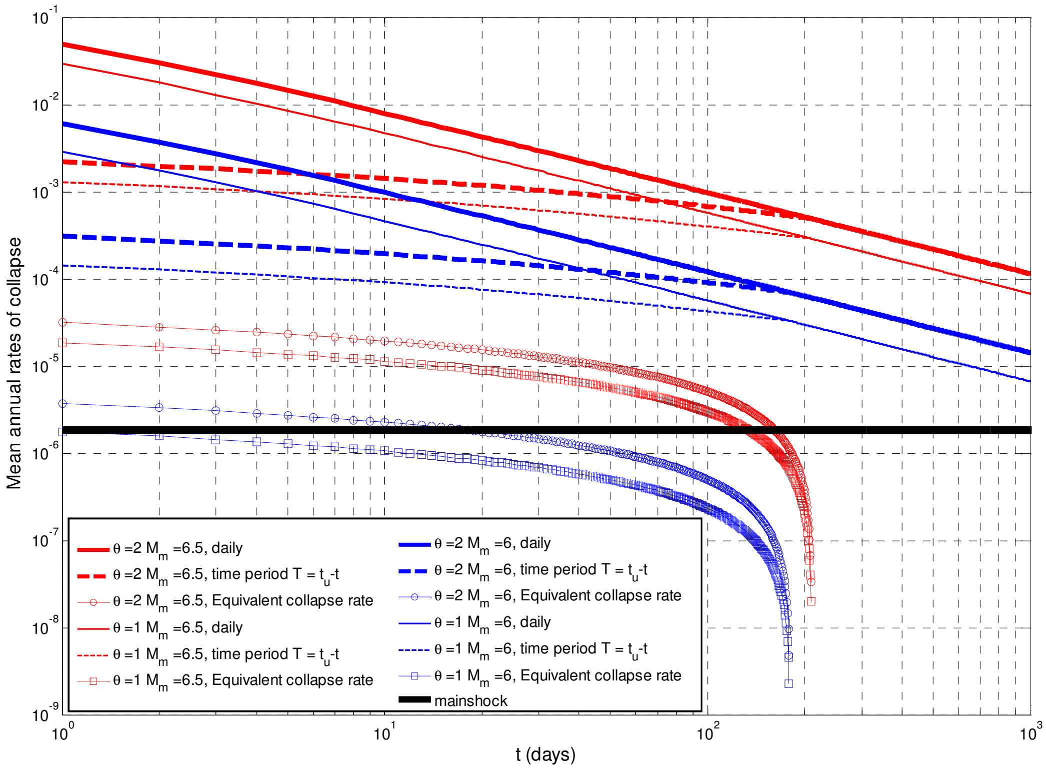

Figure 13: Mean annual frequency of collapse as a function of time elapsed from the mainshock

The equivalent mean annual rate of collapse computed with the first two criteria is much larger than the mean annual rate due to mainshock; in practice this curves intersect the mainshock level only at the end of the aftershock sequence. The criteria proposed in [12], instead, make the two risk comparable, and, for moderate earthquakes, the crossing time is shorter than the duration of the aftershocks sequence.

1. CONCLUSIONS

A critical issue in the emergency management after the earthquake is the functionality of the main infrastructure (hospitals, road network, etc.) and the decision on their usability just after the main shock. At present, a decision is take on the basis of a structure in-situ inspection; an analytical assessment is in contrast with the lack of time and data. For this reason in this paper a method that rationally combines information from the analytical approach and the in situ inspection is proposed. In particular an effective tool to speed-up the decision making phase concerning the evaluation of the seismic risk of mainshock-damaged structures due to aftershocks has been proposed. The risk is calculated combining the aftershock hazard using the Omori law and the fragility curves of the structure calculated using IDA improved by using LHS technique and updated with in-situ inspection data. The procedure has been applied to a highway r.c. bridge. The results has highlighted a high sensitivity to the Bayesian updating especially when the damage predicted by the numerical analysis does not correspond to the real damage. The mean annual rates of collapse provided by the method has shown that the risk structure change dramatically when an aftershock sequence strike the bridge and that this risk decreases with time allowing the authorities to decide if and when re-open the bridge to traffic.

AKCNOWLEDGEMENT

The work presented in this paper has been partially funded by a grant of Italian Ministry of University and Research (MIUR) in the scope of Research Programs of National Interest (PRIN 2007).

REFERENCES

[1] Gallagher R, Reasenberg P, Poland C. Earthquake Aftershocks—*Entering Damaged Buildings: ATC TechBrief 2*. Applied Technology Council (ATC), 1999

[2] FEMA. FEMA 352: *Recommended Post-Earthquake Evaluation and Repair Criteria for Welded Steel Moment-Frame Buildings*. SAC Steel Project, FEMA, 2000.

[3] G.L. Yeo, C.A. Cornell, A probabilistic framework for quantification of aftershock ground-motion hazard in California: Methodology and parametric study. *Earthquake Engng Struct. Dyn.*; 38, 45–60, 2009.

[4] G.L. Yeo, C.A. Cornell, *Stochastic characterization and decision bases under time-dependent aftershock risk in performance-based earthquake engineering*. PEER Report 2005/13, 2005.

[5] G.L. Yeo, C.A. Cornell. Building Tagging Criteria Based on Aftershock PSHA. *13th World Conference on Earthquake Engineering,* Vancouver, B.C., Canada, 2004. Paper No. 3283

[6] G.L.Yeo, and C.A.Cornell, Post-quake decision analysis using dynamic programming. *Earthquake Engng Struct. Dyn*, 38, 79–93, 2009

[7] Shotaro Kumitani, and Tsuyoshi Takada. Probabilistic Assessment of Buildings Damage Considering Aftershocks of Earthquakes. *13th World Conference on Earthquake Engineering,* Vancouver, B.C., Canada, 2004.

[8] K.R. Mackie, B. Stojadinovic, Post-earthquake functionality of highway overpass bridges. *Earthquake Engng Struct. Dyn.*; 35,77–93, 2006.

[9] P. Franchin, P.E. Pinto, Allowing traffic over mainshock-damaged bridges. *Journal of Earthquake Engineering,* 13, 585–599, 2009.

[10] R. Giannini, F. Paolacci, S. Alessandri, Post earthquake availability of damaged structures. Application to Highway Bridges. *14 ECEE*, 2010.

[11] M. Berry, M. Eberhard, M, *Performance models for flexural damage in reinforced concrete columns.* PEER Report 2003/18, 2003.

[12] G.L.Yeo, C. A.Cornell. Equivalent constant rates for post-quake seismic decision making, *Structural Safety,* vol.31, pp. 443–447, 2009.

[13] D. Vamvatsikos, C.A. Cornell, Incremental dynamic analysis. *Earthquake Eng. Struct. Dyn.* 31, 491–514, 2002.

[14] F. Sabetta, S. Pugliese, Attenuation of peak horizontal acceleration and velocity from italian strong-motion records. *Bul. of the Seism. Soc. of Am.* 77:5, 1491-1513, 1987.

[15] N.N. Ambraseys, K.A. Simpson, J.J. Bommer, Prediction of horizontal response spectra in Europe. *Earthquake Engineering and Structural Dynamics*, 25, 371 -400, 1996.

[16] N.N. Ambraseys, J. Douglas, S.K. Sarma, P.M. Smit, Equations for the estimation of strong ground motions from shallow crustal earthquakes using data from Europe and the Middle East: horizontal peak ground acceleration and spectral acceleration. *Bulletin of Earthquake Engineering* 3, 1–53, 2005.

[17] D.L. Wells, K.J. Coppersmith, New empirical relationships among magnitude, rupture length, rupture width, rupture area, and surface displacement. *Bul. of the Seism. Soc. of Am.* 84:4, 974-1002, 1994

[18] T. Utsu, The centenary of the Omori formula for a decay law of aftershock activity. *Journal of the Physics of the Earth* 43, 1–33, 1995.

[19] P.A. Reasenberg, L.M. Jones, Earthquake hazard after a mainshock in California. *Science* 243, 1173-1176, 1989.

[20] B. Lolli, P. Gasperini, Aftershocks hazard in Italy Part I: Estimation of time-magnitude distribution model parameters and computation of probabilities of occurrence. *Journal of Seismology* 7, 235–257, 2003.

[21] F. McKenna, G.L. Fenves, M.H.Scott, *OpenSees: open system for earthquake engineering simulation*. PEER, University of California, Berkeley, CA, 2007.

[22] M.J.N. Priestley, R. Verma, Y. Xiao, Seismic shear strength of reinforced concrete buildings, *ASCE Journal of Structural Engineering*, Vol. 120, No. 8, pp. 2310-2329, 1994.

[23] Gruppo di lavoro CPTI, *Catalogo Parametrico dei Terremoti Italiani, versione 2004* (CPTI04), INGV, 2004.

[24] INGV, *"Redazione della mappa di pericolosità sismica prevista dall'Ordinanza PCM 3274 del 20 marzo 2003. Rapporto conclusivo per il Dipartimento di Protezione Civile, INGV, Milano-Roma"*, INGV, Milan-Rome, Italy, 2004.

[25] R. Giannini, "*Mathazard: a program for seismic hazard analysis*", University of Roma Tre, Rome, Italy, 2000.

[26] C. Meletti, V. Montaldo, Stime di pericolosità sismica per diverse probabilità di superamento in 50 anni: valori di ag. Progetto DPC-INGV S1, Deliverable D2, http://esse1.mi.ingv.it/d2.html, 2007.

[27] R.Giannini, F.Paolacci, E.Sibilio. Experimental study on the cyclic response of an existing RC bridge pier. *14th World Conference on earthquake engineering*. Beijing, China, October 12-17, 2008.

COMPDYN 2011
III ECCOMAS Thematic Conference on
Computational Methods in Structural Dynamics and Earthquake Engineering
M. Papadrakakis, M. Fragiadakis, V. Plevris (eds.)
Corfu, Greece, 25–28 May 2011

SOFTWARE FOR MEASURING DISASTER COMMUNITY RESILIENCE ACCORDING TO THE PEOPLES METHODOLOGY

Vincenzo Arcidiacono[1]*, Gian Paolo Cimellaro[1], A. M. Reinhorn[2]

[1] Department of Structural and Geotechnical Engineering (DISTR)
Politecnico di Torino, 10129, Turin, Italy
vincenzo.arcidiacono@polito.it, gianpaolo.cimellaro@polito.it

[2] Department of Civil, Structural and Environmental Engineering,
University at Buffalo, The State University of New York,
14260-4300, Buffalo, New York
reinhorn@buffalo.edu

Keywords: recovery plan; recovery model; community resilience; resilience, disaster, loss estimation, seismic hazard.

Abstract.

Resilience is defined as the ability to mitigate hazards disposing a prompt strategy for recovering activities. Many papers are available in literature describing community resilience performances, but very few describe how to quantitative measure this index and which tools to use. The paper presents a software for evaluating community resilience index using the PEOPLES framework methodology. A critical comparison with similar softwares already available in literature is given emphasizing strengths and weakness with respect to the new proposed software, that has a user friendly graphical interface in Google earth environment. Finally the program and the methodology are tested using the case study of the 2009 Italian earthquake in L'Aquila that mainly affected historical monumental buildings in downtown L'Aquila. Four different scenario events are assumed to describe the reconstruction phase (recovery) and compared using the proposed platform.

1 INTRODUCTION

In recent years, we have seen how important is planning after disasters (e.g., L'Aquila and Haiti earthquake, Hurricane Katrina, September 11th terrorist attack, etc.), so the concept of resilience, that is the ability of social units (e.g., organizations, communities) to mitigate hazards, contain the effects of disasters, and carry out recovery activities in ways that minimize social disruption, has gained attention recognizing the fact that not all threats or disasters can be averted.

The community planning is affected by physical, social, and economic components of urban or rural communities. The main goal of this research is to develop tools that allow communities to reduce vulnerabilities while enhancing their overall resilience against extreme events and enabling sustainable development. When considering small communities such as rural communities, their residents are faced with multiple conflicting decisions when responding to natural and man-made hazards. Hazard mitigation practices of rural communities include best management practices in soil and water conservation to reduce soil erosion and flooding.

Resilience has been defined as a measure of geospatial and temporal functionality, its decay and recovery, in face of various hazards [1]. The functionality and resilience of a community depend on numerous components and dimensions. In previous research [2][3], seven dimensions of community resilience were identified and represented in the holistic, interdisciplinary framework with the acronym PEOPLES: *Population and Demographics, Environmental/Ecosystem, Organized Governmental Services, Physical Infrastructure, Lifestyle and Community Competence, Economic Development, and Social-Cultural Capital*. The PEOPLES Resilience Framework provides the basis for development of quantitative and qualitative models that measure the resilience of communities against extreme events in any or a combination of the above-mentioned dimensions, using risk assessment, loss estimation and recovery tools. The methodology has been implemented in software and the first release of it is presented for the first time in this paper. In the current version only the physical and infrastructure dimension has been developed, while other resilience dimensions have been set up in the graphical user interface waiting for approval from the scientific team of the PEOPLES framework developers. A case study of an Italian region recently affected by an earthquake has been used to prove the applicability of the developed software.

2 CRITICAL REVIEW OF CURRENT RESEARCHES

Several methods are available in literature for loss estimation methodologies. Among all the most famous is HAZUS [4], a software that was developed by the National Institute of Building Sciences (NIBS). The model uses and works on inventory of the classification of various components like population, building, transport system, lifeline utilities and hazardous materials. The building inventory is made for groups of buildings, with similar characteristic. The buildings are divided by groups of pre-defined building classes. There are 36 different *structural classes* that depend by construction, material, and structural type, while the *occupancy inventory* of the general building stock in the HAZUS methodology is prepared on the basis of its general and specific building occupancy. The building and occupancy type inventory are used, respectively, for the building risk assessment and to evaluate the potential economic losses. It is important to mention that this methodology evaluates only building risk assessment without any evaluation of the recovery plan and only a gross estimation of the recovery time.

More recently another software has been developed called *ResilUS* that is a prototype simulation model for community resilience to disasters [5][6][7]. ResilUS uses a macro-subdivision of area, like the neighborhoods subdivision, where are contained within a broader community. The model represents damage and recovery associated with a hazard event into three elements of community capital (economic, technological and human or, for businesses, individual), which is limited to buildings and lifelines (transportation network, electrical network, water network and critical facilities). ResilUS relies on two generic indicators of resilience that are the ability to perform and opportunity to perform associated with each hierarchical scale (community, neighbourhood, agent). Resilience, of agents, infrastructure, or communities, is measured in terms of some indicator of performance (e.g. level of service, building stock, income, or gross regional product). The model has four recovery curves, but currently the software *ResilUS* uses only one curve, that brings back to pre-disaster conditions.

In Europe another software package has been developed that is called *SELENA–RISe* open risk package [8][9], which was developed by the international centre for geohazards (ICG), through NORSAR (Norway) and the University of Alicante (Spain). It consists of the two separate software tools SELENA (Seismic Loss Estimation using a Logic Tree Approach) and RISe (Risk Illustrator for SELENA). SELENA is the computational platform that evaluates the building risk and potential losses (economic and casualties), while RISe converts the output files of SELENA, in order to plot on Google Earth. The software uses the HAZUS methodology to evaluate damage of the general building stock and the economic and human losses related to these physical damages. SELENA uses different building codes and models (e.g. EC8 [10], IBC-2006 [11], IS 1893 [12], CSM [13] [14], etc. The limitation of the software consists in extensive data input requirements, without a user friendly graphical interface, because it has two separate softwares, both running in MATLAB environment.

Based on the above observation there is need for a new software that takes in account the time dimension of the disaster and the entire recovery process.

3 PEOPLES FRAMEWORK

Disaster resilience is often analyzed considering technological and social units, but also considering the spatial scale of analysis, (e.g. single buildings, towns, communities, regions, country etc.). Technological aspects mainly focus on performances and interdependencies of different networks and systems. The human component is also central, because resilience depends first on the actions of people operating at the individual and neighborhood scale. Community resilience also depends heavily on the actions of different levels of government and its agencies at the local and regional scales when a disruptive extreme event occurs.

The PEOPLES Resilience Framework is built on, and expands, previous research at MCEER linking several previously identified resilience dimensions (i.e., technical, organizational, societal, and economic) and resilience properties (i.e., R^4: robustness, redundancy, resourcefulness, and rapidity) [15][16][17]. In detail, the methodology subdivides the community resilience in seven dimensions, which are listed below:

- **P** opulation and Demographics (Composition, Distribution, Socio-Economic status, etc.);
- **E** nvironmental/Ecosystem (Air quality, Soil, Biomass, Biodiversity, etc.);
- **O**rganized Governmental Services (Legal and security services, Health services, etc.);
- **P** hysical Infrastructure (Facilities, Lifeline, etc.);

- **L** ifestyle and Community Competence (Quality of Life, etc.);
- **E** conomic Development (Financial, Production, Employment distribution, etc.);
- **S** ocial-Cultural Capital (Education services, Child and elderly care services, etc.).

All dimensions are measured by functionality indices that measure the performances, so the PEOPLES Resilience Framework defines components of functionality using a geospatial-temporal distribution within its geographical influence boundaries. Interdependencies between and among these components are key to determining the resilience of communities (recovery plan). The resilience can be considered as a dynamic quantity that changes over time and across space. The PEOPLES Resilience Framework requires the combination of qualitative and quantitative data sources at various temporal and spatial scales, and as a consequence, information needs to be aggregated or disaggregated to match the scales of the resilience model and the scales of interest for the model output.

4 SOFTWARE DESCRIPTION

A software that uses the methodology of PEOPLES Resilience Framework (ArciRasilience1.0) to measure the Resilience index at the Community Scale was created.

Firstly, our interest was focused in “Physical Infrastructure” dimension, in particular in building structures, like Facilities or Health Care. The software is divided in five parts:

1. *Input data collection (e.g. building network characteristics, etc.);*
2. *Damage State Probability Analysis;*
3. *Resilience analysis;*
4. *Output data;*
5. *Decision making;*

4.1 Input data collection

Data input of physical infrastructures will be collected in a database in a central server through the access to the website of the project (www.polito.it/ICRED). The access to submit the input data from users will be controlled by a username account with password. The input data required by the program are the following:

- *Infrastructure Localization and Geometry parameters;*
- *Physical Infrastructure parameters;*
- *Damage parameters (e.g. capacity curve, damping ratio, occupancy class, construction building times, functionality losses, etc.);*

While, the services data, that are available inside the software, are the parameters that define the seismic action according to Italian Seismic Standard [18] (PGA, F_0 and T^*_c) and some parts of HAZUS database [4].

Figure 4-1: Data input interface for Localization and Geometry of Infrastructure.

Figure 4-1 shows how the geometry of the infrastructure is drawn using the Google Maps interface, while the physical infrastructure characteristics are defined using the classification given in the PEOPLES Resilience Framework [1] that will be used to evaluate the corresponding fragility curves as shown in Figure 4-2.

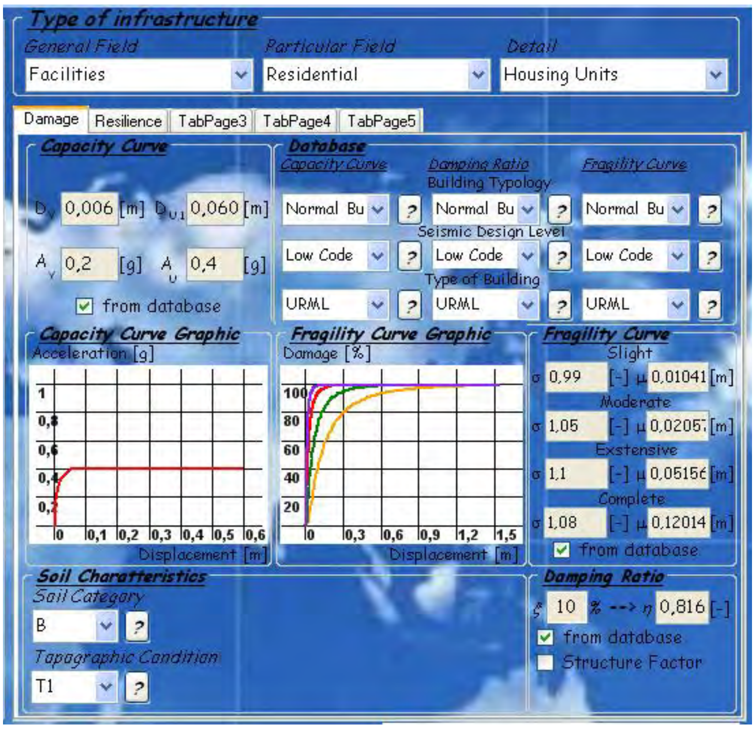

General Field: Facilities
Particular Field: Residential
Detail: Housing Units

D_y 0,006 [m] D_{u1} 0,060 [m]
A_y 0,2 [g] A_u 0,4 [g]
☑ from database

Building Typology: Normal Bu | Normal Bu | Normal Bu
Seismic Design Level: Low Code | Low Code | Low Code
Type of Building: URML | URML | URML

Slight: σ 0,99 [-] μ 0,01041 [m]
Moderate: σ 1,05 [-] μ 0,0205 [m]
Exstensive: σ 1,1 [-] μ 0,0515 [m]
Complete: σ 1,08 [-] μ 0,12014 [m]
☑ from database

Soil Category: B
Tapagraphic Candition: T1

ξ 10 % --> η 0,816 [-]
☑ from database
☐ Structure Factor

Figure 4-2: Data input interface for Damage features.

The building response is evaluated using the capacity spectrum method (CSM) rather than nonlinear time history analysis, because it is faster when several building performances need to be evaluated in a given region. When evaluating seismic response the software uses the capacity curves provided by HAZUS database [4], but they can also be assigned directly from

the users. Seismic demand is evaluated using the information provided in the Italian seismic standard, given the soil category and the topographic characteristics of the site. In the near future also the seismic demand according to the US seismic standard will be provided.
Another parameter assigned as input to evaluate the seismic response of the buildings is the damping ratio that can be assigned manually or using the default values recommended by HAZUS database [4]. The over strength factor (q) can also be assigned manually or directly evaluated according to the Italian seismic standard [18]. Also fragility curves associated to a given building typology are evaluated using the HAZUS database or assigned manually from the user. Other parameters necessary to evaluate resilience are the occupancy class, the total occupancy area, the full replacement costs, the construction building times, the recovery costs and the functionality losses (Figure 4-3).

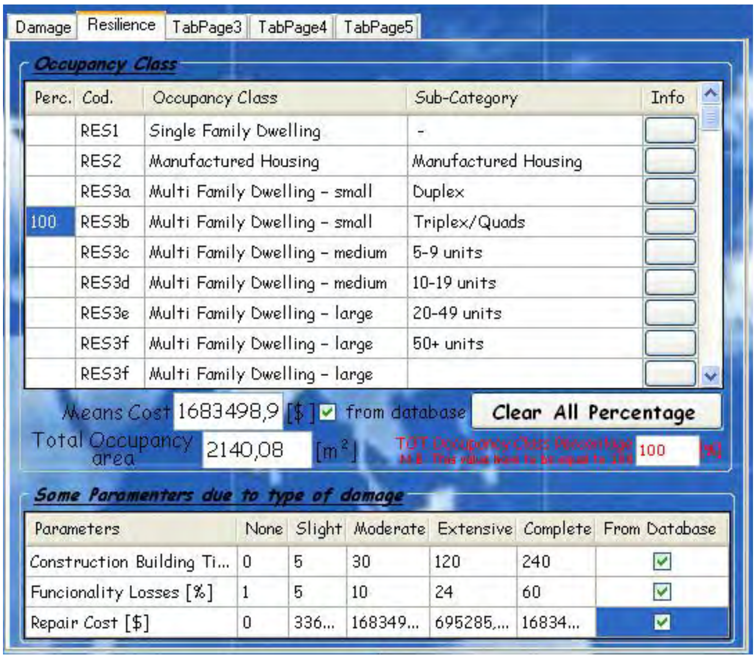

Perc.	Cod.	Occupancy Class	Sub-Category	Info
	RES1	Single Family Dwelling	-	
	RES2	Manufactured Housing	Manufactured Housing	
	RES3a	Multi Family Dwelling - small	Duplex	
100	RES3b	Multi Family Dwelling - small	Triplex/Quads	
	RES3c	Multi Family Dwelling - medium	5-9 units	
	RES3d	Multi Family Dwelling - medium	10-19 units	
	RES3e	Multi Family Dwelling - large	20-49 units	
	RES3f	Multi Family Dwelling - large	50+ units	
	RES3f	Multi Family Dwelling - large		

Means Cost 1683498,9 [$] ☑ from database

Total Occupancy area 2140,08 [m²]

TOT Occupancy Class Percentage 100 [%]
N.B. This value have to be equal to 100

Parameters	None	Slight	Moderate	Extensive	Complete	From Database
Construction Building Ti...	0	5	30	120	240	☑
Funcionality Losses [%]	1	5	10	24	60	☑
Repair Cost [$]	0	336...	168349...	695285,...	16834...	☑

Figure 4-3: Data input interface for Resilience features.

The general building stock is also classified according to the occupancy class of HAZUS, but it is divided into general occupancy and specific occupancy classes. The general occupancy classification system consists of seven groups (*residential, commercial, industrial, religion/nonprofit, government, education and lifelines*). There are 33 specific occupancy classes. While the total occupancy area is the sum of the all occupancy areas used by the respective occupancy classes presented inside the building.

Another feature is the building time for each damage state that is defined as the sum of the time spent for building cleanup and repair. If using the HAZUS database [4] these values are function of occupancy classes inside the building. The recovery costs, instead, are defined as the building repair costs due to each damage state (slight, moderate, extensive and complete). In HAZUS these values are function of full replacement cost and of the occupancy classes inside the building. Finally, the functionality losses are the percentages of the building functionality loss at a given damage state (e.g. 1% none; 5% slight; 10% moderate; 24% extensive; 60% complete). If using the internal database these values depend on the occupancy classes inside the building.

4.2 Damage State Probability Analysis

The disaster induces a different damage state for each building. The problem is to predict how the damages will be distributed in the control area. The software provides the damage state due to earthquakes, in the buildings presented in the control area. The damage state probability for each building is calculated using the following steps:

- *Evaluate the response spectrum of the building;*
- *Calculate the peak displacement response of the building;*
- *Evaluate the damage states probabilities (slight, moderate, extensive and complete) of the building;*
- *Calculate the construction building time, repair cost and the functionality of the building after disaster.*

The response spectrum of the building is evaluated according to the Italian Seismic Standard [18] in the centroid of the building perimeter. In the next version of software, it will be possible using Ambraseys AR. To evaluate the peak displacement response of the building, the software takes the data obtained from the response spectrum (function of PGA and period of the structure) and transforms them to obtain a curve function of the pseudo spectral acceleration and the pseudo spectral displacement. The peak displacement response is defined as the abscissa of intersection point between the demand spectrum curve and the capacity curve of the building.

The damage states probability (slight, moderate, extensive and complete) are the values obtained from the four fragility curves of the building substituting the peak displacement response as parameter (see Figure 4-4).

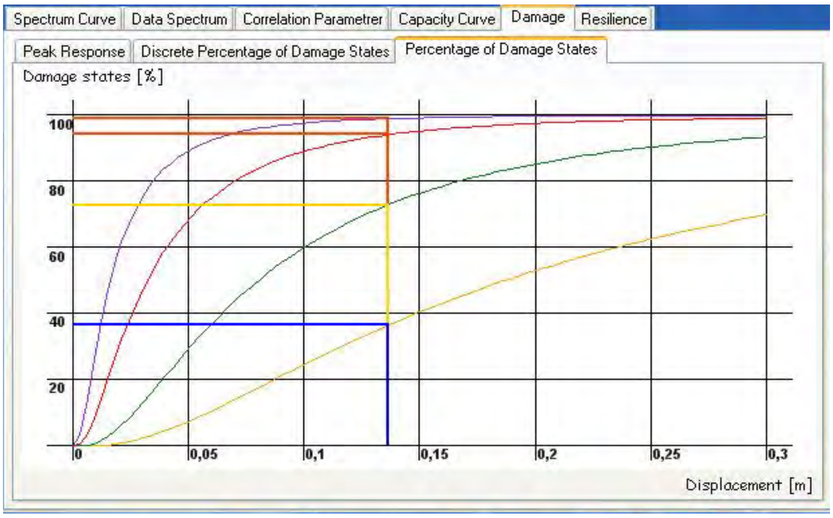

Figure 4-4: The probabilities of damage states.

The last step of damage state probability analysis is to evaluate the construction building time (which is the time spends on building cleanup and repair), the repair cost and the functionality of the building after the disaster. For the first two parameters (K_{TOT}), the software will use the same procedure of HAZUS, which consists in a summation of products between damage state probability (PDS_i) and the relative parameter (k_i) (construction buildings times or repair costs)(see Equation 1).

$$K_{TOT} = \sum_{i=1}^{4} PDS_i \cdot k_i \tag{1}$$

While for the building functionality, before the software evaluates the discrete probabilities of damage states ($DPDS_i$) (see Equation 2 and Figure 4-5) and after it uses the previous procedure (Equation 2) replacing the damage state probability with the discrete probability.

$$\begin{cases} DPDS_i = 1 - PDS_{i+1} & i = 0 \\ DPDS_i = PDS_i - PDS_{i+1} & i = 1,2,3 \\ DPDS_i = PDS_i & i = 4 \end{cases} \tag{2}$$

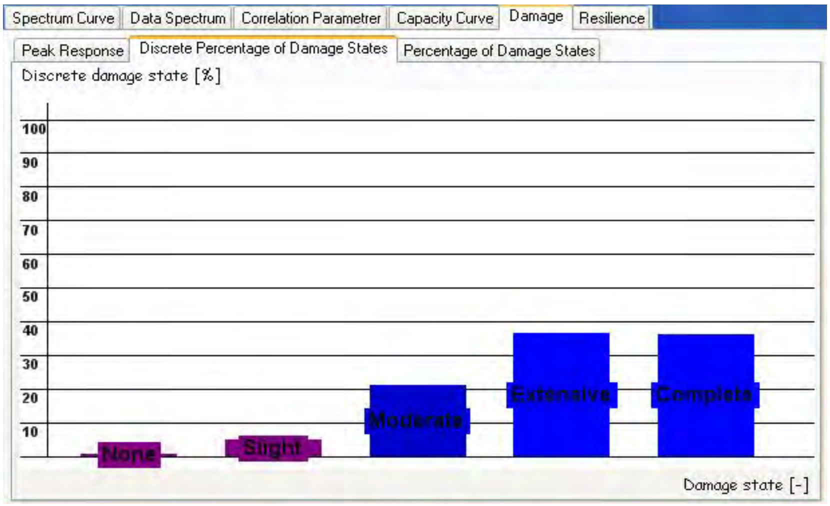

Figure 4-5: The discrete probabilities of damage states.

4.3 Resilience analysis

Resilience of the building (R_i) is defined as a function indicating the capability to sustain a level of functionality or performance for a given building, bridge, lifeline networks, or community, over a control period T_{LC} ([T_A; T_B]), that is chosen by user. This quantity is defined graphically as the normalized area underneath the functionality function $Q_i(t)$ of the building (internally integrated with a discrete Simpson integral) and is defined analytically as follows:

$$R_i = \frac{\int_{T_A}^{T_B} Q_i(T)\,dt}{T_B - T_A} \tag{3}$$

Where the functionality $Q_i(t)$ ranges from 0 to 100% (where 100% mean no reduction in performance, while 0% means total loss).

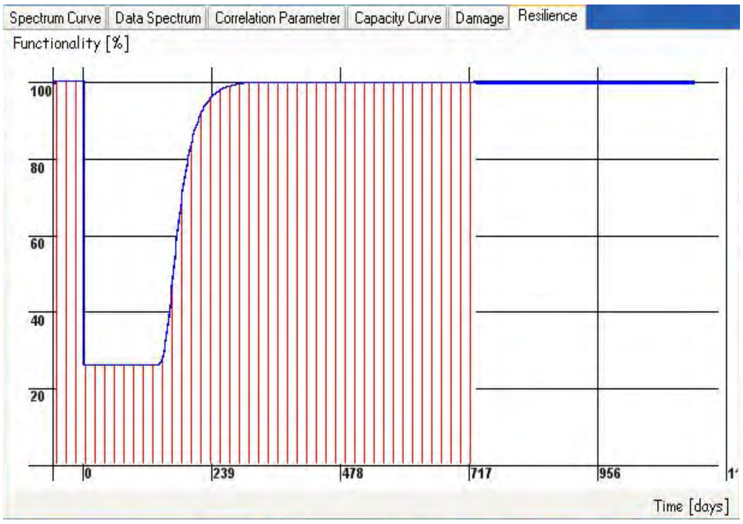

Figure 4-6: An example of recovery function.

The functionality function $Q_i(t)$ of the building is a function composed by two parts. The first part is constant, while the second one is lognormal (see Figure 4-6). The function is analytically defined as follows:

$$\begin{aligned} & Q_i(T)=1 && T<T_{Dis} \\ & Q_i(T)=F_s && T_{Dis}\leq T<T_{Ad} \\ & Q_i(T)=F_s+(1-F_s)\cdot\Phi\left(\frac{\ln(T)-\mu}{\sigma}\right) && T_{Ad}\leq T \end{aligned} \tag{4}$$

Where F_s = is the functionality of the building after disaster; Φ= is the lognormal function; σ and μ, are respectively the standard deviation and average value of the lognormal distribution; T_{Ad} and T_{Dis}, are the administrative and disaster times.

The length of the constant function is equal to the administrative time (that will be discussed in the following paragraph). While, the two coefficients of the lognormal function depend essentially from the type of infrastructure (for the μ value), the K value (ratio between construction building time CBT and average time μ) and the functionality value after building time (for σ value; see Equation 5).

$$\sigma=A\cdot\ln(K)=0.384\cdot\ln\left(\frac{CBT}{\mu}\right) \tag{5}$$

In finally, the resilience at the community scale of selected area (called community resilience R_C) is evaluated by a weighted average of all buildings resilience R_i, analytically defined as follows:

$$R_C=\frac{\sum_i R_i\cdot W_i}{\sum_i W_i} \tag{4-7}$$

where, the weight coefficients W_i depend by the type of infrastructure.

4.4 Decision making

The software can be used as decision making tools for communities to evaluate the effect of different recovery plans in terms of resilience. The software tests each possible combination of recovery processes (in agreement to the maximum possible number of simultaneous building sites in the selected area and the economic availability of the community) modifying the administrative times of each building (the administrative time is the time elapsed from the disaster to the start of repair works of the building). The software identifies as the better solution the one that has the major recovery velocity in each point of the functionality function (the recovery velocity is expressed as the value of the derivate of the functionality function). It also evaluates resilience and functionality of the buildings and the community (see Figure 4-7).

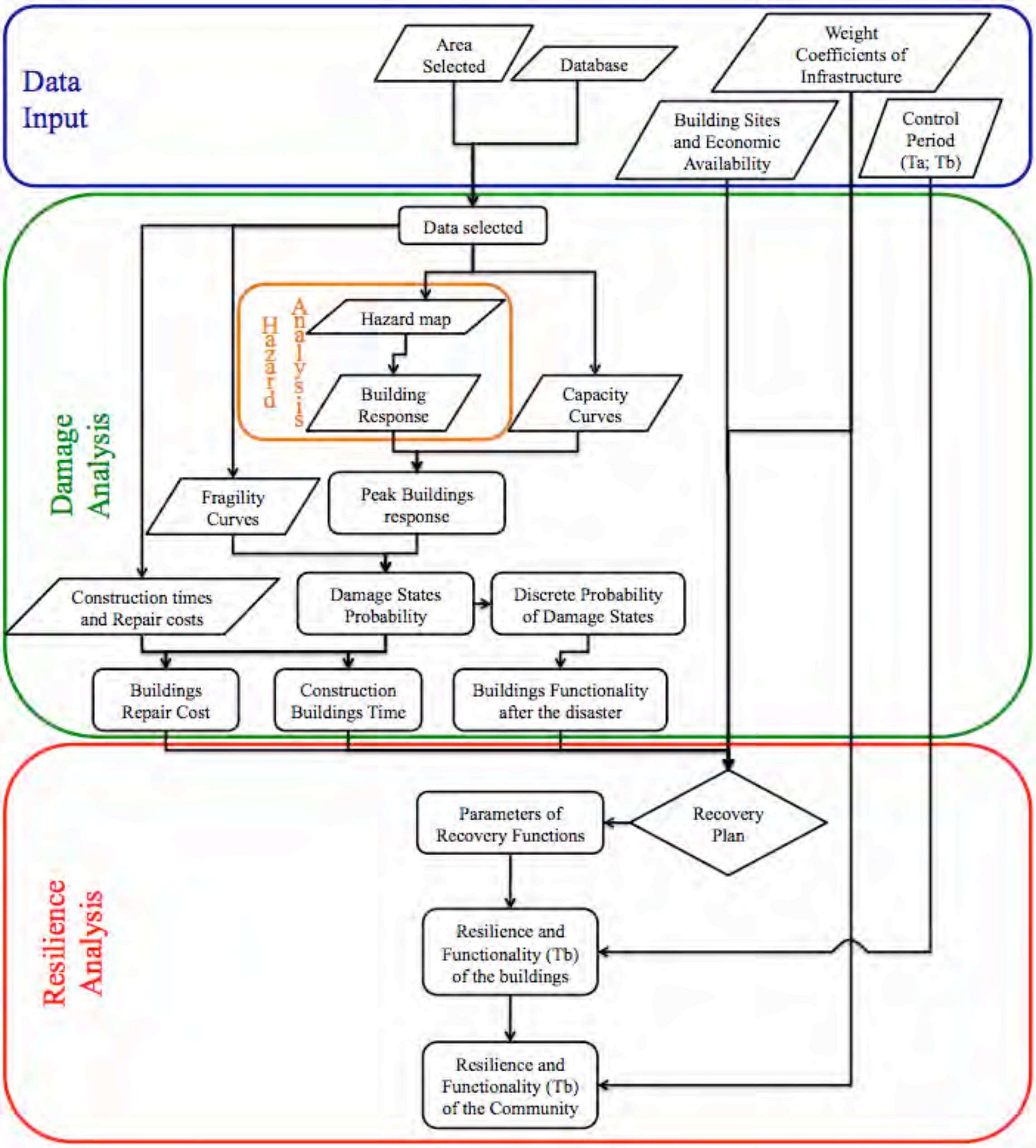

Figure 4-7: Flowchart of all steps to follow to evaluate the global resilience.

5 CASE STUDY

The software has been tested using as case study 10 buildings inside l'Aquila downtown (see Figure 5-8).

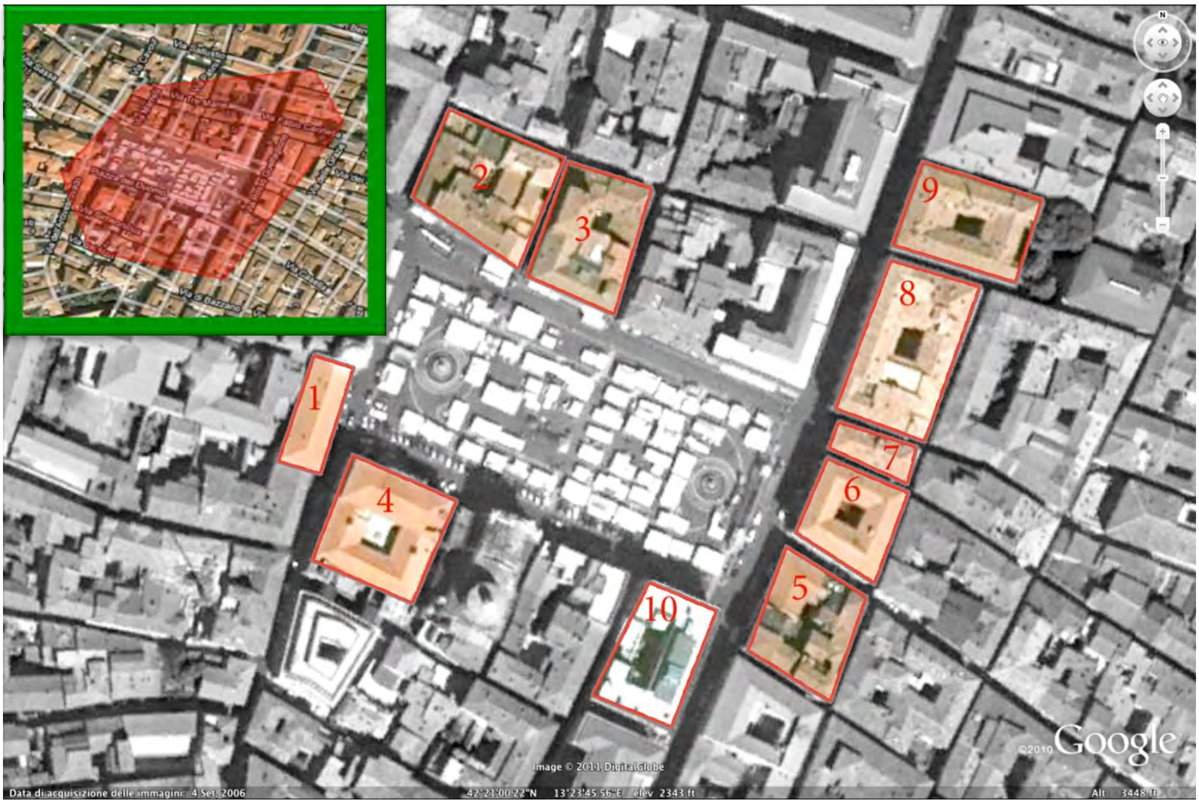

Figure 5-8: The ten buildings selected inside the city center of L'Aquila and in the high left corner there is the software interface for selected area.

The ten buildings selected have the follow features (Table 5-1; Table 5-2 and Table 5-3):

	NAME	TYPE OF INFRASTRUCTURE		
N°	Name	PEOPLES Classification		
1	Building 1	Facilities	Residential	Housing Units
2	Building 2			
3	Building 3			
4	Building 4		Commercial	Office Buildings
5	Building 5			
6	Building 6			
7	Building 7		Residential	Housing Units
8	Building 8			
9	Building 9		Commercial	Hotels - Accommodations
10	Building 10		Residential	Housing Units

Table 5-1: Data input for Localization and Type of Infrastructure.

DAMAGE FEATURES

N°	Soil Category	Topographic Condition	Building typology	Seismic Design Level	Type of Building	Description	Stories
1	B	T1	Normal Building	Low code	URMM	Unreinforced Masonry Bearing Walls	3
2					C1M	Concrete Moment Frame	4
3				High code	RM2L	Reinforced Masonry Bearing Walls with Precast Concrete Diaphragms	3
4			Special Building	Moderate code			2
5			Normal Building				3
6							
7					C1M	Concrete Moment Frame	4
8					RM2M	Reinforced Masonry Bearing Walls with Precast Concrete Diaphragms	
9			Special Building	Low code	URMM	Unreinforced Masonry Bearing Walls	
10			Normal Building	High code	C2M	Concrete Shear Walls	

Table 5-2: Data input for Damage features.

RESILIENCE FEATURES

N°	Occupancy Class	Description	Sub-category	Total Occupancy Area [m^2]
1	100% RES3b	Multi Family Dwelling – small	Triplex/Quads	2.140,08
2				6.641,45
3	67% RES3a 33% COM1	Multi Family Dwelling – small Retail Trade	Duplex Dept Store, 1 st	4.952,12
4	100% COM4	Prof./Tech./Business Services	Office, Small	3.841,74
5				4.392,80
6				2.702,28
7	75% RES3a 25% COM1	Multi Family Dwelling – small Retail Trade	Duplex Dept Store, 1 st	1.213,80
8	100% RES3b	Multi Family Dwelling – small	Triplex/Quads	6.628,45
9	100% RES4	Temp. Lodging	Hotel, medium	4.850,70
10	100% RES3b	Multi Family Dwelling – small	Triplex/Quads	4.719,35

Table 5-3: Data input for Resilience features.

The test evaluates four different recovery plans having the same limit state characteristics but different site availability - i.e. number of construction sites that might fall within the considered area.

The first and fourth scenarios have, respectively, the maximum and minimum availability, that consists having respectively a maximum of 10 and 0 building construction sites per day inside the selected area (there is not limitation for simultaneous start of construction sites). The second scenario has the maximum limit of five construction building sites per day and of four simultaneous starts of construction building sites. While, the third scenario has the limit of one building site per day (no-limit for simultaneous starts of building sites). In all cases there is no-limit on economic budget. It was found the following results that are summarized in the tables below assuming a return period for the earthquake of 2475 years and a control period of 2 years.

GLOBAL RESILIENCE OUTPUT DATA

Case:	I	II	III	IV
Community Resilience (Ta; Tb) [%]:	98,3	95,0	74,8	58,2
Community Functionality (Tb) [%]:	100,0	100,0	88,6	58,2

Table 5-4: Output data of Global Resilience for each case.

DAMAGE OUTPUT DATA FOR EACH BUILDING

Building N°	S_d [m]	S_a [g]	PDS-s	PDS-m	PDS-e	PDS-c	DPDS-n	DPDS-s	DPDS-m	DPDS-e	DPDS-c	CBT [days]	SF [%]	RC [$]
1	0,222	0,136	99	94	73	36	1	5	21	37	36	138	45,2	905294
2	0,156	0,242	100	97	71	32	0	3	26	38	32	131	48,1	2651047
3	0,745	0,041	84	55	14	2	16	29	41	12	2	31	84,9	418350
4	0,627	0,048	83	60	19	3	17	24	40	16	3	40	82,5	595000
5	0,506	0,060	90	75	36	7	10	16	38	30	7	64	74,3	1108495
6	0,506	0,060	90	75	36	7	10	16	38	30	7	64	74,3	681906
7	0,300	0,126	96	82	31	7	4	13	51	24	7	59	74,1	201859
8	0,421	0,090	91	75	27	4	9	16	48	22	4	53	77,8	983131
9	0,333	0,091	97	84	46	12	3	13	38	33	12	82	67,4	1653549
10	0,548	0,069	87	45	4	0	13	42	41	4	0	19	89,2	242968

Table 5-5: Output Damage data for each building.

Table Legend:
N°: Infrastructure number [-];
S_d: Peak displacement response [m];
S_a*:* Peak acceleration response [g];
PDS-: Probabilities of damage state (s: slight, m: moderate, e: extensive and c: complete) [%];
DPDS-: Discrete probabilities of damage state (n: none, s: slight, m: moderate, e: extensive and c: complete) [%];
CBT: Construction building time [days];
SF: Start functionality value [%];
RC: Recovery cost [$].

Figure 5-9: Histogram of discrete probability of damage states.

From the Table 5-5 and Figure 5-9 it is possible to see how are distributed the damage states in all buildings presented in the selected area. The buildings that have the higher damages are the buildings 1, 2 and 9. This result was easy to predict because the three buildings are designed with low seismic design level (low code). Instead Figure 5-10 shows the contour plot of functionality immediately after the disaster. In this case, the lower values of functionality are near buildings 1 and 2 in the plot, because the functionality is diffused through the weighted average.

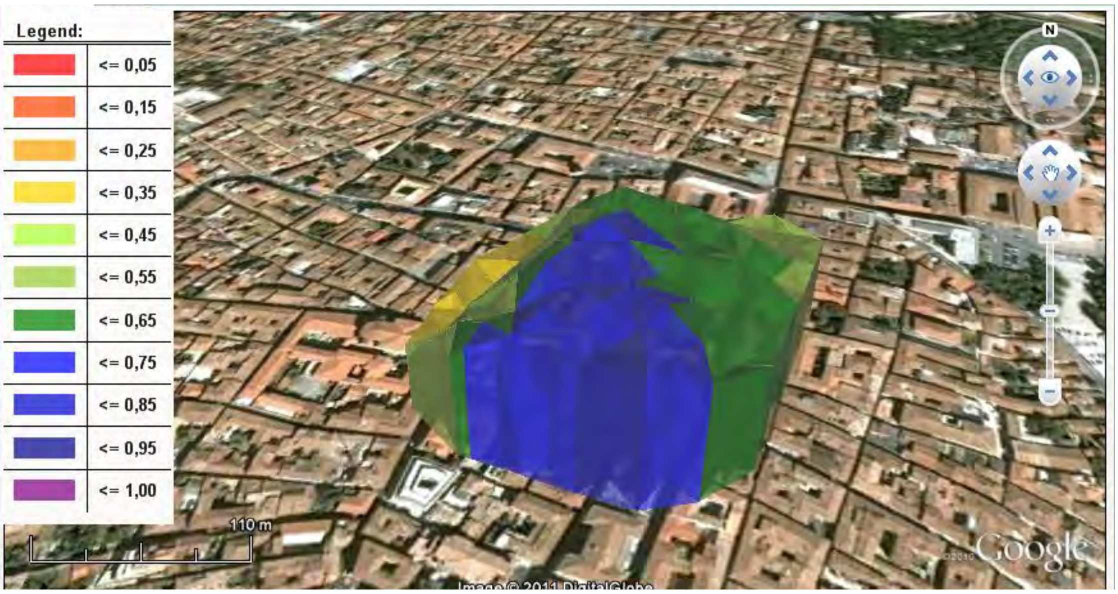

Figure 5-10: Contour plot of functionality.

RESILIENCE OUTPUT DATA FOR EACH BUILDING

Case:	I	II	III	IV	I	II	III	IV
Building N°	AT [days]				RES [%]			
1	0	133	152	inf.	95,6	82,1	80,2	45,2
2	0	91	336	inf.	96,0	87,2	63,8	48,1
3	0	0	0	inf.	99,6	99,6	99,6	84,9
4	0	0	51	inf.	99,4	99,4	97,5	82,5
5	0	34	843	inf.	98,7	96,9	61,3	74,3
6	0	51	744	inf.	98,7	96,0	61,3	74,3
7	0	34	643	inf.	98,6	96,6	61,7	74,1
8	0	0	942	inf.	98,9	98,9	64,3	77,8
9	0	66	511	inf.	97,7	93,0	61,4	67,4
10	0	0	118	inf.	99,8	99,8	97,2	89,2

Table 5-6: Output data of Resilience features for each building and each case.

Table Legend:
AT: Administrative time [days];
RES: Resilience over the control period [%].

Table 5-6 shows the administrative time, the resilience over the control period and the rank in recovery plan for each building.

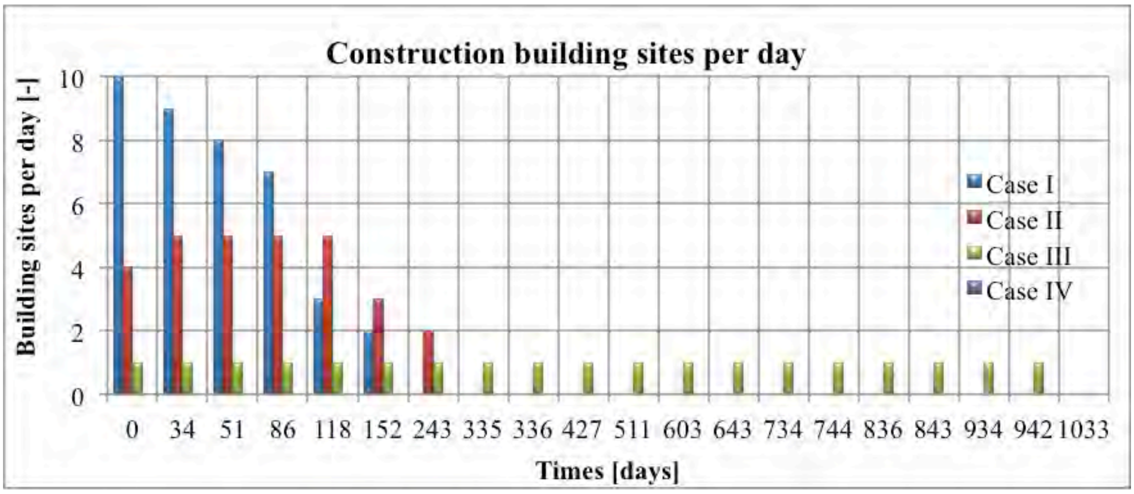

Figure 5-11: The number of building sites per day for each case.

As mentioned above, the only difference between various cases is the buildings sites availability (men / day), which is shown on Figure 5-11. Case I requests immediately an higher number men per day, while cases III, IV and II (more realistic and efficient) have a constant or homogeneous distribution in the time.

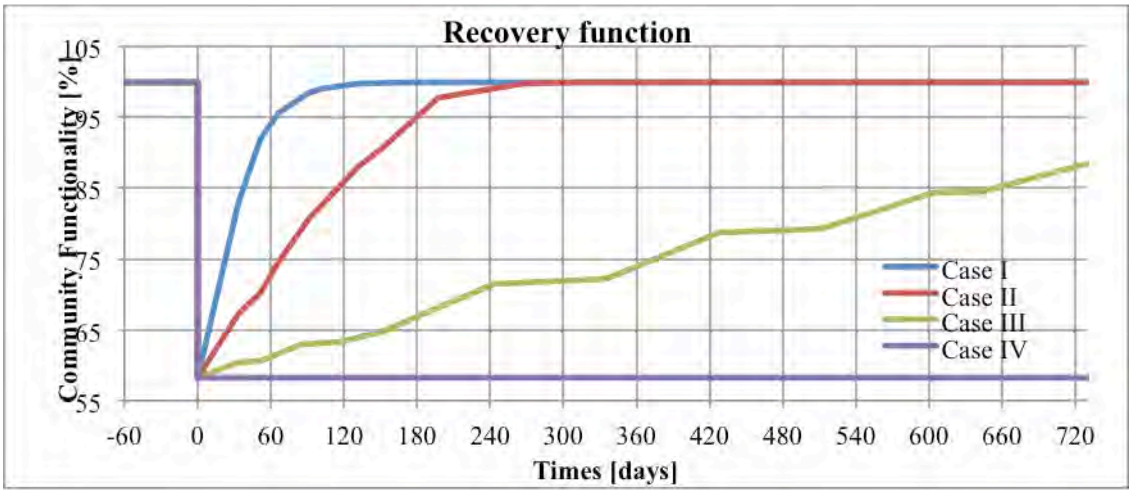

Figure 5-12: Recovery function for each case

From the Figure 5-12, that shows the four functionality functions for each case, it is possible to observe that the case I is the most resilient, while the case IV has the smallest values of resilience. The case III is like a cumulative sum of all functionality functions of the buildings, because the works follow each other sequentially.

RESILIENCE INDEX

Case:	I	II	III	IV
Community Resilience index [%]:	92,0	87,6	80,6	58,2
Time of completion of work, T_{CW} [days]:	183,9	316,8	1033,0	inf.

Table 5-7: Output data of Global Resilience for each case.

The resilience index in Table 5-7 is defined as the value of community resilience from the disaster time T_{Dis} to the time of completion of the works T_{CW} (at this time the functionality will be equal to 100% or highest value). This index decreases with decreasing of the velocity of recovery, so it is a good parameter to evaluate the performance of the community and of the chosen recovery plan.

6 CONCLUSIONS

This paper presents a software able to evaluate the disaster resilience of communities and systems in general using the PEOPLES framework methodology. The main advantage with respect to the other software already available is the simple graphical interface that uses the Google earth visualization. This platform can be used both for data input, but also for output visualization. The output file are available both in a excel format and in a KML file readable by Google Earth.

The PEOPLES framework developed in the software integrates the information from different fields in a unique function that reach results that are unbiased by uninformed intuitions or preconceived notions of how large or how small the risk is.

Finally the program and the methodology are tested using the case study of the 2009 Italian earthquake in L'Aquila. Four different scenario events are assumed to describe the reconstruction phase (recovery) and compared using the proposed platform.

Some assumptions that are made for one case can not be so important for others, so engineers and decision makers during the calculation of the community resilience index should focus on the assumptions that most influence the problem at hand.

ACKNOWLEDGMENTS

The research leading to these results has received funding from the European Community's Seventh Framework Programme - Marie Curie International Reintegration Actions - FP7/2007-2013 under the Grant Agreement n° PIRG06-GA-2009-256316 of the project ICRED - Integrated European Disaster Community Resilience.

REFERENCES

[1] G.P. Cimellaro, A.M. Reinhorn, and M. Bruneau. Framework for analytical quantification of disaster resilience. *Engineering Structures*, **32**(2010), 3639–3649, 2010.

[2] Renschler, C., Frazier, A., Arendt, L., Cimellaro, G. P., Reinhorn, A. M., and Bruneau, M. (2010). "Framework for Defining and Measuring Resilience at the Community Scale: The PEOPLES Resilience Framework." MCEER Technical Report –MCEER-10-006, pp. 91, University at Buffalo (SUNY), The State University of New York, Buffalo, New York.

[3] C. Renschler, A. Frazier, L. Arendt, G.P. Cimellaro, A.M. Reinhorn, and M. Bruneau. "Developing the "PEOPLES" resilience framework for defining and measuring disaster resilience at the community scale." *Proceedings of the 9th US National and 10th Canadian Conference on Earthquake Engineering (9USN/10CCEE),* Toronto, Canada, July 25-29, 2010, Year.

[4] FEMA. HAZUS-MH Version 1.1, FEMA`s Software Program for Estimating Potential Losses from Disasters, Technical Manual *Federal Emergency Management Agency and U.S. Army Corps of Engineers,* Washington D.C., January 2005, Available at: www.fema.gov/hazus, 2005

[5] Miles, S.B. and Chang, S.E. (2011) "ResilUS – A community disaster resilience model" *Journal of Cartography and GIS (CAGIS)*, 37(5).

[6] Miles, S.B. and Chang, S.E. (2006) "Modeling community recovery from earthquakes" *Earthquake Spectra,* 22(2) 439-458.

[7] Miles, S. B. and Chang, S. E. (2007) A Simulation Model of Urban Disaster Recovery and Resilience: Implementation for the 1994 Northridge Earthquake, MCEER Technical Report MCEER-07-0014.

[8] Lang, D. H., Gutiérrez C., F. V. and Lindholm, C. D. (2009) "RISe – Risk Illustrator for SELENA Technical User Manual v2.0" prepared at NORSAR P.O. Box 53, NO-2027 Kjeller, Norway.

[9] Molina, S., Lang, D. H., Lindholm, C. D. and Lingvall, F. (2010) "User Manual for the Earthquake Loss Estimation Tool: SELENA" NORSAR and Universidad de Alicante.

[10] EN 1998-1:2004, Eurocode 8: Design of structures for earthquake resistance — Part 1: General rules, seismic actions and rules for buildings.

[11] International Code Council (ICC) International Building Code (IBC-2006).

[12] Indian Standard IS-1893: Criteria for earthquake resistant design of structures.

[13] Applied Technology Council (1996). "Seismic Evaluation and Retrofit of Concrete Buildings Volume 1." Applied Technology Council Report No. ATC-40.

[14] Applied Technology Council (2004). "Evaluation and Improvement of Inelastic Seismic Analysis Procedures." Applied Technology Council Report No. ATC-55.

[15] Cimellaro, G. P., Reinhorn, A. M., and Bruneau, M. (2006). "Quantification of seismic resilience." Proceedings of the 8th National Conference of Earthquake Engineering, paper 1094, April 18-22, 2006, San Francisco, California. .

[16] Cimellaro, G. P., Fumo, C., Reinhorn, A. M., and Bruneau, M. (2009). "Quantification of Seismic Resilience of Health care facilities " MCEER Technical Report-MCEER-09-0009, Multidisciplinary Center for Earthquake Engineering Research, Buffalo, NY.

[17] Cimellaro, G. P., Reinhorn, A. M., and Bruneau, M. (2010). "Performance-based metamodel for health care facilities." Earthquake Engineering & Structural Dynamics, article first published online: 16 DEC 2010, DOI: 10.1002/eqe.1084.

[18] NTC 2008. Norme Tecniche per le Costruzioni.

COMPDYN 2011
ECCOMAS Thematic Conference on
Computational Methods in Structural Dynamics and Earthquake Engineering
M. Papadrakakis, M. Fragiadakis, V. Plevris (eds.)
Corfu, Greece, 25-28 May 2011

RESILIENCE-DRIVEN DISASTER MANAGEMENT OF CIVIL INFRASTRUCTURE

Paolo Bocchini and Dan M. Frangopol

Advanced Technology for Large Structural Systems (ATLSS) Engineering Research Center
Department of Civil and Environmental Engineering
Lehigh University
117 ATLSS Dr., Bethlehem, PA 18015, USA
e-mail: {paolo.bocchini, dan.frangopol}@lehigh.edu

Keywords: Resilience, Disaster Management, Optimization, Bridge Networks, Distributed Civil Infrastructure Systems.

Abstract. *After the occurrence of a natural (e.g. earthquake, hurricane, flood, fire) or technological (e.g. explosion, terrorist attack) extreme event, the distributed infrastructure systems and their individual structural components are likely to be significantly damaged. For the emergency response and the quick socio-economic recovery of the region, transportation networks, lifelines, and infrastructure in general play a role of utmost importance. For this reason, the so called "disaster management" has always to be focused on restoring as quickly as possible the proper functionality of the infrastructure under limited financial resources and other logistic constraints. The main focus of the present paper is to address this problem and provide a general framework to assist the decision making process in these critical situations. In fact, the main issue in these scenarios is to have a practical and robust way to collect and analyze data with a fast and reliable tool that can lead to quick but informed decisions.*

Several decision support systems for emergency and/or disaster management have been proposed in the last decades. The proposed approach is based on the holistic concept of resilience, which is gaining momentum as metric for the evaluation of the efficiency of the restoration activities. Resilience is used in this paper as one of the optimization criteria for the rehabilitation planning.

An illustrative example is presented to clarify the applicability of the proposed approach to transportation networks.

1 INTRODUCTION

Lately, the concept of resilience and the interest on its possible practical applications is gaining a lot of momentum. “Resilience” has become a very popular keyword for articles, symposia, workgroups, special sessions, research projects, and, in general, in the press. I civil engineering, the use of resilience is associated with disaster loss mitigation and disaster management [1, 2], especially for analyses of distributed civil infrastructure systems [3, 4] and lifelines [5].

This paper promotes a novel paradigm for the resilience-driven disaster management of civil infrastructure, with application to bridge networks. A multi-criteria perspective is proposed as optimal way to develop a framework for the quantitative assessment of resilience and its use for assisted decision making in the disaster management practice [6].

In the past years, several *systemic* definitions of resilience and frameworks for its use have been proposed. Some of the most comprehensive can be found in [7, 8, 9, 10, 11], while Rose [12] presents an interesting review of possible definitions. Section 2 focuses on the *analytical* definitions of resilience, with particular emphasis on the family of the formulation that is used in this paper. Section 3 describes the proposed multi-objective approach. Section 4 presents an illustrative example involving the post-disaster restoration of a bridge network. Finally, Section 5 collects the concluding remarks.

2 ANALYTICAL DEFINITIONS OF RESILIENCE

In the literature, several analytical definitions of resilience have been proposed and applied. Zhou et al. [13] have collected a list where the first definition of resilience dates back to 1973 [14]. The first seed of the definition of resilience that is most popular nowadays can be found in [15]: “Resilience is the ability of human communities to withstand external shocks or perturbations to their infrastructure and to recover from such perturbations”. Along the decades, several authors have focused on one or more aspects of resilience, such as the ability of a structure or system to withstand an extreme event (better called “capacity” for structural applications) or the time required to recover the original functionality (sometimes referred to as “rapidity”). In 2003, a large group of researchers introduced the concept of “resilience triangle”, to combine the various aspects associated with resilience [16]. The resilience triangle was originally used to describe the “loss of resilience” and was associated with the equation:

$$R_1 = \int_{t_0}^{t_r} [100 - Q(t)] \; \mathrm{d}t \tag{1}$$

where R_1 is the loss of resilience experienced by the system, t_0 is the time instant when the extreme event occurs, t_r is the time when the functionality of the infrastructure is fully restored, Q is the percentage “functionality” (or “quality”, or “serviceability”) of the system, and t is time. Figure 1 shows a graphical interpretation of the resilience triangle and of the resilience loss R_1 in Eq. (1). The definition in Eq. (1) has the merit of connecting analytically the concepts of resilience and functionality and has been used in several subsequent articles [17, 18, 19].

Cimellaro et al. [20, 21] proposed a different analytical formulation that focused on resilience itself, rather than on its loss:

$$R_2 = \int_{t_0}^{t_r} Q(t) \, \mathrm{d}t \tag{2}$$

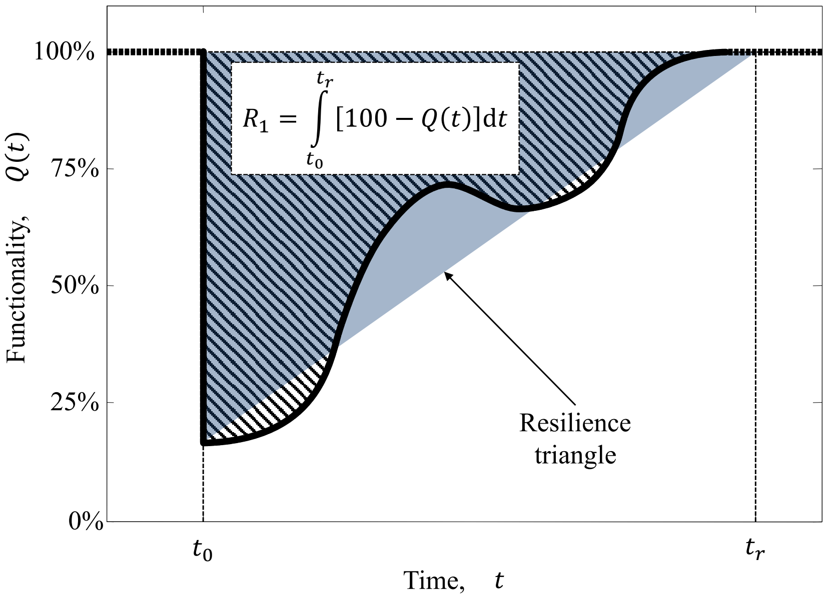

Figure 1: Resilience triangle (shaded) and resilience loss R_1 (diagonal partern)

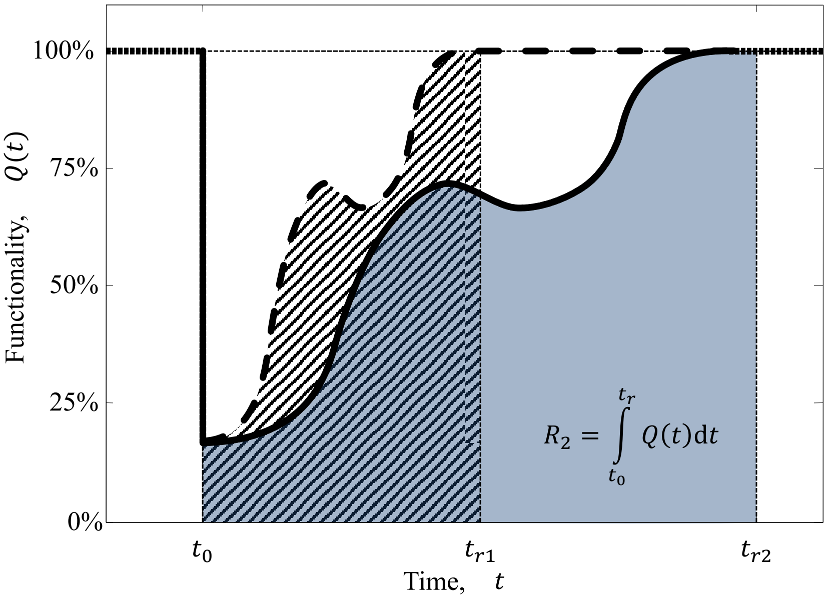

Figure 2: Resilience according to Eq. (2). The faster recovery path (dashed) yields a lower value of resilience (area with diagonal pattern) than the slower recovery path (solid).

This definition branches out from the resilience triangle and has the advantage of being able to take into account restoration patterns that bring the final functionality to a level different (i.e. lower or even higher) from 100%. However, Eq. (2) has a drawback that makes it inappropriate for some applications. In fact, the integral is computed between t_0 and t_r and this can result in low values of resilience for fast restoration strategies (see Figure 2).

To overcome the mentioned issue, Bocchini and Frangopol [22] proposed to modify the

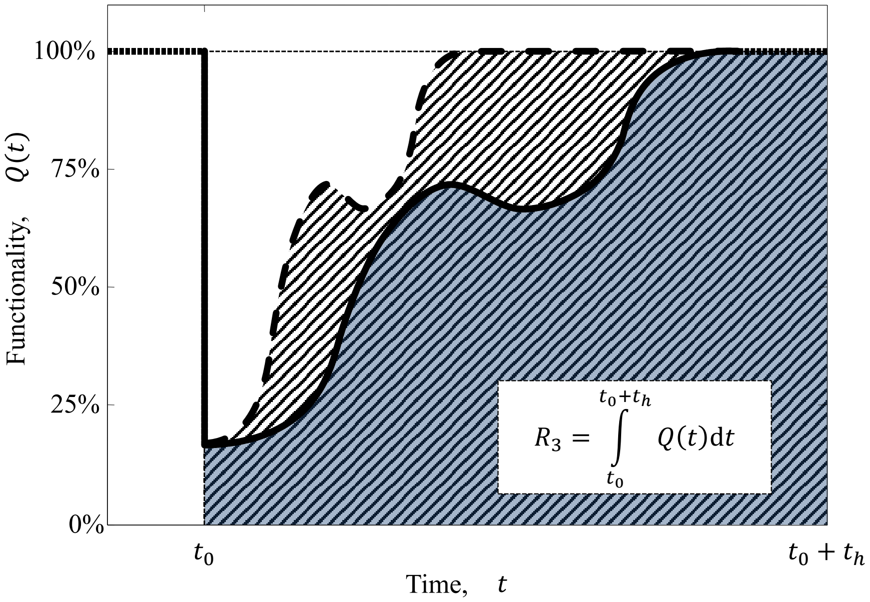

Figure 3: Resilience according to Eq. (3). The faster recovery path (dashed) correctly yields a higher value of resilience (area with diagonal pattern) than the slower recovery path (solid).

analytical definition of resilience, focusing on a fixed time horizon t_h:

$$R_3 = \int_{t_0}^{t_0+t_h} Q(t)\,\mathrm{d}t \tag{3}$$

Figure 3 shows that this definition correctly provides higher (i.e. better) values of resilience for the faster (i.e. better) recovery paths. The definition in Eq. (3) can be used to compare, rank, and optimize [22] the various disaster management strategies. The investigated time horizon t_h does not need to be chosen larger than the longest recovery time. In fact, if the recovery is not complete at $t = t_0 + t_h$, Eq. (3) is still applicable and yields, as expected, a small value of resilience. Unfortunately, R_3 still shares a shortcoming with R_1 and R_2: in all these cases resilience is measured in units of time, since $Q(t)$ is non-dimensional. Despite the fact that Eq. (3) computes correct values of resilience, these values expressed in units of time can be difficult to interpret and communicate to decision makers.

For this reason, a normalization factor was later introduced [4, 23]:

$$R_4 = \frac{\int_{t_0}^{t_0+t_h} Q(t)\,\mathrm{d}t}{t_h} \tag{4}$$

The numerator of Eq. (4) represents the area underneath the recovery path $Q(t)$; the denominator represents the value of resilience in case the event did not occur or had no effects on functionality (i.e. $100\% \cdot t_h = t_h$). Figure 4 provides a graphical interpretation of Eq. (4).

Depending on the general frameworks and applications where the analytical definitions of resilience in Eqs. (1)–(4) are used, each of them can be appropriate. However, R_4 is the most versatile and easy to use for decision makers.

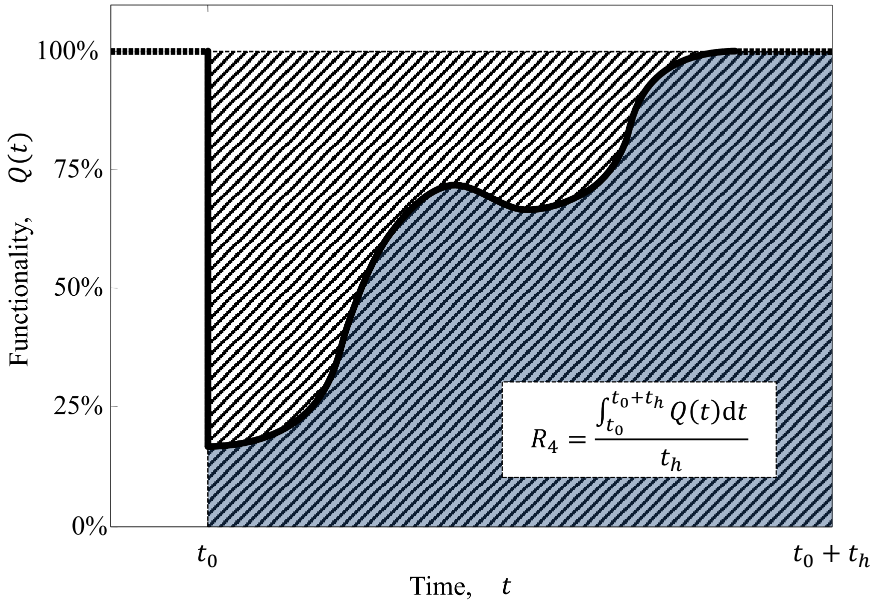

Figure 4: Resilience according to Eq. (4). The numerator of Eq. (4) is the shaded area, the denominator is the area of the large rectangle (area with diagonal pattern).

3 MULTI-CRITERIA PERSPECTIVE

Resilience is a concept that intrinsically includes several metrics. For instance, Bruneau et al. [16] define the four "properties" of resilience (i.e. "robustness", "rapidity", "redundancy", and "resourcefulness") and the four "dimensions" of resilience (i.e. "technical", "organizational", "social", and "economic"). The need of capturing all these aspects has led researchers to pursue two conflicting objectives: (i) on one hand the desire of having a synthetic, scalar index of resilience, for immediate comparison and ranking of different strategies; (ii) on the other hand the goal of representing, within a single concept, a broad set of "properties" and "dimensions". In this paper, it is proposed to reconcile these two conflicting objectives by means of a multi-criteria analysis and Pareto optimization.

Chang and Shinozuka [5] combined the concept of the resilience triangle with a probabilistic approach. To do this, they had to deviate from the basic definition in Eq. 1 and introduce acceptable thresholds for the post-event functionality $Q(t_0)$ and for the time to complete recovery t_r. This can be interpreted as a first attempt to introduce two criteria in the analysis and treat them as two separate limit states.

Similarly, Zobel [24] critics the fact that all the analytical definitions of resilience can yield the same value for very different scenarios in terms of initial loss and time to recovery, and this can be unacceptable or misleading for decision makers. Therefore, Zobel [24] proposes an "adjusted resilience function" that incorporates information on the relative importance of the time to complete recovery and the initial functionality loss, as perceived by decision makers.

The proposed approach consists in leaving the values of the important variables of the problem as separate metrics and combining them in the framework of Pareto optimization. In this way, the term "resilience" can be used to refer to the well-defined indicator R_4 in Eq. (4). Therefore, the search for the best recovery strategy should include resilience as one of its objectives, together with other objectives and constraints. For instance, for the case of disaster management of the civil infrastructure, the conflicting objectives are resilience [22], total cost of interventions [22], time to reach a target functionality level [25], and time to complete recovery [25]. As expected, resilience should be maximized, while the other values should be minimized. Moreover, Pareto optimization allows to introduce separate constraints and requirements, such as maximum cost of the interventions [22], minimum required functionality at a specific time instant [25], maximum number of simultaneous interventions on the components of a distributed system [23], and additional constraints on the individual restoration parameters. Therefore, given all the required data that depend on the specific application, the general optimization problem can be formulated as:

Find:

$$\text{parameters of the rehabilitation strategy} \tag{5}$$

so that

$$R = \text{maximum} \tag{6}$$
$$C = \text{minimum} \tag{7}$$
$$T_i = \text{minimum} \qquad \forall\ i = 1, 2, \ldots, I \tag{8}$$
$$T = \text{minimum} \tag{9}$$

subject to the constraints

$$C \leq C_{max} \tag{10}$$
$$Q(t_h^T) \geq Q_h^T \qquad \forall\ h = 1, 2, \ldots, H \tag{11}$$
$$N_{SI}(t) \leq N_{SI\,max} \qquad \forall\ t \in [t_0, t_0 + t_h] \tag{12}$$
$$\text{and constraints on the individual rehabilitation parameters} \tag{13}$$

where R is the resilience of the system, C is the total cost of the restoration interventions, T_i is the time required to reach target functionality level Q_i, T is the time of total recovery, C_{max} is the amount of available funding, Q_h^T is the target functionality level that must necessarily be provided at time t_h^T, N_{SI} is the number of simultaneous rehabilitation interventions applied to the system, and $N_{SI\,max}$ is the maximum allowable number of simultaneous interventions.

4 ILLUSTRATIVE EXAMPLE

The case of the post-disaster restoration of a bridge network is considered as a qualitative example. The functionality of the network $Q(t)$ is defined as its ability to effectively redistribute traffic flows and is a function of the total travel time spent and total travel distance covered by the network users that depart during a fixed peak traffic hour [22]. The rehabilitation strategies consist in the schedules of the interventions on the various bridges and the amount of funding invested on each bridge which, in turn, determines the quality and speed of the restoration [22].

The objectives are the maximization of the resilience R, defined as in Eq. (4), the minimization of the total cost of interventions C, the minimization of the time T_1 required to reach the functionality level $Q_1 = 50\%$, and the minimization of the total recovery time T.

The total restoration cost cannot exceed the maximum amount of funding C_{max}. Moreover, constraints on the minimum functionality level (Q_1^T and Q_2^T) at two time instants (t_1^T and t_2^T) are implemented. Finally, it is assumed that the maximum number of bridges that can undergo simultaneous interventions is $N_{SI\,max} = 5$.

Three restoration strategies are considered (namely, strategy A, B, and C) and their expected recovery paths are represented in Figure 5. All the strategies are associated with similar values

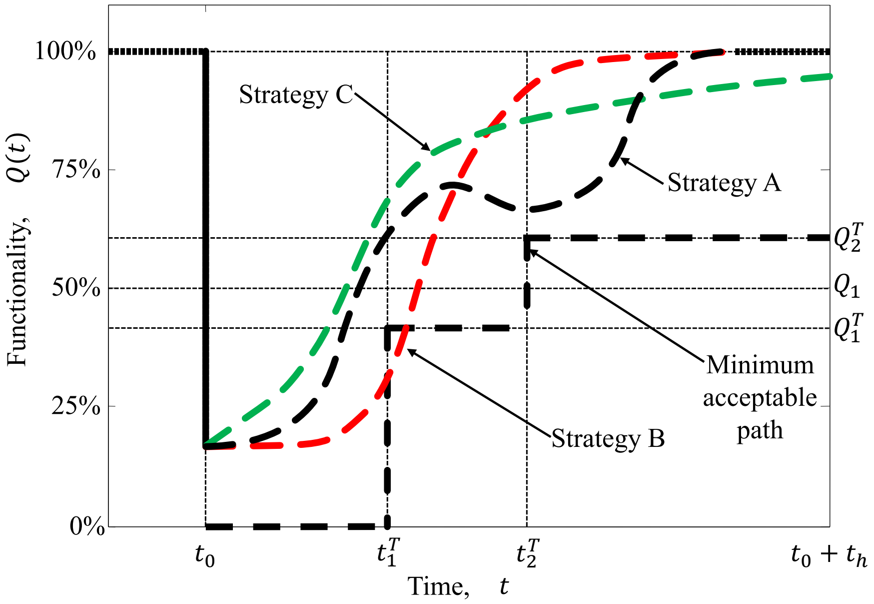

Figure 5: Three possible recovery strategies associated with similar values of resilience.

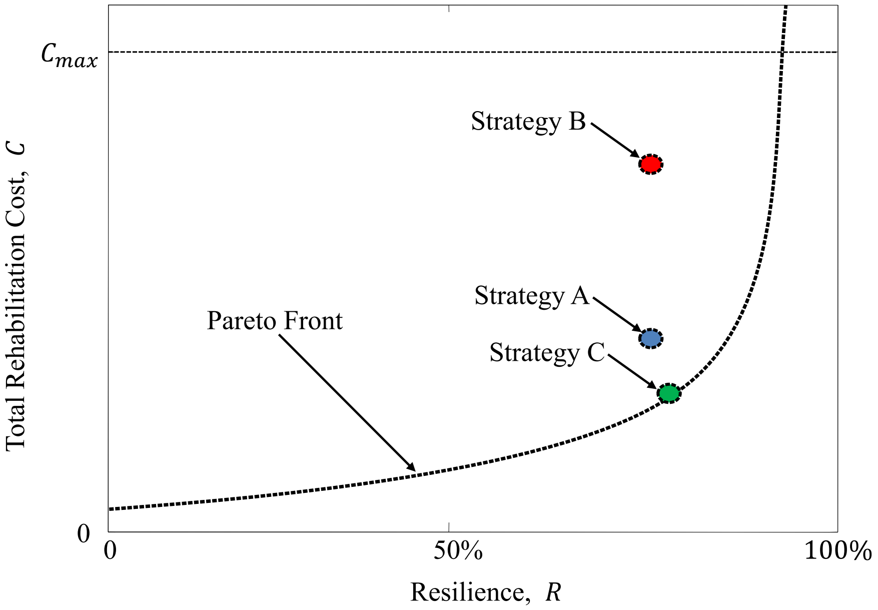

Figure 6: Pareto front in the plane of resilience and cost.

of resilience, defined by Eq. (4). Strategy A is characterized by a reduction of the functionality around time t_2^T. This usually happens when interventions start on some major bridges, requiring a (further) reduction of their flow capacity. It would be desirable to avoid negative slopes in the recovery path, and this can be required adding a constraint on the derivative of $Q(t)$. Nevertheless, strategy A yields a good value of resilience, is compatible with the requirements on the minimum functionality levels at t_1^T and t_2^T, makes the network reach $Q_1 = 50\%$ in a very short time, and the total restoration is completed significantly before the end of investigated time horizon. Strategy B has the same total recovery time as strategy A and a very similar overall

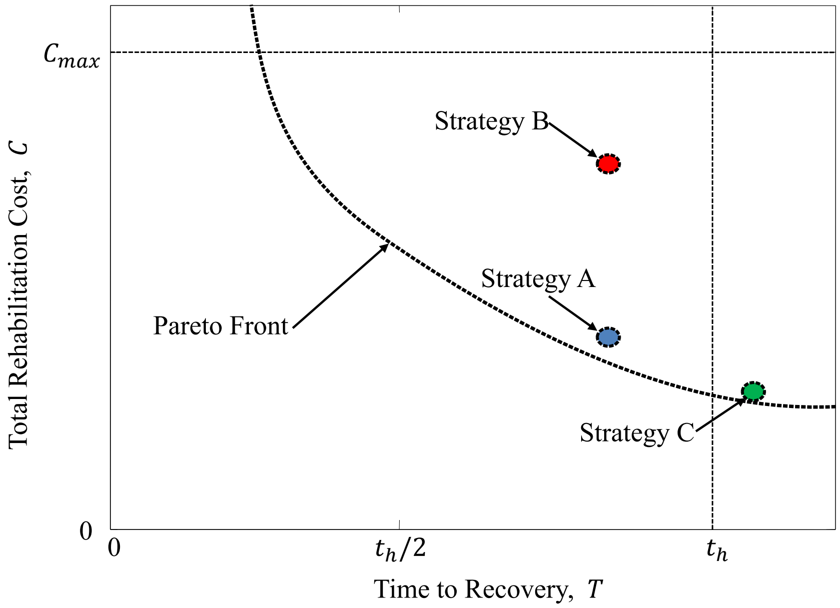

Figure 7: Pareto front in the plane of time to recovery and cost.

resilience. However, strategy B is not compliant with the constraint at time t_1^T (it crosses the dashed line, that represents the minimum required functionality in Figure 5). For this reason, strategy B should be discarded. Strategy C provides a very quick initial phase of the restoration activities and makes the network reach the values $Q_1 = 50\%$ in the shortest time, compared to the other strategies. Strategy C is also compliant with the constraints at t_1^T and t_2^T and provides a value of resilience that is slightly larger than the other strategies. This is achieved despite the fact that adopting strategy C, the network functionality is not entirely restored during the investigated time horizon: $Q(t_0 + t_h) < 100\%; \quad T > t_h$.

Figure 6 shows the Pareto front in the space of the two objectives resilience and total rehabilitation cost. A solution is said to be "Pareto-optimal" if there is no other solution that yields an improvement in one of the objectives, without worsening at least another. The front shows that to achieve higher values of resilience, more financial resources are required. All the strategies have a total rehabilitation cost that is lower than the available funding. Strategy C, in particular, requires the lowest investment and is on the Pareto front. It is very common that solutions that do not restore the entire functionality are very economical. In fact, avoiding a few very expensive bridge rehabilitation can determine a significant reduction in the cost, with a very small loss of the overall network functionality.

Figure 7 presents the Pareto front in the space of time to recovery and cost. As already mentioned, strategies A and B have very similar recovery times, while strategy C restores the entire functionality only after the end of the investigated time horizon. In this case both strategies A and C are very close to the Pareto front.

Similar plots in the spaces of the other objectives and of the design variables can be provided. Depending on the relative importance of the various objectives for the specific scenario, decision makers will choose the most convenient solution. For this example, strategy C seems to be the best compromise, for the reasons explained previously.

The procedure presented in this illustrative example can be automated by means of multi-objective genetic algorithms [26]. Numerical applications of the proposed approach to realistic bridge networks, solved by means of an automated procedure based on genetic algorithms can be found in [22, 23, 25].

5 CONCLUSIONS

A resilience-driven approach to the disaster management of the civil infrastructure has been presented. A new paradigm to the use of resilience is proposed, where resilience is one of the objectives in a multi-criteria analysis aimed at finding the best recovery path and the associated intervention strategy.

In the past, the intrinsic holistic nature of the concept of resilience has created a contrast between its *systemic definitions* (that try to be as comprehensive as possible) and its *analytical definitions* (that pursue a single scalar metric). In the proposed approach, a consistent resilience indicator is used in conjunction with other metrics and constraints that together define the best disaster management strategy. This approach reconciles the two diverging needs mentioned previously.

The framework of multi-criteria Pareto optimization appears to be the perfect paradigm to develop studies on resilience and disaster management within this novel perspective.

AKNOWLEDGMENTS

The support from (a) the National Science Foundation through grant CMS-0639428, (b) the Commonwealth of Pennsylvania, Department of Community and Economic Development, through the Pennsylvania Infrastructure Technology Alliance (PITA), (c) the U.S. Federal Highway Administration Cooperative Agreement Award DTFH61-07-H-00040, and (d) the U.S. Office of Naval Research Contract Number N-00014-08-0188 is gratefully acknowledged. The opinions and conclusions presented in this paper are those of the writers and do not necessarily reflect the views of the sponsoring organizations.

REFERENCES

[1] W. N. Carter, *Disaster management: a disaster manager's handbook*. Asian Development Bank, 1992.

[2] D. P. Coppola, *Introduction to international disaster management*. Butterworth Heinemann, 2007.

[3] D. M. Frangopol, P. Bocchini, Bridge network performance, maintenance, and optimization under uncertainty: accomplishments and challenges. *Structure and Infrastructure Engineering*, in press, 2011.

[4] G. P. Cimellaro, , A. M. Reinhorn, M. Bruneau, Framework for analytical quantification of disaster resilience. *Engineering Structures*, **32**, 3639–3649, 2010.

[5] S. Chang, M. Shinozuka, Measuring improvements in the disaster resilience of communities. *Earthquake Spectra*, **20**, 739–755, 2004.

[6] W. A. Wallace, F. D. Balogh, Decision Support Systems for Disaster Management. *Public Administration Review*, **45**, 134–146, 1985.

[7] A. Rose, S. Y. Liao, Modeling Regional Economic Resilience to Disasters: A Computable General Equilibrium Analysis of Water Service Disruptions. *Journal of Regional Science*, **45**, 75–112, 2005.

[8] S. B. Miles, S. E. Chang, Modeling Community Recovery from Earthquakes. *Earthquake Spectra*, **22**, 439–458, 2006.

[9] Z. Çağnan, R. A. Davidson, S. D. Guikema, Post-Earthquake Restoration Planning for Los Angeles Electric Power. *Earthquake Spectra*, **22**, 589–608, 2006.

[10] M. Bruneau, A. Filiatrault, G. Lee, T. O'Rourke, A. Reinhorn, , M. Shinozuka, K. Tierney, *White Paper on the SDR Grand Challenges for Disaster Reduction*. Multidisciplinary Center for Earthquake Engineering Research, University at Buffalo, The State University of New York, 2007.

[11] N. Xu, S. D. Guikema, R. A. Davidson, L. K. Nozick, Z. Çağnan, K. Vaziri, Optimizing scheduling of post-earthquake electric power restoration tasks. *Earthquake Engineering & Structural Dynamics*, **36**, 265–284, 2007.

[12] A. Rose, Defining and measuring economic resilience to disasters. *Disaster Prevention and Management*, **13**, 307–314, 2004.

[13] H. Zhou, J. Wang, J. Wan, H. Jia, Resilience to natural hazards: a geographic perspective. *Natural Hazards*, **53**, 21-41, 2010.

[14] C. S. Holling, Resilience and Stability of Ecological Systems. *Annual Review of Ecology and Systematics*, **4**, 1–23, 1973.

[15] P. Timmerman, Vulnerability. Resilience and the collapse of socieiy: A review of models and possible climatic applications. *Environmental Monograph, Institute for Environmental Studies, University of Toronto*, **1**, 1981.

[16] M. Bruneau, S. E. Chang, R. T. Eguchi, G. C. Lee, T. D. O'Rourke, A. M. Reinhorn, M. Shinozuka, K. Tierney, W. A. Wallace, D. V. Winterfeldt, A Framework to Quantitatively Assess and Enhance the Seismic Resilience of Communities. *Earthquake Spectra*, **19**, 733–752, 2003.

[17] M. Bruneau, A. M. Reinhorn, Overview of the resilience concept. *Proceedings of the* 8^{th} *National Conference of Earthquake Engineering*, San Francisco, CA, April 18–22, 2006.

[18] M. Bruneau, A. Reinhorn, Exploring the concept of seismic resilience for acute care facilities. *Earthquake Spectra*, **23**, 41–62, 2007.

[19] M. Bruneau, Enhancing the Resilience of Communities Against Extreme Events from an Earthquake Engineering Perspective. *Journal of Security Education*, **1**, 159–167, 2006.

[20] G. P. Cimellaro, A. M. Reinhorn, M. Bruneau, Quantification of seismic resilience. *Proceedings of the* 8^{th} *National Conference of Earthquake Engineering*, San Francisco, CA, April 18–22, 2006.

[21] G. P. Cimellaro, A. M. Reinhorn, M. Bruneau, Seismic resilience of a hospital system. *Structure and Infrastructure Engineering*, **6**, 127–144, 2010.

[22] P. Bocchini, D. M. Frangopol, Optimal resilience- and cost-based post-disaster intervention prioritization for bridges along a highway segment. *Journal of Bridge Engineering, ASCE*, in press and already available on line, DOI: 10.1061/(ASCE)BE.1943-5592.0000201, 2011.

[23] D. M. Frangopol, P. Bocchini, Resilience as optimization criterion for the rehabilitation of bridges belonging to a transportation network subject to earthquake. *Proceedings of the 2011 SEI-ASCE Structures Congress*, Las Vegas, NV, April 14–16, 2011.

[24] C. W. Zobel, Representing perceived tradeoffs in defining disaster resilience. *Decision Support Systems*, **50**, 394–403, 2011.

[25] P. Bocchini, D. M. Frangopol, Restoration of bridge networks after an earthquake: multi-criteria intervention optimization. *Earthquake Spectra*, Under review.

[26] K. Deb, *Multi-objective optimization using evolutionary algorithms*. John Wiley and Sons, 2001.

COMPDYN 2011
III ECCOMAS Thematic Conference on
Computational Methods in Structural Dynamics and Earthquake Engineering
M. Papadrakakis, M. Fragiadakis, V. Plevris (eds.)
Corfu, Greece, 25–28 May 2011

RISK-BASED DECISION MAKING FOR RESILIENT SYSTEMS

Yiannis Xenidis, Alkisti S. Skiadopoulou, and Demos C. Angelides

Aristotle University of Thessaloniki
Aristotle University of Thessaloniki, University Campus, 54124, Thessaloniki, Greece
e-mail: ioxen@civil.auth.gr, alkisths@civil.auth.gr , dangelid@civil.auth.gr

Keywords: Risk Analysis, Decision Making, Resilient Systems, Innovation.

Abstract. *Resilient systems present an inherent ability of recovering from a certain damage state reached due to the application of a significant stress. The quantification of a system's resilience is a difficult task to perform because of: a) the system's complexity, b) the uncertain characteristics of the excitation force, c) the lack of specific elements to measure for an accurate assessment of a system's resilience, and d) the lack of robust tools for quantifying a system's resilience. Therefore, a decision maker requires both a methodology and the tools to decide for the most effective risk-response strategy. This paper presents such a methodology for a risk-based decision making for resilient systems. The proposed methodology involves the consideration of the following parameters: i) the variability of impact upon risk occurrence, ii) the available response strategies, and iii) the preference of the decision maker with regard to the criticality of the various impacts upon risk occurrence. The proposed methodology considers the four risk-response strategies defined by the Project Management-Body of Knowledge (5th ed.), namely: a) acceptance, b) mitigation, c) transfer, and d) avoidance. Three criteria are examined, in order to determine the preference margins between these strategies: i) compliance with regulations and specifications, ii) determination based on data elaboration (e.g. statistical, empirical, etc.), and c) subjective judgment. By applying any one of these criteria for a specific risk impact, the decision maker predetermines the boundary values between the risk-response strategies. Once, the value of the impact upon risk occurrence is estimated, the decision maker is capable to decide for the respective risk-response. The proposed methodology, then, integrates the various strategies decided for the various risk impacts to one single strategy that best confronts simultaneously all the different impacts on the system. The application of the proposed methodology is demonstrated through a case study that provides with numerical results. This paper introduces a new approach that successfully incorporates into the risk-based decision making problem, the critical issue of considering margins between damage states of resilient systems for various failures that occur simultaneously under a single stress.*

1 INTRODUCTION

Infrastructure systems are characterized of great interdependencies, which are mostly identifiable, yet difficult to model. Therefore, their efficiency in improving everyday's life for people, as well as their contribution to the economy and societal wealth can only partially be estimated by traditional tools and techniques. These estimations become even more difficult when risks of all kind of nature are considered. Natural hazards like floods become more intensive due to climate changes, while earthquakes still remain difficult to foresee. Infrastructure reliability and functionality are very critical and require appropriate risk response strategies, which can successfully ensure the long-term sustainability of infrastructure systems.

Introducing the concept of resilience for infrastructure systems is a new and evolving approach that provides a different perspective to the design and monitoring of infrastructure systems [1], [2]. Resilience may be, generally, considered as a system property that allows a quick recovery after a major risk occurrence [3], [4]. The recovery can be, generally, defined as a stable system's state that allows operation to a specific service level depending on the system. Therefore, resilience does not imply a full system recovery, but rather the necessary one that ensures continuity of the system's functionality to predetermined and required levels. A comprehensive analysis of the resilience concept can be found in [4].

Measuring resilience is a difficult task, because it requires a good insight of the system's structure and operation [5]. When the system is complex and prone to inherent uncertainties with regard to its function, measuring resilience becomes a, really, rough work to do. On the other hand, while resilience is inherent to the system, there is a definite interaction between the system and the system's environment that renders the process of recovery, not solely dependent on the system's resilience, but also on the actions that aim to alleviate the risk impact, which are normally decided in the framework of a risk response action plan. Therefore, a system's safety against stresses (occurred risks) is a combination between several parameters and hardly a system's property [6].

A complementary approach to resilience measurement for ensuring infrastructure system's functionality is the application of the proper risk-response strategies against anticipated risks. A properly designed and applied risk-response strategy that successfully corresponds to the system's requirements for recovery facilitates and accelerates the system's reaction against the damage from the occurred risk. Risk-response strategies can be decided through various decision making methods. However most of them present two serious limitations when they are considered for application in resilient systems: a) they do not address, in any way, the systems' characteristics to the decision making process and b) they treat systems' complexity in a rather descriptive, than analytic fashion. The following section presents some well-established and widely applied decision making methods and argues about their limitations for resilient systems.

This paper presents a risk-based decision making approach that aims at providing risk-response decision for resilient systems that consider both the systems' characteristics and the complexity. The first feature, i.e. the systems' characteristics, is introduced in an indirect way; a risk analysis that may be performed by any traditional or innovative method produces the values of risks that the system is prone to. However, since the risk value is considered as the expected value of a risk impact and this impact is directly related to the system's characteristics, it is inferred that in an indirect way these characteristics are addressed to the decision making process. The second feature, i.e. the system's complexity, is introduced by the comparison of the best risk-response decisions for different criteria and the homogenization of these decisions to one that optimally responds to all criteria simultaneously. The final output is a single decision for responding to a specific risk that the system faces.

The proposed methodology is presented in section 3 with an application example to facilitate understanding and demonstrate the mode of application.

2 DECISION – MAKING METHODS AND THEIS LIMITATIONS FOR RESILIENT SYSTEMS

Many decision making methods have been developed that present different levels of complexity and suitability for the various decision making problems. From basic methods that apply to everyday life's occasions to more sophisticated ones that are introduced in the cases of complex problems, there are two main approaches in the philosophy of the decision making: a) the decision is made based on the preference of the expected output compared to the expected outputs of other decision alternatives or b) the decision is made based on the problem's analysis that clearly suggests the best treatment for the problem in hand. In the following subsections some well-established methods that constitute the state-of-the-art in decision making are very briefly described, in order to provide the basis for consideration of their efficiency for resilient systems.

2.1 Elementary methods

Elementary methods are mostly applied to relatively simple decision making problems and they do not require either special knowledge or specific skills. "Pros and Cons" and "weighted Pros and Cons" methods rate the advantages and the disadvantages between alternative decisions and the alternative that presents the strongest pros and the weakest cons prevails [7].

Plus/Minus/Interesting method introduces except from pros and cons, the probable impact of the alternative decisions and through simple numerical rating it does not only suggest an optimum decision among alternatives, but also examines whether the selected alternative: a) shall improve the decision situation and b) is applicable or not [8].

Payoff matrices are used in combination with optimistic, realistic or pessimistic criteria (e.g. maximax - minimin, Hurwicz criterion, maximin – minimax) to identify the best tradeoff between a decision and its output [9].

Conjunctive and disjunctive methods evaluate decision alternatives by comparison to a given threshold and only those alternatives that reach a satisfactory level compared to the threshold are acceptable for implementation [10].

The above methods are not designed for complex problems; therefore their structure prevents their application to such problems. With the exception of conjunctive and disjunctive methods, the rest of the others fail to address the system's characteristics to the decision making process in a systematic or quantified way.

2.2 Graphical methods

Graphical methods comprise influence diagrams (fault-trees, event-trees, and cause and effect diagrams) and decision-trees. They incorporate uncertainty by assigning probabilities to the different decision nodes and they can map system's processes. However, there are two major limitations for application to infrastructure systems: a) they are highly impractical for complex systems and b) the system is mapped in a rather deterministic way, i.e. each branch of a tree describes a "road map" from the initial event (decision) to the final output, which is stable and independent from interdependencies and unexpected events. Both limitations render graphical decision making methods inappropriate for application to infrastructure systems' decision situations.

2.3 Multi-Attribute Utility Theory (MAUT) methods

MAUT is a theoretical framework that can deal with complex decision problems that feature a large number of criteria and decision alternatives. MAUT methods are characterized from the use of utility functions that express the preference of the decision maker over the various decision criteria for different decision alternatives. The final decision is selected through a process that utilizes dimensions-free scales that allow for comparison between different, in nature, criteria. A great number of methods and techniques are based on MAUT such as SMART, Generalized means, UTA, AHP, etc. The main limitation of these methods, which is systemic and related to the methodological approach, is that the decision criteria are weighted according to the preference of the decision maker and the final decision is made based on the aggregate of the products between these weights and the expected values of the decision's output for the criteria. This approach overlooks the actual impact of a decision and instead it correlates it with the factual (quantitative) or judgmental (qualitative and mostly subjective) preference of the decision maker. The importance of this limitation can be understood by the following examples:

- Example A: Tom decides to go to the movies and he has to choose between two options (AL_1 and AL_2) based on the criteria of distance from home (DH) and time of the movies start off (TS). According to his preferences by using any MAUT method, the final decision will come up to a problem generally described in the following equations:

  $$AL_1 = w_{DH} \times DH_1 + w_{TS} \times TS_1 \tag{1}$$

  $$AL_2 = w_{DH} \times DH_2 + w_{TS} \times TS_2 \tag{2}$$

  In equations (1) and (2), w_{DH} and w_{TS} are Tom's weights (preferences) for each decision he used. The maximum value between AL_1 and AL_2 indicates the optimum decision for Tom. However, this optimum decision does not, in fact, considers the real values of the criteria (i.e. real distance, real start off time), but, only, some weighted values that reduce or increase the real ones according to Tom's preferences.
- Example B: A public authority decides to take measures to increase the safety of a bridge against earthquake. The appropriate measures result to two options and they are evaluated based on the criteria of bridge functionality and technical reliability (after the application of the measures). In this example, the relativity, which is an inherent feature in decisions drawn through MAUT methods may easily alter the real data and result to doubtful decisions.

The systemic limitation of MAUT methods that has been identified and described above, along with certain other limitations that each one of the methods discretely suffers from, renders them questionable for application to infrastructure systems, where real values of impact from a risk or stress should not be altered for the process of decision making.

2.4 Outranking methods

Outranking methods may also be applied to complex systems and they also use weights for the different decision criteria. However, they are significantly different to MAUT methods. The most important difference is that outranking methods do not evaluate the alternatives based on a maximum score over certain criteria with different preferences, but, instead, they make pair wise comparisons between alternatives based on actual measurements. Outranking methods, such as ELECTRE and PROMETHEE methods, are able to compare any two different alternatives fully or partially, in the case where there are no available data or information for all the criteria used. Application of these methods results to a ranking between them and the first alternative in this ranking is the selected decision. The main limitations of outranking methods are: a) complexity, b) requirement of a strong mathematical background for application, and c) computational limits, i.e. these methods are not applicable for decision problems with many alternatives. These limitations render outranking methods questionable for application to infrastructure systems.

3 A NEW APPROACH FOR RISK-BASED DECISION MAKING FOR RESILIENT SYSTEMS

In the previous section the current practice in decision making was briefly discussed and the main findings were that for various reasons the existing methods present significant limitations for application to infrastructure systems. Such limitations become more significant when considered for application with regard to the resilience of infrastructure systems. Therefore, a new approach that can be free of these limitations and applicable to these systems is required. In this section such an approach is presented and demonstrated through an application example.

3.1 Risk-based decision making process

Risk – based decision making is a process that should follow certain steps (sub-processes) as illustrated in Figure 1.

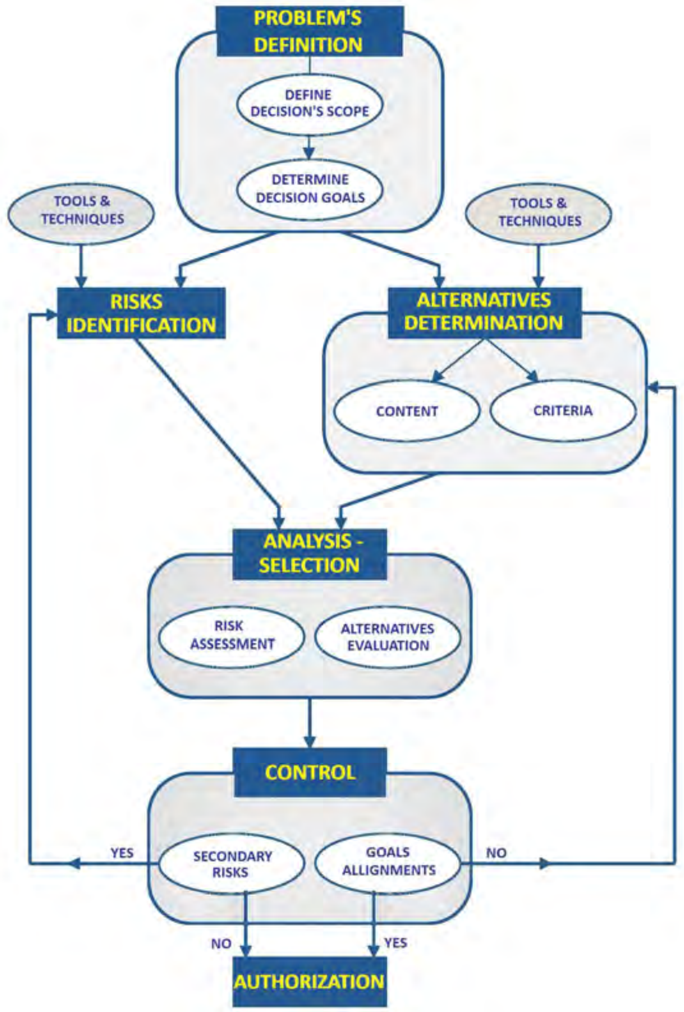

Figure 1: Risk-based decision making process flowchart

The first step is the problem's definition, which includes the clear and concise determination of the involved stakeholders' requirements. Given these requirements, the scope of the decision is defined and the determination of the respective goals to attain is achieved. Once, the decision situation problem is clearly defined, the next steps are to identify both the involved risks and the alternative decisions that can potentially serve the achievement of the goals set in the previous step. The alternative decisions must be well described in terms of their content, i.e. required processes, expected impact, etc., as well as criteria that are, one by one, associated to the predetermined goals. Both processes are performed through appropriate tools and techniques, which are extensively used in risk analysis and scenario analysis (e.g. Delphi method, SWOT analysis, information gathering techniques, etc.).The analysis that considers, simultaneously, the outputs of the previous steps, i.e. the risks and the alternative decisions, results through risk assessment and alternatives evaluation to the selection of the best decision in terms of satisfaction of the stakeholders' requirements. This decision is then checked for goals alignment and secondary risks that may arise upon its application and if the control results are acceptable then it is approved, while if not, the whole process is repeated from step 2, until it reaches acceptance.

In this paper, a new methodology is proposed that complies with the generic risk-based decision making process, as described above, and achieves to integrate the various strategies that are optimum for each different impact upon the occurrence of a specific risk to one single strategy that best confronts simultaneously all the different impacts on the system. In order to facilitate understanding, the methodology is presented through an application example.

3.2 The proposed methodology through an example of application

Suppose an infrastructure system that is of critical importance for the economic and social life of a specific area. Such a system may be a highway road, an airport, a wind farm, a public service building, etc. Infrastructure systems during their life – cycle are prone to several and different risks that can cause severe damages once they occur. Examples of such risks are all the types of failure caused by a natural hazard (earthquake, flood, fire, etc.), material failure, terrorist act, etc. The potential occurrence of one of these risks results to certain damages that are evaluated in a different way among those affected (stakeholders) by the risk event. Therefore, at every stage when a decision is required for the determination of the appropriate risk response strategy, the latter depends on the requirements and specifications set by these stakeholders.

In the case of a power plant, for example, the main priority is set to supply energy with a steady rate through an environmental friendly production process. The achievement of these goals must be ensured against a wide range of risks during the operation of the power plant. An example of one of these risks is recorded in Table 1.

Code	TECH 1.1
Name	Risk of failure due to earthquake
Class	Technical
Factors	Heavy earthquake loads that exceed the facilities' structural strength
Components	Cracks in walls, deformations, production fall
Impact	Repair costs, loss of revenue, injuries, fatalities, pollutants emissions

Table 1: A record of a risk for a power plant

Table 1 presents a hypothetical record in a risk inventory used for risk identification. The identified risk, given in the second row of the table, is classified and analyzed in terms of: a) the factors that lead to its occurrence, b) the symptoms (components) that are visible in different levels of risk occurrence and c) the impact, which is the result of the risk event upon occurrence. This type of inventory along with certain innovative notions such as the "component" term is based on current research performed by Angelides et al. [11].

The alternative decisions that need to be investigated, in relation to the identified risk, in order to determine the optimum among them that ensures the achievement of the decision's goals (i.e. constant energy supply in an environmental friendly mode) are: a) risk acceptance, b) risk mitigation, c) risk transfer, and d) risk avoidance. These alternatives are essentially the recommended risk response strategies proposed by the Project Management Body of Knowledge [12], which are apply, in general, to all types of projects or situations. Table 2 provides a detailed description of the alternative decisions in terms of content, required processes, and expected impact adjusted to the example of application.

Alternative decision	Risk acceptance	Risk mitigation	Risk transfer	Risk avoidance
Content Description	A decision that aims at assuming responsibility and liability for the negative impact upon risk occurrence. Recommended for insignificant risks	A decision that aims at the reduction of the risk to an acceptable threshold.	A decision that aims at shifting to a third party, the negative risk impact, along with ownership of the response. Risk transfer only indirectly deals with risk.	A drastic decision that aims to eliminate either the risk factors or the risk impact. It involves even project cancellation. Recommended for very significant risks.
Application mode	A. Establish a contingency reserve to use in case of failure.	A. Simplify the energy supply process. B. Reinforce critical elements of the structure. C. Design an action plan for quick – response.	A. Insurance. B. Performance bonds. C. Guarantees. D. Risk transfer contracts.	A. Establishment of the facilities to a non-seismic area. B. Change of goals.
Expected impact	Undertake the cost for the system's recovery after the occurrence of the risk	Limit the negative effect to an acceptable level	Ensure compensations from a third party for the harmed stakeholders in case of failure	Eliminate risk

Table 2: Alternative decisions for dealing with the risk of failure due to earthquake for a power plant

The alternative risk response strategies analyzed in Table 2 may be quantified either according to regulations, specifications, and legal frameworks or based on the strategy and policy of the organization that operates the power plant.

The criteria over which the alternative decisions are evaluated need to be consistent with the final decision's goals. They also need to be of quantitative nature, in order to define the thresholds that will constitute the boundaries of transition between the alternative decisions.

These boundaries, in fact, define the ranges that correspond to the respective risk response strategies or, in other words, all the estimated risks define a range from zero value to a maximum value, which is further divided to smaller ranges that each one of them corresponds to the respective decision alternative. A generic example of the quantified relation between the risks and the risk response strategies is illustrated in Figure 2 (AD: Alternative Decision).

Figure 2: Quantification of the alternative decisions for one decision criterion

For the example under study, the following criteria are set:

- Minimization of the system's recovery cost (SRC). This cost includes maintenance costs, repair/replacement costs, and loss of revenue due to the temporary halt of the energy production and supply process. The quantification of the alternative decisions with regard to the SRC criterion is based on: a) the risk analysis that is conducted by the facility's administration, and b) the attitude towards risks that the facility's administration adopts. Figure 3 illustrates a numerical example for this criterion. In Figure 3, "Ac" stands for "Risk acceptance", "M" stands for "Risk mitigation", "T" stands for "Risk transfer", and "Av" stands for "Risk avoidance". It should be noted that the ranking of the alternatives is consistent with the risk impact. Therefore, it is assumed that the smaller impact is manageable for the decision maker (risk acceptance), while the larger impact is intolerable for both the decision maker and any third party (risk avoidance).

Figure 3: Quantification of the alternative decisions for the SRC decision criterion

Any risk R that has a value R_{C_i} with regard to the SRC criterion results to the respective alternative decision according to the following relations:

$$[\,0,\,10^6\,] = \Theta^C,\ C_i \in \Theta^C \tag{3}$$

$$\forall\, R_{C_i} \in [\,0,\,20.000] \rightarrow \text{Risk acceptance} \tag{4}$$

$$\forall\, R_{C_i} \in [\,20.000,\,100.000] \rightarrow \text{Risk mitigation} \tag{5}$$

$$\forall\, R_{C_i} \in [\,100.000,\,250.000] \rightarrow \text{Risk transfer} \tag{6}$$

$$\forall\, R_{C_i} \in [\,250.000,\,1.000.000] \rightarrow \text{Risk avoidance} \tag{7}$$

- Prevention of human injury or fatality (HIF). The quantification of the alternative decisions with regard to the HIF criterion depends on the legal framework that regulates the health and safety issues in each case. An established approach to evaluate the severity of a non-fatal accident is according to the hours or days of absence from work [13]. Specific thresholds stand to differentiate between non-injuries, light injuries, fair, and severe injuries. The case of human loss is, of course, the worst scenario and the upper boundary in the HIF criterion. This quantification approach is adopted in the case of the example and Figure 4 illustrates the numerical output for this criterion. The notations in Figure 4 are identical to the respective in Figure 3.

Figure 4: Quantification of the alternative decisions for the HIF decision criterion

Any risk R that has a value R_{HL_i} with regard to the HIF criterion results to the respective alternative decision according to the following relations:

$$[\,0,\ 25.000\,] = \Theta^{HL},\ HL_i \in \Theta^{HL} \tag{8}$$

$$\forall\, R_{HL_i} \in [\,0,\ 60] \rightarrow \text{Risk acceptance} \tag{9}$$

$$\forall\, R_{HL_i} \in [\,60,\ 365] \rightarrow \text{Risk mitigation} \tag{10}$$

$$\forall\, R_{HL_i} \in [\,365,\ 5.000] \rightarrow \text{Risk transfer} \tag{11}$$

$$\forall\, R_{HL_i} \in [\,5.000,\ 25.000] \rightarrow \text{Risk avoidance} \tag{12}$$

The intervals in equations 9-12 describe respectively the following situations: a) no injury to light injury, b) light to fair injury, c) fair to severe injury, and d) severe injury to death. Again, as in the case of the SRC criterion, the ranking of the alternatives is consistent with the risk impact. Therefore, it is assumed that the smaller impact is manageable for the decision maker (risk acceptance), while the larger impact is intolerable for both the decision maker and any third party (risk avoidance).

- Prevention of environmental pollution (ENP). The quantification of the alternative decisions with regard to the ENP criterion can be based on regulations and respective legal frameworks. Another approach, which is adopted for the example, is to consider the severity of the pollution with regard to the magnitude of the area which is affected [14]. Figure 5 illustrates a numerical example for this criterion (values refer to acres). The notations in Figure 5 are identical to the respective in figures 3 and 4.

Figure 5: Quantification of the alternative decisions for the ENP decision criterion

Any risk R that has a value R_{E_i} with regard to the ENP criterion results to the respective alternative decision according to the following relations:

$$[\,0,\ 10^7\,] = \Theta^{E},\ E_i \in \Theta^{E} \tag{13}$$

$$\forall\, R_{E_i} \in [\,0,\ 10^4] \rightarrow \text{Risk acceptance} \tag{14}$$

$$\forall R_{E_i} \in [10^4, 10^5] \rightarrow \text{Risk mitigation} \tag{15}$$

$$\forall R_{E_i} \in [10^5, 5\times 10^5] \rightarrow \text{Risk transfer} \tag{16}$$

$$\forall R_{E_i} \in [5\times 10^5, 10^7] \rightarrow \text{Risk avoidance} \tag{17}$$

The same assumption made in the previous two criteria concerning the ranking of the alternatives stands for this criterion as well.

Once, the evaluation criteria of the alternative decisions are determined, the risk-based decision making process steps to the next stage, which is the analysis, based on actual risk estimations and the evaluation of the decision alternatives. It is important to notice that the process assumes the interdependency of the criteria. This assumption, although not always valid, does not reduce the effectiveness of the methodology, since the integration to one decision is independent of the interdependency between the criteria.

Risk quantification can be generally performed by the equation (18).

$$\text{Risk} = E\,[h] = \int h(\theta) \times p(\theta)\, d\theta \tag{18}$$

, where *θ*, denotes the uncertainty that characterizes the risk occurrence, which is expressed by a probability density function *p(θ)*, while the overall impact upon risk occurrence can be measured by a Risk Consequence Measure h(θ). Equation (18) expresses the expected value of the risk, which is a well – established approach on the field for risk quantification. This expected value in the case of the example under study must be estimated for the three different criteria. Therefore, the identified risk (Risk of failure due to earthquake) must be quantified in terms of impact to the system's recovery costs, the human losses and the environmental pollution. This quantification is performed by proper adjustment of equation (18). The mathematical expression for each case is given in equations (19) – (21):

$$R_{C_i} = \int h_{C_i}(\theta) \times p(\theta)\, d\theta \tag{19}$$

$$R_{HL_i} = \int h_{HL_i}(\theta) \times p(\theta)\, d\theta \tag{20}$$

$$R_{E_i} = \int h_{E_i}(\theta) \times p(\theta)\, d\theta \tag{21}$$

In equations (19) – (21), h_{C_i} measures in monetary terms the impact of the risk occurrence with regard to the SRC criterion, h_{HL_i} measures the impact of the risk occurrence with regard to the HIF criterion (the measurement is hours), and h_{E_i} measures the impact of the risk occurrence with regard to the ENP criterion (the measurement is acres). Provided that the necessary data to estimate the Risk Consequence Measures for each criterion and the probability of the risk event are available, equations (19) - (21) produce specific values that can be placed in the respective ranges of the previously defined alternative decisions for each criterion. Figure 6 illustrates graphically an example of this step of the process. As shown there, for the example under study, the same risk requires three different decisions, one for each one of the three different decision criteria: a) the proper decision with regard to the SRC criterion is “Risk acceptance”, b) the proper decision with regard to the HIF criterion is “Risk avoidance”, and c) the proper decision with regard to the ENP criterion is, again, “Risk acceptance”. It is obvious that if the analysis would indicate, also, “Risk acceptance” for the HIF criterion, then the decision maker would decide this alternative for the specific risk. However, in this case the decision maker needs to compare the alternative decisions for each criterion and select the most appropriate one that satisfies simultaneously all the criteria. While in the case of the example, the selection of "Risk avoidance" may be considered "an easy choice", since preventing human loss is a top priority, the general approach requires an objective way to compare all the alternatives for all the criteria between them. A graphical representation of all possible comparisons between any four decision alternatives for three criteria is illustrated in Figure 7.

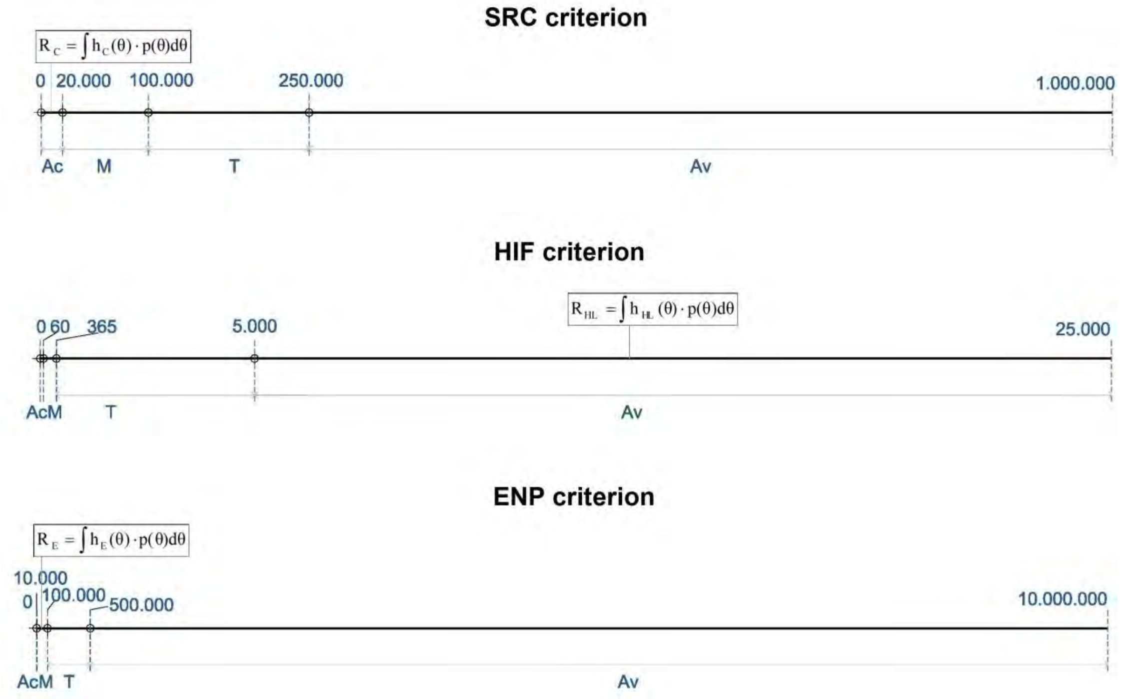

Figure 6: Assignment of risk values to the alternative decisions ranges per criterion

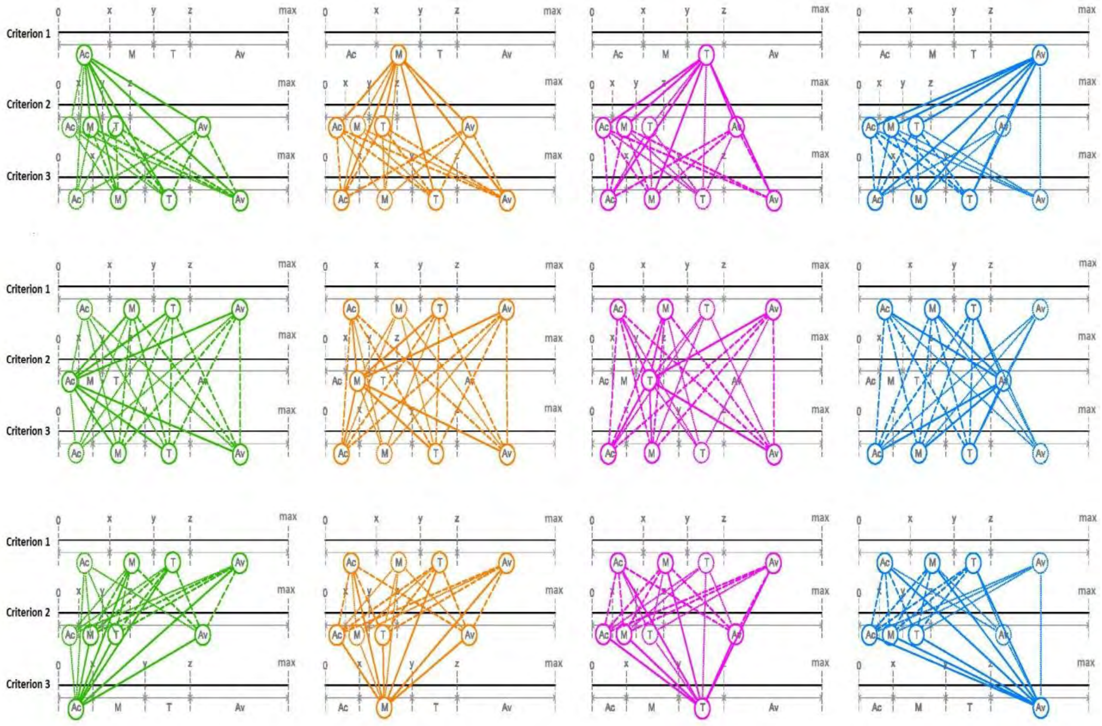

Figure 7: The possible comparisons between the alternative decisions of each criterion to the alternative decisions of the other criteria for the example under study

Due to the fact that different measures are used for each criterion, it is essential to transform the different scales from the three criteria to one single scale, in order to allow comparison between the alternative decisions. This can be easily achieved by dividing the values of the boundaries between the alternative decisions to the maximum value of the risk for each criterion. Essentially, the original scales are transformed to dimensions-free scales in the interval [0, 1], where 0 corresponds to the minimum value of the risk, 1 corresponds to the maximum value of the risk, and the values in between correspond to the boundaries of the alternative decisions. Figure 8 graphically illustrates the dimensions-free scales for each criterion.

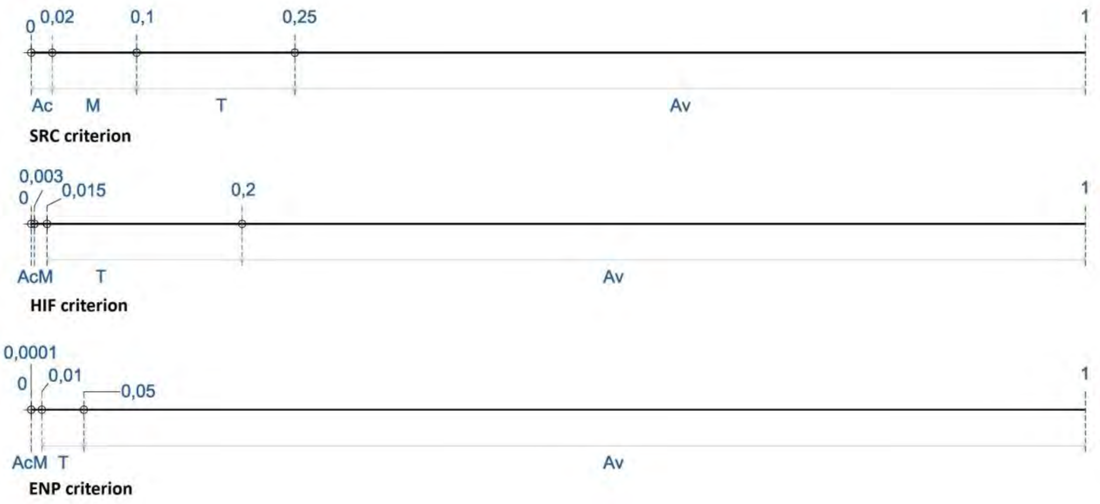

Figure 8: The dimensions-free scales for each criterion for the example under study

Another critical issue, which should be considered for the appropriate comparison between the alternative decisions, is the preference of the decision maker for the various alternatives for each criterion. For example, as stated above, it can be, generally, expected that there is a stronger preference to avoid human loss compared to the preference of spending a large amount for maintenance costs to reduce the risk of failure due to earthquake. However, it is not easy to generalize a preference, e.g. of taking measures for environmental protection (risk mitigation for the ENP criterion) compared to a fair amount of equipment replacement costs (risk acceptance for the SRC criterion). Therefore, a systematic way that will denote preference of the decision maker of the alternative decisions evaluated over different criteria is required. The proposed approach is based on the concept of utility, which addresses the preference of the decision maker between different alternative decisions. Utility theory has been used extensively with many variations in the field of decision making [15], [16], [17].

For each criterion of the alternative decisions, the decision maker defines the appropriate utility function that best represents his preference considering the parameter of risk. Figure 9 illustrates a graphical example of such functions that were selected for the example under study.

The utility functions in Figure 9 are defined in the set [0, 1] as they are in concordance with the dimensions – free scales for each criterion. Since the boundaries for each alternative decision are known from the previous steps, the overall preference of each different alternative is calculated by the area defined by the function’s curve, the *x* axis and the utility values for each boundary value of the alternative decision. Figure 10 illustrates a graphical example of this calculation and the numerical results are presented in Table 3.

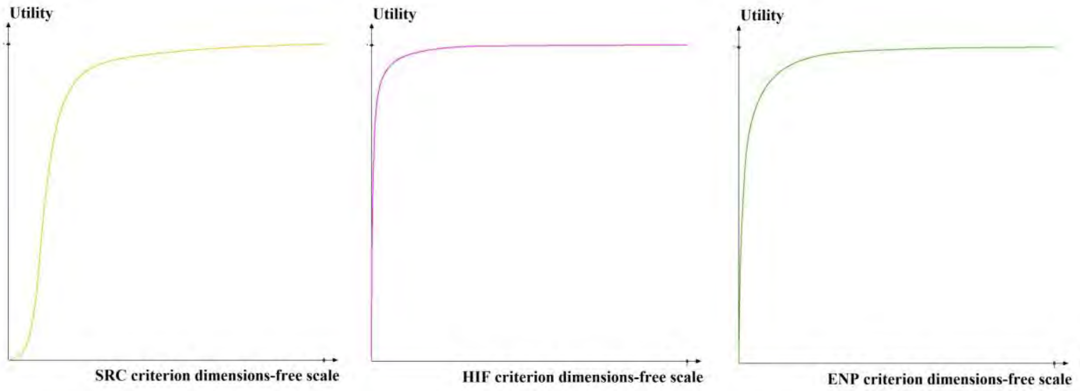

Figure 9: Utility functions for each decision criterion

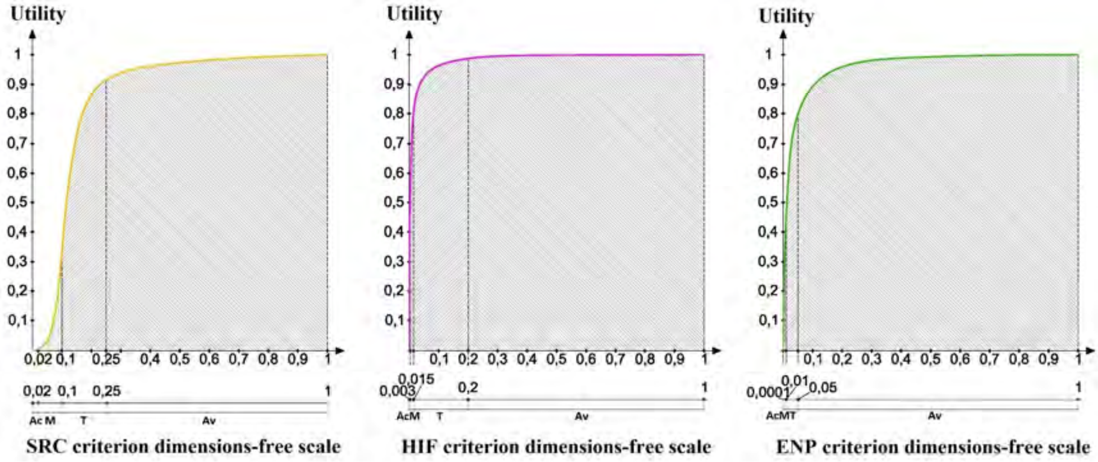

Figure 10: Calculations of the utilities of the alternative decisions for each criterion

Criterion	Alternative Decision	Utility
SRC	Risk acceptance	0.00058
	Risk mitigation	0.07361
	Risk transfer	1.13112
	Risk avoidance	7.33324
HIF	Risk acceptance	0.01106
	Risk mitigation	0.08325
	Risk transfer	1.76021
	Risk avoidance	7.98551
ENP	Risk acceptance	0.00001
	Risk mitigation	0.02922
	Risk transfer	0.27364
	Risk avoidance	9.29736

Table 3: Utility values for the alternative decisions for each criterion

The calculation of utilities for each alternative decision per criterion facilitates the comparison of the alternatives and consequently the decision making process for the decision maker. Concerning the example under study, the risk analysis indicated a risk acceptance for the SRC and ENP criteria, and risk avoidance for the HIF criterion (see Figure 6). An objective comparison between the two alternative decisions, which is based on the numerical results that are presented in Table 3, clearly suggests the “risk avoidance” decision as the most preferable (the one that corresponds to the maximum utility value).

Some interesting observations of the numerical results in Table 3 prove the logical consistency of the approach:

- In the case where each of the three criteria corresponds to a different alternative decision the most risk averse decision of all three always predominates.
- The HIF criterion, compared to the other two criteria consistently presents greater utility values for the same alternative decision. This is not the case only for the “risk avoidance” decision between the HIF and ENP criteria; however it is not unreasonable to consider a human injury or fatality as less important compared to an incident of major environmental pollution with long-term catastrophic effects on every form of life.

4 CONCLUSIONS

Infrastructure systems are very critical for the society and the economy. In a challenging situation with severe risks of different nature and magnitude, it becomes crucial to define those limit states of the systems that will ensure functionality and serviceability right after the occurrence of a risk and a fast system recovery to the operational levels before the occurrence of the risk.

Resilience is a concept that responds to the above requirements. However, due to the high complexity of infrastructure systems and their interdependencies both between the system’s parameters and between the system and its environment, the measurement of resilience becomes a very difficult task to perform. A complementary approach, which indirectly provides estimation for the system’s resilience is the application of the proper risk-response strategies against anticipated risks. Therefore, appropriate decision making is required.

Currently, several decision making methods and techniques exist that are well-established and in some cases, they are very sophisticated, in terms of methodological approach or mathematical background. However, they all present various limitations both in general and for application to infrastructure systems, in particular.

This paper presents a methodology for risk-based decision making that is characterized by the following features:

- It considers the variability of impact upon risk occurrence by using appropriate risk values, which are estimated for each criterion under study. Instead of the traditional approach, that of integrating different risk values to a single one that, allegedly, denotes an overall risk value, the proposed methodology utilizes actual risk values that correspond to the different decision criteria.
- It involves the preference of the decision maker not in a way that alters the evaluation criteria of the decision as is done in MAUT methods, but, rather, in a way that is restricted to the expression of tolerance of certain risk events in case they occur. This means that the boundaries for the alternative decisions with regard to different stresses are predefined and constant, regardless of the risk event and any per case variation of the preference of the decision maker.
- It compares preference of decisions instead of preference of alternatives. This means that the risk analysis that precedes the decision making process provides results that directly indicate the appropriate decision regarding a specific criterion and then these decisions are compared and the most preferred is selected.
- It involves risk-response strategies for which the decision maker has decided that they respond to the system’s requirements for increasing resilience.

The proposed methodology allows the overcoming of some limitations of well-established decision making methods in the problem of deciding the appropriate risk-response strategies for infrastructure systems. In this way, it becomes a potentially valuable tool for an indirect definition of resilience in these highly complex systems, which are prone to various failures that occur simultaneously under a single or multiple stresses.

ACKNOWLEDGEMENTS

This work has been supported by the Project "Integrated European Industrial Risk Reduction System (IRIS)", Nr: CP-IP 213968-2, funded by the European Union FP7.

REFERENCES

[1] E. D. Vugrin, D. E. Warren, M. A. Ehlen, R. C. Camphouse, A framework for assessing the resilience of infrastructure and economic systems, 77-116. In: K. Gopalakrishnan and S. Peeta eds. *Sustainable and resilient critical infrastructure systems: Simulation, modeling, and intelligent engineering*, Springer-Verlag Berlin Heidelberg, 2010.

[2] CIP program discussion paper series, *Critical thinking: Moving from infrastructure protection to infrastructure resilience*. George Mason University, 2007.

[3] F. Gao, *The proposed resilience analysis methodology and its application to the Susk-water pumping station*. MSc thesis, Department of Mechanical Engineering, University of Saskatchewan, Saskatoon, Canada, 2010.

[4] E. Hollnagel, D.D. Woods, N. Leveson, eds. *Resilience engineering: Concepts and precepts*, Ashgate, 2006.

[5] C.P. Nemeth, Resilience engineering: The birth of a notion, 3-9. In: E. Hollnagel, C.P. Nemeth, S. Dekker eds. *Resilience engineering perspectives: Remaining safe to the possibility of failure, Vol. I.* Ashgate, 2008.

[6] E. Hollnagel, D.D. Woods, Epilogue: Resilience engineering precepts. In: E. Hollnagel, D.D. Woods, N. Leveson, eds. *Resilience engineering: Concepts and precepts*, Ashgate, 2006.

[7] D. Baker, D. Bridges, R. Hunter, G. Johnson, J. Krupa, J. Murphy, and K. Sorenson, *Guidebook to Decision making Methods*, WSRC-IM-2002-00002, Department of Energy, USA, 2001

[8] E. De Bono, *Serious Creativity: Using the Power of Lateral Thinking to Create New Ideas*, HarperCollins Publishers Inc., 1992.

[9] A.S. Skiadopoulou, *Risk-based decision making*. MSc thesis (in Greek), Department of Civil Engineering, Aristotle University of Thessaloniki, Thessaloniki, Greece, 2010.

[10] J. Fülöp, *Introduction to decision making methods*, Working Paper 05-6, Laboratory of Operations Research and Decision Systems, Computer and Automation Institute, Hungarian Academy of Sciences, Budapest, 2005.

[11] D. Angelides, Y. Xenidis, E. Loukogeorgaki, D. Vrakas, I. Diamantoulaki, Development of the Risk Paradigm: The Risk Assessment Tool [Presentation], *IRIS European Research Project, WP-4 Meeting,* Bucharest, Romania, March 29-30, 2010.

[12] Project Management Institute, *A Guide to the Project Management Body of Knowledge, 4th Edition*. Project Management Institute, Inc., 2008.

[13] United States Department of Labor, Occupational Safety & Health Administration, Voluntary Protection Programs (VPP): Policies and Procedures Manual, 2003, Available at: http://www.osha.gov/pls/oshaweb/owadisp.show_document?p_id=2976&p_table=DIRECTIVES#appendixA [Accessed 20 October 2010].

[14] B.A. Menge, Bruce, A. M., Olson, Role of scale and environmental factors in regulation of community structure, *TREE*, **5(2)**, 52-57, 1990.

[15] J. Von Neumann, O. Morgenstern, Theory of games and economic behavior, 3rd Edition. Princeton University Press, 1944.

[16] R.L. Keeney, H. Raiffa, *Decisions with multiple objectives: Preferences and value trafeoffs*, Wiley, 1976.

[17] E. Jacquet – Lagreze, Y. Siskos, Assessing a set of additive utility functions for multicriteria decision making: The UTA method. *European Journal of Operational Research*, **10(2)**, 151-164, 1982.

COMPDYN 2011
3rd ECCOMAS Thematic Conference on
Computational Methods in Structural Dynamics and Earthquake Engineering
M. Papadrakakis, M. Fragiadakis, V. Plevris (eds.)
Corfu, Greece, 25–28 May 2011

THE P.E.O.P.L.E.S. RESILIENCE FRAMEWORK: A CONCEPTUAL APPROACH TO QUANTIFY COMMUNITY RESILIENCE

Chris S. Renschler[1*], Andrei M. Reinhorn[1], Lucy A. Arendt[2], Gian P. Cimellaro[3]

[1]MCEER - Earthquake Engineering to Extreme Events, University at Buffalo (SUNY)
Red Jacket Quadrangle, Buffalo, NY 14261, USA
{rensch, reinhorn}@buffalo.edu

[2]Austin E. Cofrin School of Business, University of Wisconsin-Green Bay
2420 Nicolet Dr, WH 460, Green Bay, WI 54311, USA
ArendtL@uwgb.edu

[3]Dept of Structural and Geotechnical Engineering, Politecnico di Torino
Corso Duca degli Abruzzi 24 - 10129 Torino, ITALY
gianpaolo.cimellaro@polito.it

Keywords: Resilience, Community, Systems, lifelines, critical facilities, functions, GIS.

Abstract. *Over the past years, the concept of resilience has gained attention recognizing the fact that not all threats or disasters can be averted. In fact, communities around the world are turning their attention to efforts and ways that can enhance their resilience against extreme events in any dimensions of life. Resilience is becoming increasingly important for modern societies as states come to accept that they cannot prevent every risk from being realized but rather must learn to adapt and manage risks in a way that minimizes impact on human and other systems. This paper presents a holistic framework for defining and measuring disaster resilience for a community at scales ranging from individual structures (e.g. hospitals) and smaller communities (neighborhoods) to entire regions. Seven dimensions of community resilience have been identified and are represented by the acronym PEOPLES: Population and Demographics, Environmental/ Ecosystem, Organized Governmental Services, Physical Infrastructure, Lifestyle and Community Competence, Economic Development, and Social-Cultural Capital. The PEOPLES Resilience Framework provides the foundation to integrate any quantitative and qualitative models that measures systems' resilience against extreme events (or disasters for that matter) in any or a combination of the above-mentioned seven dimensions. Besides a short-term gap finding analysis, this framework enables communities over the long-term to add and utilize geospatial and temporal decision-support tools that help communities in their planning efforts to assess and to enhance resilience.*

1 INTRODUCTION

Several studies on the disaster resilience of technical systems have been undertaken for quite some time [1] [2], but the societal aspects and the inclusion of various and multiple types of extreme events are new developments. This paper presents a holistic framework for defining and measuring disaster resilience for a community at scales ranging from individual structures (e.g. hospitals) and smaller communities (neighborhoods) to entire regions.

Research by the authors resulted in a) the definition of the quantitative PEOPLES Resilience Framework for communities at various scales that is based on seven distinct dimensions of resilience; b) identification of dimension subcategories and measures of functionality - at the base of resilience measurement - and related spatial-temporal scales, c) identification of gaps in definition and measurement of system functionality to determine indices and sub-indices of community resilience, and d) associated literature review [3] [4].

This new conceptual framework builds on and expands previous research at MCEER (Multidisciplinary Center for Extreme Events Research) linking the resilience dimensions (technical, organizational, societal, and economic [5]) so as to measure the disaster resilience of major components defined by the PEOPLES Resilience Framework. Seven dimensions of community resilience have been identified and are represented by the acronym PEOPLES: **P**opulation and Demographics, **E**nvironmental/Ecosystem, **O**rganized Governmental Services, **P**hysical Infrastructure, **L**ifestyle and Community Competence, **E**conomic Development, and **S**ocial-Cultural Capital.

The PEOPLES Resilience Framework provides the basis for the development of quantitative and qualitative models that already exist or will be adapted to measure continuously the resilience of communities against extreme events or disasters in any or a combination of the above-mentioned dimensions.

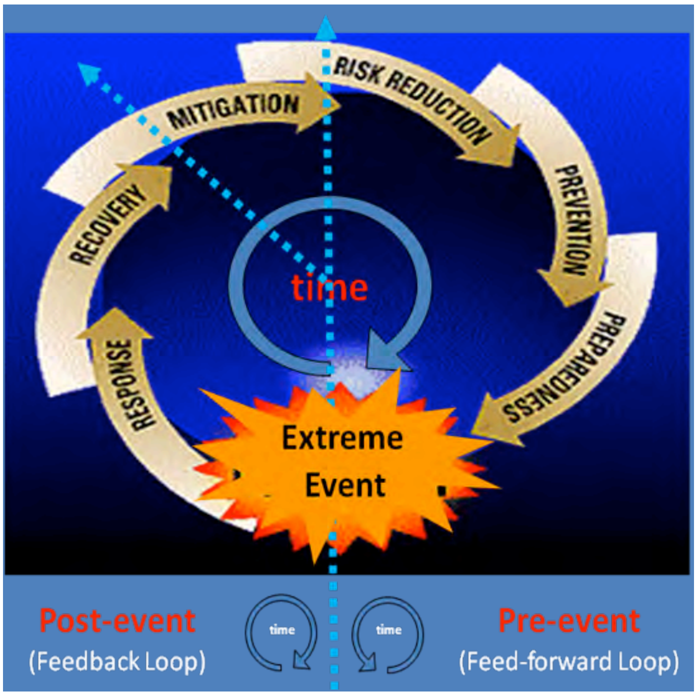

Figure 1: Extreme Events Management Cycle (Renschler et al, 2010)

This framework has been implemented in a decision-support software [6] integrating other disciplines to assess pre and post-disaster response (Figure 1) of communities in a geospatial and temporal scale. Over the longer term the software can be used as a decision support system for engineers and stakeholders as well as by emergency institutions and decision makers in general.

2 METHODOLOGY

Disaster resilience is often divided between technological units and social systems [7]. On a smaller scale, when considering critical infrastructures (for instance the closing of a local hospital), the focus is predominantly on technological and organizational aspects [8]. On a larger scale, when considering an entire community, the focus is broadened to include the interplay of multiple systems – human, environmental, and others – which combine to ensure the healthy, self-organizing functioning of a larger part of society residing in a region. At the community level, the human component is central, because in the case of a major disruptive event, in any of the seven dimensions (Figure 2) resilience depends first on the actions of people operating at the individual and neighborhood scale (Figure 3).

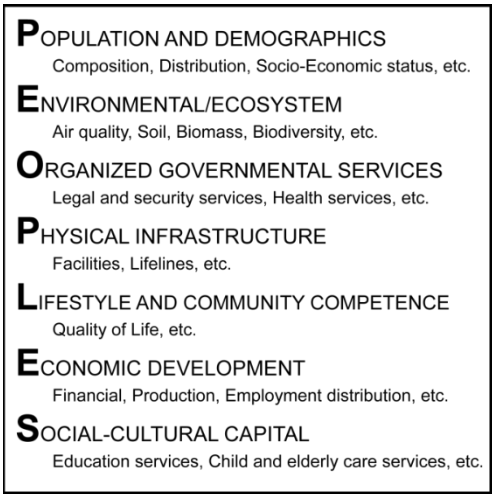

POPULATION AND DEMOGRAPHICS
Composition, Distribution, Socio-Economic status, etc.

ENVIRONMENTAL/ECOSYSTEM
Air quality, Soil, Biomass, Biodiversity, etc.

ORGANIZED GOVERNMENTAL SERVICES
Legal and security services, Health services, etc.

PHYSICAL INFRASTRUCTURE
Facilities, Lifelines, etc.

LIFESTYLE AND COMMUNITY COMPETENCE
Quality of Life, etc.

ECONOMIC DEVELOPMENT
Financial, Production, Employment distribution, etc.

SOCIAL-CULTURAL CAPITAL
Education services, Child and elderly care services, etc.

Figure 2: The PEOPLES Resilience Dimensions.

The following describes briefly each of the seven dimensions associated with the PEOPLES Resilience Framework and some potential indicators. The dimensions are neither orthogonal nor synonymous. While they are discussed as distinct dimensions and while we anticipate developing measures that are often independent, the nature of community resilience is such that interdependence between and among the dimensions is expected and necessary. The potential indicators are intended to be illustrative rather than exhaustive. Importantly, the indicators that are identified are those that may be used to describe a community and its resilience at any time, and not simply post-extreme event. Ultimately, the value of the PEOPLES Resilience Framework is that it (a) identifies the distinct dimensions and related key indicators but also (b) aggregates the dimensions in ways that reflect community realities.

2.1 Population and Demographics

A measure of functionality of population and demographics Qp within a given community could be quantified by using the social vulnerability index (SoVI) proposed by Cutter [9]. Social vulnerability (a counterpart of social resilience) is defined as the inability of people, organizations, and societies to withstand adverse impacts from multiple stressors to which they are exposed. These impacts are due in part to characteristics inherent in social interactions, institutions, and systems of cultural values. Social vulnerability is a pre-existing condition of the community that affects the society's ability to prepare for and recover from a disruptive event. It affects and is affected by both evolutionary occurrences (e.g., slow changes in median age) and transformative events (e.g., wholesale shifts in dominant ethnicity).

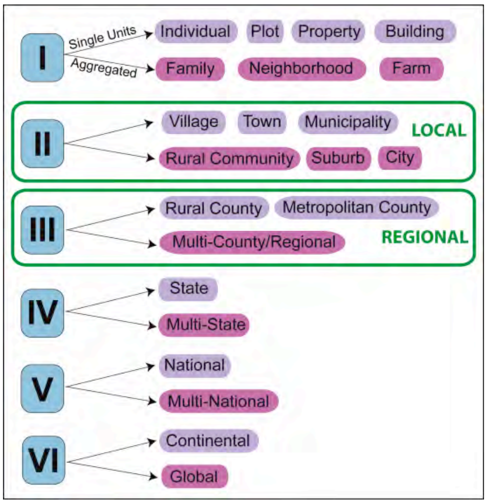

Figure 3: The Peoples Resilience Scales.

2.2 Environment/Ecosystem

Ecological or ecosystem resilience is typically measured by the amount of disturbance an ecosystem can absorb without drastically altering its functions, processes and structures [10], or by the ability of an ecosystem to cope with disturbance. In the context of the PEOPLES Resilience Framework, environmental and ecosystem resources serve as indicators for measuring the ability of the ecological system to return to or near its pre-event state.

2.3 Organized Governmental Services

In contrast to the more or less spontaneous individual and neighborhood responses to extreme events, organized governmental services are designed to allow an orderly response. Organized governmental services include traditional legal and security services such as police, emergency and fire departments and in extreme cases, the military. In this dimension, we also include the services provided by public health and hygiene departments as well as cultural heritage departments. Each of these organized government services plays a key role in sustaining communities both before and after extreme events. A good example of the necessity of a well functioning government may be seen in the devastating January 12, 2010 earthquake in Haiti. In the aftermath, the news media reported a lack of government services and orderly control, and a general perception that the government was not in a position to help its people [11].

2.4 Physical Infrastructure

The physical infrastructure dimension incorporates both facilities and lifelines. Within the category of facilities, we include housing, commercial facilities, and cultural facilities. Within the category of lifelines, we include food supply, health care, utilities, transportation, and communication networks. In terms of housing, key indicators may include proportion of housing stock not rated as substandard or hazardous and vacancy rates for rental housing [12]. In terms of communication networks, key indicators may include adequacy (or sufficiency) of procedures for communicating with the public and addressing the public's need for accurate information following disasters, adequacy of linkages between official and unofficial information sources, and adequacy of ties between emergency management entities and mass media serving diverse populations [12].

2.5 Lifestyle and Community Competence

This dimension reflects the reality that community resilience is not simply a passive "bouncing back" to pre-disaster conditions [13] but rather a concerted and active effort that relies on peoples' ability to creatively imagine a new future and then take the requisite steps to achieve that desired future. It captures both the raw abilities of the community (e.g., ability to develop multifaceted solutions to complex problems, ability to engage in meaningful political networks) and the community's perceptions of its ability to effect positive change. Communities that collectively believe that they can rebuild, restructure, and revive themselves are more likely to be persistent in the face of environmental, governmental, and other obstacles. Communities with positive experience dealing with extreme events may be more likely to possess high degrees of community competence. For example, in the wake of the 2011 earthquake and tsunami that devastated Japan, it is expected that Japan will recover relatively quickly because it has experience dealing with extreme events (e.g., the 1995 Great Hanshin or Kobe earthquake).

2.6 Economic Development

Resilient communities are characterized by their involvement in a diverse array of products and services that are both produced in and available to the community. Diversity in production and employment is linked to a community's ability to substitute goods and services and shift employment patterns as the situation demands. Efficient redundancy in operations and information systems enables relatively swift reopening of critical employers. The PEOPLES Resilience Framework incorporates three illustrative subcategories within this dimension: industry – production, industry – employment distribution, and financial services. Primary indicators of this dimension include the proportion of the population that is employed within the various industries, and the variability that might characterize a community's industrial employment distribution. This dimension is closely interwoven with the Population and Demographics dimension. For example, key indicators of economic development beyond employment and industry distribution include literacy rates, life expectancy, and poverty rates. Disaster-specific indicators related to economic development include extent of evacuation plans and drills for high occupancy structures, adequacy of plans for inspecting damaged buildings following disasters, and adequacy of plans for post-disaster commercial reconstruction [12].

2.7 Social-Cultural Capital

Measuring social/cultural capital requires acquisition of tallies, such as the number of members belonging to various civil and community organizations. It also requires surveys of community leaders and their perceptions (e.g., quality of life surveys). Communities with high degrees of social-cultural capital create “friction to exit” for their members, encouraging people to invest in those activities and organizations that make the community a “good place to live,” and encouraging people to return and reinvest in their communities after an extreme event. Disaster-specific indicators include existence of community plans targeting transportation-disadvantaged populations, adequacy of post-disaster sheltering plans, adequacy of plans for incorporating volunteers and others into official response activities, adequacy of donations management plans, and the community’s plans to coordinate across diverse community networks [12].

3 RESILIENCE COMPONENTS AND SUBCOMPONENTS

The PEOPLES Resilience Framework requires the combination of qualitative and quantitative data sources at various temporal and spatial scales, and as a consequence, information needs to be aggregated or disaggregated to match the scales of the resilience model and the scales of interest for the model output. Table 1 shows the complete list of components and sub-components. In the following sections a detailed description of each component is complemented by attempts of quantification.

4 INTEGRATION

Within the PEOPLES Resilience Framework, each dimension and its indicators or term of functionality and/or service will be represented with a GIS layer of the area of interest as suggested in the example portrayed in Figure 4, where Q_{pop} = functionality of population; Q_{env}= functionality of ecosystems; and so on. Additional terms for subcategories of resilience dimensions can be added, such as functionality of schools, dams, fire stations, oil and natural gas systems, emergency centers, communication towers/antennae, etc.

5 CONCLUSIONS

The seven dimensions of community resilience are indentified within the new PEOPLES Resilience Framework as Population and Demographics, Environmental/Ecosystem, Organized Governmental Services, Physical Infrastructure, Lifestyle and Community Competence, Economic Development, and Social-Cultural Capital.

PEOPLES builds on and expands previous research at MCEER linking the four resilience properties (robustness, redundancy, resourcefulness, and rapidity) and resilience dimensions (technical, organizational, societal, and economic) so as to measure the disaster resilience of capital assets (e.g., hospitals) and asset classes (e.g., health care facilities).

The PEOPLES Resilience Framework has been implemented in decision support software to assess pre and post-disaster response of communities. Over the longer term, the software can be used as decision support system for engineers and stakeholders as well as by emergency institutions and decision makers in general. Such a system should enable decision makers to prioritize resource allocations and take the steps needed to enhance community resilience before and after an extreme event.

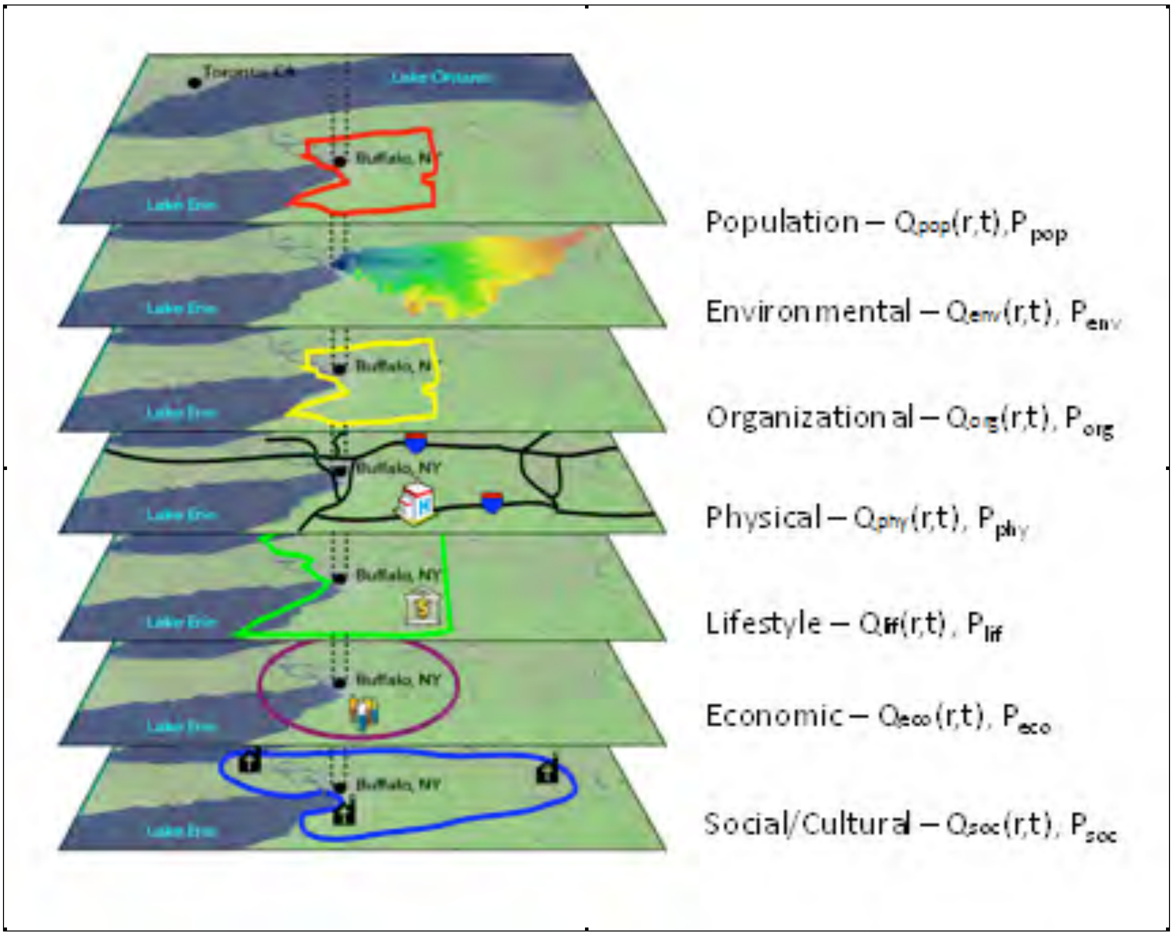

Figure 4: Layer model for Rural PEOPLES (Renschler et al, 2010)

Table 1 Complete list of components and sub-components.

- **1) POPULATION AND DEMOGRAPHICS**
  - a) Distribution/Density
    - i) Urban
    - ii) Suburban
    - iii) Rural
    - iv) Wildland
  - b) Composition
    - i) Age
    - ii) Gender
    - iii) Immigrant Status
    - iv) Race/Ethnicity
  - c) Socio-Economic Status
    - i) Educational Attainment
    - ii) Income
    - iii) Poverty
    - iv) Home Ownership
    - v) Housing Vacancies
    - vi) Occupation

- **2) ENVIRONMENTAL/ ECOSYSTEM**
  - a) Water Quality/ Quantity
  - b) Air Quality
  - c) Soil Quality
  - d) Biodiversity
  - e) Biomass (Vegetation)
  - f) Other Natural Resources

- **3) ORGANIZED GOVERNMENTAL SERVICES**
  - a) Executive/ Administrative
    - i) Emergency Response and Rescue
    - ii) Health and Hygiene
  - b) Judicial
  - c) Legal/Security

- **4) PHYSICAL INFRASTRUCTURE**
  - a) Facilities
    - i) Residential
      - (1) Housing Units
      - (2) Shelters
    - ii) Commercial
      - (1) Distribution Facilities
      - (2) Hotels - Accommodations
      - (3) Manufacturing Facilities
      - (4) Office Buildings
    - iii) Cultural
      - (1) Entertainment Venues
      - (2) Museums
      - (3) Religious Institutions
      - (4) Schools
      - (5) Sports/Recreation Venues
  - b) Lifelines
    - i) Communications
      - (1) Internet
      - (2) Phones
      - (3) TV
      - (4) Radio
      - (5) Postal
    - ii) Health Care
      - (1) Acute Care
      - (2) Long-Term Acute Care
      - (3) Primary Care
      - (4) Psychiatric
      - (5) Specialty
    - iii) Food Supply
    - iv) Utilities
      - (1) Electrical
      - (2) Fuel/Gas/Energy
      - (3) Waste
      - (4) Water
    - v) Transportation
      - (1) Aviation
      - (2) Bridges
      - (3) Highways
      - (4) Railways
      - (5) Transit
      - (6) Vehicles
      - (7) Waterways

- **5) LIFESTYLE AND COMMUNITY COMPETENCE**
  - a) Collective Action and Decision Making
    - i) Conflict Resolution
    - ii) Self-Organization
  - b.) Collective Efficacy and Empowerment
  - c.) Quality of Life

- **6) ECONOMIC DEVELOPMENT**
  - a) Financial Services
    - i) Asset Base of Financial Institutions
    - ii) Checking Account Balances (Personal and Commercial)
    - iii) Consumer Price Index
    - iv) Insurance
    - v) Number and Avg. Amount of Loans
    - vi) Number of Bank and Credit Union Members
    - vii) Number of Banks and Credit Unions
    - viii) Savings Account Balances (Personal and Commercial)
    - ix) Stock Market
  - b) Industry – Employment - Services
    - i) Agriculture
    - ii) Construction
    - iii) Education and Health Services
    - iv) Finance, Insurance and Real Estate
    - v) Fortune 1000
    - vi) Fortune 500
    - vii) Information, Professional Business
    - viii) Leisure and Hospitality
    - ix) Manufacturing
    - x) Number of Corporate Headquarters
    - xi) Other Business Services
    - xii) Professional and Business Services
      - (1) Employment Services
        - (a) Flexibilities
        - (b) Opportunities
        - (c) Placement
      - (2) Transport and Utilities
      - (3) Wholesale and Retail
  - c) Industry – Production
    - i) Food Supply
    - ii) Manufacturing ....

- **7) SOCIAL/CULTURAL CAPITAL**
  - a) Child and Elderly Services
  - b) Commercial Centers
  - c) Community Participation
  - d) Cultural and Heritage Services
  - e) Education Services
  - f) Non-Profit Organizations
  - g) Place Attachment

6 ACKNOWLEDGMENTS

The research leading to these results has received funding from the National Institute for Standards and Technology (NIST), Building and Fire Research Laboratory, Award No. 60NANB9D9155_0 and the European Community's Seventh Framework Programme - Marie Curie International Reintegration Actions - FP7/2007-2013 under the Grant Agreement n° PIRG06-GA-2009-256316 of the project ICRED - Integrated European Disaster Community Resilience.

REFERENCES

[1] S. Chang. Disasters and transport systems: Loss, recovery, and competition at the Port of Kobe after 1995 earthquake. *Journal of Transport Geography*, **8**(1), 53-65, 2000.

[2] S.B. Miles, and S.E. Chang. Modeling Community Recovery from Earthquakes. *Earthquake Spectra*, **22**(2), 439-458, 2006

[3] C.S. Renschler, A.E. Frazier, L.A. Arendt, G.P. Cimellaro, A.M. Reinhorn, M. Bruneau. A Framework for Defining and Measuring Resilience at the Community Scale: The PEOPLES Resilience Framework. MCEER Report, MCEER-10-0006. 2011.

[4] C.S. Renschler, A.E. Frazier, L.A. Arendt, G.P. Cimellaro, A.M. Reinhorn, M. Bruneau. Developing the 'PEOPLES' resilience framework for defining and measuring disaster resilience at the community scale. 9thUS and 10th Canadian Conference on Earthquake Engineering. Toronto, Canada, July 25-29 2010.

[5] M. Bruneau, S. Chang, R. Eguchi, G. Lee, T. O'Rourke, A.M. Reinhorn, M. Shinozuka, K. Tierney, W. Wallace, and D.v. Winterfelt. A framework to Quantitatively Assess and Enhance the Seismic Resilience of Communities. *Earthquake Spectra*, **19**(4), 733-752, 2003.

[6] V. Arcidiacono, G.P. Cimellaro, and A.M. Reinhorn. "A software for measuring disaster community resilience according to the PEOPLES methodology." *Proceedings of COMPDYN 2011 - 3rd International Conference in Computational Methods in Structural Dynamics and Earthquake Engineering*, Corfu`, Greece, May 26-28, 2011, 2011.

[7] G.P. Cimellaro, A.M. Reinhorn, and M. Bruneau. Framework for analytical quantification of disaster resilience. *Engineering Structures*, **32**(11), 3639–3649, 2010

[8] G.P. Cimellaro, A.M. Reinhorn, and M. Bruneau. Performance-based metamodel for health care facilities. *Earthquake Engineering & Structural Dynamics*, article first published online: 16 DEC 2010, DOI: 10.1002/eqe.1084, 2010.

[9] S.L. Cutter. Vulnerability to Environmental Hazards. Progress in Human Geography 20(4):529–39, 1996.

[10] L. Gunderson. Ecological resilience – In theory and application. Annual Review of Ecology and Systematics, 31, 425-439. 2000.

[11] D. Schwartz. A big question: Where is Haiti's government? Retrieved March 1, 2010 from:http://www.cbc.ca/world/story/2010/01/22/f-haiti-govt.html. 2010.

[12] K. Tierney. Disaster response: Research findings and their implications for resilience measures. CARRI Research Report 6. Oak Ridge, TN: Community and Regional Resilience Initiative (CARRI). URL: www.resilientUS.org. 2009.

[13] D. Brown, J., Kulig. The concept of resiliency: Theoretical lessons from community research. Health and Canadian Society, 4, 29-52.1996.

COMPDYN 2011
III ECCOMAS Thematic Conference on
Computational Methods in Structural Dynamics and Earthquake Engineering
M. Papadrakakis, M. Fragiadakis, V. Plevris (eds.)
Corfu, Greece, 25–28 May 2011

FINITE ELEMENT ANALYSIS OF BURIED STEEL PIPELINES UNDER STRIKE-SLIP FAULT DISPLACEMENTS

Polynikis Vazouras[1], Spyros A. Karamanos[2], and Panos Dakoulas[1]

[1] Department of Civil Engineering
University of Thessaly, Volos 38334, Greece
e-mail: pvazour@yahoo.gr; dakoulas@uth.gr

[2] Department of Mechanical Engineering
University of Thessaly, Volos 38334, Greece
e-mail: skara@uth.gr; www.mie.uth.gr/karamanos.htm

Keywords: Pipeline, Buckling, Seismic fault, Finite elements, Pipeline integrity.

Abstract. *The present paper investigates the mechanical behaviour of buried steel pipelines, crossing active strike-slip tectonic faults. The fault plane is vertical and crosses the pipeline axis at a certain angle. The interacting soil-pipeline system is modelled rigorously through finite elements, which account for large strains and displacements, nonlinear material behaviour and special conditions of contact and friction on the soil-pipe interface. Steel pipelines of various diameter-to-thickness ratios, and typical steel material for pipeline applications (API 5L grades X65 and X80) are considered. Most of the numerical results in the paper refer to the case where the fault plane crosses the pipeline axis at right angle. In particular, the paper investigates the effects of various soil and pipeline parameters on the mechanical response of the pipeline, with particular emphasis on pipe wall failure due to "local buckling" or "kinking" and pipe wall rupture. The effects of shear soil strength and stiffness are also investigated. Furthermore, the influence of the presence of pipeline internal pressure on the mechanical response of the steel pipeline is examined. Numerical results aim at determining the fault displacement at which the pipeline failure occurs, and they are presented in a graphical form that shows the critical fault displacement, the corresponding critical strain versus the pipe diameter-to-thickness ratio. Furthermore, results for cases where the fault plane crosses the pipeline axis at an angle different that 90-degress are presented and the corresponding failure modes are identified. It is expected that the results of the present study can be used for efficient pipeline design in cases where active faults are expected to impose significant ground-induced deformation to the pipeline.*

1 INTRODUCTION

Seismic events constitute a threat for buried pipeline structural integrity. In particular, permanent ground deformation applied on the pipeline in a quasi-static manner, and not necessarily associated with high seismic intensity, may cause serious pipeline damages, reported in numerous earthquakes, such as the 1995 Kobe earthquake [1], the 1999 Kocaeli earthquake [2] and the 1999 Chi-Chi earthquake [3].

The present paper focuses on the mechanical response of continuous (welded) buried steel pipelines crossing active strike-slip seismic faults, a particular ground-induced action, associated with axial, shear and bending loads. High stresses and strains are developed in critical locations, which are well into the inelastic range of pipe material and may cause pipeline failure. In particular, high tensile stresses may cause fracture of the pipeline wall, especially at welds or defected locations, whereas high compression stresses may cause buckling, mainly in the form of pipe wall wrinkling, a shell-type instability, referred to as "local buckling" or "kinking".

Newmark and Hall [4] were the first to attempt prediction of pipeline mechanical response under fault displacement, using a simplified analytical model of a long cable with small displacements. Their work has been extended by Kennedy et al. [5] [6] considering non-uniform friction between the pipe and the surrounding soil, and further enhanced by Wang and Yeh [7] to account for pipeline bending stiffness. Notable analytical works on the subject, based on a beam-type approach for pipeline modelling have been presented by Vougioukas et al. [8], Wang and Wang [9] and Takada et al. [10]. Kokavessis and Anagnostidis [11], presented a finite element methodology to simulate buried pipeline behaviour under permanent ground-induced actions, using contact elements to describe the soil-pipe interaction. Furthermore, Karamitros et al. [12] presented an enhanced analytical beam-type methodology, supported by three-dimensional finite element models, which employed shell elements for describing the pipe and nonlinear springs to simulate soil behavior. Liu et al. [13] presented a numerical simulation of pipelines crossing active faults through a combination of shell elements and springs, similar to the model in [12].

Experimental works on the effects of strike-slip faults on buried polyethylene (HDPE) pipelines have been reported by Ha et al. [14][15] and Abdoun et al. [16], based on centrifuge modelling of pipeline response and examined the influence of the type of faulting, the angle of strike-slip faults on the pipeline mechanical behaviour, as well as the effects of buried depth, pipeline diameter, and moisture content.

The work in the present paper is part of an extensive research effort aimed at investigating the response of buried steel pipelines crossing active faults for various soil conditions, using advanced numerical simulation tools and identifying possible failure modes, with emphasis on site conditions (i.e. the properties of the surrounding soil). The present work follows an integrated approach, which is based on modelling of the soil-pipeline system through nonlinear finite elements, accounting rigorously for (a) the inelastic behaviour of the surrounding soil, (b) the interaction and the contact between the soil and the pipe (including friction contact and the development of gap), (c) the development of large inelastic strains in the steel pipeline, (d) the distortion of the pipeline cross-section and possible local buckling formation, (e) the presence of internal pressure. The pipeline axis is assumed horizontal and crosses the fault plane at right angle. Considering a variety of soil parameters for both cohesive and non-cohesive soils, the influence of soil conditions on the pipeline structural response is examined in detail. Furthermore, the effects of pipeline diameter-to-thickness ratio D/t and steel material on pipeline response are also investigated. The numerical results are employed to develop interaction diagrams of the fault displacement causing pipeline failure with respect to the value of pipe diameter-to-thickness ratio D/t, which could be used for practical design purposes.

2 NUMERICAL MODELING

General-purpose finite element program ABAQUS [18] is employed to simulate the mechanical behavior of the steel pipe, the surrounding soil medium and their interaction in a rigorous manner, considering the nonlinear geometry of the soil and the pipe (including the cross-sectional distortions of the pipeline cross-section), through a large-strain description of the pipeline-soil system and the inelastic material behavior for both the pipe and the soil.

Figure 1 shows the elongated prismatic model considered for simulating this permanent ground-induced action, where the pipeline is embedded in the soil. The corresponding finite element mesh for the soil formation is depicted in Figure 1a and Figure 1b, and for the steel pipe in Figure 1c. Four-node reduced-integration shell elements (type S4R) are employed for modeling the pipeline cylinder, whereas eight-node reduced-integration “brick” elements (C3D8R) are used to simulate the surrounding soil. The top surface represents the soil surface, and the burial depth is chosen equal to about 2 pipe diameters, which is in accordance with pipeline engineering practice. A short parametric study demonstrated that a 60-diameter length of the pipeline (in the x direction) is adequate for the purposes of the present analysis. Furthermore, prism dimensions in directions y, z equal to 10 and 5 times the pipe diameter, respectively, are also found to be adequate. The seismic fault plane crosses the pipeline axis at a certain angle and divides the soil in two equal parts (Figure 1a). The analysis is conducted in two steps; gravity loading is applied first and, subsequently, fault movement is imposed. The vertical boundary nodes of the first block remain fixed in the horizontal direction (including the end nodes of the steel pipeline), whereas a uniform horizontal displacement due to fault movement is imposed in the external nodes of the second (moving) block (including the end nodes of the pipeline). A finer mesh was employed for the central part of the pipeline, where maximum stresses and strains are expected, with a total of 54 shell elements around the cylinder circumference in this central part, whereas the size of the shell elements in the longitudinal direction has been chosen equal to 1/26 of the pipeline outer diameter D.

Figure 2a plots the soil – pipeline system after a seismic fault movement, for a plane perpendicular to the pipeline axis. The fault movement is considered to occur within a narrow transverse zone of width w, to avoid discontinuity at the vicinity of the fault, which sometimes causes numerical problems and corresponds to a more realistic representation of the fault displacement mechanism. Following a short parametric study, the value of w has been considered equal to 0.33 m.

A large-strain J_2 flow (von Mises) plasticity model, with isotropic hardening is employed to describe the mechanical behavior of the steel pipe material, calibrated through an appropriate uniaxial stress-strain curve from a tensile test. Furthermore, an elastic-perfectly plastic Mohr-Coulomb model is considered for the soil behavior, characterized by the soil cohesiveness c, the friction angle ϕ, the elastic modulus E, and Poisson’s ratio v. The dilation angle ψ is assumed to be equal to zero throughout this study. A contact algorithm is considered to simulate the interface between the outer surface of the steel pipe and the surrounding soil, which takes into account interface friction, which is considered through definition of an appropriate friction coefficient μ. In our analysis, the value of μ is equal to 0.3. Moreover, the interface allows separation of the pipe and the surrounding soil. The analysis proceeds using a displacement-controlled scheme, which increases gradually the fault displacement d. At each increment of the nonlinear analysis, stresses and strains at the pipeline wall are recorded.

3 NUMERICAL RESULTS

Using the above numerical simulation tools, results are obtained for steel pipelines for various values of the diameter-to-thickness ratio, as well as for different soil conditions. In all cases considered in the present paper, the outer pipe diameter of the pipe D is assumed equal to 914.4 mm (36 in), whereas the pipe wall thickness ranges from 6.35 mm (¼ in) to 19.05 mm (¾ in), so that a range of D/t values between 48 and 144 is covered. This range of D/t values is typical for onshore applications (oil, gas or water pipelines). The surrounding soil has dimensions 60m×10m×5m in directions x, y, z respectively.

In sections 3.1, 3.2 and 3.3, the seismic fault plane is perpendicular to the pipeline axis and located at the middle cross-section of the pipeline. Particular emphasis is given on the effects of external pressure on the structural response. Both X65 pipelines and high-strength steel X80 pipelines are analyzed. Finally, in section 3.4, numerical results are obtained for an X65 pipeline where the fault plane crosses the pipeline axis at angles different that 90-degress, aiming at identifying the corresponding failure modes.

3.1 X65 steel pipelines in cohesive soils

A moderately thick-walled X65 pipeline is considered first, with diameter and thickness equal to 914.4 mm (36 in) and 12.7 mm (0.5 in) respectively, so that D/t =72. The API 5L X65 steel material is a typical steel material for oil and gas pipeline applications, with a nominal stress-engineering strain curve shown with solid line in Figure 3a, obtained from a uniaxial tensile test. The yield stress σ_y is equal to 450 MPa (65 ksi) followed by a plastic plateau up to 3% strain and a strain-hardening regime with a hardening modulus equal to about $E_s/300$, where E_s is the Young's modulus of the steel material. Assuming a safety (reduction) factor equal to 0.72 [21], the maximum operating pressure $p_{\max}$ of this pipeline [$p_{\max} = 0.72\times\left(2\sigma_y\, t/D\right)$] can be readily calculated equal to 9 MPa (90 barr).

The pipeline is assumed to be imbedded in a cohesive soil and to be crossing a fault zone having a width w equal to 0.33 m. At this stage, the internal pressure p is equal to zero, and a soft-to-firm clay is considered, referred to as Clay I, which under "undrained" loading conditions has a cohesion c = 50 kPa, friction angle $\varphi = 0^{\circ}$, Young's modulus E = 25 MPa and Poisson's ratio ν = 0.5. Figure 4a depicts the shape of the deformed pipeline at fault displacements d = 1 m, 2 m, 3 m and 4 m in the area near the fault. Moreover, Figure 4b depicts the shape of the deformed pipeline and the distribution of the longitudinal normal strain ε_x on its outer surface at fault displacement equal to d = 1 m and d = 4 m. The deformed shape of the pipeline at d = 1 m shows a localized deformation at point A, referred to as "local buckling" or "kinking", whereas point A is the "critical location" of the pipeline, at a distance of 5.45 m from the fault. Due to the skew-symmetry of the problem, a similar local deformation pattern occurs at point B, on the hidden side of the pipeline. Under increasing fault movement, a substantial development of this localized deformation pattern is observed, associated with the distortion of a significant part of the pipeline around this area, as shown in

Figure 4b, for a fault displacement of d = 4 m. As the pipeline length increases with continued fault movement, it results to higher tensile and smaller compressive strains in the longitudinal direction. Figure 4b, shows that for a fault displacement of d = 4 m compressive longitudinal strains are significantly lower than those corresponding to a fault displacement of d = 1 m.

Figure 5 shows the deformed shape of the pipeline at fault displacements d equal to 1 m, where a localized buckling pattern develops where the compressive stresses and strains reach a maximum value. It is also important to notice that, upon local buckling formation, the deformation of the pipeline localizes in the vicinity of the buckle, as shown in Figure 5b. The variations of longitudinal compressive and tensile strain ε_x along the two outer (most stressed) generators of the pipe cylinder are shown in Figure 6 and Figure 7 for different values of the fault displacement and for a small segment of the pipeline about the critical area. The results for the compressive strain shown in detail in Figure 6b, indicate that for a value of fault displacement greater than 0.67 m, significant distortion of the cross-section occurs due to the development of a localized wrinkling pattern (local buckling) on the pipe wall, on the compression side of the deformed pipeline. This stage is considered as the onset of local buckling.

One may notice that the value of fault displacement at which onset of localized buckling occurs (d_{cr}), referred to as “critical fault displacement”, can be defined in many ways. In the present work, the onset of local buckling is considered at the stage where outward displacement of the pipe wall starts at the area of maximum compression. At that stage, bending strains due to pipe wall wrinkling develop (Figure 6), associated with significant tensile strains at the “ridge” of the buckle, so that the longitudinal compressive strains at this location at the outer surface of the pipe wall start decreasing, forming a short wave at this location. In the present case, this stage corresponds to a fault displacement equal to 0.67m as shown in Figure 6b.

At the above stage of local buckling onset, the longitudinal strain at the location of the buckle (ε_{cr}) is measured equal to 7.7×10^{-3} .Furthermore, at this critical buckling stage, the maximum tensile strain on the opposite side of the pipe ($\varepsilon_{T,\max}$) is 5.2×10^{-3}, which is much less than the strain that would cause tensile failure in the form of rupture in a non-seriously-defected pipeline [22]. It is noted that the formation of a local buckle is undesirable because it is associated with the concentration of strain at the buckled area, which may lead to fatigue cracking under repeated loading [23]. Upon formation of the local buckle, pipe deformation concentrates around the buckled cross-section. However, further continuation of the imposed deformation results in significant tensile strains at the buckled area, decreasing the compressive strains and resulting in high local tensile stresses, on either side of the pipeline cross-section, may lead to local fracture at welds or other locations where minor defects exist.

The effects of internal pressure on pipeline mechanical behavior are investigated by considering internally pressurized pipelines imbedded in the same soil conditions (Clay I). Numerical results corresponding to a pressure level of 50 barr, which is equal to 56% of the maximum operating pressure $p_{\max}$ indicate that, despite the fact that the buckled shapes of pressurized cylinders are similar to the buckled shape of Figure 5, the corresponding values of critical fault displacement d_{cr} and the compressive strain along the critical generator of the steel pipeline are somewhat lower than the ones shown in Figure 6b. Those results indicate that, in the case of buried (confined) pipes, the presence of internal pressure results in a decrease of critical fault displacement. The decrease is attributed to the development of additional stresses and strains in the pipeline wall that cause early yielding and lead to a premature local buckling failure. For the case of $p/p_{\max}$ =0.56, the maximum strain ε_{cr} at buckling (critical strain) is equal to 8.3×10^{-3}, which is similar yet slightly higher than the critical strain for zero pressure.

The numerical results in Figure 8 and in Figure 9 refer to an X65 steel pipeline with D/t ratio equal to 72, buried in stiffer cohesive soil conditions. The values of soil parameters c, E and φ are equal to 200 kPa, 100 MPa and 0^{o}, respectively, and correspond to a stiff clay under “undrained conditions”, referred to as Clay II. The width of the fault zone is equal to 0.33 m. The numerical results indicate that pipe bending deformation in the stiff soil occurs within a shorter distance from the fault location, and the critical area is at 3.2 m from the fault. Comparison of those results with the results shown in Figures 6 and 7 demonstrates the significant effect of site conditions on the mechanical behavior of the steel pipeline. In other words, for the same fault displacement d, higher bending stresses and strains occur in the case of a stiff soil than those in the case of a soft soil. The numerical verification of the above observation is offered in Figure 8 and Figure 9, which depict the variation of longitudinal (axial) normal strain along the compression generator. Local buckling occurs when the fault displacement becomes equal to 0.23 m, which is much less than the corresponding critical fault displacement for the case of soft clay (0.67 m). The corresponding maximum compressive strain ε_{cr} that causes local buckling is equal to 7.3×10^{-3}, whereas the maximum tensile strain $\varepsilon_{T,\max}$ along the opposite generator at the stage of local buckling onset is equal to 4.8×10^{-3}. The striking difference between softer and stiffer soil conditions is attributed to the fact that a steel pipeline in a softer soil, when subjected to a fault displacement, accommodates itself easier within the deformable soil, resulting in lower bending stresses and strains, which enable the pipeline to sustain larger ground-imposed displacements.

To investigate the effects of the diameter-to-thickness D/t ratio in cohesive soils (Clay I, II), numerical results are obtained for 36-inch-diameter X65 steel pipelines with thickness ranging between ¼-inch and ¾-inch, corresponding to D/t values between 48 and 144.

The numerical results are summarized in Figure 10. In particular, Figure 10a plots the fault critical displacement, d_{cr}, normalized by the pipe diameter D, in terms of the diameter-to-thickness ratio, D/t. The results show a substantial decrease of d_{cr} with increasing value of the D/t ratio, which means that thin-walled pipelines are more prone to buckling and fail at relatively small values of fault displacement. Furthermore, stiff soil conditions result in significantly lower deformation capacity of the pipeline. In Figure 10b the corresponding critical compressive strain at the onset of local buckling, ε_{cr}, is plotted against the value of the diameter-to-thickness ratio, D/t. The results indicate that thinner pipes buckle at smaller critical strain, which is in accordance with test data and numerical results from non-confined pipes [24].

In the above results, no critical displacement or critical strain is shown for $D/t = 44$ and soft soil conditions (Clay I). In this particular case, the numerical results did not indicate local buckling; the pipeline exhibited significant ground-induced deformation without any wrinkling of the pipeline wall for fault displacements that exceed 2.5 m. The significant tensile strains developed in the pipeline due to longitudinal pipeline stretching, after a certain fault movement, are responsible for this behavior.

In Figure 10, the effects of internal pressure are also depicted. The numerical results are obtained for a pressure level equal to 56% of the maximum operating pressure, $p_{\max}$, and show that the presence of internal pressure results to a small decrease of critical fault movement, d_{cr} in Figure 10a, due to the additional stresses and strains in the pipeline wall because of pressure. Furthermore, the corresponding critical strain in the presence of pressure is similar to the corresponding critical strain for the zero pressure case, as shown in Figure 10b.

3.2 X65 steel pipelines in non-cohesive soils

The response of an X65 steel pipeline with D/t = 72 embedded in non-cohesive soils is examined, by considering representative results for two frictional soils and comparing them to those obtained for the cohesive soils. First, a granular soil is considered with a friction angle φ =30^{o}, Young's modulus E =8 MPa and Poisson's ratio ν =0.3, corresponding to loose sand and referred to as "Sand I". The relatively small value of the stress-depended Young's modulus E is justified by the shallow embedment depth of the pipeline. A small amount of artificial cohesion equal to c = 5 kPa was also included to prevent numerical difficulties associated with the behavior of a purely frictional material at very small confining stress, such as in the case of a gap opening at the pipe-soil interface. Figure 11 and Figure 12 show the variation of the axial strain ε_x along the compression and tension outer sides, respectively, of the buckled area for Sand I. The critical distance from the fault, corresponding to the point with maximum bending curvature along the pipe, is 6.1 meters. The results for the compressive strain shown in Figure 11 indicate that at a value of fault displacement equal to 0.87 m, local buckling occurs, and beyond this stage, significant distortion of the cross-section occurs due to local buckling on the pipe wall on the compression side of the bent pipeline. The shape of the developing buckling is similar to that of Clay I. The longitudinal strain at the location of the buckle (ε_{cr}) is equal to 9.7×10^{-3}. Furthermore, at the critical buckling stage (d =0.87 m), the maximum tensile strain on the opposite side of the pipe ($\varepsilon_{T,\max}$) is 6.8×10^{-3}, which is much less than the strain that would cause tensile rupture. Beyond the formation of the local buckle, pipe deformation concentrates around the buckled cross-section and the localized wrinkling pattern is further developed. Further continuation of the imposed deformation results in pipe-wall folding, which is accompanied by significant local strains (compressive and tensile) at the buckled area. Moreover, the maximum tensile strain on the opposite (tensile) side of the pipe is also significantly increased.

Similar results are obtained for an X65 steel pipeline with D/t = 72, embedded in a more dense sand with values of φ and E equal to 40^{o} and 50 MPa, respectively, referred to as "Sand II". The numerical results indicate that pipe bending deformation in Sand II occurs within a shorter distance from the fault location (5.1 m) due to the higher strength of this sand. Comparison of those results with the results in Figure 11 and Figure 12 demonstrates that for the same fault displacement d, higher bending stresses and strains occur in the case of Sand II. Furthermore, local buckling occurs when the fault displacement becomes equal to 0.70 m, which is less than the corresponding critical fault displacement for the case of loose sand (0.87 m). The maximum compressive strain ε_{cr} that causes local buckling is equal to 10.47×10^{-3}, whereas the corresponding maximum tensile strain $\varepsilon_{T,\max}$ along the opposite generator is equal to 6.98×10^{-3}.

Finally, the numerical results for the mechanical behavior of X65 pipelines in non-cohesive soils (Sand I and II) are summarized in Figure 13, in terms of the normalized fault critical displacement and the critical corresponding strain at buckling with respect to the diameter-to-thickness ratio, D/t. The results shown in Figure 13a indicate that dense soil conditions (sand II) result in lower deformation capacity of the pipeline.

3.3 Behavior of X80 steel pipelines

The behavior of buried high-strength steel (API X80) pipelines under normal fault-induced deformation is also analyzed, using the numerical tools described in the previous sections.

The nominal uniaxial tensile stress-strain relationship of the X80 material is plotted in Figure 3. The dashed material curve, which has a yield stress of 596 MPa and does not have a plastic plateau, corresponds to a cold expanded (UOE) pipe. The solid material curve with a yield stress of 550 MPa and a plastic plateau up to a strain of 1.48% represents a seamless steel pipe material. Results are obtained for 36-inch-diameter X80 steel pipelines with D/t ratios between 48 and 144. Figure 14a plots the value of the fault critical displacement, d_{cr}, normalized by the pipe diameter D, in terms of the diameter-to-thickness ratio, D/t, for the two types of X80 steel and for cohesive soil conditions (Clay I and II). As in the case of X65, the value of d_{cr} decreases significantly with increasing value of D/t, indicating that thin-walled pipelines are more vulnerable to buckling and may fail at relatively small values of fault displacement. It should be noted that for the softer Clay I material, no values of d_{cr} are given for D/t = 44 and 72, as no wrinkling of the pipeline wall was observed in this case even for fault displacements exceeding 4 m. This is attributed to the beneficial effect of tensile deformation on the mechanical behavior of those relatively thick pipes, as described in the Appendix. Naturally, the values of d_{cr} for the high-strength steel X80 pipes in Figure 14a are higher than those for the X65 pipes given in Figure 10a. Similarly, Figure 14b plots the corresponding critical axial strain, ε_{cr}, versus the diameter-to-thickness ratio, D/t, for zero internal pressure. Comparing the behavior of the two X80 materials, it is evident that both d_{cr} and ε_{cr} are higher for UOE pipe due to both increase of yield strength and higher initial post-yielding tangent modulus. The increase of buckling strength in UOE pipes is in accordance with the test data reported elsewhere [24].

3.4 Effects of the pipeline-fault crossing angle

In this section, a short parametric study is conducted to examine the effects of pipeline-fault crossing angle on the pipeline structural performance, as shown in Figure 15. The crossing angle β is the main parameter of interest; positive values of β correspond to geometries that induce tension in the pipeline, whereas negative values of β are dassociate with compression of the pipeline. A 36-inch-diameter, $1/2$-inch-thick X65 pipeline, embedded in soft-to-firm clay soil conditions (Clay I), is examined for various crossing angles.

Figure 16 shows the deformed shape of the above pipeline for a value of β equal to 25 degrees, at a fault displacement d = 2 m. At this angle, local buckling does not occur. The deformed shape shows a significant distortion of the pipeline cross-section in the form of ovalization. The amount of ovalization, defined as $ov = \Delta D/D$ (where ΔD is the change of diameter in the plane of bending), reaches a limit value of 0.15 at fault displacement of 1 m, at the area where pipe intersects with the fault. It is noted that this value of 0.15 is specified by NEN 3650 specification, as described in [25]. Under increasing fault movement, this ovalization pattern is further developed resulting in a inversion of the pipeline wall (i.e. a local “concave” deformation pattern on the pipeline wall), for a fault displacement of d = 2.53 m. Critical tension strain (3%) appears at a fault displacement d = 0.64 m, whereas a maximum tensile strain of 5% occurs at a fault displacement d = 1.42 m, at a distance 1.1 m away from fault.

The deformed shape of the above 36-inch-diameter, $1/2$-inch-thick X65 steel pipeline in Clay I soil conditions, crossing the fault plane at an angle of β equal to 45 degrees, is shown in Figure 17. The amount of ovalization reaches a critical value of 0.15 at fault displacement of 1.08 m, at the area where pipe intersects with the fault. With increasing fault displacement, this ovalization pattern is further developed. For a fault displacement equal to 4 m no “inversion” of the pipeline wall has been observed. Critical tension strain (3%) is reached at a fault displacement d = 0.37 m, whereas a maximum tensile strain of 5% occurs at a fault displacement d = 1.14 m, at the point where pipeline crosses the fault plane.

The response becomes quite different if a opposite crossing angle is considered, corresponding to a negative value of β. In this case, fault motion is associated with a decrease of length of the pipeline, resulting in the development of significant compressive stresses and strains, leading to local buckling. In Figure 18, the deformed shape of the above 36-inch-diameter $\frac{1}{2}$-inch-thick X65 steel pipeline in Clay I soil conditions, crossing the fault plane at an angle of β equal to -10 degrees, is shown. The critical fault displacement has been computed equal to 34 cm. Upon continuation of fault displacement, the buckle pattern is further developed, so that an inversion of the pipeline wall occurs at fault displacement of 75 cm in the same cross- section where buckle appears. The cross- section where maximum deformation occurs is located 7.5 meters away from fault.

4 CONCLUSIONS

Using advanced finite element simulation tools, the mechanical behaviour of buried steel pipelines crossing an active strike-slip fault was investigated. The pipeline is assumed horizontal and normal to the fault plane, an idealized case, which allows for the investigation of several soil and pipe parameters on pipeline deformation and strength. In particular, the effects of various cohesive and non-cohesive soil conditions (expressed through various values of soil cohesion, friction and stiffness parameters (c, φ, E) on the structural response of the pipe are examined, with particular emphasis on pipe wall failure.

For pipelines crossing strike-slip faults at right angle, an extensive parametric study is conducted, and numerical results are obtained for various values of D/t ratio and for X65 and X80 steel pipelines. In the majority of the cases analyzed, it is shown that the formation of local buckling due to excessive compressive strains at the pipeline wall is the governing mode of failure. The numerical results are presented in diagram form for the critical fault displacement d_{cr} and the corresponding critical strain ε_{cr}, and indicate a strong dependence in terms of the pipeline diameter-to-thickness ratio D/t.

It is concluded that, for pipelines crossing strike-slip faults at right angle, in cohesive soils, softer ground conditions result in a large deformation capacity of the pipeline, whereas stiff ground conditions decrease the critical fault displacement. Similarly, in non-cohesive soils, loose sand conditions results in larger values of critical fault displacement than in dense soil conditions. The width of the fault slip zone was found to have non-important effects for the mechanical behaviour of the pipe. It was demonstrated that the presence of internal pressure results in a small decrease of the deformation capacity, due to early yielding of the steel material. It was also concluded that high-strength X80 steel pipelines have a greater deformation capacity than X65 pipelines. Furthermore, cold-formed UOE X80 pipes exhibit better behaviour in terms of buckling than seamless X80 pipes due to strain hardening. Furthermore, the numerical results show that thick-walled pipes may not exhibit buckling; in those pipelines wall fracture may occur due to the development of excessive tensile strains.

Finally, numerical results are obtained for pipelines crossing the vertical fault at angles different that 90-degress. In “negative” values of the angle, local buckling of the pipeline wall is the dominant mode of failure; local wrinkling increases with increasing fault displacement. On the other hand, for “positive” values of the crossing angle, the behaviour is considerably different. Local wrinkling does not occur; nevertheless the pipeline exhibits a significant distortion of its cross-section, followed by the development of significant tensile strains that may lead to pipeline rupture.

REFERENCES

[1] Nakata T, Hasuda K (1995). Active fault I 1995 Hyogoken Nanbu earthquake. *Kagaku* 1995; 65:127–142

[2] Earthquake Engineering Research Institute (1999). “Kocaeli, Turkey Earthquake of August 17”, *EERI Special Earthquake Report*.

[3] Takada S, Nakayama M, Ueno J, Tajima C (1999). Report on Taiwan Earthquake, *RCUSS, Earthquake Lab. of Kobe University*; 2–9

[4] Newmark N. M., Hall W. J. (1975), “Pipeline design to resist large fault displacement”. *Proceedings of U.S. National Conference on Earthquake Engineering*; 416–425.

[5] Kennedy, R. P., Chow, A. W. and Williamson, R. A. (1977), “Fault movement effects on buried oil pipeline”, *ASCE Journal of Transportation Engineering*, Vol. 103, pp. 617-633.

[6] Kennedy R. P., Kincaid R. H. (1983). “Fault crossing design for buried gas oil pipelines”. *ASME, PVP conference*; 77:1–9

[7] Wang, L. R. L. and Yeh, Y. A. (1985), “A refined seismic analysis and design of buried pipeline for fault movement”, *Earthquake Engineering & Structural Dynamics*, Vol. 13, pp. 75-96.

[8] Vougioukas E. A., Theodossis, C., Carydis P. G. (1979), “Seismic analysis of buried pipelines subjected to vertical fault movement.”, *ASCE Journal of Technical Councils*, Vol. 105(TCI), pp. 432– 441.

[9] Wang L. L. R., Wang L. J. (1995), Parametric study of buried pipelines due to large fault movement. *ASCE, TCLEE* 1995; (6):152–159.

[10] Takada, S., Hassani, N. and Fukuda, K. (2001), “A new proposal for simplified design of buried steel pipes crossing active faults”, *Earthquake Engineering and Structural Dynamics*, 2001; Vol. 30: pp.1243–1257.

[11] Kokavessis, N. K. and Anagnostidis, G. S. (2006), “Finite Element Modelling of Buried Pipelines Subjected to Seismic Loads: Soil Structure Interaction Using Contact Elements.”, *Proceedings, ASME PVP conference*, Vancouver, BC, Canada.

[12] Karamitros, D. K., Bouckovalas, G. D., and Kouretzis, G. P. (2007), “Stress Analysis of Buried Steel Pipelines at Strike-Slip Fault Crossings.”, *Soil Dynamics & Earthquake Engineering*, Vol. 27, pp. 200-211

[13] Liu, M., Wang, Y.-Y., and Yu, Z., (2008), “Response of pipelines under fault crossing.”, *Proceedings, International Offshore and Polar Engineering Conference*, Vancouver, BC, Canada.

[14] Ha, D., Abdoun T. H., O’Rourke, M. J., Symans, M. D., O’Rourke, T. D., Palmer, M. C., Stewart, H. E. (2008), “Buried high-density polyethylene pipelines subjected to normal and strike-slip faulting – a centrifuge investigation.”, *Canadian Geotechnical Journal*, Vol. 45, pp. 1733-1742.

[15] Ha, D., Abdoun T. H., O'Rourke, M. J., Symans, M. D., O'Rourke, T. D., Palmer, M. C., Stewart, H. E. (2008), "Centrifuge Modeling of Earthquake Effects on Buried High-Density Polyethylene (HDPE) Pipelines Crossing Fault Zones.", *ASCE Journal of Geotechnical and Geoenvironmental Engineering*, Vol. 134, No. 10, pp. 1501-1515.

[16] Abdoun T. H., Ha, D., O'Rourke, M. J., Symans, M. D., O'Rourke, T. D., Palmer, M. C., Stewart, H. E. (2009), "Factors influencing the behavior of buried pipelines subjected to earthquake faulting.", *Soil Dynamics and Earthquake Engineering*, Vol. 29, pp. 415– 427.

[17] Lillig D. B., Newbury B. D. and Altstadt S. A. (2009), "The Second ISOPE Strain-Based Design Symposium - A Review.", *International Society of Offshore & Polar Engineering Conference*, Osaka, Japan.

[18] ABAQUS (2008): *Users' Manual, Version 6.7,* Simulia, Providence, RI, USA.

[19] Anastasopoulos, I., Callerio, A., Bransby, M. F., Davies, M. C., Nahas, A. El, Faccioli, E., Gazetas, G., Masella, A., Paolucci, R., Pecker, A., Rossigniol, E. (2008), "Numerical analyses of fault foundation interaction.", *Bulletin of Earthquake Engineering*, Springer, 6(4), 645-675.

[20] American Petroleum Institute (2007), *Specification for Line Pipe*, 44th Edition, ANSI/API Spec 5L.

[21] American Society of Mechanical Engineers (2007), *Gas Transmission and Distribution Piping Systems*, ANSI/ASME B31.8.

[22] Igi, S. and Suzuki, N. (2007), "Tensile Strain Limits of X80 High-strain Pipelines.", *Proceedings of the 16th International Offshore and Polar Engineering Conference*, Lisbon, Portugal.

[23] Dama, E., Karamanos, S. A. and Gresnigt, A. M. (2007), "Failure of Locally Buckled Pipelines.", *Journal of Pressure Vessel Technology,* ASME, Vol. 129, pp. 272-279.

[24] Gresnigt, A. M. and Karamanos, S. A. (2009), "Local Buckling Strength and Deformation Capacity of Pipes.", *19th International Offshore and Polar Engineering Conference*, Osaka, Japan, pp. 212-223.

[25] Gresnigt, A. M., (1986), "Plastic Design of Buried Steel Pipelines in Settlement Areas", *Heron*, Vo. 31, No. 4, Delft, The Netherlands.

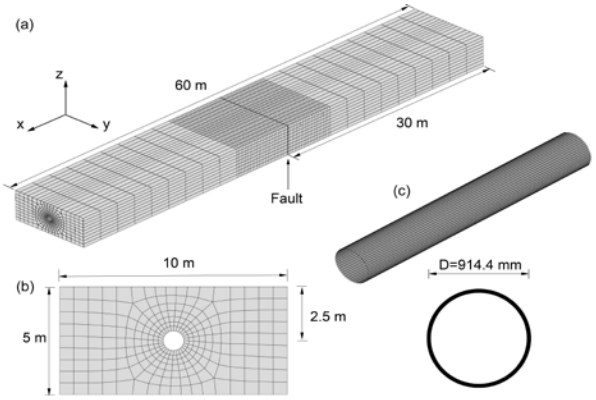

Figure 1: Finite element model of the (a) soil formation with tectonic fault, (b) soil cross-section and (c) steel pipeline.

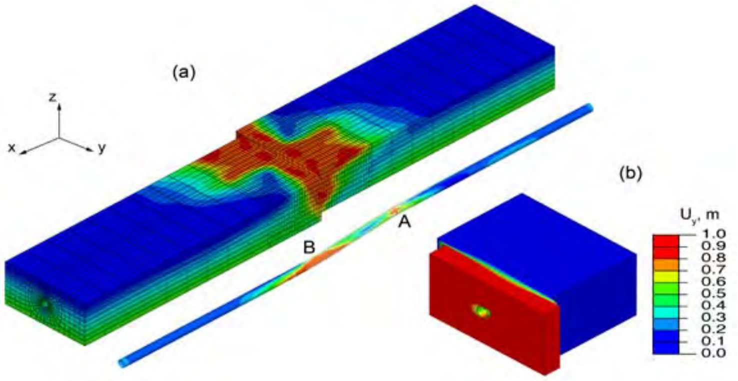

Figure 2: (a) Deformation of the pipeline-soil system after fault displacement; finite element results depict the von Mises stress. (b) Detail of fault displacement U_y (X65 pipe, $D/t = 72$, Clay I, $w = 0.33$ m, $p = 0$).

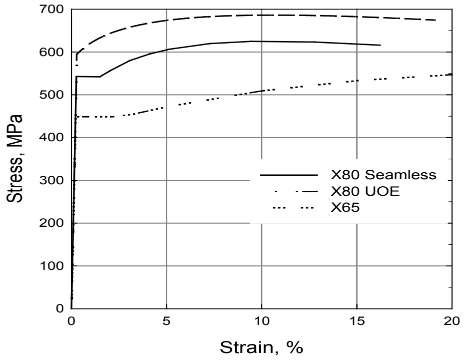

Figure 3: Uniaxial nominal stress-engineering strain curve for API 5L X65 , API 5L X80 steel.

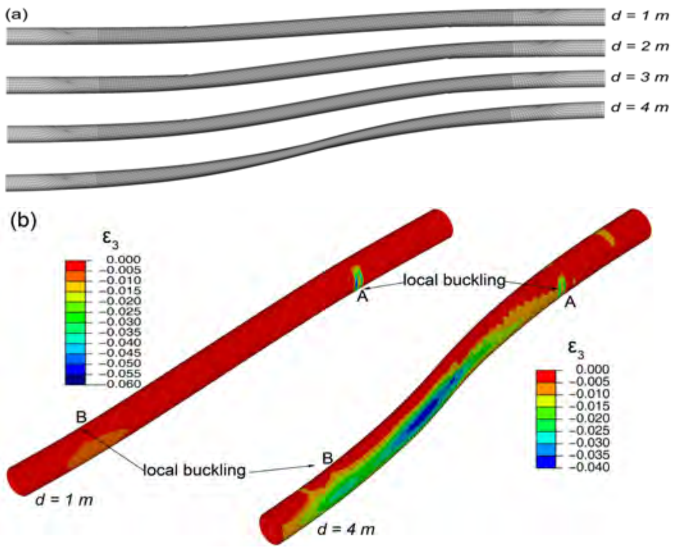

Figure 4: (a) Plan view of deformed shape of a pipeline for d = 1, 2, 3, and 4 m (b) Distribution of longitudinal normal strain ε_x for seismic fault displacement equal to 1 m and 4 m. (X65 pipe, $D/t = 72$, Clay I, $w = 0.33$ m, $p = 0$).

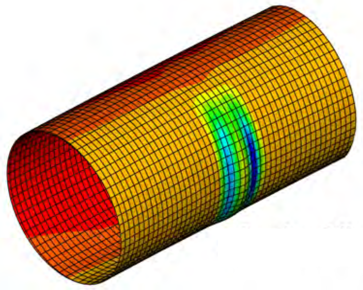

Figure 5: Details of the critical pipeline area: local buckling formation (X65 pipe, $D/t = 72$, Clay I, $w = 0.33$m, $p = 0$).

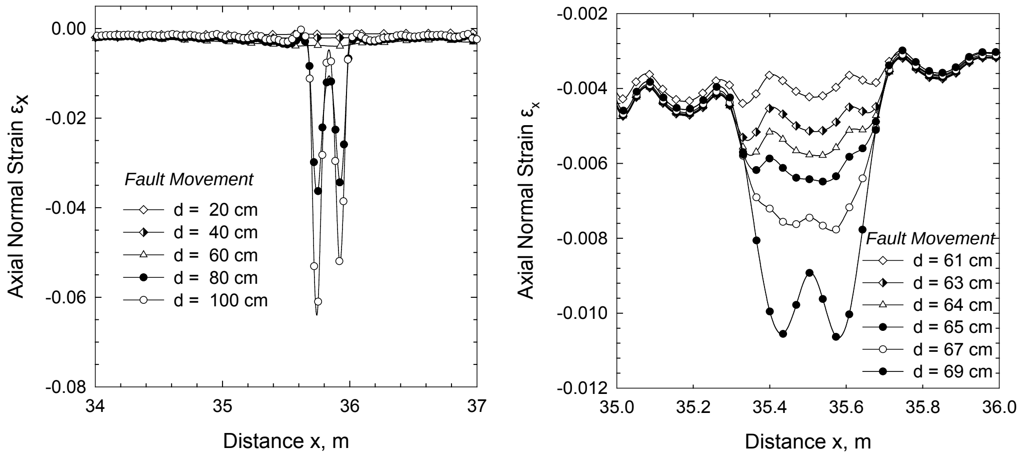

Figure 6: Variation of axial strain at the compression side of the buckled area for different values of fault displacement: (a) fault movement from 0.2m to 1.0m and (b) fault movement from 0.61m to 0.69m (X65 pipe, $D/t = 72$, Clay I, $w = 0.33$m, $p = 0$).

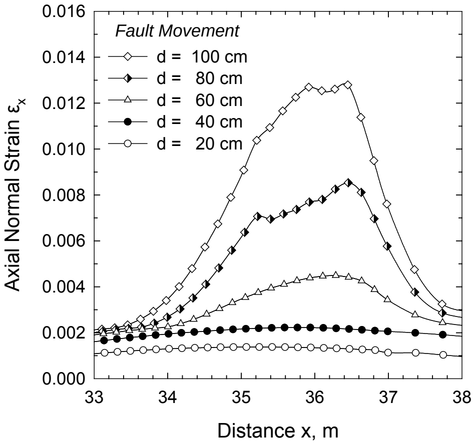

Figure 7: Variation of axial strain at the tension side of the buckled area for values of fault displacement from 0.2m to 1.0m (X65 pipe, $D/t = 72$, Clay I, $w = 0.33$m, $p = 0$).

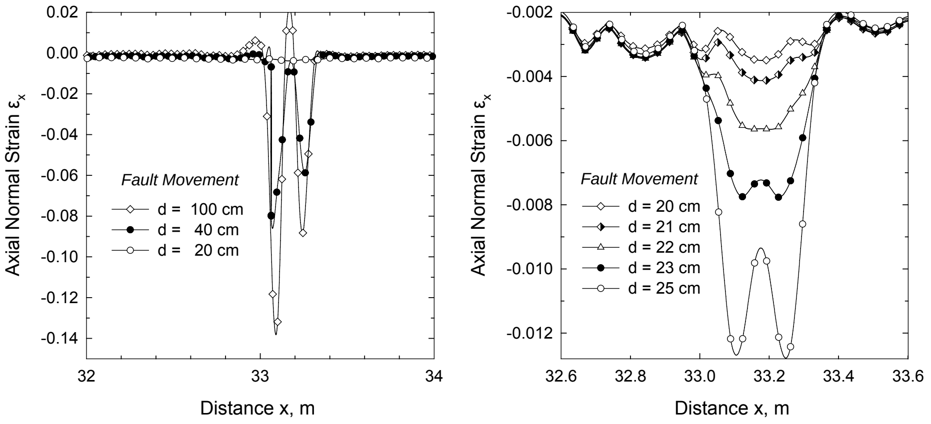

Figure 8: Variation of axial strain at the compression side of the buckled area for different values of fault displacement: (a) fault movement from 0.2m to 1.0m and (b) fault movement from 0.20m to 0.25m (X65 pipe, $D/t = 72$, Clay II, $w = 0.33$m, $p = 0$).

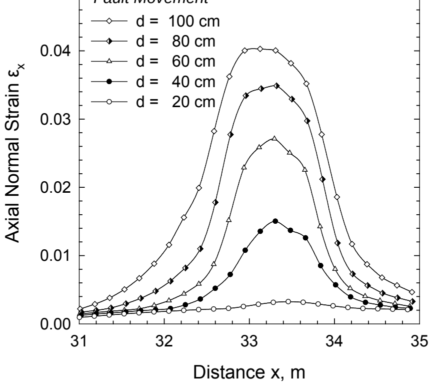

Figure 9: Variation of axial strain at the tension side of the buckled area in terms of fault displacement from 0.2m to 1.0m (X65 pipe, $D/t = 72$, Clay II, $w = 0.33$m, $p = 0$).

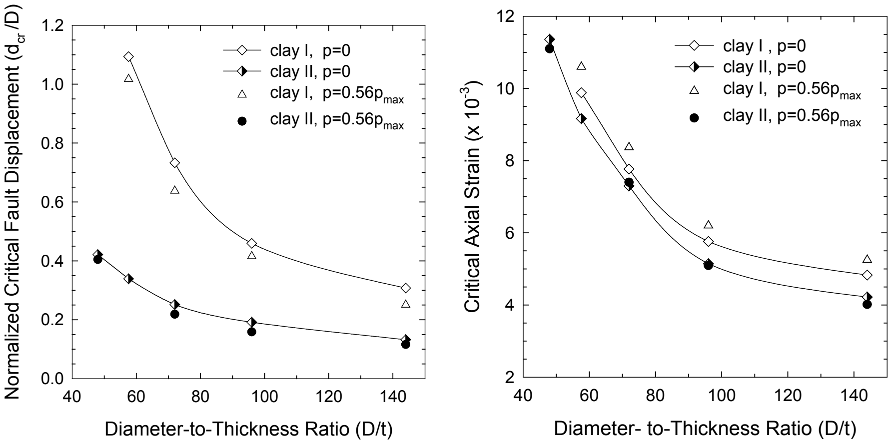

Figure 10: (a) Critical fault movement versus the diameter-to-thickness ratio D/t for clay I, II and (b) Critical axial strain versus the diameter-to-thickness ratio D/t for clay I, II (X65 pipe, $w = 0.33$m, $p = 0$ and $p = 0.56\,p_{\max}$).

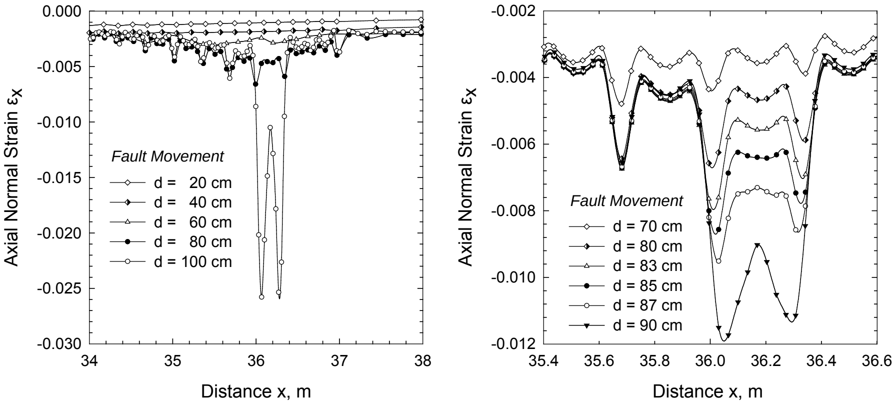

Figure 11: Variation of axial strain at the compression side of the buckled area for different values of fault displacement (a) fault movement from 0.2m to 1.0m and (b) fault movement from 0.70m to 0.90m (X65 pipe, $D/t = 72$, Sand I, $w = 0.33$m, $p = 0$).

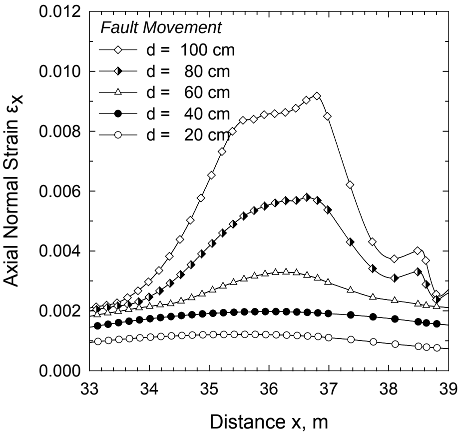

Figure 12: Variation of axial strain at the tension side of the buckled area for different values of fault displacement from 0.2m to 1.0m (X65 pipe, $D/t = 72$, Sand I, $w = 0.33$m, $p = 0$).

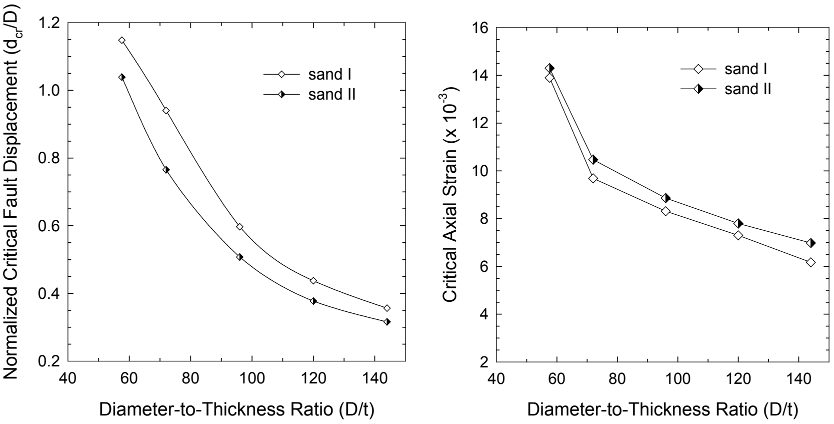

Figure 13: (a) Critical fault movement versus the diameter-to-thickness ratio D/t for sand I, II and (b) Critical axial strain versus the diameter-to-thickness ratio D/t for sand I, II (X65 pipe, $w = 0.33$m, $p = 0$).

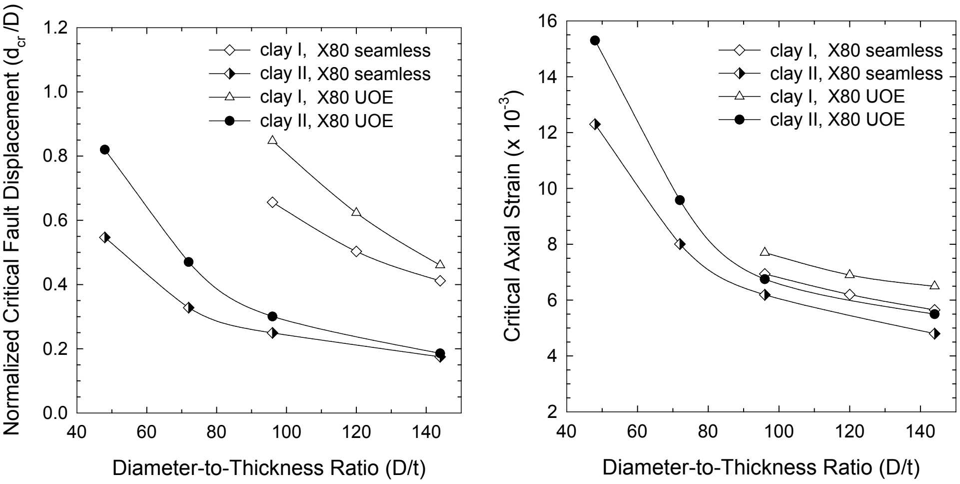

Figure 14: (a) Critical fault movement versus the diameter-to-thickness ratio D/t for two different types of X80 pipelines and (b) Critical axial strain versus the diameter-to-thickness ratio D/t for two different types of X80 (X80 pipe, $w = 0.33$m, $p = 0$)

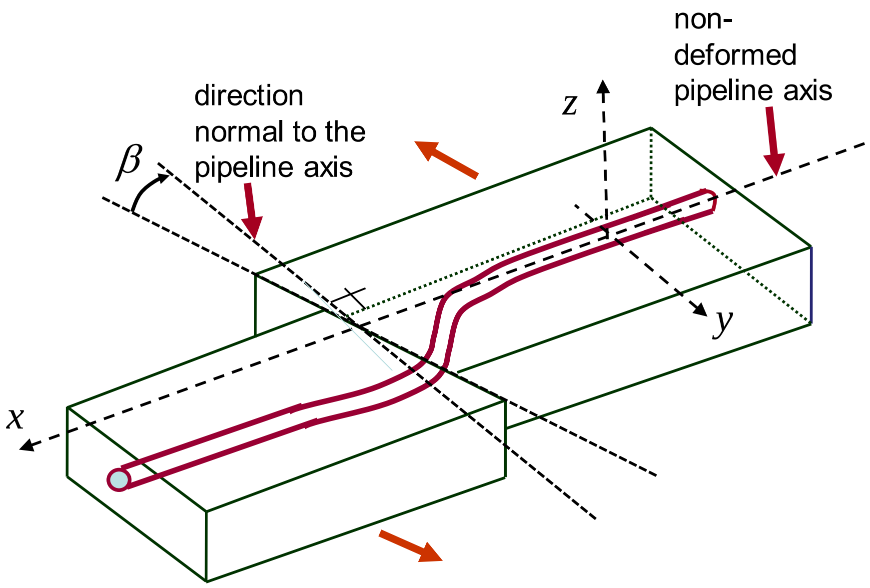

Figure 15: Schematic representation of a pipeline crossing a strike-slip fault at a certain angle.

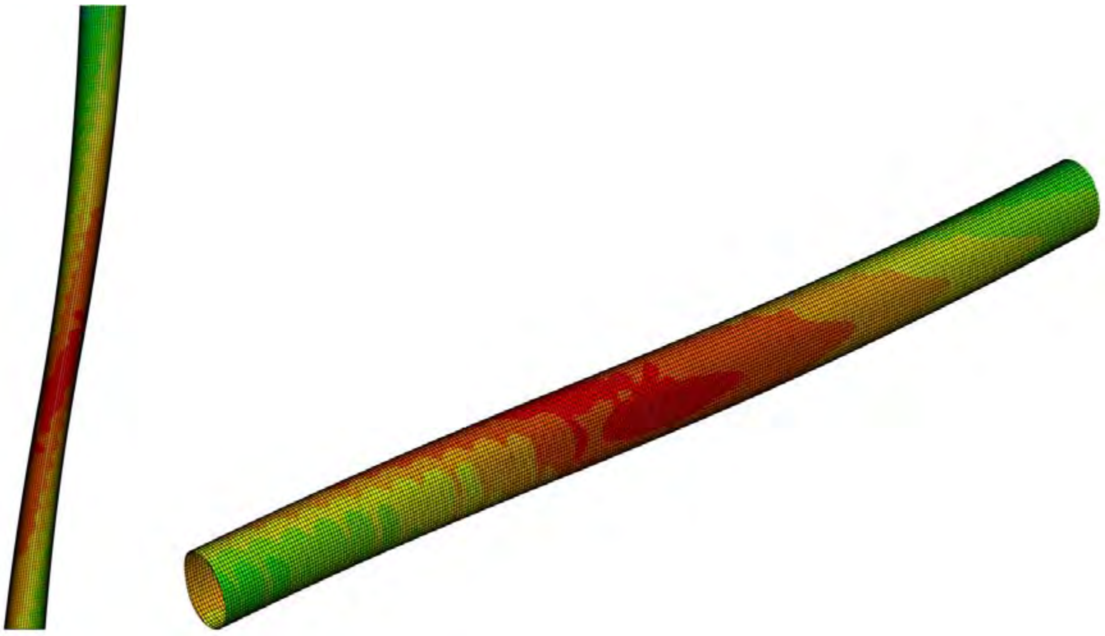

Figure 16: Deformed shape of the pipeline for β =25 degrees, at a fault displacement d = 2 m; top view (left) and three-dimensional view (right).

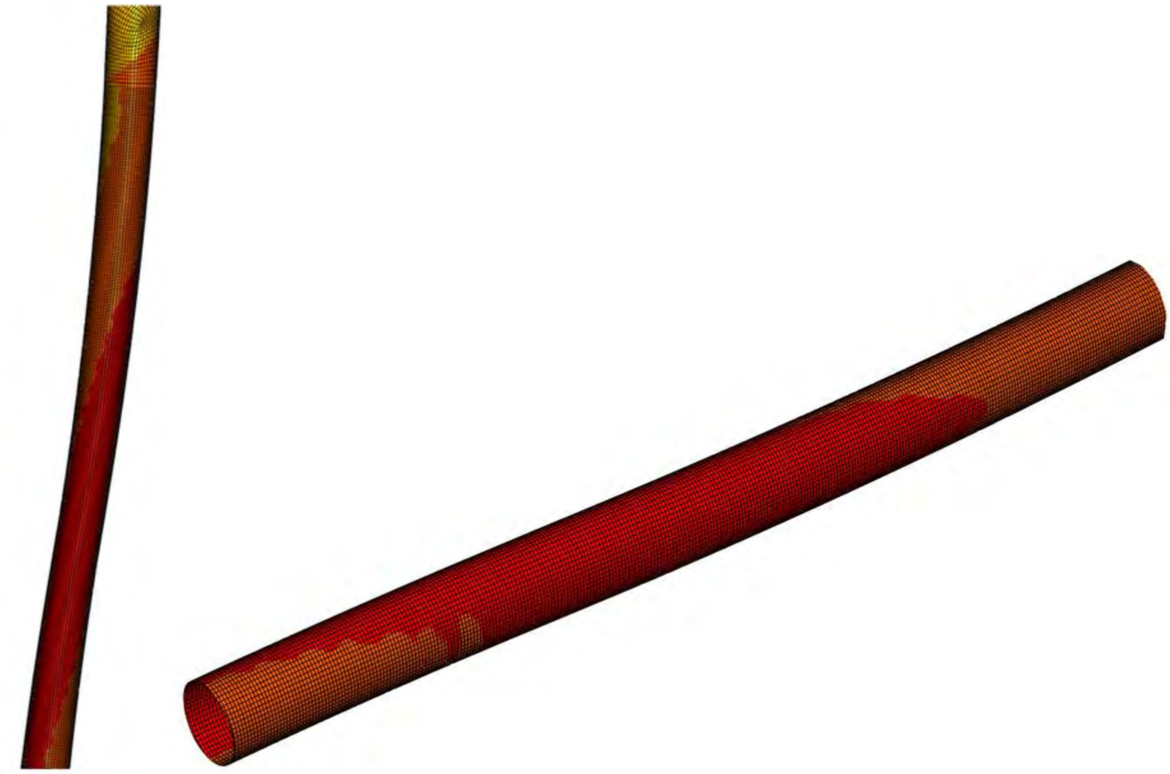

Figure 17: Deformed shape of the pipeline for $\beta = 45$ degrees, at $d = 2$ m; top view (left) and three-dimensional view (right).

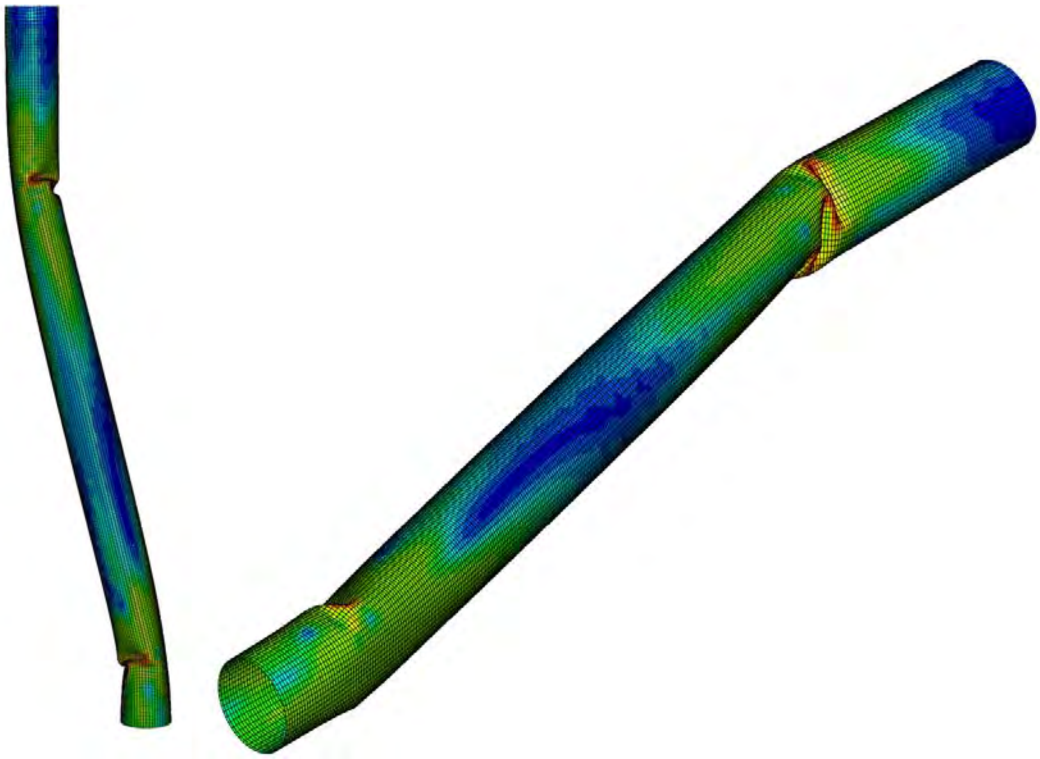

Figure 18: Deformed shape of the pipeline for $\beta = -10$ degrees, at $d = 2$ m; top view (left) and three-dimensional view (right).

COMPDYN 2011
III ECCOMAS Thematic Conference on
Computational Methods in Structural Dynamics and Earthquake Engineering
M. Papadrakakis, M. Fragiadakis, V. Plevris (eds.)
Corfu, Greece, 25–28 May 2011

SIMULATION OF INDUSTRIAL ELBOW RESPONSE UNDER STRONG CYCLIC LOADING

George E. Varelis[1], **Patricia Pappa**[1], **and Spyros A. Karamanos**[1]

[1] Department of Mechanical Engineering
University of Thessaly, Volos, Greece
{gevareli, patrpap, skara}@mie.uth.gr

Keywords: Piping, elbows, cyclic plasticity, seismic loading, buckling, ratcheting, finite elements.

Abstract. *Elbow components are widely used in industrial facilities as parts of piping/tubing systems. Their performance under severe loading conditions may be critical for the structural integrity of an industrial facility In the case of an earthquake event in addition to other service loads, such as internal pressure, they are subjected to strong repeated cyclic structural loading. When these elements are subjected to strong repeated loading, they present failure modes associated with cyclic plasticity phenomena (material degradation or cyclic creep). Furthermore, due to their flexibility, significant non-linearities occur and the elbow cross-section shape distorts as cyclic loading takes place resulting at an oval or flatten shape at the end of the loading sequence. Accumulation of plastic strains (cyclic creep or ratcheting) also takes place at the most stressed parts of the element, associated with extensive bulging of the cross-section which is more pronounced in the presence of internal pressure. The present study is numerical, based on a finite element simulation of the elbow, and investigates the elbow component behavior subjected to strong cyclic bending of various amplitudes in the presence of different levels of internal pressure. The material constitutive model has a dominant effect on the elbow response, and this is shown trough the use of 3 different plasticity models. The capabilities and drawbacks of each plasticity model regarding the simulation of cyclic plasticity phenomena are discussed in detail.*

1 INTRODUCTION

Pipe elbows constitute essential components of industrial piping systems in chemical plants, refineries and power plants. Because of their flexibility properties, they can accommodate thermal expansions and absorb other externally-induced loading. Under extreme loading conditions, such as seismic loading, elbows exhibit significant cross-sectional distortion (ovalization), associated well beyond the elastic limit of the material, which may cause failure of the piping component. Failure is in the form of excessive cross-sectional ovalization or local buckling. Therefore, their structural performance under earthquake loading conditions may be critical for the structural integrity of an industrial facility [1].

Experimental data on a series of tests on 16-inch 90 deg elbows (D/t =39 and R/t =3) under in-plane closing moments were reported by Sobel and Newman ([2], [3]) and Dhalla [4], and compared with numerical results from shell elements and simplified elbow elements. Gresnigt et al. ([5], [6], [7]) reported test data on five 30 deg, five 60 deg and one 90 deg steel elbows (R/r =6) under bending and pressure. Greenstreet [8] determined experimentally the load-deflection response of 20 carbon/stainless steel pipe elbows, under bending loading conditions, with internal pressure. Hilsenkopf et al. [9] conducted bending tests on thin-walled (D/t =89.5) stainless steel elbows and thick-walled (D/t =13.4) ferritic elbows, in connection with their functional capability. In-plane bending experiments on 90 deg elbows were reported by Suzuki and Nasu [10] and, more recently, by Tan et al. [11]. In both works, the test results were compared with finite element results. More recently, using a special-purpose "elbow" element of ABAQUS, Shaleby and Younan ([12], [13]) analyzed standalone 90 deg steel elbows (R/r =3) for a wide range of diameter-to-thickness ratios (15.5≤ D/t ≤97), under in-plane bending (opening and closing moments) and internal pressure. This work was extended by Mourad and Younan ([14], [15]) who analyzed pressurized standalone 90 deg steel elbow segments (R/r =3) under out-of-plane bending. In those works, only the curved part of the pipe was analyzed, neglecting the effects of the adjacent straight parts. Chattopadhyay et al. [16] employed twenty-node fully-integrated solid elements from a general-purpose program to analyze thick 90 deg elbows (D/t ≤25) under in-plane bending, accounting for the effects of the adjacent straight parts, and proposed simplified formulae were proposed for the collapse (limit) moment capacity in terms of pressure and the bend factor ($h=tR/r^2$). Karamanos et al. ([17], [18]) presented a numerical study of steel elbow response under in-plane bending (opening and closing) and out-of-plane bending, considering internal pressure effects. A good comparison was found between numerical results and test measurements reported by Gresnigt et al. [5]. The numerical work in Karamanos et al. ([17], [18]) was extended by Pappa et al. [19], to include the effects of external pressure on the bending response of elbows, for offshore pipeline applications.

The above works referred to monotonic loading, verifying the highly nonlinear response of steel industrial elbows under ultimate loading conditions. However, in the course of a strong seismic event, the elbows are subjected to strong repeated cyclic structural loading, associated with excursions of steel material in the plastic range. Under those severe cyclic loading conditions together with other service loads (e.g. internal pressure), the elbow may exhibit significant accumulation of plastic strain ("cyclic creep" or "ratcheting"), which eventually may lead to failure. Extensive experimental work on 2-inch pipe elbows under strong cyclic in-plane bending loading conditions has been reported by Yahiaoui et al. [20], focusing on the ratcheting behavior. The schedule of the pipes were SCH40 (Std) and SCH80 (XS), and the specimens included both long ($R = 76$mm) and short ($R = 51$mm) radius elbows. The materials were carbon steel (ASTM A106B) and stainless steel (A312 TP304L). The specimens were first pressurized, then their resonance frequency was determined and, subsequently, they were shaken under an “increasing input displacement amplitude” loading pattern. It was concluded that ratcheting in the hoop direction was more pronounced than in longitudinal direction. In short radius elbows, some ratcheting was observed at the intrados, in the longitudinal direction. It was also observed that ratcheting for carbon steel elbows initiated with the applied bending moment reached the value of plastic moment. Furthermore, no permanent cross-sectional deformation was observed. This work was continued in Yahiaoui et al. [21] for the case of elbows under out-of-plane bending moments, and similar conclusions were drawn. In a subsequent publication, the authors (Moreton et al. [22]), based on the work by Edmunds and Beer [23] attempted to predict analytically the ratcheting rate, as well as the conditions for ratcheting initiation. Slagis [24] reported experimental testing conducted by EPRI/NRC on carbon/stainless steel pipe elbows. The tests were performed through a shaking-table apparatus, simulating floor response motion, and included both component tests and piping system tests. Extensive experimental work was presented by Fujiwaka et al. [25], through a series of material tests, pipe component tests and piping system tests at room temperature and at 300^{o}C. The specimens comprised bent pipes, tees, and straight pipes, from both carbon and stainless steel material. Finite element simulations were also reported and a criterion was developed for evaluating ratcheting effects on fatigue.

Degrassi et al. [26] performed non-linear time history finite element analysis of piping system with the object of simulating ratcheting responses under seismic excitation. They simulated the seismic responses of the piping systems using the bilinear, multilinear and Chaboche models in ANSYS. Balan and Redektop [27] simulated the response of elbow specimen under cyclic bending and internal pressure with bilinear plasticity model in the finite element code ADINA. They demonstrated that the shakedown phenomenon is simulated by the bilinear model for circumferential strain at the flank. More recently, Rahman & Hassan [28] presented an extensive analytical work on cyclic behavior of steel elbows, supported by 3 experiments on 2-inch SCH10 pipes, aiming at determining the capabilities of several cyclic plasticity models in predicting the ratcheting rate.

All the above works have demonstrated that when steel elbows are subjected to strong repeated loading, they present failure modes associated with cyclic plasticity phenomena (material degradation or cyclic creep). In many instances, it has been noticed that – especially in the case of pressurized elbows – the elbow cross-section shape distorts (ovalization or flattening) or bulges as cyclic loading takes place.

The present study is part of a large European research effort, aimed at investigating the structural safety of industrial equipment structures and components, including industrial elbows. The research presented in the present study is numerical, based on a finite element modeling of 8-inch SCH40 elbows of P355 material according to EN 13480-2 (equivalent to API 5L X52), and it is motivated by the need of developing accurate numerical models for of steel elbow elastic-plastic behavior under strong cyclic bending, in the presence of different levels of internal pressure.

Following a brief presentation of elbow stress analysis and the ultimate capacity under monotonic loading conditions (closing and opening), special attention is given on the constitutive model for describing the cyclic behavior of steel material. In the present paper, linear and nonlinear kinematic hardening models are employed in terms of their capabilities and drawbacks in simulating cyclic plasticity phenomena observed in previous experimental observations. Finally, the numerical results are compared with the provisions of ASME B31.3 [29] and EN 13480-3 [30].

2 DESCRIPTION OF NUMERICAL SIMULATION

General-purpose finite element program ABAQUS is employed in the present study for the parametric study. The analysis considers nonlinear geometry through a large-strain formulation, and inelastic effects, which are accounted for through a J_2 (von Mises) plasticity model. For monotonic loading conditions isotropic hardening is employed, where the uniaxial stress-strain curve from a tensile test is considered for calibration purposes. The yield stress (σ_y) of the material is considered equal to 355 MPa, and hardening of the pipe material is assumed with a hardening modulus of about $E/200$. For cyclic loading conditions, in addition to the isotropic hardening, linear and nonlinear kinematic hardening is also employed. More details on the description and the application of those plasticity models are available in a subsequent section of the present study.

Previous numerical results indicated that pipe elbows may exhibit an unstable post-buckling response (Karamanos et al. ([17], [18])). Therefore, in the case of monotonic loading, a path-follower (Riks) algorithm is employed to trace unstable equilibrium paths and calculate the post-buckling response of the elbow members.

Four-node reduced-integration shell elements (type S4R) are employed for modeling of the pipe-elbow geometry. Several analyses have also been repeated with an eight-node element S8R, and the results were found almost identical with the results obtained through the S4R element [18]. The special-purpose "elbow" elements in ABAQUS, is not considered because of its inadequacy of simulating very accurately buckling and post-buckling elbow configurations.

The thickness of the curved part of the elbow is equal to the thickness of the straight part. Thickness variations due to the manufacturing process are not taken into account in the present analysis geometry.

In the present study, a detailed simulation the scheduled experimental procedure is conducted. In the numerical model, rigid plates are assumed to "cap" end sections A and B (Figure 1). This is achieved through the "kinematic coupling" feature of ABAQUS, which relates the degrees of freedom of the shell nodes in section B with the degrees of freedom of a reference node, which is assumed to be located at the centroid of the end-section. In case of non-zero internal pressure, the corresponding capped-end force is taken into consideration. Capped-end section A is hinged, whereas the other end-section allows for both in-plane rotation and displacement along the x-direction.

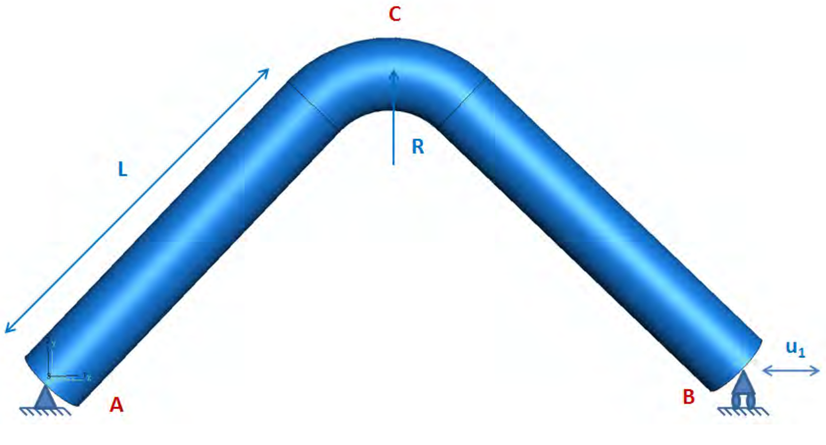

Fig. 1: Schematic representation of 90deg pipe

3 NUMERICAL RESULTS FOR MONOTONIC LOADING

Under bending loading, pipe elbows, compared with straight pipe segments, undergo very pronounced cross-sectional deformations, in the form of cross-sectional ovalization. This ovalization makes the elbow significantly more flexible, exhibiting considerably higher stresses and strains. A simple energy formulation has been proposed by Rodabaugh and George [32] to describe the mechanical behavior of elastic elbows; assuming uniform cross-sectional deformation along the elbow axis, the total potential energy of the elbow under bending and pressure is formed. Solution is obtained analytically, minimizing the potential energy, and resulted in the so-called flexibility factor, which expresses the ratio of elbow flexibility over the flexibility of a straight pipe of equal length and of the same cross-section. The same solution provides the longitudinal and hoop stresses, and the ovalization of the cross-section, and compares quite well with finite element results. For a thorough presentation of those issues, one may refer to the recent paper of Pappa et al. [19]. Among other conclusions, it is interesting to note that the flexibility factor is higher in the absence of internal pressure and is reduced when internal pressure is raised. Furthermore, the maximum circumferential stress is higher than the maximum longitudinal stress, and that the maximum longitudinal stress is considerably higher than the maximum stress of a straight pipe with the same cross-section, and does not occur at the top or the bottom of the cross-section. The significant ovalization of the elbow cross-section is mainly responsible for this behavior.

The above results refer to linear elastic analysis of standalone elbows, assuming no variation of stress and deformation along the elbow; however, in a real situation, the problem is more complicated. There are straight pipes welded to the elbow ends that influence ovalization along the elbow, whereas the severe deformation of the elbow is associated with significant inelastic deformations. Considering also the significant change of elbow geometry, it is necessary to use numerical (finite element) simulation tools in order to determine the ultimate bending moment capacity of the steel elbow.

Using the finite element simulation described in section 2, the bending response of an 8-inch short-radius SCH40 elbow is analyzed. The bend radius is 328.62 mm (equal to 1.5 times the pipe diameter D), the pipe thickness t is 8.18 mm and the material of the pipe is P355 material as described in the previous section. Each straight part of the piping specimen is 1095.4 mm (equal to 5 times the pipe diameter D).

Elbow with above characteristic is analyzed, for internal pressure levels up to 50% of the fully-plastic pressure p_y. The results focus on the ultimate capacity, the corresponding failure mode and the effects of pressure. In Figure 2, the applied in-plane closing force of thick-walled elbow is plotted in terms of the displacement of end section B. The results depicted in figure demonstrate the beneficial effect of internal pressure on the ultimate capacity of elbow. This is mainly due to the reduction of cross-sectional ovalization of the curved part. Ovalization is expressed in terms of the non-dimensional ovalization parameter (ov) defined as $\mathrm{ov} = \left| D_A - D_B \right| / 2D_m$, where D_A is the length of the deformed diameter on the plane of bending and D_B is the length of deformed diameter perpendicular to the plane of bending, both measured at the cross-section under consideration. In Figure 4, the ovalized shape of elbow is depicted. In both cases, failure is due to a plastic mechanism with four plastic hinges, which are located at the intrados, the extrados and the two “flank” locations.

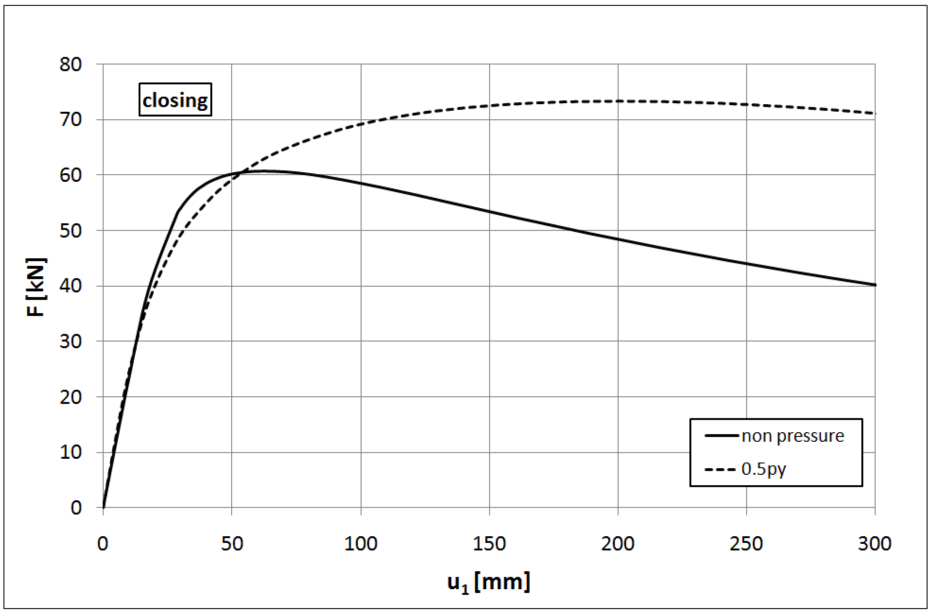

Fig. 2: Load versus end-displacement curves for two levels of internal pressure with respect to p_y .

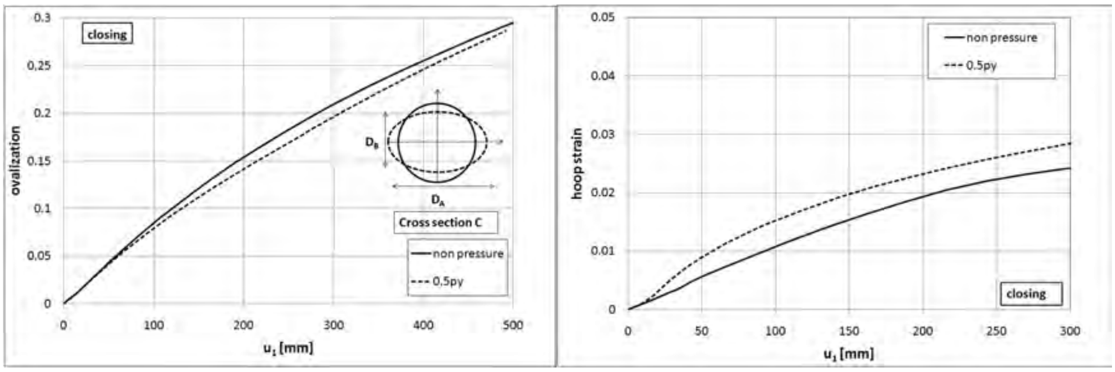

Fig. 3: Ovalization of cross section C and hoop strain of cross section C at “flank” location for two levels of internal pressure under closing bending.

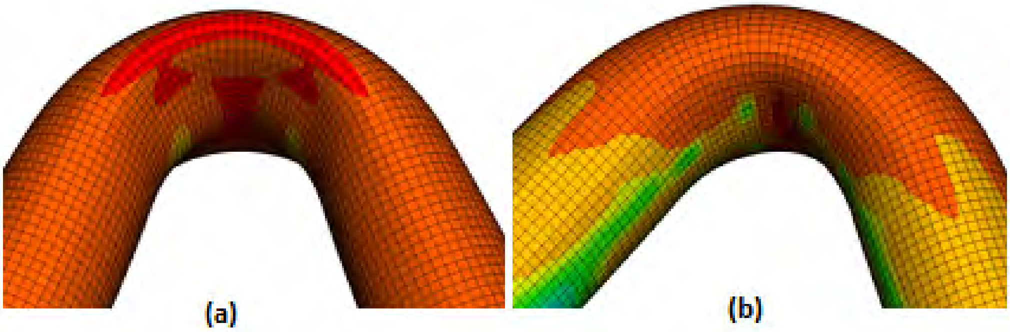

Fig. 4: Deformed three-dimensional elbow shape under closing bending moments; (a) zero pressure; (b) internal pressure 50% of p_y

The response of the elbows under opening bending moments is shown in Fig. 5, for two different pressure levels 0%, and 50% of the yield pressure p_y . In figures 5, 6 and 7, the force-displacement, ovalization–displacement and hoop strain-displacement curves are plotted. Elbows under in-plane opening moments exhibit “negative” ovalization, so that the length of the diameter on the plane of bending increases. It is noted that thick-walled pipe elbows under opening moments and internal pressure exhibit small ovalization. In Figs. 7*a* and 7*b*, the buckled shapes of elbows for zero and 50% of the fully-plastic pressure p_y opening moment bending are depicted. It is important to note that the capacity of non pressurized elbows under opening bending moments is significantly greater than the corresponding moment capacity under closing bending moments as shown in the numerical results.

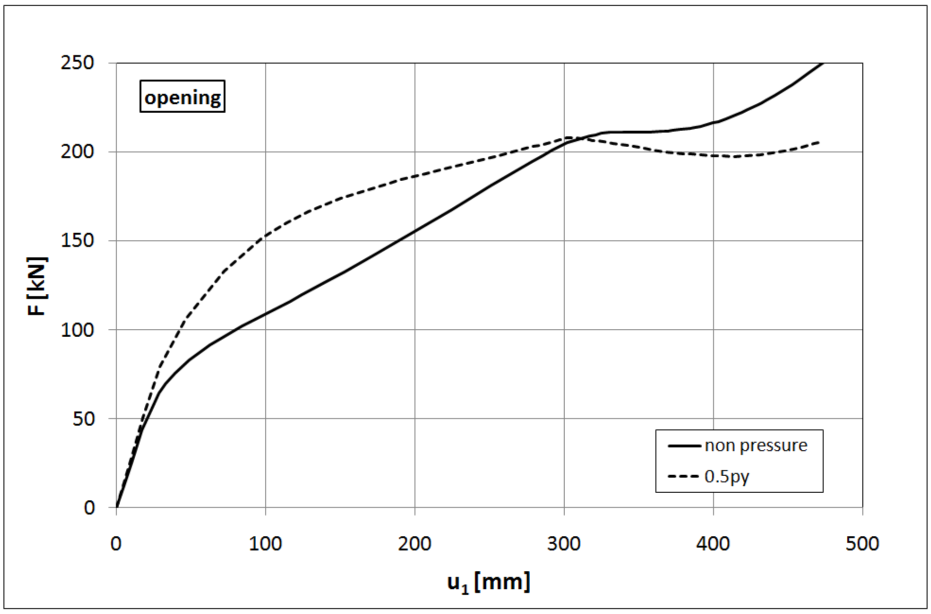

Fig. 5: Load versus end-displacement curves for two levels of internal pressure with respect to p_y .

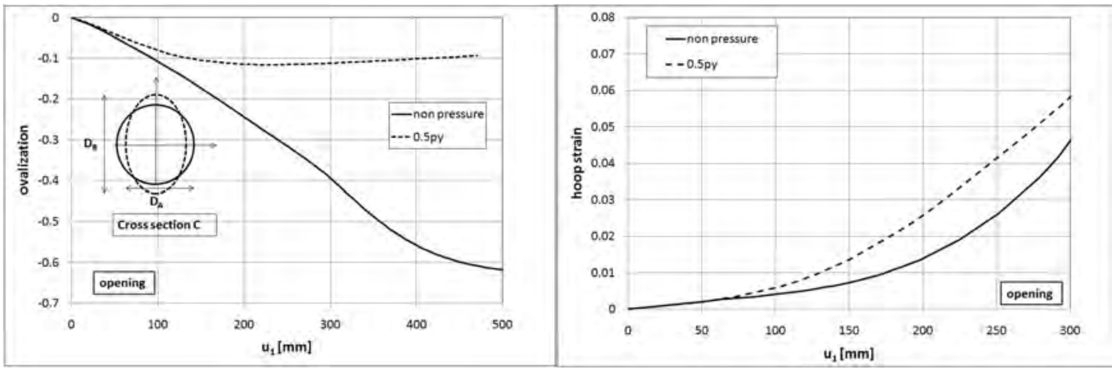

Fig. 6: Ovalization of cross section C and hoop strain of cross section C at intrados for two levels of internal pressure under opening bending.

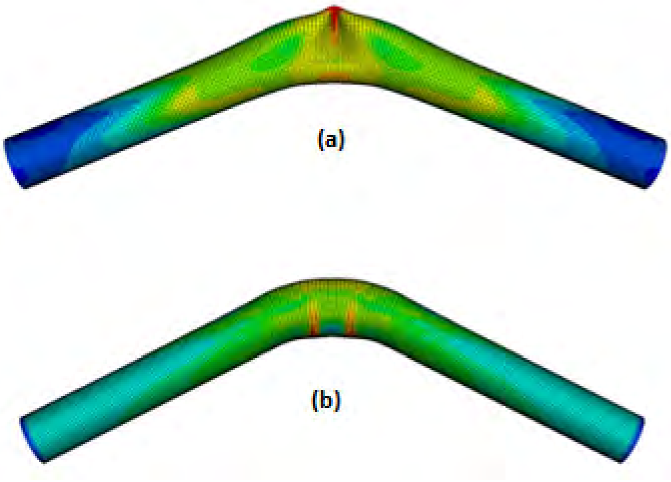

Fig. 7: Buckles under opening bending moments; (a) zero pressure; (b) internal pressure 50% of p_y .

4 MATERIAL MODELING FOR CYCLIC PLASTICITY

For the numerical simulation of the elbow performance under cyclic bending conditions in the presence of internal pressure, several cyclic plasticity models are used. The first and most traditional cyclic plasticity model adopted is a von Mises flow model with isotropic hardening. According to this model, the origin of the Yield Surface remains fixed at the stress space and it is allowed to expand as it is described by the following equation:

$$F = \frac{1}{2}\mathbf{s}\cdot\mathbf{s} - \frac{k^2(\varepsilon_q)}{3} = 0 \tag{1}$$

where $\mathbf{s}$ is the deviatoric stress tensor defined as $\mathbf{s} = \boldsymbol{\sigma} - p\mathbf{I}$ (p is the “hydrostatic” stress and $\mathbf{I}$ is the identity tensor) and k is the parameter that defines the size of the yield surface which is generally a function of the equivalent plastic strain ε_q .

An advancement of the von Mises plasticity model with isotropic hardening that overcomes the drawbacks related to its simplicity is the use of linear and nonlinear kinematic hardening rules. In this case, the Yield Surface is free to move in the stress space while its size remains constant. The yield criterion for kinematic hardening is as follows:

$$F = \frac{1}{2}(\mathbf{s}-\mathbf{a})\cdot(\mathbf{s}-\mathbf{a}) - \frac{k^2}{3} = 0 \tag{2}$$

where $\mathbf{a}$ is the back stress tensor that expresses the current center of the yield surface in the deviatoric space. The linear kinematic hardening rule is described by the following linear expression:

$$\dot{\mathbf{a}} = C\dot{\boldsymbol{\varepsilon}}^p \tag{3}$$

where C is the kinematic hardening modulus considered as constant and $\dot{\boldsymbol{\varepsilon}}^p$ is the plastic strain rate. In this case the size of the Yield Surface k is constant. When the nonlinear kinematic hardening (Armstrong-Frederick) rule is adopted, the aforementioned hardening rule is modified as:

$$\dot{\mathbf{a}} = C\dot{\boldsymbol{\varepsilon}}^p - \gamma\mathbf{a}\dot{\varepsilon}_q \tag{4}$$

where C is the linear kinematic hardening modulus and γ is the parameter that determines the rate at which the kinematic hardening modulus decreases with increasing plastic deformation. The use of the multilinear kinematic hardening rules significantly improves the capacity of the plasticity model to predict cyclic plasticity related phenomena such as the Bauschinger effect and ratcheting. The special characteristic of the adopted plasticity models have been extensively discussed by Varelis [31].

For the calibration of the above cyclic plasticity model parameters due to the lack of experimental data, the material uniaxial stress strain curve is used. The fitting of the predicted material uniaxial behavior for each plasticity model adopted to the measured values is depicted in Fig.1. The corresponding model parameter values that provide the best fit to the measured stress/strain uniaxial curve are for linear kinematic hardening $C = 1007.137$ and for nonlinear kinematic hardening σ_y=350 *MPa*, C=1500, γ=10 .

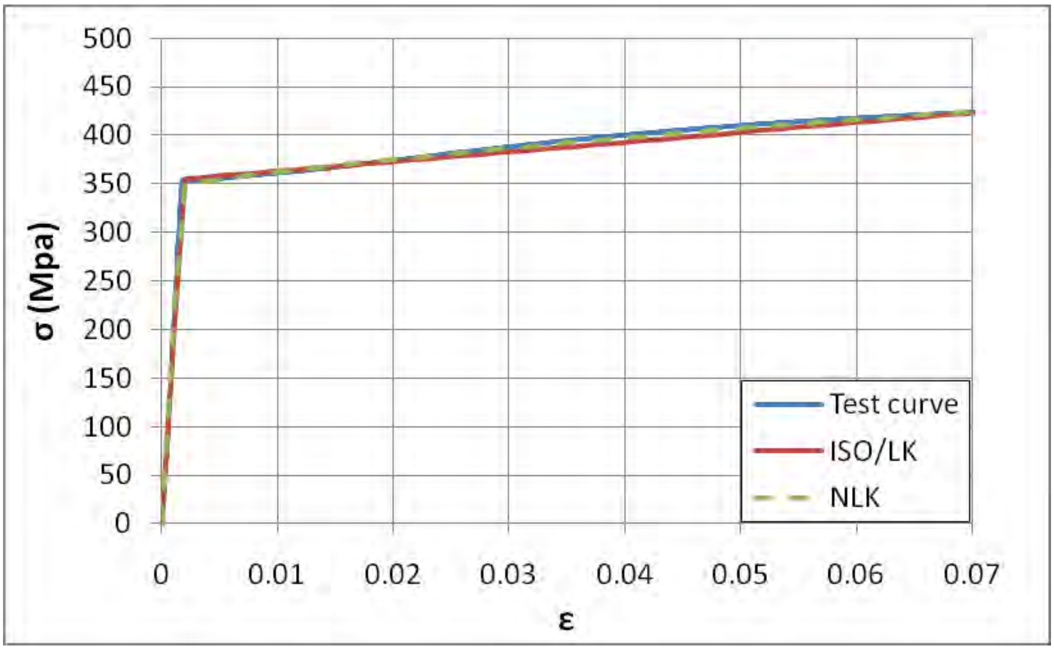

Fig. 8: Uniaxial stress-strain curve and cyclic plasticity model predictions

5 CYCLIC RESPONSE OF STEEL ELBOWS

For the examination of cyclic response of steel elbows the numerical model described above has been used. Loading is introduced by applying cyclic displacement at the one end of the elbow specimen in the absence and in the presence of internal pressure. The cyclic displacement ranges considered in the present study are ±150 mm and ±300 mm which are well beyond the elastic behavior limit of the elbow as shown in the monotonic curves presented.

The first set of simulations is conducted with zero pressure loading, while in the second simulation set a relatively high pressure of $p=14.5$ MPa is first applied and subsequently kept constant throughout the cyclic loading application. The pressure value corresponds to about 50 percent of the yield pressure of the elbow $p_y=2\sigma_y t / D$, where σ_y is the yield strength of the material (equal to 355 MPa), t is the elbow wall thickness equal to 8.179 mm and D is the elbow diameter. The result of the three cyclic plasticity models adopted are presented and discussed in detail in the following paragraphs. The numerical results of interest are the force-displacement curve, the change of the elbow diameter measured at the central cross-section in the horizontal and vertical direction, and the evolution of strain at the elbow flank.

5.1 Cyclic bending in the absence of internal pressure

The elbows are subjected to cyclic loading of alternating sign in the range of ±150 mm and ±300 mm without internal pressure. The loading begins with a closing end-displacement and continues with unloading and reverse loading for 10 complete load cycles. In Fig. 9(a) the load versus end-displacement curves for each plasticity model are presented. In Fig. 9(b) the prediction for the first loading cycle is depicted for the three material models.

It is clearly observed that the predictions of the plasticity models vary significantly. The isotropic hardening model, denoted as (ISO), predicts higher required load when reloading takes place. After a few initial load cycles the response for the remaining load cycles appears to stabilize. The models using the linear kinematic hardening rule (LK) and the nonlinear kinematic hardening rule (NLK) predict lower reaction forces compared to the ISO model and similar to each other. This can be attributed to the constantly increasing size of the yield surface assumed by the ISO due to plastic deformation increase. On the contrary, the constant size of the yield surface assumed in the case of LK and NLK model results to lower reaction forces since plastic deformations initiate at lower stress levels. Furthermore, the behavior stabilizes after a few initial load cycles as well, but the stabilized hysteresis loops predicted by the LK and the NLK model have different sizes. This is because in the case of the NLK model, the hardening modulus is continuously decreasing until it reaches a zero value as the equivalent plastic strain increases, whereas for the LK model the hardening modulus remains constant.

The prediction of cross-sectional distortion for each plasticity model is presented in Fig. 10. All three models used predict almost the same distortion values for both the horizontal and the vertical direction. Only minor differences are observed near the end of the cyclic loading history. Greater differences in predictions of the three models are observed for the strain accumulation (ratcheting) at the flank of the elbow as shown in Fig. 11. Near this area the plastic deformations are accumulated resulting to a localization of plastic deformation that might result to fracture. The main reason for the above differences is that each plasticity model predicts a different deformation shape of the elbow at the end of the loading history, as shown in Fig. 12.

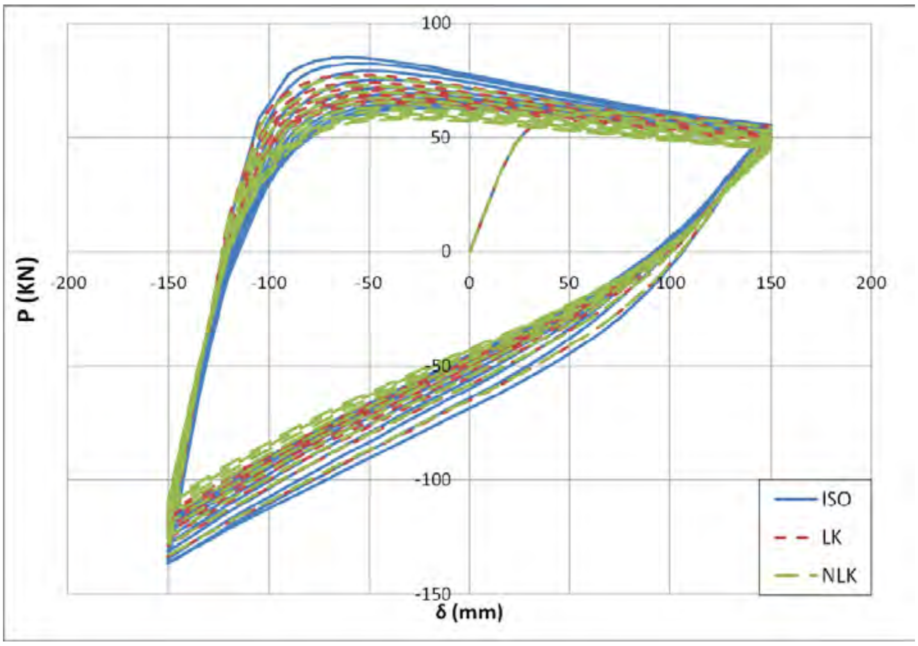

(a)

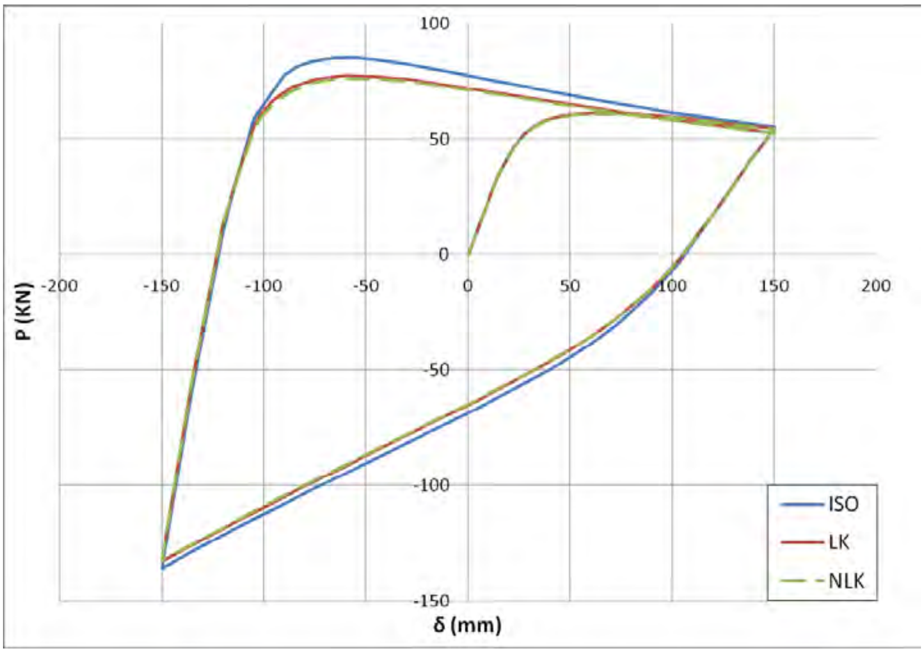

(b)

Fig. 9: Load versus end-displacement curves for displacement range ±150 mm, p=0 MPa:
(a) Complete cyclic loading (b) First load cycle

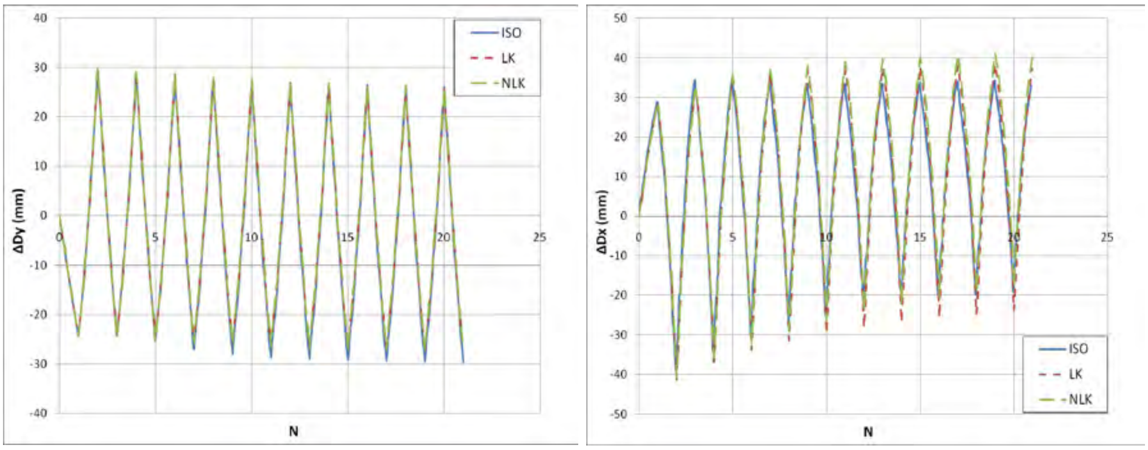

(a) (b)

Fig. 10: Cross-sectional distortion displacement range ±150 mm, p=0 MPa:
(a) Verical direction, (b) Horizontal direction

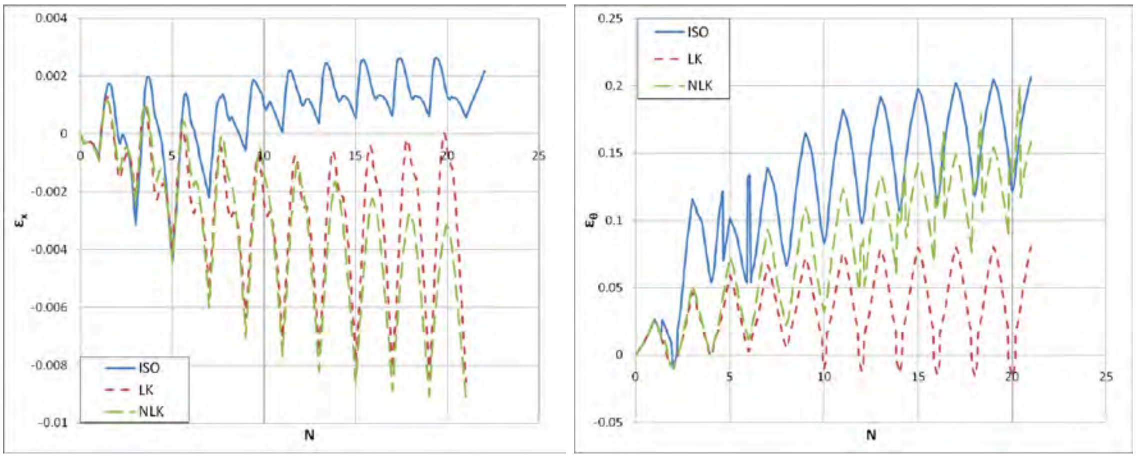

(a) (b)

Fig. 11: Strains at the elbow flank: (a) Longitudinal direction, (b) Hoop direction

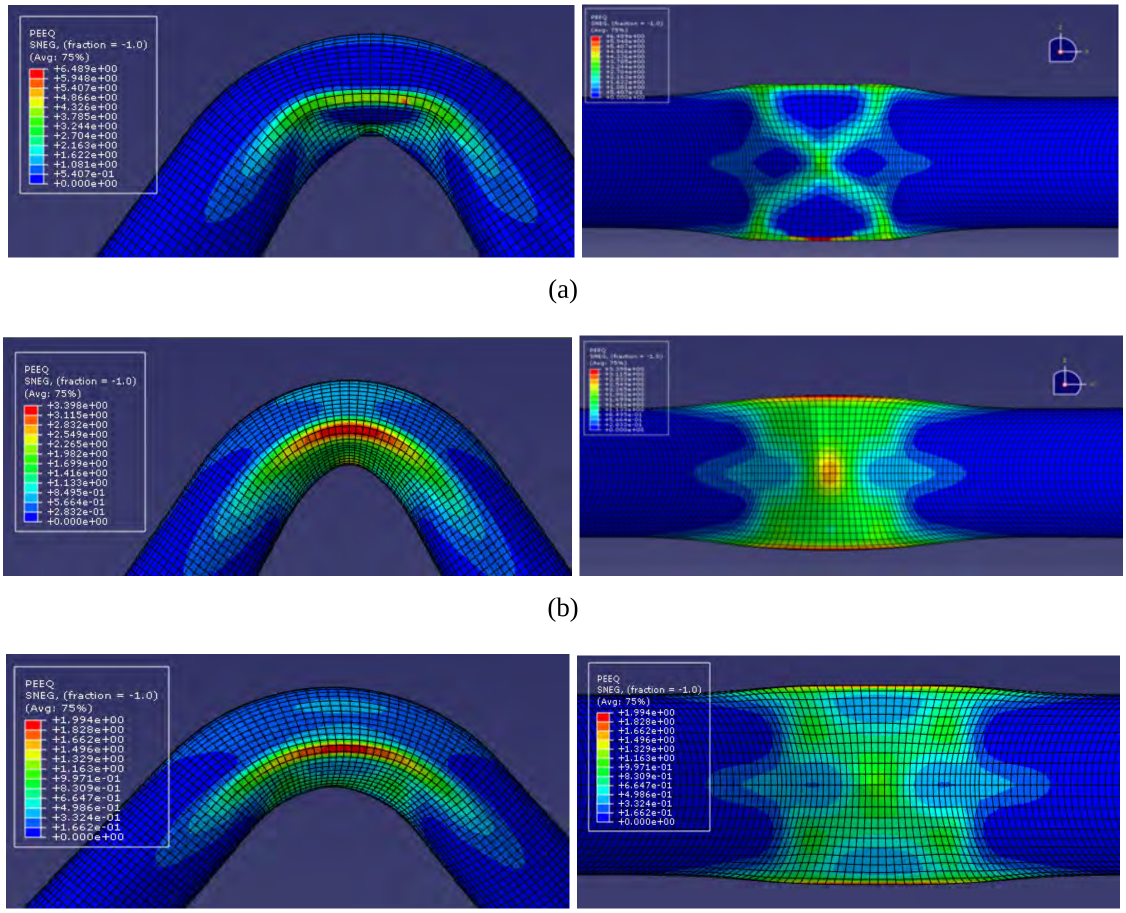

(a)

(b)

(c)

Fig. 12: Plastic deformation distribution at the end of the loading history:
(a) ISO, (b) LK and (c) NLK model predictions

The same quantities have been monitored for the ±300 mm end-displacement loading case and zero pressure. The corresponding load versus displacement curves for the entire loading history and for the fisrt load cycle only are presented in Fig. 13(a) and 13(b) respectively. Again, the ISO hardening model overpredicts the resulting end-reaction compared to the models that use the LK and the NLK rule. For this loading range as well, the same stabilization trend for the hysterisis loops is observed.

The cross-sectional distortion for the loading range of ±150 mm is also observed for the loading range of ±300 mm. The predictions of the three plasticity models presented in Fig. 14 provide close results. In Fig. 15, strain accumulation at the flank region is shown. It is noticable that the ISO madel predicts very high strain values especially near the end of the cyclic loading history, mainly in the hoop direction. It should be noted though that the predicted strain values by all models that lay or exceed the value of 20 percent are far beyond the fracture limit of the material, which indicates that a crack is propable to initiate at this region in the longitudinal direction. Finally, the significan differences observed in the strain accumulation graph of Fig. 15 can be attributed to the different deformation modes predicted by each model, which are very similar to those observed in the case of ±150 mm loading.

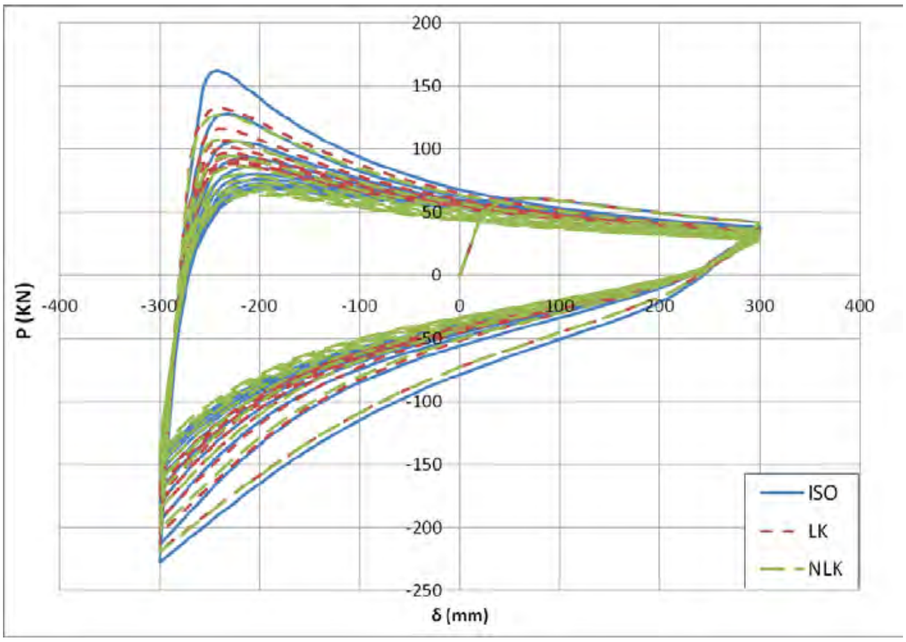

(a)

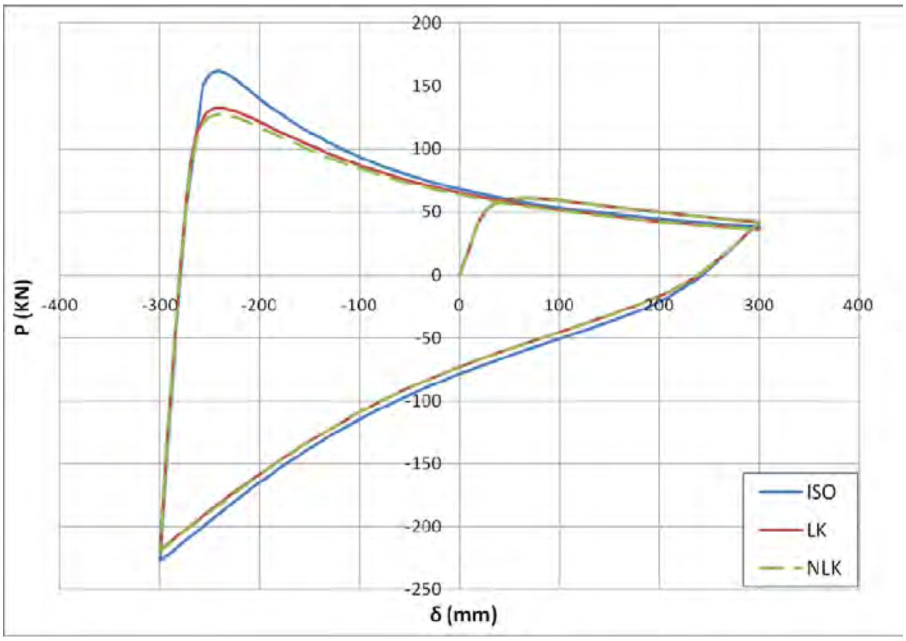

(b)

Fig. 13: Load versus end-displacement curves for displacement range ±300 mm, $p=0$ MPa:
(a) Complete cyclic loading (b) First load cycle

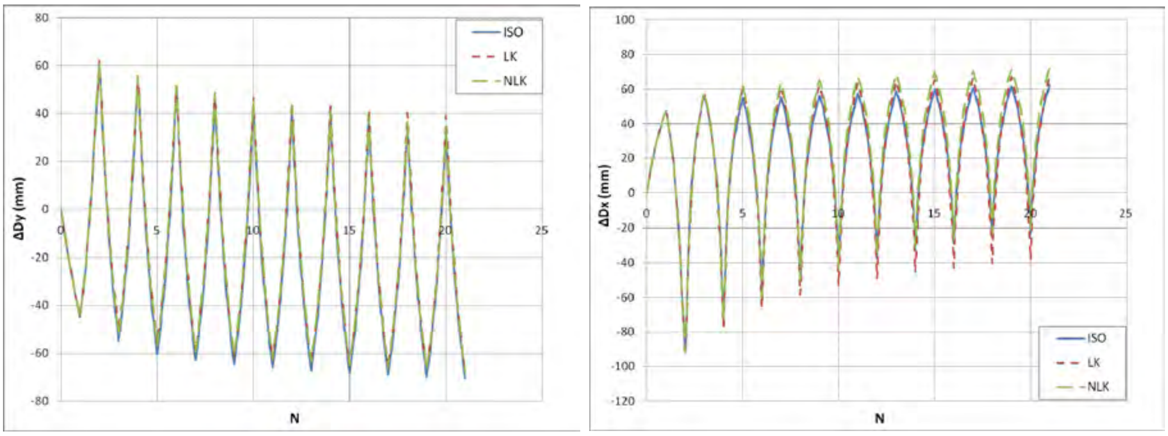

(a) (b)

Fig. 14: Cross-sectional distortion for displacement range ±150 mm, $p=0$ MPa:
(a) Vertical direction, (b) Horizontal direction

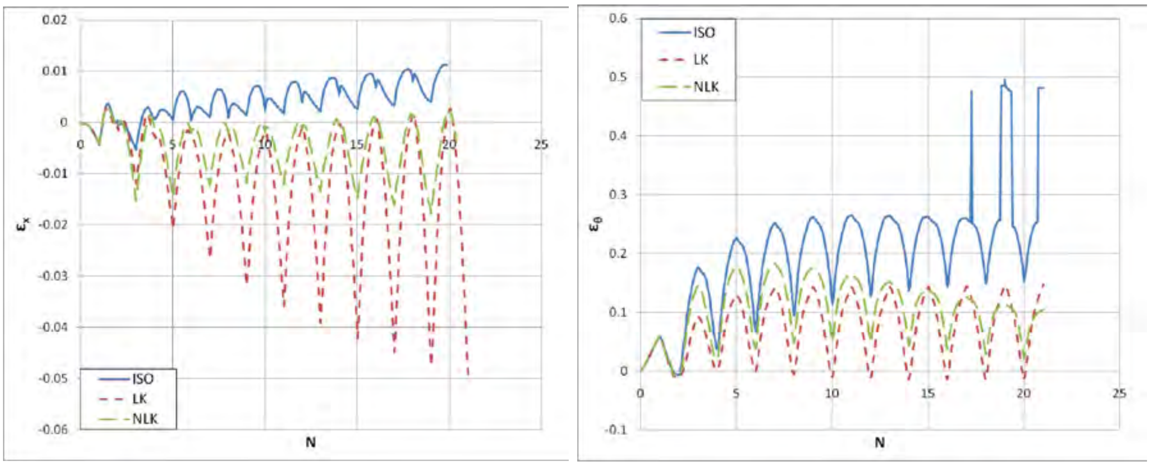

(a) (b)

Fig. 15: Strains at the elbow flank: (a) Longitudinal direction, (b) Hoop direction

5.2 Cyclic response of internally-pressurized elbows

The presence of internal pressure has significant effects on the elbow structural performance under cyclic loading conditions. The monotonic loading curves presented in a previous paragraph, indicate that due to the existence of internal pressure, the elbow capacity is increased well beyond the elastic limit. For comparison reasons, the same end-displacement ranges of ±150 mm and ±300 mm have been considered for these simulations, for a pressure level equal to $p = 14.5$ MPa.

From Fig. 16(a) it is observed that the existence of internal pressure maintains the hysteresis loops in an almost stabilized state throughout the cyclic loading history. The over-prediction of the ISO model compared to the predictions of the other two models (Fig. 16(a) and (b)) can be attributed to the constantly increasing yield surface size. This results to extensive bulging of the elbow section (Fig. 19a) and consequently to significant loss of resistance capacity observed after a few load cycles.

It is interesting to note that the predictions of the LK and NLK models as far as the final deformation state is concerned are significantly different. More specifically, the LK model predicts a local buckle oriented at the extrados of the elbow (Fig. 19(b)), while the NLK predicts a local bulging of the elbow intrados, but significantly smaller compared to the bulging predicted by the ISO model. The aforementioned differences in the deformation modes explain the differences in Figures 18 and 19 with respect to the cross-sectional distortion and the accumulation of strain at the flank region.

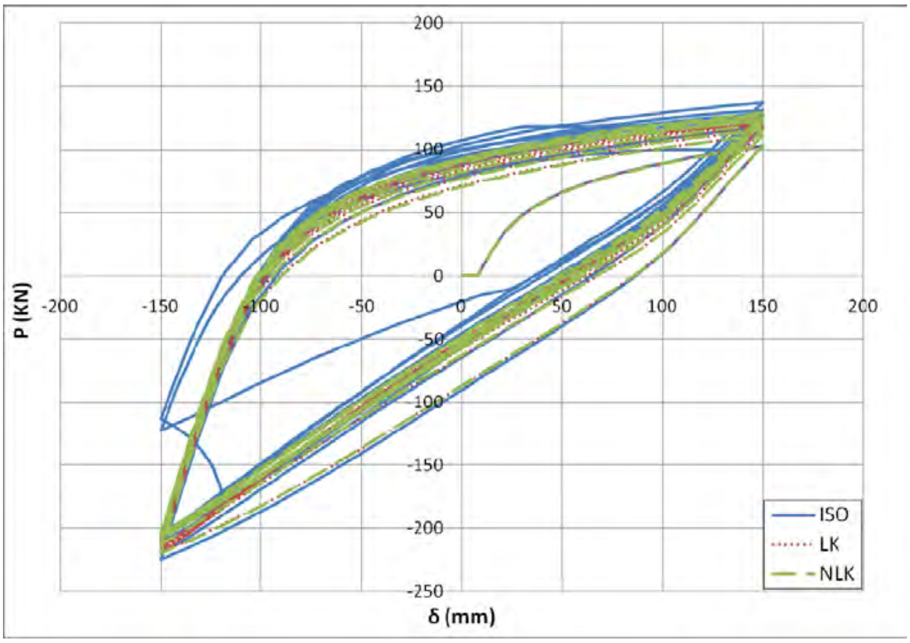

(a)

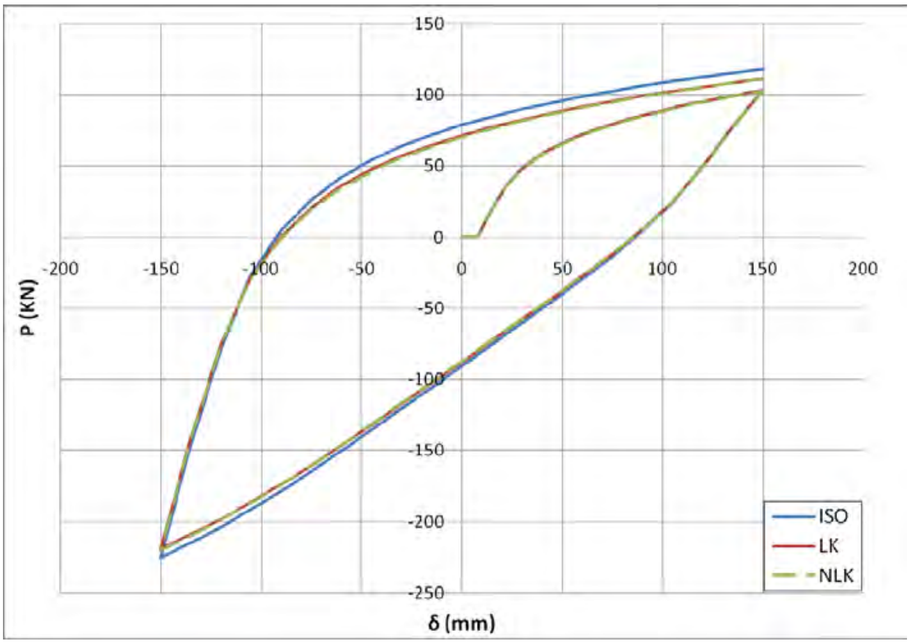

(b)

Fig. 16: Load versus end-displacement curves for displacement range ±150 mm, P=14.5 MPa:
(a) Complete cyclic loading (b) First load cycle

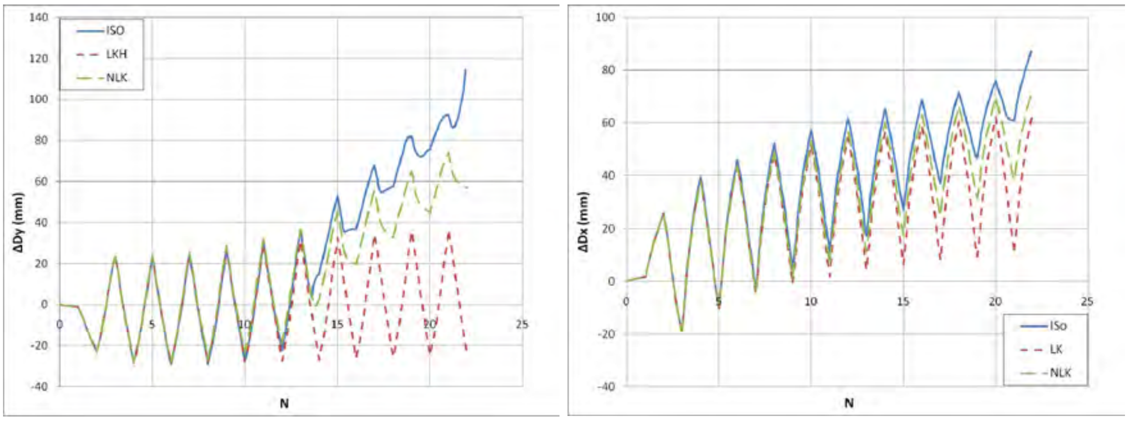

(a) (b)

Fig. 17: Cross-sectional distortion for displacement range ±150 mm, p=14.5 MPa:
(a) Vertical direction, (b) Horizontal direction

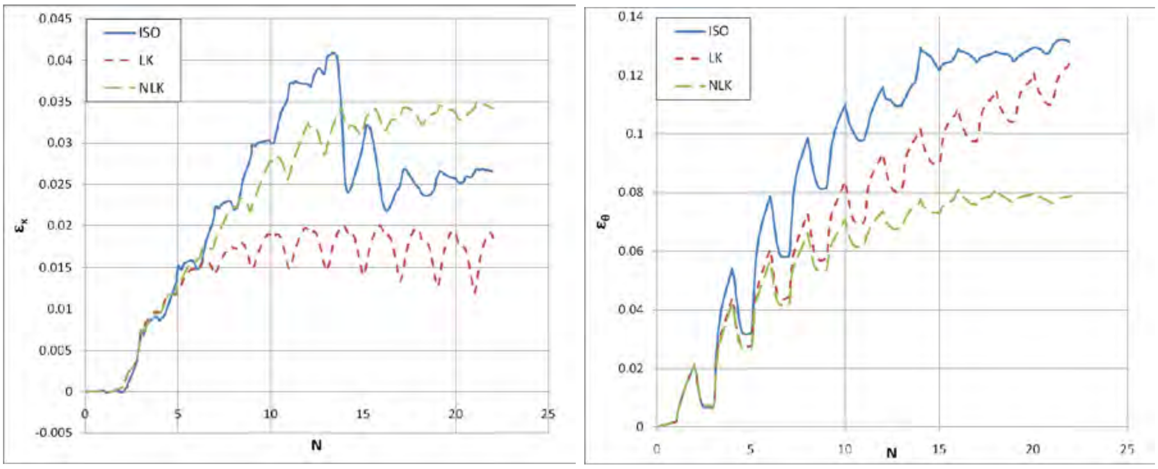

(a) (b)

Fig. 18: Strains at the elbow flank: (a) Longitudinal direction, (b) Hoop direction

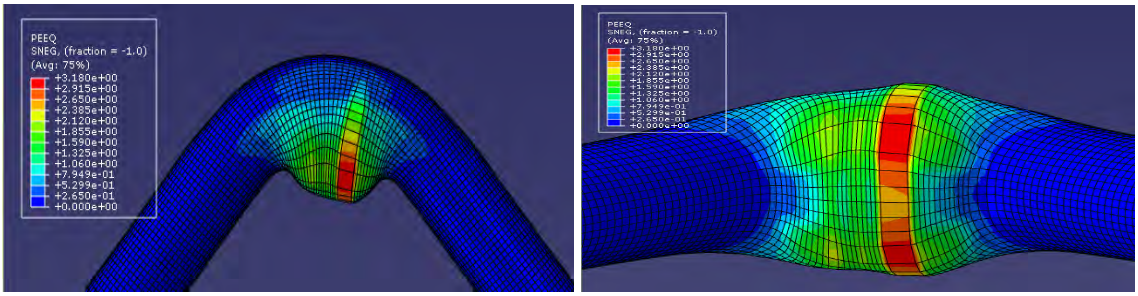

(a)

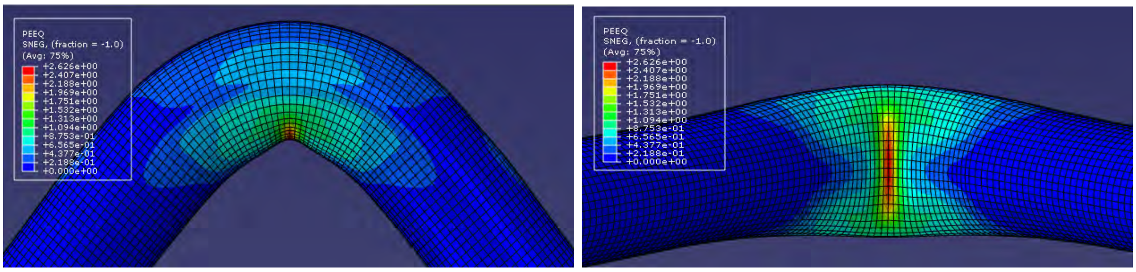

(b)

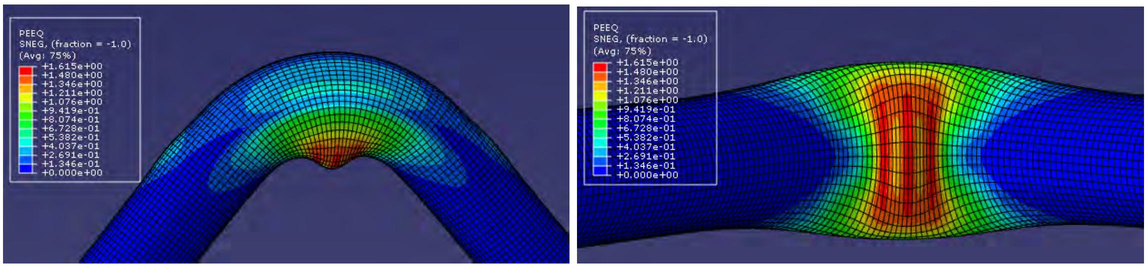

(c)

Fig.19: Plastic deformation distribution at the end of the loading history:
(a) ISO, (b) LK and (c) NLK model predictions

Finally, the end-displacement loading of ±300 mm is conducted in the presence of pressure equal to14.5 MPa. This is the most severe load combination for the elbow specimen. As illustrated in Fig. 20 to 22, the ISO and the NLK models predict extensive deformation of the material after a few initial loading cycles. The LK model predicts a smaller rate of deformation accumulation. Nevertheless, even in this case the deformation values become significant well before the end of the simulation history.

Similarly to the previous loading case, each model predicts a different deformed geometry. The ISO and the NLK models predict bulging of the elbow cross-section, while the LK model predicts a local buckle at the middle of the elbow specimen and some side buckles at the extrados of the elbow element at the connection of the straight and the curved elbow part (Fig. 23). The cross-sectional distortions as well as the longitudinal and hoop strains at the flank region are considered very high, and the rapidly increasing rate of the accumulated strains indicates the occurrence of fracture at the flank (Fig. 22).

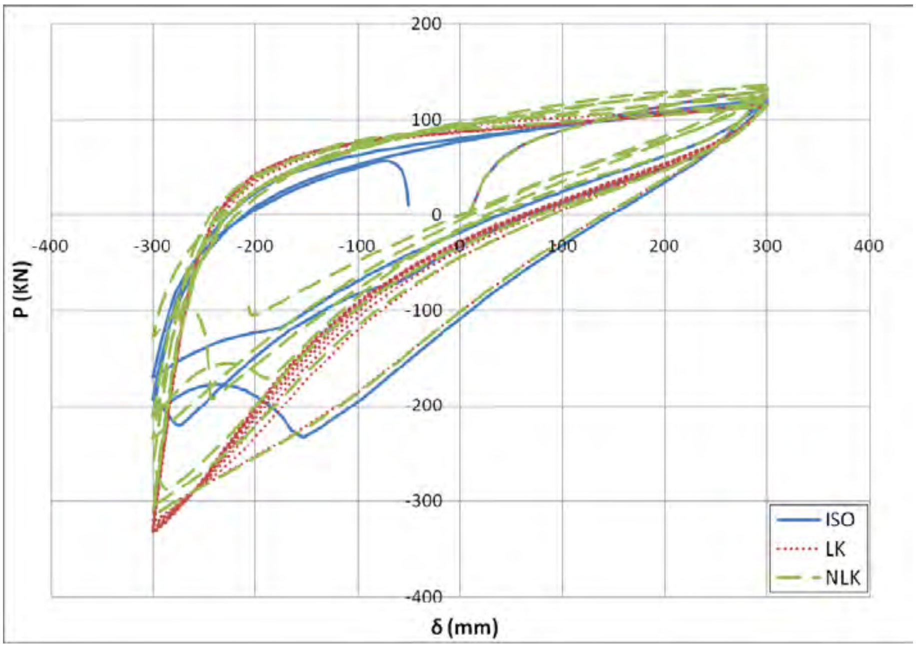

(a)

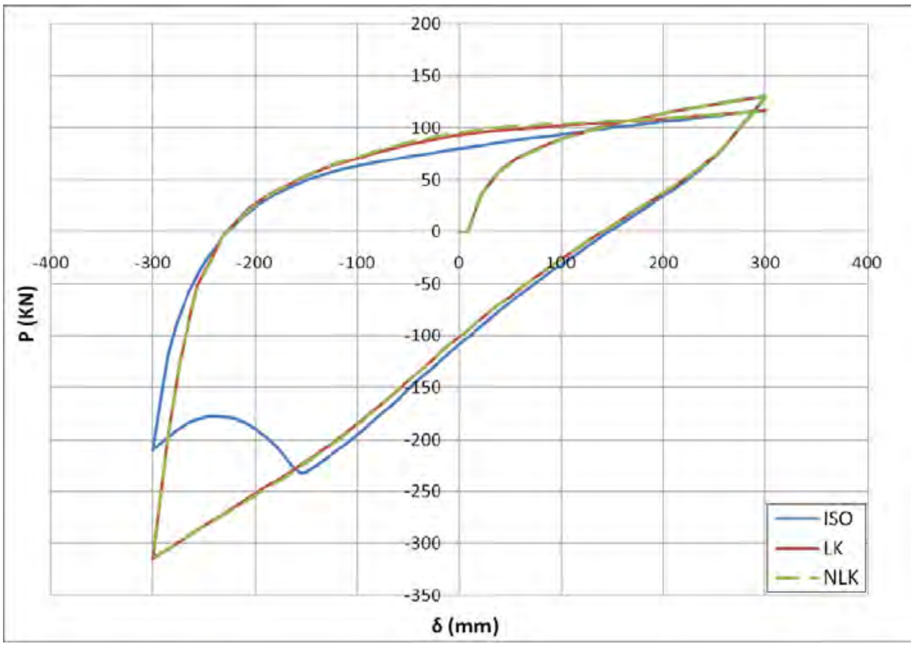

(b)

Fig. 20: Load versus end-displacement curves for displacement range ±300 mm, $p=14.5$ MPa:
(a) Complete cyclic loading (b) First load cycle

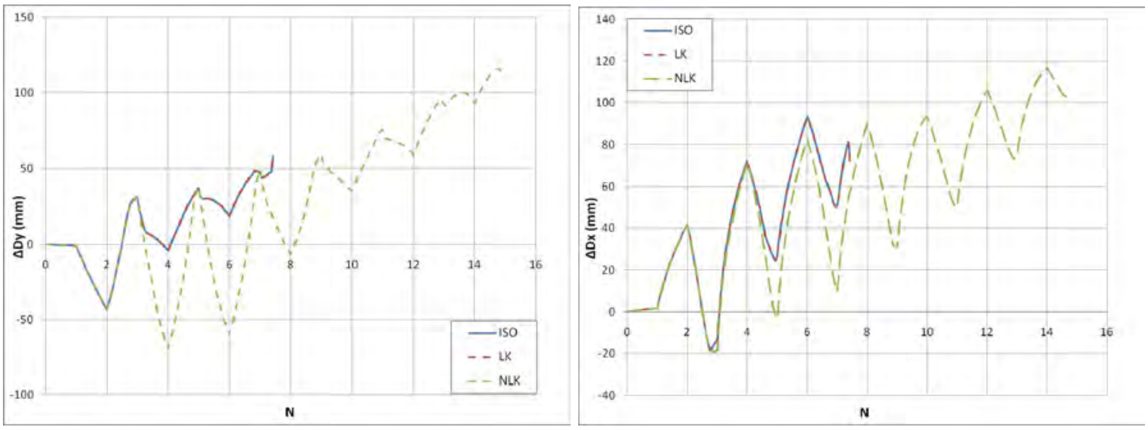

(a) (b)

Fig. 21: Cross-sectional distortion for displacement range ±300 mm, $p=14.5$ MPa:
(a) Vertical direction, (b) Horizontal direction

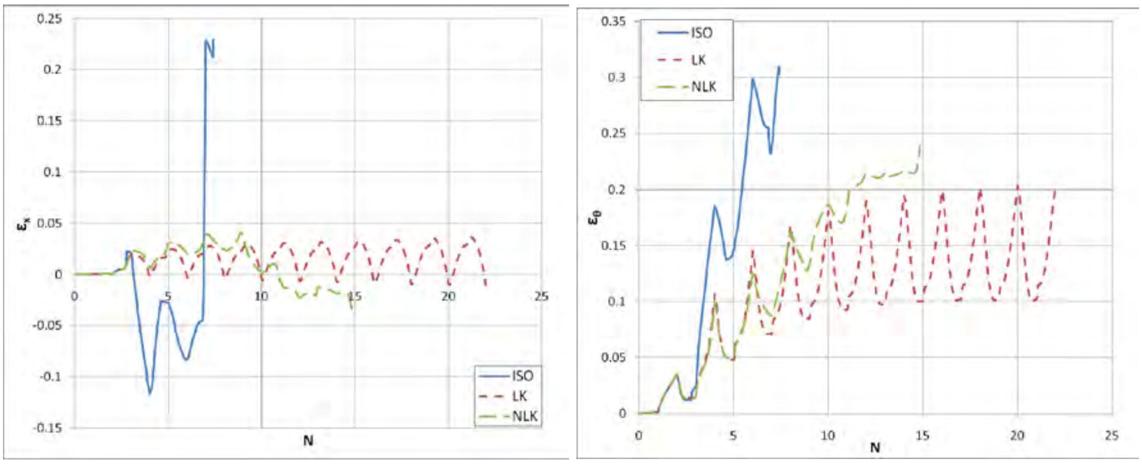

(a) (b)

Fig. 22: Strains at the elbow flank: (a) Longitudinal direction, (b) Hoop direction

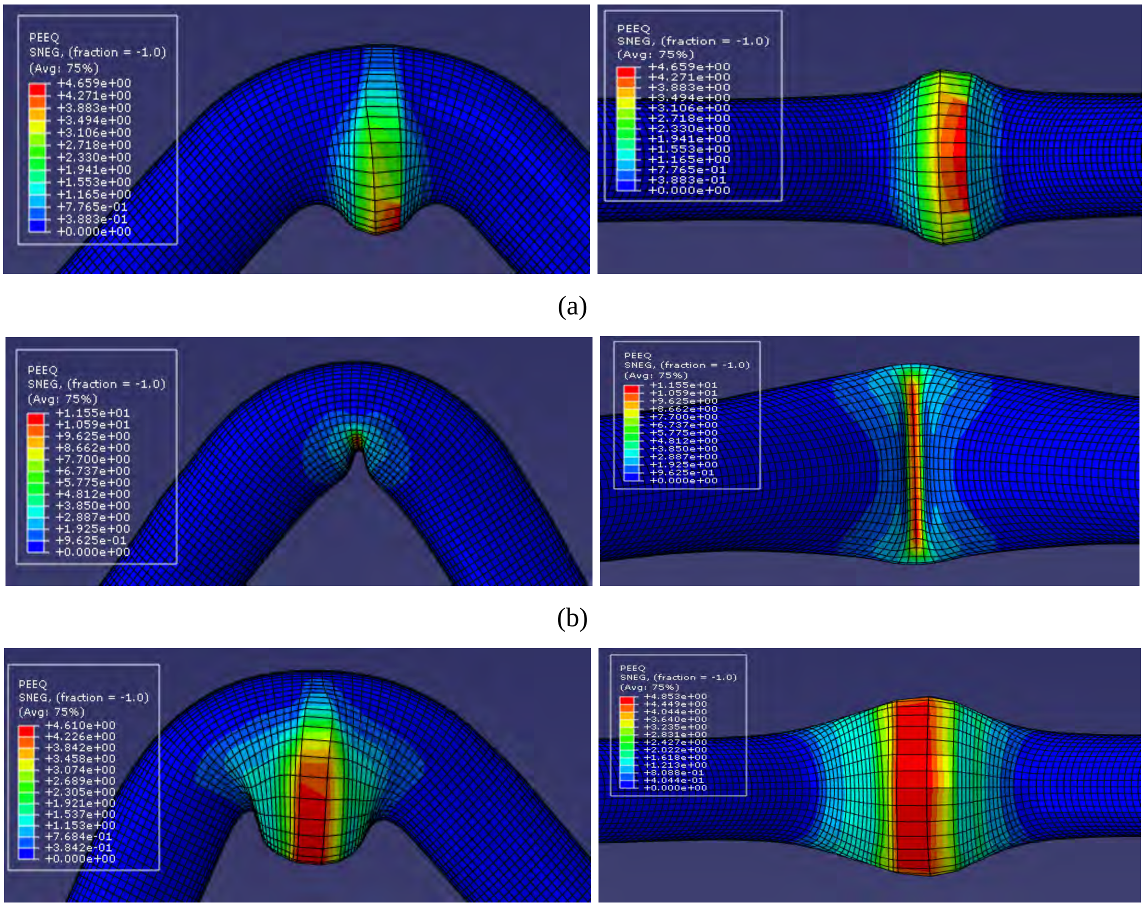

(a)

(b)

(c)

Fig. 23: Plastic deformation distribution at the end of the loading history:
(a) ISO, (b) LK and (c) NLK model predictions

Another issue examined by the present numerical simulation is whether the loading sequence influences the total specimen behavior. In all the previously analyses the loading history starts with the application of a closing moment. This sequence is now reversed and the elbow specimen is subjected to an opening moment first. In the followings, the case of ±300 mm end-displacement without pressure is presented. Similar results and conclusions are valid for the other cases examined

As in Fig. 24 to 26, the elbow performance presents the same characteristics as those presented in Fig. 13 to 15. The direct comparison between these two sets of Figures shows that only minor discrepancies exist mainly in terms of the predicted strain values. The most important one is that the ISO model predicts large strain values in the hoop direction from the first loading cycles instead of the last loading cycles as shown in Fig. 15 (b) and 26 (b). The other results for all the plasticity models adopted are only shifted by the difference in phase of the loading cycles. Finally, the deformation modes predicted by the three models are similar to those presented in Fig. 12.

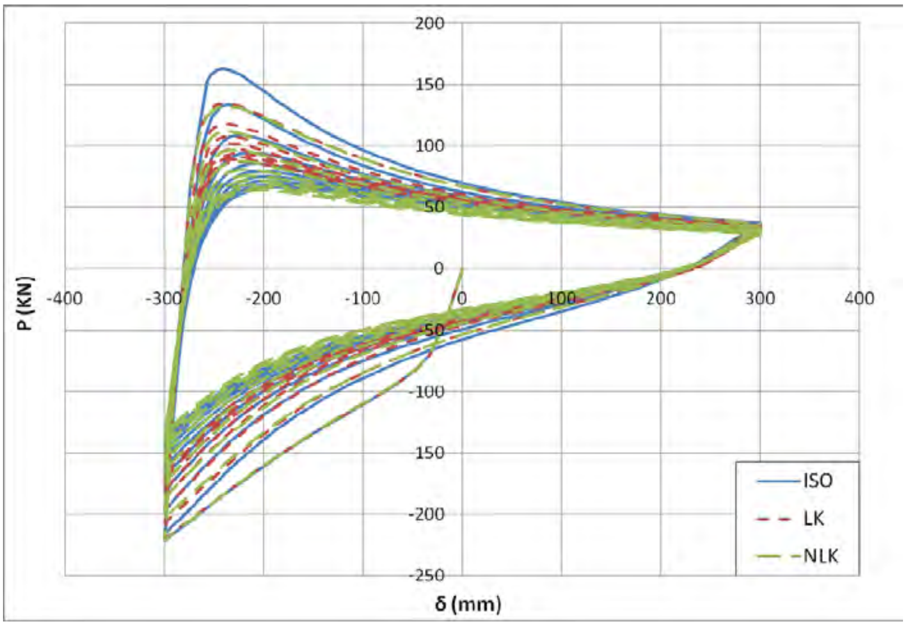

(a)

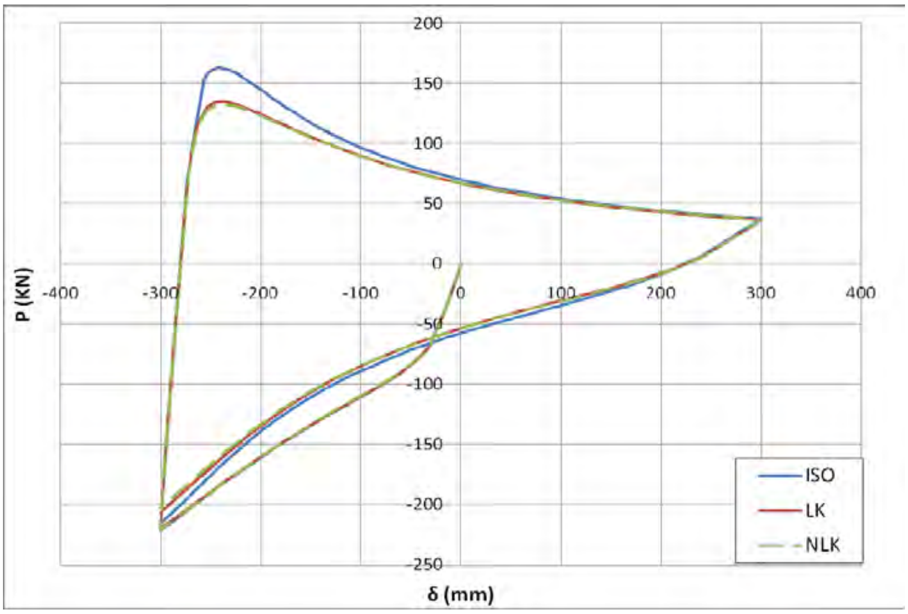

(b)

Fig. 24: Load versus end-displacement curves for displacement range ±300 mm, first opening load, $p=0$ MPa: (a) Complete cyclic loading (b) First load cycle

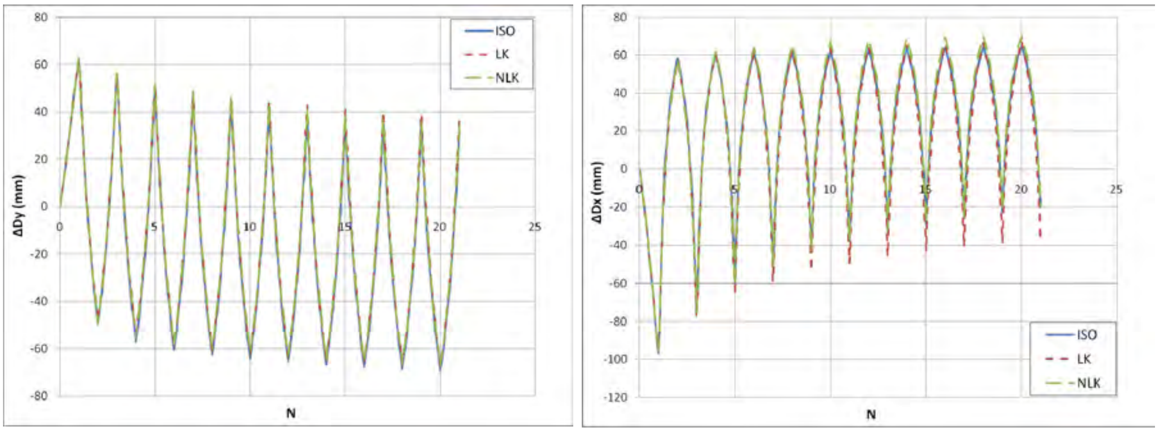

(a) (b)

Fig. 25: Cross-sectional distortion for displacement range ±300 mm, first opening load, $p=0$ MPa: (a) Vertical direction, (b) Horizontal direction

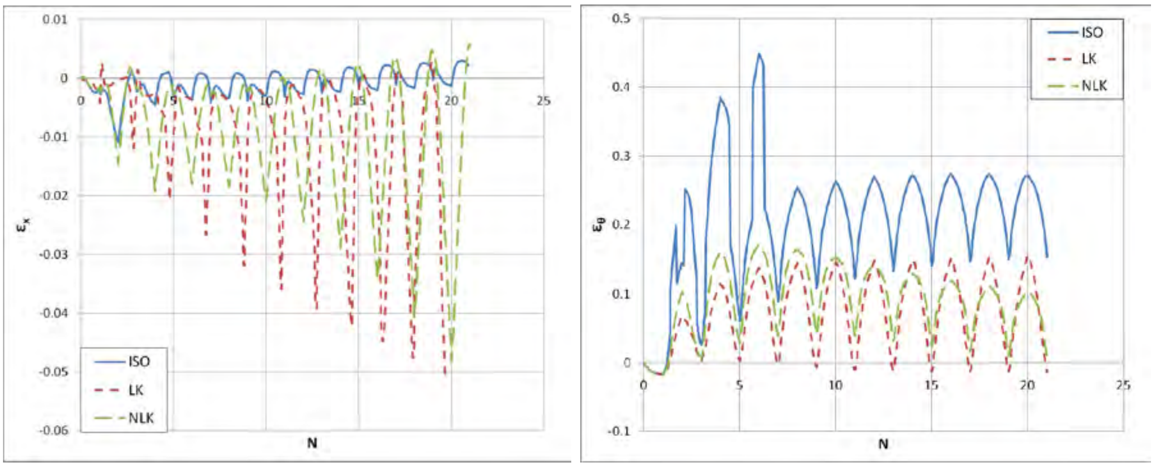

(a) (b)

Fig. 26: Strains at the elbow flank: (a) Longitudinal direction, (b) Hoop direction

6 DESIGN IMPLICATIONS

The design of process piping elbows is conducted using ASME B31.3 [29] and EN 13480-3 [30]. In both Standards the loading conditions are categorized as sustained and occasional and different design requirements are applied for each load category. In this section, using appropriate design provisions from B31.3 and EN 13480-3 and employing the numerical results the interaction between pressure and bending moment is determined.

Strong cycling loading conditions are possible to exist when severe earthquakes strike industrial facilities containing elbow specimens as the one analyzed in the present study. Therefore the applied cyclic loading is considered as occasional loading and the corresponding design rules of these two standards should be considered, as follows.

According to the B31.3 standard, in the case of occasional loading acting on an element, the sum of the longitudinal stresses, S_L, due to sustained loads, such as pressure and weight, and of the stresses produced by occasional loads, such as wind or earthquake, may be as much as 1.33 times the basic allowable stress which is given in the relevant Appendix A. In an equation form, this requirement can be written as:

$$S_{L.} + S_{L,Occ.} \leq 1.33 S_h \tag{5}$$

$S_{L.}$ can be defined as: $S_L = pD/4t$ assuming that only pressure loading and no bending loading is applied from the sustained loading case. It is worth-mentioning that there is no given formula in this standard for the calculation of the longitudinal stresses due to pressure loads. The quantity $S_{L,Occ.}$ is defined for in-plane bending as:

$$S_{L,Occ.} = \frac{\left(i_i M_i\right)}{Z},\ i_i = \frac{0.9}{\left(\frac{tR_1}{r_2^2}\right)^{2/3}},\ Z = \frac{\pi\left(D_o^2 - D_i^2\right)}{32 D_o} \tag{6}$$

where i_i is the intensification factor given in Appendix D, R_1 is the bend radius, r_2 is the elbow mean radius, D_o and D_i are the outer and inner elbow diameter respectively. Finally, the allowable stress value S_h for all the range of the operation temperatures is given in Appendix A equal to 151.68 MPa (22 Ksi).

Similar provisions exist in the EN13480-3 code, where the stresses due to occasional loading conditions are limited by the following equation:

$$\frac{p_c d_o}{4e_n} + \frac{0.75 i M_B}{Z} \leq k f_h \tag{7}$$

where p_c is the calculation pressure load, d_o is the outer elbow diameter, e_n is the nominal thickness, i and Z are the intensification factor and the section modulus defined as presented above, f_h is the allowable stress for the design temperature equal to 163.3 MPa and k is a coefficient equal to 1.2 for the design basis earthquake and equal to 1.8 for safe shut-down earthquake. It is noticeable that only the EN13480-3 code has provisions for two seismic levels resulting to a less conservative overall design of the elbow members.

The normalized moment-pressure interaction diagram by the two standards described above is presented in Fig.27. In the same graph, the numerical predictions of the developed model are also presented for the closing bending case, which is considered to be more critical than the opening bending case. The corresponding moment values have been normalized by the plastic moment equal to $M_p = \sigma_y D^2 t$, while the yield pressure $p_y = 2\sigma_y D/t$ has been used to normalize the pressure values. For the simulated range of pressure level, the corresponding allowed moment by both standards is considerably lower compared with the predictions of all models. Moreover, the beneficial effect of the internal pressure acting simultaneously with the bending loading is not recognized by any of the codes examined. This results to a different interaction curve trend. More specifically, according to the allowable stress concept that both codes are based on, as the internal pressure increases, the bending capacity of the elbow decreases. On the contrary, the numerical simulation allows for the precise prediction of the geometry change due to the combination of applied loads which has significant effect on the overall member behavior.

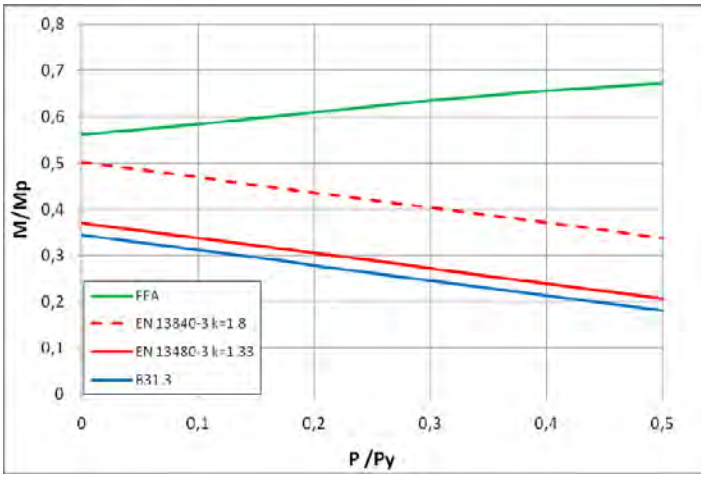

Fig. 27: Moment-pressure interaction diagram. Code provisions and FE analysis results.

7 CONCLUSIONS

In this paper, a numerical simulation of cyclic bending of industrial steel elbows was presented. Both opening and closing moment loads have been considered acting alone or in the presence of internal pressure.

The finite element model predictions regarding the monotonic behavior of the elbow indicate that the application of closing moment governs the elbow structural behavior. Moreover, the numerical results show that the presence of internal pressure increases the moment capacity of the elbow.

The predicted elbow behavior under monotonic loading in the presence of internal pressure has been also compared with the provisions of B31.3 and EN13480-3 standards. Both standards are based on the allowable stress concept and therefore are proved to be over conservative. The numerically developed moment-pressure interaction diagram shows an increase of the elbow moment capacity when internal pressure is applied. This fact contradicts the predictions of the two code provisions reported in this study where the increase of internal pressure results to a reduction of the maximum allowed pressure.

Finally, the elbow behavior under cyclic loading conditions has been extensively presented and the corresponding plasticity model predictions have been reported. The predicted hysteresis loops vary due to the different concepts each plasticity model is based on. Nevertheless, all the model predictions indicate that ratcheting takes place at the critical locations which eventually results to extensive bulging of the member and failure of the elbow.

ACKNOWLEDGMENTS

This work was carried out with a financial grant from the Research Fund for Coal and Steel of the European Commission, within INDUSE project: “STRUCTURAL SAFETY OF INDUSTRIAL STEEL TANKS, PRESSURE VESSELS AND PIPING SYSTEMS UNDER SEISMIC LOADING”, Grant No. RFSR-CT-2009-00022.

REFERENCES

[1] Suzuki, K., Earthquake Damage to Industrial Facilities and Development of Seismic Vibration Control Technology – Based on Experience from the 1995 Kobe (Hansim-Awaji) Earthquake, *Journal of Disaster Research, Vol. 1, No.2,* 2006

[2] Sobel, L. H. and Newman, S. Z., Comparison of Experimental and Simplified Analytical Results for the In-Plane Plastic Bending and Buckling of an Elbow, *J. Pressure Vessel Technology,* ASME, **102**, pp. 400-409, 1980.

[3] Sobel, L. H. and Newman, S. Z., Simplified, Detailed and Isochronous Analysis and Test Results for the In-Plane Elastic-Plastic and Creep Behavior of an Elbow, *J. Pressure Vessel Technology*, ASME, **108**, pp. 297-304, 1986.

[4] Dhalla, A. K., Collapse Characteristics of a Thin-Walled Elbow, *J. Pressure Vessel Technology*, ASME, **109**, pp. 394-401, 1987.

[5] Gresnigt, A. M. et al., Preofresultaten van Proeven op Gladde Bochten en Vergelijking Daarvan met de in OPL 85-333 Gegeven Rekenregels, [in Dutch], *Institute for Construction Materials and Structures*, TNO-IBBC, Report OPL 85-334, Delft, The Netherlands, 1985.

[6] Gresnigt, A. M., Plastic Design of Buried Steel Pipelines in Settlement Areas, *Heron*, **31**, No. 4, Delft, The Netherlands, 1986.

[7] Gresnigt, A. M. and van Foeken, Strength and Deformation Capacity of Bends in Pipelines, *Int. J. Offshore and Polar Engineering*, **5**, No. 4, pp. 294-307, 1995.

[8] Greenstreet, W. L., Experimental Study of Plastic Responses of Pipe Elbows, ORNL/NUREG-24 report, Contract No. W-7405-eng-26, 1978.

[9] Hilsenkopf, P., Boneh, B. and Sollogoub, P., Experimental Study of Behavior and Functional Capability of Ferritic Steel Elbows and Austenitic Stainless Steel Thin-Walled Elbows. *Int. J. Pressure Vessels and Piping,* **33**, pp. 111-128, 1988

[10] Suzuki, N. and Nasu,M., Non-Linear Analysis of Welded Elbows Subjected to In-Plane bending, *Computers and Structures*, **32**, No.3/4, pp.871-881,1989

[11] Tan, Y., Matzen, V.C. and Yu, L.X., Corelation of test and FEA results for the nonlinear behavior of straight pipes and elbows, *J. Pressure Vessel Technology,* ASME, **124**, pp.465-475, 2002.

[12] Shalaby, M. A. and Younan, M. Y. A., Limit Loads for Pipe Elbows with Internal Pressure Under In-plane Closing Bending Moments, *J. Pressure Vessel Technology*, ASME, **120**, pp. 35-42, 1998

[13] Shalaby, M. A. and Younan, M. Y. A., Effect of Internal Pressure on Elastic-Plastic Behavior of Pipe Elbows Under In-plane Opening Bending Moments, *J. Pressure Vessel Technology*, ASME, **121**, pp. 400-405, 1999.

[14] Mourad, H. M. and Younan, M. Y. A., Nonlinear analysis of pipe bends subjected to out-of-plane moment loading and internal pressure, *J. Pressure Vessel Technology*, ASME, **123**, No. 2, pp. 253-258, 2001

[15] Mourad, H. M. and Younan, M. Y. A., Limit-load analysis of pipe bends under out-of-plane moment loading and internal pressure", *J. Pressure Vessel Technology*, ASME, **124**, No. 1, pp. 32-37, 2002

[16] Chattopadhyay J., Nathani, D. K., Dutta, B. K. and Kushwaha, H. S., Closed-Form Collapse Moment Equations of Elbows Under Combined Internal Pressure and In-plane Bending Moment, *J. Pressure Vessel Technology*, ASME **122**, pp. 431-436, 2000.

[17] Karamanos, S. A., Giakoumatos, E. and Gresnigt, A. M., Nonlinear Response and Failure of Steel Elbows Under In-Plane Bending and Pressure., *Journal of Pressure Vessel Technology*, ASME, **125**, No. 4, pp. 393-402, November 2003

[18] Karamanos, S. A., Tsouvalas, D. and Gresnigt, A. M., Ultimate Bending Capacity and Buckling of Pressurized 90 deg Steel Elbows., *Journal of Pressure Vessel Technology,* ASME, **128**, No. 3, pp. 348-356, 2006.

[19] Pappa, P., Tsouvalas, D., Karamanos, S. A. and Houliara, S., Bending Behavior of Pressurized Induction Bends, *Offshore Mechanics and Arctic Engineering Conference,* ASME, OMAE2008-57358, Lisbon, Portugal, June 2008.

[20] Yahiaoui, K., Moffat, D.G., Moreton, D.N., Response and cyclic strain accumulation of pressurized piping elbows under dynamic in-plane bending (1996) *Journal of Strain Analysis for Engineering Design*, **31 (2)**, pp. 135-151

[21] Yahiaoui, K., Moreton, D.N., Moffat, D.G., Response and cyclic strain accumulation of pressurized piping elbows under dynamic out-of-plane bending, *Journal of Strain Analysis for Engineering Design*, **31 (2)**, pp. 153-166, 1996.

[22] Moreton, D.N., Yahiaoui, K., Moffat, D.G., Onset of ratchetting in pressurised piping elbows subjected to in-plane bending moments, *International Journal of Pressure Vessels and Piping,* **68 (1)**, pp. 73-79, 1996

[23] Edmunds, H. G. & Beer, F. J., Notes on incremental collapse in pressure vessels, *Journal of Mechanical Engineering Science,* **3(3)**, 187-199, 1961.

[24] Slagis, G.C., Experimental Data on Seismic Response of Piping Components, *J. Pressure Vessel Technology*, ASME, **120**, pp.449-455, 1998.

[25] Fujiwaka, T. Rndou, R., Furukawa, S., Ono, S., Oketani, K., Study on strength of piping components under elastic-plastic behavior due to seismic loading, PVP-Vol **137**, Seismic engineering, 1999

[26] DeGrassi, G., Hofmayer, C., Murphy, A., Suzuki, K., and Namita, Y., 2003, BNL nonlinear pre-test seismic analysis for the NUPEC ultimate strength piping test program., Transaction of the SMiRT 17 Conference.

[27] Balan, C. and Redektop, D., The effect of bidirectional loading on fatigue assessment of pressurized piping elbows with local thinned areas., *Int. J. Pres. Ves. and Piping,* **81**, pp. 235-242, 2004.

[28] Rahman, S. M. and Hassan, T., "Simulation of ratcheting responses of elbow piping components", *ASME 2009 Pressure Vessels and Piping Division Conference,* PVP2009-77819, Prague, Czech Republic.

[29] ASME B31.3, Process Piping, ASME Code for Pressure Piping, 2006.

[30] EN13480-3, Metallic Industrial Piping – Part 3: Design and calculation, 2002.

[31] Varelis, G.E., Application of the Armstrong-Frederick Cyclic Plasticity Model for Simulating Structural Steel Member Behavior, MDE Thesis, 2010.

[32] Rodabough, E.C., and George, H.H., Effect of internal pressure the flexibility and stress intensification factors of curved pipe or welding elbows., Transactions of ASME Vol. **79**, 939-948, 1957.

COMPDYN 2011
III ECCOMAS Thematic Conference on
Computational Methods in Structural Dynamics and Earthquake Engineering
M. Papadrakakis, M. Fragiadakis, V. Plevris (eds.)
Corfu, Greece, 25–28 May 2011

ANALYTICAL MODEL VERSUS NUMERICAL MODEL IN STRESS-STRAIN ANALYSIS OF BURIED STEEL PIPELINES SUBJECTED TO FAULT DISPLACEMENTS

Oleg V. Trifonov[1], **Vladimir P. Cherniy**[2]

[1,2] All-Russian research institute for natural gases and gas technologies (GAZPROM VNIIGAZ)
Razvilka poselok, Leninsky district, 142717, Moscow region, Russian Federation
{O_Trifonov, V_Cherniy }@vniigaz.gazprom.ru

Keywords: Buried steel pipeline, Active fault, Nonlinear stress analysis, Plastic strains, Pipe-soil interaction

Abstract. *In the present paper the results of the analytical model for a nonlinear stress-strain analysis of buried steel pipelines at active fault crossings are analyzed and discussed versus the numerical finite element results. The analytical model is based on the partition of the pipeline into four segments. The two segments in high curvature zones on both sides of the fault are modeled as beams in bending and tension with direct account for the axial force in the equations of motion. The two other segments are treated as beams-on-elastic foundation. The interaction of the pipeline with the surrounding soil is taken into account in axial and transverse directions using bilinear soil diagrams. The nonlinearity of the pipe steel is introduced on a cross-section level assuming a bilinear stress-strain relationship. The analysis is performed iteratively as a series of elastic solutions using a secant modulus of the pipe steel. The analysis of applicability of the proposed model to various cases of pipeline-fault intersection conditions is performed through the comparison of the results obtained with the analytical model to the results of the numerical simulation of the finite element model in ANSYS. The developed finite element model uses current technology ANSYS pipe elements with account for axial, bending, shear and torsional deformations, material nonlinearity, large displacements and strain nonlinearities. The pipe-soil interaction is modeled by the nonlinear soil spring elements. The analysis of the results allows drawing the conclusion on the applicability of the proposed analytical methodology to a wide range of conditions met in practice, at least for the preliminary assessment. The limitations of the analytical methodology and possible further refinements are also discussed.*

1 INTRODUCTION

The advancement of the gas-transport systems to the regions of high seismic activity reinforces the actuality of the research in the field of seismic analysis and design of main gas pipelines. The research methods in stress-strain analysis of pipelines can be generally divided into analytical and numerical. Giving credit for a progress in numerical finite and boundary element methods, we still have to admit the actuality of analytical models which are well suited for preliminary analysis and provide basis for more advanced numerical techniques.

It is well known that permanent ground deformation caused by relative displacements of adjacent parts of earth's crust along the fault is among the most dangerous earthquake effects and can result in a pipe failure [1]. The first paper considering a fault crossing problem analytically was published by Newmark and Hall [2]. A case of pipeline intersecting a strike-slip fault at an angle $\beta \leq \pi/2$ is studied. The axial strain component is considered to have the major effect on the pipeline. The average axial tensile strains along the effective unanchored length are calculated using the pipeline elongation due to the axial component of the fault movement and due to the second-order effects caused by lateral component of the fault movement. Since the bending stiffness and lateral pipe-soil interaction is neglected and the axial strains are averaged over the unanchored length, the maximal strains are underestimated.

Later, Kennedy et al. [3] extended the methodology proposed in [2]. The bending strains are introduced into the model based on a cable schematization. Given this assumption, adequate results can only be obtained in the case of large fault movements in projection on the axial pipe direction producing substantial axial tensile strain component.

Further advancements to the analytical models for a pipeline crossing strike-slip fault were made by Wang and Yeh [4]. Their model is based on a division of a pipe into four segments. The two segments in high curvature zone on both sides of the fault trace act as circular arcs, while the two other segments are considered as beams-on-elastic-foundation. The most significant shortcoming of the model is that the influence of axial force on the bending stiffness is neglected. Also, according to the model, the critical combination of the axial and bending strains develops at the ends of high curvature zones on each side of the fault. On the contrary, it can be shown [5, 6] that the maximal stresses and strains develop within these zones, closer to the fault intersection point.

Recently, Karamitros et al. [5] introduced a number of substantial refinements to the above mentioned methodology. In the model, the two segments in high curvature zones are considered within the elastic beam theory taking into account the pipe-soil interaction in both axial and transverse directions. The elastoplastic behavior of the pipe steel is considered within a bilinear stress-strain relationship. The analysis is performed iteratively as a series of elastic solutions using a secant modulus of the pipe steel. The results of the developed model show good agreement with the finite element results for strike-slip fault crossings over a range of fault displacements $\Delta = 0 \div 2D$, where D is the pipe diameter, and the intersection angles $\beta = 30^0, 45^0$ and 60^0.

Some essential shortcomings of the previous methodologies are addressed in the paper by Trifonov and Cherniy [6]. In particular, no symmetry condition about the intersection point is used, allowing for different types of fault kinematics to be analyzed; the tension-bending interaction is taken into account directly in the equations of motion of the two segments in high curvature zones on both sides of the fault; the contribution of transverse displacements to the axial elongation is included in calculation of axial stresses and strains. A good agreement was established between the results of the developed analytical model and finite-element model for a strike-slip and normal slip fault crossing problems.

In the present work, the application of model of the paper [6] to a strike-slip fault crossing problem is analyzed in comparison to the finite element results. In the following section the analytical model is briefly discussed. Next, in section 3 the numerical finite element model developed for the verification of the analytical methodology is presented, and the comparison of the analytical to numerical finite element results is performed. The limitations of the analytical model are also discussed. Finally, in section 4 some additional corrections to the analytical model are introduced and discussed in connection with the finite element results.

2 ANALYTICAL MODEL OF A PIPELINE CROSSING ACTIVE FAULT

2.1 Structural model of a pipeline in the fault zone

Following the papers [5, 6], a pipeline is partitioned into four segments shown in figure 1. Point B represents the intersection of the pipeline with the fault trace; points A and C are the closest points of the pipeline axis with zero transverse displacements. Points A' and C' are at a distance from A and C that is sufficient for the attenuation of transverse displacements.

As the pipeline transverse displacements relative to surrounding soil are small on the segments AA' and CC', the pipe-soil interaction can be considered as elastic and a beam-on-elastic foundation theory can be applied. The pipeline transverse displacements $w(x)$ follow the equation

$$EI\frac{d^4w}{dx^4}+kw=0 \tag{1}$$

where x is the coordinate measured from the point A (or C), E is the elastic modulus, I is the moment of inertia of the cross-section, k is the stiffness parameter of the elastic foundation. Assuming that soil resistance in considered transverse direction is characterized by a bilinear diagram with the displacement at yield w_u and corresponding force q_u, the stiffness of the elastic foundation is calculated as $k=q_u/w_u$.

The solution of the Eq. (1) is obtained with the use of the boundary conditions $w=0$ for $x=0$ and $w\to 0$ for $x\to\infty$:

$$w(x)=Ce^{-\lambda x}\sin\lambda x \tag{2}$$

where $\lambda=(k/4EI)^{1/4}$.

The segments AB and BC are analyzed as elastic beams loaded with the axial force F and distributed transverse load q. The intensity of the distributed load is equal to the limit value of pipe-soil interaction force per unit length for considered transverse pipe displacement direction relative to surrounding soil. This assumption is valid for the strike-slip fault crossing. In case of normal-slip fault with relatively small displacements an alternative partition accounting for elastic soil behavior on the segment with downward relative pipeline movement gives better results. The details on this case are given in the paper [6]. In the following, we will concentrate on the analysis of a strike-slip crossing problem.

The equilibrium equation for the beam under combined bending-tension can be obtained considering the equilibrium of the differential line element in the deformed configuration loaded with the constant axial force F and uniformly distributed transverse load q:

$$EI\frac{d^4w}{dx^4}-F\frac{d^2w}{dx^2}=q \tag{3}$$

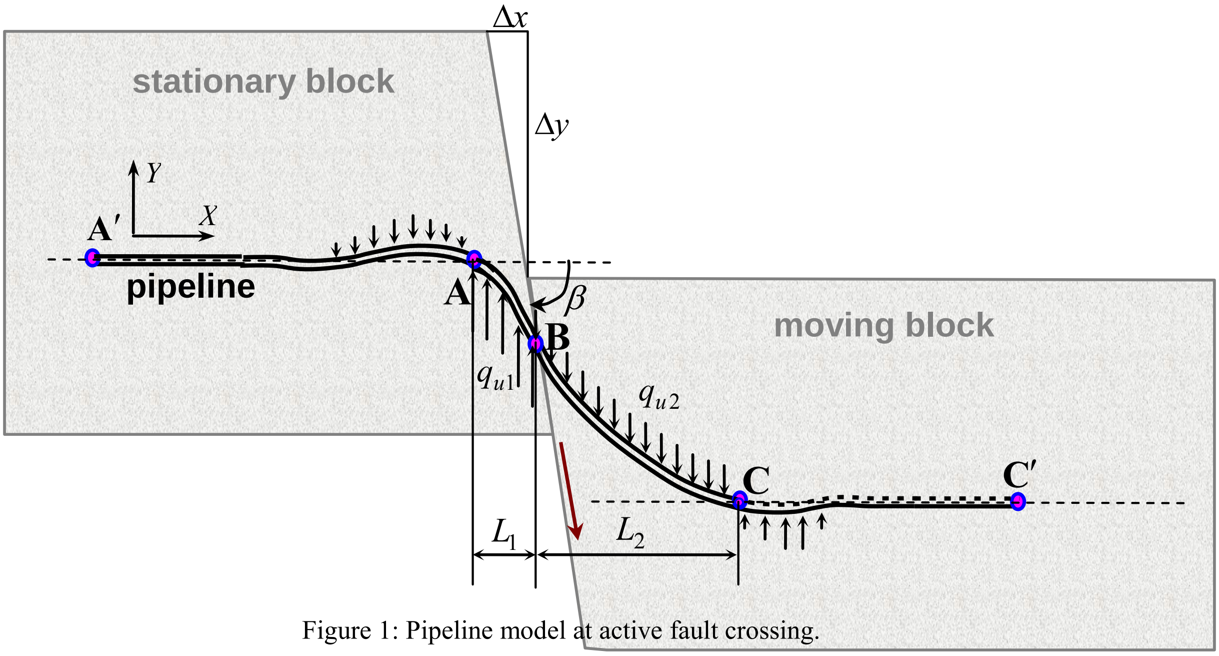

Figure 1: Pipeline model at active fault crossing.

The solution of Eq. (3) can be written in the form of initial parameters:

$$\begin{aligned} w(x) &= w(0) + \phi(0)\frac{\sinh \alpha x}{\alpha} + \frac{M(0)}{EI\alpha^2}[\cosh \alpha x - 1] + \\ &+ \frac{V(0)}{EI\alpha^3}[\sinh \alpha x - \alpha x] + \frac{q}{F}[(\cosh \alpha x - 1)/\alpha^2 - x^2/2] \end{aligned} \tag{4}$$

where $\alpha^2 = F/EI$. The parameters $\phi(0)$, $M(0)$, and $V(0)$ are the rotation angle, bending moment, and transverse force for the section with $x = 0$.

The unknown parameters in Eq. (2) and (4) written for the corresponding pipe segments together with the unknown length parameters L_1 and L_2, are found from the boundary conditions on the junction points A, B, and C . The resulting system of nonlinear algebraic equations can be solved numerically as shown in [6]. In the case of a strike-slip fault the pipeline-soil interaction forces acting on the segments AB and BC are identical. The use of symmetry condition in this case simplifies the resulting system of equations which reduces to a single nonlinear equation solved by the Newton-Raphson technique.

After the solution $w(x)$ is obtained, other quantities, such as rotation $\phi(x) = w'(x)$, bending moment $M(x) = EIw''(x)$ and transverse force $V(x) = EIw'''(x) - Fw'(x)$ can be evaluated (here the notation $w' = dw/dx$ is used). Also, the maximum bending moment $|M_{\max}|$ can be derived for each segment. Further details on the structural model and solution procedure can be found in [6].

2.2 Evaluation of the axial stress and strain

The axial force in Eq.(3) is assumed constant and equal to the axial force at the intersection of the pipeline with the fault trace. The latter is calculated by equating the geometrically required and the stress-induced (available) pipeline elongations.

The geometrically required elongation ΔL_{req} results from the fault movement in the axial direction and the pipeline elongation due to bending:

$$\Delta L_{req} = \Delta \cos\beta + \frac{1}{2}\int_x (w')^2 dx \tag{5}$$

where Δ is the fault displacement, β is the fault intersection angle. Integration in the second term in Eq. (5) is performed over the curved segments AB and BC.

The available elongation ΔL_{av} is evaluated by integrating the axial strains $\varepsilon_a(x)$ over the unanchored length L_{anch}, characterized by relative slippage of the pipe and the surrounding soil:

$$\Delta L_{av} = 2\int_0^{L_{anch}} \varepsilon_a(x)dx \tag{6}$$

In Eq. (6), it is assumed that the elongation on both sides of the fault trace is identical.

Denoting the axial force and axial stress developing at the fault intersection point by F_a and σ_a, the unanchored length L_{anch} can be calculated as:

$$L_{anch} = F_a / t_u = \sigma_a A_s / t_u \tag{7}$$

where A_s is the pipe cross-sectional area, and t_u is the limit pipe-soil interface friction.

The axial strain distribution over the length L_{anch} is obtained from the axial stress distribution

$$\sigma(x) = \sigma_a - t_u x / A_s \tag{8}$$

assuming a bilinear stress-strain relationship for the pipe steel:

$$\varepsilon_a(x) = \begin{cases} \sigma(x)/E, & \sigma(x) \le \sigma_Y \\ \sigma_Y/E + (\sigma(x) - \sigma_Y)/E_t, & \sigma(x) > \sigma_Y \end{cases} \tag{9}$$

In Eq. (9), E is the elastic modulus, E_t is the hardening parameter (plastic modulus), σ_Y is the yield stress.

Combining Eqs. (6), (8), and (9) and using the condition $\Delta L_{av} = \Delta L_{req}$, the axial stress at the fault intersection can be evaluated as [5, 6]:

$$\sigma_a = \begin{cases} [Et_u \Delta L_{req} / A_s]^{1/2}, & \Delta L_{req} \le \sigma_Y^2 A_s/(Et_u) \\ \sigma_Y(1 - E_t/E) + \\ [\sigma_Y^2((E_t/E)^2 - E_t/E) + E_t t_u \Delta L_{req}/A_s]^{1/2}, & \Delta L_{req} > \sigma_Y^2 A_s/(Et_u) \end{cases} \tag{10}$$

2.3 Modeling of the interaction between the axial and bending strains on sectional level

If the plastic strains develop in the cross-section with the maximum bending moment, the axial and bending strains become interconnected. In particular, axial strains in the vicinity of the corresponding cross-section increase locally, ensuring the equilibrium between the stress-integrated axial force and the applied axial force. To account for this effect, the stress and strain distributions over the cross-section have to be considered [6].

Under the assumption of plane cross-sections, the strain distribution on the cross-section with the maximum bending moment is given by

$$\varepsilon = \varepsilon_a + \varepsilon_b \cos\theta \tag{11}$$

where ε_a is the axial strain, and $\varepsilon_b = M_{\max} D/(2EI)$ is the maximal bending strain, θ is the polar angle of the cross-section measured from the vertical diameter (figure 2).

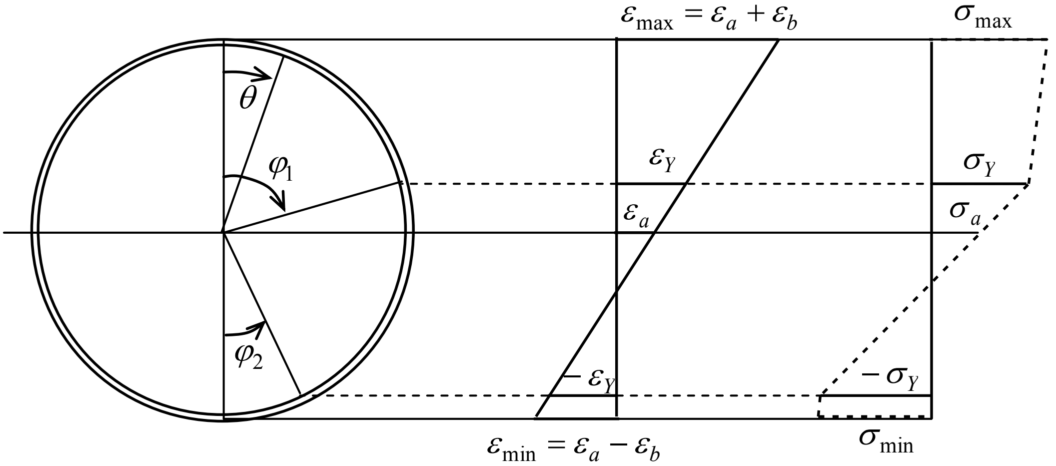

Figure 2: Stress and strain distribution over the cross-section.

In figure 2 the yield strain is denoted by ε_Y and the angles $\varphi_{1,2}$ define the portions of the cross-section that undergo yielding:

$$\varphi_{1,2} = \begin{cases} \pi, & \dfrac{\varepsilon_Y \mp \varepsilon_a}{\varepsilon_b} < -1 \\ \arccos\left(\dfrac{\varepsilon_Y \mp \varepsilon_a}{\varepsilon_b}\right), & -1 \le \dfrac{\varepsilon_Y \mp \varepsilon_a}{\varepsilon_b} \le 1 \\ 0, & 1 < \dfrac{\varepsilon_Y \mp \varepsilon_a}{\varepsilon_b} \end{cases} \tag{12}$$

Accordingly, the distribution of stresses takes the form:

$$\sigma = \begin{cases} \sigma_Y + E_t(\varepsilon - \varepsilon_Y), & 0 \le \theta < \varphi_1, \\ E\ \varepsilon, & \varphi_1 \le \theta \le \pi - \varphi_2, \\ -\sigma_Y + E_t(\varepsilon + \varepsilon_Y), & \pi - \varphi_2 < \theta \le \pi. \end{cases} \tag{13}$$

The axial force and bending moment are evaluated by the stress-integration over the cross-section with the use of Eq. (11) – (13):

$$\begin{aligned} F(\varepsilon_a, \varepsilon_b) &= 2\int_0^{\pi} \sigma R_m t d\theta = \\ &= 2R_m t[E\ \pi\varepsilon_a - (E\ - E_t)(\varphi_1 + \varphi_2)\varepsilon_a + (E\ - E_t)(\varphi_1 - \varphi_2)\varepsilon_Y - \\ &\quad -(E\ - E_t)(\sin\varphi_1 - \sin\varphi_2)\varepsilon_b], \end{aligned} \tag{14}$$

$$\begin{aligned} M(\varepsilon_a,\varepsilon_b) &= 2\int_0^{\pi} \sigma R_m t R_m \cos\theta \, d\theta = \\ &= \tfrac{1}{2} R_m^2 t [2E\,\pi\varepsilon_b - 4(E - E_t)(\sin\varphi_1 - \sin\varphi_2)\varepsilon_a + \\ &+ 4(E - E_t)(\sin\varphi_1 + \sin\varphi_2)\varepsilon_Y - 2(E - E_t)(\varphi_1 + \varphi_2)\varepsilon_b - \\ &- (E - E_t)(\sin 2\varphi_1 + \sin 2\varphi_2)\varepsilon_b]. \end{aligned} \tag{15}$$

Here, the notation $R_m = (D - t)/2$ is used.

For the evaluation of the axial strain in the cross-section with the maximum bending moment the equilibrium condition between the applied axial force and the one obtained by the integration over the cross-section is used:

$$F(\varepsilon_a,\varepsilon_b) - F_a = 0 \tag{16}$$

The Eq. (16) can be treated as a nonlinear function of ε_a and solved iteratively.

To satisfy the moment equilibrium condition

$$M(\varepsilon_a,\varepsilon_b) - M_{\max} = 0 \tag{17}$$

an iterative solution is performed using the secant Young's modulus derived from the Eq. (17):

$$E_{\sec} = \frac{M(\varepsilon_a,\varepsilon_b)D}{2I\varepsilon_b} \tag{18}$$

The specified procedure is applied separately to the segments AB and BC, yielding $\varepsilon_{a1}, \varepsilon_{a2}$ and $E_{\sec 1}$, $E_{\sec 2}$, which are applied on the next iteration.

2.4 The solution algorithm

The described model can be implemented in a computer program according to the algorithm given below. For a general fault kinematics the algorithm consists of the following steps (superscript *k* stands for the iteration number):

1. Given the fault kinematics and the intersection angle, calculate the components of fault displacements in projection on the pipe coordinate system Δx and Δy.
2. Using the transverse displacements from the previous iteration $w_1^{(k-1)}(x)$ and $w_2^{(k-1)}(x)$, calculate the elongation due to the pipe transverse displacements, the required elongation $\Delta L_{req}^{(k)}$ and axial force $F_a^{(k)}$ (section 2.2).
3. Performing the solution of the structural problem (section 2.1) using the appropriate secant moduli $E_{\sec 1}^{(k)}$ and $E_{\sec 2}^{(k)}$, evaluate the lengths of the segments AB and BC $L_1^{(k)}$ and $L_2^{(k)}$. Evaluate the transverse displacements $w_1^{(k)}(x)$ and $w_2^{(k)}(x)$.
4. Find the maximum absolute values of the bending moments on segments AB and BC $M_{1\max}$ and $M_{2\max}$. Evaluate the corresponding maximum bending strains ε_{b1} and ε_{b2}.
5. Evaluate the maximum axial strains on segments AB and BC ε_{a1} and ε_{a2} performing an iterative solution of Eq.(16) for segments AB and BC.
6. Evaluate bending moments $M_1^{(k)}(\varepsilon_{a1},\varepsilon_{b1})$ and $M_2^{(k)}(\varepsilon_{a2},\varepsilon_{b2})$ on segments AB and BC.

7. Check the moment convergence. If the convergence criterion is satisfied, proceed to the next load step or terminate the solution (step 8). Otherwise, calculate secant moduli $E_{\sec 1}^{(k+1)}$ and $E_{\sec 2}^{(k+1)}$ for segments AB and BC and go to the next iteration (step 2).
8. Output the results and stop the solution.

The initial displacement functions $w_1^{(0)}(x)$ and $w_2^{(0)}(x)$ used on the first iteration ($k=1$) for calculation of $\Delta L_{req}^{(1)}$ and $F_a^{(1)}$ are taken as zero, if the total fault displacement is applied in one step, or as the displacements calculated on the previous load step, if the total fault displacement is applied in several steps. The initial values of the secant moduli $E_{\sec 1}^{(1)}$ and $E_{\sec 2}^{(1)}$ are equal to the elastic modulus E.

The convergence of the described algorithm observed during numerical modeling is rather good for different fault intersection angles and total fault displacements. The number of iterations necessary to meet the convergence criteria ranged from 1 to 7.

3 THE RESULTS OF THE ANALYTICAL MODEL VERSUS FINITE ELEMENT MODEL

3.1 Finite element pipeline model

To analyze the applicability of the analytical model to practical cases of pipeline-fault intersection conditions, a finite element model is developed. The finite element model treats a structural problem of pipeline crossing active fault more rigorously, thus, allowing the assessment of the influence of simplifying assumptions adopted in the analytical model on the stress and strain predictions. The finite element model is implemented in ANSYS 12.1 [7]. A pipeline segment with the length 1000 m is considered. The fault intersection point is placed at the middle of the segment. The pipeline is clamped at the end on the stationary part of the fault and free at the end on the moving part of the fault.

The pipeline segment is meshed by 1000 PIPE288 elements with the concentration of elements in the near-fault zone (taken as 50 m on both sides of the fault). The PIPE288 is a three-dimensional element based on Timoshenko beam theory with axial, bending, shear and torsion deformations included. Large displacements, strains, material nonlinearity are also accounted for.

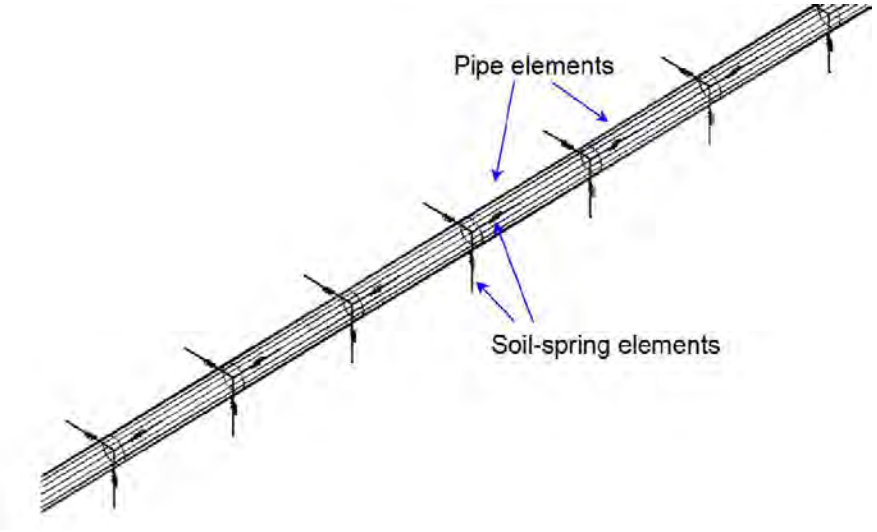

Figure 3: A fragment of the finite element model.

The pipe-soil interaction is modeled by nonlinear spring COMBIN39 elements oriented in the three orthogonal directions. The element allows for arbitrary nonlinear force-deflection curve to be used. In the analysis, an elastic-perfectly plastic diagrams with characteristics calculated according to ALA-ASCE [8] guidelines were used.

A fragment of the finite element model is depicted in figure 3.

The total fault displacement is applied in 50 steps with automatic substepping and convergence control. The fault displacement components are prescribed to the free ends of the corresponding soil-spring elements on the moving part of the fault, while the soil-spring free ends on stationary part of the fault are fixed. On each step the solution quantities are output into the data files for subsequent analysis.

3.2 Numerical results for the case of strike-slip fault crossing

The numerical examples described in this section are based on the pipeline and soil data used in the papers [5, 6]. A natural gas pipeline with the external diameter $D = 0.9144$ m, wall thickness $t = 0.0119$ m is considered. The pipeline material has the following characteristics: yield stress $\sigma_Y = 490$ MPa, elastic Young's modulus $E = 210$GPa, hardening modulus $E_t = 1.088$ GPa. The pipe-soil interaction is modeled by elastic-perfectly plastic diagrams. The corresponding parameters are calculated according to the ALA-ASCE guidelines [8] for the case of medium-density sand with friction angle 36^0, unit weight 18 kN/m^2 and pipe burial depth equal to 1.3 m.

The fault intersection angles, taken for numerical simulation in papers [5, 6], ranged from 30^0 to 60^0. A good correspondence of the analytical results to numerical results was observed. But from the practical viewpoint, the case of intersection angle close to 90^0 is an important one. Therefore, it is desirable to determine the level of accuracy of the results obtained using the proposed analytical methodology in this range of angles. The case of a strike-slip fault will be considered below as practical example.

Probably, the most representative quantity, characterizing the level of correspondence between the finite element and the analytical results, is the maximal strain in the pipe. Also, this parameter is the main characteristic used in the strain-based design procedures. Figure 4 illustrates the evolution of the maximal longitudinal strains with the fault displacement for the two values of the fault intersection angle $\beta = 30^0$ (a) and 90^0 (b). The solid line corresponds to the analytical solution while the dashed line represents the finite element solution.

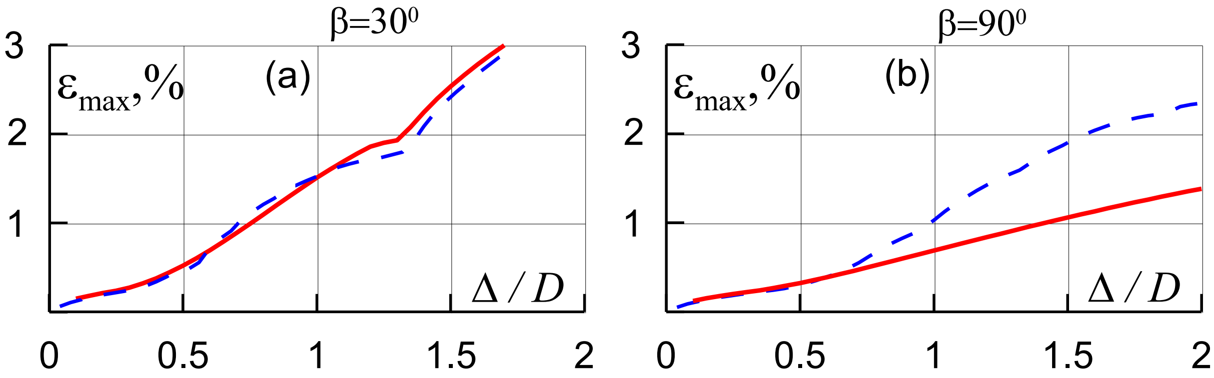

Figure 4: Comparison of the analytical (solid lines) and finite element (dashed lines) solutions for the two cases of fault intersection.

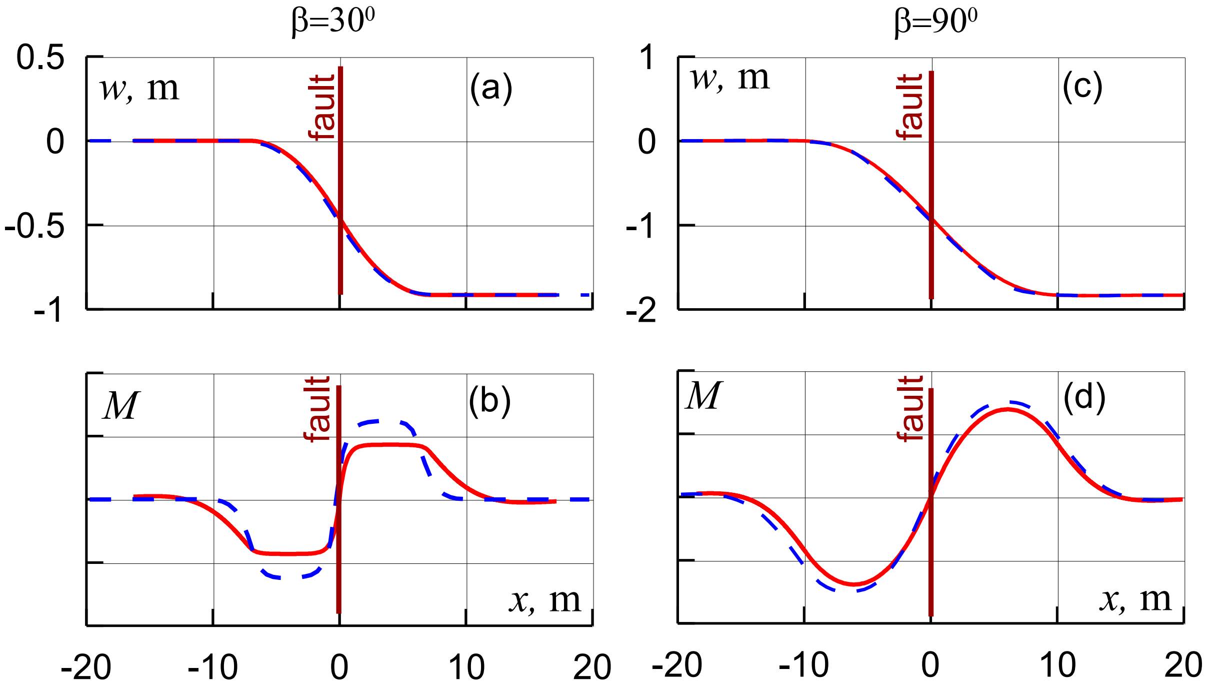

Figure 5: Distributions of the transverse displacements and bending moments in the near-fault zone.

It is seen that for the case $\beta = 30^0$ the results are rather close in the whole range of values of the fault displacements, while for the case $\beta = 90^0$ the results substantially differ starting from $\Delta / D = 0.7$. The maximal difference near 40% is observed for $\Delta / D = 2$.

To understand the cause of this discrepancy, other solution quantities were analyzed. The distributions of the transverse displacements and bending moments in the near-fault zone are depicted in figure 5. The correspondence of the finite element (dashed lines) and the analytical results is rather good in both cases.

The distributions of the longitudinal strains are shown in figure 6. Total strain is a more sensitive parameter revealing substantial differences between the rigorous numerical model and approximate analytical model for the case of $\beta = 90^0$ (figure 6, b). Surprisingly, the closeness of the results for $\beta = 30^0$ (figure 6, a) is good, especially taking into account the approximate character of the analytical model and a rather complex shape of the strain distribution. The sharp drop in strains on analytical results reflects the transition to the segments AA’ and CC’ considered as beams-on-elastic foundation with the initial Young’s modulus.

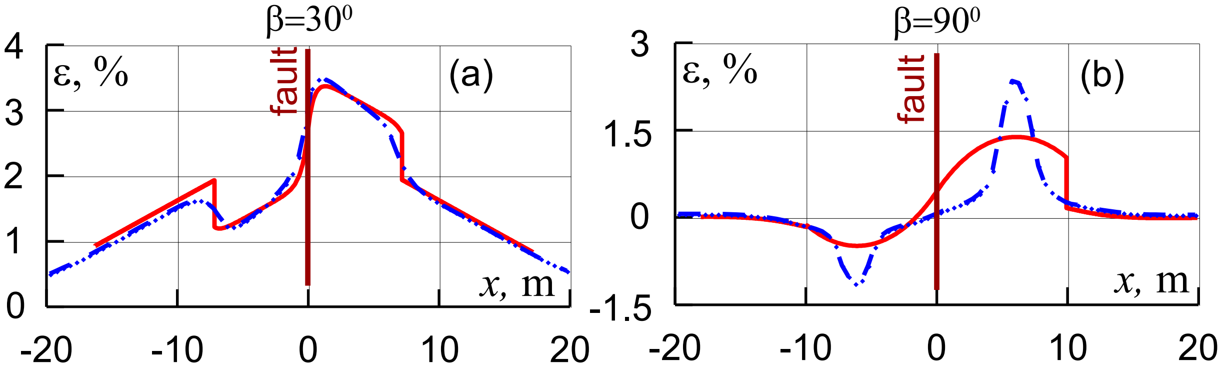

Figure 6: Distribution of the longitudinal strains in the near-fault zone.

In the case $\beta = 90^0$, numerical solution shows a concentration of deformations in relatively narrow zones on both sides of the fault. These zones do not side the fault intersection point but are rather at distance of several meters. As shown in figure 7 representing the finite element solution for plastic strains, the concentration of strains corresponds to the zones of plasticity. These zones are compact and pronounced for $\beta = 90^0$ as in this case the bending dominates, while for $\beta = 30^0$ a substantial axial component of strain causes a dramatic "stretching" of plastic zones.

In the analytical model the potentially plastic zones (segments AB and BC) are bounded by the fault intersection point and the nearest point with zero relative pipe-soil displacements in transverse direction. Thus, for $\beta = 90^0$ plastic deformations in analytical solution are spread over substantially larger length than in numerical solution. Consequently, the equivalent secant modulus is larger than the plastic modulus of the material and the maximal strains are smaller but more evenly distributed.

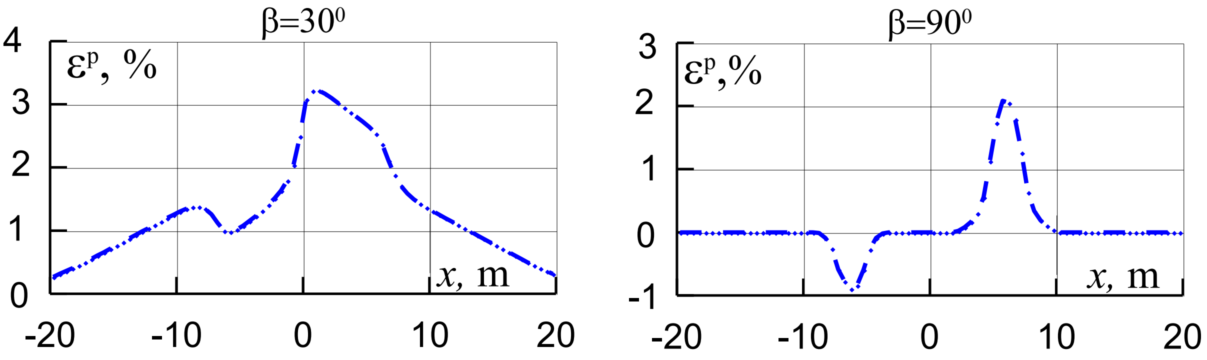

Figure 7: Distribution of the plastic strains in the near-fault zone (finite element solution).

Hence, in the situations when bending is the prevailing mechanism of deformation, the analytical model would underestimate the maximal strains. On the other hand, in situations when axial strains are significant, the analytical model would give reasonable maximal strain predictions. In the next section a correction of the analytical methodology is suggested and illustrated on numerical examples.

4 AN APPROXIMATE ACCOUNTING FOR THE STIFFNESS VARIATION WITHIN THE PROPOSED ANALYTICAL MODEL

4.1 The stiffness correction method

One of the simple ways to remedy the analytical results for the fault intersection angles close to 90^0 is based on stiffness correction within the segments AB and BC without performing any changes in the basic methodology.

For the final evaluation of strains, the initial beam is replaced by a beam with varying stiffness $EI = EI(\xi)$, where ξ is a non-dimensional coordinate within the pipeline segment. It is considered that all other loading conditions remain the same, giving an identical moment distribution along the segment. This assumption is supported by relative closeness of the moment distributions for analytical and finite element solutions shown in figure 5. Thus, it seems reasonable to state the equivalence of the bending strain energies of the initial beam with the secant stiffness and the modified beam with varying stiffness:

$$\frac{1}{2}\int_l \frac{M^2(x)}{E_{\sec} I}dx = \frac{1}{2}\int_l \frac{M^2(x)}{EI(x)}dx \tag{19}$$

Next, we adopt the following approximation of the stiffness distribution:

$$EI(\xi) = aE_{\sec}I - \omega(\xi)(aE_{\sec}I - bE_{\sec}I) \tag{20}$$

where the shape function $\omega(\xi)$ is given by

$$\omega(\xi) = \begin{cases} 0, & \xi < 0, \quad \xi > 1 \\ 16(\xi^4 - 2\xi^3 + \xi^2), & 0 \le \xi \le 1 \end{cases} \tag{21}$$

and

$$\xi = (x - x_{\max})/l_p + 0.5 \tag{22}$$

Here, l_p is the support of the function $\omega(\xi)$, $x_{\max}$ is the position of the maximum bending moment within the segment. Parameter l_p defines the length of the concentration zone.

For $x = x_{\max}$ we have: $\xi = 0.5$, $\omega(\xi) = 1$ and $EI(\xi) = bE_{\sec}I$. For $x = 0$ and $x = L$ (where L is the segment length) under the condition $l_p < L$ we have $\omega(\xi) = 0$ and $EI(\xi) = aE_{\sec}I$. Thus, the amount of stiffness variation is controlled by the parameters a and b.

As the strain concentration is connected to the strain variability within the segment and becomes higher with the strain growth, it is natural to consider the dependence of the parameters *a* and *b* on:

- Maximal bending strains within the segment ε_b;
- The parameter of unevenness taken as the ratio of average bending strains to the maximum bending strains:

$$\zeta = \varepsilon_{b,av} / \varepsilon_b \tag{23}$$

where the average bending strain is calculated as

$$\varepsilon_{b,av} = \frac{1}{L}\int_0^L \varepsilon_b(x)dx \tag{24}$$

The parameter of unevenness is plotted on figure 8, a for various fault intersection angles based on the analytical solution. It is seen that this characteristic helps to differentiate the cases where the concentration is insignificant and the ones with substantial strain concentration for large fault displacements.

Picking out the bounding levels ζ_1 and ζ_2, the following secondary parameter of unevenness is introduced:

$$C_1 = \begin{cases} a_1\zeta + b_1, & \zeta < \zeta_1 \\ 1, & \zeta \ge \zeta_1 \end{cases} \tag{25}$$

where

$$a_1 = [C_1(\zeta_1) - C_1(\zeta_2)]/[\zeta_1 - \zeta_2],\ b_1 = [\zeta_1 C_1(\zeta_2) - \zeta_2 C_1(\zeta_1)]/[\zeta_1 - \zeta_2] \tag{26}$$

Here $C_1(\zeta_1)$ and $C_1(\zeta_2)$ are the values of the parameter C_1 at bounding levels taken as $C_1(\zeta_1)=1$ and $C_1(\zeta_2)=2$. The expression (25) is illustrated in figure 8, b.

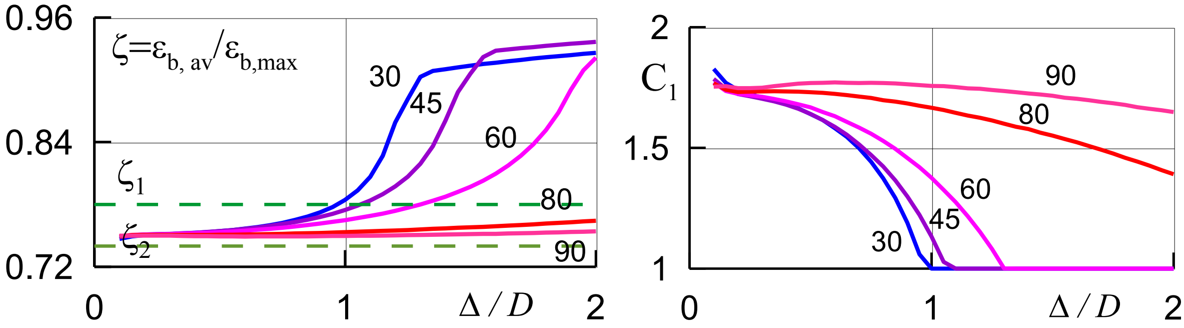

Figure 8: (a) The parameter of unevenness for various fault intersection angles. (b) Secondary parameter of unevenness.

To mitigate C_1 in the range of small strains the following parameter is used:

$$C_2 = \varepsilon_b / \varepsilon_{b,1} \tag{27}$$

where $\varepsilon_{b,1}$ – some normalizing level taken in the following equal to 0.007. The numerical values of ζ_1, ζ_2, $C_1(\zeta_1)$ and $C_1(\zeta_2)$ are based entirely on analytical solution. The numerical value of $\varepsilon_{b,1}$ defines the amount of strain concentration. Actually, this is the only parameter which is fitted using the finite element results. Finally, the following characteristic of the strain concentration is derived:

$$C_3 = \begin{cases} C_1C_2, & C_1C_2 > 1 \\ 1, & C_1C_2 \le 1 \end{cases} \tag{28}$$

The evolution of this characteristic with the fault displacement is shown in figure 9.

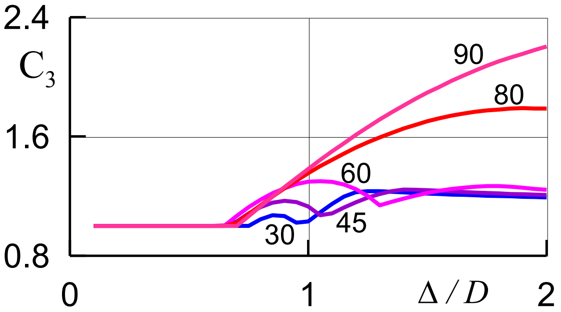

Figure 9: The characteristic of the strain concentration.

The application of the obtained strain concentration parameter within the framework of Eq. (20) is given by the relations

$$a = C_3, \quad b = 1/C_3 \tag{29}$$

Thus, in the strain concentration region the original secant stiffness is reduced in C_3 times, while outside this region it is increased in C_3 times. The proposed relations are rather approximate but at least qualitatively represent the character of the actual stiffness distribution. The application of the proposed correction technique is illustrated in the following section.

4.2 Corrected solution for various fault intersection angles

Using the proposed correction procedure, the following steps within the basic solution algorithm must be performed:

1. Given the basic solution for the prescribed fault displacement, the parameters in Eq. (20) – (22) are determined.
2. The corrected distribution of the bending strains is calculated according to the relation

$$\varepsilon_b(x) = \frac{M(x)}{EI(x)} \frac{D}{2} \tag{30}$$

3. The corrected maximal bending and total strains are then evaluated:

$$\varepsilon_b = \frac{M(x_{\max})}{EI(x_{\max})} \frac{D}{2}, \quad \varepsilon_{\max} = \varepsilon_b + \varepsilon_{a,\max} \tag{31}$$

The strain correction procedure was applied to the pipeline-fault intersection analysis of section 3.2. Figure 10 illustrates the corrected stiffness distribution for the case $\beta = 90^0$, $\Delta / D = 2$. The lengths of the curved segments AB and BC were $L_1 = L_2 = L = 9.91$ m. The parameters of Eq. (20) – (22) were found to be $C_3 = 2.18$, $l_p = 6.05$ m.

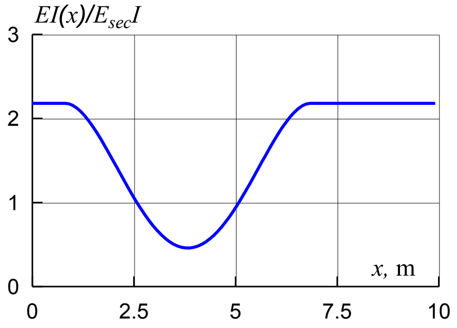

Figure 10: The corrected stiffness distribution on segments AB and BC for $\beta = 90^0$, $\Delta / D = 2$.

Figure 11 illustrates the application of the correction procedure to the analytical solution for crossing angles $\beta = 30^0$, 45^0, 60^0, 80^0 and 90^0. The maximal strains obtained with analytical model without correction (curves 1), analytical model with strain correction (curves 2), and finite element model (curves 3) are plotted against the fault displacement. It can be noted that the suggested correction procedure substantially improves the maximal strain assessment for crossing angles close to 90^0 with slight overestimate for small and moderate crossing angles.

In figure 12 the comparison of the bending strain distributions in the near fault zone is presented for $\Delta / D = 0.5, 1$ and 2 m. The numbering of curves corresponds to the figure 11. It can be concluded that the corrected strain distribution follows the exact (finite element) strain distribution quite closely for all three values of the fault displacement. In particular, for moderate strains the plastic strains are small and strain concentration is not observed. As the plastic strains caused by bending become large, the unevenness of strain distribution also grows and the effect of strain concentration is accounted for.

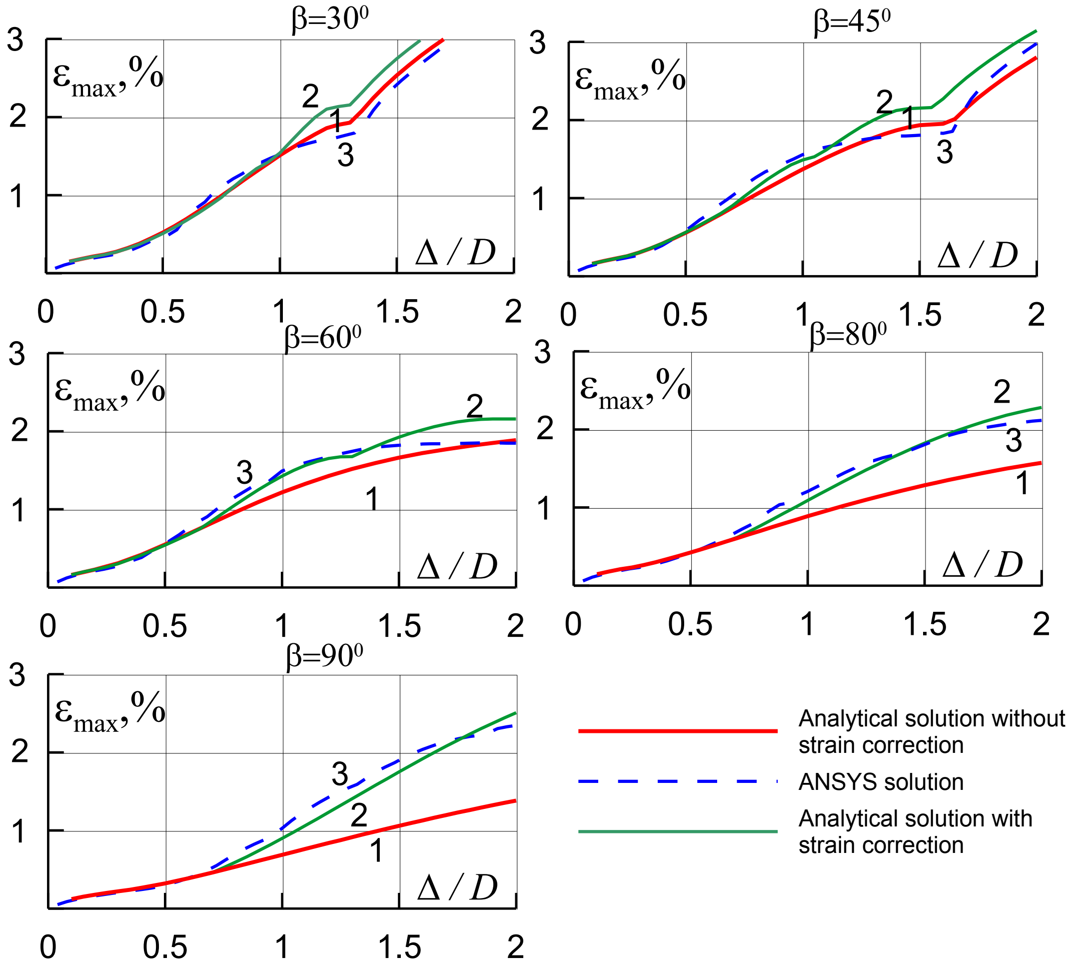

Figure 11: Evolution of the maximal strains with the fault displacement for different fault intersection angles.

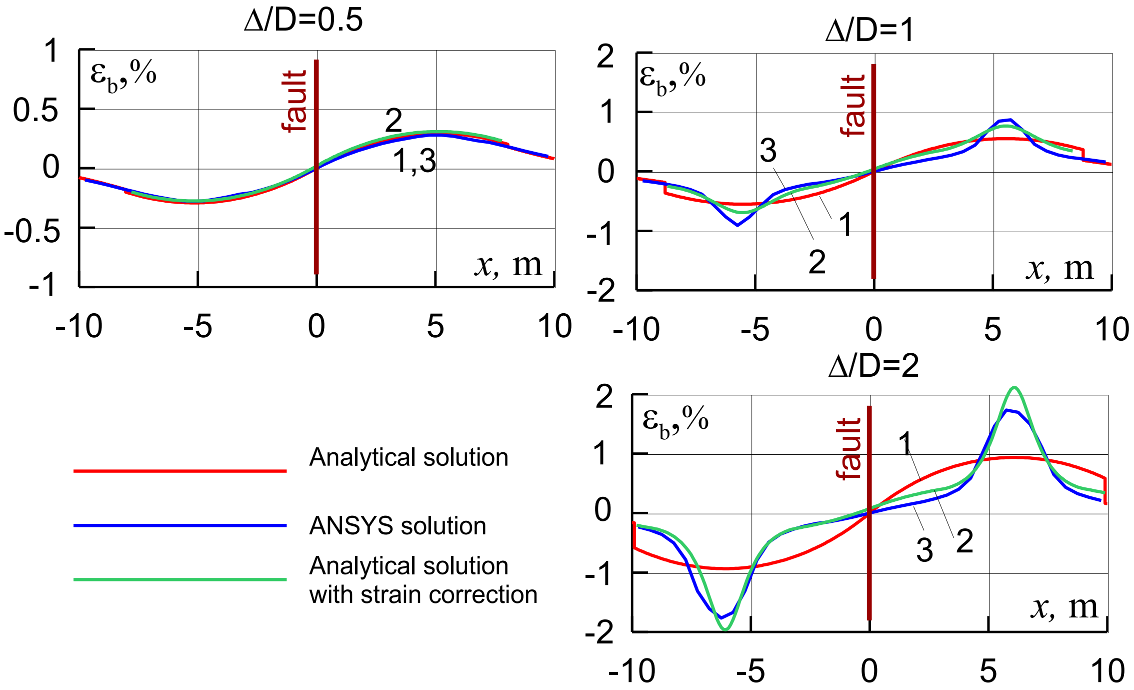

Figure 12: Bending strain distributions in the near fault zone for the case $\beta = 90^0$.

5 CONCLUSIONS

The analytical model for stress-strain analysis of pipelines crossing active faults described in paper [6] is outlined. The comparison of the numerical results obtained with the analytical model to the results of a more rigorous finite element model is performed for the case of strike-slip fault crossing at various intersection angles. The detailed analysis of the strain distributions in the near fault zone revealed the limitations of the analytical model. In particular, for the fault crossing angle close to 90^0 the difference in maximal strains is substantial for large fault displacements.

Based on the performed analysis, a strain correction procedure is suggested. The results of the numerical simulation with the use of strain correction show good correspondence with the finite element results in the range of fault intersection angles from 30^0 to 90^0 and fault displacements from 0 to $2D$ (where D is the pipe diameter). Thus, it can be concluded that the suggested procedure of strain correction extends the applicability of the original analytical model to the practically important case of pipeline crossing active fault at an angle close to 90^0. The main advantage of the proposed procedure is its simplicity and direct applicability to the original pipeline model. The main drawbacks, as they are seen to the authors, are the mostly empirical character of the correction procedure and the need to use an exact numerical solution for preliminary calibration of the strain correction parameters.

REFERENCES

[1] M.J. O'Rourke, X. Liu, *Response of Buried Pipelines Subject to Earthquake Effects*, MCEER, New York, 1999.

[2] N.M. Newmark, W.J. Hall, Pipeline design to resist large fault displacement. In: *Proceedings of the US National Conference on Earthquake Engineering.* Ann Arbor: University of Michigan, 416–425, 1975.

[3] R.P. Kennedy, A.W. Chow, R.A. Williamson, Fault movement effects on buried oil pipeline. *Transport Eng. J. ASCE,* **103**, 617-633, 1977.

[4] L.R.L. Wang, Y.A. Yeh, A refined seismic analysis and design of buried pipeline for fault movement. *Earthquake Eng. Struct. Dyn.* **13**, 75-96, 1985.

[5] D.K. Karamitros, G.D. Bouckovalas, G.P. Kouretzis, Stress analysis of buried steel pipelines at strike-slip fault crossings. *Soil Dynamics and Earthquake Engineering,* **27**, 200-211, 2007.

[6] O.V. Trifonov, V.P. Cherniy, A semi-analytical approach to a nonlinear stress-strain analysis of buried steel pipelines crossing active faults. *Soil Dynamics and Earthquake Engineering*, **30**, 1298-1308, 2010.

[7] Ansys Inc. *ANSYS Release 12.1 Documentation*, 2009.

[8] American Lifelines Alliance. *Guidelines for the design of buried steel pipes.* ASCE, 2001.

COMPDYN 2011
III ECCOMAS Thematic Conference on
Computational Methods in Structural Dynamics and Earthquake Engineering
M. Papadrakakis, M. Fragiadakis, V. Plevris (eds.)
Corfu, Greece, 25–28 May 2011

EXPERIMENTAL STUDY ON THE SEISMIC BEHAVIOR OF SHELL-BASE CONNECTIONS IN LARGE STORAGE TANKS

Gustavo Cortés[1], **Alain Nussbaumer**[2]

[1] Steel Structures Laboratory, Swiss Federal Institute of Technology at Lausanne
GC B3 505, Station 18, 1015- Lausanne, Switzerland
e-mail: gustavo.cortes@epfl.ch

[2] Steel Structures Laboratory, Swiss Federal Institute of Technology at Lausanne
GC B3 505, Station 18, 1015- Lausanne, Switzerland
e-mail: alain.nussbaumer@epfl.ch

Keywords: Unanchored tanks, shell-base connection, cyclic tests, uplifting of tanks.

Abstract. *When an unanchored tank is subjected to strong motion, the impulsive mass of the contained liquid generates a moment which if strong enough could cause partial uplift of the tank's base plate. As the tank undergoes uplifting, the shell-base welded connection is subjected to cycles of rotation which could lead to its failure. To address this issue, the Eurocode and the New Zealand's recommendations limit the rotation amplitude that the shell-base connection of a tank may undergo to 0.2 radians. This limit is obtained from the following two assumptions: (1) a plastic hinge with a length equal to twice the thickness of the base plate forms at the base plate, next to the connecting weld, and (2) the maximum strain that can be sustained by the base plate is 5%. While these two assumptions are reasonable and have been the state of practice for many years, no research work is believed to exist backing these two assumptions and therefore the 0.2 radians limit. For this reason, an experimental research was conducted to determine the real rotational capacity of shell-base welded connections found in tanks. A total of 24 shell-base connections were tested considering the bending and membrane stresses that develop at the base plate when uplift occurs. Constant amplitude tests were carried at different amplitudes of rotation in order to create curves of rotation versus number of cycles to failure. The main finding from this investigation is that the current limit of 0.2 radians is very conservative and that a limit of 0.4 radians would be more realistic.*

1 INTRODUCTION

Unanchored steel tanks are widely used to store water, gasoline and other petroleum-derived liquids. As these tanks are not anchored to the ground, they may be subjected to sliding or rocking motion. Rocking of the tank implies that the wall (shell) uplifts from the ground, causing a rotation at the junction of the shell-base connection. Design codes allow tanks to be unanchored [1, 2], however, they set a limit in the rotation amplitude that the connection may undergo. The Eurocode [1] and the New Zealand's recommendations [2] set the limit to 0.2 radians. This limit is based on two assumptions: (1) a plastic hinge with a length of twice the thickness of the base plate forms at the base plate, next to the shell-base joint, and (2) that the maximum strain at the plastic hinge is 5%. The allowed plastic rotation in the connection, θ_p, is then computed from these two assumptions, by means of equation 1.

$$\theta_p = \int_0^{2t} k \cdot dx = \left(\frac{\varepsilon}{t_{base}/_2}\right) \cdot 2 \cdot t_{base} = \left(\frac{0.05}{t_{base}/_2}\right) \cdot 2 \cdot t_{base} = 0.2rad \tag{1}$$

where dx is the length of the plastic hinge ($2t_{base}$), k is the curvature of the section ($\varepsilon/(t_{base}/2)$), ε is the maximum strain (5%) and t_{base} is the thickness of the base plate. A typical shell-base connection of a steel tank showing the assumed plastic hinge length and strain distribution is shown in Figure 1.

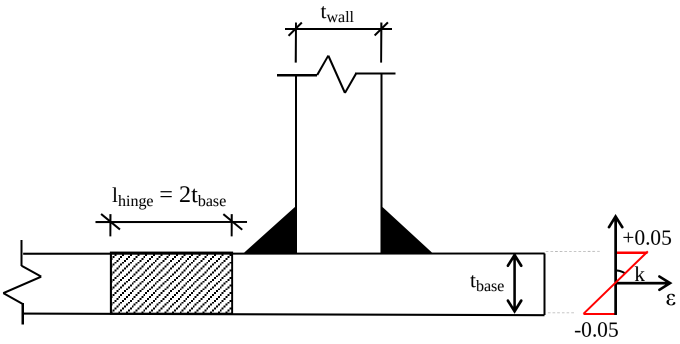

Figure 1: Shell-base connection.

The New Zealand's recommendations state that the assumptions that lead to a 0.2 radians limit should be conservative for a base plate adjacent to a well prepared weld. While the assumptions are conservative and seem reasonable, no experimental work was done to verify these limits. For that reason, an experimental work was conducted to determine the rotational capacity of the shell-base connection.

This paper summarizes the findings from the experimental work conducted on the shell-base connections. An introduction explaining the development of the current 0.2 radians limit is presented in Section 1. Section 2 presents the specimens used for testing. The loading protocol and the tests matrix are presented in Section 3. The test setup is presented in Section 4. Section 5 presents the results. Section 6 applies the findings from the experiments to estimate the rotational capacity of the connection. The conclusions are presented in Section 7.

2 SPECIMENS

Specimens were fabricated from one old tank built in 1961 and located in the city of Konolfingen, Switzerland. In addition, new specimens were fabricated in order to allow for more parameters (e.g., thickness, condition of specimen) to be tested. The new specimens were fabricated by a steel fabricator well acquainted with the fabrication process of steel tanks. Figure 2 shows two different specimens being tested. Note that the specimens are rotated 90 degrees, thus, the base is vertical and the wall is horizontal. This is explained in Section 4. 24 specimens were tested; these were divided in four types, depending on the shell-base thickness and the condition of the specimen (old vs. new). Table 1 summarizes the specimens used, their base and wall (shell) thickness, the weld size, and their condition.

Figure 2: Specimens being tested; left, view from “inside” of tank; right, view from “below” the tank’s base plate.

Type	No. of specimens	Base thickness, t_{base} [mm]	Wall thickness, t_{wall} [mm]	Weld size [mm]	Condition
1	8	6	10	4	New
2	6	8	12	6	New
3	4	10	15	7	New
4	6	7	8	7	Old

Table 1: Specimens used for experiments.

3 LOADING PROTOCOL AND TEST MATRIX

3.1 Loading protocol

When a tank undergoes uplifting of its base, the rotation induced at the shell-base connection is first resisted by bending at the base, in the region next to the weld. However, if the rotation is sufficiently large and causes yielding, the subsequent uplifting is resisted by membrane action of the base plate. The stress developed by the membrane action is normally less than 10% of the material’s yield strength, for rotations less than 0.5 radians. In addition to bending and membrane loading, circumferential compressive stresses are also developed in the base plate. These stresses may be significant for large deformations, however, that is not the case during tank uplift. In order to have a realistic scenario, both bending and tensile (membrane) loading were considered for all tests.

Experiments were loaded using two levels of membrane loading, either 10% or 50% of the specimen's base plate yield strength. While the real behavior is expected to be less than 10% of the yield strength, 50% was also studied to observe the behavior of the connection under such conservative scenario. The tests were performed at three different levels of rotation: 0.2, 0.3 or 0.4 radians. All three series were subjected to initial cycles at 0.02, 0.03, 0.05, 0.07 and 0.1 radians as shown in Figure 3. The first series continued with three cycles at 0.2 radians followed by cycles at 0.3 radians until failure. The second series continued with cycles at 0.2 radians until failure. Finally, the third series continued with three cycles at 0.2 radians, 3 cycles at 0.3 radians, and cycles at 0.4 radians until the specimen failed. Failure was achieved when total rupture of the specimen occurred.

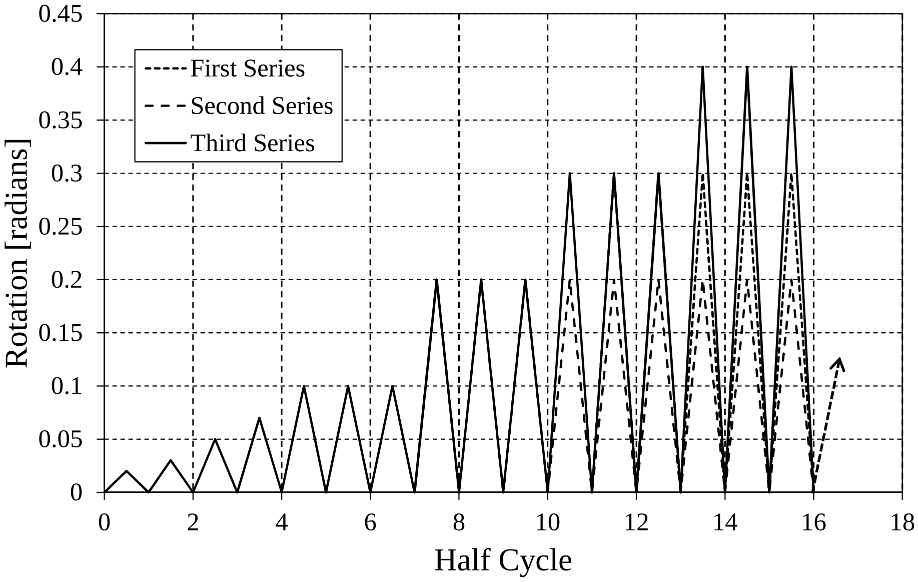

Figure 3: Loading protocol.

3.2 Test matrix

Different parameters of interest were studied in the experimental program. Specimens with different thicknesses were used to study how the thickness of the base plate affected the maximum number of cycles resisted by the specimen. The axial load applied to the bottom of the tank (membrane load) was either 10% or 50% of the nominal yield strength. Also, specimens were either newly fabricated or from an old tank. Finally, the amplitude of rotation applied was 0.2, 0.3 or 0.4 radians. The test matrix is shown in Table 2.

No. tests	Specimen condition	Base thickness t_{base} [mm]	Wall thickness t_{wall} [mm]	Tension [%P_y]	θ_p [rad]
2	Old	7	8	10	0.3
2	Old	7	8	50	0.3
2	New	6	10	10	0.3
2	New	6	10	50	0.3
2	New	8	12	10	0.3
2	New	8	12	50	0.3
2	New	10	15	10	0.3
2	New	10	15	50	0.3
2	New	6	10	10	0.2
2	New	8	12	50	0.2
2	New	6	10	10	0.4
2	Old	7	8	10	0.4

Table 2: Test matrix.

4 TEST SETUP

In order to introduce the membrane loading and the uplifting of the shell-base connection at once, a complex setup involving two actuators and a four pin frame (leveling frame) were introduced. Figure 4 shows the test setup in its displaced position. Note that the specimen was rotated 90 degrees counter clockwise, therefore, the membrane load was applied by the vertical actuator and the uplift was applied by the horizontal actuator. The leveling frame's function was to keep the specimen horizontal under all levels of uplift.

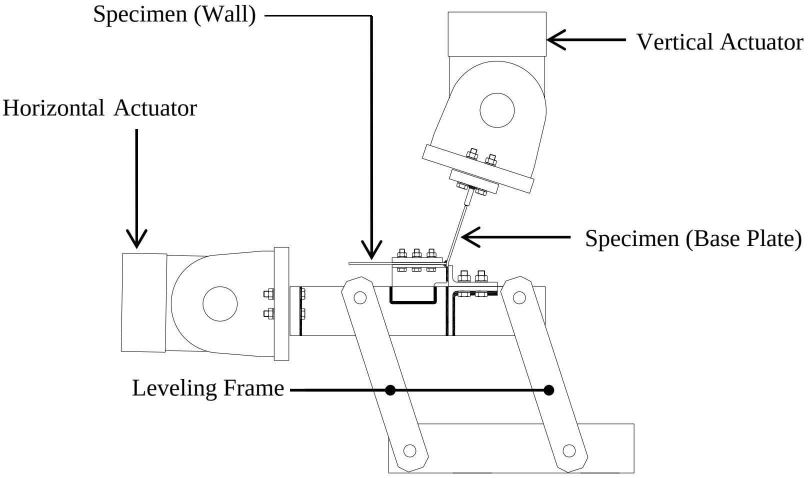

Figure 4: Test setup.

5 RESULTS

The parameter which clearly had the most influence in the number of cycles resisted by the specimens was the membrane load applied. Specimens with 50% membrane load endured between 2.5 and 9 cycles, while specimens with 10% membrane load endured between 84 and 200 cycles. In average, specimens with 10% membrane load endured 19 times more cycles than specimens with a 50% membrane load.

The thickness of the base plate was also found to influence the number of cycles resisted by a connection. For tests carried out with a membrane load of 50% of P_y, specimens with a thickness of 10mm endured about 50% more cycles than specimens 8mm thick and 183% more cycles than specimens 6mm thick. For tests carried out with a 10% of P_y membrane load, specimens with a thickness of 10mm endured 36% more cycles than 8mm thick specimens and 41% compared to 6mm thick specimens.

With the number of cycles to failure, N_f, recorded for each test (see [3] for a comprehensive discussion), plots of rotation amplitude vs. number of cycles to failure were created. Figure 5 shows the data points, the 50% confidence level (linear regression) and the 95% confidence level line for all tests carried out at a 10% of P_y membrane load. Note that the initial smaller cycles applied were considered by converting them into equivalent cycles (see [4]). From Figure 5 it can be seen that for the rotation limit of 0.2 radians, the number of cycles that may be resisted is about 342 cycles (using the 95% confidence level). It can also be seen that the connections underwent 64 cycles at 0.3 radians and about 20 cycles at 0.4 radians. Having established the relationship between rotation and number of cycles to failure, only the number of cycles that the tank is likely to undergo (for a given location) is needed to estimate the maximum rotation that the connection will undergo. Figure 5 is used in the next section to estimate a rotation limit.

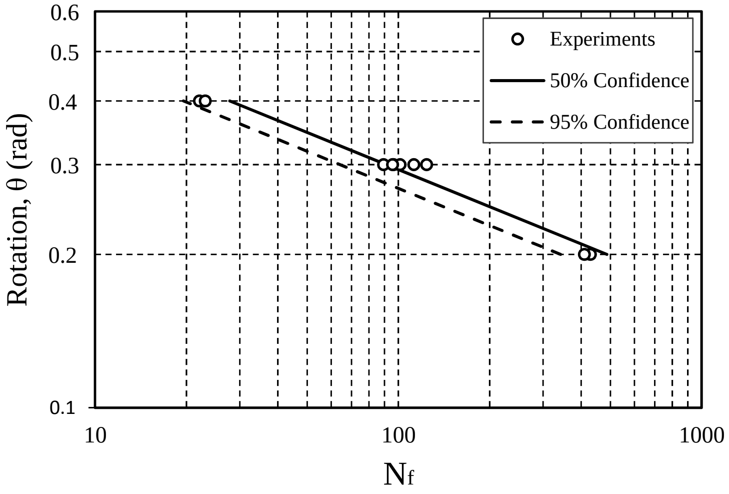

Figure 5: RN curve for shell-base connections.

6 APPLICATION

The RN curve shown in Figure 5 relates the rotation amplitude to the number of cycles (with same amplitude) that will cause failure at this rotation amplitude. It shows that at the current code limit of 0.2 radians the connection would be able to undergo about 340 cycles of equivalent amplitude. This number of cycles is clearly much greater than the expected number of cycles to which the shell-base connection of a tank would be subjected to during an earthquake. The rotation capacity of this connection can be directly obtained by entering Figure 5 with the number of equivalent cycles that it is likely to undergo for a specific site hazard.

The maximum number of cycles at the shell-base connection was estimated for the highest hazard in Switzerland [5]. To estimate the number of cycles, 2 tanks were modeled in ABAQUS and subjected to 8 ground motions. The number of cycles at the shell-base connection and their magnitude were then obtained for each ground motion. From this analysis, it was estimated that the number of cycles expected at the shell-base connection would be 4 cycles. Entering Figure 5 with this number of cycles is not possible as the range of number of cycles is between about 20 and 400 cycles. It is however clear that at a rotation of 0.4 radians (maximum tested) the tank would be able to undergo about 20 cycles which is much greater than the estimate of 4 cycles. This is a clear indication that the shell-base connection can resist at least 0.4 radians without failure.

As an alternative method for determining the equivalent number of cycles, the cyclic-demand spectrum developed in [4] could be used. The cyclic-spectrum is similar to a response spectrum, but instead of providing the acceleration for a given period of vibration, it provides the number of cycles that the structure will experience, as a function of the fundamental period of the structure. In order to apply the cyclic-demand spectrum, it was assumed that each cycle of displacement of the tank causes a cycle of rotation at the connection. This is a reasonable assumption since cycles in the shell-base connection are directly related to displacement of the tank. For full details on how to develop the cyclic-demand spectrum see [4].

The cyclic-demand spectrum was developed for the city of Sion, Switzerland, for a 2500-year return period and for 2% of critical damping. The equivalent numbers of cycles in the acceleration, velocity and displacement controlled regions (i.e., N_A, N_V and N_D) are 1.7, 1.4 and 1.1 respectively. From this analysis, the expected number of equivalent cycles was found to be about 4 cycles.

Both the time history analysis of tanks [5] and the cyclic-demand spectrum [4] estimated the number of cycles to be around 4 cycles. As mentioned before, 4 cycles is clearly much less than the 20 cycles that the connection is capable of resisting at 0.4 radians. Thus, it becomes clear that the 0.2 radians rotation limit established by the Eurocode and the New Zealand's recommendations is very conservative.

7 CONCLUSIONS

Current Eurocode and New Zealand's recommendations allow a tank to rest on ground, without anchorage, as long as uplift is limited. The uplift limit, given in terms of rotation of the shell-base connection, is set to 0.2 radians. This limit was derived from the assumptions that a plastic hinge with a length equal to twice the thickness of the base plate forms at the base plate, next to the shell, and that the maximum strain allowed in the plastic hinge zone is 5%. While both assumptions seem reasonable and have been the state of the practice for many years, to the knowledge of the authors no experimental work representing the behavior of these connections had been done to back these assumptions. With that in mind, an experimental research was performed to study the rotational capacity of shell-base connections in unanchored steel storage tanks. The experimental work included studies of connections with different shell-base thicknesses, with different amounts of membrane load and cycles at different amplitudes of rotation. In addition, new and corroded specimens were tested. The main conclusions from this experimental study are listed below:

- In average, specimens with a 10% of P_y membrane load endured 19 times more cycles than specimens with a 50% of P_y membrane load.
- The thickness of the base plate was found to influence the number of cycles resisted by a connection. Specimens with a thicker base plate endured more cycles than those with a thinner base plate.
- The main result from the experimental program was the creation of curves of rotation vs. number of cycles, called RN curves.

- The RN curves indicated that the wall-to-base connection of a tank would endure 342 cycles at the rotation limit of 0.2 radians given in the Eurocode and the New Zealand's recommendations (with 95% confidence).
- The number of cycles to which the shell-base connection of a tank will be subjected to was estimated to be about 4 cycles.
- Results from this research suggest that a limit of 0.4 radians, which was the maximum rotation angle tested, would be more realistic than the 0.2 radians limit.

Results from this research suggest that a limit of 0.4 radians would be more realistic, however, it should be noted that the results presented in this paper were drawn from a limited number of tests and therefore should be used with caution.

ACKNOWLEDGEMENTS

The authors would like to acknowledge the financial support provided by CARBURA and the Swiss Federal Office for the Environment. The authors would like to thank Dr. Praveen Malhotra for his aid in developing the cyclic-demand spectrum for the maximum hazard of Switzerland.

REFERENCES

[1] EN1998-4. Eurocode 8: Design of structures for earthquake resistance, part 4: Silos, Tanks and Pipe lines. European Committee for Standarization, Brussels; 2003.

[2] NZSEE. Seismic Design of Storage Tanks. Wellington, New Zealand: New Zealand National Society for Earthquake Engineering; 2009.

[3] G. Cortés, A. Nussbaumer, C. Berger, and E. Lattion. Experimental Determination of the Capacity of Wall-to-Base Connections in Storage Tanks. *Journal of Constructional Steel Research,* in press.

[4] P. Malhotra, *Cyclic-Demand Spectrum*, Earthquake Engineering and Structural Dynamics, 31: 1441-1457; 2002.

[5] G. Cortés, A. Nussbaumer, Seismic Behavior of Shell-to-Base Connections in Large Storage Tanks, Report No. N° IC 495-1, August 23, 2010, ICOM-EPFL, Lausanne, Switzerland; 2010.

COMPDYN 2011
III ECCOMAS Thematic Conference on
Computational Methods in Structural Dynamics and Earthquake Engineering
M. Papadrakakis, M. Fragiadakis, V. Plevris (eds.)
Corfu, Greece, 25–28 May 2011

SEISMIC ANALYSIS AND COMPONENT DESIGN OF REFINERY PIPING SYSTEMS

Fabrizio Paolacci[1]*, Md. Shahin Reza[2], Oreste S. Bursi[2]

[1]University of Roma Tre, Department of Structures
Via Corrado Segre, 00146, Rome, Italy
paolacci@uniroma3.it

[2]University of Trento, Department of Mechanical and Structural Engineering
Via Mesiano 77, 38121, Trento, Italy
oreste.bursi.@ing.unitn.it, rezam@ing.unitn.it

Keywords: Piping system, Seismic design, Dynamic analysis, Experimental test.

Abstract. *In petroleum industries, especially in refineries installations, hundreds of miles of pipes are installed to transfer row and refined material (fluid and gas) from a point to another of the plant, connecting all the components involved in the transformation process (tanks, distillations columns, furnaces, etc..).Recent seismic events showed a quite high vulnerability of these structures, where damage ranges from the simple failure of joints to the failure of supporting structures. For these reasons, initially the seismic analysis and component design of refinery piping systems is here analysed. A review of the current approaches imposed by European (EN13480:3) and American (ASME B31.3) standards is illustrated by using a proper case study of a piping system on a pipe-rack. The analysis permitted to identify the limits of the design standards and to identify the critical aspects of the problem, i.e., dynamic interaction between pipes and rack, correct definition of the response factor, strain versus stress approach. Finally, the preliminary phases of an experimental investigation on flanged joints are also illustrated.*

1 INTRODUCTION

The piping systems typically found in a refinery complex contain various components and support structures and operate in a broad range of working environments. Some common components usually used in piping systems include straight pipes, elbows, Tee-Joints, various valves, flanged joints, pressure vessels, tanks, strainers and reducers. Depending on the nature of the working fluids, piping systems are designed to work over a wide range of temperature and pressure. A typical piping system is presented in Figure 1.

A pipe-way is the space allocated for routing several parallel adjacent pipelines within process plants. A pipe rack is the structure employed for supporting the pipelines and carrying electrical and instrument trays. The pipe rack is usually made of steel or concrete frames, on top of which the pipeline rests.

Pipe racks are necessary for arranging the process and service pipelines throughout the plant, and they are used in secondary ways; principally to provide a protected location for auxiliary equipment, pumps, utility stations, manifolds, and firefighting and first-aid stations. Lighting and other fixtures can be fitted to the pipe rack columns. Air-cooled heat exchangers are often supported above pipe racks for economy of plot space.

Figure 1 Typical piping layout

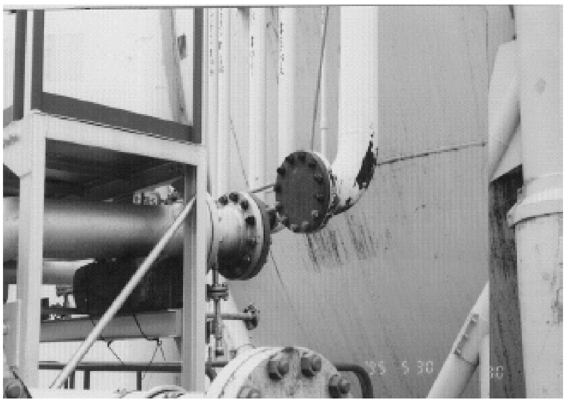

Figure 2 : Breakage of a piping flanged connection

Recent seismic events showed a quite high vulnerability of these structures, where damage ranges from the simple failure of joints to the failure of supporting structures [1],[2],[3],[4]. For example, the failure of a bolted flange connection is shown in Figure 2.

Consequences can be characterized by several degrees of severity, depending on the material delivered by pipes. For dangerous liquids or gases, even a simple failure of a joint can represent the trigger of a significant accidental chain, with severe consequences both for the environment and human lives. Unfortunately, few contributions in the literature are available, in order to clarify the seismic requirements that piping systems have to comply with. In addition, aspects like action and structural modelling have not yet been treated in a satisfactorily manner. Moreover, current American and European standards do not contain enough rules and details for a proper seismic analysis and design of piping systems.

Along these lines, some problems relevant to seismic analysis criteria of piping systems are addressed in this paper. In a greater detail, several aspects that characterise the problem are treated: 1) modelling of pipes and pipe-racks; 2) selection of the analysis method; 3) definition of the seismic action; 4) dynamic analysis of the system; 5) stress analysis of pipes; 6) definition of the ultimate capacity of pipes and joints between pipes.

To this end a representative case study of an actual piping system was analysed. The requirements of American and European codes were compared and important aspects were highlighted, like: a) dynamic coupling between pipes and pipe-rack, often erroneously neglected; b) definition of proper restraint conditions between pipes and support structures and between adjacent piping systems; c) evaluation of the ultimate capacity of pipes and joints necessary for a correct design of a structure, as suggested by modern approaches like Performance-based Engineering.

About the aforementioned item c) an experimental campaign is currently undertaken at the University of Trento in order to characterise the cyclic behaviour of flanged joints between pipes, particularly important to avoid leakage of dangerous substances during a severe seismic event. Preliminary information about the testing activity is illustrated and commented.

2 EUROPEAN AND AMERICAN STANDARS FOR THE SEISMIC DESIGN OF PIPING SYSTEMS

Nowadays, both European and American codes are available for the design of piping systems under seismic events. The main European contributions is chiefly represented by the standard EN13480, dedicated to metalling piping systems [5]. The Eurocode 8 - part 4, the European seismic code for industrial components, is also devoted to pipelines, but only of above-ground type, which differs from metallic piping system for many aspects, and then useless.

American experience on piping system is very rich, especially in terms of design standardization and seismic design calculation, and the long list of standards and codes available it is a clear demonstration of it. The main standard is represented by ASME B31.3 [6], but many other contributions and guidelines are also available [7],[8].

The seismic analysis of a piping system involves several basic steps that allow defining the proper seismic action, the suitable numerical model and analysis method and the verification format to be used. The European (EN13480:3-2002) and the American standards (ASME B31.3-2006) for piping systems differ for several of these aspects. Thus, in order to understand these differences and the consequences on the seismic response evaluation, in the following both European and American standards are applied to a representative case study.

It is necessary to stress that the American Standard does not contain explicit indications on the seismic analysis of piping systems, but rather refers to the American standard for seismic analysis of structure ASCE7-05, which includes all the required prescriptions. On the contrary the European Standard contains an entire Annex (A) dedicated to the dynamic and seismic analysis of piping systems, but does not contains explicit quantification of the seismic action. At this end the Eurocode 8 (prEN1998:1 2004) should be used.

3 DESCRIPTION OF A CASE STUDY

The piping system here analysed belongs to a refinery, whose plant view is shown in Fig.3. The supporting steel structure is composed by seven transverse moment resisting frames placed every 6 m, realized with commercial HEA/B steel profiles. In the longitudinal direction it behaves like a truss structure, which is reinforced with 6 braces (see Fig. 4, Fig.5). Horizontal bracings are also installed to avoid excessive relative displacements between the pipe supports.

The piping system presents a typical piping layout with pipes having different diameters. To simplify the analysis, only the structural contribution of 8’’ pipes has been considered, whose layout is shown in Fig. 6. The remaining pipes are considered only as weight. Several flanged elbows are present within the pipe-rack and at both the ends of the piping system.

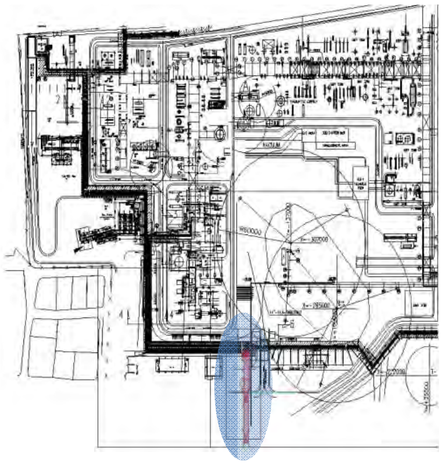

Figure 3 – Plan view of the refinery

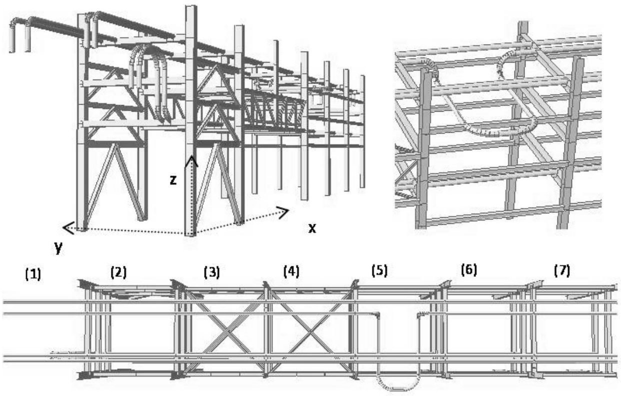

Figure 4 – The piping system

The fluids contained in the pipes are several, but essentially Amine, cooling water and high to medium pressure steam. The vertical loads corresponding to the weight of the pipes, insulation and fluid are considered as uniformly distributed equal to 12 kN/m. The main characteristics of the piping system are the following:

- Structural steel S-275 JR according to EN 10025 (2005)
- Pipe steel - ASTM A106 Grade B
- pipes with diameter of 8’’
- Pressure of the pipes: 0.5÷5 Mpa
- Temperature range 47 °C ÷360 °C.
- Seismic category of Importance Ip=1.5, PGA=0.24 g, Soil conditions: D

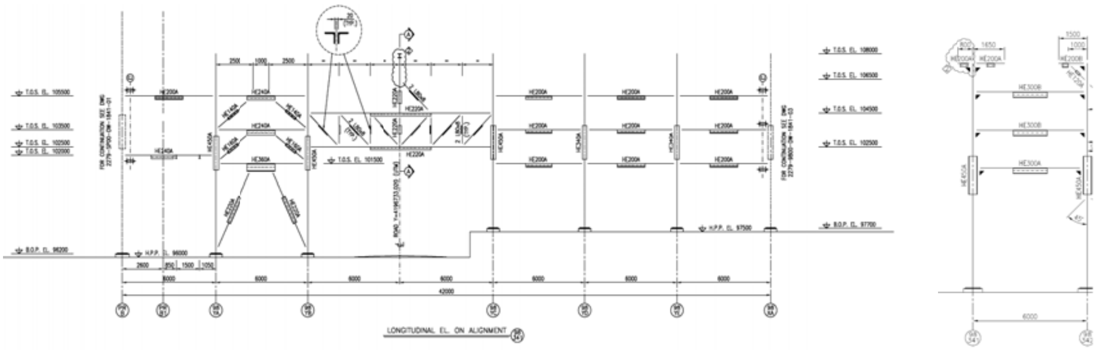

Figure 5 - The analysed piping system

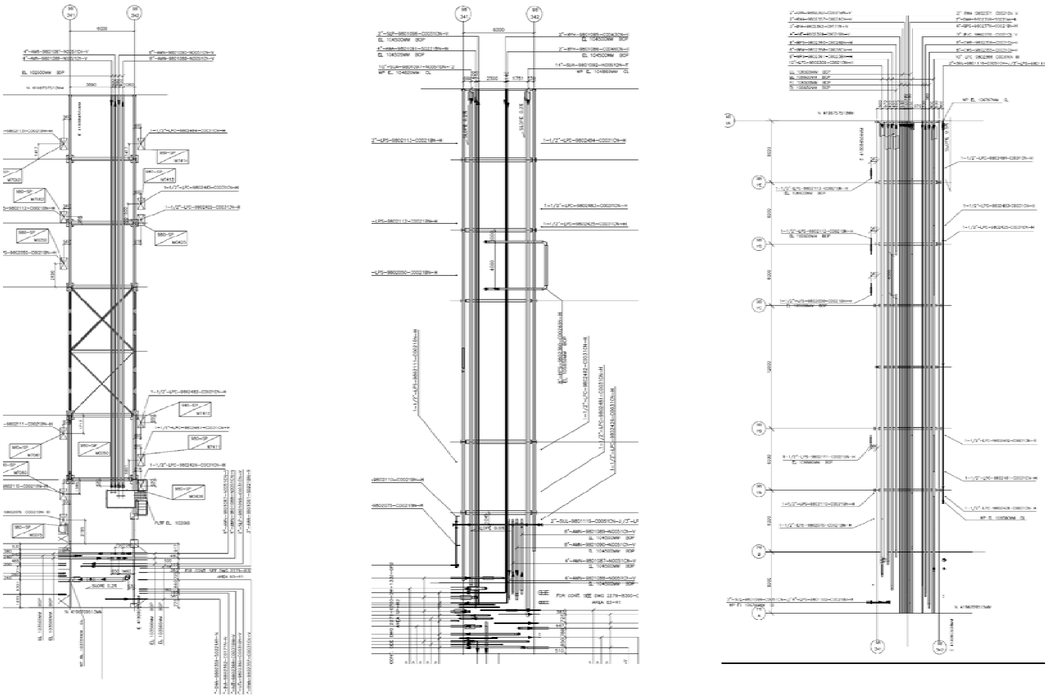

First floor Second floor Third floor

Figure 6 - The analysed piping system

4 MAIN ISSUES IN SEISMIC DESIGN OF PIPING SYSTEMS

The seismic design of a piping system entails many issues. As stated above, they are essentially related to the modelling of the structure, to a correct definition of the seismic action, to a proper analysis method to be applied, and finally, to a appropriate design method to be used. In addition, nowadays, the Load and Resistance Factor Design method (LRFD) is certainly the standard method for designing structures and the allowable stress design method is by now abandoned because often considered too much conservative. Unfortunately, this latter is still the current approach for designing a piping system. This represents a limit to be overcome. But to the purpose, it is firstly necessary to understand the limit of such an approach; and the more direct way is to apply the codes prescriptions to a case study, trying to individuate limits and drawbacks. In doing this, it seems proper to compare European and American experiences, applying both the EN13480:3 and ASME B31.3 to the case study described above along with a comparison of the results regarding all the treated aspects.

4.1 Definition of a numerical model

A synthetic scheme of what European and American standard prescribe for a correct numerical modelling of a piping system and the definition of the seismic conditions is reported in Table 1.

The table clearly shows that the suggested numerical model to use in seismic analysis is always elastic both for EN13480 and ASME B31.3. This choice comes certainly from the old way to evaluate the safety level of a structure: the allowable stress method, still diffused in designing of piping systems. Usually, only the piping system is modelled, using the supporting structure only to evaluate the seismic action at pipes level (e.g., in-structure spectra). The supporting structure (e.g. pipe-tack) is treated as elastic too. The assumption of elastic behavior would not be a strong limitation if a correct value of the behavior factor were adopted. Some comments on this aspect will be provided afterwards.

Another important aspect, often related to the assumption on the numerical model is the analysis method to be adopted. This ranges from the very simple equivalent static method to the time-History analysis. But, this aspect will be treated in the next section.

A key point in modelling a piping system is the possibility to neglect the interaction (static and dynamic) between the pipes and the supporting structure. EN13480 does not provide any indication about it, whereas ASME B31.3, by means of ASCE-07, prescribes a crude rule based on the ratio WR between the weights of pipes and supporting structure. In particular, if WR < 25% the interaction can be excluded and the piping system can be considered as a non-building structure, loaded by a seismic action coming from the supporting structure at pipes level.

This rule has been recently analysed by several authors. For example in [9] the rule has been analyzed using time-history analysis. From the results and discussion the author concluded that in some cases this decoupling rule could produce gross errors in the evaluation of the dynamic behavior of piping systems. In particular, it seems that in dynamic assessment of such systems, in addition to the primary-secondary system weight ratio criteria, attention should be paid to other aspects as “end conditions of pipes”, “relative stiffness of supporting structure to piping system” and “relative stiffness of pipes to pipe-supports”, even though only partial conclusions where reached by the authors, that suggested more investigations on this matter. In the literature many works have been dedicated to the problem of dynamic coupling between primary and secondary systems [10],[11],[12], but the results are difficult to be extended to the case of piping systems for several reasons, but mainly because in case of piping systems the secondary system is composed by more sub-systems (pipes with different diameters, different end conditions, different supports, etc..). Therefore, assumption of a single secondary system could lead to gross errors in response prediction of piping systems.

(1) elastic calculation shall be used although some part might be exhibit plastic deformations (p. 4.1), (2) SSE=safe shutdown earthquake, DBE= Occasional operation condition, (3) FF=Flexibility Factor, SIF= Stress Intensification Factor, (4) G=ground motion spectra, IS=In-structure spectra.

Code	Model type	Analysis	Seismic condition	Dynamic interaction	Relative motion	Pipe modelling
EN13480:3	Elastic (1)	Equivalent Static Modal (G,IS^4) Time-History	SSE (2) OBE	NO	YES	Beam elements (FF and SIF)
ASME B31.3	Elastic	Static Modal Time-History	SSE	YES/NO	YES	Beam elements (FF and SIF)(3)

Table 1 – Code prescriptions for numerical modelling as well as seismic conditions

Concerning the case study, applying the weight ratio rule, dynamic interaction has been considered, because WR > 25%. Moreover, for comparison, this rule has also been considered in applying the European standard. In order to evaluate the effectiveness of the weight rule, the behavior of the piping system without pipe-rack has also been analysed.

The pipes are usually connected to the pipe-rack by mechanical supports, often flexible. They are usually designed to accommodate thermal and pressure effects, avoiding excessive stress in the pipes. Unfortunately, no indications on how to model them are provided by European and American standards. Nevertheless, this is an important aspect that have to be treated with particular attention because can cause changes in dynamic behavior of the system.

Dissipative supports can be used instead of traditional ones in order to introduce artificially more damping and reduce the response of the pipes.

The analysed case present a quite stiff support systems, modelled as elastic spring in the transverse direction (Y), leaving free the relative displacements in longitudinal direction (X) and using fix restraints conditions in vertical direction. Moreover, as usual, all the rotations between pipe and pipe-rack have been unrestrained.

Another relevant aspect about modelling of piping systems is the adoption of a proper model for pipes and fittings (elbows, tee-joints, nozzles, etc..). At this regards, usually beam elements with hollow section are used for straight pipes (Fig.7). The fittings are also modelled using beam elements, but modifying the stiffness for the effect of geometry. At this regards both European and American codes define a flexibility factor (k >1) using which the moment of inertia of the pipe is reduced. In addition, to take into account the stress concentration effect, the Stress Intensification Factor (SIF) is used to increase the stress calculated using the beam theory. The value of k and SIF calculated according to EN13480 and ASME B31.3 are very similar.

In presence of high pressure condition the stiffness of the pipe could increase. To account for this effect the flexibility factor k is reduced. Unfortunately, only ASME B313.3 provides an explicit expression of the pressure reducing factor. For the analyzed case and for a pressure of 5 MPa this factor halves the flexibility.

Alternatively, it is possible to use shell elements to model fittings [13]. This approach is appropriate to account for ovalization of the section and stiffening pressure effect. For this reasons this model has been used for the case study and a comparison with beam model has been carried out (Fig. 8). We can anticipate that the numerical simulations have shown a similar behavior of both the models and the reliability of modified beam element, at least for standard fittings, like the one here analyzed. Therefore, in what follows only the results of the more refined one will be shown.

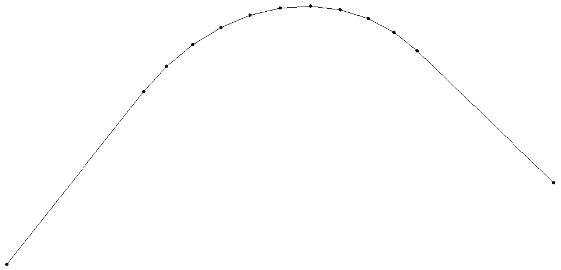

Figure 7 – Beam FEM for an elbow

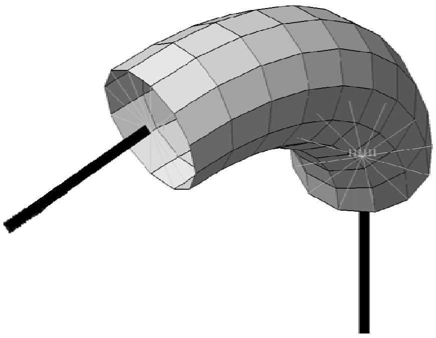

Figure 8 – Shell FEM for an elbow

A last but not less important aspect regards the boundary conditions of the pipes. In fact, because a piping system is realized by hundreds of miles of pipes, the analysis involves necessary a limited part of the structure. Consequently proper boundary conditions have to be accurately adopted to simulate the remaining part of the structure. Also for this delicate aspect no indications are provided by the European and American standards. As already shown in literature, the correct boundary conditions may cause important modifications of the dynamics of the piping system but the correct choice depends on the single case [9].

Because one of the aim of this work is to compare European and American standards, it has been decided to limit the possible cases adopting as restraint conditions of the pipe ends only hinges. In this respect, one can look at Fig. 9.

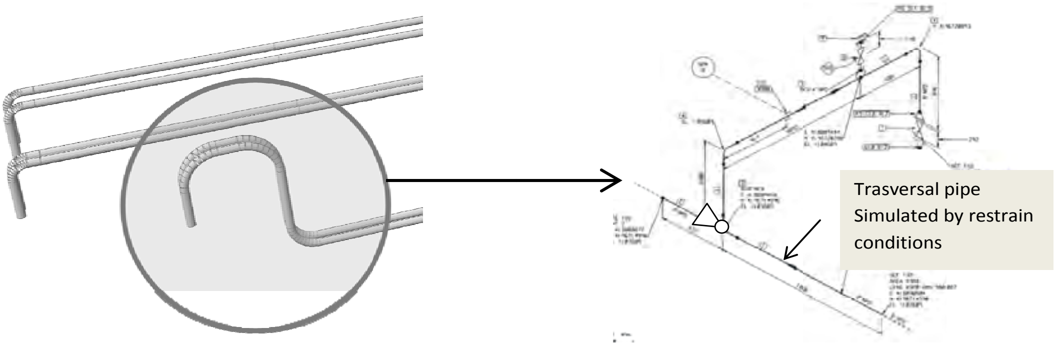

Fig. 9 – Boundary condition in one if the pipe ends

The model of the piping system and the support structure has been realized in the general purpose software MIDAS Gen [14]. It is shown in Fig. 10.

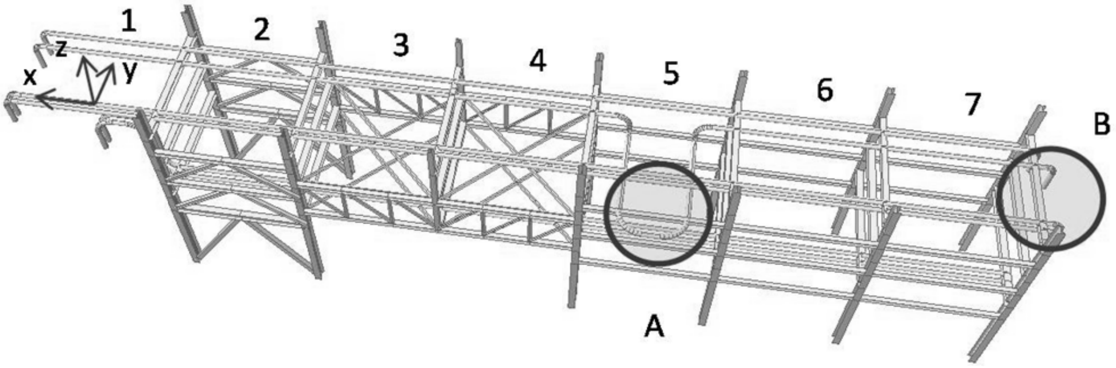

Figure 10 – The FE model of the piping system

4.2 Seismic actions and analysis methods

Both European and American standards assume the following two types of analysis mandatory for the pipes:

- Movements due to inertia effects
- Differential movement of the supports (within the supporting structure or between adjacent pipe-racks)

The first type of analysis is essentially related to the effects of the absolute acceleration on the pipe mass. The second one is due to the relative movements between two supports, within the supporting structure or belonging to adjacent structures. Often the relevant effects are due to the displacement effect rather than acceleration effects.

Concerning the case study, the entire model here considered (pipe + pipe-rack) allow identifying both the effects. On the contrary the model without considering the supporting structure, here also considered, allows identifying only the inertia effect of the pipes, unless a multi-support excitation would be used.

The seismic action for pipe-racks is usually represented by design response spectra or accelerograms (natural records or synthetic accelerograms). For the analysis of pipes only, “In-structure” spectra or “filtered response spectra” are used.

Design response spectrum method

The design spectra are the main representation of a seismic action and usually are defined by the seismic codes in terms of hazard conditions of the site, the level of dissipation capability of the supporting structure and pipes (response or behavior factor), the right level of damping to be employed, and the level of structure reliability to impose, identified by the importance factor.

For what regards the support structure, hazard conditions apart, the damping usually adopted is equal to 5%, as suggested by Eurocode 8 and 3 for steel structures, whereas the behavior factor q depends on the type of structure used for the pipe-rack. While for building-type structure this aspect has been well identified and quantified, for structures like pipe-racks, that may often be considered as non-building structure (ASCE-07:2005), the problem may be quite different.

The current American and European seismic codes provide a q factor for steel racks equal to 3 ½ and 4 respectively (Tab 2). This choice probably derives from the hypothesis of no-coupling between the rack (primary system) and the pipes (secondary system). In fact, usually the level of dynamic coupling between pipes and rack can be neglected. But in other some cases its influence cannot be excluded a priori [9].

In order to compare the results of EN13480 and ASME B31.3 the same elastic spectrum, has been here adopted defined according to prEN1998:1, and modified using the behavior factor of Tab. 2. It is shown in Fig. 13.

The spectral response of the modal oscillators and then combined to obtain the resultant response of the system. Moreover, the resultant forces and displacements from bi-directional analysis are typically obtained by the square root sum of square of the response in each direction, or by applying the so-called 100-30 rule.

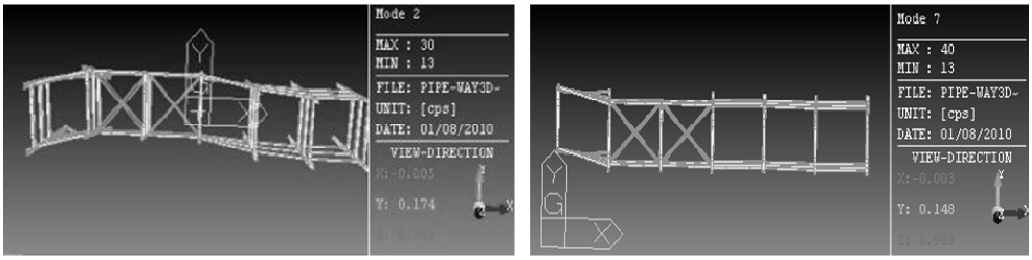

Figure 11 First two vibration modes of the pipe-rack model

In Tab.3 the main dynamic characteristics of the system are shown. As mentioned before, the modal analysis on the entire system allows highlighting the important role of the pipes in realizing structural coupling between the several frames of the pipe-rack. For example in Fig. 11 and 12 the vibration modes of the rack with and without the pipes is shown. They are quite different especially in terms of excited mass. For example, the period of the first mode of the rack with and without pipes is very similar, whereas the excited mass is higher in the first case, showing the coupling effect of the transverse frames due to the pipes.

All the results here presented have been carried out for the elbows modelled using shell elements. The results using the simpler beam elements (here not presented) are quite close to previous ones, showing their reliability.

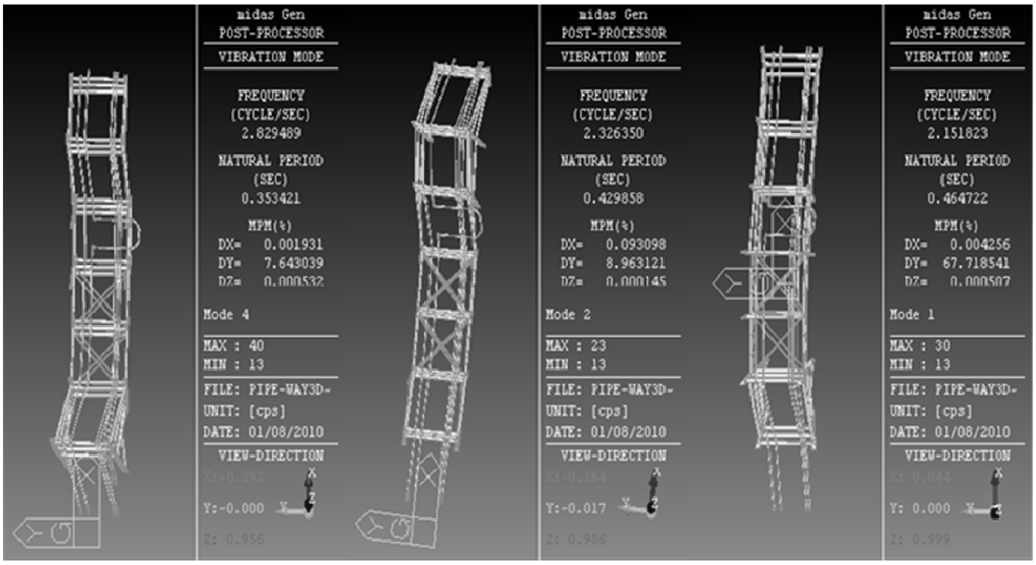

```
midas Gen
POST-PROCESSOR
VIBRATION MODE

FREQUENCY
(CYCLE/SEC)
2.829489

NATURAL PERIOD
(SEC)
0.353421

MPM(%)
DX=   0.001931
DY=   7.643039
DZ=   0.000532

Mode 4

MAX : 40
MIN : 13
FILE: PIPE-WAY3D-
UNIT: [cps]
DATE: 01/08/2010
VIEW-DIRECTION
X:-0.292
Y:-0.000
Z: 0.956
```

```
midas Gen
POST-PROCESSOR
VIBRATION MODE

FREQUENCY
(CYCLE/SEC)
2.326350

NATURAL PERIOD
(SEC)
0.429858

MPM(%)
DX=   0.093098
DY=   8.963121
DZ=   0.000145

Mode 2

MAX : 23
MIN : 13
FILE: PIPE-WAY3D-
UNIT: [cps]
DATE: 01/08/2010
VIEW-DIRECTION
X:-0.164
Y:-0.017
Z: 0.986
```

```
midas Gen
POST-PROCESSOR
VIBRATION MODE

FREQUENCY
(CYCLE/SEC)
2.151823

NATURAL PERIOD
(SEC)
0.464722

MPM(%)
DX=   0.004256
DY=  67.718541
DZ=   0.000507

Mode 1

MAX : 30
MIN : 13
FILE: PIPE-WAY3D-
UNIT: [cps]
DATE: 01/08/2010
VIEW-DIRECTION
X: 0.044
Y: 0.000
Z: 0.999
```

Figure 12 First three vibration modes of the pipe plus pipe-rack model

Code	Behavior factor R (pipe-rack)	response factor R_p (pipe)	Damping (%)	Importance F.
EN13480:3 (EC8)	4	Not indicated	5	1.5
ASME B31.3	3 ¼	6÷12	5	1.5

Tab. 2 – Behaviour factor, damping and Importance Factor

Case	Mode 1			Mode 2			Mode 3		
	f (Hz)	T(sec)	MPS(%)	f (Hz)	T(sec)	MPS(%)	f (Hz)	T(sec)	MPS(%)
TD-PR (*)	2.17	0.459	28.29	2.33	0.456	47.62	2.93	0.440	5.68
TD-PRP(*)	2.15	0.456	67.61	2.33	0.429	8.96	2.93	0.353	7.64
LD-PRP(*)	2.81	0.355	53.27	5.15	0.194	36.35	---	---	---

(*) TD-PR=Transversal direction – Pipe-rack, TD-PPR=Trans. dir. – Pipe-rack+pipes, TD-PR=Longitudinal dir. – Pipe-rack+pipes

Table 3 – First three vibration modes of the entire piping system

In-structure spectra

The in-structure spectra allow a seismic action to be defined for the single pipe at several floors of the pipe-rack, in which the pipe is placed. Both European and American codes give their explicit expressions. They are defined as the spectrum acceleration multiplied by the amplification factor AF shown in Fig. 14. The expression of the amplification factor expressed by EN13480 (EC8) and ASME B31.3 (ASCE-07) differ for the presence of the period ratio Ta/T1, presents only in the seismic European Standard which takes into account the dynamic interaction between pipes (Ta) and pipe-rack (T1). (see tab. 4).

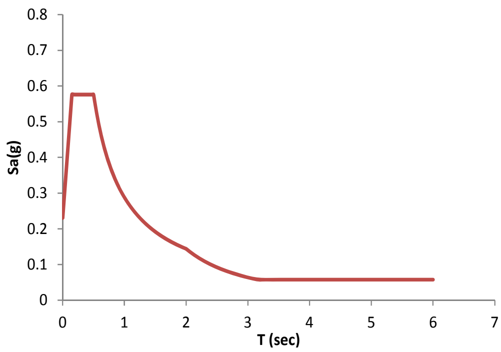

Figure 13 Eurocode 8-1 free-field elastic spectrum (Soil D)

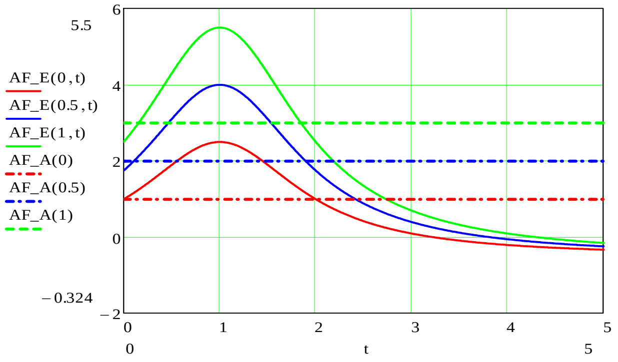

Figure 14 Amplification factor of in-structure spectra v/s T_a/T_1

In case of piping, because is generally avoided any yielding phenomenon in the pipes, the dissipation capability is generally restricted only to the supporting structure and the relative response modification factor depends on its structural configuration. In some cases dissipation phenomena may have place also in the pipes and a specific behavior factor have to be defined if the elastic analysis with response spectra is used.

The behavior factor provided by the codes, especially by the American one, seems to be overestimated. For example, ASCE-07 prescribes the use of a behavior factor 6 or 12 according to the deformability of the material used. In some cases this hypothesis may not be totally true.

For example Okeil and Tung in 1996 [15] using an idealized piping system have suggested a closed-form formula that provides the reduction factor q as function of the ductility of the support structure, μ, and the ratio f of the piping frequency and the frequency of the seismic action. The reduction q increases with the ductility, μ. Moreover, the stiffer is the piping system (low values of f) the higher is q. In any case q is never greater than 3-4. These results are in contrast with the provisions of ASCE-07.

Code	Expression	note
ASME B31.3 (ASCE-07)	$F_p=I_p\frac{0.4a_pS_{DS}W_p}{R_p}AF$ $AF=\left(1+2\frac{z}{H}\right)$	*a_p=2.5 (Tab. 13.6-1)* *S_{DS}=Maximum spectral acceleration* *W_p=Weight of the pipe* *z=height where the pipe is placed* *H=total height of the pipe-rack* *I_p=Importance factor* *R_p=response factor*
EN13480:3 (EC8)	$F_a=I_p\frac{a_gSW_p}{R_p}AF$ $AF=\left[\frac{3\left(1+\frac{z}{H}\right)}{1+\left(1-\frac{T_a}{T_1}\right)^2}-\frac{1}{2}\right]$	*a_g=Peak Ground Acceleration* *S=soil factor* *T_a=fundamental period of the pipes* *T_1=fundamental period of the pipe-rack*

Table 4 In-Structure spectra definitions

Other authors reached similar conclusions as well. For example in [16] the authors investigated on the dynamic response of a piping system on a rack with gap and with friction. By using dynamic harmonic analysis on a simple system they found that in presence of nonlinearity (friction between pipes and rack) the reduction of the acceleration with respect to the elastic case could be of the order of 2-3, value suggested also by the American Lifelines Alliance [7] and FEMA 450.

Instead of using static method employing seismic force of Tab. 4, a dynamic approach is also possible, using generated floor response spectra, whose shape is based on typical Soil-Structure interaction theory. For industrial piping systems few contributions have been found in literature [2], [3], [4], [17].

For the case study of Fig. 4**,** floor spectra have been generated by using time-history analysis. Fig. 15 shows the floor spectra for one the three accelerograms used in Time-History analysis (see next section), from which is clear the filtering effect of the pipe-rack. The maximum amplification is now restricted to the range 2-3 Hz, whereas in the ground acceleration spectra was placed in the range 2-6 Hz. The labels Frame 1, 3 and 5 correspond to the labels of the frames indicated in Fig.10. It is also possible to note the variability of the maximum amplification effect within the structure. The maximum acceleration peak is found at frame 3; this because more mass is placed there with respect to the other frames.

Because the natural frequencies of the piping systems are in the range 15-40 Hz the amplification effect due to the inertia is very limited. In fact, the maximum acceleration applied to the pipes corresponds more or less to the maximum acceleration at floor in which the pipes are placed, some peaks a part, at frequency 7 and 10 Hz.

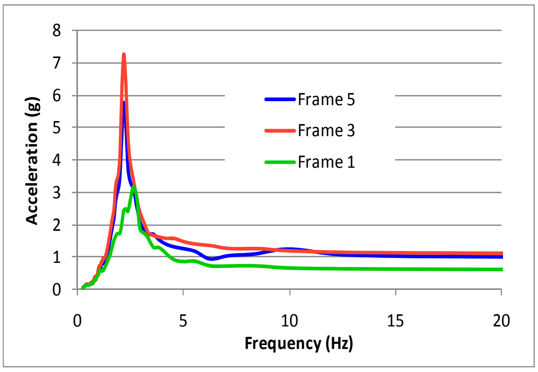

Figure 15 - Case study - Spatial variability of the floor spectra for the El-Centro earthquake

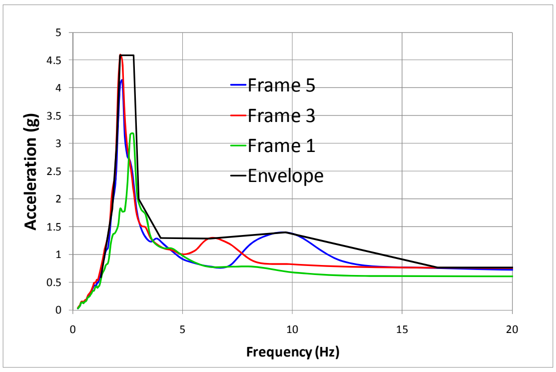

Figure 16 - Case study – Mean floor spectra for several frames and Envelope Floor Spectrum

A possible representation of floor spectra for the case-study is shown in Fig.16 as envelope of the mean spectra at several frames. This allows to account for the spatial variability of the action and its frequency content. This has been used to get the response of the pipes analyzed individually.

Time history analysis

A time history seismic input is rarely used for the design or retrofit of piping systems. Often it is used to generate facility specific response spectra analyses, or as a research tool, to study in detail the behavior of a component or system as a function of time.

Nowadays, the scientific community has widely accepted the use of natural records to reproduce a real input, for several reasons. For many engineering application, the purpose of selection and scaling of real earthquake is to fit the code design spectrum considering the seismological and geological parameters of the specific site. To comply with the seismic codes set of accelerograms, regardless its type, should basically match the following criteria:

- minimum of 3 accelerograms should be used;
- the mean of the zero period spectral response acceleration values (calculated from the individual time histories) should not be smaller than the value of ag× S for the site in question (S is the soil factor, ag is the Peak Ground Acceleration);
- in the range of periods between 0.2 T_1 and 2 T_1, where T_1 is the fundamental period of the structure in the direction where the accelerogram will be applied, no value of the mean 5% damping elastic spectrum, calculated from all time histories, should be <90% of the corresponding value of the 5% damping elastic response spectrum.

To help engineers in selecting a proper set of records, some tools have been proposed in the literature. The most recent is REXEL proposed by Iervolino et al [18].

More rarely artificial or synthetic accelerograms are used. The first ones are generated to match a target response spectrum, the second ones form from seismological source models and accounting for path and site effects. For artificial signals, even though, it is possible to obtain acceleration time series that are almost completely compatible with the elastic design spectrum, the generated accelerograms often have an excessive number of cycles of strong motion, and consequently have unrealistically high-energy content. For this reason are less used than natural records. Moreover, to generate synthetic accelerograms there is a need for a definition of a specific earthquake scenario in terms of magnitude, rupture mechanism in addition to geological conditions and location of the site. Generally, most of this information is not often available, particularly when using seismic design codes. This representation of a seismic input is rarely used.

According to the above considerations it has been decided, at least for this preliminary analysis, to use natural records and to select only three accelerograms compatible with the spectra of Fig. 13. For the case study the vertical component has been considered as negligible, so only bi-directional motion has been adopted.

The three records were taken from Pacific Earthquake Engineering Research center database (http://peer.berkeley.edu), using the following hazard and compatibility conditions (Tab. 5). In Tab. 6 the characteristics of all the selected accelerograms are shown. Fig. 17 and 18 show the elastic spectrum of two records.

Magnitude Mw	**Soil conditions**	**Distance (Km)**	**PGA (g)**	**Lower bound**	**Upper bound**
6÷7	D	0÷20	0.24	-10%	+30%

Table 5 – Hazard and compatibility conditions for natural record selection

Event	Data	Mag.	Dist. (Km)	Filter (Hz)	name
Imperial Valley	19/05/1940	7.2	13.0	0.20	El-Centro
Northridge	15/01/1994	6.7	27.6	0.14	Santa Monica
San Fernando	02/09/1971	6.6	24.0	0.50	Old Ridge

Table 6 - List of the three selected natural records

After the identification of the accelerograms, the direct integration of the equation of motion or the integration of the single modal oscillators (time-history modal analysis) can be performed. This latter is used when a limited non-linearity is present in the structure during the seismic event. Most frequently a direct integration scheme is used.

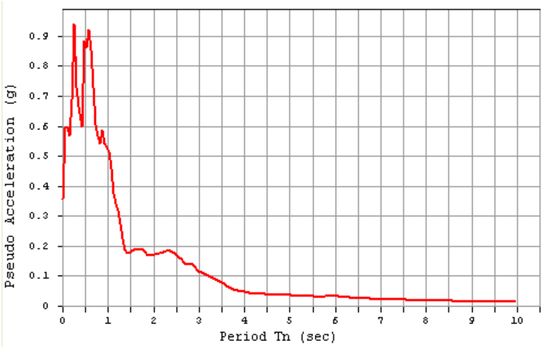

Figure 17 – Elastic spectrum of the El-Centro earthquake

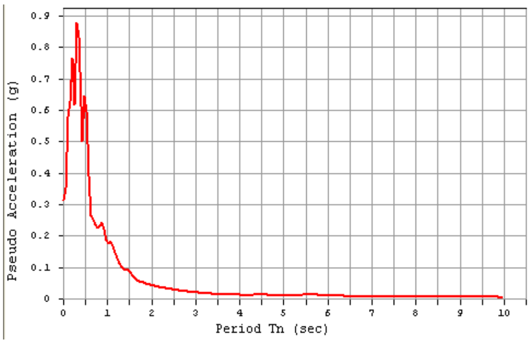

Figure 18 – Elastic spectrum of the San-Fernando earthquake

Differential movement effects

No specific indications are provided by the codes for the differential movement between two supports or between adjacent structures. Only ASCE-07 provides a simplified criterion based on the elastic analysis of the pipe-rack. Chapter 13.3.2.1 suggests evaluating the relative displacements between two connection points within the structure and at the same level using the differential movement for each vibration modes combined using appropriate modal combination procedures.

Unlike the cases of differential movements between adjacent pipe-racks connected by pipes, this effect on pipes within the structure is usually neglected. As observed above, the complete model, pipes + pipe-rack, allows to automatically accounting for this effect.

4.3 Calculation of the seismic response of the case study

The seismic analysis results of the analysed piping system using both static and dynamic methods previously described are illustrated herein.

For each analysis method the results in terms of moments are provided. In particular the maximum local moments M_y and M_z are provided for the straight pipes at each bay (1 to 7) and for the more critical elbows indicated in Fig. 10 with red circles (points A and B)

In Fig. 19 is shown, for the design conditions (PGA=0.24g, q=4, ξ=3%) the seismic response of the entire structure in terms of moments, shear and axial force for soil condition B and E, obtained using response spectrum analysis.

The maximum moment in the steel columns is about 220 kNm, very far from the ultimate moment of the steel elements. Similar results have been obtained by using T-H analysis. Therefore the support structure can be considered safe against the ultimate limit state. The soil conditions have also a limited effect both in the rack and in the pipes.

For the above observation, in what follows only the soil condition D, relative to the design conditions of the case study, have been considered.

In Tab. 7 the result of the seismic analysis of the case study of Fig. 1, in terms of bending moment in the pipes are shown. They have carried out at the several bays of the steel frame and at top floor and have obtained using all the aforementioned methods. In particular the values of damping (5%), behavior factor (q=4) and Importance factor (I_p=1.5) provides by the EN13480:3 standard and prEN1998:1 code have been used.

Firstly, a marked underestimation of the bending moment in the pipes using in-structure spectra is noticed. This is probably due to the limited mass of the pipes, which amplifies the relative displacement effects between the different support points of the pipes. In fact, by using the response spectrum method the bending moments have in mean double values.

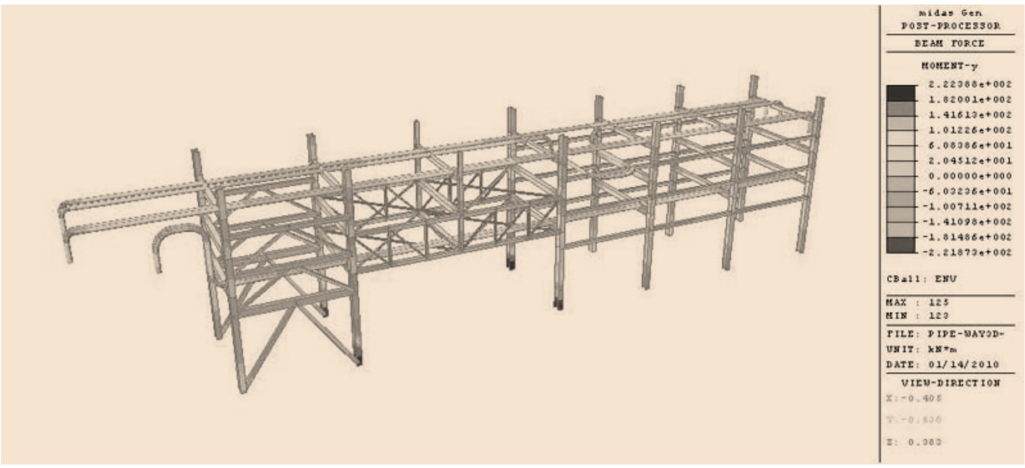

Figure 19 - Response Spectrum Analysis: Moment distribution for the Eurocode 8-1 Spectra with ξ=3%, ag=0.24g, q=4 and Soil D.

The use of dynamic analysis instead of the static one produces slight differences when in-structure spectra are used. This is due probably to the uniform distribution of the seismic force in the first case, whereas, in the second case, the distributions related to the several vibration modes is used. But substantially they provide similar results.

The time-history analysis on the elastic system produced greater values of bending moments. This is due to the absence of non-linear behavior of the structure. Because by applying to the response a reduction factor of 4, the results becomes not far to the results obtained with the response spectrum analysis and q=4, they should be considered reasonable. Further analysis will be dedicated to this aspect, modelling the analyzed structure in the non-linear range.

Method	Bay/Moment	1	2	3	4	5	6	7
Static analysis: In-structure spectra method	**M_z**	2.88	2.40	2.52	2.64	2.76	2.76	2.88
	M_y	1.56	1.56	1.20	1.32	1.44	1.20	1.44
Dynamic analysis: In-structure spectra method	**M_z**	2.10	2.30	2.30	3.10	3.30	3.00	2.30
	M_y	2.20	2.10	2.10	2.20	1.90	1.90	1.00
Dynamic analysis: Response spectrum method	**M_z**	5.30	5.50	5.50	3.50	2.90	4.80	5.80
	M_y	2.80	2.60	3.60	3.20	2.20	0.70	3.80
Dynamic method: Time-History analysis (elastic)	**M_z**	13.50	14.60	14.10	5.05	6.25	14.15	12.32
	M_y	7.30	6.65	4.45	4.65	3.05	1.70	3.85

Table 7 – Results relevant to the seismic analysis of the case study

4.4 Piping stress analysis and checks

One of the fundamental steps for the qualification of a pipe system is the fulfillment of some limits of the pipe stress or strain, for a given working condition. For a seismic action, usually two working conditions are considered:

- Operating condition or design basis earthquake condition: (OBE) is that earthquake which, considering the regional, local geology and seismology, could be reasonably expected to affect the site during the operating life of the plant. It is the earthquake during which the operating conditions of the plant can be still assured.
- Safe shutdown earthquake condition: (SSE) is the maximum ground motion for which some critical components of the plant must be designed to remain functional.

In order to evaluate the safety level stress-based or strain-based approach can be used. The first approach intends to evaluate the maximum stress in the pipes and the calculation is usually based on elastic analysis of the structure.

While stress based approach for pipelines is acceptable for a material with a well defined yield point and with a well defined yield ductility and strength, this design criteria becomes invalid when the stress in pipelines exceeds the limit under some displacement control loads, such as earthquakes and landslides [19]. In this case, strain based approach provides the design rule where the strain in the pipeline is allowed to exceed the specified yield strain provided that the safe operation can be ensured under displacement load. This method allows selected extensions to the stress-based design possibilities to take advantage of steel’s well-known ability to deform plastically, but remain a stable structure. Codes and Standards are available for the strain based design approach, see [19] for reference. With the strain-based approach maximum strain in the pipes is calculated and compared with specified strain-limits related to limit states usually identified with buckling or ovalization of the pipes. Unfortunately, this approach needs of the calculation of the seismic response in the non-linear range. This is one of the reasons because the stress approach in more used.

Only EN13480 contains explicit indications for calculating the pipe stresses limits, considering both the above conditions (OBE and SSE), whereas ASME B31.3 indicates only occasional load conditions that can be identified as OBE condition.

For the verification of the pipes against earthquake, the allowable stress approach is usually adopted and will be also adopted in the following.

Load combinations and stress calculation

The response to seismic and other loads (sustained, thermal, pressure, etc..), have to be combined. European and American code prescribe similar combinations. In this respect the seismic load prescribed by the seismic codes (prEN1998:1 and ASCE-07) can be considered as an exceptional seismic action. Under this condition, usually Load and Resistance Factor design (LRFD) approach is adopted. If the allowable stress approach is used, the seismic action has to be reduced, as usual, of a certain safety factor, typically 1.4 (see ASCE-07).

Because the allowable stress approach is wildly diffused in piping design in the following section will be used for the calculation of the stresses and the verification of the safety level. In doing this, the ASCE-07 combination formula will be adopted.

ASME B31.3 does not provide an explicit equation for calculating the longitudinal stress, whereas EN13480 provides at point 12.3.3 the formula to evaluate the longitudinal stresses due to sustained, occasional and exceptional loads (e.g. the earthquake). This comes from the beam theory and includes internal pressure P and the resultant moments due to the sustained loads (MA) and the earthquake (MB):

$$\sigma = \frac{pD}{4t} + 0.75 \times SFI\,\frac{M_A + M_B}{Z} \tag{1}$$

where *SIF* is the stress intensification factor.

Because ASME B31.1 provides a similar expression of the stress, in the following this will be also adopted for ASME B31.3.

ASME B31.3 at point 319.4.4 indicates the way to calculate the resultant moments, similar to that of EN13480:3. In particular:

$$M_R = \sqrt{\left(SIF_y \times M_y\right)^2 + \left(SIF_z \times M_z\right)^2} \tag{2}$$

This definition has also been adopted for calculating the resultant moments using EN13480.

The resultant moment and the maximum stress in the pipes using the results of spectrum analysis have been calculated for both European and American standards. In particular, the maximum stress obtained is lower than 71 MPa in the straight pipes (bay 7) and 135 MPa in the elbows (B). The stress level here calculated is greater than that determined using in-structure spectra. In any case the stresses are limited and the piping system can be considered as overdesigned.

Studies have shown that the present standards for piping system design under seismic loads are over conservative and modifications have been proposed to relax this over conservatism [20],[21]. For example, [21] has applied the present codes to calculate the stress limit on piping systems and experimental results showed significant discrepancy from the real behavior. This aspect will be treated in further studies.

Definition of the allowable stress

EN13480 includes par. 12.3.3., which is dedicated to the definition of the allowable stress calculation. They are defined according to the conditions previously recalled: Operating Basic Earthquake (OBE) and Safe Shutdown Earthquake (SSE). The basic inequality to be respected is:

$$\sigma \le k f_h \tag{3}$$

where

σ = maximum stress in the pipes due to the sustained and seismic loads.
k = 1.2 for design basic earthquake
k = 1.8 for safe shutdown earthquake
f_h = is the basic allowable stress given by code

ASME B31.3 does not provide explicit differentiation between OBE and SSE but refers to a Design Earthquake that can be identified with the OBE. It is prescribed that the maximum stress cannot be greater than 1.33 times the basic allowable stress for pipes, indicated in the Appendix A of the same code.

Code	OBE	SSE
EN13480	165.60	248.40
ASME B31.3	183.50	---

Table 8– Pipes allowable stress (MPa) for the analysed case study

Tab. 8 illustrates the capacity of the pipes evaluated using both OBE and SSE seismic condition. The comparison capacity and demand show that the verification is satisfied with a different capacity/demand ratio ρ. In particular, for EN13480 ρ=1.39 whereas for ASME B31.3 is equal to 1.36. This values of ρ show, at least in the analyzed case, a slight difference between the two codes in the evaluation of the safety level.

The above calculations confirm that using allowable stress approach and then comparing the capacity with the demand (OBE), the system is highly overdesigned. The attempt of some researchers to modified the equation (1) [21],[22] is not enough fully exploit the plastic properties of pipes. In this sense the strain-based approach is more promising, especially if the Performance-Based approach would be used to design new pipelines or to assess the seismic behavior of existing ones. This is the reason that has induced to explore the plastic behavior of pipes and pipe-joints using the way of experimental investigation. This activity has been just started and in the following section some details of on-going tests on flanged joints will be provided.

5 EXPERIMENTAL INVESTIGATIONS

5.1 Previous experimental tests

A good number of experimental tests have been performed to characterize piping systems under seismic loading and they are available in literatures, e.g., [20],[21],[22],[23],[24]. It has been found that even strong seismic excitation is not severe enough to significantly damage piping systems unless there is large differential motion of the anchorage [20], and an extremely high level of seismic input is required to introduce damage in the components of a piping system [21]. Additionally, the use of isolation systems reduces seismic demands to the piping systems [22]. Experimental tests, e.g., [20],[23] clearly show that the present design criteria of pipeline under seismic loading are overly conservative and modifications are suggested [20].

Some experimental tests have also been devoted to bolted flange connections in order to assess their behaviour under external loading, e.g., axial and bending loadings [25],[26]. Results show that flanges with lower weights, e.g., a compact VERAX VCF flange joint, have the advantage over the flanges with higher weights, e.g., an ANSI flange joint [25].

5.2 Tests to be performed in the University of Trento

The University of Trento (UniTn) will perform some experimental tests on a number of bolted flanged joints (BFJ) in order to investigate the behaviour of the joints (BFJ) under monotonic and cyclic loadings. These tests are parts of the research works of a European project, INDUSE.

Instead of using conventional thicker joints, two different thinner joints have been designed for the tests due to the fact that thinner joints are expected to exhibit better performance for regular seismic events and for relatively lower working pressure. The two designed flanges have thicknesses 18 mm (Design 01) and 27 mm (Design 02), respectively and have been designed for a pressure of 15 bar. A matlab code has been developed by UniTn to check the joints according to the Eurocode EN 1591-1. One of the joints (Design 02) satisfies the Eurocode EN 1591-1 while the other (Design 01) does not. UniTn aims at performing these experimental tests on these thinner flanges in order to characterise their behaviour in real operating conditions and to check the validity of the design rules of the Eurocode for the flanged joints.

5.3 Test set-ups and programs

Eight experimental tests on BFJs will be performed by UniTn. The test programs and loading protocols are presented in Table 9. On each type of joint four tests will be performed, two of them will be in bending loading and the other two will be in axial loading. In both of the axial and bending tests, there will be monotonic and cyclic loadings. The cyclic loading will be chosen according to ECCS 45 loading protocols [27]. The monotonic and cyclic loading protocols are presented in Fig.21. The load in the BFJs will be applied via 100 ton actuators.

(a) (b)

Figure 20: Two plate-flanges designed by UniTn for the experimental tests: a) Design 01 for a flange thickness of 18 mm, and b) Design 02 for a flange thickness of 27 mm.

Design Code	Flange Type	Type of loading		No of Tests	
Non-Standard (Design Code- EN 1591)	Plate (Design 01*)	Axial	Monotonic	2	4
			Cyclic (ECCS 45)		
		Bending	Monotonic	2	
			Cyclic (ECCS 45)		
	Plate (Design 02*)	Axial	Monotonic	2	4
			Cyclic (ECCS 45)		
		Bending	Monotonic	2	
			Cyclic (ECCS 45)		
Total No of Tests					**8**

Table 9: Number and types of tests on bolted flanged joints to be performed by UniTn

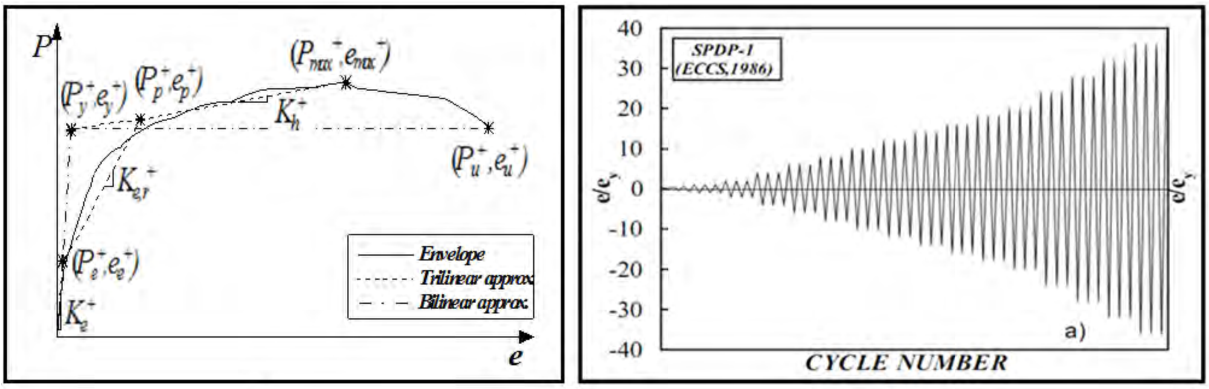

a b

Figure 21: (a) Monotonic and (b) cyclic loading protocols for the tests on bolted flanged joints.

The test set-ups for bending and axial tests are presented in Fig. 22 and 23 respectively while the real test specimens are shown in Fig. 24 and 25.

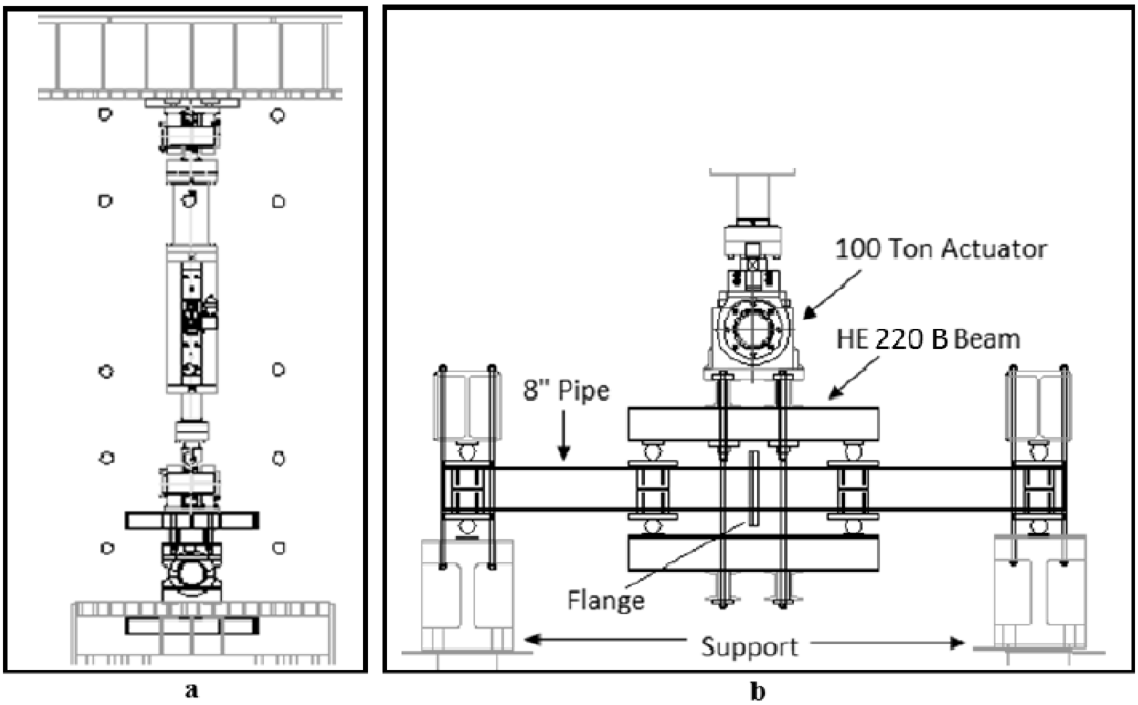

Figure 22: Set-up for bending tests: (a) front view; (b) side view.

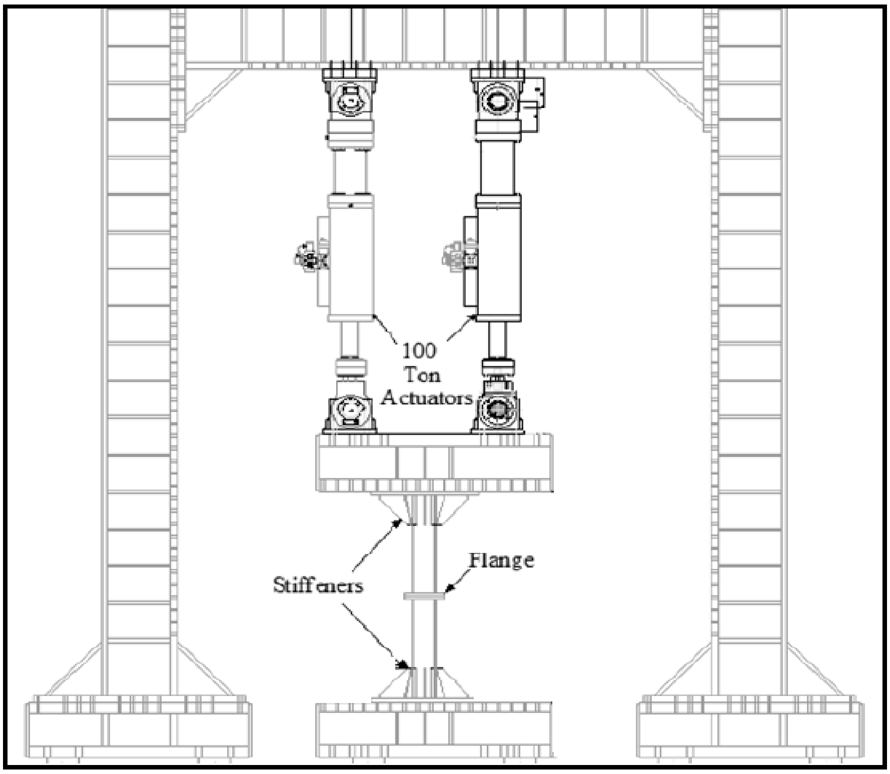

Figure 23: Set-up for axial tests.

Figure 24 Test specimens for: (a) bending tests; (b) axial tests.

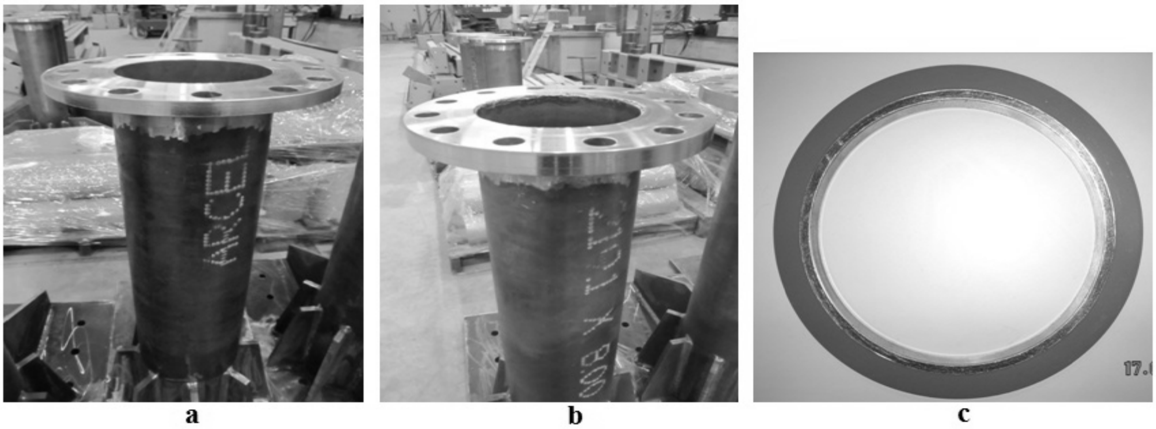

Figure 25 : (a) Flange with 18 mm thickness (Design 01); (b) flange with 27 mm thickness (Design 02); (c) a gasket

6 CONCLUSIONS

The seismic analysis of piping systems is very different from the analysis of like-building structures for which a long experience has permitted to have enough provisions for obtaining a reliable design against earthquakes. Therefore, the present contribution tried to clarify all the design steps of this type of structures and to identify all the aspect that need to be clarified. This was made through a representative case study analysed according to both European (EN13480:3) and American standards (ASME B31.3) devoted to piping systems. The comparison between EN13480 and ASME B31.3 standards showed that the two codes provide similar indications for the evaluation of the seismic response of pipelines supported by a pipe-rack. From the analysis of the results the following conclusions, considered valid for both the standards, can be drawn.

ASCE-07 provides a simple rule to establish when the dynamic coupling between pipes and supporting structure need to be considered. It is based only on a weight ratio. Actually, other ingredients should be included; for example the vibration periods range of the pipe. In the analysed case the single pipe has a limited weight and therefore short vibration periods. This means that, as already shown, the dynamic coupling between pipes and the pipe-rack is limited; whereas the relative displacements between the pipe supports would represent a more relevant effect. The pipes provide a sort of static coupling between the transverse frames. In fact, the models with and without the pipe stiffness contribution have more or less the same period, whereas the excited mass is differently distributed between the several vibration modes. Therefore, the consequence of considering the structural contribution of the pipes is the introduction of a sort of a rigid floor effect that couples the horizontal movements of the nodes of the same floor. For the above-mentioned reasons an extensive analysis on this particular but important aspect is recommended.

The in-structure spectra suggested by prEN1998:1 and ASCE-07 differs for a term that depends on the pipe-structure frequency ratio, included only in the European code. This aspect is strictly related to the previous observation on the dynamic coupling. The exclusion of the dynamic interaction could introduce a high error in the evaluation of the amplification factor of in-structure spectra. Because usually the frequency of the piping system is relatively high with respect to that of the supporting structure, the amplification effect would be relatively low. In any case, to cover all the possible cases, the use of the European formula for in-structure spectra is highly recommended. The result of this investigation suggested at point 1, should also help to clarify this important aspect toward the direction of simplified but more realistic formulas for in-structure action on pipes.

In the analysis both beam element and shell elements were used to model elbows. The comparison showed the reliability of the more simple elements based on the beam theory, at least for the simple case of elbows. For more complicated situations, the use of finite shell elements should be considered.

The behavior factor q is usually indicated by standards. In particular the values provided for piping systems by ASCE-07 seems to be too high, i.e., q=6-12. This is in contrast with the idea of avoiding yielding phenomena in the pipes and to maintain operational conditions also in case of strong seismic events. Certainly, the contribution of the supports in providing dissipation capability should be taken into account; however on the basis of several investigations found in the literature, this exclude the possibility of having so high values of q. For this reason the next step will be an investigation on the reduction factor q also considering the non-linear behaviour of pipes. This could be performed using non-linear beam elements for the straight pipes, and plastic hinges for the simulation of the elbows in the plastic range. In doing so, time-history analysis would be used, even if static non-linear analysis is nowadays very diffused, but difficult to be applied to piping systems for the presence of a uniformly distributed mass of pipes.

The usual way of designing piping systems is based on the allowable stress approach. This means that the structure is considered elastic. Consequently only an operating basis earthquake condition (OBE) can be taken into account for design. Conversely, the modern approach to the seismic design of structures is to differentiate serviceability from ultimate limit states. This latter condition could be represented, for example, by the Safe Shutdown Earthquake (SEE). The problem is that a proper definition of the deformation capability of the pipes and fittings (ovalization, etc..) in the plastic range would be necessary, and on this aspect the research has not reached solid conclusions. But the advantages would be several and first of all the design optimisation. For example in the analysed case, we are very far from the moment capacity of the bolted flanges located in the pipeline. This high level of conservatism seems to be in contrast with the modern performance based-design approach, for which a certain level of yielding in the structure is admitted according to a specific performance. For instance, it would be possible to accept in pipes a certain level of yielding on the condition that leakage would not occur, and the consequence, for example, to accept a reduction of the thickness of the flange. The experimental campaign, briefly described in the paper and that will be performed at the University of Trento in order to evaluate the cyclic behavior of flanged joints, will provide useful information for the design of the flanged joints in the more proper way. Moreover, it should allow one to link the capacity and the demand for several limit states.

ACKNOWNLEDGMENTS

This work was carried out with a financial grant from the Research Fund for Coal and Steel of the European Commission, within the INDUSE project: “STRUCTURAL SAFETY OF INDUSTRIAL STEEL TANKS, PRESSURE VESSELS AND PIPING SYSTEMS UNDER SEISMIC LOADING”, Grant No. RFSR-CT-2009-00022.

REFERENCES

[1] Suzuki K., 2006 Earthquake Damage to Industrial Facilities and Development of Seismic and Vibration Control Technology – Based on Experience from the 1995 Kobe (Hanshin-Awaji) Earthquake –Journal of Disaster ResearchVol.1 No.2, 2006, Journal of System, Design and Dynamics, N. 2, 1, 2008. 1-11

[2] Halil Sezen, M.ASCE; and Andrew S. Whittaker, M.ASCE, Seismic Performance of Industrial Facilities Affected by the 1999 Turkey Earthquake, Journal of Performance of Constructed Facilities, Vol. 20, No. 1, February 1, 2006. ©ASCE, ISSN 0887-3828/2006/1-28–36/$25.00.

[3] Sassan Eshghi and Mehran Seyed Razzaghi, The Behavior of Special Structures During the Bam Earthquake of 26 December 2003, JSEE: Special Issue on Bam Earthquake, 197-207.

[4] 2007 Niigata Chuetsu-Oki Japan Earthquake, Reconnaissance Report, http://www.grmcat.com/images/Niigata-Chuetsu-Oki-Japan-Report.pdf

[5] EN13480-3- Metallic industrial piping - Part 3: Design and calculation, June, 2002

[6] ASME Code for Pressure Piping, B31 - ASME B31.3-2006 (Revision of ASME B31.3-2004)

[7] American Lifelines Alliance - Seismic Design and Retrofit of Piping Systems, 2002.

[8] Guidelines for the Seismic Design of Oil and Gas Piping Systems, Committee on Gas and Liquid Fuel Lifelines of the ASCE Technical Council on Lifeline Earthquake Engineering, 1984

[9] Azizpour O, Hosseisni M. (2009). A verification of ASCE Recommended Guidelines for seismic evaluation and design of combination structures in petrochemical facilities, J. of Applied Sciences.

[10] Asfura, A. and Kiureghian, A. D. (1986), Floor response spectrum method for seismic analysis of multiply supported secondary systems. Earthquake Engineering & Structural Dynamics, 14: 245–265. doi: 10.1002/eqe.4290140206

[11] Burdisso, R. A. and Singh, M. P. (1987). Multiply supported secondary systems part I: Response spectrum analysis. Earthquake Engineering & Structural Dynamics, 15: 53–72. doi: 10.1002/eqe.4290150105

[12] A. Saudy, A. Ghobarah, T.S. Aziz, A modified CCFS approach for the seismic analysis of multiply supported MDOF secondary systems, Nuclear Engineering and Design, Volume 133, Issue 2, March 1992, Pages 183-197, ISSN 0029-5493, DOI: 10.1016/0029-5493(92)90179-Y

[13] DeGrassi, G. and Hofmayer, C. (2005). “Seismic analysis of simplified piping systems for the NUPEC ultimate strength piping test program,” NUREG/CR-6889, by Brookhaven National Laboratory for the US, Nuclear Regulatory Commission, December, 2005.

[14] MIDAS [2010] - Gen 2010 (v1.1), Midas Information Technology Co. Ltd., 2010

[15] Okeil A., Tung C., (1996), Effects of ductility on seismic response of piping systems and their implication on design and qualification, Nuclear Engineering and Design,166: 69-83

[16] Kobayashi H., Ochi Y., (1989), Dynamic response of piping system on rack structure with gaps and friction, Nuclear Engineering and Design,111: 341-350

[17] Ajaya K. Gupta, Jing-Wen Jaw, A new instructure response spectrum (IRS) method for multiply connected secondary systems with coupling effects, Nuclear Engineering and Design, Volume 96, Issue 1, September 1986, Pages 63-80, ISSN 0029-5493, DOI: 10.1016/0029-5493(86)90162-7.

[18] Iervolino I., Galasso C., Cosenza E. (2009). REXEL: computer aided record selection for code-based seismic structural analysis. Bulletin of Earthquake Engineering, 8:339-362. DOI 10.1007/s10518-009-9146-1

[19] Liu Bing, Liu X.J. and Zhang Hong, Strain-based design criteria of pipelines, Journal of Loss Prevention in the Process Industries 22 (2009) 884-888.

[20] Touboul F., Sollogoub P., Blay N., Seismic behaviour of piping systems with and without defects: experimental and numerical evaluations, Nuclear Engineering and Design 192 (1999) 243–260.

[21] Touboul F., Blay N., Sollogoub P., Chapuliot S., Enhanced seismic criteria for piping, Nuclear Engineering and Design 236 (2006) 1–9.

[22] Huang Yin-Nan, Whittaker Andrew S., Constantinou Michael C., Malushte Sanjeev, Seismic demands on secondary systems in base-isolated nuclear power plants, Earthquake Engineering and Structural Dynamics, Earthquake Engng Struct. Dyn. 2007; 36:1741–1761.

[23] Blay N., Touboul F., Blanchard M.T., Le Breton F., Piping seismic design criteria: experimental evaluation, 14th International Conference on Structural Mechanics in Reactor Technology (SMiRT 14), Lyon, France, August 17-22, 1997.

[24] DeGrassi G., Nie J., and Hofmayer C. Seismic analysis of large-scale piping systems for the JNES-NUPEC; ultimate strength piping test program. Office of Nuclear Regulatory Research, 2008.

[25] Nash D.H., Abid M., Combined external load tests for standard and compact flanges, International Journal of Pressure Vessels and Piping 77 (2000) 799-806.

[26] Semke William H, Bibel George D., Jerath Sukhvarsh, Guravb Sanjay B., Webstera Adam L., Efficient dynamic structural response modelling of bolted flange piping systems , International Journal of Pressure Vessels and Piping 83 (2006) 767–776.

[27] ECCS, Recommended testing procedures for assessing the behaviour of structural steel elements under cyclic loads. 1986; 45, Technical Committee 13.

COMPDYN 2011
III ECCOMAS Thematic Conference on
Computational Methods in Structural Dynamics and Earthquake Engineering
M. Papadrakakis, M. Fragiadakis, V. Plevris (eds.)
Corfu, Greece, 25–28 May 2011

THE STRAIN-BASED DESIGN OF BURIED PIPELINE SUBJECTED TO LANDSLIDES

Bing LIU [1]***, Zhangzhong WU*** [1]***, X.J., Liu*** [2]**, and *Hong Zhang*** [3]

[1] R&D Center of PetroChina Pipeline Company
Road Jinguang 51, Langfang, Hebei Province, 065000, P.R. China
kjliubing@petrochina.com.cn

[2] Liu Advanced Engineering, LLC
Houston, TX 77094-7831，USA

[3] China University of Petroleum-Beijing
Fuxue Road 18, Changping, 102249 Beijing，P.R.China

Keywords: Pipeline; strain-based design; strain limit; landslide.

Abstract. *In recent years, a number of projects have been funded in China to quantitatively evaluate the tensile and compressive strain limits of pipes and apply these limits to buried pipelines subjected to landslides. This paper covers the technical basis of strain-based design for pipelines subjected to landslides. First, finite element analyses (FEA) were conducted for a total of 594 cases covering a wide range of materials, ratios of pipe diameter to wall thickness, D/t and various internal pressures. By using the calculated data, parametric equations for strain limits of pipelines were developed. FEA analyses were also conducted for 8 cases of buried pipelines subjected to landslides. An approach for design of buried pipelines subjected to landslides using strain-based design was also proposed. It is believed that the above applications may lay the initial base of using the strain-based design method for buried pipeline subjected to landslides for pipelines in China.*

1 INTRODUCTION

With the rapid development of oil and gas pipeline industry, new trend is showing on pipelines for long-distance, large-diameter and high-operating-pressure. This requires the corresponding pipeline design guidelines and criteria to be adapted to these new situations. In the design step, not only the safety and reliability of pipeline but also its economic and efficient operation should be ensured. Most of the existing pipeline design codes are based on limiting stress criteria, which is considered acceptable for steel with a well defined yield point and a well defined ductility and strength. But the stress in pipelines may exceed the limit under some situations, such as earthquakes, landslides, and some displacement-controlled loading, such as that in laying of the submarine pipelines. In these situations, the strength design criteria based on stress is no longer valid.

Stress-based design criteria are based on the minimum yield stress for the pipeline, while strain-based design criteria are based on limit state design in displacement-controlled loading. If the safe operation can be ensured under displacement-controlled loading, the pipeline strain is allowed to exceed the specified yield strain. Although some plastic deformations occur in the pipeline, the pipeline is able to meet the operation requirements with higher operating capacity. Using stress-based design method supplemented with strain-based design method, the deformation capability of pipelines can be fully applied in security and economic design.

Limit state is a state beyond which the structure no longer satisfies the design requirements. Both Det Norske Veritas (DNV, 2000) and Canadian Standards Association (CSA, 2007) use limit state method for pipeline design. There is slightly difference in state limit classification between these codes. In DNV-OSF101 (2000), four kinds of state limits are recognized. They are serviceability limit state, ultimate limit state, fatigue limit state and accidental limit state. When limit state method is applied to the pipeline design, appropriate design criteria are presented in order to make less conservative and more flexibility for the designers.

There are many different classifications on loadings for the pipelines. Displacement-controlled loading can be defined specifically as a loading that can be reduced to zero by a change in the shape of the part of interest. On contrary, a load-control loading cannot be reduced to zero by a simple change in shape. Bigger strain may be allowed to displacement-controlled loading. The loading on a pipeline may generally be a combination of load and displacement controlled. The pressure loading is load controlled, while the soil motion around a pipeline usually causes displacement-controlled moments.

A number of natural gas and petroleum pipelines have been or will be constructed across ancient and currently active landslides in China. The pipelines studied in this paper cross numerous areas of active or potential active landslides that pose a threat to pipeline integrity. The interaction of the moving soil with the pipeline redistributes the axial force along the pipe, increasing tension in some locations and compression in others. It can also increase pipeline curvature, which induces tensile strain in half of the pipe cross-section, and compressive strain in the other half. If unmitigated, excessive tensile strain can lead to pipeline rupture. Large compressive strain may cause buckling, usually accompanied by formation of wrinkles that can rupture due to material fatigue or severe yielding.

The general framework for the application of strain-based design has been the subject of considerable researches during the past twenty years. This work has been achieved through the publication of limit state design rules for submarine pipelines. Det Norske Veritas in 1982 proposed the use of combined stress-based design criteria and strain-based design criteria. In 1996 Det Norske Veritas published a subsea pipelines limit state design criteria with many analytical methods based on a variety of load conditions. In the same year, the Canadian

Standards Association (CSA) published CSA Z662-96 (1996), which comprises strain-based design criteria for submarine pipeline design and the limit state design.

Several codes have provisions that apply of strain-based design to pipelines, including DNV-OS-F101, CSA-Z662, API RP 1111-1999, ASCE, ASME B31.8., API 1104 and ABS 2001. These codes can be placed in three general categories: those that provide a comprehensive overall pipeline standard that includes requirements both for stress-and strain-based design (DNV 2000, CSA Z662-2007), those that specifically allow strain-based design but do not provide extensive provisions related to strain-based design (B31.8, API 1104), and those provide information on strain-based design related to a specific subgroup of pipelines (ABS 2001, API RP 1111). Several organizations have current research projects that will be released to the public domain after their completion in areas that directly or indirectly impact strain-based design of pipelines. The Minerals Management Service (MMS) and the Office of Pipeline Safety (OPS) of USA co-funded EWI (2003) to provide a general guidance on strain-based design for pipelines both for the on- and off-shore environments. DNV and other organizations (Wang, Rudland and Denys, 2002; Wang and Chen, 2004; Dinovitzer and Brian, 1996; Brian and Dinovitzer, 1993; Liu, Liu and Zhang, 2007) also have some research projects about it.

In the present work the control factors of tensile and compressive strain limits of pipelines were examined first. Based on the available experiment data of full scale pipe tests under the axial tensile strain and internal pressure loading, a valid finite element model was found. Finite element analyses were conducted for a total of 711 cases covering a wide range of material, girth weld mismatch and various internal pressures. Some parametric equations were developed based on FEA. The safety factors and appropriate limits for the parametric equations have been determined based on extensive experimental data. FEA was then carried out for 8 cases of buried pipeline subjected to landslides. These examples were used to verify the method used for strain-based design of pipelines. An approach for design of buried pipelines subjected to landslides using strain-based design was also proposed. It is believed that the above applications may lay the initial base of using the strain-based design method for buried pipeline subjected to landslides for pipelines.

2 TENSILE STRAIN LIMIT

The design of pipelines using strain-based approach must count both for resistance to tension and compression along the axial direction of the pipeline. In tension, the issues relate to the failure modes of plastic collapse or fracture. Among those, ductile fracture is often found in pipelines. At its initiation, ductile fracture is not a reasonable limit state to pipeline design within the standard wall thickness regime. The crack initiation in the pipe wall does not cause leaking of product from the pipeline. However, as the fracture expands, it may reach one of these limit states.

The capacity of tensile axial strain of the pipe is affected by a large number of factors: D/t ratio, Y/T ratio, internal pressure, girth weld effect, defect size and location. More details can be found from Liu (2008) and Liu and Zhang (2008).

Wide plate test is widely used as one of the closest representations of pipeline girth weld stress state under construction and service loading conditions. Much of the test development work was done by Denys (1990).Those tests originally focused on achieving plastic collapse of the girth welds, defined as achieving a measured failure strain of 0.5% or above. In recent years, wide plate test is being increasingly used to determine failure strains beyond yield, i.e., greater than 0.5% (Wang, Chen, 2006). The wide plate tests have been designed to obtain the tensile strain limits. The more details can be found from Liu (2008), Liu and Zhang (2008).

2.1 FINITE ELEMENT ANALYSES

Finite element techniques have been widely used for shell analysis. Nowadays FEA is able to provide numerical solutions for issues with many nonlinear effects that some classical techniques cannot deal with effectively. These effects exist in the ductile fracture behavior of pipes.

In the present study, FEA analyses were conducted on quarter length specimens or pipes due to symmetry conditions. Symmetric boundary conditions were imposed on the symmetry planes. Uniform remote axial displacement was applied as the primary loading. All the analyses used a large displacement formulation implemented in ABAQUS version 6.5 (SIMULIA, 2005).

The following assumptions were made to reduce the analysis matrix to a manageable level.

Zero weld cap height was assumed. The weld cap can provide some reinforcing effects to the weld. However, the weld cap height varies around the circumference of a pipe and is process dependent. Assuming zero weld cap height leads to conservative results.

The weld bevel geometry is omitted and the weld joint is assumed to have uniform properties.

The crack-tip opening displacement (CTOD) fracture criterion is one of the fracture criteria applied to fracture of metallic materials with cracks. The failure of the pipe in this paper is defined in CTOD. The crack driving force measured in CTOD is a fundamental parameter representing the magnitude of the driving force imparted on the defect. The failure of a girth weld is assumed when the CTOD driving force reaches material's resistance measured in apparent CTOD toughness (Wang, Horsley and Cheng, 2004).

The defect is located in weld metal, not in HAZ, though it has influence on crack driving force. In this paper the weld joint is assumed to have uniform tensile properties.

Generally speaking, the higher the pipe grade, the lower the strain hardening rate and uniform strain. In this paper using the API 5L minimum yield and tensile requirements as the baseline, generic relations among pipe grade, Y/T ratio, and uniform strain are established. The stress strain curve is assumed to obey the CSA Z662 relation,

$$\varepsilon=\frac{\sigma}{E_s}+\left(0.005-\frac{F_y}{E_s}\right)\left(\frac{\sigma}{F_y}\right)^n \tag{1}$$

Where σ and ε are the stress and strain respectively. And Es is elastic modulus, Fy is effective specified minimum yield strength, and n is the strain hardening exponent. This stress strain relation has a continuous yield (no Luders extension).

It is recognized that the actual Y/T ratio of a pipe material can be different from that computed using the API 5L minimum requirements. For each pipe grade, an upper bound and a middle level Y/T ratio are also included in the analysis matrix. The lower bound Y/T ratio is computed from API 5L minimum yield and tensile requirements. The upper bound Y/T ratio is taken as the average of the lower bound Y/T ratio and unity. The middle level Y/T ratio is the averaged value of lower bound and upper bound Y/T ratios. The stress-strain curve of X60 from the API 5L as an example is given in Figure 1.

The stress-strain curves of welds used for finite element analysis are got from standard testing from X60 to X80. The yield strength values are 497MPa, 585MPa, and 662Mpa, respectively to X60, X70 and X80.

Three-dimensional FE models simulating the curved wide plate (CWP) and pipe were generated. The C3D20R element of ABAQUS was used. This is a 20-node quadratic brick element with reduced integration. The outline of a typical FE model and mesh is shown in Figure 2. The crack was meshed by Altair HyperMesh.7.0 (Altair Engineering, Inc, 2001).

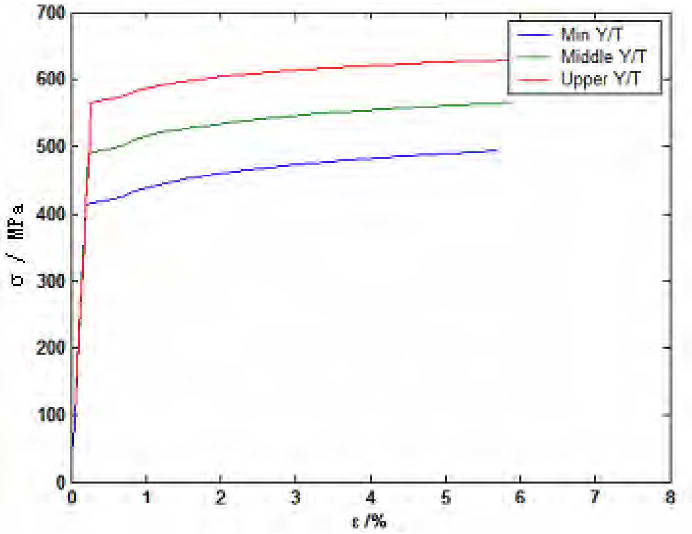

Figure 1 Stress-strain curve of X60 from the API 5L.

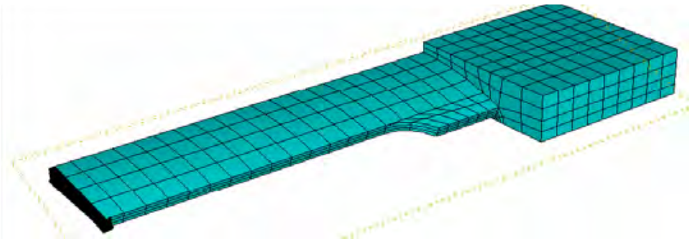

(a) The CWPs model.

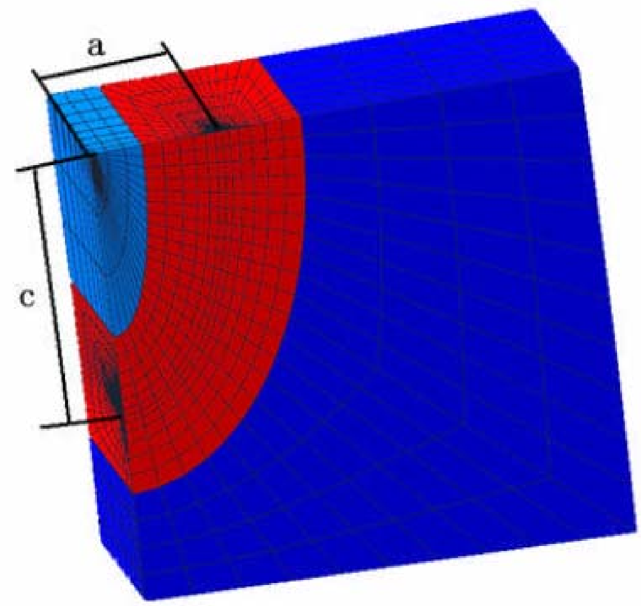

(b) The mesh of Crack tip.

Figure 2 A typical FE model and mesh.

Internal pressure was considered in the FE analysis except that for CWPs. For straight pipe, the design pressure for a given design wall thickness or the design wall thickness for a given design pressure was determined by the following design formula in this paper,

$$P_0 = 0.72\frac{2t}{D}\sigma_s \tag{2}$$

Where $P0$ is the design pressure, σs is the specified minimum yield strength (SMYS), t is the design wall thickness, D is the outside diameter of pipe.

The finite element analyses for CWPs were corresponded with CWP tests. The matrix of the finite element analysis includes:

Pipe grade

The range of pipe grades analyzed is X60, X70, and X80. Only the middle level Y/T ratios were investigated in the analysis. So the Y/T ratio, $\lambda \in [0.850, 0.917]$.

Pipe diameter and thickness

The pipe diameter ranges from 30 in. (762 mm) to 48 in. (1219 mm). The pipe thickness ranges from 9.5 mm to 17.5 mm.

The internal pressure in pipe

Assuming $\gamma \equiv Pi/P0$, where Pi is the applied internal pressure in pipe, and $\gamma \in [0,1]$.

The weld strength mismatch

The weld strength mismatch ($M=\sigma sW/\sigma sB$) ranges from 0 to 1.2. So The weld strength mismatch, $M \in [0, 1.2]$. When M is equal to zero, the result is corresponding to the plain pipe.

The defect size

The circumferential defect only is considered in this paper. Assuming $\xi \equiv 2c/t$, $\eta \equiv 2a/t$ (for buried defects, and a/t for surface defects), $\psi \equiv d/t$, so $\xi \in [1, 3]$, $\eta \in [0.2, 0.4]$, $\psi \in [0, 0.33]$, d is the depth of the defect.

Apparent CTOD（Crack Tip Open Displace）

Assuming $\mu \equiv \delta a/t$, where δa is the apparent CTOD.

Finite element analyses for a total of 450 cases produced a lot of data for a wide range of material, girth weld mismatch, various defect sizes or locations, buried or surface defects, and various internal pressures. So the tensile strain limits can be developed from finite element analyses.

$$\begin{aligned}\varepsilon_{ct\_FE} &= \mu^{0.046+0.1858\xi^{0.061}-0.549\eta^{-0.516}+e^{0.3255(1-\psi)}} \\ &\cdot\left(1+\lambda^{-7.44}\right)\cdot Exp\left[0.142(1-\gamma)-0.879(1-M)\right]\end{aligned} \tag{3}$$

Where when $M = 0$, the equation is for the pipe without weld, and when $M \neq 0$, the equation is for the pipe with weld, and $M = 1$ represents even match. And when $\psi = 0$, the equation is for the pipe with surface defect, and when $\psi \neq 0$, the equation is for the pipe with buried defect.

The equation was validated for $0.8 \le \lambda \le 0.95$, $0 \le \gamma \le 1$, $0 \le M \le 1.2$, $1 \le \xi \le 3$, $0.2 \le \eta \le 0.4$ and $0 \le \psi \le 0.3$. The strain limit is in percentage (%).

The coefficient of correlation of Eq. (3) is 0.921.

The relationship between the tensile strain limits with three defect-size factors predicted by Eq. (3) is shown in Figure 3 (a). From Figure 3 (a), it is seen that for the same type defect, the larger defect has less tensile strain capacity. For the same size defect, the surface defect is more dangerous than the buried defect.

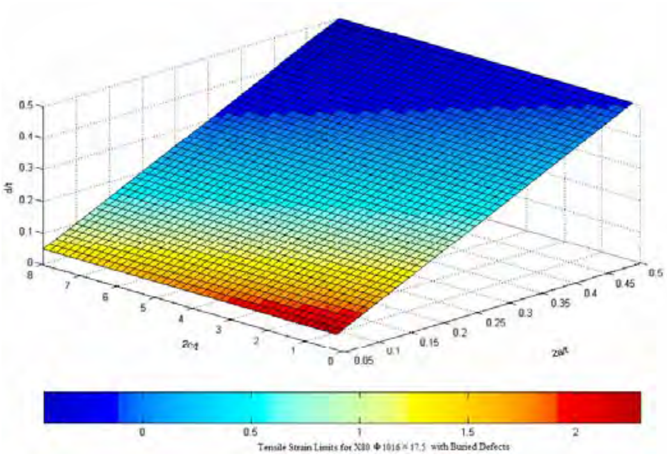

(a)The relationship between the tensile strain limits with three defect-size factors.

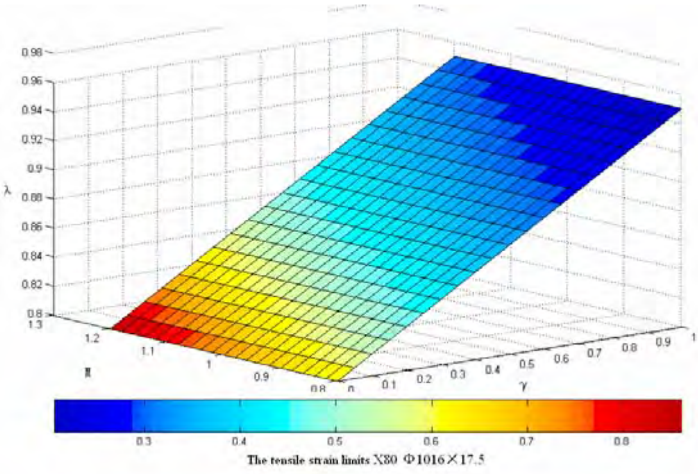

(b) The relationship between the tensile strain limits with different Y/T, girth weld mismatch, and internal pressure ratio.

Figure 3 The tensile strain limits predicted by Eq.(3).

As the curved wide plate testing can not develop the relationship between the tensile strain limit and the internal pressure of pipe, the tensile strain limits of pressurized pipes were obtained from FEA. The comparison among the tensile strain limits with the different internal pressure is shown in Figure 3 (b). The figure indicates that the higher internal pressure and the Y/T ratio reduce the ability of deformation resistance of the pipe. However the girth weld over-match does help to the ability of the deformation resistance.

2.2 The Safety Factors for the Parametric Equations

Even though the safety factor is not provided in the parametric equation, it is recommended to decrease the strain limit by 25% for the fracture process. This factor can decrease the failure probability to the unconditioned safety level in line with normal ULS checks.

3 COMPRESSION STRAIN LIMIT

In compression, the failure modes relate to varieties of buckling. Among those, local buckling is often found in pipelines. Local buckling is not, at its initiation, a reasonable limit state to pipeline design within the standard wall thickness regime. The beginning of a ripple in the pipe wall does not impede the flow of product through the pipeline. But as the buckling extends and expands, it may reach one of these limit states.

The capacity of compressive axial strain of the pipe is affected by a large number of factors: D/t ratio, Y/T ratio, internal pressure and girth weld effect. More details can be found from Liu (2008), and Liu and Zhang (2008).

3.1 FINITE ELEMENT ANALYSES

The following assumptions are made to reduce the analysis matrix to a manageable level.

1. The assumption for weld cap height is the same as that for FEA on tension.
2. The assumption on weld bevel geometry is the same as that for FEA on tension.
3. The failure of the pipe in this study is defined in limit state design, as a condition in which the structure ceases to adequately perform its function. The traditional criteria based upon ultimate strength are no longer relevant. The behaviors of the pipe in terms of the initiation and development of local deformation and wrinkling becomes a rational type of behavior upon which to base such limit state criteria.

Three-dimensional FE models simulating the pipe were generated. To focus the work on the post buckling behavior, the full length model was used. The C3D8R element in ABAQUS was used. This is an 8-node linear brick element with reduced integration in hourglass control. The meshes for CWPs are the same as used in FEA of tension. The outline of a typical FE model and mesh is shown in Figure 4.

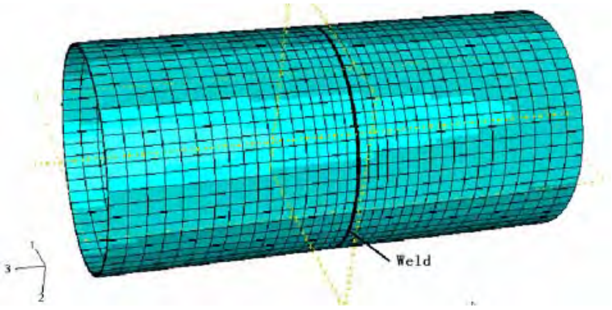

Figure 4 A typical FE model and mesh for a pipe

The finite element analysis of curved wide plate test was corresponded with testing. The analysis matrix of the additional finite element analysis as follows.

(1) Pipe grade

The range of pipe grades analyzed is X60, X70, and X80. All level Y/T ratios, including the lower bound, the middle level and the upper bound Y/T ratios were investigated. So the Y/T ratio, $\lambda \in [0.800, 0.944]$.

(2) Pipe diameter to thickness ratio

The pipe diameter ranged from 30in. (762mm) to 48in. (1219.2mm). The pipe thickness ranged from 9.5mm to 25.4mm. So the diameter to thickness ratio, $\beta \in [43.5, 88.7]$.

(3) The internal pressure in pipe

Assuming $\gamma \equiv P_i/P_0$, where P_i is the applied internal pressure in pipe, and $\gamma \in [0,1]$.

(4) The weld strength mismatch ratio

The weld strength mismatch ratio ($M = \sigma^W / \sigma^B$) ranges from 0.8 to 1.2. So The weld strength mismatch, $M \in [0, 1.2]$.
When M is equal to zero, the result is corresponding to the plain pipe.

A typical pipe post-buckling behavior from FEA is shown in Figs 5 and 6. The criteria of compressive analysis are based on the beginning of a ripple.

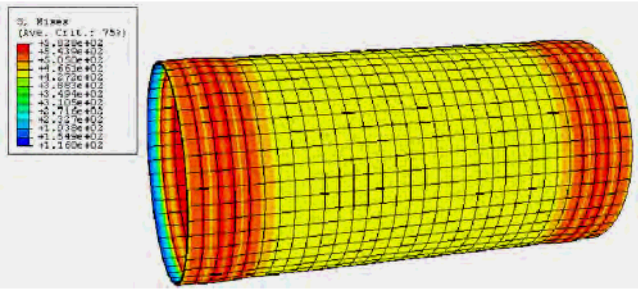

Step 1.

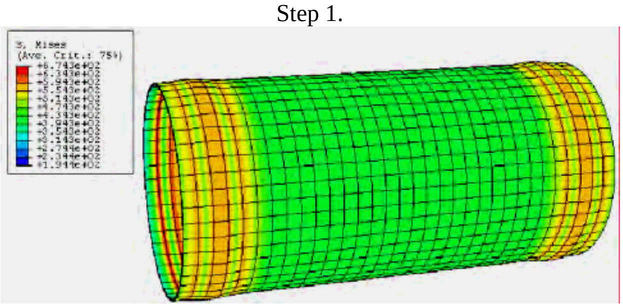

(b) Step 2.

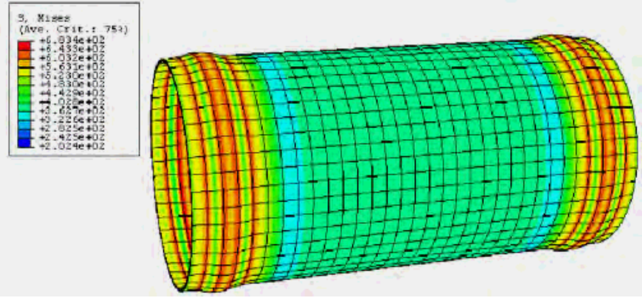

(c) Step 3.

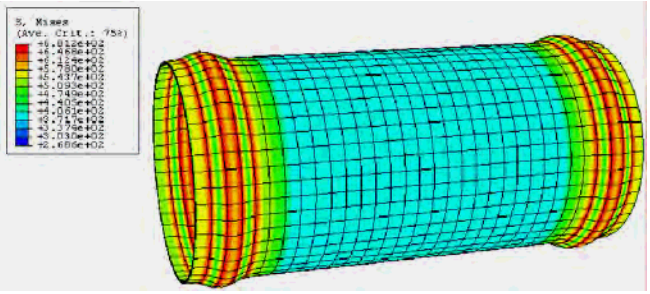

(d) Step 4.

Figure 5 The post-buckling process of pressurized plain pipe.

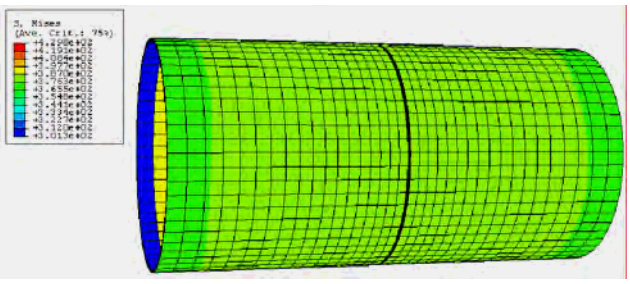

(a) Step 1

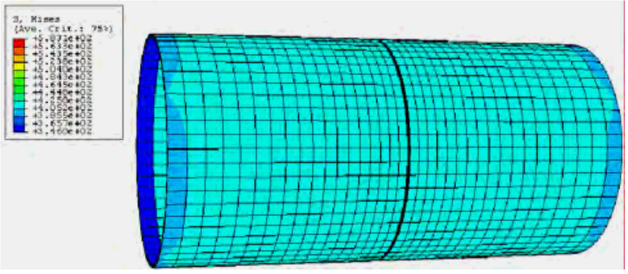

(b) Step 2.

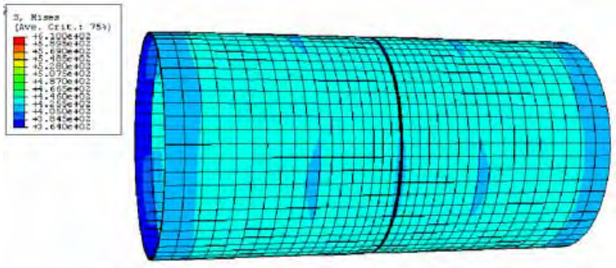

(c) Step 3.

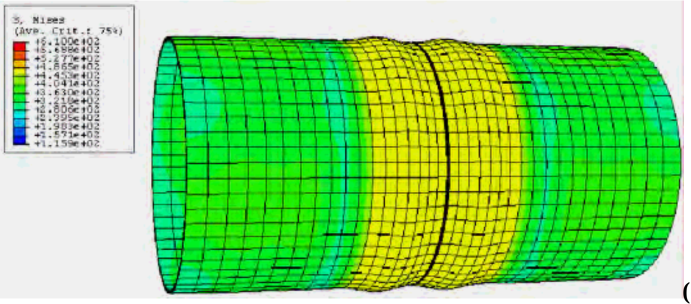

(d) Step 4.

Figure 6 The post- buckling process of pressurized weld pipe

Finite element analyses for a total of 144 cases produced data for a wide range of material, D/t ratios, weld strength mismatch ratio and various internal pressures. By using these data, the following parametric equations were developed:

$$\varepsilon_{cc\_FE} = \beta\left(7.219\lambda^{-1.1787}\right)\left(3.305\gamma^{2}-2.184\gamma+14.65\right)\left(1.63M^{2}-1.79M-0.905\right) \tag{4}$$

Where when M=0, the equation is for the NO weld pipe, and when M≠0, the equation is for the weld pipe. The equation was validated for 50≤D/t≤90, 0≤γ ≤1, and 0.80 ≤Y/T ≤ 0.93. The strain limit is in percentage (%).

The relationship between the compressive strain limits with three factors predicted by Eq. (4) is shown in Figure 7.

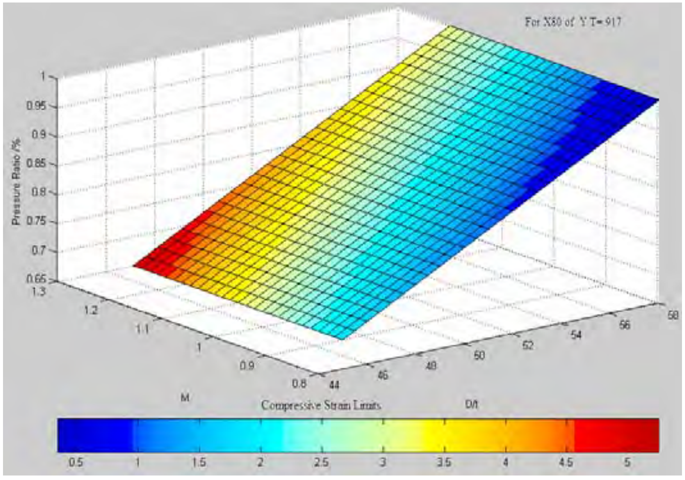

Figure 7 The relationship between the compressive strain limits with D/t, M, and the pressure ratio predicted

3.2 The Safety Factors for the Parametric Equations

Even though the safety factor is not provided in the parametric equation, it is recommended to decrease the strain limit by 25% for the post-buckling process. This factor can decrease the failure probability to the unconditioned safety level in line with normal ULS (Ultimate Limit State) checks.

4 THE RESPONSE OF BURIED PIPELINE SUBJECTED TO LANDSLIDES

4.1 The FE Model

In designing pipeline layouts, potentially unstable slope areas are commonly by-passed. In fact, as landslides are sometimes instantaneous and unexpected, enormous costs are incurred by environmental damages caused by conduit or pipeline servicing failures. Nevertheless, either for cost reasons or unclear definition of the boundaries of the unstable areas, it is not always possible to operate this way, unstable areas are not avoidable. The analysis of the problem of the interaction between landslides and pipelines is therefore of some importance. So in this part, the response of buried pipeline subjected to landslides was analyzed for the Lan-cheng-yu pipeline of China National Petroleum Corporation (CNPC).

The Lan-cheng-yu pipeline of CNPC is one of important pipelines of CNPC. It has been designed long ago, and, particularly in Sichuan across the highly unstable region of the Er-lang temple (See Figure 8), without much concern for the potential instability of the crossed slopes. As a consequence, failure is likely to occur. In the figure, the landslide is transverse across the pipeline with about 20° bevel.

To introduce the interaction model in a simple way, assume first that the free surface of the slope is planar and that its inclination with respect to the horizontal plane. The soil-pipe interaction model used in the present study is shown in Figure 9.

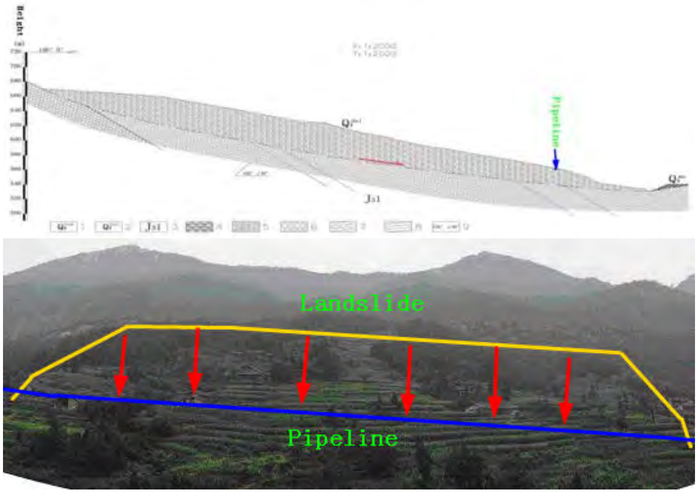

Figure 8 Er-lang temple landslide of the Lan-cheng-yu pipeline

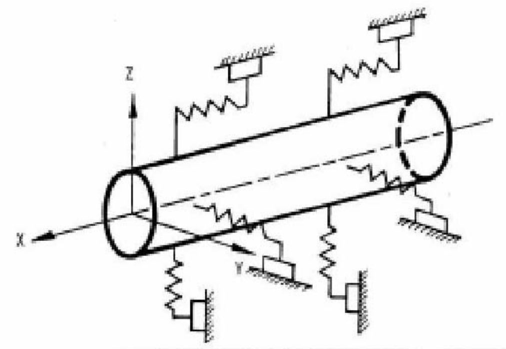

Figure 9 Simple soil-pipe interaction model used in the present study

Three-dimensional FE models simulating the CWP and pipe were generated. The PSI element was used. After FE analysis, the maximal tensile and compressive strains of the pipe were obtained as: ε_t=3.2% and ε_c=2.4%. They are the same as that calculated from Eqs (3) and (4). Using these two values, the strain based design of buried pipelines subjected to landslides was conducted.

4.2 The FE Analysis Result

In order to find the relationship between the pipe and the soil, 8 finite element analyses were done as shown in Table 1. Four of shape of FE models are set as shown in figure 9, and the others are axial across the pipeline. The width of landslides is shown in Table 1. The soil spring stiffness is shown in Table 2.

No.	Direction	Width/m	Displacement of soil/m
V1	Transverse	50	10
V2	Transverse	100	20
V3	Transverse	150	40
V4	Transverse	200	40
A1	Axial	50	5

A2	Axial	100	5
A3	Axial	150	5
A4	Axial	200	5

Table 1. The analysis matrix of the landslides.

Direction	Stress/MPa	Strain/%
Axial	42000	0.005
Vertical	-76705	-0.018
	0	0
	1252448	0.12
	2000000	0.25
Horizontal	-370638	-0.124
	0	0
	370638	0.124

Table 2. The soil spring stiffness.

As shown in Figure 10, the tensile and compressive strain limits of pipelines decrease with the increase of the transverse landslide width when the landslide width is smaller than 125m, while increase with the transverse landslide width when the landslide width is larger than 125m.

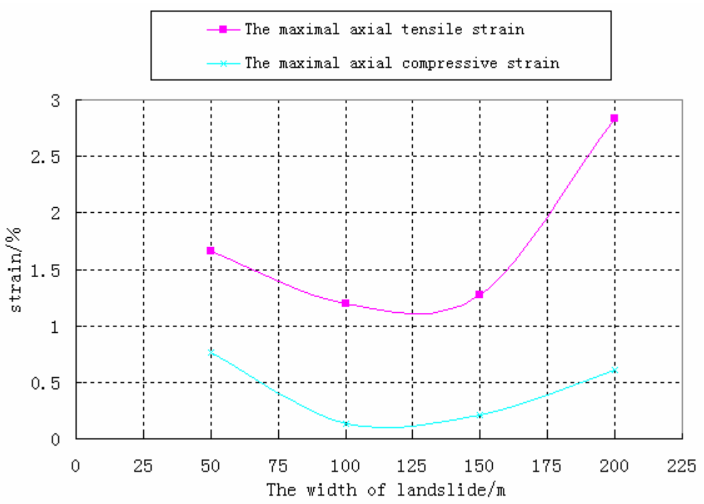

Figure 10 The relationship between the transverse landslide width and the strain of pipeline.

As shown in Figure 11, the tensile and compressive strain limits of pipelines increase with the increase of axial landslide width.

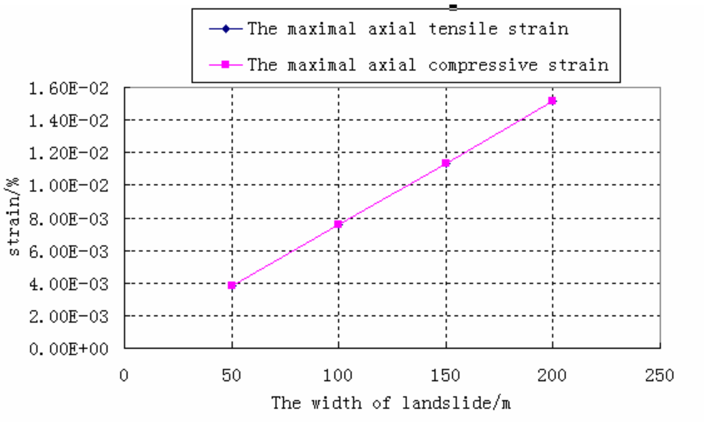

Figure 11 The relationship between the axial landslide width and the strain of pipeline.

4.3 The Strain Based Design Method of Buried Pipeline Subjected to Landslides

When the pipelines cross the area with big ground movement, the strain-based design should be considered. In the present study, the strain based-design method of buried pipeline subjected to landslides was developed. The steps of this method are listed as follows and shown in Figure 12.

Analysis steps for strain based-design of buried pipeline subjected to landslides:
(1)Estimate the location, range and magnitude of ground displacement.
(2)Estimate the strain limits.
(3)Find the material, wall thickness and depth of pipelines.
(4)Compute the soil-pipe interaction.
(5)Compute the applied strain of pipelines.
(6)Compare the strain limits and the applied strain of pipelines.
(7)Finish

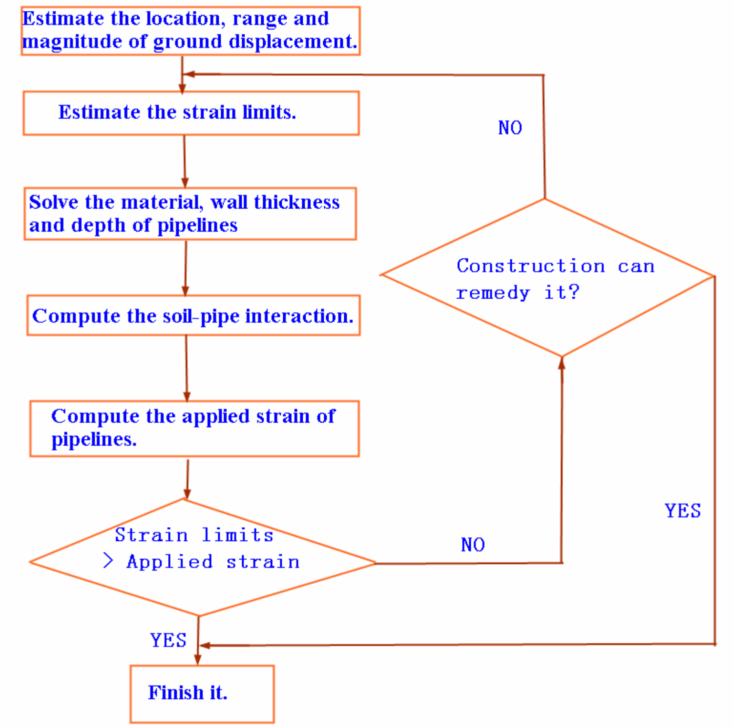

Figure 12 Strain-Based Design Method for Buried Pipeline Subjected to Landslides.

5 CONCLUSIONS

The parametric equations for the quantitative evaluation of tensile and compressive strain capacity of pipelines were proposed based on extensive FEA. The strain-based design method for buried pipeline subjected to landslides was developed. It is believed that the method presented in this paper may lay the initial basis for pipelines integrate assessment using strain-based design for pipelines in China.

6 ACKNOWLEDGEMENTS

This work was supported by China National Petroleum Corporation (CNPC). We would like thank Dr. Yong-Yi Wang, the President of Center for Reliable Energy Systems and all colleagues from R&D Center of PetroChina Pipeline Company for discussion and advising of this work， especially Dr. Bing Han.

REFERENCES

[1] Aaron S., Dinovitzer, Graville, Brian A., et al. "Strain-based failure criteria for sharp part-wall defects in pipes, "Proceedings of the 8th International Conference on Pressure Vessel Technology, ASME, 1996.

[2] Altair Engineering, Inc, "Altair HyperMesh.7.0 Users Manual," 2001.

[3] Bing Liu, X.J., Liu, Hong Zhang, "Strain-based Design Criteria of Pipelines", World Conference on Safety of Oil and Gas Industry 2007, April 10-13,2007, Gyeongju, Korea.

[4] Bing Liu, X.J., Liu and Hong Zhang. "Compressive Strain Capacity of Pipelines for Strain-Based Design", 7th International Pipeline Conference, Sept. 29-Oct.3, 2008, Calgary, Alberta, Canada.

[5] Bing Liu, X.J., Liu, Hong Zhang. "Tensile Strain Capacity of Pipelines for Strain-Based Design, " 7th International Pipeline Conference, Sep. 29-Oct.3, 2008, Calgary, Alberta, Canada.

[6] Canadian Standards Association. "Oil and Gas Pipeline Systems." ,Z662-03, Mississauga,Ontario,Canada, 2003.

[7] Canadian Standards Association. "Oil and Gas Pipeline Systems," Rexdale,Ontario,Canada,1996.

[8] Denys, R. M.. "Wide Plate Testing of Weldments, Part I, II, and III," Fatigue and Fracture Testing of Weldments. ASTM STP 1058, Eds. H. McHenry and J. Potter, ASTM, Philadelphia, 1990, pp. 157-228.

[9] EWI. Strain-Based Design of Pipelines. Report Project No. 45892GTH, October 8, 2003.

[10] Det Norske Veritas (DNV). "Submarine Pipeline Systems," HØvik Norway, 2000.

[11] Det Norske Veritas (DNV). "Rules for Submarine Pipeline Systems," HØvik,Norway,1982.

[12] Det Norske Veritas (DNV). "Rules for Submarine Pipeline Systems," HØvik,Norway,1996.

[13] Graville, Brian A., Aaron S., Dinovitzer et al. "Development of rational criteria for strain limits in pipeline welds," Report to Nova Corporation, 1993.

[14] SIMULIA, "ABAQUS Users Manual," 2005.

[15] Yong-Yi, Wang, Rudland, David Denys, et al. "A preliminary strain-based design criterion for pipeline girth welds, " Proceedings of the 4th International Pipeline Conference, Calgary, Canada, ASME, 2002.

[16] Yong-Yi, Wang, Wentao, Cheng, et al. "Tensile strain limits of buried defects in pipeline girth welds, " Proceedings of the 5th International Pipeline Conference, Calgary, Canada, ASME, 2004.

[17] Yong-Yi Wang, David J Horsley, Wentao Cheng, et al.. "Tensile Strain Limits of Girth Welds with Surface-Breaking Defects-Part 2: Experimental Correlation and Validation [C], " Proceedings of the international pipeline conference, Calgary, Alberta, Canada, September 29–October 3, 2004.

[18] Yong-Yi Wang, Wentao Cheng, Martin McLamb, et al.. "Tensile Strain Limits of Girth Welds with Surface-Breaking Defects-Part 1: An Analytical Framework[C], " Proceedings of the international pipeline conference, Calgary, Alberta, Canada, September 29–October 3, 2004.

COMPDYN 2011
3^{rd} ECCOMAS Thematic Conference on
Computational Methods in Structural Dynamics and Earthquake Engineering
M. Papadrakakis, M. Fragiadakis, V. Plevris (eds.)
Corfu, Greece, 25–28 May 2011

SEISMIC DESIGN AND RESPONSE OF HEAVY INDUSTRIAL STEEL BUILDINGS

Julien Richard[1], Sanda Koboevic[2], and Robert Tremblay[2]

[1] Hatch and Associates
Montréal (Québec) Canada
jrichard@hatch.ca

[2] École Polytechnique de Montréal
Montréal (Québec) Canada
sanda.koboevic@polymtl.ca
robert.tremblay @polymtl.ca

Keywords: irregular industrial buildings, seismic design, seismic response, steel bracing

Abstract. *Seismic behaviour of a heavy industrial building with highly irregular geometry, and mass and stiffness distribution is investigated to assess the effectiveness of current procedures for seismic design of such structures. These procedures were developed essentially for conventional commercial or residential buildings with regular and well-defined seismic force resisting systems, and their use to predict adequately deformations and forces for irregular industrial building may be questionable. The studied building is located near Montreal, Canada, and houses a vertical mechanical process representative of mining and metal refining industry. It is braced by low-ductility concentrically braced steel frames. Three-dimensional elastic dynamic time history analyses were carried out for selected acceleration records compatible with the design spectra at the site. The results are compared to those obtained from the equivalent static force procedure and the response spectrum analysis method. The study shows that the equivalent static method can adequately predict the displacements, but may underestimate column and brace axial forces. In general, response spectrum analysis method, provided appropriate prediction of the seismic response of the highly irregular structure studied.*

1 INTRODUCTION

Current code seismic design provisions for buildings in North America are mostly suited for conventional office or residential buildings framed by regular, continuous and well-defined seismic force resisting systems. Heavy industrial buildings are principally designed to ensure the functioning of an industrial process, and the structural elements are positioned to support heavy equipment and the machinery needed for operation. For these reasons, such buildings usually have complex and irregular geometries and uneven distribution of mass and/or stiffness which results in variety of dynamic characteristics that significantly differ from those found in regular structures. The application of current design provisions to industrial buildings is challenging for practicing engineers, as it requires continuous interpretation and adaptation of design rules and may result in inadequate designs [1, 2].

Structural response of steel-framed industrial buildings in past earthquakes was globally satisfactory, but the interruption of the operation was reported in many cases due to damage of individual components or connections [3]. Downtime periods may lead to loss of income for the industry, unemployment, or shortage of goods, electrical power and communications and have significant social and economical consequences. It is therefore imperative to ensure that seismic design procedures can lead to adequate performance. In view of limited data on the seismic demand imposed on industrial steel buildings by strong ground motions, it is difficult to evaluate if the seismic force and deformation demand on industrial structures can be adequately predicted using methods prescribed in current building design codes.

In this study, the seismic response of an irregular heavy industrial building is examined, and the analysis methods proposed in codes to estimate deformations and forces are critically reviewed in light of the observed response. The study is conducted for an existing building near Montreal, Canada that houses a vertical mechanical process representative of the mining and metal refining industry. Elastic three-dimensional time history analyses are carried out using a suite of ground motion records compatible with the design spectrum and the deformations, as well as axial loads in braces and columns are compared to the predictions from equivalent static force and response spectrum analysis methods. Special attention is given to the appropriate number of modes to use in response spectrum analysis and the possible impact of the direction of seismic loading on member force demand.

2 ANALYTICAL MODEL OF STUDIED BUILDING AND GROUND MOTION RECORDS

2.1 Building geometry and the analytical model

A three-dimensional view and the layout of the columns at the base of the industrial building studied are shown in Figs. 1a and 1b respectively. The main portion of the building has 37 m x 59 m plan dimensions and is 43 m high. An 8 m tall penthouse is located in the south-west part of the structure. The building also includes two extensions, one in the north-west corner (5 m x 6 m, 18 m high) and another one in the south-east corner (24 m x 8 m, 6 m high). In Fig. 1a, a more recent extension located south of column Line 11 can be seen. That addition was not considered in this study and is not shown in the other figures. With the exception of the roof level, the building does not have floors that extend through the whole building but rather a series of platform that are used to provide support and give access to different pieces of equipment. The platforms are mainly concentrated in the south and north portions of the building, leaving a large open space in the centre. Two large capacity silos (750 t and 1200 t) are located between Lines 1 and 4, and other smaller pieces of equipment are placed throughout the structure. Four low-ductility concentrically braced steel frames located on the perimeter of the building form the primarily lateral load resisting system. Additional braced frames are provided in the vicinity of the heavy equipment and large openings. The building has several irregularities as defined in the 2005 National Building Code of Canada (NBCC) 2005 [4], namely mass irregularity, in-plane discontinuity of vertical lateral load carrying elements, out-of plane offsets and torsional sensitivity.

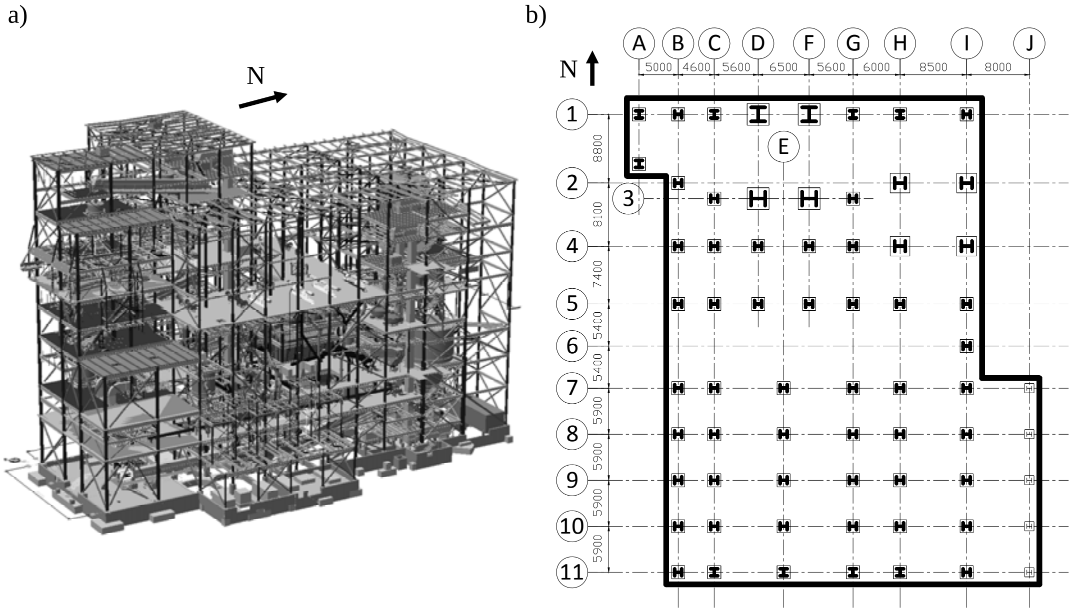

Fig. 1 Irregular building studied: a) Three-dimensional view; b) Column layout at the base.

In order to facilitate the analysis and obtain more general results that could be representative of the behaviour of similar buildings, the geometry and the secondary framing arrangements were simplified. Fig. 2 shows the final three-dimensional numerical model built with the program STAAD.Pro [5]. The model includes the columns, beams, braced frames and horizontal bracing. The members supporting the main equipment were also represented. All the platforms were included in the model, but rigid diaphragm properties were considered only for the floors with a concrete slab.

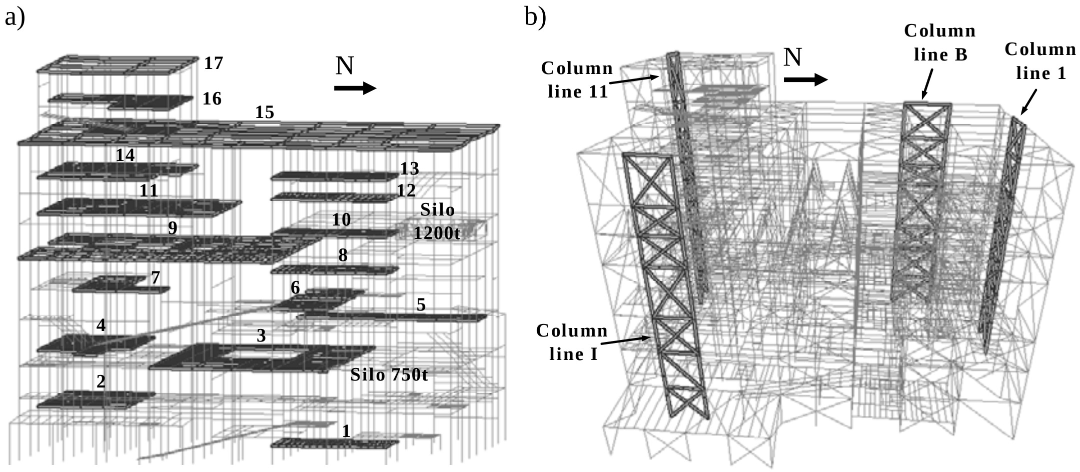

Fig. 2 Analytical model in STAAD.Pro: a) Location of platforms; b) Elevation of the braced frames studied.

The total seismic weight of the structure (W = 74200 kN) was determined as specified in NBCC 2005 and consisted of the weight of the structural members, 25% of the roof snow load and the weight of the main equipment in the fully-loaded condition. In order to include the mass of the major equipment at appropriate locations, additional nodes were introduced at the center of the gravity of the pieces of equipment considered, and linked to the rest of the structure by very stiff members. In this way, local overturning moments created by the horizontal inertia forces acting above the platforms that support the equipment could be accounted for in the analyses. The masses of the remaining equipment were assigned to the supporting columns at each floor in proportion to their tributary areas. For simplicity, the effects of accidental torsion, gravity loads and P-Delta effects were not considered in the analysis.

2.2 Selection of ground motion records

Elastic dynamic time history analyses were carried out for an ensemble of ground motions compatible with the NBCC design spectrum for a Class C site in Montreal. Due to the lack of recordings of historical ground motions rich in high frequencies, which are typical at Eastern North-American sites, simulated acceleration records were applied. Fourteen records were selected from the database described in [6] based on magnitude-hypocentral distance scenarios that dominate the seismic hazard. The records were scaled to obtain the match between the intensities of their spectra and the target design spectrum over the range of periods determined on basis of the best visual fit between the two spectra. A detail description of the ground motion selection and scaling can be found in [7]. The resulting median acceleration response spectrum of scaled records is compared to the target design spectrum in Fig. 3.

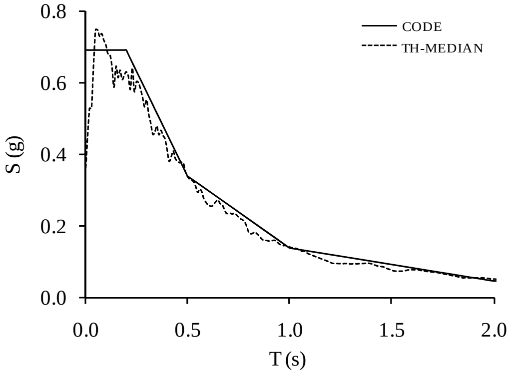

Fig. 3 Target design response spectrum (NBCC 2005) and median 5% damped elastic acceleration spectra for the ensemble of scaled ground motion

3 VALIDATION OF SEISMIC ANALYSIS METHODS USED IN DESIGN

3.1 Equivalent static force method and response spectrum method

Forces and deformations induced by seismic loads were first determined using the code equivalent static force procedure and response spectrum analysis methods. The seismic loading was not reduced to account for the ductility and the overstrength of the system so that direct comparison with the results of the elastic time history analyses could be made. Although the use of dynamic analysis is required in NBCC 2005 for an irregular building such as the one studied, the equivalent static force method was also considered as it is likely to be used by practitioners in preliminarily design due to its simplicity.

The fundamental periods were initially calculated using the NBCC empirical formula for braced frames, $T_a = 0.025h_n$, where h_n is the building height. Taking h_n = 51m for the frame height at the penthouse location and h_n = 43m elsewhere in the building, periods equal to 1.28s and 1.08s respectively were obtained. The periods were also calculated using modal analysis. The results are summarized in Table 1. The directions of the building principal modes correspond to the two orthogonal directions of the building, but modes in both directions showed torsional response. Each of the two principal modes were associated with about 54 percent of the total mass, and the contribution of higher modes was relatively small and varied between 0.1 and 7 percent (see Table 1). Thus, a large number of modes had to be considered (70 for the E-W direction and 95 for the N-S direction) to obtain the minimum 90% mass participation required by codes.

		E-W		N-S	
Mode	T_i (s)	M_i (%)	$\Sigma M_i / M$ (%)	M_i (%)	$\Sigma M_i / M$ (%)
1	1.46	0.0	0.0	0.2	0.2
2	1.38	53.2	53.2	2.1	2.1
3	1.32	1.5	54.7	63.4	65.7
4	1.11	0.2	54.8	0.2	65.9
5	1.07	7.1	62.0	0.0	65.9
6	1.05	4.2	66.2	0.2	66.1
7	1.02	0.0	66.2	0.0	66.1
8	0.98	3.8	70.0	0.7	66.9
9	0.96	0.7	70.7	5.1	72.0
…	…	…	…	…	…
70	0.38	0.1	90.0	0.1	86.2
…	…	…	…	…	…
95	0.33	0.5	92.9	0.4	90.3
…	…	…	…	…	…
126	0.26	0.3	97.1	0.1	96.1

Table 1 Results of the modal analysis: Periods and associated modal masses

Fundamental periods were also computed using the Rayleigh method: 1.29 s and 1.28 s were obtained in the E-W and N-S direction, respectively. Values from all three methods agreed well. The elastic base shear forces from the equivalent static force method ,V, were determined using the periods calculated with the Rayleigh method: V = 8900 kN along the E-W direction and V = 9000 kN along the N-S direction. Two different approaches were examined for the vertical distribution of seismic loads to assess how well they account for higher mode effects, namely (i) linear distribution with a concentrated force at the top of the structure as prescribed in NBCC 2005, and (ii) parabolic distribution, as defined in ASCE 7-05 [8].

In the response spectrum analysis, modal contributions were combined using the CQC rule assuming 5% damping in all modes. As previously mentioned, large number of modes had to be included to obtain the minimum 90% mass participation required by codes: 70 and 95 modes for the E-W and N-S directions, respectively. The base shear forces from response spectrum analysis, $V_{t,}$ were equal to 5690 kN and 6460 kN representing only 64% and 72% of the seismic base shear forces obtained from the equivalent static method in corresponding directions. When including up to 126 modes, the combined mass participation increases to 97% and 96% in each of the two directions (see Table 1) and the two associated base shear forces increased to 71% V and 79% V, respectively. Further increase in the number of modes in the response spectrum analyses did not lead to any further augmentation of the base shears. The difference between V_t and V is explained by the inherent inadequacy of the equivalent static force method to represent the dynamic response of complex structures. In this context, the requirement to scale response spectrum analysis results to the values obtained from the equivalent static force method, as currently prescribed in North-American codes, could be questioned when the number of modes used in the spectral analysis is sufficient to reach convergence. However, further investigation is needed on this subject before more general conclusions can be drawn. In this study, the results of the response spectrum analysis conducted for the number of modes engaging 90% participating mass were scaled by the V/V_t ratio, as required in NBCC 2005, and then compared with other methods.

3.2 Dynamic time-history analysis

Three-dimensional dynamic time history analysis was carried out using the modal superposition routine available in the program STAAD.Pro. Damping equal to 5% of the critical value was assigned to all modes. Preliminary analyses were performed to determine the appropriate number of modes required to adequately predict the seismic base shears, storey displacements and maximum brace forces. The number of modes was gradually increased to achieve 90% (70 modes and 95 modes in the E-W and N-S direction, respectively), 97% (126 modes) and nearly 100% (500 modes) participating mass. Increasing the participating mass from 90 to 97%, resulted in peak base shear forces increasing by as much as 25%; however, no further base shear increase was observed beyond 126 modes. Similarly, brace axial loads changed significantly until 126 modes were included but remained fairly constant when additional modes were considered. Storey displacements were the least sensitive to the number of modes selected; however, for specific building levels, it was necessary to engage 97% of the mass to avoid changes in the results. Based on these three observations, 126 modes were selected for the time history analyses performed. Comparison with the other methods was based on median results which can be considered representative in view of number of acceleration records selected. However, 84th percentile values were also tracked to illustrate dispersion. The analyses were conducted for two sets of orthogonal axes: the principal axes of the building and a set of axes oriented at 45 degrees angle with respect to the principal directions. The latter set was chosen to evaluate the impact of the direction of the analysis on the response.

3.3 Comparison of results

Following response parameters were selected for comparison between the three methods: the seismic base shear, storey displacements, and the axial forces in columns and braces of the braced frames. The results are given in Figs. 4, 5 and 6.

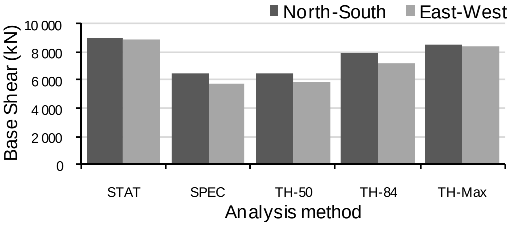

Fig. 4 Peak base shear from equivalent static force (STAT), response spectrum (SPEC) non-scaled, and time history (TH-med and TH-84th) analysis methods.

Fig. 4 shows that, regardless of the method, the seismic base shears in the two principal building directions were similar. This was expected because the corresponding building periods were comparable in the two directions. Elastic base shears calculated using the equivalent static force method exceeded the median time history results by approximately 40%, and were even slightly higher than the maximum peak values. Median results agree well with the values obtained from response spectrum analysis when no scaling of base shear is applied, confirming that the base shear estimates obtained from the equivalent static force method are probably conservative.

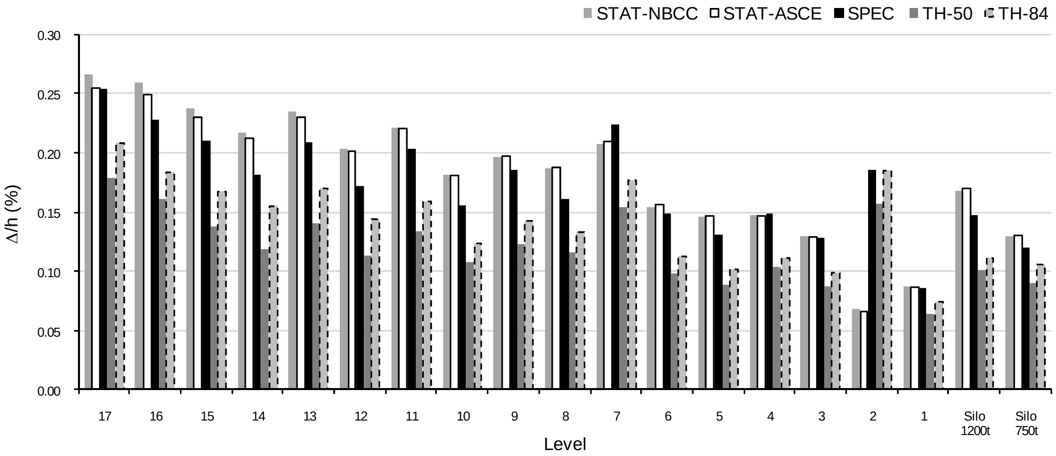

Fig. 5 Peak drift from equivalent static force (STAT), response spectrum (SPEC) scaled, and time history (TH-med and TH-84th) analysis methods and for earthquake action along the N-S direction.

Fig. 5 illustrates the calculated peak displacements under loads and ground motions applied in the N-S direction. Displacements are studied instead of inter-storey drifts, because none of the floors extended through the whole building areas. The results shown are normalized by the total storey height measured from the ground. Comparable displacement profiles were predicted from all methods employed. No significant difference was noted when using the NBCC 2005 or the ASCE 7-05 seismic force distributions in the equivalent static force method. Spectrum analysis results were slightly smaller than those obtained from equivalent static load method in all but two locations, and about 40% higher than the mean time history results. The 84th percentile values were also below the predictions of the equivalent static and response spectrum methods. These observations are consistent with those made for base shears.

Column and brace axial load profiles in the selected braced frames, shown in Fig. 6, compare well between the different methods considered. The results are shown for earthquake loads acting along the N-S direction of the building. Similar force profiles were obtained for the E-W direction, and the results are not shown herein. The response spectrum analysis values consistently exceeded the median time history results. They were even higher than the 84th percentile time history values for almost all structural elements studied. This can be explained by the scaling procedure that was applied to the response spectrum analysis results. The results from the equivalent static force method are comparable to response spectrum values for the frames oriented in the direction of the analysis. For the frames in the perpendicular direction, however, the equivalent static force method under-predicted the member forces by a large margin in some cases. This can be attributed to the inadequate treatment of higher modes and in-plane torsional effects when using an equivalent static force method for such irregular structures.

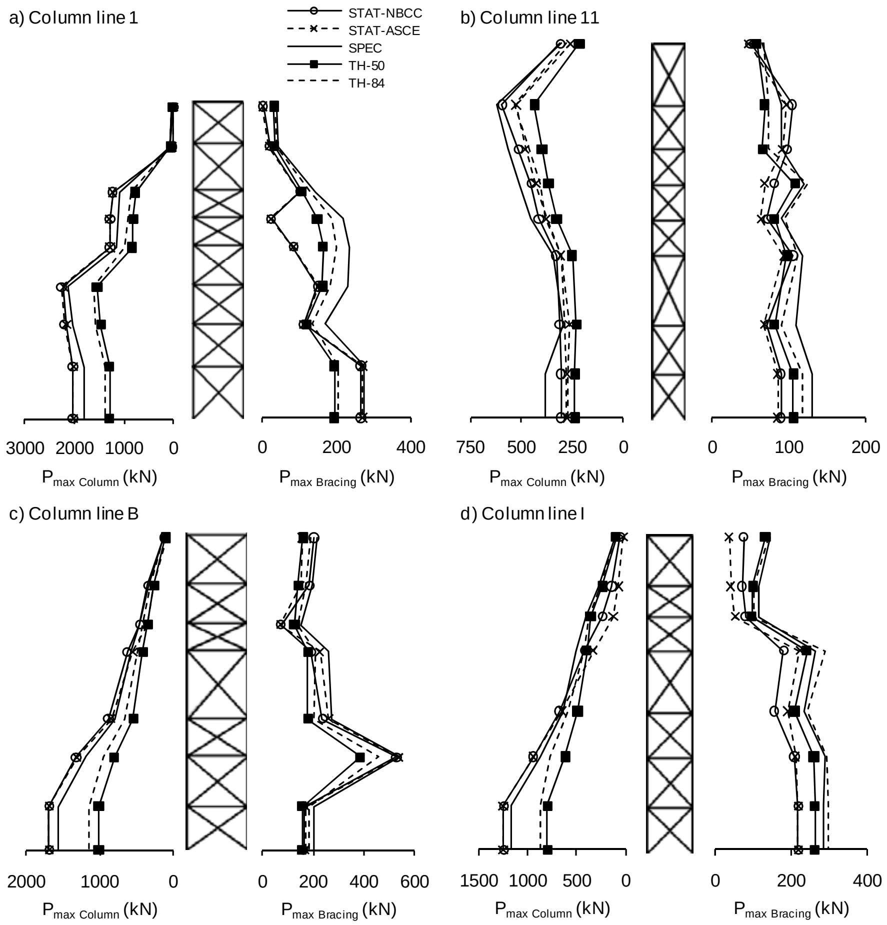

Fig. 6 Comparison of peak axial load in columns and braces induced by seismic loads acting in N-S direction: equivalent static force (STAT), response spectrum (SPEC) scaled, and time history (TH-med and TH-84th) analysis methods

3.4 Impact of the direction of analysis on column and brace forces

According to NBCC 2005, when the components of the seismic force resisting systems are orientated along a set of orthogonal axes, design seismic forces in the members of a building structure can be obtained two independent analyses performed along each of the principal axes of the structure. This condition applies for the structure studied. However, given the presence of irregularities in the structure and the fact that some braced frames shared columns in the upper part of the building, it was of interest to determine if the direction of the application of the loads could have impact on the member forces.

Fig.7 summarizes the results obtained from time history analysis for four directions of load application: two analyses along the principal axes of the building and two analyses along orthogonal axes oriented at 45 degrees angle with respect to the building principal directions. Force envelopes obtained from the response spectrum analysis are also shown for comparison. Note that column lines B and I run in the N-S direction while column Lines 1 and 11 are in the E-W direction. As expected, the highest axial loads in diagonals of the braced frame were developed when seismic action was applied in the direction of the braced frame. The same observation holds true for the columns of braced frames in the N-S direction. On the contrary, in the upper columns of the frames along the E-W direction, up to 30% higher forces were recorded under the ground motions acting in directions other than the direction parallel to the frames, including loading at 45 degrees. Such a result is explained by the fact that these columns were also part of another braced frame placed in the perpendicular direction to the studied frame. This type of framing arrangements is not uncommon in heavy industrial buildings, and caution should therefore be exercised when selecting the direction of the loading for seismic analysis. In all cases studied, member forces obtained from the response spectrum analysis were the highest and would therefore provide conservative estimates of design forces.

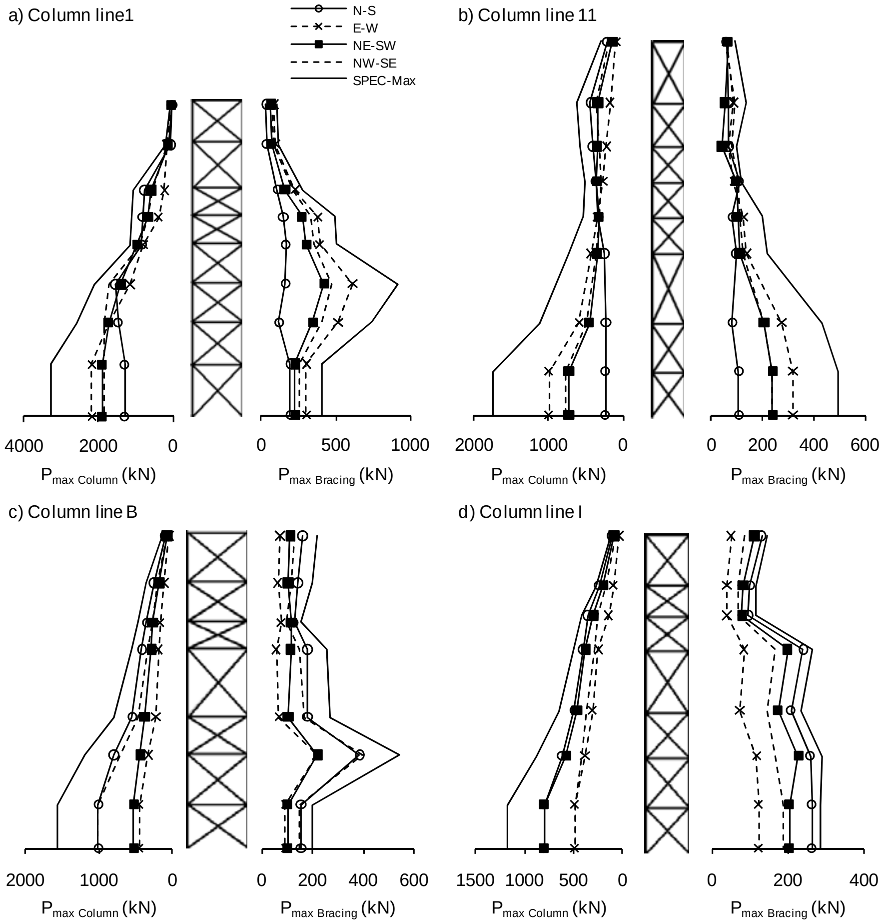

Fig. 7 Impact of direction of the analysis on peak axial load in columns and braces.

4 CONCLUSIONS

- For the building studied, the fundamental periods obtained using the code empirical formulae compared well to values from modal analysis and the Rayleigh method;
- The equivalent static force method gave reasonable estimates of deformations under seismic loads, but under-estimated the axial loads in columns and braces;
- For the response spectrum analysis method, it was necessary to include a large number of modes to engage the minimum 90% mass participation required by building codes: 70 and 95 modes, respectively, for each of the two principal directions of the building studied;

- The response spectrum analysis method provided a fair prediction of both the deformation and force seismic demand, and therefore appeared to be an appropriate method to predict the seismic response of such a highly irregular building;
- In this study, dynamic time history analysis was performed using a modal superposition technique. The results showed that member forces are sensitive to the number of modes considered in the analysis and can be significantly under-estimated if an insufficient number of modes is selected. For the building studied, the number of modes required to obtain 97% global mass participation was needed to adequately predict the base shear forces;
- The study showed that the selection of the direction in time history analysis should be done with care, as the maximum forces in components that are common to two braced frames in orthogonal directions may be induced by seismic loads acting in directions that are not parallel to the braced frame studied.
- The study was limited to a single building with specific dynamic characteristics and the results cannot be generalized before similar study is conducted on additional structures. However, the results provide insight into possible limitations of current seismic design procedures and possible directions for future investigation.

REFERENCES

[1] Daali, M., Industrial Facilities and Earthquake Engineering. *Proc., 13th World Conf. on Earthquake Eng.*, Vancouver, BC, Canada, Paper No. 330, 2004.

[2] Rolfes, J.A. & MacCrimmon, R.A., Industrial Building Design – Seismic Issues. *Iron and Steel Technology*, **4**(5): 282-298, 2007.

[3] Richard, J., Tremblay, R., Koboevic, S. and MacCrimmon, R.A., Seismic analysis and design approaches for crane-supporting steel structures. *Proc., Steel Structures in Seismic Areas (STESSA)*, Philadelphia, USA, Paper No. 0182, 2009.

[4] NRCC. NBCC 2005. *National Building Code of Canada.* National Research Council of Canada, Ottawa, ON., 2005.

[5] Bentley Systems, Inc, *STAAD.Pro. Version 20.07.03.16.* Bentley Systems, Inc., Yorba Linda,CA., 2008.

[6] Tremblay, R. Atkinson, G.M. Comparative Study of the Inelastic Seismic Demand of Eastern and Western Canadian Sites. *Earthquake Spectra*, **1**7(2): 333-358, 2001.

[7] Richard, J. *A study of seismic behaviour of industrial buildings braced with low-ductility steel framing systems*, M.Sc. Thesis, École Polytechnique, Montréal, QC, Canada (*In French*), 2009.

[8] ASCE (2005), ASCE/SEI 7-05, Including Supplement No. 1, *Minimum Design Loads for Buildings and Other Structures*, American Society of Civil Engineers, Bacon Raton, FL.

COMPDYN 2011
III ECCOMAS Thematic Conference on
Computational Methods in Structural Dynamics and Earthquake Engineering
M. Papadrakakis, M. Fragiadakis, V. Plevris (eds.)
Corfu, Greece, 25–28 May 2011

ON THE SEISMIC BEHAVIOUR AND DESIGN OF LIQUID STORAGE TANKS

Patricia Pappa[1], Daniel Vasilikis[1], Polynikis Vazouras[2], and Spyros A. Karamanos[1]

[1] Department of Mechanical Engineering
University of Thessaly, Volos, Greece
e-mail: {davasili, patrpap, skara}@mie.uth.gr

[2] Department of Civil Engineering
University of Thessaly, Volos, Greece
e-mail: pvazour@yahoo.gr

Keywords: liquid storage tank, seismic design, sloshing, finite elements, shell buckling.

Abstract. *The paper examines some special issues on the structural behaviour of upright-cylindrical liquid storage tanks, which are widely used in industrial facilities and for water storage. Two main design standards are considered: EN 1998-4, a relatively new standard, and Appendix E of API 650, which has been through substantial amendments and revisions in its new version (11th edition, 2007). There are significant differences between the two specifications, which are due to the fact that there exist several controversial issues on this subject, open to further research. These issues are (a) the number of modes necessary to estimate accurately the convective seismic force due to the hydrodynamic behaviour of the liquid containment; (b) the appropriate combination of the impulsive and the convective component of seismic force; (c) the uplifting behaviour of unanchored tanks, with emphasis on the base plate behaviour and the increase of meridional compression; (d) the choice of an appropriate reduction (behaviour) factor for calculating both the impulsive and the convective force; (e) the calculation of hydrodynamic hoop stresses due to liquid hydrodynamic motion; (f) the design of tanks against buckling at the top due to liquid sloshing; (g) the importance of nonlinear wave sloshing effects.*

The present paper is aimed at addressing the above issues based mainly on numerical simulations. To simulate the tank shell and its structural behaviour, general-purpose finite element software ABAQUS is employed, whereas to examine hydrodynamic effects, an in-house numerical technique is developed. Existing data from previous investigations are also considered. The results are aimed at better understanding of liquid storage tank seismic behaviour, bridging the gap between the two major design standards (EN 1998-4 and API 650-Appendix E), towards safer seismic design of industrial facilities.

1 INTRODUCTION

The structural response of liquid storage tanks under strong seismic loading constitutes an important issue for safeguarding the structural integrity of industrial facilities, especially in refineries and power plants. Significant damages of tanks have been reported in earthquake events [1][2]. The dominant mode of tank failure is in the form of elephant's foot buckling at the tank base. Other types of earthquake damages include buckling of the top of the tank shell, base plate failure due to uplifting, roof damage due to excessive sloshing, or shell damage at nozzle areas due to non-flexible connections with piping. Current design practice is based on the application of the API 650 provisions [3], as described in Appendix E. This Appendix has been initially incorporated in the standard in the late 70's [4], and has been substantially revised in the 11th edition published in 2007 [3] to be in accordance with the provisions of ASCE 7-05 [5]. In addition, to this standard, the newly published EN 1998-4 standard [6] contains design provisions for the seismic design of liquid storage tanks.

In the following, several issues related to the seismic analysis of liquid storage tanks and the determination of seismic action are addressed and examined, using numerical simulations. It has been recognized that there exist some specific issues that require further investigation and improvement. In particular, the following issues are addressed in the present study:

- The number of sloshing modes to be considered in convective action and their combination with impulsive action.
- The effects of shell deformation on the seismic response.
- Calculations of hoop hydrodynamic stresses
- Uplifting of unanchored tanks
- Buckling at the top of the tank
- Behavior factor of liquid storage tank and elephant's foot buckling
- Nonlinear sloshing effects

The investigation of those issues is aimed at comparing – where possible – the API 650 and the EN 1998-4 provisions for the seismic design of liquid storage tanks, towards proposing possible improvements/amendments of the EN 1998-4 standard. For this purpose, three liquid storage tanks are considered and their seismic response is simulated numerically:

(a) A moderately-broad tank, referred to as Tank I, is primarily considered. This is a 27.4-meter-diameter tank with a total height of 16.5 meters. The tank is unanchored. The filling height of the tank H is equal to 15.7, which makes an aspect ratio of the tank $\gamma\left(H/R\right)$ equal to 1.145. The tank thickness varies from 6.4 mm at its top course to 17.7 mm at its bottom course, the bottom plate is 6 mm thick, and has a 8-mm-thick annular plate.

(b) The second tank considered, referred to as Tank II, is a tall tank of 18-meter-diameter tank with a total height of 20 meters. The filling height of the tank H is equal to 19, which makes an aspect ratio of the tank H/R equal to 2.1. The tank thickness varies from 6 mm at its top course to 10 mm at its bottom course and it is anchored .

(c) The third tank, referred to as Tank III, is a very broad tank of 68-meter-diameter with a total height of 20 meters. The filling height of the tank H is equal to 19 resulting to an aspect ratio H/R equal to 0.558. The tank thickness varies from 34 mm at its top course to 38.5 mm at its bottom course.

All three of the above liquid storage tanks are existing tanks, constructed in seismic regions, and have been designed against hydrostatic pressure following the API 650 [3] methodology "Calculation of Thickness by the 1-Foot Method" in section 5.6.3, considering a liquid containment of unit gravity (water). The tanks are depicted in Figure 1.

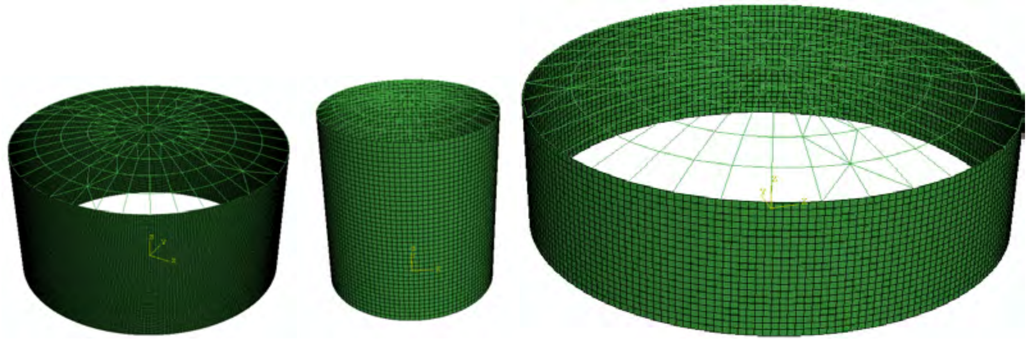

Figure 1: Tank I (left), tank II (center) and tank III (right) used for the parametric studies in the present paper.

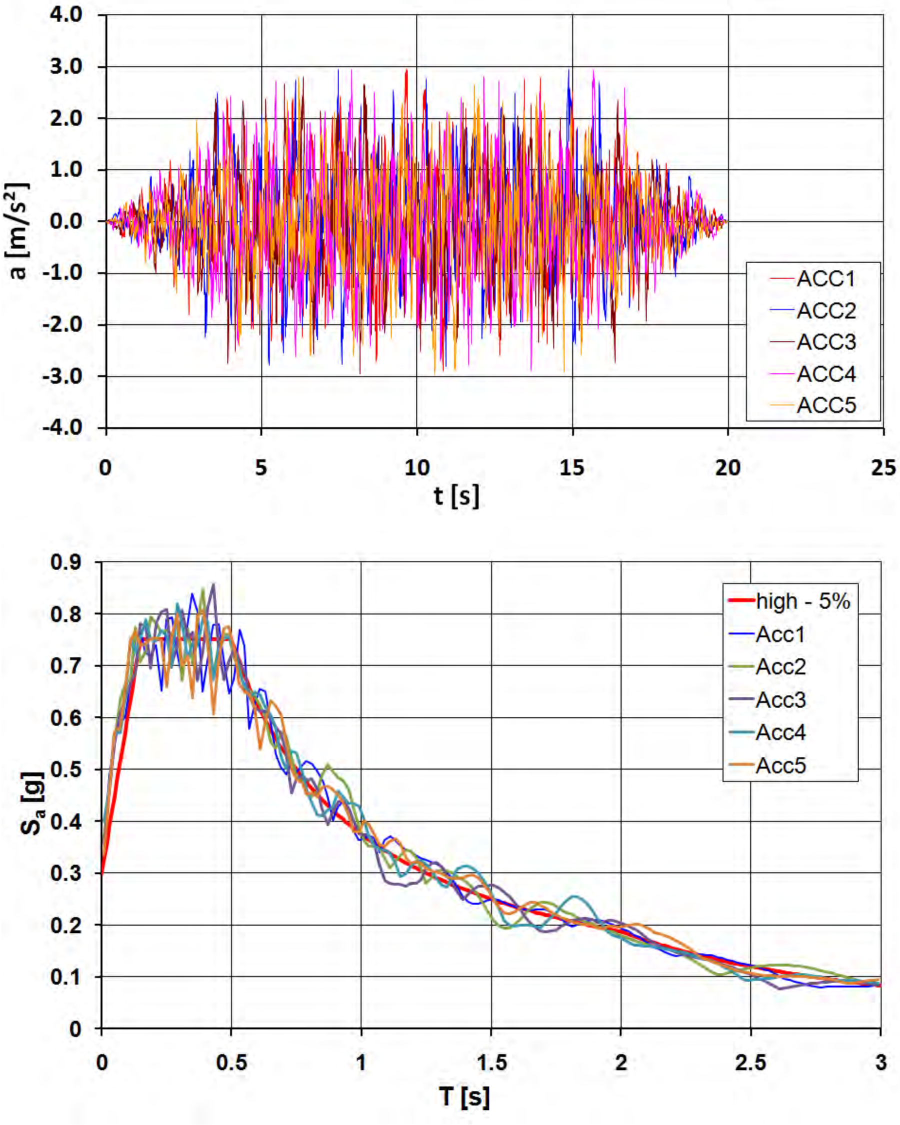

Figure 2: Artificial seismic accelerograms used in the present study (maximum ground acceleration is 0.25g) and their comparison with the 5% damping design spectrum of EN 1998-1.

2 SEISMIC DESIGN CODES FOR LIQUID STORAGE TANKS

Seismic design of liquid storage tanks in petrochemical facilities has been conducted with the relevant provisions of API 650. In particular, Appendix E of API 650 refers exclusively to seismic design, contains provisions for both determining seismic actions on tanks, as well as calculating the strength of the tank. The new edition of Appendix E includes provisions for site-specific seismic input, calculation of hoop hydrodynamic stresses, distinction between ringwall and slab overturning moments, freeboard requirements, and consideration of vertical excitation effects. The latter three issues are new, with respect to the old version of the Appendix [4], whereas the issues of uplifting/anchorage and calculation of shell compression are significantly enhanced. It should be noted that seismic action calculations in the new version of Appendix E are in accordance with ASCE 7 standard [5].

European standard EN 1998-4 [6] is part of the CEN/TC250 standards, often referred to as “Structural Eurocodes”. It includes seismic provisions for silos, tanks and pipelines. In Chapter 2 some general provisions are stated. More specific rules for the seismic design of tanks are stated in Chapter 4 (e.g. behavior factor, limit state description), whereas extensive methodologies for calculating seismic action and verifying shell buckling are presented in Informative Annex A. It has been recognized as a standard that contains state-of-the-art scientific information for determining seismic action, based on the work of Rammerstorfer et al. [7] and Scharf [8] as well as the work of Rotter [9] for shell buckling under internal pressure (elephant’s foot). However, there are some issues that need further investigation and possible improvement; a list of those issues is offered in section 1, and will be discussed extensively in the present paper.

3 SLOSHING MODES AND THEIR COMBINATION WITH IMPUSIVE MOTION

The first issue of interest concerns the number of sloshing (convective) modes to be considered for determining the convective seismic force. The three tanks under consideration have been subjected to base-ground seismic acceleration from 10 artificial earthquakes, generated from the EN 1998-1 design spectrum, as shown in Figure 2. Tables 1 and 2 show some characteristic results from 4 typical accelerograms from those earthquakes (denoted as ACC1, ACC2, ACC3 and ACC4 respectively), in terms of the maximum convective forces for several modes, the corresponding maximum impulsive force, and the maximum total seismic force. For each earthquake event the maximum convective force was calculated as the product of the “convective” accelerations and the corresponding sloshing masses:

$$F_C = \left(\sum_n \mathsf{M}_{nC} \, \ddot{u}_n \right)_{\max} \tag{1}$$

where the “convective” acceleration is calculated from the following linear oscillator equation:

$$\ddot{u}_n + 2\xi_n \omega_n \left(\dot{u}_n - \dot{X} \right) + \omega_n^2 \left(u_n - X \right) = 0 \tag{2}$$

In the above equations, the convective (sloshing) mass is computed as follows

$$\frac{\mathsf{M}_{nC}}{\mathsf{M}_L} = \frac{2 \tanh\left(k_n R \, \gamma \right)}{k_n R \gamma \left(k_n^2 R^2 - 1 \right)} \tag{3}$$

and

$$\frac{\omega_n^2 R}{g} = \left(k_n R \right) \left[\tanh\left(k_n R \, \gamma \right) \right] \tag{4}$$

is the sloshing (convective) circular frequency of the tank. Similarly, the maximum impulsive force was calculated as the product of the "impulsive" acceleration and the corresponding impulsive mass:

$$F_I = \left(\mathsf{M}_I \ddot{X}\right)_{\max} \tag{5}$$

where the "impulsive" acceleration is calculated as follows

$$\ddot{u}_I + 2\xi_I \omega_I \left(\dot{u}_I - \dot{X}\right) + \omega_I^2 \left(u_I - X\right) = 0 \tag{6}$$

In the above equation, the impulsive mass is computed as follows

$$\mathsf{M}_I = \mathsf{M}_L - \sum_{n=1,2,3,...} \mathsf{M}_{nC} \tag{7}$$

and

$$\omega_I = \frac{2\pi}{C_i}\sqrt{\frac{Et}{\rho R}} \tag{8}$$

is the impulsive circular frequency of the tank. In the above expression C_i is a nondimensional parameter that depends on the aspect ratio of the tank $\gamma = H/R$ and where t is the average thickness of the tank shell. The integration of linear oscillator equations (2) and (6) is performed through a standard central-difference numerical method. In Tables 1, 2, and in Figure 3a, Figure 3b and Figure 3c, together with the maximum convective and impulsive forces, the maximum total forces are presented, for 4 typical artificial ground acceleration inputs (denoted as ACC1, ACC2, ACC3 and ACC4 respectively), as computed by the following equation

$$F_{\max} = \left(\sum_n \mathsf{M}_{nC}\, \ddot{u}_n + \mathsf{M}_I \ddot{X}\right)_{\max} \tag{9}$$

		$F_{I,\max}$ [MN]	$F_{C,\max}$ [MN]
Tank1	*ACC1*	16.757	1.064
	ACC2	16.749	1.149
	ACC3	16.765	1.968
	ACC4	16.778	1.675
Tank2	*ACC1*	11.173	0.682
	ACC2	11.168	0.687
	ACC3	11.178	0.578
	ACC4	11.187	0.531
Tank3	*ACC1*	75.323	2.799
	ACC2	75.287	3.042
	ACC3	75.358	2.907
	ACC4	75.416	2.878

Table 1: Maximum impulsive and maximum convective force for 4 typical artificial seismic inputs (0.25g).

		$F_{C,\max}+F_{I,\max}$ [MN]	$\sqrt{\left(F_{C,\max}\right)^2+\left(F_{I,\max}\right)^2}$ [MN]	$F_{\max}\left(t\right)$ [MN]
Tank1	*ACC1*	17.822	16.792	16.888
	ACC2	17.899	16.789	17.001
	ACC3	18.734	16.881	16.823
	ACC4	18.454	16.862	17.101
Tank2	*ACC1*	11.856	11.194	11.303
	ACC2	11.856	11.189	11.632
	ACC3	11.757	11.194	10.845
	ACC4	11.719	11.200	11.620
Tank3	*ACC1*	78.123	75.376	74.689
	ACC2	78.329	75.349	75.207
	ACC3	78.267	75.415	75.364
	ACC4	78.295	75.471	76.075

Table 2: Combination of maximum impulsive and maximum convective forces.

The values in Tables 1 and 2 indicate the following

- The impulsive force is significantly higher than the convective force. Therefore, in most of the cases, refinements on the value of the convective force are of little importance on the calculation of the total seismic force.
- In the special case, of broad tanks (low values of tank aspect ratio), consideration of more than one sloshing mode (e.g. two sloshing modes) may be necessary for determining of the total seismic force, due to the appropriate determination of impulsive mass M_I in equation (7), rather than the contribution of higher modes on the value of the maximum convective force F_C.
- The combination of impulsive and convective forces should be conducted according to the SRSS rule, rather than the addition of the maximum convective and maximum impulsive forces.

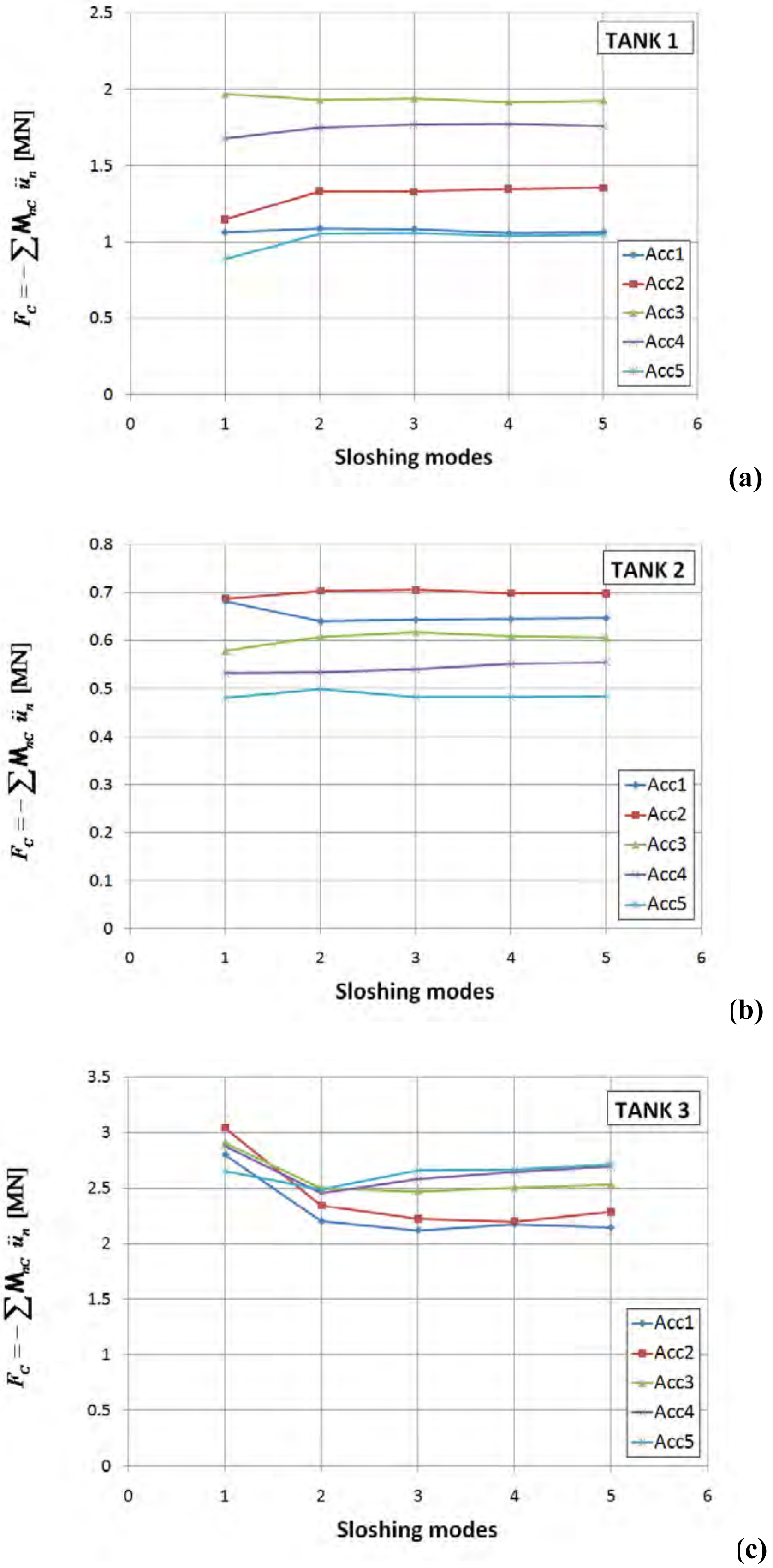

Figure 3: Effect of the number of sloshing (convective) modes on the maximum horizontal convective force for 5 typical ground acceleration excitations (a) Tank I; (b) Tank II and (c) Tank III.

4 EFFECTS OF TANK DEFORMABILITY

In the case of rigid (non-deformable) liquid containers, the impulsive motion is exactly the same as the ground motion, whereas the convective motion is determined by the solution of the hydrodynamic problem within the rigid container. However, steel tanks are not rigid, they deform due to their small thickness with respect to their diameter.

A finite element analysis, which accounted for the dynamic interaction between the liquid and the deformable tank, has been reported by Scharf [8]. Scharf's analysis it is assumed that in flexible tanks the motion of the tank-liquid system is expressed as the sum of three contributions, referred to as: „rigid impulsive’, „sloshing’ and „flexible’. The third component of liquid motion satisfies the condition that the radial velocity of the fluid along the wall equals the deformation velocity of the tank wall, as well as the conditions of zero vertical velocity at the tank bottom and zero pressure at the free surface of the fluid. The total seismic force is given by the following expression

$$F = \mathsf{M}_I\, \ddot{u}_I + \sum_n \mathsf{M}_{nC}\, \ddot{u}_n + \mathsf{M}_f\, \ddot{a}_f \tag{10}$$

In the above expression, the deformation mass M_f is multiplied by the generalized coordinate $\ddot{a}_f$, which expresses the acceleration of the container relative to its base:

$$\ddot{a}_f + 2\xi_f \omega_f \dot{a}_f + \omega_f^2 a_f = -\ddot{X} \tag{11}$$

where ω_f is the natural frequency of the deformation motion. Due to the fact that the dynamic coupling between the sloshing and the flexible components is very weak, due to the large differences between the frequencies of the sloshing motion and of the deformation of the wall, which allows determining the third component of the motion (the deformation component) independently of the others. The rigid impulsive and the sloshing components for non-deformable tanks remains therefore unaffected [10]-[12]. In the work of Scharf [8], closed-form expressions for the impulsive frequency and the deformation mass are reported, and those expressions are included in section A.3.1 of the Informative Annex A of EN 1998-4, stated below:

$$\omega_f = 2\pi \frac{\sqrt{E\left(t_{1/3}\right)/\rho H}}{2R(0.157\gamma^2 + \gamma + 1.49)} \tag{12}$$

where $t_{1/3}$ is the thickness of the tank shell at height equal to $H/3$, and

$$\frac{\mathsf{M}_f}{\mathsf{M}_L} = \psi\gamma \sum_{n=0}^{\infty} \frac{(-1)^n}{\nu_n} d_n \tag{13}$$

where

$$d_n = 2\frac{\left[\int_0^1 f(\zeta)\cos(\nu_n \zeta)\, d\zeta\right]}{\nu_n} \frac{I_1(\nu_n/\lambda)}{I_1'(\nu_n/\lambda)} \tag{14}$$

$\nu_n = (2n+1)\pi/2$, and ψ is a dimensionless parameter that depends on the shape function $f(\zeta)$ and is given by an awkward expression in EN 1998-4, paragraph A.3.1. Scharf [8] describes a tedious iterative methodology that results in the determination of shape function $f(\zeta)$.

In lieu of such a rigorous and tedious analysis described above, simplified models have also been developed to account for the interaction between the deformable cylindrical tank and the liquid. Such a model has been reported by Veletsos et al. [10], which constitutes the basis of the API 650 provisions [3] in calculating the impulsive seismic force. Similar to Scharf's formulation [8], the Veletsos' model [10] further assumes that the convective motion of the liquid remains unaffected by tank shell deformation. Therefore, the hydrodynamic solution for the rigid container is still applicable, and the tank shell deformation affects only the impulsive motion. This methodology has been adopted by the API 650 provisions, whereas the simplified methodology for deformable containers in section A.3.2.2 of EN 1998-4 is in-line with this approach. In particular, the latter provisions specify an impulsive frequency according to the equation (8), and the maximum seismic force is given by the following equation:

$$F = \mathsf{M}_I \, \ddot{u}_I + \sum_n \mathsf{M}_{nC} \, \ddot{u}_n \tag{15}$$

where the impulsive mass, the convective masses and the generalized coordinates u_I and u_n are given by equations (2) and (6) respectively. Assuming the same damping ratio for the impulsive and the deformation motion ($\xi_f = \xi_I$), one readily concludes that the two expressions (10) and (15) for the total seismic force provide identical results provided that (a) the two natural frequencies ω_f and ω_I are equal and (b) the corresponding masses M_f and M_I are equal.

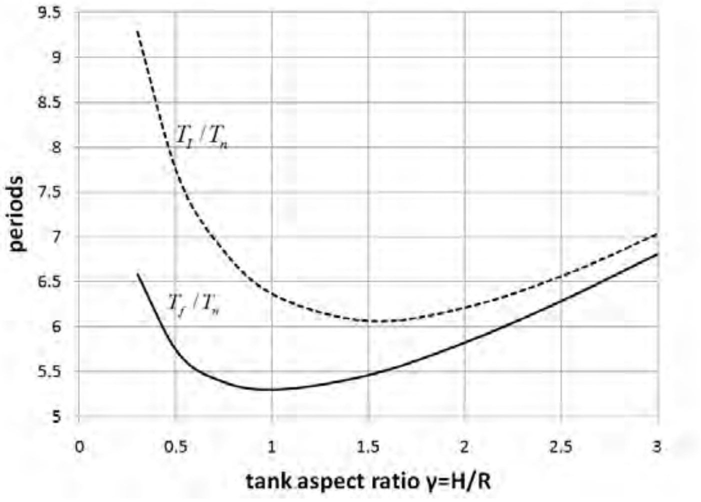

Figure 4: Comparison between the impulsive and the deformation natural periods (T_f and T_I).

The comparison between the impulsive and deformation frequencies is offered in Figure 4, in terms of the corresponding natural periods T_f and T_I, where both periods are normalized by the value of $T_n = \sqrt{\rho R H^2 / E t}$, so that $T_f^* = T_f / T_n$ and $T_I^* = T_I / T_n$, and assuming that the average thickness of the tank shell is equal to the value of $t_{1/3}$. The comparison of the two masses M_f and M_I is offered in Figure 5. The value of M_f is directly obtained by a similar graph in [8]. In the same graph, points (1) and (2) refer to the value of M_f obtained through the application of equations (13) - (14) and assuming a shape function $f(\zeta)$ equal to ζ^2 and ζ respectively.

The above comparison indicates that there exist some differences between the two natural frequencies ω_f and ω_I, and the masses M_f and M_I. However, it is the authors opinion that the simplified methodology proposed by Veletsos et al. [10] can be used for the efficient calculation of seismic action on deformable liquid storage steel tanks.

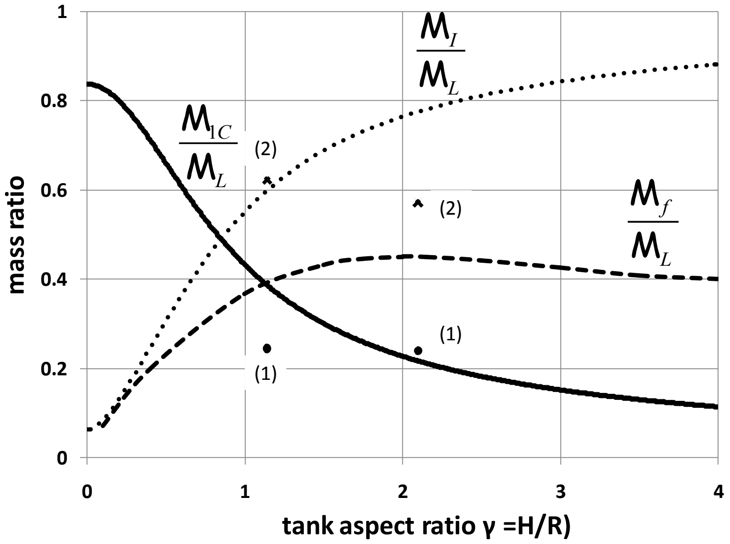

Figure 5: Comparison between the impulsive and the deformation masses (M_f and M_I).

5 CALCULATION OF HOOP HYDRODYNAMIC STRESSES

Thickness design of liquid storage tanks is based on hydrostatic pressure and the corresponding allowable stress of the tank material, as described in section E.6.1.4 of API 650. This calculation neglects the fact that during an earthquake event, additional hoop stresses will developed due to hydrodynamic loading, which need to be added to the stresses from the hydrostatic pressure and compared with the allowable stresses. A methodology for calculating hoop stresses has been proposed in the paper of Wozniak & Mitchell [13] based on the work of Veletsos [10], but up to 2007, it was not considered in design. For the first time, consideration of hoop hydrodynamic stresses and their superposition with the hydrostatic stresses is stated in the new Appendix E of API 650, 2007 edition [3]. On the other hand, there is no special provision of such a methodology in EN 1998-4 [6].

Explicit equations for computing hoop hydrodynamic stresses for the convective and impulsive component of liquid motion (denoted as σ_C and σ_I respectively) are stated in section E.6.1.4 of API 650 (not repeated herein for the sake of brevity), and should be superimposed with the hydrostatic pressure σ_h to obtain the total hoop stress σ_T in the course of seismic event as follows:

$$\sigma_T = \sigma_h \pm \sqrt{\sigma_I + \sigma_C} \tag{16}$$

The predictions of the above equation are compared with finite element results in Table 3, for the three tanks (Tanks I, II and III), which were described in section 1. Linear elastic analysis of the tanks is conducted, where the tanks are modeled with 4-node reduced-integration shell finite elements, and the hydrodynamic pressures (impulsive and convective) are applied on their lateral surface according to the following expressions. The impulsive pressure is

$$p_I(\zeta,\theta,t) = C_I(\zeta)\rho H \cos\theta \ddot{X} \qquad (17)$$

where ρ is the density of the contained liquid, H is the height from the base to the free surface of the liquid, $\zeta = z/R$ is the nondimensional coordinate along the tank height, θ is the circumferential angle, and $C_I(\zeta)$ is a function that depends on the aspect ratio of the tank. The convective pressure is

$$p_C = \rho\psi_1 \cosh(\lambda_n\gamma\zeta) J_1(\lambda_n\xi)\cos\theta \ddot{u}_{1C} \qquad (18)$$

where:

$$\psi_1 = \frac{2R}{(\lambda_1^2 - 1) J_1(\lambda_1)\cosh(\lambda_1\gamma)} \qquad (19)$$

and $\lambda_1 = 1.841$, $\gamma = H/R$, J_1 is Bessel function of the first order, $\ddot{u}_{1C}$ is the acceleration corresponding to the first sloshing mode. The above impulsive and the convective pressure distributions are imposed in the finite element model through a load-user subroutine. For simplicity, the possibility of uplifting in Tanks I and III is excluded, so that all tanks are considered mechanically anchored. The numerical results indicate a good comparison between the numerical results and the above predictions. Given the fact that EN 1998-4 does not include a methodology for calculating hoop hydrodynamic stresses, the corresponding API 650 equations can be used for an efficient prediction of hydrodynamic effects on the total hoop stress of the tank.

	Type of load	Hoop stress from finite element analysis (MPa)	Hoop stress from API 650 (MPa)
Tank I D=27.4m H=15.7m	hydrostatic pressure	116	119
	hydrostatic pressure +earthquake	140	146.3
Tank II D=18m H=19m	hydrostatic pressure	167	168
	hydrostatic pressure +earthquake	190	200.3
Tank III D=68m H=19m	hydrostatic pressure	155	164
	hydrostatic pressure +earthquake	195	203.6

Table 3: Hoop hydrostatic and hydrodynamic stresses computed from finite element models and predicted by API 650.

6 UPLIFTING EFFECTS ON UNANCHORED TANKS

In most of practical applications, relatively broad liquid storage tanks are constructed unanchored, in the sense that their bottom plate is in simple contact with the ground, without anchor bolts. In such a case, under strong seismic loading, the tank may exhibit uplifting of its bottom plate, which may result in (a) excessive stresses at the connection between the bottom plate and the tank shell, and (b) increase of the maximum compressive stress at the shell bottom. This is shown schematically in Figure 6, referring to locations 1 and 2.

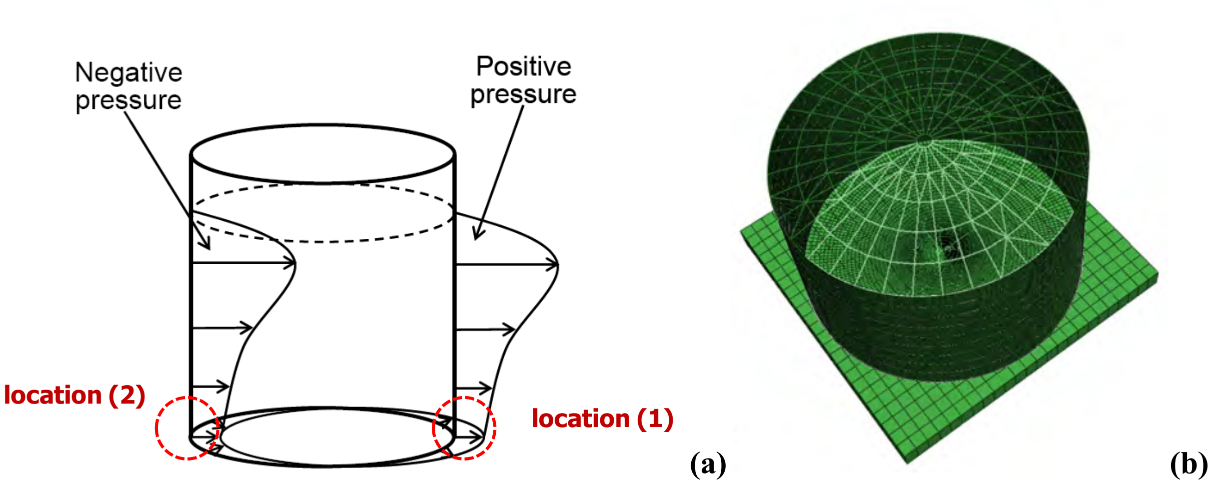

Figure 6: (a) Locations affected by uplifting during seismic action in an unanchored tank; (b) Numerical finite element model for uplifting analysis.

In current design practice, API 650 considers uplifting through the so-called anchorage ratio J defined as follows (neglecting the vertical component of seismic excitation, for the sake of simplicity):

$$J = \frac{M}{D^2 \left[w_t + w_a \right]} \tag{20}$$

If the anchorage ratio is between the values of 0.785 and 1.54, the unanchored tank is stable but its base uplifts. The corresponding compressive stress at the tank shell bottom is given by following expressions, written in more convenient terms:

- For tanks without uplifting:

$$N_{anch} = w_t + \frac{1.273M}{D^2} \tag{21}$$

- For unanchored tanks with uplifting

$$N_{unanch} = \frac{w_t + w_a}{0.607 - 0.187 \left(J \right)^{2.3}} - w_a \tag{22}$$

Paragraph A.9 of Annex A in EN 1998-4 standard describes a methodology for the uplifting effects of unanchored tanks, based on the work of Scharf [8], who conducted a finite element analysis of the tank-liquid system. These effects are presented in graphical form, where the increase of axial compressive stress due to uplifting is plotted against the overturning moment ratio M/WH .

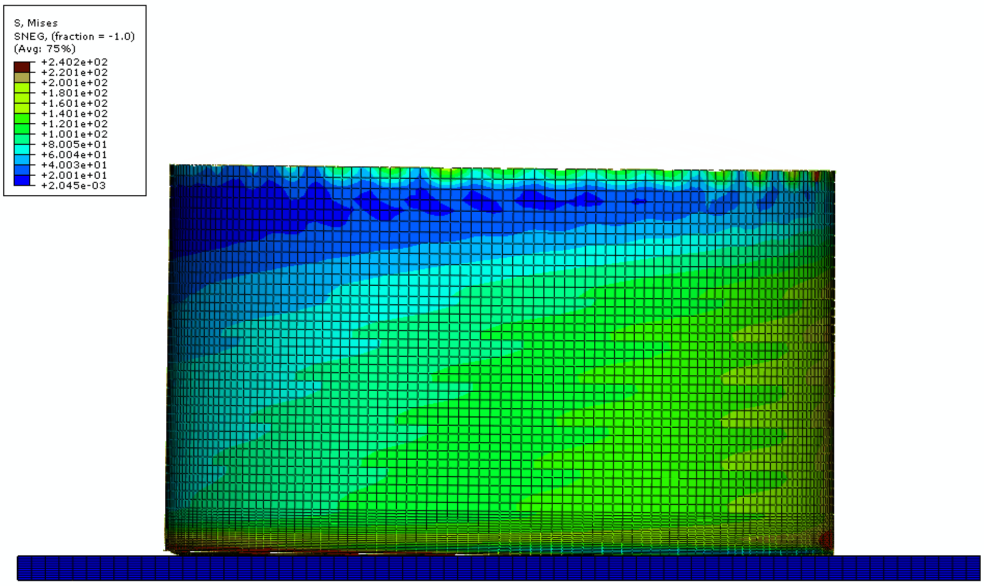

Figure 7: Finite element analysis of unanchored liquid storage tank under lateral loading.

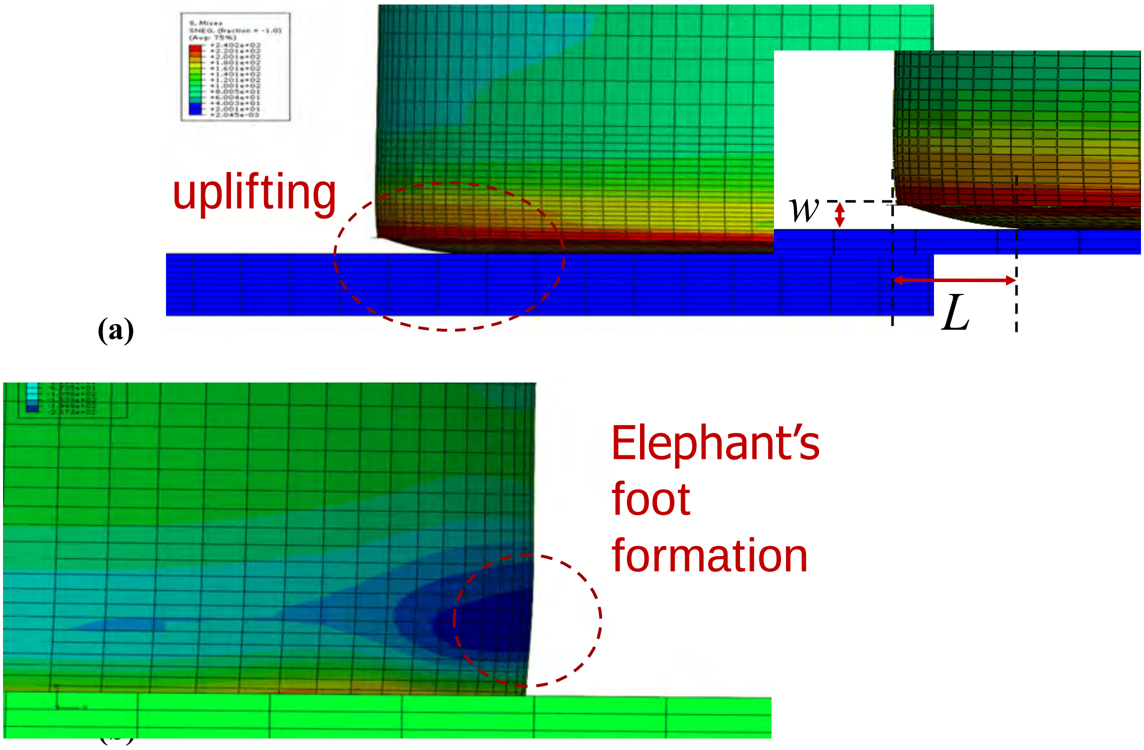

Figure 8: Finite element analysis of unanchored liquid storage tank under lateral loading; (a) uplifting of base plate, (b) development of elephant's foot at the tank bottom.

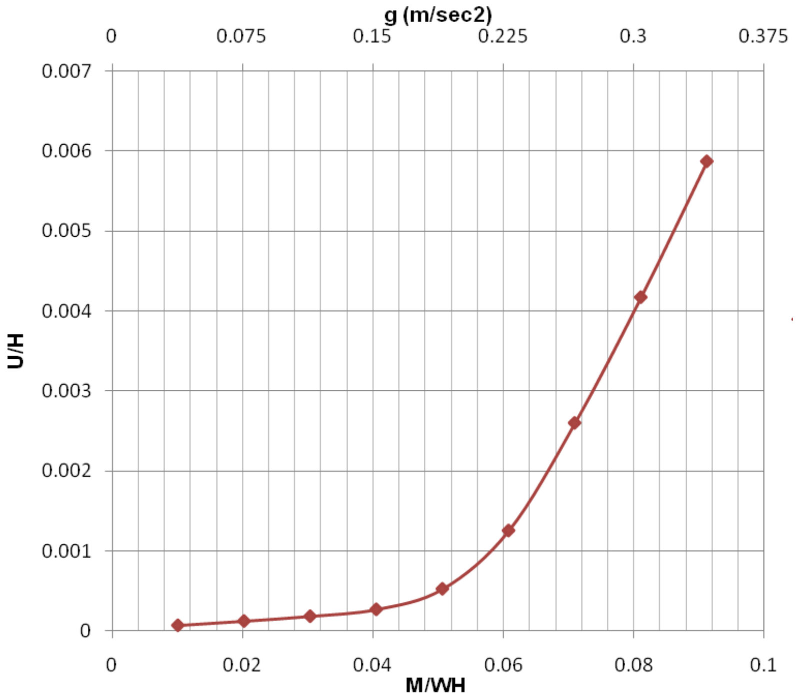

Figure 9: Overturning moment M versus top horizontal displacement U of tank, subjected to finite element pushover analysis.

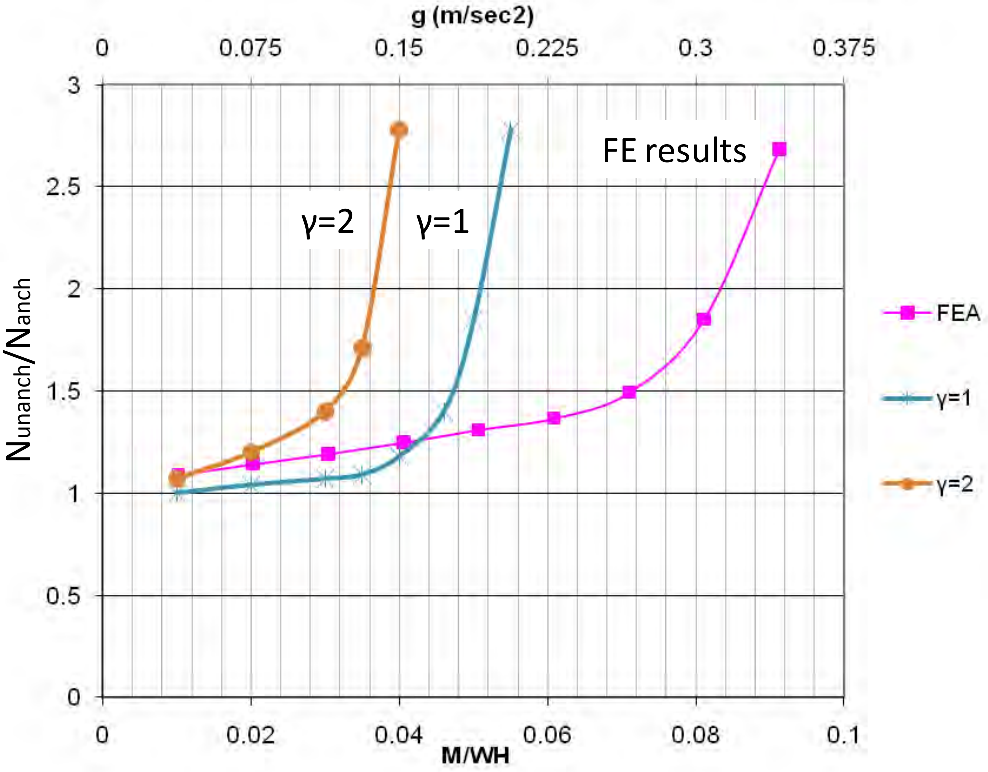

Figure 10: Increase of axial compressive stress on tank shell wall due to uplifting with respect to the overturning moment; finite element pushover analysis versus EN 1998-4 provisions.

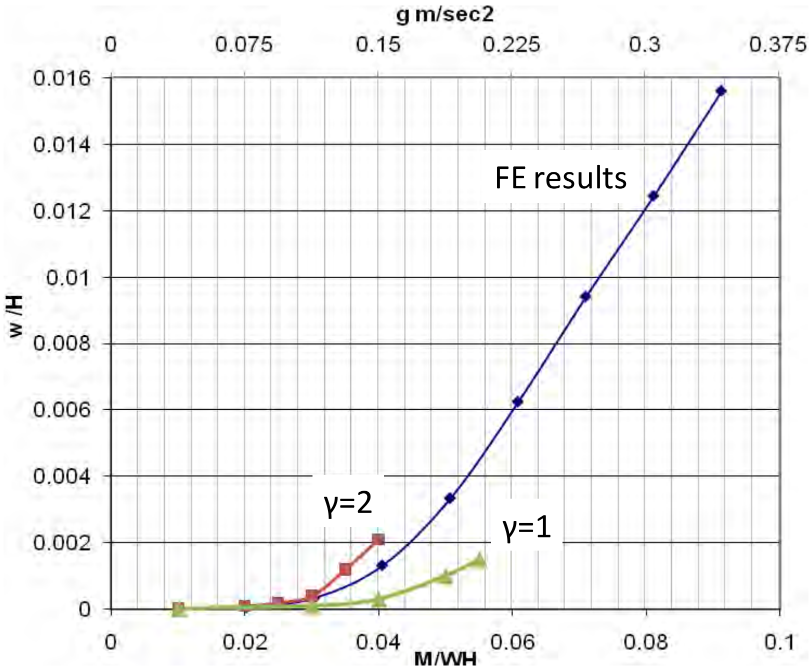

Figure 11: Uplifting size w in terms of overturning moment for Tank I; finite element pushover analysis.

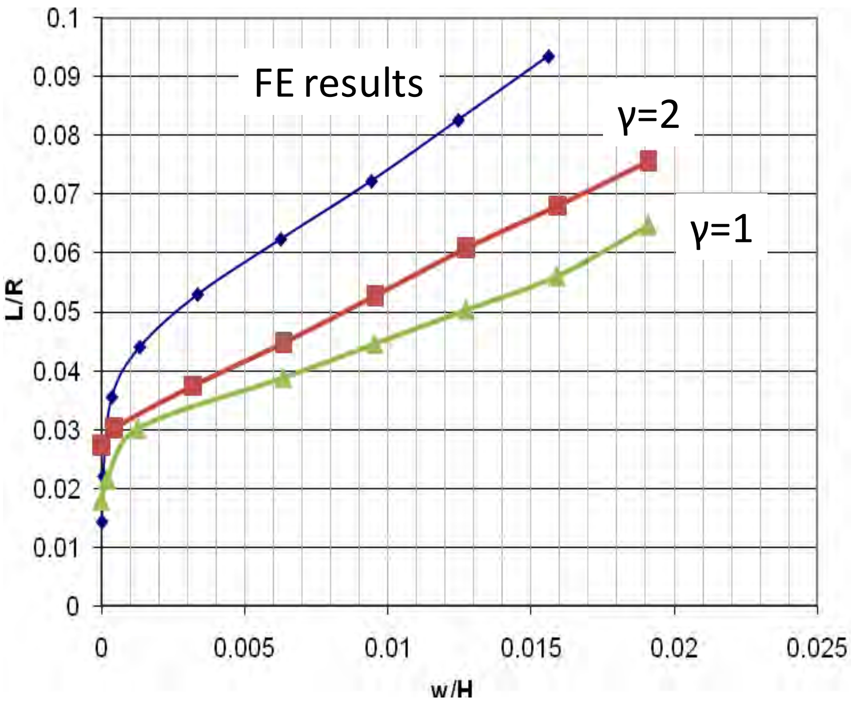

Figure 12: Uplifting length L in terms of uplifting size w for Tank I; finite element pushover analysis.

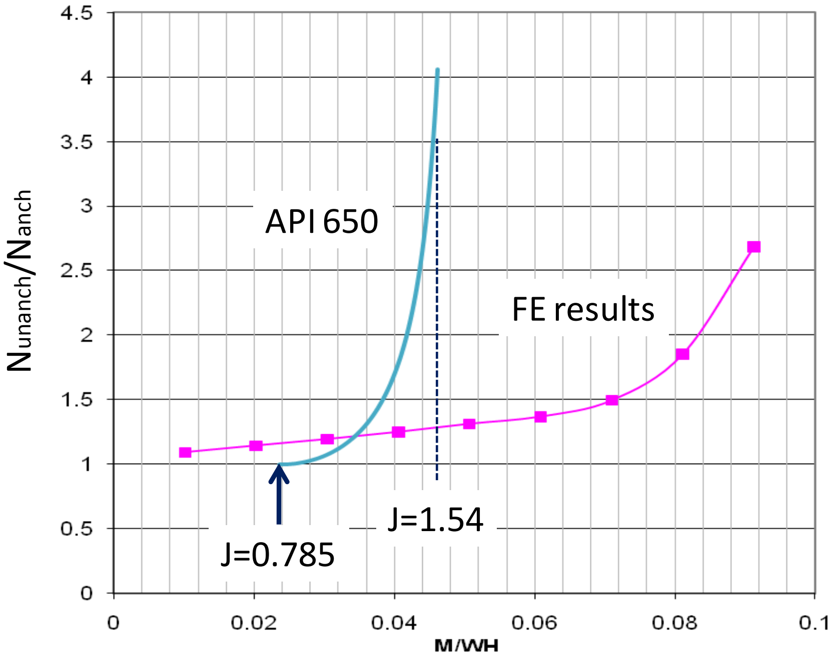

Figure 13: Increase of axial compressive stress on tank shell wall due to uplifting with respect to the overturning moment at the tank shell bottom; finite element pushover analysis versus API 650 provisions.

Herein, using more rigorous finite element simulation tools, the above API 650 and EN 1998-4 provisions for tank uplifting are evaluated. Special emphasis is given on effects of uplifting the compressive stress that causes elephant's foot buckling, which constitutes the major failure mode of the tank under strong earthquake loading. For this purpose, Tank I ($H/R = 1.145$) was simulated with shell finite elements, with the model shown in Figure 6b. All parts of the interacting system were modeled: the tank shell, the truss roof, the base plate, the annular plate, and the ground. Four-node reduced-integration shell elements are employed to model the tank shell and the base/annular plates, the truss roof is modeled with beam elements, whereas solid elements are employed for modeling the ground. Contact conditions are considered between the base/annular plate and the ground, with friction coefficient equal to 0.3, allowing for tank uplift. The analysis is nonlinear static, and the hydrodynamic pressure is applied on the tank shell and the base plate for both the impulsive and the convective component. Considering this distribution of pressure, nonlinear "pushover" analysis is conducted controlling the value of the pressure multiplier, through a Riks continuation algorithm, which allows for the detection of possible instability (buckling) phenomena at the tank shell. Figure 7 and Figure 8 show the uplifting response of Tank I, as obtained by the present finite element simulation.

Figure 9 shows the horizontal displacement of the top of the tank in terms of the normalized overturning moment at the tank base M/WH . The value of M is obtained by an appropriate integration of the pressure on the tank shell surface. The increase of axial compressive stress due to uplift is shown in Figure 10 and the numerical results are compared with the graphs in EN 1998-4. The comparison shows that the EN 1998-4 curves are quite conservative in predicting the increase of axial stress due to uplift. In Figure 11 and Figure 12, the uplift magnitude and as the uplift length are plotted. Comparing the numerical results in Figure 9 and in Figure 11, one readily observes nonlinear inelastic behavior of the tank, as soon as some uplifting of the tank starts. This is associated with inelastic deformation at the uplifted area of the base plate. Furthermore, the comparison between the numerical results and the curves of EN 1998-4 shows that the EN 1998-4 curves represent the general trend but are quite conservative in predicting the effect of uplifting on the axial compressive stress.

Finally, in Figure 13, the finite element results for the axial compressive stress increase due to uplifting are compared with the corresponding provisions of API 650, i.e. expressions (21) and (22). The comparison shows that the API 650 provisions are very conservative. However, this comparison is somewhat unfair, because the overturning moment in API 650 is calculated considering a large value of reduction factor. The value of the reduction factor is discussed in a subsequent section.

7 ELEPHANT'S FOOT BUCKLING

When subjected to earthquake loading, tanks may fail due to excessive compression at the bottom of the tank shell. This is a typical buckling mode of a thin-walled shell under the simultaneous action of meridional compression and hoop tension due to the presence of internal pressure, it is referred to as "elephant's foot buckling" and is considered as the major source of liquid storage tank failure under seismic action [14]. Figure 14 shows two characteristic cases of the elephant's foot buckling following strong earthquakes. In the following, elephant's foot is examined numerically, with emphasis on post-buckling strength.

The possibility of elephant's foot development in Tank I is examined, through the consideration of an axisymmetric finite element model. From Figure 14, it can be concluded that there is a quasi-uniform state of deformation along a significant part of the tank perimeter. Therefore, it is reasonable to assume axisymmetric conditions, for the simulation of this phenomenon, and a meridian strip of is modeled with axisymmetric shell finite elements, as shown in Figure 15. In particular, the tank area near its bottom is simulated (three bottom courses), and the compressive action is applied as external downward loading at the top of each subjected to compressive stresses. The annular plate and the base plate are modeled and frictionless contact is assumed between the plates and the foundation, allowing for uplifting.

Figure 14: Elephant's foot buckling caused by strong earthquake action.

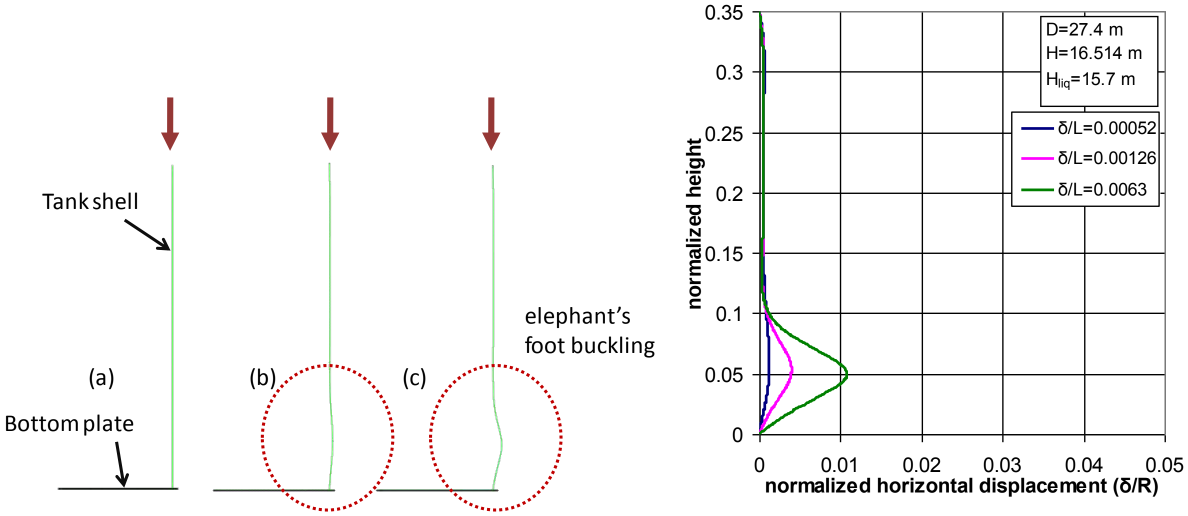

Figure 15: Development of elephant's foot, as predicted by the finite element analysis.

The results from the finite element analysis are shown in Figure 16, in terms of the equilibrium path of the applied axial stress on the tank wall in terms of the vertical and the horizontal outwards displacement of the tank wall. The most important observation refers to the fact that the The buckling shape obtained from the finite element analysis is shown in Figure 17 (in a three-dimensional form) and is very similar to observations from real earthquake events, as shown in Figure 14b. The most important observation refers to post-buckling response of the tank, which appears to be unstable; after reaching a maximum stress (load) the capacity drops very rapidly, indicating that the tank has not any ability of absorbing significant amounts of inelastic energy.

8 BUCKLING AT THE TOP OF THE TANK

Apart from elephant's foot buckling at the tank bottom, previous experience has indicated that liquid storage tanks suffer from buckling at their top. This is called "sloshing buckling" and it is shown in Figure 18. The first attempt to explain this phenomenon was report in the paper by Natsiavas and Babcock [15]. In that work, this type of buckling was attributed to the alternating sign of hydrodynamic (sloshing) pressure on the tank wall during the seismic excitation. More specifically, the tank under hydrostatic pressure exhibits tensile stresses on the tank shell that prevent buckling. However, when – in the course of a seismic event – this pressure becomes negative, i.e. directed inwards, it may overtake the internal (outward) hydrostatic pressure, so that the thin-walled tank top is locally under external pressure leading to shell buckling. It is important to note that, at the top of the tank, hydrostatic pressure is small, so that this overtaking is quite likely to occur, depending on the magnitude of the seismic action.

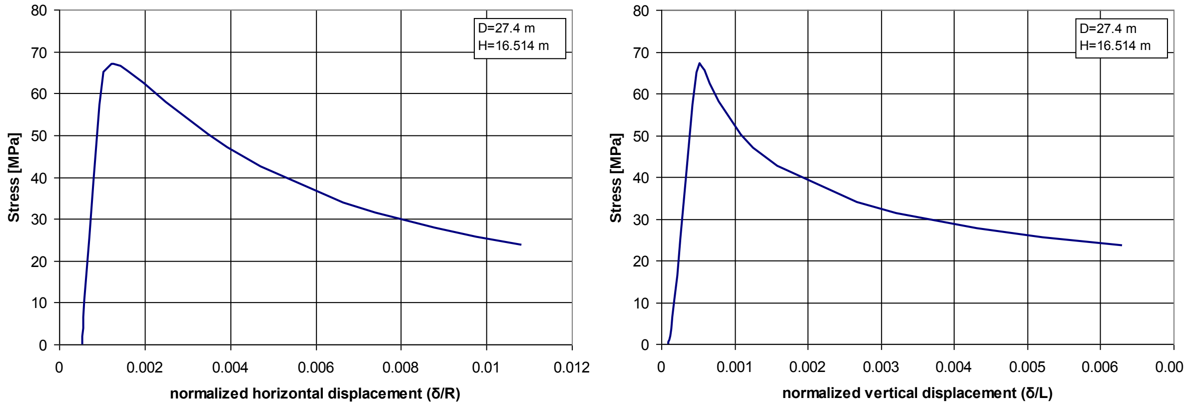

Figure 16: Compressive stress developed at the tank shell wall versus: (a) horizontal outward displacement of the wall, (b) vertical displacement at the top of the model.

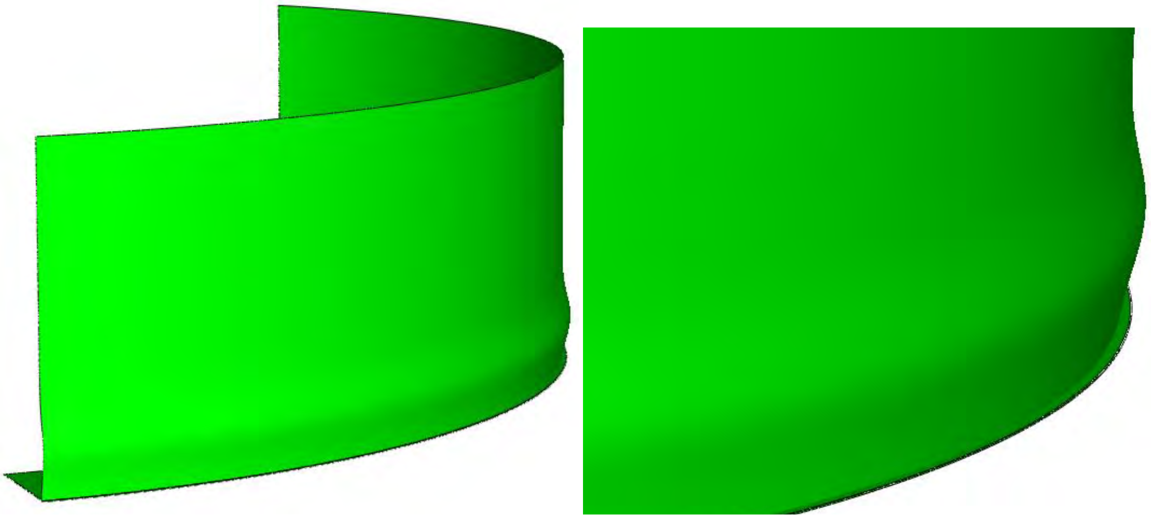

Figure 17: Elephant's foot buckling, as obtained by the finite element simulation.

To quantify this effect, Tank I is considered and the impulsive and convective pressures are computed at $\theta = 0$ and $\theta = \pi$ for 7 artificial earthquakes, corresponding to a maximum ground acceleration of 0.25g. Figure 19 shows the distribution of hydrostatic and hydrodynamic (maximum convective and maximum impulsive) pressure on the tank wall, at $\theta = 0$, for a typical earthquake. Considering that the hydrodynamic pressure are of alternating sign, the numerical results in this graph indicate that outward hydrodynamic pressures may become dominant at the top part of the tank, resulting in an external pressurization of the tank at those locations, leading to buckling. This is shown more precisely in Figure 20, where the hydrodynamic pressures are subtracted from the hydrostatic pressure. The graphs indicate that the external pressure of the tank shell extends over a significant part of its height d_C as shown in Table 4 for 10 earthquake inputs, corresponding to 0.25g.

Figure 18: Sloshing buckling at the top of a tank; Kocaeli, Turkey earthquake 1999 [1].

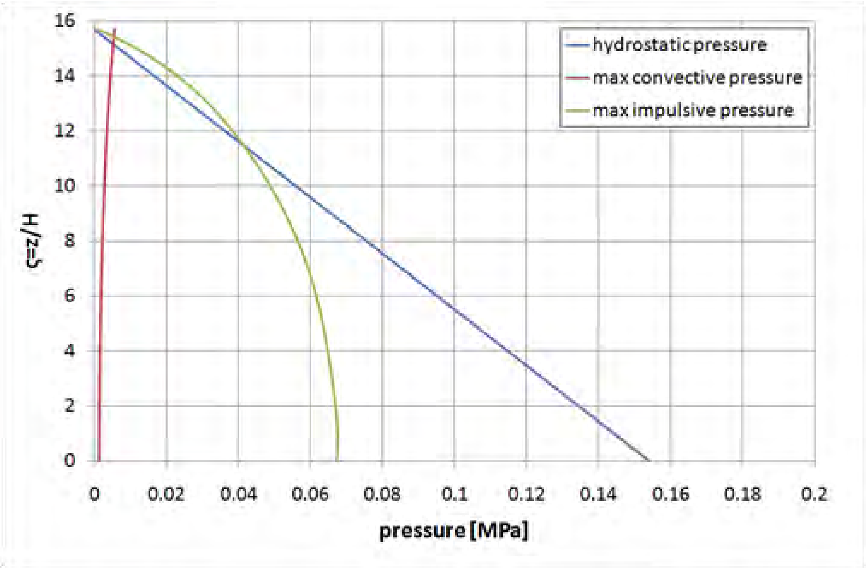

Figure 19: Distribution of hydrostatic pressure and maximum hydrodynamic pressures (impulsive and convective) along the height of Tank I for a characteristic seismic event of 0.25g.

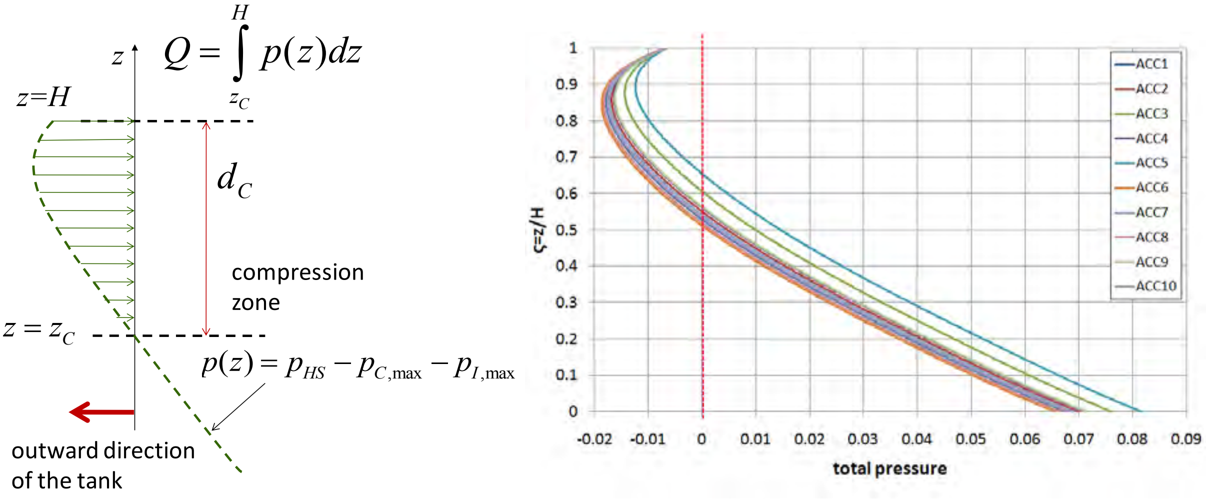

Figure 20: (a) Schematic representation of compressive (inward) pressures at the top of the tank; (b) Results from 10 artificial ground acceleration inputs (0.25g).

	Maximum impulsive acceleration [g]	**Maximum convective acceleration [g]**	**Height of compression zone d_C [m]**	**Force per unit circumferential length Q [kN/m]**
ACC1	0.790	0.05	7.40	89.35
ACC2	0.768	0.05	7.05	80.49
ACC3	0.711	0.05	6.15	60.51
ACC4	0.757	0.05	6.90	76.32
ACC5	0.660	0.05	5.40	46.05
ACC6	0.808	0.05	7.65	97.09
ACC7	0.777	0.05	7.20	84.04
ACC8	0.800	0.05	7.55	93.59
ACC9	0.754	0.05	6.85	75.20
ACC10	0.785	0.05	7.30	87.27

Table 4: Height of the compression zone at the top of the tank and corresponding inward force per unit circumferential length.

An estimate of the compressive hoop stress developed at the tank shell top can be obtained by considering the total inward force per unit circumference length Q distributed along the compression zone d_C (see Figure 20a), so that an equivalent external pressure is computed as follows

$$p_{eq} = f\frac{Q}{d_C} \tag{23}$$

where f is a factor accounting for the non-uniform distribution of pressure on the compression zone, From simple statics of thin-walled cylindrical shells, one can readily calculate the corresponding compressive hoop stress considering axisymmetric conditions around the location of maximum compression $\theta = 0$, one may assume that the top of the tank behaves as a circular under uniform external pressure and the corresponding compressive hoop stress is

$$\sigma_\theta = \frac{p_{eq}D}{2t} \tag{24}$$

Resistance of the thin-walled tank shell against this type of buckling is offered by considering one or more ring stiffeners at the top of the tank. The design of those ring stiffeners can be conducted according to the newly published ECCS European Design Recommendations for Shell Buckling [16]. It is the author's opinion that the stiffener dimensions should be increased to account for the nonlinear effects of liquid sloshing, as well as for the impulsive nature of the sloshing wave. Using the above analysis and considerations, the development of new specific rules for determining the buckling resistance of tank shell at its top is a necessity, but it is outside the scope of the present study.

9 A NOTE ON THE BEHAVIOR FACTOR FOR LIQUID STORAGE TANKS

The behavior factor to be used in the seismic design of liquid storage tanks has created quite some controversy. It is worth noticing that the API 650 provisions adopt totally different values than those of EN 1998-4, as shown in the following Table 5.

	Impulsive	Convective
API 650		
Self-anchored	3.5	2.0
Mechanically-anchored	4.0	2.0
EN 1998-4		
For all anchorage systems	1.5	1.0

Table 5: Values of behavior (reduction) factor for seismic design of liquid storage tanks.

A first observation refers to the smaller values for the convective motion in comparison with the impulsive motion. This is attributed to the fact that the convective response may not be capable at dissipating seismic energy. However, it is quite interesting to note that while EN 1998-4 specifies $q = 1$ for the convective force, the API 650 rules specify $R = 2$, which implies the presence of a dissipating mechanism in the convective (sloshing) motion.

Furthermore, there exist striking differences on the values of q and R for the impulsive component of the seismic force, which need some further investigation. The ductility of the structural system constitutes the main parameter for the reduction of the seismic force. In particular, considering elephant's foot buckling as the dominant mode of buckling, the numerical results presented in a previous section demonstrate the limited capability of the tank shell of absorbing and dissipating seismic energy due to their unstable post-buckling behavior. Communication of the authors with the API 650 drafting committee (see Acknowledgements below) indicated that the relatively high values of reduction factors R adopted by the American standards is based both on previous experience, as well as on other dissipation mechanisms such as radiation damping at the tank foundation (soil-tank interaction), the ductility of the anchor bolts, or the inelastic behavior of the base plate in the case of uplifted unanchored tanks. As far as elephant's foot buckling is concerned, the significant drop of strength following buckling, shown by the numerical results of Figure 16 are not in favor of using a value of behavior (reduction) factor significantly higher than unity. On the other hand, the moment-displacement curve of Figure 9, indicates that such a dissipating mechanism may exist in unanchored tanks exhibiting uplifting. In any case, the identification of appropriate seismic energy dissipation mechanisms that would allow the use of behavior factor larger than unity is an open research issue, which needs significant additional research effort.

10 NONLINEAR SLOSHING EFFECTS

The calculation of hydrodynamic forces described in the above sections was based on linear liquid hydrodynamic theory. The basic assumption for this theory is the small-amplitude of sloshing waves, allowing for the linearization of the liquid free-surface boundary condition. More specifically, assuming ideal fluid conditions, the liquid motion in a undeformed (rigid) container, under horizontal excitation displacement $X(t)$ in the x direction is described by the flow potential $\Phi(x, y, z, t)$, so that the liquid velocity is the gradient of Φ ($\mathbf{u} = \nabla\Phi$), which satisfies the Laplace equation in the liquid domain,

$$\nabla^2\Phi = \frac{\partial^2\Phi}{\partial x^2} + \frac{\partial^2\Phi}{\partial y^2} + \frac{\partial^2\Phi}{\partial z^2} = 0 \tag{25}$$

subjected to the following boundary conditions at the wet surface of the vessel wall

$$\frac{\partial \Phi}{\partial n} = \dot{X}\left(\mathbf{e}_x \cdot \mathbf{n}\right) \tag{26}$$

In the free-surface, the liquid should satisfy the kinematic and the dynamic boundary conditions, shown below:

$$\frac{\partial \eta}{\partial t} + \frac{\partial \eta}{\partial x}\frac{\partial \Phi}{\partial x} - \frac{\partial \Phi}{\partial z} = 0 \tag{27}$$

and

$$\frac{\partial \Phi}{\partial t} + \frac{1}{2}\left(\nabla \Phi\right)^2 + g\eta = -\ddot{X}x \tag{28}$$

If small-amplitude sloshing is assumed, then keeping only the linear terms of η and Φ in the above equations, and eliminating η, one obtained the following combined condition, widely used for linear analysis:

$$\frac{\partial^2 \Phi}{\partial t^2} + g\frac{\partial \Phi}{\partial z} = 0 \tag{29}$$

The question is whether the assumption for small-amplitude sloshing is valid or not in the course of a strong earthquake. This requires an rigorous analysis based on either an asymptotic solution or a nonlinear finite element analysis of the liquid within the container, which is outside the scope of the present study. A preliminary analysis of this type has been conducted by Chen et al. [17], where the containment of rectangular liquid storage tanks have been modeled with finite elements through an in-house moving grid methodology, and subjected to several earthquake inputs. The results indicated that:

- Nonlinear effects may be non-important for the calculation of the total seismic forces
- In strong and distant (low-frequency) earthquakes, the liquid surface elevation (sloshing wave height) can be affected. For the majority of seismic events, this effect is not very important

The above preliminary results demonstrate that the use of linear sloshing theory for determining the seismic action on the tank wall adequate, verifying the expressions proposed in current design standards, whereas the possible nonlinear sloshing effects on the sloshing wave amplitude can be accounted for through an appropriate increase of freeboard height specified by the design specifications.

11 CONCLUSIONS

In this paper several issues on the dynamic behavior of liquid storage tanks have been addressed and investigated. The main conclusions can be stated as follows:

- For the majority of tanks, consideration of only one sloshing (convective) mode is adequate for the calculation of the total seismic force.
- The combination of the convective force with the impulsive force should be conducted according to the SRSS rule, which in accordance with the design provisions of API 650, Annex E.

- Numerical results show that the EN 1998-4 provisions provide a reasonable yet conservative of the increase of axial compression due to uplifting.
- A simple methodology is presented in order to design tanks against buckling at the top, due to liquid sloshing, using the concept of "equivalent" external pressure.
- The behavior (reduction) factor for the seismic design of liquid storage tanks is a controversial issue that has not been examined thoroughly so far. Because of the relatively low post-buckling strength of the shell tank, the authors would be quite cautious in using a behavior factor greater than 1.5 for the impulsive component of motion.
- Nonlinear sloshing effects on the seismic behavior have not been thoroughly investigated so far. Limited numerical investigations, reported elsewhere, indicated that their effects on the total seismic force may not be important, but they can have significant effects on freeboard considerations.

12 ACKOWLEDGEMENTS

This work was carried out with a financial grant from the Research Fund for Coal and Steel of the European Commission, within **INDUSE** project: "STRUCTURAL SAFETY OF INDUSTRIAL STEEL TANKS, PRESSURE VESSELS AND PIPING SYSTEMS UNDER SEISMIC LOADING", Grant No. RFSR-CT-2009-00022. The authors also wish to thank Dr. Steven W. Meier, TANK INDUSTRY CONSULTANTS, INC., member of the AWWA D100 and API 650 drafting committees, for his valuable comments on the reduction (behaviour) factor for tank seismic design.

REFERENCES

[1] Suzuki K. (2002), "Report on damage to industrial facilities in the 1999 Kocaeli earthquake, Turkey.", *Journal of Earthquake Engineering*, Vol. 6, No. 2, pp. 275-296.

[2] Nielsen R. and Kiremidjian A. (1986), "Damage to oil refineries from major earthquakes.", *ASCE Journal of Structural Engineering*, Vol. 112, No. 6, pp.1481-1491.

[3] American Petroleum Institute (2007), *Seismic Design of Storage Tanks - Appendix E, Welded Steel Tanks for Oil Storage*, API 650, 11th Edition, Washington, D.C.

[4] American Petroleum Institute (2003), *Seismic Design of Storage Tanks - Appendix E, Welded Steel Tanks for Oil Storage*, API 650, 10th Edition, Washington, D.C.

[5] American Society of Civil Engineers (2006), *Minimum Design Loads for Buildings and Other Structures*, ASCE 7-05, Reston, VA.

[6] Comité Européen de Normalization (2006), *Silos, tanks and pipelines, Eurocode 8, part 4,* CEN/TC 250*,* EN-1998-4, Brussels.

[7] Rammerstorfer, F. G., Fisher, F. D. and Scharf, K. (1990), "Storage Tanks Under Earthquake Loading", *ASME Applied Mechanics Reviews,* Vol. 43, No. 11, pp. 261-283.

[8] Scharf, K. (1990), "Beiträge zur Erfassung des Verhaltens von erdbebenerregten, oberirdischen Tankbauwerken", *Fortschritt-Berichte VDI, Reihe 4. Bauingenieurwesen*, Nr. 97, VDI Verlag, Düsseldorf,.

[9] Rotter, J. M. (1990), Local Inelastic Collapse of Pressurized Thin Cylindrical Steel Shells under Axial Compression, *ASCE Journal of Structural Engineering,* Vol. 116, No.7, pp. 1955-1970

[10] Veletsos, A. S. and Yang, J. Y. (1977), “Earthquake Response of Liquid Storage Tanks”, *2nd ASCE Engineering Mechanics Conference*, Raleigh, NC, pp. 1-24

[11] Haroun, M. A. and Housner, G. W. (1981), “Seismic Design of Liquid Storage Tanks”, *ASCE Journal of the Technical Councils*, Vol. 107, No. 1, pp. 191-207

[12] Fischer, F. D., Rammerstorfer, F. G. (1999), "A Refined Analysis of Sloshing Effects in Seismically Excited Tanks"; *International Journal of Pressure Vessels and Piping*, Vol. 76, pp. 693-709.

[13] Wozniak, R. S. and Mitchell, W. W. (1978), “Basis of seismic design provisions for welded steel oil storage tanks”, *Advances in Storage Tank Design,* API 43rd mid-year meeting, Toronto, Canada.

[14] O'Rourke, M. J. and So, P. (2000), “Seismic Fragility Curves for On-Grade Steel Tanks.” *Earthquake Spectra*, Vol. 16, No. 4, pp. 801-815.

[15] Natsiavas, S. and Babcock, C. D. (1987), “Buckling at the Top of a Fluid-Filled Tank During Base Excitation”, *ASME Journal of Pressure Vessel Technology*, Vol. 109, No. 4, pp. 374-380.

[16] European Convention for Constructional Steelwork (2008), *Buckling of Steel Shells, European Design Recommendations*, 5th Edition, ECCS Publication No. 125, J. M. Rotter and H. Schmidt Eds., Brussels, Belgium.

[17] Chen W., Haroun M. A., and Liu F. (1996), “Large amplitude liquid sloshing in seismically excited tanks”, *Earthquake Engineering & Structural Dynamics*, Vol. 25, No. 7, pp. 653-669.

COMPDYN 2011
III ECCOMAS Thematic Conference on
Computational Methods in Structural Dynamics and Earthquake Engineering
M. Papadrakakis, M. Fragiadakis, V. Plevris (eds.)
Corfu, Greece, 26–28 May 2011

STUDY ON EFFECTS OF WATER DEPTH ON SEISMIC PERFORMANCE OF THE AQUEDUCT-WATER COUPLING STRUCTURE

Qiuhua Duan[1,2], **Lufeng Yang**[1], **Menglin Lou**[2]

[1] Key Laboratory of Disaster Prevention and Structural Safety of Ministry of Education,
School of Civil engineering and Archittecture, Guangxi University, Nanning 530004, P. R. China
e-mail: dqh@gxu.edu.cn , lfyang@gxu.edu.cn

[2] State Key Laboratory for Disaster Reduction in Civil Engineering,
Tongji University, Shanghai 200092, P. R. China
e-mail: lml@tongji.edu.cn

Keywords: Water Depth in Tank, Aqueduct Structure, Seismic Performance.

Abstract. *This paper uses finite element method to study how the change of water depth in tank affects the seismic performance of the aquedcut-water coupled structure. The results shows that sloshing amplitude of the water in U-shape aqueduct is very significant; the vribration frequency of the aqueduct structure is reduced due to the existence of the water body, and then the response wave shape of the aqueduct body is changed relatively. This explains that the effect of the water in the aqueduct structure has great relationship with the spectrum dynamic properties of the input earthquake wave. Water in the aqueduct plays TLD damping when the frequency scale of the input earthquake wave includes the basic frequency of the aqueduct structure and the vibration frequency of the water in the aqueduct is closed to the the basic frequency of the aqueduct structure. Finally an approximate criterion is also put forward to adjudge when the aqueduct water plays TLD damping through judging mass ratio and frequency ratio, and gives the discriminate.*

1 INTRODUCTION

The water weight on the top of the large aqueduct structures is generally heavier than structure self-weight, some reached 1.5 ~ 2.0 times as much[1]~[7]. Under the earthquake, the ground acceleration superpositons of the elastic vibration acceleration on the top of the aqueduct structure, that make fluid vibrate, which causes thus the bigger sloshing amplitude of the fluid and the sloshing of the fluid has impact on the vibration of the aqueduct structure relatively. Many scholars' research shows that[8]~[12], the role of the aqueduct water sloshing is not allowed to ignore under the earthquake, which has great threats on the security of the aqueduct structure; However in some reference[13]~[14] think the water in the aqueduct plays TLD damping on the bent-support aqueduct structural system, the sloshing of the water is stronger, and the TLD damping effect of the water on the structure is stronger.

Due to the dynamic response of the aqueduct - water coupling structure under the earthquake is complicated, involving many factors, whether the water is benefit or harm to the anti-seismic performance of the whole structure system, still remain to be further studied. In this paper, through changing the water depth in the aqueduct the anti-seismic performance of the aqueduct-water coupling structure is discussed by the analysis of many cases.

2 CALCULATION PARAMETERS AND CALCULATION CASES[15]

The aqueduct model analyzed in this paper is shown in Fig. 1 and Fig.2. The aqueduct has three spans with the length of 12.0m for each span. The U-type aqueduct body is supported with a bent via a basin-shaped rubber support. The bents of the aqueduct are H-shape with the height of 8.0m and fixed bottoms.

The U-type aqueduct section dimension: width is 8.0m, height is 6.9m, inner radius is 3.5m, out radius is 3.8m. The material parameters used in the calculation are: mass density of reinforced concrete is 2700kg/m^3, Poisson’s ratio is 0.1667.

Considering the change of the water depth in the aqueduct, the calculation conditions includes that the depth of water in the aqueduct is 0m, 2.50m, 4.41m respectively.

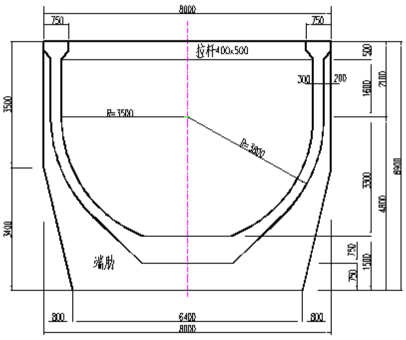

Fig. 1 Section of the aqueduct model

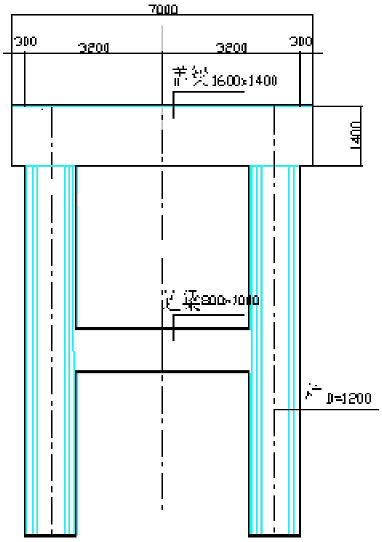

Fig. 2 Section of the bent model

3 DYNAMIC CHARACTERISTICS AND RESPONSE OF HEADINGS OF THE AQUEDUCT-WATER COUPLING STRUCTURE WHEN CHANGING THE DEPTH OF WATER IN AQUEDUCT

Figure 3 shows a three-dimensional calculation model of the bent-type aqueduct - water coupling structure, among which Figure 3 (a) is empty-aqueduct model (water depth h= 0m), Figure 3 (b) is half-aqueduct model(water depth h= 3.50m), and Figure 3 (c) is full-aqueduct model (water depth h= 4.41m).

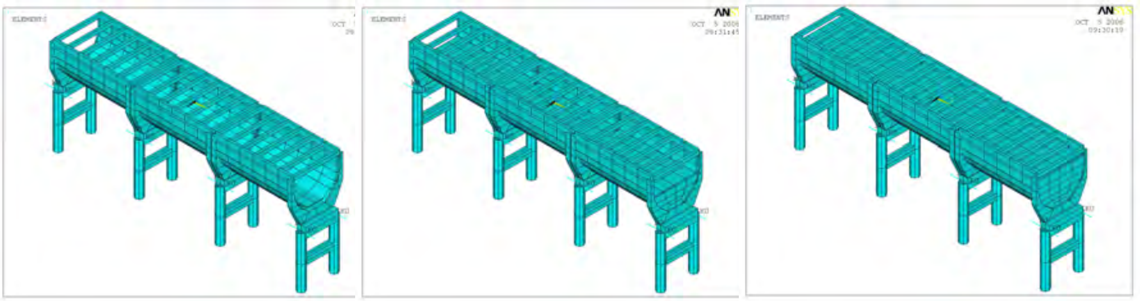
(a) (b) (c)

Fig. 3 Three-dimensional calculation model of the bent-type aqueduct - water coupling structure

3.1 Dynamic characteristics

Table 2 is the first frequency in all direction of the aqueduct structure with different water depth.

Depth of water (m)	Horizontal (X direction)	Longitudinal (Y direction)	Vertical (Z direction)
h=0	2.41	1.24	13.58
h=3.50	2.07	0.99	10.93
h =4.41	1.75	0.86	9.19

Table 1: The first frequency in all direction of the aqueduct structure with different water depth.(Hz)

From the result shown in Table 2, the whole natural frequency of the aqueduct structure is reduced following the depth of water in aqueduct is increased, these indicates that the mass of the structure is larger and the frequency of the structure is lower due to the quality of water body in the aqueduct, which is consistent with experimental results obtained. As the water depth increases from 0m to 3.50m, the whole horizontal base frequency decreases 14.1%, the longitudinal base frequency decreases 20.2%, the vertical base frequency decreases 19.5%. As the water depth increases from 3.50m to 4.41m, the whole horizontal base frequency decreases 18.3%, the longitudinal base frequency decreases 13.1%, the vertical base frequency decreases 15.9%; When the water depth increases from 0m to 4.41m, the whole horizontal base frequency decreases 27.4%, the longitudinal base frequency decreases 30.7%, the vertical base frequency decreases 32.3%.

It indicates that the vibration characteristics of the aqueduct structure in every direction are greatly affected when the depth of water in aqueduct change greatly, especially for the vertical base frequency. Therefore, the effect of the water in aqueduct on the vibration characteristics and anti-seismic performance should be not ignored.

Figure 4 represents the mode schemes of the aqueduct prototype structure in all directions. Figure 4(a)~(b) represent the first order mode schemes of the aqueduct prototype structure without water and fulled with water in X direction respectively; Figure 4(c)~(d) represent the first order mode schemes of the aqueduct prototype structure without water and fulled with water in Y direction respectively; Figure 4(e)~(f) represent the first order mode schemes of the aqueduct prototype structure without water and fulled with water in Z direction respectively. The calculation result indicates that the local modes of water sloshing appears at first when there is water in the aqueduct.

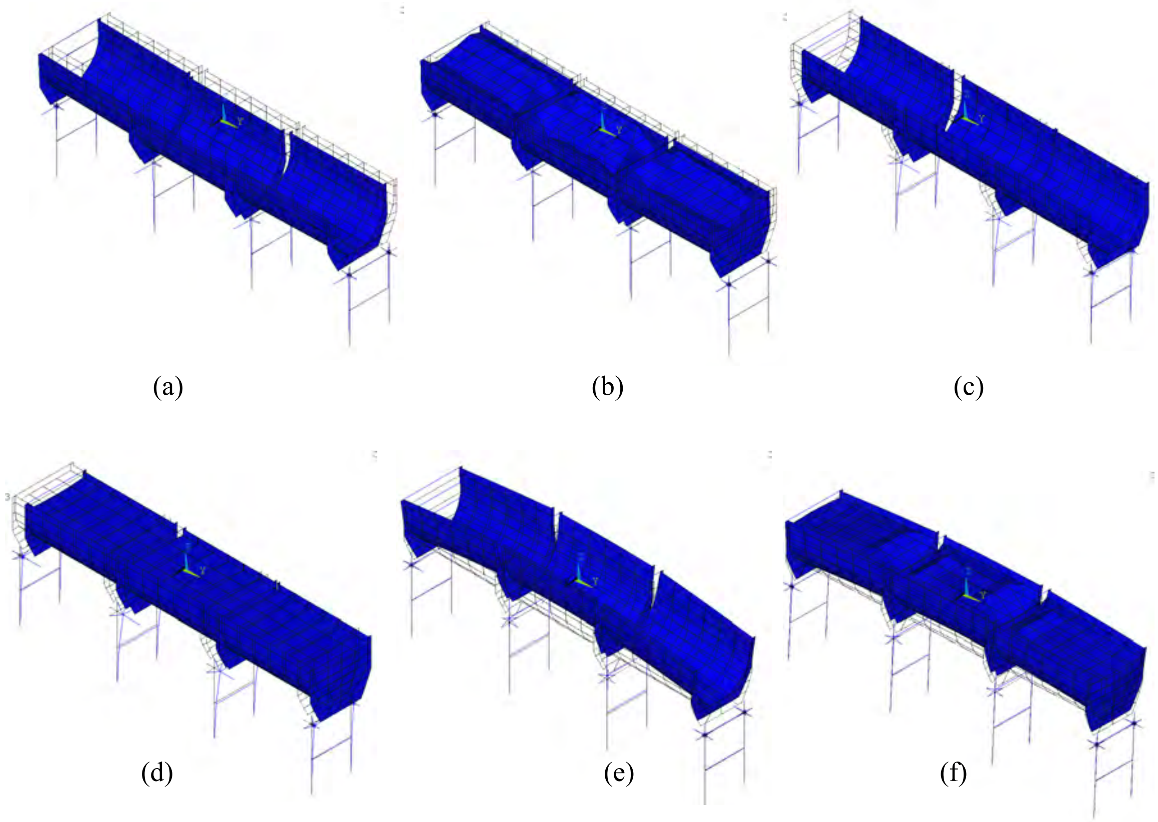
(a) (b) (c)

(d) (e) (f)

Fig. 4 Mode schemes of the bent-type aqueduct prototype structure in all directions

3.2 Acceleration response characteristics

The top point in the middle of the middle span aqueduct body is selected as research object for better descripting the effect of the water in aqueduct on the earthquake response of the aqueduct-water coupling structure. Figure 5 ~ Figure 6 show that the acceleration time-history curves of the measuring point 26 on the top of the aqueduct body under the action of EI Centro wave and ANPING wave repectively, when there is different water depth in aqueduct(*h*=0m, 3.50m, 4.41m).

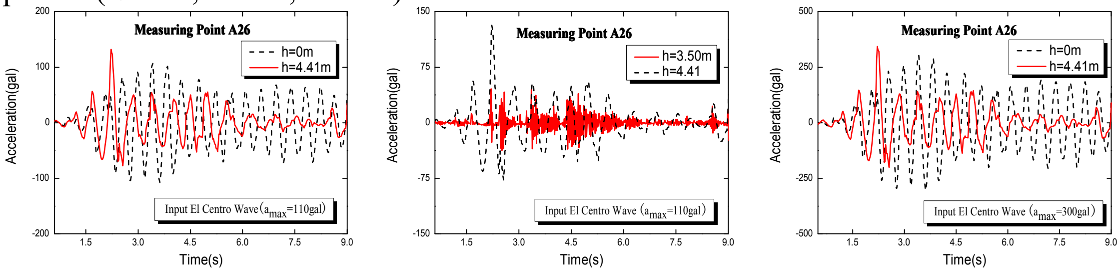

(a) (b) (c)

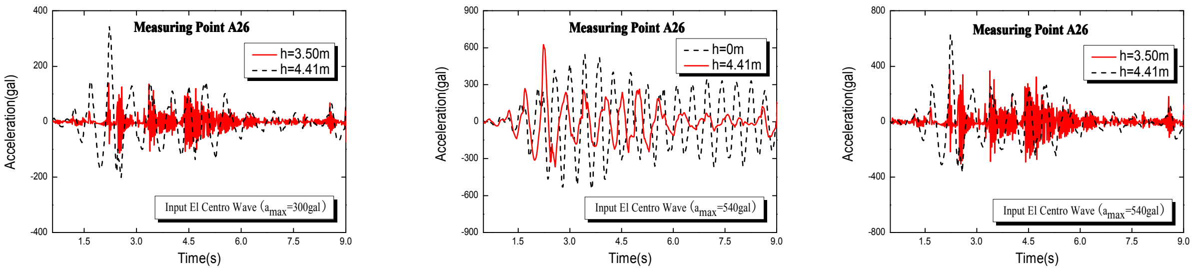

(d) (e) (f)

Fig. 5 Earthquake esponse of the aqueduct body with different water depth under El Centro wave

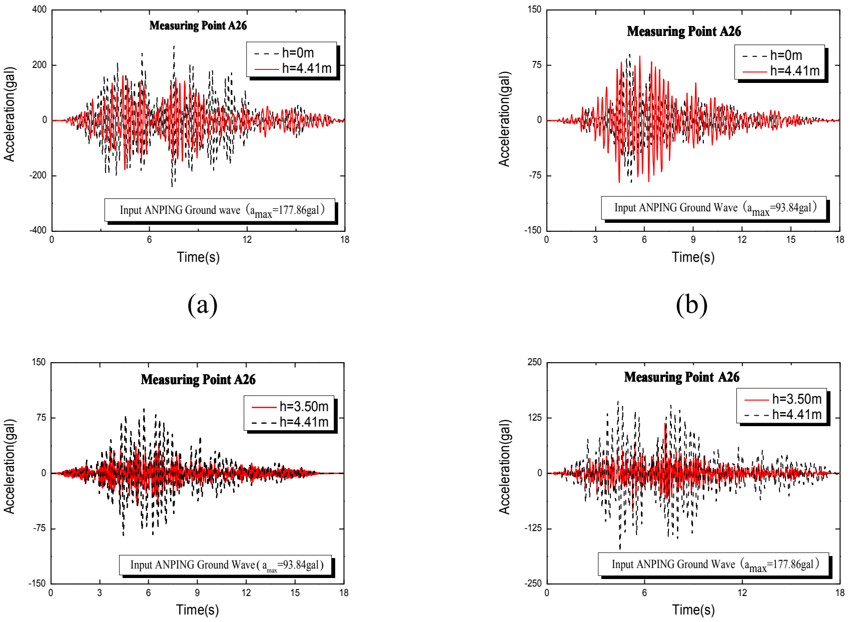

(a) (b)

(c) (d)

Fig. 5 Earthquake esponse of the aqueduct body with different water depth under ANPING wave

From figure 5~figure 6, it can be observed that the acceleration response of the measuring point A26 increases with the increasement of the peak values of the input earthquake wave. When input El centro wave, the acceleration response of the measuring point A26 with empty-aqueduct is larger than full with water, but its' response is not decrease as the water depth increase. When the water depth is 3.50m, also called half-aqueduct, the acceleration response of the measuring point A26 is smaller than full-aqueduct. When input El Centro wave of the peak accleration 110gal, the ratio of the empty-aqueduct to full-aqueduct is 1.50, the ratio of the full-aqueduct to the empty-aqueduct is 3.43; When input El Centro wave of the peak accleration 300gal, the ratio of the empty-aqueduct to full-aqueduct is 1.34, the ratio of the full-aqueduct to the empty-aqueduct is 2.88; When input El Centro wave of the peak accleration 540gal, the ratio of the empty-aqueduct to full-aqueduct is 1.06, the ratio of the full-aqueduct to the empty-aqueduct is 2.91. When input ANNPING wave of the peak accleration 93.84 gal, the acceleration response of the measuring point A26 without water is little smaller than that full of water except at 3.9~5.5 second. The acceleration response of A26 is larger that the half-aqueduct, and both peak values of the half-aqueduct and the full-aqueduct.The ratio of both peak acceleration is 4.06; When input ANNPING wave of the peak accleration 177.86 gal, the acceleration response of the measuring point A26 at full-aqueduct is much larger than that at half-aqueduct. The ratio of the peak value acceleration at the full-aqueduct to half-aqueduct is 3.27. In addition, it can be seen from the figures obviously, that the waveforms of the acceleration response of the measuring point A26 are different when the aqueduct with water and without water.

This shows that the water sloshing in aqueduct changes the dynamic characteristics of the aqueduct structure, and the water plays a TLD damping role to a certain extend, however, TLD effect is not stronger fllowing the more water sloshing more powerful. In this model, inputting El Centro wave horizontally, TLD effect reaches the strongest when the water volume is a half of the whole tank($h = 3.50$ m); The acceleration response of the aqueduct-water coupling structure increases when the aqueduct is full with water($h = 4.41$ m), but that still smaller than that when the aqueduct is empty. Because the natural frequency of the water is 1.38 Hz when the water depth is 3.50m, the natural frequency of the water is 1.09 Hz when the water depth is 4.41m, the fundamental frequency of the aqueduct structure(2.41 Hz) is closer to the natural frequency of aqueduct when the water depth is 3.50m, and then the main frequency range of El Centro wave aross the fundamental frequency of the aqueduct structure. Inputting ANPING ground wave, the water in tank does not play a similar damping effect of TLD, because of the greater difference between the main frequency range of ANPPING wave and the fundamental frequency of the aqueduct structure. In additon, the presence of water makes the vibration frequency of the aqueduct structure reduce, thus chaning the aqueduct body’s response waveform. This indicates that the effect of the water in tank on the aqueduct structure has great relationship to the spectrum dynamic properties of the input earthquake wave. When the main frequency range of the input earthquake wave across the fundamental frequency of the aqueduct structure, the virbation frequency of the water in tank and the fundamental frequency of the aqueduct structure is similar, the water in tank can play TLD damping on the aqueduct structure, but the effect at the initial stage of time-history is not significant, as the water sloshing needs a process for starting.

4 CONCLUSIONS

Numerical calculations results shows that the water in tank play a TLD damping on the aqeudcut-water coupling to some extent. The water in the aqueduct can be seen as deep TLD. Based on the hypothesis of the aqueduct-water coupling structure dynamic interaction, the water in aqueduct is ideal incompressible irrotational fluid, that the space size properties and the damping characteristics of the fluid are determined, therefore the main factors which decide when the water in aqueduct play TLD damping effect is the mass ratio(μ) and frequency ratio(β).

According to the curves of the water damping effect(η) following changes of the mass ratio and frequency under all kinds of cases, drawing the fitting curve, the discriminant of the water TLD damping is obtained as fllows:

$$\eta = 296.89\mu^2 + 329.87\mu - 48.17 \qquad (0 < \mu < 1) \qquad (1)$$

$$\eta = -3085.64\beta^2 + 3491.82\beta - 945.43 \qquad (0 < \beta < 1) \qquad (2)$$

From the discriminant (1) or (2), it can judge when the water in tank play TLD damping effect on the aqueduct structure.

REFERENCES

[1] Dogde CF, Pratt DL, Brovold FN, Wilson HO. Pipe up. *Civil Engineering*. (2):40-43, 1999.

[2] Pratt DL, Dodge Cf, Brovold FN, Wilson HO. Seismically upgrading the Mokelumne aqueducts Pipelines in the Constructed Environment. *Proceedings of the Pipeline Division Conference 1998*. ASCE, Reston, VA, USA. 405-412,1998.

[3] Zarghamee MS, Rao RS, Kan FW, Keller TO, Yako MA, Iglesia GR. Seismic risk analysis of Hultman aqueduct. *Proceedings of the Specialty Conference on Infrastructure Condition Assessment*, USA, August, 1997.

[4] Zarghamee MS, Rao RS, Yako MA, Motley EM, Garcia F, Camacho A. Seismic design of Puerto Rico's north coast superaqueduct. *Proceedings of the Conference*, ASCE, San Diego, California, 1998.

[5] Eidinger JM, Avila EA. Seismic evaluation and upgrade of water transmission facilities Technical Council on Lifeline. *Earthquake Engineering Monograph*, (15):1-19,1999.

[6] Davis C A, Cole Steven R. Seismic performance of the Second Los Angeles Aqueduct at Terminal Hill. Technical Council on Lifeline Earthquake Engineering Monograph. *Proceeding of the 5th U.S. Conference on Lifeline Earthquake Engineering*, Aug 12-14, 1999,USA.

[7] Eckhoff David W, Keaton Jeffrey R. Application of risk management and value engineering techniques to evaluation of water resources projects with special emphasis on geological hazards. *Proceedings of the ASCE 17th Annual National Conference*, Apr 17-21, 1990, USA.

[8] Li Yuchun, Lou Menglin. BEM simulation of nonlinear sloshing for aqueduct fluid. *Earthquake Engineering and Engineering Vibration*. Vol. 20(2): 51-56, 2000.

[9] Li Yuchun, Lou Menglin. Dynamic characteristics of fluid and structure interaction system for bent-type aqueduct. *Journal of Hydraulic Engineering*. Vol.12(1): 31-37, 2000.

[10] Xu Jianguo, Chen Huai, Wang Bo. Transverse seismic response of aqueducts with fluid-structure coupling. *Engineering Mechanics*. Vol. 21(6): 202-207, 2004.

[11] Xu Jianguo, Chen Huai, Wang Bo, i.e. Seismic response of large scale aqueduct with fluid-structure coupling. *China Civil Engneeing Journalr* .Vol. 38(8): 67-73, 2005.

[12] Liu Yunhe, Yu Maohong, Chen Houqun. Finite element method for transient analysis of fluid-structure coupling problem. *Engineering Mechanics*. Vol.22(6): 1-6,2005

[13] Wu Yi, Mo Haihong, Yang Chun. Dynamic characteristics of large rectangular aqueduct-water coupling system. *Earhtquake Engineering and Engineering Vibration*. Vol. 24(4): 137-142,2004.

[14] Wu Yi, Mo Haihong, Yang Chun. Analysis on tuned liquid damper effect of 3-D frame supported aqueduct. *Journal of Hydraulic Engineering*. Vol.36(9): 1115-11120, 2005.

[15] Duan Qiuhua. The shaking table test of large scale aqueduct structure and study on it's resistant for earthquake. *Doctoral dissertation.* Shanghai, Tongji University, 2008.

COMPDYN 2011
3rd ECCOMAS Thematic Conference on
Computational Methods in Structural Dynamics and Earthquake Engineering
M. Papadrakakis, M. Fragiadakis, V. Plevris (eds.)
Corfu, Greece, 25–28 May 2011

INDUSTRIAL STEEL PIPE SYSTEMS UNDER SEISMIC LOADING: A COMPARISON OF EUROPEAN AND AMERICAN DESIGN CODES

Gert J. Dijkstra[1], Benjamin Francis[1], Hildo van der Heden[1] and Arnold M. Gresnigt[2]

[1]Tebodin Netherlands BV
P.O. Box 16029 • 2500 BA The Hague • The Netherlands
g.dijkstra@tebodin.com • b.francis@tebodin.com • h.vanderheden@tebodin.com

[2]Delft University of Technology
P.O. Box 1548 • 2600 GA Delft • The Netherlands
a.m.gresnigt@tudelft.nl

Keywords: Piping System, Seismic Design, Case Studies, American Standards, European Standards, Static and Dynamic Calculation, Pipeline.

Abstract. *In the framework of the INDUSE project, which aims at innovative design methodologies for the seismic design of industrial equipment and piping systems, case studies have been carried out, performing static and dynamic seismic analyses for two existing steel pipeline systems including steel supporting structures, situated in an area of moderate seismic activity:*

a) A long aboveground 10" ammonia transmission line situated on sleepers with a vertical expansion loop and ending with a fixed point. The system may be typical for long distance above ground pipelines and for pipelines on jetties.

b) A 20" gas transmission pipeline at the interface of a buried pipeline section and an above ground piping section, including a branch connection, a vertical spring support structure and a fixed point, e.g. a tank nozzle. This system is typical for many plant piping systems.

The calculations were made using commercially available software. Both simplified static equivalent ('uniform load method') calculations as well as dynamic calculations were made in accordance with American (ASCE-7) and European (EN1998 and EN13480) earthquake design standards to identify differences in approach, differences in resulting seismic response spectra and differences in calculated results. The dynamic and static calculations were made with Caesar II software.

The results of the calculations are presented. Conclusions and recommendations are given with respect to:

- *The differences between existing earthquake design codes.*
- *The validity of the use of the "static equivalent (uniform load) method".*
- *The need to include guidelines for design and modeling in the next revisions of existing seismic design standards for (above ground) industrial piping systems.*

1 INTRODUCTION

In the framework of the INDUSE project [1], which aims at innovative design methodologies for the seismic design of industrial equipment and piping systems, a case study was carried out, performing static and dynamic seismic analyses for two existing steel pipeline systems including steel supporting structures, situated in an area of moderate seismic activity:

a) A long aboveground 10" ammonia transmission line situated on sleepers with a vertical expansion loop and ending with a fixed point. The system may be typical for long distance above ground pipelines and for pipelines on jetties.

b) A 20" gas transmission pipeline at the interface of a buried pipeline section and an above ground piping section, including a branch connection, a vertical spring support structure and a fixed point, e.g. a tank nozzle. This system is typical for many plant piping systems.

Both simplified static equivalent (‘uniform load method’) calculations as well as dynamic calculations were made in accordance with American (ASCE-7 [2]) and European (EN1998-1/4 [3],[4] and EN13480 [5]) earthquake design standards to identify differences in approach, differences in resulting seismic response spectra and differences in calculated results. The dynamic and static calculations were made with commercially available (Caesar II) software.

2 INVESTIGATED PIPE SYSTEMS

2.1 Ammonia transmission line

The 10" pipeline to transport liquid ammonia is located in the Algerian desert. It is roughly 9 km long. For practical reasons the modeled section (Figure 1) is 400 m long. Node 1 is modeled as a fixed point, node 650 allows only for rotation. As is expected with such long pipelines, there are loops to deal with thermal- and pressure expansion. Two vertical expansion loops have been modeled. The spacing between the supports in the straight pipe sections is not uniform to avoid creating any standing waves when the pipe is vibrating at a mode of its natural frequency. Relevant pipe and process data are given in Table 1.

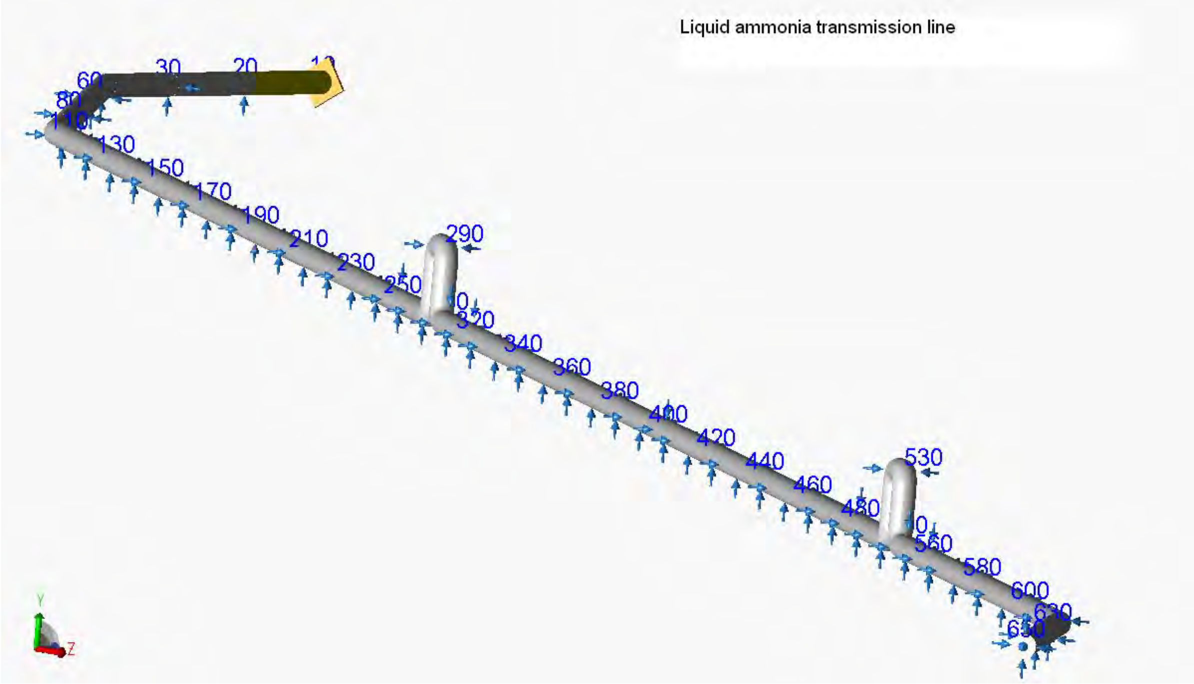

Figure 1: System layout and node numbers Liquid Ammonia line.

Pipe material	Steel A333 Gr.6
Pipe Diameter / wall thickness	10" / Std
Tensile strength, Rm	415 $\mathrm{Nmm^{-2}}$
Yield strength, Re (65°C)	232 $\mathrm{Nmm^{-2}}$
Design pressure	25 bar(g)
Design temperature	65/-35 °C
Installation temperature	40 °C
Corrosion Allowance	3 mm
Medium/ density	Liquid Ammonia, 880 $\mathrm{kg/m^3}$
Thermal Insulation	100 mm, PU Foam, 80 $\mathrm{kg/m^3}$

Table 1: Pipe and process data Ammonia line.

2.2 Gas transmission line

The gas transmission line includes an underground section and is modeled from a point underground to a (nozzle) connection (node 160) and a free end valve (node10) above ground (Figure 2). Relevant pipe and process data are given in Table 2.

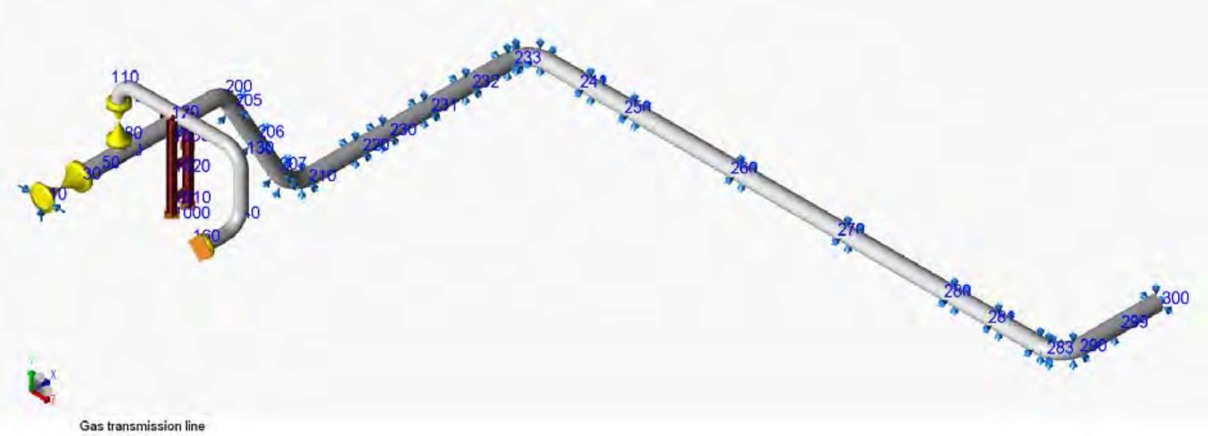

Figure 2: System layout and node numbers Gas transmission line.

Pipe material	20" ; branch 16"
Pipe Diameter / wall thickness	Sch. 60 (16.6 & 20.6mm)
Tensile strength, Rm	413 $\mathrm{Nmm^{-2}}$
Yield strength, Re (65°C)	241 $\mathrm{Nmm^{-2}}$
Design pressure	73.5 bar(g)
Design temperature	80 °C
Installation temperature	40 °C
Corrosion Allowance	1.6 mm
Medium/ density	Natural gas, 1 $\mathrm{kg/m^3}$

Table 2: Pipe and process data Gas transmission line.

The pipe is supported by two steel structures, which add a finite amount of stiffness, which have been modeled in Caesar II. The static calculation was made according to ASME B31.8:2007 [8]. For the buried pipe section, the underground pipe modeler in Caesar II calculates pseudo-supports along the pipe to mimic the behavior of the soil acting on the buried pipe. The buried pipe support distance is pre-calculated by Caesar II, based on pipe stiffness and soil characteristics. Where it is not supported, the buried pipe had six degrees of freedom. However, these are considered negligible due to the pseudo-supports.

3 MODELING THE PIPE SYSTEM BEHAVIOUR UNDER SEISMIC LOAD BY SIMPLIFIED STATIC EQUIVALENT (UNIFORM LOAD) ANALYSIS

3.1 General

Commonly used international standards for seismic design allow for a simplified static equivalent analysis method to deduce a loading value to apply to the pipe system in order to model the seismic behavior. Using this method, the systems own response to different vibrating frequencies and damping rates is ignored and instead the displacements and forces in the piping system are calculated using a single equivalent static accelerating force for each principal direction (X, Y and Z) of the seismic movements. The magnitude of the static loading is directly proportional to the element weight. Earthquake load magnitudes are given in terms of the gravitational acceleration constant, g, i.e. if an earthquake is modeled as having a 0.2 g load in a particular direction, then a factor of 0.2 of the systems weight is turned into a uniform load and applied in that particular direction. Within the framework of this study this method was worked out for the relevant American and European codes.

3.2 Uniform load analysis according to American standard ASCE-7

To determine, in the uniform load case, the overall acceleration described as a fraction of the gravitational constant g, ASCE-7 requires a number of factors to be determined. The following equations are used:

$$S_{DS} = \frac{2}{3} S_{MS} \tag{1}$$

$$S_{MS} = F_a S_s \tag{2}$$

with:

S_{DS} = *Design Seismic response acceleration*

S_{MS} = *Seismic elastic response (spectrum) ground acceleration*

S_s = *Maximum mapped response acceleration, [ms^{-2}]:* Maximum earthquake ground motion at 5% of the critical dampening applied. From ASCE-7 section 11.4.

F_a = *Site class coefficient, [-]:* This factor, normally varying between 0.8 and 2.5, is determined on the type of soil at the site of interest, The value is dimensionless.

The appropriate seismic acceleration, a_H [ms^{-2}] is found by checking the limits of the following equation, according to ASCE-7 13.3.1:

$$a_H = \frac{0.4 \cdot a_p \cdot S_{DS}}{\left(\frac{R_p}{I_p}\right)} \left(1 + \frac{z}{h}\right) \tag{3}$$

$$0{,}4 \cdot S_{DS} \le a_H \le 1{,}6 \cdot S_{DS} \cdot I_p \tag{4}$$

with:

I_p = *Importance factor* [-] : This value ranges from 1-1.5 and relates to the occupancy category which itself is dictated by the amount of risk present based on ASCE-7 table 1-1.

z/h = *Component elevation ratio* [-] : The ratio of height of the structure at the point of attachment over the average height of the supporting structure.

a_p = *Component amplification factor* [-] : Constant, based on the relationship between the piping response and the structural response for a piping system, which can be related to the response of a system as affected by the type of seismic attachment. It is determined from table 13.6-1 from ASCE-7. It is an arbitrary constant that varies depending on the mechanical components in question.

R_p = *Component response modification factor,* [-]*:* Similar to a_p this is an arbitrary constant that varies depending on the mechanical components in question. This value, too, is taken from ASCE-7 table 13.6-1.

Once a_H has been determined, the horizontal force F_p is deduced by introducing the total weight of the system, W_p, to the horizontal acceleration term in the equation:

$$F_p = a_H \cdot W_p \tag{5}$$

The uniform load shall be applied to the static analysis, independently in at least two orthogonal horizontal directions in combination with the service loads associated with the component. An additional vertical component, which is 0.2 of the horizontal loading, is applied in combination with the two separate horizontal cases.

3.3 Uniform load analysis according to the European code EN13480

EN1998-1 and -4 do not specify an equivalent static uniform load method as an alternative to dynamic analysis, however the European piping design code EN13480 calculates the uniform load magnitude in a similar way like ASCE-7. The acceleration component of the equation is based on the maximum value arising from the earthquake. The static equivalent acceleration, a_{cqi} can be found by the following equation from EN13480-3:2002, A.2.1.2:

$$a_{cqi} = k_i \cdot a_1 \tag{6}$$

with:

a_i is the acceleration defined for the level in direction i, and k_i is a factor, dependent on the degree of analyses of the natural frequencies of the system Importance factor [-].

$k_i = 1$ when system’s natural frequencies of the piping system can be shown not to coincide within 10% of the peak vibration frequencies in the response spectrum of the structure (or the peak ground acceleration if the pipe work is not mounted on a structure or building.

$k_i = 1.5$ where no check on the coincidence of piping and structure vibration characteristics has been undertaken.

For this study the factor $k_i = 1.5$ is used.

3.4 Resulting design acceleration (Uniform load method, Ammonia and Gas pipeline)

To match the original design calculations according the Algerian Earthquake resistance code RPA99:2003, made with the respective software packages AutoPIPE and ROHR2 for the Ammonia transfer line the gas transmission line, a uniform load of 0.2g and 0.14g horizontal and vertical, respectively are calculated, in order to accurately compare results. This gives three separate uniform load cases (Table 3):

Uniform load case	Horizontal acceleration ms^{-2}	Vertical acceleration ms^{-2}
ASCE-7:05	0.14	0.02
EN13480-3:2002	0.37	0.37
AutoPIPE & ROHR2 comparison	0.20	0.20

Table 3: Input seismic forces according equivalent static analyses method (uniform load case).

4 DYNAMIC MODELING OF A PIPING SYTEM UNDER SEISMIC ACTION

4.1 General

For dynamic analyses of a piping system under seismic load it is necessary to get the expected random waveform of acceleration vs. time, caused by the earthquake into a data set, such as a response spectrum. This is followed by a spectrum analyses. A spectrum analysis represents an estimate of the maximum response developed in the piping system during the transient load from the earthquake.

The response of the piping system will depend on the magnitude and the number of its modes of natural frequency (first and higher harmonics). A pipe layout showing a large number of possible natural frequencies will react different compared to piping systems having a higher natural frequency (usually more "rigid" systems).

The steps to be taken are:

- Define the *design seismic response spectra.*
- Define the range of natural frequencies (modes of vibration) of the pipe system under consideration.
- Calculate the response of the pipe system under the design acceleration related to each natural frequency.

4.2 Generation of seismic response spectra

4.2.1 Spectrum generation according to ASCE-7

A horizontal and a vertical design response spectrum are generated. Six parameters, similar to those described under 3.2 for the uniform load method, determine the shape of the (horizontal) design response spectrum according to the ASCE-7 seismic code.

4.2.2 Spectrum generation according to Eurocode 8

Eurocode 8 presents a seismic response spectrum, similar in profile to that produced using ASCE-7. However, the corresponding response amplitudes are extracted based on a different data set, in this case, from the EN1998-1 seismic code.

Once the soil type and the values of the period are selected, two curve types can be formed, Type I and Type II, depending on whether deep geology is accounted for in the calculation. However, if the geology is not known, EN1998-1: 3.2.2.2 recommends using both curve types. This study takes into account both types; this is also relevant to the vertical spectra. Contributing factors to the EN 1998-1 seismic response curve are:

- *Soil Factor S:* Ground types are described in table 3.1 and 3.3 of EN1998-1. These are based on parameters of a geotechnical nature.

- *Damping Factor η:* This is the damping correction factor of which the source is internal friction of the materials, imperfect connections between components, sliding friction, and other features. This is governed by the following expression:

$$\eta = \sqrt{\frac{10}{(5+\xi)}} \geq 0.55 \tag{7}$$

where *ξ is the damping ratio* of the structure [%]. Throughout this study, the damping ratio was set at 5%, according to EN13480-1 A.2.1.6 where a value of 5% is used for systems with a frequency below 10Hz, thus rendering the damping factor to be unity throughout.

- *Behavior Factor q:* This is the ratio between the peak ground acceleration (PGA) that produces the ultimate displacement or rotation and the PGA that produces the yielding of the first point of the structure under consideration.
- *Ground Acceleration a_g:* The design ground acceleration on type A ground is defined as:

$$a_g = \gamma_1 \cdot a_{gR} \tag{8}$$

Where γ_1 is the topographic amplification factor, which is always greater than 1.

4.2.3 Vertical design spectrum

A major difference between the ASCE-7 and EN1998-1 codes is the magnitude of a vertical component to the calculation. According ASCE-7 the vertical spectrum is set to 20% of the amplitude of the horizontal design response spectrum across the entire period range.

According to EN1998-1 two types of curves can be applied, as seen in the design spectrum for the horizontal component, namely type I & II. However, a behavior factor appears in the equation and two ground acceleration values are mentioned in the code in table 3.4 of EN1998-1, resulting in the vertical spectra, given in fig. 3a and 3b.

4.2.4 Soil type selection

The soil types selected as a basis for the calculations according ASCE 7 and EN1998-1 were best matched to each other, leading to the choice for soil type C (ASCE-7) and soil type B (EN1998-1) respectively.

Soil type C from ASCE-7 is described as "very dense soil and soft rock" with a wave velocity range, as listed in table 20.3-1 ASCE-7, lying between 365-762 ms^{-1}. EN1998-1, which is a little bit more descriptive, describes soil type B as "Deposits of very dense sand, gravel or very stiff clay, at least several tens of meters in thickness, characterized by a gradual increase of mechanical properties with depth." The shear wave velocity range in table 3.1 of EN1998-1 for soil type B is 360-800 ms^{-1}.

For both codes shear wave velocity associated with each soil type is determined in the same way, the difference being constants used to describe the same values. The following equation represents the way that shear wave velocity, $v_{s,30}$ – at 30 meters - is presented in table 3.1 (2) of EN1998-1. ASCE-7-05 presents in equation 20.4-1 an identical manner, with the thickness term h_i presented as d_i.

$$v_{s,30} = \frac{30}{\sum_{i=1,N} \frac{h_i}{v_i}} \tag{9}$$

4.2.5 Input parameters and design seismic spectrum generation

On basis of the foregoing, the input parameters for generating the design seismic response spectra are generated, Table 4 and Table 5). This results in horizontal and vertical design seismic response spectra according to both the ASCE code and the EN1998-1 code. Figure 3 and Figure 4 show the calculated horizontal and vertical design response spectra.

Parameter EN1998-1	CURVE TYPE / VALUE				Reference EN1998-1
	Type I (Horizontal)	Type I (vertical)	Type II (Horizontal)	Type II (Vertical)	
Soil Type	B	B	B	B	Table 3.1
Importance factor, γ_1	1.2	1.2	1.2	1.2	Table 2.1(3)
Ground acceleration, a_G	0.25	0.9	0.25	.45	n/a
Soil factor, $S^{1)}$	1.2	n/a	1.35	n/a	Table 3.2
$T_B{}^{1)}$ (start of acc. plateau)	0.15	0.05	0.05	0.05	Table 3.2
$T_C{}^{1)}$ (end of acc. plateau)	0.5	0.15	0.25	0.15	Table 3.2
$T_D{}^{1)}$	2	1	1.20	1	Table 3.2
Behavior factor, q	3	3	3	3	Table 6.1

$^{1)}$ Dependent on soil type

Table 4: Input parameters Seismic design spectra EN1998-1.

Parameter ASCE-7	Value	Reference ASCE-7
Soil Type	C	Table 20.3-1
Importance factor, I_p	1.25	Table 11.5-1
Site coefficient, F_A	1.1	Table 11.4-1
Site coefficient, F_V	1.5	Table 11.4-2
Maximum considered earthquake acceleration parameter, S_s	0.75	Table 11.4-1
Maximum considered earthquake acceleration parameter, S_1	0.3	Table 11.4-2
Component amplification factor, a_p	2.5	Table 13.6-1
Response modification factor, R_p	12	Table 13.6-1
Elevation ratio, z/h	1	n/a

Table 5: Input parameters Seismic design spectra ASCE-7.

For the liquid ammonia pipeline, Caesar II calculated 250 relevant modes of vibration and periods up to 0.866 seconds. Compared to this (cross country) pipeline, most plant piping systems will be smaller and more rigid (more supporting) resulting in fewer relevant modes of vibration.

To be able to see how much influence each spectra has on the piping systems output, one must look at the spectra’s period in comparison to the system’s modes of natural frequency. As can be seen in fig 3a, the blue shaded region of the curve represents the range in which this particular system’s natural frequencies lie; the bold lines are sample modes which have been highlighted. The region outside of the shaded area is above a certain cut-off period, which translates for the ammonia line to 0.866 Seconds, which is 1.154 Hz – the 1st mode of the systems natural frequency. Although the peak of the type II horizontal curve is higher, the maximum acceleration with which Caesar II calculates the system at the 1st mode of vibration is 0.15 ms^{-2} for the type I horizontal curve. The pipes natural frequency is the determining factor on how much the spectra influence the results.

The higher the mode of vibration the lower the periodicity, thus there will be a particular mode of vibration which matches the peaks of each curve. The vertical lines on the graph below represent the modes of vibration mode 1 can be seen at 0.866 seconds, the 2nd mode is visible at 0.459 seconds, the 25th and 100th modes are also represented on the graph at 0.132 and 0.060 seconds respectively. Similarly the same can be shown when comparing the ASCE-7 curve with the EN1998-1 curves.

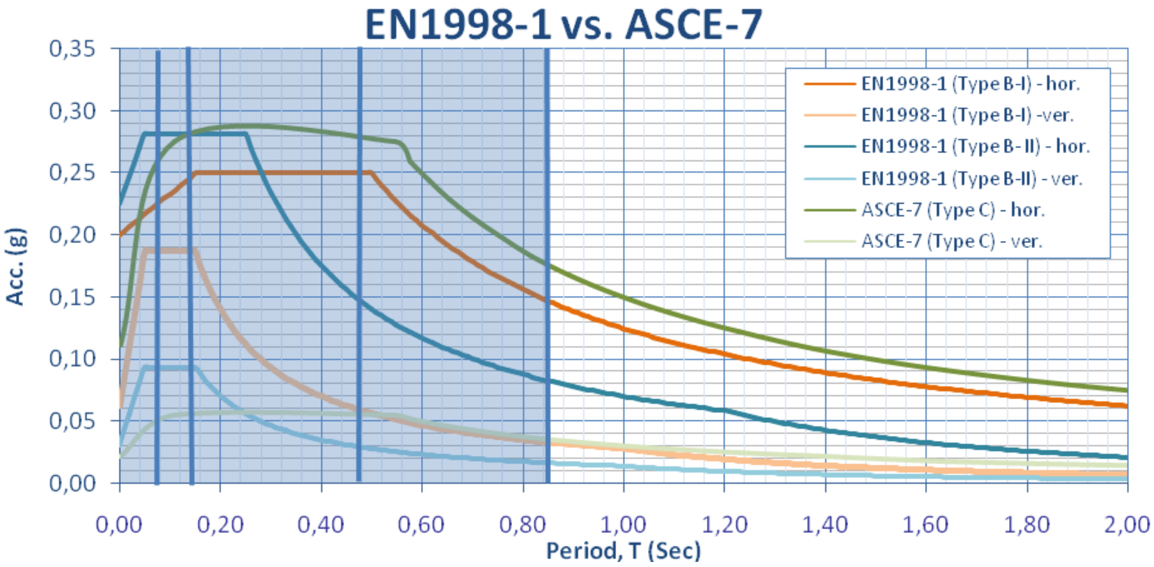

Figure 3: Horizontal and vertical seismic design spectra according EN1998-1 and ASCE-7, with natural frequency range (blue shaded) of the ammonia pipeline system.

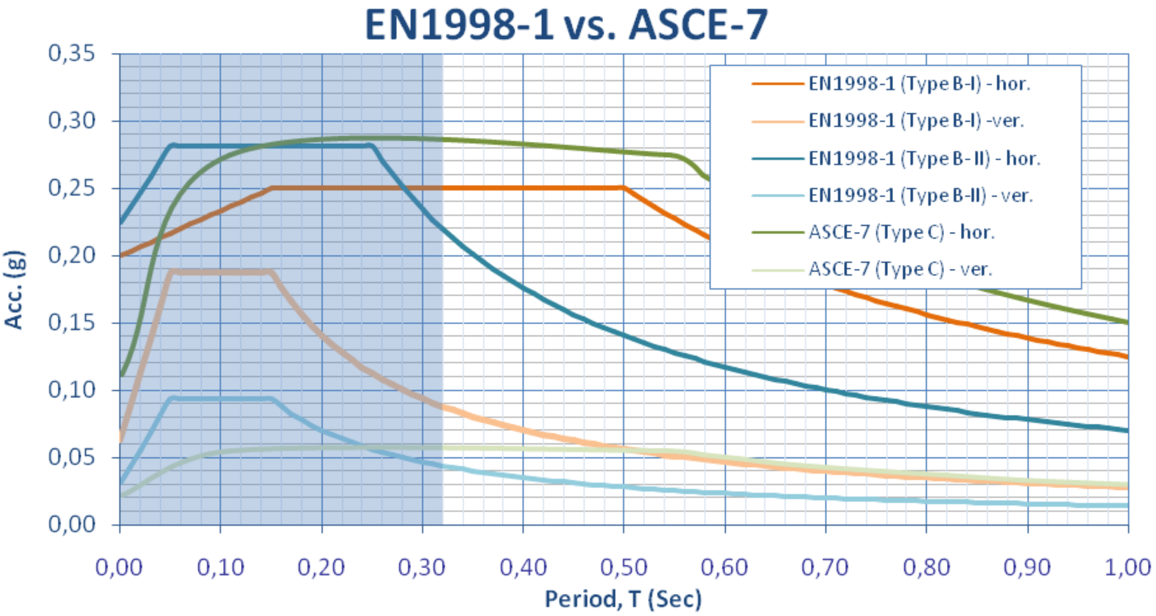

Figure 4: Horizontal and vertical seismic design spectra according EN1998-1 and ASCE-7, with natural frequency range (blue shaded) of the gas pipeline system.

The number of modes of the natural frequencies present in the gas transmission line, calculated according 4.3, are much fewer compared to the liquid ammonia transmission line. This is expected as the system is more rigid and shorter. Similarly to the curves seen in dynamic analysis of the liquid ammonia pipeline, Figure 4 shows the relevant area of the curve for the natural gas system.

It's quite clear to see from Figure 3 that natural frequency mode 1 (T~0.3 S) of the pipe system corresponds to the plateau of the response spectra EN1998, type I and ASCE 7, producing higher acceleration forces (and stress results) compared to EN1998-1 (type 2) spectra, though the latter has a larger plateau compared to EN1998 (type 1).

4.3 Modeling and determination of the range of natural frequencies of the pipe system

Calculation of natural frequencies

The system's modes of vibration will respond to the load in the exact same nature as a single degree of freedom oscillator with the generation of the response spectra, as it obeys Newton's second law for damped harmonic oscillators.

$$F(t) = m\left(\frac{d^2x}{dt^2}\right) + c\left(\frac{dx}{dt}\right) + k(x) \tag{10}$$

When calculating the modes of vibration and the fundamental frequency of the system, Caesar II, being the software package used for the dynamic calculations, will set the driving force to be zero. Also the damping factor is zero which eliminates the second term of the equation and allows Caesar II to solve the equation harmonically. For simple harmonic motion the displacement can be described as:

$$\begin{aligned} x &= x_0 \cdot Sin\ \omega \cdot t \\ \frac{dx}{dt} &= x_0 \cdot \omega \cdot Cos\ \omega \cdot t \\ \frac{d^2x}{dt^2} &= -x_0\omega^2 Sin\ \omega \cdot t \end{aligned} \tag{11}$$

Therefore, substituting in the displacement to the acceleration equation along with the stiffness and mass gives the following equation which Caesar II can use to determine the fundamental frequency:

$$\frac{d^2x}{dt^2} = -\omega^2 \cdot x \qquad \because\ \omega = \sqrt{\frac{k}{m}} \tag{12}$$

The system's overall response can be described in terms of displacement, which is shown in the equation below:

$$x = \frac{v}{\omega} = \frac{a}{\omega^2} \tag{13}$$

Where x is the displacement from response spectrum at frequency f, v is the velocity, ω is the angular frequency at which response spectrum parameters are taken and a is the acceleration from response spectrum at frequency. Caesar II completes the following steps:

1. An Eigen solver algorithm is used to extract the exact modes of vibration from the system. The subsequent modes have a characteristic frequency and mode shape.

2. The maximum response of each mode under the applied load is determined from the spectrum value corresponding to the mode's natural frequency.
3. The total system response is determined by summing the individual modal responses using the square root of the sums of the squares method, where R_i is the total response in direction, i, R_{mi} is the peak response due to mode m and n is the total number of significant modes for the particular system.

$$R_i = \pm\sqrt{\sum_{m=1}^{n} R_{mi}^2} \tag{14}$$

Figure 5 shows an example of the liquid transmission line vibrating at the fourth mode of its natural frequency. (It is easier to see in this particular piping configuration, compared to the gas transmission line).[1]

Figure 5: Caesar II representation of the fourth mode shape driven by the ASCE-7 spectra – Liquid transmission line.

The results are a statistical summation of the maximum displacements, forces, reactions, stresses, etc; the individual responses do not represent an actual physical loading case in that the maxima may all occur at different times. In this particular case, the allowable stresses for occasional loads of ASME B31.3 or ASME B31.8 will be compared to these stress analyses.

Mass point spacing

A system's modes of vibration are an inherent property of the system; however, the calculation method needs a sufficient number of mass points to estimate the system's modes of vibration.

Caesar II converts each element associated with the piping from a continuous beam element between nodes to stiffness between two masses. Supports and anchors are modeled by adding additional stiffness to the mass node. The masses assigned are only half the sum of all element masses framing into the node.

The accuracy of the model can be increased by the addition of just a few mass points to the system. There are a number of rules of thumb to follow when arranging a seismic model. There must be at least one lump mass between two pipe supports, similarly there must be an

---

[1] An accompanying video of the pipe vibrating at the listed modes is also available.

even mass distribution on bends and where there is concentration of mass, such as a flange, valve or tee. Table 6 gives the ratio to the exact solution of the number of significant nodes Caesar II can calculate depending on the number of nodes between supports.

Nodes (including end nodes)	Ratio (%)
2	69.6
3	88.5
4	93.7
5	95.7
10	97.9

Table 6: Influence of mass point spacing on calculation accuracy.

In the calculation of the liquid ammonia transfer line, having a high number of possible vibration modes, extra nodes had to be added between the supports. The average mass spacing needed is approximately 5 nodes between each supports, which gives approximately 95% ratio to the exact solution of the modes of the natural frequency. The approximate distance at which to split the sections of pipes is given by the following equation:

$$L = 9.2 \cdot \left(\frac{D^3 t}{W} \right)^{\frac{1}{4}} \tag{15}$$

where:

L = distance between two consecutive lumped masses (mm).
D = outside diameter of pipe (mm).
T = wall thickness of the pipe (mm).
W = weight per unit length of the pipe (kg.m^{-1}).

The results are only a guide, as in some cases it is impossible to split the nodes into the required distance because of the piping geometry. The lumped mass distance for the liquid ammonia transmission line was calculated to be 387 mm and the distance for the natural gas transmission line was calculated to be 480 mm.

Support modeling

Throughout both models, the types of supports which have been modeled are simplistic slide or guide supports. Only the frictional effect has been modeled along with the physical barrier which prevents the pipe moving in the specified direction. This technique is common place in pipe modeling. Where a support is very long, occasionally the stiffness factor will be modeled, however, this does not occur in the two systems studied. The aforementioned system where a steel structure has been modeled Caesar II takes into consideration the stiffness associated with the frame. When modeling the supports as slide or guide supports, the stiffness factor was assumed to be negligible.

Restrictions to modeling

Caesar II does not model any ‘slapping’ – where the pipe lifts up from a support in one time frame and slaps down on the support. The pipe must be restricted or free to move. The restraints which are non-linear in the static cases must be made active or inactive to enable an accurate dynamic analysis. It is possible to set non-linear restraints to a configuration found in the static results.

Another effect which is non-linear is the force produced from friction. These must also be set to be linear. A default setting for II is to model the supporting as having no frictional effects. If desired, Caesar II can approximate the frictional force in the dynamic case by assuming a +Y restraint the frictional value would instead be added to the X and Z directions and a spring support would be included.

It should be noted that the slapping effect does not arise in a situation where a spring hanger has been modeled in the static stage of the calculation. Therefore, if in one of the load cases a lifting of the pipe occurs at the spring support it will still be modeled as a support at the dynamic stage of the calculation.

5 CALCULATION RESULTS AND DISCUSSION FOR THE AMMONIA TRANSMISSION LINE

The effect of design acceleration on pipe stresses, forces and bending moments was calculated with special focus on the end nozzles.

The pipe stresses for all models were calculated to be within the allowable limits of the applicable design code (The results do not address the flange leak check). Table 7 shows the calculated maximum pipe stresses for both the uniform load method and the dynamic analyses. The location of the maximum stress (node number is shown in Figure 6).

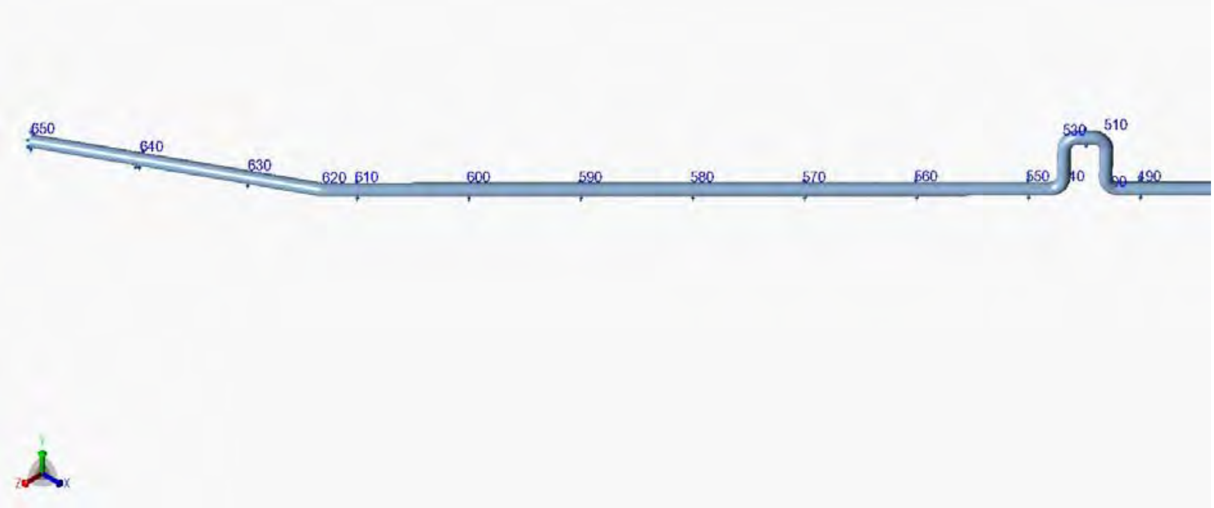

Figure 6: Ammonia transmission line including node numbering.

One can see that applying the uniform load method, the maximum stresses occur at the horizontal bend at node 610 and amount 40% -50% of the allowable code stress. The dynamic analyses however reveal a more severe picture: Maximum stresses occur now at the lower bend of the vertical expansion loop at node 550 and are not only exceeding the allowable code stress but also the yield strength. This might be an indication that for these types of pipe systems, showing high period and low natural frequencies, full dynamic analyses is always required.

Load case / Design seismic spectrum	Type of calculation	Maximum stress in node	Stress [Nmm^{-2}] *(vibration mode)* [2)]	Allowable stress [Nmm^{-2}] (ASME B31.3)	Ratio [%]
RPA99:2003 (AutoPIPE)	*Uniform load*	610	71.3	183.4	38.9
ASCE-7	*Uniform load*	610	66.1	183.4	36.0
	Dynamic	550	239.4 *(1)*	183.4	130.5
EN13480	*Uniform load*	610	91.3	183.4	49.8
EN1998-1 (Type I)	*Dynamic*	550	275.1 *(1)*	183.4	150.0
EN1998-1 (Type II)	*Dynamic*	550	354.3 *(4)*	183.4	138.8

Table 7: Calculation results for Ammonia transmission line.

Ammonia transmission line: Nozzle focus

Table 8 and Table 9 present the results for the forces and moments, calculated for respectively the uniform load cases and the dynamic cases on the nozzle (fixed point, e.g. a tank nozzle) situated at node 10 (Figure 2).

Code	F(x) [N]	F(y) [N]	F(z) [N]	M(x) [Nm]	M(y) [Nm]	M(z) [Nm]
RPA99:2003 (AutoPIPE)	15755	-5613	2190	239	6069	7209
ASCE-7	14200	-5038	-1652	173	4482	6487
EN13480	22525	-6484	-4028	335	11905	8240

Table 8: UNIFORM LOAD METHOD: Forces and moments on the nozzle at node 10.

Code	F(x) [N] *(mode)*	F(y) [N] *(mode)*	F(z) [N] *(mode)*	M(x) [Nm] (*mode*)	M(y) [Nm] *(mode)*	M(z) [Nm] *(mode)*
ASCE-7	6620 *(1)*	1434 *(14)*	2037 *(4)*	458 (*36*)	*7198 (14)*	2529 *(1)*
EN1998-1 (Type I)	7247 *(1)*	2261 *(1)*	1894 *(14)*	418 *(36)*	6561 *(14)*	3910 *(1)*
EN1998-1 (Type II)	9048 *(1)*	3381 *(1)*	2168 (*14)*	514 *(1)*	7380 *(14)*	5788 *(1)*

Table 9: DYNAMIC ANALYSES: Forces and moments on the nozzle at node 10.

It can be seen that – for this particular location, in general the uniform load cases generate higher forces and bending moments, compared to the results of the dynamic analyses, EN13480 giving the most conservative results.

[2)] An accompanying video of the pipe vibrating at the listed modes is also available.

The maximum values for the dynamic cases occur at different vibration modes. Also differences between results for the different seismic spectra can be observed. In general the calculated forces and moments are rather low.

6 CALCULATION RESULTS FOR THE GAS TRANSMISSION LINE

The effect of design acceleration on pipe stresses, forces and bending moments was calculated with special focus on tees and nozzles and on the influence of a steel support structure, modeled into the dynamic calculations.

6.1 Calculations including modeling of the steel support structure

In this case the steel supporting structure was also modeled in Caesar II, allowing deformations under load. Between the steel structure and the pipe a spring support is modeled. See Figure 7, (also for node numbers).

When removing the steel structure from the calculation, the system's overall mass will be lower. This has an effect on the system's natural frequency. Table 10 shows the calculated differences in the modes of vibration detected with and without the steel structure.

Table 11 presents the calculation pipe stresses for both the uniform load analysis and the dynamic analyses.

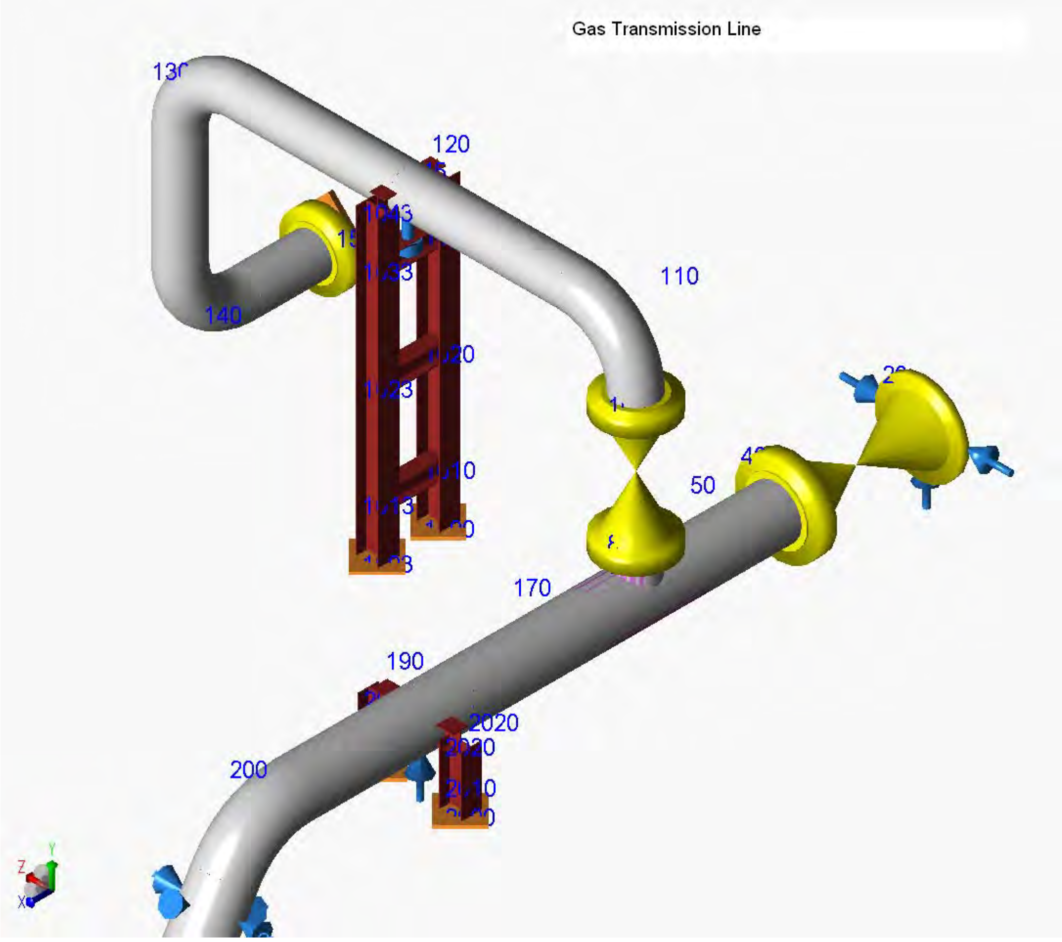

Figure 7: Detail of Gas transmission line, showing steel structure and node numbers.

Vibration Mode #	Freq. (Hz) *with steel structure*	Freq. (Hz) *no steel structure*
1	3.160	3.079
2	11.661	11.707
3	13.988	13.837
4	15.436	15.501
5	19.016	19.081
6	26.187	25.949
7	37.034	37.170

Table 10: Modes of vibration with and without steel support structure.

Design response spectrum	Calculation Method	Node nr. of max. stress	Calculated Code stress [Nmm^{-2}] / (*Vibration mode)*	Allowable stress (acc. ASME B31.8) [Nmm^{-2}]	Ratio [%]
RPA99:2003 (ROHR2)	Uniform load	50	64.0	181	35.4
ASCE-7	Uniform load	50	62.3	181	34.4
ASCE-7	Dynamic	110	18.3 *(1)*	181	10.1
ASCE-7	Dynamic [1)]	110	18.7	181	10.3
EN13480	Uniform load	50	71.6	181	39.6
EN1998-1 (Type I)	Dynamic	110	16.7 *(1)*	181	9.1
EN1998-1 (Type I)	Dynamic [1)]	110	17.0	181	9.4
EN1998-1 (Type II)	Dynamic	110	14.9 *(1)*	181	8.9
EN1998-1 (Type II)	Dynamic [1)]	110	14.9	181	8.2

[1)] No steel support structure modeled

Table 11: Gas transmission line: calculation results (Uniform Load & Dynamic).

For this more rigid pipe system, having higher natural frequencies, the uniform load method gives conservative results with stress levels about three times the maximum values of the dynamic analyses, the latter all occurring in the first mode of vibration.

As stated before it’s quite clear from Figure 4 that natural frequency mode 1 (T~0.3 S) of the pipe system corresponds to the plateau of the response spectra EN1998, type I and ASCE 7, producing higher acceleration forces (and stress results) compared to EN1998-1 (type 2) spectra. This argument holds true for the forces and moments present on the nozzle and the tee-piece. The forces and moments on the tee-piece have a maximum value at EN1998-1 (type 1) when the system is vibrating at the 1st mode of vibration.

It is also noticed that, applying the uniform load method, the maximum stresses will occur at the T-Piece (node 50), whereas the dynamic analyses shows the maximum stresses occur in the upper bend at node 110.

Comparison of the calculated stresses with and without modeling of the steel support structure shows that the differences are negligible. The (already very low) stresses in the pipe system are hardly influenced by the deformation of the steel structure under the horizontal (friction) load.

Gas transmission line: Tee focus

The 20" x 16" reducing tee piece in the gas transmission line is the subject of special attention. Table 12 and Table 13 present the forces and moments acting on the Tee at node 60 (see Figure 7) calculated with the static (uniform load) method and the dynamic analyses (between brackets the mode of vibration).

Case	F(x) [N]	F(y) [N]	F(z) [N]	M(x) [Nm]	M(y) [Nm]	M(z) [Nm]
RPA99:2003 (ROHR2)	-22031	-2838	3887	0	-48827	14800
ASCE-7	-18985	-2467	-2478	0	-33535	11869
EN13480	-34580	-3995	8794	0	-68302	23948

Table 12: Gas pipeline, UNIFORM LOAD METHOD: Forces & Moments at T-junction *(node60)*

Code/ Spectrum	F(x) [N] (mode)	F(y) [N] (mode)	F(z) [N] (mode)	M(x) [Nm] (mode)	M(y) [Nm] (mode)	M(z) [Nm] (mode)
ASCE-7	7307 (1)	13606 (1)	4025 (1)	315 (3)	14879 (2)	29182 (1)
ASCE-7 1)	7173 *(2)*	13650 *(1)*	3809 *(2)*	15726 *(3)*	7602 *(2)*	22205 *(1)*
EN1998-1 (Type I)	7602 (1)	12511 (1)	4157 (1)	340 (3)	15687 (2)	26958 (1)
EN1998-1 (Type I) 1)	7382 *(2)*	12492 *(1)*	3898 *(2)*	292 *(3)*	14944 *(2)*	26466 *(1)*
EN1998-1 (Type II)	8551 (1)	11401 (1)	4507 (1)	382 (3)	16997 (2)	24759 (1)
EN1998-1 (Type II) 1)	8331 *(2)*	11282 *(1)*	4245 *(2)*	325 *(3)*	16221 *(2)*	24041 *(1)*

1) No steel support structure modeled

Table 13: Gas pipeline, DYNAMIC ANALYSES: Forces & Moments at T-junction (node60).

The maximum values occur during the uniform load method. Comparing the results of the dynamic analyses for the different codes does not give notable differences. Comparison of the calculated forces and moments with and without modeling of the steel support structure however shows that for $F_{(y)}$ and $F_{(z)}$ and for the moments marked differences can be seen, not so much with regard to the maximum values but with regard to the direction. *The reason for this phenomenon is not yet quite clear.*

Gas Transmission line: Nozzle focus

The nozzle situated at node 160 (see Figure 7), modeled as a fixed point, is a flange connection and therefore critical with regard to possible leakage. Table 14 and Table 15 represent the results of the forces and moments, calculated for the uniform load cases and for the dynamic analyses (Between brackets the vibration mode).

Case	F(x) [N]	F(y) [N]	F(z) [N]	M(x) [Nm]	M(y) [Nm]	M(z) [Nm]
RPA99:2003 (ROHR2)	-2900	8066	-7013	-4736	8277	15637
ASCE-7	-2135	6229	-2477	-604	4519	14344
EN13480	-4908	9488	-2564	-127	5423	20083

Table 14: Nozzle focus, UNIFORM LOAD METHOD: Forces and Moments at the nozzle at node 160.

Spectrum	F(x) [N] *(mode)*	F(y) [N] *(mode)*	F(z) [N] *(mode)*	M(x) [Nm] *(mode)*	M(y) [Nm] *(mode)*	M(z) [Nm] *(mode)*
ASCE-7	4523 *(1)*	1668 *(1)*	16243 *(1)*	23074 *(1)*	20055 *(1)*	4999 *(1)*
ASCE-7 1)	4578 (1)	1419 (1)	16256 (1)	23183 (1)	20129 (1)	4967 (1)
EN1998-1 (Type I)	4307 *(1)*	1967 *(1)*	14949 *(1)*	21134 *(1)*	18414 *(1)*	5056 *(1)*
EN1998-1 (Type I) 1)	4331 (1)	1676 (1)	14881 (1)	21159 (1)	18397 (1)	5017 (1)
EN1998-1 (Type II)	4106 *(1)*	1802 *(1)*	13651 *(1)*	19167 *(1)*	16742 *(1)*	4568 *(1)*
EN1998-1 (Type II) 1)	4000 (1)	1406 (1)	13248 (1)	18738 (1)	16319 (1)	4358 (1)

1) No steel support structure modeled

Table 15: Nozzle focus, DYNAMIC ANALYSES: Forces and Moments at the nozzle at node 160.

The result for the nozzle forces are more or less in contradiction with the results of the calculated stresses in the pipes and with the forces and moments for the Tee. Here the maximum forces and moments occur in the dynamic cases. The maximum value for the moment being comparable with the result of the uniform load method (that is for the European code only), the maximum force calculated dynamically is clearly higher. The influence of the modeling of the steel substructure is negligible here.

7 CONCLUSIONS

Spectra comparison

The ASCE and EN seismic codes studied bear similar spectra, be it that that vertical spectrum of ASCE 7-05 is considerably lower than the vertical spectra acc. to EN1998-1. The results show that the EN1998-1 and ASCE-7 spectra in general yield similar stresses, forces and moments. This is due to the fact that the peaks occur roughly in the same periodicity as each other – relevant to a typical piping system with a natural frequency higher than 5Hz.

Dynamic vs. uniform load calculations

A direct comparison between the two methods of seismic calculations shows that in one case studied that the uniform load seismic calculations yielded more conservative results than the dynamic seismic calculations. This supports the already practiced method amongst engineers of rather calculating the uniform load stress then modeling the system dynamically. It is perhaps advantageous to carry out a uniform load seismic stress calculations with all earthquake prone pipelines, provided the natural frequencies are high enough.

However, for loose and long pipe systems, a dynamic analysis is of fundamental importance especially if the natural frequency is lower than 4-5Hz. In such cases the uniform load method might substantially underestimate the stresses and forces

Further investigations are required to determine safe borders for the application of the uniform load method.

Influence of supporting structure

The effect seen when a steel supporting structure is included and modeled dynamically is that the system becomes more flexible, allowing the system to vibrate freely with the supporting structure. In this particular case (the gas pipe system and the steel support structure being rather stiff), the influence on the natural frequencies appeared too little to make much difference.

Influence of design

More important than the differences between codes in seismic design spectra is the design of the piping system This is the deciding factor in whether the system will be able to withstand a particular seismic event. The philosophy of designing a system to be able to withstand loadings that occur during a static situation are that the right amount of flexibility should be included into the design e.g. to deal with expansion. This is often achieved by adding expansion loops, or by adjusting the geometry of the system. However, when a system is under seismic loading or any other dynamic situation which is likely to vibrate the system close to its natural frequency, it is desirable to design a system which is rigid. Provisions to prevent ‘slag’ between pipe and support may be necessary. This results in a trade-off between satisfying the needs of the static and dynamic analysis requirements. Often an optimum design can be found by extensive stress analysis. It is recommended to include guidelines for design in the next revision of EN1998-4 and ASCE 7-05.

Influence of computer modeling

When performing dynamic analyses it is very important to apply the correct modeling practice in order to obtain reliable results, however this is not addressed in the present codes.

Non linear modeling of supports during dynamic analyses is not possible yet with commercially available software. For systems with more modes of vibration it is also very important that a sufficient number of nodes between the supports should be applied. It should be checked whether the computer model is able to deal with slag in the supports, etc. It is advised to include recommendations for modeling in the next revision of EN1998-4 and ASCE 7-05

ACKNOWLEDGMENT

This work was carried out with a financial grant from the Research Fund for Coal and Steel of the European Commission, within INDUSE project: "Structural Safety of Industrial Steel

Tanks, Pressure Vessels and Piping Systems Under Seismic Loading", Grant No. RFSR-CT-2009-00022.

REFERENCES

[1] INDUSE, Structural Safety of Industrial Steel Tanks, Pressure Vessels and Piping Systems under Seismic Loading. *RFCS research project*, 2009-2012.

[2] ASCE 7-10, Minimum Design Loads for Buildings and Other Structures. *American Society of Civil Engineers,* May 2010.

[3] EN1998-1, Eurocode 8: Design of structures for earthquake resistance - Part 1: General rules, seismic actions and rules for buildings, *CEN*, 2004.

[4] EN1998-4, Eurocode 8 – Design of structures for earthquake resistance – Part 4: Silos, tanks and pipelines, *CEN*, 2006.

[5] EN13480-3, Metallic industrial piping - Part 3: Design and calculation, CEN, 2002.

[6] ASME B31.3:2006, Code for Pressure Piping, Process Piping, ASME, New York.

[7] ASME B31.4:2006, Pipeline Transportation Systems for Liquid Hydrocarbons & Other Liquids, ASME, New York.

[8] ASME B31.8:2007, Gas Transmission & Distribution Piping Systems, ASME, New York.

[9] E.M. Marino, M. Nakashima, et al. *Comparison of European and Japanese seismic design of steel building structures*, Engineering Structures 27 827-840, 2005.

[10] ROHR2, Pipe Stress Analysis Static and Dynamic Analysis (http://www.rohr2.com/)

[11] CAESAR II, Pipe Stress Analysis (http://www.codecad.com/Caesarii.htm)

[12] AutoPIPE, Piping Analysis (http://www.bentley.com/en-US/Products/Bentley+AutoPIPE/)

APPENDIX 1: ELASTIC RESPONSE SPECTRUM

In systems where permanent plastic deformation may be taken into account one must calculate the response spectra using the equations for Elastic response. As one can see in the equations below that when the behavior factor of the design response spectra is unity and the critical damping ratio is 5% in the elastic spectra, the plateau and decay of the curves are identical. The curve, like the design response spectra is split into four parts.

$$0 \le T \le T_B : S_e(T) = a_g \cdot S \cdot \left(1 + \frac{T}{T_B} \cdot [\eta \cdot 2.5 - 1]\right) \tag{16}$$

$$T_B \le T \le T_C : S_e(T) = a_g \cdot S \cdot \eta \cdot 2.5 \tag{17}$$

$$T_C \le T \le T_D : S_e(T) = a_g \cdot S \cdot \eta \cdot 2.5 \cdot \left(\frac{T_C}{T}\right) \tag{18}$$

$$T_D \le T : S_e(T) = a_g \cdot S \cdot \eta \cdot 2.5 \cdot \left(\frac{T_C T_D}{T^2}\right) \tag{19}$$

Damping in elastic response spectra

The determining of a spectrum with a different value of damping other than 5% is taken from the curve mentioned in EN13480 (A5.4.3) as seen in Figure 8 below.

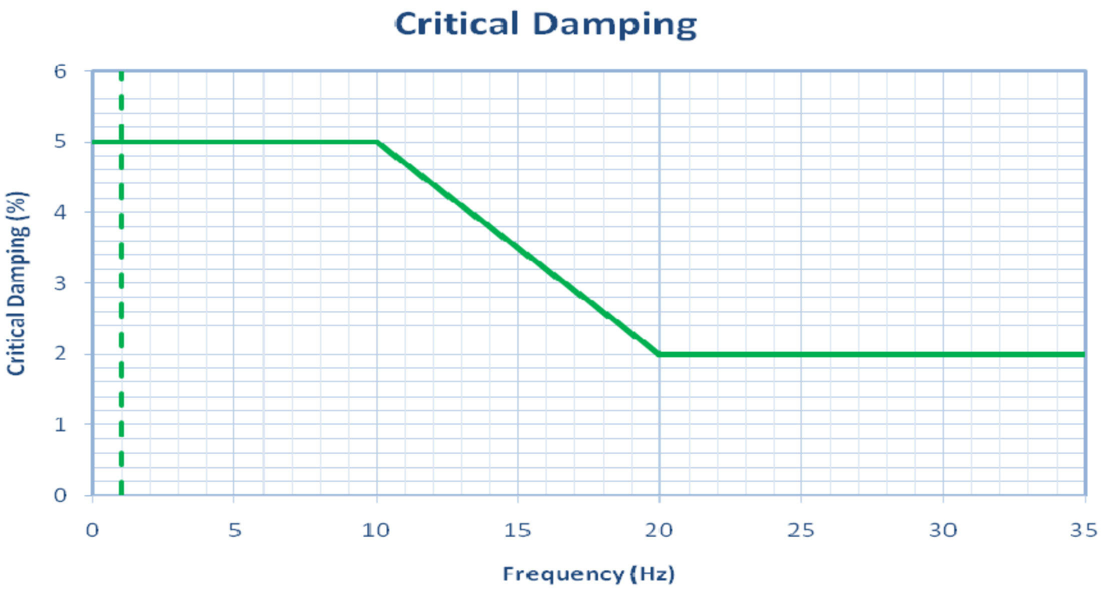

Figure 8: Critical damping.

The critical damping, η directly affects the elastic response spectra curve. The following equation simplifies the damping factor η to 1 when the critical damping ratio is 5%,

$$\eta = \sqrt{\frac{10}{(5+\xi)}} \geq 0.55 \tag{20}$$

Where ξ is the damping percentage relative to the critical damping of the system and where the critical damping is given by the following equation:

$$\xi = 2\sqrt{K \cdot M} \tag{21}$$

Where K is the stiffness of the system and M is the mass.

APPENDIX 2: JAPANESE CODE COMPARISON

A brief study between the European codes and the Japanese equivalent (BCJ) code reveals a very different approach to dynamic seismic modeling. An extensive paper already exists [9]. However, this is heavily focused on building structures and does not look at piping systems.

There seems to be a lack of a design response spectrum and an entire vertical component, whereas the European equivalent includes a design response spectrum and an elastic response spectrum, which incorporates the behavior factor, *q*. Furthermore, the Japanese codes are devoid of any importance factor. However, as can be seen from the spectra, the code is much more conservative than the European code. Assuming the average piping system’s natural frequency would not be lower than 5Hz (represented by the shaded area), one can see that the Japanese code would apply a constant load as can see at the plateau in the early stages of the BCJ curve.

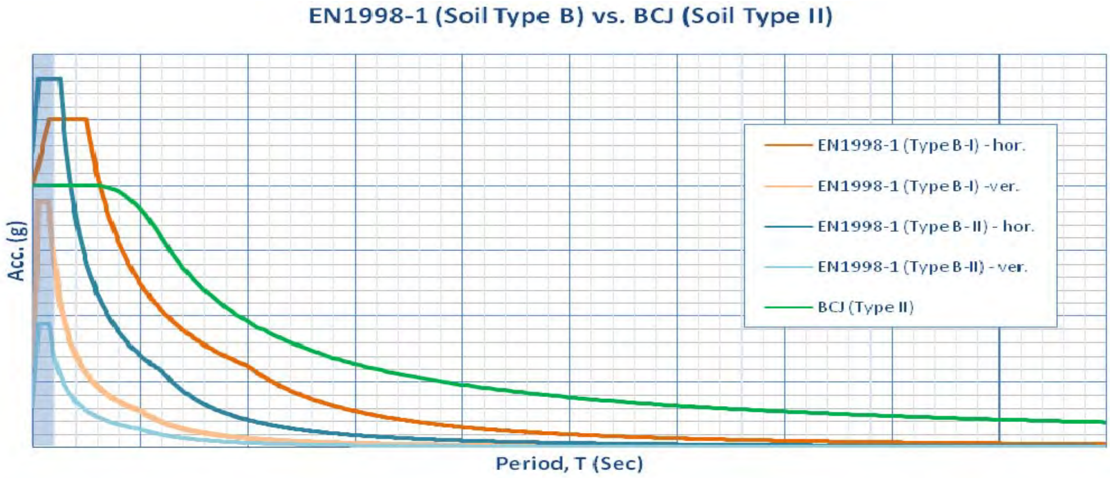

Figure 9: Comparison acceleration European and Japanese code.

COMPDYN 2011
III ECCOMAS Thematic Conference on
Computational Methods in Structural Dynamics and Earthquake Engineering
M. Papadrakakis, M. Fragiadakis, V. Plevris (eds.)
Corfu, Greece, 26–28 May 2011

SEISMIC DESIGN OF SPHERICAL LIQUID STORAGE TANKS (COMPDYN 2011)

Matthias Wieschollek[1], **Maik Kopp**[1], **Benno Hoffmeister**[1] **and Markus Feldmann**[1]

[1] Institute for Steel Structures
RWTH Aachen University
52074 Aachen, Germany
e-mail: wieschollek@stb.rwth-aachen.de

Keywords: Spherical Liquid Storage Tanks, Industrial Structures, Behaviour Factor, Sloshing Effect, Seismic Design, Earthquake Engineering.

Abstract: *Spherical storage tanks are widely used for various types of liquids, including hazardous contents; consequently these storage tanks must be adequately designed for seismic actions.*

While very detailed and specific seismic design rules for cylindrical tanks are provided by several codes, such rules are missing for spherical tanks. This paper describes the results of a survey on existing European and American Codes with regard to their applicability to spherical liquid storage tanks and provides comparison of design outcomes according to these codes. The investigations were performed on an example of an existing spherical tank which was selected to be representative for the current practice. The studies comprised numerical FE modelling and calculation as well as simplified models for the estimation of the dynamic properties of the tank structure. The applicability of behaviour factors was discussed based on proposals made by Eurocode 8. Particular attention was paid to the influence of sloshing effects for which no guidance is given in the codes. The sloshing effects were investigated according to the current state of the art based on available publications.

Finally the resistance of the tank was compared to the action effect determined from the European and American codes. The comparison of action effects obtained with and without consideration of sloshing effects showed a rather important influence of these effects on the final results.

1 INTRODUCTION

The contribution describes the results of an investigation of a representative example of a spherical liquid storage tank subjected to seismic actions. The aim of the study was to verify the applicability of existing European and American codes to spherical tanks although no particular design rules for this kind of tanks – neither for the determination of loads nor for the detailing – are provided by the considered codes. Furthermore the influence of sloshing effects was investigated according to the current state of the art [9].

2 OBJECT OF INVESTIGATION

2.1 Dimensions and load cases

The research focused on a spherical pressure vessel (material S 355) with the dimensions given below, see Figure 1. The spherical tank was supported by twelve vertical legs without additional bracings between them.

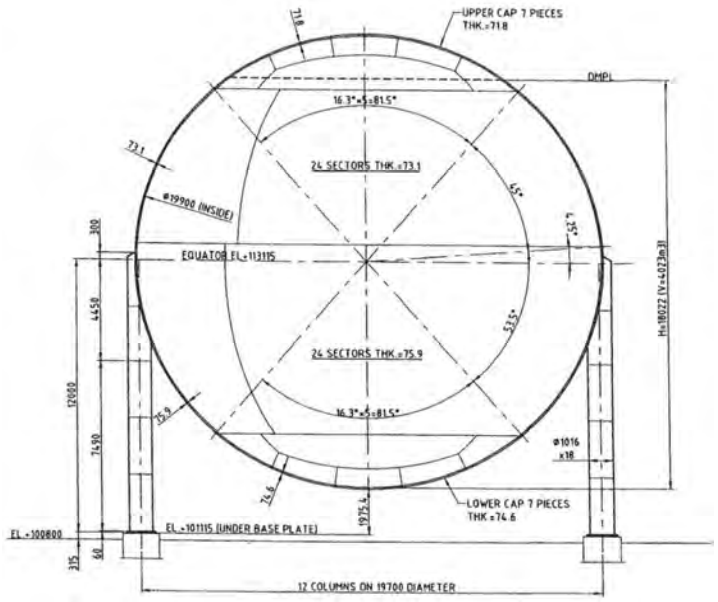

Figure 1: Spherical pressure vessel with 12 columns (inner diameter of the sphere $D_I = 19.9\ m$)

The numerical investigation considered the following load cases:

- self-weight of the structure (columns and sphere) (total weight $m = 879\ t$);
- operating load (density $\rho = 522 kg/m^3$, filling height $h_p = 18.1m$, weight $m = 2104t$);
- seismic load ($a_g = 0.24\ g \approx 2.4\ m/s^2$)

2.2 Seismic actions

In order to compare European and American standards the value of the response acceleration S_d for $T_B \leq T \leq T_C$ according to EN 1998-1:2010 (3.13) [1] was selected to be equal to S_a for $T_0 \leq T \leq T_S$ according to ASCE/SEI 7-05 (11.4-5) [4] (see Figure 2). However, the behaviour factor q is not taken into account at this point (q = 1).

$$S_d(T) = a_g \cdot S \cdot \left[\frac{2}{3} + \frac{T}{T_B} \cdot \left(\frac{2.5}{q} - \frac{2}{3} \right) \right] \quad \text{(according to EN 1998-1 (3.13))} \qquad (1)$$

$$S_a = S_{DS} \cdot \left(0.4 + 0.6 \cdot \frac{T}{T_0}\right) \quad \text{(according to ASCE/SEI 7-05 (11.4-5))} \tag{2}$$

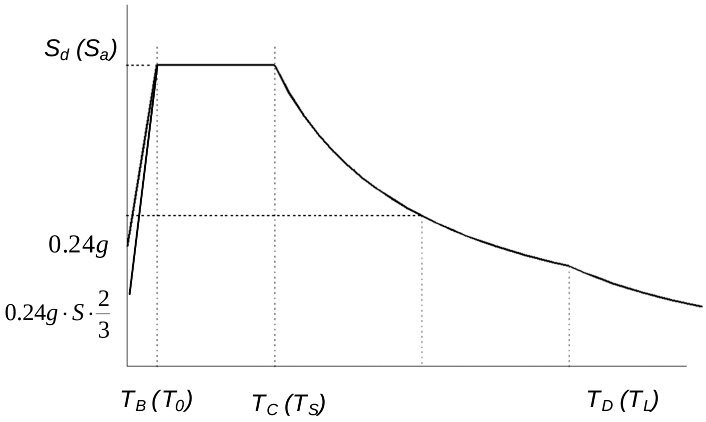

Figure 2: Elastic response spectrum according to EN 1998-1 [1] and ASCE/SEI 7-05 [4]

To consider similar ground conditions for both standards comparable locations were assumed (ground type *C* according to EC 8, part 1 [1] complies with site class *C* according to ASCE 7 [4]).

The model for the determination of the fundamental period T_1 was divided into the following sub-systems:

- ground and foundation (soil-structure interaction effects are not considered here);
- spherical pressure vessel structure;
- fluid, sloshing response, etc.

2.3 Fundamental period of the spherical pressure vessel structure

The fundamental period of the tank structure including maximum filling and neglecting sloshing effects was determined as follows (see Figure 3):

- using FEM-calculations, fundamental period was determined to $T_1 = 1.54\ s$;
- using a strut-and-tie model (single equivalent load in center of gravity) $T_1 = 1.56\ s$.

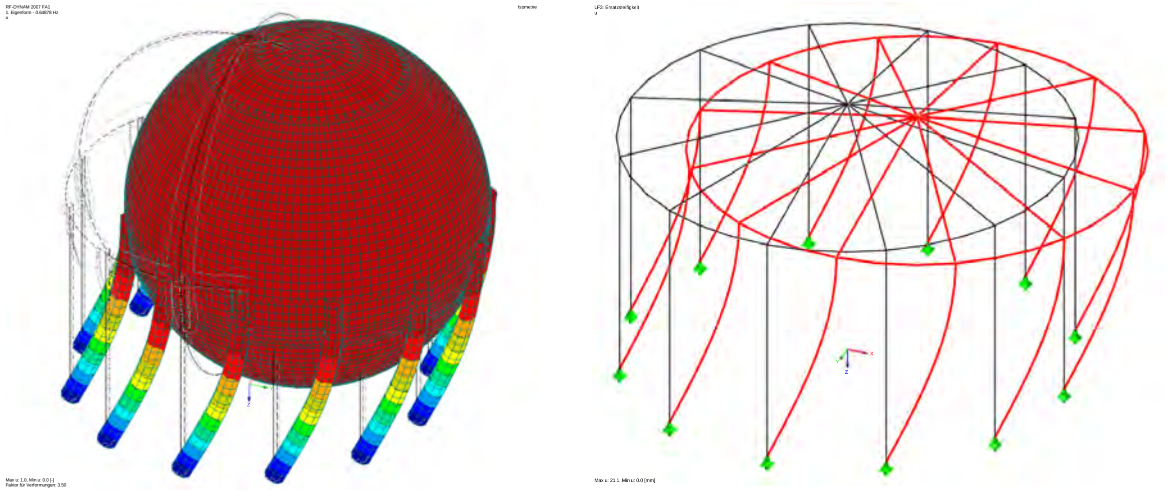

Figure 3: Ascertainment of the fundamental period T_1 based on FEM model (left) and strut-and-tie model (right)

3 SELECTION OF A BEHAVIOUR FACTOR

3.1 Basis of the behaviour factor

In the seismic design of structures the behaviour factor *q* (or response modification factor *R*) represents the dissipation capability of the structure. This dissipation capability depends on the structural type and the type of the construction (e.g.: concrete, steel, composite …). The upper limit value of *q* depends on the ductility class. EC 8, part 1 [1] differentiates between three ductility classes. Structures with small dissipation capability belong to the low ductility class (DCL). Structures belonging to DHM (medium ductility class) or DCH (high ductility class) have to fulfil minimum requirements with regard to plastic deformability (e.g. rotation capacity of the cross-sections) and with regard to detailing (e.g. capacity design of connections). In the following medium ductility class (DCM) was supposed for the steel tanks under investigation.

For structures in Europe basic seismic design rules, including seismic actions, are provided by Eurocode 8 Part 1. In the USA basic rules and seismic actions are provided e.g. by ASCE 7 [4]. With regard to tank structures EN 1998-4 [2] applies in Europe. The American standards API 620 [5] and API 650 [6] are used for the design of ground supported tanks including earthquake. Table 1 shows a compilation of references to the behaviour factor *q* respectively response modification factor *R* available the European and American standards.

Behaviour factor q	**Response modification factor R**
EN 1998-1, chap. 6.3 (steel buildings)	*ASCE/SEI 7-05, tab. 12.2 1 (general systems)*
EN 1998-4, chap. 2.4 (general)	*ASCE/SEI 7-05, tab. 15.4 2 (nonbuilding structures)*
EN 1998-4, chap. 3.4 (silos)	*API 650, tab. E 4 (ground supported, liquid storage tanks)*
EN 1998 -4, chap. 4.4 (tanks)	*API 620, tab. L 1Q and L1 R (ground supported, liquid storage tanks)*
	UBC 1997, Volume 2, tab. 16 N (general systems)
	UBC 1997, Volume 2, tab. 16 P (nonbuilding structures)

Table 1: References of behaviour factor and response modification factor

3.2 Behaviour factor *q* according to European standards

The provisions given by EC 8 for the application of behaviour factor *q* to spherical tanks are of limited precision. For elevated tanks EN 1998-4 [2], Chap. 4.4 refers to Chap. 3.4 (silos) where the application of behaviour factor *q* for an inverted pendulum (see Figure 4) is recommended. Basic definitions of an inverted pendulum system are given in EC8 Part 1. The following definitions given by Eurocode 8 are of interest for assessment of the behaviour factors of spherical elevated tanks:

- EN 1998-1 5.1.2 (1): Inverted pendulum systems – system in which 50% or more of the mass is in the upper third of the height of the structure, or in which the dissipation of energy takes place mainly at the base of a single building element.
  NOTE: One-storey frames with column tops connected along both main directions of the building and with the value of the column normalized axial load ν_d exceeding 0,3 nowhere, do not belong in this category.

- EN 1998-1 6.3.1 (5): Inverted pendulum structures may be considered as moment resisting frames provided that the earthquake resistant structures possess more than one column in each resisting plane and that the following inequality of the limitation of axial force: $N_{\mathrm{Ed}} < 0{,}3\ N_{\mathrm{pl}}, R_{\mathrm{d}}$ is satisfied in each column.
- EN 1998-4 4.4 (4): behaviour factors specified in 3.4 should be applied also to the part of the response of elevated tanks […]
- EN 1998-4 3.4 (5): For skirt-supported silos, with the skirt designed and detailed to ensure dissipative behaviour; the upper limit values of the *q* factor defined in EN 1998-1, Sections 5 to 7 for inverted pendulum structures may be used.

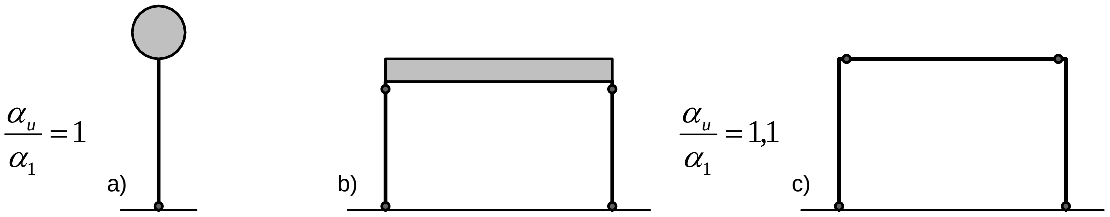

Figure 4: Inverted pendulum (a, b) and MRF (c) according to EN 1998-1, Fig. 6.5 [1]

The modal shapes obtained by the calculations using the FE-model and the strut-and-tie model however, showed that an elevated spherical tank barely behaves like an inverted pendulum as it is intentioned by EN 1998-1. Rather, the spherical tank supported by a number of columns exposes behaviour comparable to a moment resisting frame with a rigid girder. Moreover, two aspects mentioned in EC 8-1 5.2.1 – potential plastic hinges at the top of columns and more than one single resisting element – indicate a possible classification of such structures as a MRF rather than inverted pendulum. The comparison of elevated tanks to skirt-supported structures as given by EC 8-4, however, suggests the presence of one resisting element only and consequently the maximum *q*-factor of 2,0 (see Table 2), provided that the structural detailing allows for the development of a plastic mechanism.

STRUCTURAL TYPE	Ductility Class	
	DCM	DCH
a) Moment resisting frames	4	$5\alpha_u/\alpha_1$
b) Frame with concentric bracings		
Diagonal bracings	4	4
V-bracings	2	2,5
c) Frame with eccentric bracings	4	$5\alpha_u/\alpha_1$
d) Inverted pendulum	2	$2\alpha_u/\alpha_1$
e) Structures with concrete cores or concrete walls	See section **5**	
f) Moment resisting frame with concentric bracing	4	$4\alpha_u/\alpha_1$
g) Moment resisting frames with infills		
Unconnected concrete or masonry infills, in contact with the frame	2	2
Connected reinforced concrete infills	See section **7**	
Infills isolated from moment frame (see moment frames)	4	$5\alpha_u/\alpha_1$

Table 2: Table 6.2 from EN 1998-1 [1]

In fact, neither of the possible interpretations – inverted pendulum or MRF – seems to be reasonable in order to estimate the real performance of a spherical tank. The classification as inverted pendulum is probably rather conservative whereas for a classification as a frame detailing rules for the achievement of dissipative behaviour are missing.

3.3 Response modification factor R according to American standards

American standards such as ASCE 7 [4] differentiate between building and non-building structures. Table 15.4-2 in [4] contains declarations for the non-building structure types “tank” respectively “vessels”. The response modification factor for an elevated tank supported by non-braced legs yields the value *R* = 2.0 according to Table 15.4 2 in [4] (see Table 3).

Nonbuilding Structure Type	Detailing Requirements^c	*R*
Elevated tanks, vessels, bins, or hoppers:		
On symmetrically braced legs (not similar to buildings)	15.7.10	3
On unbraced legs or asymmetrically braced legs (not similar to buildings)	15.7.10	2
Single pedestal or skirt supported		
- welded steel	15.7.10	2
- welded steel with special detailing	15.7.10 and 15.7.10.5 a and b.	3
- prestressed or reinforced concrete	15.7.10	2
- prestressed or reinforced concrete with special detailing	15.7.10 and 14.2.3.6	3
Horizontal, saddle supported welded steel vessels	15.7.14	3
Tanks or vessels supported on structural towers similar to buildings	15.5.5	Use v categ resi
Flat-bottom ground-supported tanks:	15.7	
Steel or fiber-reinforced plastic:		
Mechanically anchored		3
Self-anchored		2.5
Reinforced or prestressed concrete:		
reinforced nonsliding base		2
anchored flexible base		3.25
unanchored and unconstrained flexible base		1.5
All other		1.5

Table 3: Extract from ASCE/SEI 7-05, Table 15.4 2 [4]

Ostensibly there is a good agreement between the European and the American proposal for the behaviour factor to be applied to elevated tanks ($q = R = 2.0$). In fact however, the American provisions are referring to generally shaped tanks. The detailing requirements of chapter 15.7.10 as given in the table above, are also of general nature and do not provide guidance on how to achieve a ductile behaviour in particular with regard to the connection of the legs to the shell of the tank.

3.4 Selected behaviour factor for further investigations

Considering the uncertainties related to the choice of an adequate behaviour factor and the fact that the selected example has been initially designed using elastic calculation methods the behaviour factor used in the following seismic calculations was assumed to be $q = R = 1{,}5$. Since the aim of this study was the comparison of design values resulting from the application of the European and American codes, it was important to select comparable design actions and design resistance by using the same behaviour factor for all code-based calculations. On the other hand selecting the lower bound of the available behaviour factors led to safe-sided results with regard to the intended verification of an existing spherical tank.

A more sophisticated, performance based check of the response of the spherical tank to seismic actions would require either nonlinear time-step calculations. In order to determine a realistic behaviour factor these studies would need to be extended to an incremental dynamic analysis and to other dimensions of the tanks. Such a study however was not included in the working programme of the research project.

4 SEISMIC ANALYSIS ACCORDING TO CODES

4.1 Design spectrum

In order to obtain comparable results using European and American standards the following parameters were chosen (see Table 4). The relevant design spectra according to European and American standards are shown in Figure 5. The spectra were selected such that the “plateau”-values for both codes are the same.

EN 1998-1 [1]		ASCE/SEI 7-05 [4]	
• *ground type C*	*(Table 3.1 in [1])*	• *site class C*	*(Table 20.3-1 in [4])*
$S = 1{,}0^{1)}$	*(Table 3.2 in [1])*	• *occupancy category III*	
$T_B = 0{,}2$ s	*(Table 3.2 in [1])*	$S_S = 0{,}85^{2)}$	*(Fig. 22-1 to 22-14 in [4])*
$T_C = 0{,}6$ s	*(Table 3.2 in [1])*	$S_1 = 0{,}25^{2)}$	*(Fig. 22-1 to 22-14 in [4]*
$T_D = 2{,}0$ s	*(Table 3.2 in [1])*	$T_0 = 0{,}086$ s	*(Eq. 11.4-6 in [4])*
		$T_S = 0{,}431$ s	*(Eq. 11.4-6 in [4])*
		$T_L \geq 4{,}0$ s	*(Fig. 22-15 to 22-20 in [4])*

1) This value does not agree with table 3.2 in [1] and was only chosen to fit the plateau.

2) This value was selected such that the plateau-values for both codes are the same

Table 4: Values of parameters describing the design spectrum according to EC 8 [1] and ASCE 7 [4]

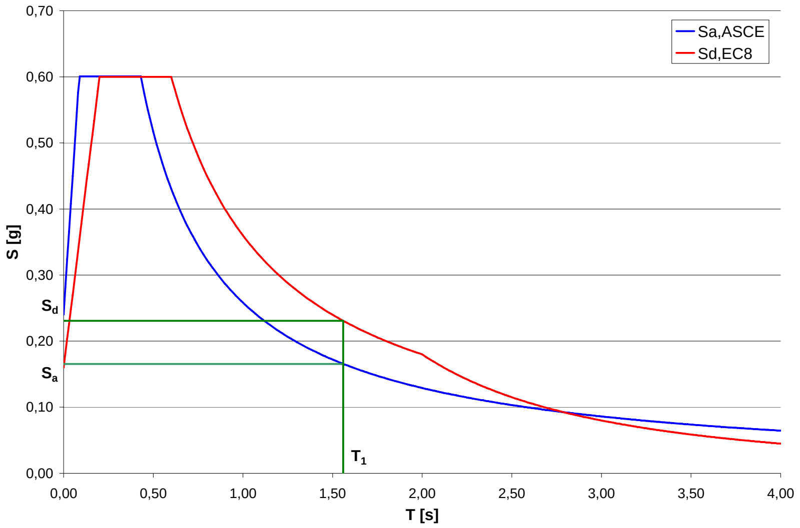

Figure 5: Comparison of the elastic response spectrum for the spherical pressure vessel according to EC 8 [1] and ASCE 7 [4]

The comparison of the spectra shows, that even with a similar plateau of 0.6g, up to T = 2.7 [s] the European spectrum leads to higher values than the American one (see Figure 5). However, the design spectrum of both standards is very dependent on the chosen parameters. Therefore the comparison of the spectra is not discussed further here. In addition for each standard the same importance factor and behaviour factor were chosen:

EN 1998-1 [1]	**ASCE/SEI 7-05 [4]**
• *importance factor* $\gamma_I = 1.25$	• *importance factor* $I = 1.25$
• *behaviour factor* $q = 1.5$	• *response modification factor* $R = 1.5$

Table 5: Importance factor and behaviour factor according to EC 8 [1] and ASCE 7 [4]

4.2 Seismic base shear force neglecting sloshing effects

A. According to European standards

The design of tanks, silos and pipeline systems is governed by EC 8, part 4 [2]. In order to obtain the seismic action effects the “lateral force method” based on linear-elastic analysis according to EC 8, part 1 [1] was used. This method is applicable for structures that respond to seismic action approximately as a single-degree-of-freedom system. This requirement is considered to be fulfilled, if the structure meets the “criteria for regularity in elevation” given in EC 8, part 1 [1] and if the fundamental periods T_1 for the two main directions are smaller than the following values:

$$T_1 \leq \begin{cases} 4 \cdot T_C \\ 2{,}0\,s \end{cases} \tag{3}$$

When neglecting the influence of sloshing the fundamental mode may be assumed as clearly governing the response. Also, the structure may be assumed as regular in plan and elevation. Thus the seismic base shear force F_b was determined as follows:

$$F_b = S_d(T_1) \cdot m \cdot \lambda \tag{4}$$

where $T_1 = 1.56\,s$ (see chapter 2.3)

$S_d(T_1) = a_g \cdot S \cdot \frac{2.5}{q} \cdot \left(\frac{T_C}{T_1}\right) = 1.51\,m/s^2$ (Eq. 13.3 in [1])

$S_d(T_1) = 0.154\,[1/s]$ (for $q = 1.5$)

$S_d(T_1) = 0.231\,[1/s]$ (for $q = 1.0$)

$m = 879 + 2104 = 2983\,t$ (see chapter 2.1)

$\lambda = 1.0$ (Ch. 4.3.3.2.2 in [1])

$F_b = 1.51 \cdot 2983 \cdot 1.0 = 4503.9\,kN$

$F_b = \gamma_I \cdot 4503.9 = 5629.8\,kN$ (for $\gamma_I = 1.25$)

In order to determine the design values for detailed verification of structural elements of the general structure the following application rules must be considered:

- combination of the effects of the components of the seismic action according to EN 1998-1 (4.3.3.5) [1] (here only the horizontal seismic acceleration is considered using the alternative combination E_{Edx} "+" $0.3E_{Edy}$, because the vertical acceleration should be taken only for horizontal or nearly horizontal structural members);

- if the accidental eccentricity of EN 1998-1(4.3.2) [1] is not taken into account by a more exact method including a 3D-model, the accidental torsional effects are accounted for by multiplying the action effects for the individual load resisting elements:

$$\delta = 1 + 0.6 \cdot \frac{x}{L_e} \tag{5}$$

where x distance of the element under consideration from the centre of mass of the building in plan, measured perpendicularly to the direction of the seismic action considered

L_e distance between the two outermost lateral load resisting elements, measured perpendicularly to the direction of the seismic action considered

- combination of the seismic action with other actions in accordance with EN 1990:2010 (6.4.3.4) [3] and EN 1998-1 (3.2.4) [1], whereas the combination coefficient for the variable action "snow load" and "wind load" is $\psi_{2,I} = 0$

With regard to the first point – combination of earthquake directions – it shall be mentioned that the initial intension of this rule was the consideration of seismic actions acting "diagonally" on structures usually rectangular in plan. Using this simplified attempt it is permitted to calculate a structure for each orthogonal direction separately and to omit the determination of the most unfavourable direction of the seismic action. Contrary to typical buildings the investigated spherical tank does not have "orthogonal" directions as it is practically rotation-symmetric. Thus there is no "unfavourable" load direction and the necessity of the combination of directions needs to be checked.

The consideration of accidental torsional effects by the simplified model was assumed to cover all eccentricities resulting from external installations, connected pipes, inspection ladders etc. and selected due to its applicability to a SDOF-model. The effects of the applied eccentricity however (+30%, see chapter 4.2 C), seem to be very much safe-sided as indicated by the results presented in Table 6.

Further investigations according to EC 8 were carried out using the strut-and-tie model in Figure 3 (right side). The results are shown and discussed in chapter 4.2 C.

B. According to American standards

The Appendix E of API 650 [6] provides only requirements for the seismic design of cylindrical tanks. Therefore the equivalent lateral force procedure of ASCE/SEI 7-05 (12.8) [4] was applied. For the investigated spherical pressure vessel the seismic base shear force V was determined as follows:

$$V = C_S \cdot W \tag{6}$$

where $T = 1.56\,s$ (see chapter 2.3)

$F_a = 1.06$ (Tab. 11.4-1 in [4])

$F_v = 1.55$ (Tab. 11.4-2 in [4])

$S_{MS} = F_a \cdot S_S = 0.901$ (Eq. 11.4-1 in [4])

$S_{M1} = F_v \cdot S_1 = 0.388$ (Eq. 11.4-2 in [4])

$S_{DS} = \frac{2}{3} \cdot S_{MS} = 0.601$ (Eq. 11.4-3 in [4])

$S_{D1} = \frac{2}{3} \cdot S_{M1} = 0.258$ (Eq. 11.4-4 in [4])

$S_a(T) = \frac{S_{D1}}{T} = 0.165[1/s]$ (Eq. 11.4-6 in [4])

$C_S = \frac{S_{DS}}{R/I} = 0.5 < \frac{S_{D1}}{T \cdot (R/I)} = \underline{0.138}$ (Eq. 12.8-3 in [4])

$W = 879 + 2104 = 2983\,t \cong 29830\,kN$ (see chapter 2.1)

$V = 0.138 \cdot 29830 = 4116.6\,kN$

Finally the horizontal seismic load effect E_h shall be determined in accordance with ASCE/SEI 7-05 (12.4.2) [4] as follows:

$$E_h = \rho \cdot Q_E \tag{7}$$

where $\rho = 1.3$ (Ch. 12.3.4 in [4])

for Seismic Design Category D (Tab. 11.6-2 in [4])

$Q_E = V = 4116.6\,kN$ (Ch. 12.4.2.1 in [4])

$E_h = 1.3 \cdot 4116.6 = 5351.5\,kN$

To determine the design values for detailed verification of structural elements of the general structure the following application rules must be considered:

- according to ASCE/SEI 7-05 (12.5) [4] for structures assigned to Seismic Design Category D, the design seismic forces are permitted to be applied independently in each of two orthogonal directions and orthogonal interaction effects are permitted to be neglected;
- according to ASCE/SEI 7-05 (12.7.2) [4] a minimum of *25%* of the filling live load shall be include within the effective seismic weight (here: *100%* of the filling live load);
- according to ASCE/SEI 7-05 (12.8.4.2) [4] accidental torsion should be taken into account by assumed displacement of the centre of mass by a distance equal to 5 percent of the dimension of the structure perpendicular to the direction of the applied forces. This approach is exactly the approach according to EN 1998-1(4.3.2) [1] and was not implemented here;
- combination of the seismic action with other actions in accordance with ASCE/SEI 7-05 (12.4.2.3) [4]: $(1.2 + 0.2\,S_{DS})\,D + \rho\,Q_E + L + 0.2\,S$, whereas the dead load D is equal to the self-weight of the tank, the live load L is equal to the filling and the snow load is zero.

This investigation is carried out using the strut-and-tie model in Figure 3 (right side). The results are shown and discussed in chapter 4.2 C.

C. Comparison of the design value

The static seismic equivalent loads are determined and combined following the rules given above. They are applied as single equivalent loads in centre of gravity of the strut-and-tie model and the action effects are calculated using linear elastic analysis. The results are given in the following Table 6, listing action effects (separated for the individual load cases) and design values (of the load combination) for both column base and column head according to European standards and American Standards respectively. The table also shows results for seismic action in 0°-direction as well as in 15°-direction. Although the static seismic equivalent loads according to European standards are approximately 5% higher than the ones taken from the American standards, the correlation of those results is good. This good correlation is due to the combination of the seismic action with other actions in accordance with ASCE/SEI 7-05 (12.4.2.3) [4].

		column base				column head			
		Eurocode		ASCE		Eurocode		ASCE	
		$\alpha = 0°$	$\alpha = 15°$	$\alpha = 0°$	$\alpha = 15°$	$\alpha = 0°$	$\alpha = 15°$	$\alpha = 0°$	$\alpha = 15°$
self-weight	N	*-732.3*		*-966.6*[1]		*-686.5*		*906.2*[1]	
	$V_x = V_y$	*0.0*				*0.0*			
	$M_y = M_x$	*0.0*				*0.0*			
operating-load	N_K	*-1753.5*				*-1753.5*			
	$V_x = V_y$	*0.0*				*0.0*			
	$M_y = M_x$	*0.0*				*0.0*			
seismic-load	N	*-1335.6*	*-1288.8*	*-1086.6*	*-1049.6*	*-1335.6*	*-1288.8*	*-1086.6*	*-1049.6*
	V_x	*609.9*		*446.0*		*609.9*		*446.0*	
	V_y	*183.0*		*0.0*		*183.0*		*0.0*	
	M_y	-				*6313.4*		*4616.4*	
	M_x	-				*1894.0*		*0.0*	
load combination	N_d	*-3821.5*	*-3774.6*	*-3806.8*	*-3769.8*	*-3553.0*	*-3514.0*	*-3746.2*	*-3709.2*
	$V_{x,d}$	*609.9*		*446.0*		*609.9*		*446.0*	
	$V_{y,d}$	*183.0*		*0.0*		*183.0*		*0.0*	
	$M_{y,d}$	-				*6313.4*		*4616.4*	
	$M_{x,d}$	-				*1894.0*		*0.0*	

[1] (1.2+0.2 S_{DS}) D (combination of the seismic action with other actions according to ASCE/SEI 7-05)

Table 6: Action effects and design values for load directions of $\alpha = 0°$ and $\alpha = 15°$ according to European and American standards

In addition a closer look at the results leads to the following recognitions:

- the methods to calculate the seismic base shear force according to European and American standards are identical, so that the differences in the results only come from the different design spectra;

- the adding of the redundancy factor ρ = 1.3 increased the static seismic equivalent load according ASCE 7 [4]; after this step the seismic loads according to Eurocode and ASCE are quite equal
- because of the accidental eccentricity, which was simplified taken into account according to the EC-8 [1], the difference between the results increased again. This becomes apparent by calculating the shear force V_x resulting from the seismic load:

$$V_x = \delta \cdot \frac{F_b}{n} = 609.9\,kN \qquad \text{(Eurocode)}$$

$$V_x = \frac{E_h}{n} = 446.0\,kN \qquad \text{(ASCE)}$$

where $n = 12$ (number of columns, see chapter 2.1)

$$\delta = 1 + 0.6 \cdot \frac{x}{L_e} = 1.3 \qquad \text{(see Eq. 5)}$$

with $L_e = 19700\,mm$ (see chapter 2.1)

$$x = \frac{19700}{2} = 9850\,mm \qquad \text{(see chapter 2.1)}$$

To design columns, bases and joints of the columns to the spherical pressure vessel the design values for α = 0° according to EC 8 are relevant. The verification of the individual members as well as the ULS verification of the vessel skin is not discussed here since the focus was only on the comparison of the different action effects.

4.3 Seismic base shear force taking into account sloshing effects

In the European as well as the American standard rules for the consideration of sloshing effect for liquids are provided for cylindrical (EC 8 und ASCE 7) respectively for rectangular (ASCE 7) tanks only. Thereby the maximum height of the sloshing wave is calculated (see equation 8 and 9) which pretend the minimum height of the freeboard. Neither in the European nor in the American standard a calculation of a seismic design shear force due to the sloshing effect is regulated.

$$d_{\max} = 0.84 \cdot R \cdot \frac{S_d(T_{c1})}{g} \qquad \text{(EC 8)} \qquad (8)$$

$$\delta_S = 0.5 \cdot D_i \cdot I \cdot S_{ac} \qquad \text{(ASCE 7)} \qquad (9)$$

For this reason the published procedure of KARAMANOS et al. [9] was used to consider the sloshing effect in seismic design of the investigated spherical tank.

e	[%]	M_{1C}/M_L	M_{2C}/M_L	M_{3C}/M_L	M_{4C}/M_L	M_{nC}/M_L	M_I/M_L
-1.0	0.0	1.00000	0.0000	0.00000	0.00000	1.00000	0.00000
-0.95	25	0.98315	0.00010	0.00000	0.00000	0.98326	0.01674
-0.90	5.0	0.96594	0.00039	0.00000	0.00000	0.96634	0.03366
-0.80	0.0	0.9338	0.00137	0.00007	0.00001	0.93184	0.06816
-0.60	20.0	0.85437	0.00434	0.00052	0.00014	0.85947	0.14053
-0.40	30.0	0.77117	0.00785	0.00140	0.00046	0.78136	0.21864
-0.20	40.0	0.67990	0.01140	0.00253	0.00094	0.69619	0.30381
0.00	50.0	0.57969	0.01458	0.00372	0.00150	0.60594	0.39406
0.20	60.0	0.46981	0.01687	0.00472	0.00202	0.49844	0.50156
0.40	70.0	0.35009	0.01753	0.00525	0.00235	0.38440	0.61560
0.60	80.0	0.22222	0.01542	0.00490	0.00228	0.26162	0.73838
0.80	90.0	0.09363	0.00919	0.00310	0.00150	0.12608	0.87392
0.90	95.0	0.03655	0.00439	0.00154	0.00076	0.05586	0.94414
0.95	97.5	0.01364	0.00185	0.00067	0.00034	0.01810	0.98190
1.00	100.0	0.00000	0.00000	0.00000	0.00000	0.00000	1.00000

Table 7: Variation of Sloshing Masses with respect to Liquid height in a Spherical Container [9]

The calculation of the relevant seismic design shear force due to the sloshing effect was performed assuming a liquid fill height of 90% which was determined to be the most unfavourable condition. The convective and impulsive masses follow from Table 7:

$$M_{nC} = 652.6[t] \tag{10}$$

$$M_I = 1239.4[t] \tag{11}$$

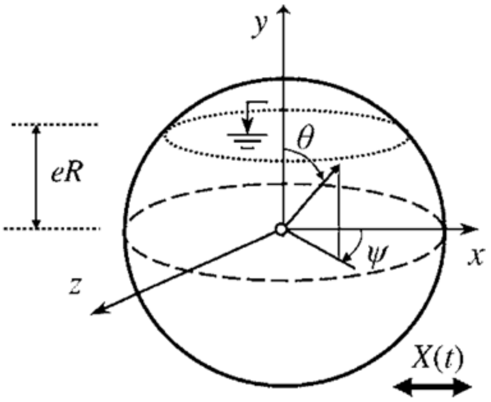

Figure 6: Configuration of a spherical container [9]

The relevant acceleration was calculated with the same assumptions regarding to the design spectrum described in Chapter 2.1.

For the convective part of the sloshing effect the periods are shown in Table 8. The angular frequencies were determined according to Table 9.

T_{1C}	T_{2C}	T_{3C}	T_{4C}
3.18	2.06	1.65	1.41

Table 8: Frist four sloshing periods for a liquid height of 90%

with:

$$T_{nC} = T_{nC} = \frac{2\pi}{\omega} \tag{12}$$

e	[%]	$\lambda_1 = \omega_1^2 R/g$	$\lambda_2 = \omega_2^2 R/g$	$\lambda_3 = \omega_3^2 R/g$	$\lambda_4 = \omega_4^2 R/g$
-1.00	0.0	1.0000	7.0000	17.0000	31.0000
-0.9	5.0	1.0347	6.5638	13.8911	26.7570
-0.80	10.0	1.0723	6.2008	11.8764	17.0320
-0.60	20.0	1.1583	5.6742	9.8543	13.8660
-0.40	30.0	1.2625	5.3683	8.9418	12.4210
-0.20	40.0	1.3924	5.2406	8.5509	11.8000
0.00	50.0	1.5602	5.2756	8.5045	11.6840
0.20	60.0	1.7882	5.4930	8.7793	12.0210
0.40	70.0	2.1232	5.9729	9.4763	12.9380
0.60	80.0	2.6864	6.9574	10.9566	14.9180
0.80	90.0	3.9595	9.4551	14.7598	20.0330
0.90	95.0	5.7615	13.1776	20.4520	27.7020
0.95	97.5	8.3121	18.5527	28.6891	38.8160
1.00	100.0				

Table 9: Variation of the first four sloshing frequencies with respect to liquid height in a spherical vessel **[9]**

The impulsive angular frequency was calculated with the stiffness of the support systems K_{bs}.

$$\omega_{(2)}^2 = \omega_I^2 = \frac{K_{bs}}{M_I} \tag{13}$$

For the evaluation of the impulsive period the support systems stiffness was determined by using the FE-model of the spherical tank. To obtain the same stiffness by hand calculation (see equation 14) the effective column height had to be $h_L = 10.39$ [m].

$$K_{bs} = \sum_{j=1}^{N} \frac{3 \cdot EI_L}{h_L^3} \tag{14}$$

This resulted in a period for the impulsive part of $T_I = 1.48$ [s]. Table 10 shows the masses and periods neglecting the sloshing effect and with consideration of sloshing. The comparison shows that the impulsive Eigen period T_I is approximately equal to the Eigen period T_1 without sloshing. In contrast, the value of the convective Eigen period T_{1C} is more than twice as large.

without sloshing				
	total mass M [t]		**period T_1 [s]**	
dynamic analysis	2919.2		1.54	
inverted pendulum	2919.2		1.56	
sloshing considered				
	convective mass M_C [t]	**impulsive mass M_I [t]**	**period T_{1C} [s]**	**period T_I [s]**
sloshing response	263.96	2644.64	3.18	1.48

Table 10: Comparison of Natural periods

Table 11 shows the ordinates S_d which were evaluated with the periods T_{1C} and T_I as well as the design spectrum according to Chapter 2.1. For the convective part the behaviour factor was set to $q = 1.0$ according to EN 1998-4, Chap. 4.4(4) [2].

$S_d(T_{1C})$	$S_d(T_I)$
0.80	2.74

Table 11: Comparison of the design response spectrum

In the calculation of the seismic design shear force F_D (equation 15) only the first convective period was taken into account. The convective and impulsive parts of the sloshing effect were combined by the “square root of the sum of the squares”-rule (SRSS):

$$F_D = \sqrt{\left(M_C \cdot S_d\left(T_{1C}\right)\right)^2 + \left(M_I \cdot S_d\left(T_I\right)\right)^2} \tag{15}$$

For the investigated spherical pressure vessel the seismic design shear force according equation 15 resulted to $F_D = 7240$ [kN]. The comparison with the seismic base shear force $F_b = 5629.8$ [kN] from Chapter 4.2 A shows that the consideration of the sloshing effect provides significantly higher earthquake loads. Thus the seismic design shear force F_D according equation 15 was used in the following stress analysis.

It needs to be mentioned, that in particular in cases where the convective period is significantly longer than the impulsive period, the application of the SRSS-rule may lead to non-conservative results because of the increased probability of the co-occurrence of the maxima of both modes (see Figure 7).

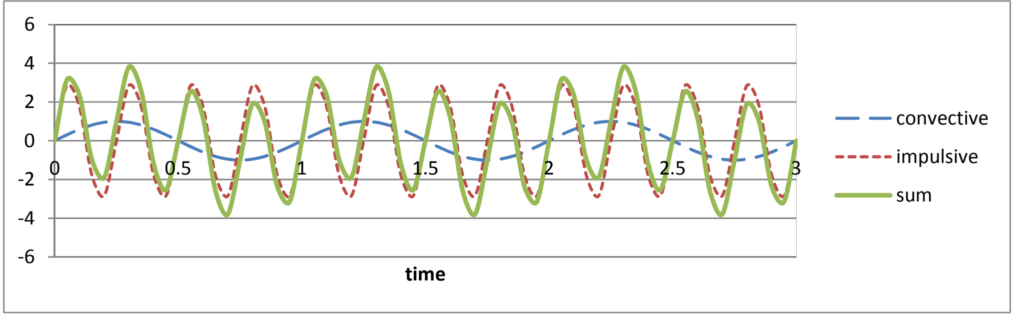

Figure 7: Simplified combination of convective and impulsive modes

4.4 Stress analysis

The stress analysis was performed using a finite element model of the spherical pressure vessel (see Figure 8). Thereto the following load cases from case study 4 were applied.

- dead load (empty weight): 815 [t]
- operating load (90% fill height): 2130 [t]
- internal pressure: 1650.0 [kN/m²]
- external pressure: 101.325 [kN/m²]
- seismic design shear force: 7240 [kN]

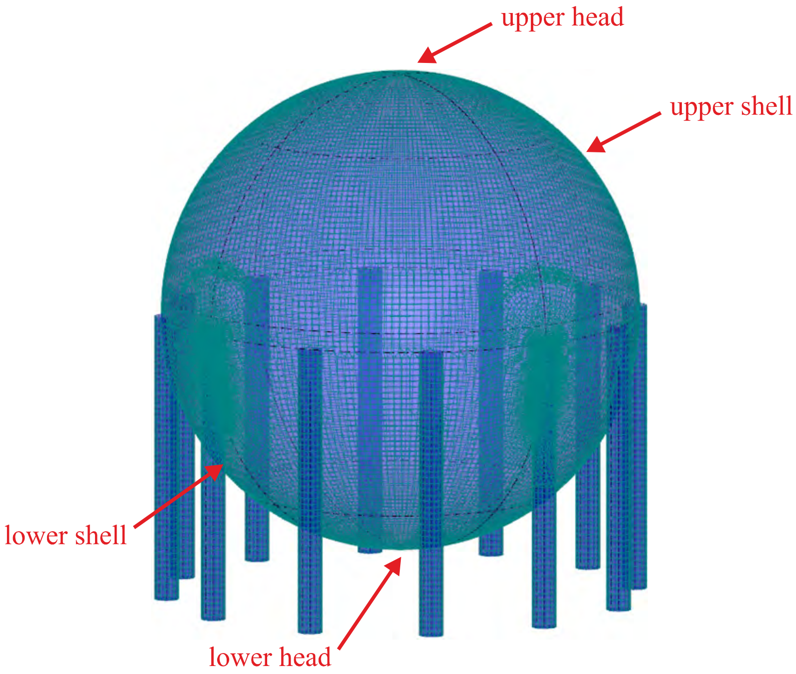

Figure 8: FE-model of the spherical pressure vessel

The tank was modelled with shell thicknesses of $t_1 = 71.8$ [mm], $t_2 = 73.1$ [mm], $t_3 = 75.9$ [mm] and $t_4 = 74.6$ [mm] (see Chapter 2.1). The vessel stresses were determined at the upper head, at the lower head as well as a two undisturbed areas of the shell. In addition stresses of the connection column-shell were determined in load direction and transverse to the load direction. The results are shown in Table 12 and Table 13.

load cases	**dead load**	**operating load**	**internal pressure**	**external pressure**	**seismic load**
	[kN/cm²]	[kN/cm²]	[kN/cm²]	[kN/cm²]	[kN/cm²]
upper head	-0.16	0.00	11.58	-0.70	0.03
upper shell	0.05	0.00	11.30	-0.69	0.09
column-shell (in load direction)	2.02	1.63	**12.68**	-0.70	**27.43**
column-shell (transverse load direction)	1.95	1.30	**12.68**	-0.68	3.98
lower head	0.17	0.42	10.96	-0.68	0.05
lower shell	0.16	0.45	11.16	-0.68	0.03

Table 12: Stresses due to load cases in different points

combination	**EN 1990,** Chap. 6.4.3.4 [3] $\Sigma G_{k,j} + A_{ed} + \Sigma 0{,}8\ Q_{k,i}$	**ASCE/SEI 7-05,** Chap. 2.4.1 [4] D + F + 0,7E	**ASME II Part-D,** Tab. 5A [7] allowable stress
upper head	9.13	11.44	34.5
upper shell	9.18	11.41	
column-shell (in load direction)	**40.90**	**35.53**	
column-shell (transverse load direction)	17.11	18.72	
lower head	9.32	11.59	
lower shell	9.48	11.79	

Table 13: Load case combination

With $G_{k,j}$ = D = dead load
A_{Ed} = E = earthquake load
$Q_{k,i}$ = F = live load

5 OVERALL CONCLUSIONS AND FUTURE PROSPECTS

With regard to the design of spherical liquid storage tanks the seismic provisions of Eurocode as well of the ASCE Code can be described as similar. The main differences in the results obtained by the application of both codes result from different input data for seismic actions. Nevertheless there are some differences within the calculation rules for spherical tanks:

- The ASCE Code provides more detailed data on the choice of a response modification factor, tanks are not classified as simple inverted pendulum systems;
- Distinction is made between braced and unbraced supports;
- Eurocode proposes the assumption of an inverted pendulum system for the behavior factor

Both codes however do not provide methods for the calculation and consideration of sloshing effects in spherical tanks. Furthermore some rules which are used in the practice design of spherical tanks need clarification or enhancement:

- Realistic assessment of the behavior factor – in fact a sphere supported by a number of legs behaves like a frame rather than like a inverted pendulum;
- The assessment of a behavior factor shall be detailing rules allowing for the achievement of a dissipative behavior; this applies in particular to the connection of the legs to the shell as well as to the foundations;
- The application of the simplified eccentricity, which was selected to allow for a simple modelling of the spherical vessel, leads to very conservative results. The application of a severe method to systems, which are obviously symmetric, shall be allowed whithout the formal requirement of a 3D-investigation;
- The need of application of the 100%-x and 30%-y seismic action with regard to rotation-symmetric structures or components shall be verified;
- Conditions for the consideration of sloshing effects shall be defined together with methods for the calculation of these effects and for the combination of the convective and impulsive modes.

6 ACKNOWLEDGEMENT

The investigations were performed within the European research project INDUSE (Structural Safety of Industrial Steel Tanks, Pressure Vessels and Piping Systems Under Seismic Loading) with the financial support by the Research Fund for Coal and Steel (RFCS) which is gratefully acknowledged.

REFERENCES

[1] EN 1998-1:2010-12: “Design of structures for earthquake resistance – Part 1: General rules, seismic actions and rules for buildings”, European Committee for Standardization, Brussels, 2010

[2] EN 1998-4:2007-07: “Design of structures for earthquake resistance – Part 4: Silos, tanks and pipelines”, European Committee for Standardization, Brussels, 2007

[3] EN 1990:2010-12: “Basis of structural design”, European Committee for Standardization, Brussels, 2010

[4] ASCE/SEI 7-05: “Minimum Design Loads for Buildings and Other Structures”, American Society of Civil Engineers, Reston, 2006

[5] API Standard 620: “Design and Construction of Large, Welded, Low-pressure Storage Tanks”, 11th Edition, American petroleum Institute, Washington D.C., 2009

[6] API Standard 650: “Welded Steel Tanks for Oil Storage”, 11th Edition, American petroleum Institute, Washington D.C., 2007

[7] ASME Boiler & Pressure Vessel Code, Section II Material, Part D – Properties (Metric), The American Society of Mechanical Engineers, New York, 2007

[8] ECCS – TC 13 Seismic Design: “ECCS Manuel on Design of Steel Structures in Seismic Zones”, No. 76, First Edition, 1994

[9] KARAMANOS, S.A.; PATKAS, L.A.; PLATYRRACHOS, M.A.: „Sloshing Effects on the Seismic Design of Horizontal-Cylindrical and Spherical Industrial Vessels“, Journal of Pressure Vessel Technology, ASME, Volume 128, Issue 3, pp. 328-340, 2006ly

COMPDYN 2011
3rd ECCOMAS Thematic Conference on
Computational Methods in Structural Dynamics and Earthquake Engineering
M. Papadrakakis, M. Fragiadakis, V. Plevris (eds.)
Corfu, Greece, 25–28 May 2011

DYNAMIC ANALYSIS OF LIQUEFIED NATURAL GAS TANKS SEISMICLY PROTECTED WITH ENERGY DISSIPATING BASE ISOLATION SYSTEMS

Vassilis P. Gregoriou[1], **Stephanos V. Tsinopoulos**[2] and **Dimitris L. Karabalis**[3]

TTA S.A. Structural Engineers
Keas 67 str.112 55, Athens, Greece
e-mail: bgregoriou@tta.gr

Department of Mechanical Engineering, Technological Educational
Institute of Patras
26334, Patras, Greece Greece
e-mail: stsinop@teipat.gr

Department of Civil Engineering, University of Patras
26500, Patras, Greece
e-mail: karabali@upatras.gr

Keywords: Seismic analysis, lead core rubber bearings, non linear viscous dampers liquefied natural gas, storage tanks

Abstract. *The time domain seismic response of a representative liquefied natural gas (LNG) tank isolated at its base level with rubber bearings is investigated. The problem is solved numerically by means of a detailed finite element model, taking into account fluid-structure interaction effects. Two types of seismic isolation systems are investigated: lead core rubber bearings and linear rubber bearings combined with non linear viscous dumpers. Both these systems are characterized by strong energy dissipation mechanisms. The isolation systems are modeled as non-linear spring-dashpot elements with properties calculated on the basis of experimental data obtained from the literature. The seismic excitation considered is an artificial accelerogram compatible with the Eurocode 8 provisions. Results concerning base shear force, sloshing vertical displacement and deflection of the inner steel container are presented. In order to measure the effectiveness of the isolation systems, percentage reductions of the peak response of all mentioned quantities are calculated using the non-isolated tank as reference.*

1 INTRODUCTION

Natural gas is a fossil fuel (90% or more methane) that is usually transported at its gaseous state through ducts from the production site to the place of its consumption. Alternatively it is possible to cool the product down to -170 ^{0}C so that it condenses to its liquid state. In that way the density of the product increases by approximately 600 times making it possible to ship it in specially designed vessels and store it in thermally insulated tanks. The stored product can then be re-evaporated in appropriate facilities and piped to the consumption. The facilities related to the unloading, storage and re-vaporisation of the Liquefied Natural Gas (LNG) are located in the same site which is usually called an LNG terminal.

LNG terminals are crucial facilities for a natural gas distribution system because, besides providing a backup in natural gas supply, they balance the difference between the demand, which varies constantly, and the supply from the international ducts, which is essentially constant. Because of the importance of the LNG tanks, very sever requirements are imposed concerning the ability of LNG tanks to withstand several postulated accidental actions such as aircraft impact, explosion, fire, major leak and earthquake. Especially for the earthquake action, LNG tanks are expected to sustain a major seismic event, of a return period of over 5000 years, up to 10000 years, without undergoing catastrophic damage, while being able to remain fully operational during a medium seismic event of a return period of around 500 years. Design issues for LNG tanks can be found in several specialized publications, e.g. Bomhard and Stempiniewski [1] and Tajirian [2].

The modern aseismic design of LNG tanks is based on base isolation and energy dissipation techniques. The seismic protection devices usually implemented in LNG tanks are either rubber-type bearings [4,2], such as lead core rubber bearings and high damping rubber bearings, or sliding-type bearings such as the friction pendulum bearings [5,2]. All the above systems feature main functions: detaching the structure from its foundation, ensuring the necessary restoring force and providing energy dissipation. Alternatively, separate energy dissipation devices can be used in combination with linear rubber bearings. The function of these devices is based either on the hysteretic behaviour of a metal or on the viscous behaviour of a fluid.

In this work, two base isolation systems, i.e., lead core rubber bearings [6] and linear rubber bearings combined with non-linear viscous dampers, are investigated numerically using the finite element method (FEM). Rubber bearings are formed by alternating layers of hot vulcanized elastomer and steel shims. The elastomer layers provide the horizontal flexibility required for the decoupling of the horizontal structural motion from the ground motion, while the steel shims ensure adequate vertical stiffness. In the case of lead core rubber bearings absorption of energy is achieved through yielding of a lead prismatic core placed in the center of the bearing. In the case of non-linear viscous dampers the energy is absorbed during the movement of a piston in a chamber filled with viscous fluid. Selective results concerning base shear force, sloshing and deflection of the inner steel container are presented.

2 DESCRIPTION AND MODELING OF LNG TANKS

A LNG storage tank has several functions related to the safe-keeping of its content: a) keeping the content from escaping to the environment, b) preventing the atmospheric air from entering the tank, c) defending the content against the effects of external events including accidents such as earthquake, fire and explosion d) maintaining the appropriate conditions in the tank particularly in respect of temperature and pressure (slightly above atmospheric). To achieve these conditions LNG tanks are usually configured as a double shell, as shown in Fig.

1. Thus, they are constituted of an outer prestressed concrete cylindrical shell which is capped by a spherical reinforced concrete dome and an inner steel cylindrical shell open at the top and closed at the bottom by a steel plate. In general the capacity of LNG tanks ranges between 50000 m^3 and 250000 m^3 with values around 150000 m^3 being the most preferable nowadays. The height to radius ("slenderness") ratio ranges from around 0.5 to around 1.5. Ratios higher than 1 allow a better use of the available land but their seismic behavior demonstrates obvious disadvantages. This is, however, what makes them good candidates for the implementation of seismic protection systems. Thus, for the "slender" tank studied in this work, the height to radius ratio is about 1.5. The inner tank height is 36.82m and its radius is 23.60m, while the outer tank height is 39.95m, and its inner radius is 24.48m. The maximum height of the liquid volume is 36.39m. The outer shell is of constant thickness 0.8m along its height, while the thickness of the inner shell increases from top to bottom from 8.0 to 25.5mm. The space between the two shells is filled with perlite to insure proper thermal insulation of the content. The outer shell seats directly on a circular foundation slab, while between the bottom of the inner container and the foundation slab there is a layer of foam glass (0.85m) for thermal insulation purposes

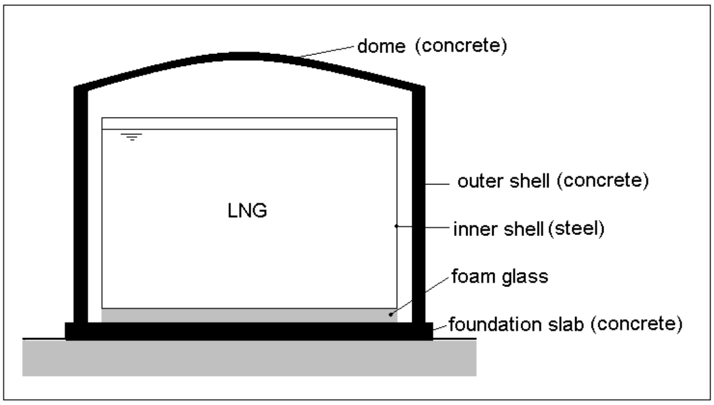

Figure 1: General configuration of an LNG tank with double shell

The seismic analysis of the selected LNG tank is performed by means of the ANSYS finite element program [8]. The outer and the inner shell as well as the dome and the foundation slab are modeled by four-nodded, 24 DOF quadrilateral shell elements. The foam glass layer is modeled by eight-nodded 24 DOF solid elements. The fluid content is modeled by eight-nodded 24 DOF fluid elements. The fluid-structure interaction is approximated by prescribing appropriate coupling equations at the nodal points on the fluid-structure interface.

3 PRELIMINARY DESIGN AND MODELING OF THE ISOLATION SYSTEMS

Both seismic isolation systems under consideration are assumed to comprise a number of similar rubber bearings, or bearings combined with dampers, uniformly distributed under the base slab. The total number of required bearings is derived from the assumption that a single bearing supports approximately 10-12 m^2 of foundation slab, at maximum. Thus, approximately 190 bearings should be used for the tank under consideration. In general dampers must be placed in two directions. The number of dampers can thus be assumed equal to double the number of bearings, though this is not necessary.

Two major assumptions are inherent in the modeling of the seismic isolation systems analyzed in the present study. The first is that the forces applied from the devices to the base slab are uniformly distributed on the entire area of the slab. The second is that the in-plane stiffness of the slab is infinite. Following these assumptions, the vertical stiffness of the bearings is simulated using Winckler type plate elements [8,9], with an appropriate foundation coefficient, while the horizontal reaction of the bearings and of the dampers is simulated using a single non-linear spring – dashpot element connected to the centre of the slab (dampers are assumed to act only in the direction of the excitation). This model for the base isolation system is illustrated in Figure 2

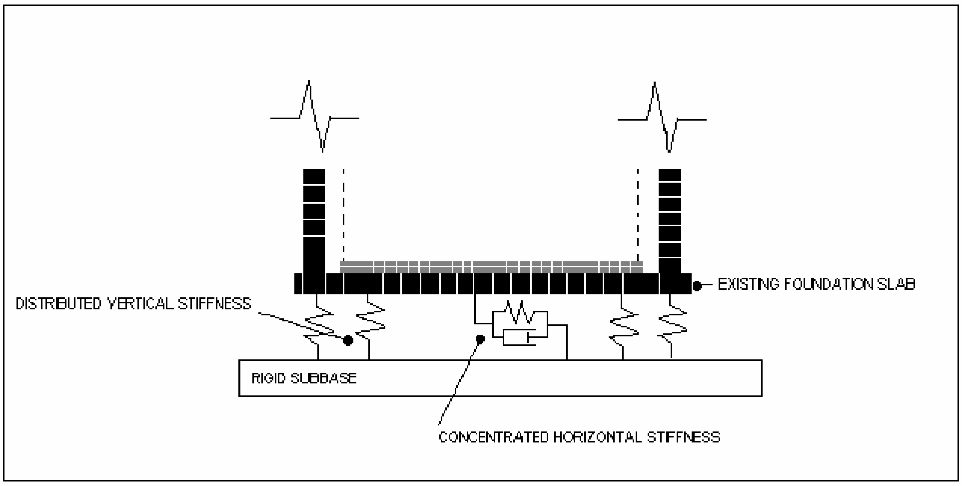

Figure 2: Modeling of the isolation systems

3.1 Vertical stiffness

The Winckler model requires the determination of the elastic foundation stiffness (EFS), which is defined as the pressure required to produce a unit normal deflection of the foundation and is given as

$$EFS = \frac{N * K_v}{A_s} \tag{1}$$

where N is the number of the installed isolators, K_v the vertical stiffness of each isolator and A_s the area of the base slab.

3.2 Horizontal stiffness of lead core rubber bearings

For isolated structures, a fundamental period, i.e. the natural period of the structure moving as an almost rigid body on the isolators, is usually selected in the range of 1.5 to 3 sec. For this study, a fundamental period of 2sec is chosen. Given the total mass M of the structure, the total horizontal stiffness K of an equivalent elastic isolation system, that would lead to a fundamental period of 2 sec, can be approximately evaluated on the assumption of an equivalent single degree of freedom system as

$$K_{eq} = 4 \cdot \pi^2 \cdot M / T^2 \tag{2}$$

The horizontal stiffness of a set of lead core rubber bearings is simulated by a bilinear elastoplastic model, as shown in Figure 4. The assumptions related to the preliminary design of the isolation system are: (a) δ_{max}=0.18 m, (b) $\lambda=K_{el}/K_{pl}=11$, and (c) ξ =40% which is reasonable for structures isolated with lead core rubber bearings [11].

The assumptions (a) and (b) made for the case of lead core rubber bearings for the determination of the parameters of the applied model, can be also employed in the case of lead core rubber bearings, where the following relationships are also used:

$$K_{eq} \cdot \delta_{\max} = K_{el} \cdot dp + K_{pl} \cdot dl \tag{3a}$$

$$dp + dl = \delta_{\max} \tag{3b}$$

$$4dp \;\; K_{el} - K_{pl} \;\; \delta_{\max} - dp \;\; - 2 \cdot \pi \cdot \xi \cdot K_{eq} \cdot \delta_{\max}^{2} = 0 \tag{3c}$$

$$F_y = K_{el} \cdot dp \tag{3d}$$

After computing the various unknown variables appearing in Eqs (3), the bilinear model of Figure (4) is implemented in the finite element model as the force-displacement relationship of a non-linear spring element connected to the centre of the foundation slab.

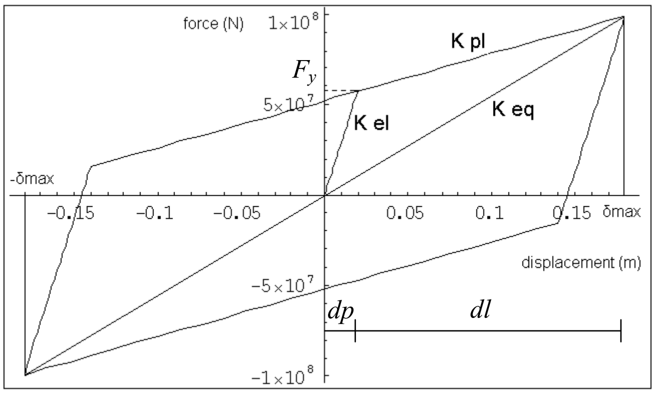

Figure 3: Energy dissipation loop for the set of lead core rubber bearings used in this work

The parameters corresponding to the model of the particular isolation system used in this work, are $K_{el} = 37.95*10^8$ N/m, $K_{pl} = 3.45*10^8$ N/m, $f_y=2.97*10^7$ N.

3.3 Horizontal reaction of linear bearings in combination with non linear viscous dampers

In the case of linear bearings the horizontal stiffness of the seismic isolation stiffness that leads to a fundamental period of T = 2 sec for a full tank is easily determined from the equation

$$Kel = 4\pi^2 (m-m_c)/T \tag{4}$$

where m is the total mass of the structure and m_c is the convective ("sloshing") mass of the liquid. The convective mass is subtracted from the total mass because it oscillates in a mode with a period much larger than the fundamental period of the isolated structure and, for this reason, is considered uncoupled from the fundamental mode of the isolated structure

In the case of application of non-linear viscous dampers the reaction force of the system is given by

$$F_d = C_{nl} v^{0.15} \tag{5}$$

where v is the velocity of the base and C_{nl} is the constant of the non linear damper system. In this work, the constants of the spring-dashpot element concentrated at the center of the slab are: $K = 5.55*10^8$ N/m, $C_{nl} = 5.25*10^7$ Nsec/m.

4 NUMERICAL RESULTS AND DISCUSSION

Time domain non-linear dynamic analyses are preformed with non-linearities concentrated at the spring simulating the isolation system. The linear acceleration method is used for the integration of the system of equations of motion while the full Newton-Raphson method is used for the solution of the non-linear systems of equations. An artificial accelerogram compatible with the EC-8 spectrum for soil type C is used as an input excitation.

In the following, selective results of the analyses of both systems investigated in this work are presented ("lrb" stands for lead core rubber bearings and "nlv" stands for non-lenear viscous dampers). In Figure 4, the base shear force below the foundation slab versus the corresponding base displacement is plotted for each isolation case. In Figure 5, the total base shear force just above the foundation slab is plotted versus time. For comparison purposes the base shear time history for the non-isolated case (fixed base conditions), is also shown. In Figure 6, time histories of base displacement are plotted for each isolation case. The time history of the horizontal displacement, relative to the base, of the inner shell at the fluid free surface level is plotted versus time in Figure 7. For comparison purposes, the horizontal displacement of the inner shell for non-isolated (fixed base conditions) is also shown. Similarly, in Figure 8 the relative displacement at 2/3 of the height of the inner shell, where the maximum deflection is observed, is illustrated. Finally, in Figure 9 the wave height at the intersection of the fluid free surface and the inner shell is plotted versus time for each isolation case and, for comparison purposes, the fixed base conditions.

From the exhibited results the following conclusions could be made: (a) in terms of base shear force, percentage reduction factors of the order of 70% are calculated for both isolation systems investigated in the present work, (b) maximum stresses in the inner shell are reduced by approximately 60%, in comparison to the non-isolated case where fixed base conditions are considered, and (c) the sloshing height remains practically unchanged in comparison to the non isolated tank.

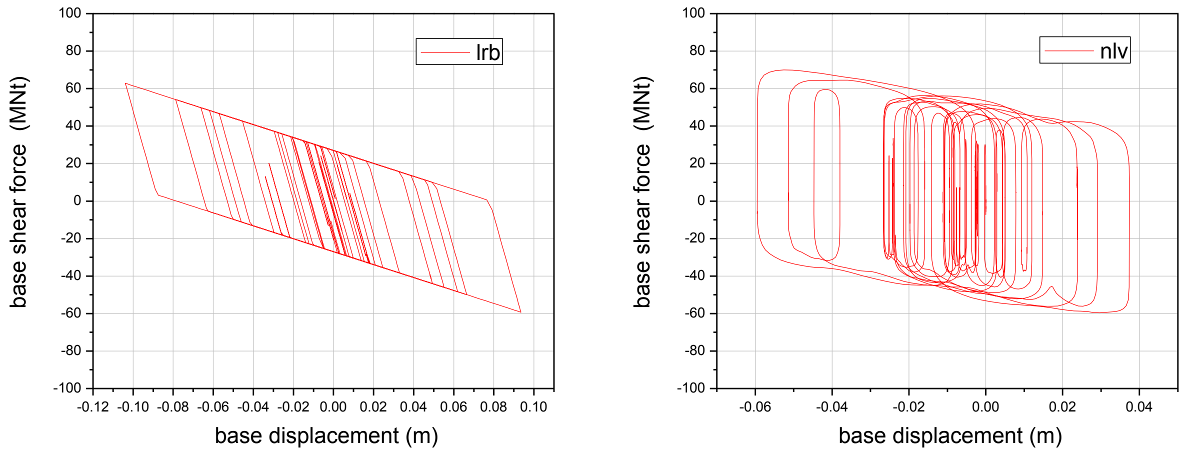

Figure 4: Base shear force below the foundation slab versus base displacement for each isolation case ("lrb" stands for lead core rubber bearings, "nlv" stands for non-linear viscous dampers)

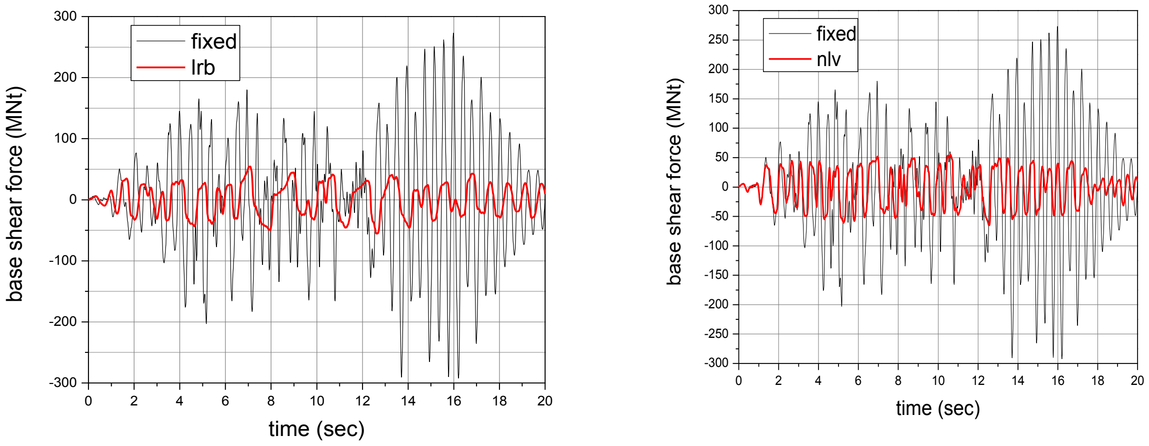

Figure 5: Time histories of total base shear just above the foundation slab for the isolated and the non-isolated (fixed base conditions) cases.

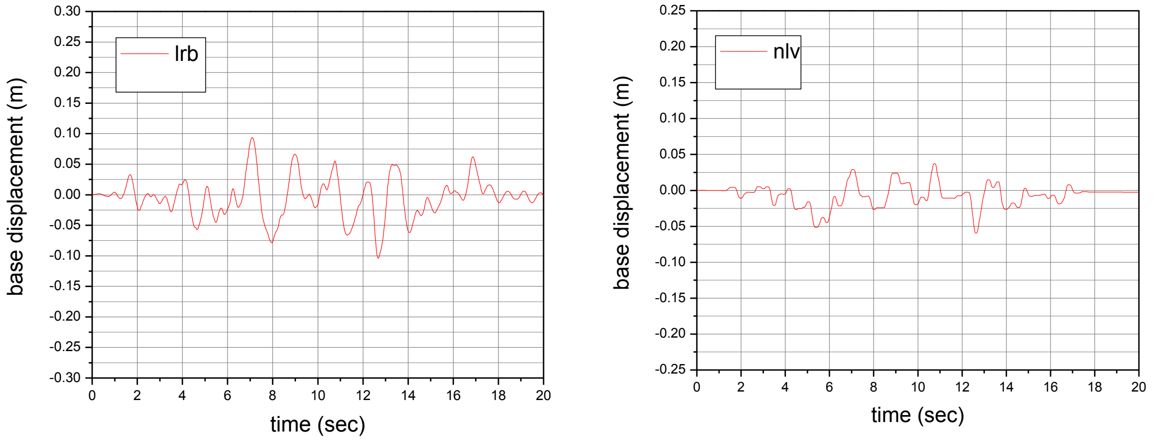

Figure 6: Base displacement time histories for each isolation case

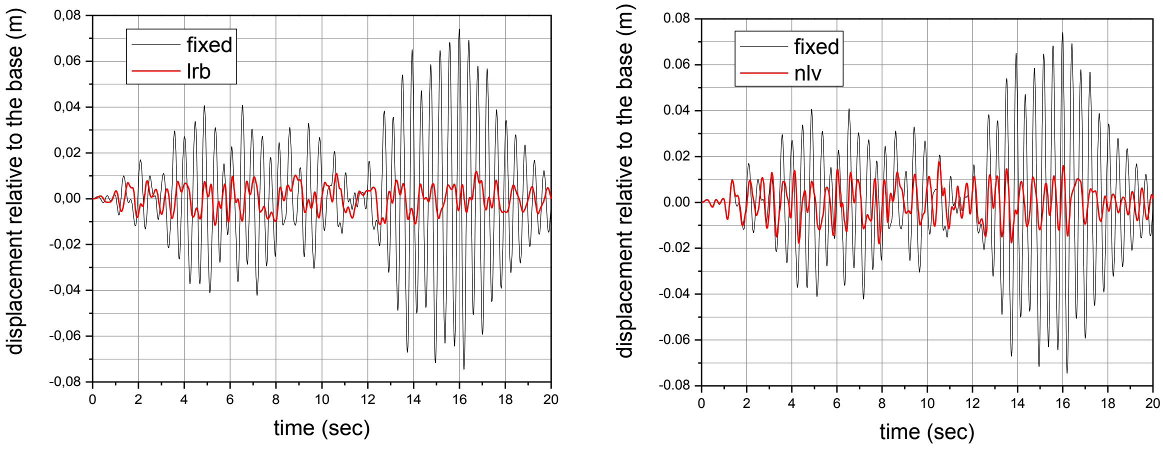

Figure 7: Time histories of the relative to the base displacement of the inner shell at the fluid free surface level

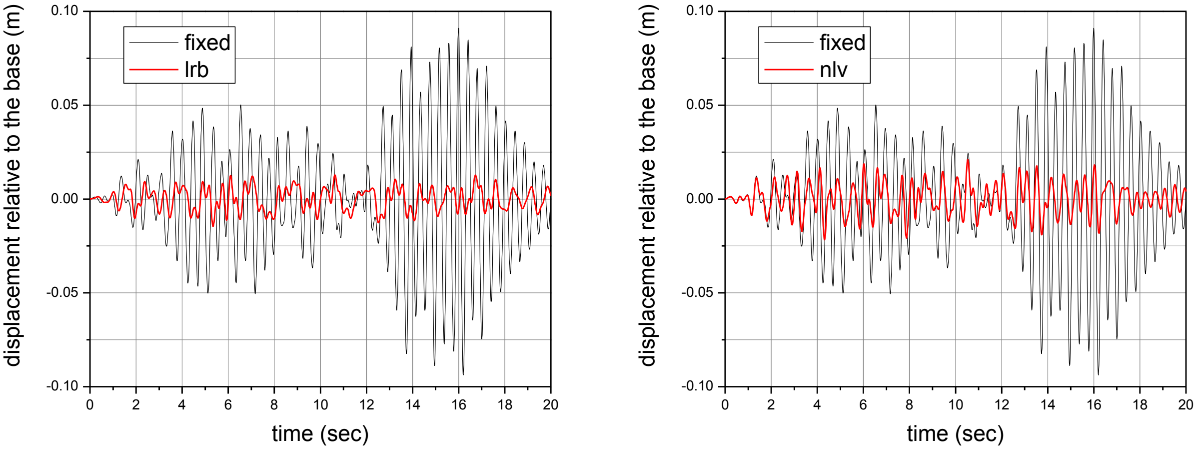

Figure 8: Time histories of the relative to the base displacement of the inner shell at 2/3 of its height

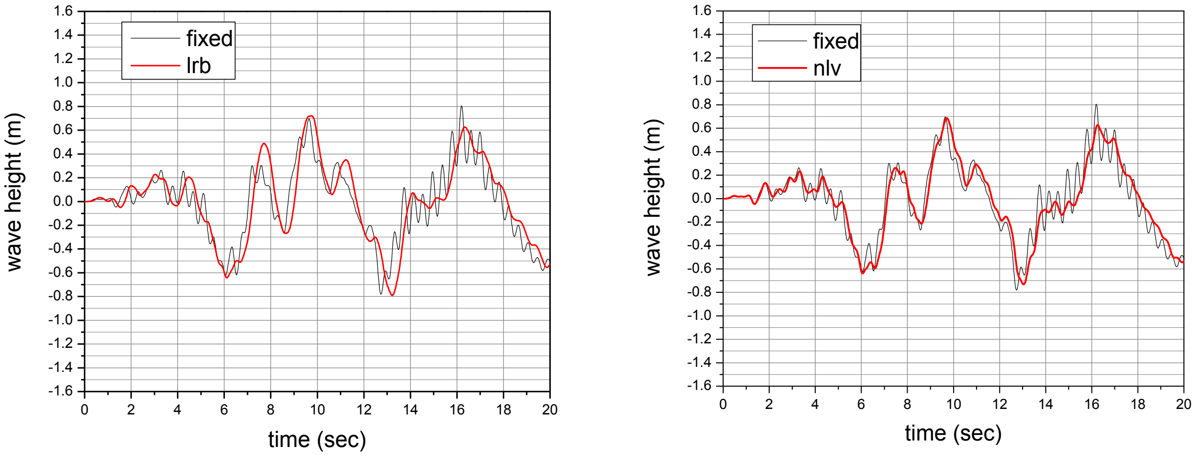

Figure 9 : Wave height time histories at the intersection of the fluid free surface and the inner shell

ACKNOWLEDGMENTS

The authors gratefully acknowledge the financial support by the Environment Programme, Global Change and Natural Disasters of the European Commission, Research Directorate General under Project INDEPTH (EVG1-CT-2002-00065) of the Fifth Framework Program.

REFERENCES

[1] Bomhard, H. and Stempniewski, L (1993) “LNG Tanks for seismically highly affected sites,” *Intl. Post-SMiRT Conference Seminar on Isolation, Energy Dissipation and Control of Vibrations of Structures*, Capri, Italy.

[2] Tajirian, F. F. (1998) “Base isolation design for civil components and civil structures,” *Proceedings of the Structural Engineers World Conference*, San Francisco, California, July.

[3] Buckle, I. G. and Mayes R. L. (1990) “Seismic Isolation History, Application, and Performance - a World View,” Earthquake Spectra 6(2), 161-201.

[4] Tajirian, F. F. (1993) “Seismic isolation of critical components and tanks,” *Proceedings of the ATC-17-1 Seminar on Seismic Isolation, Passive Energy Dissipation and Active Control*, San Francisco, California, pp. 233-244.

[5] Zayas, V. A. and Low D.S. (1995) “Application of seismic isolation to industrial tanks,” *Proceedings of the ASME/JSME Pressure Vessels and Pipe Conference*, Hawaii, PVP-Vol 319, pp. 273-244.

[6] Soong, T. T. and M. C. Constantinou, eds. (1994), *Passive and Active Structural Control in Civil Engineering, CISM Courses and Lectures No. 345*, Springer-Verlag, Wien-NewYork.

[7] European Committee for Standardisation (2002), *Eurocode 8 European Standard. Design of structures for earthquake resistance, Part 1: General rules, seismic actions and rules for buildings*, ENV1998-1-1.

[8] Swanson Analysis Systems, Inc. ANSYS (1992), *User’s Manual for Revision 5.0, Procedures*. Houston, PA.

[9] Anil K. Chopra (1995), *Dynamics of Structures: Theory and Applications to Earthquake Engineering*, Prentice-Hall, New Jersey.

[10] Naeim, F. and Kelly, J.M. (1999), *Design of seismic isolated structures: From theory to practice*, Wiley, New York.

COMPDYN 2011
III ECCOMAS Thematic Conference on
Computational Methods in Structural Dynamics and Earthquake Engineering
M. Papadrakakis, M. Fragiadakis, V. Plevris (eds.)
Corfu, Greece, 25–28 May 2011

SEISMIC ANALYSIS AND DESIGN OF INDUSTRIAL PRESSURE VESSELS

Kalliopi Diamanti[1], Ioannis Doukas[2], and Spyros A. Karamanos[3]

[1]Metallurgical Industrial Research and Technology Development Centre MIRTEC (EBETAM A.E.)
Volos, Greece
k.diamanti@ebetam.gr

[2] TechniPetroL Hellas S.A.
Athens, Greece
IDoukas@technip.com

[3] Department of Mechanical Engineering,
University of Thessaly, Volos, Greece
skara@mie.uth.gr

Keywords: Pressure Vessel, Seismic Design, Pushover Analysis, Incremental Dynamic Analysis, Sloshing.

Abstract. *The present paper focuses on the seismic analysis and design of horizontal-cylindrical and vertical-cylindrical pressure vessels. First, a comparison of the seismic provisions in ASME B&PV code and in EN 13445-3 is conducted for two specific case studies, which constitute typical vessels used in pertochemical facilities. In addition, a numerical investigation is conducted, aimed at proposing a reliable value of the behavior factor for those structures. Those issues are examined numerically, simulating the above pressure vessels with nonlinear finite element models. Finally, a methodology for determining seismic forces due to liquid sloshing horizontal-cylndrical vessels is outlined. The results of the present study can be used towards a safer and more reliable design of industrial pressure vessels under seismic action.*

1 INTRODUCTION

Seismic action constitutes a serious threat for the structural integrity of industrial facilities, such as chemical plants, refineries or power stations. In case of failure of an industrial component, there are severe consequences for the envinronment, the population, as well as in the economy. In particular, safeguading the integrity of pressure equipment is of crucial importance for the safety of an industrial facility. The general analysis and design of pressure vessels has been traditionally performed through the application of the European Standard EN 13445-3 [1] or the US code ASME B&PV Code, Section VIII (Div.1 and Div.2) [2], [3]. In those specifications, it is stated that seismic action should be taken into account for structural design, specifying an increase of stress allowables. However, no specific provisions are stated for the seismic analysis of those vessels, especially on how to compute the seismic forces and the corresponding stresses at critical locations.

In the present paper, the seismic design and analysis is conducted for two specific case studies, namely a horizontal-cylindrical and a vertical-cylindrical pressure vessel, which constitute typical vessels used in pertochemical facilities. Following a comparison of the seismic provisions in ASME B&PV code and in EN 13445-3, a numerical investigation is conducted, aimed at proposing a reliable value of the behavior factor for those structures. Those issues are examined numerically, simulating the above pressure vessels with nonlinear finite element models. Finally, a methodology for determining seismic forces due to liquid sloshing for horizontal-cylndrical vessels is outlined.

2 PRESSURE VESSEL DESIGN USING AMERICAN AND EUROPEAN CODES

A comparison of currently used European and American standards for pressure vessels design is being carried out first. The comparison is aimed at:

- outlining the current methodology for pressure vessel design with regard to seismic loading.
- summarizing the provisions of European and American standards for pressure vessel design in terms of earthquake loading.
- pin-pointing important design issues (e.g. missing links, inconsistencies) that require further investigation.

2.1 General

Both the European and the American standard for pressure vessels design, namely EN13445-3 [1], and ASME VIII Div. 1 [2] and Div. 2 [3] respectively, provide only general statements seismic loading design. The same applies for the British and the German national standards, PD5500 [4] and AD Merkblätter [5]. These main points relevant to seismic design included in EN13445-3 [1], and ASME VIII Div. 1 [2] and Div. 2 [3] can be summarized as follows:

1. Earthquake loading shall be considered where required.
2. Earthquake loads may be treated as equivalent static loads.
3. Earthquake and wind loading need not be considered to act simultaneously.
4. The standards refer to regional codes for determining the seismic load actions.
5. Higher values for the allowable stress can be used for exceptional load cases such as an earthquake.

It should be emphasized that those standards are both based on the allowable stress design framework. With respect to the above item No.5, it should be noted that ASME VIII Div. 1 allows for a general 20% increase, while in ASME VIII Div. 2 the compressive stress allowable is increased. However, in general, higher values for the allowable stresses are used in

Div.2. In the European standard an increase in the nominal safety factor for exceptional load cases is allowed but shall not be less than that for the testing load cases, which is 50%. PD5500 states that all allowable tensile stresses and stress intensities (membrane or bending, primary or secondary) may be increased by a factor of 1.2. Limitations on compressive stresses (buckling, attachments, supports and nozzles, and longitudinal compressive general membrane stress) are not hereby relaxed. In AD Merkblätter there exist relevant provisions for higher safety factor when designing for exceptional load cases.

Furthermore, it is important to notice that EN 1998-4 [6], despite its extensive provisions for liquid storage tanks, does not contain any provisions that could be applicable to pressure vessels. The only provisions that might be helpful are the ones in Annex A, section A.7 for determining forces due to liquid sloshing of the container if applicable for the container under consideration, however those provisions are quite incomplete and need significant enhancement to be used for design purposes. In practice EN1998-1 [7] is used for calculating the equivalent static loads similar to the procedure followed for buildings.

Finally, American standard ASCE 7 [8] includes pressure vessels in Chapter 15 for non-building structures. In that Chapter, guidance is given for the selection of seismic factors for calculating the base shear, element design forces. Various types of vessels are addressed, such as elevated vessels on leg or skirt supports, horizontal saddle-supported welded steel vessels and vessels supported on structural towers similar to buildings.

2.2 Description of Case Studies

Two case studies are considered in the present paper; (a) a vertical-cylindrical slender pressure vessel on skirt and (b) a horizontal-cylindrical pressure vessel on saddles. Both pressure vessels are typical vessels for petrochemical facilities.

The vertical-cylindrical pressure vessel is shown in Figure 1 (a). The vessel has an internal diameter of 3.1 m and a total height of 29.2 m. The thickness of the pressure vessel varies from 30 mm at the bottom head and 1st shell course to 28 mm for the rest shell courses and 22 mm for the top head. The skirt has a thickness of 40 mm and a height of 3 m. A corrosion allowance of 3 mm is permitted. The design pressure is 15.7 bar and the operating pressure is 7.3 bar.

The horizontal-cylindrical pressure vessel is shown in Figure 1 (b). The vessel characteristic dimensions are an internal diameter of 1.700 m and thickness of 12 mm (corrosion allowance 6 mm). The height of centerline of the vessel is 1.265 m, the length of the cylindrical part is 6.05 m and the distance between supports 3.63 m. The design and operating pressures are 8.1 and 6.2 bar respectively.

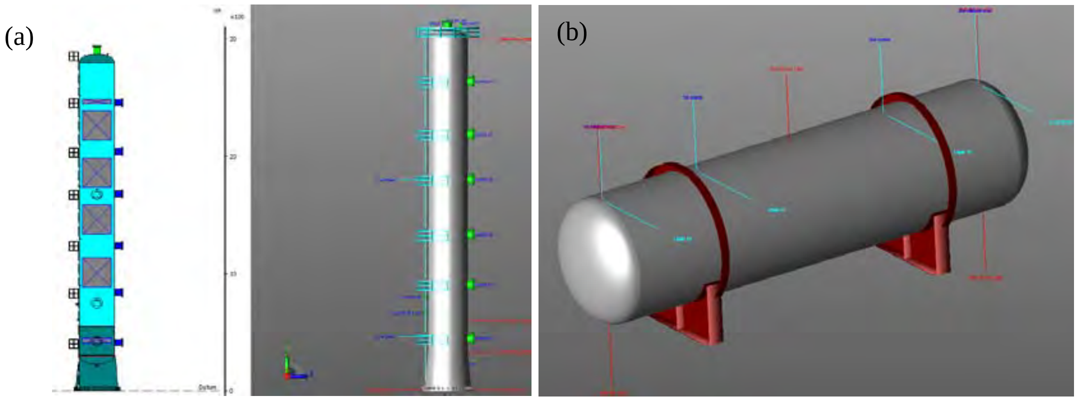

Figure 1 Sketch of (a) vertical pressure vessel on skirt support and (b) horizontal pressure vessel on saddle supports (drawings made by software PV Elite 2010).

2.3 Pressure Vessel Design for Seismic Loads

The design and analysis has been carried out using commercial design software, PV Elite [9]. Initially, in the basic design of the vessel, the thickness of the pressure vessel is determined by the maximum circumferential stress due to internal pressure. For a fair comparison between ASME Section VIII and EN13445 the selection of material, namely P265GH, was based on having similar yield strength.

The seismic input for all the seismic analysis is taken from the provisions of EN 1998-1, paragraph 3.2.2. The basic assumptions are the peak ground acceleration (equal to 0.24g), importance factor equal to 1, damping ratio equal to 5%, and soil type equal to D. Considering type 1 elastic response spectrum and taking the q factor equal to (a) 2 for skirt supported and (b) 3 for horizontal saddle supported welded steel vessel (Table 15.4-2 of ASCE-7-05, page 163), the design response spectrum is shown in the figure below. It is noted that this ASCE-7 standard is the only available source for obtaining a value of q.

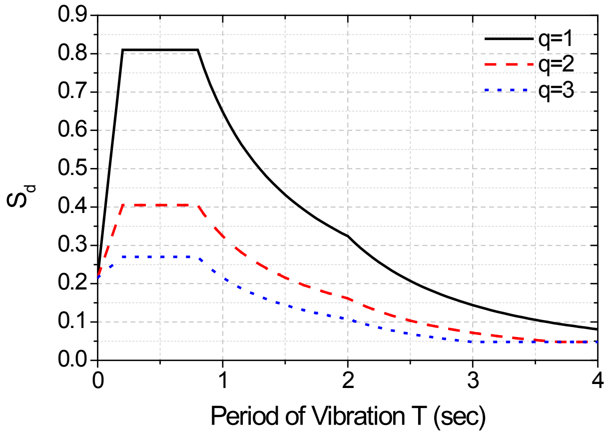

Figure 2 Design response spectrum (type1, soil D) according to EN 1998-1 (5% damping, $S = 1.35$, peak ground acceleration 0.24g), for different values of behavior factor q equal to 1 (elastic design), 2 and 3.

2.3.1. Vertical Pressure Vessel on Skirt Support

Determination of seismic forces

The fundamental period of vibration of vertical pressure vessels on skirts can be calculated using analytical expressions found in [10] for increased level of complexity (with respect to the various courses along the vessel height). The values computed by analytical expressions compare fairly well the numerical solutions calculated by finite element analysis for the vertical pressure vessel. However, it is noted that the fundamental period of the vessel is equal to 0.53 sec, which implies a rather stiff structure, corresponding to the highest part of the design spectrum. Small variations on the value of the fundamental period do not influence the value of the seismic force.

Effects of liquid sloshing

Because of the small diameter of the vessel compared to the height of the vessel as well as because of the presence of equipment inside the vessel, the effects of liquid sloshing can be neglected for this pressure vessel geometry.

Analysis of seismic forces

The general approach for treating seismic loads can be found in many text books [10], [11]. The total base shear V (the total horizontal seismic shear force at the base of the tower) is calculated by multiplying the seismic factor with the total weight of the vessel. An inverse triangular distribution of the seismic loading is assumed across the height of the vessel. A (rather small) portion F_t of the total horizontal seismic force V is applied at the top of the tower, because of the vessel cap. The remainder of the base shear is distributed throughout the length of the tower. The overturning moment is the algebraic sum of the moments of all forces. In the case of a non-uniform pressure vessel varying in diameter, thickness or weight with elevation, the vessel is divided in uniform thickness and diameter sections and the seismic forces are calculated as being proportional to the weight of each section.

The total corroded operating weight of the full vessel is 3130 kN. Considering the spectral value of the seismic factor equal to 0.405 for a fundamental period of vibration of 0.53 sec, for both horizontal directions, the combined seismic factor is : $S_d = \sqrt{S_{dx}^2 + \left(0.3S_{dy}\right)^2} = 0.423$. Therefore the total base shear force acting V is 1.3 MN. In addition, a horizontal force acting at the top of the vessel F_t is 70.7 kN to account for the vibrating mass of the top spherical cap. The seismic forces are considered for the corroded pressure vessel, which is considered the worst case scenario. The corresponding overturning bending moment is 26.1 MNm.

Calculation of seismic stresses/stress resultants and stress verification

ASME VIII Division 1 only gives general guidelines for the design of vessel supports in Annex G (nonmandatory) and some example calculations in Annex L. Specifically, § G-5 lists the load cases that should be considered for a vertical vessels supported by skirts.

ASME VIII Division 2 recommends two approaches for support design, the first in Part 4 “Design by Rule Requirements” where in §4.15.4 the loads to be considered are listed depending on the position of attachment of the vessel to the skirt. However Part 4 does not provide rules to cover all loading and geometry details. A designer can also select the approach of Part 5 “Design by Analysis Requirements” which refers to numerical analysis.

EN 13445 gives a more detailed description of the loads considered and the stresses developed for vertical pressure vessels on skirt supports in §16.12. As an alternative, “Design by Analysis” Annexes B and C may also be considered. The analysis in EN 13445 (§16.12) deals with the skirt itself and with the critical points where the pressure vessel and skirt join; for three types of skirt geometry. The method described in Annex B deals with various design checks like — Gross Plastic Deformation Design Check (GPD-DC), Progressive Plastic Deformation Design Check (PD-DC) , Instability Design Check (I-DC) , Fatigue Design Check (F-DC) , Static Equilibrium Design Check (SE-DC). The method described in Annex C, referred to as "stress analysis", involves the interpretation of stresses calculated on an elastic basis at any point in a part of a vessel, and then verification of their admissibility by means of appropriate assessment criteria.

2.3.2. Horizontal Pressure Vessel on Saddle Supports

Determination of seismic forces

The calculation of the natural frequency/period based on analytical expressions found in [10], [12] do not compare well with the predictions from finite elements analysis. It should be noted that the value of the natural period is usually rather small and – most likely – falls within the first (linearly increasing) part of the design spectrum. This means that small variations in the calculation of the natural period will result in significant differences in the value of the seismic coefficient. Because of the uncertainty in calculating the fundamental frequency of the horizontal pressure vessel on saddles supports, in this exercise we consider the maximum acceleration at the plateau of the response spectrum equal to 0.27. Therefore, the seismic force in the longitudinal and the transverse direction of the cylindrical vessel is equal to 48,9 kN for the corroded vessel.

An important note is necessary at this point. The seismic analysis is performed for the corroded state of the vessel. This is the most critical state, however because of the probabilistic nature of earthquake, it is also very conservative that the earthquake would occur at the vessel in the fully corroded state. It is a matter that requires further investigation.

Effects of liquid sloshing

It is important to note that the above calculations are based on the “worst-case scenario” of a full container. If one wishes to consider non-full container, then the accurate determination of seismic forces should account for possible sloshing effects due to liquid free surface. Those effects may be neglected if internal piping or other equipment exist within the vessel, and prevent the development of sloshing motion, as sloshing depressing devices. Otherwise, sloshing effects should be computed.

Sloshing effects can be computed through a methodology similar to the one for vertical cylindrical liquid containers, which consist on determination of sloshing (convective) frequencies and sloshing (convective) masses. Nevertheless, it should be noted that the calculation of sloshing frequencies and masses in horizontal-cylindrical containers is not trivial, due to the lack of closed form analytical solution of the corresponding hydrodynamic problem. A numerical solution of this problem leading to the calculation of sloshing frequencies and masses is offered in [13], [14] and will be outlined in a subsequent section of the paper.

Analysis of seismic forces

The two codes (ASME VIII and EN 13445) do not contain any provisions for the analysis of seismic forces and the calculation of stress resultants in the supports and the seismic stresses in the shell at the vicinity of the supports. The analysis can be conducted in a rather simple way, considering that one saddle is fixed and the other saddle is a sliding support [15], [16]. The seismic action has an overturning effect on the pressure vessel both in longitudinal and transverse direction. This effect, is described by two equivalent static forces which represent the inertia forces due to the seismic action and act at the centerline of the horizontal pressure vessel in the longitudinal and transverse directions.

Calculation of seismic stresses/stress resultants and stress verification

The design of horizontal pressure vessels supported on twin saddles used in BS5500 and ASME Division 2 has been originally developed by Zick [15]. This analysis calculates the developed stresses at critical points based on the reaction force at the saddle. Zick’s methodology was originally proposed for vertical loading of the pressure vessel, but it is straightforward to adjust this methodology to include horizontal (seismic) loading as well. Zick’s analysis is adopted in ASME VIII Div 2. On the other hand, EN13445 adopts a approach, which is based on stress resultants.

2.4 Discussion

The analysis and design of the vertical pressure vessel supported on a skirt and horizontal pressure vessel supported on saddles indicated the following issues:

- Both specifications EN 13445 and ASME VIII do not contain specific provisions for the seismic analysis of pressure vessels and the determination of seismic forces.
- Both specifications EN 13445 and ASME VIII indicate an increase of stress allowables for seismic loading. In EN13445 the safety factor can be increased up to the one used for the testing load cases for both tension and compression. In ASME VIII Div.1 a 20% increase is allowed in tension, while in ASME Div.2 no such increase is specified apart from the compression allowable used in Zick's analysis.
- The main conclusion from the above design and analysis of the two pressure vessels is a lack of guidance for choosing an appropriate value of the behavior factor q. The only source for choosing a value for the behavior factor for pressure vessels is Table 15-4.2 of ASCE 7-05, but these values are not justified. More research work is necessary towards determining appropriate values of the behavior factor q. Such an attempt will be presented in the next section of the present study.
- The calculation of the natural period of the vessel depends on the flexibility of the supports, and may affect significantly the seismic force. This causes some uncertainty in calculating the natural period especially in the horizontal vessel on saddles supports. Therefore, it would be helpful to specify one method to calculate the natural period to be used for design.
- The design procedure in ASME VIII is based on local stresses calculated from Zick's analysis. On the other hand, the design procedure in EN 13445 is based on stress resultants.

3 NUMERICAL MODELING

For analyzing the seismic behavior of the two pressure vessels, discussed above, pushover analysis and incremental dynamic analysis are employed, using a detailed finite element simulation with ABAQUS /Standard 6.10 program.

3.1 Nonlinear Pushover Analysis

A simple and efficient procedure for evaluating the performance of structural systems in strong earthquakes, used extensively for buildings, is the nonlinear static (pushover) analysis [17]. This analysis has been employed to analyze both case studies with an attempt to identify the modes of failure and study the progressive collapse after exceeding the yield limit.

Both vessels have been modeled with general-purpose finite element program ABAQUS /Standard 6.10. The nonlinear modeling accounts for geometric nonlinearities (large displacements and strains), as well as for inelastic material behavior through a von Mises plasticity material model with isotropic hardening, based on the nominal values of P265GH steel. The finite element models of both pressure vessels are given in Figure 3, where general-purpose shell elements S4R were used. An inverted triangular load distribution is applied to the vertical pressure vessel, which is fixed at its base, to represent the seismic inertia forces. For the horizontal pressure vessel a uniform load distribution either in the longitudinal x-direction or the transverse z-direction is applied and a sliding and a fixed support have been used in this model.

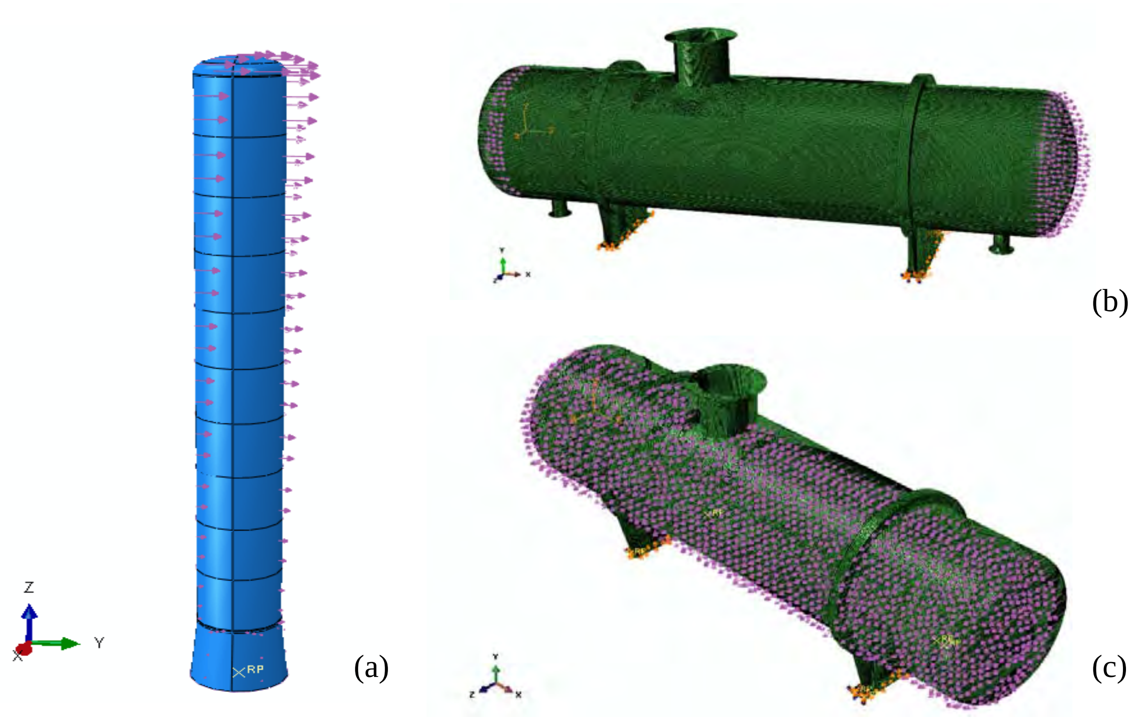

Figure 3 Finite element models for the pushover analysis of the (a) vertical pressure vessel with triangular load distribution and (b) horizontal pressure vessel with uniform load distribution in the longitudinal x-direction and (c) transverse z-direction.

The base shear taken from the reaction force at the support, in the direction of the applied loading, is plotted against the displacement at a point on the top of the vessel. A force displacement diagram is produced (pushover curve) showing the capacity of the pressure vessel to withstand a load representative of the seismic action.

For the vertical pressure vessel on skirt the load-displacement pushover curve is given in Figure 4. The seismic load calculated from the response spectra for the equivalent static analysis is equal to 1.3 MN, as stated in the previous section, considering a behavior factor q equal to 2 to account for seismic energy dissipation. The pushover analysis shows that the response of the structure is almost linear up to approximately 2.8 MN and reaches a maximum capacity at 3.8 MN. The corresponding mode of failure is buckling at the first shell course immediately above the skirt, as shown in Figure 5. The effect of internal pressure is insignificant up to the point of maximum capacity of the vessel but is beneficial for post-buckling behavior.

The horizontal pressure vessel is also analyzed using a pushover analysis. The applied load has been calculated from the response spectra approximately equal to 50 kN employing a value of q factor equal to 3. The pushover curves in Figure 6 show a deviation from linearity at approximately 300 kN for the pushover analysis in the longitudinal x-direction and 800 kN in the transverse z-direction. The mode of failure in both directions is buckling at the support plates and the stiffeners, as shown in Figure 7.

The pushover analysis for both pressure vessels shows that for the level of seismic loads used for the design of those vessels (see previous section), the behavior is elastic; in fact, the level of seismic design loads is well below the ultimate capacity level indicated by the pushover curves. For horizontal-cylindrical vessels, the pushover analysis shows a "ductile" behavior, with the vessel capable of sustaining significant deformation in the inelastic range. However, for the case of the vertical-cylindrical vessel, the maximum capacity is reached very quickly after the first-yield point, whereas the vessel resistance is significantly reduced beyond the maximum loading stage; this indicates that the vessel may not be capable of absorbing significant amount of inelastic energy.

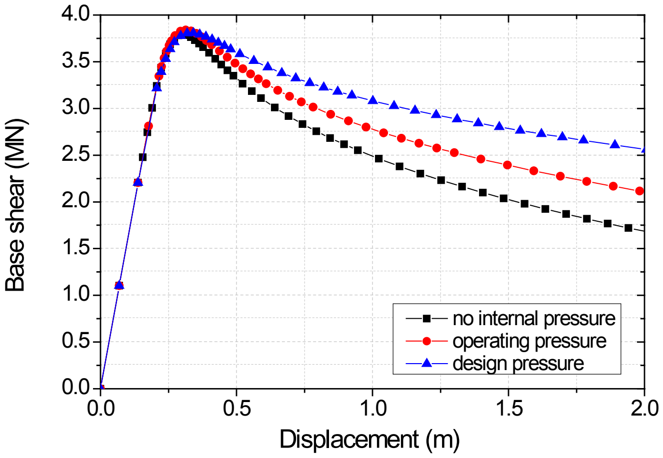

Figure 4 Results of pushover analysis for the vertical pressure vessel on skirt support.

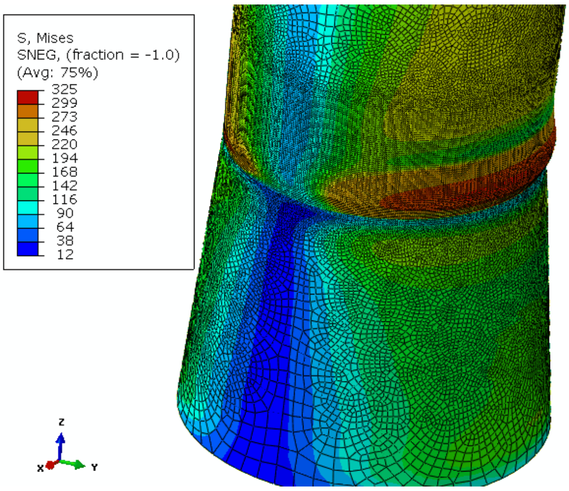

Figure 5 Von Mises stress distribution at maximum capacity (approximately 300mm displacement)

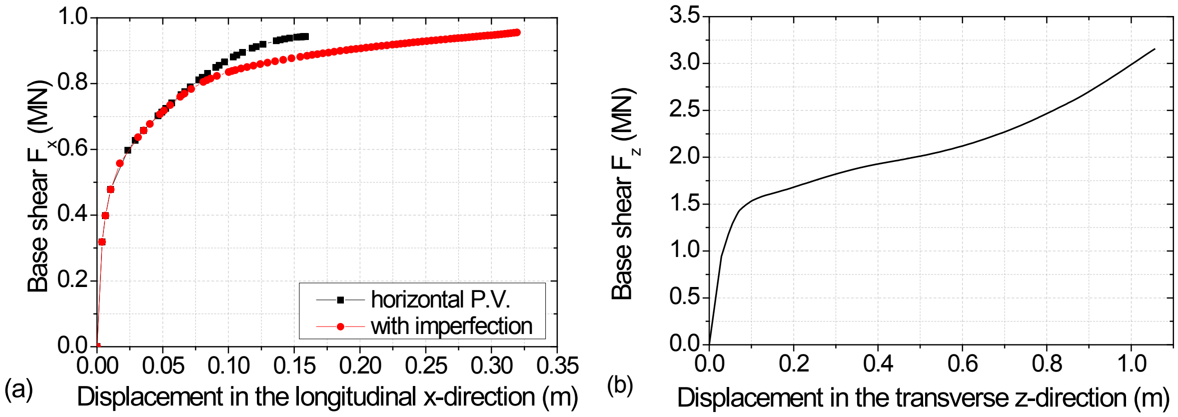

Figure 6 Results of pushover analysis for the horizontal pressure vessel on saddle supports in the (a) longitudinal x-direction and (b) transverse z-direction.

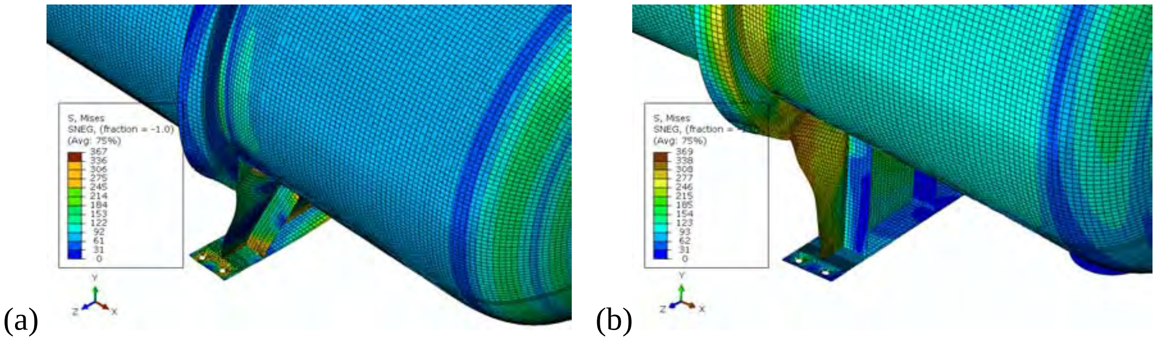

Figure 7 Von Mises stress distribution for the horizontal pressure vessel in the (a) longitudinal x-direction (approx. 10 mm displacement) and (b) transverse z-direction (approx. 50 mm displacement).

3.2 Incremental Dynamic Analysis

Time history analysis is generally a more complex and computationally expensive method of performing dynamic analysis, but is considered as most realistic for predicting the structural response of a structural system subjected to earthquake loading. In the present study, the vertical-cylindrical vessel is analyzed under incremental dynamic analysis.

The seismic input has been defined in terms of seven artificial accelerograms, corresponding to the design spectrum of EN 1998-1 for 5% damping and peak ground acceleration 0.25g. The nonlinear dynamic analysis was performed considering von Mises plasticity with kinematic hardening to describe inelastic material behavior, and a damping factor of 5%. The seven different artificial accelerograms have been considered at an increasing earthquake level, through a dimensionless "level parameter" λ, and the response of the vessel at critical locations was monitored. An example of input acceleration, and the corresponding top displacement and base shear are given in Figure 8.

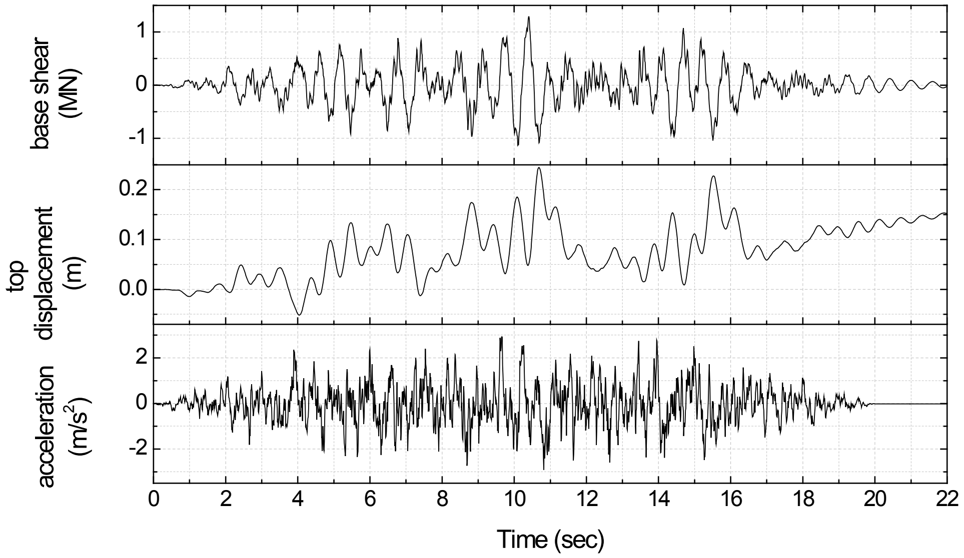

Figure 8 Imposed acceleration, predicted top vessel drift displacement and base shear in the direction of the imposed acceleration for one earthquake and level equal to 1.

Based on the previous pushover analysis, presented in the previous section, three regions of the vessel have been identified as critical, namely (a) the skirt, (b) the 1st shell course and (c) the 2nd shell course. The response of the vessel is plotted in terms of the increasing levels of seismic input is presented in the diagrams of Figure 9, Figure 10 and Figure 11 for the maximum von Mises stress, the maximum equivalent plastic strain and the maximum compressive stress and strain in the longitudinal direction, respectively. Finally, the reaction force (base shear) in terms of increasing level of seismic input is shown in Figure 12.

In order to estimate the q factor, two seismic input levels have to be identified in each of the response curves; (a) the level where transition from linear to non-liner behavior occurs (λ_e) and (b) the level at which a specific failure criterion is satisfied (λ_u). In this study, two different failure criteria, both in terms of strain, are specified as follows:

Failure criterion 1 (Rupture of vessel wall): The equivalent plastic strain reaches a value equal to 0.4%.

Failure criterion 2 (Buckling of vessel wall): The compressive strain in the longitudinal direction reaches a critical value defined by the following formula [18]:

$$\varepsilon_{22,critical} = 0.5\frac{t}{D} - 0.0025 + 3000\left(\frac{pD}{Et}\right)^2 \tag{1}$$

Furthermore, the previous pushover analyses have indicated that the critical location of the vessel is at the 1st (bottom) shell course, immediately above the skirt. At this location, the corroded thickness of the pressure vessel is 27 mm, and considering the vessel diameter (3100 mm) and its internal pressure 0.73 MPa, the critical value of compressive strain is equal to 0.24%. Using the above failure criteria, the estimated value of the q factor is given below in Table 1; the values are somewhat lower than the value of 2 suggested by ASCE 7.

	Failure criteria 1	Failure criteria 2
λ_e	1.5	1.5
λ_u	2.5	2.25
q	1.7	1.5

Table 1 Estimated q factor using incremental dynamic analysis.

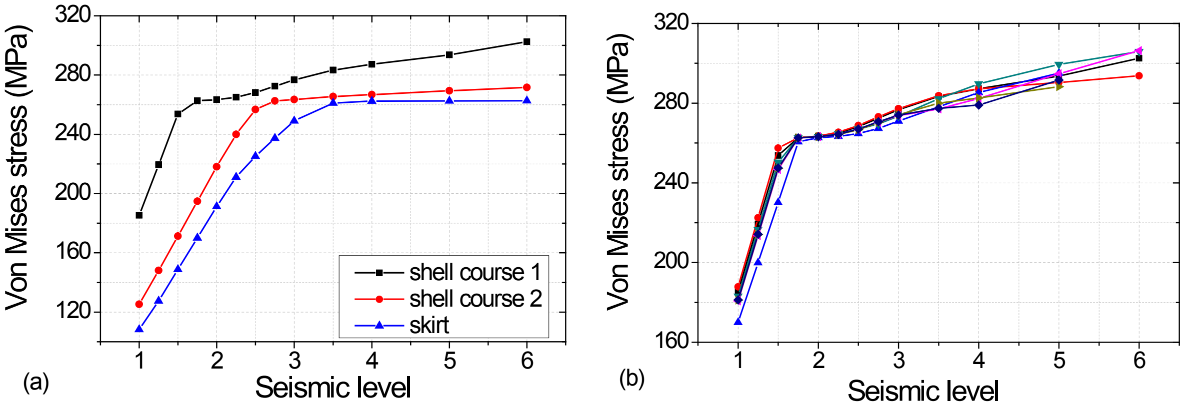

Figure 9 Maximum von Mises stress (a) at three regions of the pressure vessel for one earthquake and (b) at various levels of seismic action for 7 artificial accelerograms.

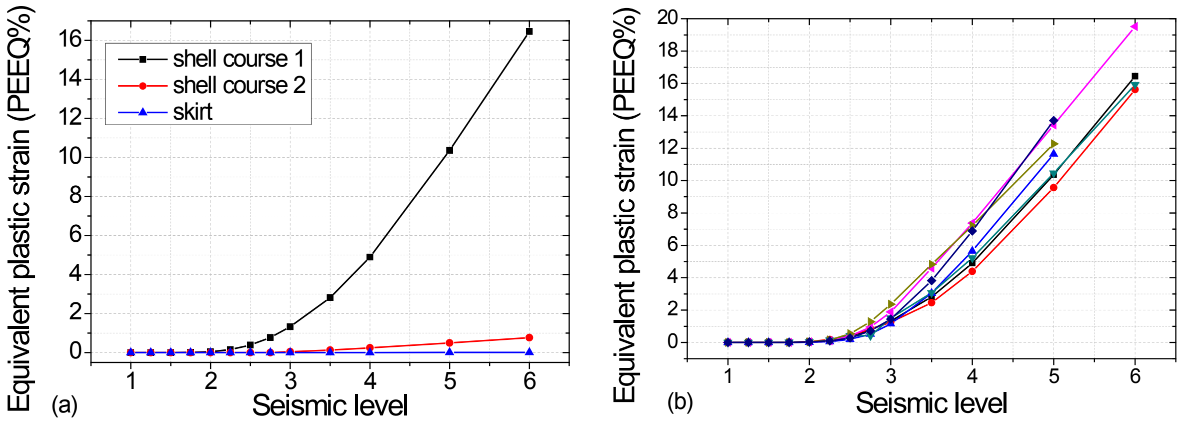

Figure 10 Maximum equivalent plastic strain (a) at three regions of the pressure vessel for one earthquake and (b) at various levels of seismic action for 7 artificial accelerograms.

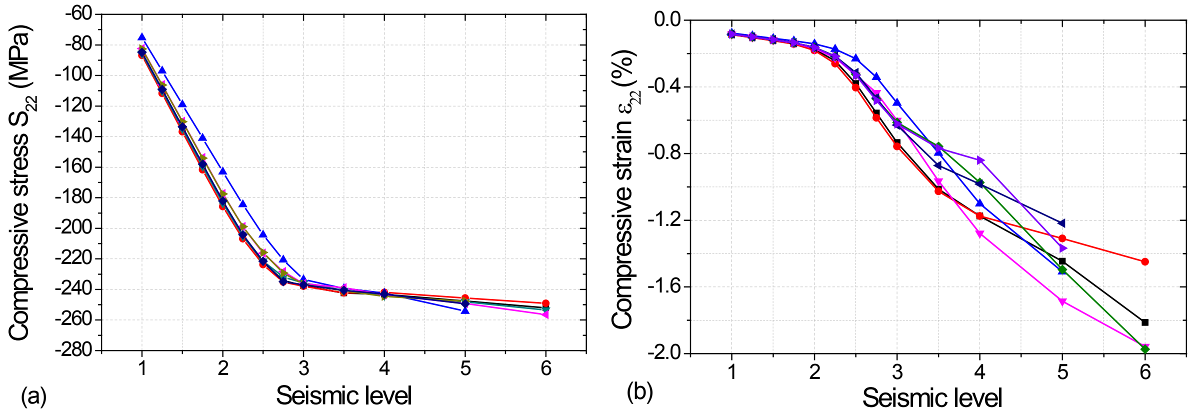

Figure 11 Maximum longitudinal compressive stress (a) and strain (b) at various levels of seismic action for the critical section shell course 1.

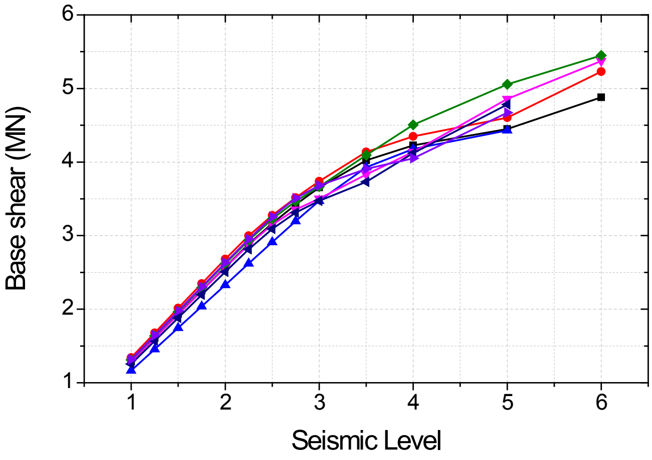

Figure 12 (a) Maximum base shear due to the seismic action.

4 HYDRODYNAMIC EFFECTS

Pressure vessels contain liquefied gas, which may interact with the steel container in the course of a strong seismic event and may cause hydrodynamic forces on the vessel wall, which should be taken into account in vessel seismic design.

For full containers, the entire liquid mass follows the motion of the container, and should be added to the container's mass. On the other hand, if one wishes to consider the container not full, then the accurate determination of seismic forces should account for possible sloshing effects due to liquid free surface. Those effects may be neglected if internal piping or other equipment exist within the vessel, which prevent the development of sloshing motion, acting as sloshing depressing devices. Otherwise, sloshing effects should be computed.

Detailed methodologies have been proposed to account for sloshing effects in vertical cylindrical liquid storage containers, which consist on determination of sloshing (convective) frequencies and sloshing (convective) masses. Those methodologies have been adopted by current design standards for liquid storage tanks (e.g. EN 1998-4 and API 650). Those provisions can be applied to vertical pressure vessels (stacks); however, the stacks are very tall, with very high value of aspect ratio H/R, so that sloshing effects are negligible. Consequently, for tall vertical cylindrical vessels, one may neglect sloshing effects and consider the entire liquid mass to vibrate with the flexible container.

On the other hand, in non-full containers of horizontal-cylindrical shape, hydrodynamic effects can be computed through a methodology similar to the one for vertical cylindrical containers. Nevertheless, in liquid containers of horizontal-cylindrical shape, the calculation of sloshing frequencies and masses is not trivial, due to the lack of closed form analytical solution of the corresponding hydrodynamic problem. A numerical solution of this problem leading to the calculation of sloshing frequencies and masses is offered in [13], [14] and is summarized in the following.

Transverse direction

The sloshing frequencies (in dimensionless form $\omega_{nC}^{2} R/g$) and the sloshing and impulsive masses M_{nC}, M_{I} respectively (normalized by the liquid mass M_{nC}/M_{L} and M_{I}/M_{L}) of a horizontal-cylindrical container ($n = 1, 2, 3, \ldots$) are shown in Figure 13. It is noticed that only one sloshing mode is necessary for the seismic analysis, and that higher modes can be neglected. The total seismic force can be computed as follows

$$F = M_{1C} S(T_C) + M_I A_g \qquad (2)$$

where the impulsive mass contains the mass of the steel, and the impulsive motion is considered as rigid so that the impulsive mass is multiplied by the peak ground acceleration A_g. Furthermore, $S(T_C)$ is the spectral value corresponding to the sloshing period T_C, which is equal to

$$T_C = \frac{2\pi}{\omega_{1C}} \qquad (3)$$

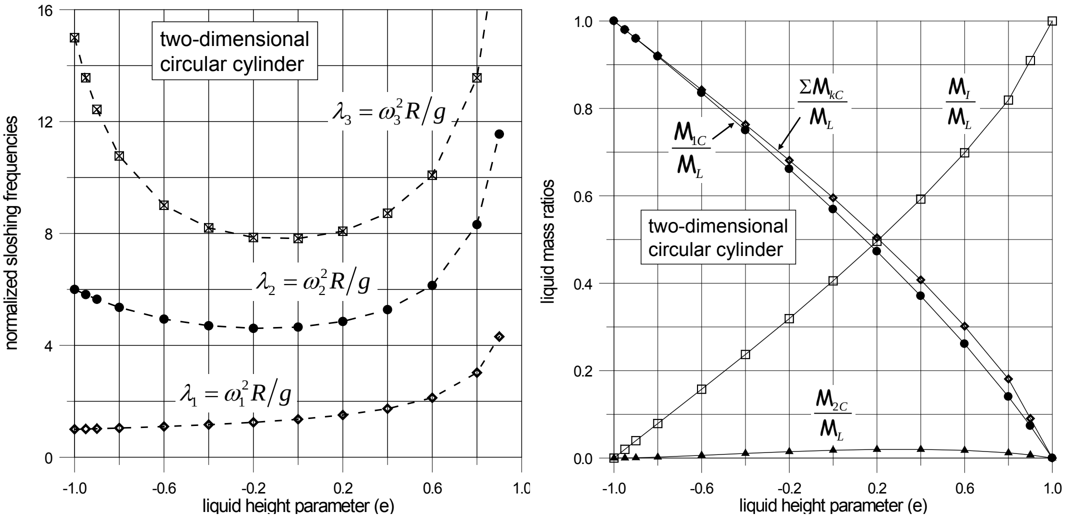

Figure 13 Sloshing frequencies and masses for horizontal cylindrical container under transverse excitation.

Longitudinal direction

The analysis presented in [13], [14] has shown that the dynamic behavior of a horizontal-cylindrical container with longitudinal excitation can be approximated with an “equivalent rectangular container”. This equivalent rectangular container has the same free surface dimensions ($2R\times L$) and the same volume as the cylindrical container. This leads to the following expression for the height of the rectangular container:

$$\frac{H_{eq}}{R}=\frac{1}{2}\left[\left(H/R-1\right)+\frac{\sin^{-1}\left(H/R-1\right)+\pi/2}{\sqrt{\left(H/R\right)\left(2-H/R\right)}}\right] \qquad (4)$$

The seismic force can be computed by equation (2), where only the first mode is considered. Expressions for the sloshing frequencies and masses in the horizontal cylindrical vessels in the longitudinal direction are stated below in a normalized form, based on the corresponding expressions for rectangular containers (e.g. see [19]):

$$\frac{\tilde{\omega}_p^2 R}{g}=\frac{\left(2p-1\right)\pi R}{L}\tanh\left[\frac{\left(2p-1\right)\pi H_{eq}}{L}\right] \qquad p=1,2,3,\ldots \qquad (5)$$

$$\frac{\tilde{M}_{pc}}{M_L}=\frac{8\tanh\left[\left(2p-1\right)\pi H_{eq}/L\right]}{\left(H_{eq}/L\right)\,\pi^2(2p-1)^3}, \qquad p=1,2,3,\ldots \qquad (6)$$

5 CONCLUSIONS

In this paper, the seismic analysis and design of two typical cylindrical steel pressure vessels used in pertochemical facilities is presented (a) a vertical vessel on skirt and (b) a horizontal vessel on saddle supports. First, the provisions of EN 13445-3 and ASME B&PV code, section VIII, for these structures are summarised and important design issues, missing links and inconsistencies are discussed. It is the authors‘ opinion that more detailed information regarding the estimation of the behavior factor for these structures should be included in the design codes, as well as more detailed guidelines for the determination of the seismic forces. An attempt to estimate the behavior factor for these structures is presented using advanced numerical tools, for pushover analysis and incremental dynamic analysis. The pushover analysis indicated that the capacity of the presure vessels is quite higher than the required strength in seismic loading. On the other hand, using incremental dynamic analysis for the vertical-cylindrical pressure vessel, the value of behavior factor calculated is somewhat below the corresponding value suggested by American standard ASCE 7.

6 ACKNOWLEDGEMENTS

This work was carried out with a financial grant from the Research Fund for Coal and Steel of the European Commission, within INDUSE project: "STRUCTURAL SAFETY OF INDUSTRIAL STEEL TANKS, PRESSURE VESSELS AND PIPING SYSTEMS UNDER SEISMIC LOADING", Grant No. RFSR-CT-2009-00022.

REFERENCES

[1] EN 13445:2002 *Unfired Pressure Vessels*, European Committee for Standardization.

[2] ASME Boiler & Pressure Vessel Code, *Section VIII Rules for Construction of Pressure Vessels, Division 1*, The American Society of Mechanical Engineers, New York, 2007.

[3] ASME Boiler & Pressure Vessel Code, *Section VIII Rules for Construction of Pressure Vessels, Division 2 - Alternative Rules*, The American Society of Mechanical Engineers, New York, 2007.

[4] PD5500:2006 *Specification for Unfired Fusion Welded Pressure Vessels*, BSI British Standards, 2006.

[5] AD Merkblätter, *Technical Rules for Pressure Vessels*, Published by Verband der Technischen Überwachungs-Vereine e.V., Essen, AD2000.

[6] Eurocode 8 – *Design of Structures for Earthquake Resistance – Part 4: Silos, Tanks and Pipelines*, EN1998-4.

[7] Eurocode 8 – *Design of Structures for Earthquake Resistance – Part 1: General Rules, seismic actions and rules for buildings*, EN1998-1.

[8] ASCE7-05, *Minimum Design Loads for Buildings and Other Structures*, Published by the American Society of Civil Engineers, 2006.

[9] *2010 PV Elite User Guide*, COADE, Engineering Physics Software, Texas.

[10] *Guidelines for Seismic Evaluation and Design of Petrochemical Facilities*, Published by the American Society of Civil Engineers, 1997.

[11] D. R. Moss, *Pressure Vessel Design Manual*, Elsevier, 3rd Edition, printed in U.S.A., 2004.

[12] W. C. Young, R. G. Budynas, *Roark's Formulas for Stress and Strain*, 7th Edition, Mc Graw Hill, 2002.

[13] S. A. Karamanos, L. A. Patkas, and M. A. Platyrrachos, Sloshing Effects on the Seismic Design of Horizontal-Cylindrical and Spherical Industrial Vessels., *Journal of Pressure Vessel Technology*, ASME, Vol. 128, No. 3, pp. 328-340, August 2006.

[14] S. A. Karamanos, D. Papaprokopiou, and M. A. Platyrrachos, Finite Element Analysis of Externally-Induced Sloshing in Horizontal-Cylindrical and Axisymmetric Industrial Vessels., *Journal of Pressure Vessel Technology*, ASME, Vol. 131, No. 5, Article Number: 051301, October 2009.

[15] L. P. Zick, Stresses in Large Horizontal Cylindrical Pressure Vessels on Two Saddle Supports, *The Welding Journal Research Supplement*, 1951.

[16] *Pressure Vessel Design – Concepts and Principles*, Edited by J. Spence and A.S. Tooth, E & FN Spon, 1994.

[17] ATC-40, *Seismic Analysis and Retrofit of Concrete Buildings*, Volume 1, Applied Technology Council, California, 1996.

[18] A. M. Gresnigt, *Plastic Design of Buried Steel Pipelines in Settlement Areas*, *Heron*, 31 (4), Delft, The Netherlands, 1986.

[19] R. A. Ibrahim, *Liquid Sloshing Dynamics: Theory and Applications*, Cambridge University Press, 2005.

COMPDYN 2011
III ECCOMAS Thematic Conference on
Computational Methods in Structural Dynamics and Earthquake Engineering
M. Papadrakakis, M. Fragiadakis, V. Plevris (eds.)
Corfu, Greece, 25–28 May 2011

BENDING CYCLIC LOADING ON PRESSURIZED ELBOWS – FINITE ELEMENT ANALYSES

Jan Ferino[1], Elisabetta Mecozzi[2], Antonio Lucci[2],Giuseppe Demofonti [2]

[1] Centro Sviluppo Materiali S.p.A
Pula, Italy
j.ferino@c-s-m.it

[2] Centro Sviluppo Materiali S.p.A
Roma, Italy
e.mecozzi@c-s-m.it, a.lucci@c-s-m.it, g.demofonti@c-s-m.it

Keywords: Instructions, ECCOMAS Thematic Conference, Structural Dynamics, Earthquake Engineering, Proceedings.

Abstract. *Industrial piping can be subjected to severe cyclic loading associated to temporary ground deformations induced by seismic activity. One of the reasons of piping failures under earthquakes can be identified in the accumulation of plastic strains along with biaxial ratcheting of elbows subjected to in-plane cyclic bending. This paper deals with the estimation, using finite element analysis, of the strain evolution in a representative OD 8" X52 grade piping section including an elbow subjected to cyclic in-plane bending and internal pressure.*

Lemaitre-Chaboche nonlinear kinematic hardening model for plasticity has been employed in FEA to represent the ratcheting phenomenon more efficiently with respect with standard kinematic hardening rule.

Numerical results provide an estimation of the plastic strain evolution at critical locations, which may result in crack formation or material damage, and valuable information to address a full future scale testing program that will be undertaken within the INDUSE project

1 INRODUCTION

CSM is involved in the European RFCS research program INDUSE [1] which is aimed at developing design guidelines and recommendations, for the seismic analysis and design of industrial equipment steel structures, such as liquid storage tanks, pressure vessels and piping. In this context, CSM is in charge to perform experimental and numerical activities on piping elbows subjected to cyclic in plane bending loading, involving large imposed displacements in the presence of internal pressure.

This paper deals with the estimation, using finite element analysis, of the strain evolution in a representative 8” piping section including an elbow subjected to cyclic in-plane bending and internal pressure. Numerical results provide an estimation of the plastic strain evolution in critical locations, which may result in crack formation or material damage, and valuable information to address the future full-scale testing program.

The behavior of pipelines under large imposed displacements typical of earthquake induced permanent ground deformations (PGD) and other seismic phenomena such as liquefaction and subsidence etc. is recognized to be one of the most important issues in pipeline research. In fact pipelines are frequently required to cross areas where human activity is very intense. Piping components such as bends and elbows connections are recognized to be critical as the deformation tend to concentrate in such locations due to their lower stiffness. It is not surprising that an important experimental and numerical activity has been undertaken in Japan as a consequence of the intense seismic activity. [2] studied the deformation and cracking behavior of induction bends X80 grade subjected to closing bending moment and internal pressure by means of experimental and numerical analysis. Closing and opening bending experiments with internal pressure were conducted by [3] while [4] studied closing bending mode by means of FEA. Ultimate bending capacity of pressurized elbows for the in plane and out of plane bending load has been extensively studied by [5]and [6] by comparing experimental results with analytical formulations and numerical FE predictions.

Several failures have also been recorded for not buried industrial subjected to repetitive alternating loads induced by temporary ground deformations (TGD). In such conditions once again piping connections are subjected to severe deformations as the presence of internal pressure causes biaxial ratcheting. Under such loading conditions trough wall cracking is reported to be one of the main causes of failure as a consequence of the accumulation of plastic strains in the hoop direction at flank position. Recently [7] studied the cyclic behavior of elbows without pressure while [8] investigated also the biaxial ratcheting effect caused internal pressure.

2 FE ANALYSIS

2.1 Geometry overview

The geometry of the piping section analyzed is shown in Figure 1 and its relevant characteristics are reported in Table 1: Relevant characteristics. The elbow element is connected to two straight pipes 1100 mm long and characterized by the same thickness. The length is enough to ensure that no stress interference in the elbow area deriving from the applied loads at the ends occurs. The bending load on pipe elbow has been obtained imposing an alternating displacement along the line
connecting the two pipe ends

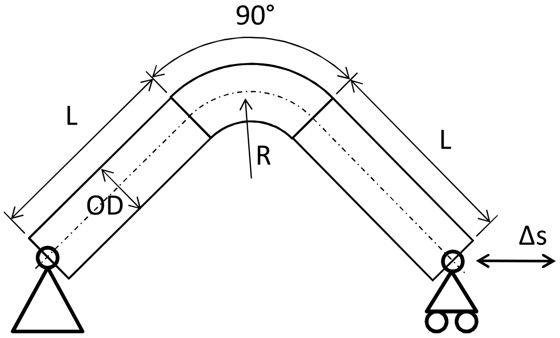

Figure 1: Overview of the studied geometry.

Outside Diameter (D) (mm)	Wall Thickness (T) (mm)	D/t	R/D	Elbow angle (°)	Straight pipe length (L) (mm)
219.1	8.2	26.7	1.5	90°	1100

Table 1: Relevant characteristics

To investigate the effect of the internal pressure during the cyclic deformation process two levels have been considered: zero pressure and a pressure associated with the 50% of SMYS design factor according to the following relation:

$$p = \frac{k \cdot SMYS \cdot 2t}{D} \tag{1}$$

with:

D : pipe outer diameter
t : Pipe wall thickness
$SMYS$: Specified Minimum Yield Strength
k : design factor

Internal pressure has been applied first and then maintained constant during the whole cyclic bending. Pressure have also been applied to the pipe ends to account for end cap effect axial induced load. A summary of the load cases analyzed have been is reported in the following Table 2

Load type	Load sequence	Displacement amplitude mm	Internal pressure MPa
Monotonic	opening mode	200mm	0 13.25 (u.f. = 0.5)
	closing mode	200mm	0 13.25 (u.f. = 0.5)
Cyclic	1st cycle opening	+/- 100 mm	0 13.25 (u.f. = 0.5)
	1st cycle closing		0 13.25 (u.f. = 0.5)
	1st cycle closing	+/- 50 mm	0 13.25 (u.f. = 0.5)

Table 2: Summary of analyzed load cases

2.2 Finite element model Description

As shown in Figure 1a representative section of a piping containing an elbow and two sleeve pipes has been modeled by using the commercial software MSC.Marc. To allow for a better estimation of the effect of the accumulated plastic strains on the wall thickness during cycling solid elements have been employed.

Exploiting the planes of symmetry of the geometry and loading conditions the modeling was limited to one fourth of the whole geometry, applying appropriate boundary conditions, thus allowing for more detailed representation of the wall thickness. The mesh adopted and a detail of the welded connection between elbow and pipes are shown Figure 2.

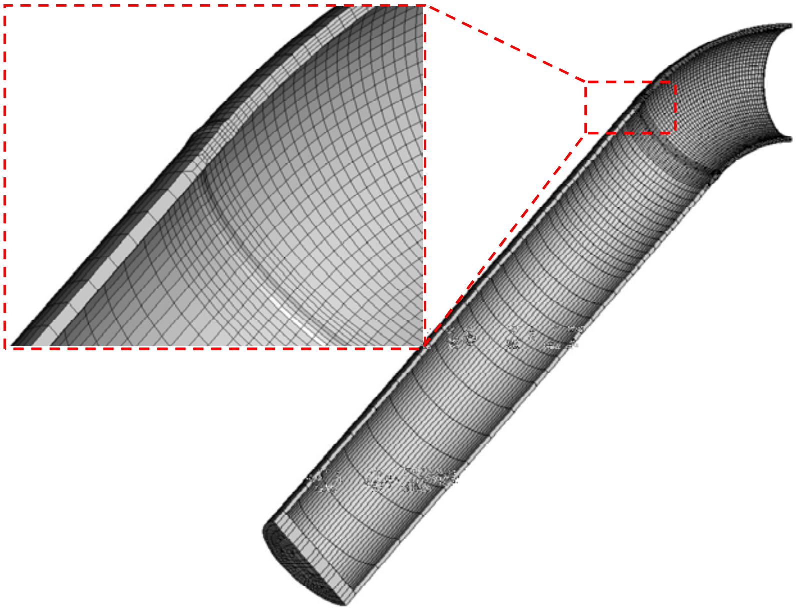

Figure 2: Overview of the mesh employed

The element type used is the three dimensional arbitrary distorted brick which is based in a full integration formulation containing 8 integration points.

To take into account the stresses and strains intensification of, the presence of the welds between the elbow and the straight pipes has been modeled adopting a 1mm increase of thickness in the weld cap. No specific material properties have been assigned to the weld.

In order to reduce calculation resources different element sizes have been used for the mesh the model along length. .

A total amount of 13609 nodes and 9674 elements have been used. More in detail the following subdivision has been implemented:

- 48 elements along elbow axial direction, with thickening close to the weld area;
- 35 elements along straight pipe axial direction, with a refining close to the weld area and a coarsening proceeding towards pipe ends;
- In the circumferential direction a number of 40 elements has been used.
- 4 elements have been used through the wall thickness for the whole elbow length,
- a gradual transition from 4 to 1 element have been adopted trough the wall thickness of straight pipe connected to the elbow;
-

The accuracy of the adopted mesh in describing the elastic plastic behavior of the piping and the concentration of stresses and strains at critical location has been verified trough sensitivity analyses.

To properly account for high deformations that are expected to occur during cyclic process, the following options have been activated for the simulation:

- large displacements;
- large strain additive strain decomposition;
- constant dilatation (incompressible material in plastic range).;

2.3 Material model employed in FEA

The currently available FE software are able to predict with good accuracy the behavior of the material in elastic-plastic regime under monotonic loading, even for a multi-axial stress state. On the other hand, cyclic behavior involves much more complex phenomena which interacts together during loading: ratcheting, hardening or softening, mean stress relaxation etc.

The non linear kinematic hardening, or Lemaitre-Chaboche rule [9] has been adopted to describe of the cyclic material properties.

This model eliminates the typical shortcomings of the standard kinematic hardening rule to describe the cyclic phenomena. Bauschinger effect is better represented as the transition from elastic to plastic regime at strain reversal is smoother, ratcheting, mean strain relaxation, cyclic hardening and softening can also be modeled.

More in detail, this model combines a non linear kinematic rule and an isotropic hardening rule so that Von Mises yield surface undergoes to the following evolution law:

$$F = J_2(\sigma_{ij} - \alpha_{ij}) - R - k = 0, \tag{2}$$

Where:

$$J_2(\sigma_{ij} - \alpha_{ij}) = \sqrt{\frac{3}{3}\left(\sigma'_{ij} - \alpha'_{ij}\right)\cdot\left(\sigma'_{ij} - \alpha'_{ij}\right)} \tag{3}$$

$\sigma_{ij'}$ and $\alpha_{ij'}$ are respectively the deviatoric components of the stress tensor and the back-stress tensor, the latter tracking the position of the centre of yield surface. R is a scalar variable which accounts for the isotropic expansion or contraction of the surface during cycling loading and is associated with the accumulated plastic strain ε_e^p and k is the initial elastic limit of the material. The evolution law for α_{ij} is:

$$d\alpha_{ij} = 2/3 \cdot C \cdot d\varepsilon_{ij}^p - \gamma \cdot \alpha_{ij} \cdot d\varepsilon_e^p \tag{4}$$

The previous equation (which was initially proposed by Armstrong-Fredrick) is composed by a linear term which is identical to the Prager rule and expresses a proportionality between σ_{ij} and ε_{ij}^p to which a nonlinear term function of the accumulated plastic strain is superimposed was initially proposed by Armstrong-Fredrick. The evolution law for the R variable is:

$$dR = b \cdot (Q - R) \cdot d\varepsilon_e^p \tag{5}$$

Current version of MSC Marc® only provides the basic Lemaitre-Chaboche rule, while more advanced versions of this model, which adopt a superposition of multiple hardening rules each with a own set of parameters exist. Following values of characteristics parameters, obtained from literature [10] have been adopted.

- k = 250 MPa;
- C = 75000 MPa;
- γ = 400.

Within the INDUSE research program base material characterization including true stress true strain monotonic curves as well as cyclic hardening and ratcheting experiments are planned allowing for Lemaitre Chaboche model parameters to be determined.

3 FE ANALYSES RESULTS

3.1 Monotonic behavior

The monotonic behavior of the piping section has been initially analyzed in order to study its basic response to simple bending in opening and closing mode. An imposed displacement of 200 mm has been applied on pipe ends and internal pressure effect have been also considered. The response in terms of applied bending moment at symmetry section of the elbow versus curvature calculated for the whole elbow length is reported in Figure 3, where the elbow curvature is initially shifted to zero for easier reading of results, it is noticeable that the effect of the internal pressure clearly influence the results.

In closing mode after the peak load is reached, there is a slow decrease of the bending moment indicating that buckling takes place. For low D/t values as in the case under study no wrinkling of the compressed side takes place, instead buckling is driven by ovalization which leads to a reduction in the section moment of inertia. Initially the material work hardening counteracts this reduction until a compensation of two competing effect is reached thus resulting in a maximum of the bending moment.

On the contrary in opening mode the moment of inertia is increased due to the orientation along the bending plane of the maximum diameter elbow. Thus work-hardening and ovalization sum their effect. In this case a collapse for high tensile strains is expected.

In closing mode an increase of internal pressure can be considered as beneficial as it increases both the peak moment and the corresponding curvature. In this case the internal pressure counteracts the ovalization of the pipe cross section which is developed along the line connecting the theoretical neutral axis on both flanks of the elbow, and is responsible of the decrease of the moment of inertia of the pipes.

In opening mode the behavior is different: at increasing bending the moment arm reduces so that always more axial tension force is needed to bend the elbow. Such high value of axial force influences the results and decreases the effect of the internal pressure. In fact passing from zero pressure to 13.2 MPa there is only a slight change in peak moment and corresponding curvature. Furthermore the pressure in this case is not beneficial as it contrast the elongation on elbow cross section along the line connecting the extrados and the intrados. In presence of pressure for the opening mode the failure mode is the necking of the intrados pipe wall as shown in Figure 6.

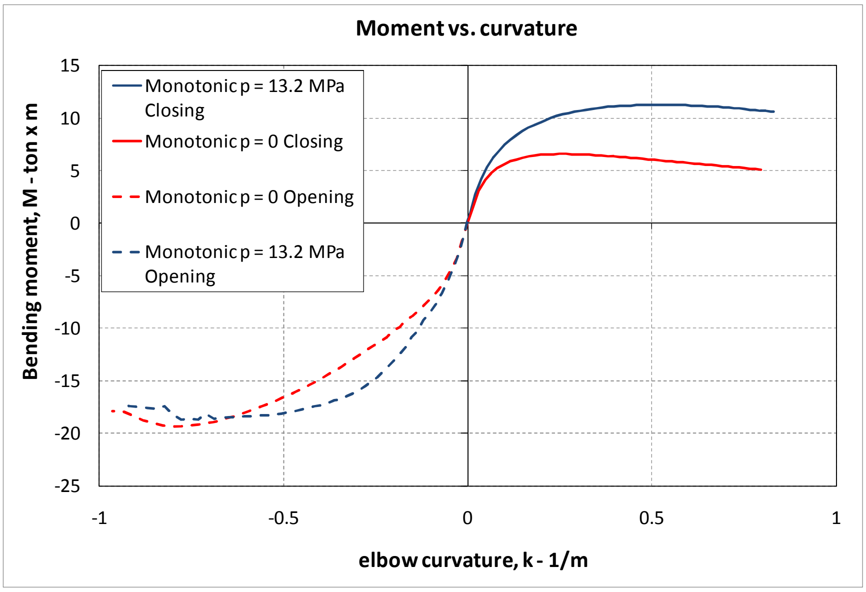

Figure 3: Monotonic bending response in opening and closing mode with and without internal pressure

Opening and closing mode ovalization shape of the elbow cross section are reported in Figure 4 together with tee original un-deformed section. In case of opening the effect of the internal pressure is clearly visible and has the effect to maintain the section more circular. In closing mode, for pressure case, the ovality at peak moment is greater because pressure allows for a larger curvature to be reached.

Errore. L'origine riferimento non è stata trovata. and **Errore. L'origine riferimento non è stata trovata.** show the critical areas, in terms of concentration of strains, of the elbow at peak moment condition with and without pressure, both in closing and opening mode. In case of closing mode the critical position is the flank of the elbow where high strains in circumferential direction are observed. In opening mode if no pressure is applied high tensile strains in axial direction are observed in the intrados of the elbow in the half length section as a result of the combined effect of bending and tensile axial load. With the internal pressure the position of the critical section moves along intrados slightly away from half-length section causing tearing of the pipe wall due to high tensile strains in axial direction.

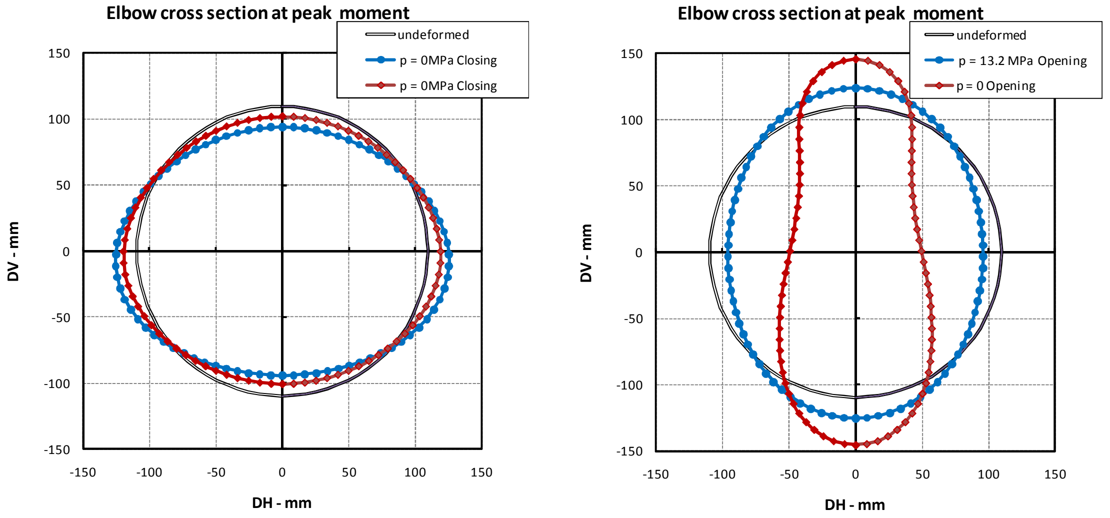

Figure 4: Cross section shape at half length of the elbow at peak bending moment in closing mode, left and in opening modem right

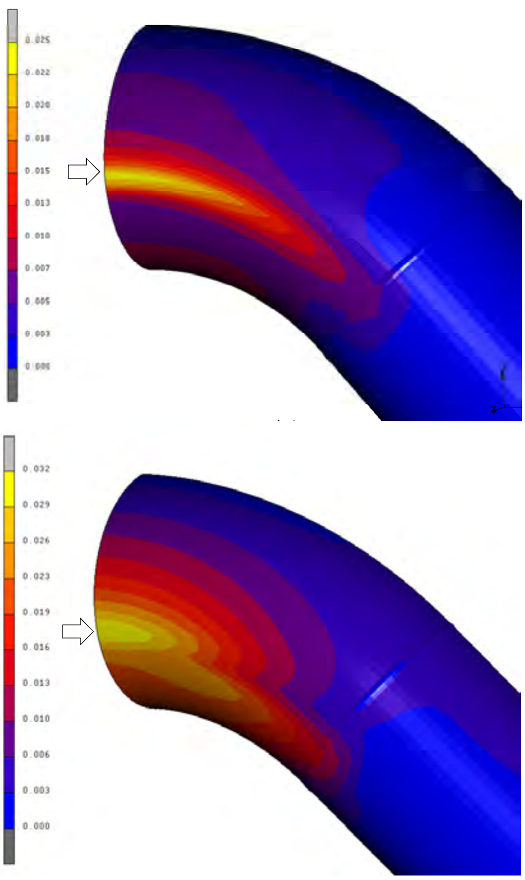

Figure 5: Accumulated equivalent plastic strains at peak closing moment at zero pressure, up and at 13.2MPa down

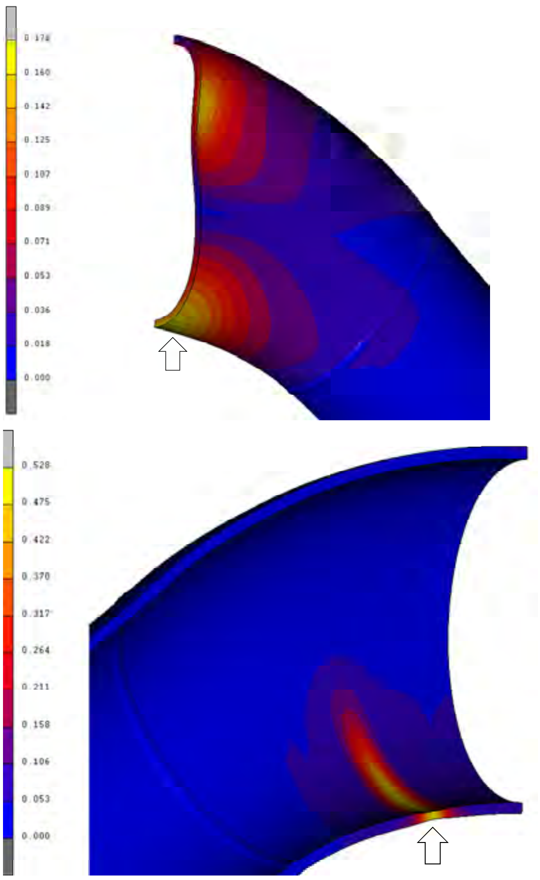

Figure 6; Accumulated equivalent plastic strains at peak opening moment at zero pressure, up and at 13.2MPa down

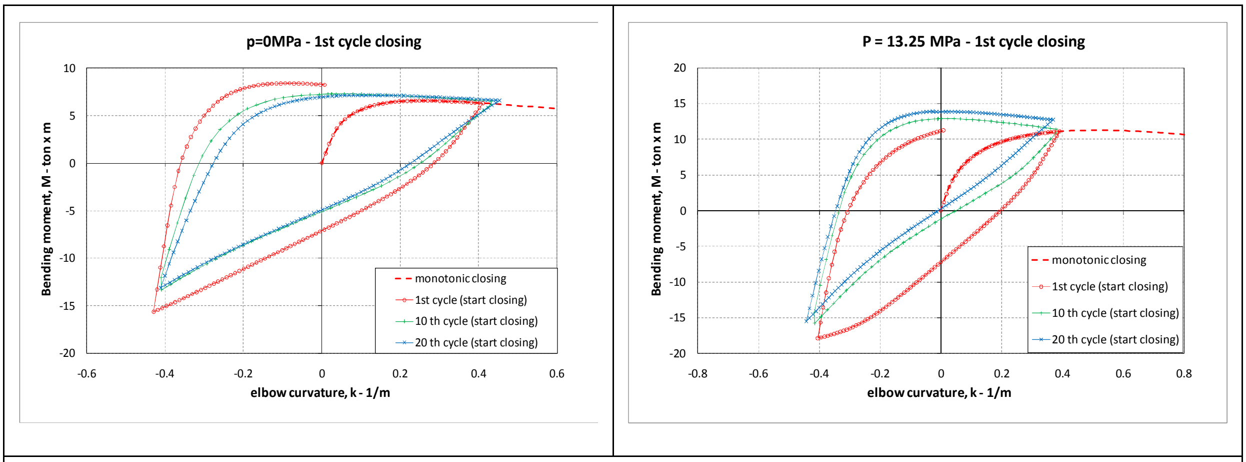

Figure 9: Cyclic response with zero pressure for cycling starting in closing mode: without pressure, left and for 13.2 MPa right.

3.2 Cyclic behavior

Cyclic behavior has been investigated for different values of internal pressure and imposed displacements of +/-100mm at one pipe end, this correspond to impose a curvature of +/-0.4m^{-1} a variation of +/-12% of the curvature at elbow yielding.

In **Errore. L'origine riferimento non è stata trovata.** the shape of the elbow cross section is reported for the zero pressure case, before cycling and after 20 cycles both for cycling starting in opening or in closing mode. The same result is reported by

, for the internal pressure case. In both cases shape differences totally have totally disappeared after 20 cycles.

The shape differs from the basic ones observed in opening and closing modes for monotonic loading, this is particularly true in the case of zero pressure case, where a downward shift of the maximum width amplitude accompanied by a high value of distortion in such locations can be reported. In general greater influence from closing mode is observed, in fact the ovality is always more pronounced along the horizontal DH diameter. This occurrence is present independently of the pressure and can be explained recalling the monotonic behavior for closing and opening bending moment reported in Figure 3: for the particular loading configuration considered, the resistance of the elbow in closing mode is much less if compared with opening mode both in terms of maximum moment than curvature. In other words a 100mm alternating displacement causes the curvature to be far beyond the curvature at peak closing moment but still below the critical curvature for opening moment.

As previously calculated, internal pressure of 13.2 MPa has the effect to introduce a constant hoop stress level of the 50% of SMYS, that in combination with stresses beyond yielding induced in longitudinal direction by bending process results in biaxial ratcheting.

Ratcheting effect is clearly visible in Figure 8 where it is possible to observe that the elbow underwent a marked cycle by cycle increase of perimeter. Furthermore hoop stress reduced the general distortion of the cross section and markedly increase the hoop deformations and consequently the perimeter.

Cyclic moment *vs* curvature diagrams for bending process starting in closing are reported in

, for 1st ,10th and 20th cycle both with zero pressure and for 13MPa of pressure. Very little difference are observed in stress strain distribution and in the moment curvature response if the load cycle starts in opening or closing mode. After a few cycles all differences disappear. and such diagrams are not reported for the opening starting mode.

If no pressure is applied the moment-curvature cycles are stable in position, while with pressure the bending moment is seen to shift in the closing moment part of the diagram. This can be explained by the increase of the moment of inertia of the pipe section caused by ratcheting. From Figure 8 in fact no decrease on DV is observed while DH increase.

To study the effect of the displacement amplitude on the cyclic bending process, two additional simulations where carried out. For the cyclic loading starting in closing mode, a displacement of +/-50mm was imposed at one pipe end, corresponding to a curvature of +/-0.2m^{-1} a variation of +/-6% of the curvature at elbow yielding.

The simulation was carried out up to 40 cycles twice the number of +/- 100mm load sequence. Deformed shapes observed at mid length are compared in Figure 10 and Figure 11 with the ones for the larger displacement case. It is possible to notice that independently of the pressure, raising the number of cycles and reducing the amplitude caused an increase of the DV diameter and a reduction on DH with respect to the lower cycles case analyzed. Furthermore in case of pressure DH is larger than un-deformed diameter.

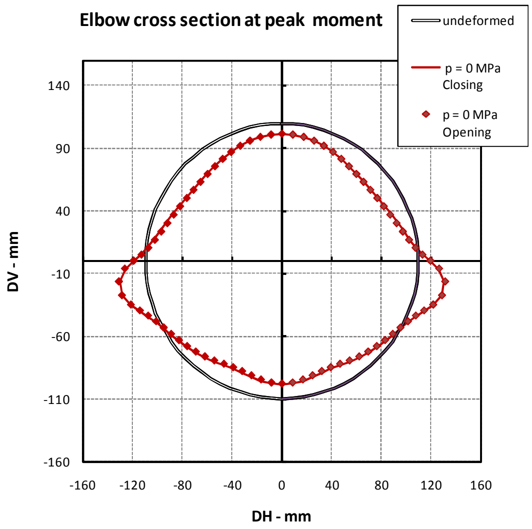

Figure 7: Cross section shape at half length of the elbow after 20 cycles for and imposed displacement of 100mm and zero internal pressure in case of 1st cycle in closing and opening mode

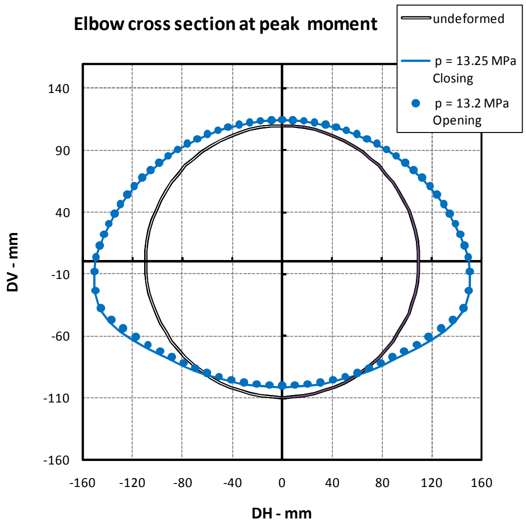

Figure 8: Cross section shape at half length of the elbow after 20 cycles for and imposed displacement of 100mm and 13.2 MPa internal pressure in case of 1st cycle in closing and opening mode

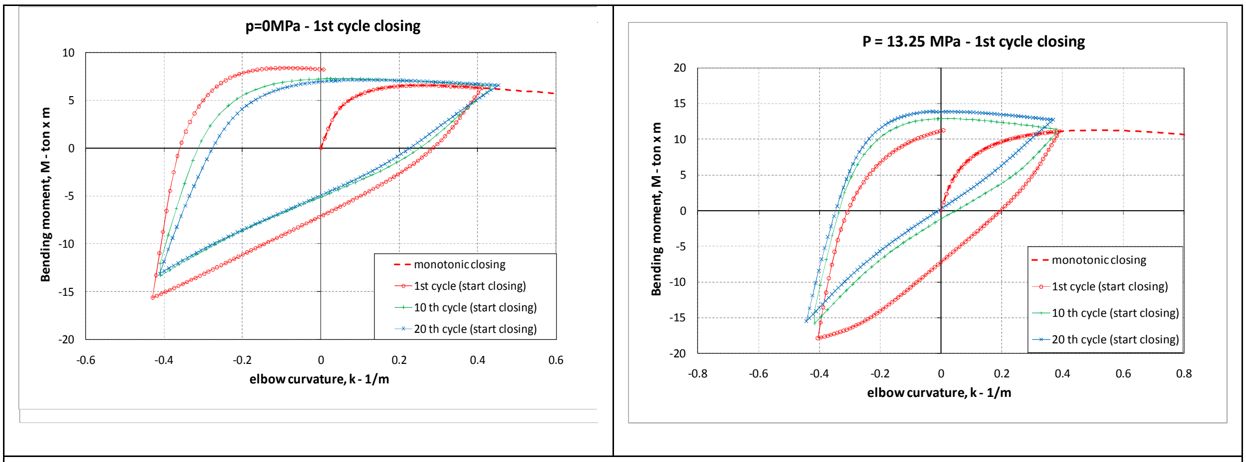

Figure 9: Cyclic response with zero pressure for cycling starting in closing mode: without pressure, left and for 13.2 MPa right.

Cyclic moment *vs* curvature diagrams for bending process starting with closing are reported in , for 1st ,10th and 20th cycles, with zero pressure and in the presence of 13.2MPa of pressure. While in absence of internal pressure the range of bending moment and curvature are stable internal pressure induces a progressive decrease of the average curvature and an increase of the bending moment at peak closing. This last effect can be explained by the increase of moment of inertia associated by DH growth due to pressure. In case of pressure cycles are also seen to translate in the opening part of the diagram indicating that a global straightening has taken place.

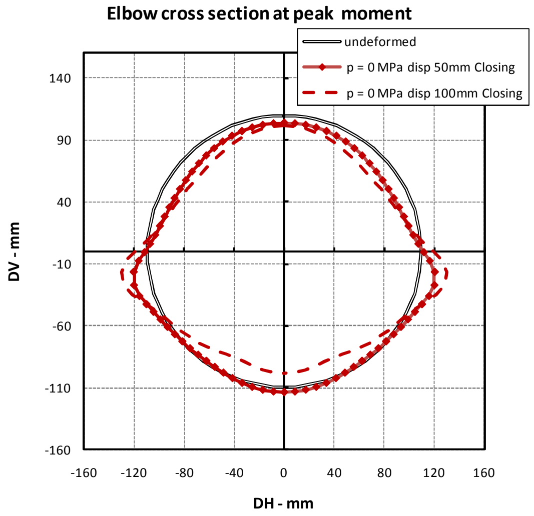

Figure 10: Cross section shape at half length of the elbow after cycling for imposed displacement of 100mm and 50mm at zero internal pressure, 1st cycle in closing mode

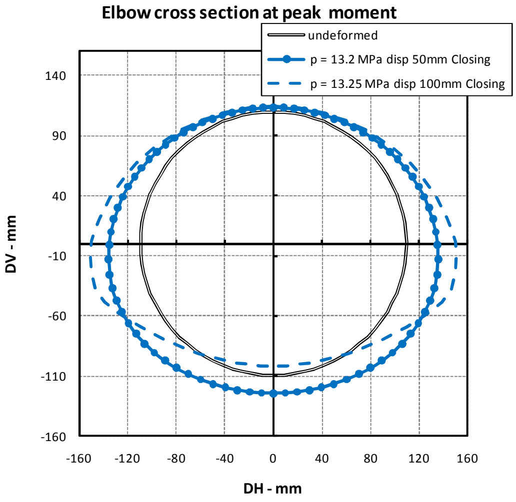

Figure 11: Cross section shape at half length of the elbow after cycling for imposed displacement of 100mm and 50mm at 13.2;Pa internal pressure, 1st cycle in closing mode

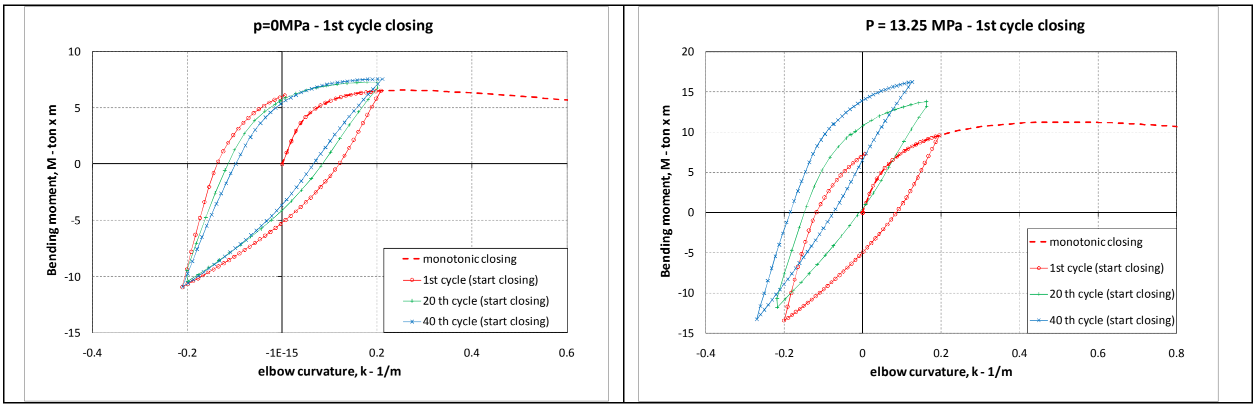

Figure 12: Cyclic response for +/50mm displacement amplitude with zero pressure for cycling starting in closing mode: without pressure, left and for 13.2 MPa right.

From Figure 13 and Figure 14 it is possible to observe the deformed shape of the elbow at the end of cycling process starting in closing mode. If no pressure is applied both load sequence lead to similar results; a sharp corner at flank is visible and high tensile hoop plastic strain is present at the external surface, while in the inner surface is compressive. When internal pressure is applied results differ for the two sequences considered: when larger cyclic curvature is imposed local buckling occurs producing an outward bulge. It is interesting to note that such behavior was not observed in monotonic compression even for larger curvatures and is to attribute to the combined effect of the steady internal pressure and accumulation of plastic strain in longitudinal direction.

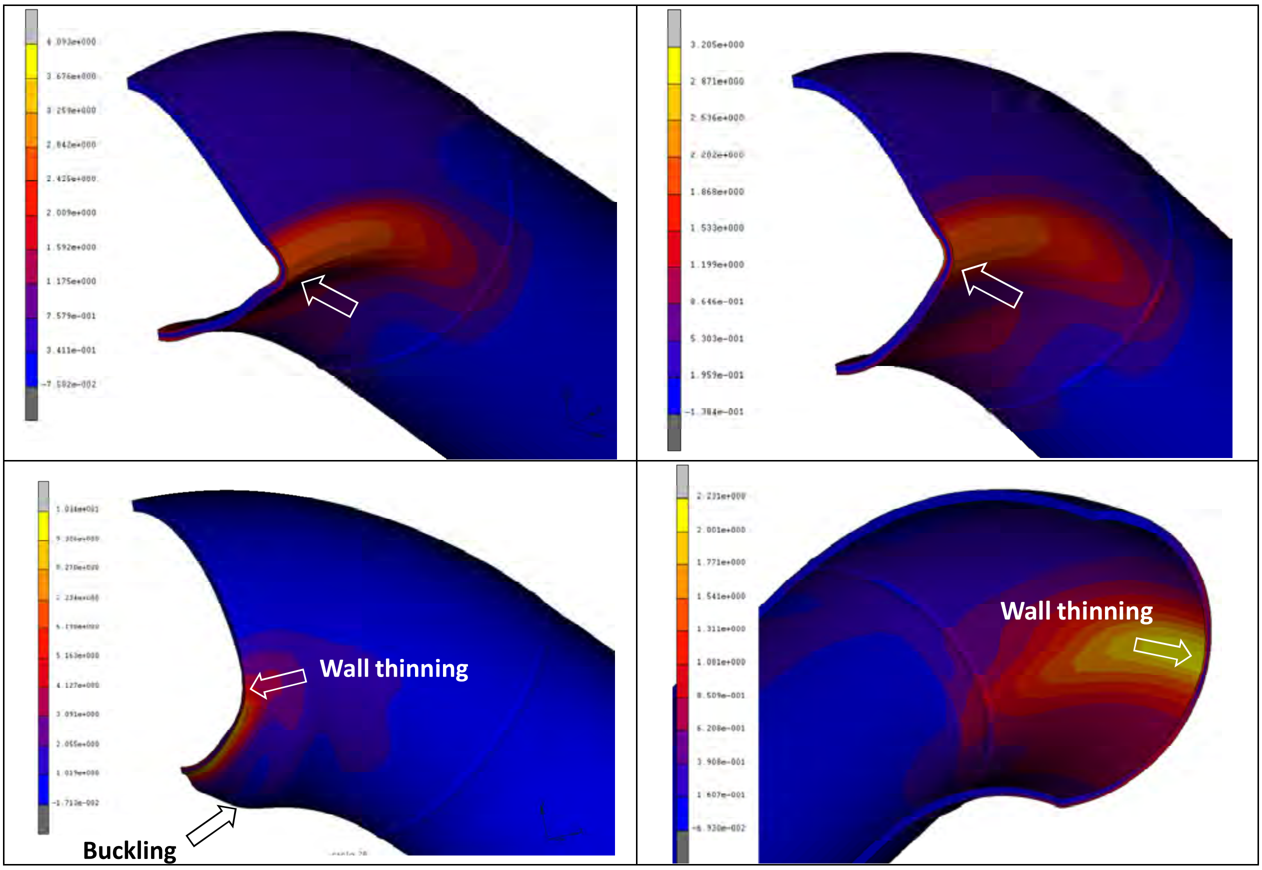

Figure 13: Accumulated equivalent plastic strains after 20 cycles at zero pressure, up and at 13.2MPa down.	Figure 14; Accumulated equivalent plastic strains after 39 cycles at zero pressure, up and at 13.2MPa down

Local strains in such critical locations have been traced along cycles in Figure 15 and Figure 16. Without internal pressure flank position is subjected to tensile hoop strain at the external surface and compressive at internal surface. Alternate tensile strains on pipe surface are to be considered critical because can induce surface cracking that can propagate through the pipe wall. For 20 cycles at larger displacement/curvature sequence tensile and compressive plastic strains have a larger range and tend to stabilize approximately at 15th cycle, while for smaller imposed curvature the range is narrower and an uniform growth is observed. It can be concluded that external surface is critical for the zero pressure case as high tensile plastic strain localize. The reduction of the imposed alternating curvature and the increase in cycle number leads to a slower and continuous increase of the mean values of the hoop strains.

As shown in Figure 16, if pressure is applied in both the internal and external pipe wall sides tensile hoop strains are detectable. For the larger displacements sequence hoop alternating range is very high in the internal surface of the pipe, so that this location has to be considered critical for crack penetration. No stabilization is observed and on both internal and external sides. When alternating displacement amplitude is reduced the rate of hoop strain growth reduces and never reaches the high values of the larger displacements sequence, even for 40 cycles. Hoop strains both in the internal and the external pipe wall are similar in value and trend being internal side slightly more critical.

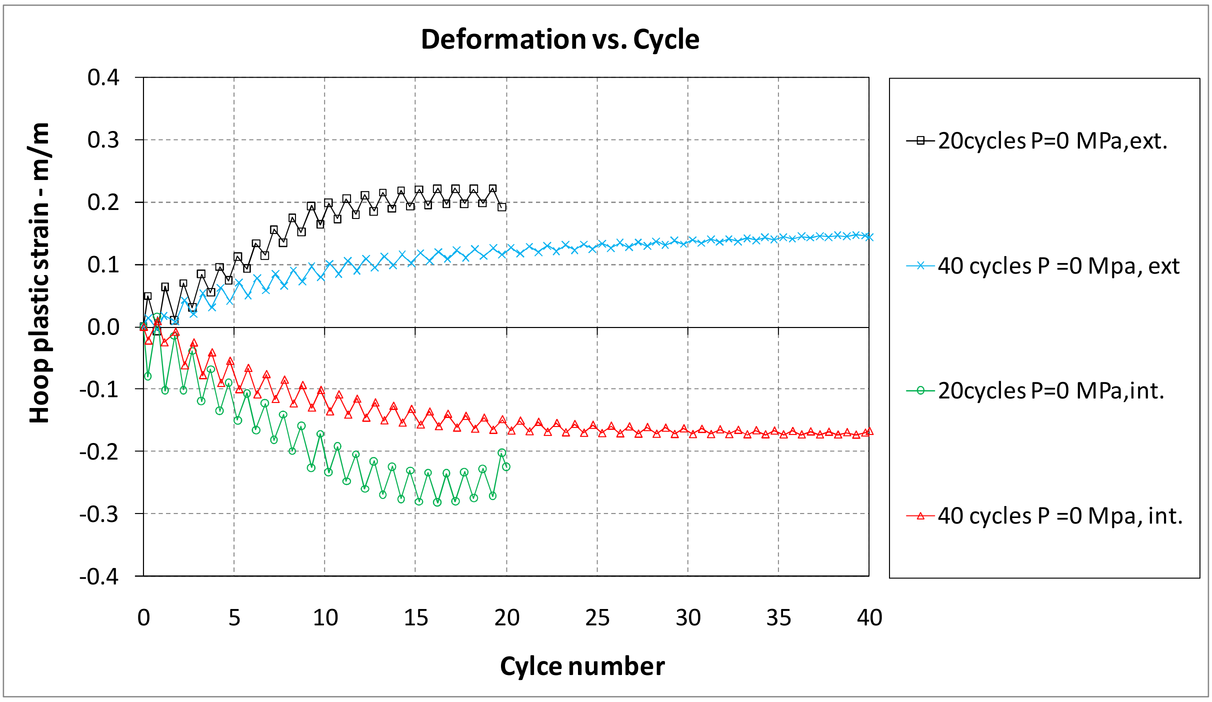

Figure 15:Hoop plastic strains at most critical locations during cycling without pressure

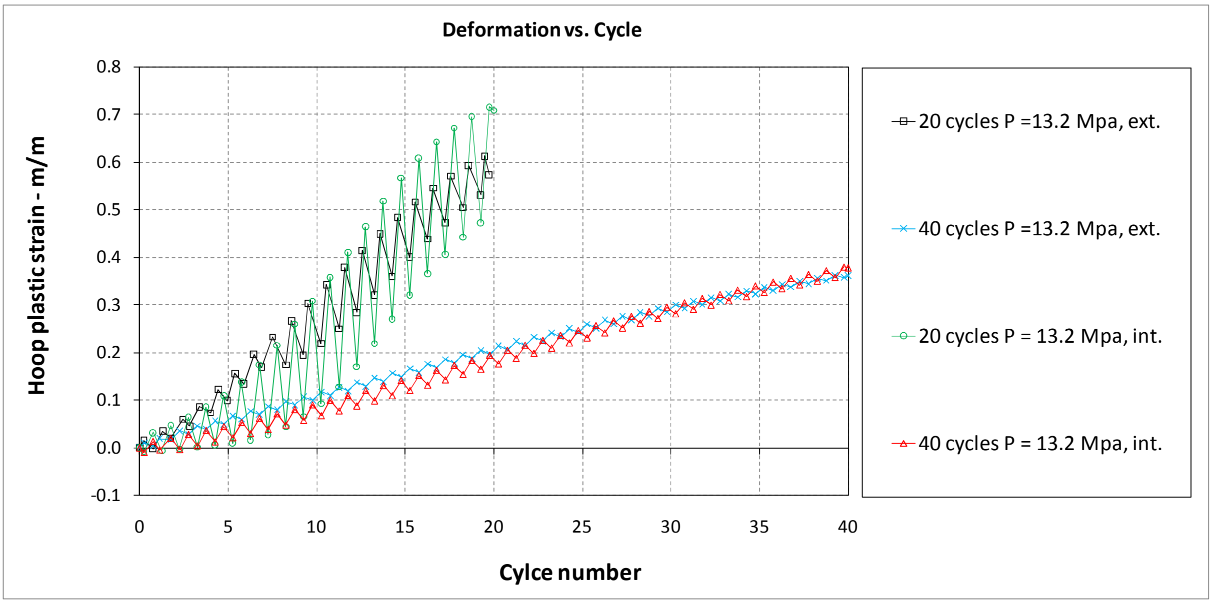

Figure 16: Hoop plastic strains at most critical locations during cycling with internal pressure

Figure 17 shows a comparison of all cyclic sequences starting in closing mode for pressurized and un-pressurized case based on the wall thickness reduction observed at mid length of the elbow.

If no pressure is applied wall thickness reduction is present in a region between the flank and the intrados. Increase of cycle number and reduction of imposed load amplitude results in a lower accumulation of strains at such locations.

The presence of the internal pressure induces high thickness reduction especially for the area between flank and intrados. Higher thickness reduction accompanied by a more irregular distribution is observed for the larger curvature sequence .In general the extrados does not seem to experience thickness significant variation as in the flank to intrados region. On the other hand, due to production process, wall thickness at the intrados pipe is slightly higher if compared with other parts of the pipe and can be considered less prone to cracking.

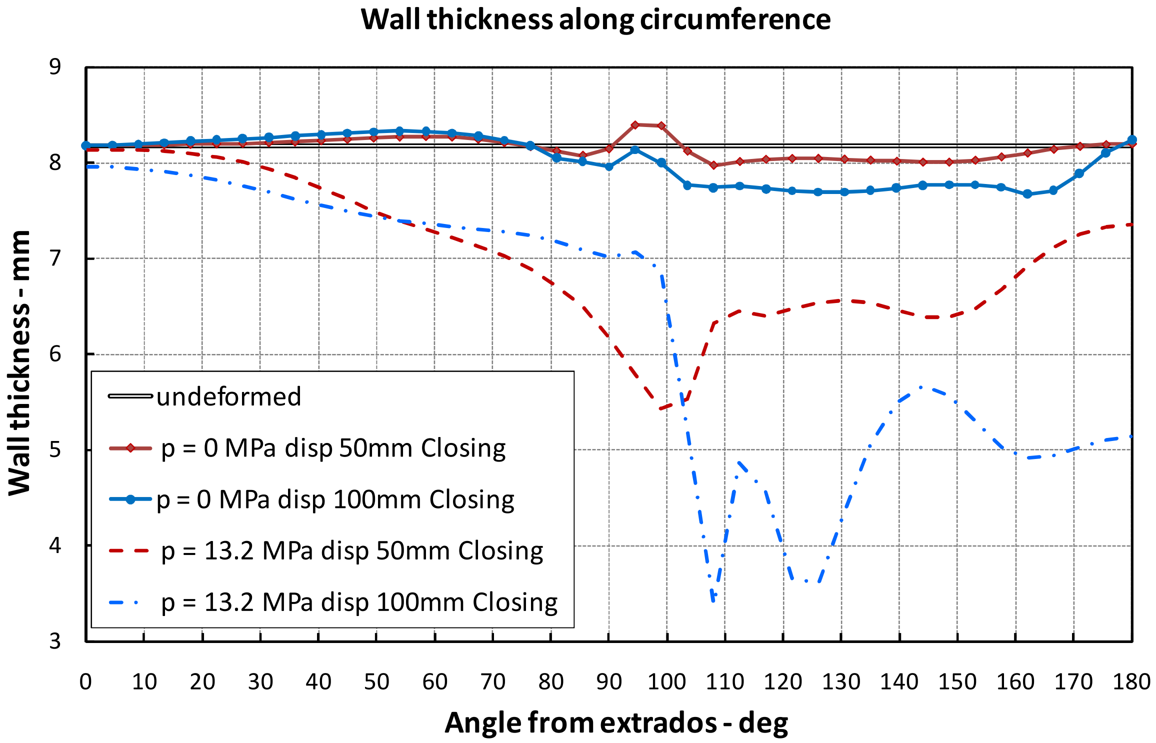

Figure 17: Wall thickness distribution along circumference

4 CONCLUSIONS

In this paper in plane bending of a representative 8” OD x 8.2mmWT grade API5L X52 industrial piping section containing a 90° elbow has been studied in this paper by means of finite element analysis, both in monotonic and cyclic conditions. The nonlinear kinematic hardening model (Lemaitre Chaboche) has been employed to take into account for biaxial ratcheting phenomenon.

Monotonic bending simulations show that opening mode show higher resistance capacity in terms of moment and curvature reached before failure, with respect to closing mode.

Cyclical load sequences starting in opening and closing mode have been investigated and after a few cycles the differences between the two load types, totally disappear.

Results show that, for the configuration presented for a symmetric alternating bending load sequence, closing bending deformation mode dominates the cyclic behavior. The most critical position is the elbow flank, both in presence and absence of the internal pressure.

The effect of the internal pressure have been investigated and results show that for monotonic case it can be considered beneficial in closing bending, while slightly negative in opening bending.

If cyclic loading is applied internal pressure induces biaxial ratcheting, causing the growth of large hoop strains that can lead to crack penetration risk. Large wall thinning is also observed.

For the particular range of imposed curvature/displacement considered the effect of reducing the cycles amplitude to one half while increasing up to twice the number of cycles, leads to a lower final accumulation of plastic strains in critical sections.

The performed analysis gave valuable information concerning stress-strain and loads to be addressed to a full scale testing activity that will be conducted within the INDUSE research program.

AKNOWLEDGEMENTS

This work was carried out with a financial grant from the Research Fund for Coal and Steel of the European Commission, within INDUSE project: “STRUCTURAL SAFETY OF INDUSTRIAL STEEL TANKS, PRESSURE VESSELS AND PIPING SYSTEMS UNDER SEISMIC LOADING”, Grant No. RFSR-CT-2009-00022

REFERENCES

[1] INDUSE-Structural Safety of Industrial Steel Tanks, Pressure Vessels and Piping Systems Under Seismic Loading, http://www.mie.uth.gr/induse;

[2] R. Muraoka, N.Ishikawa, S.Endo, M.Yoshikawa, N.Suzuki, J.Kondo, M.Takagishi, *Deformation and Ductile Cracking Behavior of X80 Grade Induction Bends*, 4th International Pipeline Conference, Calgary, Alberta, Canada September 29–October 3, 2002.

[3] C. Miki, T. Kobayashi, N. Oguchi, T. Uchida, A. Suganuma, A. Katoh, Deformation and fracture properties of steel pipe bend with internal pressure subjected to in-plane bending. *12th World Conference on Earthquake Engineering, Auckland, New Zealand, 30 January - 4 February*2000.

[4] M. A. Shalabya, M. Y. A. Younanb, *Nonlinear analysis and plastic deformation of pipe elbows subjected to in-plane bending*, International Journal of Pressure Vessels and Piping, 75,603-611,1998.

[5] S. A. Karamanos, D. Tsouvalas, A. M. Gresnigt, Ultimate Bending Capacity and Buckling of Pressurized 90 deg Steel Elbows, *J. Pressure Vessel Technology*. 128, 348-356, 2006

[6] S. A. Karamanos, E. Giakoumatos, A. M. Gresnigt, Nonlinear Response And Failure Of Steel Elbows Under In-Plane Bending And Pressure, *J. Pressure Vessel Technol*. Volume 125, 393-402, 2003

[7] K. Takahashi, S. Tsunoi, T. Hara, T. Ueno, A. Mikami, H. Takada, K. Ando,M. Shiratori, Experimental study of low-cycle fatigue of pipe elbows with local wall thinning and life estimation using finite element analysis. *International Journal of Pressure Vessels and Piping* 87 211-219, 2010.

[8] X. Chen, B. Gao, G. Chen, Ratcheting Study of Pressurized Elbows Subjected to Reversed In-Plane Bending. *Journal of Pressure Vessel Technology,*128, 525-532, 2006.

[9] J. Lemaitre, J.L Chaboche, *Mechanics of Solid Materials,* Cambridge University Press, ISBN 0-521-47758, 1994.

[10] V. Semiga, A. Dinovitza, S.Tiku, R. Batisse, M. Zarea, T. Zimmermann, *Full-scale Experimental Validation on Mechanical Damage Assessment Models,* 17th Joint Technical Meeting on Pipeline Research, Milan, Italy, May 11/15 2009.

COMPDYN 2011
III ECCOMAS Thematic Conference on
Computational Methods in Structural Dynamics and Earthquake Engineering
M. Papadrakakis, M. Fragiadakis, V. Plevris (eds.)
Corfu, Greece, 25–28 May 2011

COMPUTER MODELLING AND SEISMIC PERFORMANCE ASSESSMENT OF A BYZANTINE BASILICA

Zehra Cagnan[1]

[1] Civil Engineering Department, Middle East Technical University NCC
Middle East Technical University NCC, Kalkanli, Guzelyurt, KKTC, Mersin 10, TURKEY
e-mail: cagnan@metu.edu.tr

Keywords: Unreinforced masonry building, Seismic assessment, Historic structure.

Abstract. *Within the scope of this study, seismic performance of the St. Mamas Church (Morphu, Cyprus) that dates back to 16th Century was assessed. This structure is one of the finest examples of a three aisled basilica with a central dome that was constructed based on Franco-Byzantine type architectural style. The structure is single-story with a plan area of 19m x 8m and a height of 7.5m that utilizes thick perimeter walls together with a system of cylindrical vaults and a spherical dome. The main construction material used at this structure is local highly sandy calcarenite. With the non-destructive tests carried out, mechanical properties of the material used were identified. Among the non-destructive tests utilized; Rock Hammer, Ultrasonic Pulse Velocity, Infrared Thermography as well as Ground Penetrating Radar Tests can be listed. Based on the detailed information gathered on the structure, its 3D Finite Element model was built. With this model, seismic performance of the church was assessed with the aim of identifying critical parts of this structure. In this paper, our findings are compared with results obtained by other researchers for structures of similar geometry in Europe.*

1 INTRODUCTION

St. Mamas Church of Morphou, Cyprus is a structure that dates back to 16th Century [1]. The era in which St. Mamas Church was constructed corresponds to the latest phase of Lusignan architecture on the island (AC. 1360 to 1581). This phase is characterized by poor building quality, a reflection of impoverished conditions caused by Genoese aggression. Any stimulating contacts with Western Europe appear to have ended and the repertory of construction became almost exclusively insular in this phase [2]. However still, St. Mamas Church is considered to be one of the finest examples of the Franco-Byzantine type architecture on the island [2], which combines features of Byzantine (the dome) and Gothic (the pointed arch) characteristics in it (Figure 1b).

Structurally, St. Mamas Church belongs to the type of three aisled basilica with a dome [2]. It is a single-story structure with a plan area of 19m x 8m and a height of 7.5m that utilizes 1m thick perimeter walls together with a system of cylindrical vaults and a spherical dome (Figure 1). The aisles are separated by two colonnades of five columns. The central aisle is wider than the side aisles and bears a dome on its eastern part. The sanctuary apse is semicircular and is of the same width as the central aisle. This structure including bearing walls, internal columns as well as the roof system is made up of the local highly sandy, calcarenite stone. In the late 19th Century, a bell tower was added to the structure at the Northeastern corner as well as the porticoes on the north and west sides of the structure [1].

Historical records indicate that St. Mamas Church sustained severe damage from a fire during the Ottoman rule [2]. Some authors suggest that the dome did not exist in the initial construction but was added later by the Byzantine patrons during reconstruction of the collapsed roof after the fire. However the ornamentation of the column capitals at the bays below the dome is different, which is an indication that the position of the dome was decided beforehand during the initial construction of the structure. Today, the roof structure is in a rather deprived state due to high moisture level caused by malfunctioning drainage system. From the search of historical records, no mention of previously sustained earthquake damage could have been found, although [3] indicates that the Morphou region was shook severely by the two rather recent earthquakes of 13 June 1933 and 6 November 1968.

The present St. Mamas Church stands on the ruins of two early Christian basilicas and of a Byzantine church [1]. The non-destructive tests carried out on the structure that will be discussed in detail in the following section as well as the geotechnical and seismic tests carried out at the Church site are supportive of this statement. The geotechnical and seismic tests also indicated that soil condition at the location of interest is of NEHRP D [4] type. Due to the presence of ruins as well as the rather poor soil conditions, cracks are not absent on some of the inside columns supporting the dome structure above.

Within the scope of this study, the material and structural properties of the St. Mamas Church was investigated with the aim of assessing its seismic vulnerability as well as documenting the deterioration of this unique structure. My findings obtained based on non-destructive tests, as well as static and dynamic analyses carried out are discussed in the following sections of this paper.

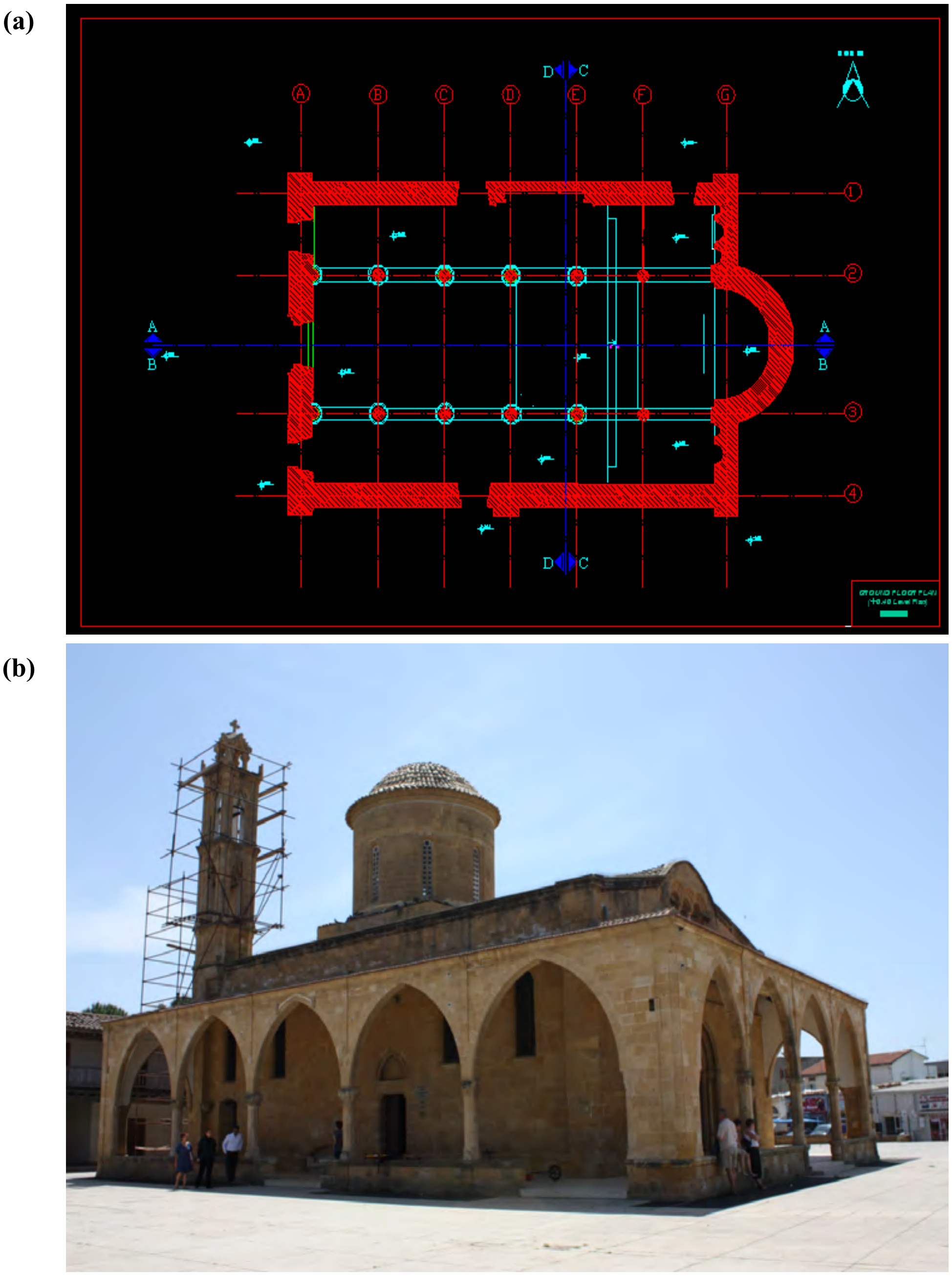

Figure 1: St. Mamas Church (a) plan view (Northern and Western porticoes are not included to the drawing), (b) picture of Northern and Western facades of the structure.

2 NON-DESTRUCTIVE TESTING

In this study, a number of non-destructive tests were employed; including rock hammer, ultrasonic pulse velocity, infrared thermography, ground penetrating radar tests with the aim of assessing the mechanical properties of the calcarenite building material of the structure. Variability of these properties throughout the structure, in addition to the degree of deterioration of the building material in different parts of the structure was studied as well.

Rock hammer test was applied to internal columns and peripheral walls of the structure. The instrument utilized for this purpose was an L-type rebound hammer with an impact energy value of 0.74nm. From each structural element 20 readings were taken, mean and standard deviation values of these readings were later computed to reach conclusions regarding relative strength values of the studied structural elements. Obtained results are summarized in Table 1 for internal columns.

	F2	F3	E2	E3	D2	D3	C2	C3	B2	B3	A2	A3
μ	9.2	13.0	11.2	12.3	10.7	17.6	11.6	14.8	9.2	14.8	8.8	6.8
σ	5.54	7.13	5.74	6.87	5.41	7.68	6.18	6.45	4.23	8.76	4.65	2.57

Table 1: Rock hammer test results (μ: mean, σ: standard deviation) for the interior columns of St. Mamas Church (The reader should refer to Figure 1a for exact locations of these columns).

Results given in Table 1 indicate clearly the considerable variability observed. This was expected as the tested material is natural hence non-uniform. Also due to structure's age, time added additional heterogeneities caused by regional decay of the material under question. The middle columns of axis 3 (F3, E3, D3, C3) have relatively higher mean strength values in comparison to the rest. This can be one reason for observed cracking on columns D2, E2, F2 (supporting the dome above) whereas their mirror image counterparts on axis 3 being crack free. The rock hammer test results obtained for peripheral walls (both interior and exterior readings) have an average value of 11 with a coefficient of variance of 20%, in this respect similar to the results obtained from the interior columns. Regarding peripheral walls, local weaknesses were observed at the sanctuary apse, where axes G and 2 meet as well as G and 3.

Ultrasonic pulse velocity test was applied to internal columns of St. Mamas Church only, at 6 different levels along each element height with an approximate spacing of half a meter. This test was especially applied around observed cracks with the aim of determining whether these cracks are running deep into the element or are just surface cracks. Obtained results are summarized in Table 2. Distribution of mean velocity values (in m/s) are in agreement with above discussed rock hammer test results. With this test, it was also observed that except from cracks of column D2, other reported cracks are probably not running very deep into the column elements. It should be noted that average results obtained for the calcarenite of St. Mamas Church in this study are almost twice as high as the velocity values obtained by [5] for the calcarenite of Saint George of Latins Church at Famagusta, Cyprus.

	F2	F3	E2	E3	D2	D3	C2	C3	B2	B3	A2	A3
μ	4956	5148	3310	4318	3735	4077	5974	6334	4659	5469	2585	3374
σ	841	1526	1524	1290	2961	1665	2631	403	1855	1730	355	1321

Table 2: Ultrasonic pulse velocity test results (μ: mean, σ: standard deviation) for the interior columns of St. Mamas Church (The reader should refer to Figure 1a for exact locations of these columns).

The malfunctioning drainage system of St. Mamas Church was already mentioned above. As presence of water accelerates deterioration of masonry and hence weakens it, variations in moisture content were documented by employing the infrared thermography technique. Results obtained indicate positive temperature gradients along the height of internal column elements suggesting moisture intake from the foundation of the structure through capillary action. However the lowest of all temperature measurements taken corresponded to the two side aisle vaults (Figure 2). On these vaults, severe discoloration was observed; the measurements obtained are the proof that these discolorations are not just stains but due to high moisture content of the masonry at these locations.

Figure 2: Pictures depicting two aisle vaults along which the lowest temperatures within the structure were detected.

The main objective of carrying out the ground penetrating radar surveys on the structure floor was to investigate the foundation type of the structure as well as existence of any possible underground structures. For this purpose a ground penetrating radar unit with a 400 MHz antenna was used that is capable of providing moderate resolution up to 5m depth. The structure floor was surveyed regularly in both North-South and West-East directions. Results indicate that the foundation system is pad foundation type with no interconnecting ground beams. Also numerous archeological remains were detected throughout the plan area of the structure. These were found to exist at two main depth levels: (i) 0.75-1.25m and (ii) below 1.5m, probably corresponding to the early Christian and Byzantine church remains mentioned above (Figure 3). Existence of such remains/cavities may give rise to settlement problems; hence the observed difference in behavior of axes 2 and 3 columns can also be attributed to differential settlement caused by these detected remains/cavities. However it should be underlined that remains detected are not localized along axis 2 only but rather distributed throughout the whole floor area.

Above, the variability of properties of structural material utilized at St. Mamas Church was discussed. In order to determine compressive strength and modulus of elasticity parameters corresponding to the structural material under investigation, rock hammer and ultrasonic pulse wave test results had to be calibrated. For this purpose three different sources of information was used: (i) official calibration data of rock hammer employed in this study [6], (ii) mechanical properties measured by [7] for local (not aged though) calcarenite, (iii) mechanical properties measured by [8] for local calcarenite (samples taken from St. Nicholas of Famagusta, Cyprus) with lower sand content. Based on this information, a compressive strength value of 10MPa, tensile strength value of 1MPa (assumed to be 1/10 of the compressive strength) and modulus of elasticity value of 2500 MPa was used in the analyses phase of this study. For columns D2, E2, F2, these values were reduced by 20% as a reflection of observed surface hardness and porosity variations. A density value of 1.7 gr/cm^3 was used throughout the whole structure.

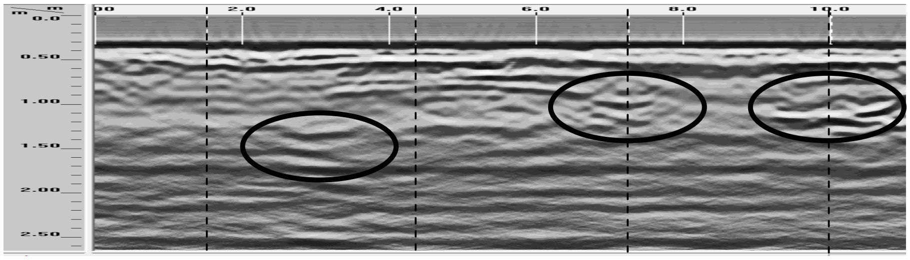

Figure 3: Ground penetrating radar survey result along axis 2. Horizontal axis represents distance along axis 2, vertical axis represents depth. Dotted black lines represent locations of columns B2, C2, D2, E2 from left to right respectively. Black ellipses close identified remains along axis 2.

3 DYNAMIC PROPERTIES

A finite element model of the structure was developed using SAP2000 software. In this model of plan area 19m x 8m, general height 7.5m that reaches 17m at the dome; all structural elements were represented by shell elements. Thicknesses of these elements vary considerably throughout the structure, i.e. 1m for peripheral walls, 0.55m for internal columns, 0.35m for the vaults and the spherical dome. The dimensions of various structural elements were quite accurately obtained with the help of a laser scanning instrument; except for the vault and dome thicknesses. As accurate dimensioning would require causing damage to the structure, these thicknesses were assumed to be 0.35m in this study. The bell tower and the porticoes were not included into the model of the church explicitly as these parts were added 300 years later to the original church building and hence are structurally independent. The effect of bell tower was taken into account indirectly as additional mass at the Northeastern corner of the structure. All peripheral and internal walls were set fixed at the foundation level in the model.

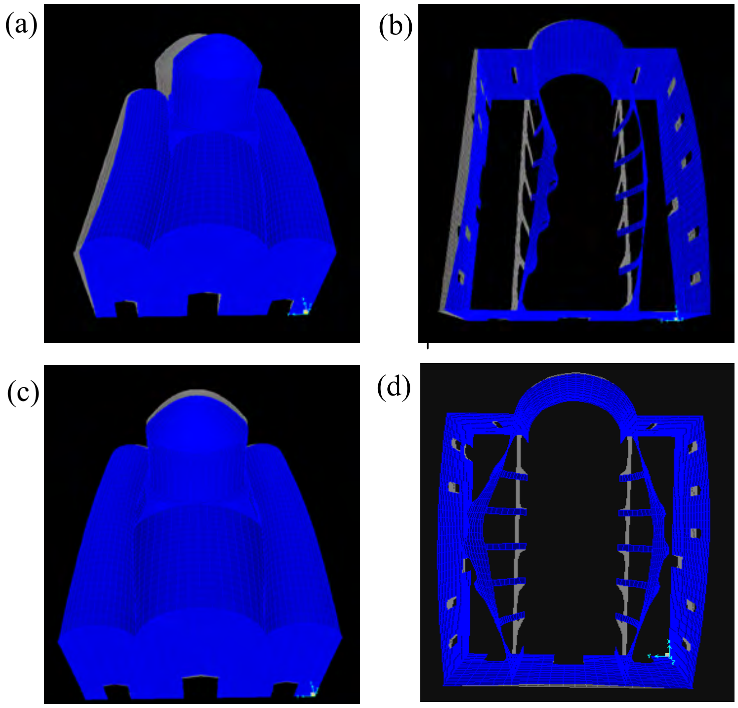

T=0.21s, U_y=59%

T=0.20s, U_y=0.05%

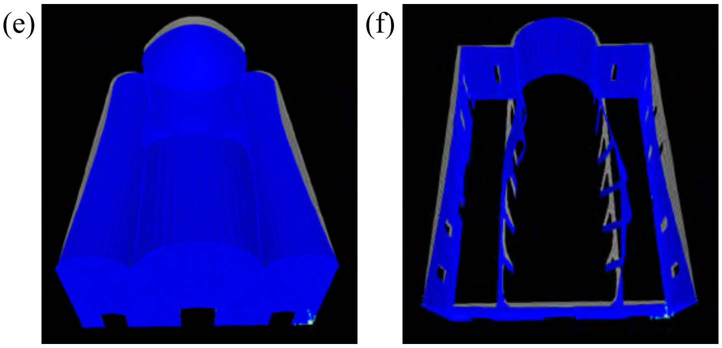

$T=0.17s$, $U_x=13\%$

Figure 4: First three eigen-modes of the structure. First column of figures illustrate the structure as a whole, second column of figures do not include the roof system (hidden from view to illustrate directly the interior elements)

Figures 4a-4f depict the first three eigen-modes of the structure obtained by the linear elastic modal analysis carried out. The translational eigen-mode in the transverse North-South direction (y direction) is the one with the longest eigen-period (Figures 4a-4b, T=0.21s). The structural response in this mode displaces the longitudinal walls mainly in an out-of-plane sense, which is achieved by the in-plane deformation of transverse peripheral walls. This first mode mobilizes approximately 59% of the total mass of the structure. This is later followed by a higher translational eigen-mode in the transverse direction that mobilizes only very small portion of the total mass and mainly causes out-of-plane deformation at internal longitudinal walls (Figures 4c-4d, T=0.20s). The translational eigen-mode in the longitudinal East-West direction (x direction) is finally reached at the third longest eigen-period (Figures 4e-4f, T=0.17s). The structural response in this mode displaces the longitudinal peripheral walls mainly in in-plane manner, with the cylindrical drum at the roof displacing in the East-West direction and the transverse peripheral walls mainly resisting with out-of-plane action. This third mode mobilizes approximately 13% of the total mass of the structure.

4 STATIC ANALYSIS RESULTS

In this part of the study, static behavior of the structure was assessed under three different loading cases. The first of these loading cases is dead load (G) that includes weight of the tile coverings on the roof as well as the weight of the bell tower. From this loading case, live loads were explicitly left out as in the absence of snow loading, which is the case for the structure of interest, the magnitude of live loads were negligible in comparison to dead loads. The second and third loading cases are the earthquake forces E_x and E_y applied in the x and y directions respectively. These earthquake forces include application of an acceleration value of 1g ($g=9.81m/s^2$) in the x and y directions. Main objective here was to determine limiting deformations in the two horizontal and vertical directions.

Results are shown in Figures 5a-5f below. Under the effect of dead load only, maximum vertical deformation of 3mm was observed at the spherical dome above the drum; whereas level of vertical deformation at the columns below supporting the drum was 2mm (Figure 5a-5b). The structure is considerably more flexible in the transverse direction than the longitudinal direction. Results also indicate that the internal colonnades are so flexible in both longitudinal and transverse directions that they contribute very little to the resistance in both of these directions. Under E_x, maximum deformation along the longitudinal axis of the structure at the dome level was determined to be 12mm whereas under E_y maximum deformation along the transverse axis of the structure at the dome level was almost twice as much approximately

22mm. Under both E_x and E_y, the deformations at the roof level below the drum were considerably lower than the aforementioned maximums, in the range of 3-4mm for E_x and 8-10mm for E_y. Under E_x, it is mainly the longitudinal peripheral walls resisting with in-plane action. Whereas under E_y, transverse peripheral walls resist with in-plane action and the longitudinal peripheral walls resist with out-of-plane action.

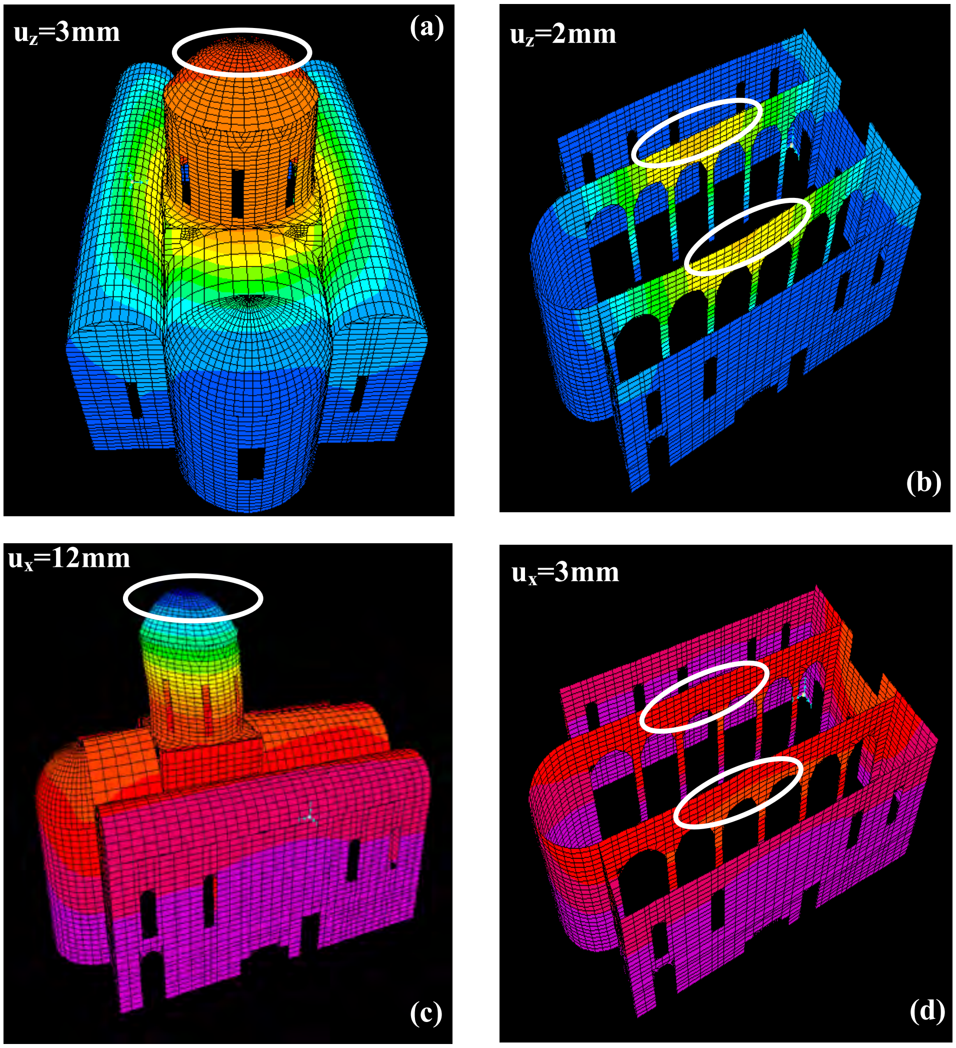

Figure 5: Deformations under (a)-(b) dead load G and (c)-(d) Earthquake load E_x. First column of figures illustrate the structure as a whole, second column of figures do not include the roof system (hidden from view to illustrate directly the deformation of interior elements)

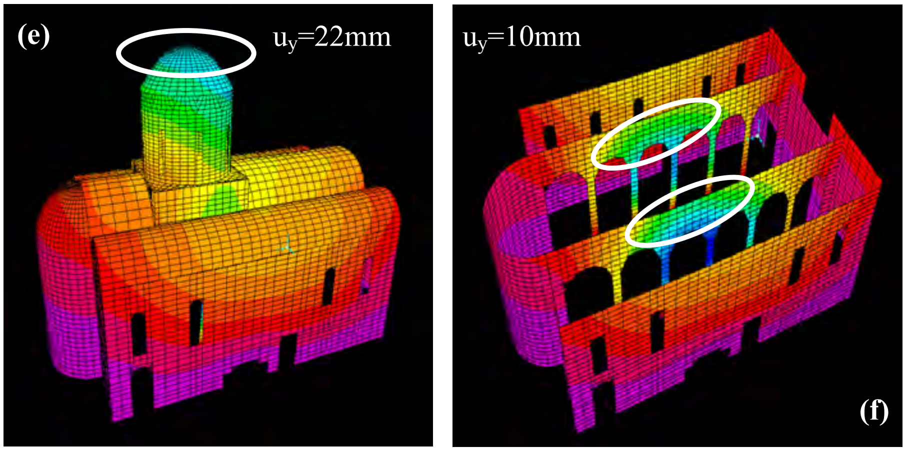

Figure 5 cont.: Deformations under (e)-(f) Earthquake load E_y. Figure on the left illustrate the structure as a whole, figure on the right do not include the roof system (hidden from view to illustrate directly the deformation of interior elements)

5 DYNAMIC ANALYSIS RESULTS

In this final phase of the study, dynamic behavior of the structure was assessed by carrying out a response spectrum analysis. According to the findings of [9], the peak ground acceleration value at the site of interest is in the range of 0.2-0.3g corresponding to a return period of 475 years. As mentioned in the introduction part of this manuscript, detailed seismological and geotechnical tests were carried out at the site of St. Mamas Church within the scope of this study. The geotechnical study included, carrying out a standard penetration test up to a depth of 30m and classification of formations based on samples taken during the test. With the seismological tests, a 2D S- and P-wave velocity profile along an axis of 50 m parallel to the structure was developed. Based on the results of both tests, soil condition at the site of interest was classified as NEHRP D, or class C of Eurocode 8. By utilizing the base response spectrum function of Eurocode 8 together with the peak ground acceleration value and the aforementioned soil type, together with the building importance factor of 1.3, the site specific response spectrum for the St. Mamas Church was developed. In addition to the horizontal loading (E_x when applied in the longitudinal direction, E_y when applied in the transverse direction) described by the response spectrum, dead load was applied to the structure with the following combinations: (1) $G+1.4E_x$, (2) $G+1.4E_y$, (3) $G+0.9E_x+0.3E_y$, (4) $G+0.9E_y+0.3E_x$. Obtained normal and shear stress distributions were investigated in detail and critical structural elements were identified.

In Figure 6, distribution of stresses is shown for peripheral walls, internal colonnades, and the roof structure. Under the average strength values given in section 2 of this manuscript, the structure is not expected to sustain any damage due to seismic loading. However as the non-destructive testing results illustrate, mechanical properties of the masonry vary considerably throughout the structure. If the lower limit strength values are considered rather than the average values obtained, several structural elements appear to be critical throughout the structure. The lower limit strength values that were employed in this study were 3MPa for compressive strength and 0.3 MPa for tensile strength. For columns D2, E2 and F2, 20% lower strength values were used to reflect non-destructive test results. The critical elements identified are the internal columns carrying the drum and the dome of the structure (D2, E2, F2, F3, E3, and F3 of Figure 1a), vicinity of openings (doors, windows, sarcophagus of St. Mamas) on the peripheral walls, base of peripheral walls and the drum-lower roof intersections of the roof structure. Based on the aforementioned lower limit strength values, masonry over limit factors (ratio of observed stress level to assumed lower bound strength value) were also computed for these critical regions. These masonry over limit factors (R_{up}) are all indicated on Figure 6 as well.

Three aisled basilicas are abundant on the island of Cyprus, as well as neighboring regions such as Balkans. One of the main aims of this study was to compare results of this study with other previously carried out studies on dynamic behavior of basilicas of similar architecture to identify commonalities as a forward attempt towards developing a vulnerability relation for this type of structures that can be utilized in aiding separation of high seismic risk structures from the rest.

In [10], behavior of three different basilicas was studied. Two of these structures had similar plan areas to that of St. Mamas Church, whereas the third structure was considerably larger. The main difference between the structures of [10] and the St. Mamas Church is that St. Mamas Church is considerably taller with a roof structure that is entirely made up of masonry which reaches a height of 17m at the semi-hemispherical dome above the drum. Whereas two basilicas of [10] (with the similar plan area as St. Mamas Church), have wooden roofs at a height of only approximately 7m. This difference between the roof structures appears to be the main reason behind different dynamic behaviors. As a result, St. Mamas Church has longer dynamic periods, as well as eigen-modes dominated by out-of-plane deformation of internal colonnades carrying the drum and the dome of the roof structure. Similarly, internal columns reach critical stress values under seismic loading whereas such behavior was not observed in the study of [10].

In [11-13], the plan area of the structure studied is very similar to that of the St. Mamas Church as well; however it only has a height of 5m with a wooden roof. Expectedly, the eigen-modes are not dominated by the out-of-plane deformation of internal colonnades supporting the roof structure. However results indicate damage incurred by internal columns due to excessive tensile stress once the peak ground acceleration level of 0.25g was surpassed (with tensile strength level corresponding to the lower bound strength level employed in this study).

In [14], structures with similar architecture were investigated both analytically and experimentally. As the plan area of the structure under consideration of [14] is much smaller than that of St. Mamas Church, direct one to one comparisons will not be made here with the findings of [14]. However in [14], it is clearly indicated that structures having a masonry roof system including a central drum and dome will sustain damage first at this critical region, in line with the observations made regarding St. Mamas Church.

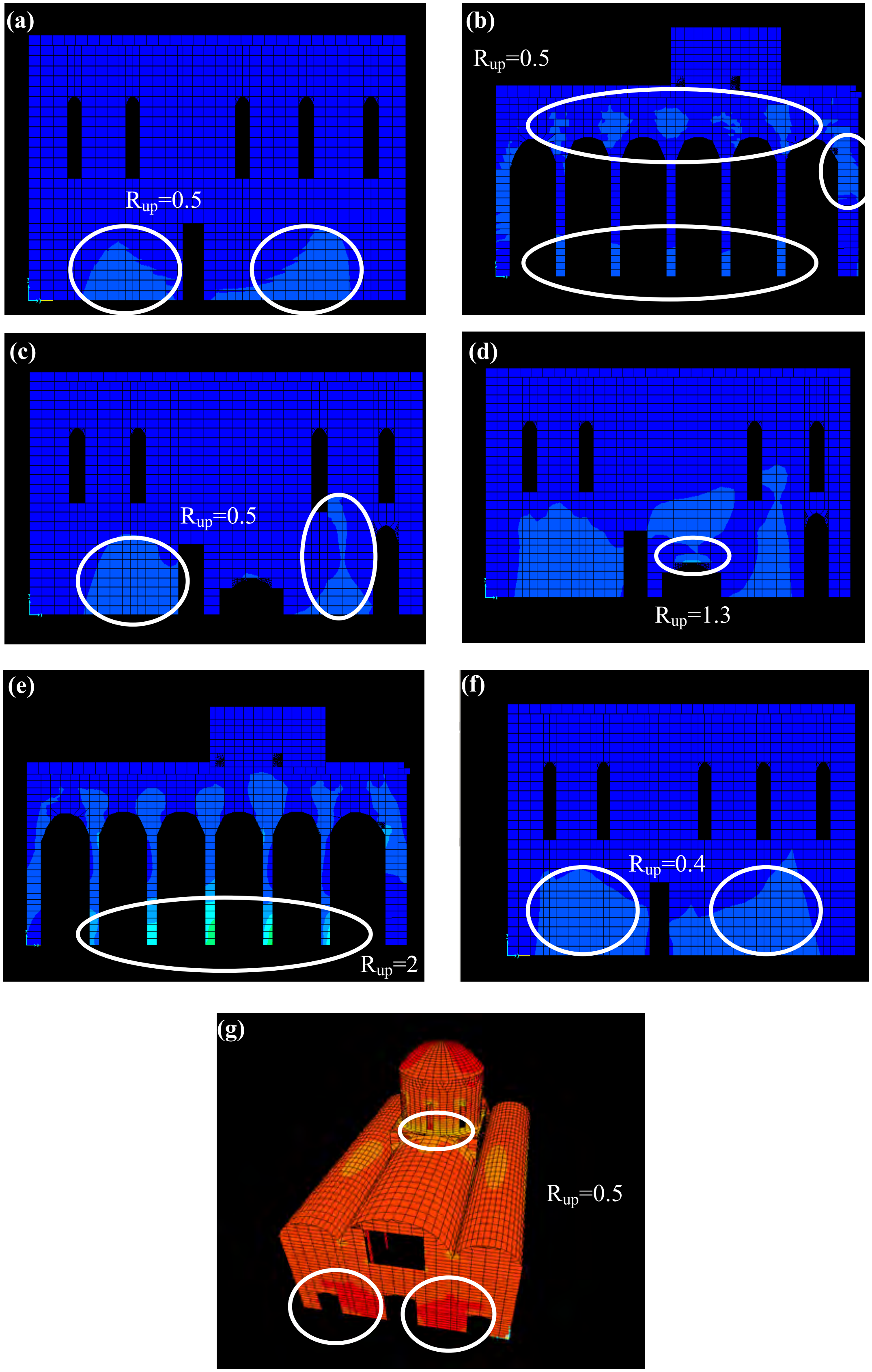
(a)
$R_{up}=0.5$
(b)
$R_{up}=0.5$
(c)
$R_{up}=0.5$
(d)
$R_{up}=1.3$
(e)
$R_{up}=2$
(f)
$R_{up}=0.4$
(g)
$R_{up}=0.5$

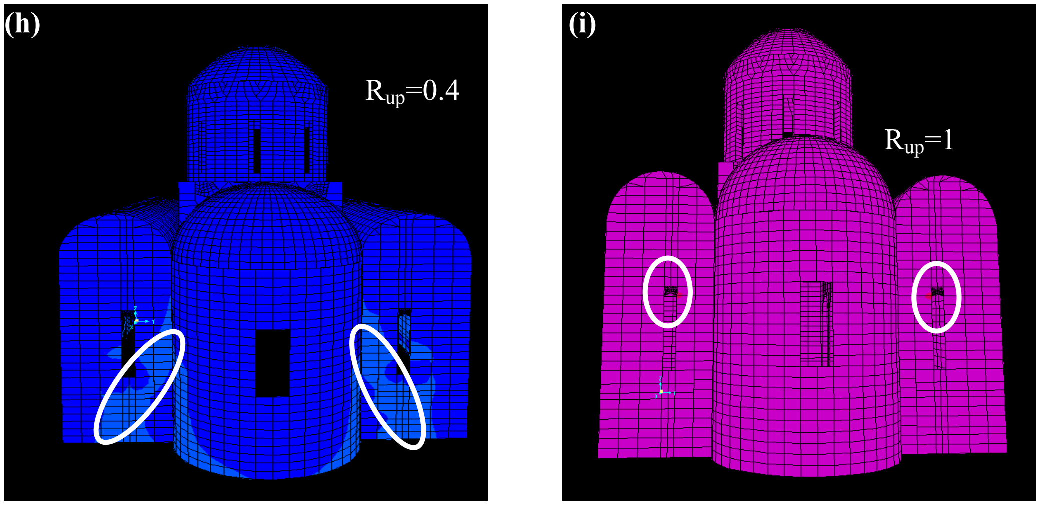

Figure 6: Stress distributions under (a)-(c) combination 3 G+0.9E_x+0.3E_y and (d)-(i) combination 4 G+0.9E_y+0.3E_x. As the structure is weaker in the transverse direction, the combination 4 yielded more critical results. Most critical regions are marked with the white ellipses, for these regions masonry over limit factors (R_{up}, ratio of observed stress to assumed lower bound strength level) are given as well.

6 CONCLUSIONS

Within the scope of this study, both experimental and analytical work had been carried out on St. Mamas Church of Morphou, Cyprus with the main objective of assessing its dynamic behavior. The following conclusions were reached:

- The non-destructive tests carried out at the structure indicated that mechanical properties of the masonry used vary considerably with coefficient of variation values computed reaching up to 60%. Based on the test results, the average compressive strength value of 10 MPa, modulus of elasticity value of 2500 MPa and tensile strength of 1 MPa were assigned to the structure. However in order to take into account the considerable variability of mechanical properties of masonry, lower bound strength values of 3 MPa for compressive strength and 0.3 MPa for tensile strength were also used.

- Dynamic analysis results indicate that as the internal colonnades of the structure are quite flexible, the structure is weaker in the transverse direction than longitudinal direction. Under the seismic loading with a return period of 475 years, the most critical elements of the structure were identified as the internal columns supporting the drum and dome of the roof system. The stress level at these columns is expected to reach twice the lower limit strength values determined. The second level critical localities are surroundings of openings such as windows, doors, sarcophagus of St. Mamas on the North façade of the church and the drum-lower roof connections of the roof system. Results indicate clearly that presence of the drum and the dome has governing effect on the dynamic behavior of the overall structure.

- Dynamic analysis results indicate the vulnerability of internal columns, hence observed cracking on these columns can not be associated with a differential settlement problem alone.

- Structures with the same architectural form as that of St. Mamas Church are abundant in Europe. Hence several studies assessing dynamic behavior of similar structures can be found in the literature. Comparison of results indicate that grouping these structures according to floor area (geometry does not vary considerably), roofing structure, material properties and developing vulnerability relations for each group would be a valuable contribution towards preservation of such monuments; as such relations would enable the preliminary categorization of structures according to their seismic risk level. With this statement of course, the intention is not to undervalue the effect of uniqueness of each structure and the effect of considerable variability of building material properties on their dynamic behaviors. However with the aim of approaching the problem of preservation from a more macro perspective, existence of such vulnerability relations would prove to be useful in preliminary categorization of these structures regarding their seismic riskiness.

7 ACKNOWLEDGEMENTS

This study is financially supported by the project entitled ‘Earthquake Vulnerability Assessment of Historical Monuments in Cyprus’ which is granted by the European Union within the scope of Cypriot Civil Society in Action Program under the award no. CRIS 2008/172-607, however the views expressed in this publication do not necessarily reflect the views of the European Union.

REFERENCES

[1] C. Enlart, *Gothic art and the Renaissance in Cyprus,* Translated and edited by D. Hunt. Trigraph, 1987.

[2] T. Kyprou, Hiera Metropolis Morphou, *Holy Bishopric of Morphou: 2000 years of art and holiness*, Bank of Cyprus Cultural Foundation, 2002.

[3] N.N. Ambraseys, Reappraisal of the seismic activity in Cyprus: 1894-1991. *Bolletino of Geofisica Teorica Ed Applicata,* **Vol.**34, 133, 41-79, 1992.

[4] Building Seismic Safety Council, *NEHRP Recommended Provisions for Seismic Regulations for New Buildings and Other Structures, FEMA-450, 2003 revision*, Federal Emergency Management Agency, Washington D.C, 2003.

[5] P.B. Lorenco, L.F. Ramos, *Preliminary report on the inspection of three Famagusta Churches*, Guimaraes, Universidade de Minho, 2008.

[6] Controls, *45-D0561 Rock classification hammer instruction manual*, 2001.

[7] O. Eren, M. Bahali, Some engineering properties of natural building cut stones of Cyprus, *Construction and Building Materials*, **Vol.**19, 213-222, 2005.

[8] Z. Cagnan, Numerical models for the seismic assessment of St. Nicholas Cathedral, Cyprus, *Soil Dynamics and Earthquake Engineering*, 2011. (submitted for publication)

[9] Z. Cagnan, G.B. Tanırcan, Seismic hazard assessment for Cyprus, *Journal of Seismology*, **Vol.** 14, 225-246, 2010.

[10] G.C. Manos, V.J. Soulis, O. Felekidou, V. Matsou, A numerical investigation of the dynamic and earthquake behavior of Byzantine and Post-Byzantine basilicas, *Proceedings of the 9th US National and 10th Canadian Conference on Earthquake Engineering, July 25-29 2010, Toronto, Canada*, 2010.

[11] C.Z. Chrysostomou, T. Demetriou, M. Pittas, A. Stassis, Retrofit of church with linear viscous dampers, *Structural Control and Health Monitoring*, Vol.12, 197-212, 2005.

[12] C.A. Syrmakezis, Seismic protection of historical structures and monuments, *Structural Control and Health Monitoring*, Vol.13, 958-979, 2006.

[13] P. Arteris, On the structural analysis and seismic protection of historical masonry structures, *The Open Construction and Building Technology Journal*, **Vol.** 2, 124-133, 2008.

[14] P. Gavrilovic, S.J. Kelley, V. Sendova, A study of seismic protection techniques for the Byzantine Churches in Macedonia, *APT Bulletin*, Vol. 34, 63-69, 2003.

COMPDYN 2011
III ECCOMAS Thematic Conference on
Computational Methods in Structural Dynamics and Earthquake Engineering
M. Papadrakakis, M. Fragiadakis, V. Plevris (eds.)
Corfu, Greece, 25–28 May 2011

SEISMIC OVERTURNING OF DAMPED ROCKING STRUCTURES

Elias G. Dimitrakopoulos[1] **and Matthew J. DeJong**[2]

[1] Univeristy of Cambridge, Department of Engineering
Trumpington Street, Cambridge, CB2 1 PZ, UK
ilias.dimitrakopoulos@gmail.com

[2] Univeristy of Cambridge, Department of Engineering
Trumpington Street, Cambridge, CB2 1 PZ, UK
mjd97@cam.ac.uk

Keywords: rocking, overturning, analytical dynamics, earthquake engineering, damping

Abstract. *Numerous structures exhibit rocking behavior during earthquakes and there is a continuing need to retrofit these structures to prevent collapse. The behavior of stand-alone rocking structures has been thoroughly investigated, but there are relatively few theoretical studies on the response of retrofitted rocking structures. In practice, despite the benefits of allowing rocking motion, rocking behavior is typically prevented instead of optimized. This paper characterizes the fundamental behavior of damped rocking motion through analytical modeling. A single rocking block analytical model is utilized to determine the optimal viscous damping characteristics which exploit the beneficial aspects of rocking motion while dissipating energy and preventing overturning collapse. To clarify the benefits of damping, overturning envelopes for the damped rocking block are presented and compared with the pertinent envelopes of the free rocking block. Finally, the same principles of controlling rocking behavior with damping are extended to a particular class of rocking problems, the dynamics of masonry arches. A pilot application of the proposed approach to masonry arches is presented.*

1 INTRODUCTION

Numerous heritage structures exhibit rocking behaviour when loaded dynamically, including monuments, towers, bridge piers, sculptures, etc. Recent earthquakes (e.g. Chile and Italy) have increased world-wide incentive to retrofit such structures to avoid collapse during dynamic loading.

The rocking dynamical response is highly nonlinear and extremely complex; the block displays numerous ways to overturn [1, 2] with respect to the number of the preceding impacts, and its response is highly sensitive on the characteristics of the dynamic loading. Most studies assume an idealized ground excitation in the form of a primary impulse [3] or harmonic loading [1]. The significant amount of research assuming harmonic loading originates from the concept that a constant frequency excitation can cause resonance. However, one main advantage of the rocking system is that constant frequency rocking resonance is impossible because the natural frequency changes with rocking amplitude. Further, harmonic ground motions which could cause rocking resonance would have to have a precise time-varying frequency, and are thus extremely unlikely [4]. Rocking behaviour is mostly affected by the distinct time-dependent characteristics of the ground excitation that are less relevant to the response of elastically deformable structures.

In contrast to the significant amount of research on the response of stand-alone rocking structures, there are only a handful of theoretical studies on the response of retrofitted rocking structures [5, 6]. In practice, rocking behaviour is typically prevented instead of limited or confined. Prevention is achieved by tying structures down, reinforcing them internally by drilling through or externally by wrapping with Fibre-Reinforce Polymers (FRP) [7].

While these methods can be effective, they can over-stiffen structures, add stress, and be destructive. More particular, Makris & Zhang [5] showed that the response of the anchored rocking block can be worse of that of the pertinent stand-alone rocking block. In addition, when earthquake loading is rare and relatively minimal, as in the UK, extensive reinforcing of a vast number of structures may be economically infeasible and too invasive for heritage structures. Hence, application of intelligent less invasive intervention methods is sought, through confinement of the rocking response instead of prevention. This research aims to lay the foundation for the development of a new class of retrofit solutions which exploit damping systems.

2 DAMPED ROCKING MOTION

Motivated by the inverse effects of adding strength to the rocking block, this research takes an alternative approach and investigates the benefits of additional damping. Consider first the free standing rocking block of Figure 1 (without dampers) subjected to a pulse-type base excitation with acceleration amplitude a_g and frequency ω_g. Assuming the coefficient of friction is high enough to prevent sliding, the rocking motion initiates when the ground acceleration $\ddot{u}_g$ exceeds the critical value: $\ddot{u}_g \geq a_{g,\,min} = g \tan\alpha$ where α is the angle of slenderness and g the gravity acceleration.

The moment equilibrium, during rocking, with respect to the pivot points O (or O' accordingly in Figure 1) gives:

$$I_0\ddot{\theta} + mgR\sin\left[\alpha\,\mathrm{sgn}(\theta)-\theta\right] = -m\ddot{u}_g R\cos\left[\alpha\,\mathrm{sgn}(\theta)-\theta\right] \tag{1}$$

where θ is the rocking rotation, I_0 the moment of inertia with respect to the pivot point, m the mass of the block, R the half-diagonal and $sgn()$ the standard sign function. The slenderness angle is defined by $\tan\alpha = b/h$, where $2b$ is the width and $2h$ the height of the block.

To complete the description of the problem, the equation of motion is complemented with a coefficient of restitution η, defined as the ratio of the pre and post impact velocities, which ranges between 0 (for perfectly plastic) and 1 (for perfectly elastic impact):

$$\dot{\theta}^{+} = \eta \dot{\theta}^{-} \tag{2}$$

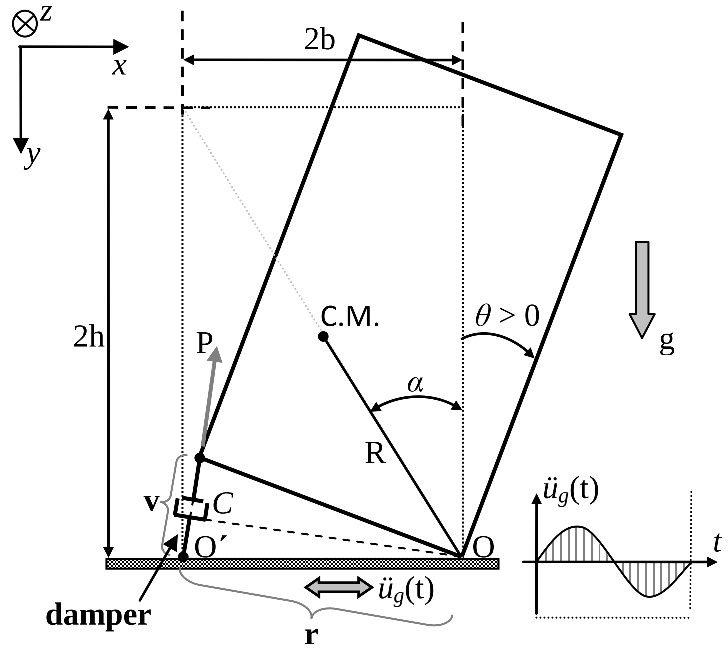

Figure 1: The rocking block retrofitted with viscous dampers at its edges.

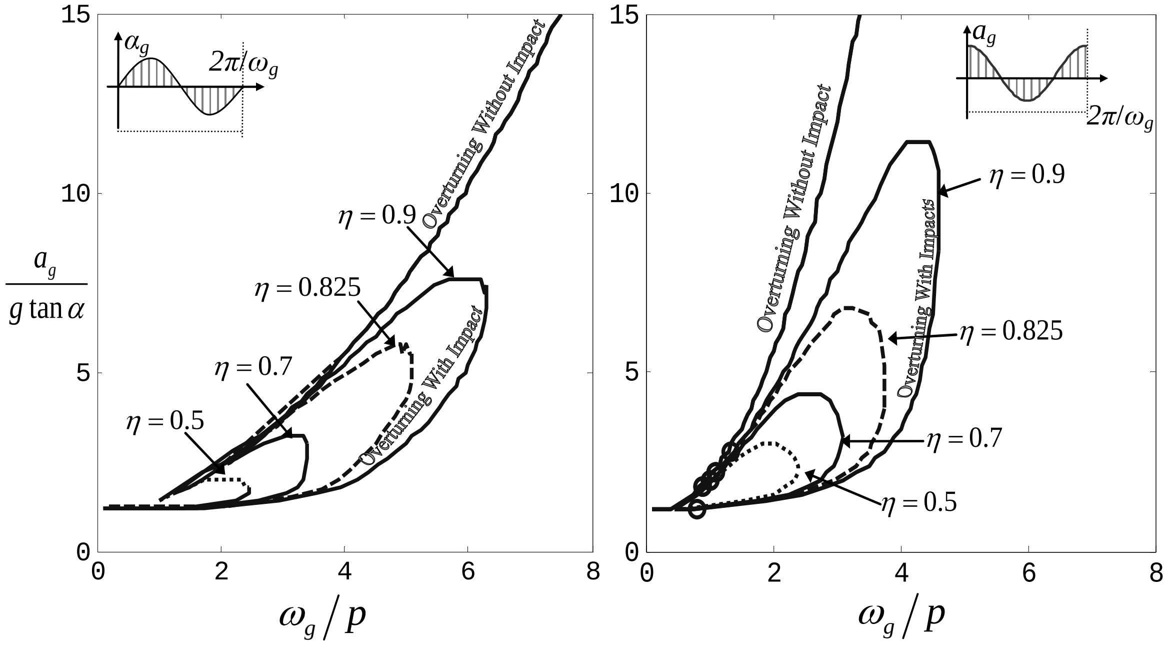

Figure 2: Overturning envelopes of the stand-alone rocking block for different coefficients of restitution η.

The present description of rocking (Equations 1 and 2), is valid under the assumption that the block is slender enough to prevent other impact behaviors to arise such as bouncing.

Figure 2 presents the overturning envelopes of the rocking block, subjected to simple trigonometric pulses, for different coefficients of restitution η. As expected, the coefficient of restitution affects the overturning of the rocking block only when impacts precede overturning. In other words, the energy is damped out of the stand-alone rigid block only during impacts. This poses a theoretical limit to reducing rocking behaviour by increasing energy dissipation at impact, as immediate overturning is unaffected.

2.1 Bilateral Viscous Dampers

As a first approach, consider a rigid block retrofitted with bilateral viscous dampers as in Figure 1. The force P of a viscous linear damper is given by:

$$P = C\dot{v} \tag{3}$$

where $\dot{v}$ is the relative velocity between the ends of the damper and C the damping constant.

Moment equilibrium of the retrofitted block (Figure 1) during rocking gives:

$$I_0\ddot{\theta} + mgR\sin\left[\alpha\,\mathrm{sgn}(\theta) - \theta\right] + P \cdot r = -m\ddot{u}_g R\cos\left[\alpha\,\mathrm{sgn}(\theta) - \theta\right] \tag{4}$$

where r is the lever of the damping force P.

Equation (4) can be written using Eq.(3)and geometric properties:

$$\ddot{\theta} = -p^2\left\{\sin\left[\alpha\,\mathrm{sgn}(\theta) - \theta\right] + \frac{\ddot{u}_g}{g}\cos\left[\alpha\,\mathrm{sgn}(\theta) - \theta\right]\right\} - p\gamma\left(1 + \cos\theta\right)\dot{\theta} \tag{5}$$

where $p = \sqrt{3g/4R}$ is the frequency parameter of the block, and $\gamma \doteq \frac{3}{2}\frac{C}{mp}\sin^2\alpha$ is a dimensionless parameter that relates the damping constant C to the mass m, slenderness α and frequency p.

2.2 Unilateral Viscous Dampers

Re-centering, i.e. limiting residual displacements despite large displacement during seismic loading, is an advantage of rocking motion. However, collapse must be prevented. Thus, to limit collapse while encouraging re-centering, unilateral viscous dampers, which are activated only during uplift, are also considered. The behaviour of such unilateral viscous dampers can be described with the help of an ad-hoc function $S\left(\theta,\dot{\theta}\right)$ defined as follows:

$$S\left(\theta,\dot{\theta}\right) = \frac{1}{2}\left[\mathrm{sgn}\left(\theta \cdot \dot{\theta}\right) + 1\right] = \begin{cases} 1 \ \textit{when uplifting} \\ 0 \ \textit{when restoring} \end{cases} \tag{6}$$

The equation of motion for the linear unilateral viscous damper is:

$$\ddot{\theta} = -p^2\left\{\sin\left[\alpha\,\mathrm{sgn}(\theta) - \theta\right] + \frac{\ddot{u}_g}{g}\cos\left[\alpha\,\mathrm{sgn}(\theta) - \theta\right]\right\} - p\gamma\left(1 + \cos\theta\right)S\left(\theta,\dot{\theta}\right)\dot{\theta} \tag{7}$$

2.3 Response of the damped rocking block to pulse-type excitations

Figure 3 presents the overturning envelopes for the bilateral damping, and Figure 4 presents the overturning envelopes for the equivalent unilateral (same γ parameter) dampers. Both figures also contain the undamped (stand-alone) rocking block envelopes. The block is excited with simple trigonometric pulses and the response is calculated by numerically solving the nonlinear differential equations of motion (Eq. 5 and 7 respectively) assuming a constant coefficient of restitution η. The behaviour is described in the dimensionless terms:

$$\frac{a_g}{g\tan\alpha},\ \frac{\omega_g}{p},\ \eta,\ \gamma=\frac{3}{2}\frac{C}{mp}\sin^2\alpha \qquad (8)$$

Similarly to the behavior of the stand-alone rocking block [3], the damped rocking block displays two different modes of overturning under a sine and a cosine pulse-excitation (e.g. Figure 3): immediate overturning without impact and overturning with at least one impact (one in the case of a sine pulse excitation and up to 2 in the case of a cosine pulse excitation). In genera land as expected, the overturning-with-impact mode is more critical since it appears for lower excitation intensities. However, unlike the case of additional strength [5], the higher the additional damping (parameter γ), the more the overturning envelopes shrink, regardless of the excitation type (sine or cosine).

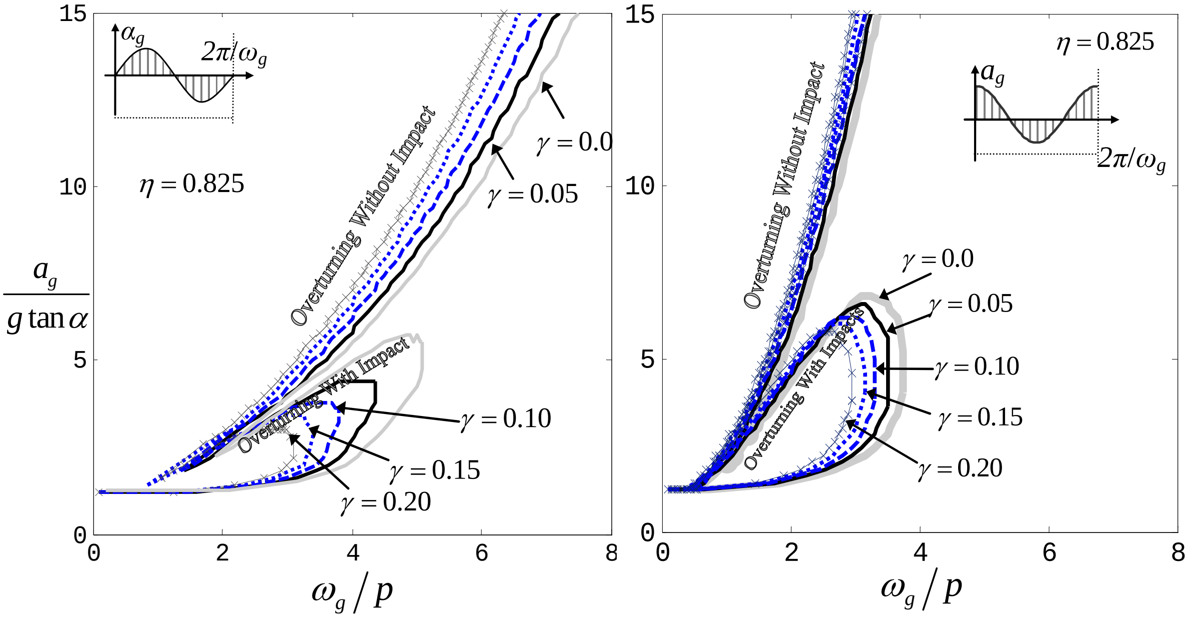

Figure 3: Overturning envelopes for the rocking block with bilateral viscous dampers. Comparison with the stand-alone rocking block (thick grey line).

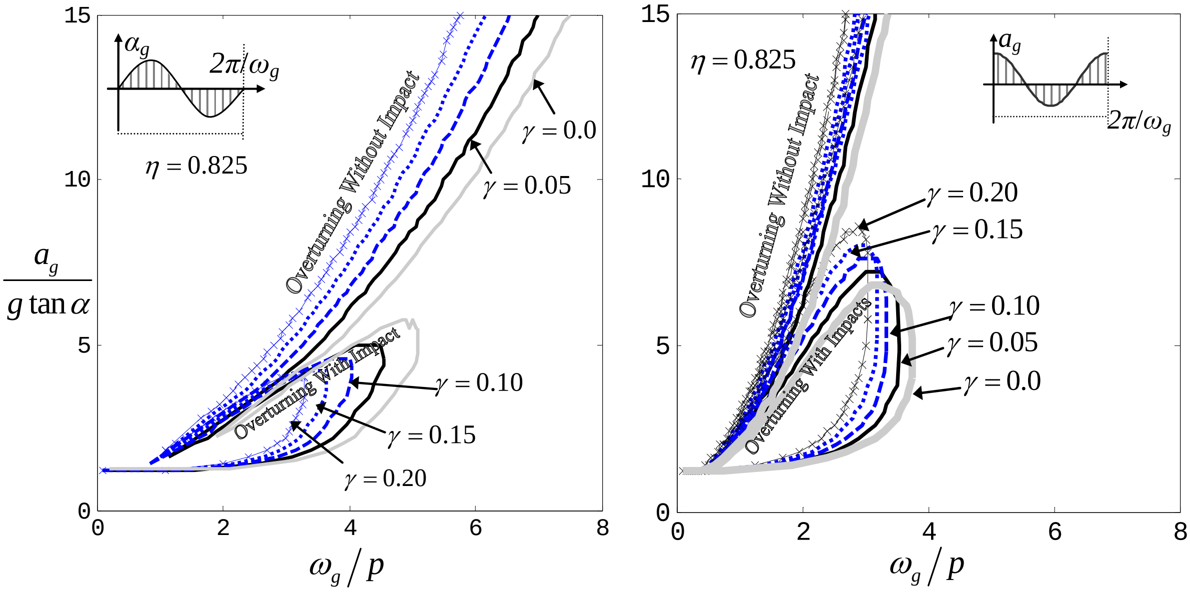

Figure 4: Overturning envelopes for the rocking block with unilateral viscous dampers. Comparison with the stand-alone rocking block (thick grey line).

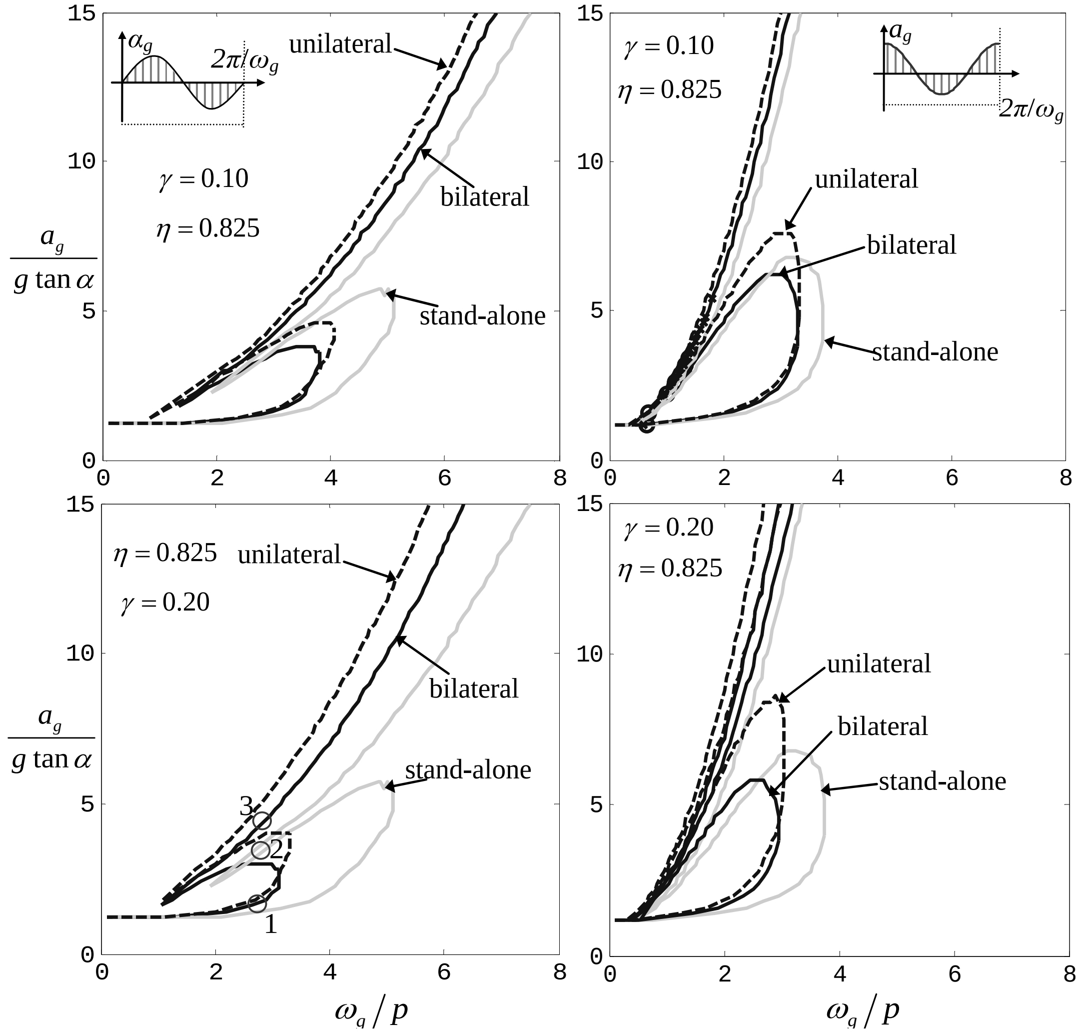

Figure 5: Comparison of overturning envelopes for the rocking block retrofitted with bilateral and unilateral viscous dampers.

In Figure 5, the overturning envelopes for bilateral and unilateral damping are directly compared. Both unilateral and bilateral dampers have a similar beneficial effect for overturning without impact. However, there is a brief change in velocity prior to overturning during which the block tries to recover. Bilateral dampers limit this recovery, while unilateral dampers allow it, making them slightly more effective.

For overturning with impact, both damping options cause a similar beneficial shift in the minimum impulses which cause overturning (the lower limit of the overturning area shifts up and left). However, bilateral dampers provide a larger decrease of the total overturning area through a larger downward shift in the upper limit of the overturning region. While may be beneficial, it should be noted that the intermediate safety area, between the two overturning basins, is a result of the highly nonlinear behavior of the rocking block and is very sensitive to the characteristics of the excitation [1, 2]. Thus, from a design perspective, it is unreliable to depend on this safety region, and the lower limit is more important. Hence, both options have a remarkably similar benefit.

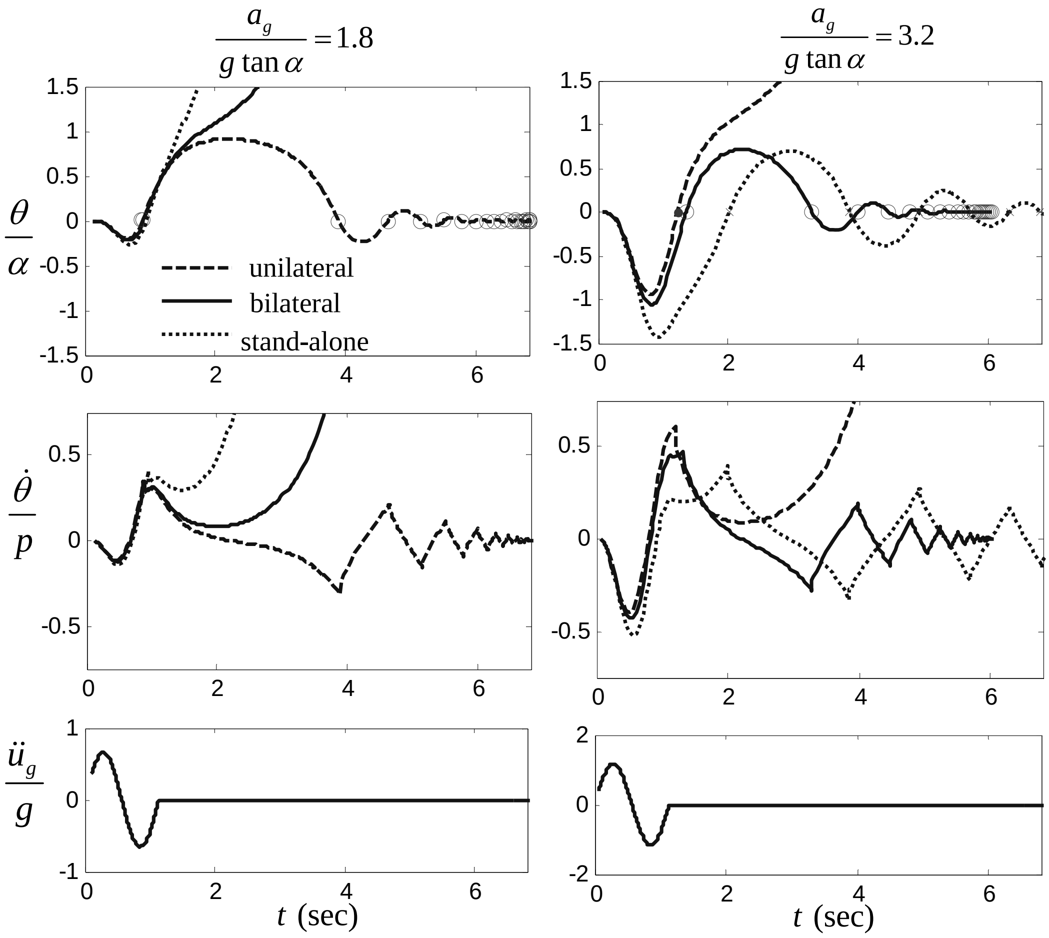

Figure 6: Rocking rotation (top) and angular velocity (middle) time-history of the rocking block (ω/p = 2.75, η = 0.825) excited with a sine pulse (bottom). Left column point 1 of Figure 5 and right column point 2 of Figure 5.

To further investigate the effects of adding damping and the sensitivity of the rocking response, Figure 6 plots the time-history response (rotation and angular velocity) of the rocking block that corresponds to the points 1 to 3 in the overturning diagram (Figure 5). For $a_g/(g\tan\alpha)$ = 1.8 and 4.6 (points 1 and 3) the stand-alone and the bilaterally damped rocking block overturn, while the unilaterally damper rocking block survives. On the contrary, for $a_g/(g\ \tan\alpha) = 3.2$ (point 2) the opposite is true: the stand-alone and the bilaterally damped block survive, while the unilaterally damped block overturns. The response is clearly highly nonlinear, and numerous instances where either the bilateral or the unilateral damper performs better can be found. As a general rule, for a given damping parameter γ the performance of the two types of damper are comparable.

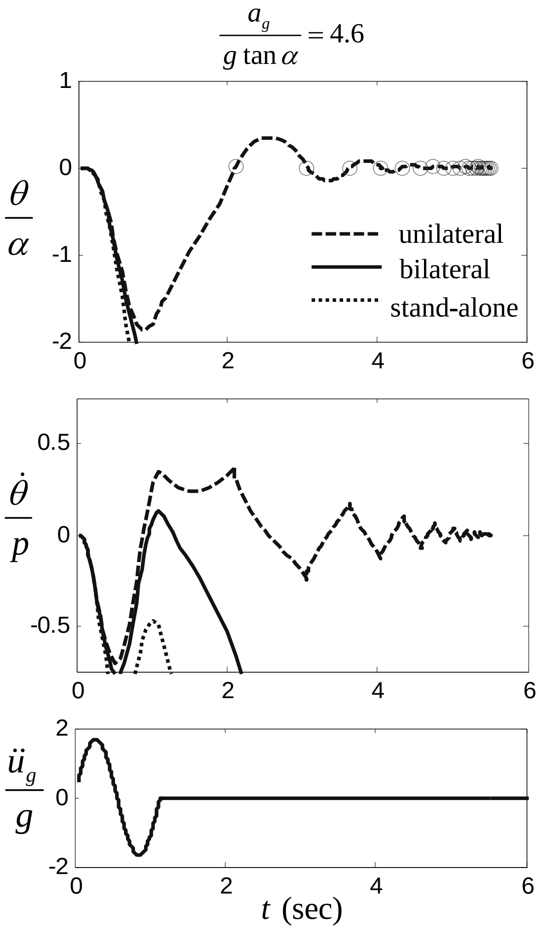

Figure 7: Rocking rotation (top) and angular velocity (middle) time-history of the rocking block ($\omega/p = 2.75$, $\eta = 0.825$) excited with a sine pulse (bottom). Point 3 of Figure 5.

3 DAMPING OF MASONRY ARCH ROCKING

The dynamics of masonry arches is a particular class of rocking problems. Under specific conditions outlined in DeJong et al. [8], Oppenheim [9] and Sinopoli [10], the dynamics of the masonry arch can be captured with a single degree of freedom model (SDOF). For single pulse dominated earthquake motions, an SDOF arch model was effective in predicting experimental collapse results for dry-stone masonry arches [8]. Further, arches are prolific in historic structures which stand vulnerable to seismic loading. Retrofit solutions which incorporate damping could potentially provide a viable solution for improving seismic safety.

As a first approach, the damping formulation presented in section 2 is here extended to masonry arches. It is assumed that linear viscous damping is added at hinging locations in the masonry arch, without considering a specific geometrical damper configuration.

The SDOF equation of motion can be derived from Hamilton's principle and Lagrange's equation:

$$\frac{\partial}{\partial t}\left(\frac{\partial T}{\partial \dot{\theta}}\right)-\frac{\partial T}{\partial \theta}+\frac{\partial V}{\partial \theta}=Q \tag{9}$$

The kinetic energy T and the potential energy V can be found in [9]. The generalized force expression is comprised of two parts: the inertial terms due to base excitation Q_g [9] and the additional damping forces Q_d. The total generalized force becomes $Q = Q_g + Q_d$.

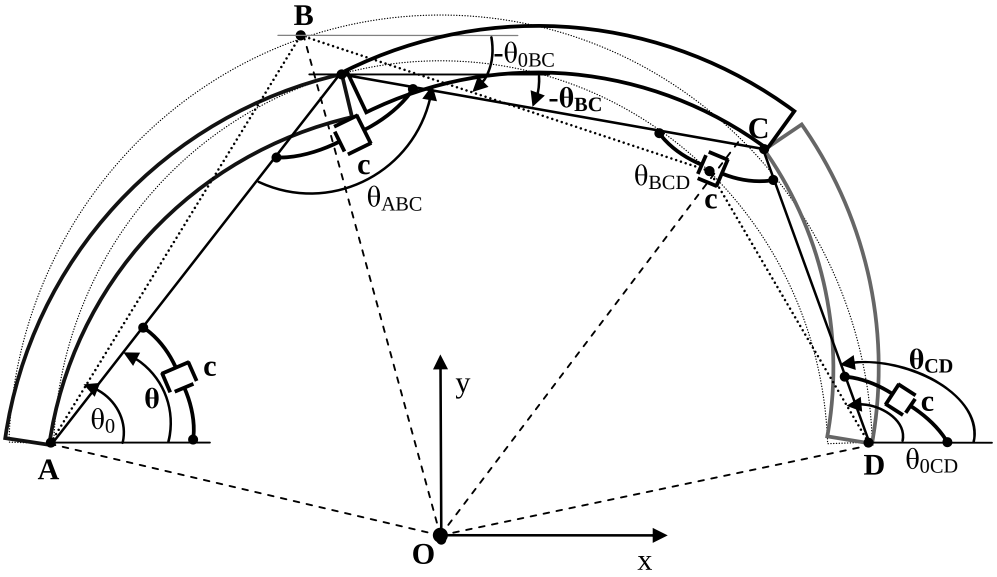

Figure 8: The four-link kinematical mechanism of a masonry arch, during rocking under base excitation. Additional linear viscous damping is assumed at hinging locations.

The damping force Q_d can be determined after calculating the work of the non-conservative forces δW_{nc} as:

$$\delta W_{nc}=Q\delta\theta=\left(Q_g+Q_d\right)\delta\theta \tag{10}$$

In particular:

$$\begin{aligned}
&Q_d\delta\theta=-c\cdot\dot{\theta}\delta\theta-c\cdot\dot{\theta}_{ABC}\left(\theta\right)\delta\theta_{ABC}-c\cdot\dot{\theta}_{BCD}\left(\theta\right)\delta\theta_{BCD}-c\cdot\dot{\theta}_{CD}\left(\theta\right)\delta\theta_{CD}=\\
&Q_d\delta\theta=-c\left[1+\left(\frac{\partial\theta_{BC}}{\partial\theta}(\theta)-1\right)^2+\left(\frac{\partial\theta_{CD}}{\partial\theta}(\theta)-\frac{\partial\theta_{BC}}{\partial\theta}(\theta)\right)^2+\left(\frac{\partial\theta_{CD}}{\partial\theta}(\theta)\right)^2\right]\dot{\theta}(t)\delta\theta\Rightarrow\\
&Q_d=-c\left[1+\left(\frac{\partial\theta_{BC}}{\partial\theta}(\theta)-1\right)^2+\left(\frac{\partial\theta_{CD}}{\partial\theta}(\theta)-\frac{\partial\theta_{BC}}{\partial\theta}(\theta)\right)^2+\left(\frac{\partial\theta_{CD}}{\partial\theta}(\theta)\right)^2\right]\dot{\theta}(t)
\end{aligned} \tag{11}$$

where θ_{AB}, θ_{ABC}, θ_{BCD}, θ_{CD} are the angles depicted in Figure 8, and c is the damping constant. After extensive algebra, the equation of motion can be written in the form:

$$M\left(\theta\right)R^3\ddot{\theta}+L\left(\theta\right)R^3\dot{\theta}^2+F\left(\theta\right)R^2g+D\left(\theta\right)R^2\dot{\theta}=P\left(\theta\right)R^2\ddot{x}_g \tag{12}$$

where $D(\theta)$ is the term introduced due to damping.

Figure 9 plots the time-history response of the masonry arch described in Oppenheim [9], to a simple sine ground motion with acceleration amplitude $a_g = 0.75\ g$ and duration $T_g = 1.0$ sec (Figure 9 bottom). The coefficient of restitution is taken as $\eta = 0.93$. The free masonry arch fails during rocking, while the addition of (linear) viscous damping at the hinging locations prevents failure.

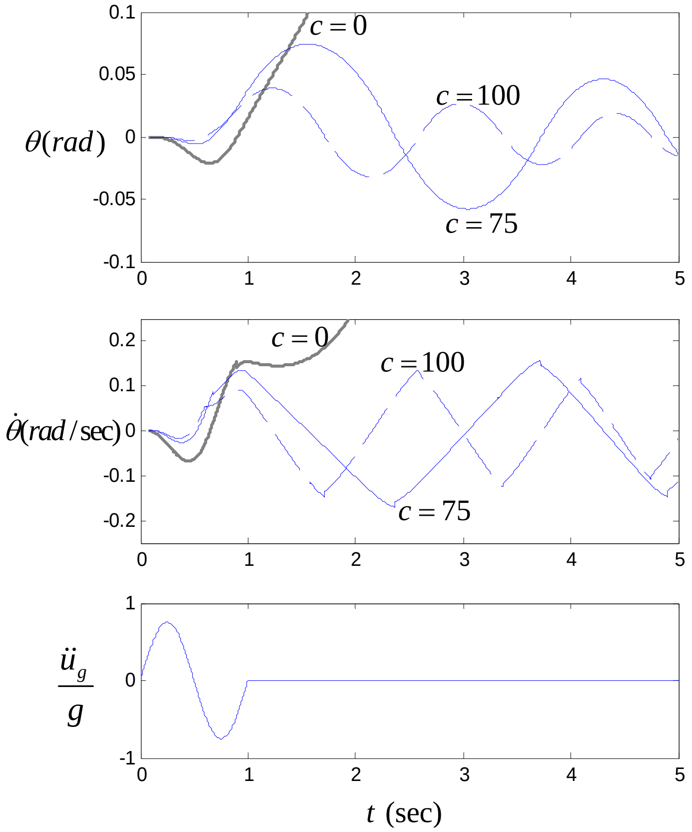

Figure 9: Rocking of the masonry arch under a sine pulse excitation (bottom). Rotation (top) and angular velocity (middle) about left hinge. While the free (c = 0) arch fails, the addition of damping (c = 75, 100 m sec kN).

4 CONCLUSIONS

In this paper the consequences of adding damping to rocking structures are investigated. Interestingly, while additional damping is already implemented in practice, to retrofit rocking structures, there is a lack of theoretical research on the subject.

The overturning envelopes of a rocking block retrofitted with bilateral and unilateral (activated only during uplift) linear viscous dampers, show a substantial enhancement of the behaviour. As a general rule, for a given damping level, the performance of the two types of damper are comparable. However, the unilateral damper delays the first appearance of overturning with impact and the first appearance of overturning without impact mode, but the area of overturning with impact is larger, compared to the pertinent bilateral damped block. Comparing with the alternative of anchoring the rocking system, the additional damping does not lead to counter effects where the behaviour of the retrofitted rocking system is actually worse than that of the stand-alone system.

The masonry arch exemplifies an alternate type of rocking structure for which added damping might be appropriate.

REFERENCES.

[1] S.J. Hogan. The many steady state responses of a rigid block under harmonic forcing. *Earthquake Engineering Structural Dynamics*, 19(7), 1057-1071, 1990

[2] R.H. Plaut. Fractal Behavior of an Asymmetric Rigid Block Overturning Due to Harmonic Motion of a Tilted Foundation. *Chaos Solitons & Fractals*. 7(2), 177-196, 1995

[3] J. Zhang, N. Makris. Rocking Response of Free-Standing Blocks under Cycloidal Pulses. *Journal Engineering Mechanics*. 127(5), 473, 2001

[4] M.J. DeJong. Seismic Assessment Strategies for Masonry Structures. PhD Thesis, Massachusetts Institute of Technology (MIT), 2009

[5] N. Makris, J. Zhang. Rocking Response of Anchored Blocks under Pulse-Type Motions. *Journal Engineering Mechanics*.127(5), 484, 2001.

[6] A. Di Egidio, A. Contento. Base isolation of slide-rocking non-symmetric rigid blocks under impulsive and seismic excitations. *Engineering Structures*. 31(11), 2723-2734, 2009.

[7] S. Pampanin. Controversial aspects in seismic assessment and retrofit of structures in modern times: understanding and implementing lessons from ancient heritage. *Bulletin of the New Zealand Society for Earthquake Engineering*. 39(2), 120-133, 2006.

[8] M.J. DeJong, L. De Lorenzis, S. Adams, J.A. Ochsendorf. Rocking Stability of Masonry Arches in Seismic Regions. *Earthquake Spectra*. 24(4), 847, 2008.

[9] I.J. Oppenheim. The masonry arch as a four-link mechanism under base motion. *Earthquake Engineering Structural Dynamics*. 21(11), 1005-1017, 1992.

[10] A. Sinopoli. A semi-analytical approach for the dynamics of the stone arch. *Proceedings of the ICE - Engineering and Computational Mechanics,* 63(3), 167-178, 2010.

COMPDYN 2011
III ECCOMAS Thematic Conference on
Computational Methods in Structural Dynamics and Earthquake Engineering
M. Papadrakakis, M. Fragiadakis, V. Plevris (eds.)
Corfu, Greece, 25–28 May 2011

SEISMIC ASSESSMENT OF 19TH CENTURY HERITAGE BUILDING THROUGH SIMULATION

Stylianos J. Pardalopoulos[1] **and Stavroula J. Pantazopoulou**[2]

[1] Demokritus University of Thrace
Dept. of Civil Engineering, 67100, Xanthi, Greece
spardalo@civil.duth.gr, pantaz@civil.duth.gr

Keywords: Assessment, Neoclassical Buildings, Deformed Shape, Modes.

Abstract. *In light of the increasing interest in rehabilitation of heritage neoclassical buildings of the 19th and 20th Century in Greece, often restricted by international treaties for non-invasiveness and reversibility of the intervention and given the practical requirements for the buildings' intended reuse, the present study focuses on the investigation of the parameters that affect the process of their seismic assessment through simulation. This class of load-bearing masonry buildings, which is also present in many European countries, are marked by carefully engineered configuration (layout in plan and elevation, systematic location of openings), that can lead to a specific type of seismic response. In the present paper, also investigated is the effect of horizontal diaphragm stiffness and connection to the walls; their contribution to dynamic response and appropriate methods of modelling are studied. Conclusions are calibrated based on comparative evaluation of the simulation results (obtained from detailed finite element modelling of a representative historic building located in the seismically active region of Thessaloniki) with the extent of actual damage patterns which have been observed due to strong earthquakes that have occurred during the buildings' lifetime. The paper also presents a relatively simple analysis procedure that for this special class of buildings can produce very dependable results compared to those obtained from time-consuming dynamic analyses, in a much easier and fast way.*

1 INTRODUCTION

Rehabilitation and retrofitting of historical and heritage structures of the 19th and 20th Century is an issue of paramount importance in countries with built cultural heritage that also suffer from high seismicity, such as the countries of the eastern Mediterranean basin. In Greece a significant number of neoclassical buildings were constructed starting immediately after the war of independence and continuing over the last two centuries. These are concentrated mainly in significant urban areas and are considered today an inseparable part of the country's inventory of historical buildings. Over the several decades of their service life, many of those buildings have undergone severe shaking during the strong earthquakes that occasionally affect the urban areas of this highly active seismic region. Yet, even today they remain in good condition, being operational in many cases. Due to those buildings' historical importance as examples of an architectural school of thought, an increasing interest for their rehabilitation has recently emerged, often regulated by international treaties for noninvasiveness and reversibility of the intervention combined with the practical requirements for the buildings' modern day intended reuse.

In the effort to assess the residual strength of neoclassical buildings, reduced from a vague undetermined value which represents the initial state and in designing the appropriate retrofit measures for upgrading, sophisticated finite element analysis programs combined with powerful computing means have become a valuable tool for Structural Engineers. Yet, despite the capabilities which can derive from the use of modern technology, the obtained results are not necessarily reliable as they often fail to recognize or reproduce important structural phenomena in the modeling process or due to lack of convergence owing to inherent limitations of the analysis algorithms. As a result, in the process of seismic assessment of historic or heritage buildings of the 19th and 20th Century the residual strength of the corresponding structure can easily be underestimated, which could lead to rather invasive choices of rehabilitation methods that can alter or destroy the unique historical or architectural features of the building in the interest of perceived needs for strength increase of the structure.

The objective of this paper is to highlight the special modeling procedures that are needed in the process of simulation of 19th and 20th century neoclassical buildings. This special class of buildings, which is similar to many historical and heritage buildings across Europe, possess special characteristics due to their design and structural configuration, whose oversight during their modeling procedure could lead to serious misinterpretation of their seismic response. Also presented is a simple and rapid analysis procedure, based on the modal characteristics of this class of buildings, which can lead to as dependable estimates as the results of complicated and time-consuming dynamic analysis.

2 OVERVIEW OF THE SPECIAL CHARACTERISTICS OF THE NEOCLASSICAL BUILDINGS DUE TO THEIR DESIGN AND CONSTRUCTION

Seismic assessment of neoclassical buildings constructed in the 19th and 20th Century is a much more demanding procedure than seismic assessment of reinforced concrete structures in that the structural system in masonry buildings is less clearly defined, whereas a profound knowledge of the design principles and the construction practices of that era is required in modeling the individual structural components to dependably reproduce the mechanics of member behavior.

Knowledge of the designing principles of the 19th and 20th Century is essential for interpretation of the dynamic response of this class of buildings. Architects of the era, being influenced by the shape and form of ancient Greek monuments, were designing neoclassical buildings that were characterized by symmetry in plan and in height, loaded with architectural features and elements inspired from archaic forms (for example colonnades, reliefs in gables, and carefully chosen aspect ratios). In the cases of single-unit buildings, the structure was designed in plan so as to have a simple geometrical shape, rectangular or prismatic, whereas multi-unit buildings were designed to have a system-plan organized in the form of an ***H*** or a ***T***, with courts located in the recesses of these shapes so that the overall plan could be thought to form a concave prism (Fig. 1). In every case, the rooms of the building were symmetrically arranged in both sides of a main corridor that was usually spanning from one end of the building to the other. Side views of the building were designed to have windows and doors symmetrically spaced with respect to a vertical axis that was intersecting the plan symmetry axis. Furthermore, the area occupied by openings (i.e. windows and doors) was gradually increased from the ground level to the top of the building (resulting to the corresponding decrease of the area of walls) to encourage a flexural-type behavior for the building in lateral vibration. Thus, buildings of that era are expected to develop favorable dynamic response during an earthquake, such as the absence of torsional effects in plan and a favorable drift distribution along the building height.

HELLENIC PARLIAMENT (1847) – ATHENS

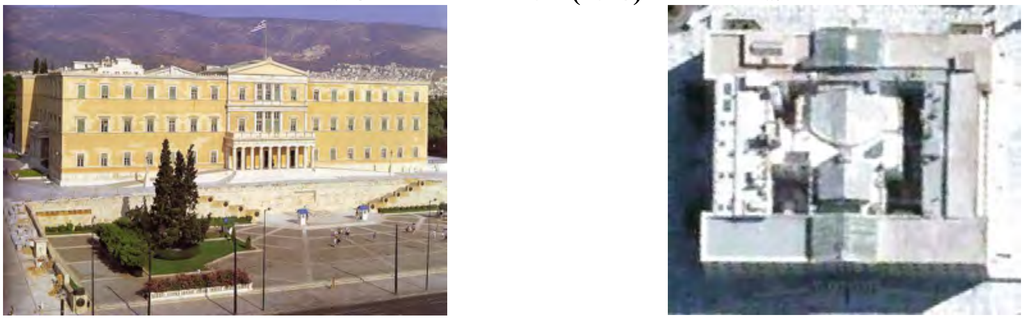

Front View [1] Plan View

MINISTRY OF MACEDONIA AND THRACE (1891) – THESSALONIKI

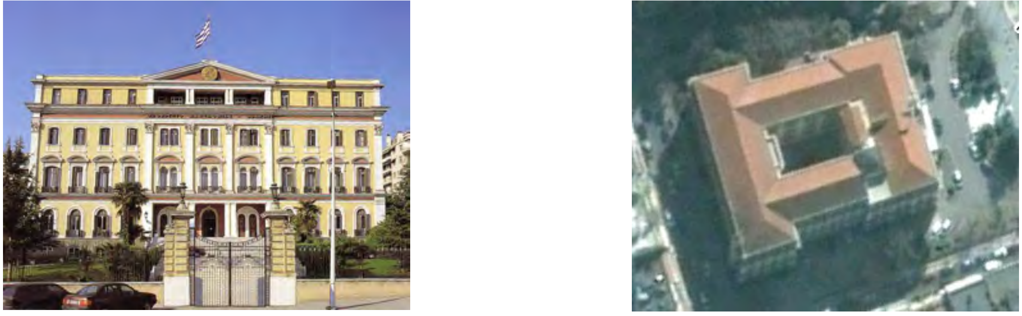

Front View [1] Plan View

PAPAFEIO ORPHANAGE (1903) – THESSALONIKI

Rear View Plan View

Figure 1: Typical monumental neoclassical buildings built in Greece during the 19th and 20th century.

The construction practice in the 19th and 20th Century was also governed by empirical principles [2 - 6], the consideration of which is essential for proper modeling of the behavioral mechanisms that are developed in neoclassical buildings during an earthquake. Starting from the foundations, different techniques were utilized according to the compressive strength of the foundation soil, in the site where the building was to be constructed. Soft soils were reinforced by driving into the ground in arbitrary manner wooden piles up to 1.30m in length, having diameters that varied from 0.15m to 0.20m, and by filling the space between the piles with gravel. Until the end of the 1860s, grids made by wooden boards of cross sectional dimensions of 80mm x 320mm, closely spaced, were utilized in medium compressed soils in order to uniformly distribute the compressive stresses of the building's walls to a wider area. In stiff soils, wooden beam grids with cross sections of 170mm up to 200mm square were utilized instead of wooden boards. Those beams were spaced at a distance which ranged from 0.45m to 1.00m and the resulting in-between space was filled with compressed gravel. When the soil stability was secured, foundation walls were constructed. Those walls were made of stone and their width was equal or greater than the width of the walls of the first storey of the building. In buildings without a basement, the depth of the foundation walls was equal to 1/7 up to 1/6 of the total building height, whereas in buildings with a basement foundation walls extended to a depth of 1.00m up to 1.20m below the basement floor. During modeling it would be wise to assume that the wooden elements (piles, boards and beams) may have undergone some extent of disintegration after those many decades of contact with the soil or the environment and therefore it would be pertinent to model contacts (structure to soil, timber elements to structure, etc.) through use of proper modeling tools (springs, etc) particularly in representing the stiffness of the foundation of such buildings.

The vertical load-resisting elements of neoclassical buildings were walls comprising stones or bricks. Walls of this type had a significantly larger thickness as compared to the infill walls of reinforced concrete buildings (ranging from 0.30m to 1.20m), whereas this thickness was gradually reduced starting from the ground floor to the top of the building. Stone walls were usually three tier walls, having an exterior facade built of large, regularly-shaped rectangular stone blocks, whereas the in-between space was filled with smaller stones of arbitrary geometry, soil and crushed bricks or tiles. To secure the uniform distribution of gravity loads to all of the three vertical layers and to avoid lateral separation of the tiers, horizontal brick lacing layers were constructed for each meter of stone wall height or so and across the entire wall thickness. In the case of brick walls, solid bricks (i.e. without holes) were mostly used. In some cases of buildings with several storeys, the brick walls of the upper storeys were made of bricks with holes (lighter), in order to effect a reduction in the magnitude of the structure's self weight in the upper storeys. Finally, to secure that crossing walls would not separate during an earthquake, timber ties comprising two longitudinal timber beams were placed along the wall's length and anchored at the external face of the crossing walls, forming a passive confining arrangement for the infilled masonry blocks. After the introduction of iron in the construction practice (in the end of the 1860s) timber ties were replaced by iron blades. Keeping in mind the construction practice of the walls of the neoclassical buildings, it is essential to model the different types of strengths of the walls. Also note that analyses procedures referring to combinations of actions in ultimate limit state design of modern buildings which have relatively small weight compared to their total volume (i.e. 1.35g) are inappropriate for neoclassical buildings, as they impose unrealistically large loads and masses to the structure.

Finally, the floor systems of neoclassical buildings built before the 1870s often had timber beams as structural elements, which were spaced at a distance of 0.60m up to 1.00m, serving to transfer the loads from the floor to the surrounding walls. When the wall thickness in two successive storeys remained constant, the timber beams of the floor between those two storeys were seated in pigeon-holes in the walls. In cases where the wall thickness in the storey above a floor level was reduced by setback of the interior façade of the wall, then the timber beams of the floor were nailed on beams parallel to the walls whose purpose was to uniformly distribute the floor loads along the length of the walls. After the 1860s the timber beams were replaced by iron elements. Two different versions of floors with iron beams were constructed. In the first case, secondary timber beams were placed between successive iron beams, to provide resistance to lateral torsional buckling in order to secure the constant spacing between parallel iron beams and also to allow timber floor planks to be supported by nailing. The second and most usual type of a floor with primary iron beams comprised brick arches spanning between parallel iron beams. Thus, consideration of the mechanisms developed in the structural system of this class of buildings, owing to the different types of floor configuration (friction between the timber beams and the walls, differential movement between the brick arches and the iron beams, etc.), is of paramount importance in the modeling procedure, as they can influence the analyses results to a significant extent.

3 EXAMPLE OF SIMULATING AND ANALYZING A NEOCLASSICAL BUILDING

To investigate the sensitivity of the analysis results obtained from simulation of neoclassical buildings with models comprising the various types of mechanisms that were discussed in the previous paragraph, a series of dynamic analyses have been performed to different types of models of a neoclassical building located in the centre of Thessaloniki. This building was constructed in 1893 in order to house the first Hellenic high school of Thessaloniki, according to the designs of Ernest Chiller, as those modified of the architects Kabanakis and Kokkinakis (Fig. 2); since its construction, the building had been continuously in operation as a school until the summer of 1978, when it suffered damage by a strong earthquake of 6.5 M_w on the Richter scale that struck the city of Thessaloniki. The epicenter of the ground motion was North-East of Thessaloniki, in the Volvi lake region.

3.1 Description of the Structural System

The neoclassical building considered in the analyses is a two-storey building with a basement and a roof, located in the centre of the city of Thessaloniki, Greece. The building has a 20.83m x 16.05m plan, symmetrical with respect to a main corridor that is spanning from the northern side of the building to the southern, whereas the external building height, including the roof, is 14.20m. The first storey comprises six rooms, symmetrically located in both sides of the storey's corridor. The second storey was originally constructed to have four halls, one big hall at each side of the corridor spanning from the front view of the building (north view) to the south and two smaller ones in the southern part of the plan. Over the years, the two big halls were divided, the eastern one with the addition of a 0.15m thick brick wall and the western one with the addition of a wooden panel. The basement comprises five rooms that were used as storage rooms and sanitary facilities, after the addition of miscellaneous infill brick walls. Floors were connected with a wooden stair in the southern part of the main corridor. The walls of the basement are made of stone, having a thickness equal to 0.75m in the perimeter of the building and 0.65m in the inner plan. Walls of the first and the second storey were built of solid brick. Perimetrical walls have 0.50m width, whereas internal walls 0.40m. Floors of the first and the second storey were made of double T iron beams having a 60mm x 180mm cross section, spaced at 0.70m along the small sides of the rooms and the corridors (i.e. having an E-W orientation over the building's corridors and a N-S orientation over the building's halls), whereas brick-arches spanning in the transverse direction between successive iron beams were encased between the upper and lower flanges of the double T beams. The total thickness of building's floors (including the finishing) is 0.33m at the location of the iron beams and 0.25m at the highest point of the arches. The last storey is covered by a roof made of timber trusses spanning in the east to west direction of the building.

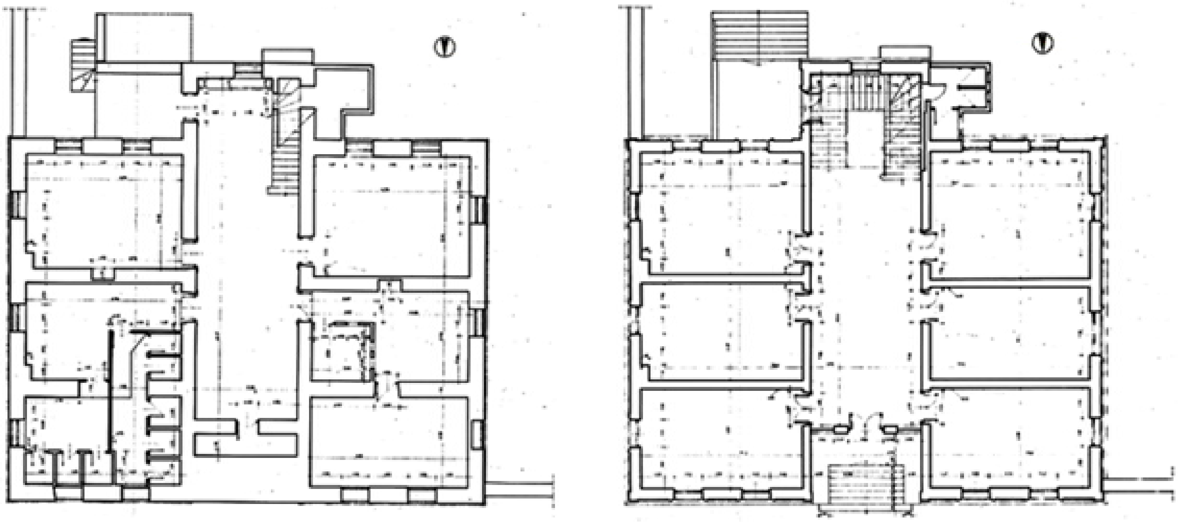

Basement plan

1st Storey plan

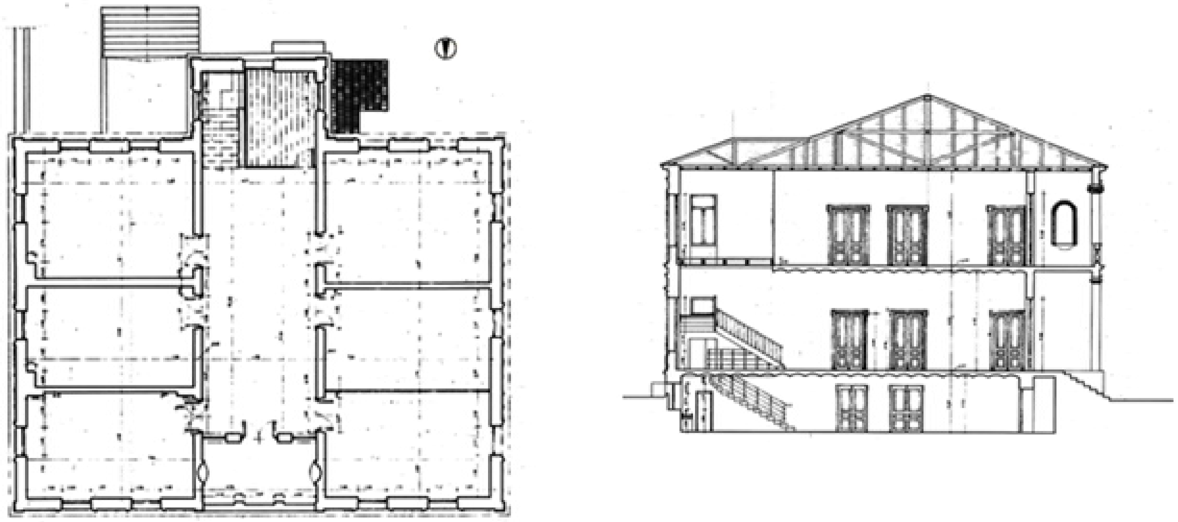

2nd Storey plan

Section along the building's corridors, facing West

Figure 2: Plan and section views of the building used for the analyses.

3.2 Description of he Structural Modes Used in the F.E. Study

To examine the degree of influence of the different mechanisms that are developed in the structural system of the building on its overall seismic response, parametric dynamic analyses were carried out using the recorded accelerations of the 1978 earthquake; results were compared with the observed damage patterns reported in post-earthquake reconnaissance of the building. Simulation and analyses were carried out using a finite element analysis program [7]. Building walls were modelled using four-node shell elements, capable of supporting forces and moments (6 d.o.f. per node). In the simulation possess, the wall thickness was reduced by 50mm from the measured dimensions in order to eliminate the plaster thickness on both sides of the walls. Thus, shell elements simulating the basement walls were assigned a thickness of

0.70m and 0.60m in the cases of exterior and interior walls respectively, whereas upper walls were modelled using a thickness of 0.45m and 0.35m for the exterior and interior brick walls of the first and the second floor. Along the basement walls, above and below the basement windows, two zones of shell elements accounting for brick lacing were used. Infill walls in the location of internal doors between the southern and the central storage rooms of the basement, the northern basement window of the west view of the building and between the northern and the central room at the east side of the corridor at the second storey were simulated using shell elements of 0.15m thickness, accounting for walls made of voided-bricks, since those additions were introduced in 1975. Timber panel divisions were omitted (in the northern and the central room at the west side of the corridor of the second floor). To investigate the degree of alteration of the building's seismic response due to the floors and the roof configuration, two model buildings were produced, *Model A* and *Model B*.

In *Model A*, the 1st and the 2nd storey floors were simulated utilizing linear elements, fixed at their ends to the shell elements of each room's wall, in order to account for the iron beams, whereas the brick arches were modelled as shell elements having a 0.16m thickness (i.e. the average thickness of the structural system of each of the two floors), accounting for voided-bricks, fixed to various points of the surrounding walls and the iron beams. Linear elements were used at the roof level, accounting for the timber beams having a 100mm square cross section over the perimeter walls and the two sides of the corridor, which were considered to be fixed at the nodes of the wall shell elements. Also included were linear elements parallel to the E-S direction of the plan, spaced at 0.60m and fixed at the nodes of the timber beams over the storey walls. These elements had the same cross section as the timber beams over the walls and modelled the horizontal members of the roof trusses.

In *Model B* (Fig. 3), gap elements were added between the nodes of the shell elements that represented the brick arches and the corresponding nodes of the iron beams, replacing the fixity condition for the same contact detail in *Model A*. Thus, gap elements were intended to model the separation between the brick arches and the iron beams when in tension whereas they were considered rigid in compression (perfect contact). Also added in *Model B* were springs between the nodes of the wall elements and the timber beams over the wall, which were meant to account for friction between the wall and the timber beams. Spring-response was described by a multi-linear force-displacement relationship (Fig. 3), that was calculated according with the development capacity over the beams' contact surfaces when accounting for friction with the building walls. In both models, the response of the shell and the linear elements was considered elastic. Modulus of elasticity of stone and bricks was considered 1000 times the value of the corresponding compressive strength, f_k; for stone f_k = 5.5 MPa, for solid bricks f_k = 4.0 MPa and for voided bricks f_k = 1.5 MPa. In the case of frame (iron and timber) elements, the modulus of elasticity was taken equal to 150 GPa for the iron beams, 10 GPa for timber in the longitudinal direction of the beams and 1GPa in the other two sectional directions. In all cases, the building load was taken equal to the self weight of the building and no variable load was considered, as during the earthquake (8pm of June 20) the school was not operational. Material density was 28.5 kN/m^3 for stone, 18 kN/m^3 for solid bricks and 14kN/m^3 for voided bricks. A roof weight equal to 1.5 kN/m^2 was assumed, uniformly distributed along the linear elements of the roof trusses according to their tributary area.

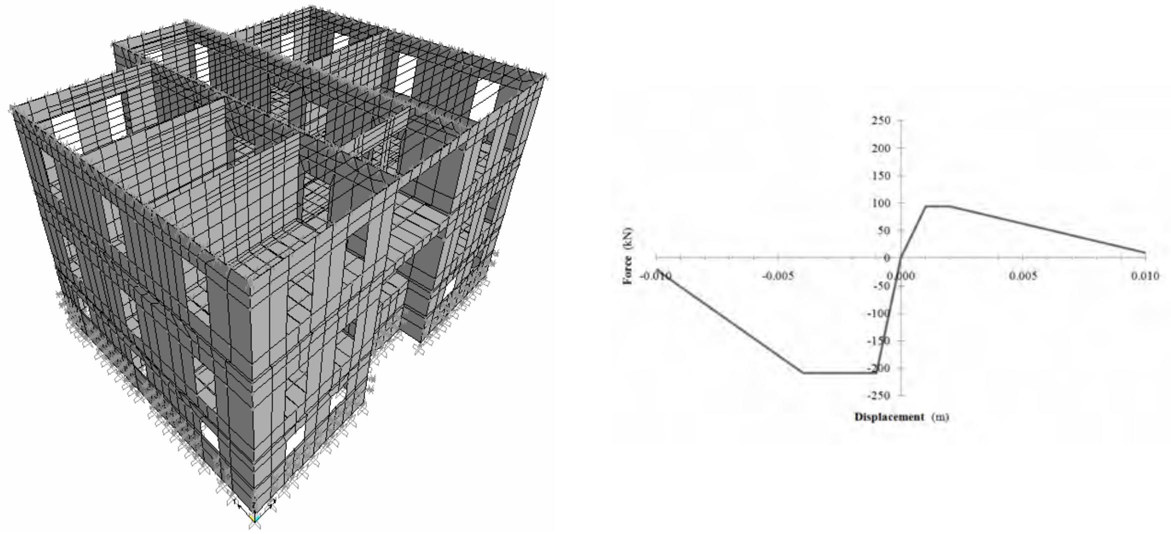

3D model view

Force-displacement relationship used in springs

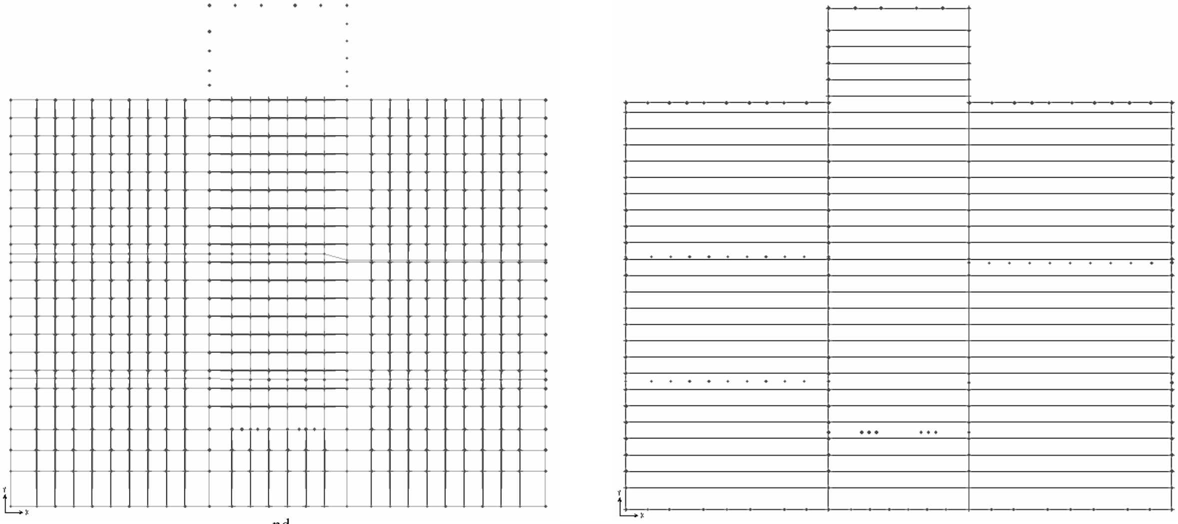

Plan of the 2^{nd} storey floor

Plan of the roof

Figure 3: Model B; Three-dimensional view of the model, plan views of the 2^{nd} storey floor, the roof and force-displacement relationship used in the friction springs that connect the timber beams with the walls of the second storey.

Parametric modal and dynamic analyses were carried out on both models. To determine the free vibration mode shapes and the natural periods, *T*, of the building, both models were subjected to Ritz-vector modal analyses, to account for the spatial distribution of the dynamic loading. Also performed were dynamic time-history analyses according to the earthquake acceleration recordings of the 1978 Thessaloniki earthquake [8]. Response spectra of the accelerations used in the analyses with respect to the building's principal directions in plan, calculated when assuming 5% damping, are presented in Fig. 4. Masses considered in the Modal and Time-History analyses were automatically calculated by the program, by multiplying each element (shell or linear) volume by their material volume mass respectively.

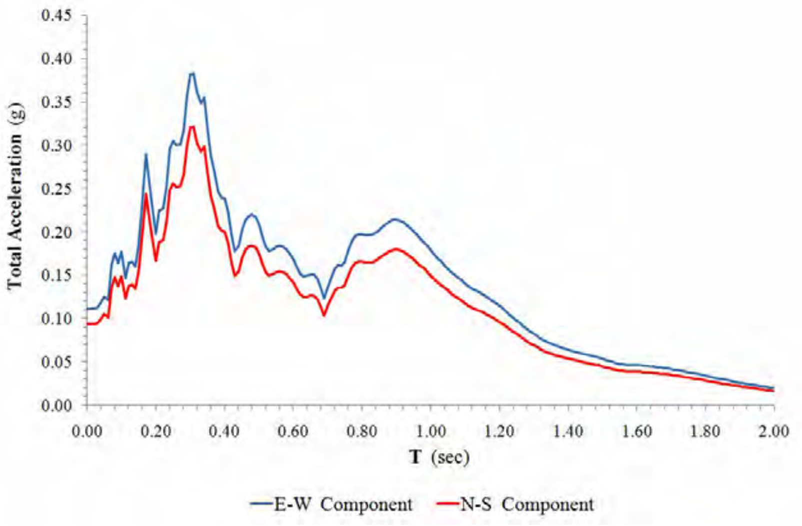

Figure 4: Elastic acceleration response spectra of the two components of the 1978 Thessaloniki earthquake that were used in the model analyses, calculated for 5% damping. The two components resulted from the same earthquake acceleration record, by projecting it to the two primary axes of the building's plan orientation.

From the results of the analyses of *Model A* and *Model B*, the following observations concerning modelling of neoclassical buildings for the purposes of seismic assessment are extracted. The first observation concerns the developed stresses in the shell elements of both models. Figure 5 presents the shear stress distribution across the walls and the floors of the two models as calculated from Time-History analyses in the time interval of the building's maximum seismic response in terms of roof displacement. As observed, the introduction of gap elements in the first and second storey floors as well as the use of friction springs in the connection of the timber beams with the second storey walls resulted in a significant reduction of the developed shear stresses of floors from *Model B* at about 50% in the first and 40% in the second floor as compared to the same shear stresses from *Model A*. Also altered were the stress distributions across the buildings floors, with *Model B* presenting a more uniform shear stress distribution than *Model A*. The same conclusions about the comparison between the magnitude of the developed stresses of *Model A* and *Model B* also apply in the developed shear stresses at the walls of the buildings, with the spread between those values being reduced to about 30%. Figure 6 illustrates the developed shear stresses on the different facades of the two models at the time of the building's maximum seismic response, together with the actual damage patterns of the building after the 1978 earthquake. From this comparison it is concluded that *Model B* correlates better with the actual damage patterns of the building than *Model A*.

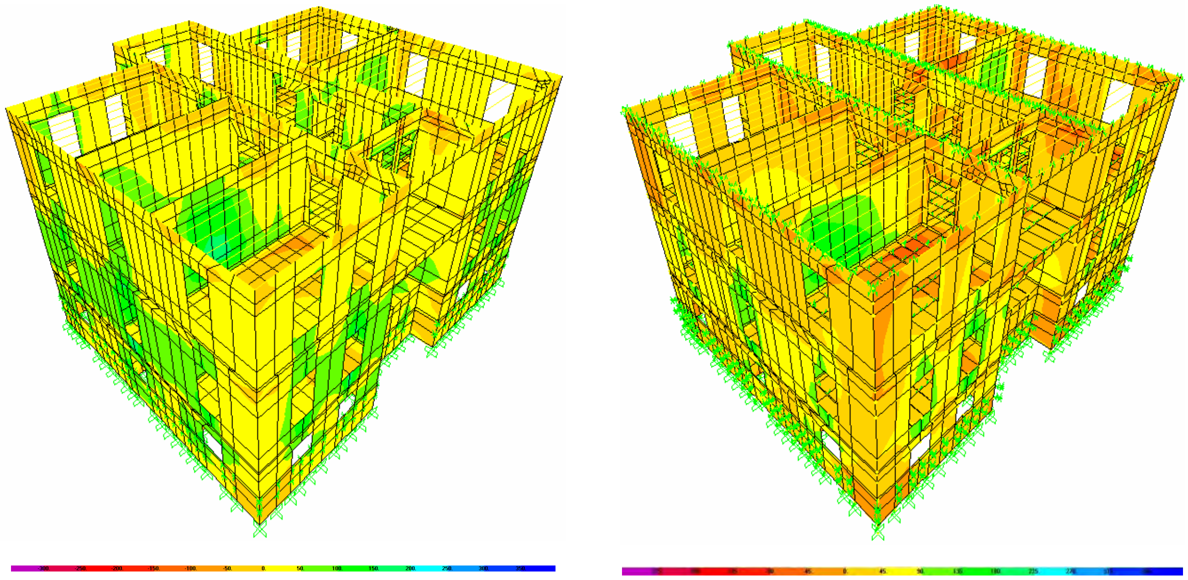

Model A – 3D view of the building

Model B – 3D view of the building

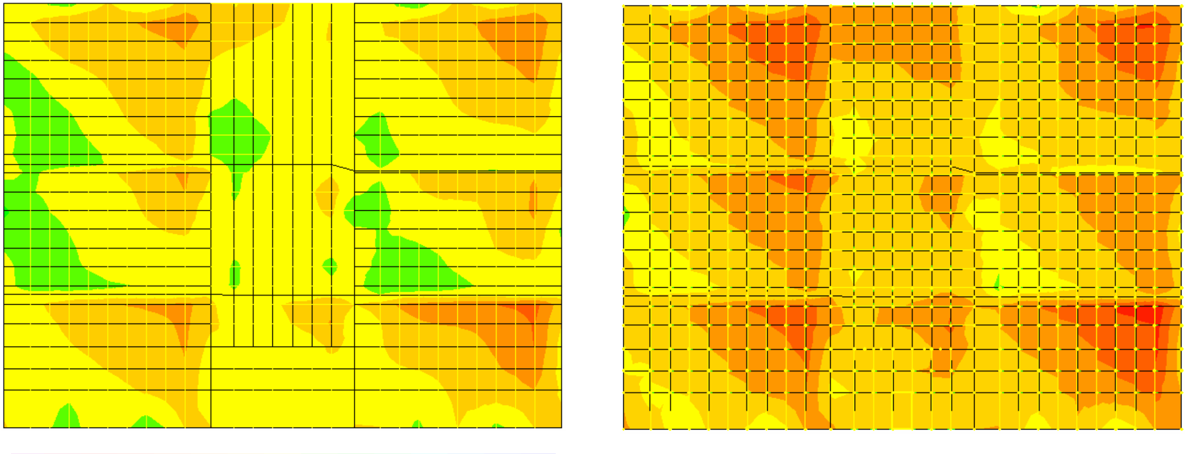

Model A – 2nd storey plan view

Model B – 2nd storey plan view

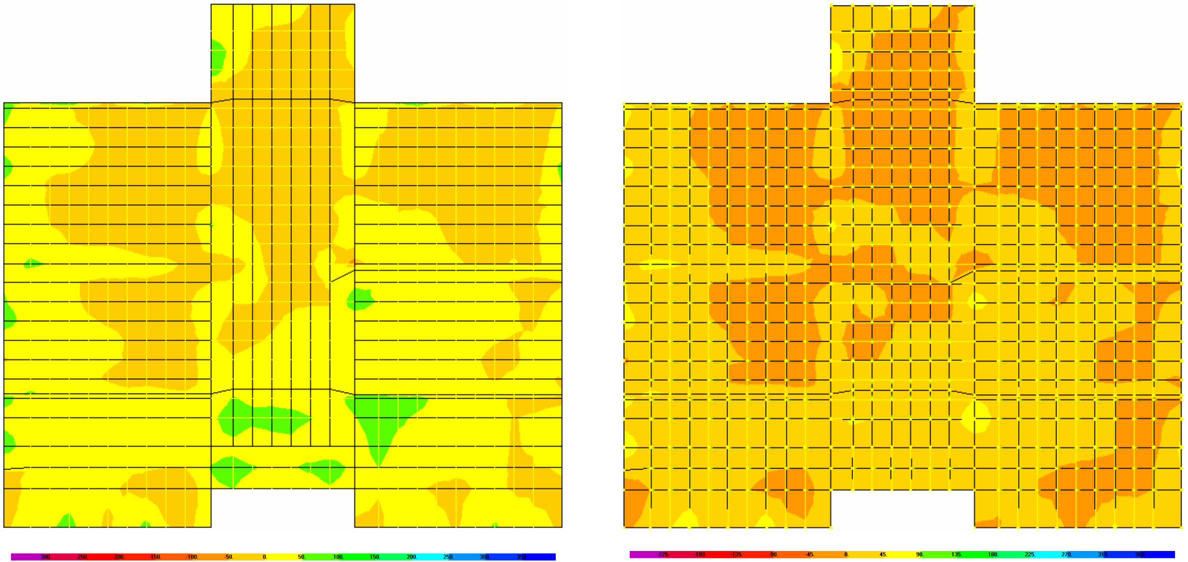

Model A – 1st storey plan view

Model B – 1st storey plan view

Figure 5: Shear stress distribution over the shell elements of Model A and Model B, as calculated at the time of the building's maximum seismic response from time-history analyses.

NORTH VIEW

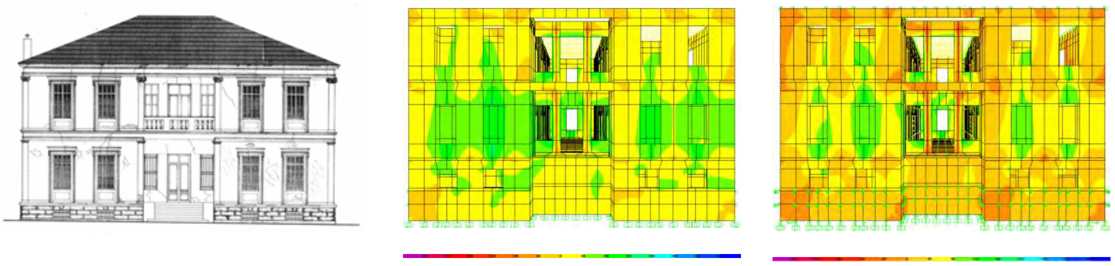

Damage pattern after the earthquake

Shear stresses in *Model A* at time of max. response

Shear stresses in *Model B* at time of max. response

EAST VIEW

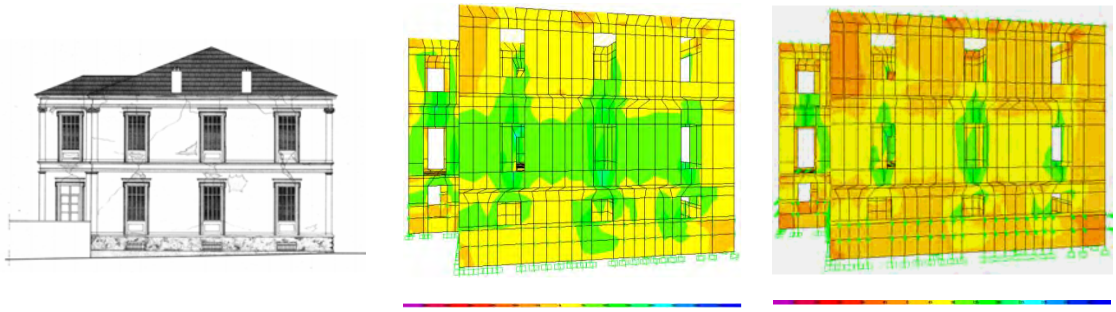

Damage pattern after the earthquake

Shear stresses in *Model A* at time of max. response

Shear stresses in *Model B* at time of max. response

SOUTH VIEW

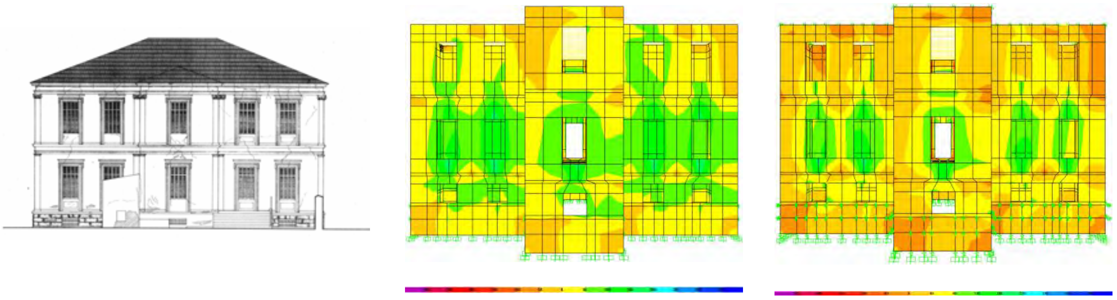

Damage pattern after the earthquake

Shear stresses in *Model A* at time of max. response

Shear stresses in *Model B* at time of max. response

WEST VIEW

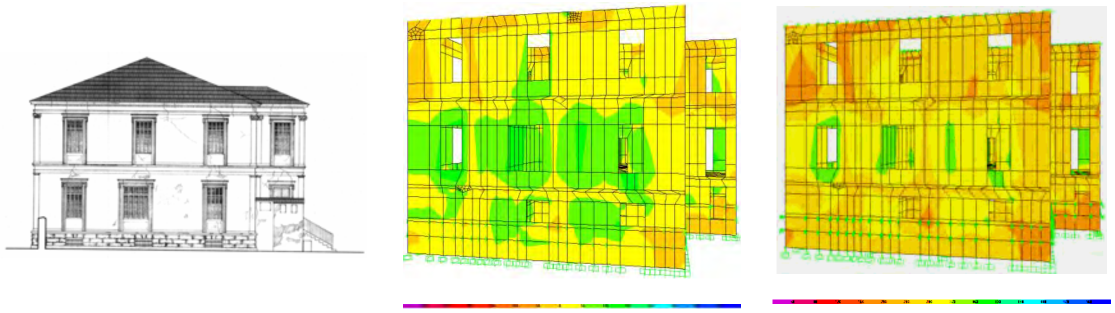

Damage pattern after the earthquake

Shear stresses in *Model A* at time of max. response

Shear stresses in *Model B* at time of max. response

Figure 6: Comparison between the damage patterns of the building after the 1978 Thessaloniki earthquake and the developed shear stresses in *Model A* and *Model B* at the time of the building's maximum seismic response in terms of roof displacement.

Modal analysis conducted on the buildings led to a large number of translational modes with closely spaced periods. This led to a group of very similar modes each having a small participation factor, leading to the requirement of including several modes in the calculation in order to mobilize the structural mass. Here an alternative approach was used to approximate the fundamental mode of vibration of the structure, by subjecting it to a notional gravitational field in the direction of lateral translation (i.e. along the longitudinal and transverse directions of the plan geometry). In light of the fact that gravitational forces are proportional to the mass of the structure, and the restoring forces in this situation are equilibrating these mass-proportional inertia forces, the deflected shape of the structure obtained from this solution is thought to be the closest approximation to the translational mode of vibration since the associated natural frequency would result from the ratio of the work-equivalent inertia force and restoring force [9]. The mass associated with this shape obtained for *Model A* of the building was estimated at 95% of the total mass, a result that suggests a fundamental inconsistency between the modal analysis and the mode approximation method; this inconsistency, which is basically owing to the discretization approach used with the finite element model, is most likely responsible for the apparently false notion that the seismic response of the neoclassical building is governed by many mode shapes with relatively small mass participation factor.

This point is documented in Figure 7 which illustrates the spread of the mass participation factors for the first 100 modes of *Model A* and *Model B* in each of the buildings' principal directions, as calculated from the results of Ritz modal analyses. Also presented are the mass participation factors in each of the corresponding directions, derived from the deformed shape of the two models after lateral loading with their self weight (a horizontally oriented gravitational field). Note that the sum of the mass participation factors of the first 100 modes of *Model A* equals to 61.4% in E-W direction and 68.6% in N-S direction, whereas the corresponding mass participation from lateral loading with the building's weight is 95.0% and 97.1% respectively. Dispersion of the results is greater between the modal analysis mass participation factor, whereas mass participation obtained from lateral loading is even greater in *Model B*; 52.8% vs. 95.2% in E-W direction and 55.9% vs. 96.9% in N-S direction respectively.

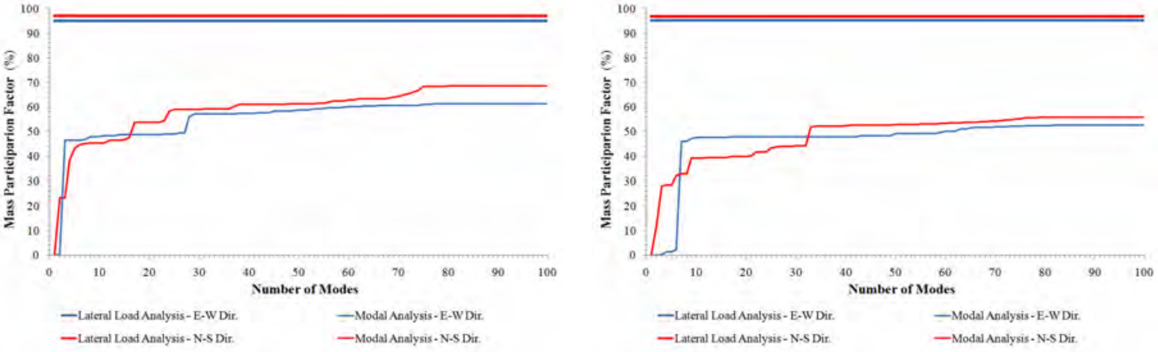

Model A *Model B*

Figure 7: Comparison between the mass participation factor for the first 100 modes of *Model A* and *Model B* obtained from Modal Analyses, and Mass participation calculated from the deflected shape when models are subjected to a horizontal gravitational field along the E-W and N-S plan directions.

Based on resent research [10] which indicated that the displacement response distribution of a structure matches very well with the shape of the principal translational mode in the corresponding direction if the mass participation factor exceeds the value of 80%, a rapid ap-

proximate method for determining the maximum seismic response of neoclassical buildings is introduced. According to this procedure, the seismic response of a neoclassical building, in terms of developed stresses or deformed shape, can be determined in a two step procedure:
(a) First a simple static analysis is performed, where the model is loaded laterally with its own self weight acting in each of the two principal directions of the plan.
(b) In each direction of the building's plan, the corresponding quantity which is investigated (nodal displacements and/or developed elements stresses/forces) is multiplied by a factor which equals to the ratio of the spectral relative displacement normalized by the peak displacement throughout the building obtained from the gravitational analysis.
Figure 8 plots the comparison between the displacement profiles obtained from time history analysis and from the proposed spectrum-based procedure for the east corner of the North façade of the building. Note the excellent correlation between the two procedures.

Model A

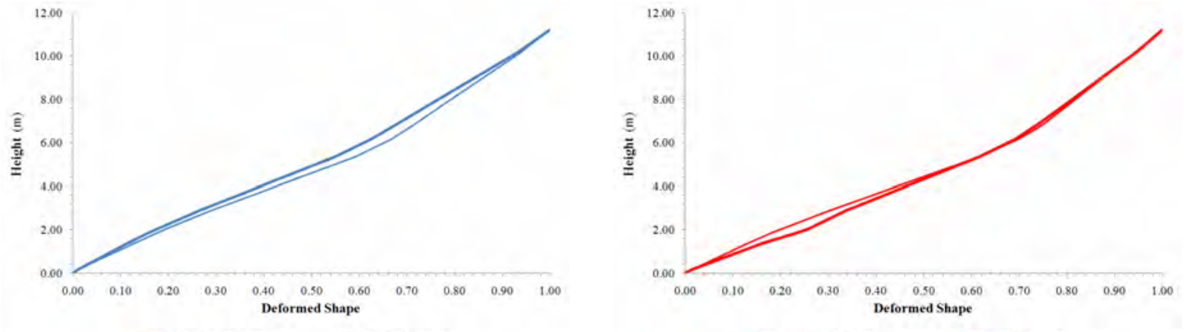

Deformed shapes in the E-W direction

Deformed shapes in the N-S direction

Model B

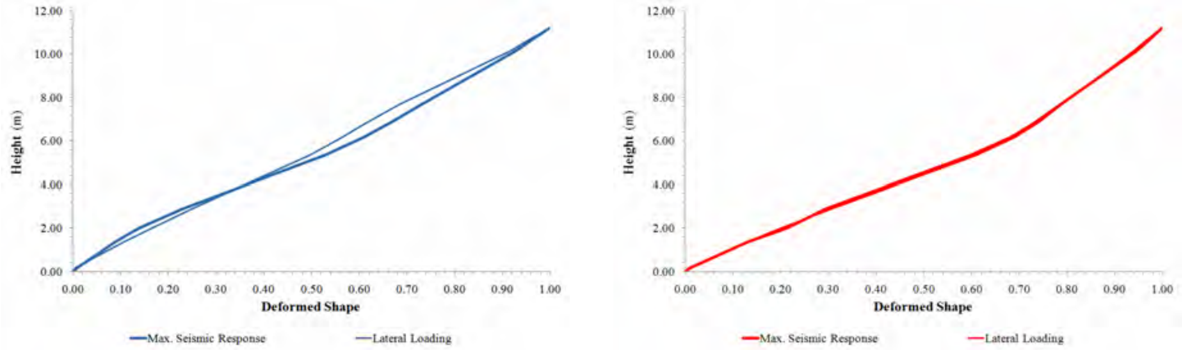

Deformed shapes in the E-W direction

Deformed shapes in the N-S direction

Figure 8: Deformed shapes of the east corner of the building's north face; Comparison between the shapes from the time-history analyses at the time of the building's maximum seismic response and the shapes from the lateral loading of the building with its self weight.

Figure 8 illustrates the displacement profiles of the east corner of the north face of *Model A* and *Model B*, for the cases of the maximum seismic response according to time-history analyses, and the deformed shape as calculated by the lateral loading of the models with their self weight. The correlation of these shapes is very good, especially in the N-S direction of the building.

In Fig. 9, comparison of the shear stress distribution along the shell elements of the building's north view between the cases examined, i.e. the results from time history analysis (at the time of peak response) against the results from the proposed spectrum-based approach is illustrated for *Model A* and *Model B*. As in the case of the comparison of the models' deformed shapes, the correlation between the shear stresses from the two analysis methods is very good.

Model A

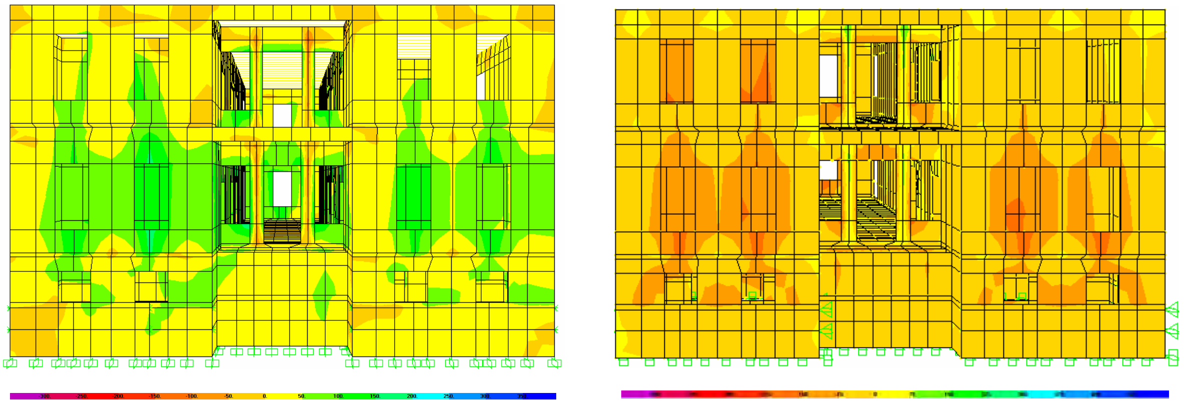

Shear stress distribution obtained from time-history analysis

Shear stress distribution obtained from lateral loading static analysis

Model B

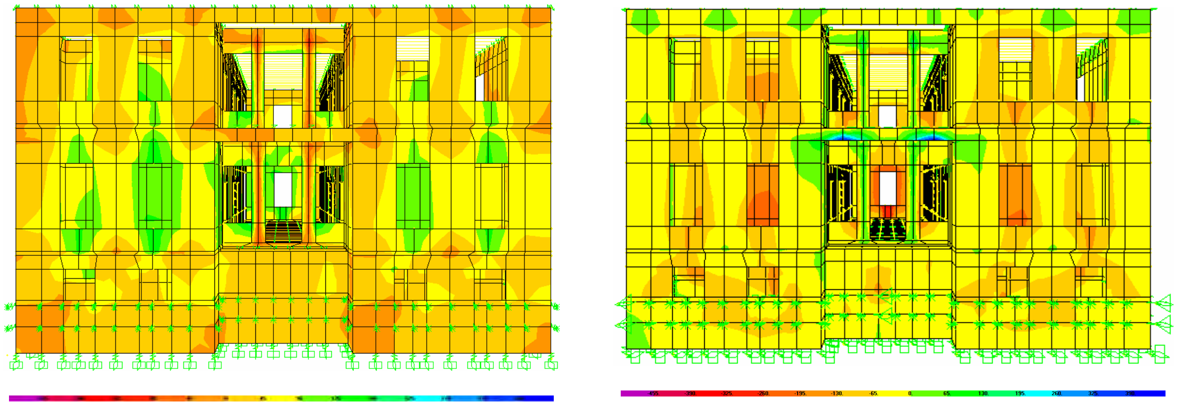

Shear stress distribution obtained from time-history analysis

Shear stress distribution obtained from lateral loading static analysis

Figure 9: Shear stress distribution at the north face of the building at the time of peak seismic response; Comparison between the results obtained from time-history analyses and static analyses with lateral loading proportional to the building's weight (a horizontal gravitational field).

4 CONCLUSIONS

Seismic assessment of neoclassical buildings of the 19th and 20th century through simulation is a very demanding task. Profound knowledge of the design and construction practices of 19th and 20th Century is essential so that the structural engineer can simulate accordingly the mechanisms that can be developed in this class of structures during an earthquake. By neglecting detailed consideration of the contact effects at the points of interaction between different materials can lead to serious overestimation of demands and a commensurate underestimation of the residual strength of the building, guiding towards severe rehabilitation methods that may alter or destroy the unique historical or architectural characteristics of the building. In the present study an example of modeling of an actual neoclassical building located in the centre of Thessaloniki, Greece, which suffered damages from the 1978 earthquake was presented, were two different types of modeling the horizontal diaphragm stiffness and the diaphragm connection to the walls were tested. According to the analyses results, the difference in the magnitude of shear stresses developed in the two models was in the range of 45% for the floor elements of the building and about 30% for the walls.

Also presented in this paper is a simple and very reliable analyses procedure, in order to determine the maximum seismic response (displacements and/or forces/stresses) of neoclassical buildings. This procedure is based on the resent research according to which the deformed shape of a building at the time of its maximum response is approximated very well by the shape of its principal translation-twisting mode if the mass participation factor is greater than 80% [10]. According to this procedure, the maximum seismic response of a neoclassical building can easily be determined from the results of a static analysis, where lateral loading of the building model is performed with its self weight, multiplied accordingly so that the horizontal displacements of the target node at the top of the building be equal to the relative displacement of the elastic spectrum used in the assessment procedure.

REFERENCES

[1] Mpiris M., Kardamitsi-Adami M., Neoclassical Architecture in Greece, Melissa Publications, 2001.

[2] Raptakis J., *Oikodomiki*, National Technical University, 1897 - 1898, Athens (in greek).

[3] Raptakis J., *Oikodomiki – Part B*, National Technical University, 1898, Athens (in greek).

[4] Raptakis J., *Oikodomiki and Construction of Various Constructions – Volume II*, National Technical University, 1903, Athens (in greek).

[5] Stougiannopoulos E., *Manual of Oikodomiki*, Perry Bros. Publications, 1889, Athens (in greek).

[6] Kriezis E., *Oikodomiki*, 1920, Athens (in greek).

[7] SAP2000, Computers and Structures, Inc., 1995 University Avenue, Berkeley, California 94704, USA.

[8] ITSAK, *Institute of Technical Seismology and Earthquake Resistant Structures*, Thessaloniki, Greece.

[9] Clough R. W., Penzien J., *Dynamics of Structures*, Second Edition, MacGraw-Hill Inc. 1993.

[10] Pardalopoulos S. J. and Pantazopoulou S.J., *Spatial Displacement Paterns of R.C. Buildings under Seismic Loads*, M. Papadrakakis et al. Computational Methods in Earthquake Engineering, Computational Methods in Applied Sciences 21, Springer, 123-145, 2010.

COMPDYN 2011
III ECCOMAS Thematic Conference on
Computational Methods in Structural Dynamics and Earthquake Engineering
M. Papadrakakis, M. Fragiadakis, V. Plevris (eds.)
Corfu, Greece, 25–28 May 2011

THREE DIMENSIONAL NONLINEAR DYNAMIC MODELING OF A VERTICALLY ISOLATED ANCIENT STATUE DISPLAYED IN A BASE ISOLATED MUSEUM BUILDING

Carlo A. Castiglioni[1], Alper Kanyilmaz[2]

[1]Politecnico di Milano

Structural Engineering Department

Piazza Leonardo da Vinci, 32 20133 Milano

castigli@stru.polimi.it

[2]Politecnico di Milano

Structural Engineering Department

Piazza Leonardo da Vinci, 32 20133 Milano

kanyilmaz@stru.polimi.it

Keywords: Seismic Isolation, Ancient Statues, Vertical Isolation

Abstract: *This research concerns with the question of how the seismic isolation methods can be applied efficiently to protect the ancient statues under both horizontal and vertical strong earthquake excitations. The results are achieved by carrying out nonlinear dynamical analyses under three dimensional earthquake ground motion data on a generic ancient statue model, considering that it is displayed in a non isolated and a horizontally isolated building. The model is developed with 8-node cubic finite elements, and placed on a rigid platform, which is modelled as an area element of rectangular shape. The isolation devices are modelled as non linear spring elements for the horizontal seismic isolation, and gap elements (compression only) for the vertical seismic isolation.*

1 INTRODUCTION

After the efficiency of seismic isolation technology has been proved for several types of structures such as bridges, buildings, power plants, etc., scientists and researchers in the field started to look for the possible ways to adapt the seismic isolation solutions and furthermore create innovative solutions for the cultural heritage of human history and art objects. The need to protect these objects against earthquakes was found inevitable since they are one of the most precious possessions of the human being on the earth.

Koumousis et al. [1], in his work for the horizontal seismic isolation of the Statue of Hermes, has designed and proved the adequacy of the FPS™ (Friction pendulum system), after carrying out numerical analyses on the 3D model of the statue. Borri and Grazini [2] have carried out static and dynamic numerical analyses for the statue of Michelangelo's David Statue. They have shown that the horizontal accelerations that could be originated by even moderate earthquakes (0.10-0.15g) can cause very high stress levels on some particular parts of the marble statue. Grazini [3] has done rocking analysis for both the non isolated and horizontally isolated statue models. Borri [2] and Grazini [3] have both pointed out the benefits of seismic isolators for the seismic protection of statues. Tadahiro and Masahiko [4] have developed seismic isolation solutions that are capable of protecting The Gates of Hell statue, which was sculpted by Augustin Rodin and owned by National Museum of Western Art, against very strong earthquakes such as the Great Hanshin Earthquake that occurred, in Kobe in 1995. Yegian et al. [5], has carried out several tests and numerical analysis for the sculptures in Nagoya Museum, with mechanical horizontal seismic isolators. In this project, the effectiveness of the horizontal seismic isolation system is investigated for isolated and non-isolated museum buildings.

Once a rigid block starts rocking, its rotation continues smoothly from point O to O', as shown in the Figure 1. If it does not fail by overturning, its rotation will change direction, and rotate otherwise, and the motion will continue in this manner, and cease some time after the ground motion comes to an end. For the rigid block to sustain this rocking motion, the energy released during the impact should be dissipated. The amount of this energy dissipation increases with the decreasing slenderness of the block [6].

The minimum rocking impulse that causes rocking of an object has been expressed by Calio and Marletta [7]. The minimum rocking impulse I_u, has been derived by equating the overturning moment due to the inertia load caused by the maximum horizontal acceleration, to the resisting moment due to the gravity as;

$$\ddot{u}_{\max}(I_r) = \frac{gb}{h} = \frac{g}{\lambda} \qquad (1)$$

Considering zero damping, the maximum acceleration is given by

$$\ddot{u}_{\max} = I\omega \qquad (2)$$

Therefore the minimum impulse that starts the rocking motion of a rigid body is represented as;

$$I_u = \frac{g}{\omega\lambda} = \frac{g}{2\pi\lambda}T \qquad (3)$$

Where,

g = gravity acceleration
h = height of the center of mass of the object
b = lateral distance between the overturning point and the center of mass
λ= h/b (slenderness ratio)
ω= natural frequency of the object
T = natural period

Calio et. al [7] concluded that the object stays in full contact with the ground until the design impulse becomes equal to the minimum rocking impulse. When the minimum rocking impulse is surpassed, the object starts rocking. Calio et al. [7] have shown that the seismic isolation significantly contributes to the stability of the object under horizontal ground motions.

Oliveto, Calio and Greco [8], have evaluated the uplift conditions for the initiation of rocking motion, considering both horizontal and vertical ground motions. They introduced a dimensionless parameter γ, to take into account the vertical accelerations of the ground motion.

$$\gamma = 1 + \frac{\ddot{v}_g}{g} \qquad (4)$$

Where

$\ddot{v}_g$ = Vertical ground acceleration (positive, when directed downwards)
g = Gravity acceleration (m/s^2)

They pointed out the significance of the vertical accelerations on the minimum rocking impulse, and expressed it through modifying the minimum rocking impulse expression;

$$I_u = \frac{\gamma g}{\omega\lambda} = \frac{\gamma g}{2\pi\lambda} T \qquad (5)$$

As it can be understood from the two expressions above, when the vertical accelerations are directed upwards (against gravity), the minimum rocking impulse decreases, therefore the initiation of rocking becomes easier for the object considered.

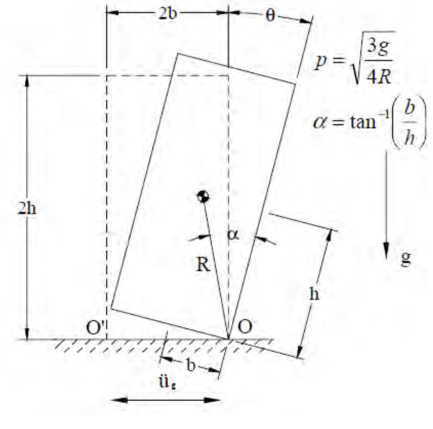

Figure 1 Rocking motion of a rigid body

This research concerns with the question of how the seismic isolation methods can be applied efficiently to protect the ancient statues subjected to both horizontal and vertical strong earthquake excitations. The study seeks to classify the effects of conditions deriving from different building types and earthquake characteristics, to design an efficient isolation system for a particular ancient statue. To achieve the results, computer models under several earthquake ground motion data are developed and compared for a generic ancient statue, considering that it would have been placed either in a non isolated or horizontally isolated building.

2 ANALYSES UNDER HORIZONTAL AND VERTICAL EARTHQUAKE EXCITATIONS

The statues are analyzed under both horizontal and vertical earthquake ground excitations, and the properties of a three dimensional seismic isolation system are decided for the protection of the statues against the three dimensional earthquake excitations.

2.1 The methodology and Ground Motion Data Used for the Analyses

The nonlinear dynamic time history analyses are performed on the 3D finite element solid model of an ancient statue (Figure 2) [9]

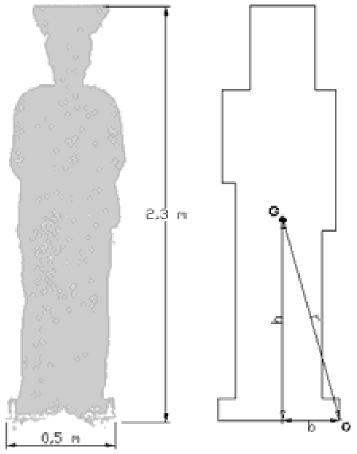

Figure 2 Ancient statue used in the numerical analysis

The model is analyzed under the three dimensional acceleration time history data of three different earthquakes which can be seen in Table 1.

Maximum Ground Accelerations (g)	Longitudinal Maximum Acceleration (g)	Translational Maximum Acceleration (g)	Vertical Maximum Acceleration (g)
Athens 1999	0,84	1,01	1,20
El Centro 1940	0,31	0,22	0,21
Aquila 2009	0,41	0,44	0,49

Table 1 Maximum accelerations used in the numerical analysis

The analyses are carried out in three stages. First, the acceleration time-history data of the earthquakes are applied to a 3 storey reinforced concrete frame which represents a generic museum building with a horizontal base isolation system. Then, the acceleration time-history data are obtained at each floor of the building model. Finally, the acceleration time-history data obtained from this model are given as the time history acceleration input to the ancient statue model. The analyses are carried out in two different parts;

1) The acceleration time-history data obtained from the non isolated building is given as the input time history data to the statues, in which case the statues are isolated against both horizontal and vertical excitations,

2) The acceleration time-history data obtained from the base isolated building is given as the input to the statues, in which case the statues are isolated against only vertical excitations.

2.2 Computer Model for the Statues with Three Dimensional Base Isolation System

The model to be analyzed under the earthquake ground motion data is developed with three dimensional 8-node finite elements, and placed on a rigid platform, which is modelled as an area element of rectangular shape (Figure 3).

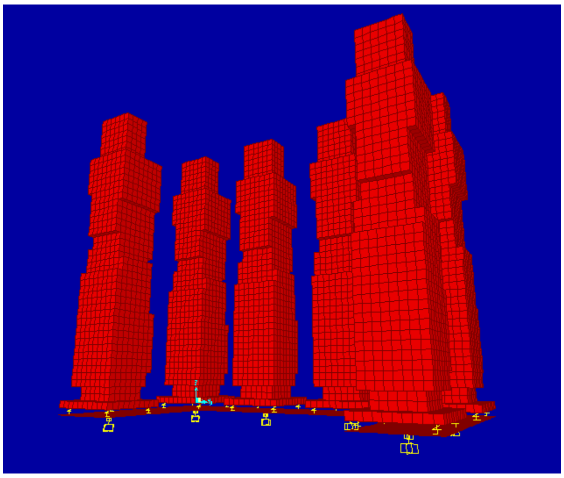

Figure 3 Three dimensional numerical model

The three dimensional seismic isolation devices are modelled as a combination of two types of elements;

1) Non linear spring elements for the horizontal seismic isolation
2) Gap elements (compression only) for the vertical seismic isolation

Horizontal seismic isolators are placed between the floor and the rigid platform on which the statues are placed. They are modeled as non-linear spring elements with initial stiffness k_e, post yield stiffness k_y and damping element with the damping coefficient c.

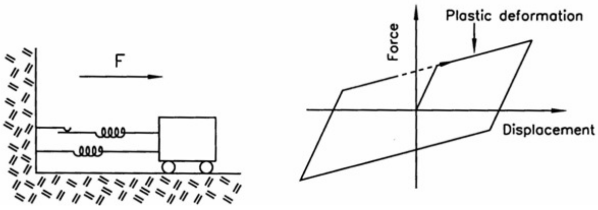

Figure 4 Horizontal isolator element

The hysteresis loop of a horizontal isolator element has a bilinear shape (Figure 4). The force deformation graph is composed of two slopes giving the 'initial' and 'yielded' stiffness respectively. The initial stiffness slope corresponds to the linear deformation; whereas the yielded stiffness slope corresponds to the plastic deformation that takes place in the isolator.

Vertical seismic isolators are placed between the rigid platform and the base of the statues. They are modeled as gap elements, which have positive stiffness values under compression, and zero stiffness under tension loads. Under compression, they show a linear behavior with spring constant k, and damping coefficient c.

2.3 Vertical Isolator Properties used in the Computer Model

The vertical isolation system consists of four springs with linear spring constant k and damping coefficient c. In the computer model, to simulate a vertical base isolation device, a gap ("compression only") element is used (Figure 5). The force deformation relationship of this element is given by;

$$f(x) = \begin{cases} k(d + open)......if : d + open < 0 \\ \hline 0,..........otherwise \end{cases} \qquad (6)$$

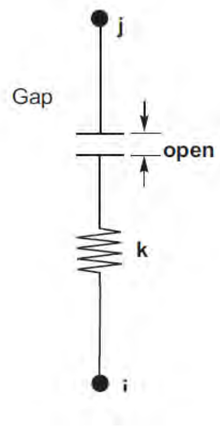

Figure 5 Vertical isolator element

As it can be seen in the Figure 6, the gap elements have a linear behavior under compression, and they can not carry any tensile load. In other words, they provide linear stiffness only under compressive loads.

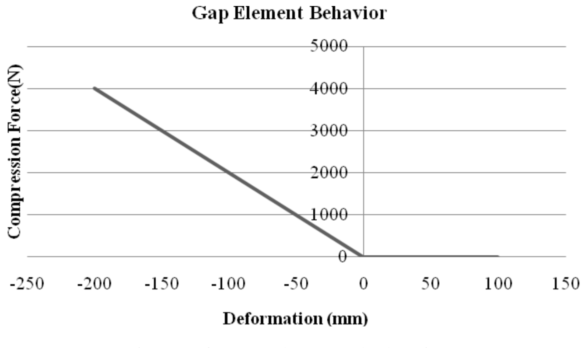

Figure 6 Gap element behaviour

In the model, thanks to the self weight of the statues, these elements are initially compressed. Therefore during the vertical earthquake excitations, they are expected to take action only in the compression range. The vertical isolator elements are constrained at the vertical (z) axis to not to permit differential displacements.

2.4 Behaviour of Three Dimensionally Isolated Statues Displayed in a Building without Horizontal Base Isolation

The analyses are carried out with different horizontal and vertical isolator elements, the properties of which can be seen in Table 2 and Table 3.

Vertical Seismic Isolation Device	Vertical Linear Stiffness(k_v) (N/mm)
Vertical Isolator 1	100
Vertical Isolator 2	50
Vertical Isolator 3	40
Vertical Isolator 4	30
Vertical Isolator 5	20

Table 2 Vertical isolator stiffnesses

Horizontal Seismic Isolation	Initial Stiffness(k_e) (N/mm)	Plastic Stiffness(k_y) (N/mm)	Yield Strength(f_y) (N/mm^2)
Isolator 4	1000	5	350

Table 3 Horizontal isolator properties

The analysis on the seismically isolated model of the statues are carried out under the acceleration time-history data obtained from the ground floor of a non-isolated building. In the Table 4 the reduced vertical accelerations can be seen for three different earthquakes and 5 different vertical isolators.

Maximum Vertical Accelerations on the Statues (Ground Floor)	Athens 1999 (g)	El Centro 1940 (g)	Aquila 2009 (g)
Earthquake Excitation:	***1,20g***	***0,21g***	***0,49g***
Vertical Linear Stiff-Stiffness (N/mm)			
100	0,79	0,17	0,21
50	0,37	0,13	0,16
40	0,32	0,13	0,16
30	0,26	0,09	0,13
20	0,24	0,05	0,09

Table 4 Maximum vertical accelerations observed on the statues at the ground floor of the museum building

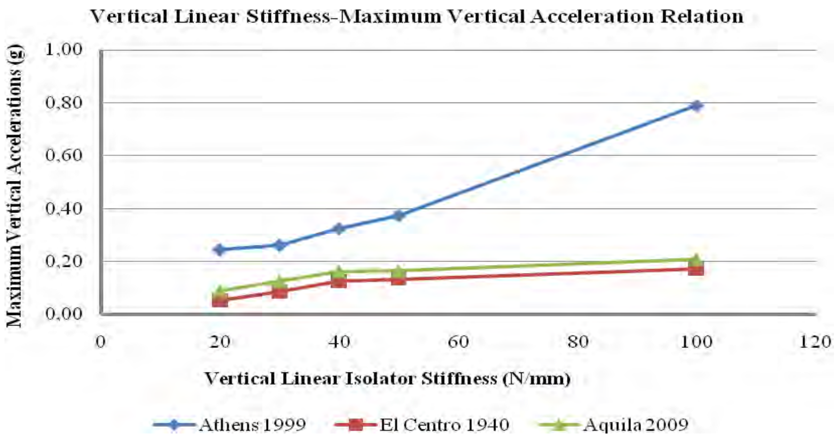

Figure 7 Vertical linear stiffness-maximum vertical acceleration relation

As it can be seen in the Figure 7 and Table 4, the vertical accelerations can be reduced significantly using vertical isolators with low stiffness values. Yet, the stiffness of the isolators must be tuned so that they must be capable of carrying the statue, under its self weight. In Table 5, the initial vertical displacements under the self weight of the statues can be seen.

Maximum Vertical Displacements at the Vertical Isolators	**Displacements Under Self Weight (cm)**
Vertical Linear Stiffness (N/mm)	
100	3,55
50	7,10
40	8,88
30	11,8
20	17,80

Table 5 Maximum vertical displacements observed at vertical isolators

Using four vertical isolator springs with the stiffness of 20 N/mm under the base of the statue, the initial vertical displacement under the self weight of the statue is 17.8 cm, whereas, it reaches up to 21.65 cm under the strongest vertical excitation (Athens 1999 Earthquake) These results show that under three earthquake excitations, the linear vertical isolator elements perform effectively, satisfying the two necessary requirements:

- They are always under compression
- Their vertical displacement values are within the limits that available products in the market can provide.

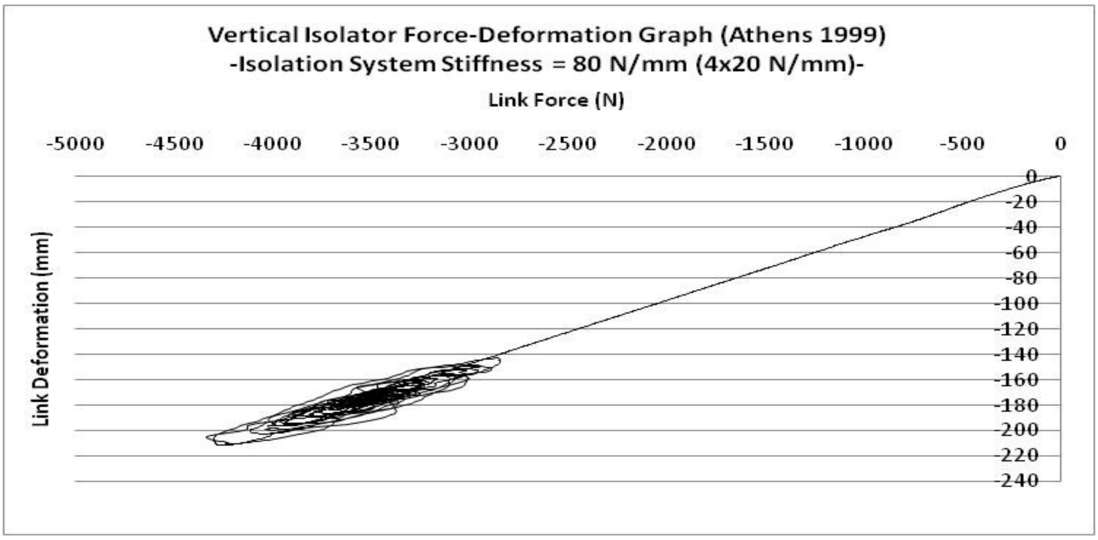

Figure 8 Vertical isolator force-deformation graph, Athens 1999 Earthquake

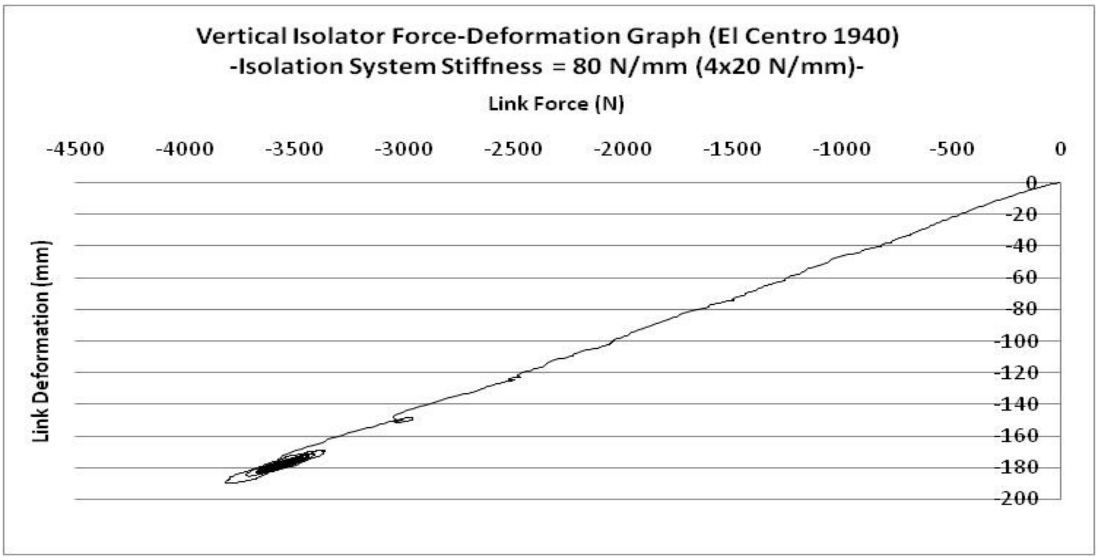

Figure 9 Vertical isolator force-deformation graph, El Centro 1940 Earthquake

From Figure 8 to Figure 10, the link-deformation graphs of the vertical isolator elements, obtained under three different earthquake ground motion can be seen. They represent the behavior of the vertical isolation system placed under each statue and composed of four isolator elements of 20 N/mm linear stiffness.

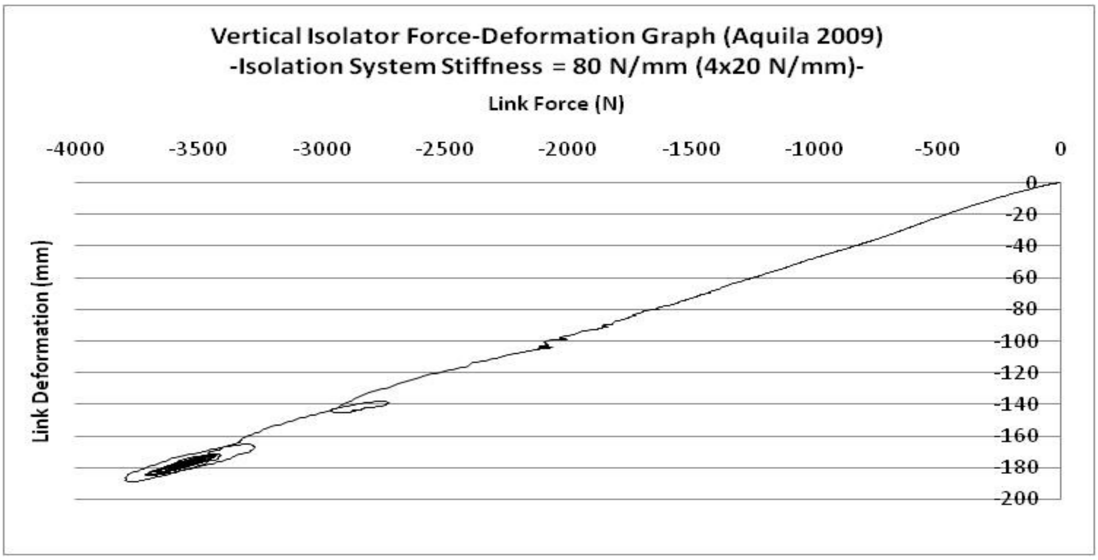

Figure 10 Vertical isolator force-deformation graph, Aquila 2009 Earthquake

In Figure 11, the displacements at the vertical isolators under the self weight of the statue obtained under three different earthquake ground motion can be seen. All the deformations observed refer to compression condition in the vertical isolation elements.

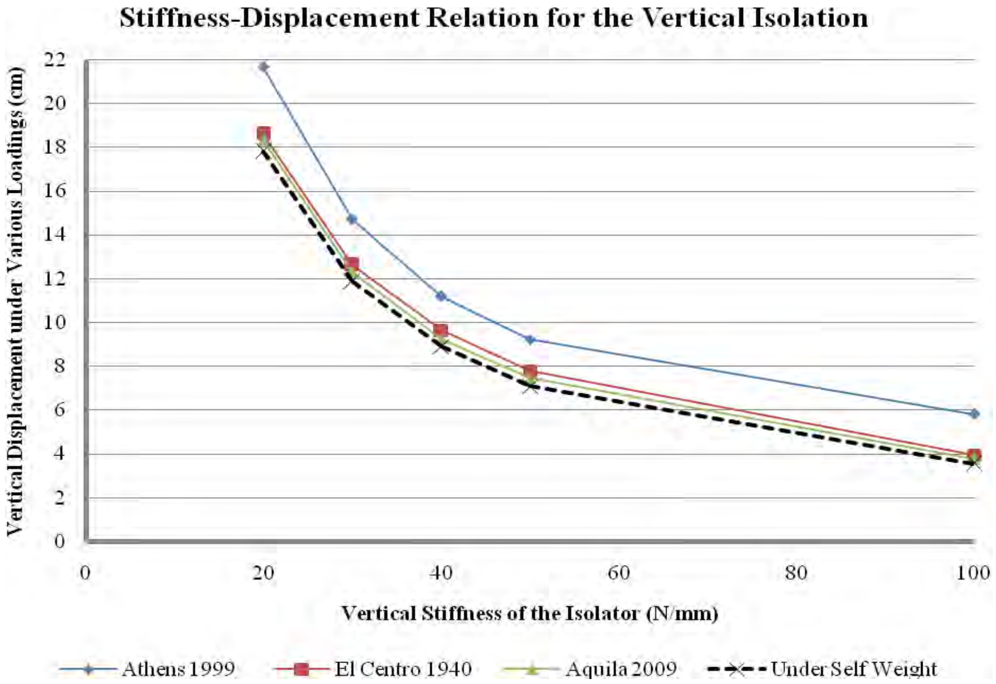

Figure 11 Stiffness-Displacement relation for the vertical isolation

From the results of the numerical analyses, it can be seen that the accelerations in any direction can be reduced significantly utilizing a three dimensional seismic isolation system. From Table 6, the amount of reduced accelerations and the percentage of reductions can be observed.

The Statues Isolated Three Dimensionally, Placed in a Non-Isolated Building	**Longitudinal Maximum Acceleration**	**Translational Maximum Acceleration**	**Vertical Maximum Acceleration**
	k_h= 5 N/mm	**k_h= 5 N/mm**	**k_v = 20 N/mm**
Athens 1999 ***reduced by:***	0,11g 87%	0,10g 90%	0,24g 80%
El Centro 1940 ***reduced by:***	0,06g 81%	0,08g 65%	0,05g 75%
Aquila 2009 ***reduced by:***	0,08g 79%	0,06g 86%	0,09g 82%

Table 6 Reductions in accelerations for the three dimensionally isolated statues placed in the non isolated museum building

The reduction of accelerations can also be seen in the Figure 12, where the peak ground and reduced vertical acceleration history data are drawn.

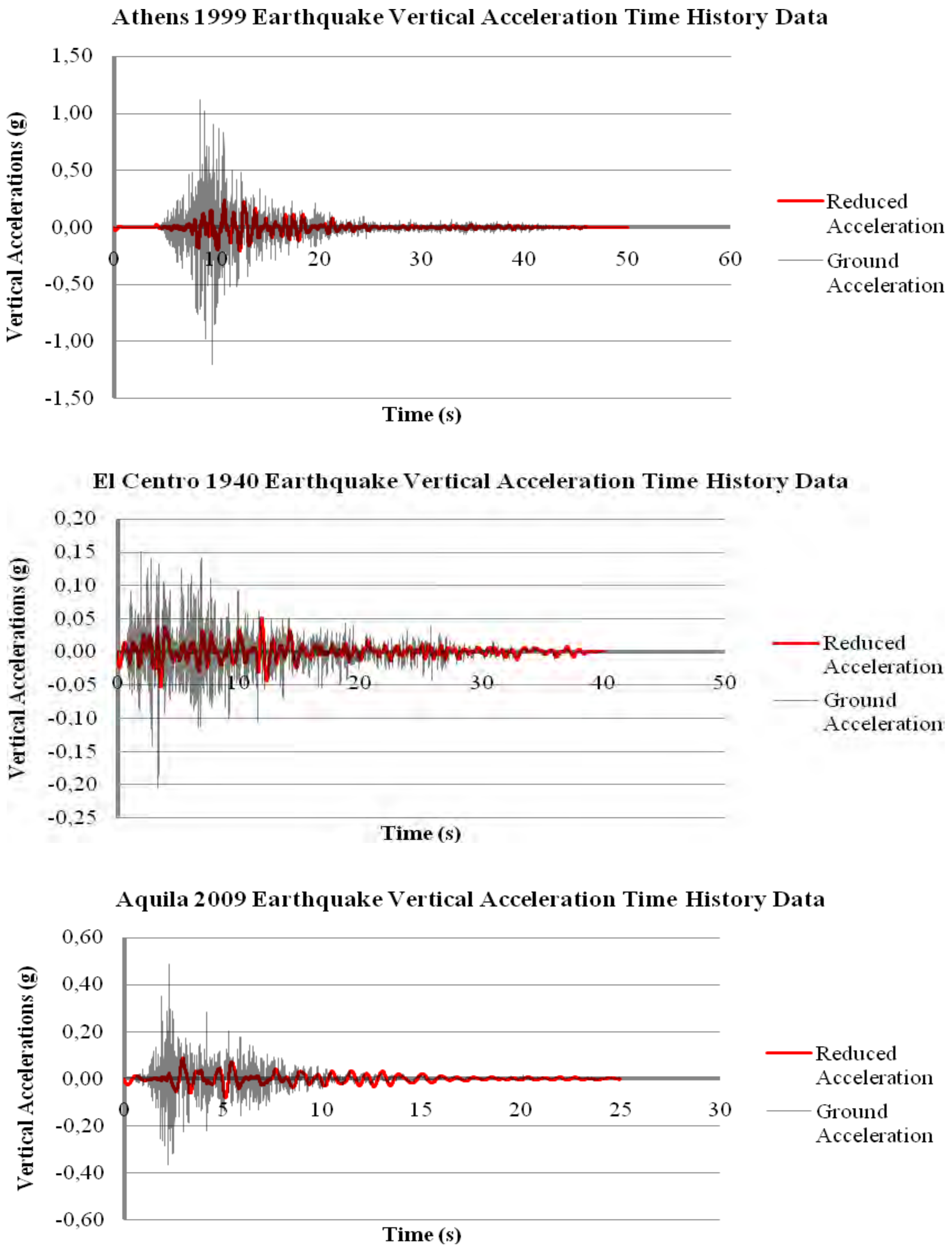

Figure 12 Reductions in Accelerations

2.5 Behaviour of Vertically Isolated Statues Displayed in a Building with Horizontal Base Isolation

In a base isolated museum building, placing the statues upon an additional local horizontal isolation system does not help reducing the accelerations, in contrary, since the frequency contents of the building and the isolated platform of statues become similar to each other, the seismic risk for the statues increase, because of a possible resonance problem. Therefore in order to achieve an effective three dimensional isolation system in a base isolated museum building, the rigid platform on which the statues are placed is restrained to the ground horizontally, and vertical seismic isolators are mounted between the statue and the rigid platform (Figure 13).

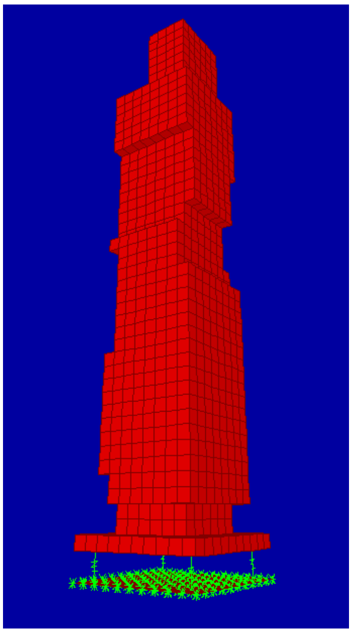

Figure 13 Vertical Isolation Model

For each statue, four vertical seismic isolator elements are used with linear stiffness values of 20 N/mm. From Table 7, the amount of reduced accelerations and the percentage of reductions in each direction can be seen. Note that in this table, the reductions in the horizontal accelerations are obtained thanks to the horizontal base isolation of the building.

Vertically Isolated Statue Placed in a Base Isolated Building	**Longitudinal Maximum Acceleration**	**Translational Maximum Acceleration (g)**	**Vertical Maximum Acceleration (g)**
Athens 1999 ***reduced by:***	0,17g 80%	0,19g 81%	0,24g 80%
El Centro 1940 ***reduced by:***	0,17g 46%	0,13g 41%	0,05g 75%
Aquila 2009 ***reduced by:***	0,08g 81%	0,04g 91%	0,09g 82%

Table 7 Reductions in accelerations for the vertically isolated statues placed in the base isolated museum building

From Figure 14, the reductions of maximum vertical accelerations that the statues experience with decreasing spring stiffness can be seen.

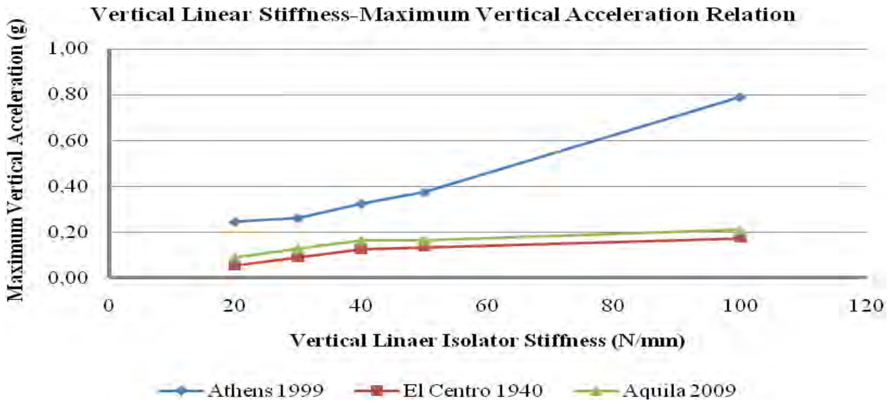

Figure 14 Vertical linear stiffness-maximum vertical acceleration relation

Therefore it can been concluded that in a base isolated museum building, adopting a vertical seismic isolation system, the accelerations that the statues experience in any direction can be lowered significantly.

3 ROCKING ANALYSES

If the vibrations are exceeded above a certain limit, the rigid blocks start "rocking". Statically, when the overturning moment caused by earthquake forces reaches the resisting moment due to the self weight, the object starts to rock. This condition can be demonstrated with the following expression for a statue shown in Figure 15 :

$$M_{overturning} = M_{resisting} \qquad (7)$$

$$h(ma_h) = b(mg \pm ma_v) \qquad (8)$$

where,
h = Height of the center of mass of the object
b = Lateral distance between the overturning point and the center of mass of the object
m = Mass of the object
g = Gravity acceleration
a_h = Horizontal acceleration
a_v = Vertical acceleration

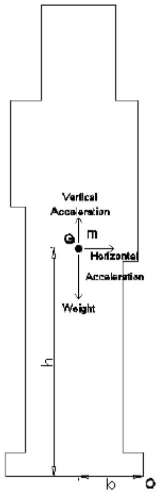

Figure 15 Ancient statue rigid body model

However, since earthquake forces are impulsive, the static approach may not give satisfying results.. Therefore, the accelerations that can start the rocking of a rigid body is estimated using “Impulsive Loading Approach”, in which the minimum impulse that a specific rigid block can tolerate is compared with the impulse caused by the maximum accelerations of the earthquake excitations.

3.1 Initiation of Rocking Motion of a Rigid Block under Impulsive Loads

A rigid block, subjected to the horizontal and vertical accelerations, can either remain in full contact with the ground or it uplifts and starts rocking. During this motion, if the acceleration impulse caused by the earthquake forces becomes larger than the minimum overturning impulse of the system, the object overturns. Otherwise, it continues rocking until the ground motion comes to the end (Figure 16). The object’s full contact to the ground can be kept, if the magnitude of the impulse remains smaller than the minimum impulse required for uplift for the object [8].

While adopting an isolation solution for the protection of ancient statues, attention must be paid to the initiation of uplift because, once the object begins rocking, it starts to have impacts while rotating from one of its corners to the other, and this action may cause serious damage to an ancient statue. In this study, assessment of the horizontal and vertical accelerations that allow the statue to remain in full contact with the ground is carried out in presence of suitable vertical isolation elements.

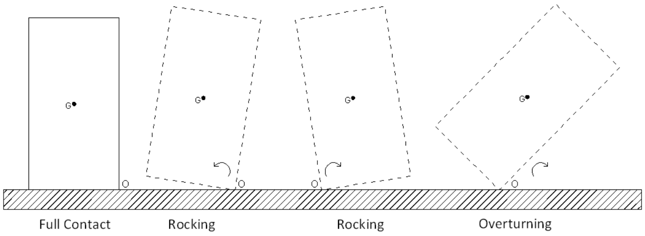

Figure 16 Rocking and overturning

For the tuning of accelerations through seismic isolation devices, the minimum impulse that can start the rocking motion of the statue is calculated and compared with the impulse caused by maximum earthquake accelerations, which is called as “design impulse”. Finally, interaction diagrams between horizontal and vertical accelerations for the specific ground motions are presented. Examining these diagrams, the allowable horizontal and vertical accelerations that can keep the statue model in full contact with the ground can be decided.

The minimum impulse that initiates the rocking motion of an object is called as the minimum uplift impulse [8]. It depends on the object’s geometric properties (slenderness), natural frequency, (stiffness and mass), and the vertical ground motions. Comparing the minimum impulse of a particular object with the impulse caused by the earthquake excitations, the probability for the initiation of rocking can be foreseen.

In the absence of damping, the minimum uplift impulse of a structure can be found according to the equation (5) in section 1, which shows that, the minimum uplift impulse decreases with the increasing natural frequency and slenderness. Also, the vertical accelerations have a direct effect on the motion. From the equation (5), it can be concluded that,

- More rigid structures (with higher natural frequency) are easier to uplift, than the flexible ones.

- More slender structures (higher h/b ratio) are easier to uplift than the less slender ones
- The upward vertical accelerations reduce the minimum uplift impulse, which results in a lower resistance to the uplift.

Thus, it can be understood that vertical accelerations of the earthquakes are very important for the uplift resistance of the object. The higher values the vertical accelerations have in the upward direction, the easier is the initiation of the uplift.

For instance, if the maximum vertical accelerations of an earthquake equals to –g, the vertical excitation parameter, γ (see equation 4) becomes zero, so does the minimum uplift impulse, I_u. This practically means "zero" resistance to uplift, therefore in such a case, even a slight horizontal impulse would be enough to start rocking of the object.

Therefore the effect of the magnitude of maximum vertical accelerations to the uplift resistance of the statue is investigated. To compare with the minimum uplift impulse of the statue, the design impulse caused by the horizontal accelerations of the earthquake excitation must be calculated. After making a comparison between these two values, the probability for the initiation of rocking for the particular object can be estimated.

3.2 Design Impulse

The maximum impulse caused by the horizontal earthquake excitation considered for the analysis is called the design impulse. To estimate the magnitude of the design impulse, the time integral of the earthquake force p(t) should be calculated.

$$\text{Earthquake Force: } p(t) = m\ddot{u}_h(t) \qquad (9)$$

$$\text{Magnitude of Design Impulse: } \int_{t1}^{t2} p(t)dt \qquad (10)$$

This integral can be estimated as the multiplication of the mass of the statue and the area under the acceleration time history graph between two successive time instants, corresponding to the maximum horizontal acceleration. As a reasonable estimation, the triangular area that is drawn in the acceleration time history diagram in Figure 17 gives the magnitude of impulse for unit mass.

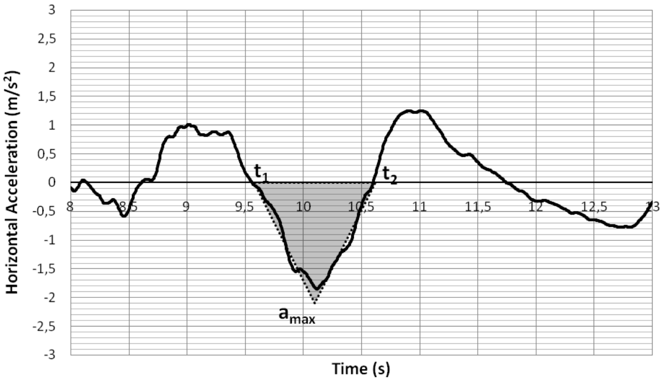

Figure 17 Impulse calculation graph

$$I_d = a_{\max} \cdot \frac{1}{2}(t_2 - t_1) \text{ (for unit mass)}$$

In the analyses, the comparison between the design impulse and the minimum rocking impulse of the statue is made by considering three different earthquake data, the properties of which are presented in the previous sections.

The comparison between the magnitude of the design impulse and the minimum uplift impulse shows if the object begins to rock or stays in full contact with the ground.

- If the design impulse is smaller than the minimum uplift impulse, the statue stays in full contact with the ground

$$I_d < I_u \rightarrow \text{Full Contact}$$

- If the design impulse is larger than the minimum uplift impulse, the object starts to rocking

$$I_d > I_u \rightarrow \text{Rocking}$$

To generalize the results for all three of the earthquake data, the same calculation procedure is applied with particular parameters of each analyses, and the results are presented as interaction graphs between the horizontal and vertical accelerations. The interaction graphs are shown in the figures 19,20 and 21. The trend line shows the intersection of the magnitudes of maximum horizontal and vertical accelerations below which the statue stays in full contact with the ground, during the specific earthquake motion. The points above the trend line represent the acceleration values that are sufficient to start the rocking motion.

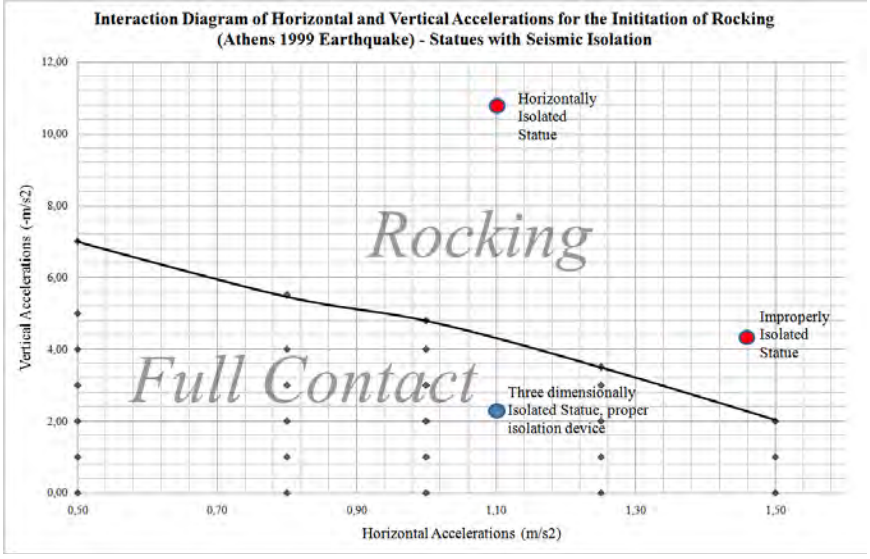

Figure 18 Interaction diagram of horizontal and vertical accelerations for the initiation of rocking

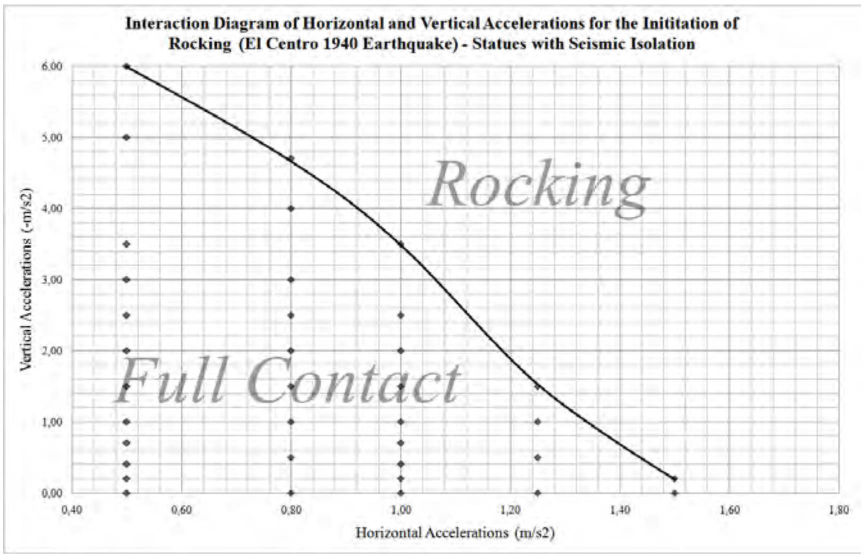

Figure 19 Interaction diagram of horizontal and vertical accelerations for the initiation of rocking

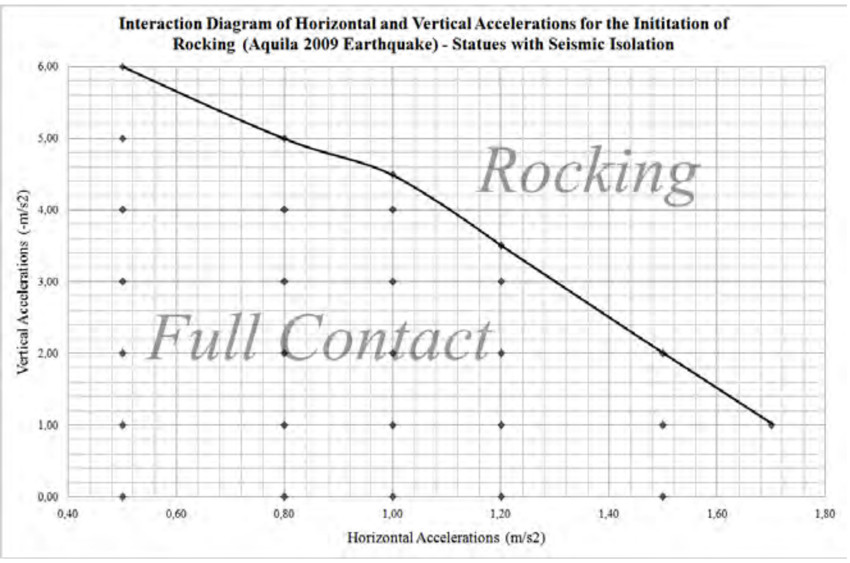

Figure 20 Interaction diagram of horizontal and vertical accelerations for the initiation of rocking

4 CONCLUSIONS

In this study, the effective ways to protect the ancient statues against three dimensional earthquake ground motions are investigated through seismic isolation methods. Several numerical analyses are carried out to understand which type of isolation system is suitable for each case. It is seen that both the horizontal and vertical accelerations transmitted to the statues can be reduced significantly, with a combination of vertical isolators at the base of the statues and horizontal base isolation system of the building. If the museum building in which the statues are to be displayed is not base isolated, then a three dimensional isolation system must be adopted for the statues.

Rocking analyses are carried out with the results obtained in each case. The results of the rocking calculations for each earthquake data are presented as interaction graphs to show the allowable accelerations under which the statues remain in full contact with the ground, and suffers no damage due to the impacts during rocking. Principally, it is understood that the vertical earthquake excitations play a very important role on the initiation of uplift of the statues.

It is shown that ancient statues can be protected against three dimensional earthquake excitations effectively, when a seismic isolation system is designed according to their particular material and geometrical properties and the characteristics of the building in which they are to be displayed.

REFERENCES

[1] Vlasis Koumousis. Seismic Isolation of the Statue of Hermes of Praxitelis at the New Museum of Olympia. İstanbul : s.n., 2007

[2] Andrea Borri, Andrea Grazini. Diagnostic Analysis of the Lesions and Stability of Michelangelo's David, Report, La stabilita' delle grandi statue, Il David di Michelangelo, 2005.

[3] Andrea Grazini. La stabilita' delle grandi statue, Il David di Michelangelo, Report, Modellazione ed Analisi Strutturale del David di Michelangelo 2005

[4] Yano Tadahiro, Higashino Masahiko. The rehabilitation of the Gates of Hell and its Seismic Strengthining by Base Isolation. 2000.

[5] Mishac Yegian, Ece Eseller, Seda Gökyer, Keith Hall, David Whelpley. Evaluation of a Mechanical Isolator for Protecting Four MFA Sculptures Against Earthquakes in Nagoya Japan, 2008.

[6] Nicos Makris, Dimitrios Konstantinidis. The Rocking Spectrum and the Shortcomings of Design Guidelines. 2001.

[7] Ivo Calio, M. Marletta. Passive Control of the Seismic Rocking Response of Art Objects. Engineering Structures, Elsevier, 2003.

[8] Giuseppe Oliveto, Ivo Calio, Annalisa Greco. Large Displacement Behavior of a Structural Model with Foundation Uplift under Impulsive and Earthquake Excitations. s.l. : John Wiley & Sons, Ltd., 2002.

[9] SAP2000 Advanced 14.1.0 Structural Analysis Program

COMPDYN 2011
III ECCOMAS Thematic Conference on
Computational Methods in Structural Dynamics and Earthquake Engineering
M. Papadrakakis, M. Fragiadakis, V. Plevris (eds.)
Corfu, Greece, 25–28 May 2011

SIMULATION FOR SEISMIC ASSESSMENT OF TRADITIONAL HOUSES IN THE HISTORICAL CORE OF THE CITY OF XANTHI BEFORE AND AFTER NON-INVASIVE STRUCTURAL INTERVENTIONS

M. L. Papadopoulos[1], S. J. Pantazopoulou[2]

[1]Demokritus University of Thrace
Vas. Sofias 12, Xanthi 67100, Greece
mipap@civil.duth.gr

[2]Demokritus University of Thrace
Vas. Sofias 12, Xanthi 67100, Greece
pantaz@civil.duth.gr

Keywords: Local Historical Structural Systems, Non-invasive interventions, Seismic behavior, Simulation models.

Abstract. *This paper examines the seismic behavior of three typical traditional houses in the old city of Xanthi using simulation models and the possibilities of restoration and optimization of the Local Historical Structural System used. For this purpose the function of their existing structural system is analyzed and their seismic behavior examined and evaluated using simulation models and time history analysis of the dynamic response to a series of ground motions. Simple, non-invasive structural interventions are selected for restoration and optimization. The seismic behavior of the improved structural system is subsequently re-evaluated using the same modeling procedures. A comparative evaluation of the results obtained from the initial and the post-intervention models is used to assess the global modification of the dynamic characteristics and the anticipated performance effected by the types of interventions examined. The variability of the results owing to parameter changes enables a first assessment of the uncertainties associated with the actual details, geometry and state of materials and the mechanical properties thereof, on the dynamic properties and dependable deformation capacity of the structure at the life-safety performance limit state.*

1 INTRODUCTION

In the framework of a comprehensive strategy for preservation of historical constructions, a decisive step is the thorough identification of the internal force path implicit in their structural system both for assessment of the deficiencies accumulated by deterioration due to ageing and systemic inadequacies, but also for evaluation of the effectiveness of alternative options for intervention and restoration. In this field of application, detailed simulation through Finite Element modeling, holds promise in promoting understanding of the global building function although at the local level there is great uncertainty with regards the accuracy of modeling a number of behavioral issues, such as interactions between components, individual member connectivity, and constitutive properties of the associated materials.

The present paper explores the use of computer-aided simulation for seismic assessment of a typical historical structural system used in construction of urban residences up to the early 1900's in the area of Xanthi, in Northeastern Greece. Objective of this effort is to identify the potential utility of such methods of analysis in the process of restoration, rehabilitation and reuse of historical or traditional houses, by enabling a better understanding of the structural function of the system of construction, but also in providing guidance for selecting the important behavioral parameters that need to be modified through interventions for improved seismic performance. By definition, when referring to monumental structures that convey a historical value for the community, a certain type of equilibrium must be sought between the need to preserve the structure as a surviving heritage exhibit, and the need to secure the safety of its inhabitants against loss of life or property in the event of a significant earthquake.

Fig. 1: Typical Samples of traditional houses in the historical center of the city of Xanthi.

In the provinces of Eastern Macedonia and Thrace in the Northeastern part of Greece, and particularly in the region of the city of Xanthi the notion of heritage construction coincides with the traditional buildings in the old city quarters and generally with buildings made with the regional historical building system (RHBS), representing the most significant (from a historical perspective) inventory of the built environment in the region. With regards to the city of Xanthi these buildings comprise a vital portion of its historical fabric, identifying the city (Fig.1). The RHBS uses as primary construction materials the stone (natural blocks or man-made solid clay-bricks) and timber (such as timber structural elements, floor ties, timber lacing elements, etc.) enhances in some situations by the use of iron clamps and ties. The art of construction with these materials, with builder functioning in a complex role of observer, creator and engineer, evolved over the years in an improved system whose performance has stood the test of time in a region of active seismic activity. It is paramount to note here, that although empirical, none of the details of the RHBS was left to chance – the contribution of these techniques therefore, in shaping the art of construction through the history of engineering is most likely their most significant attribute as a human achievement. It is noteworthy that the line of development of timber-laced construction dates back to Minoan times, continues uninterrupted in classical Antiquity and the Roman times (Fig.2), and survived till the previous century when industrialization and the emergence of reinforced concrete displaced tradition in the interest of development ([1]Vitruvius 27-23 b.C. 1997, [2] Touliatos P. 2000, [5] Langenbach R 2002, [9]Müller-Wiener, 1995). Evolution of timber laced construction became prevalent in central Europe but it is also the primary mode of traditional construction in the East (Kashmir, India, [4] Langenbach R 2000) presenting several different versions of the basic structural scheme.

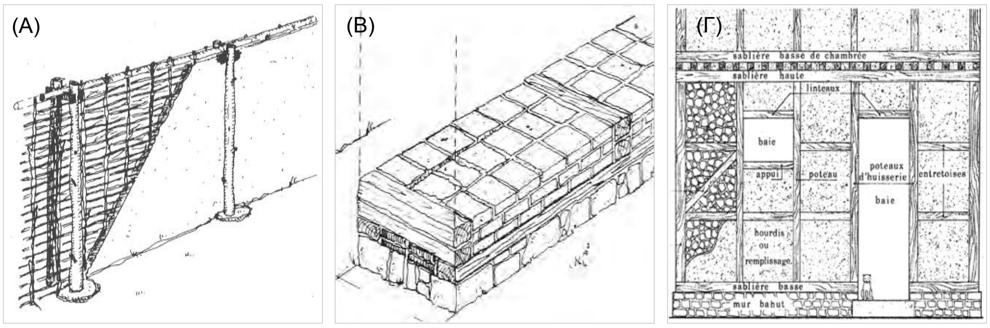

Fig. 2: (A) Early form of timber weaved walls [9], (B) Stone masonrytimber laced walls [9], (C) Timber laced walls [1].

The traditional system studied in the present paper combines a stiff load-bearing timber-laced stone-masonry wall system for the lower floor, with the upper floor made of infilled timber frame; these were known from antiquity as “opus craticium”. Today they are referred to as fachwerk, tsatmas, or half-timbered system. Interior dividing walls were made of light timber-woven gages coated with a lime-based mortar (mud-based mortar was used in poorer dwellings), usually reinforced with straw or animal hair; this is also evident in ancient monuments, but its use is found throughout southern Europe and Asia. Therefore, in construction of a traditional house these three structural forms are used selectively, combined in an overall structural system and expanded in space following well-defined rules depending on their weight, load-carrying capacity, and stiffness. The system described represents the historical city quarters of Xanthi in its entirety and is marked for the carefully organized geometry (meant to avoid irregularities and large ratios of slenderness in plan or in height, and to exploit the benefit of symmetry, the optimal distribution of mass, stiffness and ductility).

One important distinguishing characteristic is the relative compliance of connections between members, despite their robustness. This means that all members participate to lateral load resistance as there are no singularly stiff paths for the seismic load to reach the ground. We may say therefore that structures of this class survive the earthquake by practically not “taking”, or “attracting” significant forces; instead, they comply in a controlled fashion, developing wide spread low intensity damage, particularly owing to the frictional interactions between the various components which comprise different materials and types of elements. This creative combination of contact-based resistances, contributes to diffuse the strain energy imparted by the earthquake throughout the building. Thus, through this function, the absorbed energy is consumed by the extensive internal frictions that develop along the interfaces and the connections of the individual elements, materials and structural forms, leading to a large value of *equivalent* or, *effective* damping. Energy dissipation through internal friction is a characteristic mechanism for all three structural forms described (laced masonry, infilled timber frames and timber-woven walls); the process of energy dissipation may continue over a large range of deformation capacity prior to failure. Furthermore, the system is self-adjusting, since failure of the individual building components does not influence to a critical extent the other members of the system. This type of behavior to seismic loads is enhanced by the diaphragm action of the floor system, to a degree that depends on the robustness of its structure and the manner of its connection or attachment to the load bearing walls. In many of these buildings the roof timber truss is elastic and does not contribute by diaphragm action to the structure.

Note that the above observations and interpretations concern systems where the structural function has not been altered or reversed by arbitrary interventions either by the users through additions or removals of building components, inadequate or misguided retrofit of older earthquake-induced damages, or lack of maintenance. All of the above contribute to the notable performance of the traditional building system to seismic action as documented in reconnaissance studies cited in the literature that present comparative evaluations with the parallel performance of lightly reinforced – concrete construction in major seismic events which, upon collapse, have proven lethal to human life. ([8] Gülhan D, Güney I.O 2000, [7] Tobriner S. 2000, [5] Langenbach R., 2002, [3] Vintzileou E,., 2007, [4] Langenbach R., 2000, [6] Makarios T., Demosthenous M. 2004).

With regards the objective of seismic upgrading, the need to secure a level of protection to the users of a heritage building under accidental actions that is consistent with contemporary perceptions of acceptable risk, is potentially orthogonal to the spirit of international treaties for preservation and non-invasive restoration of important monuments. These usually encompass both the use, accessibility, appearance of the edifice, but also the structural function of the various components (such as foundations, ability for stress redistribution, compliance of the individual elements and connections thereof, reversibility of the intervention, compatibility (in terms of compliance and physical characteristics) of the new materials with the originals, etc.). A determining factor is the building itself and its condition.

To demonstrate the efficacy of the rehabilitation protocols their performance as a means of modifying the dynamic response and the seismic demands of the structural systems on which they are used, is evaluated through modal analysis of a number of representative traditional houses from the historical center of Xanthi. These are referred to hereon as Buildings A, B and C for convenience. Although built with similar methods of construction, each one of the three structures possesses distinguishing features that are called on here to test or to illustrate the issues of concern in the basic simulation methods employed for the purposes of assessment. Interventions considered in the analytical models are outlined below.

2 PROPOSED REHABILITATION WITH NON INVASIVE METHODS

Usual conditions imposed by international treaties on historical structures restrict the breadth and extent of interventions by the requirement of reversibility and compatibility with the existing substrate. For this reason, materials chosen must be entirely compatible in terms of the rate of strength gain in time, stiffness, porosity, adhesion, while at the same time possessing resistance to biological and chemical corrosion agents. In this work each remedial plan includes a combination of the following measures:

(a) Deep repointing in the perimeter stone walls (after removal from the joints of any old crumbled mortar and cleaning with water pressure), replacement of decayed timber lacing, repair of all timber connections.

(b) Fiber reinforced mortar coating on wall surfaces where functionally and aesthetically acceptable by the utility of the rooms and structure.

(c) Replacement of decayed timber in floor joists, diaphragms and trusses. Where needed add intermediate beams to increase the floor stiffness. Replacement of flooring and roofing interlocking planks and dense nailing on the timber beams in order to secure composite action of the floor beams.

(d) Removal of roof tiles, replacement or treatment of decayed timber elements, restructuring of the roof with water insulating membranes under the original or properly replicated tiles.

For the needs of computer assisted simulation of the rehabilitated structures, and with reference to the characteristic compressive strength of masonry defined according with EC 6 ($f_{wk}=Kf_b^{0.7}f_m^{0.3}$, short term elastic modulus $E=1000f_{wk}$, where K a parameter that depends on the type of the stone blocks (sb) and joining mortar (jm), f_b is the compressive strength of the sb's, and f_m the average compressive strength of the jm), the following properties are assumed:

-Stone masonry of lime and granite composition, f_b =20 MPa, f_m = 2MPa, K=0.45. Characteristic strength f_{wk}=4.5 MPa, E=4.5 GPa, and density γ=2200 kg/m^3.

-Solid clay bricks, f_{wk}=2.25 MPa, E=2.25 GPa, and density γ=1800 kg/m^3.

-Voided clay bricks, f_{wk}=2.25 MPa, E=2.25 GPa, and density γ=1800 kg/m^3.

-Timber lacing components, E=10 GPa, density γ=800 kg/m^3.

-Repair mortar, quality M10 (EN998-2), f_m=10 MPa, composition (lime-cement-sand volume ratios): 0.5:1.0:5.0 which is expected to give rise to an average compressive strength for the joining mortar to 3.55 MPa (based on the preceding strength equation), which is expected to impact the mechanical properties of the finished masonry wall as follows: f_b=20 MPa, f_m=3.55 MPa, K=0.45, δ=1, and a 19% increase in the characteristic strength to f_{wk}=5.358 MPa, and E=5.358 GPa.

-It is further assumed that the sectional area of the timber diaphragm elements will be doubled from the initial situation by interpolating additional joists, replacement of the flooring planks and addition of roofing layers in each floor (under the joists) and the overall stiffness of the diaphragm will be increased by means of strengthening all connections.

3 DESCRIPTION AND SIMULATION OF BUILDING A:

The building is depicted in Fig. 3. It is located in the Metropolis square, with a total height of 9.05 m from road level (i.e. 9.95 m from basement floor), with plan dimensions of 10.25 by 9.5 m, floor heights 2.4m (basement), 2.8m (first floor), 3.0m (second floor) and 1.75 m (roof). Simulation was based on the idealization of the two facades parallel to the seismic action in each case, using a series of planar frames linked by horizontal nonlinear springs that represented the diaphragm stiffness; nonlinear frame members were located on the centroidal axes of the piers, whereas connectivity was based on rigid links between members to account for the actual depth of the piers in the direction of seismic action (Fig.4). The earthquake record used to assess the peak dynamic response of the structure is the well known ElCentro (1940) NS component

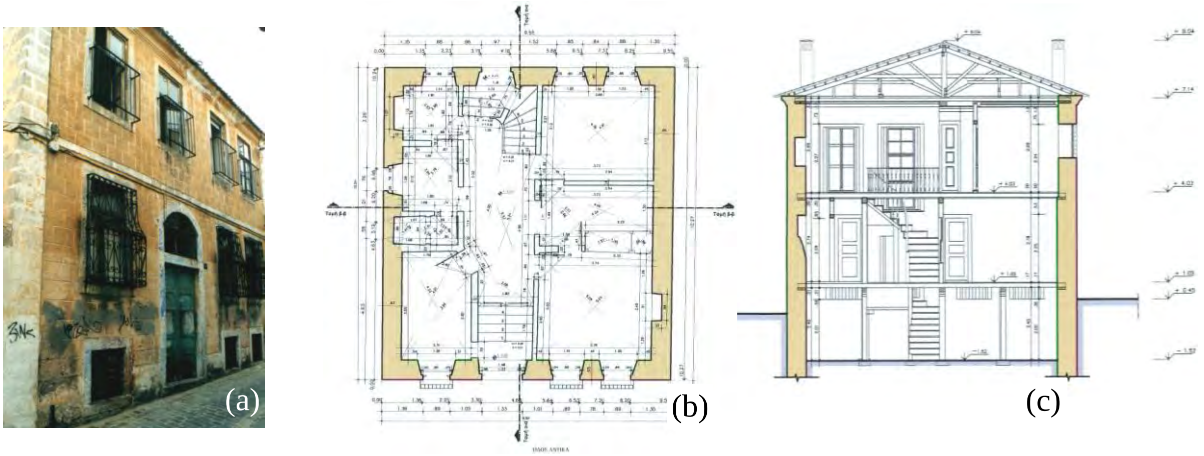

Fig. 3: Building A: (a) eastern view, (b) plan, (c) cross section

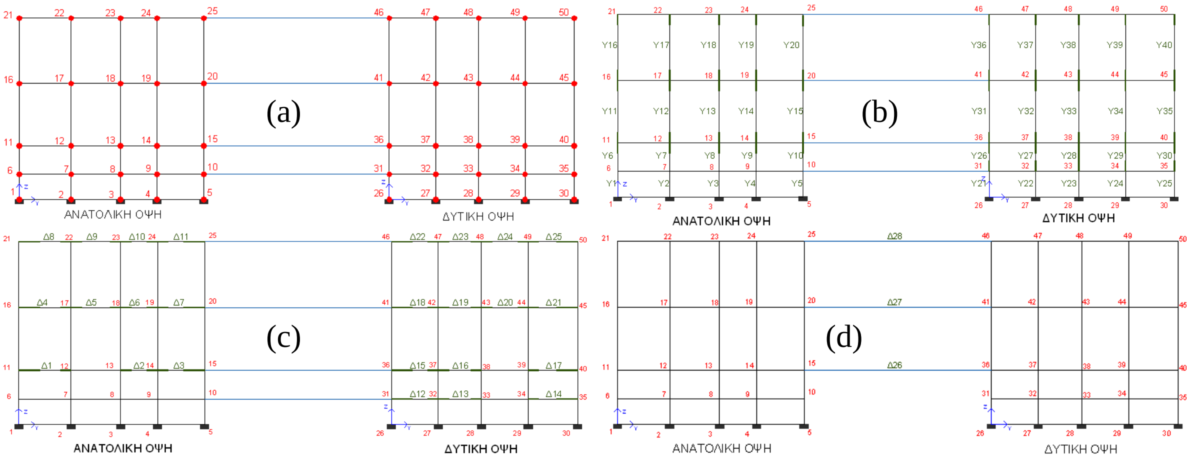

Fig. 4: Model used in simulation: (a) node numbering, (b) discretization of idealized columns, (c) idealized beams (d) connection of parallel facades using elastic links to rerpesent diaphragm action.

which is often used as a standard design earthquake motion (peak ground acceleration of 0.33g).

4 DESCRIPTION AND SIMULATION OF BUILDING B:

In the same neighborhood as building A, this structure is 12 m high (measured from the basement floor to the top), with a slightly irregular plan, having dimensions of 10.25 m (north side), 11.05 m (south side), 8.80 m (west side), and 8.35 m (east side). The building is depicted in Fig.5. Clear floor height is 2.90 m (basement), 3.4 m (first floor), 3.3 m (second floor), and 1.75 m (roof). Modeling was based on a three-dimensional idealization of the structure using a nonlinear frame-type model for each façade, where the frame elements modeling the masonry piers were located along the axes of the piers with rigid zones securing the connectivity of nodes of adjacent beams and piers (Fig. 6, 7). Diaphragm action was modeled using diagonal braces in the horizontal plane (Fig.8), whereas seismic hazard was represented by the Montenegro earthquake (1979).

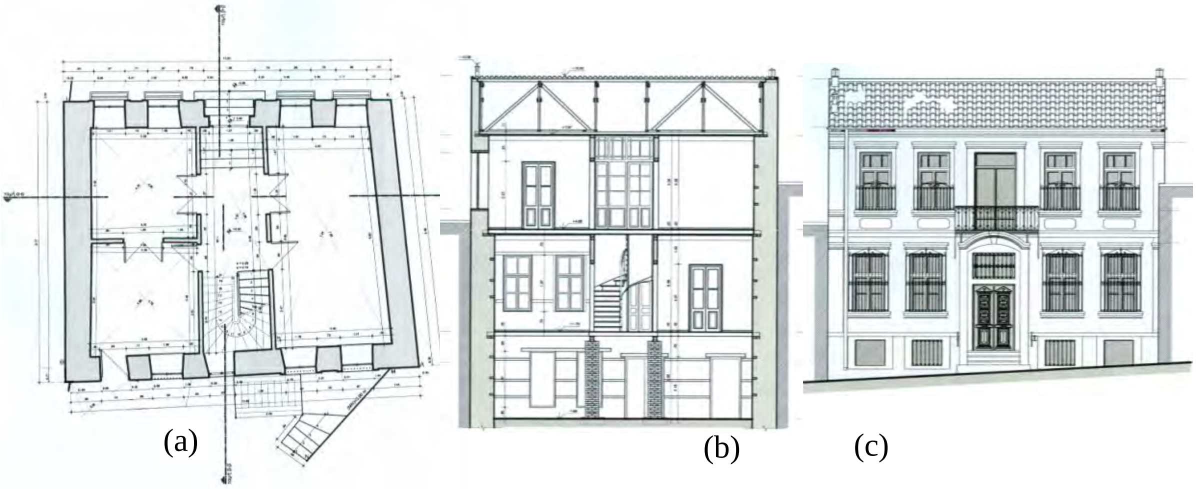

Fig. 5: Building B: (a) Plan view, (b) Cross Section, (c) View

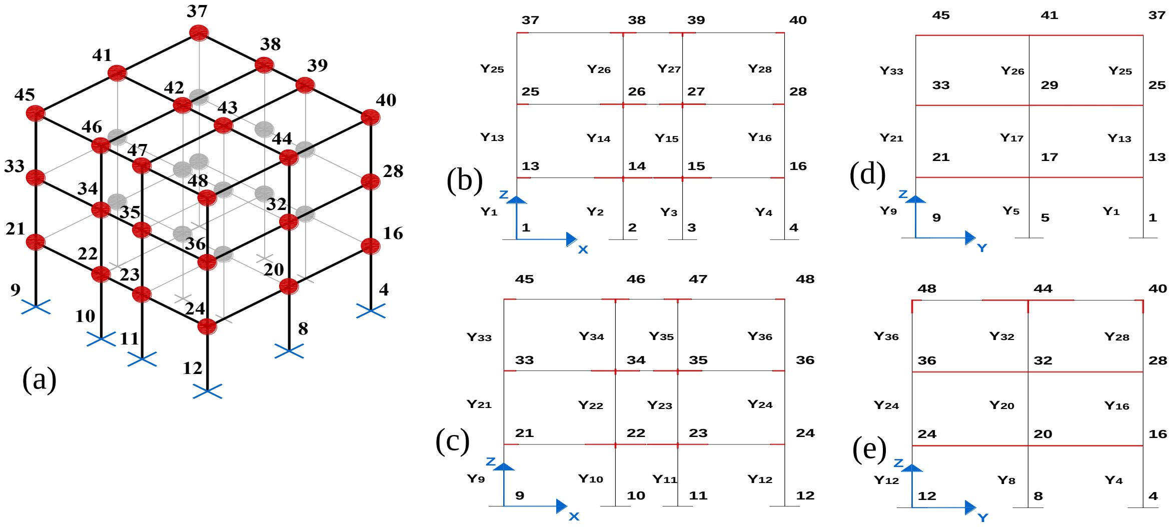

Fig. 6: (a) 3-D model, vertical elements. (b) Northern view, (c) Southern view, (d) Western view, (e) Eastern view

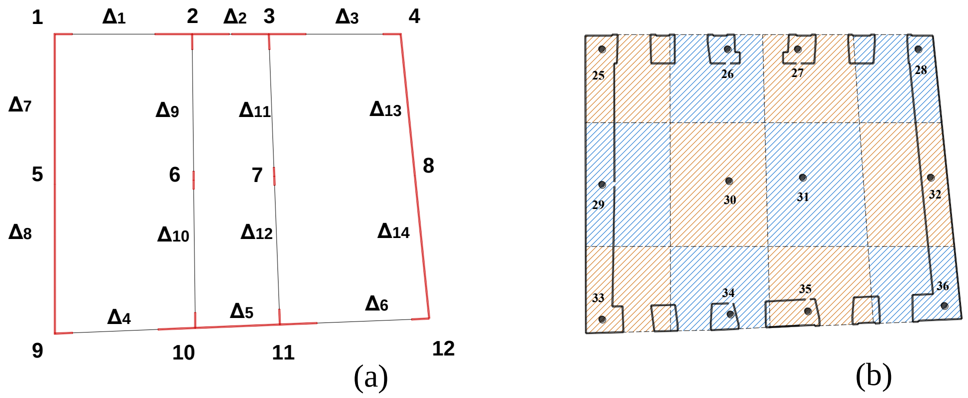

Fig. 7: (a) Horizontal members of the model at the basement level,
(b) tributary areas of idealized columns for estimation of axial loads

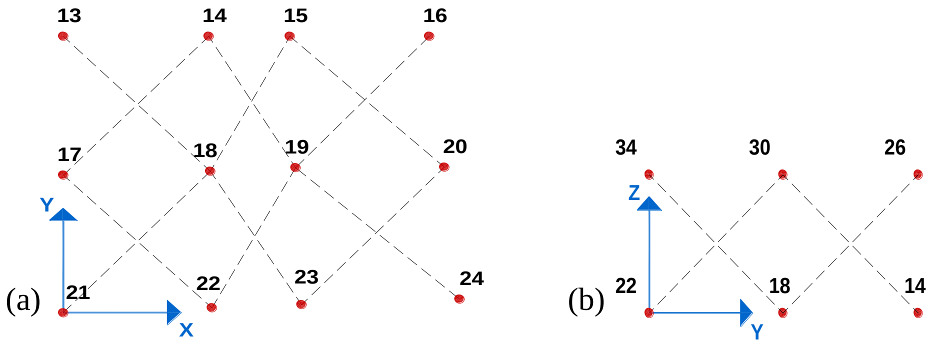

Fig. 8: (a), (b) Modelling diaphragm action through diagonal links in the horizontal plane (numbers correspond to frame nodes)

5 DESCRIPTION AND SIMULATION OF BUILDING C:

This building is located on Botsari street in the historical center of Xanthi. Its total height is 12.5 m (measured from the basement to the top), whereas plan dimensions are 12.20 m (north-south direction) by 7.65 m (east-west direction); thus the slenderness ratio for this structure was 1.63 (in the shortest plan direction). Clear storey height is 2.50 m (basement), 3.35 m (first floor), 2.95 m (second floor), 2.5 m (third floor) and 1.20 m (roof). The building is depicted in Fig. 9. This structure was modeled using 3-dimensional shell elements; finite element dimensions are in the range of 0.3 m to 0.45 m whereas timber lacing is represented by linear beam elements (Fig.10). A grillage analogy is used to model the floor beams at a spacing of 0.7m. Connection of the building along the vertical contact surfaces

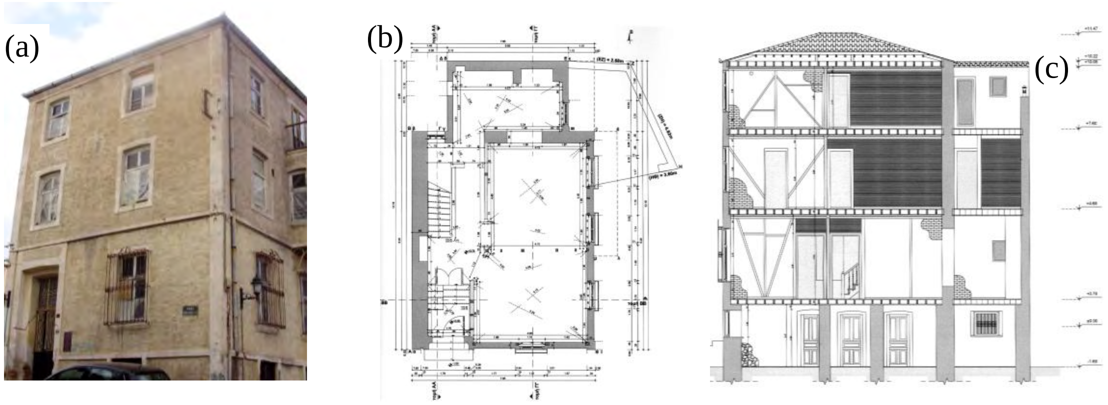

Fig. 9: Building C on M. Botsari Street: (a) South-eastern view, (b) Plan (c) Section

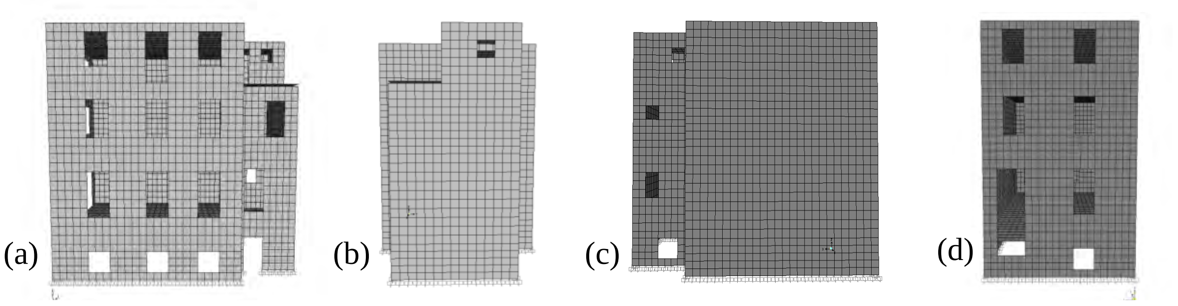

Fig. 10: Discretization of the traditional system, - Views (a) Eastern, (b) Northern, (c) Western, (d) Southern

(for the embedded depth of the basement) with the ground was modeled through one-sided nonlinear gap elements (mobilized in compression only to model bearing of the wall on soil

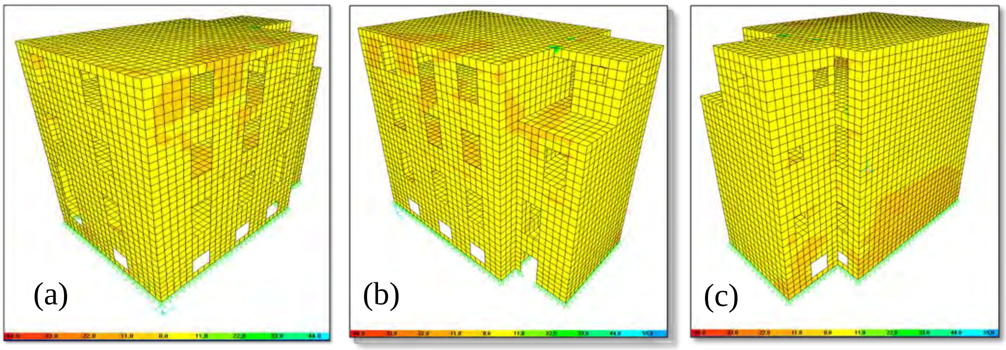

Fig. 11: Distribution of stresses σmax in the original state of the building facades

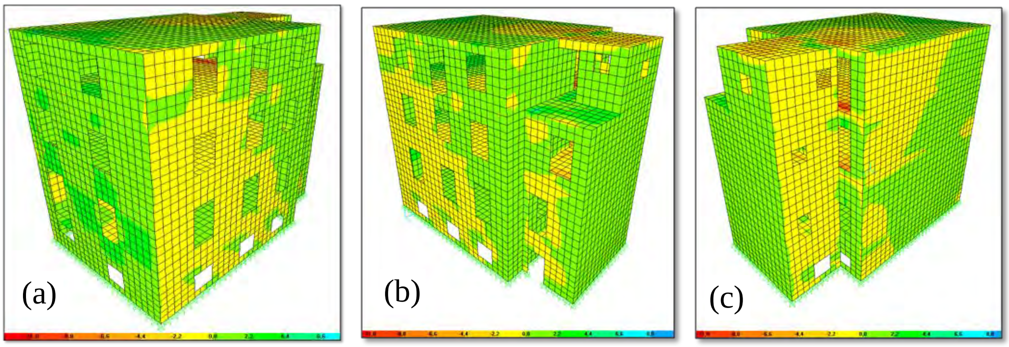

Fig. 12: Distribution of stresses σ12 in the original state of the building facades

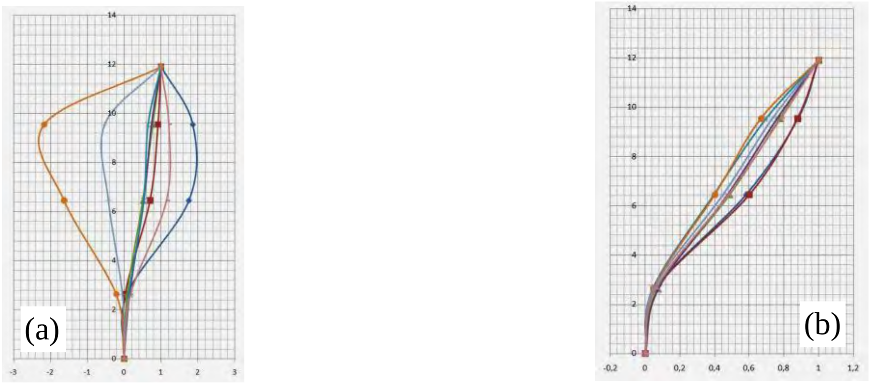

Fig. 13: (a) Lateral translational pattern U1, (b) Lateral translational pattern U2

action), whereas at the base fixity conditions were assumed against horizontal sliding. Gap element stiffness in the x and y directions are estimated from

$$\mathbf{K_x = k_x \cdot A,\ or\ K_y = k_y \cdot A}$$ **where A the tributary area of each node**

and k_x or k_y = $2.4E_s \cdot y/H^2$, where E_s the soil stiffness (estimated in the range of E_s=40000 kN/m^2), y is the distance of the gap element in consideration from the ground surface, and H the embedded height of the basement.

Flexural stiffness of the shell elements was estimated assuming cracked section (50% reduction from the reference gross value); masses are calculated from the self weight of the building, where masonry walls in the basement are 0.7m thick, reduced to a thickness of 0.25 m in the upper, clay-brick walls (from first wall upwards). The seismic hazard is represented in

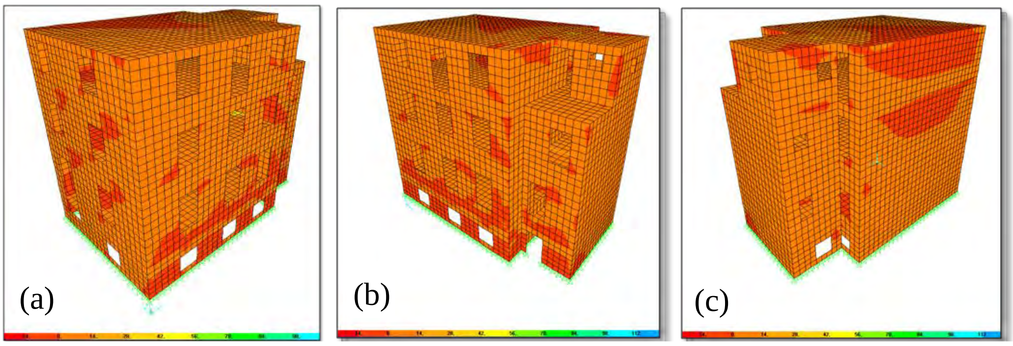

Fig. 14: Distribution of σmax on the building facades, after implementation of intended interventions

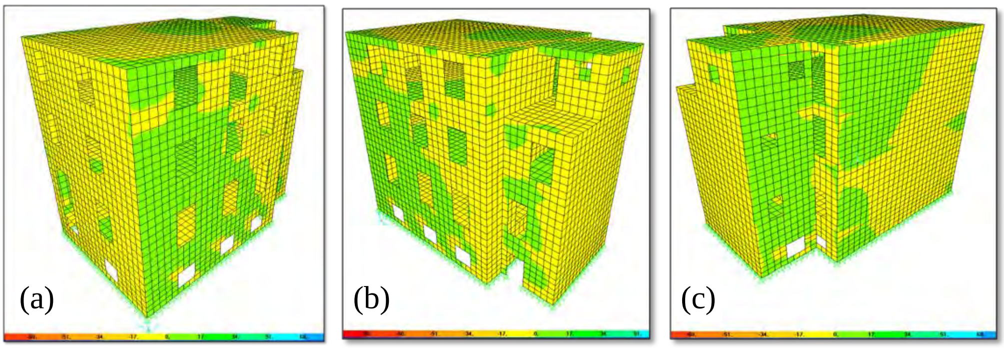

Fig. 15: Distribution of σ12 on the building facades, after implementation of intended interventions

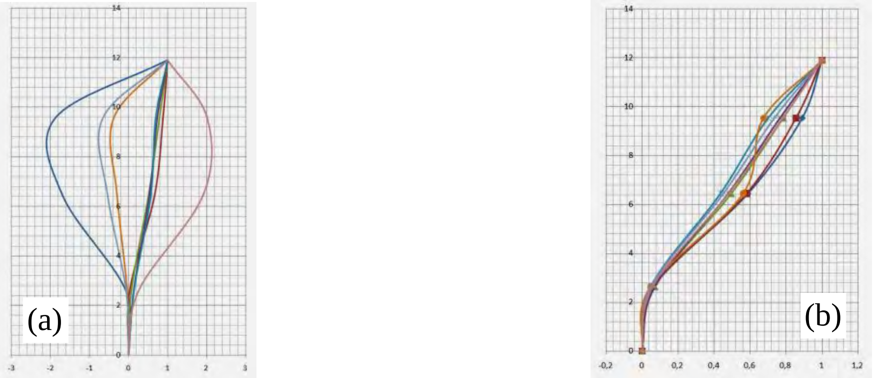

Fig. 16: (a) Lateral translational pattern U1, (b) Lateral translational pattern U2

this investigation by the nominal Greek Seismic design code spectrum (EAK 2000) using a design peak ground acceleration for the region of Thrace in the range of a_g=0.16g.

6 REDUCTION OF DISPLACEMENT DEMAND THROUGH INTERVENTION - CONCLUSIONS

The primary results of this analysis are summarized in Table 1. Values of interest is the percent reduction in the average drift for each building estimated in the as-is, as compared with the post-retrofit condition. Note that regardless of the method of modeling and simulation, the proposed interventions effectively reduce the magnitude of the demands, although they appear more effective in buildings with a frame-type tendency where stiffness enhancement was the reason for better control of displacement demand. In the case of building C, which possessed from the beginning a flexural type behavior as marked by the rather low initial period, much lower effectiveness of intervention in controlling the magnitude of the already low displacement is found. This characteristic in more prevalent in building C as compared to B

Building Code ID & slenderness ratio R (Height to smaller plan dim.)	Displ. Demand before Intervention	Displ. Demand after Intervention	Estim. Peak Drift demand before & after Interv.	Initial & Final Rotational Ductility demand
Building A, R=1.0	57 mm	9.5 mm	0.62%; 0.105%	4.3:0.7
Building B, R=1.4	35 mm	14 mm	0.29%; 0.11%	1.93:0.73
Building C, R=1.63	90 mm	60 mm	0.72%;0.48%	4.8:3.2

Table 1: Summary of the primary results of this analysis

despite the similar overall dimensions, owing to the fact that the latter is stiffened by one more diaphragm level (5 in C as compared to 4 in B) thereby rendering the upper floors at a greater risk due to the tendency for concentration of higher drift demands in the upper floors of flexural-type structures. Here, the objective is better control of demand distribution as evidenced by the deflected shape of the fundamental mode of the structure prior to and after intervention, which effectively suggests great effectiveness in the pattern of anticipated distribution of damage. Note the magnitude of estimated ductilities obtained from the post-repair drift demand assuming a drift at “yield” of the masonry structure elements in the range of 0.15% as recommended by the Greek Code for Seismic Intervention (KANEPE 2010). Note that the ductility demand is much more effectively moderated in buildings A and B, whereas the ductility demand in C is prohibitive even after the proposed rehabilitation. These simulation findings suggest that more effective strengthening measures are required in the case of building C, its primary weakness apparently being the rather low thickness (and commensurate stiffness and strength) of its free standing clay-brick walls which possess a thickness of only 0.25 m above the basement to the top of the structure without other forms of reinforcement.

REFERENCES

[1] Vitruvius, On Architecture, pp.147-175 Vol. I, Books I-V, Athens, Plethron, 1996.

[2] Touliatos P.(2000), “ Recognition and Analysis of a Local, Historic Structural System”, Proceedings of the 1st National congress for*: Appropriate Interventions for the Safequarding of Monuments and Historical Buildings,* p. 3-13, Hellenic Ministry of Culture (*4th Ephorate for Modern Monuments*) and Technical Chamber of Greece, Thessaloniki.

[3] Vintzileou E, Zagkotsis A, Repapis C, Zeris Ch (2007),“Seismic behaviour of the historical structural system of the island of Lefkada, Greece”. *Elsevier Construction and Building Materials,* 21, σ. 225-236.

[4] Langenbach R (2000), “Intuition from the past:What we can learn from Traditional Construction in Seismic Areas”, Conference Proceedings for Earthquake-safe: Lessons to be learned from traditional construction, an International Conference on the Seismic Performance of Traditional Buildings, UNESCO / ICOMOS, Instanbul, Turkey.

[5] Langenbach R (2002), "Survivors in the midst of devastation, Traditional Timber and Masonry Construction in Seismic Areas", *Conference Proceedings, 7th US National Conference on Earthquake Engineering,* Boston, Massachusetts, July 21-25.

[6] Makarios T., Demosthenous M. (2004), "Seismic response of traditional buildings of Lefkas", Proceedings of the 2nd National congress for*: Appropriate interventions for the safequarding of monuments and historical buildings,* p. 26-33 Vol. II, Hellenic Ministry of Culture (*4th Ephorate for Modern Monuments*) and Technical Chamber of Greece, Thessaloniki.

[7] Tobriner S. (2000), "Wooden Architecture and Earthquakes in Turkey: A Reconnaissance Report and Commentary on the performance of wooden structures in the Turkish earthquakes of 17 August and 12 November 1999", *Conference Proceedings for Earthquake-safe: Lessons to be learned from traditional construction, an International Conference on the Seismic Performance of Traditional Buildings,* UNESCO / ICOMOS, Instanbul, Turkey.

[8] Gülhan D, Güney I.O (2000), "The behaviour of traditional building systems against earthquake and its comparision to reinforced concrete frame systems; Experiences of Marmara earthquake damage assessment studies in Koaeli and Sakarya"*, Conference Proceedings for Earthquake-safe:Lessons to be learned from traditional construction, an International Conference on the Seismic Performance of Traditional Buildings,* UNESCO / ICOMOS, Instanbul, Turkey.

[9] Wolfgang Müller-Wiener (1995), Architecture in Ancient Greece*, pp.*70-101, University Studio Press, Thessaloniki.

[10] Prakash V., Powell G. H., Campbell S., Drain – 2dx, Version 1.02, Base Program Description and User Guide, Department of Civil Engineering, University of California, Berkeley, California, July 1992.

[11] Prakash V., Powell G. H., Campbell S., Drain – 3dx, Version 1.10, Base Program Description and User Guide, Department of Civil Engineering, University of California, Berkeley, California, August 1994.

[12] Computers & Structures Inc. SAP2000 – Structural Analysis Program, ver. 8.2, Berkeley, California, USA 2003.

[13] EN 1996, Eurocode 6, Design of Masonry Structures, 2005.

COMPDYN 2011
3rd ECCOMAS Thematic Conference on
Computational Methods in Structural Dynamics and Earthquake Engineering
M. Papadrakakis, M. Fragiadakis, V. Plevris (eds.)
Corfu, Greece, 25–28 May 2011

STRUCTURAL ANALYSIS AND DIAGNOSIS OF MASONRY TOWERS

Spyridon S. Kouris[1] and Maria K. Karaveziroglou-Weber[2]

[1] Civil Engineer MSc., Ph.D.
e-mail: spyridon.k@gmail.com

[2] Professor of Aristotle University of Thessaloniki,
Dept. of Civil Engineering, Div. of Structural Engineering,
Lab. of R/C and Masonry Structures
e-mail: mkaravez@civil.auth.gr

Keywords: masonry, monument, dynamic analysis, bell-tower, seismic strengthening.

Abstract. *The Mediterranean basin is characterized by medium up-to high level of seismic hazard but historical masonry structures, as well as a large number of old, still existing buildings, have been designed only for vertical loads; they were erected according to well established rules of common practice. In countries around the Mediterranean basin the main reason for structural failure is the combination of vertical and seismic actions. Strong earthquakes caused damages or collapse of bell towers in Greece. The few survived till today masonry "slender" campaniles are of considerable age (over one hundred years) and many of them are masterpieces of architecture in the past centuries The aim of this paper is to perform an analysis of this kind of structures. The finite element program SAP 2000 has been used for the study of the dynamic response of bell towers.*

1 INTRODUCTION

Masonry bell-towers are scattered over Greece with various densities and features from North to South. Although characterized by different stylistic decorations, age of construction and original function, their comparable geometric and structural ratios yield to the definition of an autonomous structural type. In a very concise definition, they can be described as monuments in which the total height is the prevalent dimension. Consequently, these monuments are featured by notable slenderness and this also represents one of the main differences from other historic monuments (churches, palaces, etc) or even ordinary buildings.

In Corfu, an island in north-western Greece, there exist many impressive high bell towers, which are a very important part of its main town's history, Figure 1. Bell towers are some of the only tall structures in the town, which allowed them to be invaluable surveying posts during times of war. In the past, these towers have been built as a symbol of strength, ability, and faithfulness to God (in accordance with Venice structural tradition) [1]. Their purpose lay in pointing to heaven and looking forth to survey. In times of peace, the towers were rung for celebration and mourning, to mark the hours, and in correlation with the Christian Orthodox festivals. In the past, bells were rung frequently, to call people to mass, celebrate Christian events and holidays, even just to keep time. There was at least one bell-tower in every neighborhood and typically, the inhabitants look upon their local bell tower with great pride.

Figure 1: The bell tower of St. Spyridon in the town of Corfu and the bell tower St. Mathias in the village of St. Mathias in Corfu.

Nowadays, it has become common that the bells are played automatically, and there is no reason for a bell ringer to inspect them. Since there is no bell ringer visiting the tower daily, there is no one there to observe the towers' condition and the bell-towers can easily fall into a state of disrepair. Also Corfu bell-towers were erected in areas of relatively high seismic activity. So, in addition to that, it has become evident that the bell-towers have suffered from damages and cracking caused by earthquakes and lack of repair, Figure 2. It is obvious that a seismic strengthening is essential for them, in order to avoid a total collapse and help them to survive.

Figure 2: Corfu bell-towers have suffered from damages and cracking from earthquakes.

2 DYNAMIC ANALYSIS OF A CORFU BELL-TOWER

For the investigation of a bell-tower's dynamic behavior, it is important to have a clear understanding of its structural parts. A bell tower usually consists of a strong base and a high body with the belfry. The foundation and the ground floor of the tower are constructed with heavier and thicker walls than its top parts near the belfry. Thus the most important parts of a bell tower are the base, the shaft, and the belfry. The base is usually the heaviest part and it is constructed with a non-porous stone material which should be strong enough to bear the structural pressure of the tower.

The shaft of a bell tower is by far the largest physical component of the tower. There are staircases and/or ramps that traverse the shaft, often with several landings on the way up. The shaft is usually made of bricks joined by mortar. The form and the strength of the bricks that were used varied according to the year the tower was erected, as brick manufactures improved the quality of their products over the time in order to reach a better brick resistance to higher pressures. On each of the belfry sides there was a double arch supported by a pier on either side and by a stone column in the center of the double arch. Above the belfry was the bell tower roof, a curved dome of bright red color, based on a cubic drum. The belfry is usually constructed using bricks and in many cases elaborated decorations of stone or clay are added. Generally, inside the belfry bells are supported by wooden beams.

To evaluate the dynamic behavior of a typical Corfu bell-tower, an analytical model with 3D shell and frame elements (Finite Element Method) was developed [2], Figure 3. The tower, built in 18th century, was constructed by solid bricks and lime mortar and its height is 30m approximately. The mass of masonry structure is distributed throughout the wall. So, masonry structures should be analyzed by F.E.M. with shell or solid elements.

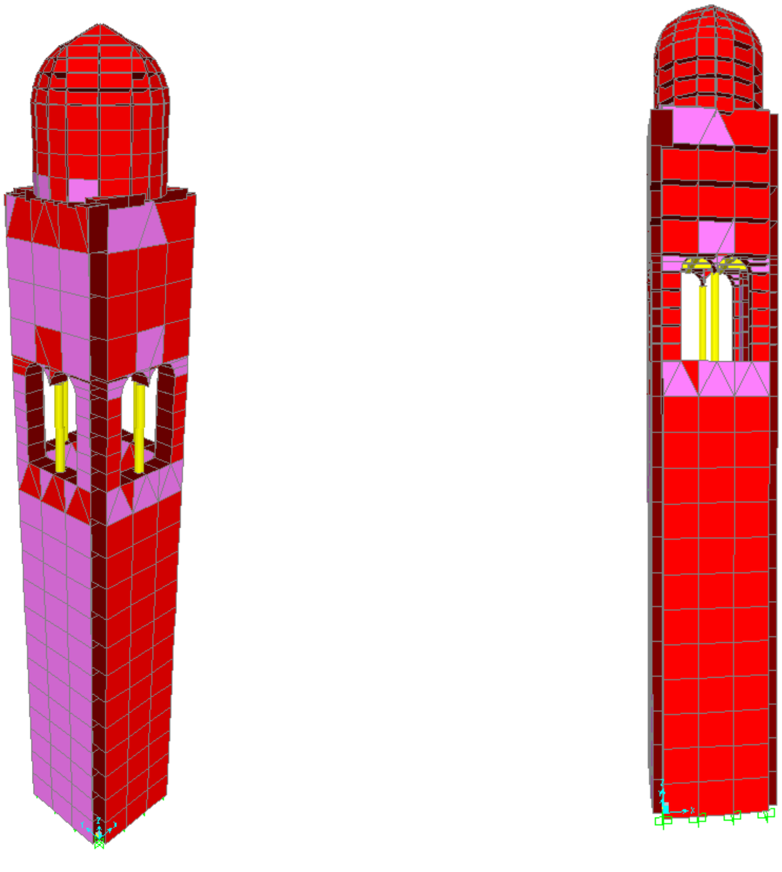

Figure 3: The analytical model with 3D shell and frame elements (F. E. M.) of the brick masonry bell tower of St. Spyridon church.

Eurocode-6 has been chosen to define the mechanical properties of masonry [3]. So, the characteristic compressive is given by relation: $f_{wc} = k \cdot f_b^{0.65} \cdot f_m^{0.25}$
where k is constant concerned with the characteristic compressive strength of masonry, f_b is the normalized compressive strength of a masonry unit and f_m is the compressive strength of

mortar. The design compressive strength is given by: $f_d=f_k/\gamma_M$ where the γ_M factor for masonry depends on the category of construction control (A↔ high, C ↔low), and the category of manufacturing control of masonry units (I↔ high quality control, II↔ normal quality control). So it was belonged in C- II category (γ_M=3.0) and group 3 (k=0.40). The modulus of Elasticity is given by: $E_{wo}=1000\ f_{wc}$ (EC-6, part 6-1, 3.8.2), but the existing pattern of cracking in vertical masonry reduces the initial module of Elasticity. We assume that the relationship between module of Elasticity of masonry with cracking and the initial could be: $E_{wcr}=2/3E_{w0}$ [2]. So, according to EC-6 [3], are computed:

- $f_{wc}=k\cdot f_b^{0.65}\cdot f_m^{0.25}$=1.977MPa, f_b=10 MPa , f_m=1.5 MPa
- γ_M=3.0, f_{wd}=1.977/3.0=0.659 MPa =0.66 MPa
- γ_s=18 KN/m^3, m_s=1.83 t/m^3, v_s=0.15
- $E_{w0}=1000\cdot f_{wc}\approx 1000\cdot 1.977\text{MPa}=1977\text{MPa}$,

Take into account the cracking on the masonry walls of the bell-tower, the modulus of Elasticity [2] was considered: $E_{wcr}=\frac{2}{3}\cdot E_{w0}=1318\text{MPa}$

As mentioned above, linear elastic analysis was carried out using SAP 2000 software [4], for bell-tower. The direction of ground acceleration corresponded to the X,Y,Z directions within SAP 2000. The elastic spectrum from Eurocode-8 [5] was used anchored to a basic ground acceleration of 0.24g in agreement with the Greek Code which defines that Corfu belongs to seismic zone II, [6]. The seismic effects were then computed according to the current Greek Code, which is in agreement with international recommendations in the field. For the modal-superposition analysis of the campanile subjected to dynamic loads, the Ritz-vector analysis was carried out, Table 1. The reason that Ritz-vectors yield such excellent results is that they take into account the spatial distribution of dynamic loading, whereas the direct use of the natural mode shapes neglects to consider this important piece of information [7]. From the results of analysis it was observed that the maximum tensile stress in the bell-tower wall occurs in and beneath the arched areas of the structure, Figures 3, 4.

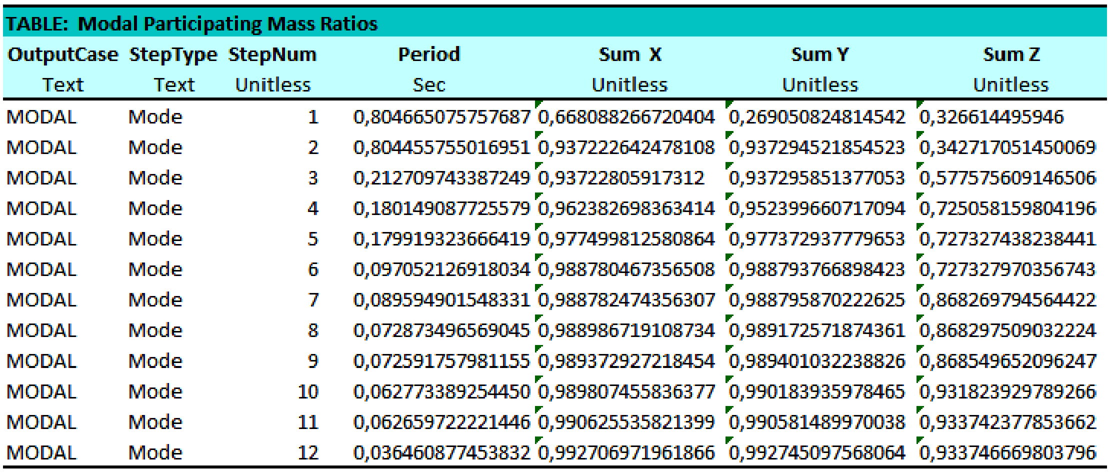

TABLE: Modal Participating Mass Ratios

OutputCase	StepType	StepNum	Period	Sum X	Sum Y	Sum Z
Text	Text	Unitless	Sec	Unitless	Unitless	Unitless
MODAL	Mode	1	0,804665075757687	0,668088266720404	0,269050824814542	0,326614495946
MODAL	Mode	2	0,804455755016951	0,937222642478108	0,937294521854523	0,342717051450069
MODAL	Mode	3	0,212709743387249	0,93722805917312	0,937295851377053	0,577575609146506
MODAL	Mode	4	0,180149087725579	0,962382698363414	0,952399660717094	0,725058159804196
MODAL	Mode	5	0,179919323666419	0,977499812580864	0,977372937779653	0,727327438238441
MODAL	Mode	6	0,097052126918034	0,988780467356508	0,988793766898423	0,727327970356743
MODAL	Mode	7	0,089594901548331	0,988782474356307	0,988795870222625	0,868269794564422
MODAL	Mode	8	0,072873496569045	0,988986719108734	0,989172571874361	0,868297509032224
MODAL	Mode	9	0,072591757981155	0,989372927218454	0,989401032238826	0,868549652096247
MODAL	Mode	10	0,062773389254450	0,989807455836377	0,990183935978465	0,931823929789266
MODAL	Mode	11	0,062659722221446	0,990625535821399	0,990581489970038	0,933742377853662
MODAL	Mode	12	0,036460877453832	0,992706971961866	0,992745097568064	0,933746669803796

Table 1: Results of dynamic analysis. Periods and Modal Participating Mass Ratios for the first 12 modes.

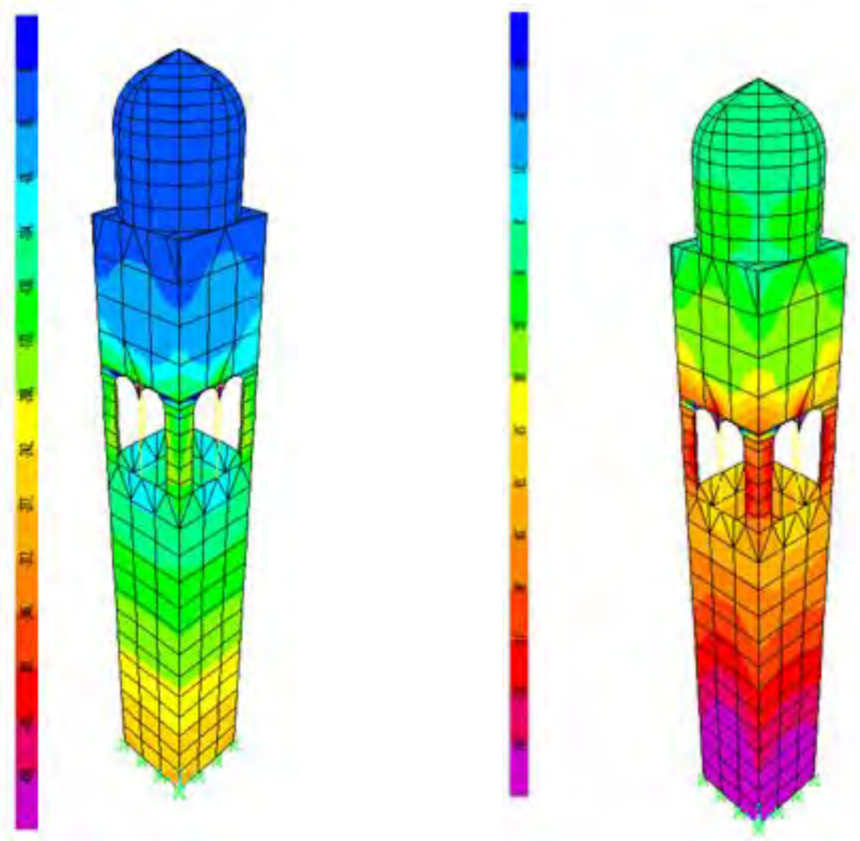

Figure 3: Stress patterns of the model under vertical loading and seismic loading correspondingly.

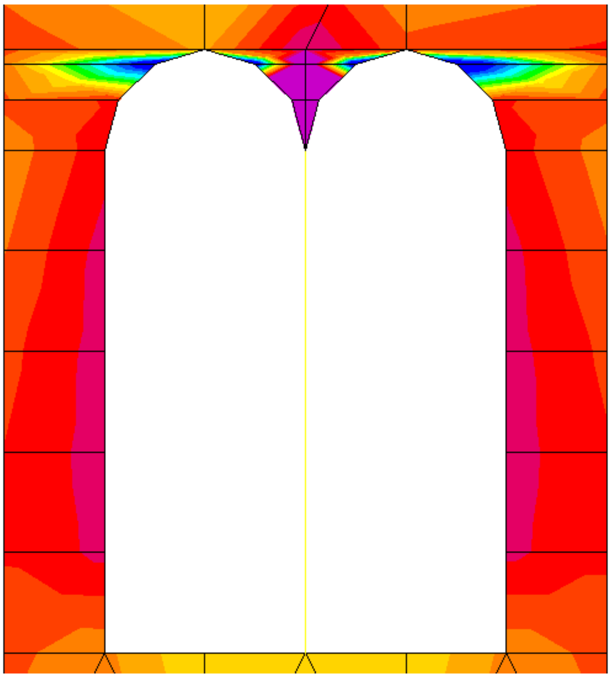

Figure 4: The maximum tensile stress in the bell-tower wall occurs in the arched areas of the structure.

3 DESIGN OF THE STRENGTHENING SCHEME

The analysis and design of strengthening scheme is a real challenge. A higher degree of damage in a historical masonry building is expected during an earthquake if the seismic resistance of the building is inadequate. The decision to strengthen it before an earthquake occurs depends on the building's seismic resistance. The structural system of deficient bell tower should be adequately strengthened in order to attain the desired level of seismic resistance. *A "Monument Safety" level corresponds to a situation in which the maximum probable earthquake (during an assigned time of reference, considerably longer than for ordinary buildings) is expected to produce repairable damages only (EC-8, Part 1-4, Annex F, F 4.4)*, [5].

The term strengthening comprises technical interventions in the structural system of a building that improves its seismic resistance by increasing the strength, stiffness and/or ductility. New codes and guidelines are founded on the concept of a structural system being designed or rehabilitated to achieve a particular level performance during an anticipated earthquake. These documents on the strengthening of existing masonry buildings, to increase its seismic resistance are:

- FEMA 273: *Guidelines for the Seismic Rehabilitation of Buildings.*
- New Zealand Draft Code [NZDC]: *The Assessment and Improvement of the Structural Performance of Earthquake Risk Buildings.*
- SERC Report: *Formulation of Guidelines for Assessment of Strength and Performance of Existing Buildings and Recommendations on Retrofitting Schemes to Ensure Resistance to Earthquake.*
- UNIDO Vol. 4: *Post-Earthquake Damage Evaluation and Strength Assessment of Buildings under Seismic Conditions.*
- EUROCODE 8: *Design Provisions for Earthquake Resistance of Structures – Part 1-4 General Rules for Strengthening and Repair of Buildings.*

The strengthening scheme of FEMA 273 [8] and EUROCODE-8 [5] consist many strengthening techniques to remedy structural deficiency, as shown in the Table 2. For monumental buildings emphasis is given to strength material type and the adequate technique to success that is the application of a strengthening mortar on the walls of the inside facade.

The simulation method for the strengthen mortar (concrete) that was proposed is based on the principals of Eurocode-6 [3] and Eurocode-2 [9]. The stress-strain diagram for the design masonry [3], Figure 5, is the same as that for the design concrete [9], Figure 6, parabolic up to 0.2%, rectangular up to 0.35%.

So a wall of masonry could be simulated as a wall of a concrete with mechanical properties of masonry, Figure 7. As a consequence of this strengthening scheme, the overall ductility of the structural system was improved. From the results of frequencies, it was observed that reinforced jacket improves the behavior of the bell-tower, Figure 8.

No	FEMA 273	EUROCODE-8
1	Infilled Openings	Reduction of the mass , particularlt at high levels, e.g., by remival of heavy rooof covering, etc.
2	Enlarged Openings	Reduction of the eccentricity between the mass and the stiffness centers, to avoid large torsional effcts, especially in buildings with strong diapfragmatic action on the floor
3	Shotcrete	Strengthening of walls by means of reinforced concrete "jackets" or steel profiles
4	Coatings for (URM) walls	Improvements of the quality of the masonry (e.g. by grouting). Due consideration should be given to the subsequent increase of stiffness and decrease of damping
5	Reinforced Cores for (URM) walls	improvements of the connections between the resisting elements (e.g. anchorage of the horizontal diaphragms in the vertical bearing elements, etc.
6	Prestressed Cores for (URM) walls	Application of vertical and horizontal confining elements to the walls
7	Braced Masonry walls	Addition of new bracing walls
8	Stiffening Elements	Improvement of the diaphragmatic action of the floors by increasing their in-plane shear stiffness and resistance
9	Enlargment of footings by placement of reinforced shotcrete or with additional reinforced concrete section	Repair or strengthening of foundation

Table 2: Strengthening techniques in accordance with FEMA 273 and EUROCODE-8

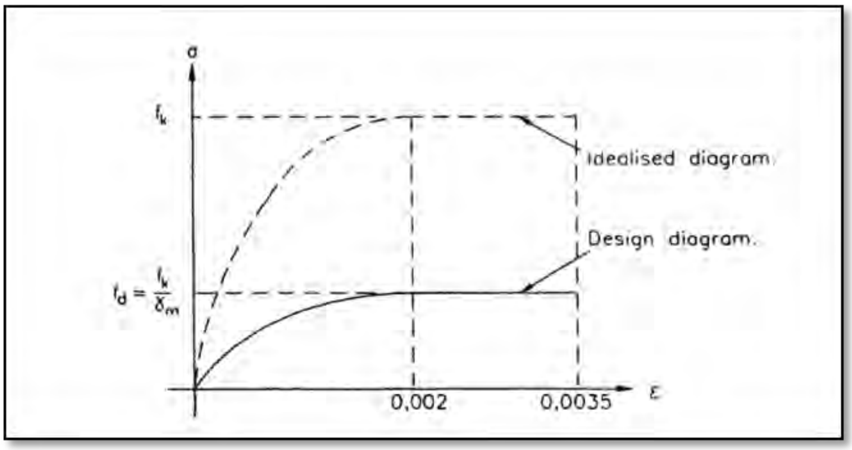

Figure 5: Stress-strain relationship for the design of masonry in bending and compression (EC-6, Part 6-1-1, section 3.8.1, fig. 3.3).

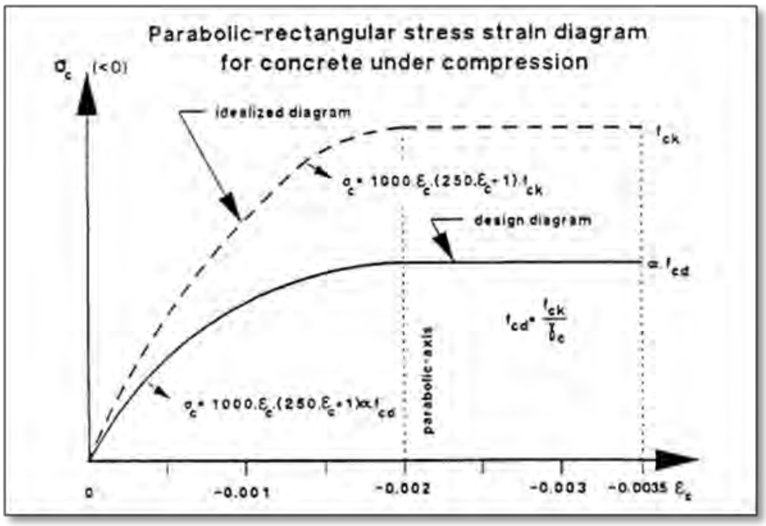

Figure 6: Stress-strain relationship for the design concrete in compression
(EC-2, Part 2-1-1, section 4.2.1.3.3, fig. 4.2).

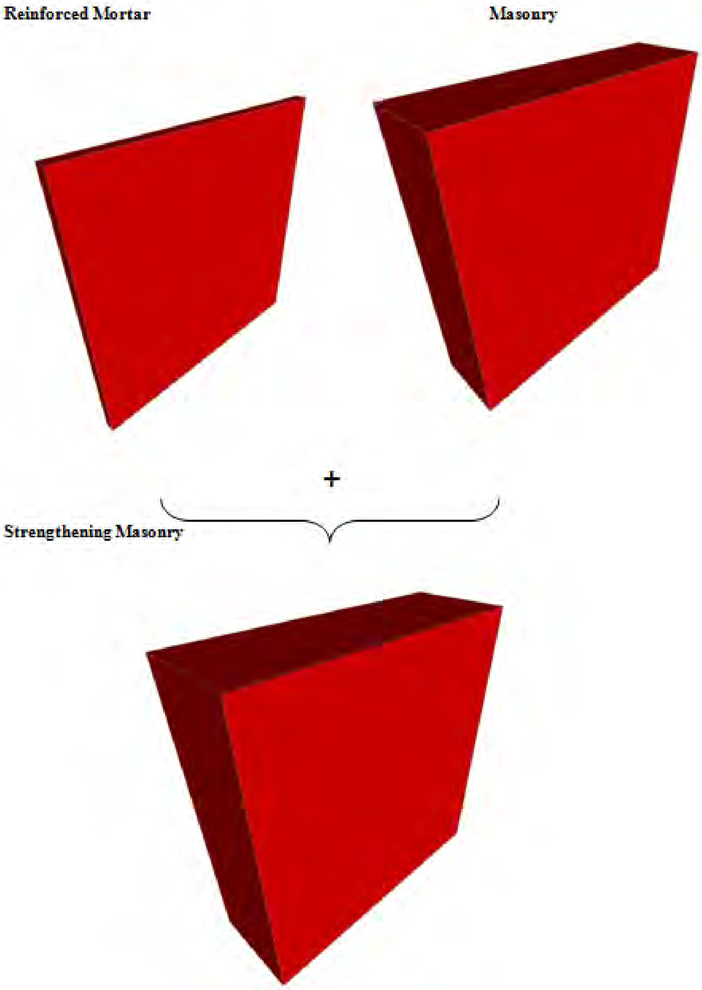

Figure 7: A simplified scheme of strengthening masonry with reinforced mortar (gunite) applying on to interior wall.

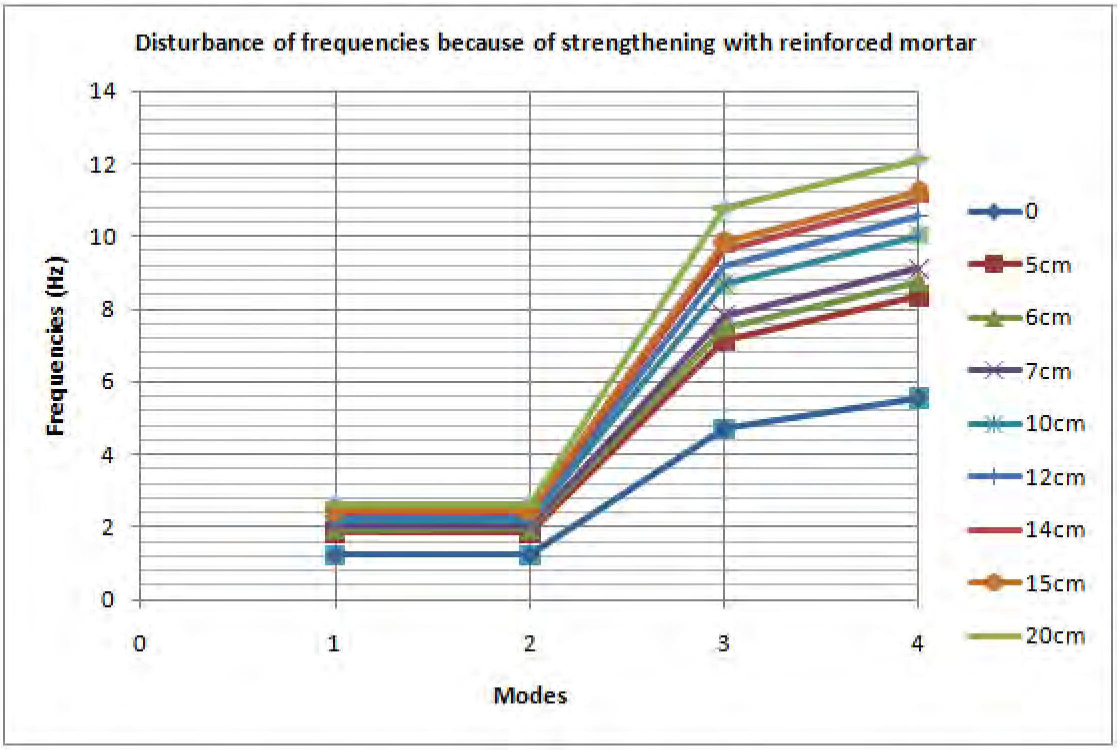

Figure 8: Results of frequencies because of strengthening scheme with different thickness of reinforced jacket.

4 CONCLUSION

In this paper it has researched the benefits of reinforced concrete strengthening of historical masonry bell towers. This method is proposed as strengthening method from FEMA 273 [8] and EUROCODE-8 [5]. The simulation method for reinforced concrete (gunite) strengthening that it proposed is based on the principals of Eurocode-6 [3] and Eurocode-2 [9]. From the results of frequencies, it was observed an increasing of the total stiffness of a bell tower and generally an improvement of the overall ductility its structural system.

REFERENCES

[1] Marion M., Milkin M., Mill E., Vitone C., *Preservation of Venetian Bell-Tower*, Venice Project Center, Italy, 2004.

[2] Kouris S.S., Karaveziroglou-Weber M., *Research on the Seismic Strengthening of Medieval Masonry Campanile*, The Structural Engineer, 87 (7) 2009, pp 20-24, 2009.

[3] Eurocode 6: *Design of Masonry Structures:* Commission of the European Communities, ENV1996.

[4] Integrated Software for *Structural Analysis and Design ANALYSIS REFERENCE MANUAL SAP 2000*, 'Computers and Structures', University Avenue, Berkeley, California, USA, 1995.

[5] Eurocode 8: *Design Provisions for Earthquake Resistance of Structures*: Commission of the European Communities, ENV1998.

[6] EAK 2000: *Greek Code for Earthquake Resistance of Structures*, OASP, Greece, 1996.

[7] Wimmer H., Majer J., Niederwanger G., *Dynamic behavior and numerical simulation of old bell-towers, in Structural Repair and Maintenance of Historical buildings*, C.A. Brebbia, Computational Mechanics Publications, pp 349-358, Southampton, UK, 1989.

[8] FEMA 273, *Guidelines for the Seismic Rehabilitation of Buildings,* USA, 1996.

[9] Eurocode 2 : *Design of Concrete Structures*: Commission of the European Communities, ENV 1992.

COMPDYN 2011
III ECCOMAS Thematic Conference on
Computational Methods in Structural Dynamics and Earthquake Engineering
M. Papadrakakis, M. Fragiadakis, V. Plevris (eds.)
Corfu, Greece, 25–28 May 2011

INTERPRETATION OF RECORDS FROM TEMPORARY AND PERMANENT INSTRUMENTATION TO IDENTIFY THE DYNAMIC RESPONSE OF A HISTORICAL BUILDING TO SEISMIC ACTIONS

D. Rinaldis[1], **P. Clemente**[2], **and G. Buffarini**[2]

[1] ENEA
Casaccia Research Centre, Via Anguillarese 301, 00123 Rome (Italy)
e-mail: dario.rinaldis@enea.it

[2] ENEA
Casaccia Research Centre, Via Anguillarese 301, 00123 Rome (Italy)
e-mail: paolo.clemente@enea.it

[3] ENEA
Casaccia Research Centre, Via Anguillarese 301, 00123 Rome (Italy)
e-mail: giacomo.buffarini@enea.it

Keywords: Seismic Input, Temporary and Permanent arrays, Experimental Dynamic Analysis, Finite Elements Model, Structural Identification.

Abstract. *The CEDRAV building in Cerreto di Spoleto, originally a monastery, was built in the 14th century on the top of a rock ridge. The two events occurred on September 26th, 1997, with magnitude Ms=5.4 and Ms=6, respectively, caused damages to it. Ambient vibration measurements were first performed by using fifteen SS-1 uniaxial velocity sensors (natural frequency 1.0 Hz) connected to five K-2 recorders and deployed in nine different configurations. Then the building was permanently instrumented by using 36 accelerometers. Results from analyses of representative seismic response data acquired from the building specific permanent deployment are also included and classified by means of cumulative normalized energy plots. The building is very complex and rigid. In fact, translational and torsional frequencies are close to one another, coupling occurs and damping ratio is low. Coupling of the frequencies and low damping are two factors that cause beating effect when shaking is strong enough. In the case of this study, the shaking levels are not large but yet the building is affected by beating effect. As stated the CEDRAV is an old buildings and has been altered repeatedly over time. This will cause dynamic interactions with other buildings or substructures during an earthquake.. On the base of recorded data a preliminary analysis in frequency domain, based on the determination of auto and cross power spectral density, has been carried out. Then the modal structure's identification has been performed by means of Ibrahim technique, working in the time domain, and Frequency Domain Decomposition technique, working in the frequency domain.*

1 INTRODUCTION

The dynamic response of the CEDRAV building in Cerreto di Spoleto (Italy), originally a monastery, built in the 14th century on the top of a rock ridge, has been deeply studied by means of experimental measurement campaigns and numerical modeling. Temporary arrays, excited by means of ambient vibration or weak motions, and a permanent array to obtain records of seismic events were deployed. Two events occurred on September 26th, 1997 (epicenter Colfiorito, distance $\approx$ 30 Km), with magnitude Ms=5.4 and Ms=6, respectively, and one on October 14th, 1997 (epicenter Sellano distance $\approx$ 10 Km), Ms=5.4. They caused damages to the building but only strong-motion records from the free-field accelerometric array were available to try to correlate the seismic input with the damage. Ambient vibration measurements were first performed by using fifteen SS-1 uniaxial velocity sensors (natural frequency 1.0 Hz) connected to five K-2 recorders and deployed in nine different configurations. Then the building was permanently instrumented by using 36 accelerometers. Transducers were installed in different locations of the structure. In particular, some of these were arranged on the perimeter walls to obtain torsional modes of the structure.

When recording seismic events, use integrated arrays is essential, i.e., to deploy free-field sensors in parallel to those in the building, to assess the ground shaking [1, 2]. It is worth noting that the structure may experience non-linear behavior during strong earthquakes. Thus, if the parameters of linear behavior are known beforehand, it may be easier to extrapolate the non-linear behavior but this process is very difficult for old damaged masonry buildings. For such cases, even for very small excitation, non-linear behavior may be experienced by the structure, which could be approximated with a pseudo-linear approach**.**

2 ENERGY PLOTS OF RECORDED EVENTS

Results from analyses of representative seismic response data acquired from the building specific permanent deployment are processed and classified by means of cumulative normalized energy plots. Recordings were obtained at 3 different level of the rock basement (CH01, CH02, CH03, CH19, CH20, CH21, CH22, CH23 and CH24 - Italic evidences sensors in the vertical direction). Data were compared with those obtained in the station "Cerreto Comune 1 Basement" of the permanent free field array for the event of January 21th, 2000. Figure 1 shows the cumulative Arias intensity for the records at the CEDRAV basement when figure 2 shows the values obtained at the free-field station: for this event the energy in the vertical component seems negligible compared to the horizontals ones. This trend is confirmed in two stations at the CEDRAV basement (CH02, CH20). Figure 3 shows instead the values of cumulative Arias intensity at the array station of "Cerreto Comune 2 Roof" for records obtained during the damaging events (September 26th and October 14th, 1997). First of all we have to outline that accelerograms were recorded by an accelerograph installed in the roof of the building. Of course a larger energy level is observed but the vertical components are still less demanding than the horizontal ones. What it is important to outline is the fact that the aftershock of October 14th was much more damaging for the historical center of Cerreto di Spoleto then the main shock of September 26th. The reason is evident looking at figure 3 where the cumulative Arias intensity evaluated from the acceleration components recorded on October 14th are 4 to 5 times larger than the ones recorded during the main shock (second shock of September 26th). This is shown as well in figure 4 where the cumulative Arias intensity of accelerometric components obtained at Borgo Cerreto Torre station are compared. Values are, of course, smaller because site effect as the hill morphology and the structural amplification are not included, but the global trend is similar.

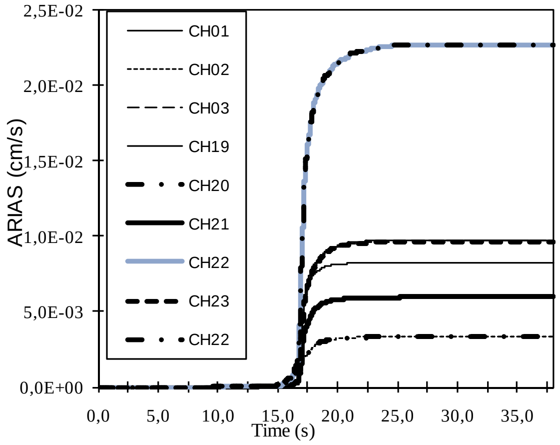

Figure 1: Cumulative Arias Intensity plots for the acceleration time histories obtained at the basement of the CEDRAV during the seismic event of the January 21st, 2001, Ml=4.

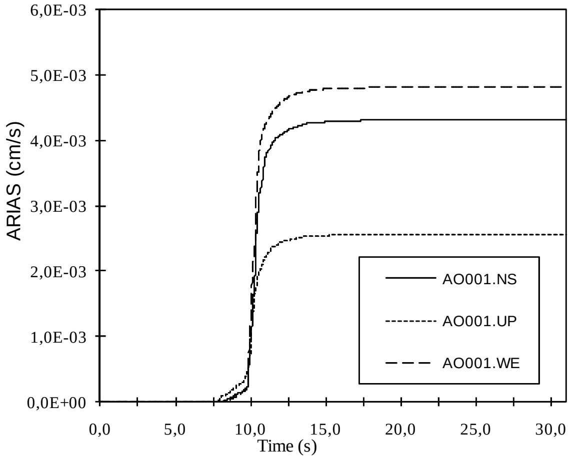

Figure 2: Cumulative Arias Intensity plots for the acceleration time histories obtained at “Cerreto Comune 1 Basement” during the seismic event of January 21st, 2001.

3 PERMANENT ARRAY VERSUS TEMPORARY DEPLOYMENT

Information on CEDRAV building may be obtained from two sources: dynamic testing of the structure (ambient and forced vibration) and analyses of data from permanent array. The second is based on strong-motion response data, which depends on a long duration project that is costly to implement and maintain. Therefore, whenever possible, low-amplitude tests are used to verify the results of analytical studies. On the other hand the seismic behavior of structural systems can be better understood if arrays of seismic sensors can be deployed throughout the structures in order to record their responses during strong shaking events. In more details, temporary arrays are generally used for dynamic characterization of structures, which can be excited by means of ambient or forced vibrations [3].

The CEDRAV building was both instrumented with a temporary deployment of velocimetric sensors in 9 configurations and then with a permanent strong-motion array of accelerometric sensors [3]. Recordings of both arrays were analyzed and compared to recover the dynamic characteristics of the building (resonance frequencies, damping, etc.) [3, 6]. Of course, the interest of results is limited by the fact that the building was not instrumented during the shocks of September 26th and October 14th, 1997. Nevertheless the following results were obtained:

a) The building is very complex and rigid; translational and torsional frequencies are close to one another;

b) Coupling occurs. Damping percentage is low. Coupling of the frequencies and the low damping are two factors that cause beating effect when shaking is strong enough. In this study, the shaking levels are not large but the building is affected by beating effect yet.

c) The results obtained from the velocimetric recordings are very similar to those obtained by means of the accelerometric recordings. The differences in the resonance frequency values are to be related to the fact that higher energy events were recorded by the temporary arrays.

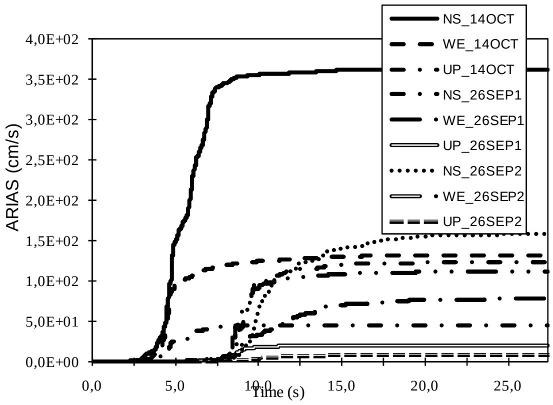

Figure 3: Cumulative Arias Intensity plots for the acceleration time histories obtained at "Cerreto Comune 2 roof" during the seismic event of September 26st, 1997 (2 shocks magnitude Ml=6 and Ml=5.4, epicenter in Colfiorito), and of October 14th, 1997 (Ml=5.4, epicenter in Sellano).

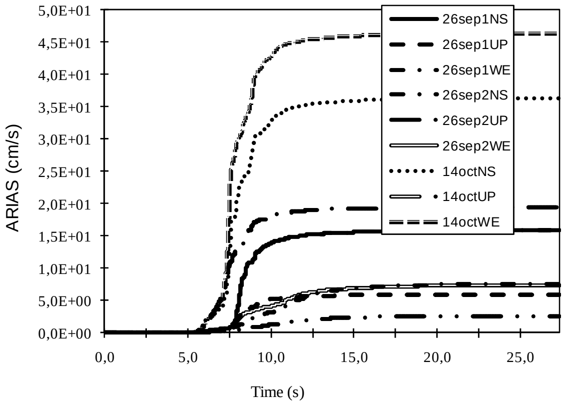

Figure 4: Cumulative Arias Intensity plots for the acceleration time histories obtained at "Borgo Cerreto Torre" during the seismic event of September 26st, 1997 (2 shocks magnitude Ml=6 and Ml=5.4, epicenter in Colfiorito), and of October 14th, 1997 (Ml=5.4, epicenter in Sellano).

Figure 5 shows velocity time-histories from the temporary array recorded at the three different levels of the building, where an approximate period of 2.5 *s* for the beatings was computed. In figure 6 the comparison between PSDs of recordings obtained from ambient noise, weak motion and impulse, produced by lifting a caterpillar tractor arm and dropping)., in Configuration1 is shown. It is clear that the most severe excitation was the impulse.

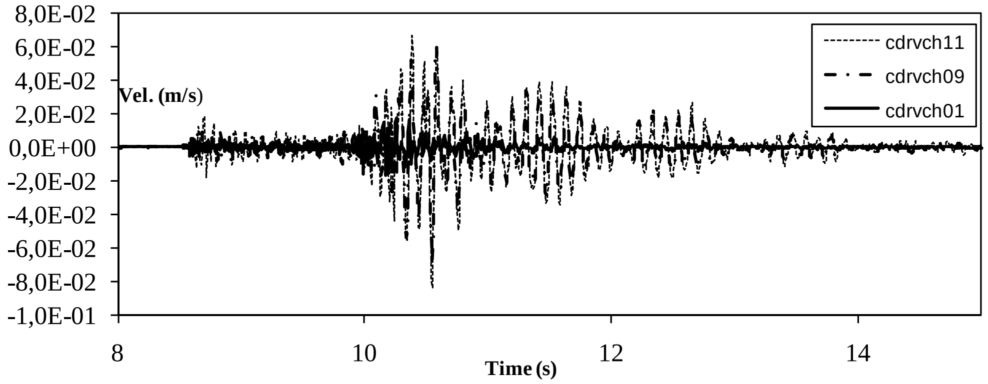

Figure 5: Velocity time-histories from the temporary array, Configuration1. Records were obtained at 3 different level (cdrvch01=basement, cdrvch09=2nd floor, cdrvch11=3rd floor).

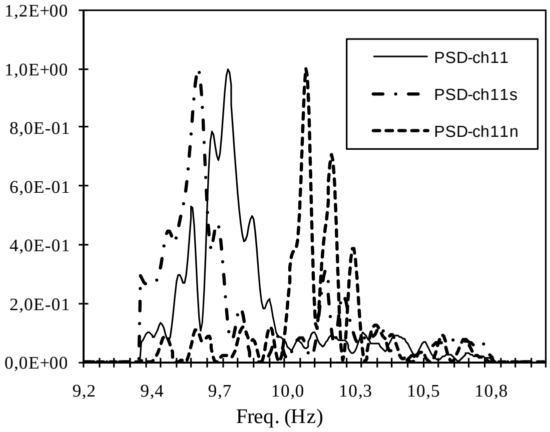

Figure 6: PSD (normalized to the peak) of time-histories from the temporary array (CH11), Configuration1. Records are obtained from weak motion, ambient noise (n) and impulse (s)

As previously stated, the 9 configurations of the temporary array were used for the dynamic characterization of the building, which have been excited by means of ambient or forced vibrations (shock) and sometimes by means of weak seismic events [1, 2, 3, 6]. The knowledge of the influence of the dynamic interactions with adjacent buildings on the modal shapes and frequencies is of fundamental importance to characterize the mechanisms that underlies the damage time history, as will results in the description of behavior of the building. It is worth pointing out that temporary arrays are useful to analyze private buildings, where sensors fixed on the structure are usually not allowed. The reason to select a certain number of configurations depends on the cost/benefit analysis: more configurations you select more accurate your analysis is, but this requires more resources to use for the analysis. So we decided to use eight configurations: four configurations to study the building behavior, and four configurations to investigate the structure-environmental built interaction [6].

The dynamic characterization of the structure, using ambient and forced vibration tests, allowed to have very important information about the health status of the structure and to point out its main dynamic characteristics. Results from Configuration 6 outline a peak at 6.2 *Hz* associated to a modal shape involving the rectangular building and the church motion, in which the structure rotate with respect to a vertical axis. Results from Configuration 8, in which CEDRAV and a smaller building connected to it by means of a masonry arch were instrumented, pointed out that the behavior of the CEDRAV wall with reference to the masonry arch depends on the analyzed event. These observations may be important to evaluate the damage induced mechanism by the October 14th 1997 event (Ml = 5.4) on the NW wall of the CEDRAV building.

4 NUMERICAL MODEL AND EXPERIMENTAL DATA

A 3D finite element model has been developed by using the computer code COSMOS with the purpose to compare the numerical results with those obtained by the experimental measures [4]. Based on standard (obtained from literature) material mechanical characteristics, the values of the frequencies for the first twenty modes were evaluated. In particular the elastic modulus was obtained equating the first resonance frequency with the experimental one. Figure 7a shows the selected finite elements representing the CEDRAV building and the environmental built and figure 7b, 7c and 7d show the first three modal shapes. In order to validate this elastic model the acceleration time-histories recorded at the basement during the June 28th 2000 event was used as seismic input for the model, and acceleration time-histories at the measurement points evaluated and compared with the experimental ones.

Subsequently it has been proceeded to the modal structure identification by means of the Ibrahim technique, working in the time domain, and the Frequency Domain Decomposition technique, working in the frequency domain.

The Ibrahim technique was much more performing then the Frequency Domain Decomposition technique due to very close peaks in the PSD of recorded accelerograms [4].

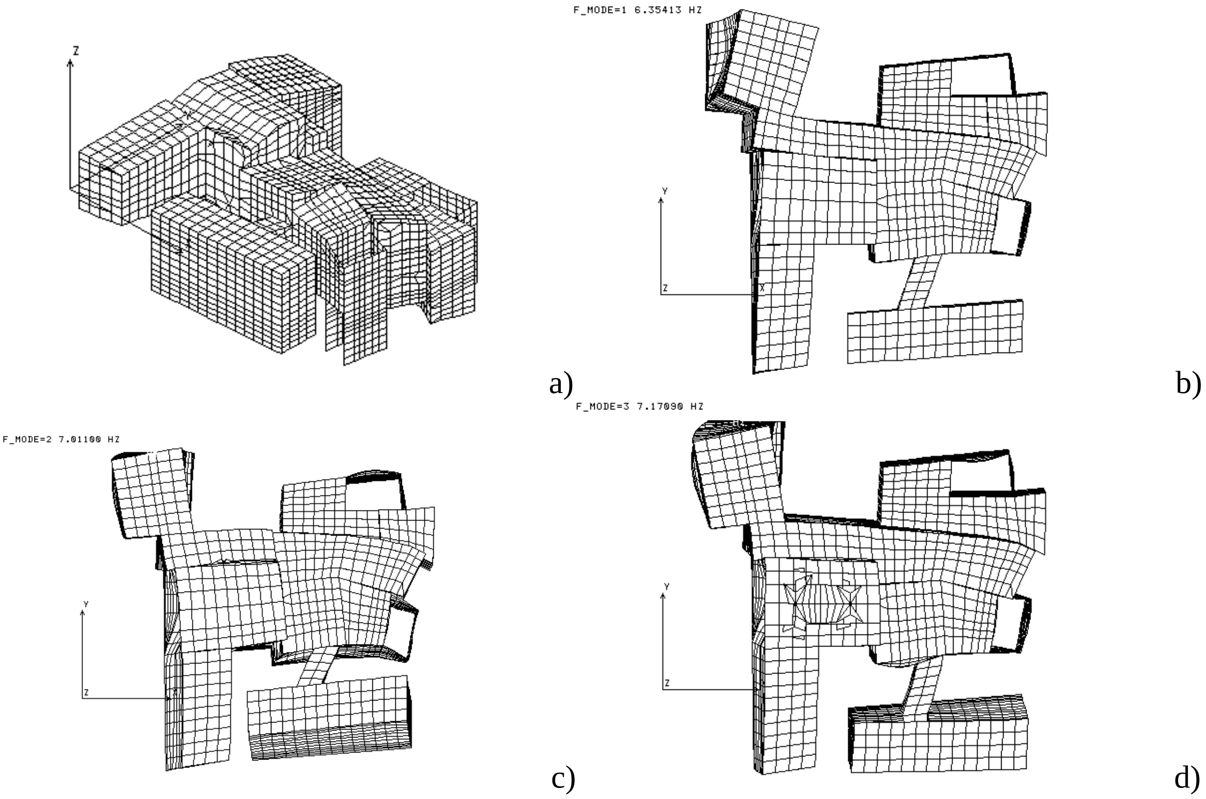

Figure 7: a) Finite elements model; b) first, c) second and d) third modal shapes.

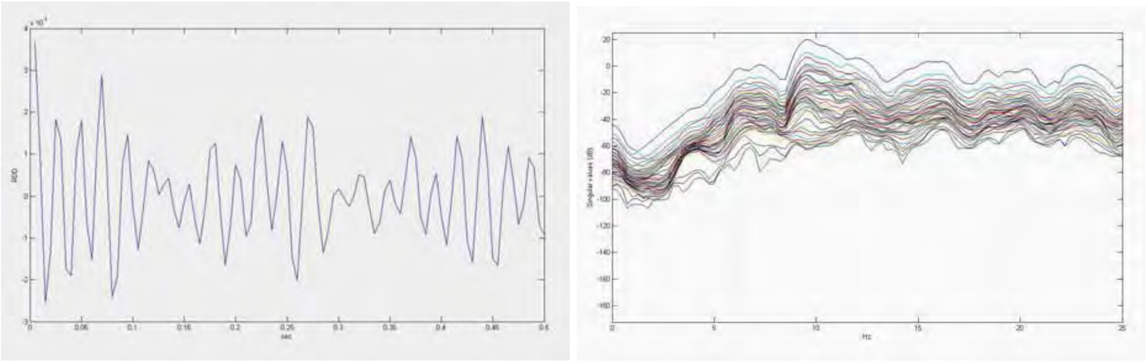

a) b)

Figure 8: a) Correlation function (Ibrahim technique) and b) singular values of power spectral density matrix function (FDD technique).

5 CONCLUSIONS

The analysis of energy plots from the main shocks of the Umbria-Marche seismic sequence outline the severity of the seismic event. The damage induced to the CEDRAV building was essentially due to the horizontal components of motion. In particular the seismic event of October 24th, 1997, was much more damaging then the main shock of September 26th, 1997, (e.g. the energy in the NS component of the acceleration of the October 14th event was double then the same component in the September 26th event). The dynamic characterization of the structure, using ambient and forced vibration tests, allowed to have very important information about the health status of the structure and to point out its main dynamic characteristics. The knowledge of the influence of building dynamic interaction in modifying the dynamic characteristics is of fundamental importance to characterize the mechanisms that underlie the damage time history. The analysis of temporary array configurations outline how important is the interaction between the building and the environmental built, to the damage mechanism of the NW wall of the building. A deeper investigation of the material mechanical characteristics and the analysis of a model as a sub-assemblies ensemble linked to identification techniques may better correlate the experimental results to the dynamic characteristics.

The health status of the building seems to be quite good. The connections between the walls are effective except for those between the main block and the two adjacent smaller blocks. The structure vulnerability is essentially related to the absence of rigid diaphragms between the walls, necessary to guarantee a suitable distribution of the seismic actions. The floors, in fact, are very flexible to satisfy this requirement. The strengthening of the building will regard essentially this aspect: the existing floors, especially the third and the fourth ones, should be substituted by new rigid floors. The connection between the floors, old and new, and the walls must be realized. The input energy was very low: more evident non-linear effects could be observed in the case of seismic actions.

REFERENCES

[1] Clemente P., Rinaldis D. (2004). “Design of temporary and permanent arrays to assess dynamic parameters in historical and monumental buildings”. Proc., North American Euro-Pacific Workshop “Sensing Issues in Civil Structural Health Monitoring”, Cshm, (Honolulu, 10-13 November), invited paper.

[2] Rinaldis, D., De Stefano and Clemente, P. (2005). ‘‘Design of Seismic Arrays for Structural Systems,’’ In: Ou, J.P., Li, H. and Duan, Z.D. (eds), Proc., 2nd International Conference on Structural Health Monitoring of Intelligent Infrastructure, (SHMII-2’2005), Nov. 16–18, 2005, Shenzhen, P.R. of China, Taylor & Francis/ Baltemia, Leiden, The Netherlands, Vol. 2, 1447–1453.

[3] Rinaldis, D., Celebi, M., Buffarini, G. and Clemente, P. (2004). ‘‘Dynamic Response and Seismic Vulnerability of a Historical Building in Italy,’’ Proc., 13th World Conference on Earthquake Engineering, Vancouver, 1–6 August, IAEE & CAEE, Mira Digital Publishing, Saint Louis, Paper No. 3211.

[4] Rinaldis D., Clemente P. and Teresi G., (2006). “Experimental Modal Analysis of the CEDRAV Historical Building”, First European Conference on Earthquake Engineering and Seismology Geneva, Switzerland, 3-8 September, Paper Number: 646.

[5] Clemente P., Rinaldis D. and Buffarini G. (2007). “Experimental Seismic Analysis of a Historical Building”, Int. J. of Intelligent Material Systems and Structures, Vol. 18, 777-784, August.

[6] Rinaldis D, Clemente P. and Buffarini G., (2010). “Dynamic Behavior of a Historical Building” , Proc. Of 7th International Conference on Structural Analysis of Historic Constructions, Shanghai, China Part 2, pp. 659-664. TTP Switzerland.

COMPDYN 2011
3^{rd} ECCOMAS Thematic Conference on
Computational Methods in Structural Dynamics and Earthquake Engineering
M. Papadrakakis, M. Fragiadakis, V. Plevris (eds.)
Corfu, Greece, 25-28 May 2011

SEISMIC VULNERABILITY ASSESSMENT OF MASONRY TOWERS: FULL NON-LINEAR DYNAMICS VS PUSHOVER ANALYSES

S. Casolo[1], **G. Uva**[2]

[1]Dipartimento di Ingegneria Strutturale, Politecnico di Milano
P.zza Leonardo da Vinci, 20133 Milano, Italy
e-mail: siro.casolo@polimi.it

[2] Dipartimento ICAR , Politecnico di Bari
Via E. Orabona, 4 70125 Bari, Italy
e-mail: g.uva@poliba.it

Keywords: Masonry towers, Belfry, RBSM, Pushover Analysis, Nonlinear Dynamic Analysis.

Abstract. *The paper concerns the seismic vulnerability assessment of masonry bell towers in Italy, which is performed by comparing full non-linear dynamic analysis and non-linear static analysis. An idealized case study is considered, in order to assess some basic and common features of the seismic structural response and to appraise the performance of the proposed approach. The reference model is supposed to be structurally independent, i.e. with no adjacent interacting construction. The geometrical dimensions are chosen in order to represent an average north-Italian masonry bell tower, without the intent to cover all the possible situations.*

The seismic response of these structures involves a coupling between flexural and axial vibration modes, the presence of shear damage patterns, and high vibration modes causing the belfry collapse. The problem is simplified by using a plane 2D scheme. A specific Rigid Body and Spring Model is adopted to describe the in-plane dynamics. Constitutive laws were assigned following a simplified heuristic approach including the main meso–scale damage mechanisms: i) very low tensile strength; ii) significant post-elastic orthotropy plus texture effects; iii) different rules for post-elastic axial and shear damage; iv) different dependence of the shear strength on the vertical and horizontal axial stress component; v) hysteretic energy dissipation due to cyclic loading. Even using a quite coarse mesh, the model is capable to describe the higher vibration modes with a reasonable computational effort and using realistic accelerograms. Non linear static analysis was performed, by using the RBSM model, obtaining the capacity curve and assessing the seismic demand. A comparison between the two approaches is proposed, in order to appraise the difference in the results and to evaluate quality and significance of results in terms of operational drawbacks and reduction of computational times. Particular attention is devoted to the fact that static non-linear analyses tends to neglect the damage effects induced by higher vibration modes, as well as the influence of the shear response on the global damage.

1 INTRODUCTION

In Italy, bell towers are a quite widespread architectural element, with peculiar morpho-typological characters, according to the geographic area.

A main issue in the seismic behaviour of slender masonry towers is the influence of the axial stresses induced by gravity loads, which are often close to the compression strength limit of the masonry material. Considering that historical masonry is typically characterized by complex geometry, irregularities and a high degree of inhomogeneity, stress concentrations can easily occur, which could even trigger a local collapse. Thence, the structural failure can be driven even by a moderate increase in the stress level, which can occur under seismic events or under long term loads. A notable example of the second case is represented by the sudden collapse of the Civic Tower of Pavia, Italy (about 900 years old), on 17 March, 1989 [1]. It is clear, therefore, that masonry towers are vulnerable also to low-intensity earthquakes, since static vertical loads combine with the dynamic loads induced by the ground motion.

The examination of the documentation about the damage caused by the 1976 Friuli earthquake [2] points out that in isolated bell towers damage patterns tend to be distributed all along the height, although it is frequently more severe at the base. This suggests the need of further investigations about the combined effects of flexural and axial actions, as well as the incorporation into the model of the higher vibration modes, which seem to be have a relevant role in the damage of the upper part, especially the tower crown and belfry [3].

Moreover, during strong earthquakes shear damages are also often observed, and in this case the reduction of the section stiffness (i.e. the loss of validity of the Eulero–Bernoulli hypothesis of plane cross-section) can significantly affect the overall response of the structure. Specific approaches are needed in order to deal with these aspects, and in particular it is paramount to model the non-symmetry in tension and compression that characterise the masonry material of which these structures are composed [4].

Finally, the investigation of the response to very strong earthquakes requires to describe the effects of the damages that cause a remarkable reduction of the material stiffness, as well as the dissipation of the seismic energy through repeated cycles of plastic deformation [5, 6]. When the tower is not particularly slender, and depending on the frequency content of the forcing actions, a material model which is capable to describe both the axial and the shear response and damage under cyclic loading is also required in order to investigate the global shear damage effects [7, 8, 9].

2 THE RBSM MODEL

The non linear behaviour of the slender medieval towers is studied by means of a specific mechanistic model made by rigid bodies and springs, RBSM which considers only the in-plane dynamics. This model is capable of describing the higher mode of vibration, as well as the combined axial and shear deformation and damage of the material by means of a simplified heuristic approach. The rigid element method (REM) [10] idealises the masonry structure as a mechanism made of rigid elements and springs. The elements are quadrilateral and have the kinematics of rigid bodies with two linear displacements and one rotation, as shown in Figure 1(b). Three springs devices connect the common side between two rigid elements or the restrained sides, as shown in Figure 1(c). These connections are two axial springs k^P and k^R, placed in the point P and R separated by a distance $2b$, and one shear device k^Q placed in the middle of the side. A volume of pertinence V^P, V^Q and V^R is assigned to each connection point. The elastic characteristics of the connecting devices are assigned with the criterion of approximating the strain energy of the corresponding volumes of pertinence in the cases of simple deformation.

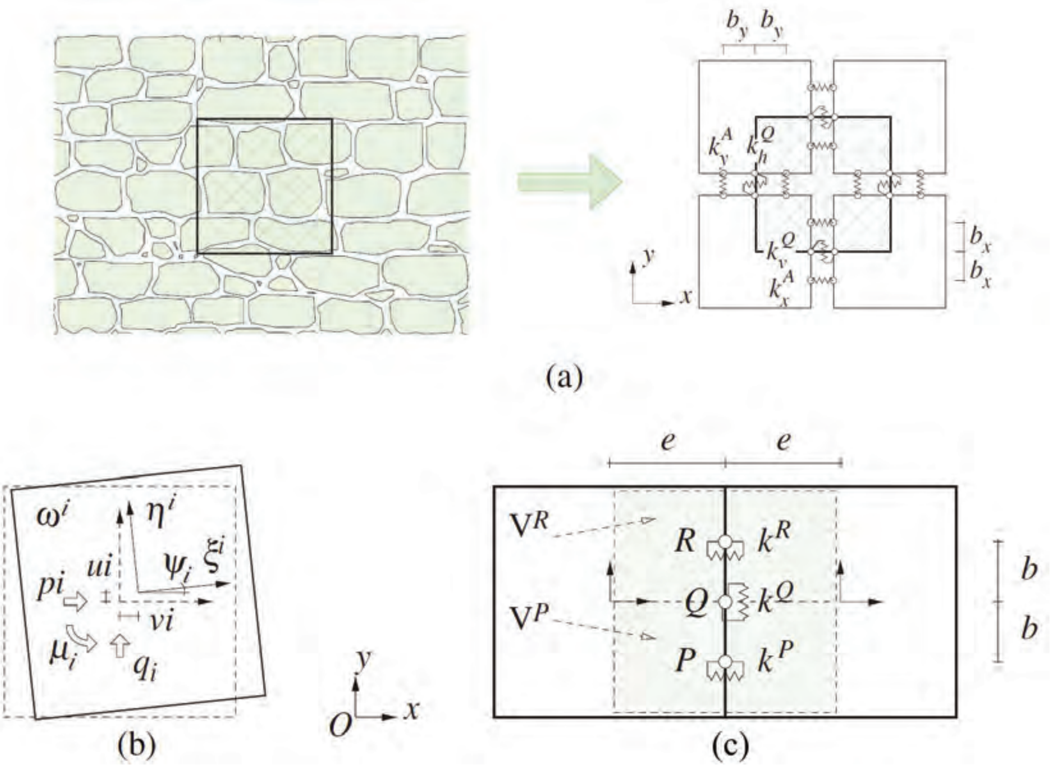

Figure 1: Scheme of a unit cell defined by four rigid elements(a), kinematics (b), disposition of the connecting spring-devices between a couple of rigid elements (c) for macroscale modelling of a representative volume of masonry [10, 11].

The conceptual core of this model is the macroscopic unit cell defined by four quadrilateral rigid elements connected to each other as shown in Figure 1(a). The cell size should be equal or larger than the minimum representative volume (RVE) of the heterogeneous solid material. In particular, the orthotropy of the shear response and the local mean rotation of the blocks, which depend on the different geometric arrangement of the vertical and horizontal material joints as well as the shape and size of the original blocks, are features that can be accounted at the macro-scale [11].

Out-of the linear elastic field, the main macroscopic constitutive aspects are: the very low tensile strength; the significant post-elastic orthotropy combined with the texture effects; the dependence of the shear strength on vertical compression stress; the progressive mechanical degradation during repeated loading; and the energy dissipation capability. To do this, a simplified heuristic approach is proposed, based on the phenomenological consideration of the main in-plane damage mechanisms that can be described at the meso–scale by adopting specific separate hysteretic laws for the axial and shear deformation between the elements. This separation reduces the computational effort, even though a Coulomb-like law is adopted in order to relate the strength of the shear springs to the vertical axial loading.

In the present work, different behaviours have been attributed to the shear connections along the vertical and horizontal directions, somewhat in the spirit of a Cosserat non-linear solid continuum material [11]. Two axial, one shear, and two in-plane flexural loadings are considered for

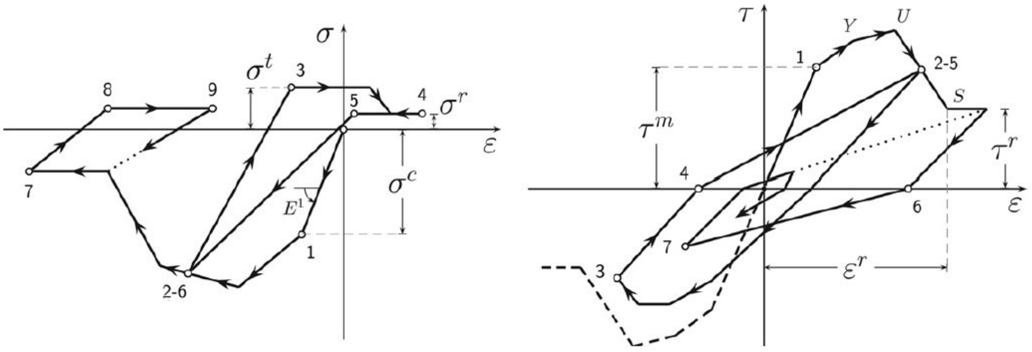

Figure 2: Schematic representation of the hysteretic rules for the axial (on the left), and the shear connecting springs (on the right).

the parameter identification [10]. The monotonic and hysteretic constitutive laws are assigned to the connecting devices adopting a phenomenological approach and separate phenomenological descriptions of the hysteresis behaviour of the axial and shear connections, as schematically shown in Figure 2. These laws are based on experimental monotonic and cyclic tests available in literature, and should be assigned to rigid elements whose size is approximately comparable to the test specimens in order to limit the problems with size effect. The plastic response of each axial connection is independent from the behaviour of any other connection, while the shear strength is related to the stresses of the axial connections according with Coulomb criterion.

It is worth noting the true discrete character of this model. In fact, during loading, relative motion between two adjacent elements always occurs, with overlapping, separation or sliding between two adjacent rigid elements; numerically, this means compression, tension or shear in the volume of pertinence of the connecting devices. This notwithstanding, the initial contacts do not change during the analysis and the global mechanism maintains the initial connectivity in order to reduce the computational effort.

3 THE REFERENCE TOWER

An idealized case study has been considered, in order to assess some basic and common features of the structural response to seismic actions and to appraise the performance of the approach proposed for the modelling. Such a reference model has been supposed to be structurally independent, i.e. with no adjacent interacting construction, and characterized by geometrical regularity both in plan and in elevation. The dimensions were chosen by looking at a number of significant examples (Fig. 3), in order to represent an average masonry bell tower located in seismic zones of Northern Italy, without the intent, of course, to cover all the possible situations. Of course, the geometry of the model was simplified by disregarding the typical structural details, like – for example – the presence of internal vaults.

On the basis of these observations, it was designed an ideal tower having a 5.30 x $5.30\ m$ square base, with a wall thickness varying from $1.00\ m$ at the base to $0.85\ m$ at the top, and having a total height of $28.50\ m$. In Figures 4 and 5, the 3D drawings and the schematic sections and plans of the tower are shown, and the geometrical characteristics are summarized in Table 1.

Figure 3: Some typical geometry and damage patterns of Italian bell-towers [2].

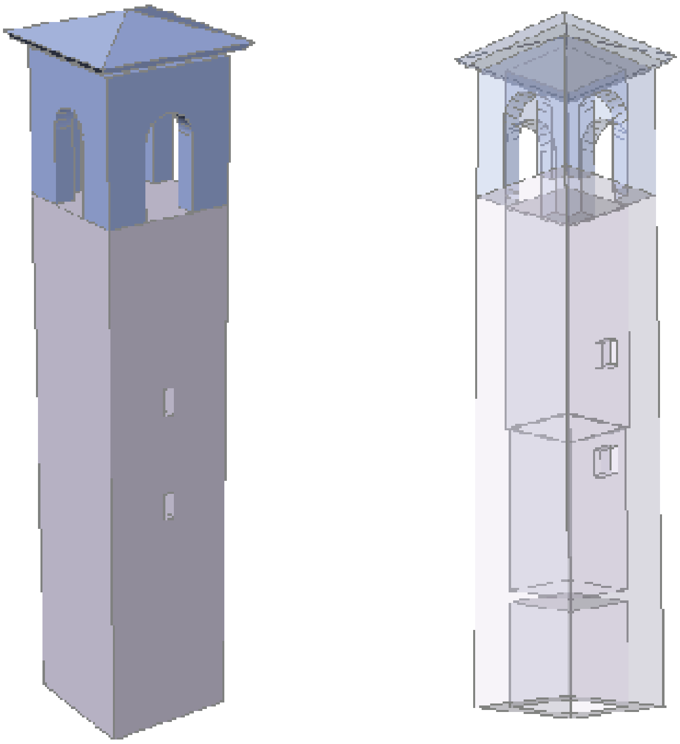

Figure 4: 3D drawing of the reference tower.

Table 1: Geometrical characteristics of the reference tower.

Total height (H)	28.50 m
Base (LxL)	5.30 m x 5.30 m
Base wall Thickness (t)	1.00 m
Wall mass density (ρ)	1900 kg/m^3
Damping (ξ)	0.05

3.1 Mechanical parameters of the masonry material

According to the constitutive model adopted for the axial and shear springs (Par. 2), a set of parameters are needed in order to define the corresponding skeleton curves and hysteretic rules [7]. The values assigned to the relevant parameters to define the masonry material of the reference tower are: compressive stress at the elastic limit: $1\ MPa$; peak compressive strength: $2\ MPa$; residual compressive strength: $0.2\ MPa$; peak tensile strength: $0.2\ MPa$; residual tensile strength: $0.02\ MPa$; shear value at the elastic limit: $0.088\ MPa$; peak shear strength on the horizontal plane: $0.097\ MPa$; peak shear strength on the vertical plane: $0.165\ MPa$; residual shear strength: $0.02\ MPa$ friction coefficient on the horizontal plane: 0.25; friction coefficient on the vertical plane: 0.05.

3.2 Preliminary characterization of the tower

Preliminarily, the analysis of the bell–tower under the only gravity loads was performed (the non structural permanent loads and the service loads were not considered, since they represent a negligible quote of the total loads). The maximum vertical displacement in this loading condition is $2\ mm$. In Figures 12, 13, 14, 15, at the left, are respectively shown the deformed shape, the normal stress map (S_{22}), the shear strain along horizotnal direction (E_{12}), the shear strain along vertical direction (E_{21}).

Then the first 3 vibration modes of the tower were determined. The corresponding natural periods are reported in Table 2 and the modes shape are shown in Figure 6.

Table 2: Natural periods of vibration of the first three modes.

Mode ♯	Period	Type
1	0.517 s	1^{st} flexural
2	0.128 s	2^{nd} flexural
3	0.079 s	1^{st} axial

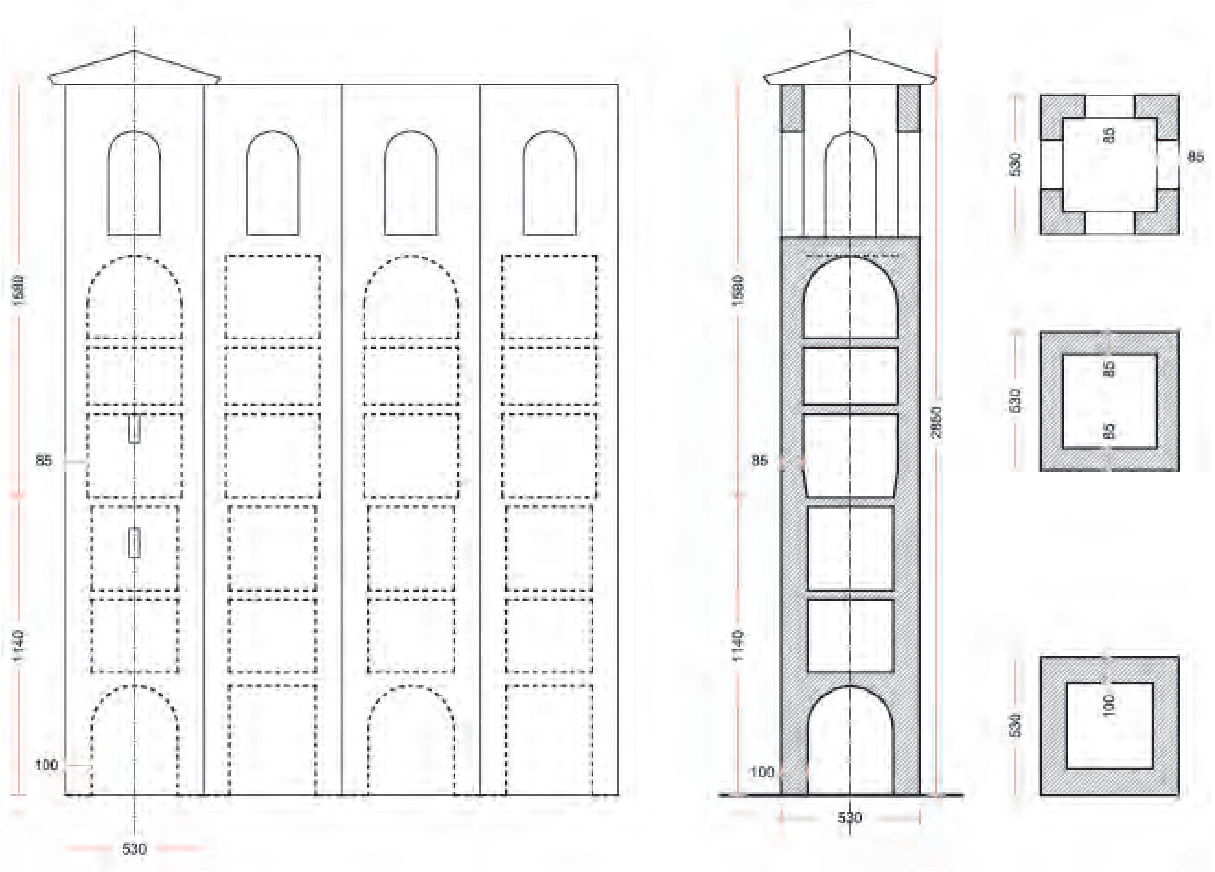

Figure 5: Schematic prospects, section and plan views of the idealized case study.

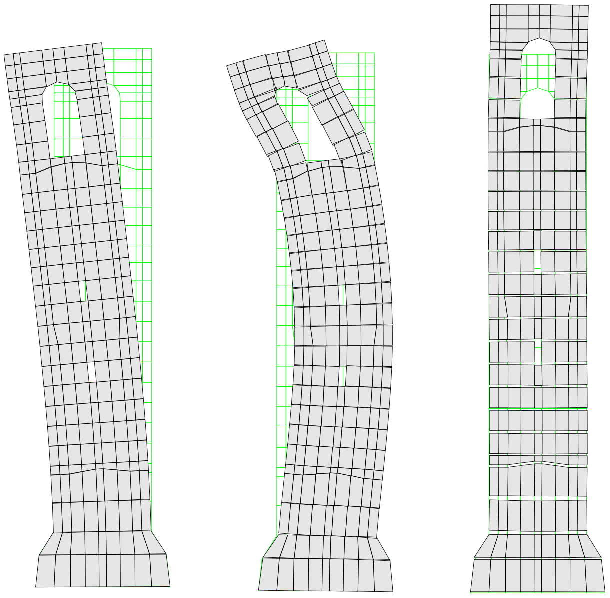

Figure 6: The first three mode shapes.

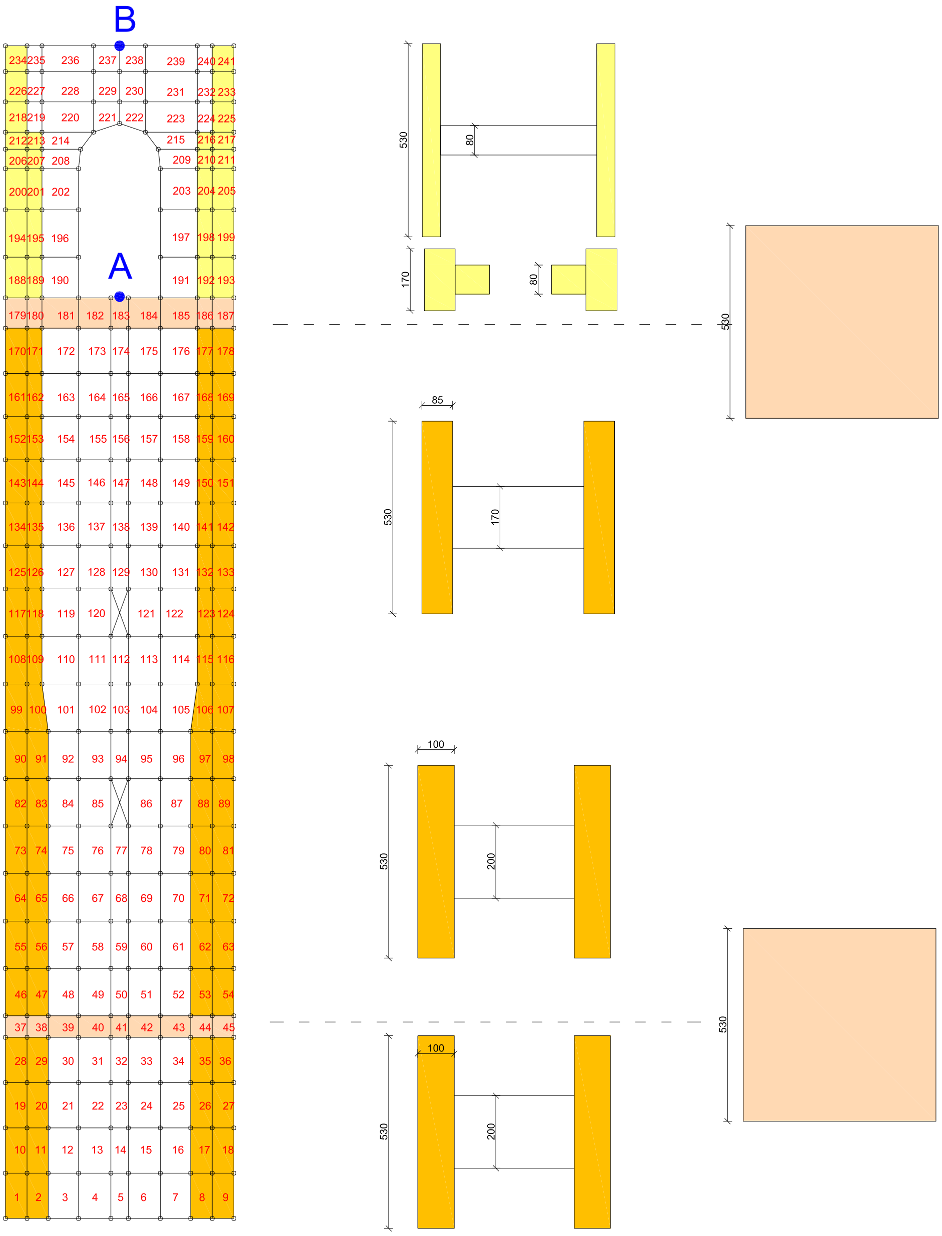

Figure 7: The mesh of the reference tower used in the numerical simulations by RBSM. The control point B, located at the top of the belfry is also shown.

4 NON LINEAR METHODS: NON LINEAR DYNAMIC VS NONLINEAR STATIC ANALYSIS

Step-by-step nonlinear dynamic analysis is hardly used in the practical application, although it is definitely the most complete and realistic approach for seismic analysis. Indeed, it presents a number of drawbacks, which actually restrict its use to advanced users and very specific case studies: adequate numerical codes, even commercial ones, are not easy available, or introduce too many complications for average end-user; the definition of the model, especially with regard to the constitutive aspects (the post-elastic, hysteretic behaviour of the structure, and the consequent energy dissipation, should be consistently reproduced) is critical; the choice of significant input accelerograms is still a controversial question; the computational cost is very high; the uncertainty about input data strongly influence the reliability of the results. Anyway, in order to predict the nonlinear structural response under strong ground motions, in the last few years simplified procedures have been proposed aimed at performing non linear analysis in a static context (Nonlinear Static Procedures - NSP), where the problem can be more easily managed, and numerical tools with a high circulation are available. These methods, generally known as pushover analyses, have recently assumed a large relevance, especially for the assessment of existing buildings [12]. In these procedures, basically, a computational model of the structure is loaded up with a proper distribution of horizontal static loads, which are gradually increased with the aim of “pushing” the structure into the nonlinear field. The basic idea is that the resulting response conveniently represents the envelope of all the possible structural responses, and can so be used to replace a full nonlinear dynamic analysis. When speaking of historical and monumental buildings, the question is even more critical: nearly all the structural analysis methods suffer from a lot of uncertainties and limitations, mainly derived from the incompleteness of the knowledge level, from the presence of widespread inhomogeneities and nonlinearities, and a complex constructive history.

4.1 Nonlinear Dynamic analyses with design–consistent artificial accelerograms

The full dynamic analyses were performed by using artificial accelerograms to represent the ground motions.

The reference design spectra used are those for the Ultimate Limit State of Life Safety for the zones 1, 2, 3 and 4 in which the Italian territory is classified, assuming an “A”–type soil and no topographic amplification effect (this corresponds to a probability of exceedance $P_{VR} = 10$ in 50 years, i.e. to a return period of the seismic action $T_R = 475$ years).

For each zone, the artificial accelerograms were generated according to the procedure proposed by Sabetta and Pugliese [13]. The resulting accelerograms have been further processed in order to improve the matching with the spectrum.

It will be now presented, as an example, the results of the analyses performed by using 4 accelerograms, one for each of the average hazard level in Italy. In Figures 11, 10, 9, 8 the input accelerograms used respectively for Zone 1, 2, 3 and 4 are shown. In the same figures, some significant outputs of the analyses are also shown: the displacement time-history for two representative points: the control point B, located at the top of the belfry and point A, at the base of the belfry (see Fig. 7); the plot of the base shear against the mean displacement of points A and B; the time hystory of the dissipated energy. For each zone, the deformed shape at the end of the dynamic analysis have been plotted in Figure 12, and also the vertical normal stress (Fig. 13), the horizontal shear stress (Fig. 14) and the vertical shear stress (Fig. 15).

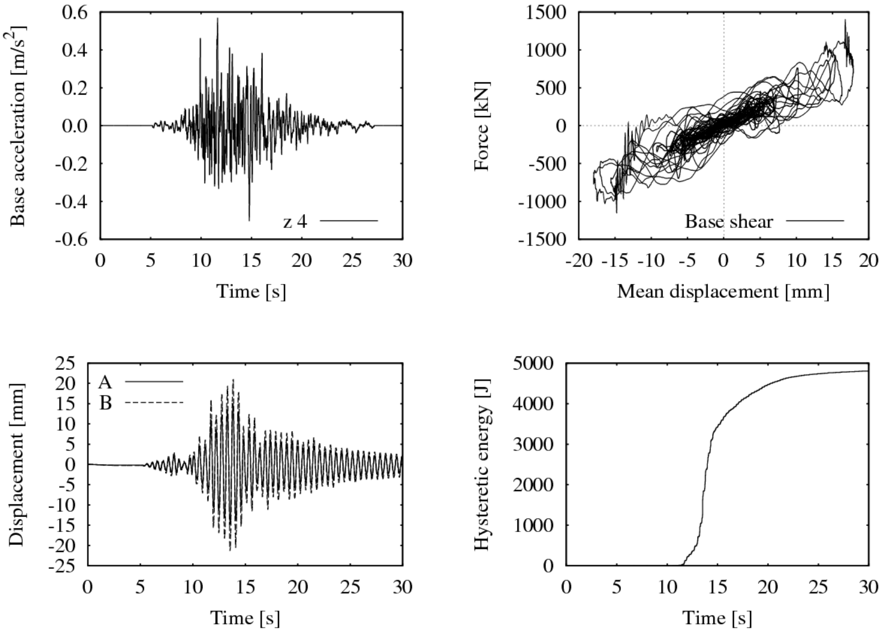

Figure 8: Input artificial accelerogram used for Zone 4; displacement time-history for points A and B (see Fig. 7); Base shear–mean displacement (points A, B) relationship; Hysteretic energy time history.

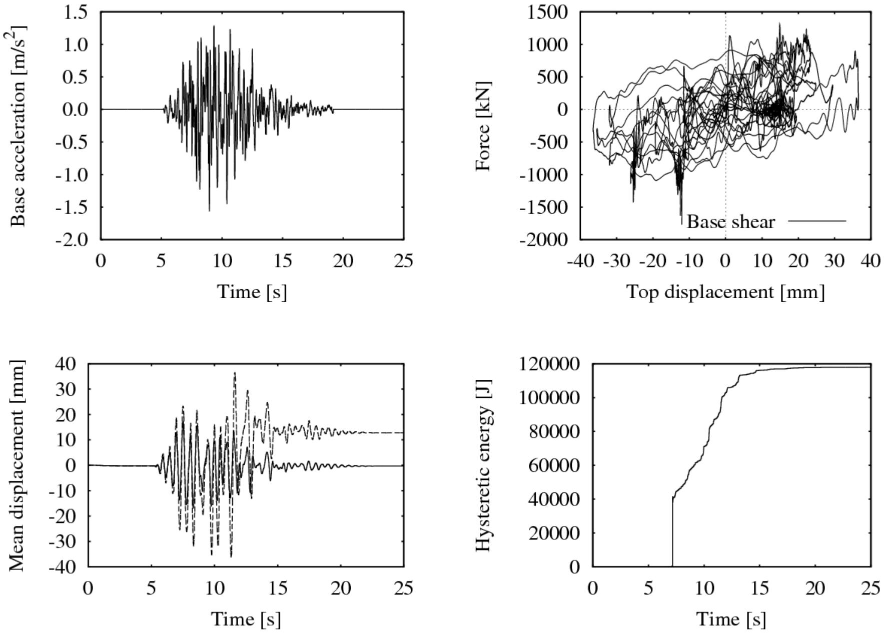

Figure 9: Input artificial accelerogram used for Zone 3; displacement time-history for points A and B (see Fig. 7); Base shear–mean displacement (points A, B) relationship; Hysteretic energy time history.

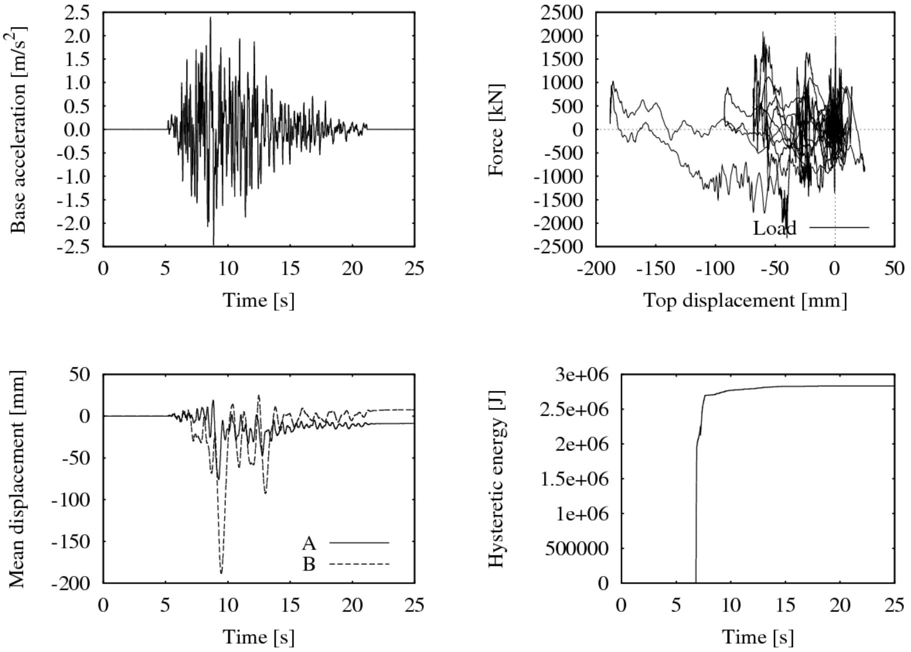

Figure 10: Input artificial accelerogram used for Zone 2; displacement time-history for points A and B (see Fig. 7); Base shear–mean displacement (points A, B) relationship; Hysteretic energy time history.

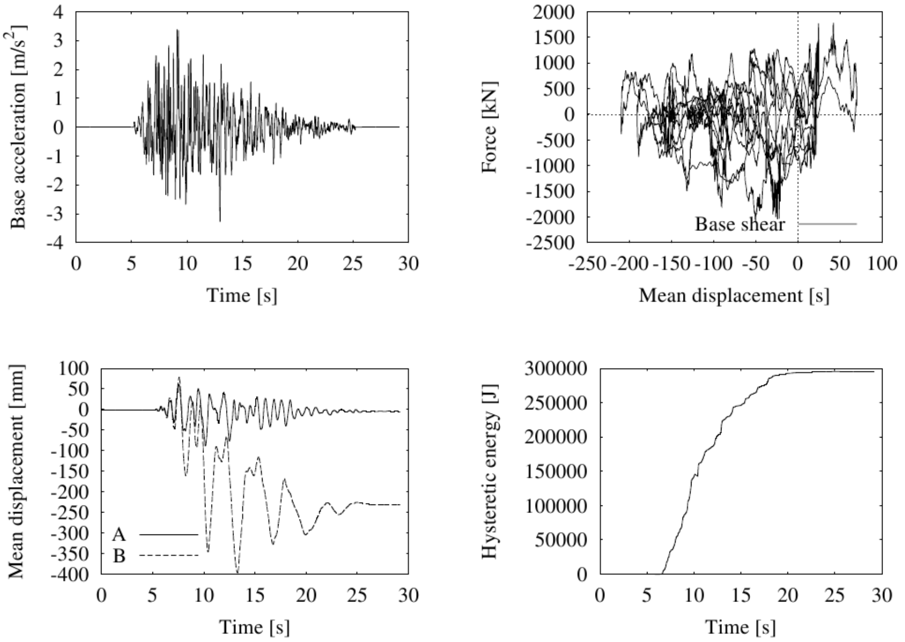

Figure 11: Input artificial accelerogram used for Zone 1; displacement time-history for points A and B (see Fig. 7); Base shear–mean displacement (points A, B) relationship; Hysteretic energy time history.

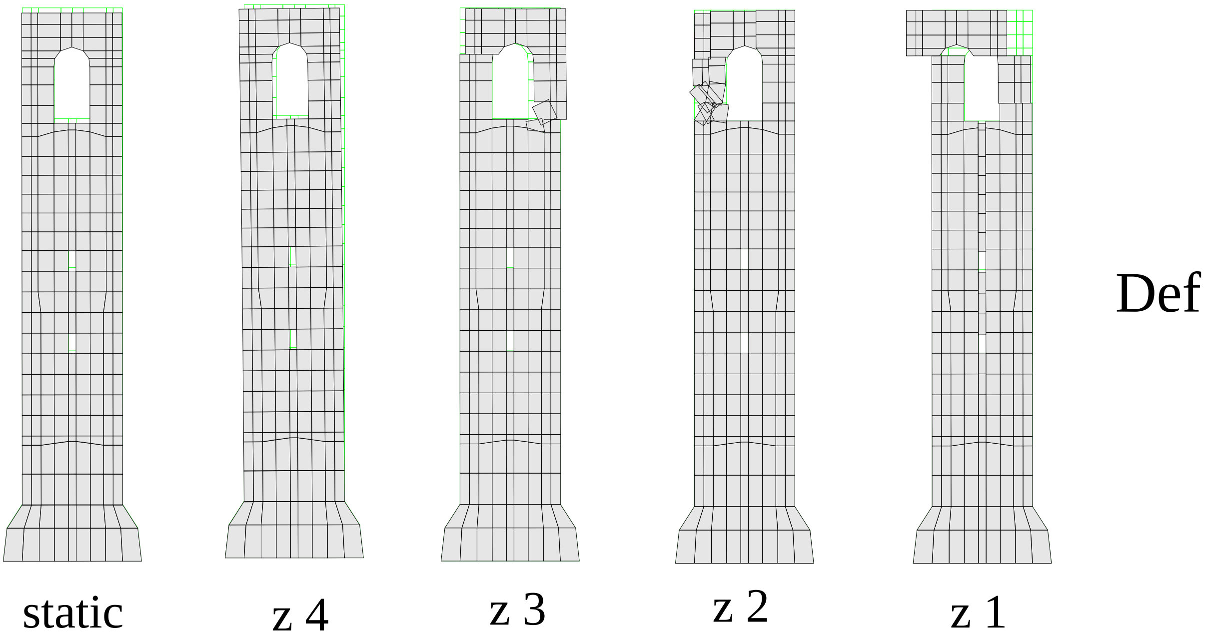

Figure 12: Deformed shapes for the static loading condition and at the end of full-dynamic analyses (Zone 4, 3, 2, 1).

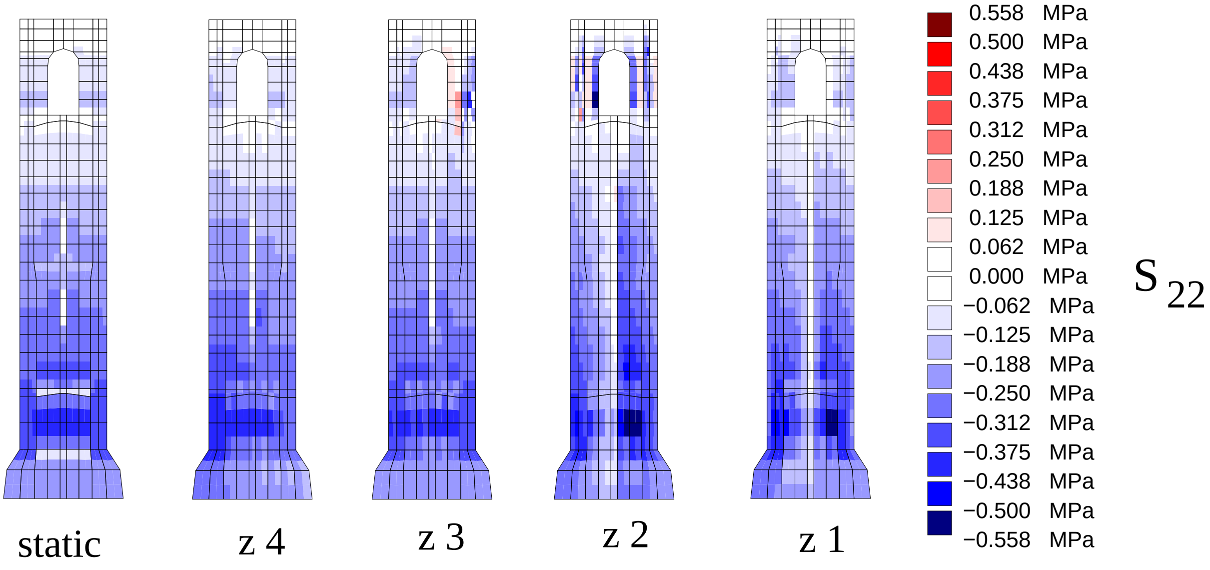

Figure 13: Normal stress along vertical direction (S_{22}) map: static load condition; ND analyses in Zones 4, 3, 2, 1.

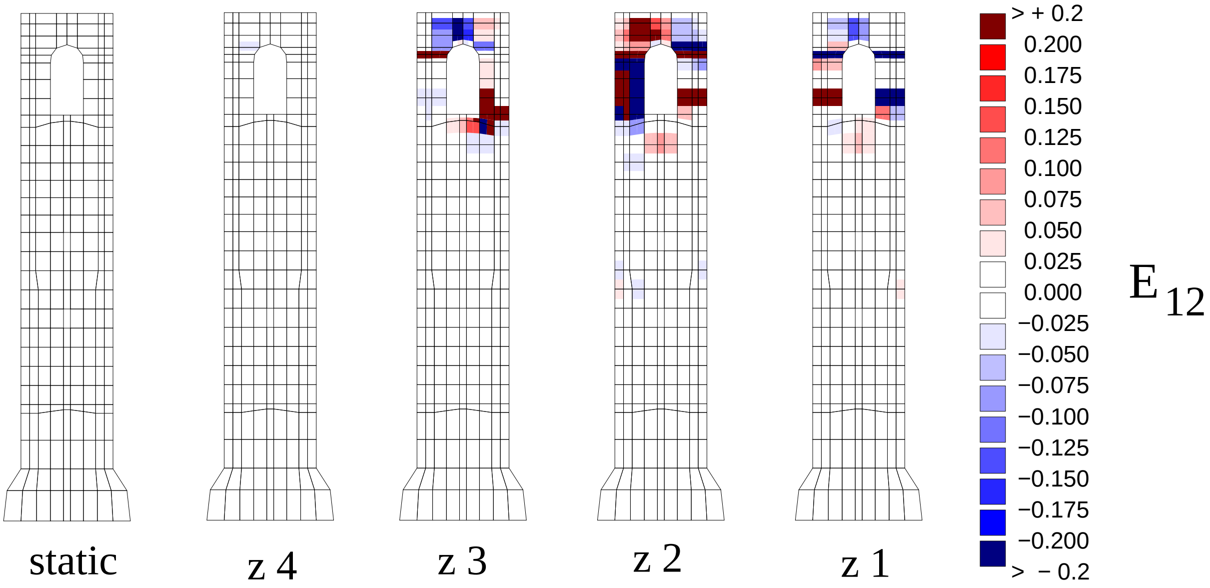

Figure 14: Shear strain along horizontal direction (E_{12}): static load condition; ND analyses in in Zones 4, 3, 2, 1.

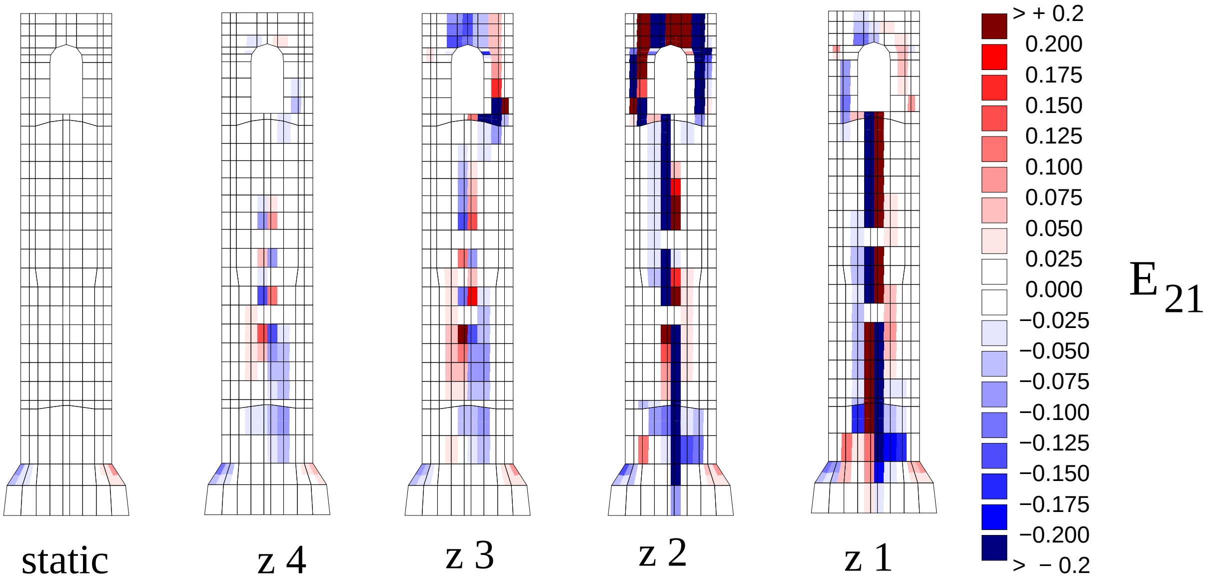

Figure 15: Shear strain along vertical direction (E_{21}): static load condition; ND analyses in Zones 4, 3, 2, 1.

The results reported in the figures clearly show the development of a global shear mechanism of damage for the tower. In Zone 4 (low seismic hazard) such a mechanism can already be appraised: by looking at Figure 15, it can be seen that the in the lower part of the tower are present significant vertical shear strains in the middle section. The relevance of the global shear collapse mechanism is progressively more evident when considering the accelerogram related to the zones 2 an 1. This is also confirmed by the normal stress map, which shows that the tower is almost split into two separate portions. This is also visible in the deformed shape of Figure 12, where, in the central thin strip, consistent vertical displacements can be observed, which suggest that a failure of the central strip has occurred .

As a consequence of this failure mode, a permanent tilt occurs for all the accelerograms. This can be clearly seen from the displacement time history of point B (Figures 8, 9, 10, 11).

For Zone 4, the permanent tilt is clearly visible in Figure 12, whereas in the other cases it is not evident because of the different metric scale adopted. In fact, for the accelerograms of zones 3, 2 and 1 there is an additional partial collapse mechanism that is activated: the failure of the belfry. The figure 14 shows the development of shear strains on the horizontal plane at the base and top of the belfry, whereas the deformed shape indicates the permanent slidings and rotations suffered by the element: actually it can be said that in these conditions the belfry is collapsed.

4.2 The pushover simulation

The non linear static analysis of the tower is now proposed, following the methods included in the European codes [12], which are based on the well-known “N2 method” [14]. The aim is to perform a critical comparison with the full dynamic analysis, appraising the reliability and relevance of the results. Analyses were performed by applying two different vertical distributions of the lateral loads: a “uniform” pattern (which will be hereafter referred to as “mode 0”), based on lateral forces that are proportional to mass regardless of elevation (uniform response acceleration); a “modal” pattern (which will be hereafter referred to as “mode 1”) corresponding to a distribution of the acceleration proportional to the 1st modal shape.

During the loading process the displacement d_c of the control point B (Fig. 7) was monitored in order to trace the pushover curve in terms of the equivalent lateral force F_b, obtaining the generalized force-displacement relationship: $F_b - d_c$.

The ultimate limit state verification then consists in checking out that the ultimate displacement capacity is larger than the corresponding displacement required by the design seismic action. It is hardly worth observing that in order to perform a nonlinear analysis, even if a static one, a proper numerical code is needed (for instance, a FE code) as well as nonlinear constitutive laws for the materials and the structural elements, able to reproduce the strength and stiffness degradation suffered by the damaged elements. Indeed, the idea of handling a nonlinear static analysis in order to take into account –at least in a simplified way– the inelastic characteristic of the structure was suggested by the availability of codes able to provide these kind of models, whereas the requirements for dynamic analyses are rather oriented to specialist users. It should be anyhow remarked that some operational drawbacks still exist, and even in the most advanced numerical formulations, it is frequent to encounter troubles in the reconstruction of the equilibrium path. In the case study, the pushover analyses were carried out by using the RSBM described in Par. 2.

The methodology includes the following steps: i) transformation of the pushover curve into a simplified bilinear force-displacement relationship for an equivalent SDOF system; ii) definition of the inelastic seismic demand for such SDOF system in the acceleration–displacement

(AD) format; iii) transformation of the displacement demand (i.e. the "target" displacement) for the SDOF system into the corresponding maximum displacement of the original structure; iv) verification of displacement compatibility (according to the current standards, for masonry structures only the global displacement checking is required, and not a specific assessment of single structural elements).

In Figure 16 the results obtained at the end of the pushover analysis performed under the modal pattern are reported: deformed shape; normal stress map; shear deformations along $Y-$axis; shear deformations along $X-$axis. The deformed shape at the end of the analysis and the corresponding maps of the axial stresses and shear deformations reveal that the collapse point is characterized by a global shear mechanism, whereas local damages involving the belfry are negligible.

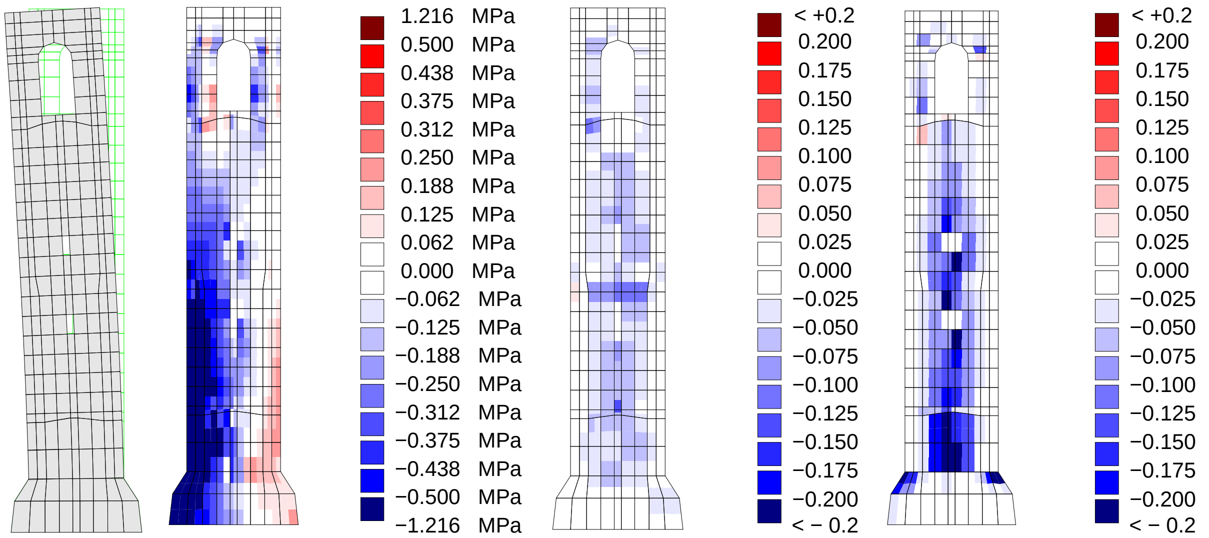

Figure 16: From left to right: results of the pushover analysis: final deformed shape; vertical axial stress; shear strain along vertical direction; shear strain along horizontal direction.

In Figure 17, the curve expressing the base reactions F_b vs the characteristic displacement d_c of the tower is shown for the loading pattern 1 (distribution of accelerations proportional to the first modal shape), which resulted to be the most demanding condition, together with the force-displacement relationship for the SDOF equivalent system ($F^* - -d^*$) , obtained by applying the modal participation factor Γ:

$$F^* = \frac{F_b}{\Gamma}; \qquad d^* = \frac{d_c}{\Gamma} \qquad \Gamma = \frac{\Sigma m_i \Phi_i}{\Sigma m_i \Phi_i^2} = 1.79 \tag{1}$$

(Φ is the 1^{st} modal shape of the structure).

The characteristic curve F^*–d^* was then transformed into the bilinear simplified relationship, also plotted in Figure 17, characterized by the yield force $F_y^* = 583.8\ KN$, by the ultimate displacement $d_u^* = 19.92\ mm$ and by the displacement at yielding $d_y^* = 15.90\ mm$ (transformation is based on an equal–energy criterion).

The elastic design spectrum in AD format is a parametric function of the natural period T^*: ($S_{de}(T^*)$, $S_{ae}(T^*)$). Thence, for the idealized bilinear system ($T^* = 0.522$ s, $m^* = \Sigma m_i \Phi_i$), the acceleration demand (strength) in the case of a perfectly elastic behaviour, and the corresponding elastic displacement demand, can be singled out. The inelastic seismic demand is

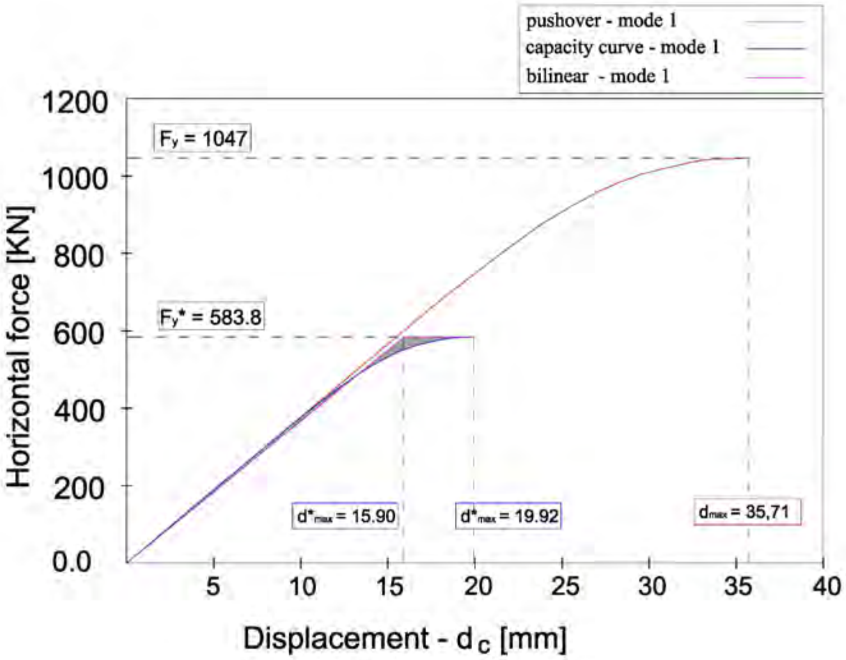

Figure 17: The pushover curve of the tower (mode 1 load pattern), the capacity curve and the equivalent bilinear curve of the equivalent SDOF system.

henceforth defined by accounting for the system ductility, depending on the range of the spectrum in which the system's period falls. The watershed is represented by the characteristic period of the ground motion T_C, defined as the transition period from the constant acceleration branch of the spectrum to the constant velocity one.

If $T^* \leq T_C$, the displacement response of the inelastic system is larger than the equal period elastic one, and can be evaluated by the following expression:

$$d^*_{\max} = \frac{d^*_{\mathrm{e}\max}}{q^*}\,(1 + (q^* - 1)\,T^*/T_C) \geq d^*_{\mathrm{e}\max} \qquad \text{where} : q^* = S_{ae}(T^*)\,m^*/F^*_y \tag{2}$$

The factor q^* represents the ratio between the force corresponding to a linear elastic response and the yielding force of the equivalent system (it will be always assumed $q^* \geq 1$).

If, instead, $T^* \geq T_C$, like in this case, the equal displacement rule applies: the inelastic displacement demand $S_d(T^*)$ is assumed to be the same as the elastic system having the same period: $d^*_{\max} = d^*_{\mathrm{e}\max} = S_{de}(T^*)$, where $S_{de}(T^*) = S_{ae}(T^*)\,(\frac{T^*}{2\,\pi})^2$.

Eventually, the displacement demand for the original structure is $d_{\max} = \Gamma d^*_{\max}$, and can be compared with the available ductility provided by the pushover analysis (Fig. 17): $d_u = 35.71\ mm$.

In Table 3 the results obtained for the four seismic design zones are reported in terms of the elastic spectral acceleration, the factor $q*$, the maximum inelastic displacement $d^*_{\max}$ of the equivalent system, and the maximum displacement d_u of the tower.

Table 3: Target displacements and actual available displacements of the structure for the different zones for the modal load distribution.

	Zone 4	*Zone 3*	*Zone 2*	*Zone 1*
$S_{ae}(T^*)$	$6.58\ m/s^2$	$4.70\ m/s^2$	$2.82\ m/s^2$	$0.94\ m/s^2$
$d^*_{et} = d^*_t$	$4.55\ cm$	$3.25\ cm$	$1.95\ cm$	$0.65\ cm$
d_u	$3.57\ cm$			

5 FINAL REMARKS

The use of the RSBM approach [10] is particularly effective for performing in-plane dynamic analyses. In the present work, its application for the seismic assessment of bell-towers has allowed to investigate the structural response under accelerograms corresponding to different levels of hazard, and to perform a nonlinear static analysis, in order to compare two different approaches.

In particular, an interesting result was related to the possible development of different collapse mechanisms. Actually, the main evidence is that while the dynamic analyses provide the presence of a local failure mode involving the belfry, which is a particularly vulnerable element of bell–towers, the pushover analyses only encounter a global shear failure mode. So, even if the results of the assessment performed in displacements terms (seismic demand vs available displacement) supplied by the nonlinear static procedure are quite comparable with the dynamic ones, the information about the damage modes is much poorer. The pushover procedure, indeed, doesn't seem to be able to describe the effect induced by earthquakes on the belfry, which are related to the higher vibration modes.

REFERENCES

[1] L. Binda, G. Gatti, G. Mangano, C. Poggi, G. Sacchi Landriani, The collapse of the civic tower of pavia: a survey of the materials and structure, Masonry International 6 (1) (1992) 11–20.

[2] F. Doglioni, A. Moretti, V. Petrini, Le Chiese e il Terremoto, Lint press, Trieste, 1994, in Italian.

[3] E. Curti, S. Lagomarsino, S. Podest, Dynamic models for the seismic analysis of ancient bell towers, in: P. Loureno, P. Roca, C. Modena, S. Agrawal (Eds.), Structural Analysis of Historical Constructions SAHC-2006, MacMillan, New Delhi, India, 2006.

[4] G. Uva, G. Salerno, Towards a multiscale analysis of periodic masonry brickwork: A fem algorithm with damage and friction, International Journal of Solids and Structures 43 (13) (2006) 3739 – 3769. `doi:10.1016/j.ijsolstr.2005.10.004`.

[5] S. Casolo, A three-dimensional model for vulnerability analysis of slender medieval masonry towers, Journal of Earthquake Engineering 2 (4) (1998) 487–512.
URL `http://www.informaworld.com/10.1080/13632469809350332`

[6] G. Magenes, G. Calvi, Cyclic behaviour of brick masonry walls, in: Proceedings of the 10^{th} World Conference on Earthquake Engineering, Madrid, 1992, pp. 3517–3522.

[7] S. Casolo, F. Peña, Rigid element model for in-plane dynamics of masonry walls considering hysteretic behaviour and damage, Earthquake Engineering & Structural Dynamics 36 (8) (2007) 1029–1048. `doi:10.1002/eqe.670`.

[8] S. Casolo, F. Peña, Dynamics of slender masonry towers considering hysteretic behaviour and damage, in: M. Papadrakakis, D. Charmpis, N. Lagaros, Y. Tsompanakis (Eds.), ECCOMAS-COMPDYN, Thematic Conference on Computational Methods in Structural Dynamics and Earthquake Engineering, Crete, Greece, 2007.

[9] F. Peña, P. B. Lourenço, N. Mendes, D. V. Oliveira, Numerical models for the seismic assessment of an old masonry tower, Engineering Structures 32 (5) (2010) 1466 – 1478. `doi:10.1016/j.engstruct.2010.01.027`.

[10] S. Casolo, Modelling in-plane micro-structure of masonry walls by rigid elements, International Journal of Solids and Structures 41 (13) (2004) 3625–3641. `doi:10.1016/j.ijsolstr.2004.02.002`.

[11] S. Casolo, Macroscopic modelling of structured materials: Relationship between orthotropic cosserat continuum and rigid elements, International Journal of Solids and Structures 43 (3-4) (2006) 475 – 496. `doi:10.1016/j.ijsolstr.2005.03.037`.

[12] Eurocode 8: Design of structures for earthquake resistance- part 1: General rules, seismic actions and rules for buildings.

[13] F. Sabetta, A. Pugliese, Estimation of response spectra and simulation of non-stationary earthquake ground motion, Bull. Seism. Soc. Am. 36 (2) (1996) 337–352.

[14] P. Fajfar, A nonlinear analysis method for performance-based seismic design, Earthquake Spectra 16 (3) (2000) 573–592. `doi:10.1193/1.1586128`.

COMPDYN 2011
3^{rd} ECCOMAS Thematic Conference on
Computational Methods in Structural Dynamics and Earthquake Engineering
M. Papadrakakis, M. Fragiadakis, V. Plevris (eds.)
Corfu, Greece, 25-28 May 2011

NUMERICAL ANALYSIS OF THE TWO BASIC COLLAPSE MECHANISM OF A TYPICAL COLONIAL FAÇADE

Siro Casolo[1], **and Fernando Peña**[2]

[1] Dipartimento di Ingegneria Strutturale, Politecnico di Milano
Piazza Leonardo da Vinci 32, I-20133 Milano, Italy
e-mail: siro.casolo@polimi.it

[2] Instituto de Ingeniería, Universidad Nacional Autónoma de México
Ciudad Universitaria, 04510 México D.F., México
e-mail: fpem@pumas.iingen.unam.mx

Keywords: Dynamics, RBSM, Façade, Masonry, Damage, Assessment.

Abstract. *The paper presents the computational modelling and the seismic damage assessment of a typology of façade that is recurring among the churches built during the colonial period in México, between* 16^{th} *and* 18^{th} *century. This typology is symmetric, with two relatively stubby bell towers on either side of the main façade itself, while the openings are usually aligned along the vertical axis of symmetry, including a portal that is much wider than the window underneath the tympanum. Even if these churches were built differently, according to the regional seismicity, this notwithstanding we considered This is an "archetype model" whose characteristics can be considered as a good basis to be representative of this typology in general, even if there is some local variability, mainly related to the regional level of seismicity.*

The main seismic collapse mechanisms of this typology tend to involve both the towers and the central part of the façade with damages that can be related both to in-plane shear actions and to the out-of-plane actions. The central part of the façade often presents damages and cracks along the symmetry axis and along the sides connecting the towers. These towers present very often a localized damage in the belfry due to flexural actions and also can present a damage mechanism related with the torsion in their middle part.

In order to study the complex nature of these damage mechanisms, we adopted two specific Rigid Body and Spring Models (RBSM) to analyse separately the in-plane and the out-of-plane dynamical behaviours. Great attention has been posed into selecting a set realistic constitutive rules to describe the main meso-scale material-damage mechanisms. The main characteristics are: i) orthotropy of the flexural and membranal response; ii) material response is strongly influenced by average vertical axial compression; iii) modelling the hysteretic energy dissipated by repeated cyclic loading.

Given a suitable discretization, these RBSM allowed us to describe realistic damage patterns and also the effects of the higher modes of vibration with a reasonable computational effort and using real accelerograms.

Figure 1: Typical colonial churches built in: a) low seismic risk zone (central Mexico), b) high seismic risk zone (Pacific coast).

1 INTRODUCTION

Ancient masonry structures frequently show extensive damages after being subjected to earthquakes, even in the case of rather moderate seismic intensity. As an example, after the earthquake of magnitude 7.0 that happened in central México on 1999, 1542 colonial churches were detected as damaged, in a radius of more than 100 km from the epicenter. The careful survey and seismic assessment of this architectural heritage affected by such a severe earthquake was a very effective way to understand the structural weaknesses of these construction. These churches, that were mainly built during the colonial period between the 16^{th} to 18^{th} centuries, are quite variable in size and in architectural style, but it is possible to identify a general recurrent typology. Clearly, we should also mention that an important factor which influenced the architectural style was the local experience of the ancient builders due to the regional seismic activity, as shown, for example in Figure 1.

In this context, and for the present study, it seemed appropriate to establish a zone of interest and a typology of church that can be considered as typical. In particular, this typology is inspired by some churches that are present in the the State of Puebla, located around 250 km from the subduction zone. In this area the main earthquakes can be qualitatively considered of "medium" intensity and quite frequent. The survey after the 1999 earthquake showed that even if the number of full collapse was relatively low, this notwithstanding the large part of the hystorical churches suffered heavy damages which had a fairly typical and specific crack pattern. In fact, in these churches the out-of-plane mechanism is rarely preminent, somewhat differently from the experience made after recent Italian earthquakes [1]. On the other hand, it was often observed a complex influence of the presence of two large and relatively stubby bell towers built symmetrically on either side of the main façade.

Figure 2: Typical colonial church of the central Mexico.

2 A TYPICAL COLONIAL CHURCH

Thousands of churches were built in Mexico from 16^{th} to 18^{th} century, and persist to date in rather good conditions; they vary in size and architectural sophistication, but follow some recurrent basic typologies. The simplest among them are rather small parochial churches which are found in every ”barrio” of Méxican towns and villages. One important factor that has influenced the evolution of their architectural features has been the experience of damage suffered from earthquake activity. In most areas of the Pacific Coast, where the recurrent destruction of the early colonial constructions produced an evolution towards low rise, heavily buttressed buildings with scarce external ornamentation. In other regions the lower concern for earthquake failures favored taller and more slender constructions, as for example in the area of Puebla, in which we are now focusing our attention.

2.1 Geometric and material description

The typical colonial church in the central Mexico has a Latin-cross floor plan. The Figure 2 shows the isometric projection of the building that we have taken as a representative example of the typology to be studied. In this example, the main nave of the church measures 20×58 m^2, while the height of the vaults is 18 m. Its two bell towers are 28 m high. The roof is constituted by a quadripartite vaulting system. A hemispherical dome is placed over the transept bay and it is supported by the drum. Small buttresses are placed along the main nave. In the first bay there is an intermediate floor for the chorus.

The façade is composed by the ”main wall”, which is connected with the towers and the frontispiece. A schematic view, in elevation and with a section in plan is shown in Figure 3. The façade has, generally, two openings: the main door and a window for illuminate the chorus. The height of the door is between five to eight meters. The main material of construction is a heterogeneous masonry constituted by stones agglutinated by lime-sand mortar. Frequently, broken clay bricks or lightweight volcanic stones were added to the masonry; this heterogeneous masonry constitutes a kind of concrete whose composition varies according to the structural element; it is lighter than normal stone masonry, and has a tensile strength bigger than brick masonry, due mainly to the absence of weak planes constituted by the mortar layers. On the

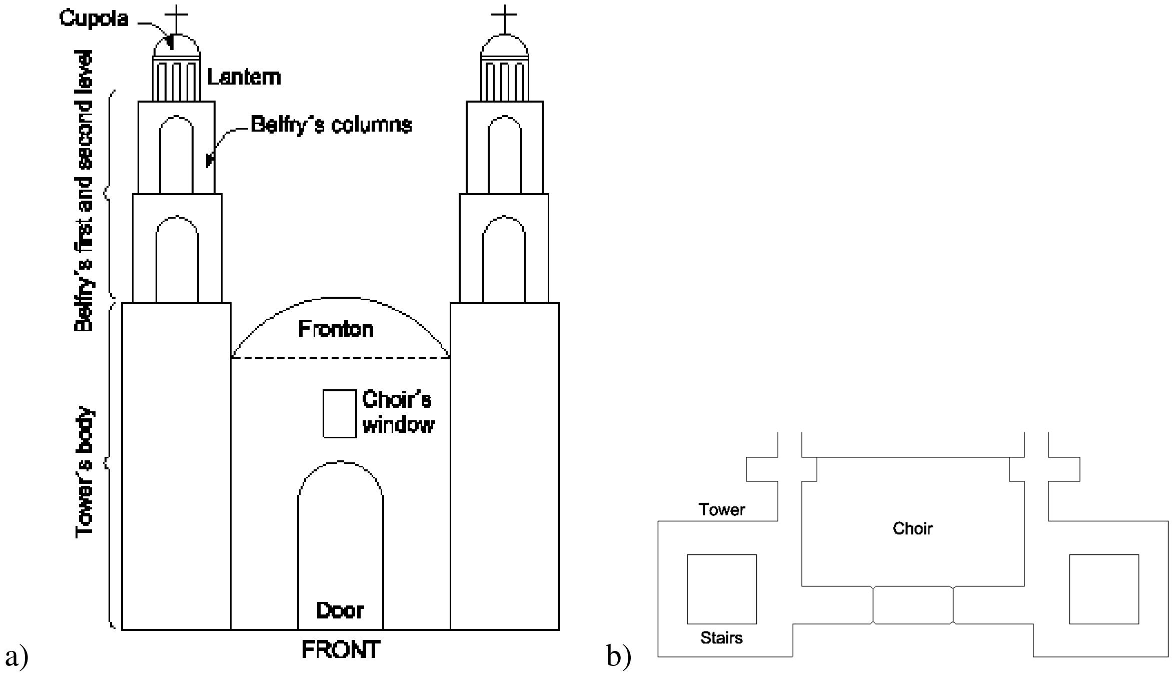

a) b)

Figure 3: Schematical representation of the façade: a) Front view, b) Plan view.

basis of these characteristics, we can consider the material as homogeneous at the macroscopic scale [2]. From the mechanical point of view, the response can be considered almost isotropic, or orthotropic as a function of different factors, such as the type of loading (e.g. in-plane or out-of-plane) and the stress condition (e.g. in the case of prevaliling compression load along vertical direction).

The bell tower can be divided in three different parts: the main body of the tower which comprises the base; the belfry which can be made as a combination of superimposed bodies; and the cover, that is often a small hemispheric dome at the top of the bell tower. In plant, the body of the towers can be treated as a square pipe, which is attached to the walls of the façade and to the lateral wall of the nave. Small openings can be found in the main body, which have the function to illuminate and ventilate the stairwell. In general, it is common that the belfry is made by two or three superimposed bodies; being the most top one smaller than the other ones. Sometimes the third body is more similar to a “lantern like” element.

2.2 Typical damages

The observation and evaluation of seismic damage suffered by typical masonry historic churches have allowed to identify their basic modes of failure and the main characteristics of their seismic response: the behaviour is governed by the low tensile and shear strength of constituting materials, which makes it difficult to guarantee the full continuity within and between structural members, in the event of strong ground motions, and leads to specific mechanisms for resisting seismic actions [1, 3].

After the earthquake of 1999, damage surveys of churches from the state of Puebla was made by different institutions, and it was possible to recover reliable data from a total of 30 churches from Puebla. It must to bear in mind that this number is not the total of churches damaged by the 1999 earthquake, especially in the State of Puebla.

The large part of these buildings presented damages on the bell towers, being one of the most damaged elements, both in the belfry and in the main body of the tower, whereas only few cases presented damages in the small dome. The bell towers are rather weak elements, in which the ground motion tends to be amplified in the upper levels. Even if they are relatively low and sturdy, damages are rather common, especially in the vertical elements and in the arches surrounding the belfry. Additionally, their bending and torsion motion tends to separate them from the rest of the church, or to generate shear cracking in the basement of the tower. The façade is typically an heavy wall, poorly connected to the rest of the temple, and the out-of-plane vibrations tend to separate it from the towers. Horizontal cracking in the frontispiece, or in the lower part of the façade weakened by large openings, is rather common, sometimes giving rise to the partial or total overturning of the façade.

3 RIGID BODY AND SPRINGS NUMERICAL MODELS

In order to cover a wide spectrum of possible mechanisms of damage two specific *rigid body spring models* (RBSM) has been considered: one for the *in-plane* [4, 5], and another one for *out-of-plane* numerical analyses [6, 7]. These two numerical models has been implemented with the aim to perform full dynamical analyses by considering non linear behaviour and the mechanical degradation of the masonry material. In the present investigation real recorded ground motions have been adopted as forcing actions.

A procedure of calibration has been performed in order to obtain a good approximation of the fundamental natural modes of vibration of the church, as it resulted from a previous research in which the complete three-dimensional building was investigated in the linear-elastic by a detailed finite element model [8]. In this process, it was also necessary to investigate and consider with some attention the influence of the lateral walls that affects the values of natural periods and modal shapes of the façade. The essential parameters assumed to describe the macroscopic masonry material behaviour are reported in Table 3. Both models were analyzed using as a forcing action the strong ground motion recorded at Ciudad Serdad during the Mexico earthquake on 15 June, 1999. The time history in terms of ground acceleration of the NS and EW components are shown in Figure 4.

Property	Magnitude	Unite
Elasticity modulus	1962	MPa
Shear modulus	817	MPa
Poisson coefficient	0.2	
Mass density	1600	kg/cm^3
Compressive strength	2943	kPa
Tensile strength	147	kPa
Cohesion	200	kPa
Friction angle	15	degree

Table 1: Mechanical properties of the masonry [9, 10]

3.1 In-plane dynamical analysis

The model implemented for the in-plane dynamic analysis is based on a RBSM approach that was specifically developed for modelling the non-linear behaviour and damage of the ma-

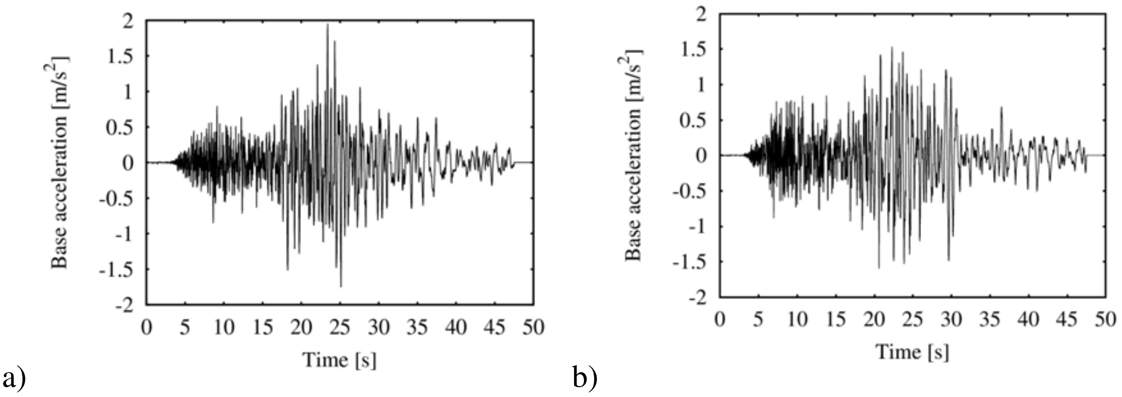

Figure 4: Acceleration time hystoris of the recording used in the analyses: a) PueCSER990615-EW component, b) PueCSER990615-NS component.

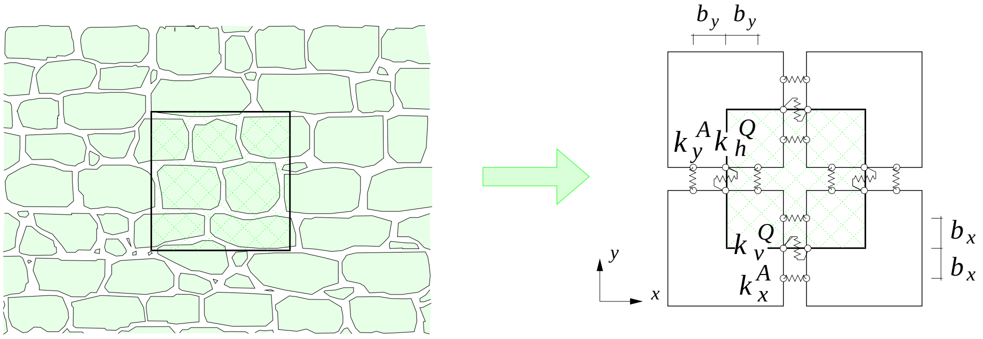

Figure 5: Schematic view of an irregular masonry and the corresponding RBSM "unit cell" made by four rigid elements [5].

sonry material [11, 4, 12, 13]. This plane model considers the heterogeneous solid material as a mechanism consisting of rigid masses connected by simple elastic-plastic springs, in the spirit of the rigid body spring model (RBSM) [14, 15, 16], and also other discrete element methods [17]. The core of the present model is the *unit cell* defined by four rigid elements connected to each other by two normal springs plus one shear spring at each side, as shown in Figure 5, on the right. Since the model is designed to work at the macro-scale, the size of the unit cell should be equal or larger than the representative volume element of the masonry. Potentially, this model allows to define the elastic characteristics of the springs by a specific procedure of identification with the objective to transfer some characteristics of the internal texture to the macro-scale model [13]. For the present case, as a first approach, and considering the observsations written in Section 2.1, the we have hypothesized a masonry texture composed by quite irregular blocks. This implies that this material presents limited effects of microstructure and the description of the global behaviour at the macro-scale can be approximated by assuming a simplified isotropic material based on the parameters reported in Table 3. On the other hand, a simplified phenomenological approach, based on the experimental tests available in the technical literature has been followed in order to model the response under the cyclic loading [18, 19, 20]. Different hysteretic rules are assumed for the axial springs and for the shear springs, as sketched in Figure 6.

A resume of the results obtained by the discrete model made by 237 rigid elements, for a

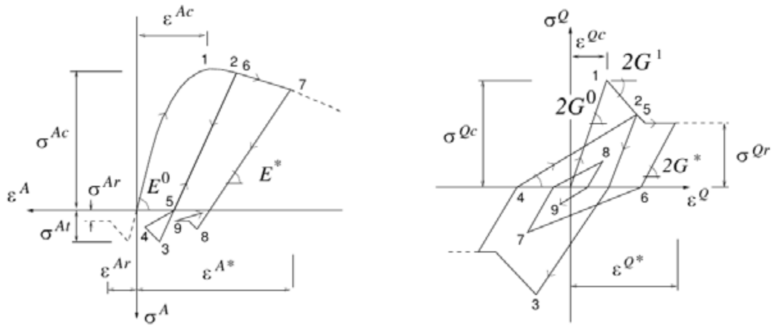

Figure 6: Hysteretic rules for axial and shear springs [5].

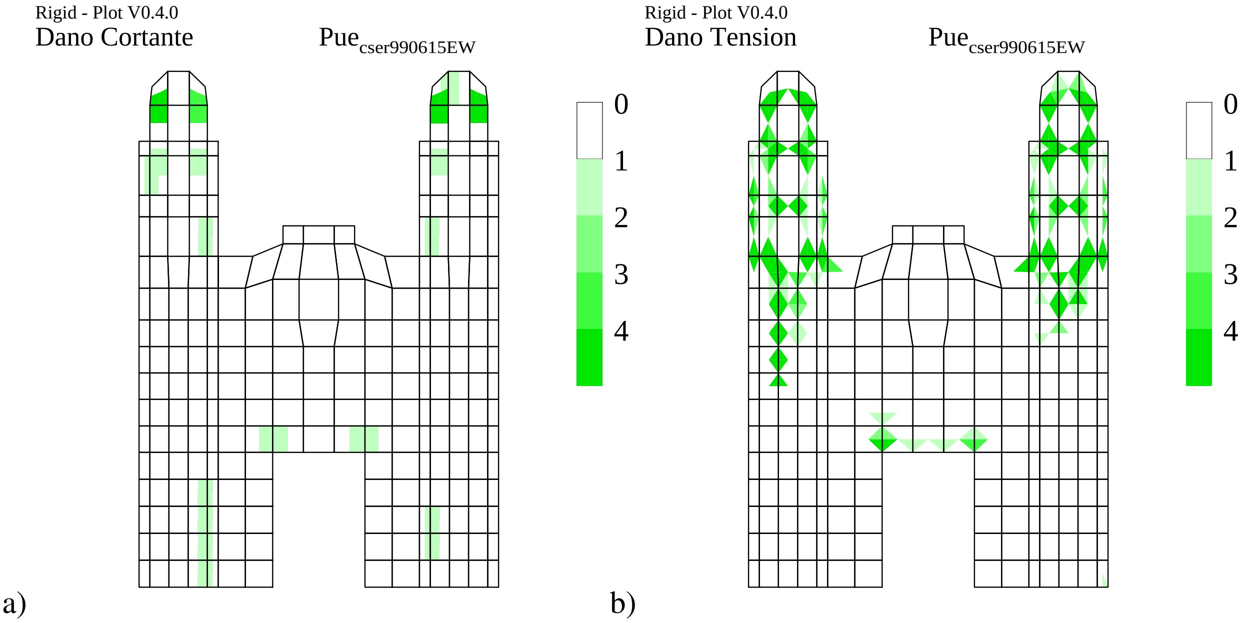

Figure 7: Damages for the in-plane model for real earthquake record: the EW component shown in Figure 4. a) Shear damage, b) Tensile damage

.

total amount of 711 degrees of freedom, is shown in Figure 7 that reports the damage patterns obtained by a full-dynamic non-linear analysis. A damage index scale $[0-4]$ has been created, as a funtion of the degradation of the mechanical characteristics of the springs of the numerical model. The main damage was related to the tensile stresses due to the belfry flexion. The belfries were the most vulnerable elements in the towers, since they present an appendix-like behaviour. A vertical cracking along the body of the tower is also present, while a slight damage zone due to shear forces is obtained in the main wall of the façade, as well as in the body of the tower. There is no compression damage in any element.

These types of damages are quite similar to the damages observed during the strong ground motions of 1999. The tower tends to separate from the rest of the structure, due to a vertical crack. Thus, this vertical crack is not due to vertical crushing, but it is due to a combination of shear actions and horizontal tensile forces. As in this particular case, it is rather common that this vertical crack appears along the body of the tower. However in some cases, the vertical crack can appear at the union of the tower with the main wall. Shear cracks are also present in the walls of the central part of the façade as well as in at the base of the tower.

3.2 Out-of-plane dynamical analysis

The out-of-plane behaviour of the masonry façade is modelled at the macro-scale level as an assemblage of quadrilateral rigid elements connected by elastic-plastic joints at which only bending and twisting movements are possible. This model was originally intended to plan out the analysis of relatively slender walls, remaining within the scope of the Kirchhoff plate model [6, 21]. In this sense, as a general rule, the wall should be regarded as a special case of a three-dimensional body $\mathcal{B} \subset \Re^3$ with one dimension - the thickness t - small compared to the other characteristic lengths. Hence, the model describes the whole structure in terms of the mid-surface $\mathcal{M} \subset \mathcal{B}$, and only the transverse displacements of this reference mid-surface are considered. For the present research, the model has been enhanced in order to be employed also in the presence of the towers, even if this case cannot be considered, at a first sight, as coherent with the terms of the Kirchhoff model. Nevertheless, we believe that the application of this model is acceptable because it is still able to describe the dynamics of these towers when their response is a mix of flexural and torsional-type. Clearly this analysis should be complemented by the in-plane analysis and morover it cannot describe the shear damages of the tower out-of the plane the façade.

Thus, a Cartesian reference frame $\{O, x, y, z\}$ is then defined so as the plane $z = 0$ is coincident with the mid-plane mapping that is parametrized by only employing the global coordinates $(x, y) \in \Omega$. The plane domain Ω is then discretized by a partition into m quadrilateral subdomains ω_i (with $i = 1, m$) such that no vertex of one sub-domain lies on the edge of another one. The mid-point of the sides of these sub-domains is the joint between the elements and is modeled as a spherical hinge from the kinematic point of view. This spherical joint allows small rotations whose axis is in the plane $z = 0$. We distinguish two components of rotation: one in which the axis is parallel to the edge of the abutting elements (flexural deformation), and the

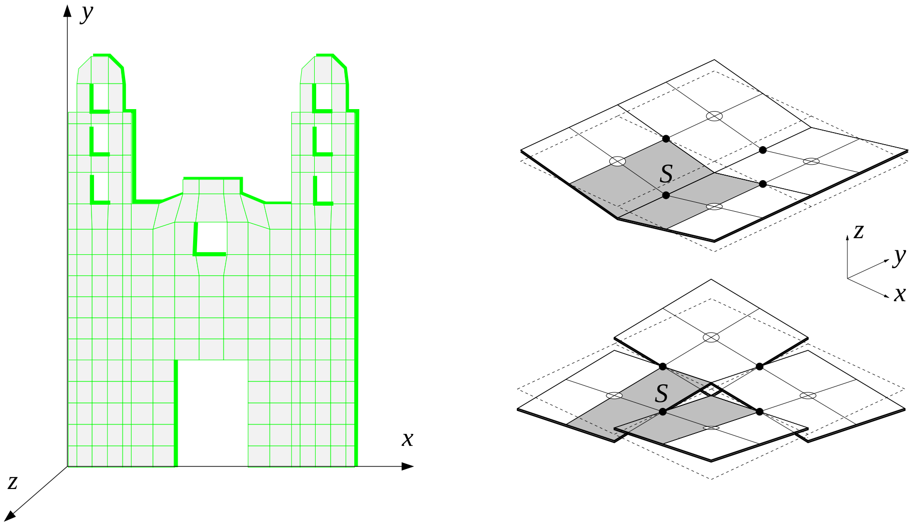

Figure 8: RBSM mesh for the out-of-plane analysis (left), and sketch of an assemblage of 4 rigid elements subjected to flexural and torsional deformation [7].

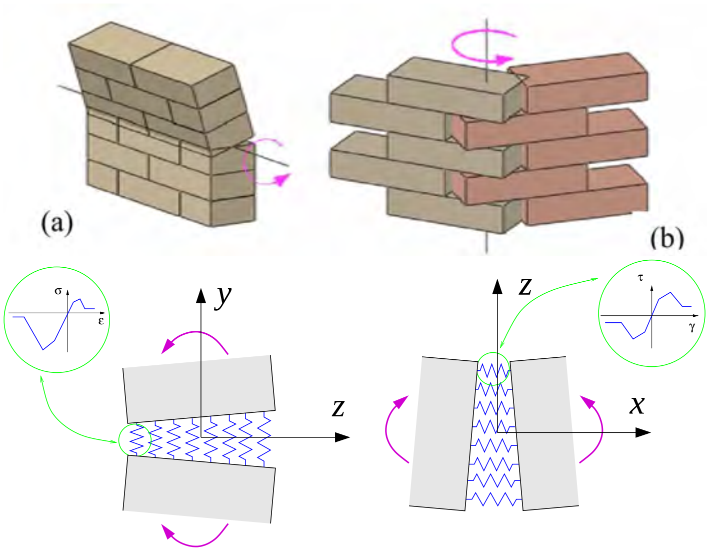

Figure 9: Heuristics of the mechanical connection between a couple of elements; corresponding layers of non-linear line-springs.

other whose axis is perpendicular to the edge (twisting deformation), as shown in Figure 8 on the right side. The allowed displacements w of the points on the reference xy plane are parallel to z; they are small when compared to the thickness and are called *deflections*. The mass is lumped into these r connection nodes, as shown in Figure 8 where the mass of the shaded area A_s is given to node S. Then, the mean bending and twisting curvature is measured at each connection joint as a function of the angle between the rigid elements.

The constitutive behavior of joints between the elements is defined on the basis of the one-to-one moment-curvature relations assigned to the bending and twisting springs placed in correspondence of each connection joint S. In the linear-elastic field, the out-of-plane constitutive behavior could be properly described by referring to the homogeneous orthotropic Kirchhoff plate model. [1]

Out-of the linear elastic field, the moment-curvature relationship assigned to each connection joint follows a piecewise linear function that is defined following an heuristic procedure in which the behavior of the wall is modelled at a sectional level by a combination of line-springs. In the Figure 9 (top) the cases of flexural damage due to rotation along an horizontal hinge (on the left side) and along a vertical hinge (on the right side) are shown. In the Figure 9 (bottom), we have sketched the different non-linear constitutive laws that are assigned to the line-spring along the vertical direction (for modelling a rotation along an horizontal hinge) and to the line-spring along the horizontal direction (for modelling a rotation along a vertical hinge).

Another aspect that must be considered in the definition of the flexural and torsional out-of-plane behaviour, is the very different effect of the in-plane vertical pressure on the response when considering the horizontal bending or the vertical bending. The geometric texture of the masonry material has also an important role in the definition of the moment-curvature rela-

---

[1] the orthotropic plate rigidities can be related to the Young moduli and Poisson coefficient according to the following relation, also recommended by M.T. Huber [22]:

$$D_{xx} = \frac{E_x J_{yy}}{1-\nu^2} \quad , \quad D_{yy} = \frac{E_y J_{xx}}{1-\nu^2} \quad , \quad D_{xy} = \nu\sqrt{D_{xx} D_{yy}} \quad , \quad D_{ss} = \frac{1-\nu}{2}\sqrt{D_{xx} D_{yy}} \tag{1}$$

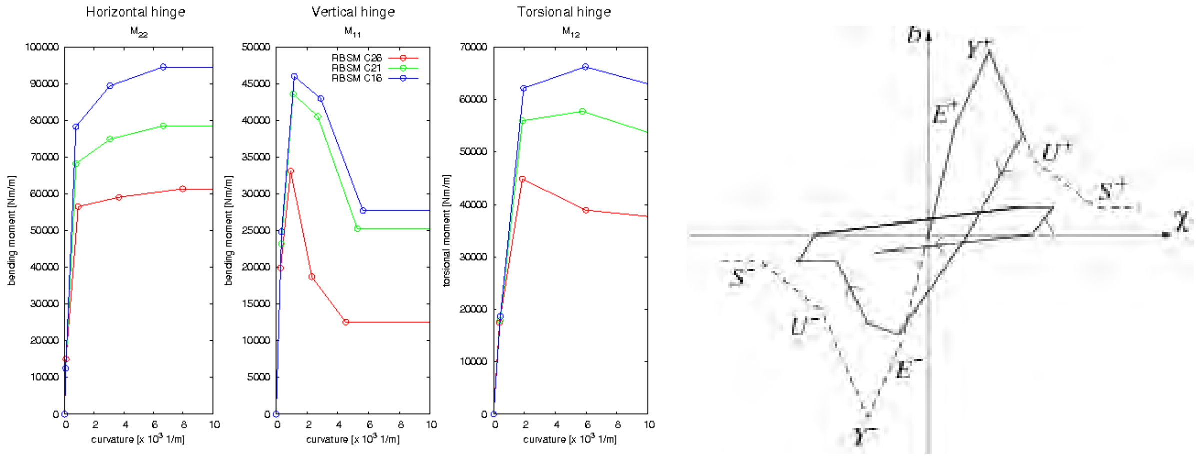

Figure 10: Skeleton curves for the relationship between bending moment and curvature in correspondence of a different vertical pressure: red=low, green=average, blue=high, (on the left side of the drawing). Scheme of hysteretic rules under cyclic loading (on the right side of the drawing).

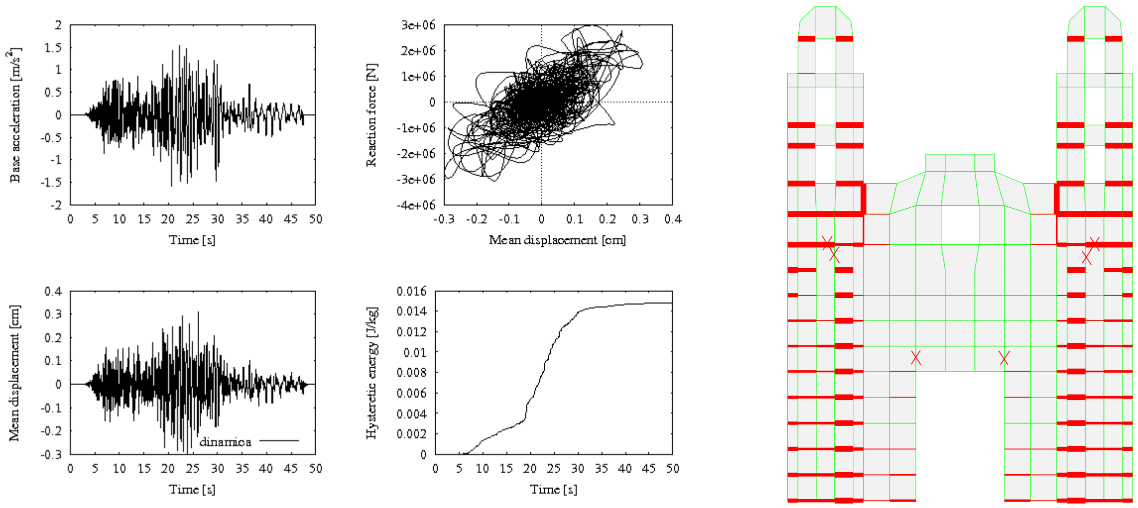

Figure 11: Scheme of damage after PueCSER990615-NS component. Map of energy dissipated.

tionship for the bending along a vertical hinge. As a consequence, the out-of-plane flexural response is strongly orthotropic and variable in the different connection points of the model [23]. In the present model, the simplified out-of-plane homogenization gives skeleton curve that are strongly related to the local vertical compression stress, as shown in Figure 10. As a first approximation, a very simple criterion was adopted here, in which the mean compression stress is assumed as directly proportional to the vertical distance of the connection joint from the upper edge of the specimen.

The non-linear dynamical analysis is performed at the macro-scale by solving the elastic-plastic problem by means of a standard full Newton-Raphson algorithm [24] until the attainment of a prefixed numerical convergence.

The Figure 11 shows a summary of the response to the NS component of the strong ground motion recorded at Ciudad Serdad during the Mexico earthquake on 15 June, 1999. On the left side of the figure, some time histories have been reported, while the drawing on the right side shows the distribution of the histeretic energy dissipated during the dynamic analysis, and it can be considered as a reasonable first indication of damage and mechanical degradation. We can observe that the damage pattern is not too much different with respect to the in-plane case already shown in Figure 7. In fact, the most vulnerable parts of the façade are again the belfries (due to out-of-plane flexure) and the joint areas between the towers and central façade. In this particular case we also note that the main body of the façade seems not to suffer from the typical out-of-plane damages that affected in many cases the Italian façades [3, 21].

4 FINAL REMARKS

The first remark of this research is that the behavior of this type of façade, very typical of the colonial churches in México, has some special features that were hardly found in previous studies that were based mainly on the surveys of the masonry churches affected by earthquakes in Italy, for which the out-of-plane collapses were often the main threat. In the present case, the presence of the towers, built in an integrated manner with the façade and not simply constructed in compliance, substantially alter the situation. In fact, on the one hand these towers provide a constraint that reduces the movement off-plan, but also they increase the in-plane actions, and are also committed themselves to a combined bending and torsion stress. We find a framework in which the shear actions have a significant role in the damage patterns, especially in the joints between the facade and towers, and moreover we observed damage due to bending-torsion in the main body of the towers. The complete picture of this behavior must therefore be studied by means of a modelling that should be able to capture all these different aspects. The application of the two models proposed here seems suitable for this purpose and it is considered promising for a subsequent and more detailed investigation of this typology.

5 ACKNOWLEDGMENTS

Financial support from the PAPIIT project of the DGAPA of the Universidad Nacional Autónoma de México under grant IN105409 “Estrategias para el modelado y análisis de estructuras históricas” is gratefully acknowledge.

REFERENCES

[1] F. Doglioni, A. Moretti, V. Petrini, Le Chiese e il Terremoto, Lint press, Trieste, 1994, in Italian.

[2] R. Meli, R. Sánchez-Ramírez, Criteria and experiences on structural rehabilitation of stone masonry buildings in mexico city, International Journal of Architectural Heritage 1 (2007) 3–28. `doi:10.1080/15583050601123118`.

[3] V. Petrini, S. Casolo, F. Doglioni, Models for vulnerability analysis of monuments and strengthening criteria, in: Bisch, P and Labbe, P and Pecker, A (Ed.), Proceedings of the Eleventh European Conference on Earthquake Engineering - Invited lectures , A A Balkema Publishers, Schipholweg 107C, PO BOX 447, 2316 XC Leiden, Netherlands, 1999, pp. 179–198, 11th European Conference on Earthquake Engineering, Paris, FRANCE, Sep 06-11, 1998.

[4] S. Casolo, Modelling in-plane micro-structure of masonry walls by rigid elements, International Journal of Solids and Structures 41 (13) (2004) 3625–3641. `doi:10.1016/j.ijsolstr.2004.02.002`.

[5] S. Casolo, F. Pena, Rigid element model for in-plane dynamics of masonry walls considering hysteretic behaviour and damage, Earthquake Engineering & Structural Dynamics 36 (8) (2007) 1029–1048. `doi:10.1002/eqe.670`.

[6] S. Casolo, Rigid element model for non-linear analysis of masonry façades subjected to out-of-plane loading, Communications in Numerical Methods in Engineering 15 (7) (1999) 457–468. `doi:10.1002/(SICI)1099-0887(199907)15:7<457::AID-CNM259>3.0.CO;2-W`.

[7] S. Casolo, Modelling the out-of-plane seismic behaviour of masonry walls by rigid elements, Earthquake Engineering & Structural Dynamics 29 (12) (2000) 1797–1813. `doi:10.1002/1096-9845`.

[8] R. Meli, F. Peña, On elastic models for evaluation of the seismic vulnerability of masonry churches., in: Lourenço, Roca, Modena (Eds.), Proceeding of Structural Analysis of Historical Constructions, Padova, Italia, 2004, pp. 1121–1131.

[9] M. Chávez, Estudio experimental de las propiedades mecánicas de mampostería de piedra natural, Master thesis, Universidad Nacional Autónoma de México, Mexico, 2005, in Spanish.

[10] F. Peña, J. Meza, Seismic assessment of bell towers of mexican colonail churches, Advanced Materials Research 133-134 (2010) 585–590. `doi:10.4028/www.scientific.net/AMR.133-134.585`.

[11] S. Casolo, F. Pena, Modelling micro-structure aspects of masonry walls by a simplified approach, in: Brebbia, CA (Ed.), Structural Studies, Repairs and Maintenance of Heritage Architecture VIII, Vol. 16 of Advances in Architecture Series, Wessex Inst Technol, WIT press, Ashurst Lodge, Southampton SO40 7AA, Ashurst, England, 2003, pp. 337–346, 8th International Conference on Structural Studies, Repairs and Maintenance of Heritage Architecture, Halkidiki, Greece, May 07-09, 2003.

[12] S. Casolo, V. Petrini, A specific model for in-plane non-linear dynamics of masonry walls including some texture effects, in: Jones, N and Brebbia, CA (Ed.), Structures Under Shock and Impact VIII, Vol. 15 of Structures and Materials, Wessex Inst Technol, WIT press, Ashurst Lodge, Southampton SO40 7AA, Ashurst, England, 2004, pp. 283–292, 8th International Conference on Structures Under Shock and Impact, Iraklion, Greece, Mar 2004.

[13] S. Casolo, Macroscale modelling of microstructure damage evolution by a rigid body and spring model, Journal of Mechancis of materials and Structures 4 (3) (2009) 551–570. `doi:10.2140/jomms.2009.4.551`.

[14] D. V. Griffiths, G. G. W. Mustoe, Modelling of elastic continua using a grillage of structural elements based on discrete element concepts, International Journal for Numerical Methods in Engineering 50 (7) (2001) 1759–1775. `doi:10.1002/nme.99`.

[15] T. Kawai, New discrete models and their application to seismic response analysis of structures, Nuclear Engineering and Design 48 (1978) 207–229.

[16] M. Ostoja-Starzewski, Lattice models in micromechanics, Applied Mechanics Review ASME 55 (1) (2002) 35–60. `doi:10.1115/1.1432990`.

[17] J. V. Lemos, Discrete element modeling of masonry structures, International Journal of Architectural Heritage 1 (2) (2007) 190–213. `doi:10.1080/15583050601176868`.

[18] G. Calvi, M. Priestley, Post collapse analyses of a medioeval masonry tower, in: Fifth North American Masonry Conference, University of Illinois at Urbana-Champaign, 1990.

[19] A. Anthoine, G. Magenes, G. Magonette, Shear compression testing and analysis of brick masonry walls, in: Proceeding of the 10th European Conference on Earthquake Engineering, Wien, 1994, pp. 1657–1662.

[20] G. Calvi, G. Magenes, Experimental research on response of urm building systems, in: U.S.-Italian Workshop on guidelines for seismic evaluations and rehabilitations of unreinforced masonry buildings., Pavia, 1994.

[21] S. Casolo, S. Neumair, M. A. Parisi, V. Petrini, Analysis of seismic damage patterns in old masonry church facades, Earthquake Spectra 16 (4) (2000) 757–773. `doi:10.1193/1.1586138`.

[22] S. P. Timoshenko, S. Woinowsky-Krieger, Theory of Plates and Shells, McGraw-Hill, 1959.

[23] S. Casolo, G. Milani, A simplified homogenization-discrete element model for the nonlinear static analysis of masonry walls out-of-plane loaded, ENGINEERING STRUCTURES 32 (8) (2010) 2352–2366. `doi:10.1016/j.engstruct.2010.04.010`.

[24] K.-J. Bathe, Finite Element Procedures in Engineering Analysis, Prentice-Hall Inc., New Jersey, U.S.A., 1996.

COMPDYN 2011
III ECCOMAS Thematic Conference on
Computational Methods in Structural Dynamics and Earthquake Engineering
M. Papadrakakis, M. Fragiadakis, V. Plevris (eds.)
Corfu, Greece, 26–28 May 2011

DYNAMIC FINITE ELEMENT ANALYSIS OF EARTH MASONRY STRUCTURES BASED ON EXPERIMENTAL MATERIAL DATA

Rogiros Illampas, Dimos C. Charmpis, and Ioannis Ioannou

Department of Civil and Environmental Engineering, University of Cyprus
75 Kallipoleos Str., P.O. Box 20537, 1678 Nicosia, Cyprus
e-mails: {rilamp01, charmpis, ioannis}@ucy.ac.cy

Keywords: Earthen Buildings, Adobe masonry, Masonry Modeling, Non-linear Dynamic Analysis.

Abstract. *Despite the fact that earthen construction is a significant feature of the international architectural heritage, the application of sophisticated analysis methods such as Finite Element (FE) modeling in the appraisal and design of adobe masonry structures has received limited attention up to this day. This paper presents some of the outcomes of an ongoing research programme at the University of Cyprus which aims to investigate the structural response of adobe construction. The behaviour of adobe masonry assemblages under the action of compressive loading-unloading cycles is hereby examined both experimentally and numerically. The development of the FE model used in the numerical simulation is based on a macro-modeling strategy while a simple elastic-plastic constitutive law is adopted. All input parameters required are derived from experimental material data. The numerical results are compared with laboratory test outcomes and useful conclusions regarding the applicability of FE modeling are deduced. The use of the formulated FE model is broadened by analyzing a complete adobe structure under various levels of seismic action. The evaluated response of the adobe structure to dynamic excitations is discussed and the constraints imposed by the model used are analyzed. Finally, critical issues that future research should address in order to enable the efficient computational analysis of earthen construction are identified.*

1 INTRODUCTION

Earth masonry composed of unfired clay bricks and earth mortar joints has been traditionally used for thousands of years. Despite its broad and extensive use in the past centuries, its applications in contemporary architecture are nowadays rather limited. However, a large heritage of adobe buildings still survives and constitutes a significant part of the global building stock and an important feature of the international architectural heritage [1]. Experience has shown that unreinforced adobe masonry construction has relatively poor response to dynamic loading and is prone to seismic damage [2-4]. This implies that there is an imminent need for protecting existing earthen buildings from the destructive effects of earthquakes.

The application of detailed/formal engineering procedures in the appraisal of mud-brick structures and the assessment of retrofitting measures is currently hindered, among others, by the absence of accurate computational methods that would account for the specific characteristics of unfired earth. Although over the last few decades the numerical modeling of conventional masonry construction has been studied in depth through academic research (e.g. [5-7]), adobe masonry has generally received limited attention. This is possibly due to its intrinsic complexity that derives from the natural randomness and inhomogeneity of earthen materials. The various constitutive models that have been applied or developed for the numerical analysis of masonry have not yet been studied in the context of earthen construction. In addition, the applicability of the Finite Element (FE) method in the structural evaluation of adobe masonry structural members and buildings has not been adequately investigated and no attempts have been made so far for calibrating and validating numerical models based on the outcomes of laboratory tests and field observations. Furthermore, the formulation of FE models is, up to this date, precluded due to the lack of adequate experimental data describing the properties of earthen materials and the structural behaviour of adobe masonry assemblages.

This paper aims to examine the structural response of earth masonry construction to compressive loading and seismic action through FE analysis. Initially a model of an adobe masonry assemblage is developed and its behaviour under the implementation of compressive loading-unloading cycles is investigated. The formulation of the model is based on the concepts of homogenized material and isotropic elastic-plastic constitutive law, while all the required input parameters are derived from laboratory tests. The numerical results obtained are compared with corresponding experimental data thus enabling the deduction of useful conclusions on the validity of the simulation procedure. In addition, a FE model of a traditional earthen building is developed and used for performing non-linear dynamic analyses. The investigation conducted involves the use of real time accelerograms from a past earthquake. The predicted response of the structure to various levels of seismic acceleration is studied and the outcomes of the FE analyses are presented and discussed. Useful comments regarding the accuracy of the numerical results are made and the technical challenges encountered when dealing with the FE modeling of earthen construction are noted. Furthermore, key issues that future research should address in order to allow for the efficient use of FE modeling in the analysis of adobe structures are identified.

2 FINITE ELEMENT SIMULATION OF ADOBE MASONRY SUBJECTED TO COMPRESSIVE LOADING AND UNLOADING

2.1 Experimental investigation of the response of adobe masonry to compressive loading and unloading

The development and calibration of a reliable FE model that would predict important aspects of the behaviour of masonry construction with adequate accuracy requires the implementation of laboratory tests [8, 9]. Experimental results can provide information regarding the material properties required for the formulation of the FE model. They can also be used for correcting the inherent deficiencies within the FE model by matching numerical outputs to measured data [9]. Within this framework an adobe masonry assemblage composed of five full-size adobe bricks and earth mortar joints has been subjected to compressive loading-unloading cycles in order to investigate its elastic and post-yield structural response. Prior to this, a number of uniaxial compression tests were also conducted on mud-brick assemblages to assess the capacity of earth masonry to bear static vertical loads [10].

The bricks used for the preparation of the specimen were supplied by a Cypriot manufacturer and belonged to the same production batch. The earth mortar had the same composition as the adobe bricks. It was prepared by mixing soil and straw fibers originating from crushed adobes with water (1155 g of water per 1850 g of solid constituents) to plastic consistency using a mechanical mixer. Stones and gravel with diameter exceeding 4 mm were not included in the mix. The mortar was applied at relatively thin layers (~ 10 mm) between the adobes. The composition of the mortar and the formation of thin joints were intentionally selected in order to replicate the form of adobe masonry that is encountered in local traditional earthen structures. The dimensions of the resulting masonry assemblage were (height x width x length) 28 x 30 x 45 cm^3. After being prepared, the assemblage was allowed to cure in the laboratory (22±2 ^oC and 42±5% R.H.) in order to ensure sufficient bonding between the adobe bricks and the mortar.

For the implementation of the compressive loading-unloading test a Lloyd LR300K universal testing machine with 300 kN capacity was used. The machine's platens have a swivel head to accommodate non-parallel bearing surfaces. Four vertical transducers were attached on each corner of the upper loading plate to record vertical displacements during the testing procedure. In addition, two horizontal transducers were placed on each side of the specimen to monitor its deformation in the transverse direction. The test setup is shown in Figure 1. Loads on the specimen were imposed using a displacement-controlled procedure. Displacement was applied at a constant rate of 0.1 mm/sec. Unloading cycles were programmed to take place successively when the load exerted reached a value of 10, 30, 50, 100, 150 and 200 kN. Figure 2 shows the stress-strain curve derived from the experimental data along with the corresponding numerical results obtained from the analysis of the FE model presented in subsection 2.2.

The results of the test indicate that the response of adobe masonry to compressive loading is non-linear and is characterized by intense plasticity and deformability. The parts of the stress-strain diagram that correspond to the application of loading show that the material exhibits progressive hardening. The form of the unloading branches reveals that when the exerted load is released, induced deformation is only partially removed, while considerable inelastic deformations remain present. Plastic deformations start to develop even when the specimen is subjected to low compressive stresses at the region of 0.08 MPa. This behaviour can be attributed to the fact that the sliding and displacement mechanisms, which take place between the soil grains due to the application of pressure, are non-reversible.

During the implementation of the test and after its completion it was noted that the specimen responded monolithically to vertical loading. Compression resulted in the compaction of adobe and mortar in the central axis of the masonry specimen. This led to the formation of a central zone within the body of the masonry assemblage where the visual distinction between the individual adobe bricks and the mortar joints was no longer feasible. No significant cracks or slips occurred at the joints during the loading procedure. Despite the fact that significant cracking and damage was recorded at the lateral sides of the adobe bricks, their central core remained sufficiently integer and did not lose coherence. This particular mode of failure experienced by adobe masonry under compression has been also noted during the execution of monotonic compression tests [10] and has been reported by other reserachers as well [11].

Figure 1: Pictures of the experimental setup used in the implementation of compressive loading-unloading tests on an adobe masonry assemblage composed of five full-size adobe bricks and earth mortar joints.

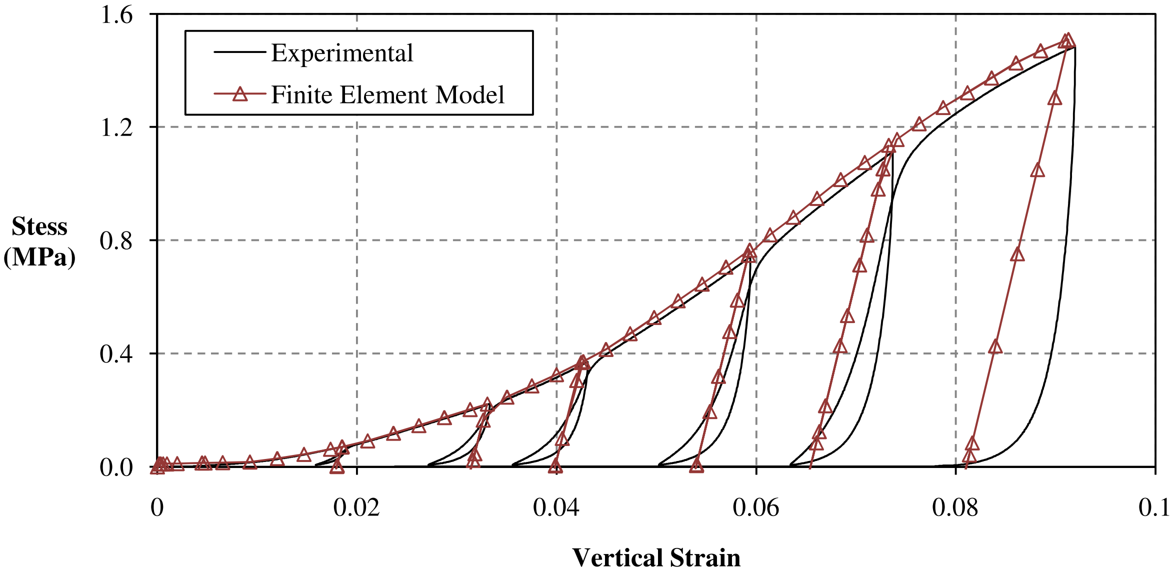

Figure 2: Experimental and numerical stress-strain curves referring to the application of compressive loading and unloading cycles on an adobe masonry specimen with dimensions (height x width x length) 28 x 30 x 45 cm^3.

2.2 Numerical simulation of compressive loading-unloading experimental test

For undertaking the numerical simulation of the experimental test on the adobe masonry assemblage, the commercial code ABAQUS CAE was employed. Both the adobe masonry specimen and the machine's steel compression plates were modeled. Since the main purpose of the current study is to examine practice-oriented analysis methods that can be applied in the appraisal and design of adobe structural members and full structures, earth masonry was numerically handled in the context of a macro-modeling strategy. The macro-modeling approach treats masonry as a fictitious homogeneous continuum and does not make any distinction between masonry units and mortar joints. Despite this rather oversimplifying assumption, macro-models have been widely used in the non-linear FE analysis of masonry structures (e.g. [12-14]) and are considered adequate for the characterization of the structural response of large-scale structural elements and full buildings [6, 7]. After all, in practice, the macroscopic structural response (estimation of forces/stresses and elastic/plastic deformations) is primarily of interest as opposed to detailed microscopic information (e.g. cracks initiation and propagation). Treating adobe masonry as a homogeneous medium is further justified by the monolithic behaviour exhibited by the tested specimen during the application of compressive loading.

All components of the FE model were discretized using 8-node 3D linear brick elements (C3D8). Each steel plate was discretized into 70 elements. A more dense FE mesh consisting of 7935 elements was used in the case of the adobe masonry specimen. It was decided to model adobe masonry using a simple isotropic Elastic-Plastic constitutive material model. The isotropic Elastic-Plastic constitutive material model available in ABAQUS CAE is based on classical metal plasticity theory and uses standard Mises yield surface with assorted plastic flow [15]. By default, when cyclic loading scenarios are examined, the aforementioned model assumes that the loading and unloading curves are parallel to the elastic loading curve (with its slope determined through the Young's modulus) [15]. The material characteristics and the elastic and inelastic properties defined in the FE model for simulating adobe masonry were assigned according to the results of laboratory tests. The density of adobe was measured following simple gravimetric methods and the Poisson's ratio was deduced from the recorded values of axial and transversal strains. The Young's modulus was derived from the stress-strain curve of the compressive loading-unloading experimental test. Its value was set to be approximately equal to the slope of the three unloading branches that were recorded after a 5% strain. In order to accommodate for the lack of elasticity that characterizes the behaviour of adobe masonry, a very low value for the yielding stress (0.01 MPa) was assigned. Post-yield behaviour was defined by providing a relation between compressive stresses and plastic strains based on the outcomes of the aforementioned laboratory test. The failure stress was computed from the results of monotonic uniaxial compression tests on mud-brick assemblages [10]. The steel plates are extremely stiff when compared to adobe masonry and were thus modeled using a Linear Elastic material model. The selected values for the properties of the adobe masonry and the steel plates are reported in Table 1. The boundary conditions provided were chosen so as to adequately simulate the test setup. The base nodes of the lower steel plate were considered to be pinned. A uniformly distributed vertical displacement was assigned to the upper steel plate. The amplitude of the displacement over time was formulated according to the mean displacement values that were computed from the data recorded by the vertically placed transducers during the experimental procedure. The contact between the adobe masonry and the steel plates was assumed to be frictionless. The FE model is shown in Figure 3. The simulated stress-strain curve is given in Figure 2.

	Adobe masonry	Steel plates
Weight per unit volume (kg/m^3)	1300	7750
Young's modulus (MPa)	135	220x10^3
Poisson's ratio	0.35	0.30
Yield stress (kPa)	10	-
Failure stress (kPa)	1650	-

Table 1: Parameter values adopted for the formulation of the FE model that was used in the analysis of adobe masonry assemblage subjected to compressive loading and unloading.

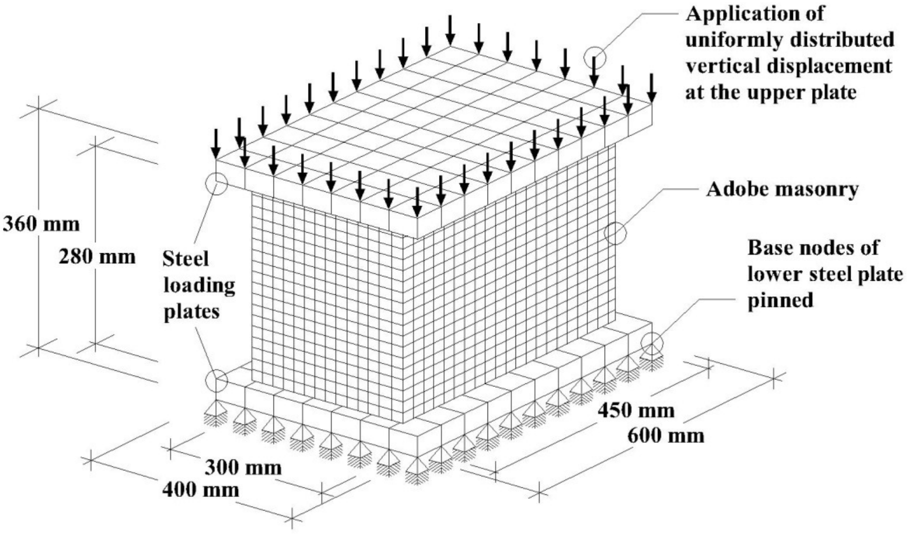

Figure 3: Finite element model used for the analysis of adobe masonry assemblage subjected to compressive loading and unloading.

The numerical results show that the FE model, although quite simplistic, reproduces very well the shape of the envelope of the experimental diagram. The difference between the ultimate stress and strain recorded during the experiment and those obtained from the numerical simulation is less than 2%. Taking into consideration the natural randomness and inhomogeneity of earth-based construction material this difference may be considered as negligible. Regarding the loading-unloading branches, these cannot be reproduced in detail by the constitutive model that has been chosen. However, despite the fact that in the FE model the loading-unloading branches coincide, they occur at approximately the same value of strain as the experimental ones. Furthermore, the stress computed by the numerical model after the end of each unloading cycle is equal to zero, as in the case of the actual masonry specimen. Therefore, the simulated response can be deemed adequate when the main aim is the macroscopic investigation of structural behaviour.

3 FINITE ELEMENT MODELING OF TRADITIONAL ADOBE STRUCTURE SUBJECTED TO SEISMIC LOADING

For examining the applicability of the formulated FE model in the assessment of the dynamic response of adobe construction, a model of a traditional earthen building was developed and analyzed under seismic excitation. The model prepared represents a “monochoro” which is the simplest and oldest typology of Cypriot earthen dwelling. A “monochoro” is a longitudinal, rectangular, single-roomed structure whose length is limited by the timber rafters of the roof. The abatements of the roof’s beams are set into the masonry and span the space between the two opposite longitudinal walls. The four load-bearing walls carry the superimposed weight of the roof.

The building that was modeled has external dimensions (height x width x length) 3.50 x 4 x 9 m^3 and its walls are 0.45 m thick. A door 2.20 m high and 0.90 m wide is located on its facade while two openings 0.80 x 0.80 m are located on the two side walls. The analysis was undertaken using the ABAQUS CAE software. The adobe walls were discretized with 3042 8-noded 3D linear brick elements (C3D8) using the same constitutive material model and input parameters as those reported in subsection 2.2. The timber elements composing the structure’s roof were not modeled because it was assumed that their limited stiffness does not enable the roof to act as a diaphragm during the application of seismic loading. In addition, no constrains were imposed on the nodes at the upper parts of the walls since it was presumed that these can oscillate freely during a seismic event. The base nodes of the walls were considered to be pinned. The unit area weight of the roof was set as 120 kg/m^2. The total weight of the roof was assigned to the upper section of the four walls in the form of uniformly distributed pressure. The FE model of the structure is shown in Figure 4. The dynamic action that was chosen for the analysis of the FE model was that of the 1978 June 20th Thessaloniki Earthquake. The duration of the seismic event was 30.59 seconds and the maximum accelerations recorded in the transverse and longitudinal directions were 0.146g and 0.139g respectively. The amplitudes of the earthquake's transverse and longitudinal components over time are presented in Figure 5. In order to investigate the response of the structure to various levels of dynamic excitation, different analyses were conducted by scaling in each case the two seismic acceleration components. The scaling factors used were: 0.25, 0.50, 1, 2 and 3.

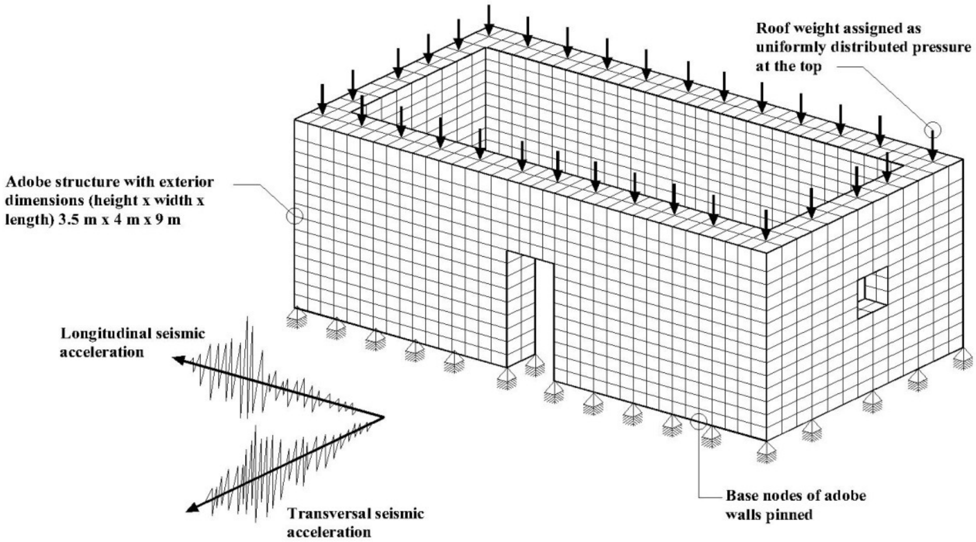

Figure 4: Finite element model used for examining the response of a traditional adobe masonry structure to dynamic loading.

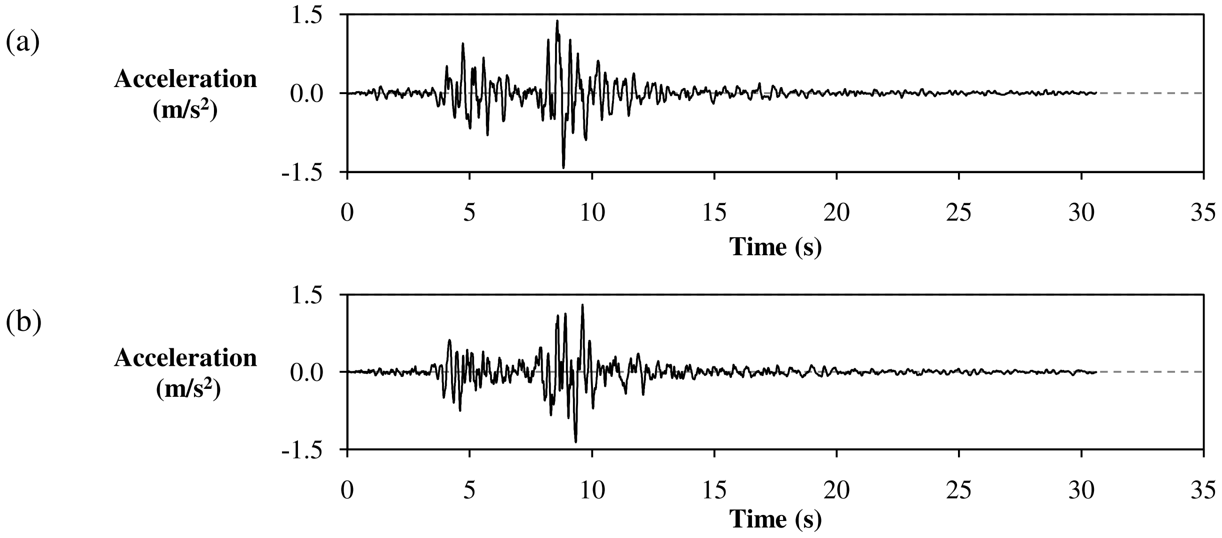

Figure 5: Transverse (a) and longitudinal (b) acceleration components of the 1978 June 20th Thessaloniki Earthquake.

The outcomes of the numerical analysis indicate that the adobe structure examined sustains considerable inelastic deformations when subjected to dynamic loading. The boundary conditions assigned at the corners and at the bottom of the model cause the walls to act as elements fully constrained on their lower part and side edges. Consequently, large displacements and deformations are encountered mainly on the central parts of the upper sections of the façade and the opposite wall (Figure 6). According to the numerical results obtained, the compressive stresses generated by the action of the 1978 Thessaloniki Earthquake do not exceed 50 kPa. However, tensile stresses up to 60 kPa develop at certain parts of the structure. After the dynamic excitation seizes, the compressive stress values encountered are below 15 kPa, but parts of the structure remain in tension (Figure 6). Figure 7 presents the transversal displacement time history of the central node at the upper part of the façade when the 1978 Thessaloniki Earthquake is applied and when the exerted accelerations are amplified by a factor of 3. The maximum transversal displacement of the same node and the out-of-plane deformation of the façade at each amplification level of the seismic action examined are reported in Figure 8. The displacementtime history results show that after the application of the maximum acceleration, the out-of-plane deformation of the façade in non reversible. An examination of the FE model during the time period of seismic loading indicates that the deformation induced does not allow the effective redistribution of loads to all parts of the structure. As a result, the loads are mainly accumulated on the opposite wall and on the two side walls. A comparison of the computed deformations at different levels of dynamic action reveals that when the maximum acceleration of the imposed excitation exceeds 0.07g, severe out-of-plane bulging develops on the façade. Between 0.14g and 0.43g non-reversible transversal displacements can reach values which range from 40 to 150 mm. It is worth noting that, according to the results yielded, the relation between the maximum applied acceleration and the maximum induced transversal deformation is not linear. The results stress out how significantly the response of masonry construction is affected by the existence of sufficient bonding between the load-bearing structural members and the diaphragmatic function at the levels of the roofs and floors.

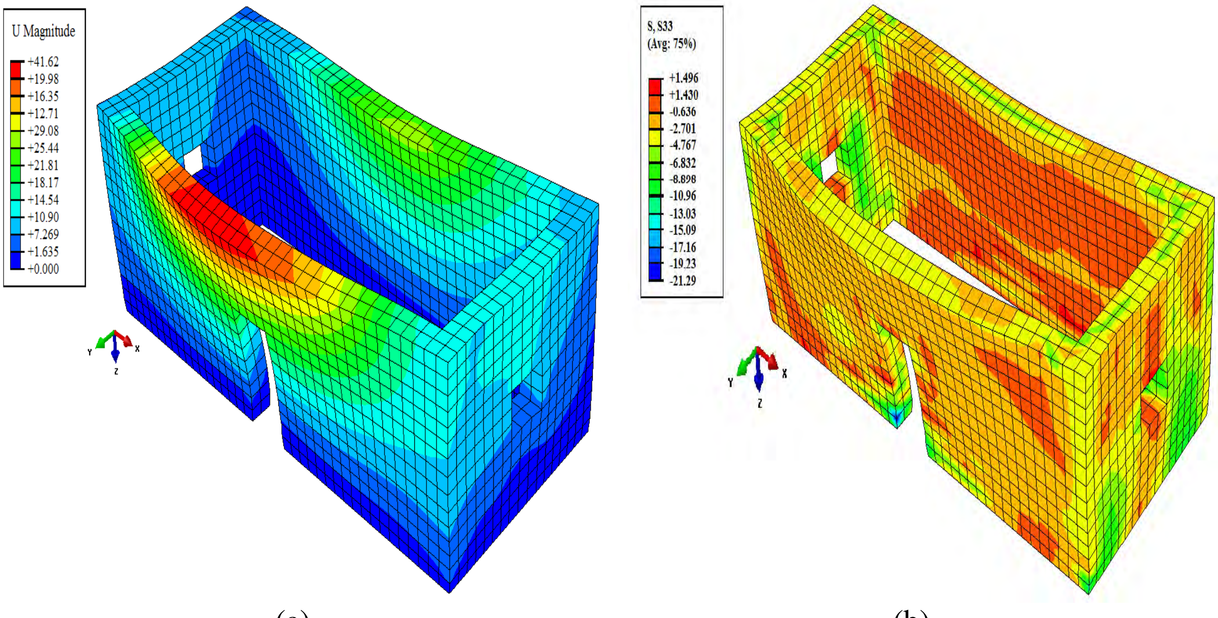

(a) (b)

Figure 6: Contour diagrams showing the distribution of transversal displacements (a) and vertical stress (b) on the adobe model structure after the implementation of non-linear dynamic analysis using the acceleration data of the 1978 June 20th Thessaloniki Earthquake.

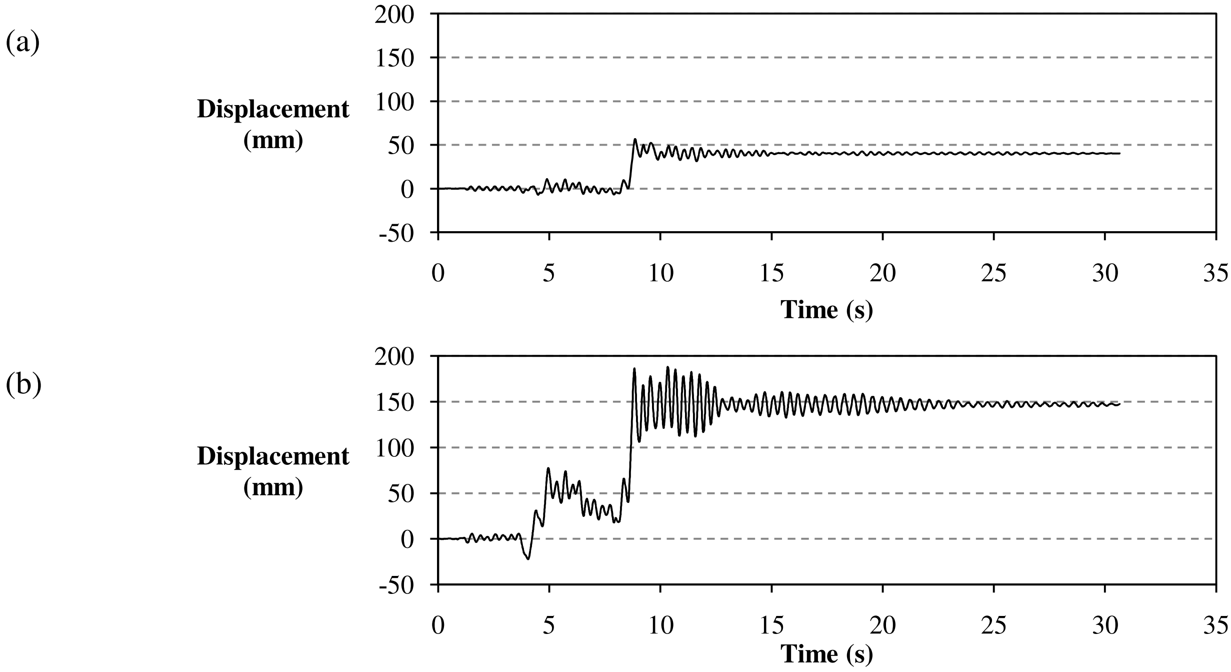

Figure 7: Transverse displacement time history for the central node at the upper part of the model structure's façade when the analysis is conducted using the acceleration data of the 1978 Thessaloniki Earthquake (a) and when the exerted accelerations are amplified by a factor of 3 (b).

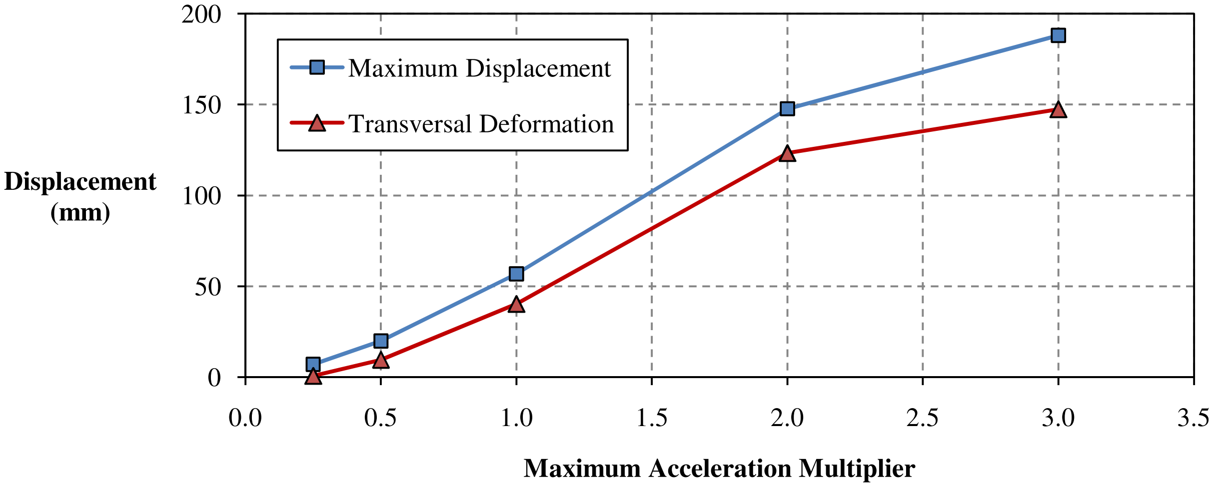

Figure 8: Maximum transversal displacement of the central node at the upper part of the model structure's façade and out-of-plane permanent deformation of the façade at different levels of seismic action. The acceleration data used are those of the 1978 Thessaloniki Earthquake while various factors have been applied in order to scale the amplitude of the dynamic excitation.

4 CONCLUSIONS AND FUTURE RESEARCH AIMS

The numerical results produced by the computational analysis of the adobe masonry assemblage specimen in ABAQUS CAE indicate that the material constitutive model and input parameters hereby suggested may correctly simulate the general behaviour of earthen construction under compressive loading. A comparison among the numerical and experimental data shows that the FE model can provide sufficiently accurate estimates for stress and deformation, especially when applied to monotonic vertical axial loading scenarios. Of particular importance is the ability of the model to predict the material's actual ultimate strength. The good agreement with experimental results and the low computational cost that results from the use of simple constitutive hypotheses appear to be very encouraging for future applications. However, concerns derive from the inability of the model to predict cyclic behaviour involving cycles of both compression and tension loading. This limitation is a product of the constraints imposed by the selected constitutive model.

Regarding the validity of the numerical results obtained from the analysis of a complete model structure, these cannot be deemed as a sufficiently accurate representation of the actual response of earthen construction, despite the fact that they appear to be in context with the general behaviour of unreinforced masonry. The computed deformations may be considered to be rather excessive with respect to the levels of seismic action examined. In an actual structure the evaluated inelastic displacements would have led to the development of significant cracking at the walls and would have probably caused the out-of-plane collapse of the façade. Although such damage mechanisms have been observed in adobe buildings [2, 3], these have occurred at seismic events where the maximum imposed acceleration was above 0.50g (e.g. Northbridge Earthquake, Iran Bam Earthquake). The overestimated displacement values can be attributed to the exclusion of the timber roof structure from the model. The latter, despite its limited stiffness, is anticipated that would have constrained, to some extent, the out-of-plane movement of the walls and would have assisted in a more effective distribution of the loads. Moreover, the boundary conditions assigned to the structure's corners cannot reproduce the actual interaction that takes place at the conjunction of perpendicular walls and force deformations to concentrate at the central part of the walls. Consequently, failure mechanisms such as the formation of detachment cracks at the interconnection of adjacent walls cannot be identified by the model. Uncertainties are also introduced by the fact that the constitutive material model selected for simulating the behaviour of adobe masonry uses a Mises yield surface, thus making no distinction between the response to compression and tension. Although adobe masonry has some considerable resistance to tensile loads, this is much lower than its compressive strength and the constitutive model should be modified in order to account for this behaviour. On the overall, it may be argued that the application of the model hereby presented in the dynamic analysis of complete structures is useful for providing qualitative information regarding the general response of adobe construction rather than accurate quantitative results.

Future work will focus on the modification of existing constitutive models and/or the development of a fully adobe masonry-oriented model that will be able to account for the specific characteristics of earthen construction. Furthermore, the construction and laboratory testing of a scaled model adobe structure in order to study its behaviour under horizontal loading has been scheduled. The experimental results that will be obtained will be used for examining the validity of the numerical data available and will be utilized in the calibration of FE models.

5 ACKNOWLEDGEMENTS

The authors would like to acknowledge financial support from the University of Cyprus, the Cyprus Research Promotion Foundation, the Republic of Cyprus and the European Regional Development Fund.

REFERENCES

[1] T. Morton, *Earth masonry – Design and construction guidelines*. Watford: IHS BRE

Press, 2008.

[2] M.R. Maheri, F. Naeim, and M. Mehrain, "Performance of adobe residential buildings in the 2003 Bam, Iran, Earthquake," *Earthquake Spectra*, vol. 21, no. 1, pp. 337–344, 2005.

[3] L.E. Tolles, F.A. Webster, A. Crosby, and E.E. Kimbro, *Survey of damage to historic adobe buildings after the January 1994 Northridge Earthquake*. Los Angeles: The Getty Conservation Institude, 1996.

[4] Y. Yucheng and Y. Liu, "Earthquake damage to and aseismic measures for earth-sheltered buildings in China," *Tunnelling and Underground Space Technology*, vol. 2, no. 2, pp. 209-216, 1987.

[5] F. Genna, Michele Di Pasqua, and M. Veroli, "Numerical analysis of old masonry buildings: A comparison among constitutive models," *Engineering Structures*, vol. 20, no. 1, pp. 37-53, 1998.

[6] P.B. Lourenco, "Computations on historic masonry structures," *Progress in Structural Engineering and Materials*, vol. 4, no. 3, pp. 301-319, 2002.

[7] M. Mistler, C. Butenweg, and K. Meskouris, "Modelling methods of historic masonry buildings under seismic excitation," *Journal of Seismology*, vol. 10, no. 4, pp. 497-510, 2006.

[8] P.B. Lourenco, J.G. Rots, and J. Blaauwendraad, "Continuum model for masonry: Parameter estimation and validation," *Journal of Structural Engineering*, vol. 124, no. 6, pp. 642-652, 1998.

[9] S. Atamturktur and J.A. Laman, "Finite element model correlation and calibration of historic masonry monuments: Review," *The Structural Design of Tall and Special Buildings*, vol. 20, no. 3, pp. 10-30, 2010.

[10] R. Illampas, I. Ioannou, and Charmpis D.C., "An assessment of the compressive strength of adobe brick assemblages," in *9th HSTAM International Congress on Mechanics*, Limassol, 12-14 July, 2010.

[11] E. Quagliarini, S. Lenci, and M. Iorio, "Mechanical properties of adobe walls in a Roman Republican Domus at Suasa," *Journal of Cultural Heritage*, vol. 11, no. 2, pp. 130–137, 2010.

[12] A. Brencich, L. Gambrotta, and S. Lagomarsino, "A macroelement approach to the three-dimensional seismic analysis of masonry buildings," in *11th European Conference on Earthquake Engineering*, Rotterdam, 1998.

[13] A. Giordano, E. Mele, and A. De Luca, "Modelling of historical masonry structures: Comparison of different approaches through a case study," *Engineering Structures*, vol. 24, no. 8, pp. 1057-1069, 2002.

[14] S. Pietruszczak and R. Ushaksaraei, "Description of inelastic behaviour of structural masonry," *International Jouranl of Solids and Structures*, vol. 40, no. 15, pp. 4003-4019, 2003.

[15] Hibbitt, Karlsson, Sorensen, Inc., *Abaqus analysis user's manual - Volume III: Materials*. Rising Sun Mills: Dassault Systemes, 2007.

COMPDYN 2011
3rd ECCOMAS Thematic Conference on
Computational Methods in Structural Dynamics and Earthquake Engineering
M. Papadrakakis, M. Fragiadakis, V. Plevris (eds.)
Corfu, Greece, 25–28 May 2011

NUMERICAL INVESTIGATION OF THE SEISMIC BEHAVIOUR OF CONNECTIONS OF ANCIENT COLONNADES

Maria-Eleni Dasiou[1], **Ioannis N. Psycharis**[2] **and Antigone Vrouva**[2]

[1] School of Civil Engineering, National Technical University of Athens
9, Heroon Polytechneiou Str., Zografos, 15780, Greece
email: medasiou@yahoo.com

[2] School of Civil Engineering, National Technical University of Athens
9, Heroon Polytechneiou Str., Zografos, 15780, Greece
email: ipsych@central.ntua.gr, a_vrouva@hotmail.com

Keywords: Monuments; restoration; fractures; connections; earthquake response.

Abstract. *As a common practice, restoration projects of ancient colonnades have to deal with joining together fragments of architectural members using threaded titanium bars (reinforcement) fixed into place with cement mortar. The basic criterion for the design of such connections is that, in case of a seismic event, the reinforcement should absorb the seismic energy and fail before the marble suffers any damage. For the dimensioning of the titanium bars, a methodology based on the capacity design philosophy is usually implemented. The accurate calculation of the forces that will be induced to the reinforcement during an earthquake is not an easy task, since the response of the structure is governed by the rocking and the sliding of the individual stone blocks.*

In this paper, the efficiency of the reinforcement used for the connection of complements, which has been calculated with the above-mentioned capacity design methodology, is investigated for selected severe seismic excitations. The analyses were performed for the case study of the restoration of the colonnades of the Southern part of the Ancient Agora of Kos in Greece. The induced forces were calculated by dynamic analyses, using an accurate numerical description of the restoration's structural scheme and earthquake motions of various characteristics, selected to be compatible with the seismological history and the soil conditions at the site. All the analyses were performed using the code 3DEC, which is based on the distinct element method and has been verified and calibrated by comparison of the numerical results with experimental data. The results show that the simplified design that is applied in practice is adequate, as the stresses induced to the reinforcement bars were always less than the ultimate strength and, in many cases, significantly less than the yield resistance as well.

1 INTRODUCTION

Ancient colonnades consist of stone blocks of different sizes and shapes made of marble, stiff limestone or porous stone, depending on the available material in the nearby region. Typically, the blocks are not connected to each other and the structure behaves as a system of discrete blocks, except of connectors (clamps and dowels) that are provided in certain places only. In current restoration practice, ancient mortises that are preserved in such places are used to connect the stone blocks with new clamps and dowels made of titanium. The basic principle that is followed for the design of the new connectors is that, in case of a seismic event, the connectors should absorb the seismic energy and fail before the surrounding marble suffers any damage.

Apart from the connectors, the use of titanium bars is also common for joining together fragmented ancient blocks or fragments of blocks with new complements so as to restore the unity of each discrete element of the ancient structure. The principle in designing the bars that are used as reinforcement is that those should bear the induced forces in a seismic event and maintain the discrete block as a whole, while the marble does not suffer any damage.

In general, the design of the restoration anticipates the following sequence of response: The joints between independent blocks are the first to be activated. This does not necessarily imply engagement of the connectors (clamps and dowels), because, typically, there is a gap between them and the mortises of the stones. However, forces are induced to the connections between blocks and new complements. When the movements of the blocks exceed certain values, the clamps and dowels are activated, reducing, in general, the forces applied to the restored interfaces of fracture. After the failure of the connectors (clamps and dowels), it is possible that rehabilitated members of the structure lose their integrity; in that event, the titanium bars of the reinforcement should yield prior to any other damage to the marble.

In order to follow the above-mentioned procedure, one should know the forces that will be induced to the connectors and the reinforcement during an earthquake. However, the calculation of these forces is not an easy task, since the response of the structure is governed by rocking and sliding of the individual stone blocks. Previous investigations [1-6] on the dynamic behaviour of single freestanding columns and sub-assemblages of ancient temples have pointed out that the response of these discrete structures is highly nonlinear and very sensitive to even small changes in the parameters. Thus, the imposed excitation and the frequency content of the ground motion, the degree of the accuracy of the numerical model concerning the geometry of the structure and the assumptions adopted in the analysis (joint properties, friction coefficient, etc.) may affect significantly the results of even rigorous nonlinear analyses. For this reason, the dynamic analyses of such structures contain an inherent uncertainty and their outcomes should be used with caution.

In practice, simplified analyses are usually applied for the design of the connections that are implemented during interventions. These analyses are based on the capacity design philosophy, thus they end up with the maximum forces that can be developed theoretically, independently of the earthquake excitation. In this paper, the response of connections of complements, which have been designed by such methodologies, under strong earthquake excitations, is investigated. For this purpose, nonlinear numerical analyses are performed using the discrete element method and the forces induced to the reinforcements are compared with their strength. The analyses are performed for the case study of the restoration of the colonnades of the Southern part of the Ancient Agora of Kos in Greece.

2 PRINCIPLES OF INTERVENTION

2.1 General philosophy

Restoration projects nowadays follow very specific guidelines in order to ascertain the required quality of the intervention. The main scope is the minimum, yet necessary and sufficient, intervention in the monument's inherent characteristics. Of main importance is the respect for the original building techniques, the original structural system and the original materials. Authenticity is a beyond debate concern and goal of the project, in order to maintain the monument at the best possible status and to minimize the alterations. Additional requirements might be reversibility, meaning the ability to revert the monument to its previous - before the restoration- state, maintenance of the structural function and consistency of the individual architectural members.

The use of new material for the complement of missing parts of structural elements is generally restricted to the absolutely necessary and must be kept in a low proportion compared to the original material. Such decisions must not be based only on stability issues, but also take under consideration the forms and volumes, the visitor's perception of the monument and aesthetic issues. It should be kept in mind that the main "recipients" of the monuments are their visitors and that the cultural heritage that they carry is not addressed to scholars and connoisseurs only, but mainly to the public.

2.2 Structural restoration

The term ‘structural restoration’ signifies the series of interventions that are necessary to ensure the bearing capacity of the structure and of its individual parts. To this end, restoration of the connectors between the structural elements and re-composition of the original geometry of the stone pieces that were retrieved during the excavation by connecting fragments and/or complement of stone elements is deemed necessary in many cases.

In antiquity, the connection elements were made of bronze or iron and were covered with lead, cast in the mortises, which after its congelation offered high insulation to the metallic connectors, protecting them from the oxidization and the corrosion. At the same time, the connectors, being ductile materials, contributed to the overall behaviour of the structure in case of an earthquake. Two types of connectors were used: dowels, which connected elements between consequent layers along the height and resisted the shear forces; and clamps, which connected stones belonging to the same layer and prevented their relative dislocation through their tensile resistance. In the ultimate limit state, the dowels and the clamps were meant to fail before the failure of the stone.

In many restorations realized in the 19th ant the 20th century, the structural steel that was used in typical constructions was applied also to monuments for the enhancement of their bearing capacity and for the connection of fragments of architectural members. The steel elements were usually cast in lead, as a follow up of the ancient practice. Cement mortars were widely used for covering mass lacks. This technique caused significant damage to the monuments, because the cast lead failed to reassure the same impermeability as the ancient one and environmental actions, due to their intense corrosive character, led to iron's oxidization and subsequently to fracture of the architectural members.

In modern restoration projects, mostly inorganic materials are adopted, in order not to provoke any additional problems in the long term. Thus, for the connections between restored members of the monument (clamps and dowels), specially formed titanium sheets are commonly used, fixed in place with the use of inorganic mortars. Similarly, for joining together fragments and/or complements, threaded titanium bars are applied.

2.3 Calculation of the reinforcement of the connections

The ancient and the new pieces are typically connected with titanium threaded bars that are inserted in properly drilled holes and fixed into place by mortar. Mortar is also used as the bonding material at the interface of the fraction. As mentioned above, a proper dimensioning of the reinforcement would require difficult nonlinear analyses, which are seldom performed in practice. Usually, analyses based on capacity design effects are performed [7, 8], which lead to the required reinforcement for resisting the maximum forces that can be induced, without restoring completely the strength of the original material. In example, the design of the connection of fractured architraves is based on the assumption that the architrave is subjected mainly to bending under increased gravity loads by a factor around 1.50; for the connection of fragments at column drums and stylobate blocks, the required reinforcement is calculated from equilibrium conditions under capacity actions that include the friction forces, assuming that sliding occurs at the joint, and the ultimate resistance of any existing dowels.

3 CASE STUDY – DESCRIPTION OF THE MONUMENT

The analyses presented herein are based on the part of the southern Arcade (Stoa) of the Ancient Agora in the island of Kos in Greece that has been proposed to be restored. The monument is situated in the center of the modern city of Kos.

An unexpectedly large number of structural members were found in situ. The location where the members were found and the study of the mortises of the connectors confirmed that they derived from specific parts of the building. Thus, the 'erection' of a small part of the Stoa was proposed, using a significant portion of the found ancient members.

The restoration project concerns three columns of the Stoa with the respective parts of the crepis and the entablature (Figure 1). In this restoration, 37 from the 62 ancient members are to be used. In addition, seven new blocks are to be used to ensure the stability of the structure and, also, for aesthetic reasons.

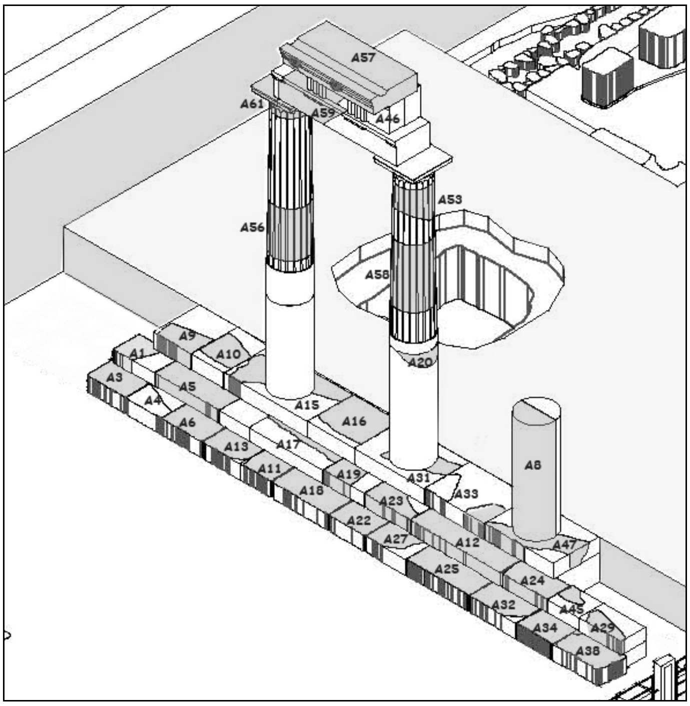

Figure 1: Drawing of the restoration proposal. The ancient members and fragments are shown in gray and the members and complements that will be made of new marble are shown in white.

The original structure rested on a two layered base of height 0.55 m, made of porous blocks that lied under the crepidoma (crepis). The crepis consisted of two steps and the stylobate. The first step had height 0.33 m and was made of gray limestone blocks of varying plan dimensions (their length was varying from 0.60 to 1.40 m and their width from 0.50 to 0.70 m). The second step had height 0.29 m and was made of marble blocks of the same overall dimensions. The stylobate was made of marble blocks of height 0.30 m, width about 1.00 m and varying length.

The marble columns of the Stoa were of doric style without fluting at their lower part, up to a height of 2.07 m. The columns consisted of four drums of uneven height with base diameter 0.78 m. The axial distance between the columns was 2.66 m and their overall height was 5.61 m. The diameter of the capital was 0.635 m and its height was 0.38 m, approximately, while the abacus had plan dimensions 0.85 m × 0.85 m and height equal to 0.11 m.

The architraves consisted of single blocks, 2.66 m in length, 0.71m in width and 0.47 m in height. The frieze was made of blocks 1.73 m in length and 0.59 m in height that included two triglyphs and two metopes. Those blocks were either single of full width (~0.47 m) or were supplemented by other blocks of approximately the same dimensions that completed the width of the layer; the latter is the case of the part of the structure that is considered in this analysis. The cornice had height 0.42 m and was projecting 0.325 m. The block that will be used in the restoration is 1.95 m long.

4 NUMERICAL ANALYSIS

4.1 General

The structural and the dynamic analysis of ancient temples or sub-assemblages of ancient temples differ significantly from the analysis carried out for modern structures, mainly because of their articulate construction. During a seismic event, rocking and/or sliding of the stones, independently or in groups, may occur, which results in highly nonlinear behaviour [1-6]. Additionally, the response is very sensitive to the details of the geometry, the characteristics of the ground motion and the joint parameters.

The complexity and the special character of the response of the structure (rocking and sliding) create computational requirements hard to meet with the incorporation of conventional software. For the numerical analyses presented herein, the code 3DEC by Itasca Consulting Group, Inc. [9] was employed, which is based on the discrete element method. The code is designed to allow significant displacements and rotations of the blocks, even total detachment. During the calculation process, the code locates the contacts between the blocks and computes the motion of each block from the forces (normal and shear) that are developed at the joints. The contacts are divided in sub-surfaces, while various types of contact are considered (apex to apex, apex to edge etc.). In this way, rocking and sliding are accurately addressed.

The code 3DEC has been verified and calibrated for the response of ancient colonnades through comparisons of the numerical results with experimental data obtained from shaking table tests performed at the Laboratory for Earthquake Engineering of the National Technical University of Athens [2, 4-6].

4.2 Numerical model

The numerical model used in the analyses was based on the actual restoration proposal. The connections between the ancient fragments and the new complements were assumed from titanium bars and were designed according to the above-mentioned methodology. The exact geometry and dimensions of the reinforcement were implemented in the numerical model (Figure 2).

The mortar typically used at the interfaces of the connected blocks was not considered, because its actual mechanical properties cannot be precisely defined. In addition, the dowels and the clamps were not included in the numerical model, because sliding can occur before these connectors are activated, since a gap of 1 to 2 cm, not filled with mortar, is commonly left between them and the edge of the mortises. Both assumptions are to the safety side and lead to the upper limit of the forces that can be induced to the reinforcement.

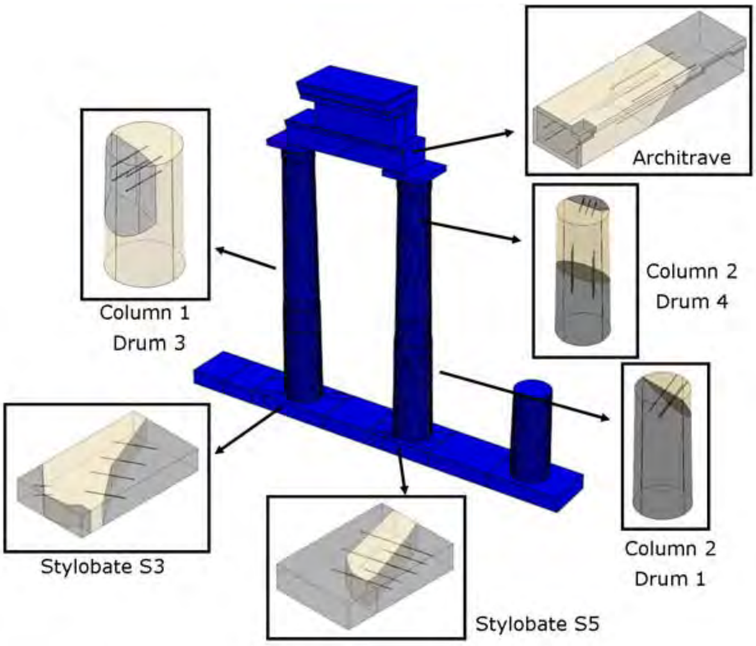

Figure 2: Numerical model used in the analyses with 3DEC. Details of the connections considered in the model are also shown.

The analyses were performed assuming that all the structural elements are rigid blocks. For rigid blocks problems, the 3DEC code gives an accurate contact formulation in which the interaction takes place at a number of contact points [9]. Each contact is assigned a contact area, which is used to calculate the local point stiffness, in terms of the user-defined stiffness of the discontinuity surface. The joint stiffness used in the model was based on former studies [2, 4-6] and was equal to 5×10^9 Pa/m in the normal direction and 1×10^9 Pa/m in the tangential direction. A 10% mass-proportional damping at ω = 0.3 Hz was also considered. The friction coefficient was taken equal to 0.75.

The reinforcement (titanium bars) were simulated as nonlinear springs for which the elastic stiffness, the yield force and the ultimate strain were assigned in both the axial and the shear directions. Since pullout test results were not available, the following theoretical expressions, given in [10] and proposed by 3DEC [9], were used to estimate the axial stiffness, K_a and the shear stiffness, K_s:

$$K_a = \pi \cdot k \cdot d_1 \tag{1}$$

$$K_s = E_b \cdot I \cdot \beta^3 \tag{2}$$

where d_1 is the diameter of the reinforcement; $k = \left[\frac{1}{2} \cdot G_\mathrm{g} \cdot E_\mathrm{b} / (d_2 / d_1 - 1) \right]^{1/2}$; G_g is the shear modulus of the grout; E_b is the Young's modulus of the reinforcement material; d_2 is the diameter of the hole; I is the second moment of area of the reinforcement element; and $\beta = \left[K / \left(4 \cdot E_\mathrm{b} \cdot I \right) \right]^{1/4}$, with $K = 2 \cdot E_\mathrm{g} / (d_2 / d_1 - 1)$.

The ultimate axial strength, P_ult, and the shear strength, $F_\mathrm{s,b}^\mathrm{max}$, of the titanium bars were calculated using the formulas proposed in [11] and [12], respectively, and adopted by 3DEC [9]:

$$P_\mathrm{ult} = 0.1 \cdot \sigma_\mathrm{c} \cdot \pi \cdot d_2 \cdot L \tag{3}$$

$$F_\mathrm{s,b}^\mathrm{max} = 0.67 \cdot d_1^2 \cdot \left(\sigma_\mathrm{b} \cdot \sigma_\mathrm{c} \right)^{1/2} \tag{4}$$

where σ_c is the uniaxial compression strength of the marble (up to a maximum value of 42 MPa); L is the bond length; and σ_b is the yield strength of the reinforcement.

4.3 Selection of base motions

For the selection of the base motions, the geological and seismological data in the area of the monument were taken under consideration. The basic ground formation in the area, where the ancient Agora is situated, is alluvial coastal depositions with significantly low mechanical properties and poor geotechnical behaviour [13-15].

There are many references of large historic earthquakes in the wider area of Kos, with magnitudes up to M = 6.5 [13-16]. During these earthquakes, ground raptures, liquefaction and collapse of many structures were reported. It should be pointed out that part of the ancient Agora collapsed in the historic earthquake of 556 A.D. [13]. In Figure 3, the map of the geological hazard of the island of Kos, according to [13], is presented. Note that a normal fault is located in a distance less than 6 kilometers from the area under consideration.

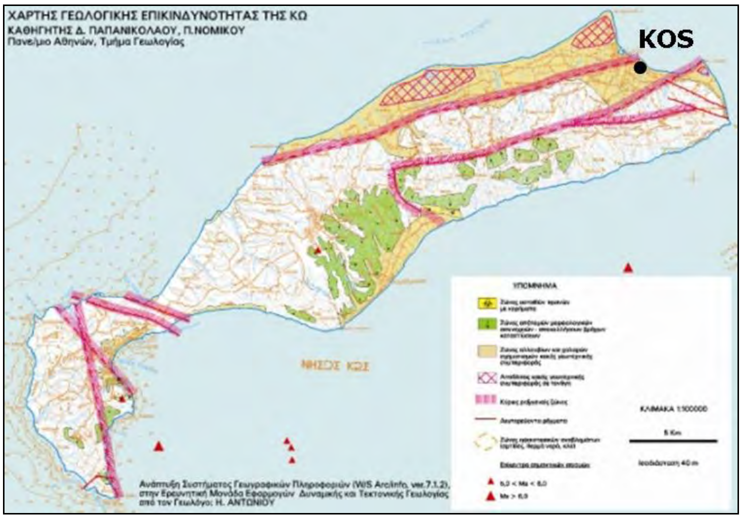

Figure 3: Seismological map of the island of Kos, showing the main faults (reproduced from [13]).

For the selection of the earthquake records to be used in the analyses, the above-mentioned seismotectonic data and the ground profile of the Ancient Agora of Kos were considered. More specifically, the following criteria were posed: adjacency to the seismic fault (near field earthquakes); magnitude around 6.5; and ground motions recorded on soft soil conditions.

Based on these criteria, six earthquake records were selected from the strong motion data bases: Cosmos Virtual Center; Pacific Earthquake Engineering Research Center (PEER); European Strong-Motion Database (ESD); National Observatory of Athens; Institute of Technical Seismology and Earthquake Resistant Structures (ITSAK), which had different characteristics and covered a wide range of spectral accelerations. Both horizontal components of each earthquake were applied as the base excitation. The selected earthquakes and their characteristics are shown in Table 1.

From the analyses performed, it was found that collapse of the structure occurs for the Sylmar, Northridge, USA earthquake. The collapse mechanism is shown in Figure 4. Since the main scope of this research was to determine the behaviour of the reinforcement assuming that collapse does not occur, this record was not further examined. The response spectra of the component that was applied in the transverse direction of the structure of the five remaining records are presented in Figure 5.

Location	Date	Fault Mechanism	Magnitude M_w	Soil Type	Distance from fault (km)
Northridge, USA/ Sylmar County Hospital	17/01/94	SS	6.7	SL	5.6
Imperial Valley, CA/ Aeropuerto Mexicali St.	15/10/79	SS	6.5	SL	0.34
Aigion, Greece	15/06/95	NM	6.3	SL or SR	6.0
Kalamata, Greece	13/09/86	NM	6.0	SL or SR	10.0
Lefkada, Greece	14/08/03	SS	5.9	SL	4.8
Athens, Greece/ Sepolia	7/09/99	NM	5.9	SL	17.0

Table 1: Selected earthquake excitations. The record in red leads the structure to collapse.

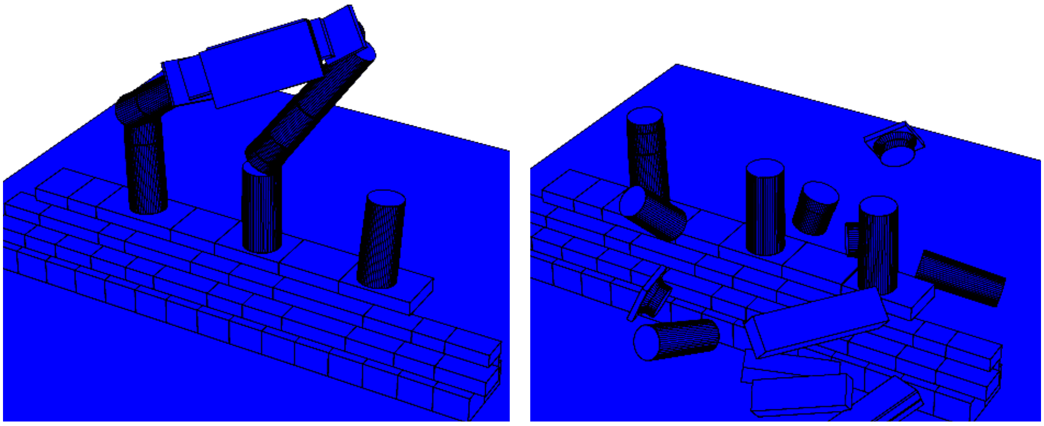

Figure 4. Collapse mechanism of the structure for the Sylmar, Northridge, USA record.

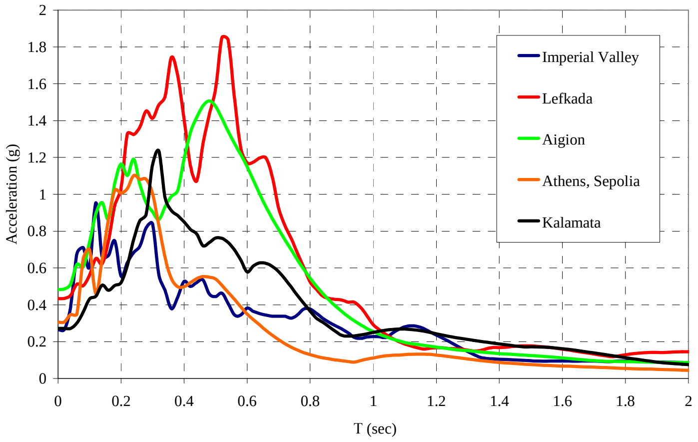

Figure 5: Acceleration response spectra for 5% damping of the component of the base motion that was applied in the transverse direction of the structure.

5 RESULTS

For all the titanium bars that were used in the connections, the time histories of the axial and the shear forces were obtained from the analyses. Indicative results are shown in Figure 6, where the time histories of the axial force of the four reinforcement bars that were used to connect the two fragmented pieces of the architrave beam are depicted.

From these results, the efficiency factor for each bar was derived as the ratio of the maximum uniaxial stress, $\sigma_{M,max}$, that was developed during each earthquake motion over the yield stress, σ_y. The uniaxial stress was calculated using the Von Mises yield criterion:

$$\sigma_M = \sqrt{\sigma^2 + 3 \cdot \tau^2} \tag{5}$$

where σ is the axial stress of the bar and τ is the shear stress. The yield stress σ_y and ultimate stress σ_u of the threaded titanium bars were taken equal to 330 MPa and 420 MPa, respectively.

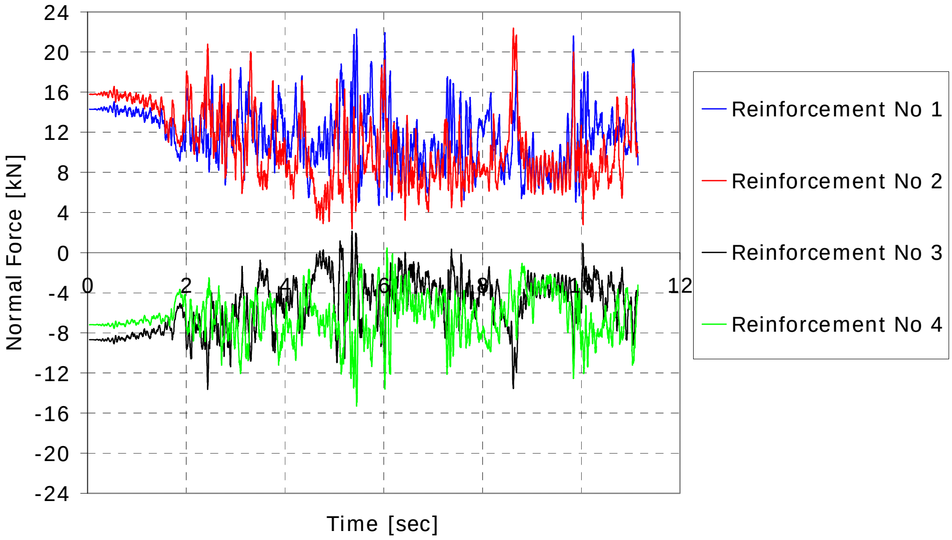

Figure 6: Time histories of the axial force of the 4 titanium bars of the architrave connection (Figure 5) for the Imperial Valley earthquake.

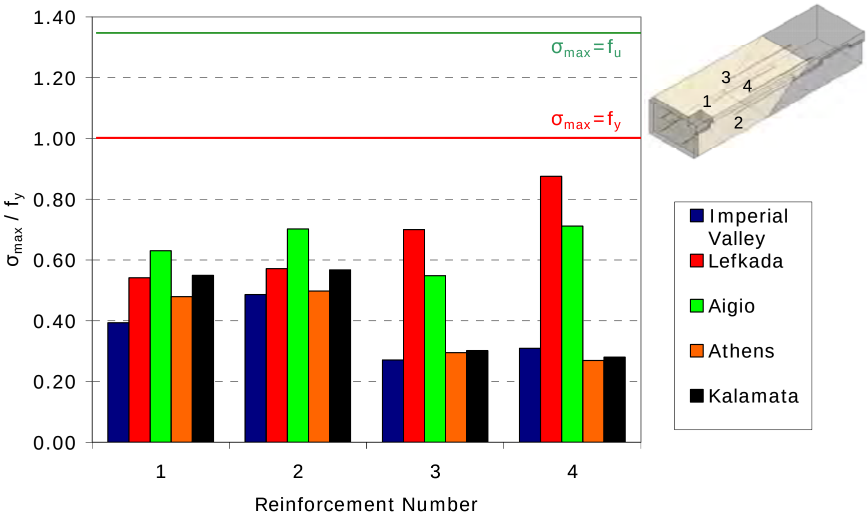

Figure 7: Accomplished efficiency factors of the four titanium bars of the architrave connection for the five earthquake excitations used in the analyses.

Figure 7 shows the accomplished efficiency factor of the four reinforcement bars applied at the connection of the architrave. None of the bars reached its yield strength for the earthquakes examined. The two lower reinforcement bars (No 1 and 2), which were in tension under gravity loads, showed an efficiency factor around 0.60, not much affected by the base motion. This value is close to $1/\gamma_G$, where $\gamma_G = 1.5$ is the load factor for the gravity loads that was used for the design of these reinforcements according to the methodology described above. The upper reinforcement bars (No 3 and 4) were stressed significantly less for three of the earthquake excitations (Imperial Valley, Athens and Kalamata), as expected; however, large stresses were induced to these bars for the Lefkada and the Aigion earthquakes, showing that large displacements occurred at the architrave during these ground motions.

Figures 8 to 10 show the efficiency factors of the reinforcement bars used for the connection of the fragments at the drums of the columns. It can be observed that significantly different stresses were induced to the titanium bars for each type of fragmentation. The worst case was observed for the fragment at the first drum of column 2 (Figure 9), in which two out of three bars yielded in most earthquakes. The smallest forces were induced to the connection of the third drum of column 1 (Figure 8), where efficiency factors less than 0.70 were achieved in most cases. Similar was the behaviour of the titanium bars of the connections at the fourth drum of column 2 (Figure 10), which were stressed significantly lower than their yield limit in most cases. It should be noted that the maximum stress was less than the ultimate limit strength of the reinforcements in all cases.

It is evident from these results that both the inclination of the connection and its position along the height of the column affect significantly the forces that are induced to the reinforcement bars. The worst case concerns fragments that form a wedge and are located at the lower part of the column, where the gravity loads are larger. During rocking, large forces are developed at such connections; this was also observed in [17].

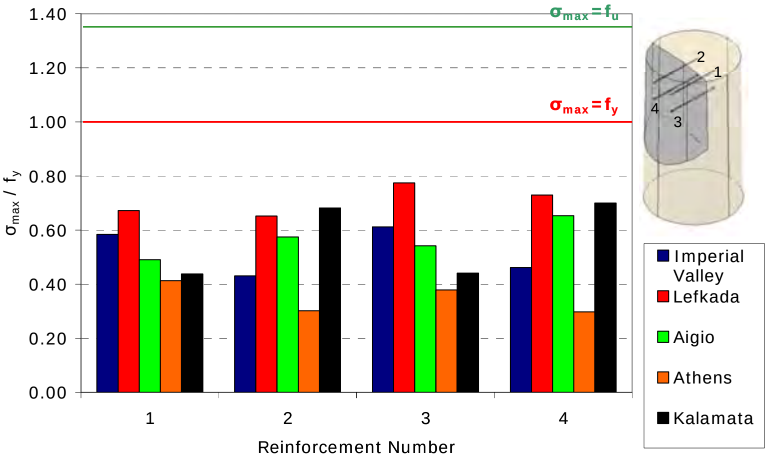

Figure 8: Efficiency factors of the four titanium bars used for the complement of the third drum of Column 1, for the five earthquake excitations used in the analyses.

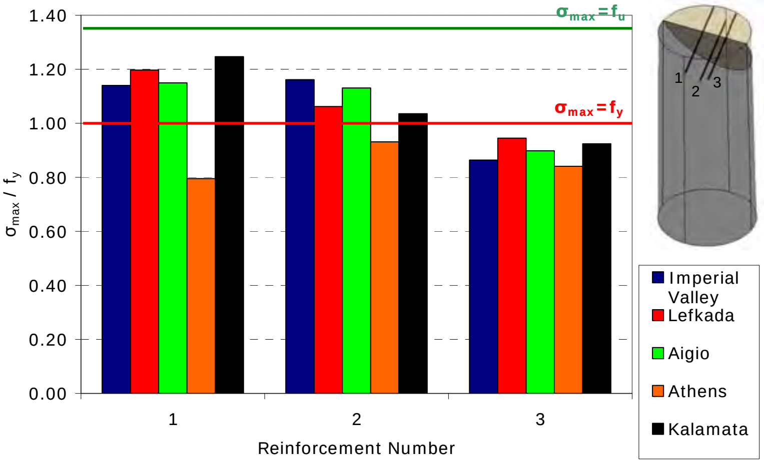

Figure 9: Efficiency factors of the three titanium bars used for the complement of the first drum of Column 2, for the five earthquake excitations used in the analyses.

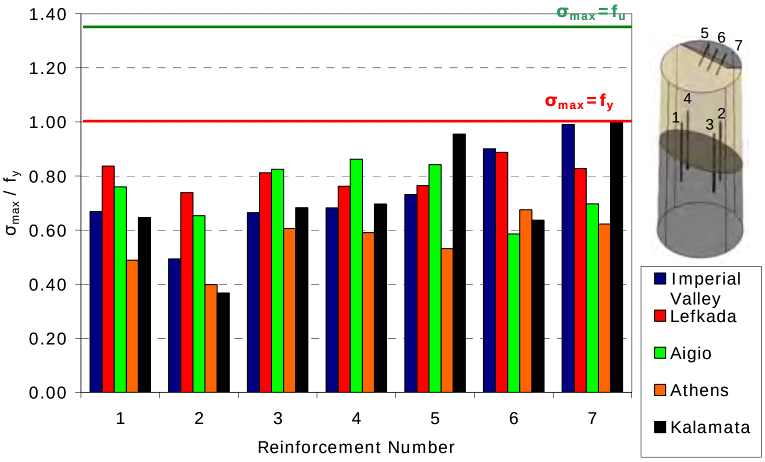

Figure 10: Efficiency factors of the seven titanium bars used for the complements of the fourth drum of Column 2, for the five earthquake excitations used in the analyses.

The results for the connections at the stylobate are shown in Figures 11 and 12. In case of S3 (Figure 11), in which extended connections were made, the stresses induced to the titanium bars were significant, more than 80% of the yield resistance in most of them (No. 1, 2, 3, 4) for all earthquake motions. In this case, the response of the reinforcement was not affected significantly by the ground motion characteristics. On the contrary, the reinforcement bars of the connection at stylobate S5 showed different behaviour for each earthquake. It is interesting to note that, although the efficiency factors attained at S5 were generally smaller than the ones at S3, probably due to the fact that the new complement was “encased” by the original block, large stresses were induced to some reinforcement bars of S3, which, in one case, surpassed the yield resistance. It should be mentioned that, for the stylobate blocks, reinforcement larger than the required according to the current design methodology was applied, in general, for constructional reasons.

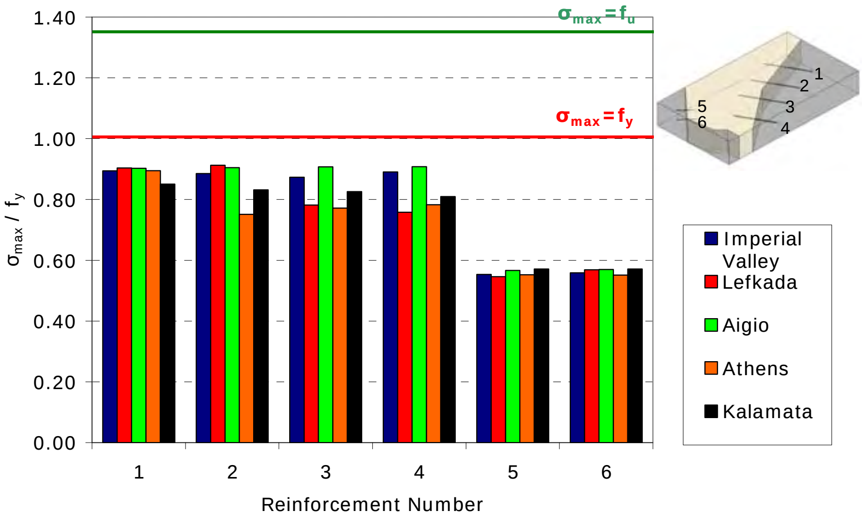

Figure 11: Efficiency factors of the six titanium bars used for the complements of the stylobate S3, for the five earthquake excitations used in the analyses.

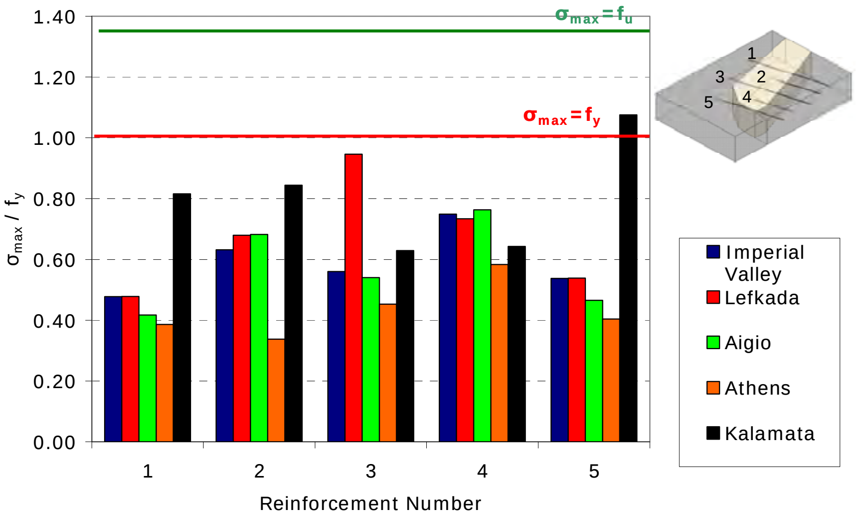

Figure 12: Efficiency factors of the five titanium bars used for the complement of the stylobate S5, for the five earthquake excitations used in the analyses.

6 CONCLUSIONS

- The simplified methodology that is used in practice for the dimensioning of the reinforcement of connections between new and old complements, which is based on the capacity design philosophy, was proved to be adequate, since the ultimate strength of the titanium bars was never reached. In most cases, the stresses induced to the reinforcement were significantly less than the corresponding yield stresses.
- The most severe situation was observed for fragments of column drums that form a wedge and are located at the lower part of the column.
- Significant stresses were observed at the connections of the stylobate, which were not expected intuitively, since only sliding can occur at these places. It should be mentioned, however, that failure of the reinforcement at such places does not, in general, puts the structure in danger of collapse.

AKNOWLEDGEMENTS

Part of the research reported herein was performed in the framework of the structural analysis of the proposed restoration of the southern Arcade of the Ancient Agora of Kos, which was financed by the Hellenic Ministry of Culture on behalf of the Archaeological Institute of Aegean Studies of Rodhes under project EL006 "Designation of the ancient Hellenistic Agora of Kos and the medieval circumferential fortifications of the city of Kos". The Supervisor of the Archaeological Institute of Aegean Studies of Rodhes, archaeologist Ag. Giannikouri has facilitated the realization of the overall project. Sincere thanks are due to the geologist D. Minos-Minopoulos for providing valuable geotechnical and seismological information on the island of Kos.

REFERENCES

[1] Psycharis I.N., Papastamatiou D.Y., Alexandris A, Parametric Investigation of the stability of classical columns under harmonic and Earthquake excitations, *Earthquake Engineering and Structural Dynamics*, **29**: 1093-1109,2000.

[2] Papantonopoulos C., Psycharis I.N., Papastamatiou D.Y., Lemos J., Mouzakis H, Numerical Prediction of the Earthquake Response of Classical Columns using the Distinct Element Method, *Earthquake Engineering and Structural Dynamics*, **31**: 1699-1717,2002.

[3] Psycharis I.N., Lemos J.V., Papastamatiou D.Y., Zambas C., Papantonopoulos C., Numerical study of the seismic behaviour of a part of the Parthenon Pronaos, *Earthquake Engineering and Structural Dynamics*, **32**: 2063-2084, 2003.

[4] Dasiou M.-E., Report in Work package 7 and Work package 8, Research Project Earthquake Protection of Historical Buildings by reversible mixed technologies (PROHITECH), 2007.

[5] Dasiou M.-E., Psycharis I. N., Vayas I., Verification of numerical models used for the analysis of ancient temples, Proceedings of PROHITECH Conference, Rome, 2009.

[6] Dasiou M.-E., Psycharis I., Vayas I., Seismic behaviour of ancient temples' columns and collonades analysis, Proceedings of 3rd Panehellenic Conference on Earthquake Engineering and Engineering Seismology, Athens, 5-7 November 2008 (in Greek).

[7] Zambas C., Study for the Restoration of the Parthenon (Vol. 3b). Hellenic Ministry of Culture, Committee for the Preservation of the Acropolis Monuments, 1994.

[8] Ioannidou, M., Paschalides, V., Mentzini M., Joining of fractured architraves with titanium reinforcement: new approach, Proceedings of the 5th International Meeting for the Restoration of the Acropolis' Monuments, Athens, Committee for the Preservation of the Acropolis' Monuments, ed., 4-6 October 2002. (in Greek)

[9] Itasca Consulting Group, Inc. *3DEC: 3-Dimensional Distinct Element Code, Theory and Background.*

[10] Gerdeen, J. C., V. W. Snyder, G. L. Viegelahn and J. Parker., Design Criteria for Roof Bolting Plans Using Fully Resin-Grouted Nontensioned Bolts to Reinforce Bedded Mine Roof, U.S. Bureau of Mines, OFR, 46(4)-80, 1977.

[11] Littlejohn, G. S., and D. A. Bruce, Rock Anchors – State of the Art. Part I: Design, *Ground Engineering*, **8** (3): 25-32, 1975.

[12] Bjurstrom, S., Shear Strength on Hard Rock Joints Reinforced by Grouted Untensioned Bolts, Proceedings of the 3rd International Congress on Rock Mechanics, Vol. II, Part B, Washington, D.C.: National Academy of Sciences, 1194-1199, 1974.

[13] Paponikolaou D., Lekkas E., Nomikou P., *Aseismic protection for the islands of Aegeon (Kos, Nisyros, Chios)*, Department of Dynamical, Tectonical and Applied Geology, National and Kapodestrian University of Athens (in Greek), 1998.

[14] Lekkas, E., Minou-Minopoulou D., Stefanodou E., *Operational organization of the Kos municipality for the protection policy and the encounter of natural and technological hazards*, Applied Research Program, Municipality of Kos, National and Kapodestrian University of Athens (in Greek), 2008.

[15] Papazahos B. & Papazahou K., *The earthquakes of Greece*. Ziti, Thessaloniki (in Greek), 1989.

[16] Zarraftis I.E., *Koia, volume A (Geographical, Historical)*, Ippokrateios Public Library of Kos, Special Historic and Folkloric Archive (in Greek), 2005.

[17] Stefanou, I., Psycharis, I. Georgopoulos, I.-O., Dynamic response of reinforced masonry columns in classical monuments, *Constructions and Building Materials*, Special Issue: Masonry Research and Practice (in print).

COMPDYN 2011
3rd ECCOMAS Thematic Conference on
Computational Methods in Structural Dynamics and Earthquake Engineering
M. Papadrakakis, M. Fragiadakis, V. Plevris (eds.)
Corfu, Greece, 25–28 May 2011

SEISMIC STRENGTHENING OF THE HISTORIC CHURCH OF STs HELEN AND CONSTANTINE IN PIRAEUS

Constantine C. Spyrakos[1*], Panagiotis D. Kiriakopoulos[2], Eleni Smyrou[3]

Department of Civil Engineering, Earthquake Engineering Laboratory (LEE), National Technical University of Athens (N.T.U.A.), Zografos 15700, Athens, Greece

[1] Professor, Director of LEE *cspyrakos@central.ntua.gr*
[2] PhD candidate *pkiriakopoulos@teemail.gr*
[3] Researcher *smiroulena@gmail.com*

Key words: Masonry historic structure, Church retrofit, Seismic strengthening, Finite elements analysis, Ambient and laboratory structural and material testing

Abstract. *The Church of St. Constantine & Helen is located in the Municipal Theater square in Piraeus. It was constructed in 1882. A series of recent earthquakes, including the Athens 1999 earthquake, strained the temple and caused serious damages. These damages are mainly attributed to the absence of particular provisions to carry the earthquake loads. In order to evaluate the earthquake vulnerability of the church, a detailed study of the masonry structure was conducted in order to determine the mechanical properties, the building construction details and the current condition of the structure as well as its dynamic behavior through in situ and laboratory testing as well as through finite element analysis. Based on the results, strengthening and repair measures are proposed, using a combination of masonry consolidation techniques, fiber reinforced plastic materials (FRP) and steel tie rods.*

1 INTRODUCTION

Newly introduced materials and technology provide engineers with the ability to repair, reinforce and restore historic buildings with a more scientific, effective and less intrusive approach. The restoration process of a heritage building that has succumbed serious damage, should be based on a reliable assessment of its state of stress and deformation before and after the intervention. Such a process usually employs computer aided methods and arithmetic models; monumental and cultural heritage buildings are often analyzed with the finite element method (FE). The method uses a model that should simulate the actual behavior of the structure for both static and seismic loads. Therefore, it is imperative that the model is developed with data collected from in-situ and laboratory testing (geometry, crack pattern, material properties, etc.) in order to obtain realistic results that can be used for repair and strengthening of the structure. [1]

2 MONUMENT DESCRIPTION

2.1 General information

The Church of St. Constantine & Helen is located in the Municipal Theater square of Piraeus. Its construction begun in 1878 and ended in 1882. It is considered as one of the most majestic temples of Piraeus and was based on the blueprints of the architect John Lazarimos. Moreover, it is characterized by a capacity of 1200 people, its impressive bell-towers and a high dome. After the end of the construction, many prominent hagiographers and marble-sculptors undertook the decoration of the temple interior.

From an architectural perspective, the temple is a “domed basilica”. Its dome is carried on four concave triangular pendentives that serve to the transition from the circular base of the dome to its rectangular base. The weight of the dome passes through the pendentives to four massive piers at the corners. The length of the temple is 29m and the width is 23m. The total height of the temple is 23.4m with the dome and the bell towers being 7.2m and 8.6m high, respectively.

Figure-1: Front view of the temple

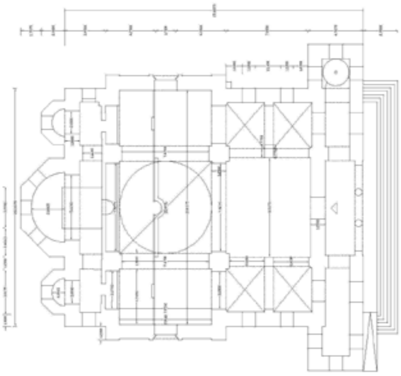

Figure-2: Plan view of the temple

2.2 Material and structural data of the church

2.2.1. Stones and mortar

At three characteristic locations of the church, the external cover of the masonry was removed at square surfaces of 50x50cm (Fig.5); two of them on masonry walls and the third on a pier. Subsequently, the stone strength was measured using a rebound hammer that was calibrated. Based on these measurements, the compressive strength of stone was estimated to be:

$$f_{bc} = 30\text{MPa}$$

Mortar samples were analyzed at the laboratories of Chemical Engineering at NTUA. The analysis procedure included three steps: (a) Natural separation of mortar-stone, (b) X-Ray diffraction, see Figure 3 and (c) Thermal analysis TG-DTG, see Figure 4. The analysis showed that mortar is hydraulic lime with a compressive strength:

$$f_{mc} = 1\text{MPa}$$

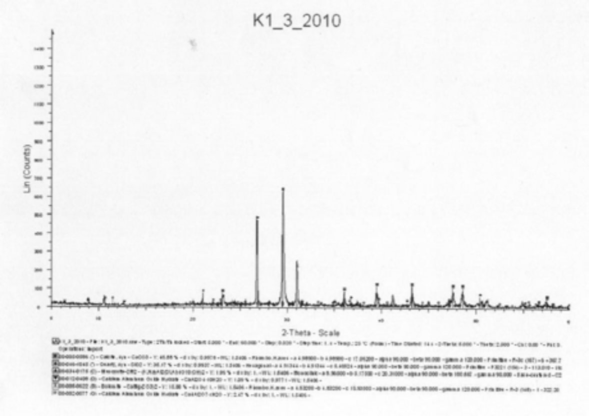

Figure-3: X-Ray analysis results

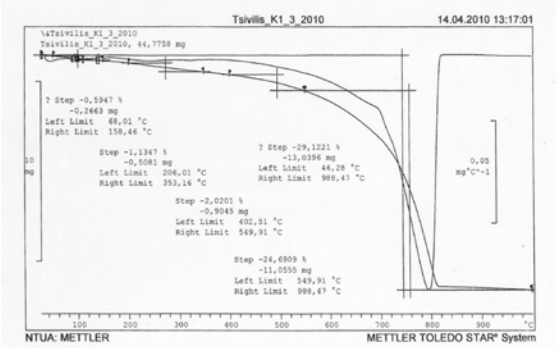

Figure-4: Thermal analysis results

2.2.2. Masonry wall type

In order to identify the transversal orientation of the materials constituting the masonry walls, drill cuttings were made and with the use of an endoscope the interior layers of the wall were inspected (Fig. 5-6). Results showed that the masonry walls are comprised of three layers. The external layers are stone of 25-30cm thickness. Moreover, the internal layer consists of solid mortar and small diameter stones.

Figure-5: Area without mortar cover

Figure-6: Inside the drill cutting

2.2.3. Masonry wall properties

In order to calculate the compressive strength of the stone masonry, the expression recommended by Tasios et. al. [2] was used:

$$f_{wc} = \frac{2}{3}\sqrt{f_{bc}} - a + \beta f_{mc} \qquad (1)$$

where:
f_{bc} and f_{mc} is the compressive strength of stone and mortar, respectively, α is a reduction factor for masonry made of natural stone (α=1) and β is a factor that accounts for the contribution of mortar on the masonry wall strength (for stone masonry β is equal to 0.5).

According to bibliography, the tensile strength of masonry and Young's modulus were calculated with the aid of equations (2) and (3). The material properties are presented in Table-1.

$$f_{tc} = f_{wc}/10 \qquad (2)$$

$$E = 1000\, f_{wc} \qquad (3)$$

Material	Property	Value
Stone	Compressive strength	30 MPa
Mortar	Compressive strength	1 MPa
Stone masonry	Density	2200 kg/m^3
	Young's modulus	3150 MPa
	Poisson's ratio	0.16
	Compressive strength	3.15 MPa
	Tensile strength	0.315 MPa
Marble	Density	2600 kg/m^3
	Young's modulus	64200 MPa

Table-1: Material properties

3 MONUMENT PATHOLOGY

A series of recent earthquakes, including the Athens 1999 earthquake, strained the church and caused serious damage. These damages are mainly attributed to the fact that there are no special provisions in the building to protect it, in case of earthquake. In particular, cracks are located in many parts of the masonry wall, both external and internal and mainly in the intrados of the arcs.


Figure-7: Sample crack at the east ceiling

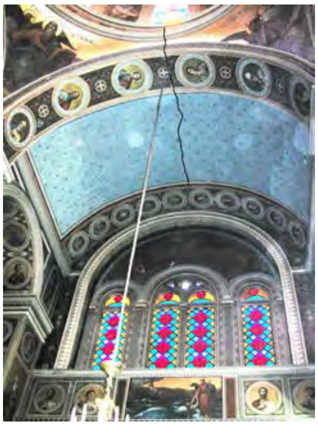
Figure-8: Sample crack at the south ceiling

Those with the largest width are located on the inner surface of the arcs, along longitudinal and transversal directions. Cracks were also developed at the triangular pendentives, which support the dome.

4 AMBIENT VIBRATIONS TESTS

To measure modes and natural frequencies of the church in its present state, ambient vibrations tests were conducted. In order to fulfill the task of the tests, there were measurements in two distinct positions, ground floor and dome level, along two directions. The results are presented in the following Tables (a) and (b) as they are obtained from the peaks in figures 9 and 10.

Mode	Modal Period (sec)	Damping Ratio (%)
1	0.372	4.5
2	0.273	3.3

(a)

Mode	Modal Period (sec)	Damping Ratio (%)
1	0.240	5.8

(b)

Table-2: Measurements at (a) transverse direction x-x’ and (b) longitudinal direction y-y’

Figure-9: Deformation function at transverse direction x-x’

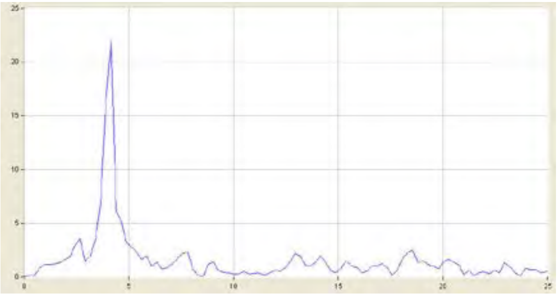

Figure-10: Deformation function at longitudinal direction y-y’

5 NUMERICAL ANALYSIS

5.1 Finite elements model

SAP2000 [3] finite element software was used to create and analyze the structure. The stone masonry and marbles were modeled by eight node solid elements with three degrees-of-freedom per node. Four-node shell elements were used to model the central dome. Two node-frame elements were used for the proper connection and collaboration of solid and shell elements [1]. The final model consists of 31055 solids, 2424 shells, 96 frame elements and 44204 nodes (Fig. 11-12).

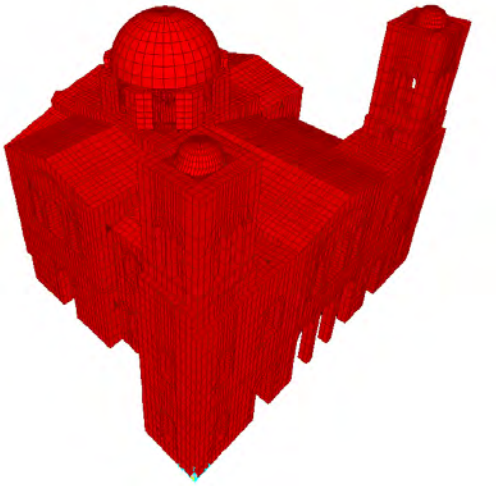

Figure-11: General view of the model

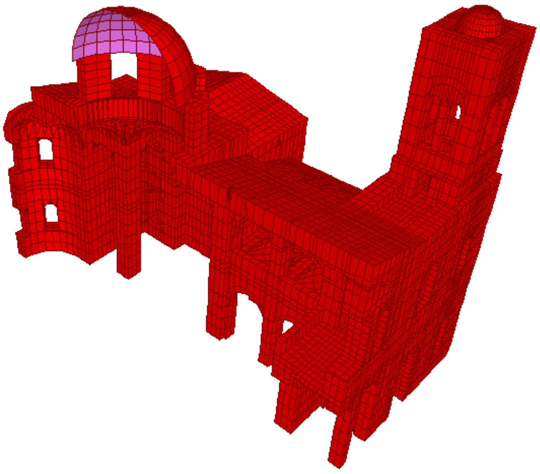

Figure-12: Section along the longitudinal direction

5.2 Response spectrum analysis

A response spectrum analysis was conducted. According to Eurocode 8-1 [4], the design spectrum Type-1 was used to calculate the seismic acceleration in both the horizontal and the vertical directions.

For the horizontal components of the seismic action the design spectrum, $S_d(T)$, is defined by the expressions (4)- (7):

$$0 \leq T \leq T_B : S_d(T) = a_g \cdot S \cdot \left[\frac{2}{3} + \frac{T}{T_B} \cdot \left(\frac{2{,}5}{q} - \frac{2}{3} \right) \right] \tag{4}$$

$$T_B \leq T \leq T_C : \ S_d(T) = a_g \cdot S \cdot \frac{2{,}5}{q} \tag{5}$$

$$T_C \leq T \leq T_D : S_d(T) \begin{cases} = a_g \cdot S \cdot \frac{2{,}5}{q} \cdot \left[\frac{T_C}{T} \right] \\ \geq \beta \cdot a_g \end{cases} \tag{6}$$

$$T_D \leq T : \quad S_d(T) \begin{cases} = a_g \cdot S \cdot \frac{2{,}5}{q} \cdot \left[\frac{T_C T_D}{T^2} \right] \\ \geq \beta \cdot a_g \end{cases} \tag{7}$$

where T is the vibration period in secs, a_g = 0.16g is the design ground acceleration for type A ground, T_B = 0.15 is the lower limit of the period of the constant spectral acceleration branch, T_C = 0.5 is the upper limit of the period of the constant spectral acceleration branch, T_D = 2 defines the start of the constant displacement response range of the spectrum, S = 1.2 is the soil factor, η is the damping correction factor with a reference value of $\eta = 1$ for 5% viscous damping, q = 1.5 the behavior factor and β = 0.2 is the lower bound factor for the horizontal design spectrum. For the vertical component of the seismic action the design spectrum $S = 1.0$, $T_B = 0.05$, $T_C = 0.15$, $T_D = 1.0$

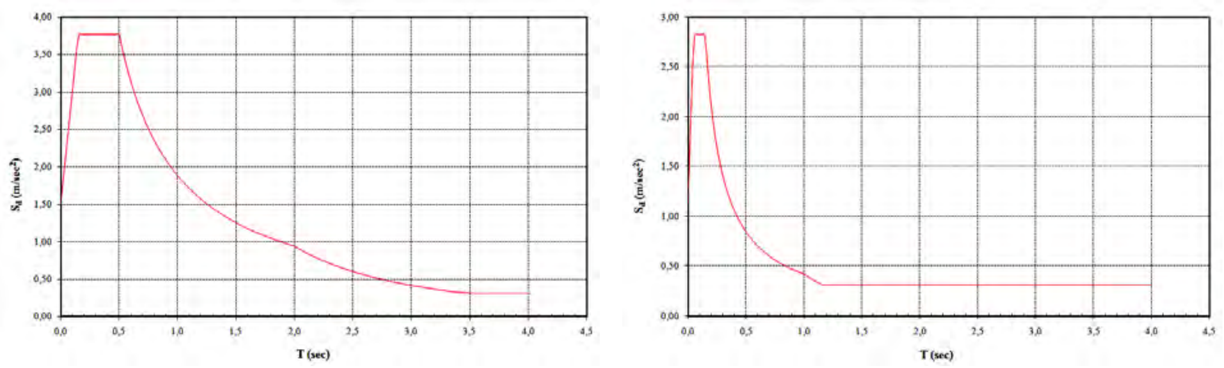

Figure-13: Design spectra for the horizontal and vertical seismic action

5.3 Analysis results

The results of modal analysis for the first three modes and the corresponding modal participating mass ratios are shown in Table-3. There is a good correlation between the measured and calculated modal periods which validates use of the model of the structure at least for static and small intensity dynamic loads.

Mode	Period (sec)	Ux	Uy	Uz	Rx	Ry	Rz
1st	0.320	0.728	0.00067	8.746E-07	0.00031	0.29906	0.2789
2nd	0.296	0.0003	0.776	1.139E-06	0.34906	0.00015	0.35204
3rd	0.228	0.032	0.00087	3.504E-07	0.00065	0.01385	0.10877

Table-3: Modal periods and participating mass ratios for displacement (U) and rotation (R)

The stresses at the transversal direction x-x’ (S11) and at the longitudinal direction y-y’ (S22) are shown in Fig. 14. With the deep blue (darkest color) are the areas where developed stresses are greater than the tensile strength of masonry. These areas are extensive and correspond to the areas where damages were observed at the temple.

(a) (e)

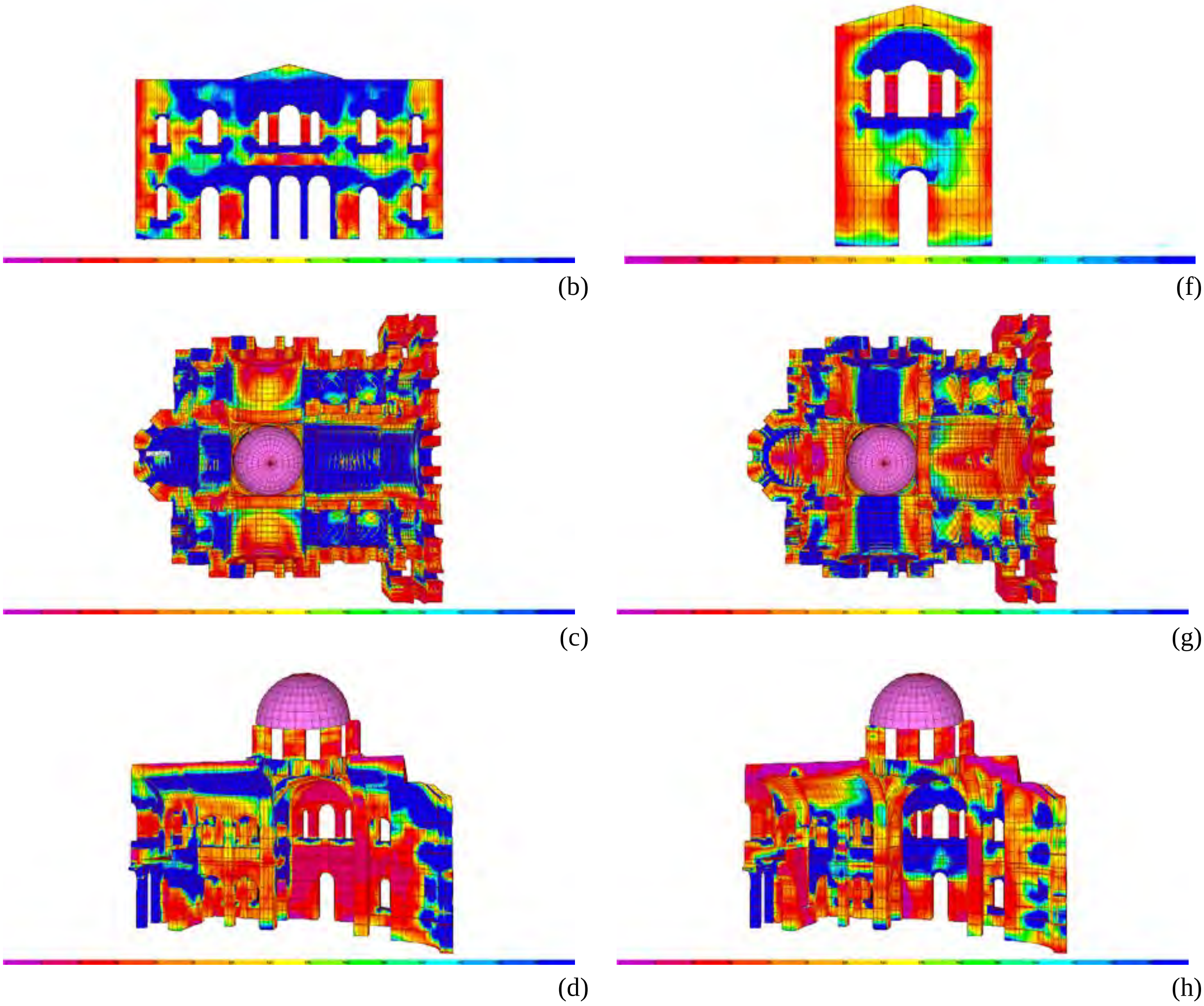

Figure-14: S11 (a-d) and S22 (e-h) stresses of the temple

It should be noted that this paper presents the first part of the analysis that was conducted for the historic structure. The second part presents a kinematic analysis as well as two displacement based analysis using frame as well as shell elements, respectively. Also, the second part elaborates on the correlation between the experiment and the analytical results and presents a comparison among the results of all three analyses.

6 REINFORCEMENT

According to the results of the analysis and the architectural- intervention restrictions imposed by the authorities that require minimum alteration of the structural configuration of the historic building and its painted walls, rehabilitation and strengthening of the church was based on a combined scheme using grout injections, CFRP and steel tie rods that complied with all limitations [5, 6]. The scheme is described in the following sections.

6.1 Grouting

The technique of grout injection in masonry through small holes drilled in the mortar at the exterior of the church walls will be used to consolidate the three leaf walls. Care will be taken to control the injection application so that the grout will not emerge on the interior surface of the walls. The compressive strength of the masonry after consolidation, $f_{wc,s}$, is calculated from [7]

$$f_{wc,s} = f_{wc,0} + 0{,}31(V_{\text{inf}} / V)\, f_{gr}^{1{,}18} \tag{8}$$

where:

$f_{wc,0}$ the compressive strength before grout injection

V_{inf} / V ratio of grout volume to masonry volume

f_{gr} compressive strength of injected material

According to the international experience for seismic strengthening of three-leaf masonry walls, consolidation of the masonry walls can be accomplished with this technique. A compressive strength of 10 MPa was used in the analysis for the injected material in order to restrain failure in the grout of the consolidated wall.

6.2 Composite materials CFRP and stainless steel tie rods

According to the analysis, undertaking of the tensile stresses can be achieved by applying sheets of fiber carbon impregnated with epoxy resins on the upper exterior surface of the church (roof) as well as at parts of the interior surfaces of certain vaults that are not decorated with historic paintings. Specifically either three or two-plies of carbon fiber reinforced plastics (CFRP), with a carbon sheet thickness of 0.17 mm is selected. The mechanical properties of the carbon fiber are: modulus of elasticity E_c= 240 GPa, ultimate strength f_j= 3500 MPa.

Also two stainless steel tie-rods F430 with a diameter of 40mm should be placed at the upper part of the arches in the interior of the church. The mechanical properties of the tie-rods are: modulus of elasticity E_c= 200 GPa, yield strength f_y= 379 MPa, ultimate strength f_u= 552 MPa.

7 ANALYSIS OF STRENGTHED STRUCTURE

The results of modal analysis for the first three modes of the strengthened structure and the modal participating mass ratios are shown in Table-4.

Mode	Period (sec)	Ux	Uy	Uz	Rx	Ry	Rz
1st	0.250	0.74	0.00045	1.639E-06	0.00021	0.30279	0.28297
2nd	0.230	0.000085	0.77	1.171E-07	0.34847	0.000047	0.3621
3rd	0.180	0.02743	0.00298	5.506E-07	0.00191	0.01185	0.10544

Table-4: Modal periods and participating mass ratios for displacement (U) and rotation (R)

Figure-15: Placement of CFRP on the intrados of the arced ceiling

Figure-16: Placement of CFRP on the arcs of central dome

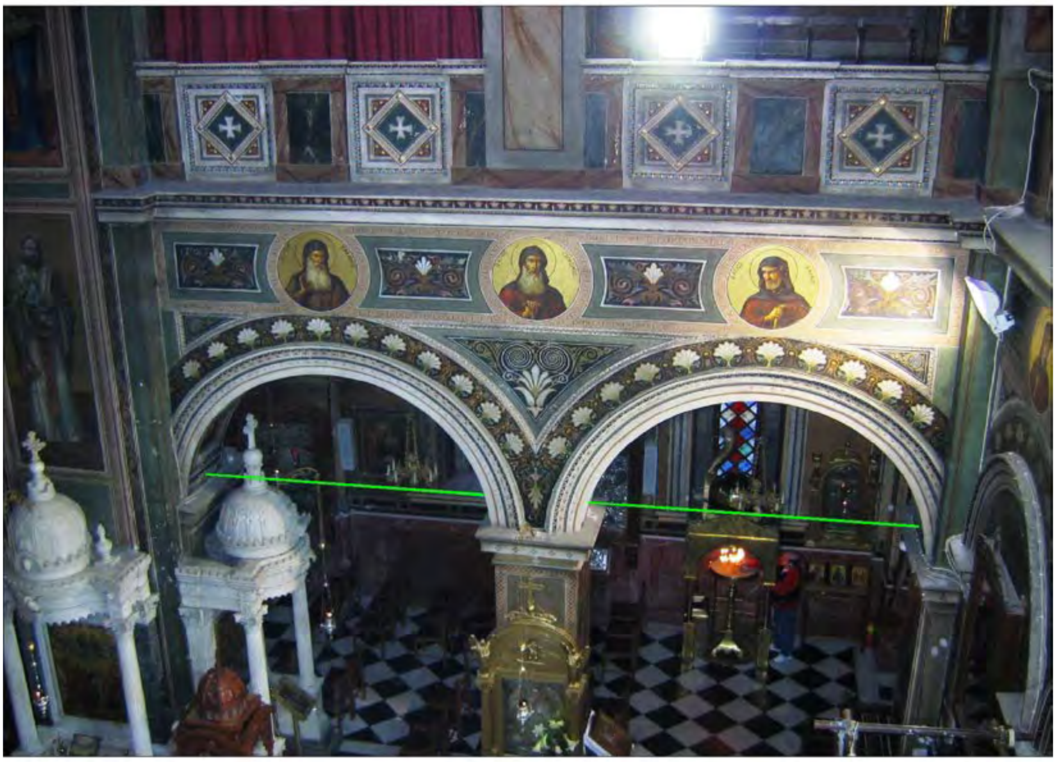

Figure-17: Placement of tie rods at arcs

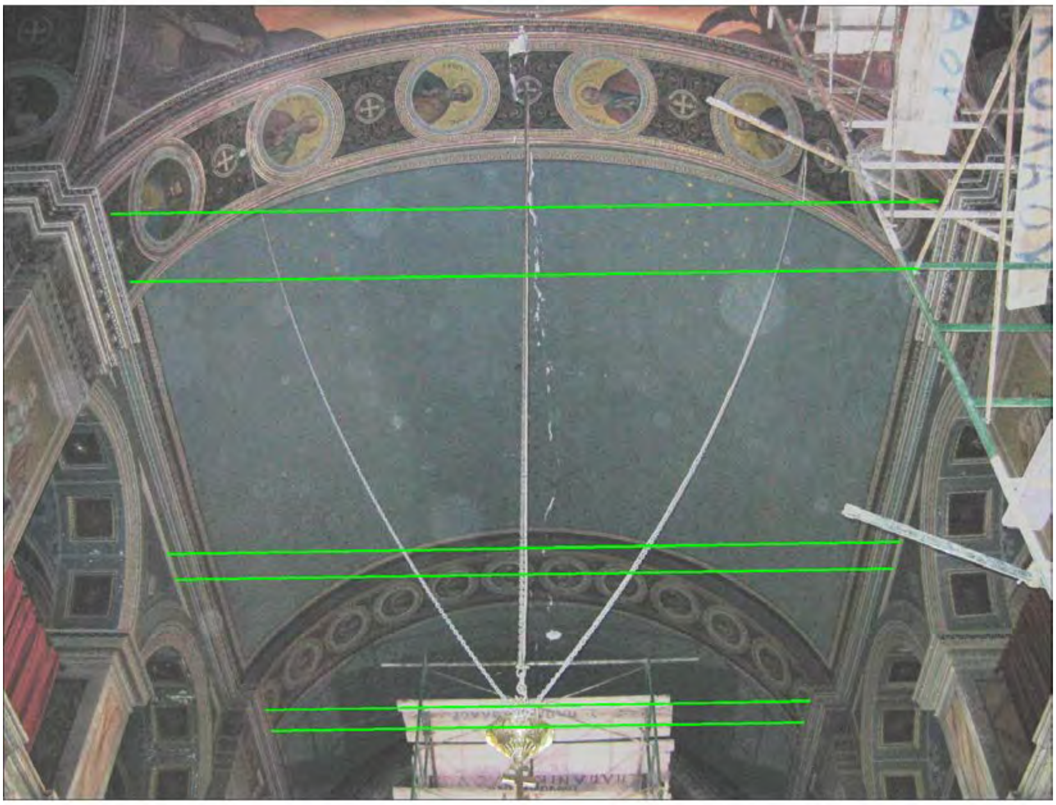

Figure-18: Placement of tie rods at the central arced ceiling

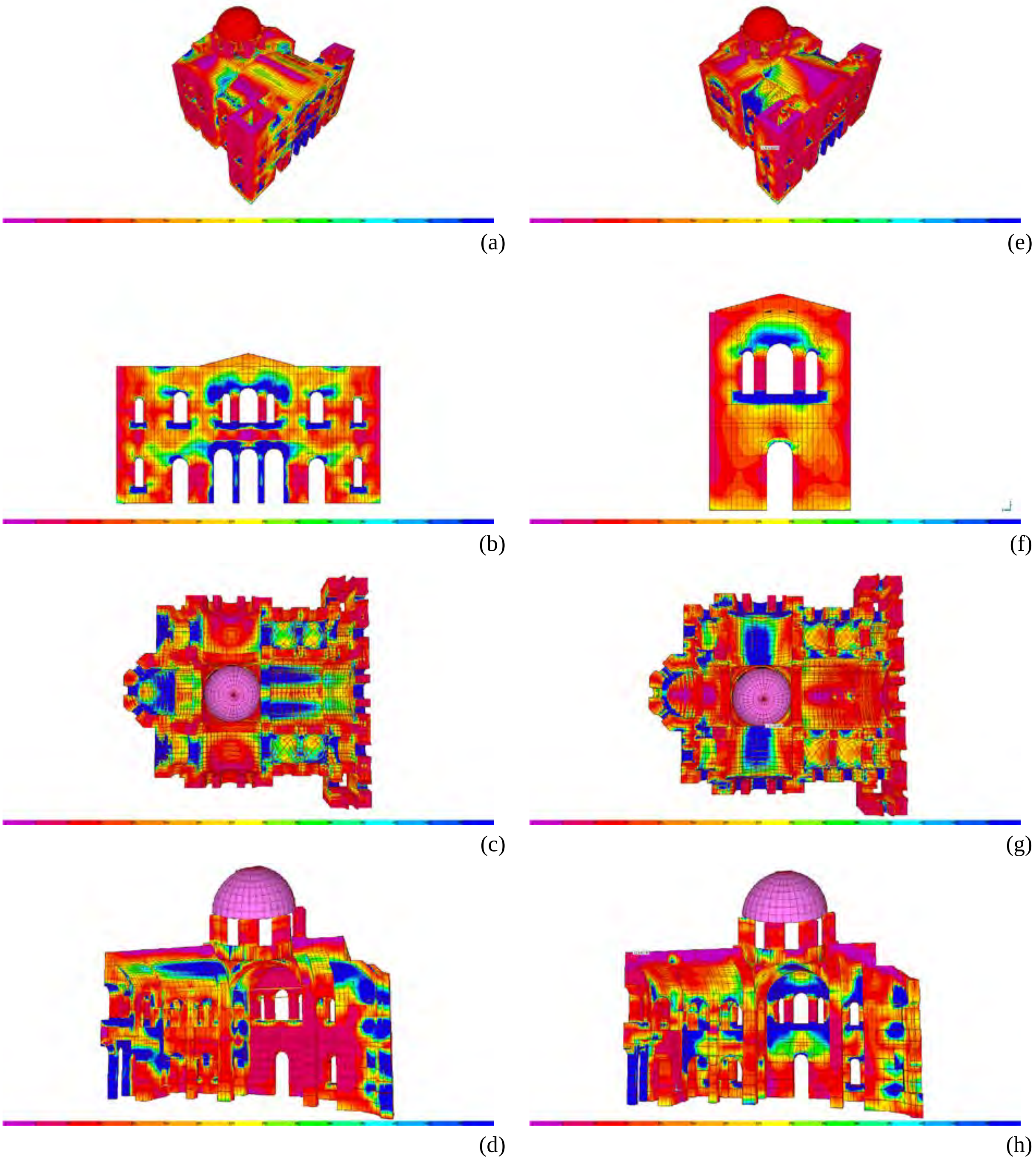

Figure-19: S11 (a-d) and S22 (e-h) stresses of the temple

Comparison between Tables 3 and 4 clearly indicates the anticipating decrease of the model periods of the strengthened structure after the interventions. According to the analysis excess of the compressive strength of the masonry does not appear after the consolidation of the walls with grout injections. Also, tensile stresses are smaller than the tensile strength attributed to the application of CFRP and tie rods. Excess of the tensile strength (10% of the tensile strength of the masonry) is limited at "secondary" places of the masonry walls for the seismic behavior and stability of the structure.

REFERENCES

[1] C.C. Spyrakos, *Finite Element Modeling in Engineering Practice,* Pittsburgh PA, 1994.

[2] Θ.Π. Τάσιος, Μ.Π. Χρονόπουλος, *Παθολογικά Αίτια και Μηχανική των Βλαβών της Τοιχοποιίας,* Υ.ΠΕ.ΧΩ.ΔΕ./ Εργ. Ωπλ. Σκυροδέματος Ε.Μ.Π., Αθήνα, 1986.

[3] SAP2000. Structural analysis program, advanced 14.1.0. Berkeley, California: Computers and Structures, Inc.; 2009.

[4] ENV 1998-1, Eurocode 8. Design of structures for earthquake resistance. Part1 General rules, seismic actions and rules for buildings. 2003. CEN.

[5] Κωνσταντίνος Σπυράκος, *Ενίσχυση Κατασκευών για Σεισμικά Φορτία*, Τεχνικό Επιμελητήριο Ελλάδας, Αθήνα, 2004.

[6] P. Foraboschi, *Strengthening of Masonry Arches with Fiber-Reinforced Polymer Strips,* J. Compos. Constr (ASCE), Vol. 8, No. 3, June 1, 2004.

[7] M.R. Valluzzi, F. da Porto, C. Modena, *Behavior and modeling of strengthened three-leaf stone masonry walls,* RILEM Materials and Structures, 37(267): 184-192, 2004.

COMPDYN 2011
III ECCOMAS Thematic Conference on
Computational Methods in Structural Dynamics and Earthquake Engineering
M. Papadrakakis, M. Fragiadakis, V. Plevris (eds.)
Corfu, Greece, 25–28 May 2011

FAST SEISMIC PERFORMANCE ASSESSMENT OF RC FRAME STRUCTURES WITH CONSIDERATION OF ALEATORY AND EPISTEMIC UNCERTAINTY BY UTILIZING PBEE TOOLBOX AND WEB APPLICATION FOR PREDICTION OF IDA CURVES

Daniel Celarec[1], **Matjaž Dolšek**[2]

[1,2] University of Ljubljana, Faculty of Civil and Geodetic Engineering
Jamova 2, SI 1000 Ljubljana, Slovenia

e-mail: dcelarec@ikpir.fgg.uni-lj.si, mdolsek@ikpir.fgg.uni-lj.si

Keywords: Epistemic uncertainty, Aleatory uncertainty, Reinforced concrete frame, Uncertainty analysis, Seismic performance, Incremental dynamic analysis

Abstract. *A simplified methodology for seismic performance assessment of structures with consideration of both aleatory and epistemic uncertainty is briefly presented. The methodology involves pushover analysis for a set of structural models and nonlinear dynamic analysis of corresponding equivalent SDOF models. However, a methodology by itself without any support of sophisticated computational software is not intended to be used for practical applications. Thus, a very efficient software tool, a PBEE toolbox [1] in conjunction with OpenSees, was used in our study in order to perform pushover analyses of required computational simulations, while nonlinear dynamic analysis are approximately computed by using a web application for prediction of IDA curves [2], which was recently developed within ICE4RISK project. Presented methodology and software tools are demonstrated by means of an example of a three-storey reinforced concrete frame building. The results of the presented example have indicated that incorporation of the epistemic uncertainty, in addition to aleatory uncertainty, slightly increases dispersion and can substantially decrease the limit-state intensities. This effect increases with the severity of the limit state. It was also proved that sophisticated software tools are important ingredient of performance-based earthquake engineering and can significantly facilitate transferring knowledge into practice.*

1 INTRODUCTION

Past investigations have shown, e.g. [1, 2], that accuracy of seismic performance assessment of structures can be reasonably improved if different sources of uncertainty are systematically incorporated within evaluation process. Thus, it is important in seismic performance evaluation to consider the effects of aleatory uncertainties, which are usually associated with random nature of earthquakes, and also the effects of epistemic uncertainties arising from incomplete knowledge of physical and modelling characteristics of structure.

Recently, several studies have been performed with a focus on comparisons between the different methods for incorporating the epistemic and aleatory uncertainties in seismic performance assessment, such as that performed by Liel at al. [3], or with the aim of defining simplified nonlinear methods for the evaluation of structural seismic performance, e.g. [4]. Nevertheless, a comprehensive seismic performance assessment with a systematic consideration of aleatory and epistemic uncertainties is from the computational point of view still very time-consuming due to numerous number of the required computational simulations, especially, if seismic response parameters are assessed by means of nonlinear dynamic analysis, such as that in [5, 6, 7]. It is therefore important to develop and use simplified procedures, which are computationally not excessively demanding, and are capable of sufficiently accurate prediction of the seismic response parameters with consideration of both types of the uncertainties.

For these reasons, this paper provides an overview of the procedure for fast seismic performance assessment of structures, which involves approximate IDA by using the web application [8], and allows incorporating the effect of both the aleatory and epistemic uncertainties. The use of the proposed methodology is demonstrated by the example of three-storey reinforced concrete (RC) frame building, which had been designed according to the Eurocode 8 requirements.

2 METHODOLOGY

The methodology for fast seismic performance assessment of buildings, which is explained in this section, involves the pushover analysis of the structure and the dynamic analysis of the equivalent single-degree-of-freedom (SDOF) model. The results of dynamic analysis are obtained by using the web application for prediction of IDA curves [8], which involves response database of SDOF model and n-dimensional linear interpolation. The effects of epistemic uncertainties are considered, by applying the pushover analysis and web application to the set of structural models, determined by utilizing the Latin Hypercube Sampling (LHS) technique [9].

2.1 Determination of set of structural models

In this study a variant of the LHS technique, which was recently proposed by Vorechovsky and Novak [9], was used. In general, two steps are needed to determine the sample of random variables, which are directly applied to the structural model. Firstly, each random variable X_i is sampled by using N_{Sim} values. The j-th sample value of the i-th random variable X_i can be obtained as follows:

$$x_{j,i} = F_i^{-1}\left(p_{j,i}\right) = F_i^{-1}\left(\frac{\pi_i\left(j\right)-0.5}{N_{Sim}}\right), \quad i=1,...,N_{Var}, \quad j=1,...,N_{Sim}, \tag{1}$$

where $\pi_i(j)$ is a random permutation of 1,…, N_{Sim}, $p_{i,j}$ is the probability that the random variable X_i is less than or equal to $x_{j,i}$ and $F_i^{-1}(p_{j,i})$ is the inverse of the cumulative distribution function (CDF) of the random variable X_i, evaluated at the probability $p_{j,i}$. The undesired correlation between the different random variables, which is introduced in the described sampling process, can be minimized by the stochastic optimization method called Simulated Annealing (see [9]). For this purpose the norm E, which is a measure for the difference between the generated and the prescribed correlation matrix, is defined by the expression:

$$E = \frac{2}{N_{Var}\left(N_{Var}-1\right)}\sqrt{\sum_{i=1}^{N_{Var}-1}\sum_{j=i+1}^{N_{Var}}\left(S_{i,j}-K_{i,j}\right)^2}, \tag{2}$$

where $S_{i,j}$ and $K_{i,j}$ are, respectively, the generated and prescribed correlation coefficients between the random variables X_i and X_j. The norm E takes into account the deviations between all the correlation coefficients, and is normalized with respect to the total number of all the correlation coefficients. It therefore represents a good measure when examples with a different number of random variables are compared. The norm E is then minimized by the stochastic optimization method known as Simulated Annealing. The result of this optimization is the optimized sample matrix **X** with N_{Sim} rows and N_{Var} columns, for which the correlation matrix is close to the target correlation matrix. More details about the LHS technique and its application can be found elsewhere (e.g. in [5, 9]).

The sample of random values is then used to generate a set of N_{Sim} structural models, which reflect the epistemic uncertainties, so that the set represents the probabilistic structural model. In a previous study [5], it was shown that if N_{Sim} slightly exceeds N_{Var}, then the optimized correlation matrix is close to the prescribed correlation matrix, and, usually, the seismic response parameters are in this case predicted with a sufficient accuracy.

2.2 Summary of the web application for prediction of IDA curves

The web application for prediction of approximate IDA curves of reinforced concrete structures, which was recently developed [8], involves response database of the equivalent single-degree-of-freedom (SDOF) model, which was computed for 30 ground motion records used by Vamvatsikos and Cornell [10].

The SDOF model was defined to be representative for reinforced concrete structure. In this case the force-displacement relationship is described by the four parameters (r_v, r_h, μ_u, α) of the pushover curve. The other two parameters of the SDOF model are the period T_1 and the ratio of the critical damping ξ. The four parameters of the force-displacement relationship are dimensionless quantities and are defined as

$$r_v = \frac{F_1}{F_2}, \quad r_h = \frac{u_1}{u_2}, \quad \mu_u = \frac{u_3}{u_2}, \quad \alpha = -\frac{k_{pc}}{k_i}, \tag{3}$$

where points (u_1, F_1) and (u_2, F_2) represent first and the second characteristic point of the idealized force-displacement relationship (Figure 1) and, respectively, roughly represent the cracking of concrete and, in the case of regular structures, yielding of reinforcements at the base of columns. The displacement u_3 is related with the displacement where the strength of the structure starts degrading, while k_{pc} and k_i are, respectively, the post-capping and initial stiffness of the idealized force-displacement relationship. With a suitable variation of the four parameters the idealized curve can be fitted to almost any pushover curve typical for reinforced concrete structures.

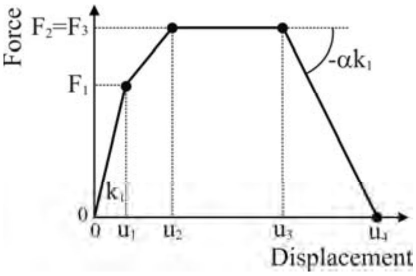

Figure 1: The idealized force-displacement relationship.

The web application was developed on the basis of the classic three-tier client-server architecture [8], which enforces a general separation of three parts: client tier (also named presentation layer or, more specifically, user interface), middle tier (business logic) and data storage tier.

The advantage of the web application for prediction of approximate IDA curves in comparison to other simplified approaches, which are based on limited parametric studies, is that the response database can be expanded by adding results of seismic response of SDOF models for additional ground motion records. Further, web application enables quadrilateral idealization of pushover curve and prediction of global dynamic instability as well as the dispersion measures, which are needed for estimation of seismic risk. These parameters are rarely estimated by simplified methods.

3 EXAMPLE

The use of the presented methodology for seismic performance assessment of structures is demonstrated by means of an example of a three-storey RC frame building, designed for the earthquake resistance according to the Eurocode 8 [11]. The seismic performance of the building is evaluated considering both the aleatory uncertainties due to the random nature of the seismic load, and the epistemic uncertainties, which relate to several sources of the uncertainty in physical characteristics of the structure and its modelling parameters. Based on the approximate IDA curves, the median seismic capacity at the ultimate limit state and the dispersion measures for demand and capacity are estimated and compared to the analysis case, in which the epistemic uncertainties are neglected. In addition, the results are also compared with the results of the N2 method [12], which was for the case of the example building previously applied in the companion study [13].

Two limit states were defined for comparison reasons between the results of the approximate IDA and results of the N2 method. The definition of the limit states differs with respect to the methods involved since the N2 method is not capable to predict global dynamic instability of the structure. In the case of the approximate IDA the limit state was therefore defined with the global stability of the structure (on the following, termed as ultimate limit state), whereas in the case of the N2 method, the limit state under consideration corresponded to the displacement at 80 % of its maximum base shear in relation to the softening part of the pushover curve (termed as near-collapse (NC) limit state). More about both limit states is explained within the related sections, for example, in section 3.4.

3.1 Description of the structure and mathematical model

The example structure is a three-storey RC frame building, which was designed for the earthquake resistance according to the Eurocode 8 [11]. The plan dimensions of the structure are 9.7×10.5 m. All three storeys are 3 m high, with monolithic slabs having a depth of 15 cm. The strength of the concrete and of the steel reinforcement amounted to 33 and 400 MPa, respectively. The masses and corresponding mass moments of inertia amounted to 94.3 t and 1667 tm^2 for the first two storeys, and 94.4 t and 1634 tm^2 for the top storey, respectively. The plan view of the building and the reinforcement of typical cross sections of the columns and beams are shown in Figure 2.

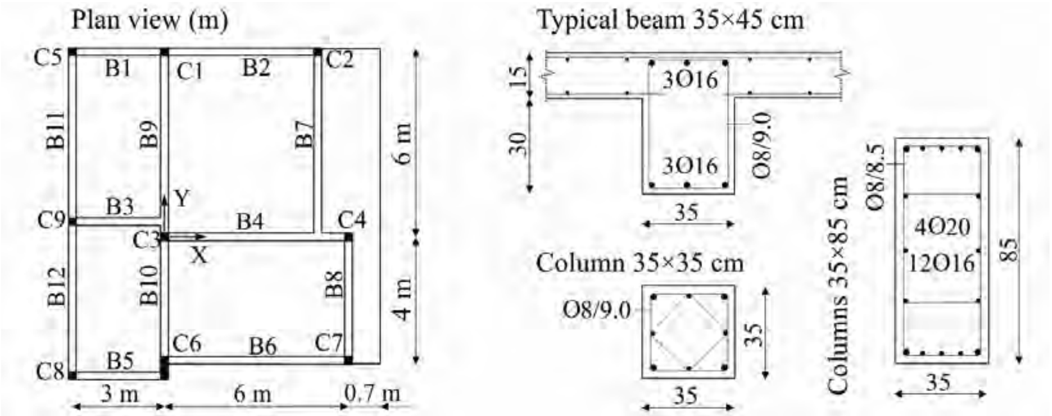

Figure 2: The plan view of the building and typical cross-sections of the columns and beams.

The structure was modelled by one-component lumped plasticity elements, which consist of an elastic beam-column element and two inelastic rotational hinges at the ends. Envelopes, describing a moment-rotation relationships of the hinges, were modelled with equivalent tri-linear relationship using effective initial stiffness of the elements. The three characteristic points of the envelopes are the yield point (Y), the maximum strength (M), and a near-collapse point (NC). The NC point represents a local near-collapse limit state in a column or beam, which is defined by the ultimate rotation θ_u, corresponding to a 20 % reduction in the maximum moment. Near-collapse rotation in the columns was estimated by means of the Conditional Average Estimator (CAE) method [14], whereas in the beams the near-collapse rotation for their hinges was determined by using the formula defined in the Eurocode 8-3 [15].

In the structural model, the rigid diaphragms were assumed at the floor levels due to the monolithic RC slabs. Consequently the masses were lumped at the mass centres. Centreline dimensions of the elements were used with the exception of beams B5 and B6 (Figure 2). These beams are connected eccentrically to column C6.

All analyses were performed with the OpenSees [16] in conjunction with the PBEE toolbox [17].

3.2 Input random variables and the set of structural models

In order to incorporate the epistemic uncertainty into the structural model, the following parameters were treated as random variables: the strength of the concrete and of the reinforcement steel, mass, effective slab width and the parameters describing the characteristic rotations in the plastic hinges, i.e. the yield and the ultimate plastic rotation. These model parameters were defined with the eight random variables, each representing individual model parameter. Note that the random variables, except for those defining the characteristic rotations in the plastic hinges, were assumed to be uncorrelated. In the study, the correlation factor between the yield and the ultimate rotation in plastic hinges was assumed to be 0.5. The statistical parameters were taken from literature and are presented in Table 1.

Utilizing the Latin Hypercube Sampling (LHS) technique [9], the selected random variables were used to generate the set of 20 structural models (simulations) in addition to the deterministic structural model in order to incorporate the selected sources of the epistemic uncertainties. Note, that the number of simulations generated is slightly higher than two times the number of input random variables. This is about the smallest reasonable number of the simulations, if using the LHS technique. A smaller number of simulations would probably lead to a significant decrease in the accuracy of the results. For more detailed discussion on the effects of number of the simulations on the results of the seismic performance evaluation when using the LHS technique, the reader is referred to the previous study [5].

Variable	COV	Distribution	Reference
Concrete strength	0.20	Normal	Melchers [18]
Steel strength	0.05	Lognormal	JCSS [19]
Mass	0.10	Normal	Ellingwood [20]
Eff. Slab width	0.20	Normal	Haselton [21]
Yield rotation:			
• columns	0.36	Lognormal	Panagiotakos and Fardis [22]
• beams	0.36	Lognormal	
Ultimate rotation:			
• columns	0.40	Lognormal	Peruš et al. [14]
• beams	0.60	Lognormal	Panagiotakos and Fardis [22]

Table 1: The statistical characteristics of the input random variables.

3.3 Results of the pushover analysis

The results of the pushover analysis are, for the simplicity reasons, presented only for the pushover analysis in positive X direction (Figure 3). The horizontal load pattern for pushover analysis was determined by the product of storey masses and the first modal shape in X direction.

The pushover curves for the deterministic structural model are compared with pushover curves of the set of 20 structural models incorporating the epistemic uncertainties (Figure 3). In addition, the 16th, 50th and 84th fractiles of the base shear given the top displacement (“fractile pushover curve”) are also shown in Figure 3. A high scatter in global ductility of the structure is observed. For example, the comparison between the fractile pushover curves and the deterministic pushover curve shows that the epistemic uncertainties mostly affect the displacement ductility of the structure. The epistemic uncertainties have moderate effect on the maximum base shear, while the difference in the initial stiffness between different structural models is almost negligible.

A large difference between the pushover curves presented in Figure 3 can be attributed to the fact that different collapse mechanisms were observed for different structural models, some of them being illustrated in Figure 4, for example at the NC limit state. The most influential parameter, which governs the type of the near-collapse mechanism of the building, is the rotation capacity of the beams. In the case, if rotation capacity of the beams is low in comparison to that of the columns, then the strength degradation of structure is a consequence of the damage in beams of the 1st and 2nd storeys. Thus, the top displacement capacity at NC limit state is low D_t = 0.18 m (Figure 4a). The opposite case, i.e. the damage in plastic hinges of the structural model with high rotation capacities of the beams, is presented in Figure 4b. In this case, the top displacement capacity at NC limit state is equal to 0.59 m.

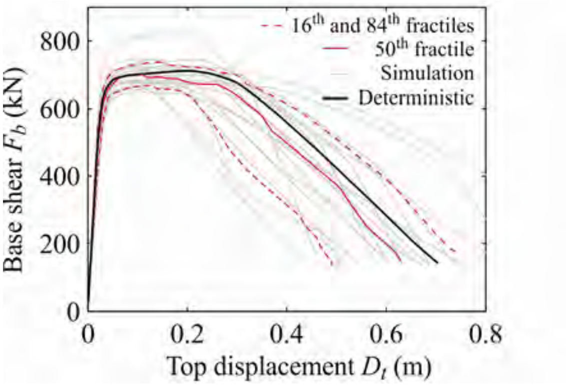

Figure 3: The pushover curves for the deterministic structural model, for the set of 20 structural models and the fractile pushover curves, representing the 16th, 50th and 84th fractiles of the base shear given the top displacement.

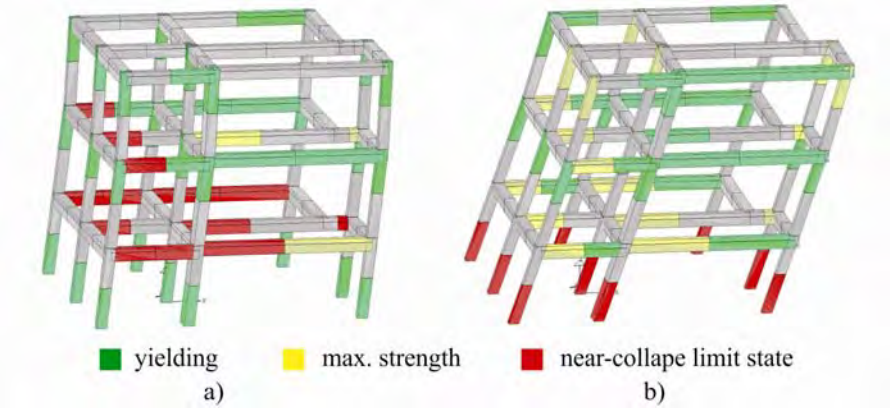

Figure 4: The damage in the plastic hinges of the building for a) the model with the smallest displacement capacity at the NC limit state, and b) for the model with the highest displacement capacity at the NC limit state. The results presented are based on the pushover analysis.

3.4 Prediction of IDA curves and definition of the ultimate limit state

The approximate IDA curves of the structure were determined by using a web application, which involves response database of the equivalent SDOF model. For that reason, the pushover curves were, for the need of the presented case study, idealized with a four-linear force-displacement relationship as presented in Figure 5. The first two points of the idealized force-displacement relationship represent the cracking (Cr) and yielding (Y) of the idealized system, the third point represents the maximum deformation capacity at the end of the plastic plateau (U), and the forth point represents a complete loss of the base shear capacity. The cracking point was defined in the elastic part of the pushover curve and corresponded to the top displacement of the structure at which the first element (column or beam) starts yielding. The yield force F_y was assumed equal to the maximum base shear obtained by the pushover analysis. The post-cracking stiffness of the idealized system was determined in such a way that the areas under the pushover curve and the idealized force-displacement relationship were equal (termed as an equal energy rule) taking into account the interval between displacement at the cracking of concrete D_{cr} and displacement at the maximum base shear D_m. Similar rule applied also in determining the third point of the force-displacement relationship. The difference between pushover curve and the idealized force-displacement relationship is small as presented in Figure 5 for the deterministic structural model.

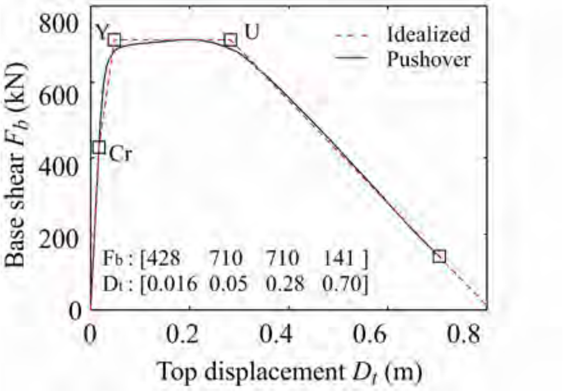

Figure 5: The pushover curve of the deterministic structural model and the corresponding idealization using a four-linear force-displacement relationship.

The modification factor Γ which relate the spectral displacement of an equivalent SDOF model to the roof displacement of the MDOF system is defined as follows:

$$\Gamma = \frac{m_{SDOF}}{\sum m_i \cdot \phi_i^2},\ m_{SDOF} = \sum m_i \cdot \phi_i, \tag{4}$$

where m_{SDOF} is equivalent mass of the SDOF model, m_i is the mass of the structure in the i-th storey and ϕ_i is the displacement in the i-th storey, normalized to the displacement at the top storey. The vector ϕ was taken equal to the first modal shape of the structure, which corresponds to translations in X direction. The additional two parameters, which also affect the dynamic response of the SDOF model, are the critical damping factor (ξ), which was in our study assumed equal to 5 %, and the period of the equivalent SDOF model (T_{SDOF}) calculated as:

$$T_{SDOF} = 2 \cdot \pi \cdot \sqrt{\frac{m_{SDOF} \cdot d_{cr}^*}{f_{cr}^*}}, \tag{5}$$

where d_{cr}^* and f_{cr}^* are, respectively, the displacement and the base shear at cracking of the equivalent SDOF model.

Using the procedure described above, the equivalent SDOF models were determined for the deterministic structural model and for 20 structural models incorporating the epistemic uncertainties. Then, by applying the web application, the IDA curves of each structural model have been approximately predicted based on the dynamic analysis of the corresponding equivalent SDOF models. Actually, the output of the approximate IDA, which is presented in the Figure 6, are the IDA points, calculated for different ground motion records and for multiple levels of seismic intensities, and the fractile IDA curves, i.e. the median IDA curve and associated 16th and 84th fractiles for the top displacements.

One of the objectives of this study was estimation of the seismic performance parameters, i.e. the median seismic capacity and the corresponding dispersion measures. These parameters have been in the case of the approximate IDA estimated for the ultimate limit state of the structure, which has been, in our case, defined with the global loss of the structural stability in relation to the approximate IDA curves. These points of the ultimate limit state are marked red in the Figure 6.

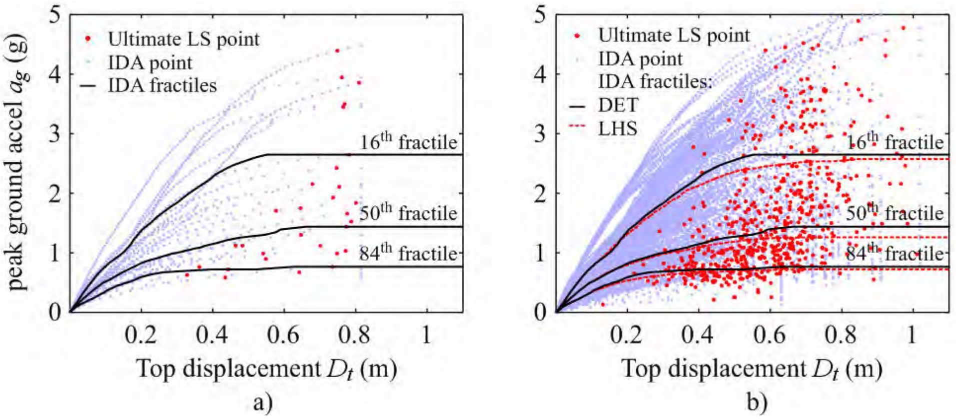

Figure 6: The fractile approximate IDA curves, collapse points and approximate IDA points for a) approximate IDA based on the deterministic structural model and b) for the approximate IDA based on the set of structural models representing the epistemic uncertainties.

Note, that such definition of the ultimate limit state is not completely realistic and probably overestimates the displacement capacity, since in the model the linear post-capping stiffness is assumed all the way to a complete loss of the base shear. Therefore the displacement, which corresponds to the global dynamic instability of structure, is probably smaller than that, which corresponds to the highlighted points in the Figure 6.

In the case if seismic response parameters were determined with the N2 method [12], which was for the same structure used in one of the previous studies [13], the displacement corresponding to the global dynamic stability of structure cannot be obtained. Usually it is conservatively assumed that this displacement corresponds to the NC limit state, as already defined above.

Nevertheless, the difference in the estimated seismic capacity, which was made due to the different definition of the limit states, is small, if expressed with the difference of predicted peak ground acceleration that cause the ultimate limit state or the NC limit-state. This is so, since the gradient of peak ground acceleration in comparison to the top displacement is low in the range of the displacements near global collapse of the structure.

By comparing the results in Figures 6a and 6b it can be concluded that a high scatter in the seismic performance of the structure arises predominantly due to the aleatory uncertainties. For example, the 16th and 84th fractiles of the approximated IDA curves for the deterministic structural model (see Figure 6a), for which only the aleatory uncertainty due to the randomness in the ground motion records were incorporated, and corresponding 16th and 84th fractiles of the approximated IDA curves incorporating both the aleatory and the epistemic uncertainties (see Figure 6b), do not differ significantly. This is observed especially for the 84th fractile and for the first part of the 16th fractile IDA curve. That means that the greatest part of the scatter in seismic performance is due to the random nature of the seismic load, whereas the epistemic uncertainties are relatively minor contributor to overall performance uncertainty. Another fact that can be concluded based on the results presented in Figure 6 is that the median seismic performance at the region of the intensities for the ultimate limit state is reduced if the epistemic uncertainties are included into the analysis. The reduction of the median seismic performance at the ultimate limit state can be visually observed as a vertical shift in the prediction of the median (50th fractile) IDA curve.

3.5 The estimation of seismic response parameters

The maximum top displacement $D_{t,C}$ at the defined ultimate limit state and corresponding peak ground acceleration $a_{g,C}$ were selected for seismic response parameters and assessed with its median value and dispersion measure. In addition, dispersion in top displacement demand was also estimated since it represents an input parameter for the seismic risk assessment if evaluated utilizing the EDP-based formulation. Note that in this case the dispersion depends on the peak ground acceleration and was for the sake of simplicity computed at $a_g = 0.4$ g.

Another distinction between the seismic response parameters was made with respect to the type of the uncertainty, which were considered in the analysis. So, the seismic response parameters were estimated, respectively, for the deterministic structural model, where only the aleatory uncertainties due to the record-to-record variability (R) were considered, and for the stochastic structural model, where both the aleatory and epistemic uncertainties (RU) were simultaneously incorporated. In addition, the results were presented also for the case if seismic response parameters were estimated by using the N2 method. In this case, the results were provided for the deterministic structural model and for the stochastic structural model with consideration of epistemic uncertainties (U).

In all cases the median and the dispersion measure of the seismic response parameters were estimated by using three different methods, all assuming a log-normal distribution of sample values. Thus the dispersion measure was defined as the standard deviation of natural logarithms. The first considered method was a so called counting method (on the following noted as M1), since 16th, 50th and 84th fractiles (y_{16}, y_{50}, y_{84}) of the seismic response parameters were determined according to the counting method and the corresponding dispersion measure was calculated as the average value of $\beta_{16} = \log(y_{50}/y_{16})$ and $\beta_{84} = \log(y_{84}/y_{50})$. The method of moments was the second method (M2) used for assessing median $\tilde{m}$ and dispersion measure β of the seismic response parameters, i.e. the 1st and the 2nd moment of the sample values:

$$\tilde{m} = \bar{m} \cdot e^{-0.5 \cdot \beta^2}, \tag{6}$$

$$\beta = \sqrt{\ln\left(\frac{\sigma^2}{\bar{m}^2} + 1\right)}, \tag{7}$$

where ($\bar{m}$) is the average value and (σ) is the corresponding standard deviation of sample values. Lastly, the third method (M3) was the maximum likelihood method, where median and corresponding dispersion were estimated as follows:

$$\tilde{m} = e^{\frac{1}{N}\sum_{i=1}^{N}\log(y_i)}, \quad \bar{m}_{\log Y} = \log(\tilde{m}), \tag{8}$$

$$\beta = \sqrt{\frac{1}{N}\sum_{i=1}^{N}\left(\log(y_i) - \bar{m}_{\log Y}\right)^2}, \tag{9}$$

where y_i is the i-th sample value and N is size of the sample.

The results for estimated median and dispersion of the seismic response parameters with respect to the three adopted methods are presented in Tables 2 and 3.The notations DET and LHS relate, respectively, to the results based on deterministic and the stochastic structural model.

It can be observed (Table 2) that the median peak ground accelerations ($\tilde{a}_{g,C}$) are very similar if estimated with the N2 method and the approximate IDA. The average value of $\tilde{a}_{g,C}$ for deterministic structural model estimated by the approximate IDA equals to 1.43 g, which is only around 6 % higher to that obtained with the N2 method ($\tilde{a}_{g,C}$ = 1.35 g). The estimated $\tilde{a}_{g,C}$ is larger if compared to that, which was obtained in the study conducted by Rozman and Fajfar [23] ($\tilde{a}_{g,NC}$ = 0.77 g), since adopted top displacement at the near collapse limit state was significantly smaller than that defined for the case of this study.

A slightly higher difference between the results of the approximate IDA and the N2 method presented in Tale 2 can be observed for the case if epistemic uncertainties are incorporated in the analysis. In that case, the average value of $\tilde{a}_{g,C}$ is reduced and amounts to 1.25 and 1.14 g if estimated by using the approximate IDA and the N2 method, respectively. However, in the contrast to the median peak ground acceleration, the predicted median displacement capacity strongly depends on the way how the limit state is defined. For example, the estimated median displacement capacity for deterministic structural model varies, respectively, from 0.39 m to 0.64 m (by the average), if calculated for the NC limit state as adopted for the N2 method, or for the ultimate limit state as adopted for the approximate IDA. Note that probably none of these values is not correct but represent more or less the boundaries in the prediction of the ultimate displacement capacity of the example structure, suggesting that the displacement at the ultimate limit state as defined in the case of the approximate IDA most probably overestimates the structural displacement capacity due to the adopted structural model, whereas the displacement capacity at NC limit state as defined in the N2 method is rather a conservative estimate for the displacement capacity.

Another phenomenon, which can be observed by comparing the results in the Table 2, is that the median seismic capacity is typically reduced if epistemic uncertainties are considered in the analysis. Thus neglecting the epistemic uncertainties leads to unsafe prediction of median capacity. In the case of the approximated IDA, the median peak ground acceleration at the ultimate limit state is, by the average, around 12 % less than that, which was estimated in the case of the deterministic model. Similar, conclusion can be made based on the results of the N2 method. A relatively high shift in the prediction of median seismic response parameters for the ultimate limit state cannot be simply ignored.

Method		$\tilde{a}_{g,C}\left(g\right)$	Δ	$\tilde{D}_{t,C}\left(m\right)$	Δ
DET + N2		1.35	-	0.39	-
LHS + N2	M1	1.15	-15 %	0.36	-8 %
	M2	1.08	-20 %	0.31	-21 %
	M3	1.20	-11 %	0.35	-10 %
DET + app. IDA	M1	1.48	-	0.71	-
	M2	1.33		0.59	
	M3	1.49		0.64	
LHS + app. IDA	M1	1.26	-15 %	0.61	-20 %
	M2	1.19	-11 %	0.53	-10 %
	M3	1.32	-11 %	0.58	-9 %

Table 2: The median seismic response parameters ($\tilde{a}_{g,C}$ and $\tilde{D}_{t,C}$) estimated by using the approximate IDA and the N2 method. The relative contribution of the epistemic uncertainties to the reduction of the median capacity is also shown and calculated as Δ = (LHS - DET) / DET.

Important results of this study are the dispersion measures in seismic demand and capacity. Based on the results presented in Table 3, the highest dispersion can be observed for the peak ground accelerations at the ultimate limit state. For example, the average β_{agCR} is 0.57 if only the results based on the second and the third statistical methods (M2 and M3) are considered.

The results of the counting method are excluded, since, it provides overestimated value for β_{agCR} if compared to that determined by the method of moment or maximum likelihood method.

Much smaller dispersion is observed for the displacement corresponding to the ultimate limit state. In this case, by the average, the dispersion in top displacement for the aleatory uncertainties amounts to around 0.24. However, the latter dispersion is slightly increased to the value of 0.26 if the epistemic uncertainties are incorporated into the model. This is true also for the IM-based response parameter. In particular, the dispersion for the peak ground acceleration at the ultimate limit state due to the aleatory and epistemic uncertainties β_{agCRU} increased, by the average, from 0.57 to 0.59. It is a very small increase in the dispersion. For the presented example can be therefore concluded that that epistemic uncertainties have in the contrast to the median estimates of seismic capacity almost negligible influence to the overall dispersion in structural seismic performance.

The dispersion measures in top displacement demand have been calculated for the peak ground acceleration 0.4 g, which approximately corresponds to the seismic intensity at which the 84th fractile IDA curve, if determined with consideration of epistemic uncertainties, becomes horizontal. However, by the average, the dispersion in the displacement demand due to the aleatory uncertainties β_{DR} amounts to 0.44. The dispersion in displacement demand due to aleaotry and epistemic uncertainty β_{DRU} cannot be determined by utilizing the method of moments or the maximum likelihood method since, for some cases, the collapse was attained at a_g=0.4 g. Therefore, β_{DRU} was estimated by using the counting method and equals to 0.49.

In addition, the Table 3 represents also the dispersion measures due to the epistemic uncertainties, which have been determined in the previous study [13] by applying the N2 method. These values amount to around 0.30 and 0.31, respectively, for the peak ground acceleration and the top displacement at the NC limit state and can be used to calculate the total dispersion in structural seismic performance by using the square root of the sum of the squares of the dispersions for aleatory and epistemic uncertainties.

Method		Peak ground accel. ($a_{g,C}$)		Displ. Capacity (C)		Displ. Demand (D)	
LHS + N2	M1	β_{agCU}	0.27	β_{CU}	0.33	β_{DU}	0.11
	M2		0.30		0.30		0.09
	M3		0.31		0.31		0.09
DET + app. IDA	M1	β_{agCR}	0.72	β_{CR}	0.25	β_{DR}	0.46
	M2		0.56		0.21		0.44
	M3		0.58		0.25		0.43
LHS + app. IDA	M1	β_{agCRU}	0.64	β_{CRU}	0.26	β_{DRU}	0.49
	M2		0.58		0.24		-
	M3		0.60		0.27		-

Table 3: The dispersion measures due to the aleatory uncertainty (randomness) $(\beta_{agCR}, \beta_{CR}, \beta_{DR})$ from approximate IDA, the dispersions due to aleatory and epistemic uncertainty $(\beta_{agCRU}, \beta_{CRU}, \beta_{DRU})$ determined based on the approximate IDA, and the dispersion measures due to epistemic uncertainty $(\beta_{agCU}, \beta_{CU}, \beta_{DU})$ determined by the N2 method.

4 CONCLUSIONS

In the presented study, a methodology for fast seismic performance assessment was presented. The procedure involves approximate IDA by using the web application. The effects of the epistemic uncertainties are considered by the set of structural models, which are determined by utilizing the Latin Hypercube Sampling (LHS) technique. The outcomes of this process are the seismic response parameters in terms of the median seismic capacity and corresponding dispersion measures, which can be estimated considering both the aleatory and epistemic uncertainties.

The use of the presented methodology was illustrated by applying it to the case of three storey RC frame building. For the example structure it was shown that the aleatory and epistemic uncertainties strongly affect the overall dispersion in seismic performance of structure. It was also shown that neglecting the epistemic uncertainty potentially leads to unsafe design, since median seismic capacity at ultimate limits state can be overestimated if epistemic uncertainties are neglected in the analysis. For example, the median seismic capacity is reduced for about 11 - 15 % if epistemic uncertainties are incorporated into the approximate IDA.

All the analyses have been performed by using the PBEE toolbox in conjunction with the OpenSees. It was proved as a very powerful toll for fast seismic performance assessment of structures, since it allows performing a numerous number of the required computational simulations enables quick post-processing of the results and damage visualization on the structure for different limit state and for different structural models.

ACKNOWLEDGEMENTS

The results presented in this paper are based on work supported by the Slovenian Research Agency (Project J2-0845, High-throughput computing environment for seismic risk assessment, http://ice4risk.slo-projekt.info/). This support is hereby gratefully acknowledged.

REFERENCES

[1] H. Aslani, E. Miranda, *Probabilistic Earthquake Estimation and Loss Disaggregation in Buildings.* The John A. Blume Earthquake Engineering Center, Department of Civil and Environmental Engineering, Stanford University, 2005.

[2] L.F. Ibarra, H. Krawinkler, *Global Collapse of Frame Structures under Seismic Excitation.* The John A. Blume Earthquake Engineering Center, Department of Civil and Environmental Engineering, Stanford University, 2005.

[3] AB. Liel, C.B. Haselton, G.G. Dierlein, JW. Baker, Incorporating modeling uncertainties in the assessment of seismic collapse risk of buildings. *Structural Safety,* **31**: 197-211, 2008.

[4] F. Jalayer, I. Iervolino, G. Manfredi, Structural modeling uncertainties and their influence on seismic assessment of existing RC structures. *Structural Safety*, **32**: 220-228, 2010.

[5] M. Dolsek, Incremental Dynamic Analysis with consideration of modeling uncertainties. *Earthquake Engineering and Structural Dynamics,* **38**(6): 805-825, 2009.

[6] D. Vamvatsikos, M. Fragiadakis, Incremental dynamic analysis for estimating seismic performance sensitivity and uncertainty. *Earthquake Engineering and Structural Dynamics*, **39**(2): 141-163, 2010.

[7] O.C. Celik, B.R. Ellingwood, Seismic fragilities for non-ductile reinforced concrete frames – Role of aleatoric and epistemic uncertainties. *Structural Safety*, **32**: 1-12, 2010.

[8] I. Peruš, R. Klinc, M. Dolenc and M. Dolšek. Innovative computing environment for fast and accurate prediction of approximate IDA curves. *Proceedings of the COMPDYN 2011, III ECCOMAS Thematic Conference on Computational Methods in Structural Dynamics and Earthquake Engineering (M. Papadrakakis, M. Fragiadakis, V. Plevris (eds.))*, Corfu, Greece, 26–28 May, 2011.

[9] M. Vořechovský, D. Novák, Correlation control in small-sample Monte Carlo type simulations I: A simulated annealing approach. *Probabilistic Engineering Mechanics,* **24** (2): 452-462, 2009.

[10] D. Vamvatsikos, C.A. Cornell, Direct estimation of the seismic demand and capacity of oscillators with multi-linear static pushovers through IDA. *Earth. Engineering & Structural Dynamics*, **35**: 1097–1117, 2006.

[11] CEN. Eurocode 8: Design of structures for earthquake resistance. Part 1: General rules, seismic actions and rules for buildings, EN 1998-1. CEN, Brussels, December 2004.

[12] P. Fajfar, A nonlinear analysis method for performance-based seismic design. *Earthquake Spectra*, **16**(3):573-592, 2000.

[13] D. Celarec, M Dolsek, A simplified Method for Seismic Performance Assessment of RC Frames with Consideration of Epistemic Uncertainties. *Proceedings of the International Symposium on Reliability Engineering and Risk Management (J. Li, Y-G. Zhao, J. Chen, Y. Peng)*, Shanqhai, China, 23-26 September, 2010.

[14] I. Peruš, K. Poljanšek, P. Fajfar, Flexural deformation capacity of rectangular RC columns determined by the CAE method. *Earthquake Engineering and Structural Dynamics*, **35**:1453-1470, 2006.

[15] CEN. Eurocode 8: Design of structures for earthquake resistance. Part 3: Strengthening and repair of buildings. *EN 1998-3*, European Committee for Standardisation, Brussels, March 2005.

[16] F. McKenna F, G.L. Fenves, Open system for earthquake engineering simulation, Pacific Earthquake Engineering Research Center, Berkeley, California, 2004. http://opensees.berkeley.edu/

[17] M. Dolšek, Development of computing environment for the seismic performance assessment of reinforced concrete frames by using simplified nonlinear models. *Bulletin of Earthquake Engineering*, **8**(6): 1309-1329 (in press).

[18] RE. Melchers, *Structural reliability analysis and prediction.* John Wiley & Sons, 1999.

[19] JCSS, *Probabilistic Model Code Part III.* Joint committee on structural Safety, 2000.

[20] B. Ellingwood, T.V. Galambos, J.G. MacGregor, C.A. Cornell, *Development of a Probability-Based Load Criterion for American National Standard A58.* National Bureau of Standards, Washington DC, 1980.

[21] C.B. Haselton, *Assessing Seismic Collapse Safety of Modern Reinforced Concrete Moment Frame Buildings*. PhD, Stanford University, 2006.

[22] T.B. Panagiotakos, M.N. Fardis, Deformations of Reinforced Concrete at Yielding and Ultimate. *ACI Structural Journal,* **98**(2): 135-147, 2001.

[23] M. Rozman, P. Fajfar, Seismic response od a RC frame building designed according to old and modern practices. *Bulletin of Earthquake Engineering,* 7: 779-799, 2009.

COMPDYN 2011
3rd ECCOMAS Thematic Conference on
Computational Methods in Structural Dynamics and Earthquake Engineering
M. Papadrakakis, M. Fragiadakis, V. Plevris (eds.)
Corfu, Greece, 25–28 May 2011

PREDICTION OF SEISMIC RESPONSE PARAMETERS OF TYPICAL MASONRY BUILDING WITH CONSIDERATION OF EPISTEMIC UNCERTAINTIES

Jure Snoj[1], **Matjaž Dolšek**[1]

[1] University of Ljubljana, Faculty of Civil and Geodetic Engineering, Jamova 2, Ljubljana, Slovenia
e-mail: jure.snoj@fgg.uni-lj.si; mdolsek@ikpir.fgg.uni-lj.si

Keywords: Seismic risk; Masonry structure; Epistemic uncertainty; Latin hypercube sampling; Pushover analysis; IN2.

ABSTRACT. *The seismic risk assessment of structures is a complex problem, which combines seismic hazard analysis, structural vulnerability analysis and analysis of socio-economic impacts. In addition, seismic risk assessment, especially in the case of old masonry buildings, is subject to many uncertainties, not only due to the random nature of earthquakes but also due to physical and modeling uncertainties related to prediction of structural vulnerability. Recent studies have shown that epistemic (modeling) uncertainties can significantly affect seismic response parameters. However, uncertainty analysis usually involves simulations, and it is therefore computationally extremely demanding, especially if seismic response parameters are computed by using nonlinear dynamic analysis. Therefore, simplified nonlinear seismic performance assessment method is used to estimate seismic response parameters for a set of structural models, which are determined by utilizing the Latin Hypercube Sampling technique. The proposed method is demonstrated by means of an example of two masonry buildings, which are modeled and analyzed by using the computer program Tremuri. Results of the study indicate that the effects of epistemic uncertainties, in addition to aleatoric uncertainties, are significant.*

1 INTRODUCTION

A substantial part of built environment is represented by masonry buildings, which were mainly constructed in the past and are therefore not earthquake resistant structures. Consequently, earthquakes endanger this part of built environment and human lives more than thought. In order to contribute to the mitigation of seismic risk, advanced methods and tools should be developed, which will enable well-informed decision making, this being the key element for the future protection of built environment against earthquakes.

Probably the simplest closed-form solution for seismic risk assessment of structures expressed in terms of the mean annual frequency of exceeding a given limit state was proposed by Cornell et al. [1]. However, the most demanding part of the risk assessment procedure, i.e. the incremental dynamic analysis (IDA) [2], which enables direct evaluation of the record-to-record variability in structural response through a set of ground motion records, can be replaced with the IN2 analysis [3, 4]. These methods were applied in the study presented in the paper. However, several methods for estimating seismic risk of masonry structures exist. For example, a methodology for deriving analytical fragility curves for masonry buildings based on stochastic nonlinear analyses was introduced [5]. The method involves consideration of aleatoric and epistemic uncertainty since the nonlinear static (pushover) analyses are used to define the probability distributions of each damage state with consideration of epistemic uncertainties, while the incremental dynamic analysis for a set of ground motion records is performed to determine the probability density function of the displacement demand.

The effects of epistemic uncertainties are usually not explicitly considered for assessment of seismic risk of structure since this task is computationally demanding and requires sophisticated software tools. Therefore, only approximate methods for seismic performance assessment of structures with consideration of epistemic uncertainties can be adopted for practical purposes. Such a method, which combines the IN2 [3, 4] and a set of structural models determined by utilizing the variant of Latin Hypercube Sampling (LHS) technique [6], is presented in this paper. In its first part the method is briefly summarized, while in the second part its use is demonstrated by means of two examples of three-storey buildings, which were analyzed by structural analysis program - Tremuri [7].

2 SEISMIC RISK ASSESSMENT METHOD

Seismic risk of a building can be, in its most basic formulation, estimated with the mean annual frequency of exceeding a defined limit state (LS), which can be determined as follows:

$$P_{\mathrm{LS}} = \int_0^\infty P\left(LS \middle| I_M = i_m\right) \cdot \left| \frac{dH\left(i_m\right)}{di_m} \right| \cdot di_m \tag{1}$$

where $P\left(LS \middle| I_M = i_m\right)$ is the probability of exceeding limit state (LS) if the intensity measure I_{M} is equal to i_{m}. Hazard function $H(i_m)$ is usually expressed in terms of mean annual frequency that the intensity measure I_{M} will be larger or equal to i_{m} and can be approximated as [1]:

$$H\left(i_m\right) = k_o \left(i_m\right)^{-k} \tag{2}$$

According to this assumption it follows, that the hazard function is linear in log-log coordinates.

The formulation of the seismic risk according to Eq.(1) is the so called IM-based formulation and requires definition of the intensity measure (i_{m}), which is the peak ground acceleration (a_g) in the case of this study. Cornell had shown that mean annual frequency of exceeding given limit state can be, according to Eqs. (1) and (2) expressed as follows:

$$\lambda_{\mathrm{LS}} = H\left(\tilde{a}_{g,LS}\right)\cdot e^{\frac{1}{2}\cdot k_{LS}^2\cdot \beta_{LS}^2} = k_o\cdot\left(\tilde{a}_{g,LS}\right)^{-k_{LS}}\cdot e^{\frac{1}{2}\cdot k_{LS}^2\cdot \beta_{LS}^2} \tag{3}$$

where $\tilde{a}_{g,LS}$ is the median value of the IM-based capacity (i.e. the median peak ground acceleration which causes the given limit state), β_{LS} is the corresponding standard deviation of natural logarithms and k_{LS} is the slope of the hazard curve, which has to be estimated for each limit state.

Many different procedures exist, which can be used in order to estimate the fragility parameters $\tilde{a}_{g,LS}$ and β_{LS}. For example, the parametric analysis method IDA, which involves the nonlinear dynamic analysis for a set of ground motion records scaled to different levels of defined intensity measure, is probably the most accurate procedure for determination of fragility parameters. However, it is computationally extremely demanding, especially, if IDA is extended by the set of structural models in order to consider effects of epistemic uncertainties [8]. Two alternative, practice-oriented approaches are the approximate IDA performed by using an equivalent single-degree-of-freedom (SDOF-IDA) model [9] and the N2 method [3,4].

The approximate IDA is more accurate, since both fragility parameters can be evaluated by taking into account the record-to-record variability. The N2 method, which was used in the paper, provides mean estimates for limit-state intensities (e.g. peak ground acceleration corresponding to limit state - $a_{g,LS}$) with respect to record-to-record variability (aleatoric uncertainty), but its dispersion has to be predetermined or assumed. Since λ_{LS} is estimated based on the median $\tilde{a}_{g,LS}$, it was conservatively assumed that $\bar{a}_{g,LS} \approx \tilde{a}_{g,LS}$.

In addition to aleatoric uncertainty, the epistemic uncertainties can also significantly affect the fragility parameters. They are knowledge-based and are most often related to the physical properties of the structure and its modelling parameters. In this study epistemic uncertainties are treated by using the LHS technique [6], which is summarized in the Section 2.1. The result of the LHS technique is N_{sim} structural models and consequently N_{sim} peak ground accelerations corresponding to predetermined limit state are obtained.

The median $\tilde{a}_{g,LS}$ and the dispersion β_{LS} in general depends on the method used for their estimation. In the case of this study the fragility parameters were estimated according to the method of moments, as follows:

$$\tilde{a}_{g,LS} = \bar{a}_{g,LS}\cdot e^{-0.5\cdot\beta_{LS}^2} \tag{4}$$

$$\beta_{LS} = \sqrt{\ln\left(\frac{\sigma^2}{\bar{a}_{g,LS}^2}+1\right)} \tag{5}$$

where $\bar{a}_{g,LS}$ and σ^2 are the sample mean and corresponding variance. In addition to LHS method, which is briefly summarized in next section, a procedure for determining the equivalent SDOF model, which is employed for estimation of the fragility parameters, is also briefly described in the Section 2.2.

2.1 Summary of the Latin Hypercube Sampling technique

The Latin Hypercube Sampling technique [10] uses stratification of the probability distribution function of the random variable X_i, therefore it requires fewer simulations as Monte Carlo method. Within the proposed methodology, the efficient LHS technique, which was recently proposed by Vořechovský and Novák [6], is used and it can be applied for any probability distribution of random variables and the target correlation matrix.

The sample matrix can be calculated in two steps. In the first step, each random variable is sampled using N_{sim} values, which is shown in Figure 1. Firstly, the codomain of the cumulative distribution function is divided into k intervals, each having the length of $1/N_{sim}$. The k-th sample value of the i-th random variable ($x_{i,k}$) is determined based on the mean probability related to each interval as follows:

$$x_{i,k} = \frac{\int_{a_{i,k-1}}^{a_{i,k}} x \cdot f_{Xi}(x)\,dx}{\int_{a_{i,k-1}}^{a_{i,k}} f_{Xi}(x)\,dx} = N_{Sim} \cdot \int_{a_{i,k-1}}^{a_{i,k}} x \cdot f_{Xi}(x)\,dx \tag{6}$$

where $f_{Xi}(x)$ is the probability density function of the random variable X_i, while $a_{i,k-1}$ and $a_{i,k}$ are the values of random variable X_i, which correspond, respectively, to the probability at the lower and the upper range of the k-th interval (Figure 1). Boundaries of the interval are estimated as follows:

$$a_{i,k} = F_{Xi}^{-1}\left(\frac{k}{N_{sim}}\right) \tag{7}$$

where $f_{Xi}(x)$ is the inverse of the cumulative distribution function of the random variable X_i.

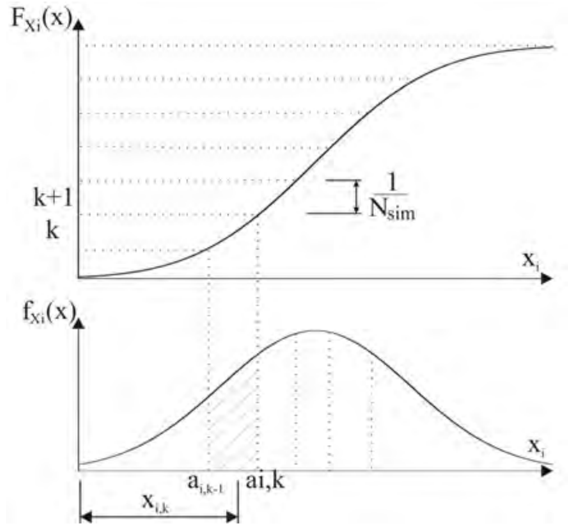

Figure 1: Sampling of random variable X_i according to the Latin Hypercube Sampling technique.

Such sampling is more accurate with respect to the sampling based on the probabilities in the middle of equidistant intervals since the influence of the data in the tails of probability density function on the variance is smaller [6].

Especially in the case of very small number of samples, undesired correlation can occur between random variables. In this case generated correlation matrix **S** significantly deviates from the prescribed (target) correlation matrix **K**. The difference between **S** and **K** is minimized by using the stochastic optimization method called "simulated annealing". It was first used in metallurgy and has some advantages, since its algorithm is very robust and it makes it possible to search for a global minimum.

In order to formulate the optimization problem, a suitable measure for difference between correlation matrices has to be defined. In the case of discussed problem, the norm E which takes into account deviations of all correlation coefficients simultaneously, is a good fitness function, which can be minimized by permutation of elements in sample matrix **X**. It is defined as follows:

$$E = \frac{2}{N_{\mathrm{var}}\left(N_{\mathrm{var}}-1\right)}\sqrt{\sum_{i=1}^{N_{\mathrm{var}}-1}\sum_{k=i+1}^{N_{\mathrm{var}}}\left(S_{\mathrm{i,k}}-K_{\mathrm{i,k}}\right)^2} \tag{8}$$

where $S_{i,k}$ and $K_{\mathrm{i,k}}$ are the coefficients of the generated and target correlation matrix, respectively, and N_{var} is the number of random variables X_i.

Optimization is an iterative procedure, where each iteration consists of two steps: mutation and selection. Mutation represents the change of the ranks of two randomly selected elements of random variable X_i, while selection makes it possible to decide if the new arrangement of the random variable X_i is acceptable or not. According to the simulated annealing algorithm, the new arrangement is automatically accepted if it results in a decrease of the norm E, otherwise new arrangement is accepted only if the random variable Z, which is defined in Eq. (9), is positive.

$$Z = e^{-\frac{\Delta E}{T}} - R \tag{9}$$

where ΔE is the difference in norms E before and after random change of the ranks, R is uniformly distributed random variable in the interval [0,1] and T is the so-called temperature, which comes from annealing in metallurgy. Note that the initial temperature has to be defined in the algorithm and it is decreased step by step after a certain number of mutations, by using a reduction factor, which has the value 0.95, as recommended in [6].

The result of the optimization is optimized sample matrix **X**, which has N_{sim} rows and its' i-th row represents i-th structural model.

2.2 The equivalent SDOF model

In this Section the definition of the equivalent SDOF model, which is determined based on the results of the pushover analysis, is briefly described. More details regarding the definition of the equivalent SDOF model can be found elsewhere [4].

It is defined that the lateral loads used in the pushover analysis correspond to the product of mass matrix **M** and the vector $\boldsymbol{\phi}$ related to assumed deformation shape, which has the value 1 at the location of the top displacement ($\varphi_n = 1$), and is assumed proportional to the first mode shape. In this case, the pushover curve corresponding to the equivalent SDOF model (F^* and m^*) is determined based on the pushover curve of the structural model by dividing the base shear F and top displacement D with the transformation factor Γ, which is defined as follows:

$$\Gamma = \frac{m^*}{\sum_{i=1}^{n} m_i \phi_i^2}, \quad m^* = \sum_{i=1}^{n} m_i \phi_i \tag{10}$$

where m_i and φ_i are masses and normalized deformations at the location of the i-th storey, and m^* is the mass of the equivalent SDOF model. The pushover curve of equivalent SDOF model has to be idealized with suitable force-displacement relationship. The corresponding initial stiffness (F_y^* / D_y^*) and the mass of the equivalent SDOF model define its period:

$$T^{*} = 2\pi\sqrt{\frac{m^{*}D_{y}^{*}}{F_{y}^{*}}} \tag{11}$$

where F_y and D_y are, respectively, yield force and yield displacement of the equivalent SDOF model.

3 EXAMPLE

The proposed methodology is demonstrated by means of seismic risk assessment of two three storey masonry buildings. Fragility parameters are estimated with approximate procedure involving N2 method. Results of both buildings are compared and the influence of epistemic uncertainties is discussed.

3.1 Description of the structures and structural models

The first example structure is a three-storey unreinforced masonry building A (Figures 2, 3 - left), which was selected from literature [11]. This building is symmetric around the Y axis and has 5.3 % of shear walls in the Y direction and 5.6 % shear walls in the X direction. Wall thickness is equal to 30 cm and storey height of all floors is equal to 2.8 m.

The second three-storey structure (building B, Figures 2, 3 - right) was derived from the geometry of SPEAR building [12], which was transformed into masonry building by adopting wall thickness equal to 30 cm, which amounted to 7.8 % of shear walls in X direction and 8.1 % walls in Y direction. The height of the first floor of the building B is 2.75 m, while the height of other stories is 3 m.

Both buildings have concrete slabs, which are considered as rigid diaphragms. At each floor level of both buildings, all walls are connected with continuous concrete beams with depth of 30 cm, which are reinforced with four 16 mm rebar (two at the bottom and two at the top) and 2 leg stirrups with 6 mm diameter at 25 cm spacing.

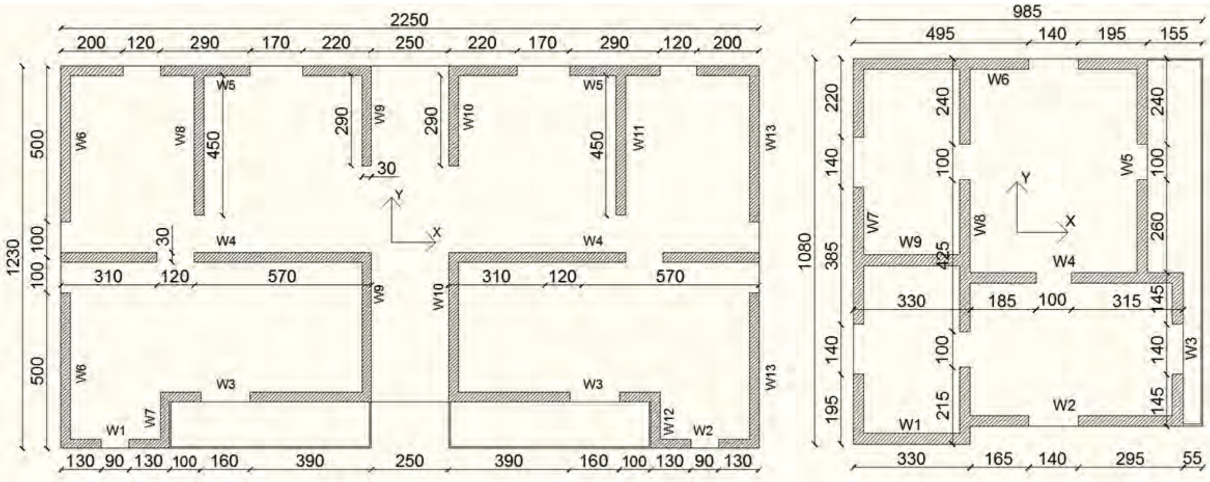

Figure 2: The plan of the building A (left) and building B (right)

Models of both buildings were made by using program 3Muri [13], specialized for seismic analysis and performance assessment of masonry structures, while the analysis was performed by using research version of the same program, Tremuri, which was developed at the University of Genoa [7]. The program is based on effective macro-element approach and enables accurate modelling, nonlinear pushover and time history analysis of masonry buildings at very small computational burden [14]. Program models nonlinear behaviour of masonry piers and lintels with flexural and shear hinges, defined by a bilinear ideally elasto-plastic moment-rotation or force-displacement relationship, where ultimate drifts are defined for sliding shear mechanism (δ_s) and for flexural collapse mechanism (δ_f).

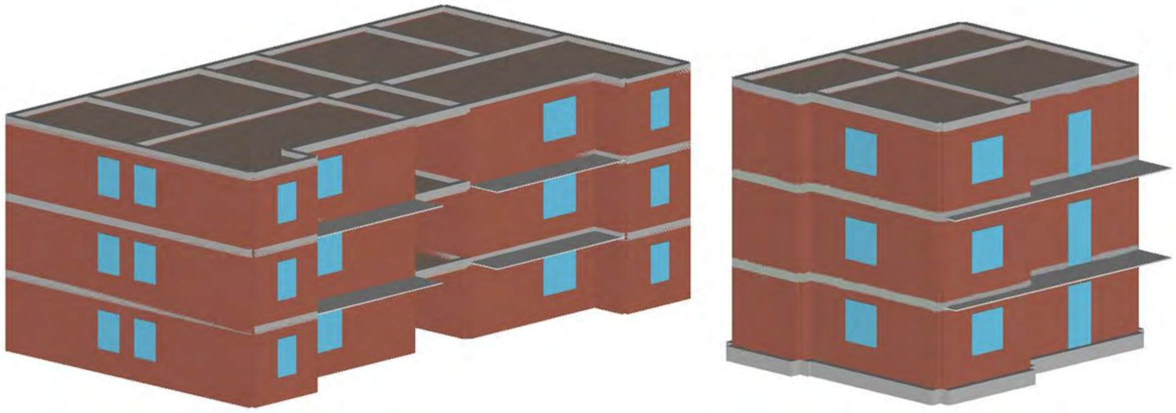

Figure 3: 3D view of the model A (left) and model B (right)

The vertical loads for both buildings, considered in the pushover analysis, are presented in the Table 1. Note that the live load was combined with the self weight by assuming combination factors 0.3 on the roof and 0.15 elsewhere.

Type of load	Building A	Building B
Self weight of masonry walls	16 kN/m^3	16 kN/m^3
Self weight and dead load of floors	5 kN/m^2	4.3 kN/m^2
Self weight and dead load of balconies	5 kN/m^2	4.3 kN/m^2
Self weight and dead load of staircase	5 kN/m^2	5 kN/m^2
Live load on floors	2 kN/m^2	2 kN/m^2
Live load on the staircase and balconies	4 kN/m^2	2.5 kN/m^2

Table 1: The self weight and the live loads used for definition of vertical load on the structure.

3.2 Uncertain parameters

In the case of this study some material and modelling parameters were considered uncertain. These parameters are: Young's modulus E, shear modulus G, compression strength of masonry wall f_m, initial shear strength f_{v0}, friction coefficient μ, nonlinear deformability parameter G_c, softening parameter β and ultimate drift ratios δ_s and δ_f that correspond to the shear and flexural collapse of masonry element, respectively.

The mean values of the uncertain parameters and corresponding coefficients of variation were adopted from literature [5] due to the lack of our own experimental data and are presented in Table 2. Normal distribution was assumed for all random variables.

Majority of the correlation coefficients between random variables was assumed 0. However, correlation coefficients between E, G, f_m, f_{vk0} were determined based on experimental data [15].

The optimized sample matrix **X** was determined according to the LHS technique, described in section 2.1, by assuming N_{sim} = 30. The norm E has a very low value of 0.0005 and the maximum difference between optimized and prescribed correlation matrix component is only 0.01. Therefore it was assumed, that the sample of uncertain parameters is appropriate for further analysis, although it cannot be claimed that the size of the sample is large enough in order to guarantee prediction of seismic response parameters with sufficient accuracy.

Thirty structural models were generated, since i-th row in optimized sample matrix **X** represented a set of input parameters for i-th model in the case of both buildings. Additionally, deterministic models with mean material characteristics were used for comparison with stochastic models.

Name of the variable	Mean	COV	Distribution	Ref
Elastic modulus E [MPa]	1620	0.08	Normal	[5]
Shear modulus G [kN/m^2]	625	0.10	Normal	[5]
Compressive strength f_m [MPa]	1.95	0.19	Normal	[5]
Initial shear strength f_{v0} [MPa]	0.153	0.16	Normal	[5]
Friction coefficient μ [-]	0.065	0.12	Normal	[5]
Deformability parameter G_c [-]	7	0.21	Normal	[5]
Softening parameter β [-]	0.3	0.17	Normal	[5]
Shear drift ratio δ_s [%]	0.4	0.10	Normal	Assumed
Flexural drift ratio δ_f [%]	0.8	0.10	Normal	Assumed

Table 2: The statistical characteristics of the input random variables.

3.3 Definiton of near collapse limit-state

The seismic risk was estimated for the near collapse (NC) limit-state, which was at the top displacement that corresponds to the 80% of the building's shear resistance, which is measured in the range beyond the post-capping point of the pushover curve. Definition of more severe limit-state, i.e. the complete collapse of building, was omitted in this study, since numerical model does not consider all phenomena, which occur in extremely nonlinear behaviour of structure.

Note that the NC limit state depends on the ultimate drift ratio, which differs for shear and flexural collapse mechanism and consequently from model to model.

3.4 Acceleration spectrum and seismic hazard

The seismic action is defined with the elastic acceleration spectrum according to the Eurocode 8 - soil type A, which is shown in Figure 4 (left).

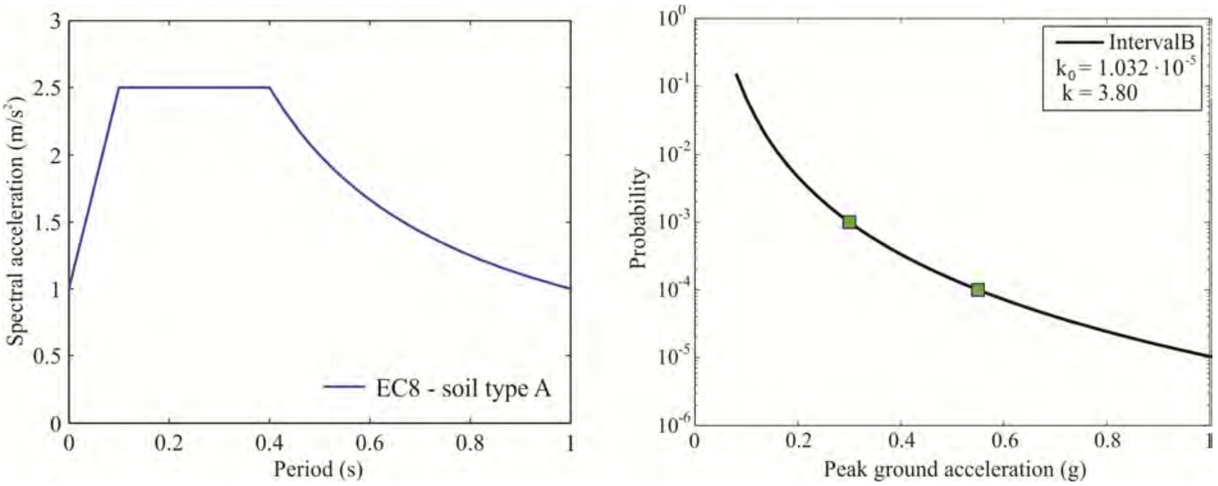

Figure 4: The Eurocode-based acceleration spectrum for soil type A (left) and the hazard curve defined based on the hazard map for return periods of 1000 and 2475 years (right).

The parameters of seismic hazard curve were computed from data, available on the website of the Environment Agency of the Republic of Slovenia [16]. The peak ground accelerations for Ljubljana, soil type A, and return periods of 475 years (10%/50), 1000 years (5%/50) and 2475 years (2%/50), amount to: 0.25 g, 0.30 g and 0.55 g, respectively. Since only two points on the hazard curve are needed in order to calculate parameters k_0 and k (Eq.(2)), it was decided to use the peak ground accelerations corresponding to the return periods of 1000 and 2475 years in order to interpolate the hazard curve in the vicinity of the limit-state intensity $\tilde{a}_{g,LS}$. The resulting curve, which is defined with parameters $k_0 = 1.03 \cdot 10^{-5}$ and $k = 3.8$, is presented in Figure 4 (right).

3.5 Pushover analysis

Pushover analyses for deterministic (mean-valued) model and 30 structural models resulting from LHS technique were performed in Y direction for a building A, and in X direction for a building B, by using the Tremuri [7]. The resulting pushover curves are shown in Figure 5. The force pattern for all pushover analyses was proportional to the product of masses and displacements at first mode shape in the Y direction.

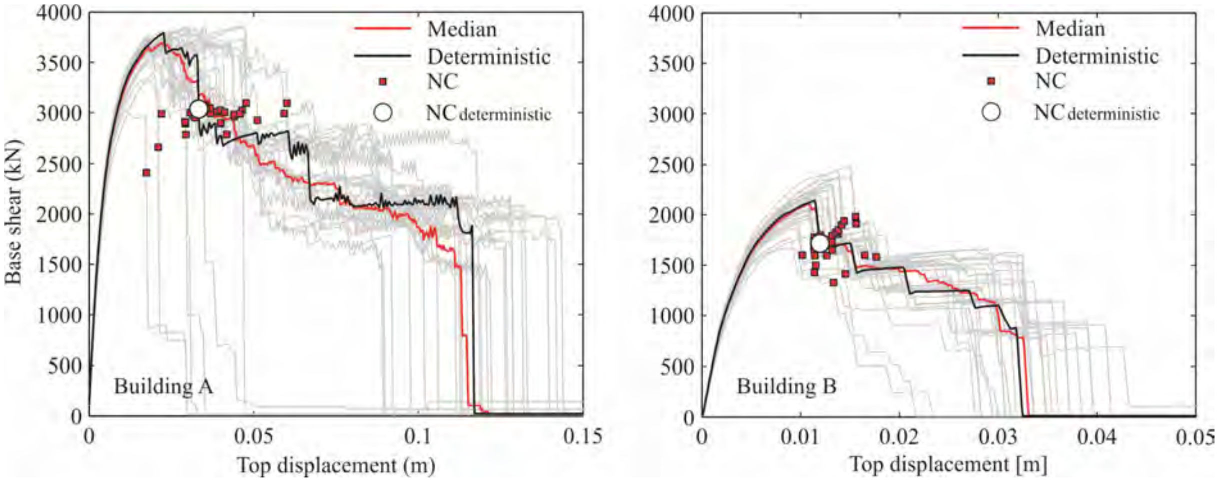

Figure 5: Pushover curves and points indicating the NC limit state for building A (left) and building B (right).

Shear resistance coefficient, which is defined as the ratio between resistance of the building and its weight, has a large value of 0.4 for a building A, and very large value of 0.6 for a building B, due to high percentage of walls in the case of both buildings. In both cases, quite small difference is observed between the median pushover curve, which represents median values of base shear at a given top displacement and the pushover curve of deterministic model.

Red points represent top displacements and corresponding base shears for the NC limit state, which is defined at 80 % of base shear resistance. Similarly, the white circle represents NC limit state of deterministic model. The coefficient of variation of the top displacement at NC limit state for building A is 0.27 and exceeds the coefficient of variation of the corresponding base shear (0.05) for more than five times. The reason for high coefficient of variation of top displacement is not only the high dispersion of the ultimate drift ratios, but also the fact, that uncertainty has the effect on the formation of different plastic mechanisms, which were in this study observed only for building A and are presented in Figures 6, 7 and 8. Different colours in piers represent different failures: red - flexural collapse, yellow - shear collapse and blue - undamaged.

In Figure 6, collapse mechanism of model A8, which occurred at the minimum top displacement ($d_{NC,SDOFA8} = 0.018$ m), is shown. Sudden large drop of base shear observed in the pushover curve is the consequence of simultaneous shear-collapse of several walls in the ground floor (for definition of walls see Figure 2 - left). Such collapse mechanism was expected since the initial shear strength of walls in model A8 is the lowest among these of 30 models and, in addition, the compressive strength and ultimate drift ratios δ_s and δ_f are also low. On the other hand (Figure 7), plastic mechanism of model A27 corresponds to the maximum top displacement ($d_{NC,SDOFA27} = 0.045$ m). At $d_{NC,SDOFA27}$ only a few elements in walls W6 and W13 fail, but at larger displacement, flexural-collapse of all piers in the second storey is observed. In this case, the initial shear strength and ultimate shear-drift ratio are very large, which governs flexural collapse and consequently NC limit-state is attained at larger top displacement. For comparison reasons, plastic mechanism of deterministic model (model A31) is also presented (Figure 8). In this case, structural elements gradually collapse in shear or in flexure at different storeys.

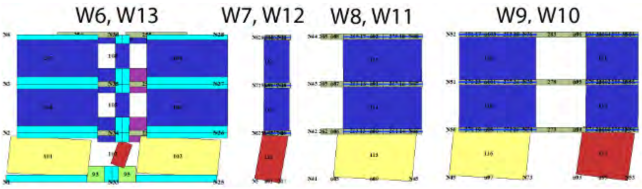

Figure 6: Plastic mechanism corresponding to the NC limit state for Model A8 - minimum top displacement.

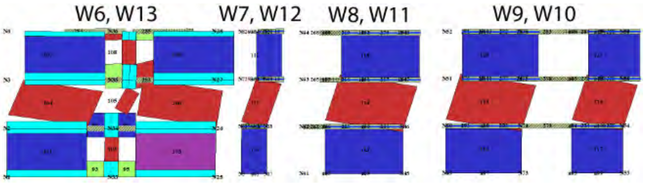

Figure 7: Plastic mechanism corresponding to the NC limit state for Model A27 – maximum top displacement.

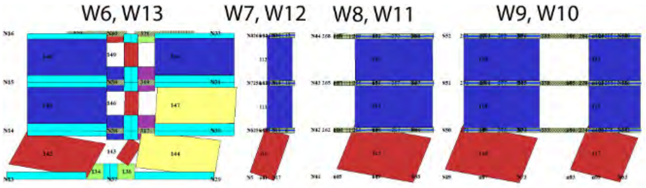

Figure 8: Plastic mechanism corresponding to the NC limit state for deterministic model A31.

In building B, the coefficient of variation in the maximum force at NC limit state is 0.09 and the coefficient of variation of the top displacement is only 0.13, which is much smaller than that obtained for building A. Namely, only one plastic mechanism forms in the case of building B - the soft storey effect in the ground floor. Firstly, element 46 (Figure 9) fails in shear and later other walls in the ground floor collapse in shear or bending. The strength of the element 46 is approximately 20 % of the strength of first storey, therefore it controls the attainment of NC limit state. In some cases the NC limit state is controlled by more than one wall, since the strength of element 46 is less than 20 % of the strength of the first storey. However, variability in NC displacements is relatively small, from 1 cm to 1.77 cm, where the smallest top displacement corresponds to the smallest δ_s.

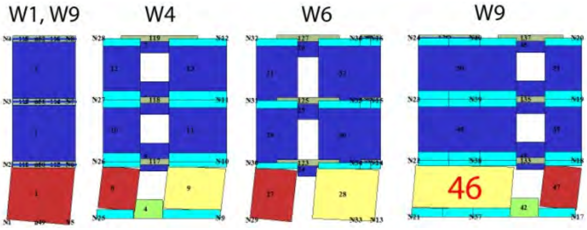

Figure 9: Plastic mechanism corresponding to the NC limit state for model B24.

In order to compute peak ground acceleration that causes the structure to violate the defined NC limit state, pushover curves were idealized using bi-linear force-displacement relationship (Figure 10). It was assumed, that initial stiffness of the equivalent SDOF model is defined based on the pushover curve at 70 % of the base shear resistance. Maximum base shear F_y of the idealized force-displacement relationship is calculated by assuming equal area under the pushover curve and idealized force-displacement relationship, if measured in the interval of displacements from 0 to the displacement d_{NC}, when maximum base shear decreases by 20 % (NC limit state (d_{NC}, F_{NC})). The described idealized force-displacement relationship of pushover curves represents input data for definition of equivalent SDOF model and is shown in Figure 10 for building A.

The force-displacement relationship of equivalent SDOF models were determined by dividing forces and displacements with the transformation factor Γ, having a mean value $\Gamma_{mean,A} = 1.33$ and $\Gamma_{mean,B} = 1.37$ for the building A and B, respectively. The masses of the equivalent SDOF models m^* of building A and B amounted to, respectively, 532 t and 230 t.

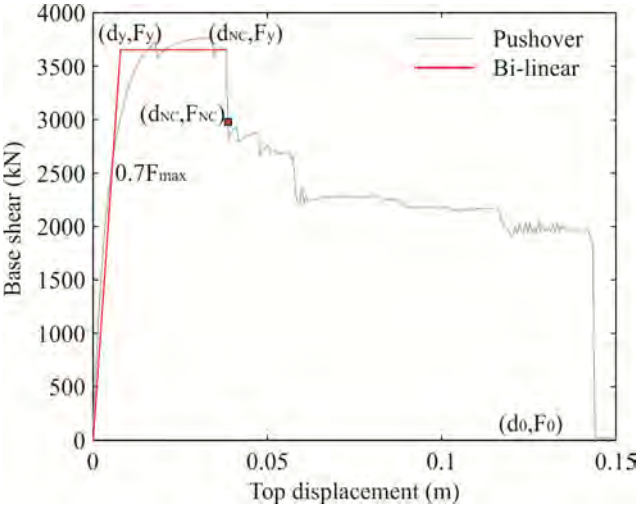

Figure 10: Idealized bi-linear force-displacement relationship of pushover curve.

3.6 Fragility parameters and seismic risk estimation

The fragility parameters were determined by utilizing the N2 method with consideration of epistemic uncertainty. The IN2 curve, as presented in Figure 11, and peak ground acceleration $a_{g,NC}^{IN2}(l)$ were determined for each model of both buildings.

In Table 3 the fragility parameters, estimated based on the procedure described in Section 2, are presented. Median peak ground acceleration and its dispersion were determined with consideration of epistemic uncertainty (U) according to Eqs. (4) and (5).

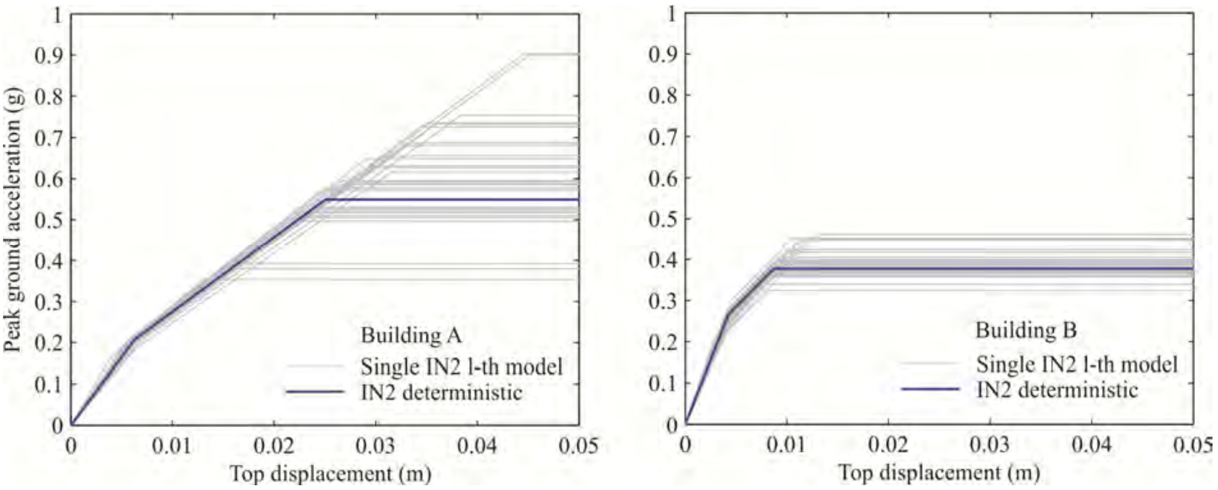

Figure 11: IN2 curves, based on 30 structural models and deterministic model for building A (left) and building B (right).

	Building A				Building B			
Method	$\tilde{a}_g(g)$		β		$\tilde{a}_g(g)$		β	
IN2$_{30}$	$\tilde{a}_{gU,A}^{IN2}$	0.59	$\beta_{U,A}^{IN2}$	0.21	$\tilde{a}_{gU,B}^{IN2}$	0.39	$\beta_{U,B}^{IN2}$	0.08
IN2$_{\text{det}}$	$a_{g,\det,A}^{IN2}$	0.55	-	-	$a_{g,\det,B}^{IN2}$	0.38	-	-

Table 3: The fragility parameters for building A and B.

High estimated median peak ground accelerations, at which the NC limit state is attained, are observed in Table 3, mainly due to the high percentage of walls in both buildings. Further, the peak ground acceleration $\tilde{a}_{g,\det,A}^{IN2}$, that corresponds to deterministic model, is slightly smaller than the median peak ground acceleration $\tilde{a}_{gU,A}^{IN2}$, which corresponds to stochastic model. An opposite was observed for building A, if fragility parameters were assessed by conducting nonlinear dynamic analysis for the equivalent SDOF model. However, the difference between $\tilde{a}_{g,\det,A}^{IN2}$ and $\tilde{a}_{gU,A}^{IN2}$ is very small.

The dispersions for $\tilde{a}_{gU}^{IN2}$ are 0.21 and 0.08, respectively, for building A and B. Quite small dispersion in the case of building B is the consequence of a small number of different plastic mechanisms that formed in this case. Namely, plastic mechanism affects displacement capacity and consequently the peak ground acceleration that causes the NC limit state.

In the Table 3, only epistemic uncertainties are considered, therefore dispersion due to aleatoric uncertainties β_R has to be assumed and in the case of presented examples equals 0.16. This value was adopted from a previous study, where approximate IDA for a single-degree-of-freedom model of the building A was performed for the 30 ground motion records. The total dispersion β_{RU}^{IN2}, which was used for calculation of seismic risk, was obtained by using SRSS rule as follows:

$$\beta_{RU,A}^{IN2} = \sqrt{(\beta_R)^2 + \left(\beta_{U,A}^{IN2}\right)^2} = \sqrt{0.16^2 + 0.21^2} = 0.26 \tag{12}$$

$$\beta_{RU,B}^{IN2} = \sqrt{(\beta_R)^2 + \left(\beta_{U,B}^{IN2}\right)^2} = \sqrt{0.16^2 + 0.08^2} = 0.18 \tag{13}$$

Mean annual frequency of exceeding the NC limit state λ_{NC} (MAF$_{\text{NC}}$), the corresponding return period T_{NC} and the frequency of exceeding NC limit state in 50 years λ_{NC}^{50} are presented in Table 4. MAF$_{\text{NC}}$ for a building B is four times higher than for building A. This is due to lower capacity of building B in terms of PGA, which has a much higher influence on result (Eq. 3) than dispersion, which is for building B smaller than that of building A.

Building	λ_{NC}	TT_{NC}(years)	λ_{NC}^{50} (%)
A	$1.28 \cdot 10^{-4}$	7800	0.64
B	$4.67 \cdot 10^{-4}$	2150	2.31

Table 4: Seismic risk in terms of mean annual frequency of exceeding NC limit state λ_{NC}, corresponding return period T_{NC} and frequency of exceeding NC limit state in 50 years λ_{NC}^{50}.

4 CONCLUSIONS

A simplified method for estimating seismic risk in combination with N2 method was used for determination of fragility parameters in the case of two three-storey masonry buildings. It was shown that the formation of plastic mechanisms has a significant effect on the estimation of fragility parameters. If only one plastic mechanism controls the seismic response of the building, the dispersion for $\tilde{a}_{gU}^{IN2}$ and the dispersion in drift capacity of the wall, which is an input parameter, are almost the same. This is not true for building A, where several plastic mechanisms were observed from pushover analyses. Since it is difficult to judge in advance, whether the modeling uncertainties affect plastic mechanism or not, it is also difficult to prescribe the dispersion measures. Therefore the use of simplified methods, which enable fast estimation of effects of epistemic uncertainties on seismic response parameters, may become more often used for risk assessment of masonry buildings.

ACKNOWLEDGEMENTS

The results presented in this paper are based on the work partially supported by the Slovenian Research Agency. The work of the first author, young researcher at ELEA iC d.o.o., was partially supported by the European Union, from the European Social Fund. This support is gratefully acknowledged.

REFERENCES

[1] C.A. Cornell, F. Jalayar, R.O. Hamburger, D.A. Foutch. Probabilistic basis for 2000 SAC Federal Emergency Management Agency Steel Moment Frame Guidelines. *Journal of Structural Engineering ASCE*, 128, 526-533, 2000.

[2] D. Vamvatsikos, C.A. Cornell. Incremental Dynamic Analysis. *Earthquake Engineering and Structural Dynamics*, 31, 491-514, 2002.

[3] M. Dolsek and P. Fajfar. Simplified probabilistic seismic performance assessment of plan-asymmetric buildings. *Earthquake Engineering and Structural Dynamics*, 36, 2021-2041, 2007.

[4] P. Fajfar. A nonlinear analysis method for performance-based seismic design. *Earthquake Spectra*, 16, 573-592, 2000.

[5] M. Rota, A. Penna, G. Magenes. A methodology for deriving analytical fragility curves for masonry buildings based on stochastic nonlinear analyses. *Engineering Structures, Early View, doi:10.1016/j.engstruct. 2010.01.009,* 2010.

[6] M. Vořechovský, D. Novák. Statistical correlation in stratified sampling. *Proc. Of 9th Int. Conf. On Applications of Statistics and Probability in Civil Engineering – ICASP 9, San Francisco, USA, Rotterdam Millpress*: 119-124, 2003.

[7] A. Galasco, S. Lagomarsino, A. Penna. Tremuri program: Seismic analyses of 3d masonry buildings. *Italy - University of Genoa,* 2009.

[8] M. Dolsek. Incremental dynamic analysis with consideration of modeling uncertainties. Earthquake Engineering and Structural Dynamics, 38, 805-825, 2009.

[9] M. Dolsek. Simplifed method for seismic risk assessment of buildings with consideration of aleatoric and epistemic uncertainty. *Submitted in Structure and Infrastructure Engineering*, 2010.

[10] M.D. McKay, W.J. Conover, R.J. Beckman. A Comparison of Three Methods for Selecting Values of Input Variables in the Analysis of Output from a Computer Code. *Technometrics*, 21: 239–245, 1979.

[11] S. Frumento, G. Magenes, P. Morandi, G.M. Calvi. Interpretation of experimental shear tests on clay brick masonry walls and evaluation of q-factors for seismic design. *EUCENTRE and University of Pavia,* 2009.

[12] ELSA - SPEAR seismic performance assessment and rehabilitation of existing buildings. *European Laboratory for Structural Assessment, Ispra*. http://elsa.jrc.ec.europa.eu/term_activity.php?id=2, 2005.

[13] S.T.A. Data. 3Muri 4.0.0. – User manual. *http://www.3muri.com/3muri/documenti/3Muri4.0_User_Manual.pdf, 2009.*

[14] A. Penna. A macro-element procedure for the non-linear dynamic analysis of masonry buildings. Ph.D. dissertation [*in Italian*]. *Italy - Politecnico di Milano*, 2002.

[15] M. Tomazevic. Potresno odporne zidane stavbe. *Ljubljana, Tehnis*, 2009.

[16] Environment Agency of the Republic of Slovenia, *http://www.arso.gov.si/potresi/potresna%20nevarnost/*, dec 2010.

COMPDYN 2011
3rd ECCOMAS Thematic Conference on
Computational Methods in Structural Dynamics and Earthquake Engineering
M. Papadrakakis, M. Fragiadakis, V. Plevris (eds.)
Corfu, Greece, 25–28 May 2011

OPTIMAL PERFORMANCE-BASED SEISMIC DESIGN OF STRUCTURES USING APPROXIMATE PERFORMANCE ESTIMATION METHODS

Athanasia Zacharenaki[1], Michalis Fragiadakis[2], Manolis Papadrakakis[1]

[1]Institute of Structural Analysis and Seismic Research, National Technical University of Athens
Iroon Polytecheiou Str., Zografou Campus, 15780, Athens, Greece
mpapadra@central.ntua.gr, azacharen@gmail.com

[2]Department of Civil and Environmental Engineering, University of Cyprus,
Nicosia 1678, Cyprus
mfrag@mail.ntua.gr

Keywords: Structural Optimization, Genetic Algorithms, Mean Annual Frequency, Pushover analysis, Incremental Dynamic Analysis.

Abstract. *We propose a new approach for the performance-based seismic design of buildings using a deterministic and a reliability-based structural optimization framework. To overcome the increased computing cost of Incremental Dynamic Analysis (IDA) we adopt an approximate seismic performance estimation tool, known as Static Pushover to IDA (SPO2IDA). The SPO2IDA tool is nested within the framework of a Genetic Algorithm resulting to an efficient seismic design procedure able to consider uncertainty. The Genetic Algorithm steps towards designs of improved performance, locating the most efficient design in terms of the minimum weight of the structure. Reliability-based constraints are considered in terms of the mean annual frequency of preset limit-states not being exceeded. A three-storey steel moment resisting frame is used to demonstrate the design algorithm proposed. The methodology presented leads to efficient real-world building designs within reasonable computing time, directly considering the seismic risk.*

1 INTRODUCTION

The design of a building structure is valued upon the extent to which regional design codes or guidelines are satisfied. This effort comes in hand with the designer's need for reducing the cost in order to obtain a more efficient design solution. Nonlinear, static or dynamic, methods of analysis are expected to lead to less costly designs using high-level performance criteria, since the engineer is allowed to have a better insight on the system's demand and capacity. Among the nonlinear performance estimation methods today available Incremental Dynamic Analysis (IDA) [1] is probably the most powerful and thorough approach.

IDA as well as other nonlinear methods of analysis requires increased computing resources. For practical applications and for designing new structures, approximating methods based on IDA have recently appeared intending to provide a fast alternative to the original method. More specifically, Dolsek & Fajfar [2] proposed the IN2 method, which is a simplified procedure that combines nonlinear static analysis with a design response spectrum. Vamvatsikos & Cornell [3,4] developed the Static Pushover to Incremental Dynamic Analysis (SPO2IDA) tool in an effort to approximate the IDA curve taking advantage information extracted from the static pushover backbone. Han & Chopra [5] proposed the MPA-based IDA method which in essence is a variation of the Modal Pushover Analysis (MPA) method. Azarbakht & Dolsek [6] proposed a method that uses a limited number of ground motions that have been appropriately selected to obtain the mean and the fractiles of the response. All the above procedures are approximate, but their results compare sufficiently to those of IDA while their cost and efficiency varies.

Evolutionary-based optimizers can handle complicated structural problems at the expense of more optimization cycles. Their rapid development made possible the solution of complex and realistic nonlinear structural optimization problems. Evolutionary Algorithms (EA) do not require the calculation of gradients of the constraints, as opposed to mathematical programming algorithms, and thus structural design code checks can be implemented as constraints of the optimization problem in a straightforward manner. Within this concept, different optimization-based seismic design procedures can be developed (Fragiadakis & Lagaros [7]).

This study discusses the use of approximating performance-estimation methods within the framework of an optimization algorithm. The resource-demanding IDA method is replaced by the Static Pushover to Incremental Dynamic Analysis (SPO2IDA) approach. SPO2IDA is employed to provide fast estimates of the mean and the dispersion of the demand at various performance levels. The constraints of the optimization problem are introduced as the exceedance of every performance level calculated either using deterministic or probabilistic design criteria. Deterministic design criteria refer to the exceedance of preset drift values that are set by the codes. Probabilistic criteria refer to the calculation of the mean annual frequency of exceedance of every limit state considering in this way the uncertainties. A Genetic Algorithm is used to handle the resulting optimum design problem. A three-storey, steel moment-resisting frame (SMRF) is used to demonstrate the proposed methodology.

2 STRUCTURAL PERFORMANCE ESTIMATION

2.1 Incremental Dynamic analysis

According to the Incremental Dynamic Analysis (IDA) method [1] the mathematical model of the structure is subjected to a suite of ground motion records incrementally scaled to different levels of seismic intensity. Recent researches show that the scaling practice is legitimate and introduces slight bias on the prediction of the structural response [10]. The building's capacity is visualised with a curve of an Engineering Demand Parameter (EDP), e.g. maximum interstorey drift ratio, versus an Intensity Measure (IM), e.g. the 5%-damped, first-mode spectral acceleration $S_a(T_1,5\%)$, representing the seismic intensity. IDA allows calculating the median (50% fractile) and also the dispersion (16%, 84% fractiles) of the building's capacity. Performance limit-states are defined on these curves by appropriate limits which are set, preferably, on the EDPs. The results of IDA can be easily combined with probabilistic seismic hazard analysis in order to estimate the mean annual frequency (MAF) of a limit-state being exceeded.

2.2 Static Pushover To Incremental Dynamic Analysis (SPO2IDA)

The Static Pushover to IDA (SPO2IDA) tool [3, 4] provides an approximate estimation of the IDA curve using the backbone of the static pushover (SPO). SPO2IDA has been verified for numerous SDOF systems and first-mode dominated structures and can be seen as a more elaborate R-μ-T relationship. More specifically, the static pushover is approximated with a trilinear or a quadrilinear envelope in order to extract the parameters that describe the SPO curve (Fig. 1). The extracted parameters are then given as input to the SPO2IDA tool to provide the fractile IDAs in normalized coordinates of the strength reduction factor R versus the ductility μ. The final approximate IDAs are obtained after a series of calculations on the available R-μ data [11].

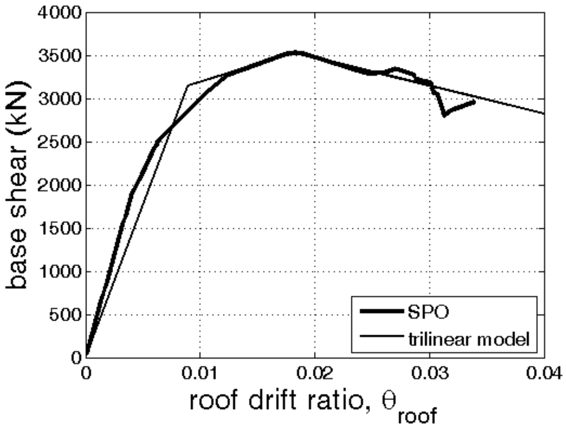

Figure 1. The SPO curve for the three-storey steel moment resisting frame and its approximation with a trilinear model.

The necessary steps to obtain the approximate IDAs are briefly summarised as follows. The process begins with approximating the static pushover curve with a multilinear envelope. Having approximated the SPO capacity curve with a trilinear model, as can be seen in Figure 1, the parameters that describe the backbone can be easily extracted. These parameters refer to the properties of the backbone curve, which initially allows for elastic behavior up to F_y , then hardens at a non-negative normalized slope of a_h while beyond this point, a negative stiffness segment starts having a normalized slope a_c [11]. These parameters are given as input to SPO2IDA to produce the median capacities. Since the capacities of SPO2IDA are in dimensionless R-μ coordinates, they have to be scaled to another pair of IM-EDP coordinates, such as the 5%-damped, first mode spectral acceleration, $S_a(T_1,5\%)$, and the maximum interstorey drift ratio, θ_{max}.

The scaling from R-μ to $S_a(T_1,5\%)$-θ_{max} is performed with simple algebraic calculations:

$$\mathbf{S_a}(T_1, 5\%) = \mathbf{R}\, S_a^{yield}(T_1, 5\%)$$
$$\boldsymbol{\theta}_{roof} = \boldsymbol{\mu}\, \theta_{roof}^{yield} \tag{1}$$

where $\boldsymbol{\theta}_{\mathrm{roof}}$ is the roof drift (displacement of the roof divided by the building height) and θ_{roof}^{yield} is the roof drift at yield, respectively. Once θ_{roof}^{yield} is known, $\boldsymbol{\theta}_{\max}$ can be extracted from the results of the SPO, since for every load increment the correspondence between the two EDPs is always available. To determine $S_a^{yield}(T_1, 5\%)$ and θ_{roof}^{yield} we assume that the yield roof drift is that of the trilinear approximation, while the $S_a^{yield}(T_1, 5\%)$ is related to the approximation of the elastic “stiffnesses” (or slopes) of the median IDA curves plotted with θ_{roof} as the EDP. The stiffness, denoted as k_{roof}, is the median value obtained using elastic response history analysis with a few ground motion records, or alternatively by using standard response spectrum analysis. An approximate relationship for k_{roof} can be found in [11]. Finally, $S_a^{yield}(T_1, 5\%)$ will be:

$$S_a^{yield}(T_1, 5\%) = k_{roof}\, \theta_{roof}^{yield} \tag{2}$$

In summary, the process of producing an approximate IDA curve from a single static pushover run involves the following steps. Initially perform a static pushover analysis with a first-mode lateral load pattern and then approximate it with a trilinear model. Next SPO2IDA will provide the IDA curves in normalized R-μ coordinates which have to be transformed in terms of $S_a(T_1,5\%)$ versus $\theta_{\max}$. This requires the elastic slope of the actual IDA, k_{roof} when θ_{roof} is the EDP. With the aid of Equations (1) and (2) we obtain the IDAs in $S_a(T_1,5\%)$-θ_{roof} coordinates. The final IDAs are obtained using the mapping between θ_{roof} and $\theta_{\max}$, available from the results of the static pushover. For a three-storey SMRF building the computing time comes down from 1.5÷2 hours required for a single IDA, to a couple of minutes, approximately two orders of magnitude less.

3 METHODOLOGY-ALGORITHM

The aim of sizing optimization problems is to minimize an objective function which, usually, is proportional to the cost of the structure. The most common objective function for steel structures is the total weight, which is considered to be directly related to the cost. The design variables are chosen to be the cross sections of the members of the structure such that the objective function can be expressed as their linear, or nonlinear, combination. Due to engineering practice demands, the members are divided into groups of design variables, thus providing a trade-off between the use of more material and the need for symmetry and uniformity due to practical considerations. Moreover, due to fabrication limitations, the design variables are not continuous but discrete. A discrete deterministic-based structural optimization (DBO) problem is formulated as follows:

$$\begin{aligned} &\min\ F(\boldsymbol{s}) \\ &\text{s.t.} \begin{cases} g_i(\mathbf{s}) \geq 0,\ i = 1,...,l \\ s_j \in R^d,\ j = 1,...,m \end{cases} \end{aligned} \tag{3}$$

where $F(\boldsymbol{s})$ is the objective function to be minimized and g_{i} are the l deterministic constraints. R^d is a given set of discrete values, and s_j is the design variables that can take values from this set. In a similar way, a discrete reliability-based (RBO) structural optimization problem is formulated as:

$$\min \; F(\boldsymbol{s})$$
$$\text{s.t.}\begin{cases} g_i(\boldsymbol{s}) \geq 0, i = 1,...,l \\ s_j \in R^d, j = 1,...,m \\ h_k(v_{\text{EDP}}(\boldsymbol{s}) \leq v_{\text{EDP}}^{\text{lim}}(\boldsymbol{s})), k = 1,...,n \end{cases} \tag{4}$$

where $F(\boldsymbol{s})$ is the objective function to be minimized, R^d is a given set of discrete values, s_j represents the design variables that can take values from this set, h_k are the n probabilistic constraints, v represents the MAF of exceedance of the k_{th} performance level and finally EDP denotes a chosen engineering demand parameter (EDP) (here is the maximum interstorey drift θ_{max}).

3.1 Solving the optimization problem using Genetic Algorithms

Genetic Algorithm (GA) [12] is the most widely used Evolutionary Algorithm. GA is a machine-learning algorithm that uses a genetic metaphor and imitates the evolution of a population. The resulting numerical tool can be used for general purposes and does not need the calculation of gradients as traditional mathematical optimizers do. Implementations of GA, typically use fixed-length character strings (binary or real-valued) to represent their genetic information. Together with a population of individuals, which undergo mutation and crossover, the GA guides the search process towards the optimum combination of the design variables. The steps of the adopted GA-based algorithm are:

1. *Initialization step:* Random generation of an initial population of the vectors of design variables s^j (j=1,…, n_{pop}). The variables are encoded as binary strings.
2. *Analysis step (Fitness evaluation):* Firstly, perform checks that do not require analysis to ensure that the design complies with the “strong-column-weak-beam” philosophy and that other detailing requirements are met. Subsequently, perform linear elastic analysis to obtain the demand for the non-seismic load combinations and then perform Static Pushover for the seismic actions. Use the SPO2IDA tool to obtain the EDP or its mean annual frequency of exceedance for every limit-state considered. For every constraint that is violated, calculate the penalties and modify the objective function accordingly (section 3.2).
3. *Selection, Generation and Mutation step:* Apply the operators of GA to create the members of the next population t^j (j=1,…, n_{pop}).
4. *Final check:* If a prespecified number of generations has been reached stop, otherwise go back to step 2.

3.2 Performance-based earthquake engineering constraints

3.2.1 Design using deterministic criteria

For structural optimization problems under earthquake loading, the constraints adopted follow the performance-based design concept where the performance of the structure is evaluated at distinct levels of seismic intensity. Three performance levels are here considered: Immediate Occupancy (IO), Life Safety (LS) and Collapse Prevention (CP). Preliminary checks are performed on every candidate design. These checks include examining whether a soft storey mechanism produced by the hinges formed in the columns rather than the beams. Also, a check whether the sections chosen are of class 1, as EC3 suggests, is carried out. This check is important in order to ensure that the members are able to develop their full plastic moment and rotational ductility. Moreover, geometrical restrictions that ensure the correct connection of the beams to the columns are performed. Another check ensuring that the bending capacity of the beams is adequate against gravity loads is also carried out. If the checks are not satisfied the design is slightly modified in order to meet the above restrictions. The capacity of the structure against seismic loads is subsequently assessed. For the three limit-states considered the first-mode spectral acceleration is computed with the aid of the EC8 elastic response spectrum. Afterwards, we determine using SPO2IDA the maximum interstorey drift demand. The latter is compared to the drift threshold values of the corresponding limit-state.

When a performance criterion is violated, a penalty, *p*, is calculated which gives a measure of the deviation of the value obtained with analysis from the acceptable threshold value. In this work the objective function is penalised as follows:

$$\overline{\mathrm{F}}(\mathbf{s}) = \begin{cases} \mathrm{F}(\mathbf{s}), & \text{if } \mathrm{s} \in \mathrm{R}^{\mathrm{d}} \\ \mathrm{F}(\mathbf{s}) \cdot \max(p), & \text{otherwise} \end{cases} \tag{5}$$

where max(p) is the maximum value of the violated constraint's penalty parameter and $\overline{\mathrm{F}}(\mathrm{s})$ is the value of the penalized objective function. The selection of the penalty parameter is significant, since a large penalty will force the design procedure to work away from the region where the global optimum is located while a small penalty will make the algorithm converge to an infeasible solution. Moreover, the penalty parameter adjusts the weight of the penalty imposed on the objective function during the optimization process.

The penalty adopted for the i-th limit state of the deterministic-based formulation of the optimization algorithm takes the form:

$$p_{\theta\max} = \frac{\theta^{\mathrm{i}}_{\max} - \theta^{\mathrm{i}}_{\lim}}{\theta^{\mathrm{i}}_{\lim}} \tag{6}$$

where $\theta^{i}_{\max}$ and $\theta^{i}_{\lim}$ is the maximum interstorey drift demand and its threshold, respectively.

3.2.2 Design using probabilistic criteria

From another point of view, the use of probabilistic criteria posess the advantage of considering uncertainties through the use of probabilities. In this way, the seismic design checks are applied on the mean annual frequency of every limit-state instead of being applied directly on the EDP. Therefore, every performance objective is realized as the exceedance probability of exceeding a specified performance level. Following this concept, for every performance level we calculate its mean annual frequency (MAF) of exccedance (v_{LS}). The calculation of the MAF can be derived using the total probability theorem:

$$v_{LS}(edp \le EDP) = \int_{0}^{+\infty} P(edp \le EDP \mid IM = im) \left| \frac{dv(IM)}{dIM} \right| \mathrm{d}IM \tag{7}$$

$P(edp \le EDP \mid IM = im)$ is the probability of limit-state being exceeded, termed also as fragility or vulnerability function, and $\left|\mathrm{d}v(IM)/\mathrm{d}IM\right|$ is the slope of the hazard curve. The absolute value is used to prevent from the negative value of the slope of the hazard curve. Equation 7 convolves the ground motion uncertainty, given through the hazard curve of the site, with uncertainties regarding the structural performance represented by the building's fragility curve.

The equation is calculated numerically since the analytical integration is not always possible. There are two ways to calculate the MAF [13]. The first way is calculating the probability that the demand exceeds the capacity of the structure, called the direct or EDP-based method, or by alternatively using the indirect or IM-based approach. The IM-based approach refers to calculating the probability that the IM will be above the random IM capacity of the structure. In this work the latter method is used, where:

$$P(edp \leq EDP \mid IM = im) = P(IM_C < IM \mid IM = im) \tag{8}$$

The mean annual frequency of exceedance of a limit-state is estimated using the statistics of the responses calculated with the aid of SPO2IDA. SPO2IDA gives an estimate of the mean value and the standard deviation of the response and may be used to calculate equation 7, for given EDP value. This is based on the assumption that the IM values are lognormally distributed. The probability of exceeding the IM capacity of the structure is thus calculated and multiplied with the slope of the hazard curve using equation 8. If $\ln(\hat{\theta}_{\max})$ and $\hat{\delta}$ are the logarithmic mean and the standard deviation of $\hat{\theta}_{\max}$ for given intensity $S_a(T_1,5\%)$, $\hat{\delta}$ is calculated as $\hat{\delta} = 0.5 \cdot \left(\ln S_a^{84\%} - \ln S_a^{50\%}\right)$ [14].

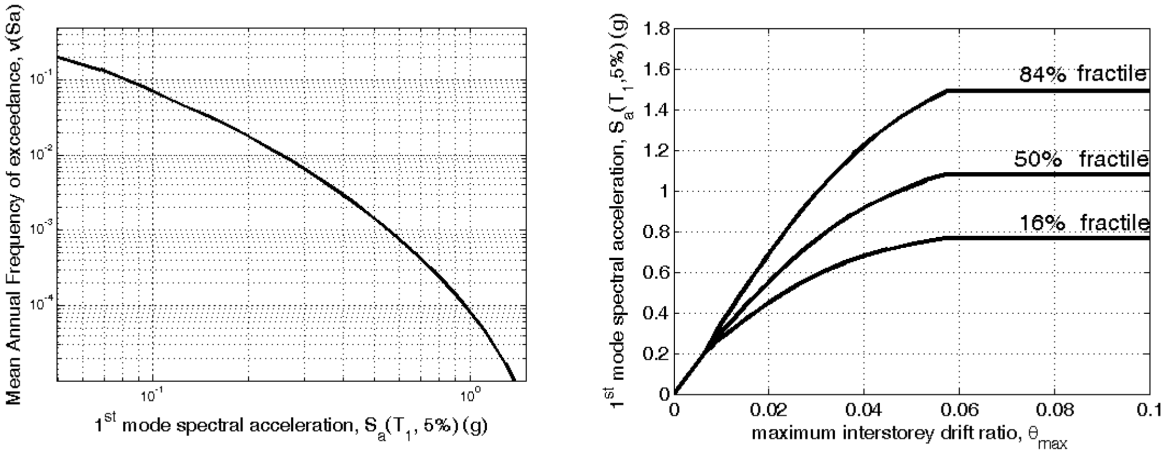

Figure 2 (a) Hazard curve for T_1= 0.93 sec, and (b) median SPO2IDA curve and its 16th and 84th fractiles.

The seismic hazard at a site can be obtained through probabilistic seismic hazard analysis (PSHA) and is represented by a hazard curve (Figure 2a). The performance levels correspond to exceedance probabilities equal to 50%, 10% and 2% in 50 years (briefly denoted hereafter as 50/50,10/50 and 2/50). For example, the IO level implies very light damage with minor local yielding and negligible residual drifts within a period of 50 years corresponding to a level of 50% probability of exceedance. Using the first-mode spectral acceleration of the structure and its period it is possible to obtain the mean annual frequency of exceedance of the ground motion *v(IM)*.

The probabilistic constraints are applied on the annual rate of the drift value being exceeded for every limit-state considered. In particular the rates used for the 50/50, 10/50 and 2/50 hazard levels are related to the return period of the limit-state being exceeded with the relationship $\tau_{LS} = 1 / \nu_{LS}$. The corresponding return periods are 72, 475, 2475 years respectively. This leads to the following probabilistic constraints:

$$\begin{aligned} \tau_{\mathrm{IO}} &\geq 72\mathrm{yrs} \\ \tau_{\mathrm{LS}} &\geq 475\mathrm{yrs} \\ \tau_{\mathrm{CP}} &\geq 2474\mathrm{yrs} \end{aligned} \tag{9}$$

The penalty adopted for the i-th limit state of the reliability-based formulation of the optimization problem is:

$$p_\tau = \frac{\tau_{\mathrm{lim}}^{\mathrm{i}} + \tau^{\mathrm{i}}}{\tau_{\mathrm{lim}}^{\mathrm{i}}} \tag{10}$$

where $\tau_{\mathrm{lim}}^{\mathrm{i}}$ is the return period of the i-th limit state set by the codes and τ^{i} is the return period of the design given by the optimization algorithm.

4 NUMERICAL RESULTS

The proposed methodology is demonstrated on a three-storey steel moment-resisting frame (SMRF) (Figure 3(a)). The frame has been designed for a Los Angeles site according to the 1997 NEHRP (National Earthquake Hazard Reduction Program) provisions. All analyses were performed on the OpenSees platform [15]. The modulus of elasticity was assumed equal to 200GPa and the yield stress f_y=235MPa. All sections are W-shaped, taken from the tables of the American Institute of Steel and Construction (AISC). The frame is assumed to have rigid connections and fixed supports. The permanent load is taken as G=5KN/m^2 and the live load is considered equal to Q=2KN/m^2. The EDP adopted is the maximum interstorey drift, $\theta_{\max}$, and the thresholds were 0.6, 1.5, and 3% for IO, LS and CP levels, respectively. This building is a first-mode dominated structure.

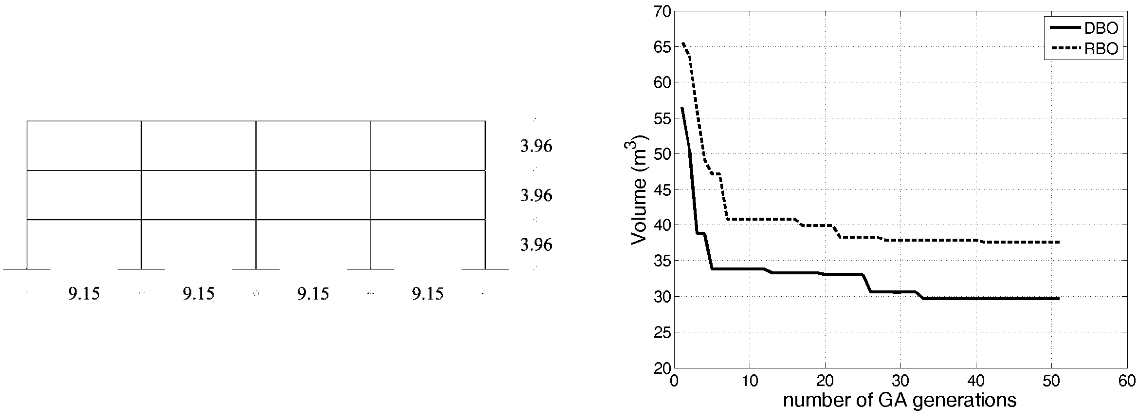

Figure 3 (a) Three-storey, steel moment resisting frame, and (b) optimization history of the three-storey frame using the deterministic-based and the reliability-based procedure.

The optimum designs obtained are shown in Table 1. As can be seen, the MAF of exceedance of the optimum design for the reliability-based optimization case satisfies the probabilistic constraints. The MAF of the optimal design using deterministic-based criteria only is given as well additionally. Figure 3(b) shows the best objective function value as the generations converge to the optimum design. It can be seen that the optimum weight reduces from 58m^3 to 29.64m^3 in the case of deterministic-based design, while for the reliability-based case, the optimum weight reduces from 65m^3 to 37.55m^3.

Case study	Volume (m^3)	Optimal design	MAF
DBO	29.64	W33×201, W27×94,W21×50, W14×30, W14×38	IO 1×10^{-2} LS 2.8×10^{-2} CP 4.7×10^{-4}
RBO	37.55	W33×263, W27×94,W21×68,	IO 1.7×10^{-3} LS 0.9×10^{-3}

W14×48,W14×26	CP	0.1×10^{-3}

Table 1. Optimal design results for the two buildings used.

Figure 4 compares the capacity curves of IDA and SPO2IDA for the optimal design of the three storey considered using the reliability-based design procedure. For the reliability-based design of the three-storey SMRF (Fig. 4) the two curves seem to be in good agreement in the elastic range. The capacity is overestimated for limit states between the elastic range and until $\hat{\theta}_{\max}$ =0.054 while beyond this value as the frame approaches collapse, SPO2IDA underestimates the capacity. These discrepancies introduce a small error in curve calculations, which is sufficient for an automatic design algorithm.

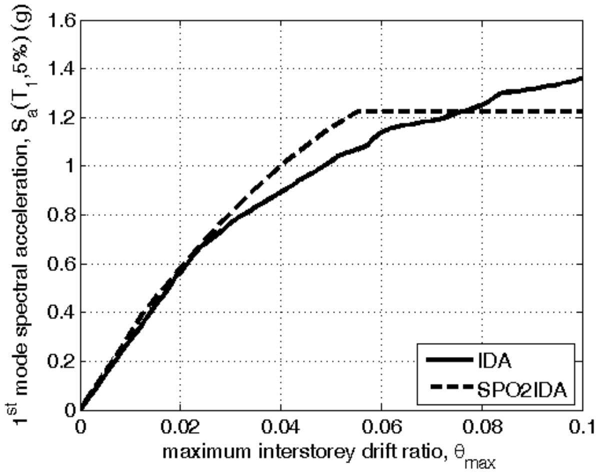

Figure 4 Median IDA curve and its SPO2IDA approximation. The curves refer to the optimal design of the three storey frame obtained by the reliability-based procedure.

5 CONCLUSIONS

A new seismic design procedure for steel moment frames has been developed. The proposed design procedure is expressed with the aid of deterministic and/or probabilistic design criteria. Both types of criteria can be imposed within the performance-based design concept as suggested by the FEMA guidelines with the latter enabling the engineer to define the return periods of preset performance levels. In this way, a common language can be used within the engineers and stakeholders during the building design procedure. The proposed algorithm uses approximate performance-estimation methods and in particular the SPO2IDA method. We have shown that the implementation of structural design code checks is possible and designs that meet the code provisions can be obtained in a straightforward manner. The mean annual frequencies of the limit-states considered are compared to preset values in order to decide whether each candidate design is acceptable. A Genetic Algorithm (GA) was implemented for the solution of the design problem leading to efficient optimal solutions through an iterative procedure. The results obtained reveal the efficiency of the proposed approach for first-mode dominated structures reducing considerably the computing time.

REFERENCES

[1] D. Vamvatsikos, C.A Cornell, Incremental Dynamic Analysis. *Earthquake Engineering & Structural Dynamics*, **31**, 491–514, 2002.

[2] M. Dolsek, P. Fajfar, Simplified probabilistic seismic performance assessment of plan-asymmetric buildings, *Earthquake Engineering & Structural Dynamics*, **36**, 2021–2041, 2007.

[3] D. Vamvatsikos, C.A Cornell, Direct estimation of the seismic demand and capacity of oscillators with multi-linear static pushovers through Incremental Dynamic Analysis. *Earthquake Engineering & Structural Dynamics*, **35**, 1097–1117, 2006.

[4] D. Vamvatsikos, C.A Cornell, Direct estimation of the seismic demand and capacity of MDOF systems through Incremental Dynamic Analysis of an SDOF Approximation. *ASCE Journal of Structural Engineering,* **131**, 589–599, 2005.

[5] S.W. Han, A.K. Chopra, Approximate incremental dynamic analysis using the modal pushover analysis procedure. *Earthquake Engineering & Structural Dynamics*, **35**, 1853–1873, 2006.

[6] A. Azarbakht, M.Dolsek, Prediction of the median IDA curve by employing a limited number of ground motion records. *Earthquake Engineering & Structural Dynamics,* **36**, 2401-2421, 2007.

[7] M. Fragiadakis, N. Lagaros, An overview to structural seismic design optimization frameworks, *Computers & Structures*, 89, 1155-1165, 2011.

[8] M. Liu, S.A. Burns, Y.K. Wen, Genetic Algorithm Based Construction-Conscious Minimum Weight Design of Seismic Steel Moment-Resisting Frames. *Journal of structural engineering* **132**, 50-58, 2006.

[9] N.D Lagaros, M. Fragiadakis, M. Papadrakakis, Y. Tsompanakis, Structural Optimization: A tool for evaluating seismic design procedures. *Engineering Structures*, **28**, 1623-1633, 2006.

[10] A. Zacharenaki, M. Fragiadakis, D. Assimaki, M. Papadrakakis, Bias introduced in the Incremental Dynamic Analysis method due to record scaling, *Bulletin of earth. Engineering*, 2011 (submitted for publication).

[11] M. Fragiadakis, D. Vamvatsikos, Fast performance uncertainty estimation via pushover and approximate IDA. *Earthquake Engineering & Structural Dynamics*, **39**, 683-703, 2010.

[12] D.E. Goldberg, *Genetic Algorithms in Search,* Optimization, and Machine Learning. Addison-Wesley Longman Publishing Co, 1989.

[13] D. Vamvatsikos, M. Dolsek, Equivalent constant rates for performance-based seismic assessment of ageing structures, *Structural Safety,* **33**, 8-18, 2010.

[14] D. Vamvatsikos, M. Fragiadakis, Incremental dynamic analysis for estimating seismic performance uncertainty and sensitivity. *Earthquake Engineering and Structural Dynamics,* **39**, 141-163, 2010.

[15] F. McKenna, G.L Fenves, The OpenSees Command Language Manual, 1.2, Edition, 2000.

COMPDYN 2011
3rd ECCOMAS Thematic Conference on
Computational Methods in Structural Dynamics and Earthquake Engineering
M. Papadrakakis, M. Fragiadakis, V. Plevris (eds.)
Corfu, Greece, 25–28 May 2011

A TARGETED NONLINEAR DYNAMIC PROCEDURE TO EVALUATE THE SEISMIC PERFORMANCE OF STRUCTURES

Dimitrios Vamvatsikos[1], **Mark Aschheim**[2], **Craig D. Comartin**[3]

[1]National Technical University of Athens
9 Heroon Polytechneiou, 157 80 Athens, Greece
divamva@mail.ntua.gr

[2]Santa Clara University
500 El Camino Real, Santa Clara, California 95053
maschheim@scu.edu

[3]CDComartin, Inc.
7683 Andrea Avenue, Stockton, California 95207-1705
ccomartin@comartin.net

Keywords: Performance-based earthquake engineering, nonlinear dynamic analysis, performance assessment, demand and capacity factored design, uncertainty.

Abstract. *The Targeted Nonlinear Dynamic Procedure is introduced to offer a practical evaluation of the seismic performance of structures. Building upon the SAC/FEMA closed-form probabilistic framework it can incorporate all important sources of variability and can be calibrated for conservatism. The hazard curve is combined with the nonlinear dynamic analysis performed for each limit-state using one or two levels of the intensity measure. This is either the elastic first-mode spectral acceleration or the more sufficient inelastic spectral displacement. From the suite of ground motion records only "targeted" subsets are used that are optimally selected to estimate the median and dispersion of the structural response. The simple factored demand and capacity checking format employed allows for a seamless integration with current engineering practice, while rational safety factors add the required degree of conservatism to account for epistemic uncertainties both for ductile and brittle modes of failure. Using a four-story reinforced concrete frame as an example, the proposed approach is shown to provide a relatively simple means to account for important sources of variability in nonlinear response history analysis. It offers powerful analysis options to a knowledgeable user in a format that can be upgraded incrementally and can provide an excellent introduction to sophisticated analysis techniques with more precisely controlled levels of conservatism.*

1 INTRODUCTION

The assessment of the seismic performance of structures is a fundamental problem in performance-based earthquake engineering (PBEE) that necessitates a compromise between cost and accuracy. Each method that has been proposed achieves a different balance between these two requirements, offering different advantages for the consideration of the engineer-user.

At the lower end of the hierarchy of methods, nonlinear static procedures (NSPs) offer considerable computational simplicity but at a certain cost in fidelity. They have limitations when predicting various engineering demand parameters (EDPs) for most structures. Also, as currently formulated, the nonlinear static procedures cannot treat uncertainty explicitly in estimating EDPs. These limitations are evident from comparisons with results from nonlinear response history analyses (NRHA).

NRHA methods lie at the opposite end of the scale, offering improved accuracy at the cost of requiring results from many ground motions to properly account for record-to-record variability. One example is incremental dynamic analysis (IDA [1]) which offers unparalleled accuracy but necessitates multiple nonlinear dynamic analyses under a suite of ground motion records scaled to several levels of the intensity measure (IM). Simpler NRHA implementations in the guidelines do exist, but they are mostly concerned with finding a single ―central" value of response (e.g. a mean or median) for a certain seismic hazard level while completely ignoring the effect of record-to-record variability and epistemic uncertainty. This has led to the familiar prescriptions such as taking the maximum of three records or the mean of seven to determine a representative ―central" response level. More recent developments, such as the Scaled NDP [2] also offer dispersion estimates but still do not offer a modern PBEE basis. Thus, practical implementation of complex NRHA methods, such as IDA, is impeded by the computational cost, while the simpler versions often seem to lack proper rigor in the wake of recent PBEE developments. We aim to offer a better alternative that strikes a favorable compromise between these two ends.

From the results of the work on the ATC-76-6 project [3] and its direct predecessors (FEMA 440/440A [4,5]), a Targeted Nonlinear Dynamic Procedure (Targeted NDP) is formulated conceptually as outlined herein. Although experience with this procedure is limited, it is expected to be more broadly applicable than predecessor nonlinear static procedures with regard to structural irregularities, component hysteretic behavior, and site-dependent ground motion characteristics (e.g. type of source mechanism and proximity to fault). At the same time, it is simpler and considerably less costly than IDA while obviously paying for it with lower accuracy. The mitigating factor though is that it is formulated to take into account epistemic uncertainties, including its inherent errors, and wherever possible shift them in such a way as to incur higher conservatism throughout its range of application. Furthermore, this implied conservatism is, to a certain degree, user-defined and can be tuned to properly cover a variety of safety requirements.

2 PROPOSED METHODOLOGY AND APPLICATION

In brief, the Targeted NDP the method is composed of 6 basic steps. At its basis lie the formation of a multi-degree-of-freedom model and its equivalent single-degree-of-freedom model, the use of subsets of records and the determination of response via NRHA:

1. Inelastic MDOF and equivalent SDOF models
2. Seismic shaking hazard and intensity measure selection
3. Stability assessment
4. Record set and subset selection
5. Nonlinear response history analyses and statistics of EDPs.

6. Safety checking

The procedure utilizes a multiple-degree-of-freedom model of the structure capable of capturing inelastic behavior and degradation at a component and system level. First mode pushover analysis of the model produces a capacity boundary for an equivalent-single-degree-freedom representation of the structure that is used to assess the potential for dynamic instability. Based on the characteristics of the structural mode, the seismic shaking hazard at the site of the structure is evaluated. This offers the fundamental consideration of uncertainty and naturally conveys the expected seismic threat level.

In the procedure described herein, two options for an intensity measure are available for scaling the ground motion records for use in nonlinear response history analyses of the MDOF model. The traditional approach, best suited when site specific ground motion records are available, is to scale records to match the spectral acceleration associated with a specific hazard level at the fundamental period of vibration of the model. This approach is sometimes referred to as $S_a(T_1)$ scaling. The alternative option is to use the peak displacement of the ESDOF model at the hazard level as the basis for scaling the ground motion records. This option allows use of a larger range of ground motion records and is sometimes referred to as S_{di} scaling.

At present we will focus on the application of the more familiar basis of $S_a(T_1)$ scaling: Two subsets of scaled ground motions are selected and median EDP's and related dispersions are estimated based on the results of nonlinear response history analyses of the MDOF model. Finally, this data is used to develop statistical representations of EDP demand and related capacities and perform safety checking in the Demand and Capacity Factored Design format introduced by FEMA-350/351 [6,7].

In the following pages the methodology will be presented in detail using the assessment of a 4-story reinforced concrete moment-resisting frame designed for California as an illustrative example.

2.1 Inelastic MDOF and equivalent SDOF models

First, a model representing the mechanical behavior of the structure to be assessed is created. The model must be capable of representing important potential inelastic mechanisms and degradation of strength and stiffness as well as P-Delta effects. The building under consideration is a 4-story reinforced concrete moment-resisting frame (RCMRF) building designed according to the 2003 IBC [8] that was developed as an archetype in FEMA-P695 [9] (see Haselton [10]).

The structural model was formed using the OpenSees platform and it is shown in Figure 1. It has accurate representation of the nonlinear behavior of beams and columns while it also incorporates nonlinear modeling of the beam-column joints. A leaning column has been included to supply any additional P-Delta forces. This is a first-mode dominated structure with a fundamental period of $T_1 = 0.86$ sec.

Conventional static pushover analysis was performed using a first-mode load pattern to develop the capacity curve of the structure shown in Figure 2. The structure was pushed well into the nonlinear range, beyond its maximum base shear capacity, to allow observation of the negative stiffness region. The resulting pushover curve is in turn fitted via a trilinear elastic-hardening-softening backbone that will serve as the capacity boundary of the equivalent SDOF (ESDOF) model that will be used for stability assessment.

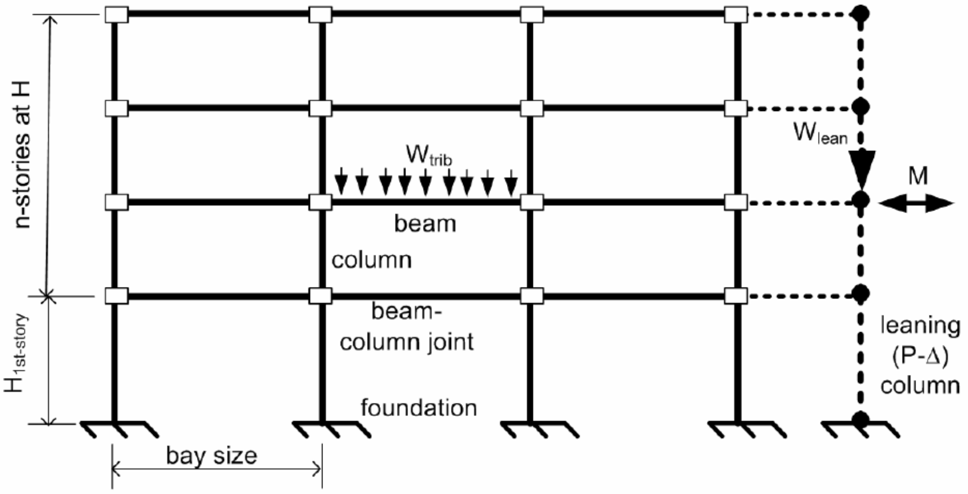

Figure 1: The four-story RC moment resisting frame building (reproduced from [8]). The bay width is 9.1m (30ft) and the story heights are 4.6m (15ft) for the first story and 4.0m (13ft) for the higher ones.

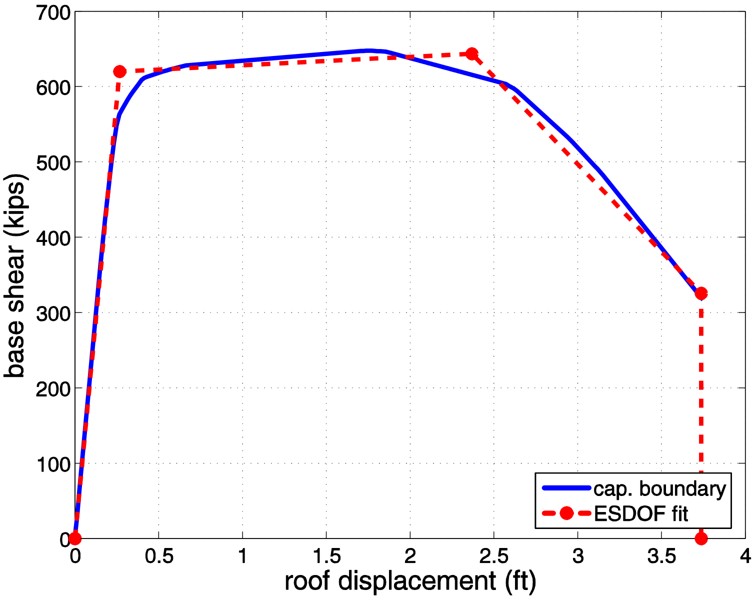

Figure 2: Capacity boundary (pushover curve) of the equivalent single-degree-of-freedom system fitted to the results of a first-mode pushover of the 4-story reinforced concrete moment frame building model.

2.2 Seismic hazard and intensity measure selection

As the next step, the seismic shaking hazard at the site of the structure is defined, allowing for the analysis results to be expressed probabilistically. Hazard may be determined from a site-specific probabilistic seismic hazard analysis. For sites within the United States, $S_a(T_1, 5\%)$ hazard data are available on the USGS website (www.usgs.gov).

Figure 3 presents an example of such data for the 4-story reinforced concrete frame structure at $T_1 = 0.86$ sec, which corresponds to the first-mode period. Mean hazard information is preferred over median data because the higher mean hazard curve also incorporates the important effect of epistemic uncertainty in the seismic hazard, as described in Cornell et al. [11]. Use of the mean hazard curve effectively allows the considerable uncertainty in seismic hazard to be addressed at this stage in a transparent way that simplifies the assessment process and avoids the need to explicitly account for seismic hazard uncertainty in subsequent steps.

Determining the seismic hazard goes hand-in-hand with selecting the intensity measure that will be used to scale the ground motion records for NRHA. Two possible choices have been considered for application with the Targeted NDP, namely the elastic spectral acceleration S_a and the inelastic spectral displacement S_{di}.

Scaling ground motions to $S_a(T_1, 5\%)$ is most appropriate where site-specific hazard data, including ground motion records, are available. Since seismic hazard data are readily available in terms of S_a, it naturally offers a very simple assessment path. Still, it is plagued by isses of sufficiency, in so far that it cannot describe adequately important seismological parameters. This may introduce a bias in the estimation of performance that is generally conservative. On the other hand, as stated by Tothong and Cornell [12], S_{di} offers advantages over $S_a(T_1, 5\%)$ in that S_{di} removes the so-called peak-valley effects associated with period elongation during nonlinear response. It can reduce the potential bias in scaling the amplitude of ground motions, thus simplifying record selection by avoiding strong emphasis on other ground-motion record properties such as epsilon [13], M_w, and distance. It is thus less restrictive than $S_a(T_1, 5\%)$ scaling as far as the selection of acceptable ground motion records. The disadvantage of the use of S_{di} as an intensity measure is the need to compute a custom-made S_{di} hazard curve that depends upon the characteristics of the ESDOF system. This may be achieved, e.g., by a probabilistic seismic hazard analysis performed using attenuation relationships for S_{di} (e.g., Tothong and Cornell [14]), or by using the ESDOF itself to determine the S_{di} from the $S_a(T_1, 5\%)$ hazard [3].

We will presently not expand further into this process which can cut down on the conservative bias induced by $S_a(T_1)$ to provide a closer estimation that is more suitable for accurate assessment. Thus we will proceed with S_a as the intensity measure, which is also the simpler version of the Targeted NDP.

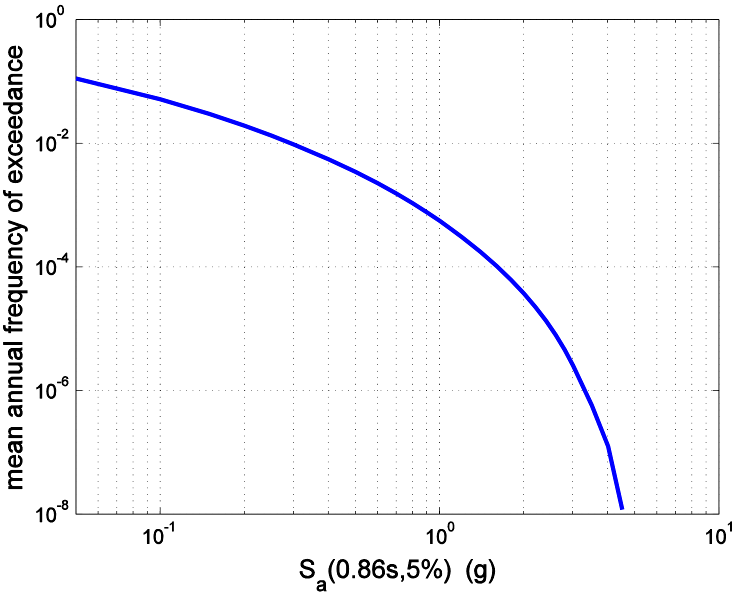

Figure 3: Seismic hazard curve for the intensity measure $S_a(T_1, 5\%)$ for T_1=0.86s .

2.3 Stability assessment

Lateral instability occurs when lateral resistance degrades due to damage caused by seismic shaking. NRHA of the MDOF system is considered the most accurate approach for assessing the likelihood of lateral instability. However, several simpler approaches based on pushover analysis may be used for this purpose—it seems that evaluation of lateral instability by pushover analysis may be more robust than evaluation of nonlinear response via NSP more generally, possibly due to the response at collapse being dominated moreso by a single mode than at lower levels of nonlinear response. Each of these pushover-based approaches makes use of the capacity boundary determined from nonlinear static pushover analysis.

One approach uses the percentile IDA curves obtained from either explicit NRHA of the ESDOF oscillator or SPO2IDA [15] relationships (the rightmost panels of Figures 4 and 5) to assess the median and distribution of collapse capacity—collapse due to lateral instability is considered to occur when the 16/50/84% IDA curves have zero slope, which indicates the corresponding percentile value of pseudo-spectral acceleration at which lateral displacements increase without limit. In case of the NRHA analyses, the record suite that will be selected for the formation of subsets for NRHA in the following section may be used for this purpose. In case of SPO2IDA though, no records are needed, as the software tool [16] is capable of instant delivery of the needed collapse capacity values in the form of the 16/50/84% percentile values of the allowable strength reduction factor.

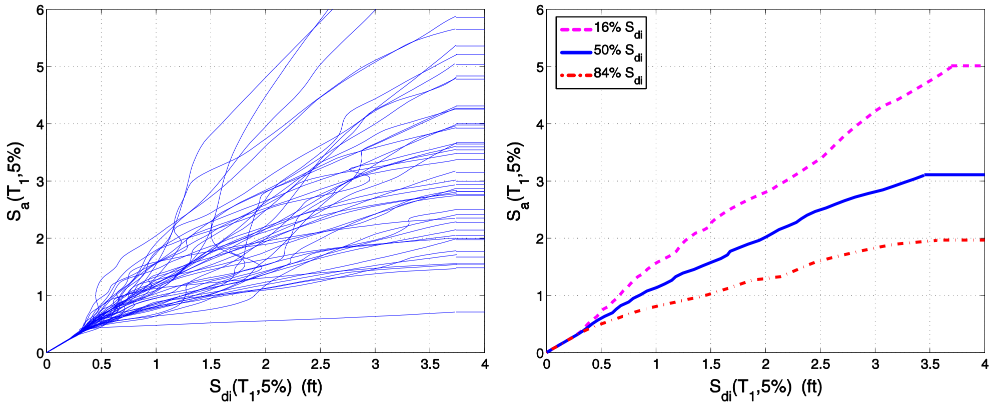

Figure 4: Complete set of 44 IDA curves and the summary 16th, 50th, 84th percentile IDA curves in S_a-S_{di} coordinates as produced by nonlinear response history analysis for the equivalent single-degree-of-freedom fitted to a 4-story reinforced concrete moment frame building model.

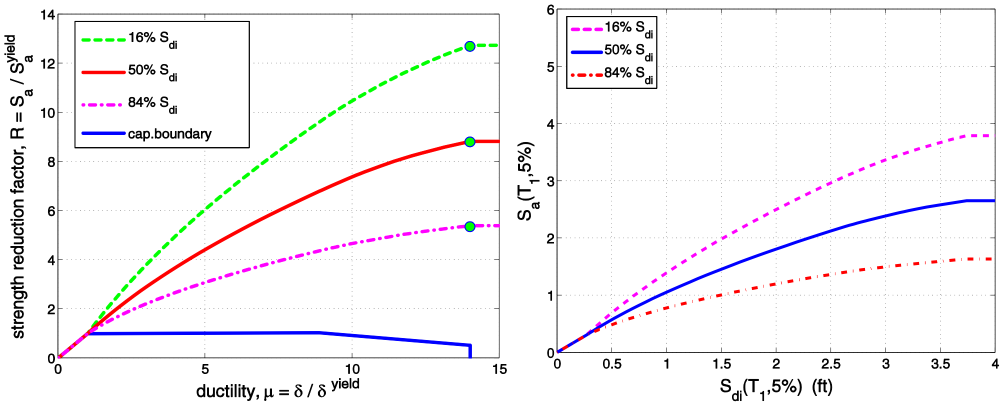

Figure 5: Percentile IDA curves in R-μ and S_a-S_{di} coordinates as produced by SPO2IDA [14] for the equivalent single-degree-of-freedom fitted to a 4-story reinforced concrete moment frame building model.

A second approach to assess the median collapse capacity does so by means of a maximum limit on strength reduction factor R_{di}, developed through a large number of SDOF simulations in FEMA P440A [5]. In this approach, $R_{di} = S_a / S_{ay}$, where S_a = the median spectral acceleration causing instability and S_{ay} = the strength of the oscillator, expressed as a spectral acceleration. Terms used in Equation 1 are defined in Figure 6.

$$
\begin{gathered}
R_{di} = \left(\frac{\Delta_c}{\Delta_y} \right)^a + b\,\frac{T_e}{3|\gamma|} + \frac{F_y}{F_r}\left(\Delta_u - \Delta_r\right)\sqrt[3]{T_e} \\
a = 1 - \exp(-dT_e) \\
b = 1 - \left(\frac{F_y}{F_c} \right)^2
\end{gathered}
\tag{1}
$$

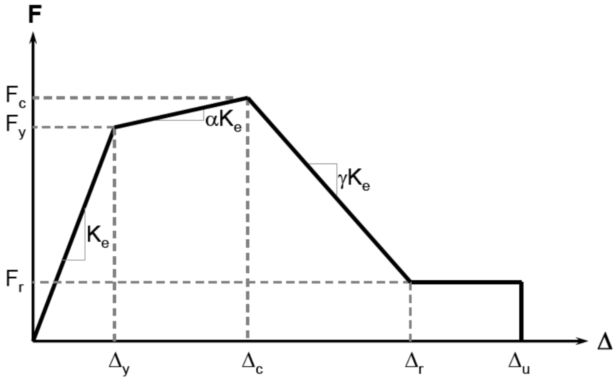

Figure 6: The backbone characteristics used in the FEMA 440A equation for maximum strength factor, R_{di}, to avoid dynamic instability.

2.4 Record Set and Subset selection

Nonlinear response history analyses of the MDOF model of the structure can be implemented at a given hazard level either by using a moderately large pool (greater than 30) of ground motion records or, more economically, by selecting subset(s) of ground motion records to estimate index values of the demand parameter distributions. The use of record subsets here follows the initial ideas presented by Azarbakht and Dolsek [17,18]. The ground motion records used in the nonlinear response history analyses are individually scaled to the target S_a or target S_{di} level, according to our choice of intensity measure.The target pseudo-spectral acceleration level $S_a(T_1)$, symbolized as S_a^{des}, is determined from the S_a hazard curve at the desired mean annual frequency of exceedance.

When using S_a as the intensity measure of choice, sufficiency (Luco and Cornell [19]) becomes an important issue. Thus, ground motion records for this approach ideally should be epsilon-consistent (Baker and Cornell, [13]) to obtain unbiased response quantity estimates. Nevertheless, ignoring this issue generally will lead to conservative estimates. A simple alternative to better control the level of conservatism is to select ground motions for which the scale factor applied to each natural (corrected) record is between 0.4 and 2.5. In our case, the far-field set of 44 records selected for FEMA-P695 [9] will be used. These motions are generally consistent with the smoothed elastic response spectrum for this site, needing scale factors within the suggested limits for reaching the design value of spectral acceleration, S_a^{des}, given by $S_a(T_1, 5\%)$ at the designated hazard level of 10% in 50yrs.

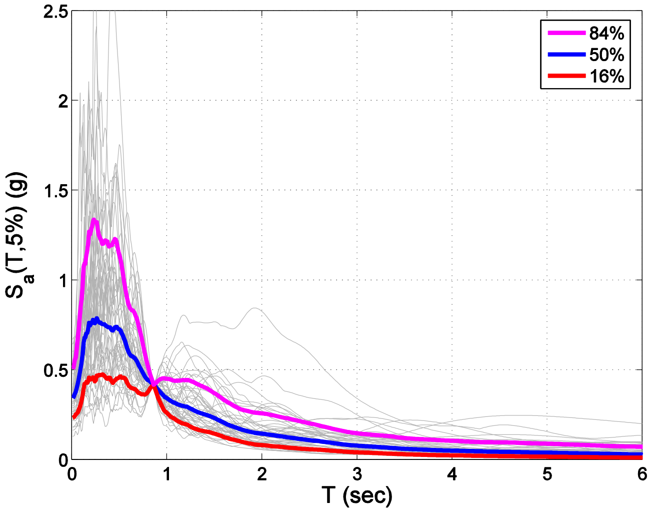

Figure 7: The 5%-damped 16,50,84% S_a spectra of the 44 records scaled to match the set median at T_1=0.86sec.

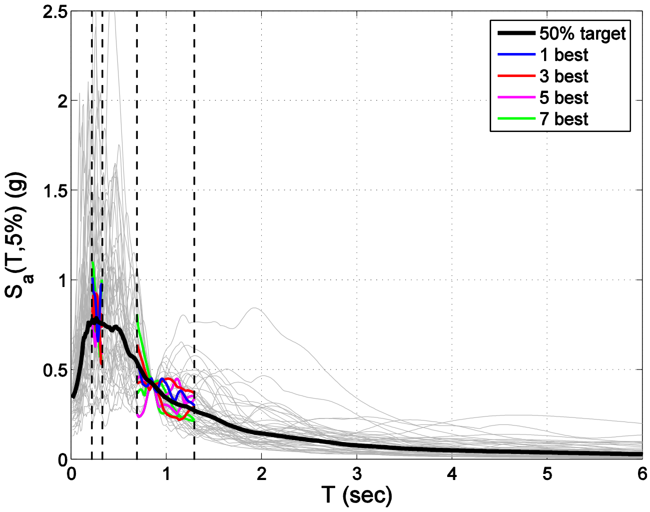

Figure 8: The 1,3,5 and 7 best record subsets A as selected to optimally match the 50% scaled-spectrum of Figure 7 in the regions of interest.

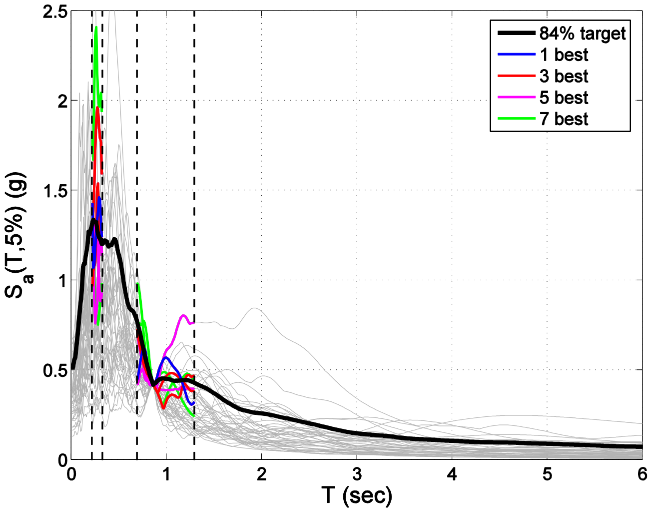

Figure 9: The 1,3,5 and 7 best record subsets B as selected to optimally match the 84% scaled-spectrum of Figure 7 in the regions of interest.

Median values of demand parameters are estimated using a subset of records whose spectra individually and collectively best approximate the median (50th percentile) spectrum; these records comprise record subset A. Where estimates of dispersion are sought, records are selected whose spectra individually and collectively best approximate a desired higher level of response spectrum (taken as the 84th percentile in this discussion); these records comprise subset B.

Subsets are selected using the elastic response spectra determined for the entire suite of ground motion records, scaled either to the target S_a value or to the target S_{di} value. The scaled elastic response spectra determined for the entire pool are used to generate 50th percentile (median) and 84th percentile spectra of S_a as a function of T. Subsets of ground motion records are selected based on how well the corresponding elastic spectra match the median or 84th percentile spectral amplitudes over a relevant period range. For records scaled to the target S_a, investigations in ATC-76-6 [3] suggest that spectral matching should be done over a period range defined by the two intervals, designed to capture both the higher mode effects and the expected lengthening of the –first-mode” after yielding. In the case of S_{di} scaling, the period range need not extend up to and past the first-mode period as the use of S_{di} is expected to directly take into account the lengthening of the –first-mode period” of the structure that occurs as inelastic response develops. Thus, the period range of interest becomes:

$$R_T = \begin{cases} [0.8T_i, 1.2T_2] \cup [0.8T_1, 1.5T_1], & \text{if } S_a \text{ - scaling} \\ [0.8T_i, 1.2T_2], & \text{if } S_{di} \text{ - scaling} \end{cases} \tag{2}$$

The lower period is T_i determined as a function of the number of stories $N_{st} > 1$, where $i = \text{ceil}\left(\sqrt{N_{st}}\right)$, –ceil” being the ceiling function that rounds up to the nearest higher integer.

To properly describe the subset selection method, the following symbols are introduced: The operator $[.]_{D,x\%}$ denotes the x percentile of dataset D, while the designations –sub” and –all” are used to distinguish the subset and the full set. Then, the selection method for S_a-scaling may be formally defined as follows: Minimize the sum of the absolute *relative* differences from the median of the elastic spectrum of the ground motion suite within the period range R_T. Formally:

$$\text{minimize} \quad \int_{R_T} \left| \frac{[S_a(T)]_{sub,x\%} - [S_a(T)]_{all,x\%}}{[S_a(T)]_{all,x\%}} \right| dT \tag{3}$$

A proper optimization to select the true optimal subsets would be cumbersome, involving a difficult combinatorial optimization problem. In its place, a simplified selection procedure is introduced that can be easily implemented, e.g. in a spreadsheet:

1. For a given $x\%$ (50/84%) fractile to be estimated, calculate the –signed” and –unsigned” objective values $S^i_{x\%}$ and $U^i_{x\%}$ for each i-th record by adapting Equation (3) with and without the absolute value, respectively:

$$S^i_{x\%} = \int_{R_T} \frac{S^i_a(T) - [S_a(T)]_{all,x\%}}{[S_a(T)]_{all,x\%}} dT \tag{4}$$

$$U^i_{x\%} = \int_{R_T} \left| \frac{S^i_a(T) - [S_a(T)]_{all,x\%}}{[S_a(T)]_{all,x\%}} \right| dT \tag{5}$$

2. Separate the records into two lists: A –negative” and a –positive” list according to the sign of the –signed” objective value. Sort each in ascending –unsigned” value.

3. Merge the two lists by selecting records alternatively from each: Start from the ―positive” list and pick the record with the lowest ―unsigned” value, then similary proceed with the ―negative” list to pick the second record. Remove them from the lists.
4. Continue with step 3 until the desired subset size is reached.

The above algorithm should be applied twice, first for $x = 50\%$ to determine subset A to estimate the median response and then for $x = 84\%$ to determine subset B and allow determination of the response dispersion. The use of 7 to 11 records in each subset appears to be adequate for many cases. There is no restriction to the maximum size of subset A or B, apart from a logical limitation of about one third the total number of records employed. The reason is that the subsets should always be small enough so that no single record appears in both A and B. Thus, for a minimum pool size of 30 records, the maximum suggested corresponding subset size is 10 for each subset. Due to the approximate nature of the results obtained with record subsets, wherever greater accuracy is required, larger subsets may be selected from an even larger pool size, or the entire pool of records may be used, disregarding subsets entirely.

The results of applying the selection algorithm for the 4-story RC building appear in Figures 8 and 9, showing the progressive selection of the 1/3/5/7 best records for subsets A and B, respectively. Obvioysly, the proposed method adopts a structure-dependent fitting range and a simple selection algorithm exploiting the relative robustness of the percentile estimators to run more efficiently. It also employs an integral over relative differences rather than plain differences. Since higher differences generally appear at the lower end of the spectrum, this distinction means that plain differences will tend to weigh lower periods more heavily than relative differences. Thus, the presented algorithm strives for more equal weighting across periods. Of course, it is conceivable that the degree of nonlinearity in the structure itself should influence the relative weighting of different areas in the spectrum, favoring, for example, the periods above T_1 when deep in the post-yield range of response versus periods around, e.g., T_2 when close to linear elastic behavior. This points to the expectation that, for the sake of simplicity, the proposed selection method may not be equally efficient at all intensity levels.

2.5 Nonlinear response history analyses and EDP statistics

Having selected the two subsets A and B, the corresponding two groups of nonlinear response history analyses are peformed. Estimates of median values of each engineering demand parameter (EDP) are given as the median of the demand parameter values obtained using record subset A as follows:

$$EDP_{50} \cong [EDP_i]_{A,50\%} \tag{6}$$

However, the estimation of the 84% needs more care, as the errors can be much higher than with estimates of the median. Consider that for a given scale factor (or intensity level) record subsets A and B have sizes N_A and N_B, respectively. Then, a relatively conservative estimate of the 84% can be made by taking the maximum of three distinct values:

1. $[EDP_i]_{B,50\%}$, the median of EDP values obtained using subset B
2. $[EDP_i]_{\max(A,B),50\%}$, the median of the N_B largest EDP values from both subsets A and B
3. $[EDP_i]_{A+B,84\%}$, the 84% of the EDP values from subsets A and B pooled together.

Care should be exercised though: the 3rd estimate is intended to be useful only for large samples, as it can become too conservative for small subset sizes, smaller than 20% of the total (e.g. N_B less than about 9 relative to a full set size of 44). On the other hand, it has to be used for larger subsets as the use of medians in the first two estimates will tend to underestimate the 84th percentile. Therefore, the combined, multi-part estimate of the 84% EDP is:

$$EDP_{84} \cong \begin{cases} \max\left([EDP_i]_{B,50\%}, [EDP_i]_{\max(A,B),50\%}\right), & \text{if } N_B < 0.2N_T \\ \max\left([EDP_i]_{B,50\%}, [EDP_i]_{\max(A,B),50\%}, [EDP_i]_{A+B,84\%}\right), & \text{if } N_B \geq 0.2N_T \end{cases} \tag{7}$$

Median and 84th percentile values are “counted” values, typically obtained by linear interpolation between the two closest values of the sample. Any collapses, assuming they are less than 10% of N_T, are still considered in the calculations as having an infinite EDP. The dispersion (aleatory randomness) in the demand parameter is thus estimated as

$$\beta_{DR} = \beta_{EDP|IM} \cong \ln(EDP_{84}) - \ln(EDP_{50}) \tag{8}$$

If the entire set of ground motion records is used to determine the MDOF response, then, allowing for modeling limitations, the evaluation procedure would be expected to introduce negligible additional uncertainty (error) in the EDP statistics. On the other hand, if the more efficient subsets are used, there is additional (non-negligible) error to consider that depends on the number of records employed in each subset and the EDP type itself. To represent this error, it is suggested that additional epistemic uncertainty dispersion is introduced in the safety checking given by

$$\beta_{SubU} = \begin{cases} 0.60 / \sqrt{\min(N_A, N_B)}, & \text{for global EDPs} \\ 0.75 / \sqrt{\min(N_A, N_B)}, & \text{for story-level EDPs} \\ 1.00 / \sqrt{\min(N_A, N_B)}, & \text{for component-level EDPs} \end{cases} \tag{9}$$

Examples of global EDPs are maxima over the entire building such as the maximum story drift or the peak roof drift over all stories; examples of story-level EDPs are story drifts and floor accelerations, and examples of component-level EDPs are member forces and section rotations.

In addition, to the two groups of NRHA corresponding to subsets A and B, in order to approximate the general shape of the IM to EDP relationship, one more group of analyses is needed. The determination of the mean annual frequency of exceedance of a demand parameter, or the required strength to ensure the capacity meets or exceeds the demand within limits implied by the mean annual frequency of exceedance at a given confidence level, necessitates the estimation of response for at least one additional seismic intensity level. When multiple intensity levels are being evaluated simulatenously (e.g., at the 50%, 10% and 2% in 50 year hazard levels) then the results at the next highest (if available) intensity level (lower probability, P_o) can be used for this purpose.

Alternatively, if the performance assessment is being made at only a single performance level (i.e., only one value of probability P_o), median response at a higher intensity level must also be determined, using a third subset of records comprising subset A scaled by a factor of 1.10 or larger. If the median capacity EDP-value for which we are testing is EDP_C then if IM^{des} (e.g. S_a^{des} for S_a-scaling) is the level of IM where we previously run subsets A and B, we can now rerun subset A at $IM' = IM^{des} \cdot EDP_C / EDP_{50}$. By virtue of Equation (6), the new set of results yields its median, EDP'_{50}, to be used in the following section.

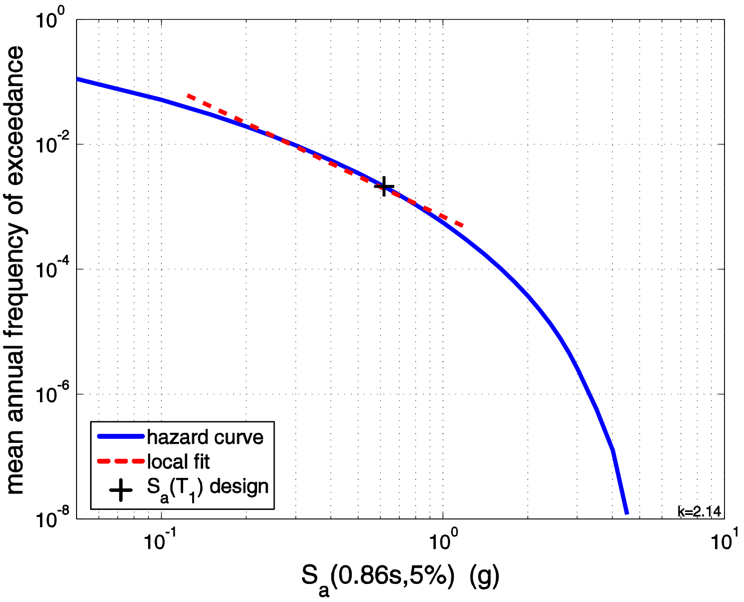

Figure 10: The mean S_a-hazard curve and the power-law approximation in the region of the 475 year intensity level.

2.6 Safety checking

Design decisions ultimately require ascertaining that a design satisfies performance expectations, and this often requires comparison of seismically induced demands with the capacities associated with the materials and components that form the structure. Although structural engineers are accustomed to treating uncertainty in demands and capacities in ultimate strength design for non-seismic loads, seismic design practice generally has neglected uncertainty, particularly on the demand side.

The Demand and Capacity Factored Design (DCFD) format developed by Cornell et al [11] is meant to be used as a check of whether a certain performance level has been violated. It cannot provide an estimate of the mean annual frequency of exceeding a given performance level. Instead, it was designed to be a checking format that conforms to the familiar Load and Resistance Factor Design (LRFD) format used in all modern design codes to check, e.g., member or section compliance. It can be represented by the following inequality:

$$FC_R \geq FD_{RPo} \cdot \exp\left(K_x \beta_{TU}\right) \Leftrightarrow \phi_R \cdot EDP_{C,50} \geq \gamma_R \cdot EDP_{50} \cdot \exp\left(K_x \beta_{TU}\right), \tag{10}$$

where FC_R is the factored capacity and FD_{RPo} is the factored demand evaluated at the probability P_o associated to the selected performance objective. The subscript R denotes that they only include aleatory uncertainties. Correspondingly, EDP_C is the median EDP capacity defining the performance level (for example, 2% maximum interstory drift for a Life Safety limit-state) and EDP_{50} is the median demand evaluated via subset A at the IM intensity level that has a probability of exceedance equal to P_o. For example, $P_o = 0.0021 \approx 1/475$ for a typical 10% in 50 years Life Safety performance level. The capacity and demand factors φ_R and γ_R are similar to the safety factors of LRFD formats and they are defined as:

$$\phi_R = \exp\left[-\frac{1}{2}\frac{k}{b_{EDP}}\beta_{CR}^2\right] \tag{11}$$

$$\gamma_R = \exp\left[\frac{1}{2}\frac{k}{b_{EDP}}\beta_{DR}^2\right], \tag{12}$$

β_{DR} is the demand record-to-record (aleatory) variability, determined according to Equation 8 from the results of NRHAs of subsets A and B. β_{CR} is the aleatory variability in the EDP-value of limit-state capacity that can be determined, e.g., from experimental tests. The parameter k is the slope of the hazard curve when plotted in log-log coordinates and depends on local seismicity and site characteristics. The slope may be derived by taking a straight-line approximation to the hazard curve in log-log coordinates, as shown in Figure 10. The approximation should closely fit the hazard curve in the region $[0.25S_a^{\mathrm{des}}, 1.5S_a^{\mathrm{des}}]$, as suggested by Dolsek and Fajfar [20]. On the other hand, following Jalayer and Cornell [21], b is estimated by taking advantage of the additional group of NRHAs performed with subset A at increased intensity IM'. Specifically, let EDP'_{50} denote the median demand parameter at the higher IM' level, then the log-slope, b, of the median demand parameter curve is estimated as follows:

$$b_{EDP} = \frac{\ln(EDP'_{50}) - \ln(EDP_{50})}{\ln(IM'/IM^{des})} \tag{13}$$

The epistemic uncertainty in demand and capacity is introduced by the total uncertainty dispersion

$$\beta_{TU} = \sqrt{\beta_{DU}^2 + \beta_{CU}^2}\ . \tag{14}$$

The two components of β_{TU} are β_{DU} and β_{CU} to address epistemic uncertainty in the demand, e.g., due to modeling parameters, and also on the EDP capacity. Any value determined or provided for β_{DU} should be inflated by β_{SubU}, which represents epistemic uncertainty associated with using record subsets to estimate demand, as given by Equation (9). The final β_{DU} value should be estimated by taking the square root of the sum of the squares of the individual components. Figure 11 provides an illustrative breakdown of the sources of variability included in the assessment and how they influence the parameters of Equation (10).

Finally, to ensure the factored capacity, FC_R, exceeds the factored demand, FD_{RPo}, with the designated MAF at a confidence level of α, we include K_x. This is the standard normal variate corresponding to the desired level α. Values of K_x are widely tabulated, and can also be easily calculated by the NORMINV function in Excel. For example NORMINV(0.9,0,1) yields $K_x = 1.28$ for $\alpha = 90\%$, while NORMINV(0.5,0,1) produces $K_x = 0$ for $\alpha = 50\%$ confidence.

Equation (10) allows a user-defined level of confidence to be incorporated in the assessment. This is a quality that may prove to be very useful since different required levels of confidence can be associated with ductile versus brittle modes of failure or local versus global collapse mechanisms. The significant consequences of a brittle or a global failure often necessitate a higher level of safety and can be accomodated with an appropriate higher value of K_x. This is fundamental in the practical application of the FEMA-350/351 [6,7] guidelines where different suggested values of the confidence level are tabulated for a variety of checking situations.

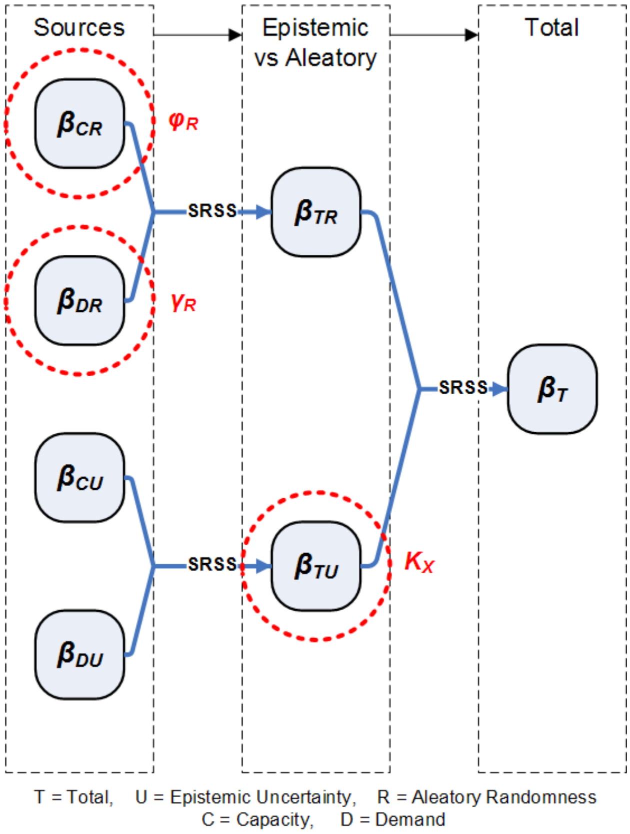

Figure 11: Breakdown of the total dispersion β_T to its four contributing sources. The circled items are the components used for the targeted NDP format.

3 ILLUSTRATIVE ASSESSMENT

The interstory drift capacity limit of 2% is subject to both aleatory randomness and epistemic uncertainty. The aleatory randomness is associated with natural variability of earthquake occurrence while epistemic uncertainty is associated with our incomplete knowledge of the seismotectonic setting (i.e. the hazard), the building and its properties. Uncertainty in the hazard is addressed by using mean rather than median hazard information (Cornell et al. [10]). The latter two sources cause the true capacity limit to be lognormally distributed with dispersions (standard deviation of the natural log of the data) that are assumed here to be β_{CU} = 30% and β_{CR} = 20%. Furthermore, based on relevant results (e.g., Liel et al [22], Dolsek [23] and Vamvatsikos & Fragiadakis [24]), we set the base value of β_{DU} at 20% as a possible estimate of dispersion due to epistemic uncertainty, associated mainly with the modeling parameters. Since we are using subsets A and B with 7 records each and assessment is peformed via a global EDP (interstory drift) this base value is inflated by β_{SubU} = 0.6 / sqrt(7) = 23%. Other sources of uncertainty that have not been accounted for may increase such estimates considerably.

Assessment based on $S_a(T_1)$ follows the basic steps discussed in the previous section. The first step is to determine the $S_a(T_1, 5\%)$ design point corresponding to the 10% in 50 years design level. This corresponds to a mean annual frequency (MAF) of λ = - ln(1 - 0.10)/50 = 0.00211 or 1/475 years, resulting in S_a^{des} = 0.62g. The stability assessment performed via SPO2IDA (Figure 5b) clearly shows that there is insigificant chance of global collapse at this intensity level, as the 16% value of collapse capacity is approximately 1.7g >> 0.62g.

Now, a straight line is fitted to the hazard curve in log-log coordinates within the ―region of interest”, defined by $\lambda_{Sa} = k_0 \cdot S_a^{-k}$. This region, according to the suggestions in Dolsek &

Fajfar [20], should be defined over the interval $[0.25S_a^{\mathrm{des}}, 1.5S_a^{\mathrm{des}}]$. The region is extended further into the lower intensities since these are the ones that have the higher probabilities of exceedance. The resulting fit appears as a red dashed line in Figure 10, corresponding to a slope of $k = 2.14$. From its relationship with the hazard curve we can tell directly that we will be overestimating the hazard more or less for any value of S_a. This observation implies that the S_a-based approach will result in a conservative evaluation.

Ground motion records are individually scaled to the S_a^{des} level in the first set of nonlinear dynamic analyses. The maximum interstory drift response $\theta_{\max}$, determined in each nonlinear dynamic analysis is the only engineering demand parameter (EDP) of interest in this example. Out of the total 14 nonlinear response history analyses, only one did not converge, signifying the occurrence of global dynamic instability. Such results are not to be excluded from the analyses. They may be considered to correspond to infinite EDP reponse and thus contribute to the estimation of the percentile values of the sample; use of percentiles is robust to infrequent infinite values The median of the maximum interestory drift values obtained with subset A is $\theta_{\max,50} = 0.0115$. Subset A together with B provide $\theta_{\max,84} = 0.0153$ via Equation (7). Thus, dispersion can be estimated as

$$\beta_{DR} = \beta_{\theta\max|Sa} = \ln\theta_{\max,84} - \ln\theta_{\max,50} = \ln(0.0153) - \ln(0.0115) = 29\%$$

If, on the other hand, collapse has been observed for more than 10% of the records, the probability of collapse should be considered explicitly with an alternative format (see Jalayer, [25]).

To estimate the slope of the median $\theta_{\max}$ versus S_a diagram, a second set of nonlinear dynamic analyses were done using ground motion records scaled to $1.10\cdot S_a^{\mathrm{des}}$ to determine the median value $\theta_{\max,50(1.10)}$. Using the full set of 44 records resulted in a median value of $\theta'_{\max,50} = 0.0124$. These median values allow the slope of the median EDP curve to be estimated as

$$b = \frac{\ln(\theta'_{\max,\ 50}) - \ln(\theta_{\max,\ 50})}{\ln(1.10)} = \frac{\ln(0.0124) - \ln(0.0115)}{\ln(1.10)} = 0.83\ .$$

In this case, an assumption of $b = 1$, as originally suggested by FEMA-350/351 [6,7], would be slightly unconservative.

Finally, factored demand and factored capacity are estimated as:

$$FD_{RPo} = \theta_{\max,50}\exp(0.5\cdot k\cdot\beta_{\theta\max|\mathrm{Sa}}{}^2/b) = 0.0115\exp(0.5\cdot 2.14\cdot 0.29^2 / 0.83) = 0.0128$$

$$FC_R = \theta_{\max,\mathrm{C}}\exp(-0.5\cdot k\cdot\beta_{CR}{}^2/b) = 0.02\exp(-0.5\cdot 2.14\cdot 0.2^2 / 0.83) = 0.0190$$

If exceedance of the 2% maximum interstory drift is assumed to involve a ductile mechanism for this building that may only produce some local problems, the probability of exceedance can be evaluated (for the purposes of this example) at a 50% confidence level. This corresponds to a lognormal standard variate of $K_x = 0$, effectively discounting in its entirety the detrimental effect of epistemic uncertainty. Thus, the evaluation inequality becomes:

$$FC_R > FD_{RPo}\cdot 1,$$

or equivalently, 0.0190 > 0.0128, which is satisfied. A result of $FC_R = FD_{RPo}$, would have indicated that the capacity is equal to the demand induced in the building, on average, at least once every 475 years, at a 50% level of confidence. The actual result indicates that the capacity exceeds the demand induced in the building at a longer mean recurrence interval.

In some circumstances a higher level of confidence for a given recurrence interval may be desired in evaluating factored capacities, especially if involving a brittle or a global collapse mechanism that will have severe consequences on the building occupants. For illustration purposes, let us assume that this is indeed the case in this situation. For a confidence level of 90%, the lognormal standard variate is $K_x = 1.28$ and the evaluation inequality becomes:

$$FC_R > FD_{RPo}\ \exp\,(K_x \cdot \beta_{TU}) = 0.0128 \cdot \exp(1.28 \cdot \mathrm{sqrt}(0.3^2{+}0.2^2{+}0.23^2)) = 0.0221$$

Since the factored capacity of 0.0190 is lower than the factored demand of 0.0221 the result is not satisfactory at the 90% confidence level. This clearly indicates that while the structure may be adequate at the 10% in 50yrs level if it presents a ductile low-consequence failure, like plastic beam hinging, it should not be considered safe if the failure mode examined is, e.g., a shear failure with important consequences.

4 CONCLUSIONS

The Targeted Nonlinear Dynamic Procedure has been introduced as an alternative to the nonlinear static procedure, offering a higher level of accuracy in seismic performance assessments within a practical format. It uses both a realistic MDOF model and its equivalent SDOF to achieve inexpensive calculations. Lateral stability assessment is performed on the equivalent SDOF, while the expensive MDOF is selectively used for nonlinear response history analysis. This is achieved by employing small subsets of ground motion records appropriately selected to match the 50/84% elastic spectra to efficiently estimate the median and the dispersion of seismic demand. The final results are integrated with seismic hazard information using the practical SAC/FEMA format to check for limit-state violations.

It is a powerful alternative to typical pushover-based methods that properly incorporates both epistemic and aleatory sources of variability while it offers a user-controlled level of confidence in safety checking. Thus, it allows proper consideration of different modes of failure (e.g., brittle versus ductile) according to their expected consequences. While not as accurate as modern PBEE approaches, it is nevertheless designed to err on the conservative side and offer an inexpensive and user-friendly method that can serve as an introduction to more sophisticated analysis techniques.

ACKNOWLEDGEMENTS

This paper relies on results obtained under Task Order 6 of the NEHRP Consultants Joint Venture (a partnership of the Applied Technology Council and Consortium of Universities for Research in Earthquake Engineering), under Contract SB134107CQ0019, Earthquake Structural and Engineering Research, issued by the National Institute of Standards and Technology. The views expressed do not necessarily represent those of the organizations identified above.

REFERENCES

[1] D. Vamvatsikos and C.A. Cornell, Incremental Dynamic Analysis. *Earthquake Engineering and Structural Dynamics*, **31**, 491-514, 2002.

[2] M. Aschheim, T. Tjhim, C. Comartin, R. Hamburger, M. Inel, The scaled nonlinear dynamic procedure. *Engineering structures,* **29**, 1422–1441, 2007.

[3] NIST, Applicability of nonlinear multiple-degree-of-freedom modeling for design. *Report No. NIST GCR 10-917-9*, prepared for the National Institute of Standards by the NEHRP Consultants Joint Venture, 2010

[4] FEMA, Improvement of nonlinear static seismic analysis procedures. *Report No. FEMA-440*, prepared for the Federal Emergency Management Agency by the Advanced Technology Council, Washington, DC, 2005.

[5] FEMA, Effects of strength and stiffness degradation on seismic response. *Report No. FEMA-P440A*, prepared for the Federal Emergency Management Agency by the Advanced Technology Council, Washington, DC, 2009

[6] SAC/FEMA, Recommended seismic design criteria for new steel moment-frame buildings. *Report No. FEMA-350*, prepared for the Federal Emergency Management Agency by the SAC Joint Venture, Washington DC, 2000.

[7] SAC/FEMA, Recommended seismic evaluation and upgrade criteria for existing welded steel moment-frame buildings. *Report No. FEMA-351*, prepared for the Federal Emergency Management Agency by the SAC Joint Venture, Washington DC, 2000.

[8] International Code Council, *2003 International Building Code,* Falls Church, VA, 2003.

[9] FEMA, Quantification of building seismic performance factors. *Report No. FEMA-P695*, prepared for the Federal Emergency Management Agency by the Advanced Technology Council, Washington DC, 2009.

[10] C.B. Haselton, Assessing seismic collapse safety of modern reinforced concrete moment frame buildings. *PhD Thesis*, Stanford University, Stanford, CA, 2006.

[11] C.A. Cornell, F. Jalayer, R.O. Hamburger, D.A. Foutch, The probabilistic basis for the 2000 SAC/FEMA steel moment frame guidelines. *ASCE Journal of Structural Engineering*, **128**, 4, 526–533, 2002.

[12] P. Tothong, C.A. Cornell, Structural performance assessment under near-source pulse-like ground motions using advanced ground motion intensity measures. *Earthquake Engineering and Structural Dynamics*, **37**, 1013–1037, 2008.

[13] J. W. Baker, C.A. Cornell, A vector-valued ground motion intensity measure consisting of spectral acceleration and epsilon. *Earthquake Engineering and Structural Dynamics*, **34**, 1193–1217, 2005.

[14] P. Tothong, C.A. Cornell, An empirical ground motion attenuation relation for inelastic spectral displacement. *Bulletin of the Seismological Society of America*; **96**, 6, 2146–2164, 2006.

[15] D. Vamvatsikos and C.A. Cornell, Direct estimation of the seismic demand and capacity of oscillators with multi-linear static pushovers through Incremental Dynamic Analysis. *Earthquake Engineering and Structural Dynamics*, **35**(9), 1097–1117, 2006.

[16] D. Vamvatsikos, *SPO2IDA software.* http://users.ntua.gr/divamva/software/spo2ida-allt.xls, 2002.

[17] A. Azarbakht, M. Dolsek, Prediction of the median IDA curve by employing a limited number of ground motion records. *Earthquake Engineering and Structural Dynamics*, **36**, 15, 2401–2421, 2007.

[18] A. Azarbakht, M. Dolsek, Progressive incremental dynamic analysis for first-mode dominated structures. *ASCE Journal of Structural Engineering*, **137**, 445–456, 2011.

[19] N. Luco, C.A. Cornell, Structure-specific scalar intensity measures for near-source and ordinary earthquake ground motions. *Earthquake Spectra*, **23**, 2, 357–392, 2007.

[20] M. Dolsek, P. Fajfar, The effect of masonry infills on the seismic response of a four storey reinforced concrete frame–a probabilistic assessment. *Earthquake Spectra*, **30**, 11, 3186–3192, 2008.

[21] F. Jalayer, C.A. Cornell, Alternative non-linear demand estimation methods for probability-based seismic assessments. *Earthquake Engineering and Structural Dynamics*, **38**, 8, 951–1052, 2009.

[22] A.B. Liel, C.B. Haselton, G.G. Deierlein, J.W. Baker, Incorporating modeling uncertainties in the assessment of seismic collapse risk of buildings. *Structural Safety,* **31**, 2, 197–211, 2009.

[23] M. Dolsek, Incremental dynamic analysis with consideration of modelling uncertainties. *Earthquake Engineering and Structural Dynamics,* **38**, 6, 805–825, 2009.

[24] D. Vamvatsikos, M. Fragiadakis, Incremental Dynamic Analysis for seismic performance uncertainty estimation. *Earthquake Engineering and Structural Dynamics* **39**:141–163, 2010.

[25] F. Jalayer, Direct probabilistic seismic aanalysis: implementing non-linear dynamic assessments. *PhD Thesis*, Stanford University, Stanford, CA, 2003.

COMPDYN 2011
3rd ECCOMAS Thematic Conference on
Computational Methods in Structural Dynamics and Earthquake Engineering
M. Papadrakakis, M. Fragiadakis, V. Plevris (eds.)
Corfu, Greece, 26–28 May 2011

NEAR-OPTIMAL BILINEAR FIT OF CAPACITY CURVES FOR EQUIVALENT SDOF ANALYSIS

F. De Luca[1], **D. Vamvatsikos**[2], **I. Iervolino**[1]

[1] University of Naples Federico II
Via Claudio, 21, 80125 Napoli, Italy
e-mail: {flavia.deluca, iunio.iervolino}@unina.it

[2] National Technical University of Athens
9 Heroon Polytechneiou, 15780 Athens, Greece
divamva@central.ntua.gr

Keywords: equivalent SDOF, bilinearization, static pushover, incremental dynamic analysis.

Abstract. *The bilinear approximation of force-deformation capacity curves is investigated for structural systems with non-negative-stiffness. This piecewise linear approximation process factually links capacity and demand; it lies at the core of the nonlinear static assessment procedures, and it has become part of seismic guidelines and codes, such as ASCE-41 and Eurocode 8. Despite codification, the various fitting rules, used to derive the bilinear representation, can produce highly heterogeneous results for the same capacity curve. This is especially valid for highly-curved backbones resulting from structural models with accurate representation of the initial, uncracked, stiffness or buildings characterized by a global collapse mechanism that leads to a gradual plasticization of the elements.*

The error introduced by the bilinearization of the force-deformation relationship is quantified by studying it at the single-degree-of-freedom (SDOF) level, away from any interference from multi-degree-of-freedom (MDOF) effects, thus avoiding the issue related to MDOF - SDOF approximation. Incremental Dynamic Analysis (IDA) is employed to enable a direct comparison of the actual backbones versus their bilinear approximations in terms of the spectral acceleration capacity for a continuum of limit-states, allowing a direct comparison of the results in terms of seismic performance.

Code-based procedures are found to be less than ideal wherever there are significant stiffness changes, while in general remaining relatively conservative. The practical fitting rules determined allow, instead, a near-optimal fit regardless of the details of the capacity curve shape.

1 INTRODUCTION

In the last decades, improvements in the computational capabilities of personal computers have allowed the employment of nonlinear analysis methods in many earthquake engineering problems. In this framework, nonlinear static analysis is becoming the routine approach for the assessment of the seismic capacity of existing buildings. Consequently, nonlinear static procedures (NSPs) for the evaluation of seismic performance, based on static pushover analysis (SPO), have been codified for use in practice. All such approaches consist of the same five basic steps: (a) perform static pushover analysis of the multi-degree-of-freedom (MDOF) system to determine the base shear versus (e.g., roof) displacement response curve; (b) fit a piecewise linear function (typically bilinear) to define the period and backbone of an equivalent single degree of freedom system (SDOF); (c) use a pre-calibrated R-μ-T (reduction factor – ductility – period) relationship for the extracted piecewise linear backbone to obtain SDOF seismic demand for a given spectrum; (d) use the static pushover curve to extract MDOF response demands; (e) compare demands to capacities; see [1] for example.

In fact, NSP is a conventional method without a rigorous theoretical foundation for application on MDOF structures [2], as several approximations are involved in each of the above steps. On the other hand, its main strength is to provide nonlinear structural capacity in a simple and straightforward way. Although several improvements and enhancements have been proposed since its introduction, any increase in the accuracy of the method is worth only if the corresponding computational effort does not increase disproportionately. Extensively investigated issues are the choice of the pattern considered to progressively load the structure and the implication of switching from the nonlinear dynamic analysis of a multiple degree of freedom (MDOF) system to the analysis of the equivalent SDOF sharing the same (or similar) capacity curve. Regarding the shape of the force distributions, it was observed that an adaptive load pattern could account for the differences between the initial elastic modal shape and the shape at the collapse mechanism [3, 4, 5]. Contemporarily, other enhanced analysis methodologies were proposed to account for higher mode effects and to improve the original MDOF-to-SDOF approximation [e.g., 6]. Regarding the demand side, efforts have been put to provide improved relationships between strength reduction factor, ductility, and period (R-μ-T relationships), to better evaluate the inelastic seismic performance at the SDOF level [7, 8].

One of the issues that have not yet been systemically investigated is the approximation introduced by the imperfect piecewise linear fit of the capacity curve for the equivalent SDOF. The necessity to employ a *multilinear* fit (an inexact, yet common, expression to describe a piecewise linear function) arises due to the use of pre-determined R-μ-T relationships that have been obtained for idealized systems with piecewise linear backbones. This has become even more important recently since nonlinear modeling practice has progressed towards realistic multi-member models, which often accurately capture the initial stiffness using uncracked section properties. The gradual plasticization of such realistic elements and models introduces a high curvature into the SPO curve that cannot be easily represented by one or two linear segments. It is an important issue whose true effect is often blurred, being lumped within the wider implications of using an equivalent SDOF approximation.

The investigation presented deals only with the bilinear approximation of the capacity curves and it is limited to non-softening force-deformation relationships. Although R-μ-T relationships that can capture far more complex backbones have recently appeared [9], the bilinear approach is by far the most widely employed in guidelines and literature [10 – 15]. The approach presented herein will be based on the accurate assessment of the effect of the equivalent SDOF fit on the nonlinear static procedure results. The latter can be achieved by proper quantification of the bias introduced into the estimate of the seismic response at the level of the SDOF itself.

Incremental dynamic analysis (IDA) [16] will be used as benchmark method to quantify the error introduced by a bilinear fit with respect to the exact capacity curve of the SDOF. Figure 1a shows a typical example, where an elastoplastic backbone fit is used according to FEMA-440 [13]. While this fit approach is meant to result to an unbiased approximation in terms of seismic performance, the median IDA results of Figure 1b show the actual error that is introduced by such code-mandated fitting rules. In most cases, they lead to an unintended and hidden bias that is generally conservative. On the other hand, this bias can become unreasonably high in many situations.

Therefore three issues come out: First, develop a methodology aimed at quantifying the bias introduced by the fitting of a capacity curve; second, assess the the error introduced by the fitting rules already employed in codes and literature; third, perform a systematical investigation aimed at providing alternative fits that can reduce this discrepancy to almost a minimum. The comparison with existing approaches will function as the benchmark to evaluate the improvement introduced by the alternative fitting rules proposed.

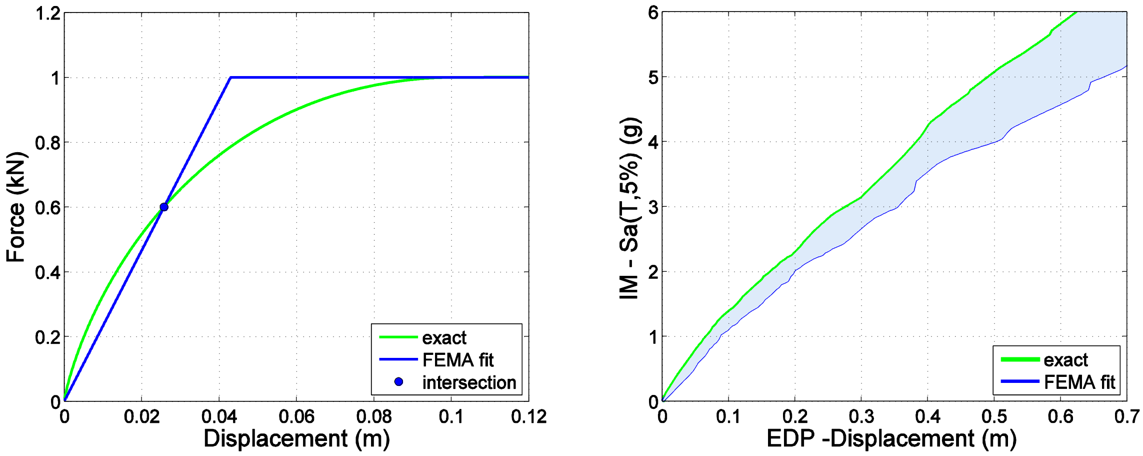

Figure 1. (a) Example of exact capacity curve versus its elastoplastic bilinear fit according to FEMA-440 and (b) the corresponding median IDA curves showing the negative (conservative) bias due to fitting for T=0.5 sec.

2 METHODOLOGY

The first main target is the quantification of the error introduced in the NSP-based seismic performance assessment by the replacement of the original capacity curve of the system, termed the “exact” or “curved” backbone, with a piecewise linear approximation, i.e., the “fitted” or “approximate” curve (e.g., Figure 1a). This will enable a reliable comparison between different fitting schemes in an attempt to minimize the observed discrepancy between actual and estimated performance. In all cases, to achieve an accurate and focused comparison of the effect of fitting only, it is necessary to disaggregate the error generated by the fit from the effect of approximating an MDOF structure via an SDOF system. Thus, all the investigations are carried out entirely at the SDOF level, using a variety of capacity curve shapes, different periods and hysteresis rules and using IDA as the method of choice for assessing the actual performance of the different alternatives.

2.1 Exact versus approximate SDOF systems

An ensemble of SDOF oscillators is considered with varying curved shapes of force-deformation backbones. They all display a monotonically decreasing stiffness that starts from elasticity and ends at a final zero or positive stiffness that remains constant for all higher deformations (e.g., Figure 1a). According to their final stiffness, these will be termed "generalized elastoplastic" and "generalized elastic-hardening" systems, respectively. They are all fitted accordingly with bilinear elastoplastic or elastic-hardening shapes.

For each considered curved backbone shape, 5% viscous damping was used and appropriate masses were employed to obtain a range of matching "reference" periods of 0.2, 0.5, 1 and 2 sec. The concept of the "reference" period, instead of the actual initial (tangent at zero displacement) period, is introduced because of the highly curved shape of some backbones. In some cases they show a strictly localized significant change in the initial stiffness, resulting in periods lower than 0.01 sec. Since this initial stiffness disappears almost immediately for any kind of loading history, a more representative reference period is required for each exact capacity curve. The reference period (*T* herein) was defined as the secant period at 2% of the displacement corresponding to the peak force capacity. Actually, in the vast majority of the cases there was insignificant difference between the initial tangent period and the reference secant period. In all cases, both the exact and the approximate system share the same mass, but, due to the lower initial stiffness of the latter, the "equivalent" period is equal to, or higher than, the "reference" one, thus replicating the approach followed in the conventional NSP methodology [2].

In order to draw general conclusions, independent of the hysteretic behavior assumed, two distinct hysteretic rules were considered for the each curved backbone and its bilinear fits. The first is a standard kinematic strain hardening model without any cyclic degradation characteristics. The second is a pinching hysteresis featuring cyclic stiffness degradation (see Ibarra et al [17]). When comparing an original system with its approximate having a piecewise linear backbone, the same hysteretic rules are always employed, so that both systems display the same characteristics when unloading and reloading in time-history analyses. In other words, all differences observed in the comparison can be attributed to the fitted shape of the approximate backbone; obviously also capturing any differences in the oscillator period.

For each exact shape of the SDOF's capacity curve and for each period value, several piecewise linear fit approximations have been considered according to different fitting rules. These include typical code-suggested fits, e.g., as laid out in FEMA-440 [13], ASCE/SEI 41-06 [14] and Eurocode 8 (EC8, [10]). In addition a multitude of different bilinear fits, with varying initial stiffness and yield point definition, have been employed in an attempt to pinpoint the consistent characteristics that can define an optimal or near-optimal fit. To enable a precise comparison that will allow distinguishing among relatively similar backbones in consistent performance terms, as it was previously stated, incremental dynamic analysis (IDA, [16]) will be employed.

2.2 Performance-based comparison via IDA

IDA is arguably the most comprehensive analysis method available for determining the seismic performance of structures. It involves performing a series of nonlinear dynamic analyses by scaling a suite of ground motion records to several levels of intensity, characterized by a scalar Intensity Measure (IM), and recording the structural response via one or more Engineering Demand Parameters (EDPs). The results typically appear in terms of multiple IDA curves, one for each record, plotted in the IM – EDP plane. These can be in turn summarized into the 16, 50, 84% fractile curves of EDP given IM (EDP|IM) or, equivalently (Vamvatsikos and Cornell [18]), as the practically identical 84, 50, 16% fractile curves of IM given EDP (IM|EDP). The summarized curves thus provide the (central value and the dispersion of the) distribution of EDP seismic demand given the IM intensity of the earthquake or, vice-versa, the distribution of a structure's IM-capacity that a ground motion should exceed to achieve the given value of EDP response.

To perform IDA for each exact and approximate oscillator considered, a suite of sixty ground motion records was used, comprised of both horizontal components from thirty recordings [19] from the PEER NGA database. They are all characterized by relatively large magnitudes of 6.5 – 6.9 and moderate distances of 15 – 35km, all recorded on firm soil and bearing no marks of directivity. Using the hunt & fill algorithm [18], 34 runs were performed per record to capture each IDA curve with excellent accuracy. The IM of choice was the 5%-damped spectral acceleration at the period T of the oscillator, $S_a(T)$, while the oscillator displacement δ was used as the corresponding EDP, being the only SDOF response of interest when applying the NSP method. To avoid the appearance of arbitrary displacement scales and units, using a normalized displacement δ_n is also attractive. Unfortunately, the concise definition of a single yield point on a curved backbone is impractical, unless tied to some preselected bilinear fitting rule; therefore using some yield displacement to normalize δ to a ductility equivalent is not possible without bias. It was chosen, instead, to normalize by the value of 0.1m that signals the onset of constant stiffness in the oscillator backbone (Figure 1a).

Once the IM and EDP are decided, interpolation techniques allow the generation of a continuous IDA curve from the discrete points obtained by the 34 dynamic analyses for each ground motion record. The resulting sixty IDA curves can then be employed to estimate the summarized IDA curves for each exact and approximate pair of systems considered. Still, in order to be able to compare an exact system with reference period T with its approximation having an equivalent period T_{eq} it was necessary to have their summarized IDA curves expressed in the same IM. In this case it is chosen to be $S_a(T)$, i.e. the spectral ordinate at the period of the curved backbone oscillator. Thus, while the approximate system IDA curves are first estimated as curves in the $S_a(T_{eq}) - \delta$ (or δ_n) plane, they are now transformed to appear on $S_a(T) - \delta$ axes. This is achieved on a record-by-record basis by multiplying all 34 $S_a(T_{eq})$ values comprising the i-th IDA curve by the constant spectral ratio $[S_a(T) / S_a(T_{eq})]_i$ that characterizes the i-th record [20].

The error is evaluated for every value of displacement in terms of the relative difference between the two system median S_a-capacities, both evaluated at the reference period T of the exact system:

$$e_{50}(\delta_n) = \frac{S_{a,50}^{fit}(\delta_n) - S_{a,50}^{exact}(\delta_n)}{S_{a,50}^{exact}(\delta_n)} \tag{1}$$

Alternatively, one could use the relative error in the median displacement response given the level of spectral acceleration:

$$e_{50}(S_a) = \frac{\delta_{n,50}^{fit}(S_a) - \delta_{n,50}^{exact}(S_a)}{\delta_{n,50}^{exact}(S_a)} \tag{2}$$

Similarly, the same definitions can be used to estimate the errors for different response or capacity fractile values, e.g., 16% or 84%, or even for the dispersion in response or capacity, which, assuming lognormality, can be defined as one half the difference between the corresponding 84% and 16% values. Thus, two different ways of measuring the discrepancy between IDA curves are available, e.g., the two median IDA curves shown in Figure 1b. In one case "horizontal statistics" are employed, working with the median EDP given IM, and in the other case "vertical statistics" of IM given EDP. As Vamvatsikos and Cornell [18] have shown, the median IDA curve is the same, regardless of how it is calculated, while, as discussed earlier, the 16, 84% fractiles are simply flipped. In addition, while there might be differences in the error estimates using these two different methods, these are only an issue of scale. Figures 2a, 2b compare the two error quantification methods for the median IDAs shown in Figure 1b. The observed trends are actually the same, but simply inverted: obviously, an overestimation in response becomes an underestimation in capacity and vice-versa.

Why then should one method be preferred over the other? There are three important reasons that make the IM-based method (IM|EDP) a more attractive solution. First, parameterizing the error in terms of the displacement response simplifies its visualization as displacement is directly mapped to specific regions of the oscillator force-deformation backbone. Thus, it is possible to see directly in Figure 2b whether the elastic or the post-elastic part is causing the accumulation of error, when it is compared vis-à-vis Figure 1a. Figure 2a is much more difficult to understand, especially if more complex backbones, than the ones used here, are considered. Second, comparing on the basis of Sa-capacity is actually directly linked to comparing in terms of the seismic performance, as expressed by the mean annual frequency (MAF) of violating limit-states defined by the oscillator displacement (Vamvatsikos [21]). An over/under-estimation of Sa-capacity maps to a consistent (although not commensurable) under/over-estimation of the MAF of limit-state exceedance. Finally, when collapse enters the problem it is obvious that the error in displacement may easily become infinite when at a given intensity level one system has collapsed, showing infinite response, while the other has not. In fact, on the contrary, this is never a problem for the Sa-based error. Although only non-collapsing systems, whose backbones never drop to zero strength, are used herein, this is another compelling reason to recommend the Sa-based comparison for general use.

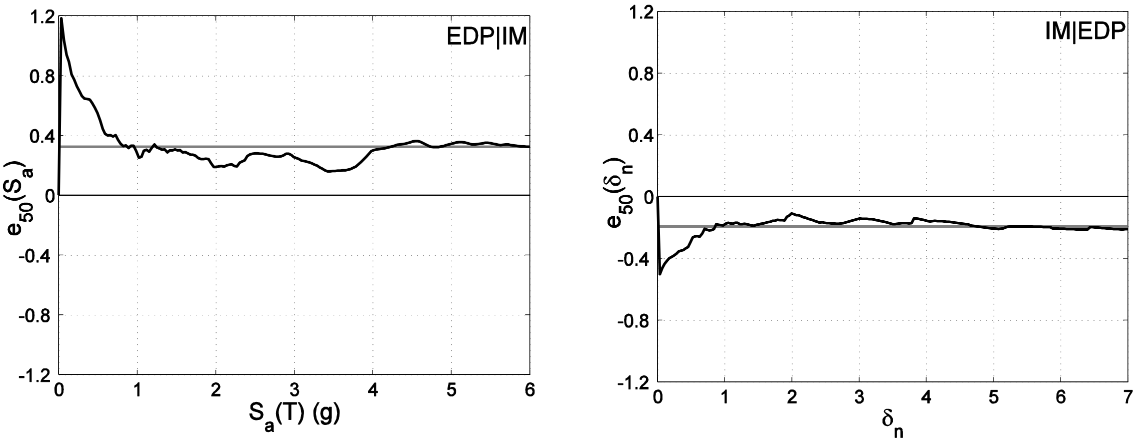

Figure 2. The relative error in the median (black line) shown versus the overall average (grey line) as introduced by the bilinear fit in Figure 1. It is expressed on the basis of (a) response given intensity (EDP|IM) and (b) intensity given response (IM|EDP).

3 INVESTIGATION OF BILINEAR FITS

Bilinear elastic-plastic or elastic-hardening fits are the fundamental force-deformation approximations employed in all NSP guidelines. The simplicity of the bilinear shape means that the only need is to estimate the position of the nominal "yield point" and select a value for the constant post-elastic stiffness. Eurocode 8 [10] suggests a piecewise bilinear fit based on the equivalence of the area discrepancy above and below the fit, assuming an elastic-plastic idealized backbone for the equivalent SDOF. This approach is similar to the original N2 method

[2]. As a consequence, EC8 prescribes an R-μ-T relationship [7] based on the elastic-perfectly-plastic fit. FEMA documents [11, 12, 13] gradually upgraded the proposed piecewise linear fit by integrating rules to account for softening behavior. According to FEMA 356 [12], the idealized relationship is bilinear with an initial slope and a post yield slope evaluated by balancing the area above and below the capacity curve up to the target displacement and calculating the initial effective slope at a base shear force equal to 60% of the nominal yield strength. The proposed graphical procedure is iterative. FEMA 440 [13] and ASCE/SEI 41-06 [14] assume the basic approach of FEMA 356 with additional rules regarding the softening behavior. In the following pages only non-softening capacity curves (generalized elastic-plastic or elastic-hardening) are investigated, thus in essence it is the original FEMA 356 and the EC8 fit rules that are tested.

In order to develop an improved bilinear fit, we choose to investigate separately the fitting of the initial "elastic" segment and then focus on the post-elastic non-negative stiffness part. Thus, we will first study generalized elastic-plastic systems, where the stiffness becomes zero beyond a displacement of 0.10 m and the target displacement is assumed to be well into the fully plastic region. Thus the post-elastic segment is fixed to have zero stiffness while the initial "elastic" part can be fitted at will. In both the FEMA and EC8 fitting rules, the fitted "elastic" stiffness can be a function of the target displacement due to the area balancing used. This can make the bilinear fitting yield different results depending on the limit-state of interest and may initially put the code-mandated fits (as implemented herein) at a slight disadvantage. It will be remedied in the second part of the study where generalized elastic-hardening systems will be tackled. They have varying post-yield stiffness and lower target displacements, allowing more fitting flexibility and providing a more rigorous comparison of code fits against any proposal for a near-optimal fit. Generally, the target, herein, is the development of a simple fitting rule that performs well for a continuum of limit states. Therefore, the performance of all rules will be carefully examined even outside the immediate region of interest defined by a target displacement.

3.1 Bilinear fits of generalized elastic-plastic systems

First a family of generalized elastic-plastic capacity curves is considered that exhibit a stiffness gradually decreasing with deformation, starting from the initial elastic and reaching zero slope. The shapes are characterized by the magnitude of the changes in stiffness. Figure 3a and 3b give an example of the shapes employed in the investigation of this family of backbones and emphasize two opposing cases. The first (Figure 3a) is not characterized by significant curvature, while the second (Figure 3b) shows a significant change in slope that can be representative of the behavior of a model that accounts for uncracked stiffness. Both the kinematic strain hardening and the pinching hysteresis are considered.

Three basic fitting rules are compared: (a) the FEMA fit (60% rule) assuming a target displacement high enough so that the slope of the second branch of the bilinear can be assumed to be zero; (b) the EC8 fit using a simple equal area criterion; (c) the "10% fit", defined so that the intersection between the capacity curve and the fitted elastic segment is at 10% of the maximum base shear. The latter is the proposal for a simple rule that can better capture the initial stiffness. Figure 3a shows that in the case in which the capacity curves are not characterized by significant stiffness changes at the beginning of the backbone, the three fits are very similar to each other. They differ significantly though when the initial backbone stiffness diminishes rapidly, as in Figure 3b. In all cases the fitted post-elastic stiffness is set to zero.

As described in the previous section, IDA is performed for each of the SDOF systems presented in Figure 3 and their fitted approximations for a range of periods. Figures 4 and 5 show the comparison in the median Sa-capacity for T equal to 0.2 and 0.5 sec, respectively. Obviously, the shapes of the backbones have a significant impact. In all cases, the error becomes significant for the shape with non-trivial curved segments. In both cases though, the maximum error appears at the earlier backbone segments. Curiously, the 10% fit leads to a remarkable decrease in the error for any deformation level, even for the highly curved shape of Figure 3b where it clearly violates any notion of equal area (or equal energy) that seems to be prevalent in current guidelines. The new fit introduced leads to a slightly non-conservative estimation of the capacity for displacements before the full plasticization (for δ_n up to 1) and only for short-period systems, $T = 0.2$ sec (Figure 4). On the other hand, even in case of highly-curved backbones (Figure 4b) only a 10% underestimation appears at most. On the contrary, it has to be noted that code approaches are always conservative for all the displacement levels and all the shapes considered, but at a cost of almost 20 – 40% underestimation of capacity. The trends identified are generally confirmed for all other periods considered (T equal to 1.0 and 2.0 seconds).

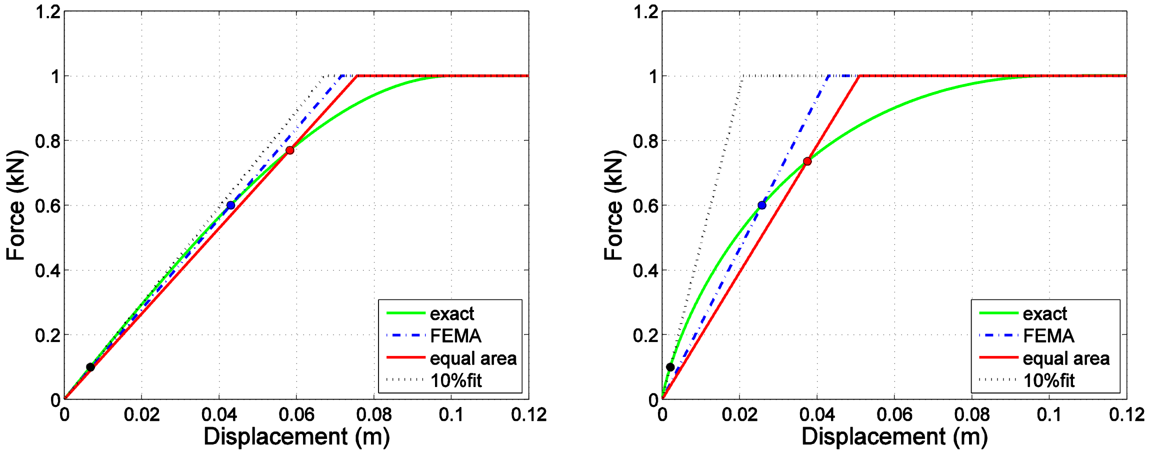

Figure 3. Comparison of generalized elastic-plastic capacity curves and their corresponding fits having (a) insignificant versus (b) significant changes in initial stiffness.

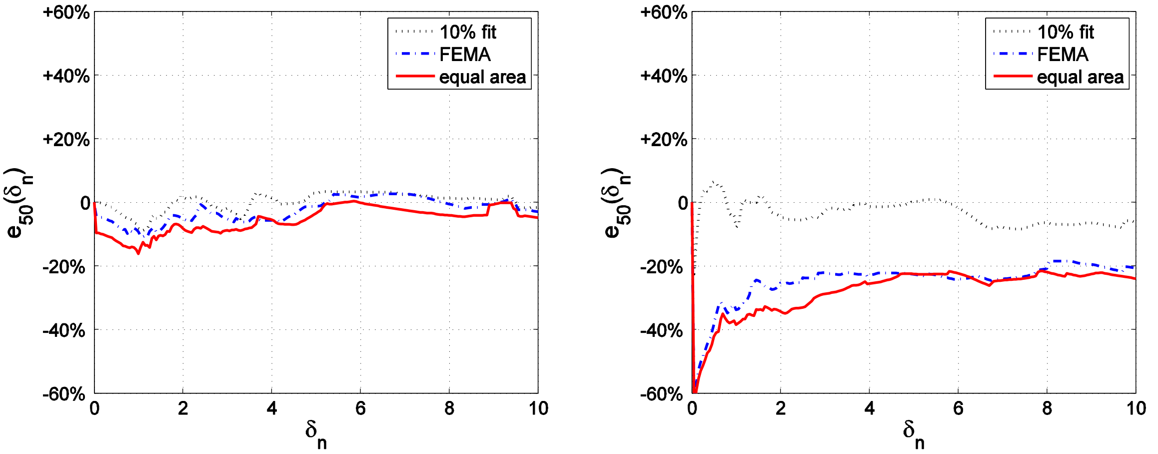

Figure 4. Median relative error comparison between the 10%, FEMA and equal area fits for $T = 0.2$ sec, when applied to the capacity curves of Figure 3: (a) insignificant versus (b) significant changes in initial stiffness.

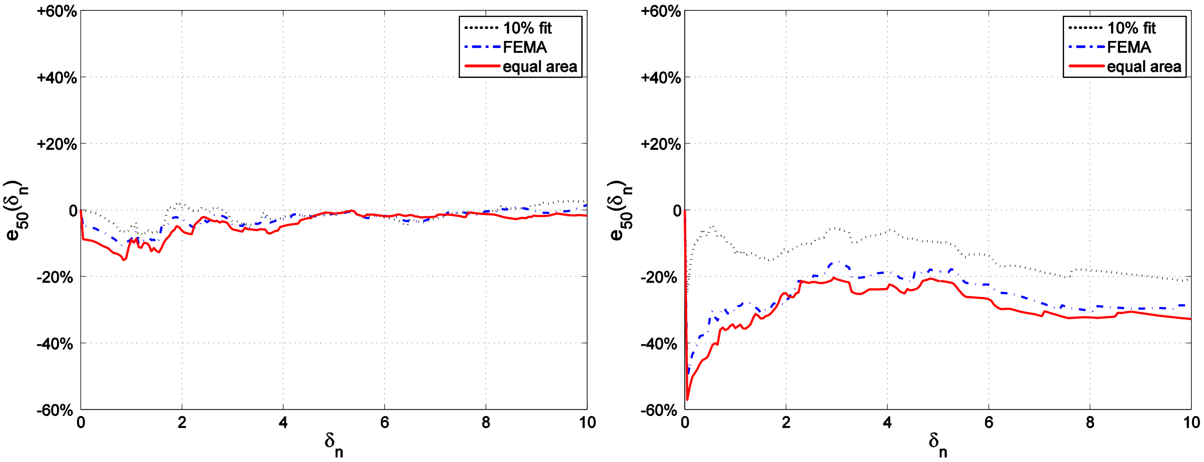

Figure 5. Median relative error comparison between the 10%, FEMA and equal area fits for $T = 0.5$ sec, when applied to the capacity curves of Figure 3: (a) insignificant versus (b) significant changes in initial stiffness.

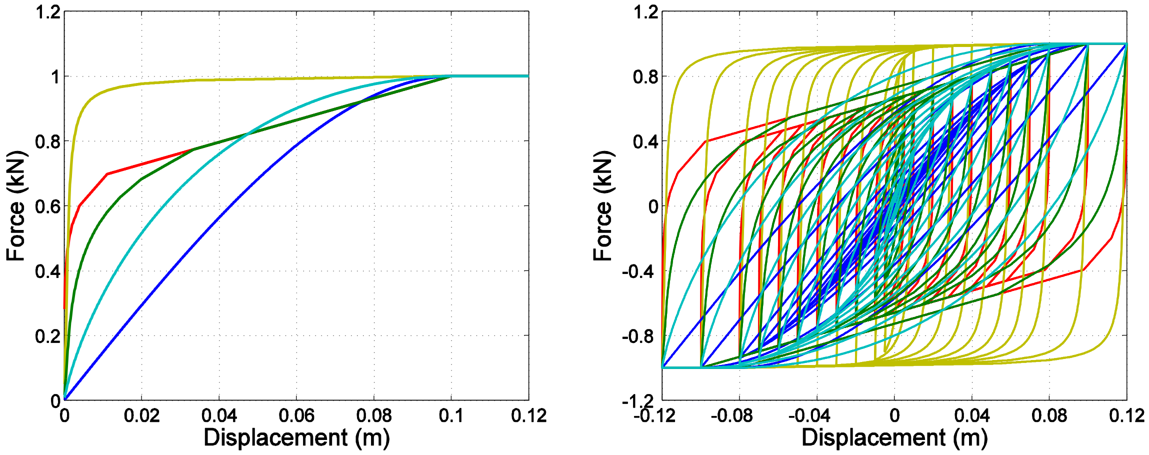

Figure 6. (a) Backbones and (b) hysteretic behavior according to standard kinematic strain hardening rule of the generalized elastic-plastic systems considered.

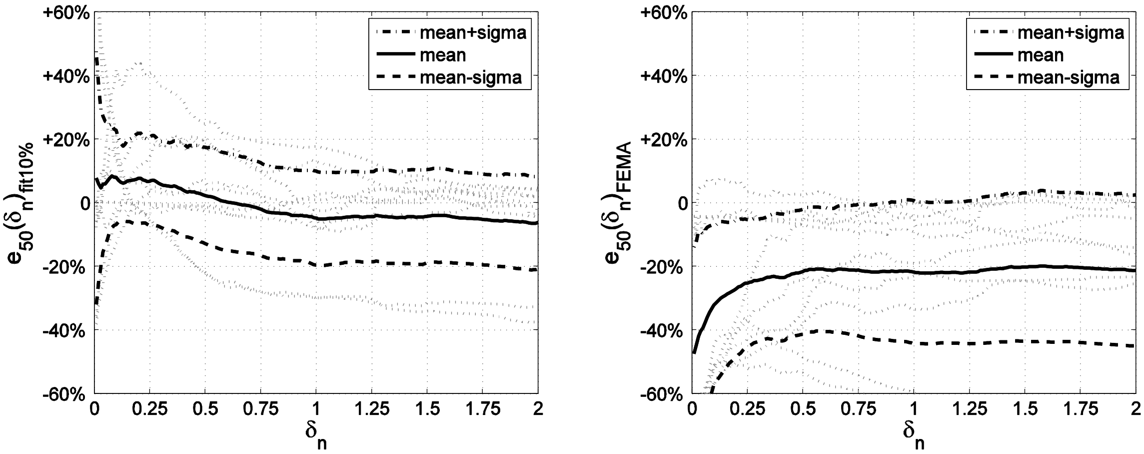

Figure 7. The median relative error for (a) the 10% fit and (b) the 60% FEMA fit, $T = 0.2$ sec, in case of elastic-plastic SDOF system family (grey dotted lines).

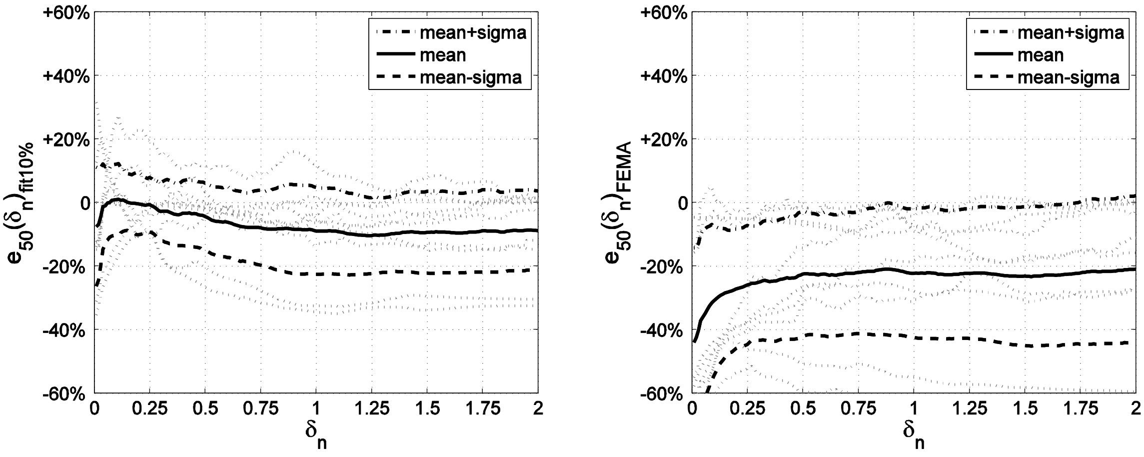

Figure 8. The median relative error for (a) the 10% fit and (b) the 60% FEMA fit, *T* = 0.5 sec, in case of elastic-plastic SDOF systems family (grey dotted lines).

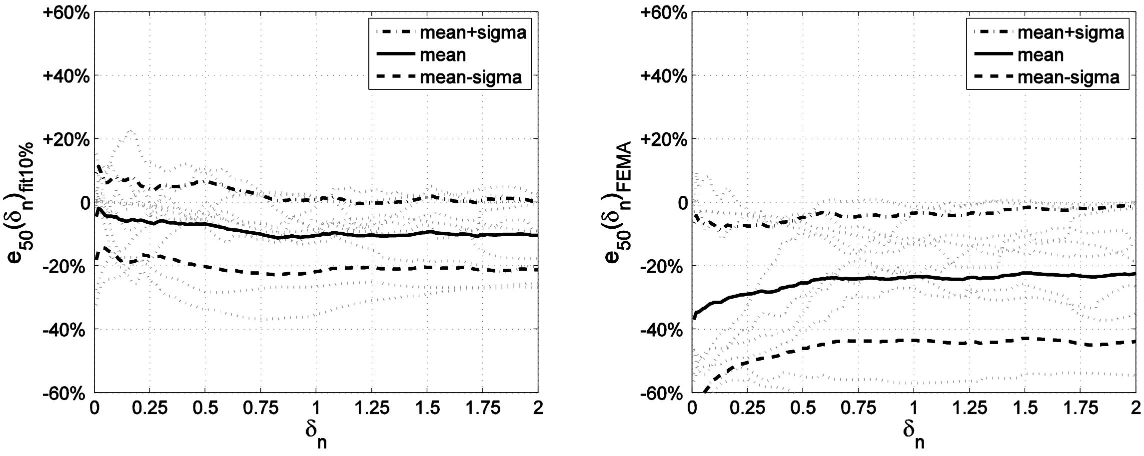

Figure 9. The median relative error for (a) the 10% fit and (b) the 60% FEMA fit, *T* = 1.0 sec, in case of elastic-plastic SDOF systems family (grey dotted lines).

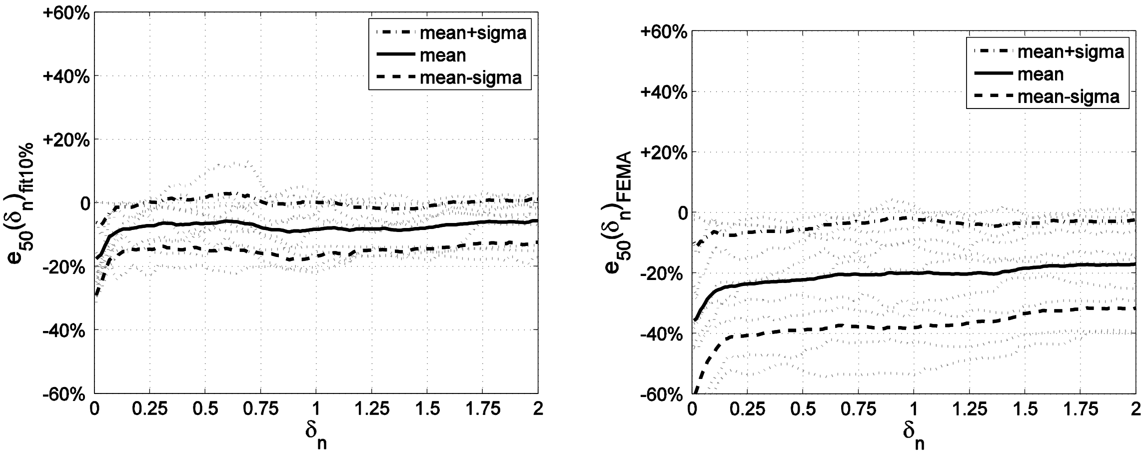

Figure 10. The median relative error for (a) the 10% fit and (b) the 60% FEMA fit, *T* = 2.0 sec, in case of elastic-plastic SDOF systems family (grey dotted lines).

Beyond the two curved shapes shown in Figures 3a, b, a number of different generalized elastic-plastic shapes were also investigated A sample of ten backbones is considered aimed at drawing out general conclusions regarding the proposal fit investigated. The sample is consists of five different shapes (see Figure 6a) times the two hysteretic rules described in section 2. In Figure 6b the standard kinematic strain hardening rule is shown for the five shapes considered.

Figure 7 to Figure 10 show the relative error on the median S_a-capacity evaluated at each period for the 10% fit proposed and the conventional FEMA fit. The bias is evaluated up to δ_n equal to 2, where most of the significant differences appear. This is evident for the two shapes in Figure 3a and 3b where it was evaluated up to δ_n equal to 10. Figure 7 to Figure 10 show grey dotted lines representing the error related to a specific shape of the backbone and to a specific hysteretic rule. The hysteretic rule chosen was found to be insignificant, as the error depends primarily on the shape of the fit; thus the two different hysteretic behaviors have been considered together to build up a heterogeneous family of generalized elastic-plastic behavior.

The 10% fit enjoys an insignificant bias on average for all the periods considered and the error introduced by the fit never exceeds 20%. FEMA fits shows a strictly negative, i.e., conservative, bias of 20% or even 60%, depending on the shape of the original backbone. Most of the bias is concentrated at the beginning of the backbone as it was already emphasized by the examples in Figure 3. Error comparisons for the S_a-capacity dispersion (record to record) are not shown as all fits roughly achieve similar performance. Some differences may appear in the region preceding the nominal yield point of the approximation. Therein the fitted system will predict no dispersion whereas the actual one shows some small variability. Still, this is to be expected and it is not important enough to make us favor one fit over another.

Summing up, it can be stated that the fit should capture as close as possible the initial stiffness of the backbone while the generally low secant stiffness assumed in most of the guidelines and codes tends to be overly-conservative. The only possible exception to this rule appears only for initially ultra-stiff systems that very quickly lose their initial properties. This is the reason why fitting the “elastic” secant at 5% or 10% of the maximum base shear, as opposed to 0.5% or 1% is considered a more robust strategy.

3.2 Bilinear fits of generalized elastic-hardening systems

The second family of shapes investigated is characterized by a generalized elastic-hardening behavior. Only the pinching hysteretic rule was considered for this family of backbones, given the insignificant differences observed earlier when compared to the kinematic hardening. Each backbone considered was characterized by different curvatures and final hardening stiffness, allowing a wide coverage of the typical shapes that can be obtained considering different structural behaviors and modeling options.

In analogy with the two examples showed in the previous subsection, two different backbones will be presented in detail from the family considered. The first (Figure 11a) is not characterized by significant changes in the stiffness, in contrast to the second (Figure 11b). The target displacement is assumed to be equal to 0.2 m. The EC8 fit is not applied as it is restricted to elastic-plastic approximations which are clearly inferior for the shapes shown in Figure 11. On the other hand, the FEMA fit rule can be applied without problems, although it might call for different approximations depending on the value of the target displacement. Still, the results and the corresponding conclusions remain the same in all cases. The alternative fit proposed, termed the “H-10%” rule, determines the initial stiffness at 10% (instead of 60%) of the nominal yield shear defined in accordance with FEMA, while the post-elastic stiffness is determined by minimizing the absolute area discrepancy between the capacity curve and the fitted line. The area minimization leads to similar results as the balancing of areas above and below the fitted line. While easy to apply graphically, the latter is an ill-defined problem that can yield mixed results: Imagine two coincident equal-size linear segments where one, the "approximation", is rotated by an arbitrary angle around the common center. Obviously, the rotated segment always satisfies the area balancing rule as a valid approximation to the original. Only when it becomes coincident does it satisfy the minimum area criterion. Thus, area minimization is algorithmically superior. The proposed H-10% procedure came out as the simplest rule with a near-minimum error for this family of backbones. While many alternatives were considered, they are not showed herein for the sake of brevity.

It has to be noted that elastic-plastic fits according to the proposal of the previous subsection have been also considered in the investigation of this family of backbones, assuming the plateau of the fit at the force corresponding to the target displacement (e.g. at 0.2m here); even if less performing than the H-10% rule, considered in the following, the still low bias of those trials compared to the FEMA-356 fitting rule, enforced the general conclusion that capturing the initial stiffness is the dominant criterion that leads to a significant bias reduction with respect to actual code fit prescriptions.

The results of the two fitting procedures (H-10% and FEMA-356) applied to the example shapes appear in Figure 11. Obviously, when the stiffness of the backbone is not characterized by abrupt changes in the curvature (Figure 11a) both fits tend to be practically the same. Figure 12 and Figure 13 show the error introduced by each fit, for both backbone shapes considered in Figure 11, in the cases of $T = 0.2$ and 0.5 sec, respectively. In analogy with the results presented for the elastic-plastic case, most of the error is concentrated at the beginning of the backbone. In the case of the backbone with low changes in the stiffness (low curvature), it can be observed that the error is very small and very similar for both fits. A higher curvature of the backbone increases the error introduced by the fit and emphasizes that although at the target displacement the backbones and their fits in both cases are coincident, this is not enough to guarantee the same error. The earlier fitted segments and especially the defined equivalent period can make a large difference. As the H-10% rule manages to capture the initial stiffness better, it provides better predictive capability for higher displacements.

The evidence, again, confirms the general trend already shown in the previous section, that it is important to capture the initial stiffness of the capacity curve to have an unbiased fit. In this case, as well, the code approach results in a conservative error that can be over 50% in the case of non-trivial shapes and at the lower displacement values (see Figure 11b). In the same range, the H-10% fit leads to a slightly non-conservative solution only for the short periods ($T = 0.2$ sec), an effect that was also observed in the elastic-plastic backbone family. Otherwise the fit remains conservative and overall it can be considered to be relatively unbiased.

In this case a sample of only four shapes is considered, the different shapes shown in Figure 14a and the pinching hysteretic rule assumed for this backbones appearing in Figure 14b. In Figure 15 to Figure 18 the relative errors in the median S_a-capacity, are compared for the four different periods and the different SDOF backbones. The importance of capturing the initial stiffness is highlighted by the results at each period, and the H-10% fit leads to a small and relatively unbiased error, which seldom exceeds 10%. In this case the sample of backbones considered for the elastic-hardening case was smaller than the elastic-plastic case but the robustness of the general results, showing the same trends in both cases, supports our remarks. It should be noted that the results of the FEMA approximation will improve somewhat at low displacements if we refit for a lower target displacement, but not enough to alter the above conclusions.

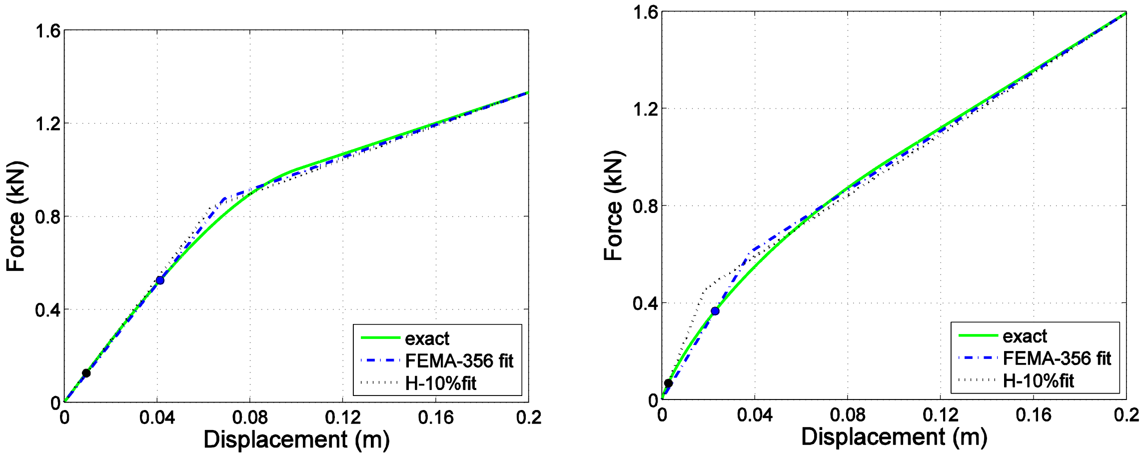

Figure 11. Comparison of generalized elastic-plastic capacity curves and their corresponding fits having (a) insignificant versus (b) significant changes in initial stiffness.

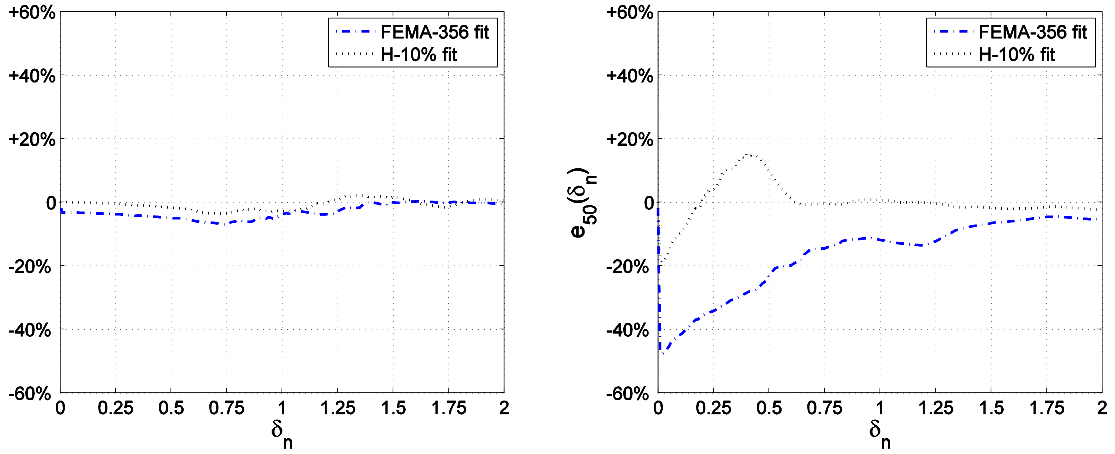

Figure 12. Median relative error comparison between the H-10% and FEMA fits for $T = 0.2$ sec, when applied to the capacity curves of Figure 10: (a) insignificant versus (b) significant changes in initial stiffness.

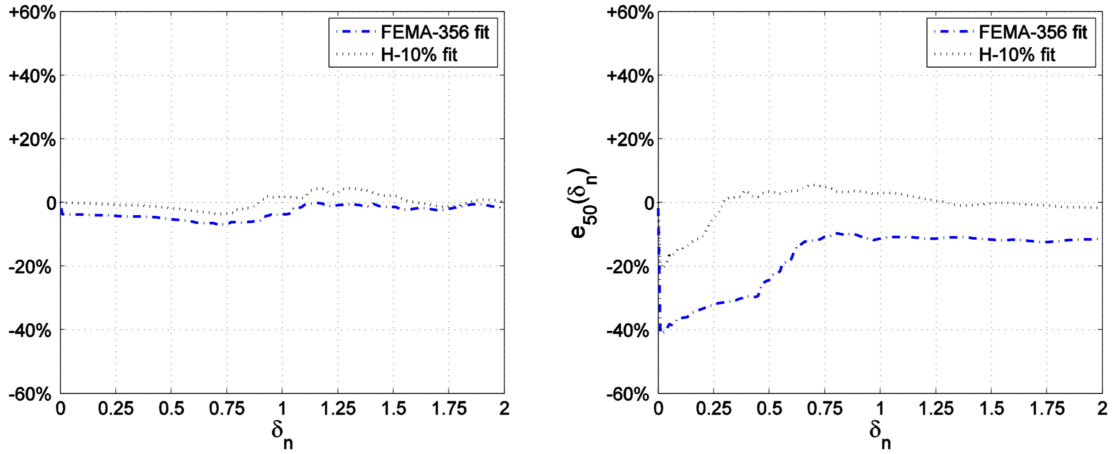

Figure 13. Median relative error comparison between the H-10% and FEMA fits for $T = 0.5$ sec, when applied to the capacity curves of Figure 10: (a) insignificant versus (b) significant changes in initial stiffness.

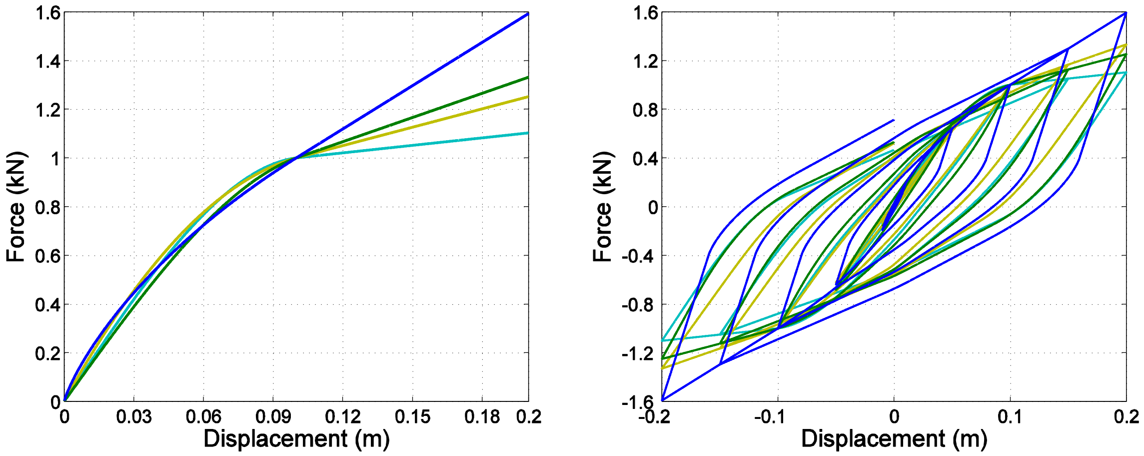

Figure 14. Backbones (a) and hysteretic behavior according to pinching hysteresis rule (b) of the generalized elastic-hardening systems considered.

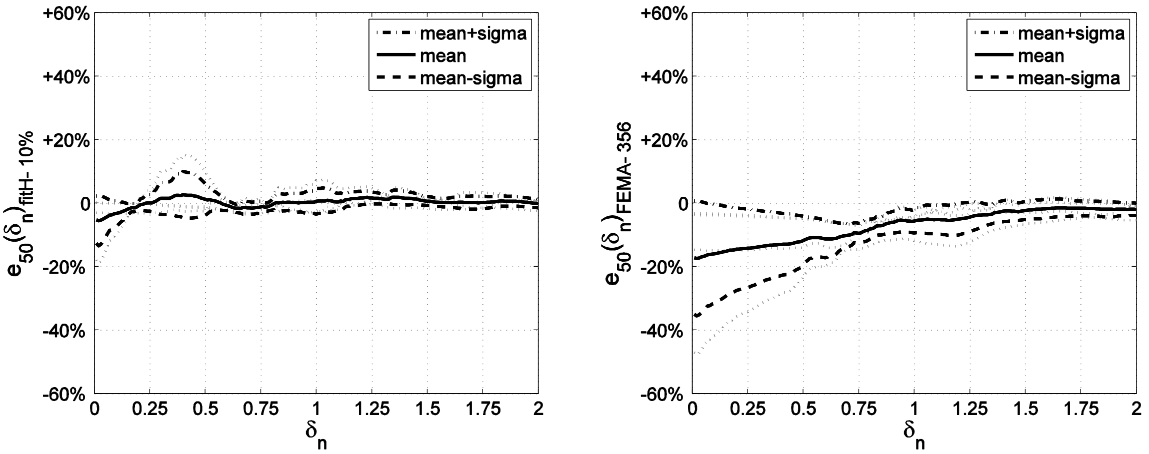

Figure 15. The median relative error for (a) the H-10% fit and (b) the 60% FEMA fit, $T = 0.2$ sec, in case of elastic-hardening SDOF systems family (grey dotted lines).

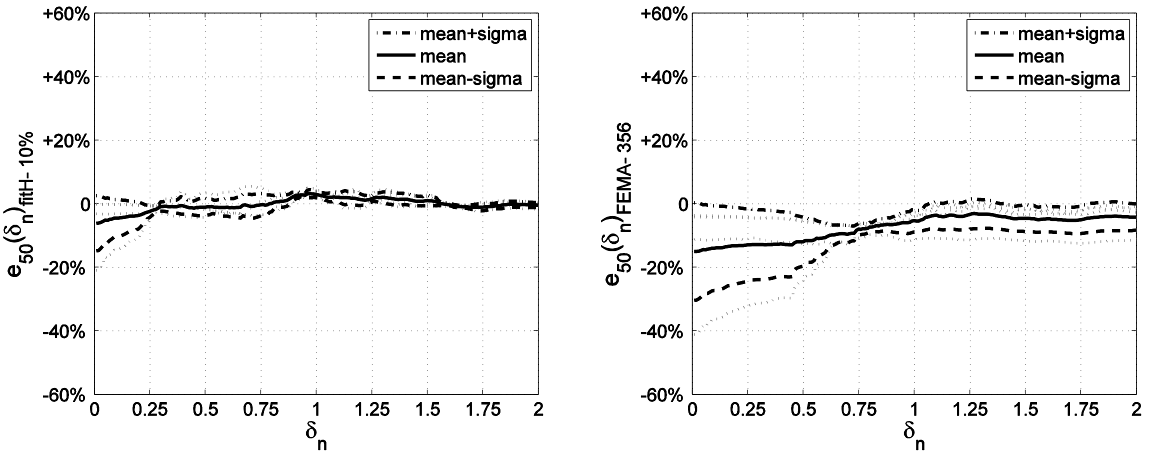

Figure 16. The median relative error for (a) the H-10% fit and (b) the 60% FEMA fit, $T = 0.5$ sec, in case of elastic-hardening SDOF systems family (grey dotted lines).

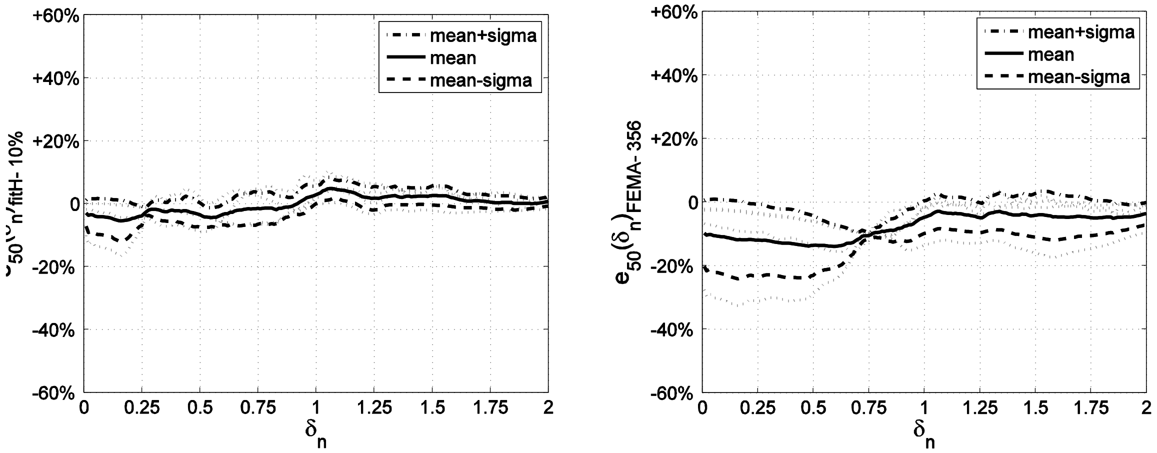

Figure 17. The median relative error for (a) the H-10% fit and (b) the 60% FEMA fit, $T = 1.0$ sec, in case of elastic-hardening SDOF systems family (grey dotted lines).

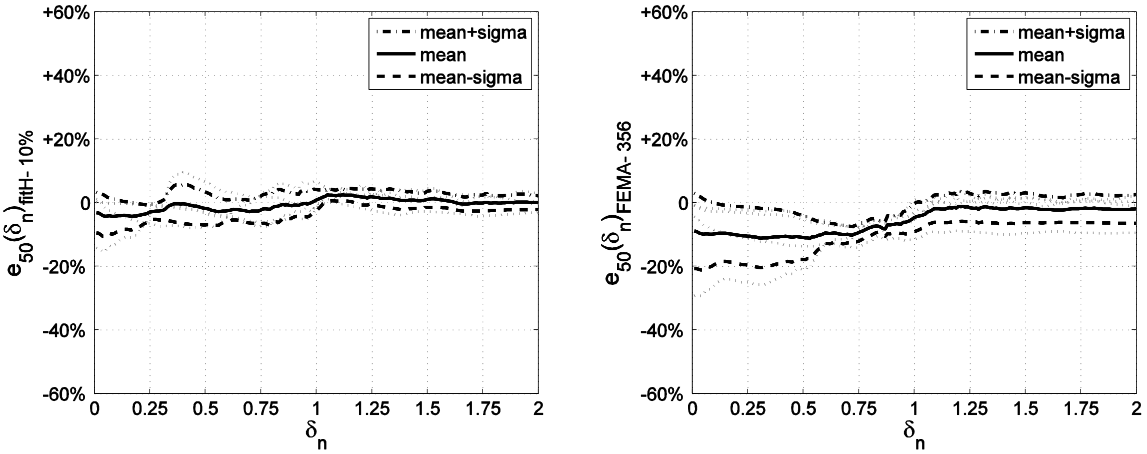

Figure 18. The median relative error for (a) the H-10% fit and (b) the 60% FEMA fit, $T = 2$ sec, in case of elastic-hardening SDOF systems family (grey dotted lines).

4 CONCLUSIONS

Structural seismic assessment based on the nonlinear static procedure is a method that, in its different versions, has become common in the last decades among researchers and practitioners. It is based on the fundamental approximation that the behavior of an MDOF system can be interpreted by the response of an equivalent SDOF. This necessitates a number of approximations at various stages of the procedure. Herein, the problem of the optimal bilinear fit to be chosen as the idealized base shear–displacement curve is systematically investigated by means of an IDA-based procedure applied to the case of non-softening capacity curves.

Assessment of different fits is achieved on an intensity-measure capacity basis that allows a straightforward comparison of the performance of structural systems characterized by different periods, in this case the period of the capacity curve and its bilinear approximation. Therefore the approach followed allows the investigation of a continuum of limit states at the SDOF level, excluding other sources of error that have already been investigated by other detailed studies.

The investigation led to the general rule and recommendation that it is fundamental to capture the initial stiffness of the capacity curve rather than aiming at balancing or minimizing the area above or below the elastic segment of the fit. A 10% of a reference value of yield base shear, i.e., the maximum attained for elastic-plastic and the nominal yield value for elastic-hardening systems, is suggested as a robust point for the intersection between the capacity curve and the fit of the elastic secant segment. The subsequent non-negative stiffness segment should be chosen to minimize the area discrepancy between the fitted and the exact model in the region of interest.

The low bias introduced by this enhanced fit is found to be an improvement with respect to existing code approaches. Essentially it can be assumed to be a near-optimal solution especially in the case of capacity curves with significant changes in stiffness, representative of modern modeling approaches that account for the uncracked section properties. The error introduced by the near optimal bilinear fit does not exceed 20% for elastic-plastic fits and it seldom exceeds 10% for systems with hardening, while codified approaches were found to be generally conservative, sometimes more than 50% for highly curved shapes.

ACKNOWLEDGEMENTS

The analyses presented in the paper have been developed in cooperation with Rete dei Laboratori Universitari di Ingegneria Sismica – ReLUIS for the research program funded by the Department of Civil Protection – Executive Project 2010-2013.

REFERENCES

[1] P. Fajfar and M. Fischinger, N2 – A method for non-linear seismic analysis of regular structures. *Proceedings of the 9th World Conference on Earthquake Engineering*, Tokyo, 111-116, 1988.

[2] H. Krawinkler and G.P.D.K. Seneviratna, Pros and cons of a pushover analysis of seismic performance evaluation. *Engineering Structures*, **20**, 452-464, 1998.

[3] J.M. Bracci, S.K. Kunnath and A.M. Reinhorn, Seismic performance and retrofit evaluation of reinforced concrete structures *Journal of Structural Engineering* **123**, 3-10, 1997.

[4] A.S. Elnashai, Advanced inelastic static (pushover) analysis for earthquake applications. *Structural Engineering and Mechanics* **12**, 51-69, 2001.

[5] S. Antoniou, R. Pinho, Advantage and limitations of adaptive and non-adaptive force-based pushover procedures. *Journal of Earthquake Engineering* **8**, 497-522, 2004.

[6] A.K. Chopra and R.K. Goel, A modal pushover analysis procedure for estimating seismic demands for buildings. *Earthquake Engineering and Structural Dynamics*, **31**, 561-582, 2002.

[7] T. Vidic, P. Fajfar, M. Fischinger, Consistent inelastic design spectra: strength and displacement. *Earthquake Engineering and Structural Dynamics*, **23**, 507-521, 1994.

[8] E. Miranda and V.V. Bertero, Evaluation of strength reduction factors for earthquake-resistant design. *Earthquake Spectra*, **10**(2), 357-379, 1994.

[9] D. Vamvatsikos and C.A. Cornell, Direct estimation of the seismic demand and capacity of oscillators with multi-linear static pushovers through Incremental Dynamic Analysis. *Earthquake Engineering and Structural Dynamics*, **35**(9), 1097-1117, 2006.

[10] Comitè Europèen de Normalisation. *Eurocode 8 – Design of Structures for earthquake resistance – Part 1: General rules, seismic actions and rules for buildings*. EN 1998-1, CEN, Brussels, 2003.

[11] Federal Emergency Management Agency (FEMA), *NEHRP Guidelines for the seismic rehabilitation of buildings*. Report No. FEMA-273, Washington, D.C., 1997.

[12] Federal Emergency Management Agency (FEMA), *Prestandard and commentary for the seismic rehabilitation of buildings*. Report No. FEMA-356, Washington, D.C., 2000.

[13] Federal Emergency Management Agency (FEMA), *Improvement of nonlinear static seismic analysis procedures*. Report No. FEMA-440, Washington, D.C., 2005

[14] American Society of Civil Engineers (ASCE), *Seismic Rehabilitation of Existing Buildings*, ASCE/SEI 41-06, Reston, Virginia, 2007.

[15] S.W. Han, K. Moon, A.K. Chopra, Application of MPA to estimate probability of collapse of structures. *Earthquake Engineering and Structural Dynamics*, **39**, 1259-1278, 2010.

[16] D. Vamvatsikos and C.A. Cornell, Incremental Dynamic Analysis. *Earthquake Engineering and Structural Dynamics*, **31**, 491-514, 2002.

[17] L.F. Ibarra, R.A. Medina, H. Krawinkler, Hysteretic models that incorporate strength and stiffness deterioration, *Earthquake Engineering and Structural Dynamics*, **34**, 1489-1511, 2005.

[18] D. Vamvatsikos and C.A. Cornell, Applied Incremental Dynamic Analysis. *Earthquake Spectra*, **20**, 523-553, 2004.

[19] D. Vamvatsikos, M. Fragiadakis, Incremental dynamic analysis for estimating seismic performance sensitivity and uncertainty. *Earthquake Engineering and Structural Dynamics*, **39**, 141-163, 2010.

[20] M. Fragiadakis, D. Vamvatsikos, M. Papadrakis., Evaluation of the influence of vertical irregularities on the seismic performance of a nine-storey steel frame. *Earthquake Engineering and Structural Dynamics*, **35**, 1489-1509, 2006.

[21] D. Vamvatsikos, Some thoughts on methods to compare the seismic performance of alternate structural designs. In: Dolsek M. (ed), *Protection of Built Environment Against Earthquakes*. Springer: Dordrecht, 2011.

COMPDYN 2011
III ECCOMAS Thematic Conference on
Computational Methods in Structural Dynamics and Earthquake Engineering
M. Papadrakakis, M. Fragiadakis, V. Plevris (eds.)
Corfu, Greece, 25–28 May 2011

FRAGILITY ASSESSMENT OF RC FRAMES COLLAPSE CAPACITY

Ilias A. Gkimousis[1], **Vlasis K. Koumousis**[1]

[1]Institute of Structural Analysis & Aseismic Research
National Technical University of Athens
Zographou Campus GR-15780, Athens, Greece
iliasgkim@hotmail.com, vkoum@central.ntua.gr

Keywords: Incremental Dynamic Analysis, Fragility Curves, Probability of Collapse, Redundancy, Stiffness Distribution, Strong Column-Weak Beam ratio

Abstract. *The inelastic behavior of reinforced concrete structures subjected to a number of strong motion excitations of escalated Intensity Measure (IM) and monitoring of characteristic Engineering Demand Parameters (EDPs) of the structure for all these different instances is presented. This provides the necessary data to estimate the overall response of a structure at a particular site of specified seismic hazard and constitutes the framework of Incremental Dynamic Analysis (IDA). In this, generation of data regarding capacity and demand evolves following a lognormal distribution while the corresponding cumulative distribution function is used to define the corresponding fragility curves. This analysis facilitates further the deduction of statistically sound estimates of the measured parameters. The hysteretic inelastic response of reinforced concrete members, i.e. beams and columns designed on the basis of Eurocodes is of primal importance. The Bouc-Wen model, as implemented in "Plastique" code is considered following the IDA procedure, the parameters of which are established based on existing experimental data. Through this modelling, a series of plane frames of different number of spans and storeys designed in a similar manner is investigated. Also, the effect of some general design code provisions on collapse capacity of these frames, such as stiffness distribution along height and strong column- weak beam ratio, are examined. Numerical results are presented and their corresponding fragility curves are derived. Interesting features are revealed, regarding the effect of each alternative design on collapse capacity, which often deviate from collapse predictions made using the static pushover analysis.*

1 INTRODUCTION

One of the main objectives of current earthquake-resistant design codes is to ensure increased levels of safety commencing with protection of human life during strong earthquakes, while reducing damage - repair cost for small and medium excitations for new and existing structures. This constitutes the framework of Performance Based Earthquake Engineering (PBEE) by defining performance levels which correspond to different damage situations. The level of collapse prevention for example, demands certain probability of collapse that does not exceed the acceptable limits set for this purpose. However, at the moment, code provisions are deterministic in nature, as they are based on return periods relating seismic excitation with specific levels of damage.

Hence, it is important to establish these probabilities and follow design methods that statistically ensure the non exceedance of the specified damage state. The Incremental Dynamic Analysis (IDA) [1, 2] addresses this issue by calculating statistical data in terms of Intensity Measure (IM) and Engineering Demand Parameters (EDPs). This is followed by a statistical analysis of the outcome and the evaluation of fragility curves [3, 4]. This procedure is capable of revealing significant probabilistic evidence of structural behaviour by defining relation between probability of collapse and ground motion IM. If fragility curves are combined with seismic hazard data from a certain region of interest, that combine the same IM with the seismic hazard, the Mean Annual Frequency (MAF) of exceeding a performance state is derived for the particular seismic hazard site.

In this paper the aforementioned methodology is used to assess collapse capacity of Reinforced Concrete plane frames designed following different considerations. It should be noted that these frames are centreline models of 3D symmetrical structures with equal inertia characteristics and fixed supports. More specifically, this study concentrates on the performance state of dynamic collapse by examining the effect of geometrical and structural frame parameters on the probability that a collapse event occurs.

2 ANALYTICAL PROCEDURE

2.1 Implementing IDA

In order to perform nonlinear elastoplastic dynamic analysis following the IDA method, the ''Plastique'' [5] program was used which employs the phenomenological Bouc-Wen hysteretic model, the parameters of which were defined as described in [6]. To establish more realistic results as the structure approaches collapse where large displacements, i.e. P-Δ effects, become significant and they were introduced according to [7]. This is a simple, approximate, non-iterative technique, where lateral forces are introduced to each storey level due to the overturning moments caused by the movement of diaphragm masses.

As far as IDA is concerned, as the scalar, escalated intensity measure (IM) the 1st eigenmode spectral acceleration with 5% viscous damping Sa (T1, 5%) was selected. Respectively, the engineering demand parameter (EDP) that measures demand on different levels of structural deterioration is the maximum interstorey drift ratio. To save computational time the haunt & fill algorithm as the method to trace IDA curves, after repeated runs, was selected [2]. This was parameterized properly to achieve as much accuracy as possible in the region of dynamic instability. Twenty accelerograms were selected for the analysis, corresponding to major earthquakes in California and they are listed in [2, 8]. They consist of relatively large magnitude excitations, moderate distances from fault, so as to avoid pulse excitations and near field effects [9]. In Figure 1, the median and the 84% percentile response spectra for all twenty excitations are presented. The only source of uncertainty used in this study is the record to record variability (aleatory uncertainty) which is sensitive to the dispersion of spectra in the region of structure's 1^{st} eigenperiod. For the selected ground motions this dispersion in their spectral accelerations is computed in terms of logarithmic standard deviation through equation (1) and the final graph is presented in Figure 2.

$$\sigma_{\ln,y} = \ln\left(\frac{y_{84}}{y_{50}}\right) \tag{1}$$

where, y_{50} are the median spectral values while y_{84} are the 84% percentile spectral values for a given eigenperiod.

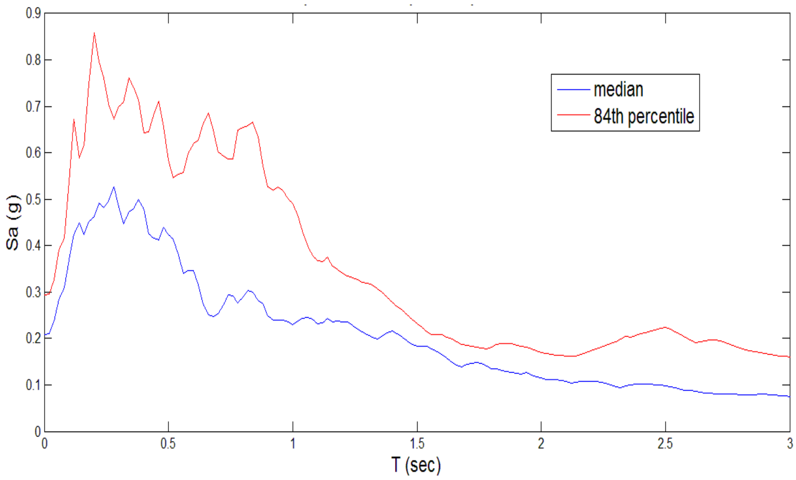

Figure 1: Median and 84% percentile response spectra for all twenty earthquakes

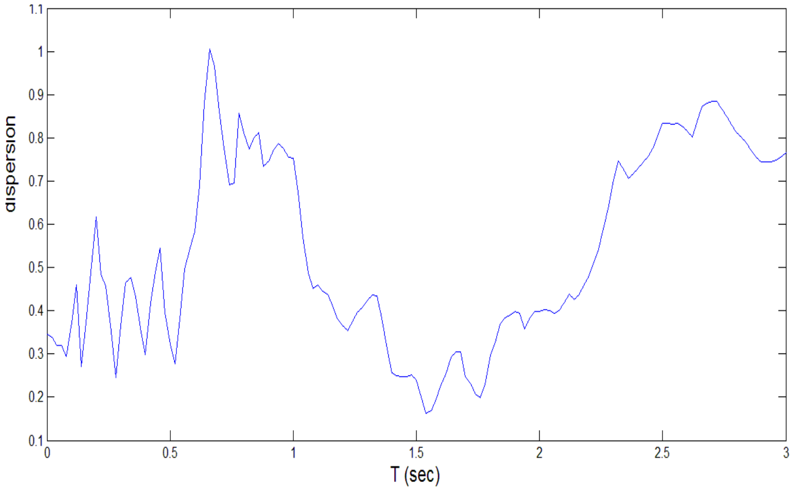

Figure 2: Dispersion of twenty acceleration spectra for the eigenperiods of interest.

2.2 Statistical evaluation

After performing the computationally demanding IDA, some very important features usually emerge with the proper statistical evaluation of the outcome. The statistical sample in this work consists of twenty spectral accelerations (Sa_c) where dynamic collapse occurred. Collapse is considered to happen, when a global or local collapse mechanism is formed, or when maximum interstorey drift ratio exceeds the value of 12%. In order to pursue analytical calculations, a lognormal distribution is fitted to the data and by calculating its cumulative distribution function (CDF) a collapse fragility curve, based on the IM approach [3, 4], is derived as follows:

$$P[Sa_c \le Sa] = \Phi\left[\frac{1}{\beta_{Sa,c}} \ln\left(\frac{Sa}{n_{Sa,c}}\right)\right] \tag{2}$$

where, $\beta_{Sa,c}$ is the standard deviation of the natural logarithm, while $n_{Sa,c}$ is the lognormal median of the data.

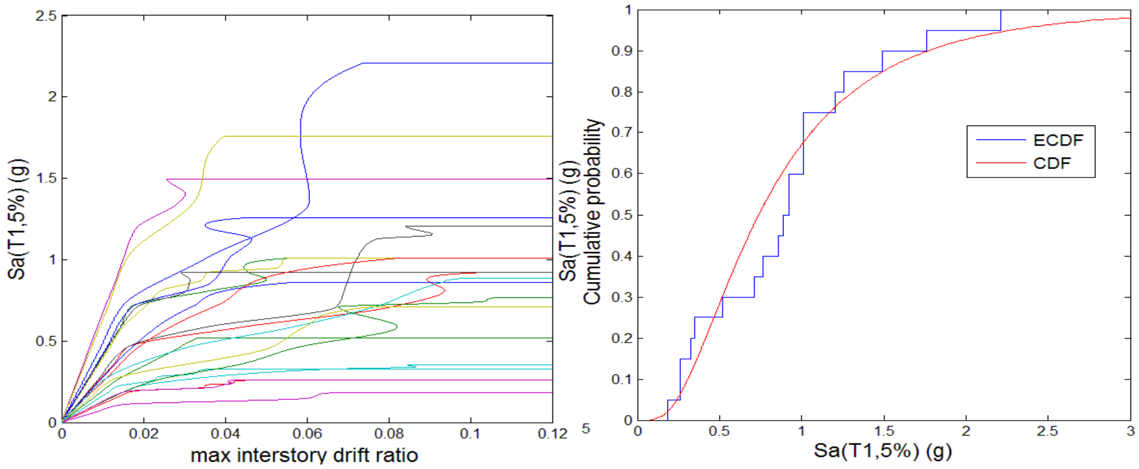

(a) (b)

Figure 3: a) All 20 IDA curves, b) Corresponding empirical and analytical fragility curves

The above described steps are presented in Figure 3, for the case of a 6-storey, 2-bay plane RC frame with first eigenfrequency, T_1= 0.639 sec. In the figure, the lognormal distribution, fitted to the data, is presented and consists the fragility curve for this frame.

Furthermore, in the literature several indices are defined that can be used to quantify the stochastic nature of fragility. To determine the most representative ones, a Probabilistic Seismic Hazard Analysis (PSHA) for the seismic site of interest is required, that provides the necessary hazard spectra and hazard curves. This data, when combined with fragility curves, can reveal the very important feature of how rarely a structure collapses when it is subjected to spectral accelerations that are possible to occur in the specific geographical region. This measure is the mean annual frequency (MAF) of collapse and its inverse is the collapse return period of the structure. In this study, the hazard curves that were implemented in the procedure are referred to the IM and are given in [10]. The indices used [11] are the median collapse spectral acceleration $(Median\,(Sa_c))$, the probability of collapse for the earthquake with probability of occurrence 10%/50 years $(P_{C|10\%/50y})$, the Margin Against Collapse (MAC) for the 10%/50 years earthquake (eq. 3) and the MAF of collapse (eq. 4). Also, the dispersion of structural behaviour according to different seismic excitations can be described through the standard deviation of the natural logarithm of the data $\left(\sigma_{\ln}\right)$.

$$MAC_{10\%/50\,years} = \frac{Median\,(Sa_c)}{Sa_{10\%/50\,years}} \tag{3}$$

where $Sa_{10\%/50\,years}$ is given in the hazard spectrum and defines the spectral acceleration that is expected to occur when the earthquake with probability of occurrence 10% in 50 years strikes.

$$MAF = \lambda_c = \int_0^{\infty} F_{C,Sa,c}(x)\, \left| d\lambda_{Sa}(x) \right| \tag{4}$$

where $F_{C,Sa,c}(x)$ is the collapse fragility curve and $\lambda_{Sa}(x)$ is the ground motion hazard curve.

3 EFFECT OF DESIGN CRITERIA IN THE COLLAPSE CAPACITY OF RC FRAMES

3.1 Effect of the number of bays and storeys

In Figure 4, eight plane RC frames of 3 and 6 storeys have been designed according to Greek codes, with number of bays ranging from 1 to 4. In order to facilitate comparison they retain the same reinforcement in the interior and exterior columns respectively.

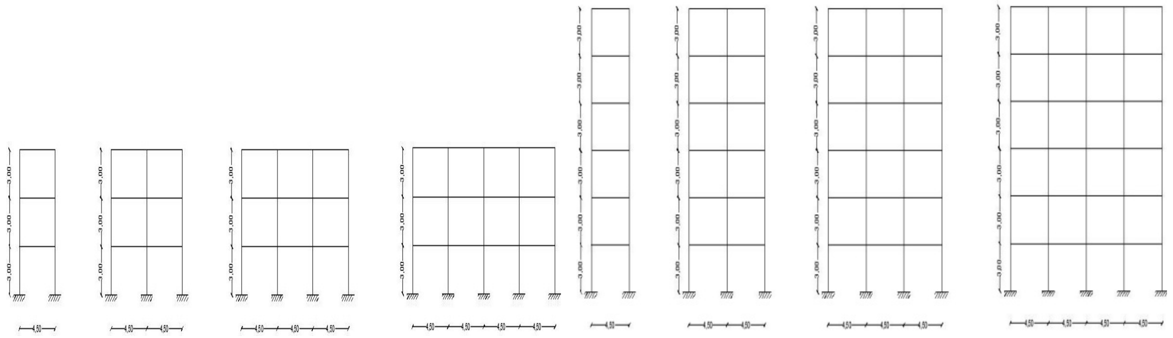

(a) (b)

Figure 4: a) 3 storey frames, b) 6 storey frames

Column sections (m)	Beam sections (m)	Bay length (m)	Storey height (m)
0.25x 0.25	0.30x0.20	4.50	3.00

Table 1: Plane frames geometrical features

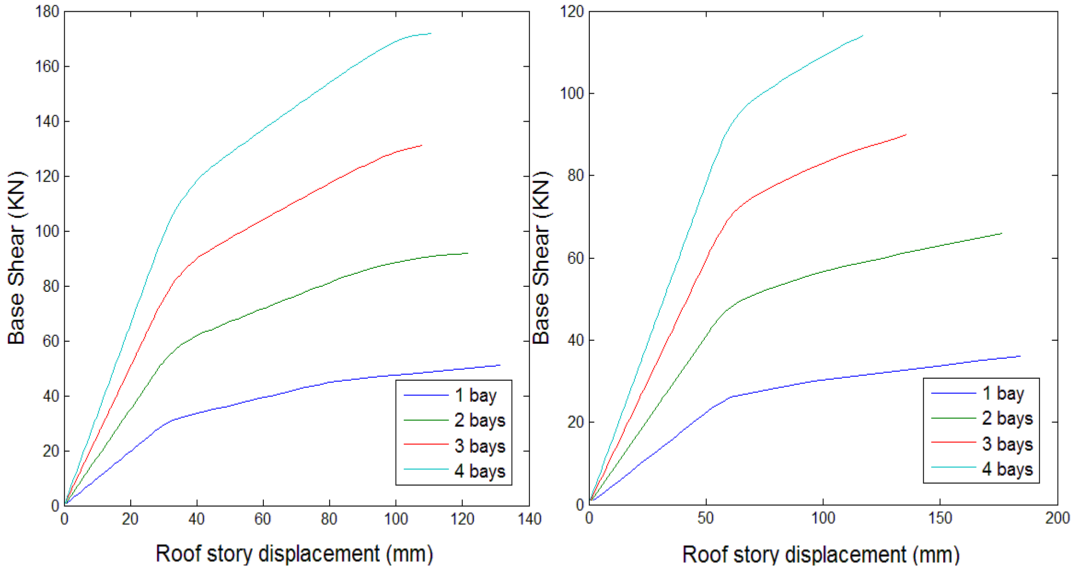

(a) (b)

Figure 5: a) Pushover curves for 3 story frames, b) Pushover curves for 6 story frames

Next, the static pushover results with triangular lateral force distribution are displayed in Figure 5. The general trend is that, as the number of bays increases, redundancy also increases and the greater possibility for force redistribution exists, resulting into higher capacity [13].

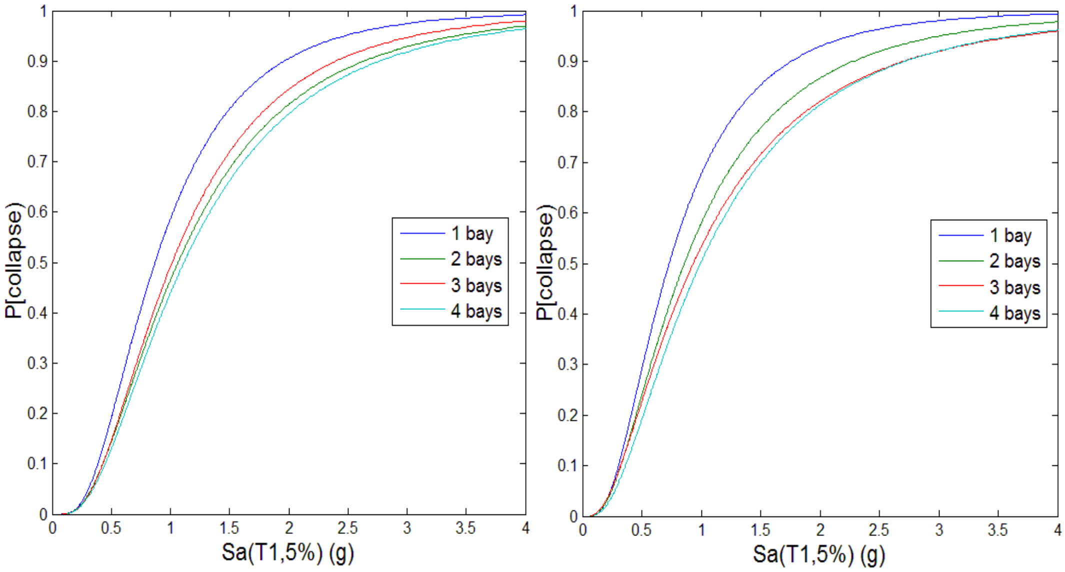

(a) (b)

Figure 6: a) Collapse fragility curves for 3 storey frames, b) Collapse fragility curves for 6 storey frames

The same frames are analysed following the IDA method. Collapse fragility curves are produced and they are presented in Figure 6. In Table 2 the probabilistic indices for collapse estimation have been calculated, together with measures of deformation such as the median interstorey drift ratio (IDR) and the median roof drift ratio (RDR). It is important to notice that the results are meant only for comparison between the different frames of the analysis as they appear inadequate to withstand the strong earthquakes of California, as they are poorly designed with the minimum code reinforcement.

Storeys	Bays	T1(sec)	Median (Sa_C)	$\sigma_{\ln}$	$P_{C\|10\%/50y}$	MAC	λ_C	Median (IDR)	Median (RDR)
3	1	0.324	0.87	0.63	74%	0.67	0.0121	0.031	0.023
	2	0.349	1.06	0.70	61%	0.82	0.0098	0.079	0.053
	3	0.357	1.02	0.67	64%	0.78	0.0103	0.054	0.041
	4	0.362	1.12	0.71	59%	0.86	0.0093	0.089	0.054
6	1	0.650	0.70	0.68	75%	0.63	0.0100	0.045	0.022
	2	0.693	0.86	0.76	65%	0.75	0.0086	0.080	0.035
	3	0.708	0.93	0.82	60%	0.81	0.0076	0.080	0.038
	4	0.717	1.00	0.77	57%	0.87	0.0068	0.076	0.040

Table 2: Collapse capacity quantification for all RC frames

A basic difference between pushover and IDA is that in the case of 3-storey frames collapse capacity does not increase with the increase of the number of bays. More specifically, the 2-bay frame exhibits smaller probability of collapse for the 10%/50 years earthquake and smaller MAF of collapse than the 3-bay frame. Comparing the two different groups of frames, the 6-storey frames result into larger dispersion of the results due to the fact that their eigenperiods represent larger spectral dispersion according to Figure 2. Also, median collapse spectral acceleration (Sa_c) takes smaller values for the 6-storey frames. Although it results that with the increase of frame height collapse capacity decreases, which is logical as P-Δ effects becomes important and also higher axial load in columns causes their ductility to diminish, this statement can't be generalised due to the limited sample of the current study. In contrast, the MAF of collapse for the 6-storey frames seems to be smaller, meaning larger collapse return periods, since smaller spectral accelerations are expected to appear in larger eigenperiods. The context of table 2 is displayed graphically in Figure 7.

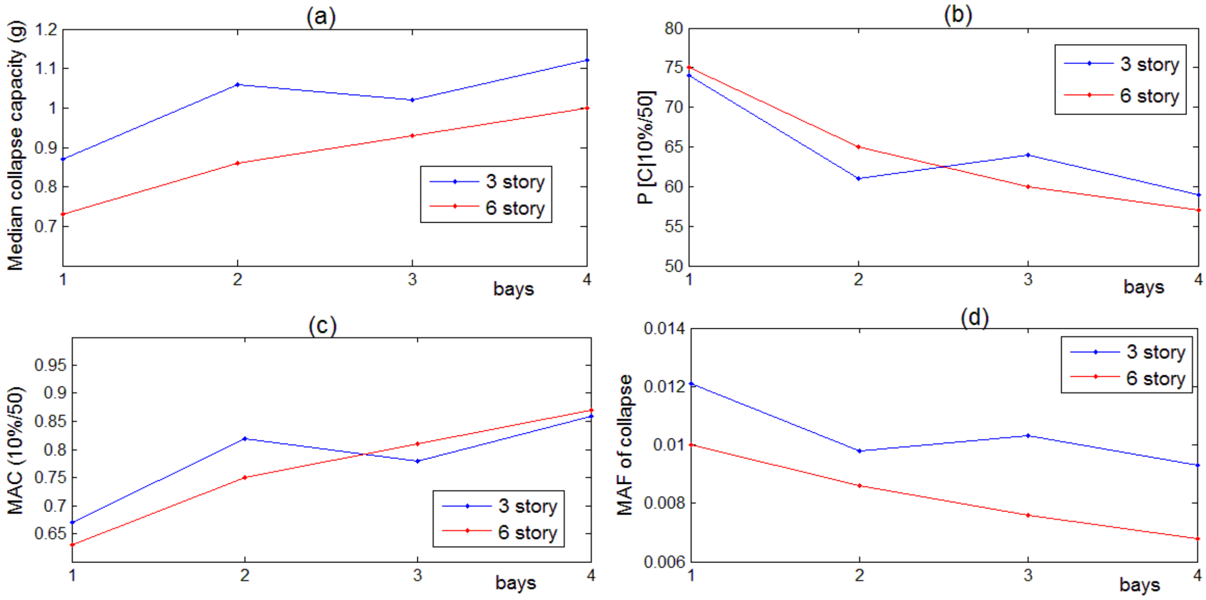

Figure 7: Effect of the number of bays and storeys in frames collapse capacity. a) Median collapse capacity, b) Probability of collapse for the 10%50 years earthquake, c) MAC for the 10%/50 years earthquake, d) MAF of collapse

The results of the last 2 columns in table 2 that refer to deformations are presented in Figure 8.

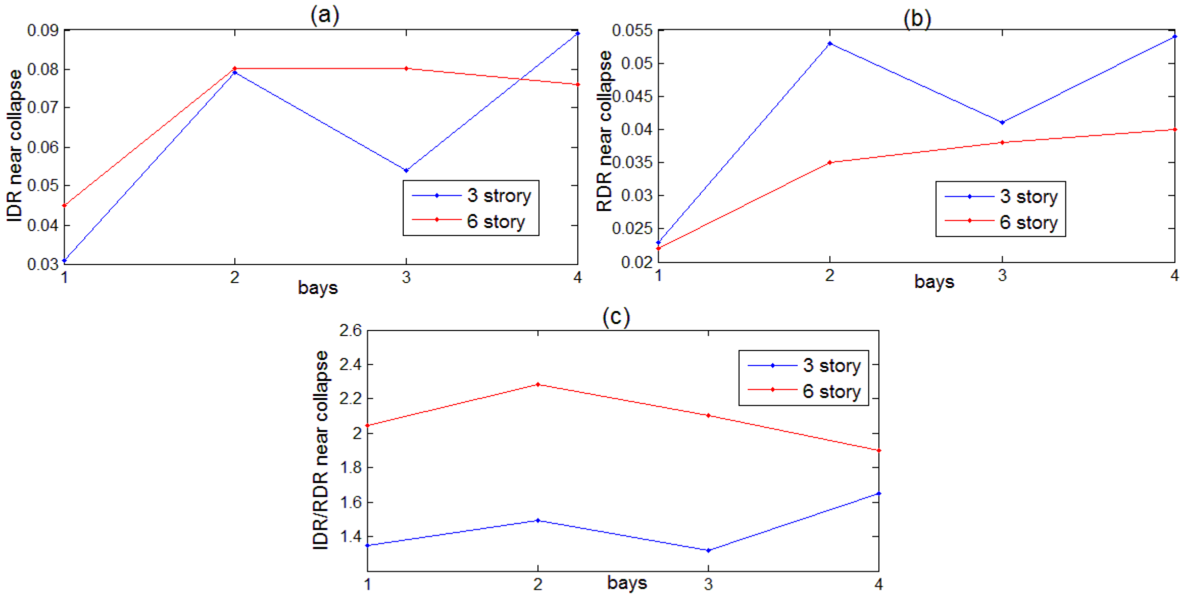

Figure 8: Effect of the number of bays and storeys in frames displacements near collapse. a) Interstorey drift ratio (IDR), b) Roof drift ratio (RDR), c) IDR/RDR

In Figure 8c, IDR/RDR ratio depicts the degree of damage accumulation in a few storeys. As the ratio becomes bigger, like in 6-storey frames, it is portrayed that damage is localized in a few storeys of the building, while in 3-storey frames damage is almost equally distributed along the height. Generally, 1-bay frames develop smaller displacements and for 6-storey frames they seem to stabilize when more bays are added. Also, 6-storey frames don't exhibit as large demands in displacements as the 3-storey frames, for the same reasons that collapse capacity in terms of spectral accelerations decreases, as it was mentioned.

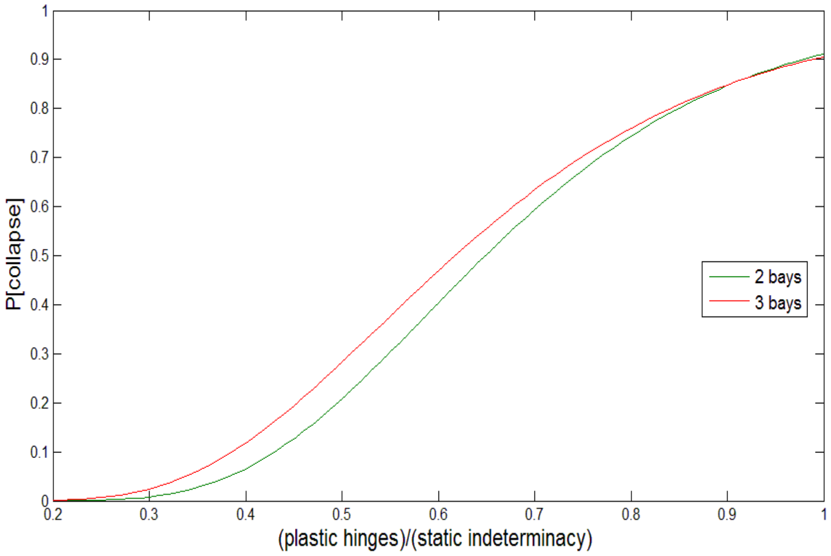

Figure 9: Number of plastic hinges involved in collapse for 2-bays and 3-bays frames

In Figures 7 and 8 it is evident that for 3-storey frames, although it was expected to develop higher strength against collapse than the 2-bay frames, the opposite happens. It is probable that this feature is caused by local collapse mechanisms that don't allow the structure to take advantage of its full redundancy. To elaborate more on this fact, the measure of structural redundancy that was given by Bertero and Bertero [14] was investigated. This measure is the number of plastic hinges n that yield or fail at structural members ends until total collapse. So, in each single record IDA run where collapse is detected, the number of formed plastic hinges is recorded. This number is divided by the number of static indeterminacy of the structure to determine the redundancy ratio. Thus, a statistical set with 20 values is formed and the results are presented in the form of a cumulative distribution function in Figure 9. It is clear that the 3-bay frame stays behind in consuming its full redundancy for a specific probability of collapse. Therefore, for a given probability of collapse, in the 3-bay frame the redundancy ratio, that expresses the cross sections that have yielded or failed, is smaller than the redundancy ratio in the 2-bay frame respectively, a fact that reveals the probabilistic nature of structural redundancy as related to seismic loading.

The nonlinear modelling of structures with the notion of plastic hinge formation reveals the estimated form of collapse. For every collapse mechanism identified in each single record IDA, the number of storeys involved in the mechanism is recorded and the results are shown in Table 3. A particular storey is assumed to participate in the collapse mechanism when at least one plastic hinge appears on its columns or on its beams.

Geometrical features		Percentages of observed plastic hinges						
Storeys	Bays	Storeys 1-1 (%)	Storeys 1-2 (%)	Storeys 1-3(%)	Storeys 1-4(%)	Storeys 1-5(%)	Storeys 1-6(%)	Percentages of storeys involved in collapse (%)
3	1	0	40	60	0	0	0	87
	2	0	25	75	0	0	0	92
	3	0	25	75	0	0	0	92
	4	0	30	70	0	0	0	90
6	1	0	0	15	15	45	25	80
	2	0	0	15	15	35	35	82
	3	0	0	10	30	35	25	79
	4	0	0	5	30	40	25	81

Table 3: Storeys involved in collapse mechanism for each frame

For example in 6-storey, 2-bay frame, plastic hinges are formed in the first 3 storeys in 15% of all the occasions, in the first 4 storeys in 15%, in the first 5 storeys in 35% and all storeys are involved in collapse mechanism in 35% of all the occasions. Also, the total percentage of storeys where plastic hinges are formed in their beams or columns is 82%. Generally, from Table 3 it is observed that the distribution of plastic hinges along height is not influenced by the number of bays and that there is a tendency for concentration of damage in higher floors. There is no case of first storey mechanism for the 3-storey frames, not first or second storey mechanism for 6-storey frames. The involvement of fifth and sixth storey is significant, since flexural strength of columns is about 3 times bigger than flexural strength of beams causing the beams in upper floors to yield faster. Finally, percentages of storeys involved in collapse for 6-storey frames are clearly smaller, a fact that comes in agreement with Figure 8(c). Hence, it is evident from a different perceptive that damage concentrates in few storeys in the case of the 6-storey frames.

3.2 Effect of stiffness distribution along height

To examine the effect of stiffness distribution along the height in RC frames collapse capacity, 2 different designs of the 6-storey 2-bay frames have been analysed. The study refers to normal, moment resisting frames, mass is considered equal in all storeys and distribution of stiffness between 2 consecutive storeys doesn't exceed 60%. Also, the same moment of inertia is attributed to the same floor's members, as all beams and columns have the same geometrical properties. In order to quantify stiffness variation for every alternative design, the indices in equations (5) to (7) are used as in [15]. These indices provide information about the form of building lateral displacements, whether they are shear-type or flexural-type dominated. Index ρ_i is defined as the ratio of the sum of stiffness ratio of all beams at floor i to the sum of the stiffness ratio of all columns at the same floor. When ρ_i equals to zero, then pure flexural-type deformation occurs and if ρ_i becomes infinite then pure shear-type deformation occurs, while intermediate values stand for a combination of the 2 types where both beams and columns deform in flexure. Index ρ_b quantifies the variation of beams stiffness and is defined as the ratio of the sum of stiffness ratio of all beams at each floor to the sum of the stiffness ratio of all beams at the first floor. Similarly, index ρ_c is defined for columns.

$$\rho_i = \frac{\sum_{story\ i\ beams} \frac{EI_b}{L_b}}{\sum_{story\ i\ columns} \frac{EI_c}{L_c}} \tag{5}$$

$$\rho_b = \frac{\sum_{story\ i} \frac{I_b}{L_b}}{\sum_{1st\ story} \frac{I_b}{L_b}} \tag{6}$$

$$\rho_c = \frac{\sum_{story\ i} \frac{I_c}{L_c}}{\sum_{1st\ story} \frac{I_c}{L_c}} \tag{7}$$

In Figure 10, all the above indices are presented for the 3 frames designed to have different stiffness variation along height. Frame (a) is the 6-storey, 2-bay frame presented in §(3.1). This frame is designed according to Greek codes with variation in columns reinforcement along height. External columns maintain the same amount of reinforcement, while the interior ones reduce steel bars diameters in the 5th and 6th floor. Frame's (b) reinforcement remains constant along height in each column so as in all storeys its index ρ_i to take approximately the same mean value with frame (a). Frame (c) is based on frame (b), but with beam cross sections varying as number of floor increases. This variation is applied only in cross sections and not in the reinforcement so as yield moment strength to remain practically constant.

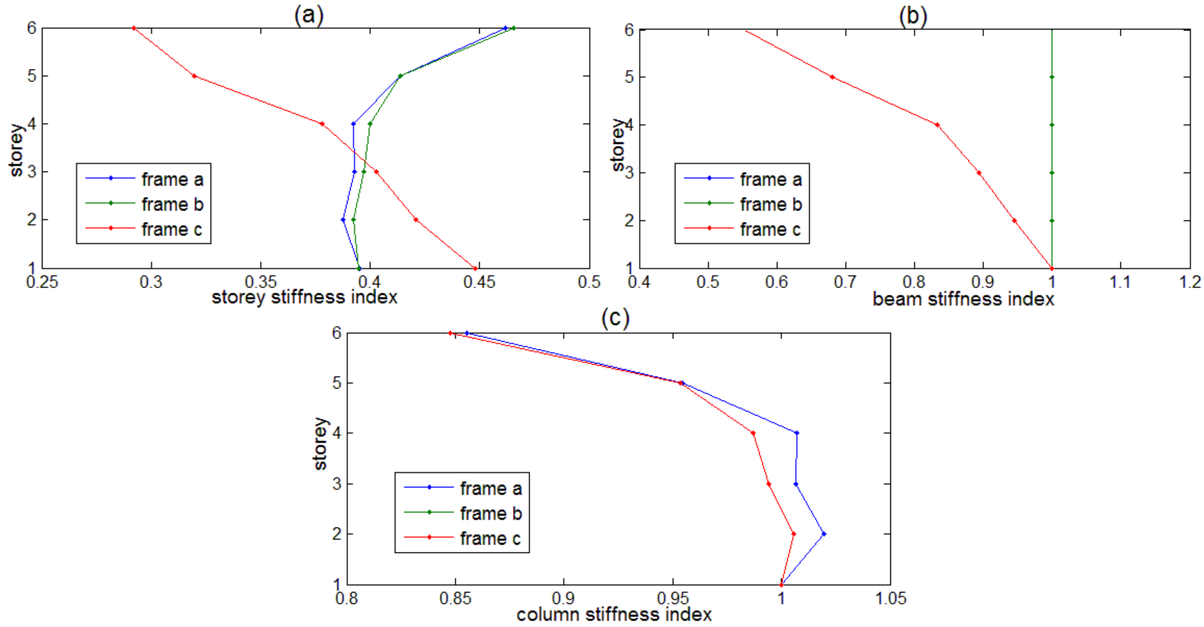

Figure 10: Variation of stiffness along height for the 3 alternative designs. a) Storey stiffness index ρ_i , b) Beam stiffness index ρ_b , c) Column stiffness index ρ_c

In the first two frames, that present constant beam stiffness in all storeys, ρ_i index attains bigger values in upper floors as reinforcement in columns decreases. On the other hand with beam cross section reduction in size in the 3rd design, index ρ_b becomes smaller as presented in Figure 10b. In the same figure, plots for frames (a), (b) are identical as their beams are the same everywhere, while in Figure 10c, plots for frames (b), (c) are identical as they have the same column properties. In general, variation of beam moments of inertia affects the frames in which beams rotations influence their deformation more than columns lateral displacements.

After performing IDA for the three frames, fragility curves are determined which are presented in Figure 11. Intuitively, one would expect that equal stiffness in each storey would have forced damage to concentrate on lower floors, dictating the collapse capacity to decrease. However, as it is portrayed in Figure 11, using the same amount of reinforcement in columns results into slight augmentation of collapse spectral acceleration. Nevertheless, there is no more collapse capacity increase when beam cross sections vary while keeping the reinforcement and the cross section of columns constant.

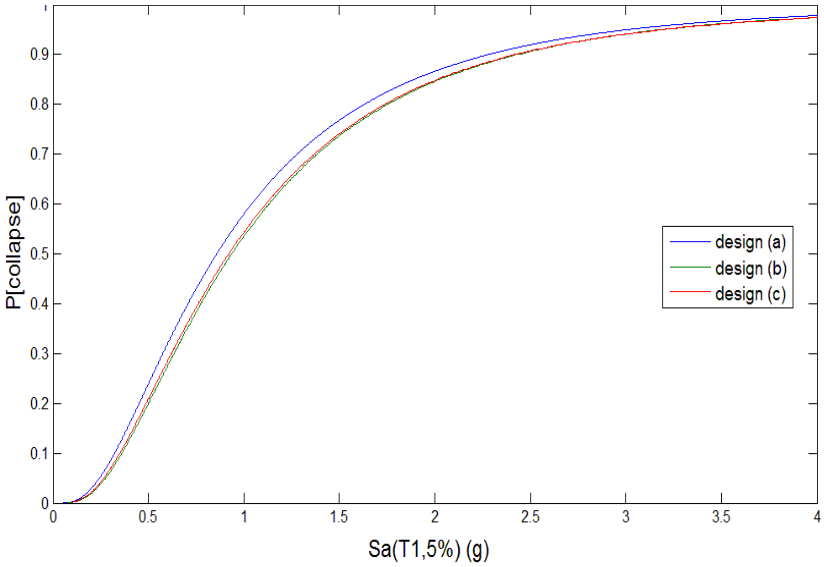

Figure 11: Fragility curves of the 3 RC frames with different stiffness variation along height

Fragility behaviour is quantified through the calculation of probabilistic indices described in §(2.2). The new outcomes are presented in table 4 below.

Frame	T1(sec)	Median (Sa_C)	$\sigma_{\ln}$	$P_{C\|10\%/50y}$	MAC	λ_C	Median (IDR)	Median (RDR)
a	0.693	0.86	0.76	65%	0.75	0.0078	0.080	0.035
b	0.694	0.94	0.74	61%	0.82	0.0072	0.080	0.046
c	0.705	0.93	0.75	62%	0.81	0.0072	0.076	0.035

Table 4: Collapse capacity quantification for the 3 different design alternatives

From Table 4 a significant feature based on IDR/RDR ratio is displayed, which describes damage localization in specific storeys. The smaller value for frame (b), meaning more similar damage distribution along height, is a main reason for the higher collapse capacity exhibited. This ratio is smaller because displacements in terms of roof drift ratio appears to be greater for frame (b) since it has less stiffness in its lower columns, facilitating in this way plastic hinge formation in these critical regions. Therefore, plastic hinges at the bottom of first floor columns helps seismic energy dissipation and is a positive feature for capacity design. More specifically, plastic hinge distribution at collapse can be found in Table 5. Generally, no significant differences are observed in the way that stiffness distribution affects plastic hinge distribution. For the case of frame (b) with uniform column reinforcement, in 50% of all the occasions plastic hinges are formed up to 5th storey. Hence, it isn't the fact that more storeys are involved in collapse mechanism which increases collapse capacity, but the fact that more columns participate in the mechanism, as they aren't as stiffened as in frame (a) where lower storey columns were designed with increased reinforcement.

	Percentages of observed plastic hinges						
Frames	Storeys 1-1 (%)	Storeys 1-2 (%)	Storeys 1-3(%)	Storeys 1-4(%)	Storeys 1-5(%)	Storeys 1-6(%)	Percentages of storeys involved in collapse (%)
a	0	0	15	15	35	35	82
b	0	0	15	10	50	25	81
c	0	0	15	10	45	30	82

Table 5: Storeys involved in collapse mechanism for each frame

3.3 Effect of the strong column-weak beam ratio

The aim of the strong column-weak beam (SCWB) design provision is to avoid localized story mechanisms and thus attain more distributed failure mechanisms. In order to study the effect of this concept, only yield moments of beams and columns are taken into account through index α [15], which is defined as the ratio of the sum of columns yield moments to the sum of beams yield moments that exist in a given joint.

$$\alpha = \frac{\sum M_{c,y}}{\sum M_{b,y}} \tag{8}$$

In this work, the alternative designs are based in the 3-storey, 3-bay frame, where beams reinforcement remains constant and only columns reinforcement varies from one design to another resulting in different α values. Lastly, index α is referred to the middle joint of the 1st floor.

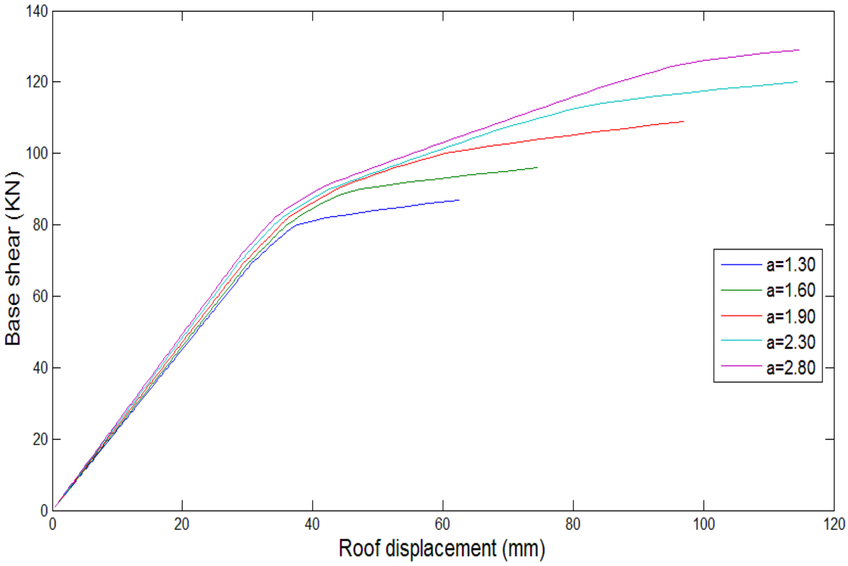

Figure 12: Static pushover curves for the different SCWB ratios

First, a static pushover analysis is performed for the five resulting RC frames and the outcome is presented in Figure 12 in order to depict the primal behaviour which will be compared with IDA. Generally, the dominant tendency is an increase of ultimate strength with the increase of column reinforcement. In addition, ductility is getting bigger and bigger up to $\alpha = 2.30$, where reinforcement area is the 2% of cross sectional area.

After performing IDA for all five frames, the fragility curves are determined which are displayed in Figure 13. Also, the accompanying probabilistic indices are included in Table 6.

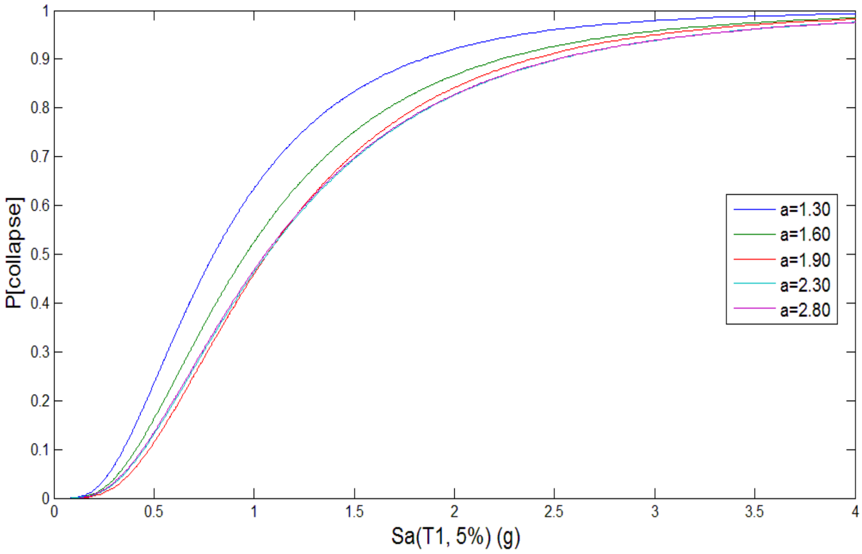

Figure 13: Fragility curves for the different SCWB ratios

α	T1(sec)	Median (Sa_C)	$\sigma_{\ln}$	$P_{C\|10\%/50y}$	MAC	λ_C	Median (IDR)	Median (RDR)
1.30	0.386	0.80	0.65	77%	0.62	0.0133	0.052	0.032
1.60	0.375	0.96	0.66	68%	0.74	0.0109	0.069	0.048
1.90	0.368	1.07	0.63	62%	0.82	0.0098	0.066	0.049
2.30	0.365	1.07	0.67	62%	0.82	0.0097	0.076	0.056
2.80	0.363	1.06	0.68	62%	0.82	0.0097	0.077	0.056

Table 6: Collapse capacity quantification for the 5 different SCWB ratios

The results in Figure 13 and Table 6 present increased collapse strength until $\alpha = 1.90$ and after that, further increase in α does not result into bigger collapse capacity, as fragility curves for $\alpha = 2.30$ and $\alpha = 2.80$ slightly differ from the fragility curve for $\alpha = 1.90$. Actually, due to larger dispersion in the last two cases, these curves present smaller collapse spectral accelerations at low collapse probabilities. Therefore, a difference in results is observed in comparison with pushover, since collapse capacity doesn't increases repeatedly when more reinforcement is added in columns. However, IDA defines a strength limit that can be assessed, meaning that the addition of more reinforcement in columns has no effect except the increase in cost. For the case of the frame studied here, this limit is accessed for $\alpha = 2$, when yield moment of columns is twice the yield moment of beams.

The results of Table 6 are displayed graphically in Figure 14. Both from Table 6 and figure 14 it is evident that there is an improvement by 15% in collapse capacity from the worst to the best design. Also an improvement of 33% at median collapse spectral acceleration and at the margin against collapse occurs, while the return period of collapse increases by 28 years. In terms of displacements, frame exhibits repeatedly larger interstorey and roof drifts up to $\alpha = 2.30$, while for $\alpha = 2.80$ no further increase occurs, which is in agreement with the static pushover results. In order to elaborate on the fact that improvement of collapse capacity is bounded up to a certain level, the results of plastic hinge formation during formation of collapse mechanisms are listed in Table 7.

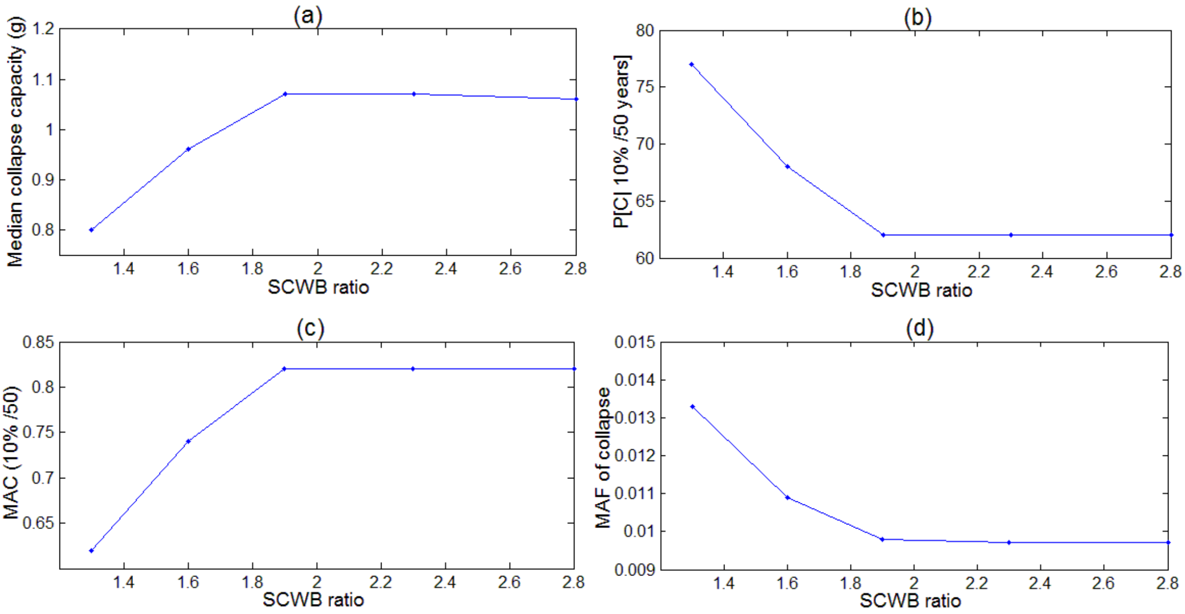

Figure 14: Effect of SCWB ratio on collapse capacity for a 3 storey, 2 bay RC frame

α	Average number of plastic hinges formed (%)	Plastic hinges percentages at columns (%)	Plastic hinges percentages at beams (%)	Capacity design violation percentages (%)
1.30	19.5	57	43	55
1.60	21	45	55	45
1.90	21	33	66	15
2.30	19.5	20	80	15
2.80	18	12	88	5

Table 7: Plastic hinge percentages at collapse

In the last column of Table 7, capacity design violation is considered to occur when a column fails prior to a beam at a given joint in the structure. Such violation can happen even if the formation of a plastic hinge at a beam isn't adequate to prevent final failure at column in the joint. As expected, more plastic hinges are formed in beams as column flexural strength increases, while the average number of total plastic hinges formed remains unaffected with SCWB ratio, meaning that only distribution of plastic hinges changes. Also, violation of capacity design regulation percentages are reduced while this ratio gets bigger. However, for values larger than 1.90 this percentage doesn't appear to differ a lot, a fact that is also portrayed by the similarity of fragility curves presented in Figure 13. Thus, it is clear that when capacity design provisions are robust, then an optimum design with respect to the probability of collapse can be achieved.

It must also be stated that an even better design can be assessed combining both beam and column flexural strength in the process and not just the SCWB ratio. Indicatively, in Figure 15 two fragility curves are presented which represent the same frame with $\alpha = 2.30$ and an alternative design where beams yield moment improved with the ratio α becoming 1.75. It is clear that this transformation increases slightly collapse capacity by increasing beam rotational capacity, justifying the claim that total structural strength is not affected only by the SCWB ratio but also by the member's strength.

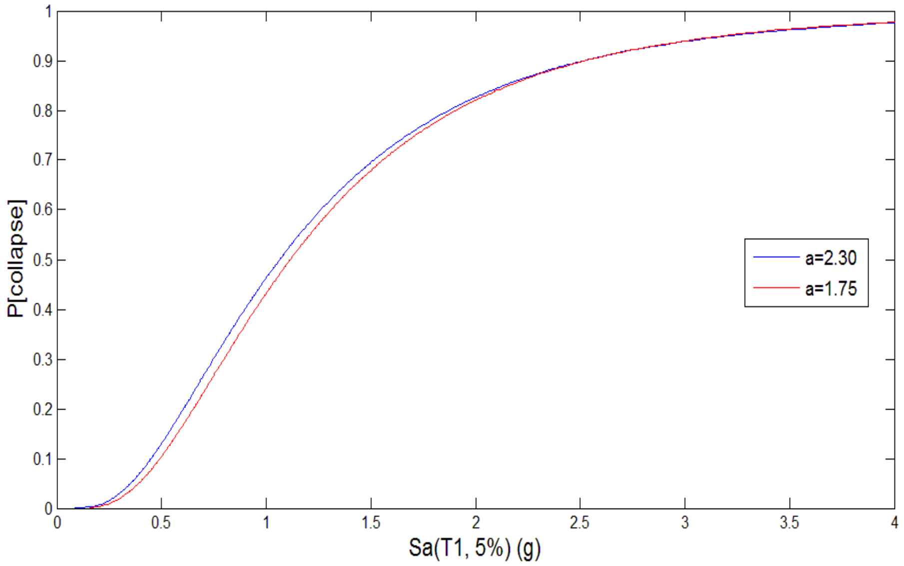

Figure 15: Fragility curves for the same frame after reducing α through beam yield moment increase

4 CONCLUSIONS

In this work fragility curves following IDA have been determined for a series of 2D RC frames to estimate the effect on their collapse capacity when some of their properties are changed. The main remarks drawn can be summarized as follows:

- For the set of frames studied in this work IDA offers similar results with pushover analysis. However, pushover analysis predicts larger differences between results in collapse capacities.
- By calculating mean values for the two groups of frames concerning 6 and 3-storey frames, 17% reduction in collapse probability assuming the 10% in 50 years earthquake occurs and 28% reduction in terms of MAF of collapse achieved when number of bays increased from 1 to 4.
- When stiffness distribution along height varies, probability of collapse reduced only 3% and MAF of collapse improved by 8%.
- With regard to the SCWB ratio, probability of collapse becomes 15% lower, while MAF of collapse is reduced by 27%. Also, it was found that there is an upper limit beyond which collapse capacity is not improving.
- By quantifying the sensitivity in collapse capacity with respect to the investigated factors, it can be concluded that the major factor is redundancy of the structure which is affected by adding more bays. Of equal importance is the SCWB ratio that affects the form of collapse mechanism throughout the structure. Stiffness distribution along the height of the structure appears to be insignificant, suggesting constant reinforcement along the height.
- More elaborate analysis should be performed to establish more general results which should be based on more representative samples and further variation of parameters.

REFFERENCES

[1] D. Vamvatsikos and A. Cornell, *Incremental Dynamic Analysis, Earthquake Eng. Struct. Dyn.* **31** (3), 491–514.

[2] D. Vamvatsikos and A. Cornell, *Applied Incremental Dynamic Analysis, Earthquake Spectra,* Volume 20, No. 2, pages 523–553, May 2004.

[3] F. Jalayer and A.Cornell, *A Technical Framework for Probability-Based Demand and Capacity Factor Design (DCFD) Seismic Formats, PEER Report* 2003/08, November 2003.

[4] F. Zareian, H. Krawinkler, L. Ibarra and D. Lignos, *Basic concepts and performance measures in prediction of collapse of buildings under earthquake ground motions, Struct. Design Tall Spec. Build.* **19***,* 167–181.

[5] Chatzi, E.N., Triantafillou S.P. and Koumousis V.K., *A computer program for 3D inelastic analysis of R/C structures*, *5th GRACM International Congress on Computational Mechanics*, Limassol, July, 2005.

[6] Charalampakis, A.E., Koumousis, V.K., (2008), *Identification of Bouc-Wen hysteretic systems by a hybrid evolutionary algorithm, Journal of Sound and Vibration,* doi:10.1016/j.jsv.2008.01.018.

[7] E.L. Wilson and A. Habibullah, *Static and Dynamic Analysis of Multi – Story Buildings, Including P-Delta effects, Earthquake Spectra, Earthquake Engineering Research Institute* Vol. 3, No. 2, May 1987

[8] D. Vamvatsikos, F. Jalayer, A. Cornell, *Application of Incremental Dynamic Analysis to an RC – Structure, FIB symposium on concrete*, 2003.

[9] H. Krawinkler, R. Medina, B. *Alavi, Seismic drift and ductility demands and their dependence on ground motions, Engineering Structures* **25** (2003) 637–653, 2003.

[10] R. A. Medina and H. Krawinkler, *Seismic Demand for Nondeteriorating Frame Structures and their Dependence on Ground Motions*, Report No. 144, *John A. Blume Earthquake Engineering Center*, December 2003.

[11] C. Haselton, G. Deierlein, *Assessing Seismic Collapse Safety of Modern Reinforced Concrete Moment-Frame Buildings, PEER Report* 2007/08, February 2008.

[12] A. Liel, C. Haselton, G. Deierlein, J. Baker, *Incorporating Modeling Uncertainties in the Assessment of Seismic Collapse Risk of Buildings, Structural Safety* **31** (2009) 197-211.

[13] M.M. Manola, V. Koumousis, *The Role of Redundancy and Overstrength in Earthquake Resisting Design, 9th International Congress on Mechanics* Limassol, Cyprus, July 2010.

[14] Bertero, R. D., and Bertero, V. V. (1999), *Redundancy in earthquake-resistant design, J. Struct. Eng.*, **125** (1), 81-88.

[15] F. Zareian, H. Krawinkler, *Simplified Performance Based Earthquake Engineering*, Report No. 169, *John A. Blume Earthquake Engineering Center*, April 2009.

[16] F. Zareian, H. Krawinkler, *Structural System Parameter Selection Based on Collapse Potential of Buildings in Earthquakes*, *Journal of Structural Engineering* ASCE/ August 2010/ **933.**

COMPDYN 2011
3rd ECCOMAS Thematic Conference on
Computational Methods in Structural Dynamics and Earthquake Engineering
M. Papadrakakis, M. Fragiadakis, V. Plevris (eds.)
Corfu, Greece, 25–28 May 2011

ANALYTICAL DISPLACEMENT-BASED SEISMIC FRAGILITY ANALYSIS OF STONE MASONRY BUILDINGS

Ahmad Abo-El-Ezz[1], **Marie-José Nollet**[2], **Miroslav Nastev**[3]

[1] Department of Construction Engineering, École de technologie supérieure, University of Québec
Montréal, Canada
e-mail: ahmad.abo-el-ezz.1@ens.etsmtl.ca

[2] Department of Construction Engineering, École de technologie supérieure, University of Québec
Montréal, Canada
e-mail: Marie-Jose.Nollet@etsmtl.ca

[3] Geological Survey of Canada, Natural Resources Canada.
Québec City, Canada.
e-mail: Miroslav.Nastev@RNCan-NRCan.gc.ca

Keywords: Seismic Risk Assessment, Fragility Analysis, Stone Masonry.

Abstract. *In an effort to reduce seismic risks, the Geological Survey of Canada has recently taken important steps by initiating a project on quantitative assessment of earthquake related risks. One of the objectives of this project is to study the seismic vulnerability of historic stone masonry buildings generally known for their poor performance during strong ground motion. This paper focuses on the development of analytical displacement-based fragility curves reflecting the characteristics of existing stone masonry buildings in Canada. The fragility analysis provides the necessary link between the building damage and earthquake intensity in a probabilistic setting, where the extent of building damage is best correlated to the amount of induced building displacement. The old historic center of Quebec City was selected as a typical study area due to the concentration of stone masonry buildings, which combined to the high heritage value increases the potential consequences of failure. Comparison was made with similar fragility curves implicit in Hazus-MH and ELER seismic risk assessment tools. Differences have been observed between the three sets of fragility curves which may lead to significantly disparate damage estimates. This comparison shows the importance of the development of fragility curves specific to the generic construction characteristics in the study area and emphasizes the need of critical use of existing risk assessment tools and generated results.*

1 INTRODUCTION

Majority of existing historic buildings in old urban centers in Eastern Canada are stone masonry structures and represent un-measurable architectural and cultural heritage. Historic stone masonry buildings were built to resist gravity loads only and generally offer poor resistance to lateral seismic loads. Damage occurred to stone masonry buildings from past earthquakes is attributed to inadequate structural integrity due to the lack of connection between stone masonry structural walls and wooden floors and roofs; and to ensuing inadequate structural resistance, which results into typical shear cracking and disintegration of stone walls and partial or total collapse of buildings [1].

The high seismic risks related to stone masonry buildings are even more increased due to their location in densely populated urban centers in a way that the consequences of failure of these structures tend to be severe with regards to human casualties, heritage damage and economic losses [2]. Seismic risk assessment of historic stone masonry buildings is therefore the first necessary step in providing mitigation plans for seismic retrofit and preservation.

In an effort to reduce seismic risks, the Geological Survey of Canada has recently taken important steps by initiating a project on quantitative assessment of earthquake related risks. One of the objectives of this project is to study the seismic vulnerability of historic stone masonry buildings. The old historic center of Quebec City was selected as a typical study area.

Seismic risk is often considered as the convolution of seismic hazard (expected ground motion at given location), exposure (demographics, buildings, essential facilities, utilities, etc.), and vulnerability (response of structures to earthquake impacts, generally defined by expected degree of damage under different levels of seismic loading). These three components are integrated to determine direct and indirect physical damage and losses. Fragility analysis is the key component in performance based seismic risk assessment. It provides the link between the two other components of the seismic risk assessment process, inventory and seismic hazard.

The most widely used risk assessment tool in North America, Hazus-MH [3], seems to not adequately represent the response of stone masonry structures to earthquake loading. It considers only one structural class for unreinforced masonry buildings, URM, mainly covering brittle brick masonry structures. The European ELER tool [4] recognizes explicitly the stone masonry as a specific structural type among the unreinforced masonry typology. URM building typologies in ELER tool cover a wide range of masonry construction encountered in Europe, such as rubble stone, adobe, simple stone, massive stone, brick masonry with wooden floors and brick masonry with reinforced concrete floors.

The objective of this paper is to introduce a procedure for the development of displacement based fragility curves for typical stone masonry buildings in Old Quebec City and to present the generated results. It was first necessary to make an inventory of the existing masonry buildings and to include their special structural and material characteristics. At the end, a comparison is made with fragility curves implicit in Hazus and ELER seismic risk assessment tools in order to assess differences and the potential disparities they may exert on damage probability estimates.

2 ANALYTICAL FRAGILITY ANALYSIS FRAMEWORK

Fragility refers to the probability of reaching or exceeding a given damage state defined as a function of earthquake loading. The output of the fragility analysis is a set of fragility curves describing different damage or limit states. Fragility curves can be obtained from empirical, judgmental, analytical, and hybrid approaches [5]. All these methods contain epistemic and aleatory uncertainties in the assessment procedures and use data including: measurement uncertainty related to observations of damage, inconsistency in the quality of available databases and related analyses, variability in the ground motions, uncertainty in experts judgment, statistical uncertainty inherent in the parameter estimates, uncertainty due to simplification of strength and stiffness models of structural materials and components, uncertainties in seismic demand and capacity of structures due to variations of their geometry and material properties, uncertainty in the definition of the damage limit states, etc.

Because of the scarcity of observational damage data in regions of moderate seismicity such as Quebec City and the subjectivity of judgmental damage data, modern risk assessment methodologies adopt analytical development of fragility curves. Analytical methods rely on structural modeling and analytical evaluation of the likelihood for a given building to experience damage by earthquakes of a given intensity and distance, as well as on consideration of related uncertainties.

The derivation process of analytical fragility curves for a particular building or building typology comprises several components: (1) buildings Inventory, (2) damage/limit state model, (3) building capacity model, (4) seismic hazard, (5) seismic demand model, and (6) fragility generation (Figure 1).

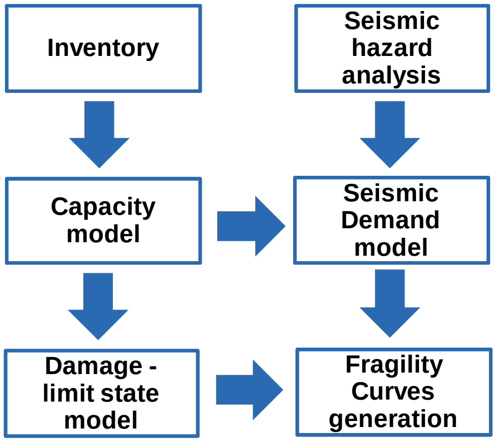

Figure 1: Derivation process of analytical fragility curves.

Fragility curves are given in the form of lognormal fragility distribution that relates the probability of being in or exceeding a given damage state for a given intensity measure (e.g., spectral inelastic displacement demand). The conditional probability of being in or exceeding a particular damage state, DS given the spectral displacement S_d is defined by the function:

$$P\left[DS \mid S_d\right] = \Phi\left[\frac{1}{\beta_{DS}}\ln\left(\frac{S_d}{\overline{S}_{d,DS}}\right)\right]$$

$$\beta_{DS} = \sqrt{CONV(\beta_C,\beta_D)^2 + \beta_T{}^2} \tag{1}$$

where: $\overline{S}_{d,DS}$ is median value of the spectral displacement at which the building reaches the threshold of damage state DS, β_{DS} is standard deviation of the natural logarithm of spectral displacement for damage state DS, and Φ is standard normal cumulative distribution function. β_{DS} describes the total variability of a fragility curve damage state. Three primary sources contribute to the total variability of any given damage state, namely, the variability in the capacity model β_C, the variability in the demand model β_D, and the variability in the threshold of a damage state from the damage model β_T. Since the seismic demand is dependent on the building capacity, a convolution process is required to combine their respective variability [6]. In the case the variability in the seismic demand, β_D, is already modeled in the Probabilistic Seismic Hazard Analysis (PSHA) process, it should be removed from β_{DS} as follows [5],

$$\beta_{DS} = \sqrt{\beta_C{}^2 + \beta_T{}^2} \tag{2}$$

3 INVENTORY OF STONE MASONRY BUILDINGS IN OLD QUEBEC CITY

A detailed inventory has been carried out to characterize the historic stone masonry buildings in Old Quebec City. Besides the field survey, the inventory consisted of review of architectural reports and dissertations, historic documents [7], and archives of the Biliothèque et Archives Nationales du Québec (www.banq.qc.ca).

Figure 2 shows the three most frequent types of stone masonry buildings, selected among the typologies reported by Vallières [7] and retained as representative structural types for the study area. These building types were constructed during the 18th and mid-19th century. The massive façade walls are relatively thick, ranging from 40 to 60 cm, and have regular window and door openings on both sides of the building. The typical story height ranges from 2.75m to 3.35m. Lateral fire walls are of the same thickness as the façade walls. The typical floor is made of wood resting on the façade walls. The massive façade and fire walls provide the buildings’ lateral resistance in both directions.

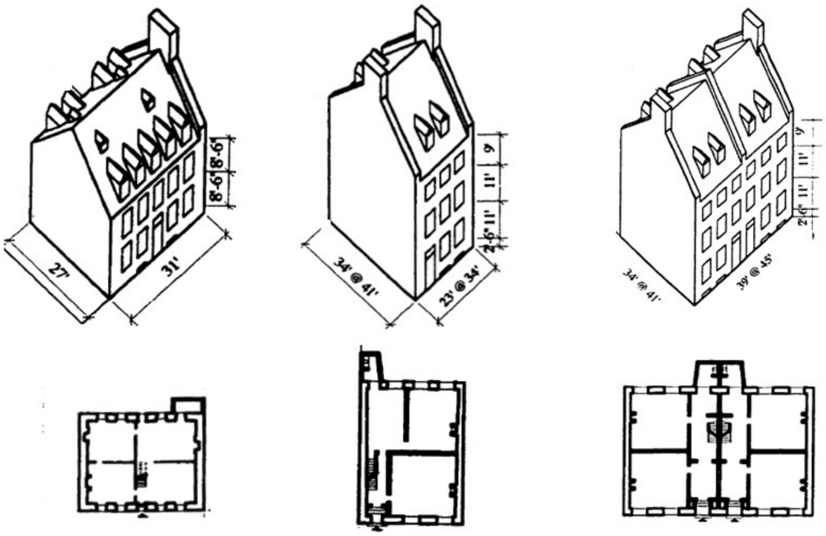

Figure 2: Main stone masonry building typologies in Old Quebec City **[7]**.

4 DISPLACEMENT-BASED DAMAGE MODEL AND FRAGILITY CURVES

The good correlation between the earthquake induced displacement and the extent of structural damage lead to the development of modern performance-based seismic assessment procedures which are based on the evaluation of the structure-specific deformation capacity and earthquake-induced displacement demand.

Recently, simplified displacement-based procedures were proposed for the risk assessment of masonry structures [8] and [9]. The procedure proposed in [9] is adopted in this study. It assumes modeling of the masonry structures by an equivalent single degree of freedom system with effective global parameters (ESDOF). The structural damage state threshold at the effective height of the ESDOF is obtained according to the assumed deformed shape of the structure. A linear shape is assumed for elastic behavior and a soft story deformed shape is assumed for inelastic behavior which is the most common failure mechanism of masonry structures under earthquake loading (Figure 3.a). Damage state drift thresholds for masonry walls are identified from experiments on masonry wall elements.

The displacement at the threshold of each damage state at the effective height of the ESDOF Δ_{DSi} , equivalent to the spectral displacement, and can be evaluated as:

$$\Delta_{DSi} = \theta_{DS1}.k_1.H + (\theta_{DSi} - \theta_{DS1}).k_2.h_s \tag{3}$$

where: H is total height of the building, h_s is height of the first story walls, θ_{DS1} is drift threshold for the first story walls at the elastic limit, θ_{DSi} is the drift threshold for the first story walls at higher damage states, k_1 is the effective height coefficient to convert the multi degree of freedom system into ESDOF, k_2 is the effective height of the first story walls going into the inelastic range when openings are present, k_2 =1.0 when there are no openings.

For a regular distribution of masses and a uniform story height, k_1 is equal to 0.667. When the mass distribution is not regular, what is common in the case of unreinforced stone masonry, the buildings are better represented by a distributed mass corresponding to the mass of the masonry walls plus lumped masses corresponding to the mass at each floor. In this case, k_1 and k_2 have to consider the different mass distributions. The computation of these two factors is explained in details by [9] and the proposed values are given in Table 1.

Damage states drift thresholds are identified on the envelope curve of stone masonry walls as shown in Figure 3.b [10] and [11]. The lateral response of stone masonry walls is strongly nonlinear. As the displacement due to cracking increases, the walls experience both strength and stiffness degradation. The thresholds on the horizontal axis correspond to flexural cracking (θ_{DS1}), shear cracking (θ_{DS2}), maximum shear strength (θ_{DS3}), and ultimate deformation at 20% loss of strength (θ_{DS4}). They are considered as respective thresholds for the slight damage state, moderate damage state, extensive damage state, and complete damage state.

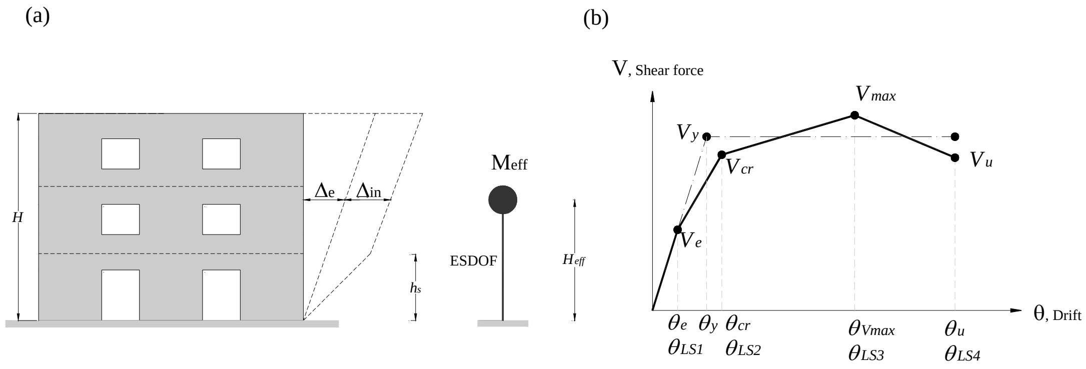

Figure 3: Simplified model for damage limit states (a), and identification of drift limits for masonry walls (b).

Number of stories	k_1	k_2
1	0.79	0.96
2	0.72	0.95
3	0.69	0.92

Table 1: Values of effective height coefficients of the ESDOF for different number of stories [9].

In the context of this study there are no laboratory test results on stone masonry walls representative for URM in the Old Quebec City, therefore damage states drift thresholds were derived from typical literature data on stone masonry wall elements [11];[12];[13]. A Matlab code [14] was used to obtain an empirical cumulative distribution (CDF) of each damage state drift threshold from collected data. The lognormal cumulative distribution was employed to fit the empirical distribution. This parametric probability distribution has the advantage of being fully defined by two statistical parameters that incorporate the central tendency (median) and dispersion (lognormal standard deviation) of the data (Figure 4.a). These values were implemented in Equation 3 as lognormal distributed random variables. The story height value was assumed deterministic as the median height from the inventory (h_s = 3.0m). The respective displacement threshold resulting data were then fitted with lognormal distributions which represent the displacement threshold fragility curves of the ESDOF (Figure 4.b).

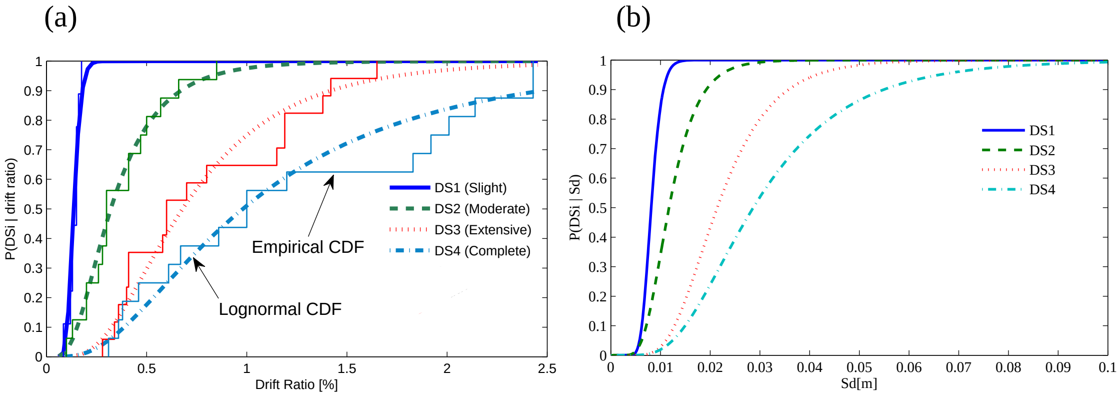

Figure 4: Drift threshold variability (a), and Displacement-based damage threshold fragility curves for two-story stone masonry buildings (b).

Figure 5 illustrates the developed fragility curves for two-story stone masonry buildings. For comparative purposes, the fragility curves for the Hazus pre-code unreinforced masonry buildings (URM) and ELER simple stone low-rise buildings are also presented. For the moderate damage state (DS2), the median displacement threshold $\overline{S}_{d,DS2}$ developed in this study is 0.7 and 3.3 fold of those implicit in Hazus and ELER, respectively. For the complete damage state (DS4), $\overline{S}_{d,DS4}$ developed in this study is 0.3 and 2.4 fold of those implicit in Hazus and ELER, respectively. The lognormal standard deviation of the moderate and complete damage state threshold are $\beta_{T,DS2} = 0.38$ and $\beta_{T,DS4} = 0.50$, respectively. This is in fair agreement with the assumed standard deviation in both Hazus and ELER for all damage states, $\beta_{T,DSi} = 0.4$. This variability can be reduced by conducting laboratory tests on typical stone masonry walls found in Old Quebec City.

One can argue that these curves can not be directly compared because of the different assumptions, information and tools used in the development process. The objective of Figure 5 is rather to show the importance for the development of specific fragility curves that reflect the generic construction characteristics for the considered study area.

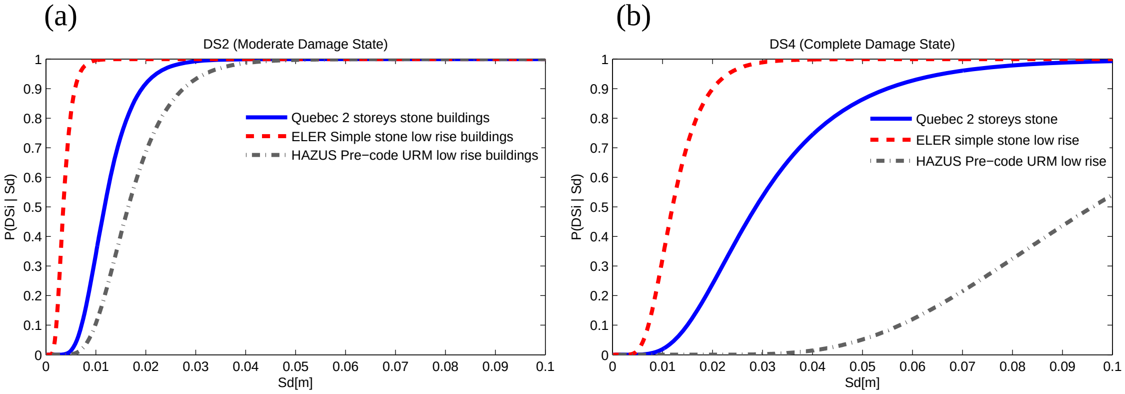

Figure 5: Comparison of fragility curves of Quebec, Hazus and ELER for (a) moderate damage state and (b) complete damage state.

5 CAPACITY MODEL

The three main typologies of existing stone masonry buildings typologies (Figure 2) were used to develop the capacity model. The variation in capacity of stone masonry buildings is relatively high since small modification in geometry or in material properties may result in different seismic resistance. Quebec City stone masonry buildings are mainly constructed from limestone and sometimes sandstone with lime mortar. However, no specific information on material mechanical properties was available. These properties were therefore obtained from the literature data [15], and may introduce significant variability in the developed capacity models.

In order to develop a representative capacity model for a building typology, a simplified mechanical model was used with some modifications [16]. The elastic deformation of the building is approximated by a linear shape up to the point where the shear capacity of the wall is reached, whereas the inelastic deformation is assumed perfectly plastic and concentrated at the first story, which is the typical damage observed in past earthquakes. The effective stiffness of the linear elastic part can be determined using secant stiffness at the capacity, V_y, and is selected such that the bilinear curve is equivalent to the experimental curve using the Energy equivalence criteria [17]. The base shear strength of the building in one direction is assumed to equal the sum of the shear strengths of the first story walls in that direction (Figure 6). Two simple criteria were used to evaluate the strength of the first story walls based on the expected failure mechanism: flexural rocking failure and diagonal cracking failure [17]. Example of the variability in capacity curves due to material uncertainty is shown in Figure 7 which presents five capacity curves corresponding to different masonry strength. More details about the development of capacity curves for the selected typologies can be found in [18].

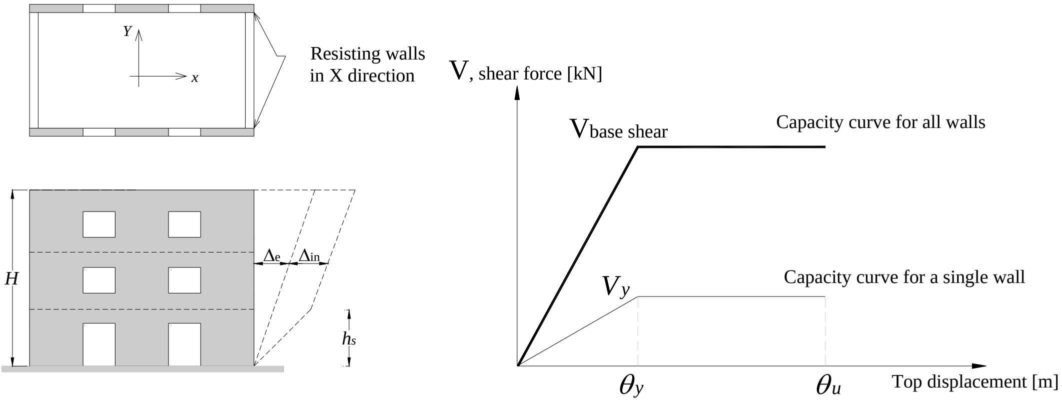

Figure 6: Simplified mechanical model for capacity curve evaluation of stone masonry buildings.

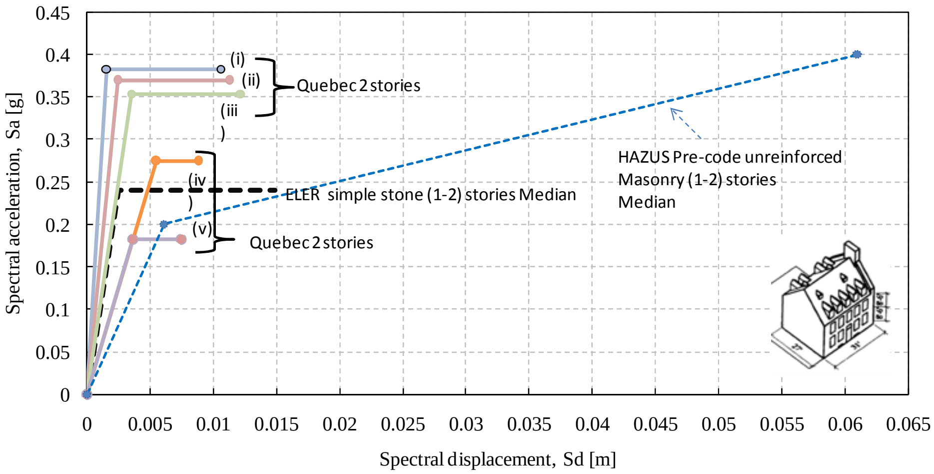

Figure 7: Variability in capacity curves for a Quebec City stone masonry typology and comparison with Hazus and ELER tools respective median capacity curves.

The fitted lognormal distributions for the capacity model parameters, the fundamental period of vibration and the yield acceleration, are shown in Figure 8. The median fundamental period of vibration for 1 to 2 story buildings considered in this study is 0.18sec, with a lognormal standard deviation of 0.34. This value is in agreement with the ELER value (0.19sec), however, it is stiffer than the respective median value implicit in Hazus (0.35sec). The median yield acceleration is 0.30g with 0.26 lognormal standard deviation, which is slightly higher than the corresponding median values implicit in ELER (0.24g) and in Hazus (0.2g) both characterized with lognormal standard deviations of 0.3.

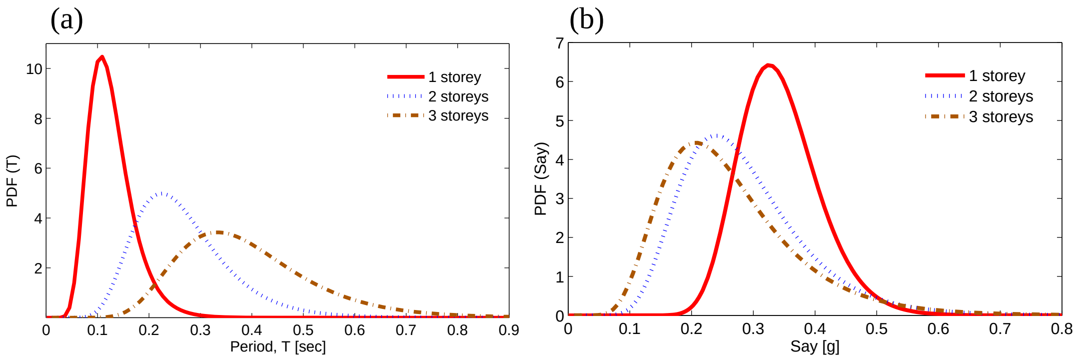

Figure 8: Statistics of the capacity model: fundamental period variation (a) and yield acceleration variation (b).

6 FRAGILITY BASED SEISMIC DAMAGE ASSESSMENT

The displacement based fragility curves with combined variability in capacity and damage state threshold, equation 2, were used for determining the damage state probabilities of two-story stone masonry buildings in Old Quebec City at a specific earthquake median uniform hazard levels with 2% probability of exceedance in 50 years obtained from PSHA [19].

The improved displacement coefficient method (DCM) presented in [20] was used to evaluate the spectral displacement demand which is the input to the displacement based fragility curves. The DCM essentially modifies the linear elastic response of the ESDOF system with 5% damping by multiplication with a series of coefficients to generate an estimate of the inelastic displacement demand S_d .

$$\begin{aligned} S_d &= C_1.C_2.S_a(T_e).\frac{T_e^2}{4.\pi^2}.g \\ C_1 &= 1+\frac{R-1}{a.T_e^2} \\ C_2 &= 1+\frac{1}{800}\left[\frac{R-1}{T_e}\right]^2 \\ R &= \frac{S_a\left(T_e\right)}{S_{ay}} \end{aligned} \tag{4}$$

where, C_1 is modification parameter which relates the expected maximum displacement of an inelastic ESDOF system with elastic-plastic hysteresis properties to the displacement calculated from the linear elastic spectral response, a is related to the type of local NEHRP soil classification (a=130 for soil class B - rock), C_2 accounts for the effects of pinched hysteresis shape, stiffness degradation, and strength deterioration on the maximum displacement response, $S_a(T_e)$ is the spectral acceleration at the effective fundamental period of the system coming from the capacity curve, and S_{ay} is the yield acceleration of the system. The median T_e and S_{ay} of the two-story stone masonry buildings were obtained from the capacity model as 0.25sec and 0.24g, respectively. The corresponding spectral acceleration $S_a(T_e)$ with 2% probability of exceedance in 50 years is 0.49g, and spectral displacement S_d is 0.01m.

The final damage state probabilities are shown in Figure 9 together with respective damage probabilities obtained from fragility curves defined in Hazus and ELER. For the given spectral displacement demand, discrete damage state probabilities are evaluated as the difference of the cumulative probabilities of reaching or exceeding successive damage states. The damage estimation obtained using Hazus shows highest probability of occurring to no damage and to slight damage, ELER yields highest probabilities to extensive and complete damage, whereas damage estimates generated by this study and for the same intensity measure (S_d=0.01m) indicate that slight to moderate damage will be the most probable damage experienced by the stone masonry buildings.

This comparative example shows the importance of the development of specific fragility curves that reflect the generic construction characteristics for the considered study area for seismic risk assessment and emphasizes the need of critical use of existing risk assessment tools and the obtained results.

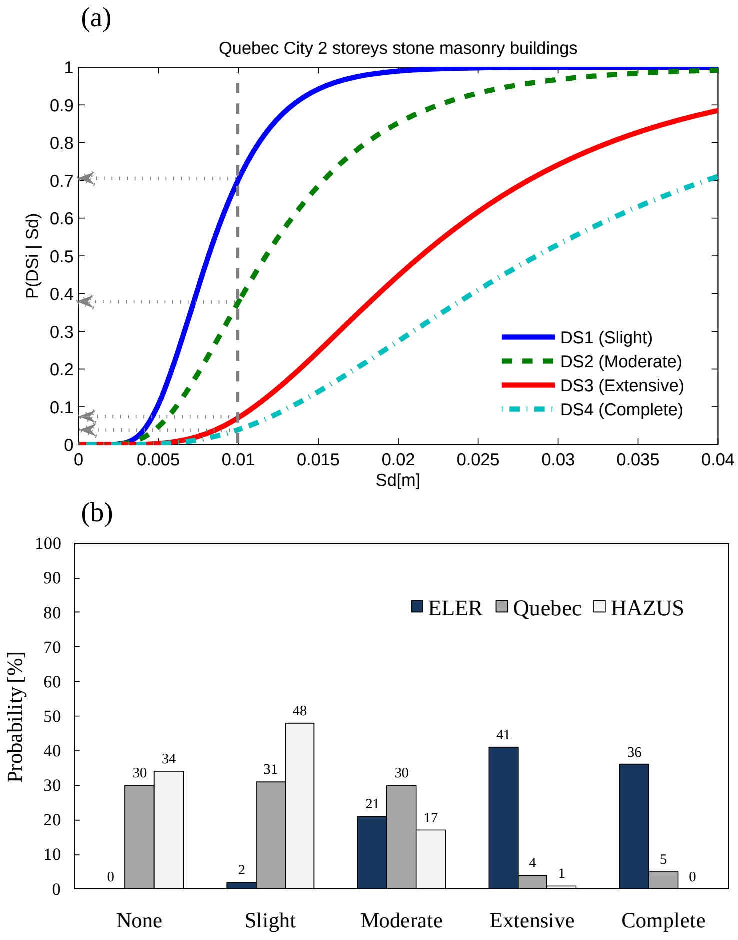

Figure 9: Damage state probabilities for Old Quebec City two-story stone masonry buildings (a), compared with respective damage states computed with fragility curves implicit in Hazus and ELER (b).

7 CONCLUSIONS

The procedure for analytical displacement based fragility analysis of stone masonry buildings in Old Quebec City is presented. The first step consisted of an inventory of existing buildings in the study area and characterization of representative typologies of stone masonry buildings. These typologies were utilized to develop a building capacity model using a simplified mechanical model with linear elastic and perfectly plastic domains which proved particularly effective for carrying out analyses of uncertainties with significantly reduced computational time.

A simplified displacement based procedure was used to develop damage state fragility curves based on drift limits of stone masonry walls which were assigned based on literature data. It is expected that using drift limits obtained from laboratory testing of stone masonry walls representative of those existing in Old Quebec City would help to reduce the uncertainties in the damage prediction. A comparison of the developed fragility curves is made with their corresponding curves in existing regional seismic risk assessment tools Hazus and ELER. Significant differences have been observed between fragility curves defined by the three methodologies. These differences were replicated in comparatively significant disparities among the estimates of the probabilities of different damages states to be experienced by stone masonry buildings in the Old Quebec City for the same seismic hazard with probability of 2% exceedance in 50 years.

REFERENCES

[1] Tomaževic.M, *Earthquake-Resistant Design of Masonry Buildings*, *Innovation in Structures and Construction, Vol. 1,* Editors: Elnashai, A.S. & Dowling, P.J., Imperial College Press, London, 268 pages, 1999.

[2] Chidiac, S.E., Foo, S., and Cheung M.S., Seismic guidelines for stone-masonry components and structures. *Proceedings of the Int. Conference on the Seismic Performance of Traditional Buildings*, Turkey, 13 pages, 2000.

[3] FEMA-NIBS, HAZUS-MH MR4: Multi-hazard Loss Estimation Methodology Earthquake Model Technical manual. *Federal Emergency Management Agency (FEMA), National Institute of Building Science (NIBS),* Washington, D.C, 712 pages, 2003.

[4] Demircioglu, M. B., Erdik, M., Hancilar, U., Sesetyan, K., Tuzun,C., Yenidogan, C., and Zulfikar, A. C., Technical Manual – Earthquake Loss Estimation Routine ELER-v2.0. *Bogazici University, Department of Earthquake Engineering, Istanbul,* 133 pages, 2009.

[5] Calvi GM, Pinho R, Magenes G, Bommer JJ, Restrepo-Velez LF, Crowley H., The development of seismic vulnerability assessment methodologies for variable geographical scales over the past 30 years. *ISET Journal of Earthquake Engineering Technology,* **43**(3), 75–104, 2006.

[6] Kircher, C. A., A. A. Nassar, et al., Development of Building Damage Functions for Earthquake Loss Estimation. *Earthquake Spectra,* **13**(4), 663-682, 1997.

[7] Vallieres, A., Processus de transformation typologique du bâti résidentiel dans l'arrondissement historique du Vieux-Québec. *Mémoire de maîtrise. Université Laval, École d'architecture*, 221 pages, 1999.

[8] Calvi, G.M., A displacement-based approach for vulnerability evaluation of classes of buildings. *Journal of Earthquake Engineering,* **3**(3), 411-438, 1999.

[9] Restrepo-Vélez, L.F., A Simplified Mechanics-Based Procedure for the Seismic Risk Assessment of Unreinforced Masonry Buildings. *Individual Study, European School for Advanced Studies in Reduction of Seismic Risk (ROSE School),* Pavia, Italy, 2003.

[10] V. Bosiljkov, A.W. Page, V. Bokan-Bosiljkov and R. Zarnic, Evaluation of the seismic performance of brick masonry walls. *Structural Control and Health Monitoring,* **17**(1), 100–118, 2010.

[11] M.Tomaževic, P.Weiss., Displacement capacity of masonry buildings as a basis for the assessment of behavior factor: and experimental study. *Bulletin of earthquake engineering,* **8**(6), 1267-1294, 2010.

[12] Tomaževič. M, Lutman. M., Heritage Masonry Buildings in Urban Settlements and the Requirements of Eurocodes: Experience of Slovenia. *International Journal of Architectural Heritage*, **1**, 108-130, 2007.

[13] Vasconcelos, G., Experimental investigations on the mechanics of stone masonry: Characterization of granites and behaviour of ancient masonry shear walls. *PhD Thesis, University of Minho, Guimarães*, Portugal, 2005.

[14] Matlab User's Guide, www. mathworks.com.

[15] Mazzon, N., Influence of Grout Injection on the Dynamic Behaviour of Stone Masonry Buildings. *Doctoral dissertation, University of Padova*, Italy, 306 pages, 2010.

[16] Lang, K.. Seismic vulnerability of existing buildings. *Swiss Federal Institute of Technology, ETHZ, Zurich*, Switzerland, 200 pages, 2002.

[17] Magenes, G. & Calvi, G.M., In-Plane Seismic Response of Brick Masonry Walls. *Earthquake Engineering and Structural Dynamics*, **26**(11), 1091-1112, 1997.

[18] Abo-El-Ezz.A, Nollet. M.J, Nastev.M., Characterization of historic stone masonry buildings in old Quebec City for seismic risk assessment. *Submitted to the Canadian Society of Civil Engineers Annual Conference*, Ottawa, June, 2011.

[19] Adams J, Halchuk S., Fourth generation seismic hazard maps of Canada: Values for over 650 Canadian localities intended for the 2005 National Building Code of Canada. *Geological Survey of Canada Open File no. 4459*, 155 pages, 2003.

[20] FEMA 440: Improvement of nonlinear static seismic analysis procedures. *Federal Emergency Management Agency, Applied Technology Council, Washington D.C.*, USA, Rep. No. 440, 2005.

COMPDYN 2011
III ECCOMAS Thematic Conference on
Computational Methods in Structural Dynamics and Earthquake Engineering
M. Papadrakakis, M. Fragiadakis, V. Plevris (eds.)
Corfu, Greece, 25–28 May 2011

FREE VIBRATION AND EARTHQUAKE BEHAVIOR OF SOLAR POWER PLANT CHIMNEYS

Christian Lang[1]

[1] L.A.W.Consulting Engineers GmbH & Co. KG
Lindenstraße 13, 67433 Neustadt / Weinstraße, Germany
e-mail: christian.lang@law-ing.de

Keywords: Solar Power Plant Chimneys, Cooling Towers, Free Vibration, Earthquake, Finite Element Modeling, Ring Elements.

Abstract. *In this paper, the basic mechanical principles for structural modeling of shells of revolution using ring elements are briefly summarized. For the representation of mechanical variables in hoop direction, Fourier series are used within this numerical model. Further, solution properties for free vibration and for transient dynamic problems are presented with special regard to ring element models. The presented algorithms are implemented in computer code ROSHE [7] which has been successfully applied to the analysis and design of a large number of cooling towers world wide. In this contribution, the challenging step from natural draft cooling towers which are currently built with standard heights up to 200 m towards large solar upwind power plant chimneys with heights of approximately 1000 m is dared. Hereby, the pre-design of a 1000 m solar chimney by Krätzig is taken as reference geometry. With this design, the dynamic behavior of this large 1000 m solar chimney subjected to horizontal earthquake acceleration is studied. The behavior of this tower is compared to dynamic behavior of cooling towers subjected to horizontal earthquake acceleration. While significant non-linear effects such as uplift from ground, cracking of columns and shell arise in cooling towers, the behavior of solar chimneys is totally different. Due to very high period of the first relevant eigenmotion, these structures behave similar to base isolated structures. The structure will not follow the ground motion in upper parts. Despite of the large height, uplift or loss of stability due to tilting will not become a problem. Tensile meridian membrane forces occur only in upper parts of the shell between 600 m and 1000 m. In this paper, the transient response of the 1000 m solar chimney is studied in comparison to a standard natural draft cooling tower of height 180 m. They are both subjected to NS component of Kern County earthquake acceleration with peak ground acceleration 0.35 g. Simplified response spectrum analysis with presentation of modal contributions is further conducted for a simplified beam model of the solar power plant chimney which confirms the obtained results. Powerful post processing tools have been developed and will be utilized within the presentation to visualize the structural response of both systems.*

1 INTRODUCTION / SUMMARY

Natural draft cooling towers up to heights 200 m are commonly found at every power plant where process water has to be cooled down. Due to their height and their slender wall thickness, they represent one of the most challenging and fascination civil engineering structure. The highest natural draft cooling tower world wide has been built at the Niederaussem power plant site close to Cologne in Germany. Cooling towers have to resist mainly dead weight, wind and earthquake action.

Recently, the discussion about solar power plant chimneys has come up again. Solar power plant chimneys use a huge circular glass roof collector to heat up the air. The air is flowing under this glass roof towards a high chimney in the middle. Due to the natural updraft effect through the chimney, the air flow is used to run several turbines which are installed at the bottom of the chimney. With such a solar chimney of height 1000 m and a collector roof of diameter 3 km, an electrical power output of 200 MWe can be generated.

For such a high structure, it must be questioned how it will behave when subjected to horizontal earthquake acceleration. Will earthquake be the dominating action? Will tilting become a problem? Which non-linear effects will occur?

For this clarification, a first step will be done within this paper. Therefore, a comparison of the structural behavior between natural draft cooling towers and solar power plant chimneys will be conducted which are both very slender shells of revolution with negative curvature.

A very simple but effective ring element model is used for this aim. Both structures are subjected to a representing earthquake acceleration (Kern County NS component) with maximum peak ground acceleration 3.50 m/s². The results for the solar power plant chimney are further confirmed by simple beam response spectrum analysis. It can be stated that tilting will not occur for the solar power plant chimney and significant tensile meridional stresses arise only in upper regions of the structure due to higher mode contribution.

2 MECHANICAL BACKGROUND AND FINITE ELEMENT CONCEPT

In Figure 1, a cut-out of a shell of revolution with its body forces and stress resultants is depicted. Internal stress resultants are described by membrane forces $n^{\alpha\beta}$ and bending moments $m^{\alpha\beta}$ which are obtained by numerical stress integration through section depth in general. They are obtained using Eq. (1) and Eq. (2) for arbitrary constitutive behavior [2].

$$n^{\alpha\beta} = \int_{-h/2}^{+h/2} \mu(\theta^3) \cdot [\delta^\beta_\lambda - \theta^3 \cdot b^\beta_\lambda] \cdot \sigma^{\alpha\lambda}(\theta^3)\, d\theta^3 \tag{1}$$

$$m^{\alpha\beta} = \int_{-h/2}^{+h/2} \mu(\theta^3) \cdot \theta^3 \cdot \sigma^{\alpha\beta}(\theta^3)\, d\theta^3 \tag{2}$$

Equations of motion are formulated using dynamic equilibrium by application of principle of virtual work with additional consideration of damping and inertia forces.

$$\begin{aligned} &\iint_A p^\alpha\, \delta u_\alpha + p^3\, \delta u_3 \;dA + \oint_C n^\alpha\, \delta u_\alpha + n^3\, \delta u_3 \;dC - \iint_A \tilde{n}^{\alpha\beta}\, \delta\alpha_{\alpha\beta} + m^{\alpha\beta}\, \delta\beta_{\alpha\beta} \;dA \\ &- \iint_A \rho h \cdot [a^{\alpha\beta}\, \ddot{u}_\alpha\, \delta u_\beta + \ddot{u}_3\, \delta u_3]\, dA - \iint_A [c_t\, a^{\alpha\beta}\, \dot{u}_\alpha\, \delta u_\beta + c_n\, \dot{u}_3\, \delta u_3]\, dA = 0 \end{aligned} \tag{3}$$

The principle of virtual work implies dynamic equilibrium in weak formulation. The equations of motion are solved by structural discretisation using finite ring elements. Further, the equations of motion are linearized to apply an implicit time integration scheme with corrective iteration steps [7], [8].

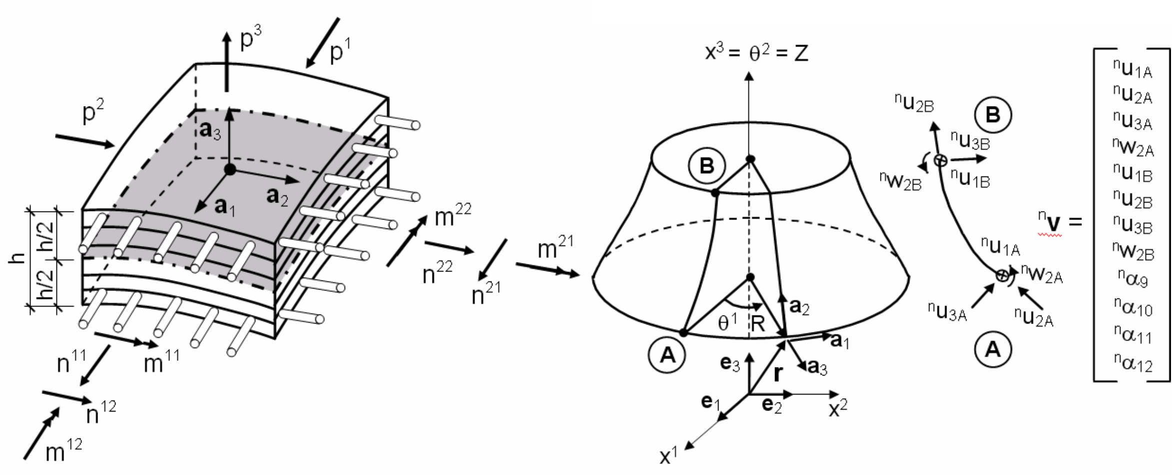

Figure 1: Numerical model for structural analysis of shells of revolution acc. to [7], [8], [9].

For structural analysis of shells of revolution, ring elements according to Figure 1 can be advantageously deployed since the computational effort is significantly decreased. The shell is described by its meridian curve. Each element possesses two nodes. Displacements are interpolated using cubic polynomials in meridian direction and a Fourier series in hoop direction. For linear elastic behavior, the structural problem is decoupled in Fourier terms: Body forces result in structural response in the same Fourier term, solely. This property is of special interest in linear earthquake analysis of shells of revolution which is conducted within this paper.

3 NUMERICAL MODELS FOR NDCT AND SPPC

In Figure 2, structural models of a modern natural draft cooling tower which has been recently built and of the pre-design of a 1000 m solar chimney by Krätzig [5], [6] are depicted.

The natural draft cooling tower consists of one upper ring beam which is modeled by a ring beam element. The double curved shell consists of 43 ring elements with a minimum wall thickness 20 cm in major parts of the shell. At its bottom, the shell is supported by V-truss columns (46 column pairs with diameter 90 cm). These truss columns are modeled by a special column macro ring element where 3D beams are coupled along the upper and lower nodal circles. The ring foundation is modeled by a ring beam element which is supported by a ring spring element to account for the elastic soil support. The geometry of the double curved middle surface of the shell is described by two hyperbolic functions below and above the throat of the shell which follows Eq. (4).

$$R(Z) = R_0 + a \cdot \sqrt{1 + \left(\frac{Z - Z_0}{b} \right)^2} \tag{4}$$

with $R_0 = -15.3644$ $Z_0 = 115.83$ $a = 51.9644$ $b = 113.9896$ below throat
$R_0 = +36.3422$ $Z_0 = 115.83$ $a = 0.25780$ $b = 8.0293$ above throat

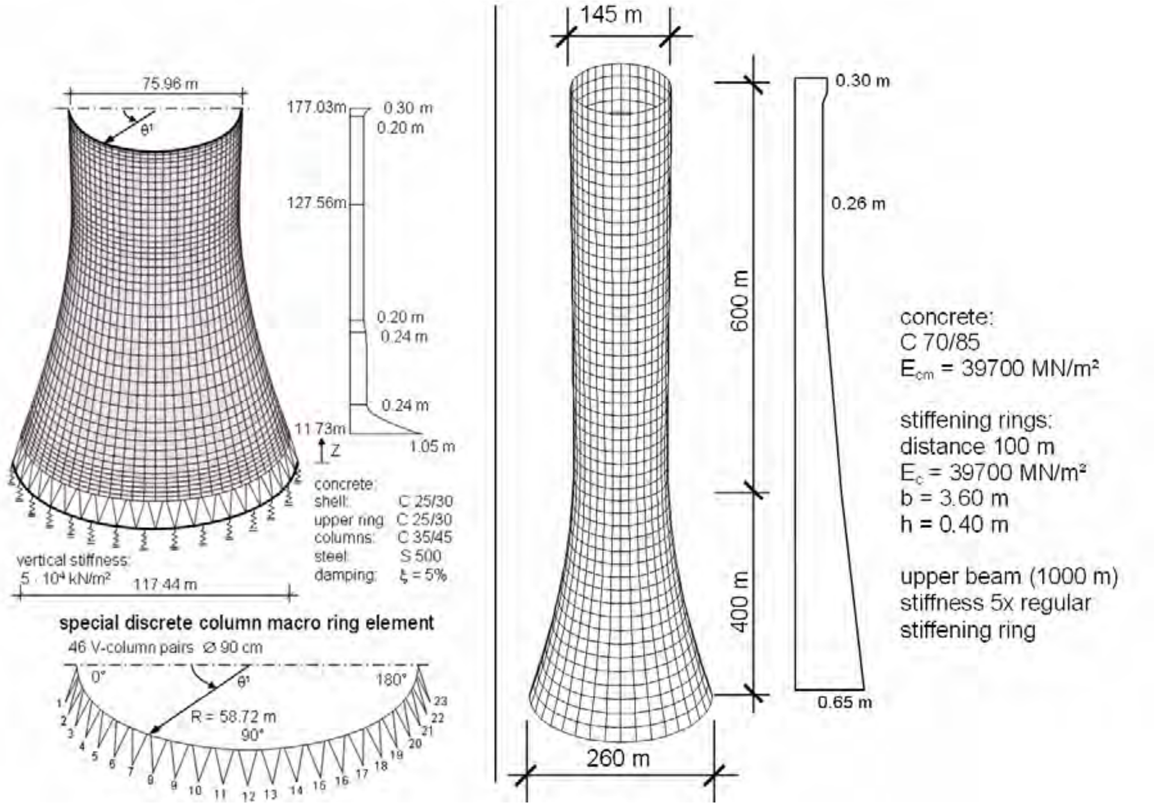

Figure 2: Structural models for earthquake analysis of NDCT and SPPC.

Further, the structural model of the 1000 m solar chimney can be found in Figure 2. This model consists of 50 shell ring elements while each element is representing a vertical section of 20 m. The base of the solar chimney is fixed. Modeling of air openings in the lower part is neglected for this study of global earthquake response behavior. The wall thickness of this 1000 m solar tower is starting at 65 cm at its bottom and reaches a minimum thickness of 26 cm in upper parts according to buckling safety requirements. At distances of 100 m, stiffening rings are attached to the shell. On top of the shell, a ring beam is attached with 5 times stiffness of standard stiffeners. A high performance concrete C 70/85 is used. All geometric and material properties are chosen according to pre-design by Krätzig, see [5], [6].

The structure is described by a double curved shell middle surface comparable to the presented natural draft cooling tower. The throat position is located at height 400 m. The geometry follows Eq. (4) with following parameters:

$R_0 = -8209.2709$	$Z_0 = 400.00$	$a = 8275.9709$	$b = 3227.9274$	below throat
$R_0 = +66.577380$	$Z_0 = 400.00$	$a = 0.1226204$	$b = 12.424908$	above throat

Although both structures are described in a similar way by a double curved shell surface (hyperbolic shape, negative curvature) with two geometric functions (below and above the throat) as can be seen in Figure 2, the earthquake behavior and structural response will be totally different due to significant discrepancies in mass and stiffness. The solar chimney will behave more or less like a very flexible cantilever beam similar to base isolated structures which can be already guessed.

4 DESCRIPTION OF EARTHQUAKE ACTION AND EQUIVALENT BODY FORCES

As reference earthquake for earthquake studies, Kern County earthquake NS component is used (21.07.1952, Taft Lincoln School, USGS Station 1095) [10]. This acceleration time history is depicted in Figure 3 with normalization to unit acceleration value 1 m/s².

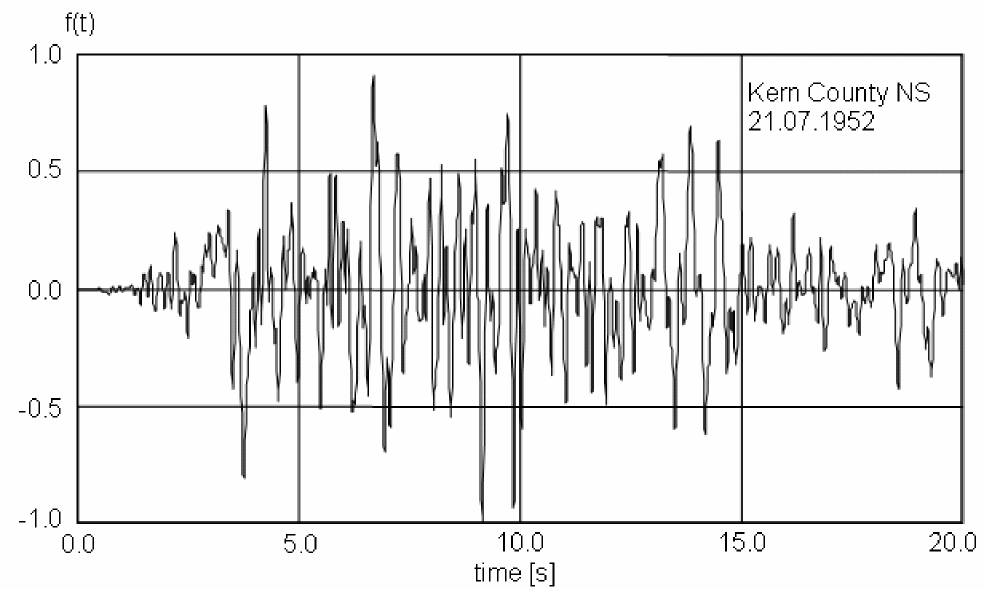

Figure 3: Acceleration time history of Kern County earthquake NS component.

Earthquake accelerations acting on a shell of revolution are described by the following body forces in tangential and horizontal direction with a_{gr} maximum ground acceleration, f(t) time history function (scaled to unit value), h shell thickness, θ^1 angle of circumference.

$p^{<1>} = +a_{gr} \cdot f(t) \cdot h \cdot \sin(\theta^1)$ tangential direction
$p^{<2>} = +a_{gr} \cdot f(t) \cdot h \cdot \cos(\theta^1) \cdot \sin(\alpha)$ meridional direction
$p^{<3>} = -a_{gr} \cdot f(t) \cdot h \cdot \cos(\theta^1) \cdot \cos(\alpha)$ normal direction
α inclination angle of meridian curve
$\tan \alpha = - dR / dZ$

Earthquake acceleration generates equivalent body forces in Fourier term n = 1, which implies circumferential distribution $\cos(n \cdot \theta^1)$ or $\sin(n \cdot \theta^1)$. Thus, for computation of linear structural earthquake response only Fourier term n = 1 is of interest so that the equations of motion can be simplified significantly.

5 EARTHQUAKE RESPONSE OF NDCT AND SPPC

5.1 Natural Eigenperiods

In Figure 4, the corresponding response spectrum for Kern County time history is presented scaled to unit ground acceleration (rigid body value at T = 0 s). Further, the response spectra according to DIN 4149 [4] for soil class A-R and C-S are presented for comparison purpose. By solving the linear eigenvalue problem of free vibration for Fourier term n = 1

$$({}^{11}\mathbf{K} - \omega^2 \cdot {}^{11}\mathbf{M}) \cdot \psi = \mathbf{0} \tag{5}$$

the governing eigenperiods and eigenmodes of both systems are obtained. The following eigenmodes can be identified:

NDCT	1st mode n = 1	motion on elastic soil support	T = 0.73 s
NDCT	2nd mode n = 1	motion on elastic column support	T = 0.40 s
NDCT	3rd mode n = 1	shell bending mode	T = 0.18 s
SPPC	1st mode n = 1	cantilever bending mode #1	T = 5.66 s
SPPC	2nd mode n = 1	cantilever bending mode #2	T = 1.36 s
SPPC	3rd mode n = 1	cantilever bending mode #3	T = 0.66 s

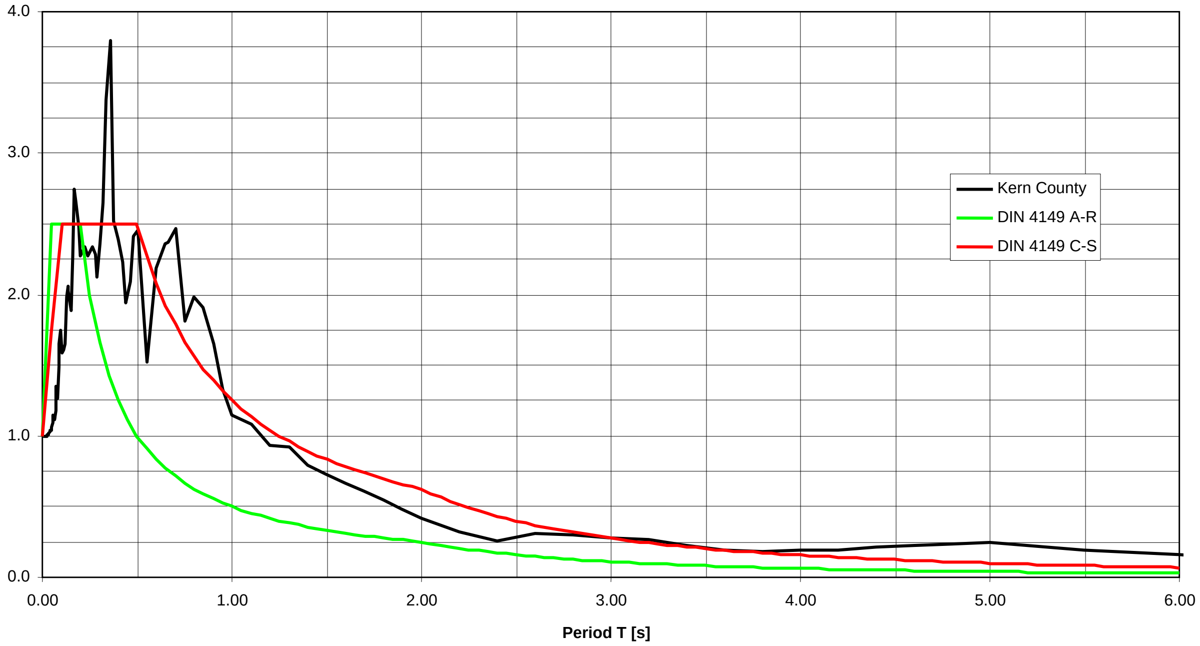

Figure 4: Eigenperiods of NDCT and SPPC with corresponding response spectra.

From natural periods, it becomes obvious that the SPPC in comparison to the NDCT is a very soft structure. The 1st period of SPPC is almost 10 times higher than the 1st period of NDCT. The SPPC is too flexible to follow the ground motion. In contrast, the NDCT is strongly affected by earthquake acceleration since the governing eigenperiods coincide with maximum response accelerations. This fact results in very high column stresses (in case of V-columns: compressive and tensile forces, in case of I-beams: bending moments).

5.2 Transient Response to Kern County Earthquake

Linear transient time history analyses have been carried out for the two presented systems NDCT and SPPC. Hereby, Kern County NS acceleration according to Figure 3 with maximum peak acceleration 0.35 g has been used as reference.

In general, the following effects can be observed for NDCT subjected to earthquake acceleration:

- uplift from ground (in case of raft foundation)
- cracking of concrete of supporting columns (exceedance of concrete tensile strength)
- cracking of shell (exceedance of concrete tensile strength)

From conducted analyses for SPPC subjected to horizontal earthquake acceleration, the following effects can be observed:

- Uplift from ground does not occur. Tilting will not become a problem since 1st period is so high that the upper structure cannot follow the ground acceleration.
- Tensile meridional forces arise only in upper parts of the structure between 600 m – 1000 m.
- Higher modes which describe higher bending modes of the cantilever system will become relevant for the structural response which can be seen from Figure 5.

In Figure 5, the structural response in terms of maximum meridional forces is depicted for both systems. For the NDCT, it can be observed that under dead weight, the complete shell is under meridional compression. Horizontal earthquake acceleration generates tensile meridional forces throughout most parts of the shell. Cracking will occur at meridional forces 0.20 m x 2.56 MN/m² = 510 kN/m. The prestressing effect due to dead weight is totally used up. For the SPPC system, it can be observed that dead weight still represents the dominating part. Tilting will not occur since the base is in compression. Assuming a tensile strength of HPC C 70/85 f_{ctm} = 4.60 MN/m², the cracking meridional force 0.26 m x 4.60 MN/m² = 1200 kN/m is not exceeded. Since the first period of the SPPC is such high, the structure cannot follow the base acceleration. Therefore, higher modes have to be considered to correctly asses the structural response in upper parts. The contribution of different vibration modes to the dynamic response can be found in Figure 5.

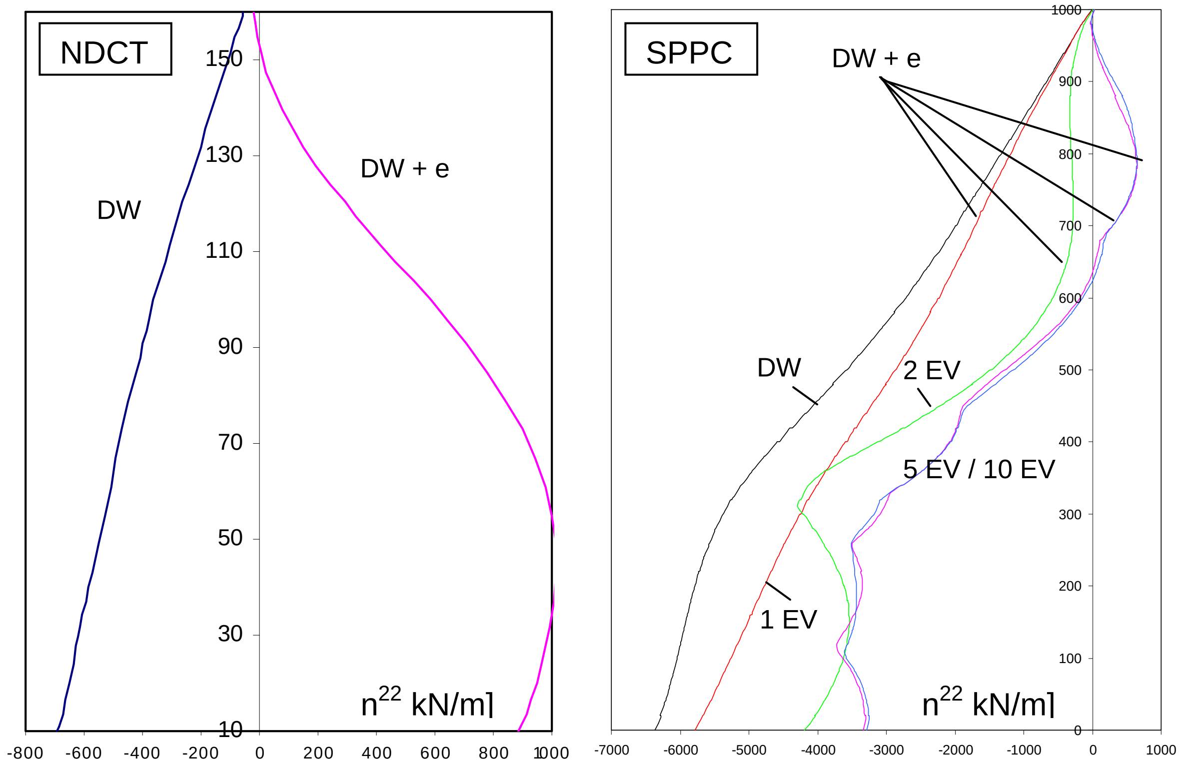

Figure 5: Meridional tensile forces due to earthquake acceleration Kern County NS component (0.35 g).

5.3 Simplified Analysis of SPPC Using Response Spectrum Method for Cantilever

The total mass of the solar power plant chimney yields approximately 501.000 t. The equation of motion for a structure subjected to earthquake motion is given in Eq. (6). By modal transformation, Eq. (7) is obtained. Hereby, the physical degrees of freedom **V** are transformed to modal coordinates q so that the system of coupled equations of motion is decoupled into independent equivalent single degree of freedom systems.

$$\boldsymbol{K}\cdot\boldsymbol{V}+\boldsymbol{C}\cdot\dot{\boldsymbol{V}}+\boldsymbol{M}\cdot\ddot{\boldsymbol{V}}=\boldsymbol{-M}\cdot\boldsymbol{I}\cdot a_{gr}\cdot f(t) \tag{6}$$

$$\boldsymbol{\psi}^{T}\cdot\boldsymbol{K}\cdot\boldsymbol{\psi}\cdot q+\boldsymbol{\psi}^{T}\cdot\boldsymbol{C}\cdot\boldsymbol{\psi}\cdot\dot{q}+\boldsymbol{\psi}^{T}\cdot\boldsymbol{M}\cdot\boldsymbol{\psi}\cdot\ddot{q}=\boldsymbol{-\psi}^{T}\cdot\boldsymbol{M}\cdot\boldsymbol{I}\cdot a_{gr}\cdot f(t) \tag{7}$$

By using the response spectrum diagram, the maximum response acceleration is obtained in dependence of the natural eigenperiod T of the considered eigenmode and in dependence of damping ratio according to Eq. (8). With this maximum response acceleration, equivalent static loads $\mathbf{H}_{E,i}$ for each eigenform i can be computed using Eq. (10).

$$\max\ddot{q}_i=\frac{\boldsymbol{\psi}_i^{T}\cdot\boldsymbol{M}\cdot\boldsymbol{I}}{\boldsymbol{\psi}_i^{T}\cdot\boldsymbol{M}\cdot\boldsymbol{\psi}_i}\cdot a_{gr}\cdot\beta(T,\xi_i) \tag{8}$$

$$H_{E,i}=\boldsymbol{M}\cdot\boldsymbol{\psi}_i\cdot\max\ddot{q}_i=\boldsymbol{M}\cdot\boldsymbol{\psi}_i\cdot\frac{\boldsymbol{\psi}_i^{T}\cdot\boldsymbol{M}\cdot\boldsymbol{I}}{\boldsymbol{\psi}_i^{T}\cdot\boldsymbol{M}\cdot\boldsymbol{\psi}_i}\cdot a_{gr}\cdot\beta(T,\xi_i) \tag{9}$$

The results from equivalent static loads for each eigenform now have to be combined again for the total solution. Results for two different methods are presented in the following: square root of sum of squares (SRSS) and sum of absolute sum.

The results of section 5.2 can be confirmed by using simplified cantilever beam analysis in conjunction with response spectrum analysis. Tilting and uplift from ground will not become a problem while tensile meridional forces arise only in the upper part of shell for the solar power plant chimney. Meridional forces using method SRSS and ABSSUM are depicted in Figure 6. ABSSUM rule provides more unfavorable results since single mode contributions are directly added assuming that maximum response for all contributing modes occurs at the same time.

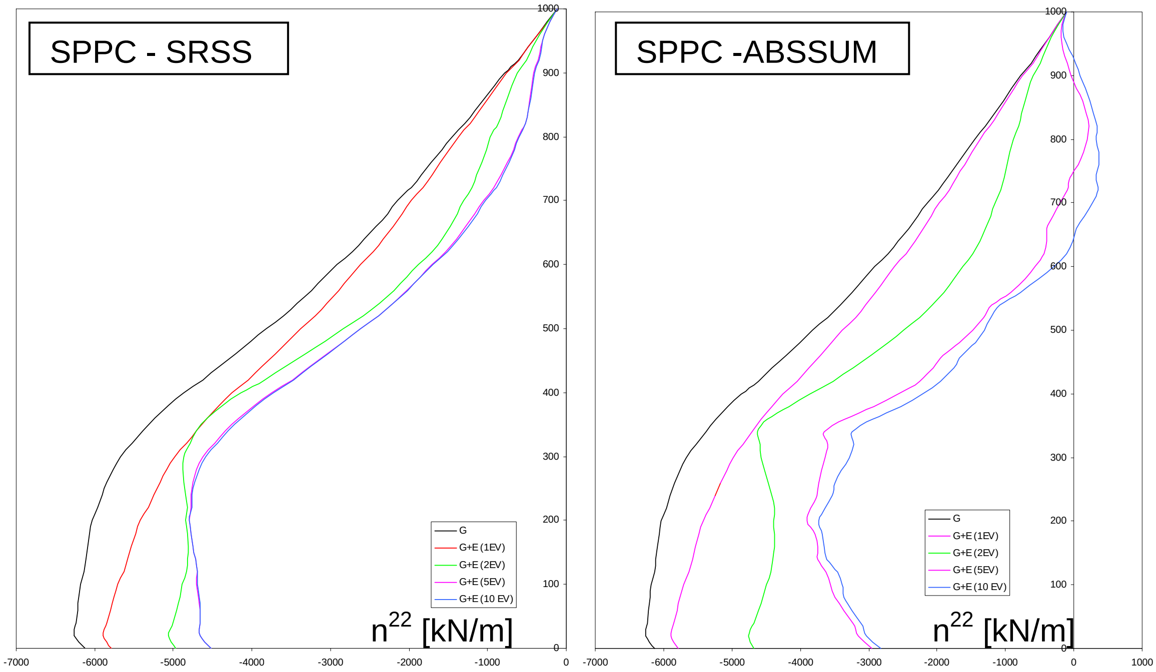

Figure 6: Simplified analysis using response spectrum analysis (SRSS and ABSSUM).

6 CONCLUSION

This contribution shall be only regarded as a first step into dynamic earthquake behavior of solar chimneys subjected to earthquake acceleration. Existing algorithms which have been developed for general shells of revolution and successfully applied to the design of a large number of natural draft cooling towers by the author world wide are deployed to this end. Although the structures SPPC and NDCT are described in a similar way by double curved hyperbolic shapes, the response to earthquake accelerations is totally different. Due to absolute values of eigenperiod, NDCTs behave more critical under earthquake acceleration than SPPCs. Non-linear effects such as uplift, cracking of shell and columns become significant for NDCT while for the analyzed 1000 m SPPC not even tilting will become a problem.

The results presented in this contribution have been obtained using transient time integration analysis for a representative earthquake acceleration time history for a full shell model (ring elements). Simplified response spectrum analysis method (hand calculation) using a cantilever beam model has been used for checking purpose which confirms the obtained results.

However, this study can be only seen as a first approach. Only a base acceleration by a rigid body ground motion has been considered (base of structure remains in original shape). Further effort has to be spent into design studies and into research in this new and demanding field of SPPC structures.

REFERENCES

[1] Th. W. von Backström et al., *State and Recent Advances in Research and Design of Solar Chimney Power Plant Technology*, VGB PowerTech 88 (2008).

[2] Y. Başar and W.B. Krätzig, *Mechanik der Flächentragwerke*, Vieweg & Sohn, 1985.

[3] A.K. Chopra, *Dynamics of structures*, Prentice Hall, 2001.

[4] DIN 4149 „Buildings in German Earthquake Areas“, April 2005, Beuth Verlag Berlin

[5] W.B. Krätzig et al., From large natural draft cooling tower shells to chimneys of solar upwind power plants, *Proceedings of the IASS Symposium 2009*, Valencia (2009).

[6] W.B. Krätzig, Kamine solarer Aufwindkraftwerke – Eine Herausforderung für den Konstruktiven Ingenieurbau, Wayss & Freytag am Donnerstag, Frankfurt am Main, 10/16/2008.

[7] C. Lang, F. Altmeyer, J. Weigl, *Finite Element Program ROSHE V 2010*, Internal L.A.W. Work Report (2010).

[8] C. Lang, R. Meiswinkel and F.C. Filippou, *Non-linear analysis of shells of revolution with ring elements*, Engineering Structures, 2002, Vol.24, No.2, 163-177

[9] C. Lang, *Beitrag zur Theorie, Numerik und Anwendung nichtlinearer Algorithmen zur statischen und dynamischen Analyse von Stahlbetonrotationsschalen*, PhD thesis, 2003, TU Kaiserslautern

[10] Strongmotion database http://peer.berkeley.edu/

COMPDYN 2011
III ECCOMAS Thematic Conference on
Computational Methods in Structural Dynamics and Earthquake Engineering
M. Papadrakakis, M. Fragiadakis, V. Plevris (eds.)
Corfu, Greece, 25–28 May 2011

COMPARISON OF DIFFERENT NON-LINEAR STATIC ANALYSIS USED FOR SEISMIC ASSESSMENT OF EXISTING BUILDINGS

A. Moshref[1], **S.M. Moghaddasi**[2], **and M. Tehranizadeh**[3]

[1] Amirkabir University of Technology (Tehran Polytechnic)
474 Hafez Ave. Tehran, Iran.
amir_moshref@aut.ac.ir

[2] Islamic Azad University Golpayegan Branch
Glopayegan, Iran P.O.BOX 87715 116
mehdi.moghaddasi@gmail.com

[3] Amirkabir University of Technology (Tehran Polytechnic)
474 Hafez Ave. Tehran, Iran.
dtehz@yahoo.com

Keywords: Retrofitting, Pushover Analysis, Moment Resisting Frames, Damage Index.

Abstract. *The present study is focused on the comparison of non-linear static analysis (Pushover) which is used by two major guidance documents, the New Zealand guideline and the US FEMA 440, on the assessment of existing buildings currently available for moment resisting concrete frames. The main purpose of the study is to trace the differences in the results produced by these two guidelines. For this, three different moment resisting concrete frames are assessed under these two guidelines to determine the PGA value that causes their collapse. In the next step, these are compared by their similar values that are determined from the nonlinear dynamic analysis in which Park and Ang damage index is used as acceptance criteria for components. As is found, the result of force based approach which is proposed by New Zealand guideline is more compatible with the nonlinear dynamic analysis.*

1 INTRODUCTION

The disastrous effects observed in recent seismic events, in terms of loss of lives as well as immediate and long-term economic damage has prompted the need to produce documents in the area of assessment and improvement of the structural performance of existing buildings in times of an earthquake. One of the earliest guidelines which has been published for the evaluation and retrofit of concrete buildings is ATC-40 [1]. After it, FEMA 273 and FEMA 356 have been published respectively as a guideline and pre-standard for the seismic rehabilitation of buildings [2,3]. In 2005, FEMA 440 has been published. The purpose of the FEMA440 has been to evaluate current non-linear static procedures (NSPs), as described in FEMA 273/FEMA 356 and ATC-40, and to develop improvements where feasible. The primary objectives were, to develop guidelines for practicing engineers on how to apply the procedures to new and existing buildings.

The first step of the assessment process in FEMA440 is definition of “Rehabilitation Objectives”; where each goal shall consist of a “Target Building Performance Level” and an “Earthquake Hazard Level”. Building performance is a combination of the performance of both structural and nonstructural components. Three performance levels are considered such as: Immediate Occupancy (IO), Life Safety (LS) and Collapse Prevention (CP) for structural components and the nonstructural performance level of a building shall be selected from five discrete performance level consisting of Operational (N-A), Immediate Occupancy (N-B), Life Safety (N-C), Hazard Reduced (N-D), and Not Considered (N-E) [4]. The seismic hazard can be represented either by an acceleration response spectrum or by acceleration time history.

Four different analysis procedures are allowed for the evaluation of the response of the buildings: the linear static (LSP), the linear dynamic (LDP), the non-linear static (NSP) and the non-linear dynamic (NDP). The two linear procedures are permitted only for buildings with “regular” structural configuration. As the non-linear dynamic procedure is the most complex, using non-linear static analysis is more common for its simplicity and ability to estimate components and system deformation demands with an acceptable accuracy.

In nonlinear static procedure the demand of the buildings is calculated by means of a pushover analysis. For this, the target displacement, which is intended to represent the maximum displacement likely to be experienced during the designed earthquake, shall be determined at first. According to this standard, the control node shall be located at the center of the roof of a building and its target displacement can be calculated by the Coefficient Method as below:

$$\delta_t = C_0 C_1 C_2 S_a \frac{T_e^2}{4\pi^2} g \qquad (1)$$

Where C_0 is a modification factor to relate spectral displacement of an equivalent single degree of freedom (SDOF) system to the roof displacement of the building, C_1 is a modification factor to relate expected maximum displacements to displacements calculated for linear elastic response, C_2 is a modification factor to represent the effect of pinched hysteresis shape, cyclic stiffness degradation, and strength deterioration on maximum displacement response, S_a is the response spectrum acceleration at the effective fundamental period and damping ratio, and T_e is the effective fundamental period of the building.

Acceptance criteria for nonlinear procedures are presented by the plastic rotation angle for the concrete components. One of the conditions which can affect the acceptance criteria of components is the conditions of transverse reinforcement. A component is conforming if, within the flexural plastic hinge region, hoops are spaced at ≤ d/3, and if, for component of moderate and high ductility demand, the strength provided by the hoops is at least threefourths of the design shear. Otherwise, the component is considered nonconforming. Where d is effective depth of the cross section.

In 1996, a draft was published for the assessment and improvement of the structural performance of earthquake risk building in New Zealand titled NZSEE 1996 [5]. This draft has been reviewed twice till now and is now available as NZSEE 2002 and NZSEE 2006 [6, 7]. The New Zealand documents concentrate only on matters relating to life safety, i.e. collapse which leads to loss of life.

Three possible approaches for performing the assessment are indicated in the document: time history analysis, force analysis and displacement analysis. The first one is the most accurate but the most complex as well, so the others are considered as the main approaches for assessments.

In the document it is stated that “the displacement based approach is generally considered to produce more rational and less conservative assessment outcome, the force based one is more familiar to designers” [7].

Five analysis methods are proposed for the evaluation of the structural response: equivalent static analysis, modal response spectrum analysis, simple lateral mechanism analysis, lateral pushover analysis and inelastic time history analysis. In this study, the proposed lateral pushover analysis is compared with the similar procedure of FEMA440.

The demands of the buildings are dependent upon the analysis method applied. In the force based approach, the acceleration response spectra are used to model the earthquake action and the demand is stated by the structural ductility factor which can be found as below:

$$k_{\mu} = \frac{C(T_1)S_P W_t (\%NBS)_t}{V_{prob}} \qquad (2)$$

Where $C(T_1)$ is the ordinate of the elastic site hazard spectrum for T_1 and for the site, W_t is total seismic weight of the structure, S_P is structural performance factor and $(\%NBS)_t$ is target percentage of new building standard which is considered equal to one in this study.

In the displacement based approach, the displacement response spectra are used to model the earthquake action and the demand is stated by the displacement at the effective height of building which is found from the spectra using the effective period and the equivalent viscous damping.

The ultimate curvature is considered as the acceptance criteria of concrete components. To calculate the ultimate curvature, having the ultimate concrete strain is inevitable. It is stated in the document that for unconfined concrete the ultimate concrete strain, ε_{cu} =0.004 and for the confined concrete, Mander model can be assumed as below [8]:

$$\varepsilon_{cu} = 0.004 + \frac{1.4\rho_s f_{yh} \varepsilon_{su}}{f_{cc}} \qquad (3)$$

Where ε_{cu} is ultimate concrete strain; ρ_s is the volumetric ratio of transverse reinforcement and can be approximated by:

$$\rho_s = 1.5A_v/b_c s \qquad (4)$$

Where A_v is total area of transverse reinforcement in a layer, s is spacing of layers of transverse reinforcement, b_c is the width of concrete core, f_{yh} is the yield strength of the transverse reinforcement, ε_{su} is the steel strain at maximum stress, and f_{cc} is the compressive strength of the confined concrete.

The document presents conditions corresponding to confined and unconfined sections. One of these conditions which are dealt with in this study is spacing of hoops. According to NZSEE guideline, when the spacing of hoops or stirrups sets in potential plastic hinge greater than or equal to d/2 or $16d_b$, the section shall be assumed as "unconfined", where d is the effective depth of section and d_b is the diameter of longitudinal reinforcement. However the sections are assumed as confined in this study.

Lupoi et al. presented a comparison of the practical applicability, the relative ease of use and the degree of agreement on the results of the methods proposed by FEMA 356, NZSEE 2002 and Japanese Standards. The PGA_f value that causes the collapse of three structures is determined based on the above mentioned documents and in comparison with each other. As it is mentioned in the paper, from the small number of cases examined, all studied structures have three stories, thus it is not possible to systematically trace the differences in the results produced by the different approaches [9]

In this study, 5, 10 and 15 story moment resisting concrete frames are assessed by the NZSEE 2006 and FEMA440 to determine the PGA_f values that cause the collapse. Then the frames are analyzed against twenty two earthquakes with the use of nonlinear dynamic analysis to determine the PGA_f value. To find, the performance of frames in the latest analysis, Park and Ang Damage Index has been used as is explained in the following paragraphs [10].

2 COMPARATIVE STUDY

This section presents the choices and assumptions made by using the above mentioned documents in order to compare results.

2.1 The studied frames

Three moment resisting concrete frames with 5, 10 and 15 stories are considered in this study. Figure 1 illustrates five-story moment resisting frame. As is shown, the frame has four bays with the width and the height of 6 and 3.2m, respectively. The design details of other frames are revealed on Table 1, 2 and 3. The gravity load containing both dead and live load is assumed 28.86 kN/m for all the levels.

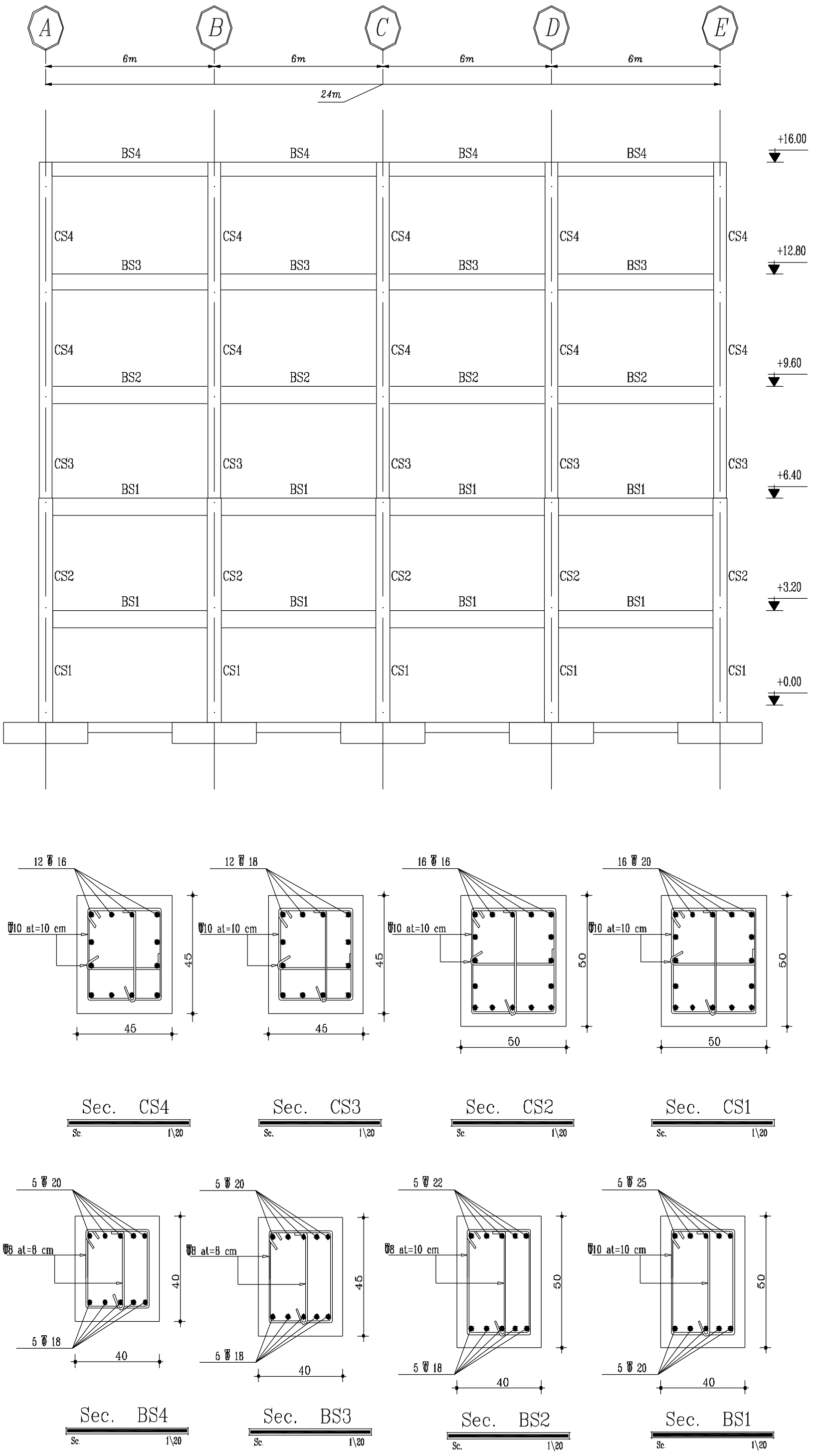

Figure 1. Details for the 5-story reinforced concrete special moment frame

Element	Story	b(mm)	h(mm)	ρ^{*}	ρ_{p}^{**}	ρ_{sh}	S(mm)
Beams	st-1	400	500	0.013	0.009	0.0014	100
	st-2	400	500	0.013	0.009	0.0014	100
	st-3	400	500	0.011	0.008	0.0009	100
	st-4	400	450	0.011	0.009	0.001	80
	st-5	400	400	0.012	0.01	0.0011	80
Columns	st-1	500	500	0.02	-----	0.0013	100
	st-2	500	500	0.013	------	0.0013	100
	st-3	450	450	0.015	------	0.0016	100
	st-4	450	450	0.012	------	0.0016	100
	st-5	450	450	0.012	------	0.0016	100

* Top Reinforcement Ratio

** Bottom Reinforcement Ratio

Table 1. Elements Properties of 5-srory Reinforced Concrete special Moment Frame

Element	Story	b(mm)	h(mm)	ρ	ρ_{p}	ρ_{sh}	S(mm)
Beams	st-1	500	600	0.010	0.007	0.0012	125
	st-2	500	600	0.013	0.009	0.0012	125
	st-3	500	550	0.012	0.009	0.0013	120
	st-4	500	550	0.012	0.009	0.0013	120
	st-5	500	550	0.012	0.009	0.0013	120
	st-6	500	500	0.013	0.009	0.0009	100
	st-7	500	500	0.013	0.009	0.0009	100
	st-8	500	500	0.011	0.008	0.0009	100
	st-9	500	450	0.011	0.009	0.0011	80
	st-10	500	400	0.011	0.008	0.0012	80
Columns	st-1	600	600	0.021	0.021	0.0016	100
	st-2	600	600	0.014	------	0.0011	100
	st-3	550	550	0.017	------	0.0014	100
	st-4	550	550	0.017	------	0.0014	100
	st-5	550	550	0.017	------	0.0014	100
	st-6	500	500	0.016	------	0.0013	100
	st-7	500	500	0.016	------	0.0013	100
	st-8	500	500	0.015	------	0.0013	100
	st-9	500	500	0.012	------	0.0013	100
	st-10	500	500	0.012	------	0.0013	100

Table 2. Element Properties of 10-srory Reinforced Concrete special Moment Frame

2.2 Term of Comparison

The comparison of selected procedures is made in terms of the PGA_f value that causes the collapse of the structures. The PGA_f has been arbitrarily related to the spectrum of Standard No. 2800-05 (Iranian code of practice for seismic resisting design of building) for the soil type 2; it is believed that the results of the comparisons would not change to any significant extent if a different reference spectrum were selected.

The PGA_f values for different approaches are determined as follow:

Element	Story	b(mm)	h(mm)	ρ	ρ_{p}	ρ_{sh}	S(mm)
Beams	st-1	500	700	0.007	0.005	0.0010	125
	st-2	500	700	0.009	0.006	0.0010	125
	st-3	500	650	0.011	0.008	0.0011	120
	st-4	500	650	0.011	0.008	0.0011	120
	st-5	500	650	0.012	0.008	0.0011	120
	st-6	500	600	0.013	0.009	0.0009	100
	st-7	500	600	0.013	0.009	0.0008	100
	st-8	500	600	0.013	0.009	0.0008	100
	st-9	500	500	0.013	0.009	0.0009	100
	st-10	500	500	0.013	0.009	0.0009	100
	st-11	500	500	0.014	0.009	0.0009	100
	st-12	500	500	0.012	0.009	0.0009	100
	st-13	500	500	0.010	0.007	0.0009	100
	st-14	500	400	0.012	0.009	0.0012	80
	st-15	500	400	0.011	0.009	0.0012	80
Columns	st-1	700	700	0.020	------	0.0014	100
	st-2	700	700	0.017	------	0.0014	100
	st-3	700	700	0.016	------	0.0014	100
	st-4	650	650	0.023	------	0.0017	100
	st-5	650	650	0.012	------	0.0017	100
	st-6	600	600	0.014	------	0.0012	100
	st-7	600	600	0.014	------	0.0012	100
	st-8	600	600	0.014	------	0.0012	100
	st-9	550	550	0.010	------	0.0010	100
	st-10	550	550	0.010	------	0.0010	100
	st-11	500	500	0.020	------	0.0018	100
	st-12	500	500	0.013	------	0.0013	100
	st-13	500	500	0.010	------	0.0013	100
	st-14	500	500	0.010	------	0.0013	100
	st-15	500	500	0.010	------	0.0013	100

Table 3. Element Properties of 15-srory Reinforced Concrete special Moment Frame

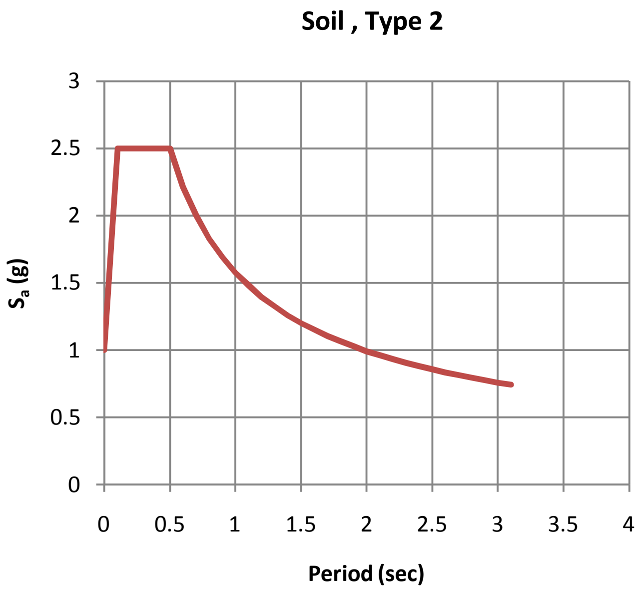

Figure 2: Standard No. 2800-05 acceleration spectrum for soil Type 2

1. The nonlinear static approach of FEMA440 (Displacement Modification):

$$(PGA_f)_{FEMA440} = \frac{(V_{prob}/W_t).(\delta_u/\delta_t)}{C(T_1)} \tag{5}$$

2. The force-based NZ procedure:

$$(PGA_f)_{NZ,force} = \frac{(V_{prob}/W_t).\mu_{sc}}{C(T_1)} \tag{6}$$

3. The displacement-based NZ procedure:

$$(PGA_f)_{NZ,displacement} = \frac{U_{el}}{C(T_{eff}).({T_{eff}}^2/4\pi^2).g\,.k(\xi_{eff})} \tag{7}$$

Where :

$$T_{eff} = 2\pi\sqrt{\frac{M_e}{K_{eff}}} \tag{8}$$

$$K_{\xi} = \sqrt{\frac{7}{2+\xi}} \tag{9}$$

3 NON-LINEAR DYNAMIC

To estimate the response of the frames under earthquake, nonlinear dynamic analysis is done using twenty-two acceleration time histories as described in Table 4. Records are selected from the PEER-NGA strong motion database which recommended by FEMAP695 [11].

Park and Ang damage index is used as acceptance criteria for components as below [10]:

$$\mathrm{DamageIndex} = \frac{\delta_{max}}{\delta_u} + \frac{\beta}{F_u.\delta_u}\int dE \tag{10}$$

Where δmax is the peak deformation, δu is the ultimate deformation capacity under monotonic loading, Fu is the calculated yield strength, β is the calibration parameter for cyclic damage and is considered to equal 0.2 in this study, and E is the dissipated energy. Maximum rotation and yield moment under monotonic loading are selected as ultimate deformation and yield strength, respectively. DI is considered equal to one for the severe damage regards to CP levels based on the classification suggested by Park et al. [12].

After doing nonlinear dynamic analysis for all above mentioned records and finding PGA_f's for each one, Minitab [13] as a software was used to fit best probabilistic distribution on 22 data's. The variability in the PGA_f is best described by a lognormal distribution so present study uses average of natural log dates instead of simply average.

ID No	**Record Seq. No.**	**Earthquake**		**File Names**	
		Year	Name	Component 1	Component 2
1	953	1994	Northridge	MUL009	MUL279
2	960	1994	Northridge	LOS000	LOS270
3	1602	1999	Duzce,Turkey	BOL000	BOL090
4	1787	1999	Hectot Mine	HEC000	HEC090
5	169	1979	Imperial Valley	H-DLT262	H-DLT352
6	174	1979	Imperial Valley	H-E11140	H-E11230
7	1111	1995	Kobe,Japon	NIS000	NIS090
8	1116	1995	Kobe,Japon	SHI000	SHI090
9	1158	1999	Kocaeli,Turkey	DZC180	DZC270
10	1148	1999	Kocaeli,Turkey	ARC090	ARC000
11	900	1992	Landers	YER270	YER360
12	848	1992	Landers	CLW-LN	CLW-TR
13	752	1989	Loma Perieta	CAP000	CAP090
14	767	1989	Loma Perieta	GO3000	GO3090
15	1633	1190	Manjil,Iran	ABBAR--L	ABBAR—T
16	721	1987	Superstition Hills	ICC000	ICC090
17	725	1987	Superstition Hills	POE270	POE360
18	829	1992	Cape Mendocino	RIO270	RIO360
19	1244	1999	Chi-Chi, Taiwan	CHY101-E	CHY101-N
20	1485	1999	Chi-Chi, Taiwan	TCU045-E	TCU045-N
21	68	1971	San Fernando	PEL090	PEL180
22	125	1976	Friuli,Italy	A-TMZ000	A-TMZ270

Table 4. Selected records for the nonlinear dynamic analysis

4 NON-LINEAR NUMERICAL ANALYSIS

Available element models generally do not accurately represent the full range of behavior (low level, frequent ground motions which contribute most to damage and financial loss as well as high level, rare ground motions which contribute most to collapse risk). Therefore, plastic hinge model to capture strength and stiffness deterioration and collapse, are used. The plastic hinge model also includes the beam-column element lumps the bond-slip and beam column yielding response into one concentrated hinge. Due to modern capacity design provisions for RC SMRF buildings, shear failure is not expected for the elements of RC SMRF buildings, so only flexural damage is modeled.

OpenSees was used for the structural analyses. P-Delta effects are accounted for using a combination of gravity loads on the lateral-resisting frame and gravity loads on a leaning column element. The model includes 5% Rayleigh damping anchored to the first and third modal periods [14]. As shown in Figure 3, plastic hinge models for beam columns have a trilinear backbone curve described by five parameters (M_y , θ_y , K_s , $\theta_{cap,pl}$, and K_c). The model captures the four important modes of cyclic strength and stiffness degradation; this is based on an energy dissipation capacity and a term that describes how the deterioration rate changes as damage accumulates. Model parameters (for initial stiffness and deformation capacity) of RC beam columns are based on recommendations from Fardis et al. [15] and Haselton calibrations to test data using the PEER structural performance database [16].

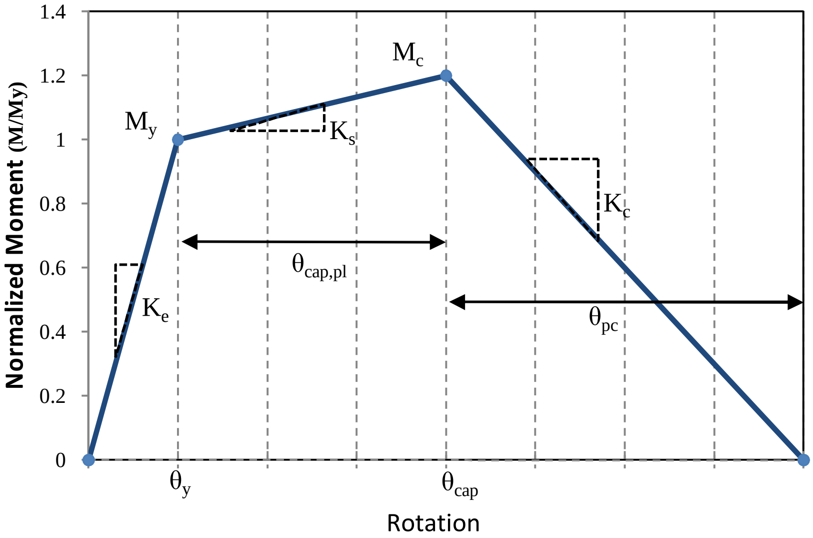

Figure 3: Monotonic backbone curve

5 DISCUSSION AND CONCLUSION

The PGA_f values that cause the collapse in the first element f the frames are reported in Table 5 and shown in Figure 4 for all the approaches. Figure 5 illustrates percent of error among each nonlinear static procedures and nonlinear time history analyses. As shown, the result of nonlinear dynamic analysis is more compatible with the New Zealand force approach and also has lower error.

No. Story	Collapse Peak Ground Acceleration (PGA_f) in Units of g				
	New Zealand		FEMA440		Time History
	Force Based	Displacement	Displacement Modification	Equivalent Linearization	
5	0.55	0.77	0.75	0.72	0.48
10	0.59	0.72	0.76	0.71	0.51
15	0.62	0.68	0.68	0.77	0.54

Table 5: The PGA_f values that cause the collapse

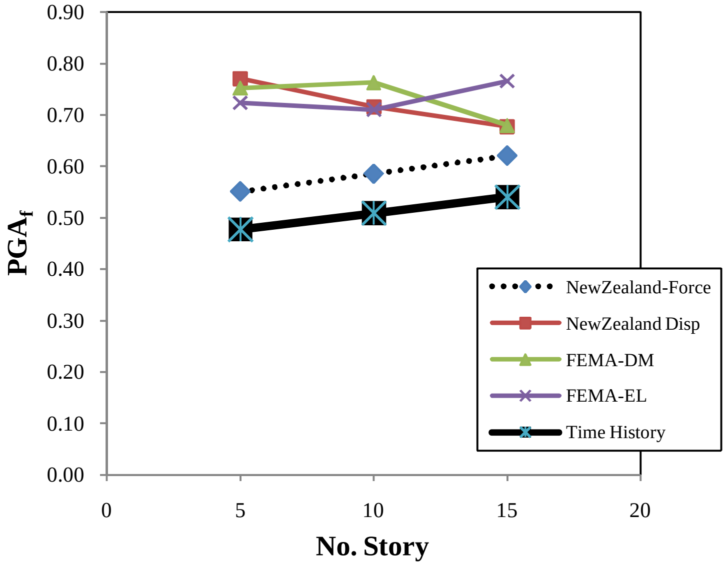

Figure 4: The PGA values cause the collapse from different approaches

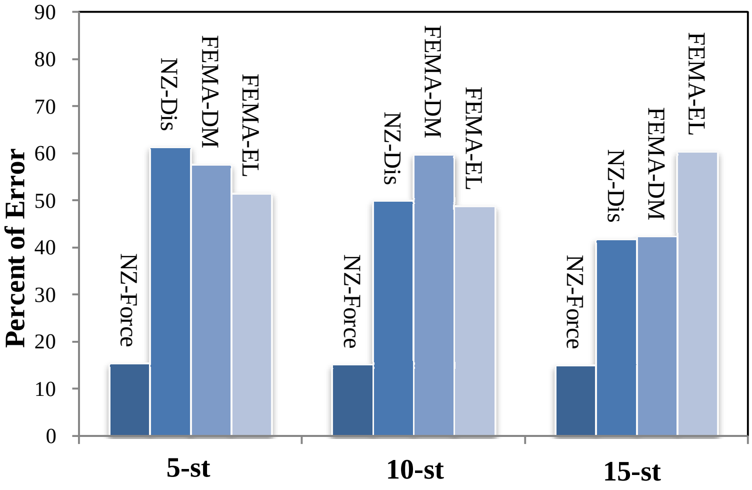

Figure 5: Error Percentage

From the figure 5, it can be concluded that the New Zealand force approach is most compatibility with the nonlinear dynamic analyses in all cases. The New Zealand displacement approach gives appropriate results for all frames but its results are not conservative.

REFERENCES

[1] ATC (1996), Seismic evaluation and retrofit of concrete buildings, Vol. 1, ATC -40, Applied Technology Council, Redwood City.

[2] Federal Emergency Management Agency (FEMA) (1997), NEHRP Guidelines for the Seismic Rehabilitation of Building, FEMA-273, Building Seismic Safety Council, Washington, DC.

[3] Federal Emergency Management Agency (FEMA) (2000), Prestandard Commentary for the Seismic Rehabilitation of Buildings, FEMA-356, Building Seismic Safety Council, Washington, DC.

[4] Federal Emergency Management Agency (FEMA) (2005), Improvement of Static Seismic Analysis Procedures, FEMA-440, Applied Technology Council, California

[5] New Zealand National Society for Earthquake Engineering (NZSEE) (1996), The Assessment and Improvement of the Structural Performance of Earthquake Risk Buildings, NZSEE 1996, Draft for General Release.

[6] New Zealand National Society for Earthquake Engineering (NZSEE) (2002), The Assessment and Improvement of the Structural Performance of Earthquake Risk Buildings, NZSEE 2002, Draft Prepared for the NZ Building Industry Authority.

[7] New Zealand National Society for Earthquake Engineering (NZSEE) (2006), Assessment and Improvement of the Structural Performance of Buildings in Earthquake, NZSEE 2006.

[8] Mander, J. B., Priestley, M. J. N. and Park, R. (1988) "Theoretical stress-strain model for confined concrete", Journal of Structural Engineering, ASCE **1l4(8)**, 1804-1826.

[9] Lupoi, G., Calvi G. M. and Pinto P. E. (2004) "Comparison of different approaches for seismic assessment of existing buildings", Journal of Earthquake Engineering, **8: 1,** 121-160.

[10] Park, Y. J., Ang A. H. S. (1985) "Mechanistic seismic damage model for reinforced concrete". Journal of Structural Engineering, **111-4**, 722-739.

[11] Peer Strong Motion Database (10 April 2010) http://peer.berkeley.edu/smcat.

[12] Park, Y. J., Ang A. H. S. and Wen, Y. K. (1985b) "Seismic damage analysis of reinforced concrete buildings". Journal of Structural Engineering, **111-4**, 740-757.

[13] Minitab 15.1.1.0, 2007. http://www.minitab.com/

[14] Miranda E. Personal communication regarding damping in buildings, 2005.

[15] Panagiotakos, T.B., and Fardis, M.N., 2001, "Deformations of reinforced concrete members at yielding and ultimate," ACI Structural Journal, 98 (2).

[16] Haselton, C.B., Mitrani-Reiser, J., Goulet, C., Deierlein, G.G., Beck, J., Porter, K.A., Stewart, J., and Taciroglu, E., 2008, An Assessment to Benchmark the Seismic Performance of a Code-Conforming Reinforced-Concrete Moment-Frame Building, PEER Report 2007/12, Pacific Earthquake Engineering Research Center, University of California, Berkeley, California.

COMPDYN 2011
3rd ECCOMAS Thematic Conference on
Computational Methods in Structural Dynamics and Earthquake Engineering
M. Papadrakakis, M. Fragiadakis, V. Plevris (eds.)
Corfu, Greece, 25–28 May 2011

DEVELOPING FRAGILITY SURFACES FOR MORE ACCURATE SEISMIC VULNERABILITY ASSESSMENT OF MASONRY BUILDINGS

Pierre Gehl[1], Serigne Sy[1], and Darius Seyedi[1]

[1]BRGM
3 avenue Claude-Guillemin, BP 36009, 45060 ORLEANS Cedex 2, France
e-mail: p.gehl@brgm.fr

Keywords: vulnerability, unreinforced masonry, fragility surfaces, ground-motion parameters

Abstract. *Usual methods for the vulnerability assessment of buildings often result in fragility curves, with respect to one intensity-measure parameter like PGA or spectral displacement. However, the seismic loading is very complex and describing it with one parameter may result in neglecting other significant characteristics of the ground motion [1]. Thus, this study proposes a methodology to develop fragility surfaces, which express the probability of damage with respect to more than one parameter, in order to better account for uncertainties related to the hazard description. The proposed methodology is applied to a model of a two-story unreinforced masonry building (real structure tested on a shaking table by [2]) and the following steps are carried out:*

- *modeling the structure with TREMURI code [3] and static pushover analysis;*
- *developing a set of models with an aleatory distribution of mechanical properties;*
- *based on Latin hypercube sampling, performing hundreds of dynamic analyses (using real and synthetic accelerograms) and assessing the damage level from each analysis;*
- *studying the ground-motion parameters: clustering methods and correlation analyses help to select the appropriate couple of variables to use in the fragility surfaces;*
- *applying the kernel estimation of density in order to get a non-parametrical distribution of damage probability and interpolation into fragility surfaces;*

The proposed framework permits us to choose a couple of ground-motion parameters that are well correlated to the dynamic response of the studied building and, in the same time, are less inter-correlated. The obtained uncorrelated intensity-measures are then used to build unbiased two-variables fragility functions, based on the couple of parameters (PGD and PGA). A comparison between the one-parameter fragility curve and "slices" of the fragility surface shows that the use of a second ground-motion parameter delivers a clearer definition of the vulnerability: the different "slices" can be seen as confidence intervals that can be of great help to public planners, especially in the case of very low probabilities for instance (i.e., extreme events).

1 INTRODUCTION

Current methods of physical vulnerabilty assessment usually result in fragility curves (probability of a given damage level with respect to an intensity-measure parameter), mostly based on parameters such as Peak Ground Acceleration (PGA) or macroseismic intensity. However, it has been recently showed that other ground-motion parameters could be more accurate descriptors of the building fragility. Besides, usual fragility curves neglect the uncertainty introduced by the use of only one parameter to represent the seismic action. Actually, due to the complexity of the seismic loading, accouting for only one parameter may neglect other important characteristics of a seismic time-history, such as the frequency or energy content of the signal.

In the scope of the seismic risk assessment at an urban or regional scale, it is crucial to use accurate information on the vulnerability of common buildings, in order to reduce the scatter in the final results. To this end, the introduction of fragility surfaces (damage probability expressed with respect to two parameters, [1]) instead of single-parameter curves could offer a better knowledge of the vulnerability of a given typology of buildings and provide the public decision-makers with more elaborate data.

Consequently, this study aims at developing a methodology to build analytical fragility surfaces for unreinforced masonry structures: this approach is tested on a two-story brick masonry building. The choice of relevant ground-motion parameters to build the surfaces requires many time-history simulations (unlike a capacity curve approach): thus, the choice of the TREMURI code ([3]) for the structural models has been guided by the use of macrocomponents of masonry panels, which enables faster dynamic calculations than more detailed modeling softwares.

2 STRUCTURAL MODEL WITH TREMURI

2.1 A brief description of TREMURI code

Several post-earthquake observations have shown that unreinforced masonry (URM) panels are composed of rigid undamaged zones, as opposed to vertical or horizontal elements (located between wall openings) that are subjected to shear forces or bending moments. This behavior has led to the developement of a masonry macromodel by [4], and later improved by [5] and [6]: this macroelement has been implemented in the TREMURI code and enables to accurately reproduce the behaviour of a masonry panel, while reducing computation times with respect to more detailed finite-element models. This equivalent-frame approach enables to discretize a masonry wall into several components (vertical elements, named ”piers”, horizontal ones, named ”spandrels”, and rigid undamageable zones), represented in Figure 1.

The nonlinear macrocomponent used here takes into account the common in-plane damage mechanisms of a masonry panel (see Figure 2), namely: shear failure (sliding or diagonal) and bending failure.

Damage by shear mechanism is achieved when the shear force of the macroelement reaches the ultimate shear strength, defined by the following criteria ([3]):

- Mohr-Coulomb criteria (for shear sliding):

$$V_u = l' t f_{v0} + \mu N \tag{1}$$

- Turnsek-Cacovic criteria (for diagonal cracking):

$$V_u = lt\frac{1.5\tau_0}{b}\sqrt{1+\frac{N}{1.5lt\tau_0}} \tag{2}$$

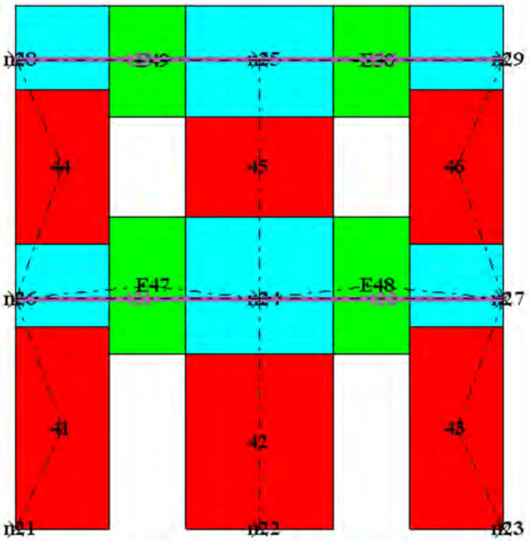

Figure 1: Example of a masonry wall and its openings, modelled into an equivalent-frame. Blue and red elements are respectively the deformable spandrels and piers, whereas the rigid zones are represented in green.

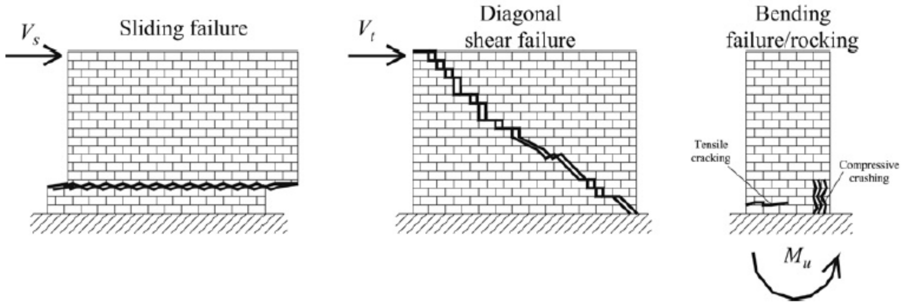

Figure 2: Various damage mechanisms considered for a masonry pier (source - [7])

Where t is the thickness of the macroelement, l its width (l' denoting the actual width of the panel that is subjected to compression), and b a shape factor (height-on-width ratio). The parameter f_{v0} is the shear stregnth without any compression, and τ_0 the shear strength when the tensile strength is reached (first diagonal cracks appearing). Finally, μ is the Mohr-Coulomb friction coefficient and N denotes the axial force that generates compression on the panel.

The ultimate bending moment, representing flexural failure, is defined by:

$$M_u = \frac{l^2 t \sigma_0}{2}(1 - \frac{\sigma_0}{0.85 f_m}) = \frac{Nl}{2}(1 - \frac{N}{N_u}) \tag{3}$$

The ultimate moment depends also on axial compression N, while σ_0 denotes current compression stress and f_m is the compression limit of the masonry.

In the case of 3D modelling, the walls are considered as bearing elements, whereas floors act as horizontal stiffening elements (flexible diaphragms governing the load distribution between the walls). One important assumption in TREMURI is that out-of-plane behavior is not taken into account: it is admitted that such a behavior is negligible due the floor diaphragms and the sound connections between horizontal and vertical components (global box-type behaviour). Thus, in-plane responses of the longitudinal walls (e.g. the ones along the direction of the seismic loading) govern most of the building behaviour: those can take various forms, depending on the type of mechanism (shear or rocking) that is predominant (see Figure 3).

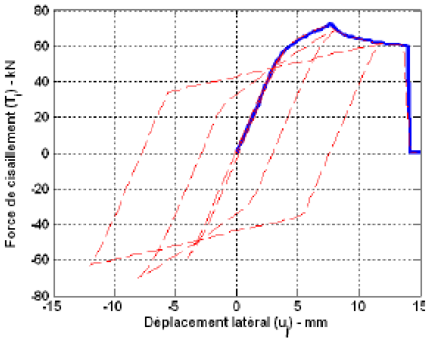

Figure 3: shear (left) and rocking (right) behavior of a single masonry macrocomponent, subject to monotonic (solid line) and cyclic (dotted line) loadings

2.2 Modeling of a two-story URM building

Using the TREMURI macroelement, a building was modeled, based on the results of an experiment in University of Pavia ([2]) on a real scale two-story URM building. The model uses the exact geometry of the real building, while the properties displayed in Table 1 were selected, based on experimental data and common features of brick masonry.

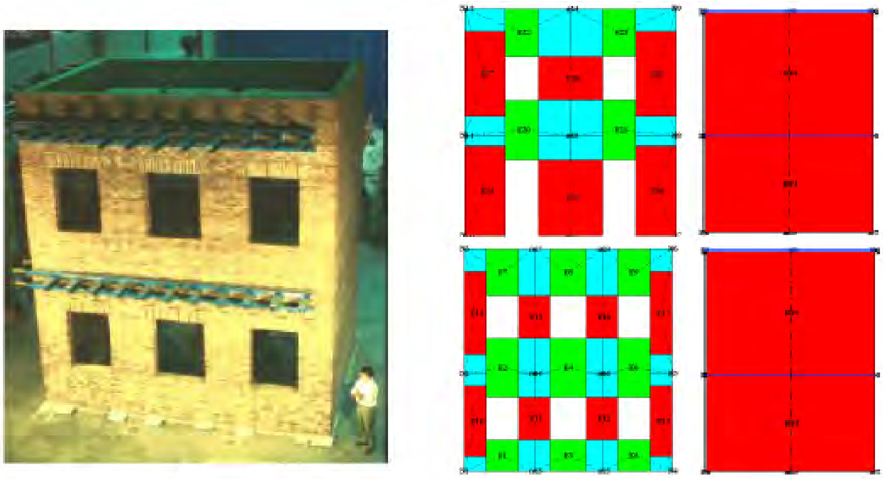

Figure 4: View of the Pavia experiment ([2]) and the corresponding TREMURI model

The structure is around 6m high, with plan dimensions of 6 by 4.4m. As axial forces are a crucial factor in the strength of the masonry, concrete blocks were added on each floor in order to account for live loads: this is traduced into the model with a vertical load of around 250 kN on each floor.

The modal analysis of the 3D model gives the first mode along the length of the building (referred to as the X-direction), for a period $T = 0.149$s (almost 90% of the building mass is concentrated in the first mode along X). The next step is to perform a pushover analysis in

	Parameter	Value
E	Young modulus	3600 MPa
G	Shear modulus	600 MPa
ρ	Density	1800 kg/m3
f_m	Compressive strength	6.2 MPa
f_{sh}	Shear strength	0.23 MPa
D_{sh}	Shear ultimate drift ratio	0.6%
D_{fl}	Rocking ultimate drift ratio	0.8%
μ	Friction coefficient	0.2

Table 1: Mechanical properties of the building model

order to obtain the building global strength and the ultimate top displacement: a progressive lateral force is applied along the X-direction, while the forces are distributed at each floor according to the first mode shape. Based on some previous studies ([8], [9]), it is admitted that the ultimate displacement is reached when the shear force falls down to 80% of its maximum value: using the equal-energy criterion, an idealized bilinear curve is then generated, yielding the elastic-limit point.

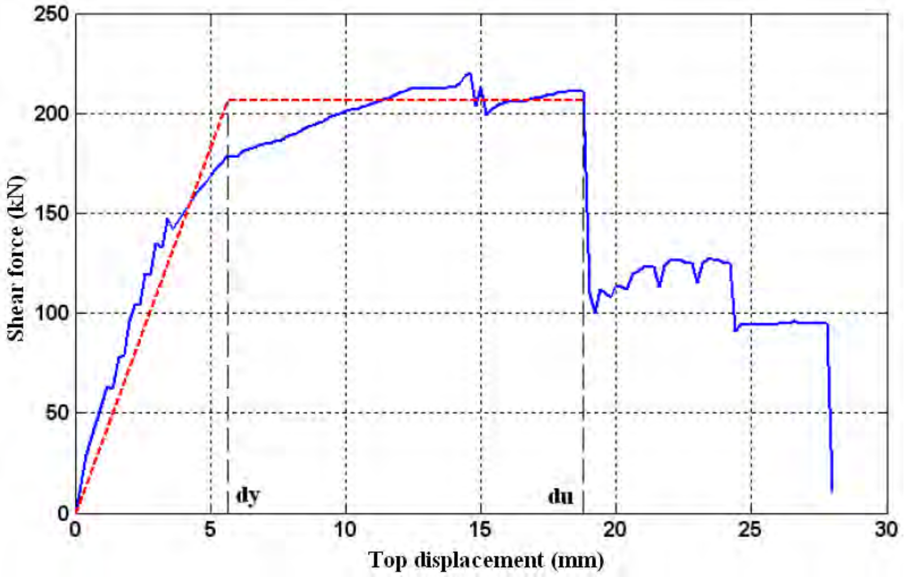

Figure 5: Pushover curve of the building model (solid line), along with the bilinear curve (dotted line). Limit-displacement values d_y = 5.6mm and d_u = 18.8mm can be identified.

The evaluation of the damage state at the building level is not trivial, as the criteria used to define the local damage level of a macrocomponent cannot be simply extrapolated to a global level. Among the numerous damage indicators available in the literature (index based on hysteretic energy dissipation [10], determinant of the stiffness matrix, maximum strain values at various locations, ...), it is chosen here to use the transient interstory drift ratio (ISDR) or floor displacements because their computation is rather straightforward and many correlations between floor displacement and damage states have been developed. The Risk-UE project ([11]) proposes some relations to link displacements d_y and d_u to the EMS-98 ([12]) damage scale (see Table 2).

Damage state	Displacement-limit	Value (mm)
Slight	$d = 0.7d_y$	3.94
Moderate	$d = 0.7d_y + 0.05(0.9d_u - 0.7d_y)$	4.59
Extensive	$d = 0.7d_y + 0.2(0.9d_u - 0.7d_y)$	6.54
Very heavy	$d = 0.7d_y + 0.5(0.9d_u - 0.7d_y)$	10.43
Collapse	$d = 0.9d_u$	16.92

Table 2: Correlation between EMS-98 damage states and the transient top displacement, for unreinforced masonry buildings, according to [11]

The recommendations from the FEMA-356 [13] document for unreinforced masonry give some values of transient ISDR corresponding to different levels of safety: 0.1% for S-1 (Immediate Occupancy) and 0.5% for S-3 (Life Safety). The results of the static analysis on the studied building give a top displacement $d = 5.8$mm for S-1 level, and $d = 20.8$ mm for S-3. Even if both damage scales are not to be compared, it appears that the FEMA criteria tend to be much less conservative than the Risk-UE values for this specific building. FEMA criteria are fixed drift ratios that are the same for a generic typology of buildings, whereas the Risk-UE values are based on the strength and the ductility of each model and may be more accurate for specific cases. Thus, the boundaries in Table 2 will be used for the rest of the study.

2.3 Development of variant models

Once the first building model is developed and validated, the uncertainties on the mechanical properties of the brick masonry can be taken into account by deriving a set of variants with respect to the basic model. Those variants are developed by sampling material properties, which are assumed to have a normal distribution. The associated coefficients of variation can be taken from various past studies ([14], [15]) and the distributions of the varying parameters are represented in Table 3.

Parameter	Mean	C.O.V.	St.-Dev. s	Lower bound	Upper bound
E (MPa)	3600	20%	720	2160	5040
G (MPa)	600	20%	120	360	840
f_m (MPa)	6.2	20%	1.24	3.72	8.68
f_{sh} (MPa)	0.23	15%	0.0345	0.161	0.299
D_{sh} (%)	0.6	10%	0.06	0.48	0.72
D_{fl} (%)	0.8	10%	0.08	0.64	0.96

Table 3: Proposed variations of some basic mechanical parameters for the masonry model

For each parameter, some bounds (set at $+/-2s$) prevent from sampling irrelevant values. We choose to generate 20 variant models out of the parametric distribution: a Latin hypercube sampling scheme is used in order to optimize the possible combinations with a reduced number of models. Thus, with 20 models, intervals of 5% can be defined and, for each parameter, an aleatory interval has been picked to sample the value for a given model. This procedure results in a total of 21 structures (one basic model plus 20 variants): for each of them, a pushover analysis is performed in order to identify the boundaries of the EMS-98 damage states.

3 NON-LINEAR DYNAMIC ANALYSES

3.1 Selection of the accelerogram datatset

The dynamic analyses on the models require a large set of seismic time-histories, in order to build consistent fragility functions. First, a sample of 120 records has been selected from the European Strong-Motion Database ([16]): these accelerograms were generated by earthquakes of magnitude (Mw) between 5.3 and 6.3, at a focal depth lower than 30km. These criteria correspond approximately to the kind of earthquakes that are to be expected in Southern France. In order to increase the size of the dataset, another series of signals has been generated, using the non-stationary stochastic procedure proposed by [17], an extension of [18]. This signal generation spans a magnitude range from 4.5 to 6.5, with the epicentral distance comprised between 10 and 100km. Also, for each magnitude-distance combination, the signal is derived for the five Eurocode-8 soil classes, in order to account for the variability in site conditions. Finally, these stochastic simulations have output 657 synthetic accelerograms, resulting in a total of 777 time-histories.

The consistency between real records and synthetic accelerograms has been checked for a wide selection of grond-motion parameters: the overall distribution of the two datasets (mean and standard-deviation) shows good agreement, except for duration-related parameters, which have a tendency to be underestimated in the synthetic signals used here ([17]).

3.2 Simulation scheme and results

The selected accelerograms are now applied at the basis of the structure, along the X-direction. The number of simulations has been optimized and the dataset of 777 accelograms has been divided into 37 groups of 21 records each. Thus, within each group, it is possible to randomly assign each accelogram with one of the 21 models. It is worth noting that the 37 groups were selected by ranking all accelerograms with respect to PGA (ground-motion parameter selected a priori to represent the ”nocivity” of the signal): this ensures that each group contains homogeneous signals, and as a result all 21 models are sujected to accelerograms with similar intensity levels.

Then, all non-linear dynamic analyses are carried out and the maximum transient displacement at the top of the building is used to identify the different damage states, based on Table 2. The results of the analyses are summed up in Table 4, in terms of relative percentage of the 777 simulation runs. It appears that more than the half of the simulations have not induced any damage to the structure. About 17% of them induce the collapse, while intermediate levels (e.g. slight to very heavy damage) are clearly underrepresented.

Damage state (EMS-98)	Percentage of runs
None	62.8%
Slight	1.8%
Moderate	5.5%
Extensive	6.1%
Very heavy	6.4%
Collapse	17.4%

Table 4: Distribution of the number of simulations that have reached the different damage states

Using these raw results, fragility curves based on a single intensity-measure parameter (for instance, PGA, as it is a widely known and usual parameter) can be built. These curves are fitted to a lognormal cumulative distribution function, as shown below:

$$P_k(PGA) = P(damage \geq D_k|PGA) = \phi[\frac{\ln(\frac{PGA}{\mu})}{\sigma}] = \frac{1}{2}[1 + erf(\frac{\ln PGA - \ln \mu}{\sigma\sqrt{2}})] \tag{4}$$

The median μ and the standard deviation σ can be defined using the maximum likelihood method, as proposed by [19]. After an optimisation procedure using the simplex method, the variables for each damage state are displayed in Table 5. The corresponding fragility curves are plotted on Figure 6.

Parameter	Slight	Moderate	Extensive	Very heavy	Collapse
μ	1.1108	1.2466	1.5724	2.1728	2.9359
σ	0.2928	0.3047	0.4146	0.4973	0.4966

Table 5: Estimated medians and standard-deviations for the fragility curves, with respect to PGA

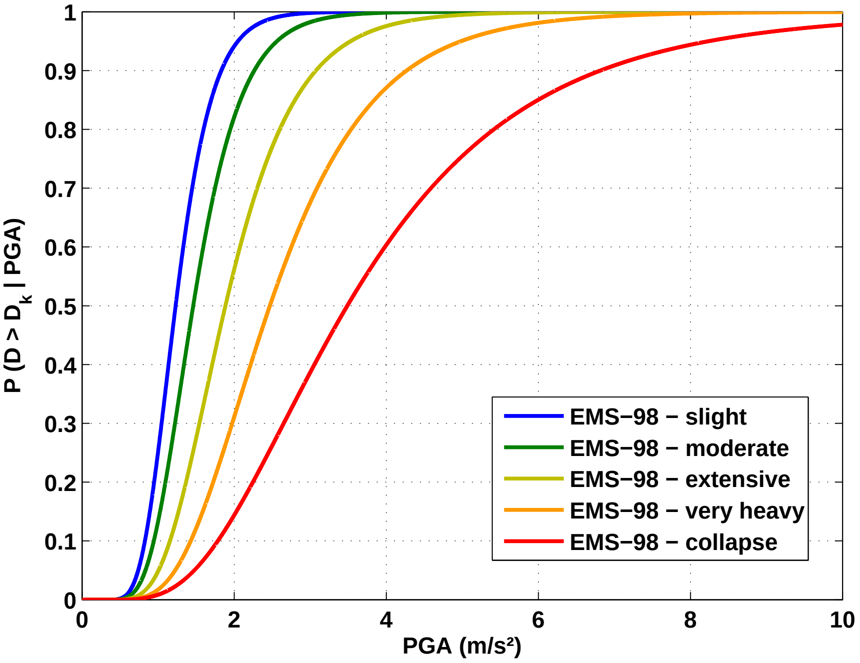

Figure 6: Analytical fragility curves for the studied low-rise URM building, with respect to PGA

4 SELECTION OF GROUND-MOTION PARAMETERS

This section is devoted to the selection of proper ground-motion parameters that could make an adequate couple of IM variables for the fragility surfaces.

4.1 Clustering of ground-motion parameters

From each of the accelerograms used in the simulations, 46 ground-motion parameters have been estimated, ranging from PGA to cyclic and duration parameters or spectral values. The first step is to rank these parameters according to their cross-correlation: The VARCLUS procedure is used to this end. It consists in a succession of principal component analyses and the merging of the parameters with strong correlation into distinct class-variables, or ”clusters”. This procedure is very helpful to reduce the high number of parameters to only 3 or 4 variables that are representative of the distribution of the studied ground-motion parameters (see Table 6).

Cluster 1	Cluster 2	Cluster 3
PGA	PGV	Duration bracketed rel.
Arias intensity	PGD	Duration uniform rel.
A95	Duration bracketed abs.	Duration significant rel.
SLOPE75	Duration uniform abs.	Nb of effective cycles
SLOPE95	Duration significant abs.	
ARMS	Sd ($T = 0.05$s to $T = 1.25$s)	
ASI	Sa ($T = 0.05$s to $T = 1.25$s)	
Cyclic damage parameters		
Sd ($T = 1.5$s to $T = 5$s)		
Sa ($T = 1.5$s to $T = 5$s)		

Table 6: Generated clusters from the accelerogram dataset and corresponding ground-motion parameters

Some of the ground-motion parameters studied above are not usual ones, and we propose here a very brief description of some of them:

- A95: the level of acceleration which contains up to 95% of the Arias intensity.
- SLOPE75 and SLOPE95: the slope of the Husid plot (e.g. cumulative Arias intensity over time) between 5% and 75% (or 95%) of the total Arias intensity.
- ARMS (Root-mean-square acceleration): the square-root of the integral of squared acceleration over time.
- ASI (Acceleration spectral intensity): the integration of the spectral acceleration between two periods (here, 0.1s and 0.5s).

More details on the way to estimate these IM parameters are given in [20]: various definitions of the duration parameters are provided, along with the different ways to count cycles.

As a result, with only 3 variables remaining, it is more straightforward to study the correlation of the ground-motion parameters with the simulation results. In Table 7, the correlation coefficients between the transient drift and the 3 class-variables are represented.

This first analysis shows that relevant ground-parameters are to be selected from both clusters 1 and 2, whereas cluster 3 is almost uncorrelated to the drift and thus has very little impact on the behavior of the structure.

	Drift	Cluster 1	Cluster 2	Cluster 3
Drift	1	0.7715	0.9043	−0.1054
Cluster 1	-	1	0.8194	−0.0794
Cluster 2	-	-	1	−0.1712
Cluster 3	-	-	-	1

Table 7: Correlation coefficients between the drift obtained from simulations and the class-variables representative of ground-motion parameters

4.2 Selection of the adequate couple of ground-motion parameters

In order to build relevant fragility surfaces, the adequate IM parameters should be both well correlated with the response of the structure (e.g. the drift) and also as uncorrelated as possible between each other. As a result, based on the cluster analysis above, one IM parameter should be selected from cluster 1 and the other one from cluster 2. To this end, we represent in Table 8 all parameters from cluster 1 and 2 that have a correlation coefficient with the drift greater than $R = 0.75$. Also, parameters like cyclic damage, signal duration or SLOPE, are discarded because their computation through usual ground-motion prediction equations is not feasible right now: thus, in the scope of a seismic risk scenario, such IM parameters would be rather useless.

	A95	PGA	Arias Int.	ARMS	Sd1.5s	Sa1.5s	Drift
PGV	0.8657	0.8657	0.8034	0.8280	0.8450	0.8446	0.9107
Sa0.5s	0.8263	0.8233	0.7751	0.7821	0.8173	0.8170	0.9006
Sd0.5s	0.8228	0.8225	0.7748	0.7815	0.8170	0.8167	0.9001
Sa0.075s	0.7978	0.7976	0.7695	0.7559	0.7880	0.7877	0.8822
Sa0.25s	0.8010	0.8046	0.7798	0.7681	0.8049	0.8046	0.8817
Sd0.075s	0.7971	0.7968	0.7687	0.7552	0.7873	0.7869	0.8816
Sa0.1s	0.7954	0.7973	0.7781	0.7618	0.7881	0.7876	0.8814
Sd0.25s	0.8006	0.8041	0.7795	0.7678	0.8045	0.8042	0.8813
Sd0.1s	0.7944	0.7964	0.7776	0.7609	0.7873	0.7869	0.8809
Sd0.75s	0.8435	0.8413	0.7703	0.7933	0.8262	0.8260	0.8713
Sa0.75s	0.8437	0.8416	0.7704	0.7934	0.8263	0.8262	0.8712
Sd1.0s	0.8547	0.8563	0.8064	0.7961	0.8554	0.8552	0.8546
Sa1.0s	0.8551	0.8567	0.8070	0.7963	0.8560	0.8558	0.8541
Sa1.25s	0.8845	0.8805	0.8109	0.8284	0.8876	0.8876	0.8447
Sd1.25s	0.8841	0.8801	0.8111	0.8280	0.8877	0.8876	0.8444
Sa0.05s	0.6758	0.6806	0.7088	0.6717	0.6962	0.6959	0.8204
Sd0.05s	0.6695	0.6745	0.7053	0.6675	0.6909	0.6906	0.8163
PGD	0.6092	0.6132	0.6601	0.6144	0.6095	0.0.6092	0.7739
Drift	0.7902	0.7841	0.7784	0.7582	0.7504	0.7498	1

Table 8: Correlation coefficients between parameters from clusters 1 and 2, and also with the drift

An obvious move would be to choose Peak Ground Velocity (PGV) as the first IM parameter, because of its good correlation with the drift: yet, this parameter is also strongly correlated with all secondary parameters from the other cluster (coefficients R above 0.8) and this would add no extra information on the seismic vulnerability of the structure. On the other hand, the PGA is quite well correlated with the drift ($R = 0.7841$) and shows also poor correlation (see Figure 7) with the Peak Ground Displacement (PGD) ($R = 0.6132$): as a result, the couple of variables (PGA, PGD) can be considered as good candidates upon which to build the fragility surfaces. One could argue that A95 and PGD would constitute a slightly better couple of parameters: yet, the parameter A95 cannot be easily obtained from ground-motion equations and its use is by far not as common as the PGA. Anyway, in a more physical sense, this means that the vulnerability of this low-rise masonry building can be well represented by both acceleration and displacement-based parameters.

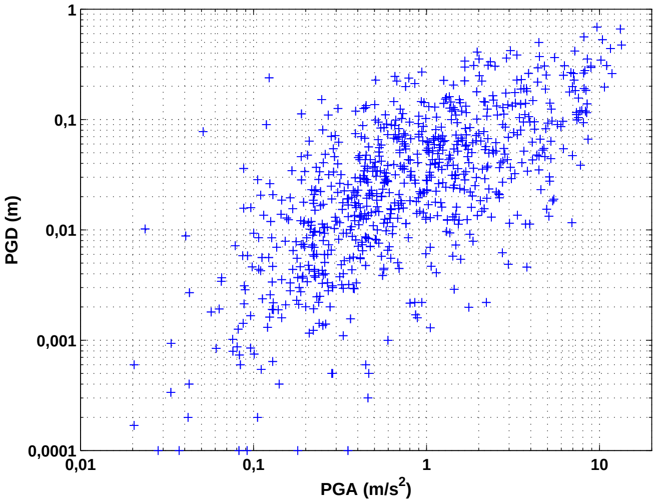

Figure 7: Distribution of the PGA and PGD values for all the accelerograms used in the simulations

5 DEVELOPMENT OF FRAGILITY SURFACES

5.1 Mathematical formulation

While fragility curves are usually represented by well-known and readily parameterizable probability distributions like the lognormal one ([21], [19]), the problem gets more complex for surfaces, where bivariate distributions must be computed. One solution is to use the kernel density estimation procedure (or Parzen-Rosenblatt method), which allows a non-parametric definition of the probability density and is thus applicable to higher-dimension problems ([22]).

Let us consider the data (PGA_i,PGD_i) corresponding to the $n = 777$ accelograms used in the simulations. Then it is possible to write a two-dimensional non-parametric estimator using the kernel density method:

$$f_h(PGA, PGD) = \frac{1}{n.\, h_{PGA,n}.\, h_{PGD,n}} \sum_{i=1}^{n} K\left(\frac{PGA_i - PGA}{h_{PGA,n}}\right) K\left(\frac{PGD_i - PGD}{h_{PGD,n}}\right) \tag{5}$$

The function K is the kernel and h is the "window", a parameter similar to the standard-deviation that controls the degree of smoothing of the estimation. K usually takes the functional form of a standard normal distribution:

$$K(x) = \frac{1}{\sqrt{2\pi}} e^{-\frac{x^2}{2}} \tag{6}$$

The window h is estimated through optimisation functions that seek to minimize the error (Mean Integrated Squared Error is used as the metric), depending on the size n of the sample and whether it is homogeneously distributed or not.

According to Table 4, intermediate damage states seem not well represented and the resulting fragility surfaces might suffer from a too large scatter. Therefore it is decided to develop only the surfaces for the damage states "slight" and "collapse". If we want to build the fragility surface corresponding to the slight damage level, we have to define first the estimator $f_{h,all}$ for the whole data (the 777 points), as well as the estimator $f_{h,slight}$ that gives the density of the records reaching or exceeding the slight damage state (e.g. 289 points). Then, the probability of the structure reaching this damage state is given by:

$$P1(PGA, PGD) = \frac{289 f_{h,slight}}{777 f_{h,all}} = \frac{h_{PGA,777}.\, h_{PGD,777}}{h_{PGA,289}.\, h_{PGD,289}}. \frac{\sum_{i=1}^{289} K(\frac{PGA_i - PGA}{h_{PGA,289}}) K(\frac{PGD_i - PGD}{h_{PGD,289}})}{\sum_{i=1}^{777} K(\frac{PGA_i - PGA}{h_{PGA,777}}) K(\frac{PGD_i - PGD}{h_{PGD,777}})} \tag{7}$$

The estimators are normalized by the size of the sample in order to get a proper cumulative distribution function, comprised between 0 and 1. In order to compare two estimators, both windows h should be the same so that densities are kept homogeneous. A high value of h denotes a small size sample or with strong disparities. Therefore the highest value of h is chosen, the limiting factor being the lowest quality estimator. We can then define:

$$\begin{aligned} h_{PGA} &= max[h_{PGA,777}; h_{PGA,289}] \\ h_{PGD} &= max[h_{PGD,777}; h_{PGD,289}] \end{aligned} \tag{8}$$

As a result, the probability of damage can finally be written as:

$$P1(PGA, PGD) = \frac{\sum_{i=1}^{289} K(\frac{PGA_i - PGA}{h_{PGA}}) K(\frac{PGD_i - PGD}{h_{PGD}})}{\sum_{i=1}^{777} K(\frac{PGA_i - PGA}{h_{PGA}}) K(\frac{PGD_i - PGD}{h_{PGD}})} \tag{9}$$

It is then possible to plot this bivariate probability function and represent it as a fragility surface (see Figure 8).

5.2 Interpretation of the results

The main motivation for developing fragility surfaces lies in a better definition of the level of seismic aggression, hence maybe a reduction of the uncertainty related to the hazard level description (usually represented by a single parameter like PGA). In order to confront both approaches, we transpose a fragility surface into 2D curves by isolating "slices" that represent the probability with respect to one IM parameter, while keeping the second one constant. An example is displayed in Figure 9, for the "slight" damage level.

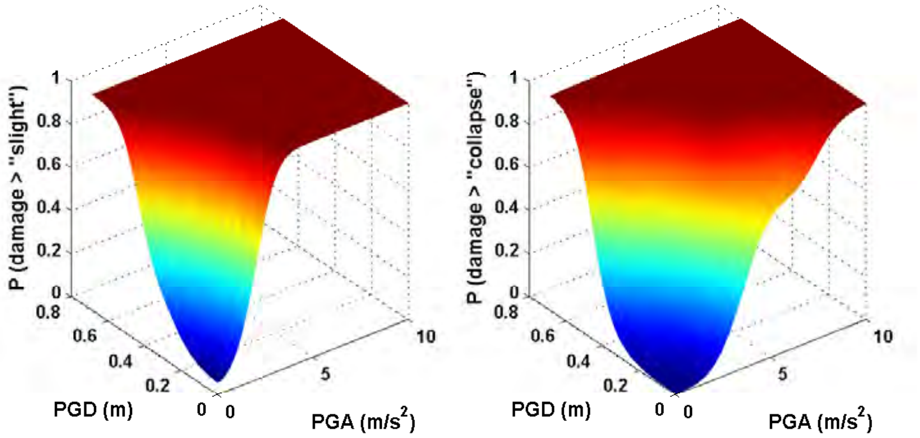

Figure 8: Fragility surfaces of the studied structure, for levels of damage ”slight” and ”collapse”

Firstly, it can be noticed that the use of a second parameter (e.g. PGD, an easily accessible variable through ground-motion prediction equations) induces a steady increase of the damage probability. For instance, in the case of small accelerations (PGA lower than $0.5m/s^2$), the single-parameter curve shows almost zero probability of damage: however, the fragility surfaces indicates that if this ground-motion is generated along with important ground deformation (e.g. $PGD = 0.1$m or 0.2m), then there is actually a non negligible probability of damage (between 10% and 20%).

The single-parameter curve does not account for the different possible values of PGD, therefore there is a tendency to neglect physical damaging phenomena related to ground displacements: the black line in Figure 9 hides indeed the epistemic uncertainty due to the absence of the second IM parameter. On the contrary, this epistemic uncertainty is well quantified by the fragility surface, which ”slices” can be seen as confidence intervals on the damage probability. According to [23], most decision makers in the field of natural risks are likely to deal with confidence intervals rather than averaged probabilities, especially in the case of rare or extreme events (on the extremities of the distribution). Let us take the example of strong accelerations (e.g. $PGA = 2.5m/s^2$): the single-parameter curve yields a damage probability of 99%. Let us assume that for this level of acceleration, it is possible to determine the PGD value with a confidence interval between 0.1m and 0.3m: thus, the fragility surface can show that the damage probability will be comprised between 95% and 100%, linking directly the uncertainty on a ground-parameter to the epistemic uncertainty on the fragility.

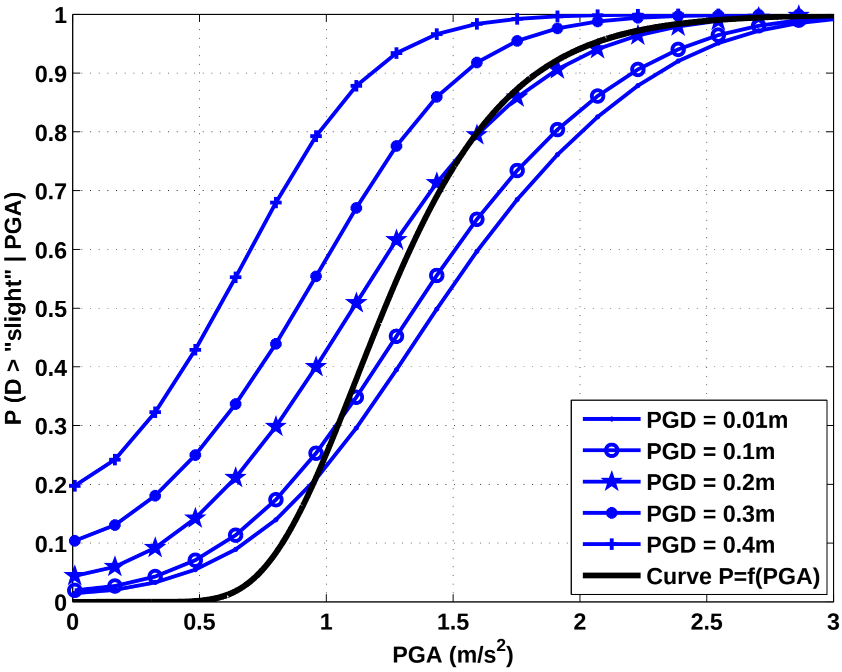

Figure 9: Single-parameter fragility curve (black line) compared to slices of the fragility surface

6 CONCLUSIONS

Starting from the use of the TREMURI code and its masonry macroelements, this study has proposed a procedure to derive analytical fragility surfaces through non-linear dynamic simulations, in the specific case of a low-rise URM building. The first steps of this procedure – such as the structural modelling, the static analyses to identify displacement boundaries for damage states, the selection of an accelerogram dataset and the time-history simulations – are the ones usually performed to develop single-parameter fragility curves.

Yet, in the case of fragility surfaces, the IM parameters are to be chosen carefully: both parameters should be well correlated with the response of the structure (e.g. top displacement or drift) in order to provide an efficient representation of the damage probability. However, there is also no point in choosing two IM paramters that are well correlated with each other, as such a surface would show nothing more than a single-parameter curve. To this end, a procedure of parameter selection has been proposed: it is based on the analysis of various ground-motion parameters and their ranking into clusters of variables. Then, a final judgement is made on the basis of correlation coefficients, in order to select the adequate couple of IM parameters.

Fragility surfaces, or in other words biviariate probability functions, have been built using a non-parametric probability density, through the use of kernel density estimators. The results have shown that these fragility surfaces can be useful in the sense that they provide a more complete description of the seismic aggression: as a result, the probability values obtained through the surfaces add another layer of information (the epistemic uncertainty related to the second IM parameter) and allow the definition of confidence intervals for the damage probabilities, which may be more interesting for decision makers than averaged probability values.

ACKNOWLEDGEMENTS

The work presented in this article has been supported by BRGM funds and by French Research National Agency (ANR) through PGCU-2007 program (project EVSIM, A mechanical approach to Evaluate Seismic Vulnerability of Masonry structures). We thank the providers of the strong-motion and the structural data used. In addition, we thank Dr Guillaume Pousse for sending us his computer program to simulate strong-motion records using his method. We thank also Prof. Sergio Lagomarsino for sharing with us the research and development version of TREMURI.

REFERENCES

[1] D. Seyedi, P. Gehl, J. Douglas, L. Davenne, N. Mezher, S. Ghavamian, Fragility surfaces for modelling the seismic vulnerability of reinforced concrete structures. *Earthquake Engineering and Structural Dynamics*, **39**, 91–108, 2010.

[2] G. Magenes, G.R. Kingsley, G.M. Calvi, Static testing of a full scale, two-story masonry building: test procedure and measured experimental response, in Experimental and numerical investigation on a brick masonry building prototype. *Report 3.0 CNR-GNDT Numerical Prediction of the experiment: 1.1 - 1.41.* 1995.

[3] S. Lagomarsino, A. Penna, A. Galasco, *TREMURI Program: Seismic Analysis Program for 3D Masonry Buildings*. University of Genoa, `http://www.stadata.com/`, 2006.

[4] K. Gambarotta, S. Lagomarsino, On dynamic response of masonry panels. *Proceedings of National Conference "Masonry mechanics between theory and practice"*, Messina, Italy, 1996.

[5] A. Penna, *A macro-element procedure for the non-linear dynamic analysis of masonry buildings*. PhD Dissertation, Politecnico de Milano, Italy, 2002.

[6] A. Galasco, S. Lagomarsino, A. Penna, On the use of pushover analysis for existing masonry buildings. *First European Conference on Earthquake Engineering and Seimology*, Geneva, Switzerland, September 3-8, 2006.

[7] V. Mallardo, R. Malvezzi, E. Milani, G. Milani, Seismic vulnerability of historic masonry buildings: a case study in Ferrara. *Engineering Structures*, **30**, 2223–2241, 2008.

[8] M.Y. Kaltakci, M.H. Arslan, H.H. Korkmaz, M. Öztürk, An investigation on failed or damaged reinforced concrete structures under their own weight in Turkey. *Engineering Failure Analysis*, **14**(6), 962–969, 2007.

[9] Y. Lu, H. Hao, P. Carydis, H. Mouzakis, Seismic performance of RC frames designed for three ductility levels. *Engineering Structures*, **23**, 537–547, 2001.

[10] Y.J. Park, A.S. Ang, Seismic damage analysis of reinforced concrete buildings. *Journal of Structural Engineering*, **111**(4), 740–757,1985.

[11] Z.V. Milutinovic, G.S. Trendafiloski, Risk-UE: An advanced approach to earthquake risk scenarios with applications to different European towns. *Technical report, European Commission, WP4 Vulnerabilty of current buildings*, 2003.

[12] European Council, European macroseismic scale (EMS-98). *Cahier du Centre Européen de Géodynamique et de Sismologie*, G. Grünthal (Eds.), 1998.

[13] ASCE, *FEMA-356: Prestandard and commentary for the seismic rehabilitation of buildings.* 2000.

[14] M. Rota, A. Penna, C.L. Strobbia, Processing Italian damage data to derive typological fragility curves. *Soil Dynamics and Earthquake Engineering*, **28**, 933–947, 2008.

[15] M. Rota, A. Penna, G. Magenes, A methodology for deriving analytical fragility curves for masonry buildings based on stochastic nonlinear analyses. *Engineering Structures*, **32**, 1312–1323, 2010.

[16] N.N. Ambraseys, J. Douglas, R. Sigbjörnsson, C. Berge-Thierry, P. Sudaholc, G. Costa, P.M. Smit, *Dissemination of European Strong-Motion Data, vol. 2, using Strong-Motion Datascape Navigator*. CD-ROM collection, Engineering and Physical Science Reseach Council, United Kingdom, 2004.

[17] G. Pousse, L.F. Bonilla, F. Cotton, L. Margerin, Non-stationary stochastic simulation of strong ground-motion time-histories including natural variability: Application to the K-net Japanese database. *Bulletin of Seismological Society of America*, **96**(6), 2103–2117, 2006.

[18] F. Sabetta, A. Pugliese, Estimation of response spectra and simulation of non-stationary earthquake ground-motions. *Bulletin of Seismological Society of America*, **86**(2), 337–352, 1996.

[19] M. Shinozuka, M.Q. Feng, H. Kim, T. Uzawa, T. Ueda, Statistical analysis of fragility curves. *MCEER Technical Report*, Department of Civil and Environmental Engineering, University of Southern California, LA, USA, 2001.

[20] J. Douglas, *Selection of strong-motion records for use as input to the structural models of VEDA*. BRGM report RP-54584-FR, 2006.

[21] M. Shinozuka, Statistical analysis of bridge fragility curves. *US-Italy Workshop on Protective Systems for Bridges*, New-York, April 26-28, 1998.

[22] E. Parzen, On estimation of a probability density function and mode. *The Annals of Mathematical Statistics*, **33**, 1065–1076, 1962.

[23] B.R. Ellingwood, K. Kinali, Quantifying and communicating uncertainty in seismic risk assessment. *Structural Safety*, **31**, 179–187, 2009.

COMPDYN 2011
III ECCOMAS Thematic Conference on
Computational Methods in Structural Dynamics and Earthquake Engineering
M. Papadrakakis, M. Fragiadakis, V. Plevris (eds.)
Corfu, Greece, 25–28 May 2011

DEVELOPMENT AND APPLICATION OF DAMAGE SPECTRA TO EVALUATE THE SEISMIC PERFORMANCE OF REINFORCED CONCRETE BUILDINGS IN GREECE

Amin Karbassi[1], **Benyamin Mohebi**[2], **Pierino Lestuzzi**[1],
and Gholamreza Ghodrati Amiri[3]

[1]Ecole Polytechnique Fédérale de Lausanne, Applied Computing and Mechanics Laboratory,
Station 18, CH-1015 Lausanne, Switzerland
{amin.karbassi,pierino.lestuzzi}@epfl.ch

[2]Iran University of Science and Technology, School of Civil Enginnereing,
P.O. box 1684613114, Narmak, Tehran, Iran
mohebi@iust.ac.ir

[3]Center of Excellence for Fundamental Studies in Structural Engineering, School of Civil Engineering,
Iran University of Science and Technology, Tehran, Iran
ghodarti@iust.ac.ir

Keywords: Damage Index, Reinforced Concrete, Seismic Vulnerability, Earthquake Scenarios.

Abstract. *Damage spectra for reinforced concrete buildings in Greece are presented in this paper based on a series of time-history nonlinear dynamic analyses for single-degree-of-freedom systems (Clough hysteresis model) with different deformation ductility and yielding capacities. The damage spectra are calculated for hundreds of horizontal ground motions recorded on rock-stiff soil in Greece since 1970's. Those damage spectra can be used in the seismic vulnerability assessment of existing reinforced concrete buildings in the country. To this end, the proposed damage spectra are evaluated via the damages observed in Athens as a result of the September 7, 1999 earthquake. The damage spectra confirm that low- to mid-rise RC buildings with lower ductility capacity experience heavy damage or collapse, as seen in the 1999 earthquake. The developed damage spectra can be also used for design purposes in the area. To this end, it is shown that the damage spectra can be used to determine what level of ductility capacity and yield strength is required to limit the expected damages to a certain accepted level according to the code provisions.*

1 INTRODUCTION

Quantification of damage potential of earthquakes can be a useful tool for those interested in seismic risk mitigation plans. A reliable estimation for such damage potential can have a wide range of application in the seismic vulnerability evaluation of existing buildings. One important application of this estimation is in scenario studies where the effects of a single earthquake, often historically significant ones, on present-day portfolios in a region are evaluated [1].

One way for quantifying the damage potential is using a damage index (DI) which has a value close to zero if the structure remains elastic, D1 damage grade of EMS-98 [2], and close to 1.0 when the structure reaches complete damage or collapse, D4 or D5 damage grade of EMS-98. Such index is known to be a function of earthquake parameters and structural properties as shown in Equation 1.

$$DI = f(M, R, \mu, T, F_y) \tag{1}$$

In Equation 1, M and R are the magnitude and source-to-site distance of the earthquake, respectively, μ is the global ductility of the structure, T is the period of vibration, and F_y is the yield strength. Several formulas are proposed in the literature to calculate the damage index ([3, 4, 5]). A very frequently-used relationship in different research works is the one proposed by Park and Ang [6] as shown in Equation 2.

$$DI_1 = \left({}^{u_{max}}\!/_{u_{mon}}\right) + {}^{\beta.E_H}\!/_{F_y.u_{mon}} \tag{2}$$

In this equation, u_{max} and u_{mon} are the maximum deformations under earthquake loads and monotonically increasing lateral loads, respectively. Moreover, E_H is the non-recoverable dissipated hysteretic energy, and β is a positive constant, which depends on structural characteristics and history of inelastic response. An advantage of the Equation 2 is that is has been calibrated with experimental data. However, in some cases, when the system remains in the elastic mode (E_H =0), the equation gives DI values way bigger than zero which can be misleading towards the behavior evaluation of the building. To overcome this problem, a modified version of the DI_1 [7] defined as follows is used here in this paper.

$$DI_2 = \left({}^{(u_{max} - u_y)}\!/_{(u_{mon} - u_y)}\right) + {}^{\beta.E_H}\!/_{F_y.u_{mon}} \tag{3}$$

The variation of damage indices over a range of structural periods for a series of single-degree-of-freedom (SDOF) systems with different ductility and yield strength values forms "damage spectra" for a region [4]. The main objective of this paper is to present damage spectra for the existing reinforced concrete buildings in Greece based on the possible different structural characteristics of that building class. To this end, a range of period, ductility and normalized yielding strength (F_y/W) is considered to develop the DI values from Equation 3 based on series of nonlinear dynamic analyses of a SDOF system using the ground motion records of earthquakes that have happened in Greece since 1970. Those DI values are later used to develop damage spectra for the studied building class and used to assess their damage potential in future events. Finally, the accuracy of the developed damage spectra is evaluated using the damages that happened in RC buildings during the 1999 earthquake in Athens.

2 APPLIED METHODOLOGY

2.1 Ground motion records and structural properties

The ground motion records used to develop the damage indices for the RC buildings are selected from the European Strong-Motion Data [8]. To this end, earthquakes with a magnitude (M_s) equal or bigger than 5 which occurred in Greece since 1970 are used in this paper (Table 1).

Date	Epicentre	M_s
17.01.1983	Kefallinia island	7.1
06.08.1983	Off coast of Magion Oros peninsula	6.7
18.11.1997	Strofades	6.7
13.05.1995	Kozani	6.6
13.10.1997	Kalamata	6.4
22.01.2002	Off coast of Karpathos	6.2
20.06.1978	Volvi	6.2
21.12.1990	Griva	6.1
23.05.1994	South Aegean	6.1
13.09.1986	Kalamata	5.8
16.10.1988	Kyllini	5.8
18.11.1992	Tithorea	5.8
18.03.1993	Kallithea	5.7
27.02.1987	Near NW coast of Kefallinia island	5.6
23.06.2001	Off coast of Rhodes	5.6
30.04.1985	Anchialos	5.4
17.09.1972	Kefallinia island	5.4
10.06.2001	Chios	5.4
19.03.1983	Heraklio	5.4
05.11.1997	Itea	5.4
23.01.1992	Kefallinia island	5.4
14.07.1993	Patras	5.4
16.06.1990	Filippias	5.3
25.10.1984	Kranidia	5.3
19.03.1991	Near SE coast of Crete	5.3
22.05.1988	Etolia	5.1
07.09.1985	Gulf of Kiparissiakos	5.1
16.09.2001	Kallirro	5.1
25.02.1994	Komilion	5.1
10.03.1981	Preveza	5.1
26.03.1993	Pyrgos	5.1
26.04.1996	Rhodos island	5.1

Table 1: List of earthquakes used in the nonlinear dynamic analysis

Consequently, 110 ground motion records recorded at various stations, located on rock or stiff soil, are chosen to perform the nonlinear dynamic analyses for a series of SDOF systems. The distribution of magnitude with source-to-site distance for those ground motion records are shown in Figure 1.

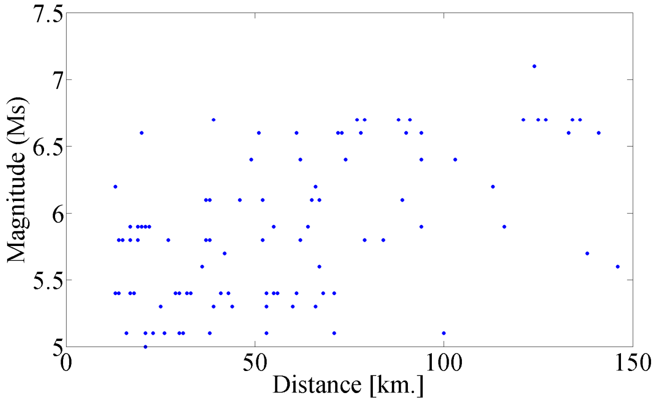

Figure 1: Distribution of the magnitude and source-to-site distance of the considered ground motion records

2.2 Structural properties of the SDOF

Taking into account that the damage spectra in this paper are being developed for RC buildings, Clough hysteresis model [9] is considered in the nonlinear dynamic analyses of the SDOF systems, performed with the computer program IDARC [10]. The structural properties of the SDOF systems are shown in Table 2.

Ductility	Period	Fy/W
2-5	0.3-1.0	0.05-0.10

Table 2: Range of the structural properties used for the RC buildings

2.3 Development of the damage spectra

As stated earlier, a damage spectrum consists of the variation of damage index values for a series of SDOF systems with various structural vibration periods. Using Equation 3, a damage index is developed from each of the 110 ground motion records shown in Figure 1 over the range of structural properties shown in Table 2. Such nonlinear dynamic analyses leads to approximately 7040 damage index values which are functions of various parameters as shown in Equation 1. An attenuation relationship is then defined (Equation 4) to estimate the variation of damage spectra with earthquake magnitude and source-to-site distance, for each ductility, yield strength, and period value.

$$log(DI_2) = C_1 + C_2.M_s + C_3.log(R) \tag{4}$$

C_1, C_2, and C_3 are regression parameters which are calculated from the regression analyses of the 7040 damage indices for different M_s and R values.

3 RESULTS

Table 3 to 6 show the values for the three coefficients C_1, C_2, and C_3 for the range of the structural properties considered in this study (Table 2).

	Fy/W=0.05			Fy/W=0.1		
T	C1	C2	C3	C1	C2	C3
0.3	-1.91	0.88	-1.96	-2.06	0.64	-1.12
0.4	-1.45	0.65	-1.45	-0.75	0.37	-1.03
0.5	-0.51	0.48	-1.39	-2.39	0.69	-1.29
0.6	-0.44	0.42	-1.31	-0.36	0.31	-1.31

0.7	-0.74	0.39	-1.06	-1.26	0.28	-0.54
0.8	-1.38	0.51	-1.17	-1.53	0.35	-0.68
0.9	-1.32	0.39	-0.79	-1.64	0.98	-3.50
1	-1.50	0.36	-0.60	-1.86	0.29	-0.47

Table 3: Values of coefficients C1, C2, and C3 for RC buildings with a ductility value of 2

	Fy/W=0.05			Fy/W=0.1		
T	C1	C2	C3	C1	C2	C3
0.3	-2.35	0.94	-2.08	-2.37	0.64	-1.12
0.4	-1.76	0.66	-1.46	-1.06	0.37	-1.03
0.5	-0.81	0.48	-1.39	-2.69	0.70	-1.29
0.6	-0.82	0.44	-1.35	-0.67	0.32	-1.31
0.7	-1.11	0.42	-1.10	-1.57	0.29	-0.54
0.8	-1.68	0.51	-1.17	-1.82	0.35	-0.68
0.9	-1.62	0.40	-0.79	-1.97	0.97	-3.42
1	-1.80	0.36	-0.60	-2.16	0.30	-0.47

Table 4: Values of coefficients C1, C2, and C3 for RC buildings with a ductility value of 3

	Fy/W=0.05			Fy/W=0.1		
T	C1	C2	C3	C1	C2	C3
0.3	-2.52	0.96	-2.16	-2.55	0.64	-1.12
0.4	-1.94	0.66	-1.46	-1.24	0.37	-1.03
0.5	-0.99	0.48	-1.39	-2.87	0.70	-1.29
0.6	-1.00	0.44	-1.35	-0.84	0.32	-1.31
0.7	-1.28	0.42	-1.10	-1.74	0.29	-0.54
0.8	-1.86	0.51	-1.17	-2.00	0.35	-0.68
0.9	-1.79	0.40	-0.79	-2.15	0.97	-3.39
1	-1.98	0.36	-0.60	-2.34	0.30	-0.47

Table 5: Values of coefficients C1, C2, and C3 for RC buildings with a ductility value of 4

	Fy/W=0.05			Fy/W=0.1		
T	C1	C2	C3	C1	C2	C3
0.3	-2.52	0.91	-2.08	-2.67	0.64	-1.12
0.4	-2.06	0.66	-1.46	-1.36	0.38	-1.03
0.5	-1.11	0.48	-1.39	-3.00	0.70	-1.29
0.6	-1.12	0.44	-1.35	-0.97	0.32	-1.31
0.7	-1.41	0.42	-1.10	-1.87	0.29	-0.53
0.8	-1.98	0.51	-1.17	-2.12	0.35	-0.68
0.9	-1.92	0.40	-0.79	-2.28	0.96	-3.37
1	-2.10	0.36	-0.60	-2.46	0.30	-0.47

Table 6: Values of coefficients C1, C2, and C3 for RC buildings with a ductility value of 5

Using the coefficient values in Tables 3 to 6 for Equation 4, the attenuation of the damage spectra with R is demonstrated in Figures 1 and 2, for the lower and upper bound values of earthquake magnitude and structural properties considered in this paper.

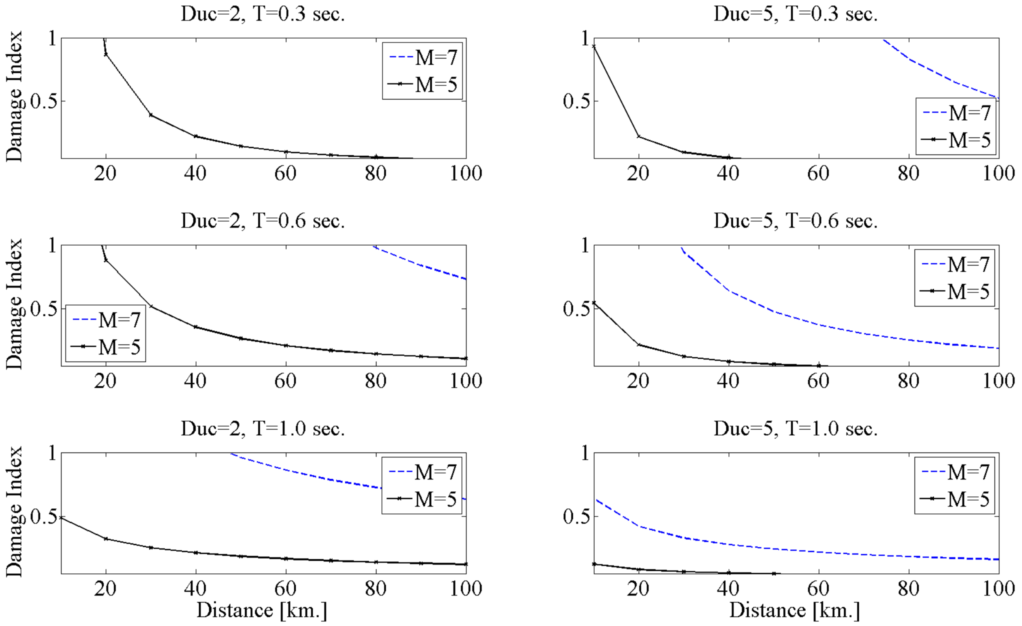

Figure 2: Attenuation of the damage spectra with source-to-site distance for structures with *Fy/W=0.05*

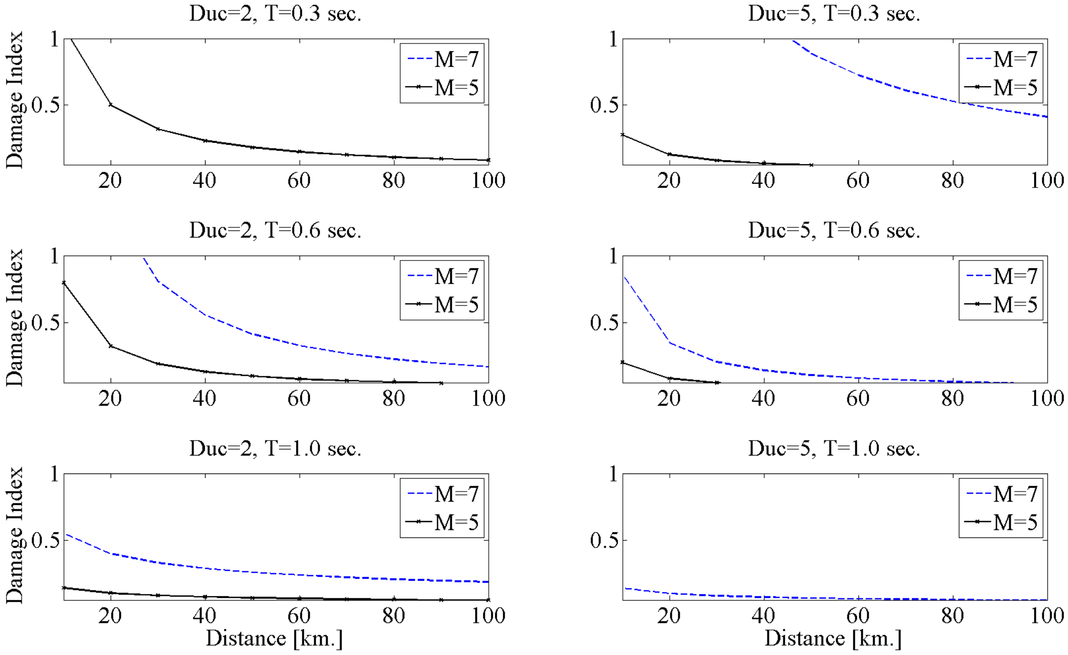

Figure 3: Attenuation of the damage spectra with source-to-site distance for structures with *Fy/W=0.1*

As seen in both Figures 2 and 3, low-rise RC buildings with 3 to 4 storeys (T_1=0.3 sec.) are completely vulnerable (DI>0.6) to big earthquakes (M>6) even at far distances. The increase of ductility, as expected, somewhat reduces such vulnerability. However, for different values of ductility, those short buildings would experience complete damage (DI>1.0) for near-to-source events and moderate damage (DI>0.5) for far-to-source ones. Mid-rise RC buildings (T_1=0.6 sec.) especially those with higher yield strength (F_y/W=0.1) and higher ductility show better behaviour as they experience slight damage (DI<0.5) even for a near-to-source event. Finally, high-rise buildings (T_1=1.0 sec) only suffer moderate to extensive damage in lower ductilities and lower yield strength. It should be noted that such conclusions are applicable to regular buildings which have high enough mass participation factor for their first mode of vibration.

4 DISCUSSION OF RESULTS

To evaluate the damage spectra developed in this paper, the damage spectra for the 1999 earthquake in Athens is compared with the observed damages from that event which happened on September 7, 1999 at 14:56 local time (11:56 GMT) with a magnitude M_w=5.9, close to the city of Athens in Greece.

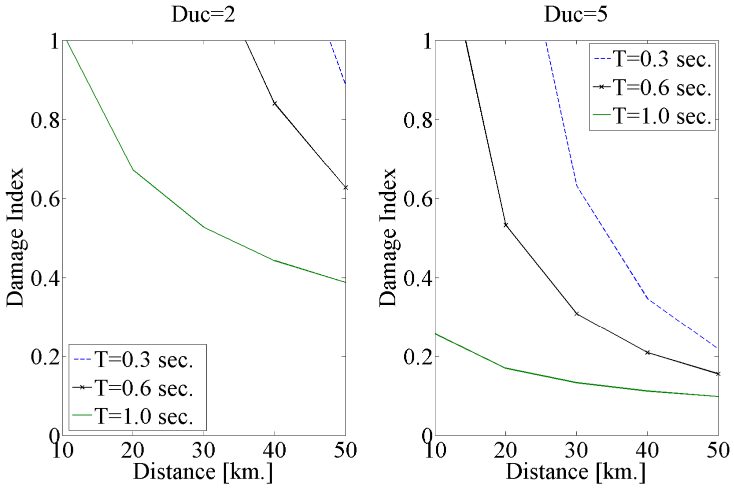

Figure 4: Attenuation of the 1999 Earthquake damage spectra with source-to-site distance for structures with *Fy/W=0.05*

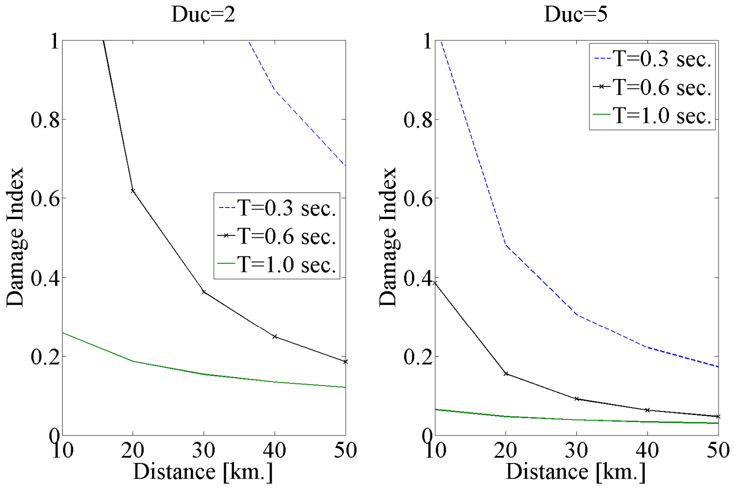

Figure 5: Attenuation of the 1999 Earthquake damage spectra with source-to-site distance for structures with *Fy/W=0.1*

It is reported that two- to five-storey RC buildings with low ductility capacity experienced the highest damage in the meizoseismal area at an epicentral distance between 10 to 20 km [11, 12]. Those were the buildings built according to the 1959 code [13], without ductility provisions, or illegally built ones with poor construction which would not fulfill the minimum requirements of the 1959 code.

Figures 4 and 5 show the attenuation of the damage spectra for the 1999 Earthquake for two different ductility values and two levels of yield strength. As seen in both figures, low- and mid-rise RC buildings (T=0.3 sec and 0.6 sec.) with low ductility capacity have DI values greater than 1.0 at epicentral distances lower than 20km. Both figures indicate that the structural damages rapidly decrease with the distance from the source.

According to the reports, no major damage was stated for bridges [11]: this is the fact seen in both Figures 4 and 5, as structures with higher periods (T =1.0 sec and bigger) have low DI values even at a close distance to the source.

The 1999 earthquake in Greece occurred at an epicentral distance of about 18 km from the historical center of Athens. The damage spectra for such a source-to-site distance are shown in Figure 6 for different ductility values. It is assumed here that the period of vibration is directly in proportion with the number of storeys (T=0.1N). In case of a similar scenario as the one in 1999, low- to mid-rise structures with low ductility capacity will experience near to collapse or complete damage. Figure 6 can also be also helpful in the design of new RC buildings in the area as it clearly states the required ductility and yield strength values for a defined accepted level of damage. For example, a 6-storey building needs to have a minimum ductility value equal to 3 ($F_y/W=0.1$) or 6 ($F_y/W=0.05$) to experience DI's lower than 0.5. Similar to the case for the 1999 Earthquake, damage spectra can be calculated for any code's design earthquake with a specific return period (magnitude), for any site (source-to-site distance) in Greece.

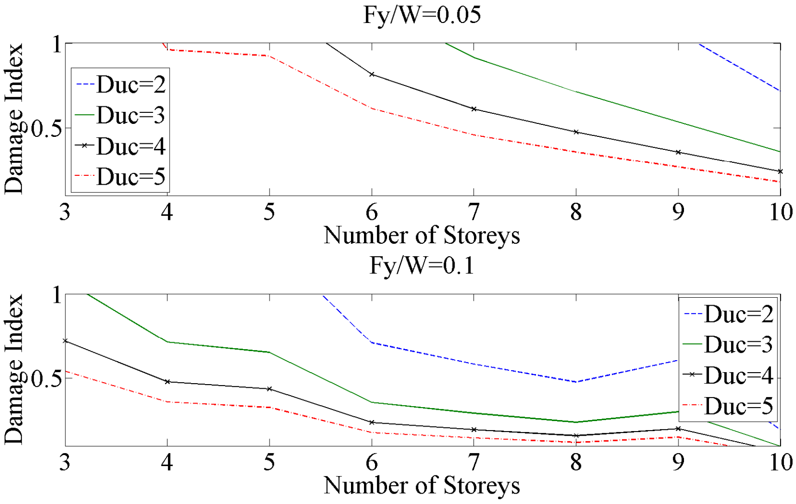

Figure 6: Damage spectra for 1999 Greece earthquake at a source-to-site distance of 18 km

5 CONCLUSIONS

- An attenuation relationship of damage spectra for RC buildings in Greece is presented in this article based on a series of nonlinear dynamic analyses using 110 ground motions records from various earthquakes which happened in the country since 1970.

- Various damage spectra can be developed from the attenuation relationship based on desired structural properties such as ductility capacity, yield strength, and the vibration period of the RC buildings.
- The calculated damage spectra show good correlation with the observed damage of the 1999 Earthquake in Greece.
- Low-rise RC buildings show high vulnerability to big earthquakes ($M_s>6$) even at far distances. In such situations, high ductility values ($\mu>5$) are required to keep the DI lower than 0.5.
- Structures with longer period of vibration (e.g., bridges) show very low damage index values in a scenario similar to the 1999 earthquake. This is in accordance with the field observation from that earthquake.
- The developed damage spectra here can be also used in the seismic design of new RC buildings in Greece: to determine the required ductility capacity and yield strength for the credible earthquake in a region based on code requirements.

REFERENCES

[1] A. Coburn, R. J. S. Spence, *Earthquake protection.* Wiley, Chichester, 1992.

[2] G. Grünthal, *European Macroseismic Scale, EMS-98*, Vol. 15. Centre Européen de Géodynamique et de Séismologie, Luxembourg, 1998.

[3] A. Ghobarah, H. Abou-Elfath, A. Biddah, Response-based damage assessment of structures. *Earthquake Engng Struct Dynamics*, **28**,79–104, 1999.

[4] Y. Bozorgnia, V. V. Bertero, Damage Spectra: Characteristics and Applications to Seismic Risk Reduction. *Jour. of Struct. Engrg.* **129**, 1330-1340, 2003.

[5] A. Massumi, E. Moshtagh, A new damage index for RC buildings based on variations of nonlinear fundamental period. *The Structural Design of Tall and Special Buildings*, doi: 10.1002/tal.656 (in Press), 2010.

[6] Y. J. Park, A. H-S. Ang, Mechanistic seismic model for reinforced concrete. *Jour. of Struct. Eng.* **111,** 722–739, 1985.

[7] S. K. Kunnath, A. M. Reinhorn, R. F. Lobo, IDARC Version 3.0: A program for the inelastic Damage Analysis of Reinforced Concrete Structures. *Technical Report NCEER-92-0022*, National Center for Earthquake Engineering Research, Buffalo, 1992.

[8] N. Ambraseys, P. Smit, R. Sigbjornsson, P. Suhadolc, B. Margaris, Internet-Site for European Strong-Motion Data. European Commission, Research-Directorate General, Environment and Climate Programme, 2002.

[9] R. W. Clough, K.L. Benuska, E.L. Wilson, Inelastic Earthquake Response of Tall Buildings. *Proceeding of the 3rd World Conference on Earthquake Engineering*, New Zealand, Vol. 11, 1965.

[10] A. M. Reinhorn, S. K. Kunnath, R. Valles-Mattox, IDARC 2D Version 7.0: user manual. Department of Civil Engineering, State University of New York at Bufallo, 2010.

[11] P. Dimitriu, C. Karakostas, V. Lekidis, The Athens (Greece) Earthquake of 7 September 1999: The Event, its Effects and the Response. Institute of Engineering Seismology and Earthquake Engineering (ITSAK), Thessaloniki, Greece, 1999.

[12] A. Elenas, Athens Earthquake of 7 September 1999: Intensity Measures and Observed Damages. *ISET Journal of Earthquake Technology*, Technical Note, **40**, 77-97, 2003.

[13] Royal Decree on the Seismic Code for Building Structures, *Government's Gazette,* Issue A, No. 36, 1959.

COMPDYN 2011
III ECCOMAS Thematic Conference on
Computational Methods in Structural Dynamics and Earthquake Engineering
M. Papadrakakis, M. Fragiadakis, V. Plevris (eds.)
Corfu, Greece, 25–28 May 2011

STRUCTURAL DYNAMIC INSTABILITY DUE TO EARTHQUAKE LOADS

Gluck N[1*], Farhat R[1], and Tzadka U.[1]

[1] Sami Shamoon College of Engineering, Dept. of Civil Engineering
Reh. Bialic – Bazel
84100 Beer Sheva, Israel, P.B. 45
mikig@sce.ac.il

Keywords: Vertical oscillations, P-Delta and Secondary Effects, Structural response, Seismic Amplification, Structural Damage,

Abstract. *From a thorough observation of the images taken after major seismic events arises the conclusion that structures collapse vertically due to their lack of stability under vertical load amplification. Overturn of buildings due to earthquake effects happens in case of weak foundations or liquefaction effects (see Niigata, Japan 1964).*

Majority of collapses occurred due to structural instability as P-Delta effects under combined horizontal and vertical loads. Worse, there must be a dynamic effect due to vertical seismic oscillations that leads to amplification of the vertical loads. Vertical effects and P-Delta phenomena are mentioned in each seismic code but the effect is dealt statically for analysis and design purposes.

It is indicated that dynamic analysis should be performed by means of step by step nonlinear analysis.

The present work is intended to initiate a methodology to use the spectral capacity demand analysis to deal with the P-Delta effects compared with the results calculated by means of step by step analysis. The nonlinear effects develop at the bar ends (beams and columns) as plastic hinges with gradual plasticization due to the lateral displacements. Bending moments and shear effects in the structural elements are monitored during the simulations performed by means of the SAP2000 – Nonlinear Software.

1 INTRODUCTION

In his paper, written in 1994, John Lawson, Vice President Kramer & Associates Structural Engineers, Inc. Tustin, California stressed that "…new provisions addressing the effects of vertical seismic acceleration should not be incorporated into the Uniform Building Code without careful consideration." Since then a lot of new research were accomplished most of them based on actual severe seismic events. Nonlinear behavior has been introduced into the methodology of the analysis of structural behavior under seismic events.

Most of the existing codes still use the conventional methodology to check or design the behavior of structures under seismic loads. Horizontal effects solely are taken into account for the seismic loads. Vertical effects are taken into account for specific elements like cantilevers, long presstressed beams or beams that support columns. The secondary effects of earthquakes are taken into account by static methods (due to the weight of each story).

The instability of structures under vertical amplification effects is evident for a lot of collapses that occurred as consequence of seismic movements. Among these effects, the damages of soft floors when the structure lost its first floor are relevant. Figure 1 visualizes some residential buildings at Loma Prieta , California which due to the collapse of their columns of the open floor destroyed the garages underneath the residences.

Figure 1. Loma Prieta, soft story collapse.

The collapse was the consequence of the P-Delta effect combined with the amplification of the vertical oscillation. Similar effects occurred during the 6.8 Richter magnitude event of the Northridge earthquake damaging multistory residential units, parking garages and freeway overpasses. Figure 2 shows the one of the damaged multistory buildings after the 24 October, 1999, 7.6 Richter Magnitude, Taipei earthquake. The structure collapsed due to the plastic hinge developed at the first storey of the building due to the P-Delta effect.

Figure 2 Taipei Structure overturning.

One of the arguments of the author of the upper mentioned paper was the example of the spectacular collapse of the California State University Northridge Parking Structure. A paper in a local newspaper attributed the collapse to the vertical ground acceleration. According to John Lawson the load factors consider the downward vertical acceleration. His reasoning is based upon the dead load of the structure of about 5.75kPa and live load of at least 2.39kPa would lead to consider an ultimate design strength of: $(1.4 \times 5.75) + (1.7 \times 2.39) = 12.113 kPa$ Since the parking structure was empty at the time of the earthquake, this ultimate strength would have been reached at $(12.113 / 5.75 - 1) = 1.1g$ of effective vertical acceleration. If we compare this effective vertical acceleration with the current UBC's 0.4g effective horizontal peak ground acceleration for Seismic Zone 4 we see that the code's load factors do provide significant reserve strength for upward vertical accelerations compared to horizontal accelerations. The main idea of the paper states "that the additional consideration must be taken on the effects of the vertical acceleration on the P-Delta effects. This situation may create a governing load condition if very large horizontal and vertical accelerations occur simultaneously". To complete this statement is the resonant state which may provide severe damage due to the loss of structural stability in any direction (horizontally or vertically).

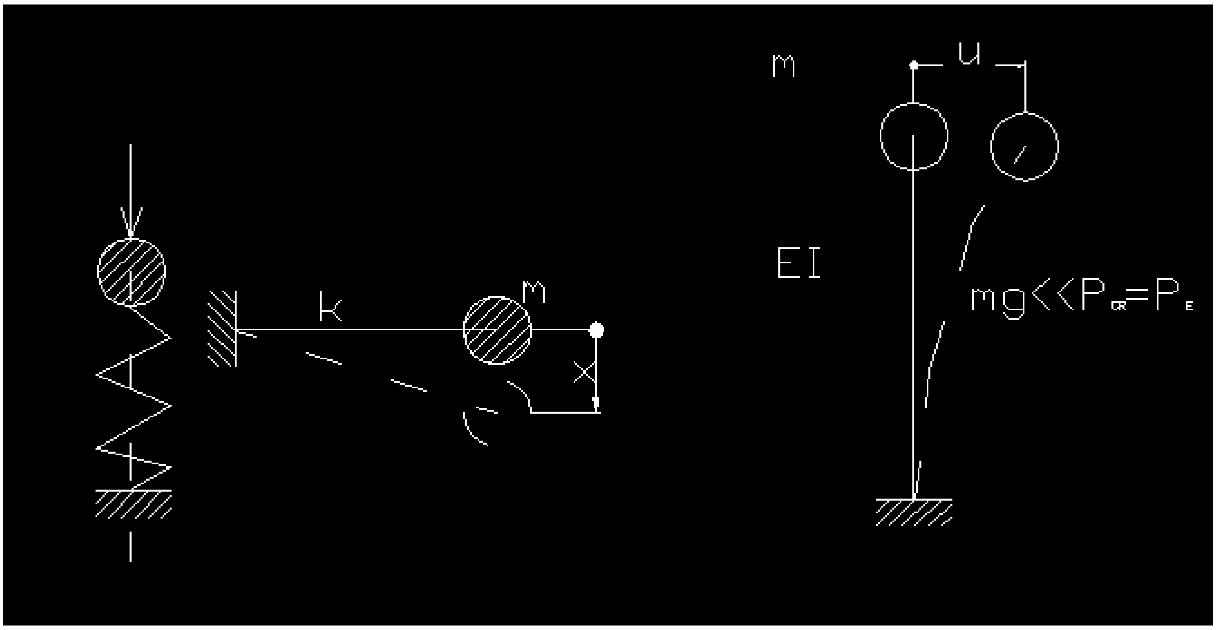

Figure 3 Static and dynamic stability for $mg << P_{cr} = P_E$

2. STRUCTURAL DYNAMIC INSTABILITY

The phenomenon of loss of stability occurs as consequence of an essential, sudden modification of the parameters defining the stationary state of the physical system. In case of a mechanical system there may be remarked two stationary states. 1) static equilibrium relative to an inertial system of coordinates, or 2) a movement mainly defined by the generalized coordinates $q, \dot{q}$ according to the minimal action defined by Hamilton.

In the first case the equilibrium loss is a static phenomenon (a sudden increase of the deformations under the critical static loads); in the second case the mechanical system has a perturbation of the main movement trough an unlimited increase of the velocity and acceleration of the system. For both cases the instability phenomenon takes place through the development of great accelerations and a gradual modification of the geometric configuration of the mechanical system and through the modification of the energetic equilibrium by the delivery of kinetical energy (the sudden feature of the loss of stability).

The dynamic systems have been classified as: autonomous systems and non-autonomous ones.

The first category comprises the systems with equation of movement according the following equation:

$$M\ddot{x}+F(P,x,\ddot{x})=0 \qquad \text{Eq. 1}$$

Where

M is the mass matrix of the system,

$x,\dot{x},\ddot{x}$ are the vectors for the displacements, velocities and the accelerations of the system,

P is the vector of the external action on the system.

Function F may be linear or non-linear according to x and $\dot{x}$ for the mechanical system. Actions which are based upon a potential (gravitation e.g.) are conservative and imply autonomous behavior.

In case of a linear elastic structure with viscous amortization the free oscillation has the following equation of movement:

$$M\ddot{x}+C\dot{x}+Kx=0 \qquad \text{Eq. 2}$$

Where

C is the damping matrix.

K is the rigidity matrix of the structure.

For positive coefficients in the damping matrix the free vibrations decay with time and the dissipated energy of the system may be expressed by a quadratic form:

$$E_d=\frac{1}{2}\dot{x}^T C\dot{x} \qquad \text{Eq. 3}$$

The instability of the shape $(x\to\infty)$ and the instability of the oscillations $(\omega\to 0)$ is attained only when the rigidity matrix K becomes singular. If we complete Eq. 2 by means of the axial force participation such as:

$-N\left(x,\frac{\partial x}{\partial z}\right)$ we define the rigidity diminution due to the axial force and thus the loss of stability may be sensed through the Equation 4.

$$\det\left|K-\lambda N\right|=0 \qquad \text{Eq. 4}$$

The increasing series of the λ values which are the roots of the equation 4 are the Eigen values for the external load.

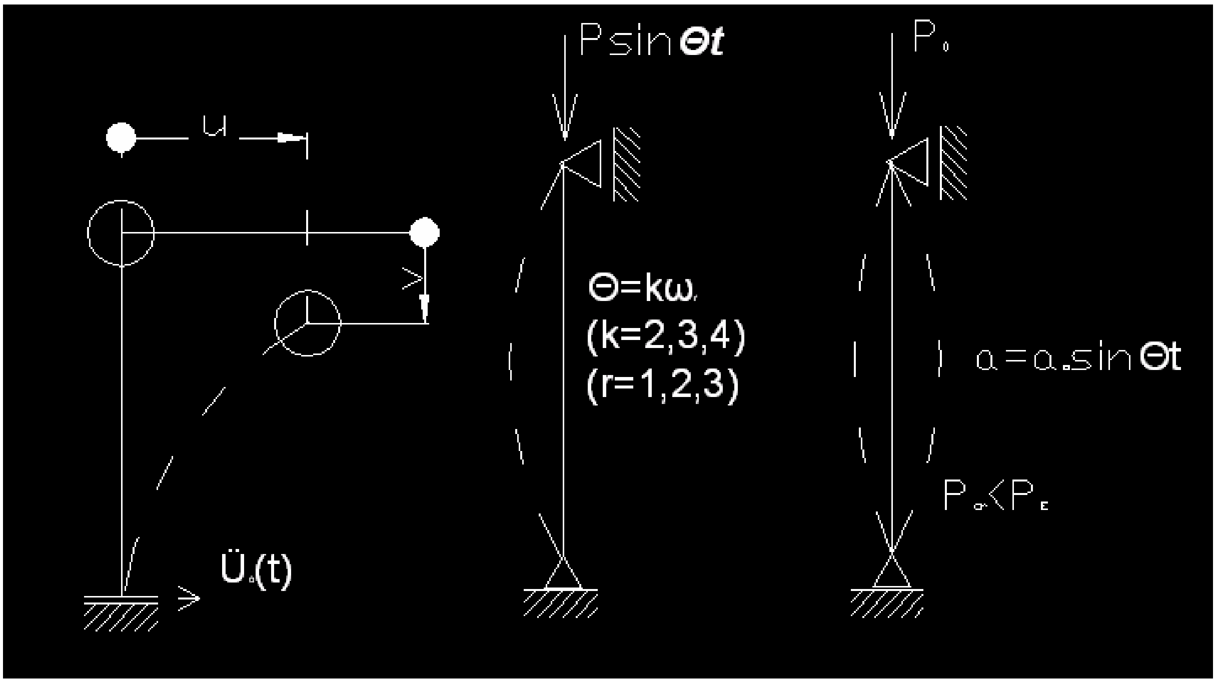

Figure 4 Column under axial load combined with oscillatory perturbation θ

An example of a non-linear system is the pendulum with an elastic wire which suffers a change of its parameters during the oscillation process. This kind of pendulum is a non-autonomous system visualized by means of the Hill type equation:

$$\ddot{\theta} + \omega(t)\theta = 0 \quad \text{Eq. 5}$$

For a non-autonomous linear system the following Equation 6 is the dynamic equilibrium :

$$M\ddot{x} + C(t)\dot{x} + K(t)x = F(t) \qquad \text{Eq. 6}$$

and gives the systems movement.

3 SECOND ORDER ANALYSIS OF THE STRUCTURAL RESPONSE

The P-Delta structural response leads to the collapse of the structure by increasing the moments and shear acting at the ends of the bars both columns and beams under seismic effects. All the codes for the seismic analysis deal in a way or in other with the structural behavior due to augmenting the static loads.

The Israeli Design Provisions for earthquake resistance of structures SI 413 takes into account the P –Delta effect by computing a coefficient that shows the ability to stand the drift the structure is going to get as result of the horizontal seismic load:

$$\theta_i = \frac{W\Delta_{el,i}K}{V_i h_i} \quad \text{Eq. 7}$$

Where:

$\Delta_{el,i}$ - the drift at the story “i” according to the elastic analysis.

V_i - the horizontal shear force at story i.

θ_i - the coefficient for the deformation at story i.

W – the total load over the floor i

K – the decrease coefficient of the loads acting on the structure.

h_i - the height for the story i.

According to SI 413 if the θ_i coefficient is less than 0.1 the structure is stable and no further analysis must be accomplished. If $0.10 < \theta_i \le 0.20$ a second order analysis must be done.

As concerns the vertical seismic oscillations certain elements must be loaded by vertical loads.

The structural stability is a function of the axial force which develops in the columns due to the amplification in vertical direction. According to Nakamura (2000) the vertical component of the tremor retains the characteristics of the horizontal tremor at the bedrock.

Based on this assumption the Eurocode 8 defines the vertical spectrum in correlation with the horizontal spectrum (Fig. 5)

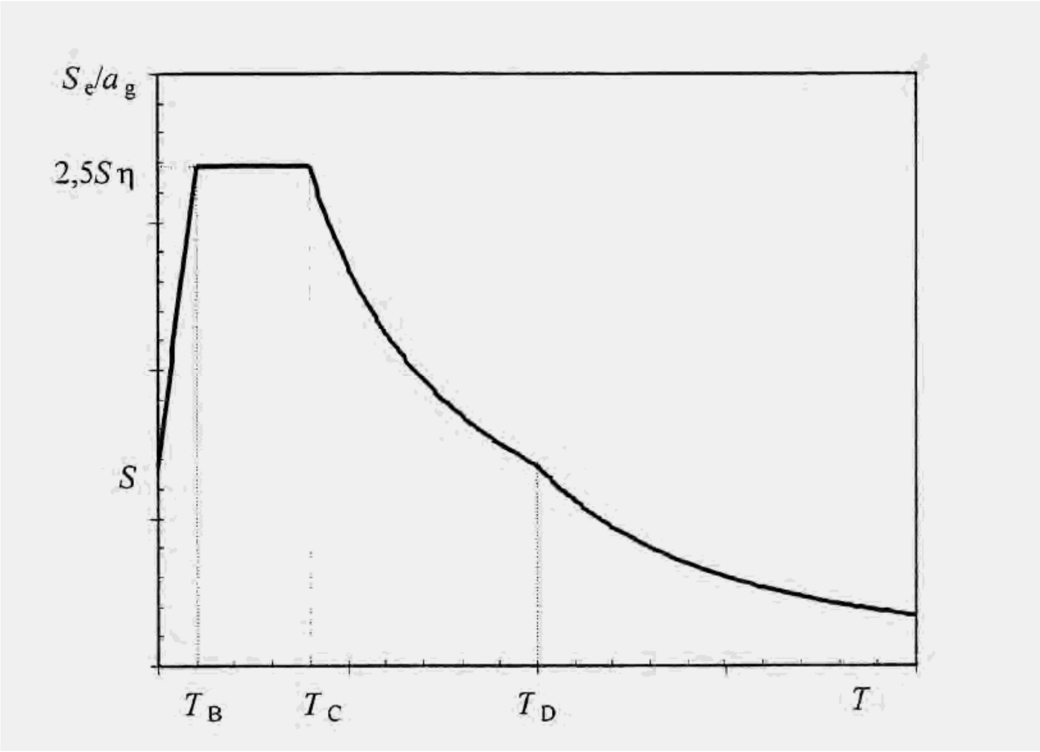

Figure 5 Shape of the elastic response spectrum

The vertical component of the seismic action shall be represented by an elatic response spectrum, $S_{ve}(T)$ derived by using the following expressions:

$$0 \le T \le T_B : S_{ve}(T) = a_{vg}\left[1 + \frac{T}{T_B}(\eta \bullet 3.0 - 1)\right](3.8)$$

$$T_B \le T \le T_C : S_{ve}(T) = a_{vg}\eta 3.0 \ (3.9)$$

$$T_C \le T \le T_D : S_{ve}(T) = a_{vg}\eta 3.0\left[\frac{T_C}{T}\right](3.10)$$

$$T_D \le T \le 4s : S_{ve}(T) = a_{vg}\eta 3.0\left[\frac{T_C T_D}{T^2}\right](3.11)$$

The values to be ascribed to T_B, T_C, T_D *and* a_{vg} for each type (shape) of vertical spectrum may be found in its National Annex.

Table 1 Recommended values of parameters describing the vertical elastic response spectra

Spectrum	a_{vg}/a_g	$T_B(s)$	$T_C(s)$	$T_D(s)$
Type 1	0.90	0.05	0.15	1.0
Type 2	0.45	0.05	0.15	1.0

Where:

$S_e(T)$ is the elastic response spectrum;T is the vibration period of a linear single-degree-of-freedom system; a_g is the design ground acceleration on type A ground $(a_g = \gamma_I a_{gR}) T_B$ is the lower limit of the period of the constant spectral acceleration branch;

T_C is the upper limit of the period of the constant spectral acceleration branch;

T_D is the value defining the beginning of the constant displacement response range of the spectrum;

S is the soil factor;

η is the damping correction factor with reference value of $\eta = 1$ for 5% viscous damping.

According ASCE/SEI 41-06 $P - \Delta$ effects shall be included in linear and nonlinear analysis procedures. For nonlinear procedures, static $P - \Delta$ effects shall be incorporated in the analysis by including in the mathematical model the nonlinear force-deformation relationship of all components subjected to axial forces.

Dynamic $P - \Delta$ effects are caused by a negative post-yield stiffness that increases story drift and the target displacement. The degree by which dynamic $P - \Delta$ effects increase displacements depends on the following:

1. The ratio of the negative post-yield stiffness to the effective elastic stiffness;
2. The fundamental period of the building;
3. The strength ratio, R;
4. The hysteretic load-deformation relations for each story;
5. The frequency characteristic of the ground motion;
6. The duration of the strong ground motion.

Because of the number of parameters involved, it is difficult to capture dynamic $P - \Delta$ effects in linear and nonlinear static analysis procedures. For the nonlinear static procedure, dynamic instability is measured by the strength ratio R. For the nonlinear dynamic procedure $P - \Delta$ effects are captured explicitly in the analysis.

The strength ratio R shall be calculated in accordance with Eq. 3-15:

$$R = \frac{S_a}{V_y / W} C_m \; (Eq.3-15)$$

Where

S_a is the response spectrum acceleration, at the effective fundamental period and damping ratio of the building in the direction under consideration;

V_y is the yield strength calculated using results of the nonlinear static procedure for the idealized nonlinear force-displacement curve developed for the building;

W is the seismic weight;

C_m is the effective mass factor. Alternatively, C_m is taken as the effective modal mass participation factor calculated for the fundamental mode using an Eigenvalue analysis.

C_m shall be taken as 1.0 if the fundamental period, T, is greater than 1.0 sec.

4 USE OF SAP2000 SOFTWARE

Building affected by seismic load both horizontally and vertically can be analyzed by means of SAP2000 software statically and dynamically. The static nonlinear methodology leads to the performance point which is placed at the intersection of the demand and capacity curves. If the capacity is determined by taking into account the $P-\Delta$ effect the capacity level is adjusted accordingly. The performance point indicates the influence of the vertical oscillations.
SAP2000 can be used for direct integration of the structural movement leading thus to the ability of the structure to withstand the seismic load till certain limit signaling the limit state of the structure.

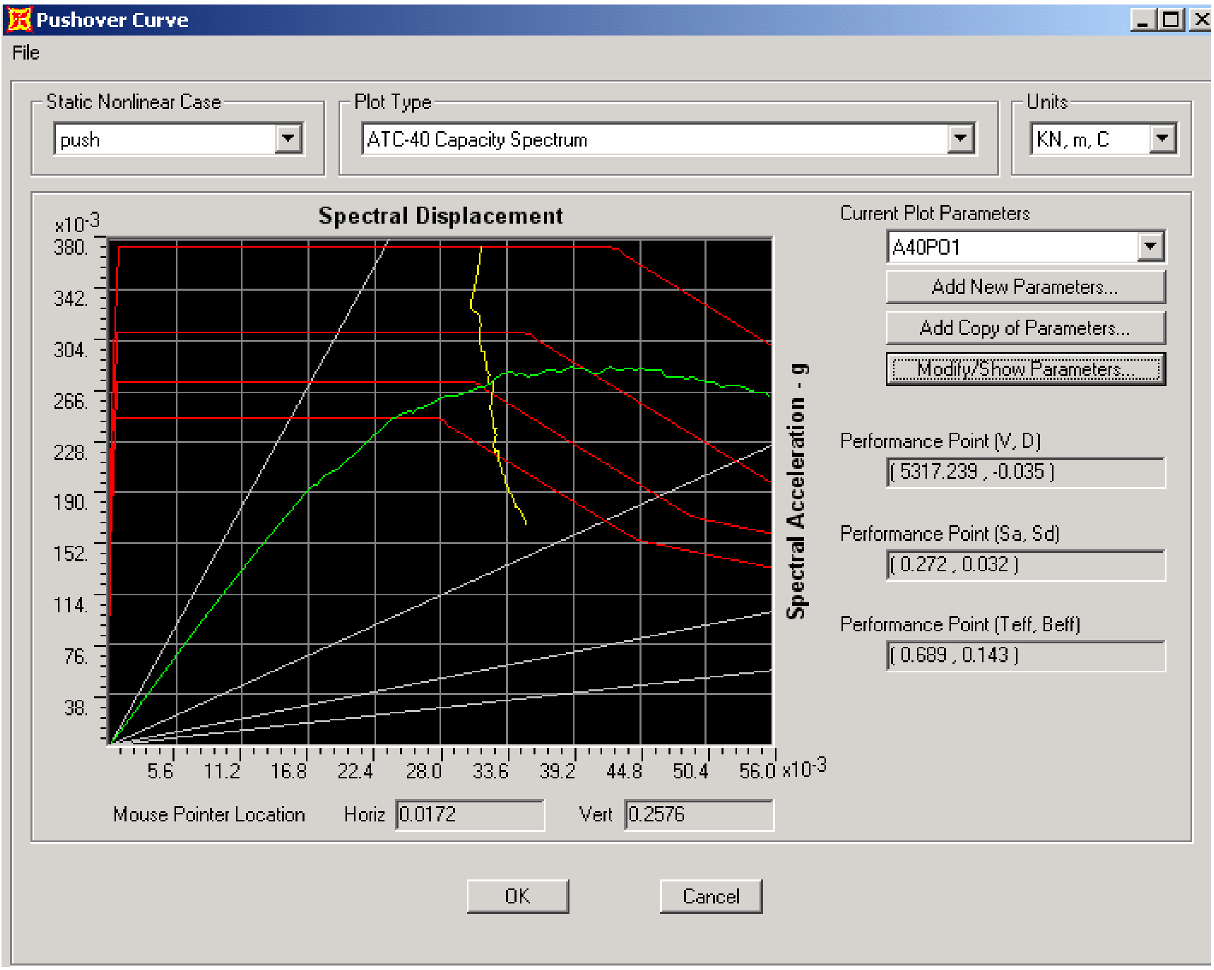

Static Nonlinear Case: push

Plot Type: ATC-40 Capacity Spectrum

Units: KN, m, C

Current Plot Parameters: A40P01

Performance Point (V, D): (5317.239 , -0.035)

Performance Point (Sa, Sd): (0.272 , 0.032)

Performance Point (Teff, Beff): (0.689 , 0.143)

Mouse Pointer Location Horiz 0.0172 Vert 0.2576

Figure 6 Static behavior under seismic load – performance point determination

5 CONCLUSIONS

Structural instability plays an important role in structural collapse. Since earthquakes are dynamic phenomena dynamic instability occurs during seismic excitations.

A thorough observation of the oscillations which occur during seismic excitations lead to the remark that both horizontal and vertical oscillations take place together.
$P-\Delta$ effects affect the stability of structures.
More, these effects are amplified during the oscillations leading to what is considered the dynamic instability due to the environmental factors and the structural abilities.
This work will be followed by further research and software for

6 REFERENCES

1 R. Marinov, Dynamic Stability Problems in Civil Engineering, Editura Technica –

2 SI 413 Design Provisions for Earthquake Resistance of Structures, 1998

3 Eurocode 8: Design of Structures for Earthquake Resistance 23.04.2004
4 SAP2000 Integrated Solution for Structural Analysis & Design, ver. 14 April 2009.
5 John Lawson, Reflections on the Effects of Vertical Seismic Acceleration, PCI Journal.

COMPDYN 2011
3rd ECCOMAS Thematic Conference on
Computational Methods in Structural Dynamics and Earthquake Engineering
M. Papadrakakis, M. Fragiadakis, V. Plevris (eds.)
Corfu, Greece, 25–28 May 2011

DEVELOPING FRAGILITY CURVES FOR A TYPICAL PILE-SUPPORTED WHARF STRUCTURE

Abdollah Shafieezaedeh[1], Reginald DesRoches[2], and Karthik Ramanathan[3]

[1] Georgia Institute of Technology,
School of Civil & Environmental Engineering, 790 Atlantic Drive, Atlanta GA 30332
a.shafiee@gatech.edu

[2] Georgia Institute of Technology,
School of Civil & Environmental Engineering, 790 Atlantic Drive, Atlanta GA 30332
reginald.desroches@ce.gatech.edu

[3] Georgia Institute of Technology,
School of Civil & Environmental Engineering, 790 Atlantic Drive, Atlanta GA 30332
karthik.ramanathan@ce.gatech.edu

Keywords: Ports, Seismic Risk Assessment, Fragility Analysis, Nonlinear Dynamic Analysis

Abstract. *Container wharves are one of the main components in port systems which are susceptible to structural damage during seismic events. Since regional economies depend largely on the operation of port systems, assessment of the vulnerability of these systems to seismic events is crucial. Seismic risk analysis provides a framework to estimate potential economic losses by incorporating the available information on structure details, soil conditions, repair cost for different components, etc. This paper studies the fragility of wharf structures for a typical pile-supported wharf as part of the NEES-GC project, Seismic Risk Mitigation of Strategic Ports. For this purpose, a two dimensional detailed model is developed for a typical pile-supported wharf structure on the west coast of the United States. The modeled structure contains a pile-deck connection model calibrated to experimental results, pile elements with spread plasticity capability and fiber sections, and soil-structure interaction elements capable of liquefaction modeling. Based on experts opinion and experimental results, a set of limit states are considered for a number of critical components of the wharf structure whose damage induce a disruption in the normal operation of ports. Using the nonlinear model and the limit states, a set of fragility curves are developed for 63 ground deformations generated for this study. The outcome of this research will help port owners to indicate the most vulnerable components of port infrastructures and invest the limited retrofit resources for risk mitigation of ports.*

1 INTRODUCTION

Seaports are intermodal transfer points in transportation networks which have a major role in the regional economy. The physical activities of ports i.e. loading and unloading of cargo, raw materials, etc are concentrated in a small geographic area and therefore, any disruption in the normal performance of structural and geotechnical components of ports may lead to partial or even full disruption of the commercial activities of the port. Historical cases of seaport damage have shown that any disruption in the activities of port infrastructures may lead to significant direct and secondary losses. Particularly poignant examples were the 1995 Kobe earthquake and 2010 Haiti earthquake in which liquefaction and lateral spreading of embankments imposed severe damage to both structural and non-structural components of ports [1,2]. Seismic risk analysis as a key component in risk mitigation efforts provides a framework to estimate potential economic losses by incorporating the available information on structure details, soil conditions, repair cost for different components, etc. In general, seismic risk of a system can be decomposed into a number of components among which is the fragility of the system. The fragility of a wharf model defines the probability of occurrence of various damage states as a function of the firm-site ground motion.

Despite the importance of ports and their vulnerability to seismic damage, a limited number of researches studied the fragility of wharves to seismic events [3,4]. The present study focuses on developing fragility curves for a typical pile supported wharf with batter piles in the west coast of the United States. This is accomplished by incorporating realistic representations of the nonlinear behavior of pile elements, nonlinear force-deformation characteristics of pile-deck connections, and nonlinear dynamic pile-soil interactions in liquefaction susceptible soils. Based on experts' opinion and experimental results, a set of limit states are considered for a number of components of the wharf structure which their damage induces a disruption in the normal operation of ports. Using the nonlinear model and the limit states, a set of fragility curves are developed for 63 ground deformations of the soil embankment and pore water pressure generated for this study through free-field analysis.

2 NUMERICAL MODELING OF A TYPICAL PILE-SUPPORTED WHARF

2.1 Structural Elements

A typical pile supported wharf in the west coast of the United States is modeled in this study. The Finite Element (FE) model of the wharf is developed in OpenSees, an object-oriented FE analysis framework [5]. The transverse section of the wharf is shown in Figure 1. Directions parallel and normal to the landside-seaside direction in the plane of the wharf deck are defined as transverse and longitudinal directions, respectively. In the longitudinal direction, wharves consist of repeating segments, referred to as strips, which are used to represent the wharf in two dimensions. The deck of the wharf and the landside crane rail are supported by pre-stressed vertical and batter piles (Figure 1). The pre-stressed piles are modeled by force-based nonlinear beam-column elements [6,7] with fiber cross-sections. The piles and the deck are connected by T-headed dowel bars which is a common connection for wharf structures. In the FE model of the wharf, these connections are modeled by a link element at the top of pre-stress piles. In order to capture the nonlinear force-deformation characteristics of pile-deck connections, the implemented procedure is calibrated with the result of a full scale test conducted by Lehman et al. [8].

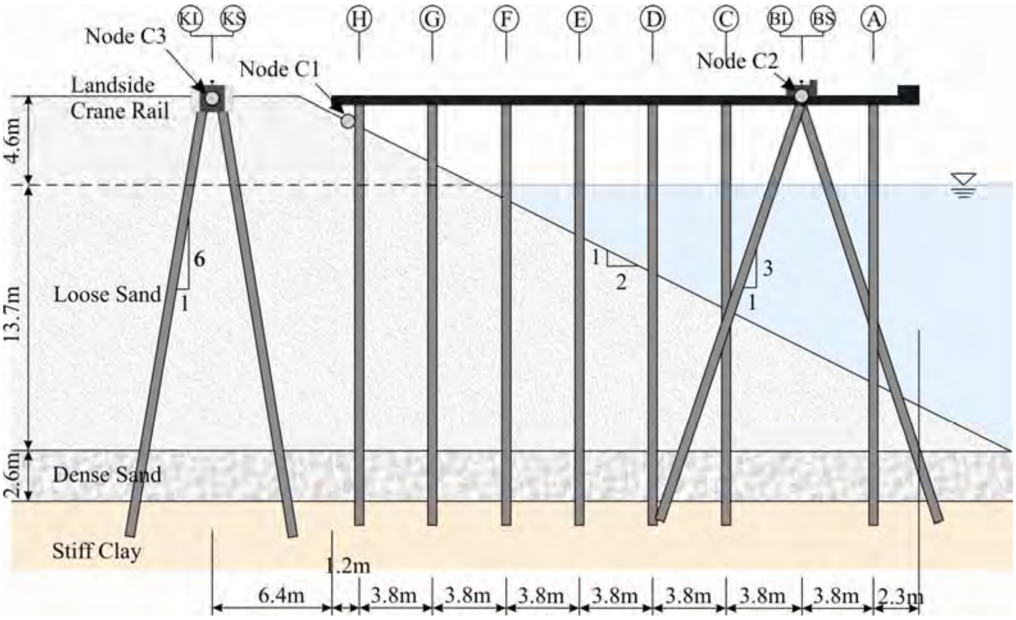

Figure 1. Configuration of the wharf and landside crane rail

2.2 Geotechnical Considerations

The profile of the soil at the location of the wharf is shown in Figure 1 which consists of three layers: a layer of loose sand in the top 18.3 m underlain by a layer of dense sand with a thickness of 2.6 m on top of a layer of clay. The water level is 4.6 m from the soil surface on the landside. Soil properties of the three layers including mass density, shear modulus, Poisson's ratio, friction angle, and undrained shear strength are presented in Table 1.

Pile-soil interaction in the horizontal direction is modeled by a series of nonlinear soil springs including macroelements [9] and conventional p-y springs [10] in sand and clay layers respectively. In the vertical direction, t-z and q-z springs are implemented to model the resistance in the face and end of the piles respectively. Soil springs are assigned at every 1 m in depth from the soil surface and their associated material properties are found for the corresponding soil layer.

Soil layer	γ (gr/cm3)	G (MPa)	ν	φ (deg)	cu (kPa)
Loose Sand	1.85	80	0.2	34	-
Dense sand	2.05	120	0.2	38	-
Clay	1.75	100	0.4	-	48

Table 1. Soil layers properties.

3 GROUND MOTIONS

Generating PSDMs for critical response measures of the wharf requires selection of representative ground motions as the inputs for nonlinear time-history analysis. A total of 63 empirical (i.e., observed) and simulated ground motions have been selected to represent a broad range of possible earthquake magnitudes and distances. The soil condition for these ground motions is typical of firm soils in coastal California. Among 63 ground motions, fifty six ground motion time-histories are empirical which are selected from the database used to develop the Next Generation Attenuation of Ground Motions (NGA) project [11]. This suite of ground motions is selected randomly from the database such that all of the earthquakes have minimum moment magnitude (Mw) of 5.5 and closest distance to the rupture (R) of 0 to 60 km. All of the selected ground motions are earthquakes within the United States except for the 1995 Kobe, Japan and 1999 Chi - Chi, Taiwan earthquakes. Furthermore, seven simulated ground motions are added to the bin to represent large magnitude California earthquakes which are not present in the NGA database. The resulting bin of empirical and simulated ground motions covers a broad range of earthquake scenarios in terms of minimum moment magnitude and the closest distance to rupture. Figure (2) presents M_w versus R for the suit of sixty three earthquakes considered in this study.

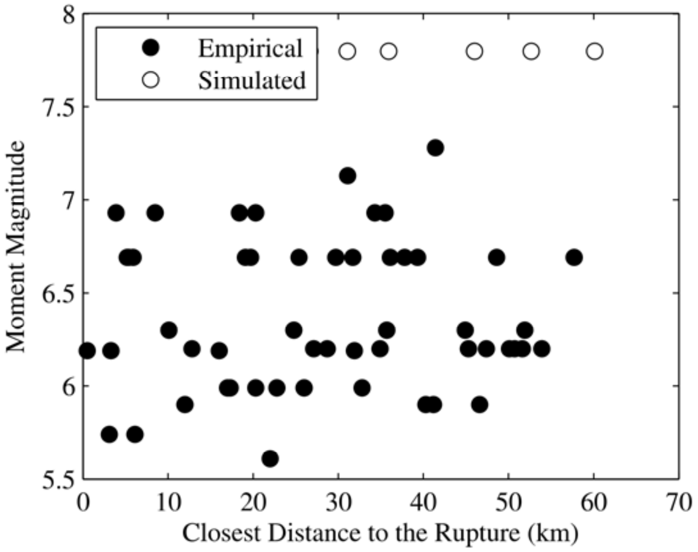

Figure 2. Moment magnitude vs. the closest distance to rupture.

The selected ground motions are used as input for numerical models of the soil embankments supporting the wharf-foundation. The nonlinear coupled ground deformation and transient pore pressure response of the wharf embankment to input ground shakings are numerically evaluated by Vytiniotis et al. [12]. The analysis uses the advanced elasto-plastic effective stress soil model proposed by Dafalias and Manzari [13]. This model is able to realistically capture the stress-strain behavior of sand during cyclic mobility events. More details about the model and assumptions together with numerical results can be found in Vytiniotis et al. [12]. Soil deformations and excess pore water pressure ratios in sand layers in the horizontal direction are applied to the far-field end of the macroelement, while for other soil springs only soil deformations are input to the model. The dynamic response of the foundation-wharf-crane system is found for time-histories of ground deformation and pore pressures within the surrounding soil medium.

4 FRAGILITY ANALYSIS FRAMEWORK

A key component in predicting the damage of a structural system when subjected to an earthquake with expected characteristics is the fragility of the system. A fragility curve describes the probability that the structure fails to satisfy a prescribed performance criterion conditioned on a seismic intensity measure (*IM*) representative of the seismic loading. In structural engineering community, it is common to define the event of a structure failing to meet a performance requirement called damage state by simply the case where demand (*D*) exceeds capacity (*C*); i.e. *C*<*D*. Assuming that both capacity and demand can be described by lognormal distributions, the probability of the structure exceeding a particular damage state for a given *IM* in closed form is

$$P(C < D \mid IM) = 1 - \Phi\left(\frac{\ln(m_C) - \ln(m_D)}{\sqrt{\beta_C^2 + \beta_D^2}}\right) \tag{1}$$

in which Φ(.) is the standard normal distribution and m and β are the median and logarithmic standard deviation respectively.

According to Equation (1), evaluation of the seismic fragilities of structures requires developing models for demand on the structural components using nonlinear time-history analysis of the wharf-foundation system as well as capacity model for the critical components.

4.1 Probabilistic seismic demand models

One of the constitutive components of the conditional probability of failure in Equation (1) is the demand model for which a probabilistic analysis is required to determine the parameters m_D and β_D. Cornell et al. [14] showed that seismic median drift demands can be represented well as a power function of *IM*.

$$m_D = a(IM)^b \tag{2}$$

where a and b are constants determined by a simple linear regression analysis of the seismic demand in the transformed logarithmic space in the following form.

$$\ln(m_D) = \ln(a) + b\ln(IM) \tag{3}$$

The assumption of demand following a lognormal distribution with respect to the IM is applied to all demand measures associated with critical wharf components including the curvature of piles and pile-deck connections and the relative displacement of the structurally separated landside crane rail with respect to the wharf. Assuming that the dispersion of seismic demand parameters is independent from the IM in the logarithmic scale, the uncertainties in the seismic demand parameters β_D in Equation (1) is determined as the logarithmic standard deviation of errors in fitting the demand models as follows.

$$\beta_D = \sqrt{\frac{\sum_{i=1}^{n}\left(\ln(D_i) - \ln\left(aIM^b\right)\right)^2}{n-2}} \tag{4}$$

Subjecting the wharf-foundation to time-histories of ground deformation and pore water pressures of the embankment soil, the dynamic response of the wharf is found using nonlinear time-history analysis and the maximum response in critical response measures are recorded. This study uses peak ground acceleration (PGA) as the *IM* which is a widely used *IM* in earthquake engineering community.

Figure (3) shows the seismic demand of the piles and pile-deck connections in terms of curvature and the relative displacement of the landside crane rail and wharf in the horizontal direction as a function of PGA. It is observed that the assumption of independence of the demand from intensity measure in the logarithmic scale is almost valid for all demand parameters. Furthermore all of the demand parameters are seen to be reasonably well described by a linear regression in the log scale which validates the assumption of demand be lognormally distributed.

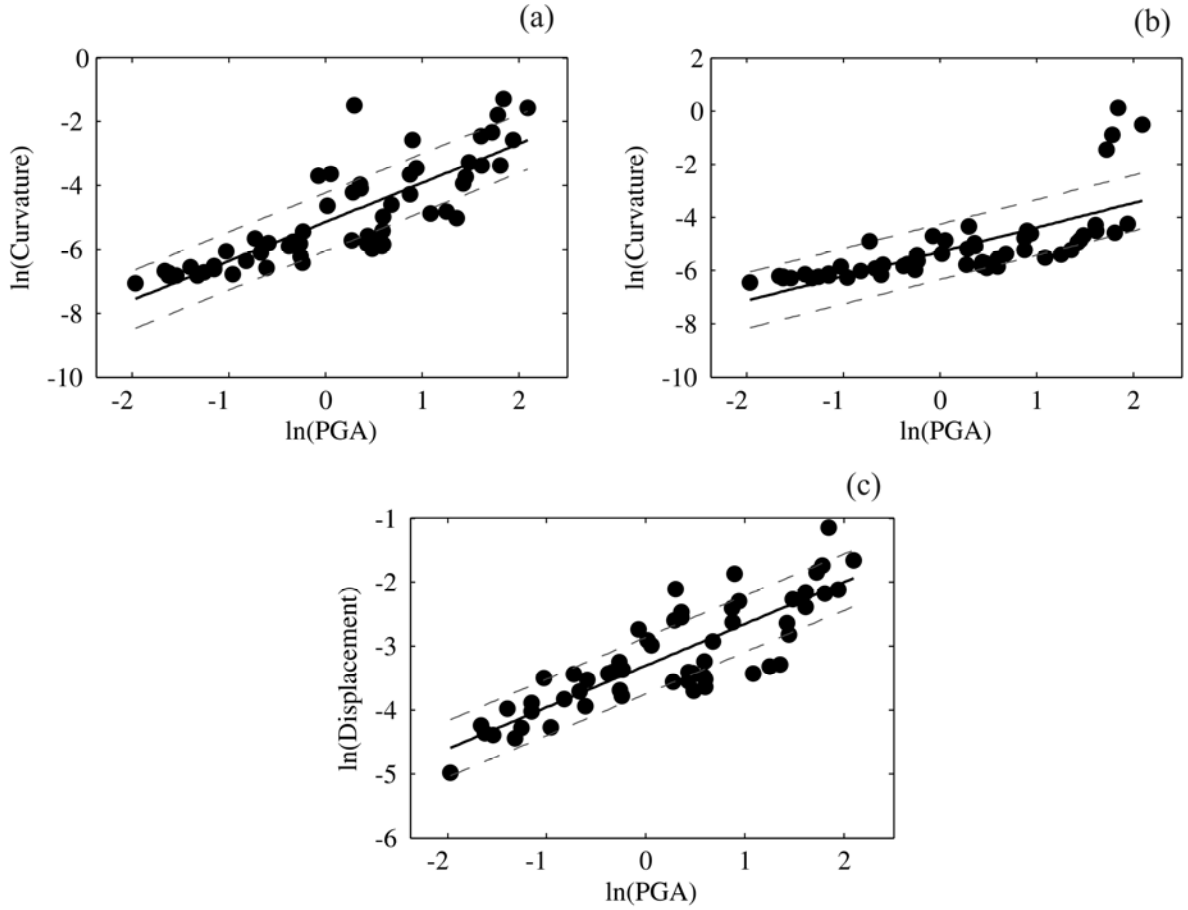

Figure 3. Probabilistic seismic demand models for (a) pile-deck connections, (b) pile sections, and (c) relative movement of the wharf with respect to the landside crane rail.

4.2 Component limit states

The study uses three damage states: slight, moderate, and extensive in which the first two states are adopted from PIANC [15]. The slight damage state has a high probability of occurrence during the life time of the wharf in which no structural damage is permitted. The moderate damage has a lower probability of occurrence compared to the slight damage state in which only reparable damages and limited residual deformations are allowed. Because of the mutual exclusiveness property of the damage states, all other damages that are more severe and consequently less probable than the ones associated with the moderate damage state falls into the extensive damage state category.

A number of response measures of the wharf that are critical in the overall structural response of the wharf and the performance of associated components such as cranes are considered in this study. As mentioned before, these critical response measures are the curvature of piles and pile-deck connections and the relative displacement of the wharf with respect to the landside rail. The limit states associated with these responses are assumed to be lognormally distributed.

The median m_C of the capacity limit state for the pile-deck connections is obtained from the experimental test conducted by Lehman et al. [8] in which the provided drift limits are converted to curvature limits at the connection using numerical simulation of the test specimen.

The curvature limit states for different pile sections are found using moment-curvature analyses. Typically the cross-section of a pile contains all or a number of the following discretized sub-regions, the cover layer of unconfined concrete, the inner core region of confined concrete, the circular layer of longitudinal reinforcing steel, and the circular layer of pre-stressing strands. In order to determine the median deformation capacity of the piles, the strain limits of the constitutive section materials provided by PIANC [15] are used to determine the corresponding section curvature. The strain limits, for each of the constitutive materials are presented in Table (2).

	Limit State		
Material Response	Slight	Moderate	Severe
Concrete extreme fiber compression strain	0.004	0.008	–
Core concrete extreme fiber compression strain	–	–	2/3 ε_{cu}
Reinforcing Steel tension strain	0.01	0.01	2/3 ε_{su}
Prestressing strand incremental strain	0.005	0.015	2/3 ε_{pu}

Table 2. Strain limits associated with defined limit states for constitutive materials of pre-stress pile sections

Performing moment-curvature analyses for different sections of the pre-stressed piles in the wharf configuration, the curvature limits are determined as the minimum of the curvatures corresponding to the strain limits of different constitutive section materials for each limit state. The derived curvature limits for all sections in the wharf are presented in Figure (4). The median of the curvature limit of different pile sections in each limit state is considered as the median m_C of the capacity limit state.

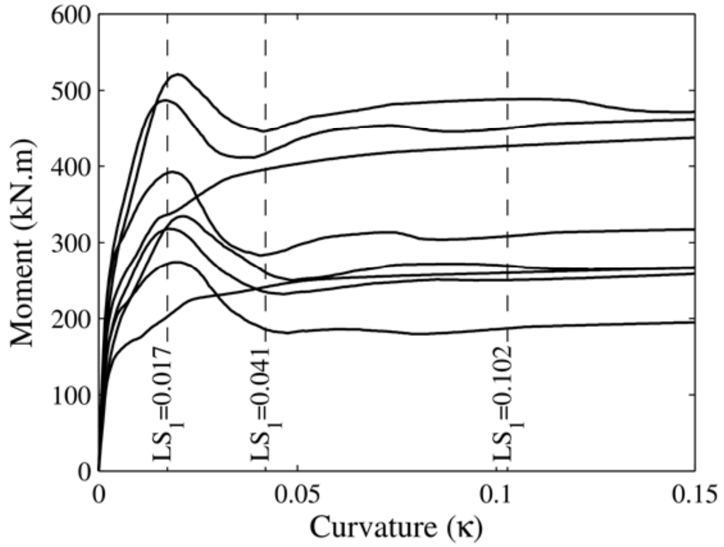

Figure 4. Moment curvature curves of different sections of the piles and the median limit states.

The median of the limit states m_C for the relative movement of the landside crane rail with respect to the wharf is provided by Werner and Cook [16] based on expert opinion. The summary of deformation limits of different wharf components associated with three limit states chosen for this study are presented in Table (3).

	Limit State		
Component	Slight	Moderate	Severe
Pile-deck connection rotation (1/m)	0.007	0.035	0.08
Pile section curvature (1/m)	0.017	0.041	0.102
Relative displacement of the landside rail with respect to wharf deck (cm)	0.3	2.5	15.2

Table 3. The deformation limits of critical wharf components corresponding to the chosen limit states.

4.3 Component fragility curves

After developing the probabilistic seismic demand models and determining the corresponding limit states of the wharf damage for the critical components, the component fragilities are constructed using the closed form given in Equation (1). Following Ellingwood [17], the dispersion in the capacity is assumed 0.2 while the dispersion in the demand is found from Equation (4).

The resulting fragility curves for pile sections, pile-deck connections and the relative displacement of the landside crane rail with respect to the wharf are shown in Figure (5)

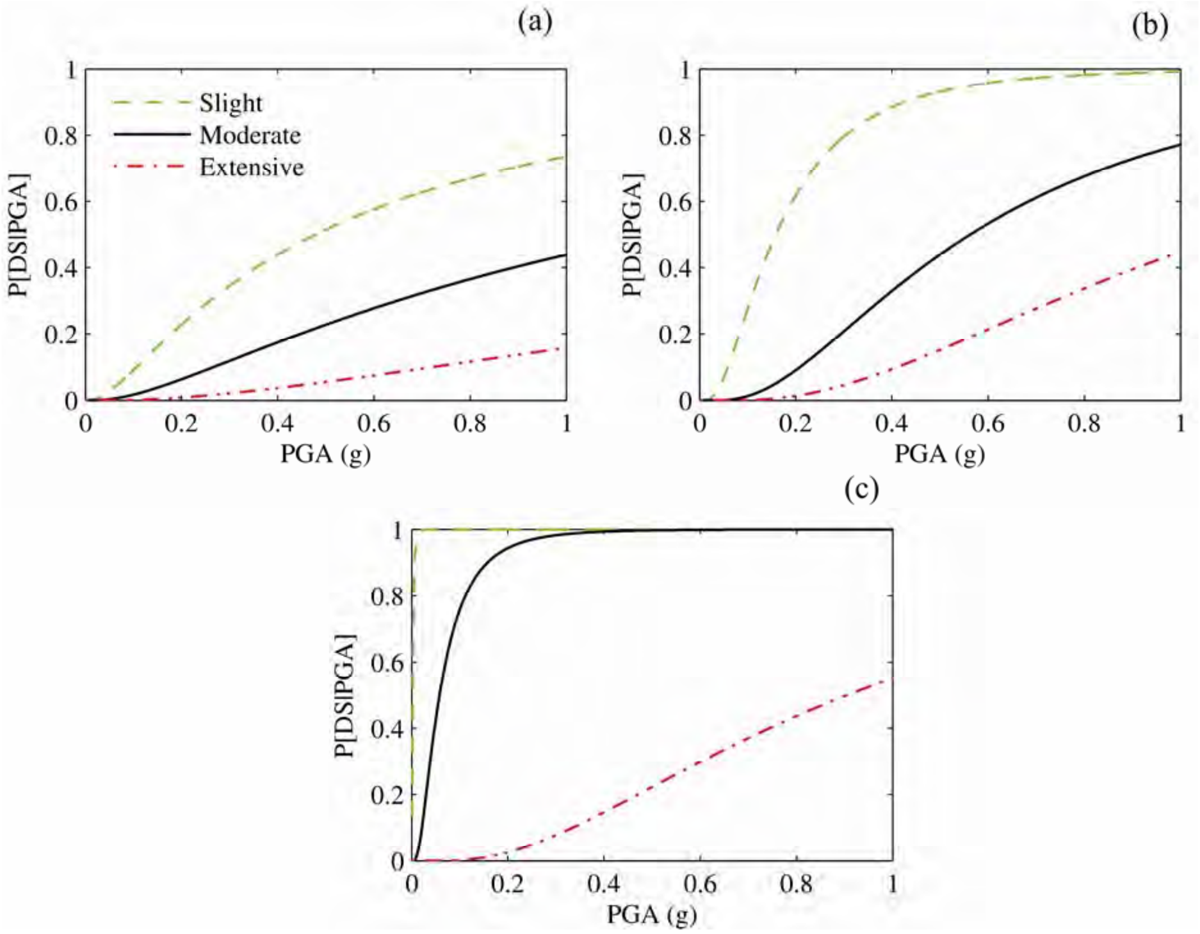

Figure 5Seismic fragility curves for (a) pile-deck connections, (b) pile sections, and (c) relative movement of the wharf with respect to the landside crane rail.

respectively. It is observed that pile-deck connections are less susceptible to damage compared to pile sections for the same intensity measure i.e. PGA. This is in large due to the considerable relative deformation of the loose and dense sand layers (Figure 1) as a result of liquefaction of the embankment. This consequently imposes large curvature demands on pile sections close to the interface of soil layers. Furthermore, the wharf damage as a result of excessive relative displacement of the wharf with respect to the structurally separated landside crane rail is seen to by highly probable. This response measure of the wharf has a large impact on the operation of the container cranes, and therefore requires more attention. A possible retrofit measure for the excessive relative displacement of the wharf can be connecting the separate landside rail and wharf using reinforced concrete.

5 CONCLUSIONS

This study presents the analytical fragility analysis of a typical pile supported wharf in the west coast of the United States. The two dimensional numerical model of the wharf used for developing fragility curves includes realistic representation of the critical wharf components including piles, pile-deck connections, and soil springs for liquefiable soils. The ground motions for time-history analysis represent a broad range of earthquake scenarios in terms of moment magnitude and the closest distance to rupture. The study presents the results of the nonlinear time-history analysis of the wharf-foundation system and the associated probabilistic seismic demand models for the ground deformations and pore water pressures of the surrounding soil medium for various seismic hazard scenarios. Using the analytical relations for the conditional probability of exceeding defined damage states, a set of fragility curves are developed for critical wharf components including piles, pile-deck connections, and the relative displacement of the landside crane rail and the wharf. It was found that the relative displacement of the wharf with respect to the structurally separated landside crane rail is the most vulnerable component in the wharf response. Furthermore, pile sections were found to be more susceptible to damage compared to pile-deck connections.

REFERENCES

[1] S.D. Werner, S.E. Dickenson, *Hyogo-Ken Nanbu earthquake of January 17, 1995: a post-earthquake reconnaissance of port facilities*. American Society of Civil Engineers, 1996.

[2] M. Eberhard, S. Baldridge, J. Marshall, W. Mooney, G.J. Rix, *The mw 7.0 Haiti Earthquake of Jauary 12, 2010, V. 1.0,* USGS/EERI Advance Reconnaissance Team Report, 2010.

[3] U.J. Na, S.R. Chaudhuri, M. Shinozuka, Performance evaluation of pile-supported wharf under seismic loading. A.K.K. Tang and S.D. Werner eds. *Lifeline Earthquake Engineering in a Multihazard Environment (TCLEE 2009)*, Oakland, USA, 2009.

[4] R.W. Boulanger, C.J. Curras, B.L. Kutter, D.W. Wilson, Seismic soil-pile-structure interaction experiments and analyses. *Journal of Geotechnical and Geoenvironmental Engineering*, **125**, 750–759, 1999.

[5] F. McKenna, M.H. Scott, G.L. Fenves, Nonlinear finite-element analysis software architecture using object composition. *Journal of Computing in Civil Engineering*, **24**, 95–107, 2010.

[6] E. Spacone, F.C. Filippou, F.F. Taucer, Fiber beam-column model for non-linear analysis of R/C frames: part I. Formulation. *Earthquake Engineering & Structural Dynamics,* **25**, 711–725, 1998.

[7] R.M. De Sousa, *Force-based finite element for large displacement inelastic analysis of frames.* Ph.D. Thesis, Department of Civil Engineering, University of California, Berkeley, CA, 2000.

[8] D.E. Lehman, E. Brackmann, A. Jellin, C.W. Roeder, Seismic performance of pile-wharf connections. A.K.K. Tang and S.D. Werner eds. *Lifeline Earthquake Engineering in a Multihazard Environment (TCLEE 2009),* Oakland, USA, 2009.

[9] Varun, D. Assimaki, A nonlinear dynamic macroelement for soil-structure interaction analyses of pile-supported waterfront structures. *International Journal for Numerical and Analytical Methods in Geomechanics,* In Press, 2010.

[10] R.W. Boulanger, C.J. Curras, B.L. Kutter, D.W. Wilson, Seismic soil-pile-structure interaction experiments and analyses. *Journal of Geotechnical and Geoenvironmental Engineering*, **125**, 750–759, 1999.

[11] B. Chiou, R. Darragh, N. Gregor, W. Silva, NGA project strong-motion database. *Earthquake Spectra*, **24**, 23-44, 2008.

[12] A. Vytiniotis, A.J. Whittle, E. Kausel, Effects of seismic motion characteristics on cyclic mobility and liquefaction. 5th International Conference on Earthquake Geotechnical Engineering, Santiago, Chile, January 10-13, 2011.

[13] Y.F. Dafalias and M.T. Manzari, Simple plasticity sand model accounting for fabric change effects. *Journal of Engineering Mechanics*, **130**, 622-634, 2004.

[14] A.C. Cornell, F. Jalayer, R.O. Hamburger, and D.A. Foutch, Probabilistic basis for 2000 SAC Federal Emergency Management Agency Steel Moment Frame Guidelines. *Journal of Structural Engineering*, **128**, 526-532, 2002.

[15] International Navigation Association (PIANC). *Seismic design guidelines for port structures*. A.A. Balkema Publishers, 2001.

[16] S.D. Werner and W.C. Cook, Wharf repair estimates for use in demonstration seismic risk analysis of port systems, Prepared for NEES-GC Project: Seismic Risk Mitigation of Port Systems, September 17, 2009.

[17] B.R. Ellingwood, O.C. Celik, K. Kinali, Fragility assessment of building structural systems in Mid-America, *Earthquake Engineering and Structural Dynamics*, **36**, 1935-1952, 2007.

COMPDYN 2011
III ECCOMAS Thematic Conference on
Computational Methods in Structural Dynamics and Earthquake Engineering
M. Papadrakakis, M. Fragiadakis, V. Plevris (eds.)
Corfu, Greece, 25–28 May 2011

IMPLEMENTATION OF A BIO-INSPIRED TWO-MODE STRUCTURAL HEALTH MONITORING SYSTEM

Tzu-Kang Lin[1], Li-Chen Yu[2], Chang-Hung Ku[3], Kuo-Chun Chang[4], Anne Kiremidjian[5]

[1]Research Fellow, National Center for Research on Earthquake Engineering,
tklin@ncree.org
[23]Graduate Student, Department of Civil Engineering, National Taiwan University,
b95501011@ntu.edu.tw,b95501031@ntu.edu.tw
[4]Professor, Department of Civil Engineering, National Taiwan University,
ciekuo@ccms.ntu.edu.tw
[5]Professor, Department of Civil and Environmental Engineering, Stanford University,ask@stanford.edu

Keywords: Structural Health Monitoring, Naïve Bayes, Bio-inspired.

Abstract. A bio-inspired two-mode structural health monitoring (SHM) system based on the Naïve Bayes (NB) classification method is discussed in this paper. For the micro-vibration mode, a two-tier auto-regression with exogenous (AR-ARX) process is used to extract the expression array from the recorded structural time history while an ARX process is applied for the analysis of the earthquake mode. The health condition of the structure is then determined using the NB classification method. To verify the performance and reliability of the SHM algorithm, a downscaled eight-storey steel building was used as the benchmark structure. The structural response from different damage levels and locations was collected and incorporated in the database to aid the structural health monitoring process. Preliminary verification has demonstrated that the structure health condition can be precisely detected by the proposed algorithm. To implement the developed SHM system in a practical application, a SHM prototype was developed, which consists of three separate modules namely, the input sensing module, the transmission module, and the SHM platform. The vibration data is first measured by the deployed sensor, and subsequently the SHM mode corresponding to the desired excitation is chosen automatically to quickly evaluate the health condition of the structure. Test results from the ambient vibration and shaking table test showed that the condition and location of the benchmark structure damage can be successfully detected by the proposed SHM prototype system, and the information is instantaneously transmitted to a remote server to facilitate real-time monitoring. Implementing the bio-inspired two-mode SHM practically has been successfully demonstrated.

1 1INTRODUCTION

Recently, an increasing number of infrastructures and buildings all over the world have been unexpectedly damaged or have collapsed due to aging and long-term material degradation. Even though most of these structures have been periodically examined or monitored using modern techniques, these catastrophic failures continue to happen. Due to the existence of a large number of aging buildings, structural health monitoring (SHM) has become an important issue in civil engineering and must go hand in hand with the current research to improve the capacity of structures and to develop a safer design method.

The multidisciplinary research field of SHM was first proposed in the area of aerospace engineering. Accompanied by the development of advanced sensors, SHM was then subsequently developed for applications such as aerospace engineering, mechanical engineering, and civil engineering. However, contrary to the other two fields, civil engineering has faced specific challenges with respect to SHM development. For example, large-scale monitoring applications in civil engineering often using customized monitoring equipment make monitoring a difficult task. Unlike the mass production frequently seen in the field of mechanical engineering where a specific SHM module can be applied to all products to save time and cost, SHM devices used in a structure are commonly customized to cater to the demand and functionality of that particular structure. In addition, the unique requirements of the exterior of structural elements such as fire proofing or indoor appearance requirements, hinder the installation of a SHM system.

The first SHM systems consisted of simple instrumentation. With development in sensor and signal processor technology, SHM systems based on these techniques were capable of detecting the structural health of aircrafts and with the help of a preventive maintenance system greatly extended the lifetime of aircrafts [Hickman et al. 1991]. In 1998, a coordination was achieved between universities, government agencies, and industry, and an innovative SHM assessment method for the overall structural condition of structures was proposed by incorporating the basic concept of system identification [Aktan et al. 1998].

To reduce both the high cost and time required for the on-site cable installation of a traditional SHM system, wireless technology was introduced in the field of SHM. For example, a new method combining the advantages of an advanced sensor and the wireless technique was proposed by Pines et al., to remotely monitor the condition of various infrastructures in 1998. Data collected by the sensors from a structure can be remotely and wirelessly transmitted back to the server and processed by the SHM system on a computer giving an indication of both the damage location and the level of damage [Pines et al. 1998]. Other SHM systems integrating sensors, micro processors, and a wireless transmitter have also been developed, and targets like high speed, accuracy, and low-cost are gradually being accomplished [Tanner 2003, Wang et al. 2007].

In subsequent years, a tiny laser scanner has been developed which can be installed in different locations of the structure for scanning cracks and monitoring fatigue. Based on its specific characteristics, the device can be incorporated in aircrafts, railways, and civil structures [Buckner et al. 2008]. Due to extensive research and subsequent achievements over the past decade, the original SHM concept for structures is being used extensively today to monitor specific structure characteristics under both ambient and forced vibrations. A study conducted by Zimmerman et al. has also proved that data can be collected reliably and processed by a pure wireless

SHM system [Zimmerman et al. 2008]. A SHM system based on a hybrid wireless network has also been verified for its feasibility in the laboratory, and several structural response parameters have been effectively monitored on site for a rapid assessment of the conditions [Mascarenas et al. 2010].

In addition to the development of the SHM system, algorithms focusing on certain specific applications have also been proposed. Contrary to the original concept wherein sensors were installed on the structure to identify the location of the damage, researchers have started to employ customized SHM software to enable a more accurate diagnosis. SHM software development was initiated in the field of aerospace engineering in the year 2000 to reduce the heavy operating and maintenance fees and to further extend the aircraft lifetime [Boller 2000]. Around the same time, various SHM algorithms for infrastructures were developed in the field of civil engineering to offer more precise detection results using certain physical SHM techniques. For example, Johnson et al. utilized local vibration signals in combination with an intelligent diagnosis algorithm to demonstrate the feasibility of a distributed SHM system for damage location and monitoring [Johnson et al. 2004]. Another algorithm based on wavelet analysis to detect the location and the level of damage for the four-story benchmark structure proposed by the American Society of Civil Engineers (ASCE) was also developed. The efficacy of this SHM system was demonstrated by drawing a comparison with an established finite element model for wind loading [Hera and Hou 2004].

Studies on the selection of proper structural parameters for the SHM have been widely conducted over the past decade. Unlike the traditional identification method, parameters selected by the genetic algorithm (GA) have shown certain unique advantages of the SHM [Udwadia and Proskurowski 1998]. The monitoring of large-scale structures is a constant challenge faced by engineers especially when the measured data contains high-frequency noise. Thus, to overcome the above problems, a new statistical SHM system based on the Support Vector Machine (SVM) was proposed. This system was found to be highly reliable under different types and different levels of noise intensity [Zhang et al. 2006]. Furthermore, a new method integrating the Autoregressive Moving Average (ARMA) models and statistical theory was used to analyze the structural response in the time domain [Carden and Brownjohn 2008].However, as mentioned above, researchers are still faced with the problem of selecting the proper parameters for the SHM algorithm.

As the bio-inspired concept was introduced in the field of engineering, researchers began to seek for possible solution inspired from the nature. The concept of gene expression monitoring was first proposed and implemented by Golub [Golub et al. 1999]. This method offered a new way to classify cancer cells and gave rise to further research in detecting diseases from a gene expression array. The results from the research ignited a new research field, and subsequent research by Slonim et al. also demonstrated the feasibility of combining the NB algorithm and the DNA array data for multi-class cancer diagnosis [Slonim et al. 2000]. In order to obtain high accuracy and overcome obstacles such as high manpower and high equipment costs for monitoring structures, a new two-mode SHM system based on bioinformatics has been proposed in this paper. The proposed system is composed of two main parts: the SHM software and SHM hardware. The basic theory of the SHM algorithm has been described in section 2. The preliminary verification of the proposed system has then been carried out on an eight-storey downscaled benchmark at NCREE in section 3. The proposed SHM system has then been implemented on a mobile SHM prototype in section 4. Section 5 discusses the practical verification of the integrated SHM system, and based on the results, a summary and conclusion have been included.

2 THE PROPOSED SHM ALGORITHM

As the bio-inspired concept for engineering is a broadly discussed topic, a novel SHM algorithm employing array expression data as the Deoxyribonucleic acid (DNA) of the structures is proposed in this research. Based on the type of vibration which can either be strong ground excitation or ambient vibration, the recorded time history is converted using an auto-regression-auto-regression with exogenous (AR-ARX) process for micro-vibration and an ARX process for earthquake excitation. The AR regression model has proven to be effective in the illustration of the structure model under pure ambient vibration while the ARX model is suitable for significant external excitation conditions [Ljung, 1986]. A series of research conducted by Sohn et al. has also demonstrated the advantage of using the chosen AR-ARX model for unknown excitation between pure ambient and strong ground excitation [Sohn et al. 2000][Sohn and Farrar, 2001]. The obtained array is then compared using the Naïve Bayes (NB) classification method which is the core of the SHM algorithm to detect the damage condition and location as shown in Figure 1. The basic description of each part is briefly summarized as follows:

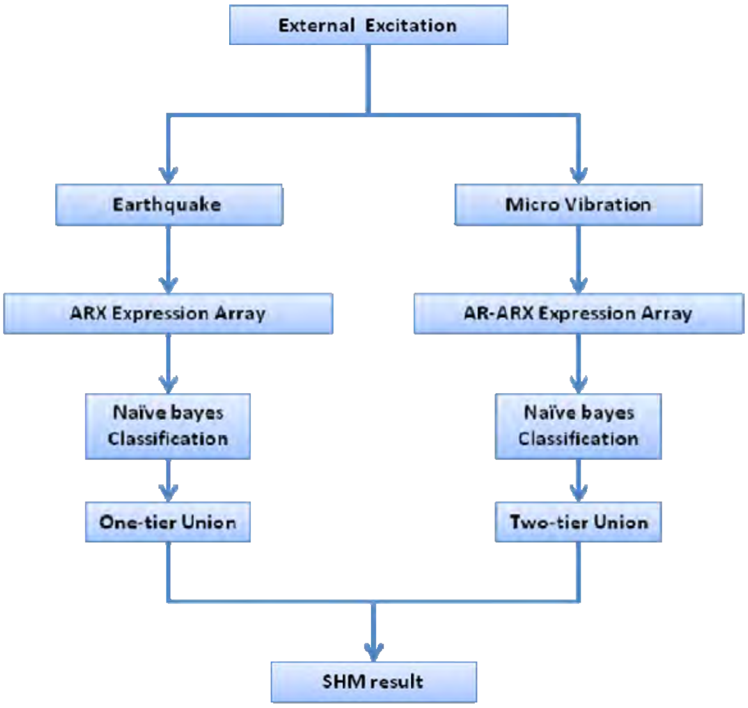

Figure 1: Flowchart of the SHM Algorithm

2.1 THE ARX EXPRESSION ARRAY

The array expression data for earthquake excitation is first extracted using the established ARX model. The measured acceleration response is used in the regression model to precisely describe the behavior of the structure.

For a single-input-single-output (SISO) system, the relationship between the input and output can be expressed as a linear differential equation, given by:

$$y(t)+a_1y(t-1)+\cdots+a_{n_a}y(t-n_a)=b_1u(t-1)+\cdots+b_{n_b}u(t-n_b)+e(t) \tag{1}$$

Where n_a and n_b represent the output and input steps used for regression, respectively.

As $e(t)$ is commonly treated as a random white-noise error in the differential equation, the model is termed the equation error model, and the adjustable parameters can be shown as:

$$\theta = [a_1 \quad a_2 \cdots a_{n_a} \quad b_1 \cdots b_{n_b}]^T \tag{2}$$

By assuming

$$A(q) = 1 + a_1 q^{-1} + \cdots + a_{n_a} q^{-n_a} \tag{3}$$

$$B(q) = b_1 q^{-1} + \cdots b_{n_b} q^{-n_b} \tag{4}$$

The equation can be rewritten as:

$$A(q)y(t) = B(q)u(t) + e(t) \tag{5}$$

The regression model described in equation 5 is a typical example of the ARX model shown in Figure 2 where the AR part is denoted by $A(q)y(t)$, and X is the external input expressed as $B(q)u(t)$. The model becomes a typical AR model if the external excitation X is excluded as depicted in Figure 3, and will be used as a part of the AR-ARX model later on.

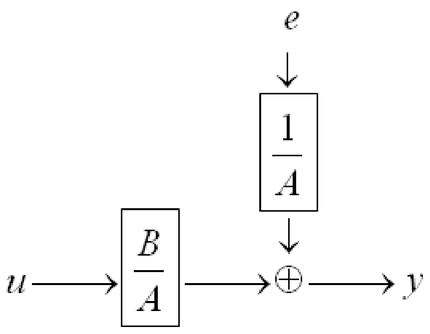

Figure 2:The ARX Model

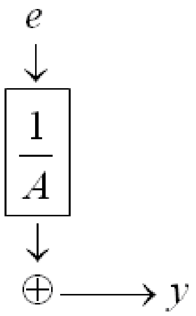

Figure 3:The AR Model

2.2 THE AR-ARX EXPRESSION ARRAY

The array expression data for the micro-vibration mode of the two-mode SHM system is extracted using the two-tier AR-ARX model. As the velocity response of the structure is more sensitive compared to the acceleration under conditions of micro-vibration, it is employed in the regression model. The AR-ARX model is explained briefly below.

The velocity response x(t) is first input to an AR regression model with p terms

$$x(t) = \sum_{j=1}^{p} \phi_{xj} x(t-j) + e_x(t) \tag{6}$$

Where $e_x(t)$ is the white-noise input signal defined as the external excitation of the AR model.

By assuming that the error generated from the model depicted in Figure 2 is the input of equation 7, the model combining these two parts represents the proposed AR-ARX model illustrated in Figure 4. The corresponding equation can be expressed as

$$x(t) = \sum_{i=1}^{n_a} a_i x(t-i) + \sum_{j=1}^{n_b} b_j e_x(t-j) + \varepsilon_x(t) \tag{7}$$

Where $e_x(t)$ is the error generated by the first AR model; n_a and n_b are the order for the input and output, respectively. The coefficients calculated from the AR-ARX model are then used in the micro-vibration mode of the SHM system.

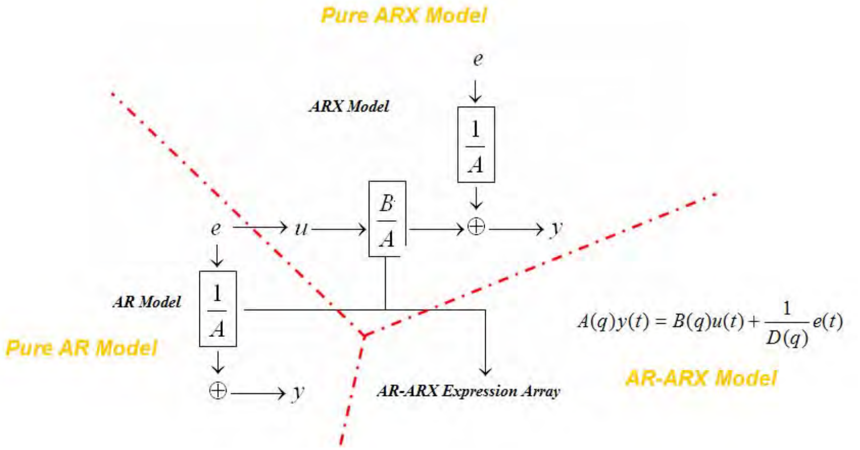

Figure 4:The AR-ARX Model

2.3 THE NAÏVE BAYES (NB) ALGORITHM

The NB algorithm which forms the core of the SHM software is a classification method established on the basics of probability theory. The a posteriori probability is estimated from the prior probability and can be expressed as a conditional probability. The test sample is inputted to the NB algorithm with a Bayes probability distribution defined by two parameters, namely, the mean value and standard deviation to determine the final probability.

The proposed methodology attempts to investigate every coefficient as the DNA of the monitoring structure as opposed to the traditional SHM method, where the health condition is usually determined by only comparing the prediction error of each pre-established regression model. The probability of a specific coefficient of the array expression data is calculated based on the presumed Gaussian distribution for an individual coefficient, which was proven to be easily satisfied. The final damage type is then determined by combining the total probability of the array expression data with the maximum a posteriori probability.

The NB algorithm can be simplified as:

$$Class(x) = \arg\max_{i} \left\{ \sum_{coefficent} \left[\log(\sigma_i^g) + 0.5\left(\frac{x^g - \mu_i^g}{\sigma_i^g}\right)^2 \right] \right\} \tag{8}$$

Where i is the array number of the test sample; μ_i^g is the mean value of class i and gth coefficient; σ_i^g is the standard deviation of class i and gth coefficient, and x^g is the gth coefficient value of the test sample.

3 PRELIMINARY VERIFICATION

To verify the feasibility of the proposed SHM system in a practical structure, a series of experiments were conducted on the eight-storey downscale specimen at the National Center for Research on Earthquake Engineering (NCREE). As shown in Figure 5, eight high-sensitivity velocity meters and eight accelerometers were deployed on the specimen to measure the floor response under micro and earthquake vibration conditions, with the sampling rate set at 200 Hz.

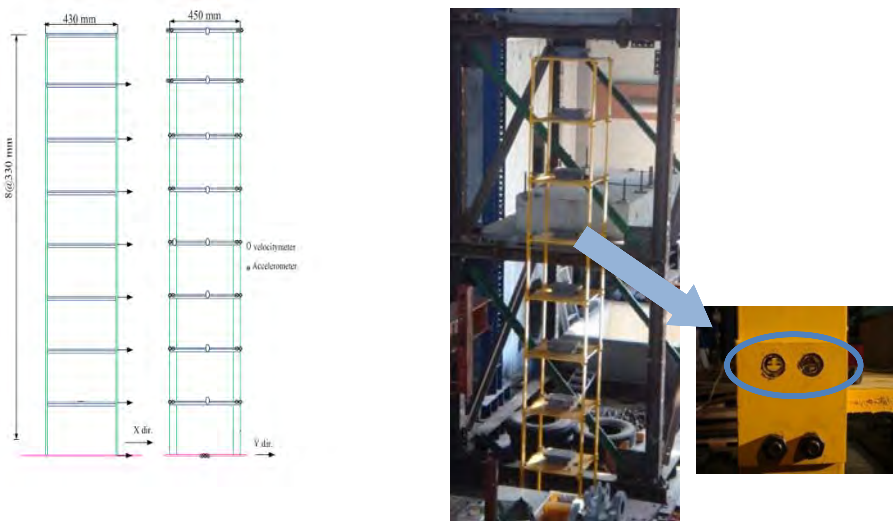

Figure 5:the eight-story SHM Benchmark at NCREE

Signals measured from the ambient vibration in the daily life are first used by the proposed system to enhance its practicability. The structural damages were classified into five major groups for 19 different damage conditions and were simulated by loosening four of the 16 bolts in each floor (1/4 of the beam-column connections). The dataset for the experiment was collected at night to avoid or substantially suppress the unwanted noise arising from machine operation or human activity in the laboratory which aimed to improve the reliability of the structural feature arrays. The 19 damage conditions are listed in Table 1, and 90 time histories each subjected to every damage condition for 20 seconds were recorded. The 19 damage conditions were achieved by switching the location of the loosened fasteners.

Concurrently, the structural response of the benchmark under earthquake excitation conditions was recorded by conducting the shaking table test at NCREE to verify the operation of the earthquake mode of the system. A list of the 11 damage conditions achieved by switching the location of the loosened fasteners is listed in Table 2, and 30 time histories including the 1940 El Centro, 1995 Kobe, TCU 072 and TCU 129 station record of the Chi-Chi earthquake were recorded for different peak ground acceleration (PGA) values for every damage condition.

Table 1: Damage Condition for the Micro-vibration Experiment

Damage Condition Number	Damage Level	Damage Location
1	Undamaged	None
2	Slight	1F
3		2F
4		3F
5		4F
6		5F
7		6F
8		7F
9		8F
10	Moderate	1 & 2F
11		3 & 4F
12		5 & 6F
13		7 & 8F
14	Severe	1 & 2 & 3F
15		4 & 5 & 6F
16		6 & 7 & 8F
17	Extreme	1 & 2 & 3 & 4F
18		5 & 6 & 7 & 8F
19	Ultimate	1-8F

Table 2:Damage Condition for the Earthquake Excitation Experiment

Damage Condition Number	Damage Level	Damage Location
1	Undamaged	None
2	Slight	1F
3		2F
4		3F
5		5F
6		7F
7	Moderate	1 & 2F
8		5 & 6F
9	Severe	1 & 2 & 3F
10		4 & 5 & 6F
11	Ultimate	1 & 2 & 3 & 4F

The micro-vibration mode of the SHM algorithm was first verified. Three fundamental parameters (p, a, and b) of the basic AR-ARX model described in equations 6 and 7, were designed to be 10-8-4 based on the rule of thumb for system identification proposed by Ljung [Ljung, 1986]. The ratio of the coefficients a and b is set to 2, and the optimal value of p is then determined. Ljung suggests that better identification results can be obtained when the sum of a and b is smaller than p. However, better structural behavior can be achieved by adjusting the value of p from 12 to 10 using an optimization process.

The advantage of utilizing array expression data for SHM was also evaluated using three different array orders, namely, 30-24-12、40-32-16， and 50-40-20 based on the format specified above to decipher the optimal array for the system while no significant difference of computation overhead was observed. To enable independent testing of the SHM system, 10 patterns selected from the database were used to verify the system performance. Figure 6 depicts the results of all 19 damage conditions which were obtained from the velocity meter located on the sixth floor (V6). The AR-ARX order increased from 30-24-12 in the top subplot to the final 50-40-20 in the bottom subplot. The 19 damage conditions are indicated in the longitudinal axis as UN, S1, S2, S3, S4, S5, S6, S7, S8, M12, M34, M56, M78, S123, S456, S678, E1234, E5678, and U12345678, where UN represents undamaged; S represents slight damage; M represents moderate damage; S indicates severe damage; E indicates extreme damage and U indicates ultimate damage. The detected damage condition is reflected in the latitudinal bar. The individual bars for each damage condition express all ten testing patterns. The numbers in the longitudinal axis represents the 19 damage conditions, and the diagnosis result is indicated in the latitudinal axis which should correspond to the same value in the X-axis. As demonstrated in Figure 6, the classification success rate can reach 100% by the proposed system for the 50-40-20 form which can be chosen as the optimal array for micro-vibration except damage conditions 3, 6, and 8 where the success rates are 80%, 90%, and 80%, respectively.

The optimal ARX configuration for earthquake excitation conditions was determined using the collected database. Similarly, the two fundamental parameters (a and b) of the basic ARX model described earlier were designed to have a form 8-4. The advantage of utilizing array expression data for SHM was again evaluated using three different array orders, namely, 48-24, 56-28, and 64-32 based on the 8-4 form. Five patterns recorded from the established database were used to verify the system performance. The ARX order was increased from 48-24 in the top subplot, to the final 64-32 form in the bottom subplot. The individual bars, as show in Figure 7, expressed all five testing patterns. The 11 damage conditions are included in the longitudinal axis as UN, S1, S2, S3, S5, S7, M12, M56, S123, S456, and U1234, where UN represents undamaged; S represents slight damage; M indicates moderate damage; S indicates severe damage, and U indicates ultimate damage. Similarly, the latitudinal bar reflects the detected damage condition while the actual damage condition is marked along the longitudinal axis. Structural damage was again correctly predicted by the system for the 64-32 form. The success rates are approximately 60% for damage conditions 8 and 9 and 80% for damage conditions 1, 2, 3, 4, and 7. This array was then chosen to represent the optimal array for earthquake excitation.

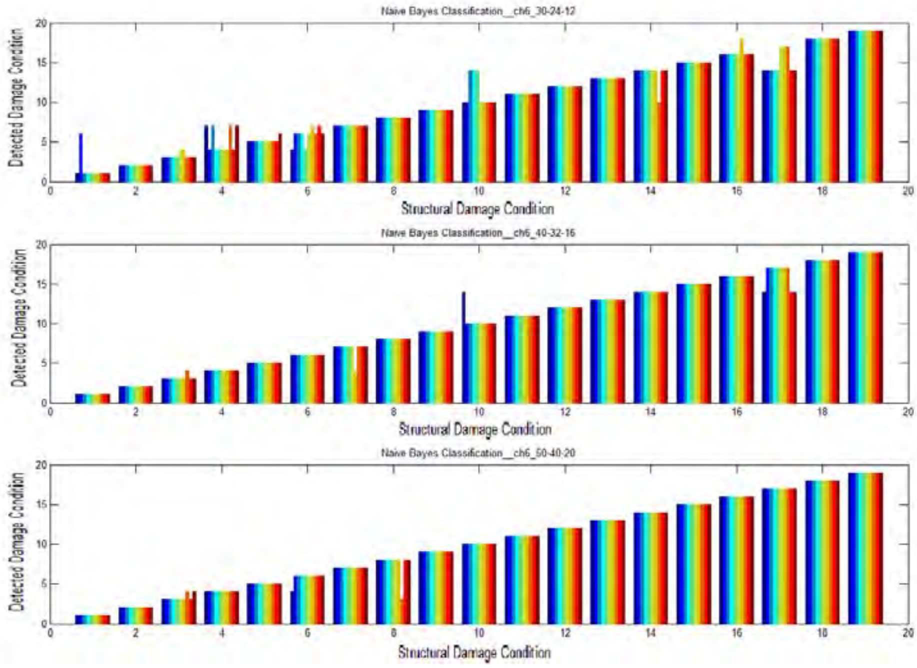

Figure 6:Verification under Micro Vibration

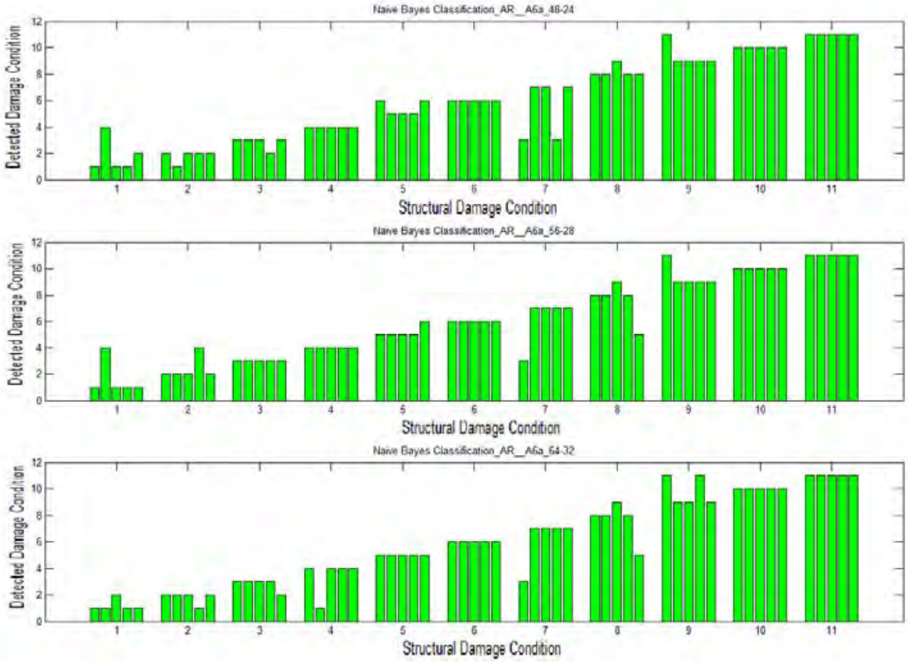

Figure 7:Verification under Earthquake Excitation

The union concept of multi-events or sensors has been introduced to achieve further improvement in the accuracy and reliability of the SHM system. The final SHM result can be determined by choosing the condition with the highest accumulated probability. Since earthquake excitations are infrequent in occurrence, only the union concept with three sensors was applied for earthquake excitation. Simultaneously, the micro-vibration mode was tested using three sensors on their respective floors (6F, 7F, and 8F) in the first union, and the results of these three different events were then combined to obtain a more accurate result. The verification of the two-mode system is summarized as follows: Table 3 shows the results obtained for earthquake excitation, and Table 4 depicts the outcome of the micro-vibration tests.

As shown in Table 3, the diagnosis result for three separate classes of earthquakes indicates almost the same damage condition and only a slight variation was observed for damage conditions 1, 3, 8, and 9. However, the approximate damage condition and location can still be rapidly and correctly determined after the occurrence of an earthquake. In addition, a more precise result can be achieved especially in the micro-vibration detection mode. Only a slight error was observed following the application of the first union of the three sensors, and the second-layer union guaranteed a reliable result. In short, the reliability of the two-mode SHM system has been demonstrated by the preliminary verification tests, indicating that the health condition of the structure under both earthquake excitation and micro-vibration conditions can be accurately detected by the proposed system.

Table 3:SHM result with the Union Concept under Earthquake Excitation Mode

Damage Condition Number	Event 1	Event 2	Event 3
1	1	1	2
2	2	2	2
3	3	2	3
4	4	4	4
5	5	5	5
6	6	6	6
7	7	7	7
8	8	8	9
9	11	9	9
10	10	10	10
11	11	11	11

Table 4:SHM result with the Union Concept under Micro-Vibration Mode

Damage Condition Number	Event 1	Event 2	Event 3	Final result
1	1 (1/1/1)	1 (1/1/1)	1 (1/1/1)	1
2	2 (2/2/2)	2 (2/2/2)	2 (2/2/2)	2
3	3 (3/3/3)	3 (3/3/3)	3 (3/3/4)	3
4	4 (4/4/4)	4 (4/4/4)	4 (4/4/4)	4
5	5 (5/5/5)	5 (5/5/5)	5 (5/5/5)	5
6	6 (4/6/6)	6 (6/4/6)	6 (6/6/6)	6
7	7 (7/7/7)	7 (7/7/7)	7 (7/7/7)	7
8	8 (8/8/8)	8 (8/8/3)	8 (8/8/8)	8
9	9 (9/9/9)	9 (9/9/9)	9 (9/9/9)	9
10	10 (10/10/10)	10 (10/10/10)	10 (10/10/10)	10
11	11 (11/11/11)	11 (11/11/11)	11 (11/11/11)	11
12	12 (12/12/12)	12 (12/12/12)	12 (12/12/12)	12
13	13 (13/13/13)	13 (13/13/13)	13 (13/13/13)	13
14	14 (14/14/14)	14 (14/14/14)	14 (14/14/14)	14
15	15 (15/15/15)	15 (15/15/15)	15 (15/15/15)	15
16	16 (16/16/16)	16 (16/16/16)	16 (16/16/16)	16
17	17 (17/17/17)	17 (17/17/17)	17 (17/17/17)	17
18	18 (18/18/18)	18 (18/18/18)	18 (18/18/18)	18
19	19 (19/19/19)	19 (19/19/19)	19 (19/19/19)	19

As mentioned above, the performance of the proposed SHM system has been successfully demonstrated in dealing with damage conditions included in the system repository. However, it is impossible to include all possible damage conditions and structure locations into the SHM database. To verify the robustness of the proposed SHM algorithm, the system was examined by utilizing several damage conditions excluded from the original database. It is expected that the approximate damage condition and location can be detected.

Three damage conditions from both the micro-vibration and earthquake excitation modes were considered, and the rest damage conditions in Tables 1 and 2 were renumbered. For the micro-vibration mode, conditions selected included slight damage on the 5th floor, moderate damage on the 3rd and 4th floors, and severe damage on the 4th& 5th& 6th floors. For the earthquake excitation mode, slight damage on the 7th floor, moderate damage on the 5th and 6th floors, and severe damage on the 4th, 5th, and 6th floors were chosen as the test conditions. The array expression data was input to the SHM algorithm to determine the corresponding damage condition. As shown in Figure 8, the detected damage conditions are indicated by conditions 5, 9 and 12 which reflect the damage condition closest to the actual damage condition with an accuracy of 100%, 70%, and 60%, respectively. Meanwhile, the damage conditions for the earthquake excitation mode shown in Figure 9 were found to be condition 5, 6, and 7 with an accuracy of 80%, 70%, and 70%, respectively. These results strongly support the reliability of the proposed SHM algorithm for use in practical applications wherein the most likely damage condition can be approximated by utilizing the inherent interpolation or extrapolation capability.

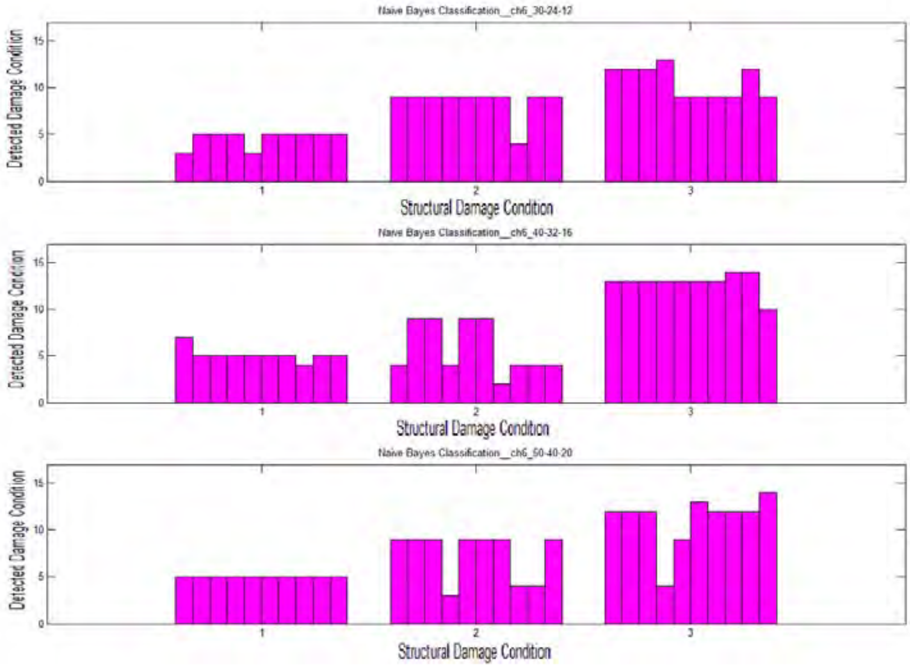

Figure 8:Verification of Unknown Damage Condition under Micro Vibration

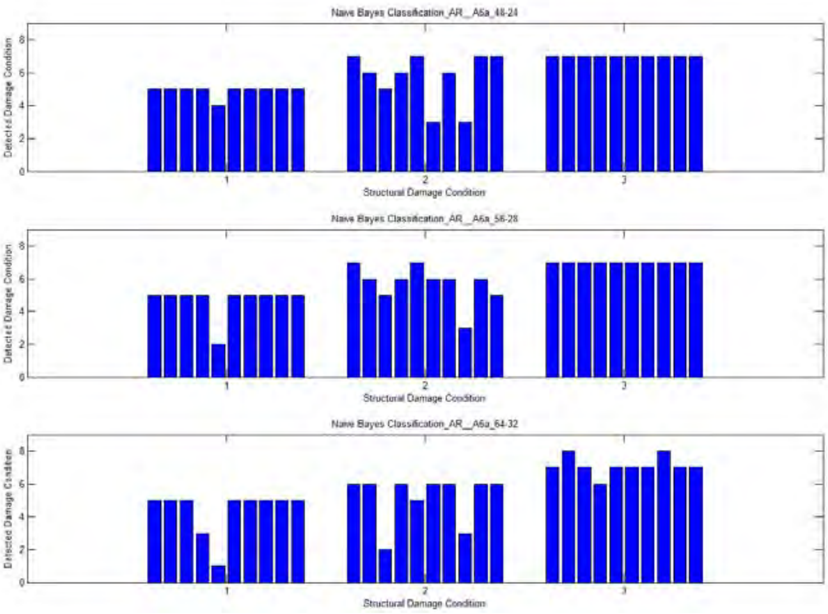

Figure 9:Verification of Unknown Damage Condition under Earthquake Excitation

4 MOBILE SHM PROTOTYPE

In order to implement the bio-inspired SHM system practically, a mobile SHM prototype was developed. As shown in Figure 10, the SHM prototype is composed of three fundamental parts including the sensing input module, the SHM platform for instrumentation and data processing, and the general packet radio service (GPRS) transmission module for conveying the final results to the remote server. To further enhance the mobility of the SHM prototype, a customized silver module depicted in Figure 10 is used for voltage stabilization and power regulation of the sensing unit and data processing center. The vibration data is first measured by the deployed sensor and is subsequently transmitted through the input module to the built-in microprocessor. The acceleration and velocity of the structure are both measured simultaneously to evaluate its structural health condition. In addition, by connecting multiple SHM prototypes, the system can be extended to form a SHM network.

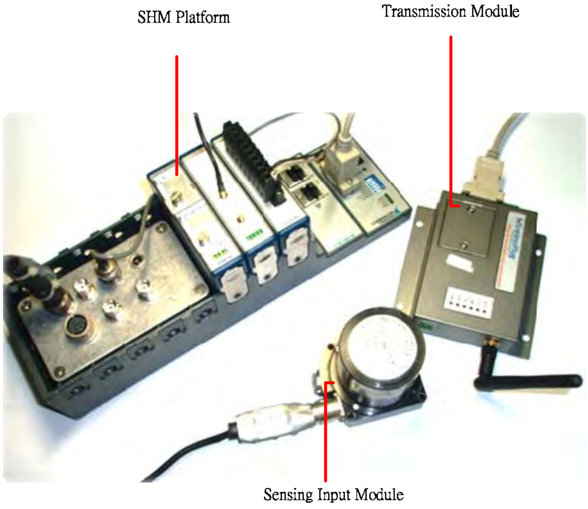

Figure 10:he SHM Prototype

The details of the customized sliver module are shown in Figure 11. A total of seven connectors are mounted in the box. Both the velocity meter and the accelerometer can be connected to the two sensor connectors located in the rightmost column for different applications. For the micro-vibration mode, two measurement resolutions can be selected by using the built-in 10 V / Kine or 1 V / Kine converters. Up to 16 sensors can be powered simultaneously by the customized unit. In addition, two optional modules, a GPS module, and a memory card module for depositing the collected raw data can be installed adjacent to the input module. These two modules enable an easy extension of the functionality and mobility of the platform.

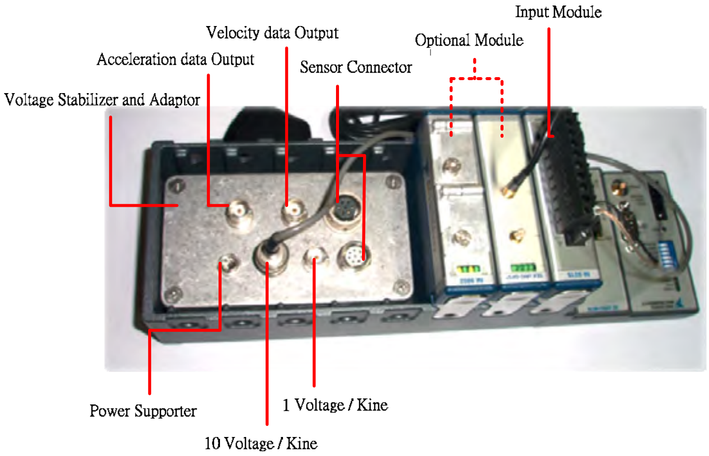

Figure 11:he SHM Monitoring Platform

In order to correctly execute the proposed algorithm in the prototype, the SHM algorithm is incorporated in the firmware of the mobile module. The corresponding software can be divided into two parts: the onsite program in the SHM platform and the demonstration program in the remote server where all the structure damage information is collected and displayed. As shown in Figure 12, the on-site program is subdivided into four parts: Data Pre-Processing, Coefficient Extraction, Health Condition Diagnosis, and GPRS & Wireless Module.

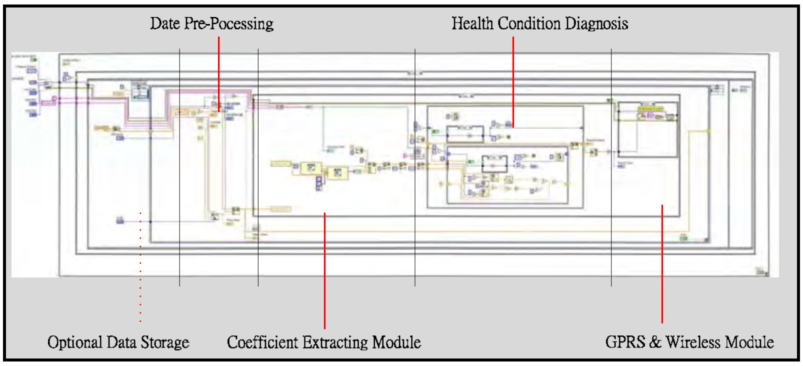

Figure 12:he On-Site Program

4.1 DATA PRE-PROCESSING

The Pre-Processing program performs three main functions: input data collection, digital filter design, and data size adjustment/setting for SHM processing. The use of the Pre-Processing program helps to eliminate the undesired noise successfully from the ambient environment to ensure clarity in the input data. In this study, the data sample rate was selected as 200 Hz, and a band-pass filter was chosen to filter out the unwanted high and low frequency sets of 90 Hz and 0.1 Hz. This also helped to eliminate errors arising from the voltage conversion between the analog and digital signals to enable accurate collection of desired data.

4.2 COEFFICIENT EXTRACTION MODULE

The Coefficient Extraction module was designed based on the two proposed SHM algorithms. In this study, the ARX and AR-ARX models are first established and then implemented with the desired order of settings. The Coefficient Extraction module assists in transforming the time history of the structural responses into array form quickly, and the damage condition of the structure can subsequently be evaluated in the next stage by making a comparison between the damage data and the collected database.

4.3 HEALTH CONDITION DIAGNOSIS

The condition and location of the structural damage are determined by the embedded NB-based SHM algorithm. By making a comparison between the arrays calculated from the previous block and the stored database, the probability of occurrence of all damage conditions for either earthquake excitation or micro-vibration modes is estimated by a designated loop, which subsequently enables the detection of the location and condition of the structural damage.

4.4 GPRS & WIRELESS MODULE

In order to achieve the goal of real-time monitoring following the analysis and classification of the damage, the GPRS Module is used to transfer the data back to the monitoring server. To ensure the security of the data being transmitted, it is encrypted. In this study, a technique to safely encrypt and decrypt the data by adding an initial AA string at the beginning of data transmission chain was developed. Only data with are equipped with this characteristic will then be received.

The mobile SHM prototype can be applied to real life structures by combining the software and hardware described above. The mobile SHM prototype has been designed to classify the structural damage condition within a span of one minute.

5 PRACTICAL VERIFICATION

The performance of the SHM prototype was tested using experimental verification. The eight-storey downscaled benchmark mounted on the shaking table at NCREE was used as the practical test structure. Structural damage testing was simulated by loosening four bolts on the third floor which represented damage condition 4. The response under both ambient and earthquake vibration modes was measured using the top three sensors (6F, 7F, and 8F) deployed on the structure.

By comparing the AR-ARX and ARX array obtained from the vibration data with the database deposited in the on-site SHM prototype, the structural health condition can be immediately evaluated. In addition, to demonstrate the feasibility of remote monitoring, the server was chosen at the headquarters of the National Science Council (NSC), and the health condition of the structure was immediately transmitted by the GPRS service, since the proposed SHM system only requires a small bandwidth. The locations of the benchmark and the monitoring server are shown in Figure 13.

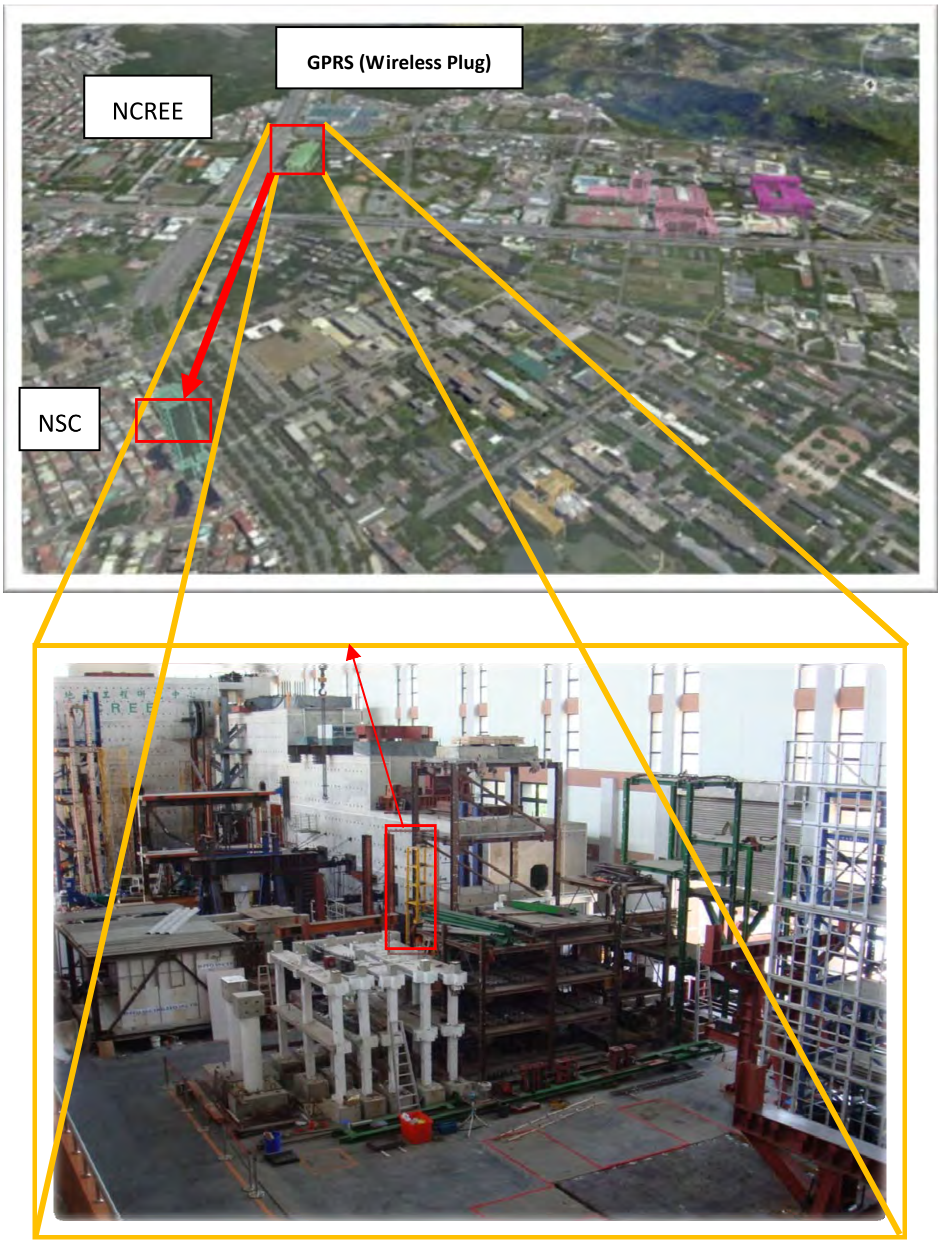

Figure 13:ocation of the benchmark and the monitoring server

The result from real-time monitoring is shown in Figure 14. It shows that SHM results can be determined by either the earthquake mode or the micro-vibration mode. The switching criterion between these two modes is set to enable an acceleration of 5 gal. If the largest measured acceleration is less than 5 gal, the structural response is measured and processed every 20 seconds, and the results are displayed sequentially in the top left-hand portion of the figure. The numbers shown in the panel represent the classification result. As mentioned in the previous section, to avoid false alarms in practical applications, the SHM algorithm operates three times a minute with the two-layer union concept to determine the condition and location of the structure damage as depicted in Figure 14. The damage level of the structure is either none, slight, moderate, severe, extreme, or ultimate, and is shown in the middle of the figure. The detected damage location is highlighted on the structure. In addition, the SHM system was also tested by shaking the benchmark structure under earthquakes. The earthquake mode was launched once the detected acceleration value became greater than 5 gal. The union result from the three different sensors is shown in the bottom-left hand corner of Figure 14. The experiment result clearly demonstrated that both the damage condition, which was slight, and the location, i.e. the third floor, could be detected with precision by the two-mode SHM system.

In addition, not only can real-time structural damage be monitored by the mobile SHM prototype, the embedded parameters can also be remotely controlled. This flexible monitoring design can make the SHM system an optimal system for facilitating varied conditions and permit the immediate evaluation of any structural damage. Characteristics like high mobility and prompts on-site processing of the proposed mobile SHM system have finally been implemented.

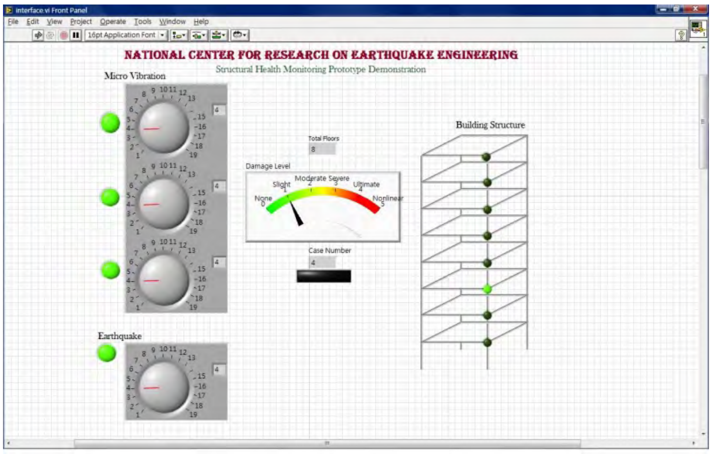

Total Floors 8

Case Number 4

Figure 14:he Real-Time Monitoring Interface

6 SUMMARY AND CONCLUSION

A bio-inspired two-mode structural health monitoring (SHM) system based on the Naïve Bayes (NB) classification method was presented in this paper. Since research focus on the bio-inspired concept for engineering has only recently evolved, a novel SHM algorithm utilizing the array expression data of the Deoxyribonucleic acid (DNA) of the structures was developed. Based on the vibration mode, the proposed SHM algorithm can switch between a two-tier AR-ARX process for micro-vibration and an ARX process for earthquake excitation. The health condition of the structure is then determined by classifying the obtained array expression data using the NB method. Moreover, the union concept in probability was introduced to improve the accuracy of the system.

To verify the performance and reliability of the SHM algorithm, a downscaled eight-storey steel building located at the shaking table of NCREE was used as the benchmark structure. The structural damage was simulated by loosening four of the 16 bolts in each floor (1/4 of the beam-column connection). The structural response was then determined for different damage levels and locations for inclusion in the structural health monitoring database. Experimental results have demonstrated that the approximate condition and location of the damage can be quickly determined immediately after the occurrence of an earthquake. A more precise result can be achieved in the micro-vibration detection mode.

To implement the proposed SHM system in a practical application, a SHM prototype consisting of three individual modules namely, the input sensing module, the transmission module, and the SHM platform was developed. The employed sensor first measures the structural response, and subsequently, the SHM mode corresponding to the excitation is chosen automatically by the system to rapidly evaluate the health condition of the structure using a preset criterion. Test results from the ambient vibration and shaking table test have shown that the condition and location of the benchmark structure damage can be successfully monitored by the SHM prototype system and can be instantly transmitted to a remote server to facilitate real-time monitoring.

Implementing the bio-inspired two-mode SHM practically has been demonstrated in this paper. The bio-inspired concept is made possible by the successful integration of software and hardware. With its unique mobility and powerful processing capacity, it is expected that the proposed SHM system can be applied to SHM networks in practical applications in the near future.

REFERENCES

[1] Hickman, G.A.; Gerardi, J.J.; Feng, Y., 1991. Application of smart structures to aircraft health monitoring, Journal of Intelligent Material Systems and Structures, v 2, n 3, p 411-430.

[2] Aktan, A.E.; Helmicki, A.J.; Hunt, V.J., 1998. Issues in health monitoring for intelligent infrastructure, Smart Materials and Structures, v 7, n 5, p 674-92.

[3] Pines, D.J.; Lovell, P.A., 1998. Conceptual framework of a remote wireless health monitoring system for large civil structures, Smart Materials and Structures, v 7, n 5, p 627-36.

[4] Tanner, N.A.; Wait, J.R.; Farrar, C.R.; Hoon Sohn, 2003. Structural health monitoring using modular wireless sensors, Journal of Intelligent Material Systems and Structures, v 14, n 1, p 43-56.

[5] Wang, Yang; Lynch, Jerome P.; Law, Kincho H., 2007. A wireless structural health monitoring system with multithreaded sensing devices: Design and validation, Structure and Infrastructure Engineering, v 3, n 2, p 103-120.

[6] Lynch, Jerome Peter; Law, Kincho H.; Kiremidjian, Anne S.; Carryer, Ed.; Farrar, Charles R.; Sohn, Hoon; Allen, David W.; Nadler, Brett; Wait, Jeannette R., 2004. Design and performance validation of a wireless sensing unit for structural monitoring applications, Structural Engineering and Mechanics, v 17, n 3-4, p 393-408.

[7] Buckner, B.D.; Markov, V.; Li-Chung Lai; Earthman, J.C., 2008. Laser-scanning structural health monitoring with wireless sensor motes, Optical Engineering, v 47, n 5, p 1-9.

[8] Zimmerman, Andrew T.; Shiraishi, Michihito; Swartz, R. Andrew; Lynch, Jerome P., 2008. Automated modal parameter estimation by parallel processing within wireless monitoring systems, Journal of Infrastructure Systems, v 14, n 1, p 102-113.

[9] Mascarenas, David D.L.; Flynn, Eric B.; Todd, Michael D.; Overly, Timothy G.; Farinholt, Kevin M.; Park, Gyuhae; Farrar, Charles R., 2010. Development of capacitance-based and impedance-based wireless sensors and sensor nodes for structural health monitoring applications, Journal of Sound and Vibration, v 329, n 12, p 2410-2420.

[10] Boller, C., 2000. Next generation structural health monitoring and its integration into aircraft design, International Journal of Systems Science, v 31, n 11, p 1333-49.

[11] Hu, N.; Wang, X.; Fukunaga, H.; Yao, Z.H.; Zhang, H.X.; Wu, Z.S., 2001. Damage assessment of structures using modal test data, International Journal of Solids and Structures, v 38, n 18, p 3111-3126.

[12] Johnson, T.J.; Brown, R.L.; Adams, D.E.; Schiefer, M., 2004. Distributed structural health monitoring with a smart sensor array, Mechanical Systems and Signal Processing, v 18, n 3, p 555-72.

[13] Hera, Adriana; Hou, Zhikun, 2004. Application of wavelet approach for ASCE structural health monitoring benchmark studies, Journal of Engineering Mechanics, v 130, n 1, p 96-104.

[14] Udwadia, Firdaus E.; Proskurowski, Wlodek, 1998. A memory-matrix-based identification methodology for structural and mechanical systems, Earthquake Engineering and Structural Dynamics, v 27, n 12, p 1465-1481.

[15] Zhang, Jian; Sato, Tadanobu; Iai, Susumu, 2006. Support vector regression for on-line health monitoring of large-scale structures, Structural Safety, v 28, n 4, p 392-406, September

[16] Carden, E.P.; Brownjohn, J.M.W., 2008. ARMA modelled time-series classification for structural health monitoring of civil infrastructure, Mechanical Systems and Signal Processing, v 22, n 2, p 295-314.

[17] Sohn, Hoon; Czarnecki, Jerry A.; Farrar, Charles R., 2000. Structural health monitoring using statistical process control, Journal of structural engineering New York, N.Y., v 126, n 11, p 1356-1363.

[18] Sohn, Hoon; Farrar, C.R., 2001. Damage diagnosis using time series analysis of vibration signals, Smart Materials and Structures, v 10, n 3, p 446-51.

[19] L. Ljung, “System Identification: Theory for the User”, Prent-Hall, Inc. Upper Saddle River, NJ, USA, 1986.

[20] T.R. Golub, D.K. Slonim, P. Tamayo, C. Huard, M. Gaasenbeek, J.P. Mesirov, H. Coller, M.L. Loh, J.R. Downing, M.A. Caligiuri, C.D. Bloomfield and E.S. Lander, “Molecular Classification of Cancer: Class Discovery and Class

Prediction by Gene Expression Monitoring", Science 15, Vol. 286. no. 5439, pp. 531-537, 10.1126/science.286.5439.531, October 1999.

[21] Donna K. Slonim, Pablo Tamayo, Jill P. Mesirov, Todd R. Golub and Eric S. Lander, "Class Prediction and Discovery Using Gene Expression Data", Annual Conference on Research in Computational Molecular Biology, Proceedings of the 4th annual international conference on Computational molecular biology, pp. 263-272, 1-58113-186-0, Tokyo, Japan, 2000.

COMPDYN 2011
3rd ECCOMAS Thematic Conference on
Computational Methods in Structural Dynamics and Earthquake Engineering
M. Papadrakakis, M. Fragiadakis, V. Plevris (eds.)
Corfu, Greece, 25–28 May 2011

COMBINATION COEFFICIENTS FOR YIELDING STRUCTURES UNDER TRI-DIRECTIONAL EARTHQUAKE EXCITATIONS

Haluk Sesigur[1], Oguz C. Celik[2], and Feridun Cili[3]

[1,2,3]Istanbul Technical University, Faculty of Architecture, Division of Theory of Structures
34437, Taskisla, Taksim, Istanbul, Turkey
e-mail: {haluk, celikoguz, cilif}@itu.edu.tr

Keywords: Spectrum Intensity, Inelastic Velocity Response Spectrum, Combination Rules.

Abstract. *Seismic regulations and guidelines for buildings and bridges prescribe simplified combination rules to obtain the maximum structural response under multi-directional earthquake effects. An unfavorable internal force usually develops under the combined effects of an earthquake motion. This study uses the spectrum intensity concept to investigate the tri-directional effects of earthquakes on structures. For this purpose, a set of recent and past thirteen earthquakes (M>6) are selected to predict tri-directional effects. Inelastic velocity response spectra for these earthquakes are numerically obtained and plotted for damping ratios of* ξ*=0.05 and 0.20, representing a wide range of damped and heavily damped (e.g. base isolated) structures. Spectrum intensities for both orthogonal and vertical directions and for the resultant direction are calculated using a computer program developed for this purpose. Unfavorable response is then calculated by equating the resultant spectrum intensity to principle direction's intensity plus the other direction's contribution as a percentage of the principle component, or equating the resultant spectrum intensity to principle direction's intensity plus a percentage of the other direction's contribution, or vice versa. The results obtained are strongly earthquake-dependent. Based on the proposed analysis way, well-known building regulations are reviewed and evaluated by emphasizing the prescribed combination rules. Numerical results show that coefficients for the tri-directional contribution varies largely in the range between 0.01~0.68 for the selected force reduction factors of* μ*=2 and 8, revealing that in some cases the code defined combination values may yield unconservative seismic designs.*

1 INTRODUCTION

Since analysis of structures under all possible angles of earthquake excitations is complex and time consuming, simplified combination rules have been developed for practical design purposes. Elastic forces and displacements are calculated based on the combination coefficients proposed by existing building codes. A structural design without considering the orthogonal earthquake effects may generally result in insufficient member dimensions, as an unfavorable internal force distribution in the structural elements would usually develop under the combined effects (bi-directional or tri-directional) of an earthquake strong ground motion.

As a common approach, the square- root-of-sum-of-squares (SRSS) procedure is based on the assumption that the actions on an element affected by earthquake excitations in two and three directions are combined. With the help of elastic velocity response spectra, Sesigur, Celik, and Cili [1,2] proposed a way of analysis for the bi-directional and tri-directional effects of earthquakes using the characteristics of the selected earthquakes. The 30% and 40% rules are simplified approximations to the SRSS and the CQC methods. Many current design codes [3 to 7] for buildings and bridges require that members should be designed for 100 percent of the seismic forces in one direction plus 30 percent of the seismic forces in the perpendicular direction (the 30% rule). ATC-32 [6] requires the 40 percent rule to be used in the design of bridges under bi-directional effects. In order to investigate the bi-directional effects of inelastic response of single degree of freedom (SDOF) structures, Sesigur, Celik, and Cili [8] presented some design recommendations.

For yielding/inelastic structures, the present study essentially aims to extend the bi-directional analysis way developed in [8] to tri-directional earthquake effects. As before, inelastic velocity response spectrum and the spectrum intensity concept (SI_H) corresponding to inelastic velocity response spectrum is used. Finally, numerical values for the combination coefficients are proposed and compared with code-defined values.

2 METHOD OF ANALYSIS

Since the velocity response spectrum is a powerful tool for estimating the damage potential of structures in the medium and long period range, the analysis method called as the spectrum intensity concept as proposed in [8] will be followed here for inelastic structures. The inelastic velocity response spectrum is obtained following the standard procedure given by Newmark [9]. The average acceleration method is used for nonlinear response analysis of SDOF system, taking $\gamma=1/2$ and $\beta=1/4$. The time step Δt is chosen as 0.02 to detect accurately the transitions from unloading to loading branches or around sharp corners of the force-deformation curves. Force-deformation relation is considered as a cyclic ideal elasto-plastic curve. Inelastic analysis is carried out by the force reduction factors of $\mu=2$ and 8, representing significantly rigid (e.g. masonry) and ductile structures (e.g. steel or RC).

Housner introduced a measure of ground motion intensity which defines the integral of the velocity response spectrum over a period range from T_1 to T_2 as the spectrum intensity (1) where SI, ξ, T, and S_v are intensity, damping ratio, fundamental period of the structure and the ordinate of the velocity spectrum respectively. T_1 and T_2 are proposed as 0.10~0.50sec and 2.50~5.00sec. This integral can be evaluated for any desired damping ratio (note that Housner recommended using $\xi=0.20$); however, to clarify the impact of damping ratio on the evaluation of this integral, damping ratios of $\xi= 0.05$ and 0.20 are chosen.

$$SI = \int_{T_1}^{T_2} S_V(\xi, T, t)\,dT \tag{1}$$

For near-fault ground motions ($L \leq 15$ km, T_0 (fundamental period of soil) ≈ 0.20sec, near the epicenter, stiff soil conditions and minimum focal depth is H=30km), one component of the spectrum intensity might be negligible, and the other could be significant, (e.g. the 10.18.1989 Loma Prieta and the 01.17.1994 Northridge earthquakes). For the far-field motions (L=40~50km, stiff soil conditions, $T_0 \approx$ 0.05~0.50sec and 2.50~6.00sec), if the horizontal components of the intensities are close to each other then both components must be taken into account, (e.g. the 05.18.1940 El-Centro earthquake). For the earthquakes with a long period, the unfavorable conditions occur in the resultant direction, (e.g. the 07.06.1964 Mexico-City earthquake). Table 1 presents the data of thirteen recorded accelerograms used in the present study. Three earthquakes that greatly affected populated areas in Turkey are also chosen.

Event	Date	Station	M	a_{max} (T)	a_{max} (L)	a_{max} (V)
El Centro	05.19.1940	El Centro	Ms=7.2	306.9	210.7	201.3
Parkfield	06.27.1966	Cholame	ML=6.1	433.2	360.0	135.5
Tokachi-Oki	05.16.1968	Hachinoe Harbour	M=7.9	229.6	180.2	114.2
San Fernando	02.09.1971	Pacoima Dam	Ms=6.6	1202.6	1137.5	685.3
Miyagi Ken Oki	06.12.1978	Tohoku University	M=7.4	258.1	203.4	152.8
Tabas	09.16.1978	Tabas	Ms=7.4	819.9	835.6	675.4
Loma Prieta	10.18.1989	Capitola	Ms=7.1	559.0	595.7	878.6
Erzincan	03.13.1992	Erzincan	M=6.9	505.5	486.1	243.0
Northridge	01.17.1994	Sylmar-Olive View	Ms=6.7	592.6	826.8	525.0
Kobe	01.16.1995	Takarazu	M=6.9	680.3	680.4	425.1
Kocaeli	08.17.1999	Yarimca	Mw=7.2	322.2	230.2	241.1
Chi-Chi	09.20.1999	CHY028-N	Ms=7.6	805.9	590.4	330.9
Duzce	11.12.1999	Bolu	Mw=7.2	713.8	806.8	198.7

Table 1. Characteristics of the selected earthquakes

In some cases, the third component (i.e. the vertical component) of an earthquake could be of great importance. For example, large span cantilevered or other structures or structures having beams or cantilevers that support heavy vertical (gravity) column loading, and structures with irregularities in elevation might be critical under the effect of vertical component of an earthquake.

As explained in [8], under tri-directional earthquake excitations and under elastic conditions, the unfavorable response of a structure could be calculated in two alternative ways: The first way is to equate the resultant spectrum intensity to principle direction's intensity plus the other direction's (i.e. the other horizontal and vertical directions) equal contributions (α) as a percentage of the principle component. The second way would be to equate the resultant spectrum intensity to principle direction's intensity plus other components' unequal contributions (i.e. λ_1 for the other horizontal component and λ_2 for the vertical component) as a percentage of the principle direction's intensity. α, λ_1, and λ_2 have numerically been calculated for each of the selected earthquake data. These coefficients can then be implemented in the combination rules to obtain the maximum response parameters. Apparently, numerical values are expected to be earthquake-dependent.

This analysis procedure will be generalized here for both tri-directional earthquake excitations and yielding/inelastic structures. A single degree of freedom (SDOF) system subjected to tri-directional strong ground motions and the evaluation of velocity spectrum intensities are illustrated in Figure 1.

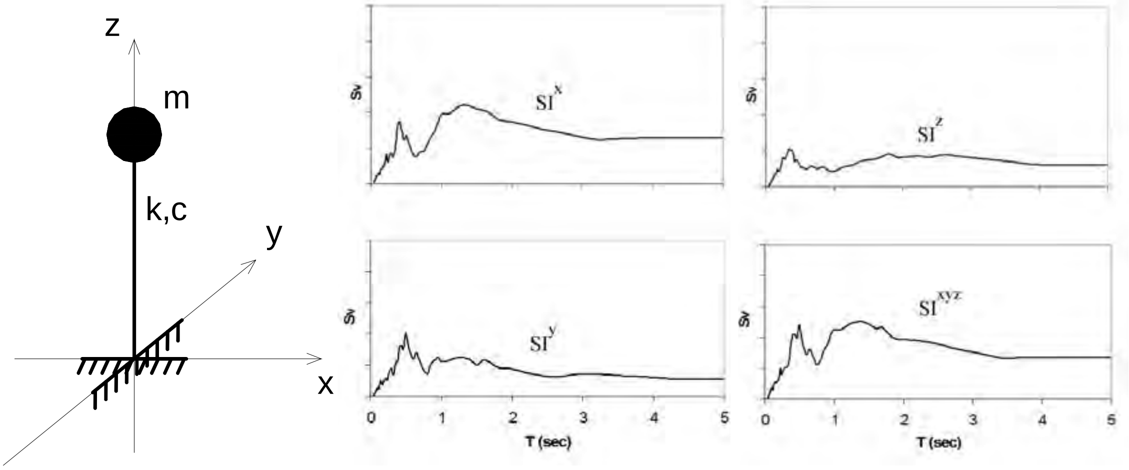

Figure 1. Single degree of freedom system under tri-directional earthquake excitation and spectrum intensities for each component and resultant

Here, x indicates the earthquake direction that produces maximum internal forces in the system. Spectrum intensities for both orthogonal and vertical directions as well as for the resultant (i.e. the unfavorable) direction are defined as SI^x , SI^y , SI^z and SI^{xyz}, respectively. Depending on these numerically obtained values, the above mentioned coefficients can then be calculated using the following equations:

$$\alpha=0.5(SI^{xyz}/SI^{x}-1) \tag{2}$$

$$\lambda_1=(SI^{xyz}/SI^{x})-(1+\lambda_2) \tag{3}$$

$$\lambda_2=(SI^{xyz}/SI^{x})-(1+\lambda_1) \tag{4}$$

For a given ground motion, the resultant inelastic velocity response ($\dot{x}_r(t)$) of a SDOF system can be calculated using the square root of the squares of each orthogonal component's contributions ($\dot{x}_1(t), \dot{x}_2(t), \dot{x}_3(t)$) as follows:

$$\dot{x}_r(t)=\sqrt{\left|\dot{x}_1(t)\right|^2+\left|\dot{x}_2(t)\right|^2+\left|\dot{x}_3(t)\right|^2} \tag{5}$$

The maximum values of the above equation for a given damping ratio and natural vibration period give the ordinates of the resultant velocity spectra. This is shown in (6).

$$(S_v)_r=\left|\dot{x}_r(t)\right|_{\max} \tag{6}$$

3 COMPUTER PROGRAM

To carry out the numerical computations, a special computer program that accepts strong ground motion data for the three components of the selected earthquakes, damping ratios, natural vibration periods, and mass as input, was coded. A flow-chart of the program is given in Figure 2. Both elastic and inelastic spectrum intensities are then calculated for the three orthogonal and resultant directions. Inelastic velocity response spectra for the selected earthquakes are numerically obtained and plotted for damping ratios of ξ=0.05 and 0.20, representing a wide range of damped and heavily damped like base isolated buildings or buildings with viscous or other type of dampers.

A similar way that was followed in the computation of spectrum intensities can be used in obtaining the maximum internal forces (E_{xyz}) in a structural member under tri-directional effects. This can be evaluated by the internal forces developed in the principal direction (E_x) plus the other direction's (both the other horizontal and vertical) contributions (λ_1, λ_2). For this purpose, α, λ_1, and λ_2 obtained through the spectrum intensity concept can be used:

$$E_{xyz} = E_x + \lambda_1 E_x + \lambda_2 E_x \tag{7a}$$

$$E_{xyz} = \lambda_1 E_y + E_y + \lambda_2 E_y \tag{7b}$$

These equations and coefficients are actually defined in Eurocode 8 [5] to take into account the tri-directional earthquake effects on structures. λ_1 and λ_2 are proposed as 0.30. On the other hand, for design purposes, the equal contributions of the other components can also be taken into account as given in (7c). Therefore, α coefficient is of special interest to evaluate the combination rules in structural codes.

$$E_{xyz} = E_X + 2\alpha E_X \tag{7c}$$

For the selected earthquake ground motions (a total of thirteen), inelastic velocity response spectra for each of the orthogonal, vertical directions and for the resultant direction are shown in Figure 3, following the procedure summarized above. Also, Figure 4 shows hysteretic curves of the elasto-plastic SDOF systems for selected earthquakes. α, λ_1, and λ_2 are numerically calculated for each of the selected earthquakes and the results are also summarized in Table 2. If λ_1 is considered as a value of 0.30 (as given in many codes), λ_2 is generally obtained as negative values that can be interpreted as the %30 rule is sufficient on the basis of spectrum intensity concept followed in this work. Therefore, the contribution of the vertical component may be neglected in most cases.

4 MULTI-COMPONENT COMBINATION RULES IN CURRENT CODES

Most design codes that address the multi-component ground motion problem, specify that the contributions to a response quantity from the orthogonal components of seismic input be combined either by the square root of sum of squares (SRSS) rule or by a percentage rule. The 30% rule is a linear approximation of the combined response. The 40% rule is also a linear approximation recommended for the analysis of nuclear and bridge structures in the ATC-32. The SRSS and 30% rules are prescribed in Eurocode 8.

The unfavorable earthquake loads are produced by the following combinations.

$$E_x,\ \lambda E_y,\ \mu E_z$$
$$\lambda E_x,\ E_y,\ \mu E_z$$
$$\lambda E_x,\ \lambda E_y,\ E_z$$

Here, E_x, E_y and E_z are internal forces developed during an earthquake loading. For practical design purposes, the λ and μ coefficients are chosen as 0.30 and 0.20 respectively. The UBC97 requires the use of either the SRSS rule or the 30% rule, but only for structures having certain types of irregularities. The current (Caltrans) bridge design specifications require the 30% rule for all structures.

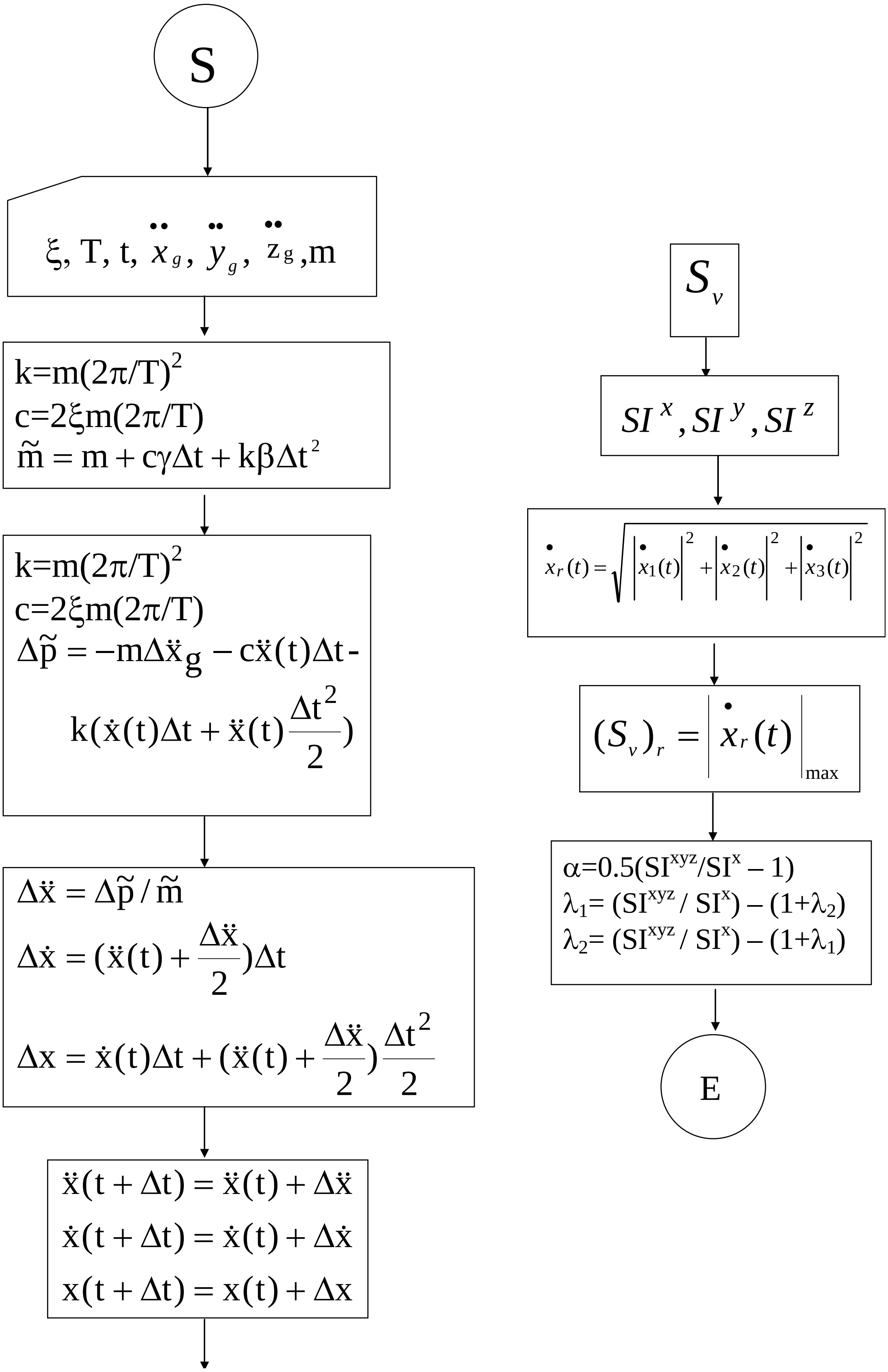

Figure 2. Flow-chart of the computer program

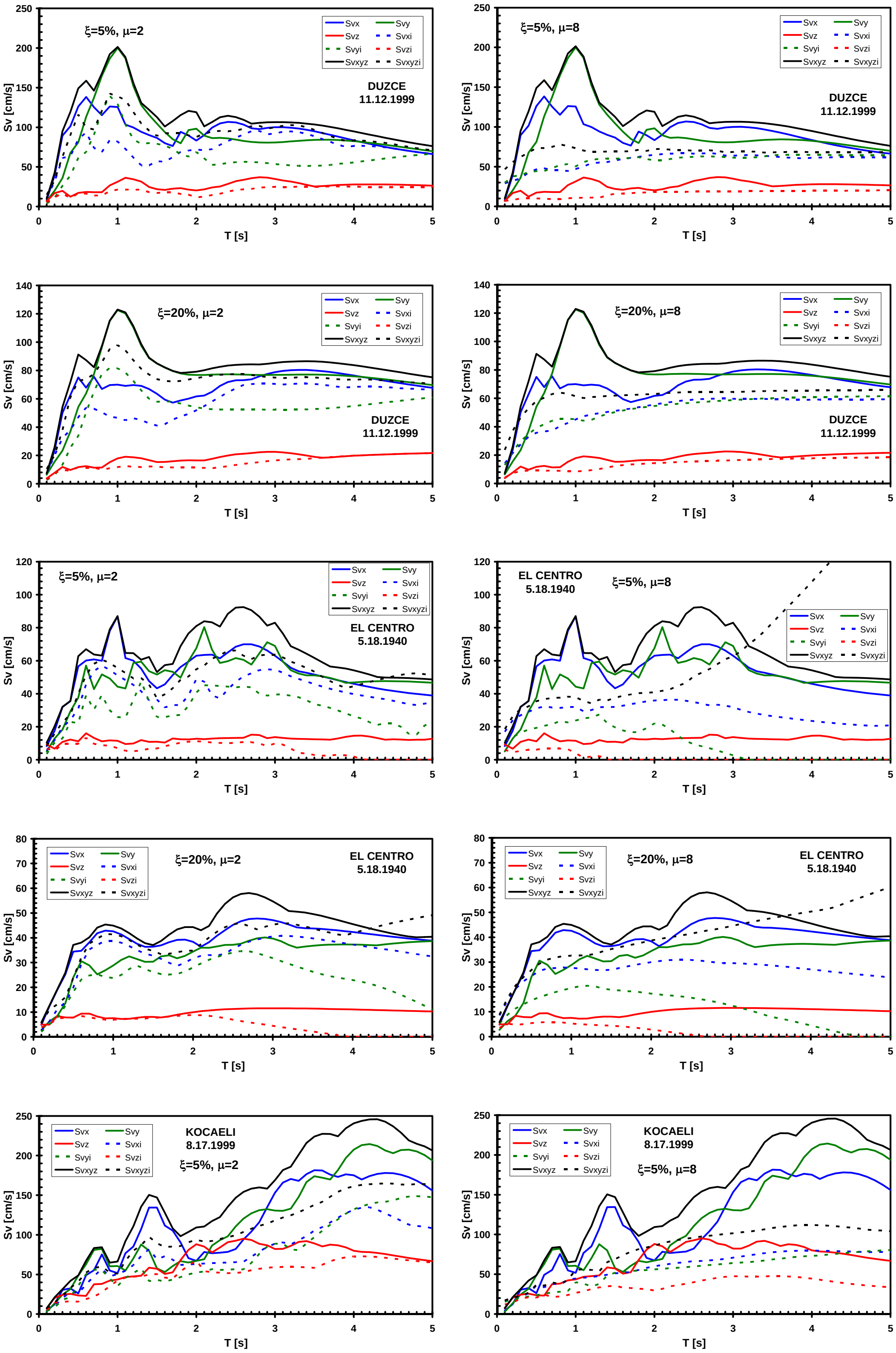

Figure 3. Elastic and Inelastic velocity response spectra for each orthogonal and resultant directions

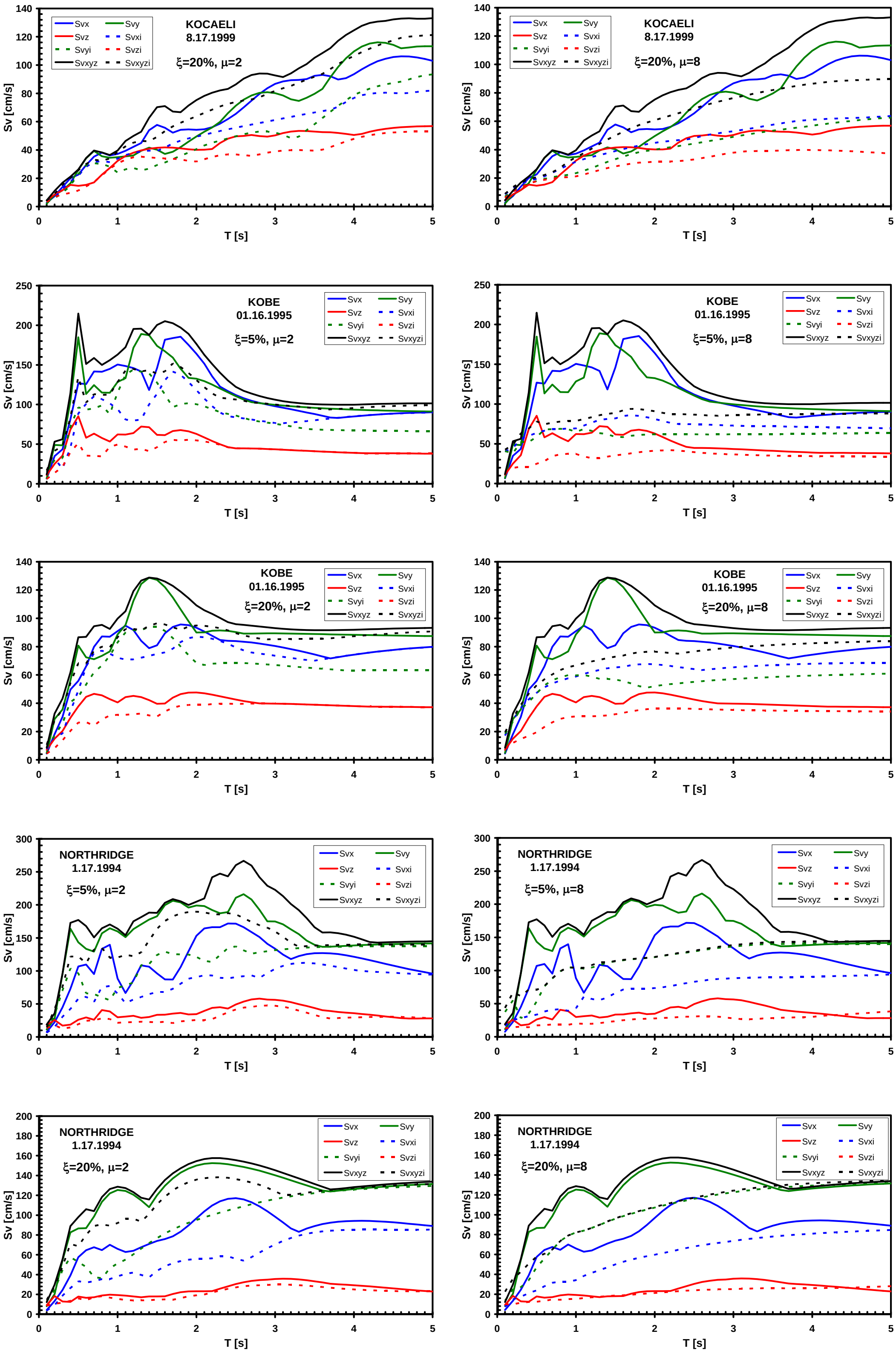

Figure 3. Elastic and Inelastic velocity response spectra for each orthogonal and resultant directions (continued)

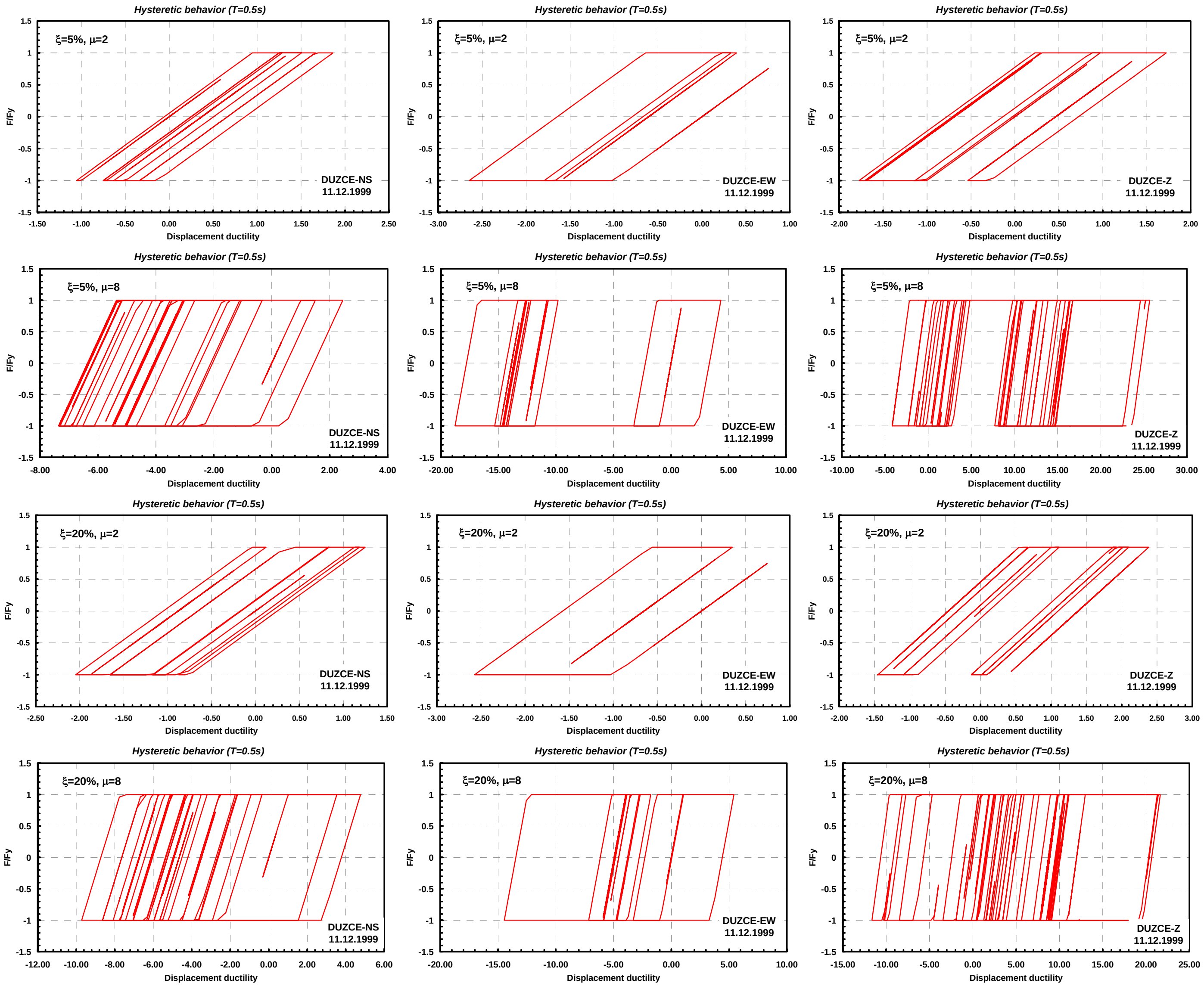

Figure 4. Hysteretic behavior of elasto-plastic SDOF systems for selected earthquakes

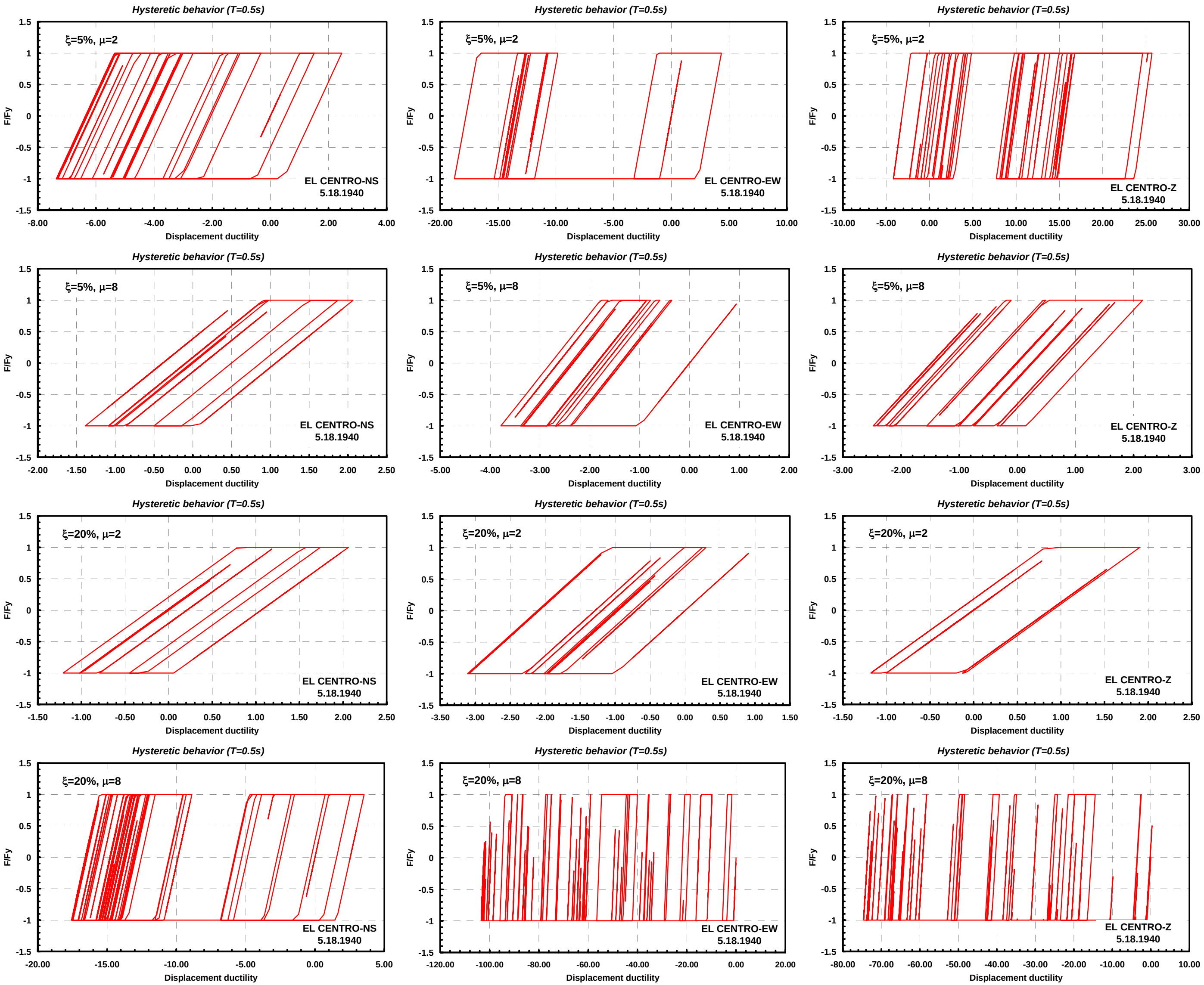

Figure 4. Hysteretic behavior of SDOF systems for selected earthquakes (continued)

	$\xi=0.05$ $\mu=1$				$\xi=0.05$ $\mu=2$				$\xi=0.05$ $\mu=8$			
	SI (cm/sec)	α	λ_1	λ_2	SI (cm/sec)	α	λ_1	λ_2	SI (cm/sec)	α	λ_1	λ_2
Elcentro	260.53	0.10	0.30	-	201.96	0.12	0.30	-	141.90	0.68	0.30	1.05
	250.64				151.85				50.19			
	60.98				30.69				6.15			
	311.96				248.77				333.57			
Parkfield	161.00	0.05	0.30	-	110.00	0.18	0.30	0.06	78.60		0.30	0.37
	133.67				100.05				82.22	0.30		
	47.63				39.12				34.20			
	175.87				149.68				131.52			
Hachinohe	109.88		0.30	-	90.72		0.30	-	70.43		0.30	0.17
	121.18	0.05			102.76	0.05			79.10	0.15		
	50.45				43.63				37.46			
	134.09				111.93				103.37			
San	702.00	0.08	0.30	-	463.00	0.23	0.30	0.17	283.00	0.51	0.30	0.71
Fernando	400.95				292.92				222.33			
	337.09				254.25				218.40			
	808.20				679.34				569.76			
Miyagi Ken	341.51	0.05	0.30	-	346.57	0.09	0.30	-	627.18	0.14	0.30	-
Oki	251.28				107.19				20.00			
	119.89				71.20				24.45			
	376.31				408.83				807.85			
Tabas	720.57		0.30	0.11	481.56		0.30	0.21	431.91		0.30	0.14
	845.36	0.10			578.54	0.13			507.67	0.11		
	324.35				250.05				189.11			
	1015.90				727.75				623.88			
Loma Prieta	990.00	0.02	0.30	-	672.00	0.05	0.30	-	473.00	0.02	0.30	-
	397.95				275.42				223.83			
	311.59				216.20				239.53			
	1032.35				741.44				495.55			
Erzincan	619.38	0.06	0.30	-	444.03	0.14	0.30	-	281.68		0.30	0.55
	483.64				397.03				322.29	0.31		
	158.94				105.90				64.12			
	692.51				564.53				520.66			
Northridge	570.00		0.30	0.23	412.00		0.30	0.43	359.00		0.30	0.37
	777.12	0.06			569.47	0.12			581.12	0.02		
	182.08				145.30				130.48			
	874.29				711.29				600.14			
Kobe	545.75		0.30	-	432.64	0.11	0.30	-	353.37	0.08	0.30	-
	552.44	0.08			411.03				302.45			
	242.05				206.86				170.00			
	637.73				526.64				412.95			
Kocaeli	575.00		0.30	0.00	395.00	0.16	0.30	0.03	301.00	0.18	0.30	0.06
	587.45	0.14			385.06				275.15			
	331.92				256.97				175.44			
	748.24				524.62				409.79			
Chi Chi	565.13		0.30	-	448.71		0.30	-	332.49		0.30	0.07
	611.64	0.08			451.53	0.13			335.62	0.18		
	216.04				148.68				145.88			
	709.30				567.17				456.80			
Duzce	452.00		0.30	-	368.00	0.12	0.30	-	286.00		0.30	-
	454.57	0.10			313.26				288.71	0.09		
	129.32				100.81				80.97			
	545.31				455.64				339.21			

Table 2. Computed spectrum intensities and combination coefficients ($\xi=0.05$)

	$\xi=0.20$ $\mu=1$				$\xi=0.20$ $\mu=2$				$\xi=0.20$ $\mu=8$			
	SI (cm/sec)	α	$\lambda 1$	$\lambda 2$	SI (cm/sec)	α	$\lambda 1$	$\lambda 2$	SI (cm/sec)	α	$\lambda 1$	$\lambda 2$
Elcentro	193.92	0.05	0.30	-	164.60	0.08	0.30	-	132.90	0.26	0.30	0.22
	162.21				118.83				57.00			
	48.25				23.25				9.99			
	214.29				192.16				202.09			
Parkfield	113.00	0.10	0.30	-	83.50		0.30	0.24	68.20		0.30	0.49
	112.18				87.96	0.23			78.12	0.28		
	32.91				31.10				30.55			
	134.75				128.72				121.76			
Hachinoe	85.70		0.30	-	71.97		0.30	-	65.73		0.30	0.05
	94.87	0.04			85.58	0.04			74.32	0.10		
	37.70				35.07				34.17			
	101.98				93.16				88.78			
San Fernando	535.00	0.08	0.30	-	375.29	0.23	0.30	0.15	262.98	0.43	0.30	0.56
	315.74				245.69				211.14			
	266.89				211.58				199.35			
	619.36				544.92				489.69			
Miyagi Ken Oki	242.82	0.03	0.30	-	239.47	0.06	0.30	-	297.62	0.07	0.30	-
	175.59				70.26				21.43			
	77.31				48.51				24.18			
	258.29				266.35				341.81			
Tabas	515.58		0.30	-	385.62		0.30	0.02	370.30		0.30	0.08
	553.83	0.09			410.66	0.12			407.62	0.13		
	216.25				180.41				160.14			
	658.28				508.51				509.60			
Loma Prieta	630.00	0.02	0.30	-	473.00	0.03	0.30	-	379.00	0.02	0.30	-
	285.96				218.48				198.80			
	220.36				168.80				202.62			
	652.58				502.19				395.67			
Erzincan	450.62	0.06	0.30	-	325.41	0.23	0.30	0.16	246.77		0.30	0.46
	364.17				304.02				278.58	0.28		
	91.05				72.95				54.18			
	506.29				476.33				434.39			
Northridge	411.00		0.30	0.23	295.00		0.30	0.60	300.00		0.30	0.45
	608.67	0.02			469.32	0.10			513.49	0.01		
	122.86				105.68				106.61			
	630.79				561.51				525.73			
Kobe	379.44		0.30	-	351.21	0.09	0.30	-	306.26	0.09	0.30	-
	432.83	0.04			325.86				271.26			
	193.77				170.00				157.10			
	466.95				412.23				359.52			
Kocaeli	333.00	0.11	0.30	-	264.00	0.17	0.30	0.05	226.00	0.18	0.30	0.06
	330.40				245.46				206.17			
	208.90				176.39				154.31			
	409.56				355.48				308.03			
Chi Chi	447.78		0.30	-	370.00	0.10	0.30	-	309.00	0.16	0.30	0.03
	448.17	0.07			340.13				295.39			
	150.35				114.35				120.31			
	512.53				442.80				410.89			
Duzce	339.00		0.30	-	284.59	0.13	0.30	-	258.60		0.30	-
	373.32	0.05			266.25				261.00	0.09		
	88.17				73.14				70.14			
	409.83				360.26				305.53			

Table 3. Computed spectrum intensities and combination coefficients ($\xi=0.20$)

The Caltrans code does not specify the SRSS rule as an alternative. There are two alternative rules prescribed in IBC2003. One of the alternative rules combines the responses with two horizontal seismic components using the SRSS rule; the result is multiplied by the redundancy coefficient and added to the effect of the vertical component, which is written as a linear term in the design load combination. The other alternative rule combines the responses with two horizontal components using the 30% rule, and adds the effect of the vertical component in the same way. In the recent Turkish earthquake code of “Specification for buildings to be built in earthquake zones” the 30% rule is prescribed.

To compare the numerical results obtained from this study, the variation of α coefficients with respect to selected damping ratios is further illustrated in Figures 5a,b. For the selected earthquake ground motions, it is observed that, for inelastic analysis, the maximum value of the coefficient α is changing wide range between 0.05~0.23 for $\mu=2$, $\xi=0.05$ and 0.02~0.68 for $\mu=8$, $\xi=0.05$, 0.03~0.23 for $\mu=2$, $\xi=0.20$ and 0.01~0.43 for $\mu=8$, $\xi=0.20$. To evaluate the contribution of the vertical component to the combination rule, λ_2 values are obtained whilst λ_1 values are taken as a value of 0.30. The results show that most of the λ_2 values are negative, hence if the orthogonal components are combined with a %30 rule, vertical component of the strong ground motion can be neglected.

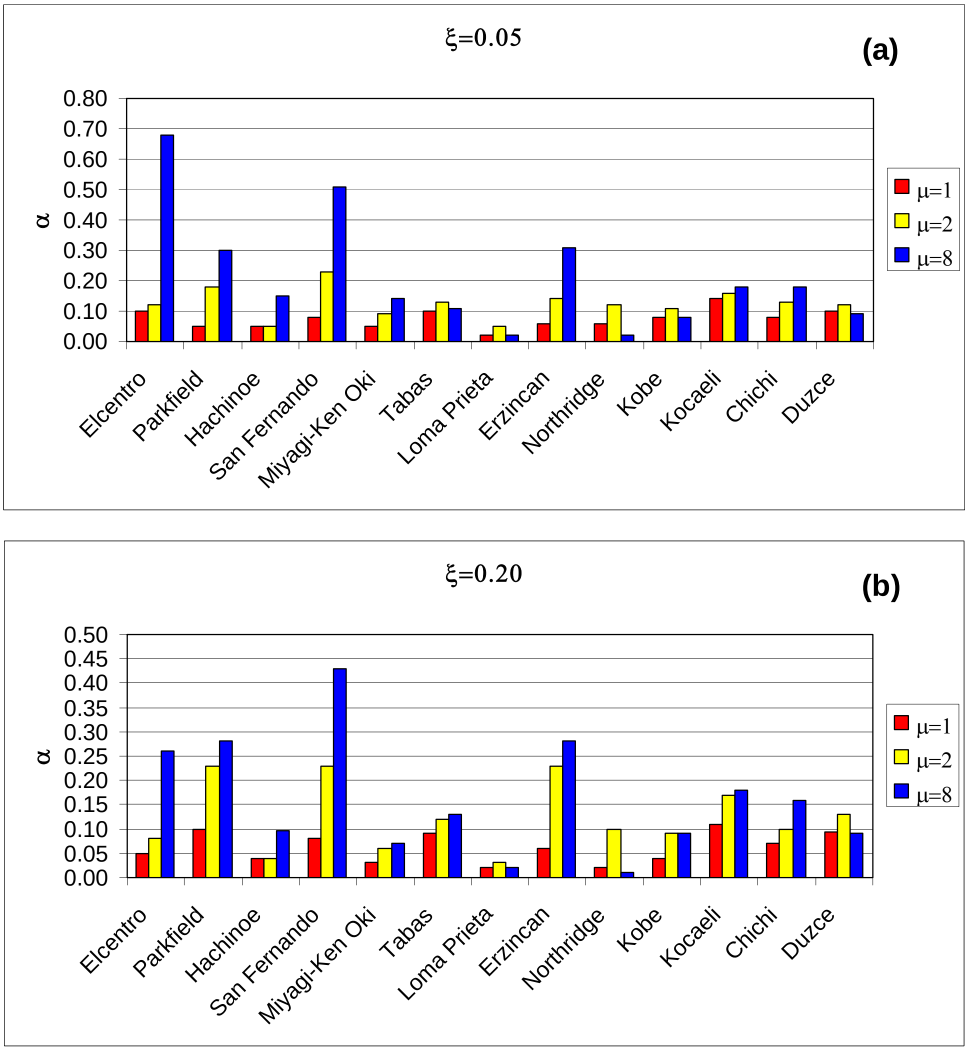

Figure 5. α coefficients for elastic ($\mu=1$) and inelastic ($\mu=2$ and $\mu=8$) systems.

5 CONCLUSIONS

Among several methods of analyses (e.g. the CQC, 30%), the Housner's spectrum intensity concept was used to investigate tri-directional earthquake effects for inelastic response of structures. For this purpose, inelastic velocity response spectra were plotted for a set of thirteen ground motions for structures having damping ratios of ξ=0.05, 0.20, and first elastic vibration periods up to T=5 sec. Spectrum intensities for both orthogonal directions and for the resultant direction were obtained. Relevant coefficients commonly used in the percentage rules recommended in building codes were numerically calculated using the velocity spectrum intensities. Obtained numerical results show that the maximum value of the coefficient α is strongly earthquake dependent and varied between 0.05~0.23 for μ=2, ξ=0.05 and 0.02~0.68 for μ=8, ξ=0.05, 0.03~0.24 for μ=2, ξ=0.20 and 0.01~0.43 for μ=8, ξ=0.20, revealing that in some cases the code defined combination values may yield unconservative seismic designs.

REFERENCES

[1] H. Sesigur, O.C. Celik, F. Cili, Review and Evaluation of Combination Rules for Structures under Bidirectional Earthquake Excitations. *13th World Conference on Earthquake Engineering*, Canada, Paper No.2079, (CD-ROM), September 2004.

[2] H. Sesigur, O.C. Celik, F. Cili, Analysis of Code Defined Combination Rules Under Tri-Directional Earthquake Excitations. *ECCOMAS Thematic Conference on Computational Methods in Structural Dynamics and Earthquake Engineering*, Rethymno, Crete, Greece, Paper No.1433, (CD-ROM), June 2007.

[3] European Committee for Standardization (ECS). Eurocode 8: Design Provisions for earthquake resistance of structures. Brussels, Belgium, 1998.

[4] ASCE/SEI 7-05. Minimum Design Loads for Buildings and Other Structures, Reston, Virginia, 2006.

[5] Ministry of Public Works and Settlement, Specification for Structures to be Built in Disaster Areas, 2006.

[6] ATC-32. Improved Seismic Design Criteria for California Bridges: Provisional Recommendations, Applied Technology Council, 1996.

[7] FEMA 356. Prestandard and Commentary for the Seismic Rehabilitation of Buildings, November 2000.

[8] H. Sesigur, O.C. Celik, F. Cili, Determination of Orthogonal Combination Coefficients Using Inelastic Velocity Response Spectra. *ECCOMAS Thematic Conference on Computational Methods in Structural Dynamics and Earthquake Engineering*, Rhodes, Greece, Paper No.465, (CD-ROM), June 2009.

[9] N.M. Newmark and E. Rosenblueth, *Fundamentals of Earthquake Engineering*, Prentice-Hall, Inc., Englewood Cliffs, N.J., 1971.

COMPDYN 2011
3rd ECCOMAS Thematic Conference on
Computational Methods in Structural Dynamics and Earthquake Engineering
M. Papadrakakis, M. Fragiadakis, V. Plevris (eds.)
Corfu, Greece, 25–28 May 2011

SEISMIC ASSESSMENT OF CONCRETE TANKS CONSIDERING FLUID STRUCTURE INTERACTION AND NONLINEAR TIME HISTORY ANALYSIS

H.Friedl[1*], M. Kwapisz[1], A. Lechner[1], R. Flesch[1]

[1]AIT Austrian Institute of Technology
Österreichisches Forschungs- und Prüfzentrum Arsenal Ges.m.b.H.
Giefinggasse 2 | 1210 Vienna | Austria

herbert.friedl@ait.ac.at
maciej.kwapisz@ait.ac.at
rainer.flesch@ait.ac.at

Keywords: Seismic assessment, fluid structure interaction, model updating, time history analysis.

Abstract. *Seismic assessment of important existing structures what are designed according to prior seismic codes or even without considering any earthquake load is one of the most important issues for minimizing the seismic vulnerability. Within this work the seismic assessment of an existing building for radioactive waste management is presented. The investigated structure is designed as a water treatment plant consisting of six collecting tanks situated in a height of 4m and is supported by eight RC columns. The building is located in the area with the highest earthquake hazard in Austria. The main goal was to analyse the whole structure under dynamic excitation during an earthquake event and in case of overloading to give recommendations for possible retrofitting solutions. An improved method for the elaboration of precise structural models is presented, which combine dynamic in-situ measurements and FE-analysis. With dynamic in-situ tests under forced excitation by usage of a reaction mass exciter, the dynamic behaviour of the structures was determined. That followed a model updating procedure to increase the reliability of the numerical investigations. The main life loads of the building are the tanks filled with water. For consideration the fluid structure interaction (FSI) during dynamic excitation an approach with usage of adequate solid elements was implemented in the structural model. In order to assess the accuracy of the chosen approach and updated finite element model, linear spectrum analysis and time history analysis were carried out. In the parametric study, the influence of a number of parameters concerning earthquake and structural characteristics on the structural responses, especially the filling level of the collecting tanks, were investigated. For the nonlinear dynamic analysis a set of different artificial time-histories, which were generated fitting to the EC8 response, were used.*

1 INTRODUCTION

Seismic assessment of important existing structures what are designed according to prior seismic codes or even without considering any earthquake load is one of the most important issues for minimizing the seismic vulnerability. Further, there are several areas in Europe, where seismic zones were upgraded during the last decade according to recent research results. Hence, the seismic assessment of important existing structures like industrial facilities processing with toxic or nuclear materials are obviously to reduce the potential risk for the population and environment. Such structures with increased risk for the population are beyond the scope of the current design codes. Considering these aspects a more detailed approach as recommended in EC8 was carried out.

1.1 Seismic Assessment in combination with in-situ tests and FE calculations

The most accurate method to assess the seismic vulnerability of existing structures is to perform field investigations in combination with numerical calculations. The goal of the tests is to identify the modal parameters of the structure under consideration. A first model of the tested structure, which was elaborated on the basis of the design - documents can be fitted to measured results by an optimisation approach. This is done by minimizing the difference between measured and calculated modal parameters. This procedure is called “model updating”. In most cases for complex structures 3D – FE models will be used. The resulting model represents very well the status of the structure at the time of the investigation concerning mass, stiffness and boundary conditions. If no reliable information about strength can be found in the design documents, realistic assumptions must be used or adequate tests have to be carried out. The updated model means a realistic linear starting point even in the case of a strong earthquake. In the presented approach the investigations started with in-situ measurements of structural- and soil response using a reaction mass exciter VICTORIA of AIT.

1.2 Investigated structure

The investigated structure is situated in Austrians highest seismic region with a maximum horizontal peak ground acceleration of 2.15m/s². With consideration the effective value and soil amplification factor a design ground acceleration of a_g=1.8m/s² results. The building is designed as a water treatment plant with six collecting tanks supported by eight RC columns. Each tank has a capacity of 80m³, with a restriction of maximum filling of five tanks at the same time it leads to additional mass of 400 to (see Figure 2). The tanks are constructed as upside down pyramids with a cubical base. The total height of the building is 7.2m, the centre of the mass in a height of about 4m. The structure is surrounded by two adjacent buildings with a height of 14.2m and the building in the background with a height of 3.3m (see figure 1). Due to different foundation and mass distribution the buildings are connected only with elastic building joints.

The main goal was to ensure the structural safety during an earthquake event. The work was done in following steps:

- FE - modelling of the building including the water tanks
- Dynamic measurement to determine the modal parameters of the building.
- Model updating approach
- Detailed investigation of the structure under the seismic loads according EC8
- Recommendations for retrofitting

2 NUMERICAL MODEL

For analysis, a three dimensional model of the building was created in ANSYS (Figure 1). This model includes only a few simplifications and thus provides very accurate results and information on the utilization of individual structural elements. For considering the real mass distribution the lightweight roof construction was modelled in a simplified manner as equivalent mass at the last slab. It was assumed that it has minor impact on dynamic and static properties of the whole building.

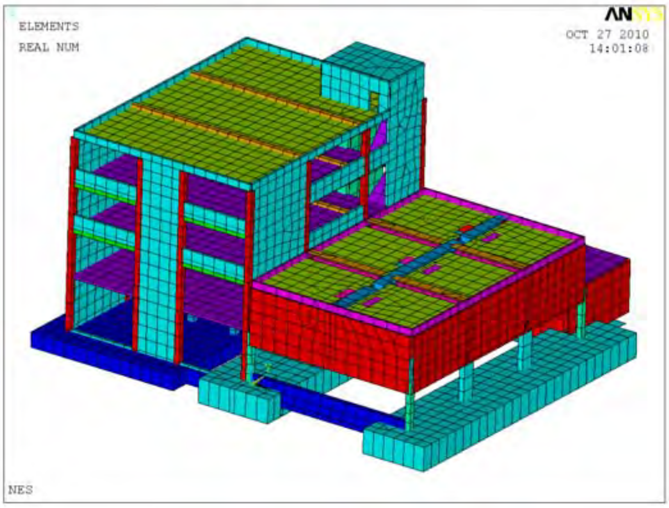

Figure 1: FE Model of entire building complex

Next to the structural system i.e. bearing walls, ceilings, beams and columns, also fluid elements (Fluid80) were implemented to model the realistic behaviour of water response in the tanks under dynamic excitation. The fluid elements are defined by eight nodes having three degrees of freedom at each node: translation in the nodal x, y, and z directions. The element input data includes eight nodes and the isotropic material properties. E_x, which is interpreted as the "fluid elastic modulus", should be the bulk modulus of the fluid (E_x=2.1E09 Pascal for water). The viscosity property is used to compute a damping matrix for dynamic analyses. A typical viscosity value for water is 1E-03 Pascal-sec. The connection between fluid and RC walls was conducted out with respect to the realistic behaviour of degree of freedom of fluid elements. At the boundary area the fluid elements have been coupled in perpendicular direction with the adjacent concrete surface elements. All other degrees of freedom are free and water can move in a realistic way under modal analysis (Figure 3) and transient analysis (Figure 8).

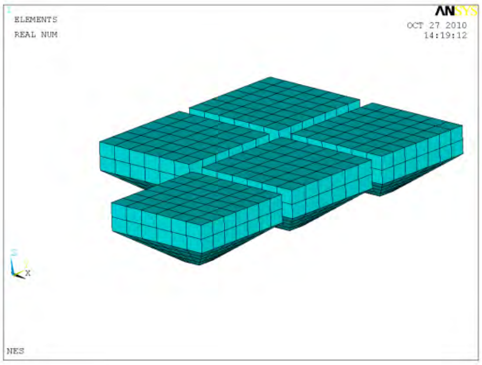

Figure 2: Fluid Elements

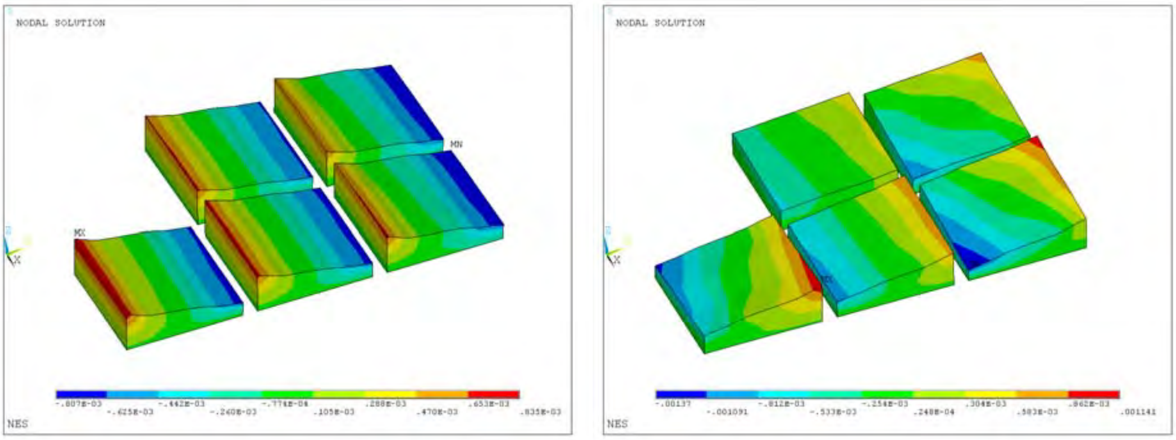

Figure 3: Movement of water – mode shapes

3 DYNAMIC MEASUREMENT

The reaction mass exciter "Victoria" was used as a vibration source to perform dynamic measurements of the building. To determine the vibration characteristics highly sensitive accelerometers were arranged at 34 points at four levels. The choice of the points was aligned to determine all representative natural frequencies and mode shapes.

Figure 4 left: connection with the building; right: position of the exciter mass

The excitation was carried out over an axial road chain between the structure and the exciter mass (Figure 4). The excitation angle of about 45° ensures to excite as many natural modes as possible.

4 MODEL UPDATING

Natural frequencies and modes shapes of the building were calculated and compared with the obtained parameters from dynamic measurement. The amount of water in the tanks during FE calculation was set to be the same as it actually was during the measurement. The calibration of the FE model was carried out with respect of the first three measured eigenmodes. In this case, the most important updating parameters were: E-modul of RC, E-modul of elastic connection between buildings and ground stiffness. Realistic maximum and minimum values of these parameters were assumed, and through series of analysis, whereas they were randomly changing, the most suitable solution was found. The natural frequencies, as well as the mode shapes of the FE model and measurement were in a good agreement (Table 1).

Mode	Natural frequency [Hz]		Deviation
	Measurement	FE model	
1	x	5.2	x
2	6,3	6,2	1,6%
3	8,7	7,6	12,6%
4	11,5	11,9	3.50%
		Average	5,9%

Table 1: Comparison of computed and measured natural frequencies

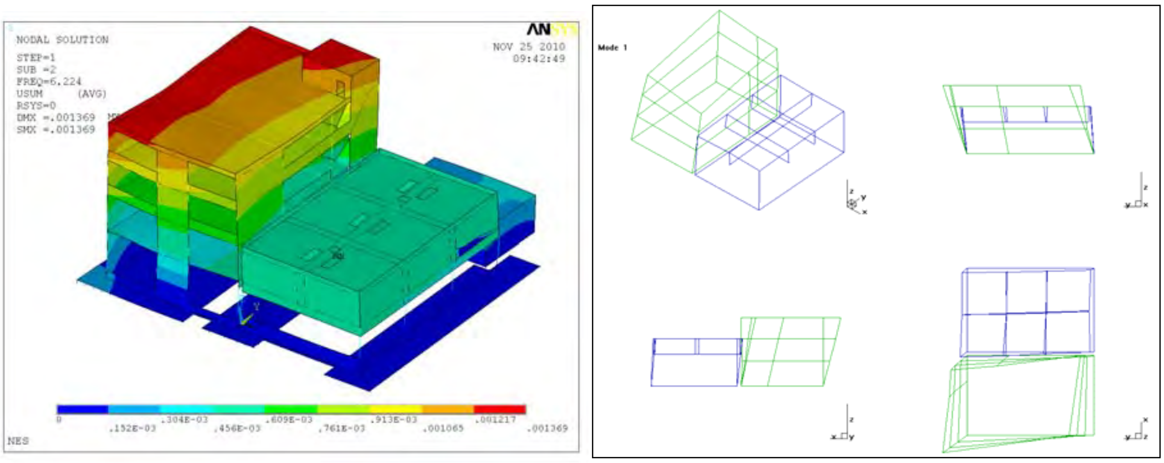

Figure 5: 2nd Mode: left: computed; right: measured

5 SEISMIC ASSESSMENT

First, a sensitivity study was carried out with the aim to identify the most unfavourable combination of filling levels. The positioning of the fulfilled tanks was varied with respect to maximum loading for each construction element and considering global torsion effects due to unsymmetrical set ups. The identification of the worst load case situations were obtained by linear spectrum analysis. Next to spectrum analysis, also transient time- history analysis was used. It was necessary to improve the behaviour of fluid elements and to allow material nonlinearities. For the nonlinear dynamic analysis a set of different artificial time-histories [1], which were generated fitting to the EC8 response, were used (Figure 6).

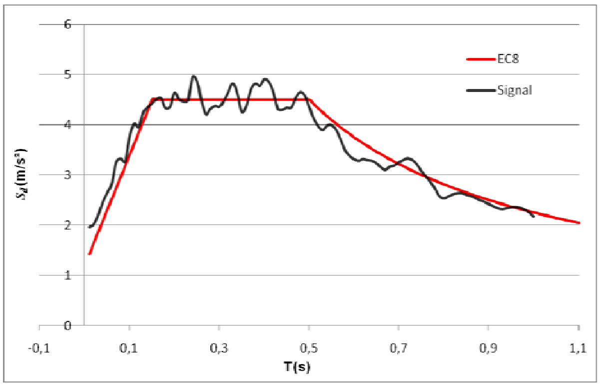

Figure 6: Response spectras

As mentioned in chapter 1.2 the building complex consists of three buildings, linked with a dilatation joint. Whereas the stiffness of this elastic material for small deformations was approximately identified by modal updating, it is difficult to assess its behaviour during the earthquake impact. Due to high deformations caused by seismic impact, connections to adjacent parts of the building may get lost during earthquake. The calculation was performed without connection to the adjacent buildings (Figure 7). Together with the high mass concentrated at the height of about 4 meters the building is extreme vulnerable to horizontal forces.

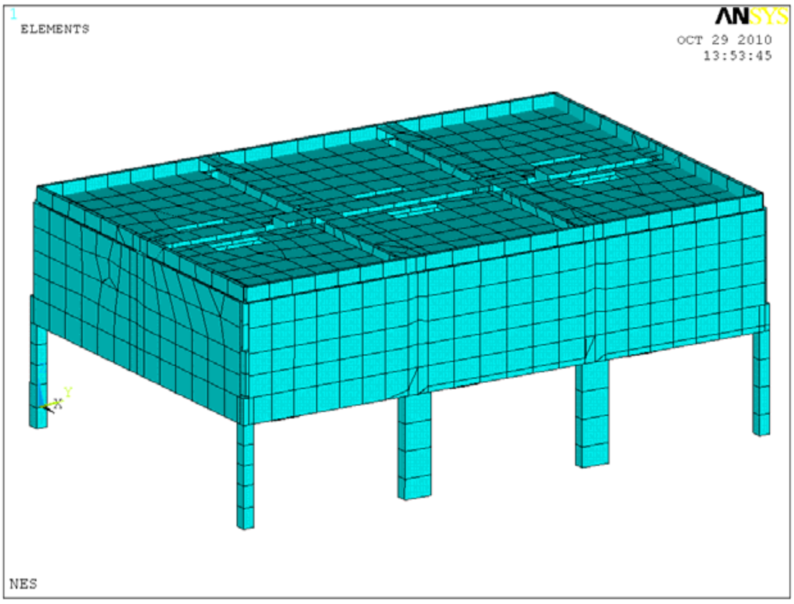

Figure 7: Water tank building treated as standing alone

The results from all transient analysis were averaged and the safety factors according the requirements of Eurocode 2 were calculated. The comparison between spectrum analysis and transient analysis types showed good agreement, with the differences about less than 20%. The deformation of the structure during time history analysis is plotted in Figure 8.

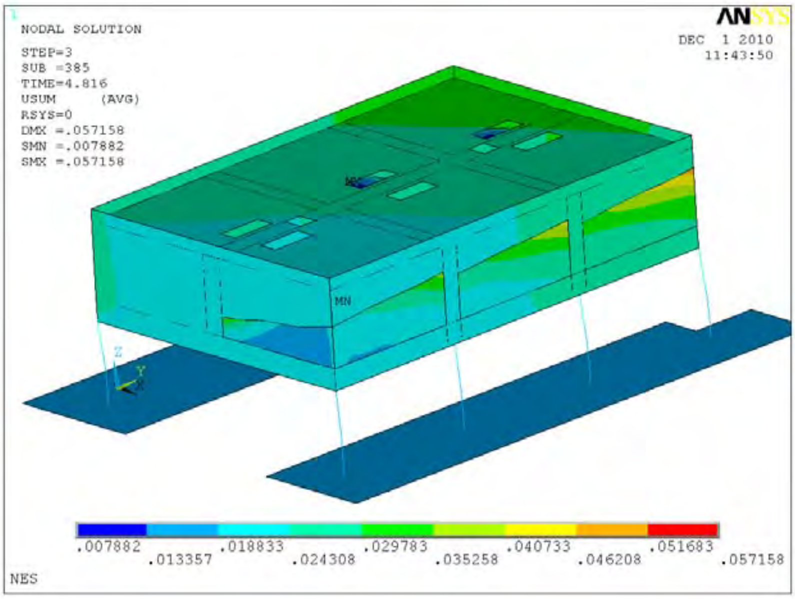

Figure 8: Deformation during time- history analysis

It is obviously that the most critical components of the structure in case of seismic impact are the eight columns in the ground floor. The structural design analyses were carried out according EC2 regarding possible shear and biaxial bending failure. An Important issue in post processing of transient analysis is the synchronism of the forces. Not only maximums are significant, but also the worst combination of all forces in time. For biaxial bending in every time step following simplified criterion (EC2) was used:

$$\left(\frac{M_{Edz}}{M_{Rdz}}\right)^{a} + \left(\frac{M_{Edy}}{M_{Rdy}}\right)^{a} \leq 1 \tag{1}$$

where:

$M_{Edz/y}$ is the design moment around the respective axis

$M_{Rdz/y}$ is the moment resistance in the respective direction

a is the exponent, which depends on the axial force

The example of time- depending bending moments (red and pink) and axial force (blue), as well as results from equation (1) are shown in Figure 9.

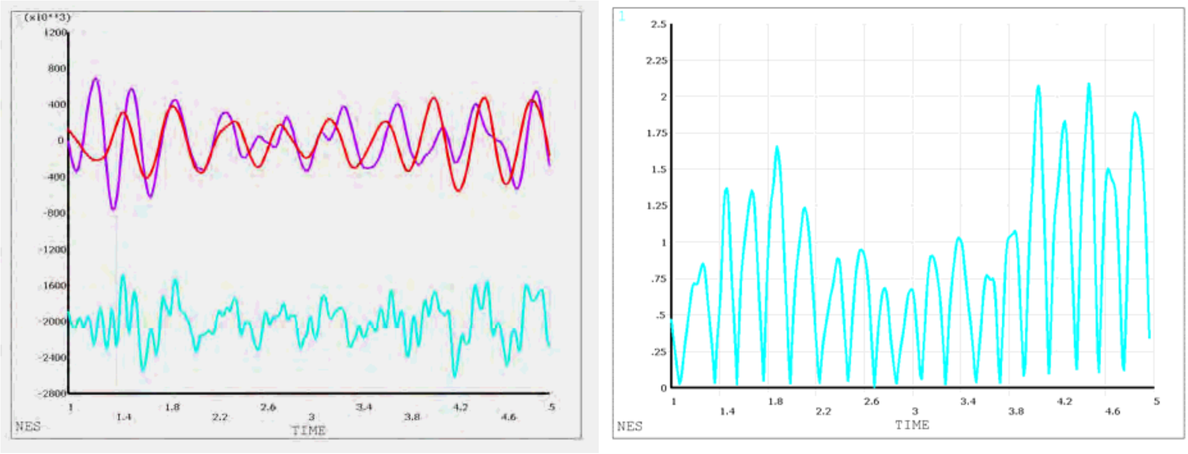

Figure 9 Left: bending moments and axial force; right: results of equation (1)

To assess the shear resistance, the equations (6.2), (6.8) and (6.9) from EC2 were used. Due to simultaneous dependency of shear and axial force, the calculation was carried out for every time step, and the worst case was taken for analysis. The structural design of the analysed columns doesn't fulfil the requirements according the standards. Furthermore the internal requirements regarding maximum deformation will exceed what will lead to damage of technical facilities and cause a potential risk for the environment.

6 STRENGTHENING RECOMMENDATIONS

Possible retrofitting designs were limited by requirement of the operator to minimize construction works inside the building due to interference with internal operation. The proposed strengthening solutions should take into account minimizing modifications for existing technical assets and facilities. Aware of these requirements also unorthodox seismic strengthening solutions, like asymmetric strengthening, were analysed. Due to asymmetric stiffening the dominant torsion mode increase the loading of the corner columns significantly. In fact of this, minor modifications of internal facilities were accepted by the operator and proper retrofitting solutions were investigated. All of the presented variants provide earthquake safety and fulfilled operator's requirements perfectly, so only simplicity of rebuilding will be the relevant criteria. Thank FE calculation a lot of various options could be investigated and optimised.

6.1 Variant 1: Additional walls

In Figure 10 the first variant is given. New walls to be built are marked in red. The torsion, caused by asymmetry, is reduced by the use of two outside walls, but could not be avoided. The big advantage is that the existing columns do not need to be replaced.

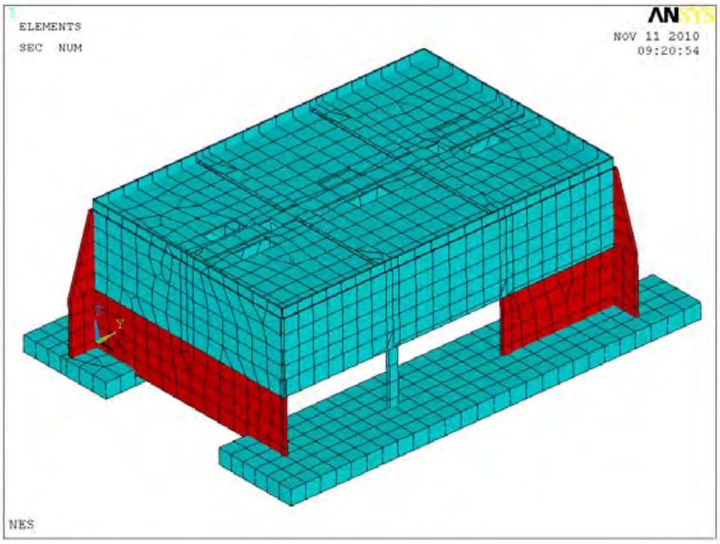

Figure 10: First retrofitting variant

6.2 Variant 2: Additional outside walls on the corners

This variant comprises adding strengthening short walls in each corner. The advantage is symmetry, disadvantage – demand to exchange of the existing columns (Figure 11).

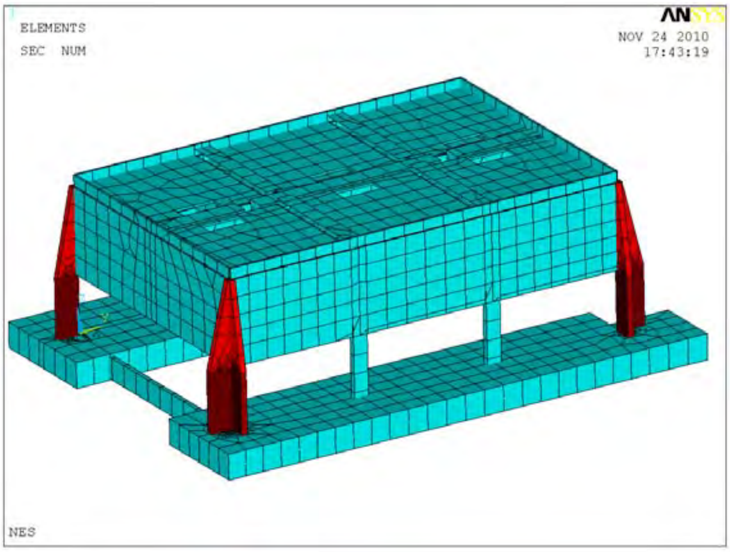

Figure 11: Second retrofitting variant

6.3 Variant 3: Connection with the other building through a damper

It occurred that coupling of both buildings would assure the earthquake safety of the water tanks. It could be achieved by implementing at least four dampers, two in each direction. Exact optimisation of dynamic parameters of dampers was not carried out in this stage.

7 CONCLUSIONS

By means of experimental modal analysis and finite element calculation a very realistic computer model for the entire building complex was created. Due to artificial excitation three mode shapes could be identified. The model adjustment was made on these three modes, whereby in addition to the Young's modulus of the materials, the elastic bearing joints to adjacent building parts and the boundary condition at the base were used as model updating parameters. The comparison of calculated with the measured mode shapes shows a very good agreement. With the improved FE model, earthquake analysis under consideration the local conditions and historical seismic events were carried out. Moreover following issues can be highlighted:

- Considering fluid structure interaction allows an adequate simulation of water behaviour under dynamic excitation and increase the reliability.
- Post- processing of transient analysis provides information about simultaneity of bending, shear and axial forces.
- Thank FE calculation a lot of various strengthening possibilities could be investigated and optimized

ACKNOWLEDGEMENT

The authors want to thank Nuclear Engineering Seibersdorf, who gave kindly their permission to publish parts of the work contracted by them to AIT.

REFERENCES

[1] Meskouris, K.: Baudynamik: Modelle, Methoden, Praxisbeispiele. Ernst & Sohn, Berlin 1999.

[2] Salajka, V.: Response of tanks with fluid to seismic excitation, Brno November 2007.

[3] He Liu and Daniel H. Schubert, “Effects Of Nonlinear Geometric And Material Properties On The Seismic Response Of Fluid-Tank Systems”, 2002 ANSYS 10th International Conference and Exhibition, April 22-24, 2002, Pittsburgh, PA.

[4] Ansys Release 11.0 Documentation for ANSYS, 2007.

[5] Flesch R., Friedl H., Campos Costa A., Candeias P., Mendes L., Eusebio M., Hoffmeister B., Oppe M., Wenzel H., Veit-Egerer R., Goretti A., Di Pasquale G., Rota M. (2007), European Manual for in-situ Assessment of Important Existing Structures. LESSLOSS, IUSS Press July 2007, Report No. 2007/02, Pavia, Italien, ISBN: 978-88-6198-006-8.

COMPDYN 2011
III ECCOMAS Thematic Conference on
Computational Methods in Structural Dynamics and Earthquake Engineering
M. Papadrakakis, M. Fragiadakis, V. Plevris (eds.)
Corfu, Greece, 25–28 May 2011

MODELLING ISSUES ON SEISMIC ASSESSMENT OF IRREGULAR RC STRUCTURES

Romain Sousa[1], **Federica Bianchi**[1], **Rui Pinho**[2], **Roberto Nascimbene**[1]
Danai Kazantzidou[3]

[1] European Centre for Training and Research in Earthquake Engineering (Eucentre)
Via Ferrata 1, 27100 Pavia
romain.sousa@eucentre.it
federica.bianchi@eucentre.it
roberto.nascimbene@eucentre.it

[2] Department of Structural Mechanics, University of Pavia
Via Ferrata 1, 27100 Pavia
rui.pinho@unipv.it

[3] ROSE School, IUSS Pavia
c/o Eucentre, Via Ferrata 1, 27100 Pavia
d.kazantzidou@meees.org

Keywords: Nonlinear Analysis, Seismic Assessment, RC Structures

Abstract. *Many existing RC structures worldwide were designed for gravity loads only, with inadequate lateral load resistance, lateral stiffness and poor detailing of the reinforcement. Moreover, the concept of regularity both in plan and elevation that characterise a good conceptual design was, in most cases, not taken into account.*

The introduction in Europe of the regulations for seismic assessment of existing structures imposed stricter performance requirements for building structures. In order to take into account the poor seismic behaviour of such buildings, recent seismic codes – namely EC8 and NTC08 (Italian code), introduce a number of prescriptions regarding issues such as analysis type, load distribution, accidental eccentricity, etc. At the same time, these codes give room for engineering judgment to be used with reference to the definition of structural and non-structural elements such as slabs or infill walls, and obviously leave it up to the analyst decisions regarding Finite Elements typology, meshing, mass modelling, etc.

The main goal of this work is thus to provide an extensive and wide evaluation on the influence of each of the abovementioned parameter on the seismic assessment of structures. For this purpose, nonlinear static procedures, as well as nonlinear dynamic analysis are performed on a real building that has also been experimentally tested in the past. The results will hopefully provide indications on the relative importance of each modelling parameter or decision.

1 INTRODUCTION

The existing building stock poses a much more serious and complex seismic safety problem when compared to safe earthquake design of new construction. Moreover, the past thirty years have witnessed such a significant increase of knowledge in the field of earthquake engineering, that even relatively modern structures may no longer meet the requisites of constantly developing regulations.

It has been recognised by the scientific community that force-based approaches for seismic assessment of structures are inappropriate. Instead, assessment methods employing displacement-based approaches, where member deformations are evaluated, tend to provide a more suitable estimation of the actual structure capacity. In order to implement this new philosophy and accurately estimate the members deformations, typically evaluated in terms of chord rotations, it is required advanced modelling capabilities that allows the structure to go behind the linear range.

Nonlinear dynamic analyses are, at the present time, the most accurate approach to evaluate the seismic response of structures. On the other hand, nonlinear static analyses (Pushover) are a simplified approach that allows the evaluation of the structure's behaviour when subjected to an increasing monotonic lateral load. Despite being considered a suitable approach for regular structures, its application on irregular structures has been pointed out as one of the main shortcomings of this type of analysis. Moreover, difficulties inherent to uncertainties in the definition of structural and non-structural elements such as slabs or infill walls, associated with modelling decisions regarding Finite Elements typology, meshing, mass modelling, etc., represents additional drawbacks.

The output of this study will hopefully provide some guidance on critical structural modelling issues that require urgent attention in order to overcome some uncertainties associated with the assessment of existing reinforced concrete (RC) structures.

2 STRUCTURAL BEHAVIOUR OF IRREGULAR RC STRUCTURES

Recent seismic events such as the 1985 Mexico, the 1994 Northridge, the 1995 Kobe and the 1999 Kocaeli earthquakes induced severe damage to non-ductile RC buildings proving that many constructions located in seismic zones are unable to withstand moderate to severe earthquakes and therefore observe significant damage and contribute to significant loss of lives.

Usually these structures were designed for gravity loads only, neglecting all the basic concepts for a good seismic behaviour such as regularity, both in plan and elevation, adequate lateral resistance systems, detailed reinforcement, etc. Because lateral actions were not taken into account in the design process, the columns cross-sections tend to be relatively small with insufficient longitudinal and transversal reinforcement. Very often these structures exhibit also a reduction in the columns cross-section over the high of the building. Consequently these elements possess reduced deformation capacity and, very often lead to soft-storey mechanisms and deformation shapes characterized by a strong torsional component.

In addition to the properties of the main structural system, there are other structural elements that, despite not being considered as part of the primary earthquake-resistant system, might modify the response of the building when the latter is subjected to lateral loads. For instance, infill panels are typically considered as secondary or non-structural elements, present only to provide a physical separation of spaces and insulation and, consequently, without any structural purpose. For this reason, generally they are not considered in the assessment procedure.

Nevertheless, in masonry-infilled RC frames, the infills might control the global response and often determine the performance and failure of the frame. Experience from earthquakes suggest that strong infill panels, although non-engineering and non-structural, often provide most of the earthquake resistance and prevent collapse of relatively flexible and weak RC structures [1]. However, very often, infills are not uniformly distributed over the plan and height, forcing the building to behave in an irregular fashion and, in this way, imposing high demands both in terms of forces and deformations, which may lead to local or global collapse of the structure. In this study, infill panels were modelled using the element proposed by Crisafulli [2].

An additional issue that requires particular attention is the way in which slabs are modelled. Very often ignored in the structural assessment process, the slab may play an important role, especially when associated to irregular buildings - its effect is mainly dependent on the relative in-plan stiffness compared with the stiffness of the vertical elements and its in-plan location. Typically three different solutions may be employed: no slab, rigid diaphragm, and an intermediate and perhaps more realistic solution, whereby the actual stiffness of the existing slab is considered. This latter solution can be implemented through the use of equivalent crossed trusses or, perhaps an easier and faster solution, by mean of nodal constraints with adjusted penalty functions. It must be pointed out that the aforementioned different assumptions do not only influence the structures global behaviour, but also at the elements level, as it will be demonstrated herein.

In order to account for uncertainties in the location of masses and in the spatial variation of the seismic motion, seismic codes such as EC8 [3] and NTC08 [4] introduce an “accidental eccentricity”, which imposes an additional torsional effect on the structure, and a number of lateral load distributions for static nonlinear analysis, aimed at reproducing higher mode effects in plan and elevation.

In summary, the importance and impact of the following structural parameters in the assessment of RC structures were assessed in the current parametric study:

- Infill panels
- Rigid/deformable slabs
- Accidental eccentricity
- Lateral distribution of loads for nonlinear static analysis

3 MODELING OF RC STRUCTURES

Supported on the exponential growth of computational capabilities witnessed in recent years, structural engineers are now able to make use of the on-going scientific developments. Moreover, practitioners are now enforced to keep themselves up to date on modelling developments and code requirements. Focused on this last observation, the present work intends to enlighten some clarification in some modelling issues, which have been proved to be crucial in seismic assessment of existing RC structures.

Nonlinear dynamic analyses are, currently, the most accurate approach to estimate the seismic behaviour of structures. Nevertheless, this advanced procedure requires high computational effort to process the analyses and, at the same time, the output extracted from the software provides information about a single seismic event. Therefore, in order to overcome these drawbacks, nonlinear static analysis, emerges as a simplified approach that allows the estimation of the capacity, defined in terms of base shear and lateral displacements, of structures subjected to increased lateral loads. The basic premise is that monotonic pushover can act as an envelope for the dynamic hysteresis.

In order to simplify the assessment procedure, a common approach consists in concentrating the mass of the structure at the beam-columns joints, rather then distributed along the elements. Following this procedure, the time taken to build-up the model as well as the processing phase might be substantially reduced. The employment of distributed mass represents a more suitable and accurate approach that enables the correct characterization of both global and local structural behaviour. On the other hand, according to previous studies, concentrating the masses at the structural joints is suitable for nonlinear static analysis since the evaluation of the mode shapes and global response of the building is consistent with the choice of distributing the lateral pushover forces in the structural joints [5]. However, because this assumption might lead to incongruences at the element level, a sensitive study making use of both approaches was carried out.

Previously, particular attention was addresses to modelling issues associated to computational performance. Nevertheless, it must be also emphasized that the time consumed during the pre- and post-processing phases may also be important. This way, and supported on the fact that beams damage are concentrated at the element ends for both static and seismic loads, a “simplified beam element”, consisting in one element defined with the beam-end-section through the entire member is evaluated. In this approach, the number of section as well as the number of elements is significantly reduced. Furthermore, the elements chord rotations can be directly obtained from the software without any additional calculations. Obviously, because in this approach the beams may not possess enough reinforcement to resist the positive moments at the mid-span, the use of concentrated mass at the beam-column joints is recommended.

In summary, the following model parameters were selected so that their influence upon the seismic response of existing RC structures is evaluated:

- Comparison between nonlinear static and dynamic analysis
- Mass modelling (lumped or distributed)
- Element meshing (“simplified beam element”)

There are many other structural issues, such as soil-structure interaction, beam-column joint behaviour, bar slippage, etc, that need also some clarification. However, due to their complexity and relative importance in practical terms, they were not included in the present parametric study.

4 PARAMETRIC STUDY

4.1 Overview

The structure under analysis in this study is the SPEAR building. The main goal of SPEAR project was contributing to the improvement of current design, assessment and retrofitting technics and the development of new simplified approaches for the seismic assessment and rehabilitation of existing building structures [6]. To enhance the issues brought by plan-irregularity in older structures, the specimen was especially designed so as to represent a typical non-earthquake resistant construction: it is a “strong beam-weak column system”, adding to the drawbacks originating from the plan eccentricity, the problems of poor local detailing, under-designed elements or joints and older construction practice.

The analysis of the structure was carried out with SeismoStruct - Finite Element package capable of predicting the large displacement behaviour of space frames under static or dynamic loading, taking into account both geometric nonlinearities and material inelasticity [7].

Lanese *et al* [8] demonstrated a good agreement between the results observed in the experimental test and the analytical ones (obtained by modelling the building in SeimoStruct). Considering the model proposed by these authors as a starting point, the building was modified in order to assess the importance of parameters mentioned before. An overview of the performed parametric study is presented in the Figure 1.

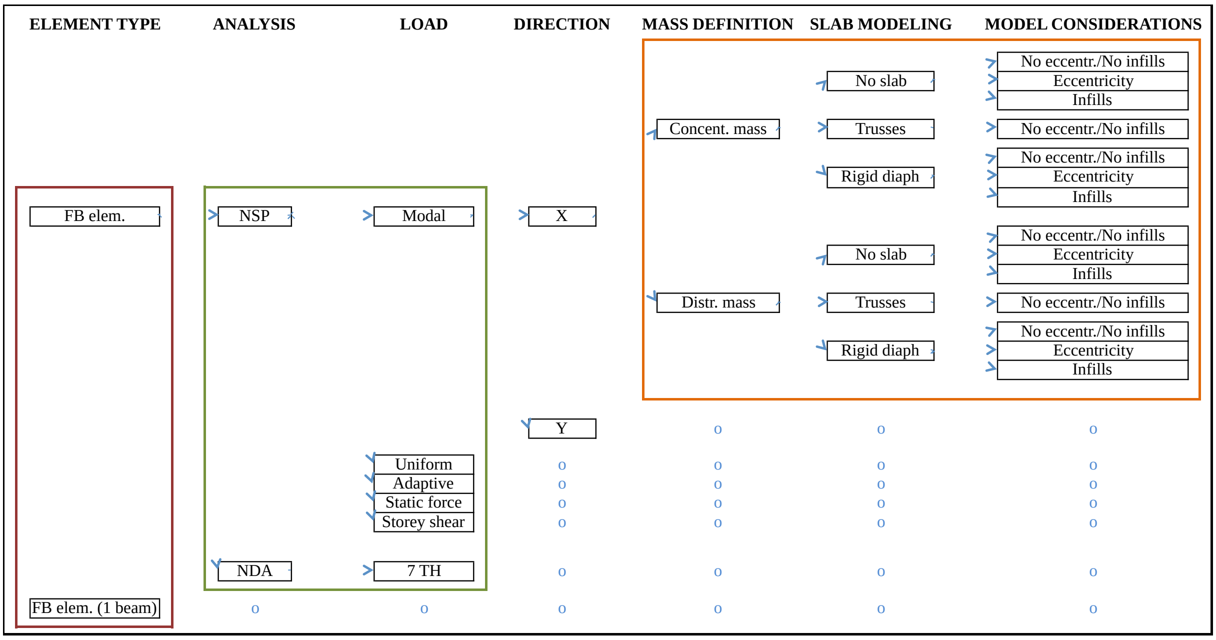

Figure 1: Parametric study flowchart.

It must be pointed out that the influence of each individual parameter was evaluated independently from the others. In order to obtain such detailed results, a total of 344 nonlinear static analyses and 224 nonlinear time-history analyses (NLTHAs) were carried out. For the sake of simplicity, only a selection of the representative results will be presented in this paper.

4.2 Building Description

The analysed structure is a three-storeys building, regular in elevation, with a storey height of 3 m. The plan configuration is non-symmetric in X and Y directions (Figure 2), with two-bay frames spanning from 3 to 6 metres.

Almost all columns have a square 250 by 250 mm cross-section; the only one that differes, column C6 in Figure 2, has a cross-section of 250 by 750 mm, which makes it much stiffer and stronger than the others along the Y direction.

The centre of stiffness (CR) (based on column secant-to-yield stiffness) is eccentric with respect to the mass centre (CM) by 1.3 m in the X direction (~13% of plan dimen- sion) and by 1.0 m in the Y direction (~9.5% of plan dimension) [6].

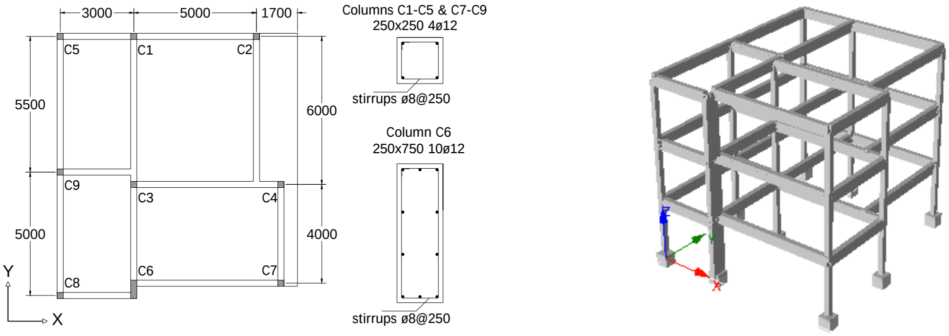

Figure 2: Building properties

4.3 Analyses Definition

As mentioned above, the structure was subjected to both nonlinear static and dynamic analyses. Regarding the former, the recent Italian code, NTC08 [4], suggests to select two of the five lateral load distributions presented hereafter:

- Distribution proportional to the static forces (triangular)
- Distribution proportional to the first mode of vibration (modal)
- Distribution proportional to the storey shear obtained from a linear dynamic analysis
- Uniform distribution
- Adaptive distribution

Note the fact that adaptive pushover, which represents an improvement with respect to conventional pushover, is introduced in this code.

In order to acquire a realistic representation of the structural behaviour during a seismic event and evaluate the performance of simplified approaches such as nonlinear static analysis, 7 real accelerograms (not scaled nor matched) were selected to perform the nonlinear dynamic analysis. The selection was such that the average response spectrums of 14 records (7 accelerograms in 2 directions) would follow, in an approximate manner, the response spectrum defined for the study (Figure 3).

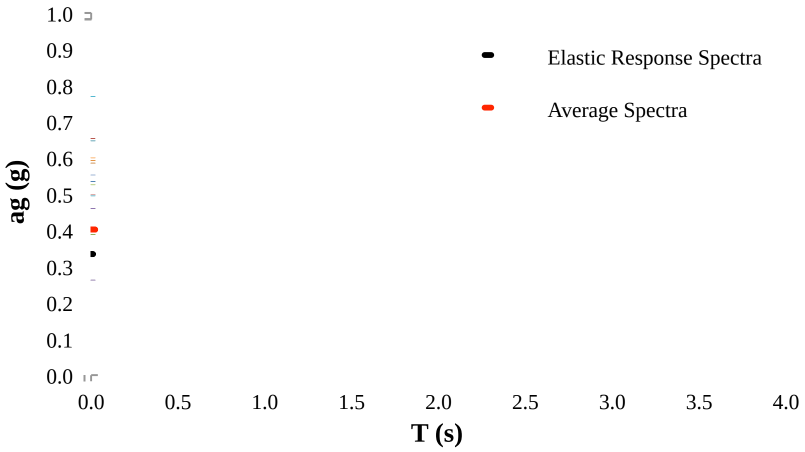

Figure 3: Individual and average acceleration spectrums selected for dynamic analysis.

The structure was then subjected, simultaneously, to pairs of bidirectional accelerations at the base in each direction (X and Y).

It must be pointed out that high deviation of individual response spectra with respect to the averaged one is difficult to avoid. Thus, high variation over the dynamic response is observed for the different accelerograms. Recall, however, that the main idea is to assess the reliability of different approaches, rather than a capacity/demand seismic compliance of the code requirements. The records main properties are presented in the following table:

Waveform ID	Earthquake Name	Date	Mw	Fault Mechanism	R (km)	PGA_X (g)	PGA_Y (g)	Site class
198	Montenegro	15/04/1979	6.9	thrust	21	0.18	0.22	A
228	Montenegro (aftershock)	24/05/1979	6.2	thrust	33	0.20	0.27	B
291	Campano Lucano	23/11/1980	6.9	normal	16	0.16	0.18	B
439	Spitak	07/12/1988	6.7	thrust	36	0.18	0.18	C
592	Umbria Marche	26/09/1997	6	normal	5	0.20	0.22	C
1228	Izmit	17/08/1999	7.6	strike slip	47	0.24	0.14	A
1314	Ano Liosia	07/09/1999	6	normal	17	0.12	0.11	B

Table 1: Main properties of selected accelerograms.

Finally, in order to make the analysis shorter, each of the records was bracketed to minimise the amount of computation required. The bracketed duration was taken to be between 5% and 95% of the total Arias Intensity as recommended by Bommer and Martinez-Pereira [9], and estimated through the software SeismoSignal [10].

4.4 Global Assessment

The first study that was carried out in order to evaluate the building response, when subjected to different modelling approaches, intends to estimate its behaviour in a global level. The results obtained through nonlinear static and dynamic analyses are presented in terms of base shear and top displacement. In the following sub-chapters, a more detailed discussion on the observed behaviour for different analysis and different parameters is presented.

4.4.1. Static and dynamic analyses comparison

Based on Figure 4, it is possible to verify that nonlinear static analyses can accurately estimate the global response of the building. In fact, the values obtained from nonlinear dynamic analyses fit in almost all cases within the five different pushover curves. Despite the difficulties to identify one pushover curve that would fit better the results obtain through nonlinear dynamic analysis, it becomes clear that the capacity curves obtained from adaptive pushover are more capable to capture the real dynamic behaviour, especially in the post-peak branch. It should be also emphasised that the capacity curves ware estimated for each direction independently, whilst in the nonlinear dynamic analysis the base excitations were applied in the two directions simultaneously.

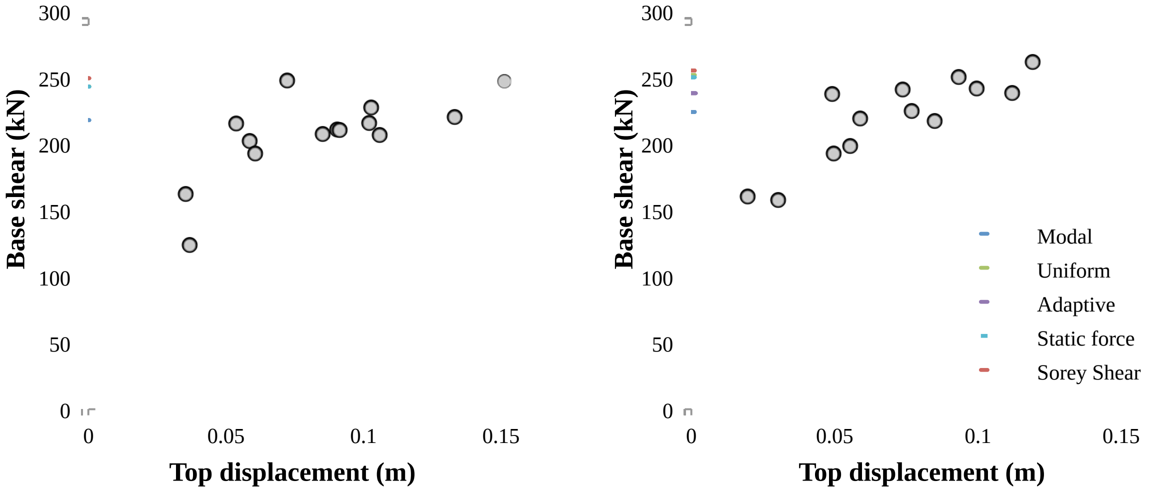

Figure 4: Comparison between nonlinear static and dynamic analysis - no slab (left) and equivalent trusses (right).

On the other hand, when in presence of infill panels within the external frames, a higher deviation from the two different approaches is identified as demonstrated in Figure 5.

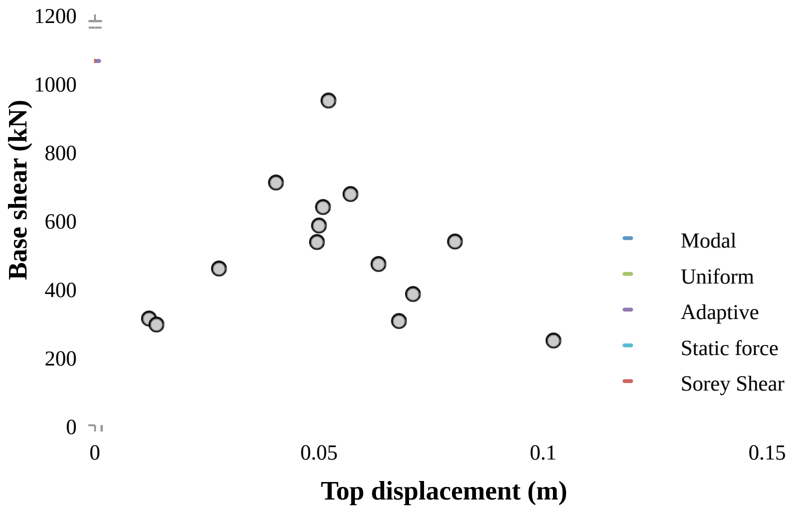

Figure 5: Comparison between nonlinear static and dynamic analysis – model with infill panels.

The main reason for the lower capacity observed during dynamic analyses is the fact that nonlinear static analyses are not able to account for the cyclic degradation both in terms of strength and stiffness of the infill panels. This effect can be clearly observed from the hysteretic behavior obtained through nonlinear dynamic analysis presented in Figure 6.

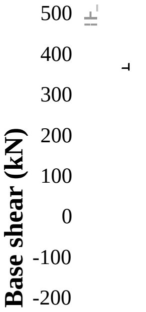

Figure 6: Hysteretic behaviour - model with infill panels.

4.4.2. Influence of accidental eccentricity

According to code prescriptions [2, 3] two different eccentricities should be considered in both directions. In fact, the one imposing an "artificial rotation" opposed to the natural deformation of the building reduces its torsional component. The results presented in Figure 7 indicate that the accidental eccentricity contribution to the global capacity, both in terms of base shear and top displacement, is not significant. Moreover, when the torsional effect is added in the opposite direction of the original building eccentricity (Acc. Ecc. 2), the buildings base shear as well as the deformation capacity is, naturally, increased.

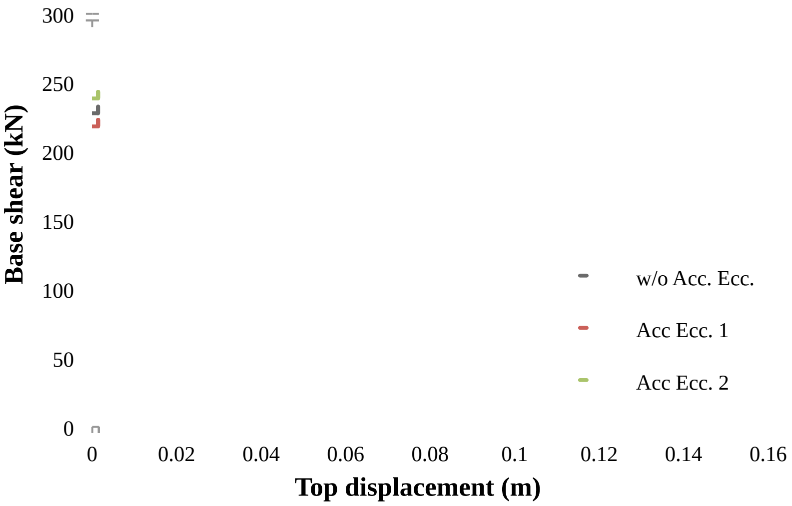

Figure 7: Capacity curves obtained with and without accidental eccentricity.

4.4.3. Slab modelling

As mentioned above, the presence of an in-plan stiff slab has a major importance especially when significant stiffness variations of the vertical elements are observed. Thus, because in Y direction one column (C6) has a flexural stiffness significantly higher than the others, the base shear increases significantly, contrary to what is observed in X direction (Figure 8). The increase in strength in the model with stiff slab can go up to 20% in comparison with the one with no slab.

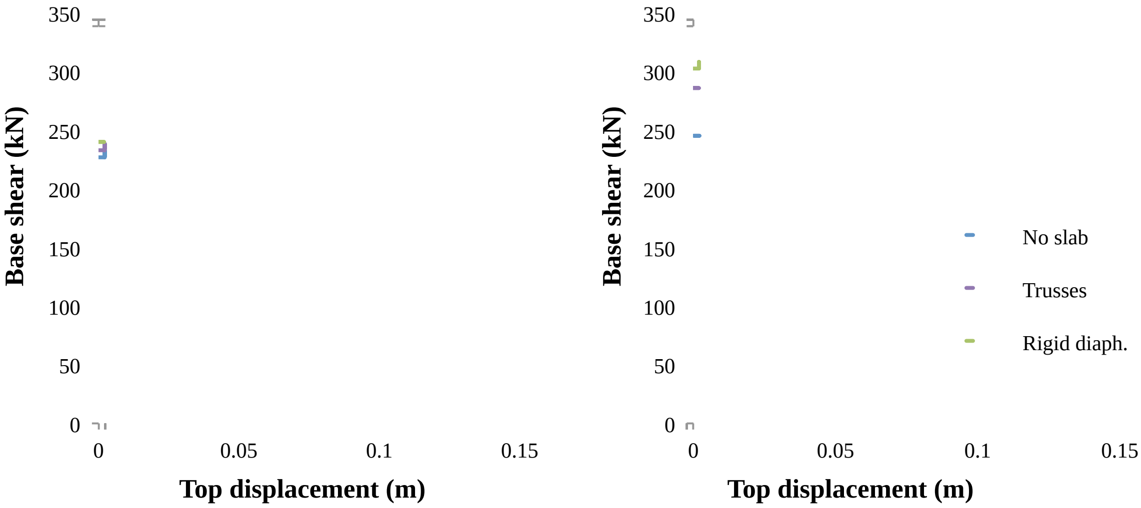

Figure 8: Capacity curves with different slab modeling in X (left) and Y (right) direction.

In the same fashion, the presence of infill panels within the RC frames will significantly increase the stiffness of the frames. However, because the panels were placed only at the external frames, the response of the building will be mainly controlled by the slab properties, rather than the infills, as illustrated in Figure 9.

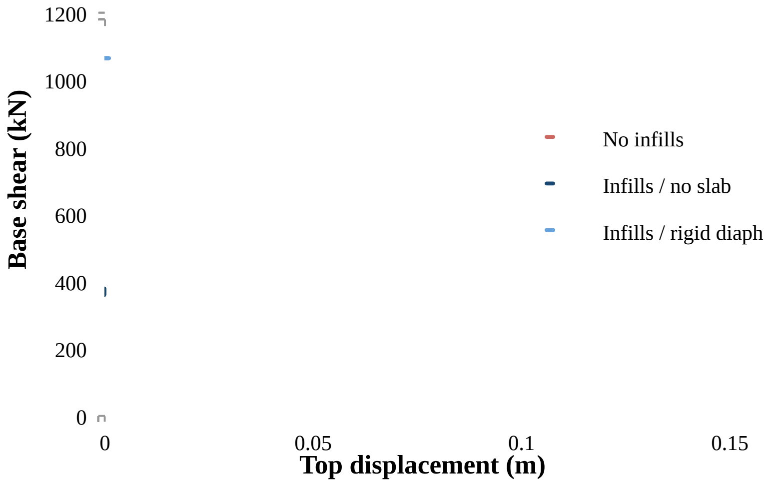

Figure 9: Capacity curves considering infilled structure with and without in-plan stiff slab.

The reason behind this peculiar behavior is the fact that without an in-plan stiff slab, the inner frame is free to deform independently from the edge ones, whilst in presence of a stiff slab the edge frames “attract” more loads and, consequently, change the overall response of the structure.

4.4.4. Mass modelling

Since no remarkable differences were observed between the different load distributions, in order to present the results in a clearer manner, only the results obtained for the main distributions (modal, uniform and adaptive) are going to be presented.

Lookong at the results presented in Figure 10, the definition of the mass as concentrated (darker color) yields slightly lower values of base shear when compared with the model with distributed mass (light color). These conservative results are, however, more noticeable in adaptive and modal distributions. This fact indicates that the results obtained with different mass approaches are affected, mainly due to variations in the modal properties of the structures, rather than different lateral load distribution.

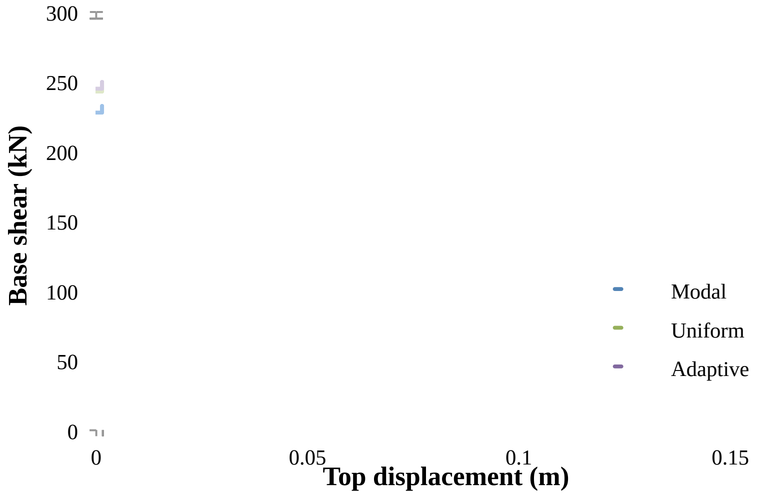

Figure 10: Capacity curves considering concentrated mass (darker color) and distributed mass (lighter color) for three different load distributions.

4.4.5. Elements meshing

Finally, the behaviour of the structure considering the simplified beam-element is evaluated. Note that, as explained in Chapter 3, this comparison is made between models with concentrated mass in order to provide consistent results. It seems clear, according to Figure 11, that implementing simplified beams has negligible influence in the global capacity of the building. This indicates, as expected, that the beams seismic response of the beams is governed by the end-section properties.

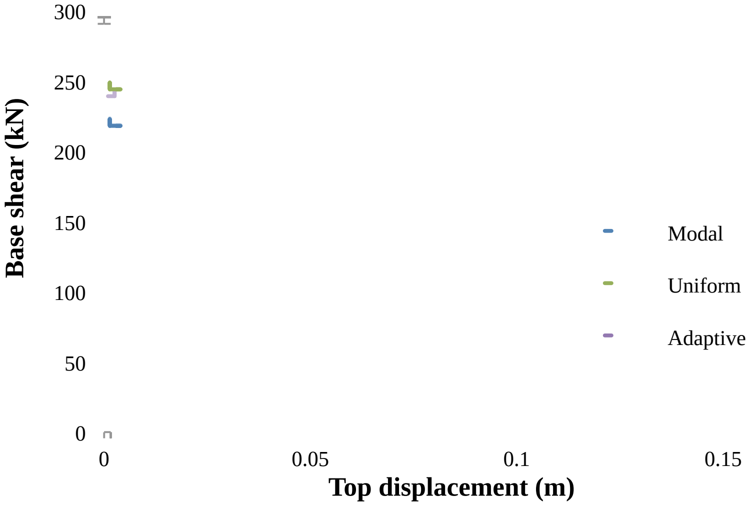

Figure 11: Capacity curves considering real beam sections (darker color) and simplified beam section (lighter color) for three different load distributions.

4.5 Local Assessment

In the previous section, the performance of the building was assessed in a global level, comparing the results obtained by both nonlinear static and dynamic analyses. In this chapter, the building performance is evaluated at the element level, and more specifically in terms of elements chord rotations. For this purpose, the performance point (PP) estimated for each of the three Limit States (LS) prescribed by EC8 (Damage Limitation (DL), Significant Damage (SD), Near Collapse (NC)) is evaluated for each capacity curve. The nonlinear static procedure (NSP) employed for this purpose was the N2 method [11], also recommended by EC8.

Because the main goal of this work is to assess the influence of different parameters and provide recommendations on how the modification in some structural and modelling aspects will affect the response of the structures, the results are presented not in terms of code compliance (capacity verification) but, instead, through a direct comparison between the chord rotations obtained from different models.

Thus, for each PP, the chord rotations for both beams and columns were evaluated and plotted as a fraction between the parameters that are being evaluated. The results close to unit indicate that no significant differences were observed between different approaches. In the following paragraphs, the results plotted from left to right, as the elements are located from the bottom to the top of the building. For simplicity, only representative plots are presented.

4.5.1. Influence of accidental eccentricity ($\theta_{originl}$ / $\theta_{w/acc. ecc.}$)

The results observed in terms of chord rotation are in line with the ones observed at the global level, indicating that no significant differences are observed when accidental eccentricity is considered. Further analyses on different structures should be performed in order to evaluate the need of considering this additional eccentricity.

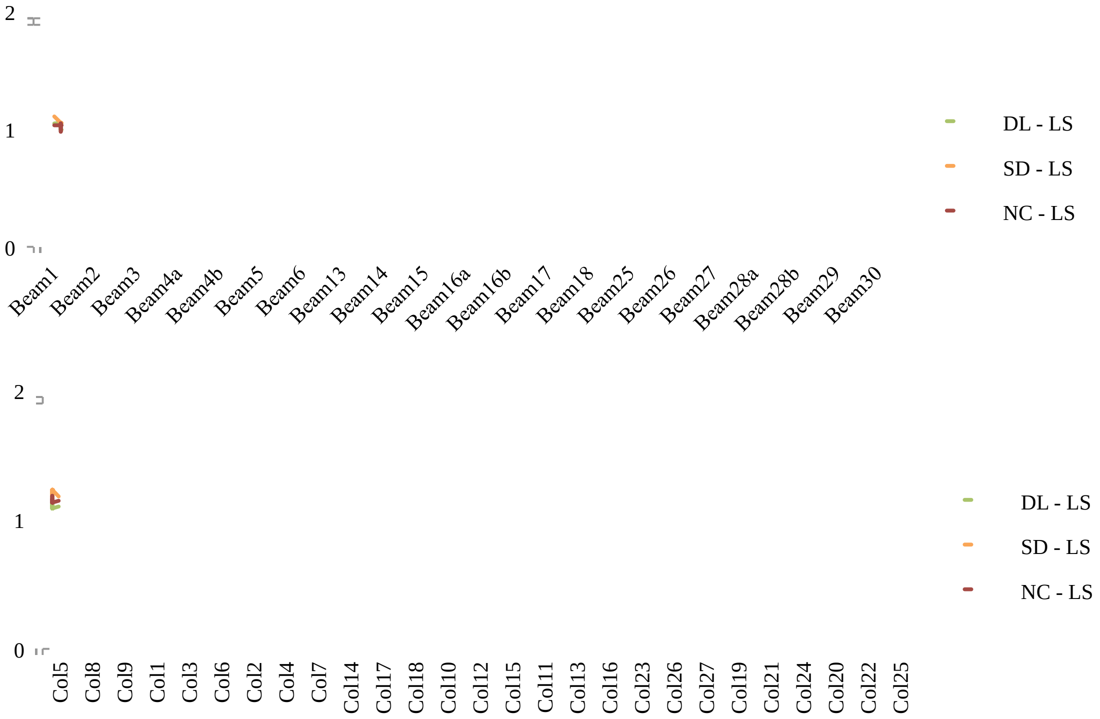

Figure 12: Beam and columns chord rotations with and without accidental eccentricity.

4.5.2. Slab modelling ($\theta_{rig.\ diaph} / \theta_{no\ slab}$)

The introduction of an in-plan stiffness slab will provide an additional axial compression force in the beam increasing, this way, its deformation capacity. At the same time, as the beams stiffness was "artificially" increased, the columns are thus forced to deform more in comparison with the configuration without slab. In this particular case, this effect is more evident at the first storey because the building exhibits a soft-storey mechanism at the ground floor.

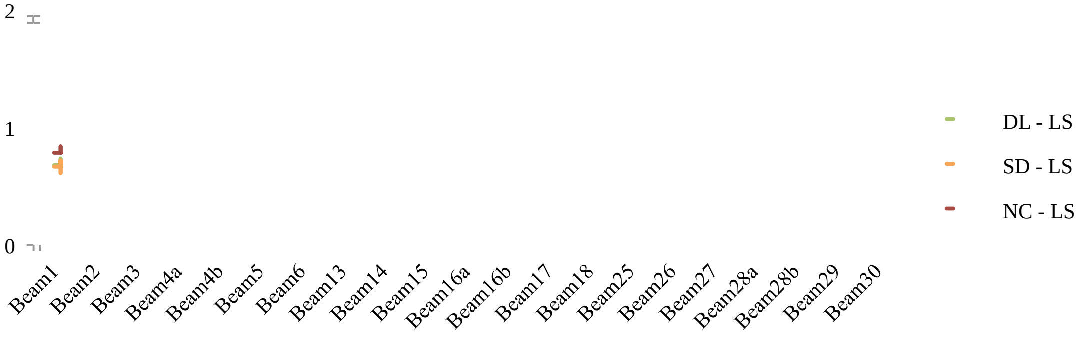

Figure 13: Beam and columns chord rotations with rigid diaphragm and without slab.

4.5.3. Mass modelling ($\theta_{concentrated}$ / $\theta_{distributed}$)

The major consequence of concentrating the mass at the beam-column joints is that no gravity moments will develop along the beams. Consequently, as seismic loads impose moments of opposite signs the both beam-ends, the deformations will also be different at each edge. Therefor, lower values of chord rotations are expected at the beam-end that has different moments signs in static and seismic load. On the other hand, in the opposite end, the results might be conspicuously non-conservative, especially in longer beams, where higher gravity moments are developed. Despite it is not possible to identify a clear trend in the columns results, it seams clear that for higher seismic intensity (NC-LS) the differences becomes less significant, indicating that, as the seismic moments are getting more relevant with respect to static ones, the outcoming variation decreases.

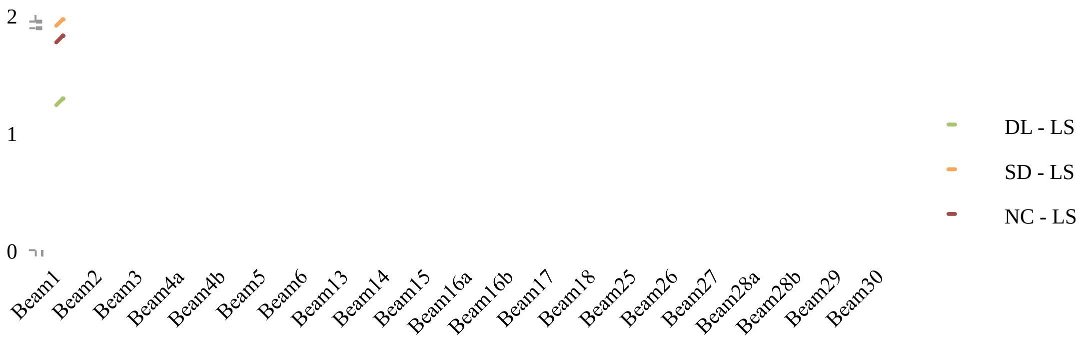

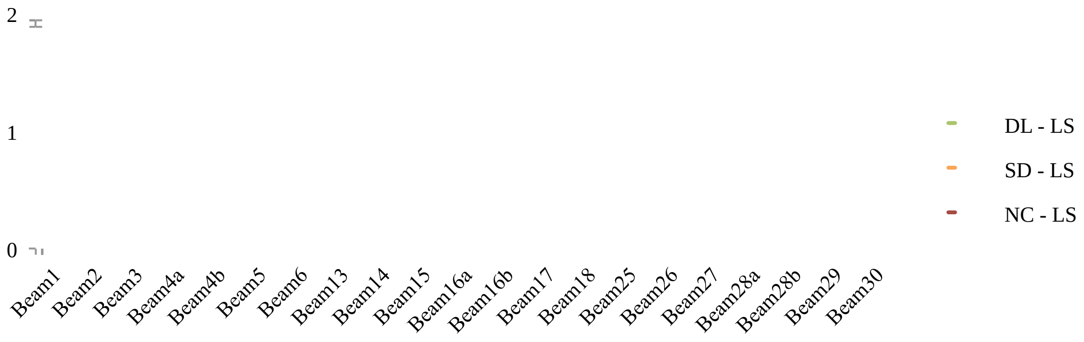

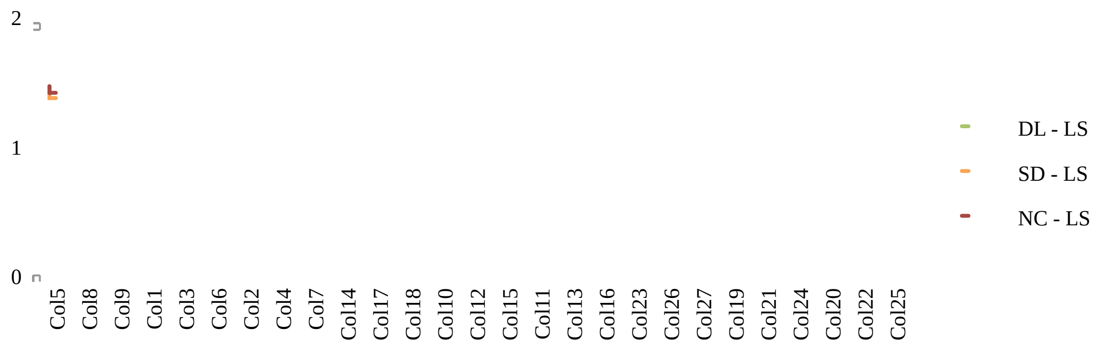

Figure 14: Beam and columns chord rotations with concentrated and distributed mass.

4.5.4. Elements meshing ($\theta_{\text{simp. beam}}$ / $\theta_{\text{real beam}}$)

Finally, the substitution of the real beams with simplified elements with the same section throughout the entire element was evaluated. The results reveal show that no differences are observed between the two approaches. This means that, in general, no loss of accuracy is observed in terms of elements chord rotations. The only exceptions, represented as spike in Figure 15, are corresponding to indirectly supported beams, in which the absence of bottom reinforcement induces a significant change in the members' deformation capacity. Therefor this approach is not suitable for cases where indirect beam supports need to be modelled.

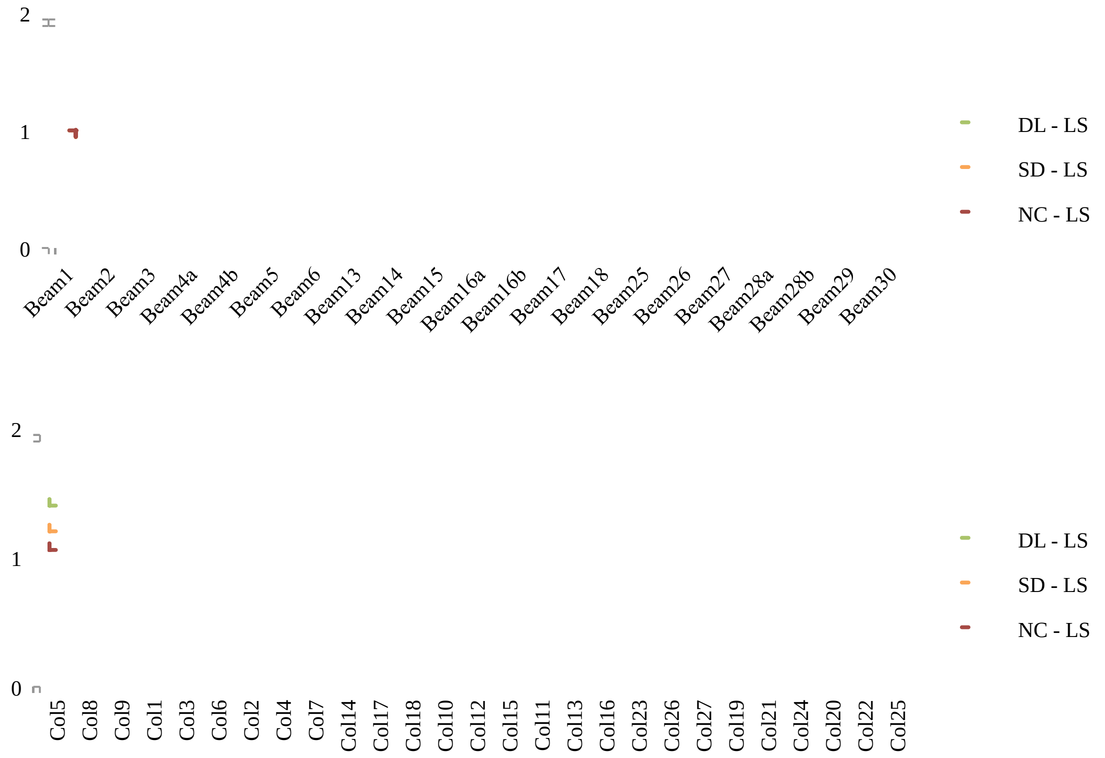

Figure 15: Beam and columns chord rotations with real beam sections and simplified beam section.

5 CONCLUSIONS

Based on the results presented in this work, the following conclusions can be made:

- The results extracted during this study indicate that nonlinear static analyses are able to accurately predict the behaviour of the buildings, even considering in-plan irregular structures.
- Between the five different load distributions used in pushover analyses, no significant differences were observed. Typically, the results obtained with adaptive distribution lie between the traditional extreme ones (modal and uniform) and seem to reproduce better the structural behaviour, especially in the post-peak branch.
- The consideration of an accidental eccentricity in the assessment of existing buildings, as prescribed by EC8, appears to have residual influence in the results obtained in both global and local analyses.
- Special attention should be addressed in the modelling of the structures slab. The results clearly indicate that both global and local behaviour of the building can be controlled by this parameter, especially because it might impose an artificial strengthening of the beams.
- The presence of infill panels significantly transforms the response of the building. The presence of these elements greatly increases the initial stiffness and strength of the structure and might attract higher seismic loads. Because infill panels loose most of its capacity after the first cycles, in order to properly capture behaviour of infilled RC structures, nonlinear dynamic analysis, rather than nonlinear static analysis should be performed in order to take into account the cyclic effects on the infill panels. Additional studies should be addressed to this topic.
- Especially when long beams are modelled, the consideration of an equivalent concentrated mass at the beam-column joints might overestimate the capacity of the elements. This issue might be bypassed if the equivalent point forces/moments obtained from gravity load are computed and applied at the joints before performing the seismic analysis. However, if this procedure is followed, the advantage (time consuming) of employing this simplification is lost.
- Finally, it was demonstrated that, in general, beams could be modelled as one equivalent element with the same section over its length. Nevertheless, this approximation is valid only if concentrated mass is implemented. Thus, because the latter approach may provide unrealistic results, the use of an equivalent beam element is not recommended.

REFERENCES

[1] T. Panagiotakos, M. Fardis, *Seimic response of infilled RC frames structures, Eleventh World Conference on Earthquake Engineering,* Acapulco, Mexico, June 23-28 1996.

[2] F.J. Crisafulli, *Seismic Behaviour of Reinforced Concrete Structures with Masonry Infills*, PhD Thesis, University of Canterbury, New Zealand, [1997].

[3] CEN (2004), Eurocode 8: *Design of structures for earthquake resistance. Part 1: general rules, seismic actions and rules for buildings*. EN 1998-1:2004 Comité Européen de Normalisation, Brussels, Belgium.

[4] Decreto Ministeriale 14/01/2008, *NTC – 08 Norme Tecniche per le Costruzioni* (in Italian)

[5] V. Mpampatsikos, *A critical review of the RC frame existing building assessment procedure according to Eurocode 8 and Italian seismic code*, MSc Thesis, Rose School, Pavia, Italy, 2008.

[6] E. Mola, P. Negro, *Full scale PsD testing of the torsionally unbalanced SPEAR structure in the 'as-built' and retrofitted configurations*, Proceeding of the International Workshop, Ispra, 4-5 April 2005.

[7] SeismoSoft, *SeismoStruct - A Computer Program for Static and Dynamic Nonlinear Analysis of Framed Structures*, Available from URL: www.seismosoft.com.

[8] I. Lanese, R. Nascimbene, A. Pavese, R. Pinho, *Numerical simulations of an infilled 3D frame in support of a shaking-table testing campaign*, Proceedings of the RELUIS Conference on Assessment and Mitigation of Seismic Vulnerability of Existing Reinforced Concrete Structures, Rome, Italy, 2008.

[9] J.J. Bommer, A. Martinez-Pereira, *The effective duration of earthquake strong motion*, Journal of Earthquake Engineering, Vol. 3, No. 2, 127–172, 1999.

[10] SeismoSoft, *Seismosignal - A computer program for derivation of elastic and costant ductility inelastic response spectra*, Available from URL: www.seismosoft.com.

[11] P. Fajfar, M, Fischinger, *N2 – A method for non-linear seismic analysis of regular buildings*, Proc., 9th World Conference on Earthquake Engineering, Tokyo, Kyoto, Vol.5, 111-116, 1988.

COMPDYN 2011
III ECCOMAS Thematic Conference on
Computational Methods in Structural Dynamics and Earthquake Engineering
M. Papadrakakis, M. Fragiadakis, V. Plevris (eds.)
Corfu, Greece, 25–28 May 2011

DEFINITION OF A PRIORITISATION PROCEDURE FOR STRUCTURAL RETROFITTING OF ITALIAN SCHOOL BUILDINGS

Barbara Borzi[1], **Paola Ceresa**[1], **Marta Faravelli**[1], **Emilia Fiorini**[1] **and Mauro Onida**[1]

[1] European Centre for Training and Research in Earthquake Engineering (EUCENTRE)
Via Ferrata, 1, 27100 Pavia, Italy
e-mail: {barbara.borzi,paola.ceresa,marta.faravelli,emilia.fiorini,mauro.onida}@eucentre.it

Keywords: Vulnerability, Seismic Risk, School Buildings, Multiphase Analysis.

Abstract. *Most of the Italian school buildings were not designed according to seismic criteria and, therefore, they are vulnerable from a seismic point of view. A clear proof of this was the catastrophic collapse of the school at San Giuliano during the October 2002 earthquake: thirty people death, twenty seven of whom were young students and one their teacher. After this seismic event, the process for identifying the most seismic vulnerable school buildings was started in Italy, with the final aim of improving their strength. Furthermore, several school buildings, mainly located in the historical centre of the town, were damaged during the recent seismic event of L'Aquila (April 6, 2009), as reported by Salvatore et al. [1]. The proposed research work was driven by the idea of defining a methodology that implements different analysis phases with an increasing level of detail such that the number of buildings analysed decreases at each phase since only the buildings most at seismic risk are considered. The implemented procedure follows some well known works published in literature [2, 3]. The definition of a prioritisation scheme of intervention is strictly due to the high number of school buildings (almost 50000) that cannot be deeply analysed considering the limited available resources. The developed tool and procedure can be very helpful since they provide information extremely important for civil protection actions.*

1 INTRODUCTION

Italian seismic provisions and seismic zonation were updated several times during the last century. Therefore, a large portion of buildings has not been designed for an adequate level of seismic resistance required under modern design provisions. The majority of the Italian school buildings are especially vulnerable to seismic ground motion since they are judged to be seismically inadequate. An ad hoc seismic risk evaluation of the school buildings becomes therefore of fundamental importance for planning an accurate rehabilitation of these buildings and for saving their occupants.

The seismic vulnerability evaluation of the school buildings is a topic that has been discussed by several authors in the last decades [2, 3, 4, 5]. However, due to the limited amount of the available data, those methodologies were applied to a Regional level only.

To the authors' knowledge, the study presented herein is the first where the maps of conditional probability of damage and seismic risk are obtained at a national level, since it has been carried out considering most of the Italian school buildings. The available data refer to the survey of all school buildings ("Anagrafe Edilizia Scolastica") carried out by the Ministry of Education ("MIUR") to identify various safety-related parameters. The collected survey forms comprise about 70% of the Italian school buildings, and contain data that allow the geographical location of the building, as well as its structural characteristics (i.e., age, number of storeys, construction type, and preservation status), its security conditions and the features of rooms and sporting facilities.

2 ADOPTED PROCEDURE

This research work describes the method proposed for identifying the most seismic vulnerable Italian school buildings and for assigning priorities for the execution of detailed inspections and structural retrofitting measures. The adopted method is based on an initial proposal by Grant et al. [2]. It comprises multiple levels of assessment of increasing level of detail, each one substantially reducing the size of the building inventory since only the buildings most at seismic risk are considered. The procedure consists of two phases which correspond to the two levels of the available building information. In both phases the seismic risk is defined considering the probability of reaching or exceeding given limit states comparing the demand with the capacity in terms of displacements. The vulnerability of the school buildings is defined computing their capacity curves (known, in the technical literature, as pushover curves). The mechanics-based methodology SP-BELA (Simplified Pushover-Based Earthquake Loss Assessment), developed for large-scale vulnerability assessment, is used for performing the simplified pushover curves [6, 7] of the analysed buildings.

In the first phase of the assessment, the capacity is computed as a function of the number of storeys, structural vertical typology, and building age written in the questionnaires of the "Anagrafe Edilizia Scolastica". Based on these data, the buildings are subdivided in classes and random populations of buildings can be generated for each building class using Monte Carlo Simulation. For each randomly generated building, a simplified pushover analysis is carried out using SP-BELA (Figure 1), leading to the definition of the displacement capacity, vibration period and viscous damping of an equivalent single degree of freedom system [6, 7].

The second phase of the procedure is based on the data collected, at Regional level, through the 2nd Level Forms [8, 9, 10] of GNDT ("Gruppo Nazionale per la Difesa dai Terremoti"). In this second phase, only masonry buildings are taken into account since the information required, in the GNDT 2nd Level Form, for reinforced concrete (RC) buildings are not enough for defining their structural capacity, whereas they allow the Conventional Resistance

("Resistenza Convenzionale") to be calculated for masonry buildings. This Conventional Resistance is the lateral strength of the weakest storey of the building divided by the building weight. Therefore, the difference with respect to the first phase of the procedure is that the resistance factor of the capacity curve is computed directly with the data available within the form of the reference school building and not computed for each random generated building stock representative of the reference school building class.

Due to the incompleteness of the available database, the second phase of the procedure cannot be applied to the overall Italian school building stock. Therefore, the estimate of the reduction of the size of the building inventory moving from the first to the second phase of the procedure cannot be carried out. The study described herein does not apply the prioritization procedure as a whole, but represents its validation in order to indentify some possible shortcomings that need improvements.

2.1 Definition of the building capacity

As discussed above, in order to compute capacity curves SP-BELA makes use of a simplified pushover methodology that can be employed in the assessment of a large number of buildings with reasonable computational effort. SP-BELA can be applied to RC [6] and masonry buildings [7], which are representative of the majority of the school buildings "as built" in Italy. The capacity curve is defined by means of the building resistance and the displacements associated to specific structural limit states (LS). Three LS conditions have been taken into account [11]:

- Light damage: the building can be used after the earthquake without the need for repair and/or strengthening.
- Significant damage: the building cannot be used after the earthquake without strengthening.
- Collapse: the building becomes unsafe for its occupants as it is no longer capable of sustaining any further lateral force or the gravity loads for which it has been designed.

The limit state conditions previously described can be related to specific prescriptions of Italian design code [12, 13]. In particular, the reference limit state conditions for RC buildings are defined in relation to the chord rotation. For masonry structures, the damage is usually related to interstorey drift capacity, and the limit conditions have been identified through results from experimental tests as described in [7].

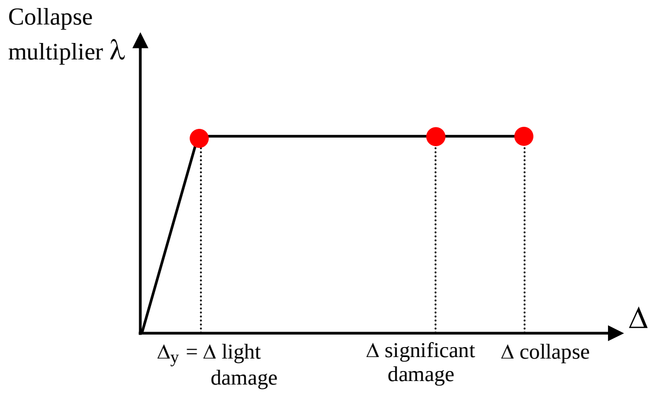

Figure 1: Capacity curve for elastic-perfectly-plastic structural behavior [7].

Within such framework, an elastic-perfectly-plastic behaviour of the structure is assumed (Figure 1), which effectively means that, in order to define the pushover curve, only the displacement capacity Δ corresponding to the three LS and the lowest collapse multiplier λ of all the considered mechanisms need to be defined. Multiplying λ by the total weight of the building gives the lateral strength of the weakest storey of the building. Therefore, λ corresponds to the Conventional Resistance of the GNDT 2nd Level Forms for the masonry buildings.

2.2 Classes of buildings

The methodology proposed in this research study for seismic risk evaluation considers 37 classes of buildings as plotted in Figure 2.

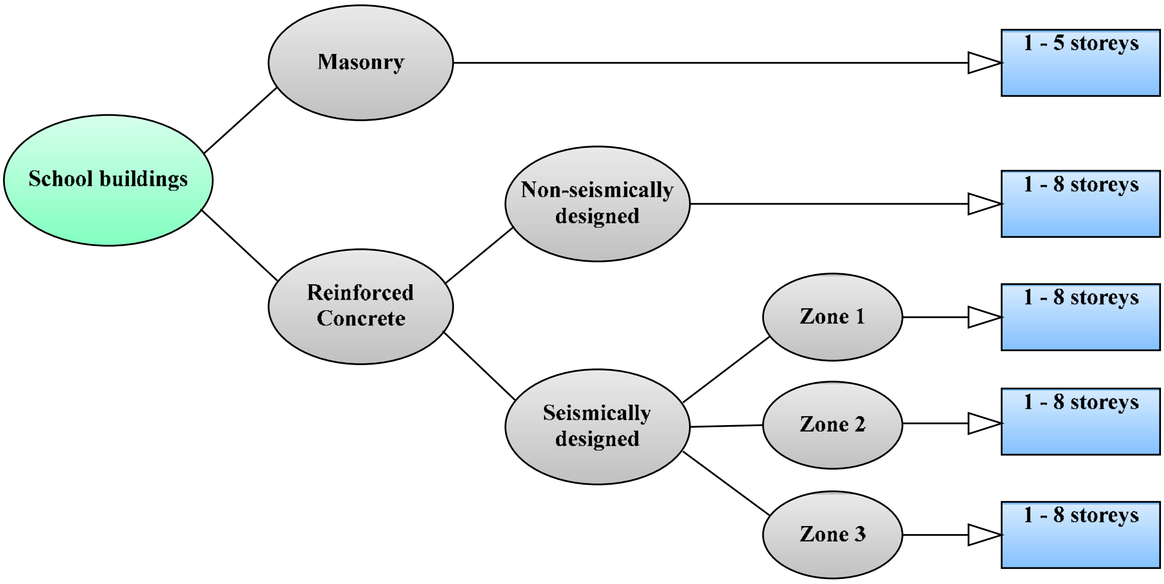

Figure 2: Classes of buildings considered in the study.

With reference to Figure 2, the masonry school buildings have been classified as a function of the number of stories (from 1 to 5), therefore five separate building classes have been defined. A different criterion has been applied for the RC buildings since they are subdivided in two main classes: RC buildings that have not been seismically designed and RC buildings seismically designed. Comparing the seismic zone to which the municipality has been assigned and the period of construction, it is possible to identify if a school building has been or not designed according to seismic design provisions. For seismically designed buildings, the seismic zone of the municipality at the period of the construction has to be taken into account since it can be used, together with the provisions of the design codes of the same period, for defining the value of the design lateral force as a percentage of the total building weight. Figure 2 refers to three seismic zones in Italy, since the fourth one [14] characterised by the smallest value of seismicity has been disregarded. In SP-BELA, the buildings are designed considering only gravity-load design before seismic classification; then following the classification and depending on the seismic zone to which the municipality was assigned, a base shear coefficient has been used to design the buildings. For buildings assigned to Zone 1, this coefficient has been taken as 10% of the weight, for buildings in Zone 2 as 7% and in Zone 3 as 4%. The number of storeys considered for RC school buildings is: 1, 2, 3, 4, 5, 6, 7, more or equal to 8 (Figure 2).

2.3 Conditional probability of damage

In SP-BELA the comparison between seismic capacity and demand is carried out in terms of displacement. The building displacement capacity has been introduced in Section 2.1. The seismic demand imposed by the earthquake to the structure is calculated with reference to the elastic spectrum related to the school building location, computed according to the formulation proposed in [12, 13]. This formulation has been obtained after the least-square interpolation of the mean acceleration spectrum derived from the probabilistic hazard study performed by DPC-INGV project [14] for a grid of points (each one at distance of 0.05 degrees) used for the whole country. The formula and the coefficients given by the Italian code [12, 13] allow the computation of the mean spectral accelerations for each point of the grid and for seismic events characterised by a return period (T_r) of 30, 50, 72, 101, 140, 201, 475, 975 and 2475 years, respectively.

In this study, the least-square interpolation method has been applied to the mean acceleration spectrum (50th percentile) plus and minus one standard deviation for deriving the parameters that allow the computation of the 84th and 16th percentile spectral accelerations, respectively. Therefore, the seismic demand imposed by the earthquake to the structure is computed with respect to the 16th, 50th and 84th percentile acceleration spectra. Flat rock soil has been assumed for the Italian territory, since no data were available for the evaluation of the effects of the site conditions where the school buildings are located.

The seismic demand is derived from the elastic response spectrum knowing the location of the school building, for a given return period and a selected percentile (16th, 50th, and 84th). From SP-BELA method, the vibration period T of the building and the equivalent viscous damping ξ are computed for each limit state. Knowing the response period, the spectral ordinate is directly derived for each LS. Knowing the equivalent viscous damping, the spectra reduction factor η, used to take into account the energy dissipation capacity of a given structure for a given LS, is then computed, as suggested for instance in [15]:

$$\eta = \sqrt{\frac{7}{2+\xi}} \tag{1}$$

For RC frames, the equivalent viscous damping ξ in Equation (1) has been obtained as a function of the ductility, using Equation (2) [15]. For masonry buildings, the damping values suggested in [16], for each limit state, have been adopted (5%, 10% and 15%, respectively).

$$\xi = 0.05 + 0.565\left(\frac{\mu - 1}{\pi\mu}\right) \tag{2}$$

The displacement spectral ordinates are defined starting from the spectral accelerations:

$$S_d = S_a\left(\frac{T}{2\pi}\right)^2 \tag{3}$$

where S_d represents the displacement demand, S_a the acceleration demand and T the period of vibration of the building.

Based on the previously introduced ingredients, the conditional probability of damage, where the condition is that a given seismic event will occurs, can been computed for the nine return periods T_r considered in the Italian seismic code [12]. Random populations of buildings are generated for each building class (1000 buildings for each one of the 37 classes shown in Figure 2) using Monte Carlo Simulation. The period of vibration T and the displacement capacity Δ at the three different damage limit states (Figure 1) can be calculated for each randomly generated building through a simplified pushover analysis performed using SP-BELA (Section 2.1). Knowing T at each LS and for a given overdamped (using Equation 1) displacement response spectrum, the displacement demand of a given building in the random population can be predicted and compared with its limit state displacement capacity. This procedure is repeated for the 1000 buildings randomly generated for each class of school buildings (Figure 2). The sum of all buildings whose displacement capacity is lower than the displacement demand divided by the total number of buildings gives an estimation of the probability of the exceeding a given limit state. The output of these computations is the conditional probability of damage, given the occurrence of a seismic event characterised by a given return period T_r.

2.4 Computation of the seismic risk

The seismic risk is computed knowing the hazard curve of the place where the school building is located. It gives the recurrence probability of a seismic event with a given level of severity in a specific exposure time t_d. Severity can be expressed in terms of the Annual Frequency of Exceedance (*AFE*), which is the reciprocal of the return period T_r. The hazard curve represents the relationship between *AFE* and a ground motion parameter, herein assumed as the spectral displacement S_d. The logarithm of the S_d and the logarithm of the corresponding *AFE* (=1/T_r) can be assumed to be linearly-related, at least for return periods of engineering interest. The gradient of the log-log hazard curve is named $-k$, according to the definition in Part 1 of the Eurocode 8 [17]. As an example, Figure 3 plots the spectral ordinates S_d for a vibration period of 0.1 seconds. Since the values are linearly related, the hazard curve is defined knowing a value of S_d corresponding to a return period T_r and the slope k of the line interpolating all the other points and passing from a reference point.

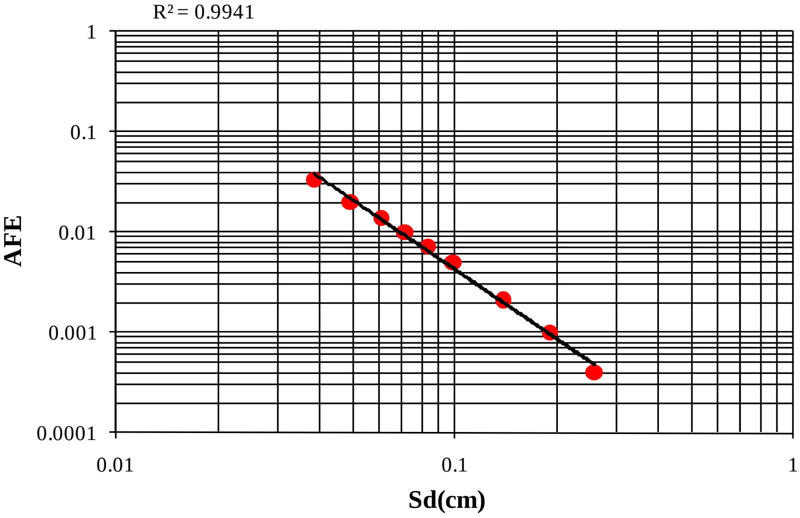

Figure 3: Relationship between the annual frequency of exceedance (*AFE*) and S_d(T=0.1 sec).

This reference point is here conventionally assumed equal to value at 475 year return period, and the hazard curve is defined by the following relationship:

$$AFE = AFE_{475}\left(\frac{S_{d475}}{S_d}\right)^k \tag{4}$$

where AFE_{475} and S_{d475} are, respectively, the annual frequency of exceedance and the spectral displacement corresponding to the 475 year return period.

Knowing the vibration period T of the structure, nine values of spectral accelerations S_a are computed in correspondence of the nine return periods T_r listed in [12]; using Equation (3), the S_a values are converted in spectral displacements S_d; the next step is the derivation, in a log-log plane, of the line interpolating these points and passing for the point computed at a 475 year return period, and the slope k is finally derived. Therefore, the hazard curve is directly derived and the displacement demand can be computed whatever return period is considered. It derives that all the events that could happen in a specific exposure time t_d can be taken into account. Hence, the seismic demand is then computed and compared with the capacity for each event, obtaining the conditional probability of exceeding a given limit state.

The seismic risk is the unconditional probability of failure of the limit state condition, because the condition on the occurrence of the seismic event is removed by considering the probability that the event occurs in the selected exposure time. For its computation, the hazard curve previously expressed as a function of the frequency has to be given in terms of probability. The occurrence of the events is assumed to follow the Poisson process, that is a memoryless distribution such that each event occurs independently of one another. Therefore, the occurrence probability (q) of an event with severity AFE, in the exposure time t_d, is given by the following equation:

$$q = 1 - e^{-t_d AFE} \tag{5}$$

Since AFE is related to the spectral displacement S_d according to Equation 4, the probabilistic hazard curve can be expressed as a function of S_d:

$$q = 1 - e^{-t_d AFE_{475} \left(Sd_{475} / Sd \right)^k} \tag{6}$$

Three exposure times t_d are taken into account in this study: 1 year, 10 years and 50 years. If, for example, the annual collapse risk has to be computed, the corresponding hazard curve is obtained from Equation 6 with $t_d = 1$. The derived curve gives the annual probability of occurrence of an event with severity AFE expressed as a function of S_d. The hazard curve has to be related to the conditional probability of collapse, i.e. the vulnerability, where the condition is the occurrence of an event for a given return period T_r. Knowing that T_r can be expressed as a function of AFE and AFE is related to S_d according to Equation 4, the conditional probability of damage is then obtained and the condition is expressed as a function of S_d. Therefore, since two curves are available – the hazard curve and the vulnerability curve – both expressed as a function of S_d, the exceedance curve of a given limit state in the exposure time t_d can be constructed as a discrete function.

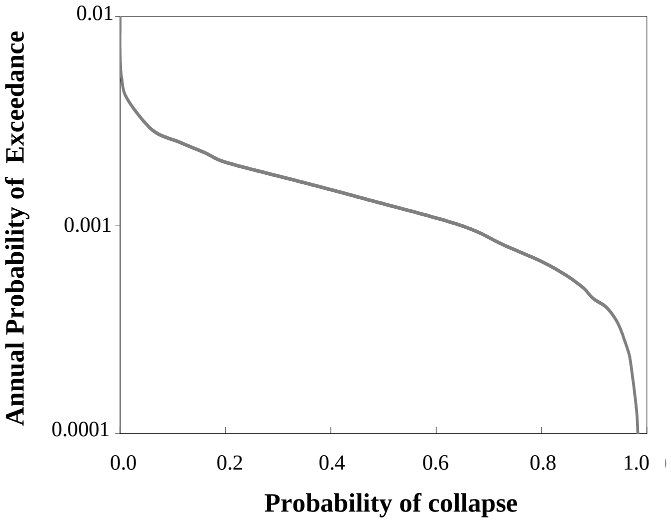

Figure 4: Exceedance curve of the collapse limit state in an exposure time of 1 year, for a given class of buildings.

Shown in Figure 4 is the exceedance curve for a exposure time t_d of 1 year and the collapse limit state. The annual seismic risk is given by the analytical integration of this curve, using the following equation:

$$Seismic\ Risk = \sum_{i=0}^{+\infty} \left[\frac{APE_{2(i+1)} - APE_{2i}}{6} \right] \cdot \left[P_{collapse_{2i}} + 4P_{collapse_{2(i+0.5)}} + P_{collapse_{2(i+1)}} \right] \qquad (7)$$

where *APE* is the annual probability of exceedance, and $P_{collapse}$ the probability of collapse.

If the exposure time t_d is different from 1 year, the ordinates of the derived plot are the probability of exceedance in the considered t_d.

3 AVAILABLE DATABASES

The procedure described for the evaluation of the seismic risk has been applied for processing the data of two databases: the survey forms of the “Anagrafe Edilizia Scolastica” (used in the first phase of the procedure) and the GNDT 2nd Level forms (used in the second phase of the procedure). The school buildings of the “Anagrafe Edilizia Scolastica” forms have been georeferenced based on the street address. Then, a correspondence between these buildings and the ones of the GNDT forms has been derived in order to compare the two sets of data. Since there is no a common identification to be associated to the school buildings of the two databases, the correspondence has been carried out using the geographical location. The georeferenced buildings belonging to the “Anagrafe Edilizia Scolastica” database are 49503, whereas the ones belonging to the GNDT database and with a correspondence in the first database are 3553.

3.1 School buildings analysed in the first phase of the procedure

As previously introduced with Figure 2, the school buildings of the “Anagrafe Edilizia Scolastica” database have been subdivided in 37 classes. However, there are 17328 buildings of this database without the specification of their structural typology or the number of storeys; therefore, they could not be introduced in one of the classes of Figure 2. Hence, some assumptions have been done in order to automatically assign the needed information for classifying these school buildings. Furthermore, additional hypotheses have been required for assigning one of the two main structural typology considered in this study (masonry and reinforced concrete) to those buildings with a mixed typology. The “reinforced concrete and masonry” or “masonry and other typology” structures have been analysed as masonry buildings, whereas the “reinforced concrete and other typology” structures have been classified as “reinforced concrete” buildings. With these assumptions, it was possible to include 7211 buildings of those 17328 without clear specifications. Therefore, there are 10117 school buildings of the “Anagrafe Edilizia Scolastica” database that cannot be analysed since there are no enough information for assigning a structural typology or because their assigned structural typology in the forms was “other”. Starting from the available 49503 school buildings of the “Anagrafe Edilizia Scolastica” database, the buildings analysed in the first phase of the procedure are 39386, subdivided in 19749 masonry structures and 19637 RC structures.

Figure 5 shows, on the left, the map with the location of the 49503 georeferenced school buildings of the “Anagrafe Edilizia Scolastica” database, and, on the right, a bar chart with the numbers of buildings considered (additionally subdivided according to their structural typology) or omitted in the proposed procedure.

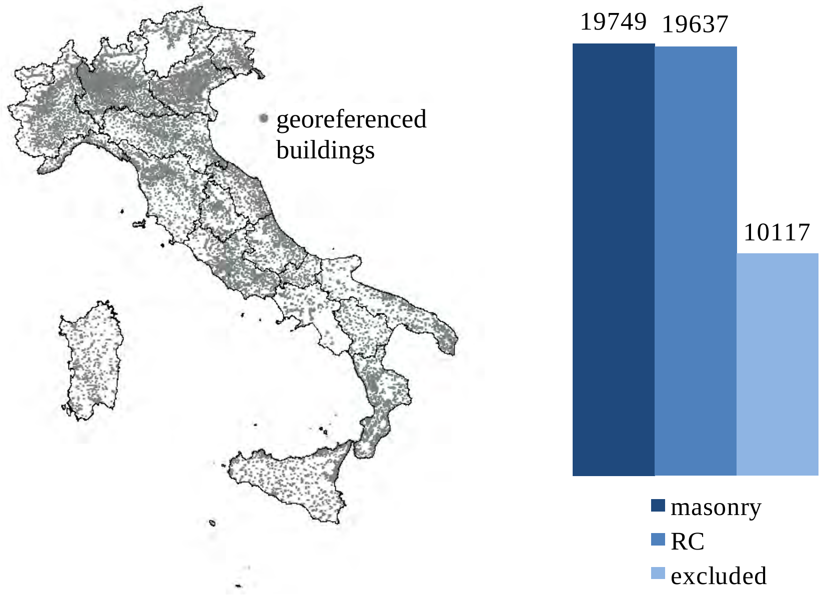

Figure 5: Georeferenced school buildings (on the left) and their classification as a function of their structural typology (on the right).

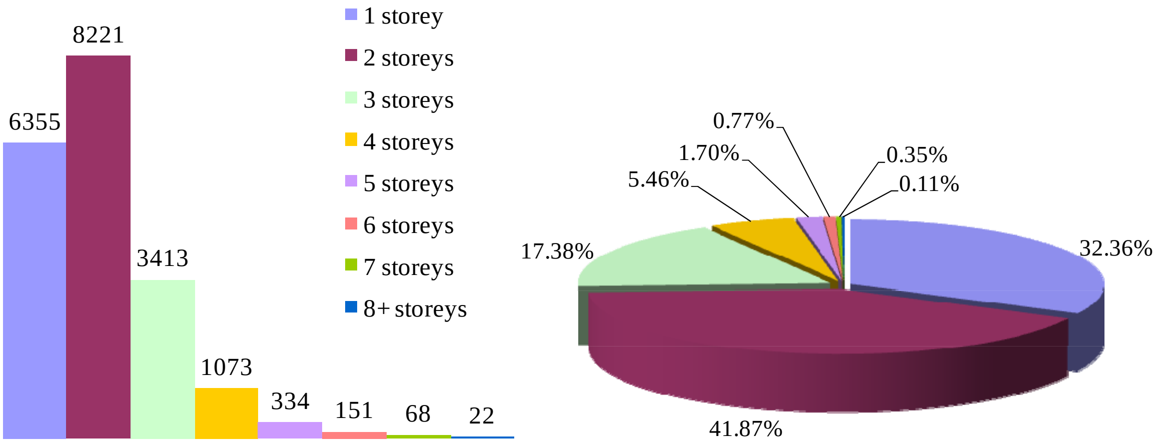

Figure 6: RC school buildings analysed in phase 1 and organised by the number of storeys.

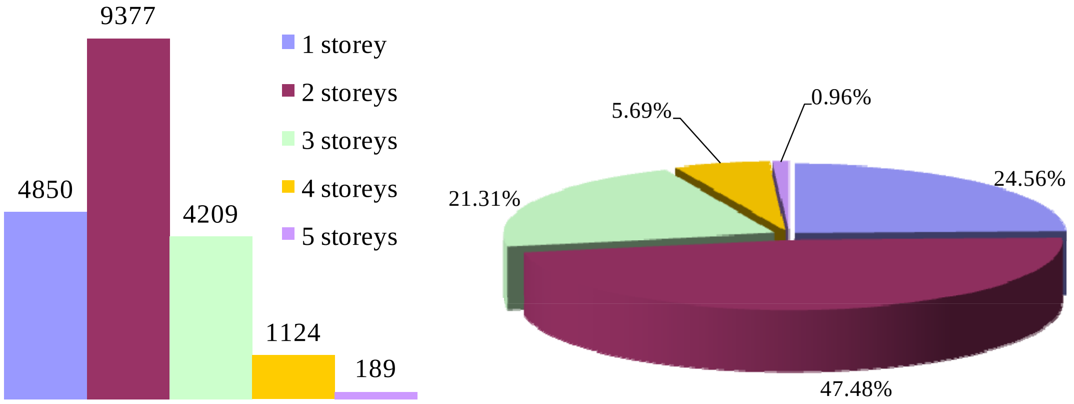

Figure 7: Masonry school buildings analysed in phase 1 and organised by the number of storeys.

Shown in Figures 6 and 7 are the RC and masonry school buildings analysed in the first phase of the procedure and divided in classes according to the number of storeys.

3.2 School buildings analysed in the second phase of the procedure

The school buildings of the GNDT database whose data of the 2nd Level forms allow the calculation of the Conventional Resistance and with a correspondence in the “Anagrafe Edilizia Scolastica” database are 3553. However, five of these masonry buildings cannot be analysed since the data of the compiled survey forms are not coherent. Therefore, the school buildings considered in the second phase of the methodology are 3548, divided in five classes according to the number of storeys (Table 1).

N° of storeys	N° of buildings
1 storey	785
2 storeys	1215
3 storeys	1156
4 storeys	356
5 storeys	36

Table 1: Masonry school buildings analysed in the second phase of the procedure.

The map shown on the left of Figure 8 gives the location of the school buildings analysed in the second phase of the methodology. In addition, the following figure shows the distribution of such buildings for the different seismic zones (from 1 to 3). It has to be pointed out that there are no school buildings belonging to seismic zone 4 (characterised by the smallest seismic hazard) since the compilation of the GNDT 2nd Level forms has been carried out only for the buildings located in zones with medium – high seismicity.

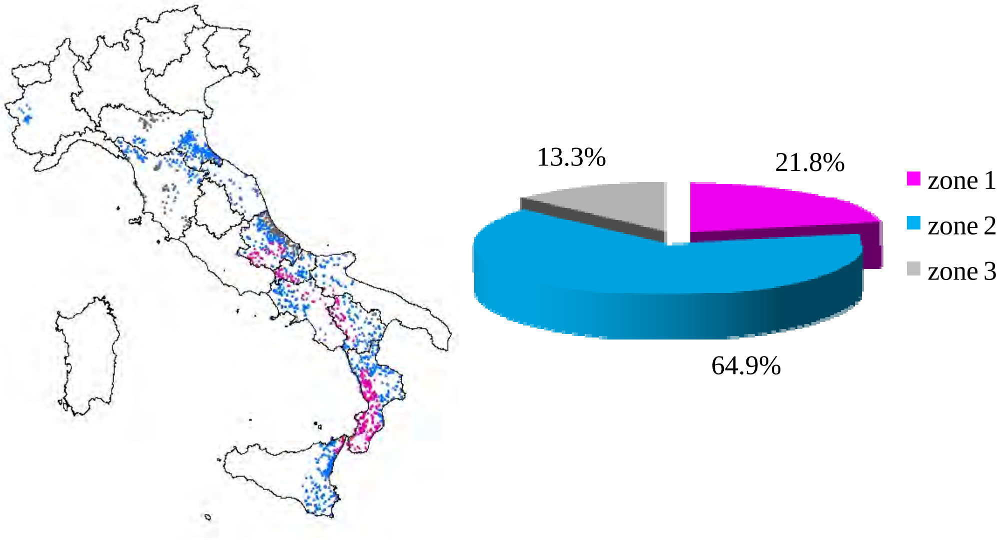

Figure 8: School buildings analysed in the second phase of the procedure and organised by seismic zone.

The Conventional Resistance has been computed for each one of the 3548 school buildings previously described. Knowing this value and its correspondence with the collapse multiplier λ (as anticipated in Section 2.1), the plateaux of the simplified capacity curve is automatically defined for each one the analysed masonry school buildings.

4 DISCUSSION OF THE RESULTS

Using the data collected during the first phase of the procedure (Section 3.1), the maps of conditional probability of damage and seismic risk have been calculated for the three limit state conditions (light damage, severe damage and collapse). The maps representing the conditional probability of damage have been computed for the 9 return periods recommended in [12]. The variability of the spectrum is taken into account considering the mean spectral accelerations plus and minus one standard deviation. Figure 9 shows the conditional probability of exceeding the severe limit state for a seismic event with a 475 year return period, computed with respect to the 16th, 50th and 84th percentile acceleration spectra.

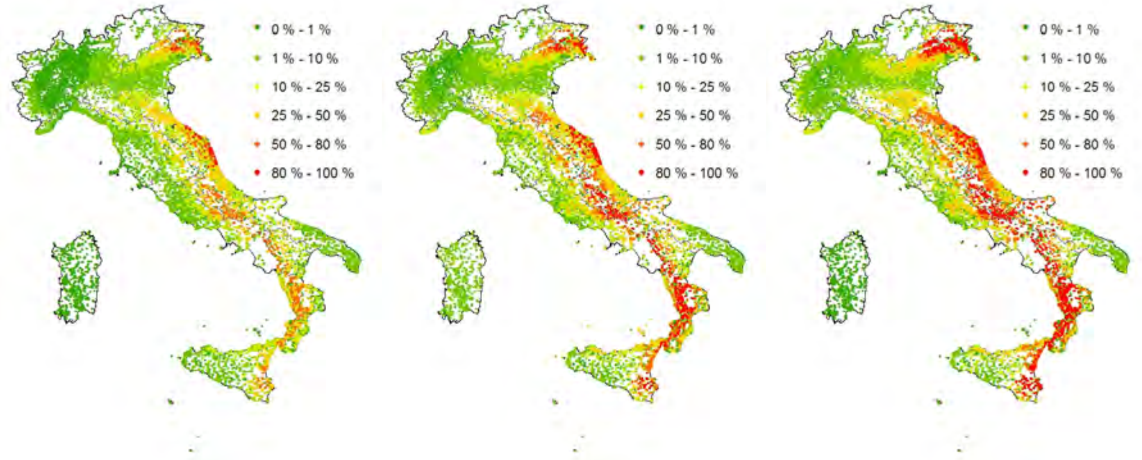

Figure 9: Conditional probability of exceeding the severe limit state computed in the first phase of the proposed procedure, for a 475 year return period (from the left: 16th, 50th and 84th percentile).

Unconditional failure probability has been then computed for the three limit state conditions and three exposure times (t_d = 1 years, 10 years, 50 years). The seismic risk maps obtained for the exposure time of 50 years are plotted in Figure 10.

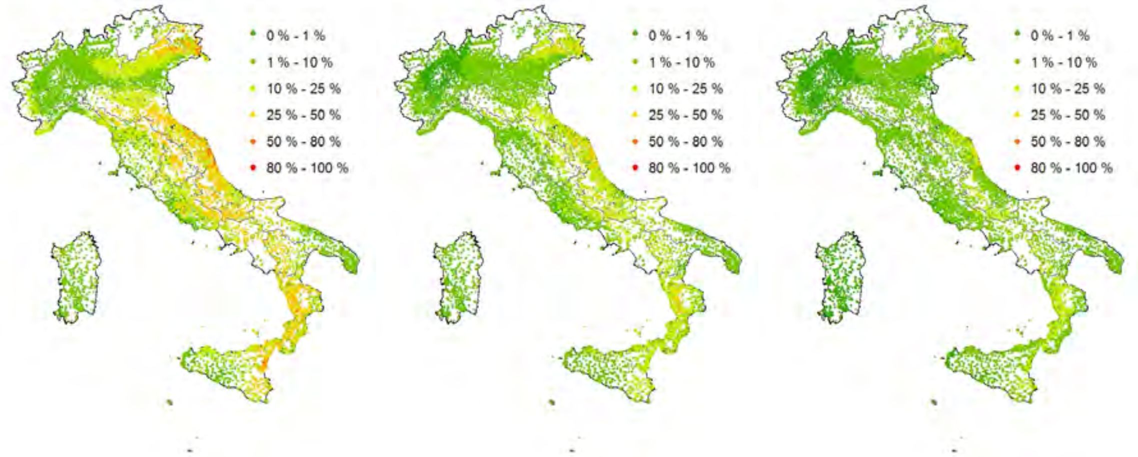

Figure 10: Seismic risk maps for the exposure time of 50 years computed in the first phase of the proposed procedure (form the left: light damage, severe damage and collapse limit state).

The results in Figures 9 and 10 show that the school buildings with the highest probability of exceeding a given limit state are located in Friuli Venezia Giulia, Marche, Umbria, Abruzzo, a reduced zone of Campania (since a small amount of “Anagrafe Edilizia Scolastica” forms have been collected in the whole of the region), the North of Puglia, Basilicata, Calabria and eastern Sicily.

As a result of the second phase of the proposed procedure, the maps of conditional probability of damage and seismic risk have been computed for the 3548 masonry school buildings accounted for. In particular, the plotted results have been calculated comparing the seismic displacement demand derived from the spectra with the seismic capacity obtained from the Conventional Resistance. The maps of Figure 11 show the conditional probability of exceeding the severe damage limit state for a seismic event with a 475 year return period (16th, 50th, and 84th percentile). The maps in Figure 12 show the unconditional failure probability for an exposure time of 50 years (light damage, severe damage, and collapse).

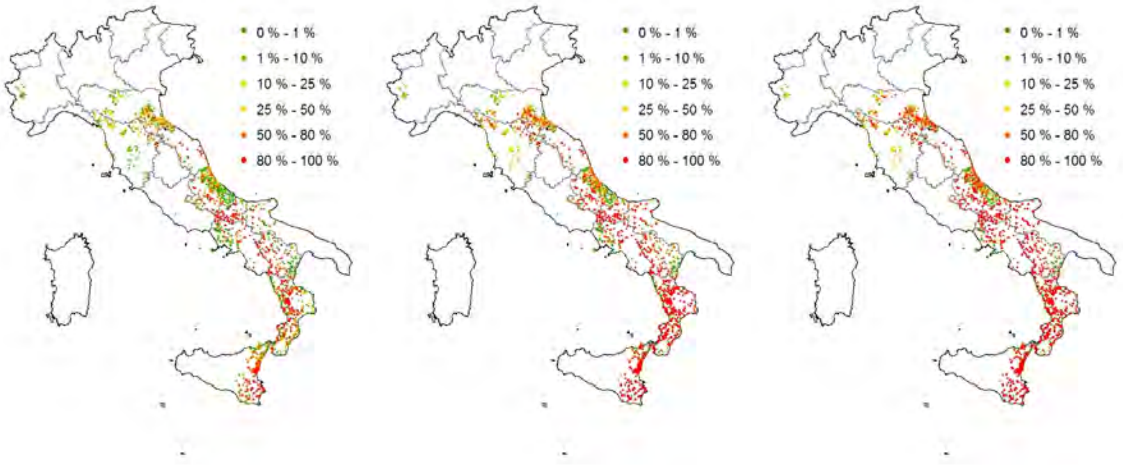

Figure 11: Conditional probability of exceeding the severe limit state computed in the second phase of the proposed procedure, for a 475 year return period (from the left: 16th, 50th and 84th percentile).

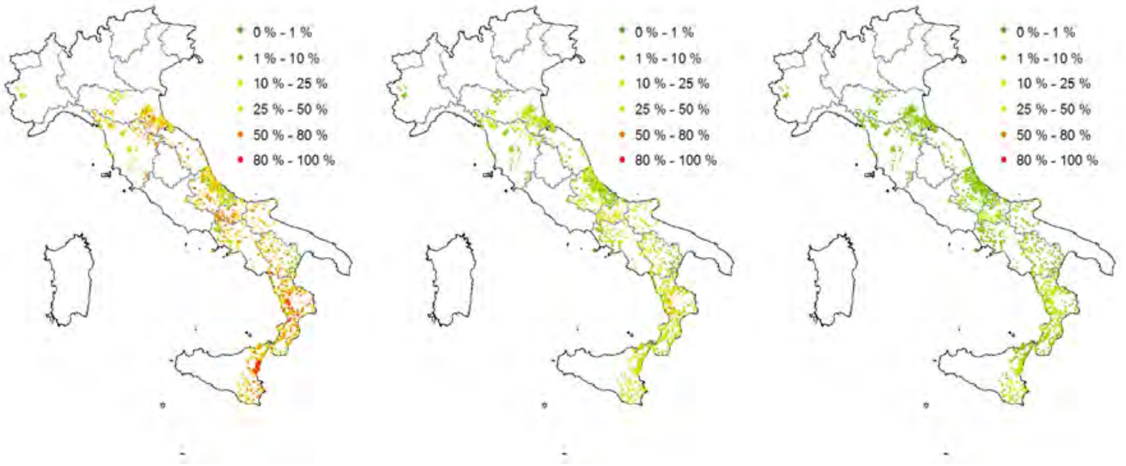

Figure 12: Seismic risk maps for the exposure time of 50 years computed in the second phase of the proposed procedure (form the left: light damage, severe damage and collapse limit state).

According to the results plotted in Figure 11 and Figure 12, the school buildings with the highest probability of exceeding a given limit state are located at the border between Emilia-Romagna and Marche, in Abruzzo, Molise, a zone of the Campania, the North part of the Puglia, Basilicata, Calabria and eastern Sicily. A further step for verifying the accuracy of the described multiphase procedure is the study of the correlation between the results of the first and second phase. The school buildings with high values of seismic risk in the second phase should be characterised by high values even in first phase; if not, it would mean that the first phase of the procedure does not allow the right identification of the highest seismic risk buildings. Therefore, the latter could not be investigated in the next phase of the analysis because they result safe.

The correlation between the results obtained in the two phases of the procedure for the 3548 masonry school buildings is plotted in Figure 13 in terms of seismic risk for an exposure time of 50 years.

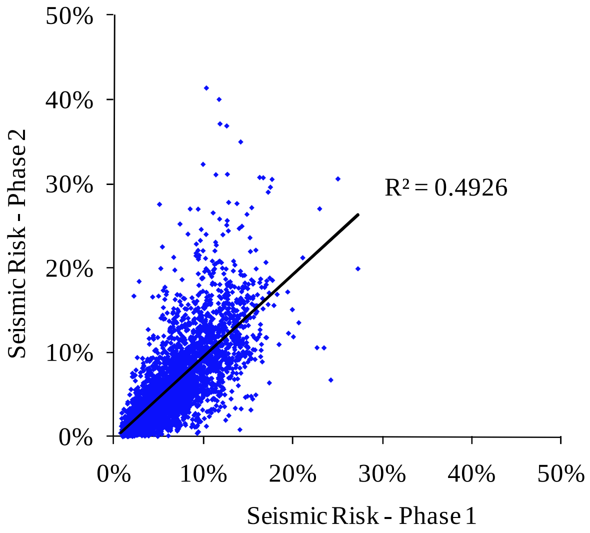

Figure 13: Correlation between the results obtained from the two phases of the proposed procedure.

Figure 13 shows that the correlation between the results from the two phases of the procedure is quite satisfactory. The data points over the line of best fit represent an underestimation of the seismic risk in the first phase of the analysis. This finding could be due to the different evaluation of the seismic vulnerability of the masonry structures. In the first phase of the procedure, good mechanical characteristics have been assigned to all the masonry buildings of the analysed five classes. In the second phase of the procedure, the Conventional Resistance is computed from the data of the survey forms and this resistance could be less than the one assumed in the first phase of the procedure, leading to more vulnerable buildings.

In order to improve the correlation between the results of the two phases of the methodology and to increase the accuracy of seismic risk maps, a refined calibration procedure is under development. This latter could give the possibility to calibrate the seismic vulnerability evaluation of the first phase of the methodology taking into account different masonry typologies also belonging to the worst classes of vulnerability. The calibration could be carried out using additional information collected in the “Anagrafe Edilizia Scolastica” database, such as the typology of the horizontal structures (e.g. the floor stiffness).

5 CLOSURE

The novelty of this research study is represented by the maps of seismic risk for school buildings at a national scale. These maps give an overall view for the definition of a prioritisation procedure for surveys and detailed structural retrofitting measures.

A multiphase procedure has been proposed for the evaluation of the amount of school buildings requiring additional investigations. The methodology implements two analysis phases with an increasing level of detail such that the number of buildings analysed decreases at each step since only the buildings most at risk are considered.

The generation of seismic risk maps at a national scale is an outcome of the first phase of the proposed procedure. The data used for the map generation are based on the collected survey forms of the 70% of the Italian school buildings. However, a reduced number of school buildings (3500) was available during the second phase of the procedure. In fact, additional information on the building resistance should be collected and used during this analysis phase. In this study, this information was available for the school buildings of some regions of Italy and for masonry structures only.

Further improvements of the proposed multiphase methodology are still required. In particular, the seismic vulnerability evaluation of the masonry structures carried out during the first phase has to be improved. The improvement should be related to the computation of the seismic vulnerability as a function of the number of storeys and additional parameters related to the quality of the masonry structures that could strongly affect the seismic response.

Finally, it should be extremely useful to complete the collection of the data related to the school building resistance in all Italian regions and for all the structural typologies in order to allow a more accurate estimate of the seismic vulnerability of these buildings and the application of the second phase of the procedure at a national scale. Therefore, it would be possible to apply the proposed procedure for the identification of the school buildings requiring priority of intervention.

ACKNOWLEDGEMENTS

The authors would like to thank the support of the Italian Department of Civil Protection (DPC – Dipartimento della Protezione Civile) through the financing of the project “Progetto Operativo d2 - Definizione delle Priorità di Intervento per Scuole Italiane”. The support of the Italian Ministry of Research and Higher Education (MIUR – Ministero dell’Università e della Ricerca) for the availability of the “Anagrafe Edilizia Scolastica” forms is also acknowledged. In closing, the authors are very grateful to Ms Miriam Colombi for the support related to the previously published works on the same topic, Ms Antonella Di Meo for finding the correspondence between the “Anagrafe Edilizia Scolastica” forms and the GNDT 2nd Level forms and Mr Marco Pagano for georeferencing the school buildings.

REFERENCES

[1] W. Salvatore, S. Caprili, V. Barberi, Rapporto dei danni provocati dall’evento sismico del 6 aprile sugli edifici scolastici del centro storico de L’Aquila. *Available on-line from www.reluis.it*, 2009.

[2] D.N. Grant, J.J. Bommer, R. Pinho, G.M. Calvi, A. Goretti and F. Meroni, A Prioritization Scheme for Seismic Intervention in School Buildings in Italy. *Earthquake Spectra*, **23**, Issue 2, 291-314, 2007.

[3] H. Crowley, M. Colombi, G.M. Calvi, R. Pinho, F. Meroni, A. Cassera, Application of a prioritization scheme for seismic intervention in schools buildings in Italy. *The 14th World Conference on Earthquake Engineering*, Beijing, China, 2008.

[4] M. Dolce and A. Martinelli, Inventario e vulnerabilità degli edifici pubblici e strategici dell’Italia centro-meridionale, Vol. II Analisi di vulnerabilità e rischio sismico. *INGV/GNDT – Istituto Nazionale di Geofisica e Vulcanologia / Gruppo Nazionale per la Difesa dai terremoti*, L’Aquila, 2005.

[5] M. Dolce, A. Masi, C. Moroni, A. Martinelli, A. Mannella, L. Milano, A. Lemme, C. Miozzi, Sisma Molise 2002. Il progetto “Scuola Sicura”: dall’indagine di vulnerabilità

sismica alla esecuzione degli interventi. *Atti del XII Convegno L'Ingegneria Sismica in Italia*, Pisa, 2007.

[6] B. Borzi, R. Pinho, H. Crowley, Simplified pushover-based vulnerability analysis for large scale assessment of RC buildings. *Engineering Structures*, **30**, Issue 3, 804-820, 2008.

[7] B. Borzi, H. Crowley, R. Pinho, Simplified pushover-based earthquake loss assessment (SP-BELA) method for masonry buildings. *International Journal of Architectural Heritage*, **2**, Issue 4, 353-376, 2008.

[8] AA.VV., Censimento di Vulnerabilità degli Edifici Pubblici, Strategici e Speciali nelle Regioni Abruzzo, Basilicata, Calabria, Campania, Molise, Puglia e Sicilia. *Dipartimento della Protezione Civile*, Roma, 1999.

[9] AA.VV., Censimento di Vulnerabilità a Campione dell'Edilizia Corrente dei Centri Abitati, nelle Regioni Abruzzo, Basilicata, Calabria, Campania, Molise, Puglia e Sicilia. *Dipartimento della Protezione Civile*, Roma, 2000.

[10] G. Zonno, coord., Rapporto Finale CNR-IRRS alla Commissione Europea. *Contratto ENV4-CT96-0279*, 95-102, 1999.

[11] G.M. Calvi, A displacement-based approach for vulnerability evaluation of classes of buildings. *Journal of Earthquake Engineering*, **3**, Issue 3, 411-438, 1999.

[12] D.M. 14.01.2008, Approvazione delle nuove norme tecniche per le costruzioni, G.U. 04.02.2008 n. 29.

[13] Circolare applicativa delle NTC08, Circolare del Ministero delle Infrastrutture e dei Trasporti 2 febbraio 2009, n. 617 recante Istruzioni per l'applicazione delle Nuove norme tecniche per le costruzioni di cui al Decreto Ministeriale 14 gennaio 2008. Suppl. Ord. n. 27 alla G.U. 26.2.2009 n. 47.

[14] INGV-DPC S1, Proseguimento della assistenza al DPC per il completamento e la gestione della mappa di pericolosità sismica prevista dall'Ordinanza PCM 3274 e progettazione di ulteriori sviluppi. Website http://esse1.mi.ingv.it, 2007.

[15] M.J.N. Priestley, G.M. Calvi, M.J. Kowalsky, Displacement-based seismic design of structures. *IUSS Press*, Pavia, Italy, 2007.

[16] L.F. Restrepo-Vélez, G. Magenes, Simplified procedure for the seismic risk assessment of unreinforced masonry buildings. *Proceeding of The 13th World Conference on Earthquake Engineering*, Vancouver, Canada, 2004.

[17] Eurocode 8, Design of structures for earthquake resistance - part 1: general rules, seismic actions and rules for buildings. *EN 1998-1:2004*, Comité Européen de Normalisation, Brussels, 2004.

COMPDYN 2011
III ECCOMAS Thematic Conference on
Computational Methods in Structural Dynamics and Earthquake Engineering
M. Papadrakakis, M. Fragiadakis, V. Plevris (eds.)
Corfu, Greece, 25–28 May 2011

SEISMIC DAMAGE ANALYSIS OF REINFORCED CONCRETE STRUCTURES WITH SUBSTANDARD DETAILING

Panagiotis E. Mergos[1], **Andreas J. Kappos**[1]

[1] Laboratory of Concrete and Masonry Structures, Department of Civil Engineering,
Aristotle University of Thessaloniki, 54124, Greece
e-mail: panmerg@yahoo.com; ajkap@civil.auth.gr

Keywords: Finite element, Reinforced Concrete, Shear-Flexure interaction, Bond-slip, Substandard detailing

Abstract. *The goal of this study is to investigate seismic behaviour of existing R/C buildings designed and constructed in accordance with standards that do not meet current seismic code requirements. In these structures, not only flexure, but also shear and bond-slip deformation mechanisms need to be considered separately and in combination. To serve this goal, a finite element model developed previously by the writers for individual non-ductile beam-column members is extended herein in order to cope with inelastic seismic analysis of complete planar R/C frames. The proposed finite element is able to capture gradual spread of inelastic flexural and shear deformations as well as their interaction in the end regions of R/C members. Additionally, it is capable of predicting shear failures caused by degradation of shear strength in the plastic hinges of R/C elements, as well as pullout failures caused by inadequate anchorage of the reinforcement in the joint regions. The finite element is fully implemented in the general inelastic finite element code IDARC2D. Then, the numerical model is calibrated against experimental data coming from three experimental plane frame structures with non-ductile detailing. It is shown that, in all cases, satisfactory correlation is established between the model predictions and the experimental evidence. The analytical results are in agreement with the experimental values in terms of stiffness, strength and displacement demands. The failure mechanism is predicted accurately for all experimental specimens. Finally, parametric studies illustrate the significance of each deformation mechanism in the seismic response of the experimental frames. It is concluded, that all deformation mechanisms, as well as their interaction, should be taken into consideration in order to predict reliably seismic damage of R/C structures with substandard detailing.*

1 INTRODUCTION

The vast majority of existing reinforced concrete (R/C) buildings was constructed prior to the development of modern seismic code provisions. The deficient design makes their structural elements susceptible to axial-flexural, shear or bond types of failure, which subsequently may lead to severe damage or collapse of the building.

Current research on seismic assessment of R/C structures is focused primarily on flexural response. Deformations caused by shear and bond-slip related mechanisms are either ignored or lumped into flexure. However, the necessary assumptions inherent to both of these approaches may drive the assessment procedure to erroneous results. This is especially the case for ‘old type’ existing R/C structures, where shear and bond types of failure cannot be precluded, due to the absence of ductile detailing and capacity design.

A significant number of analytical efforts have placed emphasis on seismic response of non-ductile R/C buildings. Among them, several studies [1-3] have demonstrated the necessity for treating individual deformation components (i.e. flexure, shear, anchorage bond-slip) in a distinct manner.

In this study, a finite element developed previously by the writers [4-7] for examining inelastic response of individual R/C beam-column members is extended herein to deal with seismic damage analysis of complete R/C frames with substandard detailing. The novel feature of the proposed finite element is the fact that it is capable of modelling gradual spread of inelastic flexural and shear deformations as well as their interaction in the end regions of R/C members. Furthermore, it has the ability of predicting shear failures caused by degradation of shear strength in the plastic hinges of R/C elements, as well as pullout failures caused by inadequate anchorage of the reinforcement in the joint regions.

The paper starts with a brief overview of the finite element model. Emphasis is placed on the abilities of the numerical model to predict brittle types of local failure (i.e. shear and bond). Moreover, the necessary alterations to the nonlinear solution algorithms are discussed in order for the proposed beam-column element to be fully implemented in a general inelastic damage analysis finite element code.

Then, with the aim to verify the capabilities of the proposed numerical model to reproduce all of the aforementioned phenomena strongly related to R/C buildings with deficient configuration, the proposed finite element is applied to the analysis of three well documented R/C frame specimens subjected to cyclic or seismic loading. Analytical results are compared with experimental recordings. It is shown that the numerical model is able to capture sufficiently experimental response in terms of strength, stiffness and displacements and to predict reliably the prevailing mode of failure for each specimen.

Finally, parametric analyses illustrate the relative importance of each deformation mechanism in the response of the examined specimens in the elastic and inelastic range. It is proven that proper modelling of all flexibility components, as well as their interaction, is a substantial prerequisite for reliable predictions of seismic response of R/C frames built with inadequate ductility capacity.

2 FINITE ELEMENT MODEL

The proposed, member-type, finite element is based on the flexibility method and belongs to the class of phenomenological models. It consists of three sub-elements representing flexural, shear, and anchorage bond-slip response (Fig. 1). The total flexibility of the finite element is calculated as the sum of the flexibilities of its sub-elements and can be inverted to produce the element stiffness matrix. Hence, it is

$$F_b=F^{fl}+F^{sh}+F^{sl} \tag{1}$$

$$K_b=F^{-1} \tag{2}$$

Where, F_b, F^{fl}, F^{sh}, F^{sl} are the basic total, flexural, shear and anchorage slip, respectively, tangent flexibility matrices. K_b is the basic tangent stiffness matrix of the element, connecting incremental moments ΔM_A, ΔM_B and rotations $\Delta\theta_A$, $\Delta\theta_B$ at the element flexible ends A and B respectively, with the following equation

$$\begin{bmatrix}\Delta M_A\\ \Delta M_B\end{bmatrix}=K_b\cdot\begin{bmatrix}\Delta\theta_A\\ \Delta\theta_B\end{bmatrix} \tag{3}$$

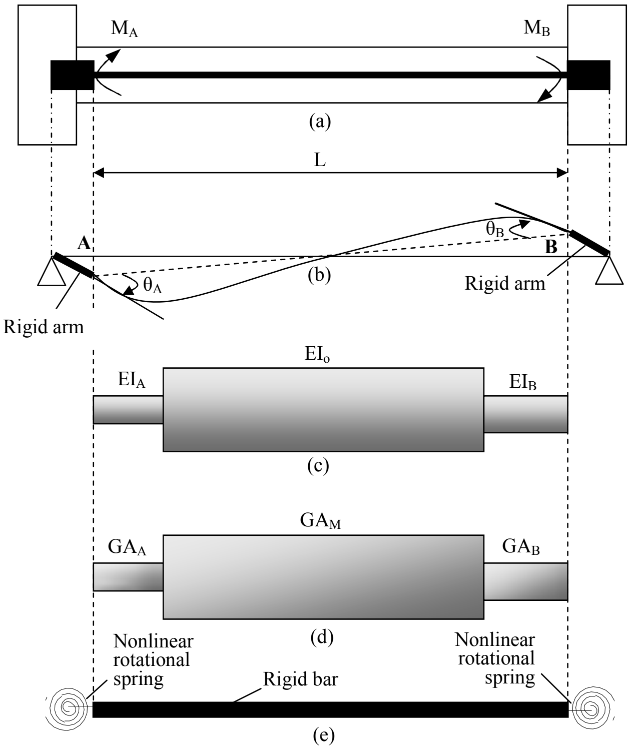

Figure 1: Proposed finite element model: a) geometry of R/C member; b) beam-column finite element with rigid arms; c) flexural sub-element; d) shear sub-element, e) anchorage bond-slip sub-element.

The local stiffness matrix K_e, relating displacements and forces at the element joints, is easily determined following standard structural analysis procedures. The components of the examined finite element, as well as their interaction, are described in the following sections.

2.1 Flexural Sub-Element

This sub-element (Fig. 1c) is used for modelling flexural behaviour of an R/C member before and after yielding of the longitudinal reinforcement. It consists of a set of rules governing the hysteretic moment-curvature (M-φ) response of the member end sections and a spread inelasticity model describing flexural stiffness distribution along the entire member.

M-φ hysteretic model (Fig. 2) is composed by the skeleton curve and a set of rules determining response during loading, unloading and reloading. M-φ envelope curve is derived by section analysis and appropriate bilinearization. Loading response is assumed to follow the bilinear envelope curve. Unloading is based on the respective Sivaselvan & Reinhorn [8] hysteretic rule adjusted for mild stiffness degradation. Reloading aims at the point with previous maximum excursion in the opposite direction.

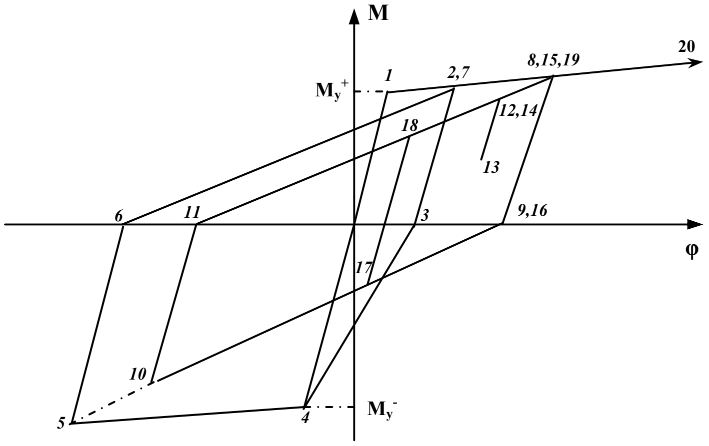

Figure 2: M-φ hysteretic model

In order to capture variation of section flexural stiffness along the concrete member, a gradual spread inelasticity model is assigned [9]. The stiffness distribution along the member is assumed to have one of the shapes shown in Fig. 3, where L is the length of the member; EI_A and EI_B are the current flexural rigidities of the sections at the ends A and B, respectively; EI_o is the stiffness at the intermediate part of the element; α_A and α_B are the yield penetration coefficients. The flexural rigidities EI_A and EI_B are determined from the M-φ hysteretic relationship of the corresponding end sections. The yield penetration coefficients specify the proportion of the element where the acting moment is greater than the end-section yield moment. These coefficients are first calculated for the current moment distribution and then compared with the previous maximum penetration lengths.

Stiffness distribution inside the inelastic zone depends on the loading state of the end section hysteretic response. In particular, Fig. 4 illustrates hysteretic response of four discrete sections located inside the plastic hinge region. It can be seen that when all sections remain in the strain hardening branch (loading state), flexural stiffness remains constant in the inelastic zone. However, in the unloading and reloading state, stiffness varies from a minimum value (corresponding to the end section) to a maximum value, which is equal to EI_o. Hence, under the general assumption that the loading state of all sections of the yielded region remains the same, it may be considered that when M-φ end section hysteretic response is on the strain hardening branch, stiffness distribution remains uniform in the inelastic zone. In the case where end-section M-φ behaviour is in the unloading or reloading state, it is assumed that the stiffness varies linearly from EI_A (EI_B) to EI_o.

Having established the stiffness distribution along the R/C member at each step of the analysis, the coefficients of the flexibility matrix of the flexural sub-element can be derived from the general Eq. (4) and Table 1, determined by applying the principle of virtual work.

$$f_{ij} = \frac{L}{12EI_o}\left(c_o + c_A \cdot \gamma_A + c_B \cdot \gamma_B\right);\ \gamma_A = \frac{EI_o}{EI_A} - 1;\ \gamma_B = \frac{EI_o}{EI_B} - 1 \qquad (4)$$

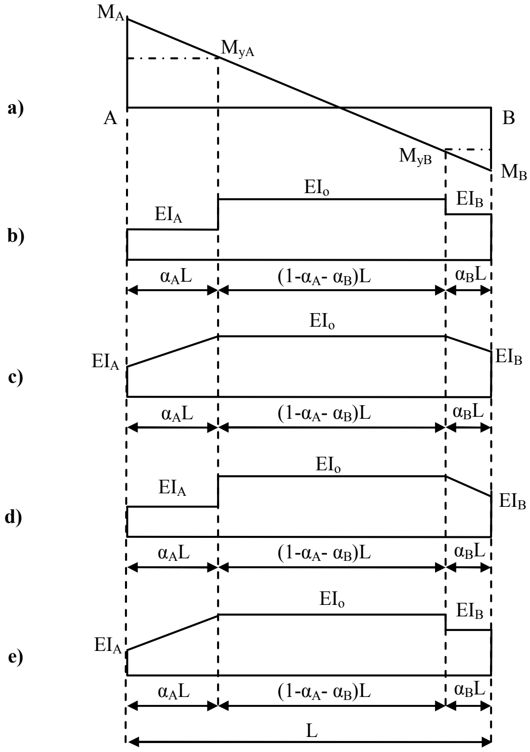

Figure 3: Element a) bending moment diagram; b) stiffness distribution when ends A and B are in the loading state; c) stiffness distribution when ends A and B are in the unloading or reloading state; d) stiffness distribution when end A is in the loading and end B is in the unloading or reloading state; e) stiffness distribution when end A is in the unloading or reloading state and end B is in the loading state.

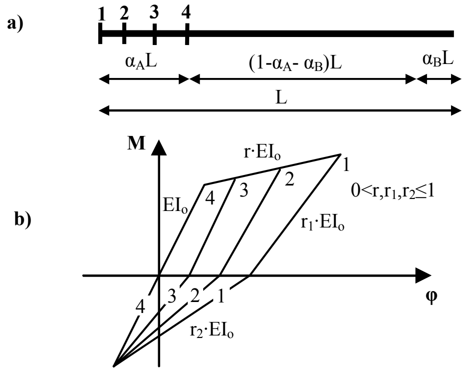

Figure 4: M-φ hysteretic response of four individual sections inside the plastic hinge region.

Flexibility matrix coefficient	Stiffness distribution	c_o	c_A	c_B
f_{11}	Fig. 2b	4	$12\alpha_A - 12\alpha_A^2 + 4\alpha_A^3$	$4\alpha_B^3$
f_{12}	Fig. 2b	4	$4\alpha_A^3$	$12\alpha_B - 12\alpha_B^2 + 4\alpha_B^3$
f_{22}	Fig. 2b	-2	$4\alpha_A^3 - 6\alpha_A^2$	$4\alpha_B^3 - 6\alpha_B^2$
f_{11}	Fig. 2c	4	$6\alpha_A - 4\alpha_A^2 + \alpha_A^3$	α_B^3
f_{12}	Fig. 2c	4	α_A^3	$6\alpha_B - 4\alpha_B^2 + \alpha_B^3$
f_{22}	Fig. 2c	-2	$\alpha_A^3 - 2\alpha_A^2$	$\alpha_B^3 - 2\alpha_B^2$
f_{11}	Fig. 2d	4	$12\alpha_A - 12\alpha_A^2 + 4\alpha_A^3$	α_B^3
f_{12}	Fig. 2d	4	$4\alpha_A^3$	$6\alpha_B - 4\alpha_B^2 + \alpha_B^3$
f_{22}	Fig. 2d	-2	$4\alpha_A^3 - 6\alpha_A^2$	$\alpha_B^3 - 2\alpha_B^2$
f_{11}	Fig. 2e	4	$6\alpha_A - 4\alpha_A^2 + \alpha_A^3$	$4\alpha_B^3$
f_{12}	Fig. 2e	4	α_A^3	$12\alpha_B - 12\alpha_B^2 + 4\alpha_B^3$
f_{22}	Fig. 2e	-2	$\alpha_A^3 - 2\alpha_A^2$	$4\alpha_B^3 - 6\alpha_B^2$

Table 1: Determination of flexural flexibility matrix coefficients

2.2 Shear Sub-Element

The shear sub-element represents hysteretic shear behaviour of the R/C member prior and subsequent to shear cracking, flexural yielding and yielding of the transverse reinforcement. This sub-element has been designed in a similar way to the flexural element described above. It consists of a hysteretic model determining V-γ (shear force vs. shear distortion) behaviour of the member ends and/or intermediate regions and a shear spread-plasticity model determining distribution of shear stiffness along the R/C member.

Shear hysteresis is determined by the V-γ skeleton curve and a set of rules describing response during unloading and reloading. The primary curve is first calculated without considering shear-flexure interaction effect. This initial envelope curve (Fig. 5) is valid for modelling shear behaviour outside the plastic hinge region for members that have yielded in flexure or the response of the entire element for members, where the longitudinal reinforcement remains in the elastic range.

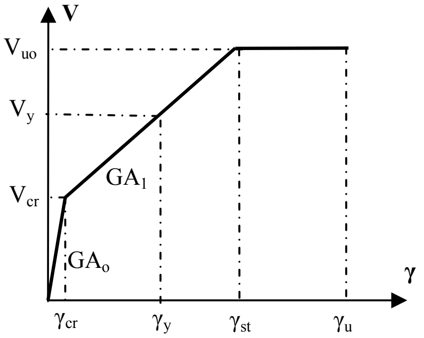

Figure 5: Initial V-γ primary curve

The V-γ initial primary curve consists of four branches (Fig. 5), but only three different slopes, as explained later on. The first branch connects the origin and the shear cracking point, which is defined as the point where the nominal principal tensile stress exceeds the mean tensile strength of concrete [10]. The second and third branches of the initial primary curve have the same slope and connect the shear cracking point to the point corresponding to the onset of yielding of transverse reinforcement, or else the point of attainment of maximum shear strength (γ_{st}, V_{uo}). The second and third branches are separated at the point corresponding to flexural yielding (γ_y,V_y). This approach is adopted in order to distinguish hysteretic shear behaviour before and after flexural yielding.

Shear strength V_{uo} is calculated by the Priestley et al. [11] approach for curvature ductility demand $\mu_\varphi \leq 3$ (i.e. no strength degradation). Shear strain γ_{st} is evaluated by the truss analogy approach and two modification factors for the member aspect ratio and normalized axial load, as proposed by the writers of this paper [5,7] on the basis of calibration studies with the experimental evidence.

The fourth branch is almost horizontal and describes shear response after yielding of transverse reinforcement and until onset of shear failure, corresponding to shear distortion γ_u. On the basis of experimental results coming from 25 R/C specimens failing in shear mode, the writers [5,7] have developed an empirical formula correlating γ_u with the level of the applied axial load, the amount of transverse reinforcement and the member shear-span. Conservatively, it is assumed in this study that shear failure coincides with onset of significant lateral strength degradation.

It is well documented [10-12] that shear strength degrades due to disintegration of the plastic hinge zones caused by inelastic flexural deformations. Hence, an R/C member originally designed with shear capacity higher than the one corresponding to flexural yielding, may eventually experience a brittle shear failure. Additionally, it has been shown experimentally [13,14] that shear distortions in the plastic hinge regions may increase rapidly (shear yielding effect) after flexural yielding, despite the fact that shear force demand remains almost constant as it is controlled by flexural yielding.

The writers have developed a methodology according to which both of these phenomena can be modelled simultaneously and in a rational manner. Following this approach, effective tangent shear stiffness GA_{eff} after flexural yielding is evaluated as a function of μ_φ. This stiffness determines modified V-γ envelope curve inside the plastic hinge regions.

Fig. 6 illustrates variation of capacity of shear resisting mechanisms (concrete V_c and truss V_s) in the plastic hinge region of a single R/C column following the Priestley et al. [11] shear strength approach (for clarity, contribution of axial load is lumped into V_c). It can be seen that after $\mu_\varphi>3$, V_s increases to accommodate both additional shear demand ΔV and additional deterioration of the concrete resisting mechanism $\Delta \text{deg} V_c$.

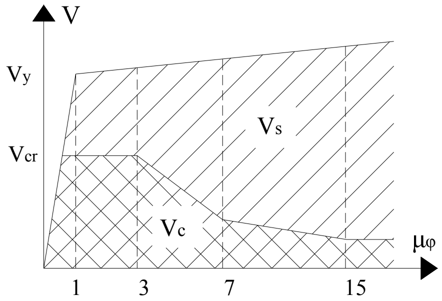

Figure 6: Variation of shear resisting mechanisms with μ_φ in plastic hinges

Generally, after shear cracking, shear strain increment $\Delta\gamma_s$ is related to the additional shear force resisted by the truss mechanism ΔV_s by Eq. (5), where GA_1 is the cracked stiffness of the initial primary curve determined by the truss analogy approach.

$$\Delta\gamma_s = \frac{\Delta V_s}{GA_1} \tag{5}$$

After flexural yielding, ΔV_s can be considered as the sum of ΔV and $\Delta \text{deg} V_c$. Hence

$$\Delta V_s = \Delta V + \Delta \deg V_c \tag{6}$$

If GA_{eff} is the tangent stiffness of the shear primary curve including shear-flexure interaction effect, it yields the same increment of shear distortions $\Delta\gamma_s$ only for the applied shear force increment ΔV (without $\Delta \text{deg} V_c$), as illustrated in Fig. 7. Consequently

$$\Delta\gamma_s = \frac{\Delta V}{GA_{eff}} \tag{7}$$

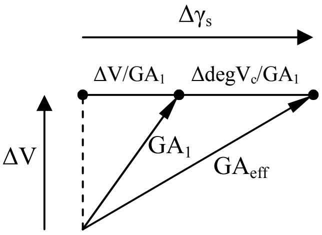

Figure 7: Definition of GA_{eff}

By joining Eqs (5-7), Eq. (8) is derived for determining stiffness of the shear envelope curve after yielding in flexure. This formula shows that GA_{eff} can only be either equal or smaller than GA$_1$. Equality holds only when the degradation of the concrete shear resisting mechanisms is negligible.

$$GA_{eff} = \frac{\Delta V}{\Delta V + \Delta \deg V_c} \cdot GA_1 \tag{8}$$

After determination of the initial and modified V-γ envelope curves, shear hysteretic response has to be established. This behaviour is characterized by significant stiffness degradation and pinching effect. In this study, the empirical model by Ozcebe and Saatcioglu (Fig. 8) is adopted for this response, properly modified by the writers [4] in order to be incorporated in the general inelastic structural analysis framework.

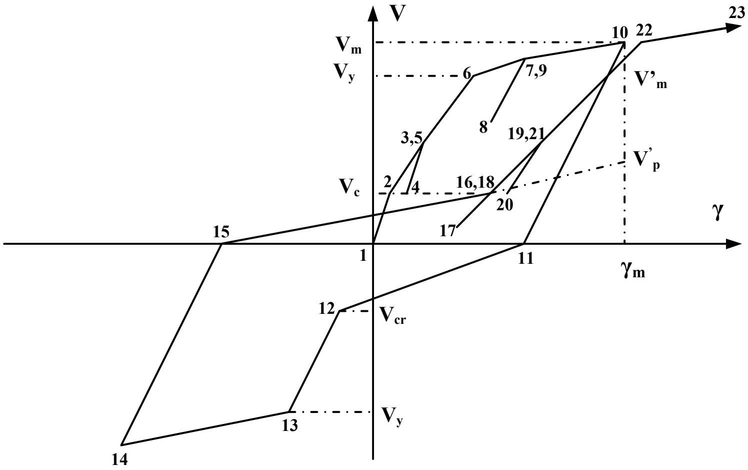

Figure 8: Shear hysteretic model

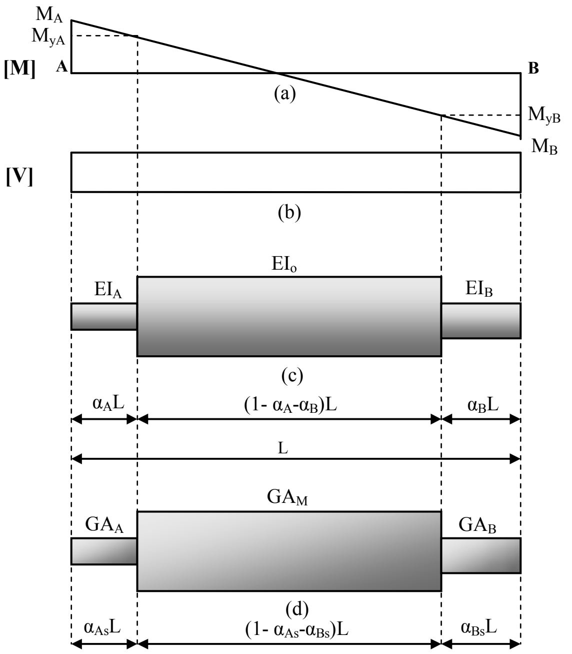

Figure 9: Spread inelasticity models: a) moment diagram; b) shear diagram; c) flexural model; d) shear model

Furthermore, following flexural deformations, inelastic shear strains tend to spread gradually from the ends to the member mid-span as the length of inelastic zones increases. The writers developed a shear gradual spread inelasticity model capable of monitoring variation of shear stiffness along the concrete member throughout the response. This is achieved by a dual coupling procedure between the flexural and shear sub-element. According to this procedure, the lengths of the inelastic zones α_{As} and α_{Bs} of the shear sub-element are defined by the respective ones of the flexural sub-element (Fig. 9). In addition, the stiffness of these zones GA_A and GA_B are determined by the modified V-γ envelope curves calculated for the curvature ductility demands of the respective ends of the flexural member model. Shear stiffness GA_M of the intermediate part of the member is determined by the initial V-γ primary curve, without considering shear-flexure interaction effect.

After determining the distribution of *GA* along the R/C member at each step of the analysis, the coefficients of the flexibility matrix of the shear sub-element are given by Eq. (9).

$$f_{ij}^{sh} = \frac{a_{As}}{GA_A \cdot L} + \frac{1 - a_{As} - a_{Bs}}{GA_M \cdot L} + \frac{a_{Bs}}{GA_B \cdot L} \quad \text{(i,j=1,2)} \tag{9}$$

2.3 Bond-Slip Sub-Element

The bond-slip sub-element accounts for the fixed-end rotations (θ_{slip}) which arise at the interfaces of adjacent R/C members due to bond deterioration and slippage of the reinforcement in the joint regions. The proposed model consists of two concentrated rotational springs located at the member-ends. The two (uncoupled) springs are connected by an infinitely rigid bar (Fig. 1e). Following this formulation, the coefficients of the bond-slip flexibility matrix F^{sl} are given simply by Eq. (10), where f_A^{sl} and f_B^{sl} are the flexibilities of the concentrated rotational springs at the ends A and B respectively. These flexibilities depend on the envelope curve and the model used to represent hysteretic behaviour of each rotational spring.

$$F^{sl} = \begin{bmatrix} f_A^{sl} & 0 \\ 0 & f_B^{sl} \end{bmatrix} \tag{10}$$

The M-θ_{slip} skeleton curve is derived on the basis of a simplified procedure [15,16] assuming uniform bond stress along different segments of the anchored rebar (Fig. 10). These segments are the elastic region L_e, the strain strain-hardening region L_{sh} and the cone penetration zone L_{pc}. The average elastic bond strength τ_{be} of ACI 408 [17] is adopted here for the elastic region, while the frictional bond τ_{bf} of the C.E.B. Model Code [18] is assumed to apply within the strain-hardening region. In the cone penetration zone, it is assumed that the acting bond is negligible.

For various levels of the applied end moment and using the results of the M-φ analysis, the stress σ_s and strain ε_s of the reinforcing bar at the loaded end are first determined. Then, by equilibrium and applying the assumed bond distribution, variation of reinforcing bar stress $\sigma_s(x)$ along the embedment length is defined as shown in Fig. 10a, where σ_y is the yield strength of steel and σ_h is the stress at the end of the straight part of the rebar anchorage. Later, by assigning an appropriate constitutive material law [19], strain distribution $\varepsilon_s(x)$ is determined, as shown in Fig. 10b, where ε_y and ε_{sh} are the steel strains at the onset of yielding and strain hardening and ε_h is the steel strain at the end of the straight part of the anchorage. It is important to note that nonlinearity of strain hardening material law should be taken into account because it influences significantly the final results [5].

Once $\varepsilon_s(x)$ is determined, slip of the reinforcement δ_{slip} can be calculated by integration along the anchored length of the bar. In the case of hooked bars, local slip of the hook should be added. This can be evaluated by the force acting on the hook $P_h=A_b \cdot \sigma_h$, where A_b is the area of the anchored bar, and an appropriate hook force-hook slip relationship [20].

Upon determination of δ_{slip}, the respective fixed-end rotation can be calculated by Eq. (11), where (d-x_c) is the distance between the bar and the neutral axis.

$$\theta_{slip} = \frac{\delta_{slip}}{d - x_c} \tag{11}$$

The envelope M-θ_{slip} curve constructed by the various points of the afore-described methodology is then idealized by a bilinear relationship for the purposes of analysis.

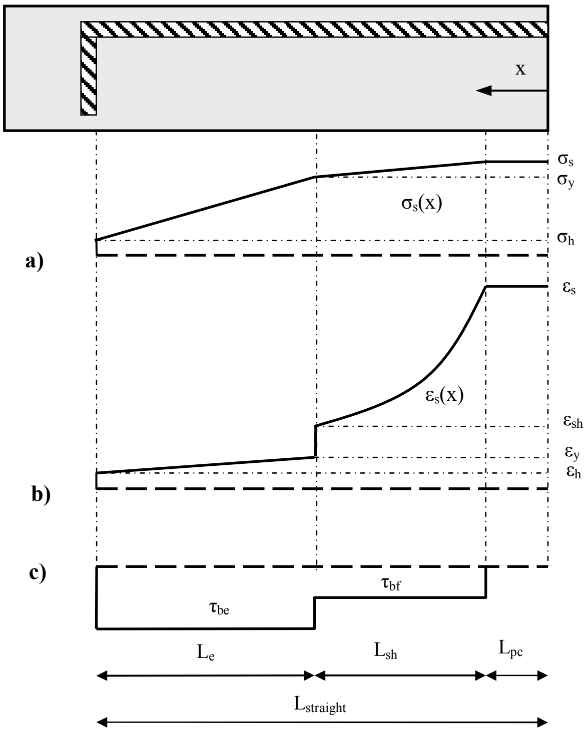

Figure 10: Reinforcing bar with 90° hook embedded in concrete; a) stress distribution; b) strain distribution; c) bond distribution.

In R/C structures with substandard detailing, anchorage-bond failures cannot be precluded. In case of straight anchorages, bond failure takes place when the anchorage length demand L_{dem} reaches the available straight embedment length $L_{straight}$. This occurs for $\sigma_s > \sigma_y$, when Eq. (12) holds, where d_b represents bar diameter. If σ_s exceeds the one corresponding to flexural failure, then bond is not the critical mode of failure for the examined anchorage.

$$\sigma_s = \sigma_y + \frac{4 \cdot \tau_{bf}}{d_b} \cdot \left(L_{straight} - L_{pc} - \frac{\sigma_y \cdot d_b}{4 \cdot \tau_{be}} \right) \tag{12}$$

For very short embedment lengths, where bond failure takes place for $\sigma_s < \sigma_y$, experimental evidence [17] shows that the assumption of uniform bond strength τ_{be} underestimates significantly the available anchorage capacity. To avoid over-conservative solutions, it is assumed in this study that actual available bond force T_d is derived from linear interpolation between the capacity bond forces corresponding to two well documented available anchorage bond lengths (Fig. 11). The first bond strength T_{d1} refers to $L_{straight}=5d_b$, where the ultimate bond stress τ_{bu} of the local bond-slip constitutive law (C.E.B. Model Code [18]) is assumed to develop uniformly. Thus

$$T_{d1} = 5 \cdot d_b \cdot u \cdot \tau_{bu} \tag{13}$$

Where, u is the bar perimeter. The second bond strength $T_{d2}=A_b \cdot \sigma_y$ refers to $L_{straight}=l_d$, where l_d is the development length (Eq. 14) corresponding to yielding of the reinforcement. Along this length, uniform bond strength τ_{be} is considered.

$$l_d = \frac{\sigma_y \cdot d_b}{4 \cdot \tau_{be}} \tag{14}$$

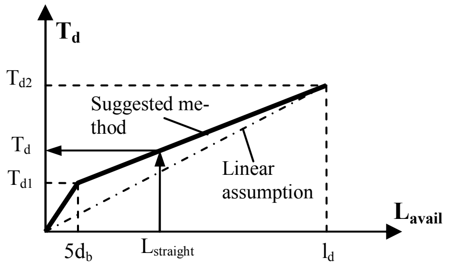

Figure 11: Determination of available straight anchorage bond strength for very short embedment lengths

In the case of deficient end hooks, anchorage failure may be assumed to develop, when the force acting on the hook reaches ultimate hook capacity P_{hu}. Depending on the range of σ_s and the available straight anchorage length $L_{straight}$, Eq. (15) holds for determining σ_s, where $L_{sh}=(\sigma_s-\sigma_y) \cdot d_b/(4 \cdot \tau_{bf})$ for $\sigma_s>\sigma_y$.

$$\sigma_s = \frac{P_{hu} + \pi \cdot d_b \cdot \tau_{be} \cdot L_{straight}}{A_{sb}} \quad \text{for } \sigma_s \leq \sigma_y$$

$$\sigma_s = \sigma_y + \frac{4 \cdot \tau_{bf}}{d_b} \cdot \left(L_{straight} - L_{pc} - \frac{\left(A_{sb} \cdot \sigma_y - P_{hu}\right)}{\pi \cdot d_b \cdot \tau_{be}} \right) \quad \text{for } \sigma_s>\sigma_y \text{ and } L_{straight}-L_{pc}-L_{sh}>0 \tag{15}$$

$$\sigma_s = \frac{P_{hu} + \pi \cdot d_b \cdot \tau_{bf} \cdot \left(L_{straight} - L_{pc}\right)}{A_{sb}} \quad \text{for } \sigma_s>\sigma_y \text{ and } L_{straight}-L_{pc}-L_{sh}<0$$

After determining M-θ_{slip} bilinear skeleton curve, bond-slip hysteretic behaviour (Fig. 12) is modelled following the suggestions of Saatcioglu and Alsiwat [21].

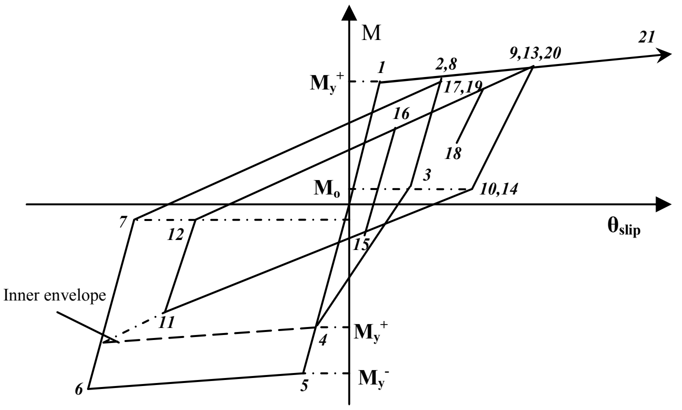

Figure 12: M-θ_{slip} hysteretic model.

3 NUMERICAL IMPLEMENTATION

The finite element model, described above, requires additional modifications to the nonlinear analysis solution algorithms in order to be implemented with consistency. It is known that during nonlinear analysis the following equation is solved in incremental form.

$$K \cdot \Delta U = \Delta F \tag{16}$$

Where K is the overall tangent stiffness matrix of the structure, ΔU is the vector of unknown nodal displacement increments and ΔF is the vector of the applied external load increments. The element stiffness matrices K_e are first calculated at the element level and later assembled into K**.**

In the case of dynamic analysis, the equivalent dynamic stiffness and external load matrices must be formed [22]. The solution of the incremental system is carried out using the unconditionally stable constant-average acceleration Newmark-Beta algorithm [23]. Viscous damping matrix is calculated by assigning the Rayleigh damping model with circular frequencies corresponding to the first and second mode of vibration.

The solution is performed assuming that the properties of the structure do not change during the analysis step. Since the stiffness of some elements is likely to change during the step t, the new configuration at t+Δt may not satisfy equilibrium. If ΔF_{ln} is the force increment vector arising from the assumption of constant stiffness during Δt and ΔF_{nl} is the force increment vector determined by the element nonlinear hysteretic laws, then an unbalanced force vector ΔF_{ub} arises, given by the following equation

$$\Delta F_{ub}= \Delta F_{ln}- \Delta F_{nl} \tag{17}$$

Typically, in the nonlinear analysis scheme, this issue is resolved by applying the one step unbalanced force correction method [22,24]. According to this technique, the unbalanced force vector is subtracted from the right part of Eq. (16) at the next time step of analysis. Despite the fact that this procedure minimizes computational effort in nonlinear analysis, it cannot be applied with consistency for finite elements composed by different sub-elements connected in series.

Fig. (13) presents determination of unbalanced forces produced by two different hysteretic laws (F-v_1 and F-v_2), which are connected in series. The two hysteretic relationships have different elastic (k_{T1} and k_{T2}) and post-elastic stiffness ($r_1 \cdot k_{T1}$ and $r_2 \cdot k_{T2}$). It can be easily extracted that for the same force increment ΔF_{ln} the restoring force increments ΔF_{nl1} and ΔF_{nl2} and consequently unbalanced forces ΔF_{ub1} and ΔF_{ub2} become different, resulting in loss of member equilibrium.

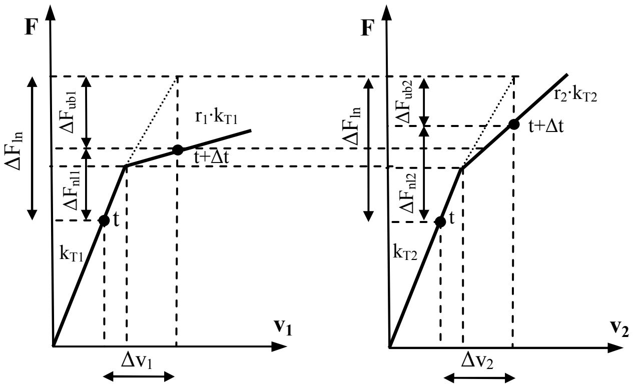

Figure 13: Unbalanced forces for two hysteretic relationships connected in series

To overcome this problem, the 'event to event' solution strategy [25] is adopted herein. This method is enhanced to cope with the finite element model proposed in this study. In accordance with this procedure, the nonlinear response of the structure is subdivided into subsequent events, which mark the change of stiffness of the entire structure. Between these events, linear behaviour is considered. To achieve this goal, each step is divided (when required) into sufficient number of sub-steps, until no event takes place during the last sub-step. For the finite element developed herein, as an event is prescribed every change in stiffness of all hysteretic responses of all three sub-elements of each beam-column model.

If the incremental load vector ΔF yields the deformation increment Δv_{mn} for the hysteretic response n of the element m, assuming constant stiffness, then the next event e force scale factor λ_{mn} corresponding to this hysteretic response is determined by

$$\lambda_{mn} = \min\left(1, \frac{v_{mne} - v_{mn}}{\Delta v_{mn}}\right) \tag{18}$$

In Eq. (18), v_{mne} is the deformation marking this event and v_{mn} is the same deformation at the beginning of the loading step. It is obvious, that the immediate next event for the entire structure will correspond to the minimum value λ_{min} of all λ_{mn}. After calculating λ_{min}, the solution algorithm implemented to each nonlinear analysis step is presented in Fig. 14.

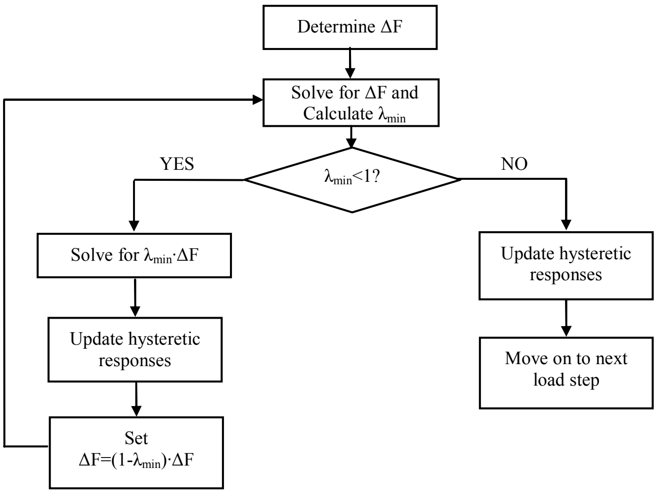

Figure 14: Event to event solution algorithm

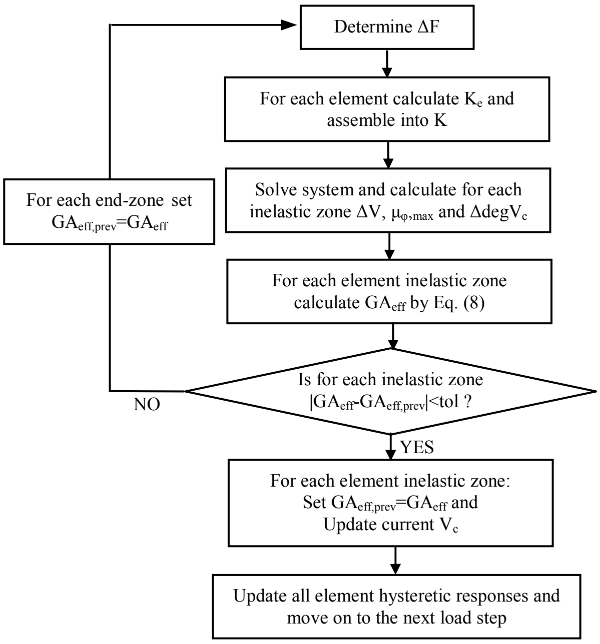

Figure 15: Shear-flexure interaction implementation algorithm

Additionally, following the procedure adopted in this study for determining tangent shear stiffness GA_{eff} after flexural yielding when accounting for shear-flexure interaction effect, it is evident from Eq. (8), that GA_{eff} becomes a function of the element shear force increment ΔV.

But if it is to be applied in the analytical procedure, ΔV will be influenced by GA_{eff} as well, since the latter will affect the flexibility matrix of the element, as given by Eqs. (1) and (9). To resolve this issue, an iterative analytical scheme, applied in the respective load step of the nonlinear analysis, is proposed herein, as detailed in the algorithm shown in Fig. 15.

Applying this procedure, it was found that numerical convergence is almost immediate. The number of iterations may increase as the influence of shear deformations on element flexibility enhances, but the additional computational cost required is justified by the significance of calculating accurately shear response in this case.

4 VALIDATION OF THE PROPOSED MODEL

The numerical model described above is implemented in the general finite element code IDARC2D developed at the State University of New York at Buffalo [22]. Then, it is validated against experimental results coming from three well documented R/C frame specimens with substandard detailing.

In addition, parametric analyses reveal the necessity of incorporating each deformation mechanism in seismic assessment of ‘old type’ R/C structures in the linear and nonlinear range of response. To this puropose, each frame specimen is examined using four different beam-column models. The F model simulates only member flexural response. The FB model incorporates flexural and anchorage bond-slip response, while the FS one applies flexural and shear flexibility. Finally, the FSB model, which is the one proposed in this study, simulates all deformation mechanisms, as well as their interaction.

4.1 Frame specimen Duong et al. (2007) [26]

A single-span, two-storey, shear critical R/C frame with a fixed base condition was constructed and tested in the facilities at University of Toronto. This test frame was 2:3 in scale and stood approximately 4.6m tall and 2.3m wide. Beams and columns had dimensions 300mmX400mm. Frame reinforcement layout is depicted in Fig. 16 as well as cross-sections detailing. The average concrete compressive strength at the time of the test was 43MPa. No. 10, No. 20 and US No. 3 were used in the specimen, with yield strengths of 455, 447 and 506MPa respectively. Further information regarding material characteristics can be found in [26].

An axial load of 420kN was applied to the top of each column and maintained in a force-controlled manner. Lateral action was applied only at the top level of the frame. Initially, the specimen was subjected to a forward lateral drift of about 1.0% (44mm) by which point significant shear damage had occurred in the beam of the first storey and failure appeared imminent. Then, the specimen was unloaded and afterwards a reverse load was applied until the frame reached the same displacement as in forward cycle. Finally, the specimen was again unloaded until approximately zero lateral force.

Fig. 17 presents the analytical finite element model used for the analysis of the frame under examination. It solely consists of six beam column elements assuring high computational efficiency. Frame joints are modelled via rigid arms at the ends of each member. Columns are assumed to be fixed into the foundation beam.

Initially and in order to investigate specimen capacity, pushover analyses are conducted for all finite element model types (F, FB, FS, FSB). Fig. 18 illustrates the lateral force-lateral top displacement curves obtained. It is clear that considering only flexural deformations leads to significant overestimation of frame stiffness, strength and displacement capacity. Incorporating fixed end rotations arising from anchorage bond-slip in model FB, reduces substantially the predicted initial frame stiffness. However, since no shear failure can be predicted, displacement capacity is grossly overestimated. Ultimate lateral strength capacity almost reaches the respective one coming from the F model. The FS analytical model predicts adequately initial frame stiffness. Nevertheless, since fixed-end rotations are not included, the model underestimates the level of lateral displacement at which shear failure is initiated (35mm instead of 44.7mm).

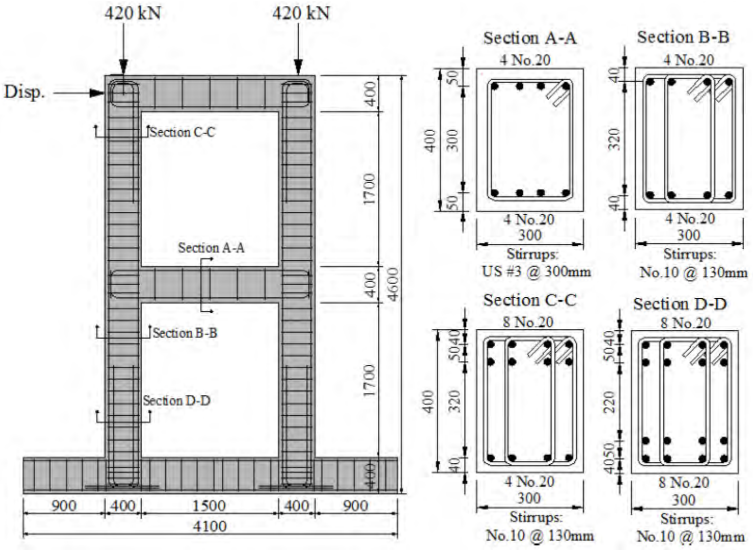

Figure 16: Duong et al. (2007) frame reinforcement layout and cross-section detailing

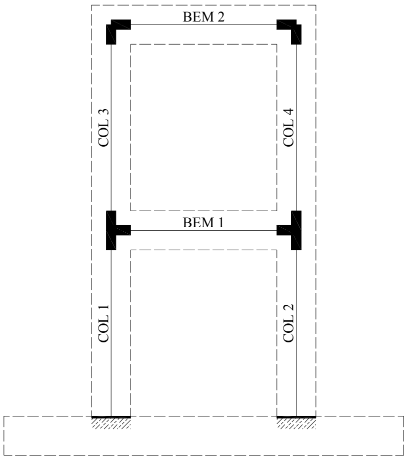

Figure 17: Duong et al. (2007) frame finite element model

The complete FSB model follows closely experimental response. Very small underestimation of initial stiffness may be attributed to the fact that the flexural pre-cracking response is not modelled in this study. The analytical model predicts accurately the lateral displacement corresponding to onset of shear failure (45mm instead of 44.7mm). Lateral strength capacity is slightly overestimated (about 10%).

For the same model, if degradation of shear strength with flexural demand is neglected, then displacement capacity becomes 159mm. On the contrary, if shear strength is assumed from the beginning of the analysis equal to its minimum value (corresponding to $\mu_\varphi \geq 15$), then displacement capacity drops to 10mm. It is recalled that the latter approach is the one adopted by modern seismic codes.

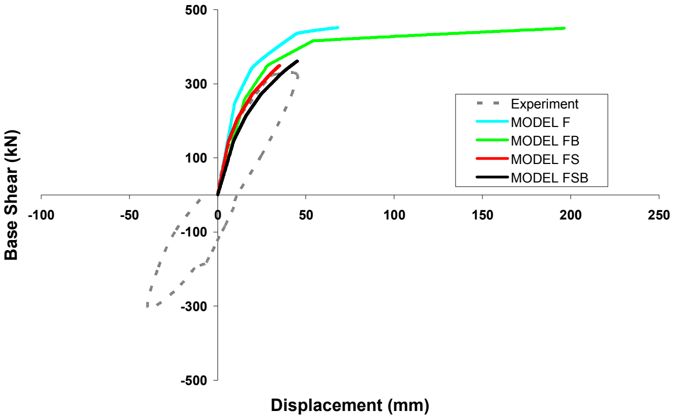

Figure 18: Pushover curves for Duong et al. (2007) frame specimen

Fig. 19 illustrates the modes of failure predicted by all analytical models at the end of pushover analysis. It is shown that while the models including inelastic shear effect (FS and FSB) predict the experimental mode of failure, which is the development of shear failure at the first-storey beam after flexural yielding, the other two models foresee erroneously a flexural failure of the same beam.

Fig. 20 compares the experimental and analytical base shear vs. top displacement response derived by the analytical models F, FB and FSB. As explained before, FS model predicted a premature shear failure and analysis had to stop prior to unloading response. It can be seen that the FSB analytical model correlates well with the experimental evidence in the whole range of response. Residual displacement after first unloading is estimated 13.5mm instead of 10.8mm. At the end of loading in the negative direction lateral frame strength is again slightly overestimated (approx. 10%). During unloading in the negative direction, initial frame stiffness is underestimated, but as an average in the whole unloading range stiffness is calculated satisfactorily. Hence, residual displacement after second unloading is found equal to 10.5mm opposed to 7.5mm. The analytical models F, FB overestimate significantly frame lateral stiffness and strength yielding higher estimates regarding total energy dissipated by the specific specimen.

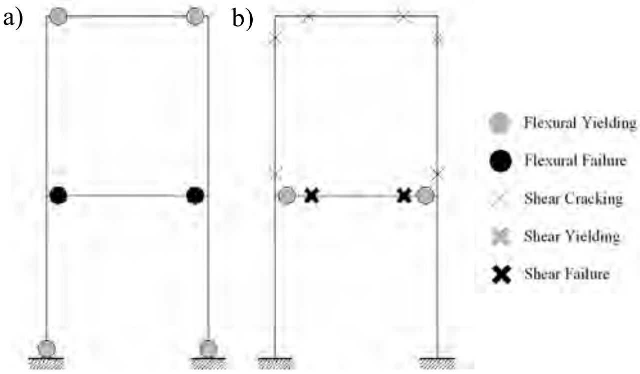

Figure 19: Predicted modes of failure for Duong et al. (2007) frame specimen by pushover analysis with a) F and FB; b) FS and FSB analytical model.

The hysteretic responses of the shear critical first storey beam produced by the FSB analytical model are presented in Fig. 21. Only one end-section is shown, since anti-symmetric response was predicted for this member. It can be inferred by this figure that the specific end-section yields first in positive bending developing high curvature ductility demand. Due to shear-flexure interaction effect, shear strains inside plastic hinge increase more rapidly than outside plastic hinge region. This increase is followed by yielding of the transverse reinforcement, which differentiates substantially shear response inside and outside the inelastic region. At peak response, maximum shear strain is 1.8% and 0.7% in the yielded and non-yielded part of the member respectively. In the negative direction, the analytical model does not predict yielding of the transverse reinforcement, as observed experimentally. This is due to the fact that μ_φ demand is not calculated to be higher than 3 and shear-flexure interaction effect is not triggered according to [11]. Hence, shear strains inside and outside plastic hinge region are estimated to be equal.

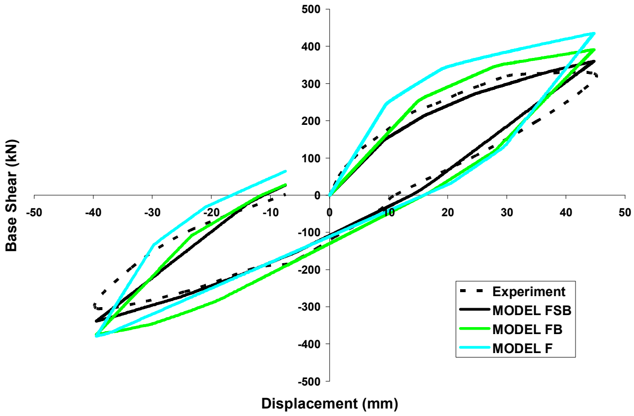

Figure 20: Pushover curves for Duong et al. (2007) frame specimen

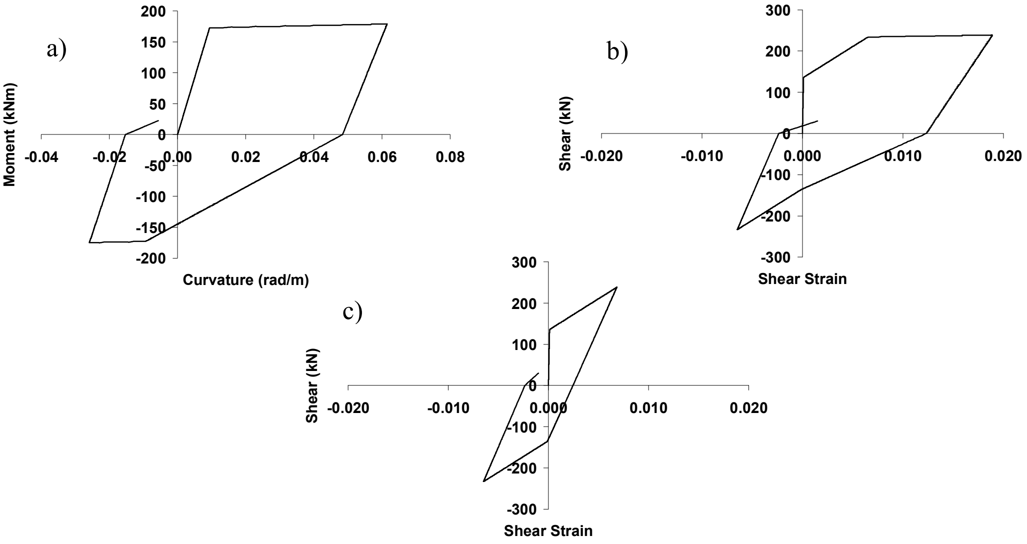

Figure 21: Duong et al. (2009) first storey beam hysteretic responses a) end-section M-φ; b) V-γ inside plastic hinge region; c) V-γ outside plastic hinge region.

4.2 Frame specimen 1 by Elwood & Moehle (2008) [27]

The specific half-scale specimen was constructed and tested on the shaking table at the University of California, Berkeley. It comprised three columns interconnected at the top by a 1.5m wide beam and supported at the bottom on footings (Fig. 22). The columns supported a total mass of 31t. To represent R/C columns typical of 1960s construction in the western United States, the central column was constructed with light transverse reinforcement having 90^o hooks (Fig. 22). The outside columns were detailed with closely spaced spiral reinforcement to ensure ductile response and to provide support for gravity loads after shear failure of the central column. The specimen was subjected to one horizontal component of the ground motion recorded at Viña del Mar during the 1985 Chile earthquake (SE32 component). The normalized central column axial load was 0.10. During testing, the central column of specimen 1 experienced a loss of lateral load capacity, apparently due to shear failure [27]. In Fig. 23, the finite element model applied for this analytical study is depicted. Its simplicity secures maximum computational efficiency. In the following, shear strength coming from transverse reinforcement of the central column is reduced to the half due to its deficient anchorage.

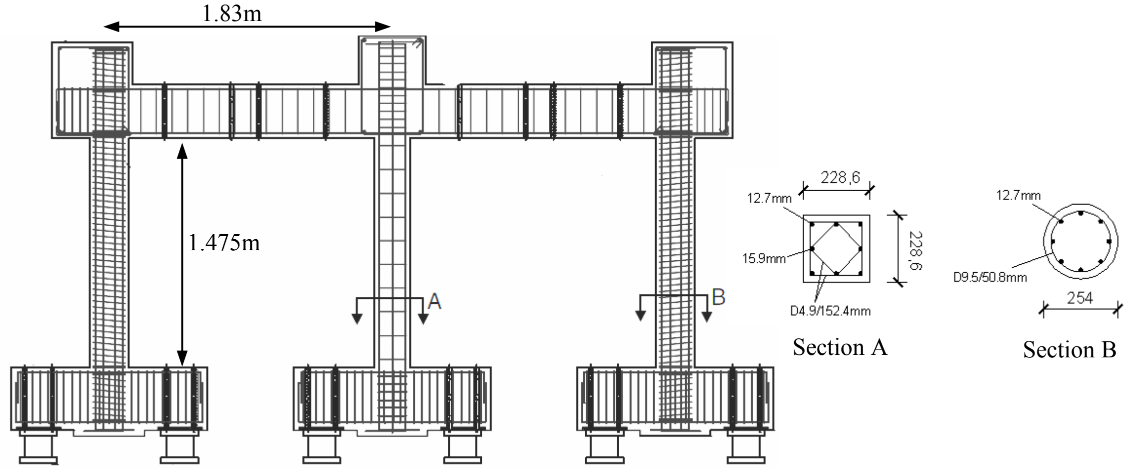

Figure 22: Elwood & Moehle (2008) frame reinforcement layout and cross-section detailing

Initially, modal response analyses were conducted including all four finite element models. Table 1 summarizes the vibration periods T estimated. The smallest period comes from the stiffest F model, which ignores shear and bond flexibility. Anchorage slip lengthens significantly the vibration period from 0.28sec to 0.33sec. On the contrary, shear deformations have minor effect on T. This is because of the fact that at this analysis stage uncracked shear stiffness is employed in the analytical model. The models FB and FSB predict well the experimental value of T ranging between 0.30sec and 0.35sec.

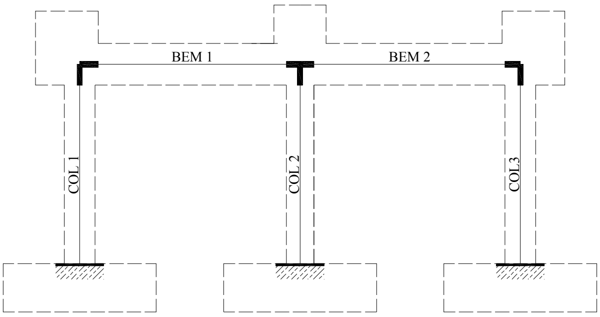

Figure 23: Elwood & Moehle (2008) frame finite element model

Model	F	FB	FS	FSB
T (sec)	0.283	0.333	0.285	0.335

Table 2: Elwood & Moehle (2008) frame predicted vibration periods

Fig. 24 presents base shear (V_{base}) vs. top displacement (Δ_{top}) relationships attained by pushover analysis of this frame as well as the experimental response recorded in the positive direction of loading. It can be seen that the F analytical model overestimates considerably initial lateral stiffness and undervalues very importantly displacement corresponding to onset of lateral failure. Inclusion of anchorage slip leads to sufficient prediction of initial stiffness until a value of $V_{base}\approx150$kN. After this level, the analytical model fails to follow closely gradual degradation of lateral stiffness and predicts a displacement capacity value of 38mm. The FS model prediction lies between the two aforementioned analytical curves. Lateral displacement capacity is found 29mm in this case. The FSB analytical model prediction converges adequately the experimental envelope for almost the entire range of response. Lateral displacement capacity is estimated equal to 46mm, which is in relatively good agreement with the experimental observation (approx. 55mm).

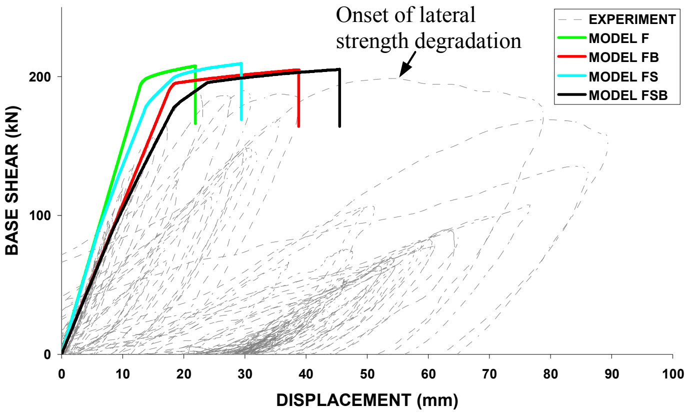

Figure 24: Elwood & Moehle (2008) frame predicted pushover curves

Fig. 25 illustrates the critical modes of failure as foreseen by the four analytical models. It is shown that the models not incorporating shear effect predict erroneously the development of flexural type of failure at the base of the central column. On the contrary, the FS and FSB analytical models drive to the experimentally observed final damage state composed by a shear failure at the top of the central column following flexural yielding.

Closing with pushover analysis, it is important to mention that if degradation of shear strength with flexural demand is neglected, the FSB analytical model predicts erroneously a flexural failure at the base of the central column for lateral displacement equal to 48mm. On the other hand, if shear strength is assumed from the beginning of the analysis equal to its minimum value (corresponding to $\mu_\varphi \geq 15$), then a shear failure is predicted corresponding to a displacement demand of only 17mm.

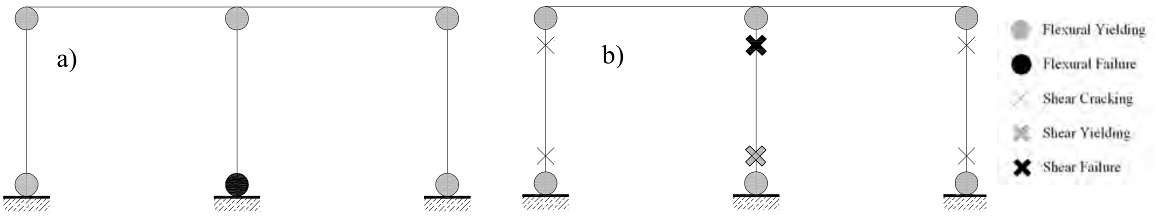

Figure 25: Predicted modes of failure for Elwood & Moehle (2008) frame specimen by pushover analysis with a) F and FB; b) FS and FSB analytical model.

Fig. 26 compares the experimental recordings and the analytical predictions produced by the proposed FSB finite element model, when the examined specimen is subjected to the ground motion component. For the analysis purposes, time step is chosen to be 0.005sec and viscous damping coefficient equal to 1% of its critical value. It can be seen that the analytical model estimates very well the displacement and base shear time histories for the major part of the response. Deviations from the experimental measurements are observed between 18.6sec and 23.1sec and between 26.0sec and 28.6sec. These time periods follow sharp excursions during which yielding of transverse reinforcement has been observed. The deviations may be attributed to the fact that the proposed finite element cannot model, in its present form, degradation of shear strength after yielding of the transverse reinforcement, as observed experimentally.

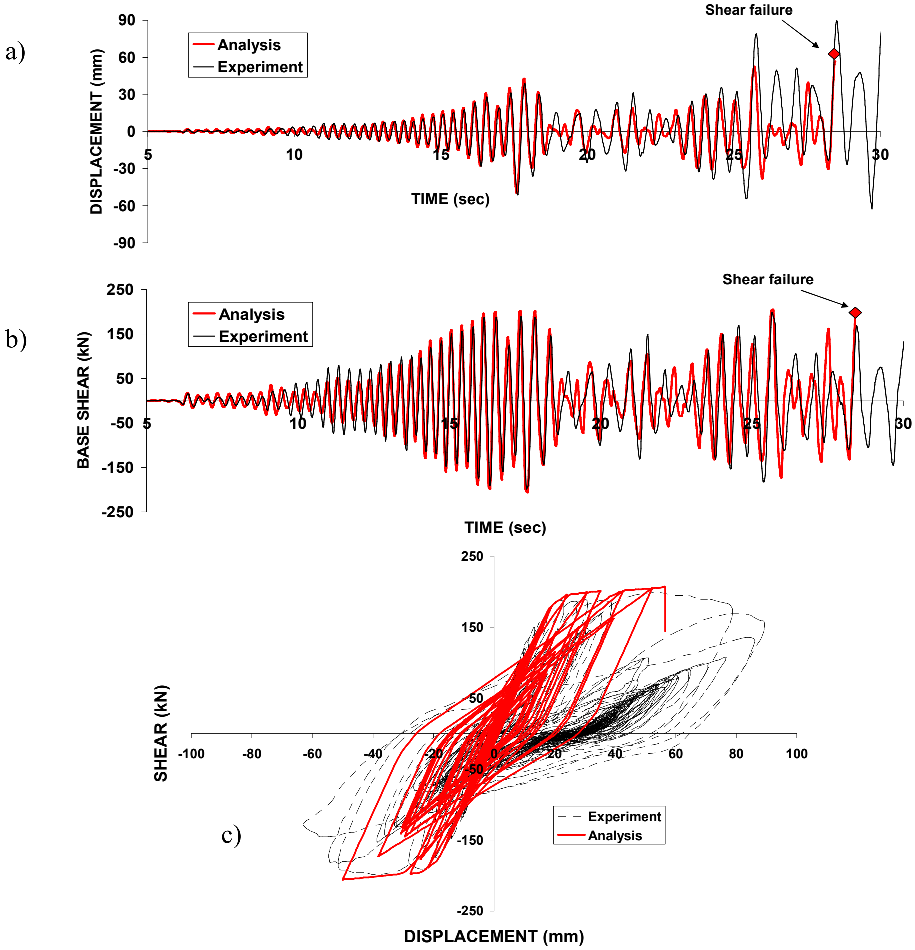

Figure 26: Elwood & Moehle (2008) frame specimen responses as recorded experimentally and predicted by FSB analytical model. a) lateral displacement time history; b) base shear time history; c) V_{base} vs. Δ_{top} response.

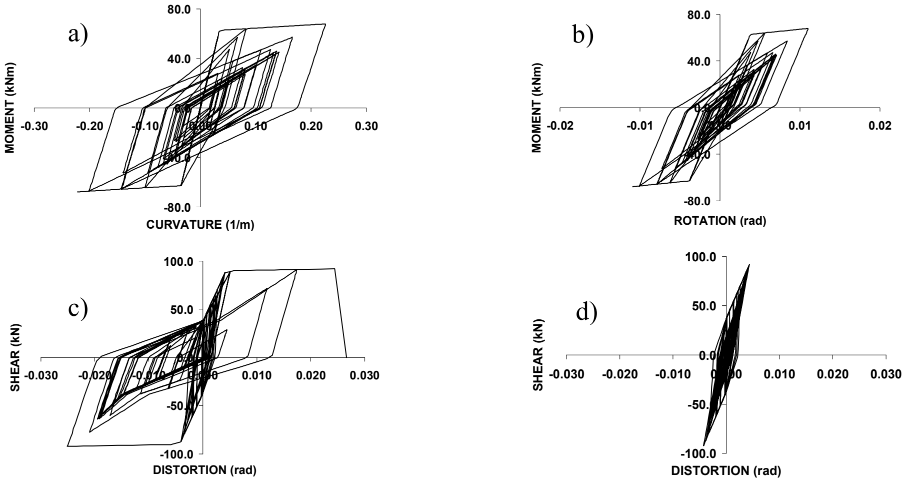

Figure 27: Elwood & Moehle (2008) central column predicted hysteretic responses. a) M-φ at the top; b) M-θ_{slip} at the top; c) V-γ at the top plastic hinge; d) V-γ outside plastic hinges

Fig. 26c compares the experimental and analytical V_{base}-Δ_{top} hysteretic relationships. It is evident that the proposed model captures sufficiently initial (elastic) stiffness, strength capacity as well as unloading and reloading response up to onset of lateral strength degradation. It must be emphasized that nonlinear dynamic analysis using the FSB model estimates accurately the magnitude of displacement corresponding to onset of shear failure and consequent lateral strength degradation, while pushover analysis yields approximately 17% underestimation of the specific response.

Fig. 27 presents hysteretic responses of the central shear-critical column, as derived by the analytical model. It can be seen that flexural yielding has been predicted at the top of the specific column followed by significant hysteretic response in flexure and anchorage slip. Due to inelastic flexural deformations, shear strength degrades in the plastic hinge of the member. Based on the shear-flexure interaction procedure proposed in this study, shear strains increase more rapidly inside than outside the inelastic zone. This phenomenon is accompanied by yielding of transverse reinforcement in the plastic hinge region driving to further differentiation of shear strains in the two discrete regions.

Finally, it is worth reporting that the predicted damage state of the examined frame from inelastic dynamic analysis is the same with the one shown in Fig. 25b, in agreement with the experimental evidence.

4.3 Frame specimen El-Attar et al. (1997) [28]

A 1/6 scale 2-storey one-bay by one-bay lightly reinforced concrete building was tested on the Cornell University shake table. The structure was designed solely for gravity loads, without regard to any kind of lateral loads. The reinforcement details (Fig. 28) were based on typical R/C frame structures constructed in the Central and Eastern United States since the mid 1900's. Model structure concrete strength was 32.3MPa (4.7ksi) and steel reinforcement yield capacity 414MPa (60ksi).

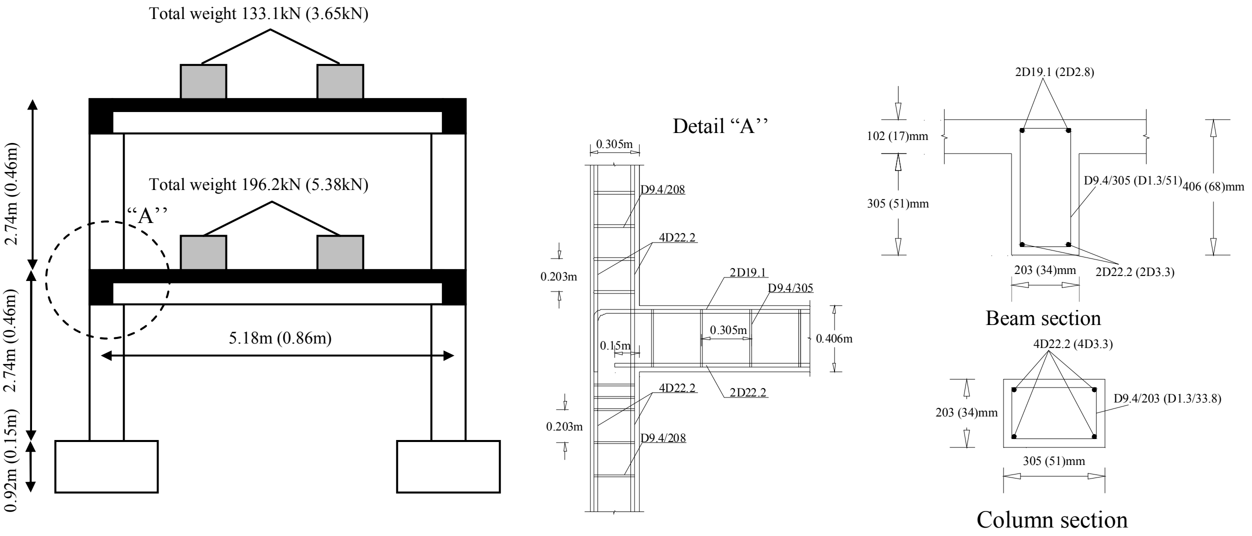

Figure 28: El-Attar et al. (1997) frame specimen configuration (values outside and inside parentheses correspond to prototype and model structure respectively).

The model structure was tested using the time-scaled Taft 1952 S69E earthquake with peak ground acceleration set in increasingly higher values. After running Taft 0.45g, wide, deep cracks were observed in the beams around the locations of discontinuous positive beam reinforcement (at the joint panels), indicating bond failure and pending pullout of these bars [28].

Fig. 29 compares frame response histories derived by the FSB analytical model and experimental recordings for the 0.36g peak ground acceleration. It is evident that the proposed model follows closely the experimental response after the first 1.5sec. Small differentiations are justifiable considering the large scale (1/6) of the examined specimen.

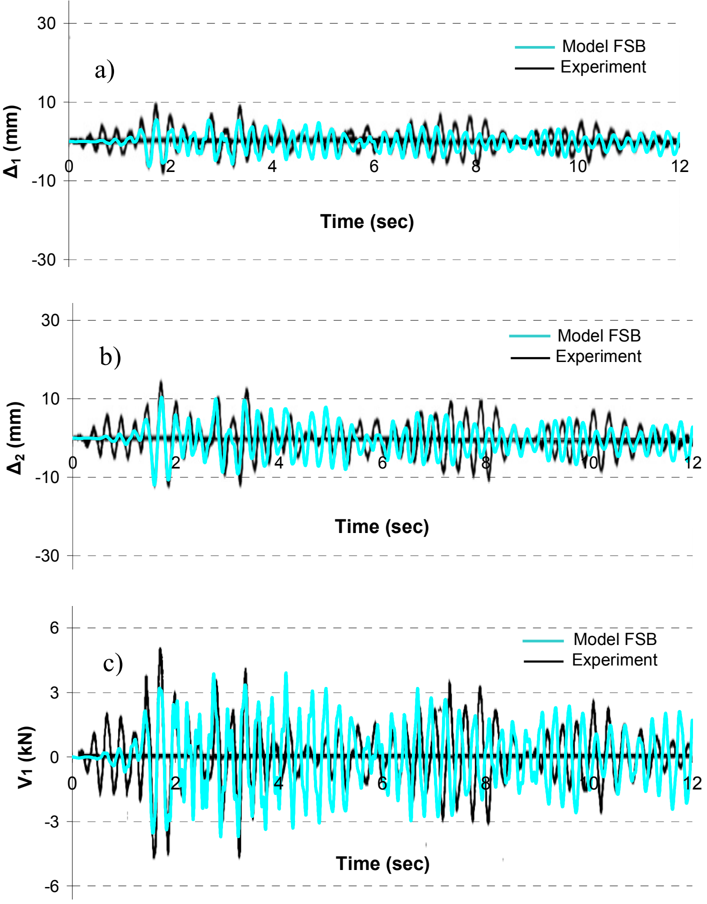

Figure 29: Comparison of El-Attar et al. (1997) frame specimen time history responses from the experimental recordings and analytical model FSB for Taft 0.36g acceleration record: a) 1st storey total displacement; b) 2nd storey total displacement; c) base shear

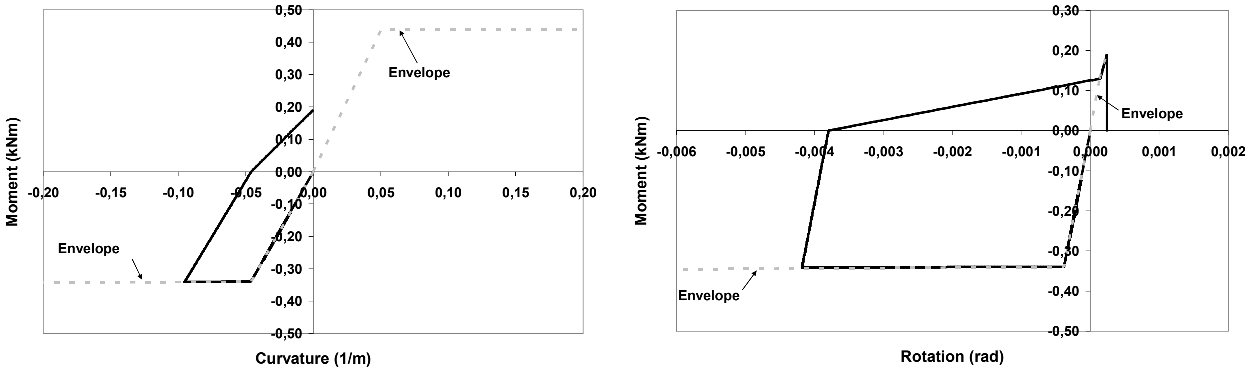

Figure 30: Hysteretic responses of left end of the 1st storey beam of the El-Attar et al. (1997) frame specimen predicted by the FSB analytical model for the 0.45g Taft acceleration record: a) M-φ; b) M-θ_{slip}

The FSB analytical model predicts the anchorage failure of the positive reinforcement at the left end of the first storey beam for the 0.45g Taft earthquake motion. This is clear by Fig.

30 presenting hysteretic M-φ and M-θ_{slip} responses of this end. It can be seen that while flexural response remains at the reloading stage, M-θ_{slip} concludes the reloading branch, moves on to the positive envelope curve and finally drives to failure, exceeding ultimate anchorage moment capacity.

5 CONCLUSIONS

A new beam-column model is introduced for seismic damage analysis of R/C frame structures with substandard detailing. This finite element models inelastic flexural, shear, and anchorage slip deformations, as well as their interaction in an explicit manner. Hence, it is capable of simulating with accuracy the seismic response of R/C frames with inadequate detailing, where shear flexibility and fixed end rotations caused by anchorage slip usually play a vital role in their response. Additionally, it is able to predict, in the general case, brittle types of failure that cannot be precluded in structures, which do not conform to modern seismic guidelines. The numerical model is implemented in a general finite element code and it is validated against experimental results from three well documented frame specimens with brittle detailing. It is concluded that the proposed model provides accurate and reliable predictions of the frame specimen responses.

REFERENCES

[1] E. Consenza, G. Manfredi, G.M. Verderame, Seismic assessment of gravity load designed R/C frames: Critical issues in structural modelling. *Journal of Earthquake Engineering,* **6**(1), 101-122, 2002.

[2] H. Sezen, T. Chowdhury, Hysteretic model for reinforced concrete columns including the effect of shear and axial load failure. *ASCE Journal of Structural Engineering*, **135**(2), 139-146, 2009.

[3] J. Pincheira, F. Dotiwala, J. Souza, Seismic analysis of older reinforced concrete columns. *Earthquake Spectra*, **15**(2), 245-272, 1999.

[4] P.E. Mergos, A.J. Kappos, A distributed shear and flexural flexibility model with shear-flexure interaction for R/C members subjected to seismic loading. *Earthquake Engineering and Structural Dynamics*, **37** (12), 1349-1370, 2008.

[5] P. Mergos, A.J. Kappos, Modelling gradual spread of inelastic flexural, shear and bond-slip deformations and their interaction in plastic hinge regions of R/C members. *In Proceedings of the 2nd Conference on Computational Methods in Structural Dynamics and Earthquake Engineering (COMPDYN),* Rhodes, Greece, 2009.

[6] P.E. Mergos, A.J. Kappos, Seismic damage analysis including inelastic shear-flexure interaction. *Bulletin of Earthquake Engineering*, 8(1), 27-46, 2010.

[7] P.E. Mergos, Assessment of seismic behaviour of existing R/C structures. *PhD thesis*, Aristotle University of Thessaloniki, Greece, 2010.

[8] M.V. Sivaselvan, A.M. Reinhorn, Hysteretic model for cyclic behaviour of deteriorating inelastic structures. *Technical report MCEER-99-0018*, University at Buffalo, State Univ. of New York, 1999.

[9] D. Soleimani, E.P. Popov, V.V. Bertero, Nonlinear beam model for R/C frame analysis. *Proc. Seventh Conference on Electronic Computation,* St. Louis, Misouri, 1979.

[10] H. Sezen, J.P. Moehle, Shear strength model for lightly reinforced concrete columns. *Journal of Structural Engineering*, **130**(11), 1692-1703, 2004.

[11] M.J.N. Priestley, F. Seible, R. Verma, Y. Xiao, Seismic shear strength of reinforced concrete columns. *Report No. SSRP-93/06*, University of San Diego, California, 1993.

[12] D. Biskinis, G. Roupakias, M.N. Fardis, Degradation of shear strength of R/C members with inelastic cyclic displacements. *ACI Structural Journal*, **101**(6), 773-783, 2004.

[13] R.G. Oesterle, A.E. Fiorato, J.D. Aristizabal-Ochoa, Hysteretic response of reinforced concrete structural walls. *Proc. ACISP-63: Reinforced Concrete Structures subjected to Wind and Earthquake Forces,* Detroit, 1980.

[14] M. Saatcioglu, G. Ozcebe, Response of reinforced concrete columns to simulated seismic loading. *ACI Structural Journal,* **86**(1)**,** 3-12, 1989.

[15] J.M. Alsiwat, M. Saatcioglu, Reinforcement anchorage slip under monotonic loading. *Journal of Structural Engineering*, 118(9), 2421-2438, 1992.

[16] S. Morita, T. Kaku, Slippage of reinforcement in beam-column joint of reinforced concrete framed. *Proc. 8th World Conf. on Earthquake Engineering*, Prentice-Hall, 477-484, 1984.

[17] ACI Committee 408, Bond and development of straight reinforcement in tension. American Concrete Institute, Farmington Hills, 2003.

[18] C.E.B., Model code for seismic design of concrete structures. 1990

[19] R. Park, R.A. Sampson, Ductility of reinforced concrete column sections in seismic design. *ACI Structural Journal*, **69**(9), 543-551, 1972.

[20] P. Soroushian, O. Kienuwa, M. Nagi, M. Rojas, Pullout behaviour of hooked bars in exterior beam-column connections. *ACI Structural Journal*, **85**(3), 269-276, 1988.

[21] M. Saatcioglu, J.M. Alsiwat, G. Ozcebe, Hysteretic behaviour of anchorage slip in R/C members. *Journal of Structural Engineering*, **118**(9), 2439-2458, 1992

[22] R.E. Valles, A.M. Reinhorn, S.K. Kunnath, C. Li, A. Madan, IDARC2D Version 4.0: A program for the inelastic damage analysis of buildings. *Technical Report NCEER-96-0010*, University at Buffalo, State Univ. of New York, 1996.

[23] N.M. Newmark, A Method of computation for structural dynamics. *ASCE Journal of the Engineering Mechanics Division*, **89**(1), pp. 67-94, 1959.

[24] A.E. Kanaan, G.H. Powel, DRAIN-2D: A general purpose computer program for dynamic analysis of inelastic plane structures. *Rep. EERC-73/06 and 73/22*, Univ. of California Berkeley, 1973.

[25] A.A. Golafshani, DRAIN-2D2: A program for inelastic seismic response of structures. *PhD Dissertation*, Dept. of Civil Engineering, Univ. of California Berkeley, 1982.

[26] K.V. Duong, S.A. Sheikh, F.J. Vecchio, Seismic behaviour of shear critical reinforced concrete frame: Experimental Investigation. *ACI Structural Journal,* Vol. **104**(3), 304-313, 2007.

[27] K. Elwood, J. Moehle, Dynamic collapse analysis for a reinforced concrete frame sustaining shear and axial failures. *Earthquake Engineering and Structural Dynamics*, **37**, 991-1012, 2008.

[28] A.G. El-Attar, R.N. White, P. Gergely, Behaviour of gravity load designed R/C buildings subjected to earthquakes. *ACI Structural Journal,* **94**(2), 1-13, 1997.

COMPDYN 2011
III ECCOMAS Thematic Conference on
Computational Methods in Structural Dynamics and Earthquake Engineering
M. Papadrakakis, M. Fragiadakis, V. Plevris (eds.)
Corfu, Greece, 25–28 May 2011

SEISMIC SHEAR DEMAND ON RC STRUCTURAL WALLS: REVIEW AND BIBLIOGRAPHY

Avigdor Rutenberg

Technion – Israel Institute of Technology
Haifa 32000 Israel
avrut@technion.ac.il

Keywords: Earthquake engineering, structural walls & wall frames, higher modes, shear demand.

Abstract: Effect of higher vibration modes on the seismic shear demand of reinforced concrete cantilever walls has been studied since the 1970's. The shear amplification becomes more important with increasing fundamental period (tall buildings) and increasing ductility demand (R or q factors). Yet, studying the relevant recommendations of structural engineering researchers and provisions of various seismic codes reveals that there is no consensus regarding the extent of shear amplification and of the inter-wall distribution of shear demand in structural systems comprising walls of different lengths.

Paper presents the available formulas for predicting shear amplification in ductile walls and dual systems (wall-frames), as well as techniques for estimating the shear distribution among interconnected unequal walls. The consideration, or absence, of these effects by leading seismic code provisions is also noted.

One effect that impacts the shear amplification is shear cracking mainly in the plastic hinge zone of the wall near the base resulting in very low effective shear stiffness. Also, deliberately allowing development of plastic hinging along the wall height (contrary to standard code requirements) has been suggested. These appear to lead to appreciably lower shear amplification than previously predicted.

Finally, an extensive bibliography (circa 100 refs.) is provided.

1 INTRODUCTION

This paper reviews the literature on the seismic shear demand on RC cantilever walls. It is mainly concerned with shear amplification due to higher vibration modes, and it also reports on the post-yield redistribution of shear demand among the walls in systems comprising several walls of different lengths. Amplification of wall shear due to higher vibration modes in the *elastic range* was not widely recognized by structural engineers until the early 1970's, although it was, or at least should have been, a known phenomenon to users of modal analysis for the seismic design of RC walls in tall buildings. However, the larger shear magnification in *yielding* flexural walls due to higher modes was first observed by New Zealand consulting engineers, which led to the 1975 pioneering paper by Blakeley et al [9]. The problem was also studied by researchers at the Portland Cement Association, and these resulted in a series of PCA reports [21, 23] and papers [22, 24] by Derecho and coworkers. The amplification tables proposed by Blakeley et al [9], the charts by Derecho et al [23], as well as later amplification expressions or charts (e.g. [29, 36, 37, 79, 81, 88, 95, 96]; and for wall-frames: [4, 38, 39, 43, 56, 81, 89]) were mainly based on results of nonlinear response history parametric studies using suites of accelerograms. Obviously, the result depended on the choice of these suites. Theoretically oriented general formulation for the shear amplification was given by Keintzel [27, 50, 51]. Extensions were proposed by Priestley [79, 80, 81], and for wall-frames by Sullivan et al [100]. Very recently Fischinger et al [32] presented a correction to Keintzel's formula, and Pennucci et al [76] modification thereof.

Shear amplification becomes more important with increasing fundamental period (tall buildings) and increasing ductility demand (R or q factors). Yet, studying the relevant recommendations of structural engineering researchers and provisions of various seismic codes reveals that there is no consensus regarding the extent of shear amplification, its height-wise variations, and the inter-wall shear demand distribution when the structural system consists of interconnected wall of different lengths.

This paper is concerned only with *shear demand* amplification on structural walls due to the effects of higher modes, but not with moment magnification along the height, which derives from the same source. Issues related to the shear capacity and post-yield shear flexure interaction are beyond the scope of the present study.

The phenomenon is described first, then available procedures to predict the amplification are presented, and relevant code provisions are briefly discussed. Shear amplification in dual or wall-frame structures is also included in the review, and post-elastic shear demand redistribution among the walls in systems with walls of unequal length is considered. The paper closes with a discussion including some unresolved issues.

The structural engineering communities in North America and in many other countries have been slow in recognizing the need to amplify shear demand, if at all. The objection of many researchers and engineers to the rather large amplification in the nonlinear range obtained from numerical simulations may perhaps explain the plethora of publications as essays in persuasion, manifested by the quite long bibliography on this rather limited problem at the end of this paper.

2 THE SHEAR AMPLIFICATION PHENOMENON

In the *linear range* the amplification of shear demand in flexural walls due to higher vibration modes has been routinely accounted for by means of response spectrum analysis. This matter is well covered in standard textbooks. Figure 1, taken from Chopra [18], shows the base shear V_b normalized by the total weight W in buildings analyzed by the modal response spectrum technique for a typical design spectrum. It can be seen that for a flexural cantilever wall ($\rho = 0$, ρ = beam to column stiffness ratio) the base shear increases appreciably with increasing natural period due the effect of higher modes compared with the design spectrum. This fact explains the requirement in many seismic codes (e.g. [16]) to permit use of the equivalent lateral force procedure only for buildings with $T_1 < \max(4T_c, 2.0\text{ sec})$, T_c = corner period to the velocity related spectral acceleration region. As can be seen, in frame structures ($\rho >> 0$) the shear amplification due to higher modes is appreciably much smaller. The main reasons for this difference are: (1) the combined effective mass of the higher modes in flexural walls is circa 35% of the total mass vs. circa 25% in frames ; (2) the period ratios of the 1st mode to the higher ones is much larger for flexural walls (e.g. $1^{st}/2^{nd} \approx 6$ vs. ≈ 3 for ideal frames). Hence, when T_1 of a flexural wall is in the velocity spectral region, the higher modes - the spectral accelerations of which are usually located at the high acceleration plateau – have a larger effect on the shear than in frames. This effect is even more pronounced when T_1 is longer so that $S_a(T_2)$ and even $S_a(T_3)$ are in the velocity spectral region. Indeed, the main effect of the higher modes is due to the 2nd mode (e.g. [50, 66, 68]) and, to a much lesser extent, to the 3rd. mode. Evidently, the shape of the spectrum also strongly affects the extent of amplification. The reader is referred to Chopra [18] and Humar & Mahgoub [41] for detailed consideration of the phenomenon. The way seismic codes consider this effect is described subsequently.

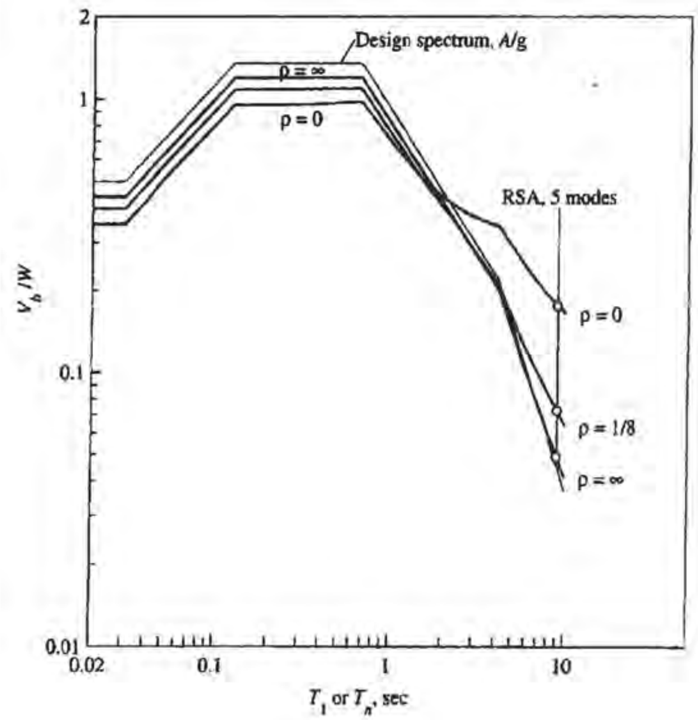

Fig. 1: Normalized base shear V_b/W for 3 values of ρ; for walls $\rho = 0$ (Chopra 2001).

As already noted, the shear amplification due to higher modes in the ***nonlinear range*** has attracted considerable interest since the Blakeley et al 1975 paper [9]. They showed, by means of nonlinear response history analysis (NLRHA), that shear demand increases with natural period and falling damping ratio. Similar results were obtained by Derecho et al [21], Keintzel [49] and Kabeyasawa [43, 44, 45], who also demonstrated that shear demand increases with ductility demand. The following explanation for the latter effect was given by Paulay & Priestley [75]. At some instants during the response the higher modes combine with the 1st mode in a height-wise force distribution similar to the 2nd mode. The higher mode shapes of hinged and fixed base cantilever are quite similar, as shown in Fig. 2, suggesting that the formation of a plastic hinge at the wall base does not significantly affect the higher modes. Hence, while the plastic hinge reduces the 1st mode shear response to the level commensurate with its flexural capacity, the response of higher modes remains circa their elastic level. In other words, the shear response can be approximated as a superposition of the 1st mode shear reduced by the force reduction factor R (q in Europe), while the higher modes' response remains elastic, thereby amplifying their shear demand relative to that due to the first mode. Note that due to the plastic hinge formation and unloading/reloading softening the periods of higher modes are also elongated, hence amplification is likely to be somewhat lowered. Similar conclusions were drawn from the response of a flexural wall with substantially reduced stiffness at its base – the plastic hinge [66]. This approach forms the basis for several analysis procedures developed to predict shear amplification, as described subsequently. As in the linear range, the base shear amplification increases with increasing natural period since higher modes become more important, and as a result the shear resultant moves downwards. Also, as in the linear range, the spectral shape plays an important role.

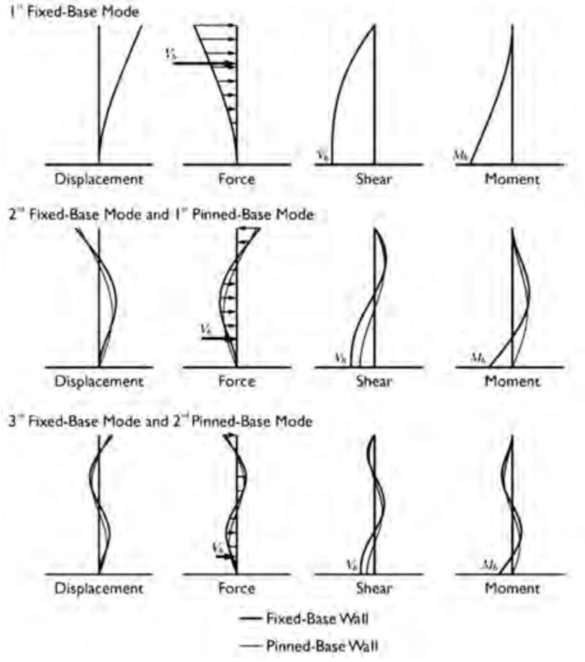

Fig. 2: Fixed base and hinged cantilever mode shapes (Wiebe & Christopoulos 2009).

It is interesting to note that base shear amplification in dual wall frame systems (WFs) is lower than in structural walls. As already observed the period ratios in frames are much lower, and their 1st mode mass participation is higher. Also, the shear demand in frames depends mainly on moment demand. Indeed, shear amplification in WFs strongly depends on the wall-to-frame shear ratio. More details on WFs are given in Section 5.

3 PROCEDURES TO PREDICT HIGHER MODES SHEAR AMPLIFICATION

The work of Blakeley et al [9] brought about changes in the provisions of the New Zealand seismic code [63] and in European model codes [13, 14]. However, the latter provisions explicitly restricted the magnifications to the equivalent lateral force (or static) procedure. This turned out to be unfortunate since the corollary was that amplification was understood not to be required when using modal analysis (as, e.g. the Israeli seismic code [97] without Amendment 3, is interpreted). It also led engineers to overlook the fact that a major part of the shear amplification due to higher modes takes place in the post-elastic range. This attitude still persists also in the National Building Code of Canada NBCC-2005 [61], which only accounts for linear multi-mode shear amplification. However, the present Canadian Concrete code CSA-A23.3-04 [19] requires considering nonlinear shear amplification, yet gives no guidance to that effect (see also [10]), although the commentary to the 1994 version of that code suggested adopting the New Zealand shear amplification formulas. Note that in the provisions and the proposals described subsequently it was tacitly assumed that the plastic hinge could form only at the wall base, and that the prescribed moment envelope took care of that.

The amplified shear V_a is given in in terms of the base shear V_d from analysis, as follows:

$$V_a = \omega_v V_d \tag{1}$$

In the New Zealand code:

$$\omega_v = \begin{cases} 0.9 + \dfrac{n}{10} & n \le 6 \\ 1.3 + \dfrac{n}{30} \le 1.8 & n > 6 \end{cases}$$

. And in CEB:

$$\omega_v = \begin{cases} 0.9 + \dfrac{n}{10} & n \le 5 \\ 1.2 + \dfrac{n}{25} \le 1.8 & n > 5 \end{cases}$$

As can be seen the NZ code is somewhat more conservative than CEB for $5< n< 15$.

In spite of their widespread use there are several problems with these formulas. First, the only governing parameter is the number of storeys, which is a crude proxy for the natural period. Also, the upper bound amplification is arbitrarily set at 1.8 for a 15 storey building. However, perhaps a more serious limitation is their independence of the excitation level, which affects the shear demand appreciably, and of the shape of the applicable response spectrum. Note also that, by today's standards, the Blakeley et al study [9] was based on a very limited data set: only 5 accelerograms, two of which were artificial. Also, bilinear moment-curvature hysteresis was assumed, while many modern studies use the modified Takeda model, considered to be more realistic. On the other hand, the bilinear model is somewhat more conservative [62].

Shear amplification design charts were presented by Derecho et al, e.g., [22, 24]. These are based on a parametric study on structural walls, 10 to 40 storey high, using the modified Takeda model for the NLRHA carried out for 6 earthquake records. They presented shear amplification relative to the base shear as evaluated by the then governing UBC provisions vs. fundamental natural period for several values of rotational ductility demand μ_r, as shown in Fig.3. Since the set of records was normalized for a given Housner spectral intensity (SI= 1.5) a correction factor (practically proportional) was provided for different SIs. One difficulty in applying this approach is its dependence on μ_r rather than on the strength reduction factor R, requiring making assumptions regarding the relation between these two parameters.

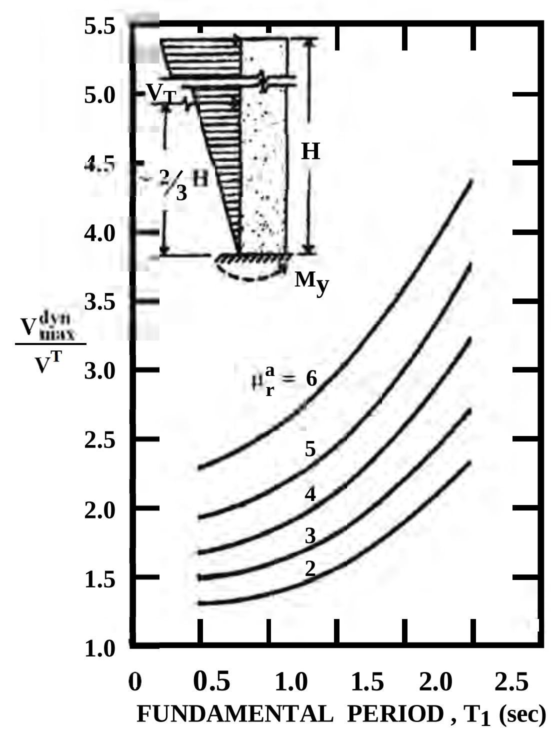

Fig. 3: Base shear demand amplification for several values of rotational ductility (Derecho et al 1981)

Based on parametric NLRHA several investigators proposed simple expressions to estimate the maximum base shear V_a by decomposing it into the 1st mode and the higher modes responses. Kabeyasawa (e.g. [43], see also [4]) gave the following expression for wall frames:

$$V_a = V_d + D_m W A_e \tag{2}$$

in which V_d = base shear of an inverted triangular loading, W = total weight, A_e = peak ground acceleration and D_m is a given factor increasing with the number of storeys (i.e., period). Based on shake-table tests Eberhard & Sozen [25] proposed $D_m = 0.3$ for 9 and 10 storey wall frames, in agreement with Kabeyasawa's results. The actual amplification in wall frames depends to a large extent on the base shear share carried by the wall. Hence the predictive ability of formulas such as Eqn. 2 is rather limited.

A similar formula for isolated walls was presented by Ghosh et al [36, 37] based on a parametric study similar to that of Derecho et al [23]:

$$V_a = M_y/0.67H + D_m W A_e \tag{3}$$

in which M_y = the yield moment at base and H = wall height. The advantage of this form is the explicit statement that the base shear is that at moment capacity level rather than at the design shear obtained from analysis, which is usually lower. For isolated walls the study by Seneviratna [95, 96], described subsequently, confirmed the equation *format* of Kabeyasawa and of Ghosh except for the short period range and for low values of R.

In 1988 Keintzel [27] proposed a simple expression for shear amplification by explicitly assuming that the 1st mode shear is limited by the flexural capacity of the wall at the base, and that the higher modes respond linearly. This formula was eventually incorporated into Eurocode 8 [15, 16]:

$$\omega_v = q \cdot \sqrt{\left(\frac{\gamma_{Rd}}{q}\frac{M_{Rd}}{M_{Ed}}\right)^2 + 0.1 \cdot \left(\frac{S_e(T_C)}{S_e(T_1)}\right)^2} \leq q \tag{4}$$

ω_v = 1st mode shear amplification factor – but see next paragraph
q = R = strength reduction (behaviour) factor
M_{Ed} = design bending moment at wall base
M_{Rd} = design flexural resistance at wall base
γ_{Rd} = overstrength factor due to steel strain-hardening
T_1 = fundamental period
T_c = higher period corner of the constant acceleration plateau (Fig. 2)
S_e (T) = Spectral ordinate (Fig. 2).

This is a very useful formula since it considers most of the parameters governing shear amplification in structural walls. It does not require exact evaluation of the 2nd mode natural period, and is practically spectrum-shape independent, in contradistinction to parametrically evaluated amplification formulas or plots, which are not (e.g. [79, 88, 95, 96]). It also accounts for the two sources of overstrength. However, it is too conservative for very tall buildings, i.e., those with T_2 in the velocity spectral region, and it is sensitive to the calculated value of the 1st mode spectral acceleration S_a, which for RC walls depends on design assumptions. It is believed that S_a at the natural period based on yield displacement should be the appropriate one (e.g. [68]). In view of the extensive use of this formula (EC8 is now applied in circa 20 countries) some background information may be in order. Based on parametric studies Keintzel assumed that the SRSS modal combination can also be applied in the post-elastic range, and also that the contributions of the first two modes are important, hence:

$$V_a = \sqrt{\left(V_{Ed,1}\right)^2 + \left(qV_{Ed,2}\right)^2} \tag{5}$$

in which $V_{Ed,i}$ are the 1st and 2nd mode shear forces from analysis. He also assumed that the contribution of the 2nd mode is 0.1 S_e (T_1)/ S_e (T_2), in which $0.1 \approx 0.32^2 \approx$ the 2nd to 1st mode mass contribution ratio squared. Considering that design flexural overstrength (M_{Rd}/M_{Ed}) affects only the 1st mode, and dividing by $V_{Ed,1}$, Eqn.4 is obtained. This development shows, as made clear by Fischinger et al [31, 32], that the amplification ω_v should factor only the 1st mode shear $V_{Ed,1}$. However, in EC8 ω_v amplifies V_{Ed} as evaluated either by the equivalent lateral force procedure (usually inversely triangular loading based on the total building weight) or by modal analysis, and, without making the distinction, evidently leads to different results. Keintzel concluded that ω_v should be bounded by q (R), but this is too low considering that the elastic bound should be based on the SRSS shear - not the 1st mode one. Note also that the present EC8 restricts the application of Eqn. 4 to walls designed for high ductility (DC-H), while for medium ductility walls (DC-M) $\omega_v = 1.5$. This has been found to be too low [31, 32, 88], suggesting that Eqn.4 should be applied also to DC-M walls, as indeed was the case in past versions of EC8.

Keintzel [50] already observed that Eqn. 4 is a simplification of an expression he considered to be more accurate. A different correction, which is based on an extensive parametric study using the Modified Takeda model and assuming hinge formation only at wall base, was proposed by Fischinger et al [32]. This correction affects the 2nd term in Eqn.4 when M_{Rd}/M_{Ed} is large, hence is of limited practical use.

A natural extension of Keintzel's formula proposed by Priestley [79], which can also predict the shear demand along the height of the wall and not only at base, is the following:

$$V_a = \sqrt{\left(V^*_{Ed,1}\right)^2 + \mu^2\left\{\left(V^*_{Ed,2}\right)^2 + \left(V^*_{Ed,3}\right)^2 + \cdots\right\}} \tag{6}$$

in which$V^*_{Ed,1}$ is the overstrength factored 1st mode design shear and μ is the displacement ductility demand. Priestley [79] reported satisfactory agreement with NLRHA results for a wide range of wall heights.

Another modification of Keintzel's formula was recently proposed by Pennucci et al [76]. The basic assumption therein is that the total response can be obtained as the absolute sum of the 1st mode shear reduced by q (denoted R_m), and of the higher modes SRSS response, which is reduced by another factor (R_p). It has similar format as Eqns. 2 and 3, and is given by:

$$V_a = \frac{V_{Ed,1}}{R_m} + \frac{\sqrt{\left(V_{pin,2}\right)^2 + \left(V_{pin,3}\right)^2 \,.....}}{R_p} \tag{7}$$

in which $V_{Ed,1}$ and $V_{pin,i}$ are the modal shear forces at their ***elastic level***, and the subscript ***pin*** denotes pin-based modal shear response. Based on parametric studies Pennucci [76] found that, as expected, the higher modes reduction factor R_p is related to R_m: large when R_m is low, and becoming smaller with increasing R_m, asymptotically reaching 1.0, i.e. linear behaviour. A considerable improvement over Eqn. 6, particularly for long periods and large strength reduction factors, and very satisfactory agreement with NLRHA results along the building height were reported. Hence, it appears that the approach can make better allowance for the period elongation due to base hinging and for the lowered stiffness of the unloading/reloading hysteresis loop (Modified Takeda). Yet, since R_p is evaluated parametrically, it is to some extnt spectrum shape dependent.

A simple formula also in the format of Eqns. 2 and 3 was proposed by Panagiotou & Restrepo [66]. It is based on the observation that the amplification can practically be accounted for by adding a factored 2nd mode shear envelope to that of the 1st mode shear at base yield. The shear demand at storey i can then be approximated as:

$$V_a = V^*_{Ed,1} + q\rho_{12}\left(\sum_{j=i}^{n}\Gamma_2\Phi_2^j\right)mSa_2 \tag{8}$$

in which ρ_{12} is a factor to be determined, and $\Gamma_2\Phi_2^i$ = min[4.28h_i/H, 0.6; -2.5h_i/H + 1.85], Γ_2 = 2nd mode participation factor, Φ_2^i = mode shape ordinate at floor i , h_i = floor height from base, H = total wall height, Sa_2 = 2nd mode spectral acceleration. Good agreement with NLRHA results for near-fault records was reported. Note, however, that the application of the formula to other cases depends on ρ_{12}, which was provided only for a small number of pulse-type near-fault ground motions.

The amplification formulas or charts given subsequently are parametrically based; hence they are only applicable to spectra having shapes that are similar to the mean spectra of the suite of records forming the data base for the NLRHA. Also, they are sensitive to the chosen damping ratios.

Base shear demand amplification charts based on 15 records for wall structures having elastic–plastic moment-rotation hysteresis designed using SRSS load pattern were provided by Seneviratna [96]. Figure 4 presents the mean amplification, defined as the ratio of the maximum base shear of the multi-degree of freedom V_b(MDOF) to the single degree of freedom (SDOF) base shear $F_y(\mu)$, vs. T_1. These are displayed for several values of μ(SDOF) - the ductility ratio of the SDOF system. It can be seen the amplification increases with T_1 and with μ(SDOF). As already observed, the amplification w.r.t the SRSS loading would be smaller since higher modes also amplify the shear in the linear range.

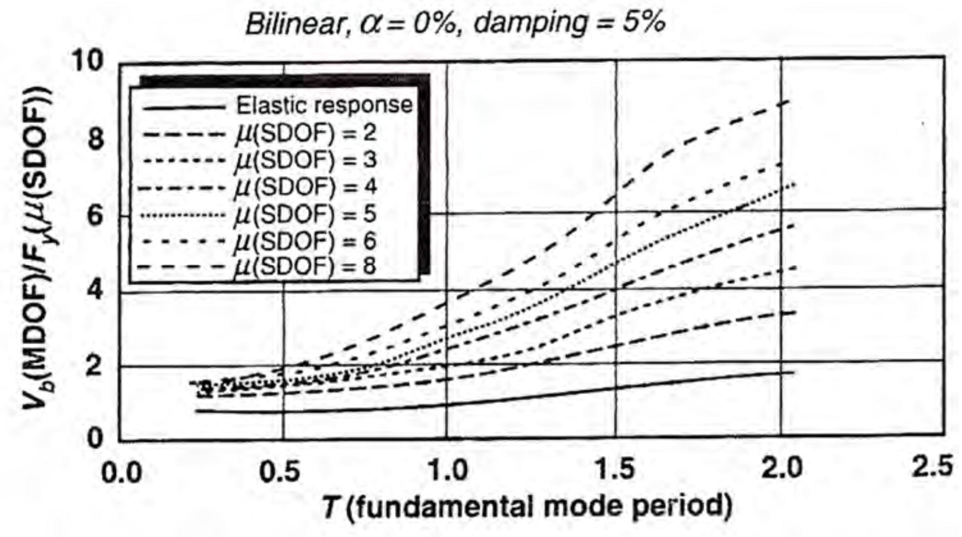

Fig.4: Base shear demand amplification for several values of displacement ductility (Seneviratna 1995)

The amplification formula provided by Priestley, [79] was based on NLRHA results for walls assuming Modified Takeda hysteresis. It has a very simple form, and is given in terms of the displacement ductility demand μ, and T_1:

$$\omega_v = 1 + \mu B_{(T)}/\Phi; \qquad B_{(T)} = 0.067 + 0.4(T_1 - 0.5) \le 1.15. \tag{9}$$

in which Φ is the flexural overstrength. Evidently, in routine analysis, μ needs to be evaluated, unless the equal displacement approximation or another conversion formula is invoked.

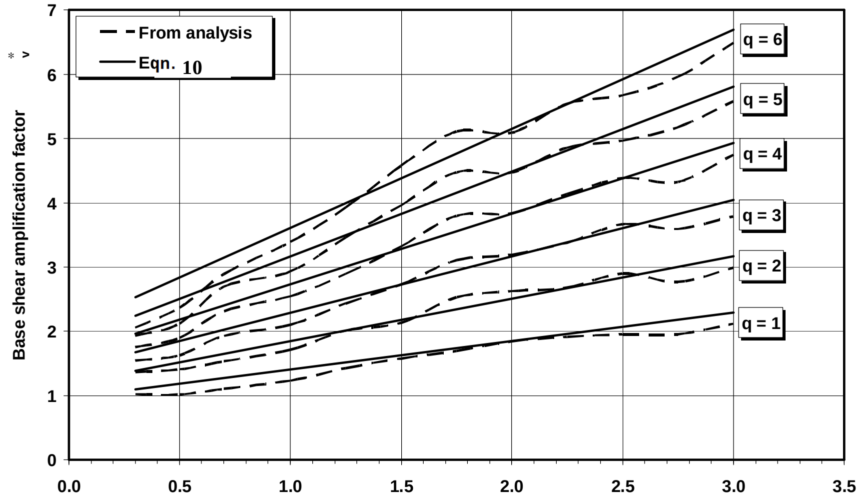

Fig. 5: Eqn. 10 - Base shear demand amplification for several values of strength reduction factor q (=R) (Rutenberg & Nsieri 2006)

A somewhat longer expression given in terms of q (or R), not incorporating flexural overstrength, was presented by Rutenberg & Nsieri [88]. It is given by:

$V_a = [0.75 + 0.22(T_1 + q + T_1q] V_d$ (10)

in which V_d is the base shear due to a triangularly distributed base shear. Eqn. 10 is shown in Fig. 5 by the straight lines. Elastic-plastic response and 5% tangent stiffness damping in the 1st and 5th modes were assumed. Note that 5% damping is now believed to be too high for very tall buildings (e.g. [92]), for which the major sources of damping have a lower effect.

4 STOREY SHEAR DEMAND

Whereas, as noted, Eqns. 6, 7 and 8 are able to predict the shear demand for the full wall height, this is not the case with the other design equations listed above, that apply only to the base shear. This is because in many cases the ω_v normalized SRSS storey shears overestimate the expected shear values for large wall portions of long period structures, as shown in Fig. 6.

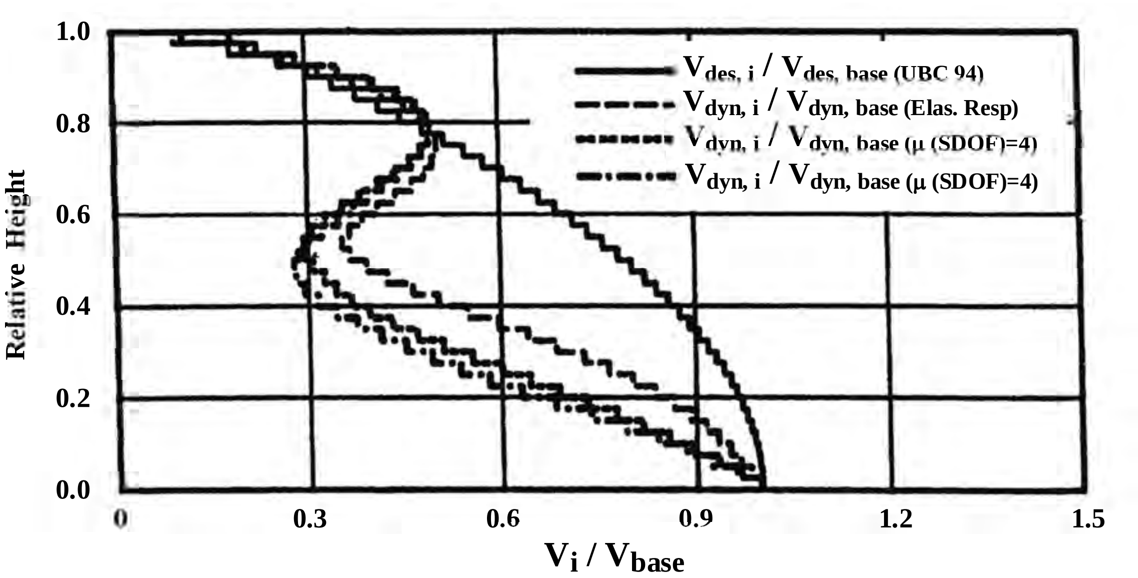

Fig.6: 40-storey wall shear envelopes: code loading design pattern, T = 2.05s: mean for $S_{1,a}$ records, bilinear, α = 0% , damping 5% (Seneviratna & Krawinkler 1997)

Apparently, this problem was first addressed by Iqbal & Derecho [42] who provided a wall height shear demand envelope that has not changed appreciably since. A design envelope as function of the fundamental period T_1 is shown in Fig. 7, in which ξ is given by:

$\xi = 1 - 0.3T_1 \geq 0.5$ (11)

Note that Eqn.11 resembles Fig. 5.4 in EC8 [16], but therein it is confined to walls in dual WF systems. A similar but straight-line envelope with the wall-top shear of:

$(0.9 - 0.3T_1) V_a \geq 0.3 V_a$, (12)

was given by Priestley et al [81] and Model Code [56].

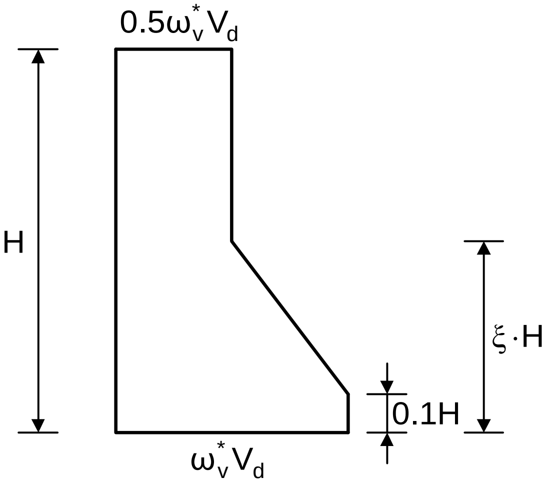

Fig.7: Shear force design envelope (Rutenberg & Nsieri 2006)

5 MORE ON DUAL WALL FRAME (WF) SYSTEMS

Some studies on dynamic shear demand amplification in WFs followed naturally from those on flexural walls, but not all. As already noted wall shear amplification in WFs was studied by Kabeyasawa (e.g. [44]) and Aoyama [4], see Eqn. 2. Paulay and his co-workers [38, 39] observed that, as in flexural walls, higher vibration modes amplified the shear force demand on the *walls* of WFs, but to a lesser extent, and proposed a simple prediction formula accounting for this response reduction. This extension of the shear amplification formula for flexural walls based on Blakeley et al [9] to walls of dual systems is also given by Paulay & Priestley [75]. This WF shear amplification factor ω_v^* is given by:

$$\omega_v^* = 1 + (\omega_v - 1)\,\eta \qquad (13)$$

in which ω_v is the free standing wall shear amplification factor and η is the fraction of the base shear carried by the walls. Although the format of this formula is appealing its predictive capability appears to be limited [89].

Alwely [3] made ω_v^* dependent on the non-dimensional frame-to-wall stiffness ratio αH, as evaluated from the linear continuum approximation (e.g. [99]). Kappos & Antoniadis [46] proposed a procedure to estimate more realistically the shear demand in the upper storeys and also a modified version of the Goodsir et al [38, 39] formula (Eqn. 13) to account for shear amplification in WFs with unequal walls. Very recently Kappos & Antoniadis [47, 48] provided formulas to improve the shear distribution match with NLRHA results all along the wall height.

The codified guidance regarding the amplification factor ω_v^* is rather limited. The New Zealand seismic code NZS 3101- 2006 [63] refers only to Paulay & Priestley [75] where Eqn. 13 is presented. Note that therein ω_v is that given by Eqn. 1. It is clearly seen that when $\eta \leq 1.0$ then $1 \leq \omega_v^* \leq \omega_v$. Eqn. 13 assumes that ω_v^*, as ω_v, is independent of the expected ductility demand or q (R). Note also that Eqn. 1 depends indirectly on T_1 through its dependence on the number of storeys n.

EC8 [16] considers WFs in which $\eta > 50\%$ as “wall–equivalent”, hence in such cases wall shear in high ductility class (DC-H) systems should be amplified per Eqn. 4.

Applicable US codes do not include dynamic shear amplification requirements even for flexural walls (except the Commentary to the 1999 SEAOC code [93]). In practice, however, amplification is considered in tall buildings design, as described subsequently. Quite recently Priestley et al [81], in the draft displacement-based seismic design code at the end of their book (also [56]), proposed a dynamic base shear amplification expression for WF walls, which requires predicting the displacement ductility demand μ_{sys} of the dual WF system. When $0.4 \leq \eta \leq 0.8$ the wall base shear amplification is given by:

$$\omega_V^* = 1 + \frac{\mu}{\Phi} C \tag{14}$$

$$C = 0.4 + 0.2(T_1 - 0.5) \leq 1.15$$

in which Φ is an overstrength factor (usually taken as 1.25). Note that ω_V^* is assumed independent of η, hence cannot be in agreement with Eq. 13.

Based on the deflected shapes observed in several time windows during NLRHA, Sullivan et al [100] recently proposed a variant of Keintzel's formula using so called "transitory inelastic modes". They concluded that the higher modes' periods elongated, and suggested that good agreement with NLRHA of the base shear per Keintzel could be obtained when the higher modes' periods were evaluated based on low post-yield secondary stiffness at wall base. This basically amounts to replacing the μ^2 factored higher modes fixed base shears (at design level) in Eqn. 6 by their thus computed counterparts.

A NLRHA based formula was very recently proposed by Rutenberg & Nsieri [89]:

$$V_a = 0.4 + 0.2(T_1 + q + \eta) + 0.13 T_1 q \eta \tag{15}$$

in which η is the elastic wall base shear to total base shear ratio. As all formulas based on NLRHA parametric studies it is applicable to design spectra similar to the mean spectrum of the suite of records used for their derivation. It was also found that the results are quite sensitive to the design yield levels of the girders over the frame height

6 EFFECTS ON SHEAR AMPLIFICATION: SEISMIC ISOLATION, MULTIPLE HINGES, ROCKING, AND SHEAR DEFORMATION

6.1 Seismic isolation, multiple hinges along height and rocking

It is often necessary to increase the strength over significant portions of the wall height if yield is to be confined - per capacity deign - to the plastic hinge zone at the base; whereas allowing yield to propagate upwards (with base level flexural strength) leads to some reduction in the shear demand, e.g., as shown in Fig. 8. Adding another plastic hinge at wall mid-height, as proposed by Panagiotou & Restrepo [67], leads to more pronounced lowering of shear demand envelope. Furthermore, when the wall is designed such that plastic hinges can develop at several locations along the height as done by Rad [82, 84], the shear demand falls appreciably, as illustrated in Figs. 9 & 10. Evidently, the last approach requires special reinforcement detailing along all the wall height.

Wiebe & Christopoulos [103] proposed a design to allow rocking of several wall segments with respect to each other in order to reduce the contribution of higher modes, using unbonded post-tensioning. Appreciable reductions in shear and bending moment were reported.

Twenty storey seismically isolated cantilever wall buildings designed with lead-plug rubber bearings were studied by Calugaru & Panagiotou [12]. Three variants were considered: single isolator at base, isolators at base and at mid height, and isolators at base and at 0.7 of height. As expected, these buildings demonstrated significant reduction in the important response parameters compared with standard fixed base, i.e. with a single plastic hinge, buildings. The buildings with dual isolation led to a further reduction in shear demand on the upper 60% of the height.

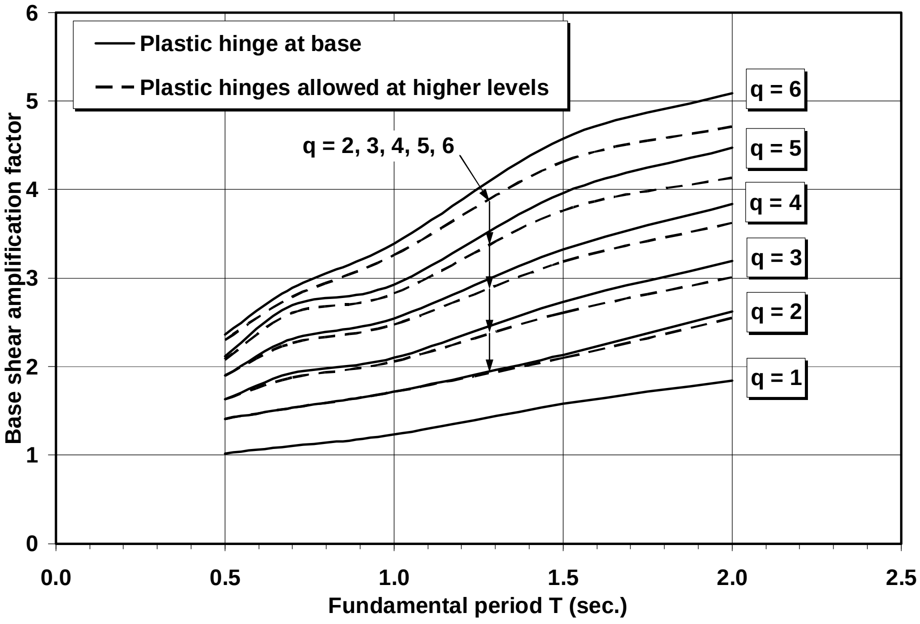

Fig.8: Plastic hinge at base only vs. plastification at higher levels –base shear flexural strength assumed over building height (Rutenberg & Nsieri 2006)

6.2 Shear deformation

Already in 1988 Eibl & Keintzel [27] observed that smaller shear rigidity lowers the higher modes dynamic amplification. In their study on the shear distribution among wall of different lengths Rutenberg & Nsieri [88] noted a substantial lowering in shear demand in cracked sections when the effective shear rigidity GA_{ve} was evaluated based on the analogous truss model [72], which is appreciably smaller than the recommended values based on the gross section (GA_{vg}) for both cracked and uncracked walls by ASCE 41-06 [6], or 50% thereof for cracked walls by EC8 [16]. Gerin & Adebar [33] provided expressions to predict the shear deformation, including shear cracking and yielding, observing that a typical effective shear rigidity of diagonally cracked concrete could approximately be taken as 10% GA_{vg}, somewhat lower than the GA_{ve} assumed by [88]. Rad & Adebar [82, 84] used effective shear stiffness as a simple way to demonstrate the significant influence of cracking on shear amplification, as shown in Fig 11. Wallace [102] suggested modelling the post-cracking shear stiffness in the plastic hinge zone as circa 2.5% GA_{vg}.

7 NOTES ON PRACTICE IN THE USA

Seismic design practice in the US, particularly in California, is highly regarded worldwide and often adopted; hence it may be useful to comment on the situation there with respect to dynamic shear amplification.

It is interesting that although researchers, code-writers and practicing engineers were exposed to the many publications on the post-yield shear demand magnification of higher modes, this has not been manifested in US seismic codes, e.g., ASCE 7-05 [5], as would be expected, particularly, since other major codes such as NZ3101 [63] and EC8 [16] included such provisions for many years. As noted, only the Commentary to the 1999 SEAOC [93] considered this issue, referring the reader to the New Zealand code. Also, shear amplification is recognized, albeit to a limited extent, by ASCE 41-06 [6] code for upgrading of existing buildings:

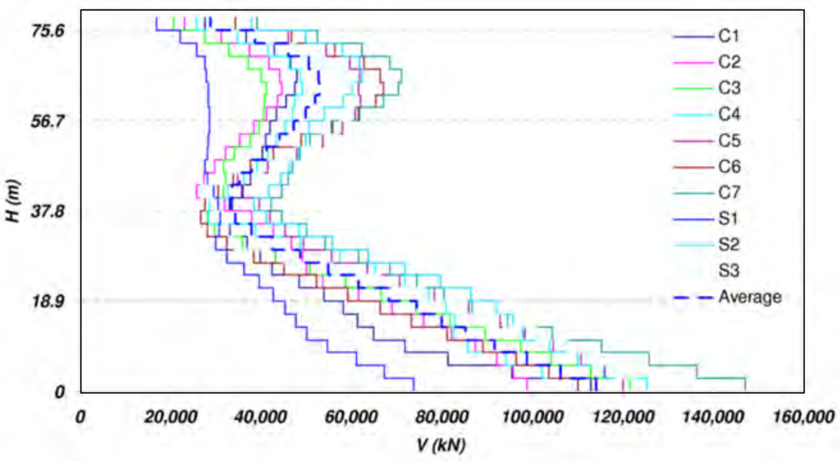

Fig. 9: Shear force envelopes with hinging permitted only at wall base, R =5 (Rad & Adebar 2008)

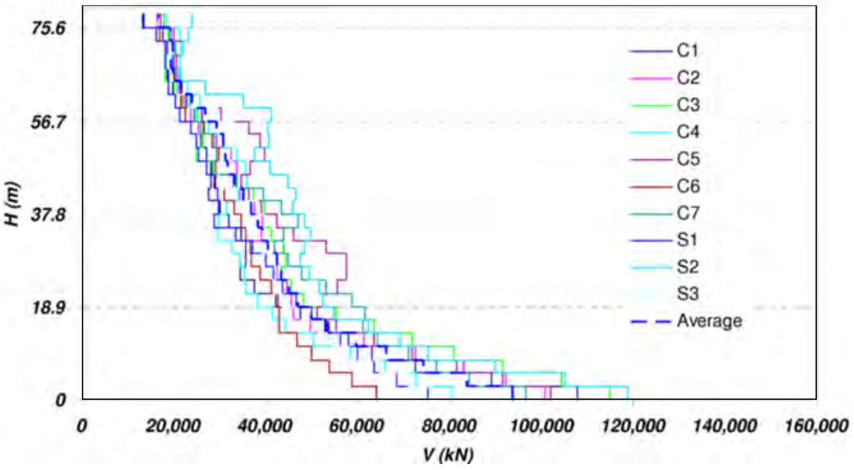

Fig. 10: Shear force envelopes, flexural hinging at many locations over height, R =5 (Rad & Adebar 2008)

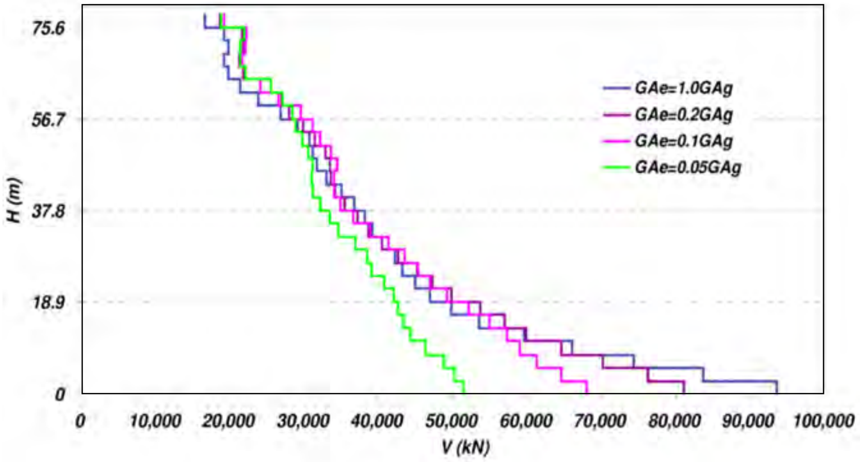

Fig. 11: Influence of effective shear stiffness on average shear force envelopes, flexural hinging at many locations along wall height, R =5 (Rad & Adebar 2008)

the shear force at the wall base is calculated assuming uniform lateral force distribution over the wall height, i.e., the shear resultant is located at wall mid-height (clause 6.7.2.4 therein) rather than at approximately its 2/3rd, thereby increasing the base shear by circa 35%. It is only when NLRHA - one of the recommended procedures by US codes - is carried out that dynamic shear amplification is accounted for. However, code based analysis per this procedure appears to be the exception rather than the rule.

The resurgence in high-rise construction in the west coast of the United States during the early and mid-2000's has led to the application of performance-based non-prescriptive design procedures ([20, 54, 94]. Such design requires using a suite of at least seven pairs of appropriate ground motion histories; hence, dynamic amplification is thereby considered. Indeed, researchers and practitioners in California were soon reporting on large higher modes magnifications [53, 57, 58, 59, 105]. For very tall buildings, circa 40 storeys, these studies predicted shear amplifications on the order of 4 relative to code. It is interesting to note that one designer [52] observed, after designing over two dozen tall buildings, that "*design which follows the prescriptive provisions of the building code will likely result in a shear capacity that falls well short of the likely demands the structure will experience during a significant seismic event. As shear failure of a structural wall is typically viewed as non-ductile, undesirable response, this outcome raises serious concerns….*"

8 POST-ELASTIC REDISTRIBUTION OF SHEAR DEMAND AMONG WALLS IN SYSTEMS WITH INTERCONNECTED WALLS OF UNEQUAL LENGTH.

The shear force distribution among the walls in regular multistorey structures laterally supported by a number of reinforced concrete cantilever walls with markedly different lengths is strongly affected by the different yield displacement levels of the walls. In the post-elastic range the share of the shear force carried by the shorter walls is larger than their share in the bending moment.

In a single storey structure the shear distribution among the walls within the elastic range is proportional to their stiffness. Following yielding of the longer wall additional loads will be carried by the shorter ones. It is evident that design for shear on the basis of relative stiffness underestimates the forces on the shorter walls since shear capacity should be made proportional to flexural strength. However, the situation in a multistory building is different as shown in Fig.12, showing a simplistic model of a two storey system supported by two walls. To fix ideas, assume Wall 2 is very much stiffer than Wall 1; hence, the horizontal force on Wall 1 is negligible so long as Wall 2 has not yielded. With Wall 2 yielding at base the force ΔH is distributed as shown in Fig.12b, where for simplicity it was assumed that the floor diaphragms are pin-connected to the walls and are infinitely rigid in plane. It can be seen that displacement compatibility requires a shear force redistribution resulting in a very large shear force acting on Wall 1.

Rutenberg and coworkers (e.g. [85, 86, 88]) demonstrated that the shear demand on the flexible walls could be very much larger than commensurate with their relative stiffness or even flexural strength. These studies were mainly carried out by means of cyclic pushover analysis on bilinear force-displacement hysteretic models. However, since redistribution is mainly due to compatibility enforcement rather than equilibrium it is sensitive to modelling assumptions. Hence further studies replaced the routine modelling (G= 0.4E, in-plane floor rigidity, bilinear hysteresis) with more realistic models. Indeed, the earlier results were shown [7, 88] to overestimate the base shear demand on the shorter wall. Beyer [7] also observed that the greatest effect was due to "locking in" of compatibility forces transmitted by the floor diaphragms. Yet, it appears that the effect of this relaxation depends on the extent of plasticity

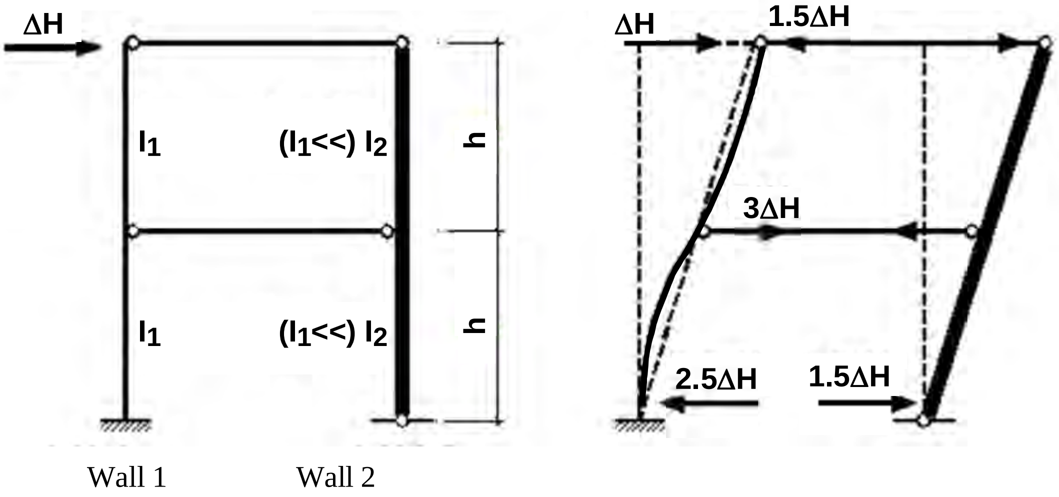

(a) (b)

Fig. 12: Two-storey wall system: (a) properties and loading, (b) floor forces and deflected shapes (Rutenberg 2004)

propagation along the wall's cross-section, which in turn depends on whether the longitudinal reinforcement is mainly concentrated at the wall ends (flanges) or is uniformly distributed, which was not considered. Also, Beyer's conclusions were obtained from a two-wall model with modest lengths ratio (1.5: 6.0m & 4.0m respectively); more pronounced stiffness differences are likely to increase the share of the short wall shear force. However, Priestley et al [81] concluded, based on Beyer's work [7], that these compatibility induced forces might normally be ignored in design. Further study on redistribution, including these effects, is now under way [8].

Beyer [7] proposed using the pushover analysis [85] to test the propensity of the shorter wall for excessive shear demand. In that procedure the resultant lateral force is located at the minimum dynamic effective height $h_{eq,\ dyn}$ given by Eqn.16:

$$h_{eq,\ dyn} = h_{eq,\ static} / \omega_v \qquad (16)$$

In which $h_{eq,\ static}$ is the height of the statically computed shear resultant, and ω_v is the dynamic amplification factor. Alternatively, $h_{eq,\ dyn}$ may be taken for the applicable spectrum from plots such as Fig. 2 in [91], if available. If the base shear on the short wall sharply increases while the base shear of the long wall drops off after formation of the plastic hinge at the base of the long wall, coupling effects are expected to be significant. Note that ω_v in Eqn. 16 is predicated on the assumption that the total base shear on a group of walls is equal to that on an isolated wall whose strength and stiffness equal the respective sums of these properties of the individual walls. This was found to be justified for the record suites used by Rutenberg & Nsieri [88].

Adebar & Rad [1], using pushover analysis, studied a two-wall system with markedly different properties (a long flanged wall and a short rectangular one). They were mainly interested in the effect of shear deformation on the response, modelling both flexure and shear with tri-linear force displacement relations, i.e., a kink at cracking and a yielding plateau (very short for shear). As expected, cracking and yielding were found to affect the shear force redistribution along the height, in some cases predicting shear failure. In particular, diagonal shear cracking led to significant shear force increase in the short wall at the 2nd floor level. Note, however, that concentrated plasticity was not accounted for.

9 DISCUSSION

In many countries dynamic shear amplification is now routinely accounted for in wall design, yet, as shown, there are large differences in the extent of amplification - from relatively low ω_v in the New Zealand code to quite high ones in EC8. As already noted, the Canadian code requires considering amplification only when the equivalent lateral force procedure is carried out, and then only the linear multi-modal effect. Interestingly, the Romanian seismic code P100-1/2006 [64], while generally adopting the EC8 provisions for RC structures, excluded Eqn. 4, based mainly on the peculiarities of the 1977 Vrancea earthquake record. Instead, it specifies $\omega_v = 1.5$ for statically computed base shear or 1.2Φ (Φ = flexural overstrength), whichever is larger [77, 104].

The very large amplifications predicted by NLRHA were met in many instances with some skepticism. For a widely expressed attitude it is perhaps best to quote Paulay [74], who wrote w. r. t. computed magnifications much larger than given in the New Zealand provisions: *"I found at that time* (early 1980's, AR) *that the duration of predicted extremely high shear demands was typically 0.02 to 0.03 seconds. So we pacified our conscience with the unanswered question: 'is this time interval long enough to enable a wall region to fail in shear?'"*. On the other hand, ignoring shear peaks with durations less than 0.03 seconds do not appear to lead to substantial reduction in shear demand. A preliminary study by Panagiotou & Calugaru [65] on records of three earthquakes showed that demand was lowered only by 6%-15%.

It has often been observed that the maximum shear may not occur simultaneously with maximum moment over the wall height; hence the large amplification factors could be questioned (e.g. [55]). Yet, simultaneous peaks at wall base level were observed in analyses by Rad [82] and Tremblay et al [101] for several historical records; and the large amplifications were evaluated for the wall base. No doubt these two issues deserve study.

The main reason for the skepticism appears to be the feeling that standard nonlinear modelling of RC walls, particularly in the plastic hinge zone, does not capture faithfully the complex response. As noted above, using the Takeda rather than the bilinear hysteresis lowers computed shear demand somewhat, and more importantly, realistic shear behaviour modelling results in substantial fall in shear demand (Fig. 11); considering shear-flexure interaction might lower it further. On the other hand, it has been demonstrated that the 5% damping routinely assumed in NLRHA is quite unconservative for tall buildings design, and damping ratios lower than 2% were reported (e.g. [92]).

Another important issue is the experimental and historical evidence for nonlinear dynamic shear amplification The study by Eberhard [25, 26, 98] on wall frames suggests that the formula proposed by Kabeyasawa (e.g. [43]) and Aoyama [4] is in approximate agreement with the experimental results. The experimental study by Panagiotou et al [66, 68, 69] did not focus on shear amplification per se, yet this phenomenon has been observed in their shake table tests. Shear amplification was also observed by Tremblay, Leger and their co-workers in an on-going shake-table testing program [55]. The large dynamic amplifications predicted by the many parametric studies listed in the bibliography and by Keintzel's formula, or variations thereof, were not observed in these studies.

On the whole it appears that the seismic performance of well-designed and constructed cantilever wall buildings has been satisfactory. Yet, damage to shear walls was reported after several earthquakes. Blakeley et al [9] referred to reports on two cases of extensive diagonal tension cracking; however, it is not clear whether those or other such failures can be attributed to dynamic shear amplification. Shear failures in walls were observed after the February 2010

Chile earthquake, but these were attributed mainly to discontinuities and similar effects such as stress concentrations near openings. Targeted studies are now under way [11].

The reader who chooses not to perform NLRHA with refined modelling may well ask which of the several formulas reviewed here he/she should adopt. In order to answer this question it is necessary to perform extensive parametric studies. On the other hand it does not appear that the differences among the several variants of Keintzel's formula are excessive. Strictly speaking, parametrically derived formulas and design charts are applicable only to the mean spectrum of their data base.

These design procedures do not account for multiple hinges when the vertical wall reinforcement follows approximately (in several steps) modal analysis moment envelope. They also do not consider wall shear cracking, which has significant effect on shear amplification, and on the response of interconnected walls. The actual impact of shear cracking on amplification depends on cyclic shear-flexure coupling; but such a model is not yet available [102].

In view of the above, it is believed that judiciously conceived NLRHA-based design can better account for the many variables affecting dynamic shear amplification.

10 ACKNOWLEDGEMENTS

The author is indebted to T. Postelnicu and D. Zamfirescu for explaining the relevant provisions in the Romanian code P100-1/2006, to M. Panagiotou for providing peak shear plots for several US records and to K. Beyer for her comments on interconnected walls. The help of R. Adoni, A. Aines and I. Elkayam is gratefully acknowledged.

REFERENCES AND BIBLIOGRAPHY

The list below, although quite extensive, is by no means exhaustive, as can be seen from relevant publications referred to in some of the listed publications. Research reports subsequently published in conference proceedings or journals are usually not included.

[1] Adebar P & Rad BR (2007). Seismic shear force distribution in high-rise concrete walls. *9th Canadian Conference on Earthquake engineering*, Ottawa, Canada.

[2] Adebar P, Mutrie J & DeVall R (2005). Ductility of concrete walls: the Canadian seismic design provisions 1984 to 2004. *Canadian Journal of Civil Engineering*, **32**, 6, 1124-1137.

[3] Alwely F (2004). Seismic behavior of ductile wall-frame structural systems. M. Sc. Thesis, Faculty of Civil & Environmental Engineering, Technion, Haifa, Israel (in Hebrew, English summary & captions).

[4] Aoyama H (1987). Earthquake resistant design of reinforced concrete frame buildings with "flexural" walls. *Journal Faculty of Engineering, University of Tokyo*, **XXXIX**, 2, 87-109. Also in: *Earthquake resistance of reinforced concrete structures*, a volume honoring Hiroyuki Aoyama, University of Tokyo, 1993.

[5] ASCE (2006) Minimum design loads for buildings and other structures. ASCE Standard ASCE/SEI 7-05. American Society of Civil Engineers, Reston, VA.

[6] ASCE (2007). Seismic rehabilitation of existing buildings. ASCE Standard ASCE/SEI 41-06. American Society of Civil Engineers, Reston, VA.

[7] Beyer K (2005). Design and analysis of walls coupled by floor diaphragms. M.Sc. thesis, Rose School, University of Pavia, Italy.

[8] Beyer K (2011). Personal communication, February.

[9] Blakeley RWG, Cooney RC & Megget LM (1975). Seismic shear loading at flexural capacity in cantilever wall structures. *Bulletin New Zealand National Society Earthquake Engineering*, **8**, 278-290.

[10] Boivin Y & Paultre P (2010). Seismic performance of a 12-storey ductile concrete shear wall system designed according to the 2005 National building code of Canada and the 2004 Canadian Standard Association standard A23.3. *Canadian Journal of Civil Engineering*, **37**, 1-16.

[11] Boroschek (2011). Personal communication, January.

[12] Calugaru V. & Panagiotou M (2010). Seismic Isolation Using Single and Dual Shear Hinging of Tall Cantilever Wall Buildings Subjected to Near Fault Ground Motions. *9th US National & 10th Canadian Conference on Earthquake Engineering*, Toronto, Canada.

[13] CEB (1980, 1983, 1985). Model Code for Seismic Design of Concrete Structures, Bulletin d'Information, Comite Europeen du Beton, No.133, 160, 165 (respectively), Lausanne, Switzerland.

[14] CEN (1988). Eurocode No 8 – Structures in seismic regions –Design. Part 1 General and building". Brussels, Belgium.

[15] CEN (1993). Eurocode 8 - Earthquake resistant design of structures. Pt. 1.3 General rules – seismic actions and general requirements for structures. Final Draft PrENV, Brussels, Belgium.

[16] CEN (2004). Eurocode 8 - Earthquake resistant design of structures. Pt. 1.3 General rules – specific rules for various materials and elements", Brussels, Belgium.

[17] Chaallal O & Gauthier D (2000). Seismic shear demand on wall segments of ductile coupled shear walls. *Canadian Journal of Civil Engineering*, **27**, 506-522.

[18] Chopra, AK (2001). *Dynamics of Structures,* 2nd edn. Prentice Hall, Upper Saddle River, NJ.

[19] CSA (1994, 2004). Design of concrete structures. Standard CAN/CSA-A23.3-04, Canadian Standards Association, Rexdale, Canada.

[20] CTBUH (2008). Recommendations for the seismic design of high-rise buildings. Council on Tall Buildings and Urban Habitat, Chicago, IL.

[21] Derecho AT et al (1978). Structural walls in earthquake-resistant buildings – Analytical investigations, dynamic analysis of isolated structural walls – Parametric Studies. Final Report to the National Science Foundation RANN, Portland Cement Association, Skokie, IL.

[22] Derecho AT, Iqbal M & Corley WG (1980). Determining design force levels for earthquake-resistant reinforced concrete structural walls. *7th World Conference on Earthquake Engineering*, Istanbul, Turkey, Vol. 5.

[23] Derecho AT et al. (1981). Structural walls in earthquake resistant buildings, dynamic analysis of isolated structural walls - development of design procedure, design force level. Final Report to the National Science Foundation ASRA, Construction Technology Laboratories, PCA, Skokie, IL.

[24] Derecho AT & Corley, WG (1984). Design requirements for structural walls in multistory buildings. *8th World Conference on Earthquake Engineering*, San Francisco, CA, Vol. 5.

[25] Eberhard MO & Sozen MA (1989). Experiments and analyses to study the seismic response of reinforced concrete frame-wall structures with yielding columns, Structural Research Series 548, Civ. Engrg. Studies, University of Illinois, Urbana, IL.

[26] Eberhard MO & Sozen MA (1993). Behavior-based method to determine design shear in earthquake-resistant walls. *Journal of Structural Engineering ASCE*, **119**, 2, 619-640.

[27] Eibl J & Keinzel E (1988). Seismic shear forces in RC cantilever shear walls. *9th World Conference on Earthquake Engineering*, Tokyo-Kyoto, Vol. VI.

[28] ***fib*** (2010). Model Code 2010, First complete draft, Vol. 2. International Federation for Structural Concrete, Lausanne, Switzerland.

[29] Filiatrault A, Anderson DL & DeVall R (1992). The effect of weak foundation on the seismic response of core wall type buildings. *Canadian Journal of Civil Engineering*, **19**, 530-539.

[30] Filiatrault A, D’Aronco D & Tinawi R (1994). Seismic shear demand of ductile cantilever walls: a Canadian perspective. *Canadian Journal of Civil Engineering*, **21**, 363-376.

[31] Fischinger M , Isakovic T & Rejec K (2010a). Seismic Behavior of RC Structural Walls and Eurocode 8 Provisions. *9th US National & 10th Canadian Conference on Earthquake Engineering*, Toronto, Canada.

[32] Fischinger M, Rejec K & Isakovic T (2010b). Shear magnification factors for RC Structural Walls in Eurocode 8. *14th European Conference on Earthquake Engineering*, Ohrid, Macedonia.

[33] Gérin M & Adebar P (2004). Accounting for shear in seismic analysis of concrete structures, *13th World Conference on Earthquake Engineering*, Vancouver, Canada.

[34] Ghorbanirenani, I et al (2009a). Distribution of inelastic demand in slender R/C shear walls subjected to Eastern North America ground motion. *ATC-SEI Conference on Improving the Seismic Performance of Existing Buildings and Other Structures*, San Francisco, CA.

[35] Ghorbanirenani I et al (2009b). Shake table tests and repair of ductile slender reinforced concrete shear walls. *9th US National & 10th Canadian Conference on Earthquake Engineering*, Toronto, Canada.

[36] Ghosh SK (1992). Required shear strength of earthquake-resistant reinforced concrete shear walls, in: *Nonlinear seismic analysis and design of reinforced concrete buildings*, P. Fajfar & H. Krawinkler eds., Elsevier, London.

[37] Ghosh SK & Markevicius VP (1990). Design of earthquake resistant shearwalls to prevent shear failure. *4th US National Conference on Earthquake Engineering*, Palm Springs, CA, Vol. 2.

[38] Goodsir WJ, Paulay T & Carr AJ (1983). A study of the inelastic seismic response of reinforced concrete coupled frame-shear wall structures. *Bulletin New Zealand National Society for Earthquake Engineering*, **16**, 3, 185-200.

[39] Goodsir WJ, Paulay T & Carr AJ (1984). A design procedure for interacting wall-frame structures under seismic actions. *8th World Conference on Earthquake Engineering*, San Francisco, CA, Vol. 5.

[40] Humar JL & Rahgozar MA (2000). Application of uniform hazard spectra in seismic design of multistorey buildings. *Canadian Journal of Civil Engineering*, **27**, 563-580.

[41] Humar J & Mahgoub MA (2003). Determination of seismic design forces by equivalent static load method. *Canadian Journal of Civil Engineering*, **30**, 287-303.

[42] Iqbal M & Derecho AT (1980). Inertia forces over height of reinforced concrete structural walls during earthquakes, in: Reinforced concrete structures subjected to wind and earthquake forces. ACI Publication SP-63, American Concrete Institute, Detroit, MI.

[43] Kabeyasawa T & Ogata K (1984). Ultimate-state design of RC wall-frame structures, *Transaction of the Japan Concrete Institute*, 629- 636.

[44] Kabeyasawa T (1987). Ultimate-state design of RC wall-frame structures, *Pacific Conference Earthquake Engineering*, Auckland, New Zealand, Vol. 1. Also in: *Earthquake resistance of reinforced concrete structures*, a volume honoring Hiroyuki Aoyama, University of Tokyo, Tokyo, 431- 440, (1993).

[45] Kabeyasawa T (1988). Evaluation of column and wall actions in the ultimate state design of reinforced concrete structures. *9th World Conference on Earthquake Engineering*, Tokyo-Kyoto, Vol. VIII.

[46] Kappos AJ & Antoniadis, P (2007). A contribution to seismic shear design of R/C walls in dual systems. *Bulletin of Earthquake Engineering*, **5**, 3, 443-466.

[47] Kappos AJ & Antoniadis PS (2010). An improved procedure for the seismic design of reinforced concrete walls in dual systems. *14th European Conference on Earthquake Engineering*, Ohrid, Macedonia.

[48] Kappos AJ & Antoniadis PS (2011). Evaluation and suggestions for improvement in of seismic design procedures for RC walls. *Earthquake Engineering and Structural Dynamics*, **40**, 35-53.

[49] Keintzel E (1984). Ductility requirements for shear wall structures in seismic areas. 8th World Conference on Earthquake Engineering, San Francisco, CA, Vol. 5.

[50] Keintzel E (1990) Seismic design shear forces in reinforced concrete cantilever shear wall structures. *European Journal of Earthquake Engineering*, **3**, 7-16.

[51] Keintzel E (1992). Advances in the design for shear of RC structural walls under seismic loading, in: *Nonlinear seismic analysis and design of reinforced concrete buildings,* P. Fajfar & H. Krawinkler eds., Elsevier, London.

[52] Klemencic R (2008). Performance based seismic design – rising. *Structure- Magazine*, June, 10-13.

[53] Klemencic R et al (2007). Performance-based design of ductile concrete core wall buildings – issues to consider before detailed analysis. *The Structural Design of Tall and Special Buildings*, **16**, 599-714.

[54] LATBSDC (2005, 2008). An Alternative Procedure for Seismic Analysis and Design of Tall Buildings Located in the Los Angeles Region, Los Angeles Tall Buildings Structural Design Council, CA.

[55] Leger P (2010). Personal communication, March.

[56] Model Code for Displacement-Based Design (2009). GM Calvi & TJ Sullivan, eds. DBD09, draft subject to public scrutiny, IUSS Press, Pavia, Italy.

[57] Moehle JP (2006) Seismic analysis design and review for tall buildings. *The Structural Design for Tall and Special Buildings*, **15**, 5, 495-513.

[58] Moehle JP (2008). Performance-based seismic design of tall buildings in the U.S. *14th World Conference on Earthquake Engineering*, Beijing, China.

[59] Moehle J, Bozorgnia Y & Yang TY (2007). The Tall Buildings Initiative. *SEAOC Convention*, Squaw Creek, CA, 315-324.

[60] Naeim F ed. (2001). *The Seismic Design Handbook*, 2nd edn. Kluwer Academic, Boston, MS.

[61] NBCC (1995, 2005). National Building Code of Canada. Associate Committee on the National Building Code. National Research Council of Canada, Ottawa.

[62] Nsieri E (2004). The seismic nonlinear behaviour of ductile reinforced concrete cantilever wall systems. M.Sc. thesis, Technion, Haifa, Israel (in Hebrew, English summary & captions).

[63] NZS (1982, 1995, 2006) “NZS 3101: Part1, Concrete Structures Standard; Part 2, Commentary on the design of concrete structures, New Zealand Standards, Wellington.

[64] P100-1/2006 (2006). Seismic design code P100 Part 1- Design provisions for buildings. Technical University of Construction, Bucharest, September, (in Romanian).

[65] Panagiotou M (2011). Personal Communication, January.

[66] Panagiotou M & Restrepo JI (2007). Lessons learnt from the UCSD full-scale shake table testing on a 7-story residential building. *SEAOC Convention*, Squaw Creek, CA.

[67] Panagiotou M & Restrepo JI (2009). Dual-plastic hinge design concept for reducing higher-mode effects on high-rise cantilever wall building. *Earthquake Engineering and Structural Dynamics*, **38**, 12, 1359-1380.

[68] Panagiotou M & Restrepo JI (2010). A displacement-based method of analysis for regular reinforced concrete wall buildings: Application to a full-scale 7-story building slice tested at UC San Diego. *Journal of Structural Engineering ASCE*, Posted ahead of print, October.

[69] Panagiotou M, Restrepo JI & Conte JP (2010). Shake table test of a 7-story full scale reinforced concrete wall building slice, Phase I: Rectangular wall. *Journal of Structural Engineering ASCE,* Posted ahead of print, October.

[70] Panagiotou M, Calugaru V & Visnjic T (2009). Higher mode effects on the seismic response of tall cantilever wall buildings subjected to near fault ground motions. *78th SEAOC Annual Convention*, San Diego, CA.

[71] Panneton P, Leger P & Tremblay R (2006). Inelastic analysis of a concrete shear wall building according to the National Building Code of Canada 2005. *Canadian Journal of Civil Engineering*, **33**, 854-871.

[72] Park R & Paulay T (1975). *Reinforced concrete structures.* Wiley, New York.

[73] Paulay T (1986). Design of R/C structural walls. *Earthquake Spectra,* **2**, 4, 810-814.

[74] Paulay T (2007). Personal communication, January.

[75] Paulay T & Priestley, MJN (1992). *Seismic design of reinforced concrete and masonry buildings*. Wiley, New York.

[76] Pennucci D, Sullivan, TJ & Calvi GM (2010). Evaluation of higher mode effects in tall building response. *14th European Conference Earthquake Engineering*, Ohrid, Macedonia.

[77] Postelnicu T (2011). Personal communication, January.

[78] Priestley MJN (2003a). *Myths and fallacies in earthquake engineering, revisited*, The Mallet Milne Lecture, 2003, IUSS Press, Pavia, Italy.

[79] Priestley MJN (2003b). Does capacity design do the job? An investigation of higher modes effects in cantilever walls. *Bulletin New Zealand Society for Earthquake Engineering*, **36**, 4.

[80] Priestley MJN & Amaris A (2003). Dynamic amplification of seismic moments and shear forces in cantilever walls. ***fib** Symposium, Concrete structures in Seismic Regions*, Athens, Greece.

[81] Priestley MJN, Calvi GM & Kowalsky MJ (2007). *Displacement-Based Seismic Design of Structures*. IUSS Press, Pavia, Italy.

[82] Rad RB (2009). Seismic shear demand in high-rise concrete walls. Ph.D. thesis, University of British Columbia, Vancouver, Canada.

[83] Rad RB & Adebar P (2006). Shear demand on high-rise concrete walls: Influence of diaphragms below grade. *8th U.S. National Conference on Earthquake Engineering*, EERI, San Francisco, CA.

[84] Rad BR & Adebar P (2008). Dynamic shear amplification in high-rise concrete walls: effect of multiple flexural hinges and shear cracking. *14th World Conference on Earthquake Engineering*, Beijing, China.

[85] Rutenberg A (2004). The seismic shear of ductile cantilever wall systems in multistorey structures. *Earthquake Engineering & Structural Dynamics*, **33**, 881-896.

[86] Rutenberg A & Leibovich E (2002a). On the lateral force distribution among structural walls in multistorey buildings. *Bulletin New Zealand Society for Earthquake Engineering*, **35**, 231-242.

[87] Rutenberg A & Leibovich E (2002b). The irregular post-yield behaviour of regular multistorey wall structures. *3rd European Workshop on Seismic Behaviour of Irregular and Complex Structures*, Florence, Italy.

[88] Rutenberg A & Nsieri E (2006). The seismic shear demand in ductile cantilever wall systems and the EC8 provisions. *Bulletin of Earthquake Engineering*, **4**, 1-21.

[89] Rutenberg A & Nsieri E (2010). On the seismic shear demand in ductile RC dual systems. *9th US National & 10th Canadian Conference on Earthquake Engineering*, Toronto, Canada.

[90] Rutenberg A, Nsieri E & Levy, R (2003). Seismic Shear Forces in Cantilever Wall Systems. *Budownictwo*, Centre of Structural Integrity, Opole Technical University, Poland, 294/2003, 43-57.

[91] Rutenberg A, Nsieri E & Levy R (2004). Seismic Shear demand on ductile systems in multi-storey structures. *13th World Conference on Earthquake Engineering*, Vancouver, Canada.

[92] Satake N et al (2003). Damping evaluation using full-scale data of buildings in Japan. *Journal of Structural Engineering ASCE*, **129**, 4, 470-477.

[93] SEAOC (1999). Recommended lateral force requirements and commentary. Structural Engineers Association of California, Sacramento, CA.

[94] SEAONC (2007). SEAONC Recommended Administrative Bulletin for San Francisco. Structural Engineers Association of Northern California, San Francisco, CA.

[95] Seneviratna GDPK & Krawinkler H (1994). Strength and displacement demands for seismic design of structural walls. *5th US National Conference on Earthquake Engineering*, Chicago, IL, Vol. 2.

[96] Seneviratna GDPK (1995). Evaluation of inelastic MDOF effects for seismic design. Ph.D. Dissertation. Stanford University. Also: Seneviratna GDPK & Krawinkler H (1997). Report 120, John A. Blume Earthquake Engineering Center. Stanford University, CA.

[97] SI 413 (1998) and Amendment No.3 (2009). Design provisions for earthquake resistance of structures. Standards Institution of Israel, Tel-Aviv.

[98] Sozen MA & Eberhard MO (1992). Design shear for earthquake-resistant walls, in: Nonlinear seismic analysis and design of reinforced concrete buildings, Report 103, John A. Blume Earthquake Engineering Research Center, Stanford University, CA.

[99] Stafford Smith B & Coull A (1991). *Tall Building Structures: Analysis and Design*. Wiley, New York.

[100] Sullivan TJ, Priestley MJN & Calvi GM (2008). Estimating the higher mode response of ductile structures. *Journal of Earthquake Engineering*, **12**, 3, 456-472.

[101] Tremblay R et al (2008). Seismic response of multi-storey reinforced concrete walls subjected to Eastern North America high frequency ground motions. *14th World Conference on Earthquake Engineering*, Beijing, China.

[102] Wallace JW (2010). Performance-based design of tall reinforced concrete core wall buildings, in: *Earthquake Engineering in Europe*, M Garevski & A Ansal eds., Springer, Utrecht, Germany.

[103] Wiebe L & Christopoulos C (2009). Mitigation of higher mode effects in base-rocking systems by using multiple rocking sections. *Journal of Earthquake Engineering*, **13**, 1, 83–108.

[104] Zamfirescu D (2011). Personal Communication, January.

[105] Zekioglu A et al (2007). Case study using the Los Angeles Tall Buildings Structural Design Council guidelines: 40-storey concrete core wall building. *The Structural Design for Tall and Special Buildings*, **16**, 583-597.

COMPDYN 2011
III ECCOMAS Thematic Conference on
Computational Methods in Structural Dynamics and Earthquake Engineering
M. Papadrakakis, M. Fragiadakis, V. Plevris (eds.)
Corfu, Greece, 25–28 May 2011

RAPID PRELIMINARY SEISMIC ASSESSMENT METHODOLOGY FOR NON-CONFORMING REINFORCED CONCRETE BUILDINGS

Stylianos J. Pardalopoulos[1], **Georgia E. Thermou**[2], **Stavroula J. Pantazopoulou**[1]

[1] Demokritus University of Thrace
Dept. of Civil Engineering 67100, Xanthi, Greece
spardalo@civil.duth.gr, pantaz@civil.duth.gr

[2] Aristotle University of Thessaloniki
Dept. of Civil Engineering, 54124, Thessaloniki, Greece
gthermou@civil.auth.gr

Keywords: Assessment, Reinforced Concrete, Buildings, Failure, Reinforcement detailing

Abstract. *In this paper, application of a rapid, yet efficient methodology for the evaluation of failure modes of lightly reinforced substandard buildings is presented. The method determines the limiting shear resistance of the structure as the least value supported by the columns' pure flexural, degraded shear, anchorage or lap-splice and joint shear resistance mechanisms. For application of the methodology only knowledge of the basic geometric and material properties of the building is required. The proposed methodology is applied to a number of Reinforced Concrete buildings that failed during past strong earthquakes for verification reasons. It is shown that the proposed methodology is ideal for rapid preliminary seismic assessment and it can be used both as a diagnostic tool for identification of the building's fragility and the prevailing mechanism of building failure.*

1 INTRODUCTION

Recent earthquakes have repeatedly illustrated the deficiencies of brittle reinforced concrete (RC) buildings built according to earlier design codes. This class of buildings, which today represents the majority of the built environment in the greatest part of the world, is typified by a number of features such as small section columns, relatively stiff beams, inadequately confined joints and insufficient anchorage of longitudinal and transverse reinforcement. Although the application of detailed assessment procedures for seismic evaluation of every single existing structure is of vital importance, the immense volume of required work makes it seem an unrealistic scenario. This difficulty could be removed by applying a rapid evaluation procedure where information readily available for most buildings will be used; in such a rapid assessment, critical features of the structure that render it more vulnerable, could be immediately identified thereby simplifying the process of singling out those structures that represent a major threat to human life in the event of an earthquake.

The objective of this paper is to present a methodology where the building's geometrical characteristics, material properties and reinforcement detailing of the structural elements are considered sufficient information so as to single out the most vulnerable buildings that are likely to collapse in a potential strong earthquake, but can also be used to determine the objectives for their rehabilitation. Existing RC buildings, "non-conforming" according to modern standards, are assessed based on prioritizing of the various alternative modes of failure. Mechanisms considered refer to column flexure, degraded shear, anchorage and lap-splice development, connection punching and exceedence of joint shear capacity; the rate of degradation of these mechanisms with increasing displacement amplitude and number of cycles is idealized through simplified mechanistic constructs which allows the prioritizing of failure modes as degradation proceeds. Furthermore, the seismic vulnerability of this category of buildings is assessed as a function of interstorey drift demand imposed by the design earthquake [1]. For confirmation, the methodology is applied to a number of RC buildings that collapsed during the 1999 Athens earthquake. Results indicated that in all cases, buildings failed in a brittle manner due to anchorage failure of column longitudinal reinforcement in the joints' regions.

2 METHODOLOGY FOR RAPID EVALUATION OF FAILURE MODES

2.1 Background information

In the first 2/3rds of the 20th century, when massive rebuilding and urbanization of cities took place throughout Southern Europe, construction details were not strictly addressed by the design codes and as such, they were seldom specified in design drawings of that era. Implementation in practice was, to a large extent, determined by the experience of the laborers and the foreman responsible for the site. Credentials were never questioned and supervision was relatively lenient; the reinforcing cages were usually assembled on site, empirically in most cases and often using makeshift tools for hook bending and bar cutting. Today, even in the rare occasion where a plan drawing from the 1960's specifies details for stirrup placement, it is questionable whether these stirrups had been actually placed as specified. Reconnaissance studies from collapsed buildings in major earthquake events suggest that at least in those, collapsed cases, there was a marked lack of, or primitive use of stirrups. But underuse of stirrups was the prevalent practice of the era. Usually stirrups were rectangular, with 90° hooks in the ends, made of smooth reinforcement, using bar sizes of $\varnothing_t$ equal to 6 mm or at best 8 mm, spaced at 250 mm to 300 mm; however, occasional examples of even wider spacing have also been cited. Steel quality was StIII (f_{yk}=420 MPa) for longitudinal reinforcement and StI

(f_{yk}=220 MPa) for stirrups, concrete quality ranged between Bn150 to Bn200 [2] (i.e. a concrete characteristic strength of 12 to 16 MPa according to today's standards). Lap splices were usually unconfined, whereas starter bars had random lengths. Joints, being considered points of reinforcement congestion since they accommodated both beam and column primary reinforcement, were usually left without stirrups, for convenience of construction. Single column footings were mostly used and, in well-attended structures, they were joined at the column base with lightly reinforced, small section connecting beams.

Despite these systematic inadequacies, the percentage of buildings that have collapsed in major earthquakes in the Mediterranean basin is relatively low when compared to the total number of available buildings that belong to this substandard construction category; this is not true in other parts of the world such as in Haiti (Port-au-Prince 2010, [3]) One issue that can be concluded, however, from post-earthquake reconnaissance evidence and forensic evaluations of collapsed buildings which led to loss of human life, is that collapse usually occurs by the formation of a mechanism before the development of any form of ductility. In this work it is demonstrated by paradigm that in most cases of such "killer collapses", displacement at the onset of failure is lower than the nominal yield displacement of the structure. This is contrary to the focus of most modern assessment methodologies that are based on comparisons between ductility demand and supply. Note that the usual point of reference in these procedures is columns where transverse reinforcement is not adequate to support shear strength under displacement reversals beyond flexural yielding of the individual members of a structure. For this reason, values of rotation capacity in what is termed "non-conforming" members are usually deemed in the range of 1% to 1.5%. This focus could be justifiable for structures with columns where the member size (in the range of 500 mm or higher) is twice that of typical stirrup spacing used in the 1960's, so that a nominal 45° shear plane in a column would intersect at least two stirrups. But in case of structures with smaller column sizes, in the range of 350 mm, as is often encountered in older residential buildings, the practical spacing of stirrups from the1960's (250 mm) could mean that a nominal potential sliding plane could be formed, intersecting no stirrup at all and therefore being unable to mobilize any form of shear resistance.

Other unfavourable characteristics of RC concrete buildings constructed prior to the introduction of capacity design principles and modern detailing practices are the relatively stiff beams intended to control serviceability requirements. For this class of buildings, a rapid evaluation for the potential mode of failure could be focused on the calculation of the limiting strength of building columns, since post-earthquake reconnaissance reports illustrate column failure as the primary cause of building collapse, being associated with the loss of gravity load-carrying capacity.

2.2 Available diagnostic tools

In light of the limited knowledge of actual construction details in older structures, preliminary assessment targeted toward identification of the most vulnerable buildings must necessarily rely on a marginal collection of data that is readily available, such as the overall geometric details of the structure (number of floors, floor height, floor area, location and gross geometry of load carrying members in plan), on the implicit assumption that all reinforcing details are represented by the historical construction information for the period and region of construction of the building studied. With these data, building seismic vulnerability is based on the following two criteria:

(a) A *stiffness index assessment*, which is used to quantify interstorey drift demand.

(b) A *strength assessment*, which is used to determine the weakest mechanism of resistance, likely to control the sequence of failure of the vertical elements of the structure.

(a) Stiffness Index Assessment: From the earliest earthquake studies the area ratio of the load-bearing elements in a structure has been used to quantify the magnitude of lateral stiffness. The importance of this parameter was reflected in the very first Seismic Codes worldwide, whereby the required floor area ratio of walls was set proportional to the number of floors in the structure, to secure adequate seismic performance. Recent studies have systematically explored the relationship of generalized stiffness, K^*, to the floor area ratios of columns, ρ_c, walls, ρ_{wc}, and infill walls, ρ_{wm}, in a structure [1]. It was shown by systematically exploring the relationship between stiffness and fundamental period, T ($T \approx 2\pi\sqrt{[0.8W/(gK^*)]}$), that the displacement demand under the design earthquake, S_d, could be expressed in terms of ρ_c, ρ_{wc}, and ρ_{wm} (where the seismic hazard is given in relative displacement vs. period spectrum coordinates). Using an estimate of the morphology of the shape of vibration of the structure (Fig. 1) it is possible to develop generic charts of the type shown in Fig. 2 that relate drift demand in the critical floor of the structure to a combined stiffness geometric index, defined as:

Dual systems:

$$k = \rho_c + \eta_{wm}\rho_{wm}^e \tag{1a}$$

$$\eta_{wm} = \frac{25E_{wm}}{E_c\left(\dfrac{h_i^2}{l_{m,ave}^2} + 2.5\right)} \;;\; \rho_{wm,i}^e = \rho_{wm,i} + \frac{\left(4\dfrac{h_i^2}{l_{m,ave}^2} + 2.5\right)}{\left(4\dfrac{h_i^2}{l_{w,ave}^2} + 2.5\right)}\frac{E_c}{E_{wm}}\rho_{wc,i} \tag{1b}$$

Frames:

$$k^{/} = \rho_c + \eta_{wm}^{/}\rho_{wm} \tag{2a}$$

$$\eta_{wm} = \frac{10 \cdot f_{wk}\sqrt{\left(1 + \dfrac{h_i^2}{l_{w,ave}^2}\right)}}{E_c\theta_1} \tag{2b}$$

where E_c, E_{wm} are the elastic moduli of concrete and masonry, respectively, ρ_c is the columns' area ratio in the floor plan, $\rho^e_{wm,}$ is an equivalent compound dimensionless area index that represents both masonry walls and RC walls expressed in terms of masonry wall properties, h_i is the storey height, $l_{m,\mathrm{ave}}$, $l_{w,ave}$ are the average length of masonry and RC wall, respectively, f_{wk} is the compressive strength of masonry and θ_1 is the estimated chord rotation demand of the first storey.

Because of inadequate shear resistance, collapse of substandard buildings in a critical earthquake could be prevented if the interstorey drift demand, θ_u, in the critical floor (if the critical floor is the first floor, $\theta_u = \theta_1$), is below the estimated drift at failure, which is given by:

$$\theta_{fail} = \frac{V_{u,.\lim}}{V_{y,flex}} \cdot \theta_{y,crit} \le \theta_{y,crit} \tag{3}$$

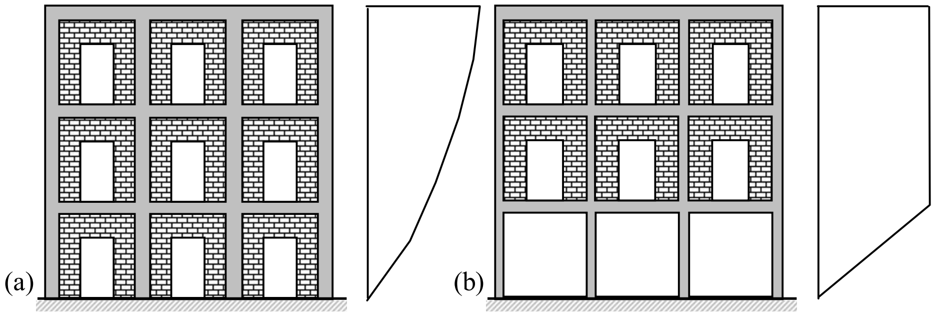

Figure 1: Lateral displacement profiles; (a) shear-type; (b) soft-storey.

In the above, $\theta_{y,crit}$ is the estimated interstorey drift at longitudinal reinforcement yielding of the critical floor – for typical frame structures (with floor heights around 3m) this is usually in the range of 0.5%. Values $V_{y,flex}$ and $V_{u,lim}$ are the estimated base shear strengths at the onset of yielding of column reinforcement and of transverse reinforcement, respectively. For typical older construction, this ratio is usually in the range of 30% - 60%, depending on the size of the columns for the typical details used in the period of reference (the ratio ≈ 30% for column section sizes in the range of 300 mm, to 60% for larger column sections in the range of 500 mm – detailed expressions for calculating these terms for each individual column are given in the following section). The plot in Fig. 2 has been drawn for the EC8 design spectrum (Type 1) using a peak ground acceleration of 0.36g; thus, demand (ordinate in the graph) should be scaled down by the ratio of $a_g/(0.36g)$ for lower levels of peak ground acceleration coefficient, a_g.

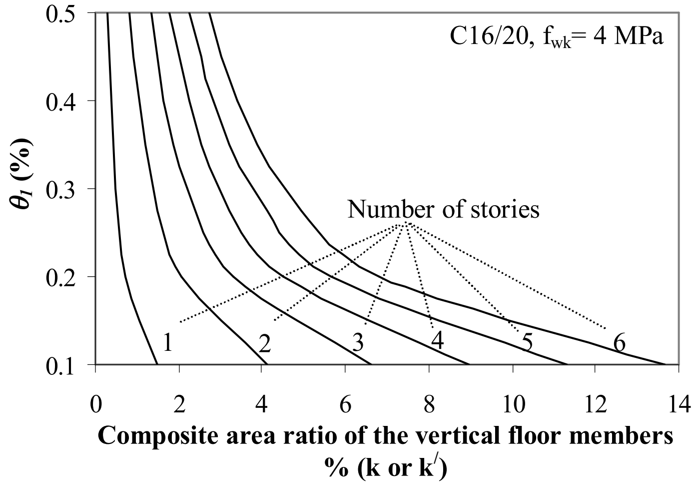

Figure 2: Vulnerability curves that relate the required composite floor area ratio of vertical members to levels of interstorey drift, $\theta_1 \leq 0.5\%$, which are of interest for buildings susceptible to brittle failures. Note that the baseline value of 0.1% is the estimated drift limit associated with diagonal cracking of unreinforced concrete flexural members.

(b) Strength Assessment: Collapse occurs when the vertical elements of the critical floor lose their load carrying capacity. This process may be initiated either by loss of lateral load resistance of the columns, or by punching and loss of support of the floor diaphragms. To be able to establish a hierarchy of possible failure modes which threatens the integrity of a structure under lateral sway, all mechanisms of response must be compared on a common basis of reference. In this study, the typical form of a moment diagram along the column lines of a swaying structure is used to establish this common frame of reference. As depicted in Fig. 3, the typical column experiences a moment reversal at the ends, owing to the transfer of moment from the horizontal to the vertical elements, occurring at the beam-column joints (in frame structures) or at the slab-column connections in flat-slab structures. The approximate location of points of inflection (zero moment) along the column length enables the establishment of a static relationship between the critical strengths of various mechanisms that could be responsible for column failure along the line of a single column, and the column shear sustained when any of these phenomena is occurring, as follows:

(i) Plastic hinging at the column end (i.e. $M_{col} = M_y$), $V^{col}_{y,flex} = 2 \cdot M_{col} / h_{st}$, where h_{st} is the deformable length of the column (i.e. the clear storey height, or free column length in captive columns).

(ii) Exhaustion of column shear strength, $V^{col}_{u,shear}$

(iii) Exhaustion of column lap-length development capacity of tension reinforcement F_b: $V^{col}_{u,lap} = 2 \cdot [F_b \cdot d \cdot (1 - 0.4 \cdot \xi) + N_{g+0.3q} \cdot (0.5 \cdot h_{st} - 0.4 \cdot \xi \cdot d_{col})] / h_{st}$ where ξ is the depth of compression zone normalized with respect the column section depth, d_{col}, and $N_{g+0.3q}$ is the axial compression load in the column owing to the combination of unfactored gravity loads plus a reduced contribution of live load (this is the average column axial load; the column axial load fluctuates about this value due to the overturning effects of the earthquake). The value of ξ ranges between 0.22 and 0.30 for columns with a reinforcing ratio of less than 1.5% and a variety of normalized axial load ratios, and for this reason the above result is not very sensitive to this parameter (Fig. 4).

(iv) Exhaustion of joint shear strength (in frame structures), $V_{j,u}$. Column shear is estimated from equilibrium of moment transfer: $V^{col}_{u,joint} = [V_{j,u} \cdot d_{beam}] / h_{st}$.

(v) Exhaustion of slab punching strength (in flat slab construction), $M_{u,slab}$. The associated column shear is again estimated from equilibrium of moment transfer (assuming this is an intermediate floor of the structure, i.e., not a roof connection): $V^{col}_{u,slab} = M_{u,slab} / h_{st}$ where $M_{u,slab}$ the strength for moment transfer of the critical punching perimeter at the slab – column connection.

Evaluation of the prevalent failure mode is obtained from the inequality:

$$V^{col}_{u,\lim} = \min\left\{V^{col}_{y,flex}, V^{col}_{u,shear}, V^{col}_{u,lap}, V^{col}_{u,joint} \text{ or } V^{col}_{u,slab}\right\} \tag{4}$$

Expressions for calculating the individual strength terms are given in the appendix. These may be subject to change as the knowledge base in reinforced concrete leads to improved models for the individual mechanisms of resistance and may differ between established code frameworks.

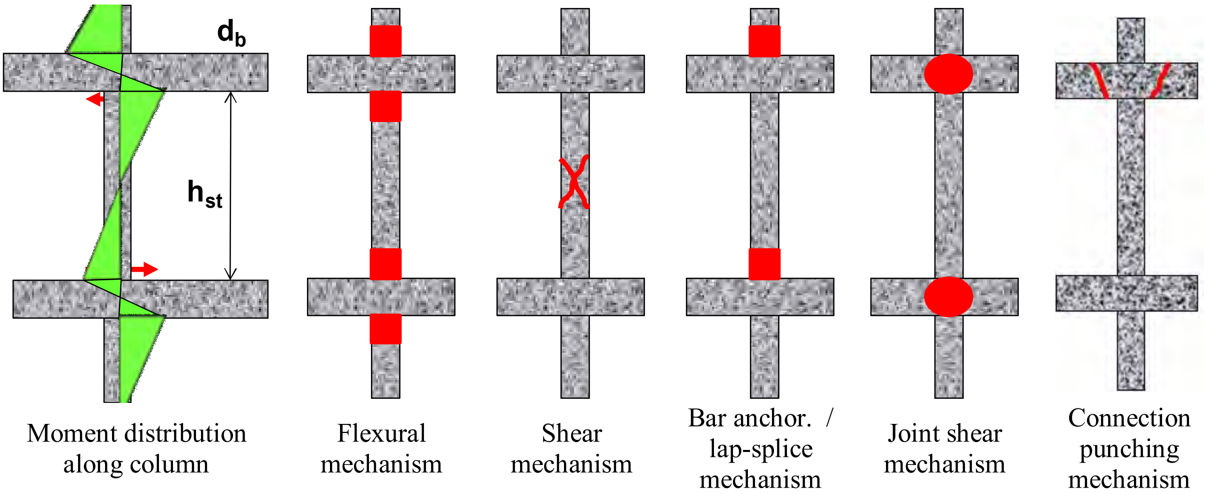

Figure 3: Moment distribution and possible failure modes of a reinforced concrete column.

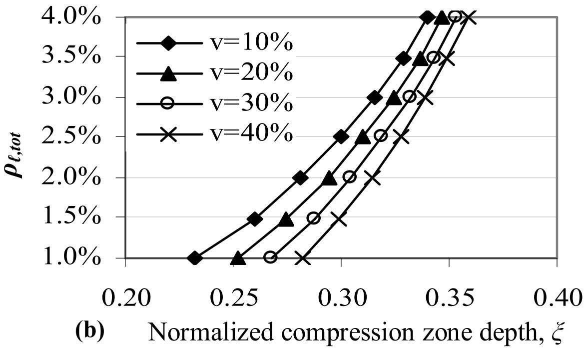

Figure 4: Relationship between ξ, $\rho_{\ell,tot}$ and normalized axial load, v, for columns.

In the following, a number of buildings collapsed during the 1999 Athens earthquake are used to illustrate performance of the proposed rapid screening approach.

3 APPLICATION OF THE METHODOLOGY

The proposed methodology for rapid evaluation of the limiting resistance of "non-conforming" RC buildings through systematic prioritizing of the individual column shear strengths is applied to two RC buildings that collapsed during the 1999 strong ground motion of Athens. Both buildings were located in the northern region of Athens, were the ground motion possessed "near-field" characteristics. The methodology is applied so as to estimate the buildings' drift at the state of their failure as well as to calculate the limiting base shear that the buildings could sustain upon failure, but also to test the ability of the methods to identify the high seismic vulnerability of such structures.

Building A was a two-storey fully symmetric in plan, industrial building, with external plan dimensions of 38.00 m by 26.00 m (Fig. 5). The first and the second storey heights were 5.40 m and 5.30 m, respectively. Building A was separated by seismic gaps from two adjacent wing buildings along the two smaller sides. The structural system was formed as an orthogonal grid of columns, beams and slabs, according to typical construction practice of RC frame structures in Southern Europe. Details of the column geometry and longitudinal reinforcement are presented in Table 1. Column stirrups were smooth, rectangular ties, approximately categorized based on site reconnaissance as Ø8/300 mm. Slab thickness was 0.15 m. All perimeter beam (PB) cross sections were 0.70 m (height) by 0.30 m (width), 0.70×0.45 m for beams spanning between columns (MB) and 0.70×0.25 m for the secondary beams (SB). During the earthquake the building collapsed without any horizontal dislocations of its structural elements, whereas the two adjacent buildings were intact. From tests of core samples, the mean value of concrete compressive strength was determined as 18.7 MPa, whereas steel yielding and ultimate stresses were found to be for the longitudinal reinforcement 431.5 MPa and 512.0 MPa, respectively, and for the stirrups 402.0 and 553.0 MPa, respectively.

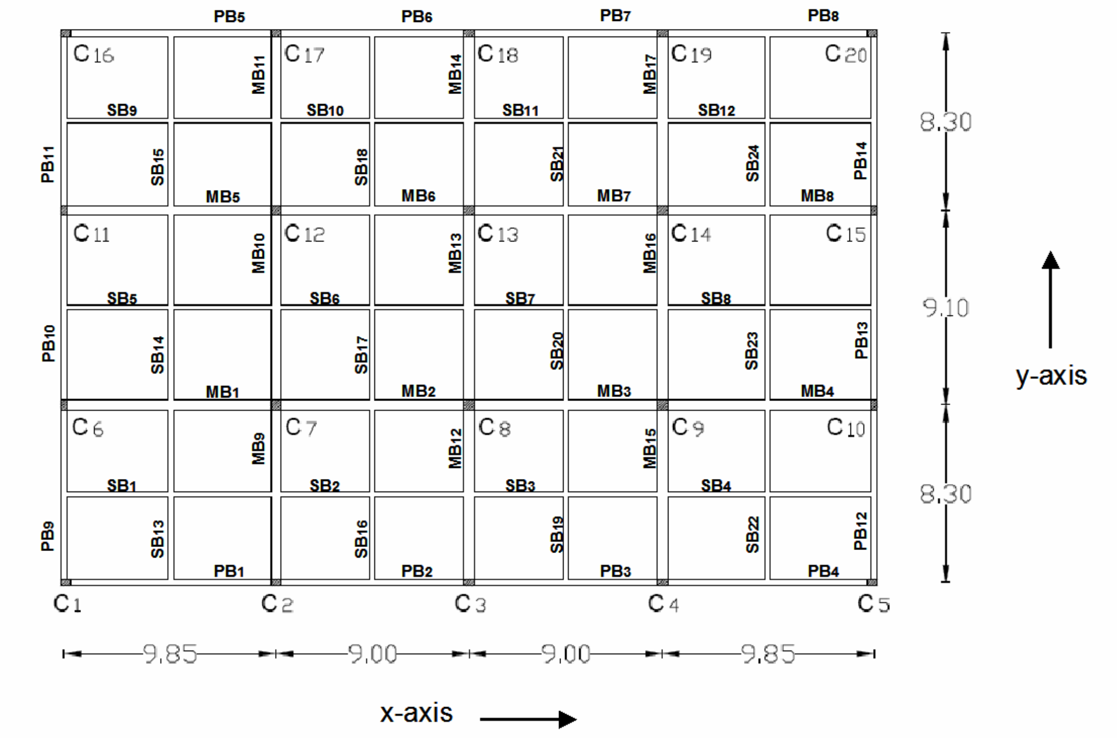

Figure 5: Plan configuration of Building A.

Column	Dimensions(mm)	Long. Reinforcement (mm)
C_1, C_5, C_{16}, C_{20}	450 / 300	4 ∅20
$C_2, C_3, C_4, C_{17}, C_{18}, C_{19}$	450 / 300	8 ∅20
$C_6, C_{10}, C_{11}, C_{15}$	300 / 450	8 ∅20
C_7, C_8, C_9, C_{12} C_{13}, C_{14}	450 / 450	12 ∅20

Table 1: Column dimensions and longitudinal reinforcement of Building A.

The results of the *strength assessment* of the first storey columns in *x* and *y* direction for Building A (Fig. 6) are presented herein. The prevailing failure mechanism for all the columns of the first storey was failure due to exhaustion of column lap-length development capacity of tension reinforcement. The total base shear that the building could sustain at the onset of this mode of failure was 1022 kN and 891 kN in x and y direction, respectively, whereas the flexural strength was estimated equal to 2094 kN and 1845 kN in x and y direction, respectively. Hence, failure was expected to occur when the imposed base shear reached 49% and 48% of the flexural resistance in x and y direction, respectively. Given the axial load of the first storey columns for the $g+0.3q$ load combination (the normalized axial load ratio was estimated as v_{ave}=0.22, W=13000 kN), the maximum peak ground acceleration that Building A could sustain was only 7.9%(=1022/13000) and 5.9%(=891/13000) of g, in the x and y directions, respectively (note that the 1999 Athens earthquake had a peak ground acceleration, pga=0.38g (Sepolia station)).

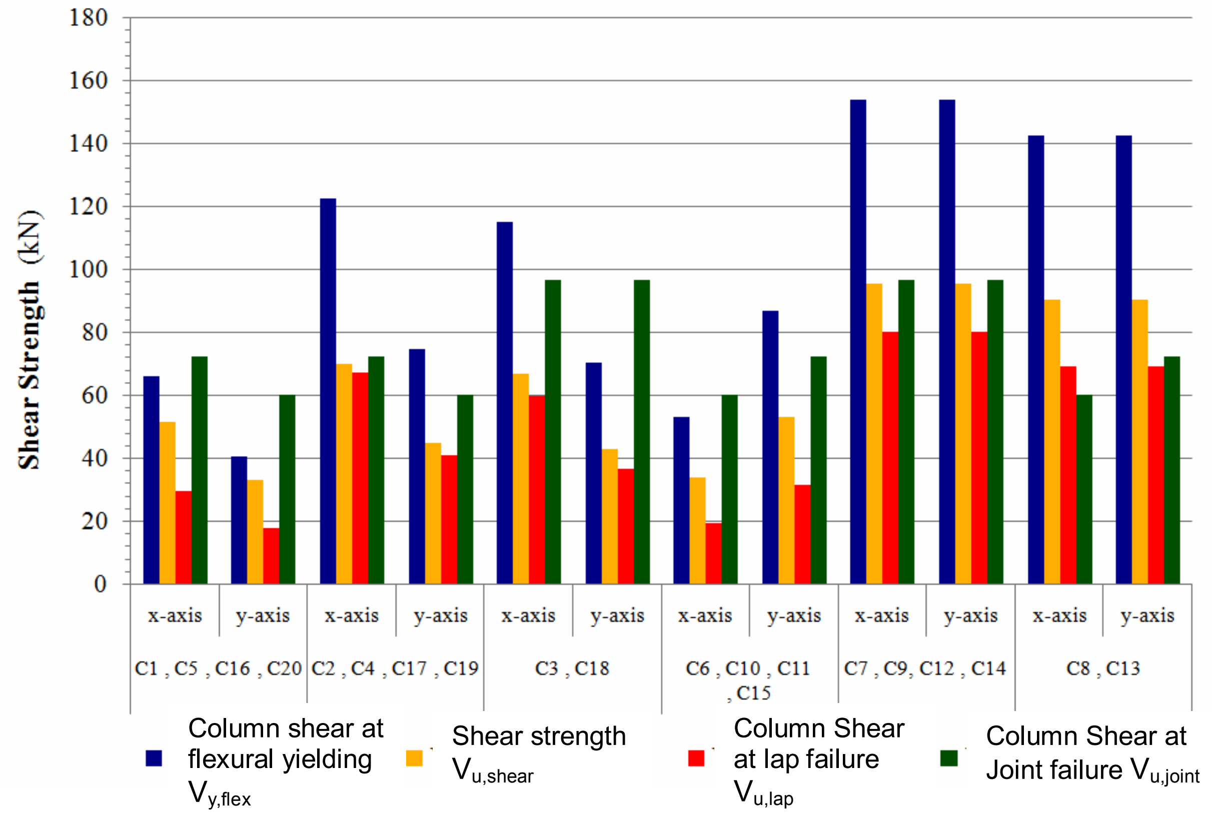

Figure 6: Strength of the columns of building A against the various mechanisms of failure; each group of bars in the chart represents the estimated column strengths against alternative failure modes, for a given column type and direction of seismic action (x or y). Labels under the bar charts identify the columns that fall under the specific category.

As calculated from the building's properties, the area ratio of the columns in both x and y directions was $\rho_{c,x}=\rho_{c,y}$=0.3%. The average nominal drift at yield, $\theta_{y,nom}$, was estimated equal to 1.26% and 1.10% in x and y direction, respectively (Table 2). Due to the premature failure of columns, failure is expected to occur at earlier drift levels. According to Eq. (3) and the results of the *strength assessment* presented in the previous paragraph, those drift levels are determined as $\theta_{fail}^{x}=1.26\cdot1022/2094=0.62\%$ and $\theta_{fail}^{y}=1.10\cdot891/1845=0.53\%$ in x and y direction, respectively.

Column	$\theta_{y,nom}^{x*}$	$\theta_{y,nom}^{y*}$
C_1, C_5, C_{16}, C_{20}	1.54%	0.99%
C_2, C_3, C_4, C_{17}, C_{18}, C_{19}	1.54%	0.99%
C_6, C_{10}, C_{11}, C_{15}	0.99%	1.54%
C_7, C_8, C_9, C_{12} C_{13}, C_{14}	0.99%	0.99%
Average	1.26%	1.10%

$\theta_{y,nom}=(2.14\varepsilon_y/d)\cdot(L_s/3)$ [4], where ε_y: steel strain at yield, d: depth of the cross secion, L_s: clear shear span length

Table 2: Nominal drift at yield for the columns of Building A.

According to the methodology developed by Thermou and Pantazopoulou [1], the vulnerability curve for Building A was estimated for Type I elastic spectrum of EC8 [5] using as peak ground acceleration the magnitude recorded in the Athens 1999 earthquake (Sepolia station) (pga=0.38g) and ρ_{wm}=0 in Fig. 7. For a drift value equal θ_{fail}^{x}=0.62% and θ_{fail}^{y}=0.53% (as defined after the reduction of nominal drift at yield due to premature failure of the columns, see Fig. 6) demand in terms of ρ_c is defined by the horizontal dashed lines in Fig. 7. The percentage of columns required in order to maintain the drift levels in the x and y direction below the failure limit would have to be equal to 0.64% and 0.75%, respectively (i.e. in order to survive the earthquake the building should have 2.1 and 2.5 times the available area ratios of columns in Building A). This leads to the conclusion that the area ratio of nonductile columns in the existing building (ρ_c=0.3%) was insufficient for the seismicity level of the Athens 1999 earthquake as evidenced by its dramatic collapse.

The vulnerability curve of Fig. 7 may be used alternatively to assess the performance of Building A by estimating the demand in terms of drift at the first storey given the percentage of columns. The vertical dashed line depicts the demand in terms of drift of the first storey, which is equal to 1.33% for ρ_c=0.3%. This means that the earthquake would require from the structure, if the structure possessed ductility, a displacement ductility value of μ=1.33%/1.26%=1.05 and μ= 1.33%/1.10%=1.2 in x and y direction, respectively. If this assessment tool would be used in practical preliminary retrofit design, it would suggest the required ductility level that should be targeted for in retrofitting the columns. This ductility limit is within the range that could be attained by the use of local interventions for seismic upgrading such as FRP jacketing, a finding that points to the criteria for establishing a retrofit scenario for structures assessed prior to the occurrence of a threatening earthquake event.

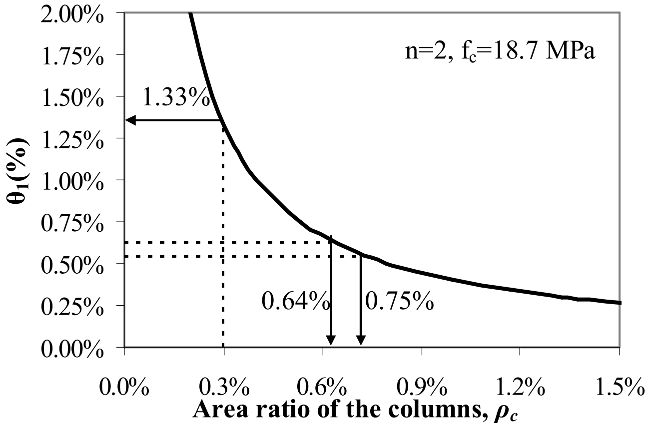

Figure 7: Vulnerability curve for Building A subjected to Athens 1999 earthquake estimated according to the methodology of Thermou and Pantazopoulou [1].

Building B was also an industrial building, having a 37.60 m by 22.80 m orthogonal plan (Fig. 8). The building had two basements and four storeys, each 2.85 m high. The structural system comprised a grid of columns which were connected with beams only along the buildings' perimeter, the beams having a section height of 0.60 m and 0.20 m web width. In the centre of the typical floor plan, columns supported a flat-plate Zoellner system, having a thickness of 0.22 m. During the earthquake the building collapsed, except for the stairwell in the corner of the plan. After tests conducted on material samples, the concrete was found to have a mean compressive strength of 20 MPa, while longitudinal reinforcement and stirrups were found to have smooth surface and were classified as S400 (f_y = 400 MPa) and S220 (f_y = 220 MPa) respectively. Column dimensions and longitudinal reinforcement details are presented in Table 3, whereas transverse reinforcement comprised Ø6/300 mm rectangular, smooth stirrups.

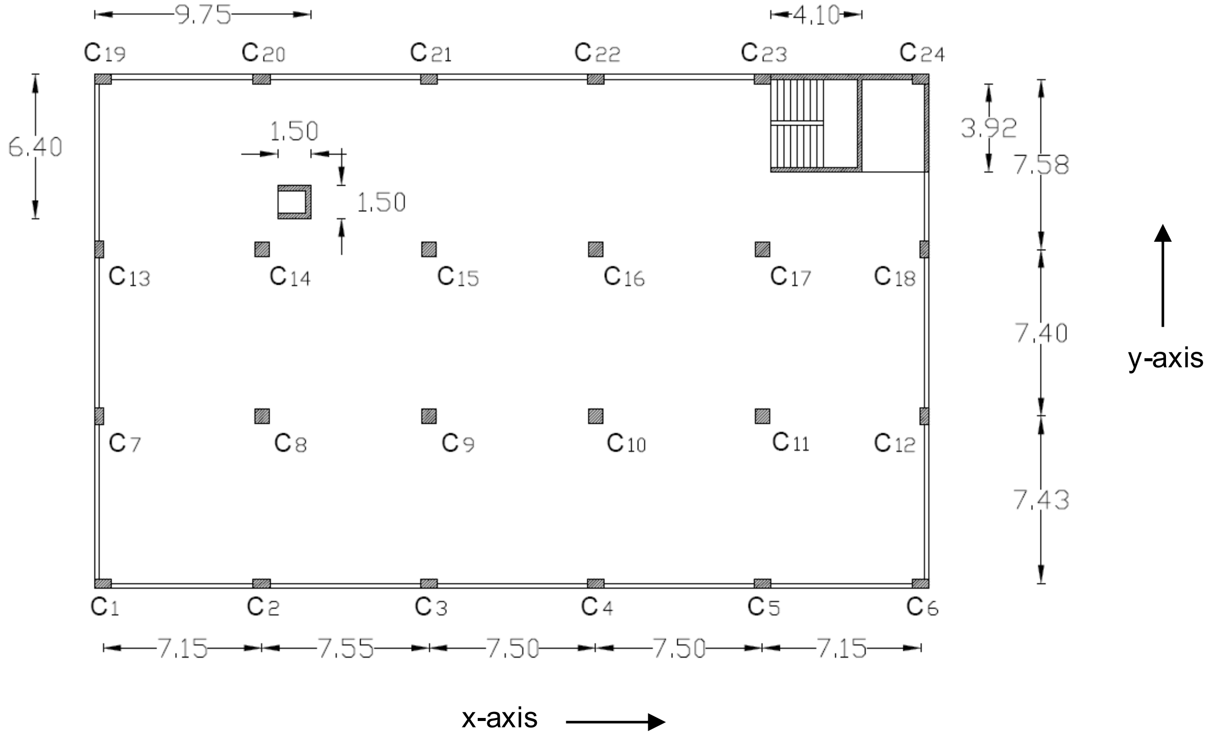

Figure 7: Plan configuration of Building A.

Column	Dimensions (mm)	Long. Reinforcement (mm)
C_1, C_2, C_3, C_4, C_5, C_6, C_{19}, C_{20}, C_{21}, C_{22}	750 / 400	8 ∅16
C_7, C_{12}, C_{13}, C_{18}	400 / 750	8 ∅16
C_8, C_9, C_{10}, C_{11}, C_{14}, C_{15}, C_{16}, C_{17}	650 / 650	8 ∅20

Table 3: Column dimensions and reinforcement of Building B.

S*trength assessment* has revealed that the prevailing failure mechanism of the first storey columns was failure due to exhaustion of slab punching strength. Note that this type of failure (lowest green bars in Fig. 8) concerns all interior columns in directions where they were not connected with beams but also exterior columns in the direction of action that bent them about their weak axis (e.g. C1 for seismic action in the y-direction). The total base shear that Building B could sustain at the onset of slab punching was 1477 kN and 861 kN in x and y directions, respectively, whereas the flexural strength was estimated equal to 4487 kN and 4136 kN in x and y direction, respectively. Thus, when the imposed base shear reached only 33% and 21% of the flexural resistance in x and y direction, respectively, failure would be anticipated. The maximum peak ground acceleration that Building B could sustain (direction *y*) for the *g+0.3q* load combination (average normalized axial load ratio v_{ave}=0.21, W=32500kN) was only 4.5 % (=1477/32500) and 2.6% (=861/32500) of g, in the x and y directions, respectively (1999 Athens earthquake, pga=0.38g, Sepolia station).

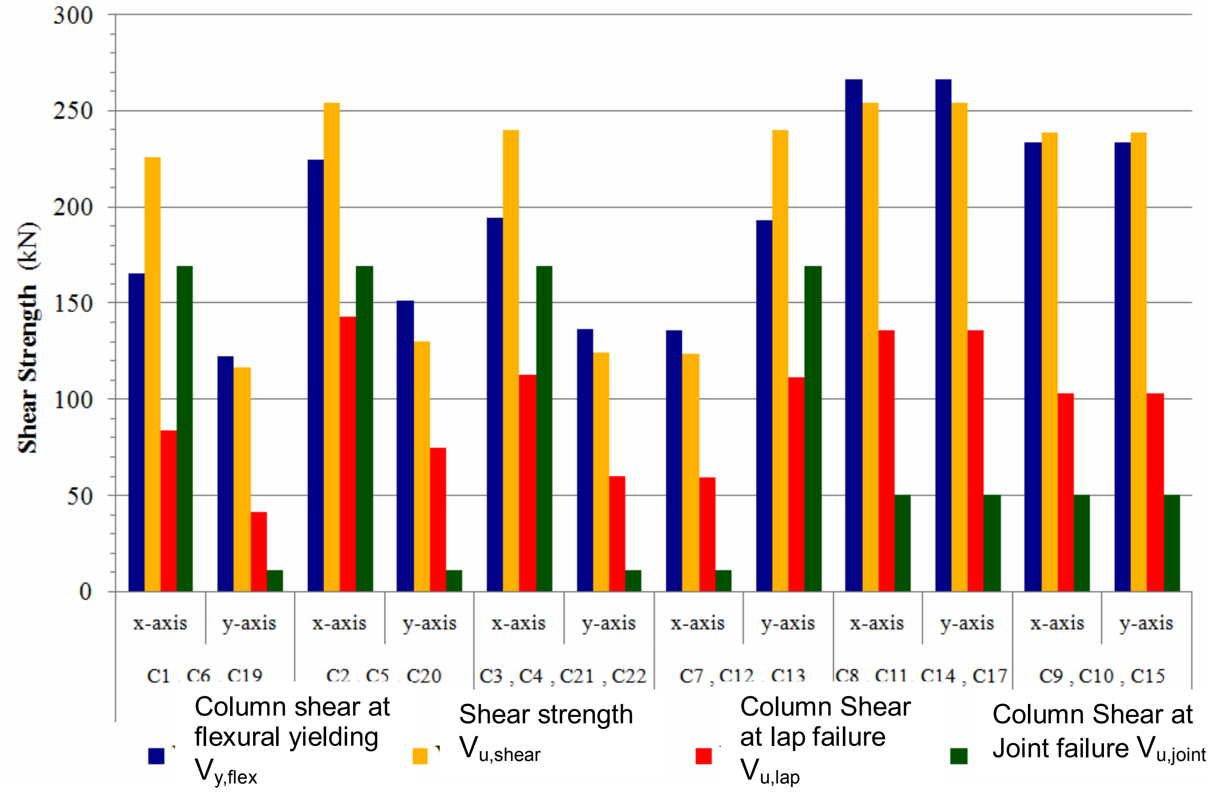

Figure 8: Strength of the columns of building B against the various mechanisms of failure; each group of bars in the chart represents the estimated column strengths against alternative failure modes, for a given column type and direction of seismic action (x or y). Labels under the bar charts identify the columns that fall under the specific category.

Stiffness assessment of Building B follows, where, according to the building's characteristics, the columns' area ratio in both x and y directions was $\rho_{c,x}=\rho_{c,y}$=0.88%, whereas the wall area ratio in x and y direction was $\rho_{w,x}$=0.35% and $\rho_{w,y}$=0.24%, respectively. In the following calculations, and in order to keep the procedure simple, only the area of columns was taken into account (the influence of the wall was considered low and further burdening the structure with torsional action due to its eccentric placement). The average nominal drift at yield, $\theta_{y,nom}$, was estimated equal to 0.42% and 0.35% in the x and y direction, respectively (Table 4). The drift levels at which failure due to premature failure of columns would be expected to occur were θ_{fail}^{x} = 0.42·1477/4487 = 0.14% and θ_{fail}^{y} = 0.35·861/4136 = 0.07% in the x and y directions, respectively.

Column	Drift at x-direction, θ_x^*	Drift at y-direction, θ_y^*
C_1, C_2, C_3, C_4, C_5, C_6, C_{19}, C_{20}, C_{21}, C_{22}	0.55%	0.28%
C_7, C_{12}, C_{13}, C_{18}	0.28%	0.55%
C_8, C_9, C_{10}, C_{11}, C_{14}, C_{15}, C_{16}, C_{17}	0.33%	0.33%
Average	0.42%	0.35%

$\theta=(2.14\varepsilon_y/d)\cdot(L_s/3)$ [4], where ε_y: steel strain at yield, d: depth of the cross secion, L_s: clear shear span length

Table 4: Column dimensions and reinforcement of Building B.

Limiting demand to avoid failure, is defined in terms of ρ_c by the horizontal dashed lines in Fig. 9 for θ_{fail}^x=0.14% and θ_{fail}^y=0.07% (these values point to significantly reduced drifts compared to the nominal drift at yield, owing to the premature failure of the columns, see Fig. 8). Thus, utilizing the vulnerability curve extracted for Type I elastic spectrum of EC8 [5] for the recorded peak ground acceleration in the 1999 Athens earthquake (pga=0.38g, Sepolia Station), it is concluded that: According to the characteristics of Building B, the percentage of required columns with the available brittle details in order to keep the drift levels in the x and y directions below the failure values would have to be 8.67% and 16.57%, respectively (9.8 and 18.7 times higher than the available area ratios of columns in the actual building). From the above, it is evident that the percentage of columns, given the mode of construction (brittle details) in the existing building (ρ_c=0.88%) was entirely insufficient for the seismicity level of the Athens 1999 earthquake.

If reversely, Fig. 9 is used to define demand in terms of drift at the first storey for the existing area ratio of columns (ρ_c=0.88%), in the hypothetical case where these possessed displacement ductility, then the vertical dashed line indicates the demand in terms drift equal to 1.36% (Fig. 9). This means that the earthquake would require from the structure, if the structure possessed ductility, a displacement ductility value of μ=1.36%/0.42%=3.2 and μ= 1.36%/0.35%=3.9 in x and y direction, respectively, a value that is somewhat excessive to be attainable by local interventions such as FRP-jacketing should such have been implemented prior to the earthquake; rather, these ductility values point to a deficiency in stiffness that could have been supplemented by infill walls in some critical bays of the lower floors, thereby mitigating the ductility demands to lower, more attainable through proper retrofit, values.

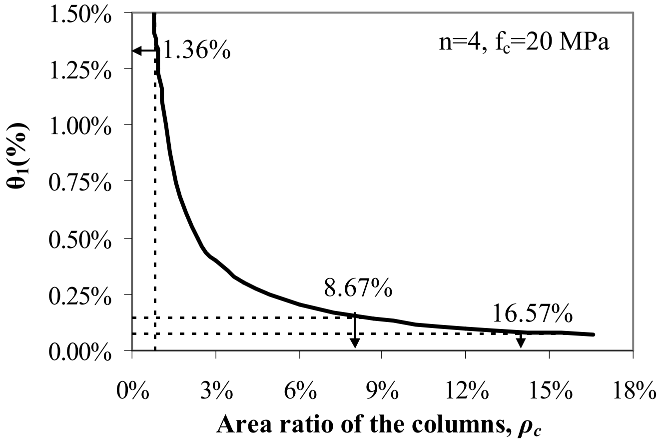

Figure 9: Vulnerability curve for Building B subjected to Athens 1999 earthquake estimated according to the methodology by Thermou and Pantazopoulou [1].

4 CONCLUSIONS

A methodology for determining the ultimate storey drift at the state of maximum seismic response and prioritizing the potential failure mechanisms in the load carrying system of concrete buildings classified as “non-conforming” according to modern standards was presented in this paper. Mechanisms considered refer to column flexure, shear, anchorage lap/splice development capacity and joint shear or slab punching strength, as failure of vertical structural elements is directly related to building severe damage or collapse. The methodology can be applied to every individual column of the building, regardless of its location; if flexural strength may be supported by the shear, anchorage, joint resistance and slab punching mechanisms, the calculated limiting strength can be compared to the developing shear force derived from a seismic analysis. However, in most cases of existing structures, brittle failure modes are prioritized to occur prior to flexural yielding, so that no ductility may be realized, whereas the building collapses at displacements lower than the yield point. In this case, the methodology may also be applied for the determination of the maximum ground acceleration that the building could sustain prior to retrofit, as illustrated it the former examples, thereby serving as a tool of rapid evaluation of the buildings’ seismic vulnerability. It is also possible to obtain, through this method, the magnitude of displacement ductility that would be required through column retrofit, in order to eliminate the risk of collapse due to excessive displacement demand.

REFERENCES

[1] G.E. Thermou, and S.J. Pantazopoulou, *Assessment indices for the seismic vulnerability of existing RC buildings*, Journal of Earthquake Engineering and Structural Dynamics, 40(3), 293-313, 2011 (early view, first published 21/7/10).

[2] Deutsches Institut für Normung (DIN). Beton un Stahlbetonbau: Bemessung und Ausführung. *DIN 1045*, Berlin, 1972.

[3] M.O. Eberhard, S. Baldridge, J. Marshall, W. Mooney, G.J. Rix, *The M_w 7.0 Haiti Earthquake of January 12, 2010*, USGS/EERI Advance Reconnaissance Team: Team Report V1-1, February 23, 2010.

[4] T. Paulay, and M. N. J. Priestley. Seismic Design of Reinforced Concrete and Masonry Buildings, 1992 (John Wiley & Sons, Inc., New York).

[5] Eurocode 8. Design of structures for earthquake resistance—Part 1: general rules, seismic actions and rules for buildings. EN1998-1-2004:E, European Committee for Standardization (CEN), Brussels, 2004.

[6] Pantazopoulou V, Syntzirma D. Code expressions for deformation capacity of lightly reinforced concrete members - a comparative study. ACES Workshop: Advances in Performance-Based Earthquake Engineering 2009, Corfu, Greece.

[7] ACI-ASCE Committee 352. Recommendations for Design of Beam-Column Connections in Monolithic Reinforced Concrete Structures, American Concrete Institute, Farmington Hills, MI, 2008.

[8] Eurocode 2. Design of concrete structures—Part 1-1: general rules and rules for buildings. EN1992-1-2005:E, European Committee for Standardization (CEN), Brussels, 2004.

APPENDIX

The following expressions can be used for calculating the individual strength terms of a column. These expressions represent the present state of the art at the field. Nevertheless, they may be subject to change as the knowledge base in reinforced concrete leads to improved models for the individual mechanisms of resistance.

(i) Calculation of column flexural yield :

Uniaxial bending [6]:

$$V^{col}_{y,flex} \approx \left[\rho_{l,tot}\cdot\frac{f_y}{f_c}\cdot(1-0.4\cdot\xi)+v\cdot\left(\frac{h_{st}}{d_c}-0.8\cdot\xi\right)\right]\cdot b_c\cdot d_c^2\cdot f_c \Big/ h_{st} \qquad \text{(A1)}$$

Biaxial bending: $V^{col}_{y,flex}$ can be considered equal to the 70% of the respective value of uniaxial bending.

where $\rho_{l,tot} = A_{s,tot}/A_g$; $A_{s,tot}$: total area of longitudinal reinforcement; f_y: steel yield stress, f_c : concrete compressive strength; ξ from Fig. 4; $v = N/(A_g f_c)$; N : compression force acting in the section from $g+0.3q$ load combination (compression as a positive value); h_{st} : clear storey height; d_c : column depth; b_c : column width.

(ii) Calculation of column shear strength [6]:

Monotonic loading:

$$V^{col}_{u,shear} = V_w + V_c \qquad \text{(A2)}$$

$$V_w = \begin{cases} 0 & for \quad d_c < S \\ A_{st}\cdot f_{st}\cdot\dfrac{d_c}{S} & for \quad d_c \geq S \end{cases} \qquad \text{(A3)}$$

Note: For 90° stirrup anchorage V_w must be reduced by 50%

$$V_c = \begin{cases} 0.5\cdot\sqrt{f_c}\cdot\left(\dfrac{d}{L_s}\cdot\sqrt{1+\dfrac{N}{0.5\cdot\sqrt{f_c}\cdot A_g}}\right)\cdot A_g & if \quad v \geq (\rho_{s1}-\rho_{s2})\cdot f_y/f_c \\ 0 & if \quad v < (\rho_{s1}-\rho_{s2})\cdot f_y/f_c \end{cases} \qquad \text{(A4)}$$

Postyielding response:

$$V_{u,shear} = 0.6\cdot(V_w + V_c) \qquad \text{(A5)}$$

where, A_{st}: area of stirrup leg; f_{st} : yield stress of stirrups; S : spacing of stirrups; L_s ($\approx h_{st}/2$): shear span length; $\rho_{s1} = A_{s1}/A_g$; $\rho_{s2} = A_{s2}/A_g$; A_{s1}, A_{s2} : area of tension and compression reinforcement, respectively.

(iii) Calculation of the longitudinal bar development capacity [6]:

At lap:

$$F_s = 1.4 \cdot \left(A_{tr} \cdot f_{st} \cdot n_{st} / n_b + p \cdot f_t \cdot L_b\right) \le f_y \cdot \left(\pi \cdot D_{b,l}^2 / 4\right) \tag{A6}$$

where, A_{tr}: total area of stirrup legs along one direction of restrain; n_b : total number of bars restrained by a total of n_{st} stirrups, $p = 2\sqrt{2}(c+D_{b,l})$; c: concrete cover; $D_{b,l}$: longitudinal bar diameter; f_t: concrete tension strength.

At anchorage in beam-column joint:

Calculate F_s as if at lap, by substituting p by the concrete cover, c, which is the actual length of the crack path.

At ultimate conditions:

$$F_s = 1.4 \cdot \left(A_{tr} \cdot f_{st} \cdot n_{st} / n_b\right) \le f_y \cdot \left(\pi \cdot D_{b,l}^2 / 4\right) \tag{A7}$$

(iv) Calculation of joint shear strength [7]:

$$V_{j,u} = \gamma_j \cdot \sqrt{f_c'}\; b_c . d_c \quad ; \quad \gamma_j = \begin{cases} 1.6 & \text{for interior joints} \\ 1.0 & \text{for exterior joints} \\ 0.6 & \text{for corner joints} \end{cases} \tag{A8}$$

(v) Calculation of slab punching strength [8]:

$$V_{u,slab}^{col} = 0.12 \cdot \min\left\{1+\sqrt{\frac{200}{d}}\ ,\ 2\right\} \cdot \left(100 \cdot \rho_l \cdot f_c^{1/3}\right) \cdot d_{slab} \cdot 0.25 \cdot u_{crit} \cdot \left(d_c + 4 \cdot d_{slab}\right) \Big/ h_{st} \tag{A9}$$

where, d_{slab}: slab depth; u_{crit}: the critical punching perimeter around the typical column in flat plate construction.

COMPDYN 2011
III ECCOMAS Thematic Conference on
Computational Methods in Structural Dynamics and Earthquake Engineering
M. Papadrakakis, M. Fragiadakis, V. Plevris (eds.)
Corfu, Greece, 25–28 May 2011

COMPUTATIONAL DAMAGE MEASURE FOR RC FRAME STRUCTURES UNDER SEISMIC LOADING

N. Celik[1]and Y. Petryna[2]

[1] Istanbul Technical University, Faculty of Civil Engineering
34469 Istanbul, Turkey
celikni@itu.edu.tr

[2] Technical University Berlin, Faculty of Civil Engineering
13355 Berlin, Germany
statik@tu-berlin.de

Keywords: damage measure, reinforced concrete frames, nonlinear dynamic analysis.

Abstract. *In the earthquake areas, the priority task in seismic design is to fulfill the safety requirements with respect to the expected earthquakes. These safety requirements will differ from each other according to the type of the earthquake and structure. For that reason, most codes for seismic design, assessment and retrofitting use the performance-based seismic design concept. In that concept, performance levels are specified ranging from fully operational to near collapse and earthquake design forces are classified. Such performance levels are then associated with a damage state with respect to a given earthquake. At that, either descriptive criteria or displacements are utilized for the damage extent instead of an explicit damage index. The aim of this work is to overview existing damage indices and to define new explicit damage indices which may be used as seismic design criteria for reinforced concrete frames.*

*Both local and global damage indices to be defined will range between 0 (*no *damage) and 1 (failure or collapse). They will be suitable for static, cyclic and dynamic computer analysis in order to be used with various existing design procedures.*

The necessary computer analyses are carried out by means of the finite element program (FRAME) developed in-house within the MATLAB environment. In that program, classical rectangular beam elements are used. Elasto-plastic bilinear moment-curvature relationships are used for the nonlinear material model including hysteretic behaviour under cyclic and dynamic loading. The stiffness matrices of the elements are obtained by use of the spread plasticity model along the length. The Newmark-Beta method with constant average acceleration is applied for the step-by-step time integration of the governing equations.

The cyclic global damage index is proposed to be composed of the separate global damage indices during positive and negative load cycles. Several test problems have been analysed to check the sensitivity of the computational global damage measure for cyclic and dynamic loadings.

1 INTRODUCTION

In the seismically active areas, it is necessary to estimate the damage level of the existing and new structures that have experienced or will experience one or more earthquakes. Most codes for seismic design, assessment and retrofitting use performance-based seismic design concept for that estimation. In that concept, various performance levels are associated with a limitation of the damage state with respect to a given earthquake. However, displacement limits are utilized for the damage state instead of computational damage measures.

The aim of this work is, therefore, to define explicit damage indices, which may be used as seismic design criteria for reinforced concrete frames. Such explicit damage criteria for design, assessment or retrofitting need mechanically well-founded damage measures, which are applicable both to individual members and entire structures.

Several damage indices for seismic assessment have previously been developed and are already well-known. A comprehensive overview can be found for example in [1, 2]. The damage indices giving quantitative information of the damage state can be local or global. A majority of the well-known damage indices usually refer to the local state of a cross-section or a structural member. Most of them are obtained from the ductility ratio or the stiffness ratio or the energy ratio defined within the moment-curvature relationship.

Only a few of the known damage indices are global, and they are usually empirical. Sometimes, they are even mechanically inconsistent, such as the combined index by [3] defined as a sum of a relative displacement and a relative energy measure. One of the consistent damage measures has been proposed by [4] for the finite element structural analysis and monotonic loading. Another consistent damage measure has been proposed in [5, 6] based on the reduction of structural stiffness. However, the structural stiffness is a multi-dimensional function and several difficulties appear by derivation of a scalar global damage index from a multi-dimensional functional.

Apparently, seismic design needs not only proper local damage indices, but also proper global ones. It is, however, hardly possible to define a global damage measure for all structural types and all structural materials such as reinforced concrete, steel and masonry. The objective of the present work is, therefore, to define proper local and global damage indices only for reinforced concrete structures. They shall vary between 0 (state without damage) and 1 (failure or collapse).

For the current study, the finite element program FRAME has been developed within the Matlab environment [7] using classical beam elements. In this program, elasto-plastic bilinear moment-curvature relationships are used for the nonlinear material model including hysteretic behaviour under cyclic and dynamic loading. The stiffness matrices of the elements are obtained by use of the spread plasticity model along the length. The Newmark-Beta method with constant average acceleration is applied for the step-by-step time integration of the governing equations. A variety of examples has been analysed by the program to check out the sensitivity of the global damage indices for reinforced concrete moment frames.

2 COMPUTATIONAL MODELS FOR MATERIAL AND MEMBER BEHAVIOUR

Both static (push-over) and dynamic nonlinear analysis procedures can be used in seismic design. The relevant nonlinear material and member models have to be defined for the nonlinear analysis. In the present work, the nonlinear material model of a reinforced concrete member is defined on the level of the moment-curvature relationship of its cross-section. For monotonic loading, the moment-curvature relationship can be defined as a piecewise linear diagram containing the characteristic points associated with the cracking, yielding and failure states of the member. However, the key issue in material modeling for cyclic and dynamic loading is the hysteretic behaviour of the material. Several hysteretic models for reinforced concrete have been developed in the past. One of the well-known hysteretic models is the model by [8], which has been then modified by several authors. Such hysteretic models are usually empirical in nature. Another well-known model is the bilinear hysteresis model on the basis of the plasticity theory. Here, the bending stiffness during elastic loading and unloading is taken as the initial bending stiffness for the monotonic loading as shown in Fig.1. In the present work, this bilinear hysteresis model will be used for the seismic analysis and determination of the damage indices under cyclic and dynamic loading.

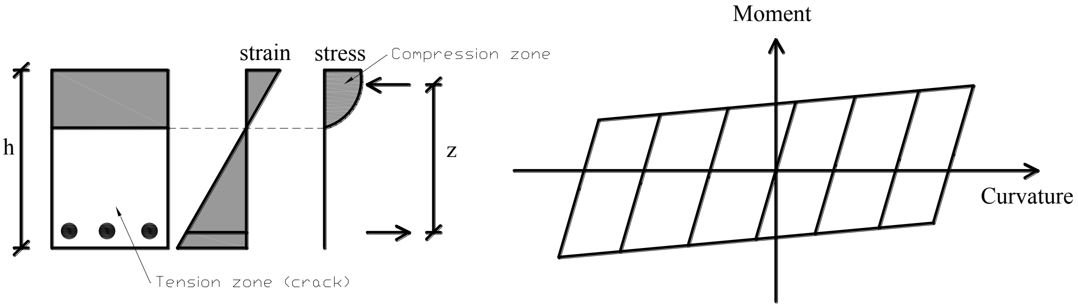

Figure 1: Material model.

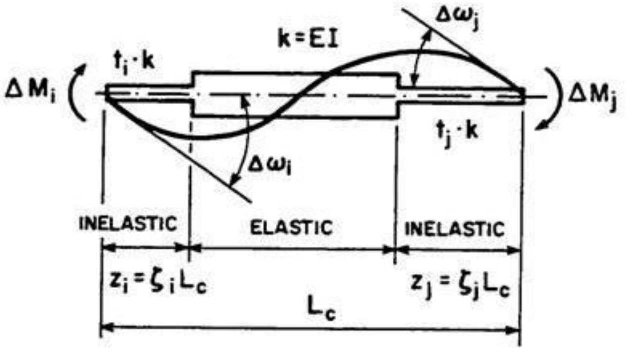

Figure 2: Member model.

The hysteretic models are usually defined for the cross-sections, but the bending stiffness of the member is needed for the analysis. Several member models for reinforced concrete have been developed until now. The member models are generally subdivided into one-component and multi- component models. In a multi-component model, the member consists of different parts acting in parallel. While one part behaves only elastically, the other behaves plastically. In a one-component model, the member consists of only one part which includes all the properties. In one variant of this model, the plasticity is assumed to occur only at the end of the member. However, it is more suitable, when plasticity is spread within the member. In this work, the spread plasticity model by [9] is used as shown at Fig.2.

3 COMPUTATIONAL DAMAGE MEASURE FOR SEISMIC LOADING

The damage in material is usually defined as softening of its stiffness and its extent can be quantified as the relative reduction of its actual modulus of elasticity (E_x) with respect to an initial value in the non-damaged state (E_0) and the critical value (E_f) at failure:

$$\mathrm{D} = \frac{\mathrm{E}_0 - \mathrm{E}_\mathrm{x}}{\mathrm{E}_0 - \mathrm{E}_\mathrm{f}} \tag{1}$$

The obvious advantage of this definition is a scalar damage index, D, ranging from 0 (no damage) to 1 (failure).

At the cross-section level, for example, at pure bending, the damage index can be derived in a similar way from the reduction of the bending stiffness EI of the beam elements:

$$D = \frac{(\mathrm{EI})_0 - (\mathrm{EI})_x}{(\mathrm{EI})_0 - (\mathrm{EI})_f} \tag{2}$$

However, these damage measures are local and it is a challenge to define a similar scalar global damage index for the entire structure. [5] showed that a scalar global damage index can be quantified by the reduction of the structural stiffness represented by some scalar characteristic values λ:

$$D = \frac{\lambda_0 - \lambda_x}{\lambda_0 - \lambda_f} \tag{3}$$

Nevertheless, the choice of λ characteristic values is a challenge. It is more suitable to define a damage index based on scalar deformation energy. [4] proposed to define a global damage index as the relative reduction of the whole structural deformation energy (W_p) with respect to an initial value in the non-damaged state (W^0_p):

$$D = \frac{W_p^0 - W_p}{W_p^0} = 1 - \frac{W_p}{W_p^0} \tag{4}$$

At that, the global damage index is a scalar varying between 0 (state without damage) and 1 (failure state). By use of the finite element simulation, this energy-based global damage index can be calculated from the actual displacement field as follows:

$$D = 1 - \frac{W_p}{W_p^0} = 1 - \frac{\sum_e a^T \int_{V_e} B^T \sigma dV_e}{\sum_e a^T \int_{V_e} B^T \sigma_0 dV_e} \tag{5}$$

where **a** stands for the nodal displacement vector, **B** for the strain shape matrix and V_e for the volume of each finite element e. Further, **σ** denotes the actual stress vector and $\boldsymbol{\sigma}_0$ the stress vector calculated for the undamaged material and the same global displacement **a**. Herein, the total potential energy W_p as well as W_p^0 is accumulated over all finite elements.

However, the local and global damage indices discussed above are suitable for the monotonic loading. They can be mainly used in the push-over analysis. Damage indices suitable for cyclic and dynamic analysis shall be properly defined. Several empirical local damage indices for cyclic or dynamic loading have previously been proposed. [10] proposed a theoretical local cyclic damage index by using the absorbed energy calculated from the moment-curvature relationship. At first, the damage indices for the positive and negative directions are separately calculated. Then, the cyclic local damage index is defined by their superposition as follows:

$$D = D^+ + D^- - D^+ D^- \tag{6}$$

This local damage index is defined on the cross-sectional level and cannot be used for the damage state of the whole structure. Nevertheless, the idea of defining two separate damage indices for positive and negative directions can be combined with the monotonic energy based global damage index [11]:

$$D_G^{\pm} = 1 - \frac{\sum_e (\mathrm{a}^{(e)\mathrm{T}} - \mathrm{a}_0^{(e)\mathrm{T}}) \cdot \mathrm{K}_\mathrm{d}^{\pm(e)\mathrm{T}} \cdot (\mathrm{a}^{(e)\mathrm{T}} - \mathrm{a}_0^{(e)\mathrm{T}})}{\sum_e (\mathrm{a}^{(e)\mathrm{T}} - \mathrm{a}_0^{(e)\mathrm{T}}) \cdot \mathrm{K}_0^{\pm(e)\mathrm{T}} \cdot (\mathrm{a}^{(e)\mathrm{T}} - \mathrm{a}_0^{(e)\mathrm{T}})} \tag{7}$$

The cyclic or dynamic global damage index can be then obtained in a similar manner from the superposition of the two separate global damage indices:

$$D_G = D_G^{+} + D_G^{-} - D_G^{+} D_G^{-} \tag{8}$$

4 EXAMPLES

4.1 RC Column

The new proposed global cyclic damage measure is applied on a canti-lever reinforced concrete column which is originally tested by [12]. The column was subjected to horizontal cyclic loading. Its geometry, reinforcement and cross-sectional properties are shown in Fig. 3 and its material properties are given in Table 1.

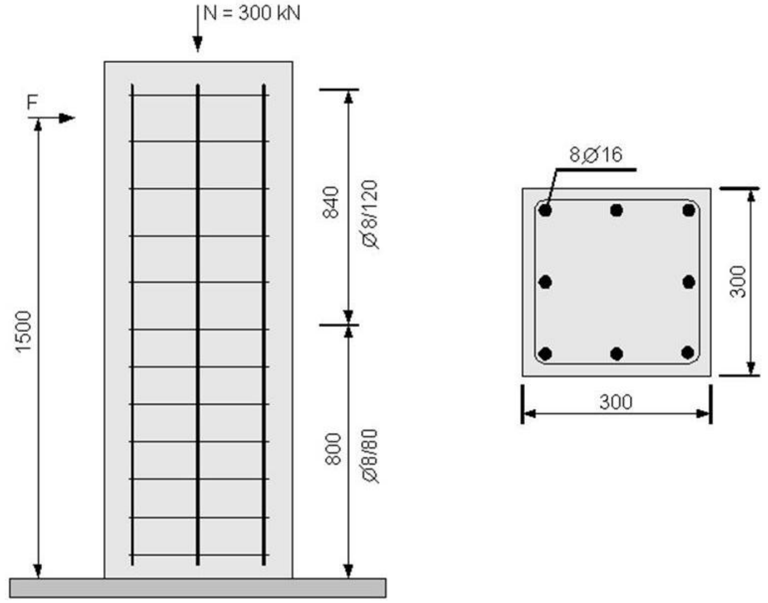

Figure 3: Geometry, cross-section and reinforcement of the RC column.

Concrete	Reinforcing steel
Young's modulus E_c = 29634M N/m²	Young's modulus E = 201000 M N/m²
compressive strength f_{cm} = 35,6 MN/m²	yielding strength f_y = 514 M N/m²
	ultimate strength f_u= 593 M N/m²
	ultimate tensile strain ε_{su} = 0.0044

Table 1: Material properties of the RC column

The moment-curvature diagram of the section at the base is given in the Fig. 4. It is in a good agreement with the bilinear hysteretic material model. It can be seen from the calculated force-displacement diagram of the upper corner that the obtained structural response correlates well with the experiment (Fig. 5). In Fig. 5, the variation of the cyclic global damage index is also shown. With each loading cycle, its value gradually increases and becomes close to 1 at failure, as expected.

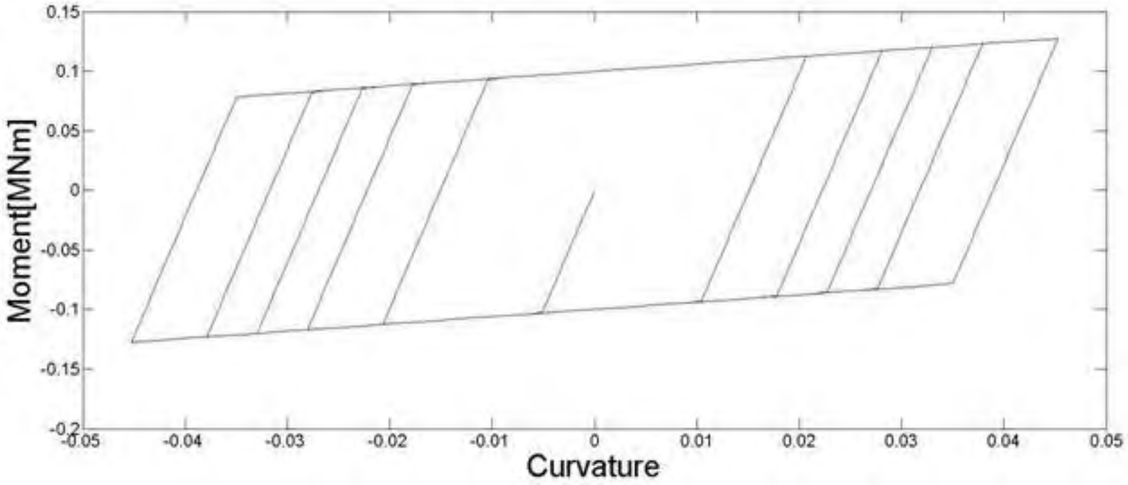

Figure 4: Moment-curvature relationship of the cross-section at the base of the RC column.

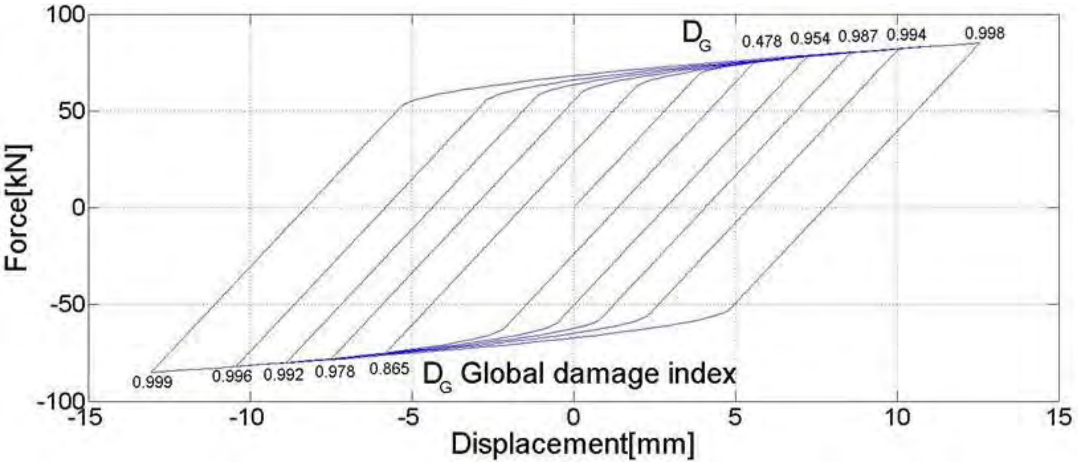

Figure 5: Force-horizontal displacement of the upper corner of the RC column.

4.2 Portal Frame

The new proposed global dynamic damage measure is applied on a reinforced concrete portal frame which is tested by [13]. The portal frame was subjected to a steady-state harmonic ground acceleration given in Fig. 8. Its geometry is given in Fig. 6 and its material properties in Table 2. The reinforcement and cross-sectional properties are shown in Fig. 7.

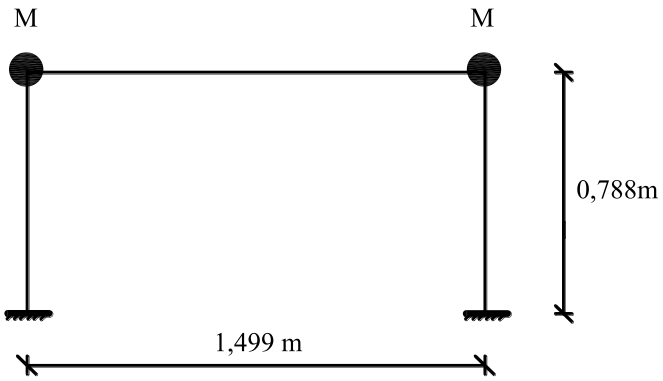

Figure 6: Geometry and mass distribution of the portal frame.

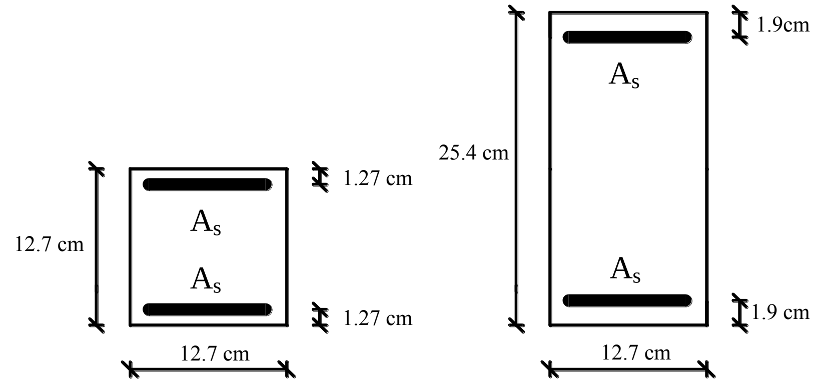

Figure 7: Reinforcement and cross-sections of the portal frame

E_s= 199948 MN/m^2
E_c= 21836 MN/m^2
f_{sy}=351.63 MN/m^2
f_{cy}= 32.75 MN/m^2
M= 972 kg
A_s= 1.43 cm^2

Table 2: Material properties of the portal frame.

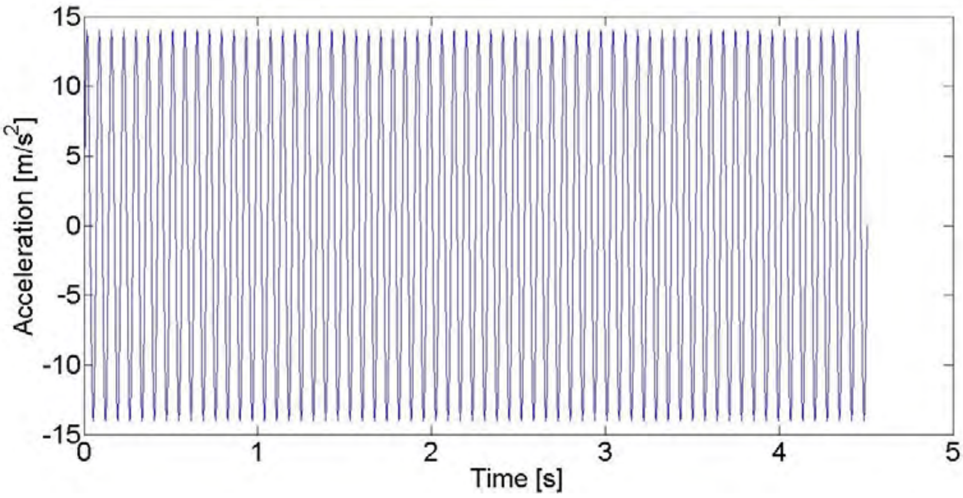

Figure 8: Base acceleration applied to the portal frame

The time-maximum horizontal displacement diagrams of the recorded and calculated response are shown in Fig.9 and 10 respectively. It can be seen from these diagrams that the obtained structural response correlates well with the experiment. In Fig. 11, the variation of the dynamic global damage index (D_G) is also shown. During the first loading cycle, the value of D_G gradually increases. After the first loading phase it becomes 0.42 and after the loading in the opposite direction it increases rapidly to 0.69. During the following loading cycles the value of D_G increases firstly by a small amount then it remains constant as expected.

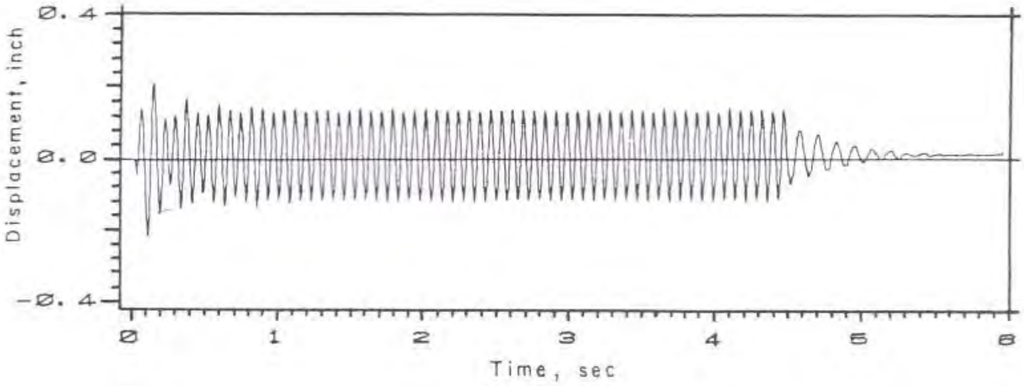

Figure 9: Recorded response.

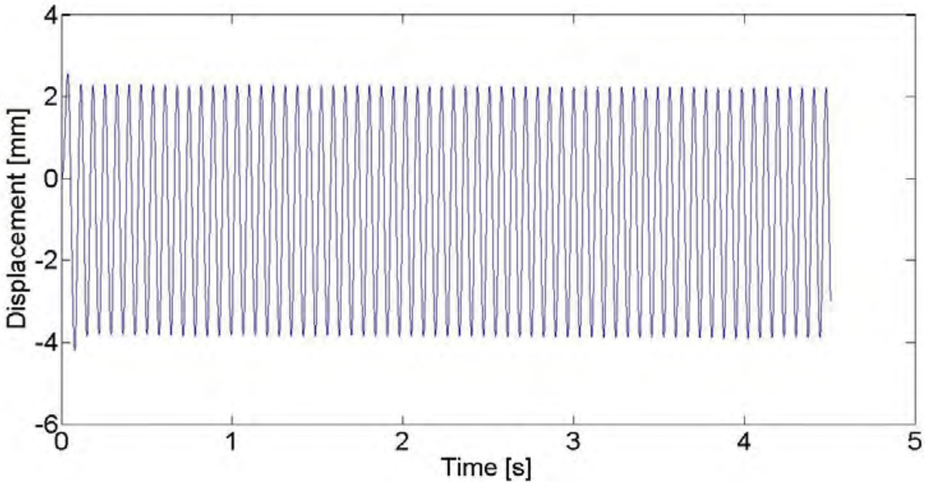

Figure 10: Calculated response.

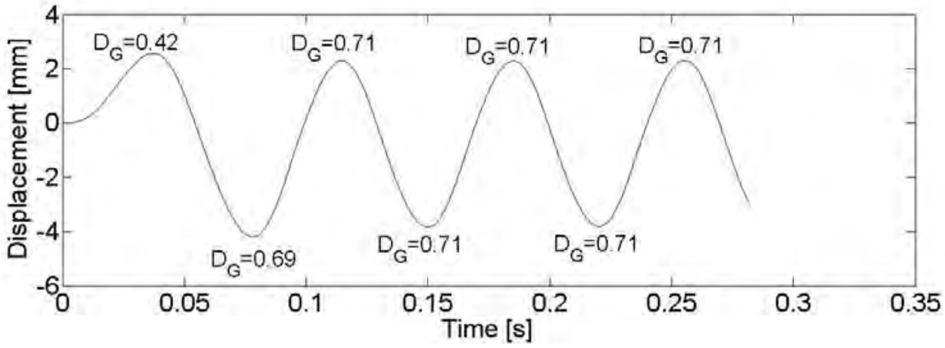

Figure 11: Displacement and global damage index under dynamic loading.

5 CONCLUSIONS

Damage measures for cyclic and dynamic loading have been proposed for reinforced concrete frames. These damage measures have been tested and compared to experiments. The proposed damage indices stand in a good agreement with the observed damage in experiments and provide a reliable damage measure for seismic design.

REFERENCES

[1] J.T.P. Yao, F. Kozin, Y.K. Wen, J.N. Yang, G.I. Schueller, O. Ditlevsen, Stochastic fatigue, fracture and damage analysis, *Structural Safety*, **3**, pp. 231–267, 1986.

[2] W.B. Krätzig, K. Meskouris, Assessment of seismic structural vulnerability as a low-cycle fatigue process, *In: Bisch Ph, editor. Proc. 11th European Conf. on Earthquake Engineering*, Paris, France, Balkema, Rotterdam, 6-11 September 1998, 161–178, 1998.

[3] Y.J. Park, A.H.S Ang, Mechanistic seismic damage model for reinforced concrete, *J. Struct. Eng.*, **111**[4], 722-739, 1985.

[4] A.D. Hanganu, E. Onate, A.H. Barbat, , A finite element methodology for local/global evaluation in civil engineering structures, *Computers & Structures*, **80[20-21]**, 1667-1687, 2002

[5] W.B. Krätzig, Y.S. Petryna, Assessment of structural damage and failure, *Archive of Applied Mechanics*, **71**, 1–15., 2001.

[6] Y.S. Petryna, W.B Krätzig, Compliance-based structural damage measure and its sensitivity to uncertainties, *Computers & Structures*, **83**[14], 1113-1133, 2005.

[7] Matlab Release R2006b –User Manual. Massachusetts, The MathWorks Inc., 2006.

[8] T. Takeda, M.A. Sozen, N. Nielsen, Reinforced concrete response to simulated earthquakes, *J. struct. div. ASCE*, **96**, 2557-2573, 1970.

[9] D. Soleimani, E.P. Popov, V.V. Bertero, Nonlinear beam model for R/C fame analysis, *Seventh conference on electronic computation St. Louis, Missouri, ASCE, New York*, 1979.

[10] I.F. Meyer, Ein werkstoffgerechtes Schädigungsmodell und Stababschnittselement für Stahlbeton unter zyklischer nichtlinearer Beanspruchung, *Dissertation, KIB-RUB SFB 151*,Mitteilung Nr. **88-4**, August 1988.

[11] N. Çelik, Y.S. Petryna, Local and global seismic damage measures for reinforced concrete frames, *International Sakarya Earthquake Engineering,*, 2009.

[12] W.B. Krätzig, I.F. Meyer, F. Stangenberg, Experimentelle Untersuchungen zur Schädigungsevolution und Instandsetzung von Stahlbetonstützen unter erdbebenähnlicher Beanspruchung, *Ruhr Universitat Bochum, SFB 151- Berichte*,1989.

[13] P. Gülkan, M. Sozen, Response and energy dissipation of reinforced concrete frames subjected to strong base motions, *Structural Research Series No:377,* University of Illinois, 1971.

COMPDYN 2011
III ECCOMAS Thematic Conference on
Computational Methods in Structural Dynamics and Earthquake Engineering
M. Papadrakakis, M. Fragiadakis, V. Plevris (eds.)
Corfu, Greece, 25–28 May 2011

SEISMIC SAFETY ASSESSMENT OF CURVED BRIDGES USING PUSHOVER ANALYSIS

Miguel Araújo[1] **and Raimundo Delgado**[2]

[1] Faculdade de Engenharia, Universidade do Porto
Rua Dr. Roberto Frias, s/n 4200-465 Porto, Portugal
maraujo@fe.up.pt

[2] Faculdade de Engenharia, Universidade do Porto
Rua Dr. Roberto Frias, s/n 4200-465 Porto, Portugal
rdelgado@fe.up.pt

Keywords: Curved Bridges, Nonlinear Analysis, N2 Pushover Method, Local and Global Capacity Demands.

Abstract. *The seismic safety assessment of bridges using nonlinear static analysis methods is not straightforward. Not only an accurate modelling of the structural frames inelastic behaviour is required, but also a correct definition of the force distribution patterns, analysis directions, reference points and target displacements that best represents its seismic structural performance. This difficulty on the pushover parameters definition increases when irregular-in-plan bridges are considered, namely curved bridges. Hence, the aim of this study is to assess the seismic safety of a set of curved bridges using the eurocode's pushover analysis method. Particular attention is paid to the RC columns biaxial behaviour modelling. The bridge structural response is evaluated in terms of global and local capacities. Comparative evaluation of the calculated response of the bridges illustrates the applicability of the N2 pushover method and the influence of the different directions of analysis in its local and global capacity demands definition.*

1 INTRODUCTION

Since the early 1960s, irregular-in-plan curved bridges have gained high popularity, particularly in the highway interchanges and urban expressways, as a result of geometric constraints, limitations of space and high density of urban traffic [1].

However, due to the relative particularity of its forms, curved bridges present an apparently different dynamic response when compared to common straight bridges, which may naturally affect its seismic behaviour. Indeed, in view of the collapse of some curved bridges during the 1971 San Fernando earthquake, United States of America, D. Williams and W. Godden [2] conducted a shaking table test study of a scaled microconcrete curved bridge model, which main objective was to evaluate the effects of both linear and nonlinear dynamic behaviour and the influence of the expansion joints to its resistance capacity. W. Tseng and J. Penzien [3] have also studied the nonlinear seismic response of long, multiple-span, reinforced concrete curved and straight bridges, and concluded, alike [2], that the ductility requirements at the column bases of curved bridges are not so critical and important compared to the levels observed in long straight bridges.

Likewise, N. Burdette and A. Elnashai [4] observed that, in the transverse direction, the curved decks provide greater stiffness to the structure through arch or catenary action, while the straight decks resists transverse forces in flexure, which allows more of the pseudostatic displacements to be absorbed by the bridge deck. However, when the longitudinal direction was analysed, the opposite was observed, that is to say, curved bridges resists inertial forces by a combination of flexural and axial stiffness of the deck, while the straight bridge deck resists these forces efficiently in pure tension and compression, giving the structure a greater stiffness longitudinally.

Therefore, the seismic response of curved bridges usually should be considered in both longitudinal and transverse directions, having the direction of the input seismic action, the planar irregularity and the two-axis related bending a great role on the maximum values of the response [5-8].

The use of nonlinear dynamic time-history analysis (THA) is, by far, the most reliable method to assess the seismic behaviour of structures, particularly the irregular ones. However, it requires a high effort of computational capacity and time, which increases when multi-directional seismic actions are considered. Thus, nonlinear static pushover analysis (PA) appears as an interesting alternative, more simple and expeditious.

The applicability of PA method to bridges has been extensively studied recently and numerous variants of the traditional method, with increasing accuracy and complexity, are available today [9-11]. However, a limited number of studies focused the use of pushover analysis in curved bridges [5, 12-14].

The seismic assessment of bridges using PA methods is not straightforward. Not only an accurate modelling of the structural frames inelastic behaviour is required, but also a correct definition of the force distribution patterns, analysis directions, reference points and target displacements that best represents its seismic structural performance. This difficulty increases when irregular-in-plan bridges are considered, since the columns tend to present biaxial behaviour and the critical input angle of the seismic action, as well as the respective direction of analysis, vary with the type and curvature of the structure.

In view of the previous considerations, the present study attempts to assess the seismic response of a set of curved bridges using the Eurocode's [15, 16] pushover method. Some practical procedures that take into account the different directions of analysis are presented and the results obtained compared to those obtained using THA. Special attention is paid to the evaluation of the seismic action critical input angle and to local and global capacities.

2 PUSHOVER ANALYSIS PROCEDURE

The PA method proposed by the Eurocode 8 is the well known N2 method, firstly developed by P. Fajfar and M. Fishinger [17] to assess the seismic behaviour of regular buildings. The Eurocode 8 presents the PA procedure for bridges in both Parts 1 [15] and 2 [16], defining, in the first, the method to determine the target displacement from the structures capacity curve and, in the second, the parameters that allow the capacity curve definition, such as the directions of analysis, reference points and load distributions.

As mentioned above, with the increasing of the curved bridges radius of curvature, the dynamic response tends to change significantly. In these cases, the principal direction of analysis is no longer the transversal one and a set of different oriented directions of analysis should be considered, in order to obtain the critical response direction. According to Eurocode 8, only two horizontal directions of analysis should be considered: a longitudinal X-direction, defined by the centres of the two end-sections of the deck; and a transverse Y-direction, that should be assumed to be orthogonal to the first.

Additionally to these directions of analysis, the Caltrans SDC [18] recommends the application of the ground motion along the principal axes of individual components. The ground motion must be applied at a sufficient number of angles to capture the maximum deformation of all critical components.

Therefore, having both normative recommendations in consideration, the steps of the PA adopted procedure are summarized in the following:

- Once defined the geometry and the structural models of all analysed bridges (Figure 2 (A)), the first step consists on the selection of the PA load distribution patterns (Figure 2 (B)). According to Eurocode 8 the pushover curves must be obtained by pushing the entire bridge structure with two load distributions patterns: a constant along the deck pattern (PAc) and a proportional to the first mode shape pattern (PAm). In spite of not being mentioned by the European Standard, it is recommended [12, 13] to carry out the pushover analysis in both positive and negative transverse direction when irregular-in-plan structures are not symmetric. Since the importance of the longitudinal response of curved bridges increases with the radius of curvature, a third pushover pattern (proportional to the mode with higher mass participation factor in the X-direction) is also proposed by some researchers [12,13] (PAxm). Finally, with the objective of capture the critical direction of the curved bridges response, a constant along the deck pattern with a variable local axis orientation (PAvoc) will be adopted as well. It should be noted that the global X-Y axis is defined by the Eurocode's directions of analysis and the local X'-Y' axis by the principal axes of individual columns elements and abutments, as presented in Figure 1.

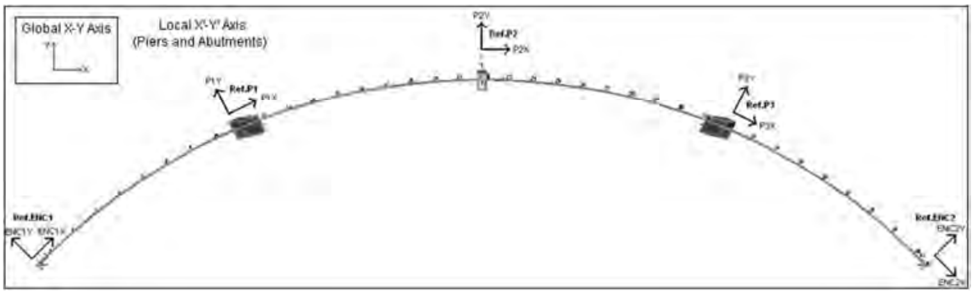

Figure 1: Local and Global axes.

- The second step concerns the construction of the total base shear vs displacement of reference point pushover curve for each considered load distribution pattern (the reference point, according to Eurocode 8, should be the centre of mass of the deformed deck) and for the various directions of analysis. The local X´-Y´ axis capacity curves are obtained from converted deck displacements and shear forces, as it is represented in Figure 2 (C).
- The last step of the presented PA procedure refers to the determination of the earthquake displacement demand associated with each pushover curve obtained previously (Figure 2 (C)). For such, the multi-degree-of-freedom (MDOF) system pushover curves must be transformed into equivalent single-degree-of freedom (SDOF) system pushover curves through a transformation factor, Γ, as it is proposed in [15]. This transformation factor depends on the normalized displacements, which should be taken as local axis converted normalized displacements depending on the direction of analysis. Once determined the target displacement for the SDOF system, d_t*, using an idealized elasto-perfectly plastic force-displacement relationship, the final MDOF system target displacement of the control node, d_t, is given by Γd_t* (Figure 2 (C)).

Previous studies [9-11] have shown that traditional PA methods generally works reasonably well when applied to bridges of regular configuration. However, T.S. Paraskeva *et al* [12] concluded that a single mode-based load pattern should not be used in bridges with strong curvature in plan, even when they qualify as regular. Hence, the results obtained using the presented PA procedures should be evaluated by comparisons with those obtained using a more accurate THA (Figure 2 (D)).

3 STRUCTURAL MODELING AND DYNAMIC CHARACTERISTICS OF THE ANALYSED CURVED BRIDGES

This study considered six different curved bridges, defined from the well-known P232 PREC8 regular bridge [19], with infinite, 1000m, 700m, 420m, 240m and 130m radius of curvature of the deck, as represented in Figures 2 (A).

The bridges were modelled using the SAP2000 analysis program considering concentrated plasticity at the columns base (Figure 3), so as to represent the Eurocode's idealized local ductility cantilever model. SAP2000 allows the definition of lumped inelastic rotational hinges through backbone uncoupled or interaction MM models and fiber models [20]. Although the use of backbone models, with Takeda's hysteretic model, ensures a lower effort of time and processing capacity, they fail to perform a 3-dimensional dynamic analysis. Thus, knowing the importance of the columns biaxial behaviour in curved bridges, a more accurate fiber hinge model was adopted. The fiber hinge computes a moment-curvature relation in any bending direction for varying levels of axial load by assigning particular material stress-strain relationships to individual discretized fibers in the cross section. The longitudinal column reinforcement stress-strain relationship was defined by a bilinear model with kinematic hysteretic behaviour, while the confined and unconfined concrete stress-strain relationships were defined by the J. Mander *et al* [21] model with Takeda's hysteretic behaviour. The lumped plasticity is assumed to occur over a plastic hinge length and is specified at the middle of the plastic hinge. The plastic hinge length was defined by the Eurocode's Annex E [16] expression. The remaining elements of the structure were taken as linear-elastic and the masses were lumped at the top of the columns and midspans (Figure 3).

The individual capacity curves of each column of the P232 Bridge, defined in terms of moment-displacement and force-displacement relationships, for both longitudinal and transverse directions, are presented in Figure 4.

(A) Geometry and Structural Models Definition

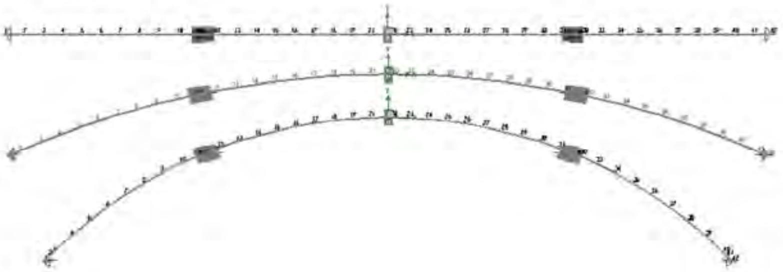

(B) Lateral Load Patterns Adopted

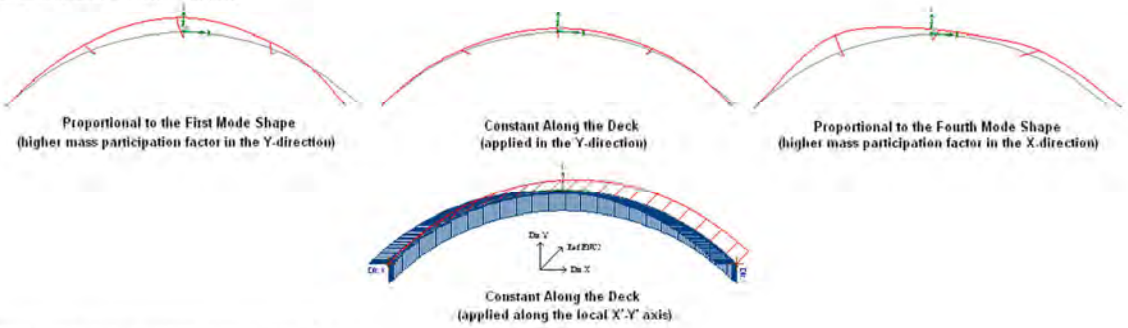

(C) Capacity Curves and N2 Method Application

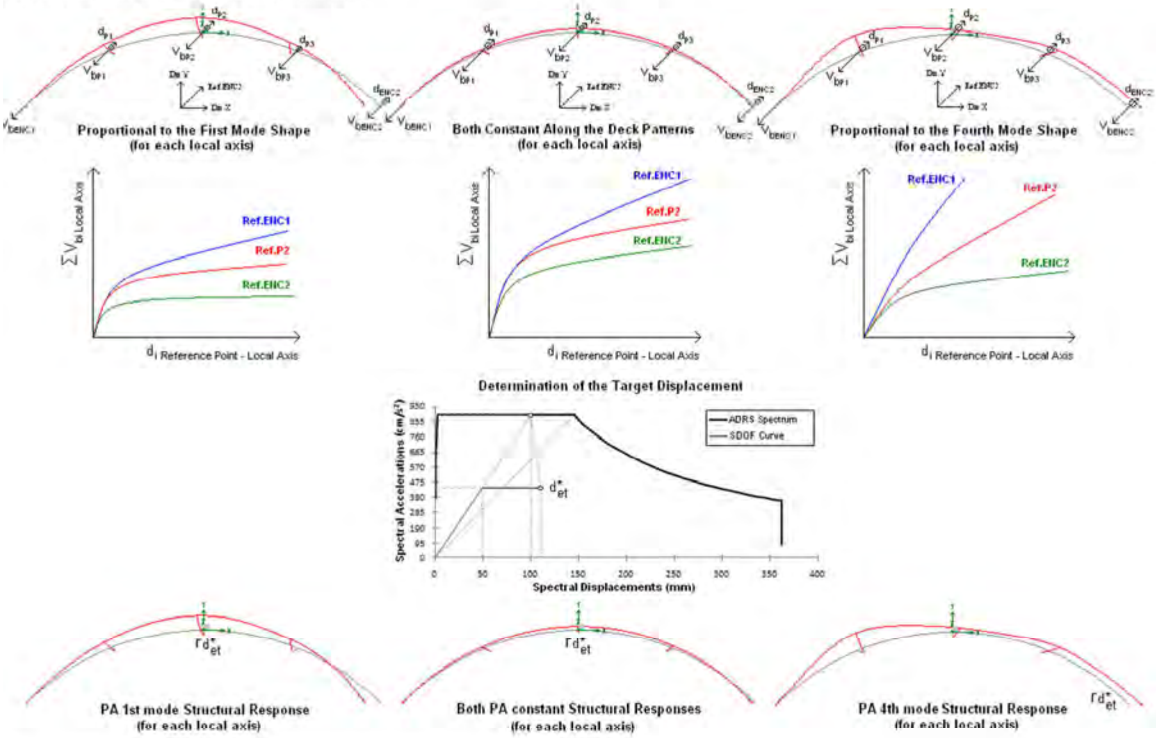

(D) Comparison with the Time-History Nonlinear Analysis (THA) Method

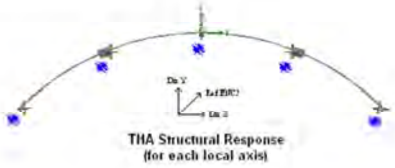

Figure 2: Analysis procedure adopted.

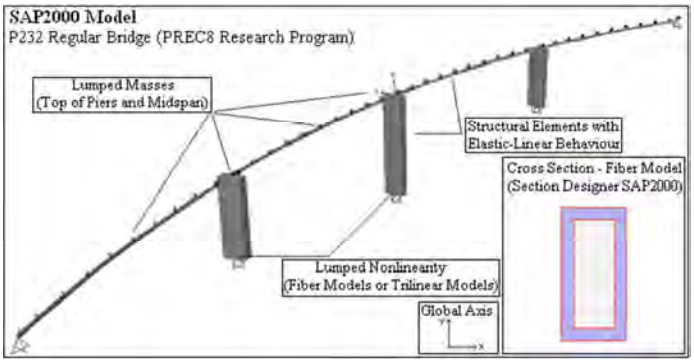

Figure 3: Structural model with concentrated plasticity at the columns base.

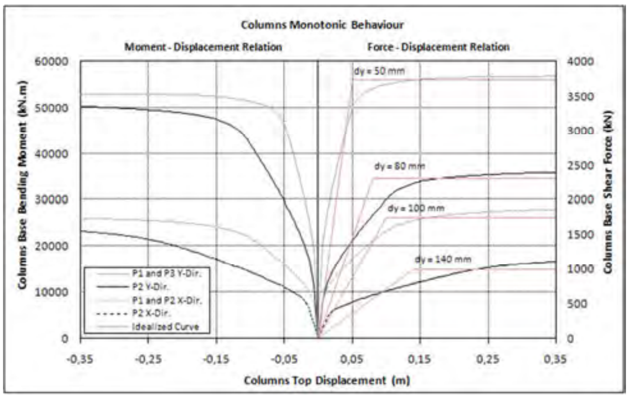

Figure 4: Capacity curves of each column in both longitudinal and transverse directions.

It is also presented in Figure 4 the yield displacements values of the RC columns in both directions, evaluated by idealising the actual F-d diagram by a bilinear diagram of equal area beyond the first yield of reinforcement, as it is proposed in [16].

With regard to the dynamic characteristics of the analysed curved bridges, it can be seen from Figure 5 a significant and expected variation on the modal eigenvalue properties with the increase of the radius of curvature. Likewise, Table 1 exhibits the evolution of the modal mass participation ratios of the 1st and 4th modes of vibration (which represents, respectively, the bridges responses on the transverse and longitudinal directions) with the curvature of the deck, being evident a counterbalanced decrease of the 1st mode importance with the increase of the 4th mode importance in the Y-direction, and the opposite in the X-direction.

Modal Mass Participation Ratios (%)				
Bridges	1st Mode of Vibration		4th Mode of Vibration	
	Y-Direction	X-Direction	Y-Direction	X-Direction
Straight Bridge	91	0	0	90
Radius = 1000m	89	1	0	64
Radius = 700m	89	2	0	58
Radius = 420m	85	5	13	40
Radius = 240m	76	14	20	42
Radius = 130m	54	34	36	23

Table 1: Evolution of the modal mass participation ratios with the curvature of the deck.

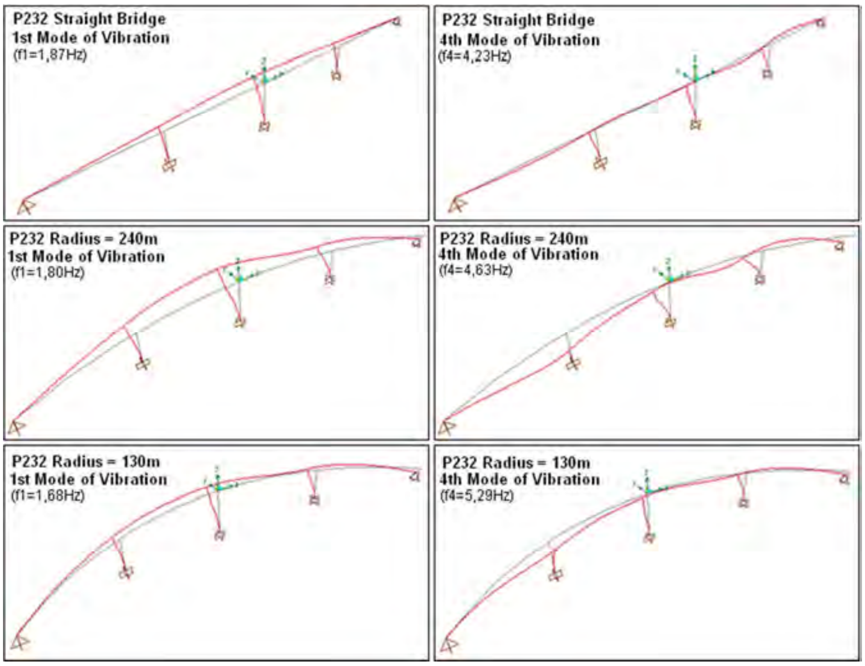

Figure 5: Transverse and longitudinal mode shapes and respective frequencies of vibration.

Before presenting the main results obtained through the adoption of the previously exposed PA procedures, some preliminary values, in terms of target displacements, are displayed in Figure 6. An evident divergence between the PAm, PAc and PAxm results is observed, particularly in the case of the PAxm results, which are well below the expected. Hence, as the PAxm results are not representative, from now on they will not be considered.

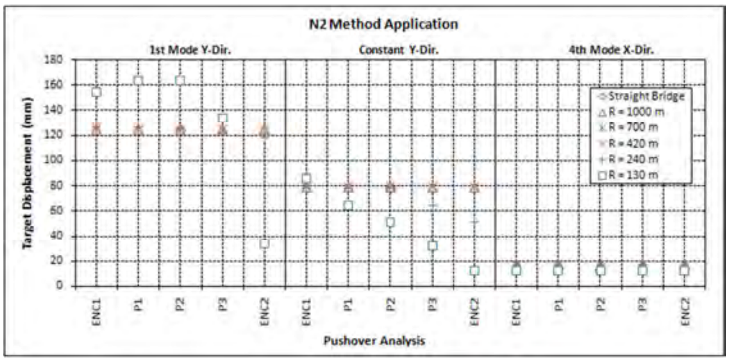

Figure 6: N2 Method application: target displacement values.

4 PUSHOVER CAPACITY CURVES

The pushover capacity curve definition step is one of the most important in the PA procedure, since it is the step that defines the structures characteristics through their total base shear vs displacements of the control node curves. As mentioned above, in order to represent the behaviour of the bridges in several directions of analysis, the construction of the capacity curves will be conducted from local axis converted deck displacements and shear forces, being the chosen local axis systems defined by the principal axes of the individual columns elements and the abutments (Figure 1). These local axis systems were obtained from the rotation of the generic global X-Y axis, with the rotation angles presented in Table 1 for each analysed curved bridge.

Local Axis Rotation (º)					
Bridges	ENC1	P1	P2	P3	ENC2
Straight Bridge	0	0	0	0	0
Radius = 1000m	5,5	3,0	0	-3,0	-5,5
Radius = 700m	8,0	4,3	0	-4,3	-8,0
Radius = 420m	13,4	7,2	0	-7,2	-13,4
Radius = 240m	23,9	12,6	0	-12,6	-23,9
Radius = 130m	44,9	23,8	0	-23,8	-44,9

Table 1: Global to local axis rotation.

Therefore, the PAm, PAc and PAvoc capacity curves, for each local axis systems and both X’ and Y’ directions, are plotted in Figures 7 to 12. Two major conclusions can be drawn by the analysis of these figures, concerning the influence of the local axis and the curvature of the deck.

Firstly, and as aforementioned above, it is easy to verify a significant variation in the curved bridges structural response with the increase of radius of curvature. If one only considers the local P2 axis results, which are identical to the global axis results, an important divergence in the Y’-direction pushover curves can be noted in the case of the PAc and PAvoc (Figures 9 and 11). For instance, under these circumstances, a similar 0,1m displacement demand at the top of the P2 central pier leads to a 25000 kN base shear in the stronger curved-in-plan bridge, while in the straight bridge it only leads to a 15000 kN base shear, representing a 40% variation. On the other hand, the X’-direction capacity curves revealed a higher divergence in the PAm (Figure 8), as expected with the evolution of the modal mass participation ratios. Thus, it can be seen that the longitudinal capacities of the analysed bridges increased, from zero (straight bridge), with the increase of the first mode X’-direction participation ratios.

The second major conclusion concerns the influence of the local axis systems in the definition of the analysed bridges pushover curves, and, consequently, on their structural capacities along the various directions of analysis. Not only can be observed from Figure 12 that bridges with stronger deck curvature tend to be more affected by different directions of analysis, but also that the direction of analysis defined by the ENC2 local axis seems to lead to lower capacity curves, while the ENC1 local axis direction of analysis lead to higher capacity curves, which is due to the higher longitudinal displacements of the ENC2 roller support.

The sequence of plastic hinge formation was also derived for both straight and higher curved bridges, as presented in Figure 13, which allows us to understand the latter conclusions. It can be noted that the sequence of plastic hinge formation is much closer to being simultaneous in the transverse direction of the straight bridge, behaving practically like an SDOF system, than in the transverse direction of the bridges with higher deck curvature for each local Y’ axis, wherein hinging is also affected by higher modes, like the longitudinal mode, and takes place at differently stages of the response. Furthermore, as also displayed in Figure 13, the hinging formation inverts its sequence with the various directions of analysis, in agreement with the respective local axis converted first mode shapes. Thus, the P3 column reaches the yielding point (at a 0,5m displacement, Figure 4) earlier in the ENC1, P1 and P2 directions, while the P2 column is the one to first yield in the P3 and ENC2 directions, wherein the bridge response has rotated from its transverse response to its longitudinal response.

Interesting results were also observed through the application of the alternative constant along the deck patterns, PAc and PAvoc, whereby the forces acting at each node are proportional to the nodal mass in the considered directions of analysis. These patterns are mainly used as a mean of identifying critical combinations of shear and flexure in each vertical element of bridge structures. The PAc and PAvoc capacity curves bring forward a higher overall strength of the system when compared to the PAm capacity curves, which may be explained by the fact that, while the first mode shape tends to present a single column with a significantly larger displacement, and so with a higher modal force, the constant patterns tends to equally distribute the inertial force at all columns, if the masses at each one are similar. As a result, for the same displacement demand, higher forces are developed in the PAc and PAvoc cases.

In terms of PAc and PAvoc capacity curves comparison, it can be verified that, as the curvature of the bridges increase, the capacity curves tend to diverge, particularly in the case of the P3 and ENC2 local axis.

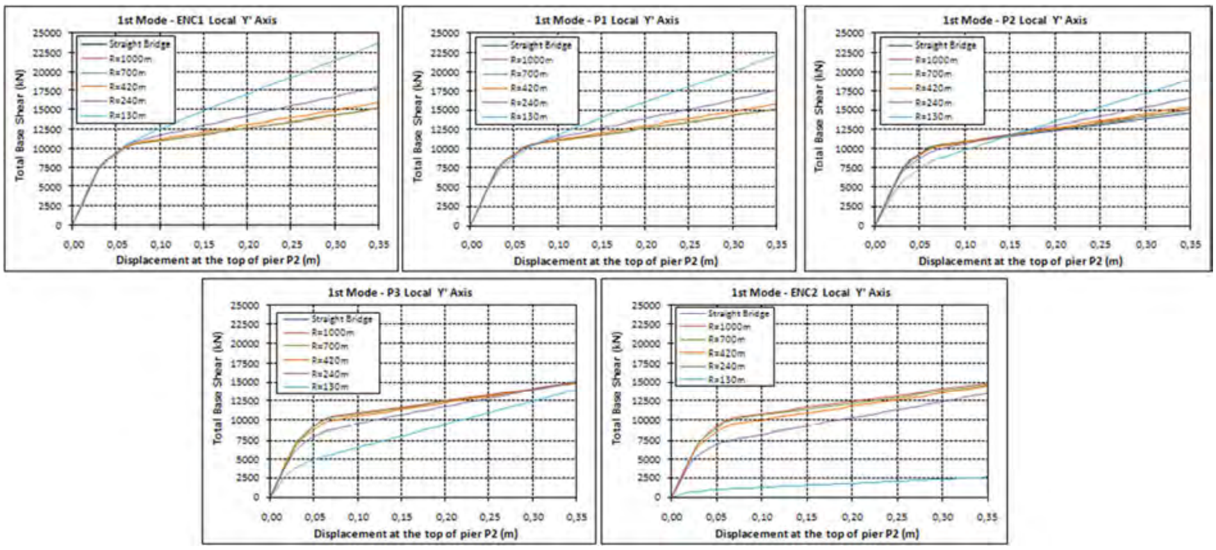

Figure 7: PAm capacity curves for each local Y’ axis.

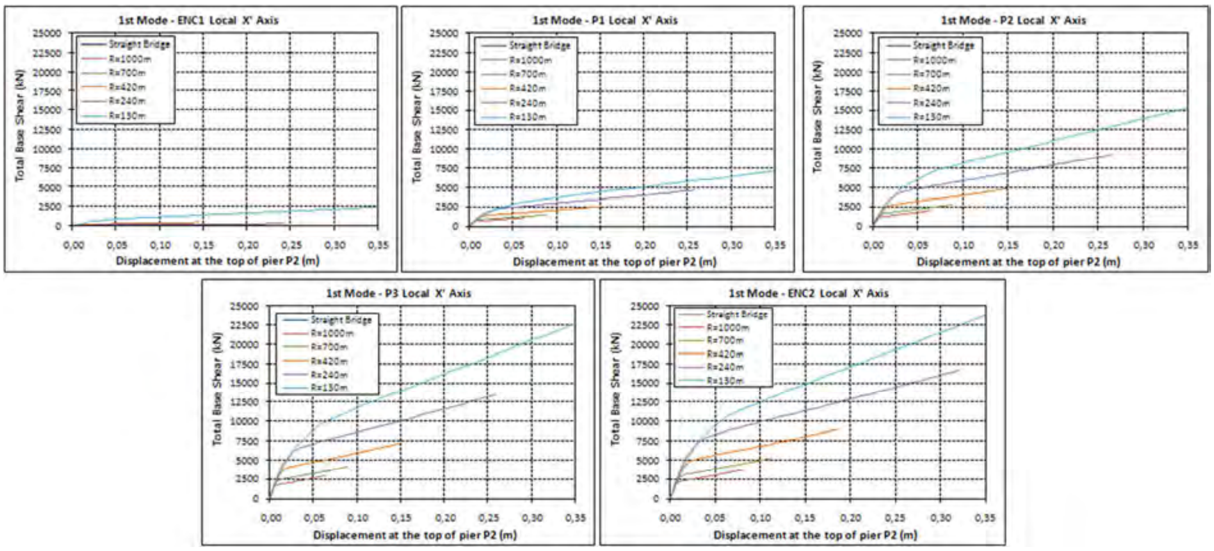

Figure 8: PAm capacity curves for each local X’ axis.

Figures 9 and 11 demonstrate that the overall strength of the bridges grows with the rotation of the local axis from ENC2 axis to ENC1 axis, namely in the case of the more curved bridges. As said before, this grow can be explained by the change in the type of the response, what, in other words, means that ENC1, P1 and P2 local axis seems to characterize the transverse response of the bridges, while P3 and ENC2 local axis seems to represent their stiffer longitudinal response. Unlike the PAc procedure, that considers converted local axis capacity curves from the global axis capacity curve, and so equally converted inertial forces, the PAvoc method admits that the same inertial forces are applied in each direction, proportionally to the lumped masses. For this reason, the PAvoc capacity curves present a higher overall strength of the system comparatively to the PAc capacity curves. This may suggest that the PAc procedure loses feasibility when applied to bridges with strong curvature in plan.

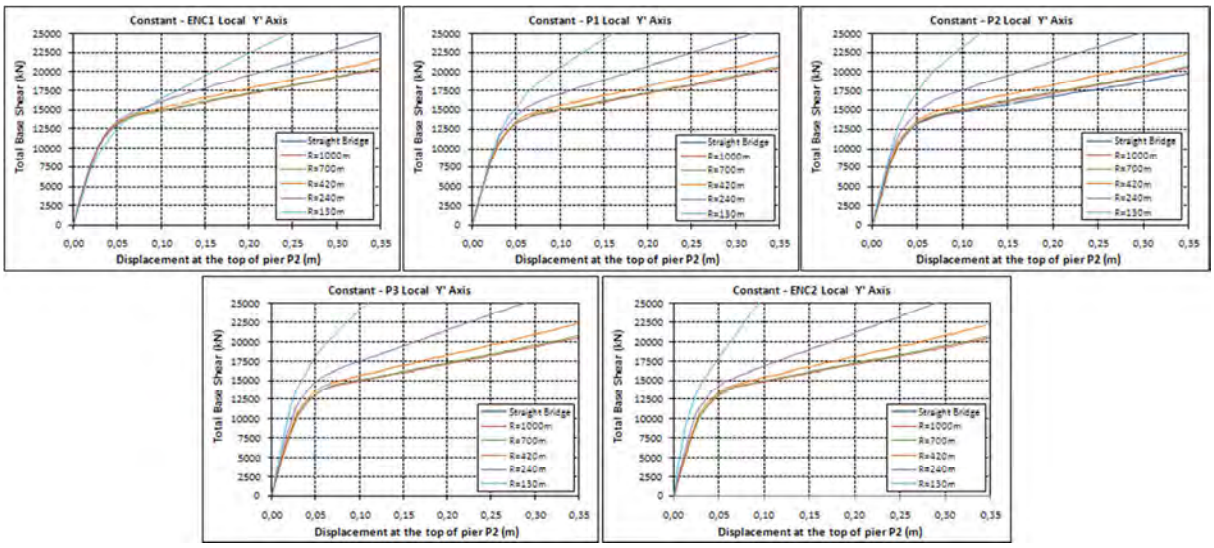

Figure 9: PAc capacity curves for each local Y’ axis.

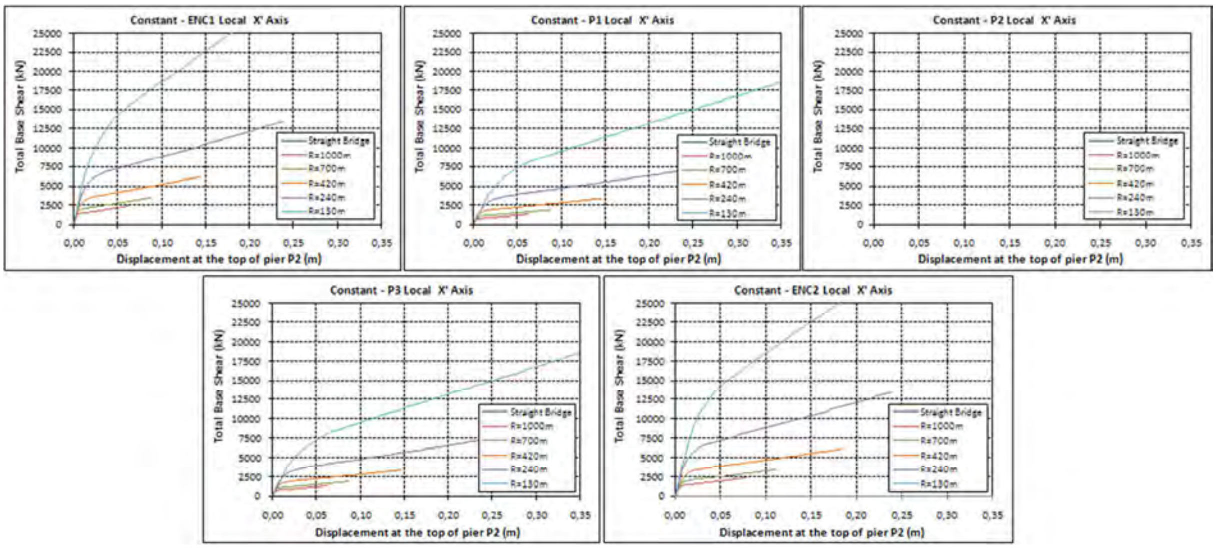

Figure 10: PAc capacity curves for each local X’ axis.

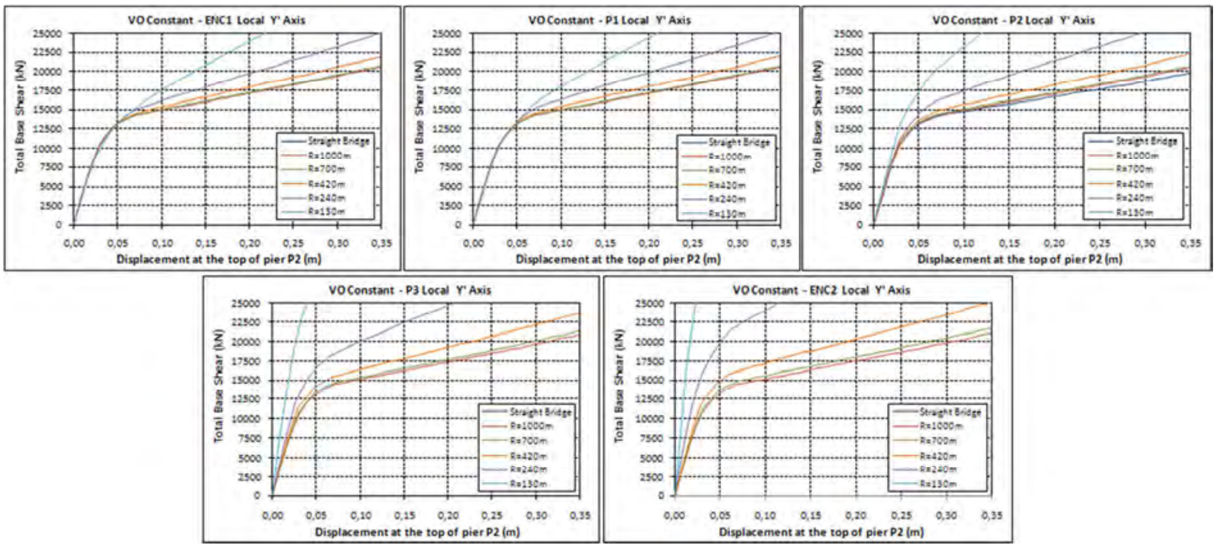
VO Constant - ENC1 Local Y' Axis

VO Constant - P1 Local Y' Axis

VO Constant - P2 Local Y' Axis

VO Constant - P3 Local Y' Axis

VO Constant - ENC2 Local Y' Axis

Figure 11: PAvoc capacity curves for each local Y’ axis.

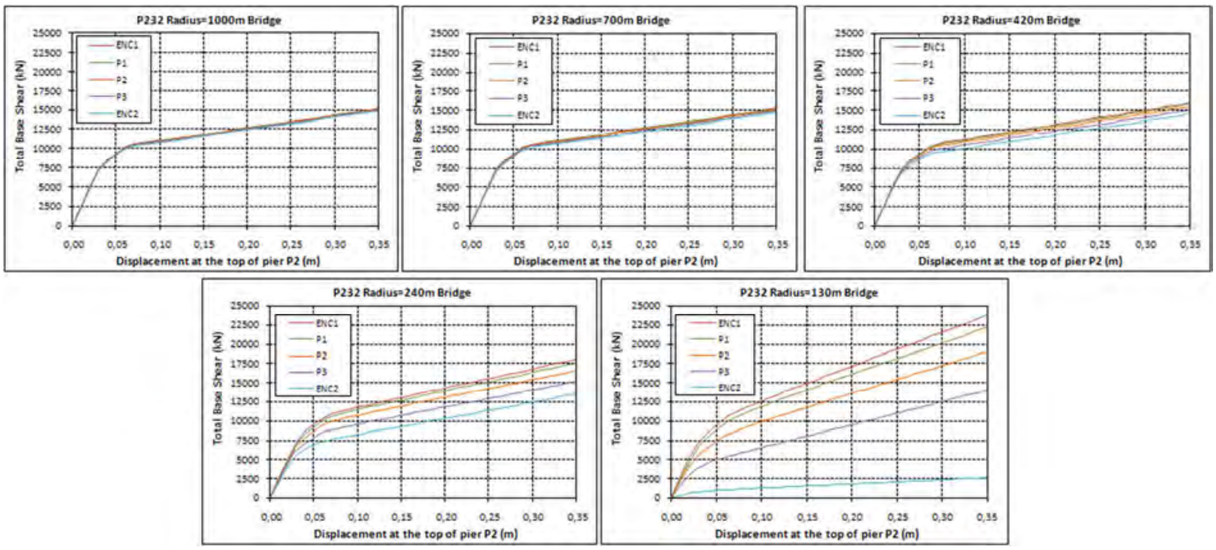
P232 Radius=1000m Bridge

P232 Radius=700m Bridge

P232 Radius=420m Bridge

P232 Radius=240m Bridge

P232 Radius=130m Bridge

Figure 12: PAm capacity curves for each analysed curved bridges in local Y’ axis.

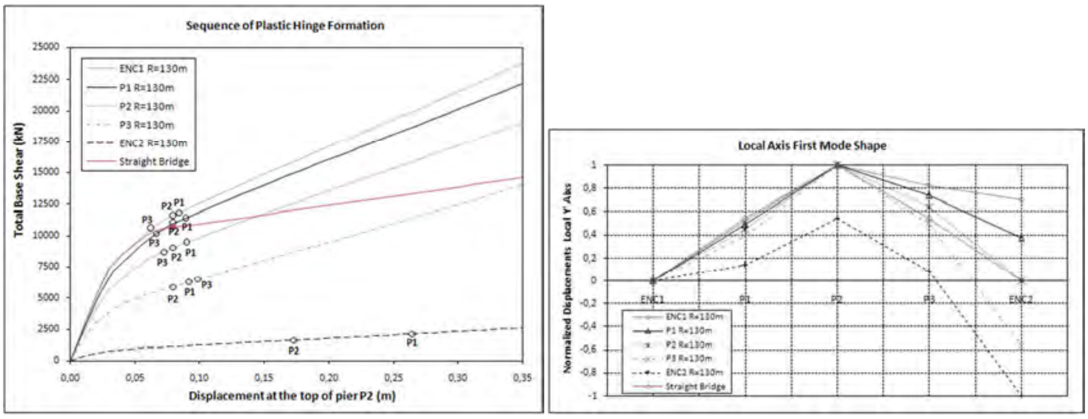
Sequence of Plastic Hinge Formation

Local Axis First Mode Shape

Figure 13: Sequence of plastic hinge formation and local axis converted first mode shapes.

5 APPLICABILITY OF N2 PUSHOVER METHOD

Previous studies [11, 12, 22] have shown that, for bridges with an effective modal mass of the fundamental mode equal or greater than 80% of its total mass, the N2 method in general works fine. Once, in short bridges the effective mass of the fundamental mode increases together with the seismic intensity, in this cases the accuracy of the N2 method also increases. Therefore, good results are expected with the application of the N2 method to bridges with high first mode modal mass participation ratios (Table 1).

However, when this fundamental mode mass ratios decrease, the higher modes start to significantly influence the response, regardless of the seismic intensity. Hence, according to [12], simplified pushover procedures should not be used in bridges with high curvature in plan.

In line with the latter considerations, a most reliable analysis procedure must be used in order to correctly evaluate the applicability of the N2 method to all analysed bridges. Thus, the nonlinear dynamic time-history analysis (THA) will serve as a benchmark for this evaluation.

5.1 Nonlinear Time-History Analysis (THA)

Contrarily to the nonlinear static analysis methods, the THA accounts for strength degradation of different elements of the bridge, as well as the influence of all modes and the characteristics of the dynamic response, making it the more accurate method of analysis. The general approach for the solution of the dynamic response of structural systems is the direct numerical integration of the dynamic equilibrium equations at a discrete point in time. Several time-integration methods are available, such as the Newmark and Hilber-Hughes-Taylor (HHT) algorithms. According to [13], the latter is more beneficial under high input ground motions, because it can reduce the high short-duration peaks in the solution, therefore it will be employed in this study. It should be noted that, if convergence problems occur during nonlinear analysis, the HHT method should be used initially with an $\alpha = -1/3$ to get an approximate solution. The analysis should then be repeated with decreasing α values to obtain greater accuracy in the results [20]. Moreover, as the results are extremely sensitive to time-step size, a time step of 0,0001s is recommended to ensure a consistent convergence of displacements [22]. A uniform damping value of 5% was assumed for all modes of vibration, as proposed by [16] for reinforced concrete structures, through the use of the Rayleigh damping coefficients. The THA was conducted considering a set of artificial records compatible with the Portuguese EC8 elastic spectrum, as presented in Figure 14.

In spite of the SAP2000 fiber model ability to represent successfully the degradation and softening after yielding, it not includes the pinching and bond slip effects. Moreover, SAP2000 requires a high effort of processing time for a cross-section discretization number of 200 fibers and the referred time step size. Therefore, the THA analysis was conducted using the SeismoStruct analysis program, well known by the scientific community.

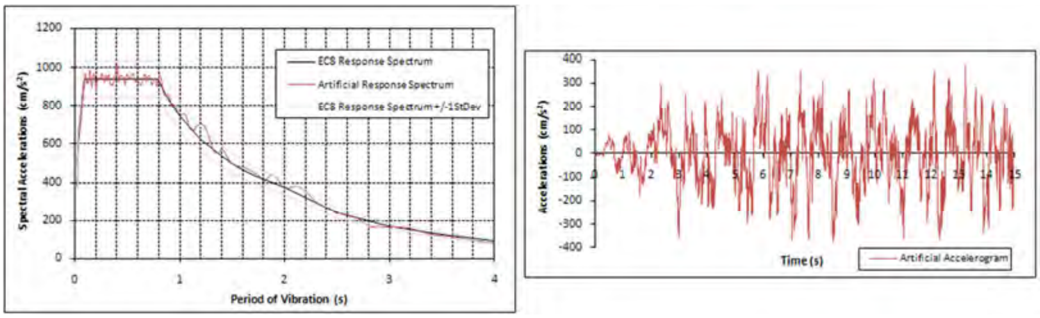

Figure 14: Seismic action adopted: EC8 response spectrum (Type 1 seismic action, Zone 1 and Ground Type D of the Portuguese National Annex) and respective generated artificial accelerogram and response spectrum.

Figures 15 and 16 depict the THA results, being evident the same conclusions drawn in the previous analysis of the pushover capacity curves. In agreement with the dynamic characteristics of the studied curved bridges, as the curvature in plan increases, the higher modes of the structure gain importance, namely the longitudinal mode of vibration. Thus, it may be seen from Figure 15 a reduction on the bridges Y-direction flexural bending moments and a contrary increase in the X-direction flexural bending moments, of approximately 40% in the P1 pier and 70% in the P3 pier, respectively. From Figure 16 it can also be observed the evolution of the longitudinal response of the various studied bridges.

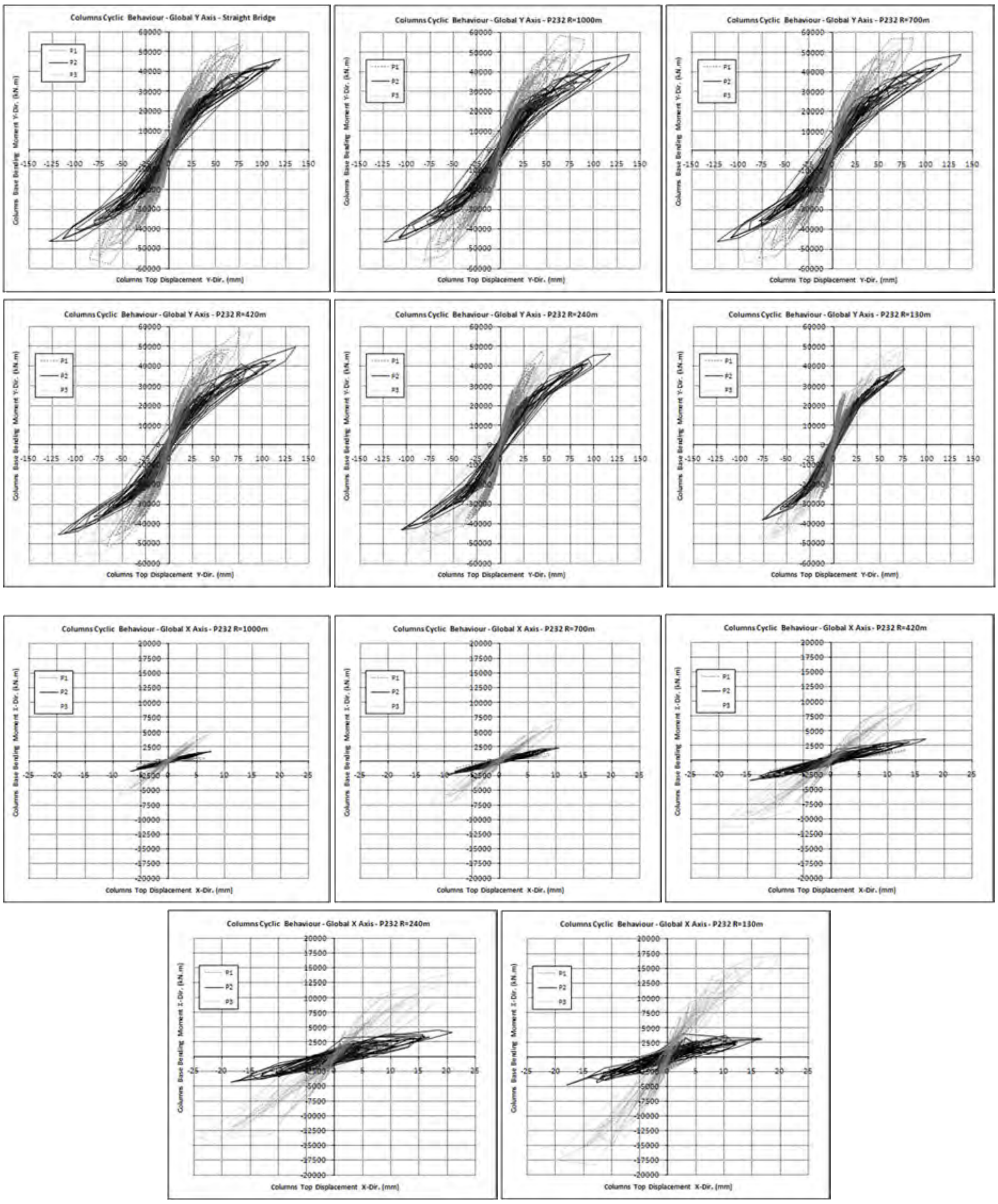

Figure 15: Columns cyclic behaviour for each analysed bridges using THA applied along the global Y axis.

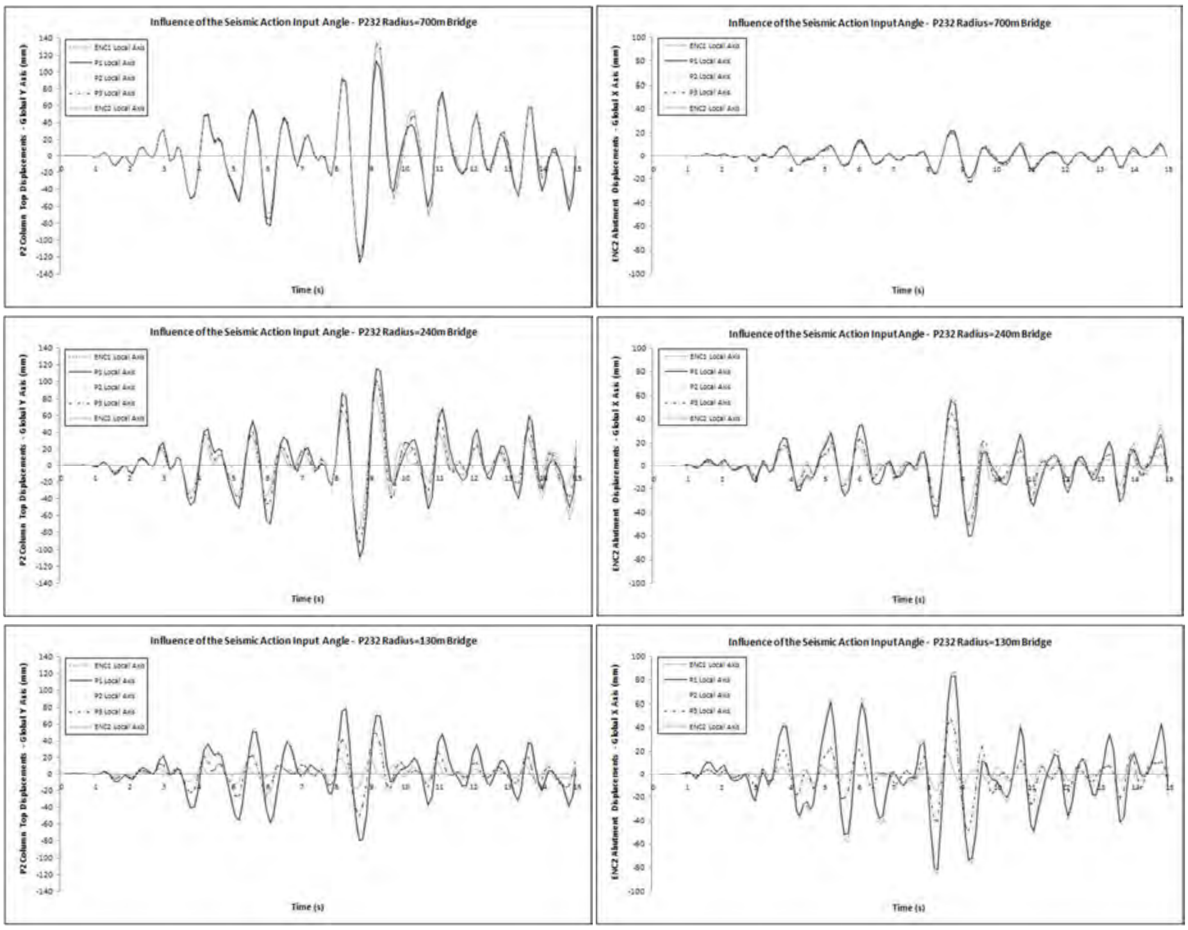

Figure 16: Influence of the seismic action input angle on the R=700m, R=240m and R=130m bridges response using the THA.

Notwithstanding, special attention should be given to the influence of the local axis systems on the bridges response. In this case, displacements variations of approximately 80%, 50% and 3% between ENC1 and ENC2 local axis systems can be observed for the Y-direction and for the bridges with radius of curvature of 130m, 240m and 700m, respectively.

5.2 Evaluation of the N2 Pushover Method by Comparisons with Time-History Analysis

During the feasibility assessment of the previously presented pushover procedures, two main comparison criteria should be taken into account: a first PA vs THA comparison criteria, which seeks the evaluation of the simplified pushover procedures by comparisons with a more refined method of nonlinear analysis; and a second PAc and PAvoc comparison criteria, which intents to evaluate the applicability of the deck displacements and shear forces conversion technique.

As mentioned above, it can be seen from Figure 17 that the PAm procedure worked very well in the case of the P232 straight viaduct, in accordance with the 91% value of the 1st mode mass participation ratio (Table 1). The bridges response is thus clearly governed by its transverse direction fundamental mode. On the contrary, the PAc procedure underestimated the deck displacements values, with an approximately 30% variation with regard to the THA result. This expected variation is due to the equal distribution of the inertial forces along the bridges piers, which allows the structure to develop a higher overall strength.

For its part, Figures 18, 19 and 20 present the response in terms of deck displacements of the bridges with a smaller curvature in plan and with a 1st mode mass participation ratio higher than 80%. In accordance with both comparison criteria, it can be firstly concluded that, in spite of the direction of analysis (seismic action input angle), the PAm procedure is the one that best fits the THA results; however a 16% variation in the Y'-direction P2 top displacements of the bridge with a radius of curvature of 420m can be observed between the use of the ENC1 and the ENC2 local axis systems, which was considered negligible. Once more, the PAc results are considerably below the THA results. Secondly, it can be observed that, not only the PAc results are identical to the PAvoc results, but also that the X'-direction displacements obtained using the PAm procedure fit quite well with the THA longitudinal displacements. Therefore, it can be concluded that the deck displacements and shear forces conversion technique leads to good results under these conditions.

Similar conclusions can be drawn from the analysis of Figure 23, where it can be seen that the differences between the PAm and the THA results are, in general, not higher than 20% (higher values are due to ENC2 local axis and to the slight stronger curvature of the R=420m bridge, which tend to increase the importance of the longitudinal response), and that the PAc vs THA displacements ratios overlap the PAvoc vs THA ratios.

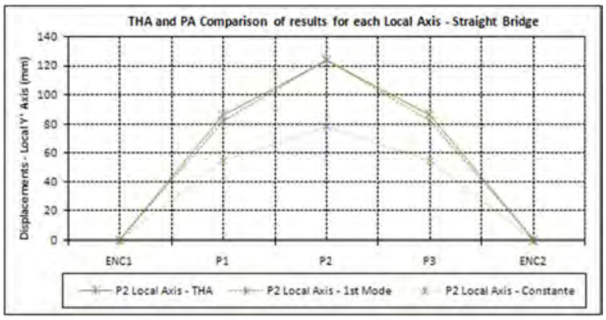

Figure 17: Response of viaduct P232, in terms of Y-direction deck displacements, calculated from PAm, PAc and THA.

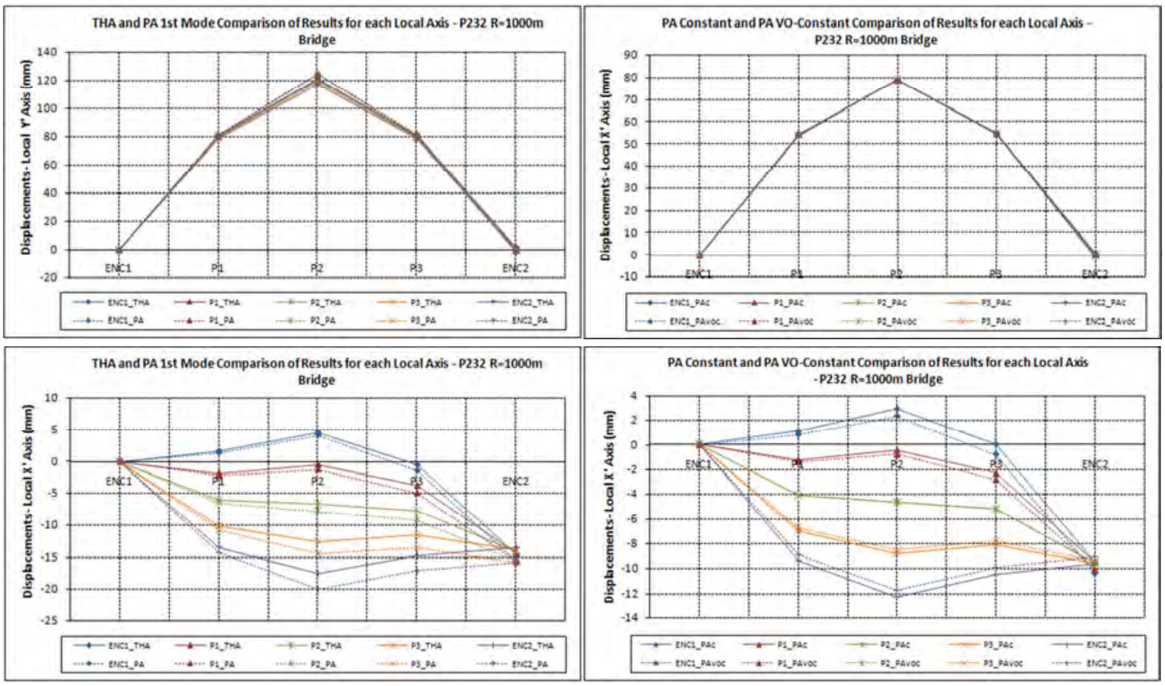

Figure 18: Response of viaduct P232 with a radius of curvature of 1000m, in terms of Y-direction and X-direction deck displacements, calculated from PAm, PAc, PAvoc and THA.

It should be noted that the outliers X'-direction ratios observed in the bridges with radius of curvature of 1000m and 700m are owing to the ratio of values that are close to zero, and so have no significance.

On the other hand, it is interesting to observe from Figure 21 that, in the case of the bridge with the radius of curvature equal to 240m, nor the application of the PAm, or the application of the PAc, leaded to perfectly good results, being evident the influence of both curvature of the deck and local axis systems in the bridge response.

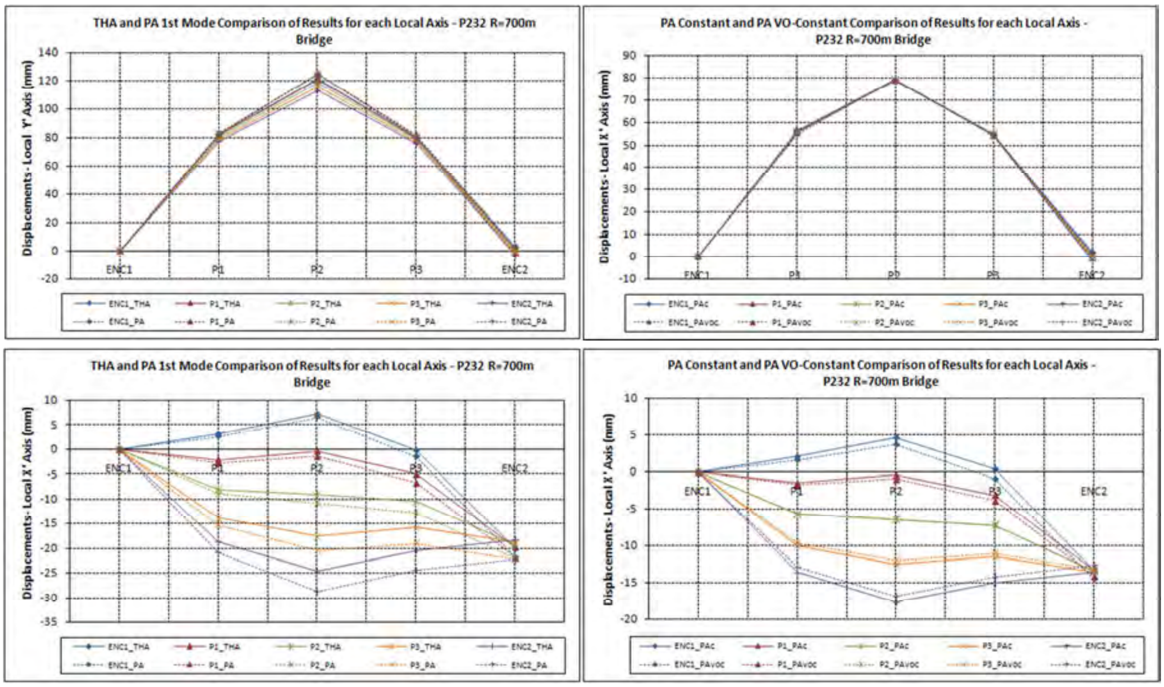

Figure 19: Response of viaduct P232 with a radius of curvature of 700m, in terms of Y-direction and X-direction deck displacements, calculated from PAm, PAc, PAvoc and THA.

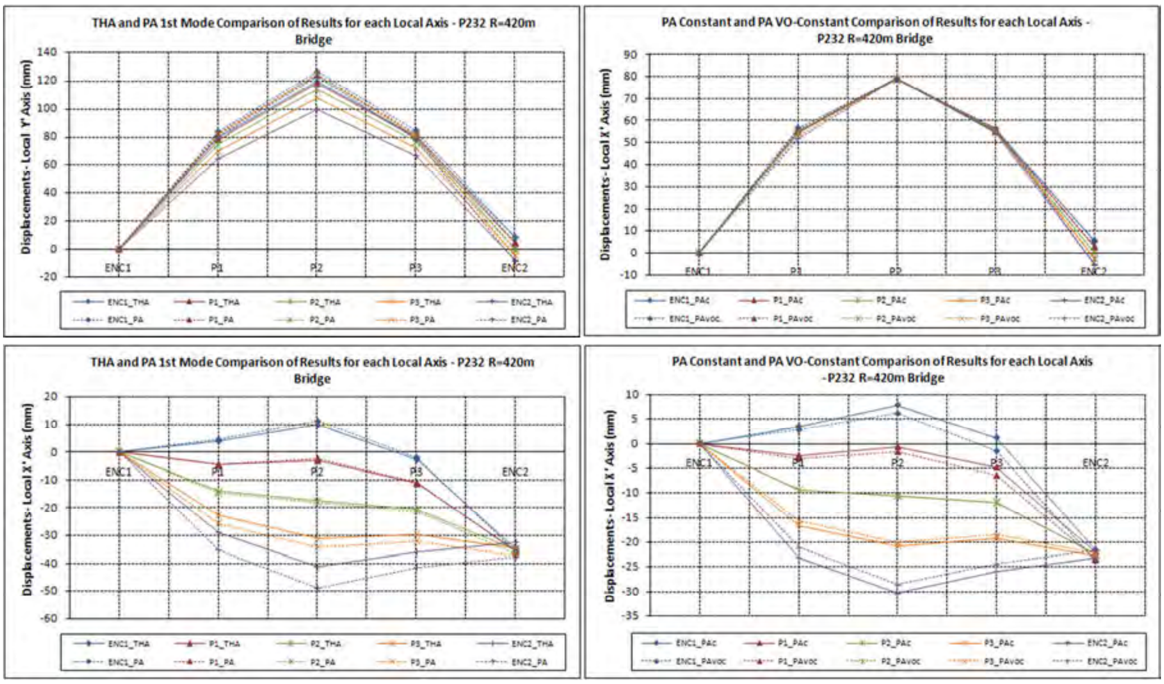

Figure 20: Response of viaduct P232 with a radius of curvature of 420m, in terms of Y-direction and X-direction deck displacements, calculated from PAm, PAc, PAvoc and THA.

Thus, while the PAm drove to relatively good results for ENC1, P1 and P2 local axis systems in both transverse and longitudinal displacements, for P3 and ENC2 local axis systems the PAm significantly overestimated the displacement demands, with a variation of 50% from the THA results in the latter case. The PAm procedure proved to be incapable of correctly reproducing the effect of the various directions of analysis in bridges with stronger curvature in plan. Although the PAc and the PAvoc procedures still to underestimate the response of the bridge, it may be noted that the results are getting closer to the THA results (Figure 23).

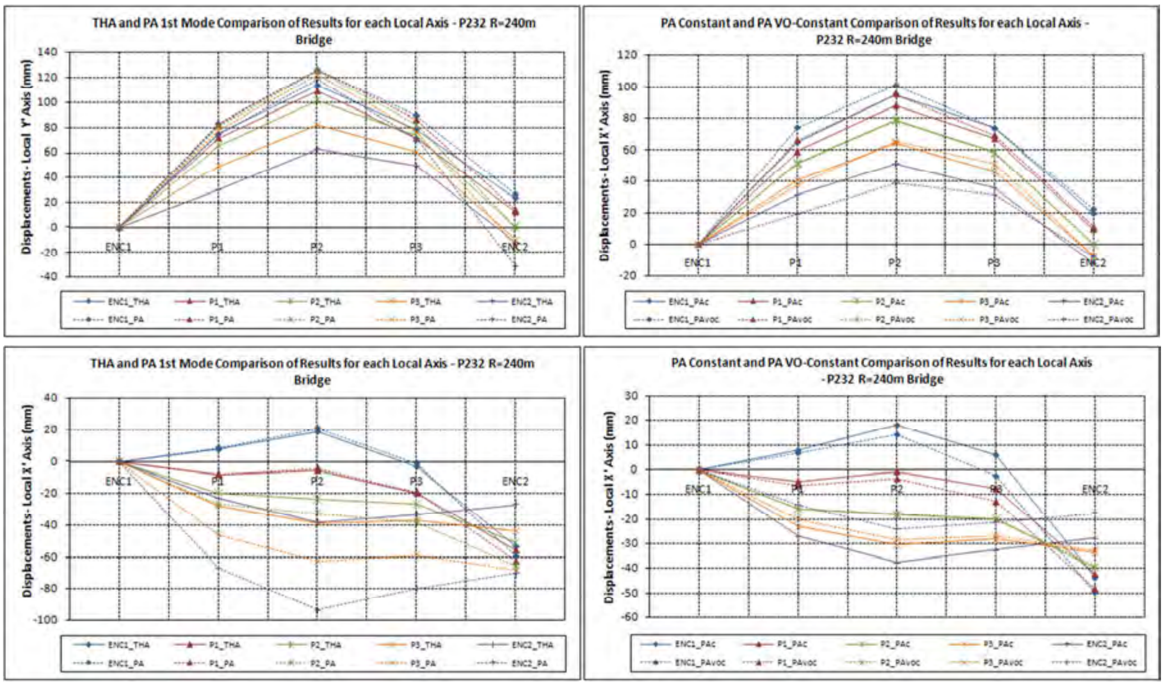

Figure 21: Response of viaduct P232 with a radius of curvature of 240m, in terms of Y-direction and X-direction deck displacements, calculated from PAm, PAc, PAvoc and THA.

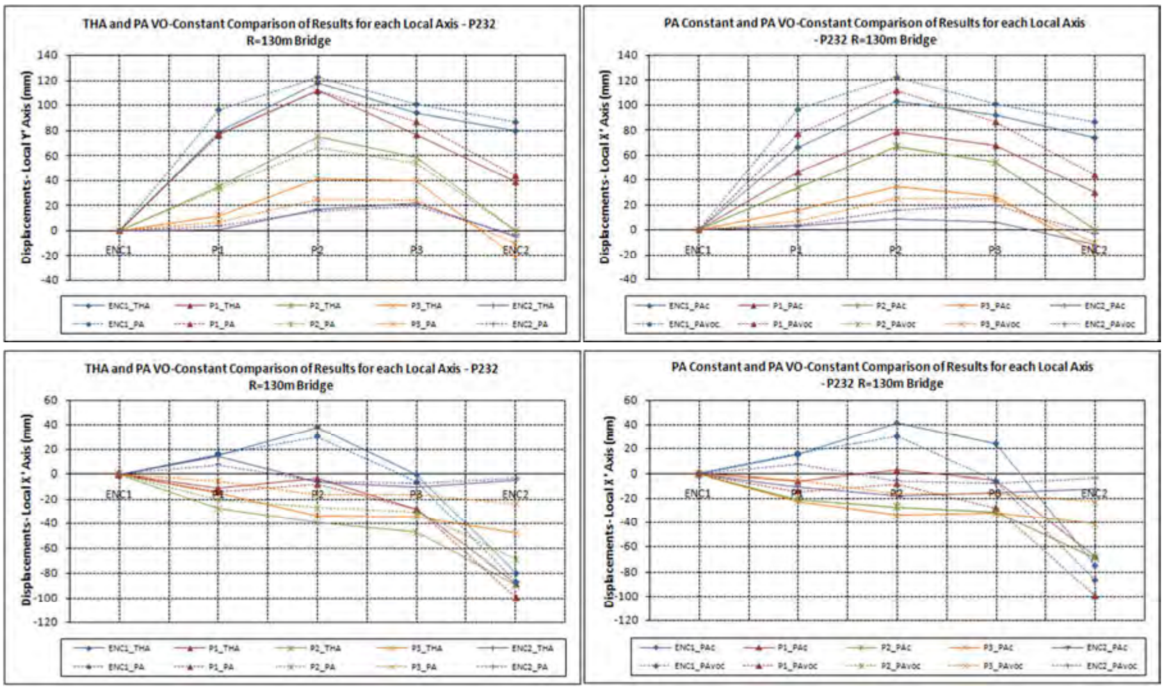

Figure 22: Response of viaduct P232 with a radius of curvature of 130m, in terms of Y-direction and X-direction deck displacements, calculated from PAc, PAvoc and THA.

It has been seen throughout this work that, for the geometric characteristics of the analysed bridges, the greater the inclination of the seismic action input angle in the direction of the left abutment, the more the curved deck will behave in flexure. Thus, the bridge response will be governed by its transverse response. On the contrary, when the seismic action is applied in the direction of the right abutment the bridge deck will behave in pure tension and the bridge response will be governed by its longitudinal response. Naturally, the validity of this statement increases with the curvature in plan of the bridge deck, such as the importance of the higher modes.

From Figures 22 and 23 it can easily be observed this influence of the local axis systems in the response of the bridge with the stronger curvature in plan, as well as the excellent approximation of the PAvoc results to the THA results and the contrary divergence of the PAm results, as already presented in Figure 6. Likewise, it can be noted that, in spite of the ability to predict the influence of the local axis systems, the PAc procedure loses accuracy when applied to bridges with a strong curvature in plan, being recommended the use of the PAvoc method in this circumstances.

A final remark regarding the third step of PA procedures, which refers to the determination of the earthquake displacement demand from the idealized SDOF system, should be taken. Not only the variation of the capacity curves with the directions of analysis (Figure 12) has an important role in the final target displacement values, but also the normalized displacements and the respective transformation factors. Thus, it was observed in stronger curved bridges that the transformation factors values decreased as the direction of the seismic action input angle rotated from the left to the right abutment, which leads to higher SDOF system idealized relationships and so to higher values of deformation energy up to the formation of the plastic mechanism, reducing the value of the target displacements. Moreover, as the final MDOF system target displacement of the control node is given by Γd_t*, smaller values of Γ conducts to smaller final displacement values. For instance, in the case of the bridge with the radius of curvature of 130m, its ENC2 local axis system transformation factor of 0,42 leaded to a higher SDOF capacity curve from a MDOF capacity curve that was significantly lower than the others (Figure 12) and to a similar SDOF target displacement comparatively to the other bridges and local axis systems. However, when the transformation factor multiplied the SDOF target displacement, it leaded to a lower final MDOF target displacement value, as displayed in Figure 6. On the contrary, bridges with not so stronger curvature in plan and identical transformation factors and capacity curves exhibit similar target displacements values.

5.3 Local and Global Capacity Demands

The modern structural design for earthquake resistance of bridges is based on the capacity design approach, which involves three main steps: (1) choose of the desirable mechanisms that best dissipate the most energy, in the present work, the plastic hinges were only considered at the columns base; (2) verification of deformation demands, the ductility demands, in terms of plastic hinge rotations or displacements, should be safely lower than the capacities of the plastic hinges; and, (3) verification of member against non-ductile failure modes, such as shear failure or joint failure. No reference will be made to step (3) in this work, however particular attention will be paid to the verification of the deformation demands of the bridge columns (step (2)) as a mean of identify the critical seismic action input angles. Therefore, Figure 24 presents the local ductility demands at the plastic hinges of the various analysed bridges, which is expressed in terms of displacement ductility factor, given by μ_d/μ_y, where μ_d is the displacement demand at each column and μ_y the yielding displacement of the same column (Figure 4).

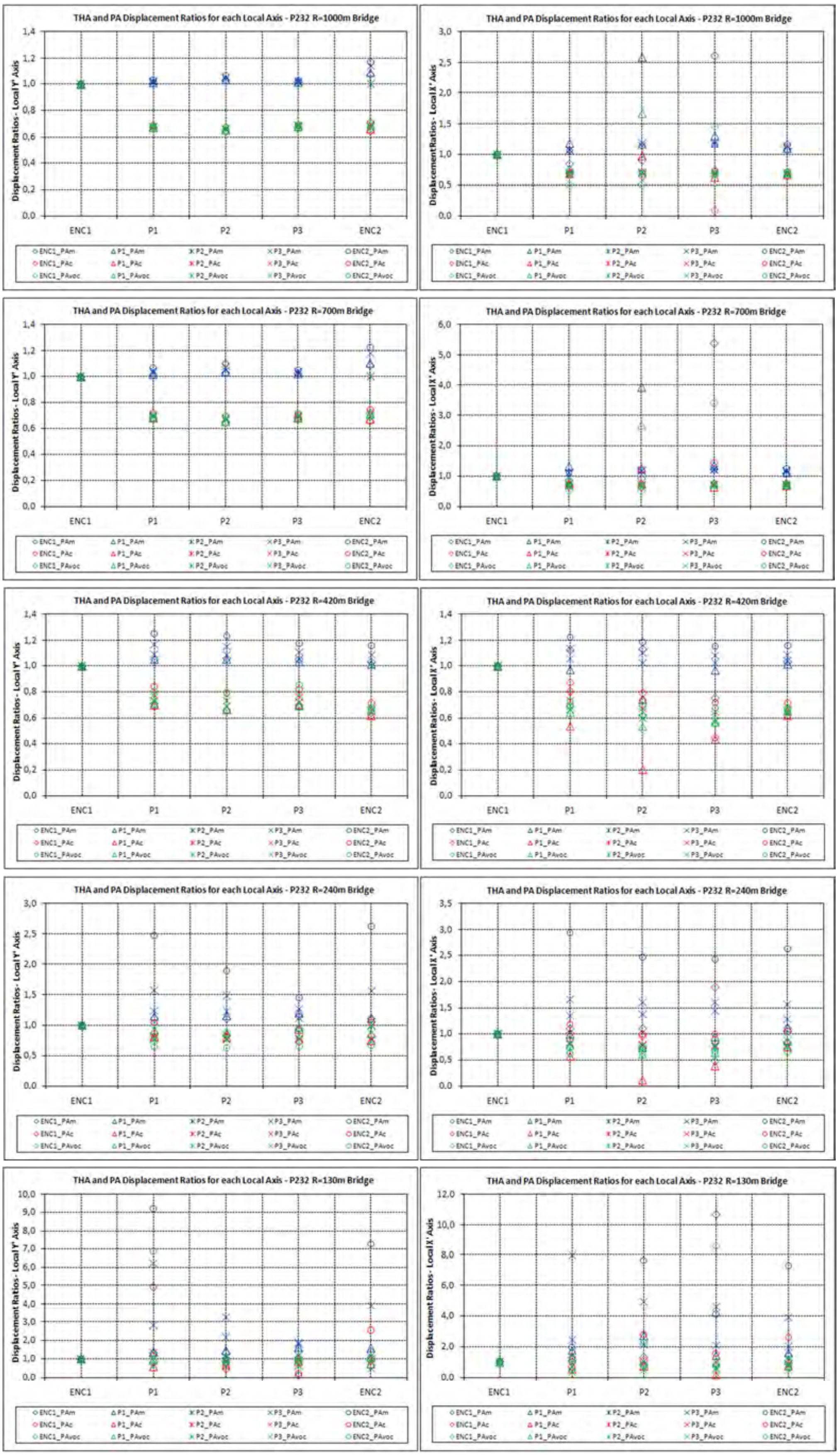

THA and PA Displacement Ratios for each Local Axis - P232 R=1000m Bridge

THA and PA Displacement Ratios for each Local Axis - P232 R=1000m Bridge

THA and PA Displacement Ratios for each Local Axis - P232 R=700m Bridge

THA and PA Displacement Ratios for each Local Axis - P232 R=700m Bridge

THA and PA Displacement Ratios for each Local Axis - P232 R=420m Bridge

THA and PA Displacement Ratios for each Local Axis - P232 R=420m Bridge

THA and PA Displacement Ratios for each Local Axis - P232 R=240m Bridge

THA and PA Displacement Ratios for each Local Axis - P232 R=240m Bridge

THA and PA Displacement Ratios for each Local Axis - P232 R=130m Bridge

THA and PA Displacement Ratios for each Local Axis - P232 R=130m Bridge

Figure 23: THA and PA displacement ratios for the various analysed bridges and for both local Y'-X' axis.

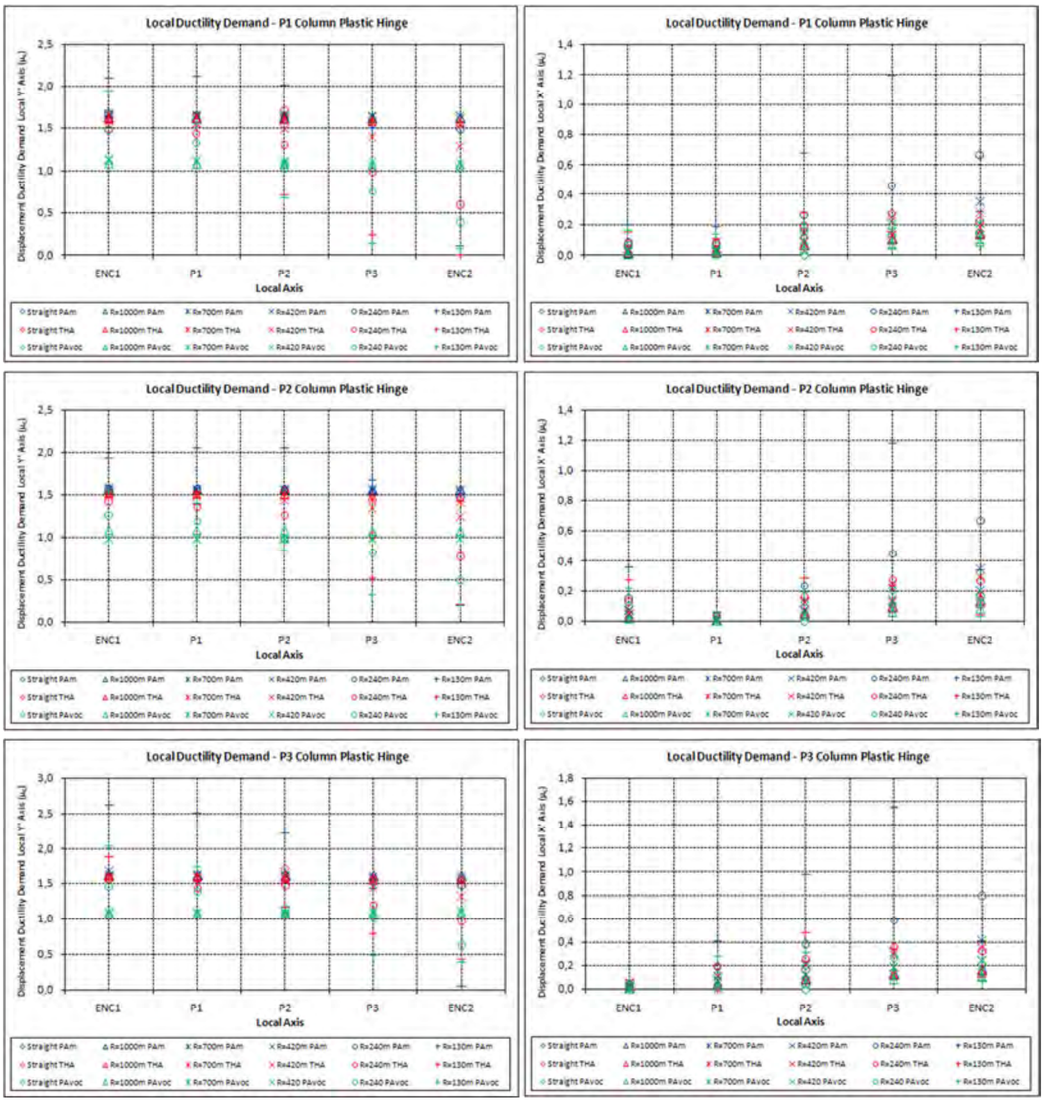

Figure 24: Local ductility demands at the columns of the various analysed bridges in both transverse and longitudinal directions.

Giving greater relevance to the THA local displacement demands, once they represent more realistically the actual seismic response of the bridges, it can be observed that, on the one hand, the transverse local ductility demands of bridges with smaller curvature in plan is similar along the various direction of analysis for each column, with a ductility factor of about 1,7. In the case of bridges with higher curvature in plan, like the bridge with a radius of curvature of 130m, the ENC1 direction of analysis is the critical one, increasing to approximately 1,9 the ductility factor of the P3 column. It should be noted that the P3 and the ENC2 directions of analysis leaded to markedly lower values of ductility demands in this type of bridges. On the other hand, the longitudinal local ductility factors are higher in bridges with stronger curvature in plan and for the P2, P3 and ENC2 directions of analysis. However, for the considered intensity level of the seismic action, the columns never experienced plastic incursions in the longitudinal direction, remaining with linear-elastic behaviour.

Finally, a global ductility demand analysis was also conducted and the results presented in Figure 25. The global ductility factors were obtained from the PAm and PAc equivalent SDOF system force-displacement relationships, as recommended in [16].

Identical conclusions may be taken regarding the local ductility demand analysis in terms of the influence of the directions of analysis and the curvature of the bridges. As mentioned above, the PAm procedure leaded to higher structural responses and to an average global ductility factor of 2,5, while the PAc procedure leaded to a lower average global ductility factor of 2, which decreased to approximately 0,5 in the bridge with a radius of curvature of 130m and for the ENC2 direction of analysis.

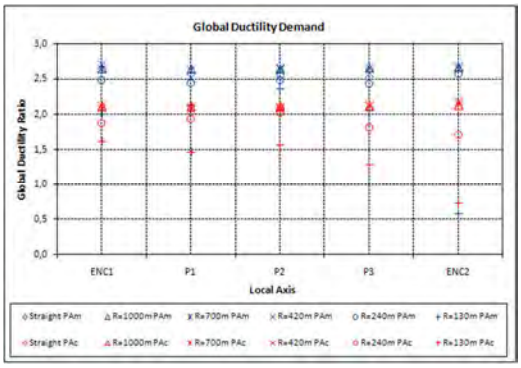

Figure 25: Global ductility demands at the various analysed bridges obtained from an equivalent SDOF system with the Eurocode's idealised elastic-perfectly plastic force-displacement relationship.

6 CONCLUSIONS

A set of short regular bridges with a radius of curvature in plan ranging between straight and 130m was selected to investigate the feasibility of the application of the N2 pushover method to curved bridges. A key issue in this work was the attempt to include the influence of different directions of analysis and seismic action input angles in the simplified PA procedures, so as to make them a reasonable alternative to the more complex and demanding, but yet reliable, THA method. The seismic response of the bridges was also evaluated in terms of its local and global capacity demands.

By applying the presented PAm, PAc and PAvoc procedures, as well as the THA, to the set of straight and curved bridges, the following conclusions were drawn:

- Complex three-dimensional structures, such as curved bridges, exhibit a multidirectional dynamic response that is more and more sensitive to earthquake directions as the level of curvature in plan increases. In the case of the bridge with the higher curvature in plan a 80% response variation between two different seismic action input directions has been observed. Therefore, a careful seismic safety assessment analysis must be conducted in these cases, otherwise the seismic response demands could be significantly underestimated.

- The Eurocode's PAm procedure proved to be quite accurate when applied to bridges with a regular curvature in plan and with a fundamental mode mass participation ratio equal or greater than 80%. On the other hand, for the same geometric type of bridges, the PAc procedure considerably underestimated its structural response, and so have no practical value. Equally, the PAxm procedure conducted to significantly low values of the response and, therefore, its use is not representative.

- With regard to bridges with a stronger curvature in plan, characterized by a decreasing importance of the fundamental mode in the dynamic response and a counterbalanced increase of the higher modes importance, the PAm provided an inaccurate estimate of the seismic response, generally overestimating it. On the contrary, as the irregularity of the curved bridges grows the PAvoc procedure is the one that best fits the more reliable THA results.

- The proposed deck displacements and shear forces conversion method, which seeks the inclusion of the various directions of analysis in the simplified pushover procedures, leaded to quite good results in bridges with regular curvature in plan and which response is governed by its fundamental mode. However, it accuracy decreased when applied to bridges with stronger curvature in plan. Thus, its application is not recommended in the latter case.
- More work is clearly required, not only to continue the investigation of the effectiveness of the Eurocode's pushover analysis method, but also the feasibility of the "conversion technique" by applying them to curved bridges with a higher degree of irregularity and different dynamic characteristics

REFERENCES

[1] M. Ahmad, L. Mark, Horizontally Curved Bridges. W. Chen, L. Duan eds. *Bridge Engineering Handbook*, CRC Press, 1989.

[2] D. Williams, W. Godden, Seismic response of long curved bridge structures: Experimental model studies. *Earthquake Engineering and Structural Dynamics*, **7**, 107-129, 1979.

[3] W.S. Tseng, J. Penzien, Seismic response of long multiple-span highway bridges. *Earthquake Engineering and Structural Dynamics*, **4**, 25-48, 1975.

[4] N.J. Burdette, A.S. Elnashai, Effect of asynchronous earthquake motion on complex bridge. II: Results and implications on assessment. *Journal of Bridge Engineering*, **13**(2), 158-165, 2008.

[5] B. Song, J.S. Pan, Q. Liu, Study on critical angle to the seismic response of curved bridges based on pushover method. *Proceedings the 14th World Conference on Earthquake Engineering*, Beijing, China, October 12-17, 2008.

[6] J. Penzien, M. Watabe, Characteristics of 3-dimentional earthquake ground motions. *International Journal of Earthquake Engineering and Structural Dynamics*, **4**(3), 365-373, 1975.

[7] E. L. Wilison, M.R. Button, Three-dimension dynamic analysis for multi-component earthquake spectra. *Journal of Earthquake Engineering and Structural Dynamics*, **10**(3), 471-476, 1982.

[8] X.A. Gao, X.Y. Zhou, Multi-component seismic response analysis of curved bridges. *Special Structures*, **22**(1), 56-59, 2005.

[9] R. Pinho, C. Casarotti, S. Antoniou, A comparison of single-run pushover analysis techniques for seismic assessment of bridges. *Earthquake Engineering and Structural Dynamics*, **36**, 1347-1362, 2007.

[10] R. Pinho, R. Monteiro, C. Casarotti, R. Delgado, Assessment of continuous span bridges through nonlinear static procedures. *Earthquake Spectra*, **25**(1), 143-159, 2009.

[11] T. Isakovic, M. Fischinger, Applicability of pushover methods for the seismic analysis of single-column bent viaducts. *Earthquake Engineering and Structural Dynamics,* **37**(8), 1185-1202, 2008.

[12] T.S. Paraskeva, A.J. Kappos, A.G. Sextos, Extension of modal pushover analysis to seismic assessment of bridges. *Earthquake Engineering and Structural Dynamics*, **35**(10), 1269-1293, 2006.

[13] A. Mwafy, A. Elnashai, W.-H. Yen, Implications of design assumptions on capacity estimates and demand predictions of multispan curved bridges. *Journal of Bridge Engineering*, **12**(6), 710-726, 2007.

[14] M. ElGawady, W.F. Cofer, R.S.-Therany, *Seismic assessment of WSDOT bridges with prestressed hollow core piles, Part II*. Technical Report, Research Project T4120, Task 7, Washington State Transportation Center (TRAC), 2009.

[15] CEN (Comité Européen de Normalisation), *Eurocode 8: Design of structures for earthquake resistance – Part 1: General Rules, seismic actions and rules for building. EN 1998-1: 2004*, CEN, Brussels, 2004.

[16] CEN (Comité Européen de Normalisation), *Eurocode 8: Design of structures for earthquake resistance – Part 2: Bridges. EN 1998-2: 2005*, CEN, Brussels, 2005.

[17] P. Fajfar, P. Gaspersic, The N2 method for seismic damage analysis of RC buildings. Earthquake Engineering and Structural Dynamics, **25**(1), 31-46, 1996.

[18] CALTRANS, *Caltrans Seismic Design Criteria, Version 1.3*. California Department of Transportation, 2004.

[19] J. Guedes, *Seismic behaviour of reinforced concrete bridges. Modelling, numerical analysis and experimental assessment*. PhD Thesis, Faculty of Engineering of Porto University, 1997.

[20] A. Aviram, K.R. Mackie, B. Stojadinović, *Guidelines for nonlinear analysis of bridge structures in California*. PEER Report 2008/03, Pacific Earthquake Engineering Research Centre, 2008.

[21] J. Mander, M. Priestley, R. Park, Theoretical stress-strain model for confined concrete. *Journal of Structural Engineering,* **114**(8), 1804-1826, 1988.

[22] A. Torres, M. Araújo, R. Delgado, Seismic safety assessment of bridges using pushover analysis. *Proceedings of the Sísmica 2010 – 8th Congress of Seismology and Earthquake Engineering*, Aveiro, Portugal, October 20-23, 2010 (in Portuguese).

COMPDYN 2011
ECCOMAS Thematic Conference on
Computational Methods in Structural Dynamics and Earthquake Engineering
M. Papadrakakis, M. Fragiadakis , V. Plevris (eds.)
Corfu, Greece, 25-28 May 2011

NONLINEAR SEISMIC ANALYSIS AND FATIGUE-ACCUMULATED DAMAGE OF STEEL FRAMES WITH END-PLATE BOLTED CONNECTIONS

Mohammad Saranik[1]*, David Lenoir[1] and Louis Jézéquel[1]

[1]Laboratoire de Tribologie et Dynamique des Systèmes
École Centrale de Lyon, 36, Avenue Guy de Collongue, 69134, Écully Cedex, France
e-mail: mohammad.saranik@ec-lyon.fr

Keywords: End-Plate connections, seismic analysis, fatigue, damage seismic, nonlinear modes, hysteretic model.

Abstract. *Analyzing damage seismic in large and complex structures is one of the most challenging problems in steel moment-resisting frame with end-plate bolted connections. The existence of structural damage in an engineering structure leads to the modification of vibration modes and global eigenvalues are usually sensitive to the degree of local damage seismic in bolted connections.*

In this analytical study, a nonlinear time history analysis which takes into account nonlinear modes and frequencies was adopted. According to this approach, the nonlinear modes and frequencies can be determined by an iterative procedure which based on the method of equivalent linearization.

However, the damage analysis of seismic response requires the introduction of efficient structural models capable of describing actual behaviour and the application of an adequate algorithm. The paper presents a Fatigue Damage-Based Hysteretic FDBH model to evaluate the seismic performance of steel moment-resisting frames. The FDBH model is an evolutionary-degrading hysteretic model based on the low-cycle fatigue LCF damage index. Hence an algorithm was developed to characterize nonlinear behaviour in structures for the purpose of either damage identification of these structures.

1 INTRODUCTION

Steel moment-resisting frame structures often are used as part of the seismic force-resisting systems in buildings designed to resist earthquakes with substantial inelastic energy dissipation. End-plate bolted connections are one of the safest and most economical options for structural steel erection. It is therefore desirable to maintain the use and economy of bolted connections as an option for seismically loaded structures [3].

Beam-column connections in steel moment frames are proportioned and detailed to resist flexural, axial, and shearing actions that result as a building sways through multiple inelastic displacement cycles during strong earthquake ground shaking. However, such inelastic action causes fatigue damage and if long enough the cumulative effect may exhaust the ductile capacity leading to fracture [4].

However, analyzing damage seismic in large and complex structures is one of the most challenging problems in steel frames with end-plate connections. Many experimental approaches confirm the presence of changes in modal parameters such as natural frequencies, mode shapes because of the damaged elements of the structure [25]. The concept of nonlinear modes was introduced for the first time by Rosenberg in 1960 [24] and has a particular interest in the study of forced responses because there are close links between the properties of the modes (shape, number) and topology forced response curves of dynamical system. In general, to access the exact solutions of nonlinear system, complex nonlinear differential equations must be solved. The nonlinear systems do not generally have access to their exact solutions in the form. Then approached methods can be used such as Ritz-Galerkin method in which the nonlinear response of the system in the physical basis is approximated by a linear combination of the normal modes and the response of the system in modal coordinates [6].

Stupnicka [26] was assumed that the nonlinear normal coordinates are associated with nonlinear normal modes. Following, the principle of nonlinear modes is used by many researchers to analyze nonlinear systems with multiple degrees of freedom [25, 21]. Dynamic analysis by finite element FE is one means of estimating the changes in the modal parameters such as natural frequencies, mode shapes and modal damping. Global eigenvalues and nonlinear modes can be determined by an iterative procedure [25].

In this paper, a nonlinear time history analysis which considers the nonlinear modes and frequencies was adopted. According to this approach, the nonlinear modes and frequencies can be determined by an iterative procedure which based on the method of equivalent linearization [25].

Moreover, the damage analysis of seismic response requires the introduction of efficient structural models capable of describing actual behavior. The paper presents a Fatigue Damage-Based Hysteretic FDBH model to evaluate the seismic performance of steel moment-resisting frames. The FDBH model is a degrading model based on two damage indices. The plastic damage index (the first index) in this model is combined with a low-cycle fatigue LCF damage index (the second index). The model can be able to calculate the fatigue-accumulated damages of structures. Hence, an algorithm was developed to evaluate the nonlinear seismic behavior of steel moment frames. Finally, a two-story steel frame will be used as an example to illustrate the proposed technique.

2 STRUCTURAL DAMAGE OF STEEL MOMENT FRAMES

The problem of damage in steel moment frames, particularly due to seismic excitation is still a challenge for engineer and researchers to investigate [16]. To understand the damage in the bolted connection, the researchers distinguish between two phenomena of damage.

The first one is the damage due to the phenomena of elasto-plasticity behaviour of the bolted connection under repeated seismic efforts. The earthquake forces cause inelastic deformations in the components of bolted connection [22]. The accumulation of plastic strains is one phenomenon of cyclic plasticity. Inelastic deformation in the end plate, in the bolts and in flanges of beams and columns can change the mechanical properties of bolted connection like the strength and the stiffness [27].

The nonlinear behaviour is mainly resulted from gradual yielding of connection and can lead to hysteretic loops at a connection under repeated loading [17]. This important feature of nonlinear connections in ductile steel frames has the capability of dissipating excitation energy by an amount equal to the enclosed loop area to stabilize the response under cyclic loading.

To describe the nonlinear behaviour of semi-rigid connection like the end-plate connection, the relationship between the moment and the relative rotation angle is used. Richard and Abbott [14] propose to represent the moment-rotation relationship by four parameters. The Richard-Abbott model represents only the monotonically increasing loading portion of the $M-\theta$ curves. However, the unloading and reloading behaviour of the $M-\theta$ curves is also essential for nonlinear seismic analysis. The subject was extensively addressed in the literature ([9]) where the unloading and reloading parts of the $M-\theta$ curves are theoretically developed using the Masing rule (see Fig.1). The unloading and reloading behaviour of an end-plate connection based on the Richard-Abbott model is described as:

$$M = M_a - \frac{(R_0 - R_p).(\theta_a - \theta)}{\left(1 + \left|\frac{(R_0-R_p).(\theta_a-\theta)}{2M_0}\right|^{\gamma}\right)^{\frac{1}{\gamma}}} - R_p.(\theta_a - \theta) \tag{1}$$

$$R = \frac{(R_0 - R_p)}{\left(1 + \left|\frac{(R_0-R_p).(\theta_a-\theta)}{2M_0}\right|^{\gamma}\right)^{\frac{\gamma+1}{\gamma}}} + R_p \tag{2}$$

where M is the connection moment, θ is the relative rotation between the connecting elements, R_0 is the initial stiffness, R_p is the plastic stiffness, M_0 is the reference moment, and γ is the curve shape parameter. (M_a, θ_a) is the load reversal point as shown in Fig.1.

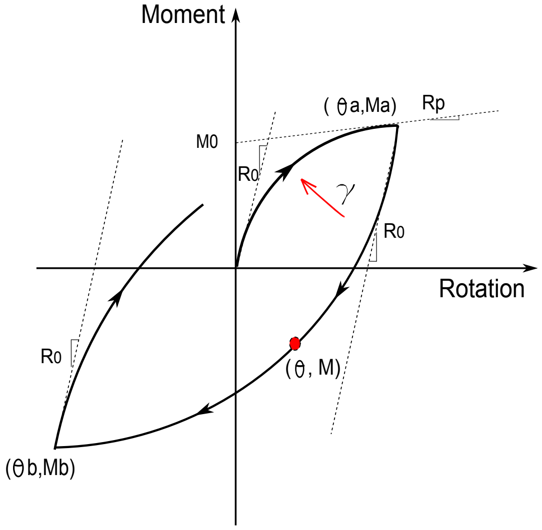

Figure 1: Nonlinear hysteretic model of end-plate connection.

The second phenomena of damage is the damage caused by low cycle fatigue. This type of fatigue causes progressive and cumulative damage in the stiffness of the bolted connection [5, 15]. Because of the stress concentration, cracks may appear in the welds which is characterised by the different stages of micro and macro crack propagation and final fracture [23]. Moreover, Bolts can loosen over time because micro-macro slip in the bolt-nut and the assembled plates [18]

Many mathematical relations have been proposed, particularly Manson-Coffin relation which describes linearly this function between the applied rotation and the number of cycles to rupture on a double-logarithmic scale [10, 11]. The information provided by the Rotation-Number of cycles curve is mainly used by engineers for the prediction of the lifetime and resistance of structures under repeated loading.

To evaluate damage more precisely, Miner's rule [11] is commonly used. According to this rule, applying a cycle n_x times with a stress amplitude which corresponds to a lifetime of N_x cycles is equivalent to consuming a portion n_x/Nf_x of the whole lifetime. This rule implies that rupture occurs when 100% of the lifetime is consumed. It describes also the phenomena of the cumulative linearity of fatigue damage if another application stress is employed. Though many models of damage have been proposed , Miner's rule is still widely used in the engineering field [15].

The fatigue problem occurs in the weaker parts of a structure and in the case of steel frames, as used in civil engineering, fatigue damage generally occurs at its connections. This indicates the importance of studying the resistance and fatigue damage of the beam-column connection in portal frame structures. Experimental tests for predicting the resistance of the beam-column connection have been published [19, 27] with the aim of identifying the key parameters of resistance of the beam-column connection. Some numerical studies have also been carried out using the finite element method to observe the behaviour of the fracture mechanism [20, 22].

The damage phenomena of elasto-plasticity behaviour and LCF due to cyclic loading may occur simultaneously. There is a strong interaction and a separation of the damage processes is impossible. Furthermore, each phenomenon alone is characterised by different aspects.

3 FBDH MODEL OF END-PLATE CONNECTION

In this study, The Richard-Abbott model has been modified to include degrading in the stiffness of the connection produced by the cumulative phenomenon of LCF. An evolutionary-degrading hysteretic model can be developed based on the LCF damage index D_n. In Richard-Abbott model, the cycle in $M - \theta$ curve begins with a secant stiffness R_0 and it changes in nonlinear way to R_p. But the connection loses part of its life in each cycle of excitation applied because of the cumulative phenomenon of LCF. For this reason the secant stiffness of the connection must be changed at the end of each cycle using an index of fatigue damage D_n to take into consideration the past lost life of the connection. The initial stiffness can be modified with the factor $(1 - D_n)$ that takes into account the effect of cumulative fatigue (see Fig.2). The following equations present the developed model for the moment-rotation relationship and the secant stiffness:

$$M^* = M_a - \frac{(R_0.(1-D_n) - R_p).(\theta_a - \theta)}{\left(1 + \left|\frac{(R_0.(1-D_n)-R_p).(\theta_a-\theta)}{2M_0}\right|^{\gamma}\right)^{\frac{1}{\gamma}}} - R_p.(\theta_a - \theta) \tag{3}$$

$$R^* = \frac{(R_0.(1-D_n) - R_p).(\theta_a - \theta)}{\left(1 + \left|\frac{(R_0.(1-D_n)-R_p).(\theta_a-\theta)}{2M_0}\right|^{\gamma}\right)^{\frac{\gamma+1}{\gamma}}} + R_p \tag{4}$$

where M^* is the degraded connection moment and R^* is the degraded secant stiffness.

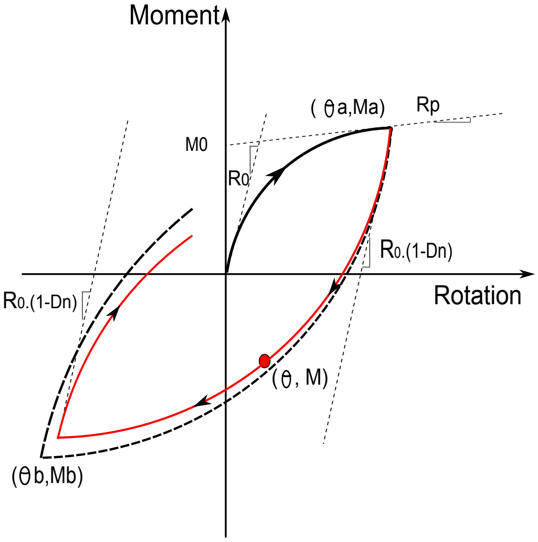

Figure 2: Fatigue Damage-Based Hysteretic model of end-plate connection.

It should be noted that the secant stiffness in Eq.(4) is modified and also with this idea, it is possible to combine the two indices by the equation:

$$D_p = 1 - \frac{R^*}{R_0} \tag{5}$$

where R_0 is the initial stiffness of the connection of connection and R^* is the tangent stiffness of the connection which depends on the index D_n.

To calculate the LCF damage index D_n, an analogous models based on the plastic connection rotation are used therein. A useful means of describing the LCF is expressed by Mander et al. [10] for a bolted connection. Thus using the well known Manson-Coffin relationship [7], the plastic rotation may be related to the number of cycles Nf by the following equation:

$$Nf = c.(\Delta\theta)^{-b} \tag{6}$$

where $\Delta\theta$ is the range of variation of rotation and c, b are parametres which depend on both the typology and the mechanical properties of the considered steel element. The parametres of Manson-Coffin relationship adopted in this study are ($c = 2.10^{-4}$) and ($b = 3$) [10].

Moreover, cumulative damage models should be used to assess deterioration and failure in structural components under arbitrary loading histories. Miner's rule is still the most used cumulative damage rule for its simplicity and efficiency in LCF region [11]. In the case of connection subjected to many cycles of rotation, Miner's rule is expressed by the following equation:

$$D_n = \sum_{x=1}^{X} \frac{n_x}{Nf_x} \tag{7}$$

where D_n is the LCF damage index, n_x is the numbre of applied cycles for a given rotation level x and Nf_x (see Eq.6) is the number of cycles to failure for roation level x according to the rotation-cycle curve given by Mander et al [10]. The rule is usually employed with the rainflow algorithm since it seems the best counting method [13].

The purpose of such model for the end-plate connection is to simulate inelastic response of structure under dynamic loading by combined damage indices.

4 NONLINEAR MODES AND FINITE ELEMENT

If a structure is properly modeled using finite element, structural damage manifests itself mathematically in the stiffness and mass matrices, and physically in its dynamic properties such as natural frequencies and mode shapes. Finite element methods (FEM) have become a standard technique for structural analyses for more than three decades. In this study, the damage in the structure is identified as a change in stiffness of the finite elements in the different beams of the FE model. The FE model of the structure is a two-dimensional model (see Fig.3) developed using the FE structural analysis program Structural Dynamics Toolbox (SDT) [28].

Consider a structure which is composed of a foundation r and a subset l of free-to-vibrate degree-of-freedom, shown in Fig.3. Ω is the interface between r and l. The equation of motion for a damped structure with N degrees-of-freedom (dof) is given as follows:

$$M\ddot{q} + \bar{C}\dot{q} + \bar{K}q = F(t) \tag{8}$$

where M, $\bar{C}$, $\bar{K}$ are respectively the mass, nonlinear damping and nonlinear stiffness matrix of the structure and $F(t)$ is the applied forces.

In this study, we adopt the hypothesis that the stiffness matrix of system is nonlinear and depends on the response of system and the nonlinear normal modes. In the case of seismic excitation applied to the foundation r, the only dynamic force of structure is the inertia force produced by basic movement. Consider the foundation of structure as immensely rigid. Therefore, the movement of the foundation r is defined as the rigid body displacements of structure.

The response of system in normal coordinate is defined as:

$$q(t) = \left\{ \begin{array}{c} q_l \\ q_r \end{array} \right\} \tag{9}$$

where q_l is the response of subset l and q_r is the response of foundation r.

The corresponding partitions of the mass, stifness matrix and the vector of external force are:

$$M = \begin{bmatrix} M_{ll} & M_{lr} \\ M_{rl} & M_{rr} \end{bmatrix}, \quad \bar{K}(q) = \begin{bmatrix} \bar{K}_{ll} & \bar{K}_{lr} \\ \bar{K}_{rl} & \bar{K}_{rr} \end{bmatrix}, \quad F(t) = \left\{ \begin{array}{c} F_l = 0 \\ F_r \end{array} \right\} \tag{10}$$

where F_r is the vector of reaction forces at the foundation r.

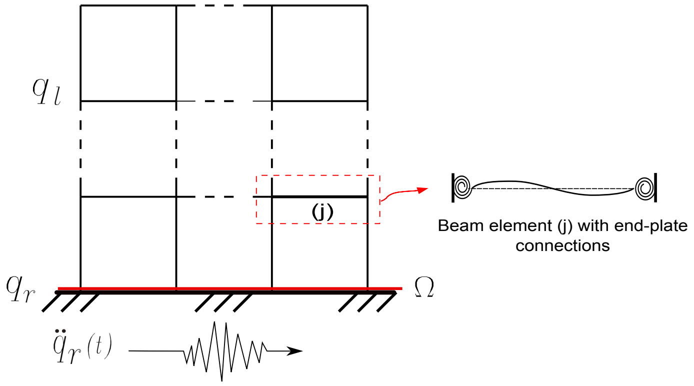

Figure 3: MDOF system

Rayleigh damping is used to represent damping in the structure. It can be written as:

$$\bar{C} = \alpha.M + \beta.\bar{K} \tag{11}$$

where α and β are the proportional constants.

According S. Setio [25], eigenvalues and eigenvectors for a nonlinear system cannot be obtained by solving the standard eigenvalue problem. As the solution of a nonlinear system depends heavily on the amplitude of motion, the frequencies and normal modes depend on the nonlinear modal amplitude. The introduction of the notion of nonlinear modes permits an extension of the method of linear modal synthesis to nonlinear cases in order to obtain the dynamical response of nonlinear multi-degree-of freedom systems.

The nonlinear normal modes and nonlinear frequencies must be calculated by an iterative procedure. In this paper, we adopted a procedure which is based on the method of equivalent linearization. For each time step of calculation, the stiffness and damping matrices of the system will be obtained which transform the nonlinear system into an equivalent linear system. The frequencies and nonlinear normal modes can then be calculated using a standard solution to the eigenvalues. A set of N nonlinear modes and frequencies are obtained according to their modal amplitudes.

Considering the FEM characteristic equation for the structure in Fig.3, the nonlinear modal problem can be written as following:

$$[\bar{K}(\eta_p, \bar{\varphi}_p(\eta_p)) - \bar{\omega}_p^2(\eta_p)M]\bar{\varphi}_p(\eta_p) = 0 \tag{12}$$

Where η_p, $\bar{\omega}_p(\eta_p)$, $\bar{\varphi}_p(\eta_p)$ are respectively the fixed structure response in modal coordinate, the nonlinear frequencies and the nonlinear normal modes.

S. Setio [25] assumes that the normal coordinates nonlinear are associated with nonlinear normal modes. In this case, the orthogonality property of eigenvectors used to treat the linear problem can be extended to nonlinear problems. This option allows to transform a system of N coupled equations of a system with N degrees of freedom in the physical basis of a set of N decoupled equations in the modal basis.

In the case of excitation at the base, the movement of the structure is the superposition of a movement training of rigid body and a movement relative to the base that can be expressed by the modes of structure fixed at the foundation r. Finally, the response of nonlinear system in normal coordinate can be obtained efficiently by superposition of modal response as follows:

$$q(t) = \Phi_r q_r + \bar{\varphi}_p(\eta_p)\eta_p \tag{13}$$

where Φ_r is rigid body modes matrix defined by the $r\ dof$ of the foundation.

The mode shapes matrix of a nonlinear structure fixed at the foundation is expressed as following:

$$\bar{\varphi}_p = \begin{bmatrix} \bar{\varphi}_{lp} \\ 0 \end{bmatrix} = \begin{bmatrix} \bar{x}_l^{(1)} & \bar{x}_l^{(2)} & \dots & \bar{x}_l^{(p)} \\ 0 & 0 & \dots & 0 \end{bmatrix} \tag{14}$$

After substituting the transformation of Eq.(13) in the equation of motion (see Eq.(8)), we obtain the following system (given the properties of rigid modes $\bar{K}\Phi_r = 0$, $\bar{C}\Phi_r = 0$):

$$\begin{bmatrix} \Phi_r^t M \Phi_r & \Phi_r^t M \varphi_p \\ \bar{\varphi}_p^t M \Phi_r & \bar{\varphi}_p^t M \bar{\varphi}_p \end{bmatrix} \begin{bmatrix} \ddot{q}_r \\ \ddot{\eta}_p \end{bmatrix} + \begin{bmatrix} 0 & 0 \\ 0 & \bar{\varphi}_p^t \bar{C} \bar{\varphi}_p \end{bmatrix} \begin{bmatrix} \dot{q}_r \\ \dot{\eta}_p \end{bmatrix} + \begin{bmatrix} 0 & 0 \\ 0 & \bar{\varphi}_p^t \bar{K} \bar{\varphi}_p \end{bmatrix} \begin{bmatrix} q_r \\ \eta_p \end{bmatrix} = \begin{Bmatrix} F_r \\ 0 \end{Bmatrix} \tag{15}$$

And also we can write:

$$\begin{bmatrix} m_{rr} & L_{pr}^t \\ L_{pr} & [m_p] \end{bmatrix} \begin{bmatrix} \ddot{q}_r \\ \ddot{\eta}_p \end{bmatrix} + \begin{bmatrix} 0 & 0 \\ 0 & [\bar{c}_p] \end{bmatrix} \begin{bmatrix} \dot{q}_r \\ \dot{\eta}_p \end{bmatrix} + \begin{bmatrix} 0 & 0 \\ 0 & [\bar{k}_p] \end{bmatrix} \begin{bmatrix} q_r \\ \eta_p \end{bmatrix} = \begin{Bmatrix} F_r \\ 0 \end{Bmatrix} \tag{16}$$

where:
$m_{rr} = \Phi_r^t M \Phi_r$ is the rigid body mass matix.
$\bar{L}_{pr} = \bar{\varphi}_p^t M \Phi_r$ is modal participation factors matrix.
$[\bar{m}_p] = \bar{\varphi}_p^t M \bar{\varphi}_p$ is the generalized mass matrix.
$[\bar{c}_p] = \bar{\varphi}_p^t \bar{C} \bar{\varphi}_p$ is the generalized damping matrix.
$[\bar{k}_p] = \bar{\varphi}_p^t \bar{K}(\eta_p, \bar{\varphi}_p(\eta_p)) \bar{\varphi}_p$ is the generalized stiffness matrix.

Eq.(16) can be expressed as the following developed form:

$$[\bar{m}_p]\ddot{\eta}_p + [\bar{c}_p]\dot{\eta}_p + [\bar{k}_p]\eta_p = -\bar{L}_{pr}\ddot{q}_r \tag{17}$$

$$F_r = m_{rr}\ddot{q}_r + \bar{L}_{pr}^t \ddot{\eta}_p \tag{18}$$

Modals movement equations of the excited structure are given by Eq.(17) where η_p is the fixed structure response in modal coordinates. The system is subjected to modal inertia forces $\bar{f}_p = -\bar{L}_{pr}.\ddot{q}_r$. The equation of movement for mode i has the following form:

$$\bar{m}_i \ddot{\eta}_i + \bar{c}_i \dot{\eta}_i + \bar{k}_i \eta_i = -\bar{L}_{ir}\ddot{q}_r \tag{19}$$

where $\bar{m}_i$, $\bar{c}_i$, $\bar{k}_i$, are respectively the modal mass, nonlinear modal damping and nonlinear modal stiffness and they can be calculated by the following equations:

$$\begin{aligned} \bar{m}_i &= \bar{x}^{(i)t} M \bar{x}^{(i)} \\ \bar{c}_i &= \bar{x}^{(i)t} \bar{C} \bar{x}^{(i)} \\ \bar{k}_i &= \bar{x}^{(i)t} \bar{K}(\eta_p, \bar{\varphi}_p(\eta_p)) \bar{x}^{(i)} \end{aligned} \tag{20}$$

In Eq.(19), $\bar{L}_{ir} = \bar{x}^{(i)t} M \Phi_r$ is the i^{th} row of the matrix $\bar{L}_{pr}$ and $-\bar{L}_{ir}.\ddot{q}_r = \bar{f}_i(t)$ is generalized force of the i^{th} mode. After solving the modal equations of motion (see Eq.(17)), the reactions at the base and the displacement of the system can be calculated.

To calculate the response of dynamical system, such as the system given by Eq.(19), which subjected to arbitrary seismic loads, temporal integration methods are considered the only methods applicable to nonlinear systems with many degrees of freedom. In this study, the Runge-Kutta method is adopted for the numerical solution of differential equations.

The incremental equilibrium equation of the dynamic system during the time Δt_n can be writhed as following:

$$\bar{m}_i.\Delta\ddot{\eta}_i + \bar{c}_{n,i}.\Delta\dot{\eta}_i + \bar{k}_{n,i}.\Delta\eta_i = \Delta\bar{f}_i(t) \tag{21}$$

where $\bar{c}_{(n,i)}$, $\bar{k}_{(n,i)}$ are the tangent properties defined at the time t_n.

In general, $\eta_{(n,i)}$, $\dot{\eta}_{(n,i)}$, $\ddot{\eta}_{(n,i)}$ at time t_n is known and Range-Kutta algorithm can be used to calculate $\eta_{(n+1,i)}$, $\dot{\eta}_{(n+1,i)}$, $\ddot{\eta}_{(n+1,i)}$ at time t_{n+1}. Once the modal displacements are obtained, the relative response of system in normal coordinates at the time t_{n+1} can be calculated by Eq.(13) as follows:

$$q_{n+1} = \sum_i^N \bar{x}^{(i)}.\eta_{n+1,i} \tag{22}$$

The stiffness matrix of system should be recalculated taking consideration nonlinear behaviour of connections. For this reason, the calculated displacements are used to calculate the internal forces of elements. From Eq.(22), the rotations of bolted connections are known and using the hysteretic model represented by Eqs.(1), (2) and (5), the connection moment $M_{j(n+1)}$, the tangent stiffness $R_{j(n+1)}$, the LCF damage index $D_{nj(n+1)}$ and the plastic damage index $D_{p_{j(n+1)}}$ of each bolted connection of the beam element (j) will be calculated at the time t_{n+1}.

A correction matrix Cr proposed by Monfortoon and Wu ([12, 8]) is adopted and it is used to modify each matrix beam of the system at the time t_{n+1}. It can take account of the flexibility of semi-rigid connections. The correction matrix Cr for the element (j) at the time t_{n+1} is presented as follows:

$$Cr_{j(n+1)} = \sum_{q} \sum_{s} c_{qs_{j(n+1)}} \text{ with } c_{qs_{j(n+1)}} = f(D_{p_{j,l(n+1)}}, D_{p_{j,r(n+1)}}, L_b) \tag{23}$$

where $D_{p_{j,l(n+1)}}$, $D_{p_{j,r(n+1)}}$ are the plastic damage indices of the connections (left l and right r, respectively) for the element (j) at the time t_{n+1}. L_b is the length of the beam element (j). The values of c_{qs} are represented by R. Hasan et al. [8] for a beam element with bolted connection at its ends.

The nonlinear matrix for the beam element (j) at the time t_{n+1} can be calculated using the correction matrix with the following equation:

$$\bar{k}_{j(n+1)} = k_j . Cr_{j(n+1)} \tag{24}$$

where k_j the standard elastic stiffness matrix for the beam element (j) [8].

The matrix $\bar{K}$ can be assembled by the stiffness matrices of each beam and column element in the system with the following equation:

$$\bar{K}_{(n+1)} = \sum_{e=1}^{n_e} \bar{k}_{e(n+1)} \tag{25}$$

where n_e is the total number of elements in the MDOF system and members are generically identified by index e.

Because we do not have nonlinear behavior in the columns, the stiffness matrix of each column element $\bar{k}_e$ is equal to the standard elastic stiffness matrix for the column element k_e.

5 ALGORITHM OF ANALYSIS

An algorithm was developed to evaluate the seismic performance of steel moment resisting frames with end-plate connections (see Fig.4). Using this algorithm, the influence of the LCF damage on the behaviour of end-plate connection is studied. To evaluate the accumulation of LCF damage, two phases of analysis have been conducted in this algorithm.

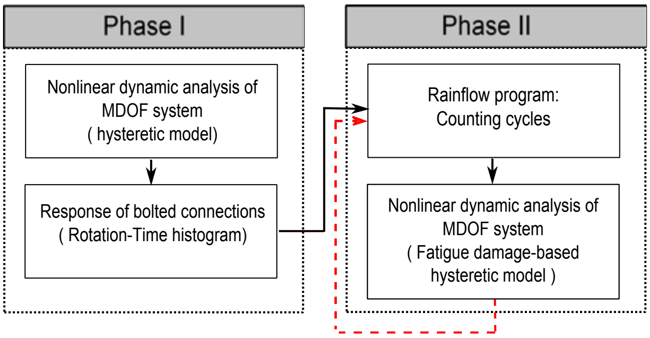

Figure 4: Flowcharte of the proposed algorithm

The objective of the first one is to prepare a nonlinear modal analysis of the structure using the hysteretic model. This phase is important to prepare the necessary data for the second phase. In this phase, the rotation-time histograms will be obtained. These histograms are necessary to prepare an analysis of LCF damage.

In the second phase, a cycle counting program (rainflow program) will be used through the Matlab toolbox offered by A. Nieslony [13]. This program analyzes the histograms to find the number of cycles counted, the corresponding rotational levels and the corresponding times. A FDBH model will be used, following in the second phase, to prepare a nonlinear modal analysis of the structure and to combine the damage caused by elasto-plastic behaviour and LCF.

In both phases, a modal analysis based on finite element code of SDT Toolbox is performed to find the dynamic response of the steel frame subjected to seismic excitation.

6 NUMERICAL EXAMPLE

In order to illustrate the application of the proposed method, a two-story steel frame is presented. The frame has end-plate bolted connections and fixed supports. The geometric, sectional properties and other pertinent information of the frames are given in Fig.5.

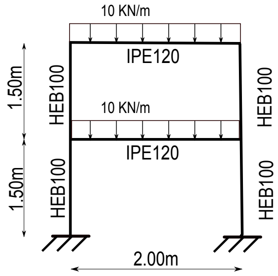

Figure 5: Two-story steel frame structure.

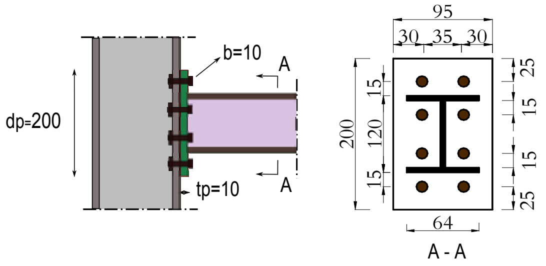

Figure 6: Parameters of the end-plate connection (in mm).

The cross sections are selected from the European section profiles. The important properties of steel used in this study are summarized in Table 1. The end-plate connection was designed for the required strength using yield-line theory.

Modulus of elasticity E (GPa)	Yield stress f_y (MPa)	Material density ρ (kg/m^3)
210	280	7850

Table 1: Properties of steel materials.

The connection parameters are represented in Fig.6 and they are set by the code EC3 to ensure a good ductile behaviour of the connection. The structure is subjected to gravity loads of the dead load plus a 10 (KN/m) live load, according to Fig.5, followed by an earthquake with a peak ground acceleration of $\ddot{q}$=0.1 g, 0.2 g and 0.36 g. An earthquake record (normalized El Centro) is used as ground motion input. A damping ratio of ξ= 0.05 is considered throughout.

The nonlinear behaviour and design limit states of the elements were modelled in accordance with the models presented above and the calculations were carried out by the code SDT Toolbox on Matlab 7.6 (R2008a).

The moment capacity of a connection depends on the strength of the individual connection elements. Various investigations have shown that the connection will begin to lose its ability to

Initial stiffness R_0 $(KN.m/rad)$	Maximum moment M_u (MPa)	Yielding moment M_y (MPa)
1.528×10^4	23.86	15.91

Table 2: Mechanical properties of the end-plate connection.

sustain further loading when one or more of the following failure modes occur: bolt failure (in tension), end plat plastic mechanism, beam and column flanges buckling. The lowest values of the moment corresponding to these failure modes will present the ultimate connection moment M_u. The equations used to evaluate M_u were adopted from EC3. The yielding moment of the connection can be evaluated as $M_y = 2/3M_u$.

Initial rotational stiffness of a connection is important and essential for the analysis semi-rigid frames. The rotational stiffness is directly related to the stiffness of each element in the connection. To evaluate the initial stiffness, the equations of EC3 are used. Based on the parameters of the connection (see Fig.6), the mechanical properties of the connection can be calculated (see Table 2). The plastic stiffness R_p is considered to be 0.

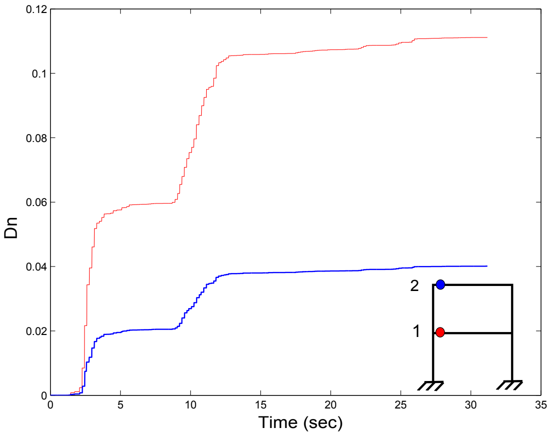

Figure 7: Low-cycle fatigue damage index of the connections (1), (2) for $\ddot{q}$=0.2 g considering the linear modes.

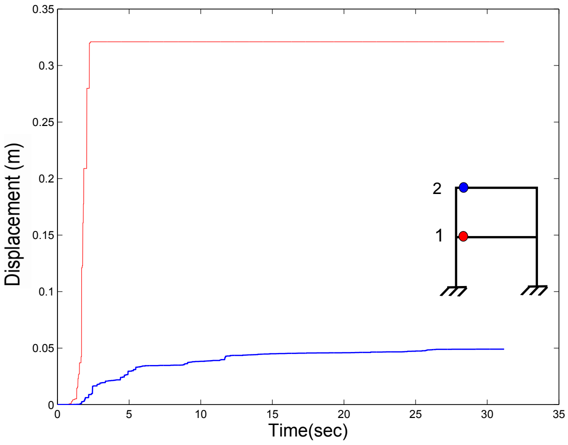

Figure 8: Low-cycle fatigue damage index of the connections (1), (2) for $\ddot{q}$=0.2 g considering the non-linear modes.

Two types of failure criteria are considered. The first one is the rotation of the connection and it must not exceed the maximum value given by the EC3 code. The maximum rotation of the connection in this study is $\theta_{max} = 0.025d_c/d_b$, according to the EC3. The second is the index D_n and it must not exceed the value of (1). If both criteria are not met, the connection will consider as a hinge. The index D_p can take value (1) but must not exceed it. In the other hand, the rigidity R_0 will be 0.

The LCF damage index of the connections (1), (2) for $\ddot{q}$=0.2 g is traced with considering and non-considering the nonlinear modes (see Figs.7 and 8). The cumulative index D_n reaches a value of 11% in the case of linear modes and it increases to a value of 32% in the case of nonlinear modes because of the modes and frequencies changes (see Figs.9).

To show the influence of the nonlinear mode in the behavior of the frame, the natural frequency of the structure as a function of time for the mode $i = 1$ is traced in Figs.9. The results are plotted for three levels of seismic excitation ($\ddot{q} = 0.1$ g, 0.2 g and 0.36 g). In the case $\ddot{q} = 0.1$ g, we note that the frequency remains constant over time (see Fig.9-a). This is because

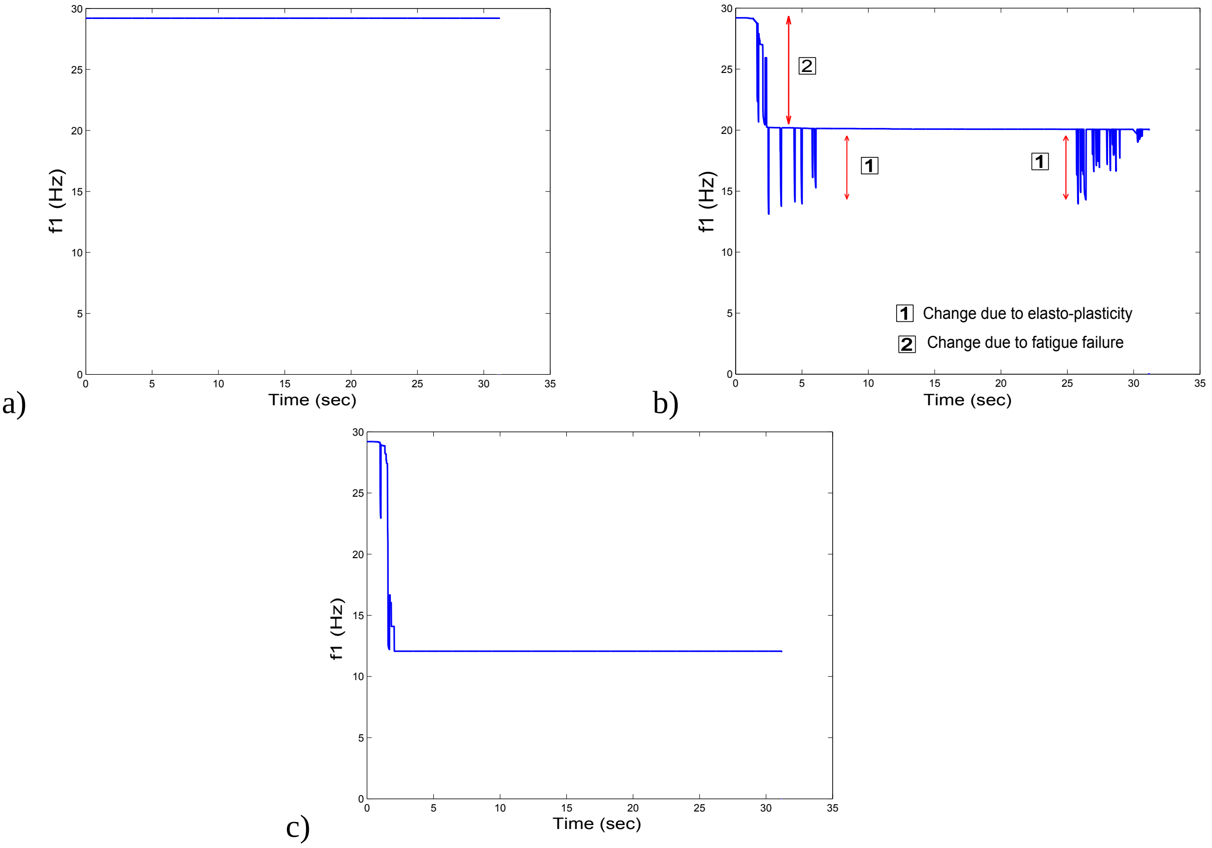

Figure 9: Natural frequency of the structure as a function of time for the mode $i = 1$ and for three cases: (a) $\ddot{q} = 0.1$ g, (b) $\ddot{q} = 0.2$ g and (c) $\ddot{q} = 0.36$ g.

the applied excitation is not very strong and it does not generate damage in modes. For the case $\ddot{q} = 0.2$ g, we can notice that two kinds of changes in the frequency of the frame (see Fig.9-b). The first is a drop in the value of frequency because the bolted connections in the frame are subjected to significant damage due to fatigue damage. The second is a cyclical change due to cyclic elasto-plastic behaviour of bolted connection into the frame.

The cyclical changes are less visible in the case of seismic excitation $\ddot{q} = 0.36$ g (see Fig.9-c). Because bolted connections (1), (2) are completely damaged and rotations reach the limit of ruin. It can also be seen that a greater drop in frequency is happened in this case.

It can be seen from Figs.9 that the analysis with nonlinear mode causes more damages in the system responses that were not taken into consideration before with the linear mode (see Figs.11 and 10).

7 CONCLUSIONS

This paper uses recent concepts in the structural damage evaluation to analyze structures under earthquake. An algorithm to study the influence of the LCF damage on the behavior of end-plate connection is used in this article and a FDBH model is adopted.

The results of this study confirm the presence of changes in modal parameters such as natural frequencies, mode shapes because of the damaged elements of the structure. Further, a drop in frequency due to the development of plastic hinges during the seismic excitation is observed in the proposed steel frame example.

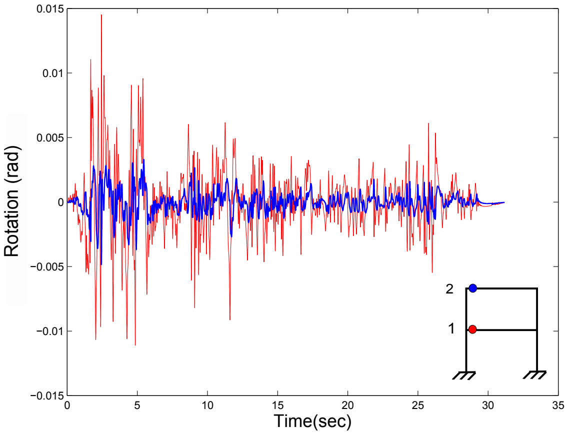

Figure 10: Rotation responses of the connections (1), (2) for $\ddot{q}$=0.2 g considering the nonlinear modes.

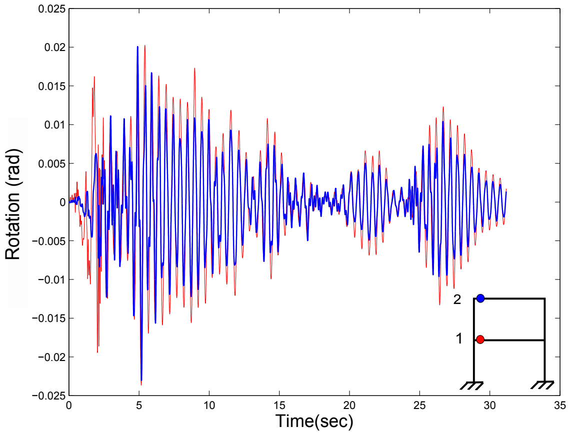

Figure 11: Rotation responses of the connections (1), (2) for $\ddot{q}$=0.36 g considering the nonlinear modes.

Moreover, the paper presents a contribution to the solution of nonlinear steel frame structures subjected to seismic excitation by the method of nonlinear modal synthesis. The introduction of the concept of nonlinear mode leads to the possibility of extending the most procedures of the method of linear modal synthesis to nonlinear cases, which involves considerable simplification in the context of the analysis of nonlinear steel frame structures.

REFERENCES

[1] Eurocode 3 (EC3), *Design of steel structures*, Part 1-1: General rules and rules for buildings, prEN 1993-1-1. 2004.

[2] Eurocode 8 (EC8), *Common unified rules for structures in seismic regions*, EN 1998-1:2004.

[3] FEMA 350, *Recommended seismic design criteria for new steel moment-frame buildings*, Washington (DC): Federal Emergency Management Agency; 2000.

[4] L. Calado, C. Castiglioni, Low cycle fatigue testing of semi-rigid beam-to-column connections, *Dans Connections in Steel Structures III*, 371–380. 1996.

[5] S.D. Campbell, R.M. Richard, J.E. Partridge, Steel moment frame damage predictions using low-cycle fatigue. *Presented at the 14th World Conference on Earthquake Engineering*, October 12-17, 2008, Beijing, China.

[6] A.K. Chopra, R.K. Goel, A modal pushover analysis procedure for estimating seismic demands for buildings. *Earthquake Engineering and Structural Dynamics*, **31(3)**, 561–582, 2002.

[7] P.P. Gillis, Manson-coffin fatigue. *Acta Metallurgica*, **14(12)**, 1673–1676, 1966.

[8] R. Hasan, L. Xu, D.E. Grierson, Push-over analysis for performance-based seismic design. *Computers and Structures*, **80(31)**, 2483–2493, 2002.

[9] J. Huh, A. Haldar, Seismic reliability of nonlinear frames with PR connections using systematic RSM. *Probabilistic Engineering Mechanics*, **17(2)**, 177–190, 2002.

[10] John B. Mander, Stuart S. Chen, Gokhan Pekcan, Low-cycle fatigue behavior of semi-rigid top-and-seat angle connections. *AISC Engineering Journal*, **31(3)**, 111–124, 1994.

[11] M.A. Miner, Cumulative damage in fatigue. *Journal of Applied Mechanics*, **12**(Trans. ASME Vol. 67), A159–A164, 1945.

[12] GR. Monfortoon, TS. Wu, Matrix analysis of semi-rigidly connected steel frames. *Journal of Structural Engineering ASCE*, **89(6)**, 13-42, 1963.

[13] A. Nieslony, E. Macha, Spectral method in multiaxial random fatigue. *Lecture Notes in Applied and Computational Mechanics*, Vol. 33, pp. 8, 2007.

[14] RM. Richardr, BJ. Abbott, Versatile elasticplastic stress-strain formula. *ASCE Journal of the Engineering Mechanics Division*, **101**(EM4), 511-515, 1975.

[15] I. Tani, D. Lenoir, L. Jézéquel, Effect of junction stiffness degradation due to fatigue damage of metallic structures. *Engineering Structures*, **27(11)**, 1677–1688, 2005.

[16] G.L. Dimitrios, H. Krawinkler, A.S. Whittaker, Collapse assessment of a 4–story steel moment resisting frame. *Conference on Computational Methods in Structural Dynamics and Earthquake Engineering*; COMPDYN 2009.

[17] Oreste S. Bursi, Fabio Ferrario, Vigilio Fontanari, Non-linear analysis of the low-cycle fracture behaviour of isolated tee stub connections. *Computers and Structures*, **80(27-30)**, 2333–2360, 2002.

[18] W. Chen, X. Deng, Structural damping caused by micro-slip along frictional interfaces. *International Journal of Mechanical Sciences*, **47(8)**, 1191–1211, 2005.

[19] E.P. Popov, S.M. Takhirov, Bolted large steel beam-to-column connection part 1: experimental study. *Engineering Structures*, **24**, 1523-1534, 2002.

[20] Christopher M. Foley, Sriramulu Vinnakota, Toward design office moment-rotation curves for end-plate beam-to-column connections. *Journal of Constructional Steel Research*, **35(2)**, 217–253, 1995.

[21] C. Gibert, Fitting measured frequency response using non-linear modes. *Mechanical Systems and Signal Processing*, **17(1)**, 211–218, 2003.

[22] A.R. Kukreti, P. Biswas, Finite element analysis to predict the cyclic hysteretic behavior and failure of end-plate connections. *Computers and Structures*, **65(1)**, 127–147, 1997.

[23] N.G. Pai, D.P. Hess, Experimental study of loosening of threaded fasteners due to dynamic shear loads. *Journal of Sound and Vibration*, **253(3)**, 585–602, 2002.

[24] R.M. Rosenberg, On nonlinear vibration of systems with many degrees of freedom. *Journal of Sound and Vibration*, **Mech.(9)**, 155–242, 1966.

[25] S. Setio, H.D. Setio, L. Jézéquel, A method of non-linear modal identification from frequency response tests. *Journal of Sound and Vibration*, **158(3)**, 497–515, 1992.

[26] W. Szemplinska-Stupnicka, The modified single mode method in the investigations of the resonant vibrations of non-linear systems. *Journal of Sound and Vibration*, **63(4)**, 475–489, 1979.

[27] K.C. Tsai, Shiun Wu, E.P. Popov, Cyclic performance of steel beam-column moment joints. *Engineering Structures*, **17(8)**, 596–602, 1995.

[28] E. BALMES, *Structural Dynamics Toolbox SDT 6.2, for use with matlab*, Software.

COMPDYN 2011
III ECCOMAS Thematic Conference on
Computational Methods in Structural Dynamics and Earthquake Engineering
M. Papadrakakis, M. Fragiadakis, V. Plevris (eds.)
Corfu, Greece, 25–28 May 2011

NEW METHOD FOR PROVIDING FAVORABLE SEISMIC PERFORMANCE IN PANEL ZONE REGIONS OF MOMENT RESISTING CONNECTIONS OF BEAMS TO FLANGED CRUCIFORM COLUMN SECTION

Rasoul Mirghaderi[1], Mohammad Motallebi[2]

[1] Assistant Professor, School of Civil Engineering, University College of Engineering,
University of Tehran, Tehran, Iran
e-mail: rmirghaderi@ut.ac.ir

[2] Graduate Student, School of Civil Engineering, University College of Engineering,
University of Tehran, Tehran, Iran
mmotallebi@ut.ac.ir

Keywords: Flanged Cruciform Column, Moment Resisting Connection, Panel Zone Region, Inclined Vertical Plates, Accordion Load Path.

Abstract. *It is common in structural design to use separate load resisting system in each principal direction of the buildings. In these systems, columns which are located in the intersection of two perpendicular axes play a significant role in resisting gravitational loads as well as seismic demands in both directions. In seismic design, it is necessary to use practically similar sections for columns in both axes.*

Flanged cruciform sections, having relatively similar behavior about both principal axes, seem to be a proper choice for this purpose. They have apparently much simpler fabrication process in beam-column joint regions than the closed box sections. Since having two perpendicular webs, usage of common doublers plates leads to discontinuation of load paths and is not applicable. On the other hand, the local increase in the web thickness is not possible in the cruciform sections built using hot rolled sections. Therefore, it is necessary to consider an alternative path to provide a suitable performance in the beam column joints.

In this paper, by means of nonlinear numerical analysis, influences of connection details on the behavior of flanged cruciform column are studied. Since dynamic behavior of flanged cruciform column is depended on the connection behavior, in order to detect column behavior, it is subjected to monotonic and cyclic lateral displacement loading. Analysis shows connection details play a significant role in moment distribution of column parts. In addition, a new load path is suggested to provide a proper way to transfer panel zone's shear force and its effectiveness in improving behavior of flanged cruciform column is presented.

1 INTRODUCTION

1.1 Column sections

It is common in structural design to use separate load resisting system in each principal direction of the buildings. In these systems, columns which are located in the intersection of two perpendicular axes play a significant role in resisting gravitational loads as well as seismic demands in both directions. In seismic design, it is necessary to use practically similar sections for columns in both axes.

W sections are not suitable since having one strong principle axis and a weak one. Their strength and stiffness about their weak principal axis is low. In addition, design and application of seismic connection to this weak axis is a complicated issue.

Box sections, although having two similar high bending and torsional strength as well as high stiffness, are not supposed as an ideal choice for above mentioned performance, due to difficulties in continuity plate fabrication and out of plane action of the column flanges in beam-column joint regions.

Flanged cruciform sections, having relatively similar behavior about both principal axes, seem to be a proper choice for this purpose. They have apparently much simpler fabrication process in beam-column joint regions than the closed box sections.

In the following the characteristics and weaknesses of flanged cruciform sections are reviewed.

1.2 Fabrication of flanged cruciform columns

This section consist of two W sections where one of these sections is cut into two pieces symmetrically at the centre line of the web along its longitudinal axis, and connected to the mid-depth of other section with welding. Fabrication procedure for this section is complicated because enough space is needed for welding of two W shape sections. Most of W12 and W14 sections are not suitable for making flanged cruciform sections due to their geometric dimensions.

1.3 Axial capacity and lateral stiffness of flanged cruciform columns

The axial capacity of column is usually calculated based on the area and compression resistance. The compression resistance depends on the effective length of the column and the radius of gyration of column section. Since this section has not minor axis and behaves similarly in both principal axes, there is no reduction in axial capacity of this columns due to buckling about minor axis.

Tahir et al, conducted experimental program to study axial capacity of these sections. They demonstrated that the behavior of the flanged cruciform column made up uniform beam sections is similar to behavior of uniform beam section with axial load bending on the major axis. Due to high lateral stiffness of this section, they suggested it for using in unbraced frames to increase stiffness of the frame and decrease sway of frame [1].

1.4 Bending capacity of flanged cruciform columns

This section consists of two W sections that are perpendicular to each other. In bending about principal axis of flanged cruciform sections, one of them bends about its major axis and other bends about its minor axis. In the analysis and design of this section ,it is a assumed that plane section of the column remains plane, so moment distribution in each part of column section follows proportionally the weak axis stiffness to strong axis stiffness ratio of W sections.

1.5 Connection of flanged cruciform columns

In order to use of flexure capacity of both perpendicular W sections at the same time, the connection of beam to columns must have enough strength and stiffness to constrain two W sections together. As the strong axis connections are investigated extensively, prequalified connections for seismic moment frames are represented in AISC prequalified connections [2, 3].

This standard mentions that the behavior of the prequalified connections with flanged cruciform columns is expected to be similar to that of a rolled wide-flange column and the behavior of the assemblies employing this section would be acceptable, as long as such column sections meet the limitations for I-shaped sections and connection assemblies are designed to ensure that most inelastic behavior occurred within the beam as opposed to the column [2].

It is necessary to study the connection characteristics needed to push two parts of section to behave in the same manner in order to whole section plane remains plane.

1.6 Panel zone regions of flanged cruciform columns

Since having two perpendicular webs, usage of the common doublers plates in both directions leads to discontinuity of load paths and is not applicable. On the other hand, the local increase in the web thickness is not possible in the flanged cruciform sections with hot rolled sections.

Therefore, in order to reduce the shear force demands on the column’s web, it is necessary to consider an alternative path that can transfer the panel zone shear force and provide a suitable performance in the beam column joints.

1.7 Objective

In this paper several moment resisting connections of beams to flanged cruciform column are developed to study their seismic performance. The design of the connection details is based on AISC prequalified procedure. A model of each connection was created and analyzed, using the finite element analysis program ABAQUS and their behavior to monotonic and cyclic lateral loading was studied. A new load path is suggested to provide a proper way to transfer panel zone shear force and its effectiveness is evaluated. In addition, moment resisting participation of each part of column section as well as shear resisting are studied.

2 DESIGN OF MOMENT CONNECTION DETAILS

Three separate specimens are adopted to examine performance of flanged cruciform column. First specimen (specimen 1) is without continuity plates, the second one (specimen 2) includes continuity plates and the third specimen (specimen 3) including continuity plates and inclined vertical plates. The details of the moment connection for specimen 1, specimen 2 and specimen 3 are shown in Figures 1(a),(b) and (c) respectively.

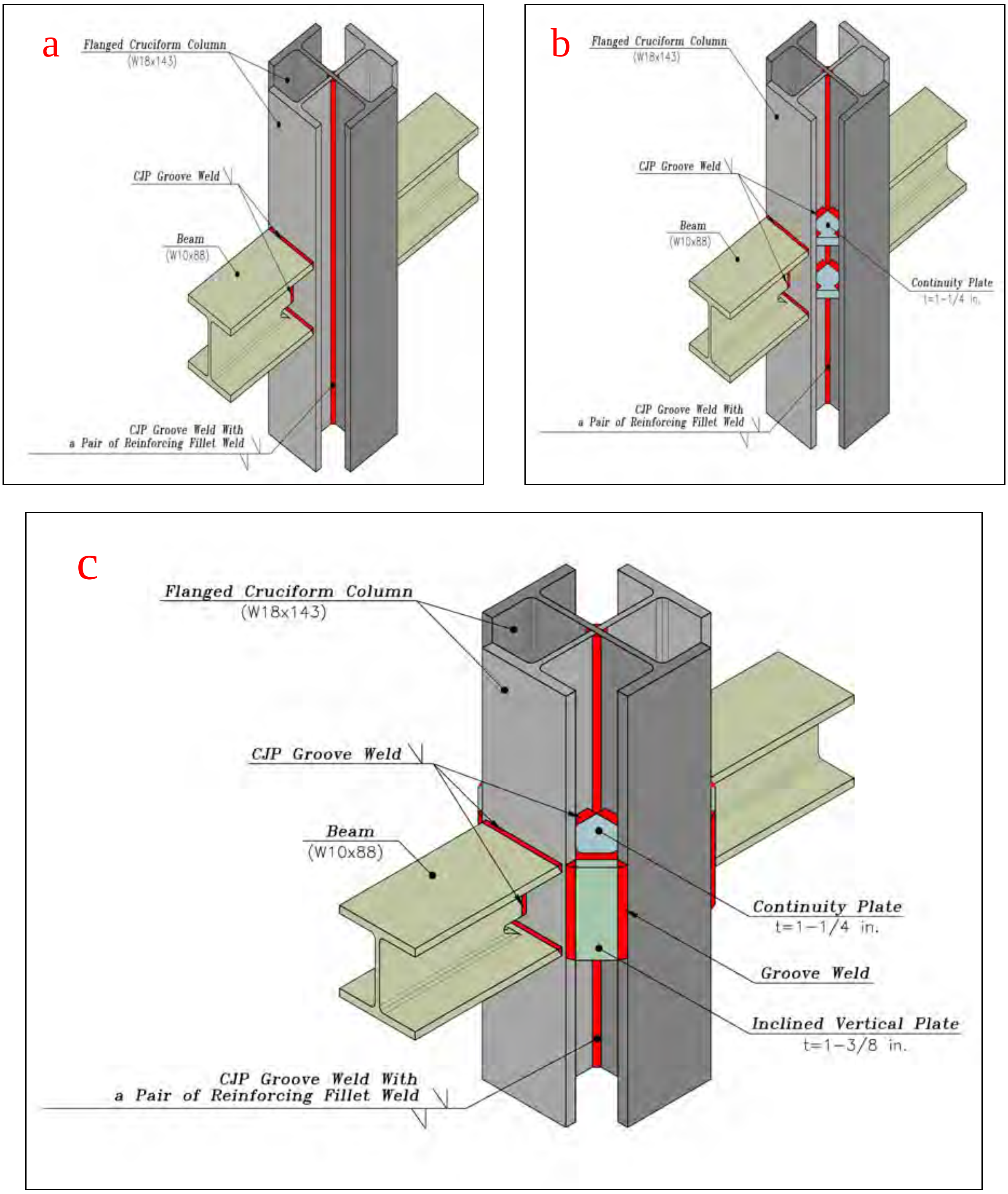

Figure 1. The details of the moment connection: (a) for specimen 1, (b) for specimen 2 and (c) for specimen 3.

As shown in Figure 1(c), inclined vertical plates with similar thickness of column flange plates, connected to flange edges of two perpendicular W sections in the panel zone region, provide a proper additional path to transfer panel zone's shear forces. Also these inclined vertical plates are welded to continuity plates. In order to show details of this specimen clearer, the details of the moment connection of specimen 3 in panel zone region are shown in Figure 2(a) and (b).

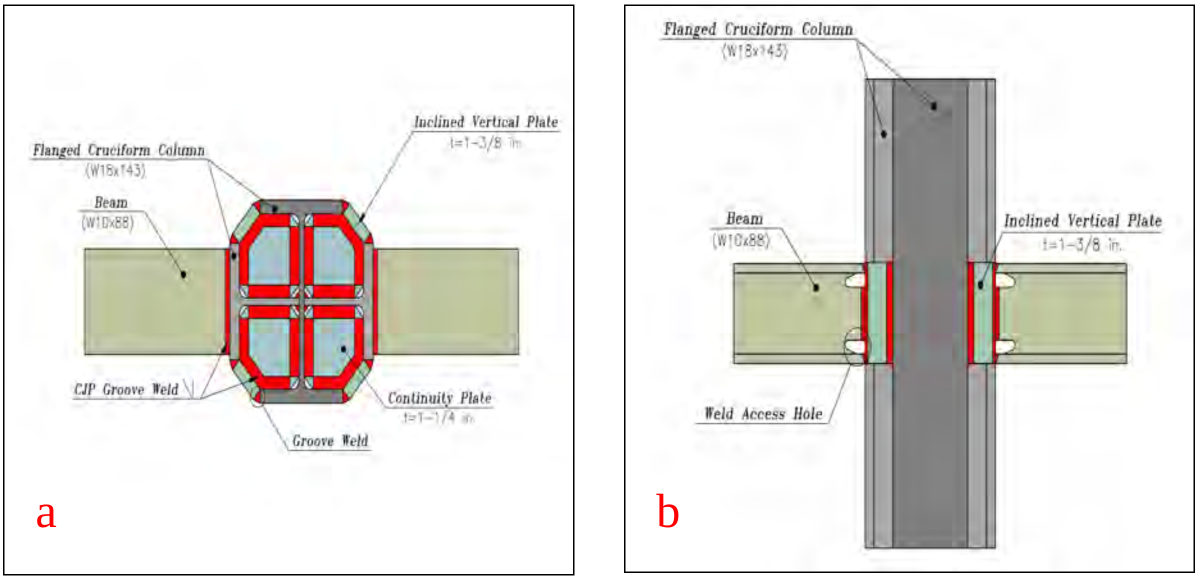

Figure 2. (a) and (b): The details of specimen 3 in panel zone region.

The specimens consist of cruciform interior connection subassemblies with beams attached to the column opposite faces. The subassemblies are extracted from interior joints of moment frames. The height of column is 160 in. and two beams 120 in. long framed into both face of column at mid height. In moment frames, deflected under lateral load, the inflection points are formed near the mid-span of beams and mid-height of columns. By this assumption, the inflection points of moment frames are considered to be the ends of subassembly beams and columns with hinged supports. The column base is supported by a hinged connection and the beam ends were supported by adjustable ones with lateral movement capability to provide the roller boundary condition. The column top end is subjected to horizontal displacement-controlled loading.

In order to avoid global and local instabilities, lateral bracing of beams and column are provided as requirements of AISC seismic provisions [4].

The flanged cruciform column consists of two W18*143 section which are suitable sections to be fabricated as flanged cruciform section. The beams in opposite side of the column are W10*88 sections. The geometric properties of the sections are shown in Table 1.

Section	d (in.)	b_f (in.)	t_w (in.)	t_f (in.)	I_x (in.^{4})	I_y (in.^{4})	Z_x (in.^{3})	Z_y (in.^{3})
W18*143	19.5	11.2	0.73	1.32	2750	311	322	85.4
W10*88	10.8	10.3	0.605	0.99	534	179	113	53.1
Flanged cruciform column(W18*143)	19.5	11.2	0.73	1.32	3061	3061	407.4	407.4

Table 1: Geometric properties of sections

To calculate geometric properties of flanged cruciform section, it is assumed that plane section of column remains plane so the second moment of area for flanged cruciform column as well as plastic section modulus are calculated by the summation of properties of area of the x–x axis and y–y axis of the corresponding w sections.

According to the AISC seismic provisions, width-thickness ratios for the flanges and web of the beam and column conform to the requirement of the seismically compact elements [4].

Material properties of all elements in the specimens are according to ASTM-A36 and showed in Table 2 [4, 5].

F_y(ksi)	F_u(ksi)	E(ksi)	ν	R_y
36	58	29000	0.3	1.5

Table 2: Material properties of all elements

In accordance with the requirements of AISC prequalified connection, the web of the tee-shaped sections shall be welded to the web of the continuous I-shaped section with CJP groove welds with a pair of reinforcing fillet welds within a zone extending from 12 in. above the upper beam flange to 12 in. below the lower beam flange [2, 3].

Welded Unreinforced flange–welded web (WUF–W) moment connections are selected to connect the beams to the column faces. In this type of connection, Beam flanges and beam web are connected to column flanges using complete-joint penetration (CJP) groove welds. These welds conform to the requirements for demand critical welds in the AISC seismic provisions. The plastic hinge location is taken to be at the face of the column [3].

The probable maximum moment at the plastic hinge, M_{pr}, is calculated in accordance with AISC prequalified connections with

$$M_{pr} = C_p R_y F_y Z_x = 8{,}543\ \text{kip} - \text{in.} \tag{1}$$

where

F_y = specified minimum yield stress of the yielding element, ksi

R_y = ratio of the expected yield stress to the specified minimum yield stress F_y ,as specified in AISC seismic provisions (presented in Table1)

Z_x = beam plastic section modulus x-axis, in.^{3}

C_{pr} = factor to account for the peak connection strength, including strain hardening, local restraint, additional reinforcement, and other connection conditions. Since experimental data shows a high degree of strain hardening, AISC prequalified connections demonstrate that the value of C_{pr} shall be taken as equal to 1.4 [3].

By dividing this value (M_{pr}) by the distance from the plastic hinge to the beam end, the corresponding shear force at the column faces (V_h) found to be 71.2 kips. The beam design shear strength (V_b) is larger than required shear strength at the column faces (V_h).

For special moment frames (SMFs), the panel zone shear force demand, per the AISC seismic provisions [4], are determined from the summation of the probable maximum moments at the face of the column and then using

$$V_{pz} = \frac{2M_{pr}}{d_b - t_{bf}} = 1{,}743\ \text{kips} \tag{2}$$

where

d_b = overall beam depth

t_{bf} = beam flange thickness

and M_{pr} is as defined previously.

The design panel zone shear strength are calculated per AISC prequalified connections with

$$V = \phi_v R_n = \phi_v 0.6 F_y t_{cw} d_c \left(1 + \frac{3 b_{cf} t_{cf}^2}{d_c d_c t_{cw}} \right) = 424.6\ \text{kips} \tag{3}$$

where

d_c= overall column depth
b_{cf} = width of column flange
t_{cf} = column flange thickness
t_{cw}= column web thickness Main headings
ϕ_v=Resistance factor for shear strength of panel zone of beam-to-column connections, AISC prequalified connections demonstrate that the value of ϕ_v shall be taken as equal to 1.0
and d_b , F_y are as defined previously [2,3,6].

Since the panel zone shear force demand are larger than the design panel zone shear strength, providing doubler plates is necessary. To detect influences of inclined vertical plates in resisting panel zone shear force demand of connection, doubler plates are not provided intentionally either specimen 1 or specimen 2.

According to AISC seismic provisions, providing continuity plates is needed in these connections [4]. In specimen 1, the continuity plates are not provided to investigate its influences on mobilizing of each part of column section. All Continuity plates are 1-1/4 in. thick which are 1/4 in. thicker than beam flange thickness and welded to column flanges and column web and inclined vertical plates with CJP groove welds.

The connection satisfy the strong column-weak beam requirement given by AISC seismic provisions [4].

$$\frac{\sum M^*_{pc}}{\sum M^*_{pb}} = 1.11 \geq 1 \tag{4}$$

Where
ΣM^*_{pb} = the sum of the moments in the beams at the intersection of the beam and column centerlines
ΣM^*_{pc}= the sum of the moments in the column above and below the joint at the intersection of the beam and column centerlines with a reduction for the axial force in the column

By extrapolation of the probable maximum moment at the plastic hinge (M_{pr}) to the centerline of the column, ΣM^*_{pb} is calculated with

$$\sum M^*_{pb} = 2(M_{pr} + \frac{V_u d_c}{2}) = 18{,}474 \text{ kips} - \text{in.} \tag{5}$$

ΣM^*_{pc} is calculated , assuming axial load is $P_{uc}= 0.3F_yA_g$, with

$$\sum M^*_{pc} = 2Z_c(F_{yc} + \frac{P_{uc}}{A_g}) = 20{,}533 \text{ kips} - \text{in.} \tag{6}$$

where
Z_c=plastic section modulus of the column, in.^{3}
F_{yc}=specified minimum yield stress of column, ksi
P_{uc}=required compressive strength using LRFD load combinations, kips
A_g=gross area of column, in.^{2}

3 ANALYTICAL STUDY

3.1 Finite element modeling

The model of each connection was created and analyzed, using the finite-element analysis program ABAQUS. In this regard the shells elements were used for modeling in order to achieve a computationally efficient model. Here, a quadrilateral four-node shell elements (S4 element) is used.

Analysis have two steps, first only column is subjected to the axial load, the top column end is loaded by imposing lateral displacement. Nonlinear geometric behavior is considered in analysis. Each model is analyzed twice, once in order to evaluate the elastic performance of connections, considering only the elastic properties of the material. An additional analysis is carried out for each model to investigate the influences of plasticization of material in connection assemblies.

While it is assumed that the connected parts were completely joined together by the welds, neither complete joint penetration welds nor fillet welds were explicitly modeled. Additionally, beam weld access holes are not included in the models.

In order to avoid global and local instabilities, the out-of-plane movement of the beam flange is restrained near the plastic hinges and beam ends. In addition lateral bracing of column is provided at the both ends of the column and near connection region.

The overall view of the finite element model of specimen 3 is shown in Figure 3.

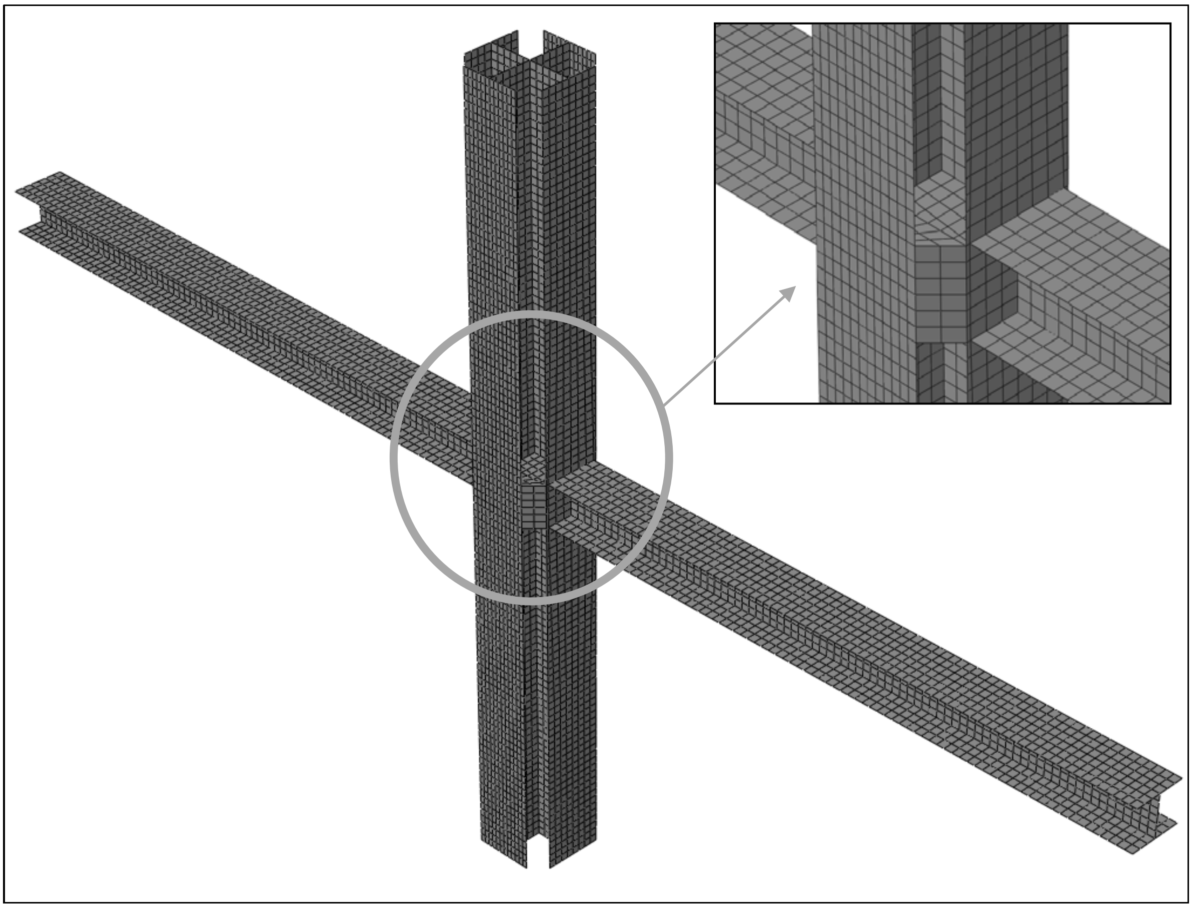

Figure 3: The overall view of the finite element model of specimen 3

3.2 Finite element analysis

A tri-linear stress-strain curve was used to represent the material properties. The Von Mises yield criterion and kinematic hardening rule were adopted to consider the plasticity behavior. The yield strength (F_y=36,000 ksi) and the ultimate strength (F_u=58,000 ksi) of the materials were considered. The Young's modulus of elasticity, tangent modulus and Poisson's ratio were assumed as 29,000 ksi, 0.01 Young's modulus and 0.3, respectively, for all materials of the analysis.

As requirements of AISC seismic provisions [4], the connection used in SMFs, must accommodate a story drift angle at least 0.04 rad. and the measured flexural resistance of the connection, determined at the column face, shall equal at least $0.80M_p$ of the connected beam at an interstory drift angle of 0.04 rad.. In all models, the top column end is loaded monotonically by imposing a displacement until 0.04 rad. of story drift angle.

Since neither specimen 1 nor specimen 2 provide sufficient panel zone shear strength, only in specimen 3, the top column end is loaded axially by $P_{uc}=0.3F_yA_g$ accompanied by a prescribed quasi-static cyclic lateral displacement. The total story drift was calculated by dividing the column tip displacement by the height of column.

3.3 Finite element analysis results

Specimen 1

As there is no continuity plate placed in this specimen, parts of section are joined by webs, the compatibility of two parts of section is not taken place sufficiently due to low out-of-plane strength of webs. Shear force and flexural moment of each part of column are presented separately to investigate moment and shear resisting participation of each part of column. Maximum shear force in the column developed in the mid height of panel zone region (Section 1) and maximum flexural moment developed in the level of continuity plates (Section 2). In both elastic and plastic analysis of specimen 1, the W section part of flanged cruciform column bent about its strong principal axis, named herein after as "strong part", resists major portion of shear force and flexural moment in the column section and the W section part of flanged cruciform column bent about its weak principal axis, named herein after as "weak part", resists only minor portion of flexural moments as well as shear forces.

The developed shear force and shear force participation ratio of each part of column at section 1 versus column tip displacement are shown in Figures 4(a) and 4(b) respectively.

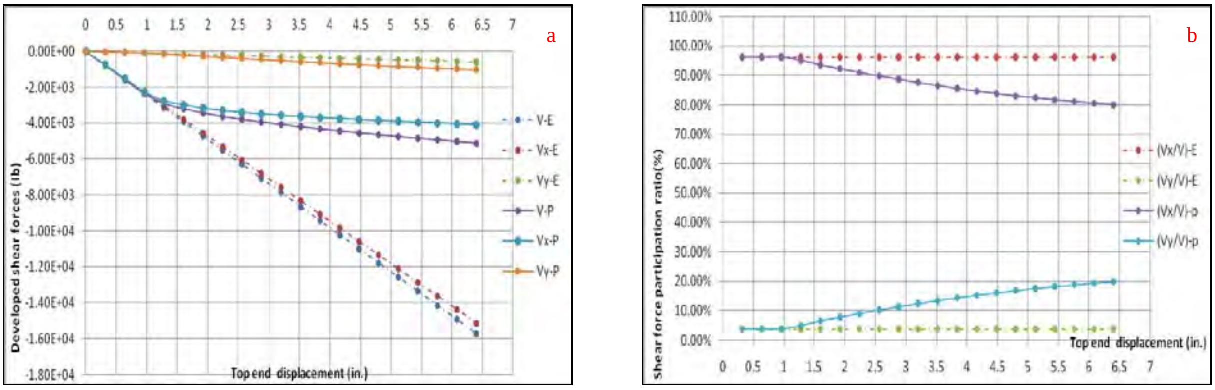

Figure 4. (a): The developed shear force of each part of column at section 1 versus column tip displacement; (b): Shear force participation ratio of each part of column at section 1 versus column tip displacement.

These figures include results of both elastic and plastic analysis to determine yielding effect of connection parts. The elastic analysis results are shown with suffix (-E) and plastic analysis results are shown with suffix (-P). In these figures (Mx) and (Vx) show flexural moment and shear forces, developed in strong part of column and (My) and (Vy) show flexural moment and shear forces, developed in weak part of column. Also (M) and (V) are resultant flexural moment and shear force, developed in the whole section of column.

In addition, the developed flexural moment and flexural moment participation ratio of each part of column at section 2 versus column tip displacement are shown in Figures 5(a) and 5(b) respectively.

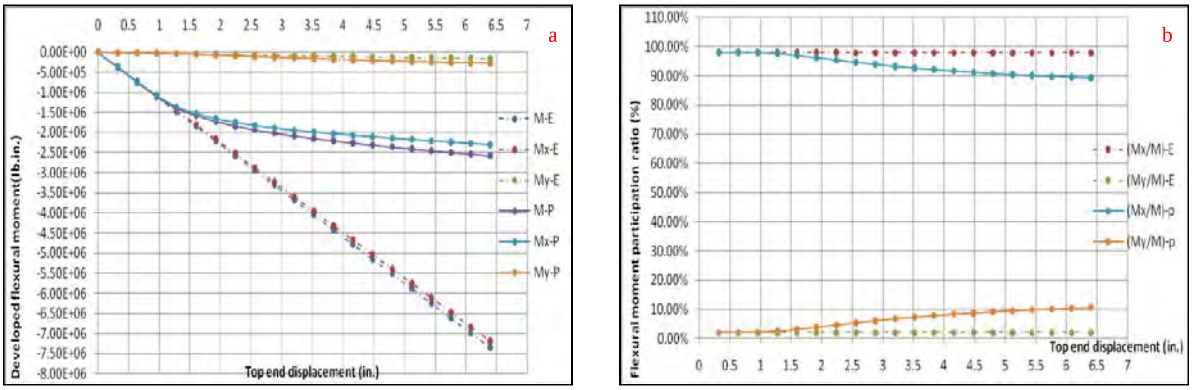

Figure 5 (a): The developed flexural moment of each part of column at section 2 versus column tip displacement; (b): Flexural moment participation ratio of each part of column at section 2 versus column tip displacement.

As shown, the compatibility of two parts of section are not remained the same which means the plane of the whole section does not remains plane and flexural moment distribution of column do not follow proportionally the weak axis stiffness to strong axis stiffness ratio of each W sections .

Due to yielding of panel zone and decrease in stiffness of strong part, the weak part participation in resisting flexural moment and shear force is higher in plastic analysis, as compared to results from elastic analysis.

Specimen 2

In this specimen which strong part and weak part are joined together through the continuity plates at beam flanges level as well as webs of two parts. Because of high in-plane capacity of continuity plates, it is predicted that the weak part has reasonably more share in the resisting flexural moment and shear force than specimen 1.

The developed shear force and shear force participation ratio of each part of column at section 1 versus column tip displacement are shown in Figures 6(a) and 6(b) respectively.

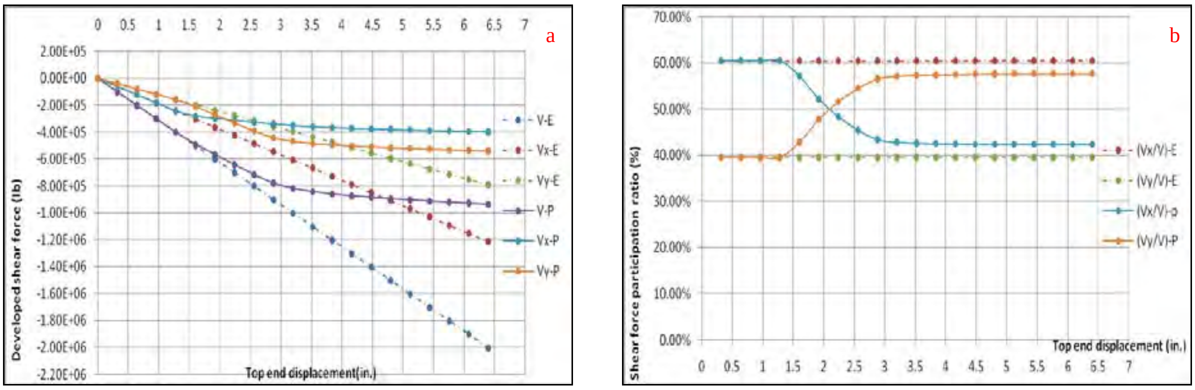

Figure 6. (a): The developed shear force of each part of column at section 1 versus column tip displacement; (b): Shear force participation ratio of each part of column at section 1 versus column tip displacement.

In addition, the developed flexural moment and flexural moment participation ratio of each part of column at section 2 versus column tip displacement are shown in Figures 7(a) and 7(b) respectively.

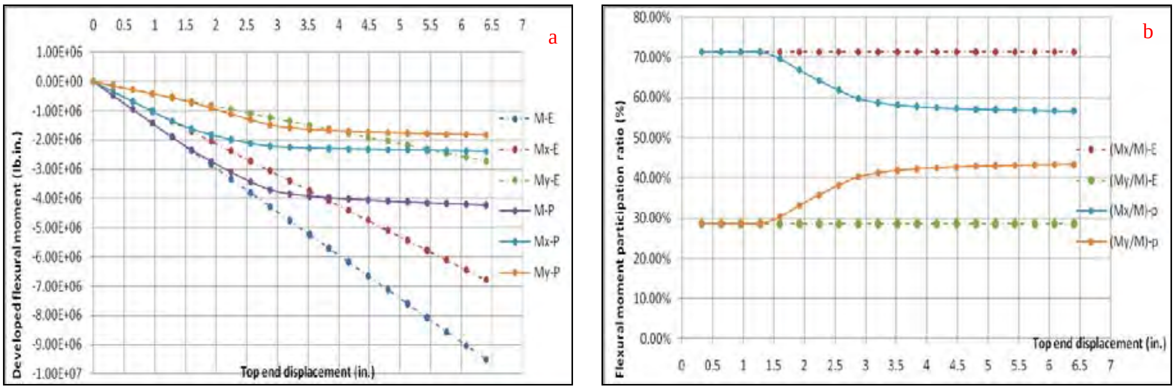

Figure 7. (a): The developed flexural moment of each part of column at section 2 versus column tip displacement; (b): Flexural moment participation ratio of each part of column at section 2 versus column tip displacement.

As shown, flexural moment distribution of column do not follow proportionally the weak axis stiffness to strong axis stiffness ratio of each W sections, so column section plane does not remains plane.

In the plastic analysis of specimen 2, as soon as panel zone start to yield, Stiffness of panel zone decreases so weak part resist more flexural moment as well as shear forces. Unlike specimen 1, panel zone yielding plays more important role in specimen 2.

Specimen 3

In this specimen, inclined vertical plates as well as continuity plates are provided. This inclined plates and flange plates of weak part create two extra load paths to transfer panel zone shear forces. In other word, there are three parallel load paths to resist shear forces of panel zone region, one directly through web of strong part and two accordion load path through inclined and flange plates.

The developed shear force and shear force participation ratio of each part of column at section 1 versus column tip displacement are shown in Figures 8(a) and 8(b) respectively.

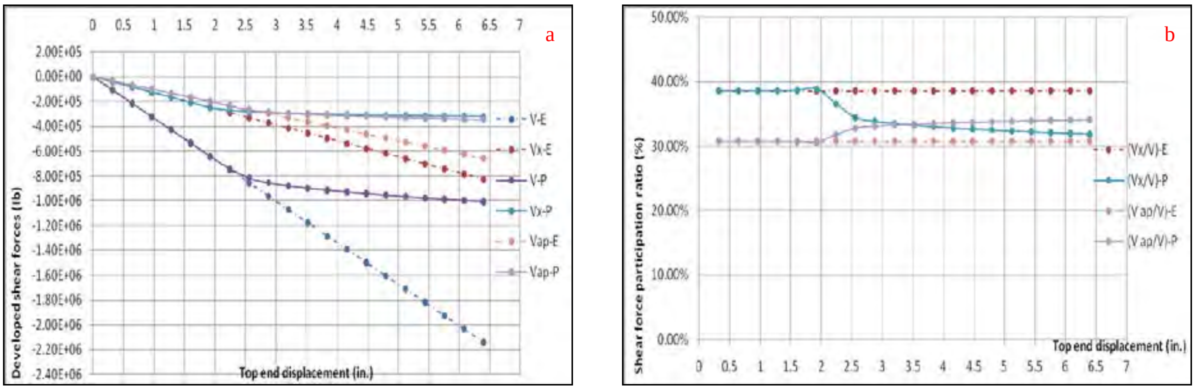

Figure 8 (a): The developed shear force of each part of column at section 1 versus column tip displacement; (b): Shear force participation ratio of each part of column at section 1 versus column tip displacement.

In these figures and (Vap) shows shear forces, developed in each accordion path of the panel zone regions. In addition, the developed flexural moment and flexural moment participation ratio of each part of column at section 2 versus column tip displacement are shown in Figures 9(a) and 9(b) respectively.

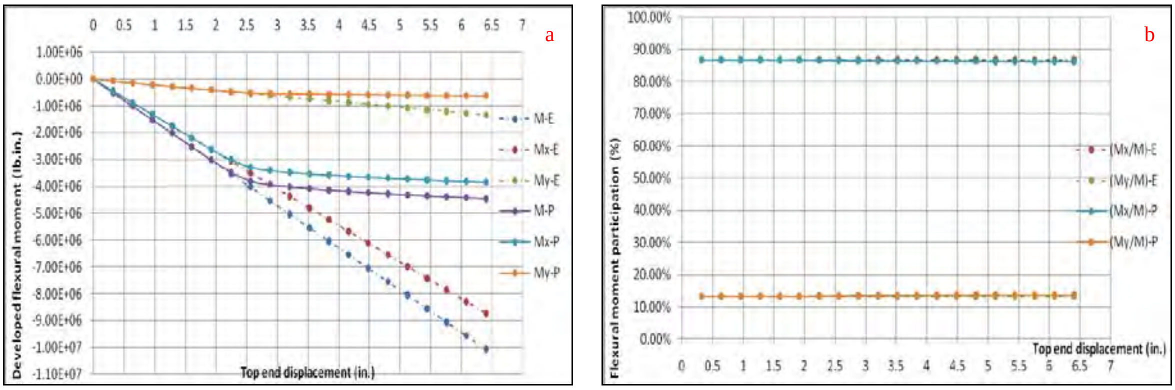

Figure 9. (a): The developed flexural moment of each part of column at section 2 versus column tip displacement; (b): Flexural moment participation ratio of each part of column at section 2 versus column tip displacement.

In the plastic analysis of specimen 3, after the yielding of web of the strong part, the flanges of weak part and inclined plates start to yield.

As shown, Although strong part web yielding cause decrease in panel zone shear stiffness, but does not considerably influence the flexural stiffness of the strong part of column, due to presence of two parallel accordion load path.

To examine connection performance in cyclic loading, this specimen is subjected to the cyclic lateral displacement loading. specimen shows quite stable inelastic behaviors and favorable energy dissipation capacities throughout cyclic loading. The connection performance exceeded the AISC seismic provision requirements.

The developed flexural moment of each part of column at section 2 versus total story drift angle of the specimens is shown in Figure 10.

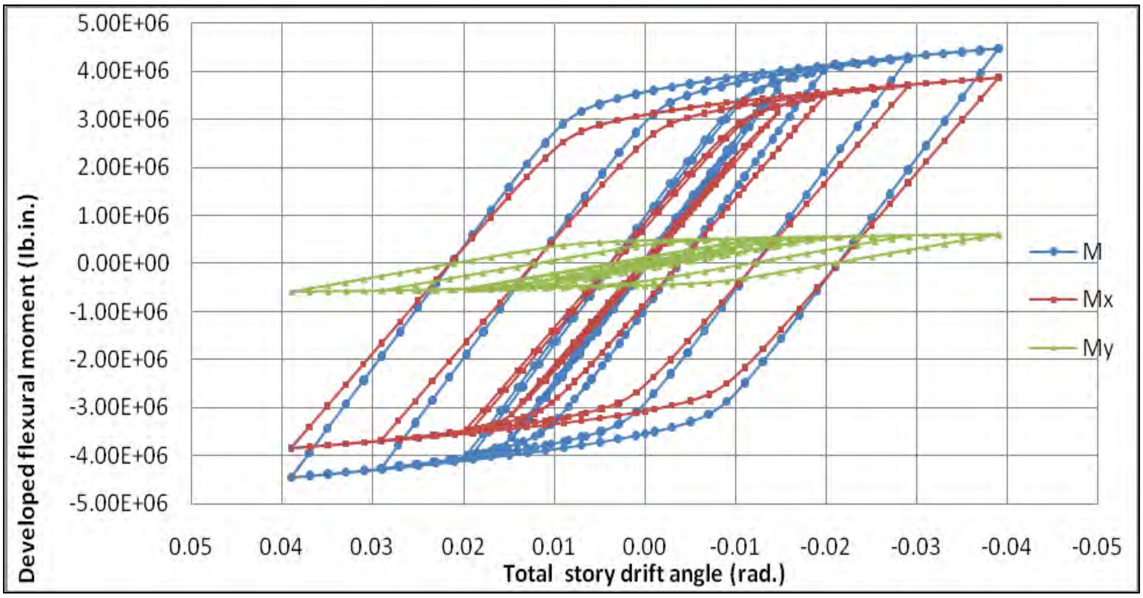

Figure 10: The developed flexural moment of each part of column at section 2 versus total story drift angle of the specimens in cyclic loading.

4 CONCLUSIONS

- While in the bending of flanged cruciform column, there is only out-of-plane bending of column web to constrain two section together and Due to low out-of-plane bending capacity of webs, extra measures is needed to push the two parts of section to behave in the same manner in order to whole section plane remains plane.
- The placement of the continuity plates in connection regions is necessary to mobilize flexural capacity of both W sections.
- Although providing continuity plates causes to develop flexural moment in both w sections, but column section plane does not still remains plane and flexural moment distribution of column does not follow proportionally the weak axis stiffness to strong axis stiffness ratio of each W sections.
- Due to the discontinuity of the load paths, it is not possible to use common doubler plates to reduce panel zone shear force in two directions and also local increase in column web thickness in the panel zone region is not possible for flanged cruciform section are fabricated from rolled sections, so it is needed to provide other paths to transfer the shear demands in panel zone regions.
- Inclined vertical plates with same thickness of column flanges, provide effective parallel accordion paths to resist panel zone shear forces. In addition, these plates cause that flexural moment participation of each part of flanged cruciform section becomes closer to the assumption of the weak axis stiffness to strong axis stiffness ratio of two perpendicular W sections.
- Due to existence of inclined vertical plates in panel zone regions, web shear yielding of strong part of column does not affect the flexural moment distribution in each part.
- These new load paths show quite stable inelastic behavior when subjected to cyclic lateral displacement loading.

REFERENCES

[1] M.M Tahir, P.N. Shek, A. Sulaiman, C.S. Tan, Experimental investigation of short cruciform columns using universal beam sections. *Construction and Building Materials,* **23**, 1354-1364, 2009.

[2] AISC/ANSI 358-05, *prequalified connections for special and intermediate steel moment frames for seismic applications*. American Institute of Steel Construction, Inc., 2005.

[3] DRAFT AISC 358-10, *prequalified connections for special and intermediate steel moment frames for seismic applications*. American Institute of Steel Construction, Inc., 2010.

[4] AISC/ANSI 341-05, *Seismic provisions for structural steel buildings*. American Institute of Steel Construction, Inc., 2005.

[5] ASTM A36/A36M - 08, *Standard Specification for Carbon Structural Steel*. American Society for Testing and Materials, 2008.

[6] AISC/ANSI 360-05, *Specification for structural steel buildings*. American Institute of Steel Construction, Inc., 2005.

COMPDYN 2011
III ECCOMAS Thematic Conference on
Computational Methods in Structural Dynamics and Earthquake Engineering
M. Papadrakakis, M. Fragiadakis, V. Plevris (eds.)
Corfu, Greece, 25–28 May 2011

EVALUATION OF ENERGY DISSIPATION CAPACITY OF STEEL FRAMES WITH STEEL SHEAR WALLS

F. Dinu[1,4], C.Neagu[2] and D. Dubina[3,4]

[1] The “Politehnica” University of Timisoara, Romania
e-mail: florea.dinu@ct.upt.ro

[2] The “Politehnica” University of Timisoara, Romania
e-mail: calin.neagu@ct.upt.ro

[3] The “Politehnica” University of Timisoara, Romania
e-mail: dan.dubina@ct.upt.ro

[4] Romanian Academy, Timisoara Branch

Keywords: Performance criteria, steel plate shear wall, energy dissipation, q factor, over-strength.

Abstract. *The papers investigates the behavior of steel frames of dissipative steel shear walls Both numerical and experimental analyses have been conducted in order to characterize in terms of energy dissipation and to evaluate the q-factor for design of these structures. The tests have been realized for two series of three-bay and two-storey frames, stiffened of Steel Plate Shear Walls. Specimens have been half-scaled and tested under monotonic and cyclic loading. A numerical model has been calibrated via test results for push over and IDA analyses. Parametric studies have been done on different frame typologies in order to obtain the q factor for such systems.*

1 INTRODUCTION

Steel plate shear walls SPSW have been used as lateral force resisting systems since 70's, but the design specifications were rather incomplete at that time. Throughout the last four decades, numerous research programs and also seismic experiences have confirmed their effectiveness. A major role on their development can be attributed to the introduction of design rules in the code provisions, e.g. AISC, 2005 [1] or NBCC, 2006 [2]. The application of SPSW system in Europe is limited, partly due to the lack of design provisions in seismic code EN 1998-1 [3]. Particularly, there are no recommendations for behavior factor and system overstrength factor, respectively. An additional problem refers to the prediction of the strength and stiffness capacity of the SPSW structures. Design practice requires simple models and conventional analysis software that are available and relatively simple to use. One of the models used to represent the behavior of SPSW is the strip model, developed by Thorburn et al., 1983 [4]. Thus, in order to model the steel plate shear walls, the steel plates are replaced by a series of truss members - strips, parallel to tension fields. A minimum of ten strips per panel are required to adequately represent the tension field action developed in the plate.

In order to address the issues presented above with regards to the performances of SPSW systems, an experimental program was developed at the Politehnica University of Timisoara, Steel Structures Laboratory. Previous research of the authors was focused on numerical investigations on SPSW systems (Dinu et al., 2009, [5]) and comparison to conventional braced systems (i.e. centrically braced frames and eccentrically braced frames). In order to evaluate the influence of beam-to-column connections on the response of the structure, two connection typologies were used, i.e. flush end plate bolted connections and extended end plate bolted connections. Structures were tested monotonically and cyclically. Behavior factors were evaluated from the cyclic test. The strip model developed by Thorburn et al. was modified based on the experimental results. In order to extend the behavior factors evaluated experimentally, a numerical study was performed. The paper summarizes the experimental program and presents the results of the numerical study.

2 EXPERIMENTAL TEST ON STEEL PLATE SHEAR WALLS

2.1 Test specimens

The steel plate shear wall specimens were extracted from a six story frame structure (Figure 1.a). The two actuators used for the tests have 1000 kN and 500 kN capacity and 360mm stroke, respectively. Due to the stroke limitation, the specimens were half-scaled. The infill plates had thickness of 2mm and 3mm, respectively. The frames are 3500 mm height and 4200 mm wide (between member centerlines) (Figure 1.b). The slenderness ratio of shear walls L/t_w amounted 595 for 2 mm panels and 397 for 3 mm panels, while the aspect ratio L/h was 0.75. In order to evaluate the contribution of the boundary frames to the strength and stiffness of the structure, two types of beam-to-column connections were used. According to EN1993-1-8 [6] classification, flush end plate connection was semi-rigid and weak partial strength ($M_{j,Rd}=0.4M_{b,Rd}$) (further refereed as semi-rigid) and extended end plate connection was rigid and strong partial strength, with a capacity almost equal to that of the connected beam ($M_{j,Rd} = 0.9M_{b,Rd}$) (further refereed as rigid). The infill panels were bolted connected to the boundary members using fish plates. Table 1 shows the thickness of the infill plates, boundary elements, beam-to-column connection types and type of loading. Table 2 shows the material properties of the specimens. As expected, the actual yield strength of the infill plates and boundary elements are much larger than the nominal values.

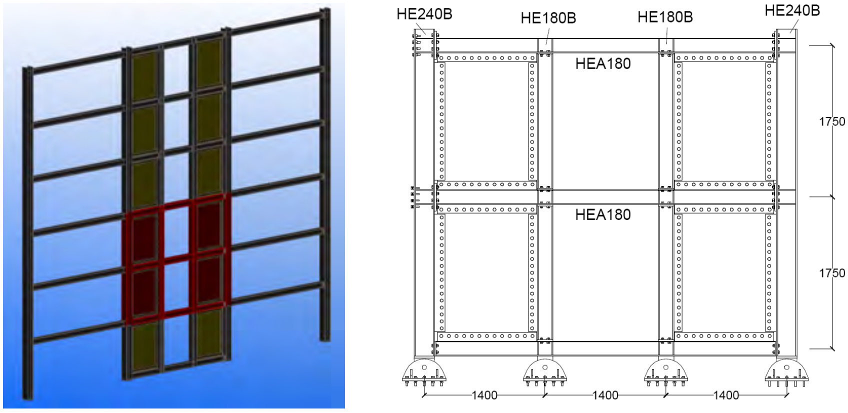

(a) (b)

Figure 1: Six story frame structure a) and half-scale test frame b)

Specimen	Infill plate [mm]	Column	Beam	Connection	Loading
R-M-T2	2	HEB240 (HEB180)	HEA180	Rigid	Monotonic
R-C-T2	2			Rigid	Cyclic
SR-C-T2	2			Semi-rigid	Cyclic
SR-C-T3	3			Semi-rigid	Cyclic

Table 1: Design of specimens

Section	Steel grade	Element	f_y	f_u	A_u	Actual steel grade
HEB240	S355	Flange	457	609	40	S460
		Web	458	609	31	
HEB180	S355	Flange	360	515	44	S355
		Web	408	540	40	
HEA180	S355	Flange	419	558	32	S420
		Web	415	542	22.5	
2 mm	S235	Infill plate	305	429	24	S275
3 mm	S235	Infill plate	313	413	25	

Table 2: Material properties

All specimens were tested monotonically and cyclically using ECCS procedure [7] but adapted to particular behavior of steel plate shears walls. The difference is the slope of initial stiffness. Thus, in the original procedure, a monotonic test is done first, in order to evaluate the force-displacement curve that is used to evaluate the equivalent yield displacement. Yield displacement D_y and corresponding yield force F_y are obtained by intersecting the initial stiffness α_y and a tangent at the curve *F-D* with a slope of 10% of the initial stiffness. Yield displacement D_y is then used to calibrate the cyclic loading history. This contains four elastic cycles ($\pm0.25D_y$, $\pm0.5D_y$, $\pm0.75D_y$ and $\pm1.0D_y$), followed by groups of 3 cycles of amplitudes multiple of $2D_y$ ($3\times2D_y$, $3\times4D_y$, $3\times6D_y$, …). Based on experimental results, the evaluation of yield displacement was adjusted to take into account the specific behavior of SPSW. Thus, the slope of initial stiffness was corrected and amounted 20% of the initial stiffness.

2.2 Monotonic test

All specimens exhibited stable force-displacement behavior. Figure 2 shows the behavior of the specimen R-M-T2 during the monotonic test. VIC-3D digital image correlation system was used for measurement of shape, displacement and strain. Areas delimited by dashed lines, magnified and represented at the right-hand side of the figures, have the dimensions of 450 mm by 550mm. As the infill plate thickness was small, some out-of-plane deflections occurred due to the fabrication (Figure 2.a), amounting approximately 8.8 mm (0.0065$\sqrt{Lh}$), where L is the distance between boundary columns centerlines and h is the story height. Up to inter-story drifts of about 0.5%, specimens were almost elastic. After this drift, some yield lines appeared in the infill plates (Figure 2.b). Out-of plane deflections corresponding to this drift were about 0.017$\sqrt{Lh}$). Some local cracks were initiated at the corners of the panels at interstory drifts of approximately 2%. The beam-to-column connections presented no damages before plastic deformations took place in panels. Local plastic deformations started to initiate at the beam flange in compression for drifts larger than 2%. For the peak capacity, the interstory drift amounted 6% approximately, while out of plate deflections amounted 0.02$\sqrt{Lh}$) (Figure 2.c). The test was stopped at a top displacement of 240mm as the force started to drop, before the attainment of full shear wall capacity (Figure 3).

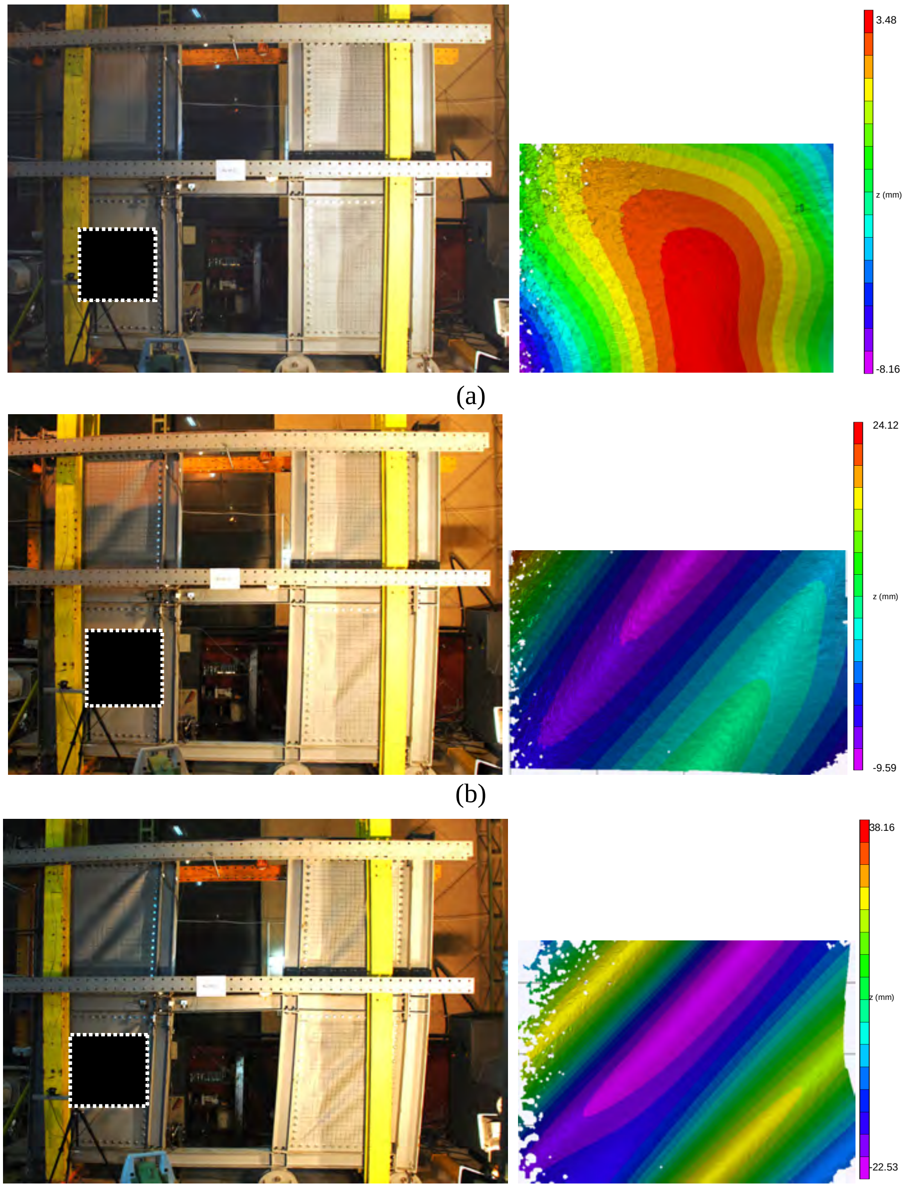

(a)

(b)

(c)

Figure 2: General view and details of the R-M-T2 specimen (VIC measurements with the scale on the right): a) initial state; b) yielding state; c) peak capacity

Results of the monotonic test were compared with the results of a pushover analysis. The strip model used in the pushover analysis was in good agreement with the initial stiffness but underestimated the strength with about 42%. When the plastic hinge was calibrated according to experimental behavior, the accuracy of the model was very much improved (Figure 3). This reduction of the panel area conservatively reduces the design strength and stiffness of the structure.

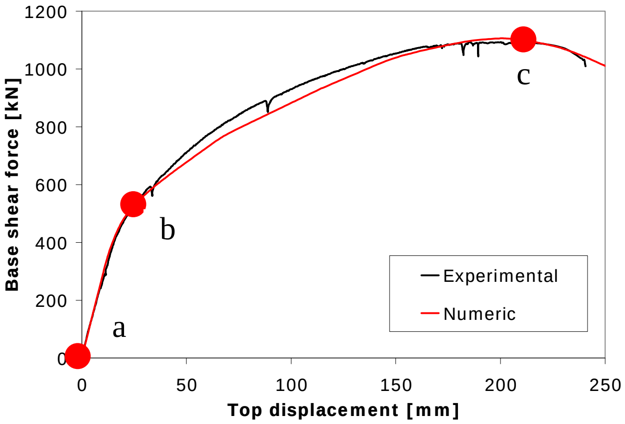

Figure 3: Comparison of experimental results for rigid specimen with 2mm thick panel and numerical results using the strip model

If Figure 2 and Figure 3 are compared, it may be seen the infill plate has out-of-plane deflections in the initial state, see Figure 2.a (it corresponds to point (a) in Figure 3). At yielding, the multiple buckle wavelengths are already visible, see Figure 2.b (it corresponds to point (b) in Figure 3). When the peak capacity is reached, the maximum out-of-plane deflections are doubled compared to yielding state, see Figure 2.c (it corresponds to point (c) in Figure 3).

2.3 Cyclic tests

In the cyclic tests, all specimens exhibited stable behavior up to cycles of 4% interstory drift. Panels yielded at approximately 0.005 of the story height. Some local cracks were initiated at the corners of the panels at drifts of approximately 2%. Local plastic deformations were observed at the beam flange in compression for rigid connections. Bolted connections between infill panels and the fish plates shown small slippages but no plastic deformations either in plates or bolts. This enabled a very easy dismantling of the steel panels after the test. Associated with a small residual drift (for rigid structure), this can assure an easy intervention to replace the damaged panels after a moderate earthquake. Some pinching was recorded in the hysteresis loops for large drifts and semi-rigid specimens, only. This can be attributed to the bolted connection between boundary beams and columns and not the slippage of the connection between infill panels and fish plates. This is particularly important at the evaluation of the q factor, as the pinching need to be taken out at the evaluation of the ultimate displacement.

Figure 4 (left) plots the hysteresis of rigid and semi-rigid specimens. Contribution of rigid connections on the ultimate capacity of the specimens is larger than in the monotonic tests. As the initial stiffness is mainly attributed to the panels, differences between rigid and semi-rigid specimens in terms of stiffness are not as important as differences in terms of strength.

The main parameters associated to the global performance of the SPSW systems are the energy dissipation and global ductility (given by behavior factor q). The cyclic tests on three SPSW systems with coupling beams have shown significant ductility and energy dissipation capacity. The specimens were capable of following large number of inelastic cycles, reaching relatively large drift values (beyond 4%). The area enclosed by a hysteresis curve is a measure of the energy dissipated by the system during a loading cycle. The hysteresis curves of all specimens are fairly wide, indicating good energy absorption of the system. In order to assess quantitatively the performance of the test specimens, the energy dissipation was calculated for each test specimen (Figure 4, right).

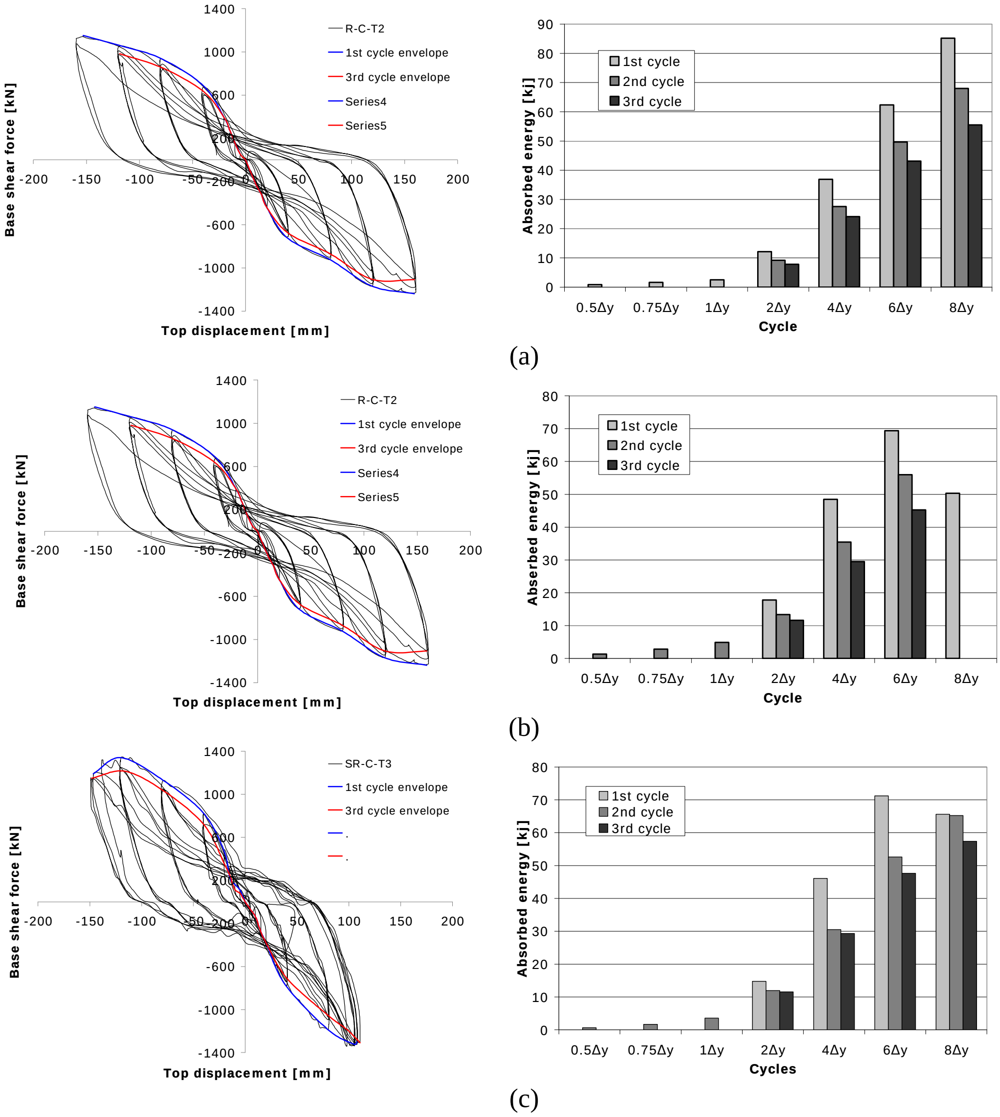

(a)

(b)

(c)

Figure 4: Histeresis curve and energy dissipation per cycles: a) R-C-T2 specimen; b) SR-C-T2 specimen; c) SR-C-T3 specimen;

An important objective of the experimental program was, also, the evaluation of the behavior factor q. The q factor can be expressed as a product of the ductility factor, q_μ, that accounts for the ductility of the structure and the overstrength factor, q_s, that accounts for the strength reserve of the structure. The overstrength may vary significantly and is affected by the contribution of gravity loads, material overstrength, structural redundancy, etc. Therefore, in order to calibrate the behavior factor q, it is more important to focus on the ductility component, which can be taken equal to the displacement ductility factor, μ. The ductility reduction factor q_μ is therefore defined as the ratio of the ultimate displacement D_u and the yield displacement

D_y. The parameter D_u corresponds to a reduction of the load carrying capacity of 10% compared to the maximum one. This reduction could be also 20%, but 10% was also imposed by the stroke limitation. The yielding displacement D_y was evaluated with ECCS methodology and the "stiffness method", where the yield point corresponds to the modification of the elastic stiffness. Based on the observation of the hysteresis curves, the ultimate displacements D_u for SR-C-T2 and SR-C-T3 were corrected to take into account the pinching during the load reversal. Table 3 presents the q_μ factor values for the specimens. Comparing the values obtained with the two methods, it may be seen the specimens have different ductility factors q_μ, with values of 4.2 and 5.2. As mentioned before, overstrength factor, q_s, depends on many factors but for a structural system it can be conservatively evaluated and prescribed in codes. For example, [2] indicates for ductile steel plate shear walls overstrength factor R_s (equivalent to q_s) equal to 1.6. Similar recommendations are given by Berman and Bruneau [8], who recommend an overstrength factor R_s=1.5. These values show SPSW structures can provide q factors similar to those corresponding to other dissipative structure, like for example moment resisting frames or eccentrically braced frames.

Structure	D_y		D_u	q_u	
	CEN	stiffness		CEN	stiffness
R-C-T2	38	31	153	4.0	4.9
SR-C-T2	33	26	163	4.9	6.3
SR-C-T3	40	33	147	3.7	4.5
Average value				4.2	5.2

Table 3: q factor values

3 EVALUATION OF PERFORMANCE OF STEEL PLATE SHEAR WALL FRAMES

3.1 Design and modeling

In order to assess the performance of steel plate shear wall structures, numerical studies using a nonlinear dynamic procedure were conducted. The geometry of the structure is presented in Figure 5. The interior bays with infill plates consist of either pinned or rigid connections. All stories are 3.5m height. The steel material for the members is S235 (f_y=235N/mm^2), S355 (f_y=355N/mm^2) and S460 (fy=460N/mm^2). The slenderness ratio L/t_w and the aspect ratio L/h of shear walls amount 420 and 0.8, respectively. The design was carried out according to EN1998-1 **Error! Reference source not found.** and P100-1 [9]. For dual frame systems of moment frames and shear walls, EN1998-1 does not provide any recommendations regarding the q factor. Thus, the results of the experimental program were taken into account, q factor of 6. A 4 kN/m^2 dead load on the typical floor and 3.5kN/m^2 for the roof were considered, while the live load amounts 2.0kN/m^2. The buildings are located in a high seismic area (i.e. the Romanian capital, Bucharest), which is characterized by a design peak ground acceleration 0.24g for a returning period of 100 years, and soft soil conditions, with a corner period T_C=1.6sec. It is noteworthy the long corner period of the soil, which in this case may affect flexible structures. For serviceability check, the returning period is 30 years, while for collapse prevention it is 475 years. Beams and columns were modeled with plastic hinges located at both ends. The shear walls were modeled with dual strip model, using 10 inclined pin-ended strips, oriented at angle α in both sides.

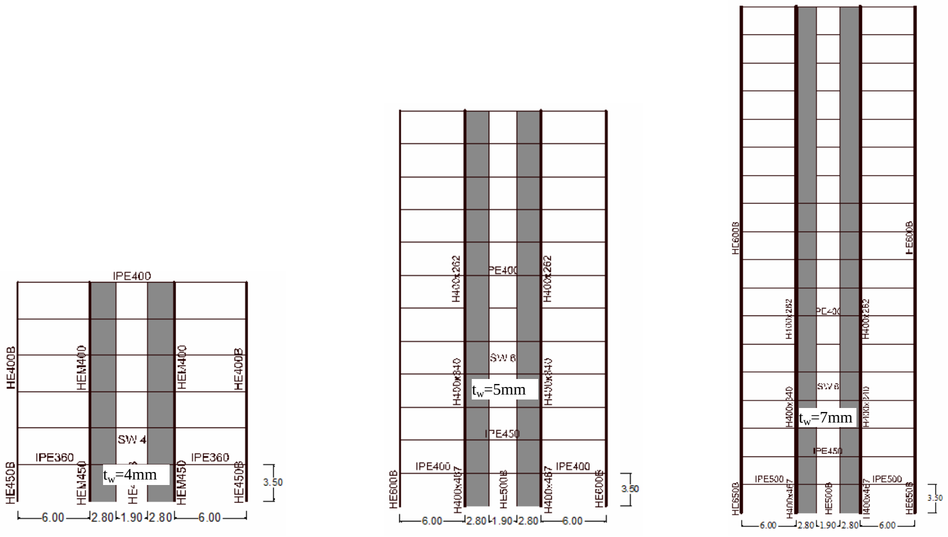

6 storey 12 storey 18 storey

Figure 5: Structural systems investigated in the numerical study

3.2 Ground motion records

A set of seven ground motions were used. Spectral characteristics of the ground motions were modified by scaling Fourier amplitudes to match the target elastic spectrum from [9], see Figure 6. This results in a group of semi-artificial records representative to the seismic source affecting the building site and soft soil conditions in Bucharest. The procedure was based on the SIMQKE-1 program (Gasparini & Vanmarcke, 1976) [10].

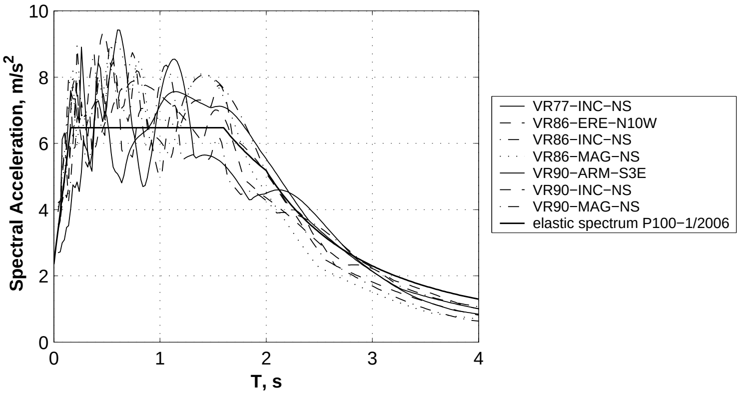

Figure 6: Elastic response spectra of semi artificial records and P100-1/2006 elastic spectrum

3.3 Analysis procedure and results

For the evaluation of the behavior factor q, acceleration time history motion records have been scaled to multiple levels, up to the collapse or the attainment of certain limiting criteria (eg. exhaustion of rotation capacity in elements). Figure 7, Figure 8 and Figure 9 show the maximum interstory drift ratio vs. spectral acceleration S_a for all structures and records. It can be seen the structure with rigid connections has smaller interstory drifts compared to the structure with pinned connections. The q factor was defined as the ratio between the acceleration leading to collapse and the acceleration leading to first yielding. Based on the results of the experimental test, first yielding forms in infill plates and corresponds to an interstory drift of 0.5%. The collapse criterion is given by the attainment of dynamic instability or plastic deformation capacity of dissipative members, steel panels and beams. For the beams, the plastic rotation capacity was considered 0.035rad. The experimental tests demonstrated that steel panels can sustain an interstory drift of 4%, which is equivalent to 0.035 radian plastic deformation in beams. Table 5 shows the values of q_μ for rigid and pinned structure. The type of ground motion affects the behavior factor q_μ. The mean values of the q_μ factor vary with the height of the structure. 12 and 18 storey structures present almost constant *q* factors while the 6 storey structure presents slightly lower values. If these values of the ductility factor q_μ are combined with the overstrength factors q_S (see section 2.3) the total q factor is obtained. It may be seen the design of SPSW structures may use similar behavior factors *q* as other dissipative structures, i.e. moment resisting frames.

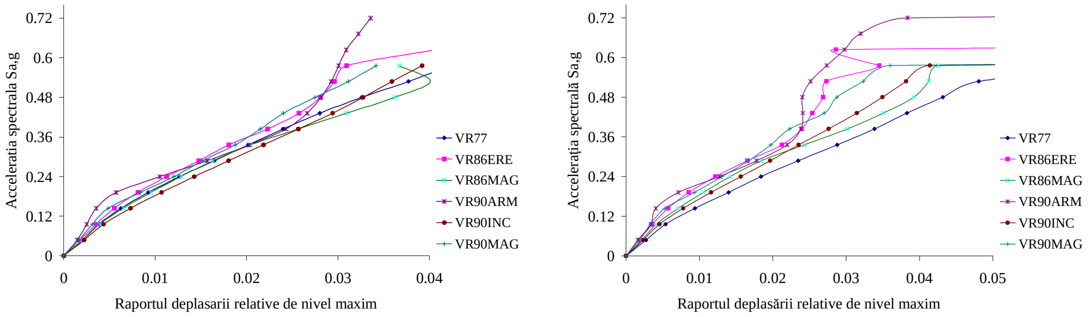

Figure 7: IDA curves: maximum interstory drift ratio vs. spectral acceleration S_a(g) for all records 6 storey structures: a) Rigid; b) Pinned

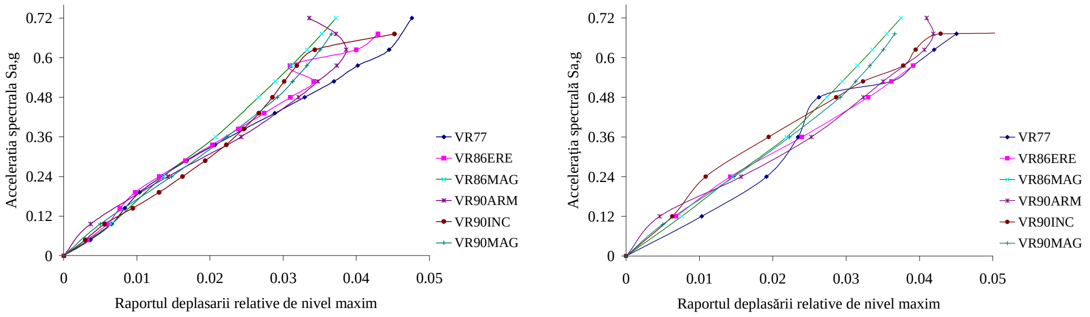

Figure 8: IDA curves: maximum interstory drift ratio vs. spectral acceleration S_a(g) for all records 12 storey structures: a) Rigid; b) Pinned

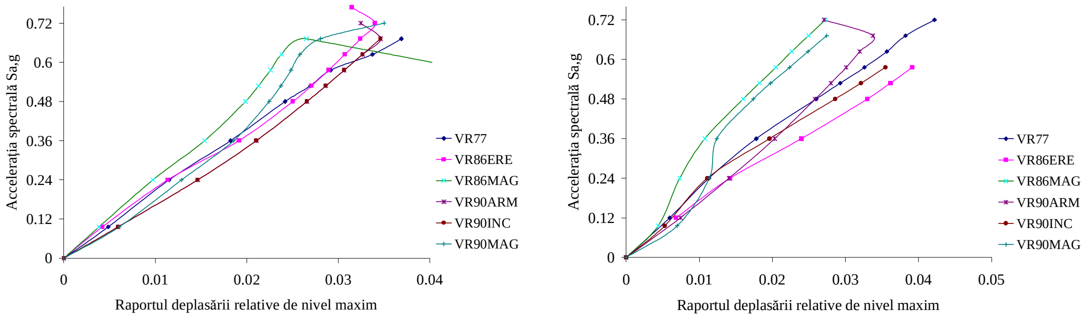

Figure 9: IDA curves: maximum interstory drift ratio vs. spectral acceleration S_a(g) for all records for 18 storey structures: a) Rigid; b) Pinned

Earth-quake	no. of Storey	Accelera-tion		q	no of. Storey	Acceleration		q	no. of Storey	Acceleration		q
		a_{gy}	a_{gu}			a_{gy}	a_{gu}			a_{gy}	a_{gu}	
VR77INC	6	0.10	0.58	6.0	12	0.10	0.53	5.5	18	0.10	0.48	5.0
VR86ERE		0.12	0.62	5.2		0.10	0.58	6.0		0.10	0.77	8.0
VR86MAG		0.10	0.58	6.0		0.10	0.72	7.5		0.13	0.67	5.1
VR90ARM		0.12	0.72	6.0		0.10	0.62	6.5		0.10	0.72	7.5
VR90INC		0.10	0.58	6.0		0.10	0.53	5.5		0.10	0.53	5.5
VR90MAG		0.12	0.62	5.2		0.10	0.62	6.5		0.10	0.67	7.0
AVERAGE				5.7				6.3				6.3

Table 4: q factors for structures with rigid connections

Earth-quake	no. of Storey	Accelera-tion		q	no. of Storey	Acceleration		q	no. of Storey	Acceleration		q
		a_{gy}	a_{gu}			a_{gy}	a_{gu}			a_{gy}	a_{gu}	
VR77INC	6	0.10	0.58	6.0	12	0.10	0.53	5.5	18	0.10	0.48	5.0
VR86ERE		0.12	0.62	5.2		0.10	0.62	6.5		0.10	0.77	8.0
VR86MAG		0.10	0.53	5.5		0.10	0.72	7.5		0.12	0.67	5.6
VR90ARM		0.12	0.77	6.4		0.10	0.72	7.5		0.10	0.72	7.5
VR90INC		0.10	0.58	6.0		0.10	0.58	6.0		0.10	0.53	5.5
VR90MAG		0.12	0.67	5.6		0.10	0.62	6.5		0.10	0.67	7.0
AVERAGE				5.8				6.5				6.4

Table 5: q factors for structures with pinned connections

4 CONCLUSIONS

Experimental and numerical investigations were conducted on dual steel plate shear wall structures. A total of 4 specimens were designed and fabricated, which included specimens of semi-rigid and rigid connections. Specimens were tested monotonically and cyclically. Rigid connections increased the “yield resistance” and the ultimate capacity of the structures. The initial stiffness was also improved when rigid beam-to-column connections were used. Behavior factor q (considering the contribution of the ductility, only) was evaluated, based on two methods. The *q* factor values indicate that SPSW structures exhibit a dissipative behavior, similar to other dissipative structures, like for example moment resisting frames. For extending the results on the behavior factor *q* for SPSW structures, a numerical study on different structures was performed. Behavior factor q varies with the height of the structures and type of ground motion. The mean values of *q* factors obtained via numerical analysis are very closed to those resulted from experimental tests.

REFERENCES

[1] AISC 341-05, *Seismic provisions for structural steel buildings*, American Institute for Steel Construction, 2005.

[2] NBCC, *National Building Code of Canada*, Institute for Research in Construction, National Research Council of Canada, Ottawa, 2005.

[3] EN 1998-1, *Design provisions for earthquake resistance of structures - 1-1: General rules - Seismic actions and general requirements for structures*, CEN, EN1998-1-1, October 1994.

[4] L. J. Thorburn, G. L. Kulak and C. J. Montgomery, Analysis of steel plate shear walls. *Structural Engineering Rep. No. 107*, Dept. of Civil Engineering, Univ. of Alberta, Edmonton, Alberta, Canada, 2003.

[5] F. Dinu, D. Dubina, C. Neagu, A comparative analysis of performances of high strength steel dual frames of buckling restrained braces vs. dissipative shear walls, *Proc. of International Conference STESSA 2009: Behavior of Steel Structures in Seismic Areas, Philadelphia*, 16-20 Aug 2009, CRC Press, Ed. F.M. Mazzolani, J.M. Ricles, R. Sause, ISBN: 978-0-415-56326-0, 2009.

[6] EN1993-1-8, *Design of Steel Structures. Part 1-8: Design of joints*, CEN, Brussels, 2003.

[7] ECCS 1985, Recommended Testing Procedures for Assessing the Behavior of Structural Elements under Cyclic Loads. *European Convention for Constructional Steelwork*. Technical Committee 1, TWG 1.3 – Seismic Design, No.45, 1985.

[8] J. Berman and M Bruneau, Plastic Analysis and Design of Steel Plate Shear Walls. *Journal of Structural Engineering, ASCE, Vol. 129, No. 11*, 2003.

[9] P100-1, Partea I: Prevederi de proiectare pentru clădiri. *Cod de proiectare seismică P100*, Romania, 2006.

[10] D.A. Gasparini and E.H. Vanmarcke, Simulated Earthquake Motions Compatible with Prescribed Response Spectra. *Research Report R76-4*. Massachusetts Institute of Technology, Department of Civil Engineering, Cambridge, Massachusetts, 1976.

COMPDYN 2011
3rd ECCOMAS Thematic Conference on
Computational Methods in Structural Dynamics and Earthquake Engineering
M. Papadrakakis, M. Fragiadakis, V. Plevris (eds.)
Corfu, Greece, 25–28 May 2011

BEHAVIOR OF CONCENTRICALLY BRACED FRAMES WITH FRICTION DAMPERS

Norin Filip-Vacarescu [1], Aurel Stratan [2], and Dan Dubina [3]

[1] Department of Steel Structures and Structural Mechanics, Faculty of Civil Engineering, Politehnica
University of Timisoara, Ioan Curea 1 Timisoara, Romania
e-mail: norin.filipvacarescu@ct.upt.ro

[2,3] Department of Steel Structures and Structural Mechanics, Faculty of Civil Engineering, Politehnica
University of Timisoara, Ioan Curea 1 Timisoara, Romania
{aurel.stratan, dan.dubina}@ct.upt.ro

Keywords: steel bracing, friction damper, .strain hardening.

Abstract. *The papers investigates the behavior of steel frames with friction dampers connected to steel braces Both numerical and experimental analyses have been conducted in order to characterize in terms of energy dissipation capacity such a type of systems and obtain an equivalent hysteric model to be used in numerical simulations. Tests have been realized for two series of brace members equipped with strain hardening friction dampers: 1st series with the brace designed to avoid buckling; 2nd series with the brace working and prone to post-elastic buckling after the damper consumed its stroke. The equivalent brace-damper model experimentally calibrated has been applied in numerical simulation of multi-storey frames in order to observe their performance in comparison with conventional centric braced systems. In the paper the test results and numerical simulations are summarized as well as the resulted conclusions.*

1 INTRODUCTION

In general damping devices can be classified according to their behavior as follows:

1. Velocity dependent devices

These devices are dependent of the velocity of application of the load. They modify their hysteretic behaviour according to velocity (Figure 1). As an example we can mention here fluid viscous dampers and fluid spring dampers.

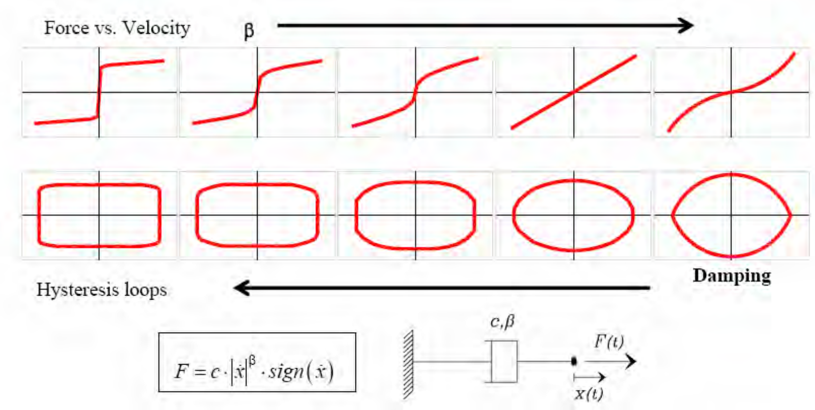

Figure 1: Influence of velocity on hysteretic behavior of fluid viscous dampers [1]

2. Displacement dependent devices

In the category enter devices non-linear behaviour such as: steel hysteretic dampers, shape memory alloy devices, and with linear behaviour such as: elastomeric viscoelastic devices. The damper to be used in the research is a strain hardening friction damper of SERB type manufactured in Romania with the hysteretic behaviour described in Figure 2.

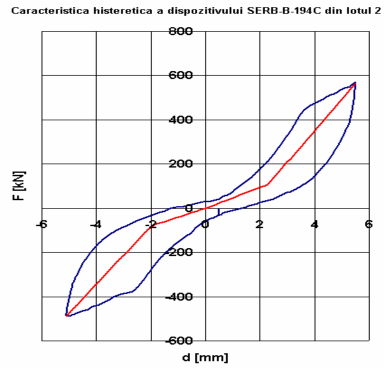

Figure 2: Hysteretic behavior of SERB type friction damper prototype

The paper analyses the behavior of steel dual frames with centrically braced frames in the mid span. The aim is to study and analyze new systems to improve the seismic behavior of steel structures

The studied frame is a dual frame with moment resisting frames and concentrically braced frames equipped with friction dampers at the base of the braces to improve their seismic response. The frame was designed according to EC3, EC8 and special considerations from the Romanian seismic design standard P100-2006 [3] for response spectra with TC=1.6.

For the experimental program a part of the braced frame was extracted and tested in laboratory both with and without damping devices (Figure 3).

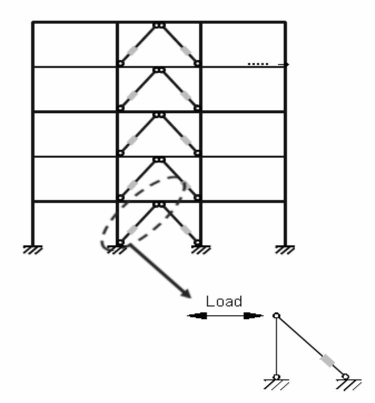

Figure 3: part of the braced frame extracted for experimental tests

2 DESIGN PRINCIPLES

For braced structural systems the seismic design concept translates in designing the braces to dissipate the energy induced by the earthquake through the formation of plastic hinges protecting the elements that are considered non-dissipative from degradation. This concept leads to the introduction of the behavior factor q that reduces the design seismic forces. Introducing damping devices in the structure leads to an increase in energy dissipation capacity of the structure. For these structures the energy dissipation devices represent „sacrificial" elements that assume the role of energy consumers entirely by plastic deformations that occur in the devices. The device prototype that is being analyzed here presents a particular pseudo-elastic behavior. This device does not have elements that yield. Instead, it consumes energy through friction from the elongation and compression of a set of steel rings around a steel core. The structures equipped with this particular type of dampers can be designed using two different concepts. A first concept is to design the braces to remain in elastic domain controlling the response of the structure solely through the friction dampers. In this case the structure has no ductile elements and is designed with a behavior factor corresponding to low dissipative structures of $1<q<2$ and benefits from the reduction of design seismic forces due to the increase in global damping. However, introducing supplemental damping in the structure leads to a much smaller reduction of design seismic loads compared to the reduction that comes from using a higher behavior factor value that corresponds to a dissipative design approach in which the brace itself is the main energy consuming element. For example an increase of damping in the structure to 15% critical damping leads to a reduction of the loads with only 35% [2]. Furthermore these types of dampers have a brittle failure that must be avoided in all configurations. All the above mentioned lead to a second design concept in which the damper has sufficient over strength compared to the brace to assure that the brace has deformation in the plastic domain and is the weaker element in the configuration. This concept should benefit in theory from both the energy dissipation capacity of the brace and the supplemental damping from the device, and the failure will occur in the brace and not in the device. For seismic motion levels corresponding to ultimate limit state the brace is the „active" element according to the dissipative design concept and for service limit state the damper is the „active" element ensuring that the brace remains in elastic domain and providing an overall damping increase. According to P100/2006 [3] the relative story drift criteria for SLS is 0.008h, where h is the story height. For the structure analyzed here this translates in a drift value of 28mm which leads to a displacement of 20mm in the brace. The damping devices were selected to satisfy this displacement criteria corresponding to SLS. Both design concept presented above will be used in the configuration of the experimental tests that will be presented further on.

3 EXPERIMENTAL PROGRAM

The experimental program is divided in two parts:
(1) experimental tests on friction dampers;
(2) experimental tests on single brace configuration with and without dampers.

3.1 Experimental tests on friction dampers

Experimental tests were performed on two dampers with maximum capacity of 800kN and 1500kN. The tests were performed in the CMMC laboratory using a cyclic load protocol. The tests were done using a load control protocol having as reference the maximum capacity of each damper Three cycles were considered at each force level (Figure 4a).

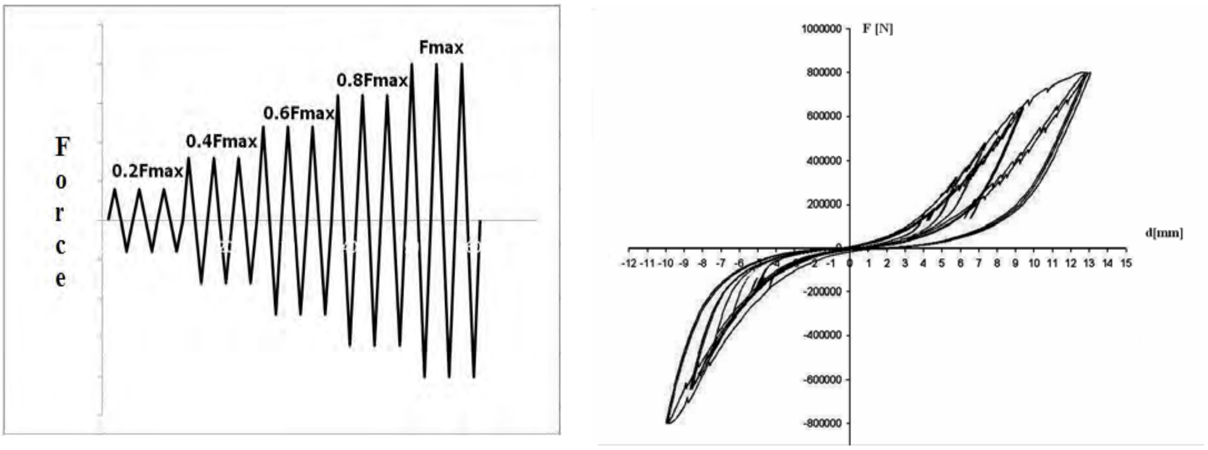

a.

b.

Figure 4: Cyclic force control load protocol (a) and force displacement curve obtained for 800kN damper (b)

The hysteretic curves obtained experimentally were in accordance to those supplied by the manufacturer (Figure 4b).

3.2 Experimental tests on single brace configuration with and without dampers

The experimental model is made from half of the beam and the brace, hinged at both ends with or without dampers installed. In the experimental program the two design concepts presented before can be found. The first concept is based on a design of the system so that energy dissipation occurs in the damper alone. This was achieved by designing the brace with sufficient over strength relative to the maximum capacity of the device. The second design concept follows both the behavior of the damper and of the beam in post-elastic domain. This was achieved by choosing the device with sufficient over strength with respect to the brace. According to these principles the cross sections of the brace were chosen as follows:
(1)„Strong” brace configuration (HEA240);
(2)„Weak” brace configuration (CHS D133x5 and HEA100)
The experimental program is detailed in Table 1:

.

No	Brace	Specimen	Damper	Type	Tests	Measured Parameters
1.	HEA 240	BDE-C	YES	cyclic	2	-relative displacement of the brace -total displacement -brace force -damper displacement -global behavior
2.	CHS, D133,t=5	B-MT, B-MC	NO	monotonic	2	
3.	CHS, D133,t=5	B-C	NO	cyclic	2	
4.	CHS, D133,t=5	BDY	YES	cyclic	2	
5.	CHS, D133,t=5	BDY	YES	cyclic	2	
6.	HEA100	HB-MT, HB-MC	NO	monotonic	2	
7.	HEA100	HB-C	NO	cyclic	1	
8.	HEA100	HBDY-C1	YES	cyclic	1	
9.	HEA100	HBDY-C2	YES	cyclic	1	

Table 1 : Experimental program for brace tests with and without dampers

3.3 „Strong” brace configuration with damper (BDE)

In order to validate the experimental behavior of the test configuration in this stage is based on the „strong” brace concept in which the brace is designed to remain in elastic domain. The aim of these tests is to study the behavior of the damper with the brace as the element with over strength. The load protocol used is identical with that used for the single damper having as reference the maximum force capacity of the damper. The experimental test configuration (Figure 5a) and total force-displacement recorded for the HEA240 brace (Figure 5b) are presented below.

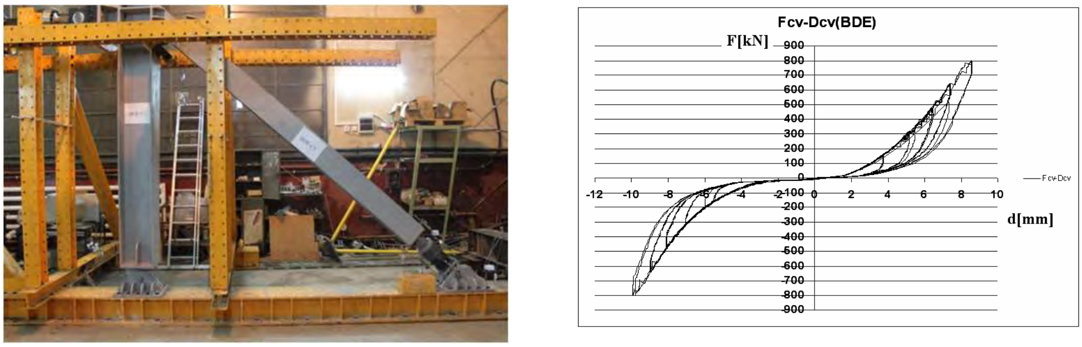

a.

b.

Figure 5: Experimental test configuration (a) and global force-displacement curves for specimen BDE (b)

The total response of the system is governed by the behavior of the damper resulting in a symmetrical behavior both in tension and in compression without strength and stiffness degradation. The brace remains in elastic domain for the entire test duration. The test was stopped when the device reached its maximum capacity. For the “weak” brace configuration two types of cross-sections for the brace were used as it was presented in the summary of experimental program. The procedure of experimental investigation was the same for the two brace types and the results showed the same global behavior of the brace with and without damper. For this reason only the experimental data obtained on HEA100 braces will be presented here.

3.4 HEA100 brace with and without damper

Monotonic tests were conducted at first for the brace without damper in order to determine the yield displacement and yield force which was used to construct the load protocol according to ECCS procedure that was used for the cyclic tests that followed. The experimental test setup had the same general configuration as the one described in the paragraph above. The behavior curves obtained for the monotonic tests and buckling of brace is presented in Figure 6a,b.

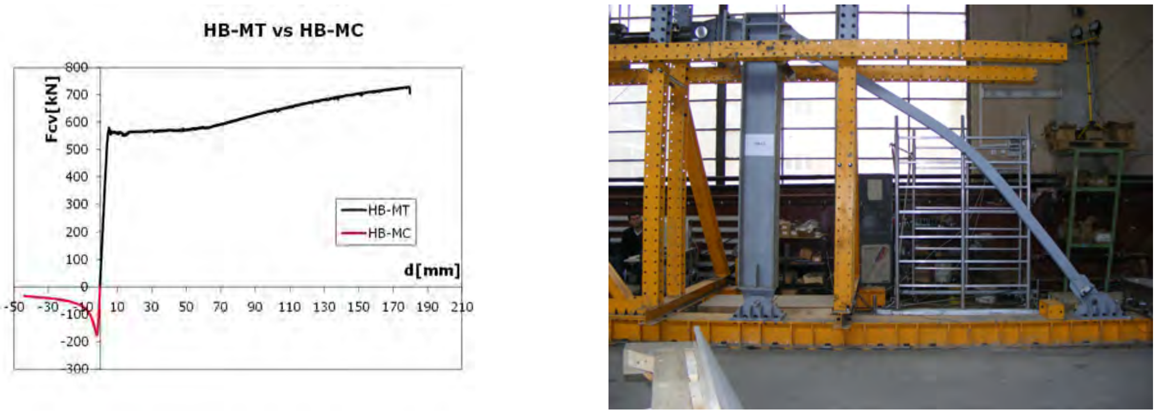

a. b.

Figure 6: Monotonic test results on HEA brace without dampers (a) and buckling of the brace in compression (b)

The load protocol for the cyclic tests was constructed using the results from the monotonic tests. The loading protocol is made according to ECCS procedure with cycles at steps of magnitude 0.25, 0.5, 0.75, 1.0, 2, 4, 6, 8 times ey with 3 cycles at each step following ey (ey-yield displacement of brace obtained from monotonic tests). The hysteretic behavior of the HEA brace without damper under cyclic load with ey=4 mm is presented in Figure 7a and the brace equipped with damper under cyclic load in Figure 7b.

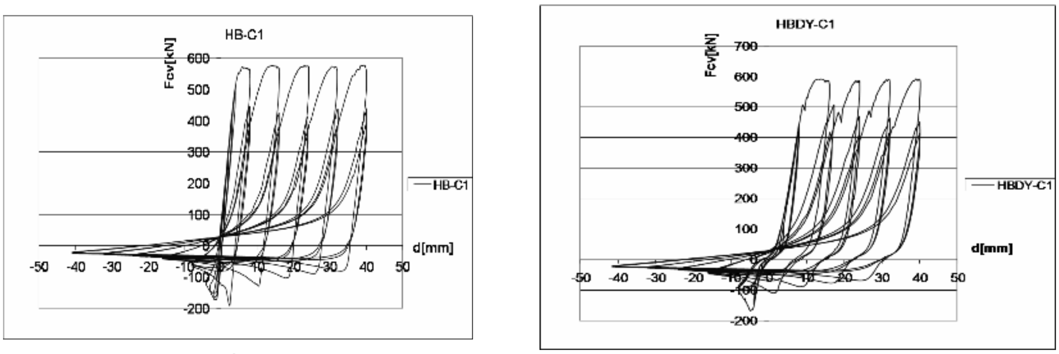

a. b.

Figure 7: Hysteretic behavior of the HEA100 beam without damper under cyclic load(a) and with damper under same cyclic load(b)

4 DISCUSSION

In order to analyze the influence of the damper on the global behavior of the brace the hysteretic behavior of the brace without damper is taken as reference curve. The behavior of the brace with damper obtained for the two design concepts of „weak” and „strong” brace is therefore compared with the hysteretic behavior of the brace without damper.

4.1 „Strong” brace with damper configuration

The behavior of the brace with dampers taken as reference is considered that recorded for double T section profile of the brace (HB-C) mainly following two parameters: recorded total force in the brace and total displacement of the brace. This is compared to the behavior recorded for the system comprised of „strong” brace (HEA240) with damper (BDE).

In this design concept the global behavior of the system of brace and damper is completely governed by the constitutive law of the damper and its properties. The system does not suffer any degradation in terms of strength and stiffness these being strictly dependent on the damper properties. The system will continue to take on load until the maximum capacity of the device is reached, with the brace remaining in elastic range. This high load carrying capacity without strength and stiffness degradation represents the advantage of this type of design concept but can also lead to an increase of the load levels in the beams and columns of the braced frame due to the pseudo-elastic behavior of the damper. Furthermore failure of this type of system is a brittle one due to failure of the device and must be avoided.

4.2 „Weak” brace with damper configuration

In this design concept the brace is allowed to have plastic deformation and the global behavior of the damper brace system is a mixed one. The weak element in this configuration is the brace which will ultimately fail. The behavior of this system is presented in Figure 8a in comparison with the behavior of the same brace, under the same load protocol but without damper.

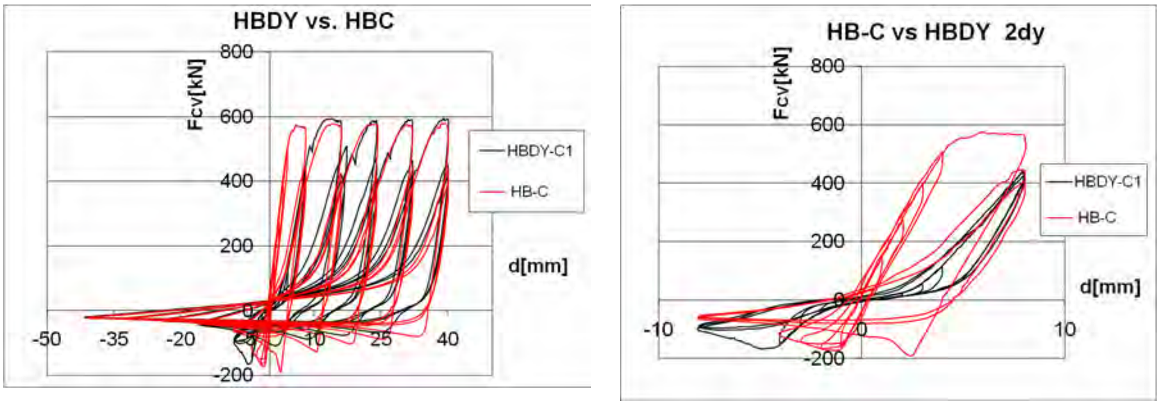

a.

b.

Figure 8: Comparison between the total hysteretic behaviors of the “weak” brace with damper and without damper (a) and hysteretic behaviors up to 2ey (b)

In both configurations the force level drops significantly after the fist cycle at each load step and the next two cycles of the same load step. The brace with damper has a higher flexibility and yields at the same load step but at a displacement of approximately 50% higher. For this system up to a level of 2ey the global behavior is governed by the behavior of the damper and by the behavior of the simple brace at higher load steps. The difference between these two systems can be observed more closely up to a level of 2ey (Figure 8b).

Up to this level the behavior is that given by the damper parameters. At tension cycles the brace remains in elastic domain and the load level in the system is significantly smaller then that of the brace without damper with a higher overall flexibility. For compression cycles the brace with damper buckles at the same load level as the one without damper but has a higher deformation capacity due to the damper properties. The experimental results are in agreement with the two design concepts considered. For the starting load levels of up to 2dy the brace remains in elastic domain and has a lower level of energy dissipation but there is a significant decrease in load level due to the damper and also an increase in flexibility. After this level the hysteretic behavior of the system is very similar to that of the brace without damper, with energy dissipation due to the formation of a plastic hinge in the brace. Failure in this design concept is represented by the failure of the brace in compression. As a preliminary conclusion it is expected that this type of damper could improve the behavior of rigid structures that are sensitive to formation of plastic hinges at levels corresponding to service limit state.

5 NUMERICAL MODELLING

The numerical modeling can be split mainly in two independent parts or stages. The first stage consists of numerical simulation of the behavior of the two elements, the brace and the damper separately, but most importantly their behavior as a whole. The second stage consists of a series of numerical simulation on the full dual frame with and without dampers in the braces. Numerical time-history analysis will be conducted using a set of recorded seismic motions scaled to the design spectra. The final stage consists of performance base evaluation of the structure with this type of damping devices and the comparison with other types of damping devices used for seismic protection.

5.1 Brace modeling

The main issue that arises with brace modeling is the accurate modeling of brace behavior at buckling. For the numerical simulation SEISMOSTRUCT version5.5 Build 10 software was used, a finite element package that uses fiber formulation. The buckling behavior of brace was modeled using geometric imperfections computed according to EN1993 1-1[4]. The brace element was divided into segments with each point having corresponding values of the imperfections computed based on a parabolic shape of the deflection with the value of the imperfection computed at midpoint of the element e_0=26.54 mm. A parametric study was conducted to determine the optimum number of elements in which the brace is to be divided and the value of the imperfections to be adopted comparing the cyclic behavior of the brace with the behavior obtained from experimental tests. The brace was divided in 2 and 4 elements and for each of the 2 models 4 values of the imperfections were considered: e_0, $e_0/2$, $e_0/3$, $e_0/4$ (Figure 9a). The material properties used were also obtained experimentally from tension tests on steel samples from the HEA100 brace.

The best results were obtained for the 2 element brace with a value of imperfection at midpoint of e0/2 (Figure 9b). Parametric studies conducted by Landolfo et.al.2010 [6] also recommended the use of 2 element division for modeling cyclic behavior of brace

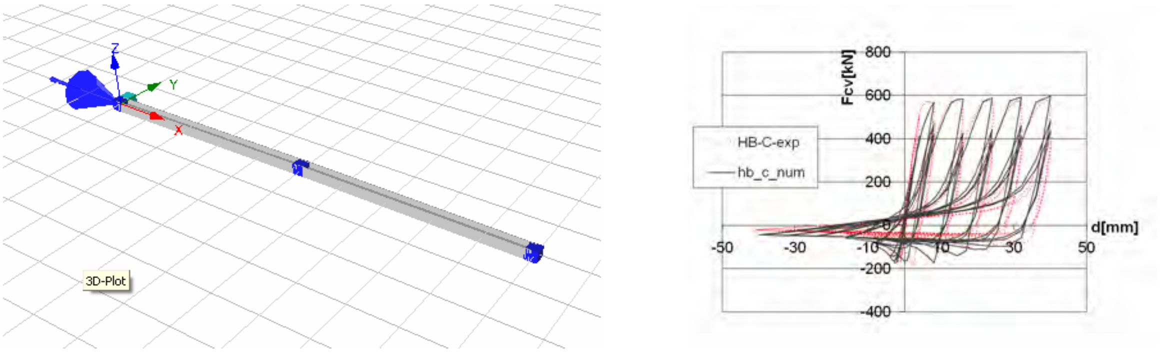

a. b.

Figure 9: Brace model in SeismoStruct (a) and comparison between cyclic behavior of brace from the numerical model with the one obtained experimentally

5.2 Damper modeling

For modeling of devices SEISMOSTRUCT software offers the use of link elements that have the possibility of defining different hysteretic behavior for each of the 6 degrees of freedom. To model the behavior of the SERB damper a combination of two parallel link elements was used. The hysteretic loops of the damper were modeled using a bilinear symmetric behavior type link (Figure 10b) combined with a gap-hook element that is employed to model the pinching of the curve (Figure 10a). These types of behavior laws were defined only for the degree of freedom corresponding to axial deformation, the other 5 degrees having a linear elastic behavior with sufficiently high stiffness as to ensure their restraint.

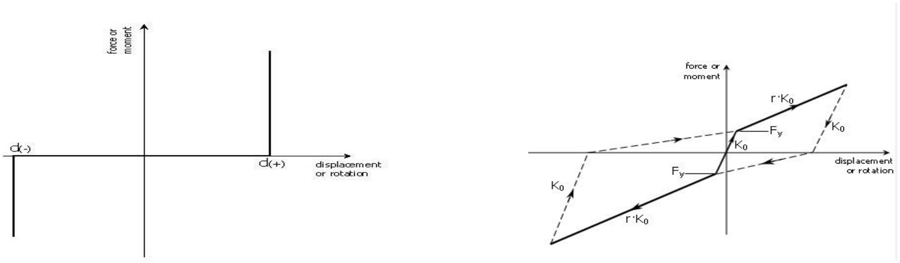

a. b.

Figure 10: Gap-hook behavior (a) and bilinear symmetric behavior of link element (b) [5]

The behavior obtained in the numerical model using the combined behavior these 2 types of link elements provide a satisfactory model behavior of the damper (Figure 11b)

5.3 Brace with damper model

The behavior of the brace with damper is obtained combining the models discussed above for the brace and the damper. The results from the numerical model were compared to the experimental results HBDY-C1 (Figure 11a).

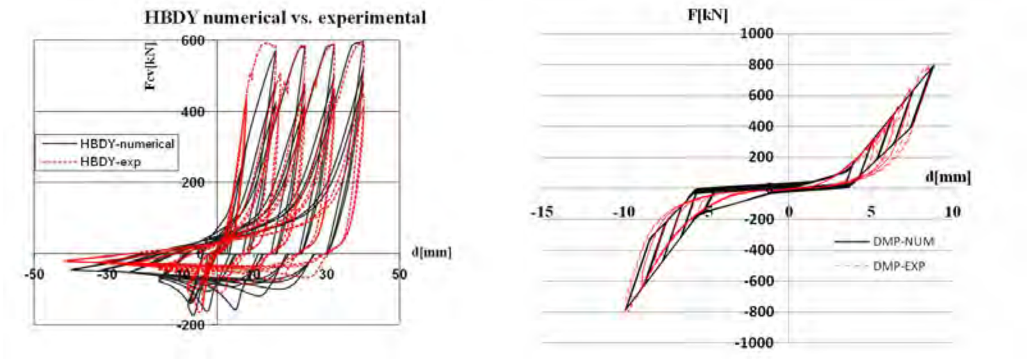

a. b.

Figure 11: Comparison between experimental and numerical behavior of HEA brace with damper (a) and comparison of the experimental and numerical damper behavior (b)

The numerical model presents the same global behavior as the one obtained from experimental data with a damper governed behavior up to 2ey and a brace governed behavior afterwards, reaching the same peak values of force for each tension cycle and with suficiently acurate modelling of sliding of the damper at zero force point transition. This two models for the brace and for the damper as presented above are employed in the overall assesment of the behavior of the full frame.

5.4 Numerical simulation on the full frame

The structure analyzed is a 5 storey plane frame extracted from a 3x3 layout with 3 spans of 6m with chevron bracing in the mid-span and a storey height of 3.5m (Figure 12a). The frame was design according to EC3 and EC8 with some special considerations from the Romanian seismic design code P100/2006 considering the design spectra for Bucharest with a corner period of TC=1.6s. Time-history analyses are conducted using two sets of seismic motions recordings scaled to the design spectra as follows: 7 recorded seismic motion characteristic for soft soil type (Bucharest) and 7 artificially generated seismic motions characteristic for stiff soil (Class B soil according to SREN1998-1) both with and without dampers (Figure 12b). The two target spectra were scaled to the fundamental period of vibration of the analyzed structure, so as to yield roughly the same design seismic forces. Three performance levels were considered for each seismic motion having an acceleration multiplier of 0.5, 1.0, 1.5 corresponding to serviceability limit state (SLS), ultimate limit state (ULS) and collapse prevention (CP) respectively. Performance based evaluation was performed using acceptance criteria for plastic deformation in the braces and plastic rotation for beams and columns according to FEMA356

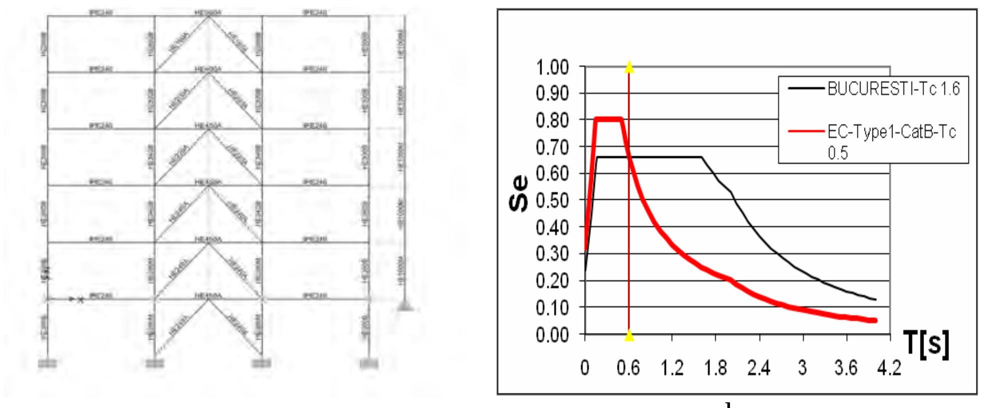

a. b.

Figure 12: Analyzed frame geometry (a) and design spectra used (b)

For the first set of time-history analysis the 7 seismic motion recordings for a soft soil type scaled for the Bucharest response spectra were used. For all 7 seismic motions used the results showed that for all performance levels the building with dampers exhibited a significant increase in drift for all 5 storeys. For SLS (0.5) the building without dampers does not form any plastic hinges in elements while the building fitted with dampers forms plastic hinges in the bracing with values of plastic deformation that check the acceptance criteria for immediate occupancy (IO) from FEMA. At ULS (1.0) both frames with and without dampers form plastic hinges in braces and in the central beams. At this level the structure with dampers has a higher number of plastic hinges in elements and a higher value of plastic deformation/rotation in elements then the structure without dampers. The values of plastic rotation for the beams exceed the acceptance criteria corresponding to life safety (LS) from FEMA 356. At collapse prevention (1.5) the behavior of both types of frames is considered unsatisfactory due to the formation of plastic hinges in central columns at most levels. As example max drift values for 3 of the 7 seismic motions with T_C=1.6s are shown in Figure 13 and values of plastic deformation/rotation for first seismic recording VR-77-INC-NS at SLS (Table 2) and ULS (Table 3, Table 4, Table 5) with and without dampers in the braces are presented.

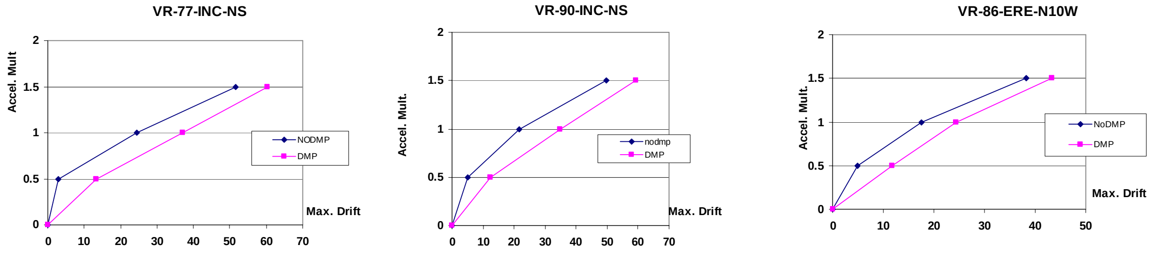

Figure 13: Comparison of the maximum drift levels for 3 of the 7 seismic motions with T_C=1.6s

BRACE Compr.	**Plastic deformation demand-SLS , mm**		**Plastic deformation capacity, mm**
LOC.	**NODMP**	**DMP**	**IO**
BR5R	-	0.43893	0.692
BR4L	-	0.75084	0.8945
BR2L	-	1.67516	1.1225

BR3L	-	1.18621	0.99125
BR5L	-	0.71606	0.692
BR(storey no.)R- right brace for selected storey			
BR(storey no.)L- left brace for selected storey			

Table 2: Plastic deformation for braces in compression at SLS for VR-77-INC-NS seismic recording (soft soil)

BRACE Tens.	**Plastic deformation demand-ULS , mm**		**Plastic deformation capacity, mm**
LOC.	**NODMP**	**DMP**	**LS**
BR1R	5.78823	2.61921	40.2283
BR2L	3.11884	0.27856	40.2283
BR2R	18.61805	11.77078	40.2283
BR3R	17.40089	18.75723	39.97
BR4R	2.69104	5.94618	39.48
BR3L	-	3.90426	39.97
BR5R	-	0.95701	39.039
BR(storey no.)R- right brace for selected storey			
BR(storey no.)L- left brace for selected storey			

Table 3: Plastic deformation for braces in tension at ULS for VR-77-INC-NS seismic recording (soft soil)

BRACE Compr.	**Plastic deformation demand-ULS , mm**		**Plastic deformation capacity, mm**
LOC.	**NODMP**	**DMP**	**LS**
BR1R	0.33586	0.90386	22.45
BR2L	0.59929	2.00463	22.45
BR2R	0.56675	2.27719	19.825
BR3R	0.52462	1.35489	17.89
BR4R	0.52487	2.18994	13.84
BR3L	0.45988	-	13.84
BR(storey no.)R- right brace for selected storey			
BR(storey no.)L- left brace for selected storey			

Table 4: Plastic deformation for braces in compression at ULS for VR-77-INC-NS seismic recording (soft soil)

BEAM	**Plastic rotation demand-ULS , mm**		**Plastic rotation capacity, mm**
LOC.	**NODMP**	**DMP**	**LS**
grc3b	-	0.009598	0.007818
grc4a	-	0.007697	0.009118
grc2a	0.01832	0.028828	0.007969
grc3a	0.004891	0.012671	0.008091
grc1a	0.021767	0.03177	0.008009
grc2a	0.01832	0.028546	0.008532
grc2b	0.008985	0.019499	0.0073
grc1b	0.011624	0.01955	0.008447

Table 5: Plastic rotation at ULS for central beams VR-77-INC-NS seismic recording (soft soil)

For the second set of time history analysis the 7 seismic motion recordings for a hard soil type scaled for the Type 1 response spectra and Class B soil according to EN 1998 were used. For all 7 seismic motions used the results showed that the building with dampers exhibited a decrease in maximum drift values for SLS and an increase for the other 2 performance levels. For SLS the frame with dampers does not form any plastic hinges in the braces as opposed to the one without dampers (Figure 14a, b). At ULS the presence of dampers continues to improve the behavior of the structure by reducing the number of plastic hinges in elements but with higher values of drift at each storey (Figure 14c, d). As example max drift values for 3 of the 7 seismic motions with T_C=0.5s are shown in Figure 15and values of plastic deformation/rotation for first seismic recording at SLS (Table 6) and ULS (Table 7, Table 8, Table 9) with and without dampers in the braces are presented.

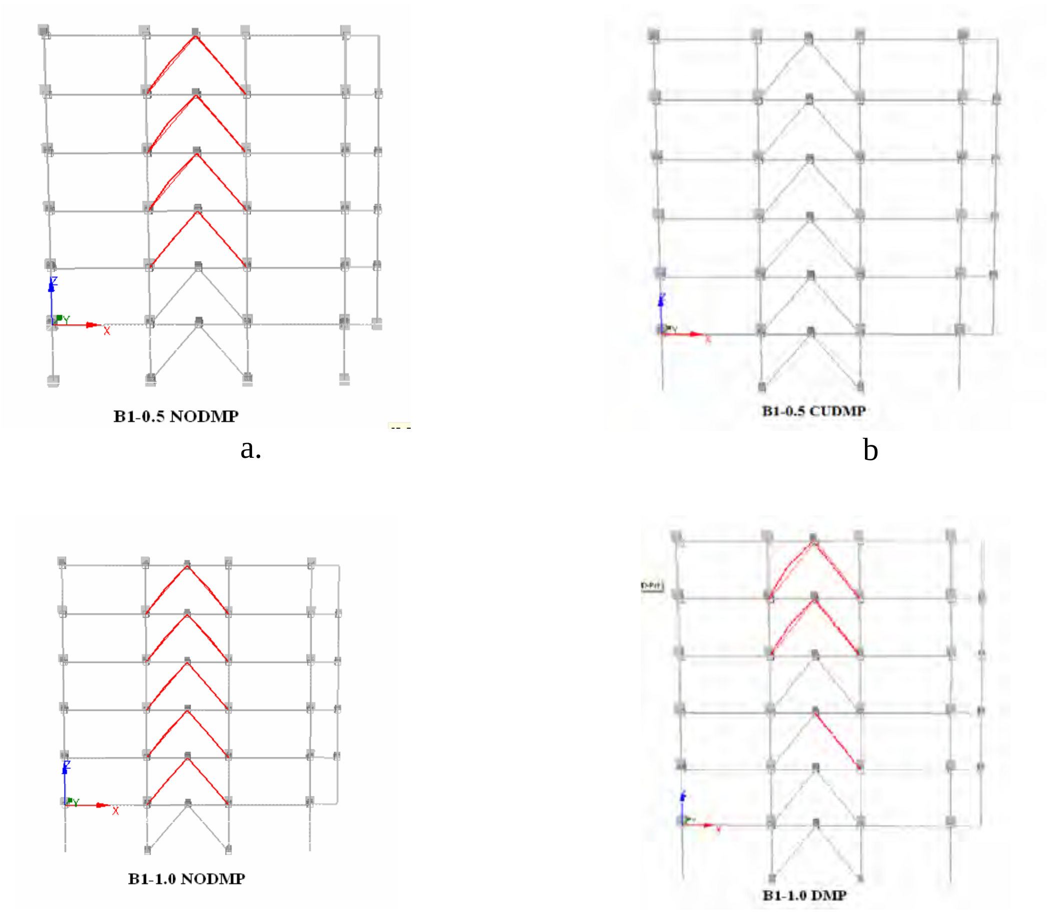

a. b

c d.

Figure 14: Plastic hinge location at SLS for the structure without dampers (a) and with dampers (b) and corresponding to ULS without dampers(c) and with dampers (d) for one of the 7 seismic motions with T_C=0.5s

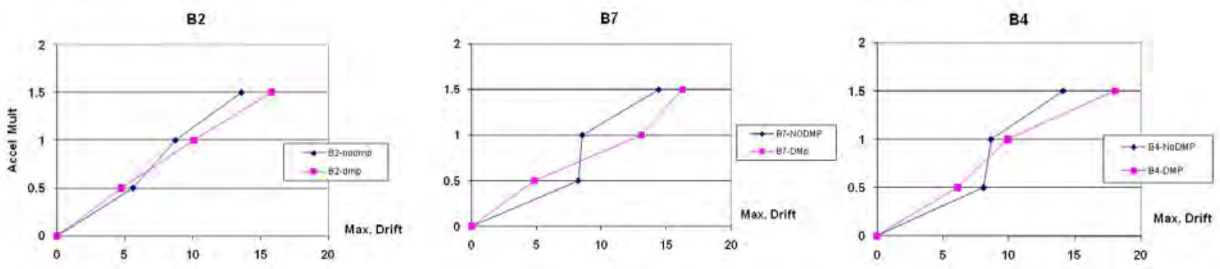

Figure 15: Comparison of the maximum drift levels for 3 of the 7 seismic motions with T_C=0.5s

BRACE Compr.	**Plastic deformation demand-SLS , mm**		**Plastic deformation capacity, mm**
LOC.	**NODMP**	**DMP**	**IO**
BR5R	0.271	-	13.84
BR3R	0.567	-	19.825
BR4L	0.682	-	17.89
BR5L	0.455	-	13.84
BR2L	0.291	-	22.45
BR(storey no.)R- right brace for selected storey			
BR(storey no.)L- left brace for selected storey			

Table 6: Plastic deformation for braces in compression at SLS for B1 seismic recording (stiff soil)

BRACE Tens.	**Plastic deformation demand-ULS , mm**		**Plastic deformation capacity, mm**
LOC.	**NODMP**	**DMP**	**LS**
BR1R	2.642	-	40.2283
BR2L	1.336	-	40.2283
BR2R	5.497	-	40.2283
BR3R	2.627	-	39.97
BR4L	2.061	1.612	39.48
BR4R	1.979	-	39.48
BR5L	3.482	4.330	39.039
BR5R	3.308	5.975	39.039
BR(storey no.)R- right brace for selected storey			
BR(storey no.)L- left brace for selected storey			

Table 7: Plastic deformation for braces in tension at ULS for B1 seismic recording (stiff soil)

BRACE Compr.	**Plastic deformation demand-ULS , mm**		**Plastic deformation capacity, mm**
LOC.	**NODMP**	**DMP**	**LS**
BR1L	0.022	-	22.45
BR2L	0.442	-	22.45
BR3L	0.351	-	19.825
BR4L	0.819	0.822	17.89
BR5L	1.216	1.395	13.84
BR5R	0.615	1.857	13.84
BR(storey no.)R- right brace for selected storey			
BR(storey no.)L- left brace for selected storey			

Table 8: Plastic deformation for braces in compression at ULS for B1 seismic recording (stiff soil)

BEAM	**Plastic rotation demand-ULS , mm**		**Plastic rotation capacity, mm**
LOC.	**NODMP**	**DMP**	**LS**
grc4a	-	0.003052	0.0091304

Table 9: Plastic rotation at ULS for central beams for B1 seismic recording (stiff soil)

At CP the global behavior of the two structures is similar, however for some of the seismic recordings for which the structure without dampers forms plastic hinges in central columns at the base of the structure the structure with dampers has no plastic hinges in columns. For all performance levels the recorded plastic deformations/rotations satisfy the acceptance criteria.

6 CONCLUSION

Experimental tests were conducted on SERB type friction damper and on damper with brace configuration. Two design concepts with “weak” and “strong” brace configuration were proposed and tested. The main purpose of the experimental program was to obtain the hysteretic behavior of the friction damping devices and the global behavior of the ensemble of brace together with damper in the two design concepts. A numerical model was developed for the brace with damper assembly and used in a performance based evaluation of the building under 2 sets of 7 recorded seismic motions scaled on 2 types of response spectra. The first set of numerical analyses showed that the frame equipped with dampers increases the flexibility of the structure, forming plastic hinges at SLS with a higher number of plastic hinges with higher values of plastic deformation/rotation in braces and beams respectively that no longer satisfy the performance criteria and generally a worse global behavior. The conclusion is that this particular type of damper is not efficient in reducing the seismic response of a building for earthquakes characterized by a high value of corner period T_C=1.6s (soft soil). The second set of numerical analyses showed that the frame equipped with dampers has a better performance avoiding the formation of plastic hinges at SLS and reducing the values of maximum drift, reducing the number of plastic hinges in elements at ULS and for some recordings avoiding the formation of plastic zones in columns at CP. The conclusion is that this particular type of damper is efficient in reducing the seismic response of a building for earthquakes characterized by short corner period T_C=0.5s (stiff soil).

REFERENCES

[1] PROHITECH, WP6 Report, *Set-up of Advanced Reversible Mixed Technologies for Seismic Protection*, edited D.Beg., P.Skuber. L.Pavlocic, University of Ljubljana Faculty of civil and geodetic engineering Slovenia

[2] EN 1998-1 2004. *Design provisions for earthquake resistance of structures: General rules - Seismic actions and general requirements for structures*

[3] P100-1/2006 *Seismic Design Code (Cod de proiectare seismică-Partea I-Prevederi de proiectare pentru clădiri*)

[4] EN 1993 1-1 *Design of steel structures. General rules for buildings*

[5] SEISMOSOFT- SEISMOSTRUCT version 5.5 build 10 *Reference Manual*

[6] R. Landolfo, M D’Aniello, F. Portioli, *Simulation of inelastic cyclic behaviour of steel concentric bracings*, 14ECEE 30.08-3.09 2010, Ohrid, T3,no.1816

[7] FEMA356 *Prestandard and Commentary for the Seismic Rehabilitation of Buildings*, Nov 2000

COMPDYN 2011
III ECCOMAS Thematic Conference on
Computational Methods in Structural Dynamics and Earthquake Engineering
M. Papadrakakis, M. Fragiadakis, V. Plevris (eds.)
Corfu, Greece, 25–28 May 2011

EXPERIMENTAL AND NUMERICAL INVESTIGATION OF NON-SEISMIC REINFORCED CONCRETE FRAMES STRENGTHENED WITH CONCENTRIC STEEL BRACES

D. Dubina[1,2], **S. Bordea**[1] **and F. Dinu**[1,2]

[1] The "Politehnica" University of Timisoara
Str. Ioan Curea 1, 300224, Timisoara, Romania
e-mail: dan.dubina@ct.upt.ro

[2] Romanian Academy, Timisoara Branch
Str. Mihai Viteazul 24, 300223, Timisoara, Romania

Keywords: reinforced concrete structure, strengthening, concentric brace, buckling restrained brace, energy dissipation, q factor.

Abstract. *Many reinforced concrete structures built before 1960's were designed to resist mainly gravity loads and wind, even if they were located in seismic zones. That is why when subjected to earthquakes of intensities even below the design level, they are at risk because of poor detailing and lack of capacity. Evaluation of such type of structures according to the present seismic design provisions leads, in most cases, to the necessity of strengthening.*

In the paper, the strengthening of non-seismic reinforced concrete frames with dissipative inverted V bracing systems is presented. Conventional concentric V braces and buckling restrained V braces are used. Portal frames with and without bracings are isolated from a real structure and tested experimentally under monotonic and cyclic loading. The tests aimed to offer information related to the real dissipation capacity of the initial unretrofitted structure and the retrofitted structures, including the effectiveness of connecting details of pre-stressed tendons, specifically designed for connecting braces in an existing frame. Both test results and numerical simulations on portal frames and on strengthened building frames have been used to evaluate the q factors.

1 INTRODUCTION

In many areas with seismic risk, the reinforced concrete structures (RC) built before 1960's were designed to resist mainly gravity loads. The main deficiencies of these structures are linked to low quality of material (poor concrete) and insufficient detailing (insufficient confinement and anchorage of the reinforcements), and thus leading to reduced local and global ductility and, finally, to a poor seismic response. When such types of structures are evaluated according to the present seismic design provisions, one finds out that, in almost all cases, strengthening is needed. Intervention strategies must be appropriately selected and applied but at the same time they must be linked to the available capacity of existing structure in terms of strength, stiffness and ductility. Reinforced concrete jacketing or FRP wrapping of existing members are among the most used strategies. Disadvantages of these strategies are linked to their irreversibility and lack of efficiency when lateral stiffness is insufficient. In these cases, the system can be improved by adding new structural elements, e.g. steel bracings, with or without local strengthening of elements with deficiencies. The main objective of the study is to validate a seismic strengthening technique for non-seismic reinforced concrete frame buildings that consists of conventional concentric V braces (CBS) or buckling restrained V braces (BRB). Numerical and experimental investigations were carried out at Politehnica University of Timisoara, within CEMSIG Research Centre (http://cemsig.ct.upt.ro) in order to study and realize this intervention [1]. The case study is represented by a historical building, erected in the first half of the XXth century. The reinforced concrete building was designed according to the Italian design code at the time but is characteristic of many reinforced concrete buildings constructed before 1970 both in Italy and in other southern European countries.

2 PERFORMANCE BASED EVALUATION AND RETROFIT OF A REINFORCED CONCRETE FRAME BUILDING

The 3 story building has plan dimensions of 23.4 by 18.4 m and 11.95 m height (Figure 1). The characteristics of rebars and concrete were considered those used in that period, i.e. concrete characteristic compressive strength f_{ck}=20N/mm^2, rebars with a characteristic yield strength f_{sk}=230N/mm^2. The specific detailing of the reinforcement is also characteristic for the design practice at that time, with poor anchorage length of the rebars at the external beam-to-column joint, the use of plane rebars (not ribbed), inclined reinforcement used for shear resistance and large spaced stirrups (15cm for columns and 25cm for beams) in plastic zones.

In the first step, the evaluation of the structural system of existing building was performed, to decide the locations of intervention. The seismic response was first evaluated using a response spectrum analysis. The seismic load for ultimate limit state verifications was defined through an elastic spectrum with the following parameters: peak ground acceleration (PGA) of 0.23g, γ_I=1.0, T_B=0.15s, T_C=0.5s, T_D=2.0s and S=1.2, where the periods T_B, T_C and T_D and the soil factor S describe the shape of the elastic response spectrum and depend upon the ground type. Considering the very poor ductility of the structure, a seismic behavior factor q = 1.5 was used. For structure strengthened with BRB, the seismic behavior factor q amounted 4, while for structure strengthened with CBS, the seismic behavior factor q amounted 2. For the steel braces, the cross sections requirements were: in X direction, ground floor = 8 cm^2, 1st level = 4 cm^2, 2nd level = 3 cm^2; in Y direction, ground floor = 6 cm^2; 1st level = 5 cm^2 and 2nd level = 3 cm^2.

Then, a detailed seismic evaluation using a static nonlinear analysis, both for initial structure and for strengthened structure, was performed. The static nonlinear procedure was based on the N2 method (EN 1998-1, 2004) [2]. Three limit states, defined as immediate occupancy (IO), life safety (LS) and collapse prevention (CP) were used. The performance based seismic evaluation implied the verification of behavior at three performance levels introduced above (i.e. IO, LS, CP), using three target displacements, one for each level. The design seismic hazard (associated to LS) corresponds to a recurrence interval of 475 years. For IO and CP, the recommendation is to use hazards with 95 years return period and 975 years return period, respectively. Table 1 shows the simplified coefficients for conversion of the peak ground acceleration (PGA) corresponding to a recurrence interval (IR) of 100 years to values of PGA corresponding to IR of 30 and 475 years. The 2D analysis was done separately on X and on Y directions for all three structural systems (MRF, MRF+BRB and MRF+CBS). The concrete material was considered unconfined and modeled using nonlinear model of Kent and Park, with no tension. Reinforced concrete members were modeled with plastic hinges concentrated at both ends. The bracing system was applied on the external frames of the RC building as an inverted V system pinned at the ends. The inelastic behavior of BRB system was modeled considering the concentrated tri-linear plasticity curve with strain hardening and strength degradation of 0.8 from maximum capacity, according to FEMA356/ASCE-41 [3]. For steel braces in tension, the modeling parameters and the acceptance criteria were based on [3] and on previous experimental tests on BRB elements (see [3]) and are summarized in Table 2. Modeling parameters and acceptance criteria for CBS were also based on [3], see Table 3.

Ratio of seismic hazard/design seismic hazard	a_g(95 years)/ a_g(475 years)	a_g (975 years)/ a_g (475 years)
Conversion coefficient	0.5	1.50

Table 1: Coefficients for conversion of PGA

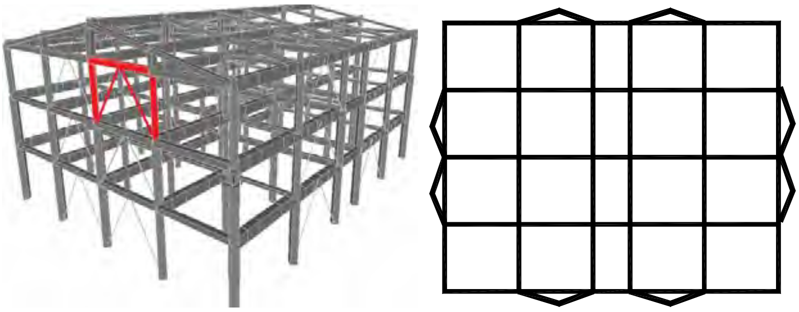

Figure 1: RC building model, with location of brace systems

BRB properties		Values of parameters
Modeling curve	Type	Tri-linear
Material	Steel	S235
Area of the core steel element	A_c [cm^2]	1x3
Core length	L_c [m]	1.7
Yielding displacement	Δ_y [mm]	1.9
Ductility displacement	μ	22
Strain hardening adjustment factor	ω	1.9
Compression adjustment factor	β	1.2
Acceptance criteria (modified FEMA356/ASCE41 for braces in tension)	IO	$0.5\Delta t$
	LS	$14\Delta t$
	CP	$18\Delta t$

Table 2: BRB modeling parameters for the analysis

CB properties		Parameters value
Material		S275
Cross section		Tube 101.6x3.6 mm
Area of the steel element	A_c [cm^2]	11.08
Length	L [m]	3.4
Acceptance criteria FEMA356/ASCE41 for braces in tension/compression	IO	$0.25\Delta_t/0.25\Delta_c$
	LS	$7\Delta_t/4\Delta_c$
	CP	$9\Delta_t/6\Delta_c$

Table 3: CBS modeling parameters for the analysis

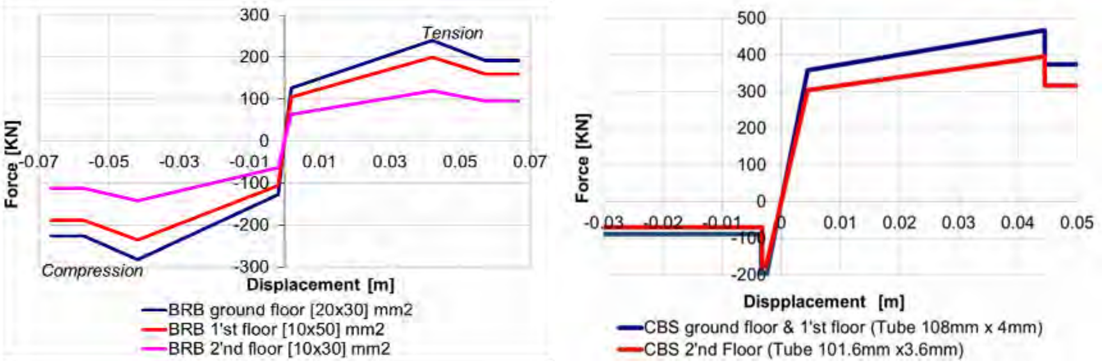

Figure 2: a) Tri-linear modeling on Y direction of: a) BRB system; b) CBS system

The results of the pushover analysis on Y direction are presented in Figure 3.a. Figure 3.b, Figure 3.c and Figure 3.d show the history of plastic hinge in the structures for LS performance level. Different symbols were used to plot the plastic rotation demand in elements: triangle shape is associated to IO, circular shape to LS and rhomb shape to CP.

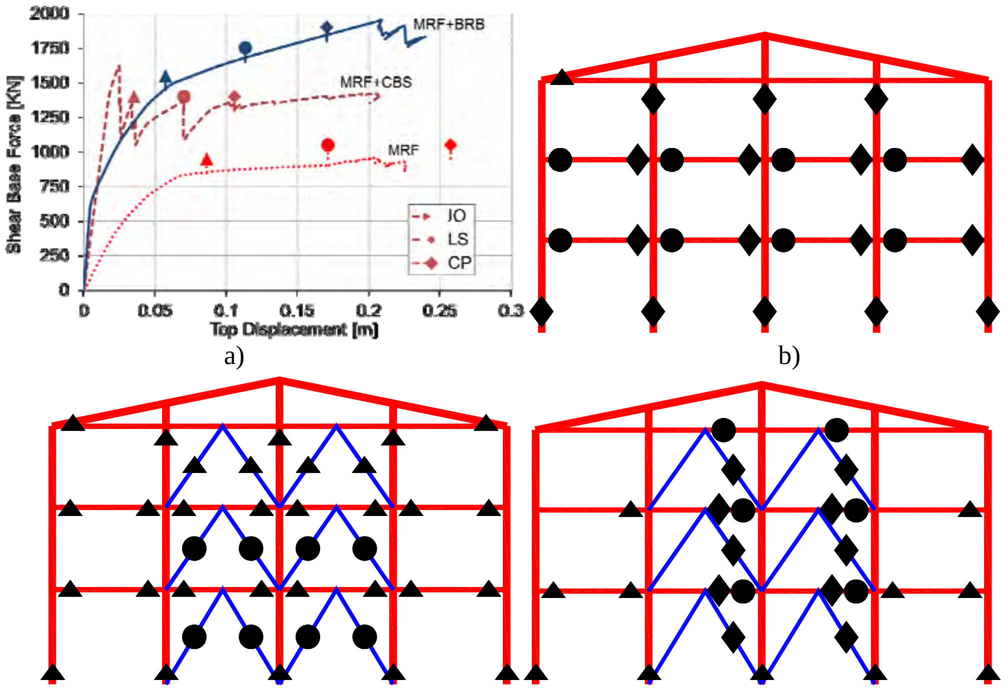

a)

b)

c)

d)

Figure 3: a) Pushover curves on Y direction; Location and stage of plastic hinges corresponding to a LS performance level for; b) MRF (frontal view on Y direction); c) MRF+BRB; d) MRF+CBS

It may be seen the initial structure MRF (Figure 3.b) has a limited ductility and does not attain the performances required for LS, as the plastic rotation demand in beams and columns exceed even CP criteria. When the structure is strengthened with BRB, the behavior is much improved. The stiffness and the strength increase and for LS performance level (Figure 3.c) there are no elements where the acceptance criteria are exceeded. When the strengthening system with CBS is used, the result is a structure with a good stiffness and strength. After the compression brace buckles, there is a reduction of the capacity. It may be noticed that even if less plastic hinges occurred in columns, beams requirements are beyond the acceptance criteria (Figure 3.d). Thus, the unbalanced vertical action effect is transferred to the beam and plastic hinges develops at the beam end and in the vicinity of brace-to-beam connection.

3 EXPERIMENTAL VALIDATION OF STRENGTHNENING SYSTEMS FOR SEISMIC RETROFIT OF A REINFORCED CONCRETE FRAME STRUCTURE

3.1 Test Specimen

Following the results of the nonlinear static analysis, a RC portal frame was isolated from the case study building (Figure 1). Six reinforced concrete frames of 3.2m height and 4.5m span were tested under monotonic and cyclic loads: two RC frames (MRF), two RC frames strengthened with BRB (MRF+BRB) and two RC frames strengthened with CBS (MRF+CBS). Results of materials testing are presented in Table 4. The BRB steel core plate (Figure 4) was divided into three main segments: the end segment (connection), the transition segment and the yielding segment. Based on the experimental results obtained on BRB elements only ([1], [5]), polyethylene foil of 1 mm thick was used as unbonding material. It should be mentioned here the BRB systems must be subjected to a technical validation procedure before intended use, which includes relevant type tests and factory control tests (see EN 15129, [4]). The core was designed for S235, but the material supplied shown larger values by more than 40% (or 100 N/mm^2).

Material		Nominal values [N/mm^2]	Test results [N/mm^2]
RC frame	Concrete (R_c)	20.5	35.5
	Beam rebars (f_y)	235	497
	Beam rebars (f_y)	235	402
	Stirrups (f_y)	235	290
BRB	Concrete (R_c)	20.5	35.1
	Steel Plate (f_y)	235	335
CBF	Tubular section (f_y)	235	248

Table 4: Material test results

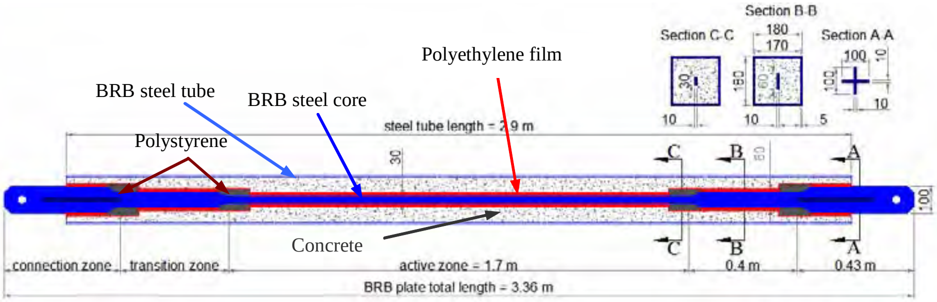

Figure 4: Details and geometry of BRB (unbonding material – polyethylene foil, 1mm thick)

The CBS were realized from circular hollow sections with S235 steel (Figure 5). The material supplied indicated the steel yield strength is very closed to the nominal values.

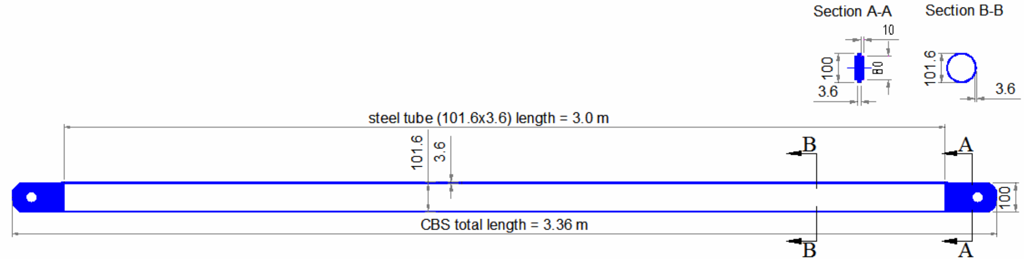

Figure 5: Details and geometry of conventional brace

3.2 Test set-up

The test set-up, the loading system and the specimens installed in testing rig are presented in Figure 6. The connection details for BRB and CBS systems are similar and use pinned connections between the brace elements and the beam and at the base of the columns. In order to prevent the slip of the connection between the braces and the RC beam, high strength pre-loaded ties have been used. The effectiveness of the connecting device has been preliminary checked by FEM simulation. Thus, a numerical simulation aimed to calibrate the level of pre-stressing forces applied in the brace - frame connecting device. Local pressure on the concrete was also checked, in order to keep the connection “elastic” (Figure 7, Figure 8).

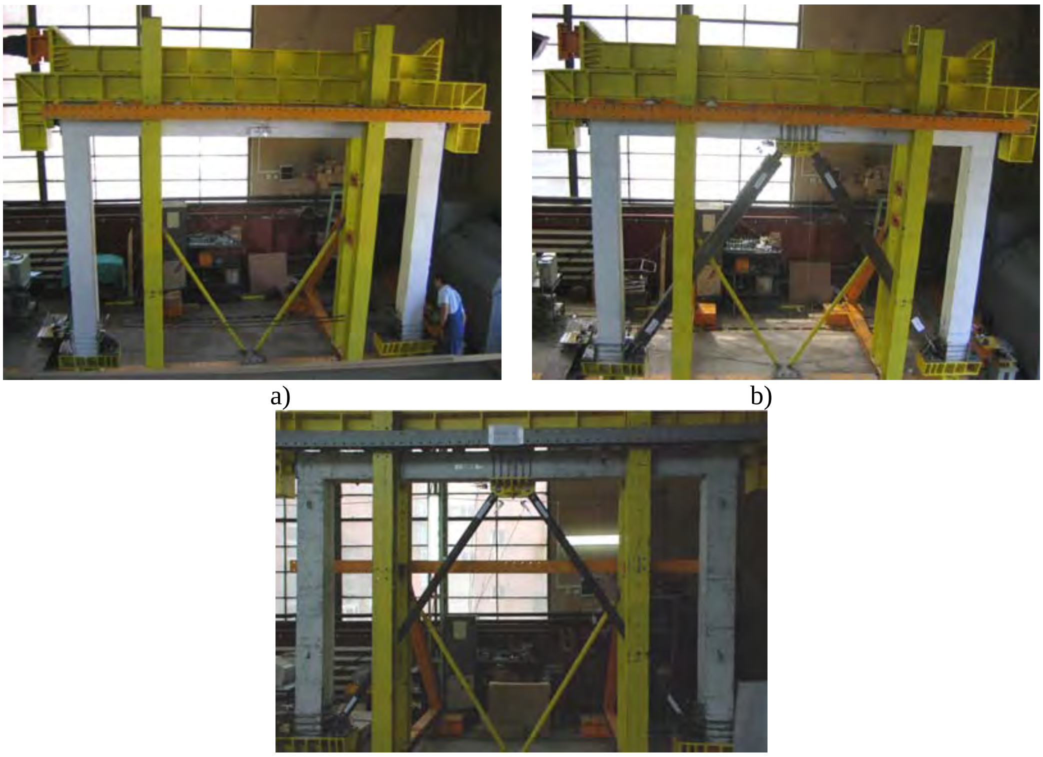
a) b) c)

Figure 6: Test set-up: a) initial RC frame without strengthening; b) RC frame strengthened with BRB; c) RC frame strengthened with CBS

During tests, the vertical and horizontal displacements of the connections were continuously recorded and plotted. Three monotonic tests have been carried out in order to evaluate the yielding point of each type of frame. The yielding displacements measured in the monotonic tests are then used in the subsequent cyclic tests to calibrate the cyclic loading history. The strain rate in the monotonic and cyclic tests was 5mm/min, so that the application of the load can be considered quasi-static.

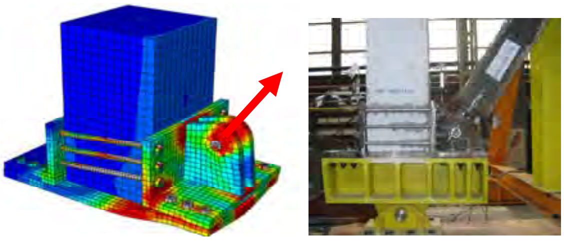

Figure 7: Column base and brace to column connection

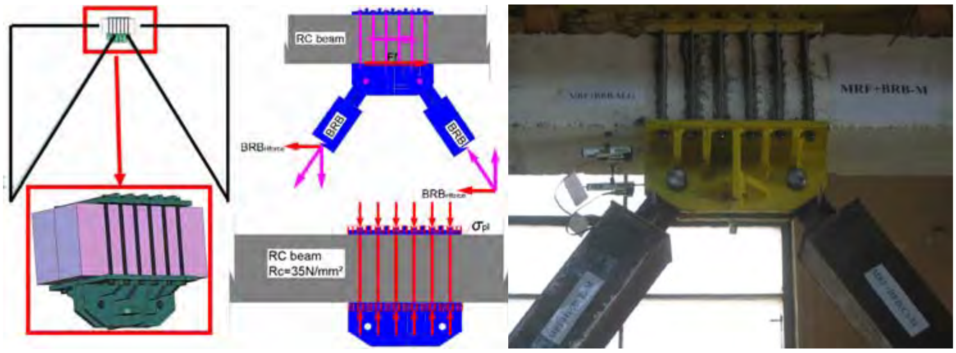

Figure 8: Beam – brace connection: pressure under the steel plate due to bolts pre-stressing

3.3 Results of monotonic tests

Figure 9 shows the force–displacement curves for the initial and strengthened frames. The effectiveness of BRB system is confirmed by the increase of both stiffness and strength. The ultimate load increases from 40kN to approximately 200 kN. The conventional brace system brings more strength and stiffness to the structure, but less dissipation capacity. The capacity increases to 230kN but the displacement corresponding to this ultimate capacity is about 50 mm, almost three times less then that corresponding to the BRB system. For the evaluation of the yield displacement (D_y) and the yield force (F_y), the ECCS methodology is used. According to this approach, yield displacement D_y and yield force F_y are obtained by intersecting the initial stiffness α_y and a tangent at the curve F - D with a slope of 10% of the initial stiffness. With the yielding point defined in this way, results D_y=29 mm and F_y=126KN for the MRF+BRB system and D_y=24mm and F_y=213KN for MRF+CBS system, respectively.

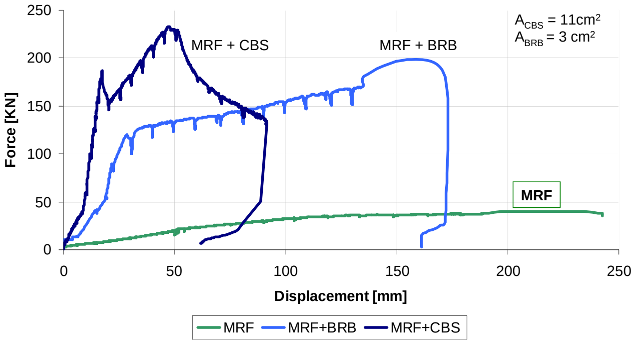

Figure 9: Force-displacement curves from monotonic tests

3.4 Results of cyclic tests

The modified ECCS loading protocol was applied in the cyclic tests. This modified procedure is characterized by a single loading at $D_y/4$, $2D_y/4$, $3D_y/4$ and D_y, followed by three repetitions of the cycles increased by $0.5D_y$ ($1.5D_y$, $2D_y$). The contribution of the strengthening systems is clearly indicated in Figure 10. The conventional brace system increases the capacity but, after few cycles in plastic range, there is an abrupt degradation in the hysteretic behavior due to the failure of the brace in compression. The frame strengthened with the BRB system has a much better behavior in terms of dissipation capacity.

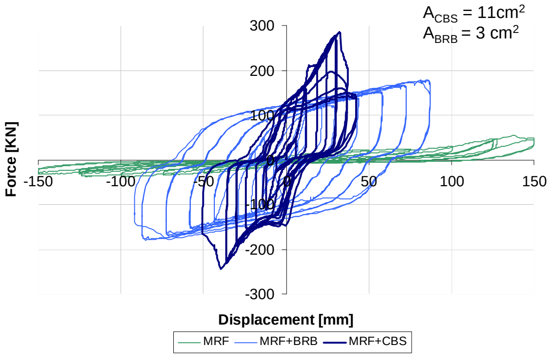

Figure 10: Hysteresis curves for initial RC frame and strengthened frames

Figure 10 shows the frames strengthened with BRB and CBS after the cyclic test. The brace in compression of the CBS system buckles and softens after few cycles and therefore the unbalanced vertical action effect is transferred to the beam. On contrary, the BRB system has a better behavior as the two braces have similar behavior and the brace in compression is protected from buckling.

a) b)

Figure 11: Photos after the test with frame strengthened with CBS a) and strengthened with BRB b)

The next photos show the cyclic damage that occurs in concrete elements, steel elements and their connections. Figure 12.a shows the crack development in initial RC frames. Bending cracks occurred first and were followed by shear cracks. The development of the shear cracks is mainly due to the inadequate distribution of stirrups. Figure 12.b and Figure 12.c show the crack development at both ends of the concrete beam and the brace connection after the test. The occurrence and development of cracks is similar to those of the initial RC frame, and were caused by the same inadequate confinement of the plastic zone. All the connections between BRB system and RC frame showed a very good behavior and there was no slippage recorded. In case of CBS system, the slippage of the brace to beam connection was about 25 mm in one direction and 10 mm in the opposite direction and is mainly due to the horizontal component of the unbalanced load that occurs after the buckling of diagonal in compression.

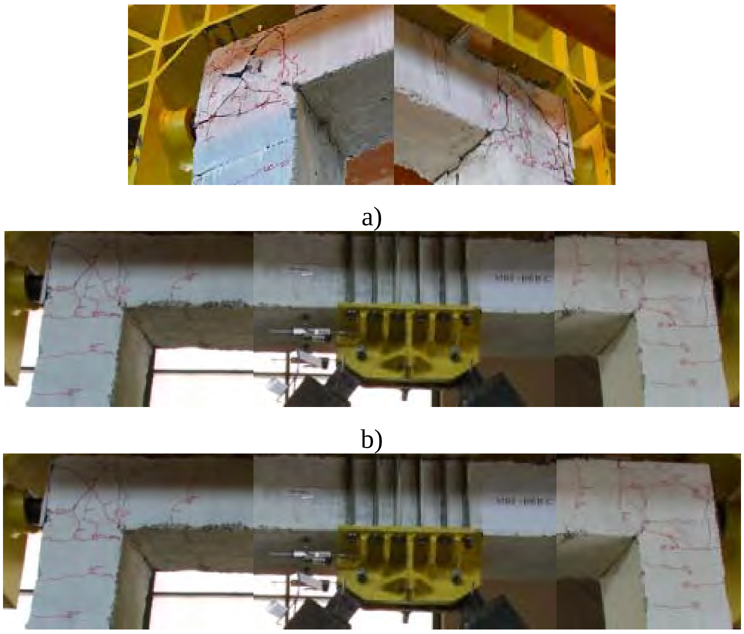

a)

b)

c)

Figure 12: Cracks in the concrete elements after the test: a) initial RC frame; b) frame strengthened with BRB; c) strengthened with CBS

4 EXPERIMENTAL EVALUATION OF Q FACTOR

The results of the experimental program were used also for the evaluation of the behavior factor q for tested structures. The q factor can be expressed as a product of the ductility factor q_μ, that accounts for the ductility of the structure and the overstrength factor q_s, that accounts for the reserve in strength of the structure (due to structural redundancy, material overstrength, member oversize due to design, other non-seismic load combinations and serviceability requirements). The overstrength may vary significantly and is affected by the contribution of gravity loads, material overstrength, etc. Therefore, in order to calibrate the behavior factor q, it is more important to focus on the ductility component, which can be taken equal to the displacement ductility factor μ. The displacement ductility factor q_μ is therefore defined as the ratio of the ultimate displacement D_u and the yield displacement D_y. Yield displacement D_y was evaluated with ECCS method (see section 3.3).

For the initial RC frame, the ultimate displacement D_u corresponds to the attainment of the ultimate strength (shear strength, Figure 12.a) and amounts 150 mm. For the frame strengthened with BRB, D_u corresponds to the failure of the BRB in tension (Figure 12.b) resulting an ultimate cycle of 86 mm. Taken into account the effect of slippage, which produces pinching in the histerezis curve (see Figure 13), D_u needs to be reduced to a value of 71 mm. For the frame strengthened with CBS, D_u corresponds to the failure of the diagonal in compression (Figure 12.c) and amounts, after the correction due to slippage, 42.2 mm. For the definition of the envelope curve, the third cycle of each step was considered. The values of the yield displacements D_y are 69.4 mm for MRF, 16.3 mm for MRF+BRB and 22.5 for MRF+CBS. The values of the behavior factor q are then calculated and results are presented in Table 5. The original unretrofitted structure has a poor behavior, characterized by a low stiffness and low dissipation capacity. As expected, the stable behavior and large ductility of BRBs leads to a q factor that can classify the strengthened structure as a medium ductility structure. When strengthened with conventional braces (CBS), the structure gains rigidity but the q factor is low, classifying the system as low dissipative.

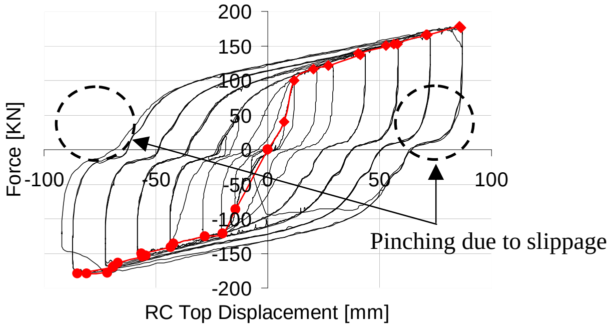

Figure 13: Envelope of the MRF+BRB cyclic test

MRF			MRF+BRB			MRF+CBS		
Dy [mm]	Du [mm]	q	Dy [mm]	Du [mm]	q	Dy [mm]	Du [mm]	q
69.4	150	2.16	16.3	71	4.3	22.5	42.2	1.8

Table 5: q factor values

In order to extend the investigation on the behavior factor q, a nonlinear dynamic analysis was employed. The results obtained so far confirmed the values obtained via experimental tests [6]. For example, for the structure strengthened with BRB, the results had shown a good agreement with experimental tests, with a mean value of q factor of 3.9.

5 CONCLUSIONS

Experimental and numerical investigations were conducted to evaluate the seismic behavior of RC frame buildings, designed for gravity loads, before and after strengthening with steel bracing systems. The preliminary analysis has shown that the RC structure is vulnerable and does not meet the seismic requirements for a moderate seismic zone. Therefore, the structural system should be adequately strengthened in order to attain the desired level of seismic resistance. Two types of strengthening techniques were considered, one with buckling restrained V braces (BRB) and one with conventional concentric V braces (CBS). The results have shown that the structure has a limited capacity, mainly due to poor detailing of the plastic zones (lack of stirrups). When the global strengthening technique is accomplished, the behavior is much improved.

A portal frame was then extracted from the building and studied experimentally. Six frames were tested, two for each type of frame, one monotonically and one cyclically. Tests have shown a very poor behavior of RC frame. The structural system should be strengthened in order to attain the desired level of seismic resistance.

Structure strengthened with BRB had a good behavior, larger rigidity, capacity and ductility compared to the initial structure. The failure was caused by the failure of the steel brace in tension. The connections between BRB and RC elements performed very well. It was also tested the workability of the system with pre-stressed ties. The connection devices used for installing BRBs within the frame took benefit from the friction resistant forces induced by the ties pretension and showed a very good behavior. In fact, reduced slips – with very small influence on the hysteretic loops of BRB system – were observed. Results recommend the application of this connecting system for such interventions. Moreover, in case of multi-story frames, such connecting systems also provide a beneficial confining effect at the frame joints, enhancing both strength and ductility of the MRF+BRB system.

Conventional brace system increases the strength and stiffness but is less ductile compared to BRB. In addition, the concrete beam should be able to support the vertical component of the unbalanced load when the compression brace buckles. The horizontal component of the same unbalanced load did also overstressed the brace-to-beam connection causing its slip. The application of such strengthening technique should therefore be done with caution, to avoid concentration of stresses and to reduce the ductility demands in critical sections.

Acknowledgement

The experimental program was done in the framework of RFCS project "STEELRETRO": Steel solutions for seismic retrofit and upgrade of existing constructions. This project was developed in the period 2007-2010 and involved 11 partners from 8 European countries.

This work was partially supported by the strategic grant POSDRU/89/1.5/S/57649, Project ID 57649 (PERFORM-ERA), co-financed by the European Social Fund – Investing in People, within the Sectoral Operational Programme Human Resources Development 2007-2013.

6 REFERENCES

[1] Bordea, S., 2010, "Dual Frame Systems of Buckling Restrained Braces", Universitatea "Politehnica" Timisoara, Teze de doctorat ale UPT, Seria 5, Inginerie Civila, Nr. 53, Editura Politehnica, 244 pagini, 199 figuri, 36 tabele, ISSN: 1842-581X, ISBN: 978-606-554-059-0

[2] EN 1998-1, 2004, "Eurocode 8: Design of structures for earthquake resistance. Part 1: General rules, seismic actions and rules for buildings" CEN - European Committee for Standardization

[3] ASCE/SEI 41-06, 2007, "Seismic Rehabilitation of Existing Buildings, American Society of civil Engineering" (superseded FEMA 356), Published by American Society of Civil Engineers, 1801 Alexander Bell Drive, Reston Virginia, 20191, www.pubs.asce.org, ISBN 13: 978—0-7844-0884-1; ISBN 10: 0-7844-0884-X, USA

[4] EN15129, 2009 „Anti-seismic devices" CEN - European Committee for Standardization

[5] Dubina, D., Bordea, S., Stratan, A., 2009, "Performance Based Evaluation of a RC Frame strengthened with BRB Steel Braces", International Conference PROHITECH, Roma, Italia, www.prohitech09.com, ISBN 978-0-415-55803-7, pp. 1009-1014.

[6] Bordea, S & Dubina, D., "Numerical and experimental evaluation of q factors for reinforced concrete frames strengthened of steel buckling restrained braces", COST Action Final Conference – Urban Habitat Constructions under Catastrophic Events, CRC Press, A Balkema Book, 16-18 September 2010, Naples, Italy, Ed. F. Mazzolani, ISBN 978-0-415-60685-1, pg. 801-807.

COMPDYN 2011
III ECCOMAS Thematic Conference on
Computational Methods in Structural Dynamics and Earthquake Engineering
M. Papadrakakis, M. Fragiadakis, V. Plevris (eds.)
Corfu, Greece, 25–28 May 2011

NONLINEAR DYNAMIC RESPONSE OF DISSIPATIVE DEVICES FOR SEISMIC RESISTANT STEEL FRAMES: EXPERIMENTAL BEHAVIOUR AND NUMERICAL SIMULATION

Alper Kanyilmaz[1], Carlo Castiglioni[2], Alberto Drei[3], Ioannis Vayas[4], Luis Calado[5], Tim Rauert[6]

[1,2,3] Politecnico di Milano
Structural Engineering Department
kanyilmaz@stru.polimi.it, castigli@stru.polimi.it, drei@stru.polimi.it

[4]National Technical University of Athens
Structural Engineering Department
vastahl@central.ntua.gr

[5]Istituto Superior Tecnico, Lisbon
Structural Engineering Department
calado@civil.ist.utl.pt

[6]RWTH Aachen - Institute of Steel Construction
tim.rauert@stb.rwth-aachen.de

Keywords: Dissipative Devices, Steel Structures, Earthquake Resistant Design

Abstract. *This study presents the preliminary numerical and experimental results of the project Fuseis carried out with the financial grant of the Research Programme of the Research Fund for Coal and Steel of the European Union (RFSR-CT-2008-00032)), initiated in July 2008 and supposed to end in July 2011, which aims at developing two innovative types of seismic resistant steel frames with dissipative fuses. The numerical model is developed using the commercial software package Perform 3D Nonlinear Analysis and Performance Assessment for 3D Structures by CS&I. The analyses are carried out using inelastic fiber sections for the fuse elements and the composite slab, and elastic steel column elements for the columns.*

1 INTRODUCTION

Steel structures in seismic zones are designed for stiffness, strength and ductility. Stiffness is required for limitation of damage of non-structural elements and reduction of the 2nd order effects. Strength is required for a safe transmission of the acting forces and moments. Ductility under cyclic loading leads to the dissipation of the input seismic energy and results in a reduction of the seismic forces. The demand for strength is therefore closely connected to the provision of ductility. The latter may result in a considerable reduction of the acting seismic forces by a factor of up to 6, according to the European and 12 according to the American Codes.

Obviously, not the entire structure shall exhibit uncontrollable inelastic deformations during a strong earthquake. Such deformations are associated with damage and shall be limited into specific zones, the dissipative zones. For that reason, the elements of the dissipative zones are weaker than their connections and the adjacent members. The latter are designed for higher forces and moments according to capacity design criteria. Table 1 shows an evaluation of the existing conventional structural systems in respect to stiffness and ductility. Strength is not evaluated since it is accepted that all systems, if properly designed, are able to resist the acting action effects. It can be seen that conventional systems have advantages and disadvantages. Moment resisting frames are ductile but usually flexible. Concentric braced frames are stiffer but less ductile due to buckling of braces. The properties of eccentric braced frames are something between the other two types. Table 1, columns 1 to 3, summarizes the properties of conventional steel frames.

	1	2	3	4
	Moment Resisting Frames	Concentric Braced Frames	Eccentric Braced Frames	FUSEIS Frames
Stifness	-	+	0	+
Ductility	+	-	+	+
Reparability	0	-	0	+
Dissipative zones	Beams	Braces	Links	Fuses

Table 1: Stiffness, ductility, reparability properties and dissipative zones of several structural systems

Inelastic deformations may develop not only under seismic loading but also in other design situations in structures exploiting plastic resistances, i.e. in frames designed according to plastic hinge theory. However, such design refers to the ultimate limit state, where the actions are magnified by the relevant safety factors. Under service conditions, inelastic deformations that may result in damage do not generally occur. Inelastic deformations leading to damage are allowed also in accidental design situations (fire, explosions etc.). When such situations actually occur, repair works are needed. However, accidental situations happen very rarely and refer only to individual structures.

Seismic loading represents a special design situation. For normal buildings, structural safety shall be assured for the design earthquake, which corresponds to rare earthquakes with usual return periods of about 500 years. Damage shall be limited for frequent earthquakes with return periods around 50 years. However, the international experience shows that the above fundamental requirements are very often not fulfilled. All over again, earthquakes occur that are much stronger than those for which the design was made. The results are well known: Structural collapses leading to loss of human life and, in much wider range, damages that require repair at high costs. Due to the population increase and the concentration in large cities, it may be stated that the seismic risk and the financial consequences increase rather than reduce over time.

For the population, and the judges, it is difficult to understand that the earthquake which had happened was the *rare* one with a return period of 500 years. This is due to the fact that the Codes rely on instrumental measurements of at most 50 years and historical data that extend over a longer period but cannot be directly transformed into engineering figures. They are therefore based rather on statistical extrapolations of natural hazards. It is observed that after a strong earthquake the region where it happened is often upgraded in the higher seismic zone.

The above descriptions and the experience show that unlike accidental loading, earthquakes lead *frequently* to damages in *large* extent. It is therefore advisable to develop structural systems that are simple to *repair*, i.e. to introduce the *reparability* as a new property. An evaluation of the conventional frames in respect to this property is made in Table 1. It may be seen that conventional frames are not well positioned according to reparability. In moment resisting frames the beams or, more usually, their connections shall be repaired. Both are elements that resist gravity loading and are difficult to repair. The same happens with eccentric braced frames where the links, the short parts of the beams, have to be repaired. In concentric braced frames, it is the braces that shall develop inelastic deformations. Damage is therefore expected in the braces, which are long and heavy elements, difficult to handle and repair.

Furthermore it has to be pointed out that, in reality, “steel structures” rarely exist by themselves (eventually just in the case of industrial buildings). Most often, in the case of high-rise buildings, housing, as well as commercial buildings, the steel beams support r.c. slabs. In this case, damage to the steel members results in damage in the r.c. slabs and in the finishes, so that repair works will be increased together with the related costs.

From other engineering disciplines, e.g. mechanical, electrical and automobile or aircraft engineering, it is well known that the best way of repair is the complete replacement of a damaged part with a new one. Such a strategy could be also envisaged in civil engineering, especially for buildings in seismic areas that are more susceptible to damage for the reasons described above. Like bumpers in cars that absorb the crash energy and are replaced afterwards, innovative devices will be developed that dissipate energy, protect the overall structure and may be dismounted and replaced after a strong earthquake.

The research proposal aims at developing two innovative types of seismic resistant steel frames with dissipative fuses. In case of strong earthquakes, damage will concentrate only in the fuses, which will be exchangeable. Repair work after a strong seismic event, if needed, will be limited only to replacing the fuses.

This study presents the preliminary numerical and experimental results of one of the two types of devices, that can be applied to the beam to column connection of moment resisting frames, as sketched in figure 1.

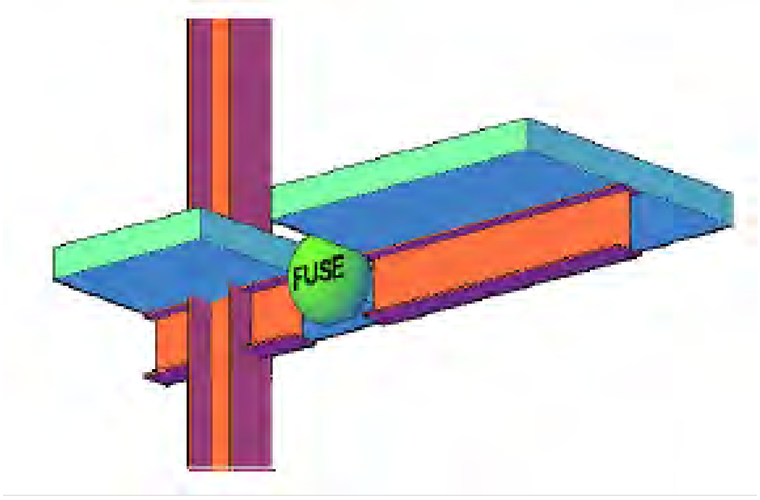

Figure 1: Fuse device placed in a moment resisting composite steel frame

2 FULL SCALE TESTS

A two dimensional composite steel frame with fuse devices has been tested in the structural engineering laboratory of the Politecnico di Milano University. The outline of the frame and its elements can be seen in figure 2.

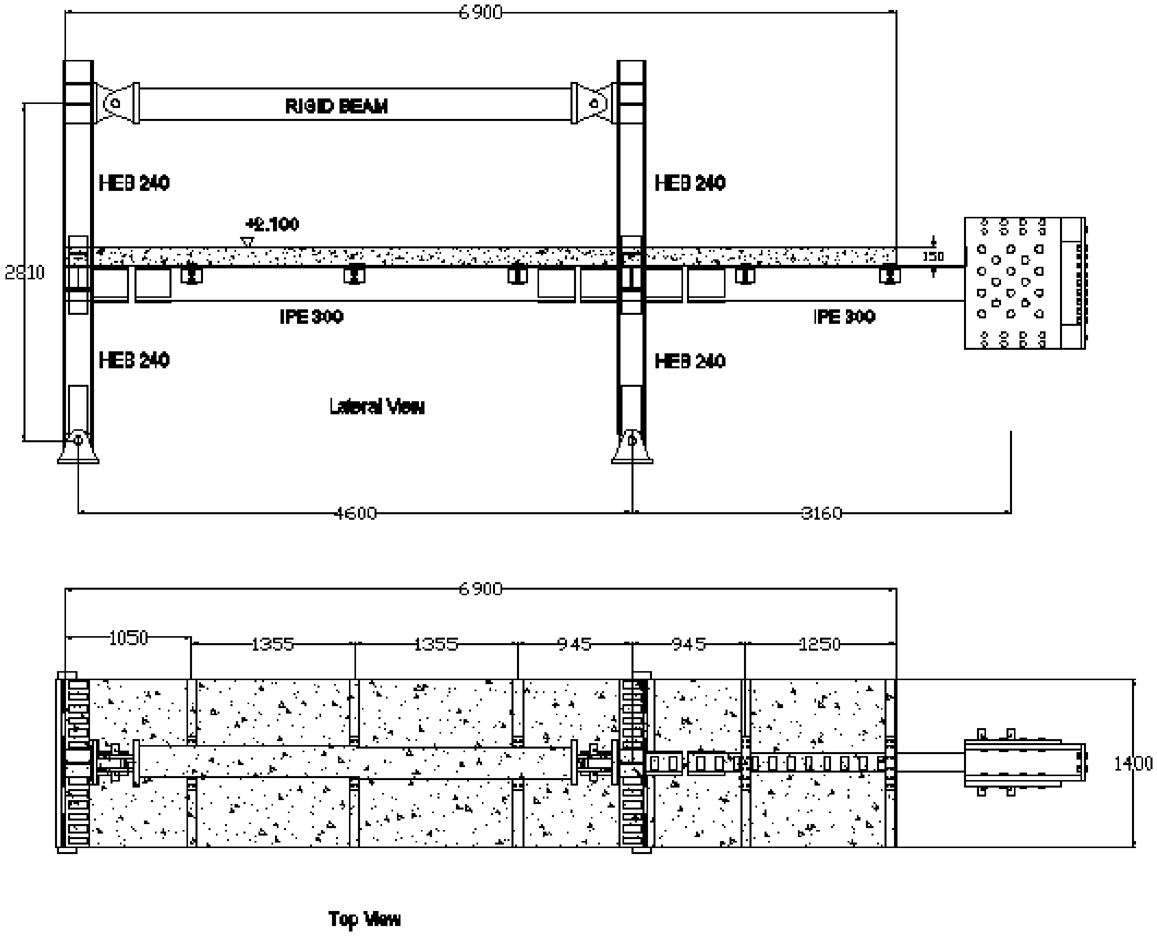

Figure 2 Full Scale Test Frame

A cyclic loading history shown in figure 3 is applied at top joint of the right side column through a load cell. The load is applied in cycles in +x and -x direction. Therefore in each cycle, in the beam and eventually in the fuse element, a positive and negative bending are observed. A maximum deflection of 110 mm (corresponding to 42 mrad in the fuse element) is imposed to the top joint.

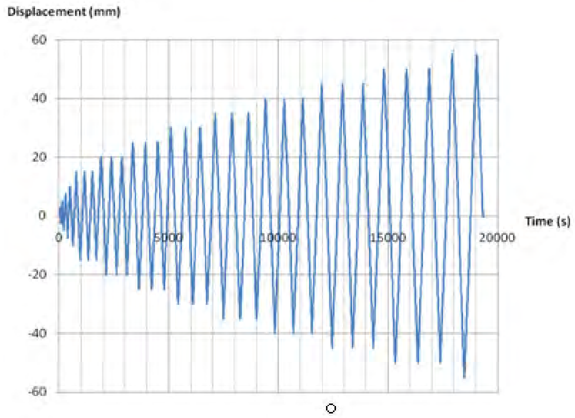

Figure 3 Cyclic loading history applied in the tests

3 NUMERICAL SIMULATION

For the design of the test specimens, a refined numerical model was set-up at Politecnico di Milano, using ABAQUS software. Such a detailed model, however, can be used only for specific research applications, but it is not a feasible model to use for engineering purposes. Therefore, the simplified model hereafter described was set up and calibrated, with the aim of using it for the simulation of multy story frame structures.

The simplified nonlinear model is developed using the commercial software package Perform 3D Nonlinear Analysis and Performance Assessment for 3D Structures by CS&I (Figure 4). The analyses are carried out using inelastic fiber sections for the fuse elements and the composite slab, and elastic steel column elements for the columns.

PERFORM-3D Version 4.0.4
Copyright 2007 Computers and Structures, Inc.
PERFORM-3D is a registered trademark of CSI. All rights reserved.

Figure 4 Perform 3D Nonlinear Analysis Software

A fiber segment is a finite length of constant cross section in a frame compound component. The key aspect of a fiber segment is how it behaves when the fiber section becomes nonlinear, through yield of it several fiber elements. In a beam fiber section, the cross section shape of the element is divided into a number of fibers, and material properties are assigned to each fiber. Each fiber segment is defined by associating it with a fiber cross section and specifying the segment length.

The behavior of a fiber segment is similar to that of a tributary length of beam with a hinge at its midpoint. Such a segment becomes nonlinear only when the hinge becomes nonlinear.

In physical terms, in a fiber segment, the cross section behavior is monitored at only one point, namely the midpoint of the segment. For instance, if a fiber section is made up entirely of steel fibers(i.e., if it models a steel section), the fiber segment yields only when the combination of axial force and bending moment at the midpoint of the segment is large enough to cause a fiber to yield.

The material types that are allowed for the fibers are: Steel material, tension-only material, buckling material and concrete material. [2]

Nonlinear element and material properties are assigned to the composite beams and the fuse elements to observe their contribution to the energy dissipation of the whole frame, during a dynamic lateral loading event. The scope is to attain the plastic behavior only at the fuse elements, and let the columns and beams of the structure behave elastically.

3.1 Properties of Structural Elements

The cross sections and material properties used in the numerical model are the same ones that are used in the full scale test model (Figure 2). HEB240 column elements are chosen as elastic type, considering that the test frame will not be suffer large axial forces. The beams and the fuses are modeled with inelastic fiber segments.

In the frame, there are three different types of beam sections. Main beams are composite steel beams that are composed of an IPE300 steel section, and a reinforced concrete slab of 150 mm thickness. The inelastic fiber section that is used for main beams are seen in the figure 5.

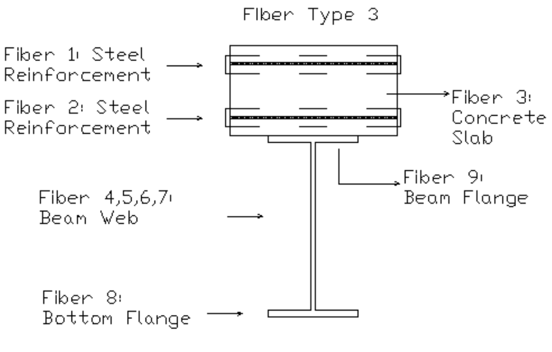

Figure 5 Cross Section Properties of fiber beam element

The short beams located between the fuse parts and the columns are also designed as fiber elements, to represent the behaviour of a composite section which consists of an IPE300 beam, steel plates attached to the flange and the web of the beam, and the concrete slab. The properties of the this beam element can be seen in figure 6.

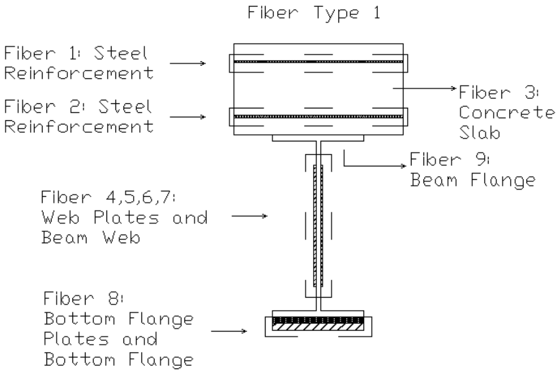

Figure 6 Cross Section Properties of fiber beam element

3.2 Fuse Element

In the model, fuse devices are modeled as short beam segments with fiber cross sections in order to simulate the plastic hinge behaviour. The fiber section used in the model can be seen in the figure 7.

They are modeled with two different fibers:

i) Inelastic steel material, non buckling type, representing the reinforcement of the slab (seismic bars) (Figure 8)

ii) Inelastic steel steel material, buckling type, representing the connection part composed of web and bottom flange plates (Figure 9)

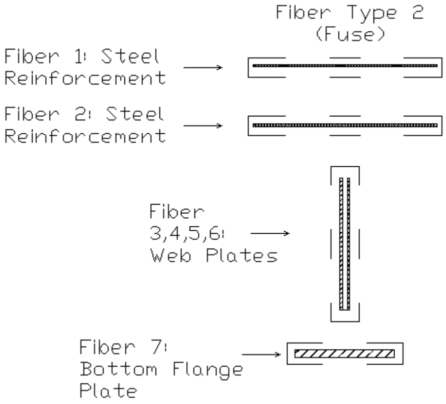

Figure 7 Definition of fibers in the fuse part

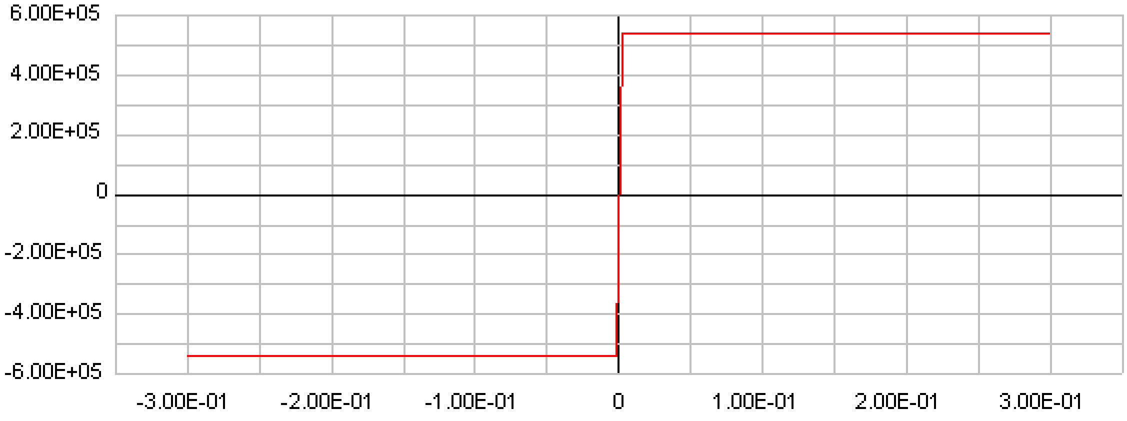

Figure 8 Force-Deformation Relationship of inelastic steel material, non buckling type used for steel reinforcement

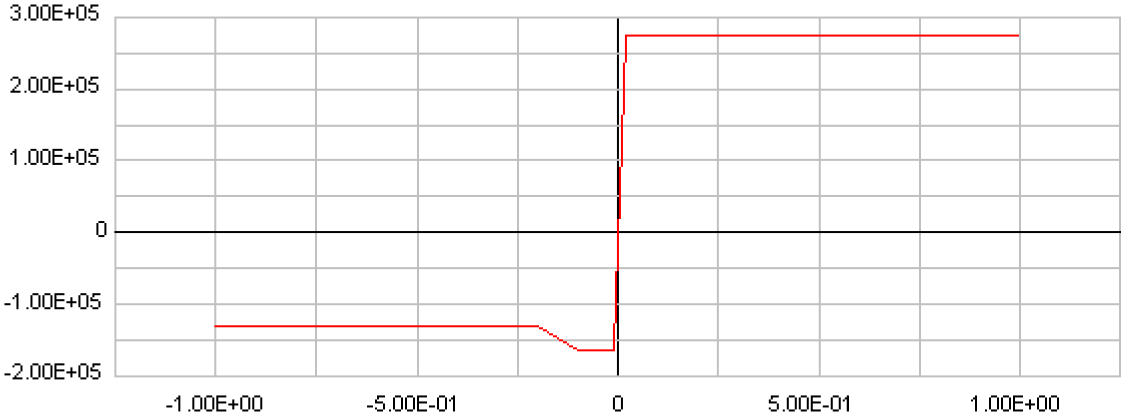

Figure 9 Force-Deformation Relationship of inelastic steel material, buckling type used for web and bottom plates of the fuse devices

The fiber of the steel reinforcement is expected to stay in the elastic range, whereas the fibers of the steel plates connected to the web and the bottom flange are expected to yield and hence dissipate energy during cyclic loading. The locations of the fiber sections can be seen in figure 10.

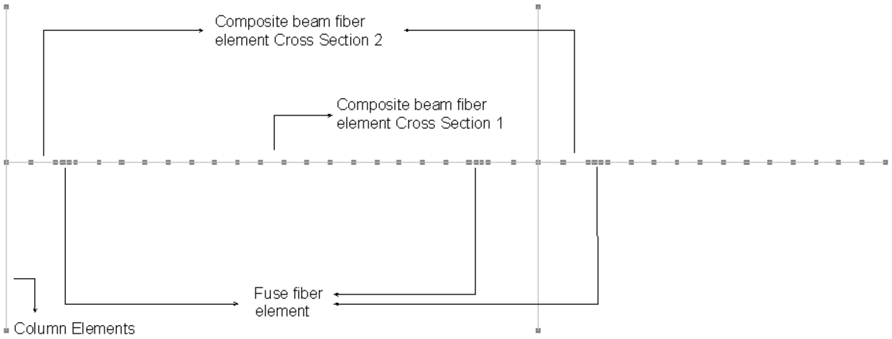

Figure 10 Fiber Segment Scheme of the Frame Model

The output time-force history of the displacement controlled push-over experiment is used as input loading history in the numerical dynamic push-over analysis. Therefore numerical analysis is carried out as force controlled push over analysis (Figure 11).

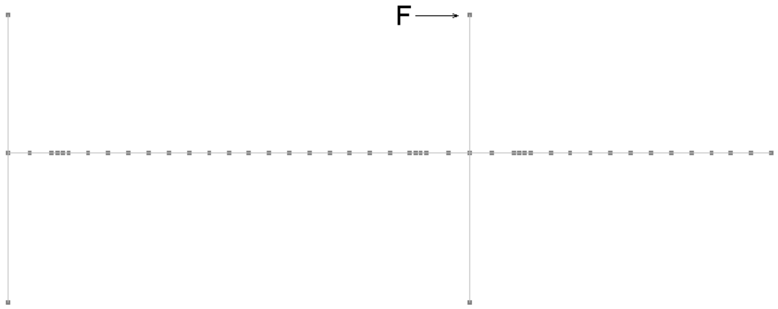

Figure 11 Force controlled push over analysis scheme

The force-time history of the cycling loading case can be seen in figure 12.

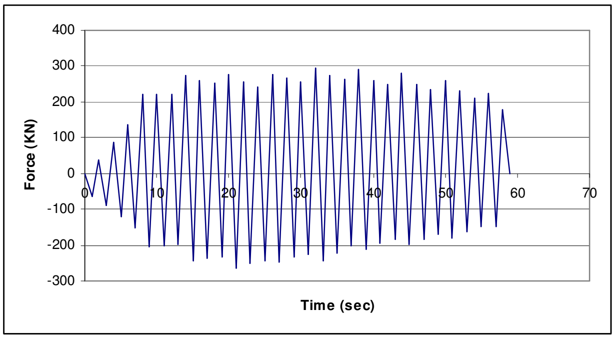

Figure 12 Cyclic loading record used in the model

4 CALIBRATION OF THE NUMERICAL MODEL

The conformity of numerical and experimental results in terms of maximum plastic moment capacity referring to the maximum rotations that the device undergo can be observed in the superposed experimental and numerical global force-displacement plots in the figure 13. The differences in the initial stiffness and amplitude of the hysteresis plots are due to inelastic effects occurring in the connections between the fuse device and the beams, that were not accounted for in the numerical model.

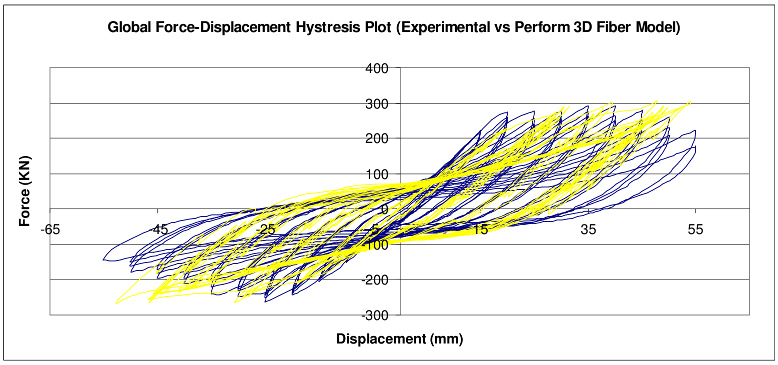

Figure 13 Experimental vs Numerical Moment-Rotation Plots

Within the remaining period of the research project, elaborating the numerical analyses further, the calibration between the analyses and experimental results are going to be improved and necessary design guides to implement the system in practice will be developed.

5 NUMERICAL ANALYSIS OF MULTISTOREY FRAMES WITH FUSES

The expected behavior of a moment resisting multistory frame under lateral loading is shown in figure 14, where a plastic hinge mechanism under collapse load is likely to occur near the beam ends at the floor levels.

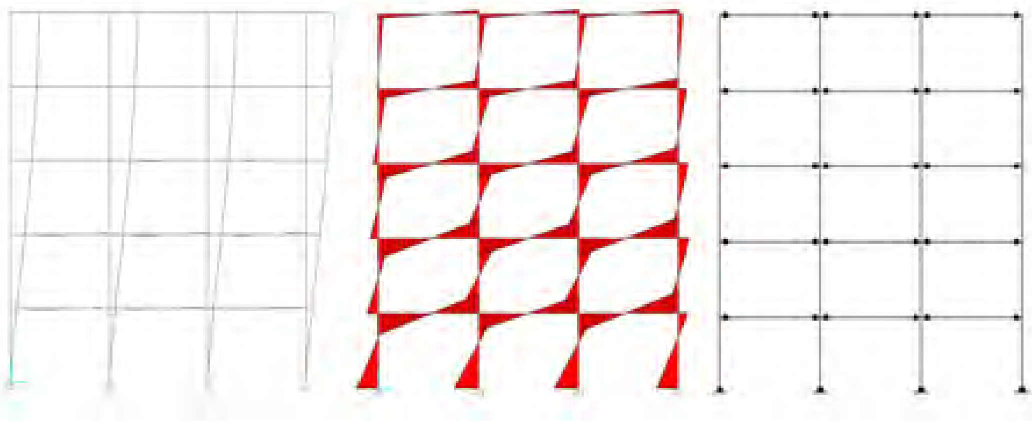

Figure 14 Deformed shape, moment diagram and location of plastic hinges observed under horizontal loading of a 5 storey moment resisting steel structure.

In order to extend the results of the numerical analyses carried for the test structure to multistory building frames and to observe the behaviour of the fuses under horizontal seismic excitations, nonlinear fiber analyses are carried out for two composite steel building frames:

1) A conventional moment resisting composite steel structure building frame
2) A moment resisting composite steel structure building frame having fuse devices, near the end of its beams.

The scope is to observe the behavior of steel building frames using inelastic fiber sections at the parts of the beams where a plastic hinge mechanism is expected to occur, and examine the contribution of fuse devices to the energy dissipation and reduction of earthquake forces in multistory buildings under horizontal earthquake excitations.

The analyses are carried out under the horizontal acceleration time history data of Kobe 1995, Aquila 2009 and Chile 2010 earthquakes. The element types and the cross sections are the same with the ones used in the numerical model of the test frame, which are described in section 2.1.

5.1 Composite Steel Building Frame without Fuses

The composite steel multistory model is analyzed with HEB240 column elements, and a composite slab element that consist an IPE360 steel beam and 150 mm thick reinforced concrete slab.

Under three earthquake excitations, the moment curvature hysteresis plots of composite beam elements are obtained. As can be understood from the moment-curvature diagrams shown in figure 15, the segments of the composite beams where the maximum moments are observed, eventually near beam ends, are plasticized.

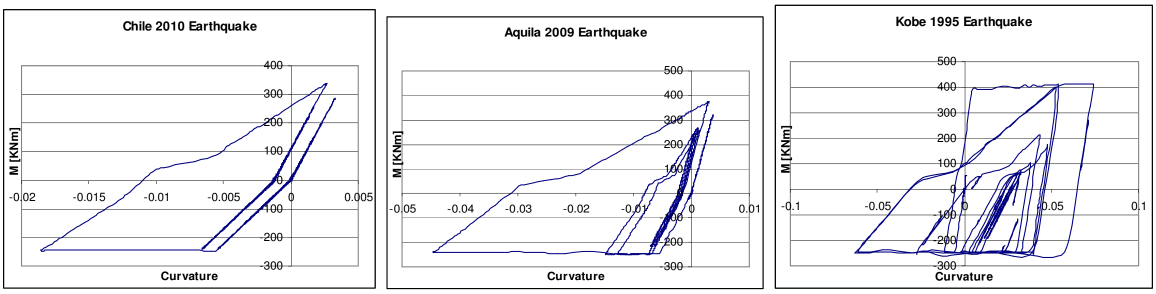

Figure 15 Moment-Curvature diagrams observed in the composite beam under three earthquake excitations

5.2 Composite Steel Building Frame with Fuses

The same building is modeled with placing the fuse devices near the end of the beams, where the plasticization is observed in the previous analysis (Figure 16). The same earthquake excitations are applied to this model as well, and the moment curvature hysteresis plots of composite beam elements and fuses are obtained.

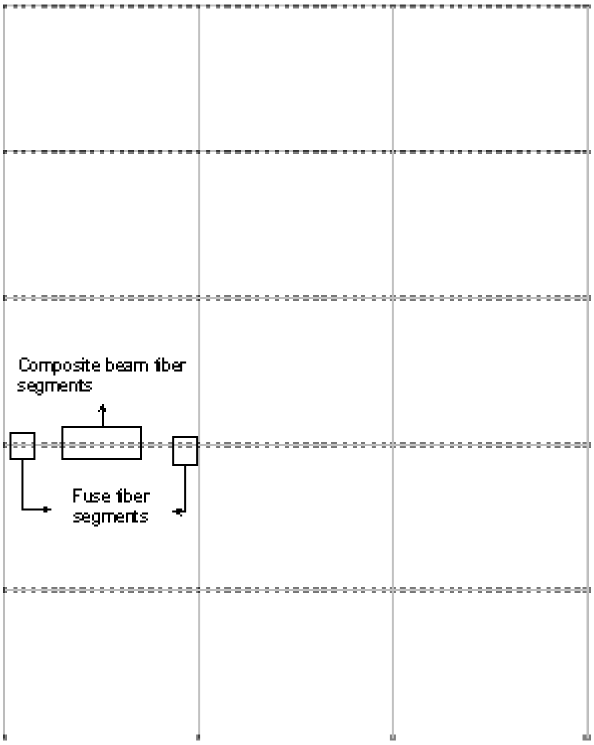

Figure 16 Moment resisting steel building frame model

As expected, the composite beams and columns showed elastic behaviour with no yielding, while the fuse parts yielded and contributed to the energy dissipation. In figure 17 and 18, the moment-curvature diagrams of the composite beams and fuse elements of the structure under lateral loading can be seen respectively.

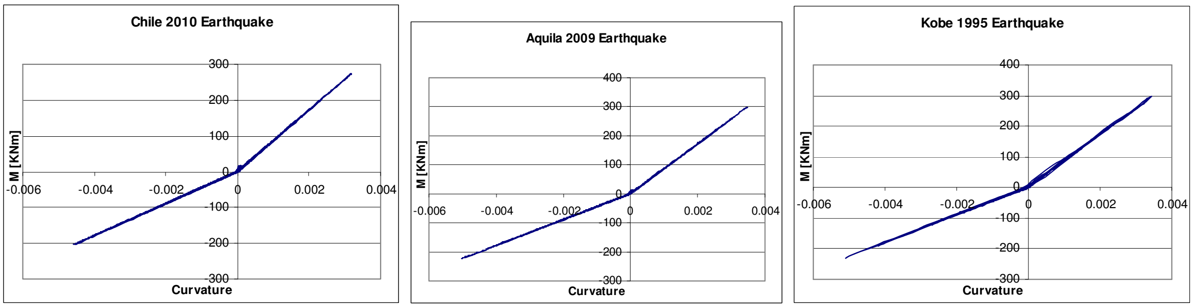

Figure 17 Moment-Curvature diagrams observed in composite slabs under three earthquake excitations

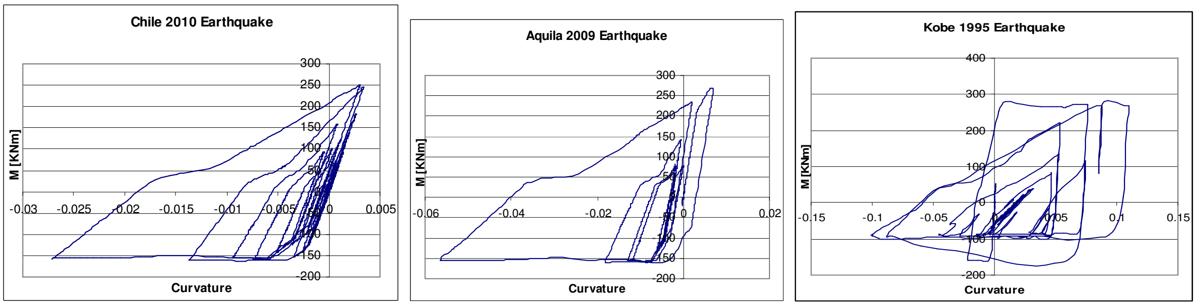

Figure 18 Moment-Curvature diagrams of the fuse devices under three earthquake excitations

From the hysteresis plots, it is seen that the plastic deformations are concentrated only in the fuse elements, whereas the composite beams remain elastic.

5.3 Comparisons between Two Building Models

A comparison between a conventional building model and a building model with fuses is made in terms of base shear forces. In figure 19, the reduction of the maximum base shear forces that take place in the building with fuses can be observed under three different earthquake excitations. Combined with the dissipative behavior of the devices, these results confirm that the fuses have an important effect in reducing the seismic forces transmitted to the structure during strong earthquakes.

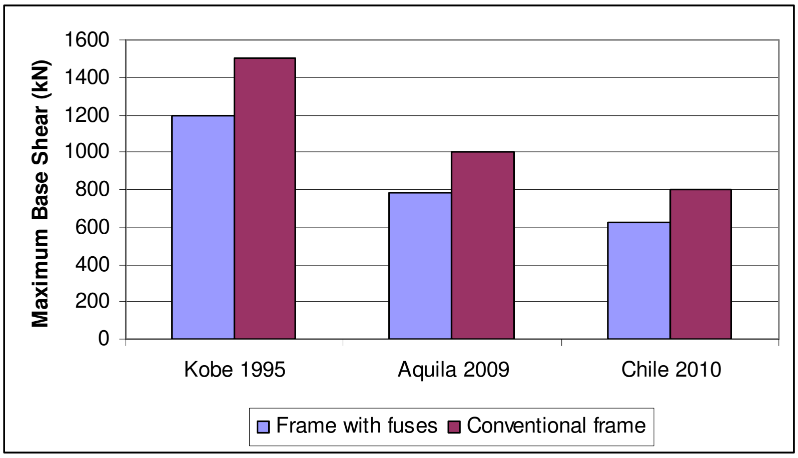

Figure 19 Comparison of maximum base shear forces between conventional and innovative structures

6 CONCLUSIONS

In this study, the preliminary results of the experimental and numerical analyses carried out for one of the two types of innovative fuse devices are presented. The ability of the fuse devices to dissipate energy and reduce the horizontal earthquake forces in steel frames is investigated. The possible damage that the main structural elements of a moment resisting steel frame would suffer during a strong earthquake is aimed to be concentrated in the fuse devices. While in the conventional moment resisting steel frames, the beams and their connections – the elements that resist gravity loading and are difficult to repair- must be repaired after a strong earthquake. In the innovative type seismic resistant steel frames with dissipative fuses, the repair work, if needed, will be limited only to the replacement of the fuses.

From the results of the nonlinear numerical analyses carried out for a simple test structure and a composite steel building frame, it can be concluded that the idea of avoiding the plastic deformations in the main structural elements of a moment resisting building frame can be achieved through concentrating the plastic deformations in “weak” elements which are to be mounted between the beam and column elements of the structure. These comparatively weaker elements, so called fuses, must be stiff enough to let the frame be stable under service loads, and also they must be the principal elements in the structure to show inelastic behaviour and dissipate the energy caused by a strong earthquake.

The numerical analyses carried out for a simple test structure which is loaded in a cyclic manner, showed that among the three elements: composite slab, column, and fuse device, the plastic deformation is observed only in the fuse device, whereas the column and the slab elements remained perfectly elastic. Finally, in order to extend these results for a multistory building frame and to observe the behaviour of the fuses under seismic excitations, a nonlinear fiber analysis is carried out for a two dimensional composite steel building frame consisting steel column elements, composite beam elements and fuse elements, under horizontal acceleration time history data of three different earthquakes. In compatibility with the results of the test structure, also in this case, the plastic deformations are only seen in the fuse devices. Moreover, through the comparison between the numerical analysis results of a conventional steel frame and an innovative type of steel frame with dissipative fuses, it is seen that the base shear forces induced by the strong earthquake motions can be reduced using fuse devices.

REFERENCES

[1] C.A. Castiglioni, I. Mazza, F. Pedrazzoli, A. Drei, M. Valente, L. Calado, M. Proença, M. Espinha: Research and results in developing innovative type of seismic resistant frames with dissipative fuses, Intermediate Report February 2010

[2] PERFORM 3D V. 4.0.4 Documentation

COMPDYN 2011
3rd ECCOMAS Thematic Conference on
Computational Methods in Structural Dynamics and Earthquake Engineering
M. Papadrakakis, M. Fragiadakis, V. Plevris (eds.)
Corfu, Greece, 25–28 May 2011

AN ANALYTICAL STUDY OF LOW CYCLE FATIGUE EFFECTS IN BUCKLING RESTRAINED BRACES

M. E. Shemshadian[1], S. Ali Razavi[2*], A. Hosseini[3], S. R. Mirghaderi[3], M. Khan Mohammadi[3]

[1]Graduate Student of Structural Engineering
Faculty of Civil Engineering, University of Tehran
Shemshadian@ut.ac.ir

[2]PHD Candidate of Structural Engineering
Faculty of Civil Engineering, University of Tehran
Arazavi@ut.ac.ir

[3]Assistant Professors,
Faculty of Civil Engineering, University of Tehran
Hosseiniaby, Rmirghaderi, Mkhan @ut.ac.ir

Keywords: Low-Cycle Fatigue, Buckling Restrained Brace, Strain History Demands, Time History Analysis, Cumulative Damage, Palmgren-Miner, OpenSees.

Abstract. *Dampers are used in structures to dissipate input energy caused by severe earthquakes. They can also reduce seismic demands on other structural elements. So dampers' life is a significant parameter to prevent the structural damages. One of the failure modes observed in the steel dampers during earthquakes, is the damage caused by cumulative effects due to few cycles of high strain amplitudes. This undesirable effect is called Low-Cycle Fatigue (LCF). In buckling restrained braced frames (BRBFs), brace element acts as a hysteretic damper and dissipates high amount of input energy by plastic axial deformations. To ensure satisfactory operation of BRB with no failure during earthquake, it is necessary to investigate LCF effects. On the other hand smaller yielding length of BRB cores imposes higher strain amplitudes and makes the LCF failure more probable.*

In the present study, a criterion to control LCF failure in BRB has been selected based on fatigue life equations recommended in the previous experimental researches. A 7 story benchmark building with BRBs as the lateral resisting system is selected. Then the yielding length of BRB has been reduced to the minimum possible based on the fatigue criterion and the building has been redesigned. Fatigue analysis has been performed on both buildings to evaluate LCF capacity. In order to evaluate fatigue effects, time history analysis have been conducted on both buildings using the open source finite element platform, OpenSees (2005). Strain history demands in each yielding segments of the braces have been extracted and the cumulative damage index of Palmgren-Miner has been calculated to estimate LCF damage index.

Results of this study show that despite the high cumulative plastic deformations the yielding segments experiences, both BRBs have proper fatigue damage indeces. Also it has been proved that developed criterion for controlling LCF failure is conservative for selected time histories and has appropriate safety factor for defining reduced core length of BRB.

1 INTRODUCTION

Braces are usually designed to act as energy dissipating members in seismic design of concentrically bracing systems. Therefore a brace is anticipated to have a stable cyclic behavior with high damping hysteresis loops. Due to buckling, the majority of the energy that could be damped in compression is lost and the brace stability is jeopardized. In Buckling Restrained Braces (BRBs), by preventing the buckling of the brace, a symmetric and stable hysteresis curve is achieved that dissipates high amount of energy in every single cycle (figure 1).

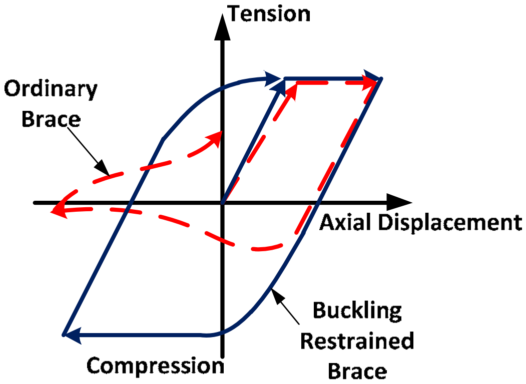

Figure 1: Cyclic behaviour of a typical BRB versus a conventional brace [1].

BRBs brilliantly solve problems of classic concentric braces, which are characterized by a pinched hysteresis loop and a small ductility due to the concentration of strain occurring when braces buckle [2]. In common BRBs, the axial deformation is distributed in a large length, so the peak strain amplitude typically falls in the range of 0.01–0.02 for usual structural applications [3]. On the other hand, the results of experimental studies on BRBs proved the capacity of core to endure the strains of higher ranges up to 0.03 or even 0.06 [3, 4]. The capacity of withstanding high strains insures the feasibility of reducing the length of the yielding segment of BRBs. Reducing the length of yielding segment in BRBs has a number of advantages. By reducing the yielding segment higher axial stiffness in brace is achieved. On the other hand, the restrained length is reduced so global encasing member can be replaced by a local one that has less weight and cost. Yielding part of BRB is the structural fuse in BRBFs and its length reduction causes a more flexible designing since in small sizes a variety of core lengths and cross sectional areas can be provided. If a fuse replacement is needed after sever earthquakes, it is enough to replace damaged fuse with a new one (only at the end of the brace) and it is not necessary to replace the whole brace [1].

The above advantages raised the interest of many researchers to investigate the possibility of reducing core length in BRBs. The majority of these studies have been carried out in recent 5 years. Table 1 summarizes some of these studies.

Researcher	Year	Location	L_c/L	Model	Max Strain
Tremblay et al.	2006	Canada	25%	Experimental & Analytical	3.4%
Mirghaderi & Ahlehagh	2008	Iran	35%	Analytical	4.3%
Ning Ma et al.	2009	China	20%	Experimental	3.4%
Mazzolani et al	2009	Italy	40%	Experimental	3.5%
Razavi & Mirghaderi	2009	Iran	20-40%	Analytical and Experimental	3-4%
Di Sarno & Manfredi	2010	Italy	20%	Analytical	1.5%

Table 1: Summary of some studies on BRB with reduced core length [3-7].

Nevertheless, reducing the yielding length imposes large strain demands on this segment which poses some concerns about Low-Cycle Fatigue (LCF) failure. However, a minimum core length is required to keep inelastic strain demand low enough such that LCF fracture of the core does not occur under a severe earthquake [3].

Since various ranges of BRB core length can be used, it is necessary to consider the effects of LCF on BRBs. Unfortunately seismic codes and specifications have not presented any distinct criterion to control these effects. So, in recent years, a series of experimental studies was accomplished on the possibility of fracture of BRBs caused by LCF. Moreover, some qualification tests with respect to LCF effects have been developed.

In the present study a series of LCF tests on BRBs are mentioned. Based on the tests results, an index to estimate fatigue life of BRBs is selected. Using this index, a criterion is presented to determine the minimum needed yielding length to prevent LCF failures. The next step is to redesign a benchmark 7 story BRBF utilizing BRBs with minimum yielding length. Time history analyses were conducted on the two buildings using the open source finite element platform, OpenSees (2005). Based on the results, an index of LCF damage is calculated for each brace to evaluate the accuracy of the presented criterion. To compare ductility demands on the primary and secondary frames, the maximum and the cumulative ductility in yielding length of BRBs were calculated.

2 LOW CYCLE FATIGUE

Common plasticity models used in civil engineering normally predict the nonlinear behavior of metallic elements under cyclic loading and commonly do not address the fatigue failure. The issue of LCF is not explicitly mentioned in seismic design standards such as Seismic Provisions for Structural Steel Buildings (AISC/ANSI 341-05) [8] and Seismic Rehabilitation of Existing Buildings (ASCE/SEI 41-06) [9]. However one of the most important issues in cyclic behavior of the metallic dampers can be the failure caused by repetitive large inelastic strains. This phenomenon is called LCF and usually occurs in members under severe cyclic loadings such as earthquake loading.

BRB dissipate energy by formation of plasticity in their core segment. As the strain amplitudes in normal BRBs are minimal, no many researches have been conducted on the LCF of normal BRBs. However when the length of the core segment is reduced the strain amplitudes rise and LCF failure could be a concern. Evaluating LCF effects requires enough data about the LCF capacity based on tests and selecting a damage evaluation process.

2.1 Low-Cycle Fatigue Capacity of BRBs

The capacity of metallic material against LCF is commonly expressed by Coffin-Manson equation [10].

$$\frac{\Delta\varepsilon_p}{2} = \varepsilon'(2N)^C \tag{1}$$

where:

- $\Delta\varepsilon_p /2$ is the plastic strain amplitude
- ε_f' is fatigue ductility coefficient
- 2N is the number of reversals to failure (N cycles)
- c is the fatigue ductility exponent

This equation is usually used to estimate the fatigue life of a specimen under constant plastic strain amplitudes. The parameters of this equation are extracted from tests. Material tests are typically conducted on small specimens which greatly differs from BRB specimens. LCF life has found to depend on many factors such as specimen shape and size, and stress concentrations [10]. Thus individual tests on steel material in BRB scale is needed to evaluate the LCF capacity of a BRB. Many researchers have attempted to investigate LCF effects in steel material or members and present a Coffin-Manson type equation to predict the fatigue life (N_f). A number of these studies will be presented.

In 2000 Nakamura et al tested five BRBs on behalf of Nippon Steel. This research intended to clarify hysteresis stability and fatigue failure characteristics of the braces by performing fatigue tests on practical scale unbounded braces [11]. Based on the test results of BRBs with different core steel grades including JIS SN400B, and LYPI00 and LYP235 a relationship between applied strain and fatigue life was presented:

$$\Delta\varepsilon_c = 0.2048(N_f)^{-0.49} \tag{2}$$

Where $\Delta\varepsilon_c$ is the strain amplitude of the core.

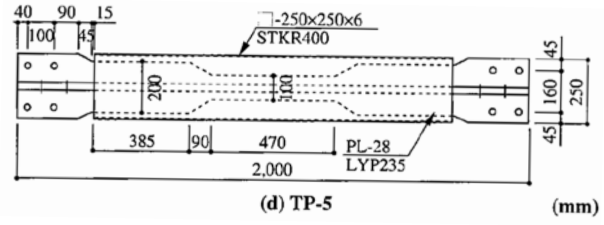

Figure 2: TP-5 specimen detail [11].

Most of failures occurred near the welding areas or reinforcing ribs that indicates stress concentration greatly decreases the fatigue properties of a BRB. The test results showed that the values of the failure cycle number (N_f) in the core model tests were 1/2 to 1/5 of those in the material tests, and those in the practical-scale tests were 1/6 to 1/10, presumably because of influences of stress concentration at the ends of the reinforcing ribs or that caused by local buckling. LYP100 and SN400B showed nearly identical plastic fatigue characteristics.

In 2002 S. L. Lin and Keh-Chyuan Tsai conducted performance tests on an all metallic detachable buckling restrained braces some of which included fatigue tests [12]. Various strain amplitudes were experimented and based on the results the following fatigue life equation was presented:

$$N = 0.0007(\varepsilon_c)^{-2.25} \tag{3}$$

Where N is the maximum tolerable cycles in strain of ε_c that occurs in BRB core.

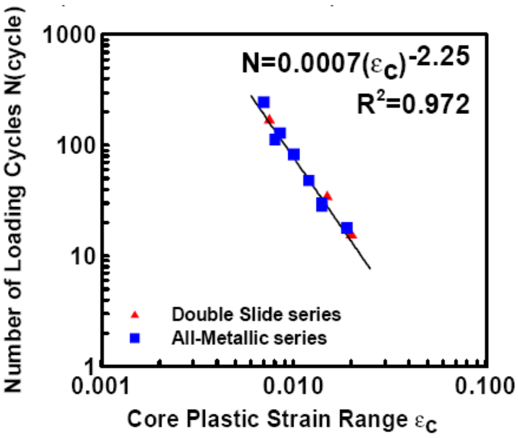

Figure 3: Number of fatigue strain cycles versus core strain relationship [13].

Other researchers have evaluated the fatigue properties of different type of BRBs. Table 2 shows a summary of the BRB fatigue studies which have presented a Coffin-Manson type equations.

Researcher	Year	Location	Equation	Material	Test Type
Nakamura et al	2000	Japan	$\Delta\varepsilon_c = 0.2048(N_f)^{-0.49}$	SN400B LYP100 LYP235	Uniaxial
Isoda et al	2002	Japan	$\Delta\varepsilon_c = 0.20(N_f)^{-0.39}$	LY225	Uniaxial
Nariharah (22278)	2002	Japan	$\Delta\varepsilon_p = 0.3770(N_f)^{-0.602}$	SN400B	Sub-assemblage
Horie et al	2003	Japan	$\Delta\varepsilon_c = 0.2(N_f)^{-0.41}$	SNB400	Uniaxial
Tsai	2003	Taiwan	$N_f = 0.0007(\varepsilon_c)^{-2.25}$	A572 GR50	Frame
Kamura et al	2009	Japan	$\Delta\varepsilon_t = 0.1128\ (N_f)^{-0.4129}$	LY100	Uniaxial

Table 2: Fatigue life prediction equations [11, 13-17].

The fatigue behavior of BRBs has been studied in other researches too. In these researches usually some extra load cycles have been exerted on the specimen after the specimen has withstood the total loading protocol for qualification test according to relevant code [18-20].

Some other researchers have reported the cumulative inelastic axial ductility capacity (ɳ) and have compared it to 200 which is noted in AISC 341-05 as a satisfactory fatigue property. It seems evaluating LCF failure only based on the cumulative inelastic axial ductility cannot consider the LCF effects completely, since strain amplitudes are of great importance in LCF failure.

From the LCF experimental studies of BRBsthe following conclusions can be derived:

- LCF capacity depends on various factors such as: the shape of core segment, the stiffness of buckling restraining mechanism, the width-thickness ratio of the axial member, clearance between the axial member and the restraining mechanism, eccentricity in the core segment, overall detailing of the BRB, the quality of manufacturing.
- Presence of any discontinuities, tack welds, attachments in core segment which is identified as protected zone per AISC 341-05 severely degrades the LCF life.

- LCF failure occurs soon after the formation of local buckling in the core segment.
- The local buckling of the core is more probable to happen at the ends of core segment [3, 21].
- Using flat plates in core segment show better fatigue properties in comparison to cruciform sections [11].
- The strain rate has minimal effect on hysteretic behavior, cyclic stress, and fatigue life for the steel plate especially when the core can dissipate heat through connections or proximity to elastic members [22].
- The overall fatigue life is somehow similar for different steel grades.

In this study the equation for fatigue life prediction presented by Nippon is adopted. Nevertheless the LCF capacity can be greatly increased if enough attention is paid to the results noted above. Though this equation is extracted for specific BRB with a special detailing, but it has been adopted for this study since it holds rational conservativeness.

2.2 Low-Cycle Fatigue Damage Evaluation

Evaluating the damage resulted from repeated cyclic loads commonly follows the Palmgren-Miner rule [23]. According to this theory the damage caused by a strain cycle is defined by the following equation:

$$D = \frac{1}{N_f} \tag{4}$$

So damage caused by "n" strain cycles is equal to:

$$nD = \frac{n}{N_f} \tag{5}$$

In order to calculate the damage index in case of several strain series with different amplitudes the, damage caused by n_i cycles at the strain of ε_{ai} is $n_iD_i=n_i/N_{fi}$. Then the overall damage of the member is equal to the summation of calculated damages [10].

$$\sum \frac{n_i}{N_{fi}} = \frac{n_1}{N_{f1}} + \frac{n_2}{N_{f2}} + ... + \frac{n_i}{N_{fi}} \tag{6}$$

Failure is probable when this summation becomes greater than 1.

When a brace is evaluated under a time history, the number of different strain amplitude is not distinctly recognized. In such cases the Rain Flow Counting Method can be applied. Rain Flow counting method is a process to calculate equivalent constant amplitude cycles for a strain or stress time history. This method has been successful [24] and is frequently used in fatigue analysis of seismic resistant systems [25, 26].

In this study the combination of Rain Flow Counting method and the Palmgren-Miner cumulative rule is applied to determine the damage index of the braces in the time history analyses.

2.3 The criterion to determine the yielding length in design procedure of the reduced core BRB

Based on the results of LCF studies, fatigue life of an element under high strain demands depends on the strain history it experiences rather than the maximum amplitude of strain. So at the first step the applicable displacement loading history on the specimen should be determined for designing purposes.

AISC 341-05 [8] suggests a loading protocol for qualification test of BRBs. When these provisions suggested, BRBs with reduced core length were not widely in use. The strain amplitudes in common BRBs are limited to 1% or 2%. Therefore seemingly the suggested protocol has not included the LCF effects. In absence of a specific criterion to control LCF failure, some researchers considered the cumulative inelastic axial deformation of the brace [4]. If the value from BRB test was much greater than 200 (AISC recommended value), they concluded that LCF failure is not probable.

In 2006 another loading protocol was presented by Tremblay et al [3] for testing series of all-steel BRBs some of which had reduced yielding length.

According to provisions of ASCE 41-06 [27], each energy dissipation device shall be loaded with 20 fully reversed cycles at the displacement in the energy dissipation device corresponding to the BSE-2 which represents an earthquake with 2% probability of exceedance in 50 years.

The provision of ASCE 41-06 which defines 20 cycles is based on the earthquake duration of the earthquake not its severity. On the other hand, the provisions of common seismic design codes are usually for design earthquakes corresponding to the BSE-1 which represents an earthquake with 10% probability of exceedance in 50 years. So in order to make the design assumptions of BRB compatible with common seismic systems, the provision of ASCE41-06 can be considered in BSE-1 instead of BSE-2. Table 3 shows loading protocols recommended by various references.

	Recommended Loading Protocol				
AISC	$2\times\Delta_{by}$	$2\times0.5\Delta_{bm}$	$2\times\Delta_{bm}$	$2\times1.5\Delta_{bm}$	$2\times2\Delta_{bm}$
Tremblay	$6\times\Delta_{by}$	$4\times0.5\Delta_{bm}$	$4\times\Delta_{bm}$	$2\times1.5\Delta_{bm}$	$4\times\Delta_{bm}$
ASCE 41-06	–	–	$20\times\Delta_{bm}$	–	–

Table 3: Comparison of loading protocols for BRB tests recommended by different references.

Δ_{by} is the projection of the story drift corresponding to the yielding of the brace on the brace direction and Δ_{bm} is the projection of design story drift on the brace direction.

As mentioned previously, the overall damage of a member is equal to the summation of calculated damages of different cycles. So the damage during the loading protocol should be calculated cumulatively. For this purpose, for each loading protocol the Palmgren-Miner equation is calculated and the result is controlled to be less than one.

3 DESIGNING AND MODELING OF A BRBF BUILDING USING REDUCED CORE BRB AND

The LCF failure is most probable in BRB with reduced yielding length, as the strain amplitudes increase. BRB with reduced yielding segment has two main parts: a short part and a long part. The short part is the restrained yielding part that yields in both tension and compression like a short BRB. This part acts as a structural fuse and is the displacement controlled (D.C.) component of the brace. The long part is the unrestrained non-yielding part without yielding or buckling. This part is expected to be elastic and is the force controlled (F.C.) component [28]. Figure 4 shows the schematic model of the Reduced Length BRB (RL-BRB), where P_y is yielding load of the brace, ε_c is maximum strain of the core, P_{cr} is critical buckling load of the whole BRB and FS is factor of safety.

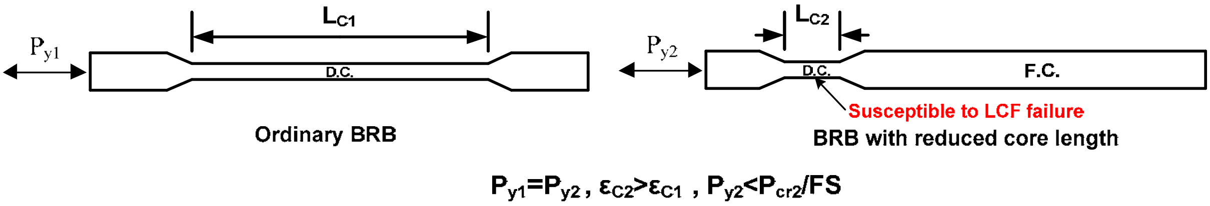

Figure 4: Schematic model of the recommended brace versus schematic model of a conventional BRB [29].

Reducing the yielding part of the BRB will affect the overall behavior of BRBF and also will make the LCF damage more possible since the core strain amplitudes will increase [30]. So the LCF property of frame with RL-BRB is investigated via nonlinear analyses. For this purpose a benchmark BRBF building was redesigned using RL-BRBs. The step by step design procedure for RL-BRBFs was completely discussed in another study by Razavi et al [28].

The original building had been selected from a Steel Tips report entitled as "Seismic Design of Buckling Restrained Braced Frames" [31]. The building is a 7 story BRBF with official application. Four sets of diagonal bracing (BF-1) in X direction and two sets of chevron bracing (BF-2) in Y direction is applied as the lateral resisting frames for a rectangular plan of 40m×25m. The total length of BF-1 braces is 7.5m in the first story and 7m in other stories. For BF-2 braces the lengths are 6.25m and 5.75m respectively. Figure5 shows the geometry of bracing bays. ASCE 7-02 [32] specifications had been used for the loading and the design procedure was originally performed according to FEMA 450 section 8.6 [33].

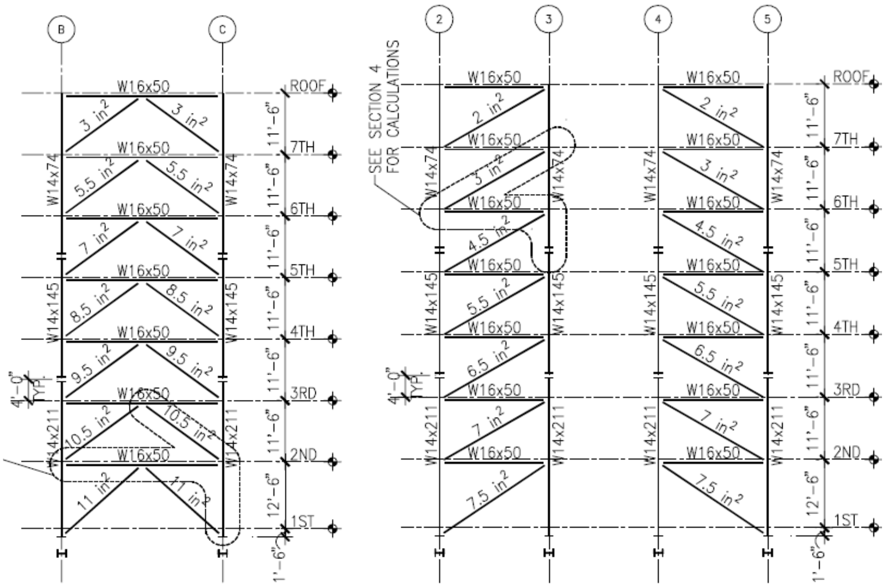

Figure 5: The elevation view of BRBF building. BF-1(left) and BF-2(right) [31].

As this study intends to study the LCF effects of the RL-BRB, the minimum length required is calculated according to the assumptions of previous sections.

In previous sections recommended equations to calculate fatigue life (N_f) of BRBs were presented. N_f can be extracted for every BRB detailing by conducting special fatigue tests. ATC 24 recommends a testing protocol for extracting the parameters in fatigue life estimation equation for steel structural elements. [34]

Tables 4 and 5 show calculated yielding lengths using different loading protocols and different N_f by applying Palmgren-Miner rule for the brace in 5th story and 4th and 5th story of BF-1 and BF-2 respectively. The lengths in the tables are calculated so that the LCF index equals 1. This means no safety factor is adopted in this stage.

	AISC	Tremblay	ASCE 41-06 (BSE-1)
Nippon	130	124	150
Isoda	115	100	171
Narihara	87	89	170

Table 4: Different yielding lengths calculated for BF-1 (cm).

	AISC	Tremblay	ASCE 41-06 (BSE-1)
Nippon	93	88	105
Isoda	81	71	122
Narihara	62	63	121

Table 5: Different yielding lengths calculated for BF-2 (cm).

Table 4 and 5 show that that different loading protocols lead to almost the same results. Using ASCE 41-06 leads in slightly longer yielding segment. In this study, yielding length calculated from the combination of AISC loading protocol and N_f from Nakamura study is selected.

Based on the selected reduced length the building with RL-BRB was analyzed and designed. Comparison of the design results showed that replacing common BRB with RL-BRB does not make a significant change in beams and columns designing. The same cross sectional area of the BRB core also obtained. The comprehensive comparison of design results is discussed by Shemshadian [30].

4 NONLINEAR DYNAMIC ANALYSES OF FRAME WITH RL-BRB

In order to investigate the LCF effects in BRBs of original and redesigned buildings, 28 nonlinear dynamic analyses (Time History Analyses) were conducted on 4 BRBFs. A set of 7 different records were used to consider the average results. These records were selected from PEER database. It was tried to select records with various frequency contents and durations in order to estimate ductility and LCF damage index more accurately. These records are introduced in table 6.

No.	Name	Year	Magnitude	Duration(sec)	Dist. (km)	PGA (g)	PGV (cm/s)	PGD (cm)
1	Duzce	1999	7.1	56	17.6	0.203	17.3	14.29
2	Imperial Valley	1979	6.5	100	43.6	0.145	14.8	8.62
3	Kobe	1995	6.9	41	15.5	0.059	6.4	2.16
4	Kocaeli	1999	7.4	30	17	0.086	8.6	5.52
5	Landers	1992	7.3	28	21.2	0.174	9.9	4.01
6	Northridge	1994	6.7	30	19.6	0.326	16.9	2.56
7	San Fernando	1971	6.6	28	21.2	0.136	4.3	1.52

Table 6: Characteristics of selected ground motions.

Since site parameters in Steel Tips report was given according to ASCE 7-02 [27], the design spectrum of this code was used for record scaling.

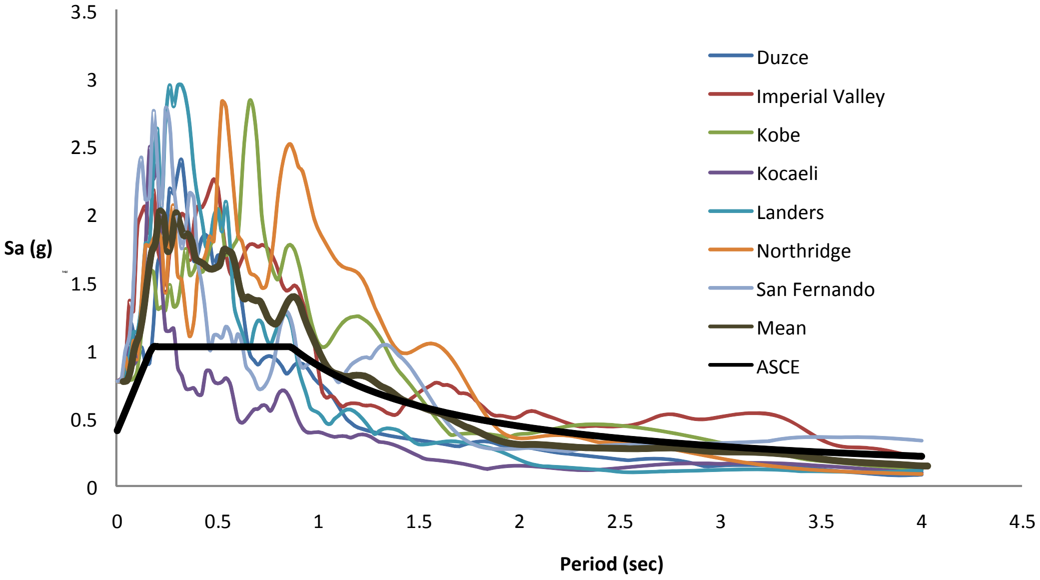

Figure 6: Response spectrum of the selected records with mean and ASCE spectrums.

The results of nonlinear time history analyses show that the maximum and residual drifts of the RL-BRBF are less than the original frame. This is the result of using RL-BRBs instead of common BRBs since RL-BRBs are stiffer [1]. On the other hand the pattern of interstory drifts is almost unchanged that indicates that replacing common BRBs with RL-BRBs does not influence the general behavior of the structure.

5 LOW CYCLE FATIGUE EFFECTS IN YIELDING LENGTH OF BRBS

The strain history of each yielding segment of BRB under each record is extracted. Then the Rain Flow Counting Method is used to calculate the equivalent strain history with complete cycles.

According to the definition of AISC 341-05, cumulative inelastic ductility under a loading is the summation of plastic ductility occurred in the member divided to deformation at beginning of yielding. The loading sequence requires each tested brace to achieve ductilities corresponding to a cumulative inelastic axial ductility capacity of 200 per AISC 341-05 specifications, [8]. Table 7 presents the cumulative inelastic ductilities for strain history of

RL-BRBs yielding length. The values justified that the yielding length of RL-BRBs will undergo large inelastic deformations under selected earthquakes .

Story	**Reduce Length**	
	BF-1	BF-2
7	193	241
6	321	351
5	303	363
4	294	360
3	337	349
2	368	262
1	187	209
Average	286	321

Table 7: Cumulative inelastic ductility in yielding length of RL-BRBs.

In order to control the LCF failure in a reduced yielding segment, LCF damage index should be calculated for equivalent strain history based on the Palmgren-Miner rule. Table 8 shows the results for RL-BRBFs considering Nakamura et al fatigue life equation. Since the tension and the compression braces behaved similarly, a single damage index was presented for every story.

Story	**Reduce Length**	
	BF-1	BF-2
7	0.05	0.07
6	0.12	0.14
5	0.12	0.16
4	0.12	0.15
3	0.14	0.13
2	0.13	0.07
1	0.05	0.06
Average	0.10	0.12

Table 8: LCF damage index for RL-BRBs.

The results confirm that LCF criterion used in design procedure of RL-BRB has an acceptable safety factor (about 6), so LCF failure does not occur under selected records. On the other hand, low damage indices show that ductility demands resulted from loading protocols in design procedure of the yielding length are much higher than ductility demands from analysis.

As an example as noted in table 9 the damage index for the brace in fifth story of RL-BRBF is 0.97. The majority of this (about 88%) is due to strain amplitudes of 1.5Δ_{bm} and 2Δ_{bm}. It can be concluded that LCF damage is the result of multiple cycles in great amplitudes.

AISC Protocol	2×2Δ_{bm}	2×1.5Δ_{bm}	2×Δ_{bm}	2×0.5Δ_{bm}
Strain in yielding segment	5.4	4.1	2.7	1.4
Palmgren-Miner fatigue index in each cycle	0.53	0.30	0.11	0.03
Palmgren-Miner fatigue in the whole protocol	0.97			

Table 9: Palmgren-Miner damage index for the brace of fifth story in RL-BRBF.

On the other hand, based on nonlinear dynamic analyses the mean calculated damage index for this brace is 0.12. For more investigation, the strain histories of this brace under Imperial Valley and Northridge records are considered (Figure 7, 8). These two records have the maximum damage indices.

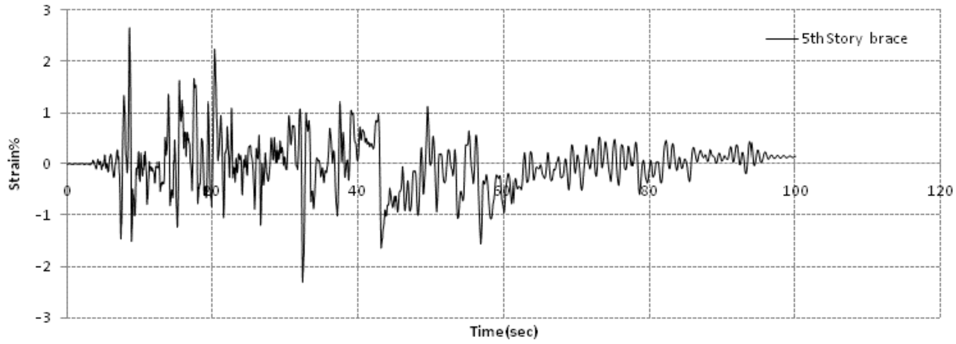

Figure 7: Strain history of fifth story brace in RL-BRBF under Imperial Valley record.

The strain history of Imperial Valley shows that the majority of strain amplitudes are less than 1% and rarely reach 2%. In other words, although the number of cycles is high (the duration of earthquake is 100 seconds) but the strain amplitudes are small.

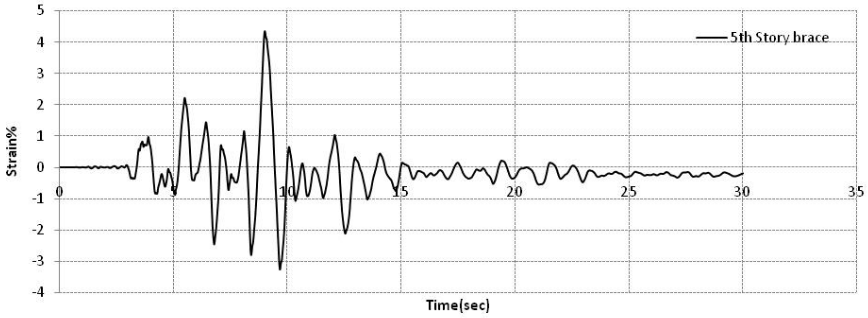

Figure 8: Strain history of fifth story brace in RL-BRBF under Northridge record.

The strain history of Northridge shows that the maximum strain amplitude is grater that 4%, but it only happens one time during the whole earthquake. Also the number of cycles in this strain history is low (the duration of earthquake is 30 seconds). In other words, although there are high strain amplitudes in strain history, but the number of these cycles is low. So, neither Imperial Valley nor Northridge record has a high damage index.

The clear difference between the damage indexes of designing and analysis is due to two possibilities. The selected records are not enough to give a general conclusion or AISC loading protocol does not include the LCF effects. It seems that AISC 341-05 does not represent a distinct criterion to control LCF failure in BRBs (especially RL-BRBs); while selecting a very short length can result in LCF failure. This topic could be a subject of research in future studies.

Finally it can be mentioned that, considering the sensitivity of LCF effects in RL-BRBs and the advantages of reducing yielding length in BRBs, there is an open space for the available seismic design codes to present some specific provisions regarding this issue.

For each brace, the mean value of maximum ductility demands from applied records were calculated and presented in Table 10. As expected the ductility demands in yielding length of RL-BRBs were much greater than the steel tips BRBs because a shorter yielding length is used. Previous studies confirm the high ductility values for BRBs with reduced yielding length [7].

Story	**Steel Tips**		**Reduce Length**	
	BF-1	BF-2	BF-1	BF-2
7	3	4	11	11
6	5	4	16	12
5	6	4	19	18
4	6	5	19	20
3	6	6	20	22
2	5	6	19	21
1	3	4	13	15

Table 10: The maximum ductility in yielding length of BRBs.

6 CONCLUSIONS

In present paper, different LCF studies on BRBs were presented and the suggested equations to estimate fatigue life of BRBs were mentioned. Using these equations and based on the rules of LCF damage estimation, a criterion was developed to determine the minimum of yielding length of the core in BRBs. This criterion was a single step of a step by step design procedure for RL-BRBFs. In order to evaluate the fatigue properties of the BRB with minimum yielding length through a time history analysis, a benchmark 7 story BRBF building was redesigned using RL-BRBs and it was tried to use the minimum possible yielding length. Then nonlinear dynamic analyses were conducted on both original and redesigned buildings. 28 analyses showed that reducing the yielding length of BRB increases the ductility demands on this part. Also the results of this damage index showed that in spite of high ductility demands, LCF effects are not critical and there is enough safety factor for LCF failure prevention. The maximum ductility of 11 to 22 (times of deformation at first yielding) and the cumulative inelastic ductility of 187 to 368 (times of deformation at first yielding) were imposed to the yielding length. The results of present study are valid for the selected records and can be extended for similar earthquakes with scientific judgments.

Key points were presented to reduce the risk of LCF failure for the BRBs. For future researches it is recommended to consider other records including artificial ones. Moreover developing a global loading protocol with enough safety factor for evaluating the LCF effects of BRBs is recommended for further researches.

REFERENCES

[1]M. E. Shemshadian, S. A. Razavi, S. R. Mirghaderi, A. Hosseini and M. Khan Mohammadi, The Advantages of Reducing the Length of Yielding Segment in Seismic Performance of Buckling Restrained Braced Frames. *Sixth International Conference of Seismology and Earthquake Engineering* Tehran, Iran, 2011.

[2]M. D’Aniello, G. Della Corte and F. M. Mazzolani, All-steel buckling-restrained braces for seismic upgrading of existing reinforced concrete buildings. *International Specialty Conference on Behaviour of Steel Structures in Seismic Area (STESSA)* Philadelphia, US, 2009.

[3]R. Tremblay, P. Bolduc, R. Neville and R. DeVall, Seismic testing and performance of buckling-restrained bracing systems. *Canadian Journal of Civil Engineering*, 33, 183-198, 2006.
[4]N. Ma ,B. Wu, H. Li, J. Ou and W. Yang, Full Scale Test of All-Steel Buckling Restrained Braces. *14th World Conference on Earthquake Engineering* Beijing, China, 2008.
[5]S. Ahlehagh, *Improvement of the Special Concentrically Braced Steel Frames Behavior by Employing Balanced Braces*. Master of Science, University of Tehran, 2008.
[6]F. Mazzolani, Innovative metal systems for seismic upgrading of RC structures. *Journal of Constructional Steel Research*, 64, 882-895, 2008.
[7]L. Di Sarno and G. Manfredi, Seismic retrofitting with buckling restrained braces: Application to an existing non-ductile RC framed building. *Soil Dynamics and Earthquake Engineering*, 2010.
[8]AISC, Seismic Provisions for Structural Steel Buildings. AMERICAN INSTITUTE OF STEEL CONSTRUCTION.2005 ,
[9]ASCE/SEI 41-06, *Seismic Rehabilitation of Existing Buildings*. American Society of Civil Engineers, 2007.
[10]R. Stephens, H. Fuchs, A. Fatemi and R. Stephens, *Metal Fatigue in Engineering*. Wiley-Interscience, 2000.
[11]H. Nakamura, Y. Maeda and T. Sasaki, Fatigue Properties of Practical-Scale Unbonded Braces.Report No. 82 *Nippon Steel*, 2000.
[12]S. L. Lin and K. C. Tsai, A Study of All Metallic and Detachable Buckling Braces. *Center for Earthquake Engineering Research, National Taiwan University*).2003 ,Chinese(
[13]K. Q. Tsai, RESEARCH AND APPLICATIONS OF DOUBLE-CORED BUCKLING RESTRAINED BRACES. 2004.
[14]K. ISODA, S. N., M. S., T. T. and H. T., Development of Unbonded Brace Damper Restrained by Channel Section Steel. Part.4 Low Cyc1e Fatigue Tests, *Architectural Institute of Japan*, 2002.(Japanese(
[15]H. NARIHARA, O. TSUJlTA and Y. S., The Experimental Study on Buckling Restrained Braces. Part 4 Low Cycle Fatigue Test on Aseismic Brace with SN400B, SN490B, *Architectural Institute of Japan*, 2002).Japanese(
[16]T. HORIE, S. MASE and T. TERADA, Development of Unbonded Brace Damper Restrained by Channel Section Steel. Part 5 Low Cycle Fatigue Tests on Unbonded Brace Dampers with SN400B, *Architectural Institute of Japan*, 2003.(Japanese(
[17]K. Hisaya, N. Takayuki, O. Koji and F. Taku, Seismic Response Control for High-Rise Buildings Using Energy-Dissipation Devices. JFE TECHNICAL REPORT, 2009.
[18]S. MERRITT, C.-M. UANG and G. BENZONI, SUBASSEMBLAGE TESTING OF COREBRACE BUCKLINGRESTRAINED BRACES.Report No. TR-2003/01, *Pacific Earthquake Engineering Research Center, University of California at Berkeley*, La Jolla, California, 2003.
[19]J. NEWELL, C.-M. UANG and G. BENZONI, SUBASSEMBLAGE TESTING OF COREBRACE BUCKLINGRESTRAINED BRACES (G SERIES).Report No. TR-06/01, *Pacific Earthquake Engineering Research Center, University of California at Berkeley*, La Jolla, California, 2006.
[20]S. MERRITT, C.-M. UANG and G. BENZONI, SUBASSEMBLAGE TESTING OF STAR SEISMIC BUCKLING-RESTRAINED BRACES.Report No. TR-2003 ,04/*Pacific Earthquake Engineering Research Center, University of California at Berkeley*, La Jolla, California, 2003.

[21]F. Mazzolani, G. Della Corte and M. D'Aniello, Experimental analysis of steel dissipative bracing systems for seismic upgrading. *Journal of Civil Engineering and Management*, 15, 7-19, 2009.

[22]P. Dusicka, A. M. Itani and I. G. Buckle, Cyclic Response of Plate Steels under Large Inelastic Strains. *Journal of Construtional Steel Research*, 63, 156-164, 2009.

[23]M. Miner, Cumulative damage in fatigue. *Journal of Applied Mechanics*, 1945.

[24]S. ARIDURU, *FATIGUE LIFE CALCULATION BY RAINFLOW CYCLE COUNTING METHOD*. Master of Science, Middle East Technical University, 2004.

[25]S. D. Campbell, R. M. Richard and J. E. Partridge, STEEL MOMENT FRAME DAMAGE PREDICTIONS USING LOW-CYCLE FATIGUE. *14th World Conference on Earthquake Engineering* Beijing, China, 2008.

[26]T. Terada, N. Satake, T. Horie, S. Mase, Y. Ogawa and K. Isoda, Low cycle fatigue characteristics and cumulative fatigue damage of unbonded brace damper buckling-restrained by channel section steel. *Journal of Architecture*, 2002.

[27]ASCE, Minimum Design Loads for Buildings and Other Structures. American Society of Civil Engineers 2005.

[28]S. A. Razavi, M. E. Shemshadian, S. R. Mirghaderi and S. Ahlehagh, Seismic design of buckling restrained braced frames with reduced core length. *The Structural Engineers World Congress* Italy, 2011.

[29]M. E. Shemshadian, S. A. Razavi, S. R. Mirghaderi, A. Hosseini and M. Khan Mohammadi, The Advantages of Reducing the Length of Yielding Segment in Seismic Performance of Buckling Restrained Braced Frames. *Sixth International Conference of Seismology and Earthquake Engineering* Tehran, Iran, May 2011.

[30]M. E. Shemshadian, *A new idea in Buckling Restrained Brace with elimination of overall restraining mechanism*. Master of Science, University of Tehran, 2011.

[31]R. Sabelli and W. Lopez, Design of Buckling-Restrained Braced Frames. *Modern Steel Construction*, 44, 67-74, 2004.

[32]ASCE, Minimum Design Loads for Buildings and Other Structures. American Society of Civil Engineers 2002.

[33]BSSC, NEHRP recommended provisions for seismic regulations for new buildings and other structures (FEMA 450). Building Seismic Safety Council, Federal Emergency Management Agency, 2003.

[34]H. Krawinkler, Guidelines for Cyclic Seismic Testing of Components of Steel Structures.ATC-24, *Applied Technology Council*, 1992.

COMPDYN 2011
III ECCOMAS Thematic Conference on
Computational Methods in Structural Dynamics and Earthquake Engineering
M. Papadrakakis, M. Fragiadakis, V. Plevris (eds.)
Corfu, Greece, 25–28 May 2011

A DETAILED 2D FINITE ELEMENT MODEL FOR THE SEISMIC ASSESSMENT OF STEEL FRAMES WITH TOP-AND-SEAT ANGLE WITH DOUBLE WEB-ANGLE CONNECTIONS

Hussam N. Mahmoud[1] **and Amr S. Elnashai**[2]

[1] University of Illinois at Urbana-Champaign
205 N. Mathews Ave., Urbana, IL 61801
e-mail: hmahmoud@illinois.edu

[2] University of Illinois at Urbana-Champaign
205 N. Mathews Ave., Urbana, IL 61801
e-mail: alenash@illinois.edu

Keywords: Semi-rigid Connections, Steel Frames, Finite Element Model, Non-linear dynamic, Time-history Analysis.

Abstract. *Early work on predicting the moment-rotation response of semi-rigid connections was conducted through simplified linearized and curve fitting models compared to experimental data. The models were developed using monotonic tests with ambiguity in the loading and boundary conditions used. As a result of such, the models often failed to predict the actual response of the connection particularly when the connection is cyclically loaded. With advancements in computational techniques and power, attention was shifted to developing 3D models which have proven to be capable of capturing the true behavior of the connection. Notwithstanding their effectiveness, 3D models are hard to construct and are computationally expensive, thus their ability to conduct large parametric studies is limited. This paper presents an overview of a new 2D inelastic finite element model (FEM) for predicting the monotonic and cyclic response of semi-rigid connections with top-and-seat angle with double web angle. The model comprises 2D plane strain elements and includes various behavioral features including bolt preload, friction between faying surfaces, connection slip, the effect of bolt-hole ovalaization and hot-rolling residual stresses in the angles. Characterized by its reduced number of nodes and elements, the model is computationally inexpensive and is capable of capturing the true behavior of the connection.*

1 INTRODUCTION

The integrity of fully-welded connections in the beam-to-column joints of steel frames under earthquake loading has come under question as many steel and composite buildings suffered severe damage in connections during the Northridge (1994) and Hyogo-ken Nanbu (1995) earthquakes. Forensic investigations following the earthquake identified failed welded beam–column connections in more than 200 buildings [1]. The failure was attributed to poor connection detailing practices and inadequate weld material properties that were common prior to the earthquake [2]. The backing bars and weld runoff tabs used to make the groove welds connecting the beams to the columns were normally left in place after completion of the weld. The existence of backing bars or welds tabs created a lack-of-fusion defect, which was large enough to originate crack growth which propagated in the heat affected zone of the weld metal and in the column flange. Studies on the weld metal used in construction, E70T-4, revealed that the weld had very low Charpy toughness [3]. Subsequently, there has been a tendency to be overly conservative in the design and detailing of these connections. Figure 1 shows a typical fractured beam-column connection in a steel moment frame during the 1994 Northridge Earthquake.

Figure 1: Fractured connection in a steel moment frame during the 1994 Northridge earthquake (crack propagated at backing bar detail and propagated in the column flange and web)

Uncertainly in the performance of welded connections spiked interest in investigating the use of bolted connections in the construction of steel frames in seismic regions. Bolted partial-strength semi-rigid connections were evaluated as a viable alternative due to their lower construction costs and simple fabrication process. Analytical and experimental studies were carried out to assess the fundamental characteristics of the connection. The cyclic behavior of the connection was evaluated through testing of beam-column subassemblies. The experimental results demonstrated the large energy absorption capabilities of these connections under cyclic loading with stable hysteretic behavior [4, 5].

The experimental results were used to develop simplified analytical and power models aimed at capturing the connection response [6, 7, 8]. The models were however developed using old tests in which high degree of uncertainty exist regarding the degree of bolt pretension and actual material properties. In addition, the tests did not cover a wide range of specimen sizes and focused on small specimens with shallow beams and thin angles. As a consequence, test data for specimens comprising deep beams and thick angles did not show good agreement with the curve-fitting models [9].

Two and Three-dimensional finite element models were developed to capture the complicated behavior of the connection such as slip, friction between surfaces in contact and prying action [10, 11, 12, 13, 14]. The component level experimental and finite element results were used for developing frame models for assessing the seismic performance of steel frames. In these models, line elements are used to represent the beams and columns and rotational springs with idealized moment-rotation relationships, obtained from the experimental results or the finite element models, are used to represent the connections [15, 16, 17]. The drawback of using such approach, in addition to idealizing the moment-rotation relationships, is that the interaction between the beam and column flanges and the angles comprising the connection is not captured. Such interaction is essential as it influences the spread of yielding in the beam. This paper presents an overview of new 2D finite element model of top-and-seat angle with double web angle connections and its use is frame analysis for the seismic evaluation of steel frames with such connections.

2 DESCRIPTION OF THE STRUCTURE

The structure considered is a 2-story, 4-bay (longitudinal) and 2-bay (transverse) steel frame. The height of the first and second story is 15 ft and 13.5 ft, respectively and the bay width is 30 ft. The outer frames are special moment resisting frames (SMRF) designed according to the Structural Seismic Design Manual, Volume 3 [18] while the inner frames are only responsible for carrying their share of gravity load.

The strong-column weak-beam design approach was used for sizing the beams and columns in the SMRFs and resulted in W18 x 40 for the beams and W14 x 159 for the columns. Following the sizing of the beams and columns, the assumed rigid connections in the frame were redesigned to reflect semi rigidity and partial strength. Three different frames are considered with the connections in each frame designed as top-and-seat angles with double web angles according to Eurocode 3 [19]. The sizes of the angles and the bolts were optimized such that the resulting connection capacity in frame 1, 2 and 3 is 30%, 50%, and 70%, respectively, of the plastic moment capacity of the beam. Plan view of the structure, an elevation of a typical SMRF, and a zoom-in of a typical connection topology are shown in Figure 2.

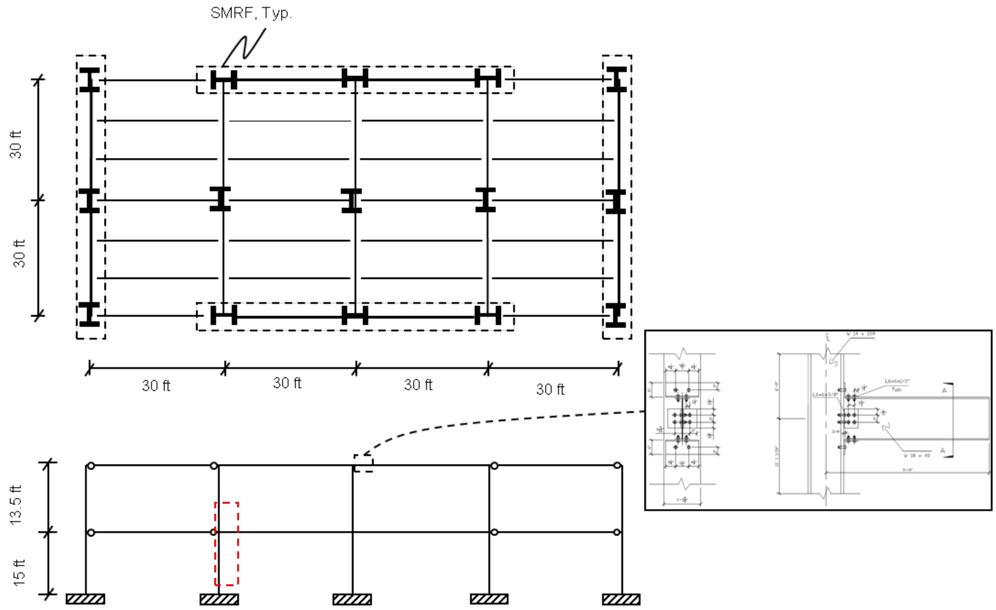

Figure 2: Plan view of the structure, an elevation of the SMRF and a zoom-in of a typical connection topology

3 ANALYTICAL MODEL

3.1 Beam-column connection model

The development of 3D finite element models for connections has been primarily driven by the notion that 2D models cannot properly capture the complex localized behavior of the connection. On the opposing side of the latter argument, 2D models may be much more efficient when compared to 3D models if the problem investigated is planar or could be idealized as planar. In addition, 3D models contain large number of nodes and elements rendering them computationally expensive and rather impractical particularly when used in parametric studies.

An inelastic finite element model is employed in the current investigation. The model comprises a 2D plane stress elements for the beam-to-column connections and 1D beam elements between subsequent connections and is developed using ABAQUS which is a general purpose commercial package [20]. The model, shown in Figure 3, includes various behavioral features namely; 1) bolt preload, 2) friction between faying surfaces, 3) connection slip, 4) the effect of bolt-hole ovalization, and 5) hot-rolling residual stresses in the angles. Figure 4 (a) shows the monotonic moment-rotation relationship (with and without slip) of a beam-column subassembly with a 30% MP_b connection capacity. Details on the model and its features are given in Mahmoud [21].

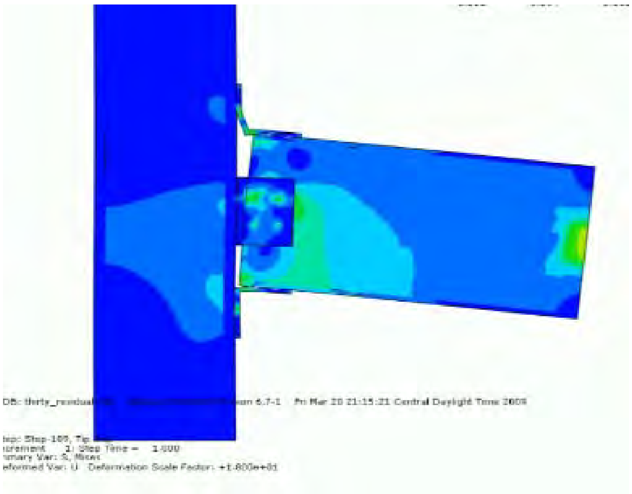

Figure 3: Finite element model of the beam-column subassembly.

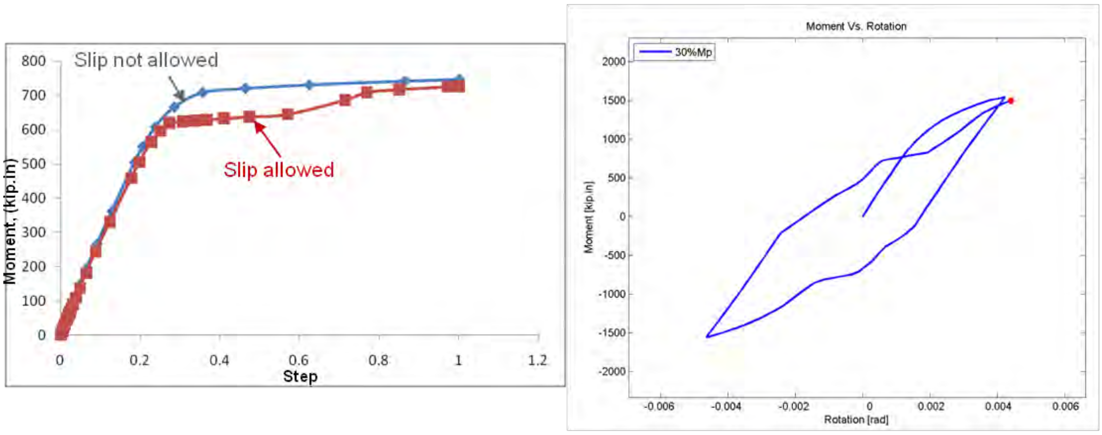

Figure 4: Moment-rotation relationship for a 30% capacity connection with and without slip.

3.2 Frame model

Analytical models of frames have utilized line elements connected with springs representing the load deformation characteristics of the connection. Due to its minimal computational demands, this modeling approach has been viewed as the best alternative for conducting frame analysis. However, the models typically represent idealized behavior and in many cases cannot capture the local response of the various connection components. Furthermore, the deformation and the spread of yielding in the beams or columns are not well represented since the interaction between the beam flanges and the top and seat angles is neither physically modeled nor accounted for. Therefore, the use of 2D or 3D finite element models when conducting time-history analysis can pay significant dividends since the localized connection behavior and its interaction with the beam and column is physically modeled.

In light of the above arguments, a multi-resolution inelastic 2D finite element model is employed for conducting time-history analysis of the steel frames with top-and-seat angles with double web angle connection as shown in Figure 5. The connections in the frame are represented through the detailed 2D finite element formulation of the beam-column subassembly described above while the beams and columns in the frame are represented using line elements.

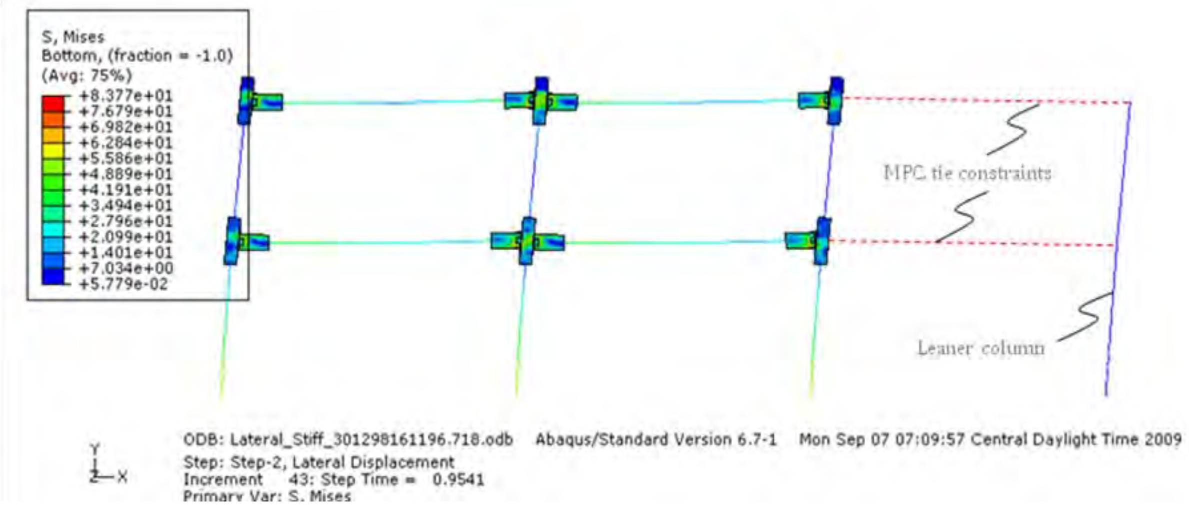

Figure 5: Frame model including a leaner column representing the gravity system.

Prior to starting the simulations, gravity loads were applied to the system using the loading combination of:

$$1.0DL + 10\,psf + 0.25LL \tag{2}$$

Where the DL indicates dead load, the 10 pfs is used for partition walls, and LL indicates live load. The resulting distributed load is listed in Table 2. Gravity loads carried by the core gravity frames were considered through the application of point loads on a leaning column modeled as a pinned rigid element and connected to the frame through tie multi point constraints.

Level	1.0 DL + Partitions (kip/in)	0.25 LL (kip/in)
Roof	0.0863	0.0013
1st	0.095	0.05

Table 1: Distributed gravity loads applied to the frames during the simulations.

4 PRELINMINARY RESULTS

4.1 Selected record and scaling

Non-linear dynamic time-history analysis was conducted to evaluate the seismic response of the frame. The structure was excited using the Northridge earthquake of 17 January 1994 with M_w of 6.69. The station used is the Arleta - Nordhoff Fire Station which is located 8.66 km away from the epicenter and measured a PGA of 0.332. To speed up the analysis, the original record was truncated where only the first 20 seconds of the record were used in the analysis since the main earthquake activities are concentrated in the first 20 seconds. In addition, to truncating the record, a scaling factor of 1.989 was applied to the record to represent a maximum considered earthquake (MCE) as per ASCE 07 [22]. The original and modified records are shown in Figure 6 (a) and (b) respectively.

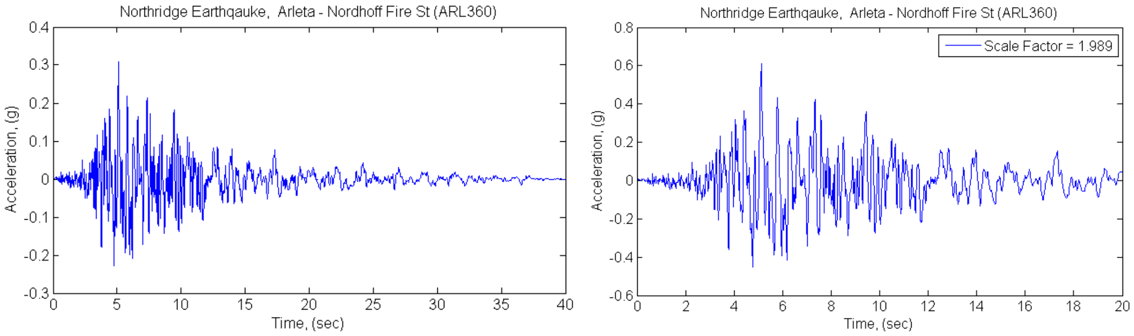

Figure 6: The Northridge earthquake used in the simulation. (a) original record. (b) modified record.

4.2 Roof displacement and Interstory drift ratios

The analysis was conducted on frames with varying connection capacity, yield strength of the connecting angles, slip in the connection and friction coefficient between the faying surfaces. Specifically, the frames were characterized by connection capacities of 30% MP_b, 50% MP_b and 70% MP_b with yield strength of 36 ksi and 50 ksi for the angles and beam elements, respectively, a friction coefficient of 0.33 and 1/16” bolt hole (i.e., a slip 1/32” on both sides of the bolt hole). The roof displacement and the interstory drift ratio of all three frames are shown in Figure 7. The maximum roof displacement experienced by the frames was 4.06 in, 5.82 in and 6.54 in, for the 30% MP_b, 30% MP_b and 30% MP_b, respectively. The resulting first floor interstory drift ratio was calculated to be 2.51%, 3.59% and 4.04% for the 30% MP_b, 30% MP_b and 30% MP_b, respectively. The roof interstory drift ratio was calculated to be 1.53%, 2.78% and 3.15% for the 30% MP_b, 30% MP_b and 30% MP_b, respectively. The calculated interstory drift ratios for all frames are below the 5% limit specified by FEMA 356 [23]

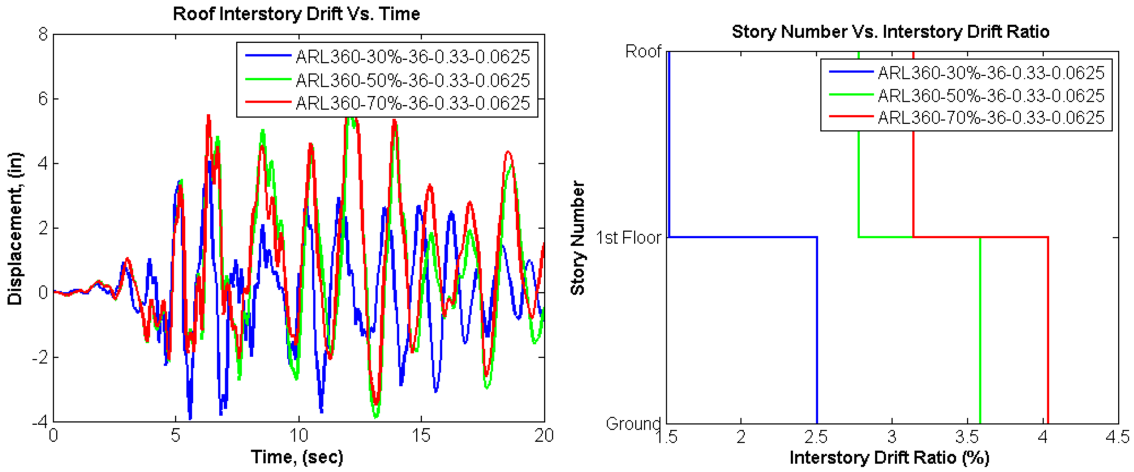

Figure 7: Roof displacement and intersotry drift ratios for all three frames

5 CONCLUSIONS

- A new beam-column connection model for top-and-seat angle with double web angle connections has been developed.
- Many inelastic features are represented in the model including hot-rolling residual stresses in the angles, bolt preload, friction between faying surfaces, connection slip and the effect of bolt-hole ovalization,
- The beam-column model was integrated in a frame model
- Non-linear dynamic time-history analysis was conducted on three different frames with varying connection capacities (30% MP_b, 50% MP_b and 70% Mp_b)
- The analysis results showed that the 30% MPb frame experienced the least roof displacement and interstory drift ratio followed by the 50% MPb frame and the 70% MPb frame respectively.
- The interstory dirft ratio for all three frames did not exceed the 5% limit defined by FEMA for MCE.

REFERENCES

[1] Whitaker, A. Gilani, A., and Bertero, V., 1998. Evaluation of Pre-Northridge Steel Moment Resisting Frame Joints, *Journal of the Structural Design of Tall Building* 7, 263–283.

[2] SAC Joint Venture., 2000. Recommended Seismic Evaluation and Upgrade Criteria for Existing Welded Steel Moment-Frame Structures, Report no. FEMA-351, Federal Emergency Management Agency, Washington, D.C.

[3] Fisher, J. W., Dexter, R. J., and Kaufmann, E. J., 1997. Fracture Mechanics of Welded Structural Steel Connections. Report No. FEMA-288 (SAC 95-09), FEMA, Washington, D.C.

[4] Azizinamini, A. and Radziminski, J., 1989. Static and Cyclic Performance of Semirigid Steel Beam-to-Column Connections, *ASCE Journal of Structural Engineering* 115, No. 12

[5] Bernuzzi, C., Zandonini, R., and Zanon, P., 1996. Experimental Analysis and Modeling of Semi-rigid Steel Joints under Cyclic Reversal Loading, *Journal of Construction Steel Research* 38, No. 2.

[6] Frye, J.M. and Morris, G.A., 1975. Analysis of Flexibly Connected Steel Frames, *Canadian Journal of Civil Engineering* 2:280–291.

[7] Richard, R.M. & Abbott, B.J., 1975. Versatile Elastic–Plastic Stress–Strain Formula", *ASCE Journal of Engineering Mechanics*, ASCE 101(4):511–5.

[8] Kishi, N. and Chen, W., 1986. Database of Steel Beam-to-Column Connection, Structural Engineering Report no. CESTR- 86-26, School of Civ. Engrg., Purdue University, West Lafayette, Ind.

[9] Leon, R.T., Hu, J.W. and Corey, S., 2004. Rotational Capacity and Demand in Top-and Seat Angle Connections Subjected to Seismic Loading, *Connections in Steel Structures V*, Amsterdam.

[10] Gendron, G., Beaulieu, D. and Dhatt G., 1989. Finite Element Modeling of Bolted Connections, *Canadian Journal of Civil Engineering* 16:172-181.

[11] Gebbeken, N., Rothert, H. and Binder, B., 1994. On the Numerical Analysis of Endplate Connections, *Journal of Construction Steel Research* 30:177–196.

[12] Sherbourne, A. and Bahaari, M., 1997. 3D Simulation of End-Plate Bolted Connections," *Journal of Structural Engineering* ASCE 120(11):3122–3136.

[13] Bursi, O.S. & Jaspart, J.P., 1998. Basic Issues in the Finite Element Simulation of Extended End Plate Connections, *Computers & Structures*. 69:361–82.

[14] Citipitioglu, A.M.., Haj-Ali, R.M. and White, D.W., 2002. Refined 3D Finite Element Modeling of Partially Restrained Connections Including Slip, *Journal of Construction Steel Research* 58:995–1013.

[15] Awkar, J. C. and Lui, E. M., 1999. Seismic analysis and response of multistory semirigid frames, *Journal of Engineering Structures* 21(5), 425-442.

[16] Salazar, A. R. and Haldar, A., 2001. Energy Dissipation at PR Frames under Seismic Loading, *Journal of Structural Engineering* 127(5), 588-592.

[17] Foutch, D. A. and Yun, S.-Y., 2002. Modeling of steel moment frames for seismic loads. *Journal of Constructional Steel Research* 58(5-8), 529-564.

[18] IBC Structural/Seismic Design Manual., 2006. Volume 3: Building Design Examples for Steel and Concrete

[19] prEN 1993-1-8. Eurocode 3., 2003. Design of Steel Structures, Part 1.8: Design of Joints, European Standard, CEN, Brussels.

[20] Abaqus/Standard Users' Manual., 2007. Version 6.7.1, Hibbitt, Karlsson & Sorensen, Inc.

[21] Mahmoud, H.N., 2011, A System Level Approach for the Seismic Evaluation of Semi-rigid Steel Frames, PhD thesis, Univ. of Illinois at Urbana-Champaign, Urbana, Illinois, (to be submitted).

[22] ASCE/SEI 7-05, 2005, Minimum Design Loads for Buildings and Other Structures, With Supplement 1, American Society of Civil Engineers, Reston, VA.

[23] FEMA 356, 2000, Prestandart and commentary for the seismic rehabilitation of buildings. Washington D.C.

COMPDYN 2011
3rd ECCOMAS Thematic Conference on
Computational Methods in Structural Dynamics and Earthquake Engineering
M. Papadrakakis, M. Fragiadakis, V. Plevris (eds.)
Corfu, Greece, 25–28 May 2011

SEISMIC RETROFIT OF EXISTING STEEL MOMENT RESISTING FRAMES WITH INNOVATIVE MATERIALS: LARGE SCALE HYBRID SIMULATION TESTS

Dimitrios G. Lignos[1], Daniel M. Moreno-Luna[2], and Sarah L. Billington[2]

[1] McGill University
817 Sherbrooke West, Room 278C, Montreal, QC, H3A 2K6
e-mail: dimitrios.lignos@mcgill.ca

[2] Stanford University
John A. Blume Earthquake Engineering Center, 439 Panama at Duena, Building 540, Stanford, CA, 94305
email 1: danielm3@stanford.edu, email 2: billington@stanford.edu

Keywords: Seismic Retrofit, Steel Moment Frames, Hybrid Testing, High Performance Fiber Reinforced Cementitious Materials.

Abstract. *This paper discusses the experimental validation of a new system for seismic retrofit of existing steel moment resisting structures. The system consists of infill panels made of a High Performance Fiber Reinforced Concrete (HPFRC) that is able to strain harden in tension. A two-phase experimental program was designed and conducted at the Network for Earthquake Engineering Simulation (NEES) facility at the University of California, Berkeley. This program utilized large-scale hybrid simulations of a 2/3-scale, 2-story steel moment frame designed in 1980s retrofitted with HPRFC infill panels. The numerical challenges during the experimental program including the development of a phenomenological model that is able to simulate cyclic deterioration of the HPFRC infill panels are summarized and validated with the available experimental data.*

1 INTRODUCTION

The goal of seismic rehabilitation strategies is to effectively upgrade seismically deficient structures that do not meet a designated performance objective. The performance objective could be achieving a specified performance level such as Immediate Occupancy (IO), Life Safety (LS) or Collapse Prevention (CP). Guidelines for seismic evaluation and rehabilitation are summarized in ATC 40 [1], FEMA 356 [2] and FEMA 440 [3].

A common way to improve the seismic performance of an existing steel moment resisting frame (MRF) involves the modification of the structural system to enhance its global strength and/or stiffness in order to avoid excessive story drift ratios during an earthquake (see FEMA 351 [4] and FEMA 547 [5]). Because MRFs are more flexible compared to other types of lateral resisting systems such as steel braced frames, an additional concern is the concentration of plastic deformations at the bottom stories due to P-Delta effects. Another common seismic deficiency in steel MRFs is brittle beam-to-column connections that are not able to develop sufficient plastic deformation capacity during an earthquake. Such types of component failures were notable during the Northridge 1994 earthquake in California (see FEMA 351 [4]) and also the Kobe 1995 earthquake in Japan. Pre-Northridge welded moment resisting connections typically consist of bolted shear tabs with full penetration welded flanges. Typical rehabilitation techniques summarized in [5] are concerned with the addition of a steel braced frame, concrete or masonry shear wall to the existing steel MRF to control excessive story deformations. Another way to improve the seismic performance of an existing steel MRF is to enhance the beam-to-column moment connections to develop a minimum plastic deformation of 2% radians. Typically, the bolted bracket (Adan and Gibb [6]) welded hunch (Gross et al. [7], Civjan et al. [8]) and RBS approach (Uang et al. [9]) are three standard connection rehabilitation techniques that are used.

Recently, High Performance Fiber Reinforced Concrete (HPFRC) materials have been utilized for seismic retrofit applications including reinforced concrete (RC) and coupled wall systems (Hung and El-Tawil [10, 11]), and steel moment resisting frames (Kesner and Billington [12]). The advantage of these composites is that they are characterized by pseudo-ductile tensile strain hardening behavior and energy absorption prior to crack localization and they exhibit little to no spalling in compression.

This paper discusses the development and experimental validation of the seismic retrofit system originally developed by [12]. A two-phase testing program was designed and executed that utilized large-scale hybrid simulations of an existing 2-story steel MRF designed in 1980s and retrofitted with the HPFRC infill panel system. These tests were conducted at the large-scale facility at the Richmond Field Station of the University of California at Berkeley, which is part of the Network for Earthquake Engineering Simulation (NEES). The hybrid simulation tests together with the experimental program that was conducted on single and double HPFRC infill panel components offered the opportunity to develop and validate 2-dimensional numerical models of retrofitted existing steel MRF with HPFRC infill panels.

2 HIGH PERFORMANCE FIBER REINFORCED CONCRETE

A modified version of the self-compacting high performance fiber-reinforced concrete mix that was developed by Liao et al. [13] at University of Michigan is used in this research. This mix has self-compacting properties and very minimal vibration is used to aid in consolidation. The mix proportion that is used has a water-to-binder ratio of 0.40 with the binder consisting of 80% type I-II Portland cement and 20% Class C fly ash. The super plasticizer used is ADVA Cast 530 and is added at 0.4% of the binder weight. A viscous agent is also used and is added at 0.49% of the binder weight. The fine aggregate is regular sand of uniform size distribution that can be easily found in any commercial precasting plant in California. A 12.7mm maximum coarse aggregate is also used, which is locally available. High strength hooked steel fibers marked as Dramix RC-80/30-BP are used in the HPFRC mix at 1.2% of the mix by volume. The minimum specified tensile strength of the fibers is 2300MPa. A regular concrete mixer that can be found in a precast plant can be utilized to mix the HPFRC material. In addition, Olsen and Billington [14, 15] and Hanson and Billington [16] have also used typical drum mixers to mix the same material. The mixing sequence is described in detail in [14, 16]. For the concrete mixes 102mmx203mm cylinders are cast and tested in compression to obtain the compression strength of the mix. A typical compression stress versus strain deformation curve for the HPRFC mix is shown in Figure 1a. To obtain the tensile properties of the same mix 76mmx76mmx305mm beams are cast and tested using 3-point bending following ASTM standard C 1609/C (ASTM [17]). The equivalent stress versus strain of a set of 4 of those beams is shown in Figure 1b. The equivalent stress is computed based on the following relationship,

$$\sigma_{b,equiv.} = \frac{Pl}{bd^2} \tag{1}$$

in which, P is the actuator load, l is the clear span length, d and b are the depth and width of the beam, respectively. As seen from the same figure the mix can carry flexural tension with a ductility range from 3 to about 6. Here, ductility is defined as the ratio between ultimate deformation prior to strength deterioration and the yield deformation of the HPRFC beam.

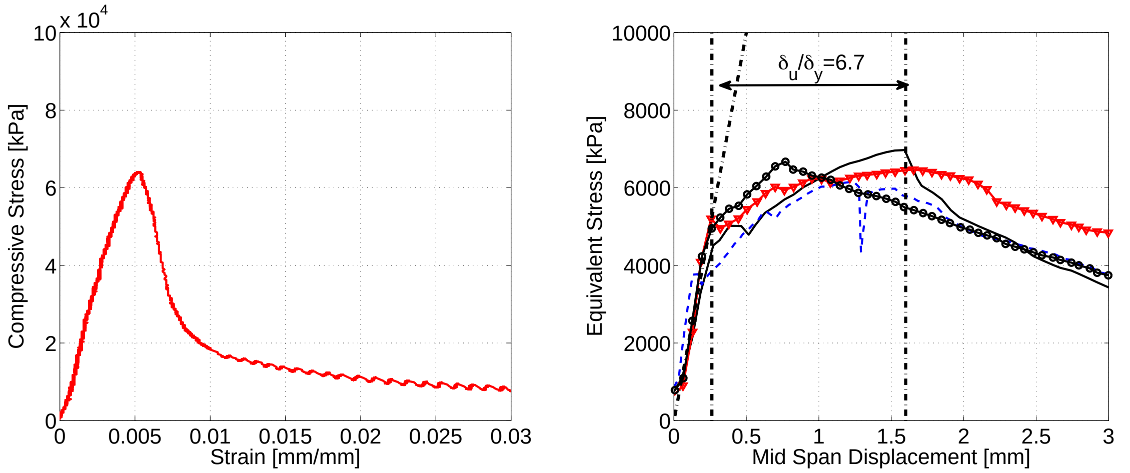

(a) Compressive strength versus strain

(b) Equivalent stress versus mid span displacement

Figure 1: Mechanical properties of High Performance Fiber Reinforced Concrete.

3 PROPOSED RETROFIT SYSTEM FOR SEISMIC REHABILITATION

The design mix discussed in Section 2 is used for the fabrication of the proposed HPFRC infill panel system for seismic retrofit of steel MRFs. This system is shown in Figure 2a. The HPFRC infill panels utilize Welded Wire Fabric (WWF) to aid in shear reinforcement and bolster flexural strength. The WWF is a single layer of 10 gauge wire on a 76mmx76mm grid. Grade 50 #3 deformed mild steel consists the primary reinforcement. Each set of two vertical HPFRC infill panels are first grouted into each of two steel channel connections that are shown in Figures 2a and 2b. These connections are pre-tensioned to about 150kN in order to avoid any slip in the connection. For this purpose a load-indicating washer is used. The top steel channel connection is field welded at the bottom flange of the upper floor steel beam.

The bottom channel connection is bolted to threaded studs that are welded to the top flange of the steel beam of the bottom story. The procedure to be used to weld these studs on the top flange of the bottom steel beam is a proven construction technique referred to by Nelson Stud Welding Inc. Holes are cored into the existing slab of a building exposing the top flange of the steel beam, and new headed studs are welded through the cored hole and then grouted in place to achieve composite construction where non-composite action was originally designed.

The two HPFRC panels are connected at mid-height of a story with a slotted connection shown in Figure 2a. This connection is utilized in order to prevent any build up of axial load in the HPFRC panels and subsequently any out-of-plane movement of the double panel system. The middle connection also guarantees that the inflection point of the bending diagram of the HPFRC double panel system stays at mid-height during the entire response history of the retrofitted steel MRF. The bolted connection details allow for damaged panels to be removed and replaced quickly after a major earthquake event provided that the residual story deformations are not large after that major earthquake event.

For panel fabrication, the infill panels are cast into plywood molds (see Figure 2c). The exposed surface of the HPFRC infill panel is finished relatively smooth without much difficulty. A number of single and double infill panels have been tested at University of Michigan in order to investigate their hysteretic response [14, 15, 16]. An example can be seen in Figure 2d. In the same figure, we have superimposed the simulated response of these panels with a phenomenological model that can capture pinching and cyclic deterioration and is utilized later to investigate numerically the seismic performance of the retrofitted steel MRF.

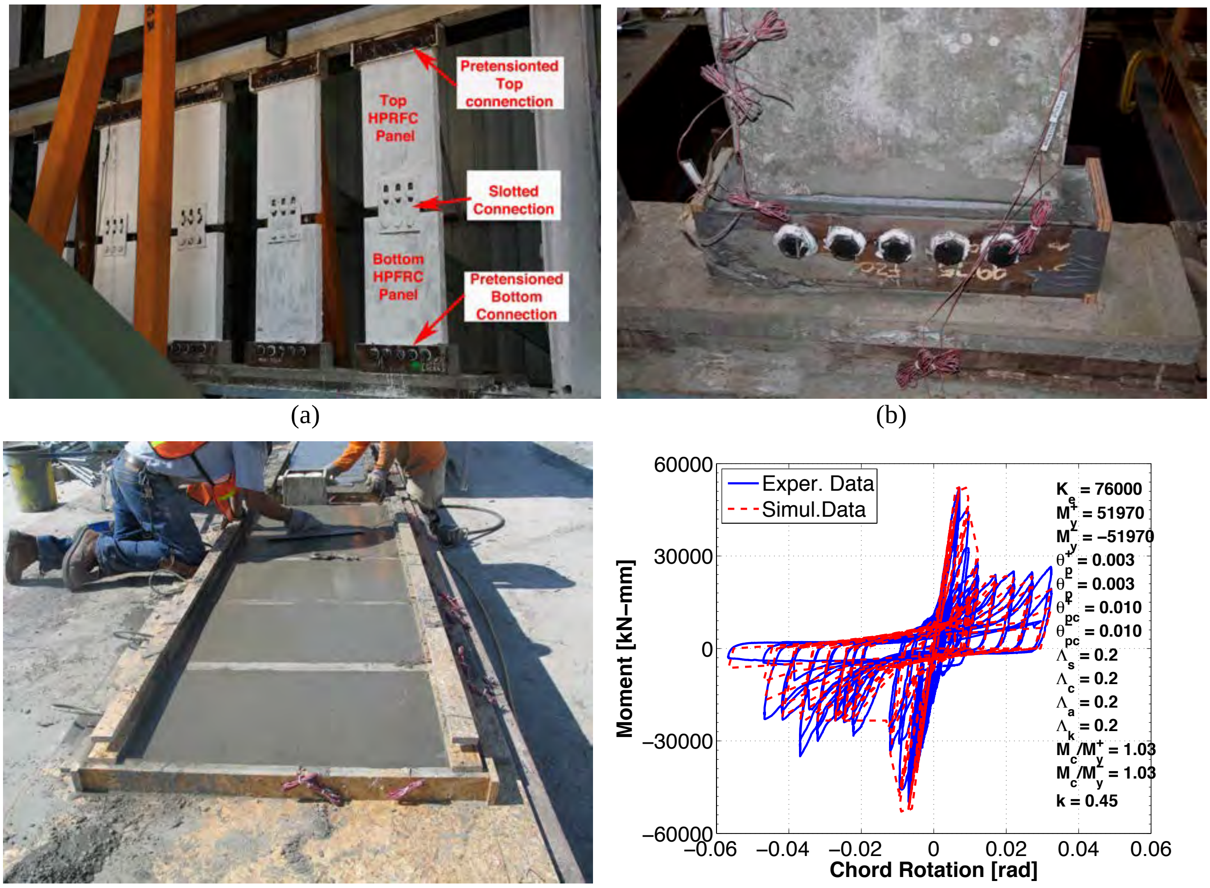

(a) (b)

(c) (d)

Figure 2: Installation, fabrication and hystereric performance of the HPFRC infill panel system for seismic retrofit applications.

4 PROTOTYPE STEEL STRUCTURE

In order to evaluate the performance of the infill panel system as part of a structural system, a prototype steel structure that was designed in California in 1980s is used. This structure, which is shown in Figure 3a in plan view, consists of perimeter steel moment resisting frames. The geometry of the East West (EW) steel MRF of the steel structure is shown in elevation in Figure 3b. The predominant period of this structure is 0.75sec. This structure does not meet the retrofit objectives per ASCE 41 [18] and FEMA 356 [2]. The EW steel MRF is modeled in the OpenSees [19] simulation platform using elastic beam column elements with nonlinear rotational springs at their ends. These springs can simulate component deterioration based on the modified Ibarra-Krawinkler (IK) model (Ibarra et al. [20], Lignos and Krawinkler [21, 22]). Panel zones are modeled with the Krawinkler model [23] as discussed in Gupta and Krawinkler [24]. The modified IK model is able to simulate fracture of steel connections based on a Coffin-Mansion fracture rule that was implemented by Lignos et al. [24]. Information related to premature steel beam-to-column connection fractures is obtained from a recently developed steel database for deterioration modeling of steel beams [21, 22].

In order to retrofit the 2-story building shown in Figure 3, a set of five panels is installed in the exterior left bay of the EW steel MRF of the prototype structure. Since there are no established design guidelines for this type of retrofit, the HPRFC infill panel system is assumed to be a deteriorating element. This assumption is valid since this retrofit system dissipates energy through multi-cracking of the HPRFC infill panels. After a few number of cycles the infill panels deteriorate as shown in Figure 2d.

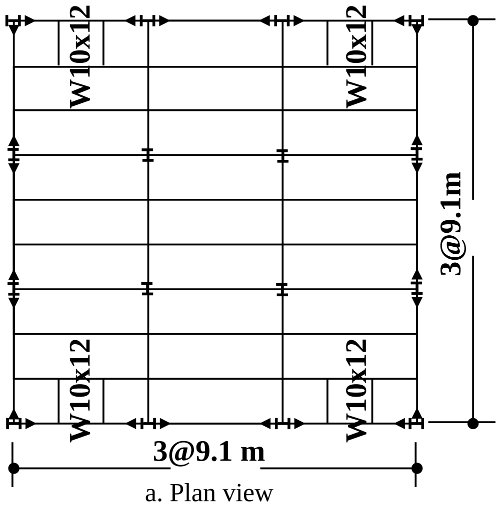

a. Plan view

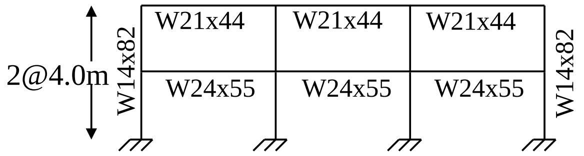

b. Elevation view

Figure 3: Plan view and elevation of the prototype steel office building designed in 1980s in California.

5 LARGE SCALE HYBRID SIMULATIONS

In order to validate experimentally the seismic performance of the retrofitted EW steel MRF discussed in Section 4, a 2/3-scale model of this moment frame is designed and fabricated. Strength and stiffness of this frame are scaled based on similitude rules discussed in

Moncarz and Krawinkler [25] and Harris and Sabnis [26]. The web and flange slenderness ratios of these sections were carefully selected in order to match the target deterioration parameters of the steel components of the prototype building shown in Figure 3b. State-of-the-art hybrid simulations are utilized in order to test experimentally the retrofitted steel MRF. The subsequent sections present aspects of hybrid testing including the hybrid model, experimental setup, and instrumentation.

5.1 Hybrid Model

Hybrid simulation is utilized in order to evaluate the seismic performance of the retrofitted steel MRF with HPFRC infill panels. Hybrid simulation is an experimentally based method for investigating the response of a structure to dynamic excitation using a hybrid model that consists of a physical and a numerical subassembly [27, 28]. The physical subassembly is tested in the laboratory. In this case, the physical subassembly is the first bay of the retrofitted steel MRF with the HPFRC panels installed. Typical A992 Gr. 50 steel is used for fabrication of the steel beams and columns of the 2/3-scale steel MRF shown in Figure 4a. Based on tensile coupon tests the yield and ultimate strengths of these components are summarized in Table 1. In order to simulate as realistically as possible the HPFRC pre-tensioned connection boundary conditions a 60mm concrete slab is cast at the base and second and third floor beams as shown in Figure 4b. In order to secure fixed conditions at the base a 51mm steel plate is used and the steel columns are welded with a typical CJP weld as shown in Figure 4c. The bolted web-welded flange beam-to-column connections of the test subassembly are welded in the field with a typical CJP weld. Figure 4d shows an example of these connections.

(a) steel MRF installed on the self-reacting platform (b) ground floor RC slab after casting

(c) fixed column base (d) beam-to-column connection and slider

Figure 4: Erection and typical connection details of the physical subassembly part of the hybrid model.

Wide Flange Section	Measured Material Properties		
	Location	σ_y (N/mm^2)	σ_u (N/mm^2)
W10x30	Flange	358	448
	Web	381	465
W14x26	Flange	363	449
	Web	385	467
W10x45	Flange	366	440
	Web	384	466

Table 1: Material properties of W sections of the physical subassembly tested in the laboratory.

The numerical portion of the hybrid model is modeled in the OpenSees [19] analysis platform in the same way that was previously discussed in Section 4. A schematic representation of the hybrid simulation technique is shown in Figure 5. As diagrammed in this figure, from a known state at instance *i* we use a numerical technique to compute a target displacement at instance *i+1*, then we use the two actuators assigned to the two horizontal degrees of freedom to impose the target displacements and measure forces and then compute the new state at instance *i+1*. The Open-source Framework for Experimental Setup and Control (OpenFresco) [29, 30] is utilized in order to conduct the hybrid simulations. As seen in Figure 5, the implementation strategy that is used separates the integrator and sub-structure processes. A three-loop architecture starts issuing actuator commands using a local estimator (predictor) of the new (target) state and then corrects the trajectory when the true target state arrives from the integrator. It should be noted that in this process the error accumulates. More details about an advanced implementation of hybrid simulation can be found in [30].

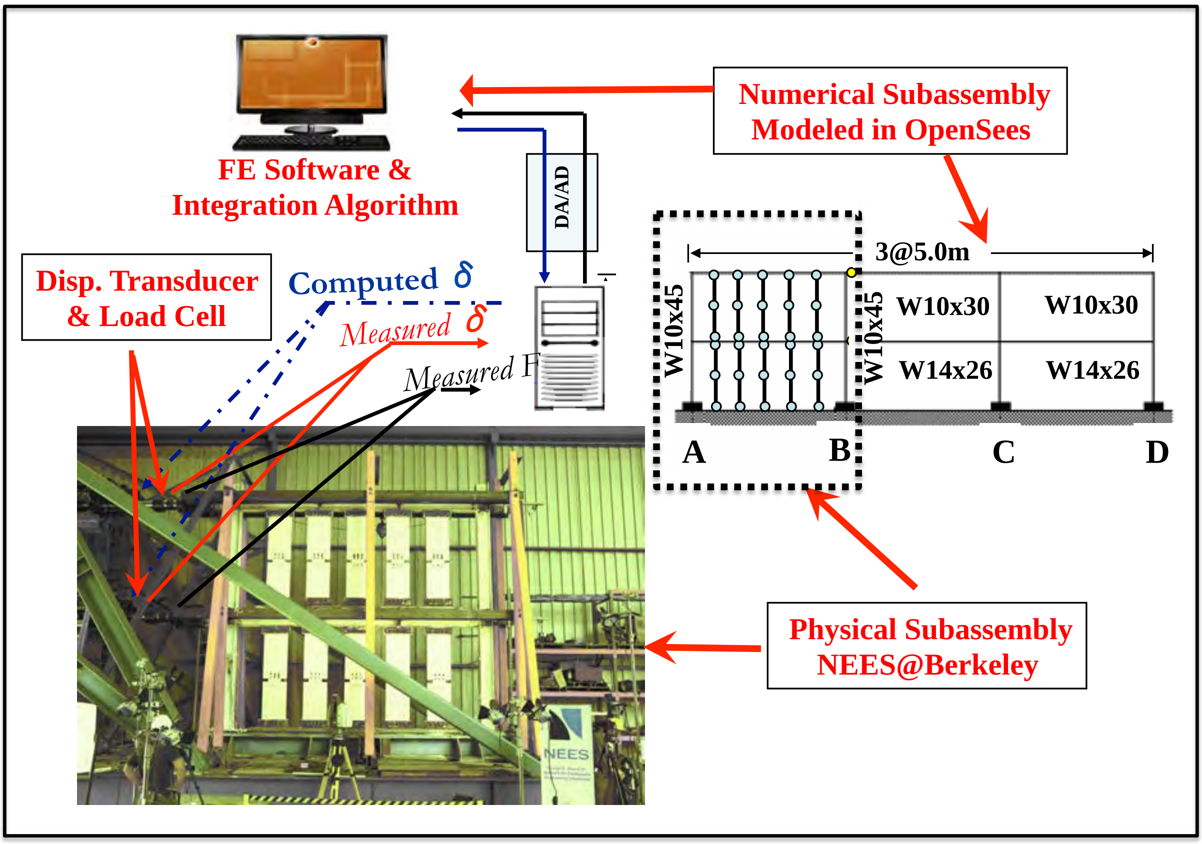

Figure 5: Schematic representation of hybrid simulation

5.2 Coupled Simulation

Prior to conducting the hybrid simulations with the physical subassembly in the laboratory, a coupled simulation was conducted with OpenFresco. The numerical subassembly of the 2-story steel MRF shown in Figure 6 is connected with a generic Super-Element within OpenSees that represents the physical subassembly tested in the laboratory. In this discussion, this is noted as the “Master Program”. The physical subassembly is also modeled in OpenSees with a separate input file that herein is called the Slave Program. The HPFRC infill panels are modeled with rigid links connecting deteriorating springs that can simulate the hysteretic response and flexibility of the HPFRC panels as shown in Figure 2d. The Master Program is responsible for imposing boundary conditions on both subassemblies. The 2-node adapter element shown in Figure 6 imposes trial displacements on the “physical subassembly”. The main information extracted from the coupled simulation is an estimate of the initial 2x2 stiffness matrix of the “physical subassembly” by holding one-degree-of-freedom at a time and applying a unit displacement to the other one. This matrix is,

$$K = \begin{bmatrix} 58.1 & -27.4 \\ -27.4 & 15.3 \end{bmatrix} \text{kN/mm} \tag{2}$$

Additional information that is extracted from the coupled simulation results is the integration method that is used during the hybrid simulation. A Newmark beta hybrid simulation implicit integrator is used with a constant number of sub-stepping [30]. Details about the assessment of coupled simulation results are given in Lignos and Billington [31].

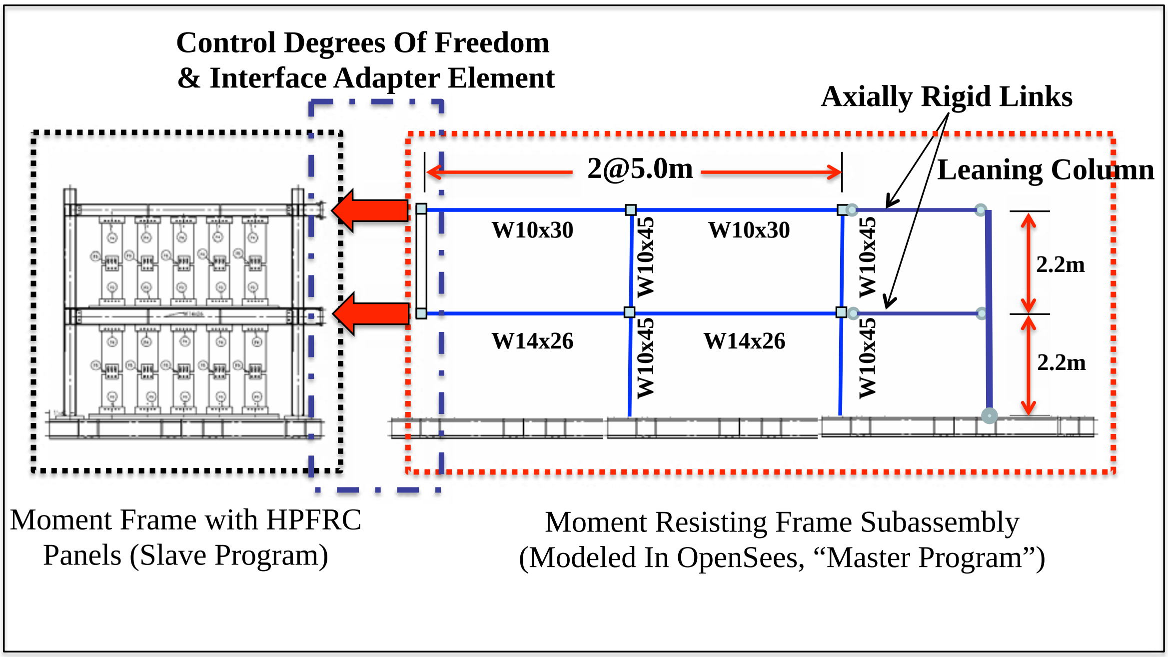

Figure 6: Schematic representation of hybrid simulation

5.3 Experimental Setup

The experimental setup of the physical subassembly tested in the Richmond Field Station at the University of California at Berkeley consists of three main parts, which are a self-reacting platform (see Figure 4a), the test frame and the lateral support system. The latter prevents any out-of-plane deformations of the test frame during the unidirectional earthquake simulation. All parts of the test setup are shown in Figure 7. Two 980kN (220-kips) dynamic actuators are connected with the test frame per floor as shown in the same figure. The self-reacting frame shown in Figure 4a was analyzed and fabricated in such a way that vertical deformations are minimized during the hybrid simulation tests. Vertical deformations of the self-reacting platform are measured with vertical LVDTs in order to make sure that they stay minimal. This platform consists of W21x166 steel sections connected together with full penetration weld. The platform is able to safely resist up to 1500kN base shear. The test frame is welded on the self-reacting platform with a 6.35mm continuous weld around the W14x311 supporting beam to guarantee full composite action between the middle interior W21x166 and W14x311 steel sections. The lateral support system consists of six triangular frames made of HSS6x6x3/8 (three on each side) and connected to each other with a longitudinal W12x26 steel beam. Lateral resistance of the lateral support frame is provided through two diagonal steel angles L6x3x1/2 that are connected at the base of the self-reacting platform. The test frame slides against this beam. The gap between the slider and the longitudinal steel beams was designed to be 6.35mm (¼”). In order to eliminate friction due to possible contact between the test frame sliders shown in Figure 4d and the W12x26 longitudinal steel beam teflon is installed in between these components. Friction forces during the hybrid simulation tests are measured through the diagonal angles that are strain gaged and calibrated to measure the force transferred to the platform due to sliding. However, during the two testing phases almost zero friction force was measured.

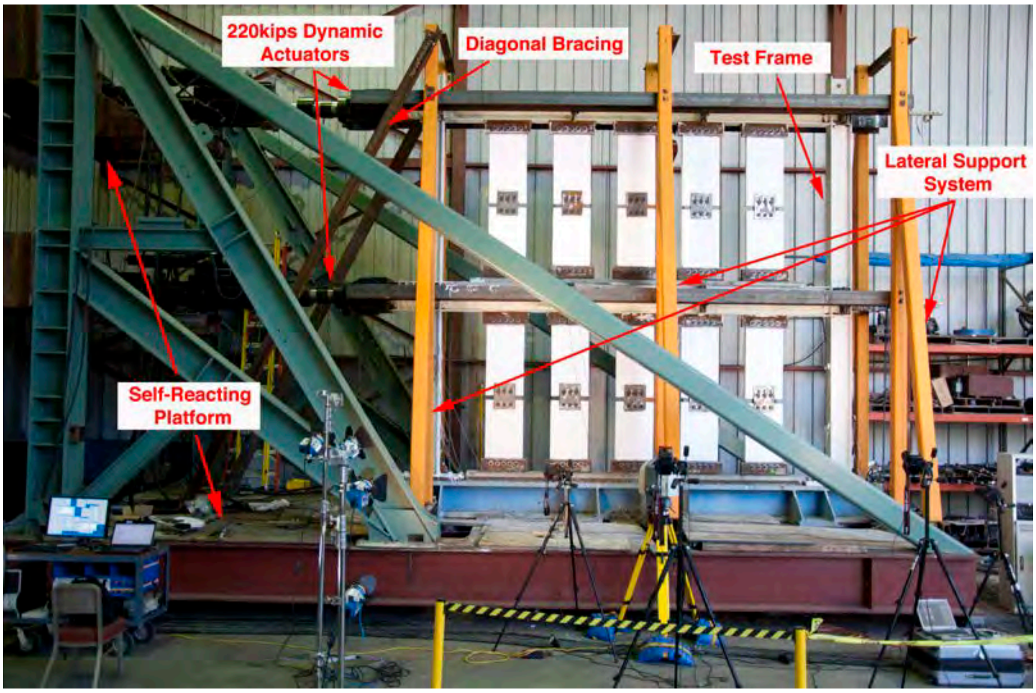

Figure 7: Experimental setup for hybrid simulation of the 2/3 retrofitted steel MRF.

5.4 Instrumentation

A total of 150 and 90 instruments are used to instrument the test frame for testing Phase I and Phase II, respectively. A laser scanner is also used that perform scan measurements of pre-defined infill panels that are likely to be damaged based on pre-test analysis predictions. The majority of instruments are strain gages to obtain strain measurements of the steel reinforcement and to obtain moment gradients in the steel columns of the test frame. One LVDT per floor is used to obtain the absolute floor displacements with respect to the “ground floor”.

Thirty-six LVDTs are attached to diagonal plastic strips to measure shear deformations in every other set of double panels per floor. A typical arrangement of these LVDTs is shown in Figure 8. Two Data Acquisition (DAQ) systems are synchronized together for the instrumentation needs of this testing series. The experimental data from both testing phases are available through the NEES central repository (www.nees.org).

Figure 8: Typical instrumentation layout of HPFRC infill panel system.

6 EXPERIMENTAL PROGRAM

Two testing phases are designed for the retrofitted steel MRF discussed in Sections 4 and 5. After the completion of testing Phase I all the HPFRC infill panels are replaced with a new set with nominally identical material properties to the ones used in testing Phase I. However, due to material variability some minor differences are noticed in the measured compressive strengths of the HPFRC panels after 28 days (see [32]). This section discusses the testing protocol used and the seismic response of the retrofitted steel MRF during the two testing phases.

6.1 Testing Protocol

Two testing phases are designed in order to conduct the large scale hybrid simulation tests of the retrofitted 2-story steel MRF. In both phases, the ground motion records are scaled appropriately to represent levels of intensity that are of particular interest to the engineering profession. Two ground motions are used for these phases. The first one is the fault normal component of the Petrolia record from the Cape Mendocino earthquake in California in 1992. The unscaled record represents a Maximum Considered Earthquake (MCE) in California with 2% probability of exceedence in 50 years at the period of interest. The second earthquake used, is the fault normal component of the Canoga Park record from the Northridge 1994 earthquake. The unscaled record of this motion represents a Design Level Earthquake (DLE) in California with 10% probability of exceedence in 50 years. The unscaled absolute acceleration and relative velocity spectra of these two motions are shown in Figures 9a and 9b, respectively. For reference, we have superimposed the predominant period of the bare steel MRF.

Testing Phase I, consists of (1) a Service Level Earthquake (SLE) with intensity equal to the 30% of the unscaled Petrolia record. This event corresponds to a 50% probability of exceedence in 50 years; (2) a DLE equal to the 70% of the unscaled Petrolia record and (3) a second DLE equal to the unscaled Canoga Park record. This event is used in order to investigate the effect of a major aftershock on the retrofitted steel MRF without replacing the

HPFRC infill panels that is likely to occur as has been illustrated during the latest earthquakes in New Zealand and Japan in 2011. Similarly, testing Phase II consists of the same SLE with testing Phase I. This part is repeated for comparison purposes. The testing protocol for this phase also consists an MCE with intensity equal to the unscaled Petrolia record in order to evaluate the seismic performance of the retrofitted steel MRF to an extreme earthquake event.

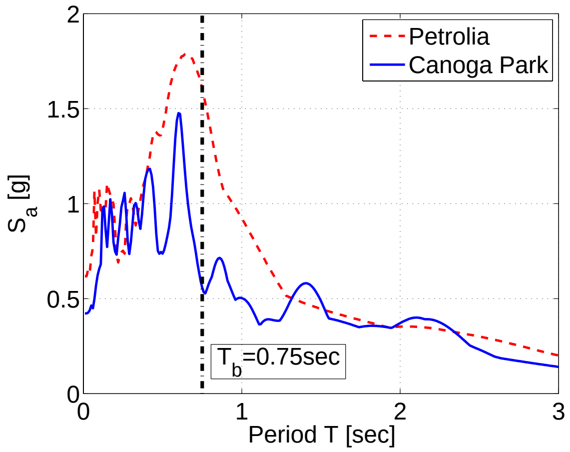

(a) Absolute acceleration spectrum

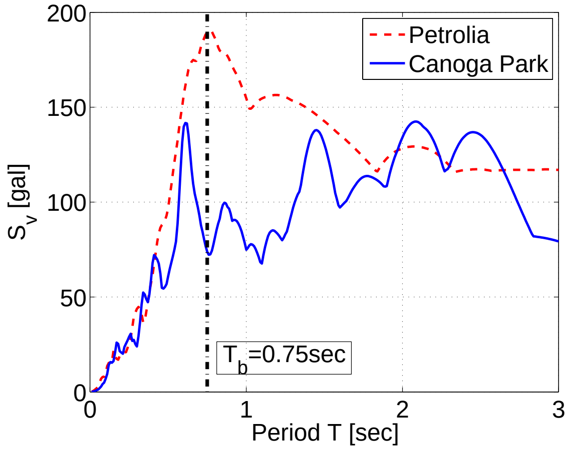

(b) Relative velocity spectrum

Figure 9: Acceleration and velocity spectra of the two ground motions used in testing Programs I and II.

7 RESULTS AND DISCUSSION

7.1 Seismic Response of the Test Frame During the Testing Program

Prior to the main testing phases the initial 2x2 stiffness of the physical subassembly was obtained by applying about one third of the yield story force per degree-of-freedom (DOF) and measuring back the relative displacements. Using the flexibility method (McGuire et al. [33]) the initial stiffness matrix is determined after coupling of the two DOF of the test frame. This matrix, which represents the Jacobian is,

$$K = \begin{bmatrix} 60.4 & -24.4 \\ -25.4 & 19.4 \end{bmatrix} \text{kN/mm} \tag{3}$$

After comparing this matrix with the one from (2) the estimated initial stiffness K based on coupled simulation is fairly close with the experimentally obtained one.

Figure 10 shows the roof drift ratio of the retrofitted steel MRF during testing Phases I and II. As seen from these figures, for both SLE phases the retrofitted test frame did not exceed more than 1% roof drift ratio. During the SLE loading, micro-cracking occurred in the HPFRC infill panels. The effect of micro cracking of HPFRC panels on the hysteretic response of the retrofitted frame can be seen in Figure 11a. This figure shows a comparison of the normalized base shear V/W versus first story drift ratio (SDR_1) during SLE for testing Phases I and II. During DLE-I (70% Petrolia) the retrofitted test frame reached slightly more than 2% rad in absolute maximum roof drift ratio and a minor residual roof drift ratio equal to 0.4% radians. Few flexural cracks were observed in the HPFRC panels. Three HPFRC infill panels failed completely at their base connection due to bending and after this failure the HPFRC panels were rocking. This implies that after DLE-I minimal to no replacement of HPFRC infill panels is needed. Without replacing any panels, the retrofitted steel MRF is subjected to a new design level earthquake (DLE-II). During DLE-II, the test frame reached a 2.5% absolute maximum roof drift ratio as shown in Figure 10a and a residual roof drift ratio of about 0.5% radians in the opposite direction compared to DLE-I. More distributed cracking was observed to the edge infill panels compared to the ones that were closer to the center of the steel beams. When reaching about 2.5% story drift ratios most of the HPFRC panels were severally damaged as discussed in [32]. These results are comparable with earlier findings of the hysteretic response of the HPFRC single and double component tests discussed in [14, 15, 16]. A comparison of peak story drift ratios between and the retrofitted steel MRF and the bare steel MRF during DLE-II is shown in figure 11b.

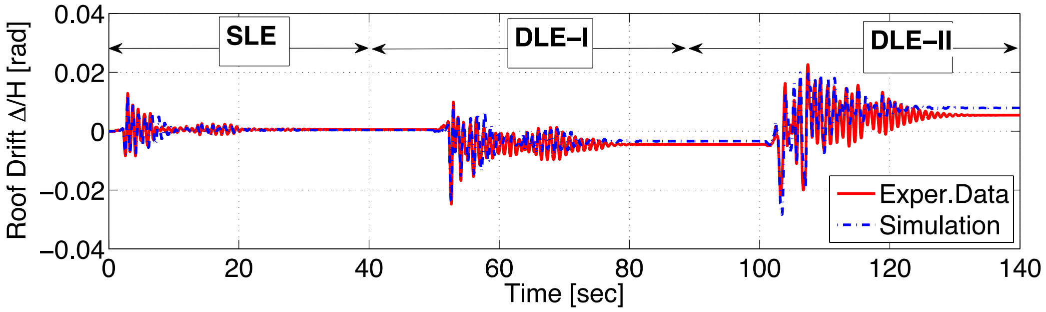

(a) Testing Phase I

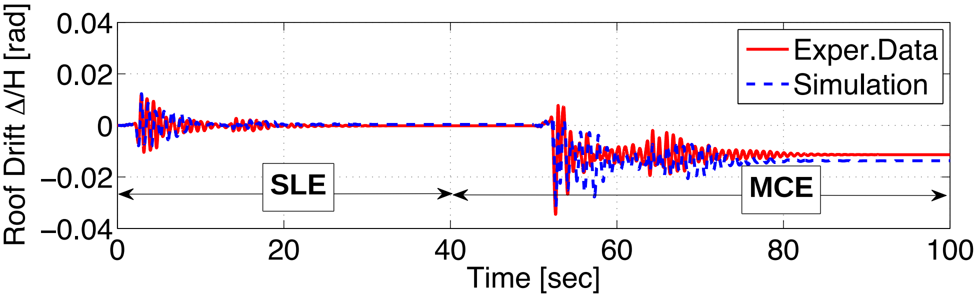

(b) Testing Phase II

Figure 10: Roof drift histories of retrofitted steel MRF during testing Phases I and II.

After the completion of testing Phase I all the HPFRC infill panels were replaced by a new set with nominally identical material properties. However, due to material variability the compressive and tensile strength of the new set was slightly lower compared to the first set of infill panels [32]. During testing Phase II, a Maximum Considered Earthquake followed the

SLE in order to investigate the performance of the retrofitted steel MRF when subjected to an extreme earthquake event. Figure 10b shows the roof drift ratio of the test frame for the MCE. In the same figure we have superimposed the simulated roof drift history of the numerical model used to simulate the seismic response of the retrofitted steel MRF during both testing phases. As seen from Figure 10 the numerical simulation results match relatively well the measured experimental data.

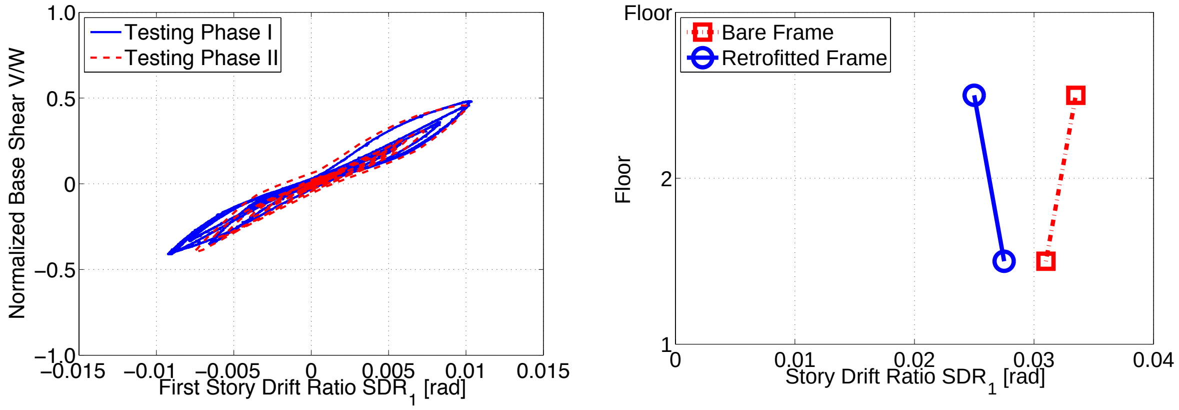

(a) (b)

Figure 11: Seismic performance of retrofitted steel MRF during testing Phase I; (a) normalized base shear versus first story drift ratio; (b) comparison of peak story drift ratios between retrofitted and bare steel MRF.

Due to large inelastic cycles prior to the main pulse of the Petrolia record (MCE) more distributed flexural cracks were developed in the HPFRC infill panels compared to Phase I. A typical damage pattern of the HPFRC infill panels after the MCE event is shown in Figure 12a. The final failure mode of a panel is the same with the one observed in Figure 12b. In some panels spalling of the reinforcement cover was observed (see Figure 12b). After the MCE event all the panels were severally damaged. The damage pattern in the HPFRC infill panels was consistent for both testing Phases I and II.

(a) multi-cracking (b) flexural crack and spalling

Figure 12: Damage pattern of HPFRC infill panels after the MCE during testing Phase II.

7.2 Structural Damage Observations and Comparison with Bare Frame Response

During testing Phase I, the structural damage that was observed to the retrofitted steel MRF was light. Yielding occurred at both the first and second floor steel beams of the steel MRF. Figures 13a and 13b shows a typical damage pattern of the first floor steel beam and column base, respectively, after the completion of testing Phase I. From Figure 13a there is no indication of local buckling in the steel beam. The hysteretic response of the corresponding numerical portion of the hybrid model indicated the same observation as shown in Figure 14a that shows the moment rotation relationship of one of the first floor steel beams that were part of the numerical portion of the hybrid model.

Looking at the normalized based shear versus first story drift ratio during testing Phase I (see Figure 14a), it can be seen that there is no indication of cyclic deterioration. The observed relatively small stiffness deterioration is attributed to the loss of stiffness from the severe damage of the HPFRC panels after DLE-II.

(a) first floor beam (b) column base

Figure 13: Structural damage observations during testing Phase I.

During testing Phase II, the structural damage that was observed to the steel MRF was very similar to that observed in testing Phase I. Again, no indication of local buckling was notable in any of the steel beam-to-column connections of the retrofitted steel frame. The lack of local buckling is confirmed from Figure 14c that shows the normalized base shear versus first story drift ratio for both the SLE and MCE loadings during testing Phase II. From this figure, there is no indication of cyclic strength deterioration. The unloading stiffness deterioration that is shown in this figure is attributed to the stiffness loss from the failure of HRFRC panels. An interesting observation during this testing phase is a dissipated energy mechanism because of yielding of the bottom flanges of the portions of the first and second floor steel beams between the steel channels. This yielding is attributed due to bending that was caused from the shear force that the individual panels carried during the MCE event (about 50kN). This yielding mechanism acted beneficially to the overall seismic behavior of the steel MRF since damage was distributed away from its the steel beam-to-column connections of the test frame. This yield mechanism is illustrated in Figure 14b.

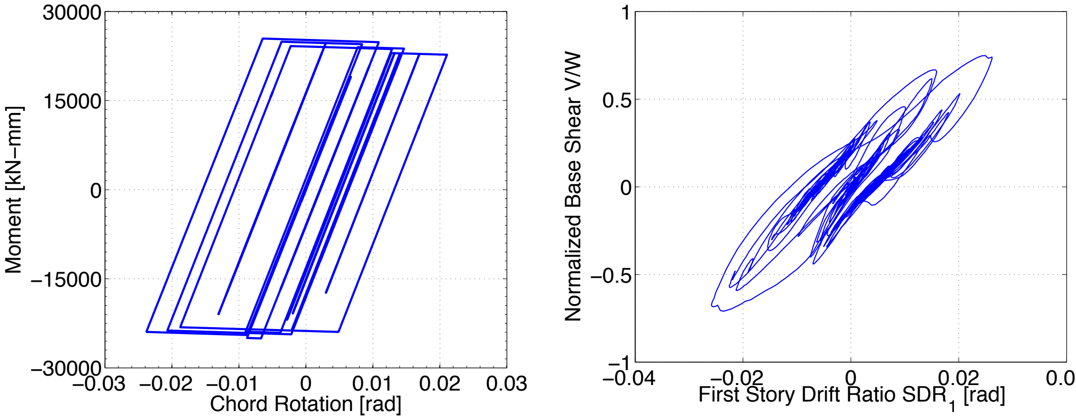

(a) Simulated moment rotation relationship of first floor steel beam during testing Phase I

(b) Normalized base shear versus first story drift ratio of the retrofitted steel MRF during testing Phase I

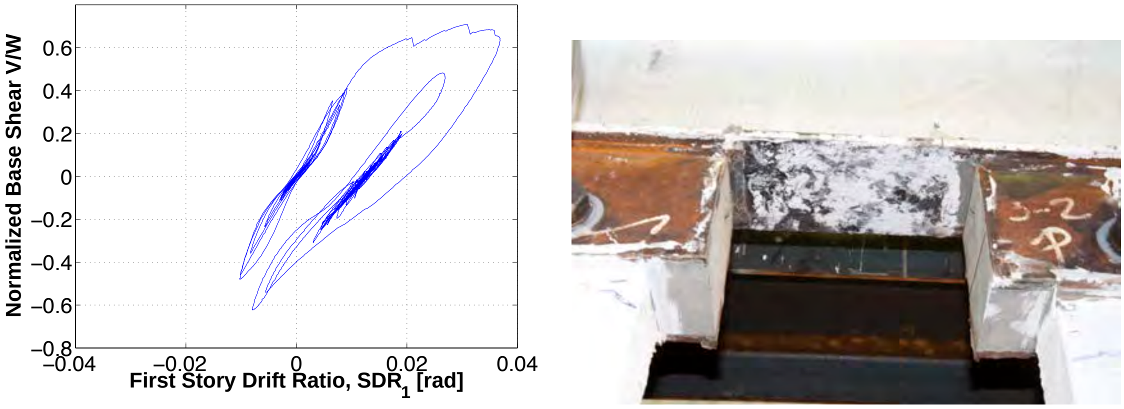

(c) Normalized base shear versus first story drift ratio of the retrofitted steel MRF during testing Phase II

(d) Observed yielding mechanism at the bottom flange of the steel beams during testing Phase II

Figure 14: Hysteretic response and observed dissipated energy mechanism during testing Phases I and II.

8 CONCLUSIONS

This paper discusses the development of an innovative seismic retrofit system for existing steel moment resisting frames designed in accordance with old seismic provisions. This system utilizes High Performance Fiber Reinforced Concrete and through multi-cracking dissipates energy during an earthquake. The proposed retrofit system was validated both numerically and experimentally through large-scale hybrid simulation tests at the NEES facility at University of California at Berkeley. Two testing phases were designed and conducted that included earthquake events of particular interest to the engineering profession. In this paper, the major computational challenges for numerical modeling of the steel moment frame and execution of the large-scale hybrid simulations were also summarized. The main findings from this research program are summarized as follows:

- Through micro cracking, the proposed infill panel system dissipates energy during service level earthquakes.
- During a Design Level or a Maximum Considered Earthquake the HPFRC infill panel system reduces seismic demands in terms of story and residual drift ratios compared to the un-retrofitted bare frame.

- Without replacing any of the HPFRC infill panels after a Design Level Earthquake the effect of an aftershock on the seismic response of a retrofitted steel MRF was simulated with a second Design Level Earthquake and its seismic performance was judged to be better compared to the bare frame.
- Regarding structural damage of the steel moment resisting frame, there was no indication of local buckling to the steel beams in any of the testing phases. The lack of local buckling in part, is attributed to the energy dissipation through micro-cracking in the HPRFC panels during the earthquake. Another reason was due to yielding of the bottom flange of the steel beams in the bare portions between the HPFRC infill panels.
- The numerical models developed to simulate the seismic response of the steel MRF and HPFRC infill panels were validated with the experimental data that became available from the large-scale hybrid simulation tests. These models can be used for further evaluation of a variety of steel buildings retrofitted with HPFRC panels in a performance-based earthquake-engineering context.

9 ACKNOWLEDGEMENTS

This study is based on work supported by the United States National Science Foundation (NSF) under Grant No. CMS-0530383 within the George E. Brown, Jr. Network for Earthquake Engineering Simulation (NEES) Consortium Operations. The Herrick Corporation in Stockton generously donated the steel frame and associated parts of the test setup, including erection. Midstate Precast generously donated the fabrication of the HPFRC infill panels. The financial support of NSF, Herrick and Midstate Precast is gratefully acknowledged. The authors also thank the undergraduate students A. Cantu, D. Ouyang, E. Flores, J. Dory, K. Morales, S. Vanderboll, William Tressler, M.S. (Stanford University), Dr. Andreas Schellenberg, Dr. Selim Gunay, Dr. Shakhzod Tachirov and the rest of the technical staff at the NEES facility at the University of California at Berkeley for their assistance with many aspects of the hybrid simulation testing program. The authors would also like to thank Mr. Ron Hamburger, Mr. David Mar and Dr. Greg Luth for their valuable input regarding the proposed testing phases of the experimental program. Any opinions, findings, and conclusions expressed in this paper are those of the authors and do not necessarily reflect the views of the sponsors.

REFERENCES

[1] ATC-40, The seismic evaluation and retrofit of concrete buildings, ATC-40, Applied Technology Council, Redwood City, CA, 1996.

[2] FEMA 356, Prestandard and commentary for the seismic rehabilitation of buildings, Washington, DC: Federal Emergency Management Agency, 2000.

[3] FEMA 440, Improvement of nonlinear static seismic procedures, Washington, D.C: Federal Emergency Management Agency, 2005.

[4] FEMA 351, Recommended seismic evaluation and upgrade criteria for existing welded steel moment-frame buildings, Washington, DC: Federal Emergency Management Agency, 2000.

[5] FEMA 547, Techniques for the seismic rehabilitation of existing buildings, Washington, DC: Federal Emergency Management Agency, 2006.

[6] S.M. Adan, W. Gibb, Inelastic cyclic testing of the Kaiser bolted bracket moment connection, *Proceedings, Structures Congress*, ASCE, 2008

[7] J.L. Gross, M.D. Engelhardt, C.M. Uang, K. Kasai, N.R. Iwankiw, AISC design guide 12, modification of existing welded steel moment frame connections for seismic resistance, *American Institute of Steel Construction*, Chicago, IL, 1999.

[8] S.A. Civjan, M.D. Engelhardt, J.L. Gross, Slab effects in SMRF retrofit connection tests, *Journal of Structural Engineering*, ASCE, 127 **(3)**: 230-238, 2001.

[9] C.M. Uang, Q.S. Yu, S. Noei, J.L. Gross, Cyclic testing of steel moment connections rehabilitated with RBS or welded haunch, *Journal of Structural Engineering*, ASCE, 126 **(1)**: 157-169, 1999.

[10] C.C. Hung, S. El-Tawil, Seismic behavior of a coupled-wall system with HPFRCC coupling beams, *Proceedings, Structures Congress*, ASCE, 2010.

[11] C.C. Hung, S. El-Tawil, Cyclic model for high performance fiber reinforced cementitious composite structures, *Proceedings, ATC & SEI Conference on Improving the Seismic Performance of Existing Buildings and Other Structures*, ASCE, San Francisco, CA, United States, 2009.

[12] K.E. Kesner, S.L. Billington, Investigation of infill panels made from engineered cementitious composites for seismic strengthening and retrofit, *Journal of Structural Engineering*, ASCE, 131 **(11)**: 1712-1720, 2005.

[13] W.C. Liao, S.H. Chao, S.Y. Park, A.E. Naaman, Self-consolidating high performance fiber reinforced concrete (SCHPFRC) - preliminary investigation, *Report UMCEE 06-02, Dept. of Civil & Environmental Engineering, University of Michigan*, Ann Arbor, MI, 2006.

[14] E.C. Olsen, S.L. Billington, Evaluation of precast, high-performance fiber- reinforced concrete infill panels for seismic retrofit of steel frame building: Phase 1- cyclic testing of single panel components, *Report No. TR 158, John A. Blume Earthquake Engineering Center, Stanford University,* Stanford CA, 2009.

[15] E.C. Olsen, S.L. Billington, Cyclic behavior of precast, self-compacting ductile concrete infill panels for seismic retrofit of steel frame buildings, *ACI Structural Journal*, 108 **(1)**: 51-60, 2011.

[16] J. Hanson, S.L. Billington, Cyclic testing of a ductile fiber-reinforced concrete infill panel system for seismic retrofitting of steel frames, *Report No. TR. 173, John A. Blume Earthquake Engineering Center, Stanford University*, Stanford, CA, 2009.

[17] ASTM, ASTM standard C 1609/C 1609M-05, Standard test method for flexural performance for fiber-reinforced concrete (Using Beam with Third-Point Loading), 2005.

[18] ASCE 41-06, Seismic rehabilitation of existing buildings, ASCE Standard ASCE/SEI 41-06, American Society of Civil Engineers/Structural Engineering Institute, Reston, VA, 2007.

[19] OpenSees, Open System for Earthquake Engineering Simulation, Pacific Earthquake Engineering Research Center (PEER), (http://opensees.berkeley.edu), 2009.

[20] L.F. Ibarra, R.A. Medina, H. Krawinkler, Hysteretic models that incorporate strength and stiffness deterioration. *Journal of Earthquake Engineering and Structural Dynamics*, EESD, 34 **(12)**: 1489–1511, 2005.

[21] D.G. Lignos, H. Krawinkler, Sidesway collapse of deteriorating structural systems under seismic excitations, *Report No. TR 172, John A. Blume Earthquake Engineering Center, Stanford University*, Stanford, CA, 2009.

[22] D.G. Lignos, H. Krawinkler, Deterioration modeling of steel components in support of collapse prediction of steel moment frames under earthquake loading, *Journal of Structural Engineering*, ASCE, (accepted for publication), 2011.

[23] H. Krawinkler, “Shear in Beam-Column Joints in Seismic Design of Frames”, *Engineering Journal*, AISC, 15 **(3)**, 1978.

[24] A. Gupta, H. Krawinkler, Seismic demands for performance evaluation of steel moment resisting frame structures, *Report No. TR 132, The John A. Blume Earthquake Engineering Research Center, Department of Civil Engineering, Stanford University*, Stanford, CA, 1999.

[25] P.D. Moncarz, H. Krawinkler, Theory and application of experimental model analysis in earthquake engineering, *Report No. TR 50, John A. Blume Earthquake Engineering Center, Department of Civil Engineering, Stanford University*, Stanford, CA, 1981.

[26] H.G. Harris, G.M. Sabnis, Structural modeling and experimental techniques, 2nd edition, CRC Press, 1999.

[27] M. Nakashima, M. Kato, E. Takaoka, Development of real-time pseudo dynamic testing. *Journal of Earthquake Engineering and Structural Dynamics*, EESD, 21**(1)**: 79-92, 1992.

[28] S.A. Mahin, P.B. Shing, C.R. Thewalt, R.D. Hanson, Pseudodynamic test method - Current status and future direction, *Journal of Structural Engineering*, ASCE, 115**(8)**: 2113-2128, 1989.

[29] A.H. Schellenberg, S. Mahin, G. Fenves, Software framework for hybrid simulation of large structural systems, *Proceedings*, *Structures Congress*, ASCE, Long Beach, CA, United States, 2007.

[30] A.H. Schellenberg, Advanced implementation of hybrid simulation, *PhD Dissertation*, Civil and Environmental Engineering, University of California Berkeley, Berkeley, CA, 2008.

[31] D.G. Lignos, S.L. Billington, Hybrid testing of a retrofitted steel moment resisting frame with high performance fiber reinforced concrete infill panels, *Proceedings 9th US National and 10th Canadian Conference on Earthquake Engineering: Reaching Beyond Borders*, July 25th-29th, Toronto, Canada, 2010.

[32] S.L. Billington, D.G. Lignos, J.V. Hanson, D.M. Moreno-Luna, Response of high performance fiber reinforced concrete infill panels retrofitting steel moment-resisting frames, *Proceedings, 8th International Conference in Urban Earthquake Engineering, Tokyo Institute of Technology*, March 7-8, Tokyo, Japan, 2011.

[33] W. McGuire, R.H. Gallagher, R.D. Zeimian, Matrix structural analysis, 2nd edition, John Wiley & Sons, Inc, 2000.

COMPDYN 2011
3rd ECCOMAS Thematic Conference on
Computational Methods in Structural Dynamics and Earthquake Engineering
M. Papadrakakis, M. Fragiadakis, V. Plevris (eds.)
Corfu, Greece, 25–28 May 2011

MEAN AND VARIABILITY RESPONSE FUNCTIONS FOR STOCHASTIC SYSTEMS UNDER DYNAMIC EXCITATION

V. Papadopoulos[1] **, O. Kokkinos**[2]

[1]Institute of Structural Analysis & Seismic Research, National Technical University of Athens
Athens, GR-15780, Greece
vpapado@central.ntua.gr

[2]Institute of Structural Analysis & Seismic Research, National Technical University of Athens
Athens, GR-15780, Greece
okokkinos@central.ntua.gr

Keywords: Dynamic Variability Response Functions; Stochastic finite element analysis; upper bounds; stochastic dynamic systems.

Abstract. *The concept of the so called Variability Response Function (VRF), recently proposed for statically determinate and indeterminate stochastic systems [1, 2], is extended in this work to linear dynamic stochastic systems. An integral form for the variance of the dynamic response of stochastic systems is considered, involving a Dynamic VRF (DVRF) and the spectral density function of the stochastic field modeling the uncertain system properties. As in the case of static systems, the independence of the DVRF to the spectral density and the marginal probability density function of the stochastic field modeling the uncertain parameters is validated using brute-force Monte Carlo simulations as well as a series of different moving power spectral density functions for the calculation of the DVRF. The uncertain system property considered is the inverse of the elastic modulus (flexibility). It is demonstrated that DVRF is a function of the standard deviation of the stochastic field modeling flexibility. The same integral expression can be used to calculate the mean response of a dynamic system using the concept of the so called Dynamic Mean Response Function (DMRF), which is a function similar to the DVRF [3]. These integral forms can be used to efficiently compute the mean and variance of the transient system response at any time of the dynamic response together with spectral-distribution-free upper bounds. They also provide an insight into the mechanisms controlling the dynamic mean and variability response. In this work this methodology is effectively utilized to estimate the stochastic dynamic response of a single degree of freedom system subjected to a) sinusoidal load at the end of its length and b) El Centro earthquake. In both cases results are drawn for different values of the stochastic field standard deviation and for various Gaussion and non-Gaussian probability distributions.*

1 INTRODUCTION

Over the past two decades a lot of research has been dedicated to the stochastic analysis of structural systems involving uncertain parameters in terms of material or geometry with the implementation of stochastic finite element methodologies (SFEM) to numerically solve the stochastic partial differential equations (PDE's) governing the respective problems. The most commonly used SFEM methods are expansion/perturbation-based [12, 13] and Galerkin-based Spectral SFEM (SSFEM) approaches [10]. Although such methods have proven to be highly accurate and computationally efficient for a variety of problems, there is still a wide range of problems in stochastic mechanics involving combinations of strong non-linearities and/or large variations of system properties as well as non-Gaussian system properties that can be solved with reasonable accuracy only through a computationally expensive Monte Carlo simulation approach [12, 11, 14, 15], limited works are dealing with the dynamic propagation of system uncertainties, most of them reducing the stochastic dynamic PDE's to a linear random eigenvalue problem [16, 17].

In all aforementioned cases, the spectral/correlation characteristics and the marginal probability distribution function (pdf) of the stochastic fields describing the uncertain system parameters are required in order to estimate the response variability of a stochastic static or dynamic system. As there is usually a lack of experimental data for the quantification of such probabilistic quantities, a sensitivity analysis with respect to various stochastic parameters is often implemented. In this case, however, the problems that arise are the increased computational effort, the lack of insight on how these parameters control the response variability of the system and the inability to determine bounds of the response variability.

In this framework and to tackle the aforementioned issues, the concept of the variability response function (*VRF*) has been proposed in the late 1980s [4], along with different aspects and applications of the *VRF* [18, 19]. A development of this approach was presented in a series of papers [1-3], where the existence of closed-form integral expressions for the variance of the response displacement of the form

$$Var[u] = \int_{-\infty}^{\infty} VRF(\kappa, \sigma_{ff}) S_{ff}(\kappa) d\kappa \tag{1}$$

was demonstrated for linear stochastic systems under static loads using a flexibility-based formulation. The basic difference of this approach with respect to previous work is that by using a flexibility-based formulation, no approximations were involved in the derivation of the resulting integral expression in Eq. (1). . It was shown that the *VRF* depends on standard deviation σ_{ff} but appears to be independent of the functional form of the spectral density function $S_{ff}(\kappa)$ modeling the inverse of the elastic modulus. The existence however of this integral expression had to be conjectured for statically indeterminate as well as for general stochastic finite element systems. A rigorous proof of such existence is available only for statically determinate systems for which *VRF* is independent of σ_{ff} as well [1]. Further investigations [7] verified the aforementioned results but showed that *VRF* has a slight dependence on the marginal pdf of the stochastic field modeling the flexibility. In [3] results were presented for general linear stochastic Finite Element systems including beams, space frames, plane stress and shell-type structures under static loads. Another important extension of the concept of *VRF* has been recently drawn [20] to determine effective material properties in homogenization problems.

The present paper extends the aforementioned approach to linear statically determinate stochastic systems under dynamic excitations. Although the derivation of an analytic expression for the variability response function of the dynamic system (*DVRF*), if possible at all, is extremely cumbersome, a numerical computation of the *DVRF* can be easily achieved to provide results for the variance time history of the dynamic system response. As in previous works [1-3], the existence of the *DVRF* and a similar to Eq. (1) integral form expression has to be conjectured. This assumption is numerically validated by comparing the results from Eq. (1) with brute force Monte Carlo simulations. It is demonstrated that the *DVRF* is highly dependent on the standard deviation σ_{ff} of the inverse of the elastic modulus and, based on numerical evidence further presented but, to this point, not to a full proof verification technique, appears to be almost independent of the functional form of $S_{ff}(\kappa)$ as well as of the marginal *pdf* of the flexibility. In addition, an integral expression similar to that of Eq. (1) is proposed for the mean system response involving a Dynamic Mean Response Function (*DMRF*), which is a function similar to the *DVRF*.

Both integral forms for the mean and variance can be used to efficiently compute the first and second order statistics of the transient system response with reasonable accuracy, together with time dependant spectral-distribution-free upper bounds. They also provide an insight into the mechanisms controlling the uncertainty propagation with respect to both space and time and in particular the mean and variability time histories of the stochastic system dynamic response.

2 DYNAMIC ANALYSIS OF A STOCHASTIC SINGLE DEGREE OF FREEDOM OSCILLATOR

For the single degree of freedom statically determinate stochastic oscillator of length L and mass Ms in Figure 1a, loaded with a dynamic deterministic load , the inverse of the elastic modulus is considered to vary randomly along the length of the beam according to the following expression:

$$\frac{1}{E(x)} = F_0(1 + f(x)) \tag{2}$$

where *E(x)* is the elastic modulus, F_0 is the mean value of the inverse of *E(x)*, and *f(x)* is a zero-mean homogeneous stochastic field modeling the variation of *1/E(x)* around its mean value F_0.

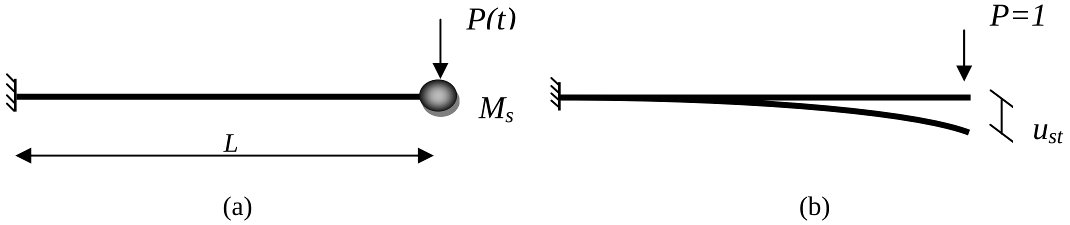

(a) (b)

Figure 1. One degree of freedom oscillator: (a) Geometry and loading (b) Static displacement for unit load

The displacement time history of the oscillator can be derived from the solution of Duhamel’s integral:

$$u(t) = \frac{1}{\omega_D}\int_0^t P(\tau)e^{-\xi\omega(t-\tau)}\sin(\omega_D(t-\tau))d\tau \tag{2}$$

where ξ is the damping ratio and $\omega_D = \omega\sqrt{1-\xi^2}$ with ω being the circular frequency of the system. Due to the system uncertainty in Eq. (2), the circular frequency ω is a random variable given by the following relation:

$$\omega = \sqrt{k / M_s} \tag{2}$$

where *k* is the stiffness of the oscillator which can be derived from the static displacement of the oscillator for a unit static deterministic load at the end of the beam (Figure 1b) as follows:

$$k = \frac{1}{u_{st}} = \left[-\frac{F_0}{I} \int_0^L (x-\alpha) M(\alpha)(1+f(\alpha)) d\alpha \right]^{-1} \tag{2}$$

where *I* is the moment of inertia of the beam and *M(α)* is the moment at position *α*.

In the general case where the load is arbitrary and the system is initially at rest, the deterministic displacement at the right end of the beam can be derived by numerically solving the Duhamel's integral. In the special case of a sinusoidal $P(t) = P_0 \sin(\bar{\omega} t)$ the solution of Eq. (3) leads to the following expression for $u(t)$:

$$u(t) = u_0(t) + u_p(t) \tag{2}$$

where

$$u_0(t) = e^{-\xi\omega t}(A \sin \omega_D t + B \cos \omega_D t) \tag{2}$$

$$u_p(t) = C_1 \sin \bar{\omega} t + C_2 \cos \bar{\omega} t \tag{2}$$

$$A = \frac{P_0}{K} * \frac{1}{(1-\beta^2)^2 + (2\xi\beta)^2} * \frac{2\beta\xi^2 - (1-\beta^2)\beta}{\sqrt{1-\xi^2}} \tag{2}$$

$$\mathrm{B} = -\frac{P_0}{K} * \frac{2\xi\beta}{(1-\beta^2)^2 + (2\xi\beta)^2} \tag{2}$$

$$C_1 = \frac{P_0}{K} * \frac{1}{(1-\beta^2)^2 + (2\xi\beta)^2} (1-\beta^2) \tag{2}$$

$$\beta = \bar{\omega} / \omega \tag{2}$$

In the trivial case in which a static load $P(t) = P_0$ is suddenly applied, the response displacement is given by

$$u(t) = \frac{P_0}{k} \left[1 - \left(\cos \omega_D t + \frac{\xi}{\sqrt{1-\xi^2}} \sin \omega_D t \right) e^{-\xi\omega t} \right] \tag{2}$$

3 RESPONSE VARIANCE AND MEAN VALUE OF THE DYNAMIC RESPONSE

Following a procedure similar to the one presented in [1] for linear stochastic systems under static loading, it is possible to express the variance of the dynamic response of the stochastic system in the following integral form expression:

$$Var[u(t)] = \int_{-\infty}^{\infty} DVRF(t, \kappa, \sigma_{ff}) S_{ff}(\kappa) d\kappa \tag{2}$$

where *DVRF* is the dynamic version of a *VRF*, assumed to be a function of deterministic parameters of the problem related to geometry, loads and (mean) material properties and the standard deviation σ_{ff} of the stochastic field that models the system flexibility. A similar integral expression can provide an estimate for the mean value of the dynamic response of the system using the Dynamic Mean Response Function (*DMRF*) [3]:

$$\varepsilon[u(t)] = \int_{-\infty}^{\infty} DMRF(t,\kappa,\sigma_{ff}) S_{ff}(\kappa) d\kappa \tag{2}$$

DMRF is assumed to be a function similar to the *DVRF* in the sense that it also depends on deterministic parameters of the problem as well as σ_{ff}. It is extremely difficult however, to prove that the *DVRF* (same counts for *DMRF*) is independent (or even approximately independent) of the marginal pdf and the functional form of the power spectral density of the stochastic field $f(x)$. As in [1-3], the aforementioned assumptions are considered to form a conjecture which is numerically validated here by comparing the results from Eqs (8a) and (8b) with brute force MCS.

The derivation of an analytic expression for the *DVRF* and *DMRF*, if possible at all, is an extremely cumbersome task. A numerical computation, however can be easily achieved, as described in the following section and then fed into the Eqs (8a) and (8b) to provide estimates of the mean and variance of the dynamic system response.

3.1 Numerical estimation of the DVRF and the DMRF using fast Monte Carlo simulation

The numerical estimation of *DVRF* and *DMRF* involves a fast Monte Carlo simulation (FMCS) whose basic idea is to consider the random field $f(x)$ as a random sinusoid [1, 2] and plug its monochromatic power spectrum into Eqs (8a) and (8b), in order to compute the respective mean and variance response at various wave numbers. The steps of the FMCS approach are the following:

(i) Generate *N* (10-20) sample functions of the below random sinusoid with standard deviation σ_{ff} and wave number $\bar{\kappa}$ modeling the variation of the inverse of the elastic modulus $1/E$ around its mean F_0:

$$f_j(x) = \sqrt{2}\sigma_{ff}\cos(\bar{\kappa}x + \varphi_j) \tag{2}$$

where *j=1,2,…,N* and φ_j varies randomly under uniform distribution in the range $[0, 2\pi]$.

(ii) Using these *N* generated sample functions it is straightforward to compute their respective dynamic mean and response variance, $\varepsilon[u(t)]_{\bar{\kappa}}$ and $Var[u(t)]_{\bar{\kappa}}$, respectively for a given time step *t*.

(iii) The value of the *DMRF* at wave number $\bar{\kappa}$ can then be computed as follows

$$DMRF(t,\bar{\kappa},\sigma_{ff}) = \frac{\varepsilon[u(t)]_{\bar{\kappa}}}{\sigma_{ff}^2} \tag{2}$$

and likewise the value of the *DVRF* at wave number $\bar{\kappa}$

$$DVRF(t,\overline{\kappa},\sigma_{ff}) = \frac{Var[u(t)]_{\overline{\kappa}}}{\sigma_{ff}^2} \tag{2}$$

Both previous equations are direct consequences of the integral expressions in Eqs. (8a) and (8b) in the case that the stochastic field becomes a random sinusoid.

(iv) Get *DMRF* and *DVRF* as a function of both time *t* and wave number κ by repeating previous steps for various wave numbers and different time steps. The entire procedure can be repeated for different values of the standard deviation σ_{ff} of the random sinusoid.

3.2 Bounds of the mean and variance of the dynamic response

Upper bounds on the mean and variance of the dynamic response of the stochastic system can be established directly from eqs (8a) and (8b), as follows:

$$\varepsilon[u(t)] = \int_{-\infty}^{\infty} DMRF(t,\kappa,\sigma_{ff}) S_{ff}(\kappa) d\kappa \le DMRF(t,\kappa^{\max}(t),\sigma_{ff})\sigma_{ff}^2 \tag{2}$$

$$Var[u(t)] = \int_{-\infty}^{\infty} DVRF(t,\kappa,\sigma_{ff}) S_{ff}(\kappa) d\kappa \le DVRF(t,\kappa^{\max}(t),\sigma_{ff})\sigma_{ff}^2 \tag{2}$$

where $\kappa^{\max}(t)$ is the wave number at which *DMRF* and *DVRF,* corresponding to a given time step *t* and value of σ_{ff}, reach their maximum value. An envelope of time evolving upper bounds on the mean and variance of the dynamic system response can be extracted from Eqs. (11a) and (11b). As in the case of linear stochastic systems under static loads [1-3], this envelope is physically realizable since the form of the stochastic field that produces it is the random sinusoid of Eq.(9) with $\overline{\kappa} = \kappa^{\max}(t)$.

4 NUMERICAL EXAMPLE

For the cantilever beam shown in Fig. 1 with length *L*=4m, the inverse of the modulus of elasticity is assumed to vary randomly along its length according to Eq. (2) with $F_0 = (1.25\times10^8 KN/m)^{-1}$ and $I = 0.1m^4$. A concentrated mass M_S=3.715 × 10^3 *Kg* is assumed at the right end of the beam. The damping ratio is taken as *ξ=5%* and the mean eigenperiod of this one d.o.f oscillator is calculated at T_0*=0.5sec.*

Three load cases are considered: LC1 consisting of a constant load $P(t) = 100$, LC2 consisting of a concentrated dynamic periodic load $P(t) = 100\sin(\overline{\omega}t)$ and LC3 consisting of $P(t) = -M_s\ddot{U}_g(t)$ where $\ddot{U}_g(t)$ is the acceleration time history of the 1940 El Centro earthquake.

The spectral density function (*SDF*) of Figure 2 was used for the modeling of the inverse of the elastic modulus stochastic field, given by:

$$S_{ff}(\kappa) = \frac{1}{4}\sigma^2 b^3 \kappa^2 e^{-b|\kappa|} \tag{2}$$

with *b=10* being a correlation length parameter.

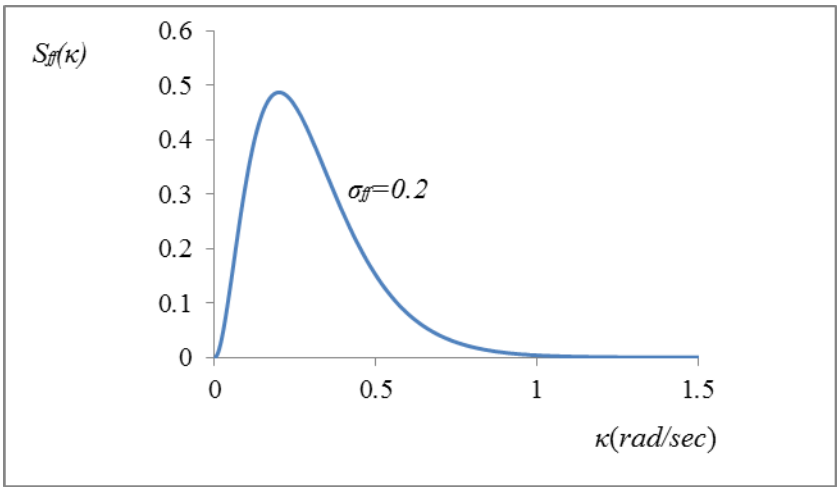

Figure 2. Spectral density function for stochastic field $f(x)$ standard deviation σ_{ff}=0.2

In order to demonstrate the validity of the proposed methodology, a truncated Gaussian and a lognormal pdf were used to model $f(x)$. For this purpose, an underlying Gaussian stochastic field denoted by $g(x)$ is generated using the spectral representation method [9] and the power spectrum of Eq. (12). The truncated Gaussian field $f_{\mathrm{TG}}(x)$ is obtained by simply truncating $g(x)$ in the following way: $-0.9 \le g(x) \le 0.9$, while the lognormal $f_{\mathrm{L}}(x)$ is obtained from the following transformation as a translation field [8]:

$$f_{\mathrm{L}}(x) = F_{\mathrm{L}}^{-1}\{G[g(x)]\} \tag{2}$$

The *SDF* of the underlying Gaussian field in Eq.(12) and the corresponding spectral densities of the truncated Gaussian and the Lognormal fields denoted $S_{f_{\mathrm{TG}} f_{\mathrm{TG}}}(\kappa)$ and $S_{f_{\mathrm{L}} f_{\mathrm{L}}}(\kappa)$, respectively, will be different. These are computed from the following formula

$$S_{f_i f_i}(\kappa) = \frac{1}{2\pi L_x}\left|\int_0^{L_x} f_i(x) e^{-i\kappa x} dx\right|^2 \; ; i = \mathrm{TG, L} \tag{2}$$

where L_x is the length of the sample functions of the non-Gaussian fields modeling flexibility. As the sample functions of the non-Gaussian fields are non-ergodic, the estimation of power spectra in Eq.(14) is performed in an ensemble average sense [8].

4.1 LC1: Constant load at the end of the beam

This load case scenario has been selected in order to further demonstrate the validity of the methodology and establish a logical continuation with previous studies related to the current work. In the case when the excitation is constant $P(t)=P_0$, and the load P_0 is suddenly applied, the response displacement is given by Eq. (7h). From this equation it can be seen that the solution degenerates to the static solution $u(t) = P_0 / k$ as time t tends to infinity. Accordingly the *DVRF* should converge to the respective static *VRF* of a cantilever beam loaded with a concentrated load at its end, given by Eq. (15) [1].

$$VRF(x,\kappa) = \left|\frac{F_0}{I}\int_0^x h(x,\xi) M(\xi) e^{i\kappa\xi} d\xi\right|^2 \tag{2}$$

where $h(x,\xi)$ is the Green function of the beam given by

$$h(x,\xi) = x - \xi \tag{2}$$

and *M(x)* is the bending moment function given by

$$M(\xi) = -P_0(L-\xi) \tag{2}$$

Validating the aforementioned expectations, figure 3 presents a 3D plot of the *DVRF* with an initial transient phase and afterwards the phase where the system is almost at rest, while figure 4 presents the coinciding *VRF* and *DVRF* obtained from Eq. (15a) and *FMCS, respectively*, when the system has approached the stationary condition at *t=10sec and* $\sigma_{ff} = 0.2$.

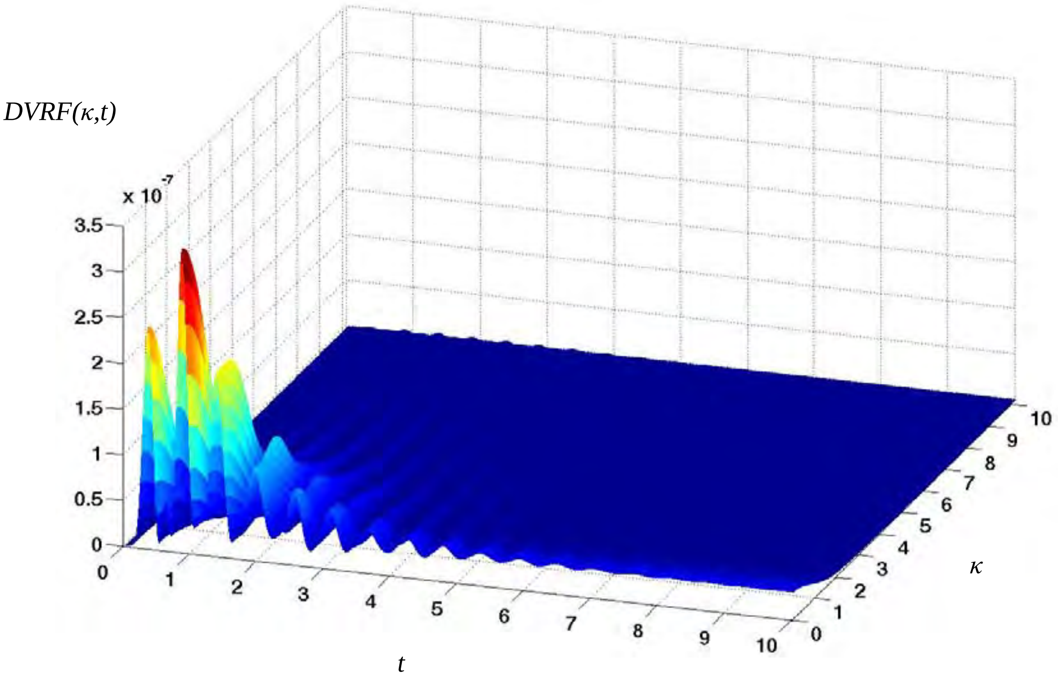

Figure 3. 3D plot of *DVRF*, as a function of frequency κ (rad/m) and time *t*(sec) for LC1 and σ_{ff}=0.2

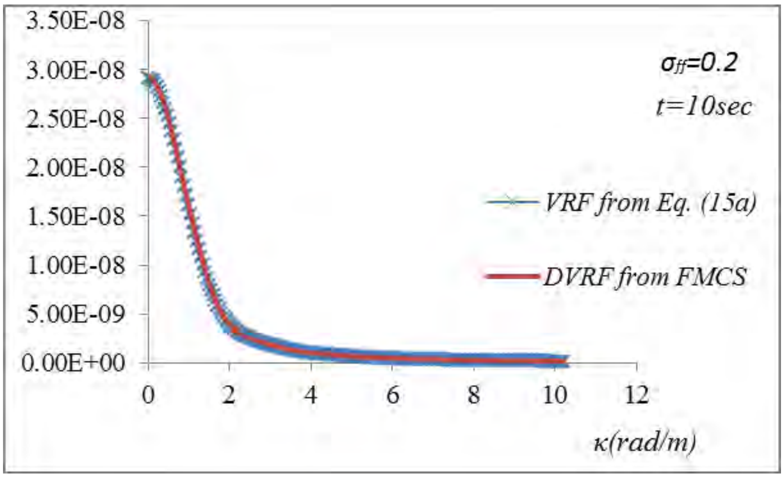

Figure 4. Values of *VRF* for static load P_0 and *DVRF* for constant load $P(t)=P_0$ at *t=10sec.*

4.2 LC2: Dynamic periodic load at the end of the beam

Figures 5 and 6 present *DMRF* and *DVRF*, respectively, computed with FMCS for a periodic load with frequency $\bar{\omega} = 2$ and three different values of the standard deviation σ_{ff} = 0.2, σ_{ff} = 0.4 and σ_{ff} = 0.6. From these figures it can be observed that *DVRF* do not follow any particular pattern with respect to any increase or decrease of σ_{ff} in contrast to *DMRF* and to what has been observed in Papadopoulos and Deodatis [2] for the corresponding static problem, albeit the mean and variability response increases as σ_{ff} increases, as shown below (Figure 8). Figures 7(a) and (b) present plots of *DMRF* and *DVRF* as a function of *t* for a fixed wave number κ*=2* and σ_{ff} *=0.2*. From the above Figures (5, 6 and 7) it appears that *DMRF* and *DVRF* have a significant variation along the wave number κ axis and the time axis *t*. Both functions and especially *DVRF* have an initial transient phase and then appear to be periodic. It is reminded here that *DVRF* and *DMRF* are functions of the imposed dynamic loading. This explains the fact that they do not approach zero with *t* increasing, since the applied dynamic load is periodic with constant amplitude which does not decay.

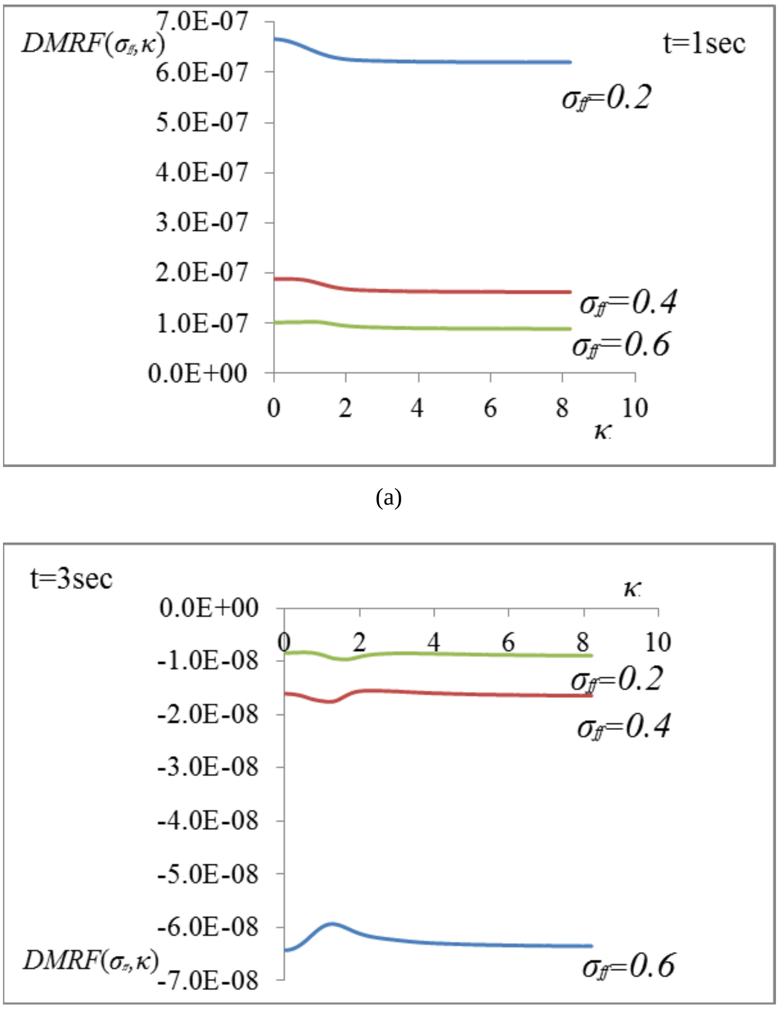

(a)

(b)

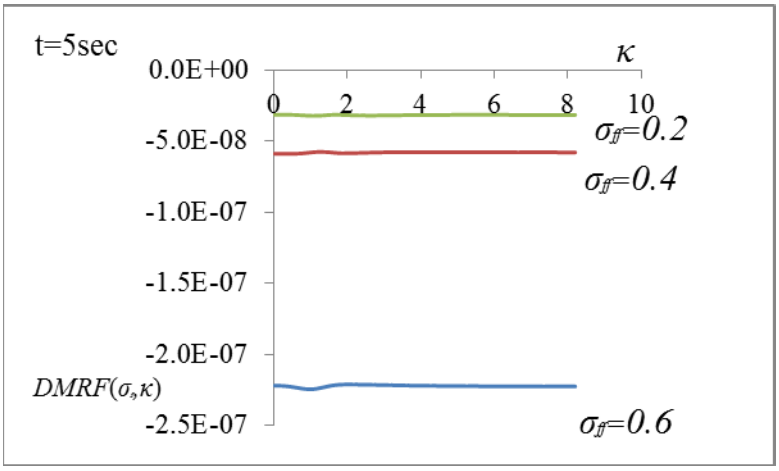

(c)

Figure 5. *DMRF* as a function of σ_{ff} for (a) t=1sec, (b) t=3sec and (c) t=5sec

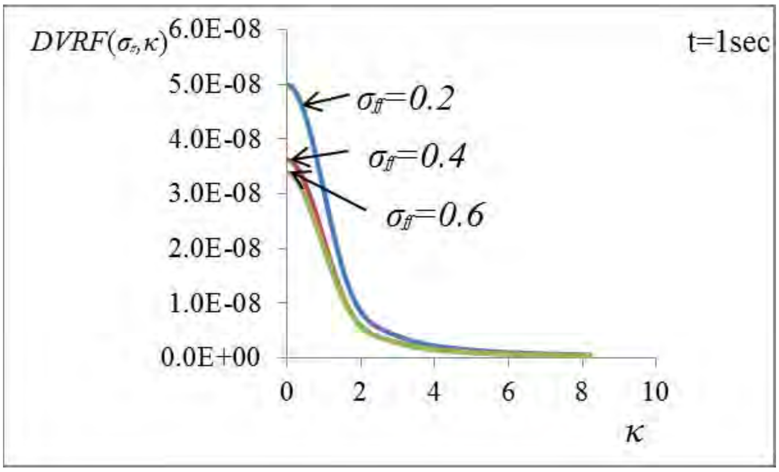

(a)

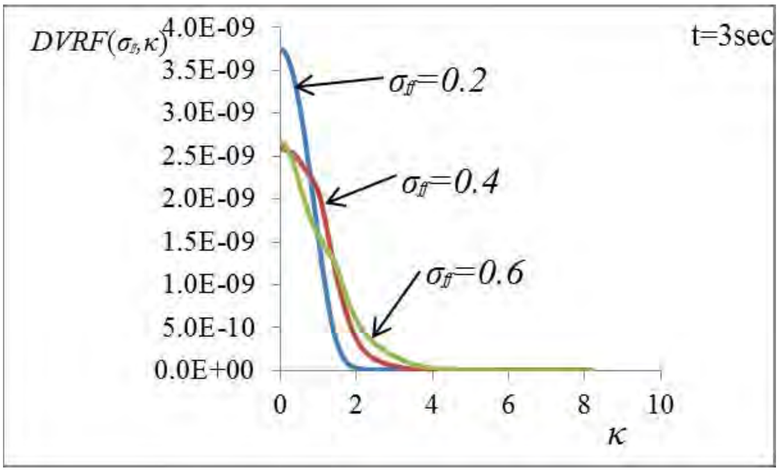

(b)

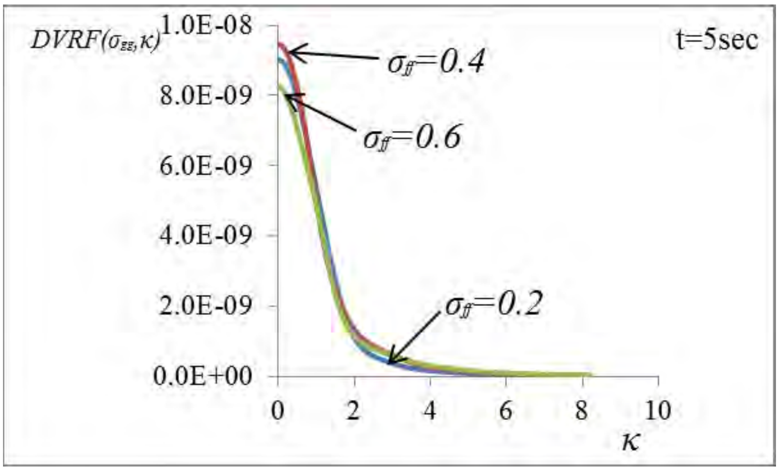

(c)

Figure 6. *DVRF* as a function of the σ_{ff} for (a) t=1sec, (b) t=3sec and (c) t=5sec

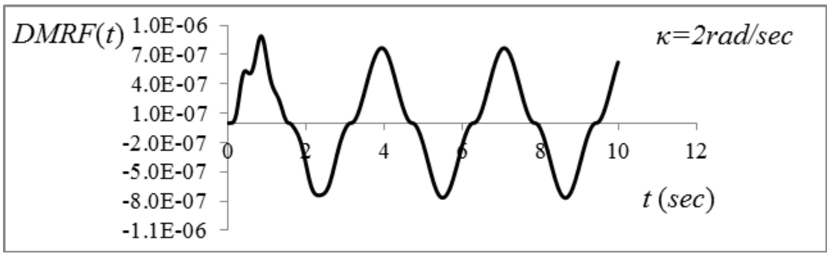

(a)

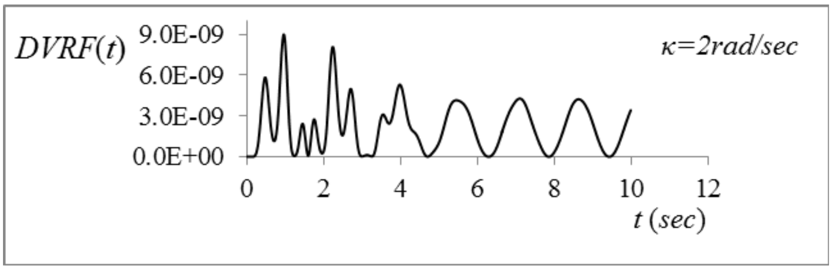

(b)

Figure 7. *DMRF* (a) and *DVRF* (b) as a function of *t* for *κ*=2 *rad/sec* and σ_{ff} = 0.2

Figures 8(a), (b) and (c) present comparatively the results of the computed response variance time histories using the integral expression of Eq.(8a) and MCS, for three different standard deviations of a truncated Gaussian stochastic field used for the modeling of flexibility. The underlying Gaussian field is modeled with the power spectral density of Eq.(12) and three different standard deviations σ_{gg} =0.2, σ_{gg} = 0.4 and σ_{gg} = 0.6. The corresponding standard deviations of the truncated Gaussian field *f*(*x*) are computed as σ_{ff} = 0.2, σ_{ff} = 0.3912 and σ_{ff} = 0.5286, respectively. Figures 9(a), (b) and (c), present the same results with Figure 6 but for the mean response of the oscillator. The deterministic displacement time history is also plotted in figure 9(d) for comparison purposes. From these figures it can be observed that the mean and variability response time histories obtained with the integral expressions of Eqs (8a) and (8b) are in close agreement with the corresponding MCS estimates. In all cases examined the maximum error in the computed *Var*[*u*(*t*)], observed at the peak values of the variance, is less than 25%, while in all other time steps this error is less than 3-4%. In the case of $\varepsilon[u(t)]$, the predictions of Eq. 8(b) are almost identical to the ones obtained with MCS, with an error of less than 3% in all cases. From Figures 9(a-d), it can be observed that in all cases, the mean response time history for all cases examined is almost identical to the deterministic one, with the exception of the first cycle where slight differences in the peak values are observed.

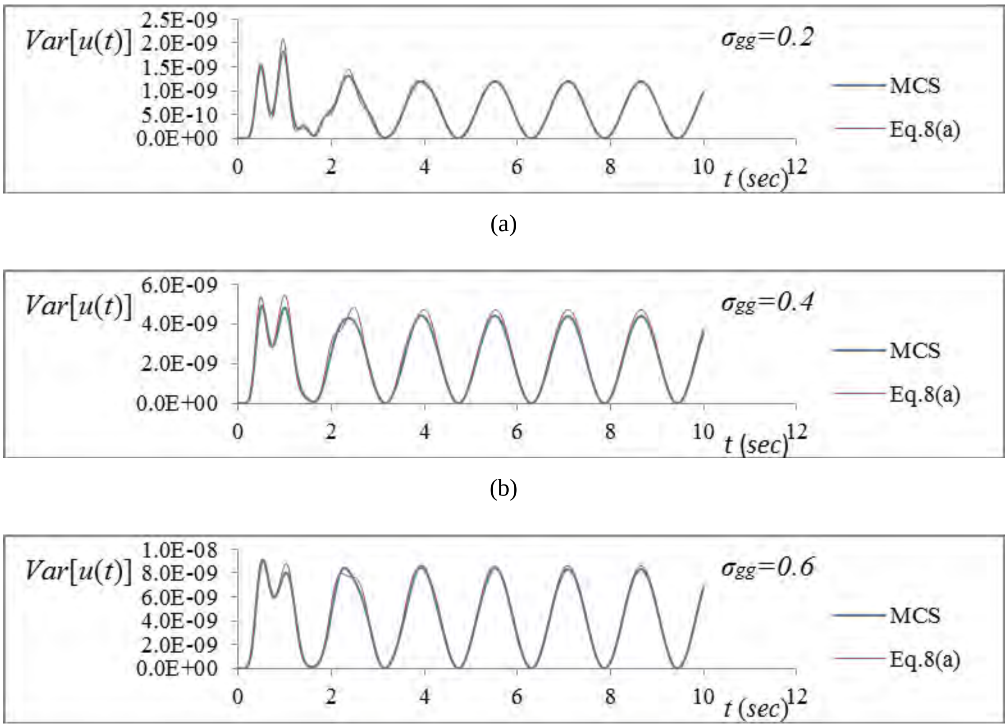

(a)

(b)

(c)

Figure 8. Time histories of the variance of the response displacement for a truncated Gaussian field with (a) σ_{gg} = 0.2, (b) σ_{gg} = 0.4, and (c) σ_{gg} = 0.6. Comparison of results obtained from eq.(11a) and MCS

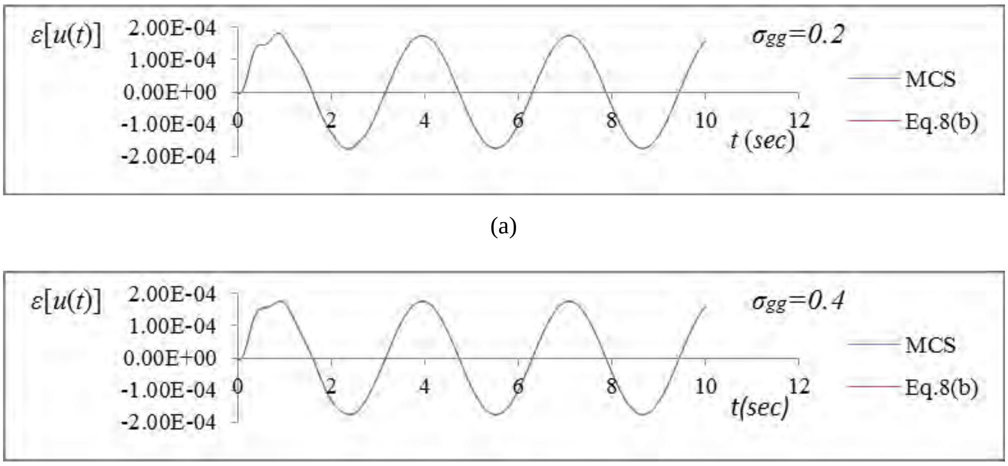

(a)

(b)

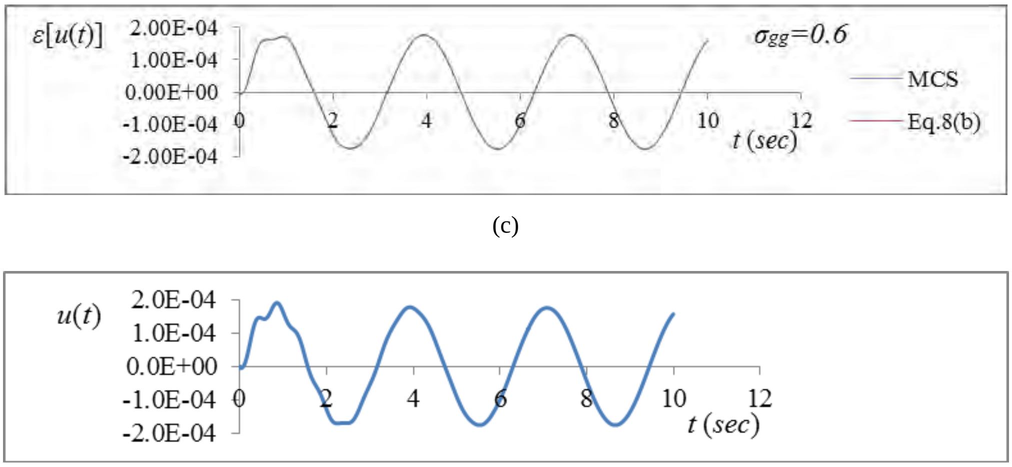

(c)

(d)

Figure 9. Time histories of: (a) mean response displacement for a truncated Gaussian field with σ_{gg} = 0.2, (b) σ_{gg} = 0.4, (c) σ_{gg} = 0.6 and (d) the deterministic displacement. Comparison of results obtained from eq.(11b) and MCS.

Figures 10(a) and (b) repeat the same comparisons with the previous figures 8 and 9 but for the case of a lognormal stochastic field used for the modeling of flexibility with σ_{ff} *=0.2* and lower bound l_b*= -0.8*. The conclusions extracted previously for the case of truncated Gaussian fields also apply here.

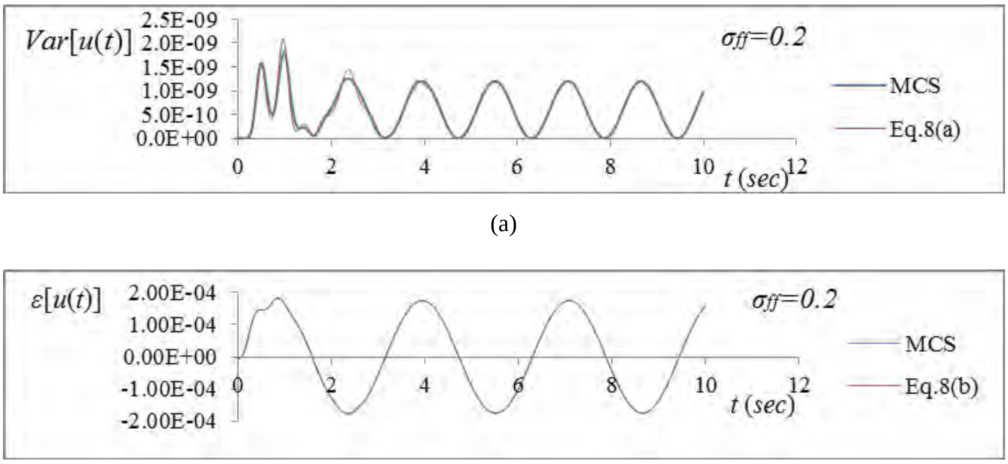

(a)

(b)

Figure 10. Comparative results from eq. 11 and MCS for a lognormal field with σ_{ff} =0.2 for (a) the variance and (b) the mean of the response displacement time history

4.3 LC3: El Centro earthquake

Figures 11 and 12 present plots of *DMRF* and *DVRF*, respectively, for the load case of the acceleration time history of the 1940 El Centro Earthquake. As in previous load case scenario, three different values of the standard deviation were used, σ_{ff} = 0.2, σ_{ff} = 0.4 and σ_{ff} = 0.6. From these figures it can again be observed that *DVRF* does not follow any pattern with respect to an increase or decrease of σ_{ff} , while in this case this is also observed for the *DMRF* at Figure 11(c) for *t*=5sec.

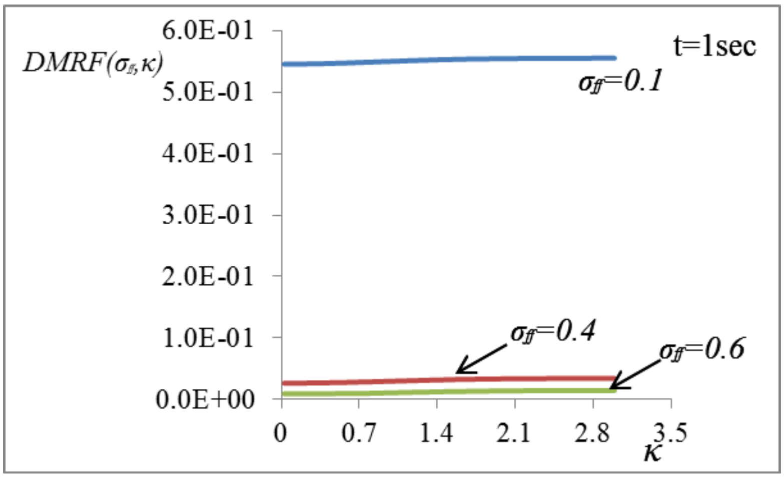

(a)

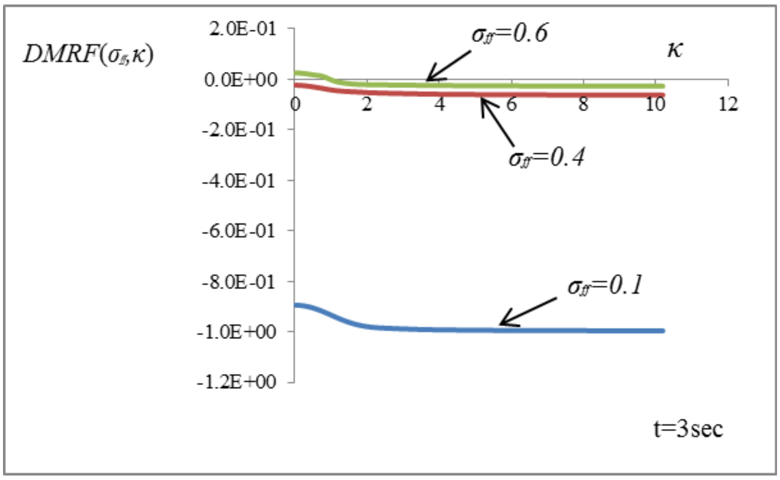

(b)

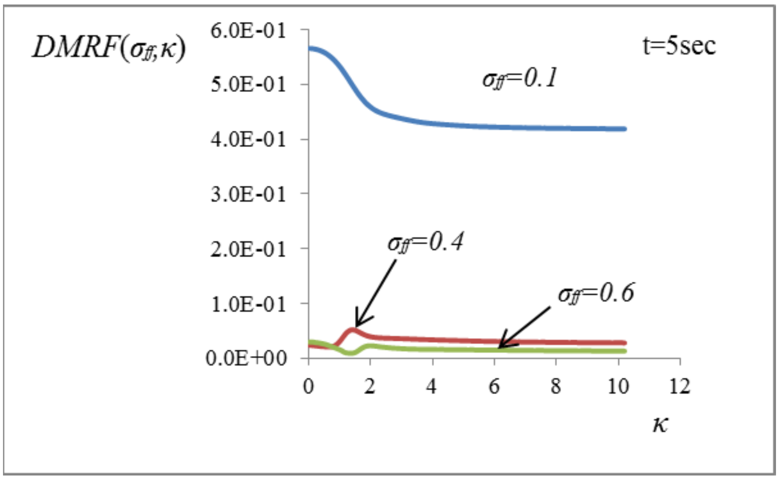

(c)

Figure 11. *DMRF* as a function of the σ_{ff} for (a) t=1sec, (b) t=3sec and (c) t=5sec

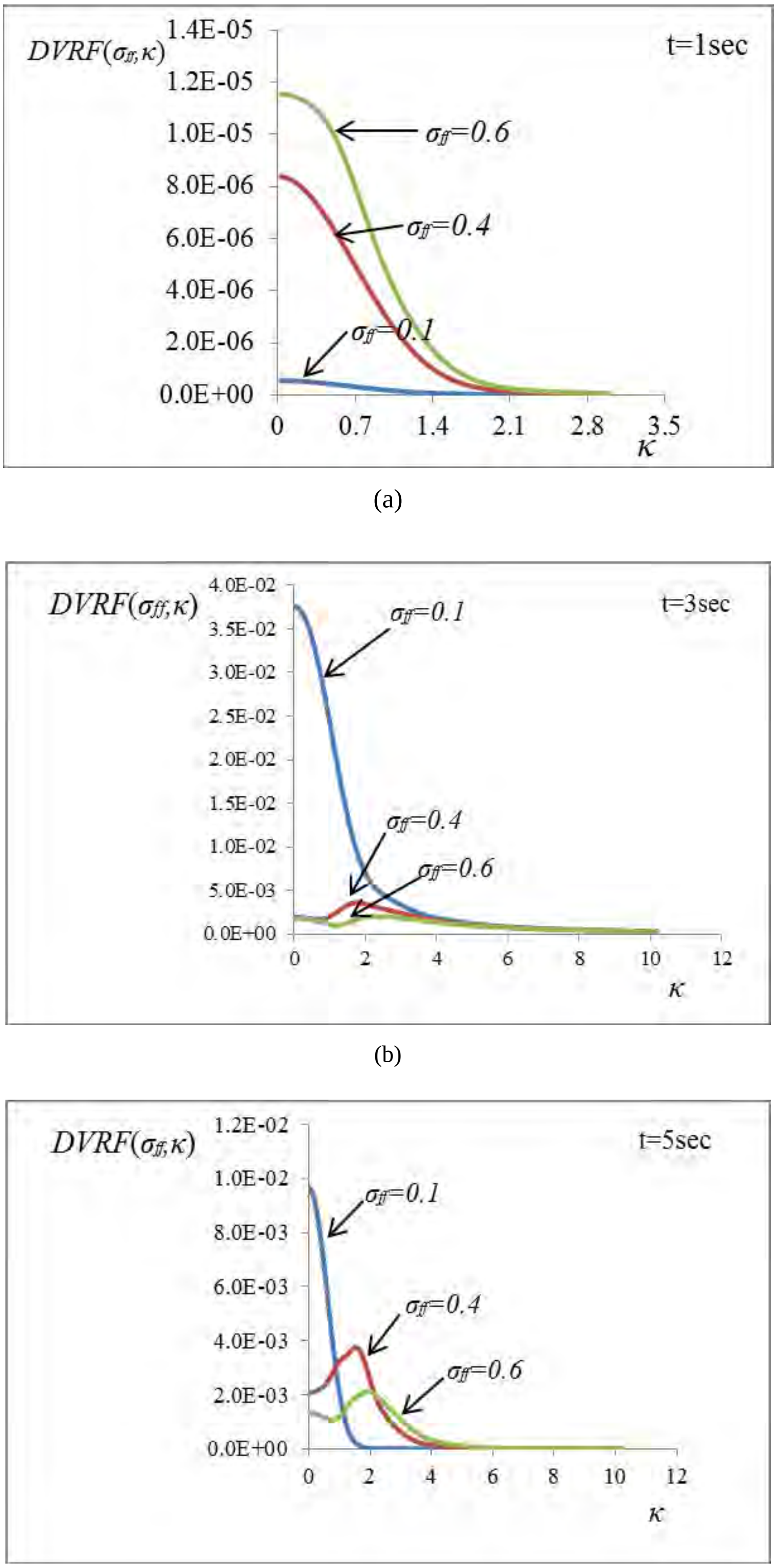

(a)

(b)

(c)

Figure 12. *DVRF* as a function of the σ_{ff} for (a) t=1sec, (b) t=3sec and (c) t=5sec

Figures 13(a) and (b) present 3D plots of the *DMRF* and *DVRF* as a function of frequency κ and time *t*(*sec*) for σ_{ff}=0.2. From these figures, as well as from figures 11 and 12, it can be observed that again *DMRF* and *DVRF* have a significant variation in both κ and t axis, without being periodic in contrast to what has been observed in LC2. In addition, both *DMRF* and *DVRF* approach a zero value with time increasing due to the fact that ground accelerations decay and vanish after some time.

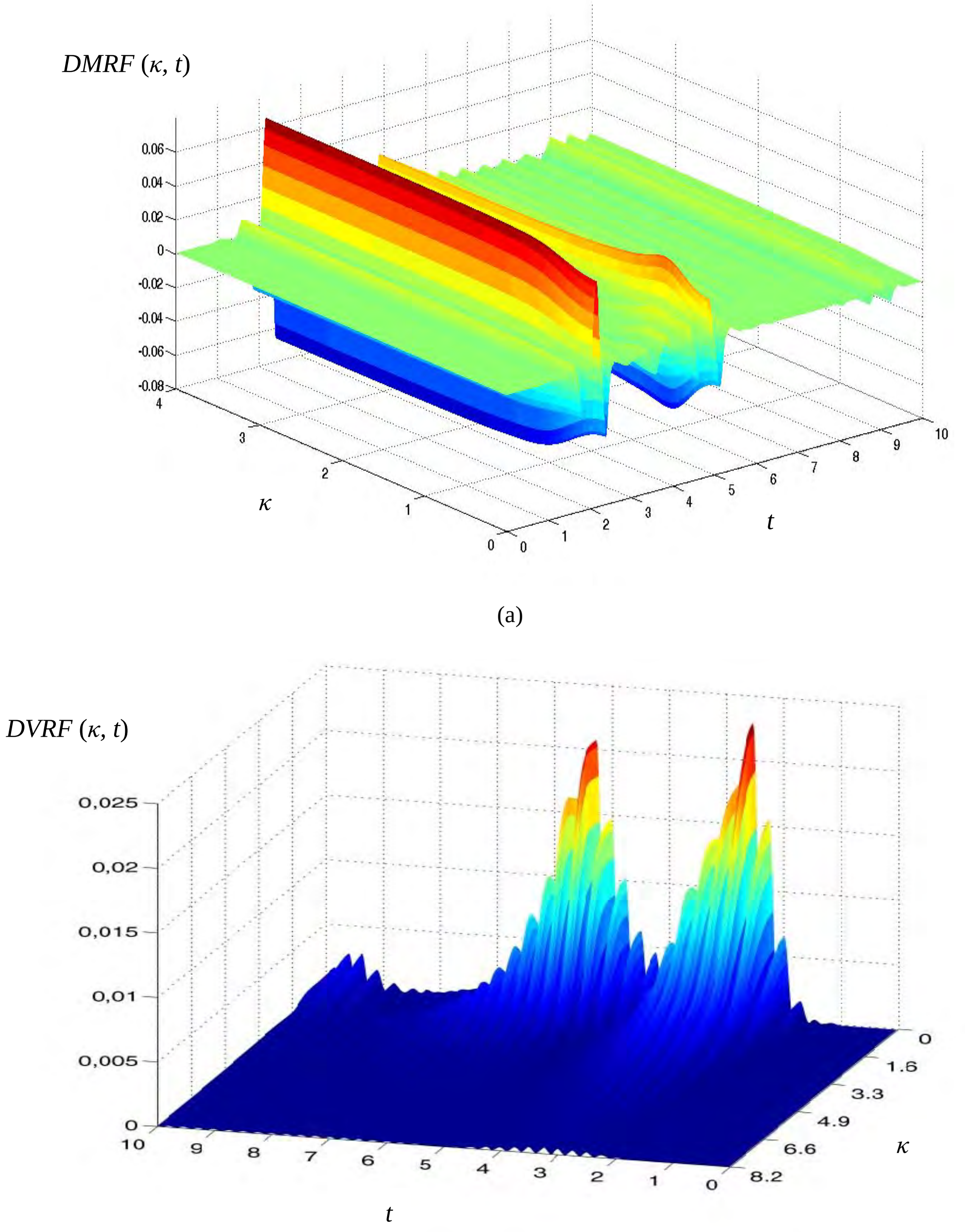

(a)

(b)

Figure 13. 3D plots of (a) *DMRF* and (b) *DVRF*, as a function of frequency κ (rad/m) and time *t*(sec) for LC3 and σ_{ff}=0.2

Figures 14(a), and 14(b) present a comparison of the response variance computed with Eq.(8a) and MCS, in the case of a truncated Gaussian stochastic field modeling flexibility with σ_{gg} = 0.4 and 0.6, while figures (15a) and (15b) present the same results for the mean dynamic response of the stochastic oscillator along with the corresponding deterministic displacement time history (figure 15(c)). Figures 16(a) and (b) repeat the same comparisons for the case of a lognormal stochastic field used for the modeling of flexibility and σ_{ff} =0.3 and lower bound l_b= *-0.8.*

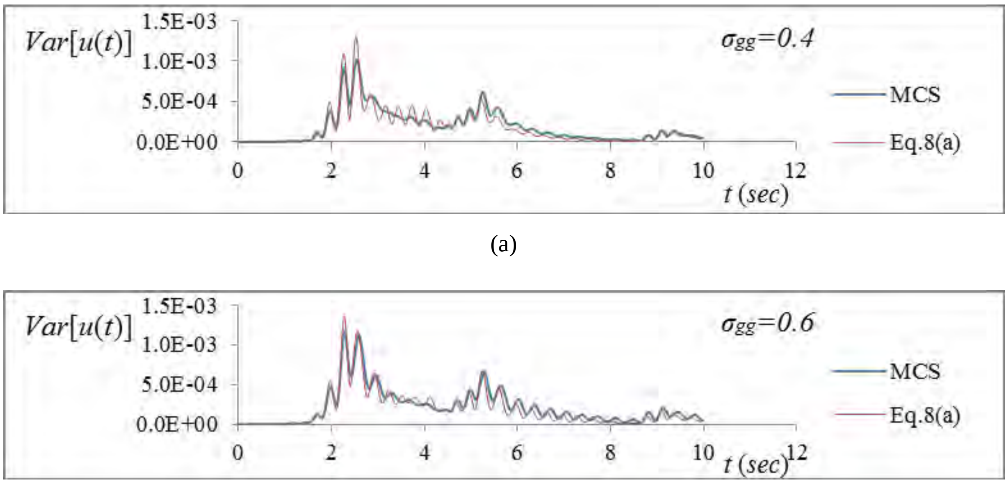

(a)

(b)

Figure 14. Time histories of the variance of the response displacement for a truncated Gaussian field for (a) σ_{gg} = 0.4 and (b) σ_{gg} = 0.6. Comparison of results obtained from eq.8(a) and MCS.

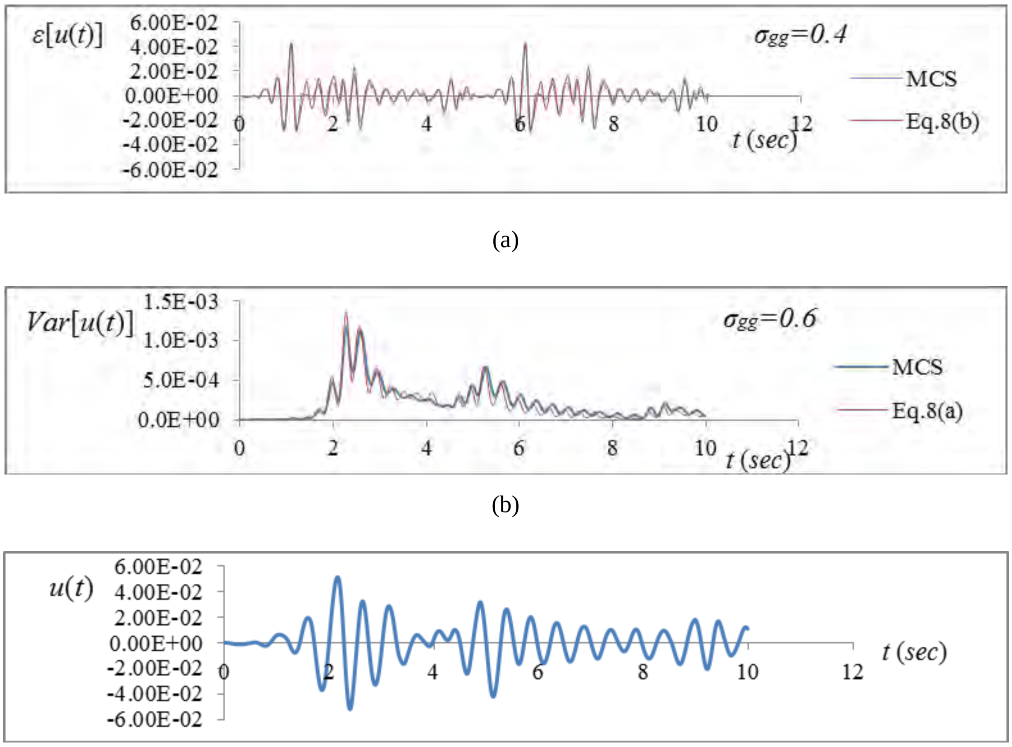

(a)

(b)

(c)

Figure 15. Time histories of the mean response displacement for a truncated Gaussian field with (a) σ_{gg} = 0.4, (b) σ_{gg} = 0.6 and (c) of the deterministic response displacement. Comparison of results obtained from eq.(8b) and MCS.

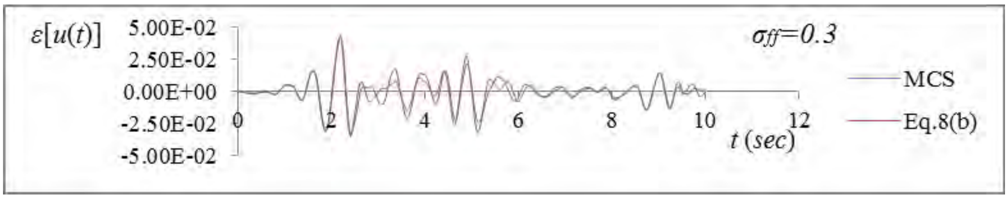

(a)

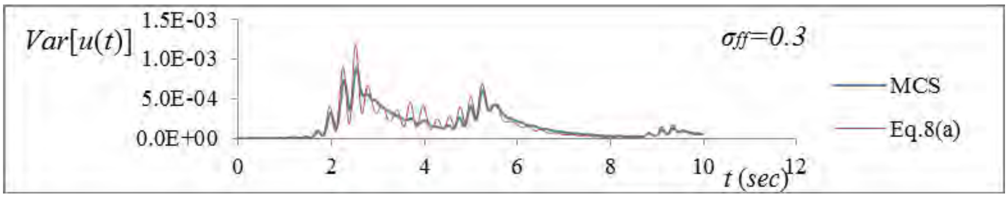

(b)

Figure 16. Comparative results from eq. 11 and MCS for a lognormal field with σ_{ff} =0.3 for (a) the variance and (b) the mean of the response displacement time history

From the above figures it can be observed that, as in LC2, the mean and variability response time histories obtained with the integral expressions of Eqs (8a) and 8(b) are in close agreement with the corresponding MCS estimates, in all cases. Again, the maximum error in the computed $Var[u(t)]$ was observed at the peak values of the variance and is less than 25%, while in all other time steps this error is less than 3-4%. In the case of $\varepsilon[u(t)]$, the predictions of Eq. 8(b) are very close to the ones obtained with MCS, with a error of less than 3% in all cases. From Figures 13(a-c), it can be observed that, in contrast to what was observed in LC2, the mean response time history differs significantly from the corresponding deterministic one, in terms of both frequencies and amplitudes.

4.4 Upper bounds on the mean and variance of the response of LC3

Spectral-distribution-free upper bounds on both the mean and variance of the response are obtained via Eqs. (11a) and (11b), respectively. Results of this calculation are presented in figures 17(a) and (b), in which the time dependant upper bounds on the mean and variance of the response displacement are plotted against time for a standard deviation σ_{ff} =0.4.

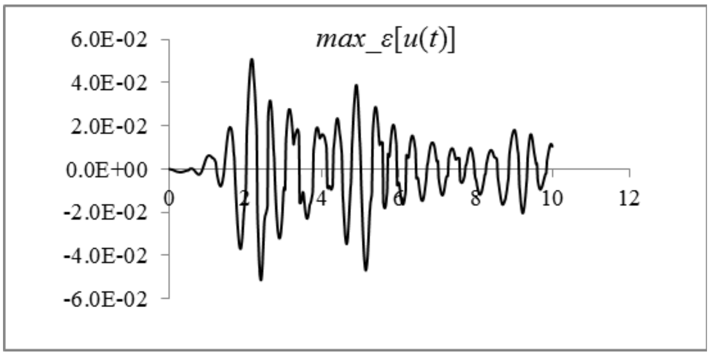

(a)

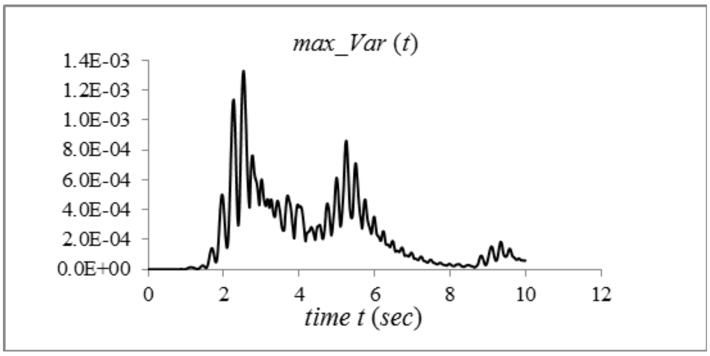

(b)

Figure 17. Upper bounds on the (a) mean and (b) variance of the response displacement for LC3 and σ_{gg}=0.4

4.5 Sensitivity analysis for LC3 using the integral expressions in Eqs 8(a) and (b)

Finally, a sensitivity analysis is performed using Eqs. (8a) and (8b) at minimum computational cost, with respect to three different values of the correlation length parameter of the *SDF* in Eq. (12) and σ_{ff}=0.2.

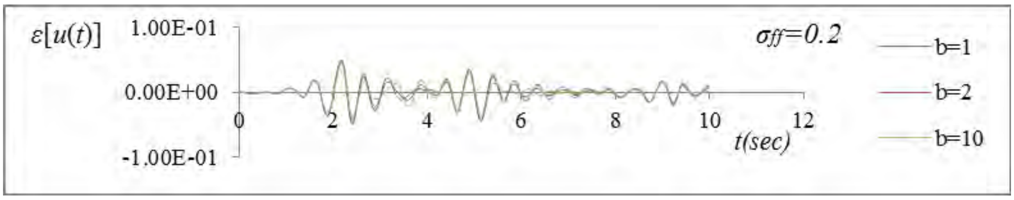

(a)

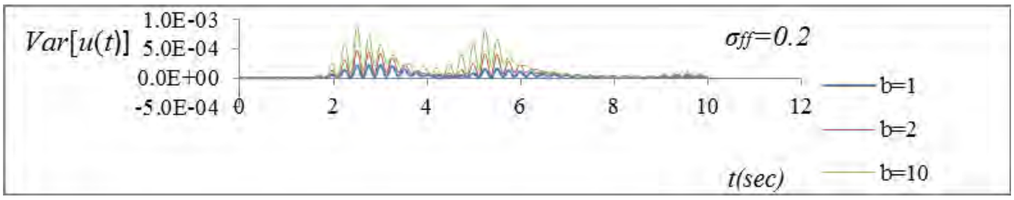

(b)

Figure 18. (a) Mean and (b) variance time histories of the response displacement computed from Eqs. (8b) and (8a), respectively for three different values of the correlation length parameter *b* of the *SDF* in Eq. (12)

5 CONCLUDING REMARKS

In the present work, Dynamic Variability Response Functions and Dynamic Mean Response Functions are obtained for a linear stochastic single d.o.f. oscillator with random material properties under dynamic excitation. The inverse of the modulus of elasticity was considered as the uncertain system parameter.

It is demonstrated that, as in the case of stochastic systems under static loading, *DVRF* and *DMRF* depend on the standard deviation of the stochastic field modeling the uncertain parameter but appear to be almost independent of its power spectral density and marginal *pdf*. The results obtained from the integral expressions are close to those obtained with MCS reaching a maximum error of the order of 20-25%.

As in the case of stochastic systems under static loading, the *DVRF* and *DMRF* provide with an insight of the dynamic system sensitivity to the stochastic parameters and the mechanisms controlling the response mean and variability and their evolution in time.

REFERENCES

[1] Papadopoulos, V., Deodatis, G. and Papadrakakis, M., Flexibility-based upper bounds on the response variability of simple beams, *Computer Methods in Applied Mechanics and Engineering*, **194**, (12-16), 8, pp. 1385-1404, 2005.

[2] Papadopoulos, V. and Deodatis, G., Response variability of stochastic frame structures using evolutionary field theory, *Comp. Meth. Appl. Mech. Eng.*, **195** (9-12), pp. 1050-1074, 2006.

[3] Papadopoulos, V., Papadrakakis, M. and Deodatis, G., Analysis of mean response and response variability of stochastic finite element systems, *Comp. Meth. Appl. Mech. Eng.* **195** (41-43), pp. 5454-5471, 2006.

[4] Shinozuka, M., Structural response variability , *J. Engrg. Mech.* **113** (6) 825-842, 1987.

[5] Deodatis, G., Graham, L. and Micaletti, R., A hierarchy of upper bounds on the response of stochastic systems with large variation of their properties: random variable case, *Prob. Engrg. Mech.* **18** (4) 349-364, 2003.

[6] Deodatis, G., Graham, L. and Micaletti, R., A hierarchy of upper bounds on the response of stochastic systems with large variation of their properties: random field case, *Prob. Engrg. Mech.* **18** (4) 365-375, 2003.

[7] Miranda, M., On the response variability of beam structures with stochastic parameters, *PhD Thesis*, ColumbiaUniversity, 2008.

[8] M. Grigoriu, *Applied Non-Gaussian Processes: Examples, Theory, Simulation, Linear Random Vibration, and MATLAB Solutions,* Prentice Hall, 1995.

[9] M. Shinozuka, G. Deodatis, Simulation of stochastic processes by spectral representation, *Appl. Mech. Rev.* **44** (4) (1991) 191-203.

[10] R. Ghanem and P.D. Spanos, *Stochastic Finite Elements: A Spectral Approach*, Springer-Verlag, Berlin (1991) (second ed.), Dover Publications, NY (2003).

[11] M. Grigoriu and Evaluation of Karhunen-Loève, spectral and sampling representations for stochastic processes, *J. Engrg. Mech. (ASCE)* **132** (2006), pp. 179–189.

[12] W.K. Liu, T. Belytschko and A. Mani, Probabilistic finite elements for nonlinear structural dynamics, *Comput. Methods Appl. Mech. Engrg.* **56** (1986), pp. 61–86.

[13] W.K. Liu, T. Belytschko and A. Mani, Random field finite elements, *Int. J. Numer. Methods Engrg.* **23** (1986), pp. 1831–1845.

[14] H.G. Matthies, C.E. Brenner, C.G. Bucher and C. Guedes Soares, Uncertainties in probabilistic numerical analysis of structures and solids – stochastic finite elements, *Struct. Saf.* **19** (1997), pp. 283–336.

[15] George Stefanou, The stochastic finite element method: Past, present and future, *Computer Methods in Applied Mechanics and Engineering*, Volume **198**, Issues 9-12, 15 February 2009, Pages 1031-1051.

[16] Ghosh, D., Ghanem, R., Red-Horse, J., Analysis of eigenvalues and modal interaction of stochastic systems(2005), *AIAA Journal*, **43** (10), pp. 2196-2201.

[17] G.I. Schueller, Model Reduction and uncertainties in structural dynamics, *Computational Methods in Stochastic Dynamics*, by M. Papadrakakis, G. Stefanou and V. Papadopoulos (Eds), Springer, 2011.

[18] F.J. Wall, G. Deodatis, Variability response functions of stochastic plane stress/strain problems, *J. Engrg. Mech.* **120** (9) (1994) 1963–1982.

[19] L. Graham, G. Deodatis, Weighted integral method and variability response functions for stochastic plate bending problems, *Struct. Saf.* **20** (1998) 167–188.

[20] S. R. Arwade, G. Deodatis, Variability response functions for effective material properties, *Probabilistic Engineering Mechanics* **26** (2011) 174-181.

COMPDYN 2011
3^{rd} ECCOMAS Thematic Conference on
Computational Methods in Structural Dynamics and Earthquake Engineering
M. Papadrakakis, M. Fragiadakis, V. Plevris (eds.)
Corfu, Greece, 25-28 May 2011

A NOVEL GALERKIN PROJECTION APPROACH FOR DAMPED STOCHASTIC DYNAMIC SYSTEMS

Abhishek Kundu[1] **and Sondipon Adhikari**[2]

Civil & Computational Engineering Research Center, Swansea University, Swansea, UK
[1]Graduate student, e-mail: a.kundu.577613@swansea.ac.uk
[2]Chair of Aerospace Engineering, e-mail: s.adhikari@swansea.ac.uk

Keywords: Stochastic dynamics, random field, spectral decomposition, Karhunen-Loève Expansion, stochastic subspace projection

Abstract. *This article provides the theoretical development and simulation results of a novel Galerkin subspace projection scheme for damped dynamic systems with stochastic coefficients. The fundamental idea involved here is to solve the stochastic dynamic system in the frequency domain by projecting the solution into a reduced finite dimensional spatio-random vector basis to approximate the response. A Nueumann expansion type of approach is used to generate the complex stochastic basis functions. The proposed method is applicable to linear dynamic systems with Gaussian and non-Gaussian random fields. Galerkin weighting coefficients have been employed to minimize the error induced due to the reduced basis and finite order spectral functions and hence to explicitly evaluate the stochastic system response. The statistical moments of the solution have been evaluated at all frequencies to illustrate and compare the stochastic system response with the deterministic case. The results have been compared to direct Monte-Carlo simulation for different correlation lengths and variability of randomness.*

1 INTRODUCTION

Due to the significant development in computational hardware it is now possible to solve very high resolution models in various computational physics problems, ranging from fluid mechanics to nano-bio mechanics. However, the spatial resolution is not enough to determine the credibility of the numerical model, the physical model as well its parameters are also crucial. Since neither of these may not be exactly known, there has been increasing research activities over the past three decades to model the governing partial differential equations within the framework of stochastic equations. We refer to few recent review papers [1–3]. Consider a bounded domain $\mathcal{D} \in \mathbb{R}^d$ with piecewise Lipschitz boundary $\partial\mathcal{D}$, where $d \leq 3$ is the spatial dimension and $t \in \mathbb{R}^+$ is the time. Further, consider that $(\Theta, \mathcal{F}, P)$ is a probability space where $\theta \in \Theta$ is a sample point from the sampling space Θ, $\mathcal{F}$ is the complete σ-algebra over the subsets of Θ and P is the probability measure. We consider a linear stochastic partial differential equation (PDE) of the form

$$\rho(\mathbf{r},\theta)\frac{\partial^2 U(\mathbf{r},t,\theta)}{\partial t^2} + \mathfrak{L}_\alpha \frac{\partial U(\mathbf{r},t,\theta)}{\partial t} + \mathfrak{L}_\beta U(\mathbf{r},t,\theta) = p(\mathbf{r},t); \quad \mathbf{r} \in \mathcal{D}, t \in [0,T] \tag{1}$$

with the associated Dirichlet condition

$$U(\mathbf{r},t,\theta) = 0; \quad \mathbf{r} \text{ on } \partial\mathcal{D}. \tag{2}$$

In the above equation $\rho(\mathbf{r},\theta)$ is the random mass distribution of the system, $p(\mathbf{r},t)$ is the distributed time-varying forcing function, $\mathfrak{L}_\beta$ is the spatial self-adjoint stochastic stiffness operator, $\mathfrak{L}_\alpha$ is the spatial self-adjoint stochastic damping operator and $U(\mathbf{r},t,\theta)$ in the stochastic response quantity to be obtained. Note that $\mathfrak{L}_\alpha(\bullet)$ and $\mathfrak{L}_\beta(\bullet)$ involve linear stochastic differential operators with coefficients $\alpha(\mathbf{r},\theta)$ and $\beta(\mathbf{r},\theta)$ as the second order random fields such that $\alpha, \beta : \mathbb{R}^d \times \Theta \to \mathbb{R}$. We assume the random fields to be stationary and square integrable. The purpose of this paper is to investigate a new solution approach for Eqn. (1) after the discretization of the spatio-random fields using the well established techniques of stochastic finite element method (SFEM) as can be found in references [4–6].

The random fields in Eqn. (1) can be discretized to represent them as spectral functions using a finite number of random variables using one of the established techniques available in literatures [4, 7]. Hence the stochastic PDE along with the boundary conditions would result in an equation of the form

$$\mathbf{M}(\theta)\ddot{\mathbf{u}}(\theta,t) + \mathbf{C}(\theta)\dot{\mathbf{u}}(\theta,t) + \mathbf{K}(\theta)\mathbf{u}(\theta,t) = \mathbf{f}_0(t) \tag{3}$$

where $\mathbf{u}(\theta,t)$ is the discretized response vector, $\mathbf{M}(\theta) = \mathbf{M}_0 + \sum_{i=1}^{p} \mu_i(\theta_i)\mathbf{M}_i \in \mathbb{R}^{n\times n}$ is the random mass matrix, $\mathbf{K}(\theta) = \mathbf{K}_0 + \sum_{i=1}^{p} \nu_i(\theta_i)\mathbf{K}_i \in \mathbb{R}^{n\times n}$ is the random stiffness matrix along with $\mathbf{C}(\theta) \in \mathbb{R}^{n\times n}$ as the random damping matrix. Here the mass and stiffness matrices have been expressed in terms of their deterministic components ($\mathbf{M}_0$ and $\mathbf{K}_0$) and the corresponding random contributions ($\mathbf{M}_i$ and $\mathbf{K}_i$) obtained from discretizing the stochastic field with a finite number of random variables ($\mu_i(\theta_i)$ and $\nu_i(\theta_i)$) and their corresponding spatial basis functions. This has been elaborated in subsection 2.1. In the present work proportional damping is considered for which $\mathbf{C}(\theta) = \zeta_1\mathbf{M}(\theta) + \zeta_2\mathbf{K}(\theta)$, where ζ_1 and ζ_2 are deterministic scalars. For the harmonic analysis of the structural system considered in Eqn. (3), it is represented in the frequency domain as

$$\left[-\omega^2\mathbf{M}(\theta) + i\omega\mathbf{C}(\theta) + \mathbf{K}(\theta)\right]\widetilde{\mathbf{u}}(\theta,\omega) = \widetilde{\mathbf{f}}_0(\omega) \tag{4}$$

where $\widetilde{\mathbf{u}}(\theta, \omega)$ is the complex frequency domain system response amplitude, $\widetilde{\mathbf{f}}_0(\omega)$ is the amplitude of the harmonic force.

Now we group the random variables associated with the mass and damping matrices of Eqn. (3) as

$$\xi_i(\theta) = \mu_i(\theta) \quad \text{and} \quad \xi_{i+p}(\theta) = \nu_i(\theta) \quad \text{for} \quad i = 1, 2, \dots, p$$

following which the expression for the linear structural system in Eqn. (4) can be expressed as

$$\left(\mathbf{A}_0(\omega) + \sum_{i=1}^{2p} \xi_i(\theta_i)\mathbf{A}_i(\omega)\right) \widetilde{\mathbf{u}}(\omega, \theta) = \widetilde{\mathbf{f}}_0(\omega) \tag{5}$$

where $\mathbf{A}_0$ and $\mathbf{A}_i \in \mathbb{C}^{n\times n}$ represent the complex deterministic and stochastic parts respectively of the mass, the stiffness and the damping matrices ensemble. For the case of proportional damping the matrices $\mathbf{A}_0$ and $\mathbf{A}_i$ can be written as

$$\begin{aligned} \mathbf{A}_0(\omega) &= \left[-\omega^2 + i\omega\zeta_1\right]\mathbf{M}_0 + \left[i\omega\zeta_2 + 1\right]\mathbf{K}_0 & (6)\\ \mathbf{A}_i(\omega) &= \left[-\omega^2 + i\omega\zeta_1\right]\mathbf{M}_i \quad \text{for} \quad i = 1, 2, \dots, p & (7)\\ \text{and} \quad \mathbf{A}_j(\omega) &= \left[i\omega\zeta_2 + 1\right]\mathbf{K}_j \quad \text{for} \quad j = p+1, p+2, \dots, 2p\,. \end{aligned}$$

The paper has been arranged as follows. In section 2 a brief overview of spectral stochastic finite element method is presented. The projection theory in the vector space is developed in section 3. In section 4 an error minimization approach in the Hilbert space is proposed. The idea of the reduced orthonormal vector basis is introduced in subsection section 5. The post processing of the results to obtain the response moments are discussed in section 6. Based on the theoretical results, a simple computational approach is shown in section 7 where the proposed method of reduced orthonormal basis is applied to the stochastic mechanics of an Euler-Bernoulli beam. From the theoretical developments and numerical results, some conclusions are drawn in section 8.

2 Overview of the spectral stochastic finite element method

2.1 Discretization of the stochastic PDE

First consider $a(\mathbf{r}, \theta)$ is a Gaussian random field with a covariance function $C_a : \mathbb{R}^d \times \mathbb{R}^d \to \mathbb{R}$ defined in the domain $\mathcal{D}$. Since the covariance function is square bounded, symmetric and positive definite, it can be represented by a spectral decomposition in an infinite dimensional Hilbert space. Using this spectral decomposition, the random process $a(\mathbf{r}, \theta)$ can be expressed [see for example, [4, 8]] in a generalized Fourier type of series known as the Karhunen-Loève (KL) expansion

$$a(\mathbf{r}, \theta) = a_0(\mathbf{r}) + \sum_{i=1}^{\infty} \sqrt{\nu_i}\widetilde{\xi}_i(\theta)\varphi_i(\mathbf{r}) \tag{8}$$

Here $a_0(\mathbf{r})$ is the mean function, $\widetilde{\xi}_i(\theta)$ are uncorrelated standard Gaussian random variables, ν_i and $\varphi_i(\mathbf{r})$ are eigenvalues and eigenfunctions satisfying the integral equation

$$\int_{\mathcal{D}} C_a(\mathbf{r}_1, \mathbf{r}_2)\varphi_j(\mathbf{r}_1)\mathrm{d}\mathbf{r}_1 = \nu_j\varphi_j(\mathbf{r}_2), \quad \forall\ j = 1, 2, \cdots \tag{9}$$

The Gaussian random field model is not applicable for strictly positive quantities arising in many practical problems. Eqn. (8) could also represent the Karhunen-Loève expansion of a non-Gaussian random field, which is also well defined. Alternatively, when $a(\mathbf{r},\theta)$ is a general non-Gaussian random field, it can be expressed in a mean-square convergent series in random variables and spatial functions using the polynomial chaos expansion. For example Ghanem [9] expanded log-normal random fields in a polynomial chaos expansion. In general, non Gaussian random fields can be expressed in a series like

$$a(\mathbf{r},\theta) = a_0(\mathbf{r}) + \sum_{i=1}^{\infty} \xi_i(\theta) a_i(\mathbf{r}) \tag{10}$$

using Wiener-Askey chaos expansion [10–12]. Here $\xi_i(\theta)$ are in general non-Gaussian and correlated random variables and $a_i(\mathbf{r})$ are deterministic functions. In this paper we use this general form of the decomposition of the random field.

Truncating the series in Eqn. (10) upto the M-th term and using the same approach for the governing PDE (1) with boundary conditions, the discretized system equation in the frequency domain (3) can be represented by Eqn. (5), with $M = 2p$ as

$$\left[\mathbf{A}_0 + \sum_{i=1}^{M} \xi_i(\theta)\mathbf{A}_i\right] \mathbf{u}(\theta,\omega) = \mathbf{f}_0(\omega). \tag{11}$$

The 'tilde' sign has been omitted from the notations of the frequency domain quantities of $\mathbf{u}(\theta,\omega)$ and $\mathbf{f}_0(\omega)$ for the sake of notational convenience and this shall be followed henceforth. The necessary technical details to obtain the discrete stochastic algebraic equations from the stochastic partial differential equation (1) have become standard in the literature. Excellent references, for example [4, 13–15] are available on this topic. In Eqn. (11), $\mathbf{A}_0$ is a complex symmetric positive definite matrix, $\mathbf{A}_i \in \mathbb{C}^{n\times n}; i = 1,2,\ldots,M$ are complex symmetric matrices, $\mathbf{u}(\theta,\omega) \in \mathbb{C}^n$ is the solution vector and $\mathbf{f}_0(\omega) \in \mathbb{C}^n$ is the input vector. For most practical applications, uncertainties are small compared to the deterministic values. Therefore, we normally have

$$\|\mathbf{A}_0\| \geq \left\| \sum_{i=1}^{M} \xi_i(\theta)\mathbf{A}_i \right\| ; \forall\ \theta \in \Theta \tag{12}$$

Here by $\|\bullet\|$ we imply the Frobenius matrix norm [16], defined as $\|\mathbf{A}\| = \mathrm{Trace}\left(\mathbf{A}\mathbf{A}^T\right)$ for any $\mathbf{A} \in \mathbb{R}^{n\times n}$. The number of terms M in Eqn. (11) can be selected based on the accuracy desired for the representation of the underlying random field. One of the main aim of a stochastic dynamic analysis is to obtain $\mathbf{u}(\theta,\omega)$ for $\theta \in \Theta$ and for all frequency value ω from Eqn. (11) in an efficient manner and is the main topic of this paper. We propose a solution technique for Eqn. (11) when $\xi_i(\theta)$ are in general non-Gaussian and correlated random variables.

2.2 Brief review of the solution techniques

The solution of the set of stochastic linear algebraic equations (11) is a key step in the stochastic finite element analysis. As a result, several methods have been proposed. These methods include, first- and second-order perturbation methods [5, 17], Neumann expansion method [18, 19], Galerkin approach [20], linear algebra based methods [21–23] and simulation methods [24]. More recently efficient collocation methods have been proposed [25, 26]. Another class of methods which have been used widely in the literature is known as the spectral methods (see [1] for a recent review). These methods include the polynomial chaos (PC) expansion [4], stochastic reduced basis method [27–29] and Wiener−Askey chaos expansion [10–12]. According to the polynomial chaos expansion, second-order random variables $u_j(\theta)$ can be represented by the mean-square convergent expansion

$$\begin{aligned} u_j(\theta) = {} & u_{i_0} h_0 + \sum_{i_1=1}^{\infty} u_{i_1} h_1(\xi_{i_1}(\theta)) \\ & + \sum_{i_1=1}^{\infty}\sum_{i_2=1}^{i_1} u_{i_1,i_2} h_2(\xi_{i_1}(\theta),\xi_{i_2}(\theta)) + \sum_{i_1=1}^{\infty}\sum_{i_2=1}^{i_1}\sum_{i_3=1}^{i_2} u_{i_1 i_2 i_3} h_3(\xi_{i_1}(\theta),\xi_{i_2}(\theta),\xi_{i_3}(\theta)) \\ & + \sum_{i_1=1}^{\infty}\sum_{i_2=1}^{i_1}\sum_{i_3=1}^{i_2}\sum_{i_4=1}^{i_3} u_{i_1 i_2 i_3 i_4}\, h_4(\xi_{i_1}(\theta),\xi_{i_2}(\theta),\xi_{i_3}(\theta),\xi_{i_4}(\theta)) + \ldots, \end{aligned} \tag{13}$$

where $u_{i_1,\ldots,i_r}$ are deterministic constants to be determined and $h_r(\ \xi_{i_1}(\theta),\ldots,\xi_{i_r}(\theta)\ )$ is the r^{th} order homogeneous Chaos. When $\xi_i(\theta)$ are Gaussian random variables, the functions $h_r(\xi_{i_1}(\theta),\ldots,\xi_{i_r}(\theta)\ )$ are the r^{th} order Hermite polynomial so that it becomes orthonormal with respect to the Gaussian probability density function. The same idea can be extended to non-Gaussian random variables, provided more generalized functional basis are used [10–12] so that the orthonormality with respect to the probability density functions can be retained. When we have a random vector, as in the case of the solution of Eqn. (11), then it is natural to replace the constants $u_{i_1,\ldots i_r}$ by vectors $\mathbf{u}_{i_1,\ldots i_r} \in \mathbb{R}^n$. Suppose the series is truncated after P number of terms. The value of P depends on the number of basic random variables M and the order of the PC expansion r as

$$P = \sum_{j=0}^{r} \frac{(M+j-1)!}{j!(M-1)!} = \binom{M+r}{r} \tag{14}$$

After the truncation, there are P number of unknown vectors of dimension n. Then a mean-square error minimization approach can be applied and the unknown vectors can be solved using the Galerkin approach [4]. Since P increases very rapidly with the order of the chaos r and the number of random variables M, the final number of unknown constants Pn becomes very large. As a result several methods have been developed (see for example [27–31]) to reduce the computational cost. In the polynomial chaos based solution approach, the *only* information used to construct the basis is the probability density function of the random variables. In the context of the discretized Eqn. (11), more information such as the matrices $\mathbf{A}_i, i = 0, 1, 2 \ldots M$ are available. It may be possible to construct alternative basis using these matrices. Here we investigate such an approach, where instead of projecting the solution in the space of orthonormal polynomials, the solution is projected in an orthonormal vector basis generated from the coefficient matrices.

3 Spectral decomposition in the vector space

3.1 Derivation of the spectral functions

Following the spectral stochastic finite element method, or otherwise, an approximation to the solution of Eqn. (11) can be expressed as a linear combination of functions of random variables and deterministic vectors. Recently Nouy [32, 33] discussed the possibility of an optimal spectral decomposition. The aim is to use small number of terms to reduce the computation without loosing the accuracy. Here an orthonormal vector basis is considered. Fixing a value of θ, say $\theta = \theta_1$, the solution of Eqn. (11) $\mathbf{u}(\theta_1)$ can be expanded in a complete basis as $\mathbf{u}(\theta_1) = \alpha_1^{(1)}\boldsymbol{\phi}_1 + \alpha_2^{(1)}\boldsymbol{\phi}_2 + \dots \alpha_n^{(1)}\boldsymbol{\phi}_n$. Repeating this for $\theta_1, \theta_2, \dots$ eventually the whole sample-space can be covered and it would be possible to expand $\mathbf{u}(\theta), \forall\theta \in \Theta$ as a linear combination of $\boldsymbol{\phi}_1, \boldsymbol{\phi}_2, \dots, \boldsymbol{\phi}_n$.

We use the eigenvectors $\boldsymbol{\phi}_k \in \mathbb{R}^n$ of the generalized eigenvalue problem

$$\mathbf{K}_0\boldsymbol{\phi}_k = \lambda_k \mathbf{M}_0 \boldsymbol{\phi}_k; \quad k = 1, 2, \dots n \tag{15}$$

Since the matrices $\mathbf{K}_0$ and $\mathbf{M}_0$ are symmetric and generally non-negative definite, the eigenvectors $\boldsymbol{\phi}_k$ for $k = 1, 2, \dots n$ form a complete basis. Note that in principle any complete basis can be used. This choice is selected due to the analytical simplicity as will be seen later. For notational convenience, define the matrix of eigenvalues and eigenvectors

$$\boldsymbol{\lambda}_0 = \operatorname{diag}[\lambda_1, \lambda_2, \dots, \lambda_n] \in \mathbb{R}^{n\times n} \quad \text{and} \quad \boldsymbol{\Phi} = [\boldsymbol{\phi}_1, \boldsymbol{\phi}_2, \dots, \boldsymbol{\phi}_n] \in \mathbb{R}^{n\times n} \tag{16}$$

Eigenvalues are ordered in the ascending order so that $\lambda_1 < \lambda_2 < \dots < \lambda_n$. We use the orthogonality property of the modal matrix $\boldsymbol{\Phi}$ as

$$\boldsymbol{\Phi}^T\mathbf{K}_0\boldsymbol{\Phi} = \boldsymbol{\lambda}_0, \quad \text{and} \quad \boldsymbol{\Phi}^T\mathbf{M}_0\boldsymbol{\Phi} = \mathbf{I} \tag{17}$$

Using these we have

$$\begin{aligned}\boldsymbol{\Phi}^T\mathbf{A}_0\boldsymbol{\Phi} &= \boldsymbol{\Phi}^T\left([-\omega^2 + i\omega\zeta_1]\mathbf{M}_0 + [i\omega\zeta_2 + 1]\mathbf{K}_0\right)\boldsymbol{\Phi}\\ &= \left(-\omega^2 + i\omega\zeta_1\right)\mathbf{I} + \left(i\omega\zeta_2 + 1\right)\boldsymbol{\lambda}_0\end{aligned} \tag{18}$$

$$\text{which gives,} \quad \boldsymbol{\Phi}^T\mathbf{A}_0\boldsymbol{\Phi} = \boldsymbol{\Lambda}_0 \quad \text{and} \quad \mathbf{A}_0 = \boldsymbol{\Phi}^{-T}\boldsymbol{\Lambda}_0\boldsymbol{\Phi}^{-1} \tag{19}$$

where $\boldsymbol{\Lambda}_0 = \left(-\omega^2 + i\omega\zeta_1\right)\mathbf{I} + \left(i\omega\zeta_2 + 1\right)\boldsymbol{\lambda}_0$ and $\mathbf{I}$ is the identity matrix. Hence, $\boldsymbol{\Lambda}_0$ can also be written as

$$\boldsymbol{\Lambda}_0 = \operatorname{diag}[\lambda_{0_1}, \lambda_{0_2}, \dots, \lambda_{0_n}] \in \mathbb{C}^{n\times n} \tag{20}$$

where $\lambda_{0_j} = \left(-\omega^2 + i\omega\zeta_1\right) + \left(i\omega\zeta_2 + 1\right)\lambda_j$ and λ_j is as defined in Eqn. (16). We also introduce the transformations

$$\widetilde{\mathbf{A}}_i = \boldsymbol{\Phi}^T\mathbf{A}_i\boldsymbol{\Phi} \in \mathbb{C}^{n\times n}; i = 0, 1, 2, \dots, M. \tag{21}$$

Note that $\widetilde{\mathbf{A}}_0 = \boldsymbol{\Lambda}_0$ is a diagonal matrix and

$$\mathbf{A}_i = \boldsymbol{\Phi}^{-T}\widetilde{\mathbf{A}}_i\boldsymbol{\Phi}^{-1} \in \mathbb{C}^{n\times n}; i = 1, 2, \dots, M. \tag{22}$$

Suppose the solution of Eqn. (11) is given by

$$\hat{\mathbf{u}}(\omega,\theta) = \left[\mathbf{A}_0(\omega) + \sum_{i=1}^{M}\xi_i(\theta)\mathbf{A}_i(\omega)\right]^{-1}\mathbf{f}_0(\omega) \tag{23}$$

Using Eqs. (16)–(22) and the orthonormality of $\boldsymbol{\Phi}$ one has

$$\hat{\mathbf{u}}(\omega,\theta) = \left[\boldsymbol{\Phi}^{-T}\boldsymbol{\Lambda}_0(\omega)\boldsymbol{\Phi}^{-1} + \sum_{i=1}^{M}\xi_i(\theta)\boldsymbol{\Phi}^{-T}\widetilde{\mathbf{A}}_i\boldsymbol{\Phi}^{-1}\right]^{-1}\mathbf{f}_0(\omega) = \boldsymbol{\Phi}\boldsymbol{\Psi}\left(\omega, \boldsymbol{\xi}(\theta)\right)\boldsymbol{\Phi}^T\mathbf{f}_0(\omega) \tag{24}$$

where

$$\boldsymbol{\Psi}\left(\omega, \boldsymbol{\xi}(\theta)\right) = \left[\boldsymbol{\Lambda}_0(\omega) + \sum_{i=1}^{M}\xi_i(\theta)\widetilde{\mathbf{A}}_i(\omega)\right]^{-1} \tag{25}$$

and the M-dimensional random vector

$$\boldsymbol{\xi}(\theta) = \{\xi_1(\theta), \xi_2(\theta), \ldots, \xi_M(\theta)\}^T \tag{26}$$

Now we separate the diagonal and off-diagonal terms of the $\widetilde{\mathbf{A}}_i$ matrices as

$$\widetilde{\mathbf{A}}_i = \boldsymbol{\Lambda}_i + \boldsymbol{\Delta}_i, \quad i = 1, 2, \ldots, M \tag{27}$$

Here the diagonal matrix

$$\boldsymbol{\Lambda}_i = \operatorname{diag}\left[\widetilde{\mathbf{A}}_i\right] = \operatorname{diag}\left[\lambda_{i_1}, \lambda_{i_2}, \ldots, \lambda_{i_n}\right] \in \mathbb{C}^{n\times n} \tag{28}$$

and the matrix containing only the off-diagonal elements $\boldsymbol{\Delta}_i = \widetilde{\mathbf{A}}_i - \boldsymbol{\Lambda}_i$ is such that $\mathrm{Trace}\left(\boldsymbol{\Delta}_i\right) = 0$. Using these, from Eqn. (25) one has

$$\boldsymbol{\Psi}\left(\omega, \boldsymbol{\xi}(\theta)\right) = \left[\underbrace{\boldsymbol{\Lambda}_0(\omega) + \sum_{i=1}^{M} \xi_i(\theta)\boldsymbol{\Lambda}_i(\omega)}_{\boldsymbol{\Lambda}(\omega, \boldsymbol{\xi}(\theta))} + \underbrace{\sum_{i=1}^{M} \xi_i(\theta)\boldsymbol{\Delta}_i(\omega)}_{\boldsymbol{\Delta}(\omega, \boldsymbol{\xi}(\theta))}\right]^{-1} \tag{29}$$

where $\boldsymbol{\Lambda}\left(\omega, \boldsymbol{\xi}(\theta)\right) \in \mathbb{C}^{n\times n}$ is a diagonal matrix and $\boldsymbol{\Delta}\left(\omega, \boldsymbol{\xi}(\theta)\right)$ is an off-diagonal only matrix. In the subsequent expressions we choose to omit the inclusion of frequency dependence of the individual matrices for the sake of notational simplicity, so that $\boldsymbol{\Psi}\left(\omega, \boldsymbol{\xi}(\theta)\right) \equiv \boldsymbol{\Psi}\left(\boldsymbol{\xi}(\theta)\right)$ and so on. Hence, we rewrite Eqn. (29) as

$$\boldsymbol{\Psi}\left(\boldsymbol{\xi}(\theta)\right) = \left[\boldsymbol{\Lambda}\left(\boldsymbol{\xi}(\theta)\right)\left[\mathbf{I}_n + \boldsymbol{\Lambda}^{-1}\left(\boldsymbol{\xi}(\theta)\right)\boldsymbol{\Delta}\left(\boldsymbol{\xi}(\theta)\right)\right]\right]^{-1} \tag{30}$$

The above expression can be represented using a Neumann type of matrix series [18] as

$$\boldsymbol{\Psi}\left(\boldsymbol{\xi}(\theta)\right) = \sum_{s=0}^{\infty}(-1)^s\left[\boldsymbol{\Lambda}^{-1}\left(\boldsymbol{\xi}(\theta)\right)\boldsymbol{\Delta}\left(\boldsymbol{\xi}(\theta)\right)\right]^s\boldsymbol{\Lambda}^{-1}\left(\boldsymbol{\xi}(\theta)\right) \tag{31}$$

Taking an arbitrary r-th element of $\hat{\mathbf{u}}(\theta)$, Eqn. (24) can be rearranged to have

$$\hat{u}_r(\theta) = \sum_{k=1}^{n} \Phi_{rk}\left(\sum_{j=1}^{n} \Psi_{kj}\left(\boldsymbol{\xi}(\theta)\right)\left(\boldsymbol{\phi}_j^T\mathbf{f}_0\right)\right) \tag{32}$$

Defining

$$\Gamma_k\left(\boldsymbol{\xi}(\theta)\right) = \sum_{j=1}^{n} \Psi_{kj}\left(\boldsymbol{\xi}(\theta)\right)\left(\boldsymbol{\phi}_j^T\mathbf{f}_0\right) \tag{33}$$

and collecting all the elements in Eqn. (32) for $r = 1, 2, \ldots, n$ one has

$$\hat{\mathbf{u}}(\theta) = \sum_{k=1}^{n} \Gamma_k\left(\boldsymbol{\xi}(\theta)\right)\boldsymbol{\phi}_k \tag{34}$$

This shows that the solution vector $\hat{\mathbf{u}}(\theta)$ can be projected in the space spanned by $\boldsymbol{\phi}_k$.

Now assume the series in Eqn. (31) is truncated after m-th term. We define the truncated function

$$\mathbf{\Psi}^{(m)}\left(\boldsymbol{\xi}(\theta)\right)=\sum_{s=0}^{m}(-1)^s\left[\mathbf{\Lambda}^{-1}\left(\boldsymbol{\xi}(\theta)\right)\mathbf{\Delta}\left(\boldsymbol{\xi}(\theta)\right)\right]^s\mathbf{\Lambda}^{-1}\left(\boldsymbol{\xi}(\theta)\right) \tag{35}$$

From this one can obtain a sequence for different m

$$\hat{\mathbf{u}}^{(m)}(\theta)=\sum_{k=1}^{n}\Gamma_k^{(m)}\left(\boldsymbol{\xi}(\theta)\right)\boldsymbol{\phi}_k;\quad m=1,2,3,\ldots \tag{36}$$

Since $\theta\in\Theta$ is arbitrary, comparing (11) and (23) we observe that $\hat{\mathbf{u}}^{(m)}(\theta)$ is the solution of Eqn. (11) for every θ when $m\to\infty$. This implies that

$$\mathrm{Prob}\left\{\theta\in\Theta:\lim_{m\to\infty}\hat{\mathbf{u}}^{(m)}(\theta)=\hat{\mathbf{u}}(\theta)\right\}=1 \tag{37}$$

Therefore, $\hat{\mathbf{u}}(\theta)$ is the solution of Eqn. (11) in probability. In this derivation, the probability density function of the random variables has not been used. Therefore, the random variables can be general as long as the solution exists.

Remark 1. The matrix power series in (31) is different from the classical Neumann series [18]. The classical Neumann series is a power series in $\mathbf{A}_0^{-1}\left[\mathbf{\Delta A}\left(\boldsymbol{\xi}(\theta)\right)\right]$, where the first term is deterministic and the second term is random. The elements of this matrix series are polynomials in $\xi_i(\theta)$. In contrast, the series in (31) is in terms of $[\mathbf{\Lambda}^{-1}\left(\boldsymbol{\xi}(\theta)\right)][\mathbf{\Delta}\left(\boldsymbol{\xi}(\theta)\right)]$, where both terms are random. The elements of this matrix series are not simple polynomials in $\xi_i(\theta)$, but are in terms of a ratio of polynomials as seen in Eqn. (39). The convergence of this series depends of the spectral radius of

$$\mathbf{R}=\mathbf{\Lambda}^{-1}\left(\boldsymbol{\xi}(\theta)\right)\mathbf{\Delta}\left(\boldsymbol{\xi}(\theta)\right) \tag{38}$$

A generic term of this matrix can be obtained as

$$R_{rs}=\frac{\Delta_{rs}}{\Lambda_{rr}}=\frac{\sum_{i=1}^{M}\xi_i(\theta)\Delta_{i_{rs}}}{\lambda_{0_r}+\sum_{i=1}^{M}\xi_i(\theta)\lambda_{i_r}}=\frac{\sum_{i=1}^{M}\xi_i(\theta)\widetilde{A}_{i_{rs}}}{\lambda_{0_r}+\sum_{i=1}^{M}\xi_i(\theta)\widetilde{A}_{i_{rr}}};r\neq s \tag{39}$$

Since $\mathbf{A}_0$ is positive definite, $\lambda_{0_r}>0$ for all r. It can be seen from Eqn. (39) that the spectral radius of $\mathbf{R}$ is also controlled by the diagonal dominance of the $\widetilde{\mathbf{A}}_i$ matrices. If the diagonal terms are relatively larger than the off-diagonal terms, the series will converge faster even if the relative magnitude of λ_{0_r} is not large.

The series in (36) approaches to the exact solution of the governing Eqn. (11) for every $\theta\in\Theta$ for $m\to\infty$. For this reason it converges in probability 1. The convergence in probability 1 is a stronger convergence than, for example, the mean-square convergence often used in the stochastic finite element analysis. Since the convergence in probability 1 automatically implies the mean-square convergence, the series in Eqn. (34) is also a mean-square convergent series.

Definition 1. The functions $\Gamma_k\left(\boldsymbol{\xi}(\theta)\right),k=1,2,\ldots n$ are called the spectral functions as they are expressed in terms of the spectral properties of the coefficient matrix $\mathbf{K}_0$ and $\mathbf{M}_0$ arising in the discretized equation.

For certain class of problems the series in Eqn. (34) can give useful physical insights into the uncertainty propagation. For structural mechanics problems, the eigenvectors $\boldsymbol{\phi}_k$ are vibrational modes [34]. Eqn. (34) says that the response of a stochastic system is a linear combination of fundamental vibrational modes weighted by the random variables Γ_k.

3.2 Properties of the spectral functions

In this section we discuss some important properties of these functions. From the series expansion in Eqn. (31) we have

$$\begin{aligned}\boldsymbol{\Psi}\left(\boldsymbol{\xi}(\theta)\right) = \boldsymbol{\Lambda}^{-1}\left(\boldsymbol{\xi}(\theta)\right) - \boldsymbol{\Lambda}^{-1}\left(\boldsymbol{\xi}(\theta)\right)\boldsymbol{\Delta}\left(\boldsymbol{\xi}(\theta)\right)\boldsymbol{\Lambda}^{-1}\left(\boldsymbol{\xi}(\theta)\right) \\ + \boldsymbol{\Lambda}^{-1}\left(\boldsymbol{\xi}(\theta)\right)\boldsymbol{\Delta}\left(\boldsymbol{\xi}(\theta)\right)\boldsymbol{\Lambda}^{-1}\left(\boldsymbol{\xi}(\theta)\right)\boldsymbol{\Delta}\left(\boldsymbol{\xi}(\theta)\right)\boldsymbol{\Lambda}^{-1}\left(\boldsymbol{\xi}(\theta)\right) + \ldots \end{aligned} \tag{40}$$

Since $\boldsymbol{\Lambda}\left(\boldsymbol{\xi}(\theta)\right)$ is a diagonal matrix, its inverse is simply a diagonal matrix containing the inverse of each of the diagonal elements. Also recall that the diagonal of $\boldsymbol{\Delta}\left(\boldsymbol{\xi}(\theta)\right)$ contains only zeros. Different terms of the series in (40) can be obtained using a simple recursive relationship [18]. The numerical computation of the series is therefore computationally very efficient. For further analytical results, truncating the series upto different terms, we define spectral functions of different order.

Definition 2. The first-order spectral functions $\Gamma_k^{(1)}(\boldsymbol{\xi}(\theta)), k = 1, 2, \ldots, n$ are obtained by retaining one term in the series (40).

Retaining one term in (40) we have

$$\boldsymbol{\Psi}^{(1)}\left(\boldsymbol{\xi}(\theta)\right) = \boldsymbol{\Lambda}^{-1}\left(\boldsymbol{\xi}(\theta)\right) \quad \text{or} \quad \Psi_{kj}^{(1)}\left(\boldsymbol{\xi}(\theta)\right) = \frac{\delta_{kj}}{\lambda_{0_k} + \sum_{i=1}^{M}\xi_i(\theta)\lambda_{i_k}} \tag{41}$$

Using the definition of the spectral function in Eqn. (33), the first-order spectral functions can be explicitly obtained as

$$\Gamma_k^{(1)}\left(\boldsymbol{\xi}(\theta)\right) = \sum_{j=1}^{n}\Psi_{kj}^{(1)}\left(\boldsymbol{\xi}(\theta)\right)\left(\boldsymbol{\phi}_j^T\mathbf{f}_0\right) = \frac{\boldsymbol{\phi}_k^T\mathbf{f}_0}{\lambda_{0_k} + \sum_{i=1}^{M}\xi_i(\theta)\lambda_{i_k}} \tag{42}$$

From this expression it is clear that $\Gamma_k^{(1)}\left(\boldsymbol{\xi}(\theta)\right)$ are correlated non-Gaussian random variables. Since we assumed that all eigenvalues λ_{0_k} are distinct, every $\Gamma_k^{(1)}\left(\boldsymbol{\xi}(\theta)\right)$ in Eqn. (42) are different for different values of k.

Definition 3. The second-order spectral functions $\Gamma_k^{(2)}(\boldsymbol{\xi}(\theta)), k = 1, 2, \ldots, n$ are obtained by retaining two terms in the series (40).

Retaining two terms in (40) we have

$$\boldsymbol{\Psi}^{(2)}\left(\boldsymbol{\xi}(\theta)\right) = \boldsymbol{\Lambda}^{-1}\left(\boldsymbol{\xi}(\theta)\right) - \boldsymbol{\Lambda}^{-1}\left(\boldsymbol{\xi}(\theta)\right)\boldsymbol{\Delta}\left(\boldsymbol{\xi}(\theta)\right)\boldsymbol{\Lambda}^{-1}\left(\boldsymbol{\xi}(\theta)\right) \tag{43}$$

$$\text{or} \quad \Psi_{kj}^{(2)}\left(\boldsymbol{\xi}(\theta)\right) = \frac{\delta_{kj}}{\lambda_{0_k} + \sum_{i=1}^{M}\xi_i(\theta)\lambda_{i_k}} - \frac{\sum_{i=1}^{M}\xi_i(\theta)\Delta_{i_{kj}}}{\left(\lambda_{0_k} + \sum_{i=1}^{M}\xi_i(\theta)\lambda_{i_k}\right)\left(\lambda_{0_j} + \sum_{i=1}^{M}\xi_i(\theta)\lambda_{i_j}\right)} \tag{44}$$

Using the definition of the spectral function in Eqn. (33), the second-order spectral functions can be obtained in closed-form as

$$\Gamma_k^{(2)}\left(\boldsymbol{\xi}(\theta)\right) = \frac{\boldsymbol{\phi}_k^T\mathbf{f}_0}{\lambda_{0_k} + \sum_{i=1}^{M}\xi_i(\theta)\lambda_{i_k}} - \sum_{\substack{j=1\\ j\neq k}}^{n}\frac{\left(\boldsymbol{\phi}_j^T\mathbf{f}_0\right)\sum_{i=1}^{M}\xi_i(\theta)\Delta_{i_{kj}}}{\left(\lambda_{0_k} + \sum_{i=1}^{M}\xi_i(\theta)\lambda_{i_k}\right)\left(\lambda_{0_j} + \sum_{i=1}^{M}\xi_i(\theta)\lambda_{i_j}\right)} \tag{45}$$

The second-order function can be viewed as adding corrections to the first-order expression derived in Eqn. (42).

Definition 4. The vector of spectral functions of order s can be obtained by retaining s terms in the series (40) and can be expressed as

$$\mathbf{\Gamma}^{(s)}(\boldsymbol{\xi}(\theta)) = \left[\mathbf{I}_n - \mathbf{R}(\boldsymbol{\xi}(\theta)) + \mathbf{R}(\boldsymbol{\xi}(\theta))^2 - \mathbf{R}(\boldsymbol{\xi}(\theta))^3 \ldots s^{\text{th term}}\right] \mathbf{\Gamma}^{(1)}(\boldsymbol{\xi}(\theta)) \tag{46}$$

where $\mathbf{I}_n$ is the n-dimensional identity matrix and $\mathbf{R}$ is defined in Eqn. (38) as $\mathbf{R}(\boldsymbol{\xi}(\theta)) = [\mathbf{\Lambda}^{-1}(\boldsymbol{\xi}(\theta))][\mathbf{\Delta}(\boldsymbol{\xi}(\theta))]$. Different terms of this series can be obtained recursively from the previous term [18].

4 Error minimization using the Galerkin approach

In subsection 3.1 we derived the spectral functions such that a projection in an orthonormal basis converges to the exact solution in probability 1. The spectral functions are expressed in terms of a convergent infinite series. First, second and higher order spectral functions obtained by truncating the infinite series have been derived. We have also showed that they have the same functional form as the exact solution of Eqn. (11). This motivates us to use these functions as 'trial functions' to construct the solution. The idea is to minimize the error arising due to the truncation. A Galerkin approach is proposed where the error is made orthogonal to the spectral functions.

We express the solution vector by the series representation

$$\hat{\mathbf{u}}(\theta) = \sum_{k=1}^{n} c_k \widehat{\Gamma}_k(\boldsymbol{\xi}(\theta))\boldsymbol{\phi}_k \tag{47}$$

Here the functions $\widehat{\Gamma}_k : \mathbb{C}^M \to \mathbb{C}$ are the spectral functions and the constants $c_k \in \mathbb{C}$ need to be obtained using the Galerkin approach. The functions $\widehat{\Gamma}_k(\boldsymbol{\xi}(\theta))$ can be the first-order (42), second-order (45) or any higher-order spectral functions (46) and $\boldsymbol{\phi}_k$ are the eigenvectors introduced earlier in Eqn. (15). Substituting the expansion of $\hat{\mathbf{u}}(\theta)$ in the governing equation (11), the error vector can be obtained as

$$\boldsymbol{\varepsilon}(\theta) = \left(\sum_{i=0}^{M} \mathbf{A}_i \xi_i(\theta)\right)\left(\sum_{k=1}^{n} c_k \widehat{\Gamma}_k(\boldsymbol{\xi}(\theta))\boldsymbol{\phi}_k\right) - \mathbf{f}_0 \in \mathbb{C}^n \tag{48}$$

where $\xi_0 = 1$ is used to simplify the first summation expression. The expression (47) is viewed as a projection where $\left\{\widehat{\Gamma}_k(\boldsymbol{\xi}(\theta))\boldsymbol{\phi}_k\right\} \in \mathbb{C}^n$ are the basis functions and c_k are the unknown constants to be determined. We wish to obtain the coefficients c_k using the Galerkin approach so that the error is made orthogonal to the basis functions, that is, mathematically

$$\boldsymbol{\varepsilon}(\theta) \perp \left(\widehat{\Gamma}_j(\boldsymbol{\xi}(\theta))\boldsymbol{\phi}_j\right) \quad \text{or} \quad \left\langle \widehat{\Gamma}_j(\boldsymbol{\xi}(\theta))\boldsymbol{\phi}_j, \boldsymbol{\varepsilon}(\theta)\right\rangle = 0 \quad \forall\, j = 1, 2, \ldots, n \tag{49}$$

Here $\langle \mathbf{u}(\theta), \mathbf{v}(\theta)\rangle = \int_\Theta P(\mathrm{d}\theta)\mathbf{u}(\theta)\mathbf{v}(\theta)$ defines the inner product norm. Imposing this condition and using the expression of $\boldsymbol{\varepsilon}(\theta)$ from Eqn. (48) one has

$$\mathrm{E}\left[\left(\widehat{\Gamma}_j(\boldsymbol{\xi}(\theta))\boldsymbol{\phi}_j\right)^T \left(\sum_{i=0}^{M} \mathbf{A}_i \xi_i(\theta)\right)\left(\sum_{k=1}^{n} c_k \widehat{\Gamma}_k(\boldsymbol{\xi}(\theta))\boldsymbol{\phi}_k\right) - \left(\widehat{\Gamma}_j(\boldsymbol{\xi}(\theta))\boldsymbol{\phi}_j\right)^T \mathbf{f}_0\right] = 0 \;\forall\, j \tag{50}$$

Interchanging the $\mathrm{E}\left[\bullet\right]$ and summation operations, this can be simplified to

$$\sum_{k=1}^{n}\left(\sum_{i=0}^{M}\left(\boldsymbol{\phi}_j^T\mathbf{A}_i\boldsymbol{\phi}_k\right)\mathrm{E}\left[\xi_i(\theta)\widehat{\Gamma}_j^T(\boldsymbol{\xi}(\theta))\widehat{\Gamma}_k(\boldsymbol{\xi}(\theta))\right]\right)c_k=\mathrm{E}\left[\widehat{\Gamma}_j^T(\boldsymbol{\xi}(\theta))\right]\left(\boldsymbol{\phi}_j^T\mathbf{f}_0\right)\quad(51)$$

$$\text{or}\quad\sum_{k=1}^{n}\left(\sum_{i=0}^{M}\widetilde{A}_{i_{jk}}D_{ijk}\right)c_k=b_j\quad(52)$$

Defining the vector $\mathbf{c}=\{c_1,c_2,\ldots,c_n\}^T$, these equations can be expressed in a matrix form as

$$\mathbf{S}\,\mathbf{c}=\mathbf{b}\quad(53)$$

with

$$S_{jk}=\sum_{i=0}^{M}\widetilde{A}_{i_{jk}}D_{ijk};\quad\forall\ j,k=1,2,\ldots,n\quad(54)$$

where

$$\widetilde{A}_{i_{jk}}=\boldsymbol{\phi}_j^T\mathbf{A}_i\boldsymbol{\phi}_k,\quad(55)$$

$$D_{ijk}=\mathrm{E}\left[\xi_i(\theta)\widehat{\Gamma}_j^T(\boldsymbol{\xi}(\theta))\widehat{\Gamma}_k(\boldsymbol{\xi}(\theta))\right]\quad(56)$$

$$\text{and}\quad b_j=\mathrm{E}\left[\widehat{\Gamma}_j^T(\boldsymbol{\xi}(\theta))\right]\left(\boldsymbol{\phi}_j^T\mathbf{f}_0\right).\quad(57)$$

Higher order spectral functions can be used to improve the accuracy and convergence of the series (47). This will be demonstrated in the numerical examples later in the paper.

Remark 2. (Comparison with the classical spectral SFEM) We compare this Galerkin approach with the classical spectral stochastic finite element approach for further insight. The number of equations to be solved for the unknown coefficients in Eqn. (53) is n, the same dimension as the original governing equation (11). There are only n unknown constants, as opposed to nP unknown constants arising in the polynomial chaos expansion. The coefficient matrix **S** and the vector **b** in Eqn. (53) should be obtained numerically using the Monte Carlo simulation or other numerical integration technique. In the classical PC expansion, however, the coefficient matrix and the associated vector are obtained exactly in closed-form. In addition, the coefficient matrix is a sparse matrix whereas the matrix **S** in Eqn. (53) is in general a fully populated matrix.

It can be observed that the matrix **S** in Eqn. (53) is symmetric. Therefore, one need to determine $n(n+1)/2$ number of coefficients by numerical methods. Any numerical integration method, such as the Gaussian quadrature method, can be used to obtain the elements of D_{ijk} and b_j in Eqn. (55). In this paper Monte Carlo simulation is used. The samples of the spectral functions $\widehat{\Gamma}_k(\boldsymbol{\xi}(\theta))$ can be simulated from Eqn. (42), (45) or (46) depending on the order. These can be used to compute D_{ijk} and b_j from Eqn. (55). The simulated spectral functions can also be 'recycled' to obtain the statistics and probability density function (pdf) of the solution. In summary, compared to the classical spectral stochastic finite element method, the proposed Galerkin approach results in a smaller size matrix but requires numerical integration techniques to obtain its entries. The numerical method proposed here therefore can be considered as a hybrid analytical-simulation approach.

5 Model reduction using a reduced number of basis

The Galerkin approach proposed in the previous section requires the solution of $n \times n$ algebraic equations. Although in general this is smaller compared to the polynomial chaos approach, the computational cost can still be high for large n as the coefficient matrix is in general a dense matrix. The aim of this section is to reduce it further so that, in addition to large number of random variables, problems with large degrees of freedom can also be solved efficiently.

Suppose the eigenvalues of $\mathbf{A}_0$ are arranged in an increasing order such that

$$\lambda_{0_1} < \lambda_{0_2} < \ldots < \lambda_{0_n} \tag{58}$$

From the expression of the spectral functions observe that the eigenvalues appear in the denominator:

$$\Gamma_k^{(1)}\left(\boldsymbol{\xi}(\theta)\right) = \frac{\boldsymbol{\phi}_k^T \mathbf{f}_0}{\lambda_{0_k} + \sum_{i=1}^{M} \xi_i(\theta) \lambda_{i_k}} \tag{59}$$

The numerator $(\boldsymbol{\phi}_k^T \mathbf{f}_0)$ is the projection of the force on the deformation mode. Since the eigenvalues are arranged in an increasing order, the denominator of $|\Gamma_{k+r}^{(1)}\left(\boldsymbol{\xi}(\theta)\right)|$ is larger than the denominator of $|\Gamma_k^{(1)}\left(\boldsymbol{\xi}(\theta)\right)|$ according a suitable measure. The numerator $(\boldsymbol{\phi}_k^T \mathbf{f}_0)$ depends on the nature of forcing and the eigenvectors. Although this quantity is deterministic, in general an ordering cannot be easily established for different values of k. Because all the eigenvectors are normalized to unity, it is reasonable to consider that $(\boldsymbol{\phi}_k^T \mathbf{f}_0)$ does not vary significantly for different values of k. Using the ordering of the eigenvalues, one can select a small number ϵ such that $\lambda_1/\lambda_q < \epsilon$ for some value of q, where λ_j is the eigenvalue of the generalized eigenvalue problem defined in Eqn. (15). Based on this, we can approximate the solution using a truncated series as

$$\hat{\mathbf{u}}(\theta) \approx \sum_{k=1}^{q} c_k \widehat{\Gamma}_k(\boldsymbol{\xi}(\theta)) \boldsymbol{\phi}_k \tag{60}$$

where c_k, $\widehat{\Gamma}_k(\boldsymbol{\xi}(\theta))$ and $\boldsymbol{\phi}_k$ are obtained following the procedure described in the previous section by letting the indices j, k only upto q in Eqs. (54) and (55). The accuracy of the series (60) can be improved in two ways, namely, (a) by increasing the number of terms q, or (b) by increasing the order of the spectral functions $\widehat{\Gamma}_k(\boldsymbol{\xi}(\theta))$.

Model reduction techniques have been widely used within the scope of proper orthogonal decomposition (POD) method [35–37]. Here the eigenvalues of a symmetric positive definite matrix (the covariance matrix of a snapshot the system response) are used for model reduction. In spite of this similarity, the reduction method proposed here is different from a POD since it only considers the operator and not the solution itself. Reduction based on eigen-solution is of classical nature in various areas of applied mathematics, engineering and physics and extensive studies exist on this topic. It should be noted that the truncation in series (60) introduces errors. A rigorous mathematical quantification of error arising due to this truncation is beyond the scope of this article. The ratio of the eigenvalues λ_1/λ_q gives a good indication, but the projection of the force on the eigenvector $(\boldsymbol{\phi}_k^T \mathbf{f}_0)$ is also of importance. Since this quantity is problem dependent, care should be taken while applying this reduction method.

6 Post processing: Moments of the solution

For the practical application of the method developed here, the efficient computation of the response moments and pdf is of crucial importance. A simulation based algorithm is proposed in this section. The coefficients c_k in Eqn. (51) can be calculated from a reduced set of equations given by (53). The reduced equations can be obtained by letting the indices j, k upto $q < n$ in Eqns. (54) and (55). After obtaining the coefficient vector $\mathbf{c} \in \mathbb{C}^q$, the statistical moments of the solution can be obtained from Eqns. (61) and (62) using the Monte Carlo simulation. The spectral functions used to obtain the vector **c** itself, can be reused to obtain the statistics and pdf of the solution. The mean vector can be obtained as

$$\bar{\mathbf{u}} = \mathrm{E}\left[|\hat{\mathbf{u}}(\theta)|\right] = \sum_{k=1}^{q} |c_k| \mathrm{E}\left[\left|\widehat{\Gamma}_k(\boldsymbol{\xi}(\theta))\right|\right] \boldsymbol{\phi}_k \tag{61}$$

where $|\bullet|$ is the absolute value of the complex quantities. The covariance of the solution vector can be expressed as

$$\boldsymbol{\Sigma}_u = \mathrm{E}\left[\left(|\hat{\mathbf{u}}(\theta)| - \bar{\mathbf{u}}\right)\left(|\hat{\mathbf{u}}(\theta)| - \bar{\mathbf{u}}\right)\right] = \sum_{k=1}^{q} \sum_{j=1}^{q} |c_k c_j| \, \Sigma_{\Gamma_{kj}} \boldsymbol{\phi}_k \boldsymbol{\phi}_j \tag{62}$$

where the elements of the covariance matrix of the spectral functions are given by

$$\Sigma_{\Gamma_{kj}} = \mathrm{E}\left[\left(\left|\widehat{\Gamma}_k(\boldsymbol{\xi}(\theta))\right| - \mathrm{E}\left[\left|\widehat{\Gamma}_k(\boldsymbol{\xi}(\theta))\right|\right]\right)\left(\left|\widehat{\Gamma}_k(\boldsymbol{\xi}(\theta))\right| - \mathrm{E}\left[\left|\widehat{\Gamma}_k(\boldsymbol{\xi}(\theta))\right|\right]\right)\right] \tag{63}$$

Based on the results derived in the paper, a hybrid reduced simulation-analytical approach can thus be realized in practice. The method is applicable to general structural dynamics problems with general non-Gaussian random fields. In the following section this approach has been applied to a physical problem.

7 Illustrative application: The stochastic dynamics of an Euler-Bernoulli beam

In this section we apply the computational method to a cantilever beam with stochastic bending modulus. Fig. (1) shows the configuration of the cantilever beam with a harmonic point load at its free end. We assume that the bending modulus is a homogeneous stationary Gaussian random field of the form

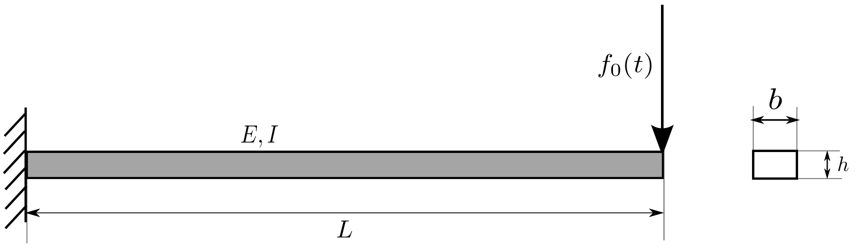

Figure 1: Schematic diagram of the Euler-Bernoulli beam with a point load at the free end.

$$EI(x, \theta) = EI_0(1 + a(x, \theta)) \tag{64}$$

where x is the coordinate along the length of the beam, EI_0 is the estimate of the mean bending modulus, $a(x, \theta)$ is a zero mean stationary Gaussian random field. The autocorrelation function of this random field is assumed to be

$$C_a(x_1, x_2) = \sigma_a^2 e^{-(|x_1 - x_2|)/\mu_a} \tag{65}$$

where μ_a is the correlation length and σ_a is the standard deviation. We use the base-line parameters as the length $L = 1m$, cross-section $(b \times h)$ $39 \times 5.93mm^2$ and Young's modulus $E = 2 \times 10^{11}$ Pa. In study we consider deflection of the tip of the beam under harmonic loads of amplitude $\tilde{f}_0 = 1.0N$. The correlation length considered in this numerical study is $\mu_a = L/2$. The number of terms retained (M) in the Karhunen-Loève expansion (8) is selected such that $\nu_M/\nu_1 = 0.01$ in order to retain 90% of the variability. For this correlation length the number of terms M comes to 18. For the finite element discretization, the beam is divided into 40 elements. Standard four degrees of freedom Euler-Bernoulli beam model is used [38]. After applying the fixed boundary condition at one edge, we obtain the number of degrees of freedom of the model to be $n = 80$.

7.1 Results

The proposed method has been compared with a direct Monte Carlo Simulation (MCS), where both have been performed with $10,000$ samples. For the direct MCS, Eqn. (23) is solved for each sample and the mean and standard deviation is derived by assembling the responses. The calculations have been performed for all the four values of σ_a to simulate increasing uncertainty. This is done to check the accuracy of the proposed method against the direct MCS results for varying degrees of uncertainty.

Fig. 2(a) presents the ratio of the eigenvalues of the generalized eigenvalue problem (15) for which the ratio of the eigenvalues is taken with the first eigenvalue. We choose the reduced basis of the problem based on $\lambda_1/\lambda_q < \epsilon$, where $\epsilon = 0.01$, and they are highlighted in Fig. 2(b) shows the frequency domain response of the deterministic system for both damped and undamped conditions. We have applied a constant modal damping matrix with 1% damping factor for all the modes. Here the mass and damping matrices are assumed to be deterministic in nature. However, the proposed theoretical approach is general and equally applicable for random mass, stiffness and damping matrices. The frequency range of interest for the present study is $0 - 600$ Hz with an interval of 2 Hz. In Fig. 2(b), the tip deflection is shown on a log

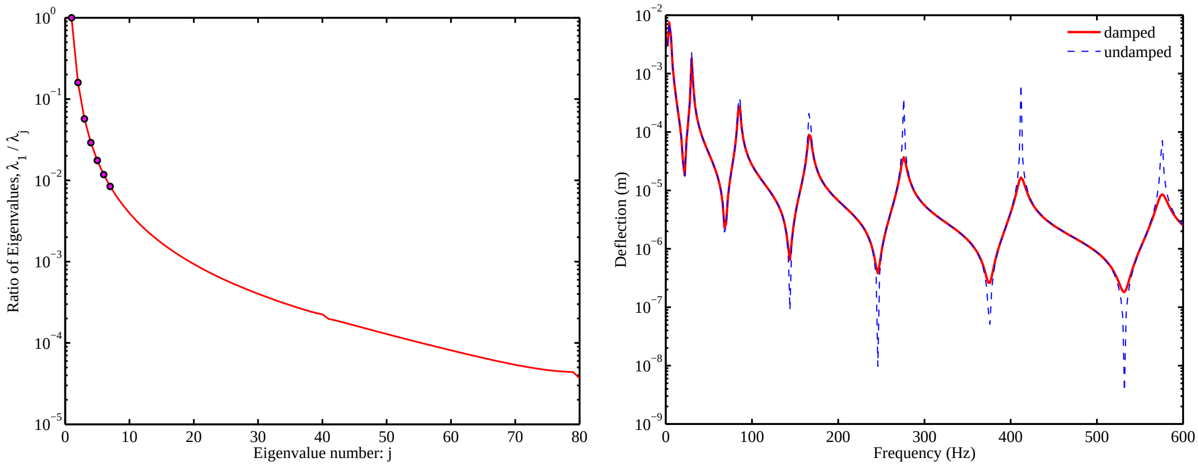

(a) Ratio of eigenvalues of the generalized eigenvalue problem.

(b) Frequency domain reponse of the tip of the beam under point load for the undamped and damped conditions (constant modal damping)

Figure 2: The eigenvalues of the generalized eigenvalue problem involving the mass and stiffness matrices given in Eqn. 15. For $\epsilon = 0.01$, the number of reduced eigenvectors $q = 7$ such that $\lambda_1/\lambda_j < \epsilon$.

scale for a unit amplitude harmonic force input. The resonance peak amplitudes of the response of the undamped system definitely depends on the frequency resolution of the plot.

The frequency response of the mean deflection of the tip of the beam is shown in Fig. 3 for the cases for cases of $\sigma_a = \{0.05, 0.10, 0.15, 0.20\}$. The figures show a comparison of the direct MCS simulation results with different orders of the solution following Eqn. (31), where the orders $s = 2, 3, 4$. A very good agreement between the MCS simulation and the proposed spectral approach can be observed in the figures. All the results have been compared with the response of the deterministic system which shows that the uncertainty has an added damping effect at the resonance peaks. This can be explained by the fact that the parametric variation of the beam, results in its peak response for the different samples to get distributed around the resonance frequency zones instead of being concentrated at a particular frequency, and when the subsequent averaging is applied, it smooths out the response peaks to a fair degree. The same explanation holds for the anti-resonance frequencies. It can also be observed that increased variability of the parametric uncertainties (as is represented by the increasing value of σ_a) results

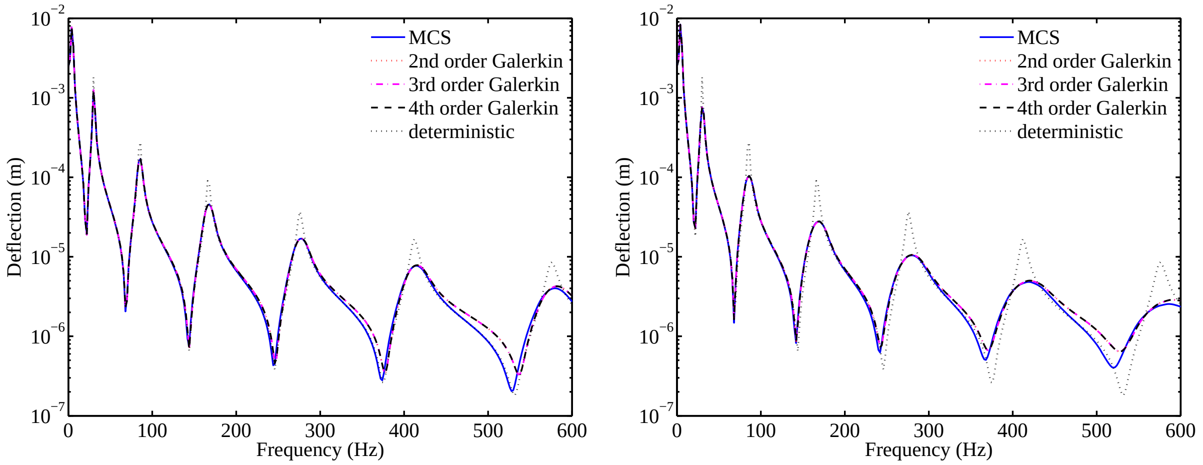

(a) Beam deflection for $\sigma_a = 0.05$.

(b) Beam deflection for $\sigma_a = 0.1$.

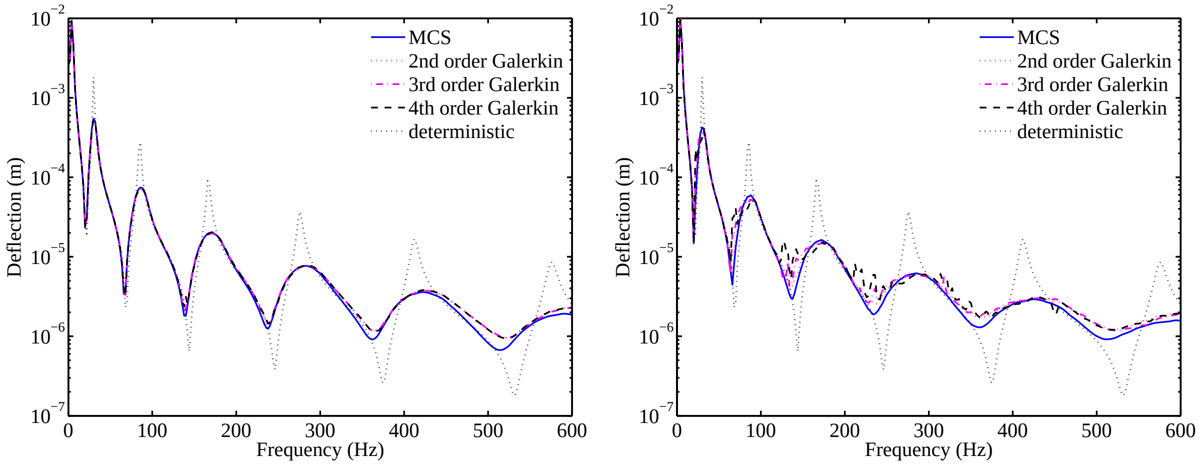

(c) Beam deflection for $\sigma_a = 0.15$.

(d) Beam deflection for $\sigma_a = 0.2$.

Figure 3: The frequency domain response of the deflection of the tip of the Euler-Bernoulli beam under unit amplitude harmonic point load at the free end. The response is obtained with $10,000$ sample MCS and for $\sigma_a = \{0.05, 0.10, 0.15, 0.20\}$. The proposed Galerkin approach needs solution of a 7×7 linear system of equations only.

in an increase of this added damping effect which is consistent with the previous explanation.

The standard deviation of the frequency domain response of the tip deflection for different spectral order of solution of the reduced basis approach is compared with the direct MCS and is shown in Fig. 4, for different values of σ_a. We find that the standard deviation is maximum at the resonance frequencies which is expected due to the differences in the resonance peak of each sample. It is again observed that the direct MCS solution and the reduced order approach give almost identical results, which demonstrate the effectiveness of the proposed approach.

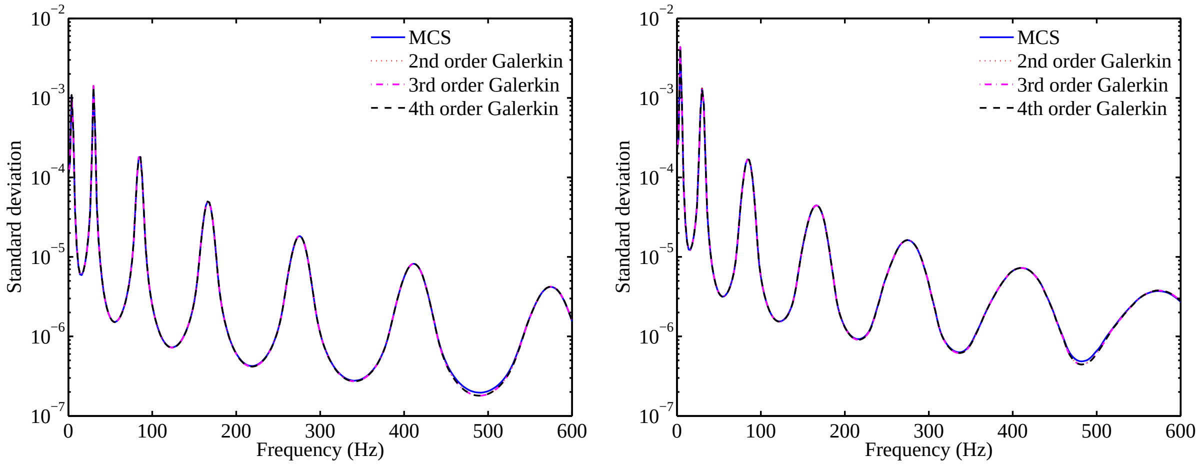

(a) Standard deviation of the response for $\sigma_a = 0.05$. (b) Standard deviation of the response for $\sigma_a = 0.1$.

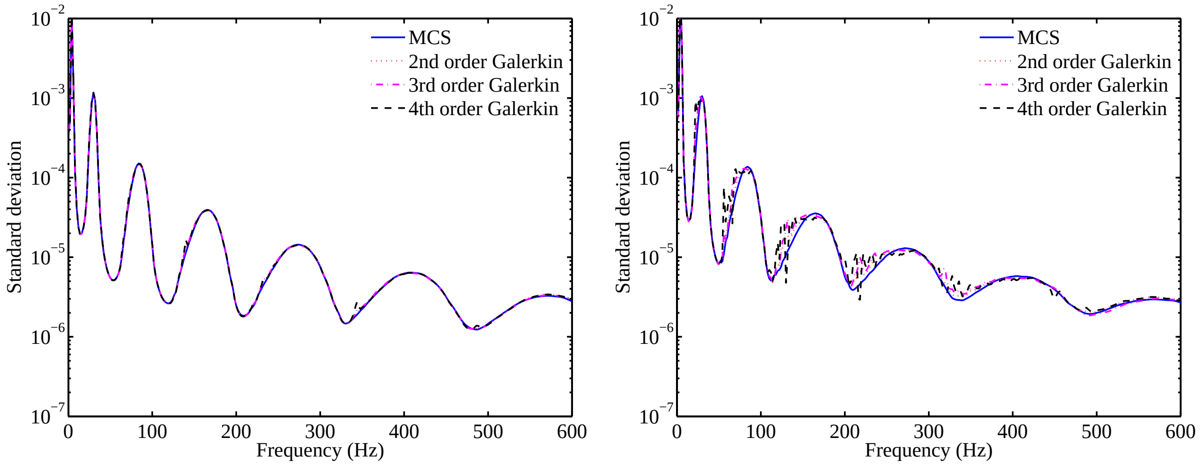

(c) Standard deviation of the response for $\sigma_a = 0.15$. (d) Standard deviation of the response for $\sigma_a = 0.2$.

Figure 4: The standard deviation of the tip deflection of the Euler-Bernoulli beam under unit amplitude harmonic point load at the free end. The response is obtained with $10,000$ sample MCS and for $\sigma_a = \{0.05, 0.10, 0.15, 0.20\}$.

Fig. 5 shows the relative standard deviation of the response of the beam at two frequencies 154 Hz and 412 Hz, which correspond to the anti-resonance and resonance frequencies of the cantilever beam respectively. The relative standard deviation values have been obtained for a set of 4 values of σ_a, which represents the different degrees of variability of the system uncertainty. The results obtained with the Galerkin approach for the different order of spectral functions have been compared to the direct MCS, and a good agreement between the two results have been obtained. It is interesting to point out here that the standard deviation decreases with the values of σ_a for the anti-resonance frequency while it increases for the resonance frequencies.

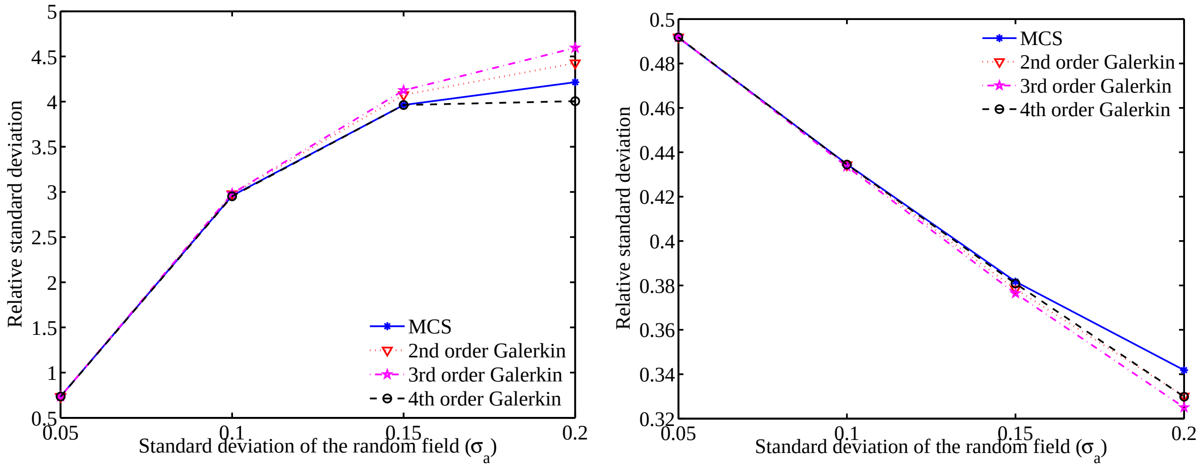

(a) Relative standard deviation at 154 Hz.

(b) Relative standard deviation at 412 Hz.

Figure 5: The relative standard deviation of the deflection of the tip (which has been obtained by normalizing the value of the standard deviation with the deterministic system response at the same frequency) versus the standard deviation (σ_a) of the random field of the Euler-Bernoulli beam under unit amplitude harmonic point load at the free end. The two frequencies, namely 154Hz and 412Hz are considered. They correspond to off-resonance and resonance frequencies respectively. The plots are shown for 4 different values of $\sigma_a = \{0.05, 0.10, 0.15, 0.20\}$ and calculated with $10,000$ random samples.

This is consistent with the results shown in Fig. 4 which shows that an increased value of the variance of the random field has the effect of an increasing added damping on the system, when an averaging is done over the sample space. Thus the resonance response is expected to reduce with the increased variability of the random field while the anti-resonance response will increase.

The probability density function of the deflection of the tip of the cantilever beam for different degrees of variability of the random field is shown in Fig. 6. The probability density functions have been calculated at the frequency of 412 Hz, which is a resonance frequency of the beam. The results indicate that with the increase in the degree of uncertainty (variance) of the system, the lower values of deflection has a higher probability which is absolutely consistent with the standard deviation curve shown in Fig. 5(a) and the comparison of the mean deflection of the stochastic system with the deterministic response in Fig. 3. This shows that the increase in the variability of the stochastic system has a damping effect on the response.

The results establish the applicability of this spectral reduced basis method with Galerkin error minimization technique as a satisfactory working model for providing solution of the stochastic structural systems. The method is found to be consistent with the direct MCS approach, while being much more computationally efficient than the latter.

8 Conclusions

We have considered the discretized stochastic partial differential equation for structural dynamic systems with generally non-Gaussian random fields. In the classical spectral stochastic finite element approach, the solution is projected into an infinite dimensional orthonormal basis functions and the associated constant vectors are obtained using the Galerkin type of error minimization approach. Here an alternative approach in the frequency domain is proposed. The solution is projected into a finite dimensional reduced vector basis and the associated complex coefficient functions are obtained. The coefficient functions, called as the *spectral functions*, are

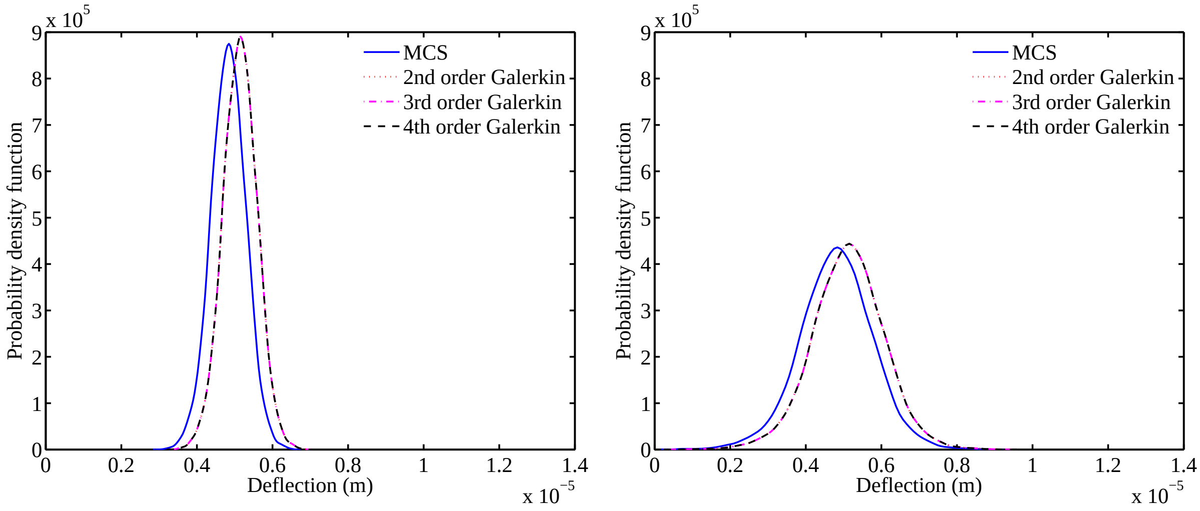

(a) PDF of the response at 210Hz for $\sigma_a = 0.05$. (b) PDF of the response at 210Hz for $\sigma_a = 0.1$.

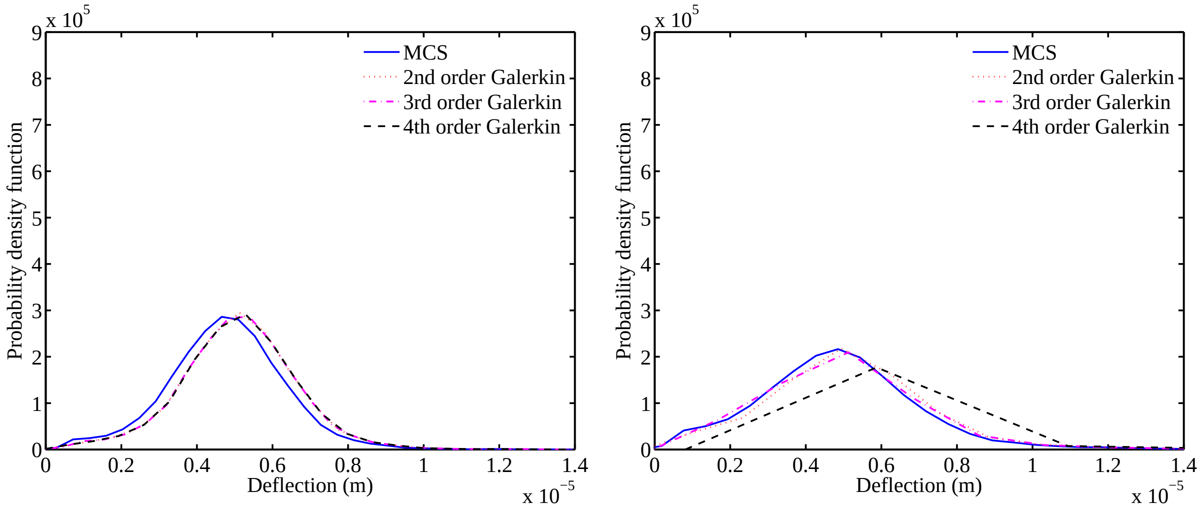

(c) PDF of the response at 210Hz for $\sigma_a = 0.15$. (d) PDF of the response at 210Hz for $\sigma_a = 0.2$.

Figure 6: The probability density function (PDF) of the tip deflection of the Euler-Bernoulli beam at 210 Hz under unit amplitude harmonic point load at the free end. The response is obtained with $10,000$ samples and for $\sigma_a = \{0.05, 0.10, 0.15, 0.20\}$.

expressed in terms of the spectral properties of the mass and stiffness matrices appearing in the discretized governing equation. It is shown that then the resulting series converges to the exact solution in probability 1. This is a stronger convergence compared to the classical polynomial chaos which converges in the mean-square sense in the Hilbert space.

Using the spectral functions, a Galerkin error minimization approach in the complex domain has been developed in a reduced vector basis. It is shown that the number of unknown constants can be obtained by solving a system of linear equations which have a dimension much smaller than the dimension of the original discretized equation. A simple numerical approach to obtain the reduced dimension has been suggested based on the ratio of the eigenvalues of the stiffness matrix corresponding to the baseline model. A numerical approach using a general-order spectral function has been developed. Based on these, a hybrid analytical-simulation approach is proposed to obtain the statistical properties of the solution.

The computational efficiency of the proposed reduced spectral approach has been demonstrated for large linear systems with non-Gaussian random variables. It may be possible to extend the underlying idea to the class of non-linear problems. For example, the proposed spectral approach can be used for every linearisation step or every time step. Further research is necessary in this direction.

Acknowledgements

AK acknowledges the financial support from the Swansea University through the award for Zienkiewicz scholarship. SA acknowledges the financial support from The Royal Society of London through the Wolfson Research Merit Award.

References

[1] A. Nouy, “Recent developments in spectral stochastic methods forthenumerical solution of stochastic partial differential equations,” *Archives of Computational Methods in Engineering*, vol. 16, pp. 251–285, 2009.
[2] D. C. Charmpis, G. I. Schueeller, and M. F. Pellissetti, “The need for linking micromechanics of materials with stochastic finite elements: A challenge for materials science,” *Computational Materials Science*, vol. 41, no. 1, pp. 27–37, 2007.
[3] G. Stefanou, “The stochastic finite element method: Past, present and future,” *Computer Methods in Applied Mechanics and Engineering*, vol. 198, no. 9-12, pp. 1031 – 1051, 2009.
[4] R. Ghanem and P. D. Spanos, *Stochastic Finite Elements: A Spectral Approach.* New York, USA: Springer-Verlag, 1991.
[5] M. Kleiber and T. D. Hien, *The Stochastic Finite Element Method.* Chichester: John Wiley, 1992.
[6] H. G. Matthies, C. E. Brenner, C. G. Bucher, and C. G. Soares, “Uncertainties in probabilistic numerical analysis of structures and solids - stochastic finite elements,” *Structural Safety*, vol. 19, no. 3, pp. 283–336, 1997.
[7] C.-C. Li and A. D. Kiureghian, “Optimal discretization of random fields,” *Journal of Engineering Mechanics*, vol. 119, no. 6, pp. 1136–1154, 1993.
[8] A. Papoulis and S. U. Pillai, *Probability, Random Variables and Stochastic Processes.* Boston, USA: McGraw-Hill, fourth ed., 2002.
[9] R. Ghanem, “The nonlinear gaussian spectrum of log-normal stochastic processes and variables,” *Journal of Applied Mechanics-ASME*, vol. 66, pp. 964–973, 1989.
[10] D. B. Xiu and G. E. Karniadakis, “The wiener-askey polynomial chaos for stochastic differential equations,” *Siam Journal on Scientific Computing*, vol. 24, no. 2, pp. 619–644, 2002.
[11] D. B. Xiu and G. E. Karniadakis, “Modeling uncertainty in flow simulations via generalized polynomial chaos,” *Journal of Computational Physics*, vol. 187, no. 1, pp. 137–167, 2003.
[12] X. L. Wan and G. E. Karniadakis, “Beyond wiener-askey expansions: Handling arbitrary pdfs,” *Journal of Scientific Computing*, vol. 27, no. (-3, pp. 455–464, 2006.
[13] H. G. Matthies and A. Keese, “Galerkin methods for linear and nonlinear elliptic stochastic partial differential equations,” *Computer Methods in Applied Mechanics and Engineering*, vol. 194, no. 12-16, pp. 1295–1331, 2005.
[14] I. Babuska, R. Tempone, and G. E. Zouraris, “Galerkin finite element approximations of stochastic elliptic partial differential equations,” *Siam Journal on Numerical Analysis*, vol. 42, no. 2, pp. 800–825, 2004.

[15] I. Babuska, R. Tempone, and G. E. Zouraris, "Solving elliptic boundary value problems with uncertain coefficients by the finite element method: the stochastic formulation," *Computer Methods in Applied Mechanics and Engineering*, vol. 194, no. 12-16, pp. 1251 – 1294, 2005.

[16] R. A. Horn and C. R. Johnson, *Matrix Analysis*. Cambridge, UK: Cambridge University Press, 1985.

[17] W. K. Liu, T. Belytschko, and A. Mani, "Random field finite-elements," *International Journal for Numerical Methods in Engineering*, vol. 23, no. 10, pp. 1831–1845, 1986.

[18] F. Yamazaki, M. Shinozuka, and G. Dasgupta, "Neumann expansion for stochastic finite element analysis," *Journal of Engineering Mechanics-ASCE*, vol. 114, no. 8, pp. 1335–1354, 1988.

[19] S. Adhikari and C. S. Manohar, "Dynamic analysis of framed structures with statistical uncertainties," *International Journal for Numerical Methods in Engineering*, vol. 44, no. 8, pp. 1157–1178, 1999.

[20] M. Grigoriu, "Galerkin solution for linear stochastic algebraic equations," *Journal of Engineering Mechanics-Asce*, vol. 132, no. 12, pp. 1277–1289, 2006.

[21] G. Falsone and N. Impollonia, "A new approach for the stochastic analysis of finite element modelled structures with uncertain parameters," *Computer Methods in Applied Mechanics and Engineering*, vol. 191, no. 44, pp. 5067–5085, 2002.

[22] C. F. Li, Y. T. Feng, and D. R. J. Owen, "Explicit solution to the stochastic system of linear algebraic equations $(\alpha_1 A_1 + \alpha_2 A_2 + \cdots + \alpha_m A_m)x = b$," *Computer Methods in Applied Mechanics and Engineering*, vol. 195, no. 44-47, pp. 6560–6576, 2006.

[23] Y. T. Feng, "Adaptive preconditioning of linear stochastic algebraic systems of equations," *Communications in Numerical Methods in Engineering*, vol. 23, no. 11, pp. 1023–1034, 2007.

[24] M. Papadrakakis and V. Papadopoulos, "Robust and efficient methods for stochastic finite element analysis using monte carlo simulation," *Computer Methods in Applied Mechanics and Engineering*, vol. 134, no. 3-4, pp. 325–340, 1996.

[25] X. Ma and N. Zabaras, "An adaptive hierarchical sparse grid collocation algorithm for the solution of stochastic differential equations," *Journal of Computational Physics*, vol. 228, no. 8, pp. 3084–3113, 2009.

[26] B. Ganapathysubramanian and N. Zabaras, "Sparse grid collocation schemes for stochastic natural convection problems," *Journal of Computational Physics*, vol. 225, no. 1, pp. 652–685, 2007.

[27] P. B. Nair and A. J. Keane, "Stochastic reduced basis methods," *AIAA Journal*, vol. 40, no. 8, pp. 1653–1664, 2002.

[28] S. K. Sachdeva, P. B. Nair, and A. J. Keane, "Comparative study of projection schemes for stochastic finite element analysis," *Computer Methods in Applied Mechanics and Engineering*, vol. 195, no. 19-22, pp. 2371–2392, 2006.

[29] S. K. Sachdeva, P. B. Nair, and A. J. Keane, "Hybridization of stochastic reduced basis methods with polynomial chaos expansions," *Probabilistic Engineering Mechanics*, vol. 21, no. 2, pp. 182–192, 2006.

[30] A. Sarkar, N. Benabbou, and R. Ghanem, "Domain decomposition of stochastic PDEs: Theoretical formulations," *International Journal for Numerical Methods in Engineering*, vol. 77, no. 5, pp. 689–701, 2009.

[31] G. Blatman and B. Sudret, "An adaptive algorithm to build up sparse polynomial chaos expansions for stochastic finite element analysis," *Probabilistic Engineering Mechanics*, vol. 25, no. 2, pp. 183 – 197, 2010.

[32] A. Nouy, “A generalized spectral decomposition technique to solve a class of linear stochastic partial differential equations,” *Computer Methods in Applied Mechanics and Engineering*, vol. 196, no. 45-48, pp. 4521–4537, 2007.

[33] A. Nouy, “Generalized spectral decomposition method for solving stochastic finite element equations: Invariant subspace problem and dedicated algorithms,” *Computer Methods in Applied Mechanics and Engineering*, vol. 197, no. 51-52, pp. 4718–4736, 2008.

[34] M. Petyt, *Introduction to Finite Element Vibration Analysis*. Cambridge, UK: Cambridge University Press, 1998.

[35] V. Lenaerts, G. Kerschen, and J. C. Golinval, “Physical interpretation of the proper orthogonal modes using the singular value decomposition,” *Journal of Sound and Vibration*, vol. 249, pp. 849–865, January 2002.

[36] M. Khalil, S. Adhikari, and A. Sarkar, “Linear system identification using proper orthogonal decomposition,” *Mechanical System and Signal Processing*, vol. 21, pp. 3123–3145, November 2007.

[37] P. Kerfriden, P. Gosselet, S. Adhikari, and S. Bordas, “Bridging the proper orthogonal decomposition methods and augmented newton-krylov algorithms: An adaptive model order reduction for highly nonlinear mechanical problems,” *Computer Methods in Applied Mechanics and Engineering*, vol. 200, no. 5-8, pp. 850–866, 2011.

[38] O. C. Zienkiewicz and R. L. Taylor, *The Finite Element Method*. London: McGraw-Hill, fourth ed., 1991.

COMPDYN 2011
III ECCOMAS Thematic Conference on
Computational Methods in Structural Dynamics and Earthquake Engineering
M. Papadrakakis, M. Fragiadakis, V. Plevris (eds.)
Corfu, Greece, 25–28 May 2011

DYNAMIC LOADS DUE TO SYNCHRONOUS RHYTHMIC ACTIVITIES OF GROUPS AND CROWDS

Vitomir Racic[1], James M. W. Brownjoh[1] and Aleksandar Pavic[1]

[1] University of Sheffield
Sir Frederick Mappin Building, Mappin Street, S1 3JD Sheffield, United Kingdom
v.racic@sheffield.ac.uk
james.brownjohn@sheffield.ac.uk
a.pavic@sheffield.ac.uk

Keywords: vibration serviceability, human-structure interaction, jumping, bouncing, forces.

Abstract. *Predicting vibration performance of civil engineering structures due to human-induced rhythmic loading is an increasingly critical aspect of the design process of structures such as sports stadia used for pop/rock concerts, floors accommodating gym and aerobic classes, and footbridges used as spectator galleries during regatta events. Two main reasons for this trend are (1) structures are becoming more slender with improvements in materials and construction techniques and modern trends in architectural design, and (2) groups/crowds are in general becoming livelier than previously was the case, i.e. their activities can become better synchronised due to the presence of various auditory and visual stimuli at above mentioned events. This paper addresses the latter issue by presenting a method to measure human bouncing and jumping forces induced by groups and ultimately crowds using motion capture technology, transferred and adapted from biomedical research.*

Compared with traditional force platform measurements, the key advantage and novelty of this method is a possibility to measure individual forces of each group/crowd member in natural environments, including real life structures. Constrains imposed by artificial laboratory settings and small size of force plates can significantly affect the quality of the force data. Results show that the new method can be used successfully to study area of significant interest and uncertainty for structural dynamics, particularly synchronisation of individual forces when people bounce and jump in groups on more or less perceptibly moving structures.

The new approach presented in this paper is a step towards more thorough and realistic mathematical models of group/crowd rhythmic loading that can be used to simulate more reliably dynamic response, thereby assessing vibration serviceability of above mentioned civil engineering structures convincingly at the design stage.

1 INTORODUCTION

In the last decade, there have been rapidly growing numbers of grandstands and entertainment venues that have failed to perform satisfactorily when occupied and dynamically excited by multiple persons and large crowds bouncing and/or jumping in unison [1-3]. These mostly vibration serviceability problems have indicated high level of uncertainty with which civil structural engineers are faced nowadays when designing any of the above mentioned structures which require vibration performance assessment.

There have been numerous attempts to provide reliable and practical descriptions of human bouncing and jumping loads by measuring the contact forces between the ground and test subjects, hence generally known as ground reaction forces (GRFs). For this purpose Ebrahimpour et al. [4] and Pernica [5] designed a 'force platform', whereas Rainer et al. [6] used the continuously measured reaction of a floor strip having known dynamic properties. Much research into GRFs has been done in the biomechanics community, as GRF patterns provide useful diagnostics in medical and sports applications [7, 8]. Therefore, it is not surprising that the present state-of-the-art equipment for the force measurements, i.e. the 'force plate', emerged from the field of biomechanics of human gait. However, there are a few disadvantages of force plates that make them less suitable in vibration serviceability assessment of civil engineering structures. Firstly, standard dimensions of force plates (typically 0.6x0.4 m) are not large enough to accommodate jumping for some individuals who must control and target their jumps to the relatively small force plate area so as to allow adequate recordings. As a result, this targeting effort can affect ability to jump naturally and therefore alter GRF patterns [8]. Secondly, force plates cannot provide accurate measurements when mounted on a flexible structure due to self-inertia. This is because they behave like 'accelerometers' and produce outputs including inertia forces of the moving support surface [9]. Therefore, a typical experimental setup includes force plates mounted on a rigid laboratory floor. However, when investigating issues related to vibration serviceability there is a growing need for measuring human-induced dynamic loading on more or less flexible surfaces in natural environments, such as office, sport facility, or a footbridge. Finally, when it comes to measuring group bouncing/jumping loads, each individual in the group must be given (at least) a force plate, which often gives financial problems.

Bearing all this in mind, one way forward is an alternative experimental approach to account for all drawbacks of force plates. Several biomechanical studies designed to estimate the contribution of motion of various body segments to vertical GRFs [10-12] offer a step in this direction. Using these biomechanical studies as a solid foundation, this paper aims to present a reader, conversant with vibration serviceability problems of civil engineering structures, with a novel method, in the context of a civil engineering application, to utilise 'free-field' measurement to obtain bouncing and jumping GRFs in a wide range of conditions. The free-field measurement applies the method to estimate the forces in the real world (i.e. naturally-occurring environments) rather than in a constrained laboratory setting. The method will also enable study of areas of significant interest and lack of knowledge, specifically human-structure dynamic interaction and coordination of movements between a number people bouncing/jumping on more or less perceptibly moving structures.

In the context of this paper, human-structure dynamic interaction aims to address two related key issues. Firstly, how perceptible structural vibrations can influence forces induced by active human occupants, and secondly, how active human occupants influence the dynamic properties (e.g. damping) of a civil engineering structure they occupy and dynamically excite.

2 THEORETICAL BACKGROUND

According to Newton [13], the origin of dynamic forces is in momentum changes, which, for constant mass, means that the force is product of mass and acceleration. As applied to the human body, the vertical force acting upon the body (i.e. vertical ground reaction force F_{GR}) can be defined as [3]:

$$F_{GR} = \sum_{i=1}^{s} m_i \left(a_i - g\right) \tag{1}$$

where g is the static acceleration due to gravity (noting that upward accelerations are defined as positive, hence g=-9.81 m/s2 in the UK), m_i and a_i are mass and acceleration of the centre of the mass of the i-th body segment and s is the total number of body segments. This relation implies that the force a person generates against the surface must react against inertia of their body, so the sum of products of masses and accelerations for all body parts must equal the GRF at all times. Similar to earthquake engineering, the only source of external excitation is the inertial force, which then generates other forces through the human body, being transmitted ultimately to the support of the body and resulting in the GRF. This is the key principle behind the idea of estimating GRFs via measuring motion of the body segments.

In this study, physical parameters associated with each rigid segment, such as mass and position of its centre, are estimated using regression equations proposed by de Leva [14], while measurement of body motion was considered using Coda [15] optical motion capture technology. More detailed explanation of different methods for estimating anthropometry of human bodies and technology for body motion tracking can be found in a comprehensive literature review article published recently by the authors [16].

3 DATA COLLECTION

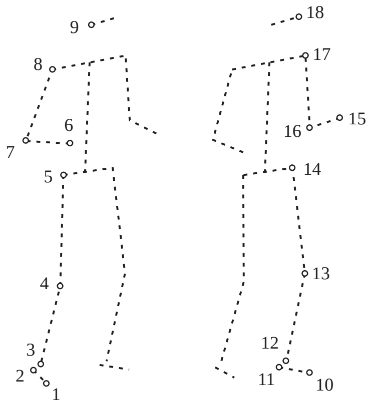

Test subject 1 Test subject 2

Figure 1: Human body model and arrangement of markers.

Two male volunteers (age 27 and 30 years, body mass 70 and 67 kg) participated in the experiment. Using the modelling strategy proposed by de Leva [14], 15 body segments and corresponding segmental masses and positions of segmental mass centres of each participant were defined. The segmentation comprised the pairs of the feet, the shanks, the thighs, the hands, the forearms, the upper-arms, as well as the pelvis, the trunk, and the head. The segmental ends were defined via nine motion tracking markers (also called ‘target’ markers) stuck to the head and major body joints such as ankle, wrist, knee or elbow, as illustrated in Figure 1. Because the number of available markers is limited, as well as to reduce the subject's preparatory time and to enable simple and time-efficient experiments, symmetry of motion in the vertical plane between the left and right body segments was assumed.

3.1 TEST STRUCTURE AND EXPERIMENTAL MODAL ANALYSIS

The test structure is a 15-tonne pre-stressed concrete slab strip situated in the Light Structure Laboratory of the University of Sheffield, UK. The slab strip is 11 m long and 2 m wide and, structurally, it presents a simply supported beam (Figures 2 and 3).

The natural frequencies, modal masses, modal damping ratios and mode shapes of the structure were determined by shaker modal testing. The modal testing is described in [3] and results are presented in Figure 2.

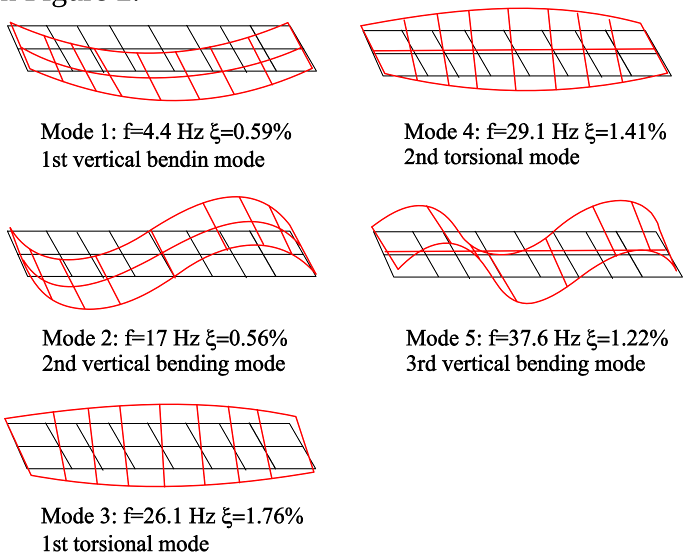

Mode 1: f=4.4 Hz ξ=0.59%
1st vertical bendin mode

Mode 4: f=29.1 Hz ξ=1.41%
2nd torsional mode

Mode 2: f=17 Hz ξ=0.56%
2nd vertical bending mode

Mode 5: f=37.6 Hz ξ=1.22%
3rd vertical bending mode

Mode 3: f=26.1 Hz ξ=1.76%
1st torsional mode

Figure 2: Experimentally estimated modal properties on the test structure (first three vertical bending modes, first two torsional modes).

Figure 3: Two test subjects jumping together on the slab strip.

3.2 BODY MOTION DATA COUPLED WITH RESPONSE MEASUREMENTS OF THE STRUCTURE

The test subjects (TSs), fully instrumented with the Coda markers, were asked to either jump or bounce alone in the mid-span of the structure (Figure 3) in response to regular metronome beats at three different tempos: 2, 2.2 and 2.5 Hz. Note that jumping and bouncing at 2.2 Hz excited the structure as near to resonance as possible by the second harmonic of the corresponding forces. On the other hand, closely spaced tempos at 2 and 2.5 Hz excited the structure out of resonance.

The Codamotion host computer enabled simultaneous acquisition of vertical movement of the body markers and response of the structure measured in the middle of the span by both a QA750 [17] accelerometer and a tracking marker. Both body motion data and vibration response were sampled at 200 Hz.

The aim was to calculate response of the structure by using the forces reproduced from the body motion data and the modal properties of the first vertical mode determined in Section 3.1. A good match between the calculated and directly measured accelerations should provide a proof that the forces can be reproduced successfully. This is the key aspect outlined in the next section, together with the possibility to use the reproduced forces in a study of human-structure dynamic interaction and synchronisation of people when jumping/bouncing in groups.

3.3 BASIC DATA PROCESSING

Movement of the skin relative to the underlying bone is one of the major sources of error when reconstructing human-induced forces from body motion data [16]. This is known as “soft tissue artefact” and is dominant during highly accelerated movements, e.g. when the feet abruptly hit the ground. Skin markers then oscillate considerably in an unsteady way with respect to the underlying bone, inducing high-frequency noise in the marker data. To filter out the noise, a fourth order low-pass digital Butterworth filter (LPF) having cut-off frequency 15 Hz was applied to accelerations of all markers. Figure 4 illustrates accelerations of the hip marker obtained with and without filtering out the noise above 15 Hz from the displacement data. It can be seen that the main visible features of the markers’ accelerations representing the whole body segment motion remain intact after the filtering.

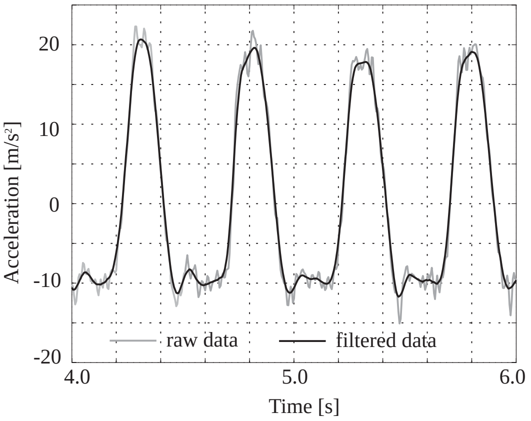

Figure 4: Raw and filtered accelerations (CF=15Hz) of a hip marker due to jumping at 2 Hz.

4 SYNCHRONIOUS VERTICAL EXCITATION

The force time histories generated in the mid-span of the structure when the test subjects were bouncing or jumping together in response to the regular metronome beats (at 2, 2.2 and 2.5 Hz) were reproduced according to Equation (1) from filtered body motion data of a kind given in Figure 4 and information about the values and locations of the segmental masses (Section 3). As an illustration, the reproduced force signals are given in Figure 5.

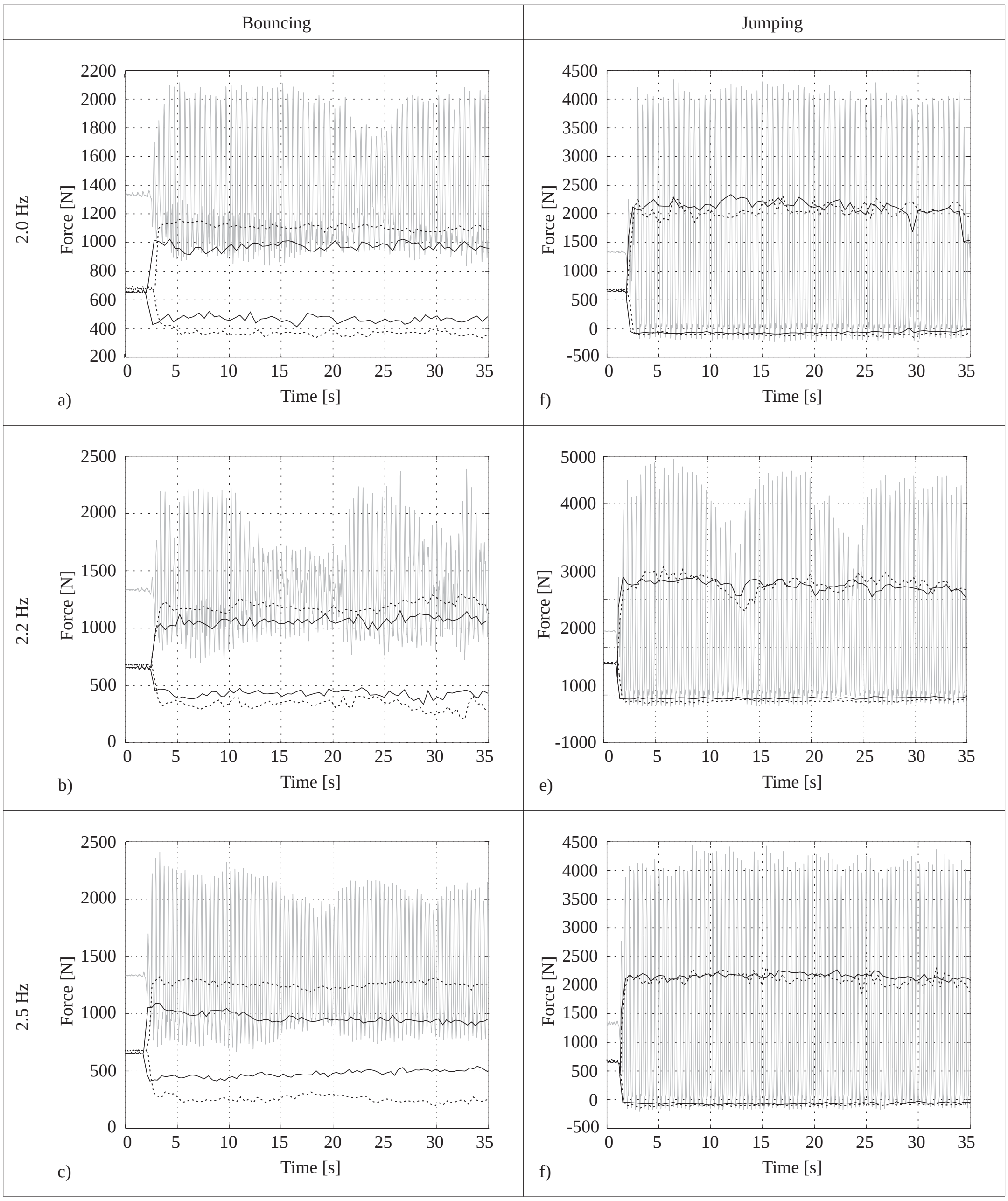

Figure 5: Force time histories generated by TS1 (black), TS2 (dashed) and their sum (grey) when (a-c) bouncing and (d-f) jumping in response to regular metronome beats at 2, 2.2 and 2.5 Hz.

The best way to check if the reproduced forces are correct is to compare responses of the structure measured directly by the accelerometers (Section 3.2) and those calculated from the corresponding SDOF model of the structure. The latter can be obtained using the reproduced forces as the forcing function together with the nonlinear modal properties of the first vertical mode given in [3].

A good match between the calculated and directly measured accelerations in the mid-span of the structure (Figure 6) strongly suggests that the forces have been reproduced successfully.

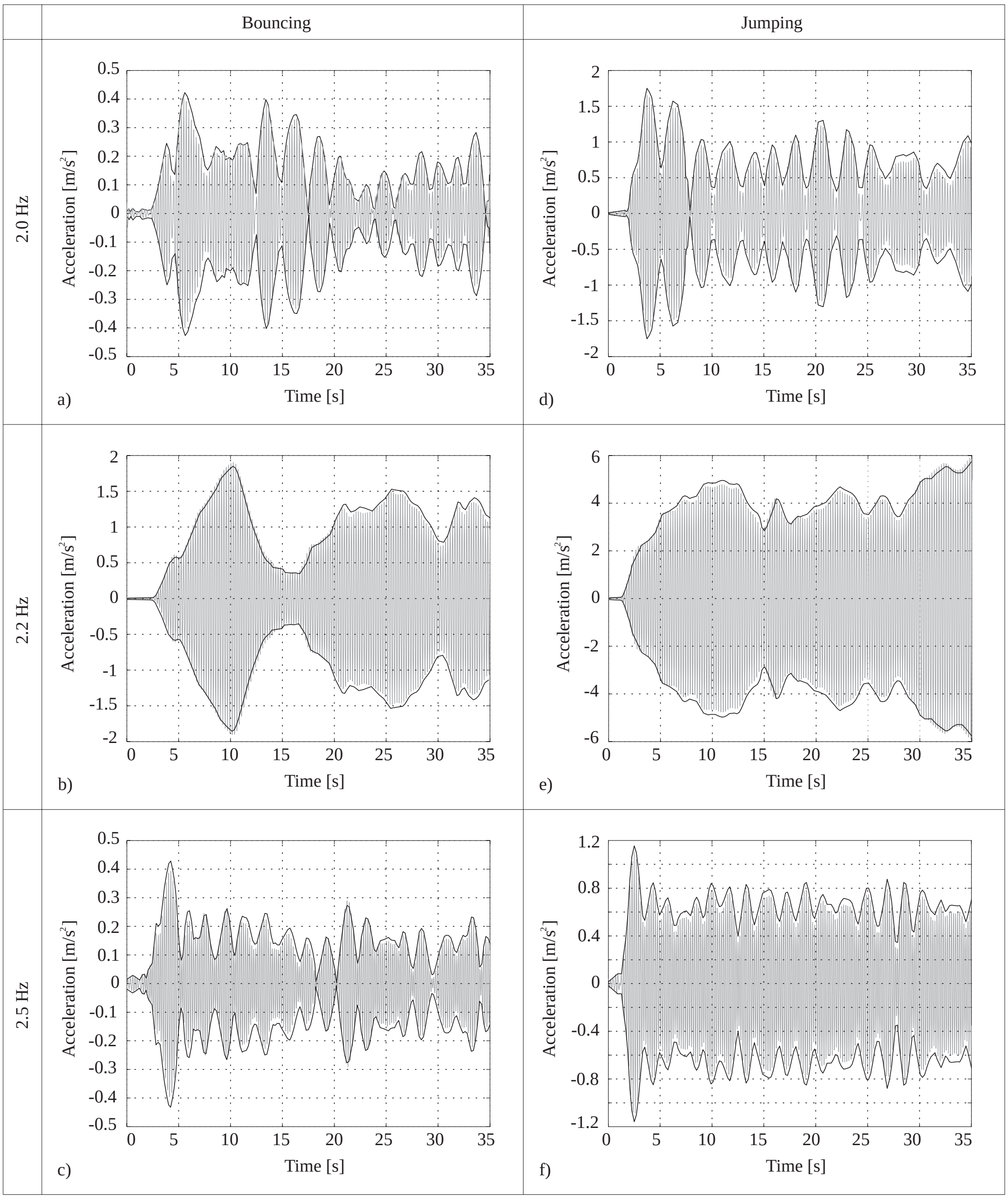

Figure 6: Measured (grey) and envelope of simulated (black) mid-span vibration response of the structure due to two persons (a-c) bouncing and (d-f) jumping together at given regular metronome beats.

Although the test subjects were following the same metronome beats when jumping and bouncing together, there was a sporadic lack of coordination between their movements, which is reflected in a lack of synchronisation of the corresponding peak force amplitudes on a cycle-by-cycle basis. Here, one jumping or bouncing cycle corresponds to a period needed to complete one jump or bounce.

In Figure 7, there are cycles for which time instants of individual peak amplitudes match well, indicating a high synchronisation level. Also, this resulted in large peak amplitudes of the total sum force for these cycles. However, because humans are not machines, despite the metronome beat they could not keep moving in synchronisation for a long time, causing peaks to diverge and their sum to decrease. After a while, the process starts to reverse, i.e. the peaks start moving towards each other and finally meet, being synchronised again. Therefore, the lack of synchronisation can be quantified through relative changes of time lags Δt_i between peaks of individual force signals on a cycle-by-cycle basis (Figures 7b and 7d). A summary of mean values and standard deviations of Δt_i values extracted from 30 s duration of all group force signals is given in Table 1.

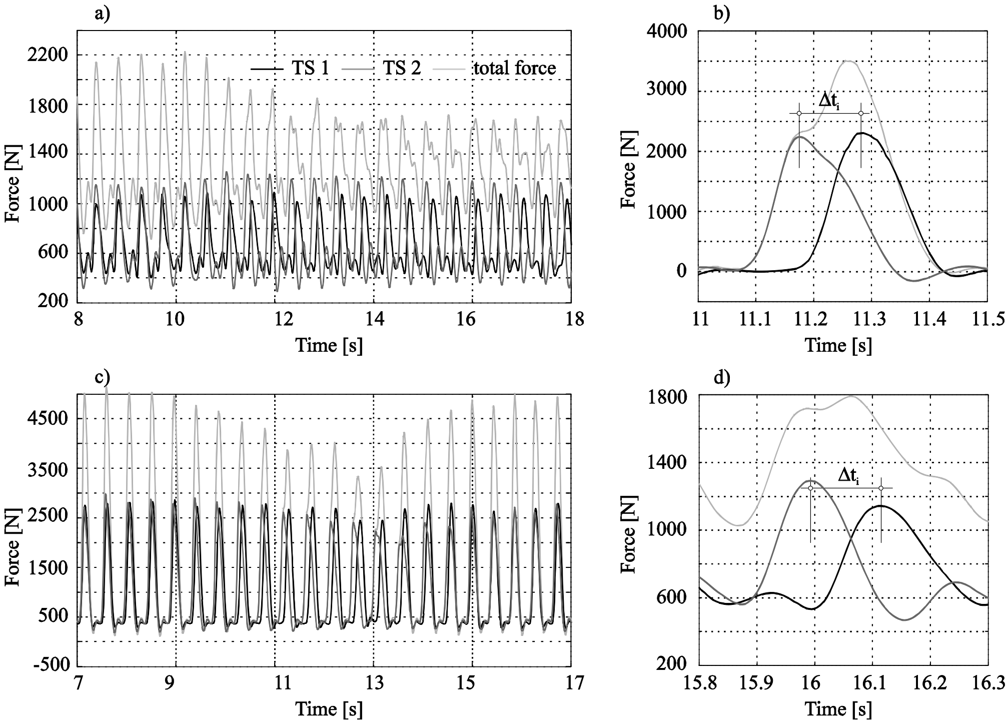

Figure 7: Synchronisation of (a-b) bouncing and (c-d) jumping forces at 2.2 Hz. Figures 5 and 7 illustrate the same data.

Table 1: Summary of statistics (mean ± standard deviation) of Δt_i:

Frequency [Hz]	bouncing [s]	jumping [s]
2.0	0.052 ± 0.036	0.039 ± 0.020
2.2	0.076 ± 0.076	0.073 ± 0.036
2.5	0.049 ± 0.024	0.022 ± 0.012

The largest values of the mean and standard deviation are for the excitation causing near-resonant response for both bouncing and jumping indicating that the synchronisation was most affected by the large structural vibrations. Also, for both resonant and non-resonant rates, synchronisation during jumping was better compared with the bouncing counterparts.

In qualitative feedback after the experiments, both test subjects agreed that non-resonant vibrations of the structure were barely perceptible, whereas the resonant response levels were perceived as rather excessive, sometimes even “scary”, thus influencing the way they were moving on the structure. Moreover, they reported that the effect was dominant for bouncing, where the feet are in permanent contact with the vibrating structure.

5 ENERGY FLOW AND POWER

A useful technique for studying human-structure dynamic interaction involves analysis of the power developed by human occupants moving on a structure and the power represented by the rate of internal energy dissipation in a structure conceptualised via damping forces [20]. Energy, with the units of Joules [J] or [Nm], is the time integral of power and is a more familiar quantity whose flow is easy to visualise. However graphical representation using power, with units of Watts [W] or [Nm/s], is simpler to study for comparative purposes.

For the slab strip, supply of energy to the structure at the point of contact is the instantaneous product of velocity $x^{\cdot}(t)$ and contact force f(t). The contact force f(t) could be obtained either directly by a load cell or reproduction from the marker motion, while velocity could be obtained by integrating accelerometer signals or differentiating contact point marker displacements. Here, the contact force is measured indirectly using Equation (1) and the velocity is obtained from displacements of a marker attached to the middle of the span where the activity was happening.

Consider an equation of motion of a SDOF system, e.g. the first mode of vibration of the slab strip excited by a jumping force at the midpoint (antinode). If the mode shape is unity scaled at the midpoint then modal and physical displacements at the mid-point are identical and can both be represented by x(t) which is a solution of the following well known differential equation [21]:

$$m\ddot{x}(t) + c\dot{x}(t) + kx(t) = f(t) \tag{2}$$

where, m, c and k are the modal mass, damping and stiffness, respectively.

Multiplying by the modal/physical velocity $\dot{x}(t)$, the equation of motion can be used to calculate instantaneous power $f(t)\dot{x}(t)$:

$$m\ddot{x}(t)\dot{x}(t) + c\dot{x}(t)\dot{x}(t) + kx(t)\dot{x}(t) = f(t)\dot{x}(t) \tag{3}$$

Here, $m\ddot{x}(t)\dot{x}(t)$ is kinetic power, $c\dot{x}(t)\dot{x}(t)$ is damping power and $kx(t)\dot{x}(t)$ is potential power.

In resonance it is well known that the inertia and stiffness forces are perfectly balanced with the interchange of kinetic and potential energy resulting in a constant value of energy and no net supply to either of them. Simultaneously, the external force simply provides positive power to compensate for the energy dissipated internally via damping (damping power):

$$\begin{aligned} m\ddot{x}(t)\dot{x}(t) &= kx(t)\dot{x}(t) \\ c\dot{x}^2(t) &= f(t)\dot{x}(t) > 0 \end{aligned} \tag{4}$$

Away from resonance in steady state the damping power is always positive (due to the square term in $c\dot{x}^2(t)$) but the external power has a zero-mean oscillating component which supplies and withdraws power during a cycle due to the imbalance of inertia and stiffness forces. During build up of response towards resonance the external force only supplies and never withdraws power to build up the constant level of total (i.e. kinetic plus potential) energy.

For the two TSs bouncing/jumping together (Figures 8 and 9), the individual cycle-by-cycle average power plots show that TS 1 was supplying energy to the system most of the time during the tests, while TS 2 was often acting as the strong damping element. This clearly explains why the resonance was very difficult to maintain for both activities. These tests also confirmed findings elsewhere [22] that the humans are characterised by huge inter-subject differences between their abilities to induce dynamic loads, to change the dynamic properties and to respond to nominally the same vibrations of the structure they occupy and dynamically excite.

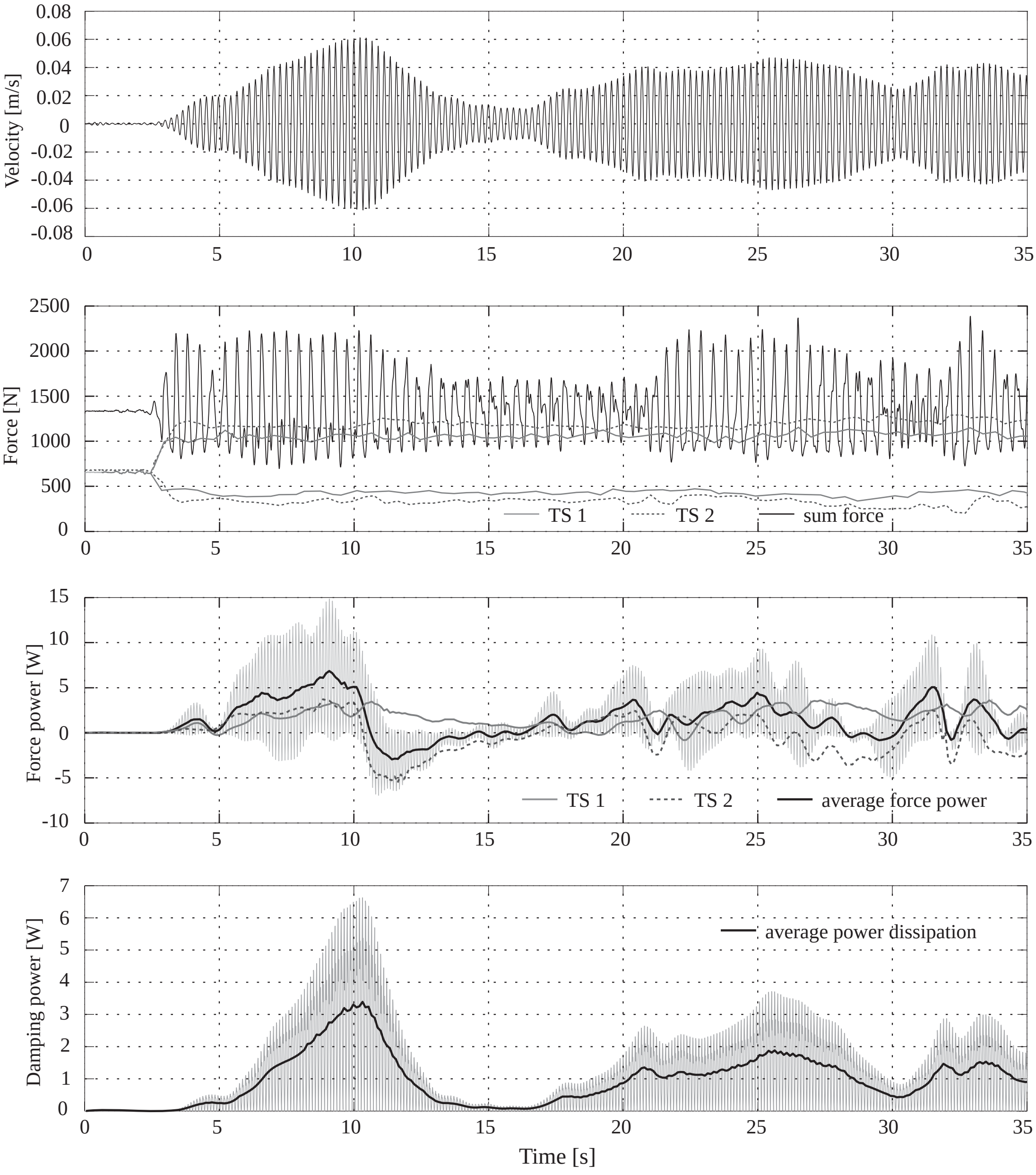

Figure 8: Energy flow and power due to both TSs bouncing together in the middle of the span at resonant rate of 2.2 Hz.

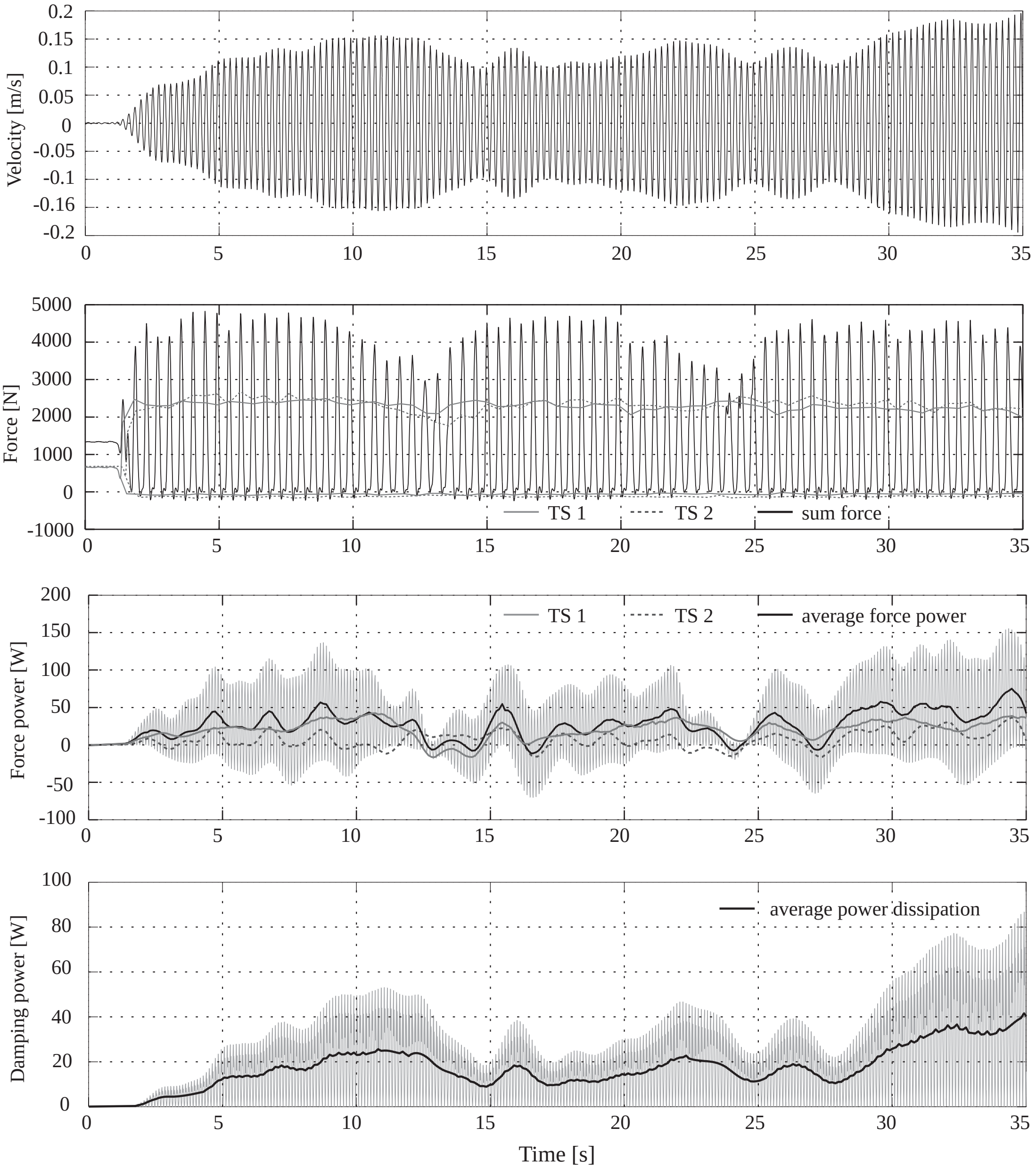

Figure 9: Energy flow and power due to both TSs jumping together in the middle of the span at resonant rate of 2.2 Hz.

6 CONCLUSIONS

This paper presents a novel method in the civil engineering context to measure indirectly bouncing and jumping GRFs by combining human body motion tracking data and known/assumed body mass distribution.

When compared with the traditional direct force measurements on floor-mounted force plates, a key advantage of the method proposed is utilisation of ‘free-field’ measurement of continuous bouncing and jumping GRFs. As demonstrated, indirect force measurements enable monitoring of people performing rhythmic activities in their natural environments, such as footbridges, grandstands, staircases and open-plan floors. Moreover, the method enables study areas of significant interest and uncertainty, specifically human-structure dynamic interaction and synchronisation between occupants when bouncing and jumping on flexible structures. Measurements have been able to show the negative cue effect of perceptible vibrations on the GRFs. Also, they indicated that in the joint human-structure dynamic system an active human can not only be the source of energy but they can also act as the strongest damping element. This happens either because the response is off-resonance or because they are out of phase with the structural motion resulting in net removal of energy. The effect is even stronger for multiple occupants due to the lack of synchronisation of their movements.

The method piloted in this paper has been validated using two male participants, who were jumping or bouncing either individually or as a pair on a realistic test structure. This means that there remains a requirement to carry out similar tests for single individuals and multiple occupants moving on a number of different, more or less vibrating real-life structures. Measurements can be used to develop and calibrate a new generation of badly needed models of rhythmic crowd loads. Therefore, this approach presents a timely opportunity to advance the whole field of vibration serviceability assessment of structures predominantly occupied and dynamically excited by bouncing/jumping humans, such as grandstands and entertainment venues.

7 ACKNOWLEDGEMENTS

The authors would like to thank Mr Christopher Middleton, Dr Ivan Munoz-Diaz and Dr Stana Zivanovic for their help in collecting the data. Also, the authors would like to acknowledge the financial support provided by the UK Engineering and Physical Sciences Research Council (EPSRC) for grant reference EP/E018734/1 (‘Human Walking and Running Forces: Novel Experimental Characterisation and Application in Civil Engineering Dynamics’).

REFERENCES

[1] V. Racic, A. Pavic, Mathematical model to generate near-periodic human jumping force signals. *Mechanical Systems and Signal Processing*, 24, 138-152, 2010.

[2] V. Racic, A. Pavic, Stochastic approach to modelling near-periodic jumping force signals. Mechanical Systems and Signal Processing, 24, 3037-3059, 2010.

[3] V. Racic, J.M.W. Brownjohn, A. Pavic, Reproduction and application of human bouncing and jumping forces from visual marker data. *Journal of Sound and Vibration*, 329, 3397-3416, 2010.

[4] A. Ebrahimpour, R.L. Sack, W.E. Saul, G.L. Thinness, Measuring dynamic occupant loads by microcomputer. In: K.M. Will, ed, *Proceedings of the Ninth ASCE Conference on Electronic Computation*, New York, USA, 328-338, 1986.

[5] G. Pernica, Dynamic load factors for pedestrian movements and rhythmic exercises. *Canadian Acoustics*, 18 (2), 3-18, 1990.

[6] J.H. Rainer, G. Pernica, D.E. Allen, Dynamic loading and response of footbridges. *Canadian Journal of Civil Engineering*, 15 (1), 66-71, 1988.

[7] D.A. Winter, *Biomechanics and motor control of human movement*, second edition. John Wiley & Sons, Toronto, Canada, 1990.

[8] J. Perry, *Gait analysis: Normal and pathological function*. Thorofare, New Yourk, USA, 1992.

[9] AMTI User manuals, Advanced Mechanical Technology, Inc., Watertown, MA, USA, 2008.

[10] A.B. Thorton-Trump, R. Daher. The prediction of reaction forces from gait data. *Journal of biomechanics*, 8, 173-178, 1975.

[11] D.I. Miller, M.A. Nissinen, Critical examination of ground reaction force in the running forward somersault. *International Journal of Sport Biomechanics*, 3, 189-206, 1987.

[12] M.M. Bobbert, H.C. Schamhardt, B.M. Nigg, Calculation of vertical ground reaction force estimates during running from positional data. *Journal of Biomechanics*, 24, 1095-1105, 1991.

[13] Sir I. Newton, *Philosophiae Naturalis Principia Mathematica (Mathematical principles of natural philosophy)*. Edmund Halley, ed., London, UK, 1687.

[14] P. de Leva, Adjustments to Zatsiorsky-Seluyanov's segment inertia parameters. *Journal of Biomechanics*, 29 (9), 1223-1230, 1996.

[15] Codamotion user manuals, Charnwood Dynamics Ltd., Leicestershire, UK, 2010.

[16] V. Racic, J.M.W. Brownjohn, A. Pavic, Experimental identification and analytical modelling of human walking forces: Literature review. *Journal of Sound and Vibration*, 326, 1-49, 2009.

[17] QA750 user manual. Washington, USA, Honeywell International, Inc, 2010.

[18] S. Yao, J.R. Wright, A. Pavic, P. Reynolds, Experimental study of human-induced dynamic forces due to jumping on a perceptibly moving structure. *Journal of Sound and Vibration*, 296, 150-165, 2006.

[19] M.J. Griffin, *Handbook of human vibration*. Academic Press, London, UK, 1996.

[20] J.M.W. Brownjohn, Energy dissipation from vibrating floor slabs due to human-structure interaction. *Shock and Vibration*, 8, 315-323, 2001.

[21] R.W. Clough, J. Penzien, *Dynamics of structures*. Mcgraw-Hill, Inc, Singapore, 1993.

[22] H. Bachmann, A.J. Pretlove, H. Rainer, Dynamic forces from rhythmical human body motions, Appendix G. In: *Vibration problems in structures: practical guidelines*, Birkhäuser Verlag, Basel, Switzerland,1995.

COMPDYN 2011
3rd ECCOMAS Thematic Conference on
Computational Methods in Structural Dynamics and Earthquake Engineering
M. Papadrakakis, M. Fragiadakis, V. Plevris (eds.)
Corfu, Greece, 25-28 May 2011

FOOTBRIDGE LATERAL VIBRATIONS INDUCED BY SYNCHRONISED PEDESTRIANS: AN OVERVIEW ON MODELLING STRATEGIES

Fiammetta Venuti[1] **and Luca Bruno**[1]

[1]Politecnico di Torino, Department of Structural and Geotechnical Engineering
Viale Mattioli 39, I-10125, Torino, Italy
e-mail: {fiammetta.venuti,luca.bruno}@polito.it

Keywords: crowd-structure interaction, complex system, synchronisation, crowd dynamics, footbridges, lateral vibrations.

Abstract. *This paper aims to provide a review and critical analysis of the state of the art concerning crowd-structure interaction phenomena on footbridges. The problem of lateral vibrations induced by synchronised pedestrians, namely the Synchronous Lateral Excitation, is specifically addressed. Due to the multi-physic and multi-scale nature of the complex phenomenon, several research fields can contribute to its study, from structural engineering to biomechanics, from transportation engineering to physics and applied mathematics. Among the different components of the overall coupled dynamical system - the structure, the crowd and their interactions - the latter ones are separately analysed from both a phenomenological and modelling point of view. A special attention is devoted to those models, which explicitly account for the interaction between mechanical and living systems.*

1 INTRODUCTION

The interaction between the structure and the crowd walking on it, and among the pedestrians within the crowd, gives rise to a multi-scale multi-physic complex dynamic system. The latter is characterised by collective phenomena that are not only due to the features of the single system components but also to their interactions. Specifically, the crowd behaviour, in particular the pedestrian force exerted on the structure, affects the structural dynamic properties and response, and the latter modifies the behaviour of the pedestrians walking on the moving structural surface.

This contribution provides a review and critical analysis of the state of the art on the modelling of the interactive dynamics involving crowds and structures, specifically focused on the so-called lively footbridges. Indeed, a specific kind of crowd-structure interaction phenomenon, the so-called Synchronous Lateral Excitation (SLE), is likely to occur on lively footbridges in the lateral direction, due to the pedestrian sensitivity to lateral vibrations which affect their balance during gait. The SLE has attracted the increasing attention of structural engineers and researchers in the last few years. While all over the 20th century the research was mainly directed towards the effects of pedestrian vertical excitation, the closure of the London Millennium Footbridge in 2000 [1, 2] focused the attention towards the problem of lateral vibration due to synchronised pedestrians. The frequency of occurrence of SLE has recently grown due to the construction of a great number of lively footbridges. In fact, bacause of the aesthetic requests for greater slenderness and lightness, newly built footbridges are often characterised by reduced mass, stiffness and damping, so that they are extremely prone to vibration.

The increasing interest for footbridge dynamics in the Civil Engineering field is testified by the growing number of papers published in international journals: a non-exaustive survey of the number of peer-reviewed papers cited in this review versus time is provided in Figure 1a. The organisation since 2002 of a specific international conference named ‘Footbridge’ mainly devoted to this issue, the recent publication of guidelines for the design of footbridges under human action [3, 4] and the start-up of dedicated European research projects [5, 6] confirm that the crowd-structure interaction is one of the topical research subjects in structural dynamics.

According to the writers’ opinion, in spite of the great scientific effort in this field and the significant advances in the comprehension of the phenomenon, the study could benefit of the contribution of other research fields to achieve general and conclusive results. First, the understanding and modelling of the multi-scale multi-physic phenomena involved by crowd-structure interaction makes it necessary to collect contributions from several research fields in a multidisciplinary frame, besides that of structural engineering: for instance, the pedestrian walking behaviour has been extensively studied in the field of biomechanics, while crowd modelling belongs to transportation, physics and applied mathematics research fields. This review aims to offer a contribution to the convergence of these knowledges: the distribution of the references cited in this work among the above mentioned research fields is shown is Figure 1b, where the papers are classified according to the journal or authors main scientific affiliation. Second, engineering and, more in general, technological sciences traditionally experience some difficulties in considering the peculiar behaviour of living systems in the interaction between inner mechanical systems and outer systems, even though this aspect is relevant in some specific cases such as the modelling of crowd and structures. It is well understood, in the case of crowd, that human and animal behaviour follow specific strategies, in some cases we can call it intelligent behaviours, that modify laws of classical mechanics [7, 8, 9, 10, 11, 12]. This is a specific characteristic of all living systems even in the case of low scales such as insects [13]

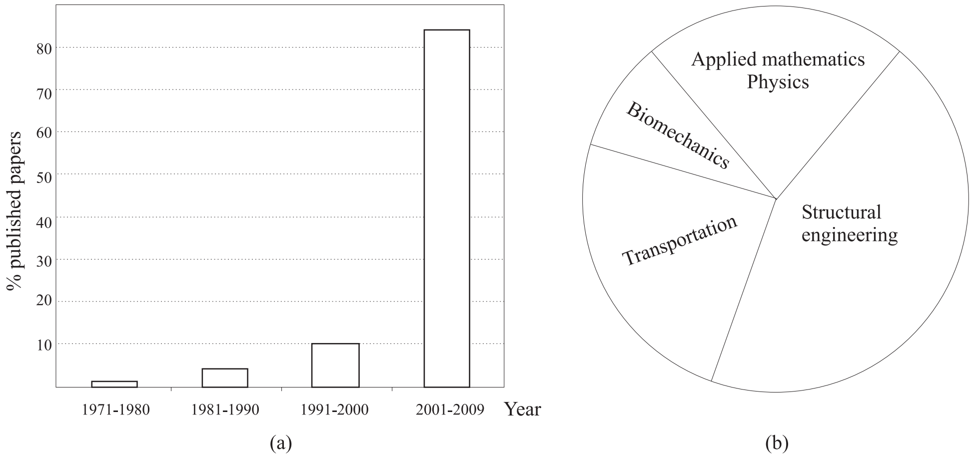

Figure 1: Published paper in the Civil Engineering field (a) and scientific affiliation of the cited references (b)

or cells [14, 15]. It is worth stressing that the coupling of living and mechanical systems is characterised by peculiar issues that have to be carefully taken into account in a comprehensive modelling approach. Summarising two specific aspects:

(i) The dynamics of living systems follows rules generated by self-organised ability, while mechanical systems follow rules of continuum mechanics according to conservation laws that provide background paradigms that are constant in time.

(ii) The overall system shows hybrid multi-scale characteristics considering that the crowd appears as a discrete system, that is, a system with finite degrees of freedom, while the modelling of structures is developed by continuum models, namely by a system with an infinite number of degrees of freedom.

Both above specific aspects are taken into account in the review proposed in this contribution.

The paper is inspired to the authors' previous review paper [16] and develops in three more Sections. Section 2 is devoted to the state of the art concerning the phenomenological analysis of the behaviour of the crowd dynamics and of the crowd-structure interaction (CSI). Section 3 is addressed to the mathematical models proposed so far to describe the different components of the overall crowd-structure system and the crowd-structure interaction models. Finally, the conclusions and some research perspectives are discussed in Section 4.

2 PHENOMENOLOGICAL ANALYSIS

This section is devoted to a review of the studies that are useful for the understanding and phenomenological description of the crowd-structure interaction phenomenon, named SLE. In the following the studies relative to the crowd behaviour, and those relative to the crowd-structure interaction are briefly analysed. A review of the studies concerning the behaviour of a single pedestrian can be found in [16] and [17].

2.1 Crowd behaviour

Crowds are complex systems, that is, large ensemble of individuals interacting in a non-linear manner. Some of the peculiar features of the pedestrian behaviour are outlined in the following [18]:

1. pedestrians in a crowd represent an example of *collective behaviour*, that is, an individual's action is dominated by the influence of his neighbours, so that the individual behaves differently from the way he/she would behave on his/her own;

2. pedestrians are *active* agents, i.e., under normal conditions without panic onset, they share the same objective of walking with the maximum velocity towards a target (e.g., doors, exit, displays), bypassing possible obstacles and avoiding the most crowded zones (see the concept of *personal space* developed in human sciences and psychology, e.g. in [19]). These strategies enable them to determine actively their walking direction and velocity, without being passively subject to the laws of inertia;

3. pedestrians are *intelligent* agents, i.e., their mind evaluates, selects, and/or makes synthesis of what it perceives according to various psychological criteria (e.g., the level of anxiety [20] or the capacity to perform ensamble evaluations [21]).

4. under normal external and subjective conditions (e.g., the area where pedestrians walk is illuminated allowing visual perception), pedestrians do not perceive the real world locally in space, due to their ability to see up to a given extent around them (the so-called *sensory region* [22]). Moreover, pedestrians react after a time interval has elapsed from the perception time (see e.g., [23, 21]). Therefore, pedestrians in a given position at a given time react to the conditions perceived in front of them at a delayed time, i.e., in a *non-local* way in both space and time ;

5. pedestrians are *anisotropic* agents, i.e., they are not equally affected by stimuli coming from all directions in space. Specifically, they distinguish between ahead and behind, in normal situations being essentially sensitive to what happens in a symmetric visual field focused on their direction of movement;

6. walking pedestrians adapt the depth and width of the sensory region to their travel purpose and to their walking speed (e.g., a pedestrian walking for leisure purposes is expected to scan a wider field than a commuter attaining a train, and the faster a pedestrian walks the deeper the space required to evaluate and react is).

Because of the crowd intrinsic multiscale features, crowd related phenomena can be schematically observed with reference to three different scales [24]:

- *macroscopic scale*, which describes the state of the ensamble of individuals with averaged quantities.

- *mesoscopic scale*, where the state of the system is identified by the probability distribution functions of the microscopic state of the individuals.

- *microscopic scale*, where the contribution of each single individual to the behaviour of the system is described.

Nevertheless, it is worth stressing that this classification obeys to conceptual, experimental and modelling requirements, while unexpected emerging phenomena, expecially in out-of-equilibrium conditions, can result from a mix of individual and collective behaviour involving several scales. In the following, the crowd behaviour is analysed from a macroscopic point of view, since experimental measurements found in literature usually refer to averaged variables, namely the crowd density, velocity and flow, which describe the macroscopic state of the crowd. In this macroscopic framework, the single pedestrian behaviour can be recovered in a limit sense, i.e. when density tends to zero.

In the following, a stationary and homogeneous pedestrian traffic flow described by macroscopic quantities is considered. The so-called *fundamental relation* is valid:

$$q = \rho v, \tag{1}$$

where q is the flow, intended as the number of pedestrians passing a cross-section of an area in a unit of time [ped/ms]; ρ is the crowd density [ped/m^2]; v is the average walking velocity [m/s]. The three variables are macroscopic characteristics of the flow: the graphical representations of their relations are called *fundamental diagrams*. It reflects one of the main feature of crowd behaviour, that is the walking velocity is affected by the crowd density, namely the higher the crowd density, the lower the walking velocity.

Looking at the flow-density diagram in Fig. 2, some relevant quantities can be identified [25]:

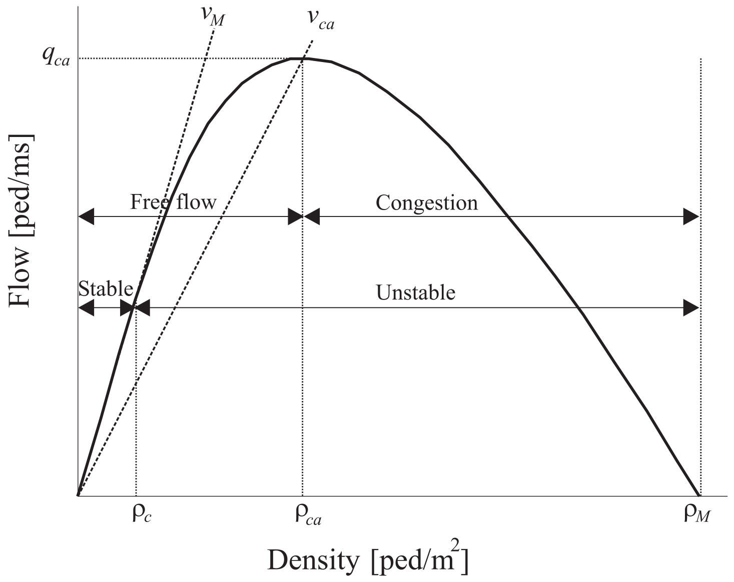

Figure 2: Flow-density fundamental diagram

- free speed v_M: the slope of the function $q(\rho)$ at the origin that corresponds to the velocity if $q = 0$ ped/ms and $\rho = 0$ ped/m^2, that is to the walking velocity of the single unimpeded pedestrian (a review of the available statistics about the single pedestrian velocity can be recovered in [16]);

- critical density ρ_c: the lower bound for unconstrained free walking. For $\rho < \rho_c$, pedestrians walk with constant free speed $v = v_M$ (*stable region*); for $\rho > \rho_c$, the walking speed decreases with increasing density (*unstable region*);

- capacity speed v_{ca} and density ρ_{ca}: the speed and density when $q = q_{ca}$, that is, the maximum flow. The region of density below ρ_{ca} is called *free flow region*, while the *congestion region* corresponds to a higher density than the capacity density;

- jam density ρ_M: the maximum admissible density corresponding to null speed and flow.

The values of the aforementioned variables are not expected to be universal, since walking behaviour is influenced by a great number of microscopic factors, such as age, culture, gender, travel purpose, type of walking facility and single or multiple walking direction [25, 26]. Many studies have been directed to the determination of a law that links the walking velocity to the crowd density. Most of these studies [26, 25] belong to the tranportation research field, with the aim of controlling the layout and dimensions of pedestrian walking facilities.

As far as the jam densities are concerned, they have been estimated to vary between 4 and 5.4 ped/m^2 [27]. The average human body has a width of 45.6 cm and a depth of 28.2 cm [27]. These dimensions refer to a motionless pedestrian. The maximum pedestrian density could be derived from the minimum average body surface (0.13 m^2): this leads to a density of 7.69 ped/m^2, that is difficult to obtain in practice, since people can hardly move at densities over 5 ped/m^2. When pedestrians are walking they require more lateral and forward space than a motionless person. The required lateral additional space has been estimated to be about 62% of the average width of pedestrians [26]. The required forward space (distance among pedestrians d) instead depends on the walking velocity: a linear relation has been proposed by Seyfried et al. [28], as a fitting to experimental data, which is valid in the $0.1 < v < 1$ m/s domain:

$$d = 0.36 + 1.06v. \tag{2}$$

The distance among pedestrians can be expressed as the sum of the step length l_p and the so-called *sensory zone* d_s, defined by Fruin [22] as ”the area required by the pedestrians for perception, evaluation and reaction”. The pioneering Fruin’s definition of this *buffer zone* quantifies one of the distinctive properties of pedestrians as active particles, i.e. their bounded visual field over which environmental information are obtained in order to draw specific, real-time strategies.

Because of the great number of factors affecting pedestrian flows, rather different experimental data and fundamental diagrams can be found in literature. Looking at the experimental data classified with respect to the kind of pedestrian traffic [29, 28, 30] (Fig. 3), it is clear that the Reimer’s measurements, reported in [29], are different from the other ones, since they refer to fast pedestrian transit in train stations and the author himself refers to them as exceptional cases: it is odd that a recent design guideline [3] only reports Reimer’s diagram. One of the first studies, which explicitly accounts for the travel purpose as a parameter that affects the fundamental diagram, was developed by Oeding [29]. He proposed an interesting diagram (Fig. 4), recently recovered in [3] and [34] , which graphs the capacity of pedestrian walkways as a function of density and traffic type. In particular he distinguished four types of pedestrian traffic (shopping, event, rush hour and factory traffic), corresponding to increasing walking velocity and capacity. The diagram also allows a classification of walking regimes to be outlined, that is: free ($\rho < 0.3$ ped/m^2); acceptable ($0.3 < \rho < 0.6$ ped/m^2); dense ($0.6 < \rho < 1$ ped/m^2); very dense ($1 < \rho < 1.5$ ped/m^2); crowded ($\rho > 1.5$ ped/m^2).

An exaustive survey of the speed-density relations proposed so far can be found in [25] and [27]. They are graphically represented in Fig. 5a, which plots the linear relations [25, 27], and in Fig. 5b, where the non-linear laws [7, 26] are reported. It should be reminded that all graphics refer to steady uniform conditions described by macroscopic quantities, therefore fluctuations are lost. Many of the studies report a linear relationship between velocity and density (Fig. 5a), according to the following form:

$$v = v_M - k\rho;\ k > 0. \tag{3}$$

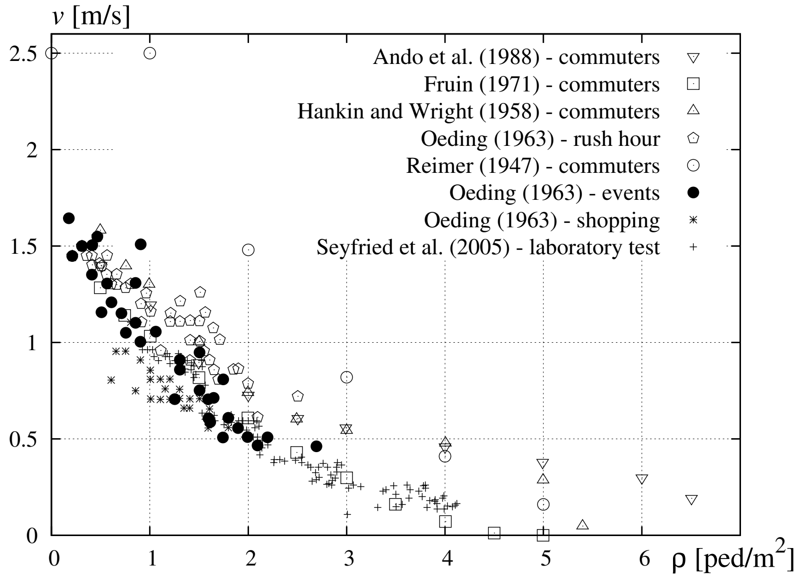

Figure 3: Speed-density relation: experimental data [31, 22, 32, 29, 33, 28]

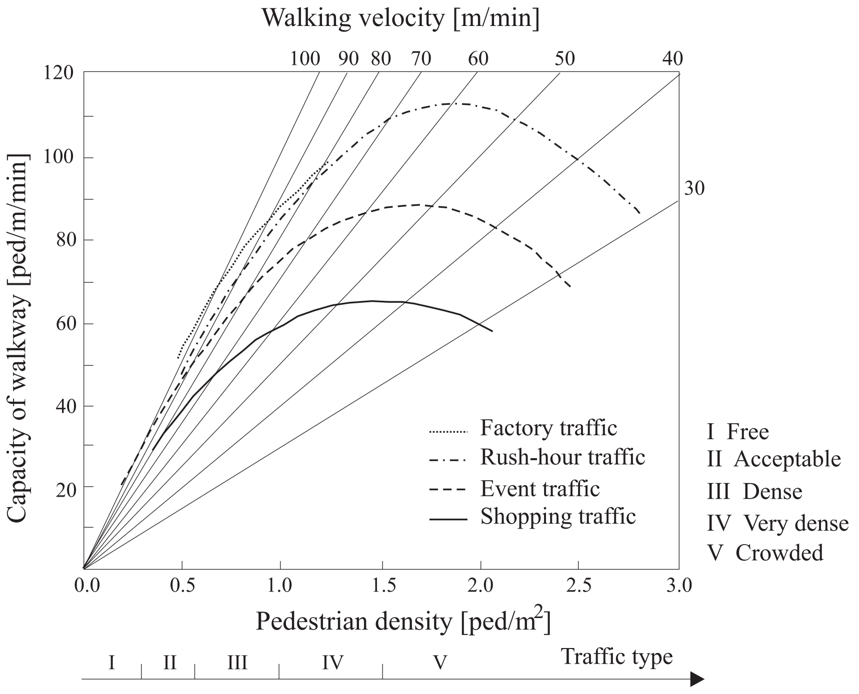

Figure 4: Relationship between bridge capacity, pedestrian density and their velocity, after Oeding [29]

Other authors have proposed non linear laws (e.g. [26]) or multi-regime models (e.g. [7]). In general, the non-linear multi-regime models are more accurate than the linear laws, since they better capture the almost constant speed at low densities and they have the upward concave form that better fits the observation data. In particular, the law proposed by Weidmann, called *Kladek formula*, has the advantage of being a continuous function of ρ, avoiding unrealistic discontinuities, such as in the Hughes' diagram. A parametrical form of the Kladek formula has been proposed in [42], in order to account for the influence on the walking velocity of both psychological and physiological factors, represented by the travel purpose and geographic area,

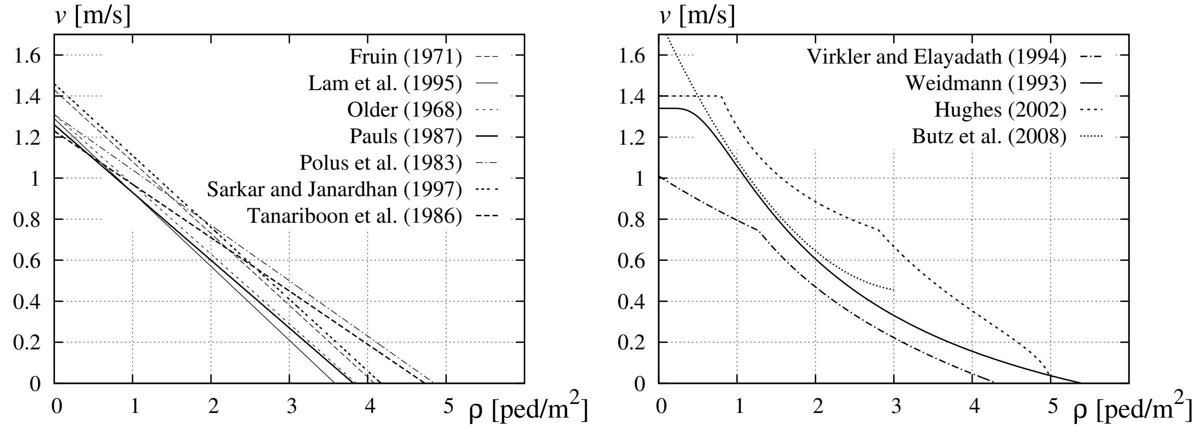

(a) (b)

Figure 5: Speed density relations in literature [7, 5, 26, 22, 35, 36, 37, 38, 39, 40, 41]: linear (a) and non linear (b)

respectively:

$$v = v_M \left\{ 1 - \exp\left[-\gamma \left(\frac{1}{\rho} - \frac{1}{\rho_M} \right) \right] \right\}, \tag{4}$$

where γ is an exponent that makes the relation sensitive to different travel purposes (leisure/shopping, commuters/events, rush hour/business), which is obtained through a fitting of the data in [22, 29]. The jam density ρ_M is expressed as:

$$\rho_M = \frac{1}{\beta_G S_m}, \tag{5}$$

where $S_m = 0.13$ m^2 is the mean surface occupied by a motionless pedestrian and the geographic area coefficient β_G is derived, considering the dimension occupied by the human body in different countries [27], as the ratio between the surface averaged per geographic area and the mean surface. It results that β_G equals 1.075 for the European and American case, while it equals 0.847 for Asian countries. The free speed v_M is expressed in the general form:

$$v_M = \bar{v}_M \, \alpha_G \, \alpha_T, \tag{6}$$

where $\bar{v}_M = 1.34$ m/s is the average free speed [27] and the coefficients α_G and α_T, which make the velocity sensitive to the geographic area and travel purpose, are determined analysing the data reported in [27] as the ratio between the proposed free speeds and $\bar{v}_M$ (Table 1).

Table 1: Coefficients of geographic area and travel purpose

	Travel purpose				**Geographic area**		
	Rush hour/ Business	Commuters/ Events	Leisure/ Shopping		Europe	USA	Asia
α_T	1.20	1.11	0.84	α_G	1.05	1.01	0.92
γ	0.273ρ_M	0.214ρ_M	0.245ρ_M				

It is worthwhile pointing out that the speed-density relations described so far refer to a one-directional flow. In a bi-directional flow, the effects due to passing pedestrians lead to a reduction of the flow capacity. Weidmann [26] estimates a capacity loss of about 4-9% in the case of equal flows in both directions (50%/50% or directional ratio = 1) and a higher capacity loss (about 14.5%) for a directional ratio of 10%/90%. This result has to be ascribed once more to the pedestrian intelligent behaviour and it follows from the self-organised phenomena which take place in the crowd: a directional ratio close to unit induces a two-lane natural configuration, where each pedestrian tends to keep his/her right due to cultural influences; low directional ratios and wide pedestrian walkways do not allow the upstream pedestrians to organise together, so that they are viewed by the main stream as moving obstacles, involving a significant capacity loss.

Finally, it is worth drawing some considerations about flow dimensionality. Many of the proposed relations refer to pedestrian movement on a plane. Seyfried et al. [28] showed that the measurement of the speed-density relation for a single-file movement of pedestrians leads to results in complete agreement with Weidmann's diagram: this means that specific two-dimensional features, such as internal friction and lateral interference, do not have a strong influence on the fundamental diagram in the considered density range.

In conclusion, it can be stated that it is not possible to determine a universally valid speed-density relation, since the pedestrian behaviour is affected by a great amount of parameters. For this reason, a specific law should be tuned in order to characterise a particular crowd condition. Furthermore, it should be borne in mind that the fundamental diagrams are derived in steady state conditions: this means that the quantities characterising the system vary slowly with respect to space and time. Therefore, fundamental diagrams, like the ones presented in this section, are not suitable for direct use in out-of-equilibrium conditions.

Althought density and velocity are the main macroscopic state variables of the crowd, other quantities are of interest in the perspective of the modelling of the crowd dynamic load acting on a structure and of the crowd-structure interaction. Among these quantities, let us recall the walking frequency, which affects in turn the pedestrian force frequency content, and a measure of the degree of synchronisation among pedestrians (e.g., the walking phase, the standard deviation of the walking frequency or, more in general, a correlation coefficient).

As for the walking frequency, it has to be intended as a vertical one f_{pv}, that is, the number of times a foot touches the ground in a time unit, while the horizontal or lateral walking frequency f_{pl} is intended as the number of times the same foot touches the ground. At the individual level (single unimpeded pedestrian at $\rho = 0$), the former depends on the free walking velocity v_M and on the step length l_s according to the fundamental walking law

$$f_{pv} = \frac{v_M}{l_s}, \tag{7}$$

where the mentioned walking parameters are random variables whose statistical moments are obtained by ensemble averaging of experimental measurements [5, 43, 44, 45, 46, 47, 48]. In the case of constrained pedestrians in a crowd ($\rho > 0$), the free speed v_M in Eq. 7 should be replaced by $v(\rho)$ and all the walking parameters should be intended as macroscopic averaged quantities. In this macroscopic framework, different empirical $f_{pv} - v$ laws have been proposed as a fitting to experimental measurements. Linear relations have been proposed, for instance, by Butz et al. [5], on the basis of the Oeding's measurements [29]:

$$f_{pv} = 0.7886 + 0.7868v, \tag{8}$$

and by Ricciardelli et al. [46]:

$$f_{pv} = 0.024 + 0.754v, \tag{9}$$

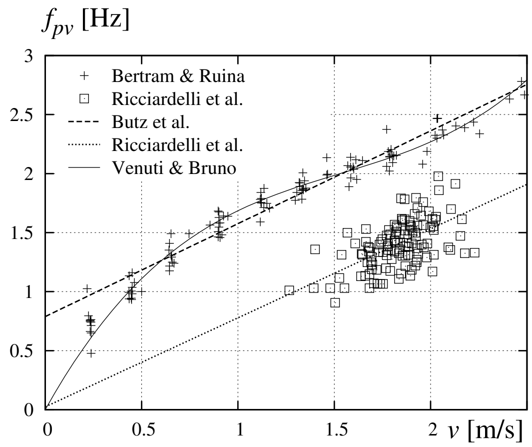

Figure 6: Examples of $f_{pv} - v$ relations

who observed that the constant value 0.024 m/s derived from the fitting can be neglected for engineering purposes. A non linear relation based on a cubic fitting to the data of Bertram and Ruina [49] has been proposed in [50]:

$$f_{pv} = 2.93v - 1.59v^2 + 0.35v^3. \tag{10}$$

The three $f_{pv} - v$ laws are compared in Fig. 6.

As for the degree of synchronisation among pedestrians in a crowd, when a pedestrian's walking is constrained because of high density values, people tend to walk with the same frequency and a null relative phase angle, that is, they synchronise to each other [51]. This behaviour is due to the attempt to avoid foot-to-foot contact in the forward direction and shoulder-to-shoulder contact in the lateral direction. Some experimental evidence of the former attempt has been obtained by Seyfried et al. [28] who observed that pedestrians tend to optimise the available forward space in case of high density, giving some overlap in the space occupied with the pedestrian in front.

So far a limited number of experimental tests has been devoted to the investigation and quantification of the synchronisation among pedestrians in dense crowds, even though it could play a crucial role in crowd-structure interaction, acting as a inner trigger of the pedestrian-structure synchronisation. In the last two years some new studies [5, 52, 53] have been carried out by means of experimental tests performed within different ranges of the crowd density. Arajo *et al.* [52] found that, in the crowd density range 0.3-0.9 ped/m^2, there is no evidence of synchronisation among pedestrians, since the standard deviation of the walking frequencies is almost constant for different densities and the phase angles are totally random. Ricciardelli and Pizzimenti [53] observed that, in the crowd density range 0.5-1.5 ped/m^2, initially different walking frequencies and phases tend to get closer for increasing crowd densities, giving rise to synchronisation nuclei within the crowd. Finally, Butz *et al.* [5] performed tests in which pedestrian streams with densities varying between 1.2 and 3 ped/m^2 walked along a 30 m long and 1.5 m wide path and their walking frequencies were measured with pressure sensors located in the right shoes. They found that the standard deviation of step frequencies for high crowd density was lower than for low density, indicating a higher correlation among pedestrians in the first case.

Besides the above mentioned experimental approach, some interesting suggestions to the comprehension of the phenomenon can be found in the fields of physics and applied mathematics. In fact, the synchronisation among pedestrians can be ascribed to *collective synchronisation* phenomena, which have been studied from the Sixties in the pioneering works of Winfree [54] and Kuramoto [55]. Collective synchronisation occurs when "an enormous system of oscillators spontaneously locks to a common frequency, despite the inevitable differences in the natural frequencies of the individual oscillators" [56]. Several examples can be found in the natural world, from the pacemaker cells in the heart, to flashing fireflies. Winfree studied the behaviour of a large population of weakly-coupled, nearly identical limit-cycle oscillators: when the spread of natural frequencies is large with respect to the coupling strength K, the system behaves uncoherently; as the spread decreases, the system behaves uncoherently until a threshold K_c is crossed (Fig. 7). Then, a small cluster of oscillators synchronises and the coherency grows towards perfect synchronisation: the threshold K_c, therefore, corresponds to a *phase transition*.

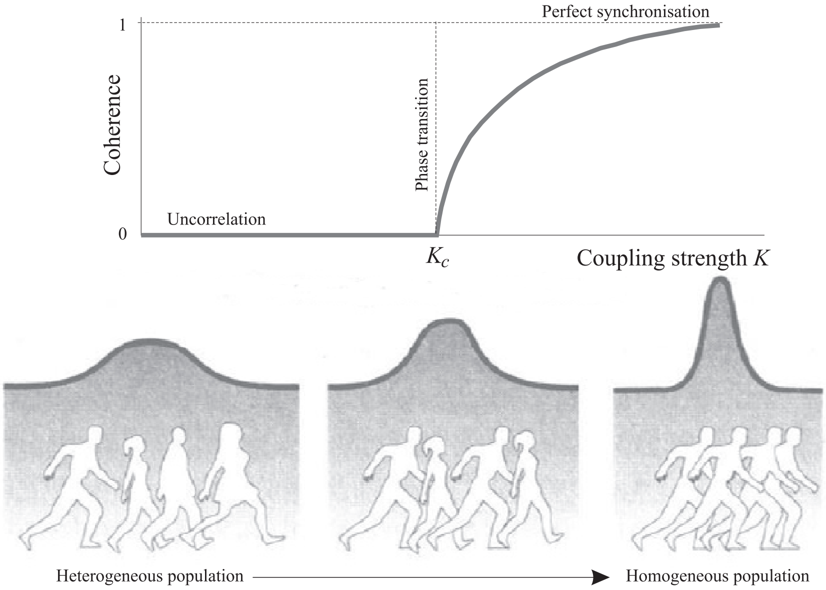

Figure 7: Schematic representation of the Winfree's model after Pizzimenti [57]

Pizzimenti [57] observed that the phase transition described by Winfree could interpret what has been observed on the London Millennium Bridge in its opening day: first, small groups of pedestrians started to synchronise; then, when the number of pedestrians exceeded a critical value, most of them were captured in the synchronisation phenomenon.

2.2 Pedestrian behaviour on a vibrating platform: crowd-structure interaction

When a pedestrian crosses a lively footbridge, he walks on a vibrating surface, therefore, if the vibrations become perceptible, human-structure interaction can occur. As stated in the Introduction, pedestrians are more sensible to lateral vibrations of the walking surface, therefore they are more likely to synchronise with the deck lateral motion. Indeed, because of the attempt to maintain body balance, the pedestrians unconsciously adapt their lateral frequency to the lateral natural frequency of the moving surface. A scheme of the pedestrian-structure synchronisation, also known as *lock-in* in structural engineering, is represented in Figure 8 [5]: if the lateral movement of the torso has the same frequency and is in phase with the deck lateral velocity, the work $W = \int_T F\dot{z}dt$ is always positive, that is, the pedestrian provides positive energy input, causing the vibrations to enlarge. As a consequence, pedestrians walk with their legs more widespread, the lateral motion of the upper part of the torso increases and the resulting lateral force grows in turn in a self-excitation mechanism, which characterises the SLE. This phenomenon is amplified if the pedestrian walks in a dense crowd, since the synchronisation among pedestrians (§2.1) can trigger or increase the effects of the pedestrian-structure synchronisation [58, 59]. So far, the phenomenon has never led to structural failure since it has a self-limited nature, that is, when the vibrations exceed a limit value pedestrians detune, stop walking or touch the handrails, causing the vibrations to decay. It is worth pointing out that the above mentioned phenomena responsible for the self limited nature of SLE are essentially due to the intrinsic features of the pedestrians that behave as active and intelligent agents (see the beginning of §2.1). Nevertheless, the resulting reduced comfort for the users has often led to a temporary closure of the footbridge in order to provide proper countermeasures, with consequent economic and social repercussions.

It is worth pointing out that human-structure interaction has also been observed by some authors in the case of vertical vibrations [60, 61]. In particular, humans' inability to synchronise their pace with vertically moving surfaces causes the vibration to diminish, as if pedestrians provide additional damping to the system. This effect, which is well-known in the case of stationary people, is not completely understood in the case of moving people and needs further investigations.

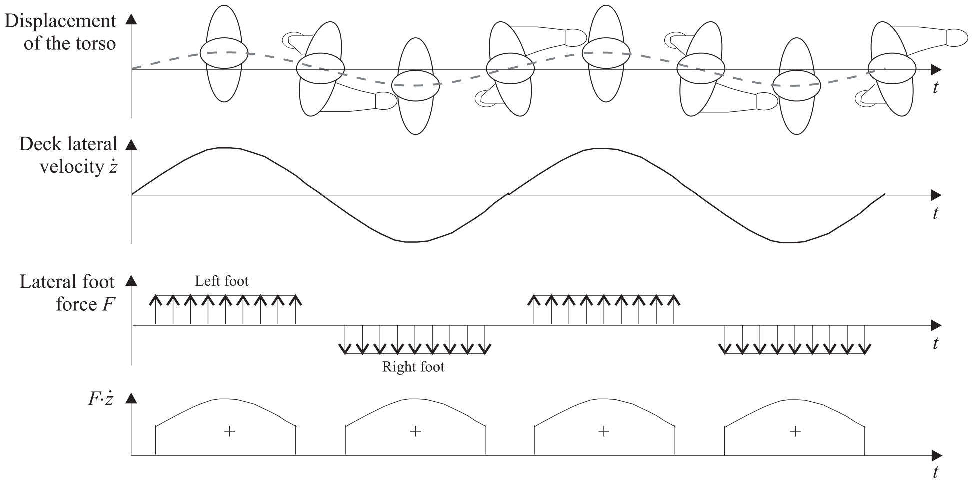

Figure 8: Schematic representation of pedestrian-structure synchronisation after Butz et al. [5]

The SLE is not related to a specific structural type, but it "could occur on any bridge with a lateral frequency below about 1.3 Hz loaded with a sufficient number of pedestrians" [1] (see [61] for a review of bridges exhibiting SLE). In the last few years, many studies have been devoted to the understanding of the SLE, mainly through an empirical approach. The experimental studies can be roughly divided into the following categories: i) laboratory tests on moving treadmills or long vibrating platforms; ii) field tests on real footbridges; iii) observation of videos recorded during real world crowd events; iv) analysis of similar phenomena occurring in nature and studied in different scientific fields.

The first laboratory experiments in the structural engineering field were carried out at London Imperial College and at the University of Southampton to explain what had happened on the London Millennium Bridge [1]. The tests at the University of Southampton involved a person walking "on the spot" on a small shaking table. The tests at Imperial College involved persons walking along a 7.2 m long platform which could be driven laterally at different frequencies and amplitudes. Similar tests on a moving treadmill were also performed by Pizzimenti [57]: the specially built treadmill (Fig. 9a) was laterally driven at different amplitude-frequency configurations. On one hand, treadmill devices permit a steady-state walking behaviour to be easily reached; on the other, they only allow the walking behavior of a single pedestrian to be explored. Moreover, the pedestrian is forced to walk at a given velocity and his/her natural behaviour is affected by the small treadmill surface. Even though these tests did not permit the behaviour of people walking in a crowd to be investigated, they allowed important results to be obtained about the behaviour of a single pedestrian, that is, the amplitude of the exerted lateral force for increasing amplitude of the platform oscillation and the probability that he/she would synchronise his/her pace to the frequency of the moving platform.

In order to better simulate the conditions that can occur on a footbridge, on which groups of pedestrians walk continuously, Setra [4] built a 7 m long and 2 m wide slab on 4 flexible blades moving laterally, in order to measure the horizontal load exerted by pedestrians and to estimate the threshold of motion perception corresponding to the triggering of the lock-in. The device was provided with access and exit ramps in order to maintain walking continuity. These tests showed that there is an acceleration threshold (around 0.1-0.15 m/s^2) above which some synchronisation arises and causes uncomfortable vibrations. A longer platform has been built during the Synpex European project [5]. The 12 m long and 3 m wide test rig was designed to vibrate both in the vertical and horizontal direction (Fig. 9b). One of the main limits of the vibrating platforms built so far is that their reduced length does not permit the synchronisation phenomena to fully develop, so that constitutive relations between the pedestrian state variables and platform motion cannot be drawn in equilibrium conditions. On the other hand, they allow experiments to be performed in a controlled environment, so that the effect of different factors can be isolated.

The phenomenon has also been studied by means of field tests. The tests carried out on the Millennium Bridge during the closure period [1] (Fig. 10) evidenced an almost linear dependence of the pedestrian force on the deck lateral velocity. In addition, the deck acceleration abruptly increased when the number of pedestrians exceeded a critical value. Several test campaigns were also carried out on the Solferino footbridge [4], leading to the following conclusions: the lock-in occurred for the first lateral mode and appeared to start and develop more easily when the step lateral frequency was lower than the deck lateral frequency; lock-in occured beyond a particular threshold, that can be determined in terms of critical number of pedestrians (as proposed in [1]) or critical value of acceleration, which seems more relevant;

(a) (b)

Figure 9: Example of treadmil and moving platform after Pizzimenti [57] and Butz et al. [5]

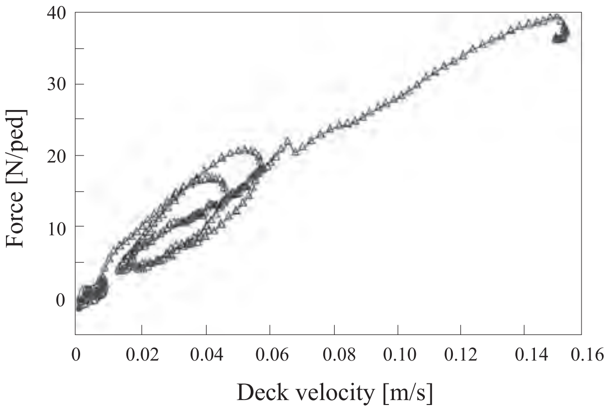

Figure 10: Lateral force per person per vibration cycle vs deck velocity, after Dallard et al.[1]

below 0.1 m/s^2, the pedestrian behaviour may be considered not related to the structure motion. Field measurements were also conducted by Nakamura [62] on the M-bridge in Japan. Accelerometers in the lateral direction were attached to the base of the handrails at five positions and accelerometers were also attached to the waist belt of a person, who walked on the bridge among other pedestrians. The measurements confirmed that the pedestrian walked at the same frequency as the girder and showed that the pedestrian's phase is between 120° and 160° ahead of the girder. A comparison between the time histories of the girder and pedestrian lateral motion also showed that the pedestrian was sometimes no longer tuned to the structure (Fig. 11): this means that he sometimes lost his balance because of large girder vibrations. By analising the behaviour of three footbridges (Millennium Bridge, T-bridge and M-bridge), Nakamura proposed a serviceability limit for lateral vibration, that is, a displacement of 45 mm (a velocity of about 0.25 m/s and an acceleration of about 1.35 m/s^2). Nakamura also observed that synchronisation is unlikely to occur at a deck natural frequency under 0.6 Hz. The same conclusion can also be inferred from the tests performed by Pizzimenti on the moving treadmill [57]. Finally, it is worth citing the experimental campaigns conducted during the Synpex project, which involved field tests on several footbridges, such as the Pedro and Ines footbridge in Coimbra (Portugal) [63] or the stress ribbon bridge at the campus of the University of Porto [64], with the aim of characterising the pedestrian perception of footbridge vibrations, validating load models and identifying the most relevant footbridge dynamic properties. Even though field tests give further information with respect to laboratory tests, it has to be pointed out that in both kind of tests the pedestrians do not walk in a completely natural way, since they are conditioned by several constraints (for instance they are asked to tune their pace to the sound of a metronome): this fact should be considered in the interpretation of the test results.

Other suggestions come from the observation of the videos recorded during crowd events or experimental campaigns. Fujino et al. [65] were the first to observe the SLE on the T-bridge in Japan, which connects a boat race stadium to a bus terminal. They recorded human passage during a congested period by means of three cameras installed on the stadium roof, synchronised to each other and connected to a computer. The motion of a selected number of pedestrians' heads were digitised from the video by means of a microcomputer [66]. The head motion time histories showed a surprising similarity, i.e. they were synchronised although the amplitudes were different. Fujino et al. estimated a percentage of synchronised pedestrians of about 20%.

Finally, as in the case of the synchronisation among pedestrians, some useful hints can be found in the wide literature about synchronisation in natural sciences [67]. The pedestrian-

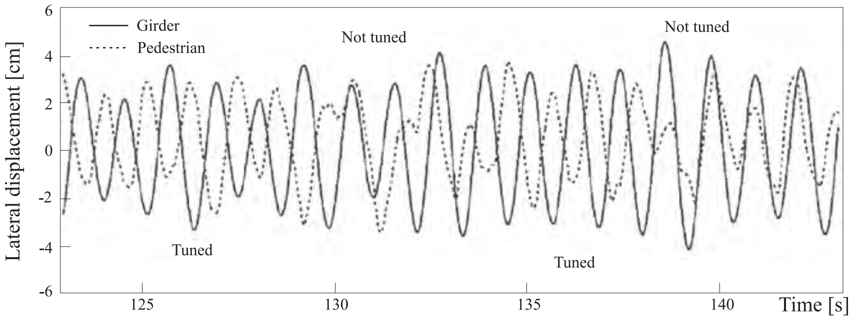

Figure 11: M-bridge: lateral displacements of girder and pedestrian at the L/4 position, after Nakamura [62]

structure synchronisation is, in fact, an example of entrainment of a self-sustained periodic oscillator by an external force, where the pedestrian is the oscillator, while the external force is represented by the structure inertial force, which is proportional to the structure acceleration. Lets ω_p be the circular frequency of the autonomous oscillator, Ω_p the frequency of the driven oscillator and ω_s the frequency of the external force. For a fixed value of the force amplitude $\bar{F}$, the frequency of the driven oscillator depends on the *frequency detuning*, i.e. on the difference $\Omega_p - \omega_s$: for small absolute value of the detuning, the external force entrains the oscillator (i.e. $\Omega_p = \omega_s$) even for low value of the force amplitude; if the detuning is above a critical threshold, the synchronisation occurs only by increasing the value of the force amplitude $\bar{F}$. Fig. 12a plots the frequency difference $\Omega_p - \omega_s$ versus ω_s for a fixed value of $\bar{F}$: the identity of frequencies that holds within a finite range of the detuning is called *frequency locking*. The trend of the frequency detuning $\Omega_p - \omega_s$ versus ω_s and $\bar{F}$ is sketched in Fig. (12b): the domain where $\Omega_p = \omega_s$ is called *synchronisation region* or *Arnold tongue* and is highlighted in grey.

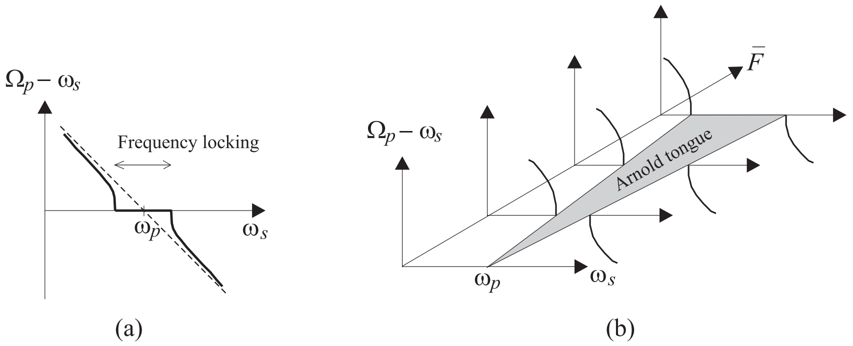

(a)

(b)

Figure 12: Frequency locking (a) and Arnold tongue (b) [67]

This framework applies to another phenomenon which has some similarities with the SLE and for this reason has inspired some authors [68, 69, 70]: it is a fluid-structure interaction (FSI) phenomenon commonly known as lock-in in Wind Engineering. In this case, the cross-flow oscillations of a bluff structure are due to and interact with the shedding of vortices in its wake. Even though the vortex-induced and crowd-induced oscillations differ in their causes and in the kind of physics they belong to (i.e. purely classical fluid and solid mechanics for FSI, hybrid classic and physics of life for CSI), they show analogous features about the structural response. In a given range of the incoming wind velocity (i.e. the synchronisation region), the vortex-shedding frequency is in fact constant and equal to the frequency at which the structure oscillates, rather than being a linear function of the wind velocity, as stated by the well-known

Strouhal law [71]. In other terms, the structural motion affects the wind flow so that synchronisation occurs and the resonance condition takes place. Furthermore, both phenomena are self-limited, in the sense that structural oscillations do not proceed to divergent amplitudes but enter a limit cycle even though the structural damping is null. These similarities brought some authors [69, 68] to propose the definition of a *pedestrian Scruton number*, in analogy to the Scruton number used in wind engineering. This number, which depends on the structural damping and on the ratio between the structure and crowd mass, can be used as an indicator of the likeliness of occurrence of SLE on a particular footbridge. According to the writers, the introduction of this sinthetic number in CSI is somewhat questionable, because the specific features of the crowd behaviour are not included in.

3 MODELLING STRATEGIES

The earlier and most common approach to deal with the problem of crowd-structure interaction considers and models the pedestrians as a simple action applied to the structure. The problem, therefore, reduces to the calculation of the structural response under the action of a suitable load model. According to this approach, several load models have been proposed (reviewed e.g. in [17]): some of them try to take into account the synchronization by means of empirical coefficients and to establish a dependence of the force on the structural response, givig rise to non linear load models. A different and more recent strategy is inspired to the one adopted for flow/wind-structure interaction problems, that is, the pedestrians are considered as a dynamical system, which has its own governing rules and that interacts with the structure system. This approach results in coupled models characterized by non-linear, multi-physic and multi-scale features and therefore require a computational approach to be solved. Moreover, special attention must be paid to the modelling of the crowd and of the interaction terms because of the special features of the crowd subsystem already mentioned in the previous sections. These modelling issues are treated in the following sections.

3.1 Crowd models

Crowd dynamics modelling is quite recent and is mainly derived from vehicular traffic modelling, which has been widely analysed in the field of applied mathematics and transportation engineering since the pioneering work of Prigogine and Herman at beginning of the Seventies [72]. An up-to-date review and critical analysis of the traffic and crowd models so far proposed can be found in Bellomo and Dogbé [73]. The literature on crowd dynamics, which has been arguably initiated by the works of Henderson (e.g. [8]), has undergone a rapid development in recent years, being motivated by the engineering demand for dimensioning of large transportation facilities, such as underground stations or airport terminals, and by safety problems, such as evacuation under panic conditions in case of danger or structural collapses.

According to the observation scales introduced in §2.1, three different kinds of modelling framework can be derived, corresponding to microscopic, mesoscopic or macroscopic description. It should be pointed out that each type of representation is chacterised by advantages and disadvantages and, at the present state of the art, it is not possible to establish the validity of a class of models with respect to the others [73]. This section is mainly devoted to the macroscopic modelling framework, since it is the only one so far used in crowd-structure interaction literature. Nevertheless, a brief description of the mesoscopic and microscopic mathematical structures is given at the end of the section in the perspective of their future application to this kind of problems. It is worth pointing out that what follows refers to modelling in normal flow condition, that is, in absence of panic, coherently with the subject of this contribution.

The representation of crowds is usually performed in two space dimension. In the writers' opinion, the particular case of interest, namely dense crowds crossing footbridges, can be represented as a monodimensional and unidirectional flow, as in the case of vehicular traffic dynamics. The flow along footbridges is mainly monodimensional because of their line-like geometry (the footbridge length is one or two order of magnitude larger than the width of the walkway) and because pedestrians usually share the main objective of crossing the bridge with maximum efficiency and minimum time [74]. Unidirectional crowd flow frequently occurs on footbridges due to the occurrence of particular events (opening day, demonstrations) or due to their specific function and location (link to transport facilities, such as railway stations or bus terminals). Indeed, most of the SLE occurrences have taken place in one of the above described conditions: for instance, the Maori demonstration on the Auckland Harbour Bridge in 1975, the London Millenium Bridge opening day in 2000 [1], the evacuation from a boat race stadium to the bus terminal in the T-bridge in Japan in 1989 [65]. Neverthless, the more general description in two space dimension is reported in the following: the monodimensional one can be easily derived as a particular case. Therefore, let us consider the system in two space dimension and let D be the domain occupied by the crowd, that can be either bounded or unbounded (Fig. 13).

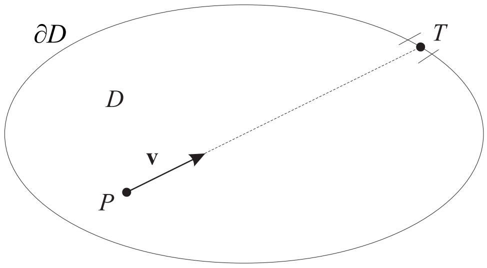

Figure 13: Geometry of the domain occupied by the crowd (P=position, T=target)

3.1.1 Macroscopic models

Macroscopic models, in analogy with the principles of fluid dynamics, refer to the derivation, on the basis of conservation equations and material models, of an evolution equation for the mass density and linear momentum, regarded as macroscopic observable quantities of the flow of pedestrians assumed to be continuous. Macroscopic models are based on the hypothesis that the crowd as a whole acts in a rational way and that all individuals have the same characteristics and share the same goal, called 'target' (T). In addition, the possibility of the presence of objects or persons that the pedestrians want to avoid should be considered in the model by introducing their repulsive effect. The general mathematical framework is given by the system of partial differential equations (PDEs), that express the conservation of mass and momentum, written in two space dimension:

$$\begin{cases} \partial_t \rho + \nabla_{\mathrm{x}} \cdot (\rho \mathbf{v}) = 0, \\ \partial_t \mathbf{v} + \mathbf{v} \cdot \nabla_{\mathrm{x}} \mathbf{v} = \mathbf{A}[\rho, \mathbf{v}], \end{cases} \tag{11}$$

where $\rho = \rho(\mathbf{x}, t)$ and $\mathbf{v} = \mathbf{v}(\mathbf{x}, t)$ are the crowd density and velocity, respectively; $\mathbf{x} = \{x, y\}$ and t are the space and time independent variables, respectively; $\mathbf{A}[\rho, \mathbf{v}]$ models the mean acceleration and square brackets indicate that it may be a fuctional of its arguments; the *dot-product* denotes inner-product of vectors. The functional dependence of $\mathbf{A}$ on its arguments is called a constitutive assumption. Different constitutive assumptions lead to different models, describing different actual situations. According to the specific constitutive assumption, models can be derived that involve only some of the two equations in (11), namely:

- First order models: only described by the first equation with a closure $\mathbf{v} = \mathbf{v}_e[\rho]$ that links the local velocity to the crowd density (e.g. [7]), where the subscript e refers to the equilibrium conditions;
- Second order models: obtained from both equations with the addition of a phenomenological relation that describes the psycho-mechanic action $\mathbf{A} = \mathbf{A}[\rho, \mathbf{v}]$ on the pedestrians, that is, the internal driving force or motivation of the pedestrian.

First order models First order models, which are reviewed in [75], need plugging experimental data into the model through the definition of a suitable closure equation. Different models can be proposed to describe the closure equation, which can be rewritten in the form:

$$\mathbf{v} = v[\rho]\mathbf{u}(\mathbf{x}), \tag{12}$$

where $\mathbf{u}(\mathbf{x})$ indicates a unit vector in the direction of $\mathbf{v}$. Three different models can be distinguished:

1. *Models of first kind.* They assume that the velocity is only a function of the local density, therefore $v(\rho)$ can be simply given by one of the speed-density relations discussed in §2.1. The pedestrians move from position P towards the target T, therefore the direction $\mathbf{u}(\mathbf{x})$ is given by:
$$\mathbf{u}(x, y) = \frac{\overrightarrow{T - P}}{\left|\overrightarrow{T - P}\right|}. \tag{13}$$
2. *Models of second kind.* They are based on the more realistic assumption that the pedestrians move towards the target with a speed that depends not only on the density but also on its gradient:
$$\mathbf{v} = v[\rho, \nabla\rho]\mathbf{u}(\mathbf{x}). \tag{14}$$
This can be achieved, for instance, by using an apparent density model [76] which is based on the concept that the pedestrians feel an apparent density ρ^*, which is larger than the real one, if the local density gradient is positive (trend to jam conditions), while it is smaller than the real one if the gradient is negative (trend to vacuum). The apparent density can be expressed in analogy with the De Angelis' proposal [77] for vehicular traffic as:
$$\rho^* = \rho\left[1 + \eta(1 - \rho)\nabla\rho \cdot \mathbf{u}\right], \tag{15}$$
where η is a positive parameter. Similar effects can be achieved through a non-local model, namely by introducing in the closure equation a space dislocation $\delta \geq 0$, as suggested in [76], so that $v = v[\rho(x + \delta, t)]$. From a phenomenological point of view, the dislocation length takes into account the non local and anisotropic pedestrian behaviour described in §2.1. A similar assumption has been made in [78] for a kinetic vehicular model, where δ is referred to as *visibility length.* A non-local crowd model has been

developed by the writers and coworkers in [18]. The space dislocation introduces in the mass conservation equation a diffusive term that has the effect of turning the hyperbolic equation into a parabolic one. The diffusive term prevents the occurrence of unrealistic shock wave phenomena, due to the fact that equilibrium conditions that correspond to a steady uniform flow are instantaneously imposed in unsteady out-of-equilibrium conditions.

3. *Models of third kind.* First-order models of crowds dynamics can be further improved observing that, in the reality, the pedestrians in a crowd do not follow a straight line towards their target. Rather, in their motion they try avoiding high density zones, in this way following minimum density paths. In this case, also the direction vector depends on the density ($\mathbf{u} = \mathbf{u}(\rho)$).

Second order models Second order models, which are reviewed in [24], need the description of the acceleration term $\mathbf{A}[\rho, \mathbf{v}]$. The acceleration can be viewed as the sum of two contributions:

$$\mathbf{A}[\rho, \mathbf{v}] = A_F[\rho, \mathbf{v}]\mathbf{u}(\mathbf{x}) + A_P[\rho, \mathbf{v}]\mathbf{u}(\mathbf{x}), \tag{16}$$

where A_F is the frictional acceleration, due to the adaptation to the mean flow velocity v_e in steady uniform flow condition, and A_P is the acceleration between pedestrians, due to the adaptation to local density gradients. For a complete review of the specific models that can be obtained from the above general expressions, the interested reader is addressed to [24, 73].

In conclusion, it should be kept in mind that the macroscopic description represents only a rough approximation of the physical reality, since the system under consideration does not satisfy the classical continuity assumption. The flow is in fact granular, which means that distances among pedestrians may not be negligible with respect to the length of the walkway, especially in low density regimes. Another drawback is that macroscopic models assume all pedestrians behaving in the same averaged way. On the other hand, these kinds of models allow a quite immediate application and are characterised by a lower computational complexity with respect to microscopic or kinetic models. Therefore, to the authors' opinion, they are suitable to be used when they have to be coupled with models describing mechanical systems, as in the case of crowd-structure interaction.

3.1.2 Mesoscopic or kinetic models

The so-called generalised kinetic models [73] describe the evolution of the probability distribution functions of the velocity and position of the pedestrians. The mathematical structure is given by a set of non-linear integro-differential equations of the type:

$$\partial_t f(\mathbf{x}, \mathbf{v}, t) + \mathbf{v} \cdot \nabla_{\mathbf{x}} f(\mathbf{x}, \mathbf{v}, t) = \mathcal{J}[f](\mathbf{x}, \mathbf{v}, t), \tag{17}$$

where $f(\mathbf{x}, \mathbf{v}, t)$ is the distribution function over the microscopic state, being $\mathbf{x}$ and $\mathbf{v}$ the position and velocity of the pedestrians at time t, and $\mathcal{J}[f]$ is an operator, in general non linear, which models the interactions among pedestrians.

The existing literature on the application of this approach to crowd dynamics is still in progress (e.g. in [80]). Guidelines and perspective ideas are reported in [73], where some kinetic models developed for vehicular traffic, such as the so-called *models with weighted binary interactions* [81] or *models with long range interaction*, are suggested as suitable to be adapted to pedestrian traffic since they include the concept of visibility zone.

3.1.3 Microscopic models

Microscopic models describe the dynamics of each single pedestrian under the action of the surrounding people. The state of the system is described by the position and velocity of each pedestrian as a function of time. Models developed at a microscopic scale are generally described by a system of ordinary differential equations (ODEs). The structure, analogous to that of Newtonian dynamics, is as follows:

$$\begin{cases} \dfrac{d\mathbf{x}_i}{dt} = \mathbf{v}_i, \\ \dfrac{d\mathbf{v}_i}{dt} = \mathbf{F}_i(\mathbf{x}_i, \ldots, \mathbf{x}_N, \mathbf{v}_i, \ldots, \mathbf{v}_N), \end{cases} \tag{18}$$

where $\mathbf{x}_i(t) = \{x, y\}_i$ is, for $i = 1, \ldots, N$, the position in D of each ith individual of a crowd of N individuals; $\mathbf{v}_i(t) = \{v_x, v_y\}_i$ is the velocity of each person; t is the time independent variable; x and y are the space independent variables.

Different modelling approaches correspond to different ways of representing the acceleration term $\mathbf{F}_i$ on the basis of the interpretation of individual behaviours. Among the different microscopic models that have been developed (e.g. [11]), it is worth citing the *social force models* (e.g. [9, 10, 82], the *cellular automata models* (e.g. [83]) and the *magnetic force models* (e.g [84]).

The solution of Eq. (18) provides the time evolution of position and velocity of pedestrians. Macroscopic quantities, such as density and mass velocity, are then obtained by suitable averaging processes performed either at fixed time over a suitable space domain or at fixed space over a suitable time interval.

The main critical aspects related to microscopic modelling consist in dealing with a large number of equations and in transferring the microscopic information to macroscopic quantities that can be observed or measured. Another issue that should be carefully considered is the heterogeneous behaviour of pedestrians, due to a change in the environmental conditions, such as the transition from normal to panic conditions.

3.2 Force models

A suitable load model should be defined in order to describe the external action that the pedestrians exert on the structure. Force models are generally classified into two main categories [85]: time domain and frequency domain force models. Time domain force models usually describe the pedestrian action as a periodic force: they can be deterministic, when a general model is proposed for each human activity (i.e. walking, running, jumping), or probabilistic, when they take into account the fact that most of the parameters that influence the human force (like body weight or walking frequency) are random variables that should be described in terms of their PDF. Assuming that the structure is a linear or linearized system, frequency domain force models could be alternatively proposed: they are based on the more realistic assumption that pedestrian loads are random processes and walking forces are represented by their PSD. This approach, which is widely used in earthquake engineering, represents a topical research axis in the case of the pedestrian vertical action [86, 87] but, to the authors' knowledge, it has never been directly applied to the SLE.

In the following, the attention will be focused on the time domain force models that have been proposed to describe the action of several pedestrians. Specifically, this section deals with those models that are specifically addressed to the SLE or that try to account for one or both synchronisation phenomena (among the pedestrians and between the pedestrians and the structure), while a critical review extended also to vertical force models can be found in [61, 17].

Bearing in mind the observation scales introduced in 2.1, it is worth pointing out that most of the design-oriented compact force models come from empirical data obtained for the single pedestrian and hence the crowd force is obtained by multiplying the single pedestrian force by an equivalent number of pedestrians. The latter is usually estimated from observation of real crowd events and, according to the authors, it can be considered as an implicit way to tackle the scaling problem involved by passing from the microscopic to the macroscopic description.

Most of the load models proposed in literature are based on some common simplifying assumptions:

- the crowd-footbridge system is modelled as a structural oscillator to which some external load is applied, therefore the crowd is viewed as an imposed load, rather than as a dynamical system;
- the structural response is dominated by one mode, therefore the structure dynamics is described by the following equation of motion:

  $$\ddot{p}_j(t) + 2\xi_j\omega_j\dot{p}_j(t) + \omega_j^2 p_j(t) = \frac{1}{M_{sj}}F_j(t), \tag{19}$$

  where $p_j(t)$ is the principal coordinate of the jth mode, ξ_j is the jth modal damping ratio, $\omega_j = 2\pi f_{sj}$ is the jth natural circular frequency being f_{sj} the natural frequency, M_{sj} is the modal mass and $F_j(t)$ the modal force;
- the crowd is uniformly distributed along the footbridge span;
- the force is periodic and represented by a Fourier series [88, 89]. Usually only a single harmonic, having the same frequency as the footbridge frequency, is retained.

In order to give a homogeneous description of the selected models, a common notation is introduced. The percentage of synchronised pedestrians is generally indicated as S, while the nomenclature S_{ps} and S_{pp} is introduced when the authors explicitly refer to the synchronisation between the pedestrians and the structure or among the pedestrians, respectively.

Before focusing on the lateral force models, it is worth citing the Matsumoto et al.'s [44] model, firstly derived for bridges vibrating in the vertical direction, since it represents one of the first attempts to model the action of several pedestrians. Assuming that the number of pedestrians per second that enter the bridge follows a Poisson distribution and that they walk with the same frequencies and random phases, the total structural response can be obtained by multiplying a single pedestrian's response by the multiplication factor $\sqrt{N}$, where N is the number of pedestrians on the bridge at any time instant. Therefore, the force exerted by N pedestrians can be expressed as:

$$F(t) = \sqrt{N}\alpha G \sin(2\pi f_p t), \tag{20}$$

where α is the Dynamic Load Factor (DLF) - i.e. the ratio of the force amplitude to the weight G of a single pedestrian ($\bar{G} = 700N$) and f_p is the walking frequency. This model considers all pedestrians as uncorrelated, therefore it is not suitable for use in the presence of synchronisation phenomena due to lateral vibrations. In fact, the application of the model to estimate the structural response on SLE test-cases [65] significantly underestimated the measured lateral vibration amplitude.

The possibility of synchronisation among pedestrians due to high crowd density (0.6-1 ped/m^2) is envisaged by Grundmann et al. [90]. Piccardo and Tubino [91] report a force model which interpret this assumption:

$$F(x,t) = S_{pp}\alpha m_c(x) g \sin(2\pi f_p t), \tag{21}$$

where g is the gravity acceleration and $m_c(x)$ is the distribution of crowd mass along the bridge. In case of uniform crowd distribution, $m_c(x)g = NG/L$. Grundmann et al. explicitly ascribe the synchronisation phenomenon to the constrained movement of pedestrians due to high crowd density: for this reason the S_{pp} notation is introduced in Eq. (21). It is worth pointing out that Grundmann et al. disregard the occurrence of crowd-structure synchronisation in the case of perceptibly moving surface: on one hand, the latter phenomenon was described for the first time in the same year by Fujino and co-workers [65] and, on the other hand, the clear distinction between the two kinds of synchronisation has been introduced later [85, 58, 59].

Since the observation of the first SLE occurrences, several models have focused the attention on the synchronisation between the pedestrians and the structure. They generally express the lateral force as a function of the structural response and assume that the pedestrians are synchronised to the structure (i.e. walk with the same frequency as the structure, that is, $f_{pl} = f_s$). Fujino et al. [65] adopted a model similar to Eq. (21), where a guess value of the DLF α has been assumed higher than the one measured on a motionless platform, in order to recover a good estimate of the structural response measured on the T-bridge. After the closure of the London Millennium Bridge and the field tests performed on it, Dallard et al. [1] observed a linear relationship between the lateral force and the local lateral velocity of the deck $\dot{z}$ (Fig. 10), after the pedestrians had synchronised to the structure. Hence, the force exerted by N uniformely distributed pedestrians synchronised to the structure is empirically modelled as:

$$F(x,t) = k_1 \frac{N}{L} \dot{z}(x,t), \tag{22}$$

where the proportionality factor k_1 has to be determined experimentally and set equal to 300 Ns/m for the Millennium Bridge. Bearing in mind that the viscous damping force is proportional to the structural velocity as well as the pedestrian force, the moving pedestrians can be viewed as negative dampers (i.e. amplifiers), providing positive energy input in agreement with the phenomenological observation described in §2.2. If the magnitude of the structural damping force is lower than the one of the pedestrian force, the system is unstable, that is, the structural response tends to infinity for small perturbations. This is not in line with the actual self-limited nature of the force, discussed in §2.2. Another drawback of the model is that it describes the pedestrian action after the lock-in triggering, while it does not permit the pre-lock-in and triggering phases to be modelled. The Dallard et al.'s load model is well-suited to obtain a stability condition for the occurrence of SLE, based on the derivation of a critical number of pedestrians N_c that trigger the lock-in. The latter is derived by setting the equality between the structural modal damping force $2\xi_j\omega_j\dot{p}_j(t)M_{sj}$ and the pedestrian modal force $F_j(t)$, where $F_j(t) = \int_0^L F(x,t)\varphi_j(x)dx$, being L the span length and $\varphi_j(x)$ the mode shape. Other authors have proposed alternative stability criteria [56, 69, 92, 93], which are useful for design purposes, but out of the scope of this review.

Piccardo and Tubino [91] proposed a refinement of Eq. (21), by expressing the DLF α as a linear function of the footbridge lateral displacement z:

$$F(x,t) = S[\alpha + k_2 z(x,t)] m_c(x) g \sin(2\pi f_{pl} t), \tag{23}$$

where $k_2 \cong 2$ m^{-1} from the experimental data in [1]. Such a simple model allows to express the pedestrian force in both cases of motionless or moving platform accounting for the self-excitation mechanism. A single synchronisation coefficient S is introduced, which seems to include both kinds of synchronisation effects. This model shows the same shortcoming as the Dallard et al.'s model, that is, the linear dependence of the DLF on the structural response causes the force to have no upper limit when the pedestrian force is higher than the damping force.

Nakamura and Kawasaki [94] proposed an improvement of the Dallard at al.'s model, in order to account for the force self-limiting. The modal force is expressed as:

$$\begin{cases} F_j(t) = S_{ps} H(\dot{p_j}) k_3(f_{sj}) \alpha M_{pj} g, \\ H(\dot{p_j}) = \dfrac{\dot{p}_j(t)}{k_4 + |\dot{p}_j(t)|}, \end{cases} \tag{24}$$

where the DLF α is taken equal to 0.04 and M_{pj} is the modal mass of the pedestrians. The percentage of pedestrians synchronised to the structure S_{ps} is assumed equal to 0.2 from the laboratory tests of Dallard et al. [1]. The function $k_3(f_{sj})$ describes how pedestrians synchronise with the bridge natural frequency f_{sj}: the authors assume that "pedestrians are most likely to synchronise at the frequency around 1.0 Hz, but it is unknown how wide the bridge frequency range around 1.0 Hz affects the synchronisation nature", so that k_3 is set constant and equal to unit in absence of experimental data. The function $H(\dot{p_j})$ describes the "pedestrians synchronisation nature": the authors assume that the pedestrians synchronise proportionally with the girder velocity at low velocity values, while, for higher values, the pedestrians feel uncomfortable or unsafe and they detune. The value of $k_4 = 0.01$ is determined by trial and error based on the T-bridge data. This model, in spite of its compact expression, provides a more accurate description of the pedestrian-structure synchronisation mechanism, which is recognised to be a function of both the deck velocity and the frequency detuning. A comparison between the force per person obtained with the models of Dallard at al. and Nakamura and Kawasaki is shown in Fig. 14.

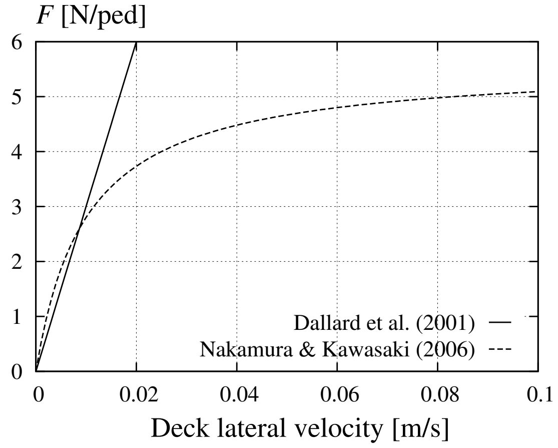

Figure 14: Comparison between the models in [1] and [94]

The models described so far explicitly take into account only one of the two synchronisation phenomena. A more advanced model was proposed by Newland [69], who expressed the lateral load as the sum of two terms, the first representing the force exerted by pedestrians on a fixed ground and the second being the component due to the deck lateral motion, under the hypothesis of small amplitudes of the deck motion ($z < 10$ mm):

$$F(x,t) = S_{pp} m_c(x) \ddot{z}_p(x,t) + S_{ps} \alpha_{ps} m_c(x) \ddot{z}(x, t-\tau), \tag{25}$$

where $z_p(x,t)$ is the displacement of the pedestrian's centre of mass on a fixed ground, α_{ps} is the ratio between the motion amplitude of the pedestrian's centre of mass and the platform (taken equal to 2/3) and τ is the time lag between the motion of the pedestrian's centre of mass and pavement. Because of the lack of data, Newland assumes $S_{ps} = S_{pp} = S$ constant in time and space. The model has the merit of recognising the different contribution of the two kinds of synchronisation and of considering the time delay of the pedestrian reaction with respect to the structural response. On the other hand, Newland assumes that the presence of the pedestrians does not modify the structural modal properties, which is questionable in the case of high crowd to structure mass ratio.

A quite different approach to account for synchronisation phenomena in the force model has been proposed by Strogatz et al. [56]. The model is explicitly formulated in a microscopic framework, where the force exerted by N pedestrians is espressed as:

$$F(t) = \sum_{i=1}^{N} F_i = \alpha G \sum_{i=1}^{N} \sin \Theta_i, \tag{26}$$

where Θ_i is the phase of the ith pedestrian, viewed as a weakly-coupled limit-cycle oscillator, according to the Kuramoto model [55]. This model expresses the Winfree's intuition about collective synchronisation ($\S 2.1$) in the phase equation

$$\frac{d\Theta_i}{dt} = \omega_i + Kr \sin(\Psi - \Theta_i), \; i = 1, \ldots, N, \tag{27}$$

where Θ_i and ω_i are the phase and natural frequency of the ith oscillator, respectively; Ψ is the mean phase; the product Kr is the effective coupling, where K is the coupling strength and r the coherence. As the population becomes more coherent, the effective coupling increases and more oscillators are involved in the synchronisation process, that is, their phases Θ_i tend to the mean phase Ψ. In the Strogatz model, the bridge motion is assumed to alter the pedestrian's gait according to a modified version of Eq. (27):

$$\frac{d\Theta_i(t)}{dt} = \omega_{pi} + k_5 z(t) \sin(\Psi_s(t) - \Theta_i(t) + k_6), \tag{28}$$

where the walking circular frequencies ω_{pi} are distributed with a Gaussian PDF; k_5 models the pedestrian sensitivity to the bridge motion analogously to the coupling strength in the Kuramoto equation; $\Psi_s(t)$ is the phase of the footbridge vibration; k_6 is a phase lag parameter. The most valuable aspect of the model lies in its reference to a well-established research field about collective synchronisation, which recognises the SLE phenomenon among other well-known examples of synchronisation in physics of life. The main shortcoming is due to the difficulty in measuring the parameters k_5, tuned according to the Millennium Bridge case study $k_5 \approx 16$ $\mathrm{m}^{-1}\mathrm{s}^{-1}$, and k_6, assumed equal to $\pi/2$. Moreover, this model does not account for the synchronisation among pedestrians induced by dense crowd. The same model has been rewritten by Bodgi et al. [95] in a macroscopic form and neglecting the phase lag parameter.

The load model proposed by the writing authors [96], unlike the ones previously described, has been conceived within the framework of a crowd-structure interaction model (§3.3). In this perspective, the scaling problem has been explicitly considered in order to assure a consistent modelling scale. Specifically, the force model is based on a macroscopic description of crowd dynamics, which means that the crowd is characterised by its density, averaged walking velocity and step frequency. Both the two types of synchronisation and the contribution of the uncorrelated pedestrians are considered. Hence, the force per unit length exerted by the crowd walking along the bridge span is given by the sum of three components:

$$F(x,t) = F_{ps}(x,t) + F_{pp}(x,t) + F_s(x,t), \tag{29}$$

where F_{ps} is the term due to the synchronisation between the pedestrians and the structure, F_{pp} is due to the synchronisation among pedestrians and F_s is the part due to uncorrelated pedestrians. F_{ps} has the same frequency f_s as the excited lateral structural mode, while the other two terms have the same frequency f_{pl} as the lateral pedestrian footstep. f_{pl} is assumed to vary as a function of the walking velocity v according to Eq. (10). It is worth stressing that the pedestrians who walk with a step frequency equal to f_{pl} are the ones not synchronised to the structure, that is, they are not made sensitive to the deck lateral motion.

Each term of the overall force is weighted on the basis of phenomenological considerations, by means of three weights, N_{ps}, N_{pp} and N_s:

$$\begin{aligned} N_{ps} &= \rho B S_{ps}, \\ N_{pp} &= \rho B S_{pp}(1 - S_{ps}), \\ N_s &= \rho B - N_{ps} - N_{pp}, \end{aligned} \tag{30}$$

where the crowd density $\rho = \rho(x,t)$ is one of the state variables of the crowd system, B is the width of the footbridge walking path, S_{ps} and S_{pp} are the synchronisation coefficients, which both vary in the [0 1] range. It is worth pointing out that these weights can be viewed, at the microscopic scale, as the number of pedestrians that are synchronised with the structure, synchronised to each other and uncorrelated, respectively. Thanks to the distinction of pedestrians in three populations, the model is able to describe the triggering of lock-in: even though no one is synchronised to the structure, the presence of a high crowd density results in a lateral force that triggers the lateral vibration of the bridge.

The pedestrian-structure coefficient S_{ps} is a function of two variables: the envelope of the deck lateral acceleration time history $\tilde{\ddot{z}} = \tilde{\ddot{z}}(x,t)$ and the frequency ratio defined as $f_r = f_{pl}/f_s$. The variation of S_{ps} versus $\tilde{\ddot{z}}$ is given by means of the piecewise function:

$$S_{ps}(\tilde{\ddot{z}}) = \begin{cases} 0 & \tilde{\ddot{z}} \leq \ddot{z}_c, \\ 1 - e^{-b(\tilde{\ddot{z}} - \ddot{z}_c)} & \tilde{\ddot{z}} > \ddot{z}_c, \end{cases} \tag{31}$$

where the second branch is obtained from a fitting of the Dallard at al.'s experimental data [1], with $b = 2.68$. Pedestrians start to synchronise with the structure for values of $\tilde{\ddot{z}}$ higher than a critical acceleration value $\ddot{z}_c$, and everyone is synchronised when $\tilde{\ddot{z}}$ reaches the maximum value $\ddot{z}_M$. $S_{ps}(f_r)$ is supposed to have a Gaussian distribution, with a variance that grows when $\tilde{\ddot{z}}$ increases:

$$\begin{aligned} S_{ps}(f_r) &= e^{[-\eta(f_r - 1)^2]}, \\ \eta(\tilde{\ddot{z}}) &= 50e^{(-20\tilde{\ddot{z}}/\pi)}. \end{aligned} \tag{32}$$

This means that, for increasing values of the deck vibration, the pedestrians who walk with a step frequency that is different from f_s gradually become involved in the synchronisation phenomenon. For $\tilde{\ddot{z}} = \ddot{z}_M$, everyone is synchronised to the structure, whatever the value of f_r. This assumption is in agreement with Fig. 12: in case of large frequency detuning, pedestrians synchronise only for high values of the driving force amplitude, that is, for high values of the deck lateral acceleration. The synchronisation coefficient $S_{ps}(\tilde{\ddot{z}}, f_r)$ is given by the product of Eq.s (31) and (32). It is worth pointing out that the proposed form of S_{ps} can be compared to the product $S_{ps}H(\dot{p}_j)k_3(f_{sj})$ in the Nakamura and Kawasaki's model (Eq. (24)).

The coefficient S_{pp} represents the degree of synchronisation among pedestrians and has been derived through a fitting of the experimental data in [5, 52], concerning standard deviation of walking frequencies as a function of the crowd density [97]. The fitting function is inspired to the trend of the coherence against the coupling strength in the Kuramoto model [55] (see Fig. 7): the coherence (i.e. S_{pp} herein) is null until the coupling strength (i.e. ρ herein) reaches a threshold value (ρ_c), which corresponds to a phase transition; for $\rho < \rho_c$ the coherence grows towards perfect synchronisation. S_{pp} is therefore expressed as:

$$S_{pp}(\rho) = \begin{cases} 0 & \rho \le \rho_c, \\ 1 - e^{a(\rho-\rho_c)} & \rho > \rho_c, \end{cases} \tag{33}$$

where a=8.868 and ρ_c is set equal to 0.6 ped/m^2 [97]. The synchronisation coefficients S_{ps} and S_{pp} can be viewed, in a statistical framework, as cumulative density functions of an exponential and a Gaussian PDF, respectively.

Hence, the components of the total force are expressed as follows:

$$F_{ps} = N_{ps}G[\alpha(\tilde{\ddot{z}})\sin(2\pi f_s t + \pi) + \alpha(\tilde{\dot{z}})\cos(2\pi f_s t)], \tag{34}$$

$$F_{pp} = N_{pp}\alpha G\sin(2\pi f_{pl} t), \tag{35}$$

$$F_s = \sqrt{N_s}\alpha G\sin(2\pi f_{pl} t). \tag{36}$$

The F_{ps} component is written, according to Pizzimenti [57], as the sum of a component 180° out-phase of the acceleration and another in-phase with the lateral velocity. The DLF of the two components are expressed as piecewise functions of the envelopes of the deck lateral acceleration and velocity time history $\tilde{\ddot{z}} = \tilde{\ddot{z}}(x,t)$ and $\tilde{\dot{z}} = \tilde{\dot{z}}(x,t)$, respectively. Their detailed description can be found in [98]: herein it is worth pointing out that their trend comes from a fitting to experimental data for moderate deck vibration and guarantees that the amplitude of F_{ps} is self-limited for higher values of the deck motion. The last feature aims at reaching the same objective as in Nakamura and Kawasaki's model, even though through a different modelling approach. The expressions of F_{pp} and F_s are inspired to the models of Grundmann et al. (Eq. 21) and Matsumoto et al. (Eq. 20), respectively. Neverthless, it is worth recalling that these two force components vanish in congested traffic condition, due to the dependence of the walking frequency on the crowd velocity v, which is in turn dependent on the crowd density ρ (Eq. 4).

With respect to the previously described force models, the last one is based on the phenomenological description of the components of the coupled crowd-structure system in their fundamental constitutive laws, rather than being empirically derived from a single case study. This feature is expected to assure a more general applicability, as shown in [96], where the model is applied to two real cases. Moreover, this model allows several features of the SLE to be accounted for: the dependence of the pedestrian force on the state variables of crowd and structure systems, namely the crowd density and footbridge lateral response; the possibility of a inhomogeneous distribution of the crowd along the deck; the existence of two kinds of synchronisation; the presence of different frequency components in the overall force; triggering of the lock-in phenomena and the resulting self-limited oscillations. On the other hand, some shortcomings should be highlighted: the validity of the basic modelling assumptions expressed in Eq.s (29,30) should be demonstrated; the model is less design-oriented than the previous ones, which have the merit of being expressed by very compact formulas; the introduction of a greater amount of constitutive laws, with respect to the previous compact models, makes it more expensive its validation since several parameters have to be experimentally measured; many of the introduced fundamental laws are expressed in a qualitative way, due to the uncomplete knowledge of the synchronisation mechanisms that drive the SLE and the scarce availability of experimental data. This latter drawback is common to all the reviewed models and makes it difficult both the modelling and the tuning of the introduced parameters.

Finally, it should be reminded that all the reviewed models neglect both the inter-subject and intra-subject variability [99]: this means that, on one hand, all the pedestrians are supposed to exert the same dynamic force and, on the other, that each feet of a single pedestrian produce exactly the same periodic force (deterministic models). These two features could be taken into account by introducing a probabilistic approach, analogously to what proposed in recent codes of practice [5, 4, 100] for both vertical and lateral action of pedestrians not synchronised to the structure: in other words, the parameters that mainly affect the human load (walking frequency, step length, dynamic load factors) are random variables and should be expressed in probabilistic terms.

3.3 Crowd-Structure Interaction models

To the authors' knowledge, the first attempt to propose a crowd-structure interaction model was made by the writing authors in [59, 101], successively developed in [42, 79] and recently adopted by other authors [102, 95] with slightly different formulation of the subsystem models. The framework is based on the so-called *partitioned approach*, which was first proposed by Park and Felippa [103, 104] and is widely used to model multi-physic coupled systems in the aerospace, mechanical and civil engineering fields, e.g. in fluid-structure interaction. According to this approach, systems are analysed through decomposition or partitioning, which is the process of spatial separation of a system into interacting components, called *partitions* or *fields*. One of the main advantages of the partitioned approach is the possibility to separately model each part of the system and to solve it with the most suitable numerical procedures. In such a way, each system component can undergo successive improvements as soon as new experimental data and modelling strategies become available. Furthermore, new components that account for emerging features of the phenomenon can be easily added to the original framework. In the case of crowd-structure interaction, the coupled system is decomposed into two physical subsystems, the Structure (S) and the Crowd (C), which interact between each other by means of forcing terms. In the following, each part of the model is described referring to the framework schematised in Fig. 15.

The Structure subsystem is modelled as a non-linear 3D damped dynamical system, whose equation of motion can be written as:

$$[m_s + m_c(\rho)]\,\partial_{tt}\mathbf{d} + \mathscr{C}\,[\partial_t\mathbf{d}] + \mathscr{L}\,[\mathbf{d}] = F(\rho, \tilde{\ddot{z}}), \tag{37}$$

where $\mathbf{d} = \mathbf{d}(\mathbf{x}, t)$ is the structural displacement, $\mathbf{x} = \{x, y, z\}$ and t are the space and time variables, m_s is the structural mass, m_c is the crowd mass, $\mathscr{C}$ and $\mathscr{L}$ are the damping and stiffness operators, respectively, and $\tilde{\ddot{z}} = \tilde{\ddot{z}}(x, t)$ is the envelope of the lateral acceleration of the deck. Eq. (37) is non-linear for two reasons: first, the forcing term F is a function of both the crowd density and the lateral acceleration of the deck; second, the overall mass m is given by the sum of the structure and the crowd mass. The latter derives from the solution of the PDE

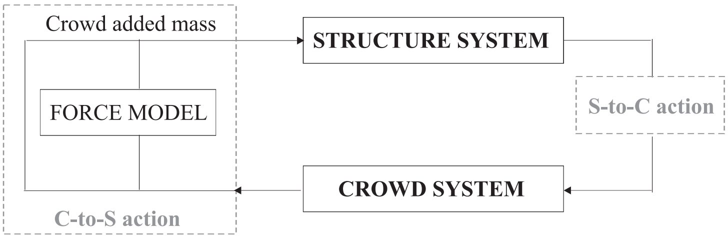

Figure 15: Framework of the time-domain coupled model

that governs the Crowd subsystem, in turn dependent on the solution of Eq. (37).

The crowd is described through a first order hydrodynamic model in the one-dimensional (1D) spatial domain. Even though crowd modelling is usually developed in 2D spatial domain, the mono-dimensional representation is more suitable to describe the phenomenon of interest, that is, dense crowd crossing footbridges, as already highlighted in §2.1. In addition, in spite of the coarse approximation of physical reality implied by the use of first order models, a relatively simple model is preferable to study the complexity of the crowd-structure coupled system. It follows that the reference framework describing the crowd dynamics is given by the 1D mass conservation equation in its Eulerian dimensional form, closed by a phenomenological relation (the closure equation) that links the mean velocity v to the mass density ρ and the lateral acceleration of the deck $\tilde{\ddot{z}}$:

$$\begin{cases} \partial_t \rho + \partial_x (\rho v) = 0, \\ v = v[\rho, \tilde{\ddot{z}}]. \end{cases} \tag{38}$$

The Structure-to-Crowd action is, therefore, expressed through the dependence of the walking velocity on the platform acceleration. Specifically, the pedestrians are assumed to adjust their step to the deck motion with a synchronization time delay τ, which is expected to be greater than the time interval between two succeeding steps ($\tau \geq 1/f_{pl}$). Therefore, bearing in mind that the pedestrians react to what they see in a suitable stretch of walkway in front of them (§3.1.1), both a space dislocation δ and a time delay τ are introduced in the closure equation:

$$v = v[\rho(x+\delta, t)]\; g[\tilde{\ddot{z}}(x, t-\tau)], \tag{39}$$

where the first term $v(\rho)$ is the speed-density relation of Eq. (4), and the second term $g(\tilde{\ddot{z}})$ is a slowing function that takes into account the sensitivity of v to the deck acceleration. The latter has a qualitative trend because of the lack of experimental data and is based on the following hypotheses:

- below the threshold of motion perception $\ddot{z}_c$, the pedestrians are not affected by the platform acceleration;
- the lateral motion of the deck reduces the walking velocity;
- after the pedestrians have stopped because of excessive lateral acceleration $\ddot{z}_M$ at time t_s, a stop-and-go time interval Δt_r should elapse before they start walking again.

It follows:

$$g(\tilde{\ddot{z}}) = \begin{cases} 1 & \tilde{\ddot{z}} \leq \ddot{z}_c \,\cap\, t \geq t_s + \Delta t_r, \\ (\ddot{z}_M - \tilde{\ddot{z}}(x, t-\tau))/(\ddot{z}_M - \ddot{z}_c) & \ddot{z}_c < \tilde{\ddot{z}} < \ddot{z}_M \,\cap\, t \geq t_s + \Delta t_r, \\ 0 & \tilde{\ddot{z}} \geq \ddot{z}_M \,\cap\, t_s < t < t_s + \Delta t_r, \end{cases} \tag{40}$$

where $\ddot{z}_c \cong 0.2$ m/s^2 [105] and $\ddot{z}_M = 2.1$ m/s^2 [62].

As far as the Crowd-to-Structure action is concerned, the scheme in Fig. 15 shows that it takes place in two ways. On one hand, the mass m is constantly updated by adding the pedestrian mass m_c to the structural mass m_s; on the other hand, a force model is proposed to determine the lateral force exerted by pedestrians on the footbridge deck [96]. The force model is the one described in §3.2 from Eq.s (29) to (36), with the following peculiarities: the space distribution of the crowd density along the bridge in any time instant is determined through the solution of Eq. (38); all the variables describing the deck motion that are introduced in the force model equations refer to the time $t - \tau$.

Further developments to this approach to crowd-structure interaction, together with proper numerical solution techniques, could provide a complementary tool to the experimental approach and a useful research tool to validate simplified load models, to reproduce the conditions of in situ tests with lower costs, to simulate scenarios which are difficult to reproduce in full scale, to simulate expected real events and to highlight emergent phenomena.

4 CONCLUSIONS

In this paper a review of the state of the art concerning the phenomenological analysis and modelling of the SLE has been proposed. Due to the multi-scale and multi-physic features of the involved complex phenomena, several scientific fields have been investigated, from biomechanics to structural engineering, from applied mathematics to transportation engineering.

The review has highlighted the still uncomplete knowledge of the mechanisms that drive the SLE, namely the synchronisation phenomena, the dependence of the force exerted by the pedestrians on the structural response, the triggering of the lock-in and the force self-limitation. The importance of a multidisciplinary approach has been outlined in this review, since many interesting suggestions can come from different research fields. Moreover, further experimental campaigns are needed in order to improve the comprehension of the phenomenon, to develop reliable models and to tune the existing ones.

As for the modelling of the parts of the complex crowd-structure system, the structural dynamic models are well-established in literature and widely applied in practice. The situation is different for the crowd models. Three modelling frameworks can be found in literature on the basis of the different observation scales (macro, meso, microscopic), but none of them have so far proved to be the most suitable to describe pedestrian traffic dynamics. The main drawback related to macroscopic models lies in the continuity assumption, which does not hold in case of very low density. On the other hand, microscopic models require handling a large number of model free parameters and equations. A further possibility for future research developments could be the proposal of a hybrid multi-scale approach: the latter could be based on the space and time combination of a microscopic description of the pedestrians in low density regime, through discrete models, with a macroscopic description of the dense crowd, through continuous first or second order models. In this framework, the hybrid approach would be dynamic, in the sense that the switch from one description to the other depends on the time and space evolution of the crowd density, that is, one of the crowd subsystem state variables. In general terms, this approach could be addressed to cope with the difficulty to describe the transition from individual to collective behaviour. Some suggestions in this direction can be found in the approach proposed in [106].

As far as the force models are concerned, the main deterministic time-domain load models specifically addressed to SLE have been reviewed. The difficulty in coupling the need for synthetic formulas to be used in design practice and the accuracy in the description of all the involved phenomena emerges from the review. On one hand, the compact models are not able to account for many of the SLE main features and are often tuned on a specific as-built structure; on the other hand, the load models proposed to tackle the above mentioned shortcomings are more demanding to be validated, due to the large number of constitutive laws introduced, and to be applied for engineering purposes. The difficulty in proposing a reliable load model for SLE is mainly related to the still uncomplete knowledge of the phenomenon. Most of the presented models can be ascribed to a macroscopic description, where inter-subject and intra-subject variability are neglected and all pedestrians are assumed to behave in the same averaged way. This assumption, which is very practical for engineering purposes, is now considered by several authors as not suitable to represent the actual nature of the pedestrian load. Therefore, a probabilistic approach to SLE could be developed.

Finally, the modelling framework proposed by the authors to develop a crowd-structure interaction model on the basis of the partitioned approach has been presented. The approach main advantage lies in the possibility to separately model each system components, which can be characterised to solve a particular problem. In the specific case dealt with in this paper, the framework has been adapted to describe the SLE phenomenon on footbridges. Both the crowd system and the interacting terms have been modelled within a macroscopic description. Even if a macroscopic approach seems more suitable in view of its practical application since it provides synthetic results on the crowd state, the coupling between the structural dynamics and a microscopic crowd modelling could be envisaged for future research perspectives. As for the interacting terms, the general framework could be improved by including new components that should account for some features so far not considered. Among others, the effects of the deck slope on the crowd dynamics is of interest due to the frequent use in civil engineering of structural types (arch structures, cable structures), which imply a deck with variable slope. The effects due to the presence of obstacles could also be modelled, since obstacles can be included in the footbridge design for architectural reasons (such as benches or lighting systems) or their presence could be used to allow control strategies of the pedestrian flow and, in turn, of the structural response.

REFERENCES

[1] P. Dallard, T. Fitzpatrick, A. Flint, S. L. Bourva, A. Low, R. M. Ridsdill Smith, M. Willford, The London Millennium Footbridge, The Structural Engineer 79 (22) (2001) 17–33.

[2] P. Dallard, T. Fitzpatrick, A. Flint, A. Law, R. M. Ridsdill Smith, M. Willford, M. Roche, The London Millennium Bridge: pedestrian-induced lateral vibration, Journal of bridge Engineering 6 (6) (2001) 412–417.

[3] Fédération Internationale du Béton, Guidelines for the design of footbridges, Fib Bullettin n.32 (November 2005).

[4] Sétra/AFGC, Passerelles piétonnes. Évaluation du comportement vibratoire sous l'action des piétons (Mars 2006).

[5] C. Butz, M. Feldmann, C. Heinemeyer, G. Sedlacek, B. Chabrolin, A. Lemaire, M. Lukic, P. O. Martin, E. Caetano, A. Cunha, A. Goldack, A. Keil, M. Schlaich, Advanced load models for synchronous pedestrian excitation and optimised design guidelines for steel footbridges (synpex), Tech. Rep. RFS-CR 03019, Research Fund for Coal and Steel (2008).

[6] HIVOSS, Design of footbridges: guideline and background documents, Research Fund for Coal and Steel, 2008.

[7] R. L. Hughes, A continuum theory for the flow of pedestrians, Transportation Research Part B 36 (2002) 507–535.

[8] L. F. Henderson, On the fluid mechanics of human crowd motion, Transportation Research 8 (1974) 509–515.

[9] D. Helbing, A mathematical model for the behaviour of pedestrians, Behavioural Science 36 (1991) 298–310.

[10] D. Helbing, P. Molnár, Social force models for pedestrian dynamics, Physical Review E 51 (5) (1995) 4282–4286.

[11] S. P. Hoogendoorn, P. H. L. Bovy, Pedestrian route-choice and activity scheduling theory and models, Transportation Research Part B 38 (2004) 169–190.

[12] P. Hoogendoorn, P. H. L. Bovy, Experiments and theory of self-organization in pedestrian flow, in: 85th Transportation Research Board Annual meeting, Washington DC, 2006.

[13] C. Detrain, J. Deneubourg, Self-organized structures in a superorganism: do ants ”behave” like molecules?, Physics of Life Reviews 3 (2006) 162–187.

[14] N. Bellomo, M. Delitala, From the mathematical kinetic, and stochastic game theory to modelling mutations, onset, progression and immune competition of cancer cells, Physics of Life Reviews 5 (2008) 183–206.

[15] D. Chowdhury, A. Schadschneider, K. Nishinari, Physics of transport and traffic phenomena in biology: from molecular motors and cells to organisms, Physics of Life Reviews 2 (2005) 318–352.

[16] F. Venuti, L. Bruno, Crowd-structure interaction in lively footbridges under synchronous lateral excitation: A literature review, Physics of Life Reviews (6) (2009) 176–206.

[17] V. Racic, A. Pavic, J. M. W. Brownjohn, Experimental identification and analytical modelling of human walking forces: Literature review, Journal of Sound and Vibration 326 (2009) 1–49.

[18] L. Bruno, A. Tosin, P. Tricerri, F. Venuti, Non-local first-order modelling of crowd dynamics: a multidimensional framework with applications, Applied Mathematical Modelling 35 (2011) 426–445.

[19] M. Dosey, M. Meisels, Personal space and self-protection, Journal of Personality and Social Psychology 11 (2) (1969) 93–97.

[20] A. Brady, M. Walker, Interpersonal distance as a function of situationally induced anxiety, British Journal of Social and Clinical Psychology 17 (1978) 127 – 133.

[21] S. M. Kosslyn, Measuring the visual angle of the mind’s eye, Cognitive Psychology 10 (1978) 356–389.

[22] J. J. Fruin, Pedestrian planning and design, Elevator World Inc., 1987.

[23] A. E. Patla, Understanding the roles of vision in the control of human locomotion, Gait & Posture 5 (1997) 54–69.

[24] N. Bellomo, C. Dogbé, On the modelling crowd dynamics from scaling to hyperbolic macroscopic models, Mathematical Models and Methods in Applied Sciences 18 (2008) 1317–1346.

[25] W. Daamen, Modelling passenger flows in public transport facilities, Ph.D. thesis, Delft University of technology, Department transport and planning (2004).

[26] U. Weidmann, Transporttechnik der Fussgänger, Tech. Rep. n. 90, ETH, Zürich (1993).

[27] S. Buchmueller, U. Weidmann, Parameters of pedestrians, pedestrian traffic and walking facilities, Tech. Rep. n. 132, ETH, Zürich (October 2006).

[28] A. Seyfried, B. Steffen, W. Klingsch, M. Boltes, The fundamental diagram of pedestrian movement revisited, Journal of Statistical Mechanics 10.

[29] D. Oeding, Verkehrsbelastung und Dimensionierung von Gehwegen und anderen Anlagen des Fußgängerverkehrs, StraSSenbau and StraSSenverkehrstechnik 22.

[30] Z. Fang, S. M. Lo, J. A. Lu, On the relationship between crowd density and movement velocity, Fire Safety Journal 38 (2003) 271–283.

[31] K. Ando, H. Ota, T. Oki, Forecasting the flow of people (in japanese), RRR, Railway Res Rev 45 (8) (1988) 814.

[32] B. D. Hankin, R. A. Wright, Passenger flow in subways, Operational Research Quarterly 9 (2) (1958) 8188.

[33] K. Reimer, Die Bewegung der Menschenmassen in Verkehrsräumen, Glasers Annalen 11 (1947) 121–131.

[34] M. Schlaich, Planning conditions for footbridges, in: Proceedings Footbridge 2002, Paris, 2002.

[35] H. K. Lam, J. F. Morrall, H. Ho, Pedestrian flow characteristics in hong kong, Transportation Research Record 1487 (1995) 5662.

[36] S. J. Older, Movement of pedestrians on footways in shopping streets, Traffic Engineering and Control 10 (4) (1968) 160163.

[37] J. Pauls, Calculating evacuation times for tall buildings, Fire Safety Journal 12 (1987) 213236.

[38] A. Polus, J. Schofer, A. Ushpiz, Pedestrian flow and level of service, Journal of Transport Engineering 109 (1) (1983) 4656.

[39] A. K. Sarkar, K. Janardhan, A study on pedestrian flow characteristics, in: Proceedings Transportation Research Board, Washington, 1997.

[40] Y. Tanariboon, S. Hwa, C. Chor, Pedestrian characteristics study in singapore, Journal of Transportation Engineering, ASCE 112 (3) (1986) 229235.

[41] M. R. Virkler, S. Elayadath, Pedestrian speed-flow-density relationships, Transportation Research Record 1438 (1994) 5158.

[42] F. Venuti, L. Bruno, The synchronous lateral excitation phenomenon: modelling framework and an application, Comptes Rendus Mecanique 335 (2007) 739–745.

[43] S. Kerr, N. Bishop, Human induced loading on flexible staircases, Engineering Structures 23 (2001) 37–45.

[44] Y. Matsumoto, T. Nishioka, H. Shiojiri, K. Matsuzaki, Dynamic design of footbridges, IABSE Proceedings P17/78 (1978) 1–15.

[45] A. Pachi, T. Ji, Frequency and velocity of people walking, The Structural Engineer 83 (3) (2005) 36–40.

[46] F. Ricciardelli, C. Briatico, E. Ingolfsson, C. Georgakis, Experimental validation and calibration of pedestrian loading models for footbridges, in: Proceedings of the International Conference on Experimental vibration analysis for civil engineering structures EVACES, Porto, 2007.

[47] C. Sahnaci, M. Kasperski, Random loads induced by walking, in: 6th International Conference on Structural Dynamics, Paris, 2005.

[48] S. Živanović, A. Pavic, P. Reynolds, P. Vuiovic, Dynamic analysis of lively footbridges under everyday pedestrian traffic, in: Proceedings 6th International Conference on Structural Dynamics Eurodyn, Paris, 2005.

[49] J. E. Bertram, A. Ruina, Multiple walking speed-frequency relations are predicted by constrained optimization, Journal of Theoretical Biology 209 (2001) 445–453.

[50] F. Venuti, L. Bruno, An interpretative model of the pedestrian fundamental relation, Comptes Rendus Mecanique 335 (2007) 194–200.

[51] A. Ebrahimpour, A. Hamam, R. L. Sack, W. N. Patten, Measuring and modelling dynamic loads imposed by moving crowds, ASCE Journal of Structural Engineering 122 (1996) 1468–1474.

[52] M. Araujo, H. Brito, R. Pimentel, Experimental evaluation of synchronisation in footbridges due to crowd density, Structural Engineering International 19 (3) (2009) 298–303.

[53] F. Ricciardelli, A. D. Pizzimenti, An experimental investigation into the interaction among walkers in groups and crowds, in: 10th International Conference on Recent Advances in Structural Dynamics RASD, Southampton, 2010.

[54] A. T. Winfree, Biological rhythms and the behaviour of populations of coupled oscillators, Journal of Theoretical Biology 16 (1967) 15–42.

[55] Y. Kuramoto, Chemical oscillations, waves and turbulence, Springer, Berlin, 1984.

[56] S. H. Strogatz, D. M. Abrams, A. McRobie, B. Eckhardt, E. Ott, Crowd synchrony on the millennium bridge, Nature 438 (3) (2005) 43–44.

[57] A. D. Pizzimenti, Analisi sperimentale dei meccanismi di eccitazione laterale delle passerelle ad opera dei pedoni, Ph.D. thesis, Universitá degli Studi di Catania, Dottorato in Ingegneria delle Strutture XVII ciclo (2005).

[58] F. Ricciardelli, Lateral loading of footbridges by walkers, in: Proceedings Footbridge 2005, Venezia, 2005.

[59] F. Venuti, L. Bruno, N. Bellomo, Crowd-structure interaction: dynamics modelling and computational simulation, in: Proceedings Footbridge 2005, Venezia, 2005.

[60] M. Willford, Dynamic actions and reactions of pedestrians, in: Proceedings Footbridge 2002, Paris, 2002.

[61] J. Brownjohn, S. Živanović, A. Pavic, Crowd dynamic loading on footbridges, in: Proceedings Footbridge 2008, Porto, 2008.

[62] S. Nakamura, Field measurement of lateral vibration on a pedestrian suspension bridge, The Structural Engineer 81 (22) (2003) 22–26.

[63] E. Caetano, A. Cunha, A. Adão da Fonseca, R. Bastos, A. Adão da Fonseca Jr, Assessment and control of human induced vibrations in the new coimbra footbridge, in: Proceedings Footbridge 2005, Venezia, 2005.

[64] E. Caetano, A. Cunha, Experimental and numerical assessment of the dynamic behaviour of a stress-ribbon bridge, Structural Concrete 5 (1) (2004) 29–38.

[65] Y. Fujino, B. M. Pacheco, S. Nakamura, P. Warnitchai, Synchronization of human walking observed during lateral vibration of a congested pedestrian bridge, Earthquake Engineering and Structural Dynamics 22 (1993) 741–758.

[66] J. Yoshida, M. Abe, Y. Fujino, K. Higashiuwatoko, Image analysis of human-induced lateral vibration of a pedestrian bridge, in: Proceedings Footbridge 2002, Paris, 2002.

[67] A. Pikovsky, M. Rosenblum, J. Kurths, Synchronization: A Universal Concept in nonlinear sciences, Cambridge University Press, Cambridge, 2001.

[68] A. McRobie, G. Morgenthal, J. Lasenby, M. Ringe, Section model tests on human-structure lock-in, Bridge Engineering 156 (BE2) (2003) 71–79.

[69] D. E. Newland, Pedestrian excitation of bridges - recent results, in: 10th International Congress on Sound and Vibration, Stockholm, 2003.

[70] A. D. Pizzimenti, F. Ricciardelli, The synchronization: the lessons of the wind engineering and their application to the crowd-structure interaction, in: Proceedings 8th Italian Conference on Wind Engineering, Reggio Calabria, 2004.

[71] E. Simiu, R. H. Scanlan, Wind effects on structures: an introduction to wind engineering, John Wiley and Sons, New York, 1978.

[72] I. Prigogine, R. Herman, Kinetic Theory of Vehicular Traffic, Elsevier, New York, 1971.

[73] N. Bellomo, C. Dogbé, On the modelling of traffic and crowds. A survey of models, speculations and perspectives, to be published.

[74] M. Brand, A. Sudbury, J. G. Sanjayan, Dynamic response of pedestrian bridges for random crowd-loading, Australian Journal of Civil Engineering 3 (1) (2007) 27–38.

[75] V. Coscia, C. Canavesio, First order macroscopic modelling of human crowds, Math. Mod. Meth. Appl. Sci. 18 (Supplement) (2008) 1217–1247.

[76] N. Bellomo, V. Coscia, First order models and closure of mass conservation equations in the mathematical theory of vehicular traffic flow, Comptes Rendus Mecanique 333 (2005) 843–851.

[77] E. De Angelis, Nonlinear hydrodynamic models of traffic flow modelling and mathematical problems, Mathematical and Computer Modelling 29 (1999) 83–95.

[78] M. Delitala, A. Tosin, Mathematical modeling of vehicular traffic: a discrete kinetic approach, Math. Mod. Meth. Appl. Sci. 17 (2007) 901–932.

[79] L. Bruno, F. Venuti, Crowd-structure interaction in footbridges: modelling, application to a real case-study and sensitivity analyses, Journal of Sound and Vibration (323) (2009) 475493.

[80] S. P. Hoogendoorn, P. H. L. Bovy, Gas-kinetic modeling and simulation of pedestrian flows, Transportation Research Record 1710 (2000) 28–36.

[81] M. Delitala, Nonlinear models of vehicular traffic flow - New frameworks of the mathematical kinetic theory, Comptes Rendus Mecanique 331 (2003) 817–822.

[82] A. Seyfried, B. Steffen, T. Lippert, Basics of modelling the pedestrian flow, Physica A 368 (2006) 232–238.

[83] V. Blue, J. Adler, Emergent fundamental pedestrian flows from cellular automata microsimulation, Transportation Research Board 1644 (1998) 29–36.

[84] S. Okazaki, A study of pedestrian movement, Architectural Space Part 2: Concentrated pedestrian movement. Trans. of A.I.J. 284 (1979) 101–110.

[85] S. Živanović, A. Pavic, P. Reynolds, Vibration serviceability of footbridges under human-induced excitation: a literature review, Journal of Sound and Vibration 279 (2005) 1–74.

[86] J. Brownjohn, A. Pavic, P. Omenzetter, A spectral density approach for modelling continuous vertical forces on pedestrian structures due to walking, Canadian Journal of Civil Engineering 31 (1) (2004) 65–77.

[87] C. T. Georgakis, E. T. Ingolfsson, Vertical footbridge vibrations: the response spectrum methodology, in: Proceedings Footbridge 2008, Porto, 2008.

[88] H. Bachmann, W. Ammann, Vibration in structures induced by man and machines, in: Structural Engineering Documents, Vol. 3a, IABSE, Zurich, 1987.

[89] A. D. Pizzimenti, F. Ricciardelli, Experimental evaluation of the dynamic lateral loading of footbridges by walking pedestrians, in: Proceedings 6th International Conference on Structural Dynamics Eurodyn, Paris, 2005.

[90] H. Grundmann, H. Kreuzinger, M. Schneider, Dynamic calculations of footbridges, Bauingenieur 68 (1993) 215–225.

[91] G. Piccardo, F. Tubino, Parametric resonance of flexible footbridges under crowd-induced lateral excitation, Journal of Sound and Vibration 311 (2008) 353–371.

[92] T. M. Roberts, Synchronised pedestrian excitation of footbridges, Bridge Engineering 156 (BE4) (2003) 155–160.

[93] T. M. Roberts, Lateral pedestrian excitation of footbridges, Journal of Bridge Engineering ASCE 10 (1) (2005) 107–112.

[94] S. Nakamura, T. Kawasaki, Lateral vibration of footbridges by synchronous walking, Journal of Constructional Steel Research 62 (2006) 1148–1160.

[95] J. Bodgi, S. Erlicher, P. Argoul, O. Flamand, F. Danbon, Crowd-structure synchronization: coupling between Eulerian flow modeling and Kuramoto phase equation, in: Proceedings Footbridge 2008, Porto, 2008.

[96] F. Venuti, L. Bruno, P. Napoli, Pedestrian lateral action on lively footbridges: a new load model, Structural Engineering International 17 (3) (2007) 236–241.

[97] L. Bruno, F. Venuti, A simplified serviceability assessment of footbridge dynamic behaviour under lateral crowd loading, Structural Engineering International 20 (4) (2010) 442–446.

[98] F. Venuti, L. Bruno, A new load model of the pedestrian lateral action, in: Proceedings Footbridge 2008, Porto, 2008.

[99] S. Živanović, A. Pavic, P. Reynolds, Probability-based prediction of multi-mode vibration response to walking excitation, Engineering Structures 29 (2007) 942–954.

[100] BSI, UK National Annex to Eurocode 1: Actions on structures - Part 2: Traffic loads on bridges, British Standard Institution, NA to BS EN 1991-2, 2003.

[101] F. Venuti, L. Bruno, N. Bellomo, Crowd dynamics on a moving platform: Mathematical modelling and application to lively footbridges, Mathematical and Computer Modelling 45 (2007) 252–269.

[102] J. Bodgi, S. Erlicher, P. Argoul, Lateral vibration of footbridges under crowd-loading: Continuous crowd modeling approach, Key Engineering Materials 347 (2007) 685–690.

[103] K. C. Park, C. A. Felippa, Partitioned analysis of coupled systems, in: Computational Methods for Transient Analysis, T. Belytschko and T.J.R. Hughes, Amsterdam, 1983, Ch. 3, pp. 157–219.

[104] K. C. Park, C. A. Felippa, C. Farhat, Partitioned analysis of coupled mechanical systems, Tech. Rep. CU-CAS-99-06, University of Colorado (March 1999).

[105] International Standardization Organization, Bases for Design of Structures Serviceability of Buildings Against Vibrations, ISO 10137 (1992).

[106] E. Cristiani, B. Piccoli, A. Tosin, Multiscale modeling of granular flows with application to crowd dynamics, Multiscale Modeling and Simulation 9 (1) (2011) 155–182.

COMPDYN 2011
3rd ECCOMAS Thematic Conference on
Computational Methods in Structural Dynamics and Earthquake Engineering
M. Papadrakakis, M. Fragiadakis, V. Plevris (eds.)
Corfu, Greece, 25–28 May 2011

THE CHALLENGES ASSOCIATED WITH THE INTRODUCTION OF A FREQUENCY DEPENDENT COUPLING INTO A PHENOMENOLOGICAL MODEL FOR VORTEX-INDUCED VIBRATION

R.H.M. Ogink[1] **and A.V. Metrikine**[2]

[1] Heerema Marine Contractors
Vondellaan 55, 2332 AA Leiden, The Netherlands
e-mail: rogink@hmc-heerema.com

[2] Delft University of Technology, Faculty of Civil Engineering and Geosciences
Stevinweg 1, 2628 CN Delft, The Netherlands
e-mail: a.metrikine@tudelft.nl

Keywords: Vortex-induced vibration, nonlinear dynamics, wake oscillator, frequency dependent coupling, fluid-structure interaction.

Abstract. *The aim of this paper is to improve the wake oscillator concept for the modeling of vortex-induced vibration of an elastically mounted cylinder in a fluid flow. To this end an attempt is made to introduce a coupling term in the wake oscillator model, that is based on a set of frequency dependent coefficients. Theoretically, it should be possible to determine these coefficients on the basis of so-called forced vibration measurements. In doing so a number of challenges are encountered. A consistent set of frequency dependent coefficients should conform to the forced vibration experiments at all amplitudes of cylinder motion and additionally it should satisfy the Kramers-Kronig relations. It has been found that it is not possible to find a set of frequency dependent coefficients with the wake oscillator model at hand that satisfies these requirements. The sensitivity of the frequency dependent coefficients to the presence of the dominant non-linearity in the wake oscillator at hand has been examined. On the basis of this analysis a new form for the wake oscillator model has been proposed.*

1 INTRODUCTION

1.1 Vortex-induced vibration

Flow over a bluff cylinder separates and vortices are formed in the wake behind the cylinder. The alternate shedding of these vortices results in an oscillating cross-flow force on the cylinder. The shedding frequency of the vortices follows the Strouhal relation and increases with increasing flow velocity. If the cylinder is mounted flexibly and the frequency of vortex shedding is close to the resonance frequency of the mounted system, the cylinder will start to vibrate in cross-flow direction. With an increase of the flow velocity the vortex shedding frequency does no longer follow the Strouhal relation, but *locks onto* the resonance frequency of the cylinder, thereby causing violent vibration of the cylinder over a wide range of flow velocities. This phenomenon is known as vortex-induced vibration (VIV). The occurrence of VIV can cause severe fatigue problems for long cylindrical structures that are exposed to air or water flow such as chimneys, railroad contact wires, the cables of stay bridges and free-hanging offshore pipelines. Recent reviews on VIV have been given by Sarpkaya [1] and Williamson and Govardhan [2].

1.2 VIV experiments

Vortex-induced vibration experiments on rigid, spring mounted cylinders can be divided into two groups, the so called *free* and *forced vibration* experiments. In a typical free vibration experiment a flexibly mounted rigid cylinder is placed in a wind tunnel or water channel. For a range of flow velocities V, the amplitude $\hat{y}$ and the frequency $f_c = \omega_c/(2\pi)$ of cylinder motion are measured. Results of two free vibration experiments performed by Khalak and Williamson [3] are plotted in Figs. 1 and 2. In these figures the flow velocity has been made non-dimensional by dividing it by the natural frequency of the spring mounted cylinder f_n and by the cylinder diameter D, that is, $V_n = V/f_n/D$. The frequency f_n is given by: $f_n = \sqrt{(k/m)}$, in which k is the spring stiffness of the mounted system and m the cylinder dry mass.

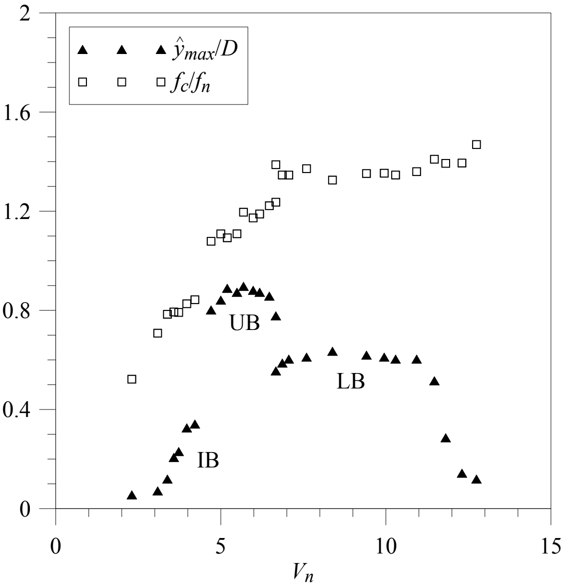

Figure 1: Amplitude and frequency of cylinder motion from the measurements of Khalak et al. [3] for $m^* = 2.4$.

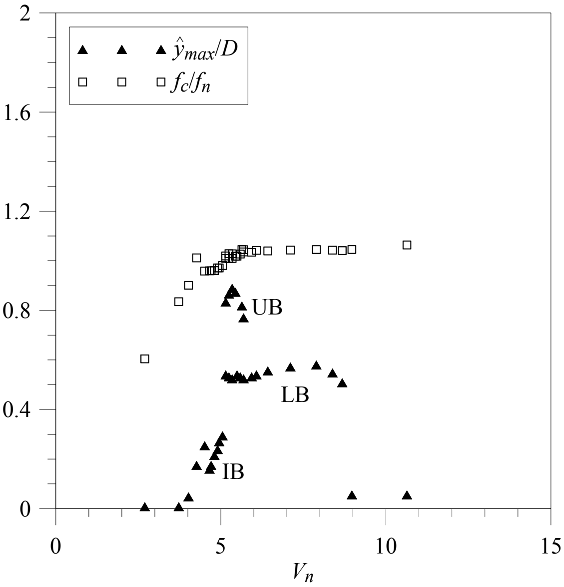

Figure 2: Amplitude and frequency of cylinder motion from the measurements of Khalak et al. [3] for $m^* = 20.6$.

The amplitude plot in Figs. 1 and 2 consists of three distinct branches, the initial, upper and lower branch, that have been marked IB, UB and LB, respectively. In the upper branch the frequency of vortex shedding f_s is very close to the natural frequency of the mounted cylinder, resulting in the cylinder motion with the largest amplitude. The frequency of vortex shedding is given by the Strouhal relation $f_s = \mathrm{St}\cdot V/D$, in which St denotes the Strouhal number. The upper branch is found for $f_s \approx f_n$ and since $\mathrm{St} \approx 0.2$, this takes place when $V_n \approx 1/\mathrm{St} \approx 5$. In the lower branch the amplitude of cylinder motion is constant over a range of flow velocities. The vortex shedding frequency is locked-in with the frequency of cylinder motion. The width of the lock-in range is dependent on the mass ratio m^*, see Figs. 1 and 2. For lower mass ratios the lock-in range is wider. The mass ratio is defined as the ratio of the cylinder mass and the mass of the displaced fluid: $m^* = 4m/(\pi\rho D^2 L)$, in which ρ denotes the density of the fluid and L the length of the cylinder.

Whereas in free vibration experiments, the coupled cylinder-fluid system sets its own frequency and amplitude, in forced vibration experiments amplitude and frequency are forced onto the system. In these experiments a cylinder is placed in a flow while it is at the same time being forced to vibrate sinusoidally in cross-flow direction with an amplitude $\hat{y}$ and a frequency $f_c = \omega_c/(2\pi)$. Typically the fluid force on the cylinder in cross-flow direction $F_y^y = \frac{1}{2}\rho D V^2 L C_y^y$ and in in-line direction $F_x^y = \frac{1}{2}\rho D V^2 L C_x^y$ are measured. In our notation C_y^y and C_x^y denote the non-dimensional fluid forces. To prevent confusion the following notation will be used consistently:

- A subscript 'x' or 'y' denotes the direction in which the fluid force is measured.
- A circumflex '^' denotes an amplitude or a processed coefficient.
- A superscript 'x' or 'y' denotes the direction in which the cylinder is forced to vibrate in the forced vibration experiment. A superscript '0' denotes a stationary cylinder.
- A second subscript '0', '1','2', etc. denotes the harmonic component for which the Fourier coefficient of the forced vibration time series has been determined.

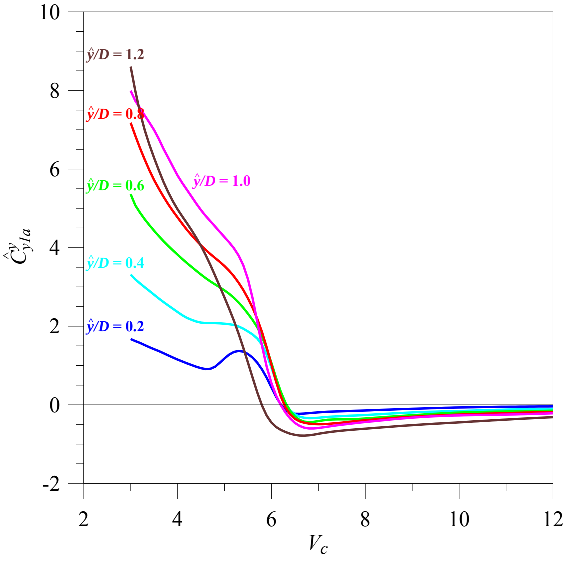

Figure 3: The cross-flow fluid force component in-phase with the cylinder acceleration from the measurements of Gopalkrishnan [4, 5].

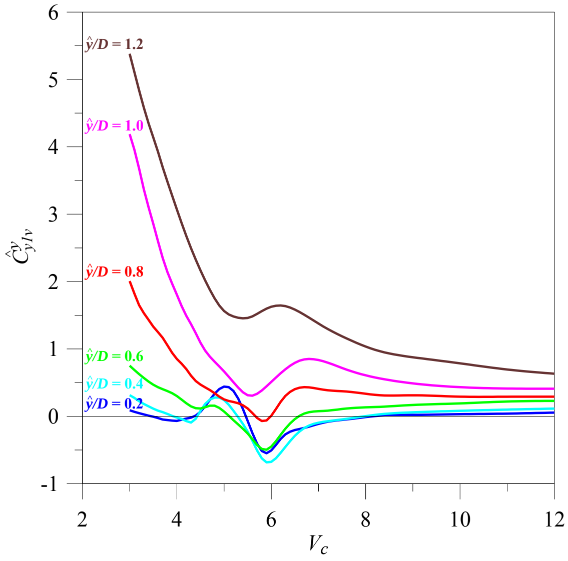

Figure 4: The cross-flow fluid force component in-phase with the cylinder velocity from the measurements of Gopalkrishnan [4, 5].

In Fig. 3 and 4, some of the results of the forced vibration measurements of Gopalkrishnan are depicted. These results have been reported in his PhD thesis [4], as well as in [5]. Gopalkrishnan measured the fluid forces on a cylinder that was pulled through a water channel and at the same time was forced to vibrate in cross-flow direction. The motion of the cylinder is given by:

$$y = \hat{y}\sin(\omega_c t) \tag{1}$$

Among other results he reported in his thesis, for a range of forced amplitudes and forced frequencies, the constant fluid force coefficient in x-direction $\hat{C}_{x0}^{y}$ and the fluid force coefficient at the first harmonic in y-direction $\hat{C}_{y1}^{y}$. He decomposed $\hat{C}_{y1}^{y}$ in a part in-phase with the cylinder acceleration (or in anti-phase with the cylinder displacement): $\hat{C}_{y1a}^{y}$, depicted in Fig. 3, and a part in phase with the cylinder velocity: $\hat{C}_{y1v}^{y}$, depicted in Fig. 4. The flow velocity in Figs. 3 and 4 is made non-dimensional by dividing it by the cylinder diameter and the frequency of forced vibration: $V_c = V/f_c/D$. Approximating C_y^y with only the first Fourier component, results in:

$$\begin{aligned} C_y^y \approx \hat{C}_{y1}^y \sin(\omega_c t + \varphi) &= \hat{C}_{y1}^y \cos(\varphi)\sin(\omega_c t) + \hat{C}_{y1}^y \sin(\varphi)\cos(\omega_c t) \\ &= \hat{C}_{y1a}^y \sin(\omega_c t) - \hat{C}_{y1v}^y \cos(\omega_c t) \end{aligned} \tag{2}$$

1.3 Semi-empirical modeling of VIV

For the description of VIV engineers rely mainly on semi-empirical models, as Computational Fluid Dynamics (CFD) codes are still computationally too expensive for the determination of fluid forces on long cylinders such as the vertical riser pipelines at sea, that are being used in the offshore oil industry. These risers can have unsupported lengths of up to 2000 meters.

The semi-empirical models can be divided into two types. The first type of semi-empirical modeling consists of applying the fluid forces measured in forced vibration experiments directly on the right-hand side of the structural equation of motion. As the force coefficient $\hat{C}_{y1v}^{y}$ is in phase with the cylinder velocity, it acts as an added damping force. So in this model cylinder motion is possible when $\hat{C}_{y1v}^{y} < 0$. Since it is not known in advance with which amplitude and frequency the cylinder will vibrate and hence which values of $\hat{C}_{y1a}^{y}$ and $\hat{C}_{y1v}^{y}$ from the measurements have to be taken, an iterative procedure is needed. The drawback of this method is that it relies on the assumption that there will be a dominant mode of vibration, as the measurements that are being used have been carried out at a single frequency of forced vibration. This assumption is questionable in the case of very long pipes, such as the deepwater risers mentioned before. These pipes have a dense spectrum of resonance frequencies and will vibrate in a combination of several modes together. The presence of a sheared incoming flow will increase the complexity of finding the dominant modes even further.

The second type of semi-empirical model is the so-called oscillator model. In this type of model, the oscillating lift force is modeled by a non-linear oscillator equation, which contains a limit cycle, so that for a stationary cylinder an oscillating lift force is found. Oscillator equations that are commonly used are the Van der Pol equation and the Rayleigh equation. A Van der Pol equation that could be used is:

$$\ddot{C}_y + \varepsilon\omega_s \dot{C}_y \left(C_y^2 - \tfrac{1}{4}\hat{C}_{y1}^2\right) + \omega_s^2 C_y = A\frac{\ddot{y}}{D} + \omega_s B\frac{\dot{y}}{D}\ , \tag{3}$$

where $\hat{C}_{y1}^{0}$ is the amplitude of the limit cycle of the unforced oscillator, which should be equal to the cross-flow fluid force coefficient at the first harmonic on a stationary cylinder, $\omega_S = 2\pi f_s$ is the vortex shedding frequency, ε is a non-dimensional tuning parameter and overdots denote derivatives with respect to time t. The right-hand side of eq. (3) models the coupling between the structural displacement y and the fluid and contains the constant non-dimensional coupling coefficients A and B.

When the model predictions are compared with free vibration experiments, it is found that the oscillator model can produce acceptable results for structures experiencing VIV in air, in which the mass ratio of the structure and the surrounding fluid is high. A major drawback of most of the existing oscillator models is however that they do not scale correctly with the mass ratio and the damping ratio of the structure and the surrounding fluid. This means that these models have to be tuned separately for every possible combination of mass and damping ratio. This severely limits the predictive capabilities of these models. Moreover, existing oscillator models are not capable of describing the amplitude branches as found in the free vibration experiments at low mass ratios and hence underpredict the amplitude of the upper branch. Because of these shortcomings oscillator models are seldom used for engineering applications.

Oscillator models do have the favorable characteristic that they do not require an assumption of a dominant frequency. They consist of a system of coupled differential equations that can simply be solved in the time domain without any initial guess of frequency or amplitude. An oscillator model that can produce acceptable results over a range of mass and damping ratios on the basis of one set of tuning parameters, could therefore be useful as an engineering tool as it can deal with motion at multiple frequencies in a computationally inexpensive manner.

In [6], we have improved the existing oscillator model of Facchinetti et al. [7] by taking account of the relative velocity between cylinder and fluid. Subsequently, we tried to improve this model by making the coupling coefficients A and B frequency dependent by means of introducing a convolution integral into the time-domain model. We strived to derive a model that scales correctly with mass ratio, can describe the results of the forced vibration measurements and can describe the upper and lower branch of free vibration. We found, however, that with using a Van der Pol or Rayleigh equation and by trying to determine the frequency dependencies of A and B on the basis of the forced vibration measurements of Gopalkrishnan, we could not find a set of consistent frequency dependencies that could be used to determine the convolution kernel that is needed. The frequency dependencies appeared to be very sensitive to the non-linearities that are present in the model.

1.4 Objective of this paper

In this paper we will give a description of the challenges that are associated with the inclusion of a frequency dependent coupling between wake and structural oscillator. Specifically, we will focus on the sensitivity of the frequency dependencies to the presence of the non-linearity in the wake oscillator. On the basis of the results, we will make a first attempt at improving the existing model.

In Section 2, the wake oscillator model that will be used is discussed and the derivations that are needed, to include frequency dependent coupling coefficients in the wake oscillator, are given. In Section 3, the frequency dependent coefficients A and B are determined and the sensitivity of these coefficients to the presence of the non-linearity in the wake oscillator is investigated and on the basis of the results of this, in Section 4 a new wake oscillator model is proposed. The conclusions are presented in Section 5.

2 WAKE OSCILLATOR MODEL WITH FREQUENCY DEPENDENT COUPLING

2.1 The wake oscillator model

The wake oscillator model that will be used is based on the model of Facchinetti et al. [7] with the additional inclusion of the relative velocity between moving cylinder and fluid. Details of the model are given in [6]. The structural equation of motion is given by:

$$m\ddot{y} + b\dot{y} + ky = F_y, \tag{4}$$

in which b denotes the structural damping coefficient. The cross-flow fluid force F_y is assumed to consist of a part due to vortex shedding F_{VY} and a part due to potential added mass F_{AY}:

$$F_y = F_{VY} + F_{AY} = \tfrac{1}{2}\rho D V^2 L\, C_{VY} - m_a \ddot{y} \tag{5}$$

The potential added mass m_a is given by: $m_a = \hat{C}_a \pi \rho D^2 L/4$, in which the potential added mass coefficient $\hat{C}_a$ has the value of 1.0. In [6] we have assumed that the non-dimensional cross-flow vortex force C_{VY} consists of a component C_{VD} in-line with the relative velocity $U = \sqrt{V^2 + \dot{y}^2}$ between moving cylinder and incoming flow and a component C_{VL} perpendicular to this relative velocity:

$$C_{VY} = \left(C_{VD} \sin\beta + C_{VL} \cos\beta\right)\frac{U^2}{V^2} \tag{6}$$

The angle β is the angle between the direction of the relative velocity and the horizontal. See Fig.5. It is given by:

$$\begin{aligned} \beta = -\arctan\left(\dot{y}/V\right),\ \sin\beta &= -\dot{y}/U = -\dot{y}\big/\sqrt{V^2+\dot{y}^2}, \\ \cos\beta &= V/U = V\big/\sqrt{V^2+\dot{y}^2} \end{aligned} \tag{7}$$

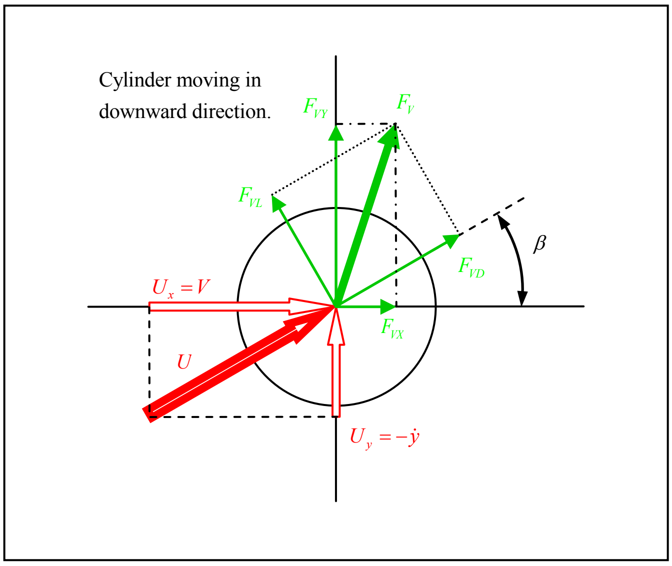

Figure 5: Definition of the angle and the decomposition of the vortex fluid force in drag, lift, horizontal and vertical direction

To complete the model description, the vortex force components C_{VD} and C_{VL} have to be defined. In [6] we have made the assumption that C_{VD} is constant and is equal to the mean drag force on a stationary cylinder and that C_{VL} can be calculated with a Van der Pol equation:

$$C_{VD} = \hat{C}_{x0}^{0} \tag{8}$$

$$\ddot{C}_{VL} + \varepsilon\,\omega_s\left(C_{VL}{}^2 - \tfrac{1}{4}(\hat{C}_{y1}^{0})^2\right)\dot{C}_{VL} + \omega_s^2 C_{VL} = \left(\frac{A}{D}\ddot{y} + \frac{B}{D}\omega_s\dot{y}\right)\cos\beta \tag{9}$$

The right-hand side of eq. (9) contains an acceleration coupling $A\ddot{y}$ and a velocity coupling $B\dot{y}$. Facchinetti et al. [7] have compared the differences on the free vibration modeling of using acceleration, velocity and displacement couplings and found that an acceleration coupling gave the best results. We have included the velocity coupling in eq. (9) for completeness, so that we have a coupling term $A\ddot{y}$ in (anti-)phase with the cylinder motion and a coupling term $B\dot{y}$ out-of-phase with the cylinder motion.

The constant coupling coefficients A and B will be made frequency dependent in Section 3. To this end we have pretuned the model to the free vibration measurements of Khalak et al. There are two ways to pretune the model. The first is to tune the model to the upper branch of free vibration and hope that by including the frequency dependencies the lower branch of free vibration can be described as well and the second way is to tune the model to the lower branch and hope that by including the frequency dependencies the upper branch can be described as well. We will call the first option *Case U* and the second one *Case L*. The values for the force coefficients $\hat{C}_{x0}^{0}$ and $\hat{C}_{y1}^{0}$ and the Strouhal number have been taken from the measurements of Gopalkrishnan.

To pretune the model, the coupled system consisting of the wake and structural oscillators, given by eq. (4) and (9) has been solved in the time domain with a fifth order Runge-Kutta routine. The initial conditions that have been used are $y(0) = \dot{y}(0) = \dot{C}_{VL}(0) = 0$ and $C_{VL}(0) = 0.01$. After a few periods of calculation the steady state is reached and the amplitude of cylinder motion has been determined by searching for the maximum recurring displacement and the frequency of cylinder motion has been determined by searching for the highest peak in the Fourier spectrum of the cylinder displacement. The results of the pretuning are presented in Figs. 6 and 7. In these figures solid lines depict results for increasing flow velocity and dashed lines results for decreasing flow velocity. The tuning parameters for the two cases are:

Case U:	***Case L:***	
$\hat{C}_{x0}^{0} = 1.1856$	$\hat{C}_{x0}^{0} = 1.1856$	
$\hat{C}_{y1}^{0} = 0.3842$	$\hat{C}_{y1}^{0} = 0.3842$	
$\mathrm{St} = 0.1932$	$\mathrm{St} = 0.1932$	(10)
$A = 4.0\cdot\frac{\hat{C}_{y1}^{0}}{2} = 0.7684$	$A = 12.0\cdot\frac{\hat{C}_{y1}^{0}}{2} = 2.3052$	
$B = 0$	$B = 0$	
$\varepsilon = 0.05\cdot\left(\frac{2}{\hat{C}_{y1}^{0}}\right)^2 = 1.3549$	$\varepsilon = 0.7\cdot\left(\frac{2}{\hat{C}_{y1}^{0}}\right)^2 = 18.9690$	

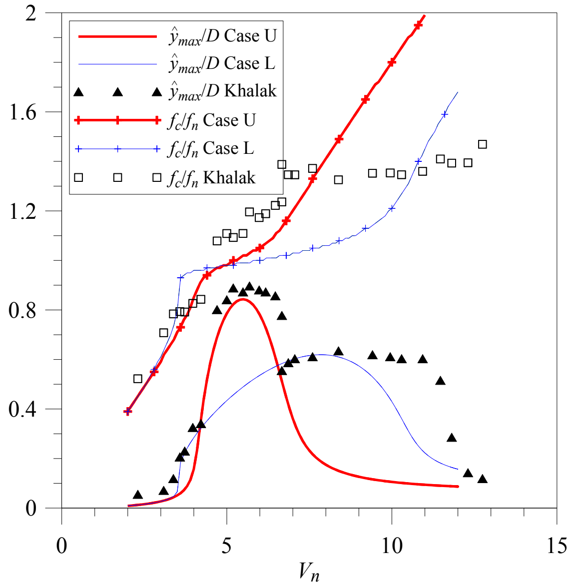

Figure 6: Pretuning of the wake oscillator model to the measurements of Khalak et al. [3] for $m^* = 2.4$.

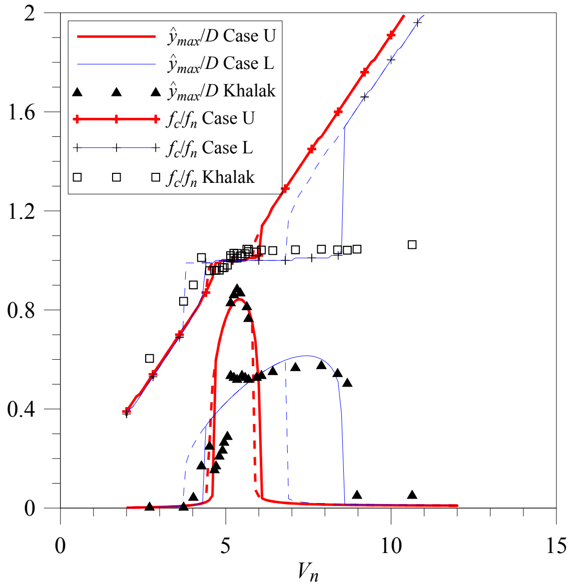

Figure 7: Pretuning of the wake oscillator model to the measurements of Khalak et al. [3] for $m^* = 20.6$.

2.2 Derivation of frequency dependent coupling

We strive to improve the wake oscillator presented in Section 2.1, by making the coupling coefficients functions of the cylinder frequency of vibration. These frequency dependent coefficients will be denoted by $\tilde{A}$ and $\tilde{B}$ for the moment. They will be determined over a range of cylinder frequencies on the basis of the forced vibration experiment of Gopalkrishnan, as will be explained in Section 3.1. The problem that is then encountered, is that if the coupled system consisting of the structural and wake oscillator is solved in the time domain, it is not known which values of the frequency dependent coefficients should be used, as the frequency of cylinder motion is not known in advance. The coupling term on the right-hand side of eq. (9) should therefore be replaced by a convolution integral. It is thus needed to derive the relation between the frequency dependent coefficients and the kernel of the convolution integral. To simplify the derivations, non-dimensional time $\tau = \omega_s t$ and non-dimensional cylinder frequency $\Omega_c = \omega_c/\omega_s$ are introduced. Substituting non-dimensional time into eq. (9) and dividing by ω_s^2 results in:

$$\frac{d^2C_{VL}}{d\tau^2}+\varepsilon\left(C_{VL}{}^2-\tfrac{1}{4}(\hat{C}_{y1}^0)^2\right)\frac{dC_{VL}}{d\tau}+C_{VL}=\left(\frac{\tilde{A}}{D}\frac{d^2y}{d\tau^2}+\frac{\tilde{B}}{D}\frac{dy}{d\tau}\right)\cos\beta \tag{11}$$

Our goal is to replace the term $\frac{\tilde{A}(\Omega_c)}{D}\frac{d^2y}{d\tau^2}+\frac{\tilde{B}(\Omega_c)}{D}\frac{dy}{d\tau}$ in eq. (11) with the convolution $\frac{1}{D}\int_0^{\tau} K(\tau-\tilde{\tau})\frac{dy(\tilde{\tau})}{d\tilde{\tau}}d\tilde{\tau}$, in which $K(\tau)$ denotes the convolution kernel. The lower limit of integration starts at $\tilde{\tau}=0$, as the cylinder cannot force the fluid, before it is moving itself. For large τ these two term should give the same results. This can be expressed as:

$$\begin{aligned}\frac{\tilde{A}(\Omega_c)}{D}\frac{d^2y}{d\tau^2}+\frac{\tilde{B}(\Omega_c)}{D}\frac{dy}{d\tau}&=\lim_{\tau\to\infty}\tfrac{1}{D}\int_0^{\tau}K(\tau-\tilde{\tau})\frac{dy(\tilde{\tau})}{d\tilde{\tau}}d\tilde{\tau}\\&=\tfrac{1}{D}\int_0^{\infty}K(\tau-\tilde{\tau})\frac{dy(\tilde{\tau})}{d\tilde{\tau}}d\tilde{\tau}=\tfrac{1}{D}\int_0^{\infty}K(\tilde{\tau})\frac{dy(\tau-\tilde{\tau})}{d\tilde{\tau}}d\tilde{\tau}\end{aligned}\qquad(12)$$

Substitution of the expression $y=\hat{y}\sin(\Omega_c\tau)$ results in the following relations:

$$\Omega_c\,\tilde{A}(\Omega_c)=-\int_0^{\infty}K(\tau)\sin(\Omega_c\tau)d\tau=A(\Omega_c)\qquad(13)$$

$$\tilde{B}(\Omega_c)=\int_0^{\infty}K(\tau)\cos(\Omega_c\tau)d\tau=B(\Omega_c)\qquad(14)$$

Eq. (13) and (14) show that, since $A(\Omega_c)$ and $B(\Omega_c)$ are the inverse sin- and cos-transform of the same kernel $K(\tau)$, these functions are not independent functions, but are in fact related to each other. This relation is known as the Kramers-Kronig relation. It can be expressed as follows, where attention has been paid to correctly include the boundaries at $\Omega=0$ and $\Omega\to\infty$:

$$\frac{A(\Omega)}{\Omega}-\lim_{\Omega\to\infty}\frac{A(\Omega)}{\Omega}=\frac{1}{\Omega}\frac{2}{\pi}\int_0^{\infty}\frac{\left(B(\tilde{\Omega})-B(\Omega)\right)\Omega}{\tilde{\Omega}^2-\Omega^2}d\tilde{\Omega}\qquad(15)$$

$$B(\Omega)-B(0)=-\frac{2\Omega^2}{\pi}\int_0^{\infty}\frac{A(\tilde{\Omega})/\tilde{\Omega}-A(\Omega)/\Omega}{\tilde{\Omega}^2-\Omega^2}d\tilde{\Omega}\qquad(16)$$

More details on the relations between $A(\Omega_c)$ and $B(\Omega_c)$ are given in [6].

3 DETERMINATION OF THE FREQUENCY DEPENDENT COEFFICIENTS *A*(Ω) AND *B*(Ω)

3.1 Method of determining the frequency dependent coefficients $A(\Omega_c)$ and $B(\Omega_c)$

It will be tried to determine the frequency dependent coefficients $A(\Omega_c)$ and $B(\Omega_c)$ on the basis of the forced vibration measurements of Gopalkrishnan. To this end, the forced vibration experiments need to be modeled with the wake oscillator model presented in Section 2. The forced vibration cross-flow fluid force C_y^y can be expressed as:

$$C_y^y=C_{VY}+C_{AY}=C_{VY}-\frac{m_a}{\frac{1}{2}\rho DV^2L}\ddot{y},\qquad(17)$$

in which C_{VY} is again given by eq. (6) :

$$C_{VY}=\left(C_{VD}\sin\beta+C_{VL}\cos\beta\right)\frac{U^2}{V^2}\qquad(6)$$

By assuming a forced vibration in the form of: $y=\hat{y}\sin(\Omega_c\tau)$, the forced vibration coefficients $\hat{C}_{y1a}^y$ and $\hat{C}_{y1v}^y$ can be calculated with:

$$\begin{aligned}\hat{C}^{y}_{y1a} &= \frac{2}{\mathcal{T}_c}\int_{\tau_0}^{\tau_0+\mathcal{T}_c} C^{y}_{y}\sin\left(\Omega_c\tau\right)d\tau \\ &= \frac{2}{\mathcal{T}_c}\int_{\tau_0}^{\tau_0+\mathcal{T}_c} C_{VY}\sin\left(\Omega_c\tau\right)d\tau + \hat{C}_a 2\pi^3\mathrm{St}^2{\Omega_c}^2\hat{y}/D\end{aligned} \tag{18}$$

$$\hat{C}^{y}_{y1v} = -\frac{2}{\mathcal{T}_c}\int_{\tau_0}^{\tau_0+\mathcal{T}_c} C^{y}_{y}\cos\left(\Omega_c\tau\right)d\tau = -\frac{2}{\mathcal{T}_c}\int_{\tau_0}^{\tau_0+\mathcal{T}_c} C_{VY}\cos\left(\Omega_c\tau\right)d\tau\,, \tag{19}$$

in which $\mathcal{T}_c = {2\pi}/{\Omega_c} = {2\pi\omega_s}/{\omega_c}$ is the non-dimensional period of forced vibration. The value of the component of the vortex fluid force in the direction of the relative velocity is again given by: $C_{VD} = \hat{C}^{0}_{x0}$. The component of the vortex fluid force perpendicular to the relative velocity will now be calculated with:

$$\frac{d^2C_{VL}}{d\tau^2} + \varepsilon\left({C_{VL}}^2 - \tfrac{1}{4}(\hat{C}^{0}_{y1})^2\right)\frac{dC_{VL}}{d\tau} + C_{VL} = \left(-\Omega_c A\frac{\hat{y}}{D}\sin(\Omega_c\tau) + \Omega_c B\frac{\hat{y}}{D}\cos(\Omega_c\tau)\right)\cos\beta \tag{20}$$

It is now possible to model the forced vibration with the help of eq. (6), (18), (19) and (20). By changing *A* and *B* in this model an error function will be minimized that characterizes the discrepancy between the model predictions and the measurements of Gopalkrishnan. The equations have been solved numerically in a similar manner as described in Section 2.1 with the value for ε and the initial values for *A* and *B* equal to the values given by (10). Then, the fluid force coefficients $\hat{C}^{y}_{y1a}$ and $\hat{C}^{y}_{y1v}$ have been calculated. When these values are known, the error can be determined as follows:

$$error = \left(\hat{C}^{y}_{y1a;\text{model}} - \hat{C}^{y}_{y1a;\text{measured}}\right)^2 + \left(\hat{C}^{y}_{y1v;\text{model}} - \hat{C}^{y}_{y1v;\text{measured}}\right)^2 \tag{21}$$

Subsequently, the error is minimized with a one-dimensional procedure that brackets the minimum and then performs a golden section search to find this minimum. This procedure is explained in detail by Press et al. in [8]. The procedure starts with changing *A* and keeping *B* constant and when under these conditions a minimum has been found, *A* is kept constant and *B* is changed. This is repeated over and over again until the error given by (21) is smaller than a preset value. Starting at $V_c = 3$ (with $\Omega_c = 1/\mathrm{St}/V_c$) and $\hat{y}/D = 0.2$, the error is minimized until it is smaller than 10^{-6}. Then at the same amplitude the reduced velocity V_c is increased with $dV_c = 0.1$ and the calculations are repeated until the whole frequency range at this amplitude is covered, each time using the final *A* and *B* at the previous frequency as the initial values for the iterative procedure at the next frequency. In this manner the frequency dependent parameters $A(\Omega_c)$ and $B(\Omega_c)$ have been determined for the amplitudes of forced motion in the range of $\hat{y}/D = 0.2$ to 1.2 with a step size of $d\hat{y} = 0.1\cdot\mathrm{D}$.

3.2 Challenges involved in determining the coefficients $A(\Omega_c)$ and $B(\Omega_c)$

It is instructive at this point to state explicitly what the difficulties are in trying to determine the frequency dependent coefficients on the basis of the forced vibration experiments. Firstly, the frequency dependent coefficients will be determined for a number of amplitudes of forced vibration. But when modeling the free vibration with the wake oscillator containing the convolution integral, *one* kernel *K* based on only *one* set of frequency dependent curves $A(\Omega_c)$ and $B(\Omega_c)$ should be able to describe the fluid force behavior for all amplitudes of cylinder motion. This implies that for all amplitudes of forced vibration the same set of curves for $A(\Omega_c)$ and $B(\Omega_c)$ should be found.

Secondly, it has been shown in Section 2.2 that $A(\Omega_c)$ and $B(\Omega_c)$ are related through the Kramers-Kronig relations. It is not possible to determine $A(\Omega_c)$ and $B(\Omega_c)$ on the basis of the forced vibration measurements over the entire frequency range from zero to infinity, as the measurements have obviously been performed over a finite frequency range. For a set of frequency dependent coefficient $A(\Omega_c)$ and $B(\Omega_c)$ that is self-consistent, it should however be possible to extend these coefficient over the entire frequency range, such that the Kramers-Kronig relations are satisfied.

If we fail to find one set of coefficients $A(\Omega_c)$ and $B(\Omega_c)$ that are valid over a range of forced vibration amplitudes, or if the set of coefficients cannot be extended over the entire frequency range to satisfy the Kramers-Kronig relation, this will be an indication that the wake oscillator model does not contain the correct non-linearities.

3.3 Results of determining the coefficients $A(\Omega_c)$ and $B(\Omega_c)$ on the basis of forced vibration measurements

The frequency dependent curves that have been found for $A(\Omega_c)$ and $B(\Omega_c)$ with the method described in Section 3.1 are depicted in Fig. 8 and 9 for *Case U* and in Fig. 10 and 11 for *Case L*. It is clear from these figures that in both cases different curves for A and B are found at different amplitudes of forcing, implying that with the current model the results of Gopalkrishnan cannot be reproduced with a single set of frequency dependent parameters. It appears that the wake oscillator as tuned in *Case U* gives better results than as tuned in *Case L*, since in Fig. 8 and 9 the spread in the curves of $A(\Omega_c)$ and $B(\Omega_c)$ for different amplitudes is one order of magnitude smaller than in Fig. 10 and 11.

In [6], we have attempted to reduce the spread in the curves of $A(\Omega_c)$ and $B(\Omega_c)$ at different amplitudes of forcing in a number of ways. This included redefining the error function that has been used in the determination procedure, retuning the model by changing the parameter values given by eq. (10) and by replacing the Van der Pol-type non-linearity in eq. (20) with a Rayleigh-type non-linearity. None of these approaches reduced the spread in the curves of $A(\Omega_c)$ and $B(\Omega_c)$ to a significant degree.

Subsequently in [6], we have described a method based on complex curve fitting with a complex polynomial that should be able to, starting with a set of frequency dependent curves that are known over only a limited range of the frequency spectrum, expand this set over the entire spectrum such that the Kramers-Kronig relations are satisfied and the inverse transform of the coefficients $A(\Omega_c)$ and $B(\Omega_c)$ can be taken to determine the convolution kernel $K(\tau)$. We found that with this method we were not able to extend the curves for the amplitudes higher than $0.6 \cdot D$ over the entire spectrum and therefore we were not able to determine a convolution kernel on the basis of these curves. For the curves plotted in Figs. 8, 9, 10 and 11 at amplitudes of $0.6 \cdot D$ and lower, we were able to extend the curves over the entire spectrum, but this could only be done with a low order polynomial and therefore a poor fit to the curves used. After determining the convolution kernel $K(\tau)$ on the basis of one of these fits, the free vibration was modeled with inclusion of the convolution coupling. The results were very poor. See Fig. 10 in [6].

We therefore came to the conclusion that the wake oscillator model given by eq. (4), (6) and (9), with or without the convolution coupling, does not contain the correct non-linearities in either the damping term in eq. (9), the coupling term in eq. (9) or both. We also noted that the wake oscillator could possibly be improvement by adding an additional oscillator, so that the fluid force is modeled with a combination of two wake oscillators.

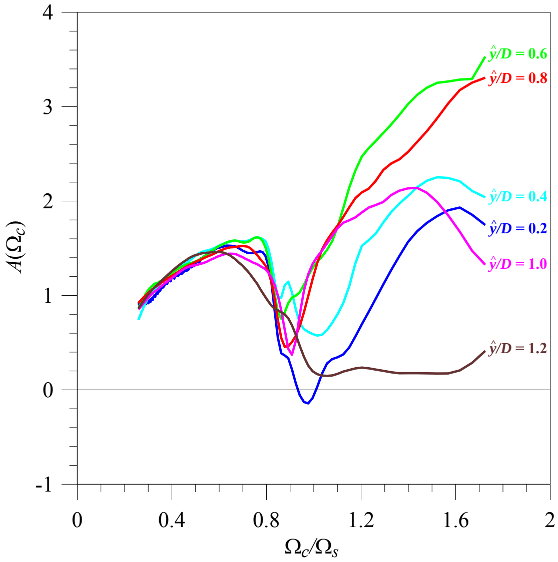

Figure 8: Curves found through a minimization procedure for the coefficient A for *Case U*.

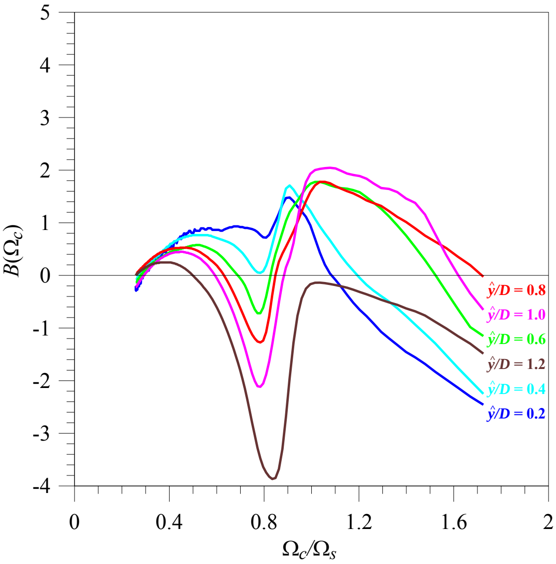

Figure 9: Curves found through a minimization procedure for the coefficient B for *Case U*.

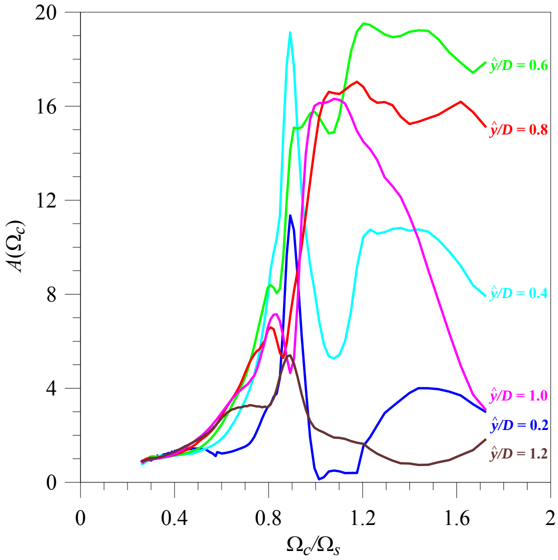

Figure 10: Curves found through a minimization procedure for the coefficient A for *Case L*.

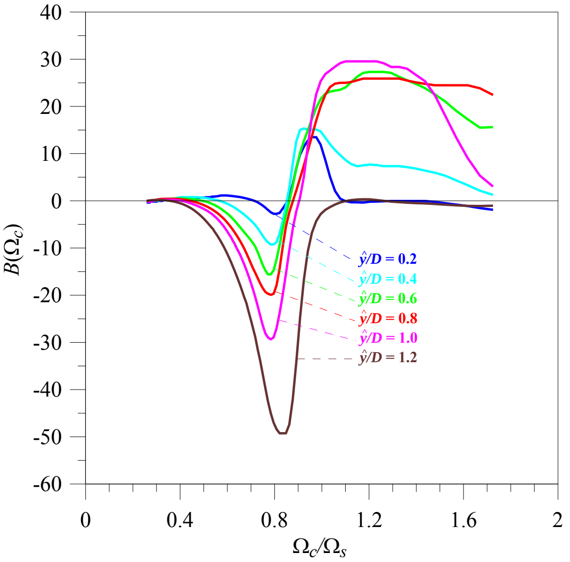

Figure 11: Curves found through a minimization procedure for the coefficient B for *Case L*.

3.4 Effect of removing the non-linearity in the damping term of the wake oscillator

It is remarkable that the spread in the curves for the frequency dependent coefficient at different amplitudes of forced vibration is an order of magnitude smaller for *Case U* compared to *Case L*. For *Case U*, the parameter ε, given by eq. (10), that multiplies the Van der Pol-type non-linearity in eq. (20) is on order of magnitude smaller compared to *Case L*. It seems, therefore, that the Van der Pol-type non-linearity in eq. (20) has a large influence on the spread of the frequency dependent curves found at different amplitudes of forced vibration. To explore whether this is indeed the case, the minimization procedure from Section 3.1 is repeated and the frequency dependent coefficients are determined anew, but in this case the non-linearity in the damping term in eq. (20) is replaced by a linear damping term:

$$\frac{d^2C_{VL}}{d\tau^2}+2\,\varepsilon\,\frac{dC_{VL}}{d\tau}+C_{VL}=\left(-\Omega_c A\frac{\hat{y}}{D}\sin(\Omega_c\tau)+\Omega_c B\frac{\hat{y}}{D}\cos(\Omega_c\tau)\right)\cos\beta \tag{22}$$

We are fully aware that it is not possible to model the free vibration with eq. (22), as this equation does not contain a limit cycle and therefore cannot model the energy input from the fluid into the structural system at low amplitudes of motion, but we only wish to investigate the effects of the presence/non-presence of this non-linear damping term on the spread of the frequency dependent coefficient at different amplitudes of forced vibration.

The frequency dependent curves that have been found for $A(\Omega_c)$ and $B(\Omega_c)$ with the help of eq. (22) are depicted in Fig. 12 to 17 for three different values of the non-dimensional damping ratio ε, namely $\varepsilon = 0.5$, $\varepsilon = 0.3$ and $\varepsilon = 0.1$. It is immediately clear from Fig. 12 to 17, that the spread in the curves for $A(\Omega_c)$ and $B(\Omega_c)$ at different amplitudes of forced vibration is of the same order of magnitude as has been found for *Case U* in Section 3.3. For decreasing damping ratio ε, the spread in the curves reduces unmistakably. Only the curves for the highest amplitude of forced vibration $\hat{y}/D = 1.2$ does not collapse onto the other curves. But additional non-linearities in the coupled structure-fluid system that are not modeled with the equations used, will certainly be present in reality. These additional non-linearities will be most visible at the higher amplitudes of cylinder motion.

The fact that a much better correspondence of the frequency dependent curves at different amplitudes of forced vibration is found when the non-linearity in the damping term in the oscillator that describes C_{VL} is removed, leads to the conclusion that this non-linearity should most likely not be included at this place. The behavior of the oscillator that describes C_{VL} appears to be linear at low amplitudes of vibration. This means that the negative damping term that models the energy input from the fluid into the structural system should be placed at a different position in the coupled fluid-structure system.

4 A FIRST ATTEMPT AT A NEW WAKE MODEL CONTAINING MULTIPLE OSCILLATORS

Based on the findings of the previous section, a first attempt is made to develop a wake oscillator model in which the oscillator that describes C_{VL} is linear in first order approximation at low amplitudes of cylinder motion. We do not wish to derive a full model at this point that is able to describe both the free and forced vibration. It is only our objective here to investigate whether focusing our attention into this direction could be worthwhile. We start with the same basic equations as before and return to the usage of dimensional time t. The equations for the structural oscillator and the cross-flow fluid force do not change and are given by:

$$(m+m_a)\ddot{y}+b\dot{y}+ky=\tfrac{1}{2}\rho DV^2L\,C_{VY} \tag{23}$$

$$C_{VY}=\left(C_{VD}\sin\beta+C_{VL}\cos\beta\right)\frac{U^2}{V^2} \tag{6}$$

It will still be assumed that: $C_{VD}=\hat{C}^0_{x0}$. For the force component C_{VL} the following equation is proposed of which the left-hand side is linear as discussed in Section 3.4:

$$\ddot{C}_{VL}+2\varepsilon_L\,\omega_s\dot{C}_{VL}+\omega_s^2C_{VL}=P_L\omega_s\,\dot{q}+\left(\frac{A_L}{D}\ddot{y}+\frac{B_L}{D}\omega_s\dot{y}+\frac{G_L}{D}\omega_s^2y\right)\cos\beta, \tag{24}$$

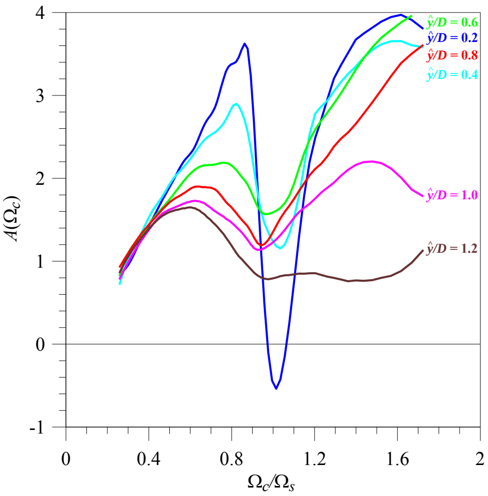

Figure 12: Curves found for the coefficient A for the linear case with $\varepsilon = 0.5$.

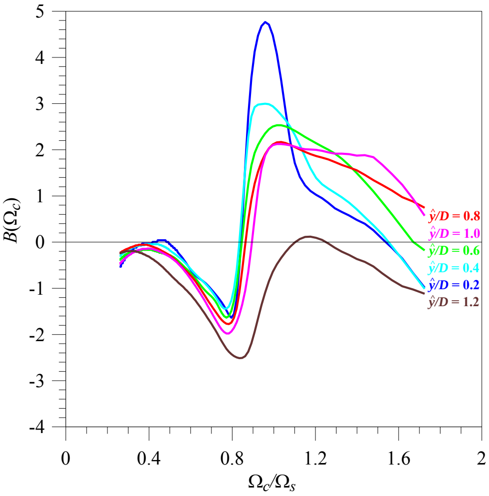

Figure 13: Curves found for the coefficient B for the linear case with $\varepsilon = 0.5$.

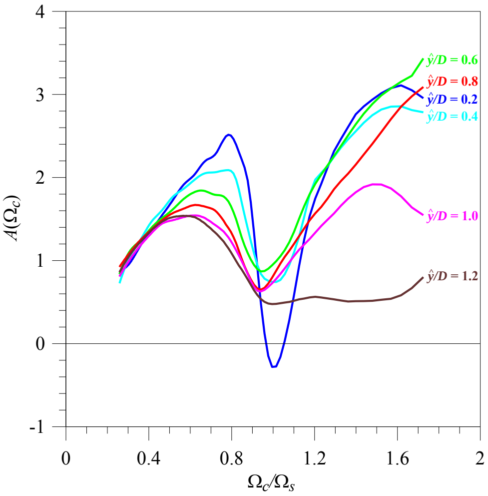

Figure 14: Curves found for the coefficient A for the linear case with $\varepsilon = 0.3$.

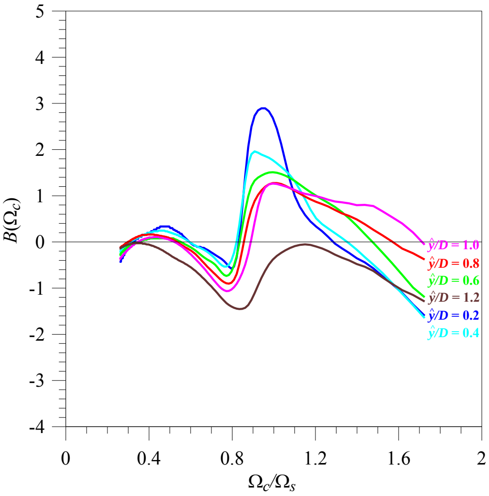

Figure 15: Curves found for the coefficient B for the linear case with $\varepsilon = 0.3$.

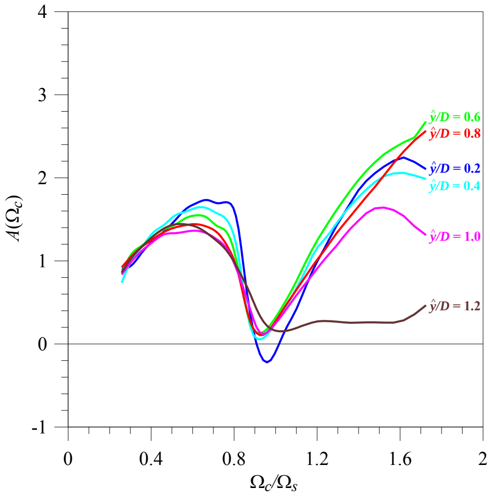

Figure 16: Curves found for the coefficient A for the linear case with $\varepsilon = 0.1$.

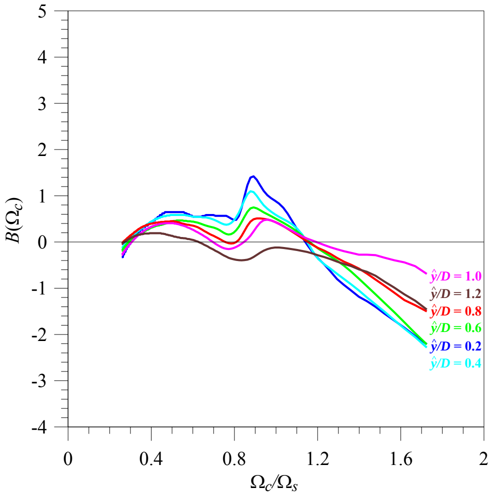

Figure 17: Curves found for the coefficient B for the linear case with $\varepsilon = 0.1$.

in which A_L, B_L, G_L and P_L are constant non-dimensional coupling coefficients and ε_L is the non-dimensional damping ratio. The non-linear damping term that is present in eq. (9) and that models the limit cycle of the cross-flow fluid force and hence the energy input from the fluid into the structural system, has been removed from eq. (24). Therefore a second oscillator is needed that reintroduces the limit cycle and thereby acts as forcing on eq. (24). The following form for this second oscillator is proposed:

$$\ddot{q} + \varepsilon_Q\,\omega_s(q^2-1)\,\dot{q} + \omega_s^2 q = \left(\frac{A_Q}{D}\ddot{y} + \frac{B_Q}{D}\omega_s\dot{y} + \frac{G_Q}{D}\omega_s^2 y\right)\cos\beta\,, \tag{25}$$

in which q is a wake variable that will be left undefined. A_Q, B_Q, and G_Q are constant non-dimensional coupling coefficients and ε_Q is a non-dimensional tuning parameter. To ensure that the cross-flow fluid force on a stationary cylinder as predicted by eq. (6) , (24) and (25) is equal to $\hat{C}_{y1}^0$, P_L should be equal to: $P_L = 2\varepsilon_L\hat{C}_{y1}^0/2 = \varepsilon_L\hat{C}_{y1}^0$.

The coupled system consisting of eq. (6), (23), (24) and (25) has been solved in the time domain and it has been tried to find values for the tuning coefficients A_L, B_L, G_L, ε_L, A_Q, B_Q, G_Q and ε_Q, such that results of the model would compare favorably with the free vibration measurements of Khalak et al. It has however been found that for the free vibration modeling this system of equations always overpredicted the amplitude of free vibration. This is likely caused by the removal of the Van der Pol-type nonlinearity from eq. (24). The presence of this term resulted in a strong damping at higher amplitudes of cylinder motion and it limited thereby the amplitude of cylinder motion that could be attained. This can be corrected by letting go of the assumption that: $C_{VD} = \hat{C}_{x0}^0$ and introducing an additional oscillator equation to describe C_{VD}. The presence of this additional oscillator will limit the amplitude of the cylinder motion. A suitable form for this oscillator is given by:

$$\ddot{C}_{VD} + 4\varepsilon_D\,\omega_s\dot{C}_{VD} + 4\omega_s^2(C_{VD} - \hat{C}_{x0}^0) = P_D\omega_s\,q\,\dot{q} + \left(\frac{A_D}{D}\ddot{y} + \frac{B_D}{D}\omega_s\dot{y} + \frac{G_D}{D}\omega_s^2 y\right)\sin\beta\,, \tag{26}$$

in which A_D, B_D, G_D and P_D are constant non-dimensional coupling coefficients and ε_D is the non-dimensional damping ratio. The inclusion of eq. (26) into the model has the added advantage that it creates the possibility to also model the oscillating components of the drag force, which are known to oscillate at even multiples of the Strouhal frequency [1, 2]. To ensure that the oscillating component of the in-line fluid force on a stationary cylinder as predicted by the present system of equations is equal to the force component $\hat{C}_{x2}^0$ from the measurements of Gopalkrishnan, P_D should be equal to: $P_D = -16\,\varepsilon_D\hat{C}_{x2}^0/4 = -4\,\varepsilon_D\hat{C}_{x2}^0$.

Again, it has been tried to tune the system of equations, now given by eq. (6), (23), (24), (25) and (26) to the free vibration experiments of Khalak et al. The results of this attempt are depicted in Fig. 18 and 19. The following values for the tuning parameters have been used:

$\mathrm{St} = 0.1932$, $\hat{C}_{x0}^0 = 1.1856$, $\hat{C}_{y1}^0 = 0.3842$, $\hat{C}_{x2}^0 = -0.0215$,
$A_Q = 1.10$, $B_Q = -0.50$, $G_Q = 0.0$, $\varepsilon_Q = 0.10$,
$A_L = 0.70$, $B_L = 0.00$, $G_L = -1.15$, $\varepsilon_L = 0.30$,
$A_D = -8.00$, $B_D = -8.00$, $G_D = 5.00$, $\varepsilon_D = 0.30$

It can be seen in Figs. 18 and 19 that the first results of the new wake model consisting of multiple oscillators seem to be very promising. It appears that with the help of multiple wake oscillators it is possible to describe the upper and lower branch of free vibration.

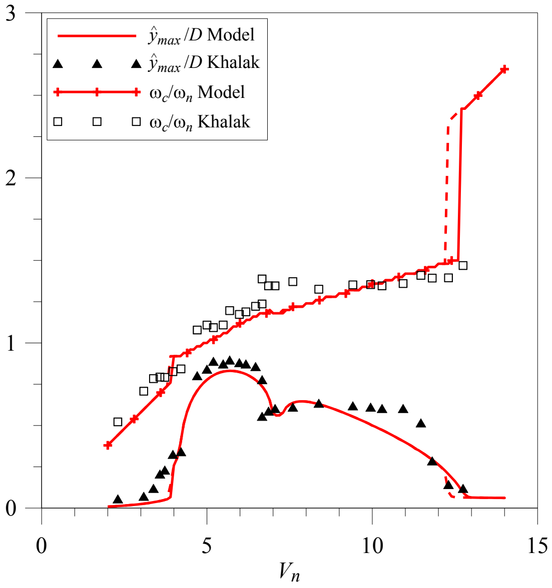

Figure 18: Comparison of the amplitude and frequency of oscillation of the multiple oscillator model with the measurements of Khalak et al. [3] for $m^* = 2.4$.

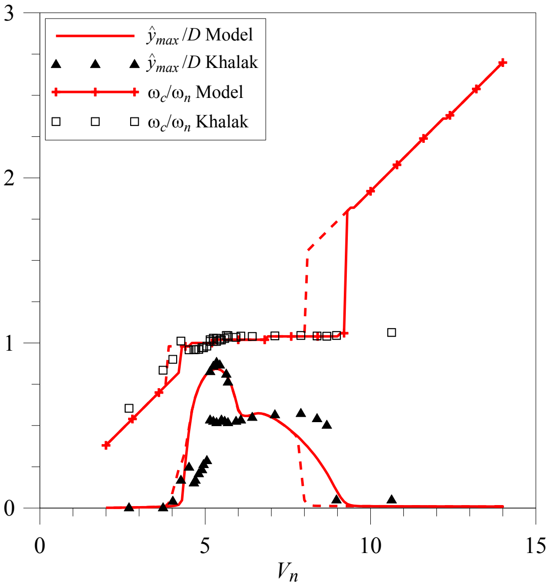

Figure 19: Comparison of the amplitude and frequency of oscillation of the multiple oscillator model with the measurements of Khalak et al. [3] for $m^* = 20.6$.

5 CONCLUSIONS

Starting with a wake oscillator model that has been developed earlier in [6] and [7] for the description of vortex-induced vibration, an attempt has been made to improve this model by making the coupling term between the structural and fluid oscillator frequency dependent. A set of consistent frequency dependent coupling coefficients is valid at all amplitudes of cylinder motion and satisfies the Kramers-Kronig relations. The frequency dependent coefficients have been determined on the basis of the results of a forced vibration experiment.

As reported earlier in [6], the sets of frequency dependent coefficients found at different amplitudes of forced cylinder motion do not correspond with each other and therefore fail the requirements mentioned above.

In this paper the influence of the presence of the dominant non-linearity in the wake oscillator on the discrepancy between the various sets of frequency dependent coefficients found at different amplitudes of cylinder motion has been examined. It has been found that removal of the dominant non-linearity reduced the discrepancy between the sets of frequency dependent coefficient.

Based on this result a new model is proposed consisting of linear oscillators for the components of the fluid forces due to vortex shedding. These oscillators are forced by the cylinder motion and a wake variable q, which is described by a Van der Pol equation. Preliminary results of this model seem to be promising.

REFERENCES

[1] T. Sarpkaya, A critical review of the intrinsic nature of vortex-induced vibrations. *Journal of Fluids and Structures,* **19**, 389-447, 2004.

[2] C.H.K. Williamson, R. Govardhan, Vortex-induced vibrations. *Annual Review of Fluid Mechanics,* **36**, 413-455, 2004.

[3] A. Khalak, C.H.K. Williamson, Motions, forces and mode transitions in vortex-induced vibrations at low mass-damping. *Journal of Fluids and Structures,* **13**, 813-851, 1999.

[4] R. Gopalkrishnan, *Vortex-induced forces on oscillating bluff cylinders, PhD Thesis*. Massachusetts Institute of Technology, 1992.

[5] F.S. Hover, A.H. Techet, M.S. Triantafyllou, Forces on oscillating uniform and tapered cylinders in crossflow. *Journal of Fluid Mechanics,* **363**, 97-114,1998.

[6] R.H.M. Ogink, A.V. Metrikine, A wake oscillator with frequency dependent coupling for the modeling of vortex-induced vibration. Journal of Sound and Vibration, **329**, 5452-5473, 2010.

[7] M.L. Facchinetti, E. de Langre, F. Biolley, Coupling of structure and wake oscillators in vortex-induced vibrations. Journal of Fluids and Structures, **19**, 123-140, 2004.

[8] W.H. Press, S.A. Teukolsky, W.T. Vetterling, B.P. Flannery, *Numerical recipes in Fortran77:The art of scientific computing, 2nd Edition*. Cambridge University Press, 1992.

COMPDYN 2011
3^{rd} ECCOMAS Thematic Conference on
Computational Methods in Structural Dynamics and Earthquake Engineering
M. Papadrakakis, M. Fragiadakis, V. Plevris (eds.)
Corfu, Greece, 25-28 May 2011

NUMERICAL SOLUTION OF THE FOKKER-PLANCK EQUATION BY FINITE DIFFERENCE AND FINITE ELEMENT METHODS - A COMPARATIVE STUDY

L. Pichler[1], **A. Masud**[2] **L. A. Bergman**[1]

[1] Department of Aerospace Engineering, University of Illinois at Urbana-Champaign
104 S. Wright Street, Urbana, IL 61801, USA
e-mail: Lukas.Pichler@ymail.com , lbergman@illinois.edu

[2] Department of Civil and Environmental Engineering, University of Illinois at Urbana-Champaign
205 N. Mathews Street, Urbana, IL 61801, USA
e-mail: amasud.illinois.edu

Keywords: Fokker-Planck Equation, Finite Difference Method, Finite Element Method, Multi-Scale Finite Element Method, Linear Oscillator, Duffing Oscillator.

Abstract. *Finite element and finite difference methods have been widely used, among other methods, to numerically solve the Fokker-Planck equation for investigating the time history of the probability density function of linear and nonlinear 2d and 3d problems, and also the application to 4d problems has been addressed. However, due to the enormous increase of the computational costs, different strategies are required for an efficient application to problems of dimension* ≥ 3*. Recently, a stabilized multi-scale finite element method has been effectively applied to the Fokker-Planck equation effectively by means of a considerably reduction of the required number of elements. Also, the alternating directions implicit method shows good performance in terms of efficiency and accuracy. In this paper various finite difference and finite element methods are discussed and the results are compared using various numerical examples.*

1 INTRODUCTION

The response of linear systems subjected to additive Gaussian white noise or linearly filtered Gaussian white noise is Gaussian. The derivation for an N-dimensional system can be found, e.g. in [1]. For the case of nonlinear systems subjected to additive Gaussian white noise, analytical solutions are restricted to certain scalar systems. It has been shown (see [2]), that the response of a multi-dimensional memoryless nonlinear system subjected to additive Gaussian white noise forms a vector Markov process, with transition probability density function satisfying both the forward (Fokker-Planck) and backward Kolmogorov equations for which numerical approximations in terms of finite element and finite difference methods can be pursued.

1.1 Scope of this work

A number of numerical methods have been introduced over the past five decades to obtain approximate results for the solution of the Fokker-Planck equation (FPE). Many of these approximations can be shown to be accurate. This work deals with a review of several finite element and finite difference methods. A comparison and assessment of different methods is carried out by means of various numerical examples including a 2d linear, 2d unimodal and bimodal Duffing oscillators, 3d linear and 3d Duffing oscillators.

The goal is to evaluate the transient solution for the probability density function (PDF) of the oscillator due to stochastic (white noise) excitation. Thus, the forward Kolmogorov or Fokker Planck equation is of interest and will be approximated within the numerical methods.

1.2 Background

The finite element method was first applied by [3] to determine the reliability of the linear, single degree-of-freedom oscillator subjected to stationary Gaussian white noise. The initial boundary problem associated with the backward Kolmogorov equation was solved numerically using of a Petrov-Galerkin finite element method.

[4] has solved the stationary form of the FPE adopting the finite element method (FEM) in order to calculate the stationary probability density function of response. The weighted residual statement for the Fokker-Planck equation was first integrated by parts to yield the weak form of the equations.

The transient form of the FPE has been analyzed by [5] using a Bubnov-Galerkin FEM. It is shown that the initial boundary value problem can be modified in order to evaluate the first passage problem. A comparison for the reliability was carried out with the results obtained from the backward Kolmogorov equation.

The drawback of the FEM is the quickly increasing computational cost with increasing dimension. Thus while 2 and 3 dimensional systems have been analyzed in the literature, the analysis of 4d or 5d problems touches the limits of today's computational capabilities and are not yet feasible.

Computationally more economical - in terms of memory requirements, and when considering the effort spent for the assembly of the mass and stiffness matrices - are finite difference methods. The application of central differences is, as expected, only feasible for the case of 2d linear systems, because of stability issues. The stability is a function of the nonlinearity and the dimension (ratio Δt and $\prod_{i=1}^{n} \Delta x_i$), thus being unfavorable to the use of this simple method.

A successful approach to overcome the limitations of simple finite differences was achieved by [6] in terms of higher order finite differences. The solution of a 4d system using higher order finite differences is reported in [6]. A comparison of various higher order FD formulations is presented in [7].

A viable approach to achieve higher accuracy is the application of operator splitting methods. Their capabilities with respect to the numerical solution of the FPE has so far received little attention. Operator splitting methods provide a tool to reduce the computational costs by the reduction of the solution to a series of problems of dimension of one order less than the original problem. Thus, more efficiency, required for the solution of problems of larger dimension ($>=3$), can be achieved. An operator splitting method for the solution of the 2d Duffing oscillator is presented in [8]. An operator splitting scheme for 3d oscillators subjected to additive and multiplicative white noise is given by [9]. The method consists in a series of consecutive difference equations for the three fluxes and is numerically stable. The ADI [10] is adopted in this paper for a series of problems and acceptably accurate results are achieved at low costs. The implementation of the method is straightforward and can be readily extended to higher dimensions.

Recent work by Masud et al. introduced a stabilized multi-scale finite element method which allows for a reduction of the number of elements for given accuracy and, thus, the efficiency of the computation can be increased by an order of magnitude when solving a 3d problem.

Several four-state dynamical systems were studied by [11, 12] in which the Fokker-Planck equation was solved using a global weighted residual method and extended orthogonal functions.

Meshless methods were proposed by [13, 14] to solve the transient FPE and [15] for the stationary FPE. Considerable reduction of the memory storage requirements could be expected due to coarse meshes employed and thus a standard desktop PC suffices to carry out the numerical analysis.

In addition, many numerical packages now provide the capability to solve partial differential equations by means of finite element and finite difference methods. However, in most cases these tools are limited to 2d and can only solve special forms of elliptic, parabolic or hyperbolic partial differential equations (PDE). The implementation of FD and FEM into computational software is shown for the cases of COMSOL (2d linear) and FEAP(general 3d).

2 THE FOKKER-PLANCK EQUATION

The Fokker-Planck equation for a n-dimensional system subjected to external Gaussian white noise excitation is given by

$$\frac{\partial p}{\partial t} = -\sum_{j=1}^{n} \frac{\partial}{\partial x_j}(z_j p) + \frac{1}{2}\left(\sum_{i=1}^{n}\sum_{j=1}^{n} \frac{\partial^2}{\partial x_i \partial x_j}(H_{ij} p)\right) \tag{1}$$

where p denotes the transition probability density function, $\mathbf{x}$ the n-dimensional state space vector and $\mathbf{z}(\mathbf{x})$ and $\mathbf{H}(\mathbf{x})$ denote the drift vector and diffusion matrix, respectively.

The normalization condition for the probability density function is given by:

$$\int p_X(\mathbf{x}) d\mathbf{x} = 1\,, \tag{2}$$

and the initial conditions are given by $p(\mathbf{x}_0, 0)$. Examples for initial conditions are, e.g., deterministic given by the Dirac delta function

$$p_X(\mathbf{x}_0, 0) = \prod_{i=1}^{n} \delta((x_i - x_{0i})) \tag{3}$$

or the n-dimensional Gaussian distribution

$$p_X(\mathbf{x}_0, 0) = \frac{1}{(2\pi)^{n/2}|\mathbf{\Sigma}|^{1/2}} \exp\left(-\tfrac{1}{2}(\mathbf{x}-\boldsymbol{\mu})^T\mathbf{\Sigma}^{-1}(\mathbf{x}-\boldsymbol{\mu})\right) \tag{4}$$

in the random case.

At infinity, a zero-flux condition is imposed:

$$p(x_i, t) \to 0 \quad \text{as} \quad x_i \to \pm\infty \quad i = 1, 2, \ldots, n \tag{5}$$

Without loss of generality, and for a better comparison, the various methods introduced in the following, will be presented for the 2d linear case,

$$\begin{Bmatrix} \dot{x_1} \\ \dot{x_2} \end{Bmatrix} = \begin{bmatrix} x_2 \\ -2\xi\omega x_2 - \omega^2 x_1 \end{bmatrix} + \begin{bmatrix} 0 \\ 1 \end{bmatrix} w(t) \tag{6}$$

The corresponding FPE is

$$\frac{\partial p}{\partial t} = -\frac{\partial(x_2 p)}{\partial x_1} + \frac{\partial\left[(2\xi\omega x_2 + x_1)\, p\right]}{\partial x_2} + D\frac{\partial^2 p}{\partial x_2^2} \tag{7}$$

which, after application of the chain rule, becomes:

$$\frac{\partial p}{\partial t} = -x_2\frac{\partial p}{\partial x_1} + (2\xi\omega x_2 + x_1)\frac{\partial p}{\partial x_2} + 2\xi\omega p + D\frac{\partial^2 p}{\partial x_2^2} \tag{8}$$

3 FINITE DIFFERENCE AND FINITE ELEMENT METHODS

Many references deal with the application of FE and FE methods to the numerical solution of the Fokker-Planck equation (see e.g. [7, 16]).

3.1 Central finite differences

In terms of central finite differences, Eq. (8) becomes:

$$\frac{p_{i,j}^{m+1} - p_{i,j}^m}{\Delta t} = -x_2\frac{p_{i+1,j}^m - p_{i-1,j}^m}{2\Delta x_1} + 2\xi\omega p_{i,j}^m + (2\xi\omega x_2)\frac{p_{i,j+1}^m - p_{i,j-1}^m}{2\Delta x_2} + D\frac{p_{i,j+1}^m - 2p_{i,j}^m + p_{i,j-1}^m}{\Delta x_2^2} \tag{9}$$

and an explicit formulation is obtained for the probability density function

$$\begin{aligned} p_{i,j}^{m+1} \;=\;& p_{i,j}^m + \Delta t\big(-x_2\frac{p_{i+1,j}^m - p_{i-1,j}^m}{2\Delta x_1} + 2\xi\omega p_{i,j}^m + (2\xi\omega x_2)\frac{p_{i,j+1}^m - p_{i,j-1}^m}{2\Delta x_2} \\ & + D\frac{p_{i,j+1}^m - 2p_{i,j}^m + p_{i,j-1}^m}{\Delta x_2^2}\big) \end{aligned} \tag{10}$$

The boundary conditions are given by $p_{i,j} = 0$ for $i, j = 1, N$. The discretization using central finite differences leads to an explicit scheme, which means that the values $p_{i,j}^{m+1}$ can be calculated directly from values $p_{i,j}^m$. Thus, the linear system of equations can be solved directly, and no inversion of the matrix relating $p_{i,j}^m$ to $p_{i,j}^{m+1}$ is required.

Explicit finite difference represents the simplest approximation; however, due to stability issues, implicit FD formulations are generally required.

Implicit, higher order finite difference schemes to solve Fokker-Planck equations have been developed by [6]. Higher order FD lead to more accurate results, but they are not used for comparison herein.

3.2 Alternating directions implicit method

The alternating directions implicit method (ADI) is a finite difference scheme, for which the finite difference steps in each direction are resolved separately and in each step implicitly for one dimension and explicitly for the others, leading to a stable finite difference formulation. The main advantages are that the resulting operational matrix is tridiagonal and, thus, its inverse can be computed efficiently. Moreover, the dimensionality of the problem is reduced by one and the problem is reduced to a series of of problems of dimension of one order less.

In Eq. (8), finite differences are first applied implicitly to the x_1-direction

$$\frac{p_{i,j}^{m+\frac{1}{2}}-p_{i,j}^{m}}{\Delta\frac{t}{2}} = \\ -x_2\frac{p_{i+1,j}^{m+\frac{1}{2}}-p_{i-1,j}^{m+\frac{1}{2}}}{2\Delta x_1} + 2\xi\omega p_{i,j}^{m} + (2\xi\omega x_2)\frac{p_{i,j+1}^{m}-p_{i,j-1}^{m}}{2\Delta x_2} + D\frac{p_{i,j+1}^{m}-2p_{i,j}^{m}+p_{i,j-1}^{m}}{\Delta x_2^2} \tag{11}$$

and then to the x_2-direction.

$$\frac{p_{i,j}^{m+1}-p_{i,j}^{m+\frac{1}{2}}}{\Delta\frac{t}{2}} = \\ -x_2\frac{p_{i+1,j}^{m+\frac{1}{2}}-p_{i-1,j}^{m+\frac{1}{2}}}{2\Delta x_1} + 2\xi\omega p_{i,j}^{m+\frac{1}{2}} + (2\xi\omega x_2)\frac{p_{i,j+1}^{m+1}-p_{i,j-1}^{m+1}}{2\Delta x_2} + D\frac{p_{i,j+1}^{m+1}-2p_{i,j}^{m+1}+p_{i,j-1}^{m+1}}{\Delta x_2^2} \tag{12}$$

Both Eq. (11) and Eq. (12) give $M-2$ tridiagonal linear systems of equations in x_1 for the $j=2,\ldots,M-1$ values of x_2 and in case of Eq. (11) to $M-2$ tridiagonal linear systems of equations in x_2 for the $i=2,\ldots,M-1$ values of x_1 and in case of Eq. (12).

The computational cost is mainly due to the n times N matrix inversions which are encountered in the n-loops solution for a full time step. n denotes the dimension of the problem and N the number of nodes per dimension.

3.3 Finite element method

Reduction of Eq. (1) to the weak form and the introduction of shape functions of C^0 continuity lead to

$$\mathbf{C}\dot{p} + Kp = 0 \tag{13}$$

where

$$C_{rs}^{e} = \int_{\Omega^e} N_r(\mathbf{x})N_s(\mathbf{x})d\mathbf{x} \tag{14}$$

and

$$K_{rs}^{e} = \int_{\Omega^e}\left(\sum_{i=1}^{n} z_i(\mathbf{x})N_s\frac{\partial}{\partial x_i}N_r d\mathbf{x} - \sum_{i=1}^{n}\sum_{j=1}^{n}\frac{\partial}{\partial x_i}N_r\frac{\partial}{\partial x_i}\left[H_{ij}N_s\right]d\mathbf{x}\right)N_r(\mathbf{x})N_s(\mathbf{x})d\mathbf{x} \tag{15}$$

The integration over time can be performed in a suitable way using the Crank-Nicholson scheme ($\theta = 0.5$).

3.4 Multi-scale finite element method

The multi-scale FEM used herein was introduced by [17] for the numerical treatment of advection-diffusion equations in fluid dynamics. Then, the methodology was extended by [18] to the special case of the Fokker-Planck equation. Finally, the method was applied for the numerical solution of the Fokker-Planck equation of a 3d linear system [19]. [20] provide an overview of stabilized finite element methods and recent developments of their application to the advection-diffusion equation.

For a description of the method the reader is referred to the aforementioned references. Basically, a multi-scale FEM means that an approximation of the error term from the traditional FE formulation is included as a fine scales into the formulation, the probability density function is then given by

$$p = \hat{p} + p' \tag{16}$$

where $\hat{p}$ represents the contribution of the coarse scale and p' the contribution of the fine scale.

3.5 Implementation within COMSOL / FEAP

The FE code COMSOL provides the possibility to solve partial differential equations in terms of finite differences. For an extensive discussion, refer to the COMSOL documentation, [21]. Fig. 1 shows the results obtained for the FPE for the 2d linear oscillator with parameters discussed later.

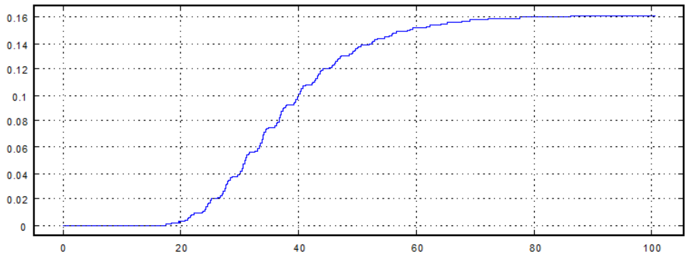

Figure 1: Probability density function $p(0,0,t)$ at central node over time.

The multiscale finite element method was implemented by Masud and coworkers into the finite element code FEAP and is used herein for comparison of the 3d examples.

4 NUMERICAL EXAMPLES

The numerical methods used in this comparison are:

1. central finite differences (FD)
2. alternating directions implicit method (ADI)
3. Bubnov Galerkin finite element method (FEM)
4. stabilized multiscale finite element method (MSFEM)

The methods 1-3 are coded in MATLAB and the analysis was carried out on a 64-bit Windows server (32GB). The results for method 4 are obtained on 32 bit Linux or Windows machines with 2GB memory using an implementation within FEAP, [18].

4.1 2-d linear oscillator

The different methods are applied to solve the FPE for the linear oscillator

$$\begin{bmatrix}\dot{x_1}\\ \dot{x_2}\end{bmatrix} = \begin{bmatrix}x_2\\ -2\xi\omega x_2 - \omega^2 x_1\end{bmatrix} + \begin{bmatrix}0\\ 1\end{bmatrix} w(t) \tag{17}$$

The parameters of the oscillator are chosen according to [5] and are given by:

μ	σ	ξ	ω	D
$[5,5]$	$\frac{1}{9}\mathbf{I}(2)$	0.05	1	0.1

Table 1: Parameter for the linear oscillator

Finite element results obtained using a 61×61 mesh are shown in Fig. 2 and Fig. 3. All results are calculated with a time increment of $\Delta t = 0.001$ and a total time of $\tau = 20$ natural periods. The state space is discretized on the domain $[-10, 10] \times [-10, 10]$;

Fig. 2 shows the evolution of the probability density function over time. In Fig. 3 the transient solution for the PDF at the origin is given. The exact stationary value at the origin is $p(0,0)_{stat} = 1.5915e{-}1$.

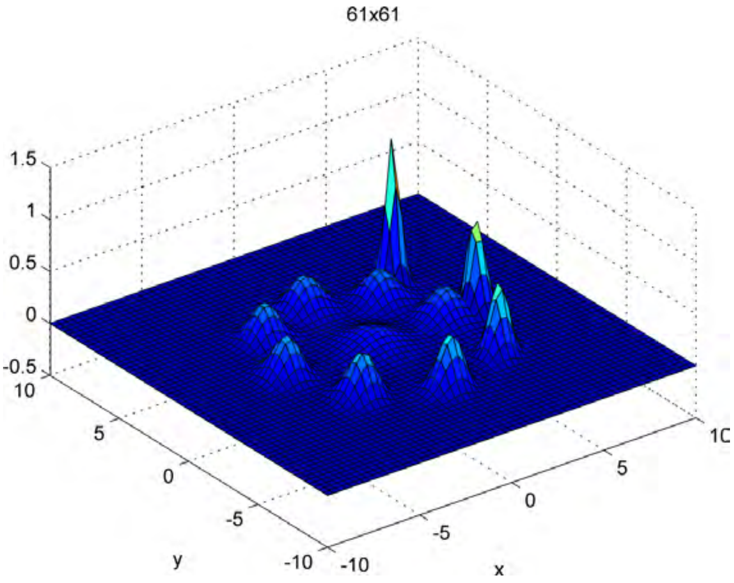

Figure 2: FEM: 61×61 - Probability density function $p(t)$ over time.

The accuracy of the numerical solutions are compared at stationarity (i.e. after t = 20 cycles) using two error measures. The first, the maximum norm

$$\|e\|_\infty = \|p^{ex} - p^{num}\|_\infty \tag{18}$$

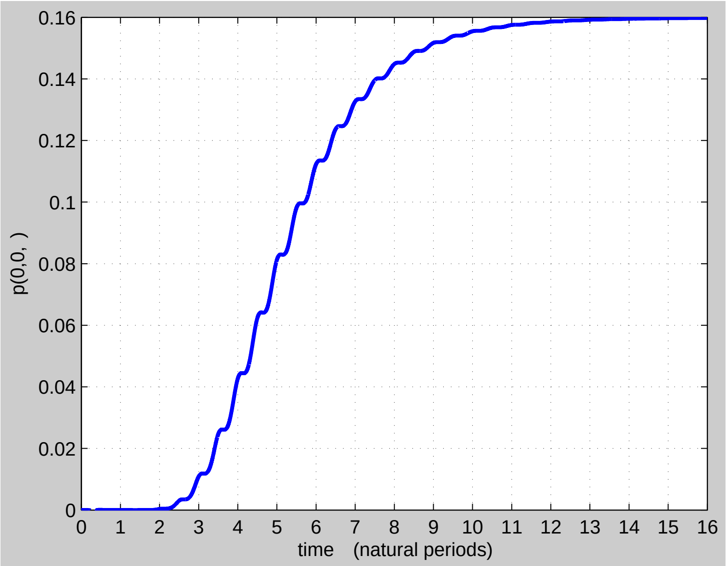

Figure 3: FEM: 61×61 - Probability density function at central node $p(0, 0, t)$ over time.

is a measure of the maximum error across the entire mesh. The second,

$$\|e\|_2 = \|p^{ex} - p^{num}\|_2 \tag{19}$$

can be used to describe the average nodal error $\bar{e} = \|e\|_2/n_{nodes}$, where n_{nodes} is the total number of nodes.

mesh	61×61		81×81		101×101		121×121	
method	$\|e\|_\infty$	$\|e\|_2$	$\|e\|_\infty$	$\|e\|_2$	$\|e\|_\infty$	$\|e\|_2$	$\|e\|_\infty$	$\|e\|_2$
FD	7.05e-3	2.99e-2	4.169e-3	2.405e-2	2.983e-3	2.201e-2	2.371e-3	2.199e-2
ADI	1.66e-2	4.61e-2	4.144e-3	2.375e-2	2.931e-3	2.149e-2	2.305e-3	2.124e-2
FEM	2.04e-3	1.00e-2	1.712e-3	1.152e-2	1.550e-3	1.370e-2	1.464e-3	1.613e-2

Table 2: Comparison of the accuracy for the linear oscillator

Table 2 correctly visualizes the increasing accuracy for all methods when the mesh is refined. It can also be seen that the FD and ADI deliver similar results. The advantage of the ADI over FD consists in the fact that the stability of the method allows one to use larger time steps. The FEM provides more accurate results for the same mesh refinement as the finite difference methods. The FEM is the preferable method to investigate the first passage problem, in case small probabilities of failure are involved and a highly accurate method is required.

Alternatively, the accuracy of the solution at stationarity can also be represented by comparison of the exact and numerical covariance matrices K_{xx}, the latter computed from FE/FD results for the PDF.

The transient solution for the probability density at the center node can be obtained with all three methods as listed in Table 2. Fig. 4 shows a comparison for the PDF at the origin using finite difference method and different mesh sizes.

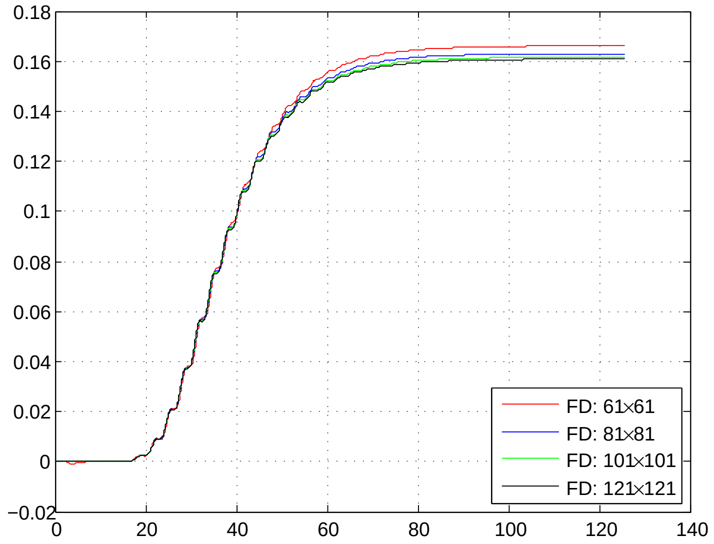

Figure 4: FD - Comparison for probability density function at central node $p(0,0,t)$ over time.

4.2 2-d Duffing oscillator

4.2.1 Unimodal

The unimodal Duffing oscillator is considered next:

$$\begin{bmatrix} \dot{x_1} \\ \dot{x_2} \end{bmatrix} = \begin{bmatrix} x_2 \\ -2\xi\omega x_2 - \omega^2 x_1 - \omega^2\gamma x_1^3 \end{bmatrix} + \begin{bmatrix} 0 \\ 1 \end{bmatrix} w(t) \tag{20}$$

The parameters of the oscillator are chosen as:

μ	σ	ξ	ω	D	γ
$[0, 10]$	$\frac{1}{2}\mathbf{I}(2)$	0.2	1	0.4	0.1

Table 3: Parameters for the unimodal Duffing oscillator

The state space is discretized on the domain $[-15, 15] \times [-15, 15]$.

It is known that central finite differences are not suited in case of nonlinearities, but ADI can be utilized nonetheless. In case the Duffing-oscillator is analyzed, it is found that the ADI can be used due to its implicit formulation with the largest time step Δt, thus providing a good compromise between accuracy and efficiency as can be seen from Table 4. The time steps used are $\Delta t = 1e-2$ (ADI), $\Delta t = 1e-3$ (FEM) and $\Delta t = 5e-4$(FEM: mesh 101).

The exact analytical expression for the stationary PDF of the unimodal Duffing oscillator of Eq. (20) is given as:

$$\begin{aligned} \sigma_{x_0}^2 &= \frac{\pi G_0}{4\xi\omega_0^3} \\ \sigma_{v_0}^2 &= \omega_0^2\sigma_{x_0}^2 \\ p_X(\mathbf{x}) = C\exp &\left(-\frac{1}{2\sigma_{x_0}^2}\left(x^2 + \frac{\gamma}{2}x^4\right) - \frac{1}{2}\sigma_{v_0}^2 v^2\right) \end{aligned} \tag{21}$$

The value of the stationary PDF at the central node is $p_{stat}(0,0) = 1.6851e-1$.

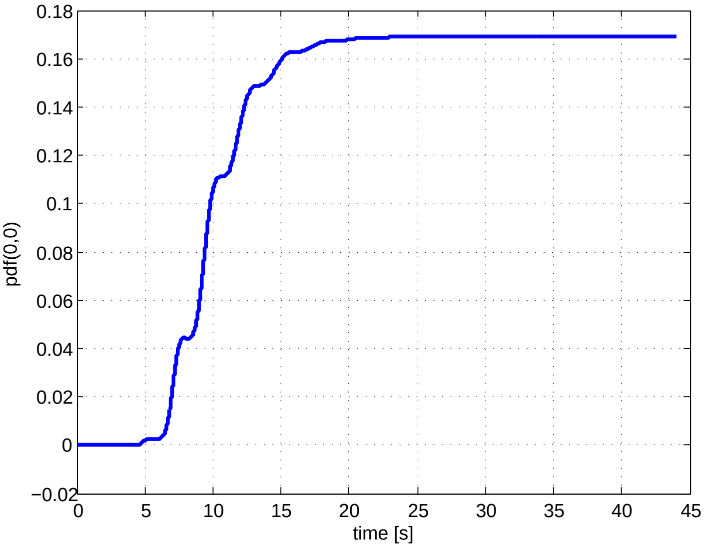

Figure 5: FEM: 101×101 - Probability density function at central node $p(0, 0, t)$ over time.

method / mesh	61×61		81×81		101×101	
	$\|\|e\|\|_\infty$	$\|\|e\|\|_2$	$\|\|e\|\|_\infty$	$\|\|e\|\|_2$	$\|\|e\|\|_\infty$	$\|\|e\|\|_2$
ADI	1.7832e-2	4.9323e-2	9.6731e-3	3.5553e-2	6.1694e-3	2.8444e-2
FEM	2.6002e-3	1.1587e-2	1.3999e-3	8.5297e-3	9.3290e-4	6.8215e-3

Table 4: Comparison of the accuracy for the unimodal Duffing oscillator

4.2.2 Bimodal

The equations for the bimodal Duffing oscillator are characterized by the changed sign of the term $\omega^2 x_1$.

$$\begin{bmatrix} \dot{x_1} \\ \dot{x_2} \end{bmatrix} = \begin{bmatrix} x_2 \\ -2\xi\omega x_2 + \omega^2 x_1 - \omega^2 \gamma x_1^3 \end{bmatrix} + \begin{bmatrix} 0 \\ 1 \end{bmatrix} w(t) \tag{22}$$

The parameters of the oscillator are chosen according to [5] and are given by:

μ	σ	ξ	ω	D	γ
$[0, 10]$	$\frac{1}{2}\mathbf{I}(2)$	0.2	1	0.4	0.1

Table 5: Parameter for the bimodal Duffing oscillator

The state space is discretized on the domain $[-15, 15] \times [-15, 15]$. Again, the ADI provides a tool for obtaining accurate results rather quickly.

In Fig. 6 the PDF is depicted for stationary conditions and a 61×61 mesh. A comparison of the evolution of the probability density function at the origin is shown in Fig. 7 for FEM and different meshes.

To compare the solution, the analytical expression according to [22] should be used. The exact analytical expression for the bimodal Duffing oscillator of Eq. (22) is given as:

$$p_X(\mathbf{x}) = C \exp\left(-\frac{1}{2\sigma_{x_0}^2} \left(-x^2 + \frac{\gamma}{2} x^4 \right) - \frac{1}{2} \sigma_{v_0}^2 v^2 \right)$$

The value of the stationary PDF at the central node is $p_{stat}(0, 0) = 8.3161e - 3$. The maximum value of the stationary PDF of the bimodal oscillator at $x_{1,2} = \pm\sqrt{1/\gamma} = \pm 3.1623$ and $y_{1,2} = 0$ is $p_{stat}(x_{1,2}, 0) = 0.1013$. A comparison of the evolution of the probability density function at the mesh point $(x = 3, y = 0)$ which is closest to the maximum of the PDF is shown in Fig. 8 for FEM and different meshes; $p_{stat}(3, 0) = 0.0988$.

method / mesh	61×61		81×81		101×101	
	$\|e\|_\infty$	$\|e\|_2$	$\|e\|_\infty$	$\|e\|_2$	$\|e\|_\infty$	$\|e\|_2$
ADI	4.7186e-2	1.8229e-1	1.1899e-2	4.2491e-2	7.5077e-3	3.0640e-2
FEM	6.8085e-3	1.9074e-2	2.6024e-3	1.1265e-2	2.8419e-3	1.3709e-2

Table 6: Comparison of the accuracy for the bimodal Duffing oscillator

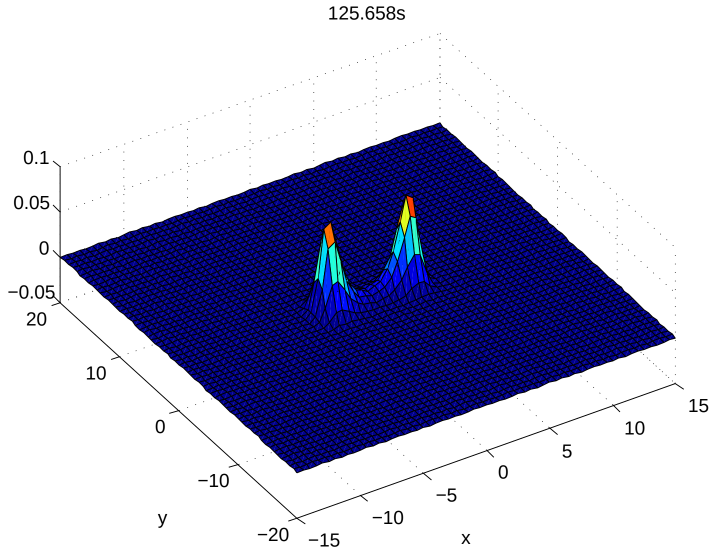

Figure 6: 61×61: Stationary probability density function p_{stat}.

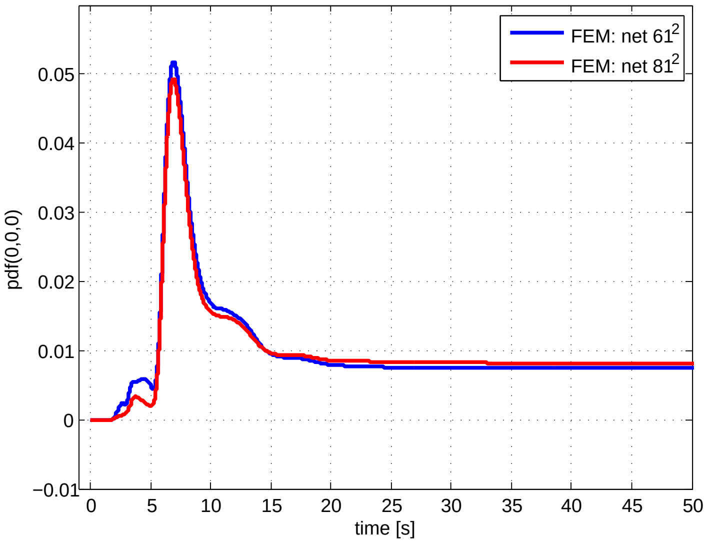

Figure 7: FEM: Comparison of the probability density function at the central node $p(0, 0, t)$ over time.

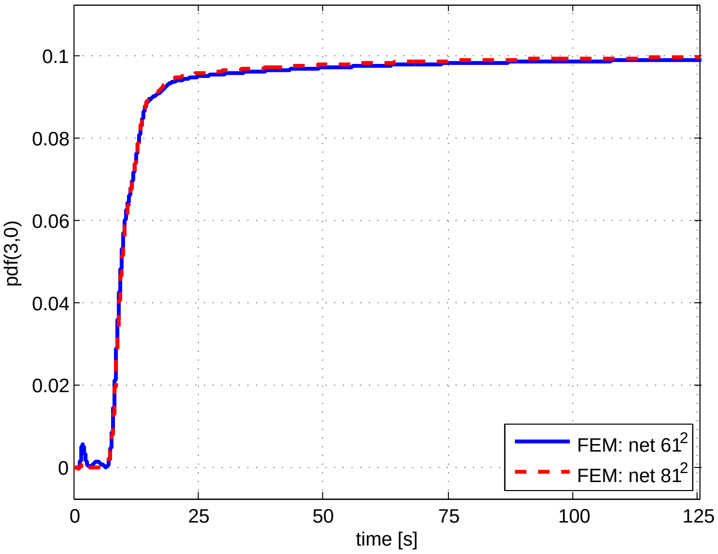

Figure 8: FEM: Comparison of the probability density function at the node $p(3, 0, t)$ over time.

4.3 3-d linear oscillator

A 3-rd state variable is introduced in terms of a low pass filter for the white noise excitation which is applied to the linear 2d system.

$$\begin{bmatrix}\dot{x_1}\\ \dot{x_2}\\ \dot{x_3}\end{bmatrix} = \begin{bmatrix} x_2 \\ -2\xi\omega x_2 - \omega^2 x_1 + x_3 \\ -\alpha x_3 \end{bmatrix} + \begin{bmatrix}0\\0\\1\end{bmatrix} w(t) \tag{23}$$

The parameters of the 3d linear oscillator are:

μ	σ	ξ	ω	D	α
$[0,0,0]$	$0.2\mathbf{I}(3)$	0.2	1	0.4	1

Table 7: Parameter for the 3d linear oscillator

Tables 8 and 9 shows a comparison of the accuracy of the results for the linear oscillator. The time step is chosen to be $\Delta t = 0.01$, and only for FEM (net 81^3) $\Delta t = 0.001$ is required. The exact stationary value of the PDF at the origin is $p(0, 0, 0) = 0.2409$.

method / mesh	25^3		41^3	
	$\|\|e\|\|_\infty$	$\|\|e\|\|_2$	$\|\|e\|\|_\infty$	$\|\|e\|\|_2$
ADI	1.8009e-1	3.6649e+0	4.8336e-2	4.8748e-1
FEM	6.5802e-3	4.6480e-2	3.5574e-3	4.6357e-2
MSFEM	1.2533e-2	5.0262e-2	memory	

Table 8: Comparison of the accuracy for the linear oscillator

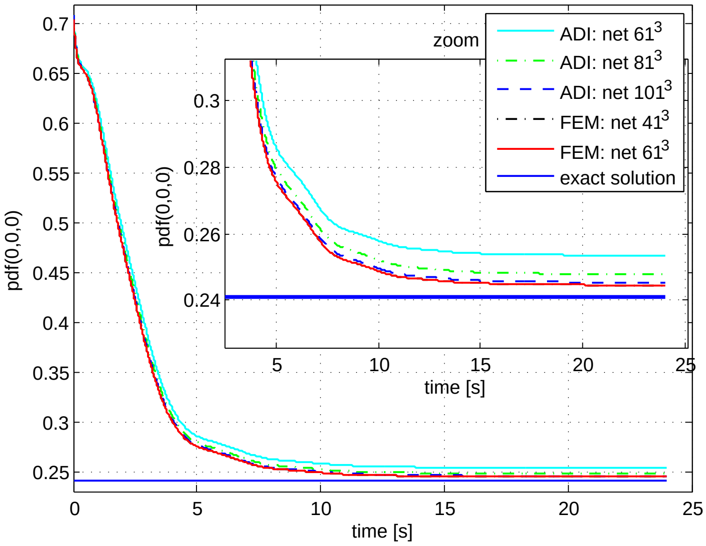

Figure 9: Probability density function at the central node $p(0, 0, 0, t)$ over time.

method / mesh	61^3		81^3		101^3	
	$\|\|e\|\|_\infty$	$\|\|e\|\|_2$	$\|\|e\|\|_\infty$	$\|\|e\|\|_2$	$\|\|e\|\|_\infty$	$\|\|e\|\|_2$
ADI	1.2542e-2	2.1170e-1	6.9165e-3	1.8067e-1	4.3899e-3	1.6063e-1
FEM	1.4081e-3	3.4554e-2	3.9016e-4	2.4920e-2		

Table 9: Comparison of the accuracy for the linear oscillator

4.4 3-d Duffing oscillator

$$\begin{bmatrix}\dot{x_1}\\ \dot{x_2}\\ \dot{x_3}\end{bmatrix} = \begin{bmatrix} x_2 \\ -2\xi\omega x_2 - \omega^2 x_1 - \omega^2\gamma x_1^3 + x_3 \\ -\alpha x_3\end{bmatrix} + \begin{bmatrix}0\\0\\1\end{bmatrix} w(t) \tag{24}$$

The parameters of the 3d Duffing oscillator are:

μ	σ	ξ	ω	D	α	γ
$[0,0,0]$	$0.2\mathbf{I}(3)$	0.2	1	0.4	1	0.1

Table 10: Parameters for the 3d Duffing oscillator

Fig. 10 shows converged results for the evolution of the PDF at the origin over time using ADI for two different degrees of nonlinearity and for the corresponding linear system ($\gamma = 0$).

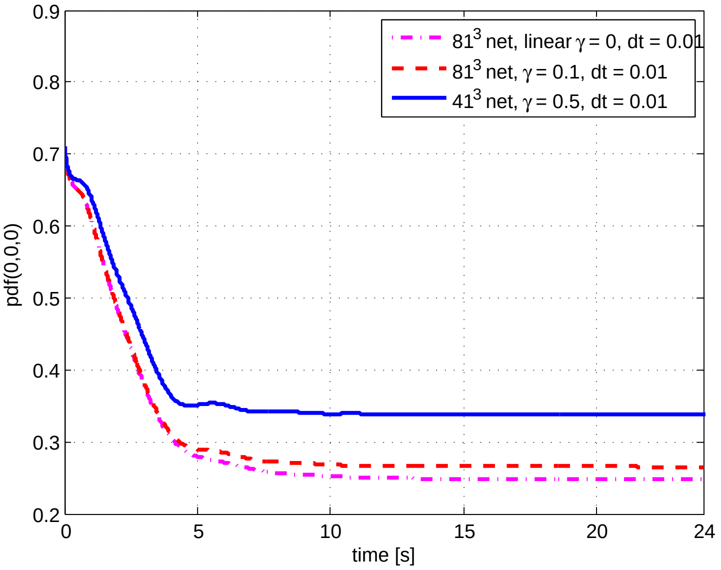

Figure 10: Probability density function at the central node $p(0,0,0,t)$ over time.

5 DISCUSSION

Despite of the greater numerical effort, the FEM is preferable over FD, because it yields more accurate results. However, at this time the FEM is only suitable for dimension ≤ 3. In the case of 3d and 4d problems, the stabilized multi-scale FEM provides a tool with a high order of accuracy, preserving numerical efficiency due to the fact that a coarser mesh size can be used.

The first effective numerical solution for 4d problems was reported by [23] in terms of high-order finite differences. The advantage of operator splitting methods including the ADI is the stability of the method, meaning that larger time steps (when compared to FEM) can be used, thus and speeding up the analysis as the dimensionality of the problem is reduced by one.

The recently introduced PUFEM (see Kumar et al.) represents a possibility to obtain good results with coarse mesh sizes. The price paid is the computational overhead required in order to allow for the proposed coarse mesh size.

From the above discussion it is clear that future developments will be bounded by the so-called curse of dimensionality for some time.

6 ACKNOWLEDGMENT

This research was partially supported by the Austrian Research Council FWF under Project No. J2989-N22 (LP, Schrödinger scholarship).

REFERENCES

[1] Y.K. Lin. *Probabilistic Theory of Structural Dynamics*. Krieger Publishing Company, 1976.

[2] Thomas K. Caughey. Derivation and application of the fokker-planck equation to discrete nonlinear dynamic systems subjected to white random excitation. *The Journal of the Acoustical Society of America*, 35(11):1683–1692, 1963.

[3] L. A. Bergman and J. C. Heinrich. On the reliability of the linear oscillator and systems of coupled oscillators. *Int. J. Numer. Meth. Engng.*, 18(9):1271–1295, 1982.

[4] R.S. Langley. A finite element method for the statistics of non-linear random vibration. *Journal of Sound and Vibration*, 101(1):41–54, July 1985.

[5] B.F. Spencer and L.A. Bergman. On the numerical solutions of the Fokker-Planck equations for nonlinear stochastic systems. *Nonlinear Dynamics*, 4:357–372, 1993.

[6] S. F. Wojtkiewicz, L.A. Bergman, and B.F. Spencer. High fidelity numerical solutions of the Fokker-Planck equation. In Shiraishi, Shinozuka, and Wen, editors, *Seventh International Conference on Structural Safety and Reliabity (ICOSSAR'97)*, 1998.

[7] P. Kumar and S. Narayana. Solution of Fokker-Planck equation by finite element and finite difference methods for nonlinear systems. *Sadhana*, 31-4:445–461, 2006.

[8] M.P. Zorzano, H. Mais, and L. Vázquez. Numerical solution of two dimensional Fokker–Planck equations. *Applied Mathematics and Computation*, 98(2-3):109–117, February 1999.

[9] Wen-Xian Xie, Li Cai, and Wei Xu. Numerical simulation for a Duffing oscillator driven by colored noise using nonstandard difference scheme. *Physica A: Statistical and Theoretical Physics*, 373:183–190, January 2007.

[10] D. W. Peaceman and H. H. Rachford, Jr. The numerical solution of parabolic and elliptic differential equations. *J. Soc. Indust. Appl. Math.*, 3:28–41, 1955.

[11] W. Wedig and U. von Wagner. Extended Laguerre polynomials for nonlinear stochastic systems. In P. D. Spanos, editor, *Computational Stochastic Mechanics*, page 293298. A. A. Balkema, Rotterdam, 1999.

[12] Utz von Wagner and Walter V. Wedig. On the calculation of stationary solutions of multi-dimensional Fokker-Planck equations by orthogonal functions. *Nonlinear Dynamics*, 21(3):289–306, March 2000.

[13] Mrinal Kumar, Suman Chakravorty, and John L. Junkins. A homotopic approach to domain determination and solution refinement for the stationary Fokker-Planck equation. *Probabilistic Engineering Mechanics*, 24(3):265–277, July 2009.

[14] Mrinal Kumar, Suman Chakravorty, and John L. Junkins. A semianalytic meshless approach to the transient Fokker-Planck equation. *Probabilistic Engineering Mechanics*, 25(3):323–331, July 2010.

[15] Mrinal Kumar, Suman Chakravorty, Puneet Singla, and John L. Junkins. The partition of unity finite element approach with hp-refinement for the stationary Fokker-Planck equation. *Journal of Sound and Vibration*, 327(1-2):144–162, October 2009.

[16] Jaap Wijker. *Random Vibrations in Spacecraft Structures Design, Theory and Applications*, volume 165 of *Solid Mechanics and Its Applications*. Springer-Verlag, Berlin/Heidelberg/New York, 2009.

[17] A. Masud and R. A. Khurram. A multiscale/stabilized finite element method for the advection-diffusion equation. *Computer Methods in Applied Mechanics and Engineering*, 193(21-22):1997–2018, May 2004.

[18] Arif Masud and Lawrence A. Bergman. Application of multi-scale finite element methods to the solution of the Fokker-Planck equation. *Computer Methods in Applied Mechanics and Engineering*, 194(12-16):1513–1526, April 2005.

[19] A. Masud and L.A. Bergman. Solution of the four dimensional Fokker-Planck equation: Still a challenge. In G. Augusti, G.I. Schuëller, and M. Ciampoli, editors, *ICOSSAR 2005 Conference*, pages 1911–1916, Rome, Italy, June 22-26 2005. Millpress, Rotterdam, ISBN 90-5966-040-4.

[20] Leopoldo P. Franca, Guillermo Hauke, and Arif Masud. Revisiting stabilized finite element methods for the advective-diffusive equation. *Computer Methods in Applied Mechanics and Engineering*, 195(13-16):1560–1572, February 2006.

[21] COMSOL. *COMSOL theory manual*, 2010.

[22] T. K. Caughey. Nonlinear theory of random vibrations. volume 11, pages 209–253. Elsevier, 1971.

[23] S. F. Wojtkiewicz, L. A. Bergman, B.F. Spencer, and E.A. Johnson. Numerical solution of the four-dimensional nonstationary Fokker-Planck equation. In *IUTAM Symposium on Nonlinearity and Stochastic Structural Dynamics : proceedings of the IUTAM Symposium held in Madras, India, 4-8 January 1999 / edited by S. Narayanan and R.N. Iyengar.*, 1999.

COMPDYN 2011
ECCOMAS Thematic Conference on
Computational Methods in Structural Dynamics and Earthquake Engineering
M. Papadrakakis, M. Fragiadakis, V. Plevris (eds.)
Corfu, Greece, 25-28 May 2011

RANDOM DYNAMICAL RESPONSE OF A MULTIBODY SYSTEM WITH UNCERTAIN RIGID BODIES

A. Batou[1], **C. Soize**[1],

[1]Université Paris-Est, Laboratoire Modélisation et Simulation Multi Echelle, MSME UMR 8208
CNRS,
5 bd Descartes, 77454 Marne-la-Vallee, France
e-mail: {anas.batou,christian.soize}@univ-paris-est.fr

Keywords: Uncertain rigid body, Random mass, Random center of mass, Random tensor of inertia.

Abstract. *This research is devoted to the construction of the random dynamical response of a multibody system with uncertain rigid bodies. We first construct a stochastic model of an uncertain rigid body by replacing the mass, the center of mass and the tensor of inertia by random variables. The prior probability distributions of the stochastic model are constructed using the maximum entropy principle under the constraints defined by the available information. The generator of independent realizations corresponding to the prior probability distribution of these random quantities are developed. Then, several uncertain rigid bodies can be linked each others in order to calculate the random response of a multibody dynamical system. An application is proposed to illustrate the theoretical development.*

1 INTRODUCTION

This study is devoted to the construction of a probabilistic model of uncertainties for a rigid multibody dynamical system made up of uncertain rigid bodies. In some cases, the mass distribution inside a rigid body is not perfectly known and must be considered as random (for example, the distribution of passengers inside a vehicle) and therefore, this unknown mass distribution inside the rigid body induces uncertainties in the model of this rigid body. Here, we propose a new probabilistic modeling for uncertain rigid bodies in the context of the multibody dynamics. Concerning the modeling of uncertainties in multibody dynamical system, a very few previous researches have been carried out. These researches concerned parameters which describe the joints linking each rigid body to the others and the external sources (see [7], [16], [3]), [12] ,[13]), but not rigid bodies themselves. In the field of uncertain rigid bodies, a first work has been proposed in [9, 10], in which the authors take into account uncertain rigid bodies for rotor dynamical systems using the nonparametric probabilistic approach [18, 19] consisting in replacing the mass and gyroscopic matrices by random matrices.

In this paper, a general and complete stochastic model is constructed for an uncertain rigid body. The mass, the center of mass and the tensor of inertia which describe the rigid body are modeled by random variables. The prior probability distributions of the random variables are constructed using the maximum entropy principle [6] from Information Theory [17]. The generator of independent realizations corresponding to the prior probability distributions of these random quantities are developed and presented. Then, several uncertain rigid bodies can be linked each others in order to calculate the random response of an uncertain multibody dynamical system. The stochastic multibody dynamical equations are solved using the Monte Carlo simulation method.

Section 2 is devoted to the construction of the mean model for the rigid multibody dynamical system by using the classical method. In Section 3, firstly, we propose a general probability model for an unconstrained uncertain rigid body and secondly, the uncertain rigid multibody dynamical system is obtained by joining this unconstrained uncertain rigid body to the other rigid bodies. The last section is devoted to an application which illustrates the proposed theory.

2 MEAN MODEL FOR THE RIGID MULTIBODY DYNAMICAL SYSTEM

In this paper, the usual model of a rigid multibody dynamical system for which all the mechanical properties are known will be called the mean model (or the nominal model). This section is devoted to the construction of the mean model for a rigid multibody dynamical system. This mean model is constructed as in ([14, 15]) and is summarized below.

2.1 Dynamical equations for a rigid body of the multibody system

Let RB_i be the rigid body occupying a bounded domain Ω_i with a given geometry. Let ξ be the generic point of the three dimensional space. Let $\mathbf{x} = (x_1, x_2, x_3)$ be the position vector of point ξ defined in a fixed inertial frame $(O\,, x_{0,1}\,, x_{0,2}\,, x_{0,3})$, such that $\mathbf{x} = \overrightarrow{O\xi}$. The rigid body class is then defined by three quantities.

(1) The first one is the mass m_i of RB_i which is such that

$$m_i = \int_{\Omega_i} \rho(\mathbf{x})\, d\mathbf{x} \quad , \tag{1}$$

where $\rho(\mathbf{x})$ is the mass density.

(2) The second quantity is the position vector $\mathbf{r}_i$ of the center of mass G_i, defined in the fixed inertial frame, by

$$\mathbf{r}_i = \frac{1}{m_i}\int_{\Omega_i} \mathbf{x}\,\rho(\mathbf{x})\,d\mathbf{x} \quad . \tag{2}$$

(3) Let $(G_i\,,x'_{i,1}\,,x'_{i,2}\,,x'_{i,3})$ be the local frame for which the origin is G_i and which is deduced from the fixed frame $(O\,,x_{0,1}\,,x_{0,2}\,,x_{0,3})$ by the translation $\overrightarrow{OG_i}$ and a rotation defined by the three Euler angles α_i, β_i and γ_i. The third quantity is the positive-definite matrix $[J_i]$ of the tensor of inertia in the local frame such that

$$[J_i]\,\mathbf{u} = -\int_{\Omega_i} \mathbf{x}'\times\mathbf{x}'\times\mathbf{u}\,\rho(\mathbf{x}')\,d\mathbf{x}' \quad , \quad \forall\mathbf{u}\in\mathbb{R}^3 \quad , \tag{3}$$

in which the vector $\mathbf{x}' = (x'_1, x'_2, x'_3)$ of the components of vector $\overrightarrow{G_i\xi}$ are given in $(G_i\,,x'_{i,1}\,,x'_{i,2}\,,x'_{i,3})$. In the above equation, $\mathbf{u}\times\mathbf{v}$ denotes the cross product between the vectors $\mathbf{u}$ and $\mathbf{v}$.

2.2 Matrix model for the rigid multibody dynamical system

The rigid multibody dynamical system is made up of n_b rigid bodies and ideal joints including rigid joints, joints with given motion (rheonomic constraints) and vanishing joints (free motion). The interactions between the rigid bodies are realized by these ideal joints but also by springs, dampers or actuators which produce forces between the bodies. In this paper, only n_c holonomic constraints are considered. Let $\mathbf{u}$ be the vector in $\mathbb{R}^{6n_b}$ such that $\mathbf{u} = (\mathbf{r}_1, ..., \mathbf{r}_{n_b}, \mathbf{s}_1, ..., \mathbf{s}_{n_b})$ in which $\mathbf{s}_i = (\alpha_i, \beta_i, \gamma_i)$ is the rotation vector. The n_c constraints are given by n_c implicit equations which are globally written as $\boldsymbol{\varphi}(\mathbf{u}, t) = 0$. The $(6n_b \times 6n_b)$ mass matrix $[M]$ is defined by

$$[M] = \begin{bmatrix} [M^r] & 0 \\ 0 & [M^s] \end{bmatrix} \quad , \tag{4}$$

where the $(3n_b \times 3n_b)$ matrices $[M^r]$ and $[M^s]$ are defined by

$$[M^r] = \begin{bmatrix} m_1[I_3] & \cdots & 0 \\ \vdots & \ddots & \vdots \\ 0 & \cdots & m_{n_b}[I_3] \end{bmatrix} , [M^s] = \begin{bmatrix} [J_1] & \cdots & 0 \\ \vdots & \ddots & \vdots \\ 0 & \cdots & [J_{n_b}] \end{bmatrix} , \tag{5}$$

in which $[I_3]$ is the (3×3) identity matrix. The function $\{\mathbf{u}(t)\,,\in[0\,,T]\}$ is then the solution of the following differential equation (see [15])

$$\begin{bmatrix} [M] & [\boldsymbol{\varphi}_\mathbf{u}]^T \\ [\boldsymbol{\varphi}_\mathbf{u}] & [0] \end{bmatrix} \begin{bmatrix} \ddot{\mathbf{u}} \\ \boldsymbol{\lambda} \end{bmatrix} = \begin{bmatrix} \mathbf{q}-\mathbf{k} \\ -\frac{d}{dt}\boldsymbol{\varphi}_t - [\frac{d}{dt}\boldsymbol{\varphi}_\mathbf{u}]\,\dot{\mathbf{u}} \end{bmatrix} , \tag{6}$$

with the initial conditions

$$\mathbf{u}(0) = \mathbf{u}_0 \quad , \quad \dot{\mathbf{u}}(0) = \mathbf{v}_0 \quad , \tag{7}$$

in which $\mathbf{k}(\dot{\mathbf{u}})$ is the vector of the Coriolis forces and where $[\boldsymbol{\varphi}_\mathbf{u}(\mathbf{u}(t), t)]_{ij} = \partial\varphi_i(\mathbf{u}(t), t)/\partial u_j(t)$ and $\boldsymbol{\varphi}_t = \partial\boldsymbol{\varphi}/\partial t$. The vector $\mathbf{q}(\mathbf{u}, \dot{\mathbf{u}}, t)$ is constituted of the applied forces and torques induced by springs, dampers and actuators. The vector $\boldsymbol{\lambda}(t)$ is the vector of the Lagrange multipliers. Equation (6) can be solved using an adapted integration algorithm (see for instance [2]).

3 STOCHASTIC MODEL FOR A MULTIBODY DYNAMICAL SYSTEM WITH UNCERTAIN RIGID BODIES

Firstly, a stochastic model for an uncertain rigid body of the multibody dynamical system is proposed and secondly, the stochastic model for the multibody dynamical system with uncertain rigid bodies is constructed joining the stochastic model of the uncertain rigid bodies.

3.1 Stochastic model for an uncertain rigid body of the multibody dynamical system

The properties of the mean model (or the nominal model) of the rigid body RB$_i$ are defined by its mass $\underline{m}_i$, the position vector $\underline{\mathbf{r}}_{0,i}$ of its center of mass $\underline{G}_i$ at initial time $t = 0$ and the matrix $[\underline{J}_i]$ of its tensor of inertia with respect to the local frame $(\underline{G}_i\,, \underline{x}'_{i,1}\,, \underline{x}'_{i,2}\,, \underline{x}'_{i,3})$. The probabilistic model of uncertainties for this rigid body is constructed by replacing these three parameters by the following three random variables: the random mass M_i, the random position vector $\mathbf{R}_{0,i}$ of its random center of mass $\mathbf{G}_i$ at initial time $t = 0$ and the random matrix $[\mathbf{J}_i]$ of its random tensor of inertia with respect to the random local frame $(\mathbf{G}_i\,, \underline{x}'_{i,1}\,, \underline{x}'_{i,2}\,, \underline{x}'_{i,3})$. The probability density functions (PDF) of these three random variables are constructed using the maximum entropy principle (see [17], [6]), that is to say, in maximizing the uncertainties in the model under the constraints defined by the available information.

3.1.1 Construction of the PDF for the random mass

(i) Available information
Let $E\{.\}$ be the mathematical expectation. The available information for the random mass M_i is defined as follows. Firstly, the random variable M_i must be positive almost surely. Secondly, the mean value of the random mass M_i must be equal to the value $\underline{m}_i$ of the mean (or nominal) model. Thirdly, as it is proven in [19], the random mass must verify the inequality $E\{M_i^{-2}\} < +\infty$ in order that a second-order solution exists for the stochastic dynamical system. In addition, it is also proven that this constraint can be replaced by $|E\{\log M_i\}| < +\infty$.
(ii) Maximum entropy principle
The probability density function $\mu \mapsto p_{M_i}(\mu)$ of the random variable M_i is constructed by maximizing the entropy under the constraints defined above. The solution of this optimization problem is the PDF of a gamma random variable defined on $]0, +\infty[$. This PDF depends on two parameters which are $\underline{m}_i$ and C_{M_i}. Since parameter C_{M_i} has no physical meaning, it is eliminated in introducing the coefficient of variation δ_{M_i} of the random variable M_i such that $\delta_{M_i} = \sigma_{M_i}/\underline{m}_i$ where σ_{M_i} is the standard deviation of the random variable M_i. Therefore, the PDF of the random mass is completely defined by the mean value $\underline{m}_i$ and by the dispersion parameter δ_{M_i}.

3.1.2 Construction of the PDF for the random position vector $\mathbf{R}_{0,i}$

In this subsection, the PDF of the random initial position vector $\mathbf{R}_{0,i}$ of the center of mass of RB$_i$ at initial time $t = 0$ is constructed.

(i) Available information
The position vector $\underline{\mathbf{r}}_{0,i}$ of the center of mass $\underline{G}_i$ at initial time $t = 0$ of the mean (or nominal) model is given. However, the real position is not exactly known and $\underline{\mathbf{r}}_{0,i}$ only corresponds to a mean position. Consequently, there is an uncertainty about the real position and this is the

reason why this position is modeled by the random vector $\mathbf{R}_{0,i}$. Some geometrical and mechanical considerations lead us to introduce an admissible domain D_i of random vector $\mathbf{R}_{0,i}$. We introduce the vector **h** of the parameters describing the geometry of domain D_i. In addition, the mean value of the random vector $\mathbf{R}_{0,i}$ must be equal to the value $\underline{\mathbf{r}}_{0,i}$ of the mean (or nominal) model. Therefore, the available information for random variable $\mathbf{R}_{0,i}$ can be written as

$$\begin{aligned} &\mathbf{R}_{0,i} \in D_i(\mathbf{h}) \quad \text{a.s.} \quad , && (a) \\ &E\{\mathbf{R}_{0,i}\} = \underline{\mathbf{r}}_{0,i} \in D_i(\mathbf{h}) \quad . && (b) \end{aligned} \tag{8}$$

(ii) Maximum entropy principle

The probability density function $\mathbf{a} \mapsto p_{\mathbf{R}_{0,i}}(\mathbf{a})$ of random variable $\mathbf{R}_{0,i}$ is then constructed by maximizing the entropy with the constraints defined by the available information in Eq. (8). The solution of this optimization problem depends on two parameters which are $\underline{\mathbf{r}}_{0,i}$ and vector-valued parameter **h**, and is such that

$$p_{\mathbf{R}_{0,i}}(\mathbf{a};\mathbf{h}) = \mathbb{1}_{D_i(\mathbf{h})}(\mathbf{a})\, C_0\, e^{-<\boldsymbol{\lambda},\mathbf{a}>} \quad . \tag{9}$$

The positive valued parameter C_0 and vector $\boldsymbol{\lambda}$ are the unique solution of the equations

$$\begin{aligned} &C_0 \int_{D_i(\mathbf{h})} e^{-<\boldsymbol{\lambda},\mathbf{a}>}\, d\mathbf{a} = 1 \quad , && (a) \\ &C_0 \int_{D_i(\mathbf{h})} \mathbf{a}\, e^{-<\boldsymbol{\lambda},\mathbf{a}>}\, d\mathbf{a} = \underline{\mathbf{r}}_{0,i} \quad . && (b) \end{aligned} \tag{10}$$

(iii) Generator of independent realizations

The independent realizations of random variable $\mathbf{R}_{0,i}$ must be generated using the constructed PDF $p_{\mathbf{R}_{0,i}}$. Such a generator can be obtained using the Monte Carlo Markov Chain (MCMC) method (Metropolis-Hastings algorithm [5]).

3.1.3 Random matrix $[\mathbf{J}_i]$ of the random tensor of inertia.

In this subsection, the random matrix $[\mathbf{J}_i]$ of the random tensor of inertia with respect to $(\mathbf{G}_i\,, \underline{x}'_{i,1}\,, \underline{x}'_{i,2}\,, \underline{x}'_{i,3})$ is defined and an algebraic representation of this random matrix is constructed. The mass distribution around the random center of mass $\mathbf{G}_i$ is uncertain and consequently, the tensor of inertia is also uncertain. This is the reason why the matrix $[\underline{J}_i]$ of the tensor of inertia of the mean (or nominal) model with respect to $(\underline{G}_i\,, \underline{x}'_{i,1}\,, \underline{x}'_{i,2}\,, \underline{x}'_{i,3})$ is replaced by a random matrix $[\mathbf{J}_i]$ which is constructed by using the maximum entropy principle.
We introduce the positive-definite matrix $[Z_i]$ independent of m_i such that

$$[Z_i] = \frac{1}{m_i}\left\{\frac{tr([J_i])}{2}\,[I_3] - [J_i]\right\}. \tag{11}$$

Then $[J_i]$ can be calculated as a function of $[Z_i]$,

$$[J_i] = m_i\{tr([Z_i])\,[I_3] - [Z_i]\} \quad . \tag{12}$$

It can be proven that $[Z_i]$ is positive definite and that each positive definite matrix $[J_i]$ constructed using Eq. (12), where $[Z_i]$ is a given positive definite matrix, can be interpreted as the matrix of a tensor of inertia of a physical rigid body for which the mass is 1 (see [1]).

The probabilistic modeling $[\mathbf{J}_i]$ of $[J_i]$ consists in introducing the random matrix $[\mathbf{Z}_i]$ and in using Eq. (12) in which m_i is replaced by the random variable M_i and where $[Z_i]$ is replaced by $[\mathbf{Z}_i]$. We then obtain

$$[\mathbf{Z}_i] = \frac{1}{M_i}\left\{\frac{tr([\mathbf{J}_i])}{2}\,[I_3] - [\mathbf{J}_i]\right\}, \tag{13}$$

$$[\mathbf{J}_i] = M_i\{tr([\mathbf{Z}_i])\,[I_3] - [\mathbf{Z}_i]\} \quad . \tag{14}$$

(i) Available information concerning random matrix $[\mathbf{Z}_i]$

Let us introduce (1) the nominal value $[\underline{Z}_i]$ of deterministic matrix $[Z_i]$ such that $[\underline{Z}_i] = (1/\underline{m}_i)\{tr([\underline{J}_i])/2[I_3] - [\underline{J}_i]\}$ and (2) the upper bound $[Z_i^{\max}]$ of random matrix $[\mathbf{Z}_i]$. Then, the available information for $[\mathbf{Z}_i]$ can be summarized as follows,

$$\begin{gathered}
[\mathbf{Z}_i] \in \mathbb{M}_3^+(\mathbb{R}) \quad \text{a.s.} \quad , \\
\{[Z_i^{\max}] - [\mathbf{Z}_i]\} \in \mathbb{M}_3^+(\mathbb{R}) \quad \text{a.s.} \quad , \\
E\{[\mathbf{Z}_i]\} = [\underline{Z}_i] \quad , \\
E\{\log(\det[\mathbf{Z}_i])\} = C_i^l \quad , \quad |C_i^l| < +\infty \quad , \\
E\{\log(\det([Z_i^{\max}] - [\mathbf{Z}_i]))\} = C_i^u \quad , \quad |C_i^u| < +\infty \quad .(e)
\end{gathered} \tag{15}$$

For more convenience, random matrix $[\mathbf{Z}_i]$ is normalized as follow. Matrix $[\underline{Z}_i]$ being positive definite, its Cholesky decomposition yields $[\underline{Z}_i] = [\underline{L}_{Z_i}]^T\,[\underline{L}_{Z_i}]$ in which $[\underline{L}_{Z_i}]$ is an upper triangular matrix in the set $\mathbb{M}_3(\mathbb{R})$ of all the (3×3) real matrices. Then, random matrix $[\mathbf{Z}_i]$ can be rewritten as

$$[\mathbf{Z}_i] = [\underline{L}_{Z_i}]^T\,[\mathbf{G}_i]\,[\underline{L}_{Z_i}] \quad , \tag{16}$$

in which the matrix $[\mathbf{G}_i]$ is a random matrix for which the available information is

$$\begin{gathered}
[\mathbf{G}_i] \in \mathbb{M}_3^+(\mathbb{R}) \quad a.s. \quad , \\
\{[G_i^{\max}] - [\mathbf{G}_i]\} \in \mathbb{M}_3^+(\mathbb{R}) \quad a.s. \quad , \\
E\{[\mathbf{G}_i]\} = [I_3] \quad , \\
E\{\log(\det[\mathbf{G}_i])\} = C_i^{l\prime} \quad , \quad |C_i^{l\prime}| < +\infty \quad , \\
E\{\log(\det([G_i^{\max}] - [\mathbf{G}_i]))\} = C_i^{u\prime} \quad , \quad |C_i^{u\prime}| < +\infty \quad ,
\end{gathered} \tag{17}$$

in which $C_i^{l\prime} = C_i^l - \log(\det[\underline{Z}_i])$, $C_i^{u\prime} = C_i^u - \log(\det[\underline{Z}_i])$ and where the matrix $[G_i^{\max}]$ is an upper bound for random matrix $[\mathbf{G}_i]$ and is defined by $[G_i^{\max}] = ([\underline{L}_{Z_i}]^T)^{-1}\,[Z_i^{\max}]\,[\underline{L}_{Z_i}]^{-1}$.

(ii) Maximum entropy principle

The probability distribution of random matrix $[\mathbf{G}_i]$ is constructed using the maximum entropy principle under the constraints defined by the available information given by Eq. (17). The probability density function $p_{[\mathbf{G}_i]}([G\,])$ with respect to the volume element $\widetilde{d}G$ of random matrix $[\mathbf{G}_i]$ is then written as

$$\begin{gathered}
p_{[\mathbf{G}_i]}([G\,]) = \mathbb{1}_{\mathbb{M}_3^+(\mathbb{R})}([G\,]) \times \mathbb{1}_{\mathbb{M}_3^+(\mathbb{R})}([G_i^{\max}] - [G\,]) \times C_{G_i} \\
\times \big(\det[G\,]\big)^{-\lambda_l} \times \big(\det([G_i^{\max}] - [G\,])\big)^{-\lambda_u} \times e^{-\,\mathrm{tr}([\mu][G])} \,,
\end{gathered} \tag{18}$$

in which the positive valued parameter C_{G_i} is a normalization constant, the real parameters $\lambda_l < 1$ and $\lambda_u < 1$ are Lagrange multipliers relative to the two last constraints defined by Eq. (17) and the symmetric real matrix $[\mu]$ is a Lagrange multiplier relative to the third constraint defined by Eq. (17). This probability density function is a particular case the Kummer-Beta matrix variate distribution (see [11], [4]) for which the lower bound is a zero matrix.

Parameters C_{G_i}, λ_l, λ_u and matrix $[\mu]$ are the unique solution of the equations

$$\begin{gathered} E\{\mathbb{1}_{\mathbb{M}_3^S(\mathbb{R})}([\mathbf{G}_i])\} = 1 \quad , \\ E\{[\mathbf{G}_i]\} = [I_3] \quad , \\ E\{\log(\det[\mathbf{G}_i])\} = C_i^{l\prime} \quad , \\ E\{\log(\det([G_i^{\max}] - [\mathbf{G}_i]))\} = C_i^{u\prime} \quad . \end{gathered} \tag{19}$$

For fixed values of λ_l and λ_u, parameters C_{G_i} and $[\mu]$ can be estimated using Eq. (19). In Eq. (19), since the parameters $C_i^{l\prime}$ and $C_i^{u\prime}$ have no real physical meaning, the parameters λ_l and λ_u are kept as parameters which then allows the ”shape” of the PDF to be controlled. If experimental data are available for the responses of the dynamical system, then the two parameters λ_l and λ_u can be identified solving an inverse problem. If experimental data are not available, these two parameters allow a sensitivity analysis of the solution to be carried out with respect to the level of uncertainties.

(iii) Properties for random matrix $[\boldsymbol{J}_i]$

It is proven in [1] that using Eq. (14) and the available information defined by Eq. (15), the following important properties for random matrix $[\mathbf{J}_i]$ can be deduced,

$$\begin{aligned} &\{\tfrac{1}{2}tr([\mathbf{J}_i])\,[I_3] - [\mathbf{J}_i]\} \in \mathbb{M}_3^+(\mathbb{R}) \quad a.s \quad , && (a) \\ &\{[\mathbf{J}_i^{\max}] - [\mathbf{J}_i]\} \in \mathbb{M}_3^+(\mathbb{R}) \quad a.s \quad , && (b) \\ &E\{[\mathbf{J}_i]\} = [\underline{J}_i] \quad , && (c) \\ &\{\lambda_l < -2, \lambda_u < 0\} \Rightarrow E\{\|[\mathbf{J}_i]^{-1}\|^2\} < +\infty \quad , && (d) \end{aligned} \tag{20}$$

in which the random matrix $[\mathbf{J}_i^{\max}]$, which represents a random upper bound for random matrix $[\mathbf{J}_i]$, is defined by

$$[\mathbf{J}_i^{\max}] = M_i\{tr([Z_i^{\max}])\,[I_3] - [Z_i^{\max}]\} \quad . \tag{21}$$

It should be noted that Eq. (20-a) implies that each realization of random matrix $[\mathbf{J}_i]$ corresponds to the matrix of a tensor of inertia of a physical rigid body. In addition, this equation implies that random matrix $[\mathbf{J}_i]$ is almost surely positive definite. Eq. (20-b) provides a random upper bound for random matrix $[\mathbf{J}_i]$. Eq. (20-c) corresponds to a construction for which the mean value of random matrix $[\mathbf{J}_i]$ is equal to the nominal value $[\underline{J}_i]$. Finally, Eq. (20-d) is necessary for that the random solution of the nonlinear dynamical system be a second-order stochastic process.

(iv) Generator of independent realizations for random matrix $[\boldsymbol{J}_i]$

The generator of independent realizations of random matrix $[\mathbf{G}_i]$ is based on the Monte Carlo Markov Chain (MCMC) (Metropolis-Hastings algorithm [5] with the PDF defined by Eq. (18). Then, independent realizations of random matrix $[\mathbf{Z}_i]$ are obtained using Eq. (16). Finally, independent realizations of random matrix $[\mathbf{J}_i]$ are obtained using Eq. (14) and independent realizations of random mass M_i.

3.2 Stochastic matrix model for a multibody dynamical system with uncertain rigid bodies and its random response

In order to limit the developments, it is assumed that only one of the n_b rigid bodies denoted by RB$_i$ of the rigid multibody system is uncertain. The extension to several uncertain rigid bodies is straightforward. Let the $6\,n_b$ random coordinates be represented by the $\mathbb{R}^{6\,n_b}$-valued stochastic process $\mathbf{U} = (\mathbf{R}_1, ..., \mathbf{R}_{n_b}, \mathbf{S}_1, ..., \mathbf{S}_{n_b})$ indexed by $[0,T]$ and let the n_c random Lagrange multipliers be represented by the $\mathbb{R}^{n_c}$-valued stochastic process $\boldsymbol{\Lambda}$ indexed by $[0,T]$. The deterministic Eq. (6) becomes the following stochastic equation

$$\begin{bmatrix} [\mathbf{M}] & [\boldsymbol{\varphi}_{\mathbf{u}}]^T \\ [\boldsymbol{\varphi}_{\mathbf{u}}] & [0] \end{bmatrix} \begin{bmatrix} \ddot{\mathbf{U}} \\ \boldsymbol{\Lambda} \end{bmatrix} = \begin{bmatrix} \mathbf{q} - \mathbf{K} \\ -\frac{d}{dt}\boldsymbol{\varphi}_t - \left[\frac{d}{dt}\boldsymbol{\varphi}_{\mathbf{u}}\right] \dot{\mathbf{U}} \end{bmatrix} \quad , \tag{22}$$

$$\mathbf{U}(0) = \mathbf{U}_0 \quad , \quad \dot{\mathbf{U}}(0) = \mathbf{v}_0 \quad , \quad a.s. \tag{23}$$

in which the vector $\mathbf{U}_0 = (\mathbf{r}_{0,1}, \ldots, \mathbf{R}_{0,i}, \ldots, \mathbf{r}_{0,n_b}, \mathbf{s}_{0,1}, \ldots, \mathbf{s}_{0,n_b})$ is random due to the random vector $\mathbf{R}_{0,i}$. For all given real vector $\dot{\mathbf{u}}$, the vector $\mathbf{K}(\dot{\mathbf{u}})$ of the Coriolis forces is random due to the random matrix $[\mathbf{J}_i]$. The random mass matrix $[\mathbf{M}]$ is defined by

$$[\mathbf{M}] = \begin{bmatrix} [\mathbf{M}^r] & 0 \\ 0 & [\mathbf{M}^s] \end{bmatrix} \quad , \tag{24}$$

in which the $(3n_b \times 3n_b)$ random matrices $[\mathbf{M}^r]$ and $[\mathbf{M}]^s$ are defined by

$$[\mathbf{M}^r] = \begin{bmatrix} m_1[I_3] & \cdots & 0 \\ & \ddots & \\ \vdots & M_i[I_3] & \vdots \\ & \ddots & \\ 0 & \cdots & m_{n_b}[I_3] \end{bmatrix} \quad , \tag{25}$$

$$[\mathbf{M}^s] = \begin{bmatrix} [J_1] & \cdots & 0 \\ & \ddots & \\ \vdots & [\mathbf{J}_i] & \vdots \\ & \ddots & \\ 0 & \cdots & [J_{n_b}] \end{bmatrix} \quad . \tag{26}$$

Random Eqs. (22) and (23) are solved using the Monte Carlo simulation method.

4 APPLICATION

In this section, we present a numerical application which validates the methodology presented in this paper.

4.1 Description of the mean model

The rigid multibody model is made up of five rigid bodies and six joints which are described in the fixed frame $(O, x_{0,1}, x_{0,2}, x_{0,3})$ (see Fig. 1). The plan defined by $(O, x_{0,1}, x_{0,2})$ is identified below as the ”ground”. The gravity forces in the $x_{0,3}$-direction are taken into account.
(i) Rigid bodies
In the initial configuration, the rigid bodies $Rb1$, $Rb2$, $Rb3$ and $Rb4$ are cylinders for which the

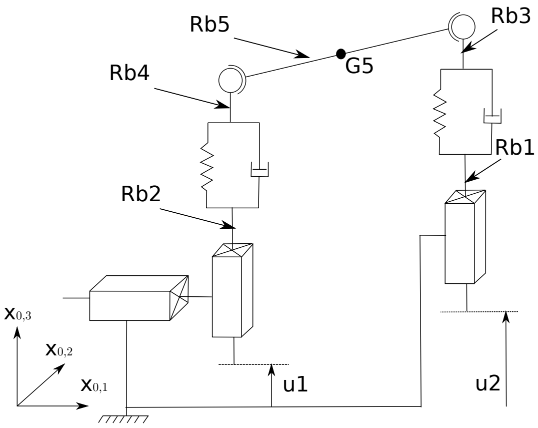

Figure 1: Rigid multibody system.

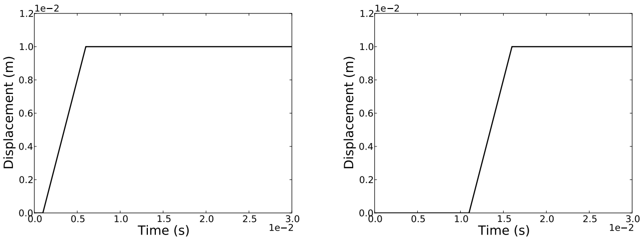

Figure 2: Imposed displacement $u1(t)$ (left figure) and $u2(t)$ (right figure).

axes follow the $x_{0,3}$-direction. In the initial configuration, the rigid body $Rb5$ is supposed to be symmetric with respect to the planes $(G5, x_{0,1}, x_{0,2})$ and $(G5, x_{0,1}, x_{0,3})$ in which $G5$ is the center of mass of $Rb5$.

(ii) Joints

$-$ The joint *Ground*-$Rb1$ is made up of a prismatic joint following $x_{0,3}$-direction. The displacement following $x_{0,3}$-direction (see Fig. 1), denoted by $u1(t)$, is imposed. The joint *Ground*-$Rb2$ is a prismatic joint following $x_{0,3}$-direction. The displacement following $x_{0,3}$-direction (see Fig. 1), denoted by $u2(t)$, is imposed. The displacement following $x_{0,1}$-direction is unconstrained. Imposed displacements $u1(t)$ and $u2(t)$ are plotted in Fig. 2 for t in $[0, 0.03]\ s$.

$-$ The joints $Rb1$-$Rb3$ and $Rb2$-$Rb4$ are constituted of 6D spring-dampers..

$-$ Finally, the joints $Rb3$-$Rb5$ and $Rb4$-$Rb5$ are $x_{0,2}$-direction revolute joints.

4.2 Random response of the stochastic model

Rigid body $Rb5a$ is considered as uncertain and is therefore modeled by a random rigid body. As explained in Section 3, the elements of inertia of the uncertain rigid Body $Rb5$ are replaced by random quantities. The fluctuation of the response is controlled by four parameters δ_{M_5} , **h**, λ_l and λ_u. A sensitivity analysis is carried out with respect to these four parameters. Statistics on the transient response are estimated using the Monte Carlo simulation method with 500 independent realizations. The initial velocities and angular velocities are zero. The observation point P_{obs} belongs to $Rb5$.

(i) Case 1: M_5 is random, $\mathbf{R}_{0,5}$ is deterministic and $[\mathbf{J}_5]$ is deterministic.

We choose $\delta_{M_5} = 0.5$. The confidence region, with a probability level $P_c = 0.90$, of the random

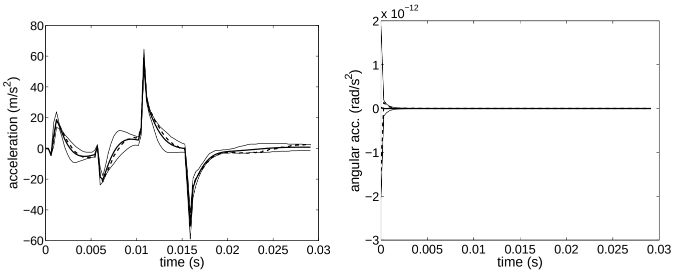

Figure 3: Random transient acceleration of point P_{obs}, Case 1: confidence region (upper and lower thin solid lines), mean response (thick solid line) and response of the mean model (dashed line); $x_{0,3}$-acceleration (left figure) and $x_{0,1}$-angular acceleration (right figure).

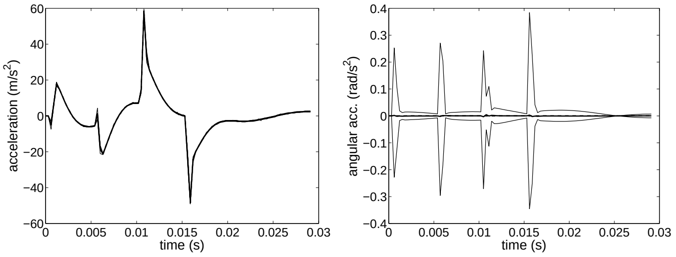

Figure 4: Random transient acceleration of point P_{obs}, Case 2: confidence region (upper and lower envelopes), mean response and response of the mean model are superimposed; $x_{0,3}$-acceleration (left figure) and $x_{0,1}$-angular acceleration (right figure).

acceleration of point P_{obs} is plotted in Fig. 3. It can be noted that the acceleration is sensitive to the mass uncertainties.

(ii) Case 2: M_i is deterministic, $\mathbf{R}_{0,5}$ is deterministic and $[\mathbf{J}_5]$ is random.

We choose $\lambda_l = -5$ and $\lambda_u = -5$ for random matrix $[\mathbf{J}_5]$. The confidence region, with a probability level $P_c = 0.90$, of the random acceleration of point P_{obs} is plotted in Fig. 4. We can remark, as it was expected, that the angular acceleration is sensitive to uncertainties on the tensor of inertia.

(iii) Case 3: M_5 is deterministic, $\mathbf{R}_{0,5}$ is random and $[\mathbf{J}_5]$ is deterministic.

The domain of $\mathbf{R}_{0,5}$ is supposed to be a parallelepiped which is centered at point $(0, 0, 0.55)$ for which its edges are parallel to the directions $x_{0,1}$, $x_{0,2}$ and $x_{0,3}$ and for which the lengths following these three directions are respectively 0.5, 0.2 and 0.02. The confidence region, with a probability level $P_c = 0.90$, of the random acceleration of point P_{obs} is plotted in Fig. 5. We can remark that the angular acceleration is sensitive to uncertainties on initial center of mass of $Rb5$.

(iv) Case 4: M_5, $\mathbf{R}_{0,5}$ and $[\mathbf{J}_5]$ are random.

The values of the parameters of the PDF are those fixed in the three previous cases. The confidence region, with a probability level $P_c = 0.90$, of the random acceleration of point P_{obs} is plotted in Fig. 6. It can be viewed that (1) the randomness on the acceleration is mainly due to the randomness of mass M_5, (2) the randomness on the angular acceleration is mainly due to the randomness of the initial position $\mathbf{R}_{0,5}$ of the center of mass and the random tensor of inertia $[\mathbf{J}_5]$.

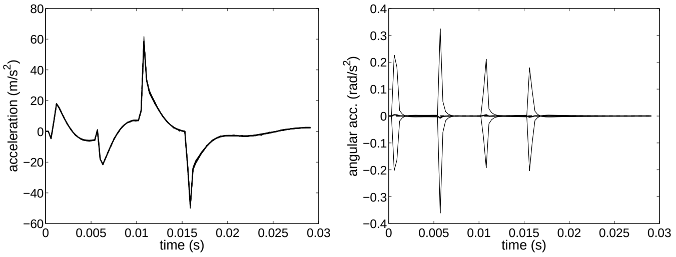

Figure 5: Random transient acceleration of point P_{obs}, Case 3: confidence region (upper and lower envelopes), mean response and response of the mean model are superimposed; $x_{0,3}$-acceleration (left figure) and $x_{0,1}$-angular acceleration (right figure).

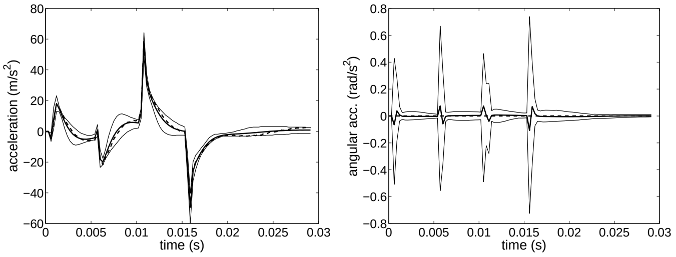

Figure 6: Random transient acceleration of point P_{obs}, Case 4: confidence region (upper and lower thin solid lines), mean response (thick solid line) and response of the mean model (dashed line); $x_{0,3}$-acceleration (left figure) and $x_{0,1}$-angular acceleration (right figure).

5 CONCLUSION

We have presented a complete and general probabilistic modeling of uncertain rigid bodies taking into account all the known mechanical and mathematical properties. This probabilistic model of uncertainties is used to construct the stochastic equations of uncertain multibody dynamical systems. The random dynamical responses can then be calculated. In the proposed probabilistic model, the mass, the center of mass and the tensor of inertia are modeled by random variables for which the prior probability density functions are constructed using the maximum entropy principle under the constraints defined by all the available mathematical, mechanical and design properties. Several uncertain rigid bodies can be linked each others in order to obtain the stochastic dynamical model of the uncertain multibody dynamical system. The theory proposed has been illustrated analyzing a simple example. The results obtained clearly show the role played by uncertainties and the sensitivity of the responses due to uncertainties on (1) the mass (2) the center of mass and (3) the tensor of inertia. Such a prior stochastic model allows the robustness of the responses to be analyzed with respect to uncertainties. If experimental data were available on the responses, then the parameters which control the level of uncertainties could be estimated by solving an inverse stochastic problem.

REFERENCES

[1] A. Batou, C. Soize, Rigid multibody system dynamics with uncertain rigid bodies, *Multibody System Dynamics*. submitted in 2010.

[2] J. Baumgarte, Stabilization of constraints and integrals of motion in dynamical systems, *Computer Methods in Applied Mechanics and Engineering*. **1**(1), 1–16, 1972.

[3] A. Carrarini, Reliability based analysis of the crosswind stability of railway vehicles, *Journal of Wind Engineering and Industrial Aerodynamics*. **95**, 493–509, 2007.

[4] S. Das, R. Ghanem, A bounded random matrix approach for stochastic upscaling, *Multiscale Modeling & Simulation*. **8**(1), 296–325, 2009.

[5] W.K. Hastings, Monte Carlo sampling methods using Markov chains and their applications, *Biometrika*. **109**, 57–97, 1970.

[6] E.T. Jaynes, Information theory and statistical mechanics, *Physical Review*. **106**(4), 620–630 and **108**(2), 171–190, 1957.

[7] L. Li, C. Corina Sandu, On the impact of cargo weight, vehicle parameters, and terrain characteristics on the prediction of traction for off-road vehicles, *Journal of Terramechanics*. **44**, 221–238, 2007.

[8] P. Masarati, M. Lanz, P. Mantegazza, Multistep integration of ordinary, stiff and differential-algebraic problems for multibody dynamics applications, *16^{-th} Congresso Nazionale AIDAA*. 24-28 Septembre, Palermo, Italy, 2001.

[9] R. Murthy, M.P. Mignolet, A. El-Shafei, Nonparametric stochastic modeling of uncertainty in rotordynamics–Part I: Formulation, *J. Eng. Gas Turbines Power*. **132**(9), 092501, 2010.

[10] R. Murthy, M.P. Mignolet, A. El-Shafei, Nonparametric stochastic modeling of uncertainty in rotordynamics–Part II: Applications, *J. Eng. Gas Turbines Power*. **132**(9), 092502, 2010.

[11] D.K Nagar, A.K. Gupta, *Matrix-variate Kummer-Beta distribution*, Journal of the Australian Mathematical Society. **73**, 11–25, 2002.

[12] D. Negrut, M. Datar, D. Gorsich., D. Lamb , A framework for uncertainty quantification in nonlinear multi-body system dynamics, *Proceedings of the 26th Army Science Conference*. Orlando, FL, 2008.

[13] A. Sandu, C. Sandu, M. Ahmadian, Modeling multibody dynamic systems with uncertainties. Part I: theoretical and computational aspects, *Multibody System Dynamics*, **23**, 375–395, 2006.

[14] W. Schiehlen, *Multibody Systems Handbook*. Springer-Verlag, Berlin, 1990.

[15] W. Schiehlen, Multibody system dynamics: roots and perspectives, *Multibody System Dynamics*. **1**, 149–188, 1997.

[16] K.P. Schmitt, M. Anitescu, D. Negrut, Efficient sampling for spatial uncertainty quantification in multibody system dynamics applications, *Int. J. Numer. Meth. Engng.* **80**, 537–564, 2009.

[17] C.E. Shannon, A mathematical theory of communication, *Bell System Technology Journal*. **27**, 379–423 and 623–659, 1948.

[18] C. Soize, A nonparametric model of random uncertainties on reduced matrix model in structural dynamics, *Probabilistic Engineering Mechanics*. **15**(3), 277–294, 2000.

[19] C. Soize, Maximum entropy approach for modeling random uncertainties in transient elastodynamics, *J. Acoust. Soc. Am.* **109**(5), 1979–1996, 2001.

COMPDYN 2011
ECCOMAS Thematic Conference on
Computational Methods in Structural Dynamics and Earthquake Engineering
M. Papadrakakis, M. Fragiadakis, V. Plevris (eds.)
Corfu, Greece, 25-28 May 2011

HERMITE POLYNOMIAL CHAOS EXPANSION METHOD FOR STOCHASTIC FREQUENCY RESPONSE ESTIMATION CONSIDERING MODAL INTERMIXING

H. Yu[1], **F. Gillot**[1], **M. Ichchou**[1]

[1]Laboratoire de Tribologie et Dynamique des Systèmes
Ecole Centrale de Lyon, 36 Avenue Guy de Collongue, Ecully 69134, France
e-mail: {hang.yu, frederic.gillot, mohamed.ichchou}@ec-lyon.fr

Keywords: SFR, Random Eigenvalue Problem, HPCEM, DSBM, Modal Intermixing.

Abstract. *The frequency response shows a big significance in estimating the structural response of linear systems subjected to dynamic loads. Its quantification is decided by the modal properties (e.g. natural frequencies and mode shapes), which are always involved in the random eigenvalue problem regarding uncertain structures. The conventional way to determine the associated stochastic frequency response (SFR) is the directly sample-based method (DSBM), which relays on Monte Carlo sampling technique and deterministic modal analysis by FEA. However, the accuracy of the DSBM is at the cost of efficiency since a large number of modal analyses are required. In this work, the Hermite polynomial chaos expansion method (HPCEM) is implemented to solve the random eigenvalue problem. The coefficients are estimated by the least square method (LSM) considering its robustness and facility. Furthermore, the modal intermixing problem is particularly considered whereby the mathematical limitation and physical validity of the HPCEM are specified. In order to fulfill the practical requirements, a univariable based strategy is proposed to avoid this issue. This strategy in conjunction with the modal assurance criterion (MAC) provides a quantitative way to define the modal intermixing. The fast modal solutions by the HPCEM will be helpful to control the dynamic response within certain frequency interval of interest during the design phase, on one hand; on the other hand, the HPCEM can also be used to evaluate the dynamic response and thereafter to improve efficiency of reliability analysis. Numerical investigations of the SFR provide the comparisons between the results obtained by the HPCEM and DSBM, which demonstrate the efficiency and accuracy.*

1 INTRODUCTION

Uncertainties are always taken into account for modern systems since there is no adequate information to precisely specify the structural parameters, boundary conditions and excitations, the randomness of which can be described by random variables or stochastic processes. Furthermore, the model uncertainties induced from the mathematical-mechanical modeling process has to be dealt with an alternative developed by Soize [17, 18] in the light of the random matrix theory. In the context of design or maintenance, how to determine the effects of uncertainties has been paid close attention to for decades.

In practical applications, complex structures or systems are always concerned. The procedure to obtain the structural response (other quantities such as the stress and deformation are also included) relays exclusively on the finite element analysis (FEA). One of the most attractive structural response of dynamical systems is the frequency response, which can provide the information of the response within certain excitation frequency interval of interest. It will be helpful to control the amplitude of the response in the design phase [19–22], regardless of deterministic systems or random systems. In cases where the uncertainties are considered, in conjunction with Monte Carlo sampling technique, huge amounts of deterministic FE analyses have to be executed so as to quantify the statistics of the structural response. The way mentioned above to determine the associated SFR is the DSBM, which is related to MCS. However, this method will not be tractable in engineering due to computationally intensive numerical simulation.

For linear structures, the frequency response is the function of the modal properties, i.e. natural frequencies, mode shapes and modal damping. As long as the statistics of the modal properties can be decided, the randomness of the SFR are readily characterized. To gain the statistics of the modal properties, the random eigenvalue problem is usually involved. From the literatures, the perturbation method [15, 23] is a classic method to solve this problem. Nevertheless, the achieved accuracy will only be satisfied for random inputs (e.g. material properties) with small coefficients of variation (COV), say less than 5% [23]. To this end, an alternative named the HPCEM [4, 5, 15] is developed to solve the random eigenvalue problem.

In current work, the HPCEM is implemented to calculate the eigenvalues and eigenfactors defined in [11]. The LSM is implemented to determine the associated coefficients. The DSBM based on Matlab in conjunction with FE-softwares is applied to prepare the small number of samples for the LSM. Moreover, the modal intermixing [14] or modal interaction [15, 16] problem is particularly considered whereby the mathematical limitation and physical validity of the HPCEM are specified. Regarding the practical applications, it is dispensable to be avoided. However, none of the above works provide an effective way to remove this issue. In this case, a univariable based strategy is proposed, the kernel of which is to keep the random eigenvalues and eigenvetors with small variability comparing to the mean model. The consistency is delineated by the MAC (modal assurance criterion) factor. In this strategy, we can check which random variable can cause modal intermixing and then avert the modal intermixing by reducing the associated variance.

In section 2, the SFR representation of multi-degree structures is addressed. Section 3 specifies the DSBM and HPCEM to solve the random eigenvalue problem and discusses the approaches to calculate the associated coefficients. In Section 4, we state the strategy to avoid the modal intermixing problem. To show the efficiency and accuracy, in Section 5, two numerical examples are investigated, which are demonstrated by comparing the results obtained by the DSBM. At last, we summarize the main findings of this work in Section 6.

2 SFR REPRESENTATION

The SFR of a linear multi-degree structure can be calculated by the modal superposition principle which is written as:

$$d_{rk}(\boldsymbol{\theta},\omega)=\sum_{j}^{N\ll n}\frac{\phi_{rj}(\boldsymbol{\theta})\phi_{kj}(\boldsymbol{\theta})\omega^{l}}{\omega_j^2(\boldsymbol{\theta})+i\cdot 2\zeta_j(\boldsymbol{\theta})\omega_j(\boldsymbol{\theta})\omega-\omega^2}, \tag{1}$$

where $d_{rk}(\boldsymbol{\theta},\omega)$ denotes the SFR at the rth degree of freedom (DOF) under the excitation at the kth DOF; $\boldsymbol{\theta}$ indicates the set of random structural parameters; ω is the excitation frequency; $\omega_j(\boldsymbol{\theta})$ is associated with the jth random natural frequency, i.e. $\lambda_j=\omega_j^2(\boldsymbol{\theta})$ is the associated random eigenvalue; $\phi_{kj}(\boldsymbol{\theta})$ represents the jth random eigenvector (mode shape) at the kth DOF; $l=0,1,2$ represent the displacement, velocity and acceleration SFR, respectively; n is the number of the DOF, while N is the number of the modes of interest.

High non-linearity has been observed in Eq. (1) so that no simple linearly approximate relation between the SFR and random parameters can be found. To this end, more attempts to solve the random eigenvalue problem have been made since the SFR is expressed explicitly by the natural frequencies and mode shapes.

3 RANDOM EIGENVALUE PRROBLEM

3.1 DSBM

Regarding the random eigenvalue problem, the simply numerical method is the DSBM. In this work, the general process is realized by Matlab and FE softwares shown in Fig.1. Matlab takes charge of generating random variables (random inputs) and FE softwares provide modal solutions. The advantages of this method are those:

- Matlab can offer commonly used random variables based on Monte Carlo sampling technique. That means we can get almost any unimodal distributed random variable of interest efficiently and accurately.
- The modal analysis is the basic module of most FE softwares. No matter how complex and large the structure is, modal solutions of FE softwares could be reasonably precise.
- There is no assumption during the whole process. Hence, all the results are accurate which can be treated as calibrations.

Because FE softwares are usually the deterministic solvers, each time they can only carry out one modal analysis associated with one set of random variables. It is obvious that, in order to gain a large number of modal solutions, the process must be repeated for many times shown in Fig. 1. As a result, this method is computationally expensive, which is not practical in engineering.

3.2 Approximate sample-based method

3.2.1 HPCEM

The generalized random eigenvalue problem of undamped multi-degree structures is given by:

$$[K(\boldsymbol{\theta})]\{\phi(\boldsymbol{\theta})\}=\lambda(\boldsymbol{\theta})[M(\boldsymbol{\theta})]\{\phi(\boldsymbol{\theta})\}, \tag{2}$$

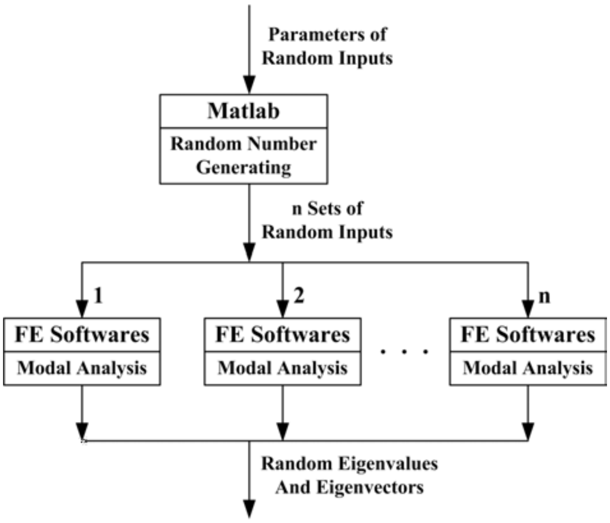

Figure 1: DSBM

where $[K(\boldsymbol{\theta})]$ and $[M(\boldsymbol{\theta})]$ are random stiffness and mass matrices; $\lambda(\boldsymbol{\theta})$ and $\{\phi(\boldsymbol{\theta})\}$ represent random eigenvalue and eigenvector respectively. Solving a random eigenvalue problem, the statistics of the eigenvalue and eigenvector must be characterized by the randomness of the structures, i.e the random inputs $\boldsymbol{\theta}$. Based on the theorem of Gameron-Martin [6], a square integrable random variable can be represented by HPC with an acceptable convergence. In case that the convergence rate is substantially slow, extensions to other orthogonal polynomials (named Wiener-Askey polynomial chaos) representation could be used according to the work [1,4,5]. Furthermore, Roger Ghanem et al [2] used HPC to express the stiffness matrix, random eigenvalues and eigenvectors to solve the random eigenvalue problem (see Eq. (2)). Inspired by these works, the jth random eigenvalue and eigenvector can reasonably be formed as:

$$\lambda_j = \sum_{p=0}^{\infty} a_p H_p(\boldsymbol{\xi}), \qquad \{\phi\}_j = \sum_{p=0}^{\infty} b_p H_p(\boldsymbol{\xi}), \tag{3}$$

where $H_p(\boldsymbol{\xi})$ is the multidimensional HPC of order p in standard normal space in which $\boldsymbol{\xi}$ represents the standard normal variables, a_p and b_p are the constant coefficients. HPC has the properties:

$$H_0 \equiv 1, \qquad \langle H_p = 0 \rangle, \qquad p > 0, \qquad \langle H_p H_q \rangle = \delta_{pq} \left\langle H_p^2 \right\rangle, \tag{4}$$

where δ_{pq} is the Kronecker delta and $\langle \cdot, \cdot \rangle$ denotes the ensemble average. This is the inner product in the Hilbert space of Gaussian random variables defined by:

$$\langle f(\boldsymbol{\xi}) g(\boldsymbol{\xi}) \rangle = \int f(\xi) g(\boldsymbol{\xi}) W(\boldsymbol{\xi}) d\boldsymbol{\xi}, \tag{5}$$

The weight $W(\boldsymbol{\xi})$ function is multidimensional Gaussian joint probability density function. Notice that Hermite polynomials are functions of standard normal random variables $\boldsymbol{\xi}$. In the original random eigenvalue problem (see Eq. (2)), random solutions are determined by random variables $\boldsymbol{\theta}$. $\boldsymbol{\theta}$ and $\boldsymbol{\xi}$ are usually not the same. Nonetheless, implementation of transformation techniques, such as Rossenblatt transformation [7] and Nataf model in [8], the random variables $\boldsymbol{\theta}$ can be transformed to standard normal random variables $\boldsymbol{\xi}$ with one to one mapping: $\theta_i \to \xi_i$. Then the Eq. (2) will be rewritten as:

$$[K(\boldsymbol{\xi})]\{\phi(\boldsymbol{\xi})\} = \lambda(\boldsymbol{\xi})[M(\boldsymbol{\xi})]\{\phi(\boldsymbol{\xi})\}, \tag{6}$$

Some analytical transformations between random variables of common univariate distributions and standard normal variables have been listed in [9, 10]. From Eq. (1), the SFR is the function of natural frequencies ω_j, and the eigenfactor defined as $\phi_{rj}\phi_{kj}$ [11]. Debusschere et al [12] indicated that multiplication of two random variables expanded by polynomial chaos can also be expanded by the same polynomial chaos. This proposition can save the CPU time. Moreover, the elements ϕ_{rj} and ϕ_{kj} from the same eigenvector which insinuates that they have the same converged rate. Consequently, we can use the HPC expansion to represent the eigenfactor directly:

$$\phi_{rj}\phi_{kj} = \sum_{p=0}^{\infty} c_p H_p(\boldsymbol{\xi}), \tag{7}$$

3.2.2 Coefficients calculation

When implementing HPC, one of the critical issues is to accurately estimate the coefficients. In the expressions of random eigenvalues and eigenfactors (See Eq. (3) and Eq. (7)), the number of the coefficients is infinite. This formula is not tractable in practice. Generally, the truncation formula is usually used. The representations of eigenvalues and eigenvectors are rewritten as:

$$\lambda_j = \sum_{p=0}^{P} a_p H_p(\boldsymbol{\xi}), \qquad \phi_{rj}\phi_{kj} = \sum_{p=0}^{P} c_p H_p(\boldsymbol{\xi}), \tag{8}$$

The total number of polynomial chaos is $N_{pc} = P + 1$ which is determined by the dimension N_{rv} of random variables $\boldsymbol{\xi}$ and the highest order N_{ho} of the HPC.

$$N_{pc} = \frac{(N_{rv} + N_{ho})!}{N_{rv}!N_{ho}!}, \tag{9}$$

Several methods can be exploited to compute the coefficients:

- Orthogonalized method [2]. This method makes use of the orthogonality of the polynomial chaos basis. Taking the inner product in Eq. (8) with H_p, we have

  $$a_p = \frac{< \lambda_j H_p >}{< H_p^2 >}, \qquad c_p = \frac{< \phi_{rj}\phi_{kj} H_p >}{< H_p^2 >}, \tag{10}$$

  The denominators in the above expressions have been calculated in [3]. However, the numerators are usually evaluated by MCS. To keep the coefficients accurate, a large quantity of samples are needed. In that case, we prefer the DSBM since the orthogonalized method takes no advantage of economy.

- Probabilistic collocation method [9, 13]. As the name defined, the collocation points are specially selected which correspond to the roots of the Hermite polynomial of one degree higher than the maximum order of current HPC expansion. With the increase of the number of random inputs and the order of the expansion, the number of available collocation points increasing exponentially. For example, in Eq. (9), for the case $N_{rv} = 5, 6$ and $N_{ho} = 2, 3$, the number of the collocation is $(N_{ho} + 1)^{N_{rv}} = 243, 4096$, whereas $N_{pc} = 21, 84$ respectively. As long as the selected number of the collocation points is equal to the number of HPC expansion terms, we could obtain the coefficients by solving a set of equations. However, different combination of collocation points may result in different coefficients. This imposes the instability of the collocation method.

- Least square method (LSM). This method belongs to parametric data fitting methods which will be representative for the whole sample population rather than precisely fitting each sample point. From this point of view, as long as the HPC expansion model can contain all information of random outputs, least square method is the first choice thanks to its facilities and efficiency. Let$\{a\} = [a_1, ...a_p, ...a_{N_{pc}}]^T$, $\{c\} = [c_1, ...c_p, ...c_{N_{pc}}]^T$ and $[H] = \{H_1, ..., H_p, ..., H_{N_{pc}}\}$. Consequently, the least square solutions of the coefficients with respect to the j^{th} set of random eigenvalues and eigenfactors are

$$\{a\} = ([H]^T[H])^{-1}[H]^T\{\lambda_j\}, \qquad \{c\} = ([H]^T[H])^{-1}[H]^T\{\phi_{rj}\phi_{kj}\} \tag{11}$$

  Here $\{\lambda_j\}$ and $\{\phi_{rj}\phi_{kj}\}$ are the m-dimension vectors, in which m denotes the number of random input samples; $[H]$ is the matrix of dimension of $m \times N_{pc}$. **For this work, LSM is utilized**. That signifies when we need M random eigenpairs, only $m \ll M$ are needed to determine the HPC representation, with which the M random eigenpairs are readily gained.

Practically, no matter what method is applied to calculate the coefficients, another critical issue is that HPC expansion can represent the random eigenvalue reasonably. In the next section, the mathematical limitation and physical validity of the HPCEM will be discussed.

4 MODAL INTERMIXING

4.1 Problem description

In random structures, the modal intermixing [14] or modal interaction [15, 16] phenomenon is usually observed when using MCS to model the uncertainties. That means, from one simulation to next, the adjacent modes may exchange whereby the random eigenvectors associated with the same order, actually, contain more than one mode. Generally, different modes behave physically different. This is exacerbated for those structures with closed space eigenvalues as the variances of random inputs increase. That is, mathematically, because the area of probability overlapping of adjacent modes become larger and larger.

Modal intermixing can strongly affect the accuracy of the HPCEM. In fact, the HPC expansion is originated to represent the solutions of random differential equations. That signifies one deterministic HPC expansion just refers to the random solutions of one family. Accordingly, for random eigenvalue problem, the accuracy of HPCEM is guaranteed by averting the modal intermixing problem. Such mathematical limitation seems to restrict wide applications of the HPCEM for random eigenvalue problem. However, this limitation has great significance in practice.

In engineering, when concerning the randomness in structures, the mean model is usually treated as a benchmark or reference. The modal behaviors of uncertain structures should be consistent with the benchmark. In that case, the modal intermixing is indispensable to avoid, the interpretation of which is that the variabilities of random eigenvalues and eigenvector should be limited in a reasonably acceptable bounds.

4.2 MAC factor

As indicated above, the variabilities of random eigenvalues and eigenvectors around the ones of mean model ought to be small in order to remove the modal intermixing issue. If this property holds, the random mode shape can be described as a linear combination [15, 19] of N mode shapes of mean model. The jth eigenvector of simulation k is formulated as:

$$\{\phi\}_j^{(k)} = \sum_{i=1}^{N} A_i^{(k)} \{\phi\}_i^{(0)}, \qquad 1 \le j \le N, \tag{12}$$

where N is the number of modes considered in Eq. (1); $A_i^{(k)}$ denotes the constant weight coefficient; $\{\phi\}_i^{(0)}$ represents the ith eigenvector of the mean model. When the behaviors of random models are identical with the ones of mean model, the effects of the other modes can be ignored, which is interpreted as the most contribution to the sample $\{\phi\}_j^{(k)}$ is from the jth mode of the mean model. In this situation, the last equation in the approximate formula is:

$$\{\phi\}_j^{(k)} \approx A_j^{(k)} \{\phi\}_j^{(0)}, \qquad A_j^{(k)} > 0, \tag{13}$$

Obviously, the angle between eigenvector $\{\phi\}_j^{(k)}$ and $\{\phi\}_j^{(0)}$ will meet $\alpha_j^{(k)} \approx 0$. In conjunction with Eq. (13), the direction cosine of these two eigenvectors has the property:

$$cos(\alpha_{jj}^{(k)}) = \frac{\{\phi\}_j^{(k)} \cdot \{\phi\}_j^{(0)}}{\left\|\{\phi\}_j^{(k)}\right\| \left\|\{\phi\}_j^{(0)}\right\|} \approx 1, \tag{14}$$

Here, $\{\phi\}_j^{(k)} \cdot \{\phi\}_j^{(0)}$ denotes the dot product and $\left\|\{\phi\}_j^{(0)}\right\|$ is the Euclidean norm. Eq. (14) is the condition to prevent the random models from the modal intermixing. It is actually a variant of the Modal Assurance Criterion (MAC) [24]. The corresponding MAC factor is defined by:

$$f_{MAC_{jj}}^{(k)} = \frac{(\{\phi\}_j^{(k)} \cdot \{\phi\}_j^{(0)})^2}{\left\|\{\phi\}_j^{(k)}\right\|^2 \left\|\{\phi\}_j^{(0)}\right\|^2} = cos^2(\alpha_{jj}^{(k)}) \approx 1 \tag{15}$$

The MAC is the criterion to check the consistency between two modes. When the value approaches unity, the consistency is well observed; on the contrary, the value is smaller than 1, the behaviors show the violation. The modal intermixing is the right phenomenon from one simulation to another that reflects the violated modes against the mean modes. Therefore, based on Eq. (15), the MAC factor is an indicator of the modal intermixing:

$$\begin{array}{ll} f_{MAC_{jj}}^{(k)} \approx 1, & \text{no modal intermixing} \\ f_{MAC_{jj}}^{(k)} < 1, & \text{modal intermixing} \end{array} \tag{16}$$

4.3 Univariable based strategy

The randomness in modal properties is induced from the random inputs. We have to note that the information of underlying physical models is usually insufficient so that uncertainties are always assumed to follow certain distribution. Mean values can be obtained readily according to the knowledge of the problems right in hand. On the contrary, it is difficult to get the precise variance since the number of sampling tests is practically small. For that reason, by means of simulation techniques, we need to carefully select the proper variance to fulfill the practical requirements, i.e. no modal intermixing.

So as to select the proper variance, a univariable based strategy is proposed to check which random input can cause the modal intermixing and determine what variance should be used. In this strategy, only one parameter is treated as random variable; others are deterministic. Special random inputs around the mean value are picked out to capture the associated modal solutions.

Let μ_θ and σ_θ be the mean and standard deviation (SD) of random variable θ. Then, the random inputs are written as:

$$\{\tilde{\theta}\} = [\mu_\theta \pm 2\sigma_\theta \quad \mu_\theta \pm 3\sigma_\theta \quad \mu_\theta \pm 4\sigma_\theta \quad \mu_\theta \pm 5\sigma_\theta]^T; \tag{17}$$

where $\{\tilde{\theta}\}$ are the selected random inputs of dimension 8. The last four elements of $\{\tilde{\theta}\}$ suggest the very rare realizations. If all the associated eigenvectors especially the ones corresponding the rare random inputs can meet the condition in Eq. (15), σ_θ is the proper SD; otherwise, a smaller SD will be used to check until the condition is satisfied. An infeasible variance is always chosen as the initial one so that the final choice will be as large as possible. Because only 8 modal analyses are required for each candidate variance, regardless of simple systems or complex systems, this strategy will be computationally efficient. Furthermore, this strategy is insensitive with distributions of random inputs since the special random inputs are determined by the mean and SD but the types of distributions. For those reasons, this strategy is very powerful to avoid the modal intermixing.

5 NUMERICAL EXAMPLES

In the following, two models are investigated to demonstrate the efficiency and accuracy of this procedure to determine the statistics of the SFR. Random structural parameters are modeled by normal, lognormal and Gamma distribution respectively for both examples.

Due to the similarity of the results, only the cases associated with normal distribution are specified. In Section 5.1, a 2-D bridge-like structure: simply supported beam is regarded. For this model, no modal intermixing problem is taken into consideration as it belongs to the structure with largely-spaced frequencies. A building-like structure: fixed support plate-beam is investigated in Section 5.2. The modal intermixing problem must be considered due to its high symmetry.

5.1 Bridge-like structure: simply supported beam

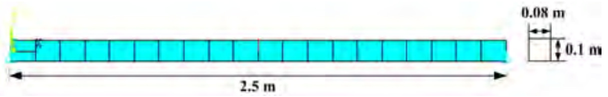

Figure 2: Beam model

A 2-D simply supported beam shown in Fig. 2. The first three modes have been used to estimate the SFR. The corresponding natural frequencies of the mean model are $\omega_1 = 321.0$ rad/s, $\omega_2 = 921.9$ rad/s and $\omega_3 = 2065.9$ rad/s. Tow deterministic parameters are: Poisson's ratio $\nu = 0.3$, modal damping ratio coefficient $\zeta = 0.05$; the other parameters are independent random variables, the mean values of which are $\rho = 7.8 \times 10^3\ kg/m^3$, $E = 2.0 \times 10^{11}$ Pa, $L = 2.5$ m, $H = 0.1$ m, $W = 0.08$ m for density, Young's modulus, length, height and width respectively. Two levels of coefficients of variance (COV), $COV = 5\%$ and $COV = 10\%$, are considered associated with each distribution. All following results are related to the node in the middle.

5.1.1 PDFs investigations

Consider normal distribution. Fig. 3(a) and Fig. 3(b) show the probability density functions (PDFs) of eigenvalues and eigenfactors for the first three modes. The perfect consistence between the distributions obtained by HPCEM and DSBM implies that HPCEM can reflect the statistics characteristics correctly. The largest error of the PDF estimation occurs for the second eigenfactor. However, it is emphasized that the magnitude is very small which contributes almost zero to the SFR. Therefore, such bad approximation of Mode 2 can be ignored. Moreover, larger COVs of eigenvalues and eigenfactors are observed as to the random inputs with large COVs. The approximate method such as perturbation method always has difficulty in dealing with larger COV problems, while the HPCEM can provide the acceptable results. Therefore, the HPCEM is a powerful tool to solve such problems.

It is revealed that the choice of the current order of HPC seems not sufficient since differences exist. Note that increasing the order of HPC is profitable in improving the accuracy. But we have to pay attention that higher order HPC signifies the more computational expense. Accordingly, there should be a trade-off between the efficiency and accuracy. The similar results of PDFs can be seen from the rest four figures in Fig. 3 corresponding the other two distributions.

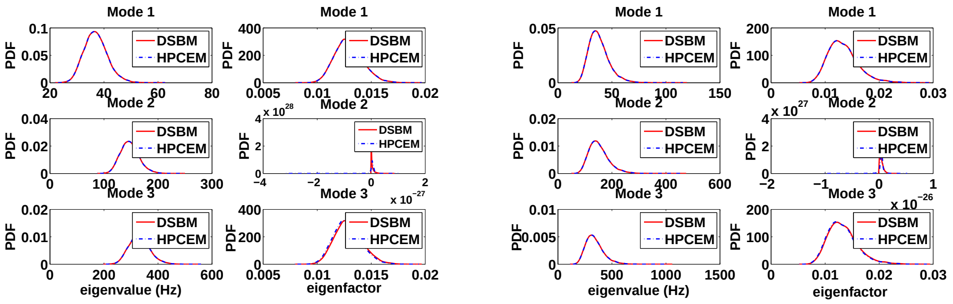

(a) Normal: $COV = 5\%$ (b) Normal: $COV = 10\%$

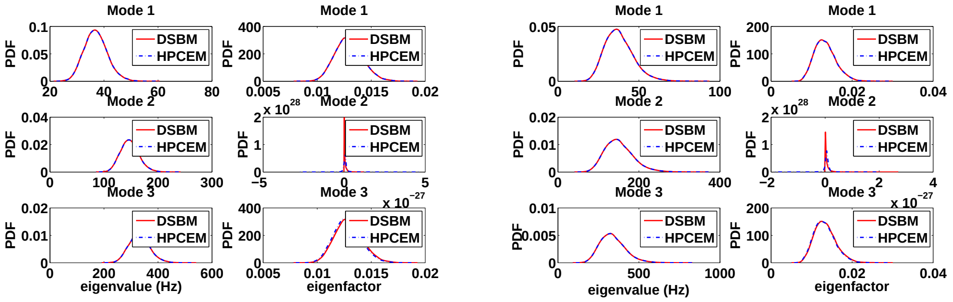

(c) Lognormal: $COV = 5\%$ (d) Lognormal: $COV = 10\%$

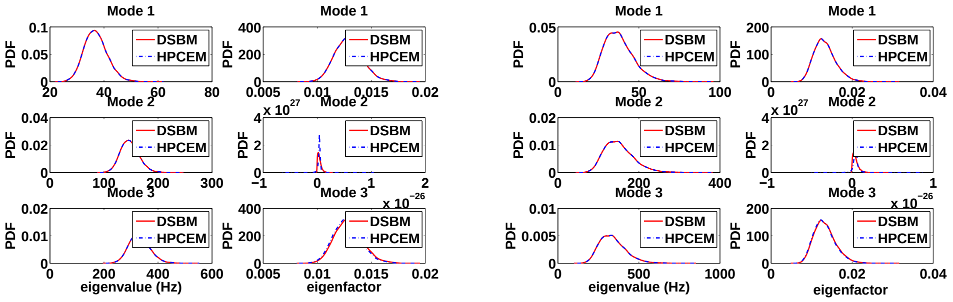

(e) Gamma: $COV = 5\%$ (f) Gamma: $COV = 10\%$

Figure 3: PDF of eigenvalues and eigenfactors based on 10000 samples

5.1.2 SFR investigations

Fig. 4 shows a comparison of the statistics of the SFR between the DSBM and HPCEM, in which the maximum, minimum, mean value of the SFR are very close to each other, respectively. The differences are observed for larger COV (see Fig. 4(b), 4(d) and 4(f)). However, the mean value comparisons represent little difference, which is very significant for reliability analysis. For smaller COV, the maximum is smaller.

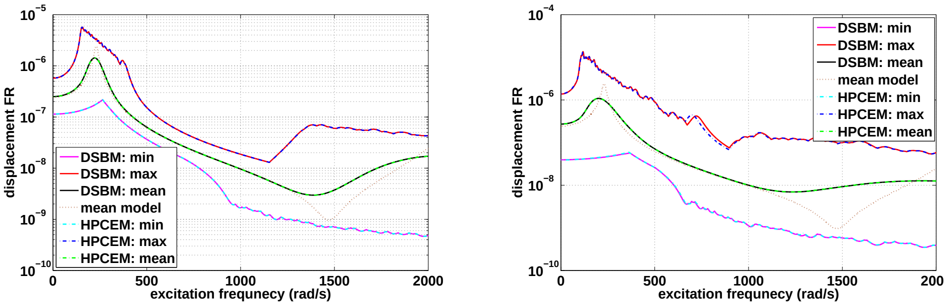

(a) Normal: $COV = 5\%$ (b) Normal: $COV = 10\%$

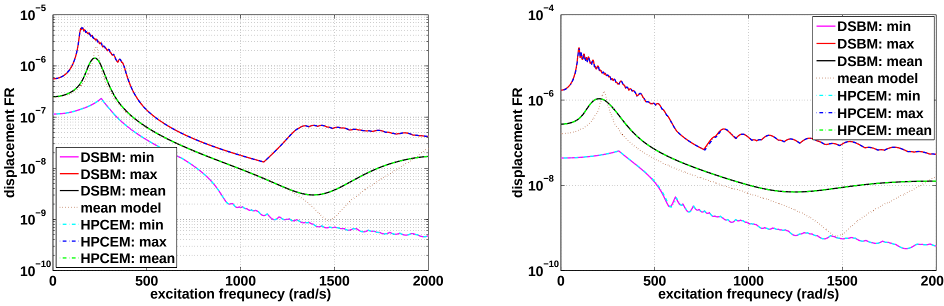

(c) Lognormal: $COV = 5\%$ (d) Lognormal: $COV = 10\%$

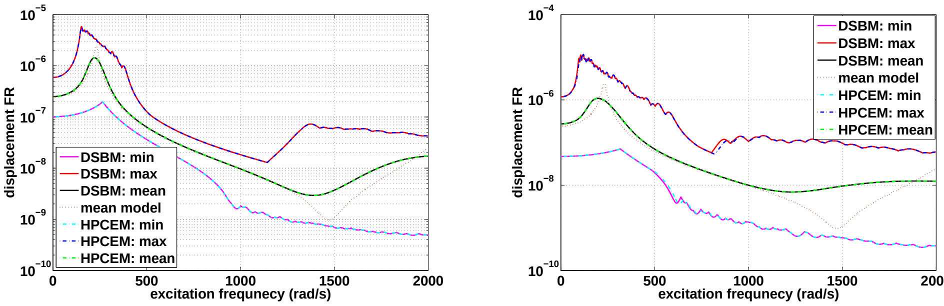

(e) Gamma: $COV = 5\%$ (f) Gamma: $COV = 10\%$

Figure 4: SFR based on 10000 samples for beam

The fourth-order HPC expansion are utilized to represent the eigenvalues and eigenfactors for all considered distributions with both COV levels. According to Eq. (9), the number of coefficients is 126. After numerical examinations, 400 samples are chosen to calculate these coefficients, which is more or less 3 times the coefficients.

In the following, a comparison of average computational time will be specified. So as to obtain the results in Fig. 4, 10^4 modal analyses are executed in the context of DSBM. Yet, for the HPCEM, only 400 modal analyses are carried out by DSBM and plus 10s to determine the coefficients and approximate 10^4 sets of eigenpairs. In conclusion, HPCEM only needs about 4% CPU time of the one needed by DSBM. Efficiency is strongly improved.

It is evident that the HPCEM could be a general method to deal with eigenvalue problem since good results are obtained for the normal, lognormal and Gamma distribution respectively. From the above, HPCEM has the capacities to estimate the SFR effectively, which is of big value concerning reliability analysis since it can save a lot of time from generating a large quantity of samples. Moreover, for structures with larger COV, it turns out that HPCEM is a powerful tool. We also find that the LSM works well in estimating the coefficients of HPC model.

5.2 Building-like structure: plate-beam

In this example, four parameters are selected as random inputs. They are: density, mean value $\mu_\rho = 7.8 \times 10^3$, $COV = 10\%$; Young's modulus, mean value $\mu_E = 2.0 \times 10^{11}$, $COV = 10\%$; beam length, mean value $\mu_{BL} = 3$, $COV = 1.75\%$; plate thickness, mean value $\mu_{PT} = 0.02$, $COV = 2\%$. The cases with random inputs following lognormal, normal and Gamma distribution are studied respectively. More information about this model are as followed: Poisson's ratio $\nu = 0.3$, modal damping ratio coefficient $\zeta = 0.01$, the height of beam is 0.04, the width of beam is 0.04 and the length of plate (square) is 5. All the unites belong to SI. Ten modes are used to calculated the displacement response. The natural frequencies of the mean model are $\omega_1 = 1.30$ rad/s, $\omega_2 = 1.31$, $\omega_3 = 1.87$, $\omega_4 = 3.99$ rad/s, $\omega_5 = 4.01$ rad/s, $\omega_6 = 5.78$ rad/s, $\omega_7 = 6.48$ rad/s, $\omega_8 = 6.50$ rad/s, $\omega_9 = 9.56$ rad/s and $\omega_{10} = 10.86$ rad/s. 294 nodes are in the FE model which is shown in Fig. 5. The results are related to node 14 in direction X. Because of high symmetry in this model, modal intermixing must be considered. The COVs mentioned above are the proper ones selected by the univariable based strategy.

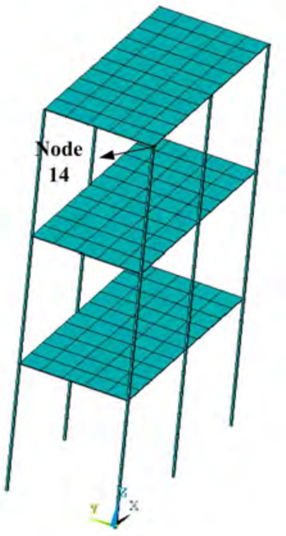

Figure 5: Plate-Beam model

5.2.1 Modal intermixing

Take the random parameter plate thickness as the example. Fig. 6 schematically describes the MAC factors with respect to 8 special random inputs. It is found that the modal intermixing always concerns the random model whose plate thickness is less than the mean value. The explanation is that as the thickness decreases, the flexibility increases since the plate belongs to thin walled structures. The associated structural behaviors can be different from the reference (mean model) more easily. Yet, as to thicker plates, the modes have a large probability to agree with the ones of the mean model.

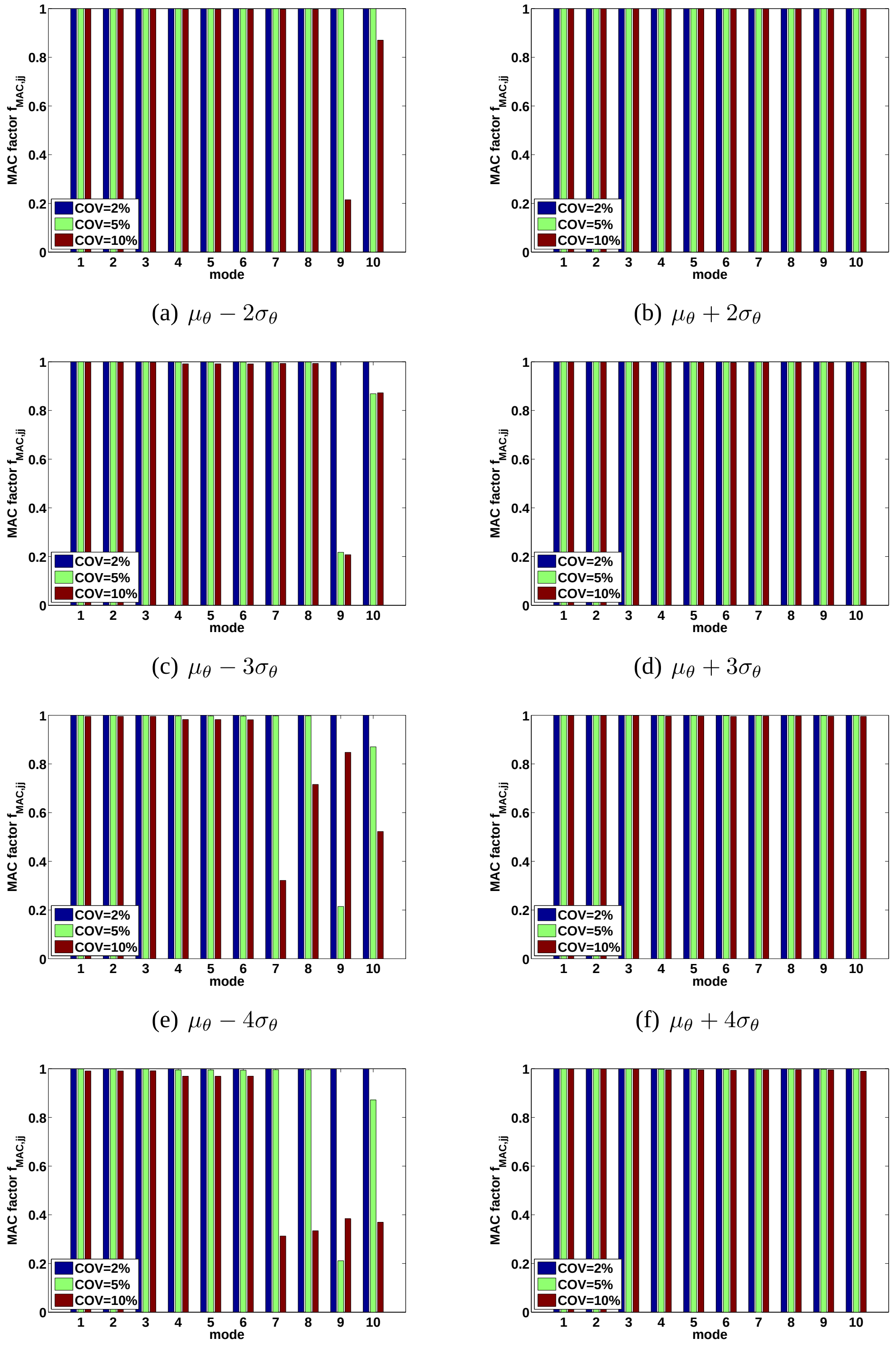

(a) $\mu_\theta - 2\sigma_\theta$ (b) $\mu_\theta + 2\sigma_\theta$

(c) $\mu_\theta - 3\sigma_\theta$ (d) $\mu_\theta + 3\sigma_\theta$

(e) $\mu_\theta - 4\sigma_\theta$ (f) $\mu_\theta + 4\sigma_\theta$

(g) $\mu_\theta - 5\sigma_\theta$ (h) $\mu_\theta + 5\sigma_\theta$

Figure 6: MAC factor comparison for 8 special random inputs

From Fig. 6, it is observed that the modal intermixing always occurs with respect to higher modes, i.e. mode 7, 8, 9 and 10. Moreover, the larger the variance is, the more probable the modal intermixing is induced. To that end, it is reasonable to avert the modal intermixing by reducing the variance.

It is also discovered that when we increase the COVs of density and Young's modulus to 30%, no modal intermixing occurs, the MAC factors of which is always similar to Fig. 6(b). In that case, the random inputs like them can be seen as the insensitive parameters; On the contrary, in cases where random inputs with large COV causing the modal intermixing can be defined as the sensitive parameters, e.g. plate thickness.

5.2.2 Cases study with different distributions

As the probabilistic information of the random inputs are priory unknown, one can choose any distribution to describe the randomness as long as the engineering requirements are fulfilled. From this point of view, like what we have done in Section 5.1, different distribution assumptions are applied so that the universality of the HPCEM is revealed again.

The accuracy investigation is shown by the comparison of the frequency response in Fig. 7 for all the three distributions. Probabilistic results (mean) obtained by HPCEM and DSBM agree with each other well. It is observed that only 6 peaks of the mean model can be told off. That implies there exists very close frequencies.

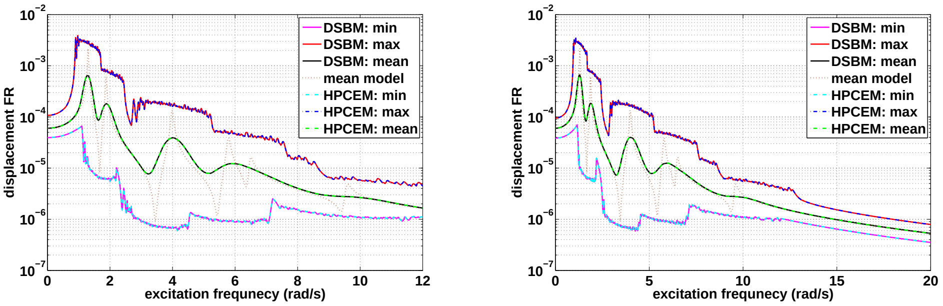

(a) Normal (b) Lognormal

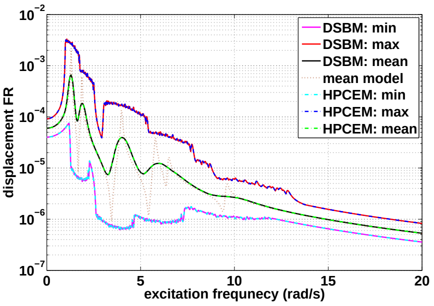

(c) Gamma

Figure 7: SFR based on 10000 samples of Plate-Beam

For this model, the fourth-order HPC expansion is utilized. Only 200 samples are needed to calculate the 70 coefficients by LSM. We have to note that the number of samples is again about 3 times of that of the coefficients. Considering the situations in Section 5.1, we recommend that the number of the samples equals more or less 3 times the number of the coefficients in order to determine the HPC model. The efficiency is still shown by the average CPU time. The DSBM needs 10^4 modal analyses, while the HPCEM only requires 200 modal analyses plus 10s to gain 10^4 sets of eigenvalues and eigenfactors. Almost 98% CPU time is saved.

6 CONCLUSIONS

This work concentrates on estimating the statistics of the SFR. The HPCEM is applied to solve the involved random eigenvalue problem, the coefficients are evaluated by the LSM. The mathematical limitation and physical validity are specially discussed by considering the modal intermixing problem, which is always encountered when using Monte Carlo sampling technique. The univariable based strategy with conjunction with the MAC is proposed to avoid the modal intermixing problem by reducing the variances of the random inputs. It is helpful to select the proper variances since no adequate information is a priori in the physical models. Comparing with the DSBM, the HPCEM is an efficient method to obtain random eigen-solutions. Several factors have significant influences on the accuracy and efficiency of HPCEM:

- The modal intermixing problem should be avoided. In cases where this problem exists, the physical behaviors associated with individual random model may differ from the mean model (benchmark) and the HPCEM in not acceptable to solve the random eigenvalue problem.
- The proper number of samples used for LSM for the HPC coefficients estimation ought to be proper. In this work, according to the simulation examinations, the number of the samples is recommended as about 3 times the number of the coefficients.
- The dimension of the underlying physical (the number of DOF) systems has a large influence of the efficiency. The larger a structure is, the more time the modal analysis needs.
- The efficiency is highly improved compared with the DSBM. However, as the number of random inputs increase,
    - the dimension of the HPC expansion increase. It signifies more time are needed to construct the HPC model which is always obtained by the expensive symbolic calculation.
    - more coefficients have to be evaluated by the LSM. In that case, more samples have to be prepared for the least square solution.

Note that the HPCEM can effectively obtain the variability of the random eigenvalues and eigenfactors, and thereafter the SFR. This achievement is very valuable for reliability analysis as well as reliability based design optimization since reliability analysis has to be carried out during each function evaluation of the optimization procedure.

REFERENCES

[1] R. Ghanmen, The nonlinear Gaussian spectrum of log-normal stochastic processes and variables. *ASME Journal Applied Mechanics*, **66**, 964–973,1999.

[2] R. Ghanem, D. Ghosh, Efficient characterization of the random eigenvalue problem in a polynomial chaos decomposition. *International Journal for Numerical Methods in Engineering*, **72**, 486–504, 2007.

[3] R. Ghanem, P.D. Spanos, *Stochastic finite elements: a spectral approach*. Dover, New York, 1999.

[4] D.B. Xiu, G.E. Karniadakis, The Wiener-Askey polynomial chaos for stochastic differential equation. *SIAM Journal on Scientific Computing*, **24**, 619–644, 2002.

[5] D.B. Xiu, G.E. Karniadakis, Modeling uncertainty in flow simulations via generalized polynomial chaos. *Computer Methods in Applied Mechanics and Engineering*, **191**, 4927–4948, 2002.

[6] R. Cameron, W. Martin, The orthogonal development of nonlinear functionals in series of Fourier-Hermite functionals. *Annals of Mathematics*, **48**, 385, 1947.

[7] M. Rosenblatt, Remarks on multivariable transformation. *Annals of Mathematical Statistics*, **23**, 470–472, 1952.

[8] P.L. Liu, A. D. Kiureghian, Multivariate distribution models with prescribed marginals and covariance. *Probabilistic Engineering Mechanics*, **1**, 105–112, 1986.

[9] S.S. Isukapalli, Uncertainty analysis of transport-transformation models. *Thesis*, 1999.

[10] B.D. Youn, K.K. Choi, An investigation of nonlinearity of reliability-based design optimization approaches. *Journal of Mechanical Design*, **3**, 401–411, 2004.

[11] H.A. Jensen, Design and sensitivity analysis of dynamical systems subjected to stochastic loading. *Computers & Structures*, **83**, 1062–1075, 2005.

[12] B.J. Debusschere, H.N. Najm, P.P. Pebay, O.M. Knio, R.G. Ghanem, O.P. Lemaitre, Numerical challenges in the use of Polynomial Chaos representations for stochastic processes. *SIAM Journal on Scientific Computing*, **26**, 698, 2004.

[13] M.A. Tatang, W. Pan, R.G. Prinn, An efficient method for parametric uncertainty analysis of numerical geophysical methods. *Journal of Geophysical Research*, **102**, 925–932, 1997.

[14] M.F. Pellissetti, G.I. Schüeller, The effects of uncertainties in structural analysis. *Journal of Structure Engineering and Mechanics*, **25**, 311–330, 2007.

[15] K. Ghosh, R. Ghanem, J. Red-Horse, Analysis of eigenvalues and modal interaction of stochastic systems. *AIAA Journal*, **43**, 2196–2201, 2001.

[16] M.-T. Yang, J.H. Grlffin, A normalized modal eigenvalue approach for resolving modal interaction. *Journal of Engineering for Gas Turbines and Power*, **119**, 647–650, 1997.

[17] C. Soize, A comprehensive overview of a non-parametric probabilistic approach of model uncertainties for predictive models in structural dynamics. *Journal Sound and Vibration*, **288**, 623-652, 2005.

[18] C. Soize, Random matrix theory and non-parametric model of random uncertainties. *Journal Sound and Vibration*, **263**, 893–916, 2003.

[19] L. Pichler, H.J. Pradwarter, C.I. Schüeller, A mode-based meta-model for the frequency response functions of uncertain structural systems. *Computers & Structures*, **87**, 332–341, 2009.

[20] D.J. Ewins, *Modal testing: theory practice and application, 2nd Edition*. Research Studies Press Ltd., 2000.

[21] B.R. Mace, P.J. Shorter, A Local modal/perturbational method for estimating frequency response statistics of built-up structures with uncertain properties. *Journal of Sound and Vibration*, **242**, 793–811, 2000.

[22] D. Moens, D. Vandepitte, A fuzzy finite element procedure for the calculation of uncertain frequency-response functions of damped structures. Part 1 - procedure. *Journal Sound and Vibration*, **288**, 431–462, 2005.

[23] G.I. Schüeller, H.J. Pradlwarter, Uncertain linear systems in dynamics: retrospective and recent developments by stochastic approaches. *Engineering Structures*, **31**, 2507–2517, 2009.

[24] Allemang, R.J.: The modal assurance criterion twenty years of use and abuse. Sound and Vibration, 14–21, August 2003

COMPDYN 2011
III ECCOMAS Thematic Conference on
Computational Methods in Structural Dynamics and Earthquake Engineering
M. Papadrakakis, M. Fragiadakis, V. Plevris (eds.)
Corfu, Greece, 25–28 May 2011

DAMAGE IDENTIFICATION FOR A REDUCED SCALE SPATIAL STEEL FRAME

Michele Betti[1], **Paolo Biagini**[1], **and Luca Facchini**[1]

[1] University of Florence, Department of Civil and Environmental Engineering
Via S. Marta 3 – 50139 Florence – Italy
e-mail: mbetti@dicea.unifi.it, paolo.biagini@dicea.unifi.it, luca.facchini@unifi.it

Keywords: Steel-Frame Structures, Damage Identification, Health Monitoring, Stochastic Subspace Identification.

Abstract. *This paper reports on an experiment carried out in the laboratory of Civil and Environmental Engineering of the University of Florence, where a reduced scale (approximately 2.5 m width × 2.5 m depth × 4.8 m height), three storey steel spatial frame was instrumented and progressively damaged by cutting one of its pillars just above the foundation; the deepness of the cut could be measured and was taken as the entity of the damage. A series of 12 accelerometers was installed on the frame and 3 more accelerometers were installed on the ground; acceleration measurements induced by ambient vibrations were recorded as the frame was progressively damaged. Acceleration signals were subsequently analyzed in both time and frequency domain (SSI, EFDD, neural networks): a frequency shift and a change in the corresponding modal shapes were observed as the damage increased. The damaged truss was also modelled by means of a FEM code and the frequency shift and the change in the modal shapes were reproduced. A genetic algorithm approach is currently being tested to try and indentify the location and entity of the damage, and is reported on.*

1 INTRODUCTION

Safety evaluation and damage assessment of existing engineering structures asks for a deeper structural analysis; usually this investigation is carried out through the finite element method techniques: a numerical model of the structure simulates the behavior of the structure (both in static and dynamic field) and it is used to predict the building response to service and exceptional loads (such as earthquakes). The correct identification of the numerical model is then a fundamental task as the modeling, even if refined from a geometrical point of view, could differ from the real structural behavior if assumptions on material, constraints, masses and stiffness are not properly evaluated. Variability of these elements can produce results that could be substantially different from the actual behavior of the structure.

To properly identify the numerical model several strategies, or methodologies, are available in the inherent literature. An effective approach to assess the structural behavior is to evaluate, by performing dynamic experimental tests, actual modal frequencies and corresponding mode shapes. Dynamic tests could be made assuming both forced (vibrodine) and/or environmental (wind or traffic) loads. This step is interesting also with respect to the so-called Structural Health Monitoring (SHM) [1] [2]. The evaluation of these quantities becomes a classical “output-only identification” problem. The identification of the FE model can thus be seen as an optimization strategy where the cost function could be assumed, f.i., the distance between the modal frequencies and mode shape obtained by experimental dynamic tests and those obtained by the numerical model. To address this optimization several approaches have been proposed in literature; among the others quite recently Facchini *et al.* [3] [4] propose a neural network approach. The “output-only” procedure could be framed as an emerging topic of both the scientific and technical community as it covers a wide range of practical problems. Effective examples can be considered, for instance, any situation where the need is felt to maintain the structure at hand operative during structural health monitoring investigation: this is the case of bridges which have to remain open to traffic during the test, as well as offshore structures (both small and medium size) ([4]) where the transport of the equipment needed for the monitoring can be extremely difficult.

In structural engineering field the most expeditive (but also, in some respects, the most “brutal”) method to approach the identification problems in case of "output only" systems is the Peak – Picking method (see e.g. Bendat & Piersol 1993 [5]). After the evaluation of the Fourier transform of the recorded signals, the eigen-frequencies of the investigated structure are assessed searching the peaks in the spectrum plot. The eigen-modes can then be determined by comparing the transfer functions of the various recordings with a reference one. The method has the advantage of being relatively simple, however in the case of complex structures it might not be able to provide significant results due to the fact that, of course, it depends on the sensitivity of the operator who has to recognize the peak of auto-spectral density. Despite its disadvantages the popularity of the method is mainly due to its simplicity as the only algorithm that is needed to convert time data to spectra is the Fast Fourier Transform (FFT).

In the last decade more advanced methods, even if more computational demanding, have been proposed. Among them it is noteworthy to remember the so-called SSI (Stochastic Subspace Identification) (see e.g. Peeters & De Roeck 1996 [6]). Starting from the consideration that in many cases of engineering interest is extremely difficult, if not impossible, to have a deterministic knowledge of the forcing process (environmental loads) the method assume a stochastic loading (often a white noise). Many applications of SSI were presented in the scientific literature showing the attractiveness of the method.

Figure 1: Three-storey investigated steel building.

The paper, discussing these problems, presents a technique for the identification of “output only” systems by means of neural networks. In a first part of the paper the experimental campaign conducted in a benchmark three-storey steel structure built at the Civil Engineering Laboratory of the University of Florence (Italy). The structure has been tested under ambient loading starting from the undamaged configuration and imposing steps of increasing damage level by incremental cuts on a steel column: the tests have been performed assuming the building being initially undamaged; successively, incremental damage states have been imposed by partially cutting one of the columns and test have been repeated. Then, a neural network based procedure has been developed to analyze accelerometer signals recorded during the experimental campaign. Results are discussed and the dynamic properties of the building are evaluated at each damage level. At the end, the ongoing research aimed to employ genetic algorithms to the structural system identification is discussed.

2 EXPERIMENTAL LAYOUT

2.1 The specimen

The case study is a three-storey steel structure (Figure 1) with profiled steel elements; this specimen has been analysed starting from an undamaged configuration and imposing increasing damage level (by progressive cutting of a column flanges).

The plane dimension of the steel frame is 2.5 m × 2.5 m. The height of the first storey is 1.64 m, while is 1.6 m for 2nd story and 1.54 for 3rd storey. The total height of the structure is 4.87 m. The layout of the specimen is shown in Figure 7. The material of steel elements was grade S235 steel with a nominal yield stress of 235 MPa. At each level a mass of about 22 kN was applied by means of concrete slabs (Figure 1) which have no structural function. The beam-to-column connections were fully welded to ensure rigidity. Column base connections were made as rigid as possible. The cross section of steel members is as follows: a) column HEB140; b) beam IPE 140; geometrical properties of member are reported in Table 1.

Properties	Columns	Beam
Section type	HEB140	IPE 140
Cross sectional area (cm^2)	42.96	16.43
	Moments of inertia (cm^4)	
Strong direction	1509	541.2
Weak direction	549.7	44.92

Table 1: Sectional properties of the structural members.

2.2 Ambient vibration test

To determine the vibration characteristics (natural frequencies and mode shapes) of the steel building model a series of ambient vibration tests were conducted.

A total of 12 uniaxial seismic accelerometers were installed on the frame (Figure 2); in particular at each level of the specimen 4 sensors have been placed to collect acceleration along the two main horizontal dimensions). The accelerometers are characterized by a 10 V/g sensitivity and a 0.1–1500 Hz frequency range.

Figure 2: Accelerometers disposition (level #1).

Test	Type of test	Load
Test # 1÷ 5	Without damage	Environmental
Test # 11÷13	Damage Level #1	Environmental
Test # 21÷23	Damage Level #2	Environmental
Test # 31÷33	Damage Level #3	Environmental
Test # 41÷43	Damage Level #4	Environmental

Table 2: Experimental campaign.

The sampling frequency during the experiment was 400 Hz and the measurement duration was selected as about 4 min for each test considering the vibration source. Table 2 reports a summary of the tests executed during the experimental campaign. The tests were performed starting from the specimen in its undamaged configuration and were repeated at four different levels of increasing damage (Figure 3÷Figure 4). The damage consisted in a progressive cut of the column flanges, as shown in Figure 3 to Figure 6.

Figure 3: Damage Level #1 (left) and Damage Level #3 (right).

Figure 4: Damage Level #4.

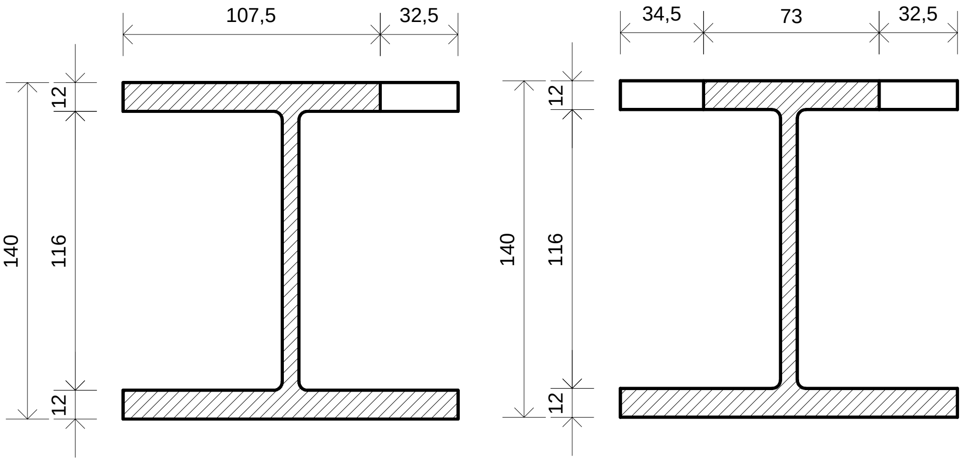

Figure 5: Damage Level # 1 and 2.

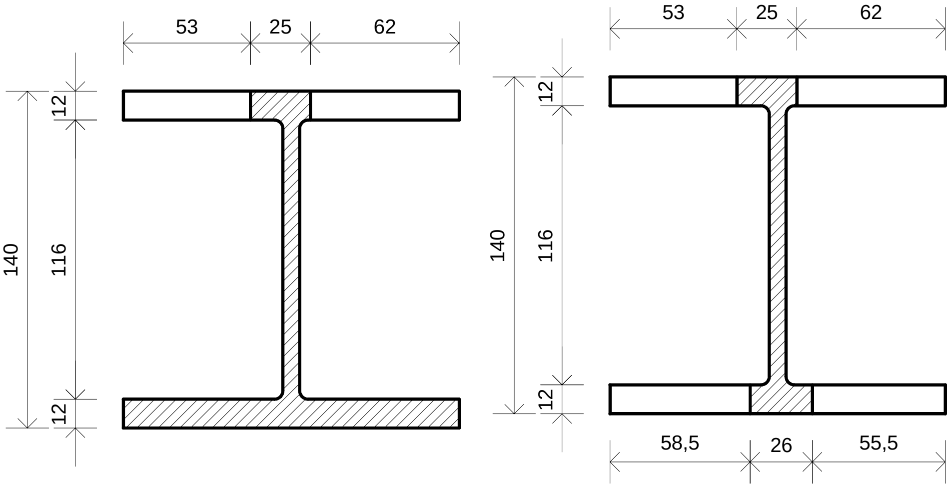

Figure 6: Damage Level # 3 and 4.

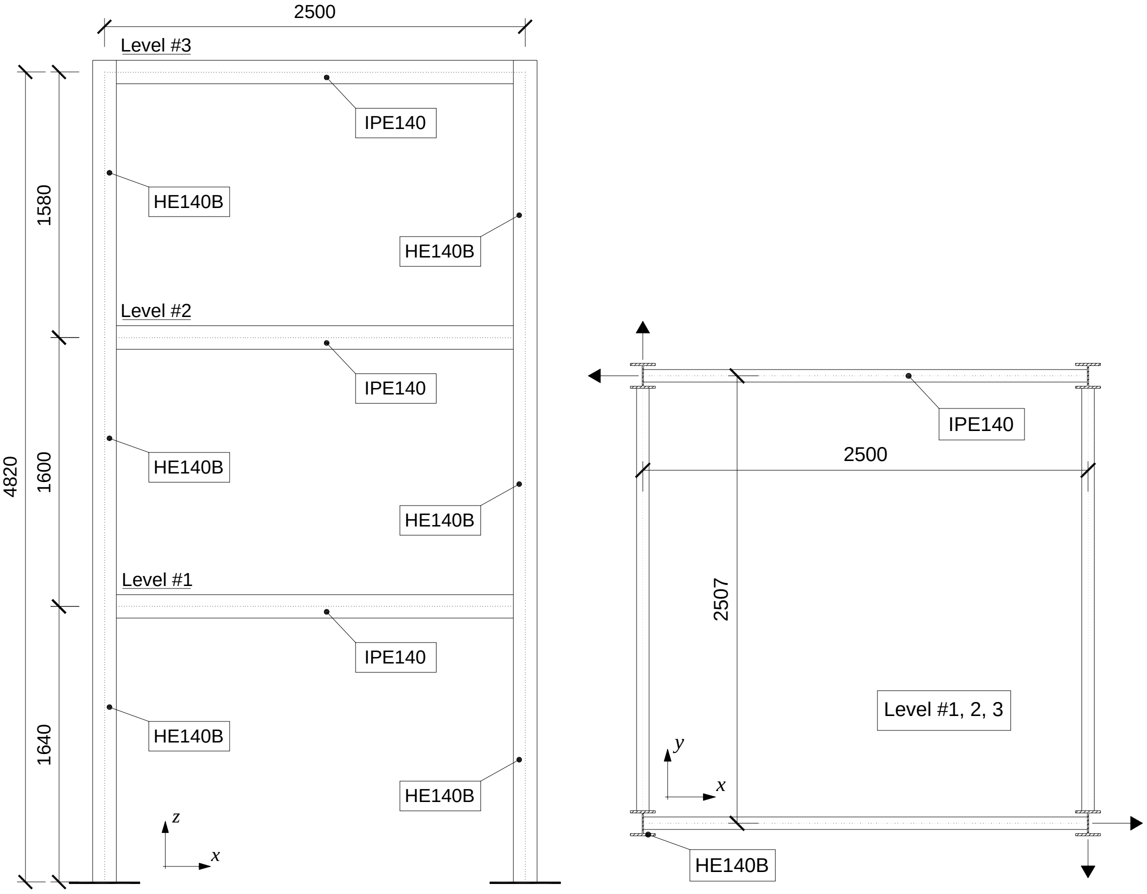

Figure 7. Specimen layout (mm).

3 NETWORK TRAINING AND SIGNAL ANALYSIS

The recognition of the structural eigenfrequencies was assisted by a neural network (described later) fed with four frequency-dependent indexes which summarize the behavior of the spectral tensor at each frequency of interest.

As a matter of fact, the response of structures with well separated eigenfrequencies and relatively low damping, when excited by random forcing processes, exhibit a spectral tensor characterized, in correspondence with the structural eigenfrequencies, by:

- the possibility to be decomposed in the tensor product of the corresponding modal shape by itself;
- a high coherence between any couple of degrees of freedom;
- a phase close to zero or to a multiple of π between any couple of degrees of freedom;
- the presence of peaks in the auto-spectral densities.

These four conditions enable to define four indexes which describe a kind of “degree of fulfillment” for each condition; the indexes were defined as follows.

The possibility to decompose the spectral tensor in the tensor product of a vector by itself can be readily checked by means of a singular value decomposition; the spectral theorem ensures that, at each frequency *f* of interest, the spectral tensor of the degrees of freedom can be decomposed as:

$$S(f)=\sum_{h=1}^{N}\lambda_h(f)\varphi^{(h)}(f)\otimes\varphi^{(h)}(f) \tag{1}$$

where $\lambda_h(f)$ are the eigenvalues and $\varphi^{(h)}(f)$ the corresponding eigenvectors. When an eigenvalue is much greater than the others the spectral tensor reduces to:

$$S(f)\approx\lambda_1(f)\varphi^{(1)}(f)\otimes\varphi^{(1)}(f) \tag{2}$$

where, without loss in generality, the eigenvalues are considered to be sorted in descending order. The first index can therefore be defined as:

$$i_1(f)=\max\left\{0 \quad 1-\frac{\left\|S(f)-\lambda_1(f)\varphi^{(1)}(f)\otimes\varphi^{(1)}(f)\right\|}{\left\|S(f)\right\|}\right\} \tag{3}$$

The degree of coherence between the various couples of signals can be checked by computing the norm of the coherence tensor; therefore the second index is defined as

$$i_2(f)=\frac{\left\|\mathbf{C}(f)\right\|}{N_{dof}} \tag{4}$$

where $\mathbf{C}(f)$ is the coherence tensor at each frequency of interest and N_{dof} the number of degrees of freedom of the structure.

The third index is a measure of the norm of the phase angle tensor, modulus π:

$$i_3(f) = \max\left\{0 \quad 1-\frac{\left\|\Phi(f)\bmod \pi\right\|}{N_{dof}}\right\} \tag{5}$$

The fourth index is derived from an index reported in Deraemaeker *et al.* (2008) [1], and is the peak index. Denoting with $S_i(f)$ the auto-spectral density to be analyzed to evaluate the peaks it is possible to define the following quantities:

$$K(f_c) = \left[\int_{f_c-\Delta f}^{f_c+\Delta f} S_i(f)\,df\right]^{-1} \; ; \; \tilde{S}_i(f_c, f) = K(f_c) S_i(f)$$

$$\mu(f_c) = \int_{f_c-\Delta f}^{f_c+\Delta f} f\,\tilde{S}_i(f_c, f)df \; ; \; \sigma^2(f_c) = \int_{f_c-\Delta f}^{f_c+\Delta f} [f-\mu(f_c)]^2\,\tilde{S}_i(f_c, f)df$$

The peak index is eventually defined by:

$$\lambda_4(f) = 1-\frac{f_c\sqrt{3}}{\Delta f}\frac{\sigma(f)}{\mu(f)} \tag{6}$$

Since as many peak indexes can be evaluated as the number of degrees of freedom, the maximum of the various indexes is taken at each frequency.

3.1 Network definition and training

The utilized network was a feed-forward back-propagation network characterized by two-hidden layers with variable number of neurons: in particular, the behavior of networks with 5, 10 or 15 neurons in both hidden layers was inspected. Hidden neurons were characterised by sigmoid activation functions.

The input layer was always composed by 4 neurons, each accepting one of the indexes i_1 to i_4. The output layer computed a linear combination of the outputs of the second layer of neurons and gave the network output, i.e. an estimate *L*(*f*) of the likelihood of finding a structural resonance at frequency *f*.

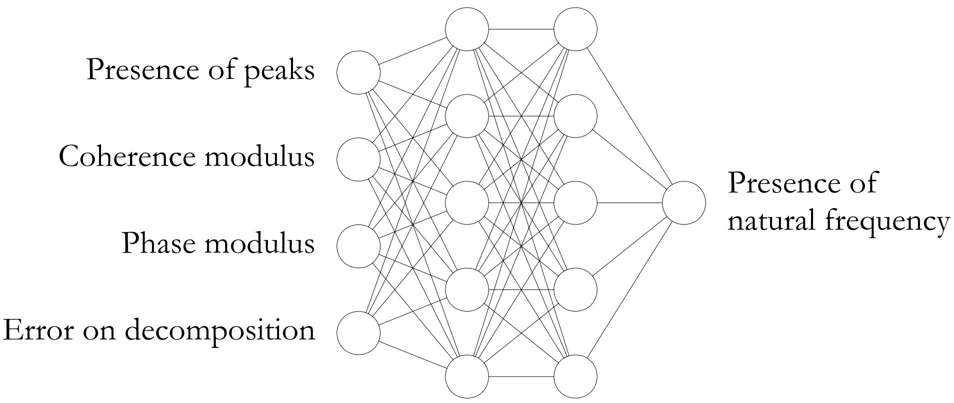

Figure 8: Example of neural architecture; here a 4-5-5-1 network is shown.

One of the major advantages of feeding the network with the four above-mentioned indexes is that training of neural network can be performed on a completely different structure, as the indexes characteristics are widely general. The possibility of training the network on a generic structure overcomes the problem that the examined structure is still widely unknown, and moreover the training structure can be built numerically, thus perfectly knowing its dynamical characteristics.

Nevertheless, the network was trained on the results obtained for the FEM model of the investigated frame *prior* to identification. In other words, a FEM model was first built on the basis of the available information for the geometry and material. Once defined the stiffness and mass matrices of the model, the frequency response functions could be evaluated, together with the first eigenfrequencies and associated modal shapes (see Figure 9).

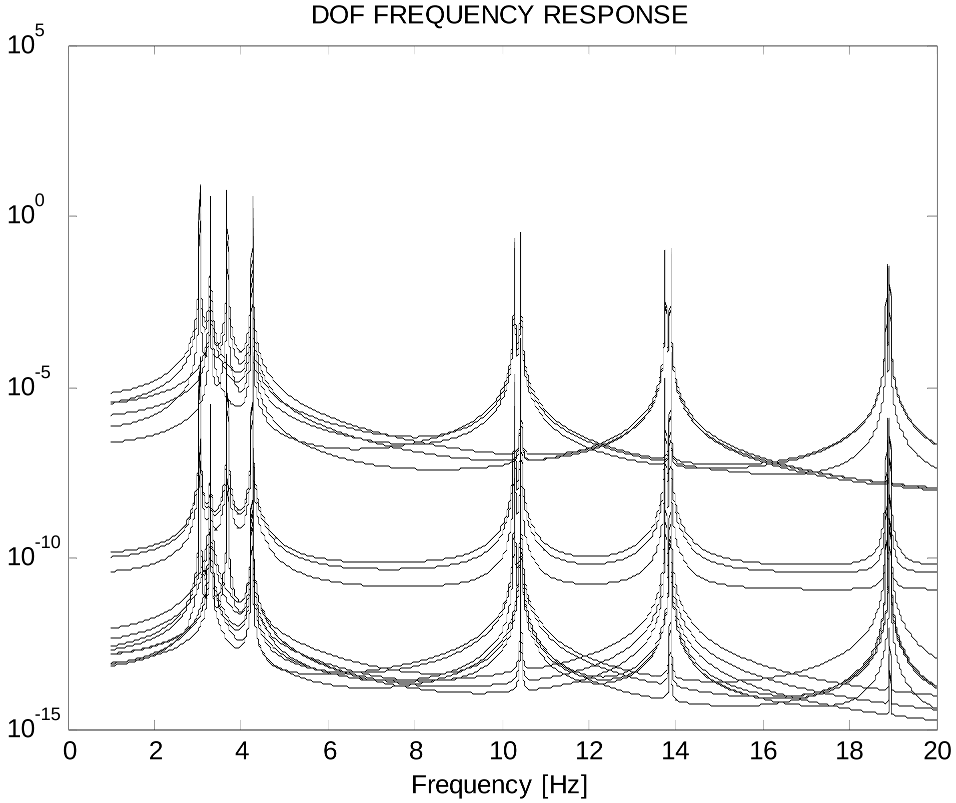

Figure 9: the response function of the structural degrees of freedom evaluated for a damping of $\nu=10^{-4}$

From the frequency response functions of the model, the four indexes $i_h(f)$ were computed, while a target function $T(f)$ for the neural network was defined as

$$T(f)=\frac{10^{t(f)}-1}{9},\quad t(f)=\sum_{h=1}^{N_r}\exp\left[-\left(f-f_{r,h}\right)^2/\sigma^2\right] \tag{7}$$

where N_r is the number of eigenfrequencies $f_{r,h}$ considered (in the case at hand, the first 10 eigenfrequencies were considered); f is the frequency and σ a proper decay parameter.

The choice of the decay parameter σ was made on the basis of some considerations on the shape of the structural FRFs; since this parameter affects the width of the peaks that indicate the resonance frequencies, σ was determined to keep as separated as possible the pairs of close resonances around 10, 14 and 19 Hz in the target function (Figure 10). Correspondingly, the target function should exhibit pairs of close peaks, which can only be possible for $\sigma^2 \leq 0.001$.

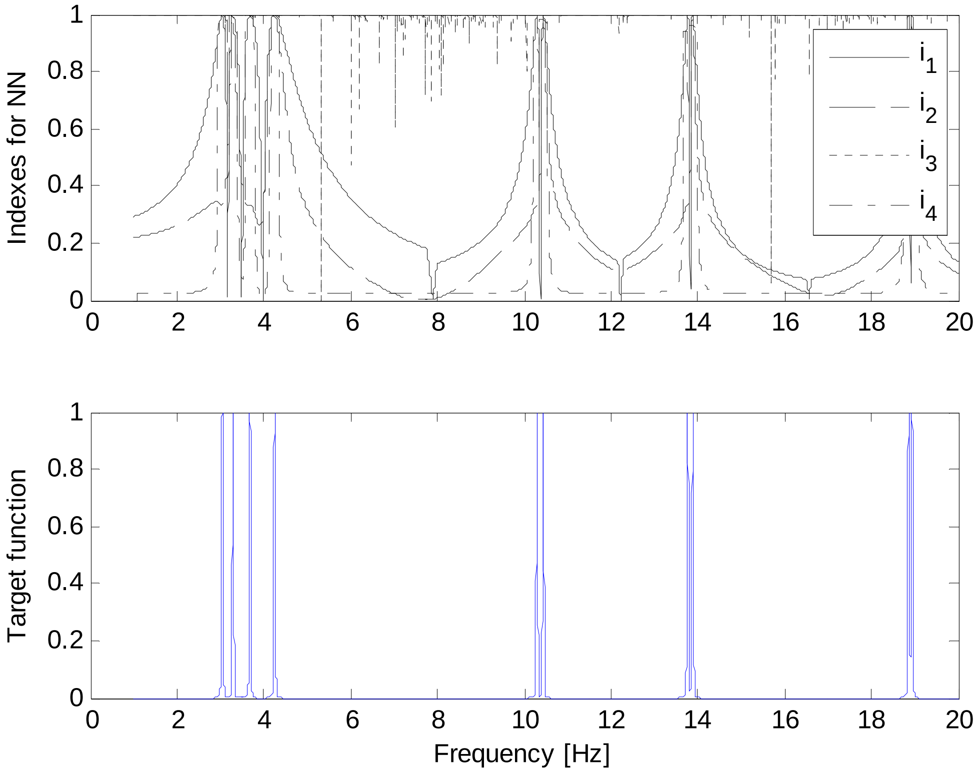

Figure 10: the four indexes obtained for the FEM model and the target function

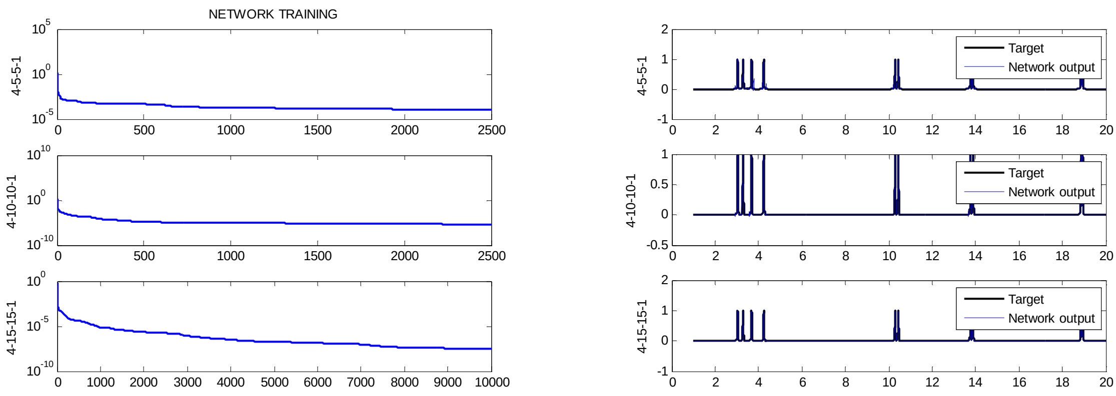

Figure 11: on the left, the performance of different networks during the training phase; on the right, the network output after the training phase (blue line) compared to the target function (thick black line)

Training was based on the Levemberg-Marquardt algorithm and employed as long as 10000 epochs in the most difficult cases.

Network validation was carried out on another structure (the shear type frame shown in Figure 12) and showed that two kinds of errors can arise: the presence of a natural frequency where there is no actual eigenfrequency, and the absence of a natural frequency where it should be present.

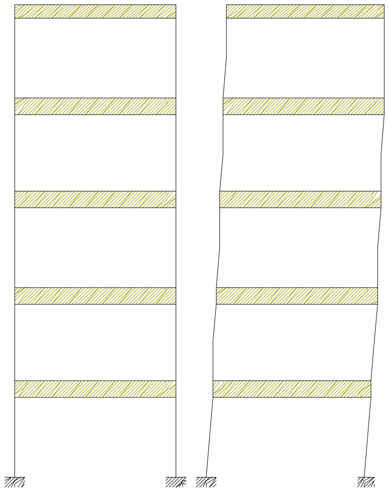

Figure 12: The validation structure with its first modal shape.

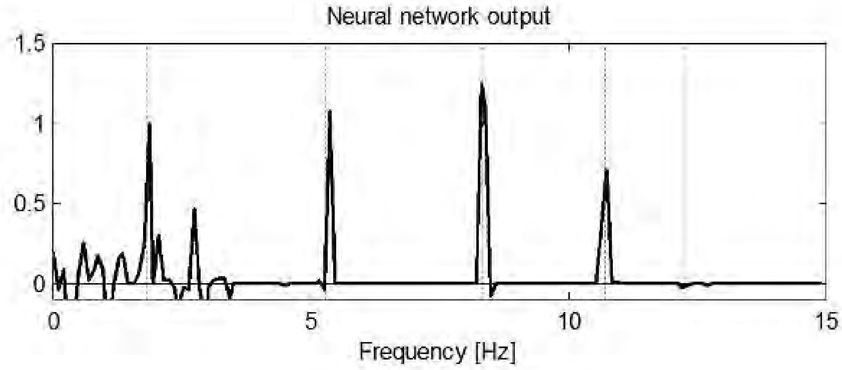

Figure 13: Example of validation of the 4-15-15-1 NN.
Structural resonances are denoted by dashed vertical lines.

Figure 13 shows an example of both types of error: at a frequency of about 3 Hz a false eigenfrequency is detected, and the last eigenfrequency is not detected at about 12 Hz. It must be noted that network validation was performed on 3 different data sets, and the other two gave good results.

The validation results show that the network output must be considered (when properly normalized) as an estimation of the probability of finding a structural resonance at a given frequency, rather than the certain presence or absence of eigenfrequencies.

In this light, it is useful to perform more than one test on the investigated structure: the analysis of the time histories of each test will give as many likelihood functions for the presence of structural resonances.

4 OUTPUT-ONLY IDENTIFICATION PROCEDURE

4.1 Signal analysis

The analysis of accelerometer signals is the first of two steps that constitute the identification procedure.

The recorded signals were transferred into a portable computer via a cross-cable. Then, the signals were digitally low-pass filtered at 12.5 Hz and resampled at 25 Hz. Spectral densities were evaluated by means of nonparametric estimation using different windows (Hanning, Hamming, DPSS and Blackman) and successively applying Fast Fourier Transform (FFT) to windowed data; with the exception of the periodogram (which is more sensitive to bias), no significant difference could be noticed in the evaluated spectral densities (Percival and Walden 1993 [8]), see Figure 14.

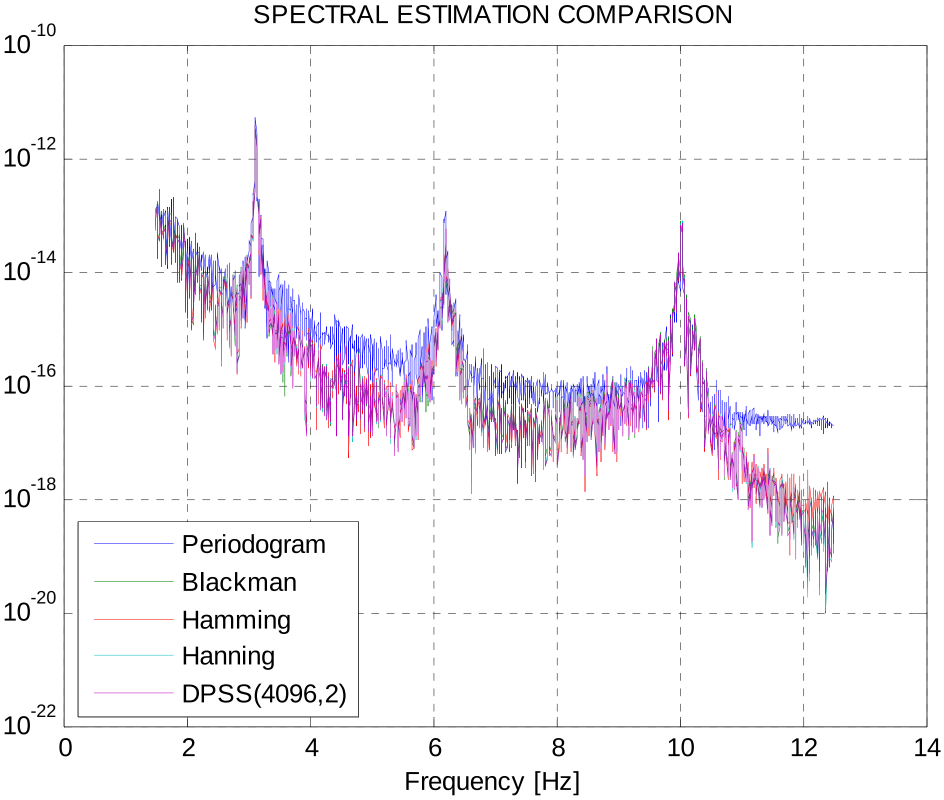

Figure 14. Comparison of the estimates of the spectral density of signal #2 with different data tapers.

The results obtained in the following analyses were also similar, so the data taper given by discrete prolate spheroidal sequences (4096,2) (Percival and Walden 1993 [8]) was adopted. The spectral densities were divided by a factor of $(2\pi)^4$ in order to evaluate the displacement spectra and the indicators previously descripted, $i_1(f)$ to $i_4(f)$, were estimated.

Figure 15 shows that the fourth index is capable of detecting resonances (one of the first identification methods, the peak picking, was based on this criterion), but shows also a certain width of its peaks, thus affecting the reliability of the estimate. The first index is close to 1 very often, but in proximity of structural resonances decreases rapidly when the frequency differs from the eigenfrequency; further useful indications come from the second and third indexes.

4.2 Combination of network output for different tests with same level of damage.

Since the neural network can undergo different kinds of errors, as pointed out before, for each level of damage several recordings of environmentally induced accelerations were taken.

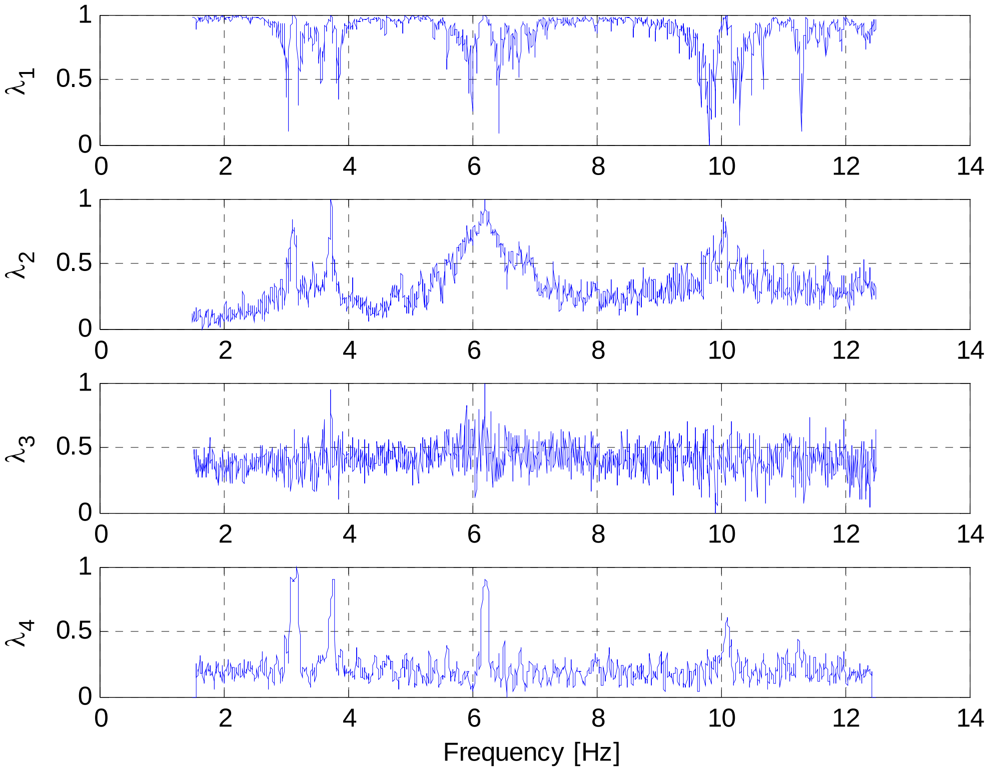

Figure 15: The four indexes as evaluated from the analysis of the signals recorded during the third test.

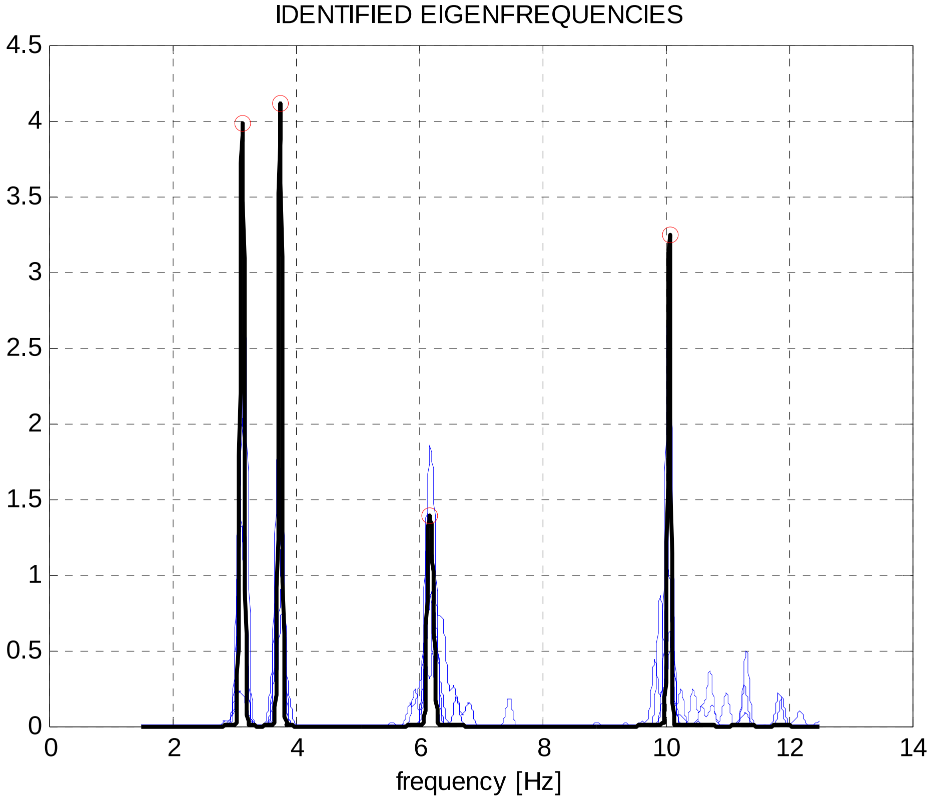

Figure 16: *Pdf* of structural resonance: first set of tests (undamaged structure)

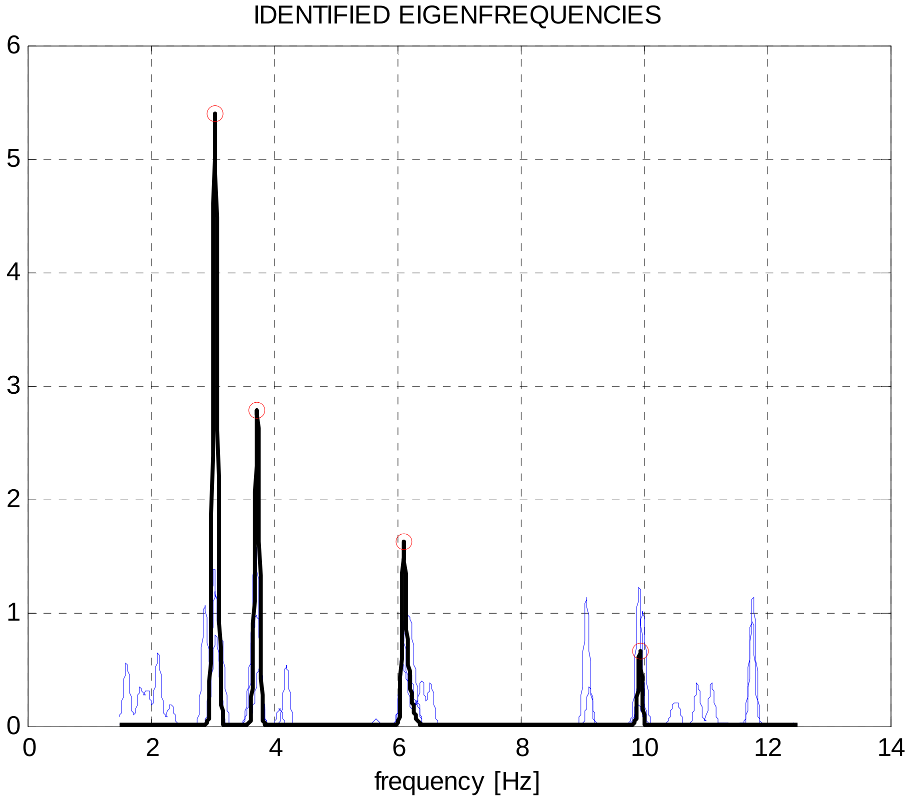

Figure 17: *Pdf* of structural resonance: third set of tests (third level of damage)

The results given by the network for each recording were therefore combined from a Bayesian point of view. Before the first recording was taken (for each level of damage), no assumptions about the distribution of structural eigenfrequencies were made, and therefore a uniform probability density for the eigenfrequency positions was considered.

The output of the neural network after each test brings information about the location of structural eigenfrequencies, but can be affected by errors. Therefore, it can be considered as an estimate of the likelihood to find a structural eigenfrequency at each frequency of interest.

The result is the final probability density function for the presence of eigenfrequencies. Figure 16 and Figure 17 show the likelihood functions coming out of each test of a given set (blue lines) and the final pdf for the structural resonances (thick black line).

It is worth spending some words on the results shown in Figure 18, where the evolution of the probability density of the first two structural eigenfrequencies is plotted.

Set #	f^1 (Hz)	f_2 (Hz)	f_3 (Hz)	f_4 (Hz)
Set #0	3.14	3.76	6.18	10.06
Set #1	3.08	3.75	6.24	9.98
Set #2	3.09	3.71	6.20	9.96
Set #3	3.05	3.74	6.11	9.94
Set #4	3.03	3.72	6.13	9.91

Table 3. Main identified frequencies.

The probability density in the undamaged state is represented by the blue line, and shows peaks located at the highest values of the two resonances; they are also more narrow than the other ones, implying a higher reliability of the estimate.

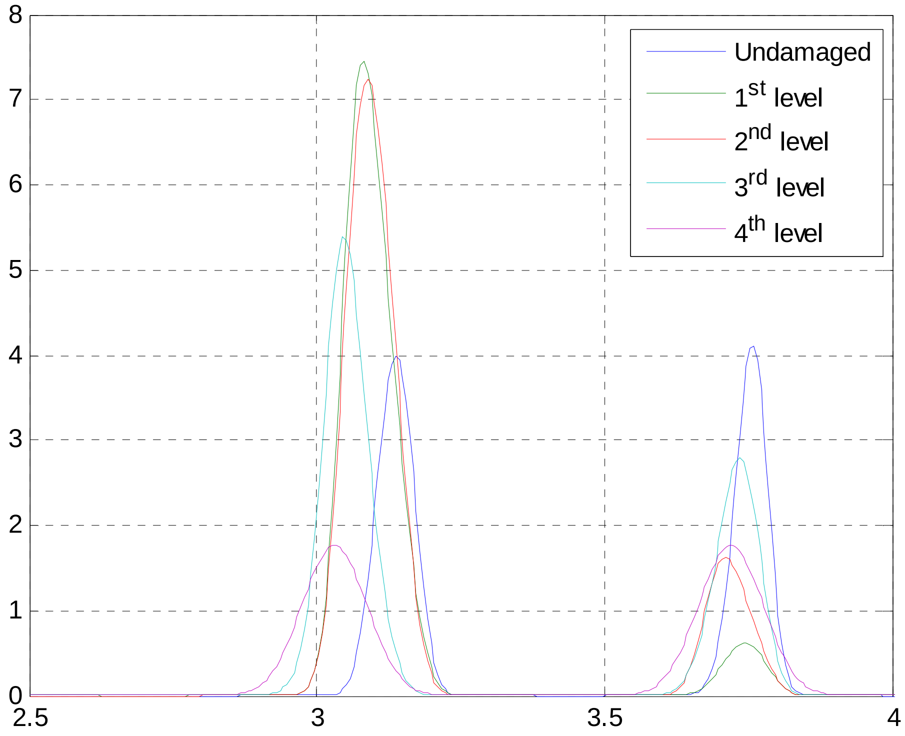

Figure 18: Evolution of probability density of the first two resonances with increasing damage

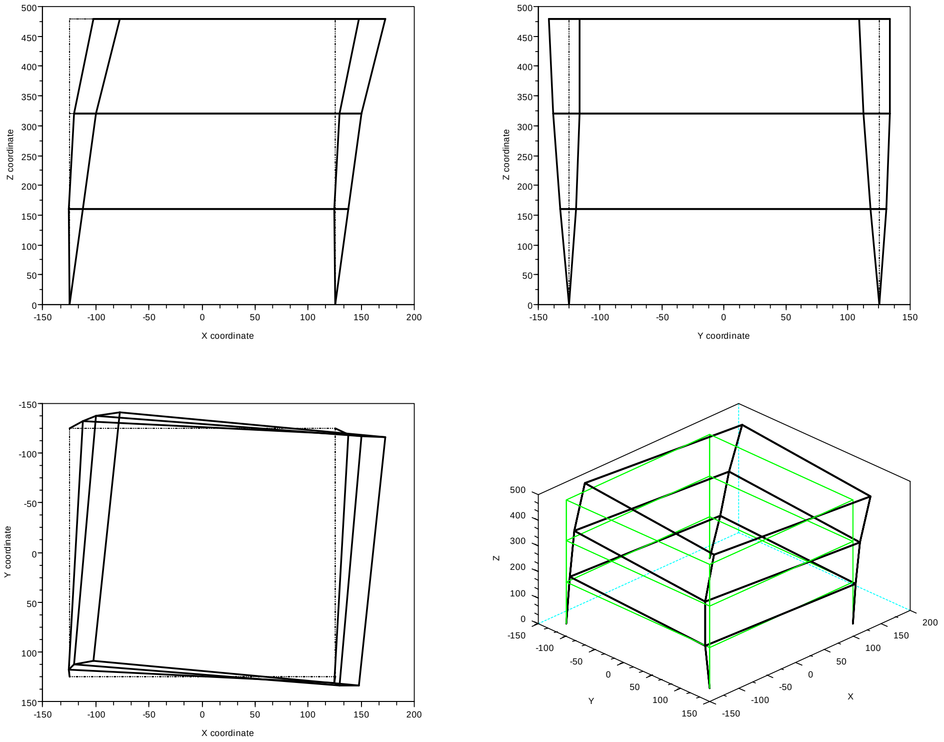

Figure 19: First bending mode (x-direction) - f_1=3.14 Hz

As it is clear also from Table 3, it is interesting to note that the second eigenfrequency estimate does not always decrease with increasing damage: as a matter of fact, it shows a minimum for set # 2 (2^{nd} level of damage). But if we look at Figure 18, it can be noticed that the peaks relative to set #1 and set #2 estimate of the second eigenfrequency are a bit wider than the others, meaning a less reliable estimate.

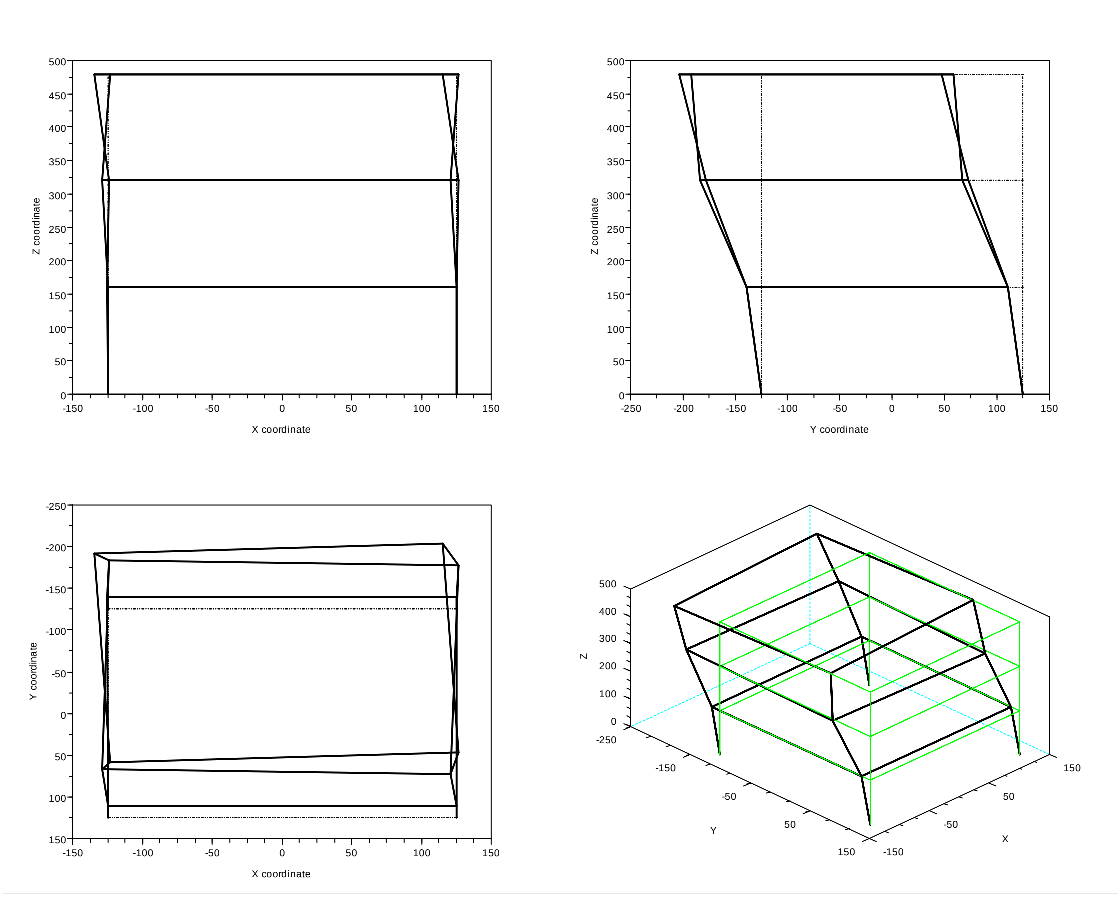

Figure 20: First bending mode (y-direction) - f_2=3.76 Hz

The same considerations hold also for the variation of the torsional frequency, f_3. The exact relation between the width of the peaks and the estimate reliability is currently under examination. Once the eigenfrequencies were estimated, the corresponding modal shapes could be retrieved by means of the spectral SVD. The first three estimated modal shapes for the undamaged state of the frame are reported in Figure 19, Figure 20 and Figure 21.

The obtained results have been compared with those given by SSI in the output-only, covariance-driven form. Even in the case of SSI the stabilization diagram can be used to define the probability density of structural resonance. The *pdf* could be built by means of a Gaussian base according to Eq. (8) where O_{min} and O_{max} represent the minimum and maximum order of the SSI model and N_f is the number of identified main frequencies.

Figure 22 is an example of the stabilization diagram and the *pdf* of structural resonance as calculated for the specimen it its initial configuration (i.e. without damage).

$$p(f) = K \sum_{h=O_{\min}}^{O_{\max}} \sum_{k=1}^{N_f} \exp\left(-\frac{(f - f_{hk})^2}{2\sigma_h^2} \right)$$

$$K = \left[\int_{-\infty}^{\infty} \sum_{h=O_{\min}}^{O_{\max}} \sum_{k=1}^{N_f} \exp\left(-\frac{(f - f_{hk})^2}{2\sigma_h^2} \right) df \right]^{-1} \tag{8}$$

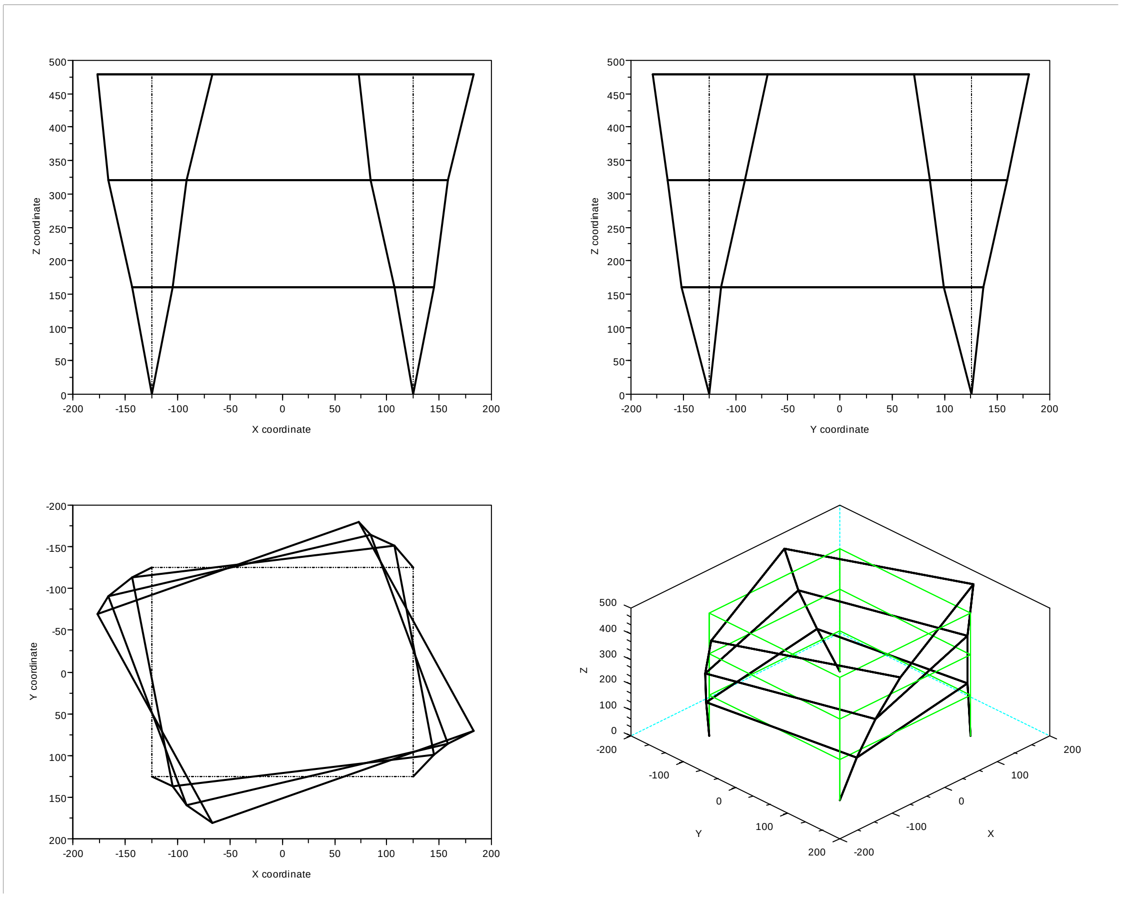

Figure 21: First torsional mode (x-y plane) - f_3= 6.18 Hz

Table 4 reports the first three identified frequencies for representative tests of each damage level. The increasing level of damage (being the column's flange cut) interests mainly the frequency in the x-direction (Figure 18) and the torsional one.

Test #	f_1 (Hz)	f_2 (Hz)	f_3 (Hz)
Test # 1	3.12	3.75	6.28
Test #32	3.08	3.72	6.16
Test #41	3.04	3.72	6.14

Table 4: Main identified frequencies (SSI).

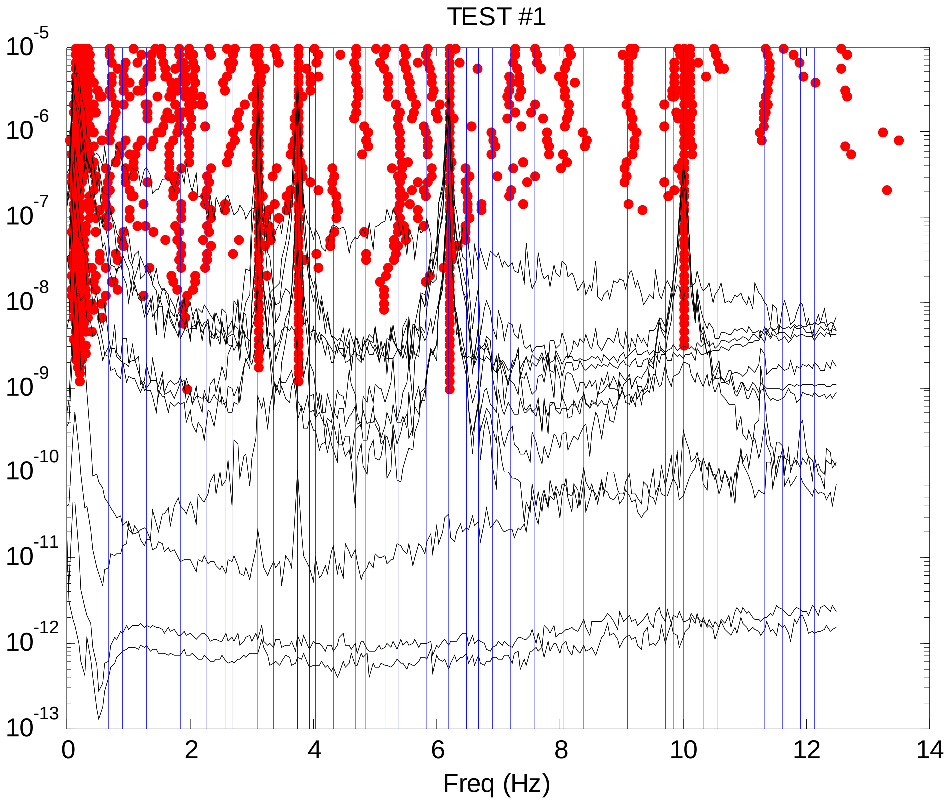

Figure 22: Stabilization diagram together with autospectra of the recorded acceleration signals: test #1

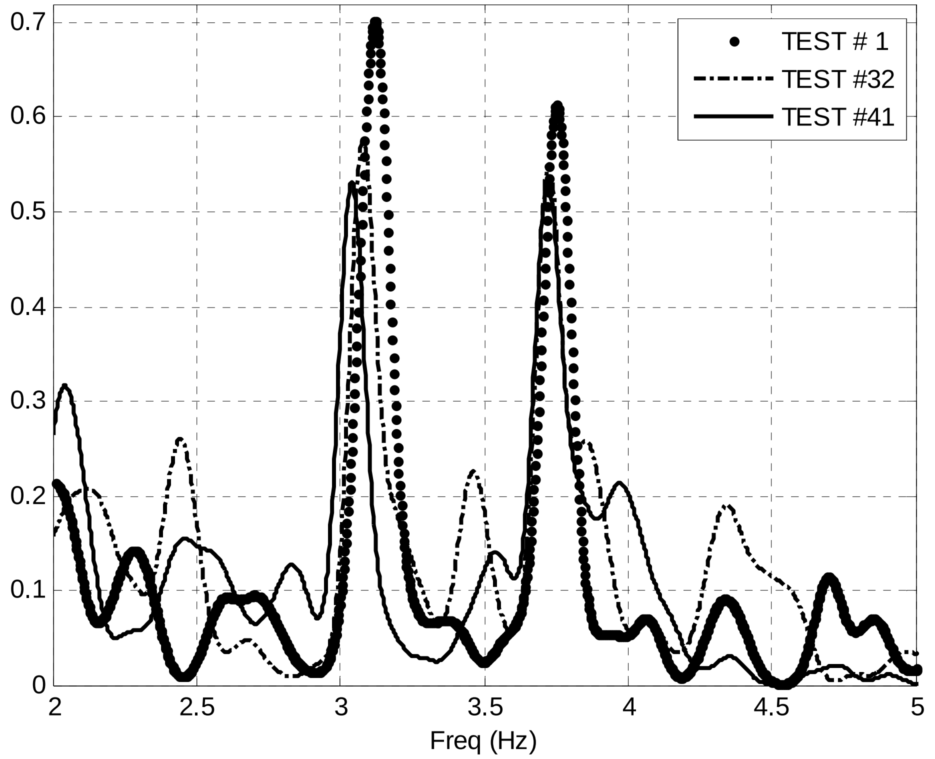

Figure 23: *Pdf* of the first two structural resonances: test #1, 32, 41

Figure 23 reports the *pdf* of the two first structural resonances in case of damage (test #32 &41) compared with the case without damage (test #1).

5 NEXT RESEARCH STEP: GENETIC ALGORITHM

Next steps of the research aim to propose the employment of genetic algorithms (GA) techniques for the identification of a finite element model of the specimen, as GA has been shown to be able to overcome the limitations of traditional methods (see e.g. Faravelli *et al.*[7]).

Genetic algorithms are based on ideas from the science of genetics and the process of natural selection. They work with an initial population (strings of zeros and ones i.e. binary strings) which may correspond to certain numerical values of a particular variable whose size is depending on the problem under consideration. The initial population is generated randomly; each string in the population corresponds to a chromosome and each binary element of the string to a gene. A new population is developed starting from the initial population according to the processed that are analogue to the fundamental genetic processes: a) reproduction based on fitness, b) crossover and c) mutation.

A set of chromosomes is selected at the reproduction stage and members of the population are chosen for reproduction on the basis of their fitness: the fittest have a greater probability of reproducing in proportion to the value of their fitness. The process of reproduction is implemented by using the crossover. Many crossover techniques are available using different data structures (single crossover point or many cross-over points). The mutation is a process where randomly a particular gene in a particular chromosome is changed. The process of mutation in a genetic algorithm occurs very rarely and hence this probability of a change in a string is normally kept very low. Nevertheless the purpose of mutation is to preserve and introducing diversity. From a computational point of view mutation should allow the algorithm to avoid local minima by preventing the population of chromosomes from becoming too similar to each other, thus slowing or even stopping evolution. Crossover and mutation represent the two special features that make different a genetic algorithm with respect to a traditional direct search procedure and make it interesting for optimization and search problems.

$$
\begin{aligned}
F &= \sum_{i=1}^{k} \left[p_{\lambda,i} \cdot \left(\frac{\lambda_{F,i} - \lambda_{Exp,i}}{\lambda_{F,i}} \right)^2 + p_{\phi,i} \cdot \left(1 - MAC(i,i)\right)^2 \right] \\
MAC(i,i) &= \frac{\left(\varphi^t_{F\,i} \cdot \varphi_{Exp\,i}\right)^2}{\left(\varphi^t_{F\,i} \cdot \varphi_{F\,i}\right) \cdot \left(\varphi^t_{Exp\,i} \cdot \varphi_{Exp\,i}\right)}
\end{aligned}
\qquad (9)
$$

CONCLUSIVE REMARKS

The paper has discussed some recent advances in case of “output-only” systems aimed at the damage identification of structural systems. To this aim the experimental campaign conducted in a benchmark three-story steel structure at the Civil Engineering Laboratory of the University of Florence (Italy) laboratory is currently carried out and has been reported on. The benchmark structure has been tested (under ambient loading) starting from the actual configuration and imposing steps of increasingly damage level by partial cuts of flanges on some steel elements (columns). Successively a neural network based procedure has been proposed and employed to analyse accelerometer signals recorded during the experimental campaign. Results are discussed and the dynamic properties of the building are evaluated at each damage level. At the end, the ongoing research step aimed to employ genetic algorithms to finite element model identification has been discussed.

ACKNOWLEDGMENTS

The authors wish to thank Mr. Saverio Giordano (Civil Engineering Laboratory of the Department of Civil and Environmental Engineering) for his precious assistance and cooperation during the whole experimental campaign.

REFERENCES

[1] A. Deraemaeker, E. Reynders, G. De Roeck, J. Kulla, Vibration-based structural health monitoring using output-only measurements under changing environment. *Mechanical Systems and Signal Processing*, **22**, 34-56, 2008.

[2] A. Alvandi, C. Cremona, Assessment of vibration-based damage identification techniques. *Journal of Sound and Vibration*, **292**, 179–202, 2006.

[3] L. Facchini, M. Betti, P. Biagini, Neural networks for output-only parameter identification. B.A. Schrefler & U. Perego eds. *8th World Congress on Computational Mechanics (WCCM8) & 5th European Congress on Computational Methods in Applied Sciences and Engineering (ECCOMAS 2008)*, Venice, Italy, June 30 – July 4, 2008.

[4] L. Facchini, M. Betti, P. Biagini, Studi recenti nell'identificazione ‘output only’ di strutture vibranti mediante l'impiego di reti neurali. A.L. Materazzi, M. Breccolotti, F. Cluni, F. Ubertini, I. Venanzi eds., *3° Workshop sui Problemi di vibrazioni nelle strutture civili e nelle costruzioni meccaniche*, Perugia, Italy, September 11-12, 2008.

[5] J.S. Bendat, A.G. Piersol, *Engineering Applications of Correlation and Spectral Analysis*. Wiley, Interscience, 1993.

[6] B. Peeters and G. De Roeck (1999), “Reference-based stochastic subspace identification for output-only modal analysis”, Mechanical Systems and Signal Processing 13(6), 855-878, 1999.

[7] L. Faravelli, F. Materazzi, M. Rarina, Genetic algorithms for structural identification. *ICOSSAR 2005*, Roma, Italy, June 19-23, 2005.

[8] D. B. Percival, A. T Walden, *Spectral Analysis for Phisical Applications*. Cambridge University Press, Cambridge 1993.

[9] R. Brincker, L. Zhang, P. Andersen, Modal Identification from Ambient Responses using Frequency Domain Decomposition. *Proceedings of the 18th International Modal Analysis Conf.*, San Antonio, USA, 2000.

COMPDYN 2011
III ECCOMAS Thematic Conference on
Computational Methods in Structural Dynamics and Earthquake Engineering
M. Papadrakakis, M. Fragiadakis, V. Plevris (eds.)
Corfu, Greece, 25–28 May 2011

THERMAL-BRIDGE SHUNT ELEMENTS MODELLING FOR SEISMIC VULNERABILITY OF BUILDINGS EVALUATION

Huyen T.T. Nguyen[1], **Frédéric Ragueneau**[1], **Damien Bahon**[2] **and Nicolas Ruaux**[2]

[1] LMT-Cachan/Ens-Cachan/Univ. P. & M. Curie/CNRS/ PRES Universud Paris
ENS-Cachan, LMT, 61 Avenue du Président Wilson
{ntthuyen,ragueneau}@lmt.ens-cachan.fr

[2] Université Paris Est, Centre Scientifique et Technique du Bâtiment
Champs sur Marne, 77447 Marne la Vallée Cedex 2
{Damien.BAHON, *nicolas.ruaux*}@cstb.fr

Keywords: building, vulnerability, constitutive equations, earthquake engineering

Abstract. *Nowadays sustainable constructions imply an objective of energetic performances by reducing the level of thermal conduction. The thermal-bridge shunt elements, an innovative technological element is under study in several countries in Europe. If the thermal benefits have already been proved, the mechanical effects of such a wall-slab connection in a building for the seismic risk have not been assessed. To evaluate the building seismic vulnerability modifications due to these thermal bridges shunt, experimental and numerical developments have to be performed. An experimental campaign is proposed to evaluate the seismic ability of such structural elements and a simplified modelling is proposed aiming at developing numerical framework able to handle parametrical and probabilistic approaches for structural analysis.*

1 INTRODUCTION

Nowadays sustainable constructions imply an objective of energetic performances by reducing the level of thermal conduction. The thermal-bridge shunt elements, an innovative technological element is under study in several countries around Europe. If the thermal benefits have already been proved, the mechanical effects of such as wall-slab connection in a building under seismic risk have not been assessed. To evaluate the building seismic vulnerability modifications due to these thermal bridges shunt, experimental and numerical developments have to be performed.

A two steps analysis is adopted in this work. In order to assess the seismic vulnerability of a building, one has to be able to perform statistic and sensitivity analysis. The numerical models to be developed should be as simple and robust as possible. Firstly the experimental analysis of reduced scale elements in comparison with 3D numerical investigations allow to determine failure mechanisms of thermal shunt elements (made of concrete and steel combinations) subject to earthquake loadings. The thermodynamic internal variables are determined in this stage. Secondly, a macro-scale model for slab-wall connection is derived following the previous analysis and based on irreversible processes thermodynamic assumptions [1]. This model accounts for damage due to shear and flexural combinations, frictional sliding and hysteresis, steel plasticity and stiffness recovery in case of alternate loadings. The finite element numerical implementation has been carried out using an implicit scheme. The model is validated thanks to experimental campaigns achieved under quasi-static loading and seismic.

2 NONLINEAR MECHANISMS IDENTIFICATION

2.1 Thermal bridge shunt elements

This new technique for buildings allows for reducing the thermal conductivity from the inside of the construction to the outside. The thermal bridges are taking place at the wall-slab connection. The role of the thermal bridges shunt elements is to break the thermal connectivity by eliminating any concrete liaison by thermal insulation passive material devices. Different solutions may be adopted, for example in figure 1 two technological solutions allowing breaking the energetic loss.

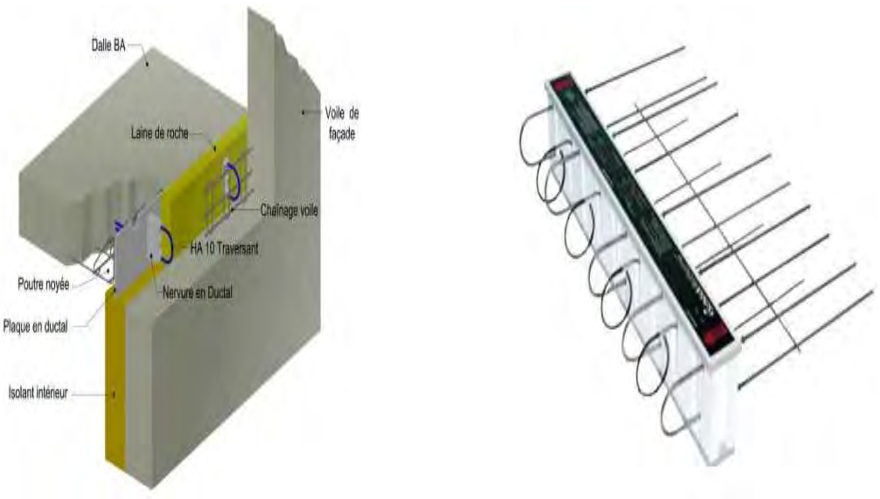

Figure 1: Thermal bridge shunt elements from Lafarge (Ruptal) (left) and Schöck (Rutherma) (right)

2.2 Experimental investigation

The experimental set-up has to be able to reproduce the load transmission mechanism between the wall and the slab when subject to lateral and horizontal acceleration motion due to earthquake loadings. A double shear test as shown in figure 2, preventing any flexion occurrence has been performed on the thermal bridge shunts elements. Four ends steel plates allows to recover the anchored boundary conditions as in the real situation.

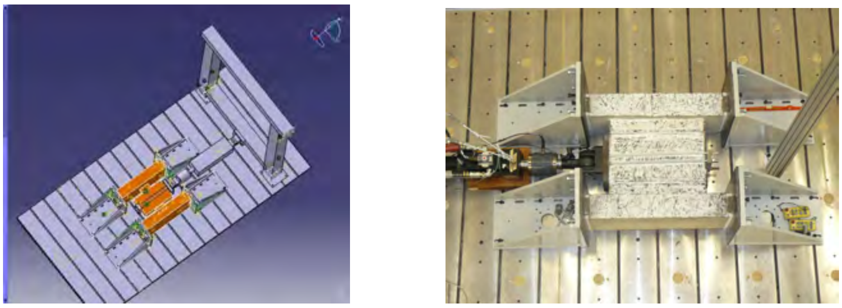

Figure 2: Experimental set-up for a double shear test

The uniaxial load is imposed by a centered hydraulic actuator. Two parallel thermal bridge shunt elements (60 cm long each) allow the load transmission to the two parallel walls. The maximum load capacity for the actuator is 25 tons. LVDT gages have been used to measure the displacements between the walls and the slab as well as digital images for numerical correlation. In the figure 3, one can appreciate an example of a global response, using normalized axis for confidentiality requirements.

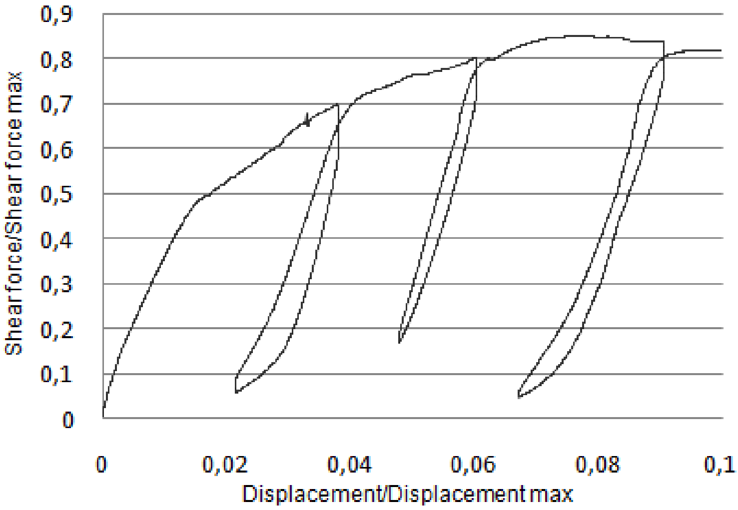

Figure 3: Experimental global response. Normalized axis

Coupling steel plasticity and concrete cracking, the main nonlinear mechanisms can be observed as: stiffness decrease, permanent displacements in unloading, hysteresis loops, nonlinear hardening and softening. This kind of experimental results can be used to develop some modeling allowing the numerical prediction of seismic behavior of building made of such innovative technological elements.

2.3 3D modeling and understanding

The objectives of this section are to proceed to 3D numerical computations on the previous case-study to be able to discriminate the different sources of nonlinearity allowing expressing a constitutive behavior for the connection.

A Finite element model has been established, thanks to the 2 axis of symmetry of the problem. Both steel and concrete have been modeled using 3D cubic elements. A plastic perfectly plastic constitutive equation has been introduced for steel and a continuum damage mechanics based model is used for concrete (wall and slab) and Ductal (connection). The different parameters introduced in the computation are given in table 1.

	Materials parameters			
	Young's modulus (GPa)	Poisson's ratio	σ compression (MPa)	σ traction (MPa)
Concrete	25	0,2	25-35	3
Ductal	45-50	0,2	100-150	8
Steel	210	0,3	σy =500 MPa	

Table 1: Material features for the 3D nonlinear computations

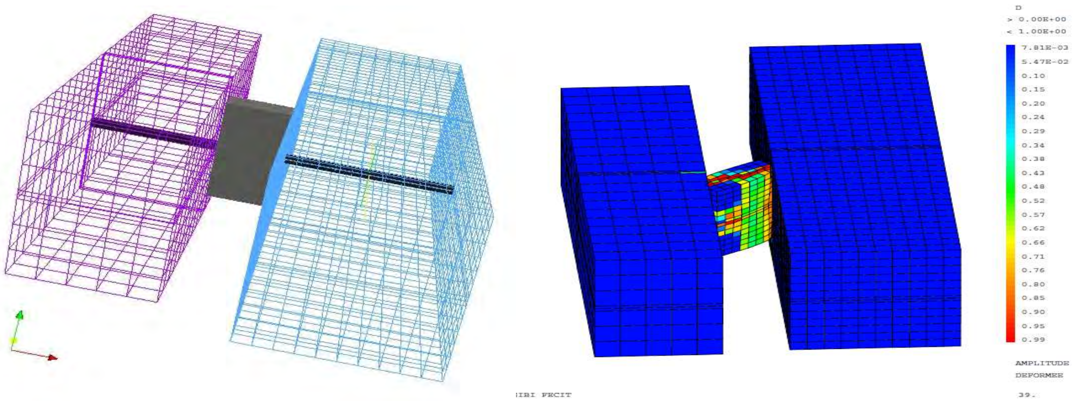

Figure 4: finite element model and results (damage map) of a shear type loading on the connection

The figure 4 presents the finite element model used in the computation as well as a damage map obtained at the end of the analysis. The damage is entirely localized in the Ductal connection zone, inducing flexion of the Ductal block. A good approximation of the experimental response can be fitted as emphasized in figure 5.

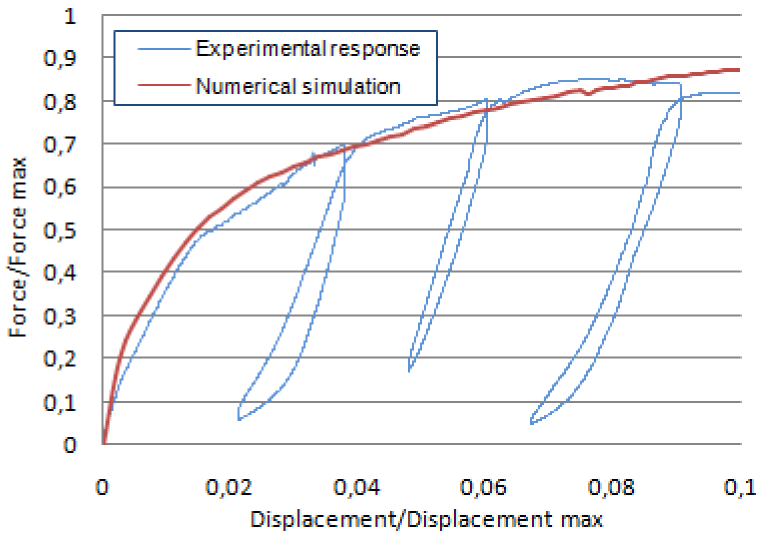

Figure 5: Correlation between 3D numerical analysis and experimental response.

These numerical results will be used in the following section to help one to identify the different evolutions laws for the constitutive equations which has to be expressed.

2.4 Micromechanical analysis

The aim of this section is to analyze the previous numerical/experimental comparisons to be able to define the number of thermodynamic variables which should be introduced in the future modeling, and to calibrate the corresponding evolution laws in case of irreversible processes. For that purpose, the nonlinear behavior of the Ductal square block is analyzed using nonlinear micromechanical models. For example, the stiffness evolution and decrease is computed in different directions according to the increase of a crack in the body. The figure 6 presents the crack propagation in the vertical direction for a vertical load applied on the block.

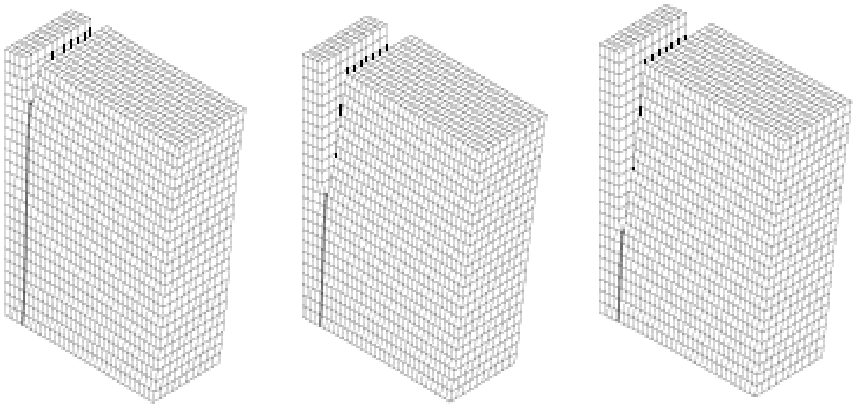

Figure 6: Crack propagation in the ductal block subject to vertical loading

The stiffness decrease is evaluated in the vertical and horizontal directions in the figures 7. Two computations are plotted in the figure 7: the results of the full 3D computation using the modeling of figure 6 and the analytical computations based on the Timoshenko’s beam theory. The main conclusion is that a kind of anisotropy appears in the behavior and should be accounted for in the future modeling. The same analysis may be carried out for a cyclic loading. The reverse loading leads to crack openings and closing in different zones of the Ductal block.

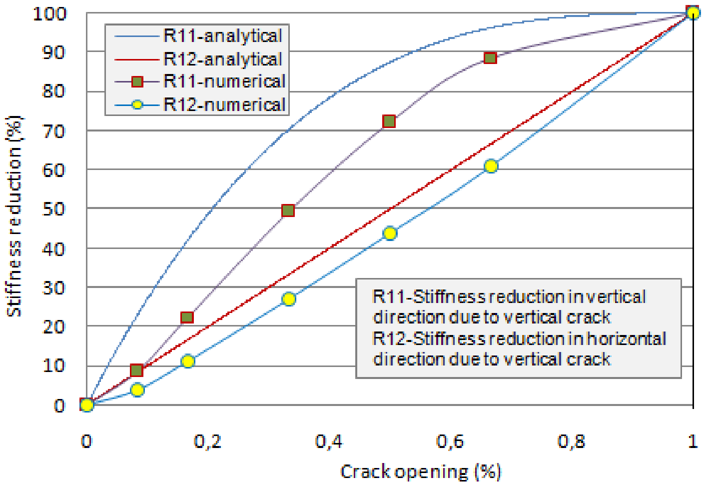

Figure 7: Stiffness reduction in different directions for a vertical crack propagation

The conclusions which could be assessed leads to the definition of two different damage variables for the two major directions of solicitations (horizontal and vertical) allowing accounting for the damage decrease in these directions. Regarding the different zones affected by crack openings and closings, two different damage variables could be introduced to account for unilateral effects and damage deactivation.

2.5 Damage evolutions

After defining the type of variables (damage ones), this section has to be able to calibrate the evolution laws of these thermodynamic quantities. Two more complete 3D computations, based on the model of figure 4, are performed to point out the effect of the steel and the Ductal block. In figure 8, the numerical results are presented by comparing the global force/displacements responses using the 3 different configurations. These comparisons allow to identify in the linear regime, the contribution of each one of the materials to the global stiffness and in the nonlinear regime to express the stiffness reduction only due to crack propagation allowing to evaluate damage variable evolution law.

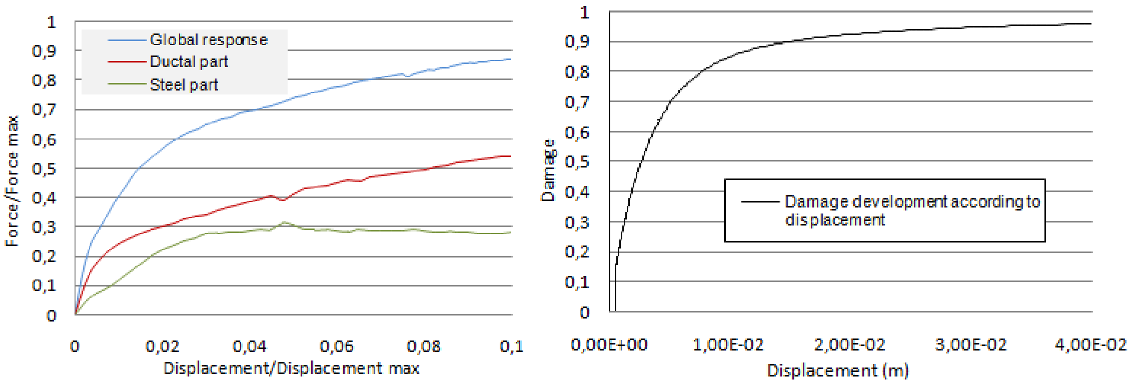

Figure 8: Contribution of the different materials to the global response (left). Damage law identification based on the numerical simulations

3 MODELLING

Regarding the ability of a model to proceed to the seismic vulnerability evaluation of a structure, the model should be, at the structural level, as simple as possible allowing performing probabilistic analysis and parametrical approaches. The choice made is to introduce the nonlinear behavior in the connection thanks global modeling based on the generalized strains and stresses concept (beam theory). The Finite Element supports are Timoshenko beams using a unique Gauss point for the numerical integration. This feature guarantees a uniform state of stresses and strains in the element.

The following sections present the thermodynamic framework detailing the developments concerning the structural element constitutive equation.

3.1 Free energy and state laws

The framework of irreversible processes thermodynamic is chosen to express the model. The previous experimental and numerical investigations allows for defining the number of thermodynamic variables, their couplings and evolutions. A choice is made concerning the thermodynamic potential from which the state laws will be derived. Expressed in different terms due to the contribution of concrete cracking, frictional sliding, steel plasticity and hardening, the potential takes the following form,

$$\rho\Psi = \frac{1}{2}K_b(1-d)D^2 + \frac{1}{2}K_b.g(d).(D-D^{\pi})^2 + \frac{1}{2}K_a(D-D^p)^2 + f(V_k) \tag{1}$$

Where ρ is the density, ψ the Helmholtz free energy, K_b et K_a are the concrete stiffness and steel stiffness respectively, D is the total displacement, D^{π} is the displacement associated to frictional sliding, D^p is the steel plastic displacement, g(d) is a function insuring the coupling between the level of damage and the friction, in a first approximation it is chosen as g(d)=d, V_k are the other internal variable linked to hardening.

From this free energy, one can obtain the expressions of the state equations by simple derivatives. The total forces vectors are expressed below:

$$F = \rho\frac{\partial\Psi}{\partial D} = \underbrace{K_b(1-d)D + K_b d(D-D_{\pi})}_{Béton} + \underbrace{K_a(D-D_p)}_{Acier} \tag{2}$$

$$F_{\pi} = -\rho\frac{\partial\Psi}{\partial D_{\pi}} = dK_b(D-D_{\pi}) \tag{3}$$

$$F_a = -\rho\frac{\partial\Psi}{\partial D_p} = K_a(D-D_p) \tag{4}$$

And the damage energy release rate,

$$Y = \rho\frac{\partial\Psi}{\partial d} = -\frac{1}{2}K_b D^2 + \frac{1}{2}K_b(D-D_{\pi})^2 \tag{5}$$

3.2 Thresholds functions and evolution laws

To define the nonlinear evolutions, one has to define thresholds function. The model is based on damage mechanics, the first and major irreversible mechanisms to be checked is damage evolution. A simple law, based on the original work of [2] allows a simple damage threshold implying associated flow rule,

$$f_{di} = Y_{di} - (Z_i + Y_0) \tag{6}$$

Z_i is the thermodynamic variable associated to isotropic hardening and Y_0 is the initial threshold.

According to associated flow rule, the damage evolution for concrete may be simply and analytically integrated to obtain a direct computation of the damage variable,

$$d_i = 1 - \frac{1}{1 + pY_{di}{}^{q}} \tag{7}$$

Where q and p are material parameters to be identified.

Concerning permanent displacements and frictional sliding, a non associated flow rule based on the works of [3] introducing nonlinear evolutions for kinematic hardening has been adopted for this study. The friction threshold stands as,

$$f_\pi = \left| F_\pi - X_b \right| \tag{8}$$

With X_b the backstress for nonlinear kinematic hardening. The plastic potential is non associated and is classically expressed as,

$$\phi_\pi = \left| F_\pi - X_b \right| + \frac{a_b}{2} X_b^2 \tag{9}$$

The evolution laws are obtained thanks to normality rules applied to the plastic potential,

$$\dot{D}_\pi = \dot{\lambda}_\pi \frac{\partial \phi_\pi}{\partial F_\pi} \quad \dot{\alpha}_b = -\dot{\lambda}_\pi \frac{\partial \phi_\pi}{\partial X_b}, \tag{10}$$

The plastic multiplier is computed using iterative procedure based on return-mapping or Newton procedures.

3.3 Cyclic response

Standing as a first validation case-study, an experimental investigation has been performed on a slab-wall connection made of Shöck thermal bridge shunt elements. A double shear tests has been performed on a mock-up. To emphasize the seismic effect, a cyclic loading has been imposed to the sample (2.5 m long and 1.6 m large). The previous model has been used to simulate the global response and the load-displacement diagram is plotted in figure 9.

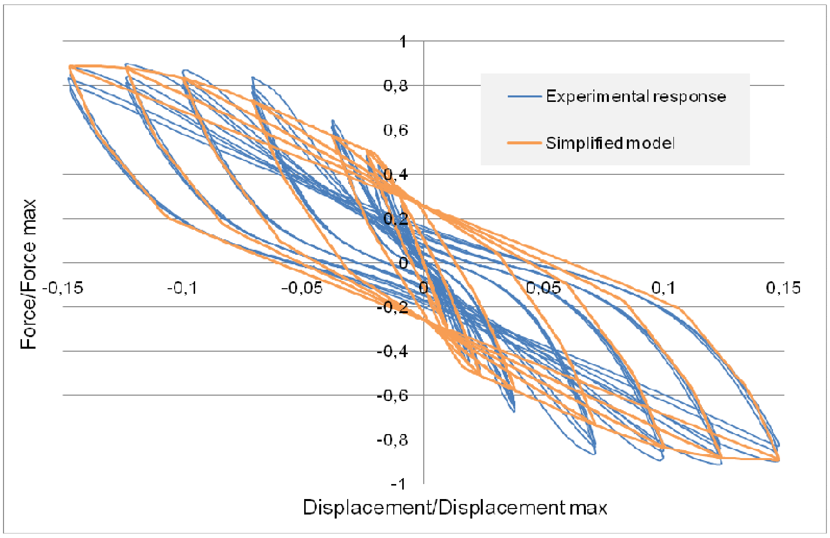

Figure 9: Cyclic loading on a Schöck thermal bridge shunt element. Comparisons between numerical simulations and experimental results.

4 CONCLUSIONS

Considering the nonlinear behavior of innovative wall-slab connection in buildings, an experimental and numerical analysis of the mechanical response of thermal bridge shunt elements is proposed in this work. The experimental part allowed assessing the ability for such structural elements to bear horizontal seismic loadings. Finite elements analysis based 3D nonlinear behaviors help one to discriminate the fundamental thermodynamic variables to be introduced and to evaluate their respective evolution laws linked to the global displacement. At last, a simplified model, based on the beam theory assumption is proposed to predict the nonlinear response of building connections subject to cyclic loading. The next step to achieve will be the assessment of building seismic vulnerability performing probabilistic and parametrical analysis.

REFERENCES

[1] B. Richard, F. Ragueneau, C. Crémona & L. Adelaide, Isotropic continuum damage mechanics for concrete under cyclic loading: stiffness recovery, inelastic strains and frictional sliding, Engineering Fracture Mechanics , 77(8), pp. 1203-1223, 2010.

[2] Laborderie C., 1991. Phénomènes unilatéraux dans un matériau endommageable, PhD thesis University Paris 6.

[3] Armstrong, P.J. & Frederick, C.O., 1966. A Mathematical Representation of the Multiaxial Bauschinger Effect, G.E.G.B., Report RD/B/N, 731.

COMPDYN 2011
III ECCOMAS Thematic Conference on
Computational Methods in Structural Dynamics and Earthquake Engineering
M. Papadrakakis, M. Fragiadakis, V. Plevris (eds.)
Corfu, Greece, 25–28 May 2011

A NEW METHOD OF GENERATION OF NONLINEAR NORMAL MODES FOR NONLINEAR DYNAMICS OF DISORDERED STRUCTURES

L. Facchini[1] , M. Rizzo[2]

[1]University of Florence,
Via S. Marta 3, 50139 Firenze, Italy.
e-mail: luca@dicea.unifi.it

[2]University of Florence,
Via S. Marta 3, 50139 Firenze, Italy.
e-mail: mrizzo@dicea.unifi.it

Keywords: Randomness, Non-linear Structural Dynamics, Invariant manifold.

Abstract. *Structural response can be affected by randomness under two different points of view – either in the forcing process and/or in the structural behaviour. Various approaches can be employed to investi-gate the structural response, among which polynomial chaos (Ghanem, Spanos [1]) and perturbation approaches (Liu et al. [2], Chiostrini and Facchini [3]) can be found.*

Both kinds of approaches require the investigation of the response variation in dependence on the (random) structural parameters, thus – often dramatically – increasing the number of degrees of freedom of the examined system.

In case of linearity of the system response, a modal reduction approach can be effectively employed together with perturbation techniques; on the other hand, for some kind of nonlinear systems, such reduction approach (Bucher [4], Geschwindner [5]) might fail to give satisfactory results unless a very large number of modes is employed in the analysis (Betti et al. [6]).

The task of reducing the number of degrees of freedom of nonlinear systems has therefore to be accomplished by means of alternative procedures, such as the introduction of nonlinear normal modes.

1 INTRODUCTION

Randomness can affect structural systems by several points of view; in particular, randomness can affect the forcing process that a system undergoes, or might as well influence the structural parameters.

The study of disordered systems, as such structures are usually referred to, is a point of concern in specialized literature: a fair amount of methods to investigate the dynamics of disordered structures can in fact be found.

One of the most common methods is taken into consideration in the present work: the first application is described in Liu et al. (1986), and subsequently enhanced in Chiostrini and Facchini (1999); it can be classified as a perturbation method and makes use of sensitivity vectors to evaluate the first two moments of the response.

Unfortunately, a severe drawback of the method is that the number of degrees of freedom of the examined structure grows rapidly for increasing number of random parameters, thus leading to the solution of very large (non) linear systems.

The idea that is introduced in the present work is to investigate the possibility to compute and apply the concept of nonlinear normal modes in order to reduce the number of degrees of freedom of the resulting system, as it has recently been examined by Rizzo (2007).

It is well known that the normal modes are of fundamental importance in the theory of linear dynamic conservative and non conservative systems, as the linear normal modes can be used to decouple the equations governing the motion and analytically evaluate the dynamic response of the examined system.

Such procedure is performed making use of modal analyses and the principle of superposition to express the response of the system as a time-dependent superposition of its modal shapes.

Clearly, such an approach is generally inapplicable in the nonlinear theory. Nevertheless, it is possible to define nonlinear normal modes (NNMs) as particular synchronous periodic solutions of the non-linear motion equations, but no link of such motions to the principle of superposition can be considered.

Several techniques can be found in specialized literature for determining the response of nonlinear systems; for free vibration problems system modes can be usefully employed to construct reduced order models: such procedures have been well developed for both linear and nonlinear systems by Vakakis (1997) and by Vakakis et al. (1996) .

One such technique, introduced by Shaw and Pierre (1991, 1993, 1993), defines the normal mode of a nonlinear oscillatory system in terms of invariant manifolds in the phase space that are tangent to the linear eigenmodes at the equilibrium point. In such a formulation, a master mode is selected, and the normal mode is constructed by a formulation in which the remaining linear modes of the system, i.e., the slave modes, depend on the master mode in a manner consistent with the system dynamics. This dependence defines the invariant manifold for the nonlinear normal mode (NNM).

The construction of the NNM invariant manifold is equivalent to the determination of the constraint relationships for all of the slave coordinates with the master coordinate; once these constraint relationships are obtained, the system dynamics can be restricted to the invariant manifold, resulting in a minimalsized model that depends only on the master coordinates. By studying the dynamics of the reduced-order model, it is possible to recover the associated modal dynamics of the original nonlinear system.

Pesheck et al. (2002) used numerical solutions of the invariant manifold equations to extend the invariant manifold approach to more general systems, including strongly nonlinear ones. In this approach, the master coordinates were expressed in polar coordinate form, and a Galerkin-based solution technique was introduced to solve the invariant manifold equations.

The present method differs from the work by present authors (2009), because the modal forms are only generated regarding the lagrangian coordinates and not regarding the total coordinate, including the derived to the first one and second order.

2 FORMULATION

A system endowed with a displacement dependent nonlinear restoring force which can be expressed by means of a nonlinear stiffness matrix is taken into consideration. The stiffness is affected by randomness in one or more of the defining parameters; such random parameters will be grouped together in the vector **b**.

In specialised literature a common approach for the study of the dynamic response of nonlinear systems is to express the dependence of the system response on the random parameters at each instant of the motion, and eventually combine such dependence with the probability distribution function of the random parameters themselves.

Several examples can be found of this approach. In the following, the method proposed by Liu *et al.* (1986) and successively modified and enhanced by Chiostrini and Facchini (1999) is considered.

Let the equation of motion of a N DOF disordered nonlinear system, where the nonlinear restoring forces depend on both the system response and the uncertain parameters grouped in the vector **b**, be given in the form:

$$\mathbf{M}\ddot{\mathbf{x}} + \mathbf{g}(\dot{\mathbf{x}}, \mathbf{x}, \mathbf{b}) = \mathbf{f}(t) \qquad \textbf{(1)}$$

The system velocity and displacement vectors are expressed by means of a second order expansion with respect to the mean value of the random parameter vector **b**:

$$x_h(t, \mathbf{b}) \cong \bar{x}_h(t) + \frac{\partial \bar{x}_h}{\partial b_i}\left(b_i - \bar{b}_i\right) + \frac{1}{2}\frac{\partial^2 \bar{x}_h}{\partial b_i \partial b_j}\left(b_i - \bar{b}_i\right)\left(b_j - \bar{b}_j\right) \qquad \textbf{(2)}$$

where the overbar denotes that the quantity is evaluated in correspondence of the expected value of the random parameters **b**. A completely analogous equation holds for the system velocity.

The response and its derivatives up to the second order can be evaluated by means of their respective equations of motion, obtained by differentiation of the system equation of motion, evaluated in correspondence of the expected values of the random vector **b**. Thus, the first group of equations is given by

$$\mathbf{M}\ddot{\bar{\mathbf{x}}} + \mathbf{g}\left(\dot{\bar{\mathbf{x}}}, \bar{\mathbf{x}}, \bar{\mathbf{b}}\right) = \mathbf{f}(t) \qquad \textbf{(3)}$$

while the second and third groups of equations can be obtained deriving equation (1) with respect to each component of vector **b** and considering again the expected value of the random vector:

$$\begin{aligned} \mathbf{M}\ddot{\bar{\mathbf{x}}},_{l} + \mathbf{C}_T\dot{\bar{\mathbf{x}}},_{l} + \mathbf{K}_T\bar{\mathbf{x}},_{l} &= \mathbf{f}_1(t) \\ \mathbf{M}\ddot{\bar{\mathbf{x}}},_{lm} + \mathbf{C}_T\dot{\bar{\mathbf{x}}},_{lm} + \mathbf{K}_T\bar{\mathbf{x}},_{lm} &= \mathbf{f}_2(t) \end{aligned} \qquad \textbf{(4)}$$

where

$$\mathbf{f}_1(t) = -\frac{\partial \mathbf{g}}{\partial b_l} \tag{5}$$

$$\mathbf{f}_2(t) = -\frac{\partial \mathbf{C}_T}{\partial b_m}\dot{\bar{\mathbf{x}}},_l - \frac{\partial \mathbf{K}_T}{\partial b_m}\bar{\mathbf{x}},_l - \frac{\partial \mathbf{C}_T}{\partial b_l}\dot{\bar{\mathbf{x}}},_m - \frac{\partial \mathbf{K}_T}{\partial b_l}\bar{\mathbf{x}},_m - \frac{\partial^2 \mathbf{g}}{\partial b_l \partial b_m}$$

The symbols $\mathbf{C}_T$ and $\mathbf{K}_T$ respectively denote the tangent damping and stiffness matrices, obtained by derivation of the nonlinear restoring function:

$$\mathbf{C}_T = \frac{\partial \mathbf{g}}{\partial \dot{\mathbf{x}}}; \quad \mathbf{K}_T = \frac{\partial \mathbf{g}}{\partial \mathbf{x}} \tag{6}$$

When the nonlinear restoring function can be expressed by only means of a response-dependent matrix times the displacement, as in:

$$\mathbf{g}(\dot{\mathbf{x}}, \mathbf{x}, \mathbf{b}) = \mathbf{g}(\mathbf{x}, \mathbf{b}) = \mathbf{K}(\mathbf{x}, \mathbf{b})\,\mathbf{x} \tag{7}$$

then the components of the tangent stiffness matrix and its derivatives can be obtained as:

$$K_{Tij} = \frac{\partial g_i}{\partial x_j} = \frac{\partial K_{ih}}{\partial x_j} x_h + K_{ij} \tag{8}$$

$$\frac{\partial g_i}{\partial b_l} = \frac{\partial K_{ij}}{\partial b_l} x_j; \quad \frac{\partial^2 g_i}{\partial b_l \partial b_m} = \frac{\partial^2 K_{ij}}{\partial b_l \partial b_m} x_j$$

$$\frac{\partial K_{T\,ij}}{\partial b_l} = \frac{\partial^2 K_{ih}}{\partial b_l \partial x_j} x_h + \frac{\partial^2 K_{ih}}{\partial x_m \partial x_j}\frac{\partial x_m}{\partial b_l} x_h +$$

$$+ \frac{\partial K_{ih}}{\partial x_j}\frac{\partial x_h}{\partial b_l} + \frac{\partial K_{ij}}{\partial b_l} + \frac{\partial K_{ij}}{\partial x_m}\frac{\partial x_m}{\partial b_l}$$

and equation (4) can be simplified in the following form:

$$\mathbf{M}\ddot{\bar{\mathbf{x}}},_l + \mathbf{K}_T \bar{\mathbf{x}},_l = -\frac{\partial \mathbf{g}}{\partial b_l} \tag{9}$$

$$\mathbf{M}\ddot{\bar{\mathbf{x}}},_{lm} + \mathbf{K}_T \bar{\mathbf{x}},_{lm} = -\frac{\partial \mathbf{K}_T}{\partial b_m}\bar{\mathbf{x}},_l - \frac{\partial \mathbf{K}_T}{\partial b_l}\bar{\mathbf{x}},_m - \frac{\partial^2 \mathbf{g}}{\partial b_l \partial b_m}$$

Equation (3) together with (4) or (8) define a set of a total of $N\left(1 + N_b + N_b^2\right)$ scalar equations which give the evolution in time of the system response and its derivatives with respect to the random parameters. N_b is in fact the number of the random parameters of the system, which correspond to the dimension of vector **b**.

For systems with many degrees of freedom, affected by randomness in one or more parameters, the number of equations grows in a way that can be hardly manageable by current computers. In order to reduce the number of equations, the non-linear normal modes of the system can be introduced.

The approach followed in the application was introduced by a series of works by Shaw and Pierre (1991, 1993, 1993).

The new formulation, regarding the work by present authors (2009), regards the resolution of the equations (7) and (7). This equations can be resolved separately. Only the equations (7) can be resolved with the use of non-linear normal mode instead the equations (7), which are decoupled from the (7) , with a non linear dynamic analysis.

The first group of equations can be resolved by a non-linear normal mode approach by means of the explicitation of the linear part of the equations of motion. The modal shapes and associated eigenfrequencies of the linearized system can be calculated, and the LHS term of system **Errore. L'origine riferimento non è stata trovata.** can be diagonalized, obtaining

$$\ddot{\boldsymbol{\eta}} + \boldsymbol{\Omega}\boldsymbol{\eta} = \mathbf{f}(\boldsymbol{\eta}) \qquad \textbf{(10)}$$

where $\boldsymbol{\eta} = \boldsymbol{\Phi}\mathbf{y}$ is the vector of the principal coordinates, $\boldsymbol{\Phi}$ is the matrix containing the linearized modal shapes of the system **Errore. L'origine riferimento non è stata trovata.** and $\boldsymbol{\Omega}$ is a diagonal matrix whose elements are ω_k^2.
If η_m denotes the master degree of freedom, its evolution in time is described by the expression:

$$\begin{aligned} \eta_m &= a\cos\phi \\ \dot{\eta}_m &= -a\omega_m \sin\phi \end{aligned} \qquad \textbf{(11)}$$

and the remaining "slave" degrees of freedom are expressed in terms of the master amplitude and phase as

$$\begin{aligned} \eta_i &= P_i(a,\phi) \\ \dot{\eta}_i &= Q_i(a,\phi) \end{aligned} \qquad \textbf{(12)}$$

The time evolution of the master amplitude and phase can be expressed by the relations

$$\begin{aligned} \dot{a} &= -\frac{f_m(\boldsymbol{\eta})}{\omega_m}\sin\phi \\ \dot{\phi} &= \omega_m - \frac{f_m(\boldsymbol{\eta})}{a\omega_m}\cos\phi \end{aligned} \qquad \textbf{(13)}$$

and also the evolution of functions P_i and Q_i in equations (12) can be obtained by the diagonalized system (10) in the form

$$\begin{aligned} \dot{P}_i(a,\phi) &= Q_i(a,\phi) \\ \dot{Q}_i(a,\phi) &= f_i(\boldsymbol{\eta}) - \omega_i^2 P_i(a,\phi) \end{aligned} \qquad \textbf{(14)}$$

Functions P_i and Q_i in equations (12) can be expressed in incremental terms, obtaining first order differential equations where the independent variable is time:

$$\begin{aligned} \dot{P}_i(a,\phi) &= \frac{\partial P_i}{\partial a}\dot{a} + \frac{\partial P_i}{\partial \phi}\dot{\phi} \\ \dot{Q}_i(a,\phi) &= \frac{\partial Q_i}{\partial a}\dot{a} + \frac{\partial Q_i}{\partial \phi}\dot{\phi} \end{aligned} \qquad \textbf{(15)}$$

When the system is subject to free oscillations and therefore $\mathbf{f}(t) = \mathbf{0}$ in equations (1) and **Errore. L'origine riferimento non è stata trovata.**, by means of the substitution of equations (13) and (14) into (15), first order differential equations are obtained for the first derivatives of functions P_i and Q_i, which are independent of time. Such equations describe the geometry of the considered non normal mode (see Pesheck *et al.* (2002) for details):

$$
\begin{aligned}
Q_i(a,\phi) &= -\frac{\partial P_i}{\partial a}\frac{f_m(\boldsymbol{\eta})}{\omega_m}\sin\phi + \frac{\partial P_i}{\partial \phi}\left[\omega_m - \frac{f_m(\boldsymbol{\eta})}{a\omega_m}\cos\phi\right] \\
f_i(\boldsymbol{\eta}) - \omega_i^2 P_i(a,\phi) &= -\frac{\partial Q_i}{\partial a}\frac{f_m(\boldsymbol{\eta})}{\omega_m}\sin\phi + \frac{\partial Q_i}{\partial \phi}\left[\omega_m - \frac{f_m(\boldsymbol{\eta})}{a\omega_m}\cos\phi\right]
\end{aligned} \tag{16}
$$

When the evaluation of the non normal mode is completely performed, the corresponding vector **y** can be evaluated by means of

$$
\begin{aligned}
\mathbf{y} &= \boldsymbol{\Phi}^t \boldsymbol{\eta} = \\
&= \boldsymbol{\Phi}^t \left[P_1 \quad \cdots \quad P_{m-1} \quad a\cos\phi \quad P_{m+1} \qquad P_{N_{tot}}\right]
\end{aligned} \tag{17}
$$

The projection in the lagrangian coordinates $\bar{\mathbf{x}}$ and the resolution of the second group of equations (13) gives the desired approximation for the dependence of the system response **x** on the random parameters vector **b**.
As outlined in the works of Liu *et al.* (1986) and Chiostrini and Facchini (1999), the response statistics can be obtained by

$$
\begin{aligned}
\mu_{x_h} &\cong \bar{x}_h(t) + \frac{1}{2}\frac{\partial^2 \bar{x}_h}{\partial b_i \partial b_j} E\left[\left(b_i - \bar{b}_i\right)\left(b_j - \bar{b}_j\right)\right] \\
\sigma_{x_h}^2 &\cong \frac{\partial \bar{x}_h}{\partial b_i}\frac{\partial \bar{x}_h}{\partial b_j} E\left[\left(b_i - \bar{b}_i\right)\left(b_j - \bar{b}_j\right)\right]
\end{aligned} \tag{18}
$$

3 APPLICATION

The method's application in the present work is make with the use of a multidimensional Duffing equation:

$$
\mathbf{M}\ddot{\mathbf{x}} + \mathbf{K}\mathbf{x} + \lambda(\mathbf{x}^{\mathbf{t}}\mathbf{C}\mathbf{x})\mathbf{K}\mathbf{x} = \mathbf{0} \tag{19}
$$

In the *2*DOF system used **M**=[1 0;0 2], **K**=[10 -5;-5 5], **C**=[1 -0.5;-0.5 1] and λ_m=0.001 and 0.01.

$$
\mathbf{M}\ddot{\mathbf{x}} + \mathbf{K}(1 + \lambda_m \mathbf{x}^t\mathbf{C}\mathbf{x})\mathbf{x} = \mathbf{0} \tag{20}
$$

$$
\begin{aligned}
&\mathbf{M}\ddot{\mathbf{x}},_{\lambda} + \mathbf{K}\left[\mathbf{x}^t\mathbf{C}\mathbf{x} + \lambda_m(\mathbf{x},_{\lambda}^t \mathbf{C}\mathbf{x} + \mathbf{x}^t\mathbf{C}\mathbf{x},_{\lambda})\right]\mathbf{x} + \\
&+ \mathbf{K}(1 + \lambda_m \mathbf{x}^t\mathbf{C}\mathbf{x})\mathbf{x},_{\lambda} = \mathbf{0}
\end{aligned} \tag{21}
$$

$$
\begin{aligned}
&\mathbf{M}\ddot{\mathbf{x}},_{\lambda\lambda} + \mathbf{K}\left[2\mathbf{x},_{\lambda}^t \mathbf{C}\mathbf{x} + 2\mathbf{x}^t\mathbf{C}\mathbf{x},_{\lambda} + \lambda_m(\mathbf{x},_{\lambda\lambda}^t \mathbf{C}\mathbf{x} + 2\mathbf{x},_{\lambda}^t \mathbf{C}\mathbf{x},_{\lambda} + \mathbf{x}^t\mathbf{C}\mathbf{x},_{\lambda\lambda})\right]\mathbf{x} \\
&+ 2\mathbf{K}\left[\mathbf{x}^t\mathbf{C}\mathbf{x} + \lambda_m(\mathbf{x},_{\lambda}^t \mathbf{C}\mathbf{x} + \mathbf{x}^t\mathbf{C}\mathbf{x},_{\lambda})\right]\mathbf{x},_{\lambda} + \\
&+ \mathbf{K}(1 + \lambda_m \mathbf{x}^{\mathbf{t}}\mathbf{C}\mathbf{x})\mathbf{x},_{\lambda\lambda} = \mathbf{0}
\end{aligned} \tag{22}
$$

The groups of equations (13), (13) and (13) are solved separately; in the first is solved the system (13) and the linear system associated gives ω_1=1.047 rad/s, ω_2= 3.377 rad/s and **Φ**=[0.369 -0.929; 0.657 0.261].

The non-linear mode shapes are generated for the first group of equation while the second and third group of equations are solved directly integrating the differential equations. this is possible because the first group of equations does not depend from the derivate ones of x. A possible future development of the method is to resolve also according to group and the third by means of use of the NNMs.

The application is made with λ_m=0.001 and are showed in figure 1, while the application with λ_m=0.01 in figure 2. The numeric simulation for the free oscillation are showed in figure 3 and 4 for λ_m=0.001 and for λ_m=0.01.

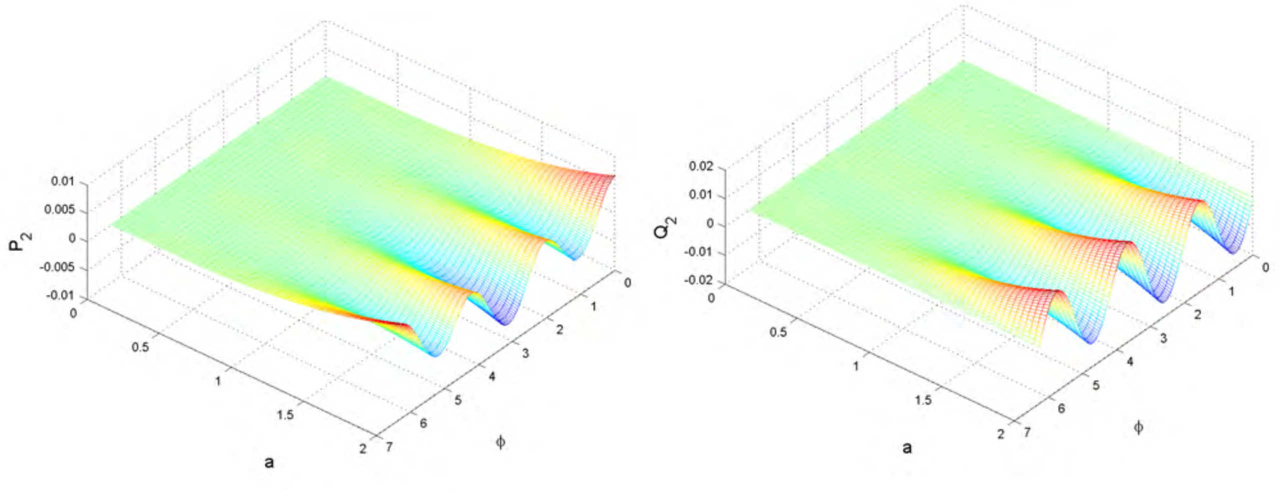

Figure 1. Non linear modal shape P_2 Q_2 for λ_m =0.001 and N_a=2, N_ϕ=4.

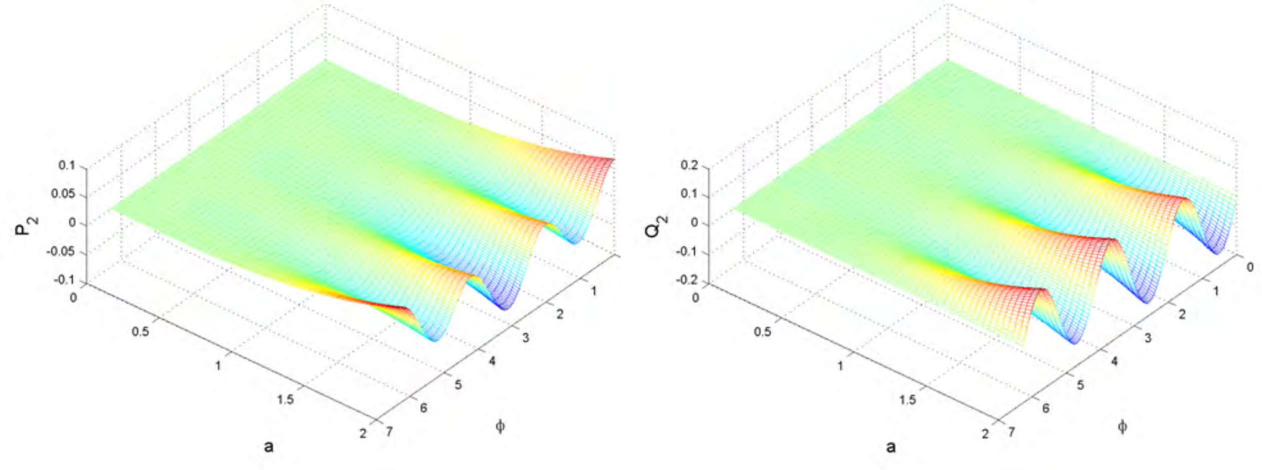

Figure 2. Non linear modal shape P_2 Q_2 for λ_m =0.01 and N_a=2, N_ϕ=4.

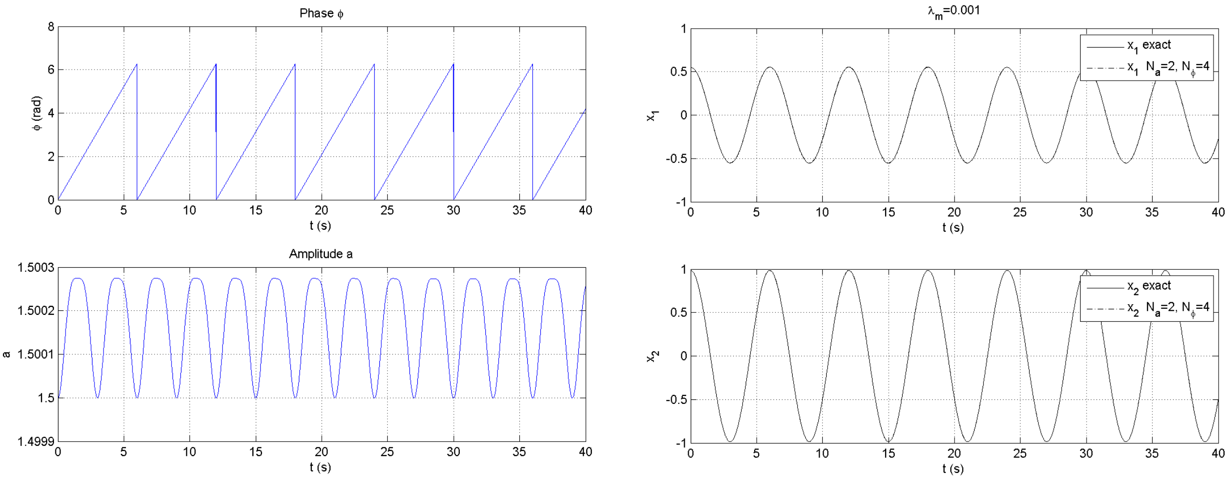

Figure 3. Numerical simulation of the amplitude *a* and ϕ and the system response **x**(t)

obtained imposing λ_m=0.001.

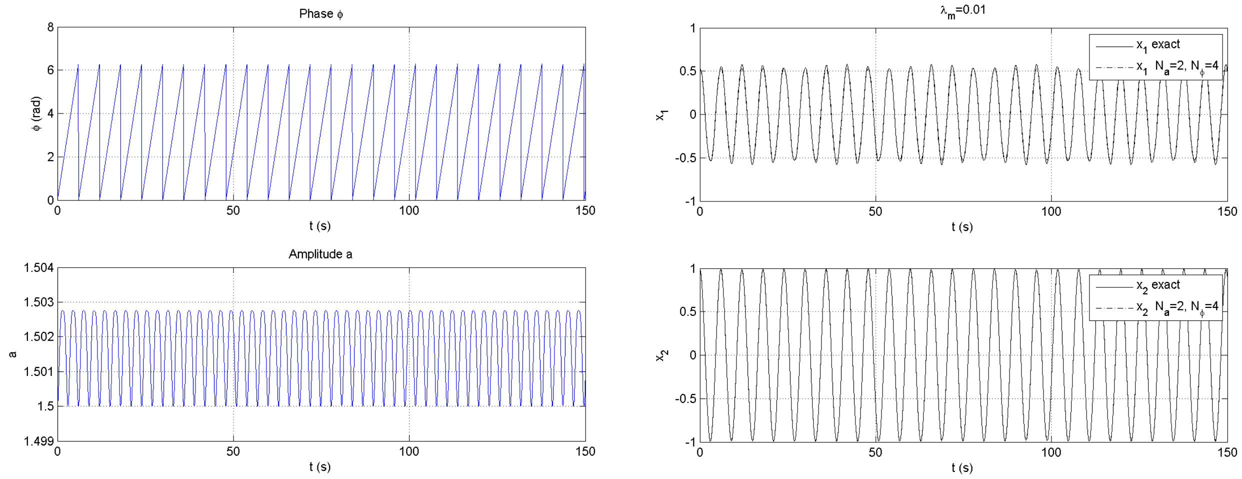

Figure 4. Numerical simulation of the amplitude *a* and ϕ and the system response **x**(t)

obtained imposing λ_m=0.01.

The method that uses the NNM's and the exact simulations in figure 3 and 4 gives results indistinguishable. In order to gain the expected value and the standard deviation of the variable ones x_1 and x_2 the following approximations in the works of Liu *et al*. (1986) and Chiostrini and Facchini (1999) are used:

$$E[x] = x(\varepsilon_m) + \frac{1}{2} x_{,\varepsilon\varepsilon} \cdot \sigma_\varepsilon^2; \quad \textbf{(23)}$$

$$\sigma_x^2 \cong x_{,\varepsilon}^2 \cdot \sigma_\varepsilon^2; \quad \textbf{(24)}$$

$$x \cong x(\varepsilon_m) + (\varepsilon - \varepsilon_m) \cdot x_{,\varepsilon} + \frac{1}{2} x_{,\varepsilon\varepsilon} \cdot (\varepsilon - \varepsilon_m)^2. \quad \textbf{(25)}$$

In the following figures the variations of x_1 are brought back and x_2 regarding λ and variable t. The variation coefficient used in the numerical simulations is 50%.

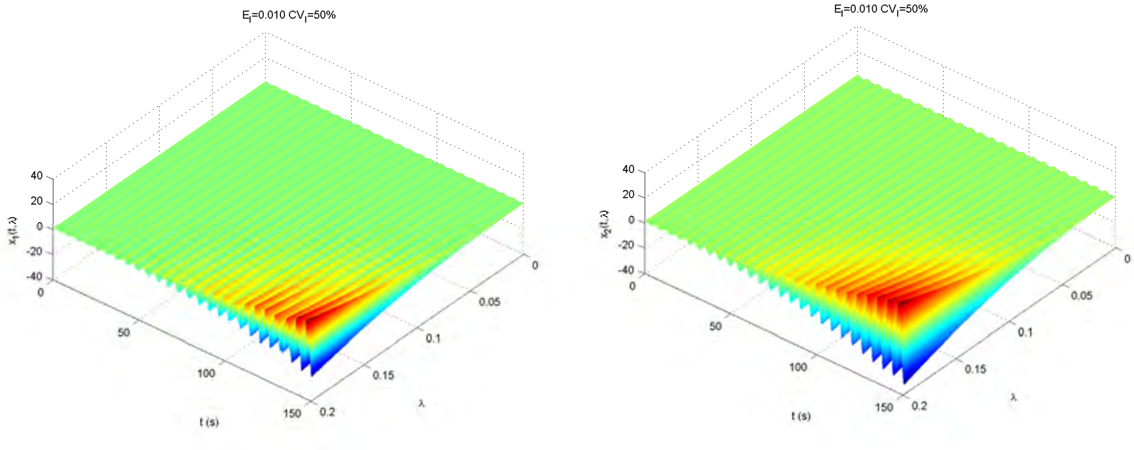

Figure 5. Numerical simulation of the system response $\mathbf{x_1}(t, \lambda)$ and $\mathbf{x_2}(t, \lambda)$ obtained with $\lambda_m = 0.01$.

In order to confront the method we have been simulated 1000 dynamic analyses with λ_m=0.01 and coefficient of variation 50%. In figure 6 the corresponding probability distribution is brought back.

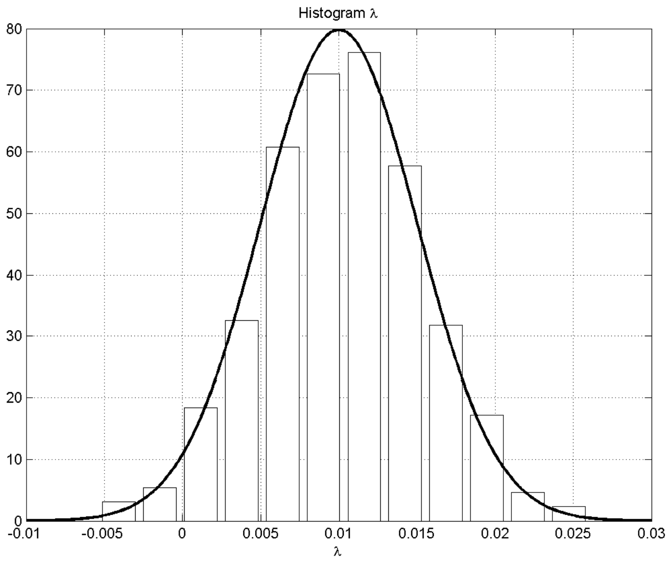

Figure 6. Normal probability distribution for the numerical simulation with $\lambda_m = 0.01$ and CV 50% .

The comparison between the adopted method and the simulations random is shown in the following figures. The method that uses the NNM's and the simulations random gives results indistinguishable.

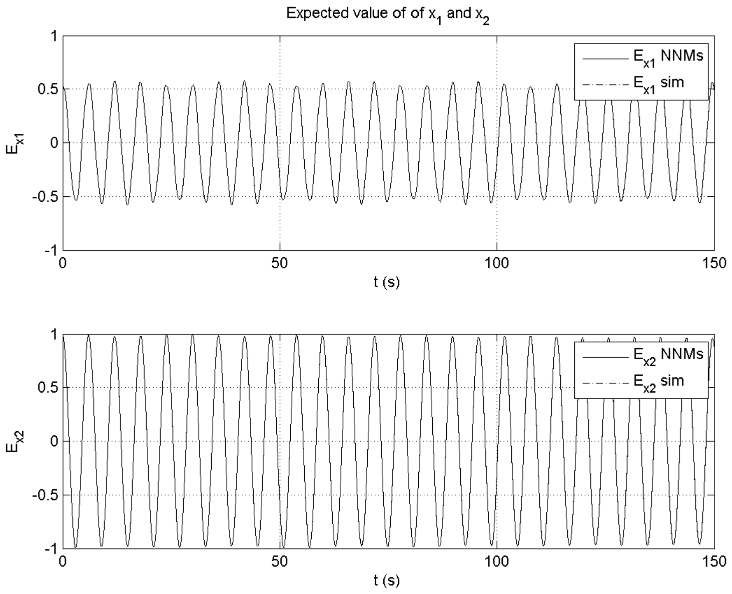

Figure 7. Numerical simulation of the expected value system response E$\mathbf{x_1}$ and E$\mathbf{x_2}$ obtained with λ_m =0.01 .

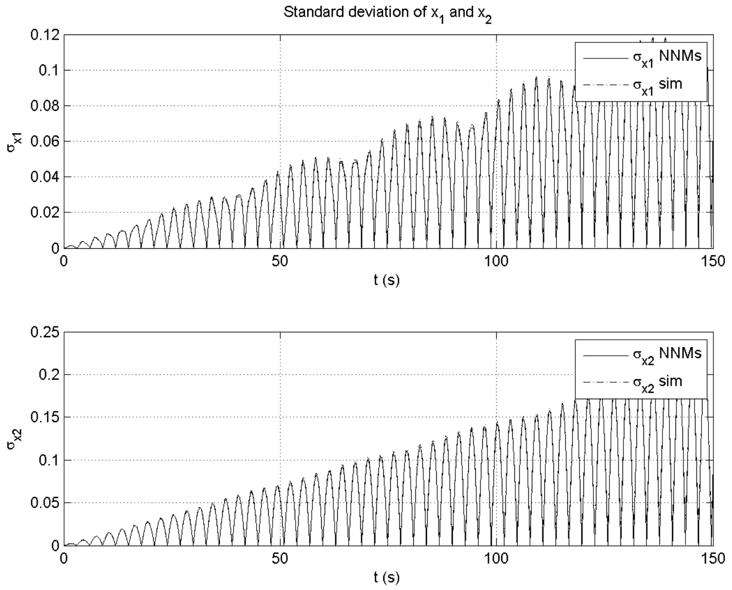

Figure 8. Numerical simulation of the standard deviation of the system response $\sigma\mathbf{x_1}$ and $\sigma\mathbf{x_2}$ obtained with λ_m =0.01 .

4 CONCLUSIONS

In the present formulation is developed a new approach that can be effectively used for the solution of the non linear dynamics of large disordered structures, when the number of degrees of freedom considerably increase owing to the presence of randomness.

The most severe problem in the present formulation is to obtain numerically the non linear modal shapes, therefore future developments of the present method will be devoted to finding a more efficient numerical method to obtain the NNM’s.

REFERENCES

[1] Ghanem R., Spanos P.D. (1991). Stochastic finite elements: a spectral approach. Springer-Verlag New York Inc., New York, 1991.

[2] Liu, W. K., Belytschko, T., Mani, A. (1986). “Probabilistic finite elements for nonlinear structural dynamics” Comp. Meth. Appl. Mech. Engng., 56, pp. 61-81, 1986.

[3] Chiostrini S., Facchini L. (1999). “Response analysis under stochastic loading in presence of structural uncertainties”, International Journal for Numerical Methods in Engineering, 46, 853-870.

[4] Bucher C. (2001). “Stabilization of explicit time integration by modal reduction”, Trends in Computational Structural Mechanics, W.A. Wall, K.-U. Bletzinger, K. Schweizerhof eds. © CIMNE, Barcelona, Spain 2001, 429-437.

[5] Geschwindner L. F. (1981). “Nonlinear dynamic analysis by modal superposition”, Journal of the Structural Division, proc. ASCE, vol. 107, no. ST12.

[6] Betti M., Biagini P., Facchini L. (2005). “Stochastic dynamics of complex uncertain systems by means of a conditional – Galerkin – RBF approach”, Proceedings of Structural Dy-namics – Eurodyn 2005, Paris, 4-7 september 2005.

[7] Shaw S.W. and Pierre C. (1994). “Normal modes of vibration for non-linear continuous systems”, Journal of Sound and Vibration, 169, 319-347.

[8] Pesheck E., Pierre C., Shaw S.W. (2002). “A new Galerkin based approach for accurate non-linear normal mode through invariant manifolds”, Journal of Sound and Vibration, 249 (5), 971-993.

[9] Facchini L., Rizzo M. (2009). “Dynamics of nonlinear disordered structures by means of nonlinear normal modes”, Proceeding of ICOSSAR 2009, Safety, Reliability and risk of structures, infrastructures and engineering systems, Furuta Frangopol Shinozuka Editors, Osaka, 13-17 September 2009.

[10] Bellizzi S., Robert Bouc R. (2005) “A new formulation for the existence and calculation of nonlinear normal modes“, Journal of Sound and Vibration 287, 545–569.

COMPDYN 2011
III ECCOMAS Thematic Conference on
Computational Methods in Structural Dynamics and Earthquake Engineering
M. Papadrakakis, M. Fragiadakis, V. Plevris (eds.)
Corfu, Greece, 25–28 May 2011

A COMPARATIVE STUDY OF UNCERTAINTY PROPAGATION METHODS IN STRUCTURAL PROBLEMS

Manuele Corradi, Marco Gherlone, Massimiliano Mattone and Marco Di Sciuva

Department of Aeronautics and Space Engineering – Politecnico di Torino
Corso Duca degli Abruzzi 24, 10129, Torino, Italy
{manuele.corradi, marco.gherlone, massimiliano.mattone, marco.disciuva}@polito.it

Keywords: Uncertainty Propagation, Epistemic Uncertainty, Aleatory uncertainty, UDR, PCE, FOSM, Evidence theory.

Abstract. Several uncertainty propagation algorithms are available in literature: (i) Monte-Carlo simulations based on response surfaces, (ii) approximate uncertainty propagation algorithms and (iii) non probabilistic algorithms. All of these approaches are based on some a priori assumptions about the nature of design variables uncertainty and on the models and systems behavior. Some of these assumptions could misrepresent the original problem and, consequently, could yield to erroneous design solutions, in particular where the prior information is poor or inexistent (complete ignorance). Therefore, when selecting a method to solve an uncertainty based design problem, several aspects should be considered: prior assumptions, non-linearity of the performance function, number of input random variables and required accuracy. It could be useful to develop some guidelines to choose an appropriate method for a specific situation.

In the present work some classical structural problems will be studied in order to investigate which probabilistic approach, in terms of accuracy and computational cost, better propagates the uncertainty from input to output data. The methods under analysis will be: Univariate Dimension Reduction methods, Polynomial Chaos Expansion, First-Order Second Moment method, and algorithms based on the Evidence theory for epistemic uncertainty. The performances of these methods will be compared in terms of moment estimations and probability density function construction corresponding to several scenarios of reliability based design and robust design. The structural problems presented will be: (1) the static, dynamic and buckling behavior of a composite plate, (2) the reconstruction of the deformed shape of a structure from measured surface strains.

1 INTRODUCTION

The design for reliability, as well as robust design, is phased in over last decades in the structural design. Although these concepts are well-known in many engineering fields, the high computational cost of the mathematical approaches needed to perform these kinds of analysis, have set back their application in the aerospace structural design. Although in this last field, the problems that deal with the input variable uncertainties are known since the beginning of the aviation history, they are coped with deterministic methods based on the safety factor approach. The diffusion of components based on composite materials, in secondary and primary aerospace structures, and the dropping of aerospace and aviation companies' profit have reawaken the interest in design philosophies that deal with the uncertainty in a more effective way. For this reason, mathematicians and researchers have been urged on the study of new numerical approaches for an accurate Uncertainty Propagation (UP) from input to output data. Traditionally, both the reliability and the robustness of a design configuration have been studied using the Montecarlo simulation; although it is the most accurate method, its computational cost could be prohibitive. For this reason several alternative approaches have been developed to face UP.

Most of the available UP algorithms have particular characteristics that make them appropriate for some specific problems but their capabilities are not fully exploited in all kinds of applications. First of all it is possible to distinguish between algorithms for the study of aleatory uncertainty and approaches that deal with the epistemic uncertainty. This classification can be based on the prior hypotheses needed to simulate the prior uncertainty. In order to model the epistemic uncertainty by means of probabilistic (aleatory) algorithms, some prior hypotheses should be adopted to transform the epistemic information into a probability distribution function (epistemic algorithms do not need such assumptions). On the other hand, a probabilistic problem may be studied by means of an epistemic algorithm if the prior probability density functions are transformed into set-based information.

The UP algorithms based on the probability theory are usually classified into five categories [1]: 1) Simulation based methods: these techniques are based on the simulation of the problem in proper trial points, selected according to the stochastic characteristics of the input variables. MonteCarlo Simulation (MCS) is certainly the most known and used of these methods. 2) Local expansion based methods: these algorithms, also known as perturbation methods, are based on the local series expansion of output functions in terms of input random parameters. The methods based on Taylor expansion, such as the FOSM (First Order Second Moment) or the SOSM (Second Order Second Moment) methods, belong to this class. 3) Most Probable Points (MPP) based methods: this class includes the First and Second Order Reliability Methods (FORM and SORM, respectively). 4) Functional expansion based methods: they rely on a stochastic expansion of the performance function. The most known method of this class is the Polynomial Chaos Expansion (PCE). 5) Numerical integration based methods: these techniques are based on the numerical solving of integral equations for the statistical moments. These methods don't yield directly the performance joint probability function, but the corresponding statistical moments; by using the Pearson System and knowing the first four statistical moments, the probability distribution function can be obtained.

Several factors affect the choice of a suitable UP approach: (i) the identification and the classification of the input uncertainty, (ii) the definition of the required outputs (the first two statistical moments in robust design and the probability density function or the most probable points in a reliability based analysis),(iii) and the mathematical characteristics of the studied model (if the first order interactions cannot be neglected the Univariate Dimension Reduction method does not yield accurate prediction while the performance function is non linear the methods based in Taylor local expansion are not accurate). This last information can be obtained using some numerical tools, such as the sensitivity analysis.

The main objective of this work is a comparative study of some of the most common and newest UP algorithms for both aleatory and epistemic uncertainties. As far as the first ones, the limits and merits of the Univariate Dimension Reduction method (UDR), of the Polynomial Chaos Expansion (PCE), and of the First Order Second Moments algorithm (FOSM) will be analyzed and discussed. These methods will be tested and compared on some numerical test functions and a classical structural problem: the probabilistic study of static, dynamic and buckling behavior of a composite plate. The sensitivity analysis has been performed in order to study the mathematical characteristics of the model. In the second part of the present work a probabilistic approach based on the UDR is compared with an epistemic approach based on the evidence theory. The structural application used as a test case for the comparison is an inverse problem: reconstruction of the deformed shape of a beam from measured surface strains using the inverse Finite elements Method (iFEM) [2][3].

2 UNCERTAINTY PROPAGATION ALGORITHMS

In this section, a review of some uncertainty propagation algorithms will be presented in order to set the framework for the assessment and comparison, through some structural applications, discussed in Sec. 3.

2.1 The Univariate Dimension Reduction method (UDR)

This method involves an additive decomposition of a multidimensional integral function to multiple one-dimensional integral functions. The technique is suitable for calculating the stochastic moments of a system response function, as Rahman and Xu have shown [4]-[6].
The stochastic moments of a probability distribution may be calculated as follows

$$m_l = \zeta[Y^l(X)] = \int_{-\infty}^{+\infty} \ldots \int_{-\infty}^{+\infty} y^l(X) f_X(X) dx \qquad l = 0,1,\ldots\ldots,m \tag{1}$$

where m_l is the lth-order statistical moment (i.e., m=1 is the mean value, m=2 is the variance, etc.), $f_X(X)$ is the system response joint probability density function, $y(X)$ is the deterministic response when the input variables assume the values collected in the vector $X = \{x_1,\ldots\ldots\ldots,x_n\}^T$, and $Y(X) = y^l(X) f_X(X)$ is the performance function. The latter can be approximated as the sum of univariate functions, each one depending on only one random variable at a time and the other variables being fixed to nominal values

$$Y(x_1,\ldots\ldots,x_n) \cong \widetilde{Y}(X) \equiv \sum_{j=1}^{N} Y(\mu_1,\ldots,\mu_{j-1},x_j,\mu_{j+1},\ldots.,\mu_N) - (N-1)\cdot y(\mu_1,\ldots\ldots,\mu_N) \tag{2}$$

where μ_j is the first moment of the stochastic variable x_j, $Y(\mu_1,\ldots,\mu_{j-1},x_j,\mu_{j+1},\ldots,\mu_N)$ is the stochastic response of the system only depending on the x_j random variable, and $y(\mu_1,\ldots.,\mu_N)$ is the deterministic response of the system depending on the nominal value of the N input variables. Adopting the dimension-reduction procedure, the expression of statistical moments (1) can be rewritten as:

$$m_l = \int_{-\infty}^{+\infty} \dots \int_{-\infty}^{+\infty} \sum_{j=1}^{N} \left(Y\left(\mu_1, \dots, \mu_{j-1}, x_j, \mu_{j+1}, \dots, \mu_N\right) - (N-1) \cdot y\left(\mu_1, \dots, \mu_N\right) \right)^l dx \tag{3}$$

To solve the univariate integration in the context of the UDR method, Xu and Rahman [4] suggest the use of the moment based quadrature rule. The evaluation of integration points x_j involves the solution of the following equation

$$x_j^n - r_{j,1} x_j^{n-1} + r_{j,2} x_j^{n-2} - \dots + (-1)^n r_{j,n} = 0 \tag{5}$$

where the coefficients r_j are solution of the following linear system of equations

$$\begin{bmatrix} \mu_{j,n-1} & -\mu_{j,n-2} & \mu_{j,n-3} & \dots & (-1)^{n-1}\mu_{j,0} \\ \mu_{j,n} & -\mu_{j,n-1} & \mu_{j,n-2} & \dots & (-1)^{n-1}\mu_{j,1} \\ \mu_{j,n+1} & -\mu_{j,n} & \mu_{j,n-1} & \dots & (-1)^{n-1}\mu_{j,2} \\ \dots & \dots & \dots & \dots & \dots \\ \mu_{j,2n-2} & -\mu_{j,2n-3} & \mu_{j,2n-4} & \dots & (-1)^{n-1}\mu_{j,n-1} \end{bmatrix} \begin{bmatrix} r_{j,1} \\ r_{j,2} \\ r_{j,3} \\ \dots \\ r_{j,n} \end{bmatrix} = \begin{bmatrix} \mu_{j,n} \\ \mu_{j,n+1} \\ \mu_{j,n+2} \\ \dots \\ \mu_{j,2n-1} \end{bmatrix} \tag{6}$$

$\mu_{j,i}$ $(i = 1, \dots, n)$ represents the i^{th} stochastic moment of the j^{th} input variable. Thus, the univariate integral can be numerically solved as

$$\int_{-\infty}^{\infty} y^l\left(\mu_1, \dots, x_j, \dots, \mu_N\right) f_{X_j}\left(x_j\right) \cdot dx_j \cong \sum_{i=1}^{n} w_{j,i} y^l\left(\mu_1, \dots, x_j, \dots, \mu_N\right) \tag{7}$$

where f_{x_j} is the probability density function of input variable x_j. The weight $w_{j,i}$ appearing in Eq. (7) are evaluated using the following expression:

$$w_{i,j} = \frac{\sum_{k=0}^{n-1} (-1)^k \mu_{j,(n-h-1)} \cdot q_{j,(ik)}}{\prod_{k=1,k\neq 1}^{n} \left(x_{j,i} - x_{j,k}\right)} \qquad q_{j,i_0} = 1\,;\; q_{j,ik} = r_{j,k} - x_{j,i} \cdot q_{j,i(k-1)} \tag{8}$$

2.2 The Polynomial Chaos Expansion (PCE)

The Polynomial Chaos Expansion was introduced by Wiener [7] and is based on the approximation of each random variable by means of a suitable polynomial expansion about centered normalized Gaussian variables.

Any set $X = \{x_1, \dots, x_n\}^T$ of independent Gaussian variables can be expressed as function of a set $\xi = \{\xi_1, \dots, \xi_n\}$ of independent normal variables

$$X = f(\xi) \tag{9}$$

Hence, a performance function $y = Y(X)$ could be transformed into a function expressed in terms of ξ and, afterwards, approximated by means of the Polynomial Chaos Expansion (PCE) on the vector space

$$Y(X) = a_0\Gamma_0 + \sum_{i_1=1}^{\infty} a_{i_1}\Gamma_1(\xi_1) + \sum_{i_1=1}^{\infty}\sum_{i_2=1}^{i_1} a_{i_1 i_2}\Gamma_2(\xi_{i_1},\xi_{i_2}) + \sum_{i_1=1}^{\infty}\sum_{i_2=1}^{i_1}\sum_{i_3=1}^{i_2} a_{i_1 i_2 i_3}\Gamma_3(\xi_{i_1},\xi_{i_2},\xi_{i_3}) + \dots \tag{10}$$

where $a = [a_0,.....,a_n]$ is the vector of the expansion unknown terms and $\Gamma_p(\xi_1,......,\xi_n)$ are the multidimensional Hermite polynomials (only if the input random variables are defined by a normal probability distribution) of order p.

Cameron and Martin have shown that this kind of series is convergent in the L_2-sense [8]. In order to simplify the notation a univocal relation between the functional Γ and a new functional Ψ is defined. Hence, the PCE expansion, expressed by Eq. (10), can be rewritten as follows

$$Y(X) = \sum_{k=0}^{\infty} \beta_k \Psi_k(\xi(X)) \tag{11}$$

In the present work the classical convention is adopted:

- $\Psi_0 = 1$: is the 0th-order polynomial
- β_k are the constant coefficients of the expansion
- Ψ_k are multivariate Hermite polynomials, orthogonal in the L_2-space. These polynomials are the product of the proper set of univariate Hermite polynomials [9].

The expansion is normally truncated at a selected order *P*

$$Y(X) \approx \hat{Y}(X) = \sum_{k=0}^{P} \beta_k \Psi(\xi)_k \tag{12}$$

The number of unknown coefficients β_k (*13*) can be evaluated using the following expression

$$P + 1 = \frac{(p+n)!}{p!n!} \tag{13}$$

The procedure described above is general, but the Hermite polynomials can be used only in the cases of input variables with Gaussian probability distribution function. Xiu and Karniadakis [9] have extended the PCE applicability to all kinds of input distribution function, adopting the Wiener-Askey scheme for non Gaussian input distribution. They have proposed to use the Askey scheme to combine the non Gaussian input distribution with orthogonal polynomial family; in this way the expansion convergence for all kind of input PDF. As well as the Hermitte polynomials are orthogonal in the Hilbert space, in the same way all polynomials, adopted in the Wiener-Askey [9] scheme are orthogonal in the Hilbert space and form an Hilbert basis of the corresponding space.

The set $\beta = \{\beta_0,.......\beta_n\}^T$ of the PCE unknown coefficients, can be approximated by a new vector $\hat{\beta}$, obtained solving the following least squares problem

$$\hat{\beta} = \arg\min_{\beta} \sum_{i=1}^{N} \left(Y(X_i) - \sum_{k=0}^{P} \beta_k \psi_k(\xi_i) \right)^2 \tag{12}$$

where N is the training points set size; generally, it is convenient that $N > p+1$.

2.3 The First Order Second Moment algorithm (FOSM)

In this approach a performance function $Y(X)$ is approximated by means of a first order Taylor-series expansion around the design point [10]

$$Y(X) \cong Y(\overline{X}) + \sum_{i=1}^{n} \left.\frac{\partial Y}{\partial x_i}\right|_{\overline{X}} (x_i - \overline{x}_i) \tag{13}$$

Substituting Eq. (13) in the expectation definition (mean)

$$E[Y(X)] = E[Y(\overline{X})] + E\left[\sum_{i=1}^{n} \left.\frac{\partial Y}{\partial x_i}\right|_{\overline{X}} (x_i - \overline{x}_i) \right] \tag{14}$$

and considering that:

$$E\left[\sum_{i=1}^{n} \left.\frac{\partial Y}{\partial x_i}\right|_{\overline{X}} (x_i - \overline{x}_i) \right] = \sum_{i=1}^{n} \left.\frac{\partial Y}{\partial x_i}\right|_{\overline{X}} E[(x_i - \overline{x}_i)] = 0 \tag{15}$$

$$E[(x_i - \overline{x}_i)] = E(x_i) - \overline{x}_i = \overline{x}_i - \overline{x}_i = 0 \tag{16}$$

the performance function mean value, estimated by means of FOSM, assumes the following expression

$$E[Y(X)] = Y(\overline{X}) \tag{17}$$

Now, given the variance definition

$$Var[Y(X)] = E\left[(Y(X) - E(Y(X)))^2 \right] \equiv \sigma^2 [Y(X)] \tag{18}$$

and substituting in it Eq. (13), the variance assumes the following expression

$$\sigma[Y(X)] = \sum_{i=1}^{n} \sum_{j=1}^{m} \left.\frac{\partial Y}{\partial x_i}\right|_{\overline{x}_i} \left.\frac{\partial Y}{\partial x_j}\right|_{x_j} \cdot COV(x_i, x_j) \tag{19}$$

where $COV(x_i, x_j)$ is the covariance matrix.

2.4 The Evidence Theory

The Evidence Theory is a non probabilistic approach, used to characterize the effect of epistemic uncertainty on a system.

Given a design variable x_1, the prior information, or evidence, consists of n intervals, obtained from s sources $\left[x_{1,i}^l, x_{1,i}^u\right]$ (with $i=1,\ldots\ldots s$) that enclose the supposed true value. Clearly, the traditional probability theory cannot handle this type of evidence, without making some assumptions that can pervert the nature of the information. Several combination rules have been formulated to handle this kind of prior information [11],[12]; in this work, the Dempster-Shafer combination rule is adopted.

When a source provides a set information, this means that the variable can assume any value inside the interval. The probability that a variable x_1 assumes the value $\bar{x}_1$ is not defined by a probability distribution function but is included between a maximum probability (plausibility), and a minimum probability (belief). In order to define the plausibility and the belief, the basic probability assignment (m) must be introduced; m defines a mapping of the variable prior information. Formally the basic probability assignment function is defined by means of the following expressions

$$m : \mathrm{P}(x_1) \rightarrow [0,1] \tag{20}$$

$$m(\varnothing) = 0 \tag{21}$$

$$m = 1 \; if \;\; \bar{x}_1 \in S_i \;\; with \; i = 1,\ldots\ldots, s \tag{22}$$

where $\mathrm{P}(x_1)$ represents the power set of x_1 (defined, according to the axiomatic set theory [12] as the set of all subset of S), while $\varnothing$ is the null set and S_i is the i-th evidence set. According to the previous equations, the basic probability assignment assumes any value included between 0 and 1; if $\bar{x}_1$ does not belong to any subset, the basic probability assignment assumes value 0, while if $\bar{x}_1$ belongs to every subset, it assumes the value 1. Once defined the basic probability assignment *m*, the plausibility and belief probability measures can be introduced. Given a set $C = [D(x_1)^-, \bar{x}_1]$, where $\bar{x}_1$ is a generic value of the variable x_1 on its domain $D(x_1)$, while $D(x_1)^-$ represents the lower domain boundary, the plausibility can be expressed by

$$Pl(C_1) = \sum_{C_1 \cap s_{x_1}^i \neq 0} m_{x_{1,i}}\left(S_{x_1}^i\right) \tag{24}$$

while the belief is defined as:

$$Bel(C_1) = \sum_{S_{x_1}^i \subseteq C_1} m_{x_1}\left(S_{x_1}^i\right) \tag{25}$$

In other words, the plausibility is the sum of all basic probability assignments of the sets $S_{x_1}^i$ which intersect the set of interest C_1, hence it represents the maximum probability that a variable x_1 assumes a given value $\bar{x}_1$. On the other hand, the belief is defined as the sum of all

basic probability assignments of the sets $S^i_{x_1}$ that $S^i_{x_1} \subseteq C_1$ hence it is a measure of the minimum probability that a variable x_1 assumes a given value $\bar{x}_1$.
The probability lies between the plausibility and the belief

$$Bel(C_1) \le P(C_1) \le Pl(C_1) \tag{26}$$

and, only when plausibility and belief are overlapped, it can be univocally defined.
In a problem with n input variables there is the need to transfer the basic probability assignment values m_{x_j}, evaluated for each variable, into an equivalent information in the n-dimensional design variables space. Assuming that all the variables are uncorrelated, the probability of each elementary set in the design variables space is defined by

$$m_{x_1,x_2,\dots\dots,x_n}\left(\left[S^j_{x_1}\right],\dots\dots\dots\dots\dots\dots,\left[S^j_{x_{n1}}\right]\right) = m_{x_1}\left(\left[S^j_{x_1}\right]\right)\cdot\dots\dots\dots\dots\cdot m_{x_1}\left(\left[S^j_{x_n}\right]\right) \tag{27}$$

Once defined the uncertainty acting on the design variables, its effects on the performance function can be evaluated. Given a generic function $y = Y(X)$, linking the output with the input variables $X = \{x_1,\dots\dots\dots x_n\}$, the evidence about y must be estimated from the joint body of evidence previously described in Eq. (27). By means of two optimization problems, for each evidence-set of the input variables space, the lower and upper boundary of the corresponding set into the output space are evaluated

$$\begin{array}{ll} find & \bar{X} = \{\bar{x}_1,\dots\dots,\bar{x}_n\} \in \Sigma_j\left(\left[S^j_{x_1}\right],\left[S^j_{x_2}\right],\dots\dots\dots,\left[S^j_{x_n}\right]\right) \\ t.c & \max/\min \ y = f(X) \ \square \\ & \qquad\qquad \Downarrow \\ & \qquad S^j_y = \left[y^j_l, y^j_u\right] \end{array} \tag{28}$$

The above optimization problems yield an evidence set on output-space S^j_y for each set Σ_j of the joint body of evidence (Fig 4.5). Hence, in order to propagate the uncertainty from in put to output two optimizations for each set Σ_j have to be performed.

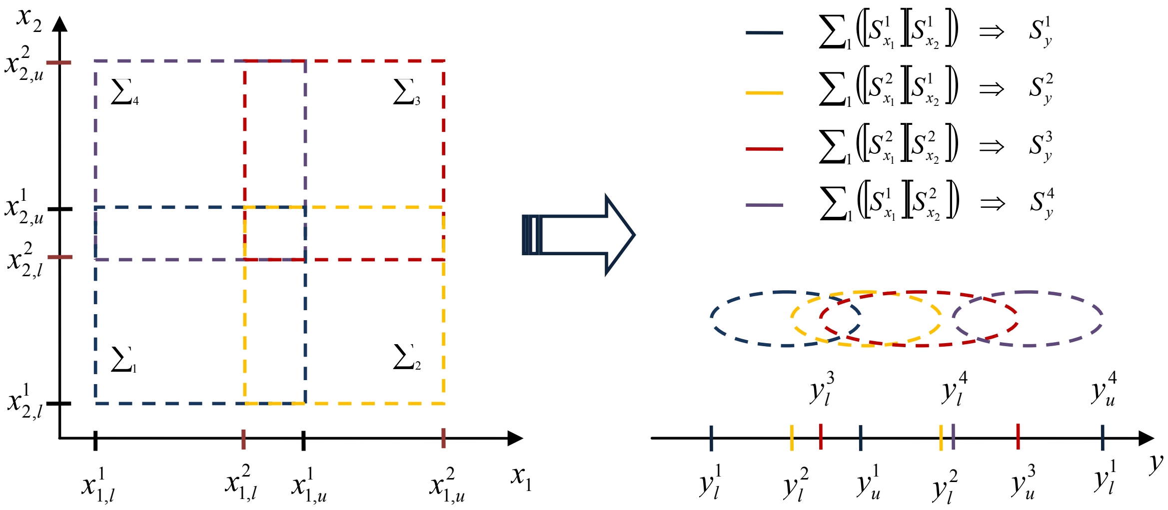

3 NUMERICAL EXAMPLES

In this section some numerical examples will be presented in order to verify the accuracy of the UP methods described above. Some test functions and a structural problem (static, dynamic and buckling behavior of a composite plate) will be the test cases considered for assessing the methods for stochastic uncertainty. A comparison between stochastic and epistemic approaches when applied to a structural shape sensing problem will be then discussed.

3.1 Test functions

Two test functions are used to compare the performance of the UP methods introduced in the previous paragraphs (Table 1).

Function	PDF	PDF Parameters
$y = x_1^k x_2^k + 2x_3^4 \qquad k = 2,3,5$	Gaussian	$\mu = [1,1,1]$ $\sigma = 0.1, 0.2, 0.4, 0.8$
$y = \sin x_1 + a \sin^2 x_2 + b x_3^4 \sin x_1$	Gaussian	$\mu = [\pi/4, \pi/4, \pi/4]$ $\sigma = 0.05, 0.1, 0.2, 0.5$

Table 1: Test functions used to test the UP methods

The first example is a three-variate function, chosen to compare the performance of the UP algorithms against the first order interaction of the input variables. The input variables follow a Gaussian distribution centered in $X = [1,1,1]$ and four values of standard deviation are tested ($\sigma = 0.1, 0.2, 0.4, 0.8$). In addition, the effect of the interactions among the variables is studied changing the value of k. The analysis of the accuracy of each method is performed comparing the predicted values of the statistical moments with those evaluated using a MonteCarlo Simulation, based on 10^6 observations. In this example the effect of an increasing input variability is combined with that of an increasing interaction effect.

In Table 2 the main effects and the interactions are listed for each value of k. These indices are evaluated by means of the Polynomial Chaos Expansion [13]. We can observe that changing the value of k the interaction $x_1 x_2$ increases its effect on the output, becoming gradually the most important factor.

	Main Effects and Interactions		
	k=2	k=3	k=5
X_1	0,011	0,0838	0,0575
X_2	0,011	0,0838	0,0572
X_3	0,9587	0,4734	0,0006
X_1X_2	0,01927	0,359	0,8808
X_1X_3	9,60E-25	8,78E-25	5,82E-04
X_2X_3	4,84E-26	8,34E-25	1,22E-03

Table 2: Main effects and interaction

In Fig (1) the errors in the estimation of the mean value are plotted in function of the input variables standard deviation and against different values of k. As a general rule, when the input variability increases, all the UP methods here discussed become less accurate. This phenomenon is negligible if the first order interactions are marginal; on the contrary, in problems

where the interaction effects are more important ($k=3$ or $k=5$) the results become more sensitive to the input variability.
As shown in Fig (1A) the UDR yields a good estimation of the mean values when the interaction between the variables is low $(k=2)$, also in the case of high input variability $(\sigma=0.8)$. Increasing the effect of interaction, the accuracy of this method greatly decays, in particular for higher values of input variability.

Similar behaviors are shown in Fig (1B-D); the output function is approximated with the Polynomial Chaos Expansion, truncated at different orders. Also in this case, for higher values of k and for a higher input uncertainty, the mean value is poorly approximated. When using the PCE, however, the reduced accuracy is not due to the interaction effects, but it is caused by the non-linearity of the output function: for example, if $k=2$ we have a 4th order function, while if $k=3$ we have a 6th order function. Hence, it is clear that a Polynomial Chaos Expansion truncated at the 5th order better describes the problem than an expansion trounced at the 2nd order, but, for $k=5$, it does not guarantee adequate accuracy. Increasing the order of the expansion, the error in the prediction gradually vanishes.

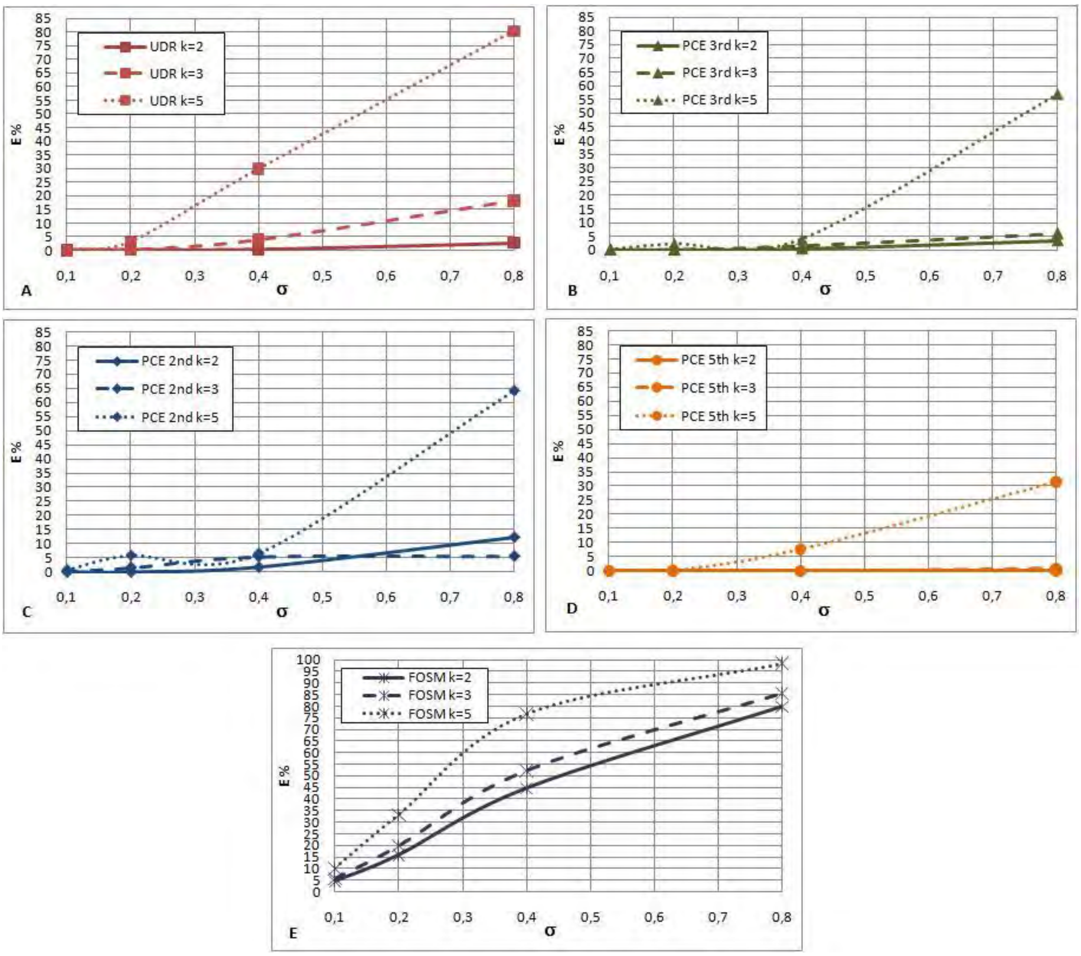

Fig 1 Error in the extimation of the output mean value: A) Error due to the Univariate dimension reduction method (UDR) B-D) Error due to the Polinomial Chaos Expansion (PCE) respectivelly of 2nd, 3rd and 5th order. E) Error due to the FOSM alghorithm

Therefore, there is a substantial difference between the UDR and the PCE. In the UDR the lack of accuracy, is inherent to its mathematical formulation and cannot be reduced. On the other hand, the accuracy of the PCE results can be improved increasing the order of the expansion.

In Fig (1E) the errors are shown on the output function mean value when computed using the FOSM algorithm. In this case the approximation is based on the hypothesis that the output function has a linear behavior in the studied domain; the errors are quite high also for small input variability levels.

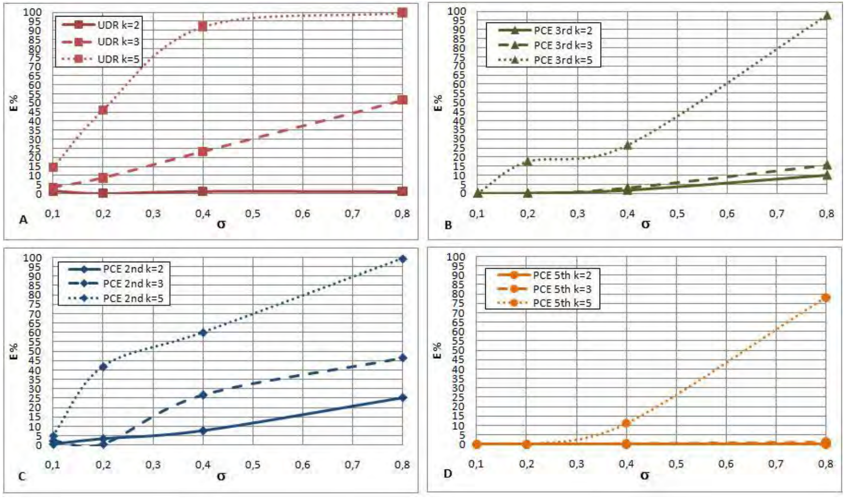

Fig 2 Error in the extimation of the output variance: A) Error due to the Univariate dimension reduction method (UDR) B-D) Error due to the Polinomial Chaos Expansion (PCE) respectivelly of 2nd, 3rd and 5th order.

The decay of UDR accuracy in the prediction of the statistical moments (due mainly to the first order effects) is more evident in the evaluation of the variance Fig (2-A) and of the higher order moments: Skewness (Fig 3-A) and Kurtosis (Fig 4-A). As already observed in the evaluation of mean value, for quite small interaction effects ($k = 2$), the UDR approximation does not affect the accuracy of the results. This is not true for the higher order moments.

Results regarding higher order statistical moments (Figs. 6.4B-D, 6.5B-D, 6.6B-D) confirm that the interaction between the variables does not affect the accuracy of the Polynomial Chaos Expansion; anyhow, a higher order expansion is required in order to have a good estimation of the variance, skewness and kurtosis.

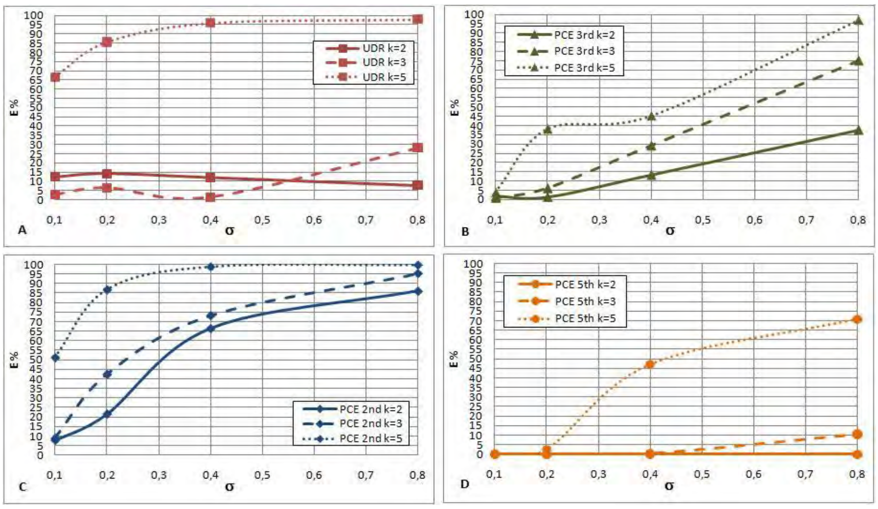

Fig 3: Error in the extimation of the output skewness: A) Error due to the Univariate dimension reduction method (UDR) B-D) Error due to the Polinomial Chaos Expansion (PCE) respectivelly of 2nd, 3rd and 5th order.

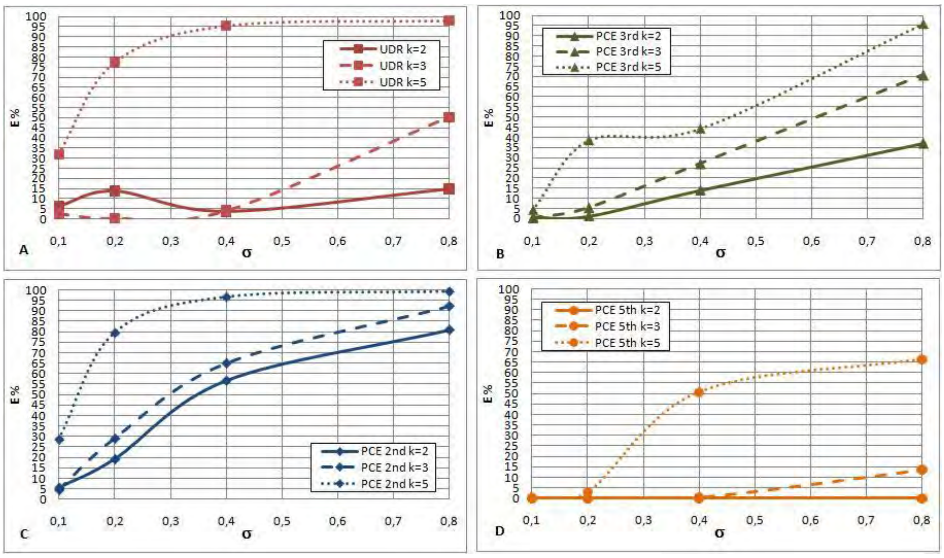

Fig 4: Error in the extimation of the output kurtosis: A) Error due to the Univariate dimension reduction method (UDR) B-D) Error due to the Polinomial Chaos Expansion (PCE) respectivelly of 2nd, 3rd and 5th order.

In Table 3 the number of observation points needed to perform each analysis are listed. The UDR methods needs only 16 observed data (it requires only $5n+1$, where n are the stocastic input variables).

FOSM	UDR	PCE 2nd	PCE 3rd	PCE 5th
49	16	31	61	168

Tab 3: Number of observations for each methods

The UDR method is the cheapest one and, as seen in the present example, if there is a negligible interaction between the input variables it yields a good estimation of the statistical moments. The computational cost of the PCE grows considerably increasing the order of expansion and the problem dimension.

The second function here considered (see Tab (1)) is the Ishigami function, commonly used to test the uncertainty propagation algorithms and the sensitivity in order to understand their behavior with non-linear and non-monotonic functions. The three variables follow a Gaussian distribution, centered in $X=[\pi/4,\pi/4,\pi/4]$; the standard deviation ranges from 0.05 to 0.5. The accuracy of each method is assessed comparing the predicted values of the statistical moments with those evaluated using a MonteCarlo Simulation, based on 10^6 observations.

In Table 6.5 the percentage errors on the estimation of the mean value and variance are listed for different values of the input standard deviation. All methods yield a good estimation of the mean value (the error is always less than 1%). The differences between the methods are more evident when considering the variance evaluation. The FOSM method yields a very poor estimation in particular for high values of input variability: for example, the error with an input standard deviation of $\sigma=0.2$ is around 12.3%, while with $\sigma=0.5$ is around 56%. The UDR method leads to a good estimation of the variance (error around 2%); there is no evident correlation between the input variability and the estimation error. The PCE is very accurate, if the order of the expansion is sufficient to describe the problem; we can observe that a 5th order expansion is very accurate in the prediction of variance, and that the 7th order expansion yields the exact solution.

Standard Deviation Input	***FOSM***		***UDR***		***PCE 2nd***	
	Mean	**Variance**	**Mean**	**Variance**	**Mean**	**Variance**
0,05	3,336E-02	1,204E+00	2,515E-02	1,934E+00	2,363E-03	2,398E-01
0,1	7,351E-02	1,968E+00	4,734E-02	1,952E+00	2,837E-02	1,997E+00
0,2	1,609E-01	1,235E+01	7,092E-02	2,162E+00	1,754E-01	2,334E+00
0,5	5,364E-01	5,575E+01	3,560E-01	1,818E+00	5,596E-01	6,521E+00
Standard Deviation Input	**PCE 3rd**		**PCE 5th**		**PCE 7th**	
	Mean	**Variance**	**Mean**	**Variance**	**Mean**	**Variance**
0,05	0,000E+00	0,000E+00	0,000E+00	0,000E+00	0,000E+00	0,000E+00
0,1	0,000E+00	2,058E-02	0,000E+00	0,000E+00	0,000E+00	0,000E+00
0,2	4,731E-03	3,456E-02	0,000E+00	3,456E-02	0,000E+00	0,000E+00
0,5	1,189E-01	2,878E+00	4,749E-03	1,641E-02	0,000E+00	2,553E-02

Tab 4: Mean values and variance estimation errors

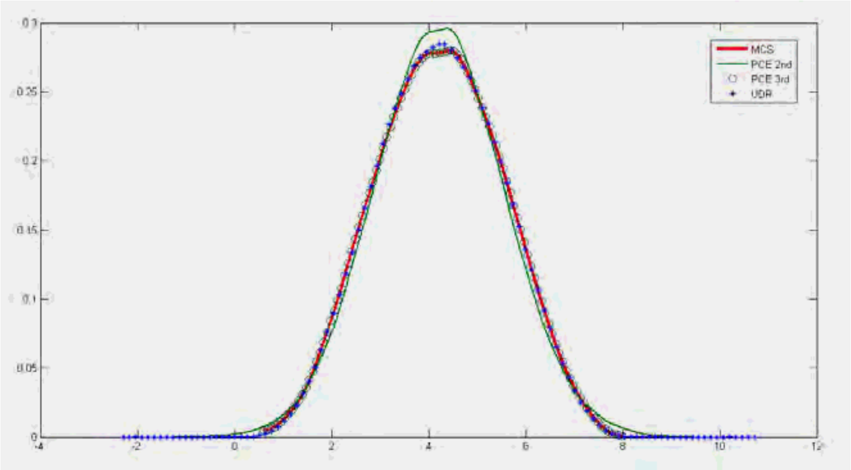

Fig 5: Probability density function in the case that all input variables have a standard deviation of 0.2

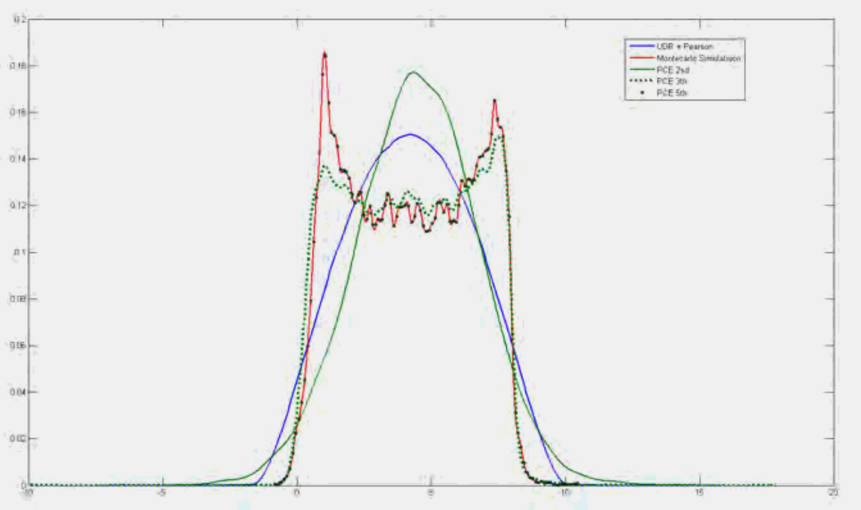

Fig 6: Probability density function in the case that all input variables have a standard deviation of 0.5.

In a robust design framework it is important the accurate evaluation of the first two statistical moments (mean and variance), but for the evaluation of the reliability degree this information

is not enough. Hence, the knowledge of the probability distribution function is needed. One of the main problems of the UDR approach is that it does not yield directly the probability distribution, but only the statistical moments. Anyway, it is possible to obtain the PDF, knowing the first four statistical moments, by means of the Pearson System. In fig (5) and fig (6) the probability distribution function, evaluated with the UDR and the Pearson System, is compared with the PDF obtained using the PCE with different expansion orders and the one obtained by means of MCS (10^6 training points). The curves plotted in Fig (5) and in Fig (6) are referred, respectively, to the case of an input standard deviation of $\sigma = 0.2$ and of $\sigma = 0.5$.
In the first case (fig 5) a good agreement among all plotted curves can be observed. The UDR method coupled with the Pearson System yields a very good approximation of the probability density function. There is only a small discrepancy in the description of the tails: the tails of PDFs, obtained with the UDR method and the 2nd order PCE, end with an asymptotic behavior, while in the one obtained with MCS the tails are limited. On the contrary there is a perfect correspondence between the probability function obtained with a 3rd order PCE and the one obtained with the MonteCarlo Simulation.
In the second case $(\sigma = 0.5)$ it is possible to appreciate a bigger discrepancy among the methods (fig 5-A). Although the UDR method is able to predict with a good accuracy the mean and the variance of the output, it fails in the estimation of the PDF. This is mainly due to the fact that the higher order moments are predicted with low-accuracy and, as well known, the Pearson System is based on the relation between skewness and kurtosis. Also the 3rd order PCE gives not an accurate probability distribution. Only by means of a 5th order PCE a good PDF approximation can be obtained.
In this example we have seen that, although the UDR approach is adequately accurate to be used in a robust design problem, it cannot be used in a reliability based problem.

3.2 Composite plate mechanical behavior

In this example the performances of UDR and PCE are tested on the static and dynamic response analysis of a symmetric composite plate $\left(0^\circ/90^\circ/90^\circ/0^\circ\right)$ with all edges clamped. The material properties, the fiber angles, and the plies thickness are considered affected by uncertainty and are described by means of Gaussian distributions. In tab (5) all plate properties are reported in terms of mean value and standard deviation. The stochastic moments of the maximum deflection (***w***), the first natural frequency (***f***), the maximum Von Misses stress (***σ_{VM}***), the maximum τ_{xz} and the maximum τ_{yz} are evaluated by means of the UDR and of the PCE. The static and dynamic responses of the plate have been obtained using the Refined Zigzag plate Theory (RZT) [14]-[18]; a Rayleigh-Ritz solution procedure has been adopted to find maximum deflection, first natural frequency and stresses distribution. The results are compared with those obtained using a MCS based on 10^5 observations.
Finally, the first four statistical moments, evaluated using the UDR and PCE, are compared with those obtained by a MonteCarlo Simulation (Tab 6). In Tab (6) one can observe that approximately all approaches give the same results, the main difference between the UDR and the 2nd order PCE is in the computational cost needed to perform the analysis, indeed are needed 71 observations and 360 training points, respectively.

		Mean	***PDF***	***SD***
Mechanical properties	**E11 [Mpa]**	1,58E+05	Gaussian	7,895
	E22 [Mpa]	9,58E+03	Gaussian	0,4792
	E33 [Mpa]	9,58E+03	Gaussian	0,4792
	G12 [Mpa]	5,93E+03	Gaussian	0,2965
	G13 [Mpa]	5,93E+03	Gaussian	0,2965
	G23 [Mpa]	3,23E+03	Gaussian	0,1613
	v12	0,32	Deterministic	-
	v13	0,32	Deterministic	-
	v23	0,49	Deterministic	-
	ρ [T/mm^3]	1,90E-09	Deterministic	-
Orientation angles	**θ_1**	0	Gaussian	3
	θ_2	90	Gaussian	3
	θ_3	90	Gaussian	3
	θ_4	0	Gaussian	3
Thicknesses	**t1 [mm]**	1	Gaussian	0,05
	t2 [mm]	1	Gaussian	0,05
	t3 [mm]	1	Gaussian	0,05
	t4 [mm]	1	Gaussian	0,05

Tab 5: Plate properties: θ_1 is the fiber orientation of the first ply, t_1 is the ply thickness

		w	f	σ_{VM}	τ_{yz}	τ_{xz}
MCS	Mean	21,37	434,24	2194,65	28,76	14,01
	Variance	3,36	200,36	13570,68	0,70	0,45
	SD	1,84	14,15	116,49	0,84	0,67
	SKW	0,01	0,04	0,23	0,15	0,16
	KURT	3,05	3,03	3,06	3,01	3,03
UDR	Mean	21,36	434,24	2194,50	28,76	14,01
	Variance	3,35	201,67	13570,68	0,78	0,45
	SD	1,83	14,20	116,49	0,88	0,67
	SKW	0,00	0,00	0,23	0,15	0,16
	KURT	3,03	3,03	3,00	3,02	3,03
2nd PCE	Mean	21,37	434,24	2194,64	28,76	14,01
	Variance	3,34	205,67	13570,68	0,72	0,45
	SDY	1,83	14,34	116,49	0,85	0,67
	SKW	0,01	0,00	0,23	0,15	0,16
	KURT	3,03	3,03	3,00	3,02	3,03

Tab 6: Stochastic moments: SD is the standard deviation, SKW is the skewness, KURT is the curtosis, w is the maximum deflection, f is the first modal frequency , VM is the maximum Von Mises stress.

3.3 Structural shape sensing

The inverse Finite Element Method (iFEM), developed by Tessler for plate and shell structures [18] and specialized by Gherlone for beams and frames [19], is aimed at the reconstruction of the displacement field of a structure starting from in situ measurements of surface strains [19]; this represents an inverse problem [20].

In the present work a cantilevered aluminum beam with a circular thin-walled cross-section, subjected to different load conditions, has been studied. In lieu of the experimental measures of surface strains, high-fidelity forward FE analyses (MSC/NASTRAN) have been carried out for the example problem (Table 7). These results have also been used to verify the accuracy of the nodal displacements and rotations obtained by iFEM.

Element type (name)	N° of elements along the external circumference	N° of elements along the beam length (L = 20) [dm]	N° of elements	N° of nodes
Shell element (QUAD4)	114	360	41,040	41,156

Tab 7: Sensor configuration: 1

The position of a strain gauge, used to measure surface strains, is defined by three coordinates: the first one, x, indicates the position along the longitudinal beam axis, the second one, θ, is an angle representing the circumferential position on the beam and the coordinate β indicates the strain gauge orientation (i.e., it represents the rotation of the strain gauge with respect to the beam axis (Fig 7). For the current application, six strain gauges are used; their nominal positions are reported in Table 8 and their location is also represented in Figure8.

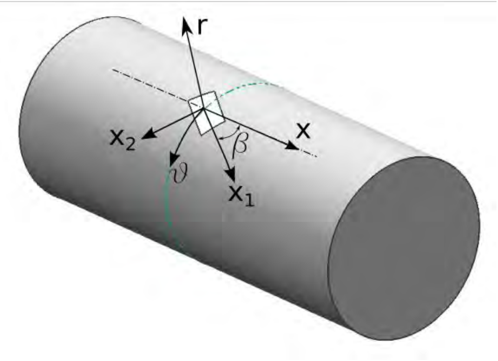

Fig 7. Location of a strain gauge on the beam external surface. [20]

Strain gauges	x	θ	β
1	10	-120	0
2	10	-120	45
3	10	0	0
4	10	0	45
5	10	120	0
6	10	120	45

Tab 8 Strain gauge nominal positions

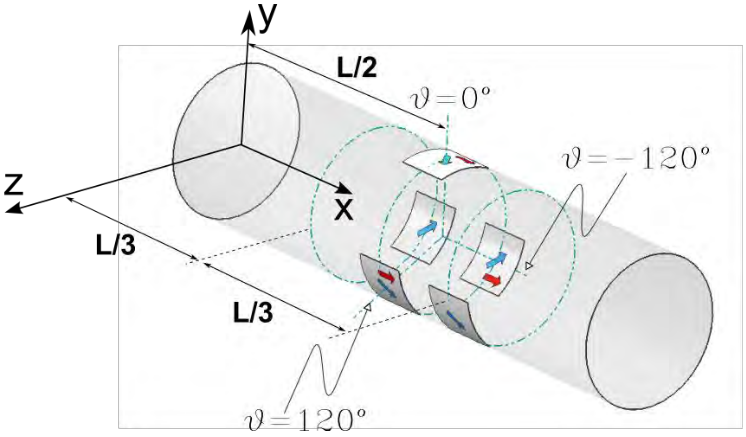

Fig 8 Sensors position [20]

In this example three different load conditions are considered (Fig (9-A)): 1) a shear force applied along y-axis, 2) the torque moment and 3) the bending moment around the z-axis. The free end displacements and rotations (Fig (9-B)) are computed by means of the iFEM and are compared with the ones obtained using the forward FEM solution. Hence, the iFEM accuracy is evaluated by means of the following error:

$$E \equiv \frac{Value(FEM) - Value(iFEM)}{Value(FEM)} \tag{29}$$

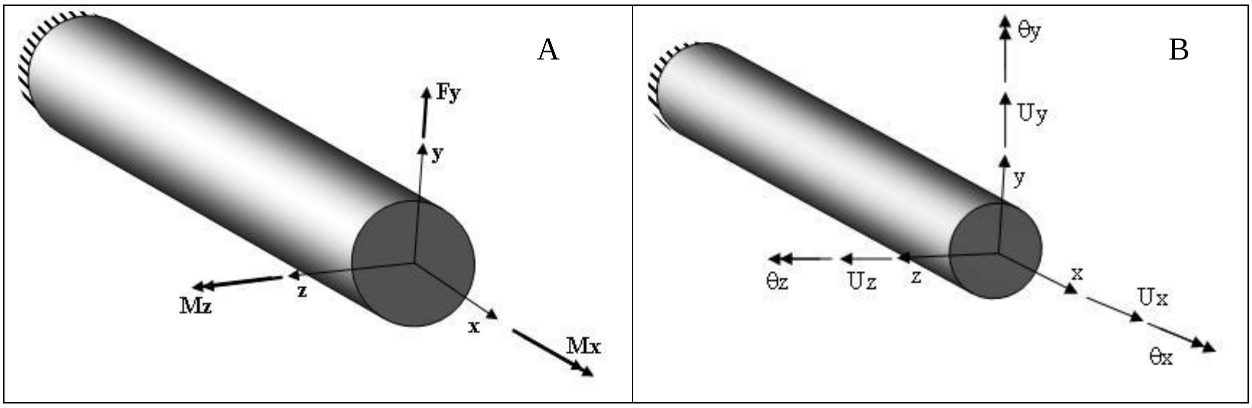

Fig 9 (A)Applied load, (B) Studied degrees of freedom.

The aim of the present application is to verify the robustness of the iFEM in evaluating the displacement field when the sensor positions are considered affected by uncertainty. For this purpose a probabilistic approach is compared with a non-probabilistic method based on the evidence theory. The main issue is the definition of the uncertainty that affects the coordinate values describing the sensors position. In order to obtain this kind of information, three technicians have been interviewed. They have given three different estimations of the error in the strain gauge location; all these experts are equally trusted. The second expert (see Tab 9) defined the errors using disjoint sets.

Expert	x [mm]		θ [°]		β [°]	
	LOWER	UPPER	LOWER	UPPER	LOWER	UPPER
1	-5	5	-5	5	-4	4
2	-5	-1	-5	5	-4	-1,5
	1	5	-5	5	1,5	4
3	-1	1	-5	5	-1,5	1,5

Tab 9: Sensor coordinates defined by means of interval sets

In order to use a probabilistic approach to propagate the uncertainty from input to output, there is the need to transform the input epistemic uncertainty into probabilistic information. Several hypotheses are then needed about the shape of the probability distribution and its standard deviation. In the present example we have assumed that the uncertainty in the sensor position is described by means of a Gaussian distribution, having the standard deviations listed in Tab (10).

Input variables	**PDF**	**Standard Deviation**
x	Gaussian	0,0233
θ	Gaussian	1,1666
β	Gaussian	1,3333

Tab 10: Probabilistic assumptions of sensor position

The information obtained by the sensitivity analysis [21] are used to select which input variables should be considered and which could be neglected during the uncertainty propagation process, performed both using the evidence theory and a probabilistic approach (the UDR method, having verified that there are not significant interactions between variables).. Then, once the first four statistical moments are known, the corresponding probability distribution function is evaluated by means of the Pearson System.

The probability that the iFEM error on the FEM reference displacements and rotations is greater than a given threshold value, is finally evaluated.

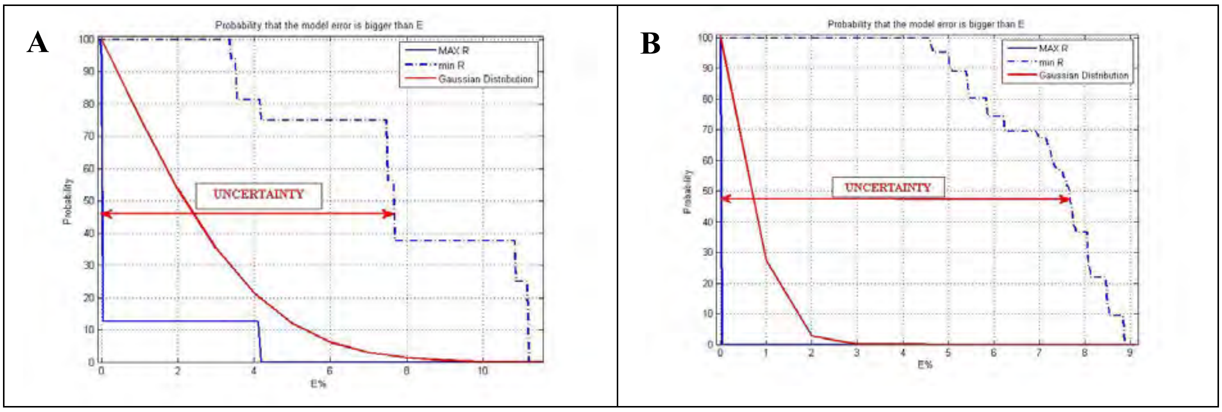

Fig 10 Shear load (Fy): Probability that the error E about Uy (A) and θz (B) is bigger than a given threshold value. Three curves are plotted: the first one represents the maximum model reliability (labeled with MAX R), the second one represents the minimum reliability of the model (labeled with min R), the red one represents the curve obtained using the assumption of the Gaussian distribution.

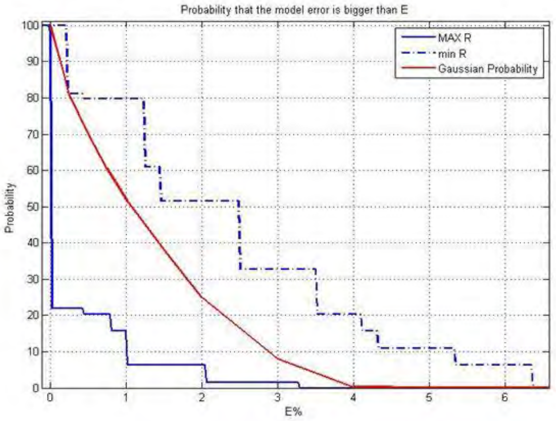

Fig 11 Torque Moment Probability that the error E about θx (B) is bigger than a given threshold value. Three curves are plotted: the first one represents the maximum model reliability (labeled with MAX R), the second one represents the minimum reliability of the model (labeled with min R), the red one represents the curve obtained using the assumption of the Gaussian distribution.

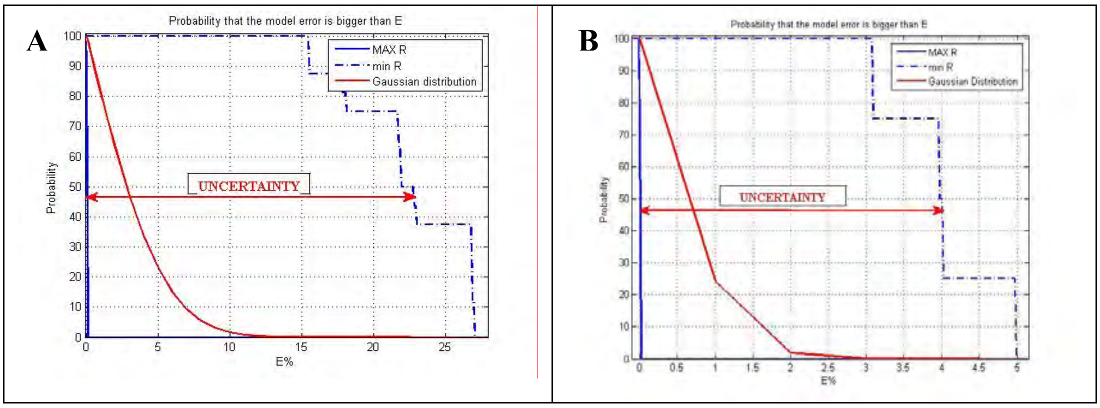

Fig 12 Bending Moment (z):): Probability that the error E about Uy (A) and θz (B) is bigger than a given threshold value. Three curves are plotted: the first one represents the maximum model reliability (labeled with MAX R), the second one represents the minimum reliability of the model (labeled with min R), the red one represents the curve obtained using the assumption of the Gaussian distribution.

The evidence theory does not furnish a unique measure of the probability, but it gives two different probability curves: the plausibility, that describes the curve of the maximum reliability of the system and the belief, that describes the minimum reliability of the system (fig 10-12). According to what it was said in Section 2.4, the true reliability curve is included between the plausibility and the belief. Actually, the area included between the maximum reliability curve and the minimum one represents a region of uncertainty; this means that, without further information, no prediction about the actual behavior of the model can be made (we only know that the true error is included between the two probability curves). For this reason, the belief curve, that represents a conservative estimation of the model behavior, is used during the design phase. In this study we have compared the results obtained assuming that the position error is described by means of Gaussian distributions with those obtained assuming that each sensor is located inside an interval. In this last case no hypothesis has been made about the probability that a sensor is in a given point (inside the region). As shown in Fig (10-12) the maximum reliability curves give almost null prediction errors, otherwise the minimum reliability curves indicate bigger probability to have large errors; in particular the evaluation of the y-displacement and z-rotation is quite sensible to the sensor position uncertainty Fig (10) and Fig (12). In most cases the reliability curves, based on the Gaussian distribution hypothesis, underestimate considerably the prediction errors. In particular the Gaussian hypothesis furnishes probability values close to those given by the maximum reliability curves.

4. Conclusion

In the present work a comparative study of some uncertainty propagation algorithms is performed and discussed.

Methods for both aleatory and epistemic uncertainty are considered; in particular, a brief review of Univariate Dimension Reduction method (UDR), Polynomial Chaos Expansion (PCE), and First Order Second Moments algorithm (FOSM) - for aleatory uncertainty - and of Evicence Theory – for epistemic uncertainty - is presented.

Then, selected example problems are considered to assess and compare the available methods; some test functions are used as preliminary test cases, then structural applications are studied, ranging from the mechanical behavior of a composite plate to the shape sensing of a beam starting from measured surface strains. As for the latter application, an epistemic uncertainty propagation approach (Evidence Theory) has been compared with a probabilistic uncertainty propagation algorithm (UDR); the considered problem is a classical example of epistemic uncertainty, therefore probabilistic approaches may be applied after introducing some prior assumptions whose correctness may not be guaranteed.

Although this study is limited to some particular examples, interesting general conclusions can be drawn.

If there is no significant interaction between variables, the UDR is the most efficient method for statistical moments estimation. Its accuracy decreases when the interactions cannot be neglected; in particular, the evaluation of the 3rd and 4th statistical moments is more sensitive to the interaction effects and, therefore, also the evaluation of the corresponding Probability Distribution Function (PDF), by means of the Pearson System, can be compromised. The accuracy and the computational cost of the PCE depend on the truncation order of the expansion. However, the PCE is a useful approach when the knowledge of the PDF is desired. Moreover, the UDR method leads to the best compromise between accuracy and computational cost when performing a probabilistic study of the mechanical behavior of a composite plate.

The transformation of the epistemic knowledge into a probabilistic knowledge could often cause a loss of information and consequently the underestimation of the uncertainty effects. The evidence theory, in the particular case of the shape sensing problem, seems to be the more robust and conservative approach. The use of a probabilistic approach is not wrong but it requires too strong prior assumptions. In other words, the correct use of the probabilistic approach would require the experimental probabilistic characterization of the sensors position.

4. References

[1] S.H.Lee, W.Chen, "*A Comparative study of uncertainty propagation methods for black-box-type problems*", Structural and Multidisciplinary Optimization, Vol 37 (3), 239-253, (2009).

[2] P. Cerracchio, M. Gherlone, M. Mattone, M. Di Sciuva, A. Tessler, "*Shape sensing of three-dimensional frame structures using the inverse finite element method*", Proc. Fifth European Workshop on Structural Health Monitoring, Sorrento, Italy, 615–620, (2010).

[3] P. Cerracchio, M. Gherlone, M. Mattone, M. Di Sciuva, A. Tessler, "Inverse finite element method for three-dimensional frame structures", DIASP Report Politecnico di Torino, 285, (2010).

[4] H.Xu, S. Rahman, "*A moment-based stochastic method for response moment and reliability analysis*", Proceedings Second MIT Conference on Compurational Fluid and Solid Mechanics, June (2003).

[5] S. Rahman, H.Xu, "*A univariate dimension-reduction method for multi-dimensional integration in stochastic mechanics*", Probabilistic Engineering Mechanics, Vol. 19 (1), 393-408, (2004).

[6] H.Xu, S.Rahman, "*A generalized dimension-reduction method for multidimensional integration in stochastic mechanics*", International Journal for Numerical Methods in Engineering, Vol. 65 (13), 1992-2019,(2004).

[7] Wiener, N., "*The Homogoeneous Chaos*", American Journal of Mathematics, Vol. 60, pp. 897–936, (1938).

[8] R.H.Cameron, W.T.Martin, "*The orthogonal development of nonlinear functionals in series of Fourier-Hermite functionals*", The Annals of Mathematics, Vol. 48 (2), pp 385-392, (1947).

[9] D.Xiu, G.M.Karniadakis, "*The Wiener-Askey Polynomial Chaos for Stochastic Differential Equations*", SIAM Journal on Scientific Computing, Vol. 24(2), pp. 619–644, (2002).

[10] M.Ticky "*Applied Methods of Structural Reliability*", Springer, (1993).

[11] J.C.Helton, J.D.Johnson, W.L.Oberkampf, C.B.Storli, "*A Sampling-Based Computational Strategy for the Representation of Epistemic Uncertainty in Model Predictions with Evidence Theory*", SANDIA REPORT, SAND2006-555, 2006. http://prod.sandia.gov/techlib/access-control.cgi/2006/065557.pdf

[12] K.Sentz, S. Ferson, "*Combination of Evidence in Dempster-Shafer Theory*", SANDIA REPORT, SAND 2002-083, 2002. http://www.sandia.gov/epistemic/Reports/SAND2002-0835.pdf

[13] T.Crestaux, O.Le Maitre, J.M.Martinez, "*Polynomial chaos expansion for sensitivity analysis*", Reliability Engineering & System Safety, Vol.94 (7), 1161-1172, (2009).

[14] Tessler A., Di Sciuva M., Gherlone M., "*Refined Zigzag Theory for Laminated Composite and Sandwich Plates*," NASA/TP-2009-215561, January (2009).

[15] Tessler A., Di Sciuva M., Gherlone M., "*A consistent refinement of first-order shear-deformation theory for laminated composite and sandwich plates using improved zigzag kinematics*," accepted for publication on Journal of Mechanics of Materials and Structures, (2010).

[16] A.Tessler, M.Di Sciuva, M.Gherlone, "*A Shear-deformation theory for composite and sandwich plates using improved zigzag kinematics*", IX International conference on computational structural Tecnology, Proceedings on Cd, Paper 30, Greece 2-5 September (2008).

[17] A.Tessler, M.Di Sciuva, M.Gherlone, "*Refined zigzag theory for homogeneous, laminate composite, and sandwich plates: a homogeneus limit methodology for zigzag function selection*", Numerical Methods for Partial differential equations, v.27 (1), 208-229, (2011)

[18] A.Tessler, J.L.Spangler, "*A least-squares variational method for full-field reconstruction of elastic deformations in shear-deformable plates and shells*", Computational methods in applied mechanical engineering. 94, 327–339, 2005

[19] P. Cerracchio, M. Gherlone, M. Mattone, M. Di Sciuva, A. Tessler, "*Shape sensing of three-dimensional frame structures using the inverse finite element method*", Proc. Fifth European Workshop on Structural Health Monitoring, Sorrento, Italy, 615–620, 2010.

[20] P. Cerracchio, M. Gherlone, M. Mattone, M. Di Sciuva, A. Tessler, "*Inverse finite element method for three-dimensional frame structures*", DIASP Report Politecnico di Torino, 285, 2010.

[21] M.Corradi, "*Uncertainty management techniques for aerospace structural design*", Ph.D. Thesis, Politecnico di Torino, February 2011.

COMPDYN 2011
III ECCOMAS Thematic Conference on
Computational Methods in Structural Dynamics and Earthquake Engineering
M. Papadrakakis, M. Fragiadakis, V. Plevris (eds.)
Corfu, Greece, 25–28 May 2011

INTRA-EVENT SPATIAL CORRELATION OF GROUND MOTION USING L'AQUILA EARTHQUAKE GROUND MOTION DATA

Gian Paolo Cimellaro[1], **Alessandro De Stefano**[2], **and Andrei M. Reinhorn**[2]

[1] Department of Structural and Geotechnical Engineering (DISTR),
Politecnico di Torino, 10129, Turin, Italy
e-mail: gianpaolo.cimellaro@polito.it

[2] Department of Civil, Structural and Environmental Engineering, University at Buffalo, The State
University of New York, 14260-4300, Buffalo, New York, USA.
e-mail: reinhorn@buffalo.edu

Keywords: intra-event, inter-event, ground motion correlation, spatial correlation, response spectra.

Abstract. *The intensities f ground motions and structural responses at two sites are correlated. The magnitude of the correlation depends on the distance between the sites and the natural vibration period of the structures. Spatial correlation of intra-event peak ground motion amplitudes at different sites is an important issue for seismic hazard and risk assessment of spatially distributed buildings and infrastructures. Correlated seismic effects cause acute concentration and accumulation of seismic losses, potentially resulting in a catastrophic event. The adequacy of the existing spatial correlation model has been checked using the L'Aquila earthquake ground motion data. Spatial correlations based on the L'Aquila earthquake data decreases gradually with increasing inter-station separation distance. At short separation distances, the estimated spatial correlation data points show large variability around the average trend. At short separation distances such as 1 km, where empirical data are limited and estimates are uncertain, discretion is required in adopting such models for seismic hazard and risk assessment of spatially distributed structures.*

1 INTRODUCTION

Traditional probabilistic seismic hazard analysis (PSHA) is often focused on a single site, however often the seismic hazard analysis for multiple sites is of interest (e.g. for regionally located building assets (portfolio) and spatially distributed systems (lifelines)) therefore correlation of ground motion intensity measures (e.g. peak ground motion, response spectra, etc.) at different location for the same seismic event need to be evaluated. Correlated seismic effects cause acute concentration and accumulation of seismic losses, and increased correlation of ground motion parameters affects the probability distribution of seismic risk for multiple structures due to the simultaneous occurrence of structural damage and collapse. The spatial intra-event correlation can be analyzed empirically for a given area, but a dense observation of records from numerous earthquakes is necessary and it has not been extensively investigated so far. The spatial intra-event correlation of ground motion parameters such as PGA have already been investigated in previous studies by Boore et al. [1] that considered particular earthquakes in California; Wang and Takada [2] considered 5 earthquakes in Japan and the Chi-Chi earthquake in Taiwan; Goda and Atkinson [3] used the K_NET and the KiK-net records collected in Japan to study spatial correlation for peak ground acceleration and pseudo-spectra acceleration. However, not many studies can be found on the correlation of the PSA at different periods and sites using a European database. Therefore this study focuses on estimating the correlation PSAs responses developing empirical equations that are able to predict the correlation coefficient considering both spatial separation distance and natural vibration periods of SDOF systems using a European earthquake set. In the paper intra-event and inter-event spatial correlation models have been proposed and calibrated using the records from the 2009 L’Aquila earthquake in Central Italy. The inter-event correlation is function of the considered ground-motion parameters, whereas the intra-event correlation is a function of the considered ground-motion parameters and the separation distance between two sites of interest. Sensitivity of the observed spatial correlation to the uncertainty in the magnitude and distance is also investigated.

2 CLASSIFICATION OF UNCERTAINTIES

Uncertainties in an attenuation relationship model (AR) can be distinguished between epistemic and aleatory uncertainty. Epistemic uncertainty results from the limited amount of observed data, while aleatory uncertainty describes the disagreement between observations and predictive models which is due to the absence of a physical explanation or due to the parameters that are not included in the predictive equations. Furthermore, the total aleatory variability [4][5] is separated in three independent components:

1. Inter-event variability (*earthquake to earthquake*);
2. Intra-event variability (*site-to-site*);
3. Variability remaining after accounting for the inter-event and the intra-event variability;

Usually the last two components are joined in a single one.

2.1 Inter-event correlation $\eta(T)$

The inter-event correlation describes the correlation among different seismic events (*earthquake –to–earthquake*) at the same site. In other words, earthquake ground motions at different sites caused by the same earthquake have something in common that depends on variation of earthquake source characteristics. So the inter-event residual $\eta(T)$ is a constant across all the sites during a given earthquake.

2.2 Intra-event correlation *ε'*(*T*)

The intra-event correlation describes the correlation among different sites (*site-to-site*) regarding the same seismic event. In other words, the intra-event variability considers the proposition that earthquake ground motion for a given event at different sites varies to some extent because of peculiarities of propagation path and local site conditions. Therefore, Tsai et al. [6] separated intra-event variability into path-to-path and site-to-site components. The site-to-site correlation depends on the ground conditions of the sites and it will decrease for sites that do not share the same geology, however a systematic research on quantifying the dependence has not been performed so far. Both inter-event and intra-event correlations can be incorporated in probabilistic seismic hazard analysis and risk assessments, because the ratio between joint probabilities and the probabilities at individual sites can vary depending on (i) inter-event correlation or ratio of inter-event and total components of variability, and on (ii) whether or not the hazard is dominated by one source or many sources.

3 DEVELOPMENT OF CORRELATION EQUATIONS

Attenuation relationships (ARs) describe the probability distribution of spectral acceleration at an individual period. A typical empirical AR at *m* locations during *n* seismic events is typically modeled explicitly as a lognormal function as follow

$$\begin{aligned} &\log_{10} S_{a,ij}\left(T_n\right) = f\left(M_j, R_{ij}, \lambda, T_n\right) + \eta_j\left(T_n\right) + \varepsilon_{ij}\left(T_n\right) \\ &i = 1,2,\ldots,m;\ \ \text{j=1,2,…,n} \end{aligned} \tag{1}$$

where $f\left(M_j, R_{ij}, \lambda, T_n\right) = \mu_{log_{10}\left(S_a(T)\right)}\left(M_j, R_{ij}, \lambda, T_n\right)$ is the predicted geometric mean of the logarithm in base 10 of the spectral acceleration Sa provided by the AR for the ith site in the jth seismic event. Equation (1) stands also if instead of Sa is considered PGA or PGV, but in these cases the equation is no longer function of T_n and it is function of the earthquake magnitude *M*, distance *R*, and a set of other explanatory variables λ such as local site conditions and faulting mechanism; $\eta_j\left(T_n\right)$ is the inter-event variability with zero mean and standard deviation $\sigma_\eta\left(T_n\right)$; $\varepsilon_{ij}\left(T_n\right)$ is the intra-event variability with zero mean and standard deviation $\sigma_\varepsilon\left(T_n\right)$. Usually the standard deviation of $\varepsilon_{ij}\left(T_n\right)$ is significantly larger than the standard deviation of $\eta_j\left(T_n\right)$, so $\varepsilon_{ij}\left(T_n\right)$ is the dominant contributor to the total $\varepsilon_T\left(T_n\right) = \eta_j\left(T_n\right) + \varepsilon_{ij}\left(T_n\right)$ that is computed for each record of the dataset at a range of periods using a given AR as follow

$$\varepsilon_T\left(T_n\right) = \frac{log_{10}\left(S_a\left(T_n\right)\right) - \mu_{log_{10}\left(S_a\left(T_n\right)\right)}\left(M, R, T_n\right)}{\sigma_{log_{10}\left(S_a\left(T_n\right)\right)}\left(M, T_n\right)} \tag{2}$$

where $\log_{10}(S_a(T_n))$ is the logarithm in base 10 of the observed spectral acceleration value, while $\mu_{log10}(S_a(T_n))$ and $\sigma_{\log10}(S_a(T_n))$ are evaluated from the AR. The uncertainty εT (Tn) comprises the inter-event $\eta(T_n)$ and the intra-event $\varepsilon_{ij}(T_n)$ uncertainty. The inter-event residual $\eta(T_n)$ is a constant across all the sites during a given earthquake. Therefore, when using records from a single earthquake, estimation of the intra-event (*site-to-site*) correlation

$\rho_\varepsilon(\Delta, T_n)$ does not require the knowledge of the inter-event residual for the earthquake. However, when the used database contains records from several earthquakes, using the same procedure the total correlation coefficient $\rho_T(\Delta, T_{n1,} T_{n2})$ between $\eta_j(T_{n1}) + \varepsilon_{ij}(T_{n1})$ and $\eta_j(T_{n2}) + \varepsilon_{kj}(T_{n2})$ for a randomly selected seismic event at two recording stations separated by the distance (km) is given by the approximated expression [7][8]

$$\rho_T(\Delta, T_{n1,} T_{n2}) = \frac{\rho_\eta(T_{n1,} T_{n2})\left[\sigma_\eta(T_{n1})\sigma_\eta(T_{n2}) + \rho_\varepsilon(\Delta, T_{MAX})\sigma_\varepsilon(T_{n1})\sigma_\varepsilon(T_{n2})\right]}{\sigma_T(T_{n1})\sigma_T(T_{n2})} \tag{3}$$

where $\rho_\eta(T_{n1,} T_{n2})$ represents the correlation between $\eta_j(T_{n1})$ and $\eta_j(T_{n2})$; $\rho_\varepsilon(\Delta, T_{MAX})$ is the intra-event spatial correlation focusing on a single vibration period T_n, and T_{MAX} is the larger between T_{n1} and T_{n2}; $\sigma_\eta(T_n)$ is the standard deviation of the inter-event residuals $\eta_j(T_n)$; $\sigma_\varepsilon(T_n)$ is the standard deviation of the intra-event residuals $\varepsilon_{ij}(T_n)$ and $\sigma_T(T_n)$ is the standard deviation of the total residuals given in equation (2). The total correlation $\rho_T(\Delta, T_{n1,} T_{n2})$ and the intra-event correlation $\rho_\varepsilon(\Delta, T_n)$ are related through Equation (3), while the inter-event component can be removed from the residuals of earthquake *j* using the estimation of $\hat{\eta}_j$ [9]

$$\hat{\eta}_j = \frac{\sigma_\eta^2 \sum_{i=1}^{n_j}\left[log_{10}\left(S_{a,i,j}(T_n)\right) - \mu_{log_{10}\left(S_a(T_n)\right),i,j}(M, R, T_n)\right]}{n_j\sigma_\eta^2 + \sigma_\varepsilon^2} \tag{4}$$

3.1 Evaluation of inter-event spatial correlation

The inter-event correlation is evaluated by using the regression residuals η(Tn) based on the selected ground motion data. For a given pair of two natural vibration periods T_{n1} and T_{n2}, $\rho_\eta(T_{n1,} T_{n2})$ is evaluated using the Pearson's linear correlation coefficient. In details, the observed values of $\rho_\eta(T_{n1,} T_{n2})$ are determined using the following step-by-step procedure:

1. Select the sites for a given earthquake;
2. Given the $S_a(T_n)$ values at several sites for one earthquake, and given the predicted value at each site using the AR, the residuals values can be determined;
3. The inter-event residual $\eta(T_n)$ is the mean of the residual values and it is associated to a given earthquake, so it will not change from site to site;
4. The inter-event residual $\eta(T_n)$ for different earthquakes is evaluated using step 2 and 3, so if n earthquakes are provided n inter-event residuals $\eta(T_n)$ are determined;
5. Repeating step 1, 2 and 3 for *m* vibration periods until a $m \times n$ matrix is determined that can be used to determine the inter-event correlation coefficient $\rho_\eta(T_{n1,} T_{n2})$ as shown in the example below.

3.2 Evaluation of intra-event spatial correlation

The intra-event correlation is evaluated by using the regression residuals $\varepsilon_{ij}(T_n)$ based on the selected ground motion data. The observed intra-event spatial correlation at a single vibration period $\rho_\varepsilon(\Delta,T_n)$ (i.e., $\rho_\varepsilon(\Delta,T_{n1,}T_{n2})$ with $T_{n1}=T_{n2}$), can be determined using the following step-by-step procedure:

1. Select the sites for a given earthquake;
2. Compute the separation distance Δ for all pairs of sites (or stations);
3. Compute the differences ε using equation (2);
4. Divide the range of Δ into bins so that the separation distance in the same bin is $\Delta \pm \delta/2$;
5. All pairs of sites that fall in the bin centered at *Δ* are used to compute the correlation function $\rho_\varepsilon(\Delta,T_n)$ that will be function of the period and the sites distance *Δ;*

In detail, the observed intra-event correlation $\rho_\varepsilon(\Delta,T_n)$ at a given vibration period is carried out by analyzing regression residuals from the AR using the following equation

$$\rho_\varepsilon(\Delta,T_n) = 1 - \frac{\left[\sigma_d(\Delta,T_n)\right]^2}{2\left[\sigma_\varepsilon(T_n)\right]^2} \tag{5}$$

where $\sigma_d(\Delta,T_n)$ represents the variance of the difference $\varepsilon_{ij}(T_n)$-$\varepsilon_{kj}(T_n)$ calculated at discrete intervals Δ; represents the variance of the difference $\varepsilon_{ij}(T_n)$-$\varepsilon_{kj}(T_n)$ calculated over the entire sample. The observed values of $\rho_\varepsilon(\Delta,T_n)$ given by equation (5) can be compared with the predicted values of the proposed model given by the following equation

$$\rho_\varepsilon(\Delta,T_n) = e^{-\alpha(T_n)\Delta} \tag{6}$$

where $\alpha(T_n)$ is the parameter that needs to be calibrated according to the earthquake data used.

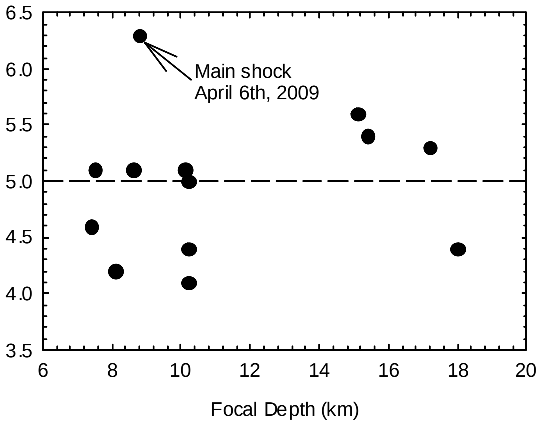

Figure 1: (Moment magnitude-focal depth) distributions of L'Aquila aftershocks.

4 L'AQUILA EARTHQUAKE DATA

All the ground motions used for the calibration of the predictive correlation models in the paper are extracted from the ITACA Database [10], http://itaca.mi.ingv.it/ItacaNet/ (last accessed January 31, 2011). The goal of the work is to investigate the intra-event and inter-event spatial correlation; therefore it is better to focus on well-recorded events that produced numerous observations at different locations such as L'Aquila 2009 earthquake. The selected ground motion set includes L'Aquila main shock and the following 12 main aftershocks and the main seismic characteristics are summarized in Table 1. All events are shallow events with a focal depth between 7 and 18 km and a moment magnitude between 4 and 6.3 as shown in Figure 1. The fault mechanism of all events is normal type. The geographical location of the aftershocks is shown in Figure 2b, while the spatial distribution of the INGV network station is shown in Figure 2a. Totally 4725 records from the 13 earthquakes have been considered for the analysis. The use of this set of record is to assess whether the observed differences in the decaying rate of the spatial correlation of the PGAs persist also for the spatial correlation of the PSAs and to calibrate the predictive correlation models for the region.

	Event (Date - Time)	Event Name	Latitude	Longitude	M_L	M_W	Depth (km)
1	2009-04-06 01:32:29	L'Aquila Main Shock	42.334	13.334	5.8	6.3	8.8
2	2009-04-06 02:37:04	Aquila	42.366	13.340	4.6	5.1	10.1
3	2009-04-06 02:37:04	Aquila	42.362	13.333	4.0	4.4	10.2
4	2009-04-06 23:15:37	Gran Sasso	42.451	13.364	4.8	5.1	8.6
5	2009-04-07 09:26:28	L'Aquila Earthquake	42.342	13.338	4.7	5.0	10.2
6	2009-04-07 17:47:37	L'Aquila Earthquake	42.275	13.464	5.3	5.6	15.1
7	2009-04-07 21:34:29	Aquila	42.380	13.376	4.2	4.6	7.4
8	2009-04-08 22:56:50	Aquila	42.507	13.364	4.3	4.1	10.2
9	2009-04-09 00:52:59	Gran Sasso	42.484	13.343	5.1	5.4	15.4
10	2009-04-09 03:14:52	Aquila	42.338	13.437	4.2	4.4	18.0
11	2009-04-09 04:32:44	Aquila	42.445	13.420	4.0	4.2	8.1
12	2009-04-09 19:38:16	Aquila	42.501	13.356	4.9	5.3	17.2
13	2009-04-13 21:14:24	Aquila	42.504	13.363	4.9	5.1	7.5

Table 1: Summary of the seismic characteristics of the 13 Earthquakes selected from the ITACA database.

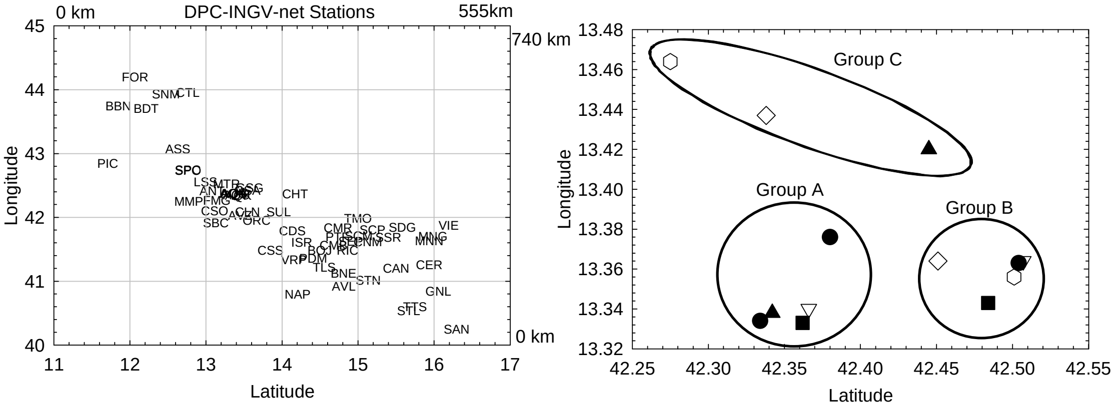

Figure 2: Geographical location of the (a) stations and of the (b) 13 aftershocks of L'Aquila earthquakes divided by groups.

5 NUMERICAL RESULTS

To investigate the variation of the empirical spatial correlation based on the residuals, statistical analysis is conducted individually for a selected major earthquake (L'Aquila Earthquake, 2009) that have a large number of records. The investigation on a single earthquake it is useful because it can provide valuable insights on the variability of spatial correlation among different sites and the dependence of spatial correlation on the vibration period for a given earthquake. To investigate the spatial correlation and carry out sensitivity analysis, a complete set of PSA responses are calculated, and the regression analysis is carried out for PSA for values of Tn ranging from 0.01 to 2 sec. The ε values were computed for each record of the dataset at a range of periods using Ambraseys AR [11]. For each record and period of the dataset, ε values were computed using Equation(2). An analysis of correlations of epsilon values has been carried out using the earthquake records in Table 1 following the procedure described above. In Figure 3 are shown the observed intra-event correlation coefficient $\rho_{\varepsilon}\left(\Delta, T_n\right)$ evaluated using equation (5), when considering only L'Aquila earthquake main shock.

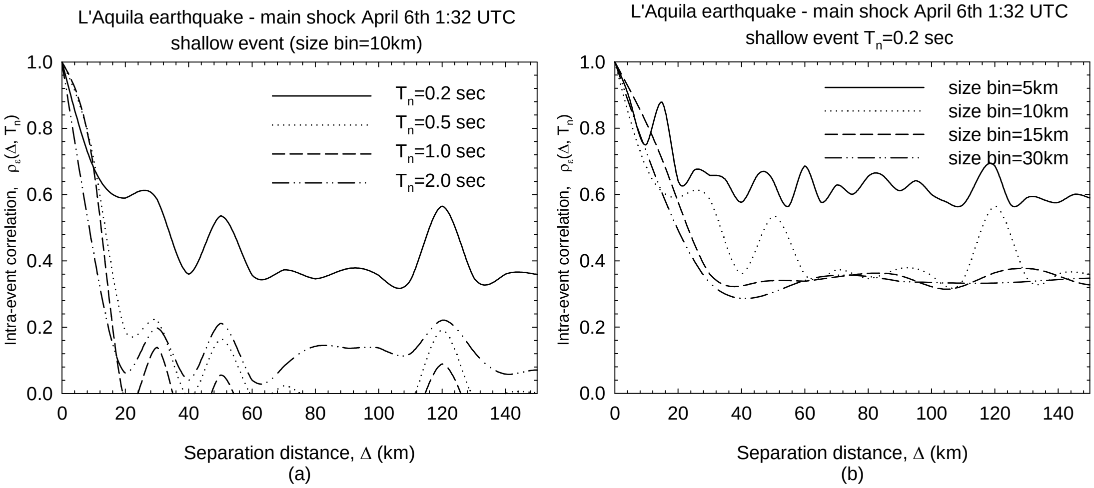

Figure 3: (a) Intra-event spatial correlation for PSA at 0.2, 0.5, 1.0 and 2 sec based on Equation (5) ; (b) Intra-event spatial correlation for PSA at 0.2 sec and different size bins at 5, 10, 15 and 30 km.

It can be observed that there is more correlation at high frequencies ($T_n=0.2s$), while at low frequencies and for separation distances more than 20 km, there is almost no correlation (Figure 3a). When considering the PSA at $T_n=0.2s$ the correlation values are stable for bin size resolutions between 10 and 30 km (Figure 3b).

When considering all earthquake set in Table 1, there is no correlation at low frequencies for distances Δ higher than 20km (Figure 4a). The correlation remains stables for values of bin size between 10 and 15 km, while it is not reliable for bin sizes higher than 30 km at high frequencies (Figure 4b).

An analysis of intra-event correlations of epsilon values at different periods has been carried out using 4725 records from the 13 earthquakes of L'Aquila region. For a given pair of two natural vibration periods T_{n1} and T_{n2}, the observed correlation coefficient $\rho_{\varepsilon}\left(\Delta, T_{n1,} T_{n2}\right)$ between $\varepsilon_{ij}(T_{n1})$ and $\varepsilon_{ij}(T_{n2})$ is evaluated using equation (5).

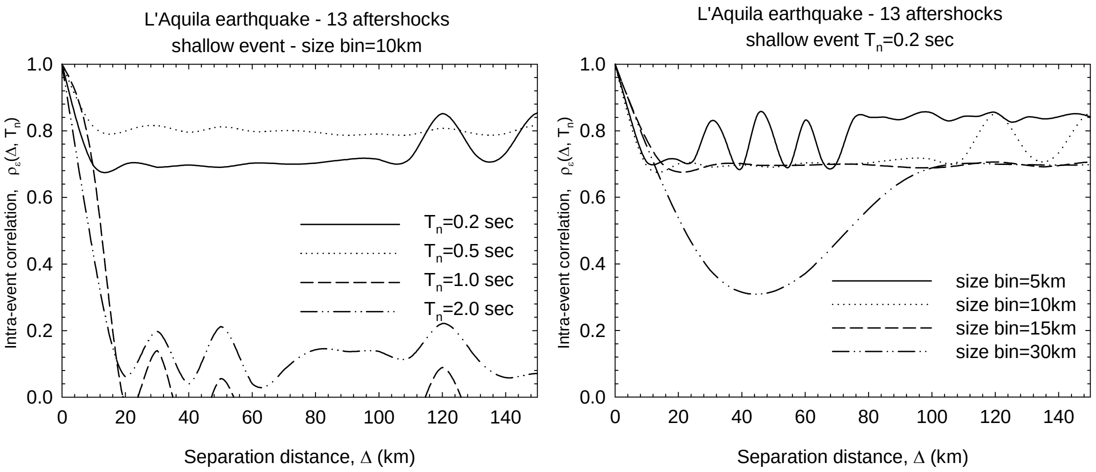

Figure 4: Intra-event spatial correlation for l'Aquila earthquake (a) for different PSAs at different periods; (b) for PSA at 0.2 sec and different size bins.

In Figure 5 are shown the observed intra-event spatial correlation $\rho_\varepsilon(\Delta, T_{n1}, T_{n2})$ for different periods and for bins separation distance of 0-20, 20-40, 40-60 and 60-80 km when all events are included. The shape of the intra-event spatial correlation is not affected significantly by the bin size resolution when all events in Table 1 are considered, while when only L'Aquila earthquake main shock is considered (Figure 6) the observed intra-event spatial correlation is affected by the bin size resolution.

Δ	A0	A1	A2	R^2
0 - 15 km	-0.0859	0.7095	1.0683	0.8613
15 - 30 km	0.8184	0.0912	0.1639	0.7443
30 – 60 km	0.6946	0.2014	0.3008	0.8738
60 – 100km	0.6137	0.2169	0.3842	0.8823

Table 2: Parameters of the correlation coefficient model for equation (7).

5.1 Proposed predictive intra-event correlation equations for ρε(Δ, Tn1, Tn2)

A correlation model of $\rho_\varepsilon\left(\Delta, T_{n1,}T_{n2}\right)$ is proposed and validated by comparison with the observed values of $\rho_\varepsilon\left(\Delta, T_{n1,}T_{n2}\right)$ obtained by Equation (5). Several linear and nonlinear equations were fitted to the observed data of the intra-event correlation coefficients and results were sorted using the r2 value as goodness of fit measure. Finally, the predictive equation was selected based on the number of parameters adopted, the simplicity and the goodness of fit. The proposed predictive intra-event correlation coefficient model between the residual values of a single horizontal component at two differing periods for L'Aquila main event is given by

$$\rho_\varepsilon\left(\Delta, T_{n1,}T_{n2}\right) = A0 + A1 \cdot e^{-T_{\min}} + A2 \cdot e^{-T_{\max}} \qquad (7)$$

where $T_{min}=min(T_1,T_2)$ and $T_{max}=max(T_1,T_2)$. The parameters of the model in Equation (7) for different distance range Δ are listed in Table 2, while results of the model for different range distances are shown in Figure 7. The r^2 value that describes the goodness of fit oscillates between 0.7443 and 0.8823 (Figure 7). The uncertainties are probably due to the fact that only the main shock is used and therefore results are sensitive to the separation distance and it is difficult to find a simple predictive model that can be adopted for different distance ranges.

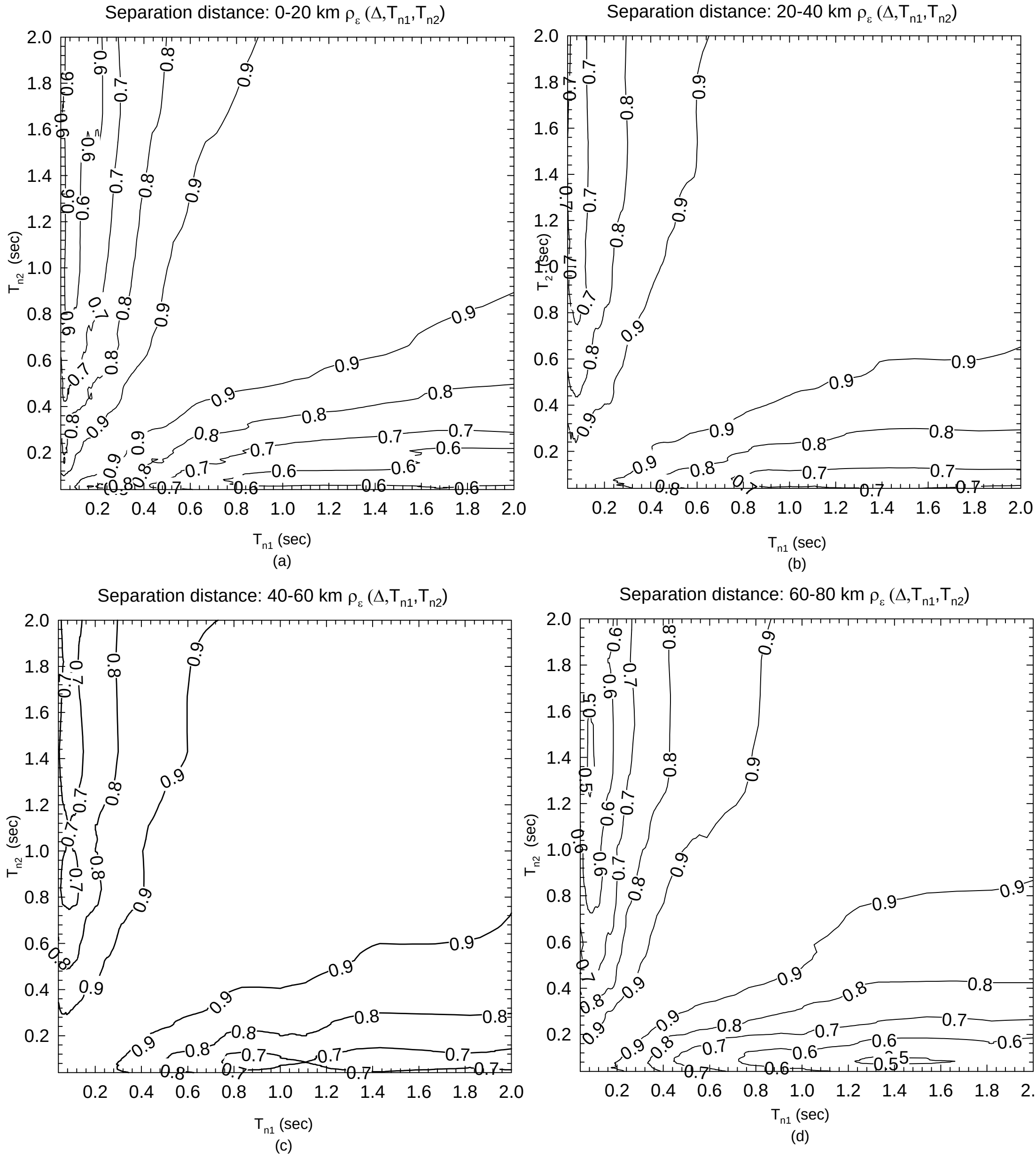

Figure 5: Observed intra-event spatial correlation ρε(Δ, Tn1, Tn2) for separation distance bins of 0-20, 20-40, 40-60 and 60-80 km for all events.

Another analytical predictive equation has been proposed by the author when all earthquakes in Table 1 area are considered.

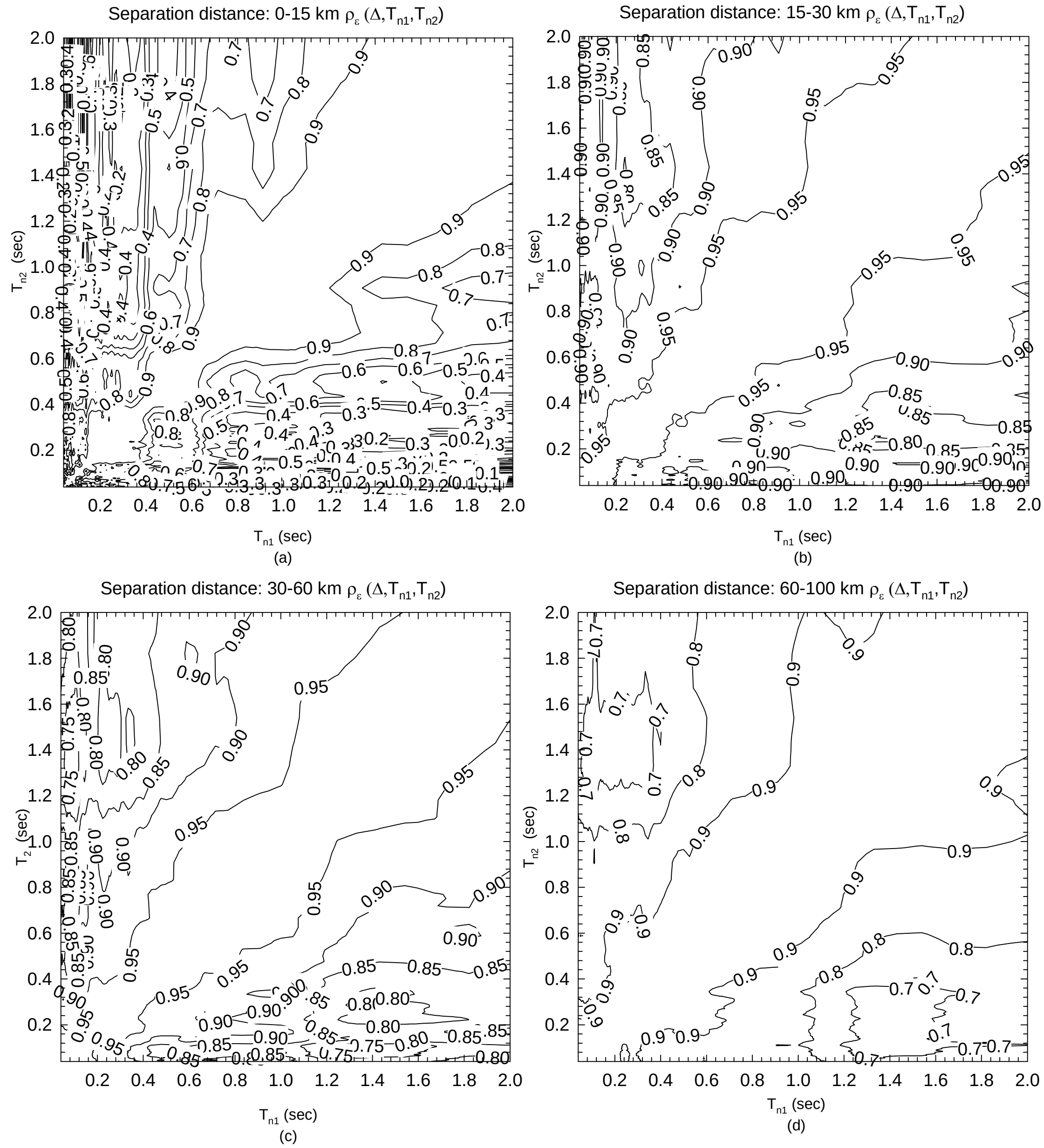

Figure 6: Observed intra-event spatial correlation ρε(Δ, Tn1, Tn2) for separation distance bins of 0-15, 15-30, 30-60 and 60-100 km for L'Aquila main shock event.

The predictive intra-event correlation coefficient model is given by

$$\rho_{\varepsilon}\left(\Delta, T_{n1,} T_{n2}\right) = \left(A0 + A1 \cdot e^{-T_{\min}} + A2 \cdot e^{-T_{\max}}\right)^{-1} \tag{8}$$

where the parameters of the model in Equation (8) for different distance range Δ are listed in Table 3, while the predicted values are shown in Figure 8 for different distance ranges. The r2 value that describes the goodness of fit oscillates between 0.9289 and 0.9496 (Figure 8), showing the robustness of the model for different distance ranges.

Δ	A0	A1	A2	R^2

0 - 20 km	0.7941	1.2669	-0.9924	0.9289
20 - 40 km	0.9180	0.7203	-0.6322	0.9496
40 – 60 km	0.9014	0.7684	-0.6587	0.9420
60 – 80km	0.8480	1.2394	-1.0756	0.8823

Table 3: Parameters of the correlation coefficient model for equation (8).

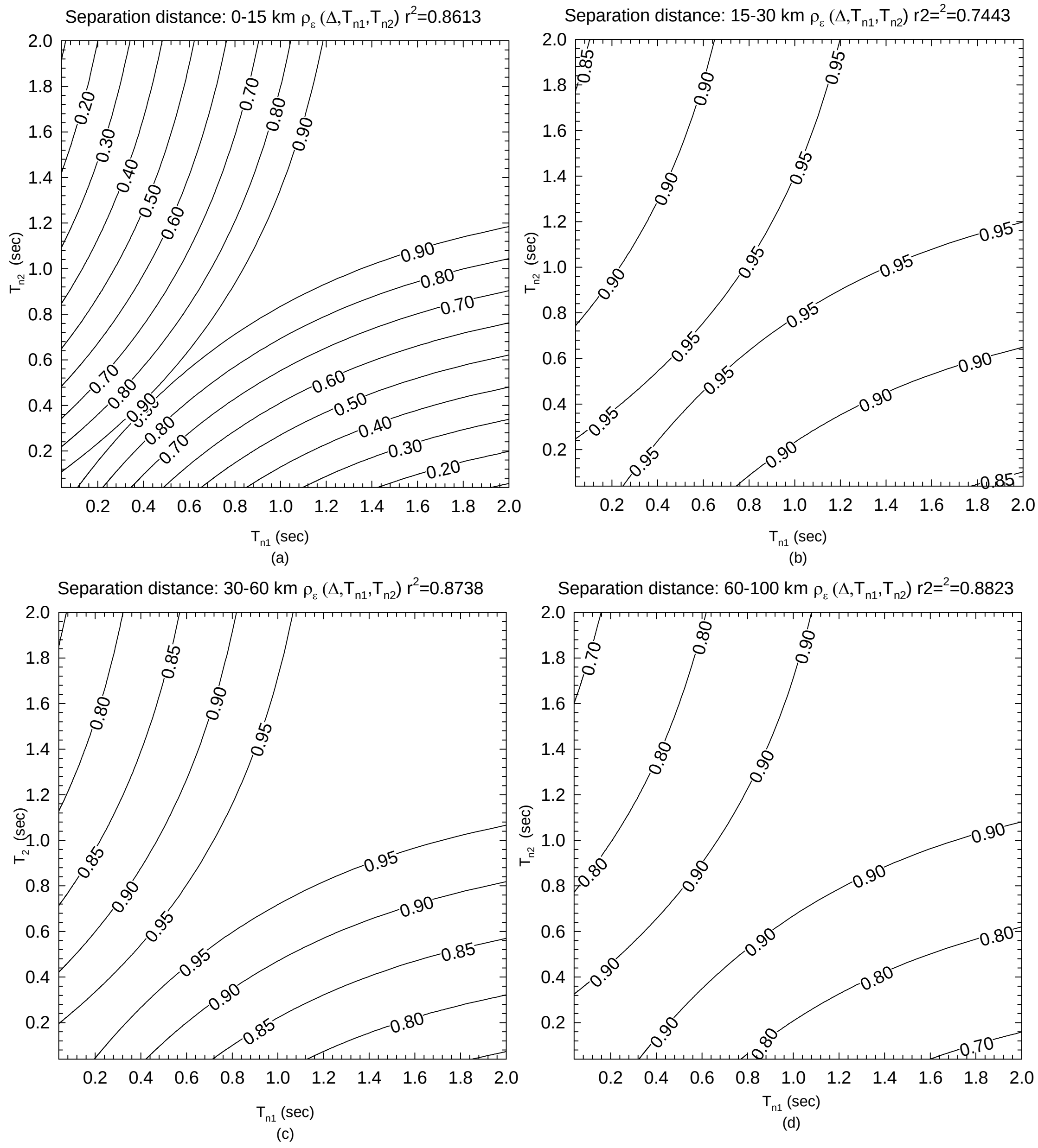

Figure 7: Intra-event spatial correlation model ρε(Δ, Tn1, Tn2) for separation distance bins of 0-15, 15-30, 30-60 and 60-100 km for L'Aquila main shock event.

5.2 Proposed predictive inter-event correlation equations for $\rho_\eta(T_{n1}, T_{n2})$

The inter-event correlation of pseudo spectra acceleration is evaluated by using regression residuals $\eta(T_n)$, based on the records from the earthquakes in Table 1 using the procedure described above. For a given pair of two natural vibration periods T_{n1} and T_{n2}, $\rho_\eta(T_{n1}, T_{n2})$ is evaluated by using the Pearson's linear correlation coefficient. The observed values of $\rho_\eta(T_{n1}, T_{n2})$ are shown in Figure 9a showing that the inter-event correlation decreases monotonically as the inter period separation distance increases. The correlation has been evaluated using the stations that were recording the seismic series of 2009 L'Aquila earthquake. To characterize $\rho_\eta(T_{n1}, T_{n2})$ the following predictive model is proposed

$$\rho_\eta\left(T_{n1,}T_{n2}\right)=e^{\left(A0+A1/T_{\min}+A2/T_{\min}^{1.5}+\cdot A3/T_{\max}+A4/T_{\max}^{2}\right)} \tag{9}$$

where the parameters of the model are respectively, A0=-0.0045; A1=-0.02256; A2=0.0036; A3=0.0165 and A4=-0.0005.

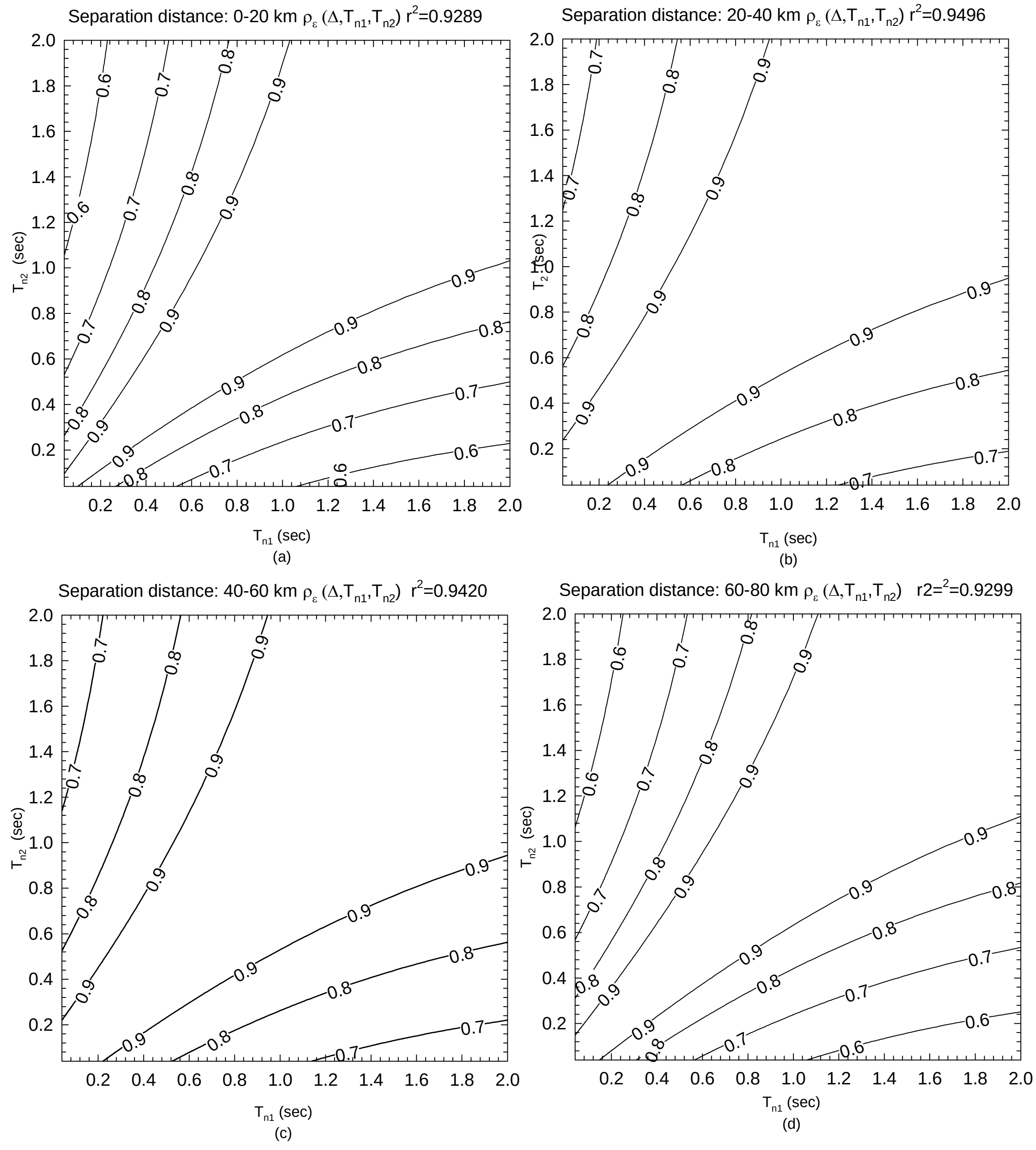

Figure 8: Intra-event spatial correlation model ρε(Δ, Tn1, Tn2) for separation distance bins of 0-20, 20-40, 40-60 and 60-80 km for all events.

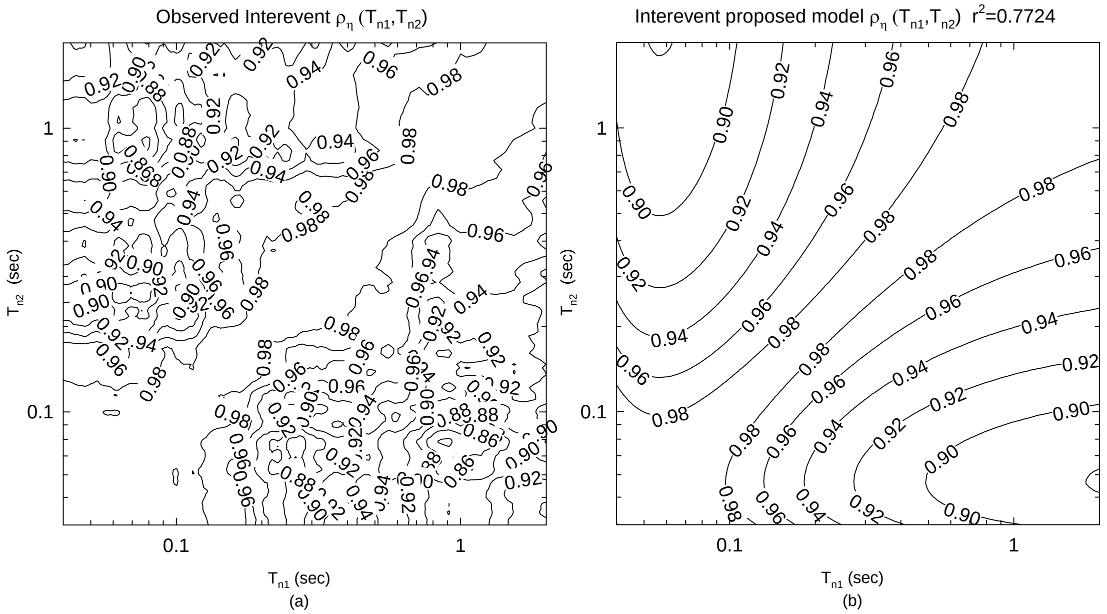

(a)

(b)

Figure 9: Inter-event correlation model ρη(Tn1, Tn2).

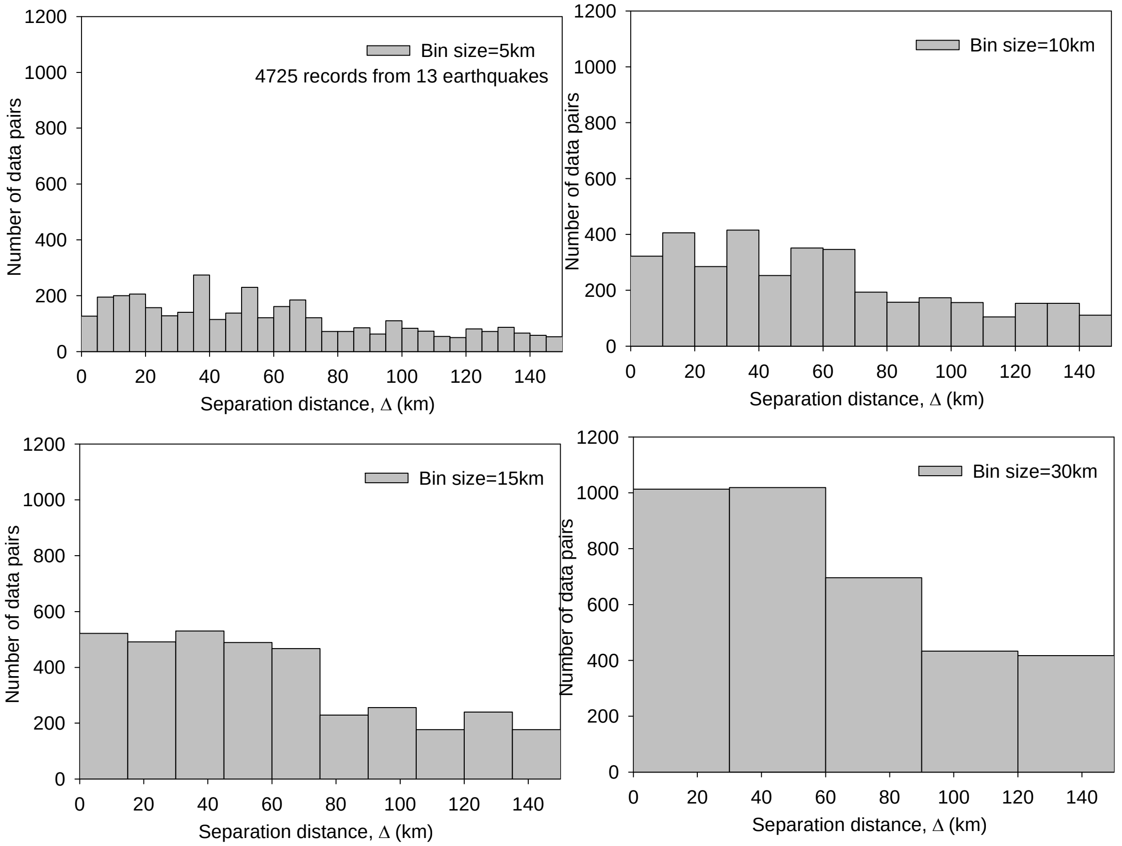

Figure 10: Histogram of the number of strong ground motion data pairs by different size bins.

The predictive values of $\rho_\eta(T_{n1}, T_{n2})$ based on equation (9) are shown in Figure 9b. The comparison of the observed and predictive values of shows a good fit (r^2=0.77) by capturing the observed values of $\rho_\eta(T_{n1}, T_{n2})$ for shallow earthquakes and for the central region of Italy however it is important to mention that results may not be stable due to the limited number of available samples.

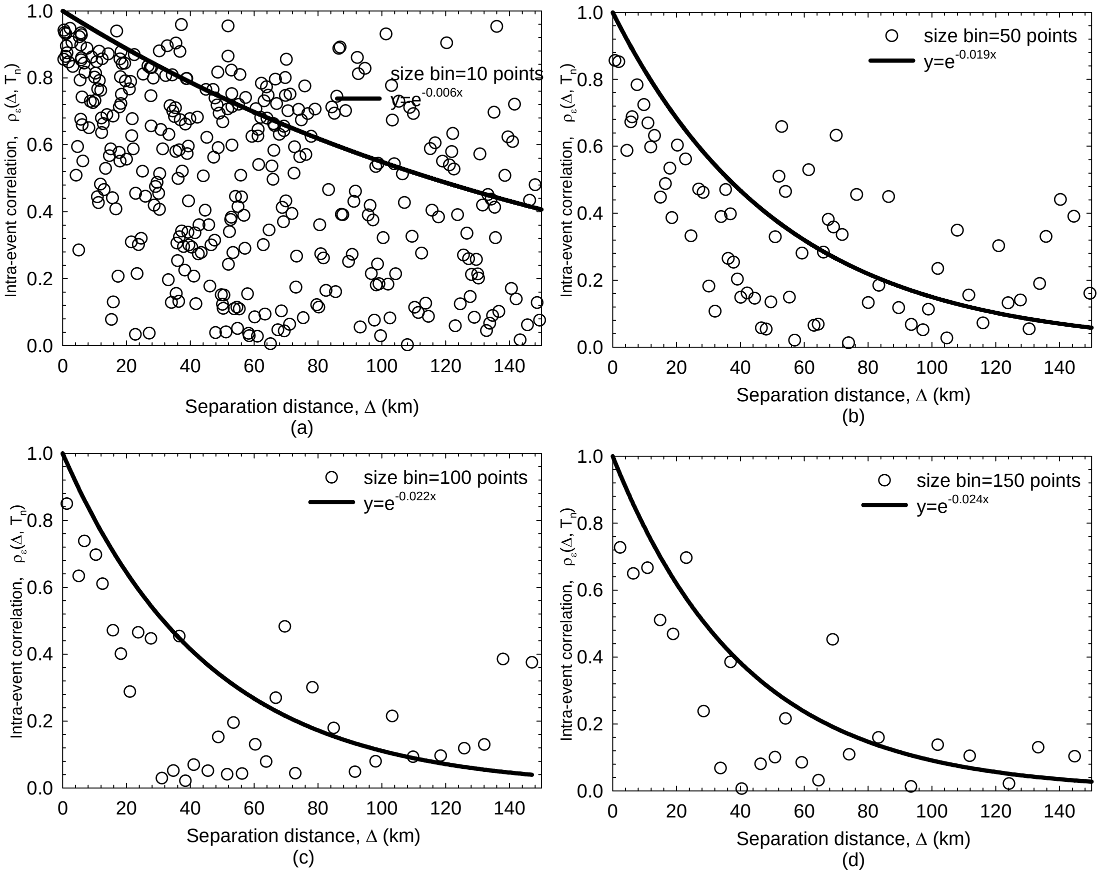

Figure 11: Overall intra-event spatial correlation for PSA at 0.2 sec using all shallow events (13 L'Aquila after-shocks) for different size bins.

5.3 Sensitivity to the size bin resolution

One of the goals of this research is to investigate the intra-event spatial correlation of L'Aquila earthquake ground motions with short separation distances; therefore it is of particular interest to inspect how many data pairs can be selected from the records using different bin size resolutions as shown in the histogram in Figure 10. In order to achieve a good estimate of the correlation coefficient at the short separation distances it is necessary at least 300 data pairs that can be obtained using a bin size resolution of 10 km. At large separation distances above 80 km the number of data pairs from the selected records reduce to half with respect to the short separation distances, regardless the bin size resolution. This brings to the conclusion that the estimation of the correlation coefficient at large separation distances is less accurate with respect to the short separation distances especially when the bin size resolution reduces to 5 km as shown in Figure 10a. This observation should be taken in account when considering results in the figures shown in the paper.

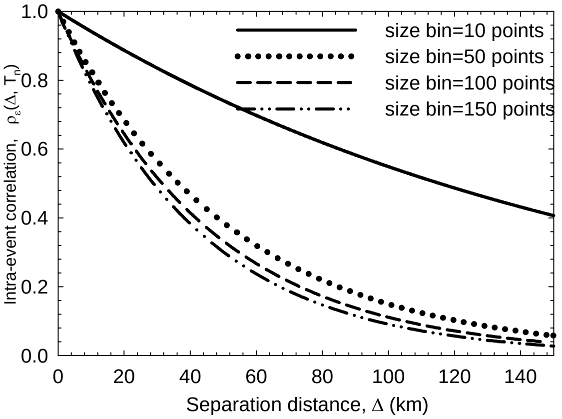

Figure 12: Comparison of fitted curves for intra-event spatial correlation at PSA of 0.2 sec and different size bins.

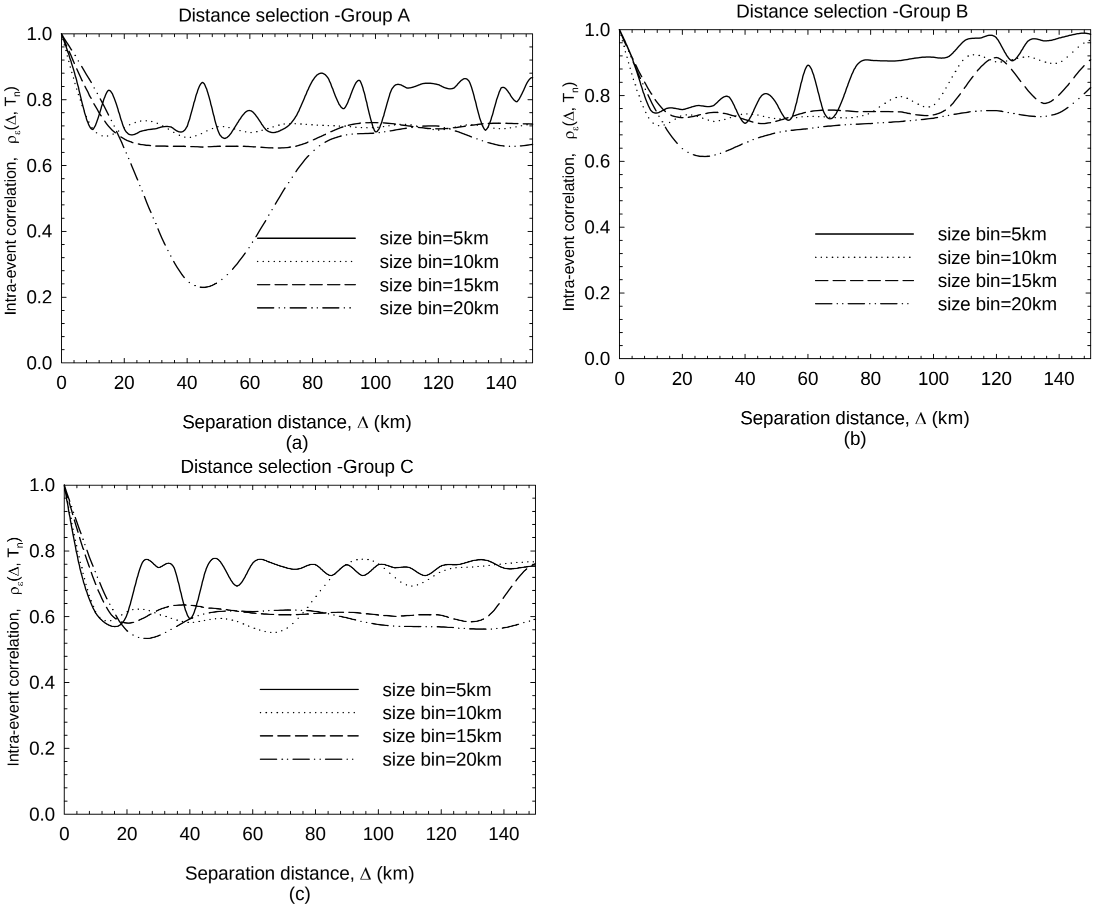

(a)

(b)

(c)

Figure 13: Intra-event spatial correlation for different size bins and PSA of 0.2 sec divided by distance selection.

Observing Figure 11 and Figure 12 it is shown that the intra-event spatial correlations based on the L'Aquila earthquakes aftershocks decrease gradually with increasing inter-station separation distance when the vibration period is 0.2 sec.

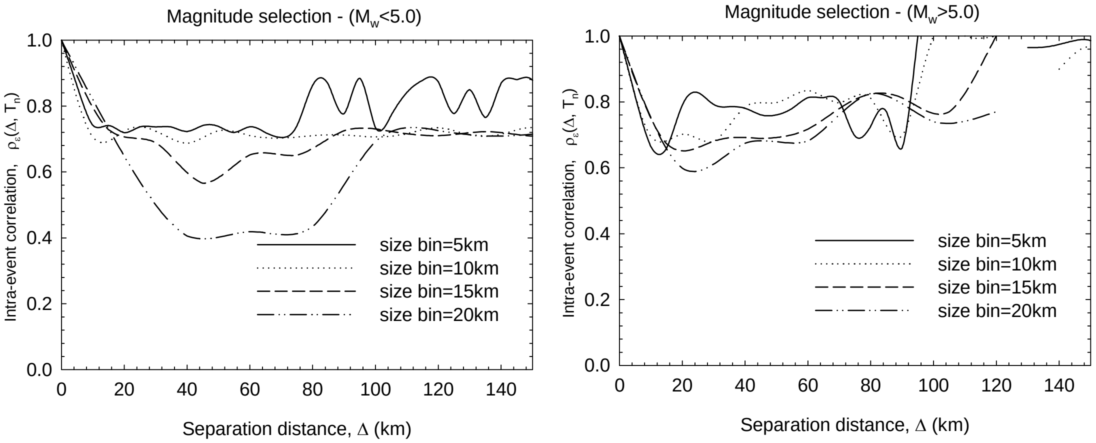

Figure 14: Intra-event spatial correlation for different size bins and PSA of 0.2 sec divided by magnitude selection.

With low resolution of the bin size (Figure 11a) the spatial correlation data points show large variability, so results due to the smaller number of available samples are not stable, therefore the parameters of the model in equation (6) given in Table 4 are uncertain, and discretion is required in adopting such models for seismic hazard and risk assessment of spatially distributed structures.

points	10	50	100	150
$\alpha(T_n=0.2s)$	0.006	0.019	0.022	0.024

Table 4: Parameters of the model for equation (6).

By increasing the bin size resolution to at least 50 points (corresponding to a bin size of about 10 km) the estimation of the parameters of the model in equation (6) is more stable, because a larger database is used and the decaying rate of the intra-event spatial correlation is more reliable as shown in Figure 12. In summary, the results reported by these research efforts reveal different rates of decay of correlation with separation distance that may be caused by regional peculiarities [3], because the site-to-site correlation depends on ground conditions of the sites and it will decrease for sites that do not share the same geology. It is also noted that the decay rate of the spatial correlation of the PSA responses depends on the natural vibration period and it is more gradual for longer natural vibration periods.

5.4 Sensitivity of observed intra-event spatial correlation to magnitude and distance

By grouping the earthquake sets according to the scheme in Figure 2b using the epicentral distance, it seems that the intra-event spatial correlation does not change with the distance when the size of the bin resolution is between 10 and 20 km as shown in Figure 13. This behavior is clear and it explained by the fact that the intra-event spatial correlation depends on the soil type and geological setting. This trend is not followed by the group A when the resolution of the bin size is 20 km that is probably too large, generating numerical errors. In Figure 14 is shown the intra-event spatial correlation coefficient is not affected by the magnitude selection. For large intensity earthquakes (with Magnitude M>5.0) the correlation increases for distances more than 100km, however, as shown before in Figure 10, the estimation of the observed intra-event correlation coefficient at large separation distances is not reliable.

6 CONCLUDING REMARKS

The paper, based on the statistical analysis of the L'Aquila earthquake records in Italy, proposes empirical intra-event and inter-event spatial correlation relations to predict the spatial correlation of the PSA responses to be used for shallow earthquakes in Central Italy.

Results of this paper show that the ground motion correlation structure is highly dependent on local geology and on peculiarities of the propagation path, however the spatial correlation coefficient decreases as the separation distance increases. The analysis results also indicate that the intra-event spatial correlation is not affected by the magnitude. A single generalized spatial correlation model may not be adequate for all European territory or similar larger areas, but it can provide a first preliminary estimation of the correlation. The characteristics are very important for assessment of seismic hazard analysis and spatially distributed systems (lifelines) and Shake Map generation. Due to the limited amount of observed data, the proposed models are affected by epistemic uncertainties. Applicability of the model to other regions remains to be tested. As future earthquakes at closely-spaced locations are recorded, these aspects of intra-event spatial correlation should be further investigated.

ACKNOWLEDGMENTS

The research leading to these results has received funding from the European Community's Seventh Framework Programme - Marie Curie International Reintegration Actions - FP7/2007-2013 under the Grant Agreement n° PIRG06-GA-2009-256316 of the project ICRED - Integrated European Disaster Community Resilience. The author is grateful to Katsuichiro Goda for valuable comments and suggestions that allow improving the paper.

REFERENCES

[1] D.M. Boore, J.F. Gibbs, W.B. Joyner, J.C. Tinsley, and D.J. Ponti. Estimated ground motion from the 1994 Northridge, California, Earthquake at the site of the Interstate 10 and La Cienega Boulevard Bridge collapse, West Los Angeles, California. *Bull. Seism. Soc. Am.*, 93, 2737-2751, 2003.

[2] M. Wang, and T. Takada. Macrospatial correlation model of seismic ground motions. *Earthquake Spectra*, 21, 1137-1156, 2005.

[3] K. Goda, and G.M. Atkinson. Probabilistic Characterization of Spatially Correlated Response Spectra for Earthquakes in Japan. *Bull. Seism. Soc. Am.*, 99(5), 3003-3020, 2009

[4] D.R. Brillinger, and H.K. Preisler. An exploratory analysis of the Joyner-Boore attenuation data. *Bull. Seism. Soc. Am.,* 74, 1441-1450, 1984.

[5] D.R. Brillinger, and H.K. Preisler. Further analysis of the Joyner-Boore attenuation data. *Bull. Seism. Soc. Am.*, 75, 611-614, 1985.

[6] C.C.P. Tsai, Y.H. Chen, and C.H. Liu. The path effect in ground-motion variability: An application of the variance-components technique. *Bull. Seism. Soc. Am.*, 96, 1170-1176, 2006.

[7] H.P. Hong, and K. Goda. Orientation-dependent ground-motion measure for seismic-hazard assessment. *Bull. Seismol. Soc. Am*, **97**, 1525-1538, 2007

[8] K. Goda, and H.P. Hong. Spatial Correlation of Peak Ground Motions and Response Spectra. *Bull. Seism. Soc. Am.*, 98(1), 354-365, 2008.

[9] N. Abrahamson, and R.R. Youngs. A stable algorithm for regression analyses using the random effects model. *Bull. Seism. Soc. Am.*, 82, 505-510, 1992.

[10] Working Group ITACA (2010) - Data Base of the Italian strong motion records: http://itaca.mi.ingv.it.

[11] N.N. Ambraseys, K.A. Simpson, and J. Bommer. Prediction of horizontal response spectra in Europe. *Earthquake Engineering & Structural Dynamics*, 25(4), 371-400, 1996.

[12] G.P. Cimellaro, I.P. Christovasilis, A.M. Reinhorn, A. De_Stefano, and T. Kirova. L`Aquila Earthquake of April 6th, 2009 in Italy: Rebuilding a resilient city to multiple hazard. MCEER Technical Report –MCEER-10-0010, State University of New York at Buffalo (SUNY), Buffalo, New York, 2010.

[13] G.P. Cimellaro, Y.-N. Huang, and A. De_Stefano. "Correlation in spectral accelerations of European ground motion records." Proceedings of the 9th US National and 10th Canadian Conference on Earthquake Engineering (9NCEE), 25-29 July, 2010, Toronto, Canada, Year.

COMPDYN 2011
3^{rd}ECCOMAS Thematic Conference on
Computational Methods in Structural Dynamics and Earthquake Engineering
M. Papadrakakis, M. Fragiadakis, V. Plevris (eds.)
Corfu, Greece, 25-28 May 2011

AN EFFICIENT META-MODELING APPROACH FOR NATURAL FREQUENCY APPROXIMATION: THE *Q*-METHOD

A. Gallina[1], **L. Pichler**[1,2], **T. Uhl**[1], **L. A. Bergman**[2]

[1]Department of Robotics and Mechatronics, AGH University of Science and Technology
al. Mickiewicza 30, 30059, Krakow, Poland
e-mail: {agallina,tuhl}@agh.edu.pl

[2] Department of Aerospace Engineering, University of Illinois at Urbana-Champaign
104 S. Wright Street, Urbana, IL 61801, USA
e-mail: Lukas.Pichler@ymail.com , lbergman@illinois.edu

Keywords: Structural Dynamics, Meta-modeling, Uncertainty Analysis, Mode Veering, Characteristic Polynomial

Abstract. *The variability and uncertainty of structural parameters have a large impact on the modal properties and need to be considered for an adequate assessment of the dynamic response. Recently, so-called modal meta-models were used to approximate the natural frequencies of structures modeled with finite elements when structural modifications are present. The present paper proposes a viable meta-modeling approach which, based on the approximation of the coefficients of the characteristic polynomial, succeeds in accurately predicting the natural frequencies of the system in presence of veering assuming stiffness variability. The meta-model is based on* m^p+p *finite element analyses, where* m *denotes the number of analyzed modes and* p *the number of parameters. The number of required analyses is independent of the model or of the complexity of the evolution of the modal parameters. Furthermore, the obtained modal meta-model is used in combination with a procedure for efficient detection of veering and crossing phenomena without resorting to time-consuming mode tracking procedures.*

1 INTRODUCTION

The evolution of the modal parameters (e.g., eigenfrequencies) as a function of changing structural parameters provides important information required for the response assessment of a structure. In many cases, the studied modal parameters show fairly smooth evolutions which suggest the utilization of direct approximations of these modal quantities as functions of the varying structural parameters, requiring only few finite element analyses. This fact proves to be especially advantageous in the case of optimization or uncertainty analysis, where many analyses with different parameter combinations need to be carried out. The utilization of approximations based on the results of several finite element runs, which are carried out according to a planned design, provides a means for reducing the computational costs. The dependence on a large number of full finite element simulations can thus be eliminated by employing fast surrogate or meta-models [1]. Relatively simple approximations based on linear regression, polynomial interpolation, kriging, radial basis functions, etc. are generally used for meta-modeling. In structural dynamics, so-called modal meta-models are introduced and refer to the case when these techniques are used to approximate modal quantities, i.e., eigenfrequencies, eigenvectors, mode shapes, modal mass, etc. Examples are the approximation of the modal parameters of a structure using linear regression with polynomial functions [2], the approximation of the eigenvalues of civil structures using polynomial functions [3] or the kriging approximation of the modal mass and stiffness as utilized in [4]. In recent investigations concerning reliability and uncertainty analysis, the linear combination of the modal parameters of a reference system is used to represent the varying modal parameters [5].

Despite the versatility and simplicity to use direct modal meta-modeling - direct refers to *direct approximation* of the response quantities of interest - recent investigations [2] have pointed out its limitations which arise when the dynamic behavior of undamped structures exhibits mode degeneration. In the presence of degenerate phenomena such as mode crossing, mode veering [6] or mode coalescence [7], the evolution of the modal parameters generally strongly varies from a smooth evolution. Consequently, the direct approximation of the modal properties gets more involved under these conditions, because only a considerably increasing number of design points can improve the quality of the approximation.

The issue of inaccurate or erroneous approximations arising from the utilization of direct meta-modeling was discussed in [8] and indirect modal meta-modeling is proposed. The idea of the indirect approach is that quantities involved in the structural eigenvalue problem are approximated before proceeding with the solution of the eigenvalue problem (see Fig. 1). As an example, in the simplest case the structural matrices (i.e., the mass and stiffness matrices) can be approximated; such approaches based on the interpolation of the structural matrices evaluated at some supporting points are used for the eigenfrequency and eigenvector approximation and are introduced in, e.g. [8, 9].

When the evolution of the eigenfrequencies is of interest, the approximation of the coefficients of a reduced characteristic polynomial can be used to analyze the influence of structural parameter changes to the eigenfrequencies. Such an approach was first introduced in [10] and a clear theoretical description of the approach in the presence of stiffness variations was presented in [11]. The proposed procedure yields very accurate predictions of the natural frequencies. It can be shown that the coefficients of the reduced characteristic polynomial demonstrate smooth behavior when linear changes are introduced for the elements of the *stiffness matrix*. Independent of the model and the complexity of the modal behavior, the procedure always requires $m^p + p$ finite element runs, where m and p are the number of analyzed modes and input parameters, respectively. Differently from a direct modal meta-modeling approach, in the indirect approach based on the approximation of the chareacteristic polynomial, no mode tracking procedure is required to account for mode switching. This means that the method does not provide any information about the physical evolution of the modes. To obtain nontheless a continuous (physical) evolution of the eigenfrequencies a step-wise procedure is applied. The procedure uses the fast predictions of the modal meta-model to identify and quantify crossing or veering phenomena. A major advantage of this approach is that the presence of the veering regions can be determined. This further allows the design of a system which is not prone to unexpected dynamic behavior associated with mode degeneration.

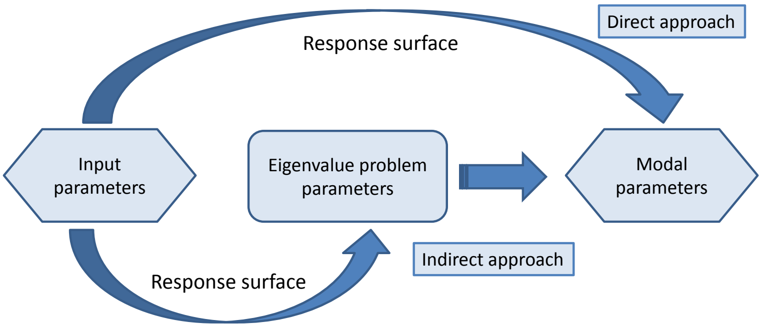

Figure 1: Modal meta-modeling: direct and indirect approaches.

In this paper, first the procedure as described in more detail in [11] is presented in Section 2 and is then combined with an algorithm for eigenfrequency loci reconstruction. This stepwise procedure (Section 3, see also [10]) allows us to detect mode degeneration within the analyzed parameter space. Finally, the effectiveness of the proposed approach is demonstrated in Section 4 for a system affected by crossing and veering.

2 THE *q*-METHOD

The q-method is a meta-modeling strategy for eigenfrequency approximation of the a structure subjected to stiffness variability. The procedure consists of directly approximating the coefficients of the system's characteristic polynomial. In the following it is shown that $m^p + p$ finite element runs provide a sufficient base for achieving a correct description of the characteristic polynomial coefficients and consequently of the eigenfrequencies evoltion, with m the number of analyzed modes and p input parameters. Moreover, a viable approach for the approximation of the coefficients is proposed.

The eigenvalue problem for a system at its nominal configuration can be written as

$$(\mathbf{K}_0 - \lambda_0 \mathbf{M}_0)\, \phi_0 = 0\,, \tag{1}$$

with $\mathbf{K}_0$, $\mathbf{M}_0$, λ_0 and ϕ_0 denoting the stiffness matrix, mass matrix, eigenvalue and eigenvector of the nominal system, respectively. A possible approximation of the modal parameters at a perturbed system configuration is obtained by applying modal reduction [12]. Modal reduction implies the definition of a eigenvector modal basis $\mathbf{\Phi}_0$ that allows one to approximate the perturbed eigevector ϕ^* as a linear combination of the assumed modal basis

$$\phi^* = \mathbf{\Phi}_0 \boldsymbol{\alpha}\,. \tag{2}$$

Under this assumption and for constant mass matrix, it is possible to write a reduced eigenvalue problem of the perturbed system as

$$\left(\mathbf{\Phi}_0^T\mathbf{K}\mathbf{\Phi}_0 - \lambda^*\mathbf{\Phi}_0^T\mathbf{M_0}\mathbf{\Phi}_0\right)\boldsymbol{\alpha} = 0\,, \tag{3}$$

with $\mathbf{K}$ and λ^* representing the stiffness matrix and the approximated eigenvalue of the perturbed system. The reduced eigenvalue problem yields very accurate modal parameters approximation as long as the analyzed eigenvectors of the perturbed system remains within the same eigenvector subspace spanned by the truncated set of nominal modes $\mathbf{\Phi}_0$. This is the case for mode veering where the eigenvectors, even though undergoing large variations within the veering region, stay and rigidly rotate within the same eigenvector subspace. Therefore, modal reduction is effective in the presence of mode veering provided that the assumed modal basis includes all pairs of eigenvectors involved in the veering phenomenon. Under this condition and using a truncated modal basis of m eigenvectors, the m modes of the system with perturbed stiffness will be studied in the following. Mass-normalizing the eigenvectors of $\mathbf{\Phi}_0$ Eq. (3) becomes

$$\left(\mathbf{K}^* - \lambda^*\mathbf{I}\right)\boldsymbol{\alpha} = 0\,, \tag{4}$$

with

$$\mathbf{K}^* \;=\; \mathbf{\Phi}_0^T\mathbf{K}\mathbf{\Phi}_0\,. \tag{5}$$

Each element k^*_{uv} of $\mathbf{K}^*$ can be written as a sum of all terms of the perturbed stiffness matrix

$$k^*_{uv} = \sum_{i=1}^{n}\phi_{0ui}\sum_{j=1}^{n}\phi_{0vj}k_{ij}\,, \tag{6}$$

with n the number of degrees of freedom of the model and ϕ_{0ui} meaning the u-th degree of freedom of the i-th mode of the modal basis. Eq. (6) shows that the k^*_{uv} are linear functions of k_{ij}. When the elements k_{ij} undergo linear changes with respect to an assumed input parameter, the elements k^*_{uv} also represent a linear behavior with respect to the same input parameter.

The characteristic polynomial associated with the reduced eigenvalue problem of Eq. (4) is given by

$$\lambda^{*m} + q_{m-1}\lambda^{*m-1} + ... + q_1\lambda^* + q_0 = 0\,. \tag{7}$$

The q coefficients (thus the name q-method) of the Eq. (10) can be expressed in terms of the elements k^*_{uv} through the relations

$$\begin{aligned} q_{m-1} =&(-1)^1\sum_{r=1}^{m}|\mathbf{K}^*_{r,r}| = (-1)^1\sum_{r=1}^{m}k^*_{rr} \\ q_{m-2} =&(-1)^2\sum_{r=1}^{m-1}\sum_{s=r+1}^{m}|\mathbf{K}^*_{\{r,s\},\{r,s\}}| \\ q_{m-3} =&(-1)^3\sum_{r=1}^{m-2}\sum_{s=r+1}^{m-1}\sum_{t=s+1}^{m}|\mathbf{K}^*_{\{r,s,t\},\{r,s,t\}}| \\ &\cdots \\ q_0 =&(-1)^m|\mathbf{K}^*|\,, \end{aligned} \tag{8}$$

with $|\mathbf{K}^*_{\{r,s,t\},\{r,s,t\}}|$ denoting the determinant of a principal minor of $\mathbf{K}^*$

$$|\mathbf{K}^*_{\{r,s,t\},\{r,s,t\}}| = \begin{vmatrix} k^*_{rr} & k^*_{rs} & k^*_{rt} \\ k^*_{sr} & k^*_{ss} & k^*_{st} \\ k^*_{tr} & k^*_{ts} & k^*_{tt} \end{vmatrix} . \tag{9}$$

According to Eq. (6) and 8, it is seen that q_{m-1} is a linear function of the factors k_{ij}, q_{m-2} a second order polynomial with interactions, q_{m-3} a third order polynomial with second order interactions, and so forth. The highest order function is due to q_0 which is a m-th order polynomial with $m-1$ order interactions. Any variation of the structural parameters which is linear with k_{ij} is related to the q coefficients by the same kind of relationship. Thus, when a number p of structural parameters are analyzed simultaneously, a correct approximation of the m coefficients q can be obtained through a set of m-th order polynomial functions with $(m-1)$th order interactions. Polynomial regression can efficiently interpolate these functions using $m^p + p$ observations.

The approximation of the q coefficients by using Eq. (8) is not handy as it involves operations with the stiffness matrix which is usually very large. A more viable approach exploits the exiting relation between the coefficients of a polynomial equation and its roots, that is between the characteristic polynomial coefficients and the eigenfrequencies associated to the reduced eigenvalue problem Eq. (4). Indeed, rewriting Eq. (10) as

$$(\lambda^* - {\lambda^*}_1)(\lambda^* - {\lambda^*}_2)...(\lambda^* - {\lambda^*}_m) = 0\,, \tag{10}$$

and solving the multiplication by binomials, it is possible to express the q in terms of the roots of λ^*. This allows one to calculate the q coefficient at the $m^p + p$ design sites directly from the results of FE analyses. Then, the q coefficients are approximated within the design space via polynomial regression and the eigenvalues at untried points are calculated by solving the approximated mth-order characteristic polynomial.

The big advantage of the proposed methodology with respect to a direct modal meta-modeling consists of being insensitive to the complexity of the modal behavior. However, it is important to bear in mind that the method is effective as long as all analyzed modes move within the subspace spanned by the same modal basis within the whole domain of interest. As mentioned above, this means also that in the presence of veering phenomena, the assumed modal basis has to accommodate aways both modes involved in the veering. The detection of coupled modes resulting from veering phenomena can be accomplished by the modal assurance criterion (MAC) matrix histogram.

From the calculation of the MAC values between every possible pair of eigenvectors and design points it is possible to assemble the MAC matrix histogram. In this matrix, each element (i.e., each histogram) shows the frequency of occurrence of a certain MAC value (see Fig. 2). The *y*-axis shows the number of occurrences and the *x*-axis labels the range of the MAC value form 0 to 1 which for convenience is subdivided into 10 parts. A dispersion on the diagonal of this matrix clearly indicates mode veering. Fig. 2 shows that the modes *j* and *k* are coupled with each other but decoupled from mode *i*.

3 MODE VEERING DETECTION

The q-method approximates the coefficients of the characteristic polynomial and can be used as an efficient tool to investigate mode degeneration phenomena. This is accomplished in the

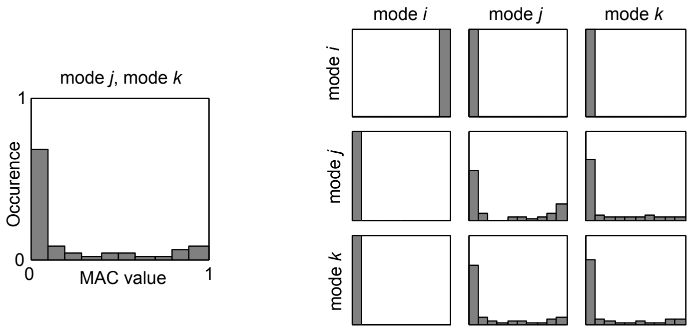

Figure 2: MAC matrix histogram. The modes *j* and *k* are coupled with each other but decoupled from *i*.

following way. The meta-model of the q-coefficients is used to evaluate the eigenfrequencies by the solution of Eq. (10). Due to the fact that no eigenvectors are calculated, no information about the presence of veering or crossing can be extracted from MAC analysis. However, the capability of the modal meta-model to correctly predicting the eigenfrequencies can be utilized for developing an efficient iterative procedure that detects possible mode degeneration within the parameter space. The step-wise algorithm is based on tangential approximations and at each step it is checked whether a change in the mode order is occurring within the range of Δ. In the sample graph of Fig. 3 this would be the case for the step ② − ③. The eigenfrequencies obtained from the q-method are denoted as f (blue: $\overline{acb}$) and g (green $\overline{dce}$) as shown in Fig. 3 and 4; the eigenfrequencies given after the construction of the eigenfrequency locus are denoted as F ($\overline{ace}$) and G ($\overline{dcb}$). The correct representation of the evolution of the modes is accomplished in the following way. First, initial values are calculated using the meta-model; they are denoted with the superscript $^{(0)}$, i.e., $F^{(0)} = f^{(0)}$ and $G^{(0)} = g^{(0)}$. Then, the new values of the eigenfrequencies at position $^{(1)}$ are calculated using finite tangential approximations

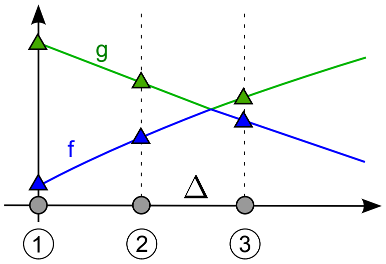

Figure 3: Step-wise algorithm.

$$F^{(1)} = \begin{cases} f^{(1)}, & \text{if } \|F^{(0)} + \frac{\partial f^{(0)}}{\partial q}\Delta - f^{(1)}\| < \|F^{(0)} + \frac{\partial f^{(0)}}{\partial q}\Delta - g^{(1)}\| \\ g^{(1)}, & \text{if } \|F^{(0)} + \frac{\partial f^{(0)}}{\partial q}\Delta - f^{(1)}\| > \|F^{(0)} + \frac{\partial f^{(0)}}{\partial q}\Delta - g^{(1)}\| \end{cases} \tag{11}$$

and

$$G^{(1)} = \begin{cases} g^{(1)}, & \text{if } \|G^{(0)} + \frac{\partial g^{(0)}}{\partial q}\Delta - g^{(1)}\| < \|G^{(0)} + \frac{\partial g^{(0)}}{\partial q}\Delta - f^{(1)}\| \\ f^{(1)}, & \text{if } \|G^{(0)} + \frac{\partial g^{(0)}}{\partial q}\Delta - g^{(1)}\| > \|G^{(0)} + \frac{\partial g^{(0)}}{\partial q}\Delta - f^{(1)}\| \end{cases} \tag{12}$$

In Eq. (11) $\frac{\partial f^{(0)}}{\partial q}$ denotes the derivative at $f^{(0)}$ and in Eq. (12) $\frac{\partial g^{(0)}}{\partial q}$ denotes the derivative at $g^{(0)}$ which are calculated numerically using a small increment ∂q; $\partial q \ll \Delta$. If the second lines of Eq. (11) and (12) appear to be correct, this is an indication of a crossing or veering occurrence within the interval Δ as shown in Fig. 4 for ② − ③.

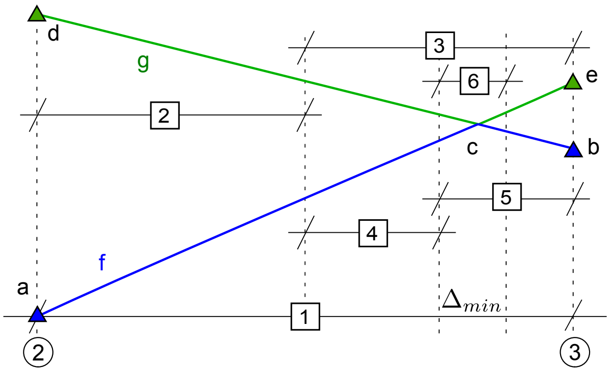

Figure 4: Bisection algorithm.

At every subsequent step, the interval is halved, until either the initial crossing is revealed to be a veering, or an established Δ_{min} is reached. In the former case, the smallest Δ_{out} is stored, and the veering point P_v is determined. Then the domain Ω_v of mode degeneration is assumed to be within the interval $[P_v - I_v, P_v + I_v]$ with $I_v = \Delta_{out}$ providing a metric for the veering intensity. In the latter case, this means that either the modes are crossing, or the modes are sharply veering within the current Δ_{min}. In both cases, the crossing/veering point P_v is determined and the domain Ω_v within which mode degeneration occurs $[P_v - I_v, P_v + I_v]$ with $I_v = \Delta_{min}$ calculated. In case of abrupt veering or crossing, a so-called veering/crossing line can be drawn by connecting the points P_v; otherwise the evaluation of the region Ω_v is more meaningful. In general, the procedure will never distinguish between mode switching and mode veering with veering region smaller than Δ_{min}, however, by reducing the value of Δ_{min} it is possible to recognize sharper and sharper veering phenomena.

4 NUMERICAL EXAMPLE

4.1 Model description

An assessment of the presented procedure and its capability to predict a physically meaningful evolution of the eigenvalue loci in the presence of veering is completed via a numerical example. A two-bay frame, modeled with finite elements provides a test case therefore; despite the simplicity of the structure, the model shows complex behavior of its modal parameters.
The frame model consists of three vertical plates which are connected through a horizontal plate. Two horizontal bars, linking the vertical plates, produce an additional weak coupling between the vertical plates. The frame is unconstrained. The underlying FE model consists of 320 shell elements and 423 nodes leading to 2538 degrees of freedom. Fig. 5 shows the FE model and Table 1 lists its properties at the nominal configuration.

The eigenfrequency loci evolution is approximated when the Young's moduli E_1 and E_2 of the plates 1 and 2 are changed. Both Young's moduli vary $\pm 30\%$ with respect to their nominal values, resulting in a range of $0.7 \cdot \mathrm{E}_{1,2} - 1.3 \cdot \mathrm{E}_{1,2}$.

Element	Young's modulus [Pa]	mass density ρ [kg/m^3]	ν	thickness[m] a,b	L[m]	H[m]
plates $1-4$	2.1×10^{11}	7860	0.3	0.002	0.2	1
bars	2.1×10^{11}	7860	0.3	$0.002, 0.0002$	0.5	-

Table 1: Nominal configuration of the frame.

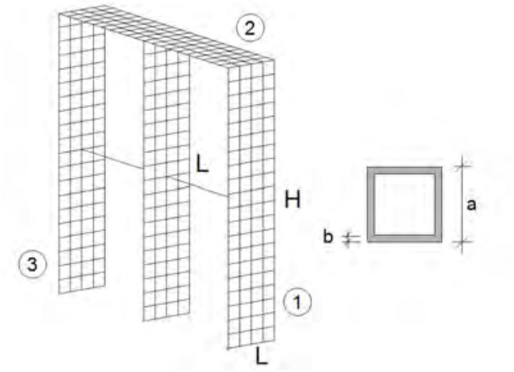

Figure 5: M-shaped frame structure.

4.2 Response surface approximation

First the MAC matrix histograms (Fig. 6) was calculated from a small number of FE runs for detecting coupled modes. The MAC matrix histogram shows a clear coupling for the modes 2 to 4. Thus, these 4 modes are selected for the further analysis.

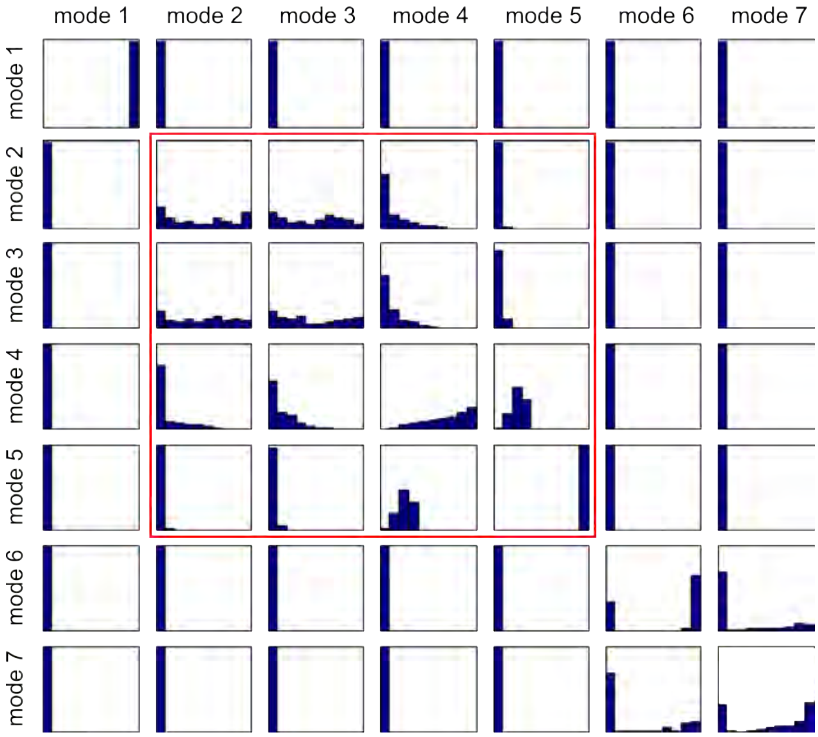

Figure 6: MAC histogram.

According to the law proposed in Section 2, $4^2 + 2 = 18$ numerical runs should suffice to accurately describe the natural frequency evolution of the analyzed modes. Thus, a 18-sample Latin hypercube sampling was carried out and 4th order polynomials (with interactions) fitted to the observations at the 18 design points via polynomial regression. The results from the q-method has been compared with the results from a direct meta-modeling approach and with the exact numerical solution calculated on a 21×21 regular grid. In particular, both meta-modeling techniques evidence high accuracy for modes 4 and 5, those not affected by degeneration (Fig. 7(a)). However, the q-method performs much better than the direct approach for modes 2 and 3, that coalesce within the parameter space as presented in Fig. 7(b). In order to assess the quality of meta-models prediction, the relative error with respect to the reference solution has been calculated at modes 2 and 3. The q-method reveals to be much more accurate than the direct method, as shown in the plots of Fig. 8.

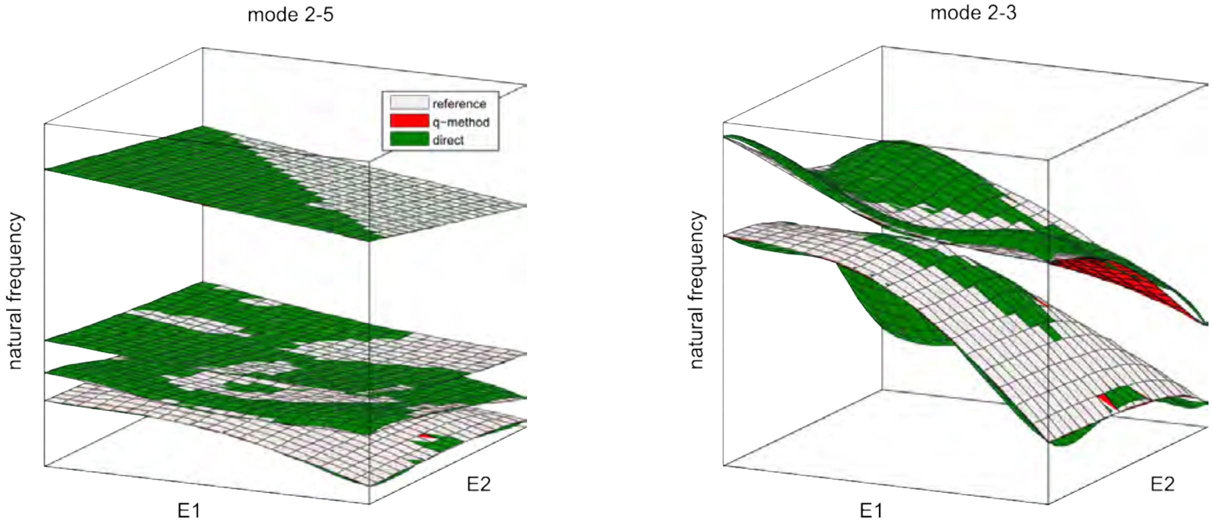

(a) (b)

Figure 7: Comparison of the eigenfrequency variation: exact solution vs. q-method and direct approximation.

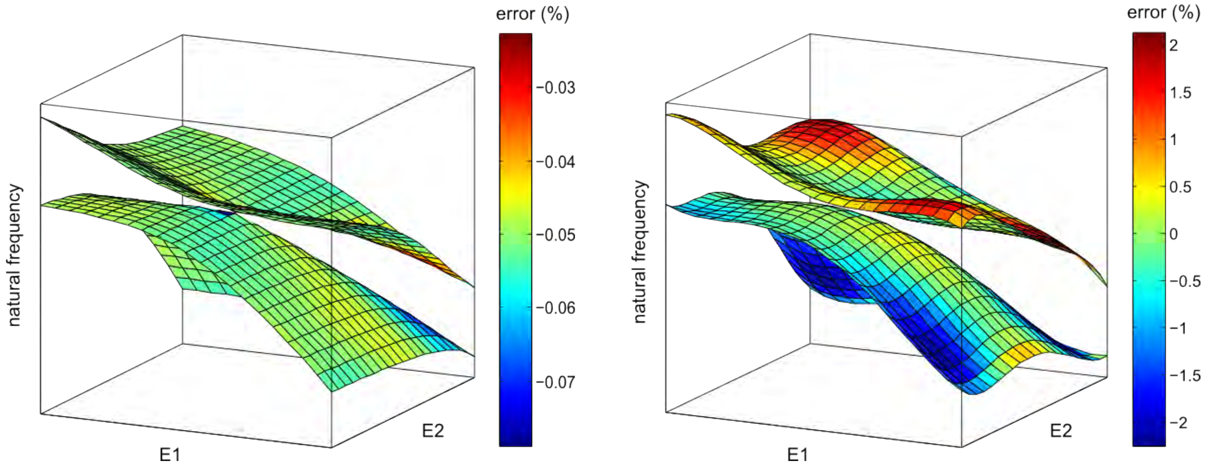

(a) q-method (b) direct method

Figure 8: Measured per cent error of the approximated responses with respect to the reference solution.

4.3 Detection of mode coalescence

The step-wise procedure was applied to a 4×20 grid which was imposed on the input parameter space. The procedure succeeded in detecting the region of mode degeneration, as presented in Section 3. The solid lines in Fig. 9 show the veering region, and the extension of the domain is given by the veering intensity $I_v = \Delta_{out}$. Close to the occurrence of mode coalescence, the veering intensity factor assumes a small value which also suggests the occurrence of abrupt veering or crossing.

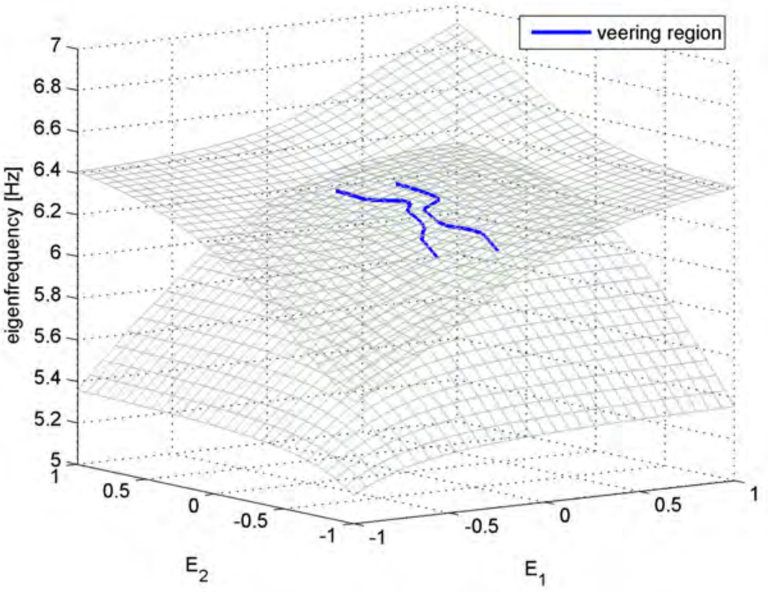

Figure 9: Spacial occurrence of coalescence.

5 CONCLUSIONS

The utilization of indirect meta-modeling for the investigation of the eigenfrequency loci evolution has been discussed in this work. A sufficient number of design sites for constructing accurate meta-models of the natural frequencies has been assessed independently of the presence of mode degeneration phenomena within the analyzed parameter space. Combined with a step-wise mode tracking procedure based on the natural frequency analysis, the modal meta-model is able to provide meaningful information about the physical mode evolution. This is an advantage with respect to direct modal meta-modeling that has difficulty in dealing with systems affected by mode veering, crossing and coalescence. A numerical example discussed the application of the methodology on a structure affected by mode coalescence. The combination of the surrogate model with the step-wise procedure provides a tool to improve the design through the identification of regions where the system dynamic behavior undergoes large modal parameter variations. In addition, it has been shown that for the examined structure, the proposed indirect meta-model is clearly outperforming a direct approximation. At present the procedure is able to only deal with systems subjected to stiffness variability. Future works will concern with the extension of the procedure to also account for mass modifications.

6 ACKNOWLEDGMENTS

This research was partially supported by the European Union under Project CIDAF7 (AG,TU) and Austrian Research Council(FWF) under Project No. J2989-N22 (LP).

REFERENCES

[1] T. Simpson, T. Mauery, J. Korte, and F. Mistree. Comparison of response surface and kriging models for multidiscilinary design optimization. Technical report, 1998. Technical Report 98-4755, AIAA.

[2] A. Gallina and T. Uhl. A modal meta-modelling for the analysis of structures subjected to input parameter variations. In *USD 2009*, 2009.

[3] J. Cheng and R.-c. Xiao. Probabilistic free vibration and flutter analyses of suspension bridges. *Engineering Structures*, 27(10):1509–1518, August 2005.

[4] M. De Munck, D. Moens, W. Desmet, and D. Vandepitte. A response surface based optimisation algorithm for the calculation of fuzzy envelope frfs of models with uncertain properties. *Computers & Structures*, 86(10):1080–1092, May 2008.

[5] L. Pichler, H. J. Pradlwarter, and G. I. Schuëller. A mode-based meta-model for the frequency response functions of uncertain structural systems. *Computers & Structures*, 87(5-6):332–341, 2009.

[6] A. W. Leissa. On a curve veering aberration. *Zeitschrift für Angewandte Mathematik und Physik (ZAMP)*, 25(1):99–111, 1974.

[7] L. Dieci and A. Pugliese. Singular values of two-parameter matrices: an algorithm to accurately find their intersections. *Mathematics and Computers in Simulation*, 79(4):1255–1269, December 2008.

[8] A. Gallina, L. Pichler, and T. Uhl. Enhanced meta-modelling technique for analysis of mode crossing, mode veering and mode coalescence in structural dynamics. *Mechanical Systems and Signal Processing*, 2011, accepted for publication.

[9] B. Goller, H.J. Pradlwarter, and G.I. Schuëller. An interpolation scheme for the approximation of dynamical systems. *Computer Methods in Applied Mechanics and Engineering*, 200(1-4):414–423, January 2011.

[10] L. Pichler, A. Gallina, and T. Uhl. Accurate modal meta-modeling procedure for representation of mode crossing and veering. In *ECCM2010 - IV European Congress on Computational Mechanic*, Paris (France), 16-21 May 2010.

[11] L. Pichler, A. Gallina, T. Uhl, and L. A. Bergman. A meta-modeling technique for the natural eigenfrequencies based on the approximation of the characteristic polynomial. *Computers & Structures*, 2011, submitted.

[12] W. Heylen, S. Lammens, and P. Sas. *Modal Analysis Theory and Testing*. Katholieke Universiteit Leuven, Departement Werktuigkunde, Leuven, 1997.

COMPDYN 2011
3rd ECCOMAS Thematic Conference on
Computational Methods in Structural Dynamics and Earthquake Engineering
M. Papadrakakis, M. Fragiadakis, V. Plevris (eds.)
Corfu, Greece, 25–28 May 2011

DAMAGE IDENTIFICATION OF MONUMENTAL MASONRY STRUCTURES: THE CASE OF FOSSANOVA GOTHIC CHURCH

F. Campitiello, M.G. Masciotta, G. De Matteis and M.Vasta

University "G. D'Annunzio" of Chieti-Pescara, Engineering Department
Viale Pindaro 42, 65123 Pescara
e-mail: mvasta@unich.it

Keywords: Masonry Structures, Earthquake Engineering, Shaking table tests, Dynamic Damage Identification

Abstract. *In the present paper, the seismic behavior of a physical 1:5.5 scaled model of the church of the Fossanova Abbey is investigated by means of numerical and experimental analyses. Aiming at defining the seismic vulnerability of such a structural typology a wide experimental campaign was carried out. The achieved experimental results lead to the definition of a refined FE model reproducing the dynamic behavior of the whole structural complex. Then, the central transversal three-central bays of the church, as it mostly influences the seismic vulnerability of the Abbey, was investigated in a more detail by means of a shaking table test on a 1:5.5 scaled physical model in the Laboratory of the Institute for Earthquake Engineering and Engineering Seismology in Skopje. In the present paper a brief review of the numerical activity related to the prediction of the shaking table test response of the model is first proposed. Then, the identification of frequency decay during collapse is performed through decomposition of the measured power spectral density matrix. Finally, the localization and evolution of damage in the structure is analyzed. The obtained results shown that a very good agreement is achieved between the experimental data and the predictive/interpretative numerical analyses.*

1 INTRODUCTION

Gothic architecture spread as from the 12th Century and broke out during the Middle Ages in the cultural and religious area of the Christianity of Western Europe, with some trespasses in the Middle East and in the Slavic-Byzantine Europe. Many important abbeys were built in those areas, providing a key impulse to the regional economy and contributing to a general social, economic and cultural development. The most interested areas sprawl from the northern Countries (England) to those facing the Mediterranean Basin (Italy), but also spread out from the Western (Portugal) to the Eastern Countries, as Poland and Hungary. Monastic orders and in particular the Cistercian one, with its monasteries, had an important role for broaden the new architectonic message, adapting to the local traditions the technical and formal heritage received by the Gothic style [1], [2] and [3] .

Gothic cathedrals may result particularly sensitive to earthquake loading. Therefore, within the European research project “Earthquake Protection of Historical Buildings by Reversible Mixed Technologies” (PROHITECH), this structural typology has been investigated by means of shaking table tests on large scale models [4]. Based on a preliminary study devoted to define typological schemes and geometry which could be assumed as representative of many cases largely present in the seismic prone Mediterranean Countries, the Fossanova cathedral, which belongs to the Cistercian abbatial complex built in a small village in the central part of Italy, close to the city of Priverno (LT), has been selected as an interesting and reference example of pre-Gothic style church [5]. In order to assess the vulnerability of the church against seismic actions a wide numerical and experimental activity was developed. Firstly, the identification of the geometry of the main constructional parts as well as of the mechanical features of the constituting materials of the cathedral was carried out. Then, Ambient Vibration Tests were performed in order to characterize the dynamic behavior of the church and to calibrate refined FE models developed by the ABAQUS code [6]. At this purpose elastic FEM analyses were performed to predict the behavior of the three-central bays of the church, which were detected as the key-part of the structural complex [7], [8]. The recognized resistant unit about transversal direction was designed in length scale 1:5.5 according to "true replica" modeling principles and tested on the shaking table in the IZIIS Laboratory in Skopje [9]. The physical model was tested and the as-built model was loaded until heavy damage occurred. The structural response of the tested physical model has been deeply investigated by means of non-linear numerical analyses that has shown good agreements with experimental measurements [10].

In this paper, the identification of frequency decay during collapse is performed through decomposition of the measured power spectral density matrix. Finally, the localization and evolution of damage in the structure is analyzed. The obtained results has shown that a very good agreement is achieved between the experimental data and the predictive/interpretative numerical analyses.

2 THE FOSSANOVA ABBEY: MODEL AND EXPERIMENTAL TEST

The Fossanova Abbey (Fig. 1) was built in the XII century and opened in 1208. The architectural complex presents three rectangular aisles with seven bays, a transept and a rectangular apse. Between the main bay and the transept raises the skylight turret with a bell tower. The main dimensions are 69.85 m (length), 20.05 m (height), and 23.20 m (width). The nave, the aisles, the transept and the apse are covered by ogival cross vaults. Detailed information on the main dimensions of the bays are provided in De Matteis et al. [6].

Figure 1. The Fossanova church.

The previously mentioned vaulted system does not present ribs, but only ogival arches transversally oriented respect to the span and ogival arches placed on the confining walls (Fig. 2). The ridge-poles of the covering wood structure is supported by masonry columns placed on the boss of the transversal arches of the nave and apse. The crossing between the main bay and the transept is covered by a wide ogival cross vault with diagonal ribs sustained by four cross shaped columns delimiting a span with the dimensions of 9.15x8.85m.

Figure 2. The vaulted system of the Fossanova church.

The main structural elements constituting the central nave and the aisles are four longitudinal walls (west-east direction). The walls delimiting the nave are sustained by seven couples of cross-shaped piers (with dimensions of 1.80x1.80 m) with small columns laying on them and linked to the arches. The bays are delimited inside the church by columns with adjacent elements having a capital at the top. The columns-capital system supports the transversal arches of the nave. The external of the clearstory walls are delimited by the presence of buttresses with a hat on the top that reaches the height of 17.90 m. The walls of the clearstory present large splayed windows and oval openings that give access to the garret of the aisles. Also the walls that close the aisles present seven coupled column-buttresses systems reaching the height of 6.87 m and further splayed windows.

During the centuries, the complex suffered some esthetical modifications: the main prospect was modified since the narthex was eliminated installing an elaborate portal with a large rose-window; a part of the roof and of the lantern were rebuilt, introducing a Baroque style skylight turret; additional modifications on the roofing of the church were applied, with the reduction of the slope of pitches and with the restoration of the same slope as in the original form.

In order to determine the actual geometry and the mechanical features of the main constructional elements, an accurate experimental activity has been developed. In particular, both in situ inspection and laboratory tests have been carried out [6, 7].

It has been determined that the basic material constituting the constructional elements of the church is a very compact sedimentary limestone. In particular, columns and buttresses are made of plain stones with fine mortar joints (thickness less than 1 cm). The lateral walls (total thickness 120 cm) consist of two outer skins of good coursed ashlar (the skins being 30 cm thick) with an internal cavity with random rubble and mortar mixture fill.

In order to inspect the hidden parts of the constituting structural elements, endoscope tests have been executed on the right and left columns of the first bay, on the third buttress of the right aisle, on the wall of the main prospect and at the end on the filling of the vault covering the fourth bay of the nave. The test on the columns (Fig. 3a) allowed the exploration of the internal nucleus of the pier, relieving a total lack of internal vacuum, with the predominant presence of limestone connected with continuum joints of mortar (Fig. 3b). The test on the buttress was performed at the level of 143 cm, reaching the centre of the internal wall. The presence of regular stone blocks having different dimensions and connected to each other with mortar joints without any significant vacuum was detected. The tests on the wall put into evidence the presence of a two skins and rubble fill. The test made on the extrados of the vault, with a drilling depth of 100 cm, allowed a first layer of 7 cm made of light concrete and then a filling layer of irregular stones and mortar with the average thickness of 10 cm to be identified. In order to define the mechanical features of the material, original blocks of stone were taken from the cathedral and submitted to compression tests (Fig. 4a). In total, 10 different specimens having different sizes have been tested, giving rise to an average ultimate strength of about 140 MPa and an average density $\gamma = 1700$ kg/m^3. Besides, based on the results obtained for three different specimens, a Young's modulus equal to 42.600 MPa has been assessed, while a Poisson's ratio equal to 0.35 has been estimated.

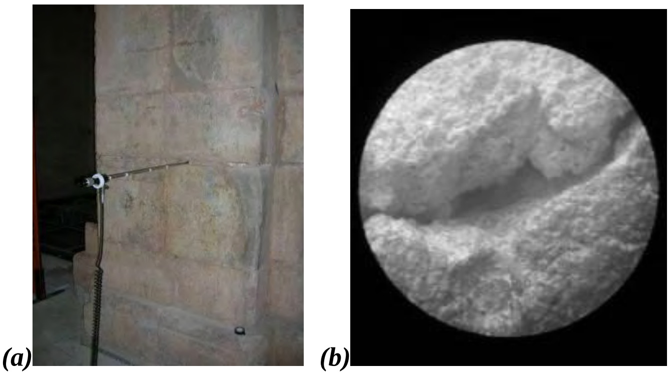
(a) *(b)*

Figure 3: Endoscope tests.

Also, mortar specimens were extracted from the first column placed on the left of the first bay, from the wall of the aisle on the right and from the wall on the northern side of the transept. The specimens were catalogued as belonging to either the external joints (external mortar) or to the filling material (internal mortar). Compression tests have been carried out according to the Italian provisions (UNI EN 1926:2001), relieving a noticeable reduction of the average compressive strength for the specimens belonging to the external mortar (3.33 MPa) with respect to the internal ones (10.30 MPa). Besides, the Young's modulus has been determined on three different mortar specimens, according to the UNI EN 1015-11:2001 provisions, providing values ranging from 8.33 MPa to 12.16 MPa.

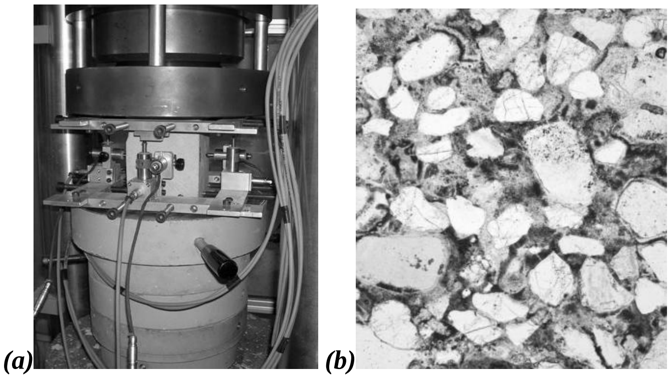

Figure 4: Compression tests on limestone (a) and microscope analysis on mortar (b).

Chemical and petrography analyses have been also performed on the mortar specimens. In particular, chemical tests were made by X rays diffractometer analysis, according to the UNI 11088:2003 provisions. The prevalence of three material, namely, quartz crystal SiO2, crystallized calcium carbonate CACO3 and some traces of felspate, was noticed. Also, a petrography study on thin sections of mortar specimens have been done by using two electronic microscopes, according to the UNI EN 932-3:1998 provisions (Fig. 4b). The analysis relieved the presence of quartz crystal sand end felspate, without any significant presence of crystallized calcium carbonate. The binding was quantified with a percentage of 60% of the total volume.

A FE model of the entire Abbey was calibrated on the basis of the in-situ experimental activity. The seismic analyses on such a model revealed that the more important structural part of the structural complex was to be recognized in the three-central bays of the main nave shown in Figure 5 [8]. For the above reason a physical model of the key-structural part was designed and constructed in the IZIIS Laboratory in Skopje (Fig. 6). The model was executed in a 1:5.5 scale ratio (length) which was the maximum value compatible with the capacity of the shaking table.

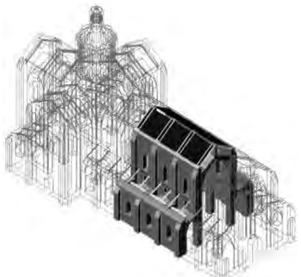

Figure 5. Recognized seismic resistant unit in transversal direction.

The Buckingham's theorem was followed to define all the physical parameters needed to the construction of the model, according to the "true replica" modeling principles. All the involved quantities was scaled on the base of the three main parameters Length (L_r=1/5.5), Mass Density (ρ_r=1) and Acceleration (a_r=1) so that for the stresses a scaling ratio σ_r=0.18 is obtained. The dimensions of the model were 3.97x4.44 m at the base, 3.67 m was the maximum height.

Fig. 6. Fossanova physical model (UPM) in scale 1:5.5 tested on shaking table.

Some simplifications were adopted in the construction of the prototype: free edges was left in longitudinal direction, in fact no boundary restrains was applied on the fronts, neglecting the longitudinal continuity as it is in the reality. Then, the wooden roof structure wasn't realized because it wasn't considered as an active element in the evaluation of the seismic vulnerability [9].

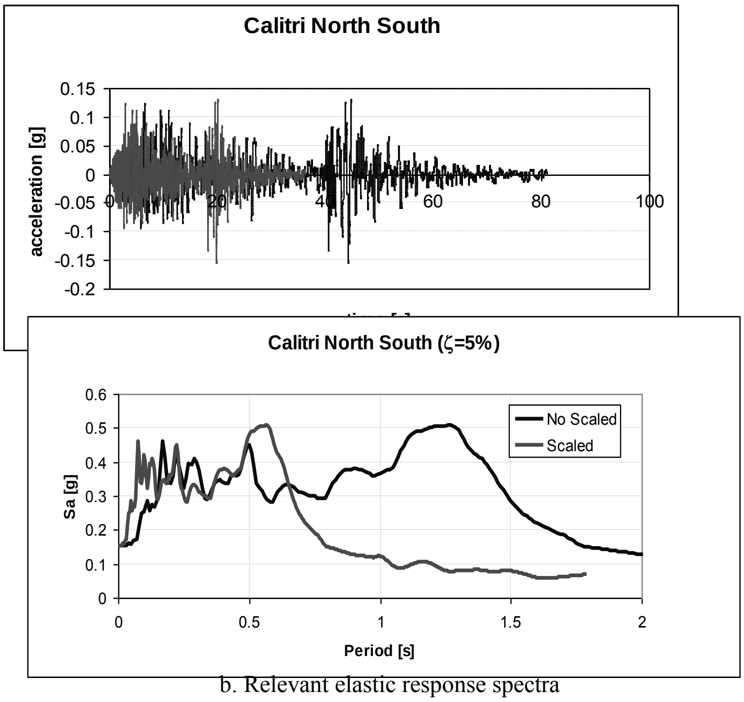

b. Relevant elastic response spectra

Figure 7. The accelerometric record (Irpinia, 1980).

The input signal of the test was assumed to be the scaled natural Calitri record (North-South direction) of Irpinia (Italy) 1980 earthquake record. The main feature of the selected earthquake are a maximum acceleration of 0.155g (compatible with seismic hazard of the site), a quite long duration time (80 sec), a high input energy for the relevant frequency (0.5Hz-10Hz) and typical two peak accelerations (or two strong motions). The record and the derived elastic spectra (with damping ratio ζ=5%) are shown in Figure 7a,b. The shaking table test was performed by considering three phases: phase 1, phase 2A and phase 2B. In the first phase the as-built unreinforced physical model (UPM) was tested and heavy damaged at the end. In the second phase (2A) the model was repaired and reinforced with carbon fiber ties. Finally, in the phase 2B, the reinforcing system was modified and the model was loaded until failure. Even though the examination of the reinforced systems is not the object of the present paper, in the following the level of input intensity which provoked serious damage to the model for every phase is listed:

- 0.14g for the original model (phase 1);
- 0.28g for the strengthened model (phase 2A);
- 0.40g for the strengthened model (phase 2B);

In particular, the maximum acceleration measured at the base of the shaking table, by means of the accelerometer “CH1” [11], versus the maximum absolute displacement measured at the top of the buttresses at each step of the phase 1 (unreinforced physical model) is shown in Figure 8. The curve can be assumed as an equivalent capacity curve for the tested UPM [10].

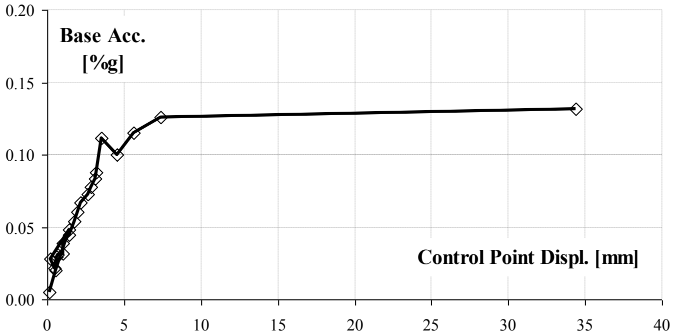

Figure 8. Equivalent capacity curve of the tested model.

3 DYNAMIC DAMAGE IDENTIFICATION

A more suitable representation of the structural response may be achieved by means of the decomposition in fully coherent independent vectors. Although the non gaussianity of the structural response vector $\mathbf{X}(t)=[X_i(t)]$ $(i=1,\dots,n)$, collecting the nodal response processes, its main characteristics can be represented by the knowledge of the second order spectral properties. To this end, let us consider the PSD matrix of $\mathbf{X}(t)$

$$\mathbf{S}_X(\omega)=\begin{bmatrix} S_{X_1}(\omega) & S_{X_1X_2}(\omega) & \cdots & S_{X_1X_n}(\omega) \\ S_{X_2X_1}(\omega) & S_{X_2}(\omega) & \cdots & S_{X_2X_n}(\omega) \\ \vdots & & \ddots & \vdots \\ S_{X_1X_n}(\omega) & \cdots & \cdots & S_{X_n}(\omega) \end{bmatrix} \tag{1}$$

The elements of $\mathbf{S}_X(\omega)$ are the direct and cross power spectral densities, defined as the Fourier transform of the correlation components

$$S_{X_1X_j}(\omega)=\frac{1}{2\pi}\int_{-\infty}^{+\infty} R_{X_1X_j}(\tau)e^{-j\omega\tau}d\tau \tag{2}$$

or equivalently, starting from measurements of the process $\mathbf{X}(t)$:

$$S_{X_1X_j}(\omega)=\frac{1}{2\pi}\lim_{T\to\infty}\frac{E[X_i(\omega,T)X_j^*(\omega,T)]}{T} \tag{3}$$

where $X_i(\omega,T)$denotes the Fourier transform of $X_i(t)$ over the observation time T

$$X_i(\omega,T)=\int_0^T X_i(t)e^{-j\omega t}dt \tag{4}$$

The psd matrix is Hermitian and non-negative definite, thus its eigenvalues $\mathbf{\Gamma}(\omega)=diag(\gamma_1(\omega)\,\gamma_2(\omega)\cdots\gamma_n(\omega))$ are real and non-negative, with orthonormal complex eigenvectors $\mathbf{\Psi}(\omega)=[\boldsymbol{\psi}_1(\omega)\boldsymbol{\psi}_2(\omega)\cdots\boldsymbol{\psi}_n(\omega)]$

$$\Psi(\omega)^{*T}\,\Psi(\omega)=\mathbf{I},\quad \Psi(\omega)^{*T}\,\mathbf{S}_X(\omega)\Psi(\omega)=\Gamma(\omega) \tag{5}$$

$$\mathbf{S}_X(\omega)\Psi(\omega)=\Psi(\omega)\Gamma(\omega) \tag{6}$$

If the eigenvalues are sorted in decreasing order, then the summation in Eq.(9) can be truncated considering only a limited number of principal components.

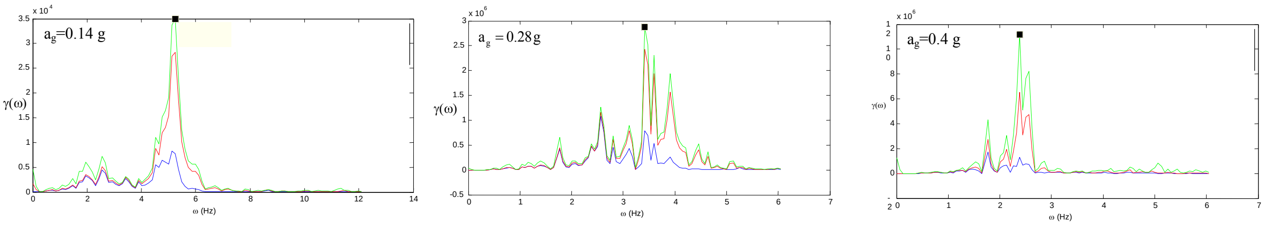

Fig.9 Response spectral eigenvalues for different values of ground peak acceleration:a_g=0.14g, a_g =0.28g and a_g =0.4g

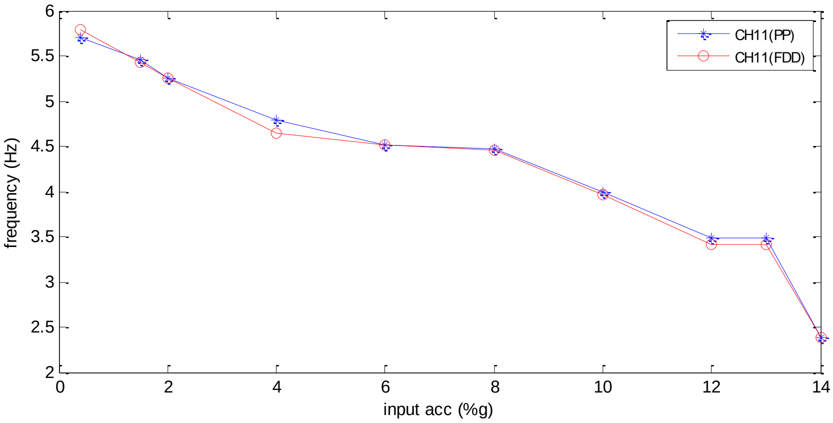

Fig.10 Comparison between experimental and identified frequency decay for different values of ground peak acceleration

Figures 9 show the response spectral eigenvalues for different values of ground peak acceleration, leading to the identification of the frequency decay, Fig. 10

Damage localization has been performed using the Parameter Method (PM) proposed by Dong et al. [14], [15] using a combination of frequency and mode shapes. The expression for the PM method is

$$\Delta\varphi = \sum_{j=1}^{n} \left[\phi_j^d \left(\frac{\omega_j^u}{\omega_j^d} \right) - \phi_j^u \right] \tag{10}$$

where ϕ is the structural mode, *n* the mode number while upper script *u,d* stands for undamaged and damage state respectively.

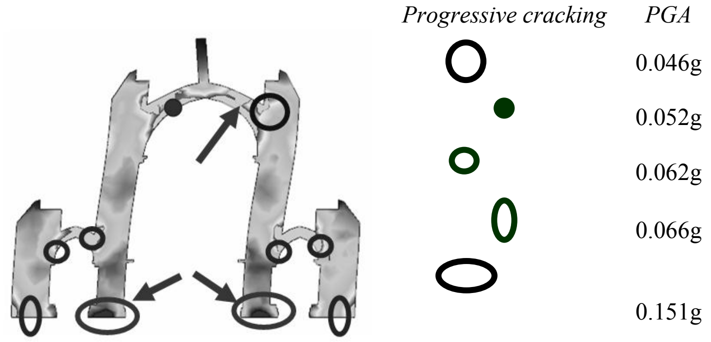

Figure 11. Progressive damage of the model with increasing PGA.

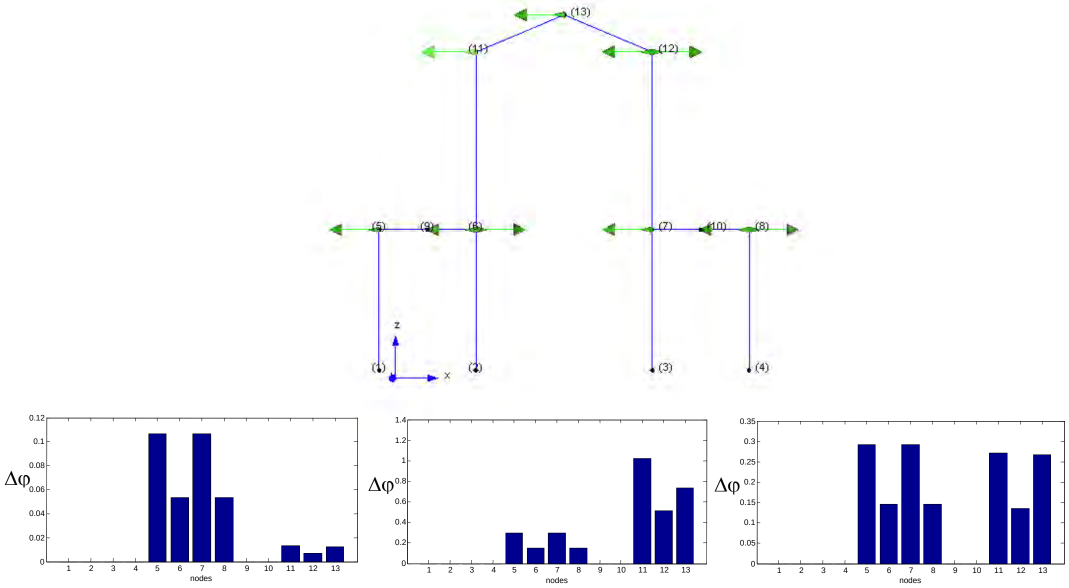

Figure 12. a) 2D finite element model [16], b) Progressive damage of the model with increasing PGA - PM method identification

Figure 11 show the FEM prediction of the progressive damage of the model with increasing PGA. In Figures 12, based on a 2D finite element model, it is shown the identification of damage location by the PM method.

CONCLUSIONS

The seismic behavior of a physical 1:5.5 scaled model of the church of the Fossanova Abbey has been investigated by means of numerical and experimental analyses. The achieved experimental results lead to the definition of a refined FE model reproducing the dynamic behavior of the whole structural complex. Then, the central transversal three-central bays of the church, as it mostly influences the seismic vulnerability of the Abbey, was investigated in a more detail by means of a shaking table test on a 1:5.5 scaled physical model in the Laboratory of the Institute for Earthquake Engineering and Engineering Seismology in Skopje. In the present paper a brief review of the numerical activity related to the prediction of the shaking table test response of the model is first proposed. Then, the identification of frequency decay during collapse is performed through decomposition of the measured power spectral density matrix. Finally, the localization and evolution of damage in the structure is analyzed. The obtained results shown that a very good agreement is achieved between the experimental data and the predictive/interpretative numerical analyses.

REFERENCES

[1] Grodecki L. *L'architettura gotica* (in Italian), Milan, 1976,.

[2] Gimpel J. *I costruttori di cattedrali* (in Italian), Jaca Book, Milan, 1982,.

[3] De Longhi F. *L'architettura delle chiese cistercensi Italiane* (in Italian), Milan, 1958.

[4] Mazzolani, F.M., Earthquake protection of historical buildings by reversible mixed technologies, in *Proc. of Behaviour of Steel Structures in Seismic Areas* (STESSA 2006), Taylor and Francis/Balkema publ., p. 11-24, 2006.

[5] De Matteis, G., Colanzi, F., Viskovic, A., Mazzolani F.M., Structural behaviour of gothic style churches in the earthquake prone Mediterranean area, in *Proc. of the Intern. Symp. Studies on Historical Heritage*, (TA-MIR), Antalya, Turkey, Sept. 17-21, 2007.

[6] De Matteis, G., Colanzi, F., Mazzolani F.M., La chiesa abbaziale di Fossanova: indagini sperimentali per la valutazione della vulnerabilità sismica, in *proc. of the Workoshop on "Design for Rehabilitation of Masonry Structures*, (Wondermasonry 2), Ischia, Italy, October 11-12, 2007.

[7] De Matteis G., Langone, I., Colanzi, F., Mazzolani, F.M., Experimental and Numerical Modal Identification of the Fossanova Gothic Cathedral, *Proc. of the 7th Inter. Conf. on Damage Assessment of Structures* (DAMAS 2007), 25th-27th June, Torino, Italy, 2007.

[8] De Matteis, G., Colanzi, F., Langone, I., Eboli, A., Mazzolani F.M., Numerical evaluation of the seismic response of the Fossanova cathedral based on experimental dynamic identification, in *Proc. of the Third Inter. Conference on Structural Engineering, Mechanics and Computation* (SEMC 2007), Sept. 10-12, Cape Town, South Africa, 2007.

[9] De Matteis, G., Langone, I, Colanzi, F., Eboli, A., Mazzolani, F.M. Seismic vulnerability evaluation of the Fossanova Gothic church. Structural Analysis of Historic Constructions, *Proc. of the 6st Int. Conf.* SAHC2008 (Eds. D. D'Ayala and E. Fodde), Bath (UK), July 2–4, CRC Press Taylor & Francis Group, 2008.

[10] De Matteis, G., Campitiello F., Eboli A., Mazzolani F.M., 2009. Analisi sismica della chiesa abbaziale di Fossanova mediante modelli numerici e sperimentali. L'Ingegneria Sismica in Italia, ANIDIS, Bologna, 2009, SM7.6.

[11]De Matteis, G., Mazzolani, F.M., Krstevska, L., Tashkov, Lj. Seismic analysis and Strengthening intervention of the Fossanova Gothic church: numerical and experimental activity. In *Urban Habitat Construction Under Catastrophic Events*, COST C26, Malta, 2008, pp. 247-254, 2008.

[12]Krstevska, L., Tashkov, L., Gramatikov, K. & Kozinakov, D. Shaking table test of Fossanova model, *PROHITECH*, Final Report. Skopje: IZIIS, 2008.

[13]Dogariu A., Dubina D. & Campitiello F., De Matteis G. FEM Modeling Masonry Shear Walls strenghtened with metal sheating - datasheet no. 2-21 Urban Habitat Construction under Catastrophic Events - COST 26 - Editors: Mazzolani et al., p. 235-240, 2008.

[14] Dong C., Zhang P.Q., Feng W.Q., Huang T.C. The sensitivity study of the modal parameters of a cracked beam. In: *Proc. of the 12th international modal analysis conference*, 1994, pp.98-104.

[15] Ramos L.F., De Roeck G., Lourenco P.B., Campos-Costa A., Damage identification on arched masonry structures using ambient and random impact vibrations, *Engineering Structures,* **32**, pp. 146-162, 2010.

[16] ARTeMIS version 5.2, Structural Vibration Solution A/S, NOVI Science Park.

COMPDYN 2011
ECCOMAS Thematic Conference on
Computational Methods in Structural Dynamics and Earthquake Engineering
M. Papadrakakis, M. Fragiadakis, V. Plevris (eds.)
Corfu, Greece, 25-28 May 2011

HIGH ORDER ABSORBING BOUNDARY CONDITIONS FOR ELASTODYNAMICS

Daniel Rabinovich[1], **Dan Givoli**[1], **Thomas Hagstrom**[2] **and Jacobo Bielak**[3]

[1]Technion — Israel Institute of Technology
Dept. of Aerospace Engineering, Technion, Haifa, 32000, Israel
e-mail: {daniel,givolid}@aerodyne.technion.ac.il

[2] Southern Methodist University
Dept. of Mathematics, SMU, Dallas, TX 75275, U.S.A.
e-mail: jbielak@cmu.edu

[3] Carnegie Mellon University
Dept. of Civil and Environmental Engineering, CMU, Pittsburgh, PA 15213, U.S.A.
e-mail: jbielak@cmu.edu

Keywords: Absorbing Boundary Condition, Elastic Waves, Elastodynamics, High-Order, Solid-Earth Geophysics, Finite elements.

Abstract. *A high-order Absorbing Boundary Condition (ABC) is devised on an artificial boundary for time-dependent elastic waves in unbounded domains. The configuration considered is that of a two-dimensional elastic waveguide. The proposed ABC is an extension of the Hagstrom-Warburton ABC which was originally designed for acoustic waves, and is applied directly to the displacement field. The order of the ABC determines its accuracy and can be chosen to be arbitrarily high. A special variational formulation is constructed which incorporates the ABC. A standard FE discretization is used in space, and a Newmark-type scheme is used for time-stepping. A long-time instability is observed, but simple means are shown to dramatically postpone its onset so as to make it harmless during the simulation time of interest.*

1 INTRODUCTION

A well-known computational technique for treating wave problems in unbounded domains is the use of Absorbing Boundary Conditions (ABCs), also known by other names such as Radiating Boundary Conditions and Non-reflecting Boundary Conditions; see the review papers [1–3]. An ABC is a condition imposed on an artificial boundary which truncates the unbounded domain, thus allowing the replacement of the original problem by another problem defined in a finite domain. The latter can then be solved using standard numerical techniques like finite element (FE) or finite difference schemes. Application areas include acoustics, oceanography, electromagnetic waves and Solid-Earth Geophysics (SEG).

In 1993, Collino [4] proposed the first genuinely *high-order* local ABC for the wave equation, which does not involve high derivatives and can be implemented up to any desired order. The key here is the use of *auxiliary variables*, which are introduced on the artificial boundary and enable the elimination of the high derivatives from the ABC equations. Various authors followed Collino in proposing different high-order ABCs; see the review in [5]. Here we concentrate on the Hagstrom-Warburton [6] high-order ABC.

The use of ABCs in SEG, for the solution of direct or inverse elastic wave problems, goes back to the seminal 1969 paper of Lysmer and Kuhlemeyer [7], who proposed a dashpot-type ABC. Despite its crude accuracy, the dashpot ABC is still used today, along with various improved ABCs and absorbing layers which have been proposed in the last four decades; see, e.g., [8–10].

In contrast to the situation with PML, the only high-order ABC developed for elastic waves to date, to the best of our knowledge, is that of Tsogka and Joly [11, 12]. Their ABC is an extension of the Collino ABC [4] to elastodynamics, and is based on using special potential functions. The ABC was incorporated in a mixed FE formulation. Very recently [13], a long-time instability has been observed in solutions generated by this scheme. We shall see that the scheme proposed here suffers from the same malady, although the onset of the instability can be postponed dramatically by using various means.

In the present paper, we propose another high-order ABC for elastodynamics, which is an extension of the Hagstrom-Warburton ABC [6]. The latter is, in turn, a high-order form of the Higdon ABC [14], and a symmetrized modification of the Givoli-Neta high-order formulation [15, 16]. This ABC, developed originally for scalar time-dependent problems and hyperbolic conservation systems, has been shown to be extremely effective in a variety of situations [6, 17–21]. Here we extend the ABC for use in elastodynamics, basing it directly on the displacement field.

2 PROBLEM STATEMENT

We consider a two-dimensional semi-infinite elastic waveguide of width b, as shown in Fig. 1(a).

In the waveguide we consider the two-dimensional (plane strain) linear equations of elastodynamics. Some boundary conditions are specified on all three boundaries. Initial conditions are also prescribed. We assume that outside a compact region, denoted Ω_0, the following simplified conditions hold: (a) the medium is *homogeneous*, namely the material properties are constant; (b) the material is *isotropic*; (c) body forces are absent; and (d) the initial values vanish. As a result of these assumptions, in the semi-infinite region outside Ω_0 the governing equations are reduced to the Navier equations.

We now truncate the semi-infinite domain by introducing the artificial boundary Γ_E, located

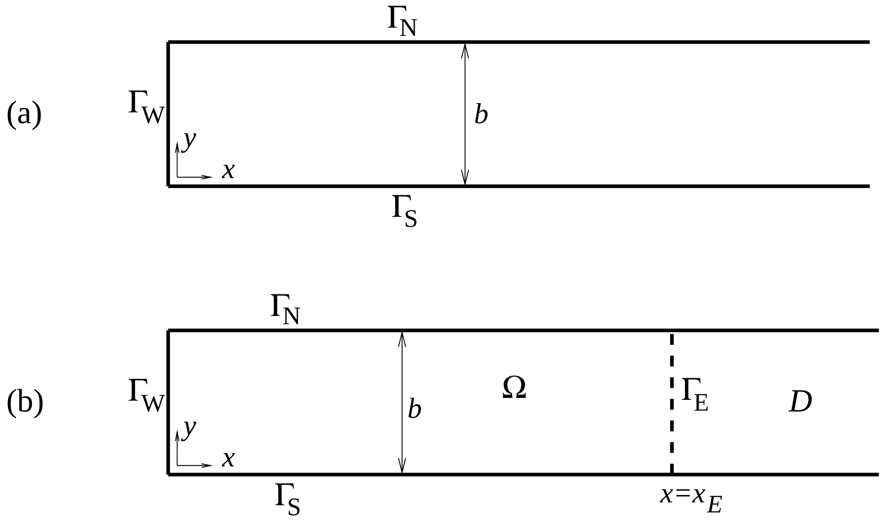

Figure 1: A semi-infinite waveguide: (a) the original setup, (b) the setup of the problem with truncated domain.

at $x = x_E$, $0 \leqslant y \leqslant b$; see Fig. 1(b). This boundary divides the original semi-infinite domain into two subdomains: the exterior domain D, and a finite computational domain Ω, which is bounded by $\Gamma_W, \Gamma_S, \Gamma_N$ and Γ_E. We choose the location of Γ_E such that Ω_0 is strictly contained in Ω.

The initial boundary value problem in Ω consists of the elastic equations in Ω, the given initial conditions, the boundary conditions on Γ_W, Γ_N and Γ_S, and an ABC imposed on Γ_E. We shall consider this ABC in the next sections.

3 THE HIGH-ORDER ABC: GENERAL APPROACH

The general approach devised in [15] and adopted in [6] to construct a high-order ABC consists of the following four steps (presented here in the context of a scalar problem, for simplicity):

Step 1. We start with a basic, low-order, ABC, $B_0 u = 0$ on Γ_E. The only essential requirement from this ABC is that it be associated with a reflection coefficient smaller than 1.

Step 2. Taking a product of operators B_j, each one of which has the same form as B_0, possibly with different coefficients, we obtain a Pth-order ABC,

$$\mathcal{B}^P u \equiv \left(\prod_{j=0}^{P} B_j \right) u = 0 \, .$$

Its reflection coefficient is the product of the reflection coefficients R_j associated with each B_j, and hence becomes exponentially small as P is increased.

Step 3. This high-order ABC is not computationally practical because it involves high-order derivatives. We introduce the auxiliary variables ϕ_j which are defined recursively; using them we eliminate all the high derivatives, and thus obtain a high-order ABC that involves only low derivatives.

Step 4. The latter high-order ABC is still not computationally practical, since it involves (in general) normal derivatives of the auxiliary variables ϕ_j on the boundary Γ_E. These derivatives do not allow us to discretize the ϕ_j on Γ_E alone. We therefore use the wave equation itself (which we prove to be satisfied by each ϕ_j) to eliminate all normal derivatives of all auxiliary variables. This finally results in a practical high-order ABC.

For details on the development of the elastic ABC based on this approach, see [22].

4 THE HIGH-ORDER ABC: FINAL FORM

The final form of the high-order ABC is as follows.
For $j = 2, \ldots, P$:

$$\begin{aligned}
&\left[\left(a_{j-1}a_j^2 + a_j a_{j-1}^2\right)(\lambda + 2\mu) + (a_{j-1} + a_j)\, c^2\rho\right] \partial_{tt}\phi_j^x - (a_{j-1} + a_j)\, c^2\mu\partial_{yy}\phi_j^x \\
&\quad = \left[a_{j-1}a_j^2(\lambda + 2\mu) - a_{j-1}c^2\rho\right] \partial_{tt}\phi_{j+1}^x + a_{j-1}a_j c(\lambda + \mu)\partial_{yt}\phi_{j+1}^y + a_{j-1}c^2\mu\partial_{yy}\phi_{j+1}^x \\
&+ \left[a_j a_{j-1}^2(\lambda + 2\mu) - a_j c^2\rho\right] \partial_{tt}\phi_{j-1}^x - a_j a_{j-1} c(\lambda + \mu)\partial_{yt}\phi_{j-1}^y + a_j c^2\mu\partial_{yy}\phi_{j-1}^x,
\end{aligned} \tag{1}$$

$$\begin{aligned}
&\left[\left(a_{j-1}a_j^2 + a_j a_{j-1}^2\right)\mu + (a_{j-1} + a_j)\, c^2\rho\right] \partial_{tt}\phi_j^y - (a_{j-1} + a_j)\, c^2(\lambda + 2\mu)\partial_{yy}\phi_j^y \\
&\quad = \left[a_{j-1}a_j^2\mu - a_{j-1}c^2\rho\right] \partial_{tt}\phi_{j+1}^y + a_{j-1}a_j c(\lambda + \mu)\partial_{yt}\phi_{j+1}^x + a_{j-1}c^2(\lambda + 2\mu)\partial_{yy}\phi_{j+1}^y \\
&+ \left[a_j a_{j-1}^2\mu - a_j c^2\rho\right] \partial_{tt}\phi_{j-1}^y - a_j a_{j-1} c(\lambda + \mu)\partial_{yt}\phi_{j-1}^x + a_j c^2(\lambda + 2\mu)\partial_{yy}\phi_{j-1}^y,
\end{aligned} \tag{2}$$

For $j = 1$:

$$\begin{aligned}
&\left[\left(a_0 a_1^2 + 2a_1 a_0^2\right)(\lambda + 2\mu) + a_0 c^2\rho\right] \partial_{tt}\phi_1^x - a_0 a_1 c(\lambda + \mu)\partial_{yt}\phi_1^y - a_0 c^2\mu\partial_{yy}\phi_1^x \\
&\qquad = \left[a_0 a_1^2(\lambda + 2\mu) - a_0 c^2\rho\right] \partial_{tt}\phi_2^x + a_0 a_1 c(\lambda + \mu)\partial_{yt}\phi_2^y + a_0 c^2\mu\partial_{yy}\phi_2^x \\
&\quad + \left[2a_1 a_0^2(\lambda + 2\mu) - 2a_1 c^2\rho\right] \partial_{tt}\phi_0^x - 2a_1 a_0 c(\lambda + \mu)\partial_{yt}\phi_0^y + 2a_1 c^2\mu\partial_{yy}\phi_0^x,
\end{aligned} \tag{3}$$

$$\begin{aligned}
&\left[\left(a_0 a_1^2 + 2a_1 a_0^2\right)\mu + a_0 c^2\rho\right] \partial_{tt}\phi_1^y - a_0 a_1 c(\lambda + \mu)\partial_{yt}\phi_1^x - a_0 c^2(\lambda + 2\mu)\partial_{yy}\phi_1^y \\
&\qquad = \left[a_0 a_1^2\mu - a_0 c^2\rho\right] \partial_{tt}\phi_2^y + a_0 a_1 c(\lambda + \mu)\partial_{yt}\phi_2^x + a_0 c^2(\lambda + 2\mu)\partial_{yy}\phi_2^y \\
&\quad + \left[2a_1 a_0^2\mu - 2a_1 c^2\rho\right] \partial_{tt}\phi_0^y - 2a_1 a_0 c(\lambda + \mu)\partial_{yt}\phi_0^x + 2a_1 c^2(\lambda + 2\mu)\partial_{yy}\phi_0^y,
\end{aligned} \tag{4}$$

These equations are accompanied by (6) and (9) which correspond to $j = 0$; namely, they connect u_i and ϕ_1^i:

$$(a_0\partial_t + c\partial_x)\, u_x = a_0\partial_t\phi_1^x \qquad , \qquad (a_0\partial_t + c\partial_x)\, u_y = a_0\partial_t\phi_1^y\ . \tag{5}$$

In addition we have the ‘closure’ conditions

$$(a_0\partial_t + c\partial_x)\, u_x = a_0\partial_t\phi_1^x, \tag{6}$$

$$(a_j\partial_t + c\partial_x)\, \phi_j^x = (a_j\partial_t - c\partial_x)\, \phi_{j+1}^x, \quad j = 1, \ldots, P, \tag{7}$$

$$\phi_{P+1}^x = 0 \quad \text{on} \quad \Gamma_E, \tag{8}$$

$$(a_0\partial_t + c\partial_x)\, u_y = a_0\partial_t\phi_1^y, \tag{9}$$

$$(a_j\partial_t + c\partial_x)\, \phi_j^y = (a_j\partial_t - c\partial_x)\, \phi_{j+1}^y, \quad j = 1, \ldots, P, \tag{10}$$

$$\phi_{P+1}^y = 0 \quad \text{on} \quad \Gamma_E\ , \tag{11}$$

as well as

$$\phi_0^x = u_x, \qquad , \qquad \phi_0^y = u_y\ . \tag{12}$$

Eqs. (1)–(12) constitute together the desired ABC on Γ_E.

5 NUMERICAL EXAMPLE

We take zero initial conditions, and we 'drive' the problem through a persistent surface force applied on the north boundary Γ_N. On this boundary we take $u_y = 0$ and the nonzero tangential traction $T_x = \sigma_{xy} = T_x^N$, where

$$T_x^N(x,t) = \begin{cases} 1 & \text{for} \quad 0 \leqslant x \leqslant 8 \\ 0 & \text{for} \quad x > 8 \end{cases} \quad , \qquad t > 0 \,. \tag{13}$$

Snapshots of the reference solution (obtained in a long domain) and the truncated-domain solution using the ABC with $P = 20$ are shown in Fig. 2. Steady state is rapidly reached due to the persistence of the applied force. In later times the solution does not change significantly, and hence no snapshots are shown after $t = 3$. It is apparent that the agreement between the two solutions is excellent.

6 LONG-TIME INSTABILITY

Numerical experiments show that our scheme exhibits a long-time instability, which causes the solution to grow exponentially after a sufficiently long amount of time. A similar phenomenon was observed with the potential-based high-order ABC of Tsogka and Joly [11, 12]. The origin of this instability is not clear yet. Nevertheless, we have found that the onset of the instability can be dramatically *postponed* by injecting small *numerical damping* into the time-stepping scheme on the boundary Γ_E. See [22] for more details.

REFERENCES

[1] D. Givoli, "Non-Reflecting Boundary Conditions: A Review," *J. Comput. Phys.*, **94**, 1–29, 1991.

[2] T. Hagstrom, "Radiation Boundary Conditions for the Numerical Simulation of Waves," *Acta Numerica*, **8**, 47–106, 1999.

[3] D. Givoli, "Computational Absorbing Boundaries," in *Computational Acoustics of Noise Propagation in Fluids*, S. Marburg and B. Nolte, eds., Chapter 5, pp. 145–166, Springer, Berlin, 2008.

[4] F. Collino, "High Order Absorbing Boundary Conditions for Wave Propagation Models. Straight Line Boundary and Corner Cases," in *Proc. 2nd Int. Conf. on Mathematical & Numerical Aspects of Wave Propagation*, R. Kleinman et al., Eds., SIAM, Delaware, pp. 161-171, 1993.

[5] D. Givoli, "High-Order Local Non-Reflecting Boundary Conditions: A Review," *Wave Motion*, **39**, 319–326, 2004.

[6] T. Hagstrom and T. Warburton, "A New Auxiliary Variable Formulation of High-Order Local Radiation Boundary Conditions: Corner Compatibility Conditions and Extensions to First Order Systems," *Wave Motion*, **39**, 327–338, 2004.

[7] J. Lysmer and R.L. Kuhlemeyer, "Finite Dynamic Model for Infinite Media," *J. Eng. Mech. Div. ASCE*, 95, pp. 859–877, 1969.

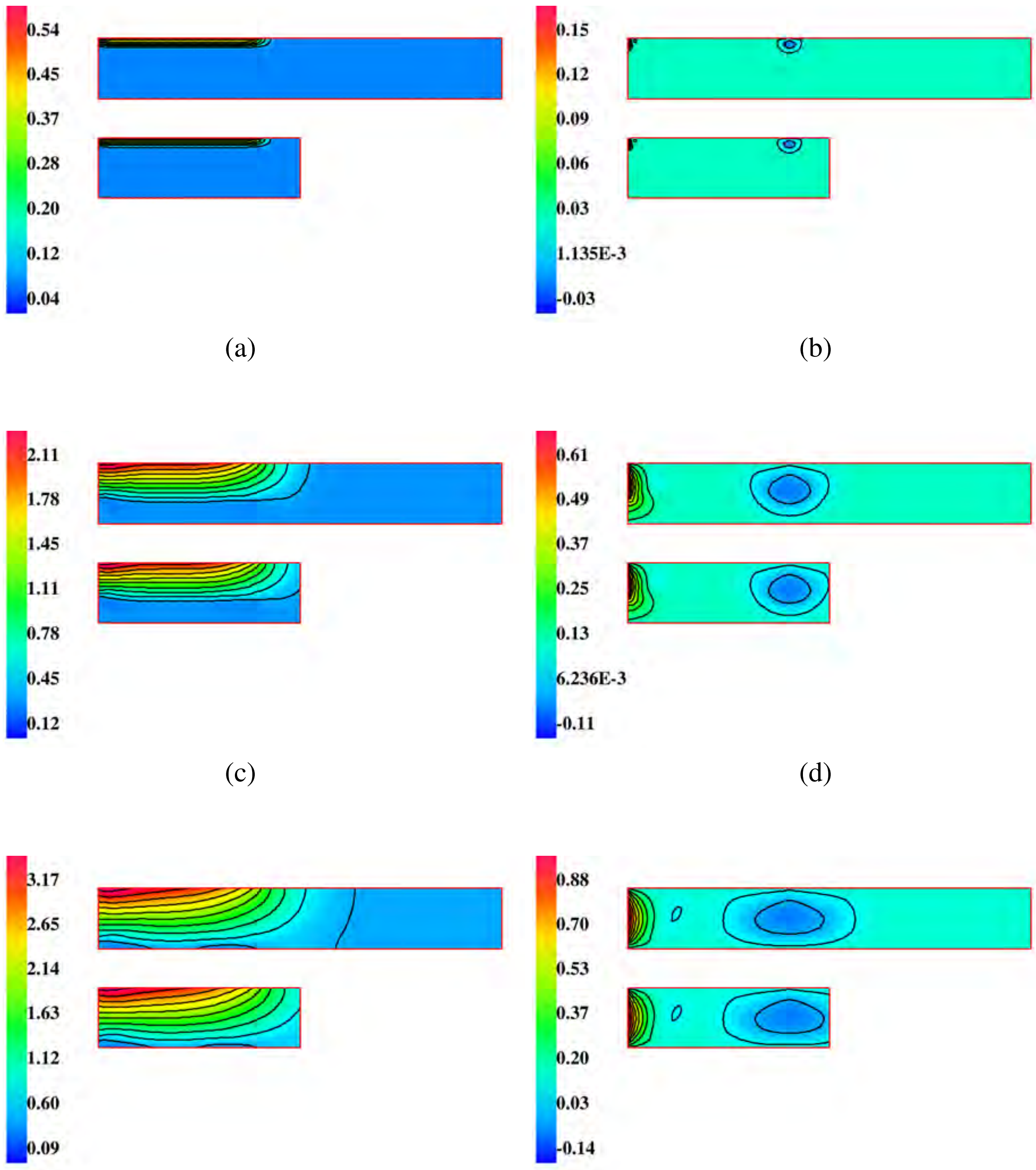

(a) (b)

(c) (d)

(e) (f)

Figure 2: Surface loading problem: snapshots of solution. (a) u_x at $t = 0.5$; (b) u_y at $t = 0.5$; (c) u_x at $t = 2$; (d) u_y at $t = 2$; (e) u_x at $t = 3$, (f) u_y at $t = 3$.

[8] H.S. Bao, J. Bielak, O. Ghattas, L.F. Kallivokas, D.R. O'Hallaron, J.R. Shewchuk and J.F. Xu, "Large-Scale Simulation of Elastic Wave Propagation in Heterogeneous Media on Parallel Computers," *Comput. Meth. Appl. Mech. Engng.*, **152**, 85–102, 1998.

[9] J. Bielak, O. Ghattas and E.J. Kim, "Parallel Octree-Based Finite Element Method for Large-Scale Earthquake Ground Motion Simulation," *Comput. Model. Engng. Sci.*, **10**, 99–112, 2005.

[10] S.M. Day, R. Graves, J. Bielak, D. Dreger, S. Larsen, K.B. Olsen, A. Pitarka and L. Ramirez-Guzmanc, "Model for Basin Effects on Long-Period Response Spectra in Southern California," *Earthquake Spectra*, **24**, 257–277, 2008.

[11] C. Tsogka, *Modélisation Mathématique et Numérique de la Propagation des Ondes Élastiques Tridimensionnelles dans des Milieux Fissurés*, PhD thesis, Paris IX, Paris, 1999.

[12] C. Tsogka and P. Joly, "Numerical Methods for Treating Unbounded Media," in *Effective Computational Methods in Wave Propagation*, N.A. Campanis, V.A. Dougalis and J.A. Ekaterinaris, Eds., Chapman & Hall CRC, 2008.

[13] P. Joly and C. Tsogka, "Higher order absorbing boundary conditions for elastodynamics," lecture, 4th Comput. Conf. on Comput. Mech. (ECCM-2010), Paris, May 16–21, 2010.

[14] R. L. Higdon, "Numerical Absorbing Boundary Conditions for the Wave Equation," *Math. Comput.*, **49**, 65–90, 1987.

[15] D. Givoli and B. Neta, "High-Order Non-Reflecting Boundary Scheme for Time-Dependent Waves," *J. Comput. Phys.*, **186**, 24–46, 2003.

[16] D. Givoli, B. Neta and I. Patlashenko, "Finite Element Solution of Exterior Time-Dependent Wave Problems with High-Order Boundary Treatment," *Int. J. Numer. Meth. Engng.*, **58**, 1955–1983, 2003.

[17] D. Givoli, T. Hagstrom and I. Patlashenko, "Finite Element Formulation with High Order Absorbing Boundary Conditions for Time-Dependent Waves," *Computer Methods in Applied Mechanics & Engineering*, **195**, 3666–3690, 2006.

[18] T. Hagstrom, M. de Castro, D. Givoli and D. Tsemach, "Local High Order Absorbing Boundary Conditions for Time-Dependent Waves in Guides," *J. Computational Acoustics*, **15**, 1–22, 2007.

[19] T. Hagstrom, A. Mar-Or and D. Givoli, "High-Order Local Absorbing Conditions for the Wave Equation: Extensions and Improvements," *J. Computational Physics*, **227**, 3322–3357, 2008.

[20] E. Bećache, D. Givoli and T. Hagstrom, "High Order Absorbing Boundary Conditions for Anisotropic and Convective Wave Equations," *J. Comput. Phys.*, **229**, 1099–1129, 2010.

[21] A. Mar-Or and D. Givoli, "High Order Global-Regional Model Interaction: Extension of Carpenter's Scheme," *Int. J. Numer. Meth. Engng.*, **77**, 50–74, 2009.

[22] D. Rabinovich, D. Givoli, J. Bielak and T. Hagstrom, "A Finite Element Scheme with a High Order Absorbing Boundary Condition for Elastodynamics," submitted.

COMPDYN 2011
3^{rd} ECCOMAS Thematic Conference on
Computational Methods in Structural Dynamics and Earthquake Engineering
M. Papadrakakis, M. Fragiadakis, V. Plevris (eds.)
Corfu, Greece, 25-28 May 2011

NON-PERIODIC HOMOGENIZATION OF THE ELASTIC WAVE EQUATION FOR WAVE PROPAGATIONS IN COMPLEX MEDIA

Yann Capdeville[1], **Laurent Guillot**[2], **and Jean-Jacques Marigo**[3]

[1]Laboratoire de Pantologie et de Godynamique de Nantes, CNRS ,France
e-mail: yann.capdeville@univ-nantes.fr

[2] Institut de Physique de Globe de Paris, France
e-mail: guillot@ipgp.fr

[3] Laboratoire de Mécanique des solides, cole Polytechnique, France
e-mail: marigo@lms.polytechnique.fr

Keywords: Seismology, Elastic waves, homogenization, non periodic, spectral elements

Abstract. *When considering numerical acoustic or elastic wave propagation in media containing small heterogeneities with respect to the minimum wavelength of the wavefield, being able to upscale physical properties (or homogenize them) is valuable, for mainly two reasons: first, replacing the original discontinuous and very heterogeneous media by a smooth and more simple one, is a judicious alternative to the necessary fine and difficult meshing of the original media required by many wave equation solvers; second, it helps to understand what properties of a medium are really "seen" by the wavefield propagating through it, which is an important aspect in an inverse problem approach. We present here a solution to solve this up-scaling problem for non-periodic complex media with rapid variations in all directions based an a non-periodic homogenization procedure. We first present a pedagogical introduction to non-periodic homogenization in 1-D, allowing to find the effective wave equation and effective physical properties of the wave equation in a highly heterogeneous medium. It can be extended from 1D to a higher space dimension and a special care of boundary conditions is required. This development can be seen as an extension of the classical two-scale periodic homogenization theory applied to the wave equation for non-periodic media. To validate this development, we then present two examples of wave propagation in 2D complex elastic models: a geometrically square model with random heterogeneities, and the Marmousi2 model. A reference solution is computed with the Spectral Element Method with meshes honoring all interfaces. Furthermore, we compare the results obtained in the homogenized model and in a low-pass filtered model with respect to the reference solution.*

1 Introduction

Being able to model and understand wave propagation in complex media is a constant concern for seismologist and the exploration community. In the recent years, advances in numerical methods have allowed to model full seismic waveform in complex media. Among these advances in numerical modeling, the introduction of the Spectral Element Method (SEM) in seismology has been particularly interesting [1]. This method has the advantage to be accurate for all type of waves and all type of media, as long as an hexahedral mesh, on which the method relies, can be designed such that all physical discontinuities are honored. In realistic media, the design of such a mesh is often impossible. For such a case, a smooth effective elastic media would solve the problem by removing the discontinuities of the elastic model while keeping the waveforms intact. Actually this problem is not limited to SEM and can be seen as a particular case of a more general problem in seismology: when an elastic model contains details much smaller than the wavelength, the model can be up-scaled consistently with the wave equation in some specific cases only: the layered media, and the periodic ones. In other words, the effective medium of a given general elastic model for a given minimum wavelength is unknown. For layered media, the up-scaling solution is known since the early work of Backus [2]. More recently, this order 0 (when referred to the homogenization theory) pioneer work has been extended to higher order, but still in the layered media case [3]. For elastic models with fast variations in several directions, the problem has been addressed for long with the two scale homogenization [4,] but is limited to the periodic media case.
In this work, we go beyond the non-periodic layered case and the high dimension periodic case with an up-scaling tool based on non-periodic homogenization.

2 Theory

We first present the homogenization method in a simple 1D periodic case and in a simplified manner. We consider a scalar wave propagating in a infinite elastic bar with ℓ-periodic elastic property $E(x)$ and density $\rho(x)$. We assume the existence of a minimum wavelength λ_m for the propagating wavefield and that $\varepsilon := \frac{\ell}{\lambda_m} << 1$. The equation of motion, driving the displacement u^ε, and the constitutive relation in the bar are

$$\begin{aligned} \rho^\varepsilon \partial_{tt} u^\varepsilon - \partial_x \sigma^\varepsilon &= f^\varepsilon \\ \sigma^\varepsilon &= E^\varepsilon \partial_x u^\varepsilon \end{aligned} \tag{1}$$

The classical periodic homogenization procedure to solve the above problem is the following:

1. The fast variable $y = \frac{x}{\varepsilon}$ is introduced;
2. The cell property $\rho(y) := \rho^\varepsilon(\varepsilon y)$ and $E(y) := E^\varepsilon(\varepsilon y)$ are defined;
3. As $\varepsilon \to 0$, y and x are treated as independent variables implying $\frac{\partial}{\partial x} \to \frac{\partial}{\partial x} + \frac{1}{\varepsilon}\frac{\partial}{\partial y}$;
4. Solutions to (1) are sought as asymptotic expansions in ε:

$$\begin{aligned} u^\varepsilon(x,t) &= \sum_{i\geq 0} \varepsilon^i u^i(x, y = \frac{x}{\varepsilon}, t) \\ \sigma^\varepsilon(x,t) &= \sum_{i\geq -1} \varepsilon^i \sigma^i(x, y = \frac{x}{\varepsilon}, t) \end{aligned}$$

5. Finally, injecting the previous expansions in 1 the series of equation to be solved for each i are:

$$\begin{aligned} \rho\partial_{tt}u^i + \partial_x\sigma^i + \partial_y\sigma^{i+1} &= f^i \\ \sigma^i &= E(\partial_x u^i + \partial_y u^{i+1}) \end{aligned} \tag{2}$$

Defining, for any function $h(x, y)$, λ_m-periodic in y, the cell average

$$\langle h\rangle (x) = \frac{1}{\lambda_m}\int_0^{\lambda_m} h(x, y)dy\,,$$

and solving the series of equations (2) up to the first order, we find that $u = \langle u^0\rangle + \varepsilon\langle u^1\rangle$ and $\sigma = \langle\sigma^0\rangle + \varepsilon\langle\sigma^1\rangle$ are solutions of the following effective wave equation:

$$\langle\rho\rangle\,\partial_{tt}u - \partial_x\sigma = f\,, \qquad \sigma = E^*\partial_x u$$

where $E^* = \langle E(1 + \partial_y\chi^1)\rangle$ is the effective elastic parameter and where χ^1 is the first order periodic corrector. χ^1 is solution of the cell problem:

$$\partial\left[E(1 + \partial_y\chi^1)\right] = 0\,. \tag{3}$$

The final order 1 solution can be obtained with

$$u^\varepsilon = (1 + \varepsilon\chi^1\partial_x)u + O(\varepsilon^2)$$

It appears that:

- in this simple 1D case, we can find an analytical solution to the cell problem leading to $1/E^* = \langle 1/E\rangle$. This result is similar to the Backus (1962)'s result. There is not such an analytical solution for higher spatial dimensions.
- at the order 0, the solutions do not depend on the microscopic scale (y) . This is still true in 2D and 3D for u^0 but not for σ^0;
- at order > 0: the boundary conditions change (e.g. Neumann condition becomes Dirichlet to Neumann);
- at order > 1: the effective equation changes (it is not the classical wave equation anymore);

Moving to the non-periodic case

When dealing with non-periodic media, the classical periodic homogenization can still be applied for the whole bar, but, then obtaining a simple constant effective media, is not really interesting. To keep the ideas of periodic homogenization and allowing a more complete effective medium, we introduce an arbitrary scale separation around a given wavelength λ_0. All scales smaller that λ_0 are considered as small scales and scales larger than λ_0 are considered as large scales. We define $\varepsilon_0 := \lambda_0/\lambda_m$. A spatial filter operator (a low-pass filter) is introduced:

$$\mathcal{F}^{\varepsilon_0}(h)(x) = \int h(x')w_{\varepsilon_0}(x - x')\,, dx'$$

where w_{ε_0} is a low-pass filter wavelet with a wave-number cutoff around $1/\lambda_0$ (see Fig. 1). $\mathcal{F}^{\varepsilon_0}$

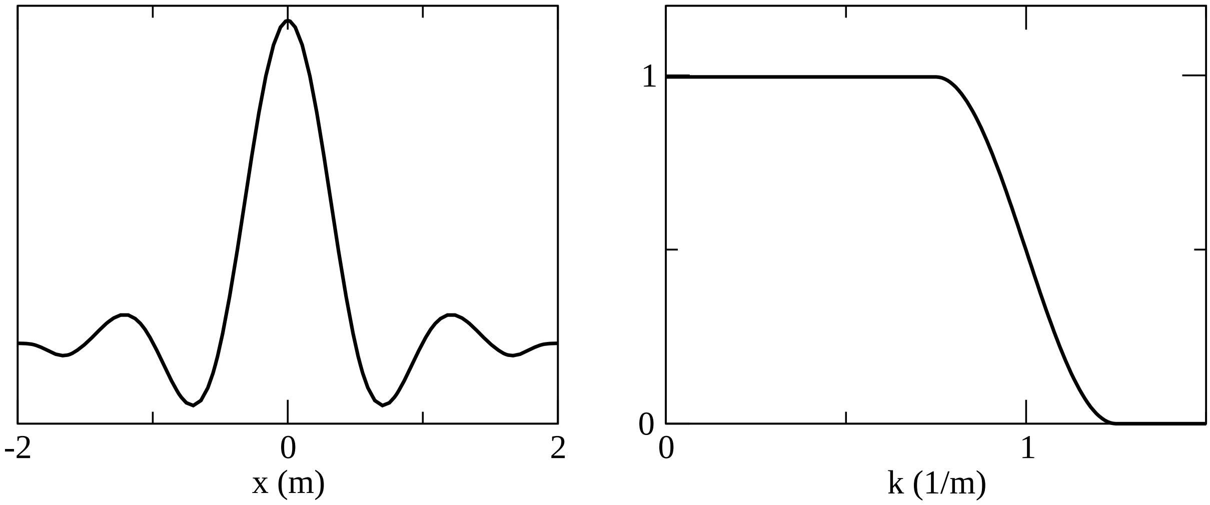

Figure 1: w wavelet example, in the space (left plot) and in the wave-number (right plot) domains, with a cutoff at $\simeq 1m^{-1}$.

allows to piratically define the slow (x part) from the fast (y part) variations. The difficulty is to define an $E^{\varepsilon_0}(x,y)$ allowing to separate the scales according to $\mathcal{F}^{\varepsilon_0}$. In the 1D case [3], this can be done using

$$\frac{1}{E^{\varepsilon_0}}(x,y) = \mathcal{F}^{\varepsilon_0}\left(\frac{1}{E}\right)(x) + \left(\frac{1}{E} - \mathcal{F}^{\varepsilon_0}\left(\frac{1}{E}\right)\right)(y) \tag{4}$$

In that case, we can readily show that

$$\frac{1}{E^{\varepsilon_0 *}} = \left\langle \frac{1}{E^{\varepsilon_0}} \right\rangle = \mathcal{F}^{\varepsilon_0}\left(\frac{1}{E}\right)$$

This effective $E^{\varepsilon_0 *}$ is smooth but allows to capture the whole wavefield for small enough ε_0. At this point, most of the periodic development is still valid and non-periodic correctors can be computed.

Going to higher dimensions

For the periodic case, 2D/3D homogenization technique exists and can be applied to the wave equation without specific difficulty. For non periodic media, the generalization of the 1D case previously presented is difficult because no analytical solution to the cell (3) problem does exist and a direct construction similar to (4) is not possible. We have nevertheless developed an un-direct construction of the elastic tensor $\mathbf{c}^{\varepsilon_0}(\mathbf{x},\mathbf{y})$ allowing non-periodic homogenization in a spatial dimension higher than 1. In the next section are shown two examples of applications in the case of the P-SV wave propagation in 2D.

Two examples

2.1 Random square example

The first model is a randomly generated 2D elastic medium. It consists of a $30 \times 30\,km^2$ square matrix of 300×300 elements of constant elastic properties surrounded by a $10\ km$ thick strip of constant elastic properties corresponding to P and S wave velocities of $5\,km^{-1}$ and

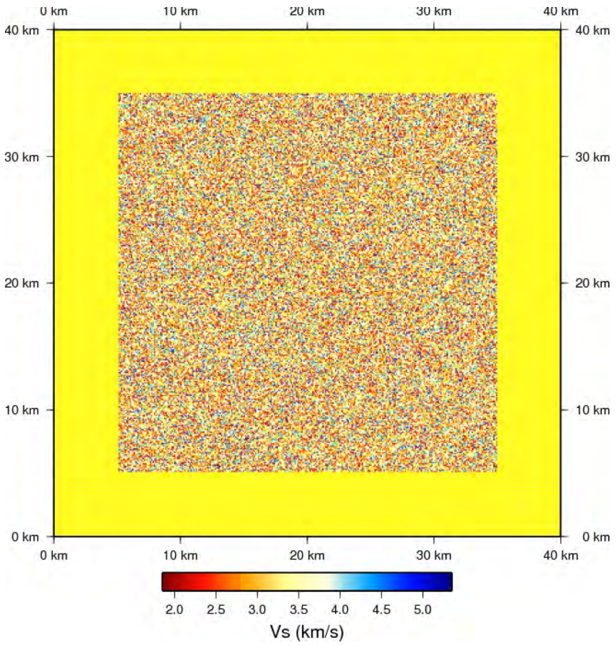

Figure 2: "Random square" model. Only V_s is presented in this plot.

$3.2\,km^{-1}$ respectively and a density of $3000\,kg\,m^{-3}$ (see Fig. 2). In each element of the matrix, the constant elastic properties and density are generated independently and randomly within $\pm 50\%$ of the outer square elastic values. We wish to propagate waves induced by an explosion located at $\mathbf{x}_0 = {}^t(20\,km, 20\,km)$ (center of the square), the source time dependence being described by a Ricker wavelet (i.e. second derivative of a Gaussian function) with a central frequency of 1.5 Hz (corresponding roughly to a corner frequency of 3.6 Hz). Ignoring the fluctuation of velocity in the inner square and far away enough from the source, we can estimate the minimum wavelength λ_m of the wavefield generated by the explosion, to be roughly equal to $800\,m$. To obtain the promised accuracy of the SEM, we must generate a mesh based on square elements that honors all physical discontinuities. In this case, the geometry is so simple that the mesh generation is trivial, nevertheless, it imposes $100 \times 100\,m^2$ elements in the random matrix. Knowing that a degree 4 spectral element (a tensorial product of degree 4 polynomial basis) can roughly handle one wavelength per element, the mesh is oversampling the wavefield by a factor 8 in each direction leading to a factor 512 in numerical cost (a factor 8 in each direction and a factor 8 in time to match the Newmark time marching scheme stability condition). For this simple 2-D case, this factor 512 can be handle and this allows to compute a reference solution. Nevertheless, one can imagine that for a 3-D case, meshing the original model can quickly be out of reach for a reasonable computing power and the temptation would be high to either use a mesh that doesn't honor the physical interfaces or to simplify the model.

We choose an $\varepsilon_0 = 0.4$ for the homogenization procedure (which means we filter out all oscillations in the medium that are twice smaller than the wavelength). The V_s and the total anisotropy (we define the total anisotropy as $\max\{|\mathbf{c}^* - \mathbf{c}^*_{iso}|\}/\max\{|\mathbf{c}^*|\}$ where $\mathbf{c}^*_{iso}$ is the closest isotope elastic tensor to $\mathbf{c}^*$) of the homogenized media are shown Fig. 3. In Fig. 4 are shown the reference solution, the result of a run in the homogenized model and in a naively "filtered model" (we defined the filtered model as $\mathbf{c}^f = \mathcal{F}^{\varepsilon_0}(\mathbf{c})$. The is a low-pass filtered version of the original model) for a receiver located in ${}^t(37\,km, 20\,km)$. It can seen that the homogenized solution is very accurate compared to the "filtered" solution.

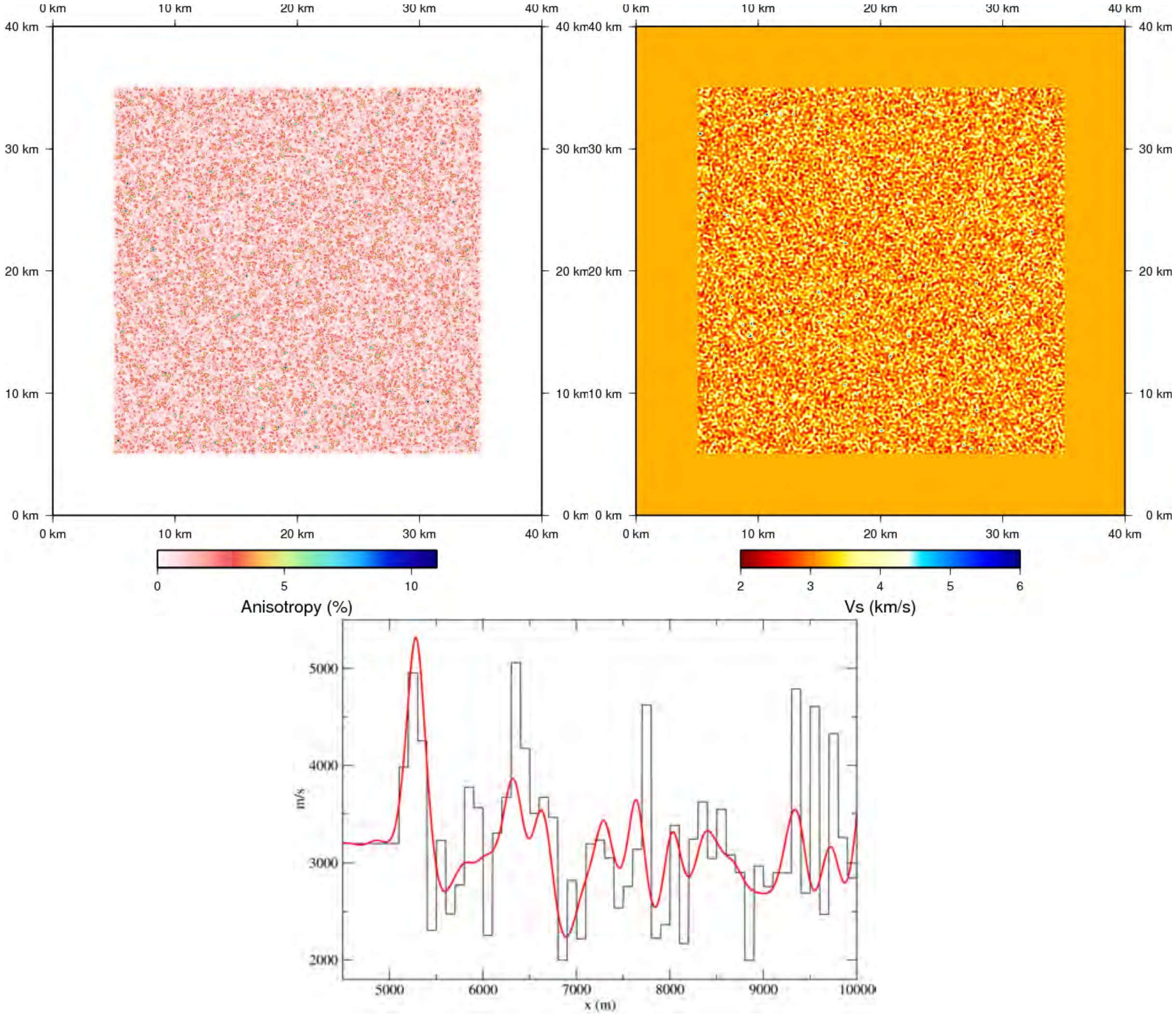

Figure 3: One of the V_s (top left plot) and total anisotropy (top right plot) of the homogenized model of the random square model. The bottom plot is a cut along $z = 32\ km$ in the original V_s (black line) and one of the V_s of the homogenized model (red line).

Marmousi2 model

Marmousi2 is a 2D elastic geological model derived by G.S. Martin from the original Marmousi model designed by the IFP (Fig. 5). The model contains thin (down to some meters) and complex structures. Even for a 2D model, the quadrangular mesh required for the Spectral Element Method is difficult to design and leads to a significant numerical cost (the reference solution computed here lasted for 7 days using 64 CPU). A sample of the mesh is shown Fig. 6, top plot. Here, the source is an explosion with, in time, a Ricker wavelet with central frequency of 6Hz (15Hz corner) leading to a minimum wavelength varying from 20m at the top of the model to 230m at the bottom. A snapshot of the propagating kinetic energy is shown in Fig. 8. The non-periodic homogenization is performed using a corner wavenumber of 0.017m^{-1} which implies a ε_0 varying from 3 at the top of the model to 0.25 at the bottom. One of the S velocity and the total anisotropy of the homogenized model are plotted in Fig. 7. For the homogenized model, the SEM mesh is a trivial regular mesh (see Fig. 6, bottom plot) leading to a lower numerical cost (1 hour using 64 CPU).

An example of traces is shown in Fig. 9. It appears that, even if the ε_0 is very poor at the

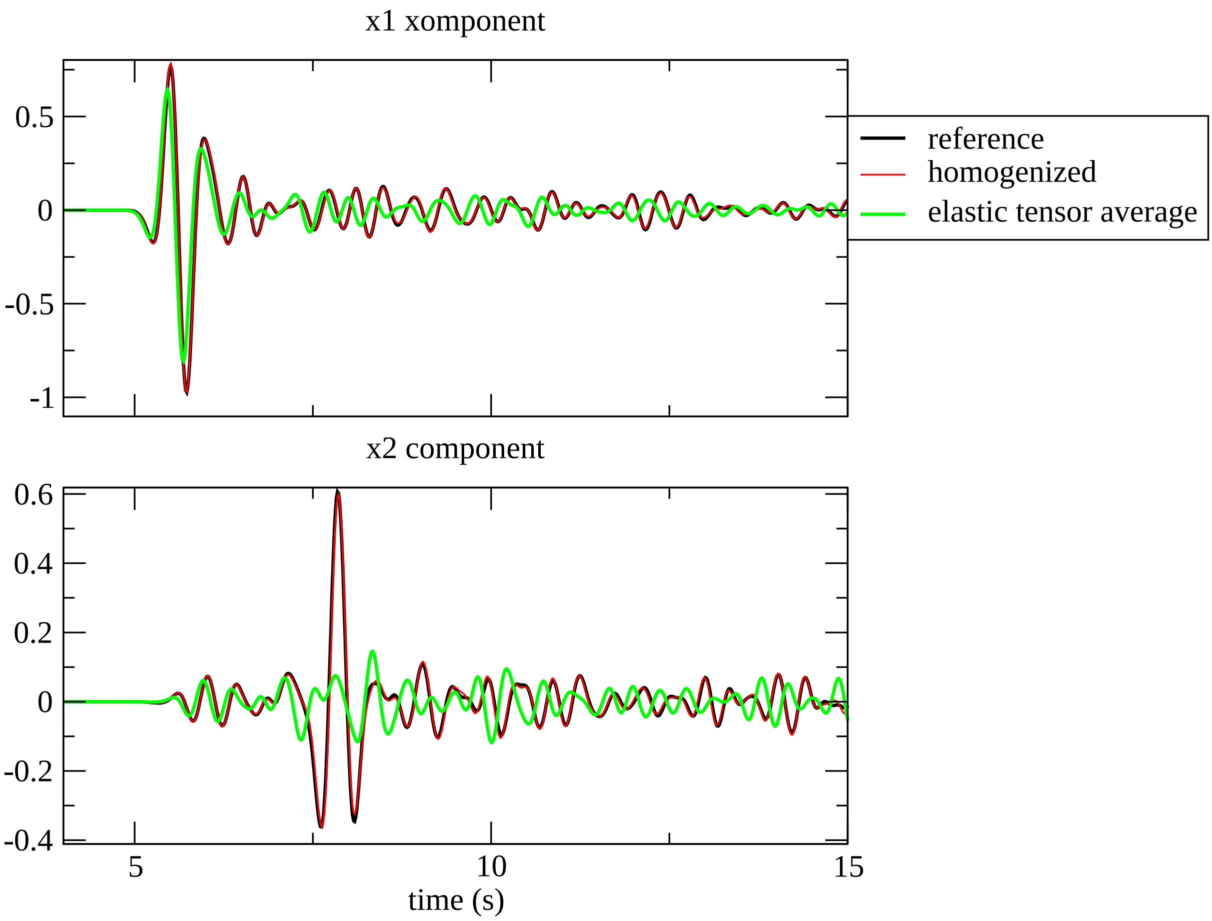

Figure 4: Traces (top: horizontal component, bottom: vertical component) for a receiver located in the middle of the model. The reference solution (black line), the homogenized solution (red line) and the “filtered” solution (green line, see text) are represented.

top of the medium, the seismograms obtained using the homogenization procedure are in very good agreement with the reference solution. The difference between those solutions and the “filtered” one is nevertheless less spectacular than for the random square example: this is due to the heterogeneities spectrum of the Marmousi2 model which has little power in the domain of the high wavenumbers.

3 Conclusions

We have presented a homogenization process for the wave equation allowing to up-scale 2D/3D non-periodic elastic models. This is a significant improvement of previous works which were limited to the layered non-periodic media case or to the 2D/3D periodic media case (more results can be found in [6, 7, 8]). To obtain a complete 2D/3D up-scaling tool, issues like boundary conditions in non-periodic 2-D/3-D cases (1-D case have been solved, [3, 5]) remain to be treated. This work should be useful for both forward and inverse problems.

4 Acknowledgments

This work was funded by the french ANR MUSE and the ANR mémé. Computations were done using the IPGP and the IDRIS clusters.

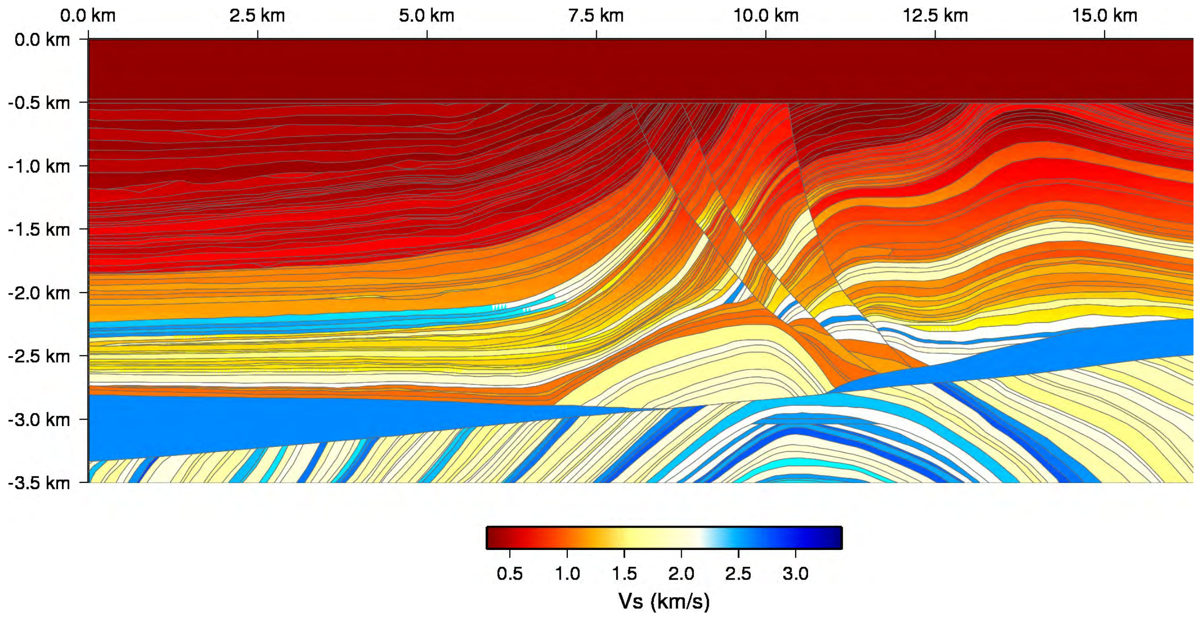

Figure 5: S velocity of the Marmousi2 model. The liquid layer has been replaced by a solid layer with slow S wave velocity.

REFERENCES

[1] Komatitsch, D. & Vilotte, J. P., 1998. The spectral element method: an effective tool to simulate the seismic response of 2D and 3D geological structures. *Bull. Seism. Soc. Am.*, **88**, 368–392.

[2] Backus, G., 1962. Long-wave elastic anisotropy produced by horizontal layering. *J. Geophys. Res. 67*(11), 4427–4440.

[3] Capdeville, Y. & Marigo, J. J., 2007. Second order homogenization of the elastic wave equation for non-periodic layered media. *Geophys. J. Int.*, **170**, 823–838.

[4] Sanchez-Palencia, E., 1980. *Non homogeneous media and vibration theory*. Number 127 in Lecture Notes in Physics. Berlin: Springer.

[5] Capdeville, Y. & Marigo, J. J., 2008. Shallow layer correction for spectral element like methods. *Geophys. J. Int.*, **172**, 1135–1150.

[6] Capdeville, Y., Guillot, L. & Marigo J. J., 2010. 1-D non periodic homogenization for the wave equation *Geophys. J. Int.* , **181**, pp 897-910.

[7] Guillot, L., Capdeville, Y. & Marigo J. J., 2010. 2-D non periodic homogenization for the SH wave equation *Geophys. J. Int.* , **182**, pp 1438-1454..

[8] Capdeville, Y., Guillot, L. & Marigo J. J., 2010. 2D nonperiodic homogenization to upscale elastic media for P-SV waves. *Geophys. J. Int.* , **182**, pp 903-922.

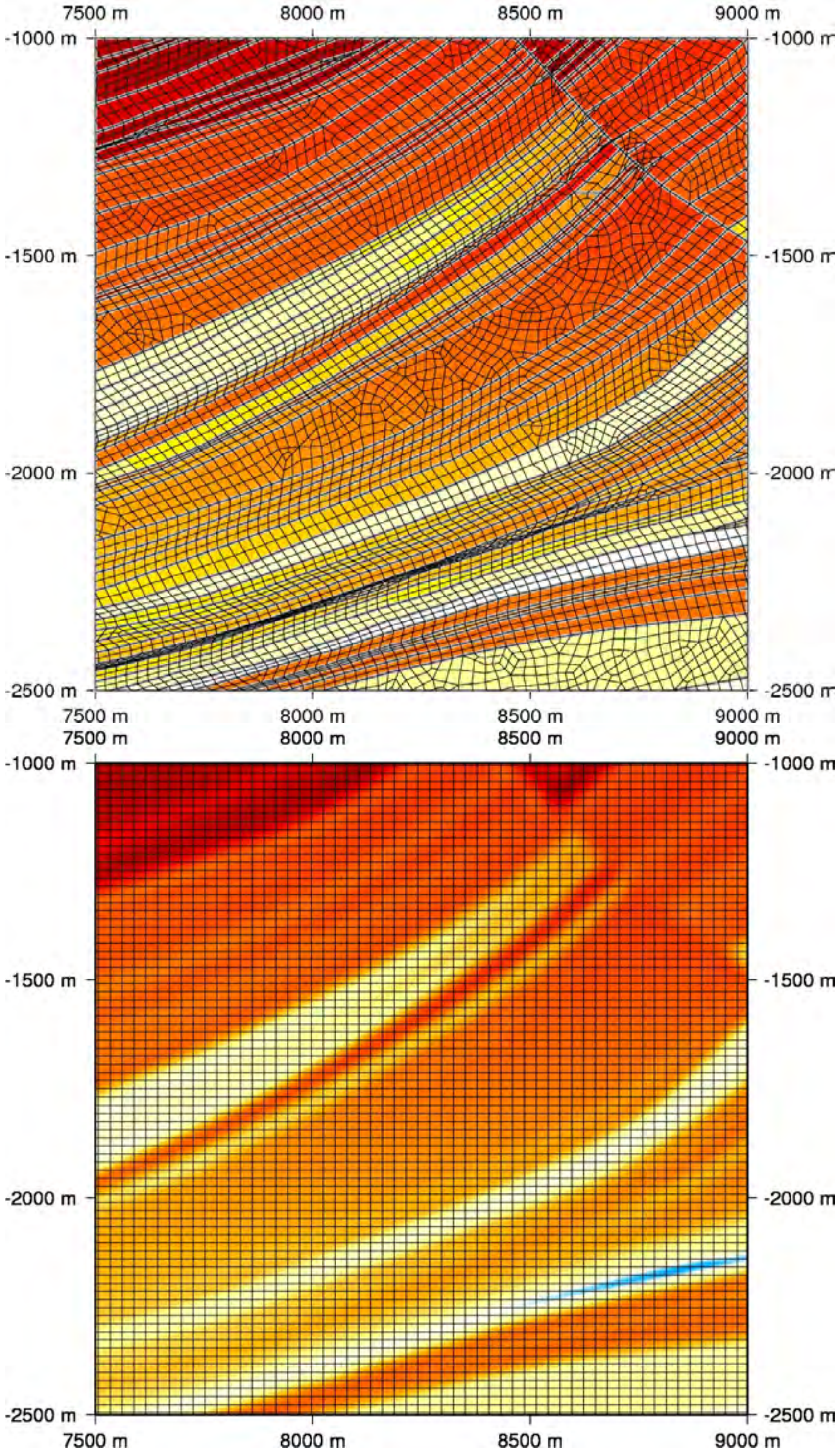

Figure 6: Sample of the SEM mesh for the original marmousi2 model (top plot) and for the homogenized Marmousi2 model (bottom plot). The back ground color is V_s.

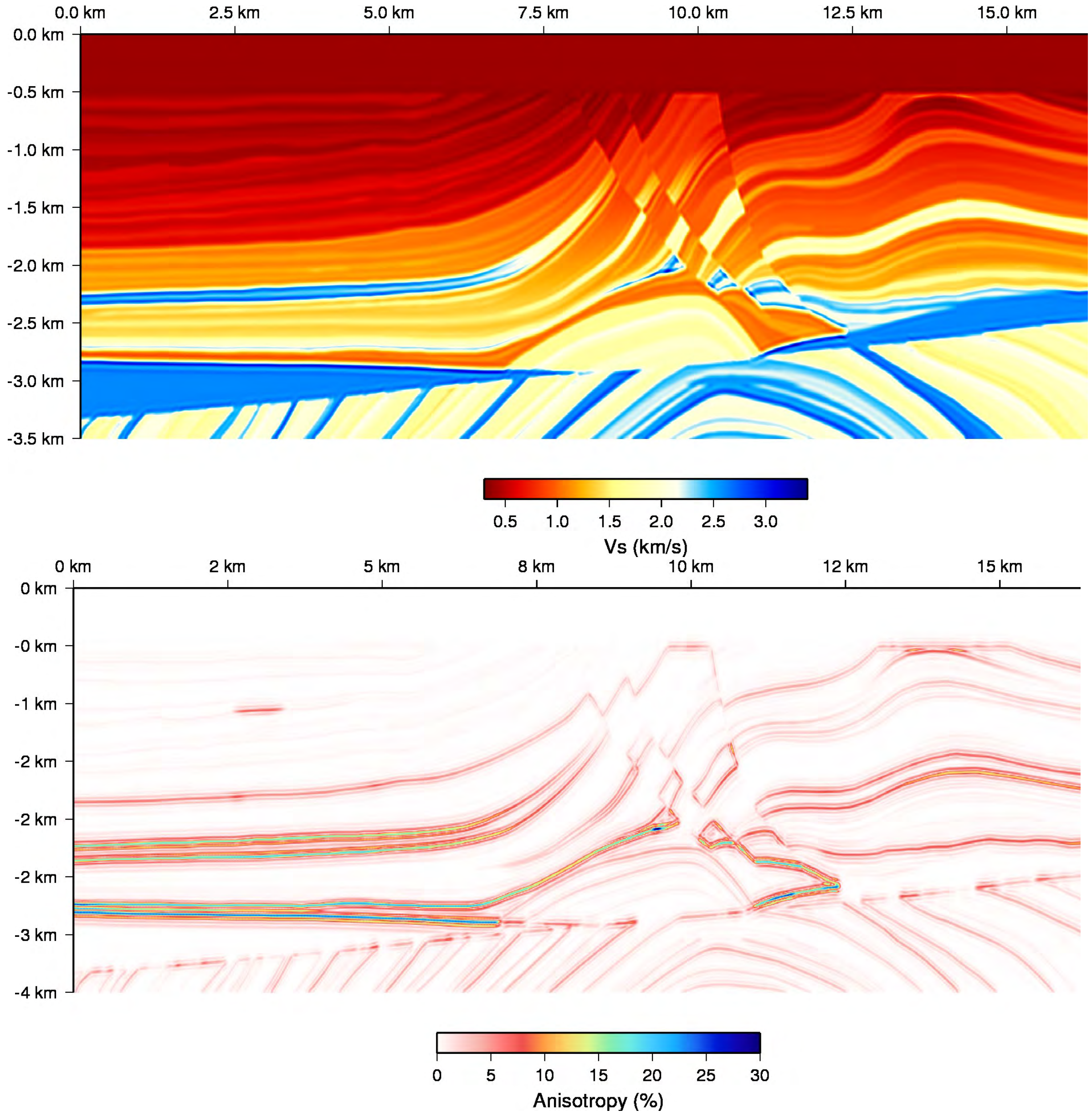

Figure 7: One of the S velocity (top plot) and the total anisotropy (bottom plot) of the homogenized marmousi2 model

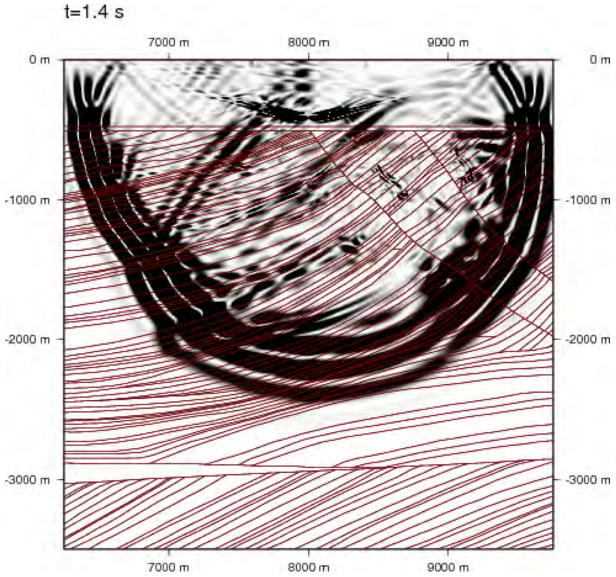

Figure 8: Snapshot of the propagating kinetic energy in marmousi2 at $t = 1.4$ s

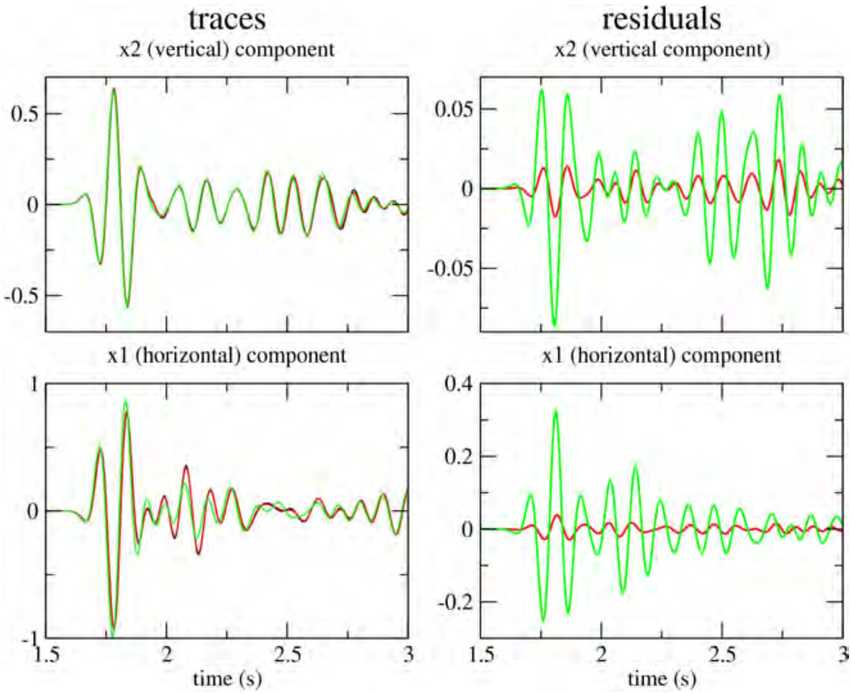

Figure 9: Traces (top: vertical component, bottom: horizontal component) for a receiver located at the middle of the model. The reference solution (black line), the homogenized solution (red line) and the "filtered" solution are represented (green line). On the right column are shown the residuals (the differences between the approximate solutions and the reference solution)

COMPDYN 2011
ECCOMAS Thematic Conference on
Computational Methods in Structural Dynamics and Earthquake Engineering
M. Papadrakakis, M. Fragiadakis, V. Plevris (eds.)
Corfu, Greece, 25-28 May 2011

REFLECTION OF PLANE HARMONIC WAVES AT A PLANE INTERFACE OF A SEMI-INFINITE LATTICE AND A SEMI-INFINITE CONTINUUM

Asiya M. Kudarova[1], **Andrei V. Metrikine**[2]

[1]Institute for Problems in Mechanical Engineering RAS
Bolshoy pr. V.O. 61, St. Petersburg, 199178, Russia
e-mail: asya.kudarova@gmail.com

[2] Delft University of Technology
Faculty of Civil Engineering and GeoSciences, P.O. Box 5048, 2600 GA, The Netherlands
e-mail: A.Metrikine@tudelft.nl

Keywords: wave reflection, dynamic coupling, discrete lattice, elastic continuum

Abstract. *Whereas the wave reflection and refraction at an interface of two continua has been studied in detail and has become a matter of text books, the wave reflection at an interface of a lattice and a continuum does not seem to have been systematically studied. The aim of this development is to close this gap. Two semi-infinite elastic media are considered in contact at a plane interface. One of these media is modelled using a rectangular network of identical masses and springs (hereafter called a lattice), whereas the other one is described by the equations of the classical elastic continuum. The wave reflection at the interface with the classical continuum is studied assuming that a plane harmonic wave falls from the lattice on the interface. The reflection coefficients for the reflected compressional and shear waves are found as functions of the wave frequency and of the incidence angle. It is shown that the reflection at low frequencies can be made very small by properly choosing the parameters of the continuum. However, the reflection coefficients inevitably grow with increase of the frequency and can reach the values close to one. This is to be expected as the classical continuum is capable of approximating a lattice only at relatively low frequencies.*

1 INTRODUCTION

The dynamic coupling of the discrete and continuum domains is widely used in concurrent multiscale simulations. The aim of such a coupling is to decrease the calculation time. This is achieved by breaking the computational domain into two parts. In the main part, where a detailed modeling is necessary, a discrete model is adopted. The rest of the domain is assumed to be occupied by a corresponding continuum. Often the role of this continuum is simply to serve as non-reflecting boundary or to pass the reflections from the outer boundaries of the computational domain. In either case the wave reflection from the fictitious boundary between the discrete and continuum domains should be minimized. This is the challenge researches are trying to cope with. A number of approaches have been introduced to couple discrete and continuum representations of materials. A coarse-grained molecular dynamics (CGMD) method has been proposed by Rudd and Broughton [3], an approach based on the Green's functions formalism has been proposed in [4] – [5] to derive the non-reflecting boundary conditions. E [6] and his co-workers contributed on the study of optimal matching conditions, Wagner and Liu introduced the bridging scale decomposition (BSL) method [7] which was developed further by Xiao and Belytschko [8]. However, most of the methods either have limitations in their application or are often too complicated to implement. Moreover, in most approaches the wave reflections either have not been yet properly studied in multidimensional cases or the non-reflecting boundary conditions have been introduced only for 1D case.

In this development a systematic investigation into the wave reflection at the interface of a square lattice composed of masses and springs and a classical isotropic continuum is presented. The parameters of the lattice are chosen such as to assure that in the long-wave approximation the lattice is reduced to the continuum, with which it is coupled. The main aim of this investigation is to demonstrate the poor ability of the classical continuum to absorb high-frequency waves in the lattice. Such demonstration is necessary to motivate the use of generalized continua at the discrete-continuum interfaces. The promising character of the latter approach has recently been demonstrated in [9], where it has been shown that the reflections from the boundary between the 1D chain of masses and springs and a gradient continuum of the second order can be eliminated at the entire frequency band.

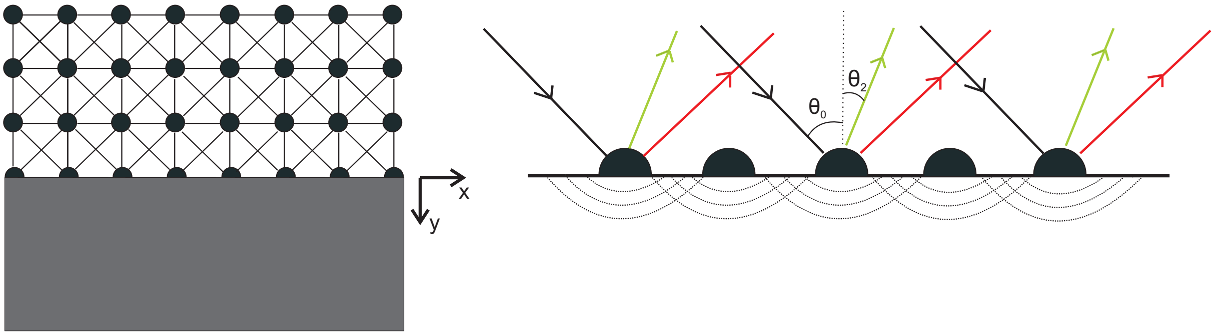

Figure 1: Coupled discrete and continuum domains (left) and wave reflection and transmission at the interface (right).

Two elastic semi-infinite half-spaces in contact are considered in this paper (see Figure 1). One of the half-spaces is described by the equations of motion of the classical continuum and another one is modelled using the system of masses and translational springs that form a so-called square lattice. It is assumed that the plane harmonic wave, either longitudinal or transversal one, propagates in the lattice towards the interface between two domains. The energy of the reflected longitudinal and transversal waves is studied as a function of the frequency and the angle of incidence θ_0 in terms of the energy reflection coefficient.

The paper is organized as follows. First, the governing equations for the lattice and the correspondence between the parameters of the lattice and of the continuum in the long-wave limit are introduced. Thereafter the propagation characteristics of the body waves in the lattice are derived. The following boundary conditions are introduced: the continuity of forces and displacements at the interface. Then the equations of motion of the continuum are solved with the certain boundary conditions and the displacements in the continuum in the form of integrals are derived. Then the integrals for the displacements at the interface are evaluated. The system of boundary conditions is applied to find the amplitudes of the reflected waves. Then the energy reflection coefficients are introduced. Finally, the results and conclusions are presented.

2 GOVERNING EQUATIONS FOR THE LATTICE

The inner cell of the square lattice consists of identical masses M and translational springs: axial κ_{axi} and diagonal κ_{dia}. The derivation of the equations of motion for the square lattice with translational and shear springs can be found in [1]. It is assumed that the dynamic behaviour of the lattice corresponds to that of the isotropic classical elastic continuum in the long-wave limit. This assumption requires the following relations between the parameters of the lattice and of the continuum [1]:

$$M = \rho d^2 h, \quad \kappa_{axi} = 2\kappa_{dia}, \quad \kappa_{dia} = h\mu, \quad 2\kappa_{dia} = h(\lambda + \mu), \tag{1}$$

where ρ is the mass density of the continuum, λ and μ are Lame's constants of the elastic continuum, d is the inter-particle distance in the lattice along the axes, h is a parameter of length in the direction normal to the $[x, y]$ plane. The introduction of this parameter is required to couple the 2D-lattice with the 3D-continuum. It follows from the equalities (1) that $\lambda = \mu$ in the continuum that corresponds to such a lattice in the long-wave limit.

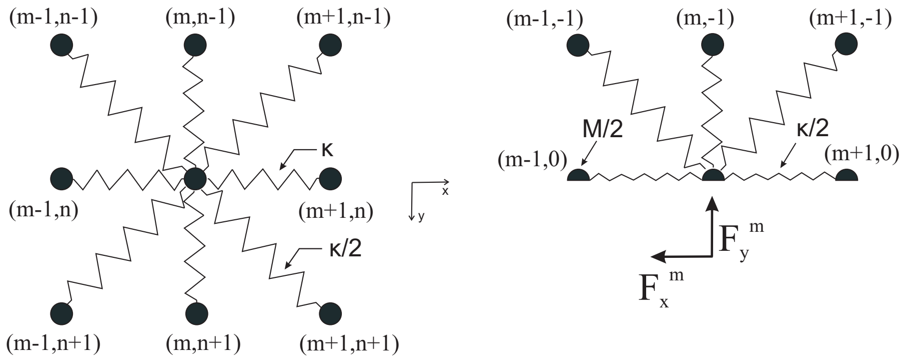

Figure 2: Inner (left) and boundary (right) cells of the lattice.

We denote $\kappa = \kappa_{axi} = 2\kappa_{dia}$. Then the equations of motion for the inner cell of the lattice (depicted in the left part of Figure 2) read

$$\begin{gathered} M \mathrm{d}_{tt} u_x^{(m,n)} = \kappa/4 \left(-12 u_x^{(m,n)} + 4 u_x^{(m+1,n)} + 4 u_x^{(m-1,n)} + u_x^{(m+1,n+1)} + u_x^{(m+1,n-1)} + \right. \\ \left. + u_x^{(m-1,n+1)} + u_x^{(m-1,n-1)} + u_y^{(m+1,n+1)} + u_y^{(m-1,n-1)} - u_y^{(m+1,n-1)} - u_y^{(m-1,n+1)} \right), \end{gathered} \tag{2}$$

$$
\begin{aligned}
M\mathrm{d}_{tt}u_y^{(m,n)} &= \kappa/4\left(-12u_y^{(m,n)} + 4u_y^{(m,n+1)} + 4u_y^{(m,n-1)} + u_y^{(m+1,n+1)} + u_y^{(m+1,n-1)} + \right.\\
&\left. + u_y^{(m-1,n+1)} + u_y^{(m-1,n-1)} - u_x^{(m+1,n-1)} - u_x^{(m-1,n+1)} + u_x^{(m+1,n+1)} + u_x^{(m-1,n-1)}\right).
\end{aligned}
$$

Here $u_x^{(m,n)}(t)$, $u_y^{(m,n)}(t)$ are the displacements of the cell with the coordinates (md, nd).

The mass of the boundary element is taken as a half of the mass of the inner cell and the stiffness of the axial springs at a boundary is taken as $\kappa/2$ (see the right part of Figure 2). The forces F_x^m, F_y^m act on the masses at the interface from the continuum. The equations of motion for the boundary cell read

$$
\begin{aligned}
\frac{1}{2}M\mathrm{d}_{tt}u_x^{(m,0)} &= -\kappa/4\left(6u_x^{(m,0)} - 2u_x^{(m+1,0)} - 2u_x^{(m-1,0)} + u_y^{(m+1,-1)} - u_x^{(m+1,-1)} - \right.\\
&\left. - u_x^{(m-1,-1)} - u_y^{(m-1,-1)}\right) - F_x^m,\\
\frac{1}{2}M\mathrm{d}_{tt}u_y^{(m,0)} &= -\kappa/4\left(6u_y^{(m,0)} - 4u_y^{(m,-1)} - u_y^{(m+1,-1)} + u_x^{(m+1,-1)} - u_y^{(m-1,-1)} - \right.\\
&\left. - u_x^{(m-1,n-1)}\right) - F_y^m.
\end{aligned}
\tag{3}
$$

We consider first a plane longitudinal incident wave that propagates towards the continuum domain with the angle of incidence $\theta = \theta_0$. Then we have two reflected waves, namely the longitudinal and transversal ones (see the right part of Figure 1). We introduce the indexes I, L and T for the incident, longitudinal and transversal waves. Then the displacements in the lattice read

$$
\begin{aligned}
u_x^{(m,n)} &= e^{\mathrm{i}\omega \mathrm{t}}\left(A_I e^{-\mathrm{i}(mK_x^I + nK_y^I)} + A_L e^{-\mathrm{i}(mK_x^L - nK_y^L)} + A_T e^{-\mathrm{i}(mK_x^T - nK_y^T)}\right),\\
u_y^{(m,n)} &= e^{\mathrm{i}\omega t}\left(B_I e^{-\mathrm{i}(mK_x^I + nK_y^I)} - B_L e^{-\mathrm{i}(mK_x^L - nK_y^L)} - B_T e^{-\mathrm{i}(mK_x^T - nK_y^T)}\right),
\end{aligned}
\tag{4}
$$

where $K_x^I = k_0 \sin\theta_0$, k_0 is a dimensionless wavenumber of the longitudinal waves (wavenumber mupltiplied by d, hereafter we will work with dimensionless wavenumbers), and according to the Snell's law $K_x^I = K_x^L = K_x^T = K_x$. The angle of reflection of longitudinal waves is then the same as the angle of incidence and $K_y^I = K_y^L = k_0 \cos\theta_0$. We denote the angle of reflection of transversal waves as $\theta = \theta_2$ and wavenumber $k = k_2$. Then $K_x^T = k_2 \sin\theta_2$, $K_y^T = k_2 \cos\theta_2$.

The wavenumber k_0 can be found numerically from the dispersion relation [1] for longitudinal waves:

$$
4\cos(k_0 \sin\theta_0)\cos(k_0 \cos\theta_0) + 2\cos(k_0 \sin\theta_0) + 2\cos(k_0 \cos\theta_0) - 8 + \Omega^2 = 0, \tag{5}
$$

where the angle of incidence θ_0 and the dimensionless frequency $\Omega = \omega d/c_T$ are input data, $c_T = \sqrt{\mu/\rho}$ is the shear wave velocity in the elastic continuum. As follows from the equalities (1), $\Omega^2/2 = \omega^2 M/\kappa$.

The reflection angle θ_2 and wavenumber k_2 can be found from the dispersion equation for transversal waves

$$
2\cos(k_2 \sin\theta_2) + 2\cos(k_2 \cos\theta_2) - 4 + \Omega^2 = 0, \tag{6}
$$

with the aid of the relation $k_2 = k_0 \sin\theta_0 / \sin\theta_2$ that follows from the Snell's law.

The dependence of the wavenumbers k_0 and k_2 on the frequency Ω for different incidence angles is depicted in Figure 2.

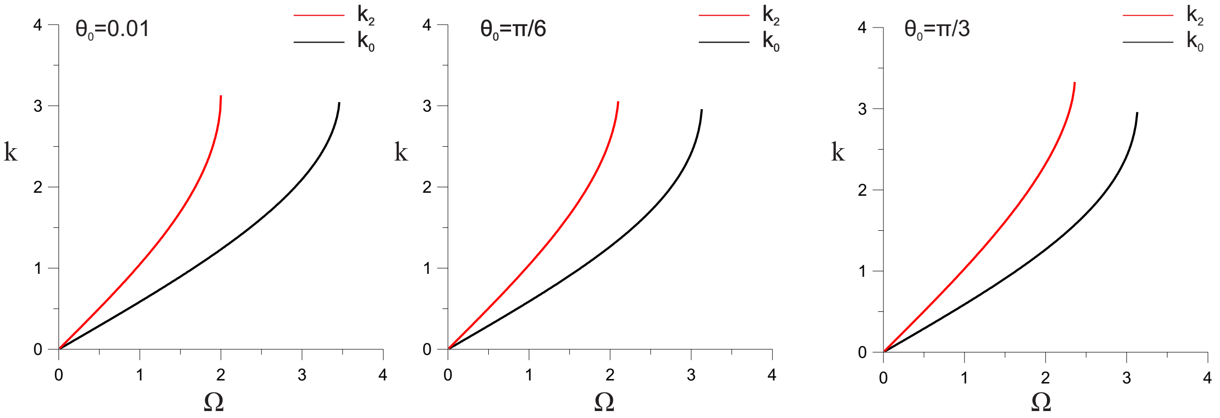

Figure 3: Wavenumbers of the longitudinal and transversal waves versus frequency for different angles of incidence

Substitution of the incident longitudinal (transversal) wave into the equations of motion (2) allows to obtain the relation between the $x-$ and $y-$components of the amplitudes of the displacements. This gives:

$$D_L = \frac{B_I}{A_I} = \frac{B_L}{A_L} = \frac{-\Omega^2/2 + 3 - \cos(K_x)(2+\cos(K_y^L))}{-\sin(K_x)\sin(K_y^L)}, \quad D_T = \frac{B_T}{A_T} = \frac{-\Omega^2/2 + 3 - \cos(K_x)(2+\cos(K_y^T))}{-\sin(K_x)\sin(K_y^T)}. \tag{7}$$

In correspondence with the incident wave the forces F_x^m, F_y^m are expressed as follows:

$$F_x^m = F_x^0(\omega)exp(-\mathrm{i}mK_x)exp(\mathrm{i}\omega t), \quad F_y^m = F_y^0(\omega)exp(-\mathrm{i}mK_x)exp(\mathrm{i}\omega t). \tag{8}$$

Substitution of the displacements (4) in the equations of motion for the boundary element (3) leads to the system of two algebraic equations with four variables, namely A_L, A_T, F_x^0, F_y^0. We need two more equations to solve the system. They come from the second set of the boundary conditions that provides the continuity of displacements at the interface $y = 0$. This will be discussed in Section 4.

3 GOVERNING EQUATIONS FOR THE CONTINUUM

Equations of motion of the elastic continuum read [2]

$$\tilde{\mu}\left(\partial_{xx}u_x + \partial_{yy}u_x\right) + \left(\tilde{\lambda} + \tilde{\mu}\right)\left(\partial_{xx}u_x + \partial_{yx}u_y\right) = \rho\partial_{tt}u_x, \quad \tilde{\mu}\left(\partial_{xx}u_y + \partial_{yy}u_y\right) + \left(\tilde{\lambda} + \tilde{\mu}\right)\left(\partial_{xy}u_x + \partial_{yy}u_y\right) = \rho\partial_{tt}u_y, \tag{9}$$

where u_x and u_y are the $x-$and $y-$ components of the vectorial displacement in the continuum. We introduce small dissipation χ: $\tilde{\lambda} = \lambda + \chi\partial_t$, $\tilde{\mu} = \mu + \chi\partial_t$. λ and μ are Lame's coefficients and $\lambda = \mu$, as it has been discussed in the previous section (1). The need to introduce a small dissipation will become clear in the course of derivation of the response of the continuum.

There is an infinite number of the points of contact between the discrete lattice and the continuum at the interface $y = 0$ (see Figure 1). At each point the forces F_x^j, F_y^j (8) act on the continuum from the lattice. We assume that there is finite contact area between each mass of the lattice and the continuum in order to avoid singularities in the solution for the classical continuum (if this were not done, the contact forces would turn to zero). For this reason we introduce parameter b — the half-width of the contact of the continuum and one particle of the lattice at the interface. We also choose the boundary conditions such as to assure that the contact force is independent of b:

$$\int_{-b}^{b} \sigma dx = \frac{F}{h}. \tag{10}$$

Then the natural boundary conditions at the interface can be formulated:

$$\sigma_{yy}(x,0) = -\sum_{j=-\infty}^{\infty} \frac{F_y^j}{2bh} H\left(b - |x - jd|\right), \quad \sigma_{yx}(x,0) = -\sum_{j=-\infty}^{\infty} \frac{F_x^j}{2bh} H\left(b - |x - jd|\right), \tag{11}$$

where $\sigma_{yy}(x,y,t)$ is the normal stress, $\sigma_{yx}(x,y,t)$ is the shear stress, $H(x)$ is the unit step function (chosen for the sake of simplicity), j is an integer.

We also impose the correspondence between the stresses σ_{yy}, σ_{yx} and the forces F_y^j, F_x^j in the long-wave limit. This can be achieved if we take $b = d/2$.

We consider the following displacement representation:

$$u_x(x,y,t) = \partial_x \Phi(x,y,t) + \partial_y \Psi(x,y,t), \quad u_y(x,y,t) = \partial_y \Phi(x,y,t) - \partial_x \Psi(x,y,t). \tag{12}$$

Then the stresses σ_{yy} and σ_{yx} are related to the displacement potentials Φ, Ψ in the following way:

$$\sigma_{yy} = \tilde{\lambda}\left(\partial_{xx} + \partial_{yy}\right)\Phi + 2\tilde{\mu}\left(\partial_{yy}\Phi - \partial_{yx}\Psi\right), \quad \sigma_{xy} = \tilde{\mu}\left(2\partial_{xy}\Phi + \partial_{yy}\Psi - \partial_{xx}\Psi\right). \tag{13}$$

This representation satisfies the equations of motion (9) if

$$\partial_{tt}\Phi - \left(\tilde{\lambda} + 2\tilde{\mu}\right)/\rho\left(\partial_{xx} + \partial_{yy}\right)\Phi = 0, \quad \partial_{tt}\Psi - \tilde{\mu}/\rho\left(\partial_{xx} + \partial_{yy}\right)\Psi = 0. \tag{14}$$

The solutions of the above equations can be found in the form

$$\Phi(x,y,t) = \phi(x,y)e^{\mathrm{i}\omega t}, \quad \Psi(x,y,t) = \psi(x,y)e^{\mathrm{i}\omega t}. \tag{15}$$

We substitute (15) in (14) and (13) in (11), then we apply the exponential Fourier transform over the spatial coordinate y defined as

$$\phi^*(k,y) = \int_{-\infty}^{\infty} e^{\mathrm{i}kx}\phi(x,y)dx, \quad \psi^*(k,y) = \int_{-\infty}^{\infty} e^{\mathrm{i}kx}\psi(x,y)dx \tag{16}$$

and obtain the equations

$$\partial_{yy}\phi^* - \zeta_L^2\phi^* = 0, \quad \partial_{yy}\psi^* - \zeta_T^2\psi^* = 0 \tag{17}$$

with the boundary conditions at the interface $y = 0$

$$\begin{aligned}
&(\tilde{\lambda} + 2\tilde{\mu})\partial_{yy}\phi^* - \tilde{\lambda}k^2\phi^* + 2\tilde{\mu}\mathrm{i}k\partial_y\psi^* = -\sum_{j=-\infty}^{\infty} F_y^0 e^{-\mathrm{i}jdK_x}\left(e^{\mathrm{i}k(jd+b)} - e^{\mathrm{i}k(jd-b)}\right)/\mathrm{i}dhk, \\
&\tilde{\mu}\left(\partial_{yy}\psi^* + k^2\psi^* - 2\mathrm{i}k\partial_y\phi^*\right) = -\sum_{j=-\infty}^{\infty} F_x^0 e^{-\mathrm{i}jdK_x}\left(e^{\mathrm{i}k(jd+b)} - e^{\mathrm{i}k(jd-b)}\right)/\mathrm{i}dhk,
\end{aligned} \tag{18}$$

where $\zeta_L = \sqrt{k^2 - \omega^2/\tilde{c}_L^2}$, $\zeta_T = \sqrt{k^2 - \omega^2/\tilde{c}_T^2}$, $\tilde{c}_L^2 = c_L^2(1 + \mathrm{i}\chi^*)$, $\tilde{c}_T^2 = c_T^2(1 + \mathrm{i}\chi^*)$, $\chi^* = \omega\chi/\mu$; $c_L = \sqrt{(\lambda + 2\mu)/\rho}$ and $c_T = \sqrt{\mu/\rho}$ are the compressional and shear wave velocities in the classical continuum, respectively.

The general solutions of the equations (17), taking into account that the functions ϕ^*, ψ^* should have finite values when y goes to ∞, can be written in the form

$$\phi^*(k,y) = A(k,\omega)exp(-\zeta_L y), \quad \psi^*(k,y) = B(k,\omega)exp(-\zeta_T y), \tag{19}$$

provided that the real parts of the radicals ζ_L, ζ_T are assumed positive.

We find the functions $A(k,\omega)$ and $B(k,\omega)$ that satisfy the boundary conditions (18). Then we substitute (15) to (12) and apply the Fourier transform to the result in order to obtain the Fourier transforms of the displacements u_x, u_y:

$$\begin{aligned} u_x^* &= (-\mathrm{i}k\phi^* + \partial_y\psi^*) = \left(F_x^0\zeta_T(2k^2e^{-\zeta_L y} - \gamma e^{-\zeta_T y}) + F_y^0\mathrm{i}k(2\zeta_T\zeta_L e^{-\zeta_T y} - \gamma e^{-\zeta_L y})\right) S, \\ u_y^* &= (\mathrm{i}k\psi^* + \partial_y\phi^*) = \left(F_x^0\mathrm{i}k(\gamma e^{-\zeta_L y} - 2\zeta_T\zeta_L e^{-\zeta_T y}) + F_y^0\zeta_L(2k^2e^{-\zeta_T y} - \gamma e^{-\zeta_L y})\right) S, \end{aligned} \tag{20}$$

where

$$S = \frac{\sum\limits_{j=-\infty}^{\infty} e^{\mathrm{i}kjd}\left(e^{-\mathrm{i}kb} - e^{\mathrm{i}kb}\right)}{\mathrm{i}dhk\mu(1+\mathrm{i}\chi^*)\Delta}, \quad \gamma = 2k^2 - \omega^2/\tilde{c}_T^2, \quad \Delta = \gamma^2 - 4k^2\zeta_T\zeta_L. \tag{21}$$

The inverse Fourier transform is applied to derive the displacements in the continuum according to the following relations:

$$u_x(x,y,t) = \frac{1}{2\pi}\int\limits_{-\infty}^{\infty} e^{-\mathrm{i}kx}u_x^*(x,y,t)dk, \quad u_y(x,y,t) = \frac{1}{2\pi}\int\limits_{-\infty}^{\infty} e^{-\mathrm{i}kx}u_y^*(x,y,t)dk. \tag{22}$$

4 COUPLING OF THE DOMAINS

The continuity of forces and displacements is required at the boundary $y = 0$. We have smeared the contact between the lattice and the continuum at the interface to avoid singularities in the solution for the continuum and this causes the ambiguity of the boundary problem statement.

We assume that the displacements of the masses at the boundary in the lattice are equal to the displacements of the continuum in the points of contact:

$$u_x^{(m,0,t)} = u_x(md,0,t), \quad u_y^{(m,0,t)} = u_y(md,0,t). \tag{23}$$

Note that one could also equate the displacements in the lattice $u_x^{(m,0,t)}$, $u_y^{(m,0,t)}$ to the displacements $u_x(md,0,t)$, $u_y(md,0,t)$ averaged over the width of the contact $2b$.

We substitute the displacements in the lattice (4) into (23) and apply the results of the previous section. Then the equations (23) transform to the following equations:

$$\begin{aligned} &A^{(f)}e^{-\mathrm{i}K_x m} = \int\limits_{-\infty}^{\infty} F^{(f)}e^{-\mathrm{i}kmd}\sum\limits_{j=-\infty}^{\infty} e^{\mathrm{i}kjd}e^{-\mathrm{i}K_x j}dk, \quad f = 1,2, \\ &A^1 = A_I + A_L + A_T, \quad A^2 = A_I D_L - A_L D_L - A_T D_T, \\ &F^1(k,\omega) = \tfrac{(2k^2-\gamma)\zeta_T F_x^0 + \mathrm{i}k(2\zeta_T\zeta_L-\gamma)F_y^0}{2\pi\mathrm{i}kdh\mu(1+\mathrm{i}\chi^*)\Delta}\left(e^{-\mathrm{i}kb} - e^{\mathrm{i}kb}\right), \\ &F^2(k,\omega) = \tfrac{-\mathrm{i}k(2\zeta_T\zeta_L-\gamma)F_x^0 + (2k^2-\gamma)\zeta_L F_y^0}{2\pi\mathrm{i}kdh\mu(1+\mathrm{i}\chi^*)\Delta}\left(e^{-\mathrm{i}kb} - e^{\mathrm{i}kb}\right). \end{aligned} \tag{24}$$

Let us multiply the left and the right parts of the equations (24) by $e^{\mathrm{i}K_x m}$ and introduce $l = j - m$. Then the equations (24) can be rewritten as follows:

$$A^{(f)} = \int\limits_{-\infty}^{\infty} F^{(f)} \sum_{l=-\infty}^{\infty} e^{\mathrm{i}l(kd-K_x)} dk. \tag{25}$$

We divide this equations by h, apply the relation $\kappa = 2\mu h$ and introduce dimensionless variables $K = kd$, $\tilde{F} = F/\kappa/h$, $b_{dl} = b/d$. After that the equations (25) take the form

$$A^1/h = C_1\tilde{F}_x^0 + C_2\tilde{F}_y^0, \quad A^2/h = C_3\tilde{F}_x^0 + C_4\tilde{F}_y^0, \quad C_3 = -C_2. \tag{26}$$

The coefficients C_1, C_2, C_4 should be evaluated:

$$\begin{aligned} C_1 &= \tfrac{1}{\pi i(1+\mathrm{i}\chi^*)} \sum_{l=-\infty}^{\infty} e^{-\mathrm{i}lK_x} \int\limits_{-\infty}^{\infty} \tfrac{F_1(K,\Omega)}{K\Delta} e^{\mathrm{i}lK} \left(e^{-\mathrm{i}Kb_{dl}} - e^{\mathrm{i}Kb_{dl}}\right) dK, \\ C_2 &= \tfrac{1}{\pi i(1+\mathrm{i}\chi^*)} \sum_{l=-\infty}^{\infty} e^{-\mathrm{i}lK_x} \int\limits_{-\infty}^{\infty} \tfrac{F_2(K,\Omega)}{\Delta} e^{\mathrm{i}lK} \left(e^{-\mathrm{i}Kb_{dl}} - e^{\mathrm{i}Kb_{dl}}\right) dK, \\ C_4 &= \tfrac{1}{\pi i(1+\mathrm{i}\chi^*)} \sum_{l=-\infty}^{\infty} e^{-\mathrm{i}lK_x} \int\limits_{-\infty}^{\infty} \tfrac{F_1(K,\Omega)}{K\Delta} e^{\mathrm{i}lK} \left(e^{-\mathrm{i}Kb_{dl}} - e^{\mathrm{i}Kb_{dl}}\right) dK, \end{aligned} \tag{27}$$

where $F_1 = \beta_T^2\sqrt{K^2 - \beta_T^2}$, $F_2 = \mathrm{i}(2\sqrt{K^2 - \beta_T^2}\sqrt{K^2 - \beta_L^2} - 2K^2 + \beta_T^2)$, $F_4 = \beta_T^2\sqrt{K^2 - \beta_L^2}$ are symmetric functions, $\beta_L^2 = \Omega^2 c_T^2/c_L^2/(1 + \mathrm{i}\chi^*)$, $\beta_T^2 = \Omega^2/(1 + \mathrm{i}\chi^*)$, $\Delta = (2K^2 - \beta_T^2)^2 - 4K^2\sqrt{K^2 - \beta_T^2}\sqrt{K^2 - \beta_L^2}$.

It has been checked that the direct numerical calculation of the sums of integrals (27) is very time-consuming because one has to take a large number of the members of summation till the sum converges. To avoid this we carry out the summation analytically. We rewrite (27) in the following way:

$$\begin{aligned} C_{1(4)} &= -\tfrac{1}{\pi\mathrm{i}(1+\mathrm{i}\chi^*)} \left(\sum_{l=1}^{\infty} \left(e^{\mathrm{i}lK_x} + e^{-\mathrm{i}lK_x}\right) \int\limits_{-\infty}^{\infty} \tfrac{F_{1(4)}(K)}{K\Delta} \left(e^{\mathrm{i}K(b_{dl}-l)} + e^{\mathrm{i}K(b_{dl}+l)}\right) dK + C_{1(4)0} \right), \\ C_2 &= -\tfrac{1}{\pi\mathrm{i}(1+\mathrm{i}\chi^*)} \sum_{l=1}^{\infty} \left(e^{\mathrm{i}lK_x} - e^{-\mathrm{i}lK_x}\right) \int\limits_{-\infty}^{\infty} \tfrac{F_2(K)}{\Delta} \left(e^{\mathrm{i}K(b_{dl}+l)} - e^{\mathrm{i}K(b_{dl}-l)}\right) dK, \\ C_{1(4)0} &= \int\limits_{-\infty}^{\infty} \tfrac{F_{1(4)}(K)}{K\Delta} \left(e^{\mathrm{i}Kb_{dl}} - e^{-\mathrm{i}Kb_{dl}}\right) dK = 2\int\limits_{-\infty}^{\infty} F_{1(4)(K)} \tfrac{e^{\mathrm{i}Kb_{dl}-1}}{K\Delta} dK. \end{aligned} \tag{28}$$

The integrands in (28) are multiple-valued functions because of the presence of the radicals. They become infinite at so-called Rayleigh poles which are the simple zeros of the equation $\Delta(K) = 0$. This equation in the case of zero damping has been examined by Achenbach [2]. There are two real roots: $K = \pm\omega d/c_R = \Omega c_T/c_R$, where c_R is the velocity of the Rayleigh waves. With non-zero damping the roots move to the lower and upper half-planes of the complex plane: $K = \pm\beta_R$, $\beta_R = \Omega c_T/c_R/(1 + \mathrm{i}\mu_{dl})$. The branch points are $K = \pm\beta_L$, $K = \pm\beta_T$. We apply the contour integration around the poles in order to evaluate the following integrals from (28):

$$\begin{aligned} &J_{1(4)}^1 = \int\limits_{-\infty}^{\infty} \tfrac{F_{1(4)}(K)}{K\Delta} e^{\mathrm{i}K(b_{dl}+l)} dK, \quad J_{1(4)}^2 = \int\limits_{-\infty}^{\infty} \tfrac{F_{1(4)}(K)}{K\Delta} e^{\mathrm{i}K(b_{dl}-l)} dK, \\ &J_2^1 = \int\limits_{-\infty}^{\infty} \tfrac{F_2(K)}{\Delta} e^{\mathrm{i}K(b_{dl}+l)} dK, \quad J_2^2 = \int\limits_{-\infty}^{\infty} \tfrac{F_2(K)}{\Delta} e^{\mathrm{i}K(b_{dl}-l)} dK, \quad J_0 = \int\limits_{-\infty}^{\infty} F_{1(4)}(K) \tfrac{e^{\mathrm{i}Kb_{dl}-1}}{K\Delta} dK. \end{aligned} \tag{29}$$

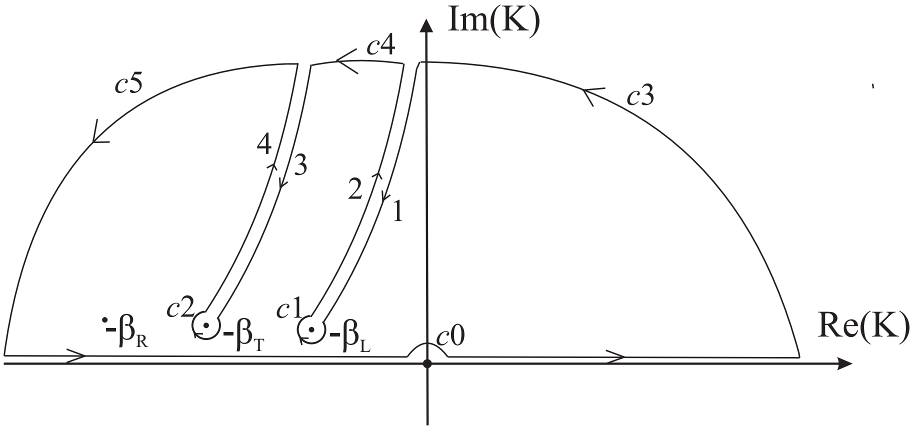

Figure 4: Contour of integration in the upper half-plane

The contour of integration and location of singular points for $J^1_{1(4)}$ are depicted in Figure 4. The contour for J^1_2 and J_0 is quite the same with the only exception that these integrals do not have a pole at $K = 0$. We integrate $J^2_{1(4)}$ and J^2_2 along the contour in the lower half-plane. The integration along the circular contours $c1$, $c2$ around the branch points vanishes as their radius decreases, the integration along the circular contours $c3$, $c4$, $c5$ vanishes as $|K| \to \infty$. Thus,

$$\oint f(K)dK = \left(\int\limits_{c0} + \int\limits_{1} + \int\limits_{2} + \int\limits_{3} + \int\limits_{4} + \int\limits_{-\infty}^{\infty}\right) f(K)dK = 2\pi\text{iRes}\left[f(K), K = -\beta_R\right], \quad (30)$$

where $\int\limits_{-\infty}^{\infty}$ is to be understood in the sense of Cauchy principal value. The pole $K = 0$ was artificially introduced as the original integrals $C_{1(4)}$ from (27) do not have this pole. In accordance with this fact the integrals around the circular contour $c0$ in the upper and in the lower half-planes have the same absolute value but are of the opposite sign and thus vanish in the sum $J^1_{1(4)} + J^2_{1(4)}$.

Im$(\sqrt{K^2 - \beta_L^2}) = 0$ on the contours of integration 1–2 and Im$(\sqrt{K^2 - \beta_T^2}) = 0$ on the contours of integration 3–4. These equalities hold true if $2\text{Im}(K)\text{Re}K = \alpha_i$, $i = 1, 2$, where $\alpha_1 = \text{Im}(\beta_L^2) = -\Omega^2\chi^* c_T^2/c_L^2/(1 + \chi^{*2})$, $\alpha_2 = \text{Im}(\beta_T^2) = -\Omega^2\chi^*/(1 + \chi^{*2})$. The general representation of K at the contours 1–4 is $K = a + i\alpha/2/a$, where $a = \text{Re}(K)$ and $\alpha = \alpha_1$ or α_2 are negative. Thus $|exp(\text{i}lK)| = |exp(-\alpha/2/a)| < 1$. Now we swap the order of summation and integration and evaluate the sums from (28) as the sums of geometric progression:

$$\sum_{l=1}^{\infty}\left(e^{\text{i}lK_x} \pm e^{-\text{i}lK_x}\right)e^{\text{i}lK} = \frac{e^{\text{i}(K_x+K)}}{1 - e^{\text{i}(K_x+K)}} \pm \frac{e^{\text{i}(K-K_x)}}{1 - e^{\text{i}(K-K_x)}}. \quad (31)$$

In the lower half-plane we have K with the opposite sign, $|exp(-ilK)| < 1$ and we can apply the formulae of the sum of geometric progression as well.

The evaluation accomplished in Eq (31) would have been impossible if no damping were present in the continuum. that is why it has been introduced in Section 3.

5 THE REFLECTION COEFFICIENTS

The amplitude reflection coefficient is found as the absolute value of the ratio of the complex amplitudes of reflected and incident waves and is given as $R_L = |A_L/A_I|$ for longitudinal wave and as $R_T = |A_T/A_I|$ for transversal wave. These coefficients can be found by solving the system of four linear equations that constitute the boundary conditions. We substitute (4) and (8) into (3) and divide the whole equations by κA_I. Then we take the equations (26) and divide them by A_I/h. Finally, we have the system of four equations:

$$\begin{cases} a_{11}\tilde{A}_L + a_{12}\tilde{A}_T + \tilde{\tilde{F}}_x = b_1, & a_{21}\tilde{A}_L + a_{22}\tilde{A}_T + \tilde{\tilde{F}}_y = b_2, \\ \tilde{A}_L + \tilde{A}_T - C_1\tilde{\tilde{F}}_x - C_2\tilde{\tilde{F}}_y = -1, & \tilde{A}_L D_L + \tilde{A}_T D_T + C_3\tilde{\tilde{F}}_x + C_4\tilde{\tilde{F}}_y = D_L, \end{cases} \tag{32}$$

where $\tilde{A}_{L(T)} = A_{L(T)}/A_I$, $\tilde{\tilde{F}}_{x(y)} = F^0_{x(y)}/\kappa/A_I$ are the unknowns and

$$\begin{aligned} a_{11} &= -\cos(K_x) - 0.25\Omega^2 + 1.5 + 0.5\exp(\mathrm{i}K_y^L)(\mathrm{i}D_L\sin(K_x) - \cos(K_x)), \\ a_{12} &= -\cos(K_x) - 0.25\Omega^2 + 1.5 + 0.5\exp(-\mathrm{i}K_y^T)(\mathrm{i}D_T\sin(K_x) - \cos(K_x)), \\ a_{21} &= D_L(0.25\Omega^2 - 1.5 + \exp(-\mathrm{i}K_y^L)) + 0.5\exp(-\mathrm{i}K_y^L)(D_L\cos(K_x) - \mathrm{i}\sin(K_x)), \\ a_{22} &= D_T(0.25\Omega^2 - 1.5 + \exp(-\mathrm{i}K_y^L)) + 0.5\exp(-\mathrm{i}K_y^L)(D_T\cos(K_x) - \mathrm{i}\sin(K_x)), \\ b_1 &= \cos(K_x) + 0.25\Omega^2 - 1.5 + 0.5\exp(\mathrm{i}K_y^L)(\mathrm{i}D_L\sin(K_x) + \cos(K_x)), \\ b_2 &= D_L(0.25\Omega^2 - 1.5\exp(\mathrm{i}K_y^L)) + 0.5\exp(\mathrm{i}K_y^L)(D^L\cos(K_x) + \mathrm{i}\sin(K_x)). \end{aligned} \tag{33}$$

The input data for the system (32) includes the angle of incidence θ_0 and the dimensionless frequency Ω. The admissible values of θ_0 are between 0 and $\pi/2$ and that of Ω are between 0 and the cut-off frequency Ω_c up to which the longitudinal waves propagate.

We consider the flux of energy through the remote area in the lattice parallel to the interface. The flux of the wave energy is proportional to the square of its amplitude. The energy reflection coefficient is found as the ratio of the energy fluxes of reflected and incident waves and is given as $P_L = R_L^2$ and $P_T = \xi R_T^2$, where

$$\xi = \frac{4D_T^2\sin(K_y^T) + \sin(K_x + K_y^T)(2D_T + D_T^2 + 1)\sin(K_x - K_y^T)(2D_T - D_T^2 - 1)}{4D_L^2\sin(K_y^L)\sin(K_x + K_y^L)(2D_L + D_L^2 + 1) + \sin(K_y^L - K_x)(1 + D_L^2 - 2D_L)}. \tag{34}$$

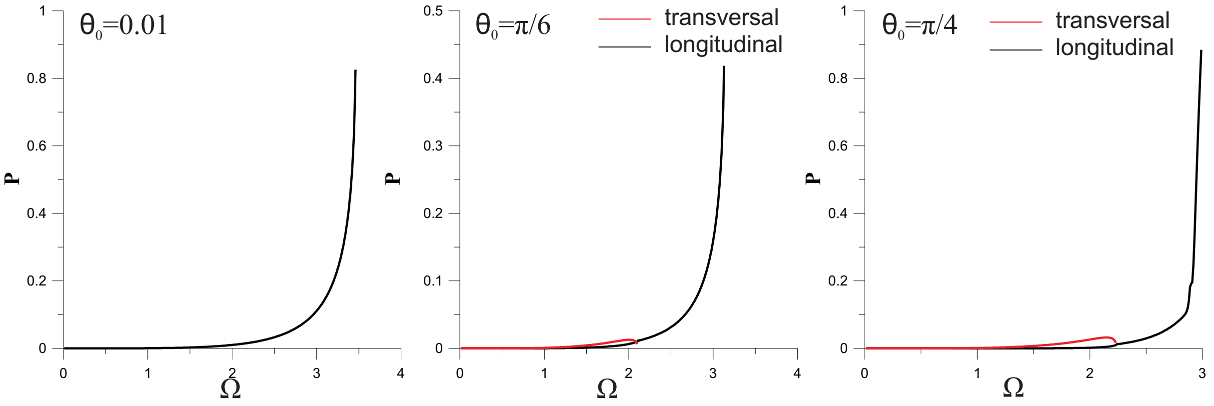

Figure 5: The energy reflection coefficients for different angles of incidence

To demonstrate the results the following parameters for the continuum are taken: $\rho = 2300$ kg/m^3, $E = 230$ GPa. As coefficient $\mu = 0.5E/(1+\nu)$ should be equal to $\lambda = \nu E/(1+\nu)(1-2\nu)$, the Poisson's ratio of the continuum is $\nu = 0.25$. The damping parameter μ^*=1000 Pa·sec. The period of the lattice $d = 0.05$ m. The values of the parameter $\mu_{dl} = \omega\mu^*/\mu = \Omega c_T \mu^*/d/\mu$ lie between 0 and 0.02 depending on the frequency Ω.

The dependence of the energy reflection coefficient P (either P_L or P_T) on the dimensionless frequency Ω for three different angles of incidence is depicted in Figure 5. One can see that there is almost no reflection at low frequencies, where the continuum is capable of approximating the lattice, and at higher frequencies the reflection grows rapidly as the dispersion properties of the lattice and the continuum differ a lot. One can also note that the reflection of transversal wave is less than that of the longitudinal one.The graph of P_T stops at a lower frequency than that of P_L as the cut-off frequency of the transversal waves is lower than that of the longitudinal waves.

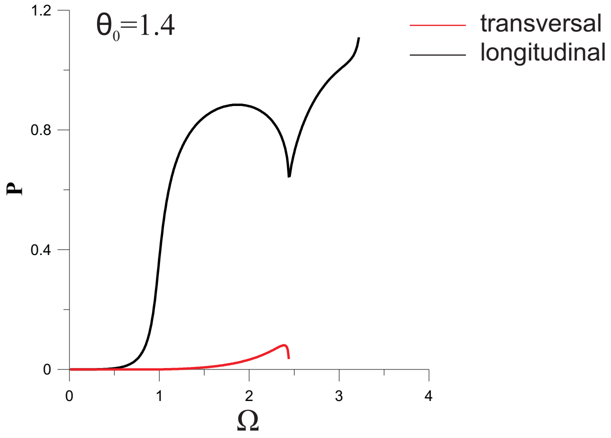

Figure 6: The energy reflection coefficient

For the angles of incidence that are larger than $\pi/4$ we have obtained non-physical results: the reflected energy exceeds the energy of the incident wave. This anomalous reflection is depicted in Figure 6. We do not yet know the genuine explanation of this result. Most likely, it is a consequence of the boundary conditions at the interface.

The case when transversal wave falls on the interface from the lattice has also been examined. The energy reflection coefficients for different angles of incidence are depicted in Figure 7.

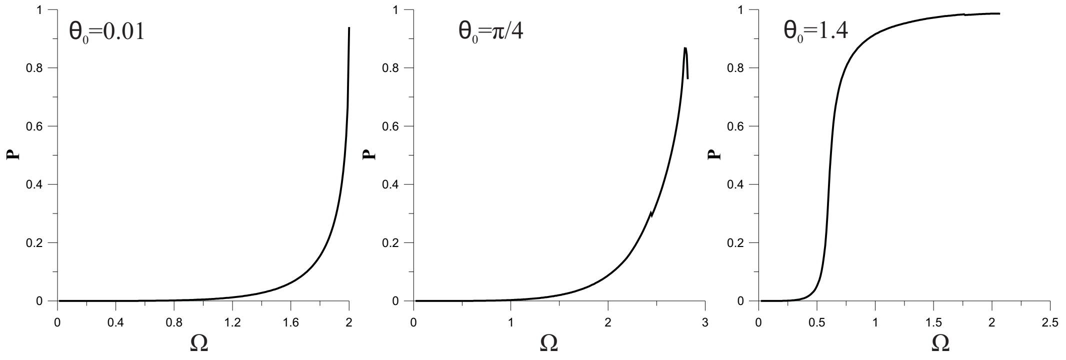

Figure 7: The energy reflection coefficients for different angles of incidence

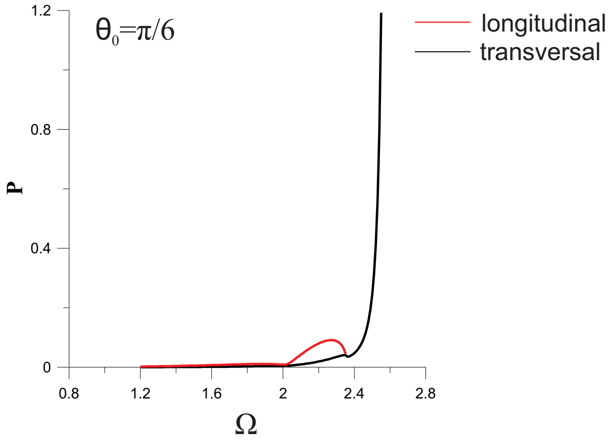

Figure 8: The energy reflection coefficient

The reflection of the longitudinal waves is negligible when $\theta_0 = 0.01$. In the cases $\theta_0 = \pi/4$ and $\theta_0 = 1.4$ the longitudinal waves do not reflect.

The anomalous reflection has also been observed in this case (see Figure 8).

6 CONCLUSIONS

The motivation for this study has been to facilitate the development of the multi-scale numerical approaches that are becoming increasingly popular in investigations into the details of dynamic deformations of various materials. Specifically, this paper is envisaged to be of interest for those researchers who employ the discrete-continuum models in order to minimize the huge computational costs associated with the detailed discrete modelling. The continuum domain in such models is introduced in order to minimize the size of the discrete domain as much as possible thereby significantly reducing the computation time. To achieve this, however, the continuum domain should not introduce spurious reflections at as broad as possible frequency range. In this paper, the capabilities of the classical continuum have been assessed to comply with this requirement. To this end, the reflection of plane harmonic waves at the interface of the square lattice and the classical continuum has been studied. A method has been proposed to couple the domains in such a manner that no singularities occur due to the point-like character of particles in the lattice. It has been shown that while the classical continuum can serve as a non-reflecting boundary for the lattice at low frequencies, it cannot absorb higher frequency waves. Moreover, it has been found that due to the ambiguity in the formulation of the boundary conditions at the discrete-continuum interface, the energy of the reflected waves can be mathematically predicted in some cases to be larger that that of the incident waves — a result that is physically unacceptable. Given the above-formulated results, it can be concluded that the classical continuum is not the most desirable model for assuring the non-reflective conditions at a wide frequency band. One of the attractive alternatives could be a gradient continuum that, according to a recent study carried out in the 1D framework [9], can be expected to match the lattice at a wide frequency band. Additionally, no singularities occur at the contact between a point load and a surface of a gradient continuum. The authors of this contribution are currently investigating whether gradient continua will be up to these expectations in the multidimensional case.

REFERENCES

[1] A.S.J. Suiker, A.V. Metrikine, R. De Borst, Dynamic behaviour of a layer of discrete particles, part 1: analysis of body waves and eigenmodes. *Journal of Sound and Vibration*, **240(1)**, 1 – 18, 2001.

[2] J.D. Achenbach, Wave propagation in elastic solids. *North-Holland Publishing Company, Amsterdam-London*, 425p, 1973.

[3] R.E. Rudd, J.Q. Broughton, Coarse-grained molecular dynamics and the atomic limit of finite elements. *Phys. Rev. B* **58**, R5893 – 6, 1998.

[4] W. Cai, M.D. Koning, V.V. Bulatov, S.Yip, Minimizing boundary reflections in coupled-domain simulations. *Phys. Rev. Lett.* **85**, 3213 – 16, 2000.

[5] E.G. Karpov, G.J. Wagner, W.K. Liu, A Greens function approach to deriving non-reflecting boundary conditions. *Int. J. Numer. Meth. Engng* **62**, 1250 – 1262, 2005.

[6] W. E, Z. Huang, Matching conditions in atomistic-continuum modeling of materials. *Phys. Rev. Lett.* **87**, 135501, 2001.

[7] Wagner, Liu, Coupling of atomistic and continuum simulations using a bridging scale decomposition. *Journal of Computational Physics* **190**, 249 – 274, 2003

[8] S.P. Xiao, T. Belytschko, A bridging domain method for coupling continua with molecular dynamics. *Comput. Methods Appl. Mech. Engrg.*, **193**, 1645 – 1669, 2004

[9] A.M. Kudarova, A.V. Metrikine, On the use of gradient continua for minimizing the wave reflection at a discrete-continuum interface. *Proceedings of XXXVIII International summer school-conference APM'2010*, 383 – 390, 2010.

COMPDYN 2011
ECCOMAS Thematic Conference on
Computational Methods in Structural Dynamics and Earthquake Engineering
M. Papadrakakis, M. Fragiadakis, V. Plevris (eds.)
Corfu, Greece, 25-28 May 2011

EXTENSION OF THE PUFEM TO ELASTIC WAVE PROPAGATION IN LAYERED MEDIA

O. Laghrouche[1], **A. El Kacimi**[1] **and J. Trevelyan**[2]

[1]School of the Built Environment
Heriot-Watt University, Edinburgh EH14 4AS, UK
e-mail: o.laghrouche@hw.ac.uk, a.elkacimi@hw.ac.uk

[2]School of Engineering and Computing Sciences
Durham University, Durham DH1 3LE, UK
e-mail: jon.trevelyan@durham.ac.uk

Keywords: Elastic waves, finite elements, plane wave basis, Lagrange multipliers, layered media, free surface, Rayleigh waves.

Abstract. *This work deals with the extension of the Partition of Unity Finite Element Method (PUFEM) to solve wave problems involving propagation, transmission and reflection in layered elastic media. Problems dealing with wave reflection at a free surface and propagation of pure Rayleigh waves are also considered. The proposed method consist to apply the plane wave basis decomposition to the elastic wave equation in each layer of the elastic medium and then enforce necessary continuity conditions at the interfaces through the use of Lagrange multipliers. The accuracy and effectiveness of the proposed technique is determined by comparing results for selected problems with known analytical solutions.*

1 INTRODUCTION

Plane wave basis finite elements capable of containing many wavelengths per nodal spacing were developed and implemented to solve wave scattering problems in homogeneous elastic media [1, 2, 3]. These elements allow us to relax the traditional requirement of around ten nodal points per wavelength and therefore lead to huge savings in computing effort. Many other techniques were developed for the same objective, such as the Discontinuous Enrichment Method [4], the Ultra Weak Variational Formulation [5] and the Partition of Unity Boundary Element Method [6], for example.

In this work, problems of practical interest such as those encountered in soil wave propagation and scattering are considered. For a layered elastic medium, the displacement field is expressed as a combination of propagating planar pressure and shear waves within each homogeneous layer. At the interface between two layers, necessary continuity conditions are enforced through the use of Lagrange multipliers, which are also approximated using the plane wave decomposition approach [7].

After presenting relevant theory, some preliminary numerical tests are carried out. The first problem deals with elastic waves propagating in a homogeneous medium and hitting a plane free surface, for angles of incidence above and below the critical angle. The second test problem concerns the propagation of pure Rayleigh waves, which are known to propagate with a specific wave number different from the pressure and shear wave numbers. Last, reflection and transmission of elastic waves at a plane interface between two elastic media will be considered. For the first two problems, there is no need to incorporate the Lagrange multipliers as no inhomogeneity is involved in the problems unlike in the third one where they are necessary to ensure compatibility conditions at the interface.

2 MATHEMATICAL FORMULATIONS

Let Ω be a space domain in $\mathbb{R}^2$ occupied by an elastic inhomogeneous medium whose elastic properties are piecewise constant such as, for example, a multilayered soil medium where each layer is homogenous. It is then adequate to assume that the domain Ω is composed of multiple homogeneous linear and isotropic subdomains Ω_j with the Lamé coefficients λ_j and μ_j, and density ρ_j. In this paper, for simplicity, the two-subdomain problem shown in Figure 1 is considered where $\Omega = \Omega_1 \cup \Omega_2$ bounded by $\Gamma = \Gamma_1 \cup \Gamma_2$ with the boundary Γ_{int} being the interface between Ω_1 and Ω_2. We will denote by $(\mathbf{i}, \mathbf{j})$ the cartesian vector system and by $\mathbf{x} = x\mathbf{i} + y\mathbf{j}$ a generic point in $\mathbb{R}^2$. We will also assume a harmonic steady state problem and hence the time variable is omitted in the formulation.

2.1 Problem formulation

Let us first consider the subdomain Ω_1 bounded by $\Gamma_1 \cup \Gamma_{int}$. The time independent displacement field $\mathbf{u}_1$ satisfies the Navier's equation

$$-\rho_1\omega^2\mathbf{u}_1 - \nabla \cdot \boldsymbol{\sigma}(\mathbf{u}_1) = \rho_1\mathbf{f}_1, \tag{1}$$

where ω is the circular frequency, ρ_1 is the density and $\mathbf{f_1}$ is the body force. The stress tensor $\boldsymbol{\sigma}$ is defined via the classical Hooke's law

$$\boldsymbol{\sigma}(\mathbf{u}_1) = \lambda_1\nabla \cdot \mathbf{u}_1 \, \mathbf{I} + \mu_1(\nabla\mathbf{u}_1 + \nabla\mathbf{u}_1^\top), \tag{2}$$

where $\mathbf{I}$ denotes the identity matrix, λ_1 and μ_1 are the Lam$\acute{e}$ coefficients, and $\nabla\mathbf{u_1} = (\nabla u_1, \nabla v_1)^\top$, with u_1 and v_1 being the horizontal and vertical components of the displacement field $\mathbf{u_1}$. The notation '$\top$' stands for the transpose of a given vector or tensor. The dot product '$\cdot$' of ∇ and the tensor field $\boldsymbol{\sigma} = (\boldsymbol{\sigma}_x, \boldsymbol{\sigma}_y)^\top$ in $\mathbb{C}^2 \times \mathbb{C}^2$ is defined by

$$\nabla \cdot \boldsymbol{\sigma} = \begin{pmatrix} \nabla \cdot \boldsymbol{\sigma}_x \\ \nabla \cdot \boldsymbol{\sigma}_y \end{pmatrix}, \tag{3}$$

with ∇ being the gradient operator. In addition to expressions (1) and (2), the formulation of the problem is completed by the boundary conditions imposed on Γ_1. Here we consider a Robin type boundary conditions such that

$$\boldsymbol{\sigma}(\mathbf{u}_1)\mathbf{n}_1 = \mathrm{i}\left[(\lambda_1 + 2\mu_1)k_1^P(\mathbf{u}_1 \cdot \mathbf{n}_1)\mathbf{n}_1 + \mu_1 k_1^S(\mathbf{u}_1 \cdot \mathbf{t}_1)\mathbf{t}_1\right] + \mathbf{g}_1. \tag{4}$$

In the above expression, i represents the imaginary number such that $\mathrm{i}^2 = -1$, $\mathbf{n_1}$ and $\mathbf{t_1}$ are the normal and tangential vectors to the boundary. The wave numbers k_1^P and k_1^S correspond to the pressure (P) and shear (S) waves, respectively. They are defined by

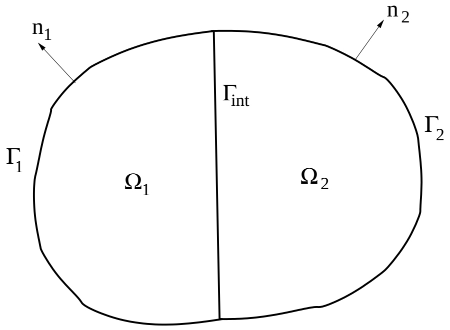

Figure 1: A two-subdomain example.

$$k_1^P = \frac{\omega}{c_1^P} \qquad \text{and} \qquad k_1^S = \frac{\omega}{c_1^S}. \tag{5}$$

The P-wave and S-wave speeds are given by

$$c_1^P = \left(\frac{\lambda_1 + 2\mu_1}{\rho_1}\right)^{\frac{1}{2}} \qquad \text{and} \qquad c_1^S = \left(\frac{\mu_1}{\rho_1}\right)^{\frac{1}{2}}. \tag{6}$$

In expression 4, the source term $\mathbf{g}_1$ will involve analytical solutions of elastic wave problems. This approach is adopted with the aim to validate the proposed method and assess its performance. But in practice absorbing boundary conditions would rather be used and would therefore involve extra numerical errors.

2.2 Weighted residual scheme

Let us multiply equation (1) by the complex conjugate of a test function $\mathbf{w}_1$

$$\int_{\Omega_1} \left(-\rho_1\omega^2\mathbf{u}_1 - \nabla \cdot \boldsymbol{\sigma}(\mathbf{u}_1)\right) \cdot \bar{\mathbf{w}}_1 \, d\Omega = \int_{\Omega_1} \rho_1 \mathbf{f}_1 \cdot \bar{\mathbf{w}}_1 \, d\Omega. \tag{7}$$

Integrating by parts over Ω_1, the following weak form is obtained

$$\begin{aligned} &-\omega^2\rho_1 \int_{\Omega_1} \mathbf{u}_1 \cdot \bar{\mathbf{w}}_1 \, d\Omega - \int_{\Gamma_1} \boldsymbol{\sigma}(\mathbf{u}_1)\mathbf{n}_1 \cdot \bar{\mathbf{w}}_1 \, d\Gamma - \int_{\Gamma_{int}} \boldsymbol{\sigma}(\mathbf{u}_1)\mathbf{n}_1 \cdot \bar{\mathbf{w}}_1 \, d\Gamma + \int_{\Omega_1} \boldsymbol{\sigma}(\mathbf{u}_1) \cdot \nabla\bar{\mathbf{w}}_1 \, d\Omega \\ &= \rho_1 \int_{\Omega_1} \mathbf{f}_1 \cdot \bar{\mathbf{w}}_1 \, d\Omega. \end{aligned} \tag{8}$$

For practicality let us express the stress tensor in terms of the displacement field by using the following expression

$$\boldsymbol{\sigma}(\mathbf{u}_1) = \lambda_1 \nabla \cdot \mathbf{u}_1 \, \mathbf{I} + \mu_1 \nabla \times \mathbf{u}_1 \, \mathbf{J} + 2\mu_1 \nabla \mathbf{u}_1, \tag{9}$$

where the matrix $\mathbf{J}$ is defined by

$$\mathbf{J} = \begin{pmatrix} 0 & 1 \\ -1 & 0 \end{pmatrix}, \tag{10}$$

and also re-write $\boldsymbol{\sigma}(\mathbf{u_1}) \cdot \nabla \bar{\mathbf{w}}_1$ in expression (8) under the following form

$$\boldsymbol{\sigma}(\mathbf{u}_1) \cdot \nabla \bar{\mathbf{w}}_1 = \lambda_1 (\nabla \cdot \mathbf{u}_1)(\nabla \cdot \bar{\mathbf{w}}_1) + 2\mu_1 \nabla \mathbf{u}_1 \cdot \nabla \bar{\mathbf{w}}_1 - \mu_1 (\nabla \times \mathbf{u}_1)(\nabla \times \bar{\mathbf{w}}_1). \tag{11}$$

Now using the boundary condition (4), the above variational formulation becomes

$$\begin{aligned}
&-\omega^2 \rho_1 \int_{\Omega_1} \mathbf{u}_1 \cdot \bar{\mathbf{w}}_1 \, d\Omega + 2\mu_1 \int_{\Omega_1} \nabla \mathbf{u}_1 \cdot \nabla \bar{\mathbf{w}}_1 \, d\Omega - \mu_1 \int_{\Omega_1} (\nabla \times \mathbf{u}_1)(\nabla \times \bar{\mathbf{w}}_1) \, d\Omega \\
&+\lambda_1 \int_{\Omega_1} (\nabla \cdot \mathbf{u}_1)(\nabla \cdot \bar{\mathbf{w}}_1) \, d\Omega - \mathrm{i} \int_{\Gamma_1} \left[(\lambda_1 + 2\mu_1) k_1^P (\mathbf{u}_1 \cdot \mathbf{n}_1)(\bar{\mathbf{w}}_1 \cdot \mathbf{n}_1) + \mu_1 k_1^S (\mathbf{u}_1 \cdot \mathbf{t}_1)(\bar{\mathbf{w}}_1 \cdot \mathbf{t}_1) \right] \, d\Gamma \\
&- \int_{\Gamma_{int}} \boldsymbol{\sigma}(\mathbf{u}_1)\mathbf{n}_1 \cdot \bar{\mathbf{w}}_1 \, d\Gamma = \rho_1 \int_{\Omega_1} \mathbf{f} \cdot \bar{\mathbf{w}}_1 \, d\Omega + \int_{\Gamma_1} \mathbf{g}_1 \cdot \bar{\mathbf{w}}_1 \, d\Gamma.
\end{aligned} \tag{12}$$

Following the same approach, a similar weak form is obtained for the subdomain Ω_2 bounded by $\Gamma_2 \cup \Gamma_{int}$ such that

$$\begin{aligned}
&-\omega^2 \rho_2 \int_{\Omega_2} \mathbf{u}_2 \cdot \bar{\mathbf{w}}_2 \, d\Omega + 2\mu_2 \int_{\Omega_2} \nabla \mathbf{u}_2 \cdot \nabla \bar{\mathbf{w}}_2 \, d\Omega - \mu_2 \int_{\Omega_2} (\nabla \times \mathbf{u}_2)(\nabla \times \bar{\mathbf{w}}_2) \, d\Omega \\
&+\lambda \int_{\Omega_2} (\nabla \cdot \mathbf{u}_2)(\nabla \cdot \bar{\mathbf{w}}_2) \, d\Omega - \mathrm{i} \int_{\Gamma_2} \left[(\lambda_2 + 2\mu_2) k_2^P (\mathbf{u}_2 \cdot \mathbf{n}_2)(\bar{\mathbf{w}}_2 \cdot \mathbf{n}_2) + \mu_2 k_2^S (\mathbf{u}_2 \cdot \mathbf{t}_2)(\bar{\mathbf{w}}_2 \cdot \mathbf{t}_2) \right] \, d\Gamma \\
&- \int_{\Gamma_{int}} \boldsymbol{\sigma}(\mathbf{u}_2)\mathbf{n}_2 \cdot \bar{\mathbf{w}}_2 \, d\Gamma = \rho_2 \int_{\Omega_2} \mathbf{f} \cdot \bar{\mathbf{w}}_2 \, d\Omega + \int_{\Gamma_2} \mathbf{g}_2 \cdot \bar{\mathbf{w}}_2 \, d\Gamma,
\end{aligned} \tag{13}$$

where all functions and parameters are defined in a similar way as for the weak form (12) replacing the subscript 1 by 2.

2.3 Compatibility conditions

At the interface Γ_{int}, between Ω_1 and Ω_2, continuity of displacements and stresses must be satisfied

$$\mathbf{u}_1 = \mathbf{u}_2, \tag{14}$$

$$\boldsymbol{\sigma}(\mathbf{u}_1)\mathbf{n}_1 = -\boldsymbol{\sigma}(\mathbf{u}_2)\mathbf{n}_2. \tag{15}$$

Let us introduce the Lagrange multiplier $\boldsymbol{\nu}$ defined by

$$\boldsymbol{\nu} = \boldsymbol{\sigma}(\mathbf{u}_1)\mathbf{n}_1 = -\boldsymbol{\sigma}(\mathbf{u}_2)\mathbf{n}_2. \tag{16}$$

The weak forms (12) and (13) become then

$$\begin{aligned}
&-\omega^2\rho_1 \int_{\Omega_1} \mathbf{u}_1 \cdot \bar{\mathbf{w}}_1 \, d\Omega + 2\mu_1 \int_{\Omega_1} \nabla\mathbf{u}_1 \cdot \nabla\bar{\mathbf{w}}_1 \, d\Omega - \mu_1 \int_{\Omega_1} (\nabla \times \mathbf{u}_1)(\nabla \times \bar{\mathbf{w}}_1) \, d\Omega \\
&+\lambda_1 \int_{\Omega_1} (\nabla \cdot \mathbf{u}_1)(\nabla \cdot \bar{\mathbf{w}}_1) \, d\Omega - \mathrm{i} \int_{\Gamma_1} \left[(\lambda_1 + 2\mu_1) k_1^P (\mathbf{u}_1 \cdot \mathbf{n}_1)(\bar{\mathbf{w}}_1 \cdot \mathbf{n}_1) + \mu_1 k_1^S (\mathbf{u}_1 \cdot \mathbf{t}_1)(\bar{\mathbf{w}}_1 \cdot \mathbf{t}_1)\right] \, d\Gamma \\
&- \int_{\Gamma_{int}} \boldsymbol{\nu} \cdot \bar{\mathbf{w}}_1 \, d\Gamma = \rho_1 \int_{\Omega_1} \mathbf{f} \cdot \bar{\mathbf{w}}_1 \, d\Omega + \int_{\Gamma_1} \mathbf{g}_1 \cdot \bar{\mathbf{w}}_1 \, d\Gamma,
\end{aligned} \tag{17}$$

and

$$\begin{aligned}
&-\omega^2\rho_2 \int_{\Omega_2} \mathbf{u}_2 \cdot \bar{\mathbf{w}}_2 \, d\Omega + 2\mu_2 \int_{\Omega_2} \nabla\mathbf{u}_2 \cdot \nabla\bar{\mathbf{w}}_2 \, d\Omega - \mu_2 \int_{\Omega_2} (\nabla \times \mathbf{u}_2)(\nabla \times \bar{\mathbf{w}}_2) \, d\Omega \\
&+\lambda_2 \int_{\Omega_2} (\nabla \cdot \mathbf{u}_2)(\nabla \cdot \bar{\mathbf{w}}_2) \, d\Omega - \mathrm{i} \int_{\Gamma_2} [(\lambda_2 + 2\mu_2) k_P (\mathbf{u}_2 \cdot \mathbf{n}_2)(\bar{\mathbf{w}}_2 \cdot \mathbf{n}_2) + \mu_2 k_S (\mathbf{u}_2 \cdot \mathbf{t}_2)(\bar{\mathbf{w}}_2 \cdot \mathbf{t}_2)] \, d\Gamma \\
&+ \int_{\Gamma_{int}} \boldsymbol{\nu} \cdot \bar{\mathbf{w}}_2 \, d\Gamma = \rho_2 \int_{\Omega_2} \mathbf{f} \cdot \bar{\mathbf{w}}_2 \, d\Omega + \int_{\Gamma_2} \mathbf{g}_2 \cdot \bar{\mathbf{w}}_2 \, d\Gamma.
\end{aligned} \tag{18}$$

It is clear from the above weak forms, (17) and (18), that the problem is augmented as the Lagrange multiplier $\boldsymbol{\nu}$ is introduced as an extra unknown in the problem. The integration of the two weak forms leads to a rectangular system of equations, where the number of unknowns exceeds the number of equations. Extra equations are therefore added by ensuring the continuity of displacements such as in expression (14). This is done through the weak form

$$\int_{\Gamma_{int}} (\bar{\mathbf{u_1}} - \bar{\mathbf{u_2}}) \cdot \boldsymbol{\delta} \, d\Gamma = 0, \tag{19}$$

where $\boldsymbol{\delta}$ is a test function in the space of the Lagrange multipliers.
In the following subsection both the displacement field and the Lagrange multiplier will be approximated via plane wave basis finite elements.

2.4 Plane wave approximation

The computational domain Ω is meshed into finite elements with n nodal points in total. We denote by N^z, $z = 1, n$, the partition of unity by polynomial finite element shape functions, and respectively by m_p and m_s the number of approximating P and S plane waves. The displacement $\mathbf{u}_j$ in a subdomain Ω_j is approximated as follows [1, 2]

$$\mathbf{u}_j = \sum_{z=1}^{n} \sum_{l=1}^{m_P} N^z A_{z,l}^P \exp(\mathrm{i} k_j^P \mathbf{x} \cdot \mathbf{d}_P^l) \mathbf{d}_P^l + \sum_{z=1}^{n} \sum_{l=1}^{m_S} N^z A_{z,l}^S \exp(\mathrm{i} k_j^S \mathbf{x} \cdot \mathbf{d}_S^l) \mathbf{d}_{S,\perp}^l. \tag{20}$$

The amplitudes $A_{z,l}^P$ and $A_{z,l}^S$, at a given node z and corresponding to P and S plane waves travelling in the directions $\mathbf{d}_P^l$ and $\mathbf{d}_S^l$, respectively, are now the unknowns of the problem. The orthogonal of a vector $\mathbf{d}$ denoted by $\mathbf{d}_\perp$ is defined by $\mathbf{d}_\perp = -\mathbf{J}\mathbf{d}$, where the rotation matrix $\mathbf{J}$, with the angle $\frac{\pi}{2}$, is given in expression (10). The directions $\mathbf{d}_P^l$ and $\mathbf{d}_S^l$ are taken uniformly distributed on the unit circle such that

$$\begin{aligned}
\mathbf{d}_P^l &= \left(\cos\theta_P^l,\ \sin\theta_P^l\right)^\top \quad , \quad \theta_P^l = \tfrac{2\pi l}{m_P} \\
\mathbf{d}_S^l &= \left(\cos\theta_S^l,\ \sin\theta_S^l p\right)^\top \quad , \quad \theta_S^l = \tfrac{2\pi l}{m_S}.
\end{aligned} \tag{21}$$

It is obvious from the above expression (20) of the displacement field that the pair of wave numbers (k_j^P, k_j^S) will take different values depending to which subdomain, Ω_1 or Ω_2, the considered finite element belongs to.

For the approximation of the Lagrange multiplier $\boldsymbol{\nu}$, the approach is inspired from previous work [7], which consists to write

$$\boldsymbol{\nu} = \sum_{z=1}^{n}\sum_{l=1}^{m_P} N^z B_{z,l}^P \exp(\mathrm{i}k^P \mathbf{x}\cdot\mathbf{d}_P^l)\mathbf{d}_P^l + \sum_{z=1}^{n}\sum_{l=1}^{m_S} N^z B_{z,l}^S \exp(\mathrm{i}k^S \mathbf{x}\cdot\mathbf{d}_S^l)\mathbf{d}_{S,\perp}^l. \qquad (22)$$

In other words, the lagrange multiplier is also approximated by sets of P and S plane waves, and the unknowns $B_{z,l}^P$ and $B_{z,l}^S$ are in a sense the amplitudes of the approximating plane waves. At the interface between Ω_1 and Ω_2, the pair of wave numbers (k^P, k^S) is chosen, for example, such that

$$k^P = \max(k_1^P, k_2^P) \qquad \text{and} \qquad k^S = \max(k_1^S, k_2^S) \qquad (23)$$

The numbers m_P and m_S of approximating plane waves may be constant or may vary depending whether the approximation is applied to the displacements fields $\mathbf{u_1}$ and $\mathbf{u_2}$ or to the Lagrange multiplier $\boldsymbol{\nu}$. Expressions (17), (18) and (19) lead to square system matrix, where the solution is obtained through a direct solver which uses a factorization of the form $\mathbf{LDL}^H$ where $\mathbf{D}$ is a real diagonal matrix, $\mathbf{L}$ is a lower triangular matrix with diagonal entries equal to 1 and $\mathbf{L}^H$ is the transpose conjugate of $\mathbf{L}$ [8]. It is worth mentioning that the element matrices are obtained via an exact integration developed in reference [2] and hence the computations are significantly faster compared to past work [1] where high order Gauss-Legendre quadrature schemes were used involving thousands of integration points per finite element.

In the next section, some preliminary numerical results validating the proposed model are presented.

3 PRELIMINARY RESULTS

The model presented above is validated by solving typical problems of practical interest such as those encountered in soil wave propagation, which involve interfaces between the soil layers and a free surface. First, SV elastic waves propagating in a homogeneous medium and hitting a plane free surface is considered. Then, a problem with pure Rayleigh waves is dealt with, where the displacement field approximation involves P and S plane waves, rather than plane waves with the Rayleigh wave number. Last, a test problem involving reflection and transmission of elastic waves at a plane interface between two semi-infinite elastic media is carried out. All considered problems have analytical solutions presented in various textbooks, such as reference [9]. To assess the accuracy of the numerical solution in percentage the following L^2 error

$$\varepsilon_2 = \frac{||\mathbf{u}-\widetilde{\mathbf{u}}||_{L_2(\Omega)}}{||\widetilde{\mathbf{u}}||_{L_2(\Omega)}} \times 100\% \qquad (24)$$

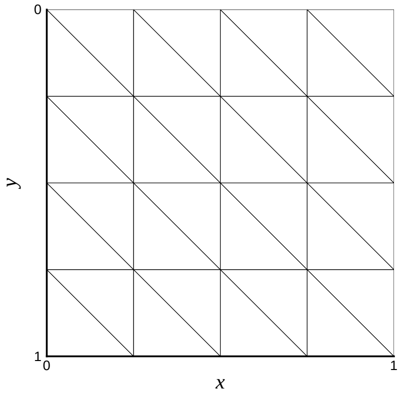

Figure 2: Mesh of the computational domain.

is used where $\mathbf{u}$ is the numerical solution and $\widetilde{\mathbf{u}}$ is the analytical solution of the considered problem. The chosen computational domain is a square of unit length. It is meshed into 3-node triangular finite elements with 32 elements and 25 nodes (Figure 2).

3.1 SV plane wave hitting a free surface

This is a common situation occurring at the soil free surface, for example. Let us consider a shear wave, SV, of unit amplitude incident with an angle β (Figure 3). In general, this leads to both reflected compression and shear waves. The compression wave potential is therefore given only by the reflected wave

$$\phi = R_P \, e^{\mathrm{i}k(-x-y\tan\alpha)}, \tag{25}$$

and the shear wave potential is the sum of the incident and the reflected waves

$$\psi = 1 \, e^{\mathrm{i}k(-x+y\tan\beta)} + R_S \, e^{\mathrm{i}k(-x-y\tan\beta)}, \tag{26}$$

where k is the wave number such that $k = k_P \cos\alpha = k_S \cos\beta$, with α being the angle of the reflected P-wave. The reflection coefficients R_P and R_S are computed by ensuring zero-stress boundary conditions at the free surface [9]. The displacements are computed via the following derivatives of the potentials

$$u = \frac{\partial\phi}{\partial x} - \frac{\partial\psi}{\partial y} \qquad \text{and} \qquad v = \frac{\partial\phi}{\partial y} + \frac{\partial\psi}{\partial x}. \tag{27}$$

Snell's law states that $c_P/\cos\alpha = c_S/\cos\beta$ and hence $\tan\alpha = (1/3\cos^2\beta - 1)^{1/2}$ for this elastic medium, with $\lambda = \mu = \rho = 1$. Consequently, the reflected compression wave exists only if the angle of incidence β reaches the critical angle $\beta_c = \cos^{-1}(1/\sqrt{3})$ and that for all angles $0 < \beta < \cos^{-1}(1/\sqrt{3})$ there is no reflected compression wave. In this latter case, $\tan\alpha$ becomes a complex number and the motion corresponding to the P-wave potential propagates along the free surface, as an edge wave, and decreases exponentially with depth, an an evanescent mode.

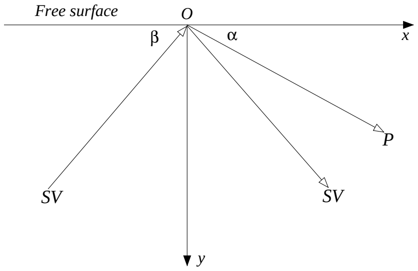

Figure 3: SV-plane wave hitting a free surface of a semi-infinite elastic medium.

Figure 7 shows, for $\omega = 30$, contour plots of the real part of the displacement for two cases of incidence. In the first case (left), the angle of incidence $\beta < \beta_c$, which means both P and S waves are reflected. In the second one, $\beta > \beta_c$ and hence only an S wave is reflected while there is an edge P-wave wave decaying exponentially with depth. In both cases, a total of 32 plane waves are used in the approximation of the displacement field $\mathbf{u}$, with $m_P = m_S = 16$. The L_2 errors, in both cases $\varepsilon_2 = 0.6\%$,show that the numerical solution is good agreement with the analytical solution of the problem.

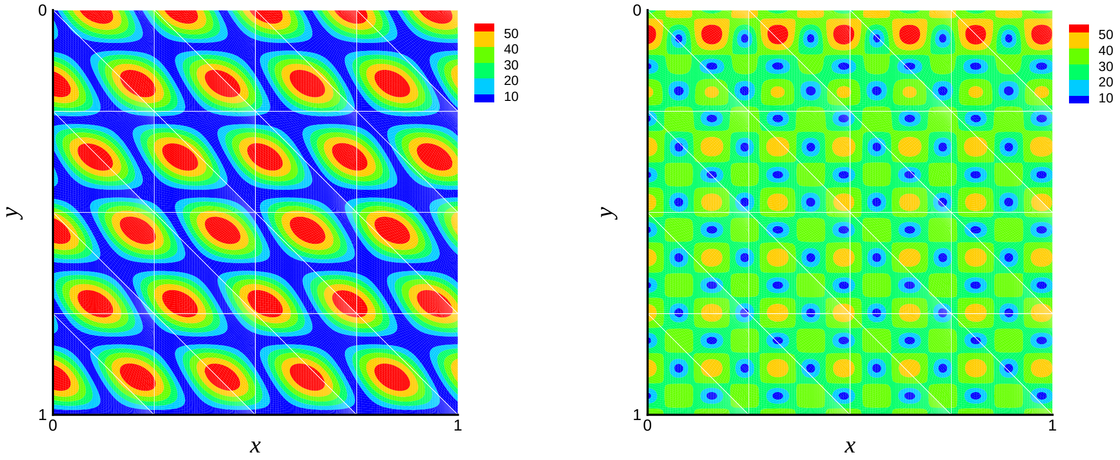

Figure 4: Real part of the displacement due to an SV-plane wave hitting a free surface of a semi-infinite elastic medium, $\omega = 30$, $m_P = m_S = 16$, (left) $\beta = 60°$, $\varepsilon_2 = 0.6\%$, (right) $\beta = 50°$, $\varepsilon_2 = 0.6\%$.

3.2 Pure Rayleigh waves

Rayleigh waves are present near the soil free surface and they decay exponentially with depth. They appear when body waves are reflected at the free surface. Part of their energy is converted into Rayleigh waves which propagate with their own wave number k_R given by the approximate expression $k_R \approx k_S/0.9194$, for the same considered material ($\lambda = \mu = \rho = 1$). The horizontal and vertical components of the displacement field caused by the Rayleigh waves are given by the following expressions [10]

$$\begin{aligned} u &= \sqrt{k_R^2 - k_S^2}\left[e^{-\sqrt{k_R^2-k_S^2}y} - \frac{2k_R^2}{2k_R^2-k_S^2}e^{-\sqrt{k_R^2-k_P^2}y}\right]e^{\mathrm{i}k_R x}, \\ v &= \mathrm{i}k_R\left[e^{-\sqrt{k_R^2-k_S^2}y} - \frac{2\sqrt{(k_R^2-k_P^2)(k_R^2-k_S^2)}}{2k_R^2-k_S^2}e^{-\sqrt{k_R^2-k_P^2}y}\right]e^{\mathrm{i}k_R x}. \end{aligned} \tag{28}$$

For the same computational domain of Figure 2, the Rayleigh induced displacements are imposed on its boundary and the model developed above is used to recover the displacement field inside the domain. It is worth pointing out again to the fact that Rayleigh waves propagate with the wave number k_R, while the plane wave approximation of expression (19) of the displacement field uses the pressure and shear wave numbers k_P and k_S, rather than k_R. Figure 5 shows two examples of numerical tests involving the Rayleigh wave problem for frequencies $\omega = 10$ and $\omega = 20$. Both figures show the displacement profile which displays ellipses with major axes normal to the free surface. Moreover, the displacements occur mainly near the free surface and decay rapidly with depth. For $\omega = 10$, only 16 plane waves are used to approximate the displacement field with $m_P = m_S = 8$, leading to an error of 0.5%. In the case of $\omega = 20$, 28 plane waves are used such that $m_P = m_S = 14$ and the L_2-error remains low as well, $\varepsilon_2 = 0.8\%$. This clearly indicates the good performance of the proposed approximation and its ability to capture Rayleigh waves in spite of the model not explicitly including the wave number k_R in the plane wave approximation (20).

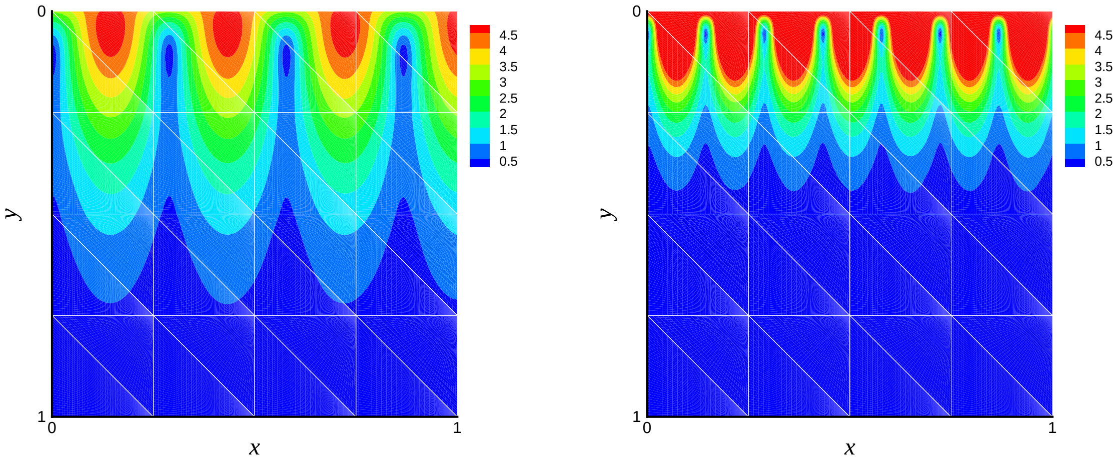

Figure 5: Real part of the displacement due to Rayleigh waves, (left) $\omega = 10$, $m_P = m_S = 8$, $\varepsilon_2 = 0.5\%$, (right) $\omega = 20$, $m_P = m_S = 14$, $\varepsilon_2 = 0.8\%$.

3.3 SV plane wave hitting a plane interface

In multilayered soils, for example, wave transmission and reflection occur at interfaces. In this sub-section, an incident elastic wave hitting a plane interface between two semi-infinite elastic media is considered. In general, this produces compression and shear waves in both media. Figure 6 shows a schematic diagram of an incident SV-plane wave hitting such interface.

For this case, the compression wave potential is therefore given by the reflected and transmitted waves

$$\phi = R_P\, e^{\mathrm{i}k(-x-y\tan\alpha)} + T_P\, e^{\mathrm{i}k(-x-y\tan\gamma)}, \tag{29}$$

while the shear wave potential is the sum of the incident, reflected and transmitted waves

$$\psi = 1\, e^{\mathrm{i}k(-x+y\tan\beta)} + R_S\, e^{\mathrm{i}k(-x-y\tan\beta)} + T_S\, e^{\mathrm{i}k(-x-y\tan\theta)}, \tag{30}$$

The wave number k is now given by $k = k_1^P\cos\alpha = k_1^S\cos\beta = k_2^P\cos\gamma = k_2^S\cos\theta$. The coefficients R_P, R_S, T_P and T_S are obtained by ensuring continuity of the displacement and stress fields at the interface [9]. The horizontal and vertical components of the displacement field, deduced from expressions (27), are imposed on the boundary of the computational domain of Figure 2 representing now two semi-infinite media in contact at the horizontal interface $y = 0.5$. Two cases are considered where a soft layer overlies a hard layer and *vice versa* with a ratio of densities of 1/3. In both cases, the SV plane wave is incident in the lower layer with $\beta = 60°$ and $\omega = 10$. A total of 24 plane waves are chosen such that $m_P = 10$ and $m_S = 14$. Figure 7 shows the numerical results of the real part of the displacement for both cases. The low L_2 errors, 0.8% and 0.7%, show the ability of the developed model to simulate such problems while ensuring continuity at the interface thanks to the Lagrange multipliers.

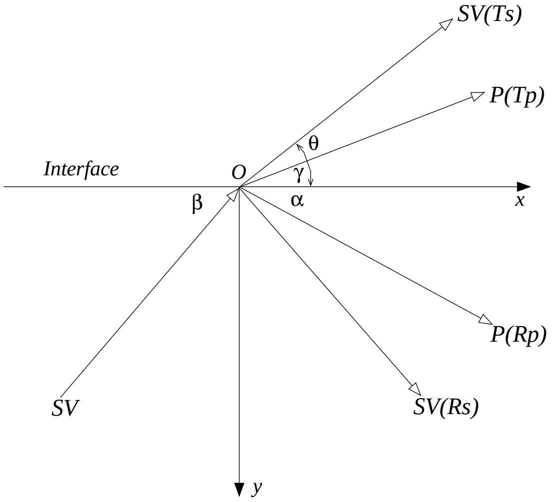

Figure 6: SV-plane wave hitting a plane interface between two semi-infinite elastic media.

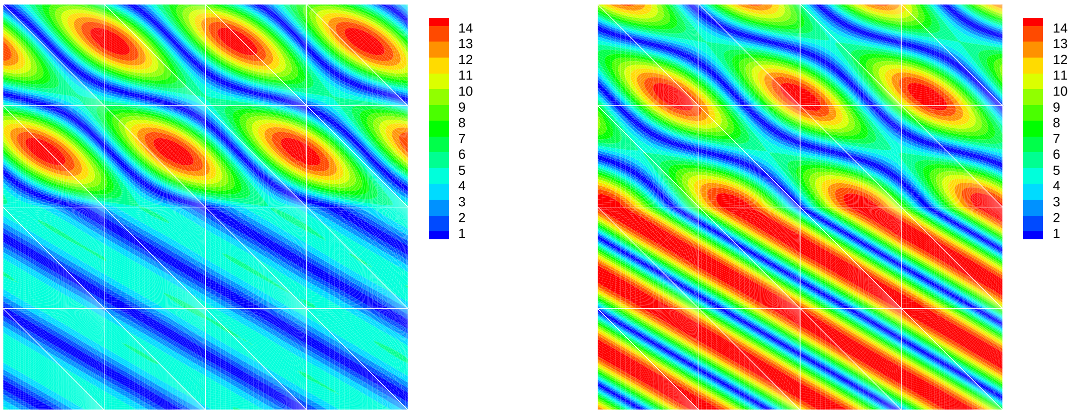

Figure 7: Real part of the displacement due to an SV-plane wave hitting a plane interface between two semi-infinite elastic media, $\omega = 10$, $m_P = 10$, $m_S = 14$, $\beta = 60°$, (left) hard layer overlying soft layer $\varepsilon_2 = 0.8\%$, (right) soft layer overlying hard layer $\varepsilon_2 = 0.7\%$.

4 CONCLUSIONS

In this work, the PUFEM is extended to deal with wave problems in elastic layered media by incorporating Lagrange multipliers to ensure compatibility conditions at the interfaces between the layers. The model is validated by considering a simple example of an SV plane wave transmitted at the plane interface between two semi-infinite elastic media. The model is also shown to deal with Rayleigh wave propagation without explicitly including its wave number in the displacement approximation. It also simulates elastic wave problems in presence of evanescent modes.

The results presented above are preliminary. They provide an indication of the ability of the PUFEM model to deal with various elastic wave problems in homogeneous and inhomogeneous media. Robustness and Accuracy of this model are currently being assessed through the consideration of different parameters such as the mesh size, the number of plane wave basis in the approximation of the displacement field and in the Lagrange multiplier, the problem frequency and the significant variations in material properties between layers.

Acknowledgements

The authors are grateful to the EPSRC for funding this work under grant number EP/I018042/1.

REFERENCES

[1] A. El Kacimi, O. Laghrouche. Numerical modelling of elastic wave scattering in frequency domain by the Partition of Unity Finite Element Method. *Int. J. Numer. Methods Engrg.* 2009; **77**:1646–1669.

[2] A. El Kacimi, O. Laghrouche. Improvement of PUFEM for the numerical solution of high frequency elastic wave scattering on unstructured triangular mesh grids. *Int. J. Numer. Methods Engrg.* 2010; **84**:330–350.

[3] A. El Kacimi, O. Laghrouche. Wavelet based ILU preconditioners for the numerical solution by PUFEM of high frequency elastic wave scattering. *Journal of Computational Physics* 2011; **230**:3119-3134.

[4] R. Tezaur, L. Zhang, C. Farhat. A discontinous enrichmment method for capturing envanescent waves in multiscale fluid and fluid/solid problems. *Comp. Meth. Appl. Mech. Engng.* 2008; **197** 1680–1698.

[5] T. Huttunen, Kaipio JP, Monk P. An ultra-weak method for acoustic fluid-solid interaction. *J. Comput. Appl. Math.* 2008; **213**:166–185.

[6] E. Perrey-Debain, J. Trevelyan and P. Bettess. P-wave and S-wave decomposition in boundary integral equation for plane elastodynamic problems. *Commun. Numer. Meth. Engng.* 2003; **19**:945–958.

[7] O. Laghrouche, P. Bettess, E. Perrey-Debain, J. Trevelyan. Wave interpolation finite elements for Helmholtz problems with jumps in the wave speed. *Comput. Meth. Appl. Mech. Engng.* 2005; **194**:367–381.

[8] P. Bettess and J.A. Bettess. A profile matrix solver with built-in constraint facility. *Eng. Comput.* 1986; **3**:209–216.

[9] W.M. Ewing, W.S. Jardetzky, F. Press. Elastic Waves in Layered Media. *McGraw-Hill Book Company*. New York, 1957.

[10] B.A. Auld. Acoustic Fields and Waves in Solids. *John Wiley and Sons*, 1973.

COMPDYN 2011
ECCOMAS Thematic Conference on
Computational Methods in Structural Dynamics and Earthquake Engineering
M. Papadrakakis, M. Fragiadakis, V. Plevris (eds.)
Corfu, Greece, 25-28 May 2011

NON-CONFORMING SPECTRAL APPROXIMATIONS FOR THE ELASTIC WAVE EQUATION IN HETEROGENEOUS MEDIA

I. Mazzieri[1,3], C. Smerzini[2], P.F. Antonietti[1],
F. Rapetti[3], M. Stupazzini[4], R. Paolucci[2] and A. Quarteroni[1,5]

[1] MOX - Modelling and Scientific Computing, Department of Mathematics, Politecnico di Milano,
P.za Leonardo da Vinci, 32, 20133 Milano, Italy.
e-mail: ilario.mazzieri@mail.polimi.it, paola.antonietti@polimi.it

[2] Department of Structural Engineering, Politecnico di Milano
P.za Leonardo da Vinci, 32, 20133 Milano, Italy.
e-mail: csmerzini@stru.polimi.it

[3] Université de Nice Sophia Antipolis, Laboratoire de Mathématiques J.A. Dieudonné,
Parc Valrose, Cedex 02, 06108 Nice, France.
frapetti@unice.fr

[4] Munich RE,
Königinstr. 107, 80802 Munich, Germany.
MStupazzini@munichre.com

[5] Chair of Modelling and Scientific Computing (CMCS),
Mathematics Institute of Computational Science and Engineering (MATHICSE),
École Polytechnique Fédérale de Lausanne (EPFL),
Station 8, 1015 Lausanne, Switzerland.
alfio.quarteroni@epfl.ch

Keywords: Computational seismology, Non-conforming approximations, Mortar Spectral Element Method, Discontinuous Galerkin Spectral Element Method.

Abstract. *Non-conforming techniques as the Mortar spectral Element Method (MSEM) or the Discontinuous Galerkin Spectral Element Method (DGSEM) are variational approaches to discretize partial differential equations, that rely on a spectral finite element approximation of a non-overlapping subdomain partition of the computational domain. In this contribution we compare and analyse MSEM and DGSEM, giving more details on the algorithmic aspects of the two non-conforming approaches, and we address their applicability and flexibility to handle seismic wave propagation problems. The numerical strategies are implemented in the spectral elements based code GeoELSE [14].*

1 INTRODUCTION

During the last three decades seismology is undergoing a major transformation at both the research and the application level. In modern seismology the classical scientific approach based on laboratory experiments has being replaced by computer simulations. Indeed, the rapid development of efficient numerical methods, gives the chance to simulate, with high resolution the complete seismic waveform field in highly heterogeneous earth media with complex geometries and up to relatively large frequencies (about 3 Hz).

The recent developments on computational seismology have been based on high-order numerical modelling of wave propagation (see, for example, [5, 12, 13, 15, 16, 17]). The reasons for using spectral element based approximations are the following. Firstly the flexibility in handling complex geometries, retaining the spatial exponential convergence for locally smooth solutions. Secondly, spectral element methods are based on the weak formulation of the elastodynamic equations involving only first-order spatial derivatives. Finally spectral element methods retain a high level parallel structure, and are therefore well suited for parallel computers.

In this paper we consider two different non-conforming high-order techniques, namely the Mortar Spectral Element Method (MSEM) and the Discontinuous Galerkin Spectral Element Method (DGSEM) to simulate seismic wave propagation in heterogeneous media. In contrast to standard conforming discretizations, as Spectral Element Method (SEM), these techniques have the further advantages that they can accommodate discontinuities, not only in the parameters, but also in the wave-field, they are energy conservative and well suited for parallel implementation. In our contribution we compare their performances when effectively applied to real problems. The paper is organized as follows. In Section 2 we recall the model problem under investigation. In Section 3 the non-conforming formulations are summarized. In Sections 4 we introduce the corresponding algebraic formulations and next, in Section 5 we describe how two efficiently implement them in a numerical code. In order to show an effective application of the methods previously described, in Section 6 a complex soil-structure interaction is studied using the MSEM and the DGSEM discretizations. Finally, in Section 7, we draw some conclusions.

2 FORMULATION OF PROBLEM

Fixing the temporal interval $(0, T]$, with $T > 0$, the equilibrium equations for an elastic medium, occupying a finite region $\Omega \subset \mathbb{R}^d$, $d = 2, 3$, subjected to an external force $\mathbf{f}$ read:

$$\rho \partial_{tt} \mathbf{u} - \nabla \cdot \underline{\sigma}(\mathbf{u}) = \mathbf{f} + \mathbf{f}^{visc}(\dot{\mathbf{u}}, \mathbf{u}), \tag{1}$$

where $\mathbf{u}$ is the displacement of the body, $\underline{\sigma}$ the stress tensor, t the time and ρ the density of the material. Since we are dealing with viscoelastic materials, we introduce in model (1) a structural damping in the form of volumetric forces $\mathbf{f}^{visc}(\dot{\mathbf{u}}, \mathbf{u}) = -2\rho\zeta\dot{\mathbf{u}} - \rho\zeta^2\mathbf{u}$, where ζ is a spatially variable (i.e., piecewise constant) suitable decay factor with dimension of inverse of the time [8]. It is worth remarking that the introduction of $\mathbf{f}^{visc}$ in (1) results in a frequency proportional quality factor, i.e. a non dispersive wave propagation (for further details see [18]).

We denote by $\Gamma = \Gamma_D \cup \Gamma_N \cup \Gamma_{NR}$ the boundary of the physical domain Ω and without loss of generality on the boundary Γ we make the following assumptions (cf [22]):

- on Γ_D the body is rigidly fixed in the space,
- on Γ_N we prescribe surface tractions ($\underline{\sigma}(\mathbf{u}) \cdot \mathbf{n} = \mathbf{t}$),
- on Γ_{NR} non-reflecting boundary conditions are imposed: cf. [27], for example.

Hereafter, an underlying bar denotes matrix or tensor quantities, while vectors are typed in bold. Moreover, we adopt the standard notation $(\cdot,\cdot)_\Omega$ to denote the L^2-inner product for scalar, vectorial and tensorial functions defined in Ω. To ease of presentation we describe the numerical methods in the case of null viscoelastic forces, i.e. $\mathbf{f}^{visc}(\dot{\mathbf{u}},\mathbf{u}) = 0$ (see Section 4.1 below for the general case).
Defining $V = \{\mathbf{v} \in [H^1(\Omega)]^d : \mathbf{v} = \mathbf{0} \text{ on } \Gamma_D\}$, the variational formulation of (1) reads:
$\forall t \in (0,T]$ *find* $\mathbf{u} = \mathbf{u}(t) \in V$ *such that*

$$\mathrm{d}_{tt}\left(\rho\mathbf{u},\mathbf{v}\right)_\Omega + \mathcal{A}(\mathbf{u},\mathbf{v})_\Omega = \mathcal{L}(\mathbf{v}), \quad \forall\, \mathbf{v} \in V, \tag{2}$$

where the bilinear form $\mathcal{A}(\cdot,\cdot) : V \times V \to \mathbb{R}^d$ is defined as $\mathcal{A}(\mathbf{u},\mathbf{v})_\Omega = (\underline{\sigma}(\mathbf{u}),\underline{\varepsilon}(\mathbf{v}))_\Omega$, and the linear functional $\mathcal{L} : V \to \mathbb{R}^d$ as $\mathcal{L}(\mathbf{v}) = (\mathbf{t},\mathbf{v})_{\Gamma_N} + (\mathbf{t}^*,\mathbf{v})_{\Gamma_{NR}} + (\mathbf{f},\mathbf{v})_\Omega$. We suppose that the strain tensor $\underline{\varepsilon}$ and the stress tensor $\underline{\sigma}$ are related through the Hooke's law

$$\underline{\varepsilon}(\mathbf{u}) = \frac{1}{2}(\nabla\mathbf{u} + \nabla\mathbf{u}^\top), \quad \underline{\sigma}(\mathbf{u}) = \lambda\nabla\cdot\mathbf{u}\,\underline{\mathrm{I}} + 2\mu\underline{\varepsilon}(\mathbf{u}),$$

where $\underline{\mathrm{I}}$ is the $d-$dimensional identity tensor and λ and μ are the Lamé elastic coefficients. We remark that for heterogeneous media ρ, λ and μ are bounded functions of the spatial variable, not necessarily continuous i.e., ρ, λ and $\mu \in L^\infty(\Omega)$. Finally, to complete problem (2), we prescribe initial conditions $\mathbf{u}_0$ and $\mathbf{u}_1$ for the displacement and the velocity, respectively.
It can be proved that the bilinear form $\mathcal{A}(\cdot,\cdot)$ is symmetric, V-elliptic and continuous. These conditions imply that problem (2) admits a unique solution, (cf. [4, 23]).
Let V_δ be a suitable finite dimensional approximation of the space V, the semi-discrete approximation of (2) reads : $\forall t \in (0,T]$ *find* $\mathbf{u}_\delta = \mathbf{u}_\delta(t) \in V_\delta$ *such that*

$$\mathrm{d}_{tt}\left(\rho\mathbf{u}_\delta,\mathbf{v}\right)_\Omega + \mathcal{A}(\mathbf{u}_\delta,\mathbf{v}) = \mathcal{L}(\mathbf{v}), \quad \forall\, \mathbf{v} \in V_\delta. \tag{3}$$

In general, in non-conforming approximations, the space V_δ is not a subspace of V. In the following section we describe how to build V_δ for both for the Mortar Spectral Element Method (MSEM) and the Discontinuous Galerkin Spectral Element Method (DGSEM).

3 NON CONFORMING FORMULATIONS

To approximate the problem (3) we start by a discretization of the spatial differential operators in Ω, that rely on a time-independent three-level spatial decomposition of the domain Ω.
At the first level, we subdivide Ω into K non overlapping regions Ω_k, $k = 1,...,K$, such that $\overline{\Omega} = \bigcup_{k=1}^K \overline{\Omega}_k$ with $\Omega_k \cap \Omega_\ell = \emptyset$ if $k \neq \ell$ and we define the skeleton of this (macro) decomposition as $\mathcal{S} = \bigcup_{k=1}^K \partial\Omega_k \backslash \partial\Omega$. Note that this decomposition can be geometrically non-conforming, i.e., for two neighbouring subdomains Ω_k, Ω_ℓ, the interface $\gamma = \partial\Omega_k \cap \partial\Omega_\ell$ may not be a complete side (for $d = 2$) or face (for $d = 3$) of Ω_k or Ω_ℓ.
To get the second level, in each Ω_k we introduce a (meso) partitioning $\mathcal{T}_{h_k}$, made by elements Ω_k^j that are image through an invertible mapping F_k^j of the reference element $\hat{\Omega} = (-1,1)^d$. The quadrilaterals Ω_k^j, if $d = 2$, or hexahedra, if $d = 3$, have typical linear size h_k and $\overline{\Omega}_k = \bigcup_{j=1}^{J_k} \overline{\Omega}_k^j$.
The third (micro) level is represented by the so-called Gauss-Lobatto-Legendre (GLL) points in each mesh element Ω_k^j. Let $\hat{\mathbf{Q}}_{N_k}(\hat{\Omega})$ be the space of functions defined on $\hat{\Omega}$ that are algebraic polynomials of degree less than or equal to $N_k \geq 2$ in each spatial variable $x_1, ..., x_d$. Thus, we set

$$\mathbf{Q}_{N_k}(\Omega_k^j) = \left\{ v = \widehat{v} \circ F_k^{j^{-1}} : \widehat{v} \in \hat{\mathbf{Q}}_{N_k}(\hat{\Omega}) \right\},$$

and we define the finite dimensional space $X_\delta(\Omega_k)$ as

$$X_\delta(\Omega_k) = \left\{ v_\delta \in \mathcal{C}^0(\overline{\Omega}_k) : v_{\delta|\Omega_k^j} \in \mathbf{Q}_{N_k}(\Omega_k^j)\ \forall \Omega_k^j \in \mathcal{T}_{h_k} \right\},$$

and finally $V_\delta = \{\mathbf{v}_\delta \in [L^2(\Omega)]^d : \mathbf{v}_{\delta|\Omega_k} \in [X_\delta(\Omega_k)]^d\ \ \forall k = 1, ..., K : \mathbf{v}_{\delta|\Gamma_D} = \mathbf{0}\}$. Here $\delta = \{\mathbf{h}, \mathbf{N}\}$ with $\mathbf{h} = (h_1, ..., h_K)$ and $\mathbf{N} = (N_1, ..., N_K)$ are K-uplets of discretization parameters. Problem (3) is then equivalent to: $\forall t \in (0, T]$ *find* $(\mathbf{u}_{\delta,1}(t), \ldots, \mathbf{u}_{\delta,K}(t)) \in V_\delta$ *such that*

$$\sum_{k=1}^{K} \mathrm{d}_{tt}(\rho \mathbf{u}_{\delta,k}, \mathbf{v}_k)_{\Omega_k} + \mathcal{A}(\mathbf{u}_{\delta,k}, \mathbf{v}_k)_{\Omega_k} + \mathcal{B}(\mathbf{u}_{\delta,k}, \mathbf{v}_k)_{\partial\Omega_k \setminus \partial\Omega} = \sum_{k=1}^{K} \mathcal{L}(\mathbf{v}_k)_{\Omega_k}, \tag{4}$$

for all $(\mathbf{v}_1, \ldots, \mathbf{v}_K) \in V_\delta$, where

$$\mathcal{A}(\mathbf{u}, \mathbf{v})_{\Omega_k} = (\underline{\sigma}(\mathbf{u}), \underline{\varepsilon}(\mathbf{v}))_{\Omega_k}, \quad \text{and} \quad \mathcal{B}(\mathbf{u}, \mathbf{v})_{\partial\Omega_k \setminus \partial\Omega} = (\underline{\sigma}(\mathbf{u}) \cdot \mathbf{n}, \mathbf{v})_{\partial\Omega_k \setminus \partial\Omega}. \tag{5}$$

Depending on the chosen non-conforming approach, the functional space V_δ is completed by additional conditions on $\mathbf{u}_{\delta,k}$, $k = 1, \ldots, K$, on the skeleton of the macro decomposition which ensure that $\mathbf{u}_{\delta,k}$ is the restriction to Ω_k of $\mathbf{u}_\delta \in H^1(\Omega)^d$. The bilinear form $\mathcal{B}(\cdot, \cdot)$ may either be zero or gather all the contributions $(\sigma(\mathbf{u}_{\delta,k}) \cdot \mathbf{n}_k, \mathbf{v}_k)_{\partial\Omega_k \setminus \partial\Omega}$, $k = 1, \ldots, K$, depending on the chosen approach. Equation (4) represents the starting point to introduce the MSEM and the DGSEM.

In the next sections we describe the two approaches. To ease the presentation, we suppose that $\Gamma_D = \partial\Omega$ and we assume that each partition $\mathcal{T}_{h_k}$ of Ω_k consists in only one element, i.e., Ω is subdivided into K non-overlapping spectral elements $\Omega_1, ..., \Omega_K$ so that $\overline{\mathcal{S}} = \bigcap_{k=1}^{K} \partial\overline{\Omega}_k \setminus \Gamma_D$. The more general case follows from similar arguments.

3.1 Mortar Spectral Formulation

In this section we introduce the MSEM for the solution of (4), see [11, 21] for a more detailed description. We denote by Γ_k^ℓ, $\ell = 1, \ldots, 2d$, the edges (faces) of each subdomain Ω_k, $k = 1, \ldots, K$, so that $\partial\Omega_k = \bigcup_{\ell=1}^{2d} \overline{\Gamma}_k^\ell$. We then identify the skeleton $\mathcal{S}$ as the union of elementary non-empty components called *mortars* (or *masters*), more precisely

$$\mathcal{S} = \bigcup_{k=1}^{K} (\partial\Omega_k \setminus \partial\Omega) = \bigcup_{m=1}^{M} \overline{\gamma}_m, \quad \text{with } \gamma_m \cap \gamma_n = \emptyset, \quad \text{if } m \neq n, \tag{6}$$

where each mortar is a whole edge (or face) $\Gamma_{k(m)}^{\ell(m)}$ of a specific element $\Omega_{k(m)}$ and m is an arbitrary numbering $m = 1, \ldots, M$, with M a positive integer. Those edges or faces Γ_k^ℓ that do not coincide with a mortar are called *non-mortars* (or *slaves*) and provide a dual description of the skeleton, as

$$\mathcal{S} = \bigcup_{m\, mortar} \gamma_m^+ = \bigcup_{n\, non\, mortar} \gamma_n^-.$$

The intersection of the closures of the mortars defines a set of vertices or *cross-points*

$$\mathcal{V} = \{\mathbf{x}_q = (\overline{\gamma}_r^+ \cap \overline{\gamma}_s^+),\ \mathbf{x}_q \notin \overline{\gamma}_m^+,\ m = 1, \ldots, M\},$$

where q is an arbitrary numbering $q = 1, \ldots, \mathtt{V}$. We define as well the set $\widetilde{\mathcal{V}}$ of *virtual* vertices (that are not cross-points) as $\widetilde{\mathcal{V}} = \{\widetilde{\mathbf{x}}_q = (\overline{\gamma}_r^+ \cap \gamma_s^+)\}$, where q is an arbitrary numbering

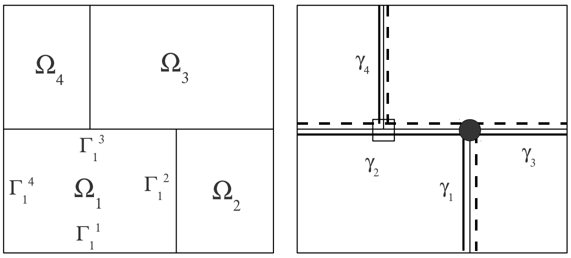

Figure 1: Nonconforming domain decomposition (left) and skeleton structure (right) showing a cross-point (●), a virtual vertex (□), the mortars (dark continuous lines) and the non-mortars (dark dashed lines).

$q = 1, \ldots, \widetilde{\mathrm{V}}$ (see Fig. 1). Let $\Lambda_\delta(\Gamma_k^\ell) = \mathbf{Q}_{N_k}(\Gamma_k^\ell)$ be the space of the traces of functions of $X_\delta(\Omega_k)$ over Γ_k^ℓ and $\widehat{\Lambda}_\delta(\Gamma_k^\ell) = \mathbf{Q}_{N_k-2}(\Gamma_k^\ell)$. We can now define the nonconforming spectral element discretization space $\widetilde{V}_\delta$ as the space of functions $\mathbf{v}_\delta \in V_\delta$ that satisfy the following additional *mortar matching condition*:

(MC) let $\mathbf{\Phi}$ be the *mortar function* associated with $\mathbf{v}_\delta$, i.e., a function that is continuous on $\mathcal{S}$, zero on $\partial\Omega$ and such that on each mortar $\gamma_m = \Gamma_{k(m)}^{\ell(m)}$ coincides with the restriction of $\mathbf{v}_{\delta,k} = \mathbf{v}_{\delta|\Omega_k}$ to γ_m; then, for all indices (k,ℓ) such that Γ_k^ℓ is contained in $\mathcal{S}$ but $(k,\ell) \neq (k(m),\ell(m))$ for all $m = 1,\ldots,M$ (that is for all indices (k,ℓ) such that Γ_k^ℓ is a *non-mortar*) we require that:

$$\int_{\Gamma_k^\ell} (\mathbf{v}_{\delta,k} - \mathbf{\Phi}) \cdot \hat{\mathbf{\Phi}}\, d\gamma = 0 \quad \forall \hat{\mathbf{\Phi}} \in [\widehat{\Lambda}_\delta(\Gamma_k^\ell)]^d, \tag{7}$$

and that

$$\mathbf{v}_{\delta|\Omega_k}(\mathbf{x}_q) = \mathbf{\Phi}(\mathbf{x}_q), \quad \forall \mathbf{x}_q \in \mathcal{V} \cup \widetilde{\mathcal{V}}. \tag{8}$$

The integral matching condition (7) represents a minimization of the jump in functions at internal boundaries with respect to the L^2 norm. The vertex condition (8) ensures exact continuity at cross-points.

The Mortar Spectral Formulation is obtained by solving in each region Ω_k the elastodynamic variational problem (4) with homogeneous Neumann boundary conditions on $\mathcal{S}$ ($\underline{\sigma}(\mathbf{u}) \cdot \mathbf{n} = \mathbf{0}$ so that $\sum_k \mathcal{B}\,(\mathbf{u},\mathbf{v})_{\partial\Omega_k \setminus \partial\Omega}$ is identically zero), and enforcing weak continuity of the displacement on $\mathcal{S}$ with *mortar condition* (7). Thus, the semi-discrete Mortar Spectral Formulation reads:

$\forall t \in (0,T]$ *find* $(\mathbf{u}_{\delta,1}(t),\ldots,\mathbf{u}_{\delta,K}(t)) \in V_\delta^{mortar}$ *such that*

$$\sum_k d_{tt}\,(\rho\mathbf{u}_{\delta,k},\mathbf{v}_k)_{\Omega_k} + \mathcal{A}(\mathbf{u}_{\delta,k},\mathbf{v}_k)_{\Omega_k} = \sum_k \mathcal{L}(\mathbf{v}_k), \quad \forall\,(\mathbf{v}_1,\ldots,\mathbf{v}_K) \in V_\delta^{mortar}, \tag{9}$$

where $V_\delta^{mortar} = \{(\mathbf{v}_1,\ldots,\mathbf{v}_K) \in V_\delta :$ the $mortar\ condition$ **(MC)** is satisfied$\}$.

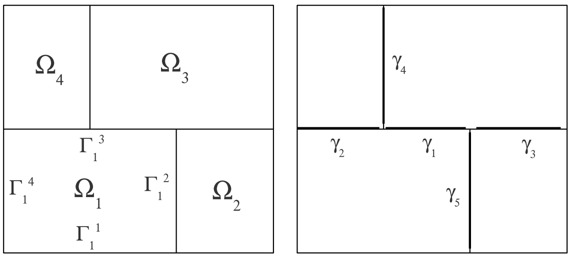

Figure 2: Nonconforming domain decomposition (left) and skeleton structure (right) showing the elementary components (dark continuous lines).

3.2 Discontinuous Galerkin Spectral Formulation

In order to introduce the Discontinuous Galerkin Spectral Formulations, we subdivide the skeleton $\mathcal{S}$ in the set of elementary components (edges if $d=2$, faces if $d=3$) as follows:

$$\overline{\mathcal{S}} = \bigcup_{j=1}^{M} \overline{\gamma}_j, \quad \text{with } \gamma_i \cap \gamma_j = \emptyset, \quad \text{if } i \neq j, \tag{10}$$

where each edge (face) is given by $\overline{\gamma}_j = (\partial\overline{\Omega}_{k(j)} \cap \partial\overline{\Omega}_{\ell(j)}) \setminus \partial\Omega$, for some different positive integers k and ℓ. Notice that this decomposition is unique (see Fig. 2). Next, we collect all the edges (faces) in the set $\mathcal{F}_I$. For regular enough functions, we use the standard notation [2] to define the jumps ($[\![\cdot]\!]$) and the average ($\{\cdot\}$) operators on each edge (face) $\gamma \in \mathcal{F}_I$.
We obtain the following semi-discrete DG Spectral Formulation:
$\forall t \in (0,T]$ *find* $\mathbf{u}_\delta = (\mathbf{u}_{\delta,1}(t), ..., \mathbf{u}_{\delta,K}(t)) \in V_\delta^{DG} \equiv V_\delta$ *such that*

$$\sum_{k=1}^{K} \left(\mathrm{d}_{tt} \left(\rho \mathbf{u}_\delta, \mathbf{v}\right)_{\Omega_k} + \mathcal{A}(\mathbf{u}_\delta, \mathbf{v})_{\Omega_k} \right) + \sum_{j=1}^{M} \mathcal{B}(\mathbf{u}_\delta, \mathbf{v})_{\gamma_j} = \mathcal{L}(\mathbf{v}) \quad \forall\, \mathbf{v} = (\mathbf{v}_1, ..., \mathbf{v}_K) \in V_\delta^{DG}, \tag{11}$$

with

$$\mathcal{B}(\mathbf{u}_\delta, \mathbf{v})_{\gamma_j} = -\left(\{\underline{\sigma}(\mathbf{u}_\delta)\}, [\![\mathbf{v}]\!]\right)_{\gamma_j} + \theta\left([\![\mathbf{u}_\delta]\!], \{\underline{\sigma}(\mathbf{v})\}\right)_{\gamma_j} + \eta_{\gamma_j}\left([\![\mathbf{u}_\delta]\!], [\![\mathbf{v}]\!]\right)_{\gamma_j}. \tag{12}$$

Here $\eta_{\gamma_j} = \frac{\alpha \mathtt{N}_\mathtt{j}^2}{\mathtt{h}_\mathtt{j}}\{\lambda + 2\mu\}_A$, where $\{\cdot\}_A$ represents the harmonic average, $\mathtt{N}_\mathtt{j} = \max(N_{k(j)}, N_{\ell(j)})$, $\mathtt{h}_\mathtt{j} = \min(h_{k(j)}, h_{\ell(j)})$ and α is a positive constant at our disposal. Corresponding to different values of θ we obtain different DG schemes, namely: $\theta = -1$ (resp. $\theta = 1$) leads to the symmetric (resp. non-symmetric) interior penalty method, while $\theta = 0$ corresponds to the so-called incomplete interior penalty method (see [2, 24, 25, 26] for more details).

4 ALGEBRAIC FORMULATION AND TIME INTEGRATION SCHEME

We discuss here the algebraic formulation of the two non-conforming approaches presented in the previous section. In particular we described how to build the linear systems coming from the mortar or DG discretization and discuss the time integration scheme.

4.1 Algebraic formulation of the problem

We denote by $D = \sum_{k=1}^{K}(N_k+1)^2$ the dimension of each component of V_δ and we introduce a basis $\{\mathbf{\Psi}_i^1, \mathbf{\Psi}_i^2\}_{i=1}^{D}$ for the finite dimensional space V_δ, where $\mathbf{\Psi}_i^1 = (\Psi_i^1, 0)^\top$ and $\mathbf{\Psi}_i^2 = (0, \Psi_i^2)^\top$. We choose the set of shape functions in such a way that they are orthonormal with respect to the L^2 inner product on the reference element.
We denote by $\{\mathbf{p}_j\}_{j=1}^{D}$ the GLL nodes of the mesh and we suppose that $\Psi_i^1(\mathbf{p}_j) = \Psi_i^2(\mathbf{p}_j) = \delta_{ij}$, for $i, j = 1, ..., D$, where δ_{ij} represents the Kronecker symbol. Dropping the subscript δ, we write the trial functions $\mathbf{u} \in V_\delta$ as a linear combination of the basis functions

$$\mathbf{u}(\mathbf{x}, t) = \sum_{j=1}^{D} \left[\begin{array}{c} \Psi_j^1(\mathbf{x}) \\ 0 \end{array} \right] U_j^1(t) + \sum_{j=1}^{D} \left[\begin{array}{c} 0 \\ \Psi_j^2(\mathbf{x}) \end{array} \right] U_j^2(t).$$

Next, we define $a_k = 1 + \sum_{j=1}^{k-1}(N_j+1)^2$ and $b_k = \sum_{j=1}^{k}(N_j+1)^2$ and we order the basis functions such that

$$\mathbf{u}_{|\Omega_k} = \left(u^1, u^2\right)^\top_{|\Omega_k} = \left(\sum_{j=a_k}^{b_k} \Psi_j^1 U_{j,k}^1 \, , \sum_{j=a_k}^{b_k} \Psi_j^2 U_{j,k}^2 \right)^\top, \quad \text{for}\, k = 1, ..., K.$$

With such a notation (11) can be rewritten as the following set of ODE

$$\left[\begin{array}{cc} \underline{\mathrm{M}}^1 & \underline{0} \\ \underline{0} & \underline{\mathrm{M}}^2 \end{array} \right] \left[\begin{array}{c} \ddot{\mathbf{U}}^1 \\ \ddot{\mathbf{U}}^2 \end{array} \right] + \left[\begin{array}{cc} \underline{\mathrm{A}}^1 + \underline{\mathrm{B}}^1 & \underline{\mathrm{A}}^2 + \underline{\mathrm{B}}^2 \\ \underline{\mathrm{A}}^3 + \underline{\mathrm{B}}^3 & \underline{\mathrm{A}}^4 + \underline{\mathrm{B}}^4 \end{array} \right] \left[\begin{array}{c} \mathbf{U}^1 \\ \mathbf{U}^2 \end{array} \right] = \left[\begin{array}{c} \mathbf{F}^{ext,1} \\ \mathbf{F}^{ext,2} \end{array} \right], \tag{13}$$

where $\ddot{\mathbf{U}}$ represents the vector of the nodal acceleration and $\mathbf{F}^{ext}$ the vector of externally applied loads. As a consequence of our assumptions on the basis functions, the mass matrices $\underline{\mathrm{M}}^1$ and $\underline{\mathrm{M}}^2$ have a block diagonal structure, i.e., $\underline{\mathrm{M}}^\ell = \mathtt{diag}(\underline{\mathrm{M}}_1^\ell, \underline{\mathrm{M}}_2^\ell, ..., \underline{\mathrm{M}}_K^\ell), \quad \text{for } \ell = 1, 2$, where each block $\underline{\mathrm{M}}_k^\ell$ is associated to the spectral element Ω_k and $\mathrm{M}_k^\ell(i,j) = (\rho\Psi_j^\ell, \Psi_i^\ell)_{\Omega_k}$, for $i, j = a_k, ..., b_k$. The matrix $\underline{\mathrm{A}}$ associated to the bilinear form $\mathcal{A}(\cdot,\cdot)$ defined in (5) takes the form

$$\underline{\mathrm{A}} = \left[\begin{array}{cc} \underline{\mathrm{A}}^1 & \underline{\mathrm{A}}^2 \\ \underline{\mathrm{A}}^3 & \underline{\mathrm{A}}^4 \end{array} \right],$$

where the block diagonal matrices $\underline{\mathrm{A}}^\ell$, $\ell = 1, .., 4$ are equal to $\underline{\mathrm{A}}^\ell = \mathtt{diag}(\underline{\mathrm{A}}_1^\ell, \underline{\mathrm{A}}_2^\ell, ..., \underline{\mathrm{A}}_K^\ell)$. The elements of the matrices $\underline{\mathrm{A}}_k^\ell$, $\ell = 1, ..., 4$ and $k = 1, .., K$, are defined by

$$\mathrm{A}_k^1(i,j) = \mathcal{A}(\underline{\sigma}(\mathbf{\Psi}_j^1), \underline{\varepsilon}(\mathbf{\Psi}_i^1))_{\Omega_k}, \quad \mathrm{A}_k^2(i,j) = \mathcal{A}(\underline{\sigma}(\mathbf{\Psi}_j^2), \underline{\varepsilon}(\mathbf{\Psi}_i^1))_{\Omega_k}, \text{ for}\, i, j = a_k, ..., b_k,$$

$$\mathrm{A}_k^3(i,j) = \mathcal{A}(\underline{\sigma}(\mathbf{\Psi}_j^1), \underline{\varepsilon}(\mathbf{\Psi}_i^2))_{\Omega_k}, \quad \mathrm{A}_k^4(i,j) = \mathcal{A}(\underline{\sigma}(\mathbf{\Psi}_j^2), \underline{\varepsilon}(\mathbf{\Psi}_i^2))_{\Omega_k}, \text{ for}\, i, j = a_k, ..., b_k.$$

We remark that the matrices $\underline{\mathrm{M}}$ and $\underline{\mathrm{A}}$ are very similar to those coming from the discretization of the elastodynamic equation (2) with the conforming Spectral Element Method (see [6, 7]).
If we are using the mortar formulation, the matrix $\underline{\mathrm{B}}$, associated to the bilinear form $\mathcal{B}(\cdot,\cdot)$ defined in (5), is the null matrix, whereas in the DG approach, is the one that takes into account of the discontinuity of the numerical solution across the skeleton $\mathcal{S}$. More precisely,

$$\underline{\mathrm{B}} = \left[\begin{array}{cc} \underline{\mathrm{B}}^1 & \underline{\mathrm{B}}^2 \\ \underline{\mathrm{B}}^3 & \underline{\mathrm{B}}^4 \end{array} \right], \tag{14}$$

where

$$\underline{\mathrm{B}}^{\ell} = \begin{bmatrix} \underline{\mathrm{B}}^{\ell}_{1,1} & \cdots & \underline{\mathrm{B}}^{\ell}_{1,K} \\ \vdots & \ddots & \vdots \\ \underline{\mathrm{B}}^{\ell}_{K,1} & \cdots & \underline{\mathrm{B}}^{\ell}_{K,K} \end{bmatrix}, \quad \text{for } \ell = 1, ..., 4.$$

In particular the elements of each block $\underline{B}^{1}_{k,n}(i,j) = \sum_{\gamma \in \mathcal{F}_I} \mathcal{B}(\mathbf{\Psi}^1_j, \mathbf{\Psi}^1_i)_{\gamma}$, $i = a_k, ..., b_k$ and $j = a_n, ..., b_n$. The elements of the matrices $\underline{\mathrm{B}}^{\ell}_{k,n}$, for $\ell = 2, 3, 4$ are defined in a similar way.
The situation is a little bit more complicated in the Mortar approach, since the weak continuity condition across the skeleton $\mathcal{S}$ does not appear explicitly in the variational equation but it is a constraint in the functional space V_{δ}^{mortar}.
To take into account the **(MC)** we have to modify the system (13) as follows. Without loss of generality let us suppose that γ_n^- is a non mortar edge contained in $\mathcal{S}$ and that it is shared by two regions Ω_m and Ω_n. We call *master* the side of γ_n^- belonging to $\overline{\Omega}_m$ and *slave* the other side. Thus, the *mortar conditions* can be recast as:

(i) $\mathbf{\Phi} = \mathbf{u}_m$ on γ_n^-,

(ii) $\int_{\gamma_n^-} (\mathbf{u}_n - \mathbf{u}_m) \cdot \hat{\mathbf{\Phi}} ds = 0 \quad \forall \hat{\mathbf{\Phi}} \in [\widehat{\Lambda}_{\delta}(\gamma_n^-)]^d$.

At the algebraic level, the condition in $(\mathbf{ii})$ is represented by the following linear system of equations

$$\begin{bmatrix} \underline{R}^1 & \underline{0} \\ \underline{0} & \underline{R}^2 \end{bmatrix} \begin{bmatrix} \mathbf{U}^1_n \\ \mathbf{U}^2_n \end{bmatrix} = \begin{bmatrix} \underline{P}^1 & \underline{0} \\ \underline{0} & \underline{P}^2 \end{bmatrix} \begin{bmatrix} \mathbf{U}^1_m \\ \mathbf{U}^2_m \end{bmatrix}, \tag{15}$$

where

$$\underline{R}^{\ell}(i,j) = \int_{\gamma_n^-} \Psi^{\ell}_j \hat{\Phi}^{\ell}_i ds \quad \text{and} \quad \underline{P}^{\ell}(i,j) = \int_{\gamma_n^-} \Phi^{\ell}_j \hat{\Phi}^{\ell}_i ds, \quad \ell = 1, 2. \tag{16}$$

By using that the shape functions are orthonormal on the reference element and suitable quadrature rules to integrate (16), (cf. [3, 11]), it is possible to easily invert the matrix $\underline{R}$ and to reduce (15) to

$$\begin{bmatrix} \mathbf{U}^1_n \\ \mathbf{U}^2_n \end{bmatrix} = \begin{bmatrix} \underline{Q}_n & \underline{0} \\ \underline{0} & \underline{Q}_n \end{bmatrix} \begin{bmatrix} \mathbf{U}^1_m \\ \mathbf{U}^2_m \end{bmatrix},$$

where $\underline{Q}_n = (\underline{R}^1)^{-1} \underline{P}^1 = (\underline{R}^2)^{-1} \underline{P}^2$. To obtain a global projection operator $\underline{\widetilde{\mathrm{Q}}}$ we proceed as follows. For each component of $\mathbf{u}$ we denote by $\mathbf{U}_{slave}$ the vector of unknowns associated to the dofs that lay on the slave side of $\mathcal{S}$ and by $\mathbf{U}_{master}$ the vector of unknowns associated to all the remaining dofs. Then, for each γ_n^- contained into the skeleton $\mathcal{S}$ we build the local projection operator $\underline{Q}_n$ and we store it into the matrix $\underline{\widetilde{Q}}$. In this way $\underline{\widetilde{Q}}$ has a block structure of the form

$$\underline{\widetilde{\mathrm{Q}}} = \begin{bmatrix} \underline{\hat{Q}} & \underline{0} \\ \underline{0} & \underline{\hat{Q}} \end{bmatrix}, \tag{17}$$

where $\underline{\hat{Q}}$ is block diagonal matrix with a block equal to the identity and the other equal to the rectangular matrix $\underline{Q}$ containing all the local matrices $\underline{Q}_n$. Thus, we have that the global linear system can be expressed as

$$\underline{\widetilde{\mathrm{Q}}}^{\top} \underline{\widetilde{\mathrm{M}}} \underline{\widetilde{\mathrm{Q}}} \ddot{\mathbf{U}}_{master} + \underline{\widetilde{\mathrm{Q}}}^{\top} \underline{\widetilde{\mathrm{A}}} \underline{\widetilde{\mathrm{Q}}} \mathbf{U}_{master} = \underline{\widetilde{\mathrm{Q}}}^{\top} \mathbf{F}^{ext}, \tag{18}$$

where the rows and the columns of the matrices $\underline{\widetilde{\mathrm{M}}}$ and $\underline{\widetilde{\mathrm{A}}}$ have been modified according to these latter assumptions on the unknown renumbering. We remark that it is possible to obtain the linear system (18) using as a basis for V_δ^{mortar}, the functions $\{\widetilde{\boldsymbol{\Psi}}_i^1, \widetilde{\boldsymbol{\Psi}}_i^2\}_{i=1}^D$, where $\widetilde{\boldsymbol{\Psi}}_i^1 = (\widetilde{\Psi}_i^1, 0)^\top$ and $\widetilde{\boldsymbol{\Psi}}_i^2 = (0, \widetilde{\Psi}_i^2)^\top$ are defined by

$$\widetilde{\Psi}_i^\ell = \begin{cases} \Psi_i^\ell & \forall i \text{ s.t } \mathbf{p}_i \text{ is a } \textit{master} \text{ node}, \\ \sum_j \underline{\hat{Q}}_{ij} \Psi_j^\ell & \forall i \text{ s.t } \mathbf{p}_i \text{ is a } \textit{slave} \text{ node}, (\mathbf{p}_j \textit{ master} \text{ node on } \mathcal{S}). \end{cases}$$

All the terms appearing in the algebraic formulations presented so fare are computed using the Gauss-Lobatto quadrature rule in which the quadrature points coincide with GLL points. We notice that since the term $\Psi_j\Psi_i \in \mathbf{Q}_{2N_k}$, for some k, the spectral mass matrix is slightly under integrated. However, since the Gauss-Lobatto rule with N_k points is exact for polynomials up to degree $2N_k - 1$, the final accuracy of spectral methods is not damaged [6].

Finally, we point out that if $\mathbf{f}^{visc} \neq 0$ we must compute the following additional external forces:

$$\begin{bmatrix} \mathbf{F}^{visc,1} \\ \mathbf{F}^{visc,2} \end{bmatrix} = - \begin{bmatrix} \underline{\mathrm{C}}^1 & \underline{0} \\ \underline{0} & \underline{\mathrm{C}}^2 \end{bmatrix} \begin{bmatrix} \dot{\mathbf{U}}^1 \\ \dot{\mathbf{U}}^2 \end{bmatrix} - \begin{bmatrix} \underline{\mathrm{D}}^1 & \underline{0} \\ \underline{0} & \underline{\mathrm{D}}^2 \end{bmatrix} \begin{bmatrix} \mathbf{U}^1 \\ \mathbf{U}^2 \end{bmatrix},$$

where the matrices $\underline{\mathrm{C}}^\ell$ and $\underline{\mathrm{D}}^\ell$, for $\ell = 1, 2$ have a block diagonal structure. Each block $\underline{\mathrm{C}}_k^\ell$ and $\underline{\mathrm{D}}_k^\ell$ is associated to the spectral element Ω_k and

$$\mathrm{C}_k^\ell(i,j) = (\rho\zeta\Psi_j^\ell, \Psi_i^\ell)_{\Omega_k}, \quad \mathrm{D}_k^\ell(i,j) = (\rho\zeta^2\Psi_j^\ell, \Psi_i^\ell)_{\Omega_k}, \quad \text{for } i,j = a_k, ..., b_k,$$

respectively. Then the discretized system becomes:

$$\underline{\mathrm{M}}\ddot{\mathbf{U}} + \underline{\mathrm{C}}\dot{\mathbf{U}} + (\underline{\mathrm{A}} + \underline{\mathrm{B}} + \underline{\mathrm{D}})\mathbf{U} = \mathbf{F}^{ext}, \tag{19}$$

where the accelerations $\ddot{\mathbf{U}}$ and the velocities $\dot{\mathbf{U}}$ are approximated as described in the next section.

4.2 Time integration

Let now subdivide into N subinterval of amplitude $\Delta t = \frac{T}{N}$ the interval $(0, T]$: the time integration scheme for (13) is achieved with the second order central difference scheme, setting $t_n = n\Delta t$:

$$\ddot{\mathbf{U}}(t_n) = \frac{\mathbf{U}(t_{n+1}) - 2\mathbf{U}(t_n) + \mathbf{U}(t_{n-1})}{\Delta t^2}, \quad \dot{\mathbf{U}}(t_n) = \frac{\mathbf{U}(t_{n+1}) - \mathbf{U}(t_{n-1})}{2\Delta t}. \tag{20}$$

Thus, the equation (13) or (18) at each time step t_n becomes:

$$\underline{\mathrm{K}}\mathbf{U}(t_{n+1}) = \mathbf{b}(\mathbf{U}(t_n), \mathbf{U}(t_{n-1}), \mathbf{F}^{ext}(t_n), \underline{\mathrm{A}}, \underline{\mathrm{B}}), \tag{21}$$

with initial condition $\mathbf{U}(t_0) = \mathbf{u}_0$ and $\dot{\mathbf{U}}(t_0) = \mathbf{u}_1$. If we adopt a fully explicit time integration scheme the matrix $\underline{\mathrm{K}}$ is the mass matrix, i.e. $\underline{\mathrm{K}} = \underline{\mathrm{M}}$, if a DGSEM is employed and $\underline{\mathrm{K}} = \underline{\widetilde{\mathrm{Q}}}^\top \underline{\widetilde{\mathrm{M}}}\, \underline{\widetilde{\mathrm{Q}}}$ for the MSEM. In particular, for the latter approach, taking advantage of the structure of $\underline{\widetilde{\mathrm{Q}}}$ it is possible to decompose the linear system (21) as follows

$$\begin{bmatrix} \underline{\mathrm{M}}_{master} & 0 \\ 0 & \underline{Q}^\top \underline{\mathrm{M}}_{slave} \underline{Q} \end{bmatrix} \begin{bmatrix} \mathbf{U}_{master}^{\mathcal{I}} \\ \mathbf{U}_{master}^{\mathcal{S}} \end{bmatrix} = \begin{bmatrix} \mathbf{b}_{master}^{\mathcal{I}} \\ \underline{Q}^\top \mathbf{b}_{slave}^{\mathcal{S}} \end{bmatrix}. \tag{22}$$

Here the superscripts $\mathcal{I}$ and $\mathcal{S}$ denote if the unknowns belong to the interior or to the skeleton of the domain. Then at each time step we solve separately the two blocks of the linear systems (22).

In particular for the non diagonal block we perform the LU-factorization with pivoting (cf [22]). To ensure stability, the explicit time integration scheme must satisfy the usual Courant-Friedrichs-Levy (CFL) condition (see [22]) that imposes a restriction on the amplitude of Δt. This limitation is proportional to the minimal distance Δx between two consecutive spectral nodes $\mathbf{p}_i$ and $\mathbf{p}_j$, with $i \neq j$, of the numerical grid, see [8]. Since GLL points are clustered near the edges of spectral elements Ω_k, where the grid size is proportional to N_k^{-2}, the stability requirement on Δt may become too restrictive for very large approximation orders N_k. In such cases an implicit time scheme is recommended.

5 HOW IMPLEMENTING THE METHODS

In this section we describe the implementation of the MSEM and the DGSEM in the spectral element code GeoELSE [14] and we compare the two different algorithms from the efficiency view point. In this context the word ”efficiency” has the meaning of low memory storage and executing program velocity. In this sense, the assembling of the matrices in (13)-(18) is performed once, outside the time loop.

After setting the initial condition $\mathbf{u}_0$ and $\mathbf{u}_1$, we build the skeleton $\mathcal{S}$ as explained in (6)-(10) for the MSEM or the DGSEM respectively. In the mortar solution scheme, see Algorithm 1, a further step is required in order to identify the *master* and the *slave* decomposition of $\mathcal{S}$.

For both algorithms we notice that in general, all the matrix-vector multiplications involving $\underline{\mathrm{M}}, \underline{\mathrm{A}}, \underline{\mathrm{B}}$ and $\underline{Q}$ have to be intended subdomains per subdomains.

Algorithm 1: Mortar Solution Scheme

```
1. Set initial conditions $\mathbf{u}_0$ and $\mathbf{u}_1$.
2. Build the skeleton $\mathcal{S}$ for the domain $\Omega$.
3. Decompose $\mathcal{S}$ into the union of master and slave edges.
4. Construct the projection operator $\underline{Q}$ for the interface unknowns $\mathbf{U}_{slave}$.
5. Perform the LU-factorization of $\underline{Q}^\top \underline{\mathrm{M}}_{slave} \underline{Q}$.
6. For each discrete time $t_n$:
    • compute the internal forces $\mathbf{F}^{int}(t_n) = \underline{\mathrm{A}}\mathbf{U}(t_n)$ ;
    • assemble external forces $\mathbf{F}^{ext}(t_n)$;
    • solve for the master unknowns $\mathbf{U}_{master}$ the systems (22);
    • perform the projection on the slave unknowns;
    • if the final time $T$ is not reached set $t_n \leftarrow t_{n+1}$ and go to 6.
```

Algorithm 2 describes the DG solution scheme. Here we denote by $\mathbf{J}(t_n) = \underline{\mathrm{B}}\mathbf{U}(t_n)$ the vector containing the interface terms. Since the matrix $\underline{\mathrm{B}}$ defined in (14) has a highly sparsity structure, it is stored taking advantage of it.

Algorithm 2: DG Solution Scheme

```
1. Set initial conditions $\mathbf{u}_0$ and $\mathbf{u}_1$.
2. Build the skeleton $\mathcal{S}$ for the domain $\Omega$.
```

3. Decompose $\mathcal{S}$ into elementary components.
4. Construct the matrix $\underline{\mathrm{B}}$ for the interface unknowns.
5. For each discrete time t_n:
    - compute the internal forces $\mathbf{F}^{int}(t_n) = \underline{\mathrm{A}}\mathbf{U}(t_n)$;
    - assemble external forces $\mathbf{F}^{ext}(t_n)$;
    - compute the jumps at the interfaces $\mathbf{J}(t_n) = \underline{\mathrm{B}}\mathbf{U}(t_n)$;
    - solve the system $\underline{\mathbf{M}}\ddot{\mathbf{U}} = \mathbf{F}^{ext}(t_n) - \mathbf{F}^{int}(t_n) - \mathbf{J}(t_n)$;
    - if the final time T is not reached set $t_n \leftarrow t_{n+1}$ and go to 4.

According to [1, 9, 10], it seems that for elastic wave propagation problems the more effective method, in term of accuracy, grid dispersion and stability is the symmetric interior penalty Galerkin method (SIPG). However, if the symmetric approach is used we recall that the constant α in (12) must be sufficiently large to guarantee consistency of the method without affecting the conditioning of the stiffness matrix in (13).

6 A SOIL-STRUCTURE INTERACTION PROBLEM

In this section we aim at studying a soil-structure interaction problem, namely the seismic response of a railway viaduct (Acquasanta viaduct, Genova, Italy). We consider the viscoelastic model (1) in the computational domain $(x, z) \in \Omega = (0, 10^4 m) \times (0, f(x))$, where f describes the top profile of the bridge and of the surrounding valley, see Fig. 3. The size of the domain is chosen in order to avoid any possible interference with reflections of the waves of interest with the spurious ones eventually arising from the absorbing boundaries. The dynamic and mechanical properties of the structure and of the surrounding soil are summarized in Table 6. Depending on the material involved, we subdivided the computational grid into different regions, as shown in Fig. 3 (top panel). Note that the mesh was designed to propagate up to about 3 Hz.

We simulate a point source load of the form $\mathbf{f}(\mathbf{x}, t) = \mathbf{g}(\mathbf{x})h(t)$, where $\mathbf{f}$ is the external force introduced in (1). The function $\mathbf{g}$ describes the space distribution of the source and often is the body force $\mathbf{g}(\mathbf{x}) = \delta(\mathbf{x} - \mathbf{x}_S)\hat{\mathbf{w}}$, where δ represents the Dirac distribution, $\mathbf{x}_S$ is the source location and $\hat{\mathbf{w}}$ is the direction of the body force. The source time history is given by a Ricker-type time function with maximum frequency $\nu_{max} = 3Hz$, defined as

$$h(t) = h_0[1 - 2\beta(t - t_0)^2]\exp[-\beta(t - t_0)^2], \tag{23}$$

where h_0 is a scale factor, $t_0 = 2$ seconds is the time shift and $\beta = \pi^2\nu_{max}^2 = 9.8696\, s^{-1}$ is a parameter that determines the width of the wavelet (23).

In Fig. 3 we show the two different computational grids used for the numerical simulations. The conforming grid, Fig. 3 left, is used with SEM discretization to produce a reference solution for the problem. It provides, in fact, a sufficiently accurate discretization, as we verified that further mesh refinements generates quasi-identical seismograms. The non-conforming grid, shown in Fig. 3 right, is used for both DGSEM and MSEM simulations.

In our analysis we choose the polynomial approximation degree as described in Table 6. It is worth highlighting that the non-conforming approximations lead to a dramatic reduction of the size of the numerical model and, hence, of the computational costs (102.640 unknowns for

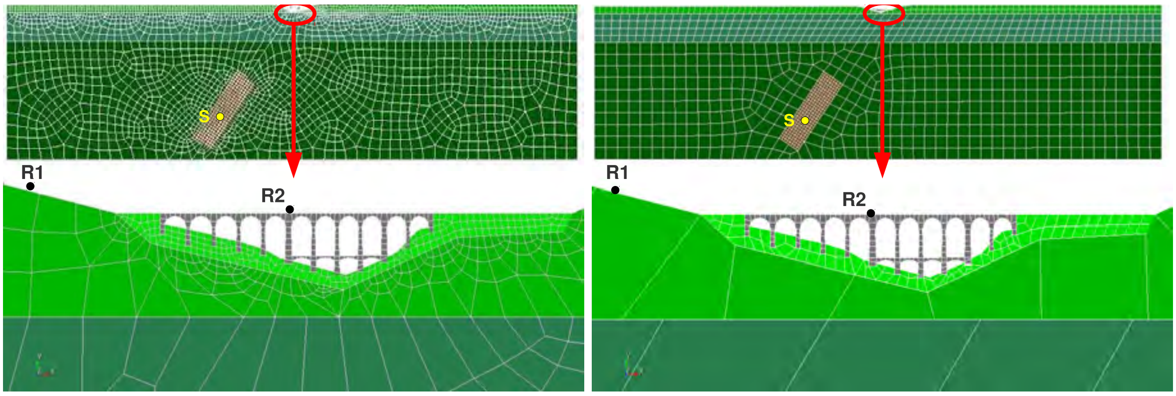

Figure 3: Conforming (left) and non conforming (right) grids. The full domain is displayed on the top and a zoom of the railway bridge is displayed on the bottom. The receivers R1 and R2, on the ground and on the bridge, respectively, are also highlighted.

Layer	$\rho\,[Kg/m^3]$	$c_P\,[m/s]$	$c_S\,[m/s]$	$\zeta[1/s]$	N [SEM]	N [MSEM/DGSEM]
1 (bridge)	1750	1218	716,7	0.6283	4	2
2 (stiff soil)	2400	1100	635	0.31416	4	2
3 (soft bedrock)	2400	1100	635	0.02513	4	4
4 (medium bedrock)	2600	1700	982	0.02284	4	4
5 (stiff bedrock)	2800	2300	1330	0.02094	4	4
6 (stiff bedrock)	2800	2300	1330	0.02094	4	4

Table 1: Dynamic and mechanical parameters and polynomial approximation degree N for each subregion of the domain decomposition (the factor ζ takes into account the visco-elastic linear soil behavior).

SEM vs. 41.322 for MSEM or DGSEM).
Such an advantage is expected to play a major role for 3D engineering applications. In Fig. 4 (resp Fig. 5 we analyse the synthetic seismograms recorded by the receiver R1 (resp. R2) on the top of the ground (resp. bridge) using the misfits criteria introduced in [19]. The results shown an excellent fit of the data for R1 and a good fit for R2. Probably, for the latter receiver, the results are affected by the grid dispersion phenomenon arising when low order polynomial approximation degrees are used [1, 9, 10].

7 CONCLUSIONS

In this paper we compared two different non-conforming high order numerical techniques, namely the Mortar Spectral Element Method and the Discontinuous Galerkin Spectral Element Method, for the approximation of the elastic wave equation in heterogeneous media. The key feature of these methods is to replace the exact continuity condition at the skeleton of the decomposition with a weak one, written in terms of the jumps of the displacements and the tractions across the interfaces. Relaxing the continuity condition is then possible, preserving the accuracy of high order methods, to deal with a geometrically non-conforming domain partitions where local meshes are independently generated from the neighbouring ones and associated with different spectral approximation degrees. Note that the subdomain partition is constructed according to the (available) material properties. Starting from a common weak formulation we describe both approaches in parallel in order to highlight their analogies and their differences. We gave a special attention to the implementation aspects of the two techniques in order to make the reader able to deal with an efficient numerical coding. Finally, we show that the MSEM and the DGSEM can be effectively used for complex seismic wave propagation problems, namely the soil-structure interaction between a valley and a railway bridge. The results, compared with those obtained with the SEM, show that both the non-conforming strategies are good in term of accuracy and computational effort. We refer to [1] for the full comparison of the methods in term of convergence, accuracy, grid dispersion and stability.

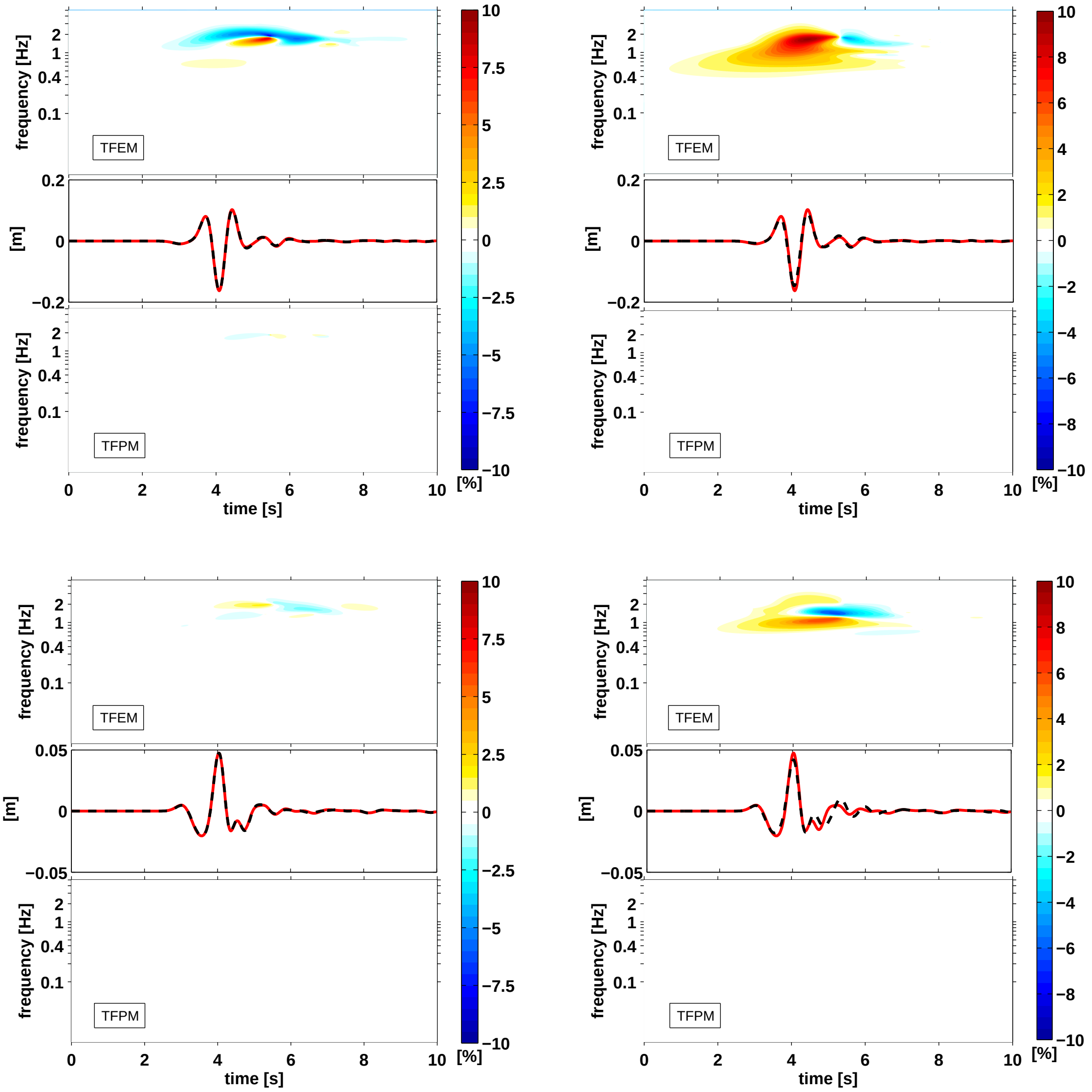

Figure 4: Analysis of the synthetic signals recorded by receiver R1, using the misfits criteria described in [19]. Comparison between the synthetic seismograms obtain with SEM and DGSEM (left) and SEM and MSEM (right). The graphics are subdivided as follows. Middle: displacement obtained using conforming (solid line) and non conforming (dashed line) approximations. TFEM: time frequency envelope misfits. TFPM: time frequency phase misfits. Top: horizontal component. Bottom: vertical component.

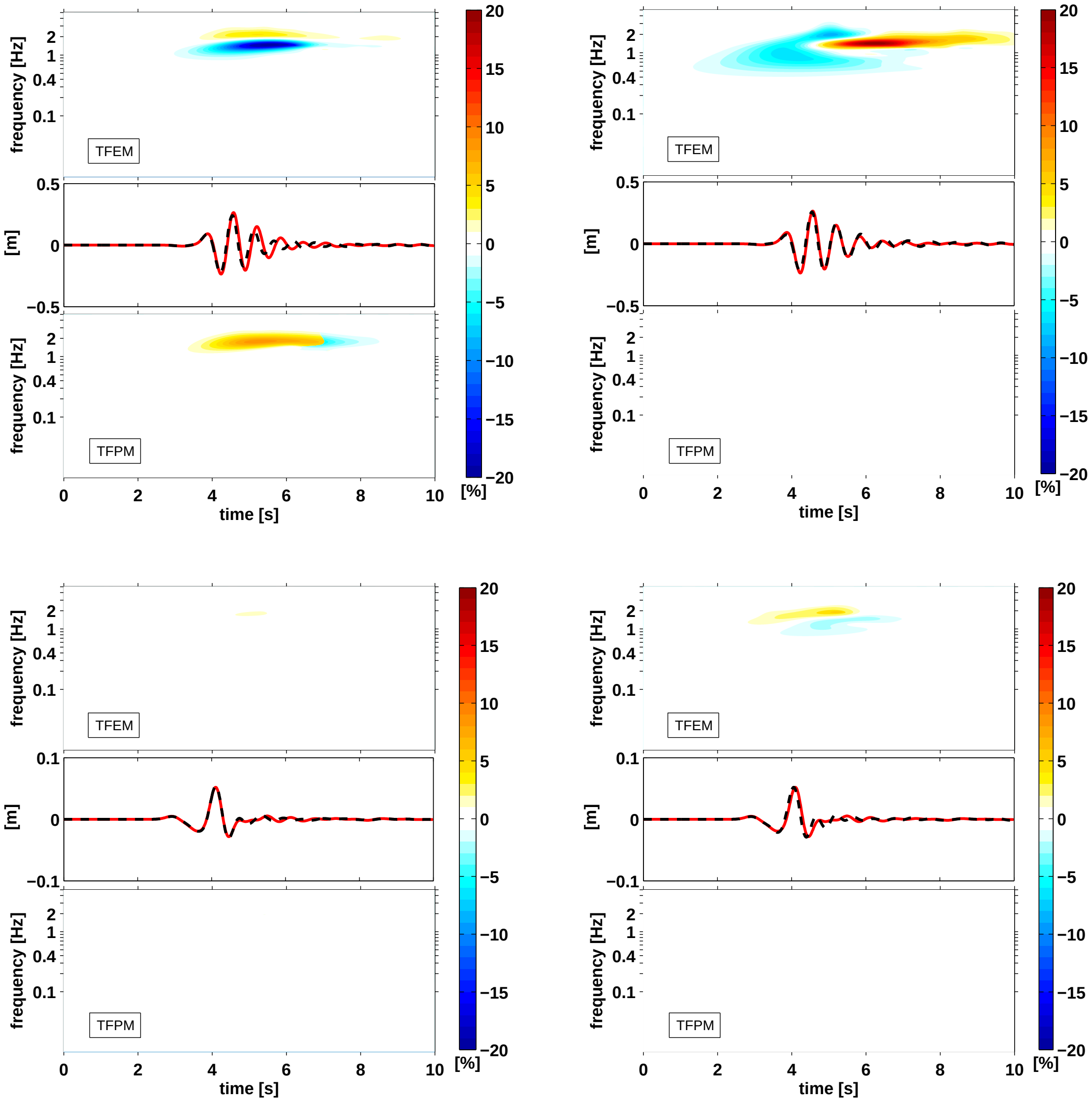

Figure 5: As in Fig. 4 but for receiver R2.

REFERENCES

[1] P. F. Antonietti, I. Mazzieri, A. Quarteroni, and F. Rapetti. In preparation.

[2] D. N. Arnold, F. Brezzi, B. Cockburn, and L. D. Marini. Unified analysis of discontinuous Galerkin methods for elliptic problems. *SIAM J. Numer. Anal.*, 39(5):1749–1779 (electronic), 2001/02.

[3] C. Bernardi, Y. Maday, and A. T. Patera. A new nonconforming approach to domain decomposition: the mortar element method. In *Nonlinear partial differential equations and their applications. Collège de France Seminar, Vol. XI (Paris, 1989–1991)*, volume 299 of *Pitman Res. Notes Math. Ser.*, pages 13–51. Longman Sci. Tech., Harlow, 1994.

[4] S. C. Brenner and L. R. Scott. *The mathematical theory of finite element methods*, volume 15 of *Texts in Applied Mathematics*. Springer, New York, third edition, 2008.

[5] E. Chaljub, Y. Capdeville, and J.P. Vilotte. Solving elastodynamics in a fluid-solid heterogeneous sphere: a parallel spectral element approximation on non-conforming grids. *J. Comput. Phys.*, 187(2): 457–491, 2003

[6] C. Canuto, M. Y. Hussaini, A. Quarteroni, and T. A. Zang. *Spectral methods*. Scientific Computation. Springer-Verlag, Berlin, 2006. Fundamentals in single domains.

[7] C. Canuto, M. Y. Hussaini, A. Quarteroni, and T. A. Zang. *Spectral methods*. Scientific Computation. Springer, Berlin, 2007. Evolution to complex geometries and applications to fluid dynamics.

[8] F. Casadei, E. Gabellini, G. Fotia, F. Maggio, and A. Quarteroni. A mortar spectral/finite element method for complex 2D and 3D elastodynamic problems. *Comput. Methods Appl. Mech. Engrg.*, 191(45):5119–5148, 2002.

[9] J. D. De Basabe and M. K. Sen. Stability of the high-order finite elements for acoustic or elastic wave propagation with high-order time stepping. *Geophys. J. Int.*, 181(1):577–590, 2010.

[10] J. D. De Basabe, M. K. Sen, and M. F. Wheeler. The interior penalty discontinuous galerkin method for elastic wave propagation: grid dispersion. *Geophys. J. Int.*, 175(1):83–93, 2008.

[11] M. O. Deville, P. F. Fisher, and E. H. Mund. *High-Order Methods for Incompressible Fluid Flow*. Cambridge Monographs on Applied and Computational Mathematics. Cambridge University Press, The Edinburgh Building, Cambridge CB2 2RU, UK, 2002.

[12] E. Faccioli, F. Maggio, R. Paolucci, and A. Quarteroni. 2-D and 3-D elastic wave propagation by a pseudo-spectral domain decomposition method. *J. of Seismol.*, 1: 237–251, 1997.

[13] M.J. Grote, A. Schneebeli, and D. Schotzau. Discontinuous Galerkin finite element method for the wave equation. *SIAM J. Numer. Anal.*, 44(6): 2408–2431, 2006.

[14] Numerical code GeoELSE: http://geoelse.stru.polimi.it

[15] J. de la Puente, M. Käser, M. Dumbser, and H. Igel. An arbitrary high-order discontinuous Galerkin method for elastic waves on unstructured meshes – IV. Anisotropy. *Geophys. J. Int.*, 169(3): 1210–1228, 2007.

[16] D. Komatitsch and J. Tromp. Introduction to the spectral-element method for 3-D seismic wave propagation. *Geophys. J. Int.*, 139: 806–822, 1999.

[17] G. Seriani, E. Priolo, J. Carcione, and E. Padovani. High-order spectral element method for elastic wave modeling. In *Expanded abstracts of the SEG, 62nd Int. Mtng of the SEG*, New Orleans.

[18] R. Kosloff, and D. Kosloff. Absorbing boundaries for wave propagation problems. *J. Comput. Phys.*, 63(2): 363–376, 1986.

[19] M. Kristeková, J. Kristek, and P. Moczo. Time-frequency misfit and goodness-of-fit criteria for quantitative comparison of time signals. *Geophys. J. Int.*, 178: 813–825, 2009.

[20] E.D. Mercerat, J.P. Vilotte, and F.J. Sánchez-Sesma. Triangular Spectral Element simulation of two-dimensional elastic wave propagation using unstructured triangular grids. *Geophys. J. Int*, 166: 679–698, 2006.

[21] Y. Maday, C. Mavriplis, and A. T. Patera. Nonconforming mortar element methods: application to spectral discretizations. In *Domain decomposition methods (Los Angeles, CA, 1988)*, pages 392–418. SIAM, Philadelphia, PA, 1989.

[22] A. Quarteroni and A. Valli. *Numerical approximation of partial differential equations*, volume 23 of *Springer Series in Computational Mathematics*. Springer-Verlag, Berlin, 1994.

[23] P.-A. Raviart and J.-M. Thomas. *Introduction à l'analyse numérique des équations aux dérivées partielles*. Collection Mathématiques Appliquées pour la Maîtrise. [Collection of Applied Mathematics for the Master's Degree]. Masson, Paris, 1983.

[24] B. Rivière. *Discontinuous Galerkin methods for solving elliptic and parabolic equations*, volume 35 of *Frontiers in Applied Mathematics*. Society for Industrial and Applied Mathematics (SIAM), Philadelphia, PA, 2008. Theory and implementation.

[25] B. Rivière, S. Shaw, M. F. Wheeler, and J. R. Whiteman. Discontinuous Galerkin finite element methods for linear elasticity and quasistatic linear viscoelasticity. *Numer. Math.*, 95(2):347–376, 2003.

[26] B. Rivière and M. F. Wheeler. Discontinuous finite element methods for acoustic and elastic wave problems. In *Current trends in scientific computing (Xi'an, 2002)*, volume 329 of *Contemp. Math.*, pages 271–282. Amer. Math. Soc., Providence, RI, 2003.

[27] R. Stacey. Improved transparent boundary formulations for the elastic-wave equation. *Bullettin of the Seismological Society of America*, 78(6):2089–2097, 1988.

COMPDYN 2011
ECCOMAS Thematic Conference on
Computational Methods in Structural Dynamics and Earthquake Engineering
M. Papadrakakis, N.D. Lagaros, M. Fragiadakis (eds.)
Corfu, Greece, 26-28 May 2011

SH SURFACE WAVES IN A HALF SPACE WITH RANDOM HETEROGENEITIES

Chaoliang Du[1,α], **Xianyue Su**[1,β]

[1]LTCS and Department of Mechanics and Aerospace Engineering,
College of Engineering, Peking University, Beijing, 100871, PR China
E-mail: [α]cldu@pku.edu.cn, [β]corresponding author: xyswsk@pku.edu.cn

Keywords: Random heterogeneities, Stochastic wave, half space, dispersion curve, frequency spectrum, SH surface wave.

Abstract. *Horizontally polarized shear waves (SH waves) do not exist in a homogeneous half space according to the traditional elastic wave theory. However, in this study, we proved both theoretically and numerically that there will be surface waves in a half space which has small, random density, but the mean value of the density is homogeneous. Historically, this type of half space is often treated as a homogeneous one with deterministic methods. In this investigation, a closed-form dispersion equation was derived stochastically, and the frequency spectrum, dispersion equation, phase/group velocity were plotted numerically to study how the random inhomogeneities will affect the dispersion properties of the half space with random density. This research may find its application in seismology, non-destructive test/evaluation, etc.*

1 Introduction

In this study, the dispersion and attenuation properties of waves propagating in a half space (see figure 1) with random heterogeneities are investigated.

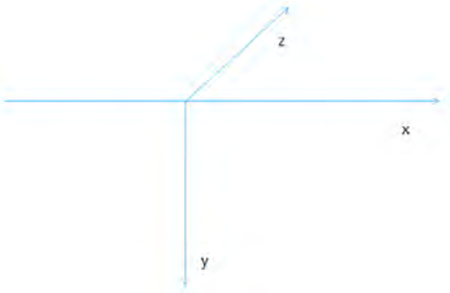

Figure 1: coordinate system of the half space

Shear horizontal surface waves (SHSW) are the most destructive waves in an earth quake and they can propagate through a very long distance without much loss of its energy. But, scientists have proved long ago that there is no SHSW in a homogeneous isotropic linearly elastic half-space [1]. However, in 1911, love predicted mathematically that SHSW could exist if the half-space is covered by a layer of a different material.

Since then, SHSW in a half space was mostly explained theoretically by Love's theory or its variant theories. But we know that the earth's surface is very complex. It is a mixture of many kinds of rocks, sands, soil, water, etc., and more complicatedly, these materials do not often distribute in deterministic ways, but distribute randomly. So do SHSW exist in such a complex, random half space?

Similar problems have been explored by some scientists. B. Collet et al. [3] studied SHSW in a Functionally Graded Material of which some material constants share the same depth-dependent function , and derived some of the depth-dependent functions which could be solved exactly. Using their solutions, they studied the influence of different inhomogeneity functions on the properties of SHSW. J. Achenbach et al. [2] studied SHSW in a purely elastic half-space whose shear modulus and mass density depend arbitrarily on the depth and gave a general solution that is quite exact for high frequencies. T.C.T. Ting [4] recently investigated SHSW in a half space of which C_{44} and ρ have the same function form, and C_{55}, C_{45} are correlated. Ting also got an asymptotic solution of general graded materials for large wave number k. Anti-plane shear waves for anisotropic graded materials have been considered for periodic half-spaces by A. Shuvalov et al. [5] and for a single plate by A. Shuvalov et al. [6]. Shear horizontal waves in functionally graded piezoelectric materials are also greatly studied by Tianjian Lu et al. [7, 8, 9].

But these researches haven't given an explicit solution of dispersion and attenuation of SHSW in a half space with random density in the depth direction by strict stochastic methods. In this study, we get the explicit dispersion equation by the first order smoothing approximation (FOSA) method. And we then analyze the dispersion and attenuation properties using the dispersion equation.

In this study we proved mathematically and numerically that SHSW could exist in a stochastically homogeneous half space. Some interesting properties of dispersion and attenuation found in this study could promote our understanding of waves propagating in a half space with random heterogeneities, e.g. earth's upper crust, alloys or composites. It will also help us to do the inverse problems, for example, to use seismic waves to detect the earth's crust structure, and to use ultrasonic waves to evaluate a structure with randomly distributed micro-cracks or heterogeneities.

2 Modeling and mathematical analysis

The fundamental dynamic equation system for statistically homogenous, isotropic, linearly elastic solid is

$$\tau_{ij,j} + \rho f_i = \rho \ddot{u}_i \tag{1}$$

$$\tau_{ij} = \lambda \epsilon_{kk} \delta_{ij} + 2\mu \epsilon_{ij} \tag{2}$$

$$\epsilon_{ij} = \frac{1}{2}(u_{i,j} + u_{j,i}) \tag{3}$$

To account for the random heterogeneities, we change the constants ρ, μ, λ in the equation system to functions of space, time and random variables.

Consider SH waves propagating in x direction in a half space (see Fig. 1).

It is known that for anti-plane waves that $u_x = u_y = 0$ and $\partial/\partial z = 0$. And if we assume that there is no body force, the equation system reduces to

$$\tau_{zj,j} = \rho \ddot{u}_z \tag{4}$$

$$\tau_{zj} = \mu u_{z,j} \tag{5}$$

in which, $j = x, y$. So the dynamic equation for SH waves in a random half space is

$$(\mu u_{z,j})_{,j} = \rho \ddot{u}_z \tag{6}$$

And the boundary condition is

$$\tau_{zy}|_{y=0} = 0 \quad i.e. \tag{7}$$

$$\mu u_{z,y}|_{y=0} = 0 \tag{8}$$

Assume here that there is randomness only in the y direction. Consider an harmonic wave motion of the form

$$u_z = f(y) exp[i(k_1 x - \omega t)] \tag{9}$$

in which, $f(y)$ is a random function. To study the surface shear wave, we assume the averaged $f(y)$ to be

$$< f(y) >= Ae^{-by} \tag{10}$$

, in which $b > 0$. Thus the mean wave motion $< u_z >$ could be written as

$$< u_z >= Ae^{-by} e^{i(k_1 x - \omega t)} \tag{11}$$

If there is no random heterogeneities in the solid, a solution of Eq. (6) would be of the form [1]

$$u_z = Ae^{-by} e^{i(kx - \omega t)} \tag{12}$$

Substituting Eq. (12) into Eq. (6), we find

$$\frac{\omega^2}{C_s^2} - k_1^2 + b^2 = 0 \tag{13}$$

For a free surface, the boundary condition at $y = 0$ is

$$\frac{\mathrm{d}u_z}{\mathrm{d}y} = 0 \tag{14}$$

The boundary condition Eq. (14) can be satisfied only if either $A = 0$ or $b = 0$. Therefore, there is no surface SH wave in an homogenous, isotropic, linearly elastic half space.

Firstly, we consider that random heterogeneities are only on the surface (as a practical example, the roughness of the earth surface could be viewed as a half space but with random density on the surface), then the boundary conditions at $y = 0$ can be written as

$$\begin{aligned} \mu\frac{\partial u_z}{\partial y} = 0 \quad &\Rightarrow \\ (\mu_0 + \epsilon\mu_1)\frac{\partial(< u_z > +\epsilon u_{z1})}{\partial y} &= 0 \end{aligned} \tag{15}$$

By averaging both sides of Eq. (15), when $y = 0$, we get

$$\mu_0\frac{\mathrm{d} < u_z >}{\mathrm{d}y} + \epsilon^2 < \mu_1\frac{\partial u_{z1}}{\partial y} >= 0 \tag{16}$$

The randomness of the surface takes effect through the term $\epsilon^2 < \mu_1\frac{\partial u_{z1}}{\partial y} >$. We assume here that

$$\epsilon^2 < \mu_1\frac{\partial u_{z1}}{\partial y} > |_{y=0} = \mu_0 A\beta e^{i(k_1 x-\omega t)} \tag{17}$$

Substituting Eqs. (17) and (11) into Eq. (16), we get

$$b = \beta \tag{18}$$

Considering Eq. (13), the dispersion equation for SH waves in a half space with random heterogeneities only on the surface is

$$\frac{\omega^2}{C_s^2} - k_1^2 + \beta^2 = 0 \tag{19}$$

Next, we will investigate the problem of the half space with random heterogeneities in the whole depth direction. Substituting Eq. (9) in Eq. (6) gives

$$(\rho\omega^2 - \mu k_1^2)f + (\mu f_{,y})_{,y} = 0 \tag{20}$$

Assuming that ρ, μ differ slightly from the mean value of them, ρ, μ can be written as

$$\begin{aligned} \rho(y) &= \rho_0 + \epsilon\rho_1(y) \\ \mu(y) &= \mu_0 + \epsilon\mu_1(y) \end{aligned} \tag{21}$$

where, ϵ is a small parameter, and

$$< \rho_1 >=< \mu_1 >= 0 \tag{22}$$

Substituting Eq. (21) in Eq. (20), we have

$$(\rho_0\omega^2 - \mu_0 k_1^2)f + \mu_0 f_{,yy} + \epsilon\left((\rho_1\omega^2 - \mu_1 k_1^2)f + (\mu_1 f_{,y})_{,y}\right) = 0 \tag{23}$$

According to FOSA theory (see Appendix A for a brief deduction of FOSA), the deterministic operator of Eq. (20) is

$$L_0(y) = \mu_0 \left(k_0^2 + \frac{\partial^2}{\partial y^2} \right) \tag{24}$$

in which,

$$k_0^2 = \frac{\omega^2}{C_s^2} - k_1^2 \tag{25}$$

and, C_s is the shear velocity of the homogeneous material without random heterogeneities,

$$C_s = \sqrt{\frac{\mu_0}{\rho_0}} \tag{26}$$

And the first order random operator of Eq. (20) is

$$L_1(y) = P(y) + \mu_1(y)_{,y} \frac{\partial}{\partial y} + \mu_1(y) \frac{\partial^2}{\partial y^2} \tag{27}$$

in which,

$$P(y) = \rho_1(y)\omega^2 - \mu_1(y)k_1^2 \tag{28}$$

Considering Eq. (22), we can see that $< L_1 >= 0$. For steady waves, G_0 can be taken as

$$G_0(y_1, y_2) = -\frac{1}{2k_0\mu_0} \sin(k_0|y_1 - y_2|) \tag{29}$$

According to the stochastic theory, the FOSA equation is

$$L_0 < f(y_1) > -\epsilon^2 \left\langle L_1(y_1) \int G_0(y_1, y_2) L_1(y_2) < f(y_2) > \mathrm{d}y_2 \right\rangle = 0 \tag{30}$$

To solve Eq. (30), let's calculate $L_1(y_1)G_0(y_1, y_2)$ first,

$$\begin{aligned} L_1(y_1)G_0(y_1, y_2) = &- \left(P(y_1) + \mu_1(y_1)_{,y_1} \frac{\partial}{\partial y_1} + \mu_1(y_1) \frac{\partial^2}{\partial y_1^2} \right) * \\ &\frac{1}{2k_0\mu_0} \sin(k_0|y_1 - y_2|) \end{aligned} \tag{31}$$

When $y_2 < y_1$

$$\begin{aligned} L_1(y_1)G_0(y_1, y_2) &= Q_1 \sin(k_0(y_1 - y_2)) + Q_2 \cos(k_0(y_1 - y_2)) \\ &= M(y_1, y_2) \end{aligned} \tag{32}$$

in which,

$$Q_1 = \left(\frac{\mu_1(y_1)k_0}{2\mu_0} - \frac{P(y_1)}{2k_0\mu_0} \right) \tag{33}$$

$$Q_2 = -\frac{\mu_1(y_1), y_1}{2\mu_0} \tag{34}$$

and, when $y_2 > y_1$

$$L_1(y_1)G_0(y_1, y_2) = -M(y_1, y_2) \tag{35}$$

Then, using Eq. (10), $L_1(y_2) < f(y_2) >$ can be expressed as

$$\begin{aligned} L_1(y_2) < f(y_2) >= & \left(P(y_2) + \mu_1(y_2)_{,y_2} \frac{\partial}{\partial y_2} + \mu_1(y_2) \frac{\partial^2}{\partial y_2^2} \right) A e^{-by_2} \\ = & A \left(P(y_2) - \mu_1(y_2)_{,y_2} b + \mu_1(y_2) b^2 \right) e^{-by_2} \\ = & N(y_2) \end{aligned} \tag{36}$$

If we assume that $\mu_1 = 0$, we could study the influence of the randomness of the density on the dispersion properties of the plate.

The random function $\rho_1(y_1;\gamma)$ is taken as Uhlenbeck-Ornstein process [10]. Although its correlation function is not mean-square differentiable, this process has been used in a number of investigations because it fits experimental data the best [11]. This process is a centered and stationary random function [10] and its correlation function is

$$\begin{aligned} R_{\rho_1(y_1;\gamma)\rho_1(y_2;\gamma)} = & \int \rho_1(y_1;\gamma)\rho_1(y_2;\gamma)\,\mathrm{d}\gamma \\ = & \zeta^2 e^{-\frac{|y_1-y_2|}{R_c}} = R(y_1 - y_2) \end{aligned} \tag{37}$$

In which, $\zeta = \sqrt{< {\rho_1}^2 >}$ and it is the standard deviation of the random density function; γ is a random variable. And R_c is the integral radius (the correlation length) of the correlation function, which physically means the scale of heterogeneity [12], and it should be positive.

From Eq. (10), we have

$$L_0 < f(y_1) >= \mu_0 \left(k_0^2 + \frac{\partial^2}{\partial y^2} \right) A e^{-by_1} = \mu_0 \left(k_0^2 + b^2 \right) A e^{-by_1} \tag{38}$$

Substituting Eqs. (31), (36) and (38) into Eq. (30), we get the dispersion equation,

$$k_0^2 + b^2 - \frac{\omega^4 \zeta^2 \epsilon^2 b}{2k_0 \mu_0^2} \left(\frac{1}{(b + \frac{1}{R_c})^2 + b^2} + \frac{1}{(b - \frac{1}{R_c})^2 + b^2} \right) = 0 \tag{39}$$

It could be seen from the dispersion equation Eq. (39) that if there is no random fluctuation, i.e. $\epsilon = 0$ or $\zeta = 0$ then $k_0^2 + b^2 = 0$ —the equation becomes the dispersion equation without random heterogeneities;

Considering the surface condition Eq. (18), the dispersion equation could be written as,

$$k_0^2 + \beta^2 - \frac{\omega^4 \zeta^2 \epsilon^2 \beta}{2k_0 \mu_0^2} \left(\frac{1}{(\beta + \frac{1}{R_c})^2 + \beta^2} + \frac{1}{(\beta - \frac{1}{R_c})^2 + \beta^2} \right) = 0 \tag{40}$$

To conveniently evaluate numerically the effect of random heterogeneities, the dispersion equation Eq. (40) is transformed into a dimensionless equation in the following.

Introduce new dimensionless variables as,

$$\begin{aligned} \overline{\omega} &= \frac{2h\omega}{\pi C_s} & \overline{k} &= \frac{2hk_1}{\pi} \\ \overline{R_c} &= \frac{\pi R_c}{2h} & \overline{\zeta} &= \frac{\epsilon\zeta}{\rho_0} \\ \overline{\mu_0} &= \frac{\mu_0}{\rho_0 C_s^2} = 1 & \overline{\beta} &= \frac{2h\beta}{\pi} \end{aligned} \tag{41}$$

From Eqs. (25) and (41), we get

$$k_0^2 = \frac{\omega^2}{C_s^2} - k_1^2 = \left(\frac{\pi}{2h}\right)^2 \left(\overline{\omega}^2 - \overline{k}^2\right) \tag{42}$$

so the dimensionless k_0 is defined as,

$$\overline{k_0}^2 = \overline{\omega}^2 - \overline{k}^2 \tag{43}$$

Using Eqs. (41), we could get the dimensionless dispersion equation from Eq. (19),

$$\overline{\omega}^2 - \overline{k_1}^2 + \overline{\beta}^2 = 0 \tag{44}$$

Using Eqs. (41) and (43), the dimensionless dispersion equation of Eq. (40) is,

$$\overline{k_0}^2 + \overline{\beta}^2 - \Lambda = 0 \tag{45}$$

Λ denote the random term,

$$\Lambda = \frac{\overline{\omega}^4 \overline{\zeta}^2 \overline{\beta}}{2\overline{k_0}} \left(\frac{1}{(\overline{\beta} + \frac{1}{R_c})^2 + \overline{\beta}^2} + \frac{1}{(\overline{\beta} - \frac{1}{R_c})^2 + \overline{\beta}^2} \right) \tag{46}$$

3 Numerical results and analysis

The SH surface waves propagating in a half space with random densities is further studied numerically. The dimensionless dispersion equation Eq. (45) is used to compute the curves. The numerical results are explained and discussed in the following.

3.1 Random heterogeneities only on the surface

The geomorphy of the earth's surface is always very complex. The reason for this complexness can come from both natural and man-made actions. In this study, we model the complex geomorphy by giving a surface parameter β. So in this section, we will study the dispersion properties for half spaces with random heterogeneities only on the surface. The dispersion curves are plotted according to Eq. (19).

From figure 2, it can be seen that the phase velocity will grow to 1 slowly, but for $\overline{k} < 2$, the phase velocity will be 0, i.e. the waves become standing waves in this circumstance.

From figure 3, it can be seen that, given a wave number, the phase velocity will decrease to 0 as the surface parameter $\overline{\beta}$ grows, i.e. the waves propagate more and more slowly when the surface becomes more and more rough, and all the waves will be blocked when $\overline{\beta}$ is large enough.

3.2 Frequency spectrum analysis

In the following, we will study the dispersion properties for half spaces with random heterogeneities not only on the surface but also in the whole half space. The related parameters are set to $\epsilon = 0.1, \overline{\zeta} = 2, \overline{R_c} = 0.4, \overline{\beta} = 2$ respectively.

From figures 4, 5 and 6, we can see that

1. As the wave number grows, the velocity will grow to a value—approximately 0.93 in this case. The reason that it can not reach to 1 could be that the waves are reflected and scattered by the random heterogeneities.

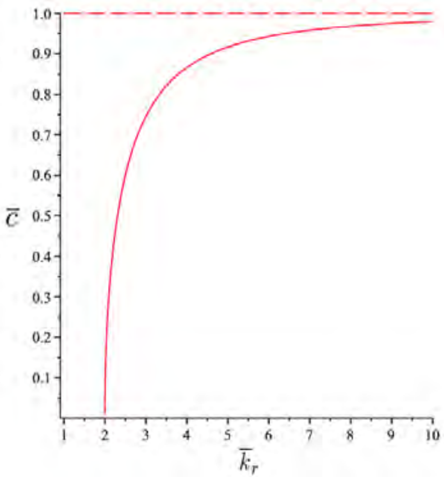

Figure 2: Normalized phase velocity—normalized wave number. $\overline{\beta} = 2$

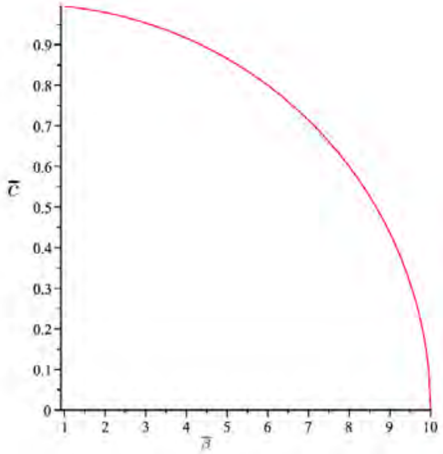

Figure 3: Normalized phase velocity—normalized surface parameter. $\overline{k} = 10$

2. The wave number does not start from 0, but 2. We can call this value the cut-off wave number. 2 is also the value of $\overline{\beta}$. From Eq. (45), we can see that the cut-off wave number equals the surface parameter.

Also, from figure 5, it can be seen that the phase velocity will decrease to 0 when the wave number decreases. This phenomenon agrees with the common knowledge that when the wave number decreases (the wave length increases), the effect of the random heterogeneities will be averaged out gradually, that is, the stochastically homogeneous half space will be more and more like a homogeneous half space, and we know that SHSW could not exist in a homogeneous half space, therefore, the phase velocity will decrease gradually to 0.

The imaginary wave number represents the attenuation rate. Therefore, we know from figure 7 that the bigger the circular frequency is, the faster the wave attenuates. This phenomenon should be caused by reflection and scattering. And from figure 6 we see that the wave length will decrease as the circular frequency grows. It is known that the smaller the wave length is, the easier the waves can be reflected or scattered by the random heterogeneities. Thus the wave attenuates more fast as the frequency grows.

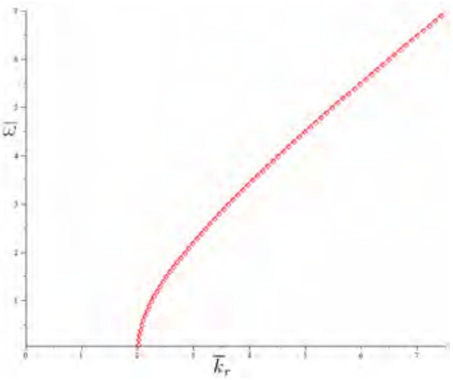

Figure 4: Normalized circular frequency—normalized wave number

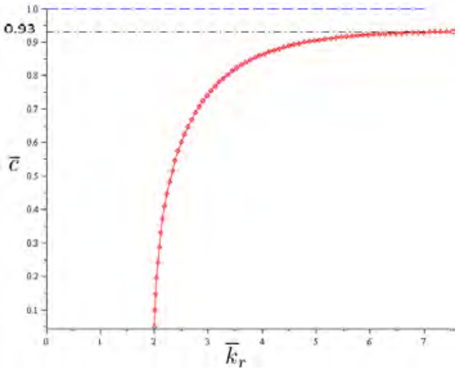

Figure 5: Normalized phase velocity—normalized wave number

4 Conclusion

In this study, we proved that SHSW could exist in a stochastically homogeneous half space. The dispersion properties of SHSW in an half space with random density in the depth direction or only near the surface have been investigated both theoretically and numerically. The first order smoothing approximation method is used to solve the random differential equation. The dimensionless dispersion equation is obtained. And the dispersion properties is further studied numerically. The phase velocity is found increasing to an asymptotic value when the wave number is bigger than a critical value—the cut-off wave number, below which the phase velocity is 0. The interesting properties of dispersion and attenuation found here will help us understanding properties of waves in a half space with random heterogeneities, e.g. the earth's crust. It will also help us to do the inverse problems, for example, to use seismic waves to detect the earth's upper crust structure, and to extract information more exactly from the acoustic testing results.

5 Acknowledgments

This study is supported by the National Natural Science Foundation of China under Grant no. 90916007.

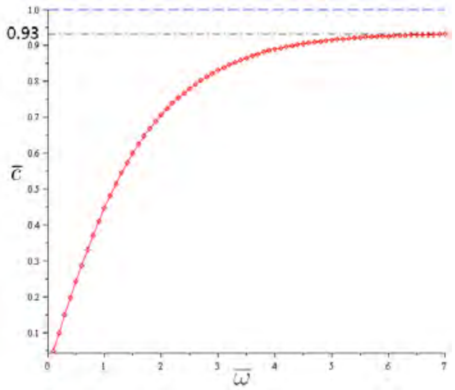

Figure 6: Normalized phase velocity—normalized circular frequency

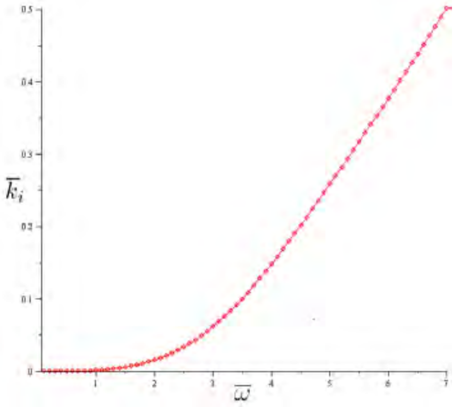

Figure 7: Normalized imaginary wave number—normalized circular frequency

REFERENCES

[1] J.D. Achenbach, *Wave propagation in elastic solids*. North-Holland Publishing Company, 1973.

[2] J. D. Achenbach, O. Balogun, Anti-plane surface waves on a half-space with depth-dependent properties *Wave Motion*, **47**, 59-65, 2010.

[3] B. Collet, M. Destrade, G.A. Maugin, Bleustein-Gulyaev waves in some functionally graded materials *European Journal of Mechanics-A/Solids*, **25**, 695-706, 2006.

[4] T.C.T. Ting, Existence of anti-plane shear surface waves in anisotropic elastic half-space with depth-dependent material properties *Wave Motion*, **47**, 350-357, 2010.

[5] A. L. Shuvalov, O. Poncelet, S. V. Golkin, Existence and spectral properties of shear horizontal surface acoustic waves in vertically periodic half-spaces *Proceedings of the Royal Society a-Mathematical Physical and Engineering Sciences*, **465**, 1489-1511, 2009.

[6] A. L. Shuvalov, O. Poncelet, A.P. Kiselev, Shear horizontal waves in transversely inhomogeneous plates *Wave Motion*, **45**, 605-615, 2008.

[7] Z.H. Qian, F. Jin, T. Lu, K. Kishimoto, Transverse surface waves in functionally graded piezoelectric materials with exponential variation *Smart Materials and Structures*, **17**, 2008.

[8] M. Eskandari, H.M. Shodja, Love waves propagation in functionally graded piezoelectric materials with quadratic variation *Journal of Sound and Vibration*, **313**, 195-204, 2008.

[9] X. Cao, F. Jin, Z.K. Wang, T.J. Lu, Bleustein-Gulyaev waves in a functionally graded piezoelectric material layered structure *Science in China Series G: Physics Mechanics and Astronomy*, **52**, 613-625, 2009.

[10] U. Frisch, *Wave propagation in random media*. Academic Press Inc., 1970.

[11] K.K. Chen, T.T. Soong, Covariance properties of waves propagating in a random medium *The Journal of the Acoustical Society of America*, **49**, 16-39, 1971.

[12] A.K. Belyaev, F. Ziegler, Uniaxial waves in randomly heterogeneous elastic media *Probabilistic Engineering Mechanics*, **13**, 27-38, 1998.

COMPDYN 2011
3^{rd} ECCOMAS Thematic Conference on
Computational Methods in Structural Dynamics and Earthquake Engineering
M. Papadrakakis, M. Fragiadakis, V. Plevris (eds.)
Corfu, Greece, 25-28 May 2011

DYNAMIC RUPTURE MODELLING ON UNSTRUCTURED MESHES USING A DISCONTINUOUS GALERKIN METHOD

Christian Pelties[1] **and Martin Käser**[1,2]

[1]Geophysics - Department of Earth and Environmental Sciences
Ludwig-Maximilians-Universität München
Theresienstrasse 41
80333 München - Germany
e-mail: pelties@geophysik.uni-muenchen.de

[2]Geo Risk - Münchener Rückversicherungs-Gesellschaft
Königinstrasse 107
80802 München - Germany
e-mail: mkaeser@munichre.com

Keywords: Dynamic Rupture, Source Physics, Earthquake Dynamics, Seismic Wave Propagation, Computational Seismology.

Abstract. *We will present recent developments concerning the extensions of the ADER-DG method to solve three dimensional dynamic rupture problems on unstructured tetrahedral meshes. A remarkable feature of this method is the combination of the DG scheme and a time integration method using Arbitrarily high-order DERivatives (ADER) to provide high accuracy in space and time with the discretization on unstructured meshes. In the resulting discrete velocity-stress formulation of the elastic wave equations variables are naturally discontinuous at the interfaces between elements. The so-called Riemann problem can then be solved to obtain well-defined values of the variables at the discontinuity itself. This is in particular valid for the fault at which a given friction law has to be evaluated. Hence, the fault's geometry is honored by the computational mesh. This way, complex fault planes can be modeled adequately with small elements while fast mesh coarsening is possible with increasing distance from the fault. A further advantage of the scheme is that it avoids spurious high-frequency contributions in the slip rate spectra and therefore does not require artificial Kelvin-Voigt damping or filtering of synthetic seismograms.*

1 INTRODUCTION

Strong ground motion models for seismic hazard assessment are based on the understanding of earthquake sources and seismic wave propagation. The state of the art is the combination of earthquake dynamics together with wave propagation in a single simulation. Synergy effects are for instance basin effects on wave propagation from finite-extent earthquake sources, high-frequency source directivity in random media and in highly heterogeneous fault zones, and rupture propagation of and seismic radiation from dynamic source models on non-planar faults utilizing slip-weakening and rate-and-state friction models.

A variety of numerical methods have been used in the past to implement the dynamics of earthquake rupture, such as finite differences (FD) [1, 2, 3], boundary integral (BI) [4, 5], finite volume (FV) [6], or spectral element (SE) [7], to name only a few commonly used methodologies. All these techniques have certain advantages and drawbacks. The most accurate and efficient method is the BI method, but it is in general not suited for handling heterogeneous media and nonlinear materials. FD schemes provide flexibility in terms of the choice in the friction law or in different material properties. However, it is difficult to apply them to non-planar faults, and computational resource issues could occur when strong material contrasts are included in the model, like sedimentary basins with extremely low wave velocities. FV methods are geometrically flexible but are only implemented as low-order accurate operators that are very dispersive. This fact affects the wave form in the nearfield and in turn the rupture front evolution. The SE method is both accurate and flexible and well suited for seismic wave propagation, but is restricted to hexahedral element types. The generation of hexahedral meshes for complicated geometries in three dimensions, such as faults with branching, and adapting smoothly the element sizes to different material properties, are still very challenging tasks and a major bottleneck.

J. de la Puente [8] presented recently an alternative for the dynamic rupture problem, based upon a discontinuous Galerkin (DG) method combined with an arbitrary high-order derivatives (ADER) time integration [9]. The DG method combines features from high-order FV and finite element methods, where a polynomial basis is used inside each element to approximate the physical variables of the elastic wave equations. This formulation enables the use of fully unstructured meshes, i.e. triangles (2D) or tetrahedrons (3D), to better fit the constraints of a given model and in particular the fault shape. Another feature of DG methods, inherited from FV methods, is the concept of numerical fluxes at element interfaces. Between any two elements the variables of the elastic wave equations are discontinuous. This is valid, as the exact solution of the elastic wave equations at a discontinuity exists, and is obtained by the solution of the well-known Riemann problem [10, 11]. At a fault the solution of the Riemann problem has to be modified to take the frictional boundary conditions into consideration. The numerical dispersion properties of a DG method and the high accuracy of the flux concept for high-order formulations are the reasons why the solution of the ADER-DG method is relatively smooth and free of spurious high-frequency oscillations compared to other methods. Therefore, it does not require artificial Kelvin-Voigt damping or filtering of the seismograms. This is an important feature, since the damping reduces the time step of a simulation and, thus, increases the computational runtime significantly.

The extension of the scheme to three dimensional problems on tetrahedral meshes was presented by *C. Pelties* [12]. In this paper, we present recent developments.

2 DYNAMICS OF FAULT RUPTURE

The kinematics of a sliding process can be described by the slip rate $\Delta v = v^{+} - v^{-}$, where $v^{+,-}$ are the velocities parallel to the fault, and the slip Δd, so that $\Delta v = \Delta \dot{d}$. We denote τ and σ the absolute shear and normal stresses on the fault, respectively.

Slip starts when the shear stress on the fault overcomes the fault strength. In the Coulomb friction model adopted here the strength is proportional to the normal stress. During active slip, the slip rate and the shear traction have opposite directions. These three phenomena are accounted for in the following expressions:

$$\begin{array}{rcl} & |\tau| \leq \mu_f \sigma \,, & \\ (|\tau| - \mu_f \sigma)\, \Delta v & = & 0\,, \\ \Delta v |\tau| + |\Delta v| \tau & = & 0\,, \end{array} \tag{1}$$

where μ_f is the friction coefficient. We adopt the linear slip weakening friction law [13]:

$$\mu_f = \begin{cases} \mu_s - \dfrac{\mu_s - \mu_d}{D_c} \Delta d & \text{if } \Delta d < D_c\,, \\ \mu_d & \text{if } \Delta d \geq D_c\,. \end{cases} \tag{2}$$

With increasing slip Δd the friction coefficient μ_f drops from the static value μ_s to the dynamic μ_d over the critical slip distance D_c, as shown in Fig. 1. Although we chose a simple friction law for demonstration reasons, the ADER-DG method is able to support any friction law.

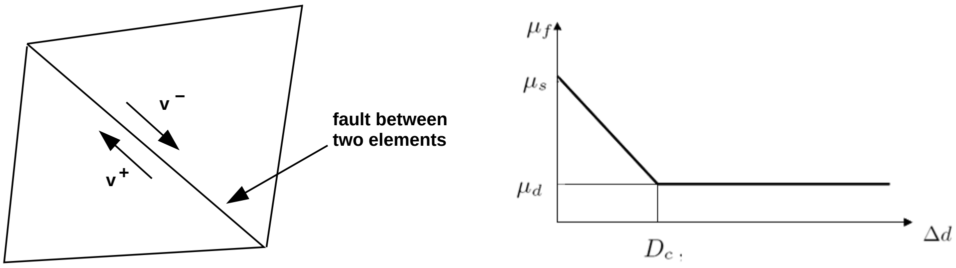

Figure 1: The left sketch gives an idea about how a fault increment is respected by the mesh. The different sides are indicated by plus and minus. On the right we plot μ_f vs. Δd for the linear slip weakening friction law.

3 FAULT DYNAMICS WITHIN THE DISCONTINUOUS GALERKIN FRAMEWORK

In contrast to other dynamic rupture implementations, like traction-at-split-node which is popular for FD methods, *J. de la Puente* [8] followed a new approach employing the concept of fluxes. In this section, we will explain the basic ideas behind this and show the extension to three-dimensional problems.

3.1 Elastic wave equations in velocity-stress formulation

Omitting external sources (e.g. moments or body forces), the three-dimensional elasticity for an isotropic medium are written in velocity-stress form as the linear hyperbolic system

$$\begin{array}{rcl}
\frac{\partial}{\partial t}\sigma_{xx} - (\lambda + 2\mu)\frac{\partial}{\partial x}u - \lambda\frac{\partial}{\partial y}v - \lambda\frac{\partial}{\partial z}w & = & 0\,, \\
\frac{\partial}{\partial t}\sigma_{yy} - \lambda\frac{\partial}{\partial x}u - (\lambda + 2\mu)\frac{\partial}{\partial y}v - \lambda\frac{\partial}{\partial z}w & = & 0\,, \\
\frac{\partial}{\partial t}\sigma_{zz} - \lambda\frac{\partial}{\partial x}u - \lambda\frac{\partial}{\partial y}v - (\lambda + 2\mu)\frac{\partial}{\partial z}w & = & 0\,, \\
\frac{\partial}{\partial t}\sigma_{xy} - \mu(\frac{\partial}{\partial x}v + \frac{\partial}{\partial y}u) & = & 0\,, \\
\frac{\partial}{\partial t}\sigma_{yz} - \mu(\frac{\partial}{\partial z}v + \frac{\partial}{\partial y}w) & = & 0\,, \\
\frac{\partial}{\partial t}\sigma_{xz} - \mu(\frac{\partial}{\partial z}u + \frac{\partial}{\partial x}w) & = & 0\,, \\
\rho\frac{\partial}{\partial t}u - \frac{\partial}{\partial x}\sigma_{xx} - \frac{\partial}{\partial y}\sigma_{xy} - \frac{\partial}{\partial z}\sigma_{xz} & = & 0\,, \\
\rho\frac{\partial}{\partial t}v - \frac{\partial}{\partial x}\sigma_{xy} - \frac{\partial}{\partial y}\sigma_{yy} - \frac{\partial}{\partial z}\sigma_{yz} & = & 0\,, \\
\rho\frac{\partial}{\partial t}w - \frac{\partial}{\partial x}\sigma_{xz} - \frac{\partial}{\partial y}\sigma_{yz} - \frac{\partial}{\partial z}\sigma_{zz} & = & 0\,,
\end{array} \tag{3}$$

where λ is the first Lamé constant and μ is the shear modulus. ρ indicates the density. The normal stress components are given by σ_{xx}, σ_{yy}, and σ_{zz}, and the shear stresses are σ_{xy}, σ_{yz}, and σ_{xz}. The components of the particle velocities in the x-, y-, and z-directions are denoted by u, v and w, respectively. These nine equations are sufficient to describe the complete wave field developing with time as described in detail in *Dumbser et al.* [14].

The physical variables $Q = (\sigma_{xx}, \sigma_{yy}, \sigma_{zz}, \sigma_{xy}, \sigma_{yz}, \sigma_{xz}, u, v, w)^T$ are approximated in the DG approach within a tetrahedral element $T^{(m)}$ by high-order polynomials

$$Q_p^m(x, y, z, t) = \hat{Q}_{pl}^m(t)\Phi_l(x, y, z)\,, \tag{4}$$

where Φ_l are orthogonal basis functions. Therefore, the physical variables are expressed within the DG scheme by a linear combination of these basis functions and time-dependent degrees of freedom $\hat{Q}_{pl}^m(t)$. The index p is associated with the unknowns in the vector Q and l indicates the l-th basis function.

3.2 Riemann problem

As mentioned above, between any two elements the variables of the elastic wave equations are in general discontinuous. This kind of problem, a discontinuous initial condition together with a partial differential equation, is called the Riemann problem. The solution of the Riemann problem at an element interface is the Godunov state and can be written in terms of explicit values as [8, 10, 11]

$$\begin{aligned}
\sigma_{xx}^G &= (\sigma_{xx}^+ + \sigma_{xx}^-)/2 + \tfrac{c_p\rho}{2}(u^- - u^+)\,, \\
\sigma_{yy}^G &= \sigma_{yy}^+ + (\sigma_{xx}^G - \sigma_{xx}^+)(1 - \tfrac{2c_s^2}{c_p^2})\,, \\
\sigma_{zz}^G &= \sigma_{zz}^+ + (\sigma_{xx}^G - \sigma_{xx}^+)(1 - \tfrac{2c_s^2}{c_p^2})\,, \\
\sigma_{xy}^G &= (\sigma_{xy}^+ + \sigma_{xy}^-)/2 + \tfrac{\mu}{2c_s}(v^- - v^+)\,, \\
\sigma_{yz}^G &= \sigma_{yz}^+\,, \\
\sigma_{xz}^G &= (\sigma_{xz}^+ + \sigma_{xz}^-)/2 + \tfrac{\mu}{2c_s}(w^- - w^+)\,, \\
u^G &= u^+ + \tfrac{1}{c_p\rho}(\sigma_{xx}^G - \sigma_{xx}^+)\,, \\
v^G &= (v^+ + v^-)/2 + \tfrac{c_s}{2\mu}(\sigma_{xy}^- - \sigma_{xy}^+)\,, \\
w^G &= (w^+ + w^-)/2 + \tfrac{c_s}{2\mu}(\sigma_{xz}^- - \sigma_{xz}^+)\,.
\end{aligned} \tag{5}$$

We assume that the fault is located exactly in the XZ-plane and ruptures purely in the Y-direction. Hence, we have to impose the shear stress σ_{xy} according to the friction law Eq. 2 and obtain the new traction value $\tilde{\sigma}_{xy}$, which in the case of rupture is different from σ_{xy}^G. In turn, this provides boundary conditions for the fault parallel-velocities. Multiplying the fourth equation of Eq. 5 by c_S/μ and subtracting the eighth equation leads to

$$\tilde{v}^+ = v^+ + \frac{c_s}{\mu}\left(\tilde{\sigma}_{xy} - \sigma_{xy}^+\right) \quad \text{and} \quad \tilde{v}^- = v^- - \frac{c_s}{\mu}\left(\tilde{\sigma}_{xy} - \sigma_{xy}^-\right)\,, \tag{6}$$

when we substitute σ_{xy}^G with its imposed value $\tilde{\sigma}_{xy}$. $\tilde{v}^-$ is obtained by summing the equations instead of subtracting them.

These expressions are crucial for the understanding of fault dynamics using fluxes, as they state that an imposed traction instantly and locally generates an imposed velocity parallel to the fault. By subtracting them, the slip rate is obtained:

$$\Delta\tilde{v} = \frac{2c_s}{\mu}\left(\tilde{\sigma}_{xy} - \sigma_{xy}^G\right)\,. \tag{7}$$

This way, the analytical form of the fault tractions is captured.

4 VERIFICATION

For most of the dynamic rupture problems there does not exist an analytical reference solution for comparison. Therefore, the Southern California Earthquake Center (SCEC) created the Dynamic Earthquake Rupture Code Verification Exercise, where different codes and methodologies are compared [15]. Here, we verify our method with the Test Problem Version 3 (TPV3).

4.1 The SCEC test case

The TPV3 uses the slip-weakening friction law in Eq. 2 and rupture on a stress-homogeneous vertical strike-slip fault set in a homogeneous full-space. The initial shear and normal stresses are assigned to be homogeneous for the 30 km long by 15 km deep fault as shown in Fig. 2, with the exception of the nucleation zone that has higher initial shear stresses. The parameters can be found in Table 1. Rupture is not allowed beyond the fault boundaries. This fault is embedded in a large computational domain of 72 km width in each spatial dimension to avoid spurious reflections from non-perfectly absorbing boundaries.

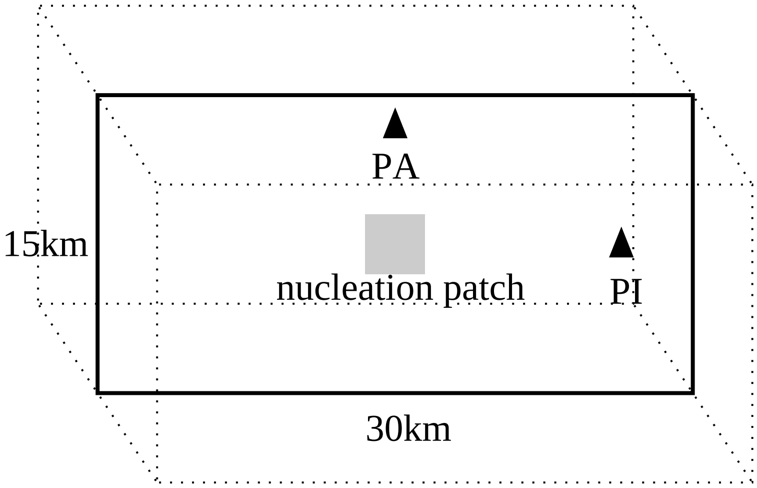

Figure 2: Sketch of the SCEC test case with the nucleation zone (grey shaded). The fault is surrounded by a box with an edge length of 72 km. The black triangles indicate the in-plane receiver (PI) and the anti-plane receiver (PA).

Parameter	Nucleation Zone	Outside Nucleation Zone
Initial shear traction (MPa)	81.6	70.0
Initial normal stress (MPa)	120.0	120.0
Static friction coefficient	0.677	0.677
Dynamic friction coefficient	0.525	0.525
Critical slip distance (m)	0.4	0.4

Table 1: Parameters describing the fault for the SCEC test case.

4.2 Results

In Fig. 3 we compare our solution (red line) with the solution of *Day et al.* [2] (black line) which was well validated during the SCEC exercises. *Day et al.* used a FD staggered-grid split node method of accuracy order 2 with a 50 m grid interval (DFM0.05). The solution produced with our DG scheme is of accuracy order 3 (ADER-DGO3) and uses a triangular mesh with an edge length of 300 m to discretize the fault, but we allow for tetrahedrons with 600 m edge length around the fault in a small box of 10 km thickness. This box is embedded in the domain of 72 km side length where we let the element edge length of the tetrahedrons quickly increase from 600 m to 3000 m to reduce the computational effort. No artificial reflexions possibly caused by the mesh coarsening are observed.

The ADER-DG solution is in excellent agreement with the solution produced by DFM0.05. This includes the arrival time of the stopping face and the stress relaxation. Furthermore, in

Fig. 4 we see that the spectral behavior of the ADER-DG slip rate solution shows the theoretically expected frequency decay [16]. No spurious high-frequency oscillations are produced. Therefore, no artificial Kelvin-Voigt damping has to be applied which would further reduce the time step size and increase the computational effort.

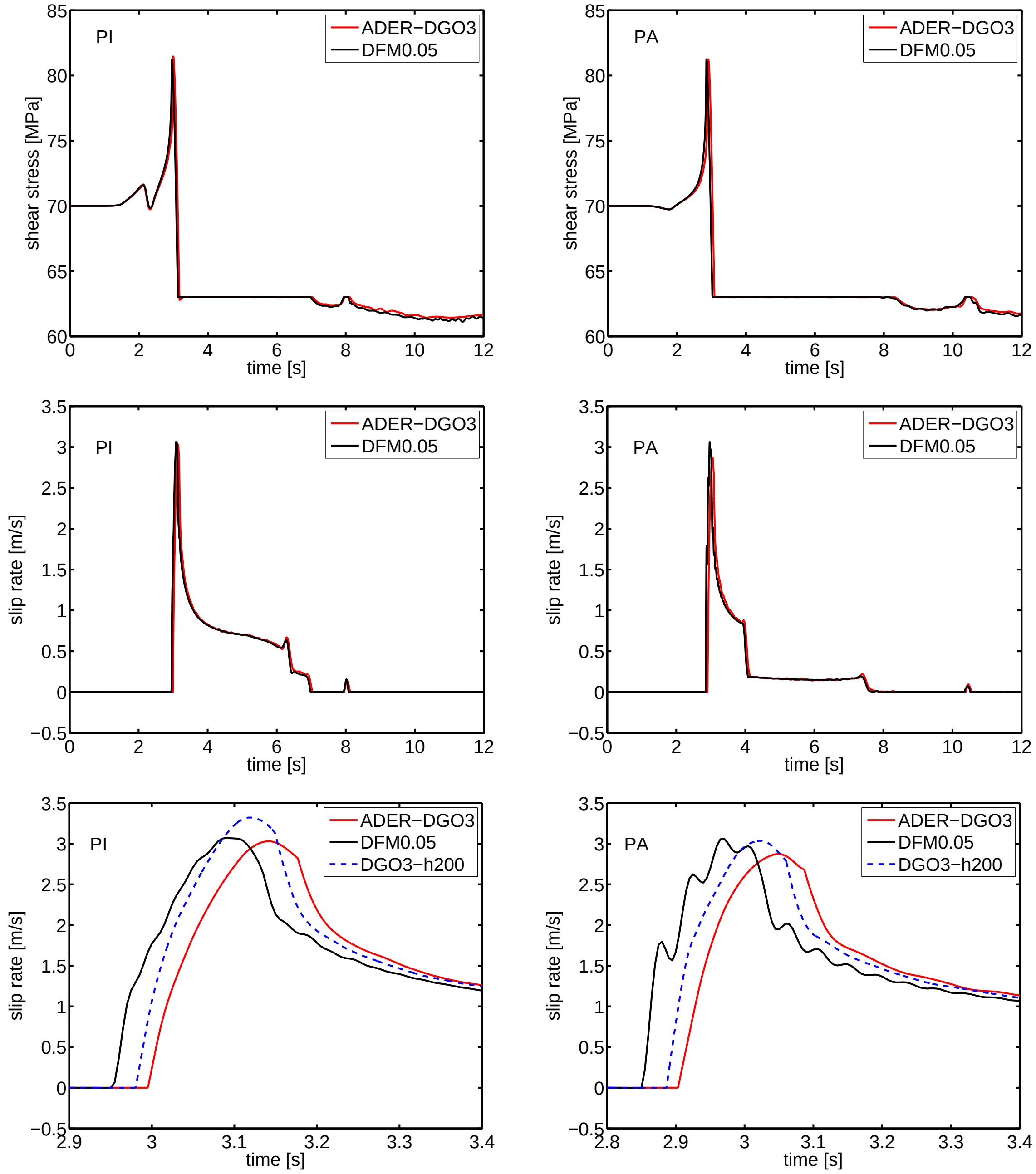

Figure 3: DFM0.05 (black line) indicates the FD staggered-grid split node method with 50 m grid interval of *Day et al.* [2]. This solution is in well agreement with the solution produced by our ADER-DGO3 scheme (red line) and a mesh spacing of 300 m at the fault. Shown is the shear stress and the slip rate. PI and PA denote the in-plane and the anti-plane receiver as shown in Fig. 2. In the bottom row we additionally plot the solution obtained with a 200 m fault discretization DGO3-h200 (blue dashed line) also with order 3 to demonstrate the trend of a convergence towards the DFM0.05 solution with increasing mesh refinement.

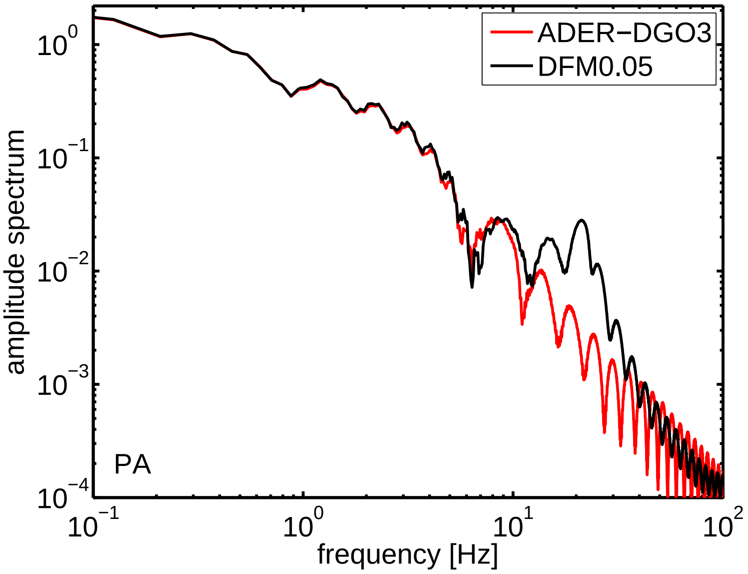

Figure 4: Spectrum of the slip rate obtained from receiver PA. The ADER-DGO3 solution does not show spurious high-frequency oscillations and, furthermore, it follows the frequency decay as theoretically expected.

5 CONCLUSIONS

We showed the successful adaption of 3D fault dynamics in the ADER-DG scheme under linear slip weakening friction. Accuracy was verified by employing the SCEC benchmark TPV3 for spontaneous rupture. Due to the properties of the Riemann problem in terms of the smoothness of the solution, the slip rate spectra remains free of spurious high-frequency oscillations. Furthermore, our implementation of the fault dynamics employing fluxes should allow for fault branching and surface rupture with little additional effort.

We conclude that the combination of meshing flexibility and high-order accuracy of the ADER-DG method will make it a very useful tool to study earthquake dynamics on complex fault systems. Future steps in the development could be the incorporation of bimaterial fault interfaces and more complex friction laws like rate- and state-dependent friction.

6 ACKNOWLEDGMENT

The authors thank the DFG (Deutsche Forschungsgemeinschaft), as the work was supported through the *Emmy Noether-Programm* (KA 2281/2-1). The data used for comparison in section 4.2 was provided by Luis A. Dalguer. Furthermore, we thank Luis A. Dalguer, Jean-Paul Ampuero, Cristóbal E. Castro and Josep de la Puente for very helpful and fruitful discussions. We also thank M. Mai for providing computational resources as many parallel tests and the SCEC benchmark have been computed on the BlueGene/P *Shaheen* of the King Abdullah University of Science and Technology, Saudi Arabia.

REFERENCES

[1] D.J. Andrews, A numerical study of tectonic stress release by underground explosions, *Bull. Seism. Soc. Am.*, 63, 1375-1391, 1973.

[2] S.M. Day, L.A. Dalguer, N. Lapusta and Y. Liu, Comparison of finite difference and boundary integral solutions to three-dimensional spontaneous rupture, *J. Geophys. Res*, 110, 2005, B12307.

[3] P. Moczo, J. Kristek, M. Galis, P. Pazak and M. Balazovjech, The Finite-difference and Finite-element modeling of seismic wave propagation and earthquake motion, *Acta physica slovaca*, 57(2), 177-406, 2007.

[4] S. Das, A numerical method for determination of source time functions for general three-dimensional rupture propagation, *Geophys. J. Roy. Astr. Soc.*, 62, 591-604, 1980.

[5] N. Lapusta, J.R. Rice, Y. Ben-Zion and G. Zheng, Elastodynamic analysis for slow tectonic loading with spontaneous rupture episodes on faults with rate- and state-dependent friction, *J. Geophys. Res*, 105, 23765-23789, 2000.

[6] M. Benjemaa, N. Glinsky-Olivier, V.M. Cruz-Atienza, J. Virieux and S. Piperno, Dynamic non-planar crack rupture by a finite volume method, *Geophys. J. Int.*, 171, 271-285, 2007.

[7] J.-P. Ampuero, Etude physique et numérique de la nucléation des séismes, Ph.D. thesis, Université Paris 7, Denis Diderot, 2002.

[8] J. de la Puente, J.-P. Ampuero and M. Käser, Dynamic rupture modeling on unstructured meshes using a discontinuous Galerkin method, *J. Geophys. Res*, 114, B10302, 2009.

[9] V.A. Titarev and E.F. Toro, ADER: Arbitrary high order Godunov approach, *J. Sci. Comput.*, 17, 609-618, 2002.

[10] E.F. Toro, *Riemann Solvers and Numerical Methods for Fluid Dynamics*, Springer, Berlin, 1999.

[11] R.L. LeVeque, *Finite Volume Methods for Hyperbolic Problems*, Cambridge University Press, Cambridge, U.K., 2002.

[12] Pelties, C., J. de la Puente and M. Käser, *Dynamic Rupture Modeling in Three Dimensions on Unstructured Meshes Using a Discontinuous Galerkin Method*, Abstract S21C-2068, AGU 2010 Fall Meeting, San Francisco.

[13] Y. Ida, Cohesive force across the tip of a longitudinal-shear crack and Griffith's specific surface energy, *J. Geophys. Res*, 77, 3796-3805, 1972.

[14] M. Dumbser and M. Käser, An Arbitrary High Order Discontinuous Galerkin Method for Elastic Waves on Unstructured Meshes II: The Three-Dimensional Case, *Geophys. J. Int.*, 167(1), 319-336, 2006.

[15] R.A. Harris, R. Archuleta, B. Aagaard, J.-P. Ampuero, D.J. Andrews, L. Dalguer, S. Day, E. Dunham, G. Ely, Y. Kase, N. Lapusta, Y. Liu, S. Ma, D. Oglesby, K. Olsen and A. Pitarka, *The source physics of large earthquakes: Validating spontaneous rupture methods*, Eos Trans. AGU, 85, 47, Fall Meet. Suppl., Abstract S12A-05, 2004.

[16] Y. Ida, The maximum acceleration of seismic ground motion, *Bull. Seism. Soc. Am.*, 63, 959-968, 1973.

COMPDYN 2011
3^{rd} ECCOMAS Thematic Conference on
Computational Methods in Structural Dynamics and Earthquake Engineering
M. Papadrakakis, M. Fragiadakis, V. Plevris (eds.)
Corfu, Greece, 25–28 May 2011

STABILIZED HYBRID AND MIXED FINITE ELEMENT METHODS FOR HELMHOLTZ PROBLEMS

Abimael F. D. Loula

Laboratório Nacional de Computação Científica
Av. Getúlio Vargas 333, Petrópolis, RJ - Brasil
e-mail: aloc@lncc.br

Keywords: Hybrid methods, Stabilization, Mixed methods, Numerical pollution, Hybridization.

Abstract. *Stabilized hybrid and mixed finite element methods are proposed for solving Helmholtz problems in heterogeneous media. The methods are based on a hybridized dual mixed formulation in velocity (flux) and pressure fields stabilized by adding least squares residual of the governed equations. The local problems, in the velocity and pressure fields, are solved at element level to eliminate these variables in favor of the Lagrange multipliers, identified as the trace of the pressure on the element edges of the finite element mesh. A global system is assembled involving only the degrees of freedom associated with the Lagrange multipliers as usually in Hybrid methods. Polynomial bases are adopted to approximate the global problem in the Lagrange multipliers. Polynomial or special bases, such as plane-wave bases, can be also used to approximate the local problems at the element level. Numerical results are reported to illustrate the potential of the proposed formulation to efficiently solve Helmholtz problems in homogeneous or heterogeneous media at medium and high frequency regimes.*

1 INTRODUCTION

The linear model for propagation of acoustic waves in an ideal compressible fluid is governed by the wave equation

$$-\Delta\varphi + \frac{1}{c^2}\frac{\partial^2\varphi}{\partial t^2} = 0, \tag{1}$$

where $\varphi(\mathbf{x}, t)$ represents small oscillations of the pressure and c is the velocity of the sound in the acoustic medium. Considering harmonic solutions in time with circular frequency ω, the pressure field is written as $\varphi(\mathbf{x}, t) = p(\mathbf{x})e^{-i\omega t}$, and the pressure amplitude p satisfies the Helmholtz equation

$$-\Delta p - k^2 p = 0, \tag{2}$$

where the parameter $k = \omega/c$, known as *wave number*, characterizes the oscillatory behavior of the solution φ.

Helmholtz problem has deserved especial attention in many physical applications associated with refraction and scattering of electromagnetic, elastic or sound waves, for example. From the numerical point of view k is a key parameter. It is well known that standard Galerkin finite element approximations deteriorate as k increases. For large values of k the solution p is highly oscillatory and, due to numerical dispersion and phase error, constructing finite element approximations for Helmholtz equation is a great challenge as reported in vast literature. See, for example, [4] and references therein. Several finite element methods have been developed to minimize the phase error. Stabilized finite element methods such as Galerkin Least-Squares(GLS) have been proposed with relative success [5]. An uniform nine node stencils with minimal pollution error, referred as QSFEM, is constructed in [6]. Variationally consistent finite element methods with stability properties equivalent to the QSFEM on uniform meshes have been proposed in [7] using a generalized GLS formulation, and in [8] using discontinuous Galerkin finite element methods. A Quasi Optimal Petrov-Galerkin (QOPG) finite element formulation for Helmholtz problem in two dimensions is introduced in [9] using polynomial weighting functions with the same support of the corresponding global test functions. The QOPG finite element formulation is naturally applied to non uniform and unstructured meshes. Generalized finite element methods using plane wave bases have been successfully developed in [3, 10, 11] to solve the Helmholtz equation with great accuracy when applied to problem with regular solutions.

Here, we consider stabilized hybrid and mixed finite element methods for solving Helmholtz problems in heterogeneous media with discontinuous wave number k. The proposed formulations is based on a hybridized dual mixed formulation in velocity (flux) and pressure fields stabilized by adding least squares residual of the governed equations. To simplify our presentation we consider as our model problem the Helmholtz equation

$$-\Delta p - k^2 p = f \text{ in } \Omega, \tag{3}$$

in a bounded domain $\Omega \subset R^2$ with a Lipschitz continuous and piecewise smooth boundary Γ subjected to Dirichlet boundary condition

$$p = g \ \text{ on } \ \Gamma = \partial\Omega. \tag{4}$$

The reminder of the paper is organized as follows. In Section 2 our model problem is presented in a mixed form and a stabilized dual mixed formulation in continuous spaces is presented. In Section 3 we review the classical dual hybrid mixed formulation. The stabilized dual hybrid mixed formulation is proposed in Section 4. The finite element approximation of the proposed dual hybrid mixed formulation is presented in Section 5. Numerical results are shown in Section 6 and some concluding remarks are presented in Section 7.

2 MIXED FORMULATION

Introducing the vector field

$$\mathbf{u} = -\nabla p$$

we can rewrite the Helmholtz equation (3) in the mixed form

$$\mathbf{u} + \nabla p = 0 \quad \text{in} \ \Omega$$

$$\mathrm{div}\mathbf{u} - k^2 p = f \quad \text{in} \ \Omega \,,$$

which will be used as the starting point to construct stabilized mixed and hybrid finite element approximations.

2.1 Dual mixed formulation

Defining the space $V = L^2(\Omega)$ of scalar functions with the corresponding inner product

$$(p, q) = \int_\Omega pq d\Omega \ \ \forall p, q \ \in V \tag{5}$$

and associated norm

$$||p||^2 = (p, p) \ \ \forall p \ \in V, \tag{6}$$

and the space $W = H(\mathrm{div})$ of vector functions:

$$H(\mathrm{div}) = \{\mathbf{v} \in [L^2(\Omega)]^2, \ \mathrm{div}\mathbf{v} \in L^2(\Omega)\} \tag{7}$$

with inner product

$$(\mathbf{u}, \mathbf{v})_{H(\mathrm{div})} = (\mathbf{u}, \mathbf{v}) + (\mathrm{div}\mathbf{u}, \mathrm{div}\mathbf{v}) \ \ \forall \mathbf{u}, \mathbf{v} \ \in W \tag{8}$$

and associated norm

$$||\mathbf{u}||^2_{H(\mathrm{div})} = (\mathbf{u}, \mathbf{u}) + (\mathrm{div}\mathbf{u}, \mathrm{div}\mathbf{u}) \ \ \forall \mathbf{u} \ \in W \tag{9}$$

we present the dual mixed formulation of our model problem as

Find $[\mathbf{u}, p] \in W \times V$ such that

$$(\mathbf{u}, \mathbf{v}) - (p, \mathrm{div}\mathbf{v}) - (\mathrm{div}\mathbf{u}, q) - k^2(p, q) - (f, q) + \int_{\partial\Omega} g\mathbf{v} \cdot \mathbf{n} ds = 0 \ \ \forall \, [\mathbf{v}, q] \in W \times V \tag{10}$$

Dual mixed problems have been usually approximated using Raviart-Thomas (RT) or Brezzi-Douglas-Marini (BDM) spaces to get accurate approximations for the gradient of the pressure field. Stability of these mixed finite element methods depends on the well known inf-sup condition which preclude many desirable combinations of velocity and pressure interpolations. Stabilized mixed formulations have been successfully introduced to overcome these limitations. See references [12, 13, 14, 16] on stabilized mixed formulations for Darcy flow.

2.2 Stabilized dual mixed formulation

In [14] an unconditionally stable mixed formulation is proposed for Darcy flow with optimal rates of convergence in $H^1(\Omega)$ and $L^2(\Omega)$ norms for same order C^0 velocity and pressure approximations. Applied to the Helmholtz problem this formulation leads to the following weak form:

Find $[\mathbf{u}, p] \in W \cap [H^1(\Omega)]^2 \times V \cap H^1(\Omega)$ such that, for all $[\mathbf{v}, q] \in W \times V$,

$$(\mathbf{u}, \mathbf{v}) - (p, \mathrm{div}\mathbf{v}) - (\mathrm{div}\mathbf{u}, q) - k^2(p, q) - (f, q) + \int_{\partial\Omega} g\mathbf{v} \cdot \mathbf{n} ds + \tag{11}$$

$$\frac{\delta_1}{k^2}(\mathrm{div}\mathbf{u} - k^2 p - f, \mathrm{div}\mathbf{v} - k^2 q) + \delta_2(\mathbf{u} + \nabla p, \mathbf{v} + \nabla q) + \frac{\delta_3}{k^2}(\mathrm{rot}\mathbf{u}, \mathrm{rot}\mathbf{v}) = 0\,. \tag{12}$$

Of course, we should not expect unconditional stability and optimal rates of convergence for same order C^0 finite element approximations of the above dual mixed formulation of the Helmholtz problem, especially for heterogeneous media. Its stability will certainly be dependent on the choice of the stabilization parameters $\delta_i,\ i = 1, 2, 3$. An other limitation of this formulation is the required C^0 approximations for both velocity and pressure which is not applicable to heterogeneous media with discontinuous material properties. In the next section we introduce hybrid formulations more appropriate to construct finite element approximations of our model problem on heterogeneous media.

3 HYBRIDIZATION

Let

$$\mathcal{T}_h = \{\mathcal{K}\} := \text{union of all elements } \mathcal{K}$$

be a regular finite element mesh on the two dimension domain Ω. To introduce the hybrid formulation we first consider equation $\mathbf{u} + \nabla p = 0$, in the local weak form

$$(\mathbf{u} + \nabla p, \mathbf{v})_{\mathcal{K}} = \int_{\mathcal{K}} \mathbf{u} \cdot \mathbf{v} d\Omega - \int_{\mathcal{K}} p \mathrm{div}\mathbf{v} d\Omega + \int_{\partial\mathcal{K}} p\mathbf{v} \cdot \mathbf{n} ds = 0,$$

defined on each element $\mathcal{K}$ using integration by parts. Considering the spaces

$$Q_{\mathcal{K}} = \{q \in L^2(\mathcal{K})\ \forall \mathcal{K} \in \mathcal{T}_h\},$$

$$U_{\mathcal{K}} = \{\mathbf{v} \in L^2(\mathcal{K}) \times L^2(\mathcal{K}), \mathrm{div}\mathbf{v} \in L^2(\mathcal{K})\ \forall \mathcal{K} \in \mathcal{T}_h\},$$

of local functions defined on each element $\mathcal{K}$ and defining the forms

$$a_{\mathcal{K}}\left([\mathbf{u}, p], [\mathbf{v}, q]\right) = (\mathbf{u}, \mathbf{v})_{\mathcal{K}} - (p, \mathrm{div}\mathbf{v})_{\mathcal{K}} - (\mathrm{div}\mathbf{u}, q)_{\mathcal{K}} + k^2(p, q)_{\mathcal{K}},$$

$$f_{\mathcal{K}}([\mathbf{v}_h, q_h]) = -(f, q)_{\mathcal{K}} - c_{\mathcal{K}}(\bar{p}, \mathbf{v}),$$

$$c_{\mathcal{K}}(\bar{p}, \mathbf{v}) = \int_{\partial\mathcal{K}} \bar{p}\mathbf{v} \cdot \mathbf{n} ds,$$

for given $p = \bar{p}$ on $\partial\mathcal{K}$ we can solve the local problems:

For each $\mathcal{K} \in \mathcal{T}_h$, find $[\mathbf{u}, p] \in U_{\mathcal{K}} \times Q_{\mathcal{K}}$, such that

$$a_{\mathcal{K}}\left([\mathbf{u}, p], [\mathbf{v}, q]\right) = f_{\mathcal{K}}([\mathbf{v}, q])\ \forall\, [\mathbf{v}, q] \in U_{\mathcal{K}} \times Q_{\mathcal{K}}.$$

Local Raviart-Thomas or BDM finite element approximations can be used to solve these local problems on each element $\mathcal{K}$. Following the classical hybrid formulation, an approximation for the pressure trace $p = \bar{p}$ on $\partial\mathcal{K}$ can be obtained by solving a global problem associated with the dual hybrid mixed formulation, as presented in the next section.

3.1 Dual Hybrid mixed formulation

To present the hybrid formulation some additional notations and definitions are need. Let

$$\mathcal{E}_h = \{e : e \text{ is an edge of } \mathcal{K} \text{ for all } \mathcal{K} \in \mathcal{T}_h\} \tag{13}$$

denote the set of all edges of all elements $\mathcal{K}$ of the mesh $\mathcal{T}_h$,

$$\mathcal{E}_h^0 = \{e \in \mathcal{E}_h \; e \text{ is an interior edge}\} \tag{14}$$

the set of interior edges, and

$$\mathcal{E}_h^\partial = \mathcal{E}_h \cap \partial\Omega, \tag{15}$$

the set of edges of $\mathcal{E}_h$ on the boundary of Ω.

Following the commonly adopted notation on DG (Discontinuous Galerkin) formulations, we consider the unit normal vectors $\mathbf{n}^1$ abd $\mathbf{n}^2$ on e pointing exterior to $\mathcal{K}^1$ and $\mathcal{K}^2$, respectively. For a scalar function φ, piecewise smooth on $\mathcal{T}_h$, with $\varphi = \varphi|_\mathcal{K}$ we define on each interior edge e

$$\{\varphi\} = \frac{1}{2}(\varphi^1 + \varphi^2), \quad [\![\varphi]\!] = \varphi^1\mathbf{n}^1 + \varphi^2\mathbf{n}^2 \quad \text{on } \; e \in \mathcal{E}^0 \tag{16}$$

and for a vector function $\mathbf{v}$

$$\{\mathbf{v}\} = \frac{1}{2}(\mathbf{v}^1 + \mathbf{v}^2), \quad [\![\mathbf{v}]\!] = \mathbf{v}^1 \cdot \mathbf{n}^1 + \mathbf{v}^2 \cdot \mathbf{n}^2 \quad \text{on } \; e \in \mathcal{E}^0. \tag{17}$$

Defining the function spaces $M = \{\mu \in L^2(e) \; \forall e \in \mathcal{E}_h^0\}$, $U = \prod_\mathcal{K} U_\mathcal{K}$, $Q = \prod_\mathcal{K} Q_\mathcal{K}$ and the bilinear and linear forms:

$$a\left([\mathbf{u}, p], [\mathbf{v}, q]\right) = \sum_\mathcal{K} a_\mathcal{K}\left([\mathbf{u}, p], [\mathbf{v}, q]\right) \;\; \forall \; [\mathbf{u}, p], [\mathbf{v}, q] \; \in U \times Q$$

$$c(\mu, \mathbf{v}) = \sum_\mathcal{K} c_\mathcal{K}(\mu, \mathbf{v}) = \int_{\mathcal{E}^0} \mu [\![\mathbf{v}]\!] ds \;\; \forall \; \mu \in M, \; \forall \mathbf{v} \in U$$

$$f([\mathbf{v}, q]) = \sum_\mathcal{K} (f, q) - \int_{\mathcal{E}_h^\partial} g\mathbf{v} \cdot \mathbf{n} ds \; \forall \mathbf{v} \in U, \; \forall q \in Q$$

the dual hybrid formulation consists in:

Find $[\mathbf{u}, p] \in U \times Q$ and the Lagrange multiplier $\lambda \in M$, such that

$$a\left([\mathbf{u}, p], [\mathbf{v}, q]\right) + c(\lambda, \mathbf{v}) = f([\mathbf{v}, q]), \; \forall [\mathbf{v}, q] \in U \times Q,$$

$$c(\mu, \mathbf{u}) = 0 \; \forall \mu \in M,$$

with $\lambda = \bar{p}$, the trace of the pressure p on $\mathcal{E}_h^0$ and $\lambda = g$ on $\mathcal{E}_k^\partial$.

3.2 Recovering the dual mixed formulation

Considering that $c(\mu, \mathbf{u}) = 0 \; \forall \; \mu \in M$ implies that $[\![\mathbf{u}]\!] = 0$ (continuity of the normal component of the velocity field $\mathbf{u}$), we note that the pair $[\mathbf{u}, p]$, solution of the above defined dual hybrid mixed method, satisfies the dual mixed formulation

Find $[\mathbf{u}, p] \in U \cap H(\text{div}) \times Q$, such that

$$a\left([\mathbf{u}, p], [\mathbf{v}, q]\right) = f([\mathbf{v}, q]) \; \forall [\mathbf{v}, q] \in U \cap H(\text{div}) \times Q$$

or, more explicitly

Find $\mathbf{u} \in W = U \cap H(\text{div})$ and $p \in V = Q$ such that

$$(\mathbf{u}, \mathbf{v}) - (p, \text{div}\mathbf{v}) = \int_{\partial\Omega} g\mathbf{v} \cdot \mathbf{n} ds \; \forall \, \mathbf{v}_h \in W$$

$$-(\text{div}\mathbf{u}, q) = -(f, q) \; \forall \, q \in V$$

which is the classical definition of the dual mixed formulation (Ravirat-Thomas) presented in Section 2.1.

4 STABILIZATION

Adding to the dual mixed formulation least squares stabilization terms defined in each element $\mathcal{K}$ and on the element boundaries we obtained the following residual form

$$a\left([\mathbf{u}, p], [\mathbf{v}, q]\right) + c(\lambda, \mathbf{v}) + c(\mu, \mathbf{u}) - f([\mathbf{v}, q]) + \sum_{\mathcal{K}} \int_{\partial\mathcal{K}} \beta(\lambda - p)(\mu - q) ds +$$
$$\sum_{\mathcal{K}} \left(\frac{\delta_1}{k^2}(\text{div}\mathbf{u} - k^2 p - f, \text{div}\mathbf{v} - k^2 q)_{\mathcal{K}} + \delta_2(\mathbf{u} + \nabla p, \mathbf{v} + \nabla q)_{\mathcal{K}} + \frac{\delta_3}{k^2}(\text{rot}\mathbf{u}, \text{rot}\mathbf{v})_{\mathcal{K}} \right) = 0 \tag{18}$$

in which the added residual forms in the interior of the element, weighted by the stabilization parameters $\delta_i, \; i = 1, 2, 3$, are the same considered in the stabilized dual mixed formulation presented Section 2.2 aiming at stabilizing the pair $[\mathbf{u}, p]$, while the residual form on the element boundaries multiplied by β is introduced to stabilize the multiplier λ.

4.1 Stabilized dual hybrid mixed formulation

Collecting appropriately the residual terms in (18) corresponding to the pair $[\mathbf{u}, p]$ and the multiplier λ, the stabilized dual hybrid mixed method can be presented as:

SDHM: Find $[\mathbf{u}, p] \in U \times Q$ and the Lagrange multiplier $\lambda \in M$ such that

$$a_\delta\left([\mathbf{u}, p], [\mathbf{v}, q]\right) + c(\lambda, \mathbf{v}) + \sum_{\mathcal{K}} \int_{\partial\mathcal{K}} \beta(p - \lambda) q ds = f_\delta([\mathbf{v}, q]) \;\; \forall \, [\mathbf{v}, q] \in U \times Q \tag{19}$$

$$c(\mu, \mathbf{u}) + \sum_{\mathcal{K}} \int_{\partial\mathcal{K}} \beta(\lambda - p)\mu ds = 0 \; \forall \, \mu \in M \tag{20}$$

where

$$a_\delta\left([\mathbf{u}_h, p_h], [\mathbf{v}_h, q_h]\right) = \sum_{\mathcal{K}} a_{\mathcal{K}}^{\delta}\left([\mathbf{u}_h, p_h], [\mathbf{v}_h, q_h]\right); \quad f_\delta([\mathbf{v}, q]) = \sum_{\mathcal{K}} f_{\mathcal{K}}^{\delta}([\mathbf{v}, q]) \tag{21}$$

with

$$a_{\mathcal{K}}^{\delta}\left([\mathbf{u}_h, p_h], [\mathbf{v}_h, q_h]\right) = a_{\mathcal{K}}\left([\mathbf{u}, p], [\mathbf{v}, q]\right) +$$
$$\frac{\delta_1}{k^2}\left(\text{div}\mathbf{u} - k^2 p, \text{div}\mathbf{v} - k^2 q\right)_{\mathcal{K}} - \frac{\delta_2}{k^2}\left(\mathbf{u} + \nabla p, \mathbf{v} + \nabla q\right)_{\mathcal{K}} + \frac{\delta_1}{k^2}\left(\text{rot}\mathbf{u}, \text{rot}\mathbf{v}\right)_{\mathcal{K}} \tag{22}$$

$$f_{\mathcal{K}}^{\delta}([\mathbf{v}, q]) = f_{\mathcal{K}}([\mathbf{v}, q]) + \frac{\delta_1}{k^2}(f, \text{div}\mathbf{v} - k^2 q)_{\mathcal{K}}$$

Considering the definitions (16) and (17) we restate problem **SDHM** as:

SDHM: Find $[\mathbf{u}, p] \in U \times Q$ and the Lagrange multiplier $\lambda \in M$ such that $\forall\, [\mathbf{v}, q] \in U \times Q$

$$a_\delta\left([\mathbf{u}, p], [\mathbf{v}, q]\right) + \int_{\mathcal{E}_h^0} \lambda [\![\mathbf{v}]\!] ds + \int_{\mathcal{E}_h^0} 2\beta\left(\{p\} - \lambda\right)\{q\} ds + \int_{\mathcal{E}_h^0} \frac{\beta}{2} [\![p]\!] \cdot [\![q]\!] ds = f_\delta([\mathbf{v}, q]) \quad (23)$$

$$\int_{\mathcal{E}_h^0} 2\beta\left((\lambda - \{p\}) + [\![\mathbf{u}]\!]\right) \mu ds = 0 \;\forall\, \mu \in M. \quad (24)$$

In Section 5 finite element approximations will be constructed for this stabilized dual hybrid formulation considering finite dimension polynomial spaces for all fields.

4.2 Hybridizable mixed DG method

Solving equation (24) for the multiplier λ we get

$$\lambda = \{p\} - \frac{1}{2\beta} [\![\mathbf{u}]\!]. \quad (25)$$

Replacing (25) in (23) yields the following stabilized mixed discontinuous Galerkin method

SMDG: Find $[\mathbf{u}, p]$ such that

$$\begin{aligned} & a_\delta\left([\mathbf{u}, p], [\mathbf{v}, q]\right) + \int_{\mathcal{E}_h^0} \left(\{p\}[\![\mathbf{v}]\!] + [\![\mathbf{u}]\!]\{q\}\right) ds + \\ & + \int_{\mathcal{E}_h^0} \frac{\beta}{2} [\![p]\!] \cdot [\![q]\!] ds - \int_{\mathcal{E}_h^0} \frac{1}{2\beta} [\![\mathbf{u}]\!][\![\mathbf{v}]\!] ds = f_\delta([\mathbf{v}, q]) \;\; \forall\, [\mathbf{v}, q] \in U \times Q \end{aligned} \quad (26)$$

Setting $\delta_i = 0$, for $i = 1, 2, 3$, the above **SMDG** formulation recovers the LDG-H (Local Discontinuous Galerkin - Hybridizable) method analyzed in [15] in the context of elliptic problems.

5 FINITE ELEMENT APPROXIMATIONS

Let us consider the finite dimension spaces

$$Q_h^l = \{q \in Q : \quad q|_{\mathcal{K}} \in \mathfrak{R}^l \;\; \forall \mathcal{K} \in \mathcal{T}_h\},$$

$$U_h^m = \{\mathbf{v} \in U : \quad \mathbf{v}|_{\mathcal{K}} \in \mathfrak{R}^m \times \mathfrak{R}^m \;\; \forall \mathcal{K} \in \mathcal{T}_h\},$$

$$M_h^n = \{\mu \in M : \quad \mu|_e \in \mathfrak{P}^n \;\; \forall e \in \mathcal{E}^0\},$$

where $\mathfrak{R}^l$ is the set of polynomial of degree less then or equal to l when $\mathcal{K}$ is a triangle or less then or equal to l in each coordinate when $\mathcal{K}$ is a quadrilateral, and $\mathfrak{P}^n$ is the set of polynomials of degree less then or equal to n on each edge e.

We can now present a finite element approximation for the stabilized dual hybrid mixed formulation introduced in Section 4.1 as:

SDHM$_h$: Find $[\mathbf{u}_h, p_h] \in U_h^m \times Q_h^l$ and the Lagrange multiplier $\lambda_h \in M_h^n$ such that

$$\begin{aligned} & a_\delta\left([\mathbf{u}_h, p_h], [\mathbf{v}_h, q_h]\right) + \int_{\mathcal{E}_h^0} \frac{\beta}{2} [\![p_h]\!] \cdot [\![q_h]\!] ds \\ & + \int_{\mathcal{E}_h^0} \lambda_h [\![\mathbf{v}_h]\!] ds + \int_{\mathcal{E}_h^0} 2\beta\left(\{p_h\} - \lambda_h\right)\{q_h\} ds = f_\delta([\mathbf{v}_h, q_h]) \;\; \forall\, [\mathbf{v}_h, q_h] \in U_h^m \times Q_h^l \end{aligned} \quad (27)$$

$$\int_{\mathcal{E}_h^0} 2\beta\left((\lambda_h - \{p_h\}) + [\![\mathbf{u}_h]\!]\right)\mu_h ds = 0 \;\; \forall\, \mu_h \in M_h. \tag{28}$$

For $n \geq l$ and $n \geq m$ we can solve explicitly equation (28), for the multiplier λ_h, obtaining

$$\lambda_h = \{p_h\} - \frac{1}{2\beta}[\![\mathbf{u}_h]\!], \tag{29}$$

which when replaced in (23) yields the following hybridizable discontinuous Galerkin method

$\mathbf{SMDG}_h$: Find $[\mathbf{u}_h, p_h] \in U_h^m \times Q_h^l$ such that

$$a_\delta\left([\mathbf{u}_h, p_h], [\mathbf{v}_h, q_h]\right) + \int_{\mathcal{E}_h^0} \left(\{p_h\}[\![\mathbf{v}_h]\!] + [\![\mathbf{u}_h]\!]\{q_h\}\right) ds +$$

$$+ \int_{\mathcal{E}_h^0} \frac{\beta}{2}[\![p_h]\!] \cdot [\![q_h]\!] ds - \int_{\mathcal{E}_h^0} \frac{1}{2\beta}[\![\mathbf{u}_h]\!][\![\mathbf{v}_h]\!] ds = f_\delta([\mathbf{v}_h, q_h]) \;\; \forall\, [\mathbf{v}_h, q_h] \in U_h \times Q_h. \tag{30}$$

Computationally, the best option to solve the systems of linear equations (28) and (29) is to solve first (28) at element level to obtain $[\mathbf{u}_h, p_h]$ in terms of λ_h, replace $[\mathbf{u}_h, p_h]$ in (29) and assemble a global system in λ_h only. After solving the global system in λ_h, the pair $[\mathbf{u}_h, p_h]$ is computed by solving the following set of local problems defined at element level.

$\mathbf{LP}_h$: For given λ_h, find $[\mathbf{u}_h, p_h] \in U_\mathcal{K}^m \times Q_\mathcal{K}^l$, at each element $\mathcal{K}$, such that

$$a_\mathcal{K}^\delta\left([\mathbf{u}_h, p_h], [\mathbf{v}_h, q_h]\right) + \int_{\partial\mathcal{K}} \beta p_h q_h ds =$$

$$f_\mathcal{K}^\delta([\mathbf{v}_h, q_h]) + \int_{\partial\mathcal{K}} \beta\lambda_h q_h ds - \int_{\partial\mathcal{K}} \lambda_h \mathbf{v}_h \cdot \mathbf{n} ds \;\; \forall\, [\mathbf{v}_h, q_h] \in U_\mathcal{K}^m \times Q_\mathcal{K}^l, \tag{31}$$

where $U_\mathcal{K}^m = \mathfrak{R}^m \times \mathfrak{R}^m$ and $Q_\mathcal{K}^l = \mathfrak{R}^l$.

This strategy, typical of hybridized mixed finite element methods, will be adopted here in the numerical experiments presented next.

6 NUMERICAL RESULTS

The parameters δ_i and β play an important role in the stability and accuracy of the proposed dual hybrid mixed formulation. However, here we will not invest in finding their optimal values. In all numerical results presented next we adopted the following choice:

$$\delta_1 = \delta_3 = -1; \quad \delta_2 = 1; \quad \beta = \frac{1}{h_e};$$

with h_e denoting the length of the edge e of the element $\mathcal{K}$. We have also adopted equal order approximations for all fields, that is, $l = m = n$.

6.1 Homogeneous media

Initially we consider Helmholtz equation, with k^2 = constant and $f(x, y) = 0$, subject to Dirichlet boundary conditions such that the exact solution is a plane wave (real part only) propagating in θ-direction:

$$w(x, y) = \cos[k(x\cos\theta + y\sin\theta)].$$

The objective is check the convergence of the proposed formulation. In this study we consider $\theta = \pi/6$, $k = 30$ and $\Omega = [0,1] \times [0,1]$. First we check the h-convergence of the stabilized formulation for $l = m = n = 2$ and a sequence of 10×10, 20×20, 40×40 and 80×80 uniform meshes. Figure 1 shows convergence results in $L^2(\Omega)$ norm (left) and $H^1(\Omega)$ seminorm (right) for the pressure approximation p_h of the stabilized dual hybrid formulation (p_{DH}) compared to the its interpolant (p_I) and the local projection (p_{LP}), obtained by solving the local problems $\mathbf{LP}_h$ replacing λ_h (approximation of the lagrange multiplier) by λ (exact value). In Figure 1 we observe pollution effects on both DH and LP solutions for coarse meshes, but these pollution effects disappear with refinement. Figure 2 show results of convergence study using a fixed 10×10 uniform mesh and varying the degree of the polynomial approximations by setting $l = m = n = 2, 3, 4, 5, 6, 7$ sequentially. We can see that highly accurate solutions are obtained by increasing the order of the polynomial approximations (l-refinement). In this study, neq is the the number of equation in the global system associated with the approximation of multiplier λ_h.

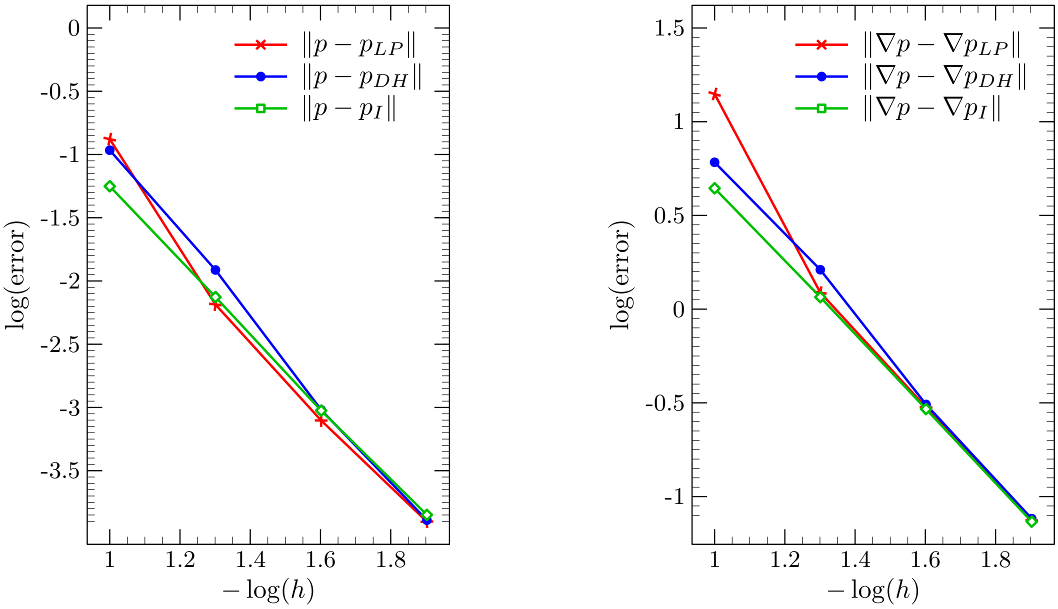

Figure 1: Convergence of the finite element approximations for the homogeneous problem with h-refinement. Error in the L^2-norm (left) and H^1-seminorm (right). Stabilized dual hybrid mixed (DH) solution compared to the local projection (LP) and the interpolant (I).

6.2 Heterogeneous media. Interface problem

We now solve Helmholtz equation in unite domain $\Omega = (-0.5, 0.5) \times (-0.5, 0.5)$ with a discontinuity in the *wavenumber*. We consider $k = k_1$ for $x < 0$, $k = k_2$ for $x > 0$ and impose Dirichlet boundary conditions, weakly as presented in the stabilized dual mixed formulation,

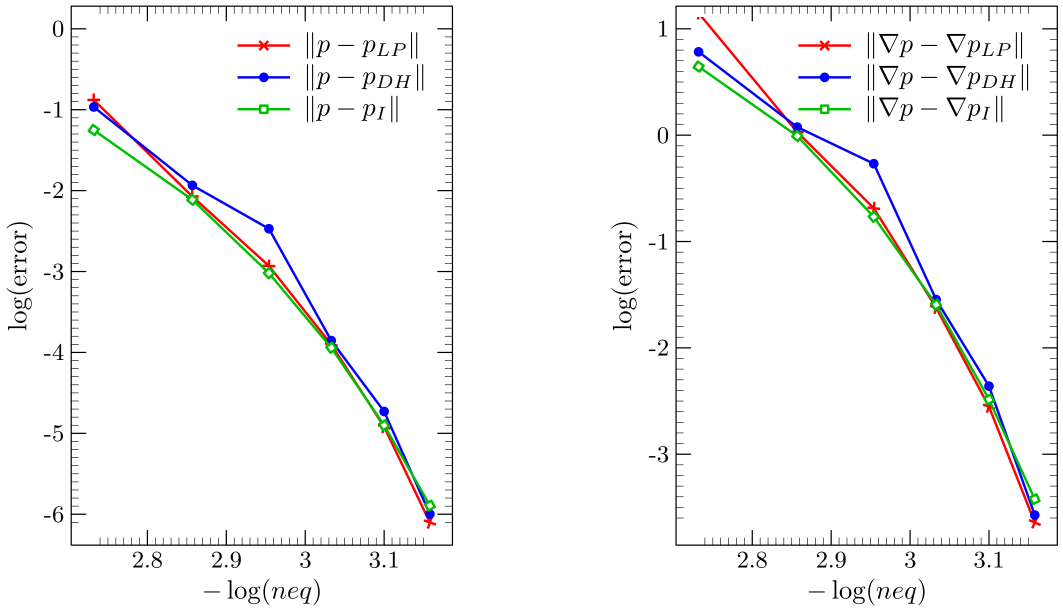

Figure 2: Convergence of the finite element approximations, with the polynomial degree l, for the homogeneous Helmholtz problem. Error in the L^2-norm (left) and H^1-seminorm (right). Stabilized dual hybrid mixed (DH) solution compared to the local projection (LP) and the interpolant (I).

such that the exact solution is given by

$$\begin{aligned}
&\text{for } x < 0 : \\
&\quad u(x,y) = \exp[-ik_1(x\cos\theta_1 + y\sin\theta_1)] + R\exp[-ik_1(-x\cos\theta_1 + y\sin\theta_1)]\,, && (32)\\
&\text{for } \ x > 0 : \\
&\quad u(x,y) = T\exp[-ik_2(x\cos\theta_2 + y\sin\theta_2)]\,, && (33)\\
&\text{with :} \\
&\quad R = (k_1\cos\theta_1 - k_2\cos\theta_2)\,/\,(k_1\cos\theta_1 + k_2\cos\theta_2) && (34)\\
&\quad T = 2k_1\cos\theta_1/\,(k_1\cos\theta_1 + k_2\cos\theta_2)\,, && (35)\\
&\quad k_2\sin\theta_2 = k_1\sin\theta_1. && (36)
\end{aligned}$$

In this study we set $k_1 = 30$, $k_2 = 20$ and $\theta_1 = \pi/6$. Again, the same sequence of uniform meshes used in the previous example is adopted in the h-convergence study for $l = m = n = 2$. From Figure 3 we can see pollution effects even higher than those observe in previous example, corresponding to the homogeneous Helmholtz problem, probably due to the an inappropriate choice of the stabilization parameters. Much more accurate solutions are obtained by increasing the degree of the polynomial approximations as shown in Figure 4 where l-convergence results are presented for this heterogeneous problem using a fixed 10×10 uniform mesh and varying the degree of the polynomial approximations by setting $l = m = n = 2, 3, 4, 5, 6, 7$ sequentially, as in the previous study of the homogeneous Helmholtz problem. Finally, we present in Figure 5 a comparison of h-refinement and l-refinement convergence results. From 5 we clearly observe that higher order are much more accurate than lower lower order polynomial approximations for the the same number of degree of freedom (neq).

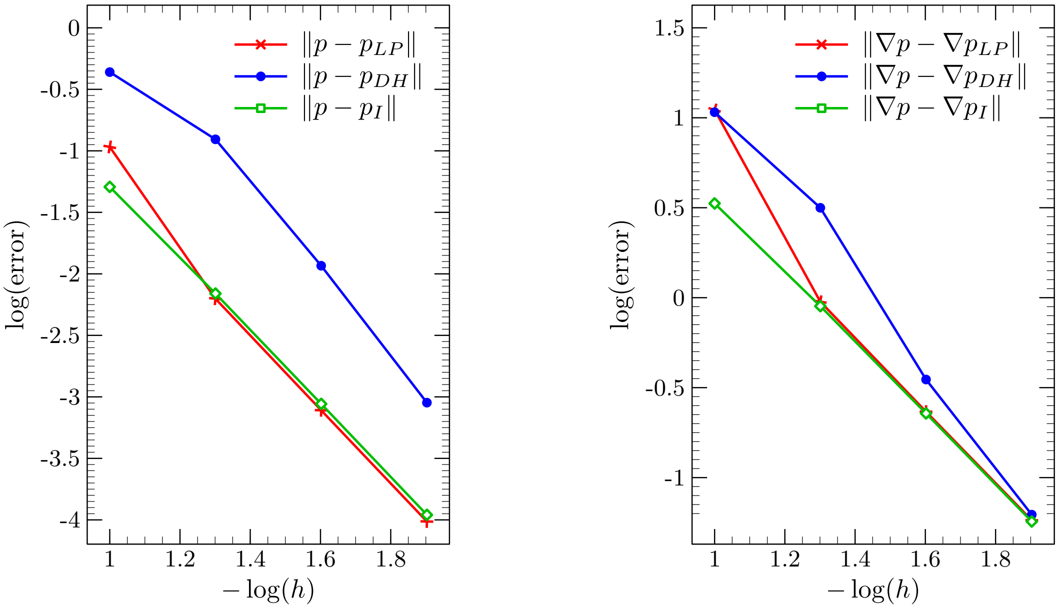

Figure 3: Convergence of the finite element approximations for the heterogeneous problem with h-refinement. Error in the L^2-norm (left) and H^1-seminorm (right). Stabilized dual hybrid mixed (DH) solution compared to the local projection (LP) and the interpolant (I).

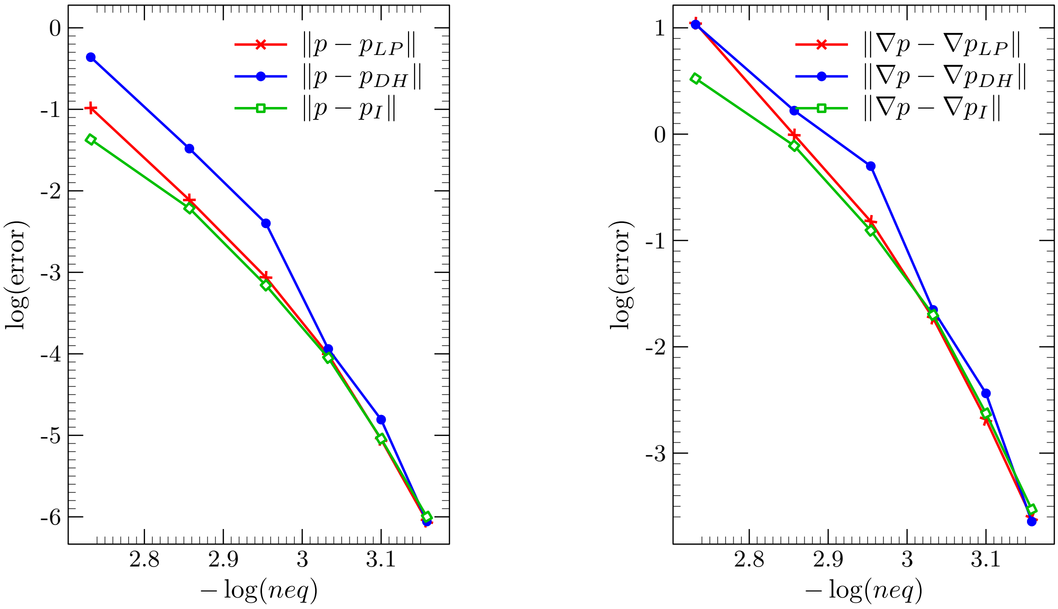

Figure 4: Convergence of the finite element approximations, with the polynomial degree l, for the heterogeneous Helmholtz problem. Error in the L^2-norm (left) and H^1-seminorm (right). Stabilized dual hybrid mixed (DH) solution compared to the local projection (LP) and the interpolant (I).

7 CONCLUSIONS

Stabilized dual hybrid and mixed finite element methods are proposed for solving Helmholtz problems in homogeneous or heterogeneous media using Galerkin and least square residual of the governing equation. Local problems, in the velocity and pressure fields, are solved at element level and these variables are eliminated in favor of the Lagrange multipliers, identified

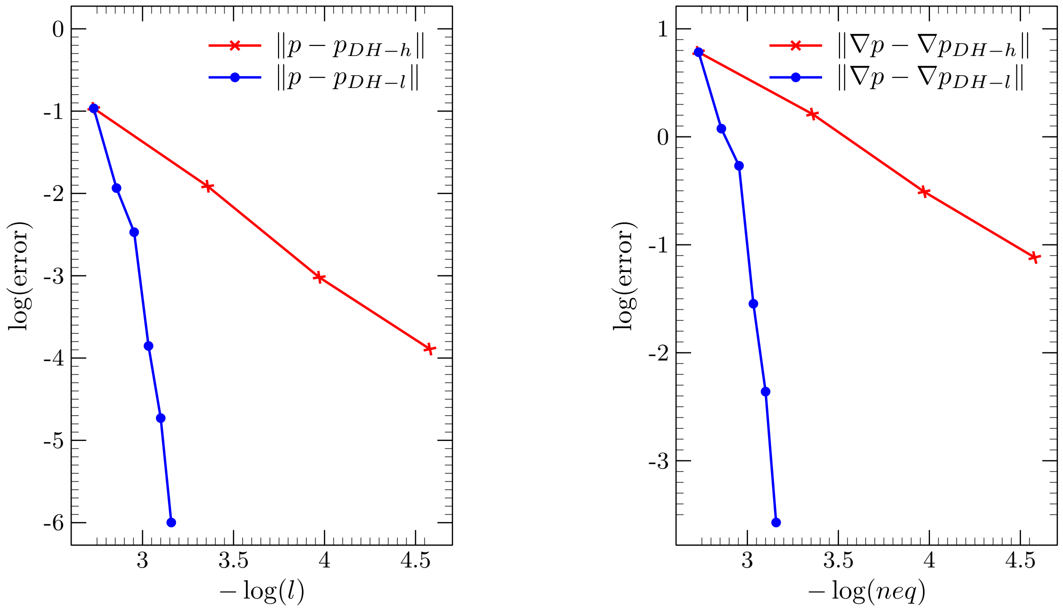

Figure 5: Convergence of the finite element approximations, with the polynomial degree l compared to h-refinement, for the heterogeneous Helmholtz problem. Error in the L^2-norm (left) and H^1-seminorm (right). Stabilized dual hybrid mixed (DH) solution and local projection (LP) corresponding to uniform meshes.

as the trace of the pressure on the element edges of the finite element mesh. A global system is assembled involving only the degrees of freedom associated with the Lagrange multipliers. Polynomial bases are adopted to approximate all fields. Numerical results are presented using equal order approximations for all fields to illustrate the potential of the proposed formulation to efficiently solve Helmholtz problems in homogeneous or heterogeneous media at medium and high frequency regimes. Higher order polynomial approximations are shown to be much more accurate than lower lower order polynomial approximations for the the same number of global degree of freedom.

REFERENCES

[1] F. Brezzi, M. Fortin, Mixed and Hybrid Finite Element Methods, in: Springer Series in Computational Mathematics, vol. 15, Springer-Verlag, New York, 1991.

[2] T.H.H. Pian, State-of-the-art development of hybrid/mixed finite element method, *Finite Elements Anal. Des.* 520, 1995.

[3] C. Farhat, I. Harari, U. Hetmaniuk, A discontinuous Galerkin method with Lagrange multipliers for the solution of Helmholtz problems in the midfrequency regime, *Comput. Methods Appl. Mech. Engrg.* **192** 31953209, 2003.

[4] Ihlenburg I, Finite Element Analysis of Acoustic Scattering, Applied Mathematical Sciences, vol. **132**, Springer-Verlag, New York, 1998.

[5] Harari I and Hughes TJR, Finite element method for the Helmholtz equation in an exterior domain: Model problems *Computer Methods in Applied Mechanics and Engineering* **87**, 59-96, 1991.

[6] Babuška I, Ihlenburg F, Paik ET and Sauter SA, A generalized finite element method for solving the Helmholtz equation in two dimensions with minimal pollution 1995, *Computer Methods in Applied Mechanics and Engineering* **128**, 325–359.

[7] Oberai AA and Pinsky PM, A residual-based finite element method for the Helmholtz equation, *Int. J. Numer. Methods Engrg.* **49**, 399-419, 2000.

[8] Loula AFD, Alvarez GB, Dutra do Carmo AG and Rochinha FA, A discontinuous finite element method at element level for Helmholtz equation, *Computer Methods in Applied Mechanics and Engineering* **196**, 867-878, 2007.

[9] Loula AFD and Fernandes DT, A Quasi Optimal Petrov-Galerkin Method for Helmholtz Problem, *Int. J. Numer. Methods Engrg.* **80**, 1595-1622, 2009.

[10] Monk P and Wang D, A least-squares method for the Helmholtz equation, *Comput Method Appl Mech Engn* **175**, 121, 1999.

[11] Gamallo P and Astley J, A comparison of two Trefftz-type methods: The ultraweak variational formulation and the least-squares method, for solving shortwave 2-D Helmholtz problems, *Int. J. Numer. Methods Engrg.* **71**, 406-432, 2007.

[12] A. Masud, T. J. R. Hughes, A stabilized mixed finite element method for Darcy flow, Comput. Methods Appl. Mech. Engrg. **191**, 4341-4370, 2002.

[13] T. J. R. Hughes, A. Masud, J. Wan, A stabilized mixed discontnuous Galerkin Method for Darcy flow, Comput. Methods Appl. Mech. Engrg. **195**, 3347-3381, 2006.

[14] M.R. Correa and A.F. Loula, Unconditionally stable mixed finite element methods for Darcy flow, *Comput. Methods Appl. Mech. Engrg.* **197**, 1525-1540, 2008.

[15] B. Cockbuen, J. Gopalakrishnan, F. Sayas, A projection-based error analysis of HDG methods, *Math. Comp.*, **27** 1351-1367, 2010.

[16] F. Brezzi, T. J. R. Hughes, L. D. Marini, A. Masud, Mixed discontnuous Galerkin methods for Darcy flow, *J. Sci. Comput.*, **22** 119-145, 2005.

COMPDYN 2011
3^{rd} ECCOMAS Thematic Conference on
Computational Methods in Structural Dynamics and Earthquake Engineering
M. Papadrakakis, M. Fragiadakis, V. Plevris (eds.)
Corfu, Greece, 25-28 May 2011

FULL-WAVEFORM-BASED INVERSION FOR SITE CHARACTERIZATION: THEORY, NUMERICAL SIMULATIONS, AND PHYSICAL EXPERIMENTS

Sezgin Kucukcoban[1] **and Loukas F. Kallivokas**[1]

[1]Department of Civil, Architectural and Environmental Engineering
The University of Texas at Austin
1 University Station, C1748
Austin, TX, 78712, USA
e-mail: {ksezgin,loukas}@mail.utexas.edu

Keywords: Full-waveform-based inversion, Perfectly-matched-layers, Site characterization, Forward transient elastic wave simulation, Mixed FEM.

Abstract. *We discuss recent progress in the full-waveform-based imaging of probed solids/soils, with geotechnical site characterization applications in mind. The primary goal is the reconstruction of the material profile of near-surface, arbitrarily heterogeneous formations using elastic waves as the probing agents.*

The problem requires efficient solutions of the forward wave simulation problem, robust strategies for tackling the inverse imaging problem, and designing of experimental protocols to best harness the limited field data that feed the imaging problem. To address the forward problem, the semi-infinite extent of the probed domains is truncated via the introduction of perfectly-matched-layers (PMLs) at the truncation interfaces. We discuss a new variational hybrid formulation for transient elastic wave simulations in PML-truncated domains that is computationally optimal when compared to competing schemes. We then discuss a full-waveform-based inversion framework driven by PDE-constrained optimization ideas: to address the imaging problem we seek to resolve simultaneously PML-endowed state and adjoint time-dependent BVPs, together with time-independent BV control problems that drive the material updates during inversion iterations. To address solution multiplicity and improve on the robustness of the inversion algorithms we deploy regularization schemes (Tikhonov and Total Variation), continuation schemes (frequency-, grid-, and regularization factor-continuations), and a new search-direction biasing scheme that seems to accelerate algorithmic convergence.

We report satisfactory results with numerical experiments targeting inversion of both smooth and sharp profiles in two dimensions, and also provide examples attesting to the quality and efficiency of the forward wave modeling.

1 INTRODUCTION

Recent advances in both algorithms and computer hardware architecture have renewed hope that problems associated with the non-invasive condition assessment of physical and biological systems are becoming more tractable with present means. The last thirty years have seen various developments aiming at the solution of such mathematically, algorithmically, and computationally challenging inverse problem that arises in various application domains ranging from seismic to medical imaging. The inverse medium problem in the context of geotechnical site characterization, reduces to the reconstruction of the soil's material profile, i.e., of the spatial distribution of the elastic material properties (Lamé parameters $\{\lambda, \mu\}$ or, to an extent, equivalently, of the P- and S-wave velocities, $\{c_p, c_s\}$).

Since the focus is on characterizing near-surface deposits, the truncation of the semi-infinite extent of the physical domain becomes necessary. We, thus, introduce perfectly-matched-layers (PMLs) [1, 2, 3, 4, 5, 6] to convert the semi-infinite physical domain to a finite computational model that mimics the physical behavior of the non-truncated domain. The PML is a truly absorbing condition, capable of handling heterogeneity, unlike any other competing methodology. The PML attenuates propagating waves without reflection from the interface for all non-zero angles-of-incidences and frequencies (Fig. 2(a)). Here, we address the numerical simulation of elastic wave motion in two-dimensional, PML-truncated, arbitrarily heterogeneous elastic media (*forward problem*). Specifically, we discuss a new hybrid, fully symmetric, variational formulation (mixed unsplit-field PML, coupled with a non-mixed approach for the interior domain) for direct transient analysis. The hybrid formulation leads to optimal computational cost and easy modification of existing interior-domain displacement-based codes to accommodate PMLs as a means of domain truncation.

To address the inverse medium problem, we favor a full waveform inversion approach that uses stress waves for interrogation, and is driven by the measurements collected directly in the time-domain at receivers on the soil's surface, as schematically shown in Figs. 1(a) and 1(b). We cast the profile reconstruction problem as a PDE-constrained least-squares misfit optimization problem [7, 8] , and then recast it with the aid of a Lagrangian, whereby the misfit functional is augmented with the side-imposition of the PML-endowed PDEs, initial, and boundary conditions via Lagrange multipliers. To enforce the stationarity of the Lagrangian, we derive next the first-order optimality conditions. Upon discretization, the coupled system results in a classic KKT (Karush-Kuhn-Tucker) system. To solve, we pursue a *reduced-space approach* in which

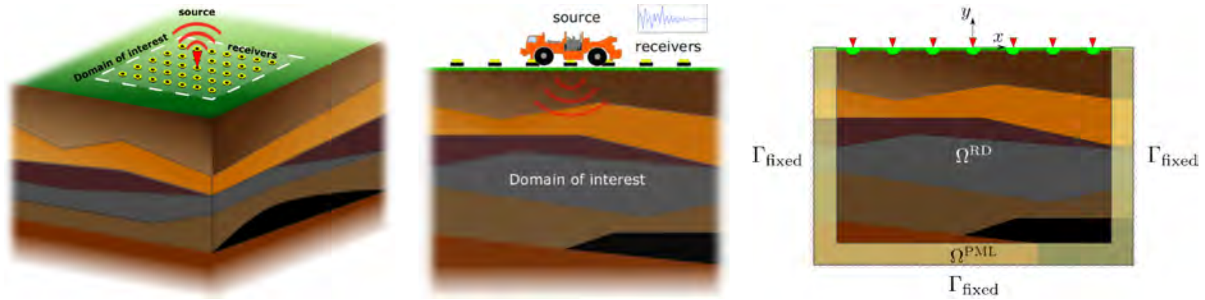

(a) (b) (c)

Figure 1: Problem definition: (a) interrogation of a heterogeneous semi-infinite domain by an active source; (b) a 2D cross-section of the domain showing one source and multiple receivers; and (c) computational model truncated from the semi-infinite medium via the introduction of PMLs

the coupled system of PDEs are solved in the reduced space of the control variables –the Lamé parameters. To alleviate the difficulties associated with solution multiplicity, we explore both Tikhonov (TN) and Total Variation (TV) regularization schemes. To aid the inversion process in reconstructing high-quality material profiles, we deploy regularization factor continuation and source-frequency continuation schemes. We present examples involving layered systems and smoothly-varying profiles, as well as layered systems containing inclusions to demonstrate the performance of the proposed inversion approach and associated algorithms.

2 2D ELASTIC WAVE HYBRID MODELING

First, the equilibrium equation and the kinematic condition combined with the constitutive law, are Fourier-transformed into the frequency-domain, to obtain

$$\mathbf{div}\,\hat{\mathcal{S}}^T + \hat{\mathbf{f}} = -\omega^2\rho\hat{\mathbf{u}}, \qquad \mathcal{D}:\hat{\mathcal{S}} = \frac{1}{2}\left[\nabla\hat{\mathbf{u}} + (\nabla\hat{\mathbf{u}})^T\right], \tag{1}$$

where $\mathcal{S}$, $\mathcal{E}$, and $\mathcal{D}$ are the stress, strain, and compliance tensors, respectively; ρ is the density of the elastic medium, $\mathbf{u}$ is the displacement vector, $\mathbf{f}$ is the load vector, and (:) denotes tensor inner product. Next, we introduce the coordinate-stretched form for each coordinate:

$$\begin{aligned} &\tilde{s} = \int_0^s \varepsilon_s(s')ds', \qquad \varepsilon_s(s,\omega) = \alpha_s(s) + \frac{\beta_s(s)}{i\omega}, \\ &\frac{d}{d\tilde{s}} = \frac{1}{\varepsilon_s(s,\omega)}\frac{d}{ds}, \qquad s = x, y, \end{aligned} \tag{2}$$

where ω denotes circular frequency, ε_s is a complex stretching function in the direction of coordinate s, and α_s and β_s denote scaling and attenuation functions, respectively. As the names imply, α_s "stretches" or scales s, whereas β_s is responsible for the amplitude decay of the propagating wave once it enters the PML.

The stretching is applied by replacing x and y in (1) with the stretched coordinates $\tilde{x}$ and $\tilde{y}$. Making use of (2), (1) can be written in terms of the non-stretched coordinates, and then, inverted back into the time domain to obtain a mixed unsplit-field PML formulation:

$$\mathbf{div}\left(\dot{\mathbf{S}}^T\tilde{\Lambda}_e + \mathbf{S}^T\tilde{\Lambda}_p\right) + a\mathbf{f} = \rho\left(a\ddot{\mathbf{u}} + b\dot{\mathbf{u}} + c\mathbf{u}\right), \tag{3a}$$

$$\mathcal{D}:\left(a\ddot{\mathbf{S}} + b\dot{\mathbf{S}} + c\mathbf{S}\right) = \frac{1}{2}\left[(\nabla\dot{\mathbf{u}})\tilde{\Lambda}_e + \tilde{\Lambda}_e(\nabla\dot{\mathbf{u}})^T + (\nabla\mathbf{u})\tilde{\Lambda}_p + \tilde{\Lambda}_p(\nabla\mathbf{u})^T\right], \tag{3b}$$

in which $a = \alpha_x\alpha_y$, $b = \alpha_x\beta_y + \alpha_y\beta_x$, $c = \beta_x\beta_y$, and $\tilde{\Lambda}_e$ and $\tilde{\Lambda}_p$ define the diagonal stretch tensors where the subscripts "e" and "p" refer to attenuation functions associated with evanescent and propagating waves, respectively. In the regular domain, $\tilde{\Lambda}_e$ reduces to the identity tensor, whereas $\tilde{\Lambda}_p$ vanishes identically. In (3), we introduce an auxiliary variable $\mathbf{S}(\mathbf{x}, t)$, which physically represent stress memories or histories, defined as

$$\mathbf{S}(\mathbf{x}, t) = \int_0^t \mathcal{S}(\mathbf{x}, \tau)d\tau \qquad \text{and consequently, } \dot{\mathbf{S}}(\mathbf{x}, t) = \mathcal{S}(\mathbf{x}, t). \tag{4}$$

Owing to the complexity of (3), one could not conceivably reduce (3) to a single unknown field, as it is routinely done in displacement-based interior elastodynamics problems, without increasing the temporal complexity. Here, we propose a hybrid approach, whereby we retain a displacement-based interior problem and couple it with the mixed unsplit PML. Thus, the

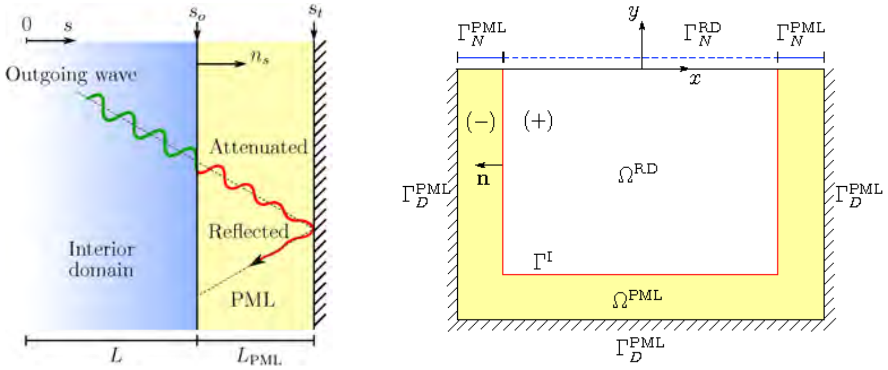

(a) (b)

Figure 2: PML-truncated semi-infinite domains in 1D and 2D

wave motion in a PML-truncated domain (Figure 2(b)) over a time interval of interest, $(0, T]$ is governed by the hybrid system of equations:

$$\mathbf{div}\left\{\mu\left[\nabla\mathbf{u}+(\nabla\mathbf{u})^T\right]+\lambda(\operatorname{div}\mathbf{u})\mathcal{I}\right\}+\mathbf{f}=\rho\ddot{\mathbf{u}} \qquad \text{in } \Omega^{\text{RD}}, \tag{5a}$$

$$\mathbf{div}\left(\dot{\mathbf{S}}^T\tilde{\Lambda}_e+\mathbf{S}^T\tilde{\Lambda}_p\right)=\rho\left(a\ddot{\mathbf{u}}+b\dot{\mathbf{u}}+c\mathbf{u}\right) \qquad \text{in } \Omega^{\text{PML}}, \tag{5b}$$

$$\mathcal{D}:\left(a\ddot{\mathbf{S}}+b\dot{\mathbf{S}}+c\mathbf{S}\right)=\frac{1}{2}\left[(\nabla\dot{\mathbf{u}})\tilde{\Lambda}_e+\tilde{\Lambda}_e(\nabla\dot{\mathbf{u}})^T+(\nabla\mathbf{u})\tilde{\Lambda}_p+\tilde{\Lambda}_p(\nabla\mathbf{u})^T\right] \qquad \text{in } \Omega^{\text{PML}}, \tag{5c}$$

subject to silent initial, and the following boundary and interface conditions:

$$\left\{\mu\left[\nabla\mathbf{u}+(\nabla\mathbf{u})^T\right]+\lambda(\operatorname{div}\mathbf{u})\mathcal{I}\right\}\mathbf{n}=\boldsymbol{g}_n \qquad \text{on } \Gamma_N^{\text{RD}}, \tag{6a}$$

$$(\dot{\mathbf{S}}^T\tilde{\Lambda}_e+\mathbf{S}^T\tilde{\Lambda}_p)\mathbf{n}=\mathbf{0} \qquad \text{on } \Gamma_N^{\text{PML}}, \tag{6b}$$

$$\mathbf{u}=\mathbf{0} \qquad \text{on } \Gamma_D^{\text{PML}}, \tag{6c}$$

$$\mathbf{u}^+=\mathbf{u}^- \qquad \text{on } \Gamma^{\text{I}}, \tag{6d}$$

$$\left\{\mu\left[\nabla\mathbf{u}+(\nabla\mathbf{u})^T\right]+\lambda(\operatorname{div}\mathbf{u})\mathcal{I}\right\}\mathbf{n}=-(\dot{\mathbf{S}}^T\tilde{\Lambda}_e+\mathbf{S}^T\tilde{\Lambda}_p)\mathbf{n} \qquad \text{on } \Gamma^{\text{I}}, \tag{6e}$$

where $\boldsymbol{g}_n$ denotes prescribed tractions. Note that the hybrid approach couples two initially-uncoupled sets of governing equations via the continuity of displacements and tractions at the interface.

We seek next the weak form, in the Galerkin sense, corresponding to the strong form (Eq. 5). We take inner products of (5) with test functions $\mathbf{w}_1(\mathbf{x})$, $\mathbf{w}_2(\mathbf{x})$, and $\mathbf{T}(\mathbf{x})$, and then integrate over Ω^{RD}, Ω^{PML}, and Ω^{PML}, respectively, where the integration by parts is applied to the equilibrium equations (5a) and (5b). By adding the equilibrium equations, the weak form of (5) can be cast as:

$$\int_{\Omega^{\text{RD}}}\nabla\mathbf{w}_1:\left\{\mu\left[\nabla\mathbf{u}+(\nabla\mathbf{u})^T\right]+\lambda(\operatorname{div}\mathbf{u})\mathcal{I}\right\}\,\mathrm{d}\Omega+\int_{\Omega^{\text{PML}}}\nabla\mathbf{w}_2:\left(\dot{\mathbf{S}}^T\tilde{\Lambda}_e+\mathbf{S}^T\tilde{\Lambda}_p\right)\,\mathrm{d}\Omega$$
$$+\int_{\Omega^{\text{RD}}}\mathbf{w}_1\cdot\rho\ddot{\mathbf{u}}\,\mathrm{d}\Omega+\int_{\Omega^{\text{PML}}}\mathbf{w}_2\cdot\rho\left(a\ddot{\mathbf{u}}+b\dot{\mathbf{u}}+c\mathbf{u}\right)\,\mathrm{d}\Omega$$
$$=\int_{\Gamma_N^{\text{RD}}}\mathbf{w}_1\cdot\boldsymbol{g}_n\,\mathrm{d}\Gamma+\int_{\Omega^{\text{RD}}}\mathbf{w}_1\cdot\mathbf{f}\,\mathrm{d}\Omega, \tag{7a}$$

$$\int_{\Omega^{\mathrm{PML}}} \mathbf{T} : \Big[\mathcal{D} : \Big(a\ddot{\mathbf{S}} + b\dot{\mathbf{S}} + c\mathbf{S}\Big)\Big] \ \mathrm{d}\Omega$$
$$= \frac{1}{2}\int_{\Omega^{\mathrm{PML}}} \mathbf{T} : \Big[(\nabla\dot{\mathbf{u}})\tilde{\Lambda}_e + \tilde{\Lambda}_e(\nabla\dot{\mathbf{u}})^T + (\nabla\mathbf{u})\tilde{\Lambda}_p + \tilde{\Lambda}_p(\nabla\mathbf{u})^T\Big] \ \mathrm{d}\Omega. \quad \text{(7b)}$$

For the mixed finite element implementation of the weak form, both $\mathbf{u}(\mathbf{x}, t)$ and $\mathbf{S}(\mathbf{x}, t)$ are treated as independent variables that need to be approximated separately now only within the PML domain. Let the basis functions be denoted by $\mathbf{\Phi}$ and $\mathbf{\Psi}$. The trial functions ($\mathbf{u}$, $\mathbf{S}$) and the test functions ($\mathbf{w}$, $\mathbf{T}$) are spatially discretized as

$$\begin{array}{lll} u_x(\mathbf{x},t) \cong \mathbf{\Phi}^T(\mathbf{x})\mathbf{u}_x(t), & u_y(\mathbf{x},t) \cong \mathbf{\Phi}^T(\mathbf{x})\mathbf{u}_y(t) & \\ S_{xx}(\mathbf{x},t) \cong \mathbf{\Psi}^T(\mathbf{x})\mathbf{S}_{xx}(t), & S_{yy}(\mathbf{x},t) \cong \mathbf{\Psi}^T(\mathbf{x})\mathbf{S}_{yy}(t), & S_{xy}(\mathbf{x},t) \cong \mathbf{\Psi}^T(\mathbf{x})\mathbf{S}_{xy}(t), \\ w_x(\mathbf{x}) \cong \mathbf{w}_x^T\mathbf{\Phi}(\mathbf{x}), & w_y(\mathbf{x}) \cong \mathbf{w}_y^T\mathbf{\Phi}(\mathbf{x}), & \\ T_{xx}(\mathbf{x}) \cong \mathbf{T}_{xx}^T\mathbf{\Psi}(\mathbf{x}), & T_{yy}(\mathbf{x}) \cong \mathbf{T}_{yy}^T\mathbf{\Psi}(\mathbf{x}), & T_{xy}(\mathbf{x}) \cong \mathbf{T}_{xy}^T\mathbf{\Psi}(\mathbf{x}). \end{array}$$

We, subsequently, obtain the *semi-discrete form* that is second-order in time and is resolved by the classical Newmark-β scheme. We note the resulting matrices are *symmetric*, and that their size is substantially smaller (up to 60% reduction in total number of unknowns in two dimensions) than that required by fully-mixed formulations (split- or unsplit-field), since the interior elastodynamics problem remains purely displacement-based.

To test the accuracy and efficiency of the hybrid formulation, we present two numerical experiments: a homogeneous semi-infinite domain (Fig. 3(a)), and a horizontally-layered medium (Fig. 3(d)). We use a Ricker pulse time signal with a central frequency $f_r = 15$ Hz as: (a) an explosive source placed at the center of the homogeneous domain, and (b) a surface stress load over a region ($-1\mathrm{m} \leq x \leq 1\mathrm{m}$) of the heterogeneous domain. The efficacy and quality of the PML is nicely corroborated by Fig. 3, which shows no discernible reflections from the PML interfaces, nor any residual reflections from the fixed external boundaries, even in the presence of heterogeneity. The various error metrics shown in Fig. 4 that include the domain energy decay, global and point-wise time-dependent norms, and a long-time stability run, all attest to the forward problem's performance.

3 THE INVERSE MEDIUM PROBLEM

We formulate the inverse problem initially as a PDE-constrained least-squares misfit minimization problem (à la [7, 8]), where the misfit is defined as the difference between the measured response ($\mathbf{u}_m$) at the receivers and a computed response ($\mathbf{u}$) that is obtained using trial distributions of the material parameters. The misfit least-squares minimization can be cast as

$$\mathcal{F} := \frac{1}{2}\sum_{j=1}^{N_r} \int_0^T\!\!\int_{\Gamma_m} (\mathbf{u} - \mathbf{u}_m)^2 \ \delta(\mathbf{x} - \mathbf{x}_j) \ \mathrm{d}\Gamma \ \mathrm{dt} + \mathcal{R}(\lambda, \mu), \tag{9}$$

and is subject to the physics of the problem, as expressed by the forward problem statement shown in the preceding section. In the above, $\mathcal{F}$ denotes the objective functional, Γ_m denotes the part of the surface Γ_N^{RD} occupied by measuring stations, N_r denotes the total number of receivers on the surface, and $\mathcal{R}$ has been introduced to alleviate the solution multiplicity. We explore both TN and TV regularization schemes.

We cast the PDE-constrained inverse medium problem (9) with the aid of a Lagrangian $\mathcal{L}$, whereby the misfit functional $\mathcal{F}$ is augmented with the side-imposition of the governing PDEs

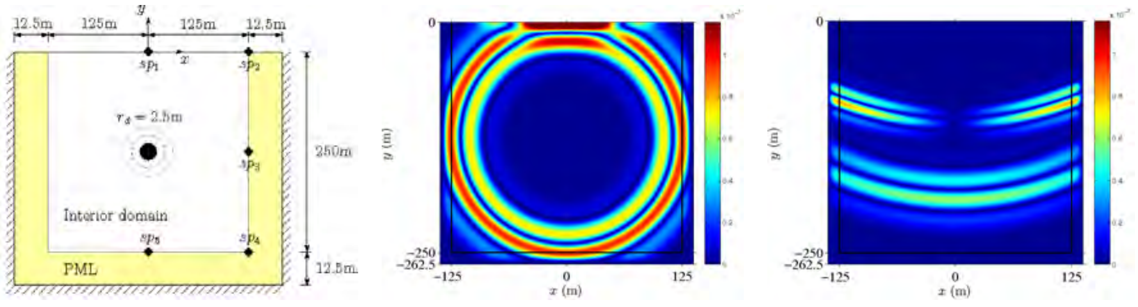

(a) Homogeneous (b) u at $t = 0.218$s (c) u at $t = 0.44$s

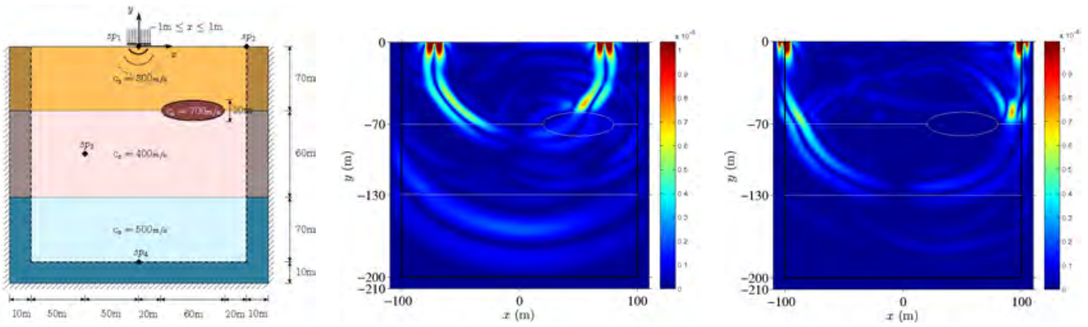

(d) Heterogeneous (e) u at $t = 0.34$s (f) u at $t = 0.45$s

Figure 3: PML-truncated medium in two dimensions

and boundary conditions via Lagrange multipliers, per:

$$
\begin{aligned}
&\mathcal{L}(\mathbf{u}, \mathbf{S}, \boldsymbol{\theta_{u1}}, \boldsymbol{\theta_{u2}}, \boldsymbol{\theta_{s}}, \boldsymbol{\theta_{b1}}, \boldsymbol{\theta_{b2}}, \lambda, \mu) \\
&= \frac{1}{2}\sum_{j=1}^{N_r}\int_0^T\int_{\Gamma_m}(\mathbf{u}-\mathbf{u}_m)\cdot(\mathbf{u}-\mathbf{u}_m)\;\delta(\mathbf{x}-\mathbf{x}_j)\,\mathrm{d}\Gamma\mathrm{d}t \;+\; \mathcal{R}(\lambda,\mu) \\
&+ \int_{\Omega^{\mathrm{RD}}}\int_0^T \boldsymbol{\theta_{u1}}\cdot\left[\mathbf{div}\left\{\mu\left[\nabla\mathbf{u}+(\nabla\mathbf{u})^T\right]+\lambda(\operatorname{div}\mathbf{u})\mathcal{I}\right\}+\mathbf{f}-\rho\ddot{\mathbf{u}}\right]\;\mathrm{d}t\,\mathrm{d}\Omega \\
&+ \int_{\Omega^{\mathrm{PML}}}\int_0^T \boldsymbol{\theta_{u2}}\cdot\left[\mathbf{div}\left(\dot{\mathbf{S}}^T\tilde{\Lambda}_e+\mathbf{S}^T\tilde{\Lambda}_p\right)-\rho\left(a\ddot{\mathbf{u}}+b\dot{\mathbf{u}}+c\mathbf{u}\right)\right]\;\mathrm{d}t\,\mathrm{d}\Omega \\
&+ \int_{\Omega^{\mathrm{PML}}}\int_0^T \boldsymbol{\theta_{s}}:\left\{\mathcal{D}:\left(a\ddot{\mathbf{S}}+b\dot{\mathbf{S}}+c\mathbf{S}\right)-\frac{1}{2}\left[(\nabla\dot{\mathbf{u}})\tilde{\Lambda}_e+\tilde{\Lambda}_e(\nabla\dot{\mathbf{u}})^T+(\nabla\mathbf{u})\tilde{\Lambda}_p+\tilde{\Lambda}_p(\nabla\mathbf{u})^T\right]\right\}\;\mathrm{d}t\,\mathrm{d}\Omega \\
&+ \int_{\Gamma_N^{\mathrm{RD}}}\int_0^T \boldsymbol{\theta_{b1}}\cdot\left\{\left(\mu\left[\nabla\mathbf{u}+(\nabla\mathbf{u})^T\right]+\lambda(\operatorname{div}\mathbf{u})\mathcal{I}\right)\mathbf{n}-\boldsymbol{g}_n\right\}\;\;\mathrm{d}t\,\mathrm{d}\Gamma \\
&+ \int_{\Gamma_N^{\mathrm{PML}}}\int_0^T \boldsymbol{\theta_{b2}}\cdot\left[\left(\dot{\mathbf{S}}^T\tilde{\Lambda}_e+\mathbf{S}^T\tilde{\Lambda}_p\right)\mathbf{n}\right]\;\;\mathrm{d}t\,\mathrm{d}\Gamma. \qquad (10)
\end{aligned}
$$

In the above and in the parlance customarily used for such problems, $\{\mathbf{u},\ \mathbf{S}\}$ are the *state variables* (s), $\{\boldsymbol{\theta_{u1}},\ \boldsymbol{\theta_{u2}},\ \boldsymbol{\theta_{s}},\ \boldsymbol{\theta_{b1}},\ \boldsymbol{\theta_{b2}}\}$ are the Lagrange multipliers or *adjoint variables* (m), and $\{\lambda,\ \mu\}$ are the *control variables* (c). We seek to satisfy stationarity of $\mathcal{L}$ by requiring that the first variations of $\mathcal{L}$ vanish.

3.1 The 1$^{\text{st}}$ optimality condition (State problem)

The variation of $\mathcal{L}$ with respect to the Lagrange multipliers must vanish; accordingly $\delta_{\mathrm{m}}\mathcal{L} = 0$. There results the *state (or forward) problem*, identical to the IBVP given by (5-6).

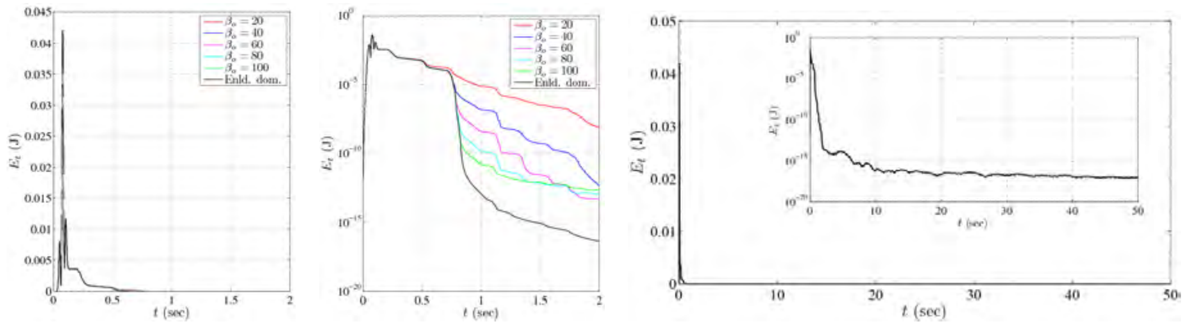

(a) Energy decay (std) (b) Energy decay (log) (c) Long-time stability

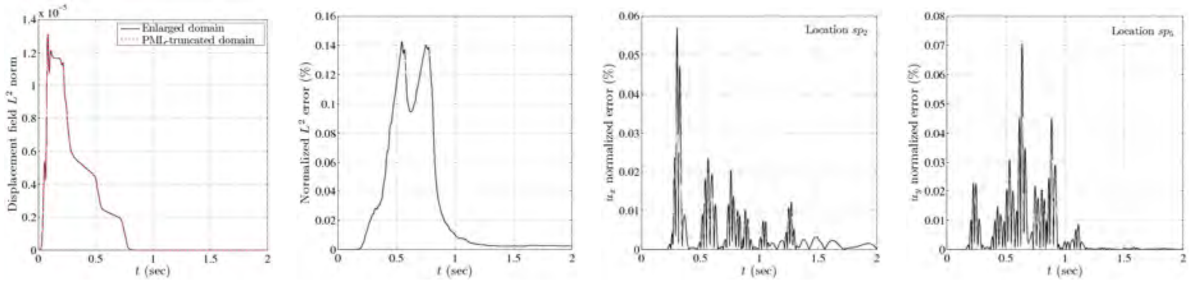

(d) Displacement norm (e) Relative error $e(t)$ (f) $e(t)$ for u_x at sp_2 (g) $e(t)$ for u_y at sp_5

Figure 4: Error metrics for homogeneous domain

3.2 The 2^{nd} optimality condition (Adjoint problem)

Similarly, we enforce the vanishing of the variation of $\mathcal{L}$ with respect to the state variables, that is $\delta_{\mathrm{s}}\mathcal{L} = 0$. There results the following *adjoint problem*:

$$\begin{aligned}
&\mathbf{div}\left[\mu(\nabla\boldsymbol{\theta}_{\boldsymbol{u1}} + \nabla\boldsymbol{\theta}_{\boldsymbol{u1}}{}^T) + \lambda\ \mathrm{div}\,\boldsymbol{\theta}_{\boldsymbol{u1}}\,\mathcal{I}\right] = \rho\ddot{\boldsymbol{\theta}}_{\boldsymbol{u1}} && \text{in } \Omega^{\mathrm{RD}},\\
&\mathbf{div}\left(-\dot{\boldsymbol{\theta}}_{\boldsymbol{s}}\tilde{\Lambda}_e + \boldsymbol{\theta}_{\boldsymbol{s}}\tilde{\Lambda}_p\right) = \rho\left(a\ddot{\boldsymbol{\theta}}_{\boldsymbol{u2}} - b\dot{\boldsymbol{\theta}}_{\boldsymbol{u2}} + c\boldsymbol{\theta}_{\boldsymbol{u2}}\right) && \text{in } \Omega^{\mathrm{PML}},\\
&\mathcal{D} \colon \left(a\ddot{\boldsymbol{\theta}}_{\boldsymbol{s}} - b\dot{\boldsymbol{\theta}}_{\boldsymbol{s}} + c\boldsymbol{\theta}_{\boldsymbol{s}}\right) = \tilde{\Lambda}_p\left(\nabla\boldsymbol{\theta}_{\boldsymbol{u2}}\right)^T - \tilde{\Lambda}_e\left(\nabla\dot{\boldsymbol{\theta}}_{\boldsymbol{u2}}\right)^T && \text{in } \Omega^{\mathrm{PML}},
\end{aligned}$$

subject to

$$\begin{aligned}
&\left\{\mu(\nabla\boldsymbol{\theta}_{\boldsymbol{u1}} + \nabla\boldsymbol{\theta}_{\boldsymbol{u1}}{}^T) + \lambda\ \mathrm{div}\,\boldsymbol{\theta}_{\boldsymbol{u1}}\,\mathcal{I}\right\}\mathbf{n} = \sum_{j=1}^{N_r}(\mathbf{u} - \mathbf{u}_m) && \text{on } \Gamma_m,\\
&\left(-\dot{\boldsymbol{\theta}}_{\boldsymbol{s}}\tilde{\Lambda}_e + \boldsymbol{\theta}_{\boldsymbol{s}}\tilde{\Lambda}_p\right)\mathbf{n} = \mathbf{0} && \text{on } \Gamma_N^{\mathrm{PML}},\\
&\boldsymbol{\theta}_{\boldsymbol{u2}} = \mathbf{0} && \text{on } \Gamma_D^{\mathrm{PML}},\\
&\boldsymbol{\theta}_{\boldsymbol{u1}} = \boldsymbol{\theta}_{\boldsymbol{u2}} && \text{on } \Gamma^{\mathrm{I}},\\
&\left\{2\mu\,\nabla\boldsymbol{\theta}_{\boldsymbol{u1}}^{sym} + \lambda\ \mathrm{div}\,\boldsymbol{\theta}_{\boldsymbol{u1}}\,\mathcal{I}\right\}\mathbf{n} = \left(\dot{\boldsymbol{\theta}}_{\boldsymbol{s}}\tilde{\Lambda}_e - \boldsymbol{\theta}_{\boldsymbol{s}}\tilde{\Lambda}_p\right)\mathbf{n} && \text{on } \Gamma^{\mathrm{I}},\\
&\boldsymbol{\theta}_{\boldsymbol{u1}}(\mathbf{x},T) = \mathbf{0}, \qquad \dot{\boldsymbol{\theta}}_{\boldsymbol{u1}}(\mathbf{x},T) = \mathbf{0} && \text{in } \Omega^{\mathrm{RD}},\\
&\boldsymbol{\theta}_{\boldsymbol{u2}}(\mathbf{x},T) = \mathbf{0}, \qquad \dot{\boldsymbol{\theta}}_{\boldsymbol{u2}}(\mathbf{x},T) = \mathbf{0} && \text{in } \Omega^{\mathrm{PML}},\\
&\boldsymbol{\theta}_{\boldsymbol{s}}(\mathbf{x},T) = \mathbf{0}, \qquad \dot{\boldsymbol{\theta}}_{\boldsymbol{s}}(\mathbf{x},T) = \mathbf{0} && \text{in } \Omega^{\mathrm{PML}}.
\end{aligned}$$

The adjoint problem is a *final-value* problem (requires reverse marching along the time line) and is driven by the misfit between the computed and observed responses at measuring stations. We note that the operators implicated in the adjoint PDEs are identical to the state operators, modulo the sign reversal for those terms implicating first-order time derivatives. By construction, the adjoint equations are also hybrid and PML-endowed, with $(\boldsymbol{\theta_{u1}}, \boldsymbol{\theta_{u2}})$ and $\boldsymbol{\theta_s}$ playing a role analogous to $\mathbf{u}$ and S of the state problem, respectively.

3.3 The 3$^{\text{rd}}$ optimality condition (Control problem)

Lastly, we impose $\delta_\lambda \mathcal{L} = 0$ and $\delta_\mu \mathcal{L} = 0$. The variations result in the following two boundary-value control problems:
λ-*control problem*:

$$- R_\lambda \Delta\lambda - \int_0^T (\operatorname{div} \boldsymbol{\theta_{u1}})(\operatorname{div} \mathbf{u})\, \mathrm{d}t = 0 \qquad \text{in } \Omega^{\mathrm{RD}}, \tag{13a}$$

$$\int_{\Gamma_N^{\mathrm{RD}}} \nabla\lambda \cdot \mathbf{n}\, \mathrm{d}\Gamma = 0 \qquad \text{on } \Gamma_N^{\mathrm{RD}}. \tag{13b}$$

μ-*control problem*:

$$- R_\mu \Delta\mu - \int_0^T \nabla\boldsymbol{\theta_{u1}} : 2\nabla\mathbf{u}^{sym}\, \mathrm{d}t = 0 \qquad \text{in } \Omega^{\mathrm{RD}}, \tag{14a}$$

$$\int_{\Gamma_N^{\mathrm{RD}}} \nabla\mu \cdot \mathbf{n}\, \mathrm{d}\Gamma = 0 \qquad \text{on } \Gamma_N^{\mathrm{RD}}. \tag{14b}$$

In writing (13) and (14), we adopted the TN scheme for regularizing the solutions. If the TV regularization were to be used instead, the first terms in (13a) and (14a) are modified, and the control problems now read

$$- R_\lambda\, \nabla \cdot \left[(\nabla\lambda \cdot \nabla\lambda + \epsilon)^{-\frac{1}{2}}\ \nabla\lambda \right] - \int_0^T (\operatorname{div} \boldsymbol{\theta_{u1}})(\operatorname{div} \mathbf{u})\, \mathrm{d}t = 0 \qquad \text{in } \Omega^{\mathrm{RD}}, \tag{15}$$

$$- R_\mu\, \nabla \cdot \left[(\nabla\mu \cdot \nabla\mu + \epsilon)^{-\frac{1}{2}}\ \nabla\mu \right] - \int_0^T \nabla\boldsymbol{\theta_{u1}} : \left(\nabla\mathbf{u} + \nabla\mathbf{u}^T\right)\, \mathrm{d}t = 0 \qquad \text{in } \Omega^{\mathrm{RD}}. \tag{16}$$

We remark that the TV scheme leads to a nonlinear operator in the control equations, as opposed to the Laplacian operator that results when TN regularization is used.

4 THE INVERSION PROCESS

To satisfy the stationarity of $\mathcal{L}$, all three problems must be solved. However, the simultaneous solution of the resulting KKT system using a *full-space method* is computationally expensive. Alternatively, a *reduced-space method*, in which the coupled system of PDEs are solved in the reduced space of the control variables, is preferable [7, 8]. The procedure is iterative: we start with an assumed initial spatial distribution of the control parameters (λ and μ) and solve the state problem. Then, we solve the adjoint problem. By doing so, we satisfy the first and second optimality conditions, and we iteratively update the control parameters using a conjugate gradient method with inexact line search so that the misfit reduces to a preset tolerance, thereby allowing the third optimality condition to be satisfied. We bring in two remedies that aid the inversion process in reconstructing high-quality material profiles: (a) a regularization factor continuation scheme to penalize high-frequency material oscillations during the early inversion stages, (b) a source-frequency continuation scheme in which a low-frequency excitation typically allows for a rough resolution of the material profile, whereas an excitation with higher-frequency components fine-tunes the profile, and (c) a search-direction biasing scheme, whereby we seek to bias the λ-search directions by the μ-search directions, effectively forcing both parameters to increase simultaneously, during the early inversion iterations. The scheme is motivated by the physics of the problem, and is described by:

$$\mathbf{d}_k^\lambda \leftarrow \|\mathbf{d}_k^\lambda\| \left[W \frac{\mathbf{d}_k^\mu}{\|\mathbf{d}_k^\mu\|} + (1-W) \frac{\mathbf{d}_k^\lambda}{\|\mathbf{d}_k^\lambda\|} \right] \tag{17}$$

where a weighted average of *unit* λ- and μ-search directions are used for the evolution of λ.

5 NUMERICAL EXPERIMENTS

To test the proposed inversion scheme, we discuss next numerical experiments, involving arbitrarily heterogeneous hosts and synthetic data. The first example is a fictitious medium that has material properties varying smoothly with depth. We reduce the half-plane, through truncation, to a $45\text{m} \times 45\text{m}$ computational domain, surrounded on its sides and bottom by a 5m-thick PML, as shown in Fig. 5(a). The material interfaces were extended horizontally into the PML, thereby, avoiding sudden material changes at the interface between the PML and the regular domain. We started the inversion process with a homogeneous profile that has both λ and μ set to 80 MPa. By applying a Gaussian pulse load with a maximum frequency of $f_r = 40$ Hz, we reconstructed the Lamé parameters shown in Fig. 6. Both Lamé parameters are satisfactorily inverted.

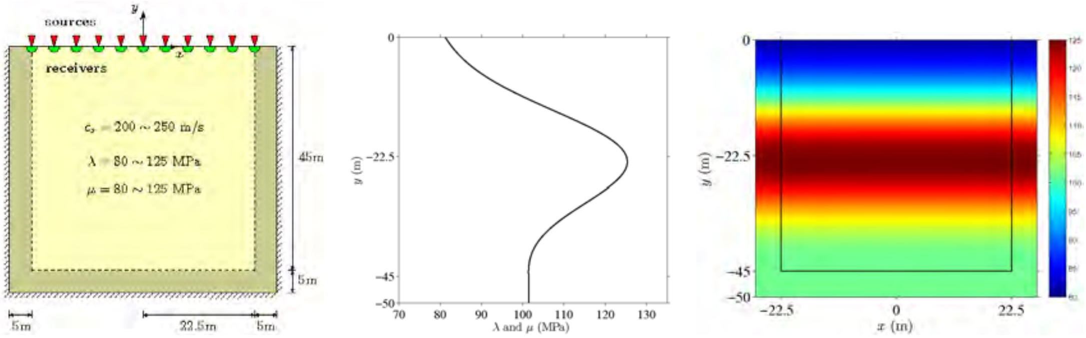

(a) Geometry (b) Cross-section (c) Target λ and μ

Figure 5: A PML-truncated semi-infinite domain in two dimensions

Example 2 involves a horizontally-layered medium with $\lambda(y) = \mu(y) = 80$, 101.25, and 125 MPa from top to bottom, as shown in Fig. 7(a). We use a source-frequency continuation scheme according to which a few time signals with different frequency content are used to probe the domain. We start the inversion process with a low-frequency source and feed the converged reconstructed λ and μ profiles as initial guesses to the problem excited with a higher-frequency source. Here, we considered four different Gaussian pulses with maximum frequencies of 10, 20, 30, and 40 Hz. Figure 8 shows the velocity profiles computed from the reconstructed Lamé parameter profiles. Both velocity profiles seem to be recovered quite satisfactorily.

The last example focuses on a layered medium with $\lambda(y) = \mu(y) = 320$, 500, 720 MPa from top to bottom and an embedded elliptic inclusion of 720 MPa in an effort to implicate arbitrary heterogeneity (Fig. 9). As in Example 2, we use a source-frequency continuation scheme with four distinct Gaussian pulses ($f_{\max} = 10$, 40, 80, and 120 Hz), to probe the

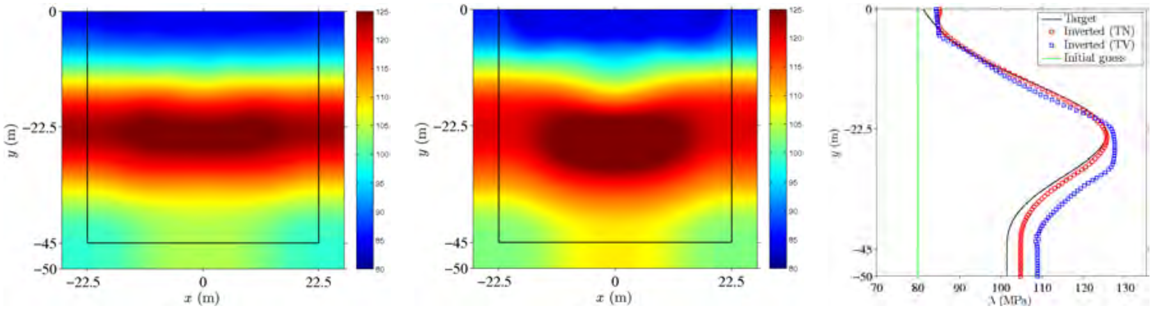

(a) λ (TN) (b) λ (TV) (c) λ at $x = 0$m

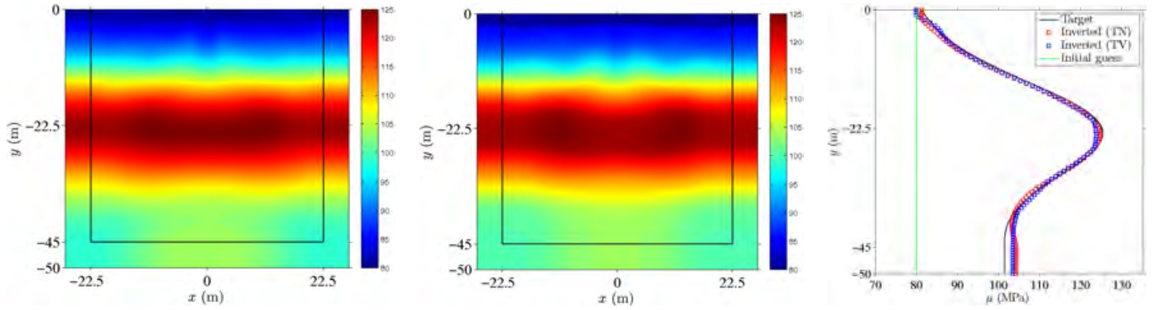

(d) μ (TN) (e) μ (TV) (f) μ at $x = 0$m

Figure 6: Simultaneous inversion for the Lamé parameters using TN and TV regularization

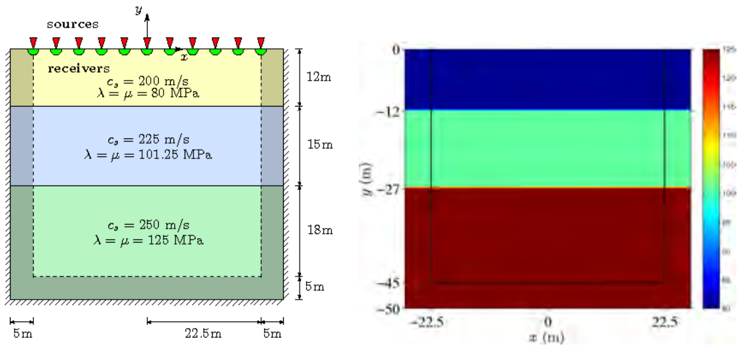

(a) Geometry (b) Target λ and μ

Figure 7: A PML-truncated horizontally-layered semi-infinite domain in two dimensions

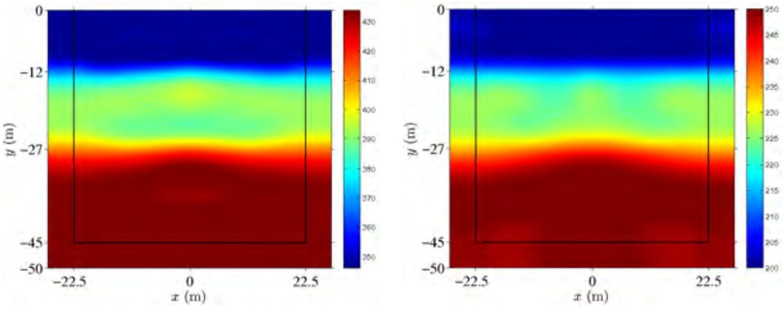

(a) c_p (m/s) (TN)　(b) c_s (m/s) (TN)

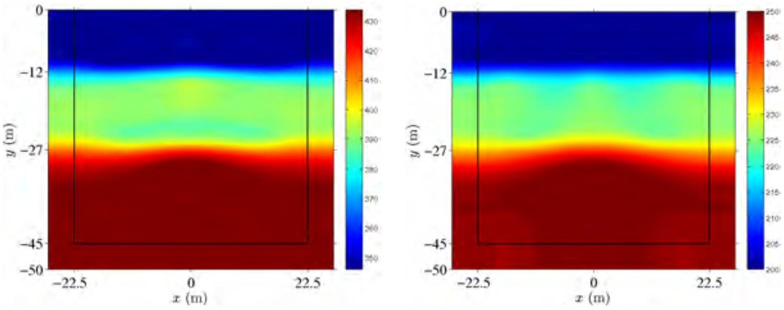

(c) c_p (m/s) (TV)　(d) c_s (m/s) (TV)

Figure 8: Velocities computed from the reconstructed Lamé parameters

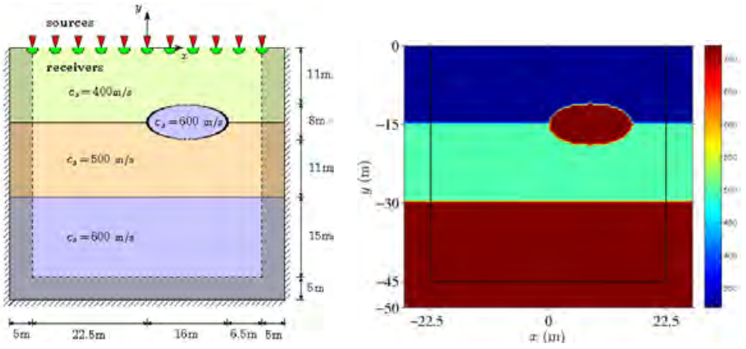

(a) Geometry　(b) Target λ and μ

Figure 9: A PML-truncated layered semi-infinite domain with an elliptic inclusion

domain. Here we opted for using the TV regularization only. We initiated the inversion process with a homogeneous medium that has $\lambda = \mu = 310$ MPa. Figure 10 provides the velocity profiles computed from the reconstructed λ and μ. Once again, both velocity profiles seem to have been recovered with moderate success.

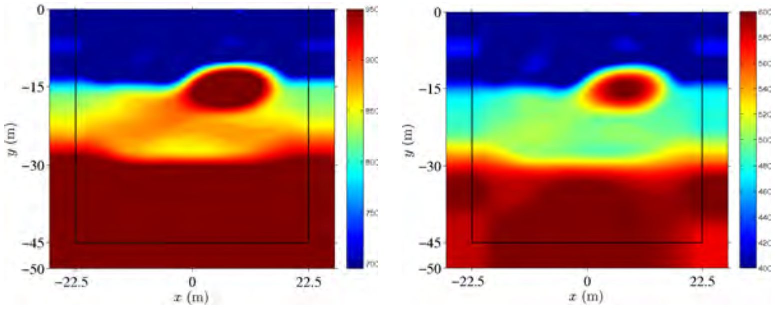

(a) c_p (m/s) (b) c_s (m/s)

Figure 10: Velocities computed from the reconstructed Lamé parameters

6 CONCLUSIONS

We discussed a full-waveform-based inversion methodology in PML-truncated elastic media, suitable for geotechnical site characterization purposes, implemented directly in the time-domain, using stress waves for probing, and driven by the measured response at receivers situated on the ground surface.

We adopted a PDE-constrained optimization approach, and discussed the implementation of the resulting first-order optimality conditions. These gave rise to: a) a state problem that was treated by the a new symmetric hybrid method developed for the forward wave simulation; b) an adjoint problem that was treated also with the hybrid method similarly to the state problem; and c) control problems that were used to update the material parameters. The continuation schemes we deployed assisted the optimizer in narrowing the initial feasibility space by presenting subsequent iterations with improved initial guesses. Though the presentation here is limited to geotechnical applications, the overall structure of the inversion scheme is modular and very flexible, and could be adopted as a solution approach for a broader class of inverse problems. Its performance can be improved by introducing a nonlinear iterative solver that would achieve convergence rates better than the conjugate gradient method used herein, possibly similar to what was proposed in [7].

We discussed our experience in reconstructing heterogeneous profiles involving smoothly-varying profiles, as well as layered systems, and layered media with embedded inclusions, in order to demonstrate the performance of the proposed inversion approach. Here, we described only the two-dimensional case, but the axisymmetric and three-dimensional cases follow directly.

REFERENCES

[1] W.C. Chew, Q.H. Liu, Perfectly matched layers for elastodynamics: a new absorbing boundary condition. *Journal of Computational Acoustics*, **4(4)**, 341–359, 1996.

[2] F. Collino, C. Tsogka, Application of the perfectly matched absorbing layer model to the linear elastodynamic problem in anisotropic heterogeneous media. *Geophysics*, **66(1)**, 294–307, 2001.

[3] U. Basu, A.K. Chopra, Perfectly matched layers for transient elastodynamics of unbounded domains. *Int. J. Numer. Meth. Engng.*, **59**, 1039–1074, 2004.

[4] D. Komatitsch, R. Martin, An unsplit convolutional perfectly matched layer improved at grazing incidence for the seismic wave equation. *Geophysics*, **72(5)**, SM155–SM167, 2007.

[5] K.C. Meza-Fajardo, A.S. Papageorgiou, A nonconvolutional, split-field, perfectly matched layer for wave propagation in isotropic and anisotropic elastic media: Stability analysis. *Bulletin of the Seismological Society of America*, **98(4)**, 1811–1836, 2008.

[6] S. Kucukcoban, L.F. Kallivokas, Mixed perfectly-matched-layers for direct transient analysis in 2D heterogeneous media. *Comput. Methods Appl. Mech. Engrg.*, **200(1-4)**, 57–76, 2011.

[7] I. Epanomeritakis, V. Akçelik, O. Ghattas, J. Bielak, A Newton-CG method for large-scale three-dimensional elastic full-waveform seismic inversion. *Inverse Problems*, **24(3)**, 34015–34040, 2008.

[8] J.W. Kang, L.F. Kallivokas, The inverse medium problem in heterogeneous PMLtruncated domains using scalar probing waves. *Computer Methods in Applied Mechanics and Engineering*, **200(1-4)**, 265–283, 2011.

COMPDYN 2011
III ECCOMAS Thematic Conference on
Computational Methods in Structural Dynamics and Earthquake Engineering
M. Papadrakakis, M. Fragiadakis, V. Plevris (eds.)
Corfu, Greece, 25–28 May 2011

HIGH-PRECISION FE-ANALYSIS FOR SEISMIC COLLAPSE SIMULATION OF STEEL BUILDING FRAMES

T. Yamashita[1], T. Miyamura[2], M. Ohsaki[3], M. Kohiyama[4], D. Isobe[5], K. Onda[6], M. Hori[7], J.Y. Zhang[8], H. Akiba[6] and K. Kajiwara[1]

[1] Hyogo Earthquake Eng. Research Center, National Research Inst. for Earth Science and Disaster Prevention
1501-21 Nishikameya, Mitsuda, Shijimi, Miki 673-0515, Japan
{tyamashi, kaji}@bosai.go.jp

[2] Dept. of Computer Science, College of Eng., Nihon University
1 Nakagawara, Tokusada, Tamura, Koriyama 963-8642, Japan
miyamura@cs.ce.nihon-u.ac.jp

[3] Dept. of Architecture, Graduate School of Eng. Hiroshima University
1-4-1 Kagamiyama, Higashi-Hiroshima 739-8527, Japan
ohsaki@hiroshima-u.ac.jp

[4] Dept. of System Design Eng., Keio University
3-14-1 Hiyoshi, Kohoku, Yokohama 223-8522, Japan
kohiyama@sd.keio.ac.jp

[5] Dept. of Engineering Mechanics and Energy, University of Tsukuba
1-1-1 Tennodai, Tsukuba 305-8573, Japan
isobe@kz.tsukuba.ac.jp

[6] Allied Engineering Corporation
Toyosu Front 9F, 3-2-20 Toyosu, Koto, Tokyo 135-0061, Japan
{onda, akiba}@alde.co.jp

[7] Earthquake Research Institute, The University of Tokyo
1-1-1 Yayoi, Bunkyo, Tokyo 113-0032, Japan
hori@eri.u-tokyo.ac.jp

[8] Dept. of Architecture and Urban Design, Ritsumeikan University
1-1-1 Noji-higashi, Kusatsu 525-8577, Japan
zhang@fc.ritsumei.ac.jp

Keywords: E-Simulator, Steel Frame, Finite Element Method, Solid Element, Parallel Computing.

Abstract. *The project of E-Simulator is under way at Hyogo Earthquake Engineering Research Center (E-Defense), which belongs to National Research Institute for Earth Science and Disaster Prevention (NIED), Japan. E-Defense facilitates the world's largest shaking table. The E-Simulator uses the parallel EF-analysis software package called ADVENTURE-Cluster (ADVC) as a platform, and we carried out elastoplastic seismic response analysis of high-rise building frame with over 70-million DOFs. In this study, we report the results of high-precision FE-analysis for simulation of dynamic collapse behavior of the 4-story steel building frame. The whole frame is discretized into hexahedral elements with linear interpolation functions. In order to improve the accuracy of collapse simulation, a new piecewise linear combined isotropic and kinematic hardening rule is implemented for steel material, and its parameters are identified from the uniaxial material test result. The stud bolts are precisely modeled using multipoint constraints and nonlinear springs. The wire-meshes in the concrete slab are modeled using hexahedral elements. The damping due to plastic energy dissipation of exterior walls is modeled by shear springs between the floors. The accuracy of the model is verified in comparison to the physical test of steel-concrete composite beam subjected to static deformation. It will be shown that elastoplastic dynamic responses of the 4-story frame can be estimated with good accuracy using a high-precision FE-analysis without resort to macro-models such as plastic hinge and composite beam effect.*

1 INTRODUCTION

A project of Earthquake Simulator (E-Simulator) is being carried out at Hyogo Earthquake Engineering Research Center (E-Defense), which belongs to National Research Institute for Earth Science and Disaster Prevention (NIED), Japan. E-Defense facilitates the world's largest shaking table, and develops the E-Simulator, a virtual shaking table, which uses numerical computation to evaluate seismic response of structures. Advantage is taken of exclusive data that are measured in shake-table experiments. The E-Simulator will be applicable to a wide range of structures, such as steel buildings, reinforced concrete structures or ground structures.

A core element of the E-Simulator is a parallel finite element (FE) analysis software package, which is called ADVENTURECluster (ADVC). ADVC is capable to be operated in a large-scale parallel computation environment; indeed, it was operated on Blue Genes in 2006 and nominated as a finalist of 2006 Gordon Bell Prizes [1], [2]. Recently, the elastoplastic seismic response analysis is carried out by using ADVC, for a detailed frame model of a high-rise building, which consists of over 70-million DOFs [3]. The detailed model is made by using solid elements, so that only constitutive relations of materials (not of structure members) are used.

It is natural to be asked whether such a massively parallel computation is needed for the estimate of seismic structure responses; a standard practice is the use of FE-analysis of fiber models. In general, FE-analysis of a fiber model is able to satisfactorily reproduce experimental data if constitutive relations of structure members are tuned up. The E-Simulator needs constitutive relations of materials instead. Even though required computation is much larger, it can reduce efforts which are made to carry out experiments needed for structure member constitutive relations.

In this study, we report E-Simulator’s recent results made for dynamic collapse behavior of a four-story steel building frame. A new constitutive model is developed for steel. A detailed and precise computer model is made for key members of the buildings, by using hexahedral elements with linear interpolation function. Large-scale parallel FE-analysis using the Coarse Grid based Conjugate Gradient (CGCG) method [1], which is fast and robust parallel solver, is applied to these models.

2 PROBLEM SETTING

The target of the E-Simulator virtual shake-table test is a frame structure for a four-story building as shown in Fig. 1 [4]; E-Defense experiments have been made using a full-scale model of this building. The height and the floor area are 14.4 m and 60 m^2, respectively.

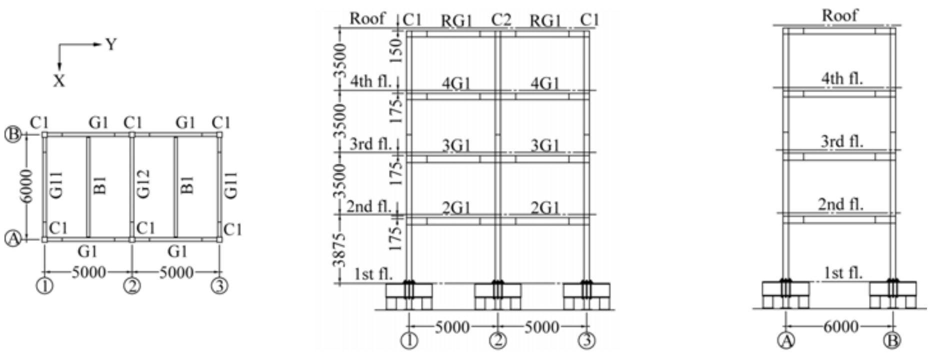

(a) Plan (1st Floor) (b) Y-elevation (longitudinal) (c) X-elevation (transverse)

Figure 1: 4-story steel frame model [4].

FE-models for this frame are presented in Fig. 2; meshes are generated using the data and documents that have been distributed for the blind analysis contest [5], [6], and all the members as well as the floor slabs are modeled in terms of 8-node hexahedral solid elements with tri-linear shape functions. The DOFs of each node are three translational displacement components.

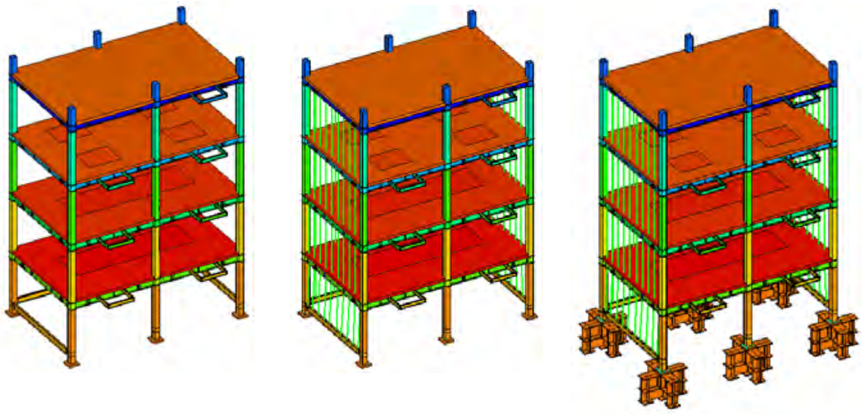

(a) Case A (b) Case B (c) Case C

Figure 2: FE-models of the three cases (drawn without mesh).

2.1 Steel Constitutive Relation

In order to improve the collapse simulation, a more accurate constitutive relation is used for steel. A piecewise linear hardening law with semi-implicit rules that is extended from the conventional combined isotropic and kinematic hardening law is implemented. The piecewise nature of the law has no theoretical background; it is more accurate representation of experimental observation of the hardening characteristics, that is, this law can simulate the yield plateau and the Bauschinger effect. Different rules are used for the first and subsequent loading states.

The parameters used in the piecewise linear law are determined from the cyclic uniaxial material test result. In the present law, it is set that there are six segments in which the hardening law is assumed to be linear, and eleven parameters including ratios between isotropic hardening and kinematic hardening are used to characterize each segment. The curve fitting is applied to determine these parameters, by minimizing the difference between the observed stress-strain relation and the computed one using an optimization algorithm. Figure 3 shows a typical example of the curve fitting for a cyclic uniaxial coupon test [7]. Note that a piecewise linear hardening law with seven segments is used in this example.

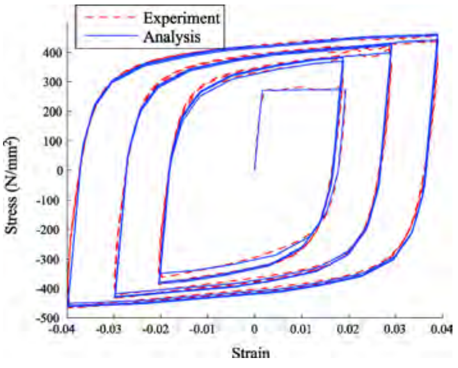

Figure 3: Parameter identification using the cyclic uniaxial coupon test [7].

2.2 Detailed and Precise Modeling

As mentioned, the E-Simulator project is aimed at developing an FE-analysis software package that uses solid elements so that the constitutive relation input is only for materials even though it results in large-scale computation. Detailed and fine meshing is needed for some structure members that have complicated configuration or complicated connection. Such detailed meshing is applied to concrete slabs and column bases as described in the followings.

While the configuration of concrete slabs of the present four-story building is relatively simple, it includes the following members that need special consideration: 1) wire meshes that are embedded in the slab to increase the stiffness; and 2) a set of stud bolts that connect the slab to beams of the floor. The wire-meshes are modeled using hexahedral elements, to evaluate accurately the reinforcement effects of the meshes; see Fig. 4. The wire-meshes are simplified, that is, the circular cross-section is changed to rectangular one and crossing reinforcements are modeled as a unified body. Figure 5 illustrates how the stud bolts are modeled. Rigid beam elements are placed at the location of the stud bolts. They are penetrated up to the second layer of the flange mesh. Note that the rigid beam should be connected to at least two nodes of the flange mesh because each node does not have rotational degree of freedom. Rigid rods are imposed to keep the distance between the beam and the slab constant. The upper end of the rigid beam is not connected to the slab, and that of the rigid rod is connected to a node of the slab mesh. The upper end of the rigid beam is connected to the upper end of the rigid rod by using the truss element. The stiffness of the truss element can be evaluated from the lateral stiffness of the stud considering the effect of the contacted concrete [8], although the lateral stiffness has not been considered for the current model yet.

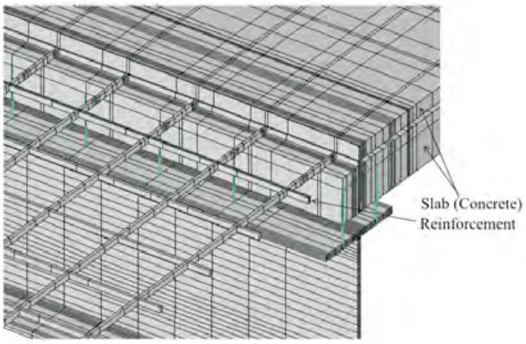

Figure 4: Composite beam.

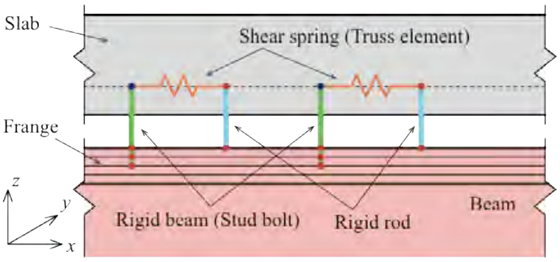

Figure 5: Modeling of stud bolt.

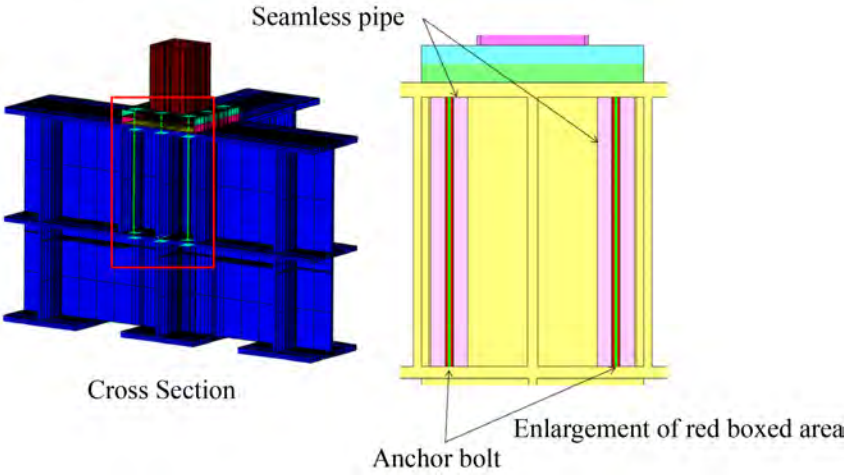

Figure 6: Column base.

Modeling of column base is illustrated in Fig. 6. The upper steel base plate and the lower mortal plate are modeled precisely. On the surface between the steel base plate and the mortar, frictionless contact condition is imposed though multipoint constraints (MPCs) are imposed for the relative displacements in horizontal X and Y directions. On the surface between the mortar and the base, the stick condition is imposed. The base plate and the base are connected by the anchor bolts that are modeled by the truss element. The base is reinforced by the seamless pipes that are also modeled by truss elements.

The extra damping of the exterior wall is due to the energy dissipation of the walls' plastic deformation. Therefore the walls are modeled by elastoplastic shear springs; see Fig. 2 (b) and (c).

Table 1: Model types.

Case	**Column base**	**Stiffness of exterior wall**	**Slab**	**Hardening law for steel**
Case A	Fixed.	Ignored.	No stud bolts, no wire-meshes	Isotropic hardening
Case B	Rotational spring based on the recommendation by Architectural Institute of Japan [9].	Shear spring (truss element) connecting the flanges of the beams in the upper and lower floors. Parameters are identified from the experimental results [10].	No stud bolts, no wire-meshes	Isotropic hardening
Case C	Solid model. Beam element for the anchor bolt with pretension. Contact with small friction between the lower face of base plate and the upper face of base.		With stud bolts and wire-meshes	Piecewise linear combined isotropic and kinematic hardening law with semi-implicit rules

3 RESULTS

In order to study the accuracy of the modeling of the column base, the slab, and the exterior wall, the three models, which are explained in Table 1, are made. Figure 2 depicts FE-models of these three cases.

3.1 Evaluation of Natural Period

If DOFs of the analysis model is large, there is always a possibility that mistakes are made in the pre-process of the model. Natural periods and modes are first examined in the E-Simulator project, in order to find out apparent errors in the pre-process.

Assuming linear elasticity, first 6 eigen-values are computed for the stiffness matrix, from which the natural periods and the associate modes are computed. The results are summarized in Table 2 and Fig. 7. The natural periods observed in the E-Defense experiment are also included in the table. As is seen, the E-Simulator model reproduces natural periods fairly well.

Table 2: Four lowest natural periods for Cases A, B, C and experiment.

Case	**Natural period**			
	1st	**2nd**	**3rd**	**4th**
Case A	0.8389	0.8144	0.5700	0.2702
Case B	0.8303	0.8203	0.5555	0.2700
Case C	0.7836	0.7653	0.5298	0.2549
Experiment [10]	0.80	0.76	---	---

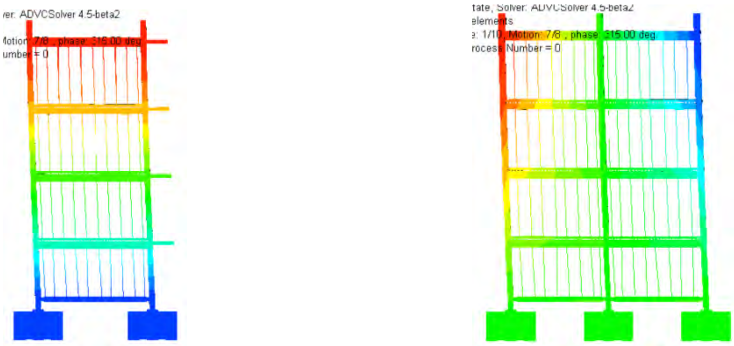

(a) 1st mode

(b) 2nd mode

Figure 7: Two lowest eigenmodes of Case C.

3.2 Time-history Analysis for Nonlinear Collapse Behavior

Here only the results of the time-history analyses for the two models, Cases A and B are shown. The results of Case C will be shown in the presentation. Input strong ground motions are the JR-Takatori wave of the 1995 Hyogo-ken Nanbu Earthquake; the motions are scale by 0.6. The acceleration record measured on the shaking table of the E-Defense experiment is used rather than the numerically scaled ground motion record of the earthquake; see Fig. 8, where the EW, NS, or UD direction correspond to X-, Y-, or Z-directions, respectively. The duration of the motion is 20 s. The Rayleigh damping is used, where the damping factors are 0.02 for the 1st and 4th modes, which are the two lowest modes in the X-direction. The Hilber-Hughes-Taylor method is employed for the time integration; the parameters are $\alpha = -0.05$, $\beta = (1-\alpha)^2/4 = 0.275625$. A super-computer SGI Altix 4700 Intel Itanium 1.66 GHz, 1 node × 256 core, in NIED is used for computation. The computation time is 2,414 s for static analysis for self-weight, and average of 1,106 s for one step (Δt = 0.01 s) of the time-history analysis.

The time histories of inter-story drift angles and shear forces of the first story are plotted in Figs. 9 and 10, respectively. Better agreement with the experiment results is observed for Case B, than Case A. The maximum and minimum values of the inter-story drift angle are {0.01089, –0.01357} rad in the X-direction, and {0.02300, –0.007942} rad in Y-direction, whereas the experimental results are {0.0121, –0.0122} rad in X-direction, and {0.0190, –

0.00933} rad in the Y-direction. Moderately accurate values are obtained by the E-Simulator. Note that residual deformation is observed only in the Y-direction. The story shear forces are calculated by the summation of the products of concentrated mass of each layer and the acceleration at the center of gravity of each layer. The maximum and minimum values of the shear forces are {1142, –1153} kN in the X-direction, and {1385, –1229} kN in the Y-direction. The measured values in the experiment are {1169, –1173} kN in the X-direction, and {1423, –1058} kN in the Y-direction. The shear forces are estimated with good accuracy.

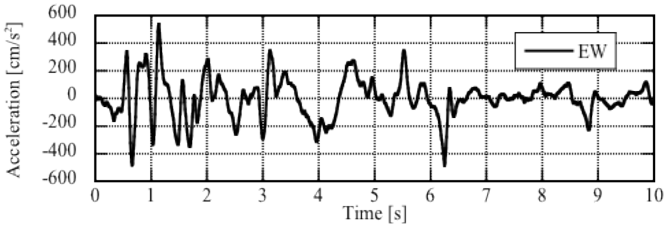

(a) X-direction

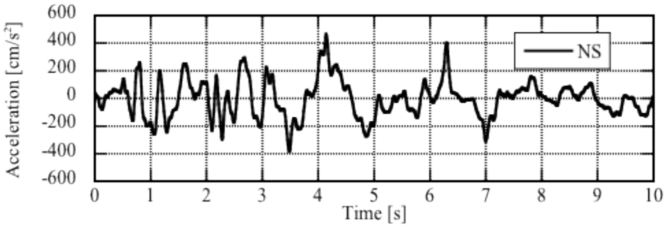

(b) Y-direction

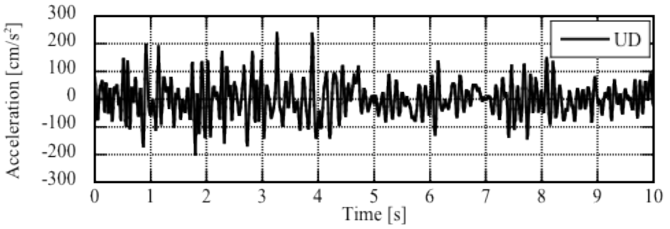

(c) Z-direction

Figure 8: Input acceleration.

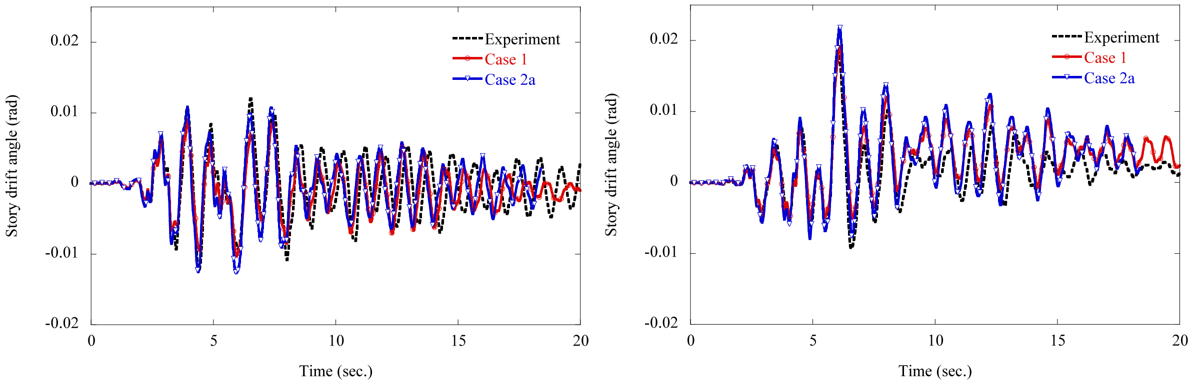

(a) X-direction

(b) Y-direction

Figure 9: Time-history of interstory drift angle of the 1st story.

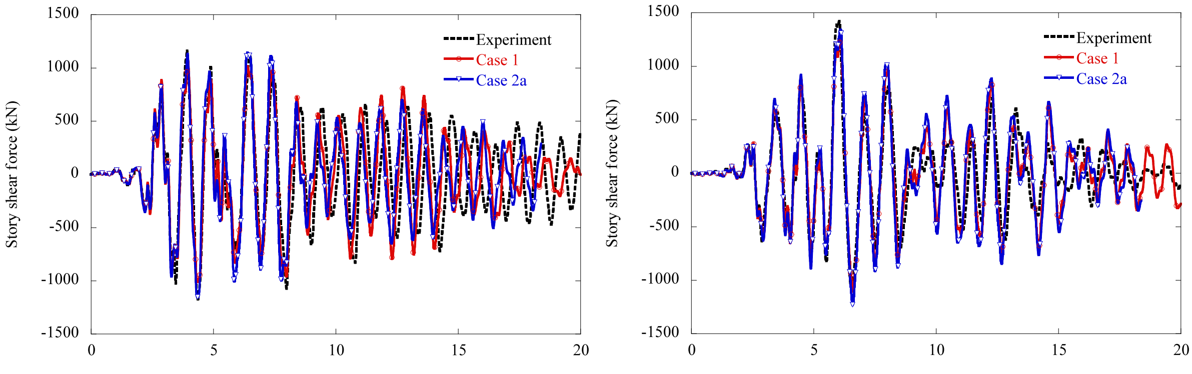

(a) X-direction (b) Y-direction

Figure 10: Time-history of shear force of the 1st story.

4 CONCLUSIONS

- A virtual shake-table test has been carried out using the prototype of the E-Simulator for investigation of elastoplastic dynamic behavior of the 4-story frame model as the specimen of full-scale shake-table test conducted in September 2007 at E-Defense. It has been shown that the large-strain elastoplastic dynamic behaviors can be estimated with good accuracy based on the solid elements and the constitutive relations of the steel material without resort to macro models and empirical parameters such as plastic hinge and stiffness amplification factor of the composite beam.

- The stiffness and strength of the exterior walls are modeled by elastoplastic shear springs. Hence, the use of ambiguous equivalent damping factor due to the friction and plastic deformation of the nonstructural components will be avoided by elaborating the model. This spring model will be further replaced by a solid model that is under development.

- The rotational spring at the column base is replaced by a precise model with hexahedral elements, multipoint constraints and truss elements. Contact between the base plate and the mortar is also considered. This model may reproduce the local behaviors such as collapse behavior at the column base.

- The effect of the wire-mesh on the stiffness of the concrete slab is considered by using a precise model of hexahedral elements. Also, the stud bolts that connect the concrete slab and the beam are modeled by the rigid beams and the truss elements. Contact between the concrete slab and the column is also considered. These modeling approaches may reproduce the behaviors of the composite beam.

5 ACKNOWLEDGEMENTS

This study is a part of E-Defense Seismic Experimental Study and Simulation System Construction Project conducted by E-Simulator Production Committee (Leader: Prof. Muneo Hori, The University of Tokyo). The authors acknowledge the valuable contribution from the committee members, and the financial support by NIED. The contribution by Dr. Yuyama of Allied Engineering Corporation for computation and mesh generation is also acknowledged.

The authors also acknowledge the valuable information from the NEES/E-Defense collaborative research program on steel structures (Leader: Prof. Kazuhiko Kasai, Tokyo Institute of Technology), which was pursued by the Analysis Method and Verification Working Group (Leader: Prof. Motohide Tada, Osaka University) and Building Collapse Simulation

Working Group (Leader: Prof. Keiichiro Suita, Kyoto University). The authors would like to show sincere appreciation to Prof. Satoshi Yamada of Tokyo Institute of Technology, Japan, who has provided us with the experimental results of steel materials.

REFERENCES

[1] H. Akiba, et al., Large scale drop impact analysis of mobile phone using ADVC on Blue Gene/L, *Proc. International Conference for High Performance Computing Networking and Storage (SC06)*, Tampa, 2006.

[2] M. Ogino, R. Shioya, H. Kawai, and S. Yoshimura, Seismic response analysis of nuclear pressure vessel model with ADVENTRUE System on the Earth Simulator, *Journal of The Earth Simulator*, **2**, 41-54, 2005.

[3] M. Ohsaki, T. Miyamura, M. Kohiyama, M. Hori, H. Noguchi, H. Akiba, K. Kajiwara and T. Ine, High-precision finite element analysis of elastoplastic dynamic responses of super-highrise steel frames, *Earthquake Engineering & Structural Dynamics*, **38**, 635-654, 2009.

[4] M. Tada, M. Ohsaki, S. Yamada, S, Motoyui, and K. Kasai, E-Defense tests on full-scale steel buildings: Part 3 – Analytical simulation of collapse, *Proc. Structures Congress 2007*, ASCE, Long Beach, 2007.

[5] M. Ohsaki, K. Kasai, Y. Matsuoka, and J. Y. Zhang, Results of recent E-Defense tests on full-scale steel buildings: Part 2 – Collapse simulation and blind analysis contest, *Proc. Structures Congress 2008*, ASCE, Vancouver, 2008.

[6] T. Hikino, M. Ohsaki, K. Kasai and M. Nakashima, Simulation of E-Defense full-scale shake-table test results of moment-resisting steel frame, *Proc. Behavior of Steel Structures in Seismic Areas*, STESSA 2009, Philadelphia, Taylor & Francis, 137-143.

[7] S. Yamada, T. Imaeda and K. Okada, Simple hysteresis model of structural steel considering the Bauschinger effect, *Journal of structural and construction engineering*, AIJ, **559**, pp. 225-232, 2002. (in Japasese)

[8] K. Yamanobe, Y. Yoshitaka, A. Wada, 2-Dimensional elasto-plastic analysis of steel frames with composite beams incorporating structural non-linearity of headed studs, *Journal of structural and construction engineering*, AIJ, **502**, 135-140, 1997. (in Japanese)

[9] Architectural Institute of Japan (AIJ), Recommendations for the Design and Fabrication of Tubular Structures in Steel, AIJ, 1990. (in Japanese)

[10] Y. Matsuoka, T. Matsumiya, K. Suita, and M. Nakashima, Test on seismic performance evaluation of exterior ALC walls with opening: E-Defense experimental projects for steel buildings – Part 14, *Summaries of technical papers of Annual Meeting Architectural Institute of Japan*, **C-1**, 1081-1082, 2007. (in Japanese)

[11] S. Yamada, K. Suita, M. Tada, K. Kasai, Y. Matsuoka and Y. Shimada, Collapse experiment on 4-story steel moment frame: Part 1 Outline of test results, *Proc. The 14th World Conference on Earthquake Engineering*, pp. S17.1.4, 2008.

COMPDYN 2011
ECCOMAS Thematic Conference on
Computational Methods in Structural Dynamics and Earthquake Engineering
M. Papadrakakis, M. Fragiadakis, V. Plevris (eds.)
Corfu, Greece, 25-28 May 2011

APPLICATION OF PDS-FEM TO SEISMIC FAILURE ANALYSIS OF REINFORCED CONCRETE BRIDGE PIER

M. Hori[1], K. Oguni[2], Y. Takahashi[3], T. Maki[4], S. Okazawa[5] and T. Yamashita[6]

[1] 1Earthquake Research Institute, University of Tokyo,
Yayoi 1-1-1 Bunkyo, Tokyo, 113-0032, JAPAN,
hori@eri.u-tokyo.ac.jp.
[2]Department of System Design Engineering, Keio University,
3-14-1 Hiyoshi, Kohoku, Yokohama, Kanagawa, 223-8522, JAPAN,
oguni@sd.keio.ac.jp.
[3]Disaster Prevention Research Institute, Kyoto University,
Gokasho, Uji, Kyoto, 611-0011, JAPAN,
yos@catfish.dpri.kyoto-u.ac.jp.
[4]Division of Environmental Science and Infrastructure Engineering, Saitama University,
255 Shimo-Okubo, Sakura, Saitama, 338-8570, JAPAN,
maki@mail.saitama-u.ac.jp.
[5]Department of Transportation and Environmental Systems, Hiroshima University,
1-4-1 Kagamiyama, Higashi-Hiroshima, Hiroshima, 739-8527, JAPAN,
okazawa@hiroshima-u.ac.jp

[6]National Research Institute for Earth Science and Disaster Prevention,
1501-21 Nishikameya, Mitsuda, Shijimi, Miki, Hyogo, 673-0515, JAPAN,
tyamashi@bosai.go.jp.

Keywords: PDS-FEM, crack, concrete, seismic structure analysis

Abstract. *Particle-Discretization-Scheme (PDS) is a new discretization scheme which uses a pair of basis functions that discretize a function and its derivatives using characteristic functions, and PDS-FEM is an FEM which is implemented with PDS. It is straight forward to numerically solve a crack problem by means of PDS-FEM. This paper presents an application example of PDS-FEM to seismic structure response analysis of an RC bridge pier. A sophisticated non-linear elasto-plastic constitutive relation is used for concrete, and a detailed model is made. It is shown that the processes in which the pier is damaged and partially failed due to seismic loading are computed. Large plastic deformation as well as initiation and growth of local cracks in concrete are computed.*

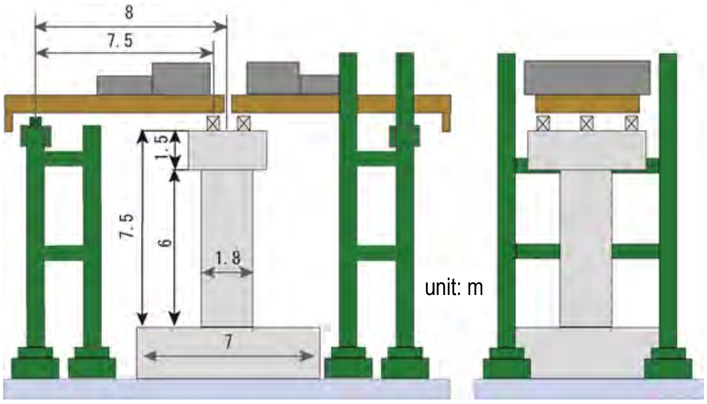

Figure 1: Schematic view of C1-1 Reinforced Concrete Bridge Pier.

1 INTRODUCTION

Earth Defense (E-Defense)[1] is the world largest shaking table that is capable to shake a full scale four story building. A project of Earthquake Simulator (E-Simulator) is aimed at building a virtual shaking table which numerically computes seismic response of a structure which even E-Defense cannot shake[2]. A solid element finite element method is used in E-Defense, so that only material constitutive relations are implemented in it even though large scale numerical computation is inevitable. ADVC is used as a base finite element analysis method in E-Simulator.

Reinforced concrete pier is a core target of E-Defense as well as E-Simulator. As an example, C1-1 Reinforced Concrete Bridge Pier, which was shaken by E-Defense, is presented in Fig. 1; the height of the pier reaches 7.5 m. There are two major characteristics in concrete materials. The first is brittle failure that is induced by single or multiple cracking. Closure of cracking or contact of crack surfaces is important as well as initiation and propagation of cracks.The second is constitutive relations (CCR), which expresses transition from elastic state to elasto-plastic state that accompanies material damage.

The implementation of cracking treatment and a sophisticated CCR into E-Simulator is thus needed. Cracking treatment of E-Simulator is made by applying a new discretization scheme, called Particle Discretization Scheme (PDS). PDS is implemented in E-Simulator. The most complicated but most reliable CCR is being implemented.

This paper briefly reports the current state of implementing PDS and CCR into E-Simulator. Concise but rigorous formulation for PDS and CCR is presented in Section 2. An example problem of seismic structure analysis of a concrete pier is solved in Section 3. This problem uses an E-Defense experiment of a real scale reinforced concrete pier.

2 FORMULATION

2.1 PDS

The main idea of PDS is the use of a characteristic function as a basis function of discretization[3, 4]. Let us denote by D and $\{\Phi^\alpha\}$ the analysis domain and a set of sub-domains of D, repsectively (D is decomposed into $\{\Phi^\alpha\}$). A basis function is ϕ^α, a characteristic function of Φ^α. A discretized function is thus expressed in terms of sub-domain-wise constant functions. This function has discontinuities across $\partial\Phi^\alpha$'s. Derivative of a function is computed by using a different domain decomposition of D. Denoting this decomposition by $\{\Psi^\beta\}$, the derivative is expressed in terms of ψ^β, which is a characteristic function of Ψ^β.

The implementation of PDS to FEM is straightforward. For simplicity, we consider the case that D is a linearly elastic body, and define the following functional for displacement, strain and stress ($\mathbf{u}$, $\boldsymbol{\epsilon}$ and $\boldsymbol{\sigma}$) is used:

$$J(\mathbf{u},\boldsymbol{\epsilon},\boldsymbol{\sigma}) = \int_D \frac{1}{2}\rho\dot{\mathbf{u}}\cdot\dot{\mathbf{u}} - \frac{1}{2}\boldsymbol{\epsilon}:\mathbf{c}:\boldsymbol{\epsilon} + \boldsymbol{\sigma}:(\boldsymbol{\epsilon} - \boldsymbol{\nabla}\mathbf{u})\,\mathrm{d}v, \tag{1}$$

where $\mathbf{c}$ and ρ are elasticity and density, $\boldsymbol{\nabla}\mathbf{u}$ is the gradient of $\mathbf{u}$, and $\cdot$ and $:$ stand for the first- and second-order constraction. The variation of this J leads to the wave eqution,

$$\rho\ddot{\mathbf{u}} - \boldsymbol{\nabla}\cdot(\mathbf{c}:(\boldsymbol{\nabla}\mathbf{u})) = 0. \tag{2}$$

Discretizing $\mathbf{u}$ in terms of $\{\phi^\alpha\}$ and discretizing $\boldsymbol{\epsilon}$ and $\boldsymbol{\sigma}$ in terms of $\{\psi^\beta\}$, we now compute variation for the discretization coefficients and obtain

$$[M][\ddot{u}] + [K][u] = [f] \tag{3}$$

where $[u]$ is a vector for the coefficient of ϕ^α for discretized $\mathbf{u}$ and $[f]$ is a vector of the corresponding nodal force; $[M]$ is a diagonal mass matrix and its diagonal term is $\rho\Phi^\alpha$ with Φ^α standing for the volume of the sub-domain Φ^α; and $[K]$ is

$$k_{ij}^{\alpha\alpha'} = \sum_\beta c_{ipjq}\, b_p^{\beta\alpha}\, b_q^{\beta\alpha'} \tag{4}$$

with $b_p^{\beta\alpha} = \int_D \psi^\beta(\boldsymbol{\nabla}\phi^\alpha)_p\,\mathrm{d}v$.

When a traction-free crack is initiated or propagated onto a facet of $\partial\Phi^\alpha$, the constribution of $\boldsymbol{\nabla}\phi^\alpha$ in the integral of $b_p^{\beta\alpha}$ which is used in Eq. (4) is dropped. Additional boundary tractions need to be discribed on the facet, so that the traction free boundary conditions are met. As an approximation, the traction that has acted befor cracking is cancelled. In this manner, the reduction of $[K]$ and the change in $[f]$ due to the crack initiation or propagation can be rigorously computed in PDS-FEM.

2.2 CCR

Maekawa and his group[5, 6, 7] have proposed the most sophisticated and reliable CCR, which has the following two key relations:

$$\boldsymbol{\sigma} = \mathbf{c}:\boldsymbol{\epsilon}^E, \quad \mathrm{d}\boldsymbol{\epsilon}^P = \boldsymbol{\ell}:\mathrm{d}\boldsymbol{\epsilon}^E, \tag{5}$$

where d stands for the increment, superspcrit E or P designates elastic or plastic parts, respectively; $\mathbf{c}$ and $\boldsymbol{\ell}$ are functions of $\boldsymbol{\epsilon}^E$ which have been determined as experimental relations. An elasto-plasticity or instantaneous modulus tensor which gives strain increment-stress increment relation is thus given as

$$\mathbf{c}^{EP} = (\mathbf{c} + (\boldsymbol{\nabla}\mathbf{c}):\boldsymbol{\epsilon}^E):(\mathbf{I} + \boldsymbol{\ell})^{-1}. \tag{6}$$

where $\boldsymbol{\nabla}\mathbf{c}$ is a six-order tensor which gives the derivative of $\mathbf{c}$ with respect to $\boldsymbol{\epsilon}^E$ and $\mathbf{I}$ is the fourth-oder symmetric unit tensor.

As is seen, $\mathbf{c}^{EP}$ is not symmetric. Furthermore, it loses the positive-definiteness as $\boldsymbol{\epsilon}^E$ increases. The loss of the positive-definiteness will be a bottle neck for a solver which uses a conjugate gradient (CG) method or its extension. Beside the loss of symmetry and positive-definiteness, the numerical computation of $\mathbf{c}^{EP}$ is not trivial since it involves the computation of derivatives and an inverse tensor.

Table 1: Material properties used in numerical simulation.

a) concrete

Young's modulus	25,200 MPa
Poisson's ratio	0.2
compression strength	29.4 MPa
density	2,300 kg/m^3
critical strain for tensile failure	0.001339

b) steel

Young's modulus	197,100 MPa
Poisson's ratio	0.3
density	7,930 kg/m^3

The authors are proposing reformulation of Maekawa's CCR, assuming that an experimental relation between plastic and elastic invariants is a yield function, i.e., $J_2^P - H(J_2^E) = 0$, with H being an experimentally determined function and J_2 being the second invariant of the deviatoric part; this function yields a consistency condition that fully determines plastic strain increment. Indeed, when $\mathrm{d}\boldsymbol{\epsilon}^P = \mathrm{d}g\,\mathbf{d}$ is assumed with $\mathbf{d}$ being a second-order tensor which is experimentally determined, the increment of this yield function produces $\mathrm{d}g\frac{\mathbf{e}^P\mathbf{d}}{2J_2^P} = H'\,\frac{\mathbf{e}^E\mathrm{d}\mathbf{e}^E}{2J_2^E}$. Thus, the reformulated elasto-plasticity tensor is

$$\mathbf{c}^{EP} = (\mathbf{c} + (\boldsymbol{\nabla}\mathbf{c}):\boldsymbol{\epsilon}^E):(\mathbf{I} - \mathbf{L}). \tag{7}$$

where $\mathbf{L} = \Big(DP\,\boldsymbol{\delta} + \frac{\mathbf{e}^E}{J_2^E}\Big) \otimes \Big((\frac{\mathbf{e}^E\mathbf{e}^P}{H'\,J_2^P} + 2)^{-1}\mathbf{e}^E\Big)$.

Unlike the original equation, Eq. (6), $\mathbf{c}^{EP}$ of Eq. (7) does not involve computation of the inversion. Explicit expression of $\boldsymbol{\nabla}\mathbf{c}$ is obtained to further reduce numerical computation. Finally, the stress increment-strain increment is rewritten as

$$\mathrm{d}\boldsymbol{\sigma} = \mathbf{c}:\boldsymbol{\epsilon} + \mathrm{d}\boldsymbol{\sigma}^*, \tag{8}$$

where

$$\mathrm{d}\boldsymbol{\sigma}^* = -\mathbf{c}:\mathrm{d}\boldsymbol{\epsilon}^P + (\boldsymbol{\nabla}\mathbf{c}:\boldsymbol{\epsilon}^E):\mathrm{d}\boldsymbol{\epsilon}^E. \tag{9}$$

Since $\mathbf{c}$ always satisfies the symmetryc and the positive-definiteness, a solver based on the CG method is applicable.

3 NUMERICAL SIMULATION RESULTS

As an illustrative example of PDS-FEM implemented with Maekawa's CCR, we compute the seismic response of the C1-1 which is shown in the introduction; see Fig. 1. The material properties of concrete and steel are summarized in Table 1. Linear tetrahedron elements are used, and the element number, the node number and the degree-of-freedom are 29,740,000, 4,860,000 and 14,580,000, respectively. Concrete and rebars are separately discretized; see Fig. 2. The input strong ground motion is presented in Fig. 3.

A super-computer SGI Altix 4700 Intel Itanium 1.66 GHz, 1 node × 256 core, is used for the computation. It takes 300 s for the computation of linear response at one increment of 0.01 s. The CPU time increases when plastic deformation becomes large as well as cracking takes place in the element. Cracking or the reduction of the element stiffness matrix is made according to the strength of material criterion; if the principal value of the element stress reaches the critical value of the strength, cracking takes place on a facet that is close to the principal value. It should be emphasized that the value of the reduced components of the element that suffers cracking is rigorously computed by using Eq. (4).

First, we examine the quality of the model. Eigen-values and eigen-vectors of the linear elastic deformation is computed, and the eigen-values are converted to the natural frequencies.

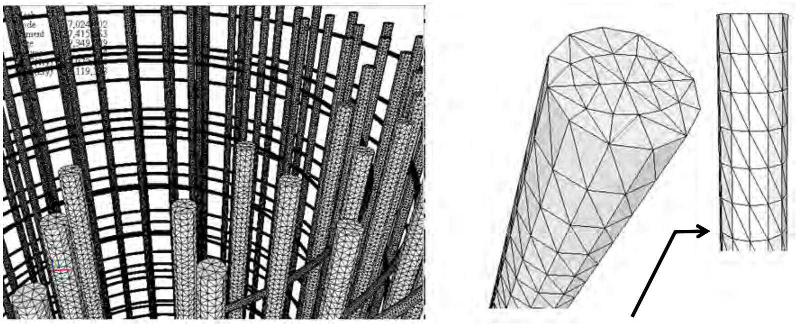

a) steel bar embedded in pier

b) surface covered by rectangular elements of 15 x 7.4 mm

Figure 2: Examples of meshes used in analysis model.

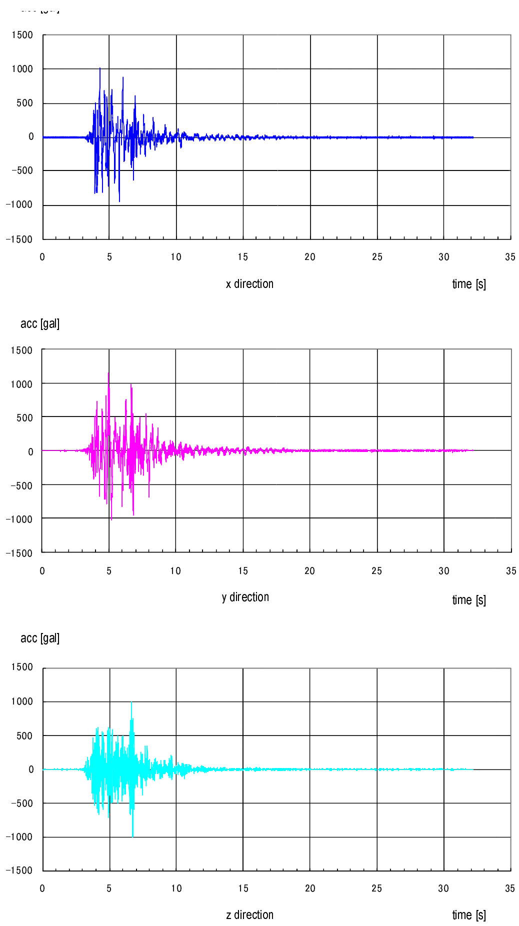

Figure 3: Input strong ground motion; time series of acceleration.

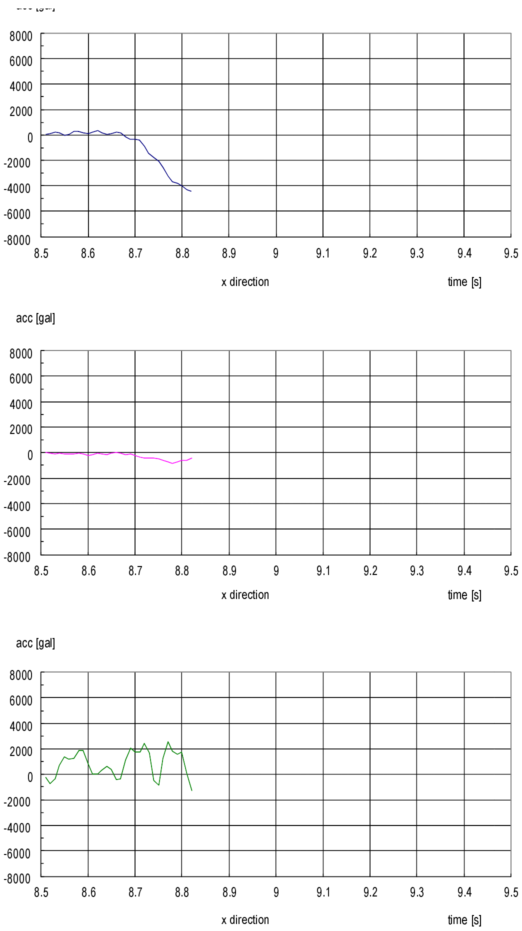

Figure 4: Seismic structure response computed for analysis model.

Table 2: First five natural frequencies of analysis model.

	frequency Hz	mode
1	2.58	1st bending normal to bridge axis
2	2.62	1st bending parallel to bridge axis
3	9.08	torsion
4	24.1	2nd bending normal to bridge axis
5	29.4	2nd bending parallel to bridge axis

Table 3: Number of broken element.

	number of broken elements		CPU time for 0.01 [s]	
time [s]	30 facets	60 facets	30 facets	60 facets
0.800000	0	0	360	420
0.810000	0	0	420	420
0.820000	0	0	420	360
0.830000	0	0	360	360
0.840000	0	0	420	480
0.850000	124	124	1200	1140
0.860000	1,778	2,055	8640	5340
0.870000	4,255	4,366	17400	9420
0.881914	7,094	7,170	24780	15600
0.891914	7,118	7,071	23340	13020
0.901914	21,867	22,654	67800	38640
0.911914	20,273	20,181	72180	38100
total	62,509	63,621		

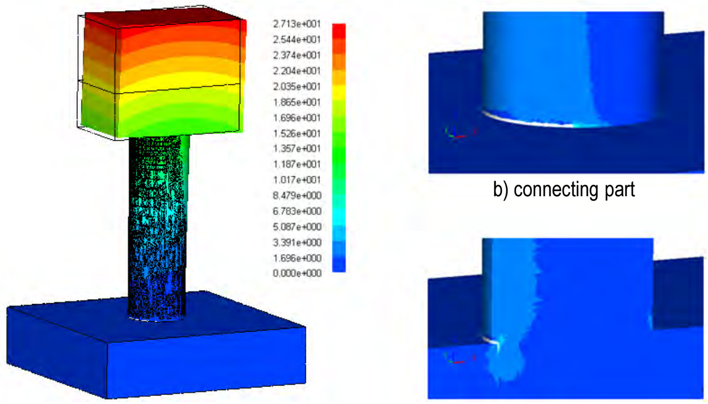

b) connecting part

a) whole view

c) cross section at connecting part

Figure 5: Schematic view of cracking at t =8.81 s.

The first five natural frequencies are shown in Table 2. These values are slightly larger than the experimentally measured data of the natural frequencies of the C1-1. The mode that corresponds to the natufral frequency is described in the table.

At this moment, the numerical computation is finished up to the input of first large shaking. The response of the top part of the pier is shown in Fig. 4. This response will be compared with the experimental data of E-Defense.

In PDS-FEM, cracking is made element-wise. The stiffness element and the nodal force increment are changed when one facet of an element is broken. Thus, it could take an unacceptable CPU time if non-linear computation is made every time one facet is broken, in order to carry out the most accurate computation. In this paper, we use the simultaneous cracking by specifying the maximum number of the facets of elements that are broken during one increment (0.01 s). The results of the number of broken element are summarized in Table 3, where the maximum number of the facets which are broken simultaneously is set as 30 or 60. As is seen, the number of the broken element does not differe significantly for the two cases. From now on, we set the maximum number as 60.

A schematic view of cracking is presented in Fig. 5; a) is the whole view of the pier and b) and c) are the closed-up view of the connecting part. The spatial distribuiton of the vertical normal

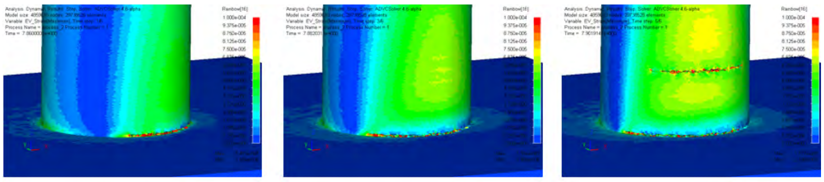

0.86 [s] 0.88 [s] 0.90 [s]

a) surface

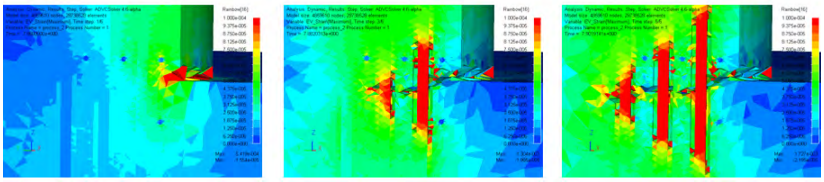

0.86 [s] 0.88 [s] 0.90 [s]

b) stress distribution inside of column

Figure 6: Distribution of broken elements.

stress component is shown. On the surface of the pier, cracking takes place at the connecting part (Fig. 5b)). The crack penetrates inside the pier (Fig. 5c)). The time series of cracking is presented in Fig. 6; a) is for the broken elements on the surface that have cracking and, and b) is for the broken elements inside the pier. The spatial distribution of the vertical normal stress component is plotted, to show that the stress is carried by steel rebars when cracking takes place in concrete.

We first have to admit that the results presented here are tentative and that a systematic evaluation will be made when the numerical computation is finished. At this momenet, however, it is shown that PDS-FEM is capable to simulate *multiple* cracking. In concrete, the crack tip is not broken uniformly, and a few parts of the crack tip are broken. By choosing suitable facets, PDS-FEM computes this cracking. Branching of cracks frequently occurs in concrete, and this cracking is computed, as well. It is certanily true that a model with the same configuration but different meshinng will produce different processes of cracking since PDS-FEM sues mesh boundary (or $\{\partial\Phi^{\alpha}\}$) as candidates of crack facets. A Monte-Carlo simulation of evaluating cracking processes or crack paths will be made by using a few models of the C1-1.

4 CONCLUDING REMARKS

This paper presents an application example of PDS-FEM to the seismic structure response analysis of the C1-1 that was shaken by E-Defense. A sophisticated CCR is implemented into ADVC, and detailed model is constructed. While the numerical computation is not finished, multiple cracking that is often observed in concrete is reproduced.

A sysmatic comparsion of the numerical results of PDS-FEM with the experimental data will be made, in order to clarify the limitations of PDS-FEM and to improve the treatment of cracking. A Monte-Carlo simulation of using different meshing will be made, as well, in oder to evaluate the variability of failure processes.

REFERENCES

[1] E-Defense, Hyogo Earthquake Engineering Research Center (E-Defense), National Research Institute of Earth Science and Disaster Prevention (NIED), Japan, http://www.bosai.go.jp/hyogo/ehyogo/index.html, as of 28 October 2009.

[2] Ohsaki, M., Miyamura, T., Kohiyama, M., Hori, M., Noguchi, H. Akiba, H., Kajiwara, K. and Ine, T.: High-precision finite element analysis of elastoplastic dynamic responses of super-highrise steel frames, *Earthquake Engineering & Structural Dynamics*, 38, 635–654, 2009.

[3] Hori, M., Oguni, K. and Sakaguchi, H.: Proposal of FEM implemented with particle discretization for analysis of failure phenomena, *Journal of the Mechanics and Physics of solids,*, Vol. 53(3), pp. 681–703, 2005.

[4] Wijerathne, M.L.L., Oguni, K. and Hori, M.: Numerical analysis of growing crack problems using particle discretization scheme, *International Journal for Numerical Methods In Engineering,* DOI: 10.1002/nme, 2009.

[5] Maekawa, K. and Okamura, H.: *Nonlinear Analysis and Constitutive Models of Reinforced Concrete,* Giho-Do, 1991.

[6] Maekawa, K., Okamura, H. and Pimanmas, A.: *Non-Linear Mechanics of Reinforced Concrete,* Taylor & Francis, 2003.

[7] Maekawa, K., Ishida, T. and Kishi, T.: *Multi-Scale Modeling of Structural Concrete,* Taylor & Francis, 2008.

COMPDYN 2011
III ECCOMAS Thematic Conference on
Computational Methods in Structural Dynamics and Earthquake Engineering
M. Papadrakakis, M. Fragiadakis, V. Plevris (eds.)
Corfu, Greece, 25–28 May 2011

SEISMIC RESPONSE ESTIMATION OF A NUCLEAR POWER PLANT STRUCTURE CONSIDERING NEARBY FAULT BASED ON A MULTISCALE APPROACH

Pher Errol B. Quinay[1], **Tsuyoshi Ichimura**[2], **and Muneo Hori**[2]

[1] Earthquake Research Institute, University of Tokyo
1-1-1 Yayoi, Bunkyo-ku, Tokyo 113-0032, Japan
equinay2@eri.u-tokyo.ac.jp

[2] Earthquake Research Institute, University of Tokyo
1-1-1 Yayoi, Bunkyo-ku, Tokyo 113-0032, Japan
{ ichimura, hori }@ eri.u-tokyo.ac.jp

Keywords: Fault-structure system, multiscale, nuclear power plant.

Abstract. *An approach to estimate the response of a model of nuclear power plant (NPP) that includes the rupture of a nearby fault using a multiscale approach is demonstrated. The conceptual model is the fault-structure system: a system that models the 3D fault rupture process, wave propagation through the irregular crust structure, effect of local geologic setting at the NPP location, and response of NPP structure. A multiscale method, called Macro-Micro Analysis is employed, which resulted to reduction in computation cost. A reproduction of a recent earthquake event in Kanto region is performed to check the earthquake wave propagation and compare the resulting synthetic seismogram to the recorded seismogram in an observation station. A scenario earthquake simulation is then conducted and the response of NPP under this scenario is obtained. Results have revealed irregular structure deformation caused by the varying phase and amplitude characteristics of the input wave caused by the scenario earthquake.*

1 INTRODUCTION

Estimating the seismic response of nuclear power plant (NPP) structures poses a big computational challenge because of the need to account for the geologic settings of the site. Past earthquakes generated from the nearby fault have shown that NPP is vulnerable to large deformations and large amplitude acceleration. To obtain a reliable structure response, the components of seismic analysis should be modeled with high resolution. It is known that the input ground motion is affected by the following factors: fault-rupture process, irregular crust structure, soft basin layer, and site-specific conditions such as topography and nature of soil at site vicinity. Thus, aiming to model all processes related to these factors is desirable, but as mentioned, to satisfy the high resolution modeling, a large computational environment is needed.

In computation, the above problem is called fault-structure system (FSS). FSS is a conceptual model that includes modeling all the significant processes in the problem of seismic wave propagation and seismic response of structure. The aim of this approach is to account for the three-dimensional (3D) variability of each process (as examples: radiation of seismic waves from the source, response of structure with geometrical irregularities). To reduce the heavy demand for computational resources, a multiscale-based method, called the Macro-Micro Analysis (MMA) has been proposed by Ichimura and Hori [1]. MMA decomposes the FSS problem into two scales and refines the solution as each scale is solved. It is noted that MMA's applicability has been earlier demonstrated on the analysis of large-scale underground structure [1]. This study extends the applicability of this multiscale approach to NPP seismic response estimation.

2 METHODOLOGY

2.1 Multiscale Approach and the Macro-Micro Analysis

It can be observed that two length scales are being considered when solving the FSS – the geologic-length scale (for seismic wave propagation) and engineering-length scale (for seismic structural response). In these two scales, the spatial dimensions would vary from about 10^5 meters for the domain size for seismic wave propagation to about 10^{-1} meters for the structure mesh to obtain high resolution output. Thus, if all components are simultaneously solved, the resulting computation cost can be very high which may not be practical to run in the present computational environment. MMA derives the mathematical basis for performing a multiscale approach applicable to these two scales that reduces the cost of solving the FSS.

The MMA applies the perturbation technique to the elastodynamic problem,

$$d_i\left(c_{ijkl} d_l\left(u_k\right)\right) - \rho \ddot{u}_j = 0 \tag{1}$$

where c_{ijkl}, ρ, $u_k, d_i,$) are the component of elasticity tensor, mass density, displacement component, partial differentiation, and temporal differentiation, respectively.

The singular perturbation expansion method [2] expands the solution u_k of the wave equation as,

$$u_k \approx u_k^{(0)} + \varepsilon u_k^{(1)} + ... \tag{2}$$

where $u^{(0)}$ is solution at low resolution, $u^{(1)}$ is solution at high resolution, and $\varepsilon = X_i/x_i$ is a very small parameter (<<1) that relates the slow spatial variable, X to fast-changing variable, x.

Using Equation (2) on Equation (1) results to two equations that first, computes the solution in the domain of the slow spatial variable, and then refines this solution using the properties near the structure:

$$D_i\left(C_{ijkl} D_l u_k^{(0)}\right) - R \ddot{u}_j^{(0)} = 0 \tag{3}$$

$$d_i\left(c_{ijkl}\left(d_l u_k^{(1)} + d_l u_k^{(0)}\right)\right) - \rho\left(\ddot{u}_j^{(1)} + \ddot{u}_j^{(0)}\right) = 0 \tag{4}$$

where D_i is differentiation with respect to X_i , R is the effective density, and C_{ijkl} is the equivalent elasticity tensor in the domain of the slow spatial variable. Equation (3) and Equation (4) are called the Macro and Micro analysis of the MMA, respectively. Figure 1 shows the schematic of the MMA in relation to FSS. The details of derivation of these equations can be found in Ichimura and Hori [1, 3]

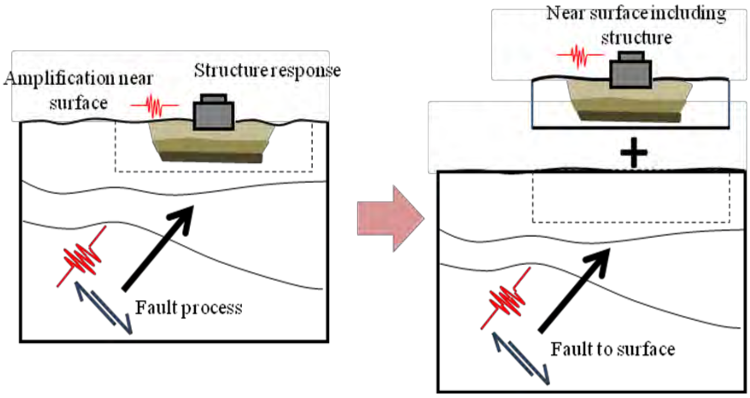

Figure 1: Decomposition of FSS (left) to Macro Analysis (bottom right) and Micro Analysis (top right).

2.2 Computing the Macro and Micro Analysis

In MMA, modeling the earthquake wave generation and propagation (Macro analysis) includes accounting for the fault-rupture settings and the properties of irregular crust structure and basin velocity structures. Given Equation (3), the spatial component is discretized using the Galerkin method, and the time integration method used is Newmark-β (β=1/4) method. A Rayleigh damping term is added to account for material (layer) damping:

$$\left(\mathbf{K}+\frac{2}{\Delta t}\mathbf{C}+\frac{4}{\Delta t^2}\mathbf{M}\right)\mathbf{u}^{n+1}=\left(\frac{2}{\Delta t}\mathbf{C}+\frac{4}{\Delta t^2}\mathbf{M}\right)\mathbf{u}^{n}+\left(\mathbf{C}+\frac{4}{\Delta t}\mathbf{M}\right)\mathbf{v}^{n}+\mathbf{M}\mathbf{a}^{n}+\mathbf{f}^{n} \tag{5}$$

where **K**, **C**, **M**, **u**, **v**, **a**, **f**, *n*, Δt are stiffness matrix, Rayleigh damping matrix, mass matrix, displacement vector, velocity vector, acceleration vector, external force vector, temporal counter, and time step size, respectively.

In the Macro analysis simulation, the response at the nodes that are shared with the boundary of the Micro model is stored as input boundary condition for the Micro analysis. The Micro model includes the site-specific conditions such as soft soil layers that will add to the coarse solution of Macro analysis as refinement. The Micro analysis is carried out following Equation (4). Discretization in space using the Galerkin method and in time using Newmark-β (β=1/4) method, results to an equation similar to Equation (5) without the external force term.

In Macro and Micro modeling, hybrid-grid FEM (HyFEM) [3] is implemented to reduce memory usage and computation time. HyFEM uses the background cell, voxel [4], and octree technique [5] for finite element mesh arrangement and for the analysis, element-by-element method [6] and preconditioned conjugate gradient method (PCG) are implemented. For the details of the Macro and Micro analysis and implementation of the computation techniques, the reader is referred to the following related papers: [1, 3, 7, 8].

3 APPLICATION EXAMPLE

3.1 Reproduction of observed ground motion

The Macro analysis code is validated for application to earthquake simulation by conducting a reproduction of an observed earthquake event. An earthquake that occurred on May 9, 2010 in Tokyo is selected. For the simulation, a region that includes a small part of Kanto region is selected, as shown in Figure 2. The crust layer information derived by Tanaka et al. [9] for this selected region is given on Table 1. The earthquake information (fault parameter) were taken from F-NET [10], and the recorded seismograms on seismic station TKY 021 (about 14.4 km from the epicenter) were taken from K-NET [11]. This earthquake is modeled as a double-couple point source with settings as given in Table 2. In this simulation, the target accuracy is 0.5 Hz. Time step size is 0.01 seconds and total time duration is 40.96 seconds. The criterion for spatial discretization is 10 elements for one wavelength (minimum element size is 100 m). The iterative solver is PCG method with convergence criteria of $1\text{x}10^{-6}$.

Layer	P-wave velocity (m/s)	S-wave velocity (m/s)	Density (kg/m^3)	Quality factor
1	1850	500	1950	60
2	2560	1000	2150	150
3	3200	1700	2300	200
4	5800	3360	2700	500
5	6600	3700	2800	600
6	8040	4480	4400	800

Table 1. Layer material properties used in reproduction of observed earthquake [9].

Date	2010/05/09
Latitude	35.6757 N
Longitude	139.6613 E
Depth	26.73 km
Source time function	$M_o(2t^2/T_o^2)\ \ 0 \le t \le T_o/2$
	$M_o(1-2(t-T_o)^2/T_o^2)\ \ T_o/2 \le t \le T_o$
	$M_o\ \ \ t \ge T_o$
Magnitude	Mw = 3.8
Strike, Dip, Rake	253^o, 17^o, 39^o
Rise time, To	0.18 sec

Table 2. Observed earthquake properties [11].

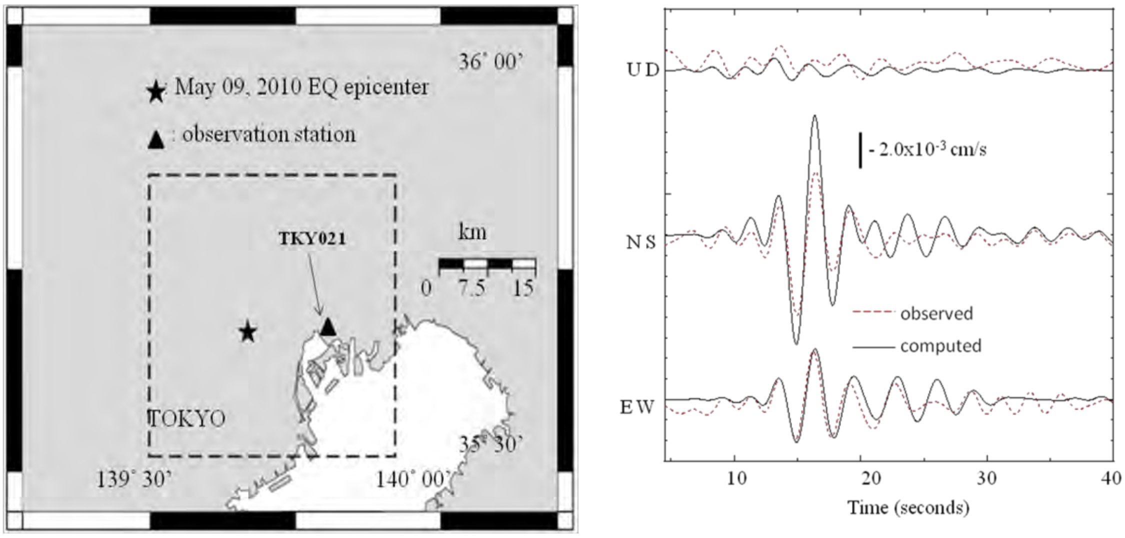

Figure 2: Reproduction of observed earthquake: Left: simulation region and location of epicenter and observation point; Right: comparison of observed and synthetic seismograms at observation station TKY021 (bandpass-filtered [0.0Hz-1.0Hz]).

Figure 2 (right) shows the comparison between the observed and computed (synthetic) seismograms. The comparison shows both agreements and disagreement in amplitude and wave phases at different points, wherein the disagreements can be attributed to the uncertainty in the crust structure data (verified at less than 0.5Hz) and earthquake parameters (moment tensors were derived from inversion analyses using horizontal layered velocity structure [10]). Nevertheless, the results validate the application of Macro analysis code for earthquake wave propagation simulation and for estimating the input boundary condition to the Micro analysis.

3.2 Scenario earthquake and response estimation of NPP

In this section, a scenario earthquake simulation is conducted to perform the complete Macro-Micro Analysis for NPP. For this scenario earthquake, several of the fault parameters are based from the CDPC report for East-Central Tokyo Earthquake Scenario [12] (fault dip and rake, fault rupture speed and fault depth). The fictitious problem setting (as shown in Figure 3) is that the position of the NPP is 13.0 km from the epicenter of a reverse fault close to the surface. The scenario is generated from rupture of a fault plane (modeled as a sequential rupture of points in the fault plane) of about 1.8 km x 1.8 km in dimensions that dips at 45^0 from the horizontal plane (see Figure 3). The depth of the top portion of the fault is about 6 km and rupture propagation speed from the hypocenter (at the depth of 7.2 km) is 2.5 km/s. The details of the point source settings are shown on Table 3.

Hypocenter depth	7.20 km
Rupture speed	2.5 km/s
Source time function	$M_o(2t^2/T_o^2)\ \ 0 \leq t \leq T_o/2$ $M_o(1-2(t-T_o)^2/T_o^2)\ \ T_o/2 \leq t \leq T_o$ $M_o\ \ \ t \geq T_o$
Magnitude	$M_W = 5.3$
Strike, Dip, Rake	30^o, 45^o, 90^o
Rise time, To	0.216 sec

Table 3. Scenario earthquake point source setting

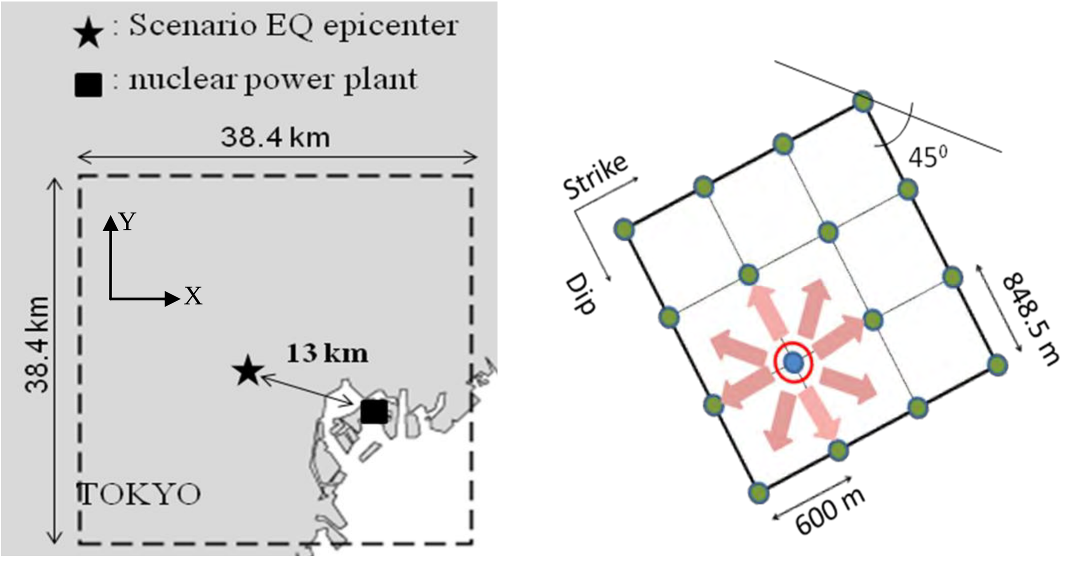

Figure 3: Fictitious problem settings for the scenario earthquake simulation. Left: The relative location of the fault-plane epicenter and the NPP; Right: The fault-plane showing the point sources (in green) that have varied rupture starting time. Hypocenter is encircled in red. Settings of each point source are given on Table 3.

The same model domain and crust layer properties as 3.1 are used. The target accuracy is set at 0.5 Hz. The time increment is 0.01 seconds and total time step is 2048. Criterion for spatial discretization is ten (10) elements for one wavelength (minimum element size is 100 m). The iterative solver is PCG method with convergence criteria of $1\text{x}10^{-6}$. Figure 4 shows the Micro model derived from the Macro model (with location of NPP embedded on engineered fill) and the configuration of the NPP meshed model. The material properties of the NPP and engineered-fill are given on Table 4.

Material	P-wave velocity (m/s)	S-wave velocity (m/s)	Density (kg/m3)	Quality factor
Engineered fill	1500	400	1600	50
NPP	3373	2127	2500	200

Table 4. Material properties

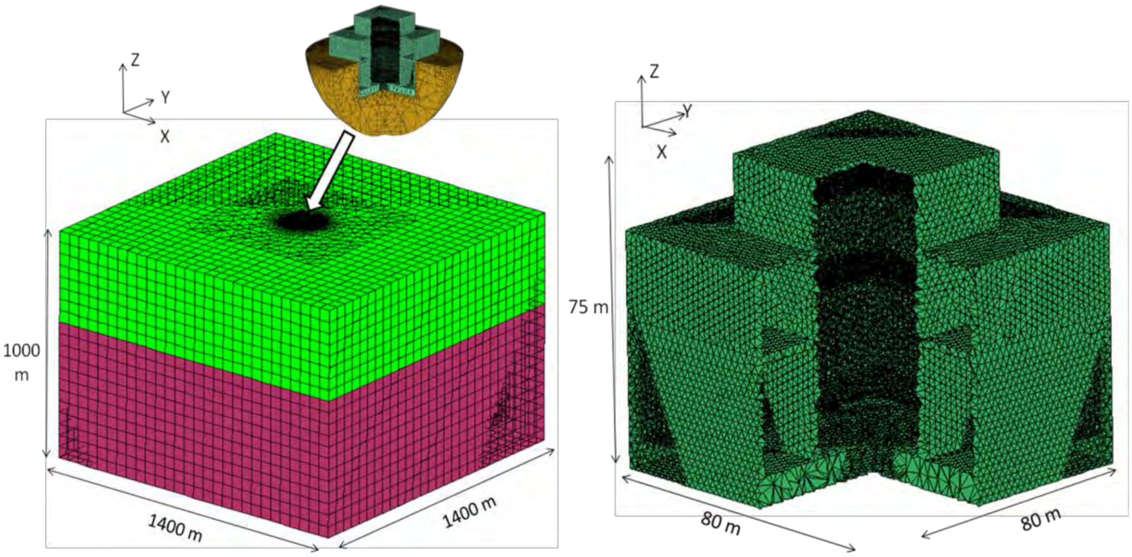

Figure 4: Micro analysis FEM models. Left: the micro model includes two crust layers which are derived from the Macro Analysis model. The location of NPP partially-embedded in an engineered-fill is located at the center of the Micro model; Right: The meshed NPP model and dimensions. The embedded portion is 36.0m from the bottom.

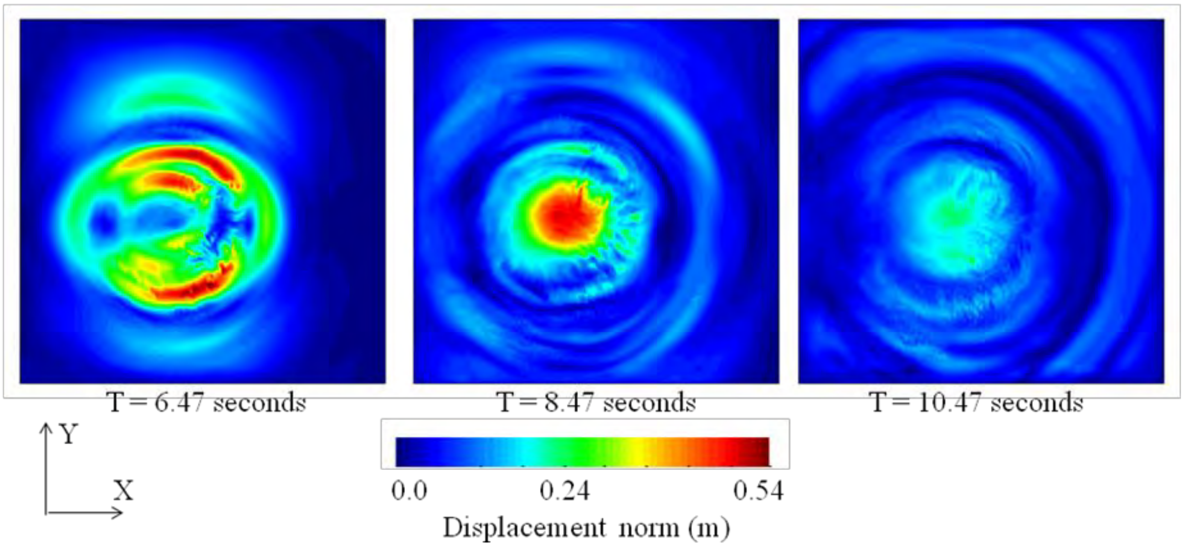

Figure 5: Snapshots of simulation result at surface: displacement norm. The wavefield is made complicated by the effect of the earthquake source, irregular crust structure, and surface topography.

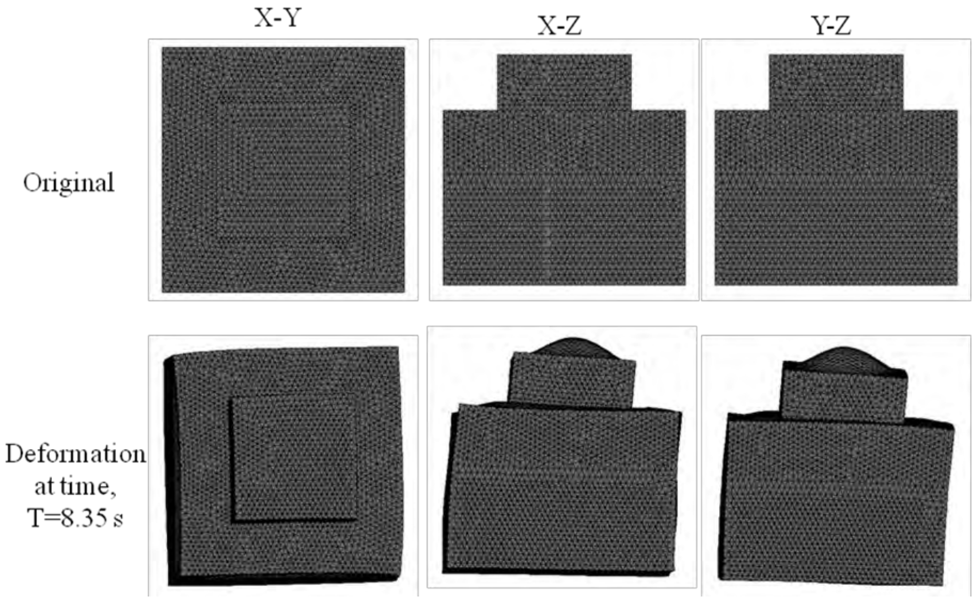

Figure 6: NPP structure deformation (x1500) at time, T = 8.47 seconds. Shown are deformations viewed at three orthogonal directions. Both lateral and vertical deformations are significant because of the effect of configuration of fault plane and direction of rupture.

Figure 5 shows snapshots of the waves at different time intervals as outputted by the Macro Analysis. The corresponding structure response at a given time, as outputted by the Micro Analysis is shown on Figure 6.

Implementing the FSS for estimating the seismic response of NPP from a rupture of a nearby fault is an advantage because the three-dimensional variation of the input wave can be modeled. As shown in Figure 6, the deformation of the NPP varies on all three orthogonal views, evident that the input wave varies in amplitude and phase characteristics in all its spatial components. For an actual NPP, which is geometrically-irregular, the response can be more complicated, and modeling by FSS can aid in identifying the critical locations of the NPP based on the scenario earthquake.

In solving the FSS in a multiscale manner, analysis in geologic- and engineering-length scales are solved efficiently, leading to reduction in computation cost. Thus this methodology would allow for simulations aiming for higher target frequency, which will improve the seismic response estimation of NPP. Given the results presented here, FSS analysis is now being studied for extension to fracture analysis of NPP structures. Moreover, to further reduce the computation time in modeling and analysis, shared and distributed memory parallelization is presently being implemented to the MMA codes.

4 CONCLUSION

An approach to estimate the response of NPP that includes the rupture of a nearby fault using a multiscale approach is presented. This approach, called the FSS, models the important processes related to earthquake wave propagation and seismic response of NPP structure. A multiscale method, called Macro-Micro Analysis is used which resulted to reduction in computation cost. A reproduction of a recent earthquake event in Kanto region is performed to check the earthquake wave propagation and compare the resulting synthetic seismogram to the recorded seismogram in an observation station. A scenario earthquake is then conducted and the response of NPP under this scenario is obtained. Results have shown irregular structure deformation caused by the varying input wave characteristics of the scenario earthquake. These results emphasize the importance of three-dimensional modeling of different components of earthquake wave propagation and structure response for reliable estimation of future strong ground motions.

Acknowledgement

The authors acknowledge the support from the CREST project and Japan Atomic Energy Agency (JAEA).

REFERENCES

[1] T. Ichimura, M. Hori, M., Structural seismic response analysis based on multiscale approach of computing fault-structure system, *Earthquake Engineering and Structural Dynamics*, 38, 439-455, 2009.

[2] D. R. Smith, *Singular Perturbation Theory, An Introduction with Applications*, Cambridge University Press: Cambridge, 1985.

[3] T. Ichimura, M. Hori, J. Bielak, J., A hybrid multiresolution meshing technique for Finite Element three-dimensional earthquake ground motion modeling in basins including topography,” *Geophysical Journal International*. 177, 1221-1232, 2009.

[4] K. Koketsu, H. Fujiwara, Y. Ikegami, Finite Element simulation of seismic ground motion with a voxel mesh, *Pure and Applied Geophysics*, Vol. 161, pp.2183-2198, 2004.

[5] J. Bielak, O. Ghattas, E.J. Kim, Parallel Octree-based Finite Element Method for large-scale earthquake ground motion simulation, *Computer Modeling in Engineering and Sciences*, Vol. 10, 99-112, 2005.

[6] J. M. Winget, and T. J. R. Hughes, Solution algorithms for nonlinear transient heat conduction analysis employing element-by-element iterative strategies,” *Computer Methods in Applied Mechanics and Engineering*., 52, 711-815, 1985.

[7] T. Ichimura, M. Hori, Macro-Micro Analysis method for wave propagation in stochastic media, *Earthquake Engineering and Structural Dynamics*, 35, 419-432, 2006.

[8] T. Ichimura, M. Hori, H. Kuwamoto, Earthquake motion simulation with multiscale Finite-Element Analysis on hybrid grid,” *Bulletin of Seismological Society of America*, Vol. 97, No. 4, 1133-1143, 2007.

[9] Y. Tanaka, H. Miyake, K. Koketsu, T. Furumura, T. Hayakawa, T. Baba, H. Suzuki, T. Masuda, The DaiDaiToku integrated model of the velocity structure beneath the Tokyo Metropolitan Area (2),” *Abstracts of the Japan Geoscience Union Meeting*, S116-P014, 2006.

[10] F-net Broadband Seismograph Network, Japan National Research Institute for Earth Science and Disaster Prevention, http://www.fnet.bosai.go.jp/freesia/

[11] K-net Kyoshin Network, Broadband Seismograph Network, Japan National Research Institute for Earth Science and Disaster Prevention, http://www.k-net.bosai.go.jp

[12] Central Disaster Prevention Council (CDPC) (2004), Working Report on Near-field Earthquake beneath Central Tokyo,
http://www.bousai.go.jp/jishin/chubou/shutochokka/12/shiryo2-2.pdf (in Japanese).

COMPDYN 2011
III ECCOMAS Thematic Conference on
Computational Methods in Structural Dynamics and Earthquake Engineering
M. Papadrakakis, M. Fragiadakis, V. Plevris (eds.)
Corfu, Greece, 25–28 May 2011

SEISMIC PERFORMANCE ANALYSIS OF UNDERGROUND RAMP TUNNEL STRUCTURE USING 3-D MASSIVE NUMERICAL COMPUTATION

Hiroshi Dobashi [1], Yoshihiro Terashima [2], Muneo Hori [3], Tsuyoshi Ichimura [3],

Naoto Ohbo[4], Takemine Yamada[4] and Takashi Obara[4]

[1] Metropolitan Expressway Co., Ltd.
1-4-1 Kasumigaseki, Chiyoda-ku, Tokyo 100-8930, Japan
h.dobashi118@shutoko.jp

[2] Shutoko Engineering Co., Ltd.
3-10-11 Toranomon, Minato-ku, Tokyo 105-0001, Japan
y.terashima@shutoko-eng.jp

[3] Earthquake Research Institute, University of Tokyo
1-1-1 Yayoi, Bunkyo-ku, Tokyo 113-0032, Japan
{hori , ichimura}@eri.u-tokyo.ac.jp

[4] Kajima Technical Research Institute, Kajima Corporation
1-2-7 Motoakasaka, Minato-ku, Tokyo 107-8388, Japan
{ohbo, takemine, obarat}@kajima.com

Keywords: Underground structure, Ramp tunnel, Three-dimensional analysis, FEM, Seismic response analysis, Massive numerical computation.

Abstract. *There is increasing concern about the three-dimensional finite element analysis of large underground tunnels due to the threat of a nearby earthquake generating large strong motion on the tunnel with spatial variation. Using a new numerical analysis method based on massive numerical computation, we carried out a 3-D seismic response analysis of an underground ramp tunnel structure. Based on the finite element method, this method can analyze a large-scale computer model consisting of a nearby ground structure as well as the entire tunnel structure to be studied. As expected, the 3-D seismic response of the tunnel is complicated due to the complex configuration of the tunnel structure. While the intensity of response is smaller than the design criterion, the calculations show large deformation and stress for the part where the ramp tunnel passes through the interface between soft and hard ground layers, with stress and section force varied on the connection with the ramp tunnel. These results suggest that 3-D seismic response analyses should be performed for underground tunnels with complicated configuration which could be subjected to a nearby earthquake.*

1 INTRODUCTION

The working report of the International Tunneling Association (ITA) in 2001 [1] was a state-of-the-art review of earthquake-induced damages and researches on earthquake-resistant designs of tunnels, focusing on practice in the US. In order to perform rational earthquake-resistant design of large tunnels, the report suggested that appropriate aseismic investigations are needed which correctly evaluate the 3-D earthquake motions, response characteristics of the tunnel and dynamic interaction between the tunnel and ground. Since several subway stations were damaged during the Hyogoken-Nanbu Earthquake in 1995 [2], more attention has been paid to the aseismic capability of underground structures. Large-scale underground infrastructures are now being planned and constructed in many countries, and aseismic measures have been employed in many large-scale tunnels such as the Trans-Tokyo Bay Highway tunnel [3] and the Marmaray tunnel crossing the Bosphorus strait [4]. In order to perform rational earthquake-resistant design of large tunnels, we propose a 3-D numerical analysis.

We have developed a large-scale 3-D numerical analysis technique for practical design, and are researching application of the technique to the earthquake-resistant design of actual large tunnels having complicated structures [5, 6]. To make effective use of the expressway networks in metropolitan Tokyo efficiently, a circular route of highway network is being constructed to carry traffic away from the city center. The construction uses tunnels to help preserve the environment. In the case of a highway tunnel, a number of ramp tunnels are necessary for the main tunnel to access the ground surface. These ramp tunnels diverge from and merge into the main tunnel, and pass through several ground layers between the main tunnel and the ground surface. In addition, sections of the ramp tunnels vary in a complex manner and so their seismic response is very complicated. We have been investigating the seismic response of ramp tunnels and the dividing and merging parts between the ramp tunnels and main tunnel.

This paper outlines our large-scale 3-D dynamic FEM analysis technique, and the results of a full-scale 3-D seismic response analysis of a center-ramp-type road tunnel and the surrounding ground. The tunnel is being constructed as part of the Yamate tunnel of the Tokyo Metropolitan Expressway. In past studies [5, 6] the tunnel structure was simplified, but in the present study a very detailed model of the tunnel structure was used to quantitatively evaluate the seismic behavior for practical design. Based on the results, the deformation, displacement, stress and section force of the tunnel structure are evaluated, and the applicability of 3-D numerical analysis for the aseismic design of large tunnels is investigated.

2 3-D DYNAMIC FINITE ELEMENT ANALYSIS METHOD

The material is assumed to be linearly elastic. By reducing the continuous system to a discrete idealization and employing Newmark’s β method in the time domain ($\delta = 1/2$, $\beta = 1/4$), the governing equation can be expressed as:

$$\left(K + \frac{2}{\Delta t} C + \frac{4}{\Delta t^2} M \right) u^{n+1} = \left(\frac{2}{\Delta t} C + \frac{4}{\Delta t^2} M \right) u^n + \left(C + \frac{4}{\Delta t} M \right) v^n + M a^n , \tag{1}$$

where K, M, C and Δt are global stiffness matrix, lumped mass matrix, Rayleigh damping matrix and time increment. u, v, and a are displacement vector, velocity vector, and acceleration vector, respectively. Rayleigh damping is defined as C = aK + bM using K and M, and parameters a and b are determined such that the damping can be appropriately set.

To solve the problem of many degrees of freedom, Ku is built by the element-by-element method [7], and the preconditioned conjugate gradient method [8], which is an iterative analysis method, is adopted. As stiffness matrix of element is evaluated step-by-step, K need not be kept in memory and therefore the problem of significantly many degrees of freedom is overcome. In addition, a combination of non-structure elements and structure elements is used to reduce the computation cost in evaluating stiffness matrix of element in the element-by-element method. Structure elements are used in the large region without approximation of geometrical shape, and non-structure elements are used in the narrow region with complicated shape close around the structure. As there is a single shape of structure element, the number of element stiffness matrixes needed to be kept in memory is the same as the number of materials, and thus the computational cost for the element stiffness matrix is significantly reduced. In this study, second-order tetrahedron elements are used for the non-structure elements, and hexahedron isoparametric elements (voxel elements) for the structure elements. As second-order tetrahedron elements are used for non-structure elements, the response variation in the complicated region close to the structure can be simulated with relatively few elements.

3 ANALYSIS METHOD

The numerical analysis was applied to the center-ramp type road tunnel of the Yamate Tunnel of the Tokyo Metropolitan Expressway, as shown in Fig. 1. The geological section of the ground around the tunnel is shown in Fig. 2. The two main tunnels (outside diameter 12.83 m), 7.25 m apart, employ steel segments. The RC divergence/confluence part and exit/entrance tunnel (called “ramp tunnel” hereafter) are constructed between the two main tunnels. As shown in the figure, the ramp tunnel extends to the surface with a complicated, and varied cross-section of structure. The ground between the main tunnel and ramp tunnel varies from a hard layer with Vs of 400 m/s or more to a soft sedimentary layer with Vs of around 150 m/s. Past studies [5, 6] have clarified that the local structure such as the transverse section depends on the response of the tunnel as a whole. Therefore, the external appearance of the tunnel and main internal structure are very finely modeled, except for some detailed structures that would not affect the main response characteristics.

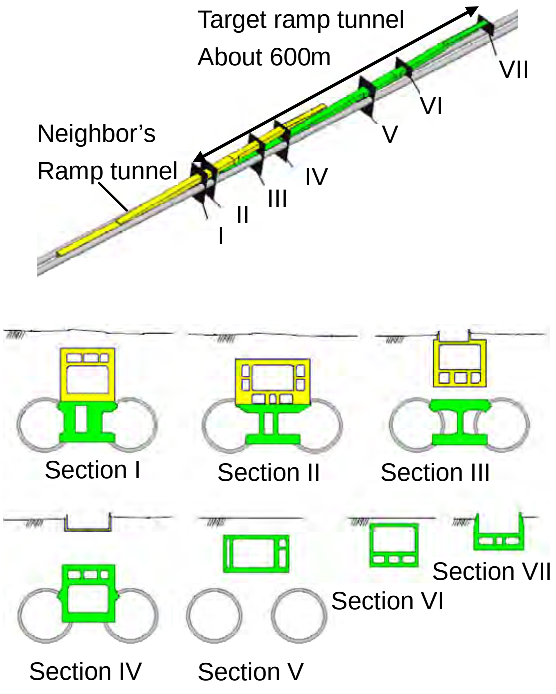

Figure 1: Overview of target ramp tunnel structure in the Tokyo Metropolitan Expressway Central Circular Route: the Yamate Tunnel.

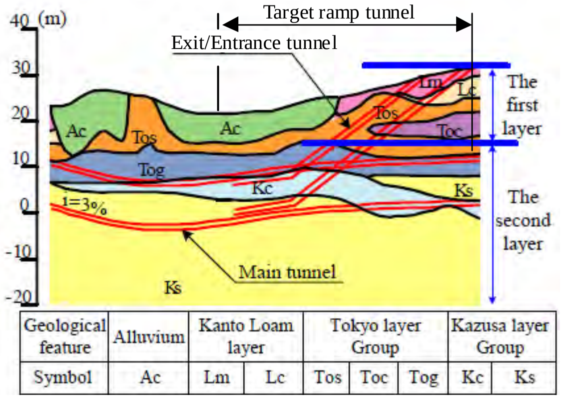

Figure 2: Vertical section of geological profile.

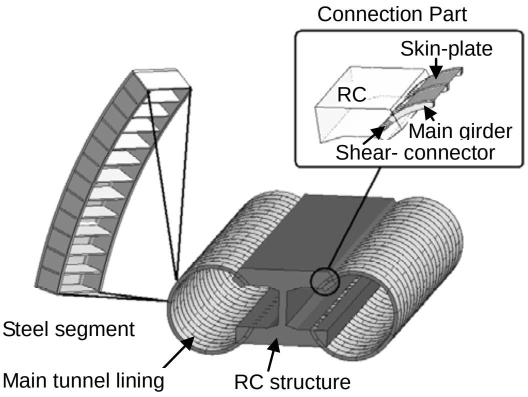

Figure 3: Connection part between main tunnel and RC structure.

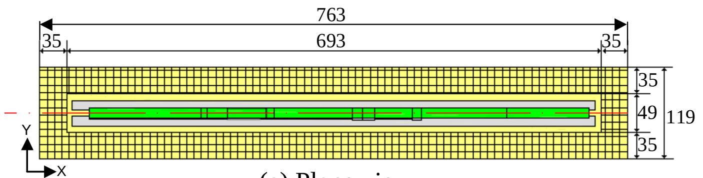

(a) Plane view

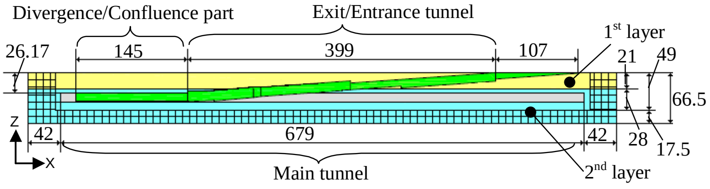

(b) Side view

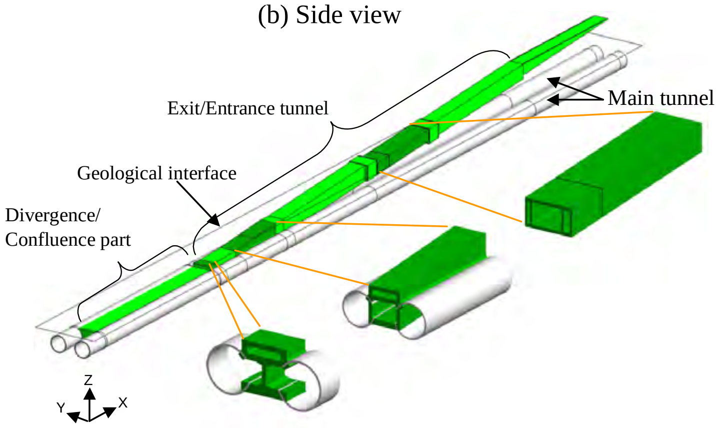

(c) Bird's-eye view for the tunnel structure

Figure 4: Overview of numerical model.

The connection part between the ramp tunnel and main tunnels is important in terms of transferring seismic loading, and therefore the new type of connection structure where a part of the steel shell is embedded in the RC structure is also modeled in detail as shown in Fig. 3. The numerical analysis model is generated as shown in Fig. 4, based on the results of studying the appropriate range for the numerical model used for dynamic analysis [5]. The design strength of concrete in the RC structure is 40 N/mm^2 (40 MN/m^2). As parameters used in the analysis, the elastic constants and Poisson’s ratio corresponding to the design strength are employed. As shown in Fig. 3, the steel segment of the main tunnel consists of main girders and skin plates. For simplicity, the steel segment section is modeled as a solid with the lining being the same thickness as the height of the girders. The elastic constant is determined such that the in-plane bending stiffness of the solid section model is the same as that of the original steel segment. The mass of the solid section model is set such that the unit weight in the longitudinal direction of the tunnel remains the same as the original steel segment (see Table 1). As for Poisson’s ratio, the value for steel (of which the segment is made) is used. As the shear-wave velocity impedance ratio is significantly different, the ground is set as a two-layer model with the upper boundary of the Tog layer as the geological interface between the two layers. A level 2 acceleration wave is used as input motion, as described later. An earthquake response analysis of the free field is performed first using SHAKE, and the converged stiffness and damping ratio are obtained. The parameters for 3-D analysis are determined based on the converged stiffness and damping ratio of the free field, so that the maximum response of the linear analysis matches that obtained through analysis by SHAKE. Therefore, the nonlinear behavior of the ground could be approximately simulated through linear analysis. The parameters for 3-D analysis are listed in Table 2.

Based on the fundamental frequency of ground (0.7 Hz) obtained by analysis using SHAKE, and the predominant frequency range of earthquake waves, the upper limit of the frequency range within which an accurate analysis is assured, is set as 2 Hz. Assuming that the analysis is accurate if the wavelength can cover 10 elements, the element size is set at

	Real structure	Model
Structure	Girders and skin plate	Isotropic solid body
Thickness of lining (mm)	530	530
Thickness of girder (mm)	43	-
Area of cross section (m^2)	0.0493	0.6360
Second moment of area (m^4)	0.001304	0.014888
Modulus of elasticity (N/m^2)	2.10×10^{11}	1.84×10^{10}
Flexural rigidity (Nm^2)	2.738×10^8	2.738×10^8
Mass density (kg/m^3)	7850	609
Mass per unit length (kg/m)	387	387

Table 1: Modelling of main tunnel lining.

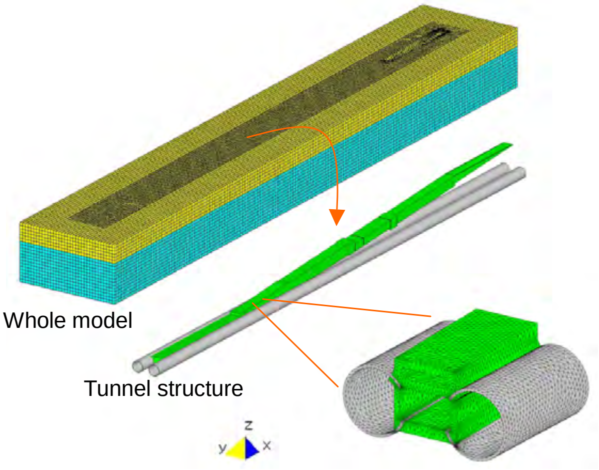

Figure 5: Finite element mesh.

	Mass density ρ (kg/m^3)	Shear wave velocity Vs (m/s)	Poisson's ration v	Damping factor α* (1/sec)
Main tunnel	609	3372	0.30	2.0
Ramp tunnel	2500	2299	0.15	2.0
1st ground layer	1500	60	0.45	2.0
2nd ground layer	2000	400	0.45	2.0

*: Layleigh's mass damping factor

Table 2: Material properties for the analysis.

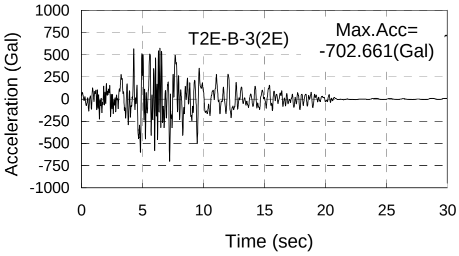

Figure 6: Maximum design earthquake: T2E-B-3.

3.5 m for second-order elements, and 1.75 m for first-order elements. In the meshing of the structure part, at least one element is placed in the cross-section direction to appropriately simulate the distribution of the stress and section force of the structure, and the mesh size is 1 m. It was confirmed that the accuracy of displacement is appropriate and the distributions of stress and section force are tolerable. Figure 5 shows the 3-D finite element model of the structure and ground. The total number of nodes and the total number of elements are 2,638,078 and 2,268,533, respectively. As for the input wave, the maximum design earthquake (T2E-B-3) with maximum acceleration of 702.7 Gal is employed, which is one of the largest earthquake ground motions assumed in current earthquake-resistant design in Japan (Fig. 6). The input wave is epicentral earthquake ground motion (directly underneath type), and the duration of main shaking is 10.23 seconds with a time interval of 0.01 second. The seismic response of free-field ground is performed first, and the input wave is applied at the depth of the bedrock in the actual earthquake-resistant design, which is 5 m below the bottom of the main tunnel. The seismic response at the depth corresponding to the bottom of the 3-D numerical model is computed, which is used as the input wave for the 3-D analysis. Two cases are analyzed: one with the input direction perpendicular to the tunnel longitudinal axis, and the other parallel with the tunnel longitudinal axis.

4 ANALYSIS RESULTS

Figure 7 shows the deformation and displacement of the tunnel when the response of the ground is large. The response of the entrance/exit part of the tunnel in the upper ground layer, where the response is remarkable, is large in the direction of the input wave. When the direction of the input wave is along the tunnel longitudinal axis, compressive stress and

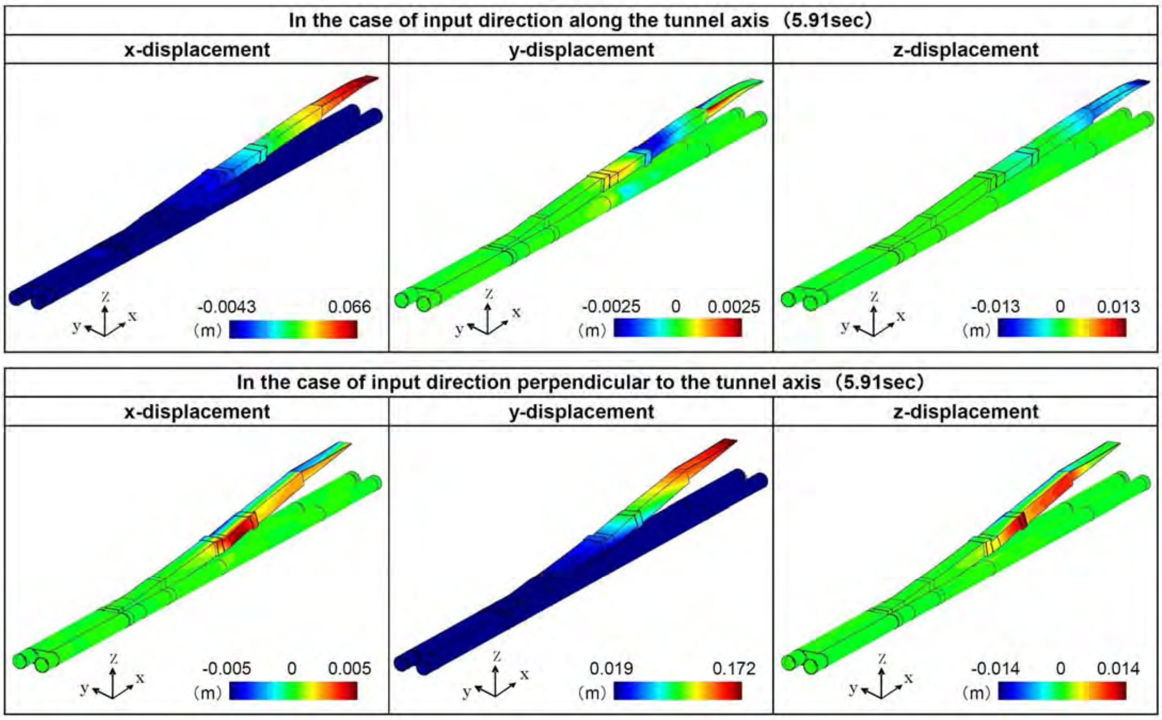

Figure 7: Deformation and displacement of the tunnel.

tensile stress are observed in the tunnel. When the input direction is perpendicular to the tunnel longitudinal axis, the tunnel deforms in the direction perpendicular to the tunnel longitudinal axis, and sectional shear deformation of the tunnel can be observed together with bending and rotating deformation. When the input direction coincides with the tunnel longitudinal axis, the displacement in the x-direction significantly varies at the location where the tunnel structure changes, and also in the area from the ground layer boundary to the middle depth of the upper layer. Due to the large stiffness of the tunnel in the longitudinal direction, the displacement of the tunnel is 0.09 m at the ground surface level, contradicting the larger displacement of the free field ground, which is 0.21m. On the other hand, when the input direction is perpendicular to the tunnel longitudinal axis, the displacement in the y-direction of the tunnel at the ground surface level is 0.17 m, indicating that the tunnel closely follows the ground deformation in the direction of the input wave. In comparison to 0.17 m which is the displacement of the tunnel in the y-direction, the perpendicular displacements in the x-direction and z-direction are 0.005 m and 0.014 m, respectively, and are symmetrically distributed about the central axis of the tunnel. When the input direction is perpendicular to the tunnel axis, a larger response concentrates in the part of the tunnel where the structure is varying, and in the part of the ground where the ground condition is changing.

Figure 8 shows the distribution of stress. The area subject to large stress is shown enlarged in Fig. 9. The main component of stress (with the maximum value shown in parentheses) is σ_{xx} (27 MN/m^2) when the input direction is along the tunnel axis, and the normal stresses are σ_{xx} (25 MN/m^2), σ_{yy} (34 MN/m^2), σ_{zz} (41 MN/m^2) and shear stress is σ_{yz} (29 MN/m^2) when the input direction is perpendicular to the tunnel axis. In each case, the stress in the RC structure is large, and the maximum value is 63–102% of the design strength of concrete. Though the response tends to be large on assumption of the conventional design earthquake assuming plane wave, the increase in stress due to earthquake should be taken into account in the design.

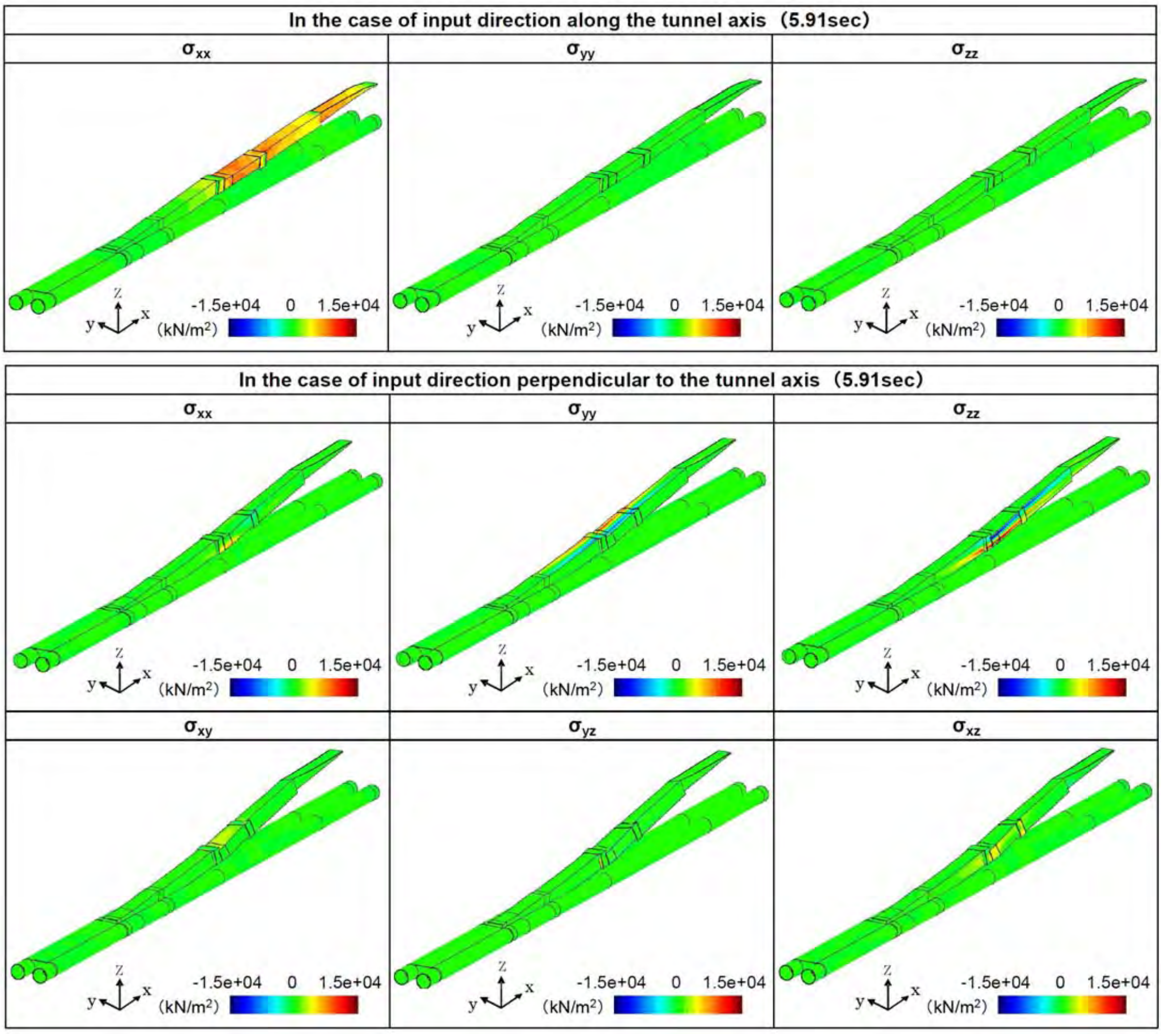

Figure 8: Stress of the tunnel.

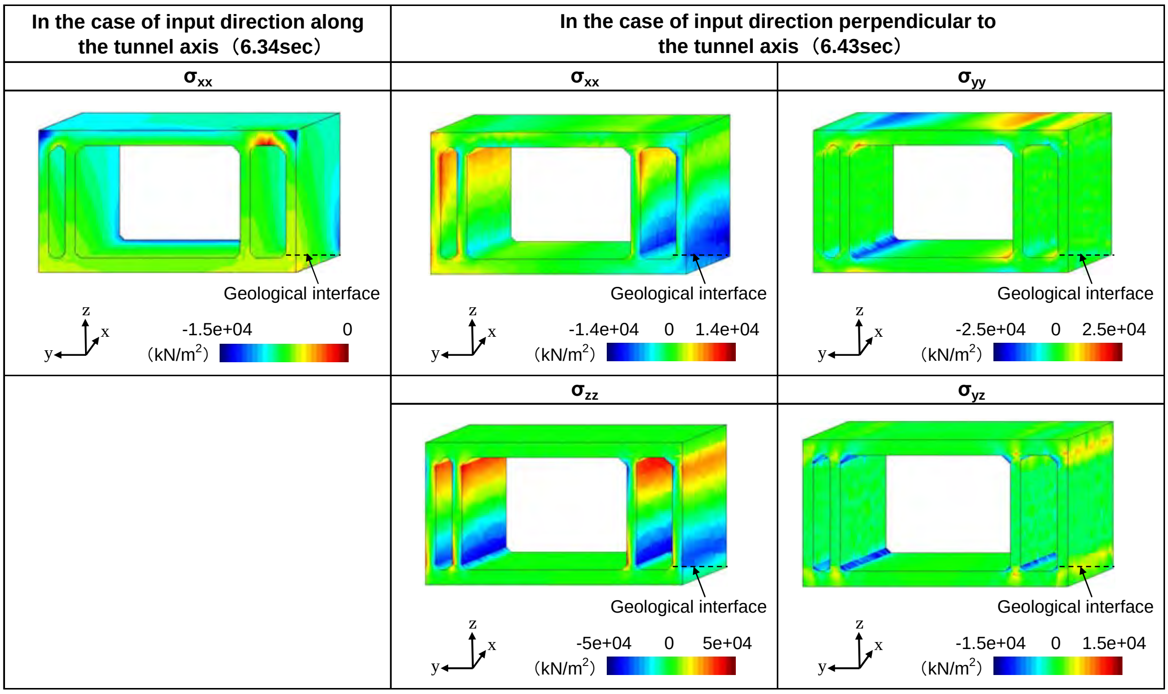

Figure 9: Stress of the tunnel around geological interface at the time when the maximum stress occurs

When the input direction is along the tunnel axis, as shown in Fig. 9, σ_{xx} is not evenly distributed in the transverse section, and becomes large at the corners in some sections. On the other hand, when the input direction is perpendicular to the tunnel axis, the sign of the stress on the left part of the tunnel section differs from that on the right part due to bending in the longitudinal direction of the tunnel, and large stress occurs in the lower part of the side wall of the tunnel above the ground layer boundary. In addition, bending moment is large at the end of the structure member due to the shear deformation of the transverse section of the tunnel, resulting in large fringe stress σ_{yy}, σ_{zz} in the slab and side wall. σ_{yz} is shear stress in the transverse section of the tunnel. In this analysis, although the distribution of stress is reasonably smooth, slight dispersion can be observed in the area with stress concentration due to the use of single elements in the direction of thickness of the tunnel. Therefore, the maximum value of stress may depend on the way of meshing; finer meshing could improve the accuracy of analyzing stress in the stress concentration area.

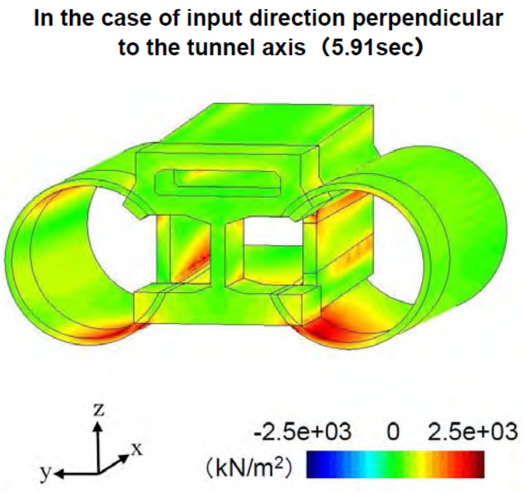

Figure 10: Mises stress around nose point

Figure 10 shows the distribution of Mises stress at the nose part which connects the divergence/confluence part and the exit/entrance tunnel. The distribution of section force in the connection part along the tunnel axis is shown in Fig. 11. It can be seen that the stress locally varies at the nose part where the tunnel section changes (Fig. 10). As for the distribution of section force in the connection part, the section force varies around the nose part and over the middle wall al-though the transverse section is constant (Fig. 11). By carrying out a 3-D analysis using a more detailed model for the local structure in the connection part, a structure with rational cross-section for the connection part to assure the capacity of the connection structure can be determined.

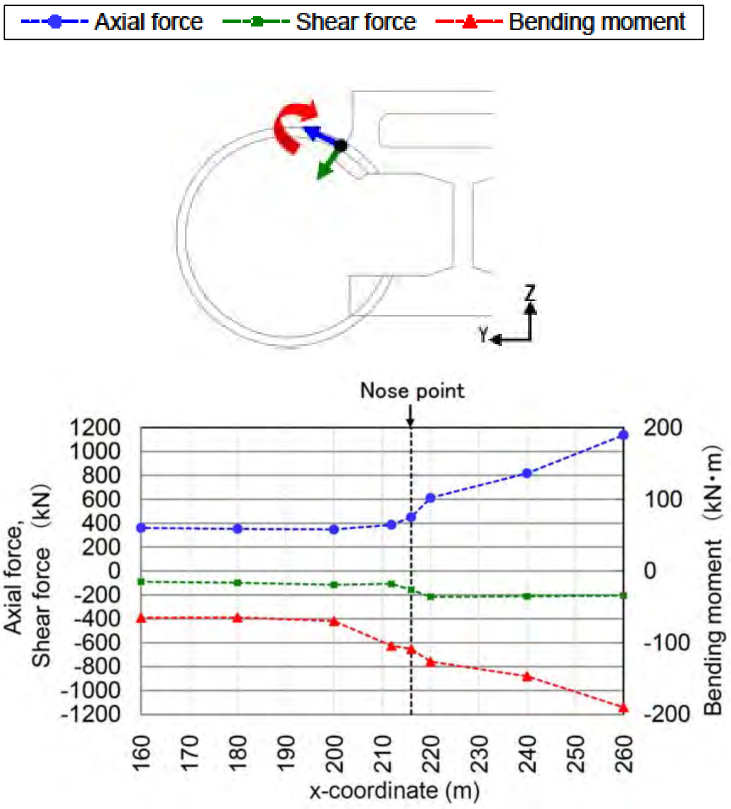

Figure 11: Section force at connection part around nose point

The above stress and section forces are induced due to 3-D interaction. Especially, the shear deformation of ground concentrates in the tunnel within the upper ground layer, and stress in the tunnel significantly increases in the part where the structure varies. It is difficult to rationally evaluate these kinds of behavior by the 2-D response-seismic-coefficient method, which is currently used in practical design, or by the response displacement method for investigating the behavior in the longitudinal direction, where the tunnel and ground are modeled using beam and spring elements. 3-D analysis could identify the location where the aseismic capacity needs to be clarified, and thus it is possible to evaluate their aseismic capability. In addition, the conventional aseismic design method using simplified models tends to overestimate the seismic response [1], and it is possible to perform a more rational design of tunnel structure and to reduce the construction cost by using 3-D analysis. In the actual design of the tunnel in this study, the structure joint is placed in the transverse section of the tunnel at the location of the ramp tunnel above the ground layer boundary to enhance the aseismic capacity of the ramp tunnel around the ground boundary, based on the results of 3-D analysis of the response.

5 CONCLUSIONS

We have developed a large-scale 3-D dynamic FEM analysis technique, and used it to analyze the earthquake response of a center-ramp type road tunnel (ramp tunnel of the Yamate Tunnel of the Tokyo Metropolitan Expressway) with a complicated structure. We clarified that the ramp tunnel with complicated structure displays complex 3-D behavior, and the 3-D analysis could quantitatively evaluate the seismic behavior. In addition, by carrying out seismic response analysis using a full-scale model of the tunnel and ground, it is possible to evaluate the displacement, stress, and section force of the tunnel more precisely, and to determine the location where displacement and stress significantly increase. In order to increase the evaluation accuracy, the forces in the tunnel computed by 3-D analysis could be used as external loading forces for a separately generated detailed model of the local part of the tunnel structure taking nonlinearity into consideration, and thus it is possible to optimally design the tunnel. Through 3-D numerical analysis, a more suitable aseismic design of large tunnel with complicated structure could be realized, and 3-D numerical analysis is an effective approach to rationalize the tunnel structure in the practical design.

REFERENCES

[1] Y.M.A. Hashash, J.J. Hook, B. Schmidt, J.I.C. Yao, Seismic design and analysis of underground structures, *Tunnelling and Underground Space Technology*, Vol.16, 247-293, 2001.

[2] H. Iida, T. Hiroto, N. Yoshida, M. Iwafuji, Damage to Daikai Subway Station, Soils and Foundations, *Special Issue on Geotechnical Aspects of the January 17 1995 Hyogoken-Nambu Earthquake,* Japanese Geotechnical Society, 283-300, 1996.

[3] F. Tatsuoka, K. Uchida, T. Ouchi, Geotechinical engineering aspects of Trans-Tokyo Bay Highway project, *An International Conference on Geotechnical and Geological Engineering(GeoEng 2000)* , Melbourne, Australia, 19-24 November, 2000.

[4] H. Belkaya, I. H. Ozmen, I. Karamut, The Marmaray Project: Managing a large scale project with various stake holders, *Proceedings of the World Congress on Engineering 2008(WCE 2008)*, London, U.K., 2 - 4 July, 2008.

[5] H. Dobashi, E. Ochiai, T. Ichimura, T. Yamada, Y. Yamaki, N. Ohbo, M. Moriguchi, H. Itami, M. Hori, 3D FE Analysis of seismic response of complicated large-scale ramp tunnel structure, *ECCOMAS Thematic Conference on Computational Methods in Structural Dynamics and Earthquake Engineering (Compdyn2007)*, Rethymno, Crete, Greece, 2007.

[6] H. Dobashi, T. Hatsuku, T. Ichimura, M. Hori, T. Yamada, N. Ohbo, M. Moriguchi, H. Itami, Full 3D seismic response analysis of underground ramp tunnel structure using large-scale numerical computation, *The 14th World Conference on Earthquake Engineering*, Beijing, China, 2008.

[7] J.M. Wenget, T.J.R.Hughes, Solution algorithms for nonlinear transient heat conduction analysis employing element-by-element iterative strategies, *Computer Methods in Applied Mechanics and Engineering*, 711-815, 1985.

[8] H.A. van der Vost, Bi-CGSTAB: A fast and smoothly converging variant of Bi-CG for the solution of nonsymmetric linear systems, *SIAM Journal on Scientific Computing*, Vol.13, No.2, 631-644, March, 1992.

COMPDYN 2011
III ECCOMAS Thematic Conference on
Computational Methods in Structural Dynamics and Earthquake Engineering
M. Papadrakakis, M. Fragiadakis, V. Plevris (eds.)
Corfu, Greece, 25–28 May 2011

INTEGRATED SYSTEM FOR EARTHQUAKE IMPACT ASSESSMENT

S. L. Lin[1], A. S. Elnashai[2], J. Li[3], and B. F. Spencer[4]

[1] University of Illinois at Urbana-Champaign
205 N Mathews Ave, Urbana, IL 61801, USA
e-mail: slin30@illinois.edu

[2] University of Illinois at Urbana-Champaign
205 N Mathews Ave, Urbana, IL 61801, USA
{aelnash, jianli3, bfs}@illinois.edu

Keywords: NISRAF, Earthquake Impact Assessment, Hybrid Simulation, Hazard Characterization, Model Calibration, Hybrid Fragility Analysis, Uncertainty Quantification.

Abstract. *NEES Integrated Seismic Risk Assessment Framework (NISRAF) integrates several components in order to obtain the most reliable earthquake impact assessment results: hybrid simulation with free-field and structural sensor measurements, hazard characterization, system identification-based model updating technology, hybrid fragility analysis, and impact assessment tool. Software has been built and verified, concurrently, via applications to an actual test bed in California. Regional impact assessment results of the Los Angeles area under the 1994 Northridge earthquake, using the generated hazard map and fragility curves, showed reasonable accurate, although conservative. Also, the implemented uncertainty quantification analysis aids decision-makers to judge the estimated losses easily and quickly, which will contribute to the development of more suitable and more confident recovery plans and emergency responses.*

The novelty of the proposed system derives primarily from the integration of components of earthquake impact assessment—most of which have not been deployed in such an application before. To achieve seamless integration and to arrive at an operational system, several components were used innovatively, tailored to perform the role required by NISRAF. The integrated system brings the advanced tools of earthquake hazard and structural reliability analyses into the context of societal requirement for accurate evaluation of the impact of earthquakes on the built environment.

1 INTRODUCTION

The 2008 Sichuan, China, earthquake caused thousands of deaths and over $150 billion economic losses [1]. In 2010 an earthquake in Port-au-Prince, Haiti, killed more than a quarter of million people, and resulted in losses over $14 billion [2]. These catastrophes show the severe damage earthquakes can inflict. Since 1960s, practitioners and researchers—through field investigations after devastating earthquakes, along with theoretical and experimental studies—have significantly improved our understanding of earthquakes and strategies to mitigate the impact. Examples of disciplinary developments are strong-motion measurements, system identification, model updating, structural performance evaluation through experimental and analytical simulations, fragility derivation, and the development of consequence estimation software.

The above component-specific studies allow researchers to focus on a particular problem at a fundamental level. Even though these specific studies have progressed considerably and produced mature research results, uncertainties remain in their outcomes not only because of their inherent characteristics, but also because of the interactions between them. For example, the derivation of fragility curves requires that a large amount of simulations be performed. It is essential to have an accurate structural model which closely represents the response of the real structure. In most fragility simulations, however, either a very simplified structural model is used or a complicated numerical model is used without being calibrated to measured response. Such methods, therefore, introduce significant and by-and-large unquantifiable uncertainties in the derived fragility curves. Moreover, the fragility curves heavily depend on input ground motions, particularly when the fragility curves are defined in terms of peak ground acceleration (PGA) [3]. The ground motion is in turn influenced by source, path, and site characterization, each of which is a formidable challenge in its own right. The realism of both model and input is therefore essential to the accuracy and applicability of the ensuing fragility relationships.

Earthquake impact assessment is the basis for emergency planning, mitigation, response, and recovery. The realism of the outcome, such as the effect on civil infrastructure systems, economy, and societal activities, is the essential ingredients to developing plans that adequately protect vulnerable communities. As mentioned above, significant progress has been made in earthquake impact assessment, including consequence estimation methodology as well as developing software that provides decision-makers with a tool to assess the impact [4]. Generally, the impact assessment software is composed of three main components: namely, (i) Hazard, (ii) Fragility, and (iii) Inventory. Among these, the inventory can be improved through the development and application of survey methods and technologies. This renders the accuracy of the assessment dependent on the reliability of the fragility curves and hazard characterization. Unquantifiable uncertainty and inaccuracies in the latter two components of hazard and fragility lead to earthquake impact assessments—that are unreliable and that do not form a viable basis for societal readiness.

2 METHODOLOGY

To reduce the above-mentioned uncertainties and unreliability in impact assessment, an integrated framework is proposed, developed, and demonstrated via application to an actual test bed. Figure 1 illustrates the proposed framework and how its components are combined to achieve the main goal of this research. As can be seen, the proposed framework, referred to as NEES Integrated Seismic Risk Assessment Framework (NISRAF), integrates hybrid simulation with free-field and structure sensor measurements, hazard characterization analysis, system identification-based model updating technology, hybrid fragility analysis, and earthquake impact assessment tools. The procedure is specifically proposed and programmed for ease of use.

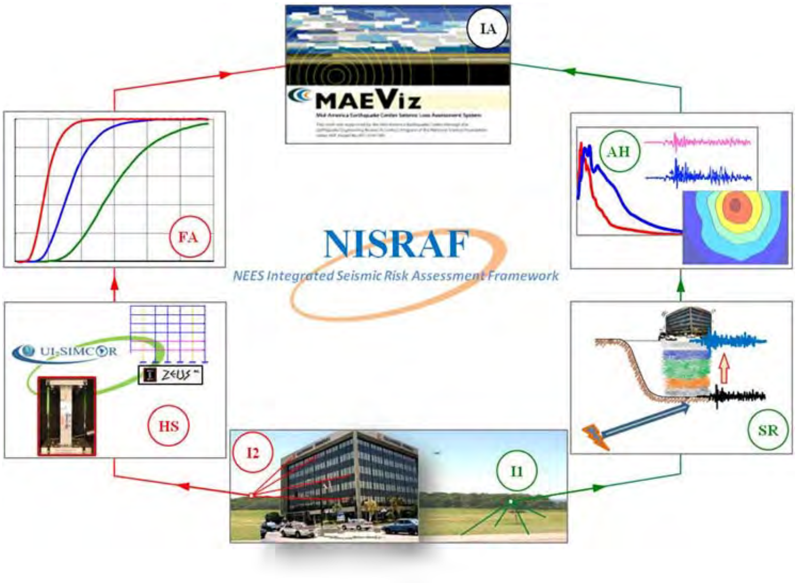

Figure 1: Schematic of the proposed integrated framework

In the schematic representation of the integrated framework given in Figure 1, free-field measurements (**I1**) along with nonlinear site response analysis (**SR**) are used to generate the advanced hazard map and ground motion records (**AH**). The measured and synthetic records are then used as seismic inputs in hybrid simulation and fragility analysis. Meanwhile, the structural model is calibrated with the measured structural response (**I2**). Next, hybrid simulations (**HS**) are performed with the most critical component of the structural system tested in the laboratory and the remainder of the structure simulated analytically. These simulations are conducted to derive the mean seismic intensity value (PGA, for example) of the corresponding performance limit state. The fragility curves (**FA**) of the structure are then generated using the hybrid simulation data and the dispersions from the literature. Finally, the derived fragility curves and the calibrated hazard map are fed into the impact assessment tools, such as MAEviz [5] (**IA**) to evaluate the seismic losses.

The integrated system provides an opportunity to bring together all the sub-disciplines, capitalizing on the respective advances of each sub-discipline. This method of integration is not only intended to provide a tool, but it is also intended to stimulate the sub-communities of researchers to investigate the problems at the interfaces between them. Through this systematic and transparent framework, uncertainties from each sub-discipline can be managed more effectively and the use of the instrumentation will increase. For example, the reliability of probabilistic seismic hazard can be significantly improved through the use of free-field strong-motion measurements. Analytical and hybrid (analytical-experimental) simulations can be more realistic due to calibration with system identification results from sensor measurements. The uncertainties resulting from deriving fragility relationships can be greatly reduced through the use of more reliable representation of hazard and more accurate structural models. Confidently, with seismic hazard from field measurements and fragility curves from more accurate models, NISRAF can significantly improve upon earthquake impact assessment results with higher reliability. In the subsequent sections, the methodologies and techniques utilized in each component will be discussed and then followed by the development and implementation of this integrated framework.

3 ADVANCED COMPONENTS UTILIZTED IN NISRAF

To achieve a seamless integration and to arrive at an operational and verified system, several components were used innovatively, tailored to perform the role required by NISRAF. The integrated system brings the advanced tools of earthquake hazard and structural reliability analyses into the context of societal requirement for accurate evaluation of the impact of earthquakes on the built environment.

3.1 Advanced hazard analysis

Owing to uncertainties from seismo-tectonic, earthquake energy attenuation and site conditions, it is difficult to estimate accurately the ground motion parameters. Many methods for seismic hazard analysis have been developed over the past decades, such as the Deterministic Seismic Hazard Analysis (DSHA) and Probabilistic Seismic Hazard Analysis (PSHA). Due to the probabilistic nature and the simple assumption for the local site effect, i.e. site coefficients F_a, F_v [6], uncertainties remain in the procedure and outcome. To reduce these uncertainties, an hazard characterization analysis component, including site response analysis is proposed.

As shown in Figure 3, this approach is composed of (i) seismic hazard analysis, (ii) synthetic ground motion generation, (iii) site response analysis, and (iv) hazard map generation. First of all, the natural records are directly investigated to evaluate the hazard characterization. Synthetic records of different hazard levels are then generated to evaluate the hazard as well as to provide various ground motions for further use in hybrid simulation and fragility curves derivation. Step-by-step procedure to generate synthetic ground motion with the advanced method is given below:

Step 1: At the beginning of the analysis, the user is prompted to define the seismic parameters (magnitude, distance, fault mechanism and site condition).

Step 2: User specified response spectra or spectra based on strong motion attenuation relationships (the Next Generation Attenuation (NGA) models [7], for example) and the predicted duration [8] are produced.

Step 3: Finally, synthetic ground motions for different hazard levels are generated through SIMQKE [9] based on the information defined previously.

Subsequently, both the natural and synthetic records are ready to be modified to reflect the local site effect. DEEPSOIL [10]—a 1-D site response analysis program—is implemented in NISRAF to conduct the site response analysis.

In addition to the hazard analysis, synthetic ground motion generation and site response analysis, the advanced hazard characterization method also provides a function to generate hazard map, which is the exposure of the impact assessment. To generate the hazard map, users are prompted to define the scenario events, the site conditions and the region of interest. The hazard map is then generated and shown on NISRAF.

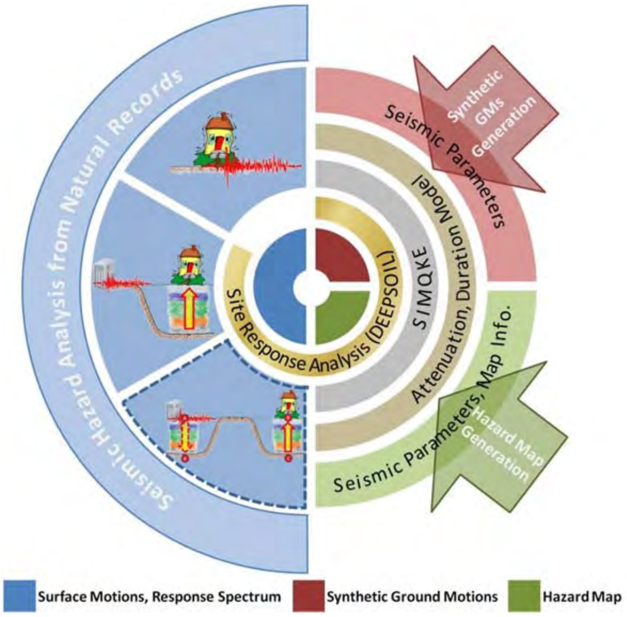

Figure 2: Methodology and procedures of the advanced hazard characterization analysis method

3.2 Efficient model calibration

Finite element model simulation provides a powerful way to understand the response of structures. Unfortunately, even well-constructed models may produce significant differences in some dynamic response predictions, in particular when the structure behaves nonlinearly. The difference is from the uncertainties of the material, boundary conditions and the contribution of the non-structural elements in the real structures. In order to overcome this drawback, a model calibration component based on the experimental or real response—which is composed of system identification and model updating techniques—is proposed. The following sections give an overview of these techniques.

System Identification

Among the many state-space based system identification methods, the Eigensystem Realization Algorithm (ERA) [11] is implemented in NISRAF due to its wide application and good performance in multi-input multi-output (MIMO) problems. The basic idea of ERA is to find a minimum realization of the system (a state-space representation with minimum dimensions) using the Singular Value Decomposition (SVD) on the Hankel matrix built by the Markov parameters (impulse response functions), so that the modal properties can be extracted from the realized minimum state-space representation.

A two-step strategy is applied to filter out computational and noise modes. Since more singular values are retained, more potentially genuine modes can be identified. In NISRAF, the dimension of the realized system N is increased until an adequate number of modes are included. For each particular order of a system, three commonly used mode accuracy indicators, namely Modal Amplitude Coherence (MAC) [11], Extended Modal Amplitude Coherence (EMAC), and Modal Phase Colinearity (MPC) [12] are used to filter out the computational or noise modes. The retained modes are then deemed trustable and a stabilization diagram is plotted for further confirmation. All modes—which are based on the idea that a genuine mode should always be identified with a different order of realized system, as long as the system order is adequate for that mode—are gathered in this diagram. Among the same order of modes identified and plotted in the stabilization diagram, the one with highest EMAC value is then selected as the confirmed mode.

Model Updating

Model updating aims to minimize the discrepancies between the numerical and real model by adjusting the stiffness and mass matrices. The objective function is formed as a linear combination of the natural frequency residuals and mode shape residuals, with different weighting factors for each residual.

$$F(x) = w_f \sum_{k=1}^{N_f} \left(\frac{f_{ak} - f_{ek}}{f_{ek}} \right)^2 + w_m \sum_{k=1}^{N_m} \frac{cos^{-1}(\sqrt{MAC_k})}{(\pi/2)} \tag{1}$$

f_{ak} and f_{ek} denote the analytical and experimental natural frequencies; w_f and w_m are weighting factors applied to the frequency residuals and mode shape residuals, respectively. *MAC* (Modal Assurance Criteria) is a measurement of mode shape discrepancy and is defined as [13].

$$MAC_i = \frac{(\emptyset_{ai}^T \emptyset_{ei})^2}{(\emptyset_{ai}^T \emptyset_{ai})(\emptyset_{ei}^T \emptyset_{ei})} \tag{2}$$

$\emptyset_{ai}$ and $\emptyset_{ei}$are analytical and experimental mode shapes. *MAC* = 1 means $\emptyset_{ai}$ and $\emptyset_{ei}$are perfectly matched; *MAC* = 0 means they are orthogonal. It is known that *MAC* is rather insensitive to the change of mode shape. It is also noted that the *MAC* is actually the square of the inner product between the two mode shape vectors. Therefore, the objective function for the mode shape residual is formed as the normalized angle between the two mode shape vectors, which are much more sensitive to the changes in the mode shape.

3.3 Advanced hybrid fragility analysis

Fragility, or vulnerability, presents the probability of reaching or exceeding a specific performance level under a specific seismic hazard. Fragility curves relate the effects of seismic hazard to the damage of the structures. Through the application of fragility curves, loss from earthquake hazard is estimated.

Generally, fragility curves are sub-divided into four categories based on data sources, namely empirical, judgmental, analytical, and hybrid fragility curves [14]. Empirical fragility curves are developed through field investigations after earthquakes—are the most realistic. However, this observation data is scarce and clustered in the low damaged range. Judgmental fragility curves are based on expert opinion, and are therefore subjective. Unlike the empirical and judgmental fragility curves, analytical fragility curves are more general, curves are allowed to be generated for different limit states and different structural types, although at a higher computation cost. Due to this limitation, most analytical fragility curves are generated either by simple models or by complicated models without calibration to the real structural response, which can result in uncertainties in these curves.

To reduce the uncertainties, a hybrid fragility analysis method is proposed. In this approach, hybrid simulation with critical element tested in the laboratory and the rest simulated in the calibrated finite element model is performed to evaluate the structural response. By scaling ground motions, several hybrid tests are conducted to reach the target structural response. The PGA of the scaled ground motion is then assumed as the mean PGA for the current limit state. Here, the target structural response is defined for different limit states, such as interstory drift angle of 0.7% for immediate occupancy limit state for steel moment frame building. With the mean PGA values and the dispersions from similar structures found in the literature, the fragility curves are generated based on the lognormal distribution assumption. Figure 3 illustrates the methodology and procedures of the proposed advanced hybrid fragility analysis method.

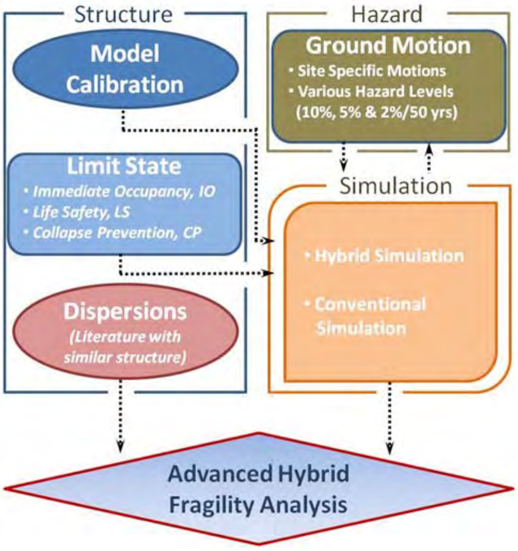

Figure 3: Methodology and procedures for the advanced hybrid fragility analysis

4 NEES INTEGRATED SEISMIC RISK ASSESSMENT FRAMEWORK

NISRAF, a software package with a graphical user interface (GUI) under the MATLAB environment has been developed for the purpose of making impact assessment more efficient and more reliable. Several components—instrumentation, advanced hazard characterization, system identification, model updating, hybrid simulation, advanced hybrid fragility analysis and impact assessment tools—have been implemented and tailored with novel methods to build the seamless, transparent and extensible framework. Figure 4 shows several components with GUI implemented in NISRAF.

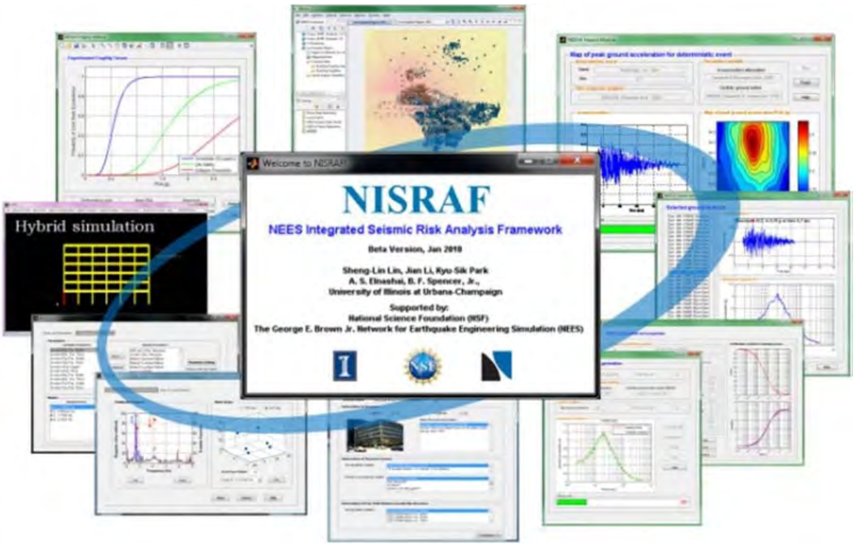

NISRAF

NEES Integrated Seismic Risk Analysis Framework

Beta Version, Jan 2010

Sheng-Lin Lin, Jian Li, Kyu-Sik Park
A. S. Elnashai, B. F. Spencer, Jr.,
University of Illinois at Urbana-Champaign

Supported by:
National Science Foundation (NSF)
The George E. Brown Jr. Network for Earthquake Engineering Simulation (NEES)

Figure 4: Components with GUI in NISRAF

Several advanced features contained in this integrated framework are given below:

1. *Open source software with friendly GUI:* In NISRAF, each component (module) is developed separately before being incorporated into the framework. Consequently, it is easy to understand and maintain. This software, as well as the source code, will be open to the public. The open source feature will allow NISRAF to be utilized efficiently, as well as improve its integrity and robustness.
2. *Extensible and accessible:* As mentioned previously, each component is developed and verified separately. Hence, it is extensible and accessible to any of the latest research findings and program techniques.
3. *Efficient and reliable impact assessment:* This is the first time that all the components for impact assessment are integrated and work seamlessly in just one software platform. Concurrently, the integrated feature brings the most advanced tools of earthquake hazard and structural reliability analyses into the context for accurate evaluation of impact assessment. Surely, with these seamlessly integrated advanced techniques, which provide a more accurate hazard and structural model and hence generate superb fragility curves, the assessment of earthquake impact will be more efficient and more reliable

As mentioned previously, this is the first time to integrate all components of earthquake impact assessment in one analysis platform. Through NISRAF, uncertainties from hazard and fragility can be reduced or managed efficiently; therefore the results from impact assessment can be more realistic and reliable. Meanwhile, NISRAF provides a chance for seismologists, geotechnical and structural earthquake engineers, structural control and impact assessment experts to ameliorate algorithms in order to bring out more confident assessment results. Through its extensible and accessible feature, the new or improved algorithm can be easily incorporated into NISRAF.

5 CASE STUDY

NISRAF has been successfully developed and demonstrated via a heavy-instrumented building in Burbank, California [15]. Earthquake impact assessment on a single building provides the possible damage and loss under scenario or historical earthquake events for this specific building. It indeed provides valuable information to reduce and mitigate losses in particular for the essential buildings, such as hospitals and schools. However, regional impact assessment—seismic losses for a region, especially urban area—is more valuable for decision-makers to develop emergency response and recovery planning. In this section, earthquake impact assessment in the Los Angeles area was carried out; comparison and uncertainty were also presented and discussed, respectively.

5.1 Introduction

Los Angeles, California—a high seismic urban region—was selected to demonstrate the regional impact assessment. Near one million inventory data exported from HAZUS-MH was used as the inventory input. The hazard map of PGA for the 1994 Northridge earthquake in the Los Angeles area and fragility relationships for all building types and code levels were fed into MAEviz to perform earthquake impact assessment. Reference was made to Lin [15] for more detailed information about the generation of the hazard map. Below, fragility relationships utilized in this application will be illustrated, followed by the discussion on the impact assessment result and uncertainty analysis in NISRAF.

5.2 Parameterized fragility method

A database contained fragility relationships for all building types is an essential ingredient of regional impact assessment. The proposed advanced hybrid fragility analysis provides an alternative method to derive more reliable fragility relationships. Definitely, this hybrid approach can be applied to any other building types to generate the related fragility curves. However, considerable time and effort are required. For the mid-rise steel moment resisting frame building in Los Angeles area, its fragility relationships have been generated in order to demonstrate fully the hybrid fragility analysis implemented in NISRAF [15]. Extension of the database for fragility relationships to other building types is underway. Currently, an alternative method to derive fragility relationships for other building types is the Parameterized Fragility Method, PFM [16]. In the following paragraphs, PFM will be reviewed first, followed by the derivation of fragility relationships for other building types using PFM.

Parameterized Fragility Method, an analytical fragility analysis approach, derives fragility curves through dynamic time history analysis on a single-degree-of-freedom (SDOF) model. It is, therefore, parameters corresponded with structure types and ground motions representative of site hazard characterization are essential for this methodology’s use in regional impact assessment.

In HAZUS-MH, 36 building types (from W1: wood, light frame to MH: mobile homes) are defined [17]. Meanwhile, structural parameters (i.e. period, yield and ultimate strength) for 36 building types under 4 code levels (i.e. pre-code, low-code, moderate-code, and high-code) are tabulated. However, the majority of these parameters are based on engineers’ opinions and experts’ judgment. To be more realistic and reasonable, the latest research findings on structural capacity were incorporated. For example, parameters for wood frame and unreinforced masonry buildings were replaced according to the more comprehensive investigations [18, 19]. In addition, sets of ground motions specific for Los Angeles area were used as earthquake demand when performing dynamic time history analysis in PFM.

Consequently, fragility relationships for 36 building types under 4 code levels particularly for the Los Angeles area were generated based on structural parameters and specific ground motions.

5.3 Assessment results and comparison

The MAEviz interface depicted in Figure 5 presents the distribution of the direct economic building loss for the Los Angeles area in the 1994 Northridge earthquake, using the hazard map and fragility curves generated by NISRAF. The mean total loss was 20.7 billion dollars. Table 1 provides a comparison of the direct economic building loss of the study area between NISRAF and observed data. In this table, Lower_B. and Upper_B. stand for Lower Bound and Upper Bound, respectively. In general, results of Lower_B. and Mean NISRAF loss provide bounding values of the observed loss. Therefore, NISRAF predicted reasonable accurate and modestly conservative assessment results for the Los Angeles area in the 1994 Northridge earthquake.

Table 1: Direct economic building loss (Los Angeles county under the 1994 Northridge earthquake)

	Observed*	NISRAF		
		Lower_B.	Mean	Upper_B.
Dollar in Millions	18,500	17,938	20,706	23,474
Difference (%)	0.00	-3.13	10.65	26.89

**[20]*

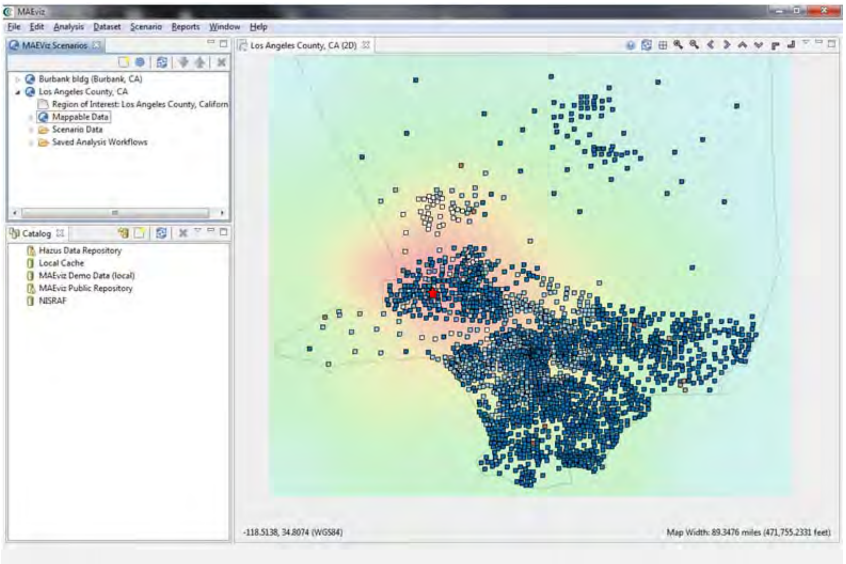

Figure 5: Earthquake impact assessment in Los Angeles area

5.4 Uncertainty analysis

Earthquake impact assessment is essential for disaster planning as well as developing risk reduction policies and emergency responses. As mentioned previously, an impact assessment package is composed of seismic hazard, fragility function, and inventory data. Mathematically, the loss estimation can be described by the following equation [21]:

$$P[Loss] = \sum_{s}\sum_{LS}\sum_{d} P[Loss|D=d]\cdot P[D=d|LS]\cdot P[LS|IM=s]\cdot P[IM=s] \qquad (3)$$

where $P[\blacksquare]$ is the probability of loss (direct or indirect loss from the earthquake events), IM is the intensity measure of the seismic hazard (PGA or S_a), and s is the realization of the intensity measure. $P[LS|IM=s]$ is the conditional probability of reaching or exceeding structural limit states, and $P[D=d|LS]$ is the conditional probability of reaching damage. Here the term $P[LS|IM=s]$ refers to fragility or vulnerability discussed in previous section.

Due to the random nature and limited knowledge in earthquake engineering, numerous assumptions are made and many approximated methods are applied when performing impact assessment. Therefore, various types (aleatory and epistemic) of uncertainties exist in earthquake impact assessment, for example, the prediction of seismic intensity, the generation of fragility functions, the assumption of distribution of damage ratio, the inventory uncertainties and others. With additional investigation and knowledge, it is definitely possible to reduce the epistemic uncertainties, such as by providing more realistic seismic hazard characterization, more reliable fragility relationships generated through NISRAF, and more accurate inventory data. Nevertheless, uncertainties are unavoidable, particularly in the case of aleatory uncertainties (randomness).

One advanced feature of MAEviz that distinguishes it from HAZUS-MH is its uncertainty quantification analysis, which not only provides users with the mean value of the predicted losses, but also the uncertainty information (the standard deviation values). With this contribution of uncertainty analysis in MAEviz, NISRAF—to be consistent with its user-friendly feature—presents the uncertainties through an intuitive and friendly interface [15], as shown in Figure 6. Through this intuitive interface, a pie-chart of different losses (i.e. structural, non-structural, and contents) is presented. Also, losses with upper-bound and lower-bound vary with the different confidence level which was selected by the users.

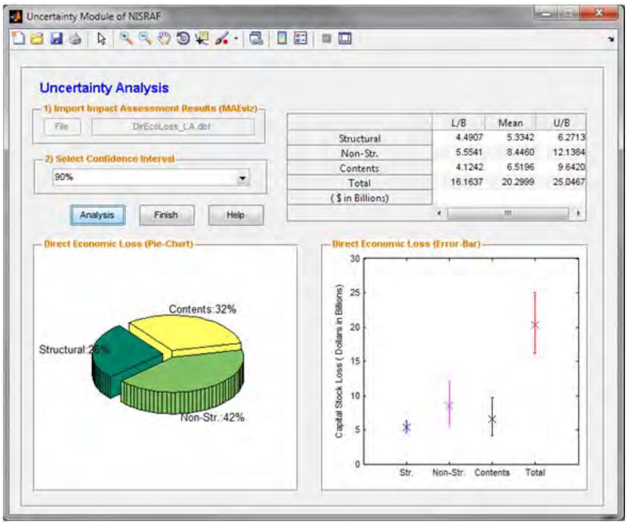

Uncertainty Module of NISRAF

Uncertainty Analysis

1) Import Impact Assessment Results (MAEviz): DirEcoLoss_LA.dbf

2) Select Confidence Interval: 90%

	L/B	Mean	U/B
Structural	4.4907	5.3342	6.2713
Non-Str.	5.5541	8.4460	12.1384
Contents	4.1242	6.5196	9.6420
Total	16.1637	20.2999	25.0467
($ in Billions)			

Figure 6: Uncertainty qualification analysis in NISRAF

The actual test bed in California, the regional impact assessment in the Los Angeles area, was carried out to demonstrate the integrated framework as well as its components. This example demonstrated not only the seamlessly-integrated, extensible, and transparent framework, but also that all the elements required for impact assessment can be performed under just one software platform. Consequently, the reasonable accurate, although conservative impact assessment results confirmed one of the advanced features of NISRAF, which is more efficient and more reliable impact assessment. Meanwhile, the implemented approximate uncertainty quantification analysis can assist decision-makers to judge the losses easily and quickly, which will contribute to the development of more suitable and more confident recovery plans and emergency responses.

6 CONCLUSIONS

NISRAF is intended to serve as a user-friendly software platform through which impact assessment can be efficiently and reliably performed by combining hazard (exposure) and fragility (sensitivity), to provide assessment of impact on the built environment at the regional scale. Concurrently, it is intended to extend the state-of-the-art hybrid simulation approach to fragility analysis, and propose refined methods for hazard characterization and model calibration. The successful completion of the development of the framework and verification of its components demonstrates that these objectives have been achieved. In addition, the application of NISRAF will be a stimulus for cooperation between not only for geotechnical and structural earthquake engineers, and impact assessment experts, but also for seismologists and structural control researchers improving their algorithms in order to pursue the ultimate goal of accurate and reliable earthquake impact assessment.

ACKNOWLEDGEMENTS

This research was supported by National Science Foundation, Grant Number 0724172 (NEES Simulation Development), Dr. Joy M. Pauschke, Program Director.

REFERENCES

[1] United States Geological Survey (USGS), Magnitude 7.9-Eastern Sichuan, China, http://earthquake.usgs.gov/earthquakes/eqinthenews/2008/us2008ryan/#summary, 2008.

[2] United States Geological Survey (USGS), Magnitude 7.0-Haiti Region, http://earthquake.usgs.gov/earthquakes/eqinthenews/2010/us2010rja6/#summary, 2010.

[3] Kwon, O. S., and Elnashai, A. S., The effect of material and ground motion uncertainty on the seismic vulnerability curves of RC structure, *Engineering Structures*, **28**(2):289-303, 2006.

[4] Molina, S., Lang, D. H., and Lindholm, C. D., SELENA – An open-source tool for seismic risk and loss assessment using a logic tree computation procedure, *Computers & Geosciences*, **36**:257-269, 2010.

[5] Mid-America Earthquake Center (MAE Center), *Mid-America Earthquake Center Seismic Loss Assessment System, MAEviz v3.1.1*, University of Illinois at Urbana-Champaign, Urbana, IL, 2007.

[6] Federal Emergency Management Agency (FEMA), *NEHRP (National Earthquake Hazard Reduction Program) Recommended Seismic Provisions for New Buildings and Other Structures*, Report No. FEMA P-750, Washington D.C., 2009.

[7] Power, M., Chiou, B., Abrahamson, N., Bozorgnia, Y., Shantz, T., and Roblee, C., An Overview of the NGA Project, *Earthquake Spectra*, **24**(1): 3-22, 2008.

[8] Kempton, J. J. and Stewart, J. P., Prediction Equations for Significant Duration of Earthquake Ground Motions Considering Site and Near-Source Effects, *Earthquake Spectra*, **22**(4), 985-1013, 2006.

[9] Gasparini, D. A., and Vanmarcke, E. H., *Simulated Earthquake Motions Compatible with Prescribed Response Spectra, Evaluation of Seismic Safety of Buildings Report No.2*, Massachusetts Institute of Technology, 1976.

[10] Hashash, Y., Groholski, D.R., Phillips, C.A., and Park, D., *DEEPSOIL V3.5beta, User Manual and Tutorial*, Department of Civil and Environmental Engineering, University of Illinois at Urbana-Champaign, Urbana, IL, 2009.

[11] Juang, J. N., and Pappa, R. S., An eigensystem realization algorithm for modal parameter identification and model reduction, *Journal of Guidance, Control, and Dynamics*, **8**(5): 620-627, 1985.

[12] Pappa, R. S., and Elliott, K. B., Consistent-mode indicator for the eigensystem realization algorithm, *Journal of Guidance, Control, and Dynamics*, **16**(5): 852-858, 1993.

[13] Allemang, R. J., and Brown, D. L., A Correction Coefficient for Modal Vector Analysis, Proceedings, *International Modal Analysis Conference*, Orlando, FL, 110~116, 1982.

[14] Rossetto, T., and Elnashai, A., Derivation of Vulnerability Functions for European-type RC Structures Based on Observational Data, *Engineering Structures*, **25**(10):1241-1263, 2003.

[15] Lin, S.-L., *An Integrated Earthquake Impact Assessment System*, Ph.D. dissertation, Civil Engineering, University of Illinois at Urbana-Champaign, Urbana, IL, 2010.

[16] Jeong, S. H. and Elnashai, A. S., Probabilistic fragility analysis parameterized by fundamental response quantities, *Engineering Structures*, **29**:1238-1251, 2006.

[17] Federal Emergency Management Agency, *HAZUS-MH technical manual*, FEMA, Washington, D.C., 2006.

[18] Gencturk, B. E. and Elnashai, A. S., Development and application of an advanced capacity spectrum method" Engineering Structures, 30:3345–3354, 2008.

[19] Frankie, T. M., *Simulation-Based Fragility Relationships for Unreinforced Masonry Buildings*, MS thesis, Department of Civil and Environmental Engineering, University of Illinois at Urbana-Champaign, Urbana, Illinois, 2010.

[20] Cmerio, M. C., Landis, J. D., Firpo, C. J., and Monzon, J. P., Residential Earthquake Recovery, *California Policy Seminar*, University of California, Berkeley, CA, 1996.

[21] Ellingwood, B. R. and Wen, K. Y., Risk-benefit-based design decisions for low-probability/high consequence earthquake events in Mid-America, *Progress in Structural Engineering and Material*, **7**:56-70, 2005.

COMPDYN 2011
III ECCOMAS Thematic Conference on
Computational Methods in Structural Dynamics and Earthquake Engineering
M. Papadrakakis, M. Fragiadakis, V. Plevris (eds.)
Corfu, Greece, 26–28 May 2011

ISSARS: AN INTEGRATED SYSTEM FOR STRUCTURAL ANALYSIS AND EARTHQUAKE RECORDS SELECTION

Evangelos I. Katsanos[1], Anastasios G. Sextos[2], and Thomas Notopoulos[3]

[1] Civil Engineer, M.Sc., PhD Candidate, Division of Structural Engineering,
Department of Civil Engineering, Aristotle University of Thessaloniki, 54124 Greece
katsanos@civil.auth.gr

[2] Assistant Professor, Division of Structural Engineering,
Department of Civil Engineering, Aristotle University of Thessaloniki, 54124 Greece
asextos@civil.auth.gr

[3] Civil Engineer, Division of Structural Engineering,
Department of Civil Engineering, Aristotle University of Thessaloniki, 54124 Greece
thomasnotos@gmail.com

Keywords: strong motion, earthquake record selection, Eurocode 8, FEMA P-750, structural analysis, response spectra, spectral matching.

Abstract. *Despite the major advancements in earthquake engineering research and the novelty of most modern seismic codes, the selection of the earthquake ground motions used for the design or assessment of structures in the framework of structural analysis still induces significant dispersion in the calculated dynamic response of structures. For this reason, the current study presents a new, freely available, computational system developed for improving the reliability of the code-based earthquake record selection and scaling procedure, as a means to reduce the resulting structural response scatter. Through a set of preliminary criteria, related to the magnitude, epicentral distance, soil conditions, intensity measure (i.e., PGA), components of excitation (2D or 3D) and structural system (building or bridge), the proposed algorithm searches through internet the entire PEER-NGA Strong motion Database for appropriate seismic records and then ranks them in terms of their spectral matching to a target response spectrum within a prescribed frequency range. A key feature of the software is that it implements the new Application Programming Interface (API) of the computer program SAP2000 and proceeds in applying the selected records to the finite element model that the designer is assumed to have prepared at the background. In this way, both the variation of the response quantities in the time domain and the relative structural response dispersion under various records are automatically retrieved. The presentation concludes with a demonstration regarding the assessment of a real, irregular in plan, multi-storey, RC building, where the importance of adopting a structure-specific earthquake record selection process is highlighted.*

1 INTRODUCTION

During the last decades, elastic and inelastic dynamic analyses have been made feasible for the design and assessment of complex structures with thousands of degrees of freedom, thanks to the rapid evolution in computational processing power and the enhancements in engineering software. As a result, the vast majority of modern seismic codes prescribes the application of the response history analysis as an equally eligible method to assess the response of a structural system. However, current research work [1]-[3] has demonstrated that among all possible sources of uncertainty stemming from the structural and soil material properties, the design and analysis assumptions and the earthquake-induced ground motions, the latter seems to affect most seriously the structural response variability, as determined by the dynamic analyses. Therefore, the selection of a “reliable” set of earthquake ground motions for conducting response history analysis becomes an important prerequisite as it affects the reliability of the procedure as a whole.

This truly complex task, which is still undertaken by the engineers without detailed seismic code guidelines, cannot be accomplished without understanding the fundamental concepts behind selection and scaling of earthquake records and their implication in the predicted structural response. For this reason, numerous alternative methods have been proposed for enhancing the reliability of the earthquake records selection and scaling process, most of them being summarized recently by Katsanos et al. [4].

Quite typically, implicit parameters such as the earthquake magnitude *M* and the source-to-site distance *R* are widely used as preliminary criteria combined with desirable filters that are related to the soil conditions of the site of interest, code or seismic hazard prescribed levels of different intensity measures, as well as of the seismotectonic environment features (i.e. the source mechanism, the path of seismic waves, strong-motion duration). Nevertheless, the concurrent application of all the above parameters significantly restricts the number of the records eligible for selection and thus relaxation of these criteria may be inevitable to ensure a reasonable number of records for dynamic analyses. Furthermore, research work has shown that application of site-specific *M-R* criteria did not reduce the structural response discrepancy in various structural systems, while highlighted the relative independence of nonlinear response on the distance (e.g. [2, 5 and 6]) with the exception of cases where the cumulative damage measures are of interest [7] or for structures where the contribution of higher modes is significant [2].

As the most common earthquake record selection procedures involve spectral matching of the average response spectrum of the records to be used, with a target, code-prescribed or seismic hazard-defined elastic response spectrum [8, 9], or even a conditional mean spectrum [10], recent work evolved to develop methods for quantifying (e.g. [11, 12]) and/or optimizing [13,14] this spectrum compatibility.

Especially in case of the performance-based design approach, the selection of acceleration time series is considered with the goal of accurate prediction of the structural response at a specified ground motion intensity measure, IM. The Peak Ground Acceleration of records and some other characteristic parameters (i.e. the spectral acceleration, SA) have been used as suitable IMs (e.g. [2]). Nevertheless, advanced intensity measures, including information about the spectral shape and structural characteristics, are expected to be preferable for records selection and scaling procedures resulting in a more accurate and reliable estimate of the seismic demand [6,15,16].

Despite the aforementioned state-of-the-art evolution in this quite recent research field, a rather rough framework is prescribed by most of the modern seismic codes concerning the motions to be used for time history analysis while most of the aforementioned record selection methods proposed in the literature have not yet been incorporated in the codes. Furthermore, specific guidelines of the codes have been proven either inadequate or misleading [17]. In fact, most of the current earthquake resistant codes share a lot of similar provisions, thus revealing that most probably, specific selection provisions have been widespread among seismic codes used in other parts of the world without systematic review, needless to say, quantification of their implications in structural design and assessment [8].

Along these lines, this paper presents a new, freely available, computational scheme for selecting and scaling earthquake records which aims at maximizing both the applicability and efficiency of the code-based earthquake record selection procedure, while minimizing the potential scatter that is commonly induced in structural response. More specifically, the proposed Matlab-based software **ISSARS** (**I**ntegrated **S**ystem for **S**tructural **A**nalysis and **R**ecord **S**election) utilizes the extensive PEER-NGA ground-motion database to form suites of records complying with specific criteria while exhibiting spectral matching with a user defined target spectrum. These suites of records, which have been ranked based on their compatibility with the design spectrum, can be further used as the required seismic loading for the dynamic analyses of a structural model studied. This is made feasible by using the Applications Programming Interface (API) of the finite element program SAP2000 [18] to run numerical analyses at the background and quantify the produced discrepancy of structural response as a part of the earthquake record selection process.

To this end, the scope of the paper is to present the integrated, computational system developed that permits:

(a) the rapid code-based selection of earthquake records required for the design and assessment of buildings and bridges, that are characterized by best matching with a target response spectrum at specific structural periods and;

(b) the automatic prediction of the impact that the selected suites can have on the dispersion of the structural response of the specific structure under study. This can be used as an additional criterion before finally approving an eligible earthquake record suite.

An illustrative example regarding the application of the current integrated system for the case of a real, irregular in plan, multi-storey, RC building, in Thessaloniki, Greece is also presented in order to highlight the above advantages. The description of the computational framework and the application case study are presented in the following.

2 CODE-BASED FRAMEWORK FOR EARTHQUAKE RECORD SELECTION

As already mentioned, the computational framework developed aims to maximize the applicability and efficiency of the code-based earthquake record selection procedures with emphasis on those prescribed in Eurocode 8, Part 1 for buildings, Eurocode 8, Part 2 for bridges [19] and NEHRP Recommended Seismic Provisions for New Buildings and Other Structures [20], abbreviated in the following as FEMA P-750. According to EC8 Part1, the seismic motion to be used for response history analysis may be either artificial, simulated or recorded, depending on the application nature and the information available at the location of the structure. It is notable that the use of artificial records is described in more detail in EC8 Part1 compared to the use of real and simulated records. FEMA P-750 and EC8 Part2 limit the use of simulated seismic motions only in cases of inadequate number of real accelerograms, the latter being selected in terms of magnitude, fault distance and source mechanisms that control the hazard at the site of interest. The source mechanism and path characteristics are also adopted as preliminary criteria, while EC8 Part1 imposes compatibility with the soil category at the location of the building studied.

Concerning the spectral matching procedure, FEMA P-750 guidelines are almost identical to those in EC8 Part2 for bridges; in particular, the SRSS spectrum is determined by taking the square root of the sum of squares of the 5%-damped elastic spectra of each selected component of the horizontal motions and then, the average values of the SRSS spectra of the individual earthquakes define the final average spectrum. Spectral matching is imposed within the period range $0.2T_1 – 1.5T_1$ where T_1 is the fundamental period of the structure. On the other hand, EC8 Part1 requires that the mean 5%-damped elastic spectrum, calculated from all the response spectra of the individual records, has to be compatible with the target spectrum. However, the period range of the foreseen spectral matching is wider (i.e., $0.2T_1$ - $2T_1$). The comparative presentation of the above criteria is made in Table 1.

Seismic code	Selection criteria	Ensemble Spectrum	Spectral matching period range	Lower bound
EC8 Part1	source mechanism, soil type	mean of individual spectra	$0.2T_1$ - $2T_1$	$0.9 \cdot SA_{design}$
EC8 Part2	source mechanism, M, R	mean of SRSS spectra	$0.2T_1$ - $1.5T_1$	$1.3 \cdot SA_{design}$
FEMA P-750	source mechanism, M, R	mean of SRSS spectra	$0.2T_1$ - $1.5T_1$	$1.17 \cdot SA_{design}$

Table 1: Earthquake record selection and spectral matching criteria prescribed in the seismic codes studied herein.

FEMA P-750 also specifies that each one of the recorded ground motions can be scaled by different factors as a means to facilitate spectral matching, while Eurocode 8 prescribes the use of a unique scaling factor, uniformly applied to all the selected records. In addition, both Eurocode 8 and FEMA P-750 share identical provisions concerning the post-processing of the structural analysis results. More specifically, they require that the maximum of the structural response quantities arising from the individual response history analyses has to be used as the design value, when the number of records n is between $3 \le n \le 6$, while the average of the response quantities from all analyses has to be computed in case that more than 7 records are used.

3 OVERVIEW OF THE PEER-NGA STRONG MOTION DATABASE

The computational framework developed for earthquake record selection and structural analysis utilizes online the PEER-NGA Next Generation Attenuation strong-motion database [21,22] (PEER-NGA, Copyright © 2005, The Regents of the University of California, available in http://peer.berkeley.edu/peer_ground_motion_database). Currently, the data-set consists of 3551 publicly available, three-components seismic records (i.e., about 10650 individual earthquake acceleration time series) that have been recorded during 173 shallow crustal earthquakes from active tectonic regions world-wide. As can be seen in Figure 1, most of these earthquakes have occurred in California. The corresponding seismic events range in magnitude from 4.2 to 7.9 and cover epicentral distances in the range 0.2km-600km (detailed distribution is illustrated in Figures 2 and 3).

Besides the magnitude and the distance, the earthquake database contains basic information about the seismic source including date and time of the event, hypocenter location, faulting mechanism, seismotectonic environment and others. Detailed data about 1600 strong-motion stations are also provided (i.e. site characterizations, surface geology, shallow subsurface conditions, the location of the instrument inside the structure's installation place). Furthermore, each acceleration time-history has been corrected for the response of the strong-motion instrument itself and filtered out the noise included. As a result, all the above features of the NGA-Strong Motion Database enable to conduct a reliable and efficient searching for "suitable" earthquake accelerograms among the thousands of available records.

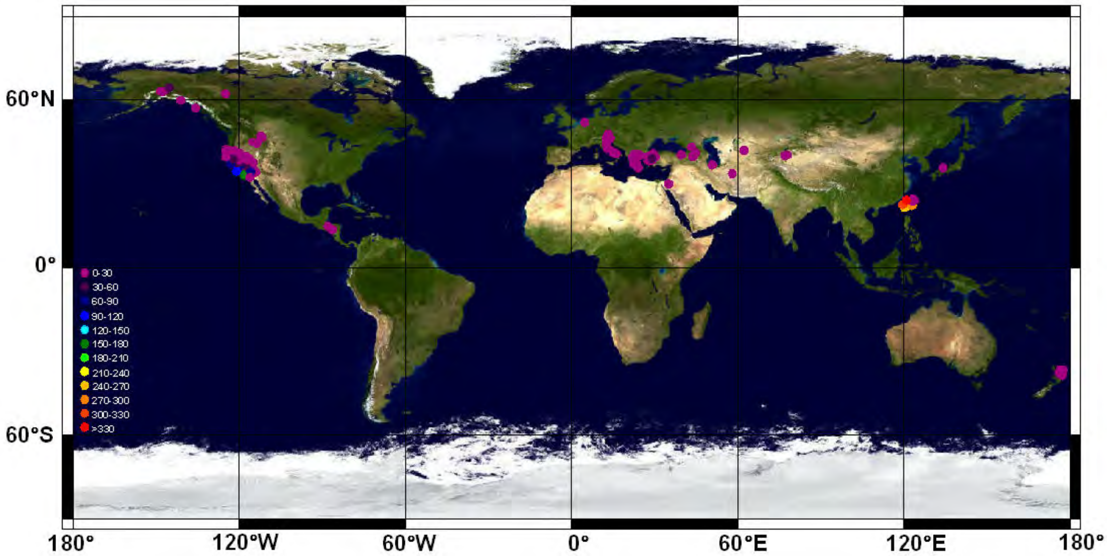

Figure 1: World map illustrating the distribution of the seismic events associated to the 173 earthquakes stored in the PEER-NGA database (distribution computed based on the information available online in http://peer.berkeley.edu/peer_ground_motion_database).

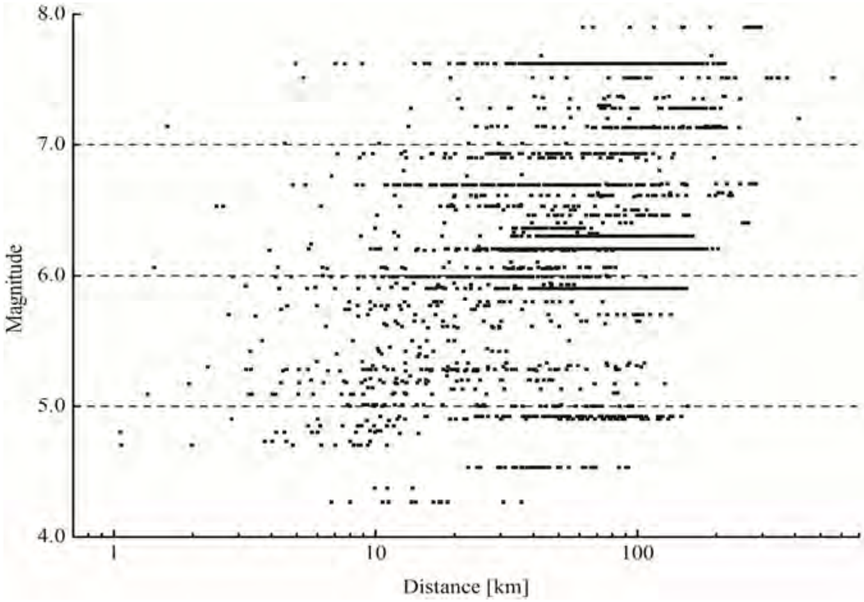

Figure 2: Magnitude and Distance distribution of strong motion records available in the PEER-NGA database (distribution computed by the ISSARS software based on the information available online in http://peer.berkeley.edu/peer_ground_motion_database).

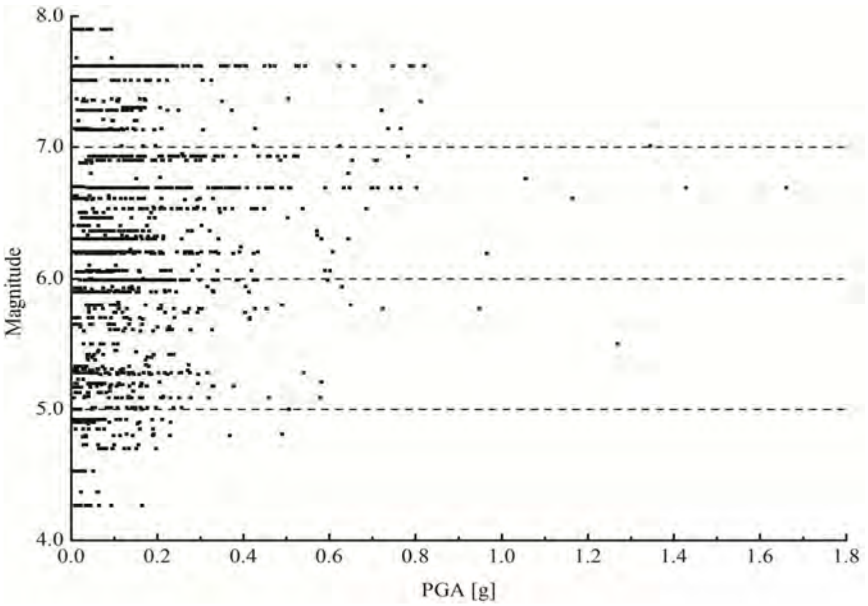

Figure 3: Magnitude and Peak Ground Acceleration distribution of strong motion records available in the PEER NGA database (distribution computed by the ISSARS software based on the information available online in http://peer.berkeley.edu/peer_ground_motion_database).

4 OVERVIEW OF THE COMPUTATIONAL FRAMEWORK DEVELOPED

The computer program ISSARS has been developed in Matlab programming environment, utilizing a series of scripts assembled and coordinated within a graphical environment. It consists of two major modules, (a) the Ground-Motion Selection Module, which is oriented to search for suitable seismic waves that comply with specific criteria and target spectrum, and (b) the Structural Analysis Module which enables automated finite element analysis of the structure under study and quantification of the record set-depended structural response scatter. Additionally to the above, an auxiliary visualization module permits the quick visualization of the generated response spectra, their means as well as the target spectrum. These modules are described in more detail below.

4.1 Ground-Motion Selection Module

The earthquake magnitude, M, and the epicentral distance, R, of the seismic events, the peak ground acceleration, PGA, of the strong-motion records as well as the site classification, S, of the recording instruments constitute the preliminary criteria for records searching through the web-based NGA-Strong Motion Database. Most of these seismological parameters, which are familiar to the structural engineers, are usually determined either through a site-specific deterministic seismic hazard analysis, SHA, or resulted from the disaggregation of a probabilistic SHA. Apart from the above criteria, both the earthquake name and the region of the seismic event can be used as a means to further refine the searching criteria.

After the establishment of the preliminary seismological criteria, the algorithm core script requires the determination of the seismic code-based parameters, which are necessary for the calculation of the target response spectrum and the consecutive implementation of the spectral matching procedure. Since both Eurocode 8 (including Part1 and Part2) and FEMA P-750 provisions can be considered, the present software may be used for the design or assessment of structures both in Europe and the U.S.

In the first case of applying the Eurocode 8 procedure for selecting earthquake records, the calculation of the elastic, damped, code spectrum involves the definition of: (a) the spectrum type, (b) the importance factor of the structure studied, (c) the site classification, (d) the viscous damping and (e) the reference peak ground acceleration. On the other hand, the determination of the FEMA P-750-based target spectrum requires, apart from site classification, some characteristic seismic ground motion values, such as, the mapped uniform-hazard ground motion parameters (S_{SUH}, S_{1UH}), the mapped risk coefficients (C_{RS}, C_{R1}), the mapped deterministic ground motion parameters (S_{SD}, S_{1D}) as well as the mapped long-period transition period (T_L). Regardless of the seismic code adopted, the fundamental dynamic characteristics of the structure under study have also to be defined.

Based on the aforementioned preliminary criteria and spectrum-related parameters, ISSARS connects to the online PEER-NGA-Strong Motion Database [21] and defines the eligible seismic events (Figure 4). The user chooses any number *s* (or the entire group) of the compatible motions and the records are grouped into appropriate suites ("bins") of *m* records. The number of the suites formed, $N_{tot.suites}$, is given by the following factorial formula:

$$N_{tot.suites} = \binom{s}{m} = \frac{s!}{m!(s-m)!} \tag{1}$$

The number *m* of records forming each suite of ground motions is taken by default equal to 7 according to Eurocode 8 and FEMA P-750 provisions about the minimum value of strong-motions that allows for the definition of the design response value as the average of the response quantities from all the analyses. This number can be easily modified through the code scripts. However, it has to be noted that for cases that *m*>7, it is quite possible that the fit of the average spectrum of the suite to the target one will be eventually inferior, unless the list of the selected seismic events is relatively large. Kottke and Rathje [23] showed that if *m* exceeds 10, a larger list of records than 70 may be necessary to achieve adequate spectral convergence. Such a number of records is often difficult to be achieved given the multiple selection criteria applied while at the same time leads to an increased number of response history analyses.

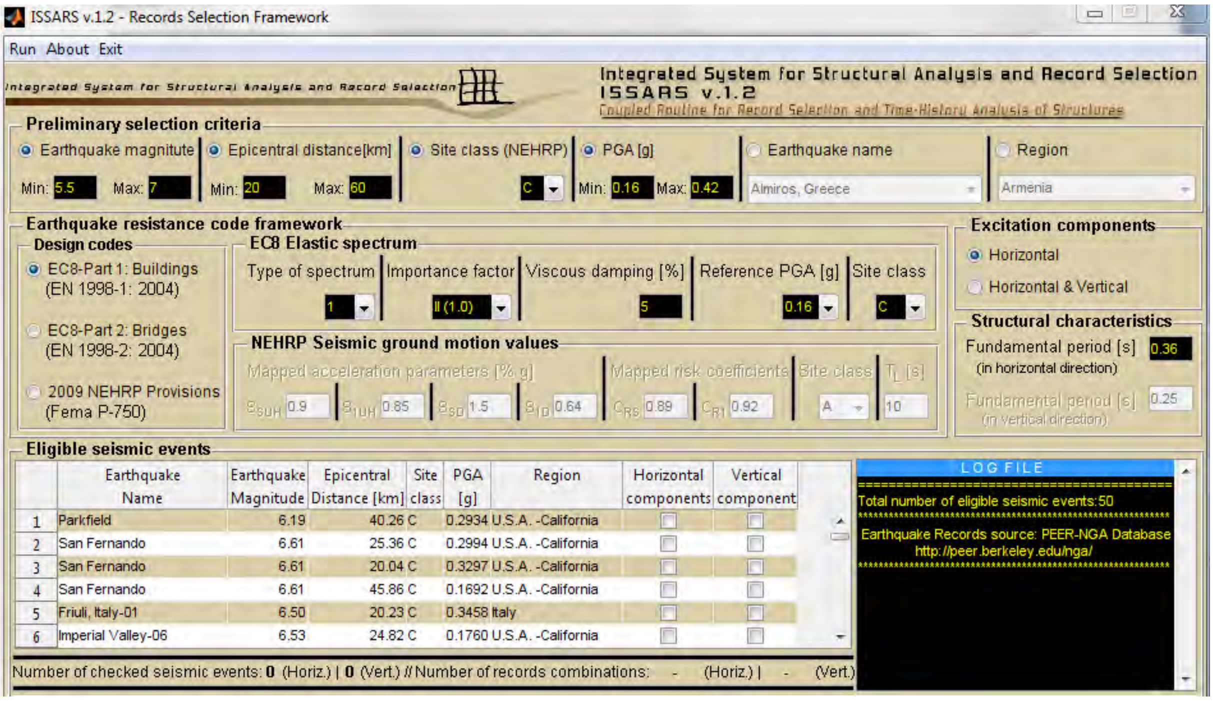

Preliminary selection criteria

● Earthquake magnitute — Min: 5.5 Max: 7
● Epicentral distance[km] — Min: 20 Max: 60
● Site class (NEHRP) — C
● PGA [g] — Min: 0.16 Max: 0.42
○ Earthquake name — Almiros, Greece
○ Region — Armenia

Earthquake resistance code framework

Design codes
● EC8-Part 1: Buildings (EN 1998-1: 2004)
○ EC8-Part 2: Bridges (EN 1998-2: 2004)
○ 2009 NEHRP Provisions (Fema P-750)

EC8 Elastic spectrum
Type of spectrum: 1
Importance factor: II (1.0)
Viscous damping [%]: 5
Reference PGA [g]: 0.16
Site class: C

NEHRP Seismic ground motion values
Mapped acceleration parameters [% g]: S_{SUH} 0.9, S_{1UH} 0.85, S_{SD} 1.5, S_{1D} 0.64
Mapped risk coefficients: C_{RS} 0.89, C_{R1} 0.92
Site class: A
T_L [s]: 10

Excitation components
● Horizontal
○ Horizontal & Vertical

Structural characteristics
Fundamental period [s] (in horizontal direction): 0.36
Fundamental period [s] (in vertical direction): 0.25

Eligible seismic events

	Earthquake Name	Earthquake Magnitude	Epicentral Distance [km]	Site class	PGA [g]	Region	Horizontal components	Vertical component
1	Parkfield	6.19	40.26	C	0.2934	U.S.A. -California	☐	☐
2	San Fernando	6.61	25.36	C	0.2994	U.S.A. -California	☐	☐
3	San Fernando	6.61	20.04	C	0.3297	U.S.A. -California	☐	☐
4	San Fernando	6.61	45.86	C	0.1692	U.S.A. -California	☐	☐
5	Friuli, Italy-01	6.50	20.23	C	0.3458	Italy	☐	☐
6	Imperial Valley-06	6.53	24.82	C	0.1760	U.S.A. -California	☐	☐

Number of checked seismic events: **0** (Horiz.) | **0** (Vert.) // Number of records combinations: - (Horiz.) | - (Vert.)

```
LOG FILE
================================================
Total number of eligible seismic events:50
************************************************************
Earthquake Records source: PEER-NGA Database
http://peer.berkeley.edu/nga/
************************************************************
```

Figure 4: Preliminary seismological criteria, Code-based parameters and list of eligible seismic events.

Having formed all the eligible suites of *m* records, the average spectra for each suite are calculated and the appropriate scaling factors sf_{avg} (unique for each suite), required to comply with the spectral matching criteria (Table 1), are computed as follows:

$$sf_{avg} = \left\{ \min\left(\frac{Sa_{avg}(T_i)}{Sa_{target}(T_i)} \right) \right\}^{-1}, \; i = 1 \; to \; N \tag{2}$$

where $Sa_{avg}(T_i)$ is the ordinate of the average response spectrum of the records suite corresponding to the period T_i, Sa_{target} is the spectral acceleration of the code spectrum derived at the same period and *N* is the number of values within the code-imposed range of periods (Table 1). The suites, which consist of scaled of motions, are then ranked according to their "goodness-of-fit" to the target spectrum. The level of spectral matching between the scaled average spectra of the record combinations and the target spectrum is quantified by the expression of the normalized root-mean-square-error, *NRMSE*, also used by Iervolino *et al.* [24].

$$NRMSE = \sqrt{\frac{1}{N} \sum_{i=1}^{N} \left(\frac{S_{avg}(T_i) - S_{target}(T_i)}{S_{target}(T_i)} \right)^2} \tag{3}$$

The final list of the eligible suites of *m* records, appropriately ranked according to the spectral matching criterion of Eq. (3), is shown in Figure 5. Additionally, the algorithm provides an extensive output data file that includes all related input data (i.e. the preliminary seismological criteria, the seismic code parameters and the dynamic characteristics of the structural system under study) and the associated meta-data concerning the eligible seismic events and their acceleration time series as well as the final hierarchy of the suites formed (Figure 6).

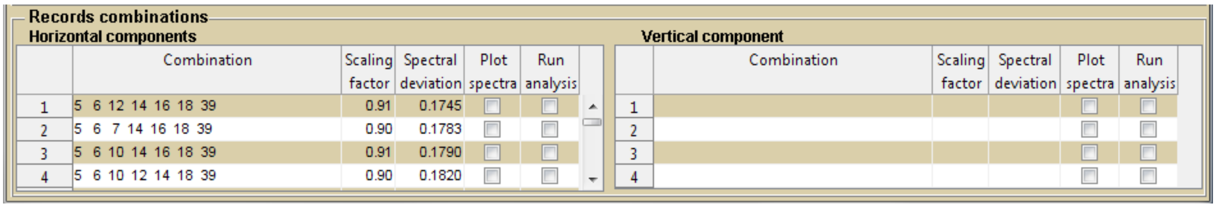
Records combinations

Horizontal components

	Combination	Scaling factor	Spectral deviation	Plot spectra	Run analysis
1	5 6 12 14 16 18 39	0.91	0.1745	☐	☐
2	5 6 7 14 16 18 39	0.90	0.1783	☐	☐
3	5 6 10 14 16 18 39	0.91	0.1790	☐	☐
4	5 6 10 12 14 18 39	0.90	0.1820	☐	☐

Vertical component

	Combination	Scaling factor	Spectral deviation	Plot spectra	Run analysis
1				☐	☐
2				☐	☐
3				☐	☐
4				☐	☐

Figure 5: Final list of the ground motion suites formed, as they are ranked according to the spectral matching criterion of Eq. (3).

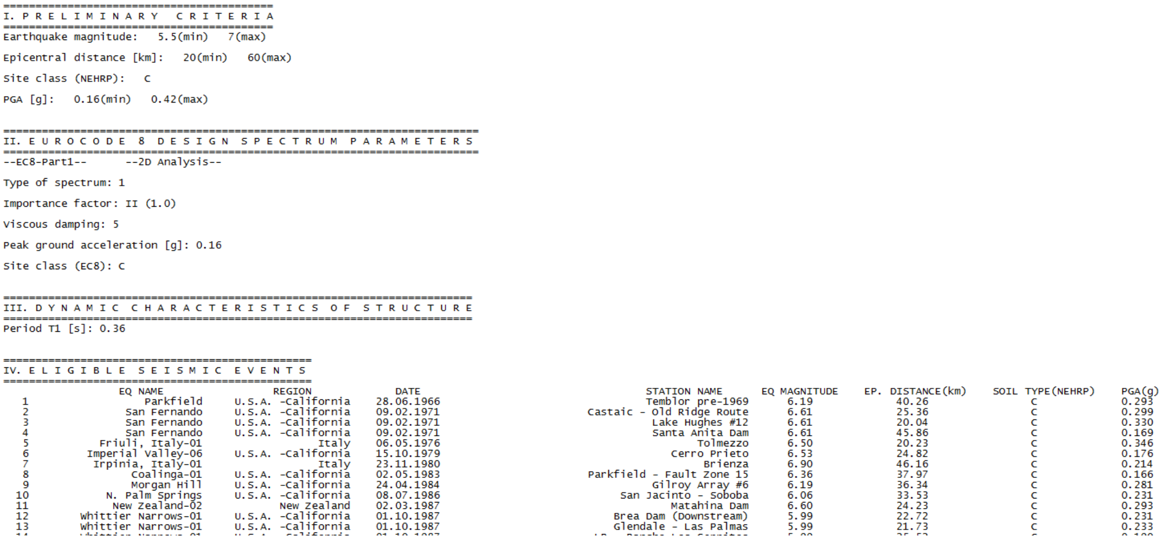
```
===========================================
I. P R E L I M I N A R Y   C R I T E R I A
===========================================
Earthquake magnitude:   5.5(min)   7(max)

Epicentral distance [km]:   20(min)   60(max)

Site class (NEHRP):   C

PGA [g]:   0.16(min)   0.42(max)

===========================================================================
II. E U R O C O D E  8  D E S I G N  S P E C T R U M  P A R A M E T E R S
===========================================================================
--EC8-Part1--      --2D Analysis--

Type of spectrum: 1

Importance factor: II (1.0)

Viscous damping: 5

Peak ground acceleration [g]: 0.16

Site class (EC8): C

==========================================================================
III. D Y N A M I C  C H A R A C T E R I S T I C S  O F  S T R U C T U R E
==========================================================================
Period T1 [s]: 0.36

=================================================
IV. E L I G I B L E  S E I S M I C  E V E N T S
=================================================
              EQ NAME              REGION          DATE                      STATION NAME        EQ MAGNITUDE    EP. DISTANCE(km)    SOIL TYPE(NEHRP)    PGA(g)
  1          Parkfield    U.S.A. -California   28.06.1966            Temblor pre-1969       6.19            40.26                C              0.293
  2       San Fernando    U.S.A. -California   09.02.1971    Castaic - Old Ridge Route      6.61            25.36                C              0.299
  3       San Fernando    U.S.A. -California   09.02.1971            Lake Hughes #12        6.61            20.04                C              0.330
  4       San Fernando    U.S.A. -California   09.02.1971            Santa Anita Dam        6.61            45.86                C              0.169
  5   Friuli, Italy-01                 Italy   06.05.1976                   Tolmezzo        6.50            20.23                C              0.346
  6 Imperial Valley-06    U.S.A. -California   15.10.1979               Cerro Prieto        6.53            24.82                C              0.176
  7  Irpinia, Italy-01                 Italy   23.11.1980                    Brienza        6.90            46.16                C              0.214
  8        Coalinga-01    U.S.A. -California   02.05.1983   Parkfield - Fault Zone 15       6.36            37.97                C              0.166
  9        Morgan Hill    U.S.A. -California   24.04.1984           Gilroy Array #6         6.19            36.34                C              0.281
 10     N. Palm Springs   U.S.A. -California   08.07.1986      San Jacinto - Soboba         6.06            33.53                C              0.231
 11     New Zealand-02           New Zealand   02.03.1987               Matahina Dam        6.60            24.23                C              0.293
 12 Whittier Narrows-01   U.S.A. -California   01.10.1987       Brea Dam (Downstream)       5.99            22.72                C              0.231
 13 Whittier Narrows-01   U.S.A. -California   01.10.1987       Glendale - Las Palmas       5.99            21.73                C              0.233
```

Figure 6: ISSARS's output file.

The computational time, required for calculating 480700 suites of scaled records (formed for the case of 25 selected seismic events), is about 60 seconds on a 8GB RAM 1.60 GHz quad core processor. This computational efficiency permits the concurrent use of the software for multiple ranges of preliminary criteria.

4.2 Visualization Module

The results of the previous module can be visualized by calling the plot module. For each one of the formed suites of records, ISSARS provides a figure illustrating (a) the target spectrum, (b) the code-imposed lower bound of the design spectrum (necessary for the spectral matching procedure, Table 1), (c) the individual 5% damped response spectra of all records within a given suite (d) the average spectrum of the suite, and (e) the scaled average spectrum. This schematic illustration of the calculated spectra (Figure 7) enables a preliminary but useful visual assessment regarding the "goodness-of-fit" of a particular suite of records to the target spectrum, which may reveal period ranges of inappropriately unsuccessful fit that may be otherwise suppressed by the averaging *NRMSE* values of Eq. (3).

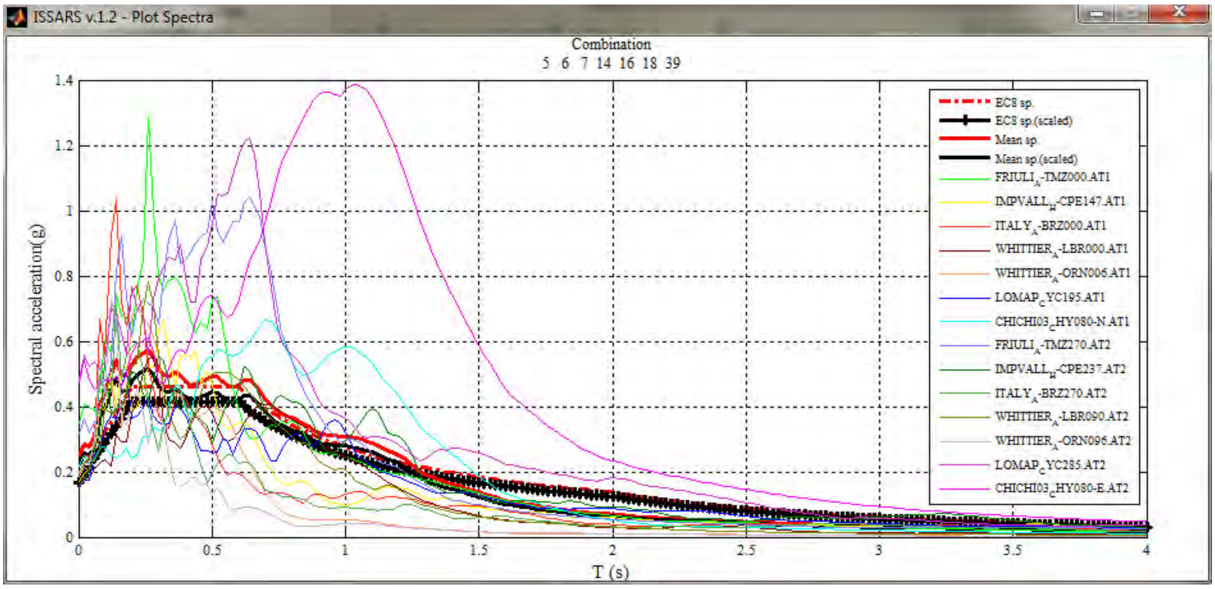

Figure 7: Sample plot of individual, average and target spectra computed for each suite.

4.3 Structural Analysis Module

Although it is not explicitly stated in modern seismic codes, one of the main objectives of selecting and scaling accelerograms is to form suites of records that will eventually induce adequately stable estimates of the predicted elastic or inelastic structural response; otherwise, the associated dispersion in response quantities may undermine the reliability of the predicted design values [25, 26]. At the same time, the consideration of the structural response variability in the decision-making procedure for selecting earthquake records is only implicitly considered by seismic codes through the rough estimate of the fundamental period and the associated period range for spectral matching.

In the computational framework developed, the discrepancy induced in the response quantities by the selection of a given suite of records, is quantified and utilized as a selection criterion itself. This is made feasible by using the recently introduced Application Programming Interface (API) of the finite element software SAP2000 [18]. This API permits the execution of specific build-in functions to run and control SAP2000 in the background, during the execution of the Matlab script, provided that the designer/engineer has developed and made available the finite element model of the structure in advance.

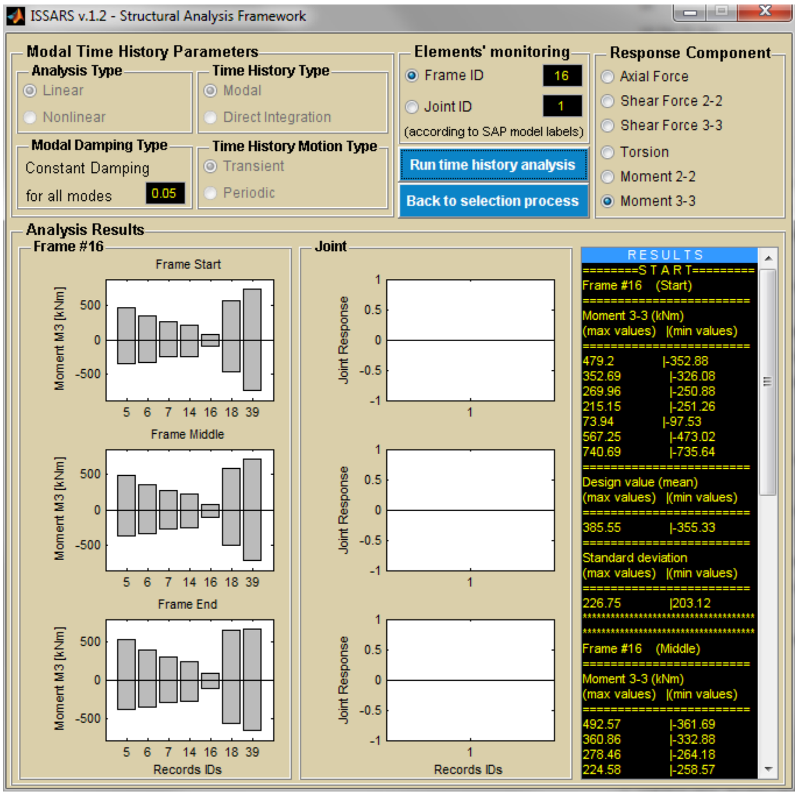

Modal Time History Parameters

Analysis Type
● Linear
○ Nonlinear

Time History Type
● Modal
○ Direct Integration

Modal Damping Type
Constant Damping
for all modes 0.05

Time History Motion Type
● Transient
○ Periodic

Elements' monitoring
● Frame ID 16
○ Joint ID 1
(according to SAP model labels)

Response Component
○ Axial Force
○ Shear Force 2-2
○ Shear Force 3-3
○ Torsion
○ Moment 2-2
● Moment 3-3

```
========S T A R T=========
Frame #16    (Start)
========================
Moment 3-3 (kNm)
(max values)   |(min values)
========================
479.2           |-352.88
352.69          |-326.08
269.96          |-250.88
215.15          |-251.26
73.94           |-97.53
567.25          |-473.02
740.69          |-735.64
========================
Design value (mean)
(max values)   |(min values)
========================
385.55          |-355.33
========================
Standard deviation
(max values)   |(min values)
========================
226.75          |203.12
*************************************
*************************************
Frame #16    (Middle)
========================
Moment 3-3 (kNm)
(max values)   |(min values)
========================
492.57          |-361.69
360.86          |-332.88
278.46          |-264.18
224.58          |-258.57
```

Figure 8: Structural Analysis Module.

Through this interactive link, response history analyses are performed using the record suites, which are defined according to the preliminary criteria set and the “goodness-of-fit” ranking system, while the Matlab-based script retrieves post-processing structural analysis data, such as the action effects (i.e. forces and displacements) maxima, monitored at the frames and joint locations (Figure 8). Another advantage of the interactive record selection procedure is that, it can be followed, regardless of the complexity of the finite element model, that is, the type of the structure, the number of degrees of freedom, its geometry, the potential for material or geometrical nonlinearities, the consideration of soil flexibility, the direction of excitation or any unconventional structural characteristic. The complexity of the structure is resolved by the designer and once the finite element model is made available to the Matlab script, the structure-specific earthquake record selection runs effortlessly.

5 APPLICATION OF THE PROPOSED COMPUTATIONAL FRAMEWORK FOR THE ASSESSMENT OF AN EXISTING RC STRUCTURE

In an attempt to illustrate the applicability of the proposed computational framework, a demonstration is presented herein for the case of an existing, multi-storey R/C building, located in Thessaloniki, Greece. The overview of the case study as well as the results derived are presented in the following.

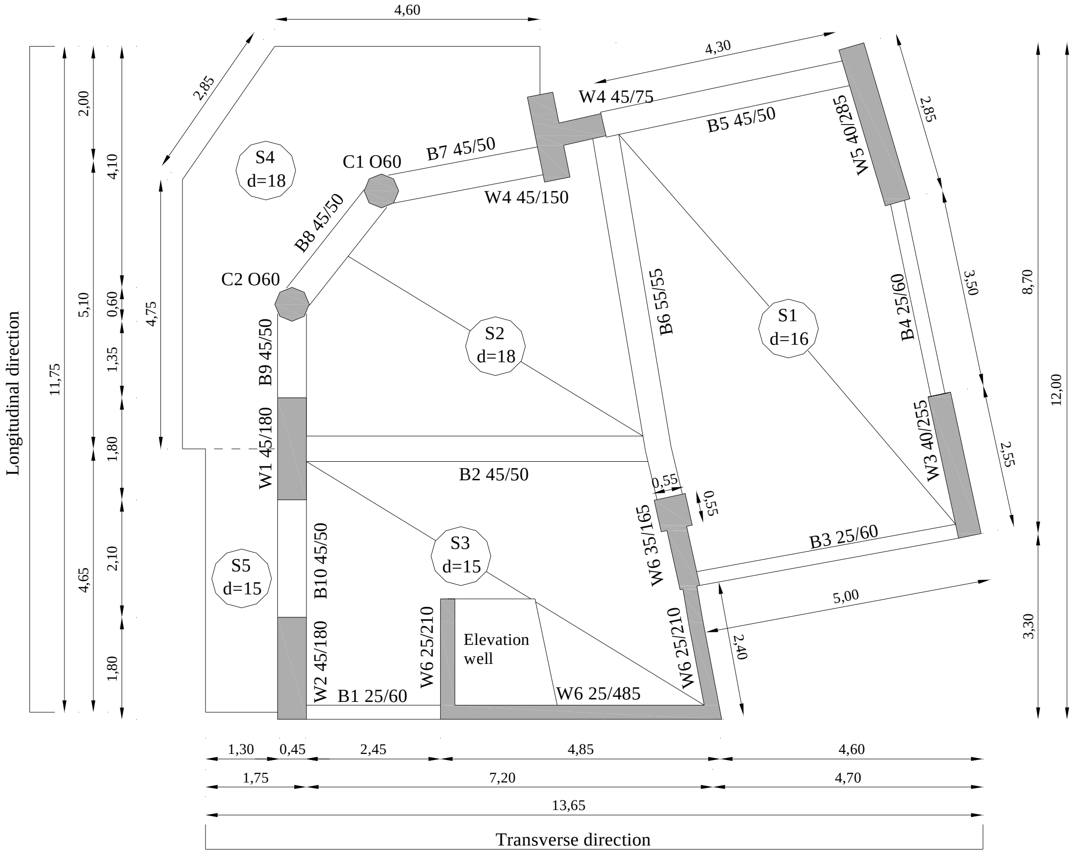

Figure 9: Plan view of the typical floor of the case study building.

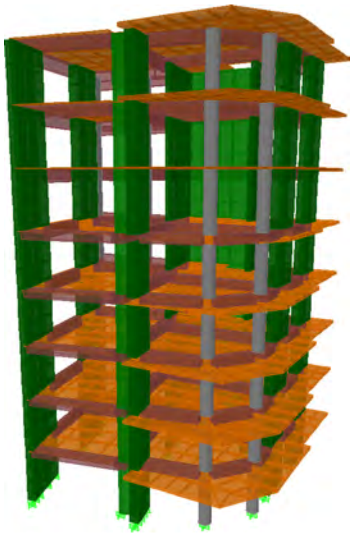

Figure 10: A 3-Dimensional finite element model of the building under study.

5.1 Case study building: Structural configuration and numerical modeling aspects

The building studied is an irregular in plan, seven-storey R/C dual system, with a pilotis and a basement, which is located in the city of Thessaloniki, in Greece, whose plan view is presented in Figure 9. The total area of the typical storey is 135.0 m^2 and the storey height is 3.0 m. The lateral strength of the building is provided by four shear walls of relatively equally dimensions and a reinforced concrete core eccentrically. The concrete class used was C20/25 (i.e., compressive strength $f_c'=20\ N/mm^2$), and St.III steel bars (i.e. yield strength $f_y'=500\ N/mm^2$) were applied for the longitudinal and transverse reinforcement. The building under study was constructed in 2008 according to the latest version of the Greek Seismic Code EAK2000 [27] which is currently in parallel enforcement with the Eurocodes. The design ground acceleration, a_g, has been set equal to 0.16g as corresponding to the lowest seismic hazard category in Greece. The soil conditions have been classified as category C according to both EAK2000 and EC8 site categorization. Figure 10 illustrates the fixed-base model [28], developed with the use of SAP2000 finite element software [18] using both frame elements for the beams and the columns and shell elements for the shear walls and slabs.

5.2 Coupled earthquake record selection and structural analysis

After the development of the finite element model of the building studied, a seismic scenario was determined for the seismic hazard of the particular site using the following seismological criteria: (a) earthquake magnitude, $6.5 \leq M \leq 7.5$, (b) source-to-site distance, $20 \leq R \leq 50$ (km), (c) peak ground acceleration, PGA≥0.16g and (d) soft soil conditions, corresponding to Eurocode 8 soil category C. Regarding the target spectrum, the EC8 5% damped, elastic spectrum was defined for soil category C while the reference peak ground acceleration value was taken equal to 0.16g for the reason described previously. The fundamental period of the structure was found equal to 0.621s and was used to establish the EC8 prescribed spectral matching period range (i.e. $0.2T_1=0.12s<T<2T_1=1.24s$). Based on the above, ISSARS was performed to search online within the PEER-NGA Strong Motion Database and 36 different seismic events have been returned as eligible. Analytical description of the resulting sample is summarized in Table 2. It is notable that each one of these eligible earthquakes consists of two horizontal seismic records, which are required for the bi-directional seismic loading of the particular multi-storey R/C building.

Due to the enormous computational cost that would be required in case of calculating all the possible records suites from the 36 eligible seismic events (i.e., 8,347,680 suites of seven pairs of horizontal components of strong motions would be required), 28 different earthquakes were selected, leading to the generation of 1,184,040 suites of records (Figure 11). The required computational time for this calculation did not exceeded 120-150 s using a 8GB RAM 1.60 GHz quad core processor.

In the following, ranking of the suites of records took place in terms of their spectral compatibility to the Eurocode 8 target spectrum and according to the hierarchical concept adopted. The first suite of records, characterized by the highest matching score, was selected as the first candidate for the dynamic analysis of the structure under study. More specifically, the seven pairs of strong motions, which are included in the first suite, were automatically transferred and applied as the seismic excitation of the case study finite element model, thus, seven bi-directional, elastic response history analyses were performed in the background using the Structural Analysis Module and the built-in API functions of the SAP2000 program. The results of these consecutive analyses were returned, processed and finally presented by ISSARS (Figure 12) in the form of maximum absolute values of all response quantities at the monitored frames and joints, as well as their average values and standard deviations. The designer may also choose alternative top ranked suites of earthquake records, compare the resulting discrepancy of the computed response quantities and decide on the most representative combination (suite) of records to be eventually used for design or assessment purposes.

No.	Earthquake	Recording Station	M	R	PGA	Used
1	KC 21.07.1952	Taft Lincoln School	7.36	43.49	0.173	Yes
2	SFE 09.02.1971	Castaic-Old Ridge R.	6.61	25.36	0.299	Yes
3	SFE 09.02.1971	Lake Hughes#12	6.61	20.04	0.330	Yes
4	SFE 09.02.1971	Santa Anita Dam	6.61	45.86	0.169	Yes
5	FR 06.05.1976	Tolmezzo	6.50	20.23	0.346	Yes
6	TAB 16.09.1978	Dayhook	7.35	20.63	0.351	Yes
7	IV 15.10.1979	Cerro Prieto	6.53	24.82	0.176	Yes
8	IR 23.11.1980	Brienza	6.90	46.16	0.214	Yes
9	NZ 02.03.1987	Matahina Dam	6.60	24.23	0.293	Yes
10	LP 18.10.1989	Anderson Dam	6.93	26.57	0.238	Yes
11	LP 18.10.1989	Coyote Lake Dam	6.93	30.78	0.295	Yes
12	LP 18.10.1989	Gilro-Gavilan Coll.	6.93	28.98	0.334	Yes
13	LP 18.10.1989	Hollister-South & Pine	6.93	48.24	0.279	Yes
14	LP 18.10.1989	San Jose-S.T. Hills	6.93	20.13	0.283	Yes
15	LP 18.10.1989	Saratoga-Aloha Ave	6.93	27.23	0.382	Yes
16	CM 25.04.1992	Shelter Cove Airport	7.01	36.28	0.195	Yes
17	LAN 28.06.1992	Lucerne	7.28	44.02	0.721	Yes
18	NOR 17.01.1994	Big Tujunga, Angeles	6.69	31.55	0.200	No
19	NOR 17.01.1994	Castaic - Old Ridge R.	6.69	40.68	0.490	Yes
20	NOR 17.01.1994	Glendale - Las Palmas	6.69	29.72	0.256	Yes
21	NOR 17.01.1994	LA-City Terrace	6.69	39.15	0.267	Yes
22	NOR 17.01.1994	LA-Cypress Ave	6.69	33.25	0.206	Yes
23	NOR 17.01.1994	LA-Fletcher Dr	6.69	30.27	0.207	Yes
24	NOR 17.01.1994	LA-Temple & Hope	6.69	32.72	0.165	No
25	NOR 17.01.1994	LA-Univ. Hospital	6.69	36.47	0.349	Yes
26	NOR 17.01.1994	La Crescenta - N.Y.	6.69	27.83	0.173	No
27	NOR 17.01.1994	Lake Hughes#12A	6.69	40.65	0.215	Yes
28	NOR 17.01.1994	Lake Hughes#9	6.69	44.77	0.169	No
29	NOR 17.01.1994	Manhattan Beach	6.69	38.69	0.166	No
30	NOR 17.01.1994	Moorpark-Fire Station	6.69	31.45	0.229	No
31	NOR 17.01.1994	Pasadena-N. Sierra	6.69	44.01	0.234	Yes
32	NOR 17.01.1994	Point Mugu-Lag Peak	6.69	48.28	0.175	No
33	NOR 17.01.1994	San Gabriel-E Grand	6.69	44.32	0.209	No
34	DZC 12.11.1999	Lamont 375	7.14	24.05	0.737	Yes
35	MAN 20.06.1990	Abbar	7.37	40.43	0.505	Yes
36	HM 16.10.1999	Hector	7.13	26.53	0.306	Yes

Table 2. Description of eligible seismic events as derived by the application of the seismological criteria adopted in the current algorithm.

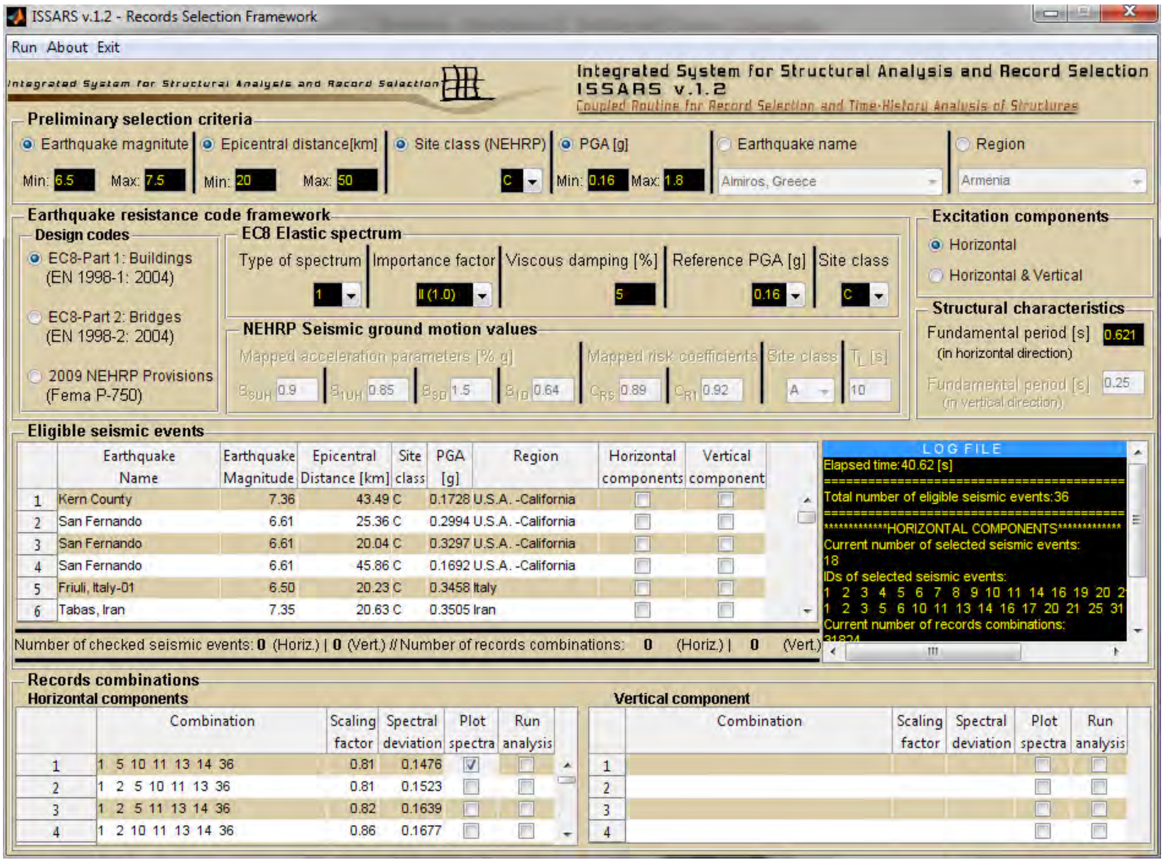

Preliminary selection criteria

● Earthquake magnitute Min: 6.5 Max: 7.5
● Epicentral distance[km] Min: 20 Max: 50
● Site class (NEHRP) C
● PGA [g] Min: 0.16 Max: 1.8
○ Earthquake name Almiros, Greece
○ Region Armenia

Earthquake resistance code framework

Design codes
● EC8-Part 1: Buildings (EN 1998-1: 2004)
○ EC8-Part 2: Bridges (EN 1998-2: 2004)
○ 2009 NEHRP Provisions (Fema P-750)

EC8 Elastic spectrum
Type of spectrum: 1
Importance factor: II (1.0)
Viscous damping [%]: 5
Reference PGA [g]: 0.16
Site class: C

NEHRP Seismic ground motion values
Mapped acceleration parameters [% g]: S_{SUH} 0.9, S_{1UH} 0.85, S_{SD} 1.5, S_{1D} 0.64
Mapped risk coefficients: C_{RS} 0.89, C_{R1} 0.92
Site class: A
T_L [s]: 10

Excitation components
● Horizontal
○ Horizontal & Vertical

Structural characteristics
Fundamental period [s] (in horizontal direction): 0.621
Fundamental period [s] (in vertical direction): 0.25

Eligible seismic events

	Earthquake Name	Earthquake Magnitude	Epicentral Distance [km]	Site class	PGA [g]	Region	Horizontal components	Vertical component
1	Kern County	7.36	43.49	C	0.1728	U.S.A. -California	☐	☐
2	San Fernando	6.61	25.36	C	0.2994	U.S.A. -California	☐	☐
3	San Fernando	6.61	20.04	C	0.3297	U.S.A. -California	☐	☐
4	San Fernando	6.61	45.86	C	0.1692	U.S.A. -California	☐	☐
5	Friuli, Italy-01	6.50	20.23	C	0.3458	Italy	☐	☐
6	Tabas, Iran	7.35	20.63	C	0.3505	Iran	☐	☐

Number of checked seismic events: **0** (Horiz.) | **0** (Vert.) // Number of records combinations: 0 (Horiz.) | 0 (Vert.)

```
LOG FILE
Elapsed time:40.62 [s]
==========================================
Total number of eligible seismic events:36
==========================================
************HORIZONTAL COMPONENTS************
Current number of selected seismic events:
18
IDs of selected seismic events:
1  2  3  4  5  6  7  8  9 10 11 14 16 19 20 2
1  2  3  5  6 10 11 13 14 16 17 20 21 25 31
Current number of records combinations:
31824
```

Records combinations

Horizontal components

	Combination	Scaling factor	Spectral deviation	Plot spectra	Run analysis
1	1 5 10 11 13 14 36	0.81	0.1476	☑	☐
2	1 2 5 10 11 13 36	0.81	0.1523	☐	☐
3	1 2 5 11 13 14 36	0.82	0.1639	☐	☐
4	1 2 10 11 13 14 36	0.86	0.1677	☐	☐

Vertical component

	Combination	Scaling factor	Spectral deviation	Plot spectra	Run analysis
1				☐	☐
2				☐	☐
3				☐	☐
4				☐	☐

Figure 11: Application of ISSARS for the case of an existing, irregular in plan, multi-storey, RC building (Ground-motion selection module)

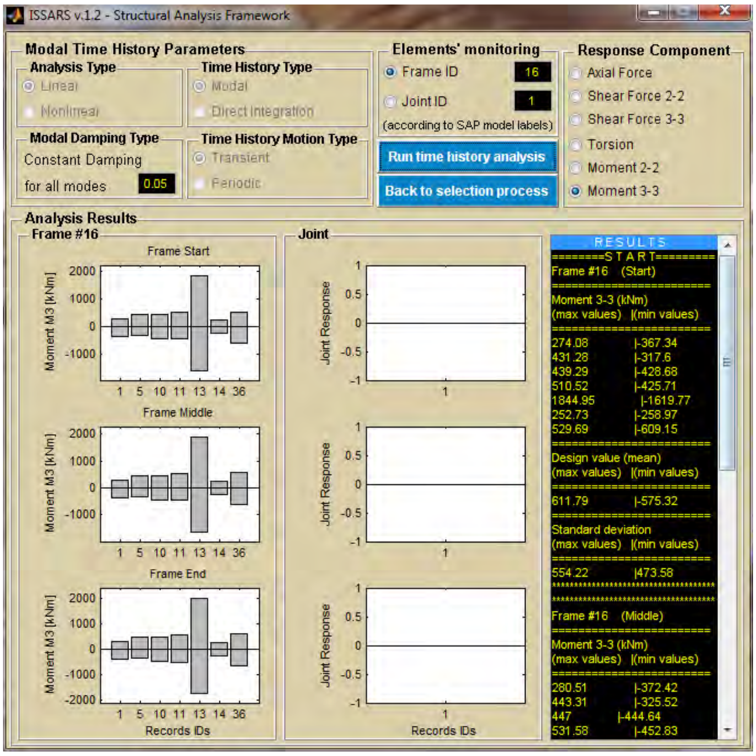

Modal Time History Parameters

Analysis Type: ● Linear ○ Nonlinear
Time History Type: ● Modal ○ Direct integration
Modal Damping Type: Constant Damping for all modes 0.05
Time History Motion Type: ● Transient ○ Periodic

Elements' monitoring
● Frame ID 16
○ Joint ID 1
(according to SAP model labels)

Response Component
○ Axial Force
○ Shear Force 2-2
○ Shear Force 3-3
○ Torsion
○ Moment 2-2
● Moment 3-3

```
RESULTS
========S T A R T========
Frame #16   (Start)
========================
Moment 3-3 (kNm)
(max values)  |(min values)
========================
274.08        |-367.34
431.28        |-317.6
439.29        |-428.68
510.52        |-425.71
1844.95        |-1619.77
252.73        |-258.97
529.69        |-609.15
========================
Design value (mean)
(max values)  |(min values)
========================
611.79        |-575.32
========================
Standard deviation
(max values)  |(min values)
========================
554.22        |473.58
******************************
******************************
Frame #16   (Middle)
========================
Moment 3-3 (kNm)
(max values)  |(min values)
========================
280.51        |-372.42
443.31        |-325.52
447        |-444.64
531.58        |-452.83
```

Figure 12: Application of ISSARS for the case of an existing, irregular in plan, multi-storey, RC building (Structural analysis module).

6 CONCLUSIONS

An integrated computational system that couples the code-based earthquake records selection procedure and the structural response is developed and presented herein as a means to increase both the applicability and the effectiveness of the current state-of-the-practice in conducting response history analyses. The proposed Matlab-based algorithm utilizes the online PEER-NGA strong motion database in order to search for compliant strong motions, which are required for the seismic loading of dynamic analyses. After an initial records filtering procedure in terms of magnitude, epicentral distance, soil conditions, intensity measure, components of excitation (2D or 3D) and structural system (building or bridge), the eligible acceleration time series are grouped into numerous suites and finally ranked on the basis of their spectral similarity with the design spectrum. Through the recently released Application Programming Interface (API) of the computer program SAP2000, the selected records are applied to excite the finite element model that the designer is assumed to have prepared at the background. The variation of the response quantities in the time domain are automatically computed and the relative structural response dispersion under various records sets is assessed. The presentation concludes with a demonstration assessment of an existing, irregular in plan, multi-storey, RC building, where the importance of adopting a structure-specific earthquake record selection process is highlighted. It is deemed that the structure-specific earthquake record selection procedure presented herein is a promising alternative to the existing procedures and a significant improvement compared to the conventional application of the current seismic code provisions.

REFERENCES

[1] A.S. Elnashai, D.C. McClure, Effect of modelling assumptions and input motion characteristics on seismic design parameters of RC bridge piers. *Earthquake Engineering and Structural Dynamics* **25**(5), 435–63, 1996.

[2] N. Shome, C.A. Cornell, P. Bazzurro, J.E. Carballo, Earthquakes, records and nonlinear responses. *Earthquake Spectra* **14**(3), 469–500, 1998.

[3] J. Padgett, R. Desroches, Sensitivity of seismic response and fragility to parameter uncertainty. *Journal of Structural Engineering* **133**(12), 1710–1718, 2007.

[4] E.I. Katsanos, A.G. Sextos, G.D. Manolis, Selection of earthquake ground motion records: a state-of-the-art review from a structural engineering perspective. *Soil Dynamics and Earthquake Engineering* **30**(4), 157–169, 2010.

[5] H. Krawinkler, R. Medina, B. Alavi, Seismic drift and ductility demands and their dependence on ground motions. *Engineering Structures* **25**, 637-653, 2003.

[6] J. Baker, C.A. Cornell, A vector-valued ground motion intensity measure consisting of spectral acceleration and epsilon, *Earthquake Engineering and Structural Dynamics* **34**, 1193-1217, 2005.

[7] P. Bazzurro, C.A. Cornell, Seismic hazard analysis of nonlinear structures. I: Methodology, *Journal of Structural Engineering*, ASCE **120**(11), 3320-3344, 1994.

[8] K. Beyer, J.J. Bommer, Selection and scaling of real accelerograms for bidirectional loading: a review of current practice and code provisions, *Journal of Earthquake Engineering* **10**(1), 13-45, 2007.

[9] P.K. Malhotra, Strong-motion records for site-specific analysis, *Earthquake Spectra* **19**(3), 557-578, 2003.

[10] J. Baker, The Conditional mean spectrum: A tool for ground motion selection, *Journal of Structural Engineering*, ASCE doi:10.1061/(ASCE)ST.1943-541X.0000215, 2010.

[11] F. Naeim, A. Alimoradi, S. Pezeshk, Selection and scaling of ground motion time histories for structural design using genetic algorithms, *Earthquake Spectra* **20**(2), 413-426, 2004.

[12] R.R. Youngs, M.S. Power, G. Wang, F.I. Makdisi, C.C. Chin. Design ground motion library (DGML) - Tool for selecting time history records for specific engineering applications, in *SMIP Seminar on Utilization of Strong-Motion Data*, 2007

[13] A. Kottke, E.M. Rathje, A semi-automated procedure for selecting and scaling recorded earthquake motions for dynamic analysis, *Earthquake Spectra* **24**(4), 911-932, 2008.

[14] N. Jayaram, T. Lin, J. Baker, A computationally efficient ground-motion selection algorithm for matching a target response spectrum mean and variance, *Earthquake Spectra* 2010 (in press).

[15] N. Luco, C.A. Cornell, Structure-specific scalar intensity measures for near-source and ordinary earthquake ground motions, *Earthquake Spectra* **23**(2), 357-392, 2007.

[16] P. Tothong, N. Luco, Probabilistic seismic demand analysis using advanced ground motion intensity measures, *Earthquake Engineering and Structural Dynamics* **36**, 1837-1860, 2007.

[17] A.G. Sextos, E.I. Katsanos, G.D. Manolis, EC8-based earthquake record selection procedure evaluation: Validation study based on observed damage of an irregular R/C building, *Soil Dynamics and Earthquake Engineering* **31**, 583-597, 2011.

[18] CSI, Computers and Structures, *SAP2000: Integrated Software for Structural Analysis and Design*, ver.14, Berkeley, California, U.S.A., 2010.

[19] EC8, 2004. *Eurocode 8: Design provisions of structures for earthquake resistance. Part 1: General rules, seismic actions and rules for buildings. Part 2: Bridges*, Final Drafts pr EN1998-1 and -2, European Committee for Standardization (CEN), Brussels, Belgium.

[20] FEMA P-750, 2009. *NEHRP Recommended Seismic Provisions for New Buildings and Other Structures*, Building Seismic Safety Council, Washington, D.C., U.S.A.

[21] B. Chiou, R. Darragh, N. Gregor, W. Silva, NGA project strong motion database, *Earthquake Spectra* **24**(1), 23-44, 2008.

[22] M. Power, B. Chiou, N. Abrahamson, Y. Bozorgnia, Th. Shantz, Cl. Roblee, An overview of the NGA Project, *Earthquake Spectra* **24**(1), 3-21, 2008

[23] A. Kottke, E.M. Rathje, A semi-automated procedure for selecting and scaling recorded earthquake motions for dynamic analysis, *Earthquake Spectra* **24**(4), 911-932, 2008.

[24] I. Iervolino, G. Maddaloni, E. Cosenza, Eurocode 8 compliant real record sets for seismic analysis of structures, *Journal of Earthquake Engineering* **12**, 54-90, 2008.

[25] N. Luco, C.A. Cornell, Structure-specific scalar intensity measures for near-source and ordinary earthquake ground motions, *Earthquake Spectra* **23**(2), 357-392, 2007.

[26] Y.-N. Huang, A.S. Whittaker, N. Luco, R.O. Hamburger, Scaling earthquake ground motions for performance-based assessment of buildings, *Journal of Structural Engineering, ASCE* doi:10.1061/(ASCE)ST.1943-541X.0000155, 2009.

[27] EAK, *Hellenic Antiseismic Code*, Earthquake Planning and Protection Organization, Ministry Of Public Works, Athens, Greece, 2003.

[28] A. Petropoulos, *Earthquake-induced pounding of adjacent reinforced concrete buildings through dynamic inelastic analysis.* MSc Thesis, Department of Civil Engineering, Aristotle University of Thessaloniki, Greece (*in Greek*), 2008.

COMPDYN 2011
3rd ECCOMAS Thematic Conference on
Computational Methods in Structural Dynamics and Earthquake Engineering
M. Papadrakakis, M. Fragiadakis, V. Plevris (eds.)
Corfu, Greece, 25–28 May 2011

USING THE NEW SAP2000 OPEN APPLICATION PROGRAMMING INTERFACE TO DEVELOP AN INTERACTIVE FRONT-END FOR THE MODAL PUSHOVER ANALYSIS OF BRIDGES

A. G. Sextos[1] and G. K. Balafas[2]

[1] Assistant Professor, Division of Structural Engineering
Department of Civil Engineering, Aristotle University of Thessaloniki, 541 24 Greece
e-mail: asextos@civil.auth.gr

[2] Civil Engineer, Division of Structural Engineering
Department of Civil Engineering, Aristotle University of Thessaloniki, 541 24 Greece
e-mail: balgior@civil.auth.gr

Keywords: modal pushover analysis, bridges, seismic assessment, software development, SAP2000, API.

Abstract. *Seismic assessment of bridge structures often requires inelastic (static or dynamic) analysis methods to be used, in order to draw a realistic evaluation of the structural behaviour beyond the elastic range. While the widely-used non-linear static (pushover) analysis provides a low-computational-cost approach to this direction, it is inherently limited by the assumption that the structure's response is solely controlled by its fundamental mode. This limitation is raised by an extension of the "standard" pushover analysis (SPA) to take into consideration the effect of higher modes , a method known as Modal Pushover Analysis (MPA). This method however, can often prove to be time-consuming and strenuous both for pre- and post processing. The latter, provided the motivation for investigating the feasibility to take advantage of the recently released SAP2000 application programming interface (API) in order to develop a new computational tool that implements the MPA specifications for evaluating the seismic behavior of bridges in an organized and automatic fashion. The paper concludes with the application and demonstration of the software developed, for the case of an existing reinforced concrete bridge located along the Egnatia Highway in Greece.*

1 INTRODUCTION

Nonlinear static procedures have become a commonly used tool for assessing the seismic performance of buildings and bridges. Nevertheless, its main advantage of lower computational cost, compared to non-linear time-history analysis (NL-THA), is counter-balanced by its inherent restriction to those structures, wherein the fundamental mode dominates the response. To this end, Modal Pushover Analysis, as introduced by Chopra and Goel [1], [2] for buildings and extended by Paraskeva et al. [3], [4] for bridges, is deemed a useful alternative, as it can provide a reliable estimate of the non-linear structural response, based on the repeated application of a given nonlinear static analysis procedure for each of the significant vibration modes of the structure, followed by an adequate combination of the results. However, this procedure is time-consuming and the significant effort required for pre- and post-processing of the required and obtained data, respectively, quite often cancels the advantage of simplicity compared to the non-linear time-history analysis.

This limitation is raised herein by making use of the new SAP2000 [5] Application Programming Interface (API), for developing an interactive front-end for the modal pushover analysis of bridges. This API was recently introduced by CSI, the developer of the finite element code SAP2000, and grants access to the SAP2000 advanced numerical modules, thus permitting pre- and post-analysis computations to be efficiently programmed. An introduction to using this new computational tool is made herein and the capabilities that are opened for developing third-party earthquake engineering applications to be coupled with SAP2000 are also discussed. Subsequently, the architecture of the front-end is presented in detail, presenting the implementation approach that was followed and the way that the procedure's specifications where encapsulated into the software.

Finally, the front-end developed is also applied for the assessment of seismic response of an existing bridge structure in Greece, which is presented in this paper for testimonial purposes. It is shown that with the use of the new SAP2000 API and the aforementioned interactive front-end, the time and effort required for studying the inelastic response of bridges through a modal pushover analysis scheme is greatly reduced.

2 STANDARD AND MODAL NONLINEAR ANALYSIS

2.1 Nonlinear Static (Pushover) Analysis

When it comes to estimating the nonlinear behavior of structures that are subjected to seismic forces, pushover analysis is the most widely-used method, capable of providing a reliable estimate of the structural capacity. During this procedure, monotonically increased lateral loads are statically applied to the structure, in an invariant pattern that aims to resemble the distribution of the fundamental mode forces that the structure is subjected to when excited seismically along a given direction. Under the increasing load application, a series of plastic hinges develop at critical sections of the structure, leading force redistribution and gradually to a failure mechanism. As a result, it is possible to obtain the non-linear relationship between the lateral force applied and the deformation of the structure which is monitored at a specific location, usually expressed in the form of the pushover curve, that is, a "base reaction versus control node displacement".

By converting the base shears and roof displacements obtained to equivalent spectral accelerations and displacements ($S_a(T)$ and $S_d(T)$) and superimposing an earthquake demand curve (typically the prescribed seismic hazard spectrum for the site), the non-linear (pushover) analysis can then provide an estimation of the inelastic response of the structure at a given level of target earthquake intensity. It is therefore a useful structural assessment tool as it offers a number of advantages, primarily being the fact that:

- it is a conceptually simple methods which is straightforward to apply low computational cost, in comparison to the nonlinear response history analysis (NL-RHA).
- the results obtained by SPA can be easily post-processed and interpreted, especially compared to NL-RHA. It is recalled that the latter method leads to time variant action effects (i.e., forces and displacements) and computing the statistics of response can be a demanding task. Moreover, the inelastic response results obtained by NL-RHA are very sensitive to both the characteristics (i.e, frequency content, amplitude, duration etc) of the suite of earthquake ground motions used and the assumptions made in modelling the cyclic response of RC members; thus the discrepancies associated with structural response are often large.

On the other hand, the applicability of nonlinear static analysis is limited by its:

- incapability of considering the contribution of higher than the fundamental modes and insensitivity to the dynamic characteristics of the structure.
- problematic application to three-dimensional, non-symmetrical or irregular systems.

As a result, in most realistic cases, “standard” nonlinear static (pushover) analysis (SPA) can only provide a rough estimate of the inelastic response, and more accurate procedures have to be followed.

2.2 Modal Pushover Analysis for the seismic assessment of bridges

Given the above limitations, as already mentioned, Chopra & Goel [1], [2] developed an improved Modal Pushover Analysis (MPA) procedure where the total seismic demand of inelastic systems is computed based on the combination of individual “modal” demands. With a series of adaptations and further assumptions, the method was extended for the assessment of the inelastic response of bridges ([3], [4]). The main steps of this method are summarized in the following [3]:

- *Step 1*: Calculation of the “elastic” natural periods T_n and the modes φ_n of the bridge. Due to the physical characteristics of bridges, the number of modes that need to be taken into account during the procedure may reach even a few hundred modes, until the total mass contribution sums up to a level of at least 90%, which is considered to be adequate.
- *Step 2*: Separate SPA are performed for each significant mode of the bridge, from which the base shear force – control node displacement relationship $(V_{bn} - u_{rn})$ is extracted, in order to form the pushover curve that corresponds to each mode.
- *Step 3*: The pushover curve is transformed appropriately into an idealized bilinear equivalent, so that the yield point and the ductility factor can be obtained.
- *Step 4*: The earthquake displacement demand is defined. The idealized pushover curve of the multi-degree-of-freedom (MDOF) system is converted into a capacity diagram of the equivalent single-degree-of-freedom (SDOF) system, using the following relationships:

$$S_a = \frac{V_{bn}}{M_n^*} \tag{1}$$

$$S_d = \frac{u_{rn}}{\Gamma_n \cdot \varphi_{rn}} \tag{2}$$

wherein S_a and S_d are the spectral acceleration and displacements, correspondingly, φ_{rn} is the value of φ_n at the monitoring point, $M_n^* = L_n \cdot \Gamma_n$ is the effective modal mass, $\mathrm{L_n} = \varphi_n^T \cdot m$, $\Gamma_\mathrm{n} = L_n / M_n$ and $\mathrm{M_n} = \varphi_n^T \cdot m \cdot \varphi_n$ is the generalized mass, for the nth natural mode. In this way, by applying the capacity spectrum method ([6], [7]) it is possible to estimate the displacement demand corresponding to the applied earthquake intensity.

- *Step 5*: The displacement demand of the nth mode inelastic SDOF system that was calculated in the previous step is converted back to the peak displacement of the monitoring point u_{rn} of the MDOF representing the actual bridge.
- *Step 6*: The values of the desired responses r_n are extracted from the analysis step at which the displacement at the monitoring point is equal to u_{rn} defined in Step 5.
- *Step 7*: Steps 3 to 6 are repeated for all the modes considered “important”.
- *Step 8*: An appropriate modal combination rule, such as SRSS or CQC, is applied to the peak modal responses r_{no} (i.e., for displacements and plastic hinge rotations) that correspond to each “important” mode, in order for the total value of the desired response to be estimated.

The procedure described briefly in the aforementioned steps is subjected to a number of important key-factors that should be taken into account while performing the analysis, such as the appropriate selection of the monitoring point (i.e., deck mass center, top of the nearest pier, location of maximum displacement etc) for each pushover analysis or the rule that is used during the idealization of the pushover curves. Further investigation of the details that describe MPA is beyond the scope of the present work. However, wherever applicable, additional reference to the specifications, which were followed along the development of the MPA software, will be made.

3 INTRODUCTION TO THE SAP2000 APPLICATION PROGRAMMING INTERFACE

Facing the challenge of developing new, more accurate and, inevitably, more sophisticated procedures for the needs of structural engineering does not come at no cost; the need for computational power and the subsequent requirement to embrace bleeding-edge technology tools and resources are demanding. Reversing the argument, it is this vey availability of increasingly productive computational systems that motivates the researchers to investigate more advanced and optimized tools for the assessment of structures, leading in this way to a recursive pattern of development and adoption of new information technologies achievements. Furthermore, the need of simplifying the application of available procedures and making effective use of the computational methods already established is not to be neglected, as this can greatly improve the productivity and quality of performing every-day tasks. In this direction, the recently introduced computational tool SAP2000 API, which accompanies the structural analysis software SAP2000 as of version 11, has come to significantly expand the usage of its parent-application into wider research fields beyond the structural analysis framework currently established.

3.1 Description of the SAP2000 API

The SAP2000 Application Programming Interface (API) is a programming tool which aims to offer efficient access to the analysis and design technology of the SAP2000 structural analysis software, by allowing, during run-time, a direct bind to be established, between a third-party application and the analysis software itself [Fig. 1]. Additionally, through the use of this API, one has the option of developing plug-ins, which extend the program's usability and are totally embedded within the SAP2000 environment. In terms of computer programming, the API consists of a software library that offers access to a collection of objects and functions capable of “remotely” controlling the way that the SAP2000 behaves, thus, overriding the standard point-and-click procedure. A highlight of the main features that the API provides are summarized below:

- Direct, fast and robust coupling with the SAP2000 design and analysis methods.
- Two-way data flow as it can be used to facilitate both pre- and post-processing procedures.
- No need of using intermediate files, which reduces significantly the time needed for data exchange when working on large models.
- Compatibility with most major programming languages.
- Concurrent data transfer and control of a structural model by different third-party applications.
- Development of third-party applications that will remain compatible with future releases of SAP2000.
- Ability to develop a custom interface for SAP2000, calibrated to the user's needs, or to embed one in an application that allows for user programming.

3.2 Using the SAP2000 API

In order to make use of the above SAP2000 API features for developing new computing tools, usually a solid programming background is required, as the process may prove demanding, in terms of programming skills. However, this is not always the case, when it comes to simple computing tasks. In either case, the SAP2000 API offers a broad range of programming languages that it can be used which cover the vast majority of the modern software development options including Visual Basic.NET, Visual Basic for Applications (VBA), Visual C#, Visual C++, Visual Fortran and Matlab.

To get started with, accessing the API requires nothing more than a functional SAP2000 installation, as all the components that it consists of are automatically installed during the main program's setup. Using it, however, depends at large on the programming language that the developer is familiar with and the programming environment that is selected for this purpose. Different integrated development environments (IDEs) offer several options in order for the programming project to link successfully with the API and, additionally, in each case the syntax to be used and the potential planning of the application to be developed differ according to the language's standards. One should bear in mind, however, that in order to make effective use of the API it may be appropriate that the programming style, to which one is accustomed to, has to be adapted to the way the API is structured, due to its non-deviant attitude, regarding the SAP2000 approach to designing an assessing a structure; in any case though, the steps necessary to accomplish a task via the API resemble vastly the corresponding point-and-click procedure required by the standard usage of the parent-application.

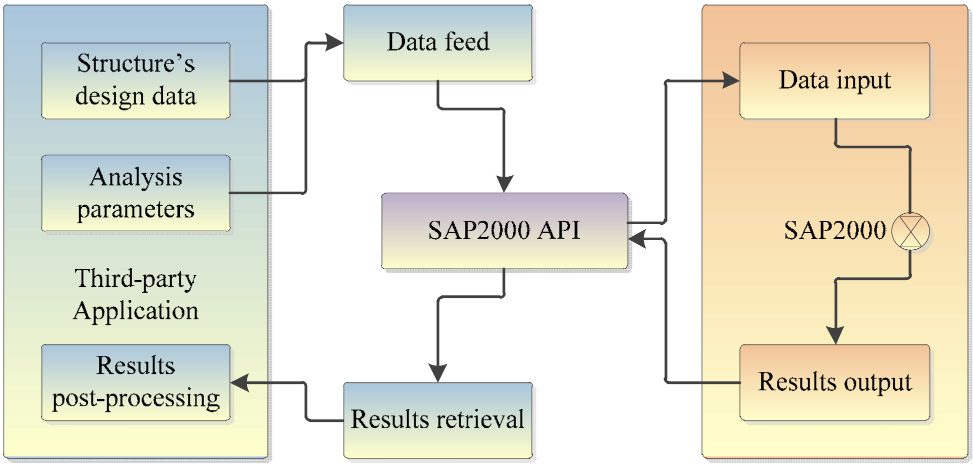

Figure 1: Application binding and typical data flow using the SAP2000 API.

As a general assistant in utilizing the SAP2000 API, a detailed documentation file is also provided along with the installation (SAP2000_API_Documentation.chm) including all the required information that will assist in getting accustomed to the API programming. This guide is to be used side-by-side when developing SAP2000 collaborated software, as it contains a full list of every single function provided, accompanied by its exact syntax, a detailed description of the arguments that it handles and a commented example of usage.

4 MODAL PUSHOVER ANALYSIS IMPLEMENTATION

Implementing an innovative scientific method requires thorough planning and well-balanced decisions to be made, regarding the usability, flexibility and layout of the final product. Developing software capable of applying the MPA procedure to bridges involves taking into account a considerable amount of analysis parameters, storing and manipulating a large number of variables and ensuring that access is granted to important information at every stage of the analysis. Herein, an effort for simplicity and integrity to be respected has been made, while fulfilling the need for optimizing and supervising the applied procedure.

4.1 Software architecture

The scheme chosen, so as to implement the MPA method, consists of an application arranged in modules, separated according to the tasks that are intended to perform. The analysis flow is controlled through an interactive graphical user interface (GUI), which consists of a main window that contains all the components necessary to define and review the analysis procedure. Linked to the interface is an external graphics component, which is used in order to visualize the bridge's deck deformation during the various analysis cases, while the pre- and post-processing is made entirely inside a separate dynamic link library (DLL) that binds the interface with the SAP2000 software. This is accomplished through the use of the SAP2000 API, which aims to regulate the flow of data within the bipartite scheme [Fig. 2].

The user is expected to interact entirely with the interface provided, while SAP2000 runs silently in the background of the operating system's desktop, throughout the analysis runtime. What is more, the required actions related to the manipulation of the SAP2000 model file are transferred, via the API, to the MPA software's interface. However, if needed, the user is allowed to bring the SAP2000 interface to the foreground, in order to make explicit definition of any advanced parameters that the MPA software does not provide, gaining, thus, complete control over the procedure.

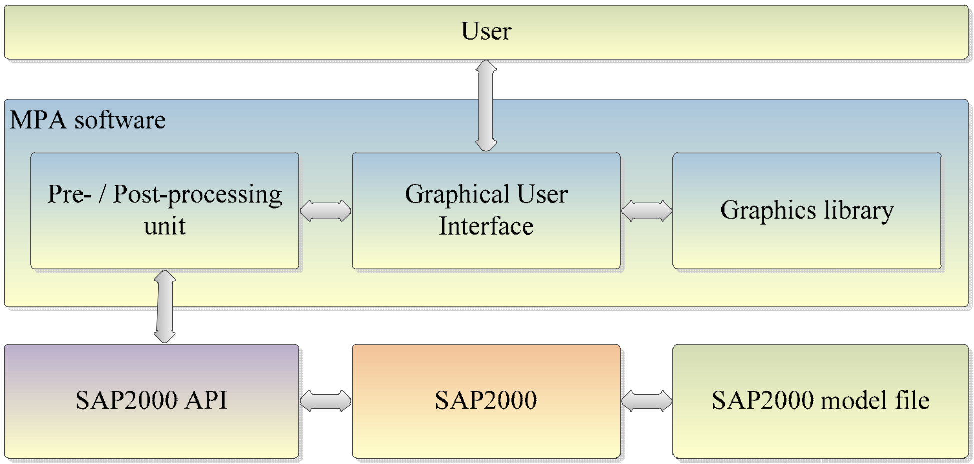

Figure 2: Modal Pushover Analysis software structure.

4.2 Description of the implementation

Researching and developing an innovative computational method is one thing, implementing one, however, into productive software requires combining a variety of different development tools in a way that sticks to the procedure. Furthermore, using the SAP2000 API, while expands greatly the computational power that lays before the engineer, raises the limitation of having to follow the SAP2000-way of arranging the analysis flow. In respect to the MPA procedure and taking the above into consideration, the approach that was selected in order to implement the analysis method concluded to an application providing the following features:

- Direct collaboration between the application and the SAP2000 suite, by making use of the dynamic data exchange capabilities that the API offers.
- SAP2000 model's loading and specification of the appropriate analysis parameters.
- Automated selection of the modes which are deemed as ”important”, allowing the user to interfere manually as needed.
- Automated creation of the necessary analysis cases, modal and non-linear, as well as using pre-run, user-specified cases.
- Visualization of intermediate steps' results, where applicable, in order to provide adequate information for the user's supervision of the procedure.
- Embedded calculation of the Design Spectrum required for the analysis, according to the EC8-Part 1 specifications [8], or making use of a spectrum data-file.
- Automated application of an appropriate combination rule, in order to calculate the analysis' final results – SRSS and CQC included.
- Visualization of the final deck deformed shape.
- Results' extraction to file, using plain text or comma-separated values format.

Finally, the implementation of the aforementioned was arranged as described by the following flowchart [Fig. 3]:

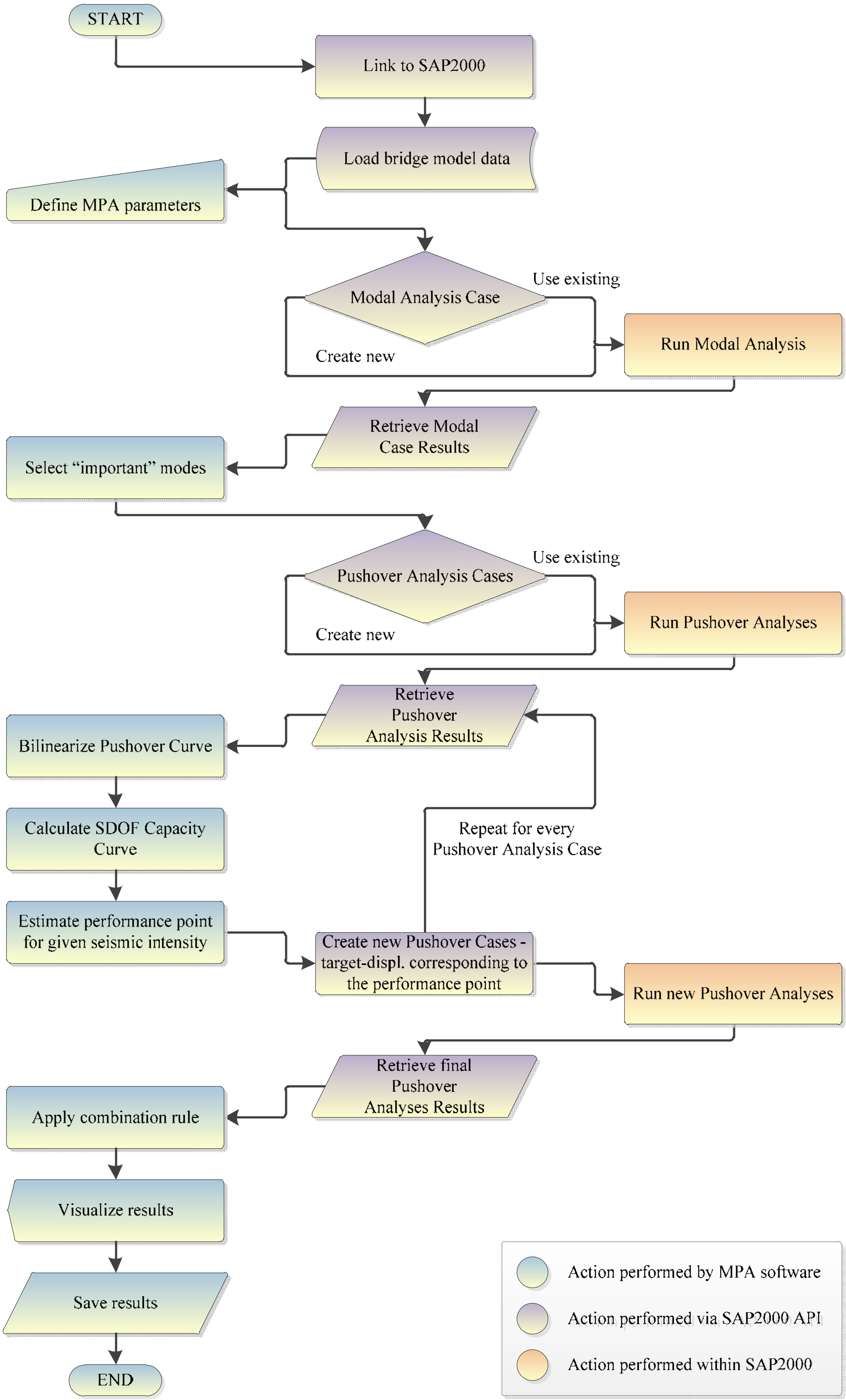

Figure 3: Modal Pushover Analysis software flowchart.

5 APPLICATION FOR THE CASE OF AN EXISTING BRIDGE

In order to investigate the accuracy and efficiency of the software developed around the MPA procedure, it was deemed appropriate to estimate the seismic assessment of an actual bridge structure, whose physical characteristics result to a reasonable contribution of higher modes. What follows is the description of the analysis procedure through the MPA software.

5.1 Description of studied bridge

The bridge selected for this task is a typical straight, three-span, symmetrical bridge, constructed of reinforcement concrete, that belongs to the highway network of EGNATIA ODOS A.E. (bridge T7). Its length sums up to 99.00m, divided into spans of 27.00 – 45.00 – 27.00 m, while the deck consists of a 10.00 m wide pre-stressed concrete box girder section. The deck has a slope of 7%, along the longitudinal direction, and it is supported by two solid piers of circular section, P1 and P2, of length 7.94 m and 9.34 m, accordingly, which are linked in a monolithic way, while each of the bridge’s edges, A1 and A2, lay on two laminated elastomeric bearings [Fig. 4].

5.2 Preparation of the bridge model

Prior to performing any task within the application, it is necessary to have the structural model of the bridge properly prepared, in accordance to certain standards that will allow for its usage. This can be summarized into the following steps:

- Definition of the geometrical characteristics of the structure, within the SAP2000 application, including the applied sections, the required non-linear hinges etc.
- Creation of a new object group, named “DECK”, to which all the nodes, that the bridge's deck consists of, will be assigned.
- Definition of the gravity loads of the structure, in the form two Load Patterns named “G” and “Q”, referring to the constant and moving loads applied, accordingly.
- Subsequently, a new non-linear load case named “GRAV” is required in order for the gravity loads to be applied, which, however, can be created either manually or automatically via the MPA software's interface, at a later stage of the procedure.
- Saving the model into a new file, with the extension “.sdb” and terminating the execution of SAP2000.

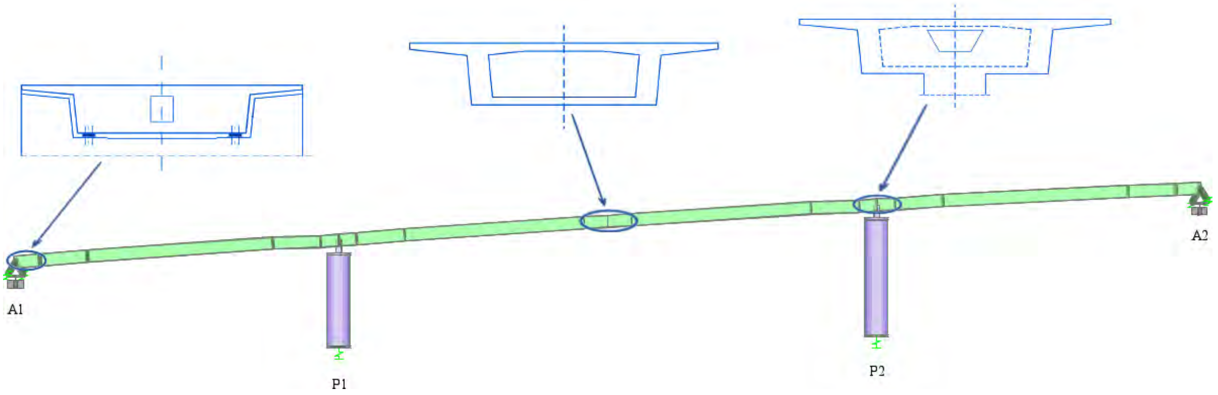

Figure 4: Three-span bridge model for the case of the T7 bridge along the Egnatia Highway in Greece.

After performing the steps described above, and in order to bring the model into a form able to be utilized, the file can be loaded into the MPA software. This is accomplished by running the application and using the menu “File → Open”, which will prompt for locating the file previously created. Following this, SAP2000 will be executed at the background of the operating system’s desktop and, via the API, the bridge model will be eventually loaded. When every parameter needed has been retrieved, the un-deformed shape of the bridge’s deck will be displayed at the center of the main window.

5.3 Definition of analysis parameters

Coming after the proper setup of the bridge model is the definition of the MPA parameters that is accomplished through the “Options” window, which emerges by selecting the submenu “Analysis → Options”. The parameters to be applied are grouped into tabs, in accordance with the intermediate stages of the MPA procedure. An effort has been made, in order to keep the analysis parameters required to a minimum, self-explanatory but adequate level.

For the bridge that was selected for testimonial reasons, the selected options defined in the “General” options tab will lead to a MPA along the “Y” directional “Degree Of Freedom” (DOF) of the bridge, as defined by SAP2000, using the “Advanced Solver” offered by the same analysis software and applying a “SRSS” combination rule at the end of the procedure, in order for the final displacement of the deck nodes to be estimated [Fig. 5a].

Subsequently, the parameters required for performing the modal analysis are defined as creating a new Modal Load Case, which will calculate the structure's natural modes up until the 99% of the participating mass ratio of the structure is reached, according to the preselected direction (Y). Among the modes that will be retrieved, those that sum up to a level of 97% will be selected as “important”, excluding those that participate less than 1%, in order to avoid computational instability during the remaining procedure [Fig. 5b].

Regarding the intermediate pushover analysis cases, for this particular bridge P – Δ effects are excluded, while the monitoring point is defined, for each case, as the node that presents maximum modal displacement according to the corresponding mode. Additionally, the previously-defined Load Case “GRAV”, referring to the gravity loads, is selected as the starting point of each Pushover Analysis case [4][Fig. 6a].

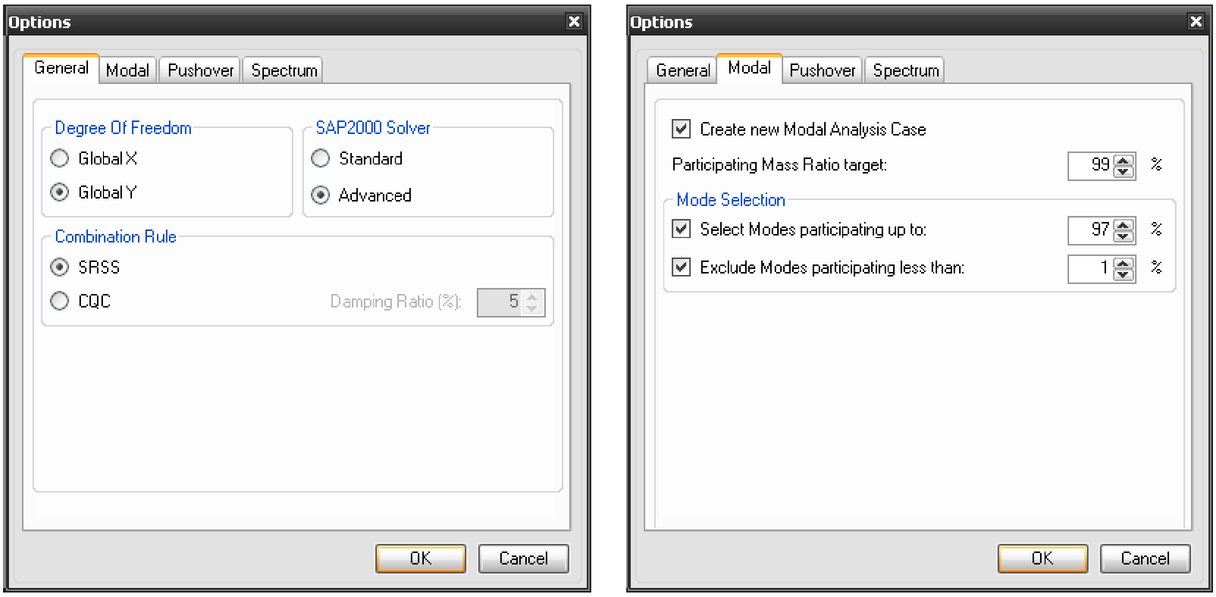

Degree Of Freedom
○ Global X
● Global Y

SAP2000 Solver
○ Standard
● Advanced

Combination Rule
● SRSS
○ CQC
Damping Ratio (%): 5

☑ Create new Modal Analysis Case
Participating Mass Ratio target: 99 %

Mode Selection
☑ Select Modes participating up to: 97 %
☑ Exclude Modes participating less than: 1 %

Figure 5: Definition of General and Modal Analysis parameters.

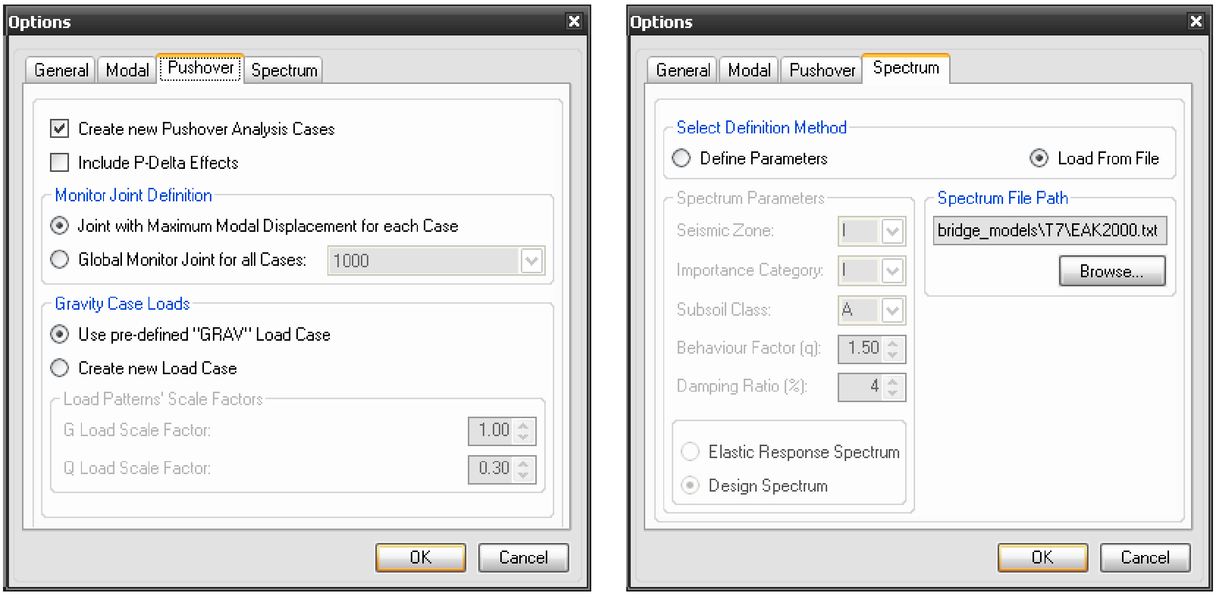

☑ Create new Pushover Analysis Cases
☐ Include P-Delta Effects
Monitor Joint Definition
● Joint with Maximum Modal Displacement for each Case
○ Global Monitor Joint for all Cases: 1000
Gravity Case Loads
● Use pre-defined "GRAV" Load Case
○ Create new Load Case
Load Patterns' Scale Factors
G Load Scale Factor: 1.00
Q Load Scale Factor: 0.30

Select Definition Method
○ Define Parameters ● Load From File
Spectrum Parameters
Seismic Zone: I
Importance Category: I
Subsoil Class: A
Behaviour Factor (q): 1.50
Damping Ratio (%): 4
○ Elastic Response Spectrum
● Design Spectrum
Spectrum File Path
bridge_models\T7\EAK2000.txt

Figure 6: Definition of Pushover Analysis cases and Design Spectrum parameters.

Finally, using the “Spectrum” tab, an appropriate Design Spectrum data file is located on the system, which will be used in order to define the displacement demand for a given earthquake intensity. Alternatively, a spectrum following the EC8 specifications could be defined through the appropriate field that is provided [Fig. 6b].

5.4 Performing the analysis

After the parameters’ definition is complete, selecting the menu “Analysis → Run → Modal Analysis” triggers the MPA procedure to begin, by firstly performing the Modal Analysis. With the completion of the analysis, the modal data of the bridge are retrieved and a list of the computed modes is displayed, allowing for the viewing of the mode-shapes through the main window's graphics component. What comes next is the selection of the modes considered “important”, according to the user's preference; this can be done in addition to the program's prior automatic selection, which resulted, in this case, in pre-selecting the first three modes of the bridge, summing up to a percentage of 97.4% total mass contribution of the structure [Fig. 7].

When the desired modes have been selected, through the “Analysis → Run → Pushover Cases” sub-menu, the procedure continues to performing the separate Pushover Analysis Cases, one corresponding to each selected mode. This stage is the most time-consuming of the MPA procedure and it vastly depends on the bridge's characteristics as well as on the “SAP2000 Solver” engine that was previously selected [Fig. 8].

By completing this step, the MPA software automatically proceeds to retrieving the pushover curves, for each case, their bi-linearization, according to the FEMA 356 [6] specifications, and the estimation of the peak displacement of the monitoring point. Subsequently, the desired node displacements are extracted and the analysis concludes by applying the combination rule that was selected, in this case a SRSS combination [Fig. 9].

The results of the MPA procedure, as well as the results of the intermediate non-linear static cases can be reviewed by the time the analysis is complete. By selecting the menu “View”, the user is capable of exploring the individual steps performed, which will provide useful data, adequate to indicate whether the analysis followed the desired or estimated route. Moreover, a graphical display of the deck's final deformed shape, as assessed by the MPA software, is available for visual evaluation of the analysis results. Finally, by selecting the sub-menu "File → Export Results", the estimated displacement of the deck's nodes can be saved in a file, using either a simple text format (.txt) or a "comma-separated values" format (.csv), which is suitable for inserting the extracted data in a spreadsheet application, should any further processing is considered necessary.

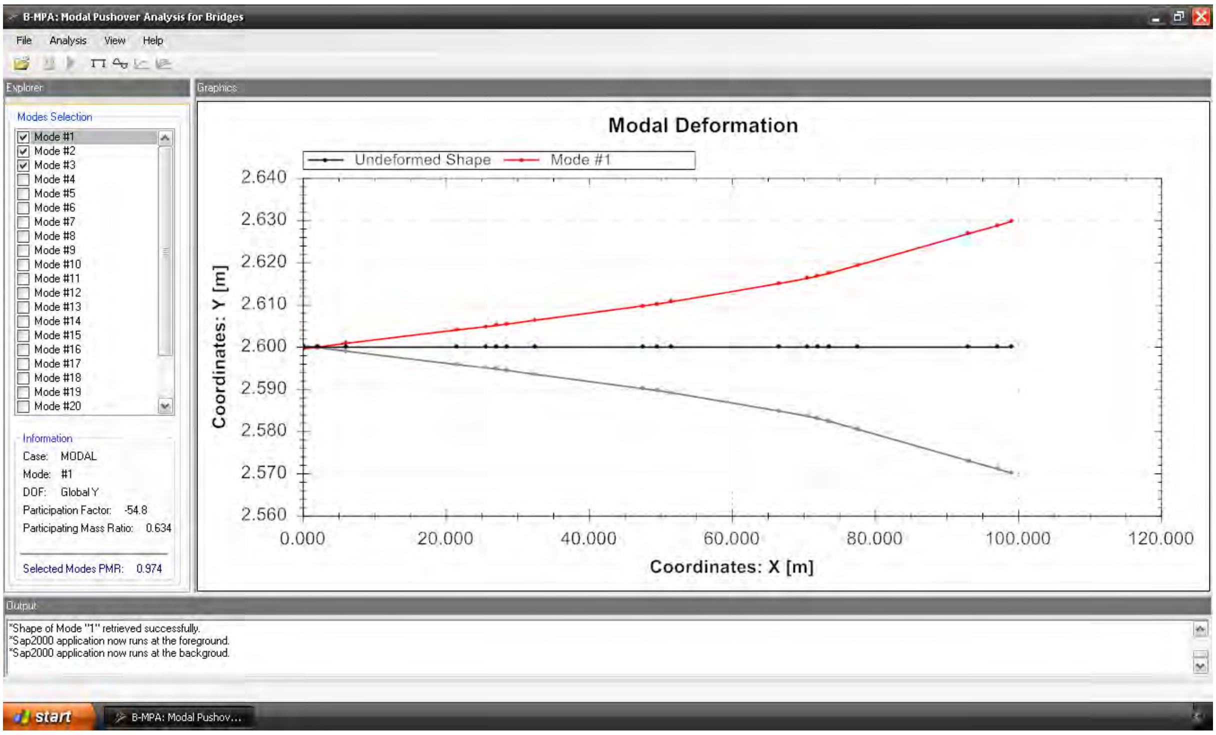

☑ Mode #1
☑ Mode #2
☑ Mode #3
☐ Mode #4
☐ Mode #5
☐ Mode #6
☐ Mode #7
☐ Mode #8
☐ Mode #9
☐ Mode #10
☐ Mode #11
☐ Mode #12
☐ Mode #13
☐ Mode #14
☐ Mode #15
☐ Mode #16
☐ Mode #17
☐ Mode #18
☐ Mode #19
☐ Mode #20

Information
Case: MODAL
Mode: #1
DOF: Global Y
Participation Factor: -54.8
Participating Mass Ratio: 0.634

Selected Modes PMR: 0.974

```
*Shape of Mode "1" retrieved successfully.
*Sap2000 application now runs at the foreground.
*Sap2000 application now runs at the backgroud.
```

Figure 7: Selection of "important" modes, after the completion of Modal Analysis.

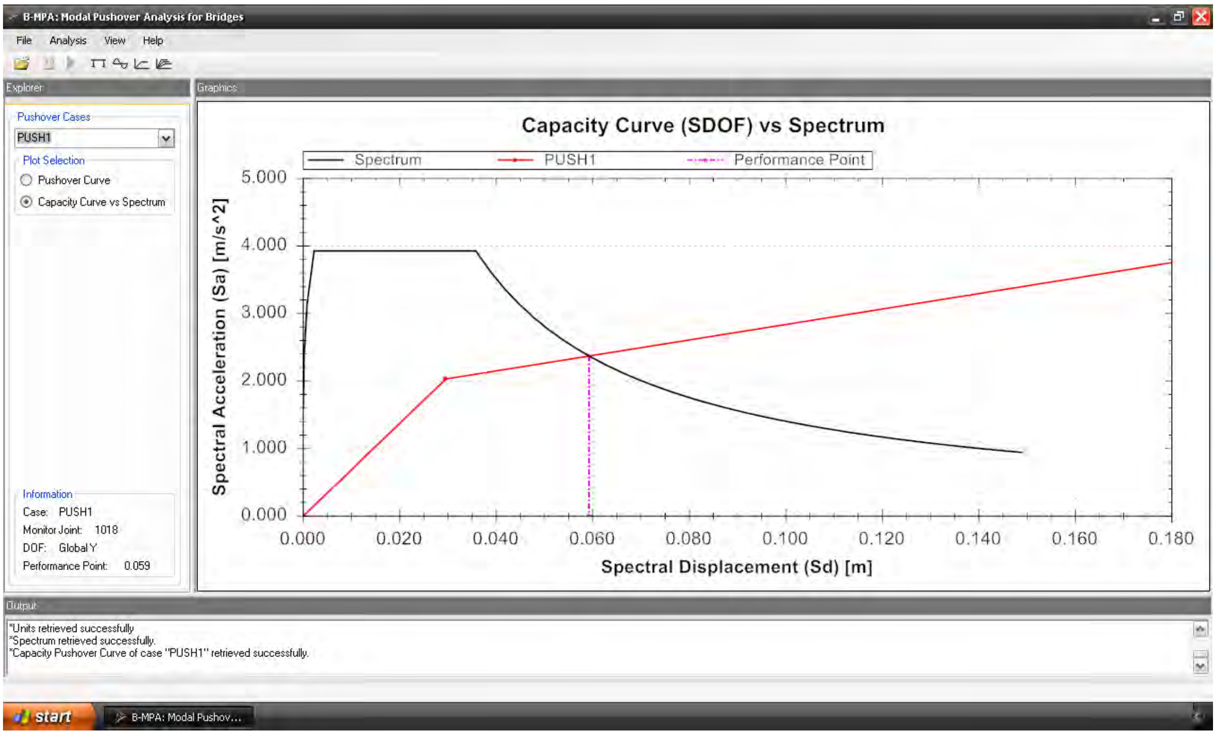

Pushover Cases: PUSH1

○ Pushover Curve
● Capacity Curve vs Spectrum

Information
Case: PUSH1
Monitor Joint: 1018
DOF: Global Y
Performance Point: 0.059

```
*Units retrieved successfully
*Spectrum retrieved successfully.
*Capacity Pushover Curve of case "PUSH1" retrieved successfully.
```

Figure 8: Estimation of the earthquake demand of the equivalent inelastic SDOF system.

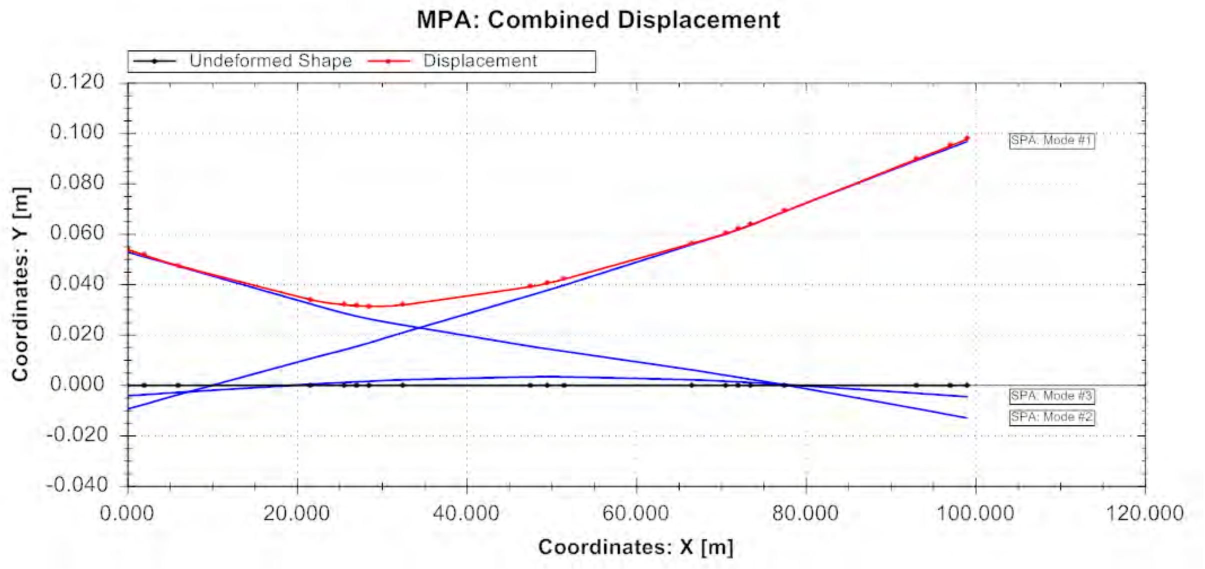

Figure 9: Modal Pushover Analysis software results visualization.

6 CONCLUSIONS

The aim herein was to introduce a new, effective approach to developing software for the seismic assessment of bridges, by implementing modal pushover analysis. The aforementioned was achieved by making use of some of the latest technology available in software development for engineers, such as the SAP2000 Application Programming Interface. In order to fulfil the targeted scope, a new application has been developed, capable of controlling the SAP2000 workflow through its API, while performs pre- and post-processing of the relative data. What is to be noted is that, as the use of generic programming tools has solely been made, the following conclusions are to be taken into account in virtually every case of modern procedures' implementation, through SAP2000 API, and are summarized as such:

- MPA proved a balanced example of a procedure strenuous enough, yet able to be divided to logical, repetitive subtasks, in order for being worthy of implementing via SAP2000 API. What is more, the benefits that occur by automating the procedure include the potential of improving faster and more efficiently its further, in-depth investigation.
- Developing software that is built around the SAP2000 platform, through its API, is considered feasible and, with most modern programming languages being supported, getting started with developing new earthquake engineering software should be a fast and effective task, at least for an engineer with reasonable programming skills.
- As the SAP2000 API is a generic programming tool able to control the internal structure of the analysis software that is bound to, programming style may need to be adapted to the API’s guidelines, in order to allow for a productive development route. Moreover, prior experience to using the SAP2000 application is considered necessary, as the API’s approach “mimics” the standard point-and-click procedure.
- Thorough consideration of every aspect, regarding the method’s specifications, prior to commencing any engineering programming attempt, is crucial and can make the difference between easy-flowing and stalling development; setting clear and realistic goals during planning the software is essential, in order to achieve a well-balanced relationship

between time investment and productivity. Furthermore, forming collaborative development teams of experts, covering every scientific aspect encountered, is an effective the path to be taken, if possible, in order to maintain a flexible, and productive scheme.

- Finally, the importance of human supervision over the application of any scientific procedure, performed by computational tools, is not to be neglected, especially in cases that quantifying a problem's solution approach cannot be deemed adequate; the user's capability of parameterizing appropriately the MPA procedure, selecting applicable analysis variables, interfering with the software's pre-selected options and, above all, interpreting the analysis results to a meaningful perception are the most important factors of the analysis.

7 ACKNOWLEDGEMENTS

The authors would like to acknowledge the contribution of Andreas Kappos, Professor at the Civil Engineering Department of Aristotle University Thessaloniki and Mrs. Themelina Paraskeva, Ph.D. candidate at the same department for their precious feedback regarding the applicability and efficiency of the software developed.

REFERENCES

[1] A. K. Chopra, R. K. Goel, A modal pushover analysis procedure for estimating seismic demands for buildings. *Earthquake Engineering & Structural Dynamics*, **31**, 561–582, 2002.

[2] R. K. Goel, Chopra, A. K. Role of Higher-"Mode" Pushover Analyses in Seismic Analysis of Buildings. *Earthquake Spectra,* 21(4), 1027-1041, 2006.

[3] T. S. Paraskeva, A. J. Kappos, A. G. Sextos, Extension of modal pushover analysis to seismic assessment of bridges. *Earthquake Engineering & Structural Dynamics,* **35**:1269-1293, 2006.

[4] T. Paraskeva, A. J. Kappos, Further development of a multimodal pushover analysis procedure for seismic assessment of bridges. *Earthquake Engineering & Structural Dynamics*, 211-222, 2010.

[5] Computers and Structures, Inc., *SAP2000, Integrated Finite Elements Analysis and Design of Structures, Detailed tutorial including pushover analysis.* Computers and Structures, Inc., Berkeley, CA, USA, 1998.

[6] K.K. Sasaki, S.A. Freeman, T.F. Paret. Multimode pushover procedure (MMP)—a method to identify the effects of higher modes in a pushover analysis. Proceedings of the 6th US National Conference on Earthquake Engineering, Seattle, Paper No. 271, 1998.

[7] Applied Technology Council (ATC), *Seismic Evaluation and Retrofit of Concrete Buildings. ATC-40,* Redwood City, CA, 1996.

[8] EC8, *Design of structures for earthquake resistance, Part 1: General rules, seismic actions and rules for buildings.* European committee for standardization, Brussels, 2002.

COMPDYN 2011
3rd ECCOMAS Thematic Conference on
Computational Methods in Structural Dynamics and Earthquake Engineering
M. Papadrakakis, M. Fragiadakis, V. Plevris (eds.)
Corfu, Greece, 25–28 May 2011

A COMPUTATIONAL FRAMEWORK FOR THE ASSESSMENT OF EARTHQUAKE-INDUCED ROCKING IN CIDH PILE SUPPORTED BRIDGES

Anastasios G. Sextos[1], Elli-Konstantina V. Mylona[2] and George E. Mylonakis[3]

[1]Assistant Professor, Dept. of Civil Engineering, Aristotle University Thessaloniki
Tel:+30-2310-995697, fax:+30-2310-995769
e-mail: asextos@civil.auth.gr

[2] Civil Engineer-MSc, Ph.D. Candidate
e-mail: mylonae@civil.auth.gr

[3]Associate Professor, Dept. of Civil Engineering, University of Patras
Tel: +30 2610 996542, 6550, fax: +30 2610 996576
e-mail: mylo@upatras.gr

Keywords: pile foundation, kinematic interaction, rocking, soil-structure interaction

Abstract. *The scope of this study is to investigate the response of RC bridges, founded on single cast-in-drilled-hole (CIDH) piles, under simultaneous earthquake-induced translational and rocking excitation. This rotational excitation results from pile bending under vertically propagating S-waves which, in turn, is dependent on pile's relative flexibility with respect to the surrounding soil, a phenomenon known as "kinematic interaction". Typically, the rotational component of seismic excitation of the superstructure is not taken into consideration; neither is it prescribed in any of the modern seismic codes, despite the fact that analytical solutions have been proposed in the literature. Moreover, the potential impact of such a pile-induced rocking of CIDH supported bridges has also not been quantified yet. Along these lines, an effort is made in this paper to present an analytical and computational framework for parametrically studying both: (a) the nature of the rotational excitation component and: (b) the additional displacement demand imposed to the superstructure. For this reason, a Matlab-based program is developed and the lateral response of multiple 4-DOF oscillators representing typical bridge structures is analytically studied, for various scenarios of excitation frequencies, superstructure height and soil stiffness. The resulting displacement demand is then compared to the displacements that would develop by ignoring the rotational component of ground excitation). From the set of parametric analyses conducted, it is concluded that ignoring kinematically induced rocking, transverse deck displacements may be significantly increased, especially in frequencies associated with the dynamic characteristics of the soil and the superstructure.*

1 INTRODUCTION

Bridge construction industry comprises nowadays the second most demanding construction sector in terms of overall investment; therefore, the safety of bridges constitutes a field of extensive research worldwide. Following a series of catastrophic earthquakes around the world (San Fernando 1971, Loma Prieta 1989, Costa Rica 1990, Northridge 1994, Kobe 1995, Kocaelli 1999, Chile 2010, Japan 2011) that caused serious damage and collapse in numerous bridges, the safety issue becomes more emerging. The reason is that bridges are part of commercial and transportation networks whose vulnerability determines the level of social impact that can be caused by a seismic event. As a result, nearly all modern seismic codes prescribe means to ensure a target level of performance related to bridge integrity and serviceability for various levels of earthquake loading, so that the probability of massive human loss is reduced and the disruption of the social and financial activity is as limited as possible.

Bridges, despite their relatively simple structural system compared to buildings, may exhibit quite complex seismic response due to their larger dimensions, their various non-linear mechanisms (stoppers, shear keys, gaps, bearing-type connections), the more significant contribution of higher modes, their higher sensitivity to the spatially variable properties of the surrounding soil and ground motion, the high soil compliance, as well as to the overall topography of the area crossed. As a result, it is not uncommon that the overall superstructure-foundation-subsoil system is studied as a whole and the dynamic interaction among its subcomponents is taken into consideration. Research on the dynamic interaction of such systems has long been studied; significant progress was achieved thanks to field observations, structural health monitoring data and strong ground motion records obtained during major seismic events [1-3]. Moreover, analytical solutions and advanced numerical simulation models have been developed [4-6] with particular emphasis on the response of pile foundations [7-14], lateral spread of soil [15], lateral excitation in layered deposits [16-19] and soil liquefaction [20-23]. Experimental results, involving complex bridge structures and pile foundations, are also currently available [24-26] while significant research effort was shed light in the nature of kinematic soil-pile interaction [27-31].

Despite the extensive research, an issue that has not yet been thoroughly studied is the additional rocking that is imposed to the bridge superstructure due to earthquake-induced pile bending. In particular, it is well known that the presence of a pile foundation modifies the amplitude and frequency content of the incoming seismic waves, thus resulting into a “Foundation Input Motion” that is different from the free field one, while analytical expressions have been proposed for computing the aforementioned additional pile head rotation [32]; still, however, there is no comprehensive approach available for practical purposes that can simultaneously account for the translational and rotational component of seismic acceleration neither has this effect ever been quantified for the case of realistic structures. This approach would be of particular use, especially for bridges supported on cast-in-drilled-hole (single) pile foundations, a common design alternative, primarily in the U.S.

Along these lines, the scope of this paper is to:

(a) present a comprehensive methodology and computational framework for considering the translational and rotational excitation of the soil-pile-superstructure system, and

(b) highlight those cases where ignoring the rotational component of seismic excitation, the displacement demand imposed to the superstructure may be significantly underestimated.

The fundamental concepts of the approach as well as the parametric analysis scheme and the subsequent results, are presented in the following.

2 PROBLEM VARIABLE DEFINITION

The study of pile-induced pier rocking requires definition of different variables that can be grouped into four major categories, specifically relating to the soil, the foundation, the superstructure (in terms of both material and geometry) and seismic excitation (primarily defined in terms of frequency). It is noted that some of these variables are dimensional, while others are dimensionless, as summarized in Table 1 below. The fundamental dimensions of the variables involved are mass (M), time (T) and length (L).

Variable category	**Variable**	**Dimensions**	**Fundamental dimensions**	**Kind of variable**
Super-structure	Modulus of elasticity, E	kN/m^2	M,T, L	Dimensional
	Mass of superstructure, m	t (of mass)	M	Dimensional
	Pier height, h	M	L	Dimensional
	Pier density, ρ	kg/m^3	M, L	Dimensional
	Pier material damping, ζ	%	-	Dimensionless
Founda-tion (RC CIDH pile)	Modulus of elasticity, E_p	kN/m^2	M,T, L	Dimensional
	Pile diameter, d_p	M	L	Dimensional
	Poisson's ratio, v_p	-	-	Dimensionless
	Density, ρ_p	kg/m^3	M, L	Dimensional
	Material damping, ζ_p	%	-	Dimensionless
Soil	Modulus of elasticity, E_s	kN/m^2	M,T, L	Dimensional
	Stratum thickness, H_s	M	L	Dimensional
	Poisson's ratio, v_s	-	-	Dimensionless
	Density, ρ_s	kg/m^3	M, L	Dimensional
	Material damping, ζ_s	%	-	Dimensionless
Excitation	Cyclic frequency, ω	T	T	Dimensional

Table 1: Problem Variables

Due to the fact the seismic excitation is assumed sinusoidal, its cyclic frequency, ω, is used to characterize the excitation; the amplitude of the pulse is irrelevant since the analysis is linear elastic. Based on the above, a total number of 11 dimensional and 5 dimensionless variables is derived, in particular: E, m, h, ρ, E_p, d_p, ρ_p, E_s, H_s, ρ_s, ω and ζ, v_p, ζ_p, v_s, ζ_s respectively. Eventually, it is only 9 out of 11 different dimensional variables that remain as part of the problem, due to the fact that the (concrete) material between the superstructure and the pile is identical, hence, it can be assumed that $E=E_p$.

In the framework of the parametric analysis conducted herein, the modulus of Elasticity of concrete was taken equal to E_p=29GPa, thus corresponding to a concrete strength of f_c=20MPa, while the stiffness of the soil, as expressed by the shear wave velocity V_s, was assumed to parametrically vary between 100 and 250 m/sec. It is recalled out that circular frequency of the soil ω_{soil} is expressed as:

$$\omega_{\mathrm{soil}} = 2\pi V_s/4H \tag{1}$$

where H the (uniform) soil stratum thickness, as defined in Table 1.

3 ANALYSIS OUTLINE

Rocking of a bridge supported on CIDH piles occurs along both longitudinal and transverse direction, however the latter is more critical the lower level of redundancy. It is therefore the transverse response of the bridge that is studied herein, assuming a 4-degree-of-freedom oscillator, with translational and rotational DOFs at the locations of its two concentrated masses, one at the top of the pier and one at its bottom as it is seen in Figure 1 (m, J_m, m_p and J_{mp} being the mass and moments of inertia of the pier top and base respectively, h denotes the oscillator height, e the eccentricity that eliminates the conjugation stiffness term K_{xr}, E the pier modulus of elasticity, ζ the damping ratio, b the pier diameter, and D the pile diameter. The spring properties required for providing the translational (K_{xx}) and rotational (K_{rr})

stiffness of the soil-pile system are derived using appropriate equations from the literature [32].

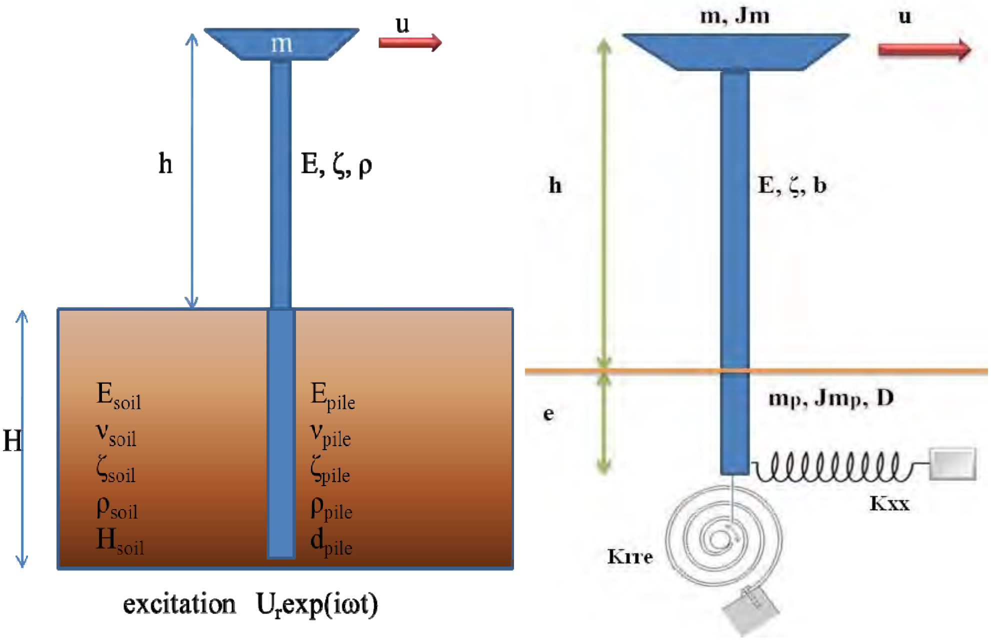

Figure 1: Overview of the system studied and the related variables and degrees of freedom.

The so-called kinematic response factors, I_u for the translational and I_θ for the rocking seismic component which express the frequency-dependent translational and rotational amplification of motion compared to that of the free-field are also derived based on expressions proposed in the literature [32]. As the pile of diameter *d* is assumed to be excited by vertically propagating, harmonic S-waves with amplitude U_r and frequency ω, the rotation that is eventually imposed to the superstructure can be simply derived as [18]:

$$\theta(t) = 2I_\theta(\omega)U_{ff}(z=0)/d_p \tag{2}$$

for each time step, *t* of the incoming harmonic motion. The overall process to derive the rotational excitation time history can be summarized in the following successive steps described below.

1st step: Assessment of the relevant problem variables (related to the soil, foundation, superstructure and seismic excitation) as it described in Table 1.

2nd step: Calculation of the pile moment of inertia and mass:

$$\begin{gathered} I_p=\pi {d_p}^4/64 \\ m_p=25\left(\frac{\pi {d_p}^2}{4}\right)L/g \end{gathered} \tag{3}$$

where L: length of the pile (assumed equal to the thickness of the stratum, H_s)
g: acceleration of gravity

3rd step: Assessment of soil modulus of elasticity E_s and shear wave velocity V_s

4th step: Calculation of the free field motion at the surface (z=0) for each frequency ω in the time domain [33]:

$$U_{ff} = U_r e^{i\omega t} = \left(\frac{U_g}{cos \frac{\omega}{V_s} L} \right) cos\left(\frac{\omega}{V_s^*} z \right) e^{i\omega t} \tag{4}$$

where U_{ff}: free-field motion amplitude
U_g: amplitude of the bedrock motion (i.e., base of the soil stratum)
z: depth from the ground surface

5th step: Calculation of the foundation impedance functions assuming a Beam on Dynamic Winkler Foundation [34]:

$$S_x = k_x(\omega) + i\omega c_x(\omega)$$

where $k_x = \delta E_s,\ \delta = 1.67 (\frac{E_p}{E_s})^{-0.053}$

$$c_x(\omega) = 2 a_0^{-1/4} \rho_s V_s d_p \left[1 + \left(\frac{V_{La}}{V_s} \right)^{5/4} \right] + 2\zeta_s \frac{k_x}{\omega} \tag{5}$$

$a_0 = \frac{\omega d_p}{V_s}$ and $V_{La} = \frac{3.4 V_s}{\pi(1-v)}$

6th step: Calculation of the translational, kinematic interaction factor for a free head single pile [35]:

$$I_u(\omega) = \frac{k_x + i\omega c_x}{E_p I_p (q^4 + 4\lambda^4) - m_p \omega^2} \cdot \left[1 + \frac{1}{2} \left(\frac{\omega}{V_s \lambda} \right)^2 \right] \tag{6}$$

where: $q = \frac{\omega}{V_s}$ and $\lambda = \left(\frac{k_x + i\omega c_x}{4 E_p I_p} \right)^{1/4}$ (7)

7th step: Calculation of the rocking, kinematic interaction factor for a free head single pile [35]:

$$\mathrm{I}_\theta(\omega) = \frac{\mathrm{k_x + i\omega c_x}}{\mathrm{E_p I_p (q^4 + 4\lambda^4) - m_p \omega^2}} \cdot \left(\frac{\omega}{\mathrm{V_s}} \right)^2 \cdot \frac{d_p}{\lambda} \tag{8}$$

8th step: Calculation of the imposed rotation [18]:

$$\theta(t) = \frac{I_\theta(\omega) U_{ff}(t, z=0)}{d_p/2} \tag{9}$$

9th step: Calculation of the translational (K_{xx}) and rotational (K_{rr}) stiffness properties of the soil-pile system springs according to Maravas et al. [32]. It is noted that the discrete sign e which refers to the dynamic impedance terms after appropriate spring-pile head eccentricity and stiffness decoupling:

$$\begin{gathered}K_{xx} = 4E_pI_p\lambda^3\\ K_{xr} = 2E_pI_p\lambda^2\\ K_{rr} = 2E_pI_p\lambda\\ K_{xxe} = K_{xx}\\ K_{xre} = 0\\ K_{rre} = K_{rr} - 2K_{xr}\cdot e + K_{xx}\cdot e^2\\ e = \frac{K_{xr}}{K_{xx}} = \frac{1}{2\lambda}\end{gathered} \tag{10}$$

where K_{xx}: translational stiffness of the soil-pile system along the x direction
K_{xr}: coupled rotational-translational stiffness of the soil-pile system
K_{rr}: rotational-translational stiffness of the soil-pile system
K_{rre}: uncoupled rotational stiffness of the soil-pile system
e: spring-pile head eccentricity

Having defined the translational and rotational foundation input motion and the dynamic properties of the flexible supported bridge structure along the transverse direction, the dynamic response of the 4DOF system can be analytically defined. The equation of motion has the general form:

$$M\cdot\ddot{u} + C\cdot\dot{u} + K\cdot u = p(t) \tag{11}$$

while the initial conditions can be set cast as, $u(0) = 0$ and $\dot{u}(0) = 0$. In this case, the matrix of the displacements relative to the moving base takes the following form, $u = [u\ \theta\ u_p\ \theta_p]^T$ where (u, θ) represent the displacement and rotation of the deck mass and (u_p, θ_p) of the foundation mass respectively. The solution of the equation of motion (11) is given from the well-known Duhamel's integral:

$$q_n(t) = \frac{1}{M_n\omega_{dn}}\int_0^t \tilde{p}_n(\tau)\cdot e^{-\zeta\omega_n(t-\tau)}\, sin\omega_{dn}(t-\tau)d\tau, \qquad n = 1,2,3,4 \tag{12}$$

Thus, the ultimate, geometric coordinates of the vector u(t) can be written as:

$$u(t) = \textstyle\sum_{n=1}^{N}\varphi_n\cdot q_n(t) \tag{13}$$

Assuming that due to the elastic response of the system considered, the damping matrix, C, equals to $C=2m\zeta\omega$, the mass matrix is quadratic and given as:

$$M = \begin{bmatrix} m & 0 & 0 & 0\\ 0 & Jm & 0 & 0\\ 0 & 0 & m_p & 0\\ 0 & 0 & 0 & Jm_p\end{bmatrix} \tag{14}$$

The computation of the stiffness matrix requires the calculation of its individual values, i.e. the generalized stiffness factors of the system, $K_s = [k_{ij}]$, where i,j=1,2,3,4. The ultimate stiffness matrix diversifies for each excitation frequency, as the foundation impedance is frequency dependent. In general however, stiffness matrix maybe written in the following form:

$$K=\begin{bmatrix} \frac{12EI}{h^3} & \frac{6EI}{h^2} & \frac{-12EI}{h^3} & \frac{6EI}{h^2} \\ \frac{6EI}{h^2} & \frac{4EI}{h} & \frac{-6EI}{h^2} & \frac{2EI}{h} \\ \frac{-12EI}{h^3} & \frac{-6EI}{h^2} & \frac{12EI}{h^3}+K_{xx}(\omega) & \frac{-6EI}{h^2} \\ \frac{6EI}{h^2} & \frac{2EI}{h} & \frac{-6EI}{h^2} & \frac{4EI}{h}+K_{rre}(\omega) \end{bmatrix} \tag{15}$$

It is noted that the external load vector *p(t)* considers both the translational and rotational component of seismic excitation, which for the purpose of linear elastic analysis, can be decoupled and then the individual structural response due to base translation and rotation be superimposed. For instance, the translational seismic component is:

$$-m\cdot\delta\cdot\ddot{u}_0(t) \tag{16}$$

where m is the oscillator (deck) mass, δ the vector of rigid body displacements and $u_0(t)$ the base excitation time history, which is in turn equal to the second derivative of the free-field ground displacement expressed by equation (4). The vector of rigid body displacements, in this case, receives the following form for a unit displacement of the oscillator base.

$$\delta=[1\ 0\ 1\ 0]^T. \tag{17}$$

Similarly to the above, the rocking excitation component is induced separately in the right-hand side of the equation of motion, while the rocking acceleration results from the double derivative of the rotation, with respect to time, as it has been calculated from equation (9) above. For a unit rotation of the pier base, vector δ takes the following form:

$$\delta=[h\ 1\ 0\ 1]^T. \tag{18}$$

and the two equations of motion for the two distinct translational and rotational base excitation mechanism can be written as:

$$\begin{gathered} M\cdot\ddot{u}(t)+2m\zeta\omega\cdot\dot{u}(t)+K\cdot u(t)=-M\cdot\delta\cdot\ddot{u}_{ff}(t,z=0)\cdot I_u \\ M\cdot\ddot{u}(t)+2m\zeta\omega\cdot\dot{u}(t)+K\cdot u(t)=-M\cdot\delta\cdot\ddot{\theta}(t)=-M\cdot\delta\cdot I_{\varphi}(\omega)\cdot\frac{\ddot{u}_{ff}(t,z=0)}{d_p/2} \end{gathered} \tag{19}$$

4 COMPUTATIONAL FRAMEWORK

The above analysis steps are implemented computationally through a specifically developed graphical MatLab environment, a sample of which is illustrated in Figure 2. The user defines the properties of the pile (i.e., modulus of elasticity, diameter, length, density and damping ratio), soil data (expressed in terms of the ratio E_p/E_s, Poisson's ratio, damping, density and shear wave~~s~~ velocity) and the desired excitation frequency range. In turn the program returns the variation of the translational and rotational kinematic interaction factors (I_u and I_φ) with the dimensionless frequency $\omega d/V_s$. The translational and rotational excitation time histories are also computed to be used as the foundation input motion to the (spring-supported) superstructure.

Following the computation of the kinematic interaction factors, the seismic response of the 4DOF system representing the pier-foundation-soil is derived for each excitation frequency (Figure 3). The fundamental period of both the fixed and flexibly supported structure is also computed and the maximum response quantities are derived and stored. The resulting displacement maxima are compared to the deck displacements that would have been derived if the conventional approach (i.e., translation-only foundation input motion) was followed. Results are plotted in appropriate diagrams of dimensionless quantities as will be described below.

5 ANALYSIS RESULTS

Having established the analytical and computational framework, a detailed parametric analysis scheme was formed and the effect of rotational excitation was investigated. In particular, the parametric study was performed by modifying four analysis parameters, related to the:

- *Soil stiffness*: of the upper soil layer (taken uniform along the pile height) expressed in terms of shear wave velocity V_s which was taken equal to 100m/sec or 250m/sec, thus corresponding to very soft and medium soft soil conditions respectively. It is noted that the above variation of soil stiffness corresponds to a modulus of Elasticity of the soil E_s, between 2.9MPa (very soft clay) to 29MPa (moderately soft clay), in other words, to a dimensionless variable Ep/Es lying within the range of 100-1000. (*2 cases*)
- *Pier Height*: taken equal to 5m, 7.5m, 12.5m and 20m leading, after appropriate mass modification, to fundamental periods in the transverse direction between the range 0.4-2.5sec. (*4 cases*)
- *Frequency of excitation*: harmonic pulses were used ranging between (0.1-2.0sec), that is, having frequencies 0.5,1,2,3,4,5,6,7,8,9 and 10Hz. (*11 cases*)
- *Excitation component*: the flexibly supported pier was excited in the transverse direction by (a) the translational, (b) the rotational and (c) the combined translational and rotational components of the foundation input motion. (*3 cases*)

The analysis of the above 2 x 4 x 11 x 3 = 264 parametric analysis were plotted in a normalized ratio, versus the dimensionless frequency term ($\omega D/V_s$). The ratio adopted for illustrating the relative effect of the different (i.e., translational and rotational components of the kinematically modified seismic wave field) was:

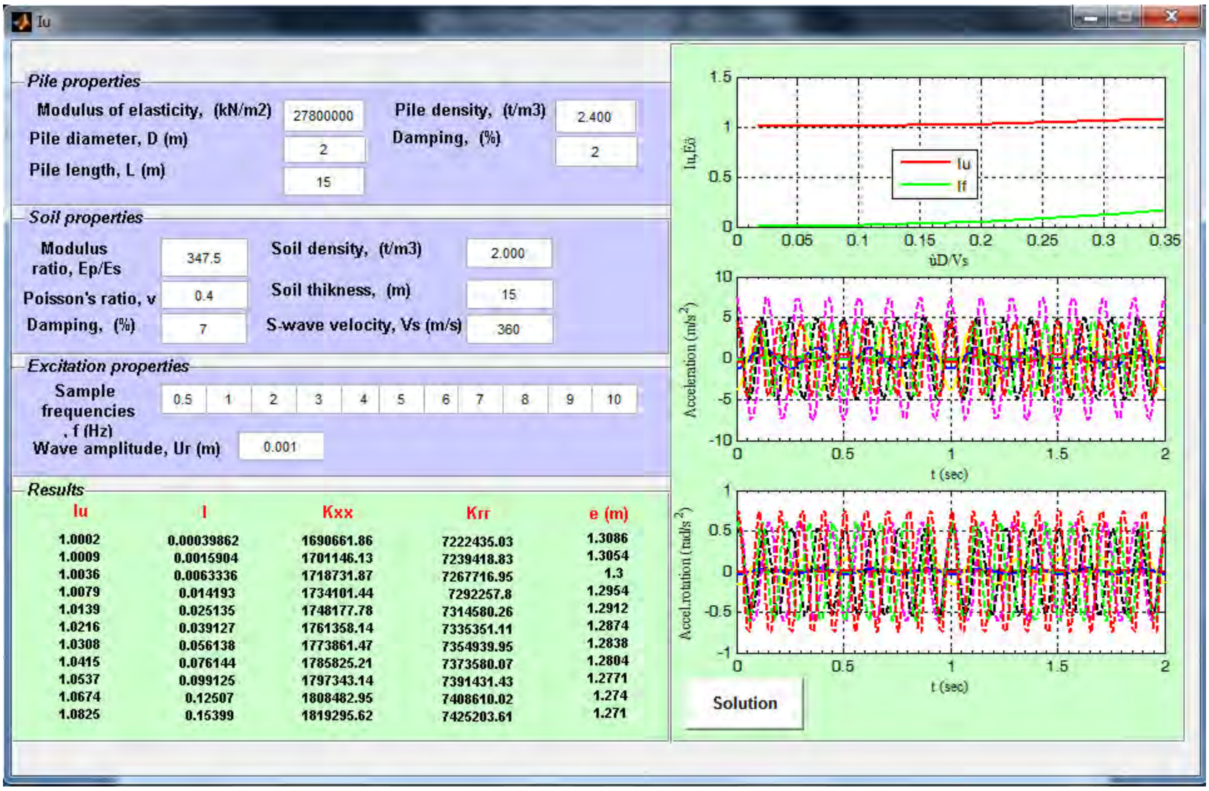

Pile properties

Modulus of elasticity, (kN/m2): 27800000
Pile density, (t/m3): 2.400
Pile diameter, D (m): 2
Damping, (%): 2
Pile length, L (m): 15

Soil properties

Modulus ratio, Ep/Es: 347.5
Soil density, (t/m3): 2.000
Poisson's ratio, v: 0.4
Soil thikness, (m): 15
Damping, (%): 7
S-wave velocity, Vs (m/s): 360

Excitation properties

Sample frequencies, f (Hz): 0.5, 1, 2, 3, 4, 5, 6, 7, 8, 9, 10
Wave amplitude, Ur (m): 0.001

Results

Iu	I	Kxx	Krr	e (m)
1.0002	0.00039862	1690661.86	7222435.03	1.3086
1.0009	0.0015904	1701146.13	7239418.83	1.3054
1.0036	0.0063336	1718731.87	7267716.95	1.3
1.0079	0.014193	1734101.44	7292257.8	1.2954
1.0139	0.025135	1748177.78	7314580.26	1.2912
1.0216	0.039127	1761358.14	7335351.11	1.2874
1.0308	0.056138	1773861.47	7354939.95	1.2838
1.0415	0.076144	1785825.21	7373580.07	1.2804
1.0537	0.099125	1797343.14	7391431.43	1.2771
1.0674	0.12507	1808482.95	7408610.02	1.274
1.0825	0.15399	1819295.62	7425203.61	1.271

Figure 2 : MatLab application for computing the translational and rotational interaction factors (I_u, I_φ) and the subsequent uncoupled dynamic impedance matrix terms (K_{xx}, K_{rre}).

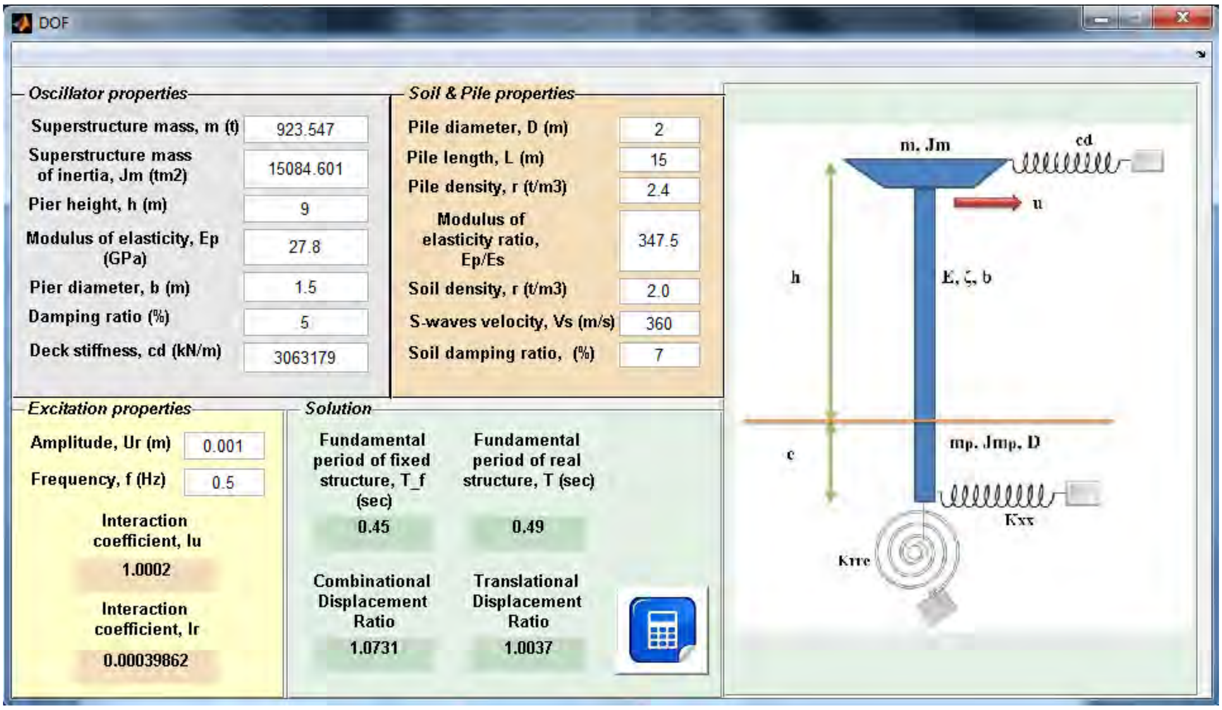

Oscillator properties

Superstructure mass, m (t): 923.547
Superstructure mass of inertia, Jm (tm2): 15084.601
Pier height, h (m): 9
Modulus of elasticity, Ep (GPa): 27.8
Pier diameter, b (m): 1.5
Damping ratio (%): 5
Deck stiffness, cd (kN/m): 3063179

Soil & Pile properties

Pile diameter, D (m): 2
Pile length, L (m): 15
Pile density, r (t/m3): 2.4
Modulus of elasticity ratio, Ep/Es: 347.5
Soil density, r (t/m3): 2.0
S-waves velocity, Vs (m/s): 360
Soil damping ratio, (%): 7

Excitation properties

Amplitude, Ur (m): 0.001
Frequency, f (Hz): 0.5
Interaction coefficient, Iu: 1.0002
Interaction coefficient, Ir: 0.00039862

Solution

Fundamental period of fixed structure, T_f (sec): 0.45
Fundamental period of real structure, T (sec): 0.49
Combinational Displacement Ratio: 1.0731
Translational Displacement Ratio: 1.0037

Figure 3 : MatLab-based solution of the soil-pile-superstructure system under combined translational and rotational excitation.

$$\boldsymbol{I_u = \frac{u_{max,\ FIM,u}(t)}{u_{max,ff}(t)}} \tag{20}$$

expressing the maximum displacement in time of the deck (pier top) when the kinematic interaction between the soil and the pile is taken into consideration and the deck is excited exclusively by the translational component of the foundation input motion (F.I.M.), over the maximum displacement in time of the deck due to free field base excitation (a ratio essentially identical to the standard kinematic interaction factor I_u of equation (6)), and

$$\boldsymbol{I_{u+\theta} = \frac{u_{max,\ FIM,u+\theta}(t)}{u_{max,ff}(t)}} \tag{21}$$

expressing the maximum displacement in time of the deck (pier top) when the kinematic interaction between the soil and the pile is taken into consideration and the deck is excited by both the translational and the rotational component of the foundation input motion (F.I.M.), over the maximum displacement in time of the deck due to free field base excitation.

The absolute values of pier top displacements are also plotted so that the relative contribution of each excitation component can be assessed. The results are discussed in the following.

5.1 Very Soft Soil, V_s=100m/s

The first set of figures (Figures 4,6,8,10) illustrates the kinematic interaction factors for translational or combined translational base excitation of the bridge pier under study, together with the corresponding absolute displacements of the deck (Figures 5,7,9,11) for decreasing pier heights (i.e., 20m, 12.5m, 7.5m, 5.0m) and a constant, uniform soil profile of V_s=100m/sec. A first observation is that the kinematic interaction factors are significantly higher in the case of combined translational and rotational foundation input motion compared to the conventional approach of translational base excitation only, for the whole dimensionless frequency range $0<\omega D/V_s<1.4$. These factors, $I_{u+\theta}$, can exceed the value of 10, at specific frequencies, for the case of a very flexible pier (h = 20m) and decay to 6.5 for the case of stiffer bridge structures (h = 5m) in contrast to the translational kinematic interaction factor which does not exceed 2 in the entire frequency range. This situation is also confirmed by the absolute displacement depicted in Figures 5, 7, 9 and 11 where it is clear that the deck displacements are dominated by the base rotational excitation.

It has to be noted that such a significant effect of rotational excitation cannot be generalized, as the case studied clearly represents the extreme condition where the structure is excited at a single and critical frequency (in contrast to the broad frequency content of an actual earthquake loading), in the transverse direction which is more prone to base rotations due to limited redundancy, while the pier height is significant (h = 20m) and at the same time, the soil is very soft (V_s = 100 m/sec). One could even argue that in such cases of soft soil profiles, a single CIDH pile wouldn’t be a desirable foundation type anyway. As a general trend though, the aforementioned diagrams are

indicative of the fact that the earthquake –induced head rotation of a (single) CIDH pile imposes, apart from the inertial component, an additional rigid body motion to the pier-deck superstructure which has a direct effect on the pier deck displacements as it is proportional to the pier height (i.e., the displacement vector $\delta_{rocking}=[h\ 1\ 0\ 1]^T$). As a result, the importance of rotational foundation input motion in piles casted in soft soils is non-negligible under certain circumstances and has to be further studied.

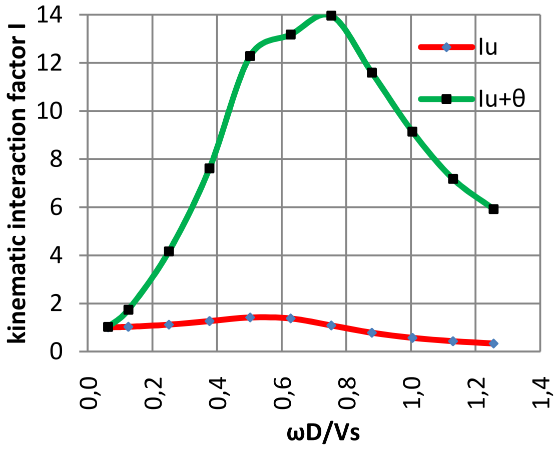

Figure 4: Displacements ratio as function to dimensionless frequency for V_s=100m/s, h=20m.

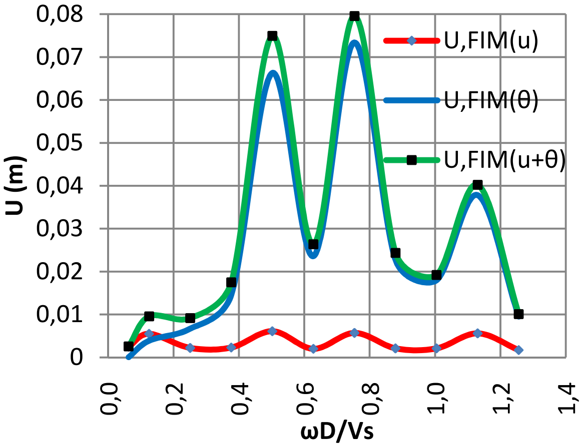

Figure 5: Absolute displacements as a function of dimensionless frequency for V_s=100m/s, h=20m.

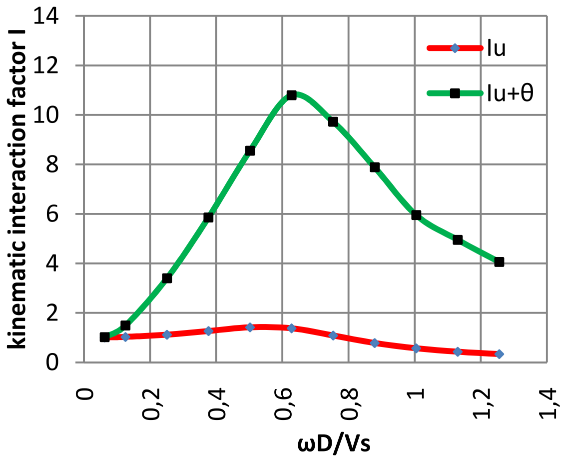

Figure 6: Displacements ratio as a function of dimensionless frequency for V_s=100m/s, h=12.5m.

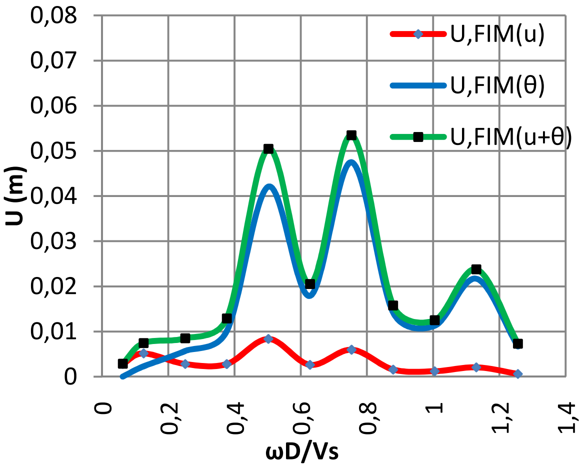

Figure 7: Absolute displacements as a function of dimensionless frequency for V_s=100m/s, h=12.5m.

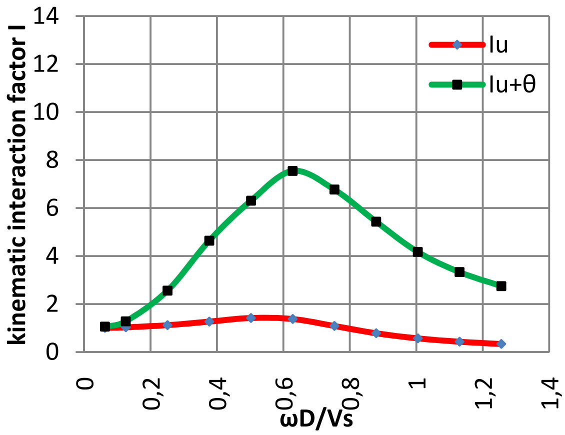

Figure 8: Displacements ratio as a function of dimensionless frequency for V_s=100m/s, h=7.5m.

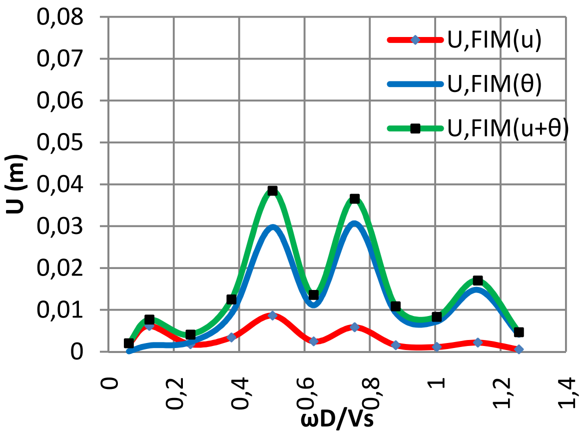

Figure 9: Absolute displacements as a function of dimensionless frequency for V_s=100m/s, h=7.5m.

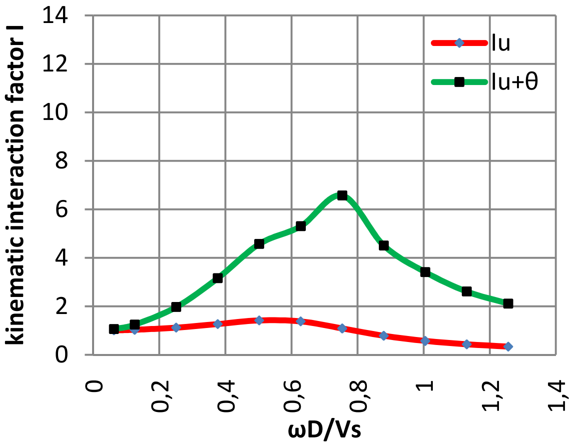

Figure 10: Displacements ratio as a function of dimensionless frequency for V_s=100m/s, h=5m.

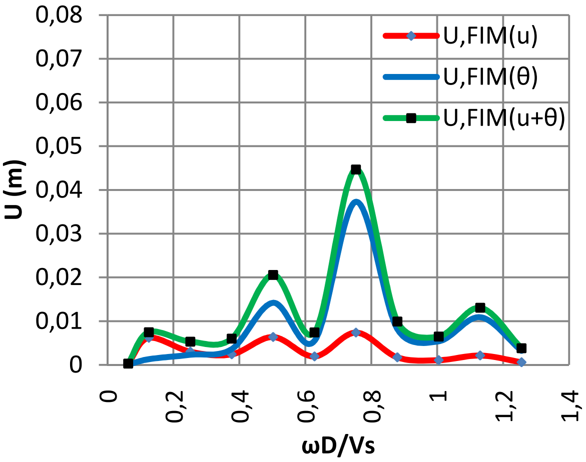

Figure 11: Absolute displacements as a function of dimensionless frequency for V_s=100m/s, h=5m.

5.2 Medium Soft Soil, Vs=250m/s

Similarly to the case of soft soil, the same set of parametric analyses were conducted for the case of medium soil, characterized by a shear wave velocity of 250m/sec. The corresponding variation of the kinematic interaction factors with and without the effect of rotational excitation as well as the variation of the absolute bridge deck displacements with the dimensionless frequency is illustrated in Figures 12,14,16,18 and 13,15,17,19 respectively. Again, the impact of rotational excitation on the overall pier top displacements is clearly visible: the combined kinematic interaction factor $I_{u+\theta}$ ranges from 3.8 to 8, always being higher than the conventional I_u which does not exceed 1.1 along the entire frequency range and for all pier heights. On the other hand, as anticipated, this effect of the rotational component of foundation input motion, although significant, is lower than the one observed for the case of soft soil, and as such it is expected to be smaller for stiffer soils as well. The overall (i.e., rigid body and inertial) mechanism described previously, in which the rotational excitation affects the transverse bridge deck displacements, is again confirmed.

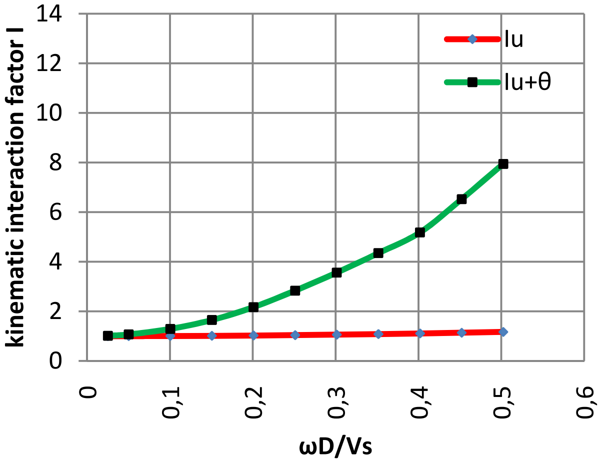

Figure 12: Displacements ratio as a function of dimensionless frequency for V_s=250m/s, h=20m.

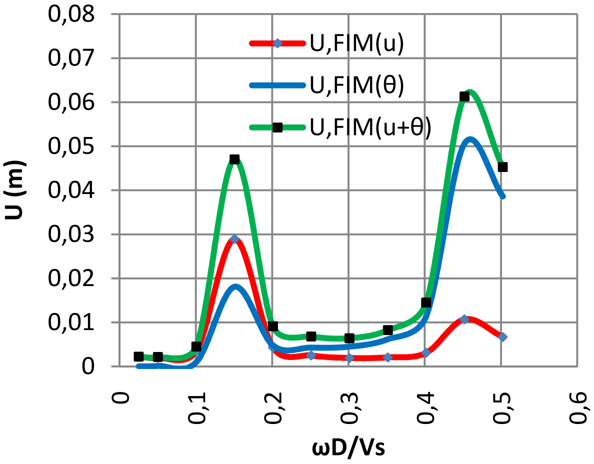

Figure 13: Absolute displacements as a function of dimensionless frequency for V_s=250m/s, h=20m.

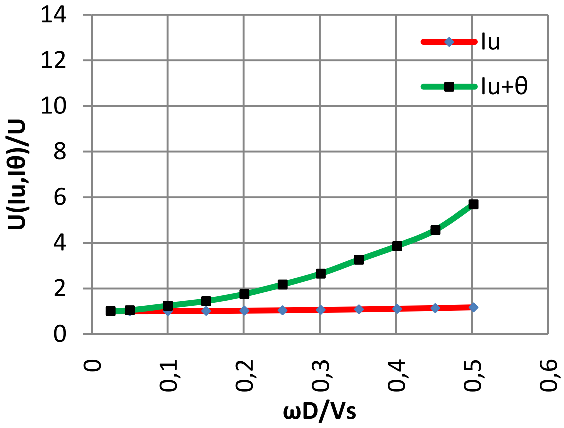

Figure 14: Displacements ratio as a function of dimensionless frequency for V_s=250m/s, h=12.5m

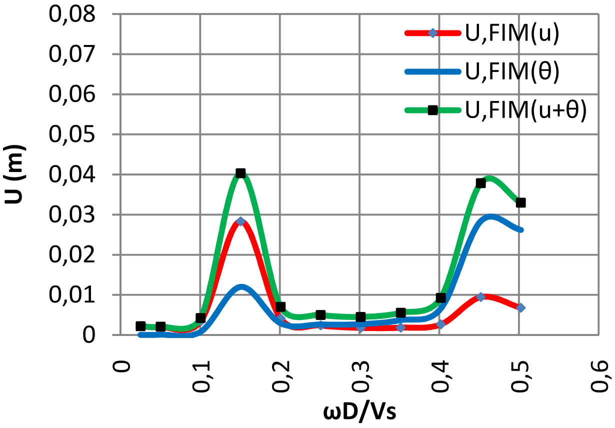

Figure 15: Absolute displacements as a function of dimensionless frequency for V_s=250m/s, h=12.5m.

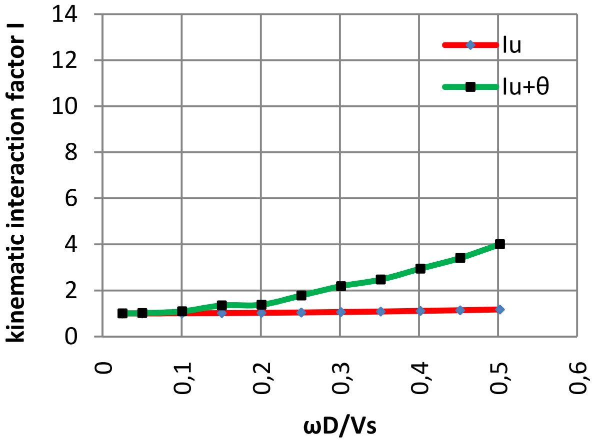

Figure 16: Displacements ratio as a function of dimensionless frequency for V_s=250m/s, h=7.5m

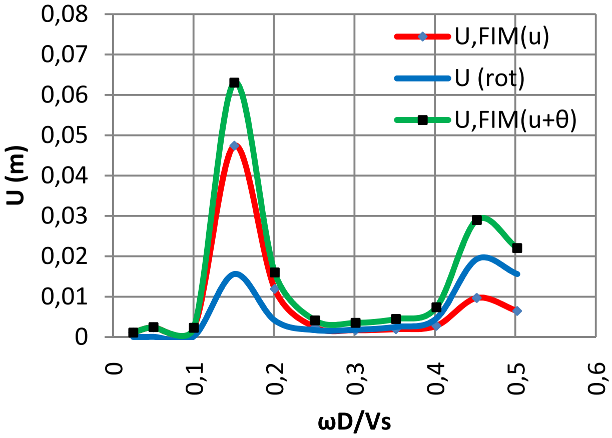

Figure 17: Absolute displacements as a function of dimensionless frequency for V_s=250m/s, h=7.5m.

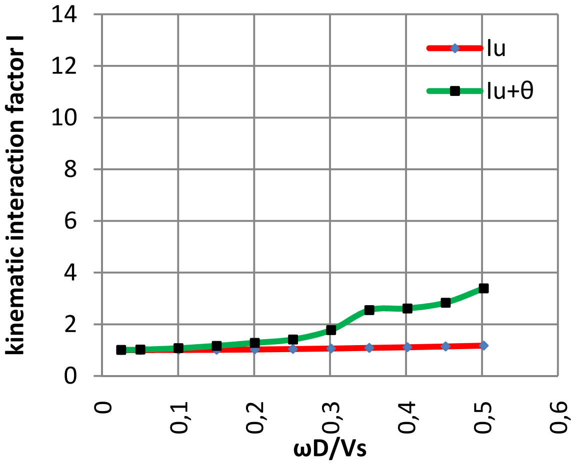

Figure 18: Displacements ratio as a function of dimensionless frequency for V_s=250m/s, h=5m

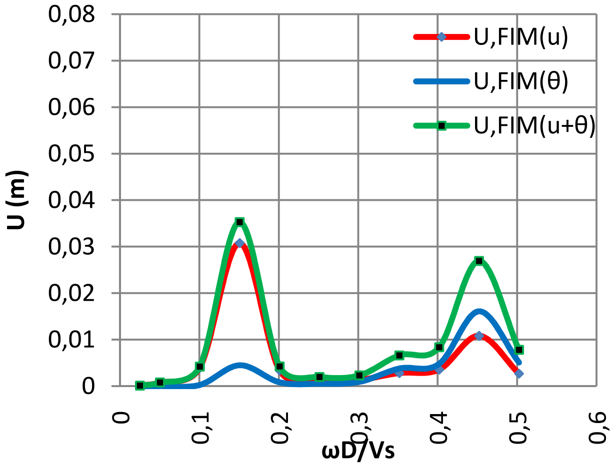

Figure 19: Absolute displacements as a function of dimensionless frequency for V_s=250m/s, h=5m.

6 CONCLUSIONS

A comprehensive analytical study was presented for the rocking effects of seismic motion in reinforced concrete bridges supported on cast-in-drilled-hole piles in homogeneous soil deposits. The study focuses on a 4-degree-of-freedom spring-supported pier subjected to simultaneous translational and rotational foundation input motion. The analytical approach is implemented into a comprehensive computational framework, programmed in Matlab environment, with the use of which a set of linear, elastic analyses was performed for different soil types, dynamic characteristics of the bridge and frequencies of harmonic excitations.

Through the above set of parametric analyses it is concluded that the combined consideration of the translational and rotational seismic components produced by the kinematic response of the pile foundation to vertically propagating S-waves, may reveal specific combinations of excitation frequency content and dynamic characteristics where the additional transverse deck displacements induced by the base rotation can indeed dominate the system response. It was also confirmed that the effect of the rotational component is higher for cases of soft soil profiles and flexible, tall piers.

Further research is certainly needed for quantifying the importance of the rotational excitation, in case of more complex seismic motions, structural systems and foundation types.

REFERENCES

[1] M. Celebi, A.M. Eeri, Real-time seismic monitoring of the New Cape Girardeau (MO) bridge, *Earthquake Spectra*, **22**(3), 2006.

[2] G. Mylonakis, C. Syngros, G. Gazetas, T. Tazoh, The role of soil in the collapse of 18 piers of Hanshin expressway in the Kobe earthquake, *Earthquake Engineering and Structural Dynamic*s, **35**(5), 547-575, 2006.

[3] N. Makris, G. Gazetas, E. Delis, Dynamic soil-pile-foundation-structure interaction: records and predictions, *Geotechnique*, **46**(1), 33-50, 1996.

[4] A. Kotsoglou, S. Pantazopoulou, Response simulation and seismic assessment of highway overcrossings, *Earthquake Engineering & Structural Dynamics*, **39**(9), 991-1013 2010.

[5] A.G. Sextos, K.D. Pitilakis, A.J. Kappos, Inelastic dynamic analysis of RC bridges accounting for spatial variability of ground motion, site effects and soil–structure interaction phenomena. Part 1: Methodology and analytical tools, *Earthquake Engineering and Structural Dynamics*, **32**(4), 607-627, 2003.

[6] A.G Sextos, A.J Kappos, K.D Pitilakis, Inelastic dynamic analysis of RC bridges accounting for spatial variability of ground motion, site effects and soil–structure interaction phenomena. Part 2: Parametric study, *Earthquake Engineering and Structural Dynamics*, **32**(4), 629-652, 2003.

[7] Y.X. Cai, P.L. Gould, C. S. Desai, Nonlinear analysis of 3D seismic interaction of soil–pile–structure systems and application, *Engineering Structures*, **22**, 191-199, 2000.

[8] E. N. Rovithis, K. D. Pitilakis, G. E. Mylonakis, Seismic analysis of coupled soil-pile-structure systems leading to the definition of a pseudo-natural SSI frequency, Soil Dynamics and Earthquake Engineering, **29**(6), 1005-1015, 2009.

[9] B. Maheshwari, K.Z. Truman, M.H. El Naggar, P. L. Gould, Three-Dimensional nonlinear analysis for seismic soil–pile-Structure interaction, *Soil Dynamics and Earthquake Engineering*, **24**(4), 343-356, 2004.

[10] G. Gazetas, Seismic Response of End-Bearing Single Piles, *International Journal of Soil Dynamics and Earthquake Engineering*, **3**(2), 82-93, 1984.

[11] E. A. Ellis, S.M. Springman, Modeling of soil-structure interaction for a piled bridge abutment in plane strain FEM analyses, *Computers and Geotechnics*, **28**, 79-98, 2001.

[12] N. Makris, G. Gazetas, Dynamic pile-soil-pile interaction. Part II: lateral and seismic response, *Earthquake Engineering & Structural Dynamics*, **21**(2), 145-162, 1992.

[13] D. Badoni, N. Makris, Pile-to-pile interaction in the time domain-non-linear axial group response under harmonic loading, *Geotechnique*, **47**(2), 299-317, 1997.

[14] K. K. Koo, K.T. Chau, X. Yang, Lam S.S., Y.L. Wong, Soil-Pile-Structure interaction under SH wave excitation, *Earthquake Engineering & Structural Dynamics*, **32**(3), 395-415, 2003.

[15] T. Abdoun, R. Dobry, Evaluation of pile foundation response to lateral spreading, *Soil Dynamics and Earthquake Engineering*, **22**, 1051-1058, 2002.

[16] D. Badoni, N. Makris, Nonlinear response of single piles under lateral inertial and seismic loads, *Soil Dynamics and Earthquake Engineering*, **15**, 29-43, 1996.

[17] G. Mylonakis, G. Gazetas, Lateral vibration of internal forces of grouped piles in layered soil, *Journal of Geotechnical and Geoenvironmental Engineering*, **125**(1), 16-25, 1999.

[18] Z. Yang, B. Jeremic, Numerical analysis of pile behavior under lateral loads in layered elastic-Plastic soils, International *Journal for Numerical and Analytical Methods in Geomechanics*, **26**(14), 1385-1406, 2002.

[19] A.J. Kappos, A.G. Sextos, Effect of foundation compliance on the lateral load response of R/C bridges, *Journal of Bridge Engineering*, **6**, 120–130, 2001.

[20] S. Miwa, T. Ikeda, T. Sato, Damage process of pile foundation in liquefied ground during strong ground motion, *Soil Dynamics and Earthquake Engineering*, 26(2-4), 325-336, 2006.

[21] J. Berrill, S. Yasuda, Liquefaction and piled foundations: some issues, *Journal of Earthquake Engineering*, **6**(1), 1-41, 2002.

[22] S. Bhattacharya, S.P.G Madabhushi, M. Bolton, An alternative mechanism of pile failure in liquefiable deposits during earthquakes, *Geotechnique*, **54**(3), 203-213, 2004.

[23] W.D.L Finn, N. Fujita, Piles in liquefiable soils: Seismic analysis and design issues, *Soil Dynamics and Earthquake Engineering*, **22**, 731-742, 2002.

[24] R. Ranf, H. Shin, M. Eberhard, P. Arduino, S. Kramer, Experimentally based evaluation of soil-foundation-structure interaction for a reinforced concrete bridge, *8th National Conference on Earthquake Engineering*, San Fransisco, U.S, 2006.

[25] K. Chau, C. Shen, X. Guo, Nonlinear seismic soil–pile–structure interactions: shaking table tests and fem analyses, *Soil Dynamics and Earthquake Engineering*, **29**(2), pp. 300-310, 2009.

[26] N. Kamijo, H. Saito, K. Kusama, O. Kontani, R. Nigbor, Seismic tests of a pile-supported structure in liquefiable sand using large-scale blast excitation, *Nuclear Engineering and Design*, **228**(1-3), 367-376, 2004.

[27] K.J. Bentley, M.H. El Naggar, Numerical analysis of kinematic response of single piles, *Canadian Geotechnical Journal*, **37**, 1368-1382, 2000.

[28] G. Mylonakis, A. Nikolaou, G. Gazetas, Soil-pile-bridge seismic interaction: kinematic and inertial effects. Part I: soft soil, *Earthquake Engineering and Structural Dynamics*, **26**, 337-359, 1997.

[29] F. Dezi, S. Carbonari, G . Leoni, Kinematic bending moments in pile foundations, *Soil Dynamics and Earthquake Engineering*, **30**(3), 119-132, 2010.

[30] G. Mylonakis, G. Gazetas, Kinematic Pile Response to Vertical P-wave Seismic Excitation, *Journal of Geotechnical and Geoenvironmental Engineering,* **128**(10), 860-867, 2002.

[31] F. Dezi, S. Carbonari, G. Leoni, Static equivalent method for the kinematic interaction analysis of single piles, *Soil Dynamics and Earthquake Engineering,* 1-12, 2010.

[32] A. Maravas, G. Mylonakis, D. Karabalis, Dynamic characteristics of structures on piles and footings, *4th International Conference on Earthquake Geotechnical Engineering*, 2007.

[33] J.M. Roesset, *Soil amplification in earthquakes,* Numerical Methods in Geotechnical Engineering, C. S. Desai and J. T. Christian, eds., McGraw Hill, New York, Chapter 19, 639-682, 1977.

[34] R. Dobry, E. Vicente, M.J. O'Rourke, J.M. Roesset, Horizontal stiffness and damping of single piles, *Journal of Geotechnical Engineering Division,* American Society of Civil Engineers, **108**(3), 439-459, 1982.

[35] G. Gazetas, R. Dobry, Simple Radiation Damping Model for Piles and Footings, *Journal of Engineering Mechanics,* ASCE, **110**(6), 937-956, 1984.

[36] S. Nikolaou, G. Mylonakis, G. Gazetas, T. Tazoh, Kinematic pile bending during earthquakes: analysis and field measurements, *Geotechnique,* **51**(5), 425-440, 2001.

COMPDYN 2011
III ECCOMAS Thematic Conference on
Computational Methods in Structural Dynamics and Earthquake Engineering
M. Papadrakakis, M. Fragiadakis, V. Plevris (eds.)
Corfu, Greece, 25–28 May 2011

A ROUGH COLLAPSE ASSESSMENT OF EARTHQUAKE EXCITED STRUCTURAL SYSTEMS VULNERABLE TO THE P-DELTA EFFECT

Christoph Adam[1], **and Clemens Jäger**[2]

[1] Department of Civil Engineering Sciences, University of Innsbruck
Technikerstr. 13, 6020 Innsbruck, Austria
e-mail: christoph.adam@uibk.ac.at

[2] Department of Civil Engineering Sciences, University of Innsbruck
Technikerstr. 13, 6020 Innsbruck, Austria
e-mail: clemens.jaeger@uibk.ac.at

Keywords: Collapse Capacity Spectrum, Equivalent Single-Degree-of-Freedom System, Global Collapse Capacity, Non-Deteriorating Inelastic Component Behavior, P-Delta Effect, Planar Multi-Story Frame Structure.

Abstract. *This paper addresses the prediction of the seismic collapse capacity of flexible non-deteriorating multi-story frame structures with regular layout, which are vulnerable to the destabilizing effect of gravity loads. The proposed time-saving and yet sufficient accurate methodologies are based on an equivalent single-degree-of-freedom system capable to cover the significant dynamic properties of the structure, and collapse capacity spectra. For a series of generic frame structures the global collapse capacity is assessed both with the proposed methodologies and the computationally expensive Incremental Dynamic Analysis procedure. From the outcomes of both methods it can be concluded that in the initial design process the proposed methodologies are an appropriate tool to assess sufficiently accurate the collapse capacity of P-delta sensitive regular moment resisting frame structures subjected to severe earthquake excitation.*

1 INTRODUCTION

Prediction of sidesway collapse of a structural building induced by severe earthquake excitation is the most prominent challenge in earthquake engineering [1]. Sidesway collapse may be the consequence of successive reduction of the lateral load bearing capacity due to strength and stiffness degradation. In very flexible buildings the destabilizing effect of gravity loads may lead to a negative post-yield stiffness, and thus, the structural collapse capacity is exhausted at a rapid rate when driven into its inelastic range of deformation even for stable hysteretic component behavior [2]. In many buildings the components are successively deteriorated until gravity takes over, and consequently the structure collapses. [1]

The focus of this paper is on the prediction of earthquake induced sidesway collapse of non-deteriorating flexible frame structures, which are vulnerable to the destabilizing effect of gravity loads, or, expressed in other words, vulnerable to the global P-delta effect. For a realistic *elastic* building the P-delta effect is usually negligible. However, it may become of significance for inelastic structural behavior when P-delta induces a negative post-yield slope of the lateral load-displacement relationship.

In earthquake engineering the global P-delta effect has been studied analytically, numerically, and experimentally in a series of papers. Representatively, the publications of Jennings and Husid [3], Bernal [4, 5], MacRae [6], Gupta and Krawinkler [7], Vian and Bruneau [8], and Lignos et al. [9] are cited. Asimakopoulos et al. [10], Villaverde [11], Ibarra and Krawinkler [12], Krawinkler et al. [1], and Haselton et al. [13] provide profound insights into the literature on studies dealing with dynamic collapse of earthquake excited structures. In comprehensive parameter studies, Adam and Jäger [14, 15, 16] treat rigorously the effects of P-delta on the collapse capacity of non-deteriorating SDOF systems, and the results are graphically displayed by means of collapse capacity spectra. In further studies, Adam and Jäger [2, 17] propose the collapse capacity spectrum methodology, based on an equivalent single-degree-of-freedom system and collapse capacity spectra, in an effort to determine the global collapse capacity of regular multi-story frame structures vulnerable to P-delta both time-efficient and yet accurate.

In the presented contribution the application of the original collapse capacity spectrum methodology as introduced in [2, 17] is described in detail. Additionally, a simplified collapse capacity spectrum methodology is recommended. The underlying concepts of equivalent single-degree-of-freedom (ESDOF) systems and collapse capacity spectra are reviewed. Both collapse capacity spectrum methods are evaluated for a series of generic frame structures, and the outcomes are set in contrast to “exact” collapse capacities of corresponding IDA studies.

2 GLOBAL COLLAPSE CAPACITY

2.1 Initial assessment of the structural vulnerability to global P-delta effects [2]

At first it must be assessed whether the considered structure is vulnerable to P-delta effects. Strong evidence delivers the result of a global pushover analysis [7]. During this nonlinear static analysis gravity loads are applied, and subsequently the structure is subjected to lateral forces. The magnitude of these forces with a predefined invariant load pattern is amplified incrementally in a displacement-controlled procedure. As a result the global pushover curve of the structure is obtained, where the base shear is plotted against a characteristic deformation parameter. In general the lateral displacement of the roof is selected as characteristic parameter. It is assumed that the shape of the global pushover curve reflects the global or the local mechanism involved when the structure approaches dynamic instability.

In Figure 1 the effect of gravity loads on the global pushover curve of a multi-story frame structure is illustrated. Figure 1(a) shows the global pushover curve, where gravity loads are either disregarded or of marginal importance. The pushover curve of Figure 1(b) corresponds to a very flexible multi-story frame structure with a strong impact of the P-delta effect leading to a reduction of the global lateral stiffness. In very flexible structures gravity loads even may generate a negative post-yield tangent stiffness as shown in Figure 1(b) [18]. If severe seismic excitation drives such a structure in its inelastic branch of deformation a state of dynamic instability may be approached, and the global collapse capacity is attained at a rapid rate. From these considerations follows that a gravity load induced negative post-yield tangent stiffness in the global pushover curve requires an advanced investigation of P-delta effects [7].

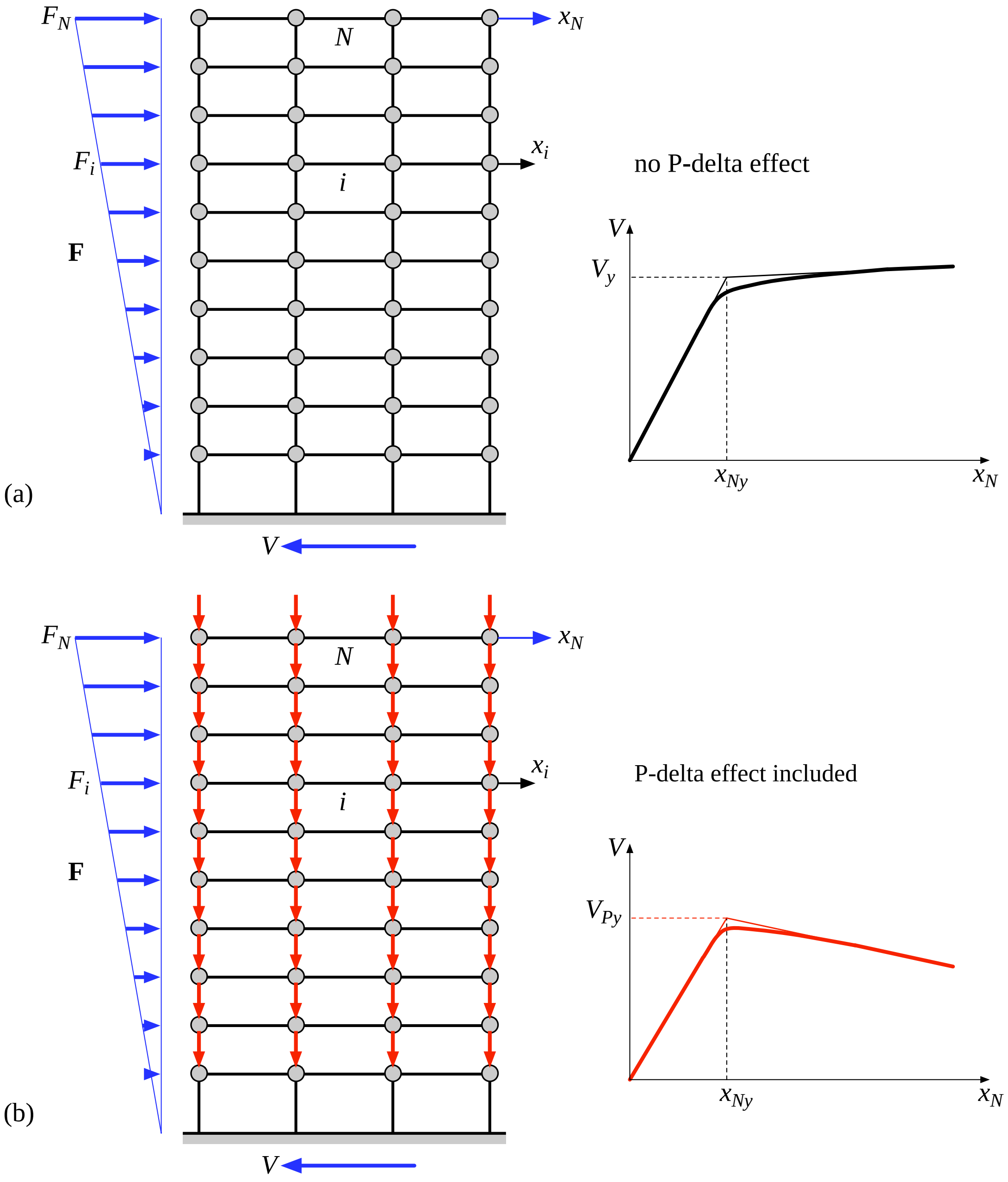

Figure 1: Multi-story frame structure and corresponding global pushover curves. (a) Pushover analysis disregarding P-delta. (b) Pushover analysis considering P-delta [2].

2.2 Assessment of the global collapse capacity

In the most general approach the Incremental Dynamic Analysis (IDA) procedure [19] is applied to determine the smallest earthquake intensity, which leads to structural collapse [2]. Thereby, for one acceleration time history of an earthquake record dynamic time history analyses are performed repeatedly, where in each subsequent run the intensity of the ground motion is incremented. As an outcome a characteristic seismic intensity measure is plotted against the corresponding maximum characteristic structural response quantity for each analysis. The procedure is stopped when the response grows to infinity, i.e. structural failure occurs. The corresponding intensity measure of the ground motion is referred to as collapse capacity of the building for this specific ground motion record. There is no unique definition of intensity of an earthquake record, however, the normalized 5% damped spectral acceleration at the structure's fundamental period $S_a(T_1)$ normalized by the product of the gravity of acceleration g and the base shear coefficient γ, $S_a(T_1) / (g\ \gamma)$, is widely accepted to characterize the intensity appropriately. γ is defined as ratio between yield base shear V_y (from the pushover curve without P-delta) and total weight W ($\gamma = V_y / W$).

Since the result of an IDA study strongly depends on the selected record, IDAs are performed for an entire set of n ground motion records, and the outcomes are evaluated statistically. In particular, the median of the sorted individual collapse capacities CC_{MDOF}^{i}, $i = 1,\ldots, n$, is considered as the representative collapse capacity for the examined structure and the regarded set of ground motion records,

$$CC_{MDOF} = med\left\langle CC_{MDOF}^{i}, i = 1,....,n \right\rangle \ , \quad CC_{MDOF}^{i} = \left.\frac{S_{a,i}}{g\gamma}\right|_{collapse} \tag{1}$$

Further significant statistical values of the collapse capacity are 16% and 84% percentiles of the individual outcomes, CC_{MDOF}^{16} and CC_{MDOF}^{p84}, respectively.

The IDA procedure requires the numerical solution of the equations of motions in each time step of each time history analysis, and as a consequence, is both time-consuming and computationally expensive. Thus, in [2, 17] for regular multi-story frame structures the so-called collapse capacity spectrum methodology has been proposed to obtain a quick but yet accurate approximation of the collapse capacity without performing time history analyses. The proposed methodology is based on the observation that the global P-delta effect is mainly governed by the fundamental mode. This holds also true if higher modes play a significant role in the dynamic structural response. Consequently, the collapse capacity is assessed utilizing an equivalent single-degree-of-freedom (ESDOF) system, and a collapse capacity spectrum [14, 15, 16]. This methodology is particular useful in engineering practice, because the structure can be evaluated with respect to its seismic collapse capacity in the initial design process.

3 FUNDAMENTALS OF THE COLLAPSE CAPACITY SPECTRUM METHODOLOGIES

3.1 Equivalent single-degree-of-freedom system

The ESDOF system is based on a time-independent shape vector $\boldsymbol{\phi}$, which describes the displacement vector $\mathbf{x}$ of the N-story MDOF frame structure regardless of its magnitude,

$$\mathbf{x} = \boldsymbol{\phi} x_N \ , \quad \phi_N = 1 \tag{2}$$

and on global pushover curves of the MDOF structure disregarding and considering gravity loads. In the corresponding pushover analyses the lateral load pattern must be selected to be affine to the displacement vector $\mathbf{x}$,

$$\mathbf{F} = \boldsymbol{\phi} F_N \tag{3}$$

and thus to the shape vector $\boldsymbol{\phi}$. x_N denotes the roof displacement, and F_N is the peak magnitude of the pushover load at the top of the frame structure, see Figure 1. The components ϕ_i of the shape vector $\boldsymbol{\phi}$ and the story masses $m_i, i = 1,...,N$, of the MDOF structure enter mass and participation factor of the ESDOF system. Transformation of bilinear idealizations of the global pushover curves, Figure 2(a), into the domain of the ESDOF system renders its backbone curves, Figure 2(b). However, consideration of the P-delta effect in the ESDOF system is not straight forward, because in contrast to a real SDOF system an ESDOF does not exhibit a unique stability coefficient. This behavior can be led back to the underlying global pushover curves with and without gravity loads. In a bilinear approximation of the pushover curves the stability coefficient θ_i in the post-yield range of deformation is larger than the elastic stability coefficient θ_e: $\theta_i > (>) \theta_e$ [18], compare with Figure 2(a). Thus, in [12, 2] it is proposed to assign an auxiliary backbone curve to the ESDOF system, which yields the backbone curve with applied gravity load by means of a single auxiliary stability coefficient θ_a [15]. Backbone curves of the ESDOF system are depicted in Figure 2(b): The blue bilinear curve represents the auxiliary backbone curve, and the corresponding red graph is the backbone curve with applied gravity load. For details of the ESDOF system it is referred to Fajfar [20], Adam et al. [21], and Ibarra and Krawinkler [12].

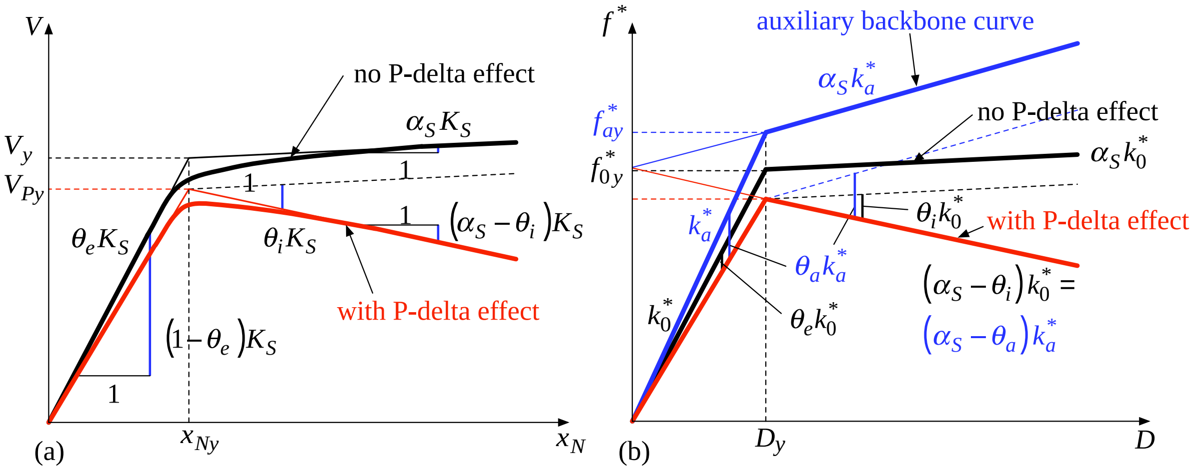

Figure 2: (a) Pushover curves with and without considering P-delta of a multi-story frame structure. (b) Backbone curves of the corresponding equivalent single-degree-of-freedom system.

The essential parameters of the ESDOF system required for the application of the collapse capacity spectrum methodology are the period T_a of the auxiliary ESDOF system, the auxiliary stability coefficient θ_a, and coefficient λ_{MDOF}. λ_{MDOF} transforms the collapse capacity from the SDOF domain into the domain of the MDOF system [2]. In [21, 12] these parameters are derived as:

$$T_a = 2\pi \sqrt{\frac{1-\alpha_S}{\upsilon}} \sqrt{\frac{x_{Ny}}{V_y}} \sqrt{\sum_{i=1}^{N} \phi_i m_i} \quad , \quad \theta_a = \frac{\theta_i - \theta_e \alpha_S}{\upsilon} \quad , \quad \upsilon = 1 - \theta_e + \theta_i - \alpha_S \qquad (4), (5), (6)$$

$$\lambda_{MDOF} = \frac{\left(\sum_{i=1}^{N} \phi_i m_i \right)^2}{\sum_{i=1}^{N} m_i \sum_{i=1}^{N} \phi_i^2 m_i} \tag{7}$$

Thereby, x_{Ny} denotes the roof displacement at onset of yield of the global pushover curve (without P-delta), see Figure 1.

If all story masses are equal, $m_i = m_s$, $i = 1,...,N$, than the expressions T_a and λ_{MDOF} reduce to

$$T_a = 2\pi \sqrt{\frac{1-\alpha_S}{\upsilon}} \sqrt{\frac{x_{Ny}}{V_y}} \sqrt{m_s \sum_{i=1}^{N} \phi_i} \quad , \quad \lambda_{MDOF} = \frac{\left(\sum_{i=1}^{N} \phi_i \right)^2}{N \sum_{i=1}^{N} \phi_i^2} \tag{8), (9}$$

For a linear shape vector with components $\phi_i = i / N$, $i = 1,...,N$, and constant story height *h*, period T_a and coefficient λ_{MDOF} read as:

$$T_a = 2\pi \sqrt{\frac{1-\alpha_S}{\upsilon}} \sqrt{\frac{x_{Ny} m_s}{2V_y}} \sqrt{N+1} \quad , \quad \lambda_{MDOF} = \frac{3}{2} \frac{N+1}{2N+1} \tag{10), (11}$$

If the number of stories N is larger than 9, λ_{MDOF} can be approximated according to

$$\lambda_{MDOF} \underset{\forall N>9}{\approx} \frac{3}{4} \tag{12}$$

3.2 Collapse capacity spectrum

In [14, 15] it is shown that the record dependent collapse capacity of a real non-deteriorating SDOF system with bilinear backbone curve, which is vulnerable to the P-delta effect, is governed by the following quantities:

- Initial period of vibration T
- Viscous damping coefficient ζ
- Negative post-yield stiffness ratio $\theta - \alpha$
- Hysteretic loop

If the collapse capacity of a system with assigned hysteretic loop and fixed parameters ζ and $\theta - \alpha$ is plotted against the period of vibration, the resulting graph is referred to as collapse capacity spectrum for an individual ground motion record. Statistical evaluation of individual collapse capacity spectra, which belong to a specific set of earthquake records, leads to median, 16% and 84% percentile collapse capacity spectra. In [15] a rigorous study of the impact of the parameters specified above on collapse capacity spectra is presented.

In an effort to provide engineers a tool, which allows a quick estimation of the collapse capacity, in the same publication [15] design collapse spectra with a “smooth” shape have been derived via non-linear regression analyses. For a certain set of parameters an analytic relation for base case median design collapse capacity spectra are defined. The impact of parameters, which differ from the base case, is considered by influence coefficients. For details see again [15]. Exemplarily, Figure 3 shows median design collapse capacity spectra (marked by circles) for a series of post-yield stiffness ratios $\theta - \alpha$, and the corresponding design collapse capacity spectra depicted by full lines. These collapse capacity spectra are based on the ATC63 far-field set of 44 ordinary ground motions [22], and have been derived for SDOF systems with bilinear hysteretic loops, and a viscous damping coefficient of $\zeta = 0.02$.

Application of design collapse capacity spectra is simple. An estimate of the elastic period of vibration *T*, damping coefficient ζ, stability coefficient θ, and hardening ratio α of the actual SDOF structure is to be determined. Subsequently, from the chart the corresponding collapse capacity *CC* can be read. Furthermore, in [15] analytic approximations of fragility curves based on a log-normal distribution of the collapse capacities are presented.

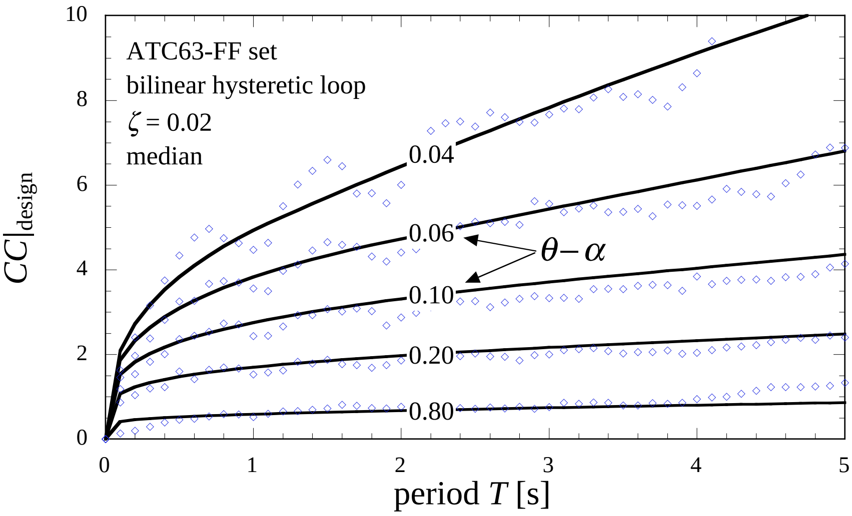

Figure 3: Median collapse capacity spectra (blue circles) and corresponding design collapse capacity spectra. Underlying parameters specified in the figure.

4 COLLAPSE CAPACITY SPECTRUM METHODOLOGIES

4.1 Original collapse capacity spectrum method

The procedure to derive an estimate of the collapse capacity of an MDOF frame structure based on the corresponding ESDOF system and collapse capacity spectra can be summarized as follows [2, 17]:

- Derive global pushover curves of the MDOF structure without and with gravity loads with an appropriate horizontal load pattern, e.g. according to the fundamental mode shape. If the post-yield stiffness of the gravity loaded structure is negative, determine the global collapse capacity as subsequently described.
- If feasible, perform a bilinear approximation of the pushover curves and identify the global hardening ratio α_S, and the elastic and inelastic stability coefficient θ_e and θ_i, respectively.
- Derive the auxiliary stability coefficient θ_a according Eq. (5), and derive the negative post-yield stiffness ratio $\theta_a - \alpha_S$.

- Select the shape vector ϕ affine to the horizontal load pattern of the pushover analyses, and derive the period T_a of the auxiliary ESDOF system according to Eqs (4), (8), or (10).
- Consult the appropriate design collapse capacity spectrum with respect to the underlying ground motion set, viscous damping ζ, hysteretic loop, and the negative post-yield stiffness $\theta_a - \alpha_S$, and read at the period T_a the median collapse capacity *CC*.
- Derive the coefficient λ_{MDOF} according Eq. (7), (9), or (11) and transform *CC* into the domain of the ESDOF system [2]:

$$CC_{ESDOF} = \frac{CC}{\lambda_{MDOF}} \tag{13}$$

  This outcome is an estimate of the actual median collapse capacity $CC_{MDOF} \approx CC_{ESDOF}$.
- If required, determine the 16% and 84% collapse capacities CC_{ESDOF}^{p16} and CC_{ESDOF}^{p84}, respectively, in analogy to the relations for a real SDOF system as derived by Adam and Jäger [15]:

$$CC_{ESDOF}^{p16} = CC_{ESDOF} / s_l^* \ , \quad s_l^*(T_a) = \frac{10}{7} T_a^{1/20} \tag{14, 15}$$

$$CC_{ESDOF}^{p84} = CC_{ESDOF} s_u^* \ , \quad s_u^*(T_a) = \frac{3}{2} T_a^{1/20} \tag{16, 17}$$

- Assuming that the uncertainties in the collapse capacities follow a log-normal distribution derive the fragility curve from [15]

$$\ln N(m, \sigma^2) \tag{18}$$

  with

$$m = \ln\left(CC_{ESDOF}\right) \ , \quad \sigma = \ln\sqrt{s_l^* s_u^*} \tag{19, 20}$$

4.2 Simplified collapse capacity spectrum method

In the following, a further simplification of the collapse capacity spectrum method for an even faster assessment of the global collapse capacity is suggested.

Inspection of Eqs (4), (8), and (10) reveals that only for large stability coefficients, i.e. $\theta_a - \alpha_S >> 0$, the P-delta effect has a severe impact on the auxiliary period T_a. However, for flexible systems the gradient of collapse capacity spectra is small, if $\theta_a - \alpha_S >> 0$, as it can be seen from Figure 3. Consequently, the collapse capacity *CC* is not much affected, if an approximation of the period enters the collapse capacity spectrum. Thus, it is proposed that a rough estimate of the fundamental structural period without taking account the gravity loads can be utilized instead of the auxiliary period T_a. This period replaces T_a in all relations of the original collapse capacity spectrum methodology.

A second simplification concerns the negative post-yield stiffness ratio. It can be shown that the auxiliary stability coefficient is always in-between the elastic and the inelastic stability coefficient. Hence, $\theta_i - \alpha_S$ is always larger than $\theta_a - \alpha_S$. Assuming that $\theta_i - \alpha_S$ is the characteristic post-yield stiffness ratio, the corresponding collapse capacity estimation is more conservative compared to the value based on $\theta_a - \alpha_S$. For a fast and rough assessment of the collapse capacity the negative stiffness ratio derived according to $\theta_i - \alpha_S$ may be utilized.

Finally, for an initial collapse assessment a transformation coefficient of $\lambda_{MDOF} = 3/4$ may be employed, compare with Eq. (12).

5 EVALUATION OF THE COLLAPSE CAPACITY SPECTRUM METHODOLOGIES

For several generic multi-story frame structures as depicted in Figure 4(a) the original collapse capacity spectrum methodology and its simplified counterpart is evaluated setting its results in contrast with the “exact” collapse capacity based on IDAs. All stories of the single-bay structures of *N* stories are of uniform height *h*, and they are composed of rigid beams, elastic flexible columns, and rotational springs at the ends of the beams. Nonlinear behavior at the component level is modeled by non-degrading bilinear hysteretic behavior of the rotational springs (compare with Figure 4(b)) to represent the global cyclic response under seismic excitation. The strength of the springs is tuned such that yielding is initiated simultaneously at all spring locations in a static pushover analysis (without gravity loads) under an inverted triangular design load pattern. To each joint of the frames an identical point mass $m_i / 2 = m_S / 2$, $i = 1, ..., N$, is assigned. The bending stiffness of the columns and the stiffness of the springs are tuned to render a straight line fundamental mode shape. Identical gravity loads are assigned to each story to simulate P-delta effects. This implies that axial column forces due to gravity increase linearly from the top to the bottom of each frame. The frame structures have a fundamental period of vibration of $T_1 = 0.2\,N$, which makes them rather flexible.

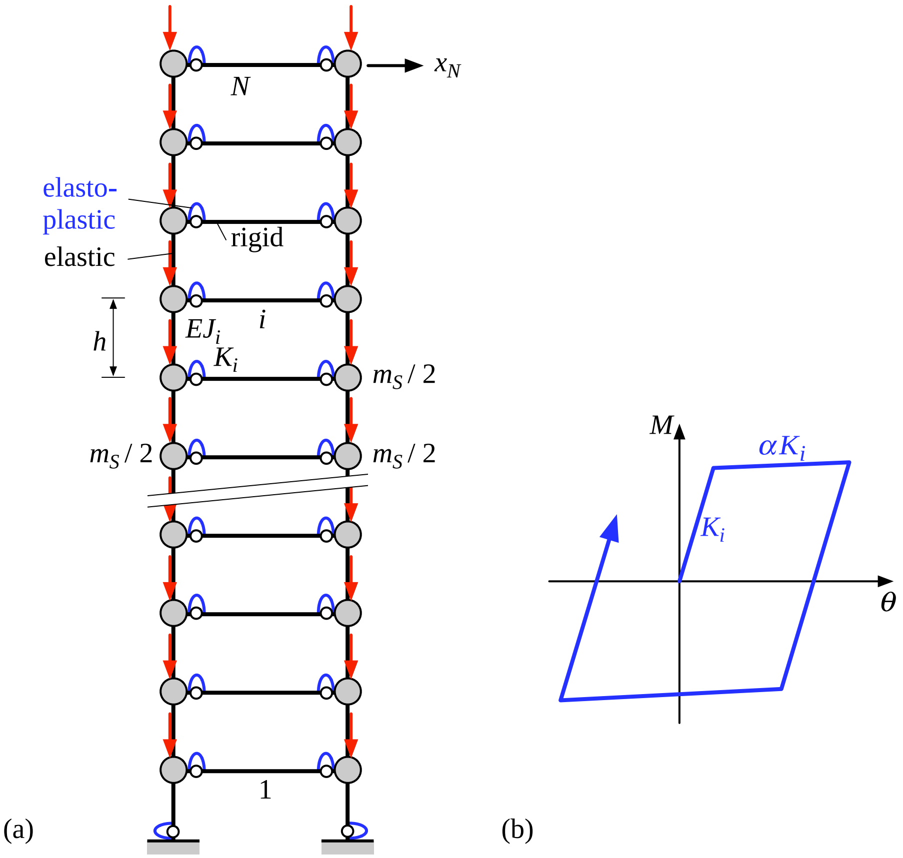

Figure 4: (a) Planar generic multi-story frame structure. (b) Bilinear hysteretic loop of the rotational springs.

In a first example problem an 18-story frame structure is considered. The fundamental period is $T_1 = 3.6$ s. The hardening coefficient of all rotational springs is chosen to be $\alpha = 0.01$, the ratio of dead load plus life load to dead load is $\vartheta = 1.0$. Structural damping is considered by means of mass and stiffness proportional Rayleigh damping of 2% of the first mode and 2% of that mode, where the sum of modal masses exceeds 95% of the total mass.

In Figure 5 the outcomes of an IDA procedure utilizing the 44 records of the ATC63-FF set are shown. Each IDA curve displayed with light gray lines belongs to a specific record. Thereby, the non-dimensional excitation intensity $S_a / \left(g\gamma\right)$ is plotted against the normalized roof displacement x_N / S_d. S_a and S_d are the spectral acceleration and spectral displacement, respectively, at the period $T = T_1$ of the 5% damped response spectrum of the considered record. The lowest intensity, where a specific IDA curve exhibits a horizontal tangent, is the collapse capacity of the MDOF structure for the corresponding earthquake record. This figure reveals the large record dependent dispersion of the individual collapse capacities. A blue fat line represents the median IDA curve. From the results the “exact” median collapse capacity of $CC_{MDOF} = 3.33$ can be identified. Additionally, fat black lines correspond to the 16% percentile and 84% percentile IDA curves. The 16% percentile and 84% percentile collapse capacities are $CC_{MDOF}^{16} = 2.33$ and $CC_{MDOF}^{84} = 5.45$, respectively.

The assessment of the collapse capacity according to the collapse capacity spectrum methodology requires the identification of the elastic and the inelastic stability coefficient, and the global hardening ratio from global pushover curves without and with P-delta effect. The pushover curves of the structure are depicted in Figure 6. The parameters are determined as: $\theta_e = 0.073$, $\theta_i = 0.222$, $\alpha_S = 0.013$. Subsequent evaluation of Eqs (5) and (10) yields the auxiliary stability coefficient and the auxiliary period, respectively: $\theta_a = 0.195$, $T_a = 3.35$ s. The transformation coefficient λ_{MDOF}, Eq. (11), is derived as 0.770. The required post-yield stiffness ratios are: $\theta_a - \alpha_S = 0.182$, $\theta_i - \alpha_S = 0.209$.

Figure 7 shows the utilized 2% damped median design collapse capacity spectra for bilinear hysteretic behavior and the ATC63-FF record set [15]. Herein, it is illustrated, how the median collapse capacities for the proposed methodologies are determined.

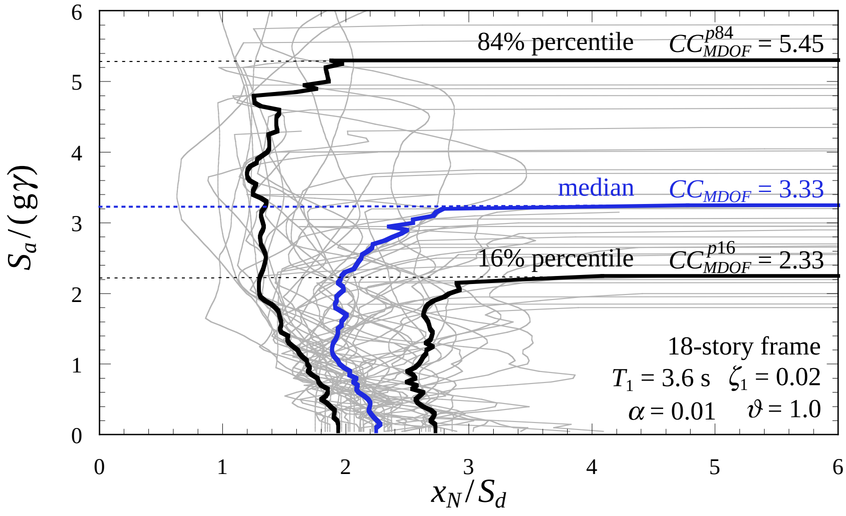

Figure 5: IDA curves for 44 ground motions of the ATC63-FF set. Median, 16% percentile, and 84% percentile IDA curves. Generic 18-story frame structure with a fundamental period of vibration of 3.6 s.

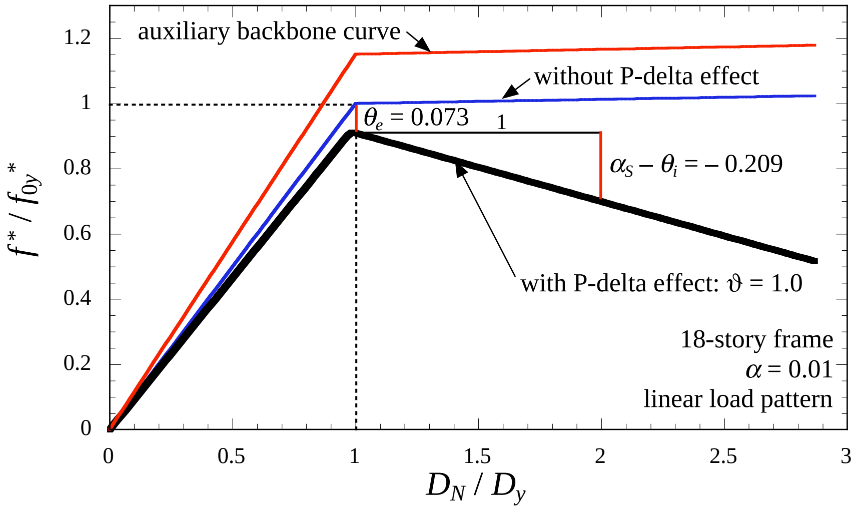

Figure 6: Backbone curves of the equivalent single-degree-of-freedom system for a generic 18-story frame structure.

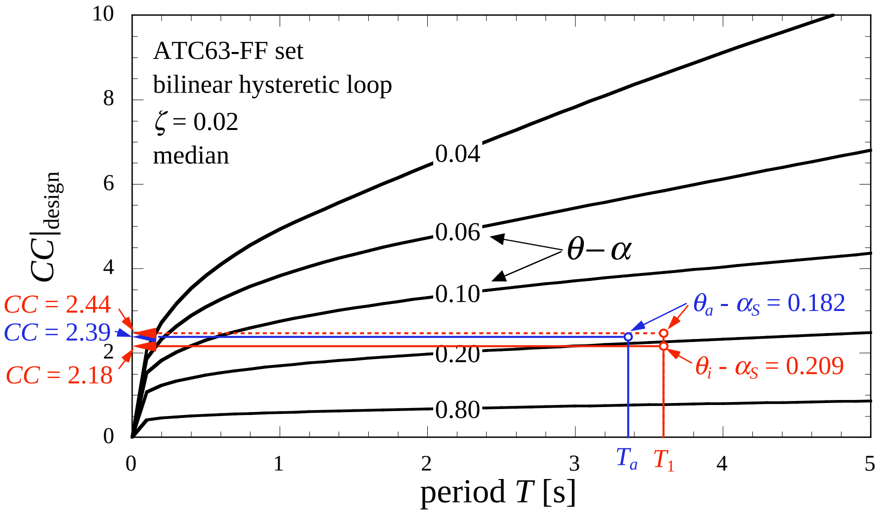

Figure 7: Median design collapse capacity spectra applied for prediction of the median collapse capacity of a generic 18-story frame structure. Different collapse capacity spectrum methodologies.

In Table 1 the outcomes of different collapse capacity assessment methodologies are specified. The collapse capacity of the second column corresponds to the “exact” outcome of an IDA study based on the 44 earthquake records of the ATC63-FF set, whereas the results of columns three, four and five are based on ESDOF systems and collapse capacity spectra. Furthermore, in this table the underlying parameters of the different collapse capacity spectrum approximations are listed.

Inspection reveals that the median collapse capacity of the third column, CC_{ESDOF} = 3.10, determined by the original collapse capacity methodology, is about 93% of the “exact” counterpart, and thus a conservative estimate. The simplified collapse capacity spectrum methodology yields a median collapse capacity CC_{ESDOF} = 2.91, compare with column five. An “intermediate” simplified capacity spectrum methodology, where the negative post-yield stiffness of the auxiliary ESDOF $\theta_a - \alpha_S$, and the fundamental period T_1 of the frame structure enters the collapse capacity spectrum leads to CC_{ESDOF} = 3.16, which is the approximation closest to the “exact” outcome. The difference between the “exact” and approximated percentile collapse capacities is of the same order as for the median values, compare with Table 1.

Figure 8 shows the counted collapse fragility curve from the IDA study, and several approximated “smooth” fragility curves of the considered 18-story frame structure. The blue line is a “best fit” of the counted fragilities employing the maximum likelihood method. The black and red lines are based on log-normal approximations taking into account different values of the percentiles. The fragility curves according to the collapse capacity spectrum methodologies (displayed in red color) are derived employing Eqs (14) to (20). The curve displayed in black color has been derived using counted median, 16% and 84% percentiles from the IDA study.

Subsequently, the median collapse capacity of 12 generic multi-story frame structures vulnerable to P-delta is evaluated. The number of stories N ranges from 15 to 24. Spring hardening ratios α of 1%, 2%, and 3% are employed, and viscous damping ζ_1 of the fundamental mode of 2% and 5% is taken into account. The considered dead load plus life load to dead load ratios ϑ are 1.0, 1.2, and 1.4. In Table 2 the properties of the individual frames are specified.

Methodology	IDA study	Original collapse capacity spectrum methodology	Simplified collapse capacity spectrum methodology	Simplified collapse capacity spectrum methodology
Period		$T_a = 3.35$ s	$T_1 = 3.60$ s	$T_1 = 3.60$ s
Post-yield stiffness ratio		$\theta_a - \alpha_S = 0.182$	$\theta_a - \alpha_S = 0.182$	$\theta_i - \alpha_S = 0.209$
Transformation coefficient		$\lambda_{MDOF} = 0.770$	$\lambda_{MDOF} = 0.770$	$\lambda_{MDOF} = 3/4$
CC from spectrum		2.39	2.44	2.18
Median collapse capacity	$CC_{MDOF} = 3.33$	$CC_{ESDOF} = 3.10$	$CC_{ESDOF} = 3.16$	$CC_{ESDOF} = 2.91$
16% percentile collapse capacity	$CC^{16}_{MDOF} = 2.33$	$CC^{16}_{ESDOF} = 2.04$	$CC^{16}_{ESDOF} = 2.07$	$CC^{16}_{ESDOF} = 1.91$
84% percentile collapse capacity	$CC^{84}_{MDOF} = 5.45$	$CC^{84}_{ESDOF} = 4.94$	$CC^{84}_{ESDOF} = 5.05$	$CC^{84}_{ESDOF} = 4.65$
CC_{ESDOF} / CC_{MDOF}	1	0.93	0.95	0.87
$CC^{p16}_{ESDOF} / CC^{p16}_{MDOF}$	1	0.88	0.89	0.82
$CC^{p84}_{ESDOF} / CC^{p84}_{MDOF}$	1	0.91	0.93	0.85

Table 1: Median, 16% percentile, and 84% percentile collapse capacity of a generic 18-story frame structure. “Exact” outcome of an IDA study, and results from collapse capacity spectrum methodologies based on equivalent single-degree-of-freedom systems.

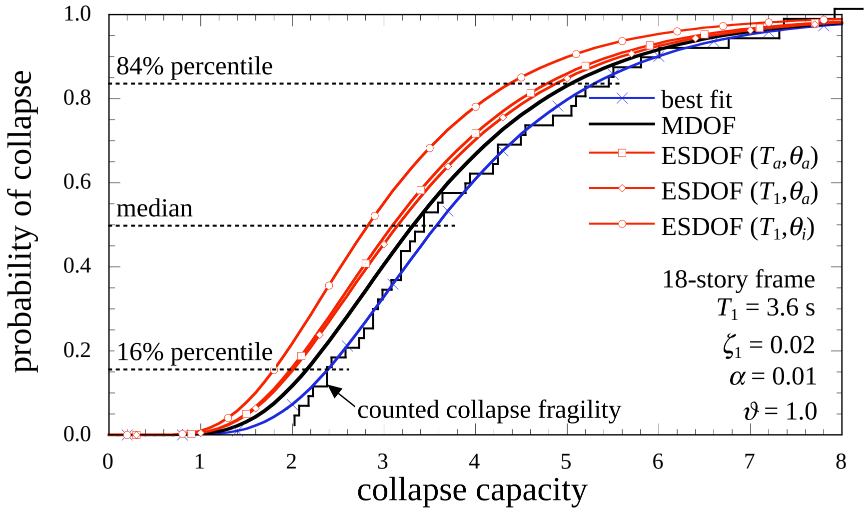

Figure 8: Counted fragility curve and "smooth" approximations based on log-normal distribution of an generic 18-story frame structure.

Frame ID	Number of stories N	Fundamental period T_1 [s]	Spring hardening ratio α	Damping ratio ζ_1	Gravity load ratio ϑ
1	18	3.6	0.03	0.05	1.0
2	18	3.6	0.03	0.05	1.2
3	18	3.6	0.03	0.05	1.4
4	15	3.0	0.03	0.05	1.0
5	21	4.2	0.03	0.05	1.0
6	24	4.8	0.03	0.05	1.0
7	18	3.6	0.02	0.05	1.0
8	18	3.6	0.01	0.05	1.0
9	18	3.6	0.03	0.02	1.0
10	18	3.6	0.03	0.02	1.2
11	18	3.6	0.01	0.02	1.0
12	18	3.6	0.02	0.02	1.2

Table 2: ID and properties of the considered generic multi-story frame structures.

Figure 9 shows for each frame the median collapse capacity from an IDA study of the actual multi-story structure (black bar), and from application of the collapse capacity spectrum methodologies (colored bars). The outcomes of the original collapse capacity spectrum methodology, based on the auxiliary structural period T_a and the auxiliary stability coefficient θ_a, are depicted in red. The blue bar corresponds to results from the simplified collapse capacity spectrum methodology utilizing the fundamental structural period T_1 and the inelastic stability coefficient θ_i. The collapse capacities depicted in green are derived from an "intermediate" simplified collapse capacity spectrum methodology, where T_1 and θ_a enter the analysis. It is readily observed that the 15-story frame (frame ID 4) exhibits the largest global collapse capacity. The median collapse capacity of structures with ID 3, 6, and 12 is of the same magnitude. Comparison reveals that for all considered structures the "exact" IDA results are of the same magnitude as their counterparts of the collapse capacity spectrum methodologies.

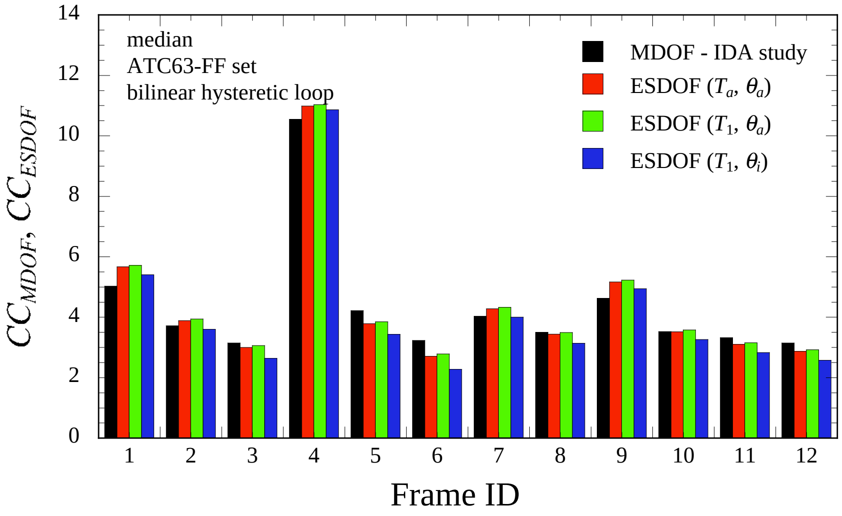

Figure 9: Global collapse capacities for a series of generic multi-story frame structures according to Table 2. "Exact" outcome from IDA studies, and results from collapse capacity spectrum methodologies based on equivalent single-degree-of-freedom systems.

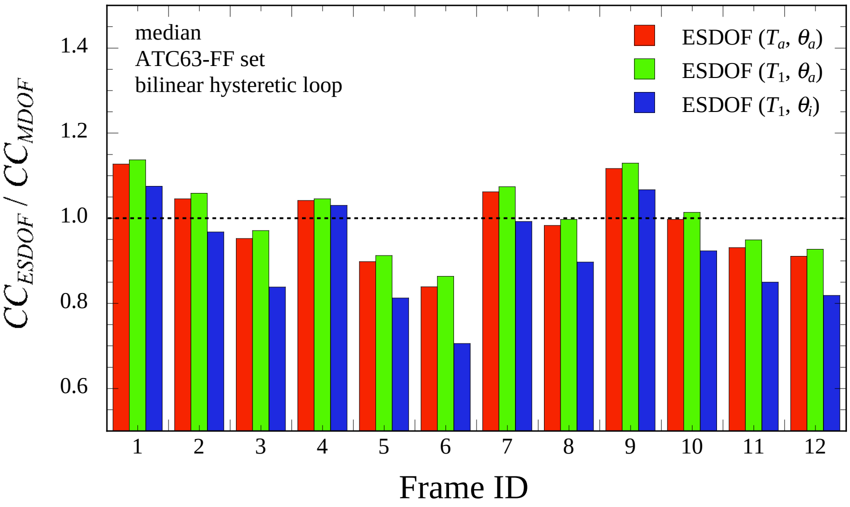

Figure 10: Global collapse capacity ratios for a series of generic multi-story frame structures according to Table 2. Results from collapse capacity spectrum methodologies based on equivalent single-degree-of-freedom systems related to the "exact" outcome from IDA studies.

The difference in percent of the individual results for each frame is illustrated in Figure 10, where the ratios of collapse capacities from ESDOF considerations to the "exact" outcomes are shown. A ratio of one implies that both considered methods predict the same collapse capacity. If the ratio is smaller than one, the collapse capacity is underestimated by the collapse capacity spectrum methodology, i.e. the outcome is conservative compared to the "exact" value. It can be seen that for frames 1, 2, 4, 7, and 9 the collapse capacity spectrum methodologies lead to slightly non-conservative predictions up to 12%. For frames 5 and 6 predictions are very conservative.

Setting in contrast the results of the individual collapse capacity spectrum methodologies for each frame separately reveals that the simplified method renders the smallest collapse capacity, and thus, for some structures over-conservative predictions.

However, taking into account the underlying simplifications it can be concluded that all applied collapse capacity spectrum methodologies are capable to yield a collapse capacity estimate, which is sufficiently accurate for the initial design process of buildings.

6 CONCLUSIONS

The seismic collapse capacity of a series of non-deteriorating multi-story frame structures vulnerable to the destabilizing effect of gravity loads was assessed employing the collapse capacity spectrum methodology, a simplified subspecies of this methodology, and the IDA procedure. Evaluation of the results reveals that both the original and simplified capacity spectrum methodology render sufficient accurate estimates of the global collapse capacity, and thus can be utilized efficiently in the initial design process of buildings.

REFERENCES

[1] H. Krawinkler, F. Zareian, D.G. Lignos, L.F. Ibarra, Prediction of collapse of structures under earthquake excitations. M. Papadrakakis, N.D. Lagaros, M. Fragiadakis eds. *2nd International Conference on Computational Methods in Structural Dynamics and Earthquake Engineering (COMPDYN 2009),* Rhodes, Greece, June 22-24, 2009, CD-ROM paper, paper no. CD449, 2009.

[2] C. Adam, C. Jäger, Seismic induced global collapse of non-deteriorating frame structures. Papadrakakis, M., Fragiadakis, M., Lagaros, N.D., eds. *Computational Methods in Earthquake Engineering*, pp. 21 - 40, Springer, 2011.

[3] P.C. Jennings, R. Husid, Collapse of yielding structures during earthquakes. *Journal of the Engineering Mechanics Division, Proc. ASCE* **94**, 1045-1065, 1968.

[4] D. Bernal, Amplification factors for inelastic dynamic P-Δ effects in earthquake analysis. *Earthquake Engineering and Structural Dynamics* **15**, 635-651, 1987.

[5] D. Bernal, Instability of buildings during seismic response. *Engineering Structures* **20**, 496-502, 1998.

[6] G.A. MacRae, P-Δ effects on single-degree-of-freedom structures in earthquakes. *Earthquake Spectra* **10**, 539-568, 1994.

[7] A. Gupta, H. Krawinkler, *Seismic demands for performance evaluation of steel moment resisting frame structures*. Report No. 132. The John A. Blume Earthquake Engineering Research Center, Department of Civil and Environmental Engineering, Stanford University, Stanford, CA, 1999.

[8] D. Vian, M. Bruneau, Tests to structural collapse of single degree of freedom frames subjected to earthquake excitation. *Journal of Structural Engineering* **129**, 1676-1685, 2003.

[9] D.G. Lignos, H. Krawinkler, A. Whittaker, Prediction and validation of sidesway collapse of two scale models of a 4-story steel moment frame. *Earthquake Engineering and Structural Dynamics*, accepted for publication.

[10] A.V. Asmialopoulos, D.L. Karabalis, D.E. Beskos, Inclusion of P- Δ effect in displacement-based seismic design of steel moment resisting frames. *Earthquake Engineering and Structural Dynamics* **36**, 2171-2188, 2007.

[11] R. Villaverde, Methods to assess the seismic collapse capacity of building structures: State of the art. *Journal of Structural Engineering* **133**, 57-66, 2007.

[12] L.F. Ibarra, H. Krawinkler, *Global collapse of frame structures under seismic excitations*. Report No. PEER 2005/06, Pacific Earthquake Engineering Research Center, University of California, Berkeley, CA, 2005.

[13] C.B. Haselton, A.B. Liel, G.G. Deierlein, Simulating structural collapse due to earthquakes: Model idealization, model calibration, and numerical simulation algorithms. Papadrakakis M., Lagaros, N.D., Fragiadakis, M., eds. *2nd International Conference on Computational Methods in Structural Dynamics and Earthquake Engineering* (*COMPDYN 2009*), June 22-24, 2009, Rhodes, Greece, CD-ROM paper, paper no. CD497, 2009.

[14] C. Adam, P-delta effects in earthquake excited structures. Yamanaka, H., Morikawa, H., Satoshi, Y. eds. Proc. *Sixth International Conference on Urban Earthquake Engineering*, Tokyo Institute of Technology, Japan, March 3-4, 2009, pp. 231 – 234, 2009.

[15] C. Adam, C. Jäger, Seismic collapse capacity of basic inelastic structures vulnerable to the P-delta effect. *Earthquake Engineering and Structural Dynamics* (submitted for publication).

[16] C. Adam, C. Jäger, Collapse capacity spectra for finite ductility thresholds, to be published.

[17] C. Adam, C. Jäger, Assessment of the dynamic stability of tall buildings subjected to severe earthquake excitation. *Highrise Towers and Tall Buildings 2010*, International Conference at the Technische Universität München, Germany, April 14 - 16, 2010, CD-ROM paper, 8 pp., 2010.

[18] R.A. Medina, H. Krawinkler, *Seismic demands for nondeteriorating frame structures and their dependence on ground motions*. Report No. 144. The John A. Blume Earthquake Engineering Research Center, Department of Civil and Environmental Engineering, Stanford University, Stanford, CA, 2003.

[19] D. Vamvatsikos, C.A. Cornell, Incremental dynamic analysis. *Earthquake Engineering and Structural Dynamics* **31**, 491-514, 2002.

[20] P. Fajfar, Structural analysis in earthquake engineering - a breakthrough of simplified non-linear methods. *12th European Conference on Earthquake Engineering*, CD-ROM paper, Paper Ref. 843, 20 pp., Elsevier, 2002.

[21] C. Adam, L.F. Ibarra, H. Krawinkler, Evaluation of P-delta effects in non-deteriorating MDOF structures from equivalent SDOF systems. *13th World Conference on Earthquake Engineering*, August 1 - 6, 2004, Vancouver B.C., Canada. DVD-ROM paper, 15 pp., Canadian Association for Earthquake Engineering, 2004.

[22] FEMA P695 - Quantification of Building Seismic Performance Factors. Federal Emergency Management Agency, Washington D.C., 2009.

COMPDYN 2011
III ECCOMAS Thematic Conference on
Computational Methods in Structural Dynamics and Earthquake Engineering
M. Papadrakakis, M. Fragiadakis, V. Plevris (eds.)
Corfu, Greece, 25–28 May 2011

USABILITY OF PUSHOVER ANALYSIS FOR ASYMMETRIC BASE-ISOLATED BUILDINGS

Vojko Kilar[1], **David Koren**[1]

[1] University of Ljubljana, Faculty of Architecture
Zoisova 12, SI-1000 Ljubljana, Slovenia, EU
e-mail: vojko.kilar@fa.uni-lj.si, david.koren@fa.uni-lj.si

Keywords: Base Isolation, Asymmetric Buildings, Pushover Analysis, N2 Method, Torsion.

Abstract. *The paper deals with the applicability of a simplified nonlinear method (N2 method) to base-isolated plan-asymmetric building structures. In the first part of the paper the modifications that have been implemented into the originally proposed N2 method – such as the new three-linear idealization and inclusion of isolator damping by reduction factor* R_ξ *– are shortly described. In the paper the proposed procedure is used for the seismic analysis of a base-isolated 4-storey RC asymmetric building isolated with lead rubber bearings (LRBs). For the base isolation system we have considered three different types of isolators with different stiffness. The results of nonlinear dynamic time-history analyses are compared with the results of the N2 method in terms of obtained top, base and relative displacements. Comparisons of the results of the simplified method with the ‘exact’ results of the nonlinear dynamic analyses have shown a very good agreement. It has been shown that the presented simplified approach might be a valuable tool for design, analysis and verification of the behavior of symmetric as well as moderately asymmetric base-isolated structures.*

1 INTRODUCTION

Over the last decade simplified non-linear methods based on pushover analysis, the equivalent single degree of freedom (SDOF) system, and the response spectrum approach have been implemented in guidelines, standards and codes for the seismic resistant design of new buildings and the evaluation of existing buildings. One of these simplified non-linear methods is the N2 method, which has been successfully applied to the analysis of symmetric [1] and asymmetric buildings (extended N2 method – [2]) with different building system types. The method combines the pushover analysis of a multi degree of freedom (MDOF) model with the response spectrum analysis of an equivalent SDOF model. In the paper the method is applied for symmetric and moderately asymmetric base-isolated structures with the mass centre of the superstructure coinciding to the stiffness centre of the isolation system. The modifications of original method include: 1) a new three-linear idealization of the pushover curve based on the first yield of the superstructure, and 2) the introduction of the reduction factor R_ξ to account for damping of isolators [3,4].

2 PROPOSED CAPACITY CURVE FOR BASE-ISOLATED STRUCTURES

For the idealization of the capacity curve of a base-isolated structure the authors have considered that the first yielding point of the superstructure is far more important that the "average yielding" point of the structure used for bilinear idealization in the original N2 method for fixed base structures. In this way the N2 method should be able to detect the first yielding of the superstructure, as well as to estimate the behavior of the superstructure further into the nonlinear range directly in relation to the first yielding of the superstructure.

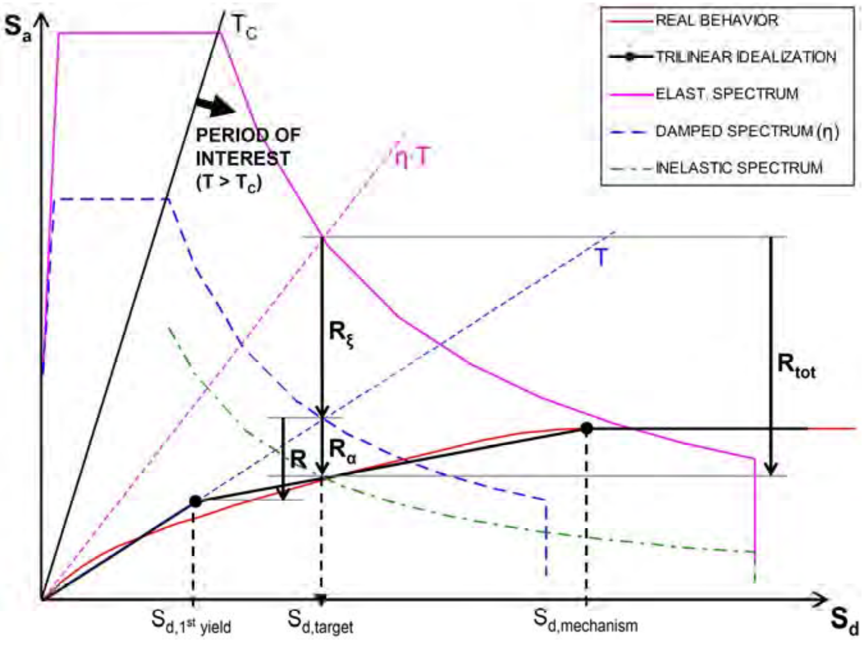

Figure 1: Idealized capacity curve of base-isolated structures and estimation of target top displacement.

The first yielding of the superstructure is determined by a pushover analysis for the selected lateral load distribution. The initial stiffness is obtained by equalizing the areas below and above the actual pushover curve of the base-isolated structure. The secondary slope is obtained in such a way that it best fits the real pushover curve. Alternatively it can be determined from the failure mechanism obtained by pushover analysis. After the mechanism has occurred, a zero slope is suggested. A consequence of such idealization is a much more pronounced hardening secondary slope which does not correspond to the assumptions used in the original N2 method (see Figure 1). A similar model with a higher secondary slope was suggested also by [5] for structures with incorporated hysteretic dampers. It should be noted that the range of interest for base-isolated structures is practically limited to the secondary hardening part of the idealized curve, since it is not expected that base-isolated structures would experience damage close to the failure mechanism.

3 DESCRIPTION OF THE PROCEDURE

Due to the non-zero hardening slope α, the actual reduction factor R_α is smaller than the assumed factor R from original N2 method. The relations between R and R_α depend on the hardening slope α and can be obtained by using equation (1). Assuming that the equal displacement rule applies the equations can be obtained by using relatively simple geometric relations.

$$R_\alpha = \frac{R}{\alpha R - \alpha + 1} \tag{1}$$

The use of the N2 method remains practically the same as was suggested in the original N2 method [1]. The inelastic spectra can be obtained as:

$$S_a = \frac{S_{ae}}{R_{tot}} \tag{2}$$

where R_{tot} can be obtained as a product of the reduction factor R_ξ and the reduction factor R_α:

$$R_{tot} = R_\xi \cdot R_\alpha \tag{3}$$

R_α represents the reduction due to the nonlinear behavior and damping of the superstructure, whereas R_ξ represents the strength reduction due to the higher damping of the isolators:

$$R_\xi = \frac{1}{\eta^2}\text{, where } \eta = \sqrt{10/(5+\xi)} \geq 0.55 \tag{4}$$

where η is the correction factor which takes into account damping effects (see [6], equation (3.6)) and ξ is the damping of the isolation system. A graphical representation of the procedure is presented in Figure 1. The reduction factor that relates the proposed procedure with the quantities from the general N2 method can be expressed as a product of R_ξ and R. It should be noted that the damping of the isolation system ξ used in equation (4) depends on the achieved base displacement D_d. In our study we have obtained it by means of Jacobsen's equation [7]:

$$\xi_{LRB}(D_d) = \frac{4\,Q\,(D_d - D_y)}{2\,\pi\,K_{eff}\,D_d^2} \tag{5}$$

where D_y and K_{eff} are the yield displacement and effective stiffness of the selected LRB isolator and Q is its characteristic strength. Since the actual base displacement D_d it is not known in advance, some iteration steps are required in order to obtain the correct results. In each step the top displacement of the MDOF system is obtained as $D_{top} = \Gamma \cdot S_d$, whereas the corresponding base displacement can be obtained by pushover analysis. The new damping value is then calculated by substituting D_d in equation (5) by the obtained D_{base}, until a satisfactory agreement is reached.

The extension of the N2 method to fixed base plan-asymmetric building structures has been described in detail in [2]. It has been proposed to combine the results obtained by usual 3D pushover analysis with the results of a linear dynamic (spectral) analysis in order to determine the torsional correction factor (c_T) to correct the results obtained by pushover analysis. This factor is defined as the ratio between the normalized top displacements obtained by elastic modal analysis and by pushover analysis (equation (6)). The normalized top displacement is the top displacement at an arbitrary location divided by the top displacement at the centre of mass (CM). If the normalized top displacement obtained by elastic modal analysis is smaller than 1.0, it is suggested to assume it to be equal to 1.0. This recommendation, which in case of base-isolated structures seems to be too conservative, was not applied in the presented case study. Correction factors are defined for each horizontal direction separately and they depend on the considered location in the plan. Then all the relevant quantities obtained by pushover analyses for considered location (e.g. distance from the CM) should be multiplied with appropriate torsional correction factor for this location in order to obtain the target values of relevant quantities.

$$c_T = \frac{\bar{u}_e^{top}}{\bar{u}_{push}^{top}} \qquad \bar{u}^{top} = \frac{u^{top}}{u_{CM}^{top}}; \text{ if } \bar{u}_e^{top} < 1.0 \text{, take } 1.0 \tag{6}$$

In the presented case study we have used the same presumptions as for symmetric base-isolated structures and we have treated the frame in the vertical plane passing through the CM in the same manner as the frame in a symmetric structure. All quantities were therefore observed in this plane, where also the horizontal loads for pushover analysis have been also applied [8, 9].

4 CASE STUDY: A BASE-ISOLATED RC FRAME STRUCTURE

4.1 Building description

A four-storey base-isolated RC frame building, which is presented in Figure 2, was used as a test example. The symmetric variant of the same structure was already used for example in [4], where all data about the geometry, masses, and periods can be found, as well as some design details for the fixed-based variant of the building (a_g = 0.35g). More detailed data about asymmetric variants can be found in [10]. For the purpose of this study, only one-directional asymmetry was introduced by moving the mass centre CM by 10% (A10), 20% (A20) or 30% (A30) of the larger floor plan dimension (L_x). The torsional to lateral frequency ratio (Ω_s) of the original (symmetric) superstructure amounts to 1.0.

4.2 Base isolation system

A widely used base isolation system, consisting of an orthogonal mesh of RC foundation beams and 24 identical round lead rubber bearings, was used. In order to verify the applicability of the proposed simplified N2 method, the stiffness of the isolator compound was intentionally varied so as to correspond to three different protection levels: a) "Hard" isolators (H), which cannot adequately protect the superstructure; b) Elastic limit or “normal” (N) isolators, which have been designed to bring the symmetric superstructure subjected to the design ground acceleration (a_g = 0.35g, soil class B and q = 1) exactly to the limit of its elastic range; c) "Soft" isolators (S), which could be actually used in practice. The used isolators are described in detail in [4]. The positions of individual isolators have been adjusted for the given eccentricity level of the superstructure (Figure 2) in order to ensure that the centre of the isolation system CI corresponds to the centre of mass of the superstructure CM. In this case, torsion is a consequence of the eccentricity between the CS and CM of the superstructure.

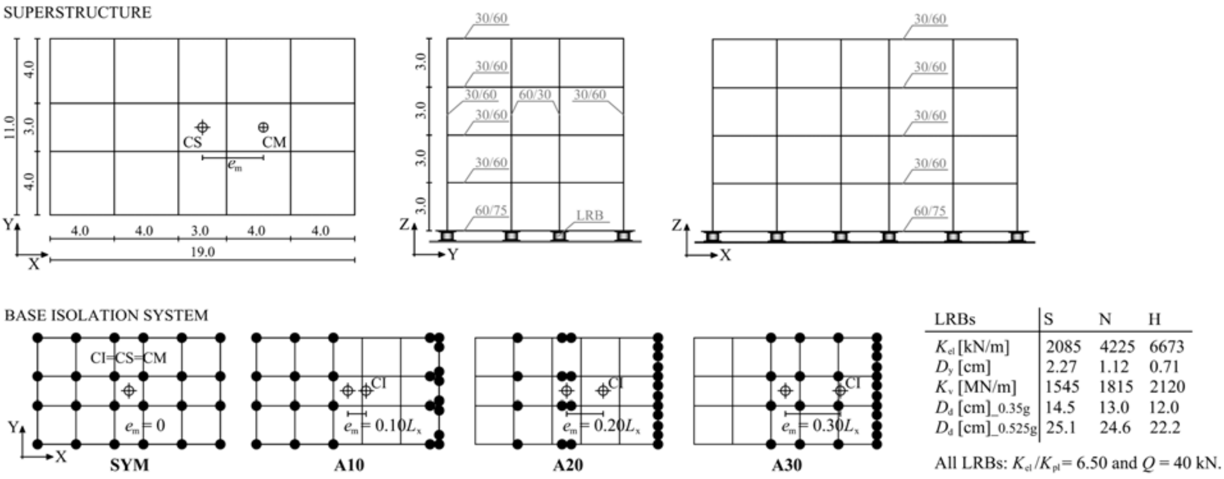

LRBs	S	N	H
K_{el} [kN/m]	2085	4225	6673
D_y [cm]	2.27	1.12	0.71
K_v [MN/m]	1545	1815	2120
D_d [cm]_0.35g	14.5	13.0	12.0
D_d [cm]_0.525g	25.1	24.6	22.2

All LRBs: $K_{el}/K_{pl} = 6.50$ and $Q = 40$ kN.

Figure 2: Geometry, basic characteristics and positions of LRBs for the analyzed structural variants.

4.3 Mathematical modeling and seismic ground motions

The nonlinear analyses were performed using the program SAP2000 (v12.0.1) [11]. The nonlinear behavior of the superstructure was modeled using bi-linear moment hinges without a load drop, located at both ends of each beam and column. An ensemble of seven accelerograms was used to represent the seismic action (2 from Friuli 1976, 3 from Montenegro 1979, 1 from Banja Luka 1981 and 1 from Vrancea 1986). The accelerograms were further modified to match the target EC8 [6] elastic spectrum for soil type B, scaled to a peak ground acceleration of $a_g = 0.35$g (considered as the design basis earthquake – DBE) and 0.525g (considered as the maximum credible earthquake – MCE). More detailed data about the used ground motion records can be found in [3, 4, 10]. Only uni-directional input has been considered where the N-S components of the accelerograms were applied in the Y direction of the building. For the pushover analyses three different lateral load distributions were investigated: (a) "triangular"; (b) "1st mode"; and (c) "PSC" – the proposal of the Protective Systems Committee of SEAONC [12].

4.4 Comparison of selected top, base and relative displacements

The results are presented in terms of the maximum top, base and relative displacements of the base-isolated structure where the relative displacements of the superstructure were calculated as the maximum total difference between the top and base displacements (in NLDA they do not necessarily occur at the same time). Figures 3-6 present comparisons of the displacements and ductility factors obtained by the extended N2 method and NLDA for selected analyzed models. The displacements are presented as absolute values at the CM (u_{CM}), and as normalized values (u/u_{CM}) for the flexible and stiff sides, in order to present the effects of the torsional twist. In the presented results, the correction factor c_T was taken exactly as calculated from equation (6), taking into account the obtained top displacements.

Observing the displacements at the CM (Figures 3 and 4), it is evident that the softer isolators – as expected – result in larger top and base displacements and smaller relative displacements than the harder ones. It can be seen that the agreement between the results of NLDA and the ext. N2 method is fairly good, and within the standard deviation boundaries until the eccentricities of the superstructure do not exceed a certain level for selected type of isolator (approximately 20% for normal and 15% for hard type of isolator). For larger eccentricities, where much more damage occurs in the superstructure, all the displacements obtained by the ext. N2 method tend to be underestimated. The best results were obtained in the case of the 1^{st} and PSC distributions, which give similar results, whereas the results of triangular distribution tend to be underestimated, especially for the top and base displacements. Similar conclusions were obtained in the case of the symmetric base-isolated structures [3, 4].

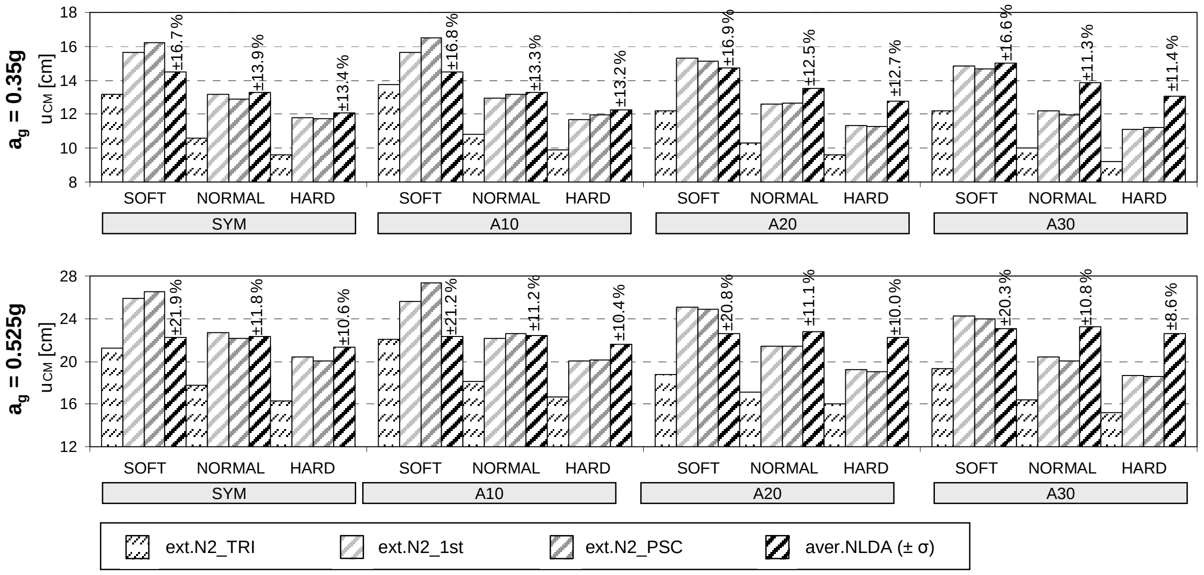

Figure 3: Top displacements (at the CM).

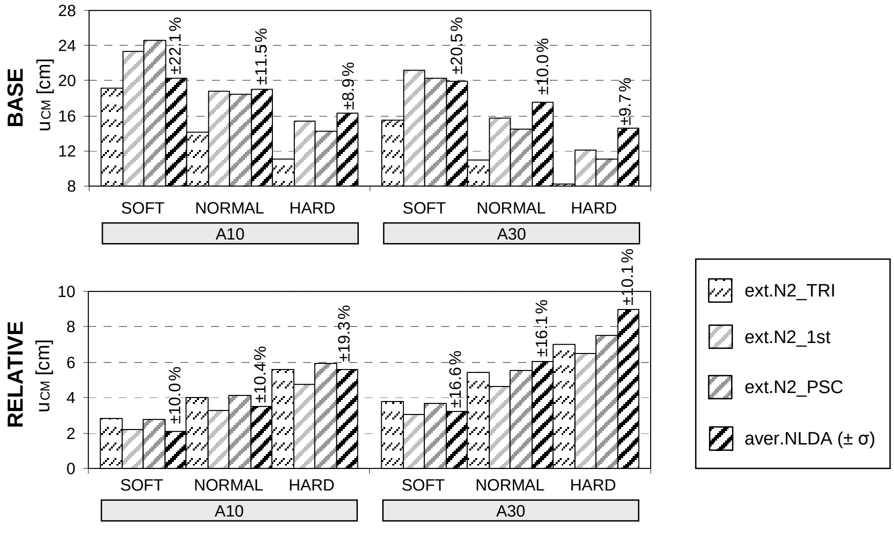

Figure 4: Base and relative displacements (at the CM) for a_g = 0.525g.

Observing the normalized displacements (Figure 5) it can be seen that, on the flexible side, the agreement with the results obtained by NLDA is very good; although it appears that the ext. N2 method slightly underestimates the demands for eccentricities equal to 20% or larger. The severest effects of torsion were observed in the case of the harder types of isolators. The amplification factors are in very good correlation with those obtained by NLDA. There is no significant difference between the lateral load distributions; however the best correlations with NLDA were obtained for the 1^{st} mode and PSC distribution.

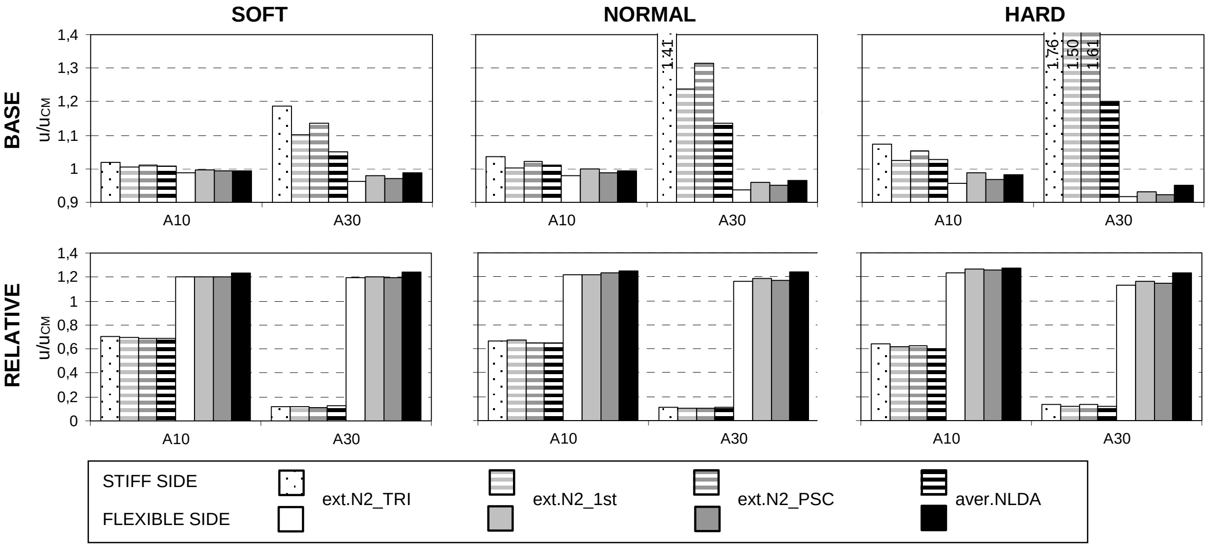

Figure 5: The torsional amplification factors for the base and relative displacements for $a_g = 0.525g$.

In Figure 6 the rotational ductility factors obtained by the ext. N2 method (for the PSC lateral load distribution) are presented and compared with the average ductility factors obtained by NLDA for $a_g = 0.525g$. The damage patterns are shown for all analyzed types of isolators but only for the A10 model and they are presented for the stiff as well as the flexible frames. It can be seen that there is more damage in the case of harder isolators, whereas in the case of soft isolators the structure practically remains elastic (ductility < 1.0). In all the analyzed cases, it turns out that the ext. N2 method is able to follow the spread of damage in the superstructure with sufficient accuracy. The agreement with the results obtained by NLDA is satisfactory, and the results obtained by the ext. N2 method remain conservative for presented eccentricity (A10). In the case of larger eccentricities, however, it was shown that the ductility factors (damage patterns) obtained by the ext. N2 method may slightly underestimate the response of the superstructure. In all cases the obtained correction factors (c_T) have values which are close to 1.0, which means that in all these cases the usual 3D pushover analysis would give similarly good results.

In the presented case study we have analyzed the base isolation system with the CI corresponding to the CM and we have treated the frame in the vertical plane passing through the CM as the plane under observation where also the horizontal loads for pushover analysis have been applied. In general, the distribution of the isolators could be also asymmetric where the CI does not correspond to the CM. In our previous studies we have found out that the distribution CI=CS or even CI=-CM are even more effective for the protection of the superstructure because they minimize the rotations of the superstructure [10]. In those cases where the CI does not correspond to the CM, we have proposed that the loads for pushover analysis should be applied at the plane through the mid-point between the CI and the CM (Figure 7) where also all quantities should be observed [9]. The point of application of the lateral loads might be eventually also determined with higher accuracy considering additional influencing parameters, but here we should be also aware of the limitations of simplified methods to follow all the changes of parameters in complex dynamic nonlinear 3D structural response.

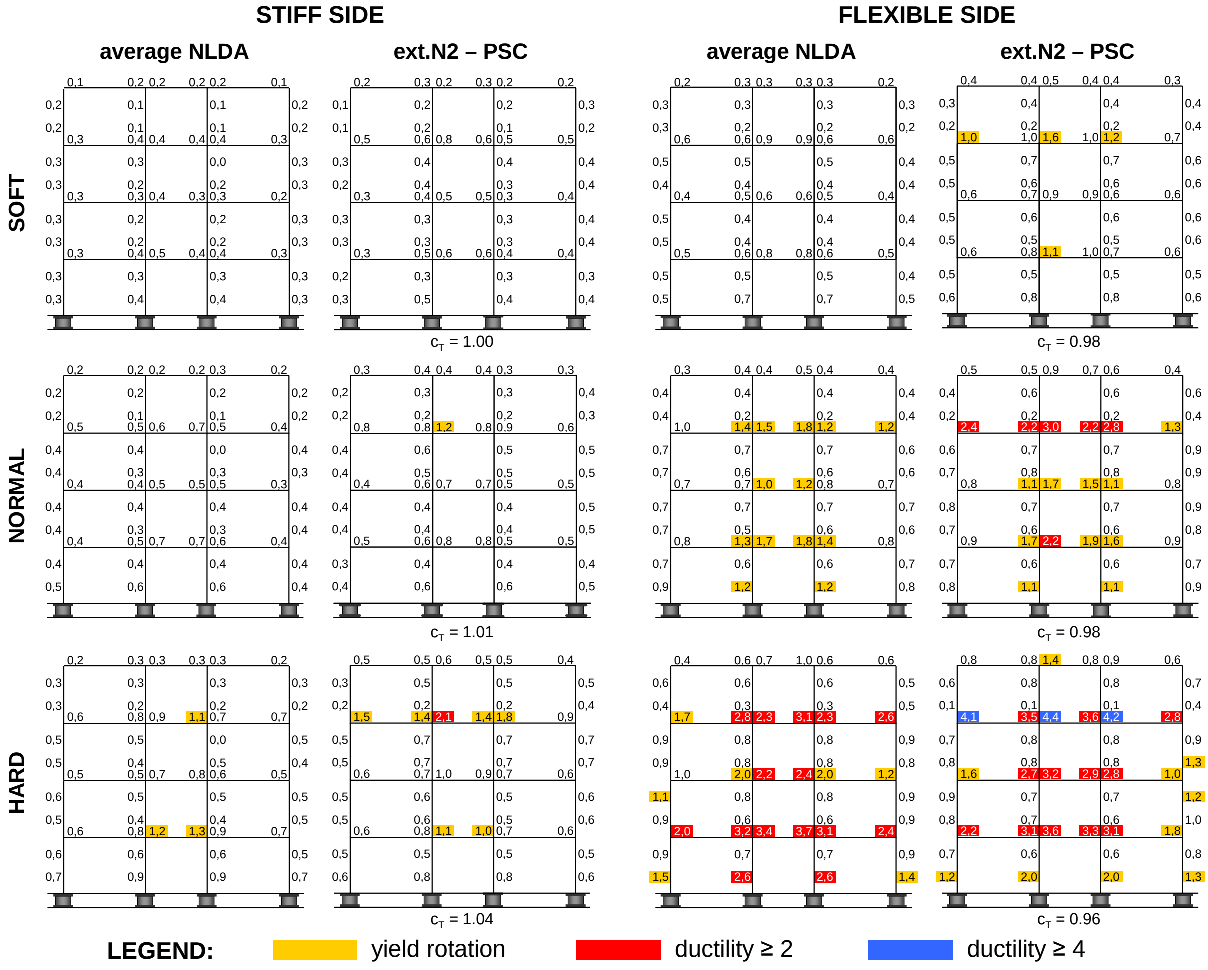

Figure 6: Maximum ductility factors for the stiff and flexible side, for the model A10 and a_g = 0.525g.

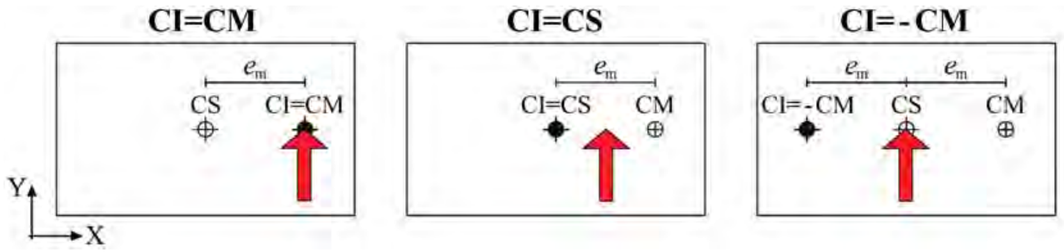

Figure 7: Points (vertical plane) of lateral load application in case of different positions of the center of the isolation system (CI).

5 CONCLUSIONS

It was found that the proposed N2 method procedure provides results which are in very good agreement with the results obtained by NLDA, if the eccentricity of the superstructure is moderate (e.g. in extreme cases limited to approximately e_m = 20%). In case of larger eccentricities all the displacements obtained by the ext. N2 method tend to be underestimated, especially in the cases with harder isolators, where the superstructure is exposed to deeper nonlinear behavior and consequently, the centre of stiffness of the superstructure (CS) is shifted towards the stiff side. The influence of different lateral load distributions and the effect of the ground motion intensities on the torsional amplifications were shown not to be very important. However, the distribution with additional force at the base (PSC) tends to work better, while the triangular load distribution seems less appropriate. For the analyzed CI=CM distribution of the isolators, the usual 3D pushover analysis yields good results, and the usage of the correction factor c_T is not absolutely necessary. The originally proposed ext. N2 method requires that the corrected displacement on the stiff side should not be taken smaller as in CM. For base-isolated structures this requirement leads toward a considerable overestimation of displacements on the stiff side, which is, however, on the conservative side.

REFERENCES

[1] P. Fajfar, A nonlinear analysis method for performance-based seismic design. *Earthquake Spectra,* **16** (3): 573-592, 2000.

[2] P. Fajfar, D. Marušić, I. Peruš, Torsional effects in the pushover-based seismic analysis of buildings. *Journal of Earthquake Engineering,* **9** (6): 831-854, 2005.

[3] V. Kilar, D. Koren, Seismic assessment of base isolated structures using N2 method. M. Papadrakakis, N.D. Lagaros, M. Fragiadakis eds. *2nd International Conference on Computational Methods in Structural Dynamics and Earthquake Engineering (COMPDYN 2009 - ECCOMAS Thematic Conference),* Rhodes, Greece, June 22-24, 2009.

[4] V. Kilar, D. Koren, Simplified inelastic seismic analysis of base-isolated structures using the N2 method. *Earthquake Engineering and Structural Dynamics,* **39** (9), 967-989, 2010.

[5] M. Nakashima, K. Saburi, B. Tsuji, Energy input and dissipation behaviour of structures with hysteretic damping. *Earthquake Engineering and Structural Dynamics,* **25** (5), 483-496, 1996.

[6] CEN, European Committee for Standardization, *EN-1998-2 – Eurocode 8: Design of structures for earthquake resistance. Part 1: General rules, seismic actions and rules for buildings.* 2005.

[7] A.K. Chopra, *Dynamics of structures: theory and applications to earthquake engineering.* Prentice-Hall, Ltd., 1997.

[8] D. Koren, V. Kilar, Simplified seismic analysis of asymmetric base isolated frame buildings using the N2 method. Proceedings 14th European Conference on Earthquake Engineering (14ECEE), Ohrid, Macedonia, 30 Aug – 3 Sep, 2010.

[9] D. Koren, V. Kilar, The applicability of the N2 method to the estimation of torsional effects in asymmetric base-isolated buildings. *Earthquake Engineering and Structural Dynamics,* **(in press)**, 2010.

[10] V. Kilar, D. Koren, Seismic behaviour of asymmetric base isolated structures with various distributions of isolators. *Engineering Structures,* **31** (4), 910-921, 2009.

[11] CSI Computer & Structures Inc., *SAP 2000: Linear and nonlinear static and dynamic analysis and design of three-dimensional structures.* Computer & Structures, Inc., Berkeley, California, 2008.

[12] Structural Engineers Association of Northern California (SEAONC), *Tentative Seismic Isolation Design Requirements.* San Francisco, California, 1986.

COMPDYN 2011
3rd ECCOMAS Thematic Conference on
Computational Methods in Structural Dynamics and Earthquake Engineering
M. Papadrakakis, M. Fragiadakis, V. Plevris (eds.)
Corfu, Greece, 25–28 May 2011

Evaluation of a Modified-SSAP in estimating seismic demands of a torsionaly flexible building

Mohammad Ebrahimi K.[1*], **Abdoreza S. Moghadam**[2]

[1]Science and Research Branch, Islamic Azad University
Simoonbolivar Blvd.,Poonak, Tehran, Iran
Mohammad.ebrahimi.k@gmail.com

[2]International Institute of Earthquake Engineering and Seismology (IIEES)
South Dibaji St., Farmaniye, Tehran, Iran
moghadam@iiees.ac.ir

Keywords: Torsinaly flexible, asymmetric buildings, SSAP, Modified-SSAP

Abstract. *Storey Shear-Based Adaptive Pushover (SSAP) procedure has originally been developed for estimating seismic demands of planar frames. An extension and modification of the SSAP, has recently been proposed to estimate seismic demands of asymmetric buildings, represented by a 3D structural model. In order to investigate the capability of the proposed Modified-SSAP in severe mass asymmetric buildings, in the current paper, the method is evaluated for a 12-story asymmetric reinforced concrete moment resisting building with a torsionaly dominant fundamental natural mode, representing torsionaly flexible buildings. Results of the storey drift predictions of the Modified-SSAP are compared with Nonlinear Response History Analysis (NRHA) as well as estimations of the well-known Modal Pushover Analysis (MPA) procedure, subjected to a set of seven near-field ground motions. Alternative correction factors for the target displacement to improve the results are also examined. An acceptable compatibility of storey drift estimations of pushover procedures is observed, while Modified-SSAP is more compatible with the results of rigorous NRHA when proper correction factors for the target displacement are applied.*

1 INTRODUCTION

Conventional pushover analysis procedures are based on the assumption that the structure predominantly vibrates in a single mode. This assumption is not straightforward particularly for tall and irregular buildings. In recent years many attempts has been made worldwide to take the higher modes effects and the changes of modal characteristics into consideration while structure responds in inelastic range. Many of the proposed methods enjoy from strong theoretical background and acceptable degree of accuracy. However, they have merely been introduced to estimate seismic demands of planar frames. In this respect, development of the nonlinear static methods, originally for planar frames, so that are able to analysis of irregular building represented by 3D structural model has been considered. Backed by an extensive range of studies N2 method [1] has been extended for asymmetric buildings based on the assumption that torional effects in the elastic and inelastic domains are very close and mostly overestimated by an elastic analysis [2]. The well-known modal pushover analysis [3] has also been developed for asymmetric building [4] by extending the formulations in accordance with dynamics of structures theories. An alternative of conventional capacity spectrum method in an adaptive framework [5] has also been proposed another indication of development of conventional methods.

Storey Shear-Based Adaptive Pushover (SSAP) originally has been proposed for planar frames taking into account reversal signs of applied load pattern as well as changes in modal attribute within inelastic range [6]. In this paper an extension of the SSAP introduced first in [7] has been summarized. The extension has been done through extending the formulations based on structural dynamics theory. Modifications for load pattern and target displacement have also been proposed [7] which are currently in their premature stages of development. In the current study, a torsionaly flexible 12 storey building subjected to uni-directional excitation is validated by extended SSAP. Proposed Modifications of load pattern and target displacement are further evaluated for the example building when standard design spectrum is utilized in the algorithm of the method. Therefore the accuracy of the method is investigated by using standard design spectrum instead of individual spectrum.

2 SUMMARY OF THE EXTENDED SSAP METHOD

The overall trend of the procedure is similar to its original for planar frames developed by Shakeri et al. [6], except the fact that formulations have been converted to three dimensional based on the concepts of structural dynamic. Extended story shear-based adaptive pushover analysis to asymmetric plan buildings under uni-directional excitation can be summarized in the following steps:

Step 1: Create a 3D structural model incorporating nonlinear material characteristics.
Step 2: Perform a nonlinear static analysis to consider gravity loads on the structure.
Step 3: Compute instantaneous natural frequencies, ω_n and mode shapes, $\emptyset_n$ by performing an eigenvalue analysis using the current stiffness characteristics of the structure.
Step 4: For a selected number of modes considered, compute modal story forces and torques associated with the global x,y, and z directions using the following equation:

$$\boldsymbol{f}_{nx} = \Gamma_n \boldsymbol{\phi}_{nx} \boldsymbol{m} A_n \qquad \boldsymbol{f}_{ny} = \Gamma_n \boldsymbol{\phi}_{ny} \boldsymbol{m} A_n \qquad \boldsymbol{f}_{n\theta} = \Gamma_n \boldsymbol{\phi}_{n\theta} \boldsymbol{I}_o A_n \tag{1}$$

Where $\boldsymbol{f}_{nx}$and $\boldsymbol{f}_{ny}$ are the vectors of modal story forces, $\boldsymbol{f}_{n\theta}$ is the vector of torsional moments at each floor diaphragm. $\boldsymbol{\phi}_{nx}$, $\boldsymbol{\phi}_{ny}$, and $\boldsymbol{\phi}_{in\theta}$ are three sub vectors of the n-th instantaneous translational and torsional natural mode shapes associated with x, y, and z directions, respectively. A_n is the ordinate $A(T_n, \xi_n)$ of the earthquake pseudo-acceleration response spectrum for the n-th mode single degree of freedom system. $\boldsymbol{m}$ is the diagonal sub matrix of the global mass matrix, $\boldsymbol{M}$, with $m_{ii} = m_i$, the lumped mass at the i-th floor diaphragm:

$$\boldsymbol{M} = \begin{Bmatrix} \boldsymbol{m} \\ \boldsymbol{m} \\ \boldsymbol{I}_o \end{Bmatrix} \tag{2}$$

$\boldsymbol{I}_o$ is a diagonal matrix with $I_{ii} = I_{oi}$, the polar moment of inertia of the i-th floor diaphragm about a vertical axis through the center of mass. Γ_n is the modal participation factor obtained as the following:

$$\Gamma_n = \frac{L_n}{M_n} \qquad M_n = \boldsymbol{\phi}_n^T \mathbf{M} \boldsymbol{\phi}_n \qquad L_n = \begin{cases} \boldsymbol{\phi}_{xn}^T \mathbf{m1} & for\ \ddot{u}_{gx}(t) \\ \boldsymbol{\phi}_{yn}^T \mathbf{m1} & for\ \ddot{u}_{gy}(t) \end{cases} \tag{3}$$

Step 5: Calculate modal story shears of x and y directions and summation of torsional moments of the considered story and all upper storeys:

$$SS_{inx} = \sum_{k=i}^{N} f_{knx} \qquad SS_{iny} = \sum_{k=i}^{N} f_{kny} \qquad SM_{in\theta} = \sum_{k=i}^{N} f_{kn\theta} \tag{4}$$

Step 6: Combine the story shear forces and torsions obtained by Eq. (4) using modal combination rules such as SRSS and CQC to define forces and torsional moment of each floor diaphragm. In this study the SSRS rule has been used because of its simplicity as the following:

$$SS_{ix} = \sqrt{\sum_{n=1}^{m} {SS_{inx}}^2} \qquad SS_{iy} = \sqrt{\sum_{n=1}^{m} {SS_{iny}}^2} \qquad SM_{i\theta} = \sqrt{\sum_{n=1}^{m} {SM_{in\theta}}^2} \tag{5}$$

Step 7: Define the amount and sign of the incremental load pattern, including forces in translational directions and torsional moments about a vertical axis through the center of mass, by subtracting the consecutive story shears and moments:

$$\begin{array}{llll} F_{ix} = SS_{ix} - SS_{(i+1)x} & F_{iy} = SS_{iy} - SS_{(i+1)y} & F_{i\theta} = SM_{i\theta} - SM_{(i+1)\theta} & i = 1,2,\dots,(i-1) \\ F_{Nx} = SS_{Nx} & F_{Ny} = SS_{Ny} & F_{N\theta} = SM_{N\theta} & i = N \end{array} \tag{6}$$

Step 8: Use any appropriate quantity to normalize the lateral load patterns. As an alternative lager value of the base shear associated with x and y directions can be taken for normalizing the lateral loads pattern using the following equations:

$$V = \max\left(\sum F_{ix}\ , \sum F_{iy}\right) \tag{7}$$

$$\bar{F}_{ix} = \frac{F_{ix}}{V} \qquad \bar{F}_{iy} = \frac{F_{iy}}{V} \qquad \bar{F}_{i\theta} = \frac{F_{i\theta}}{V} \tag{8}$$

Step 9: Consider an incremental base shear and multiply it to the normalized lateral loads pattern to obtain forces and torques which are applied in each step to each floor diaphragm:

$$\Delta F_{ix} = \Delta V_b \times \bar{F}_{ix} \qquad \Delta F_{iy} = \Delta V_b \times \bar{F}_{iy} \qquad \Delta F_{i\theta} = \Delta V_b \times \bar{F}_{i\theta} \tag{9}$$

Where ΔV_b is the incremental base shear and ΔF_{ix} , ΔF_{iy} , $\Delta F_{i\theta}$ are the i-th components of the incremental applied loads at each step.

Step 10: Apply the scaled incremental load profile (Eq. 9) to the structural model considering $P - \Delta$ effects; compute displacements, inter-story drifts, element forces, etc.

Step 11: compute the assumed fundamental mode shape vector for step k employing the following equation:

$$\emptyset^{\mathrm{k}} = \mathbf{M}^{-1}\boldsymbol{F}^{k} \tag{10}$$

Where k denotes the step number, $\emptyset^{\mathrm{k}}$ is the assumed mode shape at step k, $\mathbf{M}^{-1}$ is the inverse of the global mass matrix, and $\boldsymbol{F}^{k}$ is vector of total forces applied up to the step k, consisting of three sub vectors, as it is shown by Eq. 11.

$$\boldsymbol{F}^{\boldsymbol{k}} = \begin{Bmatrix} \boldsymbol{F}_x^k \\ \boldsymbol{F}_y^k \\ \boldsymbol{F}_{\boldsymbol{\theta}}^k \end{Bmatrix} \tag{11}$$

Step 12: Based on the assumed fundamental mode shape (Eq. 10), convert base shear of the Multi Degree Of Freedom (MDOF) system to the equivalent force of the Single Degree Of Freedom (SDOF) system using the following equation:

$$F^* = S_a = \frac{V_b}{M^*} \tag{12}$$

Where F^* is the equivalent force of the SDOF system, V_b is the base shear of the applied forces in the direction of excitation, and M^* is the effective modal mass considering the mode shape acquired by Eq. (10).

Step 13: Calculate the equivalent displacement of the SDOF system by means of an energy concept using Eqs. (13) to (15).

$$\sum_{i=1}^{N}\left(\left(F_i^{(k-1)} + \frac{1}{2}dF_i^{(k)}\right) \times \Delta d_i^k\right) = \left(\sum_{i=1}^{N}\left(F_i^{(k-1)} + \frac{1}{2}dF_i^{(k)}\right)\right) \times \Delta D^k \tag{13}$$

$$\Delta D^{(k)} = \sum_{i=1}^{N}\left(\left(F_i^{(k-1)} + \frac{1}{2}dF_i^{(k)}\right) \times \Delta d_i^k\right) / \left(\sum_{i=1}^{N}\left(F_i^{(k-1)} + \frac{1}{2}dF_i^{(k)}\right)\right) \tag{14}$$

$$D^{(k)} = D^{(k-1)} + \Delta D^k \tag{15}$$

where $F_i^{(k-1)}$: the existing story force in the direction of excitation at the end of step $k - 1$, $dF_i^{(k)}$: incremental applied force in the story i at step k, Δd_i^k: incremental displacement of the story i in the direction of the excitation due to increased applied load at step k, ΔD^k: incremental displacement of the equivalent SDOF system at step k, $D^{(k)}$ displacement of the equivalent SDOF system at step k.

Step 14: Go back to step 3 and repeat the process until an extreme value of base shear is achieved or the structure fails.
Step 15: Develop the Force-Displacement curve, ($F^* - D$ curve) of equivalent inelastic SDOF system with unit mass based on the computed values in steps 12 and 13 in the previous cycles and idealize it as a bilinear curve.
Step 16: compute the peak inelastic displacement of the equivalent SDOF system by performing a nonlinear time history analysis to obtain the target displacement. Alternatively, target displacement can be computed by plotting the capacity curve (i.e. $F^* - D$ curve) against the inelastic acceleration-displacement response spectra.
Step 17: Determine the corresponding step to the target displacement in the pushover procedure and obtain the interested pseudo seismic demands.

3 DESCRIPTION OF PARAMETRIC STUDIES

3.1 Structural system

A twelve-storey moment resisting concrete frame has been selected with a structural plan as shown in Fig. 1. A distance equal to 10% of the plan dimension has been considered between the centre of mass (CM) and centre of stiffness (CS). Since the first natural vibration mode of the structure is dominantly torsional the building is considered as a torsionaly flexible structure. Fig. 2 demonstrates the natural vibration modes of the structure. The building has been loaded as majority of common residential buildings are loaded in Iran. However, polar moment of inertia has been multiplied to represent a torsinaly flexible structure. Nonlinear behaviour of the structure occurs at discrete hinges at both ends of beam and column elements which were defined in accordance with provisions of FEMA356 [8]. First 10 natural vibration modes of the structure have been considered to implement the SSAP method.

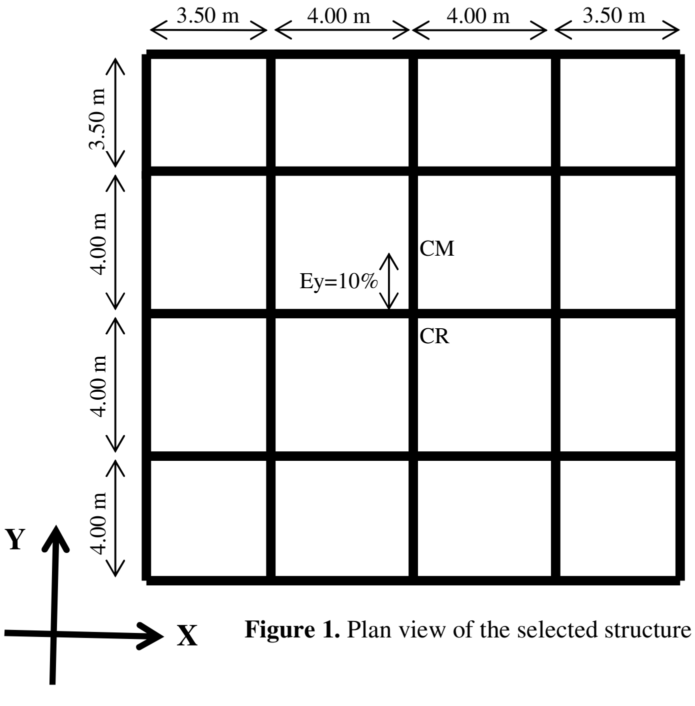

Figure 1. Plan view of the selected structure

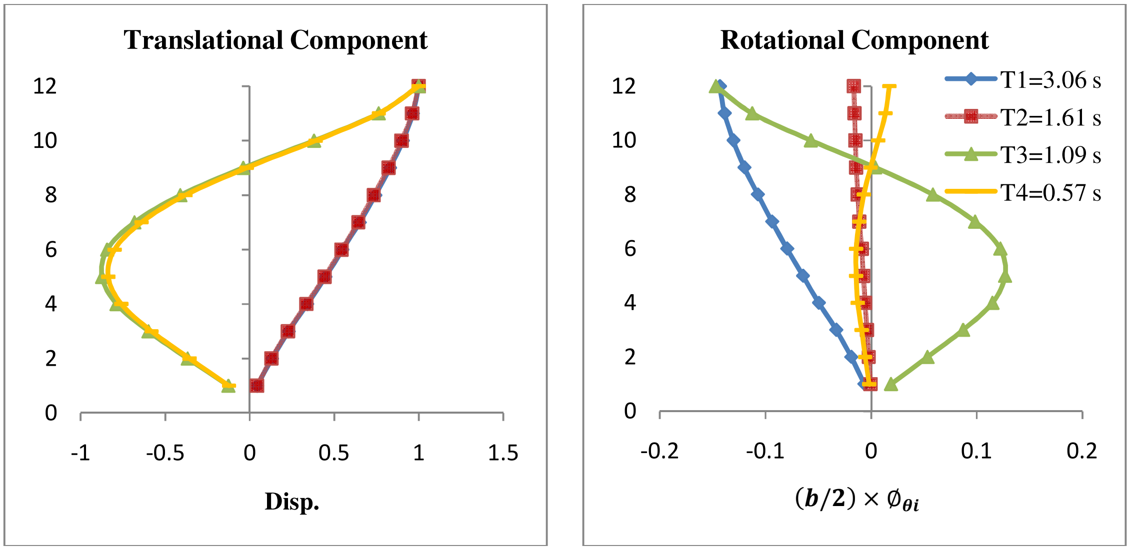

Figure 2. Natural periods and modes of vibration of the selected torsionaly flexible structure

3.2. Ground motions

The building is subjected to a set of seven near-field seismic actions in the X-direction where torsion occurs throughout the analysis. Table 1 depicts the ensemble of selected motions. In addition, Fig.3 depicts pseudo-acceleration response spectrum of the records along with the design response spectrum of FEMA356 [8] for site class D in a high seismic region having short period response spectral acceleration (S_s) equal to 2.05g and spectral acceleration response at a period of 1 (S_1) equal to 0.82g. In order to ensure that the building responds within the inelastic range, records have been scaled such that the acceleration response spectrum of individual records are identical to pseudo acceleration response spectrum of FEMA356 at the structural fundamental period.

Table-1. List of selected ground motions

Eq#	Earthquake	Magnitude (Mw)	Station name	Distance (km)	PGA (g)
1	Cape Mendocino 1992/04/25	7.1	89156 Petrolia	9.5	0.662
2	Coyote Lake 1979/08/06	5.7	47380 Gilroy Array #2	7.5	0.339
3	Erzincan, Turkey 1992/03/13	6.9	95 Erzincan	2.0	0.515
4	Northridge 1994/01/17 12:31	6.7	24279 Newhall - Fire Sta	7.1	0.59
5	Kobe 1995/01/16 20:46	6.9	0 Nishi-Akashi	11.1	0.509
6	N. Palm Springs 1986/07/08 09:20	6.0	5071 Morongo Valley	10.1	0.218
7	Gazli, USSR 1976/05/1	6.8	9201 Karakyr	Hypocentral (3.0)	0.718

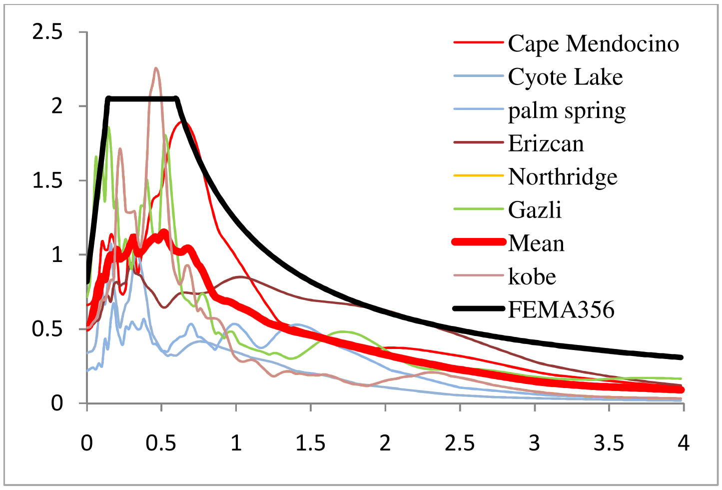

Figure 3. Pseudo-acceleration response spectrum of selected records along with the mean spectrum and FEMA356 design spectrum

4 RESULTS OF NUMERICAL STUDIES

4.1. SSAP method via FEMA356 standard spectrum

Previous studies conducted to validate the SSAP procedure and its extended form (e.g. [6] and [7]) have been done by utilizing response spectrum of individual records, i.e. response spectrum of each record is used for A_n in eq. 2.1. One the main purposes of the current paper is to make the SSAP more practical. In this regard, the response spectrum of FEMA356 [8] has been used for the SSAP method instead of utilising individual spectrum for each record. Therefore, seven NLRHA have been performed and storey drifts were compared to the results of SSAP. To compute the target displacement, NLRHA of equivalent single degree of freedom system has been done. Since SSAP is performed once for seven earthquakes, mean of maximum displacement response of the equivalent single degree of freedom system from NLRHA of seven ground motions is taken as the target displacement. Fig.4. demonstrates the storey drift predictions of the extension of SSAP method versus mean of NLRHA obtained from seven ground motions selected for the study. As it is indicated in the figure, SSAP estimates are fairly acceptable at lower storeys while results are markedly under estimated at the upper storeys up to a level of roughly 60 percent at both flexible and stiff edges of the plan.

4.2. Modified-SSAP method via FEMA356 standard spectrum

Modifications already been defined in [7] to improve results of the extended form of SSAP are evaluated in this section while design spectrum is used in the method. To find the best matched storey drift profiles between pushover analysis and NLRHA, correction factor of the load pattern is applied and target displacement amplification is then evaluated such that best results for the pushover are obtained. To modify the load pattern, applied force to the top level is amplified based on the instantaneous period of first natural vibration mode, i.e. eq. (9) is replaced by the following equation:

$$\begin{cases} \Delta F_{ix} = \Delta V_b \bar{F}_{ix},\ \Delta F_{iy} = \Delta V_b \bar{F}_{iy},\ \Delta F_{i\theta} = \Delta V_b \bar{F}_{i\theta} & i = 1,..,N-1 \\ \Delta F_{ix} = \Delta V_b \bar{F}_{ix}(1+0.9T_1),\ \Delta F_{iy} = \Delta V_b \bar{F}_{iy}(1+0.9T_1), \Delta F_{i\theta} = \Delta V_b \bar{F}_{i\theta}(1+0.9T_1) & i = N \end{cases} \quad (16)$$

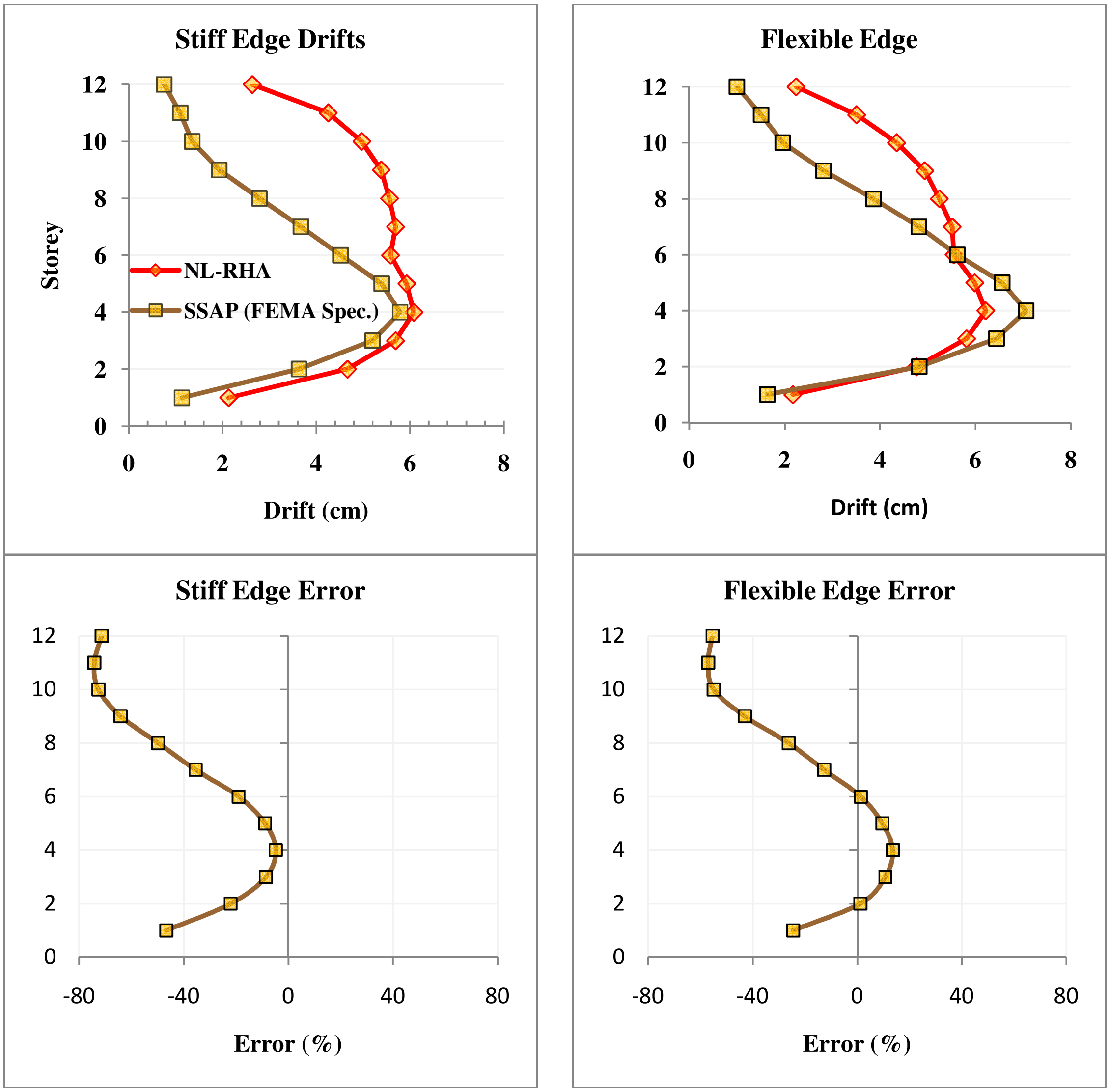

Stiff Edge Drifts

Flexible Edge

Stiff Edge Error

Flexible Edge Error

Figure 4. Height-wise storey drift predictions and errors of extended SSAP in comparision with mean of NLRHA from seven ground motions

where T_1 is instantaneous period of the first mode at each step obtained by stiffness characteristics of the structure at the end of the previous step.

As in the case of extended SSAP method described earlier, pushover analysis is performed once and the storey drift predictions of Modified-SSAP is compared with the mean of the results of NLRHA from seven ground motions. Figure 5 illustrates height-wise distribution of storey drifts in both flexible and stiff edges of the plan for SSAP when the modification factor of load pattern has been implemented in the algorithm. In order to be able to investigate the influence of the response spectrum shape in accuracy of the applied load pattern, depicted also in Figure 5 is a comparison of Modified-SSAP using FEMA356 spectrum as well as mean spectrum of the seven selected records. In both cases, target displacement correction factors have been multiplied which can lead to the best possible compatibility of the result compared to NLRHA. In this respect, correction factor 1.45 has been multiplied to target displacement

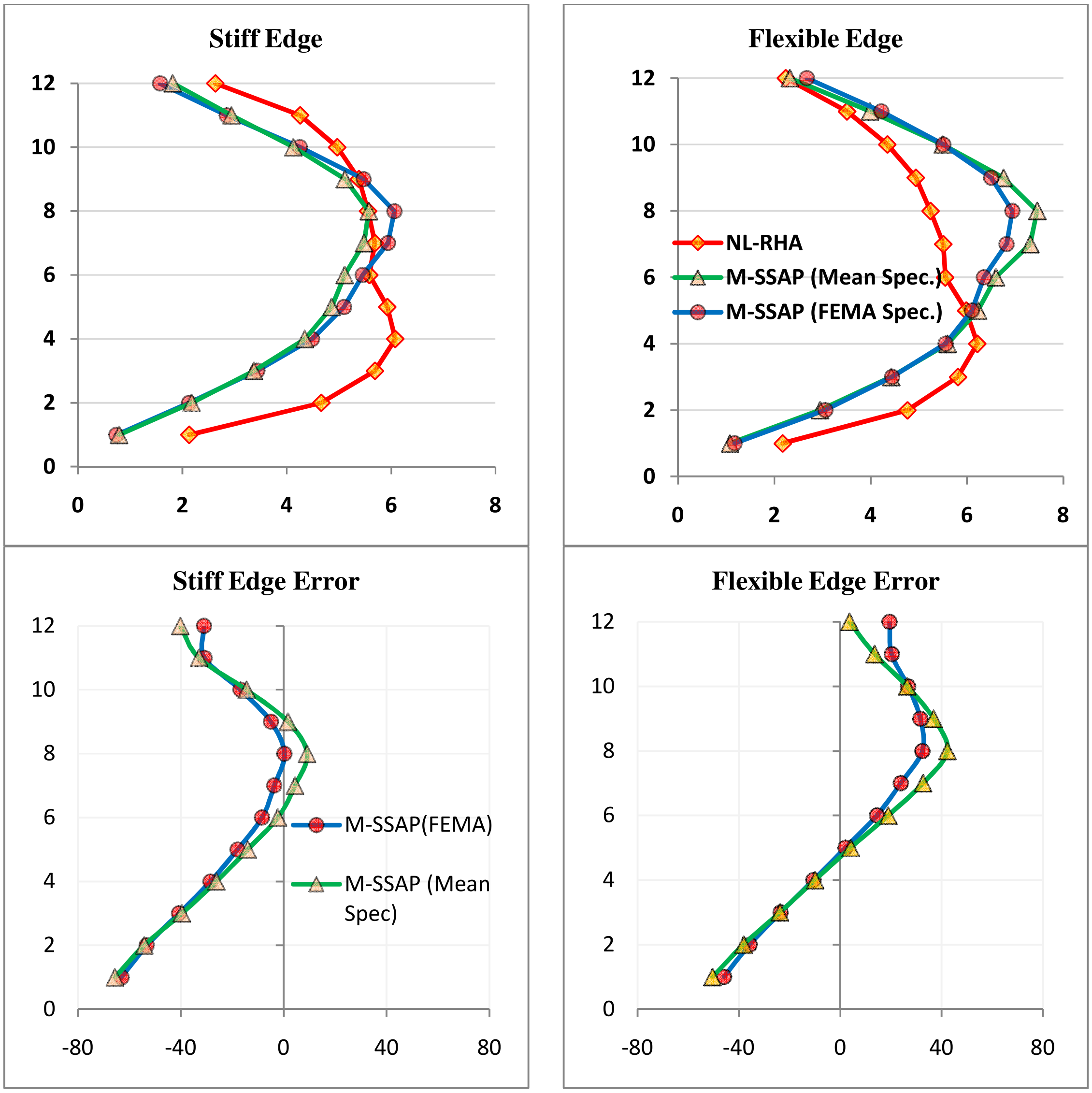

Figure 5. Height-wise storey drift predictions and errors of Modified- SSAP using mean as well as FEMA spectra in comparision with mean of NLRHA from seven ground motions

when the mean spectrum is used, and correction factor 1.5 has been used for the FEMA356 spectrum. Errors of the pushover analyses with respect to NLRHA have also been depicted in the figure. Clearly, it is expected to see much better results in the case where mean spectrum is utilised in the method. However a small difference is observed using two different spectra. This implies that design spectra can be used in the SSAP method while errors do not dramatically increase. The observation is important as far as the applicability of SSAP practically is concerned.

Comparison of figure 4 and 5 indicates that implication of modification of load pattern has been effective to improve the storey drift profile of the example building. Nevertheless, errors in the lower levels have been increased particularly in stiff edge. As it can be seen in the figure the little quantities of storey drifts in lower storey makes the errors larger while the differences are not very big. Therefore, definition of the error percentage as the ratio of drifts difference between pushover analysis and NLRHA should be taken into consideration.

5 CONCLUSIONS

A twelve storey building with torsinaly dominant fundamental natural mode was evaluated in the paper by extended SSAP and NLRHA. FEMA356 design spectrum was used in SSAP to investigate the applicability of design spectra in the procedure algorithm instead of utilizing individual records spectra. Relatively acceptable degree of compatibility of results was observed in lower levels while results deteriorated in upper storeys. Mutliplying the load pattern at the top storey by a factor related to the instantaneous period of the structure appeared to be effective to improve the compatibility of SSAP and NLRHA for the example building. However, modification factor leads to the underestimation of drift responses in lower storeys. Also, flexible edge estimates were better compatible to those of stiff edge. The impact of the selection of response spectrum on the accuracy of procedure seemed to be negligible.

Following the results of the example building studied in the paper, modifications of the original algorithm of the SSAP for planar frames looks to be a promising approach to improve the results of SSAP method. Needless to say that a very wide range of study is required to find most suitable correction factors for load pattern as well as target displacement.

REFERENCES

[1] Fajfar A Nonlinear Analysis Method for Performance Based Seismic Design. Journal of Earthquake Spectra,Vol. 16, No. 3, pp.573-592, 2000.

[2] Fajfar P, Marusic D, Perus I. Torsinal effects in the pushover-based seismic analysis of buildings. J Earthquake Eng 9(6):831-854, 2005.

[3] Chopra, AK. Goel, RK. A modal pushover analysis procedure for estimating seismic demands for buildings, *Earthquake Eng & Struct Dyn* 31:561-582, 2002.

[4] Chopra, AK. Goel, RK. A modal pushover analysis for estimate seismic demands for unsymmetric-plan buildings, *Earthquake Eng Struct Dyn* 33:903-927, 2004.

[5] Casarotti, C. Pinho, R. An adaptive capacity spectrum method for assessment of bridges subjected to earthquake action”, *Bull Earthquake Eng* 5:377-390, 2007.

[6] Shakeri, K. Shayanfar, MA. Kabeyasawa, T. A story shear-based adaptive pushover for estimating seismic demands of buildings, *Eng Struct* 32:174-183, 2010.

[7] Ebrahimi K., M. Moghadam AS. An enhanced pushover procedure for asymmetric buildings”, *Proceedings of the 14th European conference on earthquake engineering*, Ohrid, Macedonia, paper No. 455, 2010.

[8] FEMA356, Prestandard and commentary for the seismic rehabilitation of buildings, *FEMA356, Washington (DC) Federal Emergency Management Agency*, 2000.

COMPDYN 2011
3rd ECCOMAS Thematic Conference on
Computational Methods in Structural Dynamics and Earthquake Engineering
M. Papadrakakis, M. Fragiadakis, V. Plevris (eds.)
Corfu, Greece, 25–28 May 2011

COMPARATIVE ASSESSMENT ON MODELING APPROACHES FOR THE SEISMIC RESPONSE OF RC SHEAR WALLS

C. Stathi[1*], M. Fragiadakis[2], A. Papachristidis[1] and M. Papadrakakis[1]

[1] Department of Civil Engineering, NTUA, Iroon Polytechneiou 9, 15780, Zografou, Athens, Greece
e-mail: {cstathi, aristidi, mpapadra}@central.ntua.gr

[2] Department of Civil and Environmental Engineering, University of Cyprus, P.O. Box 20537, 1678 Nicosia, Cyprus
mfrag@mail.ntua.gr

Keywords: Shear Walls, Shear Deformations, Fiber Elements, RC Structures, Slender Walls.

Abstract. *Shear deformations may considerably affect the capacity and the failure mode of reinforced concrete members. Simplified beam-column models typically are not able to capture this effect and usually are suitable only for members that exhibit a flexure-dominated response. Modeling approaches of increasing complexity for the simulation of reinforced concrete shear walls are compared in this work. More specifically, we compare the common fiber beam element, a simplified fiber beam element based on the Timoshenko theory that considers separately shear and bending deformations and a third Timoshenko beam element where a multidimensional concrete law is used. The various approaches are discussed and compared against experimental results. It is worth noting that experiments implemented for the comparison exhibit different failure modes, flexural as well as shear failure. The numerical study provides an insight to the efficiency of the above methods in terms of computing demand, accuracy and ease of implementation.*

1 INTRODUCTION

Recent earthquakes have demonstrated that often reinforced concrete (RC) members fail under shear. Moreover, shear walls increase the stiffness and the deformation capacity of RC structures when subjected to inelastic cyclic deformations such as those imposed by strong seismic ground motions. Therefore, proper modeling of members of the effect of shear is essential for the seismic capacity assessment of RC structures.

Four alternative modeling approaches for the simulation of reinforced concrete frame members are here compared. The first approach is the common fiber-based beam element where shear effects are neglected. The second approach is also a fiber beam-column formulation, based on the Timoshenko theory. This element uses the fiber approach to capture bending and a separate shear force-shear strain relationship (V-γ) to capture the shear in the section level. Since separate laws are used for the fibers and the shear effect, this approach is called the “decoupled approach” [1, 2]. A more elaborate approach, also based on a Timoshenko fiber beam-column formulation, is adopted. In the latter case, a three-dimensional constitutive law for the concrete fibers is used, thus offering a full coupling between bending and shear strains [2, 3]. Our study includes also the Multiple-Vertical-Line-Element Model (MVLEM) approach as discussed by Massone and Wallace [4]. MVLEM is a macro-model element, able to incorporate important response parameters such as confinement, nonlinear shear behavior and migration of the neutral axis.

After a brief presentation of the models adopted, a comparative assessment on RC members subjected to different loading is presented. To evaluate the effectiveness and the reliability of the modeling approaches, our results are compared with available experimental data.

2 FINITE ELEMENT FORMULATIONS

The beam-column formulations implemented follow the force-based formulation, also known as flexibility formulation [5] for fiber-based, beam-column elements. Compared to displacement-based elements, this approach improves considerably the accuracy and the efficiency of the analysis [2, 3]. According to the force-based approach, the element flexibility matrix is calculated after integrating the section stiffnesses $\mathbf{k}_{\text{sec}}$, as:

$$\mathbf{F}_{\text{N}} = \left[\int_{-1}^{1} \mathbf{b}^{\text{T}}(\xi) \left[\mathbf{k}_{\text{sec}} \right]^{-1} \mathbf{b}(\xi)\, d\xi \right] \tag{1}$$

where $\mathbf{F}_{\text{N}}$ is the element flexibility matrix and $\mathbf{b}(\xi)$ is the force shape function matrix which calculates the section forces from the element forces. The element natural stiffness matrix is therefore calculated as:

$$\mathbf{K}_{\text{N}} = \left[\mathbf{F}_{\text{N}} \right]^{-1} \tag{2}$$

The element Cartesian stiffness is obtained from the expression:

$$\mathbf{K} = \mathbf{a}_{\text{N}}^{T} \mathbf{K}_{\text{N}} \mathbf{a}_{\text{N}} \tag{3}$$

where $\mathbf{a}_{\text{N}}$ contains algebraic calculations and relates the displacements in the local cartesian and the natural system. The section stiffness matrix $\mathbf{k}_{\text{sec}}$ of Equation (1) is obtained as the partial derivative of the section forces $\mathbf{D}_{\text{sec}}$ over the section deformations $\mathbf{d}_{\text{sec}}$, and is calculated as [2,3]:

$$\mathbf{k}_{sec} = \int_{A} \mathbf{a}_{S}^{T} \mathbf{C}\, \mathbf{a}_{s}\, dA \tag{4}$$

where $\mathbf{C}$ is the material constitutive matrix and $\mathbf{a}_{\text{s}}$ is the section strain distribution matrix.

$$\boldsymbol{\varepsilon}(\xi, y, z) = \mathbf{a}_s(y, z)\mathbf{d}_{\sec}(\xi) \tag{5}$$

More details about the fiber element formulation and the notation used above can be found in [2, 3].

2.1 Fiber element based on Euler-Bernoulli beam theory

The simplest force-based fiber element formulation (Bernoulli EB) is based on the Euler-Bernoulli assumption and therefore shear deformations are neglected. In this case, the section stiffness will be:

$$\mathbf{k}_{sec} = \int_A \mathbf{a}_{s,EB}^T \mathbf{C}\, \mathbf{a}_{s,EB}\, dA = \sum_{i=1}^{nfib} \begin{bmatrix} E_i A_i & -y_i E_i A_i & z_i E_i A_i \\ -y_i E_i A_i & y_i^2 E_i A_i & -y_i z_i E_i A_i \\ z_i E_i A_i & -y_i z_i E_i A_i & z_i^2 E_i A_i \end{bmatrix} \tag{6}$$

where **C** is a scalar and equal to the tangent Young modulus E_i of the i$^{\mathrm{th}}$ fiber, A_i is the area of the fiber, and y_i, z_i denote the coordinates of the fibers with respect to the centroid of the cross-section.

In Eq. (6) $\mathbf{a}_{\mathrm{s,EB}}$ is the section strain distribution matrix of Eq. (5) which here takes the form:

$$\mathbf{a}_{s,EB}(y, z) = \begin{bmatrix} 1 & -y & z \end{bmatrix}. \tag{7}$$

2.2 Decoupled fiber element

This model consists of a shear spring connected in series with a beam-column element. This idea was initially presented by Marini and Spacone [1]. In order to take into consideration shear strains, a phenomenological *V-γ* shear law is implemented at the section level, and therefore the shear strains are uncoupled from axial and bending strains. This is a simplifying assumption that maintains all the advantages of fiber elements in terms of robustness and simplicity of the material laws adopted. The section stiffness will be:

$$\mathbf{k}_{sec} = \begin{bmatrix} \mathbf{k}_{\sec}^{EB} & 0 & 0 \\ \mathbf{0} & dV_y / d\gamma_{xy} & 0 \\ \mathbf{0} & 0 & dV_z / d\gamma_{xz} \end{bmatrix}. \tag{8}$$

where $\mathbf{k}_{\sec}^{EB}$ is the stiffness matrix of Eq. (6) and *dV/dγ* is the slope of the *V-γ* relationship.

A bilinear or a trilinear *V-γ* relationship can be used as discussed in a following section. In the linear elastic range *dV/dγ* is equal to the product of the shear modulus times the area of the section (*GA*). It is noted that since this approach (Decoupled TB) is based on the Timoshenko assumption, the elastic stiffness of the element is different than that of the Euler-Bernoulli case.

2.3 Shear-Deformable fiber element

Compared to the previous two elements this is a more elaborate formulation that considers the axial-moment-shear interaction. In this case the material matrix **C** has dimensions 3×3 and is given by the expression:

$$\mathbf{C} = \frac{\partial \boldsymbol{\sigma}}{\partial \boldsymbol{\varepsilon}} = \begin{bmatrix} C_{11} & C_{12} & C_{13} \\ C_{21} & q_y C_{22} & C_{23} \\ C_{31} & C_{32} & q_z C_{33} \end{bmatrix}. \tag{9}$$

In Eq. (9) in order to take into consideration that the shear stresses are not constant throughout the section, as Timoshenko beam theory assumes, the scaled shear stress distribution factors q_y, q_z are introduced. Moreover, the section strain distribution matrix of Eq. (5) takes the form:

$$\mathbf{a}_s(y,z) = \begin{bmatrix} 1 & -y & z & 0 & 0 \\ 0 & 0 & 0 & 1 & 0 \\ 0 & 0 & 0 & 0 & 1 \end{bmatrix} = \begin{bmatrix} \mathbf{a}_{s,EB} & 0 & 0 \\ \mathbf{0} & 1 & 0 \\ \mathbf{0} & 0 & 1 \end{bmatrix}. \tag{10}$$

Eq. (10) leads to the section stiffness matrix:

$$\mathbf{k}_{sec} = \int_A \mathbf{a}_s^T \mathbf{C}\, \mathbf{a}_s dA = \sum_{i=1}^{nfib} \begin{bmatrix} C_{11}^i \mathbf{a}_{s,EB}^T \mathbf{a}_{s,EB} & C_{21}^i \mathbf{a}_{s,EB} & C_{31}^i \mathbf{a}_{s,EB} \\ C_{21}^i \mathbf{a}_{s,EB}^T & q_y C_{22}^i & C_{23}^i \\ C_{31}^i \mathbf{a}_{s,EB}^T & C_{32}^i & q_z C_{33}^i \end{bmatrix}. \tag{11}$$

where y and z are the coordinates of an arbitrary point in the section.

Complicated materials are often described in the 3D continuum, thus hampering their application to structural elements such as beams, plates or shells. In order to incorporate a 3D material law we impose a condition of transverse equilibrium at every monitoring section [6].

$$\sigma_{y,c} A_{y,c} + \sigma_{y,s} A_{y,s} = 0 \Leftrightarrow \sigma_{y,c} + \rho_v \sigma_{y,s} = 0\ . \tag{12}$$

where $\sigma_{y,c}$ and $\sigma_{y,s}$ are the stresses developed in the concrete and the stirrups respectively, $A_{y,c}$ and $A_{y,s}$ are the area of concrete and the stirrups, respectively, in the monitoring vertical section and ρ_v is the shear reinforcement ratio.

2.4 The Multiple-Vertical-Line-Element Model approach

The generic Multi-Vertical-Line-Element model (Figure 1) consists of a series of truss elements (or macro-fibers) connected to infinitely rigid beams at their top and bottom. The number of truss elements can be increased to obtain a more refined description of the wall cross section. The shear response of the wall element is simulated with a horizontal spring, as originally suggested by Vulcano *et al.* [7].

The relative rotation between the top and bottom end of the wall element occurs around a point placed on the central axis of the element at height $h_c = c \times h$, where h is the height of the shear wall. A suitable value of parameter c is based on the expected curvature distribution along the element height. Although an accurate assessment of c is not necessary, if we use a moderate number of MVLEM elements within the yielding region are used, a value of c=0.4 is recommended based on experimental results [8, 9].

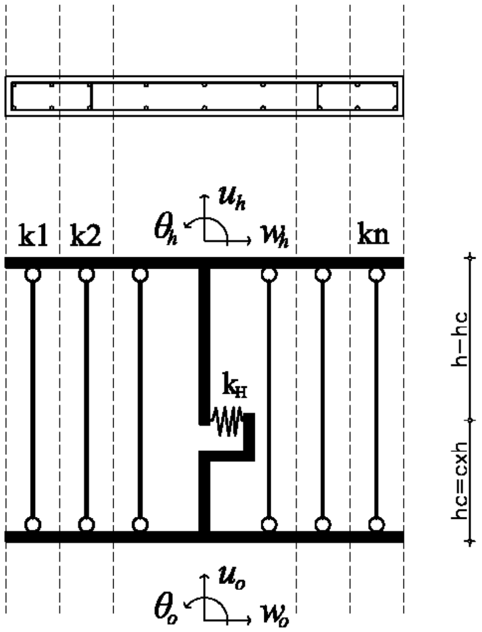

Figure 1: Schematic representation of the MVLEM.

The shear wall is modeled as a stack of *m* elements, placed one upon the other [4, 8]. A single two-dimensional MVLEM has 6 degrees of freedom, located at the center of the rigid beams of its top and its bottom cross-sections (Figure 1). In order to calculate the strains of the truss elements, it is assumed that the top and bottom sections remain plane. The stiffness matrix of an MVLEM element, will be:

$$\mathbf{K}_e = \mathbf{e}^T \mathbf{K} \mathbf{e} \,. \tag{13}$$

where **e** is a transformation matrix used to extract the extension and the relative rotations at the two ends from the element Cartesian degrees of freedom (Figure 1). The transformation matrix **e** is given by the formula:

$$\mathbf{e} = \begin{bmatrix} 0 & -1 & 0 & 0 & 1 & 1 \\ -1/h & 0 & 1 & 1/h & 0 & 0 \\ -1/h & 0 & 0 & 1/h & 0 & 1 \end{bmatrix} \tag{14}$$

and the element stiffness matrix $\mathbf{K}_e$ of Eq. 14 will be:

$$\mathbf{K} = \begin{bmatrix} \sum_{i=1}^{n} k_i & -\sum_{i=1}^{n} k_i x_i & \sum_{i=1}^{n} k_i x_i \\ -\sum_{i=1}^{n} k_i x_i & k_H c^2 h^2 + \sum_{i=1}^{n} k_i x_i^2 & k_H c(1-c) h^2 - \sum_{i=1}^{n} k_i x_i^2 \\ \sum_{i=1}^{n} k_i x_i & k_H c(1-c) h^2 - \sum_{i=1}^{n} k_i x_i^2 & k_H (1-c)^2 h^2 + \sum_{i=1}^{n} k_i x_i^2 \end{bmatrix} \tag{15}$$

where k_H is the stiffness of the horizontal spring, k_i is the stiffness of the i^{th} truss element and x_i is the distance of the i^{th} truss element to the central axis of the MVLEM element.

3 MATERIAL MODELS

The uniaxial stress-strain relationship used for the concrete fibers follows the modified Kent and Park model [10]. In the coupled shear-deformable fiber element where a 3D material law is necessary, the same relationship for each of the principal axes is adopted, while in order to take fracture into consideration, a three-dimensional rotating crack model is employed [2, 3]. Although this is not strictly a multidimensional concrete law, this approach is able to yield robust results of increased accuracy. The hysteretic response of reinforcing steel follows according to the stress–strain relationship proposed by Menegotto and Pinto [11], as extended by Filippou *et al.* [12] to include isotropic strain hardening.

When a shear *V-γ* law is used for the decoupled–shear deformable beam element, a bilinear curve is defined. Two different approaches for calculating the *V-γ* law were examined. The first approach is based on the shear law proposed by Gerin and Adebar [13] and the second approach is discussed in Mergos and Kappos [14]. The two different *V-γ* curves are shown in Figure 2.

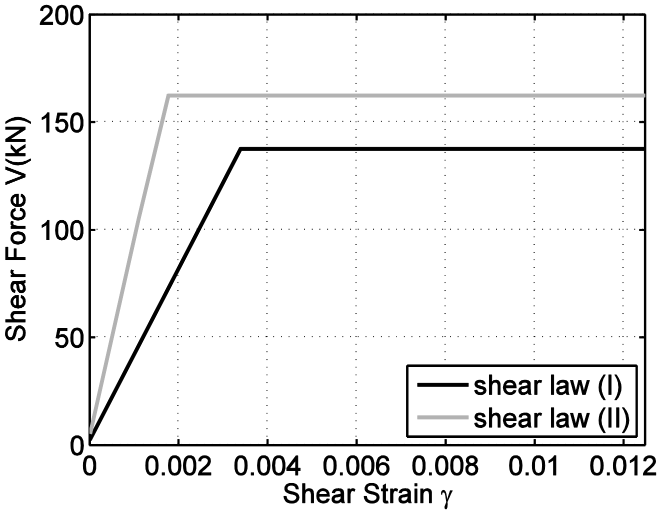

Figure 2: Shear force versus shear strain *(V-γ)* relationship used for the shear component is obtained as discussed in [13] and [14].

According to the first approach [13], the envelope is primarily defined by the shear stress and strain at yield, which are used to estimate the ultimate shear strain. The first branch connects the origin with the peak point (V_{Rd}, γ_y). The section shear capacity V_{Rd} was calculated according to Eurocode 2 (2004) [15], while the shear strain at yield is given by the following equation:

$$\gamma_y = \frac{f_y}{E_s} + \frac{v_y - n}{\rho_v E_s} + \frac{4 v_y}{E_c} \tag{16}$$

where f_y is the reinforcement yield stress, E_s is the reinforcement modulus of elasticity, v_y is the applied shear stress(at yield), n is the vertical axial compression, ρ_v is the vertical reinforcement ratio and E_c is the tangent stiffness of the concrete. The ultimate shear strain γ_u is obtained using the shear strain at yield from the following relationship for the shear strain ductility μ_γ:

$$\mu_\gamma = \frac{\gamma_u}{\gamma_y} = 4 - 12\frac{v_y}{f_c} \tag{17}$$

Here perfect plasticity is assumed, so the section shear capacity at ultimate strain coincides with that of the shear strain at yield (V_{Rd}=V_u).

According to the second approach discussed in [14], the bilinear curve is defined by a cracking point and the failure point. The shear force at cracking is given by the relationship of Sezen and Moehle [16]:

$$V_{cr} = \frac{f_{ctm}}{L_s / h} \sqrt{1 + \frac{N}{f_{ctm} \cdot A_g}} \cdot 0.80 A_g \tag{18}$$

where f_{ctm} is the mean concrete tensile strength, N is the compressive axial load, L_s/h is the shear span ratio, and A_g is the gross area of the concrete section. Assuming a parabolic shear strength distribution along the cross section, the initial shear stiffness GA_{eff} is calculated as $GA_{eff} = G\cdot(0.80A_g)$ where G is the elastic shear modulus. The second and third branches share the same slope, connecting the cracking point to the failure point, and separated at the flexural yielding point (V_y,γ_y). The mean shear strain γ_u is estimated using the truss analogy [17, 18]:

$$\gamma_u = \frac{V_{cr}}{GA_{eff}} + \frac{V_{Rd,s}}{\left(d - d'\right)} \cdot \left(\frac{s}{E_s \cdot A_{sw} \cdot \left(\cot\theta\right)^2} + \frac{1}{E_c \cdot b \cdot \left(\sin\theta\right)^3 \cdot \cos\theta \cdot \cot\theta} \right) \tag{19}$$

where A_{sw} is the area of the transverse reinforcement oriented parallel to the shear force, d-d' is the distance between the centers of the longitudinal reinforcement, s the spacing of transverse reinforcement, b is the width of the cross-section, E_c is the elastic modulus of concrete, E_s the elastic modulus of steel, θ is the angle defined by column axis and the direction of the diagonal compression struts and $V_{Rd,s}$ is the shear strength contributed by the transverse reinforcement [15].

4 NUMERICAL EXAMPLES

A numerical investigation has been carried out using two RC shear walls and an RC column specimen. The two shear walls (denoted as SW30 and SW33) were tested under monotonic and cyclic loading by Lefas and Kotsovos [19], while the RC column was subjected to cyclic loading by Xiao *et al*. [20].

The dimensions and the arrangement of the reinforcement of the wall specimens are shown in Figure 3. They are 0.65m wide, 1.3m high and their thickness is 0.065m. Both walls were monolithically connected to a beam in their base. The vertical and the horizontal reinforcement comprises of high-tensile deformed steel bars of 8mm and 6.25mm diameter, respectively. Additional reinforcement in the form of stirrups confine the wall edges using mild steel bars of 4mm diameter. The properties of the reinforcing bars are shown in Table 1. The cube strength f_{cu} at the day of testing was 30.1 MPa for the SW30 and 49.2 MPa for the SW33 shear wall.

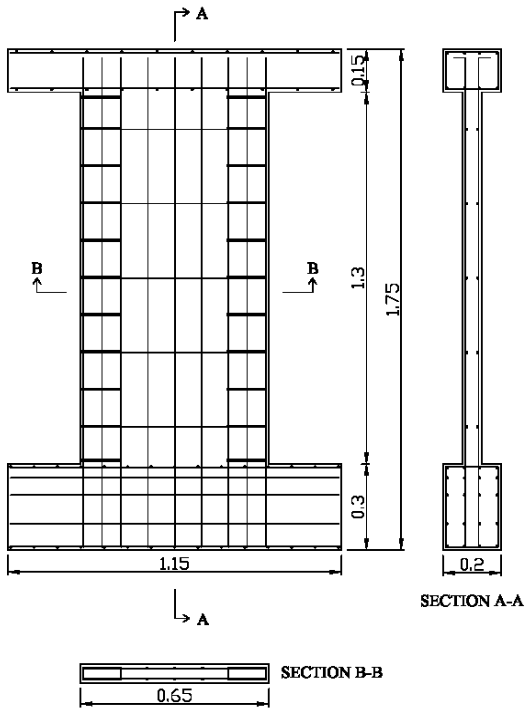

Figure 3: Geometry and reinforcement of the shear wall specimens.

Diameter(mm)	f_{sy} (MPa)	f_{su} (MPa)
8	470	565
6.25	520	610
4	420	490

Table 1: Properties of the reinforcing bars.

The SW30 wall was modeled using the Bernoulli EB, Decoupled TB and Shear-deformable TB simulation with a single force-based element. For all elements five Gauss-Lobatto integration points were used. For the MVLEM approach, one macroelement has been adopted. The analysis results of all models are compared to experimental results and are summarized in Figure 4. Considerable differences between numerical and experimental results for both stiffness and ultimate strength are observed for the Bernoulli EB model. The Decoupled TB model curve gives improved results but still is not able to closely predict the experimental results. The curve obtained by the shear-deformable fiber element exhibits good accuracy compared to the experimental curve. Implementing the MVLEM approach, the discrepancy for the ultimate strength is reduced, but the stiffness is overestimated for displacements between 5 and 10 mm.

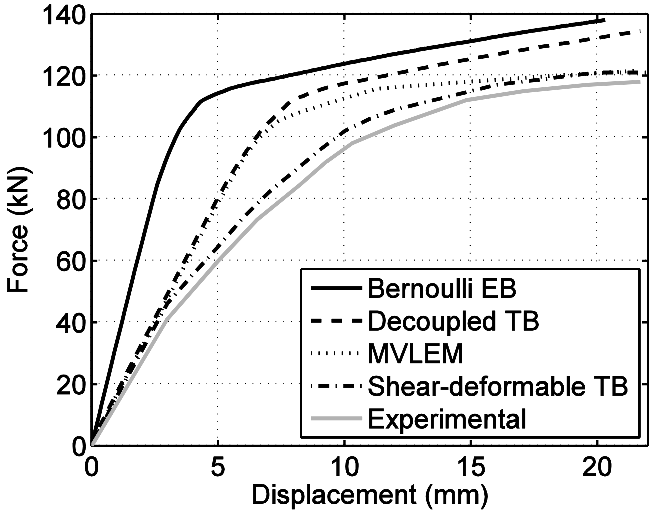

Figure 4: Experimental and numerical results for specimen SW30.

The sensitivity of the numerical results to the shear law assigned to the shear spring for the Decoupled TB element is shown in Figure 5. The results correspond to the to the two different envelope curves of Figure 2 and are compared with experimental results and those of the common fiber element (Bernoulli EB). It can be observed that numerical models overestimate the initial stiffness and the ultimate strength of the wall compared to the experimental results. However, they give a more representative response compared to Bernoulli EB model, since shear deformations have been taken into consideration, even though the model neglects the interaction between moment and shear.

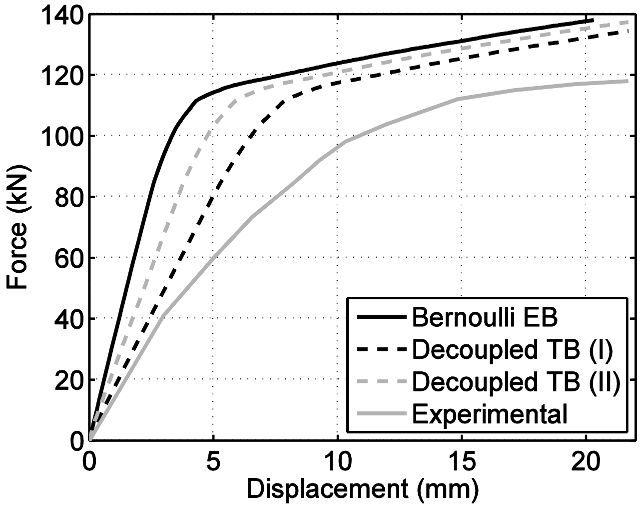

Figure 5: Influence of the shear – law used for the decoupled shear–deformable element on SW30 shear wall.

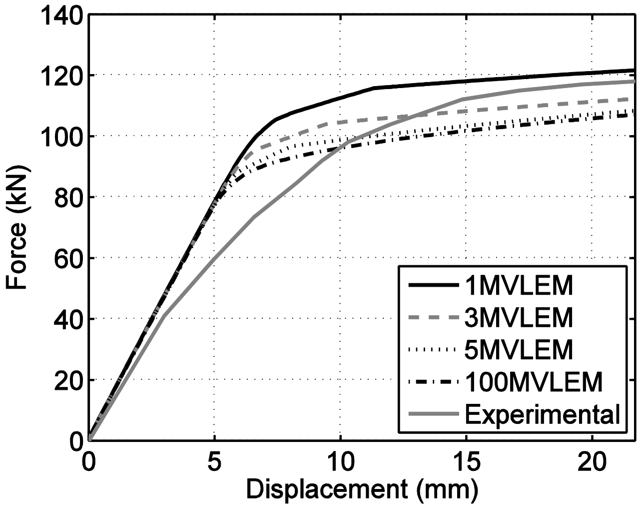

Figure 6: Influence of the number of MVLEM elements used for the uncoupled shear–deformable element on SW30 shear wall.

A parametric study on the sensitivity on the number of MVLEM elements is shown in Figure 6. The initial stiffness is correctly calculated regardless of the number of MVLEM elements. Contrary to the initial stiffness, the ultimate strength is affected by the number of elements. When one MVLEM element is implemented, the ultimate strength is overestimated, while increasing the number of elements leads to underestimating it. The more elements are implemented for the analysis, the underestimation is increased and converges to the curve of the 100 elements. It is worth noting that analyses with 20, 27, 42 MVLEM elements was conducted and the results were similar to those of the 100 elements.

The second shear wall specimen (SW33) is similar to the first but is subjected to cyclic instead of monotonic loading. The history of the displacement which was forced at the top of the wall is shown in Figure 7.

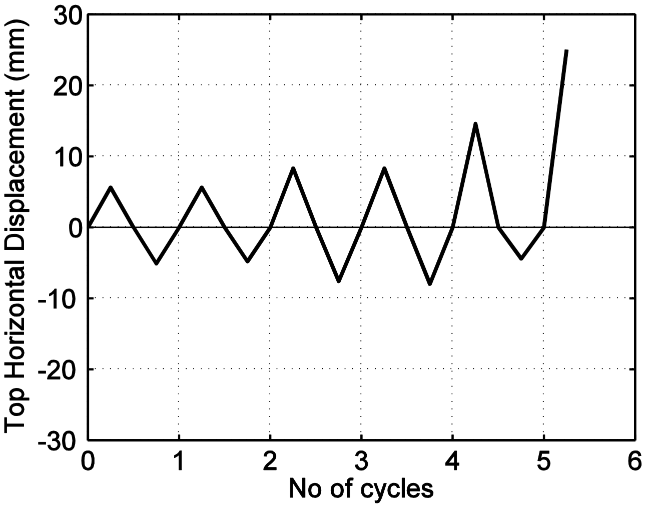

Figure 7: The displacement history adopted of the cyclic tests.

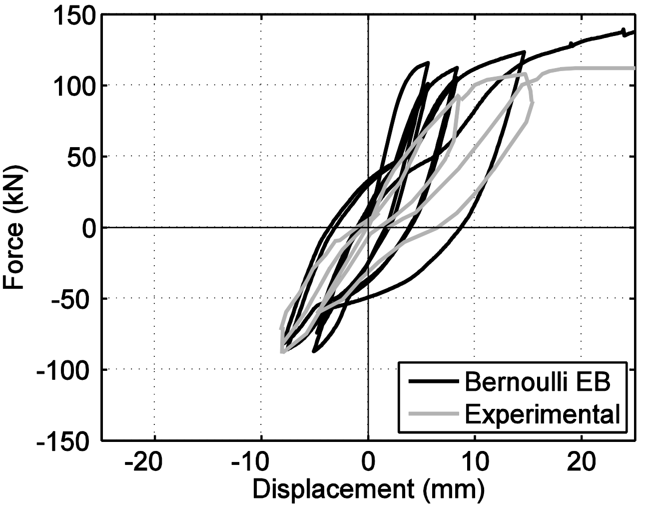

Figure 8: Experimental and numerical results for specimen SW33 of the Bernoulli EB model.

According to Figure 8, the Bernoulli EB model overestimates both stiffness and ultimate strength. When the Decoupled TB (Figure 9) is implemented, a clear improvement on the stiffness prediction can be observed. However, again the ultimate strength is overestimated. Good agreement with experimental results in the prediction of the wall flexural behavior has been obtained with the MVLEM (Figure 10). The difference on the ultimate strength has been reduced, while the stiffness is predicted sufficiently in comparison with the Bernoulli EB and the Decoupled TB models.

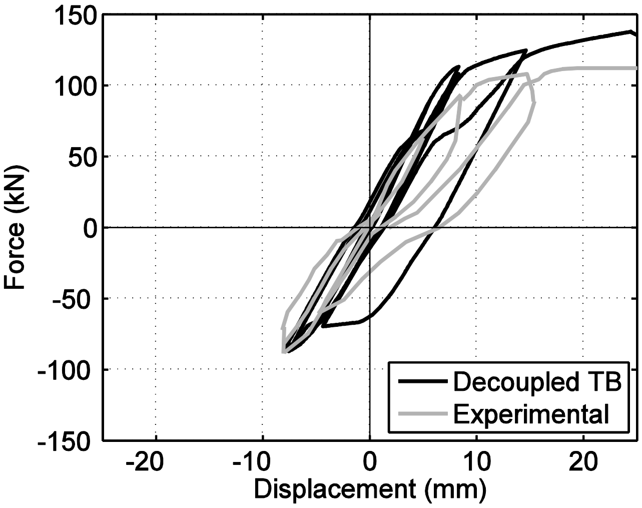

Figure 9: Experimental and numerical results for specimen SW33 implementing Decoupled TB.

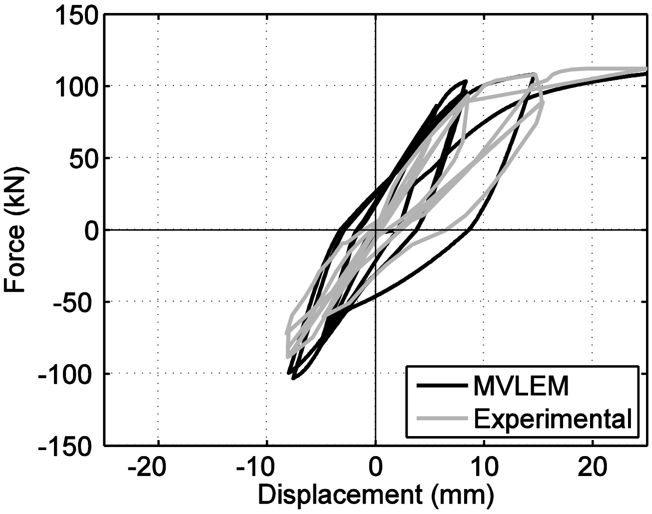

Figure 10: Experimental and numerical results for specimen SW33 implementing MVLEM model.

The next specimen examined is an RC column. The column is 0.61m wide, 1.83m high and 0.406m thick. The vertical and horizontal reinforcement consists of steel bars of 22Φ19.05mm and 1Φ6.35mm/107mm diameter, respectively. The yield strength f_{sy} of the vertical and horizontal reinforcement is 470MPa and 324MPa respectively. The cube strength f_{cu} at the day of testing was 32.75 MPa. The reason for examining this specimen was that sudden loss of strength was observed during the experiment, due to the opening of large shear cracks which lead to shear failure mode.

Implementing the Bernoulli EB model, an overestimation on stiffness, strength and dissipated energy is observed (Figure 11). As far as the Decoupled TB model is concerned, sensitivity to the adopted shear law curve was detected as in the previous specimens. Consequently, numerical results obtained for different shear law curves will also be presented. The first shear law curve was obtained according to reference 12, while the second is adopted as proposed for a similar cross-section in reference [1] (Figure 12).

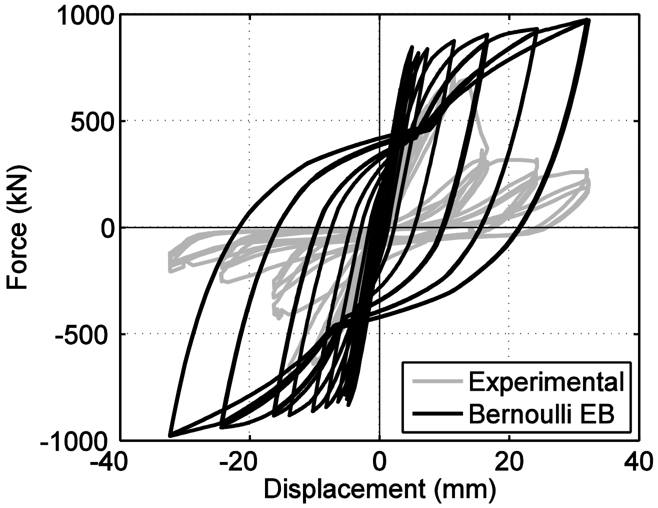

Figure 11: Experimental and numerical results for specimen SW33 implementing Bernoulli EB.

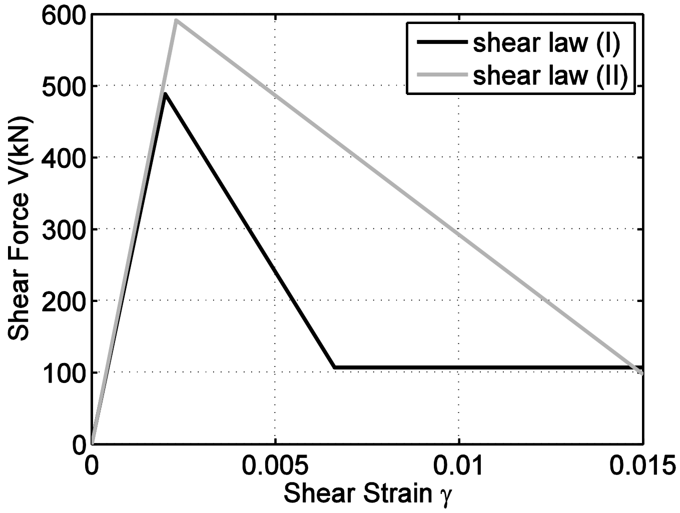

Figure 12: Shear force versus shear strain *(V-γ)* relationship used for the shear component (I: Gerin and Adebar [13], II: Marini and Spacone [1].

Despite the fact that strength is underestimated, a clear improvement is noticed in the prediction of stiffness and energy dissipated when Decoupled TB model (I and II) is adopted compared to Bernoulli EB model (Figures 13 and 14). According to Figures 13 and 14 the load-displacement curves follow the trends imposed by the shear *V-γ* curves, since the failure mode of this specimen is shear.

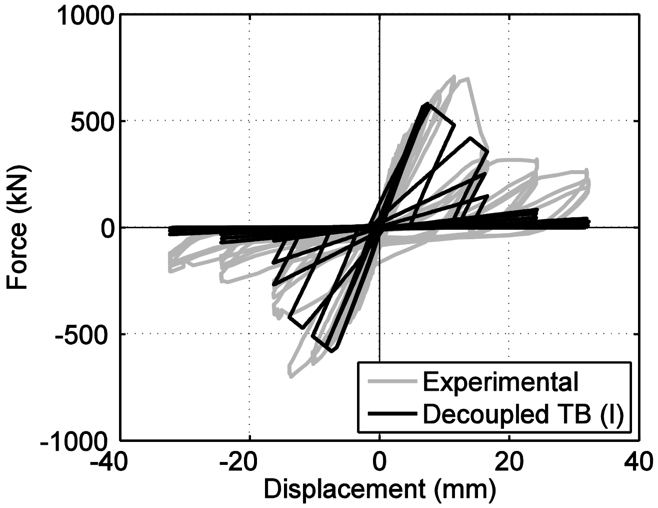

Figure 13: Experimental and numerical results for RC column specimen implementing the Decoupled TB shear law I [12].

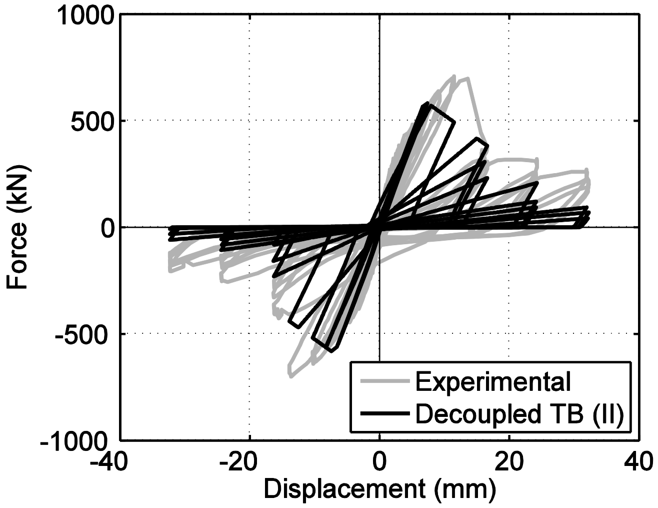

Figure 14: Experimental and numerical results for RC column implementing the Decoupled TB shear law II [1].

When the MVLEM (I and II) model is adopted (Figures 15 and 16), considerable underestimation of the strength was again observed, while the calculation of the stiffness and energy dissipation is improved compared to Bernoulli EB model, regardless of the shear model. The results shown has been obtained with the *V*-*γ* curve of reference [12, 1].

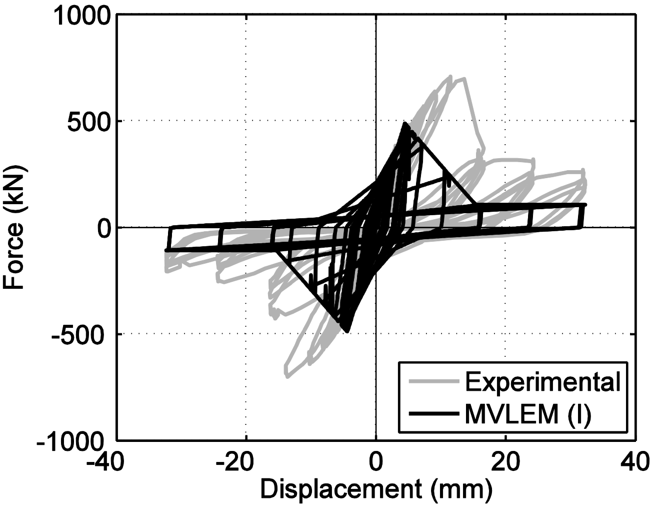

Figure 15: Experimental and numerical results for RC column specimen implementing MVLEM shear law I [12].

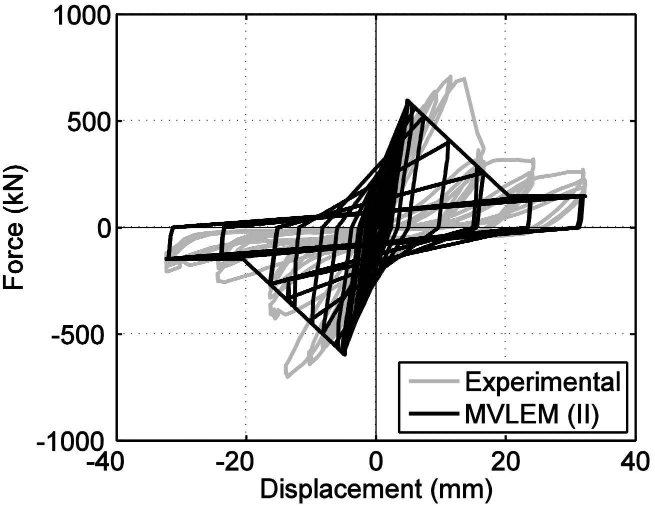

Figure 16: Experimental and numerical results for specimen R5 implementing MVLEM shear law II [12].

5 CONCLUSIONS

Several modeling approaches for the modeling of RC shear walls have been compared. In order to validate the numerical results monotonic and cyclic experimental data were adopted. The analyzed walls exhibited flexural as well as shear failure modes. It is shown that the beam element based on the Euler-Bernoulli theory, although suitable for its simplicity, is not capable to properly simulate various phenomena related to shear effects and therefore produced erroneous predictions. No particular advantage was observed implementing beam element based on Timoshenko beam theory, with no coupling between shear and flexural deformations, despite the fact that a slight improvement in stiffness prediction is apparent compared to the Euler-Bernoulli EB model. The MVLEM model predicts relatively accurately the wall response as identified from the previous seen work. However, no damaging effects were captured. Sufficient results were obtained but still there are differences from the experimental results. The shear-deformable fiber element proved to be more suitable to predict the inelastic static behavior of slender walls. It successfully balances the simplicity of a beam model and the refinements offered by a 3D law, while it enables modeling some important features which are ignored by other models.

ACKNOWLEDGMENTS

The work presented in this paper is co-financed by Greece and the European Union in the frame of Operational Programme Education and Lifelong Learning “HRAKLEITOS II”.

REFERENCES

[1] A. Marini, E. Spacone, Analysis of Reinforced Concrete Elements Including Shear Effects, *ACI Structural Journal,***106**, 645-655, 2006.

[2] A. Papachristidis, M. Fragiadakis, M. Papadrakakis, A 3D fiber beam-column element with shear modeling for the inelastic analysis of steel structures, *Comput. Mech.*, **45**, 553-572, 2010.

[3] A. Papachristidis, M. Fragiadakis, M. Papadrakakis, *Inelastic Analysis of Frames under Combined Bending, Shear and Torsion, Computational Methods in Earthquake Engineering, M. Papadrakakis, M. Fragiadakis, N.D. Lagaros (Eds.),* Springer-Verlag, Berlin, 2011 .

[4] L. Massone, J. Wallace, Load-Deformation Responses of Slender Reinforced Concrete Walls, *ACI Structural Journal*, **101**, 103-113, 2004.

[5] E. Spacone, F.C. Filippou, F.F. Taucer, Fibre Beam-Column Element for Nonlinear Analysis of R/C Frames, *Part I. Formulation. Earthquake Eng Struct Dyn* **25**, 711-725, 1996.

[6] M. Petrangeli, V. Ciampi, Equilibrium based Iterative Solutions for the Non-Linear Beam Problem, *Int J Numer Methods Eng* **40**, 423-437, 1997.

[7] A. Vulcano, V.V. Bertero, V. Colotti, Analytical Modeling of RC Structural Walls, Proceedings, *9th World Conference on Earthquake Engineering, V. 6,* Tokyo-Kyoto, Japan, 1988.

[8] K. Orakcal, J.W. Wallace, J.P. Conte, Nonlinear Modeling and Analysis of Reinforced Concrete Structural Walls, *ACI Structural Journal*, **101**, 688-698, 2004 .

[9] K. Orakcal, J.W. Wallace, Modeling of Slender Reinforced Concrete Walls, *Proceedings, 13th World Conference on Earthquake Engineering*; Vancouver, Canada, 2004, paper No. 555.

[10] Kent D.C., Park R., Flexural members with confined concrete, *Journal of structural Division ASCE*, **97**, 1964-1990, 1971 .

[11] M. Menegotto, E. Pinto , Method of Analysis for Cyclically Loaded Reinforced Concrete Plane Frames Including Changes in Geometry and Non-Elastic Behavior of Elements Under Combined Normal Force and Bending, *IABSE Symposium on Resistance and Ultimate Deformability of Structures Acted on by Well-Defined Repeated Loads*, Lisbon, Portugal, 1973, (15-22).

[12] F.C. Filippou, E.G. Popov, V.V. Bertero, *Effects of Bond Deterioration in Hysteretic Behavior of Reinforced Concrete Joints , EERC Report No. UCB/EERC-83/19*, Earth-

quake Engineering Research Center, University of California, Berkeley, Calif., 1983, 184 pp.

[13] M. Gerin, P. Adebar, Accounting for Shear in Seismic Analysis of Concrete Structures, *Proceedings, 13th World Conference on Earthquake Engineering*, Vancouver, B.C. Canada, August 1-6 2004, Paper No.1747.

[14] P.E. Mergos, A.J. Kappos, A Distributed Shear and Flexural Flexibility Model with Shear-Flexure Interaction for R/C Members subjected to Seismic Loading, *Earthquake Engng Struct. Dyn.*, **37**, 1349-1370, 2008 .

[15] Eurocode 2 (2004): Design of concrete structures ENV 1992-1-1, European Standard, European Committee Standardization.

[16] H. Sezen, JP. Moehle, Shear Strength Model for Lightly Reinforced Concrete Columns, *Journal of Structural Engineering*, **130**, 1692-1703, 2004.

[17] R. Park, T. Paulay, *Reinforced Concrete Structures*, Wiley: New York, 1975.

[18] MJ. Kowalsky, MJN. Priestley, *Shear Behaviour of Lightweight Concrete Columns under Seismic Conditions, Report No. SSRP-95/10*, University of San Diego, San Diego, CA, 1995.

[19] D. Lefas, M. Kotsovos, Strength and Deformation Characteristics of Reinforced Concrete Walls under Load Reversals, *ACI Structural Journal*, **87**,716-726, 1990.

[20] Y. Xiao, MJN. Priestley and F. Seible, Steel jacket retrofit for enhancing shear strength of short rectangular reinforced concrete columns, Report No. SSRP-92/07, University of California, San Diego, 1993.

COMPDYN 2011
3rd ECCOMAS Thematic Conference on
Computational Methods in Structural Dynamics and Earthquake Engineering
M. Papadrakakis, M. Fragiadakis, V. Plevris (eds.)
Corfu, Greece, 25–28 May 2011

SEISMIC ASSESSMENT OF STEEL MOMENT FRAMES USING SIMPLIFIED NONLINEAR MODELS

Dimitrios G. Lignos[1], **Christopher Putman**[2], **and Helmut Krawinkler**[3]

[1] McGill University
817 Sherbrooke West Room 278C, Montreal QC, H3A 2K6
e-mail: dimitrios.lignos@mcgill.ca

[2] Degenkolb Engineers
1300 Clay Street, Suite 900, Oakland, CA, 94612, United States
cputman@degenkolb.com

[3] Stanford University
473 Via Ortega, Room 231, Stanford, CA, 94305, United States
e-mail: krawinkler@stanford.edu

Keywords: Simplified modeling, nonlinear static procedures, multi-modal static procedures, gravity system, seismic demands, steel moment resisting frames.

Abstract. *The effectiveness of simplified nonlinear models for seismic assessment of steel moment frames using single and multi-mode nonlinear static methods compared to nonlinear response history analysis is discussed in this paper. Results of studies of different steel archetype buildings with perimeter steel moment resisting frames are compared with those from nonlinear response history analysis (NRHA). Simplified modeling of gravity systems is also discussed. It is demonstrated that the nonlinear static procedure (NSP) has many limitations for quantitative assessment of moment frame demands even for relatively low-rise structures. But it has much value in understanding important behavior characteristics that are not being explored in a NRHA in which engineers usually focus on a "blind" demand/capacity assessment rather than interpretation and visualization of behavior. The conclusion is that both NSP and NRHA have intrinsic value and that it is advisable to employ a combination of both to understand seismic performance and quantify important engineering demand parameters. This study is part of a recent National Institute of Standards and Technology (NIST) funded project through a joint venture partnership of the Applied Technology Council (ATC) and Consortium of Universities for Research in Earthquake Engineering (CUREE) on improvement of nonlinear multiple-degree-of-freedom modeling for design decisions of regular and irregular structural systems (NIST GRC 10-917-9).*

1 INTRODUCTION

Performance Based Earthquake Engineering (PBEE) concepts have been adopted by a number of engineering guidelines such as [1-7] for seismic evaluation and rehabilitation of steel and reinforced concrete structures. A common procedure for a structural engineer to conduct such an evaluation is to utilize nonlinear static procedure (NSP), which is also referred in the literature as pushover analysis. In U.S. practice, a pushover analysis is typically based on an invariant lateral load pattern that is applied along the height of a structure, which is pushed to a pre-defined target roof displacement. Many researchers have conducted extensive research on the evaluation of seismic demands of structural systems with nonlinear static procedures based on invariant load patterns, e.g., [8-12]. In these studies major drawbacks of these procedures to predict seismic demands of structures have been summarized. Others [13-16] have conducted research on enhanced NSPs that account for higher mode effects and either retain the simplicity of invariant load patterns or employ adaptive procedures in which the lateral load pattern varies during the nonlinear analysis. Typically, these methods improve the prediction of engineering demand parameters compared to the single mode PA. The value of NSP is in the fact that this procedure permits inspection of response and is a relatively simple approximate tool to identify critical regions of a structural system in which the potential for significant strength or stiffness discontinuities is relatively high.

In FEMA-440 [5] the major differences between results obtained from nonlinear static and nonlinear response history analysis (NRHA) were attributed to a number of reasons such as the effect of component deterioration on the seismic response of a structural system [6]. Other reasons for differences between NRHA and NSP in prediction of seismic demands of a structural system are (1) P-Delta effects, (2) inaccuracies in the prediction of target roof displacement at which structural response is to be evaluated, and (3) multi-degree-of-freedom (MDOF) effects. In order to improve nonlinear MDOF modeling for structural engineering design practice for better estimation of the seismic response of structural systems such as steel and reinforced concrete moment resisting frames (MRFs) and reinforced concrete and masonry shear walls, the National Institute of Standards and Technology (NIST) initiated a program of focused studies [18]. This paper summarizes one of the analytical studies conducted as part of this program, which addressed the minimum level of MDOF modeling sophistication and appropriateness of nonlinear methods for seismic evaluation of special steel MRFs. This study investigates the effect of higher modes and gravity system as part of the lateral resisting system on engineering demand parameters (EDPs) of steel MRFs such as story drift ratios, story shear forces, overturning moments, residual story drift ratios and absolute floor accelerations along the height of steel MRFs. The investigation is based on simplified nonlinear models of steel MRFs.

2 ARCHETYPE STEEL BUILDINGS

The steel buildings used for evaluation of EDPs predicted with NRHA and NSP procedures are two-, four- and eight-story special MRFs. The structural systems are perimeter moment frame systems of a set of archetype steel buildings designed as part of the NIST [19] project. These structures comprise 3-bay steel MRFs with Reduced Beam Sections (RBS) designed in accordance with AISC 358-05 [20]. A plan view of a typical archetype is shown in Fig. 1. The three steel buildings that are utilized in this study are designed based on Response Spectrum Analysis (RSA) for seismic design category D_{max}. This corresponds to a design spectral acceleration at short period, S_{DS}, and at a period of 1second, S_{D1}, equal to 1.0g and 0.60g, respectively. More details on the design of the archetype steel buildings are summarized in [19, 21]. In the subsequent discussion and figures, the two-, four- and eight-story steel MRFs are denoted as 2-RSA-D_{max}, 4-RSA-D_{max} and 8-RSA-D_{max}, respectively.

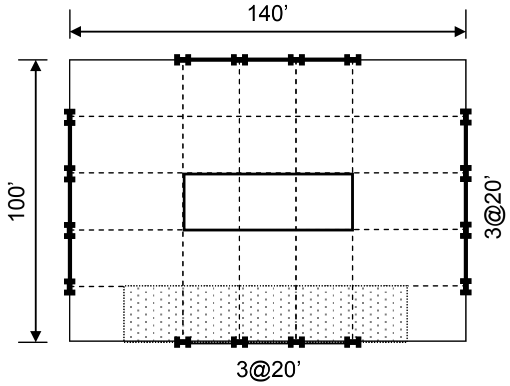

Figure 1: Plan view of typical archetype building with perimeter moment resisting frames.

3 MODELING OF ARCHETYPE STEEL MOMENT RESISTING FRAMES

In order to model the seismic response of the perimeter steel MRFs discussed in Section 2, two analytical models are utilized. Both models are two-dimensional (2-D). In the first analytical model all components (beams, columns and panel zones) of the steel MRF are modeled explicitly. The second model is a single bay simplified frame whose properties are tuned to represent the detailed steel MRF. In both models P-Delta effects are simulated with a leaning column that is connected to the steel MRF with axially rigid links. These links have hinges at their ends. The subsequent sections discuss details of these two analytical models.

3.1 Three-bay steel moment resisting frame model

The steel MRF in the East-West loading direction (see Fig. 1) is modeled in a customized version of DRAIN-2DX (Prakash et al. [22]). This numerical model consists of elastic beam-column elements with concentrated plastic hinge springs at their ends. These springs simulate the hysteretic response a steel component (beam or column) subjected to cyclic loading including strength and stiffness deterioration based on the modified Ibarra-Krawinkler (IK) deterioration model [23, 24]. Panel zones are modeled with the model discussed in [25], which explicitly represents panel zone shear distortions including the possibility of nonlinear behavior during an earthquake. The exact location of the RBS section is also incorporated in the model. The deterioration parameters of beams with RBS and steel columns are determined by multivariate regression equations that have been developed based on information retrieved from a recently developed database for deterioration modeling of steel components [24, 26]. These analytical models were used extensively for quantification of building seismic performance factors using the FEMA P-695 methodology [19].

3.2 Simplified single-bay frame model

To reduce the computational effort in estimating seismic demands of the steel MRFs with NRHA and evaluate the effectiveness of simpler representations of the 3-bay steel MRFs discussed in Section 3.1, a simplified model as shown in Fig. 2 is developed. In this model a single bay frame in a manner represents the three-bay moment-resisting frame so that overturning moment and column axial deformation effects are adequately represented. Luco et al. [27] developed similar models for computing the seismic inelastic demands of steel MRFs. P-Delta effects are simulated with a leaning column that is always present in the numerical model. Strength and stiffness properties of the gravity framing that is not part of the moment resisting frame can be represented with the fishbone model shown at the right of Fig. 2. Lumping together multi-bay frames into a single bay frame can be accomplished by the following rules:

$$\sum EI_i/L_i = EI/L \tag{1}$$

$$\sum M_{p,i} = M_p \tag{2}$$

in which I_i and L_i is the moment of inertia and length of the *i*-th beam in a story, respectively, and EI/L and M_p are the stiffness and plastic moment of the single bay beam. For steel columns,

$$\sum EI_i = 2EI \tag{3}$$

$$\sum M_{pc,i} = 2M_{pc} \tag{4}$$

in which $M_{pc,i}$ is the plastic moment of the *i* –th column of the multi-bay frame and M_{pc} is the plastic moment of the single bay column in the presence of an axial load. For taller steel MRFs in which overturning moment and axial deformations in columns are important, these effects can be approximated by setting *L* of the single bay frame equal to the distance between end columns of the multi-bay frame, and setting the area of the single bay column equal to the area of the end column of the multi-bay frame. This simplification is based on the assumption that overturning effects are resisted mostly by the exterior columns of a steel MRF. The approximations summarized herein are reasonable if all bays of the steel MRFs are of about equal width, and become more approximate when spans of the steel MRF vary considerably. Ignoring panel zone shear deformations and using centerline dimensions for beams and columns introduce additional approximations to the analytical models.

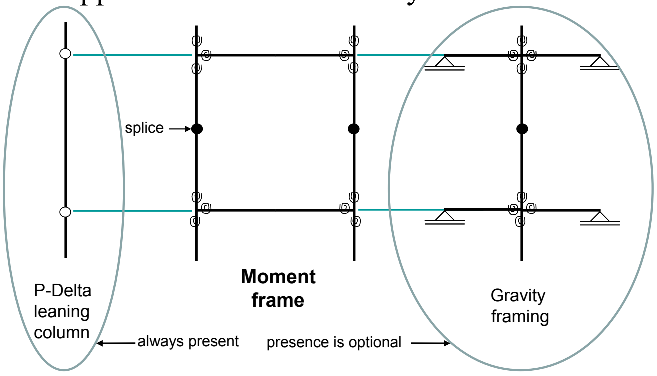

Figure 2: Simplified model with P-Delta column and gravity framing fishbone model.

Figure 3a shows a comparison between the pushover curves of the 3-bay four-story steel MRF and the simplified 1-bay model. In this figure, the base shear V is normalized with respect to the seismic weight W of the steel MRF. The base shear V is computed from the inertia forces only (V_I). The roof drift θ_r is defined as roof displacement δ_r over the total height *H* of the steel MRF. As seen from this figure, the response of the 1- and 3-bay models is almost identical. The 1-bay models are implemented in the OpenSees [28] simulation platform whereas the 3-bay models are implemented in Drain-2DX [22]. The base shear histories for a single ground motion obtained from the 3-bay model developed in Drain-2DX (ATCW 3-Bay) and the 1-bay model developed in OpenSees are shown in Fig. 3b. . Simulations are carried out for the FEMA P-695 [7] set of 44 ground motions for three scale factors (0.5, 1.0 and 2.0). Note that a scale factor SF=2.0 corresponds to approximately a maximum considered event (MCE) in California. A comparison between absolute peak overturning moments (OTM) obtained for the eight-story 3-bay and 1-bay frames is shown in Fig. 3c. In both static and dynamic analysis the seismic response based on the 1-bay and 3-bay models is almost identical, providing confidence in both the simulation platforms and in the ability of the simplified model to represent the response of the 3-bay steel MRF.

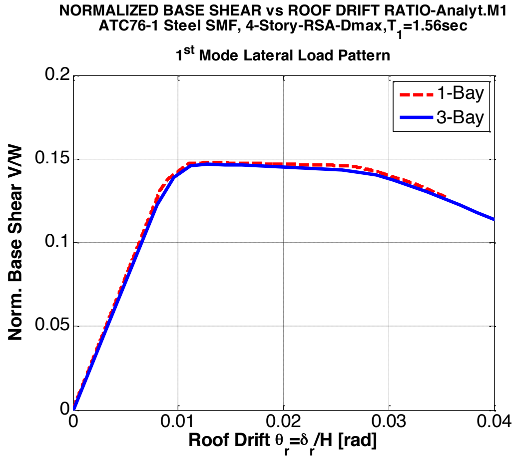

(a) Comparison of pushover curves between 1-bay and 3-bay models of the four-story steel MRF

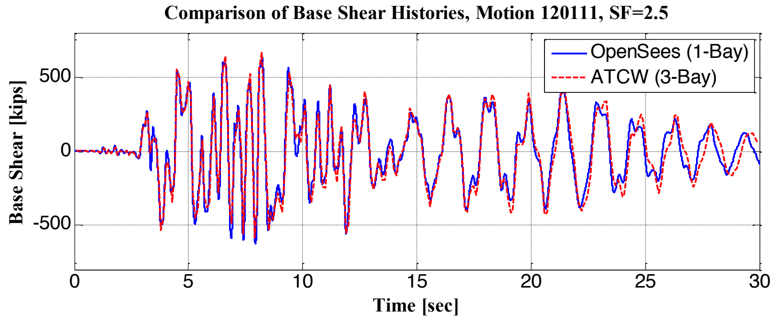

(b) Base shear history of the four-story MRF models for a single ground motion

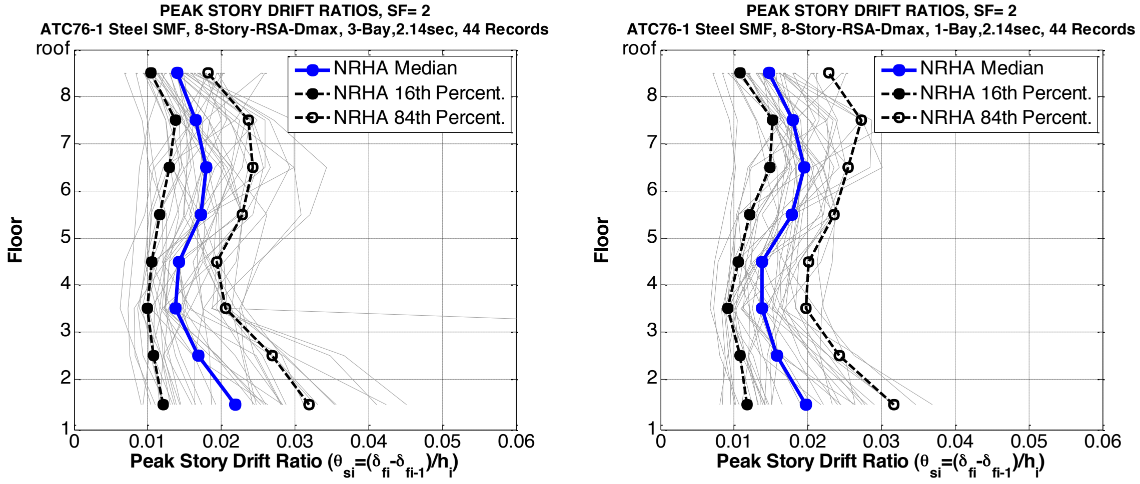

(c) Comparison of overturning moments obtained from NRHA of 3-bay and simplified 1-bay model

Figure 3: Comparison of response predictions using the 3-bay and 1-bay simulation models.

4 SEISMIC ASSESSMENT OF STEEL MOMENT RESISTING FRAMES

This section focuses on evaluating the seismic response of steel MRFs with simplified models discussed in Section 3.2. The assessment is based on a comparison between NSP and NRHA results. Feasibility and limitations of the NSP is illustrated with the case studies that were investigated. Since the emphasis is on simple methods that can assess multi-mode effects on the seismic response of steel frame structures the modal pushover analysis (MPA) [13] is also evaluated. Two main options are used for modeling the components of the steel MRFs discussed in Section 3. These options are summarized as follows:

- **ASCE41:** all the steel components are modeled in accordance with ASCE/SEI 41-06 [3] utilizing the component model shown in Fig. 4a. Note that a post-capping stiffness obtained by linearly connecting peak point C and point E of the generic ASCE/SEI 41-06 model is used. This modification is made in order to provide a better match with data and analysis models developed in the past decade [23, 24] and also to avoid numerical stability problems in the analysis.
- **Analyt.M1:** all the steel components are modeled with the modified IK component model [24]. For this purpose, a monotonic backbone curve is used as shown in Fig. 4b. This option is the same as the ATC-72-1 [29] analysis Option 1. Cyclic deterioration is not reflected in the component model for monotonic response and subsequently in the NSP. However, in the NRHA the component model deteriorates cyclically based on rules discussed in [23, 24]. For comparison purposes in the same figure we have superimposed the modified backbone curve based on the IK model (see Fig. 4b) based on the ATC-72 [29] analysis option 3.

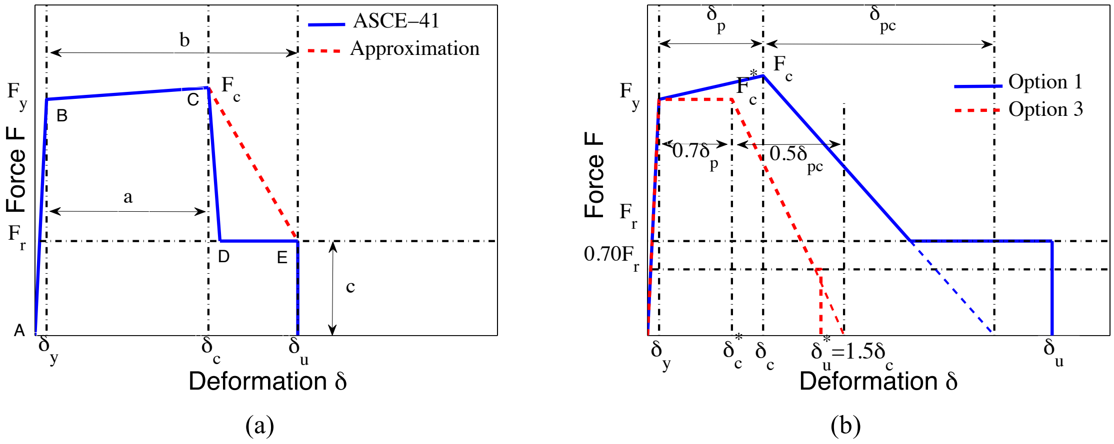

(a) (b)

Figure 4: Steel component models; (a) ASCE 41; (b) Modified IK model, Options 1 and 3.

The following two options are used to determine the target roof displacement for the NSP:

- **ASCE41**: Target displacement obtained from ASCE/SEI 41-06 [3] coefficient method.
- **EqSDOF:** Target displacement based on median displacement obtained from NRHA of the first mode equivalent Single-Degree-Of-Freedom (SDOF) system using the 44 ground motions of the FEMA P-695 [7] set and the analysis tool IIIDAP (Lignos [30]). Equivalent SDOF properties are obtained from the base shear without P-Delta V_I – roof displacement pushover curve (not the base shear including P-Delta $V_{I+P\text{-}\Delta}$ – roof displacement pushover curve), which implies that P-delta effects are accounted for approximately in the properties of the equivalent SDOF system.

Note that for the MPA procedure only the Analyt.M1-EqSDOF option was explored. This implies that the pushover analysis is conducted with the Analyt.M1 model, and the target displacement for the individual modes is determined from an equivalent SDOF analysis with the analysis tool IIIDAP [30], which computes inelastic response of SDOF systems with due consideration given to deterioration. The cyclic deterioration parameter λ [26] is set equal to the median value for steel components obtained from a steel database for deterioration modeling (Lignos and Krawinkler [26]).

4.1 Single mode nonlinear static analysis procedure

Figures 5a and 5b show the pushover curves with ($V_{I+P\text{-}\Delta}$) and without P-Delta (V_I) effects for the four-story steel MRF based on the ASCE-41 and Analyt.M1 component models, respectively. In the same figures we have superimposed the idealized trilinear curve based on the ASCE-41-06 [3] criteria. These figures show that the NSP based on the ASCE41 component model underestimates the post-yield strength and deformation capacities compared to the Analyt.M1 model. The implication is that the target roof displacements predicted from the equivalent SDOF systems shown in Fig. 5c and 5d are different for large ground motion demands.

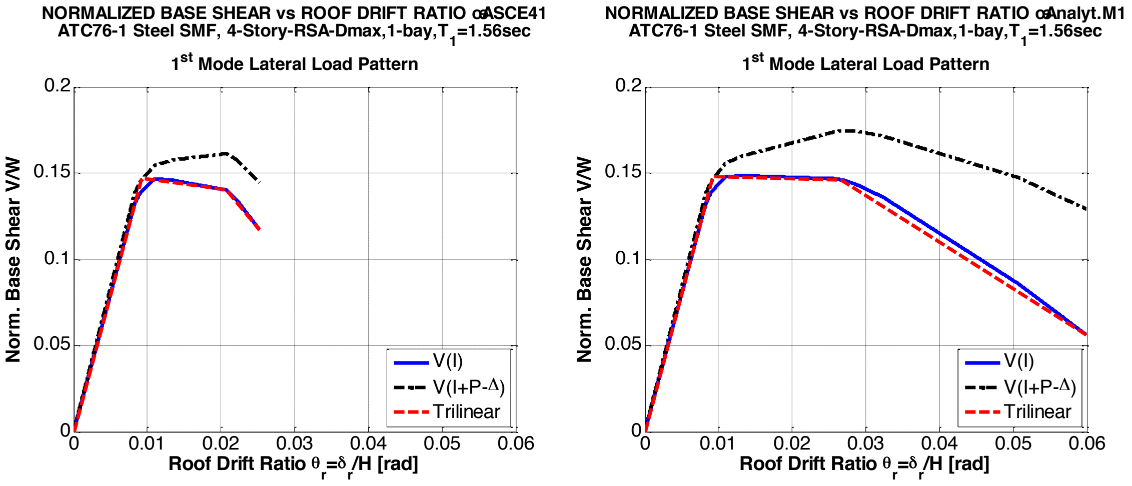

(a) ASCE-41 component model (b) Analyt.M1 component model

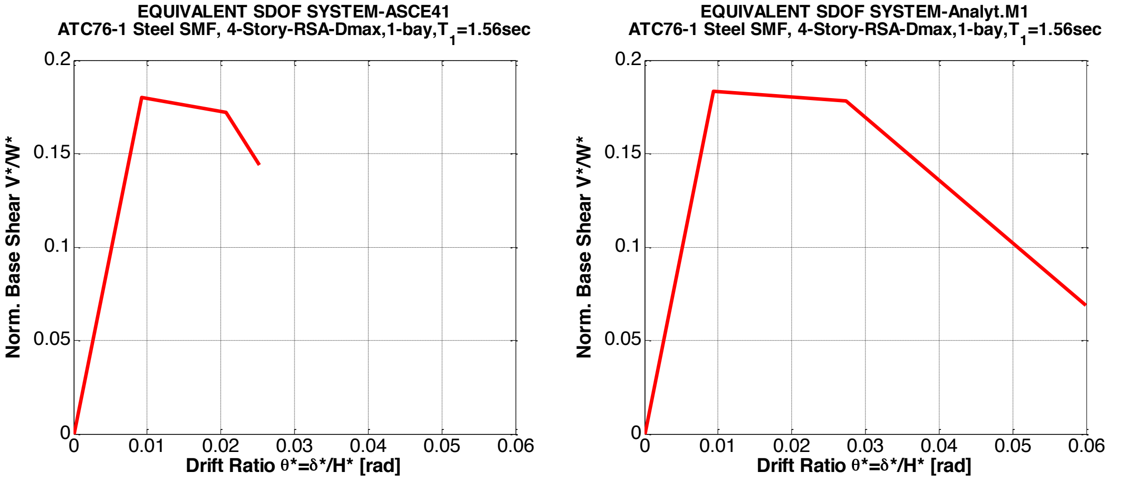

(c) ASCE41 component model (d) Analyt.M1 component model

Figure 5: Single mode pushover curves and equivalent SDOF systems for the 4-story-RSA-Dmax steel MRF.

The use of the pushover curve based on the ASCE-41 component model (see Fig. 5a) together with the equivalent SDOF model for target displacement prediction (ASCE41-EqSDOF) may provide performance estimates that are lower than might be justifiable. For a scale factor SF = 2.0 the EqSDOF leads to 33 collapses, which are a direct consequence of the relatively short yield plateau obtained from using ASCE41 component models in the pushover analysis. For all options, NSP story drift predictions show a significant deviation from median NRHA values (Fig. 6a, 6b). In the inelastic range (SF = 2.0) drifts in the lower stories are overestimated and drifts in the upper stories are underestimated. Results are illustrated for the two- and four-story steel MRFs but the same observation applies for the eight-story MRF.

Nonlinear static procedure story shear predictions for the four-story steel MRF show poor correlation with NRHA results in the inelastic range (SF = 2.0). This can be seen in Fig. 6c and 6d. Story shears are consistently underestimated, particularly in the upper stories. The reason is dynamic redistribution, which amplifies story shear forces compared to those obtained from a predetermined lateral load pattern. If story shears are an important performance consideration, then the validity of quantitative values obtained from a pushover analysis diminished for this 4-story steel SMF. Similar observations apply to floor OTMs, which control axial forces in columns of frame structures. In the upper stories, the NSP predictions are less than half those obtained from NRHA (see Fig. 6e and 6f). The situation is better at the base, because absolute maximum shear forces in individual stories occur at different times. The outcome is that even for relatively low-rise steel MRF structures NSP predictions may provide misleading quantitative information, particularly for force quantities.

The all-important issue of lateral load pattern is not explored here. Previous work [5] has addressed this issue and came to the conclusion that variations in invariant lateral load patterns do not improve the accuracy of EDP predictions. The load pattern applied in all cases discussed here is the pattern structured after the elastic first mode deflected shape, as recommended in [3].

4.2 Incorporation of gravity system in analysis model

Gravity system components must have sufficient strength and deformation capacity to resist tributary gravity loads at the maximum drifts computed for the lateral load resisting system. The structural engineer typically decides weather or not to include contributions of the gravity system to lateral stiffness and strength of a building. It is recommended to incorporate the gravity system in the analytical model of the structural system because the analysis might expose weaknesses that are not evident from inspection. An incentive for incorporating the gravity system is its potential benefit in decreasing drift demands and increasing collapse capacity. This might be particularly attractive if the pushover curve exhibits an early negative tangent stiffness that may lead to large displacement amplification or even collapse. The negative stiffness will be reduced potentially by incorporating the gravity system or might even turn into a positive stiffness (Gupta and Krawinkler [31]).

A simple way to incorporate the gravity framing is by means of the “fishbone” arrangement shown earlier in Fig. 2. In order to prevent accumulation of large axial force in the column of the fishbone, an arrangement with two beams is preferred. In this arrangement all beams are lumped into a single beam (I/L of beam = $\Sigma EI_i/L_i$ of all beams), all columns are lumped into a single column (I of column = ΣI_j of all columns), and all gravity connections are lumped into two connections represented by rotational springs.

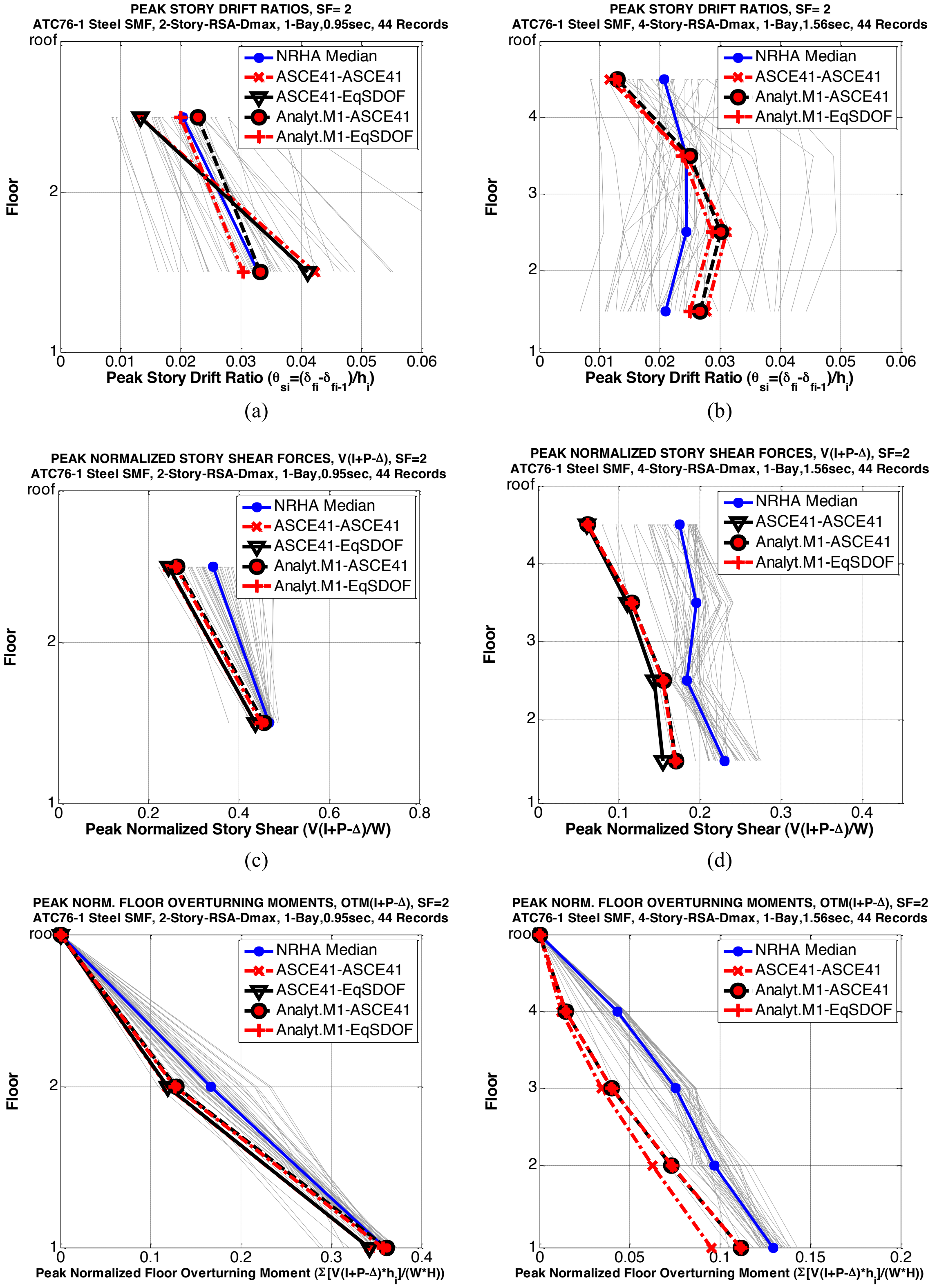

(a) (b)

(c) (d)

(e) (f)

Figure 6: Comparison between NSP and NRHA predictions for EDPs of the two and four-story steel MRFs for SF=2.0.

Beams can be represented usually by elastic elements, provided the connections of beams to columns are weaker than the beams. Column bending strength should include the effects of tributary axial forces due to gravity loads. Post-yield properties of the columns should be based on average plastic hinge properties of the column sections. For modeling of the 4-RSA-D_{max} gravity system, a preliminary design of the gravity beams and columns is performed using tributary areas deduced from the plan view shown in Fig. 1. Since only half of the structure is modeled, the spine (column) of the "fishbone" represents 6 gravity columns and four moment frame columns bending about the weak axis. The beam represents 7 gravity beams.

Connection properties were estimated from tests summarized in Liu and Astaneh-Asl [32, 33]. The cyclic behavior of a typical steel shear tab connection is shown in Fig. 7a. From this figure, the hysteretic response of the gravity connection is pinched. Utilizing the pinching04 model in OpenSees [28] the simulated response of this connection matches the experimental results fairly accurately. However, because of the complex behavior of these connections, greatly simplified and generally conservative models can also be employed that are easily utilized by the engineering profession; thus, a simple elastic-perfectly plastic spring model superimposed on the experimental results is also used. The yield rotation for this spring is 0.008, which is about the same as the yield rotations of the beams of the steel MRF. Pre-capping plastic rotation θ_p is 0.10 and post-capping θ_{pc} is assumed as 0.15. The yield strength is a compromise between positive and negative strength values that can be sustained at very large inelastic rotations. This model ignores the additional strength at relatively small rotations. A comparison of pushovers without and with gravity system is presented in Fig. 7b. In this example not much is gained in pushover strength and deformation capacity by incorporating the gravity system in the analysis model.

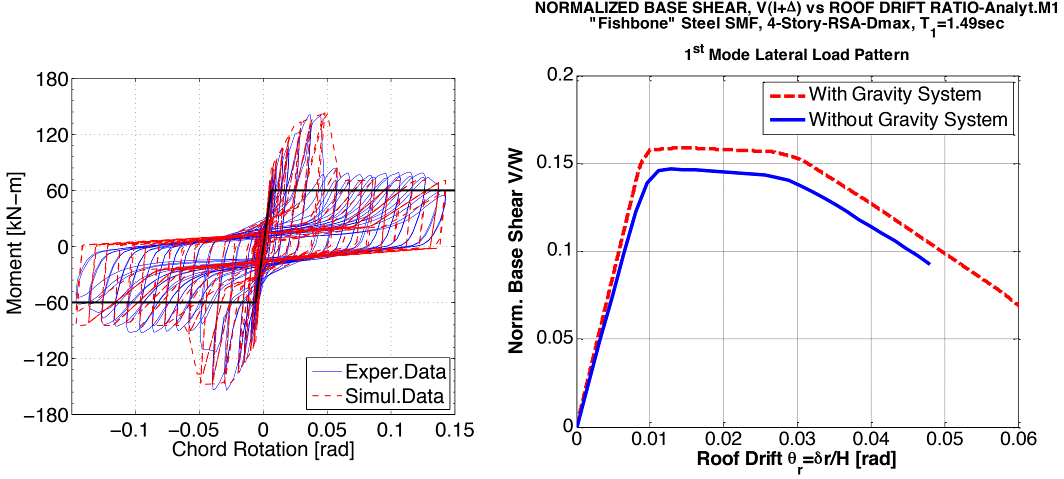

(a) Hysteretic response of a shear connection (data from [32,33])

(b) Comparison of pushover curves of four-story steel MRF with/without gravity system

Figure 7: Effect of gravity system on global pushover of the four-story steel MRF.

The gain in peak story drift ratios when incorporating the gravity system in this example is seen in Fig. 8, which show NRHA and NSP results for a ground motion scale factor SF = 3.0. For this large ground motion scale factor the maximum response is mostly in the negative tangent stiffness region of the pushover (roof drift > 3% as seen from Fig. 7b). Figure 8a shows the median story drift ratios along the height of the bare four-story steel MRF for the set of 44 ground motions for SF=3.0. This scale factor represents the median collapse capacity of this steel MRF, because collapse occurred under 22 of 44 ground motions. Incorporation of the gravity system reduced the number of collapses from 22 to 11, which has a significant effect on the probability of collapse. The median roof drift is reduced from 0.049 to 0.034, and the effect of the gravity system on peak story drifts can be inspected from the figure. The observations made here are case specific, and the benefit gained from incorporating the gravity system may depend strongly on the structural configuration.

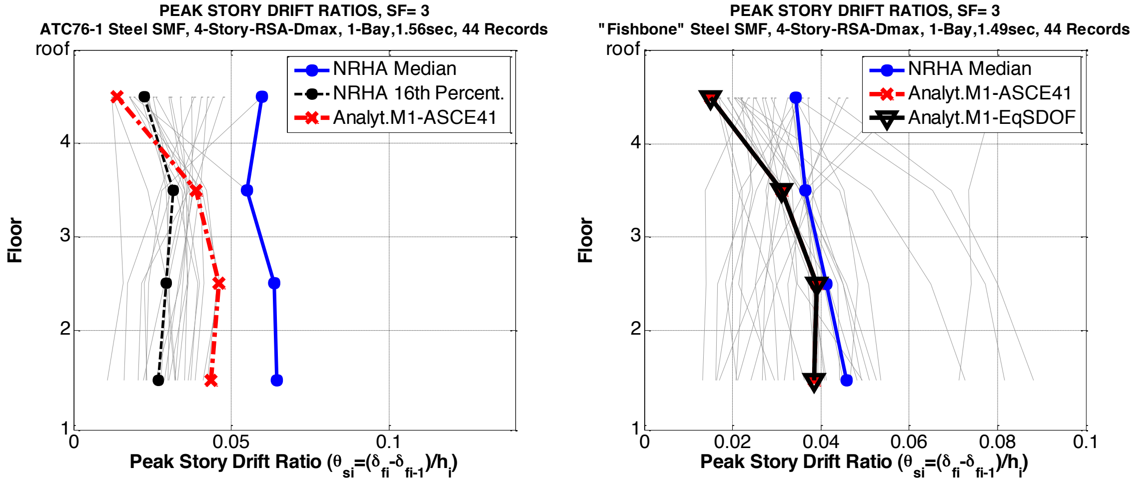

(a) Bare steel MRF (b) Steel MRF with gravity system

Figure 8: Effect of gravity system on story drift ratios of the four-story MRF for SF=3.0.

4.3 Multi mode nonlinear static procedures

In this section, the assessment of the four- and eight-story steel MRF based on the MPA procedure is discussed. The basic steps for seismic evaluation of the peak response of a structural system using MPA are summarized in [13,18]. Figures 9a and 9b show the pushover curves of the four-story steel MRF using the 1st and 2nd mode lateral load pattern. The idealized equivalent SDOF systems based on the Analyt.M1 component model are shown in Fig. 9c and 9d for the 1st and 2nd mode load pattern, respectively. The IIIDAP program was used to compute median displacements for the equivalent modal SDOF systems using the 44 FEMA P695 ground motions.

Based on Goel and Chopra [34] an improved estimate of plastic hinge rotations and member forces using MPA into the inelastic range can be obtained by computing plastic hinge rotations from the total story drifts [36]. However, this will require an additional nonlinear static analysis. For simplicity purposes, this approach was not implemented in the results presented in this section. But in many cases, particularly for low-rise regular structure, the higher mode target displacement obtained from the equivalent SDOF system is less than the yield displacement, which implies that the higher mode contribution is elastic. If this is the case, all deformations and forces obtained from the MPA are modal combinations of inelastic first mode contributions and elastic higher mode contributions. In general, this is a preferred procedure compared to the elastic response spectrum analysis (RSA) in which all modal contributions are assumed to be elastic up front [18].

The results presented in this section are for the four- and eight-story steel MRFs. Note that their seismic response has not entered the negative tangent stiffness region. The following summary observations are made on the benefits of MPA predictions for steel SMFs compared to single mode NSP predictions:

1. In all cases investigated the MPA led to improved EDP predictions compared to the single mode NSP options. The MPA employed here is based on the component model used in the NRHA (Analyt.M1) and on predicting modal target displacements from NRHA of equivalent modal SDOF systems.

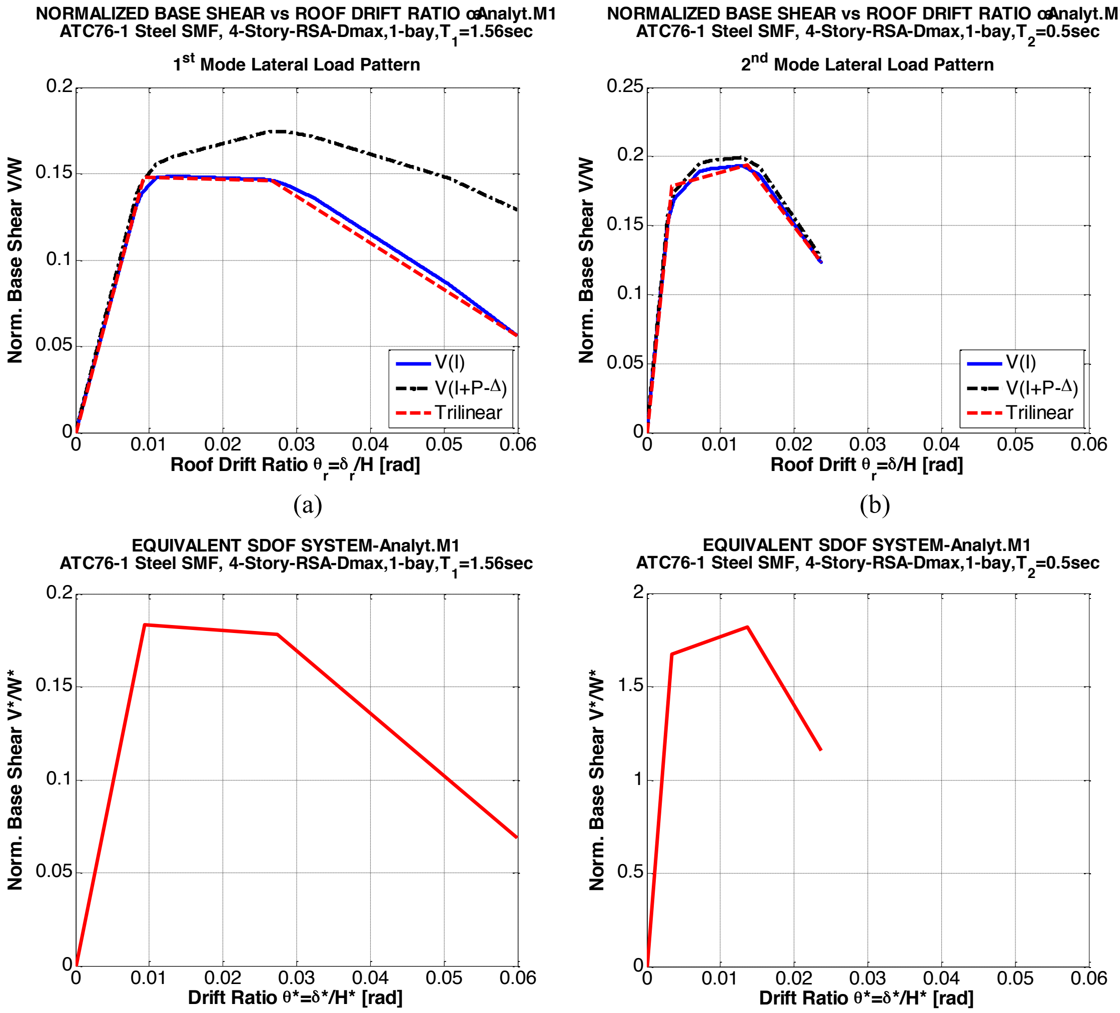

(a) (b)

(c) (d)

Figure 9: Pushover curves for 1st and 2nd lateral load pattern of the 4-story-RSA-Dmax steel MRF together with equivalent SDOFs.

2. Incorporation of the second mode led to considerable improvement in EDP predictions. Consideration of the 3rd mode did not change the results by much even for the eight-story steel MRF (see Fig. 10).
3. In the case of the four-story steel MRF (see Fig. 10a, 11c, 10e) the improvement of all story-based EDP predictions compared to NSP predictions is remarkable. In the eight-story steel MRF the MPA significantly improved story drift ratios (Fig. 10b), shear force (Fig. 10d), and overturning moment predictions in the upper stories (Fig. 10f), compared to NSP. But predicted drifts based on MPA in the lower stories are more than 50% larger than those obtained from NRHA for a ground motion scale factor of 2.0. The reason is that for this scale factor the first mode pushover shows large amplification of story drifts in the lower stories, which is not present in the NRHA. This shows the sensitivity to invariant load patterns, which is present as much in the MPA as it is in a single mode NSP.
4. The second mode contribution was elastic, which simplifies the modal combination and avoids ambiguities that might be caused by displacement reversals sometimes observed in inelastic higher mode pushover analyses.

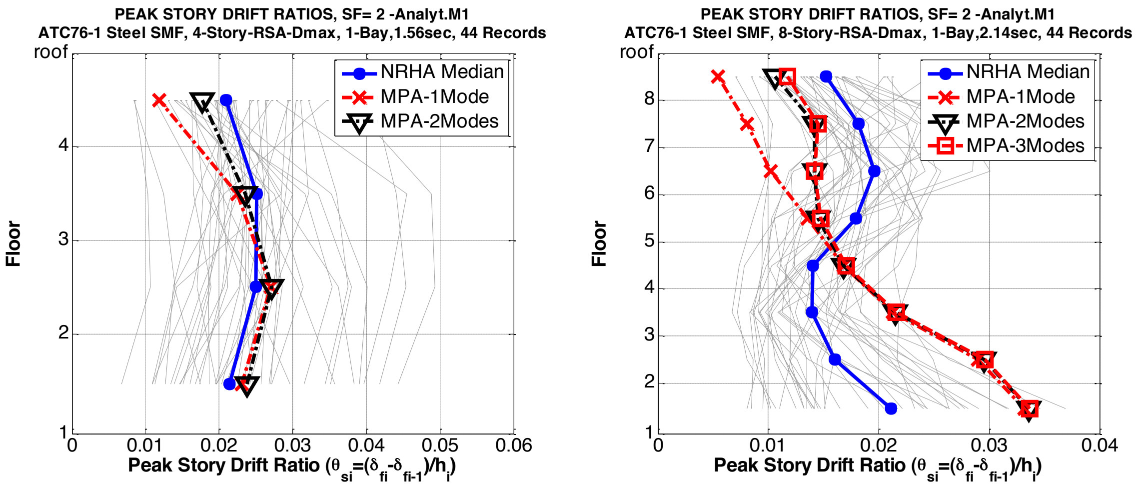

(a) four-story steel MRF (b) eight-story steel MRF

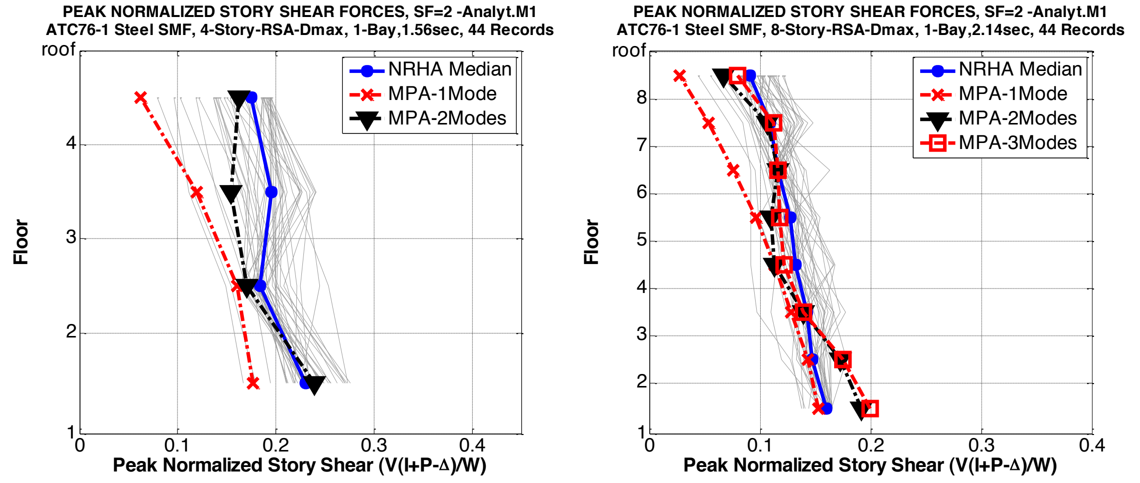

(c) four-story steel MRF (d) eight-story steel MRF

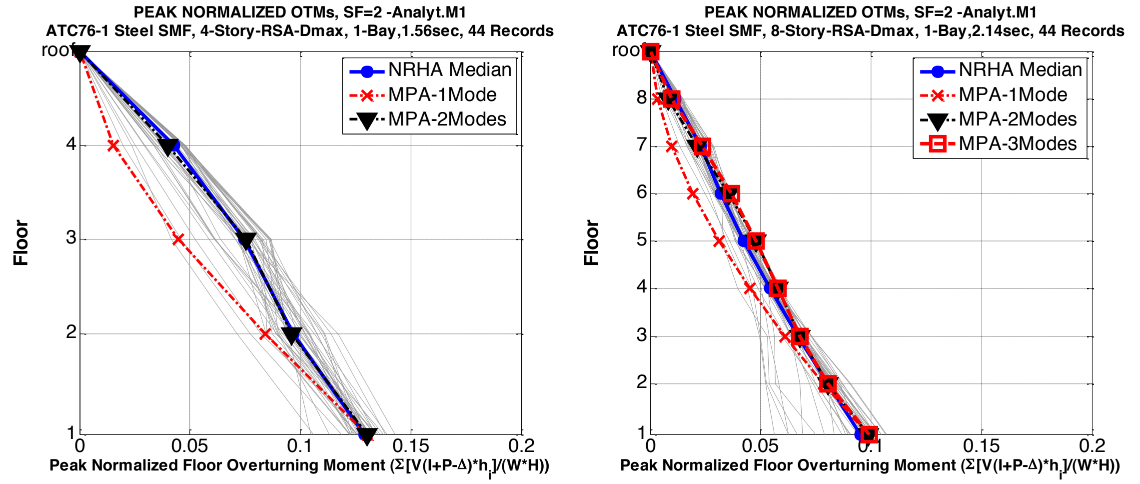

(e) four-story steel MRF (f) eight-story steel MRF

Figure 10: Peak EDPs for the four and eight-story steel MRF as predicted with NRHA and MPA for SF=2.0.

4.4 Residual deformations and absolute acceleration demands

Figure 11 shows residual story drift ratios and peak absolute floor accelerations along the height of the four-story steel MRF for SF=1.0 and 2.0. It is noteworthy that the maximum absolute floor acceleration does not vary radically over the height of the four-story MRF, and that it is distributed almost uniformly over the height for a ground motion scale factor of 2.0 at which the structure responds in the highly inelastic range. Similar observations are made for all structures in this study. It is a shortcoming of the NSP that it does not provide any estimation of these two important EDPs, considering the increasing importance of floor acceleration and residual drift in loss assessment of structures [37-39], and the importance of floor accelerations in estimating diaphragm forces.

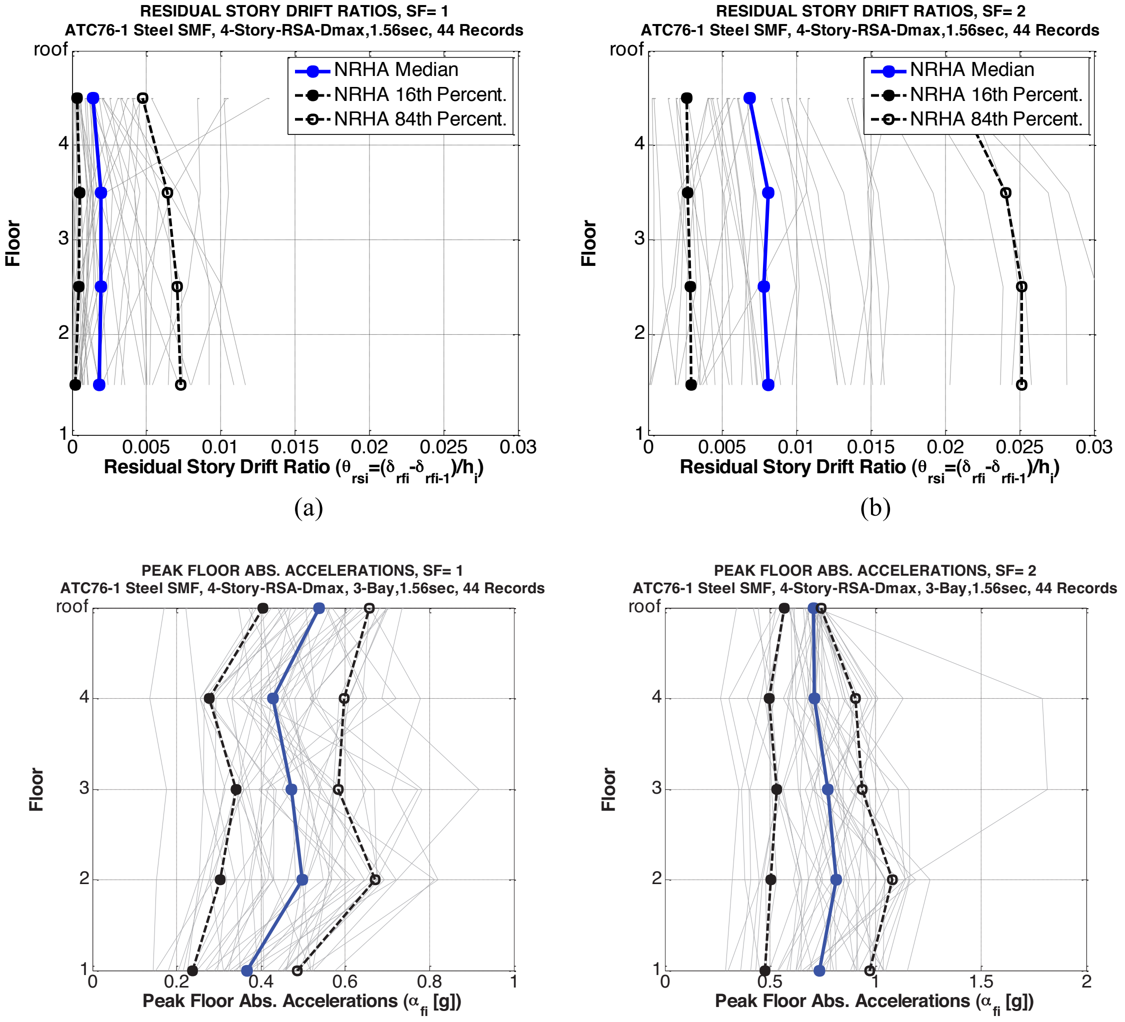

(a) (b)

(c) (d)

Figure 11: Residual story drift ratios and peak floor accelerations for the four-story MRF for SF=1.0 and 2.0.

5 CONCLUSIONS

This paper presents an assessment of simplified techniques for the seismic evaluation of steel moment resisting frames. This assessment is based on direct comparison of engineering demand parameters such as story drift ratios, story shear forces and overturning moments as predicted with nonlinear single and multi mode static procedures and nonlinear response history analysis. The analytical models employed in this study are 2-dimensional models of two, four and eight-story archetype steel buildings designed as part of NIST [19]. Detailed 3-bay models and simplified 1-bay "models of the steel MRFs of these buildings are utilized, with the results being almost identical. Modeling of gravity framing can be achieved by means of a simple fishbone model. The main findings from the results presented here, which are representative for regular moment frames only, are summarized as follows:

- For regular frames of 4 and more stories, results from a single mode pushover analysis with an invariant load pattern do not correlate well with median results from nonlinear response history analysis. This holds true for story drifts, shear forces, and overturning moments.
- Modal Pushover Analysis leads to improved EDP predictions compared to the single mode NSP options by incorporating the second mode in the analysis in addition to the first mode. The second mode contribution is elastic for the cases evaluated in this study, which simplifies the modal combination.
- The sensitivity to invariant load patterns in single mode NSP and MPA typically leads to amplification of story drifts in lower stories compared to NRHA.
- Incorporating the effect of gravity system into the analytical model of the structural system typically leads to a reduction in story drift ratios compared to the bare frame only. This reduction may not be very important, except when the ground motion intensity is large and collapse becomes an issue. Further studies need to be conducted to address in detail the effect of gravity system on the seismic response of steel MRFs.
- Nonlinear static analysis procedures are not capable of providing relevant information on residual drifts and floor accelerations. These two EDPs are very important in loss assessment of buildings; the former for nonstructural acceleration sensitive damage, and the latter for assessing the need for demolition.
- In the authors' opinion, the main value of a nonlinear static (pushover) analysis is to inspect the load-deformation response at a global and local level for the purpose of evaluating behavior characteristics such as importance of P-Delta effect, global yielding, and post-yield and post-capping strength and stiffness characteristics, and for detection of potential strength and stiffness discontinuities that might adversely affect dynamic response. Quantification of demand parameters from pushover results is questionable for structures that have considerable higher mode effects and/or significant strength or stiffness discontinuities. Such quantification can be obtained, approximately, from NRHA using simple component models such a bilinear hysteresis model, and a small set of spectrum-matched ground motions. More accurate assessment of demand parameters, including measures of uncertainties, will necessitate more accurate structural modeling for NRHA and ground motions that represent the intensity characteristics and record-to-record variability inherent in seismic hazard.

ACKNOWLEDGEMENTS

This paper relies on results obtained under Task Order 6 of the NEHRP Consultants Joint Venture (a partnership of the Applied Technology Council and Consortium of Universities for Research in Earthquake Engineering), under Contract SB134107CQ0019, Earthquake Structural and Engineering Research, issued by the National Institute of Standards and Technology. The views expressed do not necessarily represent those of the organizations identified above.

REFERENCES

[1] ATC, “Seismic evaluation and retrofit of concrete buildings,” ATC 40 Report, Volumes 1 and 2, Applied Technology Council, Redwood City, CA., 1996.

[2] ASCE, “Seismic evaluation of existing buildings,” ASCE Standard ASCE/SEI 31-03, American Society of Civil Engineers/Structural Engineering Institute, Reston, VA., 2003.

[3] ASCE, “Seismic rehabilitation of existing buildings,” ASCE Standard ASCE/SEI 41-06, American Society of Civil Engineers/Structural Engineering Institute, Reston, VA., 2007.

[4] FEMA, “NEHRP guidelines for the seismic rehabilitation of buildings,” FEMA 273 Report, prepared by the Applied Technology Council for the Federal Emergency Management Agency, Washington, D.C., 1997.

[5] FEMA, “Improvement of nonlinear static seismic analysis procedures,” FEMA 440 Report, prepared by the Applied Technology Council for the Federal Emergency Management Agency, Washington, D.C., 2005.

[6] FEMA, “Effects of strength and stiffness degradation on seismic response,” FEMA P-440A Report, prepared by the Applied Technology Council for the Federal Emergency Management Agency, Washington, D.C., 2009.

[7] FEMA, “Quantification of building seismic performance factors,” FEMA P-695 Report, prepared by the Applied Technology Council for the Federal Emergency Management Agency, Washington, D.C., 2009.

[8] M. Saiidi, M.A. Sozen, “Simple nonlinear seismic analysis of R/C structures,” *Journal of the Structural Division,* ASCE*,* 107 (**ST5**), pp. 937–951, 1981.

[9] P. Fajfar P. Gaspersic, “The N2 method for the seismic damage analysis of RC buildings,” *Earthquake Engineering and Structural Dynamics,* EESD*,* 25 **(1)**, pp. 31–46, 1996.

[10] R.S. Lawson, V. Vance, H. Krawinkler, “Nonlinear static pushover analysis — why, when and how?,” *Proceedings 5th US Conf. Earthq. Engng* Chicago, IL, **(1)**, pp. 283–292, 1994.

[11] J.M. Bracci, S.K. Kunnath, A.M. Reinhorn, “Seismic performance and retrofit evaluation of reinforced concrete structures,” *Journal of Structural Engineering,* ASCE*,* 123 **(1)**, pp. 3–10, 1997.

[12] H. Krawinkler, G.D.P.K. Seneviratna, “Pros and cons of a pushover analysis for seismic performance evaluation,” *Journal of Engineering Structures*, 20 **(4-6)**, pp. 452-464, 1998.

[13] A.K. Chopra, R.K. Goel, “A modal pushover analysis procedure for estimating seismic demands for buildings,” *Earthquake Engineering and Structural Dynamics*, EESD, 31 **(3)**, pp. 561-582, 2002.

[14] B. Gupta, S.K. Kunnath, “Adaptive spectra-based pushover procedure for seismic evaluation of structures,” *Earthquake Spectra,* 16 **(2)**, pp. 367–392, 2000.

[15] K.K. Sasaki, S.A. Freeman, T.F. Paret, “Multimode pushover procedure (MMP)—a method to identify the effects of higher modes in a pushover analysis,” *Proceedings of*

the 6th U.S. National Conference on Earthquake Engineering, Seattle, Washington, 1998.

[16] S. Antoniou, R. Pinho, "Development and verification of a displacement-based adaptive pushover procedure," *Journal of Earthquake Engineering*, 8 **(5)**, pp. 643-661, 2004.

[17] S. Antoniou, R. Pinho, "Advantages and limitations of adaptive and non-adaptive force-based pushover procedures," *Journal of Earthquake Engineering* 8 **(4)**, pp. 497-522, 2004.

[18] NIST, "Applicability of nonlinear multiple-degree-of-freedom modeling for design, GCR 10-917-9," prepared by the NEHRP Consultants Joint Venture for the National Institute of Standards and Technology, Gaithersburg, MD, 2010.

[19] NIST, "Evaluation of the FEMA P-695 methodology for quantification of building seismic performance factors, GCR 10-917-8," prepared by the NEHRP Consultants Joint Venture for the National Institute of Standards and Technology, Gaithersburg, MD, 2010.

[20] AISC, "Prequalified Connections for Special and Intermediate Steel Moment Frames for Seismic Applications," AISC 358-05, American Institute of Steel Construction, Inc., Chicago, IL, 2005.

[21] D.G. Lignos, C. Putman, F. Zareian, H. Krawinkler, "Seismic evaluation of steel moment frames and shear walls using nonlinear static analysis procedures," *Proceedings ASCE Structures Congress*, Las Vegas, April 14th-16th, 2011.

[22] V. Prakash, G.H. Powell, S. Campbell, "DRAIN-2DX: Basic program description and user guide," *Report No. UCB/SEMM-1993/17*, University of California, Berkeley, CA, 1993.

[23] L.F. Ibarra, R.A. Medina, H. Krawinkler, "Hysteretic models that incorporate strength and stiffness deterioration," *Journal of Earthquake Engineering and Structural Dynamics*, EESD, 34 **(12)**, pp.1489–1511, 2005.

[24] D.G. Lignos, H. Krawinkler, "Deterioration modeling of steel components in support of collapse prediction of steel moment frames under earthquake loading," *Journal of Structural Engineering*, ASCE, (accepted for publication), 2011.

[25] H. Krawinkler, V.V. Bertero, E.P. Popov, "Shear behavior of steel frame joints," *Journal of the Structural Division,* ASCE, **101** (11), pp. 2317–2336, 1975.

[26] D.G. Lignos, F. Zareian, H. Krawinkler, "A Steel component database for deterioration modeling of steel beams with RBS under cyclic loading," *Proceedings ASCE Structures Congress,* Orlando Florida*,* May 12th-15th*,* 2010.

[27] N. Luco, Y. Mori, Y. Funahashi, A. Cornell, M. Nakashima, "Evaluation of predictors of non-linear seismic demands using 'fishbone' models of SMRF buildings," *Earthquake Engineering and Structural Dynamics*, EESD, 32 **(14)**, pp. 2267-2288, 2003.

[28] F. McKenna, "Object oriented finite element programming frameworks for analysis, algorithms and parallel computing," *Ph.D. Dissertation*, University of California, Berkeley, CA, 1997.

[29] PEER/ATC, "Modeling and acceptance criteria for seismic design and analysis of tall buildings," PEER/ATC-72-1, prepared by the Applied Technology Council in coopera-

tion with the Pacific Earthquake Engineering Research Center, Redwood City, CA, 2010.

[30] D.G. Lignos, "Interactive interface for incremental dynamic analysis, IIIDAP: Theory and example applications manual, Version 1.1.5," Department of Civil and Environmental Engineering, Stanford University, CA, 2009.

[31] A. Gupta, H. Krawinkler, "Dynamic P-Delta effects for flexible inelastic steel structures," *Journal of Structural Engineering*, ASCE, 126 **(1)**, pp. 145-154, 2000.

[32] J. Liu, A. Astaneh-Asl, "Cyclic testing of simple connections including effects of slab," *Journal of Structural Engineering*, ASCE, 126 **(1)**, pp. 32-39, 2000.

[33] J. Liu, A. Astaneh-Asl, ''Studies and tests of simple connections, including slab effects.'' *Report No. UCB/CEE-Steel-99/01*, University of California, Berkeley, CA, 1999.

[34] R. K. Goel, A. K. Chopra, "Extension of modal pushover analysis to compute member forces", *Earthquake Spectra*, 21, pp. 125-140, 2005.

[35] A.K. Chopra, "Dynamics of structures. Theory and applications to earthquake engineering", *3rd Edition*, Pearson Prentice Hall, Upper Saddle River, NJ, 2007.

[36] A. Gupta, H. Krawinkler. "Seismic demands for performance evaluation of steel moment resisting frame structures (SAC Task 5.4.3)," *Report No. 132*, John A. Blume Earthquake Engineering Center, Stanford University, Stanford, CA., 1997.

[37] S. Pampanin, C. Christopoulos, M.J.N. Priestley, "Residual deformations in the performance-seismic assessment of frame structures," *Report No. ROSE-2002/02*, European School for Advanced Studies in Reduction of Seismic Risk, Pavia, Italy, 2002.

[38] H. Aslani, E. Miranda, "Probabilistic earthquake loss estimation and loss disaggregation in buildings," *Report No. 157*, John A. Blume Earthquake Engineering Center, Stanford University, Stanford, CA, 2005.

[39] C.M. Ramirez, E. Miranda, "Building-specific loss estimation methods & tools for simplified performance-based earthquake engineering," *Report No. 173*, John A. Blume Earthquake Engineering Center, Stanford University, Stanford, CA, 2009.

COMPDYN 2011
3rd ECCOMAS Thematic Conference on
Computational Methods in Structural Dynamics and Earthquake Engineering
M. Papadrakakis, M. Fragiadakis, V. Plevris (eds.)
Corfu, Greece, 25–28 May 2011

SIMPLIFIED METHOD FOR SEISMIC PERFORMANCE ASSESSMENT OF SKEWED BRIDGES

Peyman Kaviani[1*], Farzin Zareian[2], Ertugrul Taciroglu[3], Majid Sarraf[4]

[1] University of California – Irvine
E/4130 Engineering Gateway, Irvine, CA 92697-2175, USA
pkaviani@uci.edu

[2] University of California – Irvine
E/4141 Engineering Gateway, Irvine, CA 92697-2175, USA
zareian@uci.edu

[3] University of California – Los Angeles
5731E Boelter Hall, Los Angeles, CA 90095-1593, USA
etacir@ucla.edu

[4] PARSONS – Irvine
2201 Dupont Drive, Irvine, CA 92656, USA
majid.sarraf@parsons.com

Keywords: Skewed Bridges, Response History Analysis, Structural Dynamics, Earthquake Engineering.

Abstract. *Damage and seismic movements observed in bridges in recent earthquakes have indicated that the response and failure modes of bridges with skew-angled abutments are significantly different from those of bridges with normal abutments. One significant manifestation of this difference is the inherent tendency of skewed bridges to rotate about their vertical axes under seismic excitation. In this study, with the aforementioned field observations in mind, we have conducted parametric response-sensitivity analyses in an effort to identify the key parameters that control the seismic behavior of skewed bridges. This paper describes our simplified modeling technique, which takes bridge-abutment interaction into account, along with the analysis results. Three short bridges located in California were used as subjects. These bridges have different arrangements of number of spans and number of columns per bent; and through nonlinear time-history analyses, we investigated the sensitivity of their various responses to variations in parameters such as torsional stiffness, span arrangement, column height, abutment skew angle, and ground motion characteristics.*

1 INTRODUCTION

Bridge with skew-angled abutments (“skewed bridges”) are constructed to accommodate geometry constraints resulting from the alignment of a waterways or roadway crossing that occurs at an angle that is different form 90 degrees. In the present study we consider only “seat-type” abutments, which are very common in construction practice in California. A seat-type abutment is simpler to construct compared to an “integral abutment.” It reduces service and seismic demands on foundations and allows the superstructure to move freely under thermal, and low-intensity mechanical (service or seismic) loads [1]. Despite having a fair amount of knowledge on the response of bridges with normal abutments [2], the engineering community still lacks quantitative knowledge on the seismic performance of skewed bridges with adequate certainty. As a result, somewhat gross approximations are employed in their design, and the implications of these approximations are not completely understood [3]. There has been a recent surge of studies that were aimed at providing guidelines for nonlinear seismic response-history analysis of regular bridges, primary motivated by developments in performance-based earthquake engineering (PBEE) [4-8]. The present study follows in the footsteps of these efforts, and provides an initial attempt at applying PBEE concepts to skew-angled bridges.

In a seat-type abutment (Figure 1), exterior shear keys are used to counter the deck movement along the transverse direction. They are proportioned and detailed to act as fuses that will break off under the design earthquake [9]. In the longitudinal direction, a backwall that holds an engineered backfill in place is designed to break off and allow the mobilization of the soil mass, which, in turn, generates passive resistance. Observations from past earthquakes indicate [10-12] that one of the primary causes of unseating of the skewed bridges is the pronounced in-plane rotation caused by the eccentric passive resistance of the backfill [13-16]. Post-earthquake reconnaissance reports also suggest that this rotational mode of response is exacerbated once the bridge is subjected to near-field motions [17]. However, there still remains significant uncertainty in predictive models that needs to be alleviated and addressed in order to better quantify such behavior.

In the present study, we adopt a performance-based seismic assessment approach, which starts with the selection of a representative suite of critical ground motions and repeated nonlinear response-history analyses of models with varied parameters. The output is a statistically scattered collection of response metrics. The trends in these measures are what we seek to identify. In what follows, we first describe the details of our modeling approach and the ground motion selection procedures. We then summarize and discuss the results.

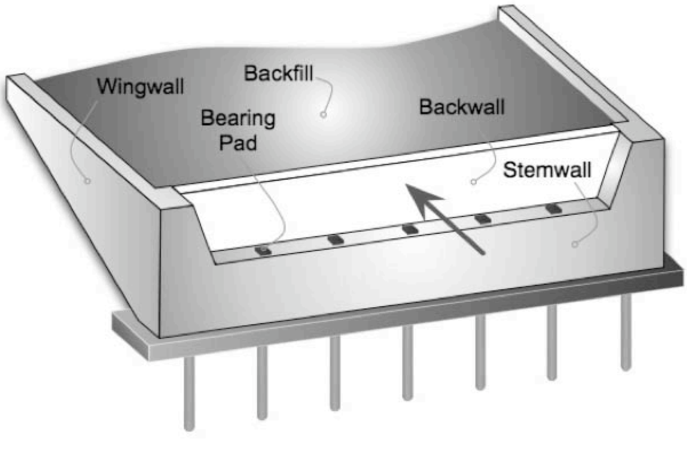

Figure 1: Configuration of typical seat-type abutment (adopted from [2]).

2 ANALYTICAL MODEL

For the present study, we have selected three actual bridges as seeds for our parametric response-sensitivity analyses. These bridges are recently designed and built (ca. 2000) in Southern California, at regions with high seismicity. The first bridge is the *Jack Tone Road Overcrossing*, which over-crosses Route 99 at the City of Ripon. It has a typical configuration encountered frequently in California. Its total length is 67.2 m, consisting of two (33.1m and 34.1 m) spans with a single column. It has seat-type abutments with four elastomeric bearing pads on each seat. The superstructure is a three-cell continuous reinforced concrete box-girder. The bent-cap is integral with the deck and the concrete column. The column has a 1.68-m diameter and is supported on steel piles. Its longitudinal reinforcing steel ratio is approximately 2%.

The second bridge is the *La Veta Avenue Overcrossing*. It is also a two-span structure; but it is supported on a multi-column bent. As such, it has a larger global torsional stiffness than the single-column Jack Tone Road Bridge. The third bridge is the *Jack Tone Road Overhead*. It is a three-span and multi-column bridge, and has the largest global torsional stiffness among the three bridges studied here.

A representative analytical model used in the parametric studies is displayed in Figure 2. The modeling platform is OpenSees [18], which provides an adequate element and material response library, and enables scripted execution of repetitive nonlinear response-history analyses in which the model parameters and input ground motions can be systematically varied. The present modeling assumptions follow the general guidelines suggested in Caltrans' Seismic Design Criteria document [3], and the studies by Aviram *et al.* [6] and Kaviani *et al.* [19-20].

The superstructure is modeled as a three-dimensional spine that follows the alignment of the bridge with line elements located at the centroid of the cross-sections. The model features various nonlinear elements, which capture the behavior of components that significantly impact the response. These include column plastic hinges, transverse and longitudinal springs that mimic passive abutment reaction, and abutment gap elements. As no damage or significant nonlinear behavior is expected within the superstructure and the foundation system, the superstructure elements, the cap beam, and the foundation springs are all considered as linear elastic elements.

2.1 Column Bent Modeling

Progression of column yielding and damage is expected under strong ground motions, and thus nonlinear fiber-based force-based beam finite elements are used to represent the columns (Figure 3). In order to achieve a more realistic representation of their response, the beam finite elements representing them are endowed with the ability to respond inelastically at every quadrature point. All fiber sections are assigned with the *UniaxialMaterial* model tag of OpenSees [18]. Three different constitutive rules are used depending on which material a given fiber of the cross-section represents—*viz.*, (*i*) confined concrete, (*ii*) unconfined concrete, and (*iii*) steel rebar.

The specific beam finite element of the OpenSees library used in the simulations is the *NonlinearBeamColumn*, which has a force-based formulation that enables a more accurate accounting of the moment distribution within the element [21]. A single force-based element with 10 quadrature points is used per column, and this is usually deemed to provide adequate accuracy. In order to model the portion of the column-bent embedded in the superstructure, a rigid element is attached to the top of the nonlinear beam-column element. The length of this rigid element was set equal to the distance between the centroid of the soffit-flange of the superstructure box-girder and the column top.

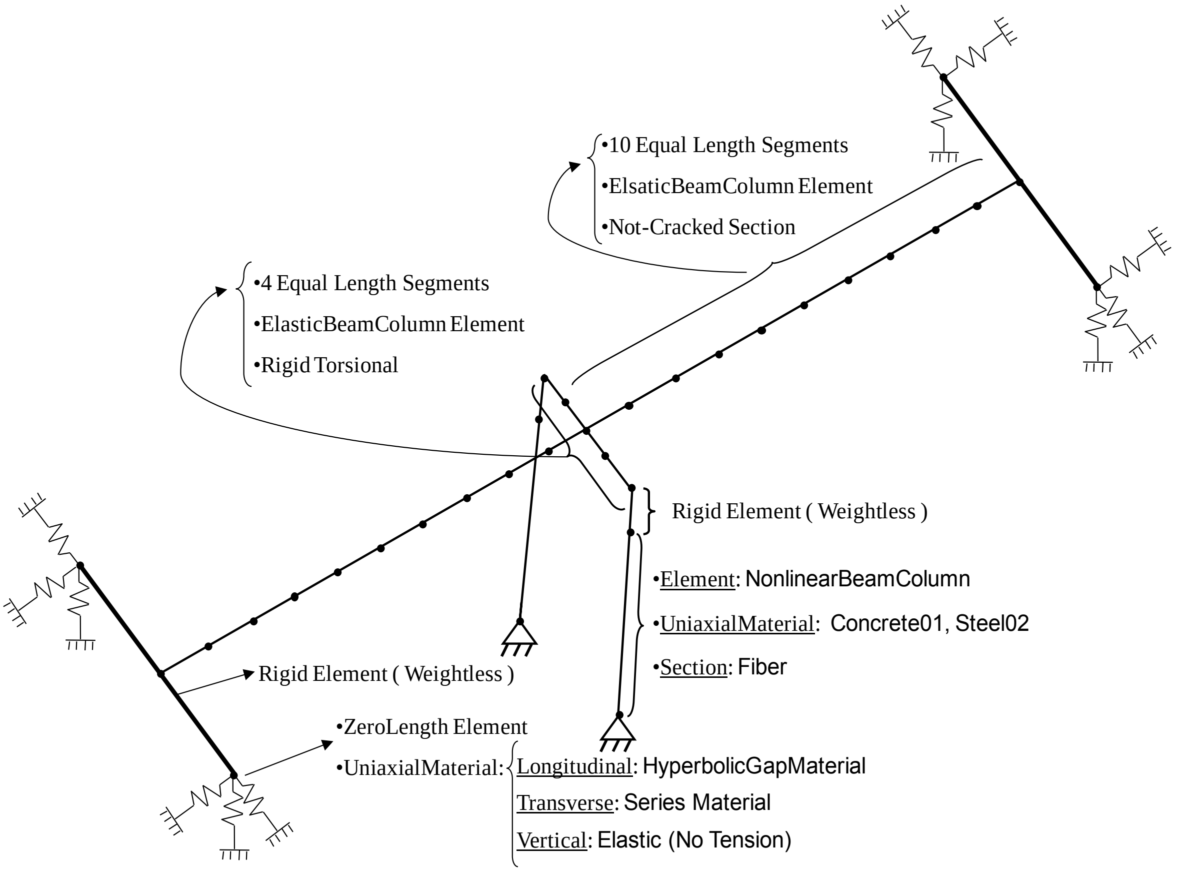

Figure 2: Typical analytical model used for nonlinear time-history analysis of skewed bridges.

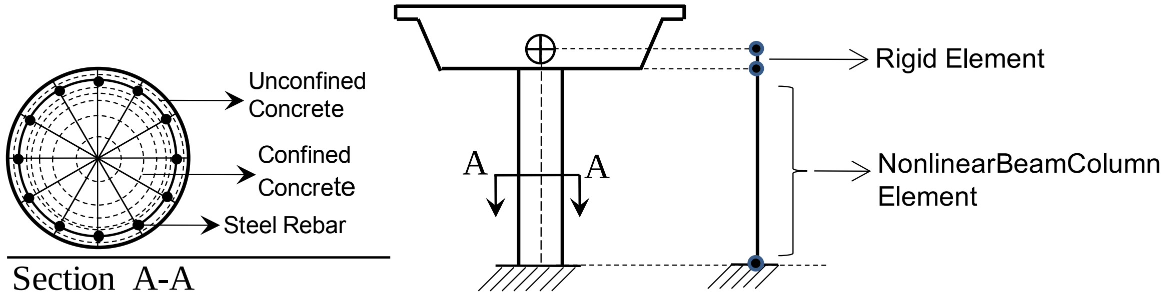

Figure 3: Column analytical modeling scheme.

2.2 Abutment Modeling

The model of the abutments is adopted from a simplified modeling technique (Figure 4) as recommended by Preistley et al. [22] and Aviram et al. [6]. Each abutment is modeled with a massless rigid element of length equal to the superstructure width, connected through a rigid joint to the superstructure centerline, and with a zero-length element at each.

In the longitudinal direction, the response is governed by a zero-length, tension-free (gap) element. In compression, it behaves as an elastic-perfectly-plastic material once the gap is closed. The gap size is proportional to the expansion joint detail as shown on the bridge as-built plans. The stiffness and the equivalent yield strength are defined according to Section 7.8 of Caltrans SDC [3]. The rotation about the longitudinal direction is not allowed.

In the transverse direction, the behavior is characterized as elastic compression-only response. The abutment stiffness and the backwall strength for the longitudinal direction are modified by corresponding wall effectiveness factor (C_L) of 2/3 and participation factor (C_w) of 4/3. The wingwall length is assumed to be 1/3 times the back wall length.

In the vertical direction, only simple elastic material properties associated with the bearing pads are included upon assuming that the response in this direction does not significantly impact the horizontal movements,

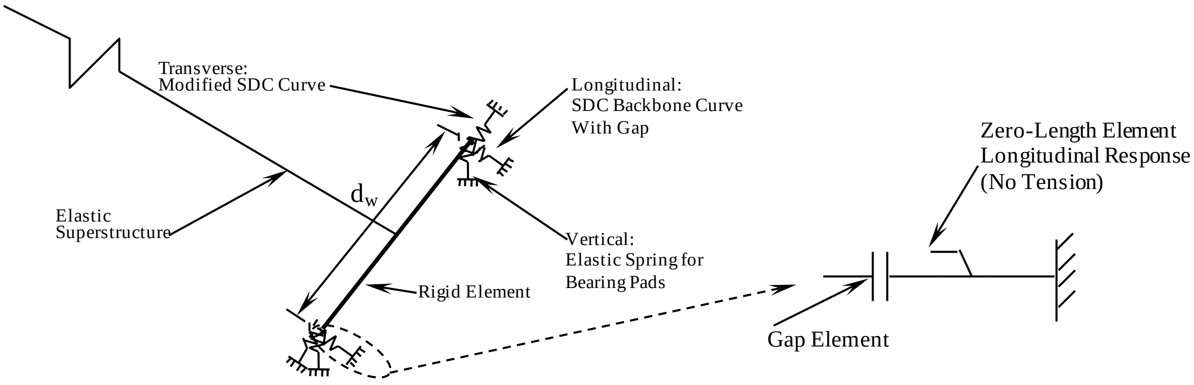

Figure 4: Simplified abutment model

3 GROUND MOTIONS

To investigate the sensitivity of bridge responses to a sufficiently diverse range of ground motions that are representative of those recorded in California, three sets of ground motions were selected from the “EQ Library” that was developed as part of the *PEER Transportation Research Program* [23]. These sets are denoted as “Soil,” “Rock,” and “Pulse.” Each set comprises forty ground motions. Figures 5, 6, and 7 show the fault-normal and fault-parallel spectra for these three ground motion sets, respectively. The EQ Library motions do not represent motions that are specific to the site of the bridges considered in this study; they are generic and are merely used to observe the general trends within the seismic responses. The ground motions in the EQ Library are originally selected from a subset of the PEER NGA Project ground motion library [24] representing mid- to large-magnitude earthquakes occurring at close distances. Selected motions have a variety of spectral shapes, durations, and directivity periods. For each set, the mean and variance of the natural logarithm of spectral acceleration match the generic $M_w = 7$ and $R = 10$ km scenario for California.

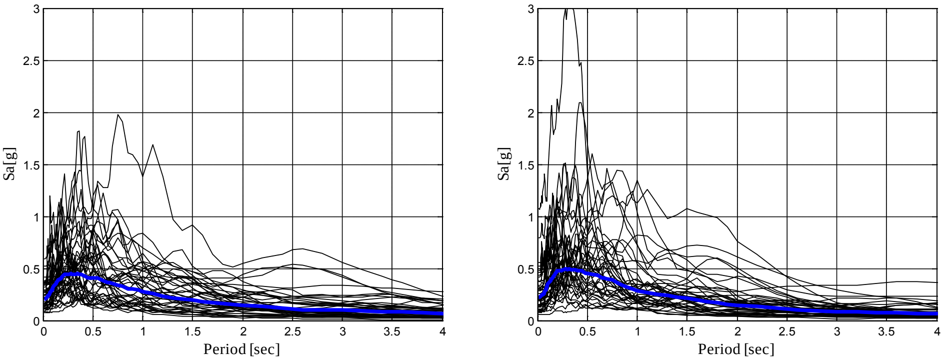

(a) (b)

Figure 5: Response spectra of Soil-type ground motions:
(a) Fault-normal component, (b) Fault-parallel component

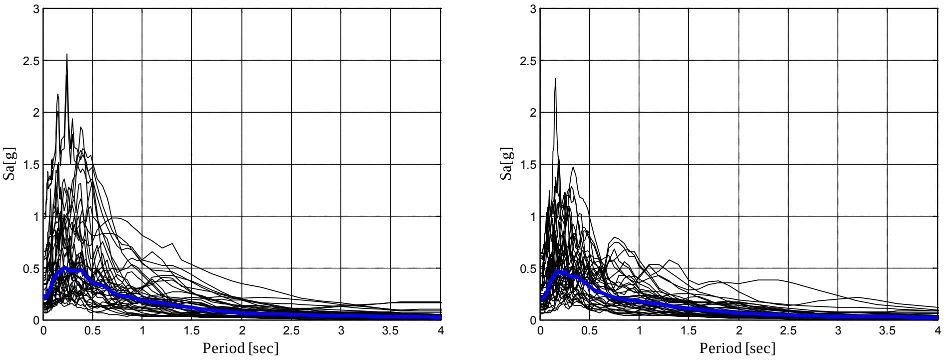

(a) (b)

Figure 6: Response spectra of Rock-type ground motions:
(a) Fault-normal component, (b) Fault-parallel component

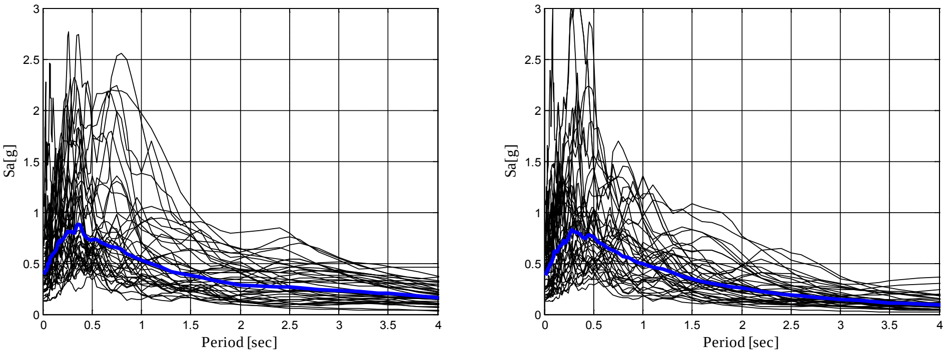

(a) (b)

Figure 7: Response spectra of Pulse-type ground motions:
(a) Fault-normal component, (b) Fault-parallel component

4 OBSERVATIONS

We investigated the sensitivities of seismic responses of the specimen skewed bridges to variations in their structural properties by analyzing each instance of the models under each ground motion. The four response measures—henceforth referred to as *Engineering Demand Parameters* (EDPs)—that we selected were the maximum values of deck rotation, column drift ratio, abutment unseating, and transverse abutment displacement.

4.1 Deck Rotation

The results indicate that deck rotation is highly sensitive to bridge structural properties and ground motion characteristics. Figure 8 shows the variation of deck rotation as a function of abutment skew angle of the Jack Tone Road Overcrossing for different types of ground motion. The solid lines show the estimated median, and the individual data points are depicted with solid dots on the plot. Figures 8(a) and 8(b) show deck rotation variation due to the abutment skew angle increment; however, they differ in span arrangement. In the asymmetrical span arrangement of the bridge (Figure 8(b)), the span lengths differ by 20%.

Results in Figures 8(a) and 8(b) indicate that by increasing the abutment skew angle from 0^{o} to 30^{o}, the median estimate of deck rotation increases, regardless of the type of applied ground motion or span configuration. However, for higher skew angles ranging from 30^{o} to 60^{o}, the deck rotation increases for the symmetric-span configurations (i.e., Jack Tone Overcrossing); whereas the increasing trend continues on for the asymmetrical one. This behavior is particularly pronounced for pulse-like ground motions.

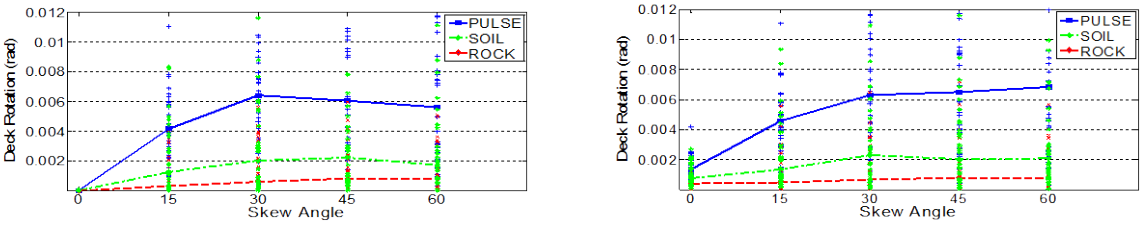

(a)

(b)

Figure 8: Deck Rotation Sensitivity to span arrangement: (a) Symmetrical spans, (b) Asymmetrical spans

The effect of abutment gap-size variation on the selected EDPs is shown in Figure 9. Four abutment gap-sizes (0.25, 0.5, 1.0, and 2.0 in.) are investigated. For deck rotation, it is observed that for skew angles less than 40°, the curves corresponding to different abutment gap-sizes are approximately matched. However, for larger skew angles the bridge with the 0.25-in. gap distance rotates more, in comparison to that with a 2-in. gap. This trend indicates that with reducing gap-distance, the bridge rotates more for higher skew angles. Less gap-distance between the deck and the backwall results into more effective impact forces impose to the superstructure by backfill soil.

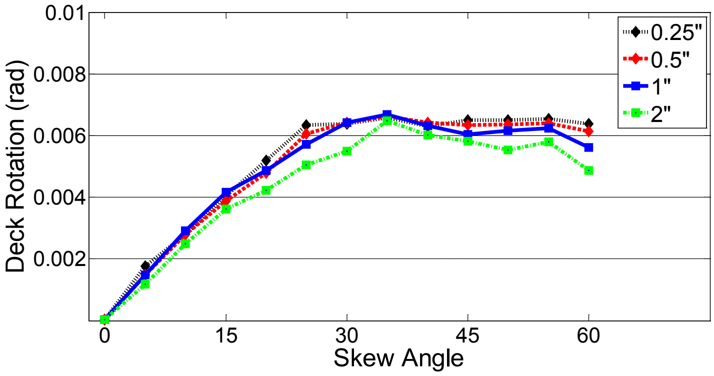

Figure 9: Deck rotation sensitivity to abutment gap size

Considering the variations in column height, the general observation is that for a given skew angle, bridges with taller and more flexible columns tend to have larger deck rotations. Figure 10 shows this general trend.

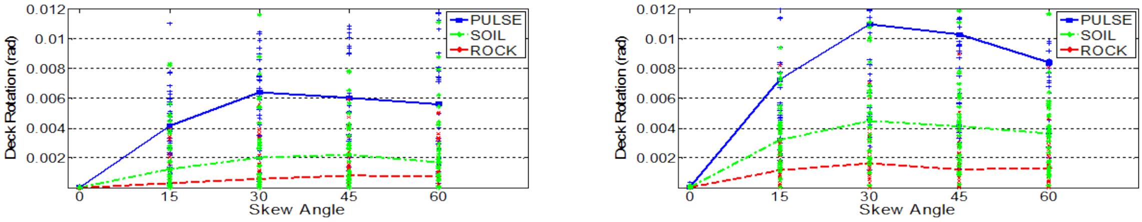

(a)

(b)

Figure 10: Deck rotation sensitivity to column bent elevation: (a) Lower column, (b) Higher column

4.2 Column Drift Ratio

Results for the two-span single-column bridge (i.e., Jack Tone Overcrossing) indicate that the column drift ratio (CDR) for smaller values of column height is insensitive to abutment skew angle (Figure 11). This behavior is likely due to the particular mode shape of vibration for the single column bridge in which the rotation of the deck increases as the skew angle increases, but the column usually remains near the center of rotation. However, for higher columns (Figure 12), CDR increases with increasing skew angle. For instance, for lower values of column height (the actual height of the Jack Tone Overcrossing), the CDR varies smoothly around 4%. However, for higher values (as a common assumption in design practice, we considered higher-level height of the columns as eight times its diameter), the CDR ranges from 2.5% to more than 4%; and it has greater values for the 60° skew angle. This trend demonstrates that if column stiffness is decreased, then the sensitivity of CDR to abutment skew angle increased.

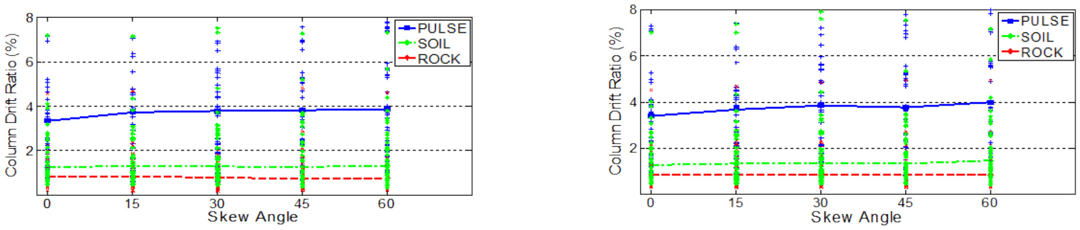

(a)

(b)

Figure 11: Column drift ratio sensitivity (lower column) to span arrangement:
(a) Symmetrical spans, (b) Asymmetrical spans

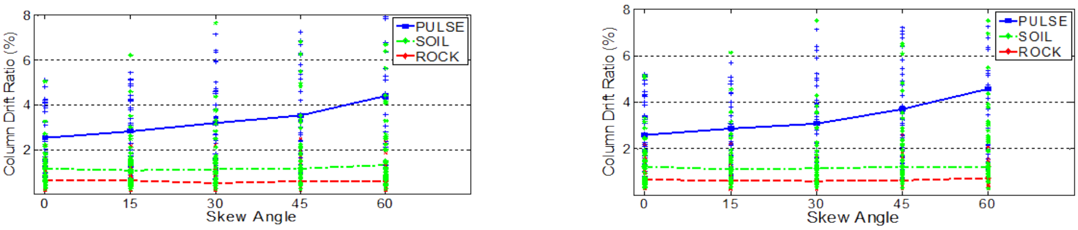

(a) (b)

Figure 12: Column drift ratio sensitivity (higher column) to span arrangement: (a) Symmetrical spans, (b) Asymmetrical spans

4.3 Abutment Unseating

As displayed in Figure 13, incidence of the unseating of abutment is increased by skew angle, particularly for the higher range of skew angles. As expected, the abutment unseating increases with increasing skew angles, because the effective stiffness of the abutment in the longitudinal direction is reduced for larger skew angles.

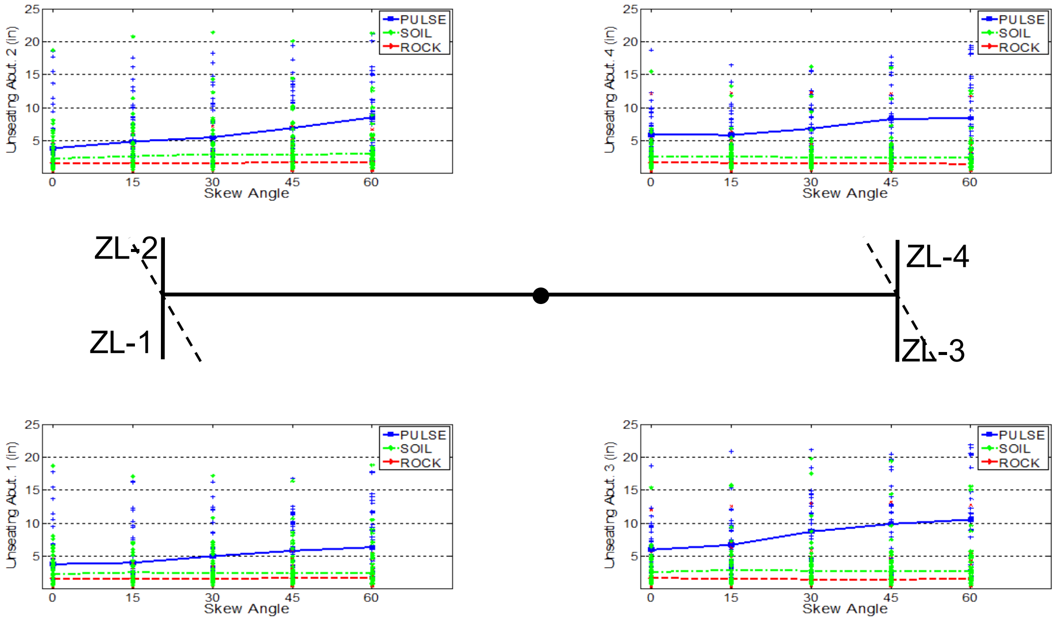

Figure 13: Abutment unseating for symmetrical span arrangement (recorded form the ZeroLength elements, located at each abutment corner)

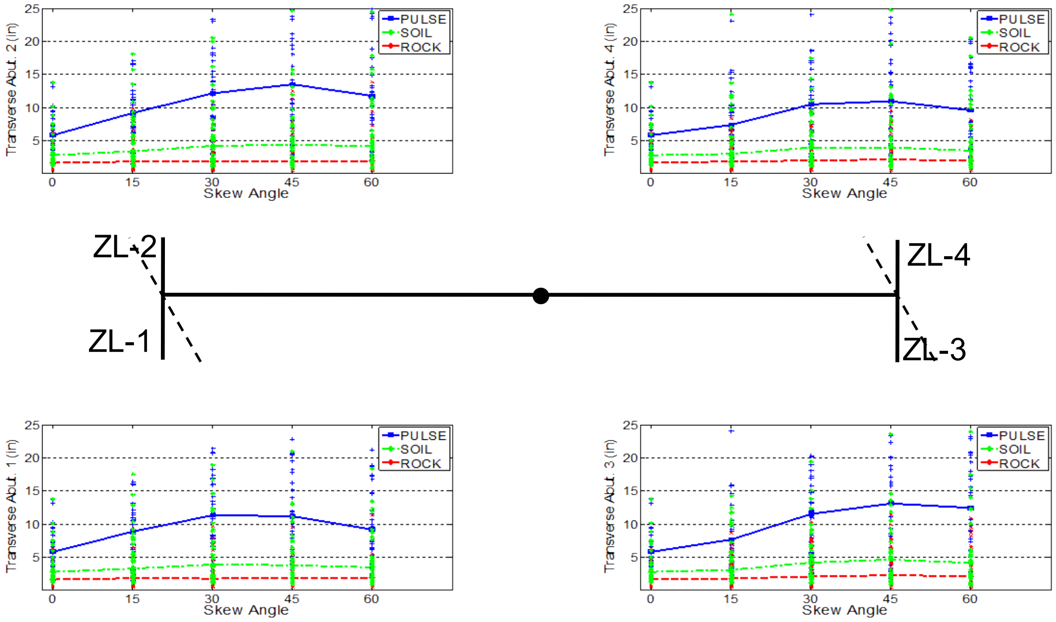

Figure 14: Transverse abutment displacement for symmetrical span arrangement (recorded form the ZeroLength elements, located at each abutment corner)

4.4 Transverse Abutment Displacement

As the deck rotational response here is calculated by dividing the difference between abutment transverse displacements at both ends of the bridge to the bridge length, the abutment transverse displacement is expected to follow a similar trend as the deck rotation. As expected, the transverse abutment displacement increases with increasing skew angle from 0° to 30°, but slightly decreases thereafter, particularly for symmetrical span arrangements (Figure 13).

5 SUMMARY

In this study, we investigated the sensitivity of seismic response of skewed bridges to variations in critical parameters using simulations carried out as nonlinear time-history analyses. Seismic response parameters that we looked into include deck rotation, column drift ratio, abutment unseating, and transverse displacement of abutment. We used three bridges located in California as seeds for our parametric study. These bridges mainly differ in their global torsional resistance. Multiple analytical bridge models were generated from each of three seed bridges by varying the original bridges’ geometrical properties, which included abutment skew angle, span arrangement, and column height. In addition, we studied effects of ground motion characteristic on the seismic response of skewed bridges by introducing three types of ground motions into our response-sensitivity analyses. These were soil-site, rock-site, and pulse-like ground motions. We observed that less gap size between the deck and the backwall results in more effective impact forces that mobilize the backfill soil and leads to higher deck rotation; especially when the bridge is subjected to pulse-like ground motions. Column drift ratio is significantly sensitive to the column height, abutment skew angle, and number of columns in each bent. Abutment unseating increases by increasing skew angle, particularly for bridges with tall columns.

ACKNOWLEDGEMENTS

This study is based on work supported by the by the PEER Transportation Research Program under Grant No. UCLA-45782. This financial support is gratefully acknowledged. Any opinions, findings, and conclusions or recommendations expressed in this paper are those of the authors and do not necessarily reflect the views of sponsors.

REFERENCES

[1] Caltrans, *Memos to Designers 5-1*. California Department of Transportation, Sacramento, 1996.

[2] A. Shamsabadi, P. Khalili-Tehrani, J.P. Stewart, E. Taciroglu, Validated simulation models for lateral response of bridge abutments with typical backfills. *ASCE Journal of Bridge Engineering*, **15**(3), 302-311, 2010.

[3] Caltrans SDC (ver. 1.4), *Caltrans Seismic Design Criteria Version 1.4*. California Department of Transportation, Sacramento, 2006.

[4] A. Kotsoglou, S. Pantazopoulou, Response Simulation and Seismic Assessment of Highway Overcrossings. *Earthquake Engineering and Structural Dynamics*, **39**(9), 991-1013, 2010.

[5] N. Johnson, M.S. Saiidi, D. Sanders, Nonlinear Earthquake Response Modeling of a Large-Scale Two-Span Concrete Bridge, *ASCE Journal of Bridge Engineering*, **14**(6), 460-471, 2009.

[6] A. Aviram, K. R. Mackie, B. Stojadinović, Guidelines for Nonlinear Analysis of Bridge Structures in California. *PEER Report 2008/3*, Pacific Earthquake Engineering Research Center, 2008.

[7] K. R. Mackie, B. Stojadinovic, Performance-Based Seismic Bridge Design for Damage and Loss Limit States, *Earthquake Engineering and Structural Dynamics*, **36**(13), 1953-1971, 2007.

[8] T. S. Paraskeva, A. J. Kappos, A. G. Sextos, Extension of Modal Pushover Analysis to Seismic Assessment of Bridges. *Earthquake Engineering and Structural Dynamics*, **35**(10), 1269-1293, 2006.

[9] A. Bozorgzadeh, S. Megally, J. I. Restrepo, S. A. Ashford, Capacity Evaluation of Exterior Sacrificial Shear Keys of Bridge Abutments. *ASCE Journal of Bridge Engineering*, **11**(5), 555-565, 2006.

[10] M. Yashinsky, *Performance of highway and railway structures during the February 27, 2010 Maule Chile earthquake*. EERI/PEER/FHWA Bridge Team Report, 2010. http://peer.berkeley.edu/publications/chile_2010/reports_chile.html

[11] K. Kawashima, S. Unjoh, J. Hoshikuma, K. Kosa, *Damage of transportation facility due to 2010 Chile earthquake (April 5, 2010)*. Bridge Team Dispatched by Japan Society of Civil Engineers, 2010. http://peer.berkeley.edu/publications/chile_2010/reports_chile.html

[12] P. C. Jennings, J. H. Wood, *Engineering Feature of the San Fernando Earthquake*. EERL 71-02, Pasadena, California, 1971.

[13] J. Y. Meng, E. M. Lui, Seismic Analysis and Assessment of a Skew Highway Bridge. *Engineering Structures*, **22**, 1433-1452, 2000.

[14] R. R. Wakefield, A. S. Nazmy, D. P. Billington, Analysis of Seismic Failure in Skew RC Bridge. *ASCE Journal of Structural Engineering*, **117**(3), 972-986, 1991.

[15] A. A. Ghobarah, W. K. Tso, Seismic Analysis of Skewed Highway Bridges with Intermediate Supports. *Earthquake Engineering and Structural Dynamics*, **2**(3), 235-248, 1974.

[16] P. C. Jennings, J. H. Wood, Engineering Feature of the San Fernando Earthquake. *EERL 71-02*, Pasadena, California, 1971.

[17] A. Shamsabadi, K. M. Rollins, M. Kapuskar, Nonlinear Soil–Abutment–Bridge Structure Interaction for Seismic Performance-Based Design. *ASCE Journal of Geotechnical and Geoenvironmental Engineering*,**133**(6), 707-720, 2007.

[18] F. McKenna, G. L. Fenves, M. H. Scott, Open System for Earthquake Engineering Simulation. University of California Berkeley, California, 2000. http://opensees.berkeley.edu

[19] P. Kaviani, F. Zareian, M. Sarraf, Comparison of Seismic Response of skewed Bridges to Near vs. Far Field Motions. *7th International Conference on Urban Earthquake Engineering & 5th International Conference on Earthquake Engineering*, Tokyo, Japan, March 3-5, 2010.

[20] P. Kaviani, F. Zareian, M. Sarraf, P. Pla-Junca, Sensitivity of Skewed-Bridges Response to Seismic Excitations. *14th European Conference on Earthquake Engineering*, Ohrid, Republic of Macedonia, August 30- September 3, 2010.

[21] A. Neuenhofer, F. C. Filippou, Evaluation of Nonlinear Frame Finite-Element Models, *Journal of Structural Engineering, ASCE*, **123**(7), 958-966, 1997.

[22] M. J. N. Priestly, F. Seible, G. M. Calvi, *Seismic Design and Retrofit of Bridges*. John Wiley & Sons, Inc., New York, 1996.

[23] N. Jayaram, S. Shahi, J. Baker, *Ground Motion for PEER Transportation Research Program*, 2010. http://peer.berekeley.edu/transportation/gm_peer_transportation.html

[24] PEER, Pacific Earthquake Engineering Research Center: PEER NGA Database. University of California, Berkeley, 2010. http://peer.berkeley.edu/nga

COMPDYN 2011
III ECCOMAS Thematic Conference on
Computational Methods in Structural Dynamics and Earthquake Engineering
M. Papadrakakis, M. Fragiadakis, V. Plevris (eds.)
Corfu, Greece, 25–28 May 2011

DIRECT DISPLACEMENT-BASED SEISMIC ASSESSMENT OF MULTI-SPAN SIMPLY SUPPORTED DECK BRIDGES

D.Cardone[1], V. Capone[1] , G.Perrone[1], and L.Petrini[2]

[1] DiSGG, University of Basilicata
Viale dell'Ateneo Lucano, 85100 Potenza, Italy
donatello.cardone@unibas.it, vito.capone@inwind.it, giuseppe.perr@alice.it,
[2] DIS – Politecnico di Milano
P.zza Leonardo Da Vinci 32, 20133 Milano, Italy
lpetrini@stru.polimi.it

Keywords: Seismic Assessment, Bridges, Damage States, Nonlinear Time History Analysis

Abstract. *Traditional seismic assessment is based on a simple comparison of estimated base shear capacity and base shear demand specified by a seismic code. The required code base shear is found by reducing the elastic base shear force corresponding to the elastic stiffness of the structure, by a code-specified force-reduction or behaviour factor. The problems with this approach are that no assessment is made of the actual collapse mechanism, inelastic deformed shape and ductility demand of the structure. In recognition of the limitations of force-based design and assessment methods, several researchers have started proposing displacement-based approaches for earthquake engineering evaluation and design, with the aim of providing improved reliability in the engineering process by more directly relating computed response and expected structural performance. The need for accurate seismic assessment methods is particularly important for bridges, due to the crucial role that some bridges (especially highway bridges) have after an earthquake, for allowing the civil protection interventions and first aid organizations. In Italy, many of these "strategic" bridges have been built without antiseismic criteria and, therefore, they need to be assessed against seismic risk. In this extent, the development of an assessment procedure which gives reliable results and, at the same time, is sufficiently simple to be applied on a large population of bridges in a short time is very useful. In this paper a Direct Displacement-Based Seismic Assessment (DDBA) procedure satisfying the aforesaid requirements is proposed. In the paper, the proposed DDBA procedure is applied to a number of bridge configurations derived from a 4-span reinforced concrete simply-supported deck bridge of the A16 Italian highway. Some analyses are also repeated following the traditional force-based seismic assessment approach. Finally, the predictions of the proposed DDBA procedure are compared to the results of nonlinear time history analyses.*

1 INTRODUCTION

Recent earthquakes have repeatedly demonstrated the seismic vulnerability of existing bridges, due to their design based on gravity loads only or inadequate levels of lateral forces [1]. Many bridges are of great importance after an earthquake for guaranteeing civil protection interventions and first aid organizations. As a consequence, they have to be in service immediately after the earthquake. In Italy, as well as in other seismic countries, many bridges have been built before the '80s, without antiseismic criteria. Therefore, they must be seismically assessed and, if needed, retrofitted. From this point of view, the development of seismic assessment procedures which give reliable results and, at the same time, are sufficiently simple to be applied to a large stock of bridges could be very useful.

In recognition of the limitations of force-based design and assessment methods, several researchers have started proposing displacement-based approaches for earthquake engineering evaluation and design, with the aim of providing improved reliability in the engineering process by more directly relating computed response and expected structural performance. A rather complete literature review of the subject is reported in Calvi [2], where most displacement – based approaches proposed in the literature, are summarized, critically reviewed and compared, to favour code implementation and practical use of rational and reliable methods. One of the most developed displacement-based methods is the Direct Displacement-Based Design (DDBD) approach proposed by Priestley et al. [3]. A Model Code for the DDBD of structures has been recently published [4], as part of the 2005-2008 RELUIS project.

In this paper, a Direct Displacement-Based seismic Assessment (DDBA) procedure is presented and applied to a number of bridge configurations derived from a multi-span reinforced concrete bridge of the A16 Italian highway. The predictions of the proposed procedure are then compared to the results of nonlinear time-history analysis carried out using a set of seven accelerograms compatible with the Eurocode 8 [5] response spectrum. In addition, a comparison with the traditional force-based approach has been made for a number of selected case studies.

2 DIRECT DISPLACEMENT BASED ASSESSMENT PROCEDURE (DDBA)

The fundamentals of proposed DDBA procedure are derived from previous studies by Petrini et al [6]. In particular, the proposed procedure is based on an Iterative Eigenvalue Analysis (IEA) to obtain the target displacement profile of the bridge, corresponding to a selected Performance Level (i.e. target displacement) of the structure. The Multi Degree of Freedom (MDOF) model of the structure is then converted into an equivalent Single Degree of Freedom (SDOF) system, according to the principles of the DDBD [7], [8]. Hence, the Peak Ground Acceleration (PGA_{PL}) corresponding to the selected Performance Level (PL) is evaluated.

In this paper, the proposed DDBA procedure is specialised to multi-span reinforced concrete simply-supported deck bridges. In particular, the influence of the bearing devices placed between pier/abutment and decks is taken into account. At this stage of the study, the attention is focused on the transverse response of the bridge.

The proposed DDBA procedure can be summarized in three main steps:

(i) Structural modelling, through the acquisition of structural information;

(ii) Derivation of the bridge target displacement profile associated to a selected performance level of the structure, through an Iterative Eigenvalue Analysis (IEA);

(iii) Evaluation of the corresponding PGA value, based on the comparison between the seismic capacity of an equivalent SDOF model of the structure and the seismic demand of the expected ground motions represented by an overdamped elastic response spectrum.

2.1 Structural Modelling and Damage States

The bridge model has been purposely kept as simple as possible in order to reduce the complexity of the analysis. In accordance with the structural component modelling approach [1], the bridge structure has been divided in a number of independent rigid diaphragms, modelling the bridge decks, mutually connected by means of a series of nonlinear springs, modelling bearing devices and piers (see Fig. 1). Obviously, different modelling strategies can be pursued without influencing the core of the proposed DDBA procedure. Table 1 summarises the basic modelling assumptions adopted in this study for each bridge component, to describe their monotonic and cyclic behaviour, within modal and nonlinear dynamic analysis, respectively.

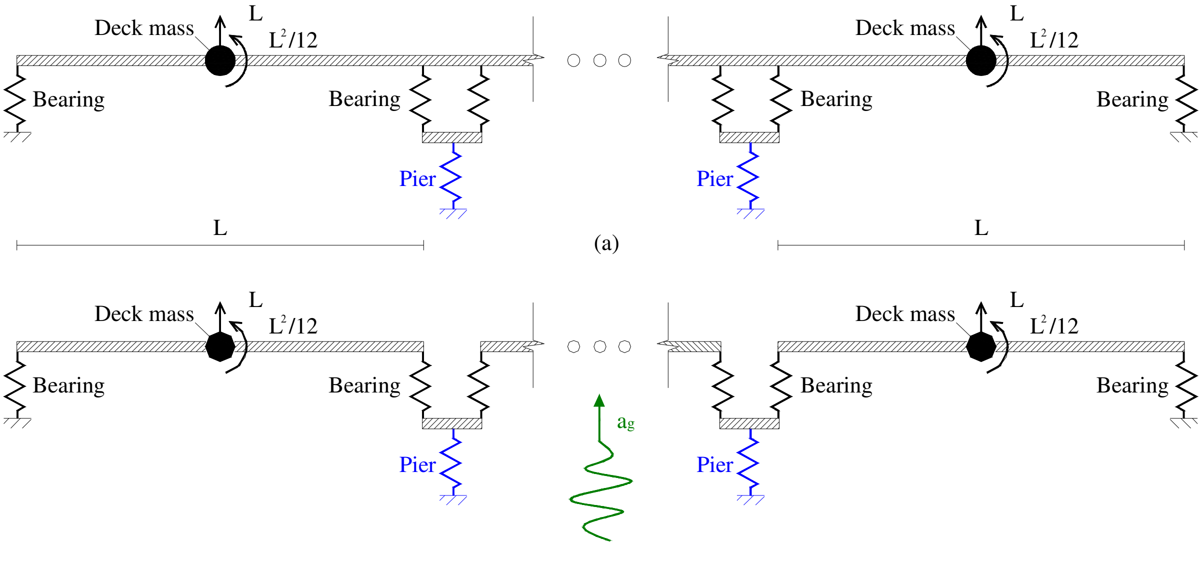

(b)

Figure 1: Schematization of multi-span simply supported (a) continuous and (b) isostatic deck bridges.

COMPONENT	MODELLING ASSUMPTIONS	DAMAGE STATES
Foundations/ Abutments	Infinitely rigid and resistant.	-
Deck	Diaphragm behaviour. Lumped translational and rotational masses.	-
Piers	Nonlinear force-displacement behaviour. Flexural behaviour based on moment-curvature analysis. Shear strength, lap-splice effects, buckling of bars and P-Δ effects considered.	Plastic hinge formation. Ultimate rotation capacity. Shear failure.
Bearing devices	Mechanical behaviour described by means of nonlinear force-displacement relationships.	Device failure. Post-failure sliding.

Table 1: Types of bridge components and basic modelling assumptions considered in the procedure.

The translational and rotational mass of each deck have been lumped as shown in Figure 1. Decks and foundations have been considered as infinitely rigid and resistant. Piers have been modelled with nonlinear springs characterized by a bilinear backbone curve. In this study, the lateral force-displacement relationships of the piers have been derived based on preliminary elasto-plastic pushover analyses of the piers, schematized as elastic beams with plastic hinges at the end(s). The plastic hinge behaviour has been derived from a moment-curvature analysis of the critical cross section(s) of the pier, considering the axial force due to gravity loads and the effects of concrete confinement and steel strain-hardening. In this study, reference to the models by Mander et al. [9] and Menegotto-Pinto [10] has been made for confined/cover concrete and steel, respectively. Lap-splices and buckling effects have been also considered in the moment-curvature analysis (see Fig. 2(a)). The moment-curvature relationship thus obtained has been properly bilinearized (see Fig. 2(a)) and then converted in the moment-rotation behaviour of the plastic hinge, whose length has been evaluated according to the formula proposed by Priestley et al. [1]. P-Δ effects due to gravity loads and premature shear failure have been considered in the pushover analysis (see Fig.2(b)). As far as the cyclic behaviour of the piers is concerned, reference to the Takeda degrading-stiffness-hysteretic model has been made [11] (see Fig. 2(c)).

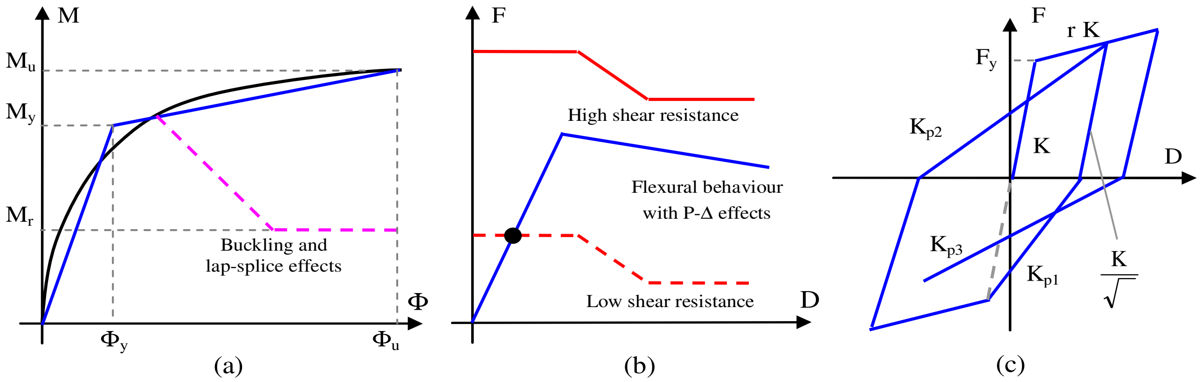

Figure 2: Pier modeling: (a) Moment-curvature analysis of the critical section, (b) force-displacement behaviour taking into account possible shear failure, (c) Takeda degrading-stiffness-hysteretic cyclic model.

The nonlinear behaviour of the bearing devices has been defined based on a comprehensive survey of the Italian highway bridge inventory. In particular, two different types of bearing devices have been considered, i.e.: (i) steel hinges and (ii) neoprene pads.

Steel hinges have been assumed to remain linear elastic up to failure (Fig. 3(a)), which is usually brittle, being due to the attainment of the shear strength (F_u) of the device. The shear stiffness has been estimated based on the geometric details available. During the analysis, the maximum shear force has been monitored. When the shear strength was prematurely exceeded, a post-failure frictional behaviour, corresponding to sliding between deck and pier cap, has been considered (Fig. 3(a)).

A linear visco-elastic behaviour has been considered for neoprene pads (Fig. 3(b)), whose shear stiffness (K) has been evaluated based on the dimensions (cross section area and thickness) of the pads and shear modulus (G) of neoprene. In this study, a shear modulus of 1 MPa and a viscous damping ratio (ξ) of 6% have been assumed for neoprene pads. The horizontal strength of the bearing system has been computed as the lowest between the shear resistance of the neoprene pads and the friction resistance between neoprene and concrete sliding surfaces. The shear resistance of neoprene pads has been associated to the attainment of a shear strain of 150%. The friction coefficient between neoprene and concrete has been taken equal to 70%.

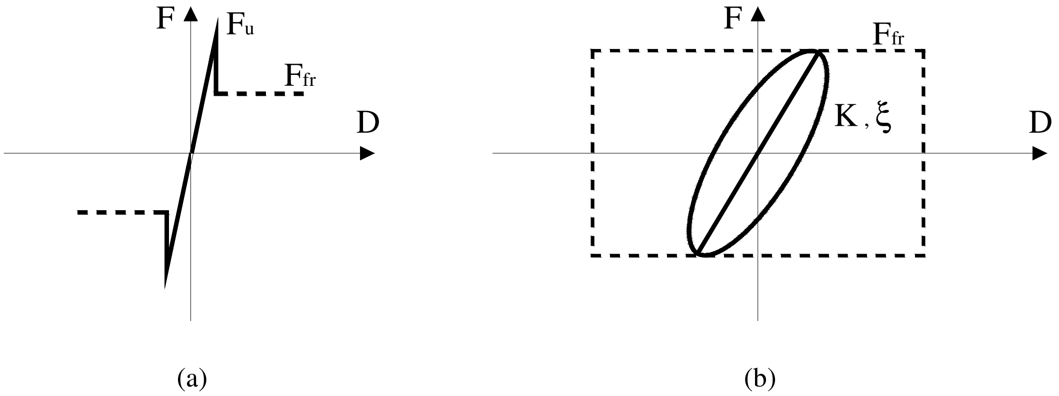

Figure 3: Force-displacement behaviour of (a) steel hinges, (b) neoprene pads.

A number of Damage States (DSs) have been defined for piers and bearing devices. The DSs have been grouped in three different Performance Levels (PLs) (see Tab. 2), based on the consequences in terms of damage that the attainment of each DS can produce. Obviously, this division is only formal and it is made only for the sake of clarity. The first Performance Level (PL1) includes post-earthquake Damage States in which only very limited structural damage has occurred (e.g. pier yielding, attainment of the horizontal strength in neoprene pads,….). The second Performance Level (PL2) includes post-earthquake Damage States in which significant damage to some structural elements has occurred but large margin against either partial or global collapse still remains (e.g. 50% of the ultimate ductility demand in piers, large post-failure displacements in neoprene pads,….). The third Performance Level (PL3) includes post-earthquake Damage States in which the structure continues to support gravity loads but retains no margin against collapse (e.g. collapse of steel hinges, pier collapse due to the attainment of ultimate ductility or shear strength, …).

PL1 (Slight Damage State)	PL2 (Moderate Damage State)	PL3 (Severe Damage State)
○ Pier yielding ○ Neoprene pad failure	○ 50% ultimate ductility of piers ○ Large post-failure displacements in neoprene pads	○ Pier collapse ○ Steel hinge failure

Table 2: Performance Levels of the structure and Damage States of piers and bearing devices.

2.2 Iterative Eigenvalue Analysis (IEA)

An eigenvalue analysis is initially performed assuming the elastic stiffness of piers and bearings. The resultant mode shape in the transverse direction is recorded as the displacement pattern of the bridge. Next, in order to obtain the target displacement profile, the displacement pattern is scaled, based on the displacement corresponding to the attainment of a given DS in a (trial) critical element (pier or bearing) of the bridge. The element that first reaches a predefined target displacement amplitude in the current displacement pattern is recognized as the critical element of the bridge and its displacement is the critical displacement Δ_{cr}. The displacements of the other piers and bearings are obtained from Δ_{cr} in proportion to the mode shape (ϕ_i):

$$\Delta_i = \frac{\Delta_{cr}\phi_i}{\phi_{cr}} \tag{1}$$

where ϕ_i is the component of the mode shape vector related to the i-th pier or bearing, ϕ_{cr} is the component of the mode shape vector related to the critical pier, Δ_i is the displacement of the i-th structural element.

Next, the secant stiffness of each element corresponding to the displacements Δ_i are found:

$$K_i = \frac{F_i}{\Delta_i} \tag{2}$$

where F_i is the force value corresponding to the pier displacement Δ_i found on each force-displacement curve. New secant stiffness values are used in the next eigenvalue analysis and a new displacement shape is obtained. The iterative procedure continues till there is no significant change in the displacement shape. The iterative procedure normally converges in 3-5 iterations.

At this point, the effect of higher modes must be checked and if needed the bridge displacement shape must be revised. If the mass participation ratio at the end of the IEA process is lower than 65-70% of the total mass, higher mode effects shall be considered. To this end, reference has been made to the so-called Effective Mode Shape (EMS) method [12], in which the displacement of each element (piers and bearings) is calculated with the following equation:

$$\Delta_{i,j} = \phi_{i,j} \cdot PF_j \cdot S_{d,j} \tag{3}$$

where the index i represents the element number and the index j represents the mode number, $\Delta_{i,j}$ is the displacement of the i-th element for the j-th mode, $\phi_{i,j}$ is the modal displacement of i-th element for the j-th mode, PF_j is the participation factor of the j-th mode and $S_{d,j}$ is the spectral displacement for the j-th mode obtained by entering the 5% damped elastic displacement spectrum with the modal period of the j-th mode. The final displacement shape of the bridge, considering the higher mode effects, is calculated by any appropriate modal combinations (SRSS, CQC etc.) of these displacements.

2.3 Evaluation of the PGA associated to given Damage States of the structure

The equivalent SDOF displacement of the bridge (Δ_e) is derived, from the displacement profile obtained at the end of the IEA, through the following equation:

$$\Delta_e = \frac{\sum_j \left(m_j \cdot \Delta_j^2 + \mathrm{I}_j \cdot \delta_j^2 \right)}{\sum_j m_j \cdot \Delta_j} \tag{4}$$

where m_j and Δ_j are the translational mass (μL) and the horizontal displacement of the centre of mass of the j-th deck, respectively, I_j and δ_j are the rotational mass ($\mu L^3/12$) and the rotation around the vertical axis of the j-th deck, respectively. The force level associated to Δ_e is given by the global base shear (V_b) obtained at the end of the IEA.

The equivalent SDOF mass (m_e) is then given by:

$$m_e = \frac{\sum_j m_j \cdot \Delta_j}{\Delta_e} \tag{5}$$

The next step of the procedure is to determine the seismic demand associated to each DS, represented by a reference over-damped elastic response spectrum. This step requires the evaluation of the equivalent viscous damping of the bridge by the combination of the damping contributions of each structural member (piers and bearings). The equivalent damping of the bearing devices can be calculated through the well-known Jacobsen approach [13]:

$$\xi_{b,j} = \frac{E_{visc} + E_{hyst} + E_{fr}}{2\pi \cdot F_{b,j} \cdot \Delta_{b,j}} \tag{6}$$

in which E_{visc}, E_{hyst} and E_{fr} identify the energy dissipated by the device, through its viscous, hysteretic or frictional behaviour, in a cycle of amplitude $\Delta_{b,j}$, being $\Delta_{b,j}$ the displacement of the device and $F_{b,j}$ the corresponding force level.

As far as piers are concerned, reference has been made to the following relationship:

$$\xi_{p,k} = 0.05 + \frac{1}{\pi}\left(1 - \frac{(1-r)}{\sqrt{\quad}} - r \quad\right) \tag{7}$$

which relates the equivalent hysteretic damping of the pier to its displacement ductility (μ) and post-yield hardening ratio (r). The aforesaid relationship has been derived by Kowalski et al. [14], by applying the Jacobsen's approach to the Takeda degrading-stiffness-hysteretic model.

The global equivalent damping of the bridge ξ_e is calculated by weighting the damping contributions based on the energy dissipated by each structural element:

$$\xi_e = \frac{\sum_{j=1}^{nb} \xi_{b,j} F_{b,j} \Delta_{b,j} + \sum_{k=1}^{np} \xi_{p,k} F_{p,k} \Delta_{p,k}}{\sum_{j=1}^{nb} F_{b,j} \Delta_{b,j} + \sum_{k=1}^{np} F_{p,k} \Delta_{p,k}} \tag{8}$$

Once the equivalent damping of the bridge has been determined, the corresponding demand spectrum can be derived from the reference 5%-damping normalized response spectrum, using a proper damping reduction factor [15].

The final step of the procedure is to determine the PGA value associated to the selected DS.

From a graphical point of view, the PGA associated to a selected Performance Point (PP) can be evaluated through a translation of the over-damped Normalized Response Spectrum (NRS in Fig.4) to intercept the selected PP, whose coordinates are the equivalent SDOF displacement Δ_e and the spectral acceleration:

$$S_e = \frac{V_b}{m_e} \tag{9}$$

where V_b is the total base shear of the structure corresponding to the deformed shape resulting from IEA

From an analytical point of view, the PGA associated to a selected Performance Point (PP) can be determined as the ratio between the spectral acceleration S_e corresponding to the selected PP and the normalized spectral acceleration at the effective period of vibration (T_e) and global equivalent damping (ξ_e) of the structure:

$$PGA = \frac{S_e}{S_{e1}(T_e, \xi_e)} \tag{10}$$

being:

$$T_e = 2\pi \cdot \sqrt{\frac{m_e}{K_e}} \tag{11}$$

and K_e is the equivalent SDOF stiffness given by:

$$K_e = \frac{V_b}{\Delta_e} \tag{12}$$

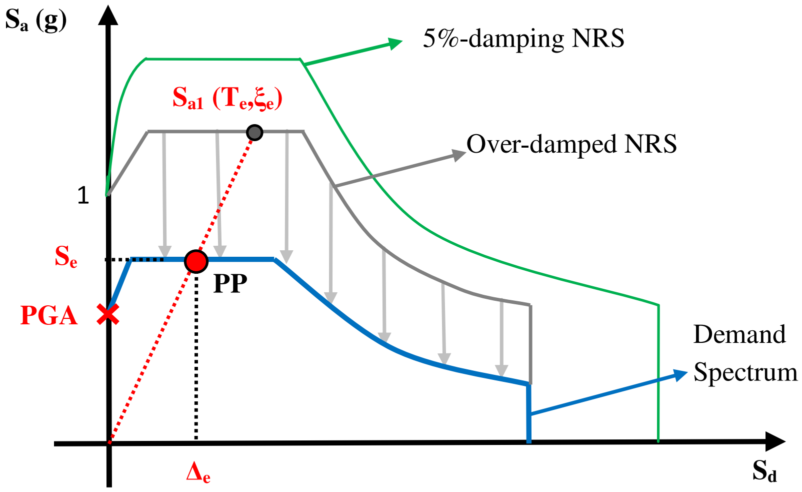

Figure 4: Evaluation of the PGA associated to a selected PP.

3 COMPARISON WITH NTHA RESULTS

3.1 Case Studies

The proposed DDBA procedure has been applied to a number of bridge configurations derived from a Reinforced Concrete (RC) bridge of the A16 Italian highway (Fiumarella viaduct). The Fiumarella viaduct is a 4-span simply-supported isostatic deck bridge of 135m total length, featuring two seat-type abutments and three identical frame-type piers characterised by five RC columns with 1.2m diameter circular cross section and 3.2m effective height. The longitudinal reinforcement ratio of each column is equal to 0.44%. The transverse reinforcement is realised by 10mm diameter hoops at 20mm spacing. The bridge presents steel bearings acting as a pendulum in the longitudinal direction and as a fixed steel hinge in the transversal direction. The yield strength of the reinforcing steel (type AQ50-60) is equal to 270 N/mm2. As far as concrete is concerned, a compression strength of 35 N/mm2 has been assumed, based on the design data available.

A set of nine bridge configurations have been derived from the real bridge configuration (F1 in Tab. 3). They are summarized in Table 3. The schematic layout of the ten bridge configurations is shown in Fig. 5. In the bridge configuration F2 neoprene pads have been considered in place of steel hinges. The stiffness of each line of neoprene pads has been assumed equal to 35000 KN/m, based on a comprehensive survey of similar Italian highway viaducts. The configurations from F3 to F10 have been derived from the configurations F1 and F2 by changing the pier layout (pier heights equal to H-2H-3H or H-3H-2H, with H = 3.20 m) and considering both isostatic and continuous decks.

BRIDGE CONFIGURATION	DECK	PIER LAYOUT (*)	BEARINGS
F1	Isostatic	H-H-H	Steel Hinges (SH)
F2	Isostatic	H-H-H	Neoprene (N)
F3	Isostatic	H-2H-3H	Steel Hinges (SH)
F4	Isostatic	H-2H-3H	Neoprene (N)
F5	Continuous	H-2H-3H	Steel Hinges (SH)
F6	Continuous	H-2H-3H	Neoprene (N)
F7	Isostatic	H-3H-2H	Steel Hinges (SH)
F8	Isostatic	H-3H-2H	Neoprene (N)
F9	Continuous	H-3H-2H	Steel Hinges (SH)
F10	Continuous	H-3H-2H	Neoprene (N)

* H=3.20 m

Table 3: Main characteristics of the analyzed bridges

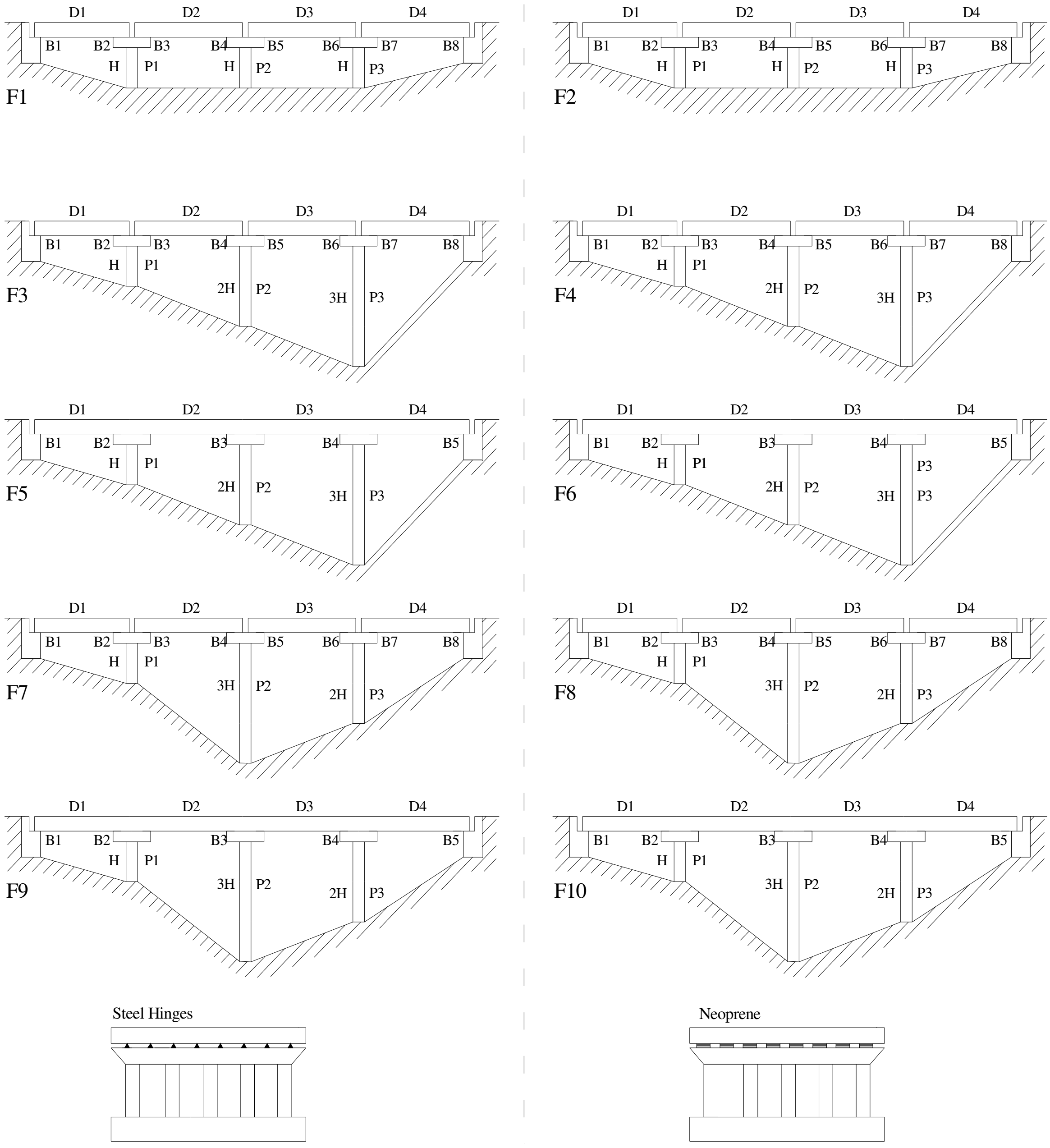

Figure 5: Schematic Layouts of the examined bridges.

3.2 Application of the DDBA procedure

Figure 6 shows the displacement profiles obtained at each step of the IEA for the bridge configurations with irregular pier layouts. As can be seen, the displacement profile considerably changes considering the inelastic behaviour of the bridge elements, since plastic deformations are mainly concentrated in a few elements, due to the irregular bridge configuration. The most significant changes, however, take place in the first 2-3 steps of the analysis. The comparison between the initial and final displacement profile emphasizes the differences between the traditional force-based approach, based on the elastic response of the structure reduced by a proper behaviour factor, and the proposed DDBA procedure, based on the use of an inelastic displacement profile scaled at a given target displacement amplitude.

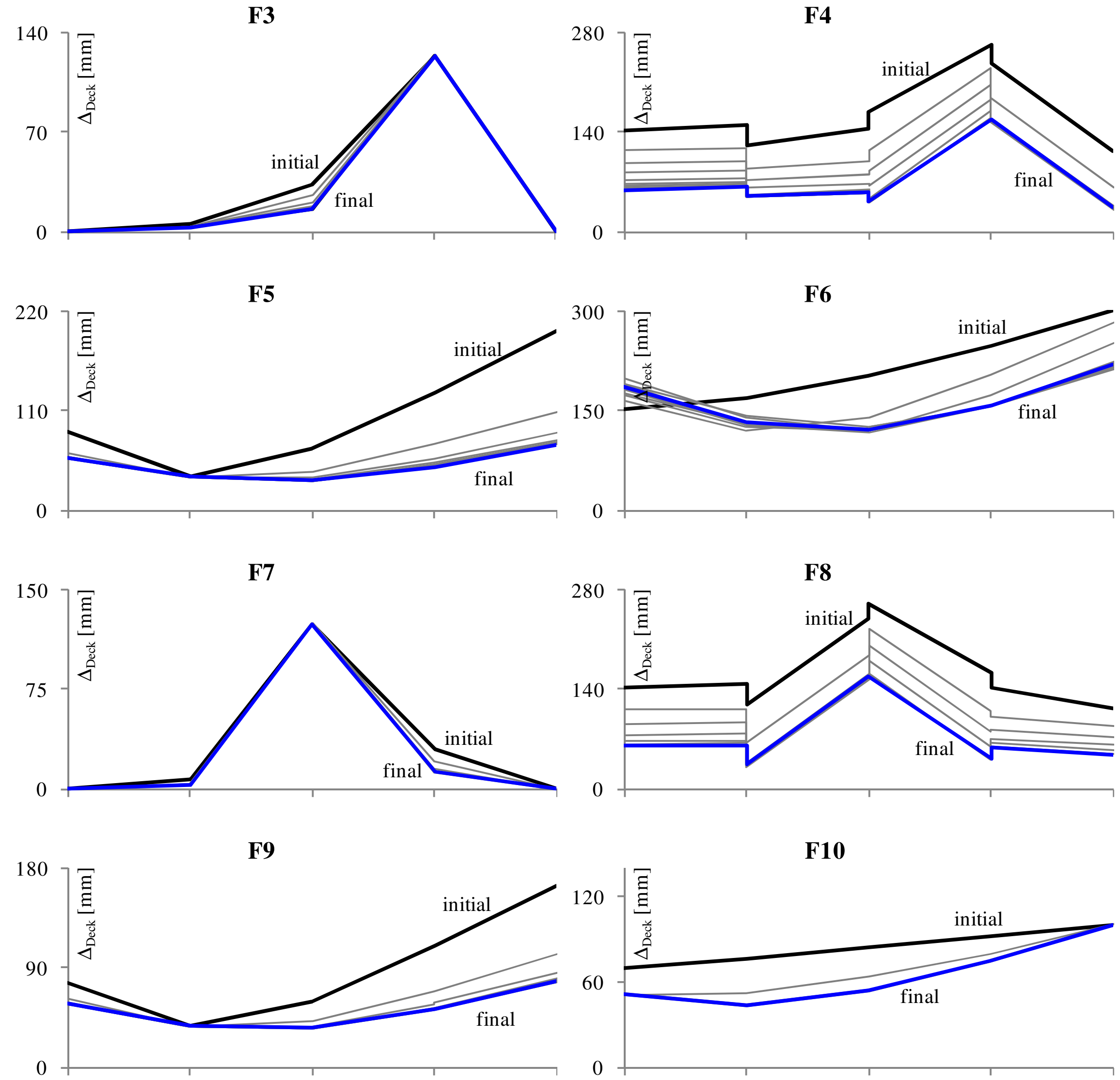

Figure 6: Displacements profiles of the bridge configurations with irregular pier layouts at each step of the IEA.

Table 4 summarizes the results obtained from the application of the DDBA procedure to the case studies described in the paragraph 3.1. The results are expressed in terms of PGA values associated to a number of PLs, corresponding either to pier collapse or failure of neoprene pads. The critical element of the bridge, where first the selected damage state is reached, is also specified in Tab. 4. The PGA values listed in Tab. 4 have been used to scale the accelerograms for nonlinear time-history analysis.

BRIDGE CONFIGURATION	DECK	PIER LAYOUT*	BEARINGS	PERFORMANCE LEVELS	PGA VALUES
F1*	Isostatic	H-H-H	SH	PL3: collapse of P2	0.565 g
F2	Isostatic	H-H-H	N	PL1: elastic limit of B4 PL2: Large displacement on B4	0.206 g 0.538 g
F3	Isostatic	H-2H-3H	SH	PL3: collapse of P3	0.447 g
F4	Isostatic	H-2H-3H	N	PL3: collapse of P3	0.442 g
F5	Continuous	H-2H-3H	SH	PL3: collapse of P1	0.491 g
F6	Continuous	H-2H-3H	N	PL3: collapse of P1	0.626 g
F7	Isostatic	H-3H-2H	SH	PL3: collapse of P2	0.459 g
F8	Isostatic	H-3H-2H	N	PL3: collapse of P2	0.415 g
F9	Continuous	H-3H-2H	SH	PL3: collapse of P1	0.472 g
F10	Continuous	H-3H-2H	N	PL2: Large displacement on B4	0.405 g

* H=3.20 m

Table 4: Performance levels, damage states and corresponding PGA values for the examined bridges.

3.3 Comparison with NTHA results

Comprehensive nonlinear response Time-History Analyses (NTHA) have been carried out to assess the accuracy of the proposed DDBA procedure. The bridge models for NTHA have been implemented in SAP2000_Nonlinear [16], adopting the same modelling assumptions made in the IEA within the proposed DDBA procedure. The NTHA have been performed using a set of 7 artificial accelerograms strictly compatible, on average, with the 5%-damped acceleration response spectrum provided by Eurocode 8 for soil type B [5]. The input ground motions have been scaled to the PGA values provided by DDBA for the calculated PLs (see Tab. 4). A total of 77 NTHA (10 bridges * 7 accelerograms * 1-2 damage states) have been carried out. The accuracy of the proposed procedure has been evaluated by comparing the bridge displacement profile expected based on DDBA with the envelope of the maximum bridge displacements (averaged on 7 accelerograms) obtained from NTHA.

A preliminary comparison between DDBA predictions and NTHA results has been made considering an elastic performance level of the structure (corresponding to the shear failure of neoprene pads at 0.206g for the bridge configuration F2 of Tab. 4), in order to select the best modal combination rule between SRSS and CQC. The comparison is shown in Figure 7. As can be seen, the CQC combination rule leads to errors less than 10% while the SRSS combination rule leads to errors up to 30%.

In Figure 8, DDBA predictions and NTHA results are compared for the PL3 of the bridge configuration F1 (regular pier layout and isostatic decks supported by steel hinges in the transverse direction), representing the real Fiumarella viaduct. Based on the DDBA outcomes, the critical pier, where collapse first takes place, is the pier P2 at 0.565g PGA. Piers P1 and P3, on the contrary, undergo negligible plastic deformations. The comparison between expected and ‘actual’ deformed shapes clearly points out the great accuracy of the DDBA in the prediction of the PGA values associated to severe damage states. Indeed, the percent errors in the evaluation of the ‘actual’ maximum deck displacements do not exceed 14% and, on average, they result of the order of 9%. The NTHA results also confirm that pier P2 is the critical element of the bridge with ductility demands that differ from those derived from DDBA less than 8%. It is worth to observe that in Figures 7-17 displacement profiles and bridge coordinates are reported in two different scales. From a graphical point of view, this determines a distortion of the deformed shape of the bridge that considerably amplifies the rotations of the decks.

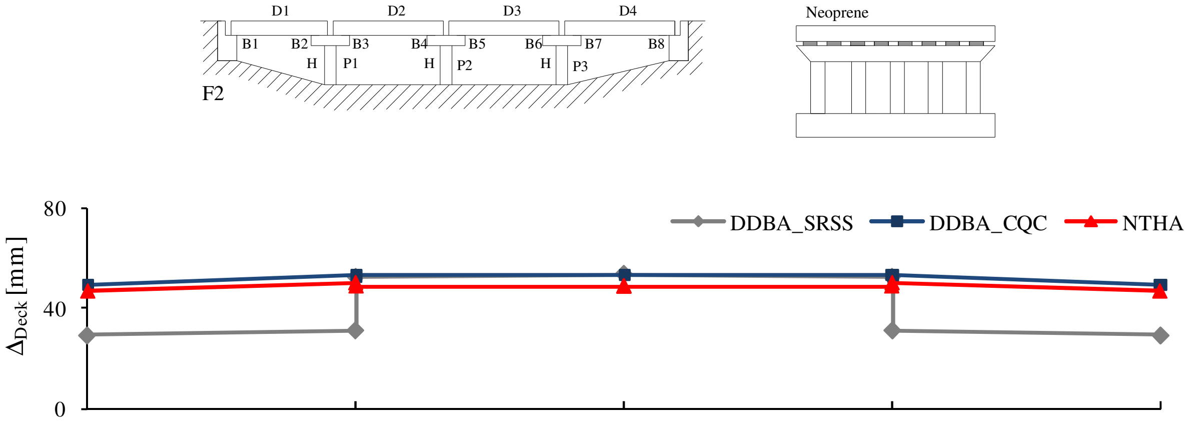

Figure 7: Comparison between NTHA results and DDBA predictions using the CQC and SRSS combination rule.

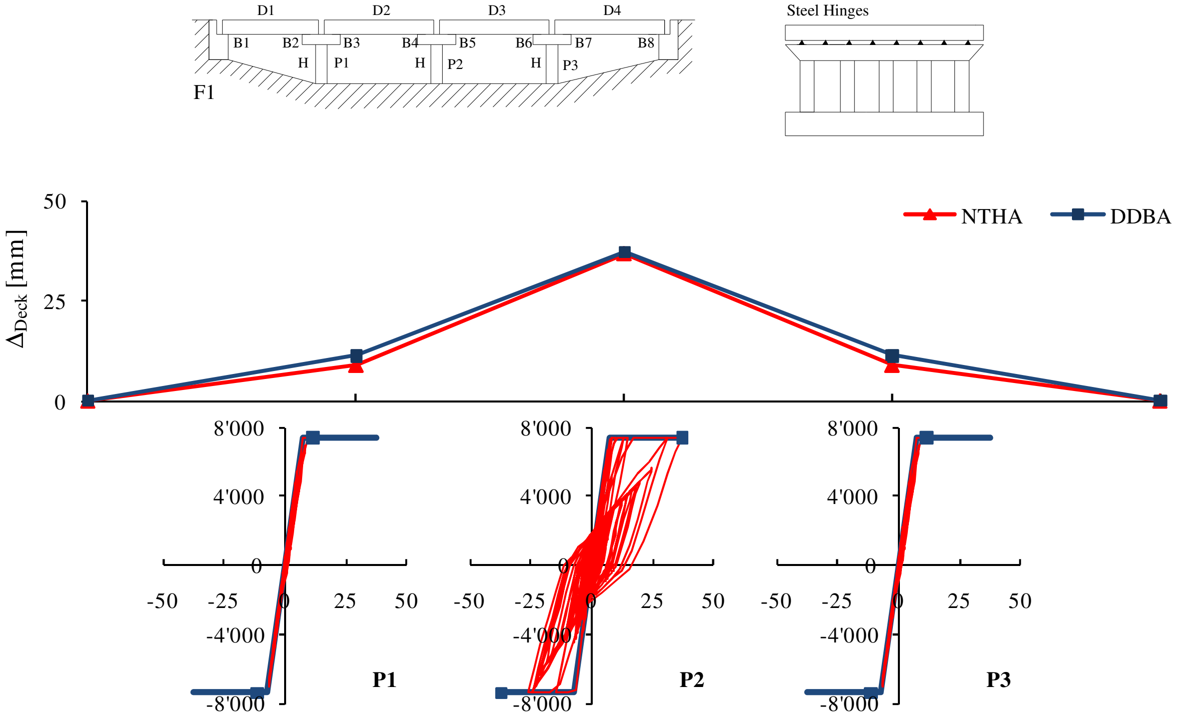

Figure 8: Comparison between DDBA predictions and NTHA results (average maximum values) in terms of deformed shape of the bridge and cyclic behaviour of some structural elements (F1 bridge configuration at PL3, PGA =0.565 g).

Similar observations can be made examining the seismic response of the bridge configuration F2 (see Fig.9), differing from the bridge configuration F1 for the pier-deck connections (neoprene pads instead of steel hinges). A moderate damage state (PL2), corresponding to a post-failure displacement of 100 mm in the bearing devices B4 and B5, occur at 0.538g. No plastic deformations are registered in the piers. The percent errors between DDBA predictions and NTHA results do not exceed 14% and, on average, result of the order of 9%.

The same level of accuracy in the prediction of the 'actual' maximum deformed shape of the bridge is found considering irregular pier layout and multi-span simply-supported continuous deck (Figs. 9-17). As a matter of fact, indeed, the percent errors between DDBA predictions and NTHA results never exceed 20% and, on average, result lower than 15%. Also the critical element of the bridge is always captured correctly.

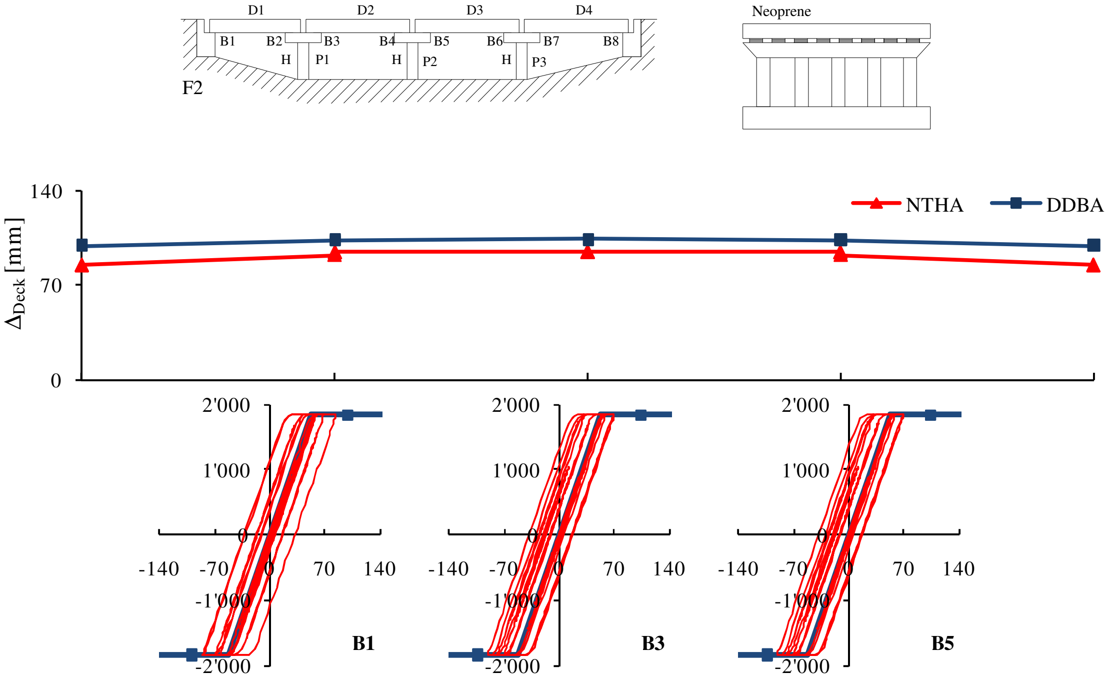

Figure 9: Comparison between DDBA predictions and NTHA results (average maximum values) in terms of deformed shape of the bridge and cyclic behaviour of some structural elements (F2 bridge configuration at PL2, PGA =0.538g).

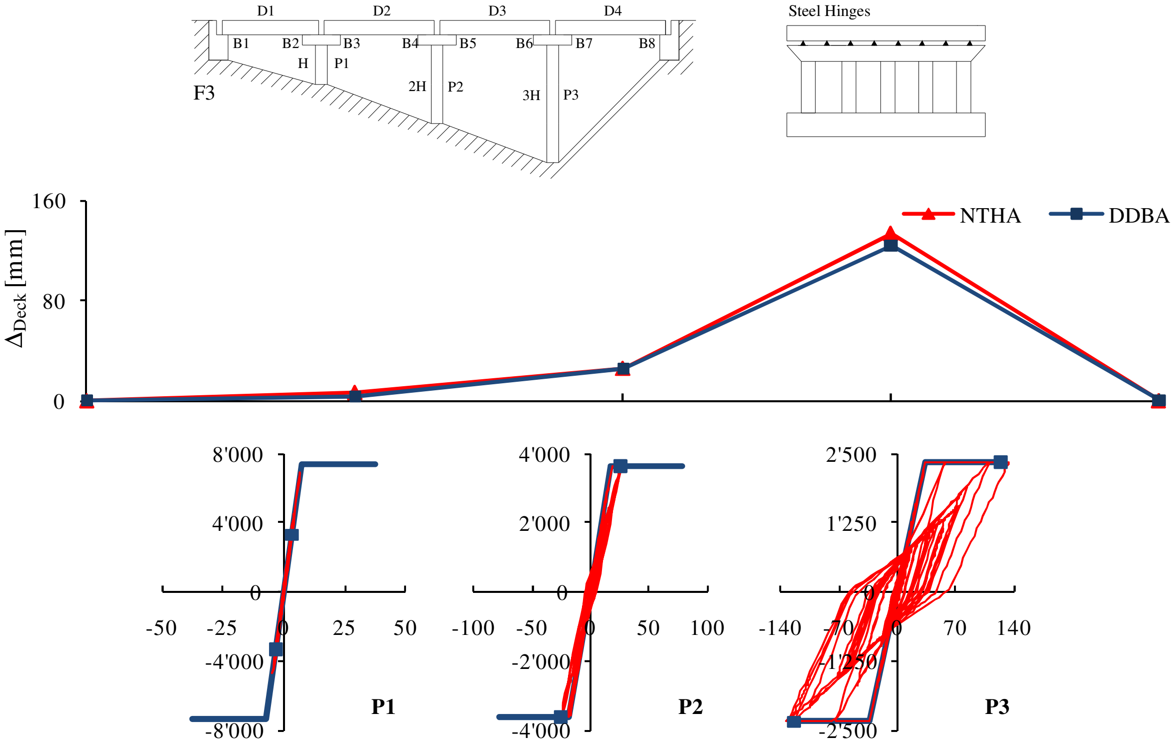

Figure 10: Comparison between DDBA predictions and NTHA results (average maximum values) in terms of deformed shape of the bridge and cyclic behaviour of some structural elements (F3 bridge configuration at PL3, PGA =0.447 g).

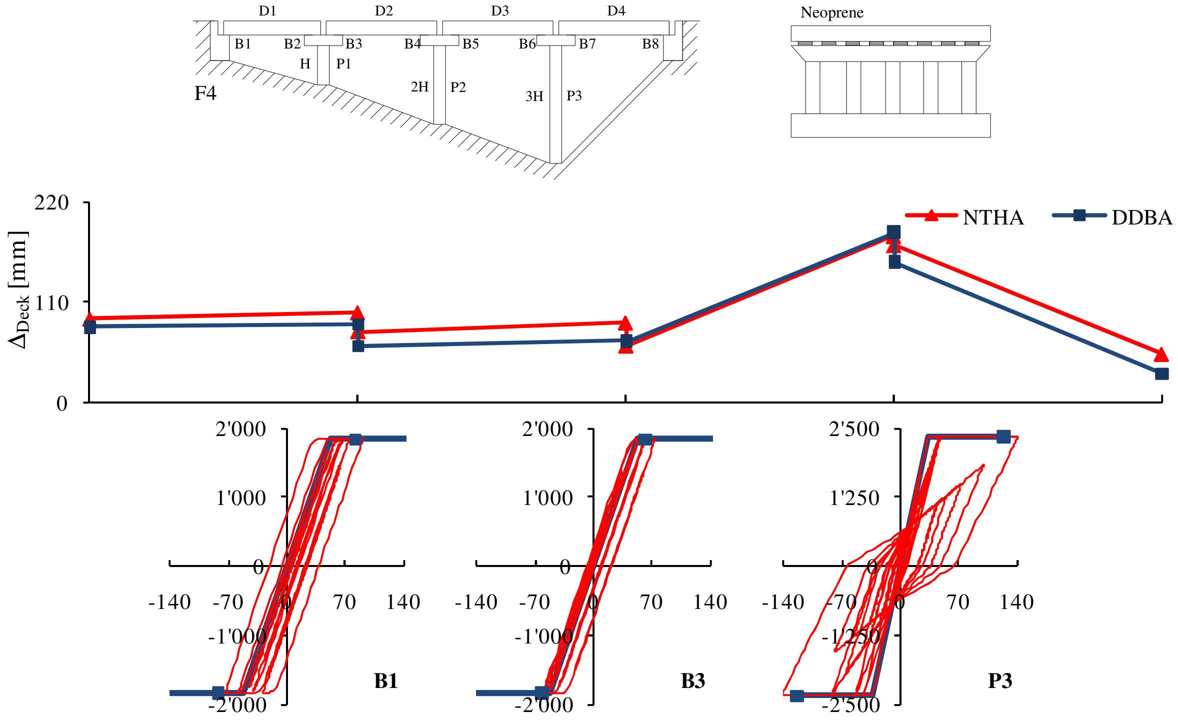

Figure 11: Comparison between DDBA predictions and NTHA results (average maximum values) in terms of deformed shape of the bridge and cyclic behaviour of some structural elements (F4 bridge configuration at PL3, PGA =0.442 g).

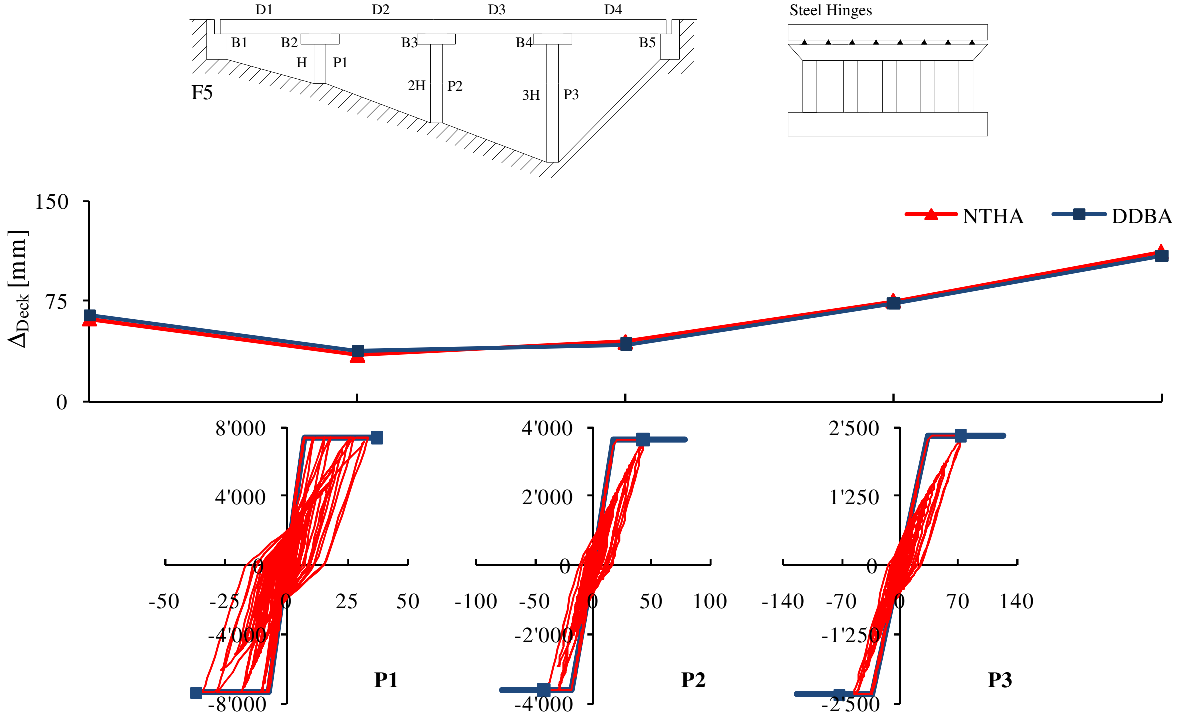

Figure 12: Comparison between DDBA predictions and NTHA results (average maximum values) in terms of deformed shape of the bridge and cyclic behaviour of some structural elements (F5 bridge configuration at PL3, PGA =0.491 g).

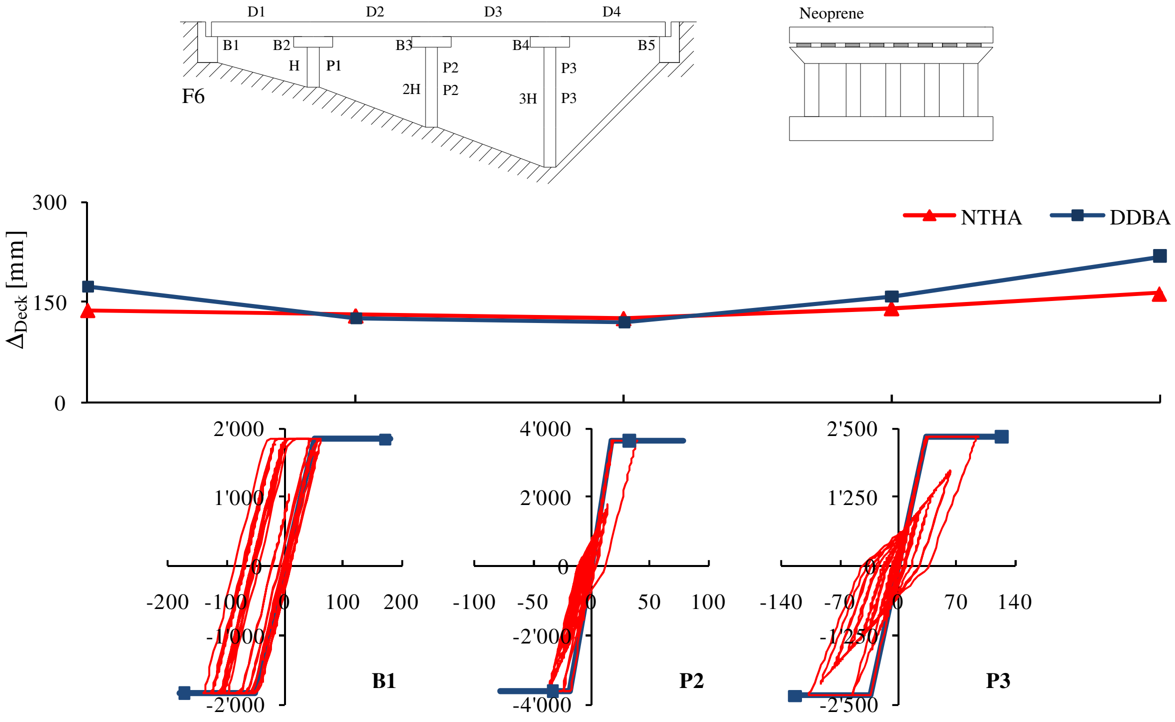

Figure 13: Comparison between DDBA predictions and NTHA results (average maximum values) in terms of deformed shape of the bridge and cyclic behaviour of some structural elements (F6 bridge configuration at PL3, PGA =0.626 g).

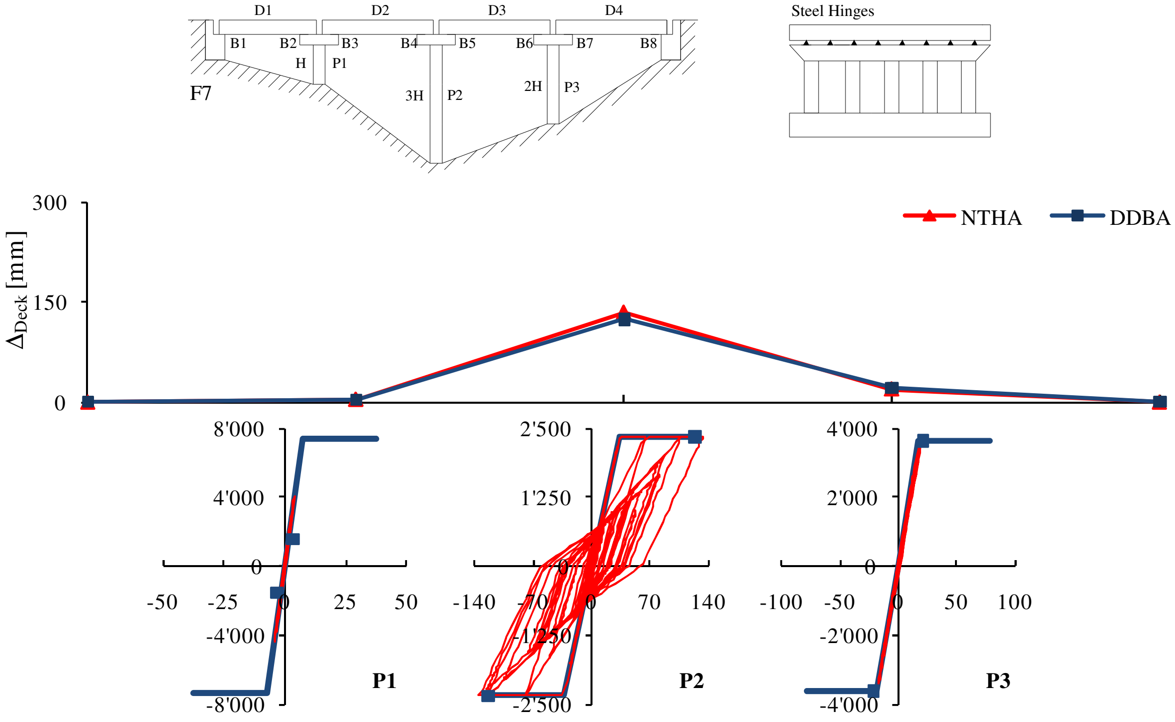

Figure 14: Comparison between DDBA predictions and NTHA results (average maximum values) in terms of deformed shape of the bridge and cyclic behaviour of some structural elements (F7 bridge configuration at PL3, PGA =0.459 g).

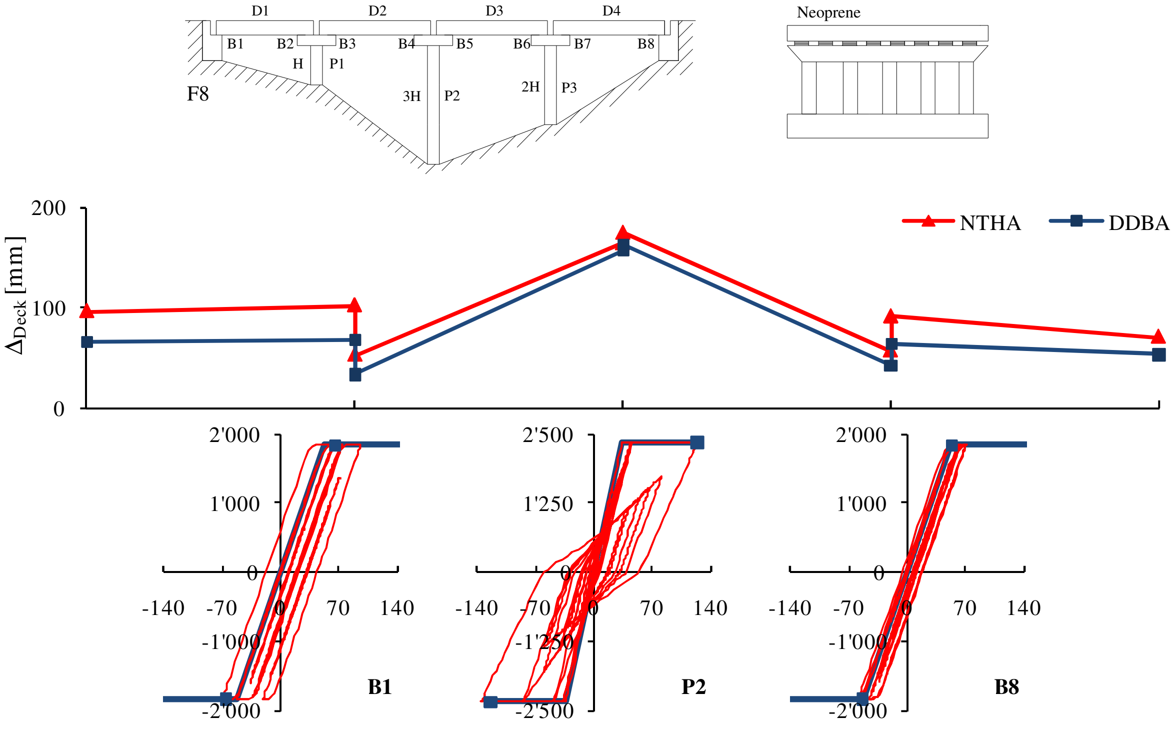

Figure 15: Comparison between DDBA predictions and NTHA results (average maximum values) in terms of deformed shape of the bridge and cyclic behaviour of some structural elements (F8 bridge configuration at PL3, PGA =0.415 g).

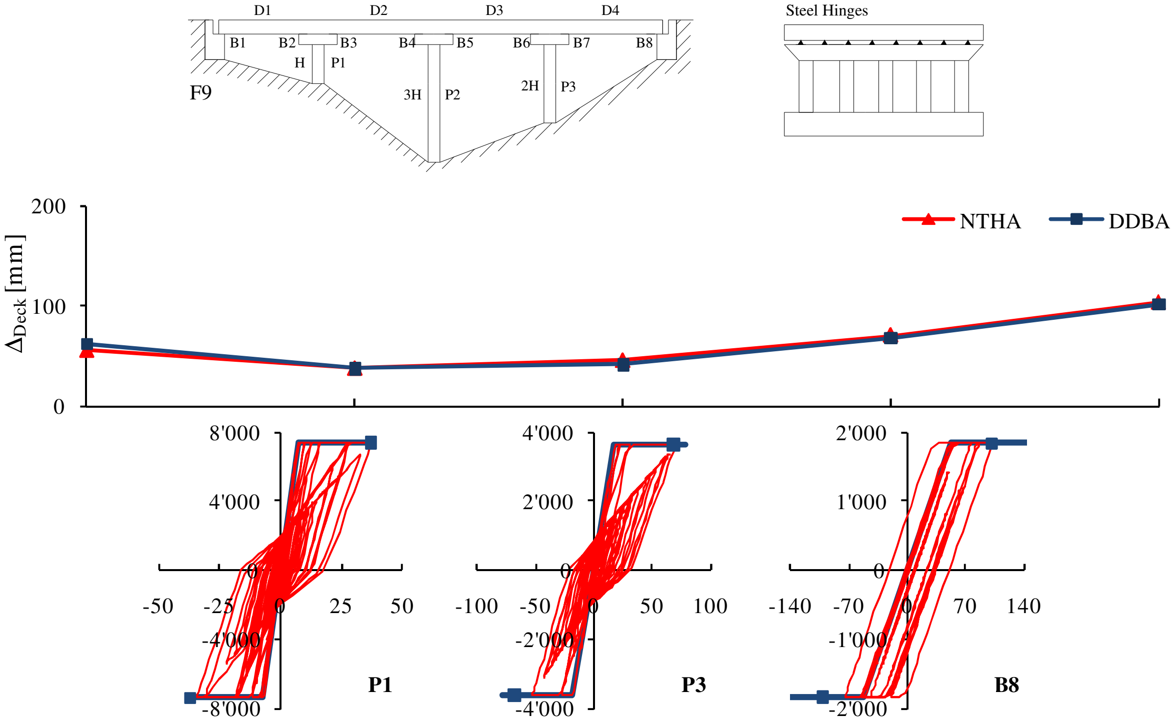

Figure 16: Comparison between DDBA predictions and NTHA results (average maximum values) in terms of deformed shape of the bridge and cyclic behaviour of some structural elements (F9 bridge configuration at PL3, PGA =0.472 g).

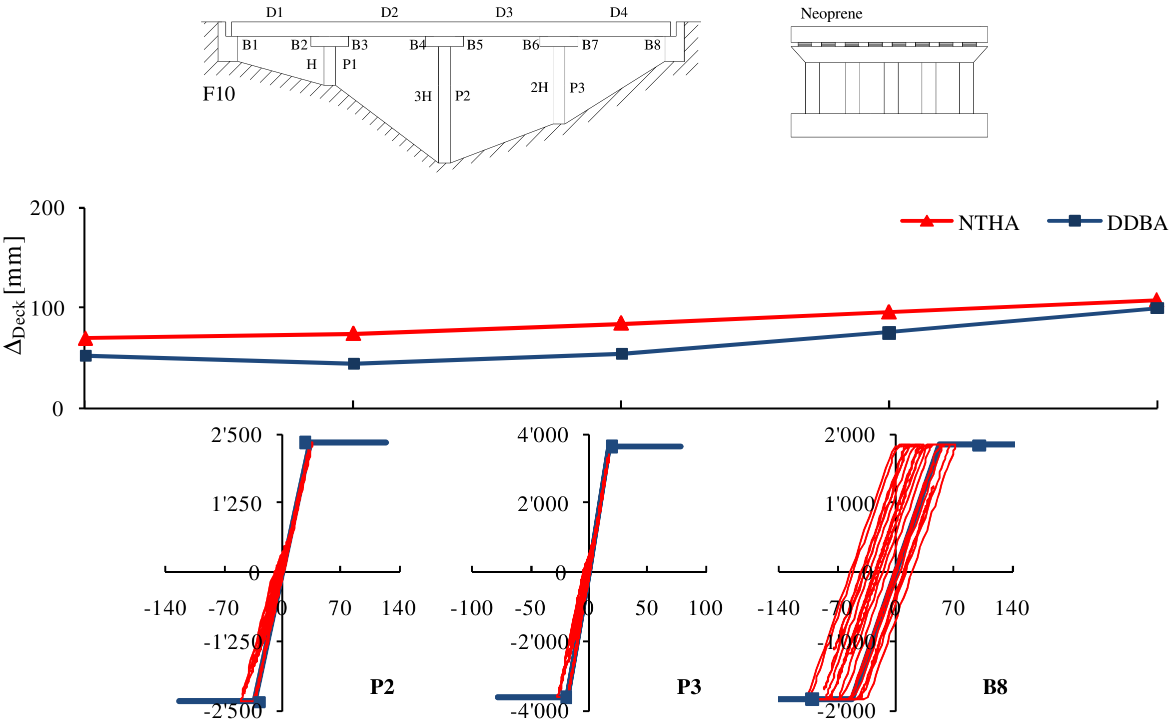

Figure 17: Comparison between DDBA predictions and NTHA results (average maximum values) in terms of deformed shape of the bridge and cyclic behaviour of some structural elements (F10 bridge configuration at PL2, PGA =0.405 g).

For more clarity, in Table 5 the average errors (ERR_{av}) between DDBA and NTHA results, computed based on the deformed shape of the entire bridge, and the error relevant to the critical element of the bridge (ERR_{cr}) are summarised for the ten bridge configurations considered.

BRIDGE CONFIGURATION	DECK	PIER LAYOUT (*)	BEARINGS	PL	PGA	ERR_{av}	ERR_{cr}
F1	Isostatic	H-H-H	SH	PL3-P2	0.565 g	5.01%	1.44%
F2	Isostatic	H-H-H	N	PL1-B4 PL2-B4	0.206 g 0.538 g	5.79% 8.64%	9.86% 9.69%
F3	Isostatic	H-2H-3H	SH	PL3-P3	0.447 g	0.72%	7.19%
F4	Isostatic	H-2H-3H	N	PL3-P1	0.442 g	15.71%	12.81%
F5	Continuous	H-2H-3H	SH	PL3-P1	0.491 g	1.97%	8.02%
F6	Continuous	H-2H-3H	N	PL3-P3	0.626 g	11.97%	15.59%
F7	Isostatic	H-3H-2H	SH	PL3-P2	0.459 g	1.21%	8.05%
F8	Isostatic	H-3H-2H	N	PL3-P2	0.415 g	21.38%	8.16%
F9	Continuous	H-3H-2H	SH	PL3-P1	0.472g	2.32%	0.61%
F10	Continuous	H-3H-2H	N	PL2-B8	0.405g	27.06%	6.81%

* H=3.20 m

Table 5: Comparison between DDBA and NTHA results: average error and error relevant to the critical element.

In Figure 18 the results derived from DDBA are compared to those abtained applying the traditional Force-Based seismic Assessment (FBA) approach, consisting in a Response Spectrum analysis, considering three different behaviour factors, equal to 1 (elastic behaviour), 1.5 and 3.5, respectively. The comparison is made for two different bridge configurations (F4 and F6 respectively) in terms of base shear of each pier and abutment. As can be seen, the accuracy of the FBA approach is very sensible to the definition of an appropriate behaviour factor and, in the investigated cases, is rather low. Assuming q = 1.5, for instance, the FBA approach captures with good accuracy the maximum base shear of the piers P1 and P2 while it considerably overestimate (by 90%) the maximum base shear of the pier P3. On the contrary, assuming q = 3.5 the FBA approach captures with good accuracy the maximum base shear of the pier P3 while it largely underestimate (by 40%) the maximum base shear of the piers P1 and P2.

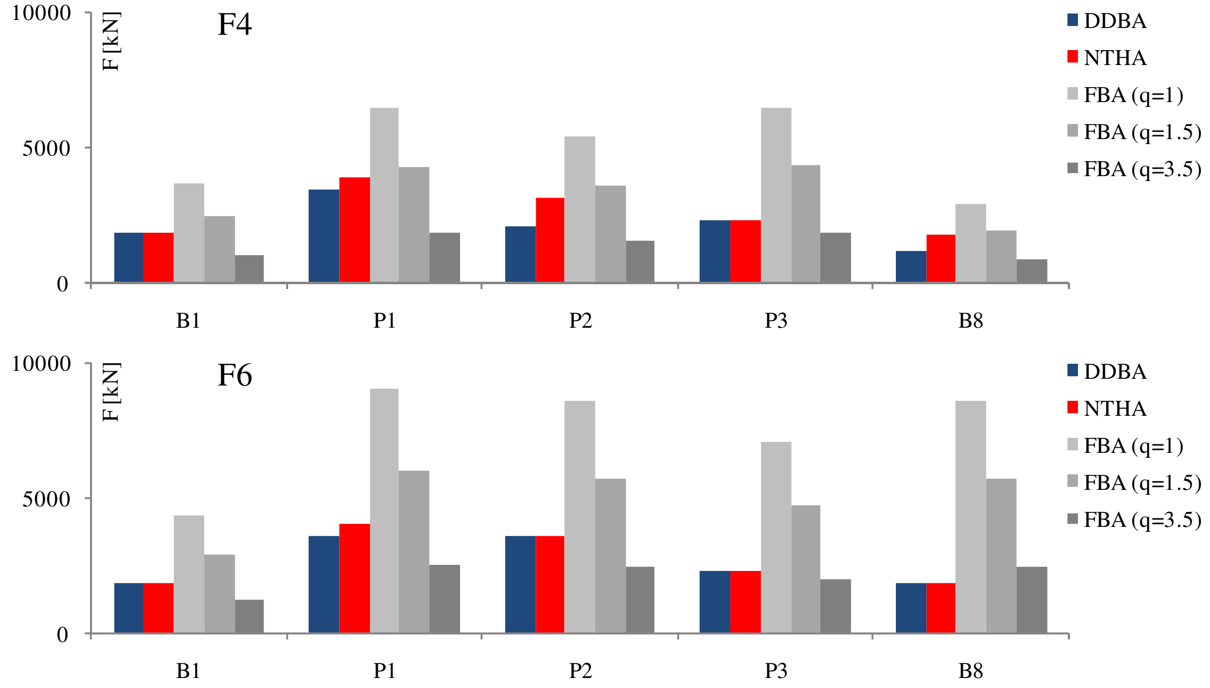

Figure 18: Comparison between DDBA, FBA and NTHA results (average maximum values) in terms of base shear of piers and abutments.

4 CONCLUSIONS

A Direct Displacement-Based Assessment (DDBA) methodology for the seismic evaluation of multi-span simply-supported deck bridges has been proposed. The proposed DDBA procedure provides the PGA values associated to given Damage States (DS) of the critical elements of the bridge (piers, bearing devices,....). The target displacement profile of the bridge corresponding to the selected DS is determined through an Iterative Eigenvalue Analysis (IEA).

In the paper, the proposed DDBA procedure has been applied to a set of ten multi-span simply-supported deck bridges, differing in pier layout (regular or irregular), bearing type (neoprene pads or steel hinges) and deck type (isostatic or continuous). The predictions of the DDBA procedure have been compared to the results of Nonlinear response Time-History Analyses (NTHA), carried out using a set of seven accelerograms, compatible with the EC8-soilB response spectrum, scaled to the PGA values provided by DDBA procedure for selected DSs. The comparison between DDBA predictions and NTHA results confirms the good accuracy of the proposed procedure in predicting the PGA values associated to slight-to-severe Damage States, regardless pier layout, bearing type and deck type. In all the examples of application considered, indeed, the DDBA correctly identify the critical element of the bridge, where first a given DS is reached. The displacement profile of the bridge predicted by the DDBA (including joint displacements, top pier displacements, bearing device displacements and deck rotations) is in good agreement with the maximum deformed shape of the bridge found with NTHA, with errors that do not exceed 15 %. Meanwhile, the accuracy of the traditional force-based seismic assessment approach is very sensible to the definition of an appropriate behaviour factor and, in the investigated cases, rather low.

Although the proposed methodology appears very promising, there are a number of aspects that require further investigation. Works are still in progress and additional numerical studies are being to be carried out, in order to fully verify the proposed procedure. Future research shall focus also on the influence of different modelling assumptions and modelling approaches.

Finally, considering that the proposed DDBA procedure for multi-span reinforced concrete bridges is very simple and it can be applied to bridges with different typologies with small revisions, the use of this procedure is recommended when the time and conditions are limited to perform more detailed nonlinear analyses.

5 ACKNOWLEGEMENTS

This work has been carried out within the RELUIS 2010-2013 research program, Project AT1_L2_Task7, funded by the Italian Civil Protection Department.

REFERENCES

[1] M.J.N. Priestley, F. Seible, G.M. Calvi, *Seismic Design and Retrofit of Bridges*, John Wiley & Sons, 1996.

[2] G.M. Calvi, (Editor), Displacement-based Seismic Design of RC Buildings, *FIB Bulletin 25*, fib, Lausanne, 2003.

[3] M.J.N. Priestley, G.M. Calvi, M. Kowalski, *Displacement based seismic design of structures*. IUSS Press, Pavia, Italy, 2007.

[4] G.M. Calvi, T.J. Sullivan, *A model code for the Displacement-Based Seismic Design of Structures, DBD09 – Draft Issued for Public Enquiry*, IUSS Press, 2009.

[5] CEN - Comité Europeen de Normalization, *Eurocode 8: Design of Structures for Earthquake Resistance - Part 1: General rules, seismic actions and rules for buildings*, PrEN 1998-1: 2005, CEN, Brussels, Belgium, 2005.

[6] L. Petrini, O.B. Şadan, G.M. Calvi, Direct Displacement-Based Seismic Assessment Procedure for Multi-Span Reinforced Concrete Bridges, *13th Italian conference of earthquake engineering*, 28 June 2009 – 2 July 2009.

[7] M.J.N. Priestley, Performance Based Seismic Design, 2000, *12th World Conference on Earthquake Engineering*, Keynote Address, Auckland, 2000.

[8] A. Shibata, M. Sözen, Substitute Structure Method for Seismic Design in Reinforced Concrete, *ASCE Journal of Structural Engineering*, 102(1), 1-18, 1976.

[9] J.B. Mander, M.J.N. Priestley, R. Park, Theoretical Stress-strain Model for Confined Concrete, *Journal of the Structural Division*, ASCE, Vol. 114. n° 8, 1988;

[10] M. Menegotto, P.E. Pinto, Method of analysis of cyclically loaded RC plane frames including changes in geometry and non-elastic behavior of elements under normal force and bending, *Preliminary Report, IABSE*, Vol. 13, pp. 15–22, 1973.

[11] R.K. Dowell, F.S. Seible, E.L. Wilson, Pivot Hysteretic Model for Reinforced Concrete Members, *ACI Structural Journal*, Vol. 95, pp. 607–617, 1998.

[12] M.J. Kowalsky, A displacement-based approach for the seismic design of continuous concrete bridges, *Earthquake Engineering and Structural Dynamics*, 31:719–747, 2002.

[13] L.S. Jacobsen, Steady Forced Vibrations as Influenced by Damping, *Transactions ASME*, Vol.51, p227, 1930

[14] M.J. Kowalsky, M.J.N. Priestley, G.A. MacRae, Displacement-based design of RC bridge columns in seismic regions, *Earthquake Engineering and Structural Dynamics*, 24(12):1623–1643, 1995.

[15] D. Cardone, M. Dolce, M. Rivelli, Evaluation of reduction factors for high-damping design response spectra, *Bulletin of Earthquake Engineering*, Vol. 9, issue 1, pp. 273-291, Springer Ltd, Dordrecht, 2008.

[16] Computer and Structures, inc., *SAP2000 Advanced: Static and Dynamic Analysis Finite Element Analysis of Structures*, University Ave. Berkeley, CA, 2005.

COMPDYN 2011
3^{rd} ECCOMAS Thematic Conference on
Computational Methods in Structural Dynamics and Earthquake Engineering
M. Papadrakakis, M. Fragiadakis, V. Plevris (eds.)
Corfu, Greece, 25–28 May 2011

FRAGILITY CURVES FOR TYPICAL MULTISPAN SIMPLY SUPPORTED BRIDGE CLASSES IN MODERATE SEISMIC ZONES: PRE- AND POST-SEISMIC DESIGN CONSIDERATIONS

Karthik Ramanathan[1], **Jamie E. Padgett**[2], **and Reginald DesRoches**[1]

[1] School of Civil and Environmental Engineering, Georgia Institute of Technology
790 Atlantic Drive, Atlanta, GA 30332-0355.
e-mail: karthik.ramanathan@gatech.edu, reginald.desroches@ce.gatech.edu

[2] Department of Civil and Environmental Engineering, Rice University
6100 Main Street, MS-318, Houston, TX 77005.
e-mail: jamie.padgett@rice.edu

Keywords: Fragility curves, analytical modeling, seismic design, non-seismic design, bridge classes, HAZUS-MH comparison.

Abstract. *Multispan simply supported concrete and steel girder bridges are common bridge types in Central and Southeastern United States. Probabilistic seismic risk assessment of these bridge classes is essential due to an increased awareness of the seismic hazard in the region. This study focuses on developing and comparing fragility curves for seismically and non-seismically designed bridges that are common in the region. Detailed three dimensional nonlinear analytical models, which account for the nonlinear behavior of the columns, girders and abutments, are developed in OpenSEES platform. Unlike most previous studies, the fragility curves are developed considering a wide range of material and geometric uncertainties in the stochastic analyses coupled with considerations of vulnerability of multiple components in defining bridge system performance. The results provide insight into the level of uncertainty introduced in the analysis of fragility curves for portfolios of bridges with the use of three dimensional analytical models and nonlinear time history analyses. Component and system fragility curves are obtained and are compared for the case of non-seismically and seismically designed bridge classes and with those currently used in HAZUS-MH.*

1 INTRODUCTION

Fragility curves, which are conditional probability statements that give the likelihood that a structure will meet or exceed a specified level of damage for a given ground motion intensity measure, have found widespread use in probabilistic seismic risk assessment of highway bridges. The conditioning parameter is typically a single intensity measure such as peak ground acceleration (PGA) or spectral acceleration at the geometric mean of the longitudinal and transverse periods ($S_{a\text{-}gm}$). They are a fundamental building block used in multiple (current and potential future) applications including emergency response, design support such as performance based earthquake engineering, planning support involving assessment of traffic impacts and possible economic losses post a seismic event, and policy support.

The earliest attempt to formalize seismic risk assessment procedures is found in the seminal work by Whitman et al. [1]. Since then several attempts have been made to quantify the risk to highway infrastructure systems. The Applied Technology Council took the first step in performing seismic risk assessment [2] of infrastructure for the state of California using damage probability matrices and restoration functions. Since then several committees constituted by ATC have been solely devoted to the risk assessment of lifelines. The ATC 25 report [3] introduced the concept of continuous fragility functions for lifeline systems including bridges by performing regression on the discrete values of damage probability matrices. Further attempts to push forward the seismic risk assessment methods were made by the Federal Emergency Management Agency (FEMA) by the constitution of a committee of experts and introduction of a Geographic Information Systems (GIS) based risk assessment software, Hazards United States [4] in 1997. Since then HAZUS has undergone several improvements and revisions and now includes models for estimating potential losses from a variety of natural disasters like earthquakes, floods and hurricanes.

Over the years, structural fragilities have been determined in a variety of ways. The ATC 13 Report documents risk assessment of the infrastructure stock in California essentially based on expert opinion. A panel of 42 experts was assembled to develop damage probability matrices for bridge infrastructure based on their expertise. This technique has several major concerns since the procedure is totally subjective and depends on the number of experts queried and therefore is based on expertise and experience of the individuals with little correlation to actually observed earthquake damage. The 1989 Loma Prieta, 1994 Northridge and 1995 Kobe earthquakes were watersheds for fragility research. Several researchers [5, 6, 7, 8, 9, 10] developed empirical fragility curves based on actual damage data observed in these earthquakes. Although the adopted procedure differed slightly among the researchers, the general essence was the same. Basoz and Kiremidjian [5] assembled damage frequency matrices and performed a logistic regression analysis to develop fragility curves while Shinozula et al. [9] used the Maximum Likelihood Method to estimate the parameters of a lognormal probability distribution describing the fragility curves. Der Kiureghian [7] employed a Bayesian approach in order to develop fragility curves. However, lack of sufficient damage data, discrepancies in the damage assessments in the aftermath of a seismic event, variation in the ground motion intensities at the damage sites depending on the earthquake source are some of the limitations of this technique for developing fragility curves.

Advances in modeling capabilities coupled with lack of sufficient earthquake damage data drove the development of fragility curves using analytical methods. Yu et al. [11] used simple single-degree-of-freedom models and elastic response spectrum analysis to develop fragility curves for highway bridges in Kentucky while Hwang et al. [12] furthered this approach with slight modifications. Dutta [13] and Basoz and Mander [14] used the Nonlinear Static Procedure commonly referred to as the Capacity Spectrum Method (CSM) to develop fragilities for highway bridge classes in the United States. Currently these values are employed in HAZUS-MH for seismic risk assessment of highway infrastructure systems. Several researchers resorted to more reliable yet computationally expensive techniques like Nonlinear Time History Analysis (NLTHA) and Incremental Dynamic Analysis (IDA) to develop fragility curves. Mackie and Stojadinovic [15] employed NLTHA and IDA to develop fragility curves. These formed the basis of a rational methodology to evaluate damage potential and to assess probable highway bridge losses for critical decision making regarding post earthquake safety and repairs to highway networks. Nielson et al. [16], Padgett et al. [17], Ramanathan et al. [18] employed NLTHA to develop fragility curves for as-built and retrofitted bridge classes in Central and Southeastern United States (CSUS) accounting for multiple component vulnerability.

This study develops analytical fragility curves for seismically (S-) and non-seismically (NS-) designed multispan simply supported (MSSS) bridge classes in the CSUS to provide new insight on the relative vulnerability of these classes of bridges considering distinct levels of seismic design. The following eleven states are considered in the analysis: Arkansas, Alabama, Georgia, Illinois, Indiana, Kentucky, Missouri, Mississippi, North Carolina, and South Carolina. A detailed review of bridges in the NBI [19] in the CSUS region shows MSSS concrete and steel girder bridge classes account for approximately 20% of the bridges in the region. In 1990, bridges in the CSUS began incorporating seismic details. The bridges in the CSUS built prior to 1990 have several known seismic deficiencies which include non-ductile steel bearings, short seat widths, non-ductile columns, high pounding potential and the increased potential for the toppling of rocker bearings [20]. Some of the changes post-1990 included the component design forces, design of columns and foundation, bearing types, and treatment of liquefaction and liquefaction induced ground movement. A review of the evolution in seismic design practices in the region reveals that the predominant difference between seismically and non-seismically designed bridges is associated with the detailing aspects in the columns and the replacement of the steel rocker bearings with elastomeric bearing pads with steel dowels, as presented in detail in the next section of the paper. Bridge piers designed in the CSUS after 1990 have greater splice lengths and transverse reinforcement ratios in the longitudinal and transverse directions, when compared to the respective values in columns designed prior to 1990. The steel rocker bearings are often replaced with elastomeric bearing pads with steel dowels. Their flexibility allows the superstructure to be decoupled from the substructure yet they may also render susceptibility to large deck displacements as well as the potential for bearing walk out from under the girders.

While previous studies [16, 21, 12] have evaluated the seismic response and fragility of various bridge classes common to the CSUS, there is very little research that explores the differences in performance of typical CSUS bridge classes built with and without seismic detailing. This paper addresses this gap by investigating the influence of seismic detailing of the two multispan bridge classes on the seismic performance, as well as the failure probability through the development and comparison of fragility curves.

2 PRE- AND POST-SEISMIC DESIGN CONSIDERATIONS IN CSUS

This paper assesses the effect of seismic design detailing on typical MSSS concrete and steel girder bridge classes in the CSUS through the development of analytical fragility curves. As previously stated, the predominant difference between the non-seismically (NS-MSSS) and seismically (S-MSSS) designed bridges considered in this study is associated with the enhanced ductility characteristics of the columns in terms of detailing aspects and the replacement of non-ductile steel bearings with elastomeric bearing pads having steel dowels. Bridges constructed prior to 1990 in the CSUS region are typically not designed for the adequate seismic hazard in the region. Non-seismically designed bridges with steel girders in their superstructure typically use one of the two general classes of steel bearings, viz. high type and low type. Both of these bearing types include a fixed or pinned type bearing and an expansion type bearing with the difference being the type of motion associated with the latter. In the case of high type bearings, the motion associated with the expansion bearing is based on a rocking mechanism while it is characterized by sliding in the case of the low type bearing. In the case of MSSS steel girder bridge class, these bearing types are replaced by elastomeric bearing pads with steel dowels in addition to the reduced transverse reinforcement spacing in the columns. The relative flexible nature of these elastomeric bearings allows the superstructure to be decoupled from the substructure, and hence these bearings are susceptible to large deformations, which will be illustrated in subsequent sections of the paper. However, these large deformations could cause unseating of the bridge girders and may also result in bearings walking out from under the girders. In case of both NS- and S-MSSS concrete girder bridges, the bearings adopted were elastomeric bearing pads with steel dowels.

The reduced spacing of the transverse reinforcement in the columns is the primary difference considered between seismically and non-seismically designed columns in both bridge class columns. It is well known that column transverse reinforcement has a major impact on the shear resistance, and ductility capacity of bridges. Prior to 1990, bridge columns in the CSUS typically had transverse reinforcement which consisted of #13 bars at a spacing of 305 mm on center. Whereas, in case of the seismically designed bridges, the spacing of the #13 stirrups is as close as 76 mm on center thereby making flexure the predominant behavioral mode. In either case, the bridges have multi column bents often consisting of a rectangular reinforced concrete bent beam (Figure 1) supported by 914 mm diameter circular columns. The effect of closely spaced transverse reinforcement is incorporated by an increase in the confined compressive strength of concrete and ductility by specifying higher ultimate strain using the concrete model proposed by Mander et al. [22]. Further details can be found in [18]. In the case of the seismically designed columns, the confined compressive strength, f_{con} is approximately 33% larger than characteristic concrete strength, f'_c and the ultimate strain, ε_{cu} is approximately 0.05. Whereas, in the case of the non-seismically designed bridge columns, f_{con} is approximately 7.1% larger than f'_c and ε_{cu} is only about 0.012. Other column details such as lap splices in plastic hinge regions are not considered explicitly in the current study's column models.

3 SEISMICALLY AND NON-SEISMICALLY DESIGNED BRIDGE CLASS CASE STUDIES

The following sections present detailed information on the bridge class characteristics, analytical modeling procedures and provide some insight on the change in dynamic characteristics with the incorporation of seismic design principles. It moves on with the development of PSDMs and having characterized damage, demonstrates the development of component level fragility curves, which provides a means to look at the relative vulnerability of components in the seismic and non-seismically designed bridges.

3.1 Bridge Class Characteristics

Basic geometric characteristics of the bridge, such as number of spans, span length, deck width, and column height are analyzed and empirical cumulative density functions (CDF) are developed for each of these parameters. Twelve representative bridge configurations are generated using Latin Hypercube sampling from these empirical CDFs for the geometric parameters. The distributions are consistent with those presented in [16] to facilitate comparison.

Based on the inventory analyses, analytical bridge models are created with three spans and zero skew across all bridge classes as these were the most likely bridge configurations. Typical details for these bridge classes can be found in [21, 16], and these are consistent with [12] for Memphis, TN and [23] for Southern IL. The pre- and post-seismic design considerations for the respective bridge classes were discussed in the preceding section.

3.2 Analytical Bridge Models

The typical layout of a three span zero skew bridge is shown in Figure 1. The bridges are modeled in three dimensions using the finite element platform OpenSEES [24] incorporating both geometric and material nonlinearities. The superstructure is modeled using elastic beam-column elements with mass lumped along the centerline. This is typical as the composite slab and girder generally behave linearly. Pounding between the decks is considered using the contact element approach developed by Muthukumar and DesRoches [25]. This approach explicitly accounts for the effects of loss of hysteretic energy. Rayleigh damping is used in the model but is treated as a random variable. Nonlinear beam column elements with fiber defined cross sections are used to model the columns. The nonlinear hysteretic behavior of these columns is captured using a distributed plasticity element. Fiber defined cross sections enable specifying different properties for cover concrete and confined concrete. The differences in the modeling of the seismically and non-seismically designed columns are incorporated using the concrete model. The effect of the closely spaced transverse reinforcement in the case of the seismically designed bridge columns is accounted for by using the confined concrete model discussed in the previous section.

The bearings, both steel and elastomeric bearing pads with steel dowels, are modeled using nonlinear translational springs. In case of the elastomeric bearings, this accounts for the contribution of the elastomeric pads in addition to the steel dowels in the bearing elements. The behavior of steel bearings in both longitudinal and transverse directions is modeled according to the recommendations of Mander et al. [26] stemming from an experimental study. Abutments provide both longitudinal and transverse restraint to the bridge superstructure under loading in both directions. The longitudinal resistance is comprised of both passive and active components. The former is partially provided by soil and by the piles while the latter is provided only by the piles. This study adopts the recommendations of Caltrans [27] in estimating the stiffness of the abutments which are modeled using nonlinear translational springs. Further, the Caltrans recommendations [27] suggests that the effect of wing-walls decreases as the width of the abutment increases and therefore the transverse resistance is conservatively assumed to be provided solely by the piles. The foundation system of most of the highway bridges in CSUS consists of piles [12] which are modeled using nonlinear translational and rotational springs. The stiffness used here is the average stiffness by considering both rigid and flexible nature of the piles. The composite behavior is then computed following some basic geometry based equations presented in [28].

3.3 Deterministic Bridge Responses

In order to understand the effect of seismic detailing principles on the dynamic characteristics of the bridge, one sample set of responses from the NLTHA is compared prior to presenting the PSDMs. In this sample, identical geometries of seismically and non-seismically designed bridges with all the variables set to their median values are subjected to the same ground motion with geometric mean of the PGA of two orthogonal components equal to 0.62g . Therefore, the only distinction rests with the incorporation of seismic provisions viz., enhanced ductility in the columns in all bridge classes and replacement of steel bearings with elastomeric bearing pads in the steel bridge classes.

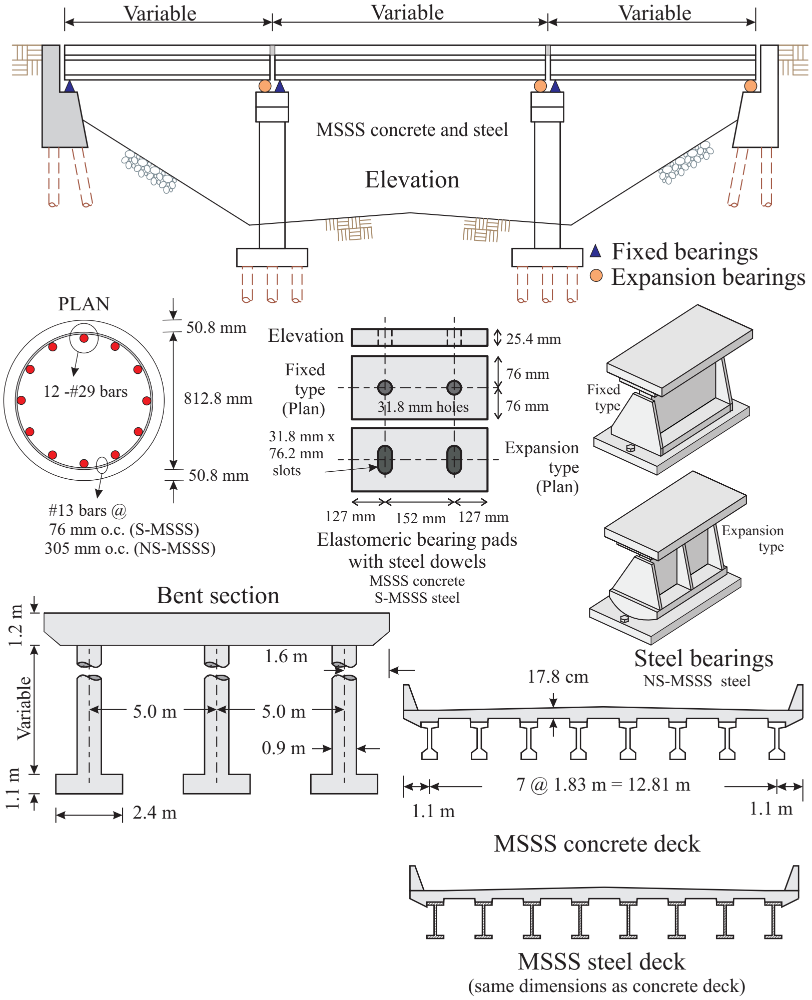

Figure 1: Configuration details of seismically and non-seismically designed bridge classes.

Figure 2 shows various component responses in the MSSS steel girder bridge. Figures 2(a) shows that the column demand is substantially greater in non-seismically designed bridge when compared to its seismic counterpart. In the transverse direction, the seismically designed column experiences a slightly higher moment demand but by far the non-seismically designed column has a much higher curvature demand. The reduced demand on the columns in the seismically designed bridge is due to the increased demand on the bearings. As seen in Figures 2(b) and 2(c), the elastomeric bearing pads in the seismically designed bridge experiences a large force and displacement demand when compared to the brittle steel bearings in the non-seismically designed bridge. The elastomeric bearings have a well defined hysteresis as seen in the figures thereby causing much of the seismic energy to dissipate through enhanced displacement capabilities. It must be noted that in case of steel bearings the internal hysteresis loop captures the frictional component of its response and this frictional force is a function of the normal force that it experiences. In this bridge type, the fixed bearings are typically located at the abutments and the end span, in this case is shorter than the middle span, thereby having a smaller mass and producing smaller reactions leading to narrow hysteresis loops as depicted in Figure 2(b). This leads to difference in the demand models for these components, as will be shown subsequently in this section. In this case, the abutment response in longitudinal direction is seen to be dominated by passive action as shown in Figure 2(d). The transverse response is characterized by piles alone and in this case, although not shown here, it is seen that the pile action of the abutments never exceeded the linear range with maximum deformations less than 6 mm in either case of seismic and non-seismically designed bridges. Greater pounding action was seen in the non-seismically designed bridge when compared to the seismically designed bridge. Pounding typically causes the passive action of abutments to engage while doing very little to engage the active action. This is depicted in Figure 2(d) where the non-seismically designed bridge has a very dominant passive response (negative quadrant) when compared to the seismically designed bridge. Further, the seismically designed bridge shows very little active response (positive quadrant) which is absent in the case of the non-seismically designed bridge. The transverse load path does not interfere much with pounding and hence very little force gets transmitted to the abutments thereby resulting in the linear response of the abutment piles as seen in this case.

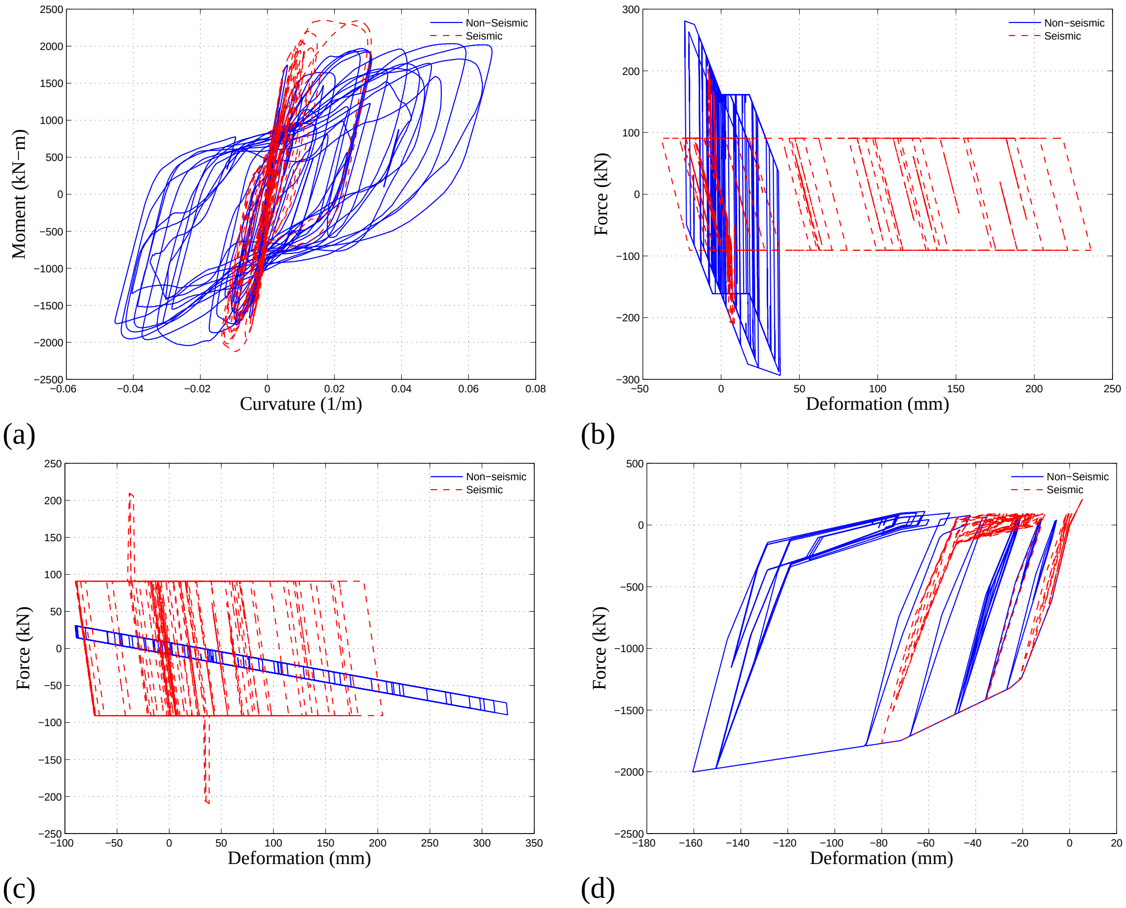

(a)

(b)

(c)

(d)

Figure 2: MSSS steel girder bridge component responses for (a) transverse column response, (b) transverse fixed bearing response, (c) longitudinal expansion bearing response, and, (d) longitudinal abutment response.

The component responses from seismically and non-seismically designed MSSS concrete girder bridges with identical geometries and median parameters is shown in Figure 3. As seen in almost all figures 3(a) through 3(d), there is no major difference in demand in the seismically and non-seismically designed bridge. Seismically designed column is seen to have a slightly greater demand in the transverse direction although both the columns have almost similar demands in the longitudinal direction. The elastomeric bearing pads in the seismically designed bridge were observed to have slightly larger displacement demands when compared to their presence in the non-seismically designed bridge maintain the same force demands. Passive action dominated the abutment response in the longitudinal direction as in the case of steel girder bridges, with the abutments in the seismically designed bridge experiencing slightly greater demands when compared to non-seismically designed bridge. The abutment piles were seen to respond in the elastic range in both the bridges considered similar to steel girder bridges. Therefore, it can be concluded that in case of concrete girder bridge class, the seismic design does not lead to a significant change in the demands and this is reflected in the PSDMs developed subsequently in this section. Instead the change in capacity due to seismic detailing of components is more critical for the concrete bridges.

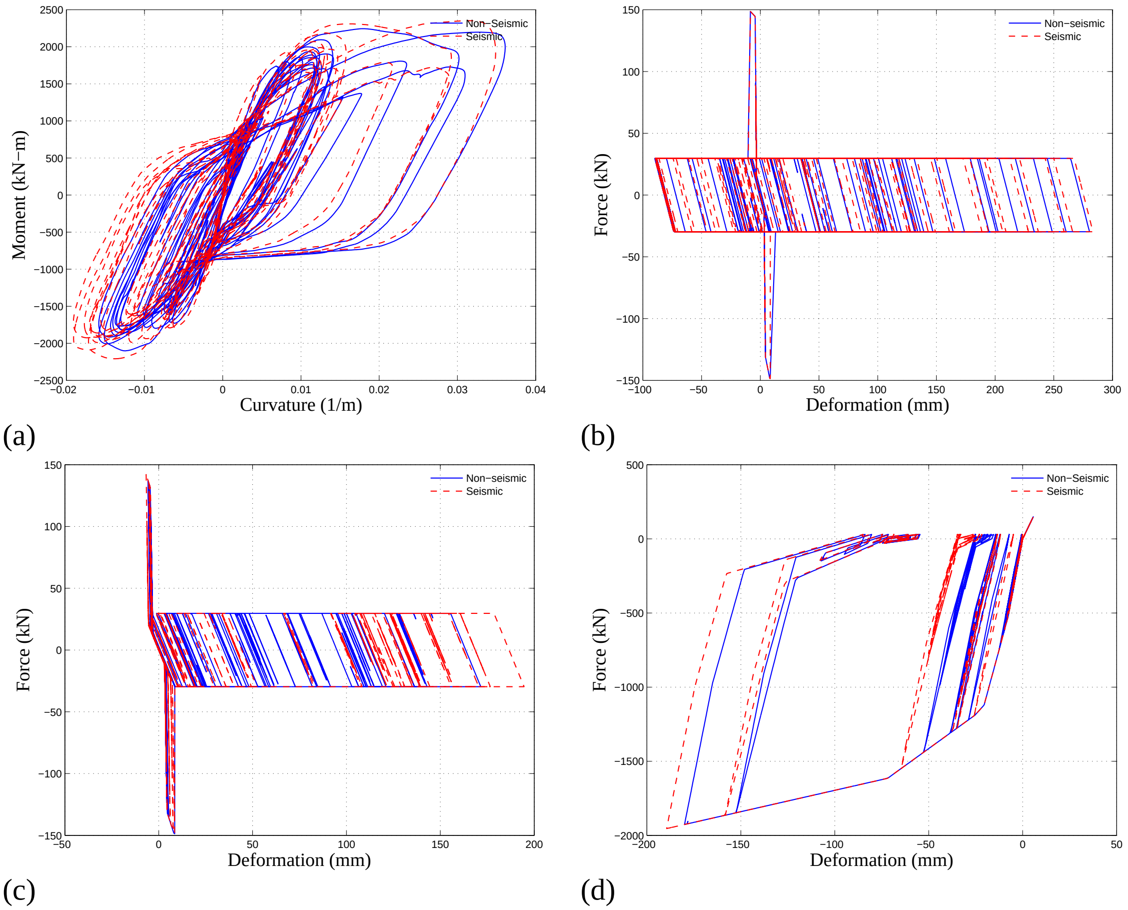

(a) (b)

(c) (d)

Figure 3: MSSS concrete girder bridge component responses for (a) transverse column response, (b) longitudinal fixed bearing response, (c) transverse expansion bearing response, and, (d) longitudinal abutment response.

3.4 Ground Motion Suite

240 ground motions developed by Fernandez and Rix [29] are used to perform NLTHA. These are probabilistic ground motions developed for selected cities within the Upper Mississippi Embayment including Memphis, TN; Jonesboro, AR; Jackson, TN; Blytheville, AR; Paducah, KY; Cape Girardeau, MO, and Little Rock, AR. Ground motions developed for

Memphis, TN included both Lowlands and Uplands soil profiles since portions of the city are in each soil type. The CSUS ground motions in this database were generated by scaling recorded ground motions for Western United States (WUS). Thus this process provides CSUS ground motions with realistic phase, amplitude relationships between components and frequency-to-frequency variability [29]. The ground motions are probabilistic motions consistent with hazard levels of 10%, 5% and 2% probability of exceedance in 50 years, corresponding to return periods of 475, 975 and 2475 years. 10 motions for each intensity level were generated for every city making it 240 in total. The suite of ground motions is intended to represent the epistemic and aleatoric variability characterized in the soil attenuation relationships developed for the region. Each of the synthetic ground motion was used to generate two orthogonal components following the procedure outlined by Baker and Cornell [30]. The geometric mean of the PGA values of the orthogonal components varies between 0.08g and 1.46g.

3.5 Probabilistic Seismic Demand Models (PSDM)

A PSDM is a conditional statement of the probability that a component experiences a demand for a given IM level, illustrating the importance of the IM as a conditional parameter in the probabilistic model. Hence, the choice of ground motions, definition of the class of structures, formulation of a nonlinear analysis model, and choice of IM and demand measure (DM) pairs form the key aspects of the approach. Padgett et al. [31] and Shafieezadeh et al. [32] explored IMs for portfolios of bridges with geometric variation and concluded that PGA is an optimal IM for probabilistic seismic demand analysis of classes of bridges. This study uses PGA as the IM to develop PSDMs and fragility curves subsequently. The estimation of the median demand, expressed in Equation (1) is based on a power-law model proposed by Cornell et al. [33].

$$S_D = a(IM)^b \tag{1}$$

where, S_D is the median demand, IM is the intensity measure chosen, a and b are the power-law model parameters. By expressing the median demand in logarithmic space, the variation of S_D with the IM takes a linear form and this facilitates the evaluation of the parameters a and b using a simple linear regression analysis. In order to describe the uncertainty about the demand, the logarithmic standard deviation, commonly referred to as the dispersion, $\beta_{\mathrm{D|IM}}$, needs to be evaluated, which is expressed in Equation (2). Having estimated, S_D and $\beta_{\mathrm{D|IM}}$, the PSDM can be formulated as shown in Equation (3):

$$\beta_{D/IM} = \sqrt{\frac{\sum_{i=1}^{N}\left(\ln d_i - \ln a(IM)^b\right)^2}{N-2}} \tag{2}$$

$$P[D \geq d \mid IM] = 1 - \Phi\left(\frac{\ln(d) - \ln(S_D)}{\beta_{D|IM}}\right) \tag{3}$$

where, $\Phi(\bullet)$ is the standard normal cumulative density function and S_D is shown in Equation (1).

This study considers various geometric and material variabilities in the fragility analysis. As stated previously, twelve representative bridge realizations are created by sampling on the geometric variables obtained from the inventory analyses. In addition to these geometric variations, several other uncertainties are propagated as listed in Table 1. The bridge realizations together with the uncertainties presented in Table 1 are used to create 240 bridge models which are then randomly paired with 240 Rix ground motions to create 240 bridge – ground motion pairs which are statistically significant and nominally identical.

Uncertainty parameter	Units	Sampling distribution	Distribution parameters	
Concrete compressive strength	MPa	Normal*	$\mu = 33.5$	$\sigma = 4.3$
Reinforcing steel yield strength	MPa	Lognormal†	$\lambda = 6.14$	$\zeta = 0.03$
Elastomeric bearing shear modulus	MPa	Uniform‡	$\alpha = 0.69$	$\beta = 2.07$
Elastomeric bearing coeff. of friction		Lognormal	$\lambda = 0$	$\zeta = 0.1$
Dowel bar strength	MPa	Lognormal	$\lambda = 4.49$	$\zeta = 0.03$
Gap at the dowels	mm	Uniform	$\alpha = 0$	$\beta = 50.8$
Steel fixed bearing coeff. of friction				
Longitudinal direction		Lognormal	$\lambda = -1.56$	$\zeta = 0.5$
Transverse direction		Lognormal	$\lambda = -0.99$	$\zeta = 0.5$
Steel expansion bearing coeff. of friction				
Longitudinal direction		Lognormal	$\lambda = -3.22$	$\zeta = 0.5$
Transverse direction		Lognormal	$\lambda = -2.30$	$\zeta = 0.5$
Passive abutment stiffness	kN/mm/m	Uniform	$\alpha = 11.5$	$\beta = 28.8$
Active abutment stiffness	kN/mm/m	Uniform	$\alpha = 2.2$	$\beta = 6.6$
Translational foundation stiffness	kN/mm/pile	Uniform	$\alpha = 28$	$\beta = 84$
Rotational foundation stiffness	kN-m/rad	Uniform	$\alpha = 3\,(10)^5$	$\beta = 9.1(10)^5$
Deck mass ratio		Uniform	$\alpha = 0.9$	$\beta = 1.1$
Damping ratio		Normal	$\mu = 0.045$	$\sigma = 0.0125$
Gap at internal hinges	mm	Normal	$\mu = 25.4$	$\sigma = 4.3$
Gap between deck and abutment	mm	Normal	$\mu = 38.1$	$\sigma = 5.8$
Earthquake angle of incidence	rad	Uniform	$\alpha = 0$	$\beta = 2\pi$

*Normal distribution is characterized by the mean, μ, and standard deviation, σ.

†Lognormal distribution is characterized by the parameters, λ and ζ, which are the mean and standard deviation, respectively, of the associated normal distribution.

‡Uniform distribution is characterized by the lower, α, and upper bound, β.

Table 1: List of uncertainties considered in fragility analysis.

A full NLTHA is performed for each bridge – ground motion pair and the maximum demand placed on various components is recorded. In total, 1920 NLTHA are performed for the seismically and non-seismically designed bridges in the four bridge classes considered. Researches in the past [16, 17, 18] have indicated the necessity to consider the vulnerability of several key components to assess system level performance and hence this study considers multi-component vulnerability. Table 2 details the demand parameters used to assess component demands for various bridge components considered in this study. Having performed NLTHA and recorded peak component demands, PSDMs are determined according to the procedure described in the previous section, according to the formulations in Equations (1), (2) and (3).

Demand measure	Abbreviation	Units
Column curvature ductility demand	μ_ϕ	
Longitudinal fixed bearing deformation	δ_{fl}	mm
Transverse fixed bearing deformation	δ_{ft}	mm
Longitudinal expansion bearing deformation	δ_{el}	mm
Transverse expansion bearing deformation	δ_{et}	mm
Passive abutment deformation	δ_p	mm
Active abutment deformation	δ_a	mm

Transverse abutment deformation	δ_t	mm

Table 2: Bridge component demand measures.

Figure 4 illustrates a few sample PSDMs for S-MSSS and NS-MSSS concrete and steel girder bridge classes for the columns and bearings. There is a very minor difference in demand in S-MSSS and NS-MSSS concrete bridges as seen in Figures 4(a) and 4(b). This is expected since the initial stiffness for both cases is identical, and the maximum compressive strength only shows in small difference between the seismically and non-seismically designed bridge columns. The critical effect of the non-seismically designed column is not necessarily an effect on the demand but rather a reduction in capacity. Hence, limit states are most critical when considering changes only in column detailing. However, in the case of the steel bridges, an appreciable difference in demand curves is observed as shown in Figures 4(c) and 4(d) for MSSS steel girder bridges. The difference in the dynamic characteristics of the bridge and the change in load path, as explained in the early parts of this section, are the predominant reasons for the difference in demand models.

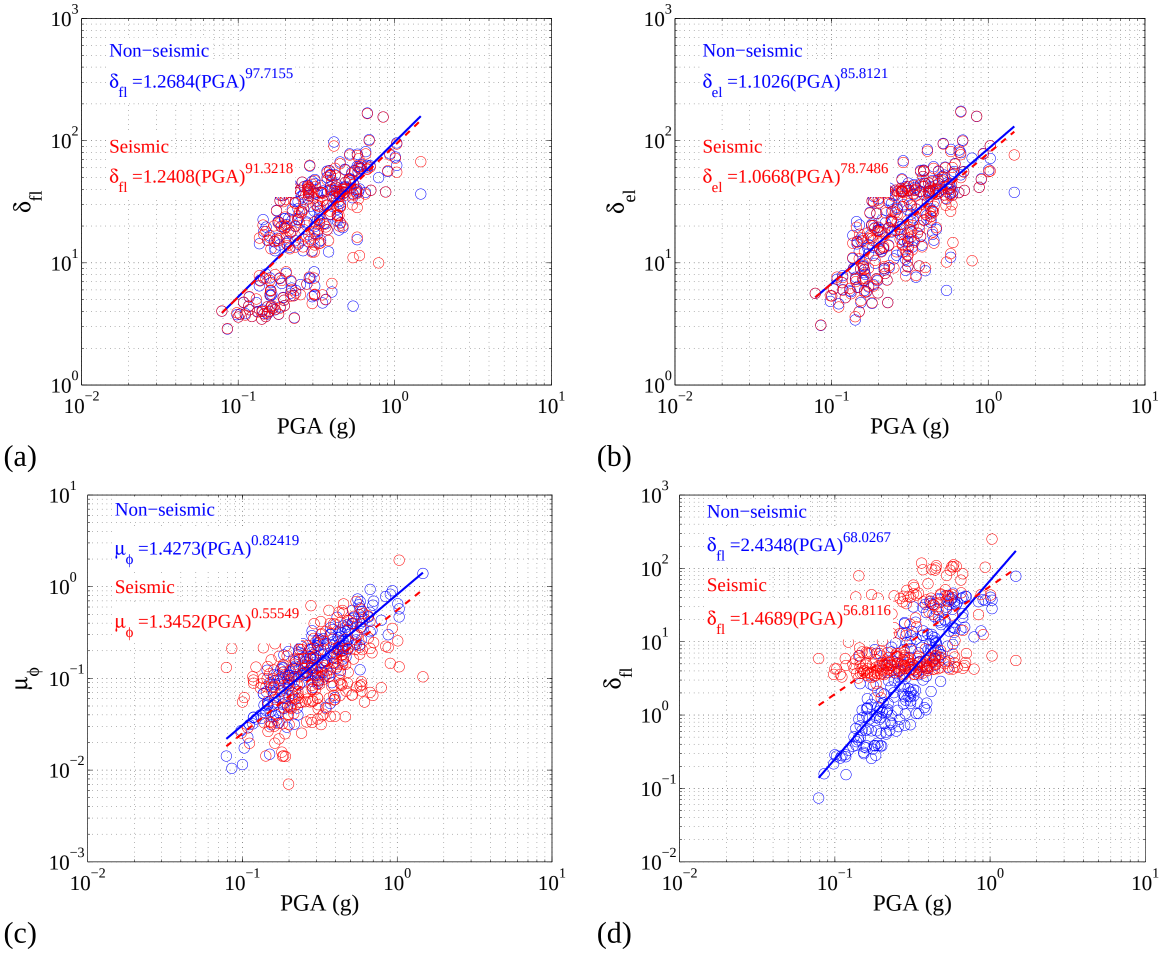

Figure 4: Probabilistic seismic demand models for (a) longitudinal fixed bearing response in MSSS concrete, (b) longitudinal expansion bearing response in MSSS concrete, (c) columns in MSSS steel, and (d) longitudinal fixed bearing response in MSSS steel.

3.6 Component Damage States

The components considered in this study are columns, fixed and expansion elastomeric bearings and abutments (active and passive as well as transverse).The component limit states are also assumed to be lognormally distributed. The median, S_c and the dispersion, β_c values of the capacity limit states are obtained from experimental results and are truly prescriptive. The study uses four damage states; slight, moderate, extensive and complete, comparable to those found in HAZUS-MH. Table 3 summarizes the limit states adopted for the various bridge components. The damage state definitions provided in Table 3 stem from recommendations from previous studies [12, 21, 16, 18] and results from experimental tests. The damage states for columns are quantified using curvature ductility and the results presented in the table below for seismically and non-seismically designed columns stem from the recommendations of [12] and the Pacific Earthquake Engineering Research (PEER) Center's column structural performance database [34]. Steel fixed and expansion bearings have damage states prescribed in terms of displacements and the values shown in Table 3 are obtained from experimental tests conducted on similar bearings [26]. The bearing damage states for elastomeric bearing pads and those for the abutments are consistent with those presented in [16].

Component	Slight		Moderate		Extensive		Complete	
	S_c	β_c	S_c	β_c	S_c	β_c	S_c	β_c
Columns								
Non-seismically designed	1.0	0.25	1.58	0.25	3.22	0.47	4.18	0.47
Seismically designed	1.0	0.25	5.11	0.25	7.50	0.47	9.00	0.47
Elastomeric bearing pads with steel dowels								
Fixed bearing – Long. (mm)	30.0	0.25	100.0	0.25	150.0	0.47	255.0	0.47
Fixed bearing – Trans. (mm)	30.0	0.25	100.0	0.25	150.0	0.47	255.0	0.47
Expansion bearing – Long. (mm)	30.0	0.25	100.0	0.25	150.0	0.47	255.0	0.47
Expansion bearing – Trans (mm)	30.0	0.25	100.0	0.25	150.0	0.47	255.0	0.47
Steel bearings								
Fixed bearing – Long. (mm)	6.0	0.25	20.0	0.25	40.0	0.47	255.0	0.47
Fixed bearing – Trans. (mm)	6.0	0.25	20.0	0.25	40.0	0.47	255.0	0.47
Expansion bearing – Long. (mm)	6.0	0.25	20.0	0.25	40.0	0.47	255.0	0.47
Expansion bearing – Trans (mm)	30.0	0.25	100.0	0.25	150.0	0.47	255.0	0.47
Abutments								
Passive response (mm)	37.0	0.25	146.0	0.25	1000	0.47	1000	0.47
Active response (mm)	9.75	0.25	37.9	0.25	77.2	0.47	1000	0.47
Transverse response (mm)	9.75	0.25	37.9	0.25	77.2	0.47	1000	0.47

Table 3: Prescriptive bridge component limit states.

3.7 Component Fragility Curves

Fragility curves at the component level are derived based on the formulation presented in Equation (4) to provide a basis of comparison for the effect of seismic detailing on component vulnerability for the various bridge classes.

$$P[D > C \mid IM] = \Phi\left(\frac{\ln(S_D/S_c)}{\sqrt{\beta_{D|IM}{}^2 + \beta_c{}^2}}\right) \tag{4}$$

Figure 5 plots the component fragilities for the S-MSSS concrete and steel girder bridges at the two intermediate limit states. In the case of the S-MSSS steel bridge class, the elastomeric expansion bearings are the most vulnerable component at the slight damage state whereas the elastomeric fixed bearings tend to be the most vulnerable component at all the other damage states as shown in Figures 5(a) and 5(b). This should be expected as there was considerable demand imposed on the bearings as illustrated in Section 3.5 and Figure 2. In the case of NS-MSSS steel, the columns tend to be the most vulnerable component at lower damage states while the longitudinal expansion bearing response dominates the system fragility at higher damage states. This shift in vulnerability may be attributed to the change in dynamic characteristics and resulting demands imposed on the components due to the consideration of seismic design principles. In the case of the S-MSSS concrete bridge class, as shown in Figures 5(c) and 5(d), the expansion bearings tend to dominate the vulnerability in the slight and moderate damage states but the fixed bearings dominate the vulnerability in the case of the extensive and complete damage states. In contrast, columns tend to dominate the vulnerability of the system at all damage states.

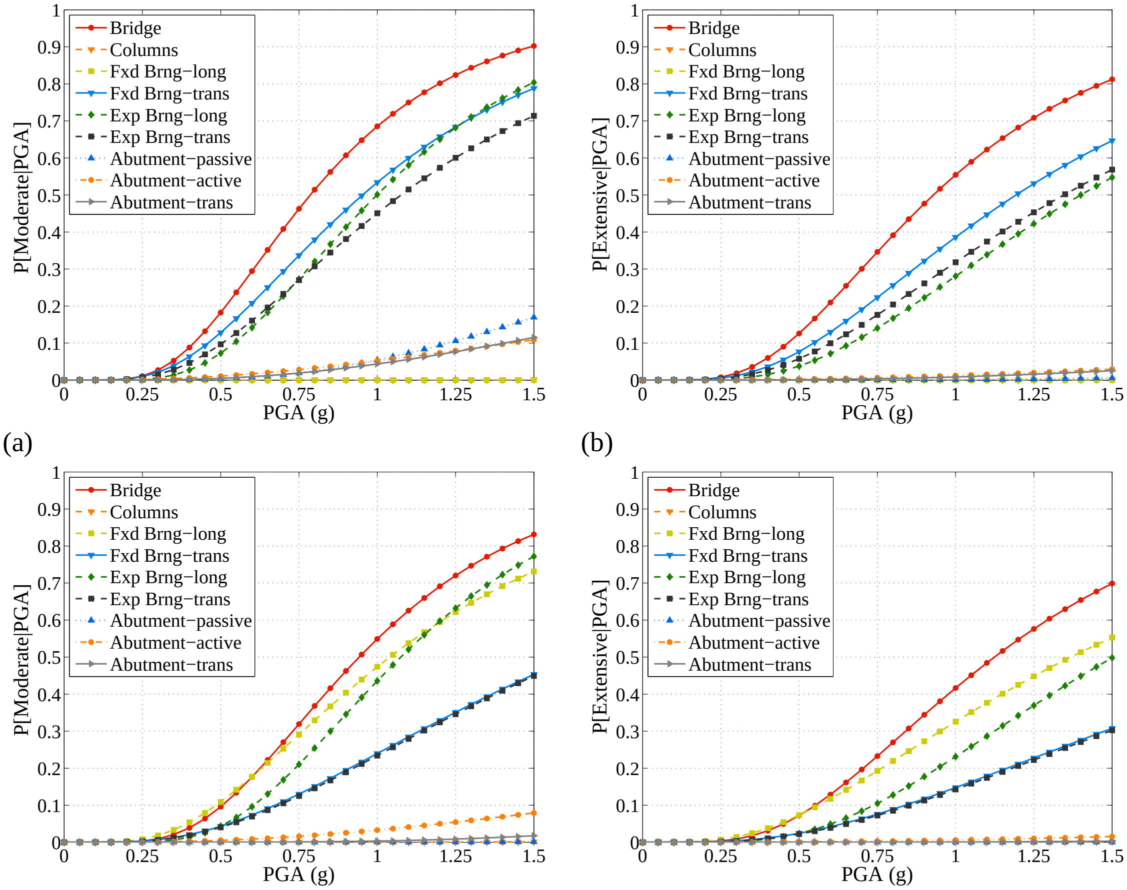

(a)

(b)

(c)

(d)

Figure 5: Bridge and component fragility curves for S-MSSS steel girder bridge class for (a) moderate, and (b) extensive limit states, and for S-MSSS concrete girder bridge class for (c) moderate, and (d) extensive damage states.

4 BRIDGE SYSTEM FRAGILITY CURVES

4.1 Comparison of System Fragility for Seismically and Non-seismically Designed Bridge Classes

The logical step that succeeds the determination of component fragilities is to integrate these to enable the macroscopic view of the bridge as a system. Several researchers [16, 35, 21] have proposed techniques to develop fragility curves for the bridge as a system. Mackie and Stojadinovic [35] used the first order reliability method in developing fragility curves while Choi et al. [21] considered first order bounds for series systems. The present study uses the approach developed by [16]. The estimate of system fragility curves is facilitated through the development of joint probabilistic seismic demand model (JPSDM), recognizing that the demands on various components have some level of correlation. A Monte Carlo simulation is then used to compare realizations of the demand (using the JPSDM defined by a conditional joint normal distribution in the transformed space) and statistically independent component capacities to calculate the probability of system failure. Samples (10^6 in this case) are drawn from both the demand and capacity models and the probability of demand exceeding the capacity is evaluated for a particular IM value. The procedure is repeated for increasing values of the IM. Regression analysis is used to estimate the lognormal parameters, median and dispersion, which characterize the bridge system fragility. The methodology presented in this section is used to develop system fragility curves for seismically and non-seismically designed bridges within the fore mentioned bridge classes by considering multiple component vulnerability. The CDFs that define the probabilities of exceeding a limit state, LS, can then be plotted based on the Equation (5), where λ_i and ζ_i are the median and dispersion, respectively, of the i^{th} limit state.

$$P[LS \mid IM] = \Phi\left(\frac{\ln(IM) - \ln(\lambda_i)}{\zeta_i}\right) \tag{5}$$

Figure 6 shows the system fragility curves for seismic and non-seismically designed MSSS concrete and steel girder bridge classes. In the case of the MSSS concrete bridge class, a very minor difference is seen in the curves at slight damage state. This is because the elastomeric expansion bearings dominate the vulnerability at this limit state followed by elastomeric fixed bearings. Hence, a significant improvement is not seen due to seismic detailing of the columns which has little effect on the demand and more effect on the capacity. On the contrary, in case of the MSSS steel bridge class, significant differences are observed in the curves at all damage states as shown in Figure 6(b). These differences may be attributed predominantly to the replacement of the non-ductile steel bearings with elastomeric bearing pads. This is not the case in their concrete bridge counterparts as the only difference between seismic and non-seismic design is with respect to the column ductility enhancement. Steel bearings are the most vulnerable components in case of NS-MSSS steel bridge class and hence their replacement along with seismic detailing of columns produces a significant reduction in the vulnerability of the system as a whole. This is seen in Figure 6(b).

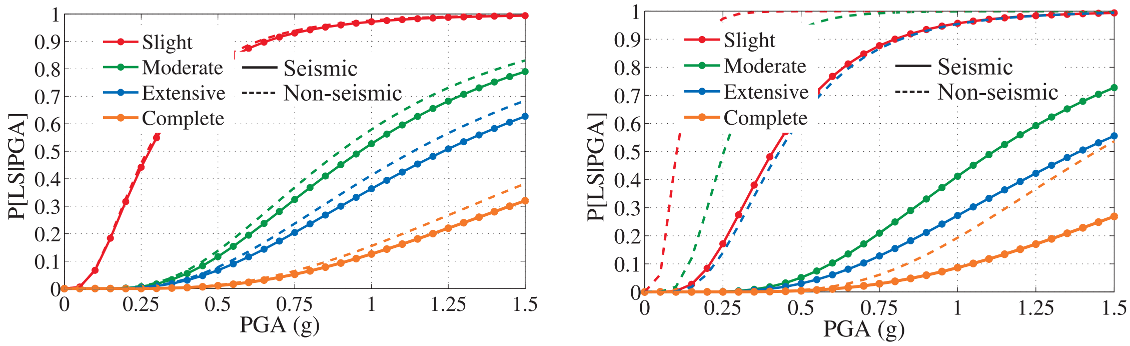

(a)

(b)

Figure 6: Bridge system fragility curves for seismically and non-seismically designed (a) MSSS concrete girder bridge class, and (b) MSSS steel girder bridge class.

In the case of all the bridge classes, with and without seismic design, the dispersions associated with various limit states fall in a narrow range and hence a single constant dispersion value is chosen to characterize the bridge fragility curves. For example, in the case of the S-MSSS concrete girder bridge class, the dispersion values for slight, moderate, extensive and complete damage states are 0.50, 0.56, 0.52, and 0.55 respectively. In this case, a constant dispersion equal to the mean value, 0.53 in this case, is chosen for the curves corresponding to all the limit states. The median values of fragility curves for the bridge system for various bridge classes along with the dispersions is tabulated in Table 4. It can be seen that incorporation of seismic design principles tends to increase the dispersion about the median fragility. In this study, the parameters included in the uncertainty analysis are the same for both seismic and non-seismically designed bridges, and these were obtained from a sensitivity study presented in [16] that was primarily aimed as non-seismically designed bridge classes. The dispersions associated with the various damage states are similar for seismically and non-seismically designed bridge classes.

Bridge class	Seismically designed*					Non-seismically designed					Percent change in λ			
	λ_s†	λ_m	λ_e	λ_c	ζ	λ_s	λ_m	λ_e	λ_c	ζ	λ_s	λ_m	λ_e	λ_c
MSSS concrete	0.37	0.94	1.12	1.66	0.53	0.34	0.84	0.99	1.41	0.46	8.8	11.9	13.1	17.7
MSSS steel	0.41	1.12	1.39	2.09	0.52	0.10	0.26	0.43	1.45	0.46	310	331	223	44.1

*The subscripts s, m, e, c for the median values denote slight, moderate, extensive and complete damage states, respectively.

†Median values are reported as proportions of acceleration due to gravity, *g*.

Table 4: Median and dispersion values for bridge class fragility and percentage change in median values of between seismically and non-seismically designed bridge classes.

A simple technique to compare differences in the fragility curves is to evaluate the relative change in the median value of the fragility curves. This facilitates comparison between the bridge classes as well as for seismic and non-seismic detailing of a given bridge type. A positive change indicates a less vulnerable structure while a negative change indicates a more vulnerable structure. The percentage change in median values for the seismically designed bridges with respect to their non-seismic counterparts is also reported in Table 4. As mentioned previously, significant improvements in the median values are seen in case of the steel bridges in comparison to the marginal improvements in case of concrete bridges. The higher percentage increase in case of steel bridges can be attributed to the seismic detailing provisions in the columns and replacement of the steel bearings with the elastomeric bearing pads.

The results show that the difference in the median values is well pronounced at higher damage states when compared to lower states. This can be attributed to the fact that the actual distinction in performance is predominant when significant nonlinearity occurs and this is seen typically at higher damage states. Hence, the effect of seismic design is well pronounced at the higher damage states.

4.2 Comparisons with HAZUS

As mentioned in Section 1 of the paper, the fragility curves currently used in the risk assessment software, HAZUS, were developed by Basoz and Mander [14] using the nonlinear static procedure, commonly referred to as the Capacity Spectrum Method. These fragility curves, akin to the ones developed in this study are applicable to a class of bridges. The dispersions for the system fragility curves obtained in this study are in the range of 0.5-0.6 (see Table 4) and this is in good agreement with the value of 0.6 proposed by Basoz and Mander [14]. Table 5 shows the median value of fragilities obtained from this study along with the values used in HAZUS-MH. The percentage change in the median values of the present study with respect to those in HAZUS-MH is also presented. A positive change in the median values indicates a less vulnerable structure while a negative change indicates a more vulnerable structure.

Bridge class	Source	Median (g) values				Percentage change (%)			
		λ_s	λ_m	λ_e	λ_c	λ_s	λ_m	λ_e	λ_c
S-MSSS concrete	Proposed	0.37	0.94	1.12	1.66	-17.8	23.7	6.7	8.50
	HAZUS	0.45	0.76	1.05	1.53				
NS-MSSS concrete	Proposed	0.34	0.84	0.99	1.41	30.8	14.0	25.0	16.9
	HAZUS	0.26	0.35	0.44	0.65				
S-MSSS steel	Proposed	0.41	1.12	1.39	2.09	-8. 9	47.4	32.4	36.6
	HAZUS	0.45	0.76	1.05	1.53				
NS-MSSS steel	Proposed	0.1	0.26	0.43	1.45	-61.5	-25.7	-2.3	23.1
	HAZUS	0.26	0.35	0.44	0.65				

Table 5: Median values of fragility curves obtained in this study and those from HAZUS.

For the seismically and non-seismically designed bridge classes, this study shows that the bridges are much less vulnerable in the complete damage state. The difference in median values proposed in this study to those reported in HAZUS-MH could be attributed to a variety of reasons. This study adopts nonlinear time history analyses while the fragilities reported in HAZUS-MH are derived using nonlinear static procedure. The differences are also attributed to the consideration of multiple components in estimating the overall system vulnerability and differences in the limit state values. Further, this study considers a much broader list of geometric and material variables in the fragility framework in addition to inclusion of key bridge class attributes based on a detailed NBI bridge inventory. The hallmark of this study is that it also includes considerations of seismic, non-seismic, and general design features exclusive to bridge classes predominant in CSUS making these fragility estimates more suitable to this region.

5 CONCLUSIONS

This study presents an analytical method for the development of fragility curves for seismically and non-seismically designed bridge classes in the central and southeastern United States. Two typical multispan bridge classes are considered that include simply supported concrete and steel girder bridges. Detailed three dimensional finite element models which account for the nonlinear behavior of the column, girders, and abutments, are developed in the OpenSEES platform. Fragility curves are developed from nonlinear time history analyses using a suite of 240 ground motions developed by Fernandez and Rix [29] for selected cities within the Upper Mississippi Embayment. The uncertainty analysis includes a range of material and geometric parameters and the fragility curves are developed considering multiple component vulnerability using the joint probabilistic seismic demand model approach developed by Nielson and DesRoches [16]. The predominant difference between seismically and non-seismically designed bridges is associated with enhanced ductility characteristics of the column in all the bridge classes considered. In the case of steel girder bridge class, the non-ductile steel bearings prevalent in non-seismically designed bridges are replaced with elastomeric bearing pads with steel dowels in bridges designed post 1990.

The following are some of the important conclusions that can be drawn from the present study. Significant reduction in the vulnerability is seen in both the bridge classes considered in this study with seismic design principles used in their design. The percentage change in the median values is as high as 300% for almost all damage states in the case of steel girder bridges and it is to the order of 15% in the case of their concrete counterparts. The big increase in steel bridges may be attributed to enhanced column ductility performance and replacement of non-ductile steel bearings with elastomeric bearing pads. Comparisons are made between the proposed fragility curves and with those presently adopted by HAZUS-MH. For the seismically and non-seismically designed bridge classes, this study yields significantly fewer vulnerable bridge classes at the complete damage state. The results from this study yield significantly less vulnerable seismically designed bridge fragilities in comparison to HAZUS-MH. The differences in median fragilities may be attributed to the difference in the adoption of analyses techniques, definition of system vulnerability, range of parameters considered in the stochastic analysis at the least. This study considers seismic, non-seismic, and general design features exclusive to bridge classes predominant in CSUS making these fragility estimates more suitable to this region.

REFERENCES

[1] R. V. Whitman, J. M. Biggs, J. E. Brennan III, A. C. Cornell, R. L. de Neufville, and E. H. Vanmarcke, Seismic Design Decision Analysis. *Journal of Structural Engineering*, 101, 1067-1084, 1975.

[2] ATC, 1985. Earthquake Damage Evaluation Data for California, *Report No. ATC – 13*, Applied Technology Council, Redwood City, CA.

[3] ATC, 1991. Seismic Vulnerability and Impact of Disruption of Lifelines in the Coterminous United States, *Report No. ATC – 25*, Applied Technology Council, Redwood City, CA.

[4] FEMA, 2003. *HAZUS-MH MR1: Technical Manual.* Federal Emergency Management Agency, Washington, DC.

[5] Basoz, N., and Kiremidjian, A. S., 1997. Evaluation of Bridge Damage Data from the Loma Prieta and Northridge CA Earthquakes, *Report No. MCEER-98-0004*, MCEER, Buffalo, NY.

[6] Yamazaki, F., Hamada, T., Motoyama, H., and Yamauchi, H., 1999. Earthquake Damage Assessment of Expressway Bridges in Japan, *Technical Council on Lifeline Earthquake Engineering Monograph*, 16, 361-370.

[7] Der Kiureghian, A., 2002. Bayesian Methods for Seismic Fragility Assessment of Lifeline Components, *Acceptable Risk Processes: Lifelines and Natural Hazards*, Monograph No. 21, A. D. Kiureghian ed., Technical Council for Lifeline Earthquake Engineering, ASCE, Reston, VA.

[8] Shinozuka, M., Feng, M. Q., Kim, H.-K., and Kim, S.-H., 2000. Nonlinear Static Procedure for Fragility Curve Development, *Journal of Engineering Mechanics*, **126(12)**, 1287-1296.

[9] Shinozuka, M., Feng, M. Q., Kim, H., Uzawa, T. and Ueda, T., 2003. Statistical Analysis of Fragility Curves, *Report No. MCEER-03-0002*, MCEER, Buffalo, NY.

[10] Elnashai, A., Borzi, B., and Vlachos, S., 2004. Deformation-Based Vulnerability Functions for RC Bridges, *Structural Engineering and Mechanics*, **17(2)**, 215-244.

[11] Yu. O., Allen, D. L., and Drnevich, V. P., 1991. Seismic Vulnerability Assessment of Bridges on Earthquake Priority Routes in Western Kentucky, *3rd US National Conference on Lifeline Earthquake Engineering*, Los Angeles, CA.

[12] Hwang, H., Jernigan, J. B., and Lin, Y. W., 2000. Evaluation of seismic damage to Memphis bridges and highway systems, *Journal of Bridge Engineering* **5(4)**, 322-330.

[13] Dutta, A., 1999. On Energy Based Seismic Analysis and Design of Highway Bridges, *Ph.D. Thesis*, State University of New York at Buffalo, Buffalo, NY.

[14] Basoz, N., and Mander, J. B., 1999. *Enhancement of the Lifeline Transportation Module in HAZUS, Report No. Draft #7*, National Institute of Building Sciences, Washington, DC.

[15] Mackie, K., and Stojadinovic, B., 2005. Fragility Basis for California Highway Overpass Bridge Seismic Decision Making, *PEER Report 2005/02*, Pacific Earthquake Engineering Research Center, University of California, Berkeley, CA.

[16] Nielson, B. G., and DesRoches, R., 2007. Analytical Seismic Fragility Curves for Typical Bridges in the Central and Southeastern United States, *Earthquake Spectra* **23**, 615-633.

[17] Padgett, J. E., and DesRoches, R., 2008. Methodology for Development of Analytical Fragility Curves for Retrofitted Bridges, *Earthquake Engineering and Structural Dynamics*, **37(8)**, 1157-1174.

[18] Ramanathan, K., DesRoches, R., Padgett, J. E., 2010. Analytical Fragility Curves for Multispan Continuous Steel Girder Bridges in Moderate Seismic Zones, *Transportation Research Record* 2202, 173-182.

[19] U.S. Department of Transportation, Federal Highway Administration, 2009. *National Bridge Inventory Data*, Washington, DC, available at: http://www.fhwa.dot.gov/bridge/nbi/ascii.cfm.

[20] DesRoches, R., Choi, E., Leon, R. T., Dyke, S. J., and Aschheim, M., 2004. Seismic Response of Multiple Span Steel Bridges in Central and Southeastern United States. I: As Built, *Journal of Bridge Engineering* **9(5)**, 464-473.

[21] Choi, E., DesRoches, R., and Nielson, B., 2004. Seismic Fragility of Typical Bridges in Moderate Seismic Zones, *Engineering Structures* **26(2)**, 187–199.

[22] Mander, J. B., Priestley, M. J. N., and Park, R., 1988. Theoretical stress-strain model for confined concrete, *Journal of Structural Engineering* **114(8)**, 1804-1826.

[23] Bignell, J. L., LaFave, J. M., and Hawkins, N. M., 2005. Seismic vulnerability assessment of wall pier supported highway bridges using nonlinear pushover analysis, *Engineering Structures* **27**, 2044-2063.

[24] McKenna F., Scott M., and Fenves G. L., 2010. Nonlinear Finite-Element Analysis Software Architecture Using Object Composition, *Journal of Computing in Civil Engineering* **24(1)**, 95-107.

[25] Muthukumar, S., and DesRoches, R., 2006. A Hertz contact model with non-linear damping for pounding simulation, *Earthquake Engineering and Structural Dynamics* **35**, 811-828.

[26] Mander, J. B., Kim, D. K., Chen, S. S., Premus, G. J., 1996. Response of steel bridge bearings to reversed cyclic loading, *Technical Report NCEER 96-0014*, Buffalo, NY.

[27] Caltrans, 1990. *Caltrans Structures Seismic Design References*, First Edition, California Department of Transportation, Sacramento, CA.

[28] Ma, Y., and Deng, N., 2000. *Deep Foundations*, *Bridge Engineering Handbook*, Chen, W.-F., and Duan, L. (editor) CRC Press.

[29] Fernandez, J. A., and Rix, G. J., 2006. Probabilistic Ground Motions for Selected Cities in the Upper Mississippi Embayment, available at: http://geosystems.ce.gatech.edu/soil_dynamics/research/groundmotionsembay/.

[30] Baker, J., and Cornell, A. C., 2006. Which Spectral Acceleration Are You Using? *Earthquake Spectra* **22**, 293-312.

[31] Padgett, J. E., Nielson, B. G., and DesRoches, R., 2008. Selection of optimal intensity measures in probabilistic seismic demand models of highway bridge portfolios, *Earthquake Engineering and Structural Dynamics* **37**, 711-725.

[32] Shafieezadeh, A., Ramanathan, K., Padgett, J. E., and DesRoches, R., 2010. Fractional Order Intensity Measures for Probabilistic Seismic Demand Modeling Applied to Highway Bridges, *Earthquake Engineering and Structural Dynamics*, In Press.

[33] Cornell, A. C., Jalayer, F., Hamburger, R. O., and Foutch, D. A., 2002. Probabilistic basis for 2000 SAC Federal Emergency Management Agency steel moment frame guidelines, *Journal of Structural Engineering* **128**, 526-532.

[34] Berry, M. P., and Eberhard, M. O., 2004. *PEER Structural Performance Database User's Manual*, Pacific Earthquake Engineering Research Center, University of California, Berkeley CA.

[35] Mackie, K., and Stojadinovic, B., 2004. Fragility curves for reinforced concrete highway over-pass bridges, *13th World Conference on Earthquake Engineering, August 2004*, Vancouver, B.C., Canada.

COMPDYN 2011
III ECCOMAS Thematic Conference on
Computational Methods in Structural Dynamics and Earthquake Engineering
M. Papadrakakis, M. Fragiadakis, V. Plevris (eds.)
Corfu, Greece, 25–28 May 2011

AN IMPROVED DISPLACEMENT-BASED SEISMIC DESIGN METHODOLOGY FOR BRIDGES ACCOUNTING FOR HIGHER MODE EFFECTS

Andreas J. Kappos[1], **Konstantinos I. Gkatzogias**[1], **and Ioannis G. Gidaris**[1]

[1] Aristotle University of Thessaloniki
Laboratory of Reinforced Concrete & Masonry Structures, 54124, Greece
ajkap@civil.auth.gr; kgkatzog@gmail.com; igidaris31@gmail.com

Keywords: Displacement-Based Seismic Design, Bridges, Reinforced Concrete, Higher Mode Effects.

Abstract. *Weaknesses of existing methods for direct displacement-based design (DDBD) of bridges are pointed out and an improvement is suggested to account for higher mode effects, the key idea being not only the proper prediction of a target-displacement profile through the effective mode shape (EMS) method (wherein all significant modes are considered), but also the proper definition of the corresponding peak structural response. The proposed methodology is then verified by applying it to an actual bridge wherein the different pier heights and the unrestrained transverse displacement at the abutments result in an increased contribution of the second mode. A comparison between the extended and the 'standard' DDBD is conducted, while further issues such as additional design criteria leading to optimum design, the proper consideration of the degree of fixity at the pier's top, and the effect of the deck's torsional stiffness are also investigated. The resulting designs are evaluated using nonlinear response-history analysis (NLRHA) for a number of spectrum-compatible motions. Unlike the 'standard' DDBD, the extended procedure adequately reproduced the target-displacement profile providing at the same time a good estimate of results regarding additional design quantities such as yield displacements, displacement ductilities etc., closely matching the results of the more rigorous NLRHA. However, the need for additional iterations clearly indicates that practical application of the proposed procedure is feasible if it is fully 'automated', i.e. implemented in a software package.*

1 INTRODUCTION

Although force-based design methods still remain the norm in existing national seismic codes, during the past decade several research groups have developed alternative, performance-based, evaluation and design procedures [1], based directly on displacements and/or deformations. In this context, Moehle [2] proposed a general framework for earthquake-resistant design of structures based on drift control, with the seismic demand given by displacement response spectra, while Priestley and co-workers proposed the so-called direct displacement-based design (DDBD) for the design of fundamental mode dominated structures, which may be reduced to 'equivalent' linear single-degree-of-freedom (SDOF) systems [3 - 6]. The DDBD procedure starts from a target displacement, consistent with a deformation capacity ensured by an appropriate detailing of the structure. Estimating a reasonable value for the yield displacement, the target displacement translates into a displacement ductility demand and a corresponding equivalent damping ratio, which is used to reduce the selected displacement spectra, to account (indirectly) for non-linear hysteretic behaviour. Entering this response spectrum with the aforementioned target displacement (expressed in terms of the displacement of the equivalent SDOF system) the effective period (secant value at target displacement) of this system is determined; subsequently, the yield strength corresponding to the previously defined peak displacement and the secant stiffness calculated from the effective period, are found and used to apply a 'traditional' equivalent lateral force design of the structure. Calvi and Kingsley [7] were the first to extend this methodology to multi-degree-of-freedom (MDOF) structures which can be reduced to an equivalent SDOF system using an assumed deformed configuration of the structure. For buildings, this deformed configuration is that corresponding to a predefined plastic mechanism and is dominated by the fundamental mode. This version of the DDBD methodology, accompanied with tables for easier implementation of the procedure for different performance levels, was incorporated in the SEAOC [8] recommendations (referring only to buildings).

As far as bridges are concerned, the early work by Kowalsky et al. [5] dealing with isolated columns modelled as SDOF systems was later extended by Kowalsky [9] and Dwairi and Kowalsky [10], who introduced the effective mode shape (EMS) method to identify the displacement pattern and hence the displacement profile of a bridge at the beginning of the design process. Displacement pattern scenarios for continuous bridge structures subjected to transverse seismic excitation were also investigated in the latter study [10] through the use of nonlinear response-history analysis, while the recent study by Kappos et al. [11] identified required extensions and/or modifications of the aforementioned DBD procedure (see next section), for it to be applicable to actual bridges wherein the simplifying assumptions made at various stages of the procedure do not really hold. Finally, the book by Priestley et al. [12] presents a detailed treatment of the DBD procedure and its application to different structural types, mainly focussing on buildings, but also addressing bridges.

So far, the vast majority of the work performed on this topic does not consider higher mode effects, given the procedure’s inherent limitation (resulting from the equivalent SDOF approach) to structures wherein the fundamental mode dominates the response. In a recent study, Adhikari et al. [13] introduced some additional considerations to account for higher mode effects on flexural strength of plastic hinges in the case of long-span concrete bridges with limited-ductile piers. Following the suggestion of Priestley et al. [12], Adhikari et al. used a response-spectrum analysis (RSA), after completion of the DDBD procedure, with two different design spectra (a 5%-damped design spectrum and a design spectrum with damping value obtained from the DDBD procedure) to determine the design responses (elastic and inelastic) at critical locations of the bridge as combinations of several modes.

In view of the aforementioned limitations of DDBD and the fact that bridges are structures wherein higher modes usually play a more critical role than in buildings, the present study attempts to refine and extend the procedure for bridges proposed by Dwairi and Kowalsky [10] and extended by the writers [11], to account for higher mode effects, not only regarding the proper definition of a target-displacement profile (comprising non-synchronous displacements, since all significant modes are considered), but also the proper definition of the corresponding peak structural response. The extended modal procedure proposed herein follows the general framework introduced in previous studies of Chopra and Goel [14] on buildings and Paraskeva et al. [15] on bridges, noting that these studies deal with the pushover procedure, rather than with design based on elastic analysis. The efficiency of the proposed methodology is then assessed by applying it to an actual bridge, whose different pier heights and the unrestrained transverse displacement at the abutments result in an increased contribution of higher modes. Some additional issues such as the proper consideration of the degree of fixity at the pier's top and the effect of the deck's torsional stiffness are also investigated, and comparisons between the extended modal and the 'standard' DDBD method are made. Design results are finally evaluated with the aid of nonlinear response-history analysis.

2 LIMITATIONS OF THE EXISTING DIRECT DBD PROCEDURE

The direct DBD method of Kowalsky [9] and Dwairi & Kowalsky [10] aims at designing a bridge to achieve a prescribed limit state that may be defined directly from displacements or derived from strain criteria under the selected design earthquake. The procedure utilizes the elastic displacement spectra reduced for an equivalent damping value, and the secant stiffness at the selected design displacement. Hence the stiffness of the bridge is not fixed at the beginning of the procedure (as in force-based design, FBD) but is derived in the process through the effective period (secant value). This is achieved by reducing the multi degree of freedom (MDOF) structure to an equivalent single degree of freedom (SDOF) system. The equivalent SDOF inelastic response is represented by the secant stiffness at peak response and equivalent damping, meant to account for hysteretic energy dissipation.

The crucial assumption involved in the above procedure is that this SDOF system suffices for capturing the displacement response of the bridge (which is typically inelastic, for all limit states beyond that corresponding to full serviceability); this implies that a single mode (which might, in fact, be a fictitious one, see subsequent sections) is used for deriving the properties of the equivalent SDOF system. The idea of the 'effective mode shape' (EMS) proposed in [9], building on concepts previously put forward by Calvi & Kingsley [7], is a useful one in this respect; it involves the estimation of a fictitious mode shape of the (inelastically responding) bridge by a statistical combination of individual modes. It is important to note that these modes are also fictitious ones, since they are not the (elastic) normal modes of the bridge but they are derived by eigenvalue analysis of a bridge model wherein yielding members (such as piers and, wherever applicable, abutments) are modelled with their secant stiffness at the intended displacement that generally exceeds the yield displacement, hence inelastic response is foreseen. It is clear from the foregoing summary of the procedure that, in general, a substantial number of iterations would be required to define effective mode shapes consistent with the inelastic response of the bridge to the design earthquake, even more so when multiple earthquake intensities are considered for checking multiple limit states (performance requirements). This important limitation of the method has been remedied to a certain extent by the 'calibration' of inelastic displacement patterns carried out by Dwairi & Kowalsky [10] who performed response-history analyses of four-span bridges with regular and irregular pier configurations, and with different support conditions at the abutments, for a set of 12 recorded motions from all over the world.

To simplify things and improve convergence of the procedure, the existing DDBD methodology assumes that the transverse response of single-column piers monolithically connected to the superstructure is that of a simple cantilever. This simplifying assumption can lead to conservative design of the piers, since the consideration that pier behaviour is that of a simple cantilever usually results to significant increase in the required steel ratio at the base of the pier. Additionally, the assumption of the simple cantilever implies that the superstructure has zero or significantly small torsional stiffness; in the common case of box-girder type decks this situation can be realistic only in the case of yielding of the superstructure's transverse reinforcement (Katsaras et al. 2009). However, this situation is not permitted by current seismic codes, wherein the superstructure is required to remain (essentially) elastic under the design earthquake. Moreover, proper consideration of the expected moment pattern in the piers has a significant importance in the case of the DBD procedure, as it affects the yield displacement (hence the displacement ductility demand) and the flexural stiffness of the piers. Although the previous aspects are identified by Priestley et al. [12], no specific guidelines are given for taking into account the degree of fixity at the pier's top.

A more general limitation of all DBD procedures is the (hardly ever mentioned in the previously cited publications on DBD) fact that not all bridges are, or should be made, displacement-controlled. There are two typical 'scenarios' wherein DBD is meaningless:

First, the case of regions of low, moderate, and even moderate-to-high seismic hazard, where the maximum displacement defined by the pertinent design spectrum is too low, even when no additional viscous damping (accounting for inelastic response) is introduced. Just as an example, seismic Zone I in Greece (which is the country with the highest seismicity in the European Union) is characterized by a design PGA=0.16g and a design spectrum, according to Eurocode 8 (CEN, 2005) for the common case of ground C, that results in a maximum elastic displacement (for 5% damping) of only 119 mm at a period T_D=2.0 sec (the Eurocode 8 recommended value for the threshold of the constant displacement branch of the spectrum). This is lower than the yield displacement of the pier of even a bridge with relatively short piers like the overpass reported later in the paper. In fact, to make DBD relevant to the common bridge configurations studied by the authors, higher seismic hazard (Zones II and III) and more conservative assumptions (T_D=4.0 sec) for the displacement spectrum had to be used. For bridges with (relatively) tall piers even these conservative assumptions cannot lead to meaningful DBD.

Second, the configuration of the bridge, including support conditions, which must also account for soil-structure interaction (SSI), should be such as to permit substantial displacements, accompanied by inelastic action. The case of bridges with tall piers has been mentioned previously, another case is that of bridges with transverse displacement blocked at the abutments. For instance, in the bridge studied in a later section, which is a typical overpass structure, blocking of transverse movement through stoppers at the (seat-type) abutments leads to very small displacements of the piers subsequent to their yielding, as most of the base shear developed after that stage goes to the abutments.

Last and not least, for DBD procedures for bridges to be suitable for practical design, they should be enriched with additional design criteria that would avoid the situation (that the authors have encountered on several occasions in their case-studies) wherein the advantages of DBD (with respect to FBD) are lost when minimum requirements for dimensioning and detailing of reinforced concrete (R/C) members are applied, in line with current practice.

The extensions to the Kowalsky et al. method introduced by the authors in [11] and here aim at remedying some of the aforementioned limitations.

3 PROPOSED EXTENSIONS TO THE 'STANDARD' DDBD

Various design criteria (complementary to those already included in the procedure of Kowalsky et al. and recently proposed by the authors [11]) are briefly reviewed herein; they can be deemed as guidelines that can assist the practicing engineer to achieve an efficient design, regarding both performance and economy. The extension (to account for higher-mode effects) of the displacement based design procedure for bridges with monolithically connected single-column piers to the superstructure, is then proposed, wherein the degree of fixity to pier top provided by superstructure rigidity is taken into consideration.

It is clear that not only the complexity but also the challenge of the design procedure derives from the multiplicity of 'solutions' to the design 'problem'. An ideal solution would satisfy all design criteria; nevertheless such an outcome (if at all feasible) would require numerous iterations. Therefore, the pragmatic approach is to meet as many criteria as possible with the least number of iterations. The additional design criteria proposed herein for the 'standard' DDBD method are as follows:

i. $\boldsymbol{V_{pier} \geq V(\rho_{req}=\rho_{min})}$**:** The shear carried by each pier (V_{pier}) should exceed, for the sake of economical design, the shear (and hence the moment) that corresponds to the minimum required longitudinal reinforcement ratio, $V(\rho_{req}=\rho_{min})$. Otherwise, code minimum requirements will prevail and any benefits of DDBD will probably vanish.

ii. $\boldsymbol{V_{Abt} \leq V_u}$**:** The shear carried by each abutment (V_{Abt}) should not exceed the ultimate shear (V_u), which is directly related to the 'weakest link' of the superstructure-abutment-backfill (SAB) system. For instance, in the case of a bearing-supported superstructure (with or without seismic links), it can be assumed that the SAB system will respond quasi-elastically ($K_{SAB} = K_{Bearings}$) until the closure of the gap between the deck and the abutment or seismic link; thus, V_u can be calculated from the ultimate force that can develop in the elastomeric bearings placed at the abutment, or the resistance of the seismic link. Activation of the abutment-backfill system can in turn determine V_u; this is also the 'weakest link' in the case of a monolithic superstructure-abutment connection.

iii. $\boldsymbol{k_{eff} \geq k(T_{eff}=T_D)}$**:** Calculated supporting member (pier/abutment) secant stiffnesses (corresponding to the target-displacement profile), and hence the secant stiffness (k_{eff}) of the equivalent SDOF system (see Step 3 in next section) should not correspond to an effective period (T_{eff}) longer than the threshold (T_D) of the constant displacement branch of the design spectrum (see next section and Figures 2, 4). For very long T_{eff} the target displacement has to be reduced, which generally results in a longitudinal reinforcement increase and hence in less economical design. It should be stressed here that the choice of a proper T_D is essential for DDBD to be meaningful (see also section 'Evaluation of the proposed procedure in the case of an existing bridge').

iv. $\boldsymbol{\Delta_{pier} \leq \Delta_D}$ and $\boldsymbol{\mu_{pier} \leq \mu_u}$**:** The pier target-displacements should not exceed the corresponding 'damage-based' displacements (Δ_D), determined either from strain-based criteria [16] or drift-based criteria. P-Δ effects should also be considered. In addition, an ultimate displacement ductility value, determined by the designer (taking into account the detailing rules used in dissipating zones), should specify the upper limit in pier displacement ductilities.

v. $\boldsymbol{\Delta_{Abt} \leq \Delta_D}$**:** As in design criterion (ii), the abutment target-displacements should not exceed the corresponding 'damage-based' displacements (Δ_D), defined with due consideration of the SAB system configuration. Referring to the common case of a bearing-supported superstructure, Δ_D is calculated in terms of the maximum acceptable shear strain ratio (γ_u), given the bearing horizontal stiffness.

In the extensions of the 'standard' DDBD method presented herein, the parameter of the equivalent cantilever length (h_{eq}), which is the distance from the pier base to the contraflexure point (see Fig. 1), is introduced to take into account the degree of fixity at the top of the pier.

Figure 1 represents the modelling of a pier with a rigid base and monolithically connected to the deck, whereas possible moment diagrams under transversal loading are also illustrated. It is obvious that a pier moment diagram consists of two different components; the bending moment derived from the inertial horizontal forces F, acting on the mass centroid (G), and the bending moment induced from the eccentricity of the latter forces with respect to the shear centre, in the usual case wherein the shear centre does not coincide with the mass centroid. The final moment diagram depends on the cracked torsional stiffness of the bridge deck, the superstructure-abutment connection and the pier-superstructure relative stiffness; likewise it is required to properly account for the degree of fixity at pier's top and hence for the pier's transverse response regarding its flexural stiffness (k_{pier}) and yield displacement ($\Delta_{y,pier}$), according to Equations (1) and (2), (referring to case (b) in Figure 1, similar relations can be derived for the other cases).

$$x_k = \frac{h_{eq}}{h} = \frac{h_{eq}}{h_{clear} + h_G}, \quad k_{eq} = \frac{3EI}{h_{eq}^{\ 3}}, \quad k_{pier} = x_k k_{eq} \tag{1}$$

$$x_{\Delta y} = \frac{L_{eq}}{L_{eff}} = \frac{h_{eq} + 0.022 f_y d_{bl}}{h_{clear} + h_G + 0.022 f_y d_{bl}}, \quad \Delta_{y,eq} = \frac{\varphi_y L_{eq}^{\ 2}}{3}, \quad \Delta_{y,pier} = \frac{1}{x_{\Delta y}} \Delta_{y,eq} \tag{2}$$

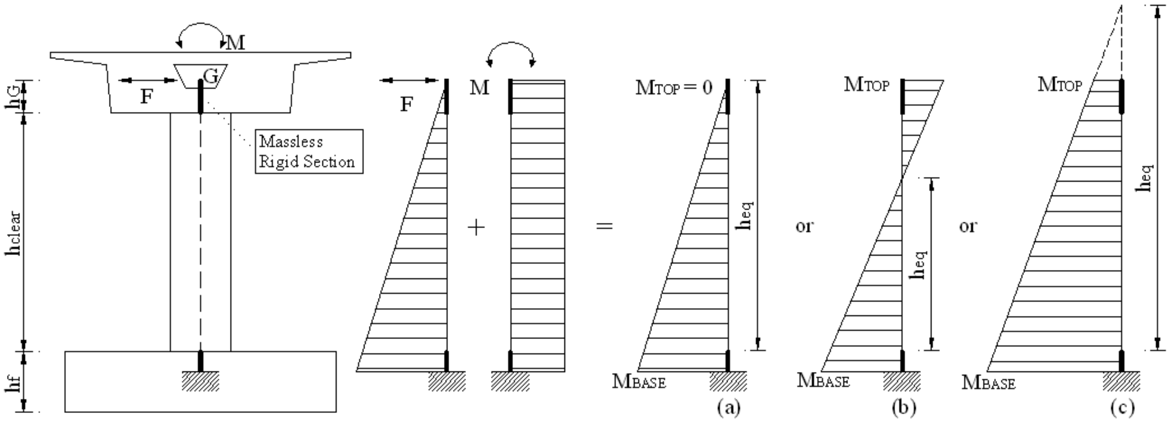

Figure 1: Pier modelling and transverse response accounting for the deck's torsional stiffness.

In Equations (1) and (2) E is the elasticity modulus of concrete and I is the moment of inertia of the pier cross-section (modified for cracking effects wherever necessary), φ_y is the yield curvature, f_y is the longitudinal bar yield stress and d_{bl} is the longitudinal bar diameter.

4 A MODAL DDBD PROCEDURE FOR BRIDGES

An extension of the DDBD methodology to bridge structures, wherein consideration of higher mode effects is deemed indispensable, is proposed herein. Procedures supplementary and/or alternative to those included in the 'standard' DDBD, are presented in this section, while an application of the suggested methodology to an actual bridge is given in the following section. For the sake of completeness (and the benefit of the reader) all steps of the procedure (including those that are essentially the same as in the 'standard' method [9, 10, 11]) are summarized in the following.

Step 0 - Definition of initial input parameters: General input parameters concerning the geometry (e.g. column height and diameter in piers with cylindrical columns), the mass properties (e.g. translational mass and mass moment of inertia), and material properties are defined. An initial estimate of the column cross-section is required. As a starting point, the output of the dimensioning of the deck and the piers for the Ultimate and Serviceability Limit States under the pertinent combinations of permanent and transient actions can be used. Then, single or multiple performance levels are set as design objectives, by designating the targeted damage states ('damage-based' displacements) for selected seismic hazard levels (elastic displacement response spectra).

Step 1 – Selection of the displacement pattern: The step prescribed in the 'standard' DDBD procedure, involves the computation of the relative pier-deck stiffness (RS) and the determination of whether the bridge has a rigid or a flexible displacement pattern, as suggested by Dwairi et al. [10]. Given that the procedure proposed here is intended for bridges where higher mode contribution should not be ignored, the flexible displacement pattern scenario is adopted, disregarding the relative stiffness parameter. This means that this step is essentially redundant, nevertheless it is deemed advisable to retain it, as it is always useful for the designer to have a proper indication of the relative stiffness of the deck.

Step 2 – Definition of target-displacement profiles: The iterative effective mode shape (EMS) method is followed, according to the following steps:

i. Evaluation of mode shapes *(Φ_j)*: Due to the unavailability of the member effective properties at the start of the process a first estimation is required. Based on current seismic design practice for bridges it can be assumed that the superstructure will respond essentially elastically, regarding its flexural stiffness, while for its torsional stiffness it is proposed to assume 20% of the uncracked value, based on the ratios (10÷30%) of cracked-to-uncracked torsional stiffness just after concrete cracking, estimated by Katsaras et al. [17]. On the other hand, it is suggested that a secant flexural stiffness equal to $10\%EI_g$ be applied to columns expected to deform inelastically, while 60% of the uncracked section stiffness is suggested for columns that are expected to remain elastic. The reduction in the effective axial [18] and shear [19] stiffness of the column(s) can be considered proportional to the reduction in the effective flexural stiffness. Once the structure properties have been established, the eigenvalue problem can be solved, hence the mode shapes Φ_i can be obtained.

ii. Evaluation of modal participation factors *(Γ_j)*: The modal participation factors can be computed using standard procedures, i.e. Equation (3), where $\boldsymbol{m}$ represents a diagonal mass matrix and $\boldsymbol{\iota}$ is a unit vector.

$$\Gamma_j = \frac{\boldsymbol{\Phi}_j^T \boldsymbol{m}\boldsymbol{\iota}}{\boldsymbol{\Phi}_j^T \boldsymbol{m}\boldsymbol{\Phi}_j} \tag{3}$$

iii. Evaluation of peak modal displacements *($u_{i,j}$)*: The peak modal displacements are computed according to Equation (4), where index i represents the joint number associated with a lumped mass, as per the inertial discretization, index j represents the mode number, $\Phi_{i,j}$ is the modal factor of joint i and mode j, and S_{dj} is the spectral displacement for mode j obtained by entering the 5%-damped design spectra with the period obtained from modal analysis.

$$u_{i,j} = \Gamma_j \Phi_{i,j} S_{dj} \tag{4}$$

iv. Evaluation of expected displacement pattern: The displacement pattern (δ_i) is obtained by an appropriate combination of the peak modal displacements, such as the SRSS combination given by Equation (5); CQC combination is expected to yield better results when the natural frequencies of the participating modes in the response are closely spaced.

$$\delta_i = \sqrt{\sum_j u^2_{i,j}} \tag{5}$$

It is noted that a displacement pattern derived from the above procedure accounts for the effect of all significant modes (e.g. those needed to capture 90% of the total mass in the transverse direction); therefore, it does not correspond to an actual inelastic deformed shape of the bridge, particularly so in the case of asymmetric systems. To obtain the target displacement profile (Δ_i), the displacement pattern given by Equation (5) is scaled such that none of the member (pier or abutment) displacements exceed the target displacements obtained based on strain or drift criteria:

$$\Delta_i = \delta_i \frac{\Delta_{D,c}}{\delta_c} \tag{6}$$

where $\Delta_{D,c}$ and δ_c are the 'damage-based' displacement and the modal value at the critical mass *c* (whose displacement governs the design), respectively. Finally, peak modal displacements ($u_{i,j}$) are scaled to N modal target-displacement profiles ($U_{i,j}$) utilizing the same scaling coefficient as that used to obtain the target-displacement profile in Equation (6):

$$U_{i,j} = u_{i,j} \frac{\Delta_{D,c}}{\delta_c} \tag{7}$$

An immediate consequence of the aforementioned procedure is that the combination of the N modal target-displacement profiles ($U_{i,j}$) yields the target-displacement profile (Δ_i); hence, in the case the SRSS combination rule is used:

$$\Delta_i = \sqrt{\sum_j U^2_{i,j}} \tag{8}$$

Step 3 – Definition of N+1 equivalent SDOF structures: These structures are established based on equal work done by the MDOF bridge and the equivalent SDOF structure, according to Calvi & Kingsley [7]. Each of the *N* SDOF structures is related to the corresponding modal target-displacement profile ($U_{i,j}$), whereas the additional SDOF is related to the target-displacement profile (Δ_i). Utilizing Equations (9) and (10), an equivalent system displacement (Δ_{sys}, $U_{sys,j}$), mass (M_{sys}, $M_{sys,j}$) and location (x_{sys}, $x_{sys,j}$) of the SDOF across the MDOF bridge deck is computed for each of the *N+1* SDOF structures. In Equations (9) and (10), m_i is the mass associated with joint *i*, and *n* is the number of joints as per the inertial discretization.

$$U_{sys,j} = \frac{\sum_{i=1}^{n} m_i U_{i,j}^{\ 2}}{\sum_{i=1}^{n} m_i U_{i,j}},\ M_{sys(j)} = \frac{\sum_{i=1}^{n} m_i U_{i,j}}{U_{sys,j}},\ x_{sys,j} = \frac{\sum_{i=1}^{n}\left(m_i U_{i,j} x_i\right)}{\sum_{i=1}^{n}\left(m_i U_{i,j}\right)} \tag{9}$$

$$\Delta_{sys} = \frac{\sum_{i=1}^{n} m_i \Delta_i^2}{\sum_{i=1}^{n} m_i \Delta_i},\ M_{sys} = \frac{\sum_{i=1}^{n} m_i \Delta_i}{\Delta_{sys}},\ x_{sys} = \frac{\sum_{i=1}^{n}\left(m_i \Delta_i x_i\right)}{\sum_{i=1}^{n}\left(m_i \Delta_i\right)} \tag{10}$$

Step 4 – Estimation of equivalent viscous damping levels: Utilizing the target displacement (Δ_i) and the modal target-displacement profiles ($U_{i,j}$), the ductility level is calculated for each member (for each of the $N+1$ profiles), according to Equation (11) and in line with the equivalent cantilever concept (Equation (2)). The height of the equivalent cantilever cannot be determined at the initial stage of design, therefore either preliminary structural analyses should be performed for each of the $N+1$ equivalent structures under lateral loads compatible with the corresponding profile, or an assumption that the height of the equivalent cantilever equals the height of the pier, should be made during the first iteration. The first approach is strongly recommended for the case of significant higher mode effects, since it reduces the number of iterations required to achieve convergence.

$$\mu_{\Delta_i} = \Delta_i/\Delta_{yi},\ (or\ \mu_{\Delta_i} = U_{i,j}\ /\ \Delta_{yi,j}) \tag{11}$$

Yield curvatures in Equation (2) are estimated using Equation (12), where ε_y is the reinforcement yield strain and D is the diameter of a circular section; similar equations are provided for different section shapes [12, 19].

$$\varphi_y = 2.25\varepsilon_y/D \tag{12}$$

The displacement ductility ($\mu_{\Delta,i}$) of each pier should be compared with μ_u, (see design criterion iv). If any $\mu_{\Delta,i}$ exceeds μ_u, the designer should revise either the target-displacement profile (by reducing the pier limit-state displacements) or the yield displacements (by reducing the pier cross-section).

Several relationships [20 - 23] between hysteretic damping and ductility have been proposed. The one obtained by Dwairi [20] based on Takeda's hysteretic model [24], given by Equation (13), is used here. Additional elastic viscous damping (ξ_v) up to 5% should be added to the hysteretic damping in line with the approach proposed by Grant et al. [25].

$$\xi_i = \xi_v + \frac{50}{\pi}\left(\frac{\mu_\Delta - 1}{\mu_\Delta}\right)\% \tag{13}$$

These damping values need to be combined in some form to obtain system damping for each of the $N+1$ equivalent SDOF structures. A weighted average can be computed, as given by Equation (14), where $W_i\ /\Sigma W_k$ is a weighting factor, based on the work (W_i) done by each member (Equation (15)), according to the Kowalsky [9] approach.

$$\xi_{sys} = \sum_{i=1}^{n}\left(\frac{W_i}{\sum_{k=1}^{n} W_k}\xi_i\right),\quad \xi_{sys(j)} = \sum_{i=1}^{n}\left(\frac{W_{i,j}}{\sum_{k=1}^{n} W_{k,j}}\xi_{i,j}\right) \tag{14}$$

$$W_i = V_i\Delta_i,\quad W_{i,j} = V_{i,j}U_{i,j} \tag{15}$$

Calculation of the weighting factors obviously requires the knowledge of member forces (V), which are not known at the current step. As a starting point, it can be assumed that the seismic force carried by the abutments is equal to 30% of the total seismic force carried by the bridge and column shears are inversely proportional to column heights, as illustrated by Equation (16) [9], where μ is less than one for elastic columns and equal to one for columns that have yielded. In subsequent iterations, system damping is computed in proportion to the member forces obtained from structural analyses.

$$W_i = \mu_{\Delta_i}\Delta_i/h_{eq,i},\quad W_{i,j} = \mu_{\Delta_i}U_{i,j}/h_{eq,ij} \tag{16}$$

Step 5 – Determination of the equivalent structures effective periods: Utilizing the *N+1* system target-displacements (Δ_{sys}, $U_{sys,j}$), levels of system damping (ξ_{sys}, $\xi_{sys,j}$), and elastic response spectra for the chosen seismic demand, the effective periods (T_{eff}, $T_{eff,j}$) of the equivalent structures are determined from the design spectrum as shown in Figure 2.

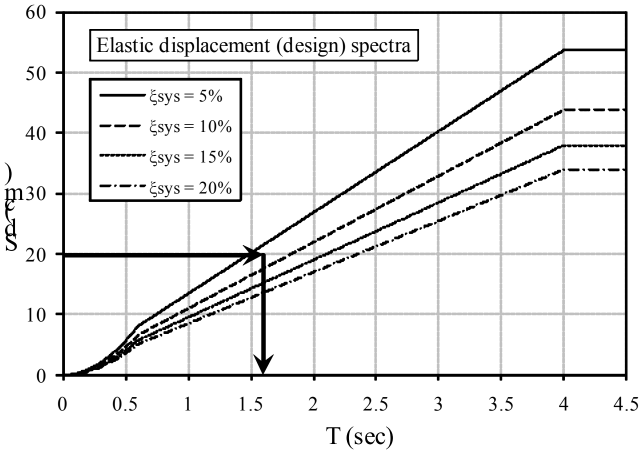

Figure 2: Effective period evaluation based on DDBD procedure.

Once again, revision of the target-displacement profile is required when the calculated target displacements exceed the displacement that corresponds to the corner period (T_D) (see design criterion iii). Once the effective periods have been determined, effective stiffnesses (k_{eff}, $k_{eff,j}$) and design base shears (V_B, $V_{B,j}$) are computed by Equations (17) and (18), respectively.

$$k_{eff} = 4\pi^2 M_{sys}/T_{eff}^{\ 2},\ k_{eff,j} = 4\pi^2 M_{sys,j}/T_{eff,j}^{\ 2} \tag{17}$$

$$V_B = k_{eff}\Delta_{sys},\ V_{B,j} = k_{eff,j}U_{sys,j} \tag{18}$$

Step 6 – Verification of design assumptions: Design base shears (V_B, $V_{B,j}$) are distributed in proportion to the inverse of the column height according to Equation (19), which is based on the simplifying assumption that all columns have the same diameter and longitudinal reinforcement steel ratio, zero post-elastic slope of the force-displacement response, mass small enough such that inertia forces due to self-weight can be neglected, and the same end-fixity conditions. In Equation (19) μ_i and μ_k are less than one for elastic columns and equal to one for columns that have yielded and F_{Abt} represents the total force carried by the abutments. Member cracked section stiffnesses are computed for each of the *N+1* profiles, using Equations (20) and are compared to assumed values of Step 2. If the values related to the target-displacement profile (Δ_i) differ significantly, computed secant stiffnesses ($k_{eff,i}$) are utilized in the EMS to obtain revised target-displacement profiles (Δ_i, $U_{i,j}$). Steps 2 to 6 are repeated by changing column secant stiffnesses until the target profile (Δ_i) stabilizes. Although a strict approach requires iteration within Steps 2 to 6 until all profiles (Δ_i and $U_{i,j}$) stabilize, the implementation of the proposed methodology in the next section indicates that whenever Δ_i stabilizes, $U_{i,j}$ are also practically stabilized, hence Δ_i can be used as the sole convergence criterion.

$$V_{B,k} = \left(V_B - F_{Abt}\right)\frac{\mu_{\Delta,k}}{h_k}\Big/\sum_{i=1}^{n}\frac{\mu_{\Delta,i}}{h_i},\ V_{B,kj} = \left(V_{B,j} - F_{Abt,j}\right)\frac{\mu_{\Delta,kj}}{h_k}\Big/\sum_{i=1}^{n}\frac{\mu_{\Delta,ij}}{h_i} \tag{19}$$

$$k_{eff,i} = V_{B,i}/\Delta_i,\ k_{eff,ij} = V_{B,ij}/U_{i,j} \tag{20}$$

Step 7 - Structural analysis: Once the target-displacement profile (Δ_i) stabilizes, base shears ($V_{B,j}$) are distributed as inertia forces to the masses of the MDOF structure in accordance with the modal target-displacement profiles ($U_{i,j}$), as given by Equation (21) [7]. In this equation $F_{i,j}$ are the bent inertia forces, $V_{B,j}$ are the design base shears, indices i and k refer to joint numbers, and n is the number of joints.

$$F_{k,j} = V_{B,j}\left(m_k U_{i,j}\right) \Big/ \sum_{i=1}^{n} (m_i U_{i,j}) \tag{21}$$

N structural analyses (as many as the significant modes) are performed on the bridge under the inertia loads, to obtain the 'modal' base shear for each column. Secant stiffnesses $k_{eff,ij}$ obtained from the iteration within Step 6, at which stabilization of Δ_i (hence stabilization of $U_{i,j}$ as mentioned in Step 6) was observed, should be used in each of the N structural model analyses, in order to be consistent with the DDBD philosophy. Afterwards, displacements derived from the N structural analyses are compared with the corresponding profiles $U_{i,j}$. In the case of significantly different displacements, reasonable values for column secant stiffnesses are assumed and analyses are conducted until convergence is achieved. Once the displacement profiles obtained from structural analyses converge to the assumed modal target-displacement profiles, column secant stiffnesses and abutment forces from each analysis are compared with the values assumed at Step 6, at which stabilization of $U_{i,j}$ was achieved. It is reminded that during the first loop of iterations the seismic force carried by the abutments is assumed equal to 30% of the total seismic force carried by the bridge for all the $N+1$ cases. In case of significant discrepancy, the target-displacement profile is revised utilizing the EMS method and forces from structural analyses. Steps 2 to 7 are repeated, until column secant stiffnesses and abutment forces converge.

In order to perform the new loop of iterations and the new EMS in particular, previous loop secant stiffnesses ($k_{eff,i}$) (Step 6) can be assumed as a starting point. Furthermore, revised equivalent cantilever heights are computed according to the results of the N structural analyses, which were previously performed, as far as the modal target-displacement profiles ($U_{i,j}$) are concerned, whereas in the case of the target-displacement profile (Δ_i), proper values of the equivalent cantilever heights can be approximately determined by combining the peak 'modal' responses (N structural analyses). Following the same approach, the force carried by the abutments and the base shear distribution for each of the $N+1$ cases required in the subsequent steps are determined from analysis results, instead of utilizing Equation (19), which, given the diversity of the column end-fixity conditions, is not accurate.

Step 8 - Design of the MDOF structure: The MDOF bridge is designed in accordance with capacity design principles and also design criterion (i), such that the desired failure mechanism, as well as economical design are achieved. The response quantities of design interest (displacements, plastic hinge rotations, internal pier forces) are determined by combining the peak 'modal' responses (the N structural analyses), using an appropriate modal combination rule (e.g. SRSS or CQC), superimposed with the pertinent combinations of permanent and transient actions. To meet design criterion (i) the target-displacement profile and/or the pier cross section are revised and Steps 1 to 8 are repeated.

5 EVALUATION OF THE PROPOSED PROCEDURE IN THE CASE OF AN EXISTING BRIDGE

5.1 Description of studied bridge

To investigate the accuracy, efficiency, and also the practicality, of the proposed procedure it was deemed appropriate to apply it to an actual bridge structure, whose different pier heights and the unrestrained transverse displacement at the abutments result in an increased contribution of the second mode. The selected structure (known as the T7 Overpass), is quite common in modern motorway construction in Europe. The 3-span structure of total length equal to 99 m (see Figure 3), is located in northern Greece and is characterized by a significant longitudinal slope (approximately 7%). The deck consists of a 10 m wide prestressed concrete box girder section with a variable geometry across the longitudinal axis of the bridge (see Figure 3). The two piers have a cylindrical cross section, a common choice for bridges both in Europe and in other areas, while the pier heights are unequal (clear column height of 5.94 and 7.93 m), due to the deck's longitudinal inclination. The deck is monolithically connected to the two piers, while it rests on its abutments through elastomeric bearings; movement in both the longitudinal and the transverse direction is initially allowed at the abutments, but transverse displacements are restrained in the actual bridge whenever the 15 cm gap shown in Figure 3 is closed. In applying the proposed design procedure to this bridge, the gap size, as well as the characteristics of the bearings are treated as design parameters. The piers and the abutments are supported on surface foundations (footings) of similar configuration.

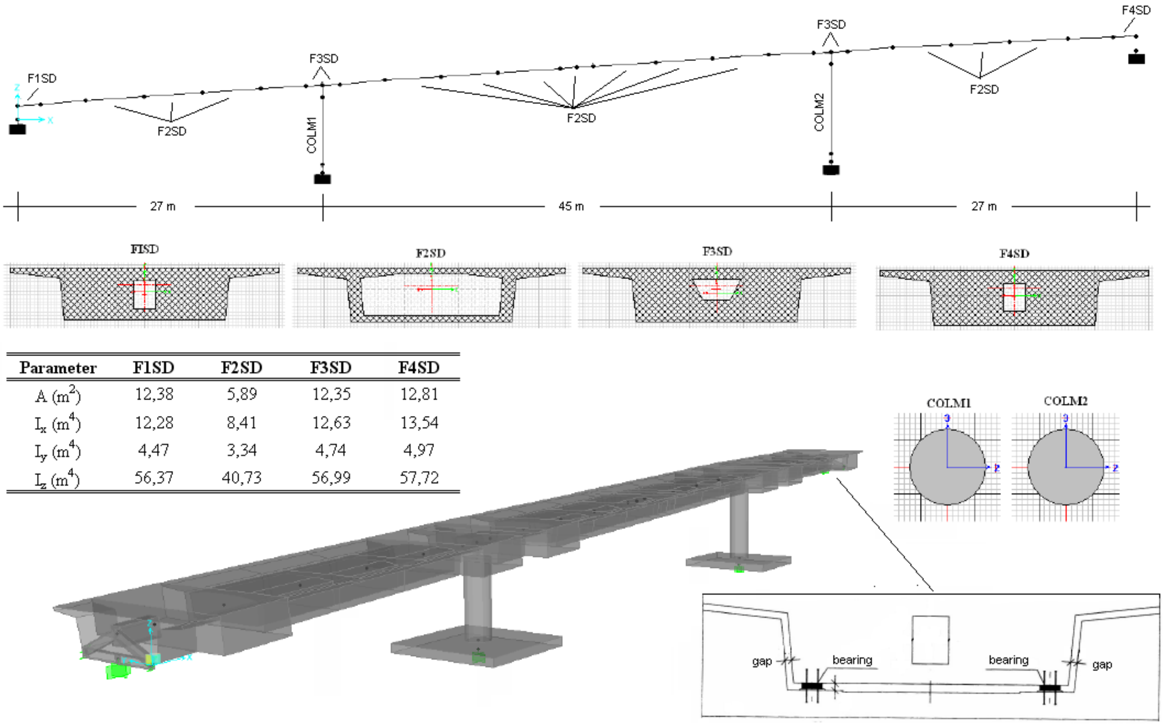

Parameter	F1SD	F2SD	F3SD	F4SD
A (m^2)	12,38	5,89	12,35	12,81
I_x (m^4)	12,28	8,41	12,63	13,54
I_y (m^4)	4,47	3,34	4,74	4,97
I_z (m^4)	56,37	40,73	56,99	57,72

Figure 3: Layout of the bridge configuration and finite element modelling.

T7 Overpass was designed using DDBD, both in the form proposed by Dwairi and Kowalsky [10], and its modified version proposed herein, for two different seismic zones. The Greek Seismic Code (EAK2000) elastic spectrum [26] for Zone II (PGA of 0.24*g*) and III (PGA of 0.36*g*) was the basis for seismic design; it corresponded to soil conditions category 'B' of the Code, which can be deemed equivalent to subsoil class 'B' of older drafts of Eurocode 8-2 and closer to 'C' in the final version of the Eurocode [27]. The bridge was designed as a ductile structure implying that plastic hinges are expected to form in the piers, while P-Δ effects were taken into consideration. A further parameter that was investigated in applying the DDBD was the effect of the girder's torsional stiffness.

In the analyses presented in the following, the focus is on the transverse response of the bridge, as it is well known (e.g. Reference [28]) that this is the response most affected by higher modes; additional analyses in the longitudinal direction were also conducted [29], however due to space limitations and the fact that longitudinal design was found to be less critical, these analyses are not presented herein. The analysis was carried out using the SAP2000 software [30]; the reference finite element model (Fig. 3) involved 32 non-prismatic 3D beam elements. Preliminary analyses accounting for soil-structure interaction (SSI) effects, using an appropriate foundation compliance matrix, have shown that due to the relatively stiff soil formations underneath the studied bridge, SSI had little effect on the response; hence these effects were subsequently ignored in the design (and assessment) of the bridge.

5.2 'Standard' direct displacement-based design (DDBD)

A 'standard' DDBD [9, 10, 11] was first performed, mainly to show the inefficacy of the procedure, which arises from its inherent restriction to structures wherein the fundamental mode dominates the response, as previously pointed out by Calvi & Kingsley [7]. In the case of T7 Overpass, the transverse response is determined by two dominant modes (see Figure 5). A 'damage control' limit state that corresponds to a drift ratio of 3%, was considered; qualitatively, 'damage control' implies that only repairable damage occurs in the columns. The design displacement spectrum was derived from the pertinent elastic acceleration response spectrum (see Figure 4), using the well-known equation $S_d(T) = S_a(T)/\omega^2$

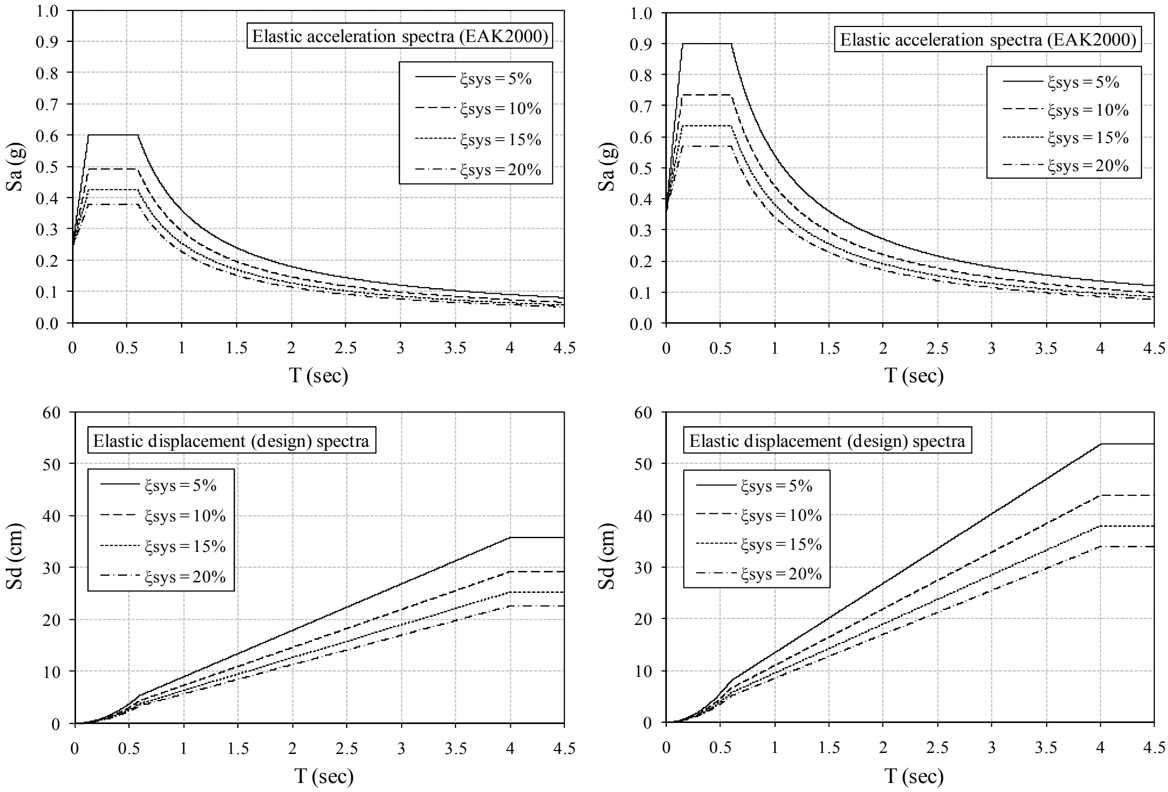

Figure 4: Elastic acceleration (according to EAK2000, Soil Type B) and displacement response spectra; left: Zone II (PGA=0.24*g*), right: Zone III (PGA=0.36*g*).

A significant modification was made to the spectrum used for design, i.e. the corner period in S_d was taken equal to 4.0 sec, according to SEAOC's [8] recommendations, which is substantially higher than the values of 2.5 and 2.0 specified by EAK2000 and EC8, respectively. This modification is not only in line with recent research findings, but also necessary for DDBD to be meaningful (short corner periods lead to small displacement values in the period range that is common to DDBD, which relies on secant stiffness values at the maximum displacement). Moreover, the modification to the elastic acceleration spectrum, required to account for ductile response through an increased effective damping ratio, was made using the damping modifier (η) adopted in the final version of EC8, i.e. Equation (22) below, where ξ_{sys} is the viscous damping ratio of the structure, expressed as a percentage.

$$\eta = \sqrt{10/(5+\xi_{sys})} \tag{22}$$

As previously mentioned, the mechanical characteristics of the elastomeric bearings are a design parameter, hence an initial estimate is required. A rational choice of the elastomer (rubber) cross-sectional area can be made from the design for axial loading, while, regarding the transverse modes of the bridge (Figure 5), the total thickness (t_r) of the elastomer should provide the target-displacement profile with adequate displacements at the abutments, so that the 'damage-based' displacements (Δ_D) of each column, related to the acceptable drift ratio, could be attained, and a reasonable longitudinal reinforcement ratio could be obtained for the pier. The elastomeric bearings chosen herein are rectangular in shape (350 · 450 mm) with t_r of 88 mm, horizontal stiffness of 2506 kN/m and equivalent viscous damping ratio equal to 5%; two bearings are placed at each abutment, as shown in Figure 3. The maximum acceptable shear strain ratio (γ_u), from which the 'damage-based' displacements of the bearings are derived, is taken equal to 2.0. Introducing the 3% drift ratios for the columns, the 'damage-based' displacements of all members (piers or abutments) were calculated and are shown in Table 1; a diameter of 2.0 m was initially assumed for the two columns.

Damage-based displacements				
Member	Abt_1	Col._1	Col._2	Abt_2
Δ_D (m)	0.176	0.218	0.278	0.176

Table 1: 'Damage-based' displacements related to the 'damage control' limit state.

In order to obtain the target-displacement profile for the inelastic system, the EMS method was utilised. It was assumed that the superstructure will respond essentially elastically, as far as its flexural stiffness is concerned, while its torsional stiffness was set equal to 20% of the uncracked section torsional stiffness [17]. A secant flexural stiffness equal to 10% the gross value was applied to the columns (both of them are expected to deform inelastically), while the reduction in the effective axial and shear stiffness was considered to be proportional to the reduction in flexural stiffness. Figure 5 illustrates the target-displacement profile derived from applying the EMS repeatedly until convergence was achieved (four iterations were needed in total); displacement patterns, peak modal displacements and modal mass participation factors for each mode are also shown. Convergence was checked with regard to stabilization of the target-displacement profile or the column secant stiffness from one iteration to the next. Discrete dots on the graphs represent the points of the deck's axis passing from its mass centroid, corresponding to the centres of elastomeric bearings and columns.

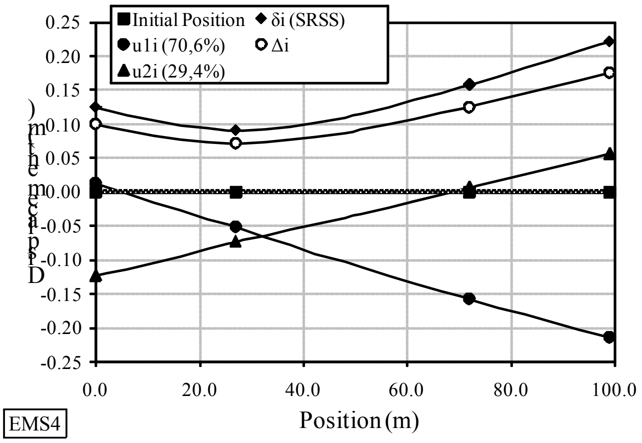

Figure 5: Displacement profile: Peak modal displacements $u_{i,j}$, displacement pattern δ_i and target-displacement profiles Δ_i, estimated iteratively from EMS method.

The next step of the 'standard' DDBD method involves structural analysis of the bridge under the inertia loads given by Equation (21), (where, in the 'standard' procedure $U_{i,j}$ corresponds to Δ_i), to obtain the design base shear of each column. In Figure 6 the displacement profile derived from structural analysis Δ_i (SA1), is compared with the target-displacement profile Δ_i (EMS4). The discrepancy between the two profiles reveals one of the main deficiencies of the standard DDBD, i.e. its inability to predict the peak structural response (in terms of displacements and hence internal member forces), on the basis of which design will be carried out.

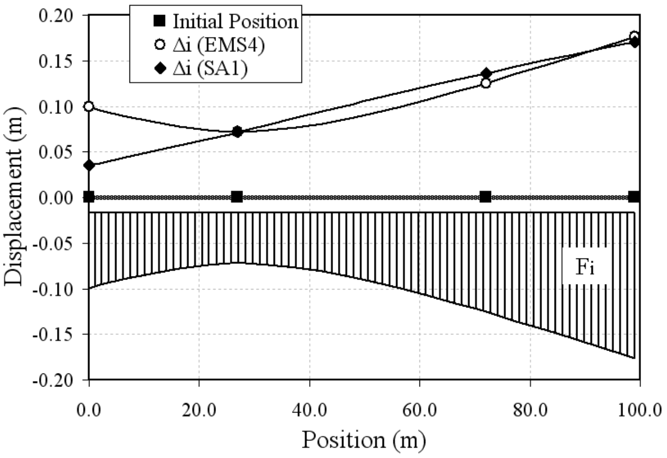

Figure 6: Structural analysis displacement profile (SA1) compared with target-displacement profile (base shear distribution (F_i) as inertia forces to the masses of the MDOF structure is also illustrated).

The target-displacement profile, which generally reflects the ultimate limit state (in terms of displacements) of the structural members, was constructed from the combination of the peak modal displacements (according to the SRSS rule), and then scaled in such a way that none of the member displacements exceeds the 'damage-based' design values. By following this procedure, the target-displacement profile never reflects an actual deformed shape of the structure; instead, it represents a fictitious deformed shape comprised of non-simultaneous displacements, which is deemed to reflect the peak (and non-simultaneous) structural member response. Therefore, in cases (like here) where more than one mode dominates the response, a static structural analysis under a modal combination of seismic lateral forces such as those given by Equation (21) (whose distribution is also shown in Figure 6), cannot, under any circumstances, produce the target-displacement profile.

A final remark regarding the above, is that the above discrepancy in the displacement profiles is due neither to errors in the estimation of the equivalent cantilever heights nor to the approximate base shear distribution according to Equation (19). In fact, additional iterative structural analyses wherein secant stiffnesses are modified, as required by the DDBD, in this case can only lead to convergence in terms of one critical member displacement (the first member that reaches its limit state) rather than in terms of the entire target-displacement profile, which is determined from the contribution of all significant modes.

5.3 Modal direct displacement-based design (MDDBD)

The proposed extended DDBD procedure was applied to the T7 Overpass as follows.

Step 0: As in the 'standard' DDBD, a 2.0 m column diameter was assumed as a starting point. However, seismic design for Zone II resulted in column longitudinal reinforcement ratios less than the minimum required by E39 [18] and other codes. Due to the fact that providing the minimum required ratio, would obscure the concepts of DDBD (regarding the target profile, displacement ductilities etc.) and aiming at an optimum design (see design criterion i), a 1.5 m column diameter was subsequently used. Preliminary structural analyses were performed for each of the three equivalent SDOF systems (N+1, considering the first 2 modes), under lateral loads compatible with the modal profiles and their SRSS combination, to obtain the equivalent cantilever heights and the uncracked stiffnesses ($K_{g,i}$), according to Equation (1). The assumed characteristics of the elastomeric bearings, the design spectrum and the 'damage-based' displacements were determined as in the standard DDBD.

Steps 2 to 6: The previously described EMS methodology was applied. In order to establish the initial displacement profiles, a modal analysis was conducted where member stiffnesses were set as in the standard DDBD. The peak modal displacements ($u_{i,j}$), the displacement pattern (δ_i), the target-displacement profile (Δ_i) and the modal target displacements profiles ($U_{i,j}$) were determined by Equations (4 to 7) respectively, and presented herein in Figure 7, and it is clear that the abutments are the critical elements. The three equivalent SDOF systems were defined in accordance with Equations (9) and (10).

Once the target-displacement profiles were established, the individual member ductility values (Equations (11)) were calculated along with the corresponding equivalent viscous damping values (Equation (13)), where elastomeric bearings were assumed to respond elastically ($\xi_{Abt}=5\%$). Assuming that 30% of the total shear is carried by the abutments (in all 3 cases), the equivalent system damping values were obtained from Equations (14) and (16) for the first iteration and Equation (15) thereafter. The effective periods at maximum response were then obtained from Figure 4. This was then followed by the calculation of secant stiffnesses at maximum response (Equation (17)). Design base shears were calculated from Equation (18) and member shear forces from Equation (19). It is noted, that in the case of modal target-displacements with different signs, Equation (23) was used in lieu of (19).

$$V_{B,j} - F_{Abt,j} = V_{B,1j} + V_{B,1j}, \quad V_{B,1j} \big/ V_{B,2j} = -\left(\frac{\mu_{\Delta,1j}}{h_{eq,1j}} \Big/ \frac{\mu_{\Delta,2j}}{h_{eq,2j}} \right) \tag{23}$$

As soon as base shears for the SDOF systems are defined, the fraction of the shear carried by the abutments can be recalculated using the following equation

$$\begin{aligned} x_{Abt}(\%) &= F_{Abt}/V_B = \sum F_{Abt,i}/V_B = \sum\left(2k_h\Delta_{Abt,i}\right)/V_B \\ x_{Abt,j}(\%) &= F_{Abt,j}/V_{B,j} = \sum F_{Abt,ij}/V_{B,j} = \sum\left(2k_h\Delta_{Abt,i}\right)/V_{B,j} \end{aligned} \tag{24}$$

In Equation (24), k_h represents the bearing's horizontal stiffness (for one bearing). If the revised fractions differ significantly from the assumed values (30%), Steps 4 and 5 are repeated until fractions of x_{Abt} stabilize. It is clear than in the case of seat-type abutments with bearings the design is simplified on the grounds that the shear carried by the abutment is known from the first iteration. The column secant stiffness values can be recalculated at this point since column forces and member displacements are now known (Equation (20)). This is then followed by a revised modal analysis with the new secant stiffness properties resulting into new target-displacement profiles (Δ_i, U_{ij}). In total, four iterations were needed until Δ_i stabilized. The finally derived (from all iterations) profiles are illustrated in Figure 7. It is evident (from Iterations 3 and 4), that whenever Δ_i stabilizes, $U_{i,j}$ also stabilize.

Step 7: Once the target-displacement profile (Δ_i) stabilized, two structural analyses of the MDOF structure were performed under the inertia forces of Equation (19), utilizing the secant stiffnesses ($k_{eff,ij}$) from the 4th Iteration. Due to the inconsistency of the derived displacements ($U_{an,ij}$) with the corresponding modal target-displacements ($U_{i,j}$), the two analyses were repeated with revised secant stiffnesses until convergence was achieved. Since the final secant stiffnesses of columns differed significantly from the assumed ones, Steps 1 to 7 were repeated, so long as new equivalent cantilever heights and column shear distribution were defined from the results of the structural analyses.

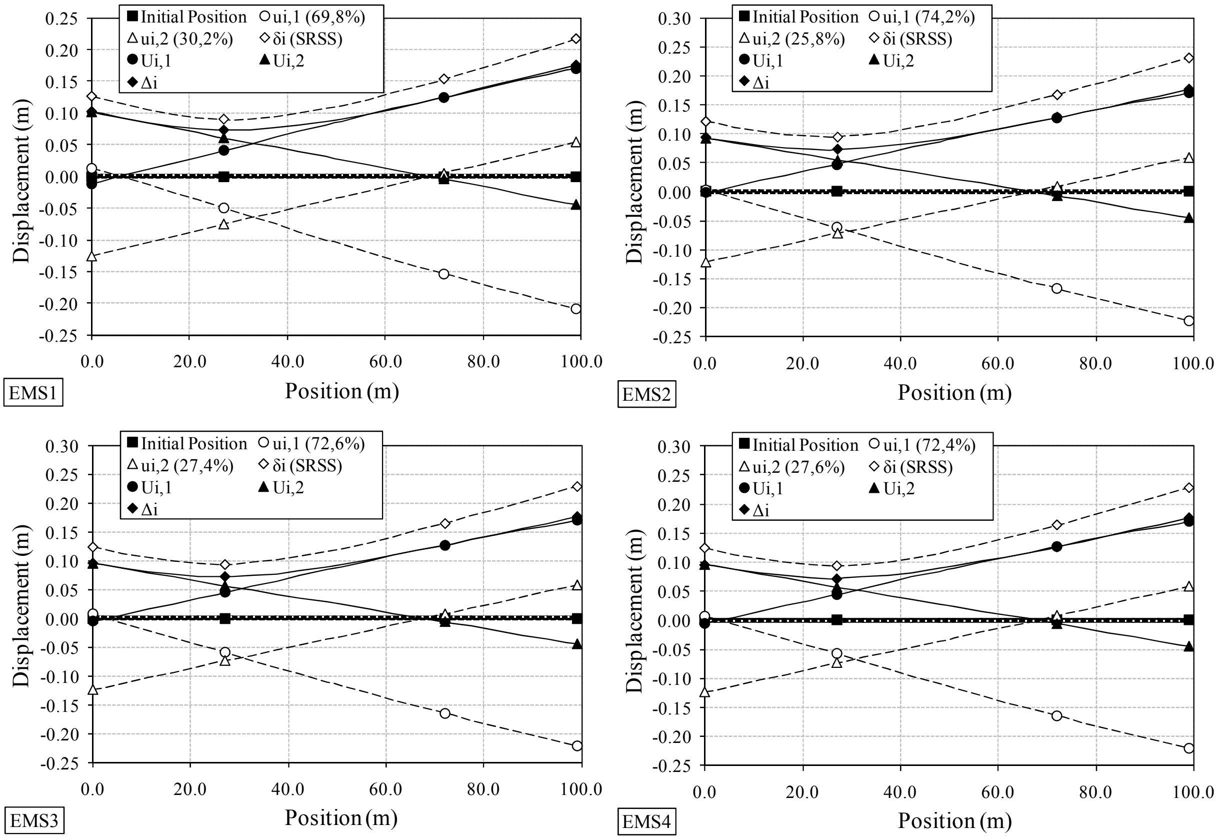

Figure 7: Displacement profiles: Peak modal displacements $u_{i,j}$, displacement pattern δ_i, modal target-displacement profiles $U_{i,j}$ and target-displacement profiles Δ_i, successively derived from EMS.

The new loop of iterations attempts to reduce the discrepancy resulting from the equivalent cantilever height updating (which does not change much the initially assumed value), and the shear distribution effect according to Equation (19), but not the fraction of the shear carried by the abutments, since this is considered known, as already discussed. The results from the final iterations are summarised in Figure 9(a) in the next section, where the target-displacements profiles (Δ_i) and the profiles derived from structural analysis ($\Delta_{i,an}$) are shown. It is noted that $\Delta_{i,an}$ is derived from the SRSS combination of $U_{ij,an}$.

Step 8: The response quantities of design interest (rotations, pier forces) are determined by combining the peak 'modal' responses (from the two structural analyses), using the SRSS combination rule, superimposed with the pertinent combinations of permanent and transient actions. P-Δ effects were also taken into account, and it is verified that the stability index satisfied $\theta_\Delta \leq 0.20$. Finally, the design procedure yielded a longitudinal steel ratio of 9.8‰ and 12.4‰ for Col_1 and Col_2, respectively. The ratio of Col_1 is just slightly less than the minimum required ratio (1%), according to E39 and the Eurocode.

The whole procedure was repeated for the case of Zone III, (PGA of 0.36*g*), in which case a 2.0 m column diameter was selected. The target-displacements profiles (Δ_i) and the profiles derived from structural analysis ($\Delta_{i,an}$) are shown in Figure 9(b). In this case the design procedure yielded a longitudinal steel ratio of 11.5‰ and 19.0‰ for Col_1 and Col_2, respectively.

Furthermore, the effect of the girder's torsional stiffness throughout the suggested methodology was investigated. The design procedure was repeated assuming zero deck torsional stiffness, which results to cantilever action of the columns (see Figure 1(a)), and using a simplified stick model of the deck, supported on elastic translational spring elements, representing the abutments and the piers. It is clear, that such an approach simplifies the design procedure, since iterations with respect to the equivalent cantilever heights are no longer required. In Figure 8, the derived target-displacement profile (Δ_i) is compared with the corresponding profile of the previous (general) case, where deck torsional stiffness was set equal to 20% of the uncracked value. Despite the slight discrepancy in column displacements (ascribed to the different participation factors of the first two modes), the simplified design procedure yielded a longitudinal steel ratio of 42.2‰ and 62.3‰ for Col_1 and Col_2, respectively, attributed mainly to the increased required ratios of the secant-to-uncracked column stiffnesses ($K_{eff,i}/K_{g,i}$) (resulting from the significant reduction of $K_{g,i}$). It is seen that despite the fact that a zero torsional stiffness assumption simplifies the design procedure, it also overestimates the required longitudinal steel ratios and leads to uneconomical design.

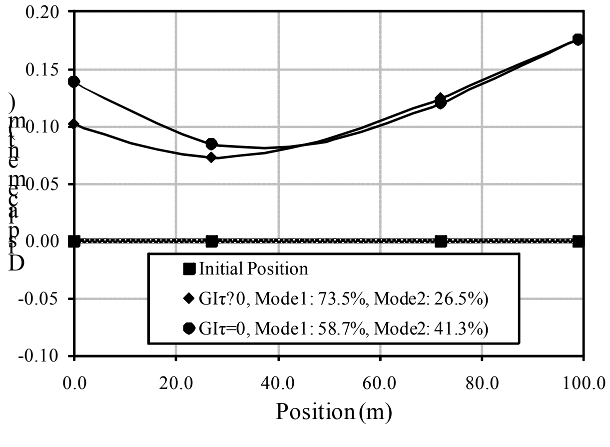

Figure 8. Target-displacement profile (Δ_i) in the case of finite and zero deck's torsional stiffness (GI_τ), (Zone II, D = 1.5 m, in both cases).

5.4 Assessment of MDDBD by NLRHA

The proposed DDBD procedure was assessed using nonlinear response-history analysis (NLRHA) for artificial records closely matching the design spectrum. The artificial records were generated with the computer program SIMQKE [31], while nonlinear analyses were carried out using the SAP2000 software [30]; appropriate nonlinear links were introduced in the finite element model (Figure 3) for response-history analysis, in line with the well-known lumped plasticity approach. The assessment focussed mainly on the target-displacement profiles and on design quantities such as yield displacements, displacement ductilities, stiffnesses, and magnitude of forces developed in critical members of the bridge.

Since the primary objective of the assessment was the study of the transverse bridge response under a seismic excitation which matches as closely as feasible the 'design excitation' (i.e. the design spectrum), one set of NLRHAs was performed for each case (Zone II, III), using artificial records compatible with the design spectra (Figure 4). The set consisted of seven artificial records that fitted the linear design S_a spectra of Figure 4. The Hilber et al. a = -0.1 integration method was selected in SAP2000 [28], which utilises lumped plasticity elements (NLLinks) with rotational spring. Herein, the Takeda degrading-stiffness model [22], also assumed for design (to estimate ξ_i), was adopted. Moment-rotation (M-θ) relationships, assigned to NLLinks used in the finite elements models, were defined from moment-curvature analyses performed for each pier section, utilizing the computer program RCCOLA-90 [32].

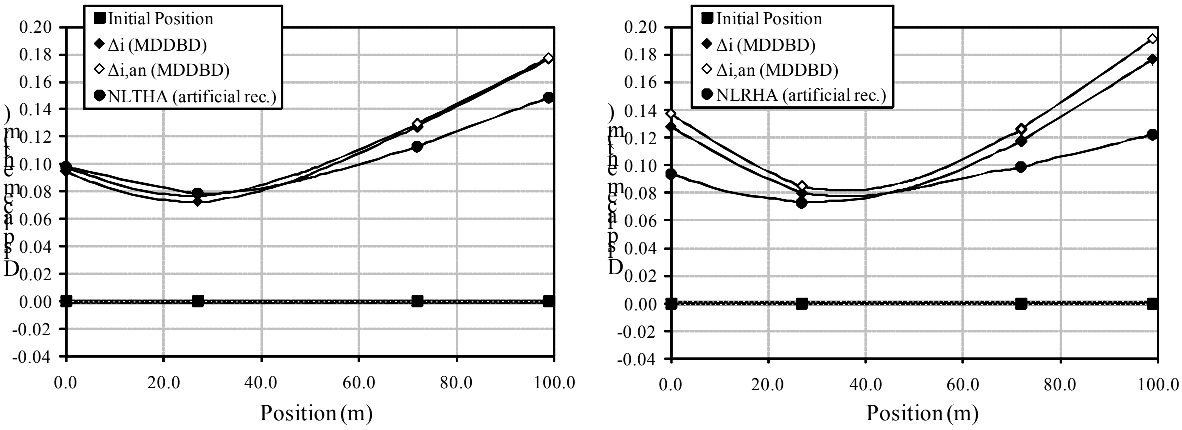

(a) Zone II (PGA=0.24*g*) (b) Zone III (PGA=0.36*g*)

Figure 9: Nonlinear response history maximum displacements: (a) Zone II (PGA=0.24*g*), (b) Zone III (PGA=0.36*g*), compared with target-displacements profiles (Δ_i) and displacement profiles obtained from structural analyses (Δ_{ani}) of Modal DDBD.

In Figure 9 the target-displacement profiles and the displacement profiles obtained from structural analyses within the MDDBD procedure are compared with the displacement envelopes from NLRHA; it is noted that the deck displacements shown in the figures as the NLRHA case are the average of the maximum displacements recorded in the structure during the seven RHAs of each set. It is observed that the target-displacement profiles derived from MDDBD tend to match that obtained from NLRHA, more so in the case of Zone II. The main difference between MDDBD and NLRHA is noted towards the abutments of the bridge (critical members of design), with differences diminishing in the area of the piers. These differences may be attributed to a higher mode contribution (modes not taken into account in the MDDBD) and/or to the contribution of the first two modes with different participation factors than those obtained from the EMS method. However, the displacement demand in the critical member (the one that governs the design – herein Abutment 2) obtained from NLRHA, never exceeds the design displacement, indicating a safe design. A minor exceedance was only observed in the case of Col_1 (see also Figure 10).

Similar conclusions are drawn with respect to the other design quantities; yield displacements, displacement ductilities, bearing shear strain and column drift ratios obtained from NLRHAs were compared with those estimated at the design stage. Figure 10 (supplemented by Table 2) illustrates the correlation in the above quantities, in the case of Zone II. Again, curves shown in the figures as the NLRHA case are the average of the quantities recorded in the structure during the seven RHAs (either at the time step each member enters the inelastic range or at the time step of maximum response), whereas curves shown as MDDBD were computed from the results of structural analyses. It is clear that MDDBD predicts very well, (i.e. matches closely the values from the NLRHA approach), the quantities related to member yielding, which implies the effectiveness of the equivalent cantilever approach in capturing the degree of fixity at the top of the piers, despite the fact that during the design procedure the equivalent cantilever heights are computed according to moment diagrams at maximum response (and not the response at the time of yielding). Finally, difference in member shear force at maximum response is mainly attributed to the consideration of strain hardening in M-θ relationships used in the assessment, whereas MDDBD assumes zero post-elastic slope of the member force-displacement response. In conclusion, the overall agreement between MDDBD and NLRHA is deemed satisfactory.

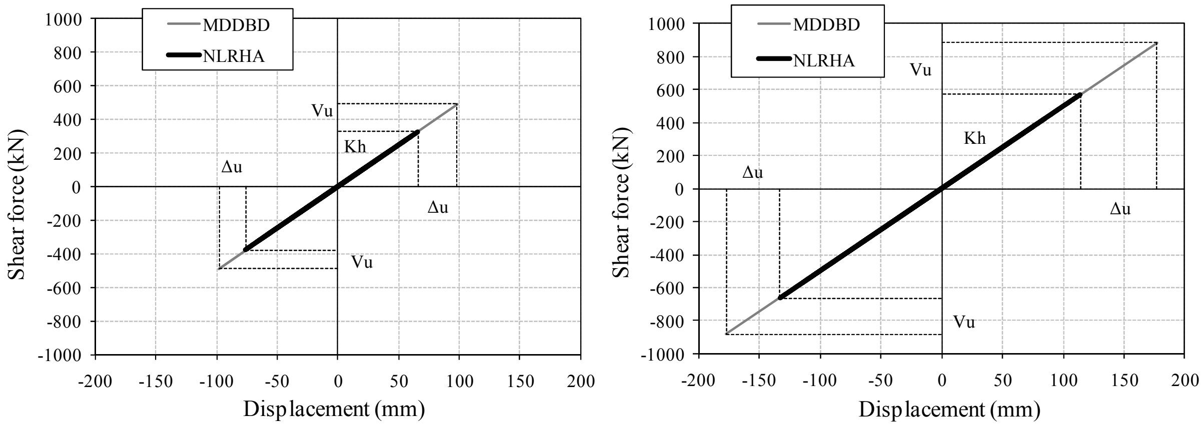

(a) Abutment 1

(b) Abutment 2

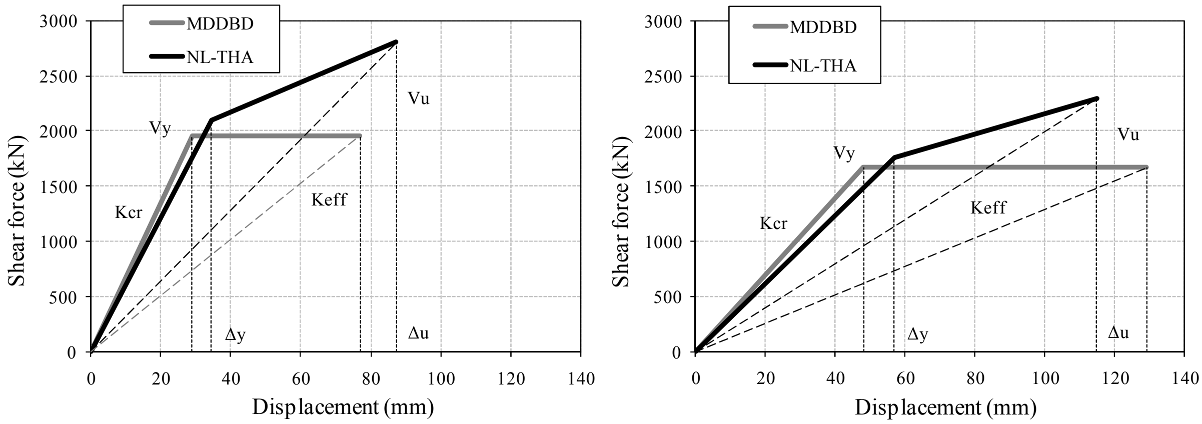

(c) Column 1

(d) Column 2

Figure 10: Member shear force-displacement curves derived from modal direct displacement-based design (MDDBD) and nonlinear response history analyses (NLRHA) in the case of artificial records and Zone II (PGA=0.24*g*).

Member	Abutment 1		Abutment 2		Column 1		Column 2	
	MDDBD	NLRHA	MDDBD	NLRHA	MDDBD	NLRHA	MDDBD	NLRHA
Δ_y (mm)					29	35	48	57
V_y (kN)					1958.6	2102.3	1668.5	1757.1
Δ_u (mm)	98	76	177	133	77	87	129	115
V_u (kN)	489.5	378.8	882.6	663.7	1958.6	2804.3	1668.5	2291.2
K_h (kN/m)	5011.4	4980.8	5011.4	4986.9				
K_{cr} (kN/m)					67537.6	60839.1	34760.4	30929.6
K_{eff} (kN/m)					25436.2	32119.7	12934.1	19981.0
μ_Δ					2.66	2.53	2.69	2.02
γ% (γ_u=2.0)	1.11	0.86	2.01	1.51				
Col. Drift (%)					1.06	0.92	1.06	1.21

Table 2. Design quantities in the case depicted in Figure 10.

6 CONCLUSIONS

An existing displacement-based methodology (DDBD) was extended here to account for higher mode effects in the case of bridges. Its feasibility and accuracy were evaluated by applying it to an actual bridge wherein the first two modes dominate the transverse response. The key issue in this extension was the proper definition of N+1 target-displacement profiles and equal in number equivalent SDOF structures for performing the EMS and estimating the peak 'modal' earthquake forces; the peak 'modal' response was then obtained by conducing N structural analyses, (as many as the significant modes), on the MDOF. Additional issues addressed included the columns' degree of fixity, introducing the concept of the equivalent cantilever heights, and the base shear distribution according to the results of structural analysis. The significance of a rational consideration of the superstructure torsional stiffness throughout the design procedure was also underlined.

By applying DDBD and MDDBD, as well as NLRHA, to the aforementioned bridge, it was concluded that:

- The DDBD method failed to reproduce, through the structural analysis, the target-displacement profile (Δ_i), which was anticipated given the fact that the latter represents a fictitious profile consisting from non-synchronous displacements, and eventually reflects the peak (and non-synchronous) structural member response. On the contrary, MDDBD is intrinsically capable of meeting this goal, by producing the target-displacement-profile (Δ_i) and hence the peak structural response.
- The MDDBD provided also a good estimate of results regarding not only the displacement profile but also additional design quantities such as yield displacements, displacement ductilities, values of stiffness and magnitude of member forces, closely matching the results of the more rigorous NLRHA, and indicating at the same time the validity of the equivalent cantilever concept.
- Investigation concerning the effect of the girder's torsional stiffness throughout the suggested methodology revealed the significance of a properly selected value according to the current bridge design philosophy. In contrast, the simplified design procedure, based on the assumption of a simple cantilever column behaviour under lateral earthquake forces, resulted in significantly overestimated longitudinal steel ratios.
- On the basis of the results obtained for the studied bridge, MDDBD can be further simplified, as far as the required iterations in the EMS methodology (Steps 2 to 6) are con-

cerned. Given that whenever the target-displacement profile Δ_i stabilized, the modal target-displacement profiles $U_{i,j}$ also stabilized, Δ_i (and hence the characteristics of the corresponding SDOF) should be used as the sole convergence criterion during Steps 2 to 6. $U_{i,j}$ and hence the remaining SDOFs should be used only in the last iteration (i.e. during the 4th iteration of Figure 7, instead of the 1st, 2nd, 3rd and 4th) in order to define the peak 'modal' earthquake forces (base shears of Equation (18)). This simplification reduces the amount of required calculations.

- More work is clearly required, to further investigate the effectiveness of MDDBD by applying it to bridge structures with higher mode contribution (even more significant that in the bridge studied here), since MDDBD is expected to be even more valuable for the proper estimation of the actual inelastic response and hence for the efficient design of bridges with significant higher modes. Further investigation is also required in the case of different abutment type configuration (i.e. superstructure's transverse displacement restrained at the abutments through seismic links – activation of the abutment-backfill system), where the shear carried by the abutment is not known during the design procedure.
- The MDDBD method proposed herein, as a rule requires a substantial number of iterations; therefore an implementation of the proposed procedure in a software package would significantly increase its usefulness in practical design.

ACKNOWLEDGEMENTS

The contribution of Asst. Prof. A. Sextos and Dr. I. Moschonas (from the Department of Civil Engineering of the Aristotle University of Thessaloniki) to the computational aspects of this work is gratefully acknowledged.

REFERENCES

[1] T.J. Sullivan, G.M. Calvi, M.J.N. Priestley, M.J. Kowalsky, The limitations and performances of different displacement based design methods. *Journal of Earthquake Engineering*, **7**(1), 201–241, 2003.

[2] J.P. Moehle, Displacement based design of RC structures subjected to earthquakes. *Earthquake Spectra*, **8**(3), 403–428, 1992

[3] M.J.N. Priestley, Myths and fallacies in earthquake engineering – Conflicts between design and reality. *Proceedings of the Tom Paulay Symposium – Recent Developments in Lateral Force Transfer in Buildings*, San Diego, 229–252, 1993.

[4] M.J.N. Priestley, Performance based seismic design. *Proceedings of the 12th World Conference on Earthquake Engineering*, Auckland, NZ, Paper No.2831, 2000.

[5] M.J. Kowalsky, M.J.N. Priestley, G.A. MacRae, Displacement-based design of RC bridge columns in seismic regions. *Earthquake Engineering and Structural Dynamics*, **24**(12), 1623–1643, 1995.

[6] M.J. Kowalsky, M.J.N. Priestley, Experimental verification of direct displacement-based design and development of approach for multiple degree of freedom systems. *Proceedings of the National Seismic Conference on Bridges and Highways, Progress in Research and Practice*, Federal Highway Administration, Sacramento, CA, 651–665, 1997.

[7] G.M. Calvi, G.R. Kingsley, Displacement based seismic design of multi-degree-of-freedom bridge structures. *Earthquake Engineering and Structural Dynamics*, **24**, 1247–1266, 1996.

[8] Seismology Committee of Structural Engineers Association of California (SEAOC), *Recommended Lateral Force Requirements and Commentary (Blue Book)*, Sacramento, California, 1999.

[9] M.J. Kowalsky, A displacement-based design approach for the seismic design of continuous concrete bridges. *Earthquake Engineering and Structural Dynamics*, **31**, 719–747, 2002.

[10] H. Dwairi, M. Kowalsky, Implementation of inelastic displacement patterns in direct displacement-based design of continuous bridge structures. *Earthquake Spectra*, **22**(3), 631–662, 2006.

[11] A.J. Kappos, I. Gidaris, K.I. Gkatzogias, "An Improved Displacement-Based Design Procedure for Concrete Bridges", *3rd International Conference on Seismic Retrofitting*, Tabriz, Iran, 20-22 October 2010.

[12] M.J.N. Priestley, G.M. Calvi, M.J. Kowalsky, *Direct displacement-based design of structures*. IUSS Press, Pavia, Italy, 2007.

[13] G. Adhikari, L. Petrini, G.M. Calvi, Application of direct displacement based design to long span bridges. *Bulletin of Earthquake Engineering*, **8**(4), 897–919, 2010

[14] A.K. Chopra, R.K. Goel, A modal pushover analysis procedure for estimating seismic demands for buildings. *Earthquake Engineering and Structural Dynamics*, **31**(3), 561–582, 2002.

[15] T.S. Paraskeva, A.J. Kappos, A.G. Sextos, Extension of modal pushover analysis to seismic assessment of bridges. *Earthquake Engineering and Structural Dynamics*, **35**(11), 1269-1293, 2006.

[16] M.J. Kowalsky, Deformation limit states for circular reinforced concrete bridge columns. *Journal of Structural Engineering*, **126**(8), 869-878, 2000.

[17] C.P. Katsaras, T.B. Panagiotakos, B. Kolias, Effect of torsional stiffness of prestressed concrete box girders and uplift of abutment bearings on seismic performance of bridges. *Bulletin of Earthquake Engineering*, **7**:363–375, 2009.

[18] Ministry of Public Works of Greece, *Guidelines for Earthquake Resistant Design of Bridges (E39)*, Athens, 2007, (in Greek).

[19] M.J.N. Priestley, F. Seible, G.M. Calvi, *Seismic Design and Retrofit of Bridge Structures*. Wiley, New York, 1995.

[20] H.M. Dwairi, *Equivalent Damping in Support of Direct Displacement-Based Design with Applications to Multi-Span Bridges*. Ph.D. dissertation, North Carolina State University, Raleigh, NC, 2004.

[21] C.A. Blandon, M.J.N. Priestley, Equivalent viscous damping equations for direct displacement-based design. *Journal of Earthquake Engineering*, **9**, 257-278, 2005.

[22] C. Guyader, W.D. Iwan, Determining equivalent linear parameters for use in a capacity spectrum method of analysis. *Journal of Structural Engineering*, **132**(1), 59-67, 2006.

[23] H.M. Dwairi, M.J. Kowalsky, J.M. Nau, Equivalent Damping in Support of Direct Displacement-Based Design. *Journal of Earthquake Engineering*, **11**, 512–530, 2007.

[24] T. Takeda, M. Sozen, N. Nielsen, Reinforced concrete response to simulated earthquakes. *Journal of the Structural Division, ASCE*, **96**(12), 2557–2573, 1970.

[25] D.N. Grant, C.A. Blandon, M.J.N. Priestley, *Modeling Inelastic Response in Direct Displacement-Based Design*. Report No. ROSE 2004/02, European School of Advanced Studies in Reduction of Seismic Risk, Pavia, Italy, 2004.

[26] Ministry of Public Works of Greece, *Greek Seismic Code-EAK 2000*, Athens, 2000 (amended June 2003), (in Greek).

[27] CEN (Comité Européen de Normalisation), *Eurocode 8: design of structures for earthquake resistance–Part 2: Bridges*, Brussels, 2005.

[28] M. Fischinger, D. Beg, T. Isakovic, M. Tomazevic, R. Zarnic, Performance based assessment—from general methodologies to specific implementations. *International Workshop on PBSD, Bled, Slovenia*, 293–308, 2004 (published in PEER Report 2004-05 (UC Berkeley)).

[29] K.I. Gkatzogias, *Displacement-based design of RC bridges*. M.Sc. Dissertation, Aristotle University of Thessaloniki, 2009, (in Greek).

[30] Computers and Structures Inc, *SAP2000: Three Dimensional Static and Dynamic Finite Element Analysis and Design of Structures*. Computers and Structures Inc.: Berkeley, CA, 2009.

[31] E.H. Vanmarcke, *SIMQKE*: *A Program for Artiificial Motion Generation*. Civil Engineering Department, Massachusetts Institute of Technology, 1976.

[32] A.J. Kappos, *RCCOLA-90: A Microcomputer Program for the Analysis of the Inelastic Response of Reinforced Concrete Sections*. Imperial College, London, 1996. (Revised at the Department of Civil Engineering, Aristotle University of Thessaloniki, Greece, 2002).

COMPDYN 2011
III ECCOMAS Thematic Conference on
Computational Methods in Structural Dynamics and Earthquake Engineering
M. Papadrakakis, M. Fragiadakis, V. Plevris (eds.)
Corfu, Greece, 25–28 May 2011

BLIND PREDICTION OF A FULL-SCALE RC BRIDGE COLUMN TESTED UNDER DYNAMIC CONDITIONS

Federica Bianchi[1], **Romain Sousa**[1] **and Rui Pinho**[2]

[1] European Centre for Training and Research in Earthquake Engineering (Eucentre)
Via Ferrata 1, 27100 Pavia, Italy
e-mail: {federica.bianchi, romain.sousa}@eucentre.it

[2] Department of Structural Mechanics, University of Pavia
Via Ferrata 1, 27100 Pavia, Italy
e-mail: rui.pinho@unipv.it

Keywords: RC bridge column, Blind Prediction, Fiber Element, Dynamic non-linear analysis, Shaking Table.

Abstract. *The definition of appropriate modelling approaches combined with a consistent software framework is a topic of major importance in the present days for structural engineering in general and, particularly, for earthquake engineering. The accuracy of the results obtained in the recent "Concrete Column Blind Prediction Contest 2010" for a full-scale reinforced concrete bridge column tested on the NEES Large High-Performance Outdoor Shake Table, seems to indicate that current modelling strategies are on the right track. The 1.2 m diameter cantilevered column spans 7.2 m from the footing. A massive 230 tonne reinforced concrete block supported by the column generates the inertial forces to mobilize the column capacity. Seismic performance was investigated under 6 ground motions, starting with low-intensity shaking and bringing the column progressively to near-collapse conditions. Based on the obtained results from the pre-contest simulation, as well with the post-contest analysis, it was possible to extract some important conclusions regarding the application of several strategies, namely the use of different type elements, element discretization, constitutive laws for materials.*

1 INTRODUCTION

In 2010 a blind prediction contest was announced and sponsored by PEER and NEES. The aim of the contest was to predict failure mode and several response quantities for a full-scale reinforced concrete bridge column. The specimen, subjected to six uniaxial earthquake ground motions, was tested in September 2010 on the NEES Large High-Performance Outdoor Shake Table located at UCSD's Englekirk Structural Engineering Center, starting with low-intensity shaking and bringing the column progressively to near-collapse conditions.

In order to prepare the analytical model, the organizing committee provided all the relevant input data, such as construction details, material properties and base excitation records. Based on the obtained informations, the FE model of the bridge column was prepared using a fiber-based Finite Elements computer program. Several modelling strategies (e.g. different type elements, element discretization, constitutive laws for materials, damping, etc.) were studied in order to obtain the best representation of the real structure. A nonlinear dynamic time-history analysis was performed for predicting the failure mode of the structure. Because the actual loadings were determined during the course of the testing, after the pre-test the organizing committee provided each participant with the registered records. The analytical model was thus updated and another nonlinear dynamic time-history analysis was carried out considering the actual loading.

The analytical results, in terms of displacements at the top of the column and base shear, were compared with experimental ones to assess the nonlinear response prediction capabilities of the adopted modelling strategy.

2 DESCRIPTION OF THE SPECIMEN

The test specimen is a full-scale RC bridge column (see Figure 1) [1] which details are consistent with current Caltrans design practice. The 1.2 m diameter cantilevered column spans 7.2 m from the footing, as shown in Figure 2. A massive 230 tonne reinforced concrete block supported by the column generates the inertial forces to mobilize the column capacity.

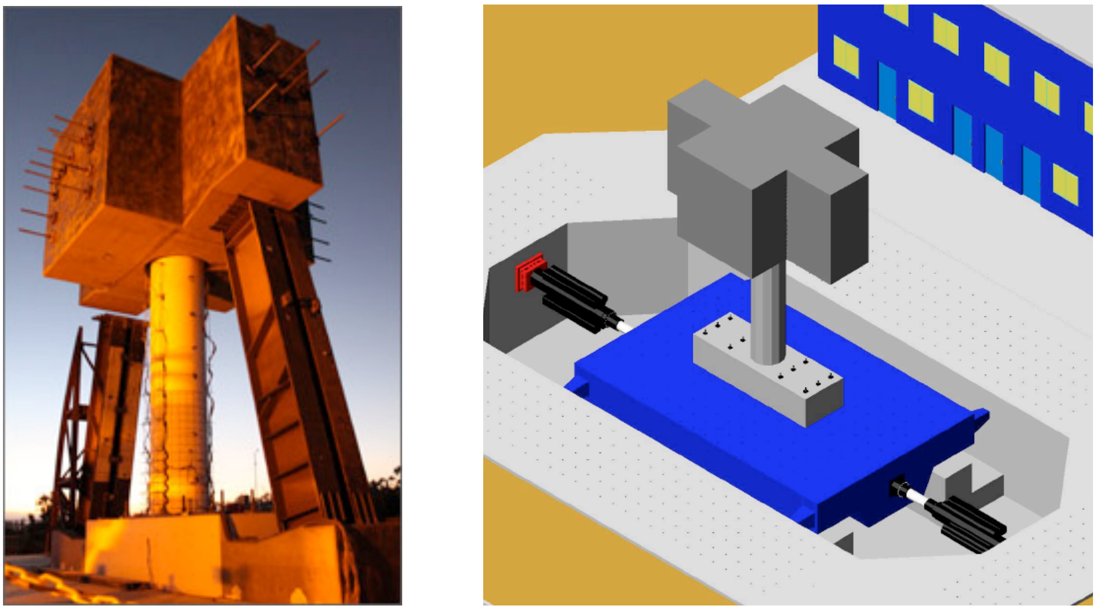

Figure 1: Full-scale reinforced concrete bridge column tested on the NEES Large High-Performance Outdoor Shake Table at UCSD's Englekirk Structural Engineering Center [1].

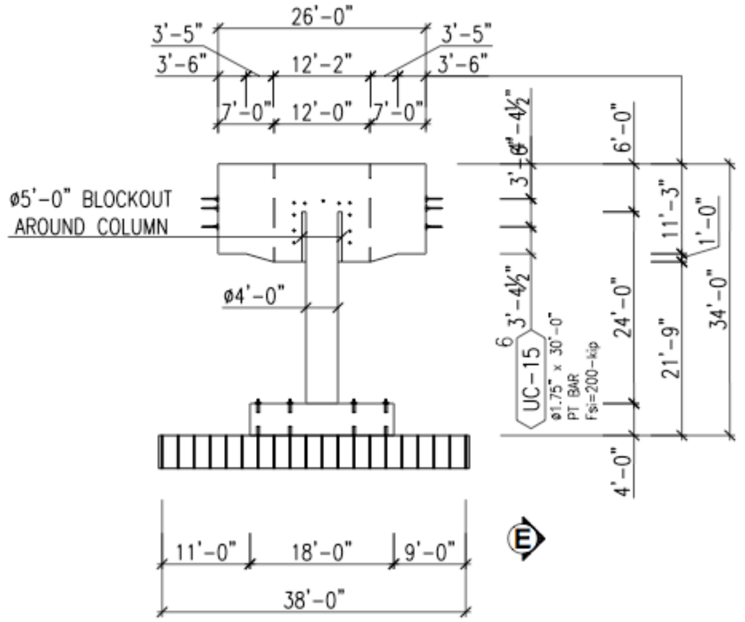

Figure 2: RC bridge column specimen configuration [1].

The concrete used for the construction of the column was normal-weight with a cylinder compressive strength of 41500 kPa.

The reinforcement of the column consisted of eighteen No. 11 continuous bars (see Figure 3), as longitudinal reinforcement and butt-welded No. 5 double hoops, spaced at 152-mm on-center (see Figure 3), as transverse reinforcement. The steel was A706 grade 60 for both longitudinal and transverse reinforcement.

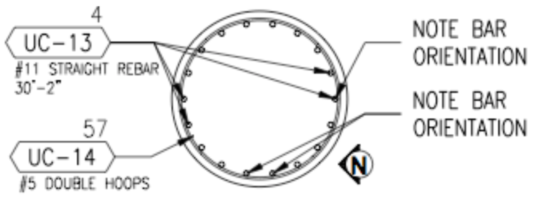

Figure 3: Reinforcement details for the RC bridge column [1].

3 FINITE ELEMENTS MODELLING OF THE RC BRIDGE COLUMN

3.1 Selection of the Finite Elements computer program

The software employed in this work for modelling the behavior of the RC bridge column is SeismoStruct [2], a fiber-based Finite Elements computer program for seismic analysis of framed structures, which is freely downloadable from the Internet. The program is capable of predicting the dynamic behavior of any framed type of structural configuration, accounting both for geometric nonlinearities and material inelasticity.

In the following paragraphs, a description of the constitutive laws for materials, type elements and element discretization is given.

3.2 Section and materials

In the model, the column cross-section was defined through a 1.22 m diameter reinforced concrete circular section with a concrete cover of 0.06667 m and the longitudinal reinforcement which reproduces the layout of the test specimen, as shown in Figure 3.

The stress-strain behavior of the reinforcing steel (see Figure 4(left)) was described by the nonlinear model of Menegotto and Pinto [3], as modified by Filippou *et al.* [4] including isotropic strain hardening effects.

The constitutive law employed for defining the concrete material is a nonlinear constant confinement concrete model that follows the relationship proposed by Mander *et al.* [5], later modified by Martinez-Rueda and Elnashai [6] for numerical stability reasons under large displacements/deformations (see Figure 4(right)). This is a uniaxial model in which a constant confining pressure is assumed through the entire stress-strain range.

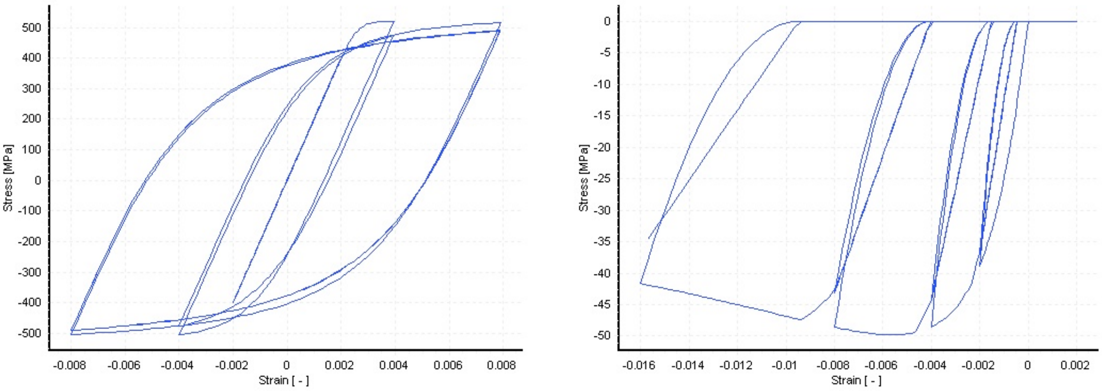

Figure 4: Menegotto-Pinto steel model, with Filippou isotropic hardening (left) and nonlinear constant confinement concrete model (with $k_c = 1.2$) (right).

Some mechanical characteristics of the materials, such as yield strength, ultimate stress and strain for the steel, cylinder compressive strength and strain at peak stress for the concrete, were provided by the organizing committee. The other model parameters were calibrated and set as shown in Table 1 and 2.

Parameter	Steel
Modulus of elasticity (kPa)	2.00E+008
Yield strength (kPa)	518500
Strain hardening parameter	0.008
Transition curve initial shape parameter (default value)	20
1st transition curve shape coefficient (default value)	18.5
2nd transition curve shape coefficient (default value)	0.15
1st isotropic hardening coefficient	0
2nd isotropic hardening coefficient	1
Specific weight (kN/m^3)	77

Table 1: Parameters for Menegotto-Pinto steel model.

Parameter	Concrete (conf)	Concrete (unconf)
Cylinder compressive strength (kPa)	41500	41500
Tensile strength (kPa)	0	0
Strain at unconfined peak stress (m/m)	0.0028	0.0028
Constant confinement factor	1.2	1
Specific weight (kN/m^3)	23.6	23.6

Table 2: Parameters for the nonlinear constant confinement concrete model.

The tensile strength of the concrete was ignored for the numerical stability of the analysis.

3.3 Element type and discretization

Two different FE formulations can be selected within the software for implementing distributed inelasticity frame elements, the classical displacement-based (DB) formulation (e.g. Hellesland and Scordelis [7], Mari and Scordelis [8]) and the more recent force-based formulation (e.g. Spacone *et al.* [9], Neuenhofer and Filippou [10]).

In the present study, a 3D inelastic beam-column element with displacement-based (DB) formulation and capable of capturing both geometric and material nonlinearities was selected for modelling the cantilevered column. The number of fibers used in section equilibrium computations was set to 300, in order to guarantee an adequate reproduction of the stress-strain distribution across the element cross-section, considering the shape and material characteristics of the latter and the degree of material inelasticity that is likely to be reached.

The structural member was appropriately subdivided into eight elements of different length (see Figure 5), in order to accept the assumption of a linear curvature field inside each of the sub-domains.

3.4 Applied mass and boundary conditions

In order to perform the nonlinear dynamic time-history analysis required for the blind prediction, it was necessary to define the mass elements. The mass of the column was automatically computed by the program knowing the material's self weights, while the additional mass coming from the reinforced concrete block supported by the column, was applied in a lumped fashion at the top node (see Figure 5). The applied values are summarized in Table 3.

Lumped mass	Concrete block
Translational mass (tonne)	228
Rotational mass (tonne × m^2)	885

Table 3: Computed masses.

Modelling of the footing under the column was ignored; hence the column base node was considered as fully restrained against rotations and translations (see Figure 5).

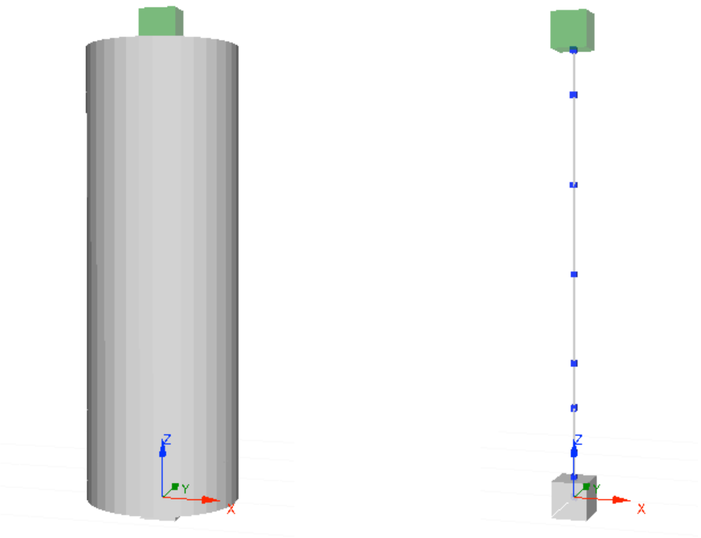

Figure 5: Bridge column FE model with finite element discretization.

3.5 Applied dynamic loading

For post-test response prediction, the actual ground motions were applied as dynamic loading. Time history analysis was carried out for a single input record consisting of an assemblage of the six accelerograms provided by the organizing committee. Ten seconds of delay were left between one motion and the one immediately after (see Figure 6) in order to damp out the structure motion.

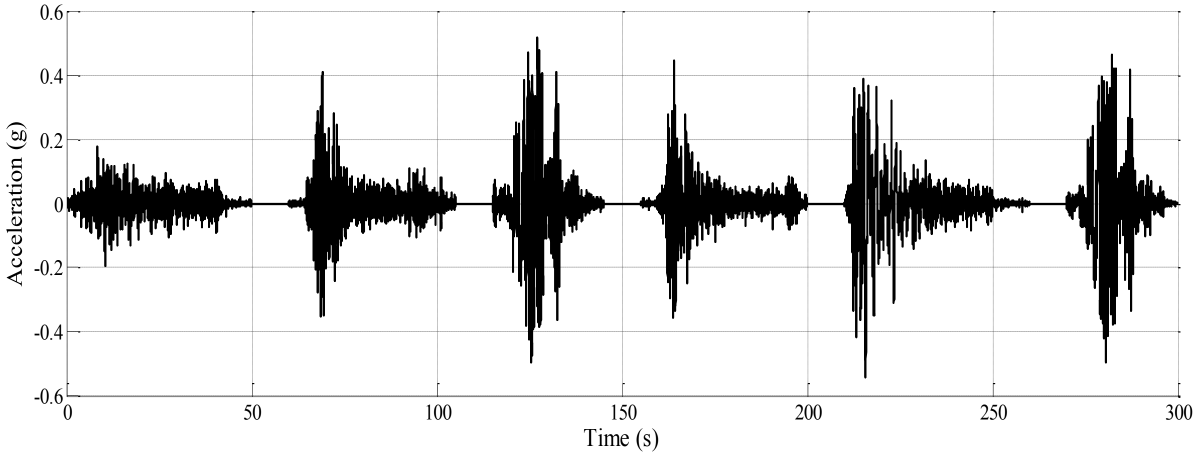

Figure 6: Actual acceleration records.

The time step for the dynamic analysis was set as 0.00390625 s, coincident with the input record sampling time step.

3.6 Damping, Integration Algorithm and Convergence Criterion

In addition to the hysteretic damping, which was implicitly accounted for by the cyclic material relationships, a small amount of non-hysteretic equivalent viscous damping (1%) was also introduced in order to improve the numerical stability of the dynamic nonlinear analyses. A tangent stiffness-proportional viscous damping model was employed, as suggested by Priestley and Grant [11] and Hall [12].

Regarding the numerical integration scheme, the Hilber-Hughes-Taylor algorithm (Hilber *et al.* [13]), with an alpha coefficient equal to -0.1, was adopted.

Finally, the displacement/rotation based scheme was selected as convergence criterion.

4 COMPARISON BETWEEN NUMERICAL AND EXPERIMENTAL RESULTS

After the submission of the post-test analytical results, the organizing committee provided all the responses of the column, in terms of maximum/minimum values and time histories, for each ground motion.

The experimental time histories of column top displacement and base shear were compared with the numerical ones; they are presented in the following figures. It is observed that the numerical predictions matched relatively well the experimental results. In particular, there is a good agreement between both the amplitude and the frequency content of the response when the column is subjected to earthquake 1, 3, 5 and 6 (see Figures 7, 8, 9 and 10, respectively).

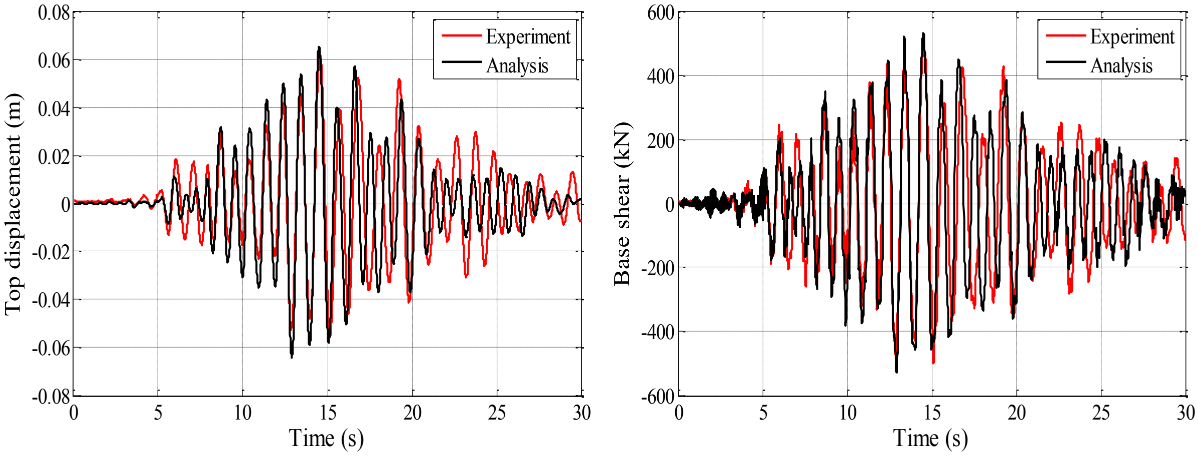

Figure 7: Top displacements (left) and base shear during earthquake 1

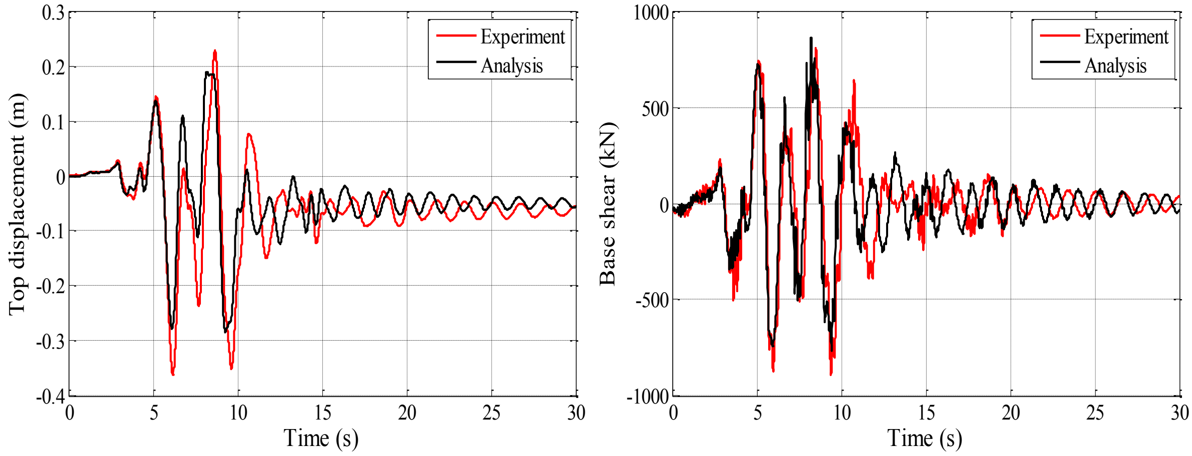

Figure 8: Top displacements (left) and base shear during earthquake 3

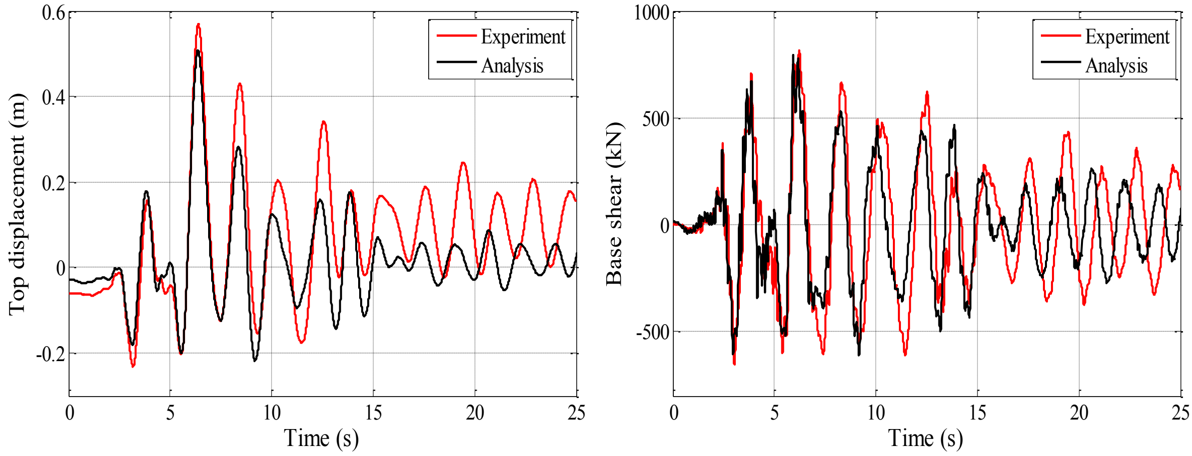

Figure 9: Top displacements (left) and base shear during earthquake 5

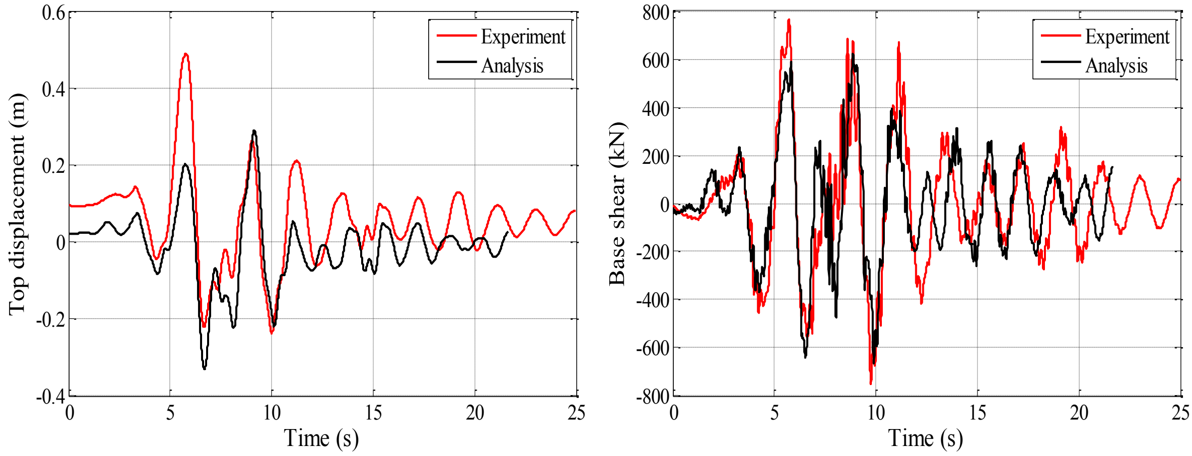

Figure 10: Top displacements (left) and base shear during earthquake 6

5 CONCLUSIONS

This work described the blind prediction of the dynamic response of a full-scale RC bridge column tested on the NEES Large High-Performance Outdoor Shake Table located at UCSD's Englekirk Structural Engineering Center. The results show that the definition of appropriate modelling approaches combined with a consistent software framework led to a relatively accurate prediction of the global nonlinear dynamic response of the column.

REFERENCES

[1] NEES@UCSD, *Concrete Column Blind Prediction Contest*. Available from: http://nisee2.berkeley.edu/peer/prediction_contest [2010].

[2] SeismoSoft, *SeismoStruct – A Computer Program for Static and Dynamic nonlinear analysis of framed structures*. Available from: http://www.seismosoft.com [2008].

[3] M. Menegotto, P.E. Pinto, Method of analysis for cyclically loaded R.C. plane frames including changes in geometry and non-elastic behaviour of elements under combined normal force and bending. *Symposium on the Resistance and Ultimate Deformability of Structures Acted on by Well Defined Repeated Loads*, International Association for Bridge and Structural Engineering, Zurich, Switzerland, pp. 15-22, 1973.

[4] F.C. Filippou, E.P. Popov, V.V Bertero, Modelling of R/C joints under cyclic excitations. *ASCE Journal of Structural Engineering*, Vol. 109, No. 11, pp. 2666-2684, 1983.

[5] J.B Mander, M.J.N. Priestley, R. Park, Theoretical stress-strain model for confined concrete. *Journal of Structural Engineering*, Vol. 114, No. 8, pp. 1804-1826, 1988.

[6] J.E. Martinez-Rueda, A.S. Elnashai, Confined concrete model under cyclic load. *Materials and Structures*, Vol. 30, No. 197, pp. 139-147, 1997.

[7] J. Hellesland, A. Scordelis, Analysis of RC bridge columns under imposed deformations. *IABSE Colloquium*, Delft, pp. 545-559, 1981.

[8] A. Mari, A. Scordelis, Nonlinear geometric material and time dependent analysis of three dimensional reinforced and prestressed concrete frames. *SESM Report* 82-12, Department of Civil Engineering, University of California, Berkeley, 1984.

[9] E. Spacone, V. Ciampi, F.C. Filippou, Mixed formulation of nonlinear beam finite element. *Computers & Structures*, Vol. 58, No. 1, pp. 71-83, 1996.

[10] A. Neuenhofer, F.C. Filippou, Evaluation of nonlinear frame finite-element models. *Journal of Structural Engineering*, Vol. 123, No. 7, pp. 958-966, 1997.

[11] M.J.N. Priestley, D.N. Grant, Viscous damping in seismic design and analysis. *Journal of Earthquake Engineering*, Vol. 9, Special Issue 1, pp. 229-255, 2005.

[12] J.F. Hall, Problems encountered from the use (or misuse) of Rayleigh damping. *Earthquake Engineering and Structural Dynamics*, Vol. 35, No. 5, pp. 525-545, 2006.

[13] H.M. Hilber, T.J.R. Hughes, R.L. Taylor, Improved numerical dissipation for the time integration algorithms in structural dynamics. *Earthquake Engineering and Structural Dynamics*, Vol. 5, No. 3, pp. 283-292, 1977.

COMPDYN 2011
III ECCOMAS Thematic Conference on
Computational Methods in Structural Dynamics and Earthquake Engineering
M. Papadrakakis, M. Fragiadakis, V. Plevris (eds.)
Corfu, Greece, 25–28 May 2011

GENERALIZED FRAGILITY CURVES FOR BEARING-SUPPORTED SKEW BRIDGES, FOR ARBITRARY ANGLE OF INCIDENCE OF THE SEISMIC ACTION

Ioannis F. Moschonas[1], **Andreas J. Kappos**[1]

[1] Department of Civil Engineering
Aristotle University of Thessaloniki, Greece
imoschon@civil.auth.gr; ajkap@civil.auth.gr

Keywords: Bridges, Vulnerability assessment, Fragility curves, Pushover analysis, Damage states, Angle of Incidence.

Abstract. *In a previous work by the authors and their co-workers an analytical methodology for the derivation of seismic fragility curves for bridges was proposed. Bridges were classified into three main categories according to their seismic energy dissipation mechanism: bridges with yielding piers of the column type, bridges with bearings and non-yielding piers of the wall type, and bridges with bearings and yielding piers of the column type. Then, damage states were defined using deck displacement at characteristic points of 'typical' bridge pushover curves, which are related to the seismic energy dissipation mechanism, consistently with the proposed classification scheme. Only one horizontal component of the seismic action was considered to act along the principal directions of the bridge. This methodology was subsequently extended by the authors to take into account the angle of incidence of the seismic action, considering only the single-component case. In the present work the methodology is further extended to the general case wherein the minor principal horizontal component of the earthquake is also taken into account (dual-component seismic action). Furthermore, damage states for bridges with bearings are redefined in a broader manner, to take into account biaxial shear effects, and all possible failure mechanisms of the bearings. The methodology is applied here to a skew bridge, subjected to either single- or dual-component seismic action. The main difference between straight and skew bridges is that the modal principal bridge directions are rotated with respect to the geometric principal bridge directions, for a specific angle of incidence. The proposed methodology is formulated in terms of modal principal directions. The CQC rule is used for the combination of the projections of the control point displacement and of the base shear in the single-component case, while in the dual-component case the SRSS rule is used and it is found adequate for all excitation angles. From the derived generalized fragility curves it is concluded that when the minor principal horizontal component of the earthquake is taken into account, bridge fragility is significantly increased, while it remains practically unaffected by the angle of incidence.*

1 INTRODUCTION

Various analytical methodologies proposed in the past for the vulnerability/fragility assessment of bridges in Europe [8], the US [6, 9, 10, 13], and Japan [4], address only one horizontal component of the seismic action (single-component seismic action) acting along the longitudinal or transverse direction of the bridge. Hence, an issue that has to be addressed is the assessment of bridge vulnerability/fragility in the general case where the seismic excitation acts at an arbitrary angle. The first attempt in this direction was made by Shinozuka et al. [12] who proposed an analytical methodology based on dynamic inelastic analysis for single-component seismic action. Damage states were defined only for bridges with inelastic piers, in terms of displacement ductility of pier critical sections.

Recently the authors have developed a methodology for the derivation of fragility curves for arbitrary angle of incidence of the seismic action [7] extending their previously proposed methodology [8], which is based on static nonlinear (pushover) analysis. At first, static nonlinear analysis was extended to take into account the angle of incidence of the seismic action; it is noted that on this topic only two previous attempts have been made in [14] and [15], both of them focusing on the estimation of the critical angle of incidence of the seismic action, rather than on the derivation of pushover curves. Two methodologies were proposed for deriving pushover curves for arbitrary angle of incidence of the single-component seismic action. According to the first one, an effective mode shape is determined in the direction of the seismic action, while according to the second one the response along the principal bridge directions is combined in order to derive the response in the direction of the earthquake. The two methods were both applied to a symmetric overpass bridge and the results were evaluated against those from nonlinear response-history analysis (NLRHA). It was concluded that the first method is valid only in the period range where the equal displacement approximation is valid, while the second one is valid for all periods. Besides the extension of static nonlinear analysis, damage state definitions were also extended to take into account the effect of the angle of incidence of the seismic action.

In the work presented herein, the methodology for the derivation of static pushover curves and fragility curves for arbitrary angle of incidence of the seismic action is extended to account for dual-component seismic action. Static nonlinear analysis for arbitrary angle of incidence is carried out using the second of the previously proposed methods [7], due to its broader range of application; the method is further extended to account for biaxial bending effects in critical pier sections and for biaxial shear effects in the bearings. Regarding damage state definitions, in particular for bearing-supported bridges, damage states are defined taking into account the biaxial deformation of the bearings. Furthermore, the last damage state is defined on the basis of the ultimate shear deformation, as it is derived considering all possible failure mechanisms of the bearings. Finally, the proposed methodology is applied to a skew bearing-supported bridge and conclusions are drawn regarding the effect of dual-component action and of angle of incidence.

2 METHODOLOGY FOR THE DERIVATION OF FRAGILITY CURVES

2.1 Modelling of the seismic action

The earthquake ground motion is analyzed into three principal components E_I, E_{II} and E_{III} linearly independent (or statistically linearly uncorrelated) directed along a set of principal axes *O-I-II-III*. Components E_I and E_{II} are the horizontal ones, with the first one having the maximum intensity (E_I = major horizontal component, E_{II} = minor or secondary horizontal component).

The simpler approach is to consider only the major horizontal earthquake component (single-component seismic action) acting at an angle *a* with respect to the bridge longitudinal axis (Fig. 1). Thus, the axis system *O-I-II-III* is considered identical with system *Oξηζ* which is rotated by an angle *a* with respect to the bridge axes *Oxyz*. Thus, the major earthquake component E_I acts along *Oξ* axis and for this reason it will be referred to as $E_ξ$.

The proposed methodology for deriving pushover curves for arbitrary angle of incidence of the seismic action described in the following paragraphs is based on the combination of longitudinal and transverse responses. Therefore, it is more convenient to analyse the major earthquake component into two components $E_x=E_ξ\cdot\cos a$ and $E_y=E_η\cdot\sin a$ (Fig. 1) acting along the longitudinal and transverse direction, respectively. Components E_x and E_y have identical time-histories (accelerograms), thus they are linearly dependent or statistically linearly fully correlated.

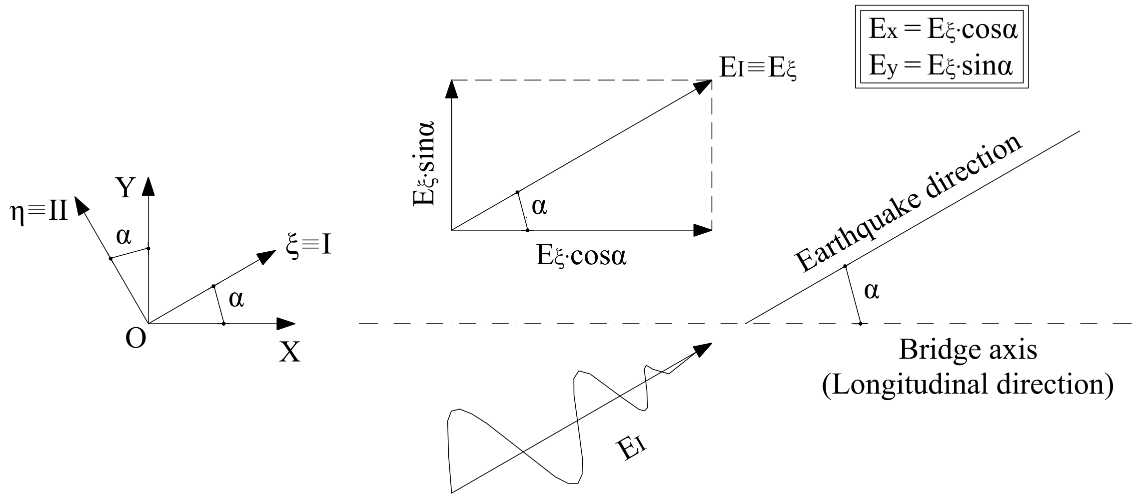

Figure 1: Single-component seismic action acting at an arbitrary angle of incidence.

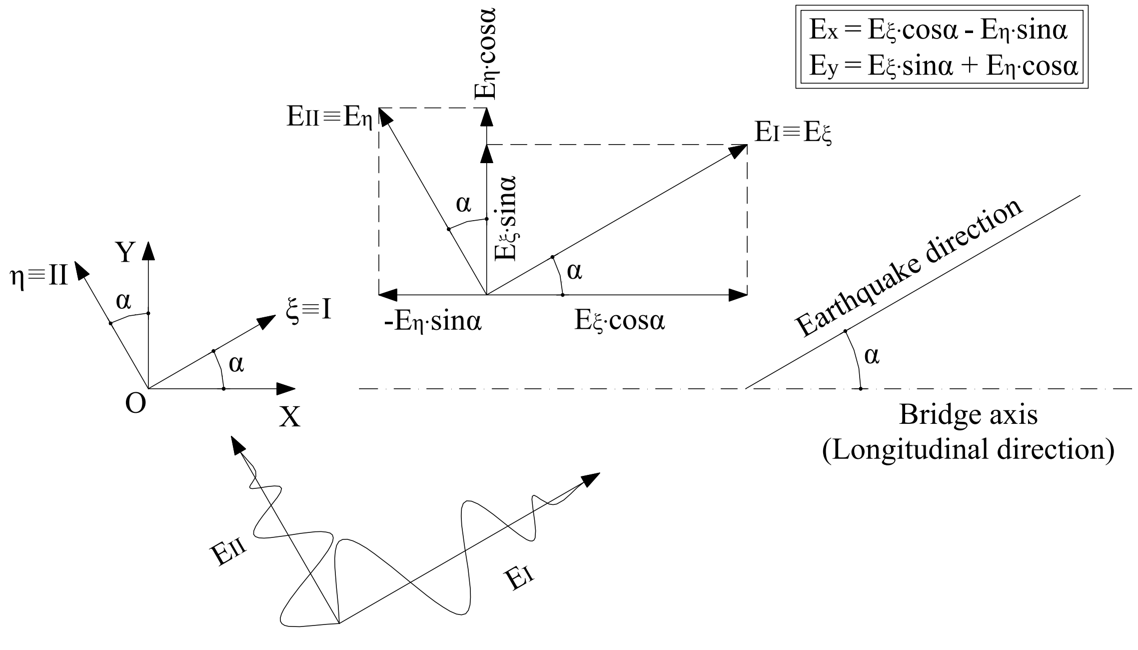

Figure 2: Dual-component seismic action acting at an arbitrary angle of incidence.

In the general case the minor horizontal earthquake component, $E_{II} \equiv E_{\eta}$, is also considered (dual-component seismic action) (Fig. 2) and it is normal to the major horizontal component E_I, which acts at angle a with respect to the longitudinal bridge axis X (i.e. the minor component acts at an angle α with respect to the Y-axis). The components acting along the longitudinal and the transverse bridge directions are $E_x = E_{\xi} \cdot \cos\alpha - E_{\eta} \cdot \sin\alpha$ and $E_y = E_{\xi} \cdot \sin\alpha + E_{\eta} \cdot \cos\alpha$. These components are a linear combination of E_{ξ} and E_{η}, thus they are linearly dependent or statistically linearly correlated. For excitation angles 0°, 90°, 180° and 270° components E_x and E_y become identical with the principal horizontal components $E_I \equiv E_{\xi}$ and $E_{II} \equiv E_{\eta}$, thus they have quite different time-histories, i.e. they are linearly independent or statistically linearly uncorrelated.

Only natural earthquake records can be analyzed into principal components. Hence, in the case where a code-type response spectrum, or spectrum-compatible artificial accelerograms are utilized, a proper value for their intensity ratio is required; based on the available literature [5] a value of 0.70 can be reasonably adopted.

2.2 Derivation of pushover curves

Having modelled the seismic action appropriately, i.e. analyzing it into the components acting along the longitudinal and transverse directions, the next step for the derivation of pushover curves for arbitrary angle of incidence of the seismic action is to take into account the interaction between biaxial bending moments and axial force (PMM interaction) at critical pier sections and/or the interaction between biaxial shear forces and axial force (PFF interaction) in the bearings.

In the first step of the method, the bridge is analyzed for a low earthquake intensity level (e.g. 0.1g) for which the response along both principal bridge directions remains within the elastic range. Then, the displacements of the selected control point along the longitudinal and transverse bridge directions, $u_{L,el}$ and $u_{T,el}$, are calculated using elastic response spectra, and from them the corresponding rotations ($\theta_{x,el}$ and $\theta_{z,el}$) and moments ($M_{x,el}$ and $M_{z,el}$) of the critical pier sections, as well as the corresponding shear deformations ($\gamma_{x,el}$ and $\gamma_{z,el}$) and forces ($F_{x,el}$ and $F_{z,el}$) in the bearings along their principal axes, are estimated. The moment ratio $M_{x,el}/M_{z,el}$ (Fig. 3) and the bearing shear force ratio $F_{x,el}/F_{z,el}$ remains constant also for higher earthquake intensity levels so long as the loading is monotonically increasing and the response along both principal bridge directions remains elastic. For a certain earthquake intensity level the pier critical section, or an individual bearing, yields under a moment M^{y}_{int} (Fig. 3) or force F^{y}_{int}, respectively (the subscript *int* indicates that the point lies on the interaction curve). This means that the critical section or the bearing yields under biaxial conditions earlier than in the case where the moment vector is normal, or the force vector is parallel, to one of the principal directions. Then, the (idealised as bilinear) M-θ or F-γ diagrams along the principal directions of critical pier sections or bearings are modified using the reduced values of yield moments or yield forces, respectively.

Finally, the selection of an appropriate axis to project the displacement of the control point and the base shear force of the bridge along the longitudinal and the transverse direction is needed, so that the pushover curve can be plotted. An obvious choice is the axis $O\xi$ of the major earthquake component $E_I \equiv E_{\xi}$. From the two approaches proposed in [7] the one based on the combination of responses along the bridge's principal directions is used here, for the reasons explained earlier in the paper. The successive steps of the methodology proposed for deriving the pushover curve are the following:

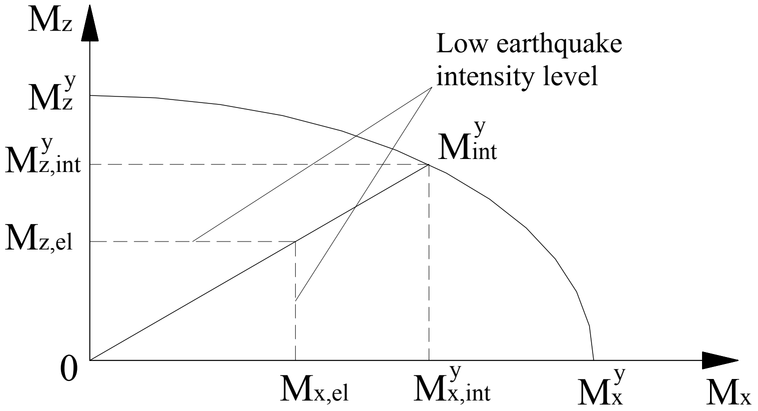

Figure 3: Elliptically idealised moment interaction diagram of a critical R/C pier section.

Step 1: For a given dual-component seismic action E (code-type spectra or natural records) whose major component acts at an angle a, the corresponding component response spectra E_x and E_y (Fig. 2) are calculated and are scaled to increasing levels of earthquake intensity (0.1g, 0.2g,…, $A_{g,u}$·g) until the bridge reaches its ultimate point (bridge failure) at the intensity level $A_{g,u}$.

Step 2: For a low earthquake intensity level (e.g. 0.1g), for which bridge response along both its principal directions remains elastic, the moments $M_{x,el}$ and $M_{z,el}$ of critical pier sections and the shear forces $F_{x,el}$ and $F_{z,el}$ of bearings along their principal directions are calculated. The resulting moment ratios $M_{x,el}/M_{z,el}$ and shear force ratios $F_{x,el}/F_{z,el}$ are subsequently used in the corresponding interaction diagrams (Fig. 3) to reduce yield moments of critical pier sections and/or yield shear forces of bearings; the reduced values are introduced in the M-θ or F-γ diagrams for the principal directions of critical pier sections and of individual bearings.

Step 3: A ‘standard’ pushover analysis is performed separately along the longitudinal (0°) and the transverse direction (90°), for lateral force patterns compatible with the corresponding prevailing mode. Then, the derived pushover curves are idealised as bilinear ones [11] and they are converted to spectral pushover curves (‘capacity curves’ [3]) of the inelastic equivalent SDOF corresponding to the prevailing mode of each principal bridge direction.

Step 4: At each earthquake intensity level the displacement $u_{L,max}$ along the longitudinal direction and $u_{T,max}$ along the transverse direction are calculated using inelastic spectra. Then, the corresponding base shears V_{bL} and V_{bT} are extracted from the database of each individual pushover analysis and the projections of these two quantities on the axis of earthquake action (Fig. 2) are taken, i.e.

$$u_{L,proj} = u_{L,\max} \cdot \cos\alpha,\ V_{bL,proj} = V_{bL} \cdot \cos\alpha \tag{1}$$

$$u_{L,proj} = u_{T,\max} \cdot \sin\alpha,\ V_{bT,proj} = V_{bT} \cdot \sin\alpha \tag{2}$$

Then, the projections are combined using the SRSS rule, the CQC rule or the ABS rule, since these response quantities are not simultaneous, for the calculation of the displacement u_ξ and the base shear force $V_{b\xi}$ in the earthquake direction. In case of the SRSS rule, u_ξ and $V_{b\xi}$ are calculated using the following relationships:

$$u_\xi = \sqrt{u_{L,proj}^2 + u_{T,proj}^2} = \sqrt{u_{L,\max}^2 \cdot \cos^2\alpha + u_{T,\max}^2 \cdot \sin^2\alpha} \tag{3}$$

$$V_{b\xi} = \sqrt{V_{bL,proj}^2 + V_{bT,proj}^2} = \sqrt{V_{bL}^2 \cdot \cos^2 \alpha + V_{bT}^2 \cdot \sin^2 \alpha} \tag{4}$$

Step 5: Step 4 is repeated for all earthquake intensity levels (0.1g, 0.2g,…, A_{gu}·g) until the bridge reaches its ultimate point in either principal direction. The pushover curve referring to the earthquake direction is plotted using u_ξ–$V_{b\xi}$ points.

2.3 Definition of damage states

The first step for defining damage states is their qualitative (descriptive) definition. Here the corresponding definitions of HAZUS [3] are adopted which are based on bridge damage data from the Loma Prieta and Northridge earthquakes [1]. Thus, four damage states, in addition to the No-Damage state (DS0), are defined: Minor/Slight Damage (DS1), Moderate Damage (DS2), Major/Extensive (DS3) Damage, and Failure/Collapse (DS4).

Then, damage state descriptive definitions are quantified in terms of bridge deck displacement δ_ξ (global damage parameter) along the earthquake direction. Apart from bridge damage, i.e. damage developed due to plastic hinge formation in the piers and/or yielding of bearings, damage developed at the abutment-backfill system due to its activation after the longitudinal gap closure is also taken into account. Damage states due to bridge damage are defined using bridge deck displacement δ_ξ at characteristic points of 'typical' bridge pushover curves for a given earthquake direction *a*, which are defined on the basis of the seismic energy dissipation mechanism consistently with the classification scheme proposed in [8]. Damage states due to damage developed at the abutment-backfill system are also defined using bridge deck displacement, and complement the corresponding damage state definitions referring to bridge damage. The final threshold value of displacement for each damage state is taken as the minimum of the two threshold values for damage to the bridge (piers, bearings) and damage to the abutment-backfill system.

2.3.1 Bridges with yielding piers of the column type

In bridges with inelastic piers of the column type the 'typical' pushover curve for seismic action acting at an angle *a* along the axis $O\xi$ is shown in Fig. 4. The first branch of the pushover curve corresponds to all the seismic intensity levels for which the response in both bridge directions remains in the elastic range, and terminates at the first plastic hinge formation (Point A). The second branch of the pushover curve corresponds to the successive plastic hinge formation (development of plastic mechanism) and terminates at the intensity level for which the last plastic hinge forms (Point B). The third branch of the pushover curve terminates at the first failure of a pier (Point C). Subsequent to this point progressive failure of the bridge occurs, with successive pier failures, as shown in Fig. 4.

Idealizing the pushover bridge curve as bilinear, the second branch corresponding to the plastic hinge formation stage (branch AB) is reduced to a single point (named conventional yield point) and the branch after Point C corresponding to the failure mechanism is reduced to another single point (named bridge ultimate point) using a strength drop criterion for the bilinearization and the assumption of equal areas between the initial and the idealised pushover curves [11]. The four damage states are then defined on the bilinearised bridge pushover curve as described in Table 1. The first damage state (DS1: Minor Damage) is defined at the elastic branch (at 70% of conventional yield displacement, since, as described previously, actual yielding occurs before the conventional yield point), while the last damage state (DS4: Failure/Collapse) is defined at the ultimate bridge point, defined as previously. The two intermediate damage states (DS2: Moderate Damage and DS3: Major/Extensive Damage) are defined differently for high ductility bridges ($\mu_u \geq 3.0$) and for low-to-moderate ductility bridges (μ_u<3.0). More specifically, in high ductility bridges intermediate damage states are defined at bridge displacements corresponding to ductility levels 1.5 and 3.0, while in low-to-moderate ductility bridges are defined at displacements equally spaced (1/3 and 2/3) along the post-yield branch.

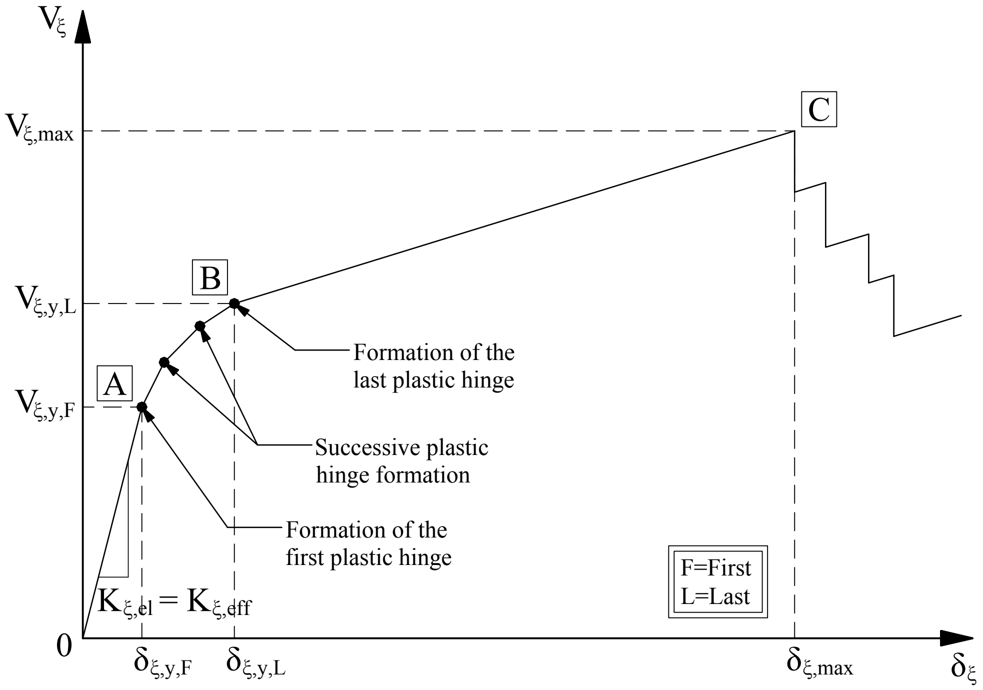

Figure 4: 'Typical' pushover curve of bridges with yielding piers of the column type.

a/a	Damage State	Threshold values of δ_ξ	
		$\mu\geq3.0$	$\mu<3.0$
DS1	Minor/Slight	$> 0.7\cdot\delta_{\xi,y}$	$> 0.7\cdot\delta_{\xi,y}$
DS2	Moderate	$> 1.5\cdot\delta_{\xi,y}$	$> \delta_{\xi,y} + (1/3)\cdot(\delta_{\xi,u} - \delta_{\xi,y})$
DS3	Major/Extensive	$> 3.0\cdot\delta_{\xi,y}$	$> \delta_{\xi,y} + (2/3)\cdot(\delta_{\xi,u} - \delta_{\xi,y})$
DS4	Failure/Collapse	$> \delta_{\xi,u}$	$> \delta_{\xi,u}$

Table 1: Damage state definitions for bridges with yielding piers of the column type.

2.3.2 Bridges with bearings and non-yielding piers of the wall type

In this type of bridge the shape of the 'typical' pushover curve is similar to that of the previous type, replacing yielding and failure of critical pier sections with yielding and failure of bearings (or groups of bearings in the common case where more than one bearings are placed at the top of a pier) (Fig. 5-solid line). Whenever seismic links (stoppers) are present at the top of the piers an apparent hardening-softening is noticed due to their successive activation and failure, respectively (Fig. 5-dotted line, see discussion in [8]).

Damage states for this bridge type are defined as follows: Firstly, damage states for a single bearing are defined (Table 2) using shear deformation, γ_{bi}, as damage parameter. Then, the deformation of the equivalent single bearing, γ_{eq}, is calculated as the average of the deformations of all bridge bearings, i.e.

$$\gamma_{eq} = \frac{\sum_{i=1}^{N} \gamma_{bi}}{N} \tag{5}$$

where: γ_{bi} = shear deformation of single bearing i
γ_{eq} = shear deformation of the equivalent single bearing and
N = total number of bridge bearings

hence damage state definitions for the single bearing (Table 2) can be used also for the entire bridge. Alternatively, the corresponding bridge displacement δ_ξ (Table 2) can be used for damage state definitions. More specifically, the first damage state is defined using the yield shear deformation γ^{y}_{int}, which lies on the interaction curve and is derived for low earthquake intensity level. The other three damage states are defined reducing the threshold values for the uniaxial shear deformation of bearings (1.5, 2.0 and γ_u) using the minimum of the ratios $\gamma^{y}_{x,int}/\gamma^{y}_{x}$ and $\gamma^{y}_{z,int} / \gamma^{y}_{z}$ (Table 2).

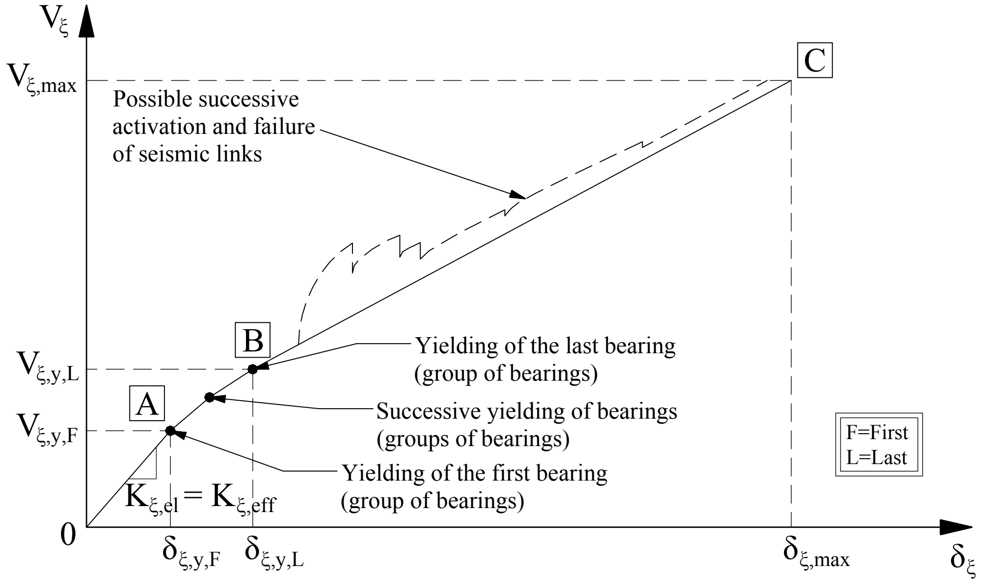

Figure 5: 'Typical' pushover curve of bridges with bearings and non-yielding piers of the wall type.

a/a	Damage State	Threshold values of	
		γ_{bi}, γ_{eq}	δ_ξ
DS1	Minor/ Slight	$> \gamma^{y}_{\text{int}}$	$> \delta_\xi(\gamma_{eq,DS1})$
DS2	Moderate	$> 1.5 \cdot \min\left[\gamma^{y}_{x,\text{int}} / \gamma^{y}_{x}, \gamma^{y}_{z,\text{int}} / \gamma^{y}_{z}\right]$	$> \delta_\xi\left(\gamma_{eq,DS2}\right)$
DS3	Major/ Extensive	$> 2.0 \cdot \min\left[\gamma^{y}_{x,\text{int}} / \gamma^{y}_{x}, \gamma^{y}_{z,\text{int}} / \gamma^{y}_{z}\right]$	$> \delta_\xi\left(\gamma_{eq,DS3}\right)$
DS4	Failure/ Collapse	$> \gamma_u \cdot \min\left[\gamma^{y}_{x,\text{int}} / \gamma^{y}_{x}, \gamma^{y}_{z,\text{int}} / \gamma^{y}_{z}\right]$	$> \delta_\xi\left(\gamma_{eq,DS4}\right)$

Table 2: Damage state definitions for bridges with bearings and non-yielding piers of the wall type

2.3.3 Bridges with bearings and yielding piers of the column type

In this bridge typology the seismic energy is dissipated due to the inelastic behaviour of both piers and bearings. Thus, the shape of a 'typical' bridge pushover curve (Fig. 6) is similar to the previous bridge types. Here, the second branch represents both the successive plastic hinge formation and yielding of bearings. In addition, the slope of the first branch is smaller than in the case of bridges with yielding piers of the column type due to the significantly lower stiffness of pier-bearings systems, thus ultimate displacement ductility in bridges with yielding piers of the column type is usually small, but is also a rather inappropriate indicator of the bridge's response. Damage states are defined using the corresponding definitions of bridges with yielding piers of the column type (Table 5, typically the μ_u<3.0 case applies).

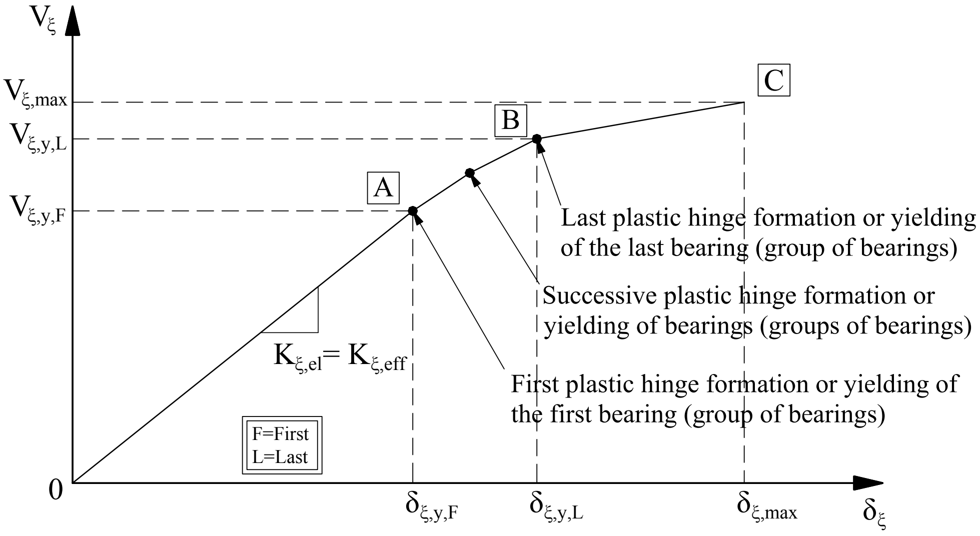

Figure 6: 'Typical' pushover curve of bridges with bearings and yielding piers of the column type.

a/a	Damage State	Threshold values of δ
DS1	Minor/Slight	$> 0.7\cdot\delta_{\xi,y}$
DS2	Moderate	$> \delta_{\xi,y} + (1/3)\cdot(\delta_{\xi,u} - \delta_{\xi,y})$
DS3	Major/Extensive	$> \delta_{\xi,y} + (2/3)\cdot(\delta_{\xi,u} - \delta_{\xi,y})$
DS4	Failure/Collapse	$> \delta_{\xi,u}$

Table 3: Damage state definitions for bridges with bearings and yielding piers of the column type.

2.3.4 Damage due to abutment-backfill system activation

In case the abutment-backfill system is taken into account in the analysis model ('full-range analysis') the typical bridge pushover curve in the longitudinal direction has the shape shown in Fig. 7 (a bilinear force-displacement, V-δ, diagram is assumed for the abutment-backfill system). For deck displacements smaller than the longitudinal gap, δ_{gap}, the pushover curve is derived on the basis of bridge response. After the activation of the abutment-backfill system, its response is combined with bridge response and the pushover curve is derived adding the corresponding shear forces of bridge and abutment-backfill system for each value of bridge displacement.

Damage states are defined differently in the case where the abutment-backfill system is modelled (full-range analysis) and in the case where the abutment-backfill system is not directly included in the model (approximate analysis). In the former case (full range analysis) the first damage state is defined on the basis of the displacement at the longitudinal gap closure, δ_{gap}, the last damage state is defined on the basis of the ultimate displacement of the abutment-backfill system, if it is smaller than the ultimate bridge displacement δ_{max}, and the two intermediate damage states are defined at displacements equally spaced along the post-yield branch of the 'typical' bridge pushover curve after the activation of the abutment-backfill system. In the latter case (approximate analysis) the first damage state initiates at the gap closure, δ_{gap}. The two intermediate damage states are defined increasing the threshold value of the first damage state by 10% and 20%, while the last damage state is defined as the maximum of $a\cdot\delta_u$ (which is an estimate for the ultimate displacement of the abutment-backfill system, see [8]) and $1.1\cdot\delta_{DS3}$. When bridge ultimate displacement is smaller than these two values, δ_u is used to define the threshold of the final damage state.

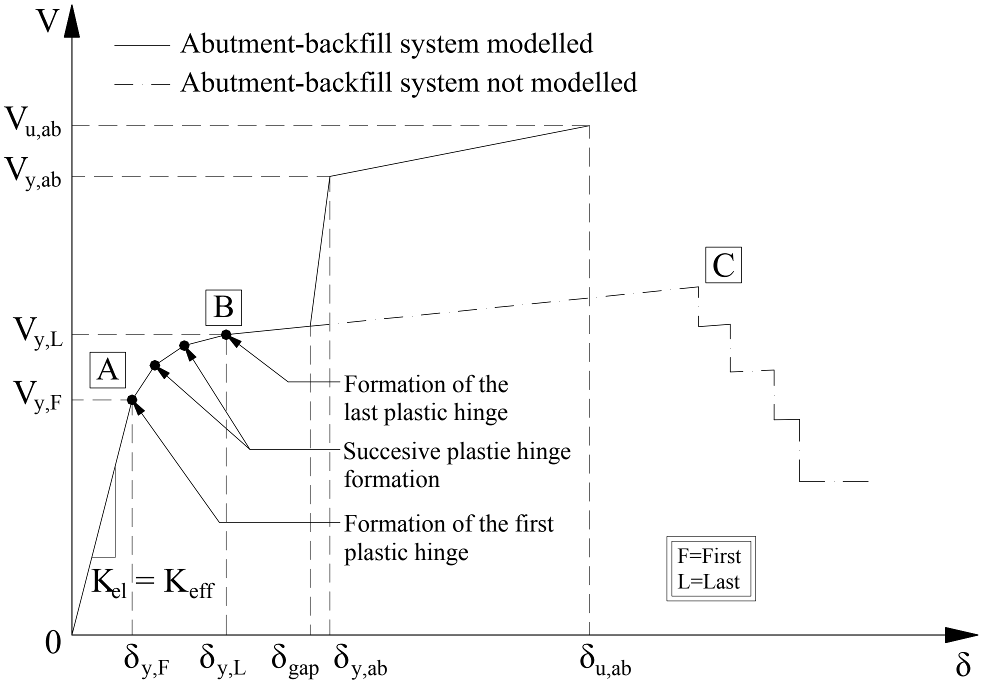

Figure 7: 'Typical' pushover bridge curve (here bridge with yielding piers of the column type) taking into account the abutment-backfill system.

a/a	Damage State	Threshold values of	
		Full range analysis	*Approximate analysis*
DS1	Minor/Slight	$> \delta_{gap}$	$> \delta_{gap}$
DS2	Moderate	$> \delta_{y,ab} + (1/3)\cdot(\delta_{u,ab} - \delta_{y,ab})$	$> 1.1\cdot\delta_{gap}$
DS3	Major/Extensive	$> \delta_{y,ab} + (2/3)\cdot(\delta_{u,ab} - \delta_{y,ab})$	$> 1.2\cdot\delta_{gap}$
DS4	Failure/Collapse	$> \delta_{u,ab}$	$> \begin{cases} \delta_u,\ when\ \delta_u < 1.1\cdot\delta_{\Sigma B3} \\ \max\{a\cdot\delta_u,\ 1.1\cdot\delta_{\Sigma B3}\} \end{cases}$

Table 4: Damage state definitions for damage developing at the abutment-backfill system.

The effect of the angle of incidence of the seismic action is taken into account by modifying bridge deck displacements estimated from static nonlinear analysis. More specifically, bridge displacement δ_ξ in the earthquake direction a, is firstly projected on the longitudinal bridge direction ($\delta_\xi\cdot\cos\alpha$ –Fig. 8a) and then it is increased by the displacement caused by the rotation of the bridge deck ($B\cdot\sin\theta$ – Fig. 8b). Hence, the bridge displacement $\delta_{\xi,Br}$, used in order to take into account the damage caused by the activation of the abutment-backfill system is

$$\delta_{\xi,Br} = \delta_\xi \cdot cos\,a + B \cdot sin\,a \tag{6}$$

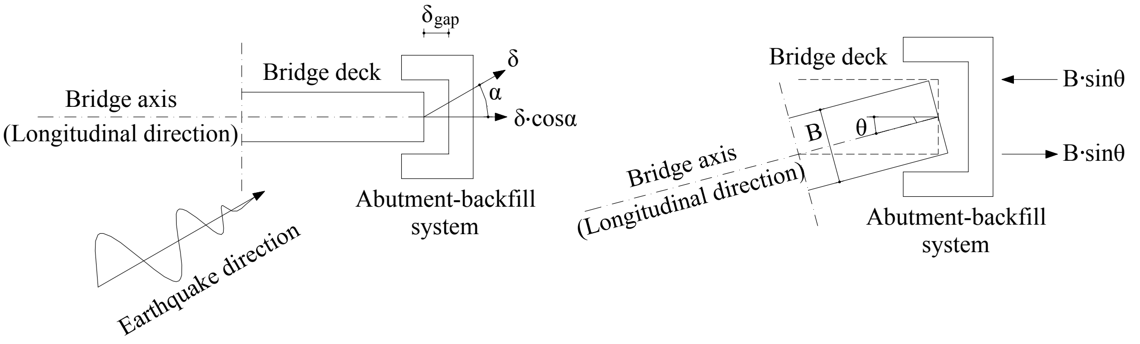

a. Projection of bridge displacement on the bridge axis

b. Increase of bridge displacement due to deck rotation

Figure 8: Calculation of bridge displacement for the activation of the abutment backfill system.

2.4 Derivation of fragility curves

The starting point for the derivation of fragility curves is the quantification of the exceedance of a given damage state, which is materialized using damage parameters, here bridge displacement δ_ξ along the axis $O\xi$ (Fig. 2) of the major horizontal component of the earthquake. Peak ground acceleration A_g is selected as the earthquake intensity parameter, but other quantities could also have been used (e.g. spectral displacement S_d).

The available bridge capacity that corresponds to the threshold of damage state i (i=1,2,3,4) is quantified through the bridge displacement δ_ξ used for the damage state definitions (Tables 1 to 4). Correspondingly, bridge response for a given earthquake intensity level A_g is quantified through bridge displacement $\delta_{\xi,Br|Ag}$, as it is calculated from bridge analysis for earthquake intensity A_g. Thus, the exceedance of a damage state can be represented by the following relationship

$$\delta_{\xi,Br|Ag} \geq \delta_{DSi} \tag{7}$$

and the probability of exceedance is written

$$P\left(\delta_{\xi,Br|Ag} \geq \delta_{DSi}\right) = P_f \tag{8}$$

In order to derive a fragility curve quantification of the total uncertainty is also needed. Here, since the probability density function is idealised as lognormal (as in most previous studies on bridge fragility), the total uncertainty is represented by the total lognormal standard deviation β_{tot}, which is assumed equal to 0.6 in line with previous studies [3]. The probability of exceedance using the median values of damage parameter (bridge displacement in the earthquake direction δ_ξ) can be written as:

$$P_f = \Phi\left[\frac{1}{\beta_{tot}}\cdot\ln\left(\frac{\delta_{\xi,Br,m|Ag}}{\delta_{DSi,m}}\right)\right] \tag{9}$$

The next step is the correlation of damage parameter (δ_ξ) with earthquake intensity parameter (A_g), which is achieved through the median damage evolution curve (or primary fragility curve, Fig. 10), which is the plot of the median value of bridge deck displacement versus the corresponding earthquake intensity parameter (here A_g). Fig. 9 shows the estimation of bridge displacement for increasing earthquake intensity levels using inelastic demand spectra in the region where the equal energy approximation is valid (i.e. for T≤0.5-0.6

sec) and elastic demand spectra in the region where the equal displacement approximation is valid (i.e. for T>0.5-0.6 sec). From the median damage evolution curve, given the threshold value of bridge deck displacement for a specific damage state, the corresponding median value of A_g can be estimated (Fig. 10). For example, the median threshold value of A_g for damage state DS2 for bridges with bearings and elastic piers of the wall type is the direction of the piers is that corresponding to $\delta_{DS2} = \delta(\gamma_{eq} = 1.5)$.

Hence, the damage state probability can be written in terms of peak ground acceleration A_g as follows:

$$P_f = \Phi\left[\frac{1}{\beta_{tot}} \cdot \ln\left(\frac{A_{g,m}}{A_{g,DSi,m}}\right)\right] \tag{10}$$

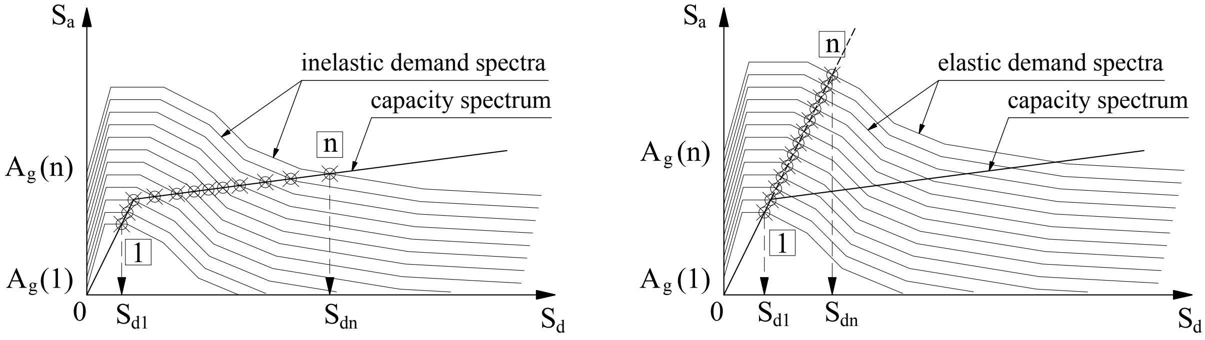

a. $T \leq$ 0.5-0.6 sec b. $T >$ 0.5-0.6 sec

Figure 9: Estimation of target displacement for increasing earthquake intensity levels

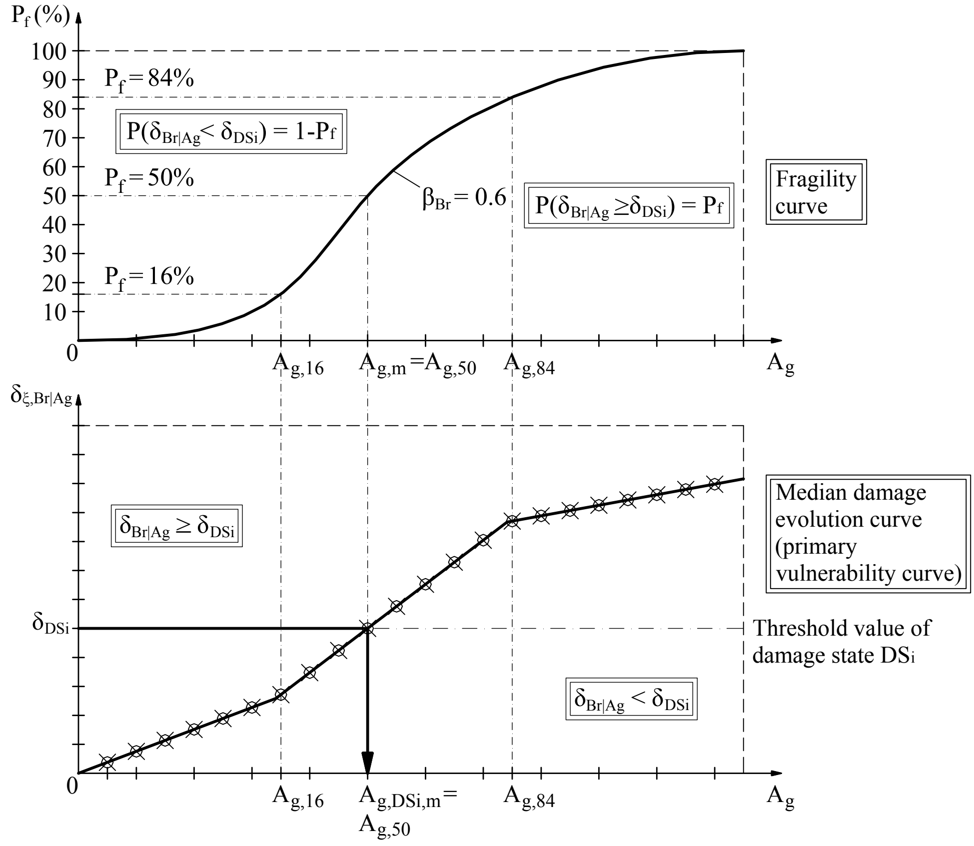

Figure 10: Median damage evolution curve (primary vulnerability curve) and fragility curve.

The plot of equation (10) is the fragility (probabilistic vulnerability) curve, of the specific damage state (Fig. 10). For the derivation of generalized fragility curves the proposed methodology is applied for various values of the angle of incidence of the seismic action between 0° and 180°.

3 APPLICATION OF THE PROPOSED METHODOLOGY TO SKEW BRIDGES

In a previous study by the authors [7] the proposed methodology was applied to a straight overpass bridge subjected to single-component seismic action. Here, the methodology is applied to a skew bridge subjected to either single- or dual-component seismic action.

3.1 Description and modelling of the selected bridge

The selected bridge is a 5-span bridge of 180m total length (5×36) that crosses Kosynthos River in North-Eastern Greece (Thrace), and is part of the Egnatia Motorway. The deck consists of a system with 6 simply-supported precast-prestressed beams connected through a continuous R/C slab (Fig. 11) and rests through common elastomeric bearings 400×500×181 (elastomer thickness 77mm) on four piers of the wall type with rectangular solid cross section 1.2×14.7m (Fig.12). Piers are inclined at an angle of 110° with respect to the bridge's longitudinal axis, i.e. there is a skew of 20^o (Fig. 13).

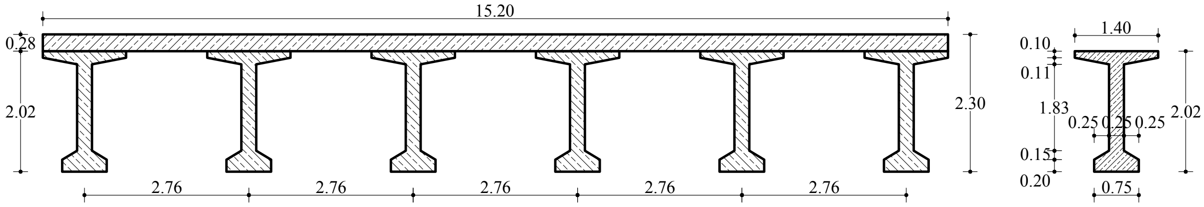

Figure 11: Deck section of Kosynthos bridge

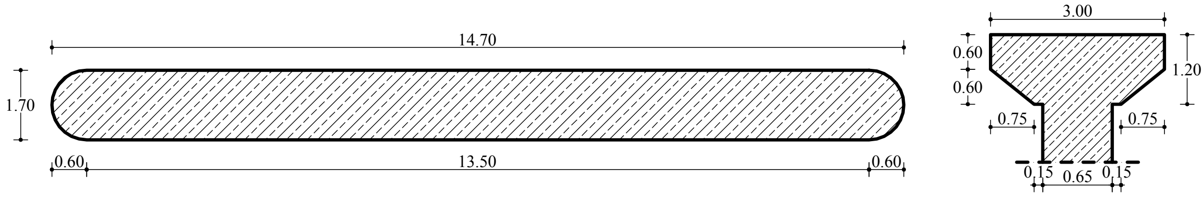

Figure 12: Wall-type pier section of Kosynthos bridge

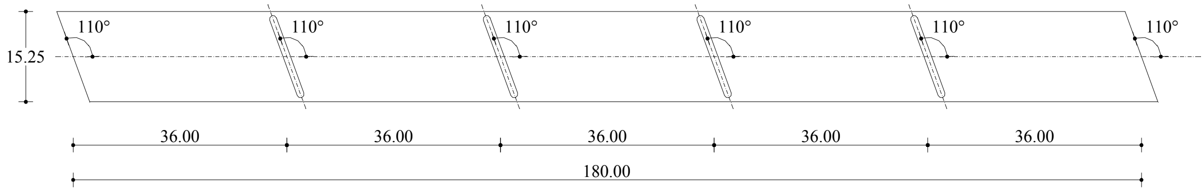

Figure 13: Inclination of pier in Kosynthos bridge with respect to the geometric longitudinal axis (Plan View)

The bridge deck rests on the abutments through common elastomeric bearings 400×600×226(110). The deck movement along the longitudinal direction is permitted up to the closure of a 100mm gap, while in the transverse direction it is unrestrained.

The Kosynthos bridge was modelled using the software package SAP2000 Nonlinear [2] (Fig.14a). Precast deck beams and piers are modelled with frame elements, while the continuous deck slab is modelled with shell elements. Bridge bearings are modelled with Link elements with length equal to the total thickness of rubber in each bearing. The base of Link elements is connected through rigid-arms to the top of piers (Fig. 14b). The behaviour of bearings is considered as linear, which is a reasonable and common assumption for low-damping bearings (here the equivalent viscous damping is only about 5%).

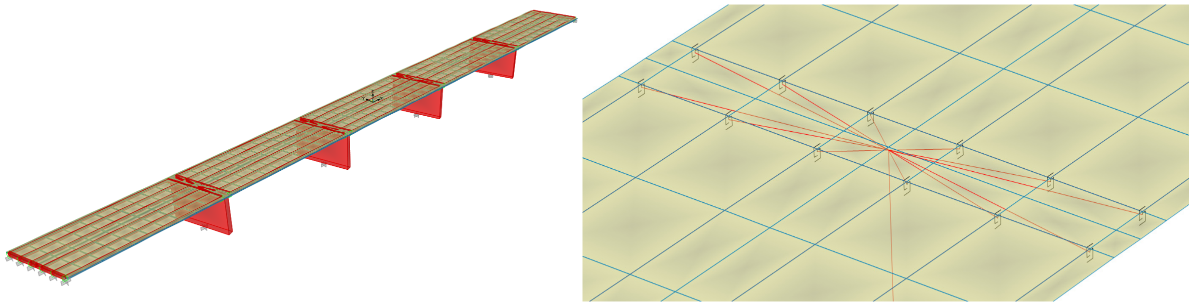

a. Finite element model

b. Modelling of pier-to-deck connection (through elastomeric bearings)

Figure 14: Modelling of Kosynthos bridge.

3.2 Application of the proposed methodology

The proposed methodology is applied twice, considering the seismic action either as single- component or as dual-component, for three different greek earthquakes using the records described in Table 5. For each of the three pairs, principal horizontal components are derived. The corresponding response spectra are shown in Fig. 15 for the case of Thessaloniki earthquake; it is worth pointing out that due to its different frequency content the minor component has larger spectral displacement values than the major one.

Place	Station	Date	Time	M	R [km]	Orientation	A_g [g]
Thessaloniki	City Hotel	20/6/78	08:03:21	6.1	29	N-S	0.139
						E-W	0.146
Kalamata	OTE Building	13/9/86	17:24:31	5.8	10	N80E	0.240
						N10W	0.272
Athens	Sepolia (Garage)	7/9/99	11:56:50	5.8	21	LONG	0.326
						TRANS	0.310

Table 5: Selected greek earthquakes.

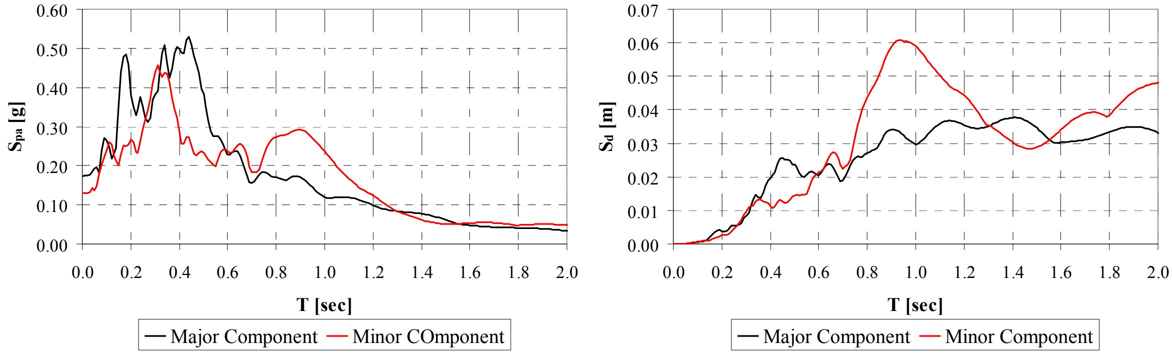

a. S_{pa}-T

b. S_d-T

Figure 15: Elastic response spectra of principal horizontal components of Thessaloniki earthquake.

For the derivation of pushover curves for arbitrary angle of incidence of the seismic action, the modal characteristics of the bridge have to be determined. The prevailing mode in the longitudinal direction is translational and the bridge deck moves as a rigid body at an angle of 20° with respect to the longitudinal axis (Fig. 16). The transverse prevailing mode is also translational but the deck moves as a rigid body at an angle of 110° with respect to the longitudinal axis (Fig. 17) or at an angle of 20° with respect to the geometric transverse axis, i.e. normal to the longitudinal prevailing mode. The two prevailing modes define the modal principal axes of Kosynthos bridge (Fig. 18, system O-*M*1-*M*2), which are rotated at an angle of 20° with respect to the geometric principal axes (Fig. 18, system *Oxy*). The rotation of the modal principal axes with respect to the geometric principal axes is due to the bridge skewness.

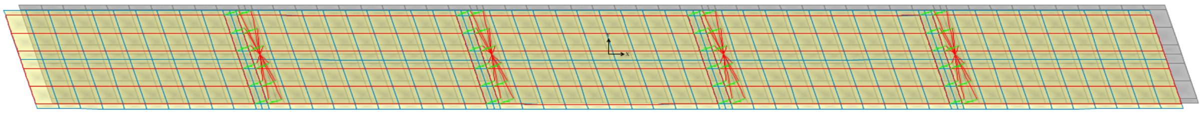

Figure 16: Prevailing longitudinal mode of Kosynthos bridge

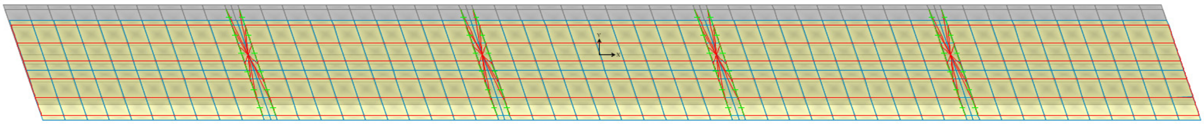

Figure 17: Prevailing transverse mode of Kosynthos bridge

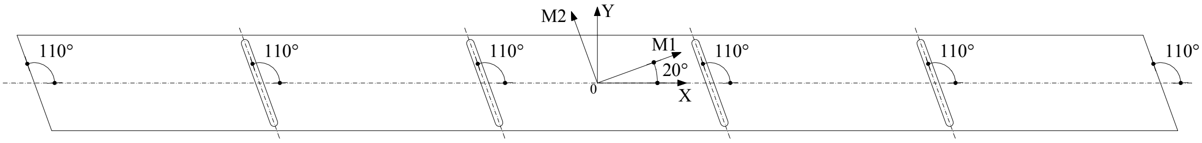

Figure 18: Geometric and modal principal axes of Kosynthos bridge

Regarding the periods of the two prevailing modes it is noticed (Table 6) that they differ only by 6.4%, something that is usual for bearing-supported bridges [8]. In addition, modal participating mass ratios are 100% for both prevailing modes along the corresponding modal principal axes, while with respect to the geometric principal axes they are $\varepsilon_x = \varepsilon_{M1} \cdot cos^2 20°$ = 88.3% and $\varepsilon_y = \varepsilon_{M1} \cdot sin^2 20°$ = 11.7% for the longitudinal prevailing mode and $\varepsilon_x = \varepsilon_{M2} \cdot sin^2 20°$ = 11.7% and $\varepsilon_y = \varepsilon_{M2} \cdot sin^2 110°$ = 88.3% for the prevailing transverse mode.

Prevailing mode	T [sec]	ε_x [%]	ε_y [%]	ε_{M1} [%]	ε_{M2} [%]
Longitudinal	1.376	88.3	11.7	100	0
Transverse	1.288	11.7	88.3	0	100

Table 6: Modal characteristics of the two prevailing modes of Kosynthos bridge

For force distribution consistent with the longitudinal and the transverse prevailing mode the bridge deforms only along the direction of modal principal axis *O-M*1 and *O-M*2, respectively. Thus, in order to apply the proposed methodology the modal principal directions are used instead of the corresponding geometric ones. Biaxial effects in the bridge bearings are ignored to simplify the procedure, keeping the modal principal axes constant; it is also noted that no information on shear and axial force interaction in bearings is available in the literature. The derived pushover curves, using the deck mass centre as control point, along the modal principal directions are linear because the behaviour of common elastomeric bearing is considered as linear.

Then, the proposed methodology is applied for excitation angles from 0° to 110°, and the results are evaluated against those from linear dynamic analyses. In the single-component case the CQC rule is used for the combination of the projections of displacements of the control point and of base shears, because the earthquake components acting along the modal principal directions have identical accelerograms, hence identical response spectra, and the correlation of modal responses is significant (the modal correlation coefficient [16] is ρ_M = 0.696). Conversely, for the dual-component case the SRSS rule is adopted, ignoring the correlation of the earthquake components acting along the modal principal directions and the correlation of modal responses.

The key results from the application of the proposed methodology, i.e. displacement δ_ξ of the control point (deck mass centre) along the earthquake direction and the shear deformation of the equivalent single bearing γ_{eq} along the geometric principal directions, against the corresponding ones from the dynamics analyses, are shown in Tables 7 and 8 for single- and dual-component seismic action, respectively.

Focussing first on the results for the simpler case of the single-component seismic action, it is seen from Table 7 that the differences for δ_ξ are small for all excitation angles and vary from 0.0% for a=110° to 7.3% for a=60°. With respect to γ_{eq}, differences are similar to those for δ_ξ, varying from 0.0% for a=110° to 5.5% for a=60°.

When the minor principal horizontal component of the earthquake is also taken into account, differences are larger than in the single-component case, still small enough to be acceptable, varying from 0.1% for a=110° to 15.5% for a=45° for the displacement of the control point, and from 0.2% for a=110° to 13.1% for a=30° for the deformation of the equivalent shear bearing. Furthermore, differences are maximized for excitation angles a=30°, 45° and 60°, i.e. the region where correlation between the earthquake components acting along the modal principal bridge directions is maximized, something anticipated due to the use of the SRSS rule where the aforementioned correlation is ignored.

α [°]	δ_ξ [m]		Difference	$\gamma_{eq}=\max[\gamma_{eq,x}, \gamma_{eq,y}]$		Difference
	Static	Dynamic	[%]	Static	Dynamic	[%]
0	0.01598	0.01648	3.0	0.1517	0.1568	3.3
15	0.01645	0.01654	0.5	0.1494	0.1511	1.1
20 (M1)	0.01649	0.01656	0.4	0.1464	0.1467	0.2
30	0.01636	0.01656	1.2	0.1378	0.1354	1.7
45	0.01579	0.01655	4.6	0.1177	0.1132	3.8
60	0.01533	0.01654	7.3	0.1302	0.1378	5.5
75	0.01551	0.01659	6.5	0.1491	0.1553	4.0
90	0.01619	0.01667	2.9	0.1585	0.1623	2.4
105	0.01672	0.01676	0.3	0.1577	0.1587	0.6
110 (M2)	0.01677	0.01676	0.0	0.1549	0.1549	0.0

Table 7: Comparison between static and dynamic analysis results – Single-component seismic action.

The derived pushover curves for various excitation angles between 0° and 110° with a step of 15° (including the directions of modal principal directions) are also linear since the behaviour of common elastomeric bearings is considered as linear for both the single- and dual-component case. The most critical and least critical directions regarding bridge failure (bridge ultimate point) are for a=90° ($A_{g,u,min}$=2.80g) and a=45° ($A_{g,u,max}$=3.80g) for single-component seismic action, and for a=30 ($A_{g,u,min}$=1.80g) and a=75° ($A_{g,u,max}$=2.02g), i.e. for the excitation angles where the maximum and the minimum value of the shear deformation of the equivalent single bearing is reached, for the dual-component action (Tables 7 and 8).

α [°]	δ_ξ [m]		Difference	γ_{eq}=max[$\gamma_{eq,x}$, $\gamma_{eq,y}$]		Difference
	Static	Dynamic	[%]	Static	Dynamic	[%]
0	0.01696	0.01790	5.2	0.2297	0.2306	0.4
15	0.01601	0.01692	5.4	0.2319	0.2225	4.1
20 (M1)	0.01651	0.01655	0.3	0.2299	0.2168	5.7
30	0.01858	0.01651	11.1	0.2483	0.2158	13.1
45	0.02101	0.01775	15.5	0.2433	0.2342	3.7
60	0.02129	0.01820	14.5	0.2285	0.2436	6.2
75	0.01927	0.01780	7.7	0.2220	0.2445	9.2
90	0.01698	0.01658	2.4	0.2318	0.2401	3.4
105	0.01629	0.01646	1.0	0.2321	0.2356	1.5
110 (M2)	0.01677	0.01678	0.1	0.2315	0.2318	0.2

Table 8: Comparison between static and dynamic analysis results – Dual-component seismic action.

Finally, generalized fragility curves for various excitation angles are derived (Figures 19 to 26) for both the single- and the dual-component case. The corresponding median damage state threshold values of peak ground acceleration are shown in Table 9. It is observed that in the case of single-component seismic action, for all damage states, the critical bridge direction is *a*=90°, while the less critical direction is *a*=45°. When the minor principal earthquake component is also taken into account the critical direction is *a*=30° while the least critical one is *a*=75°. It is also observed that for both in single- and dual-component seismic action the most critical and the least critical directions are similar with those resulting from the pushover curves, because the ultimate bridge point and the damage state definitions are based on the shear deformation of the equivalent single bearing.

α [°]	Singe-Component Seismic Action				Dual-Component Seismic Action			
	DS1	DS2	DS3	DS4	DS1	DS2	DS3	DS4
0	0.132	0.989	1.319	2.951	0.087	0.653	0.871	1.948
15	0.134	1.004	1.338	2.995	0.086	0.647	0.862	1.930
20 (M1)	0.137	1.025	1.366	3.058	0.087	0.653	0.870	1.947
30	0.145	1.089	1.452	3.249	0.081	0.604	0.806	1.803
45	0.170	1.274	1.699	3.803	0.082	0.616	0.822	1.840
60	0.154	1.152	1.536	3.437	0.088	0.656	0.875	1.959
75	0.134	1.006	1.342	3.003	0.090	0.676	0.901	2.016
90	0.126	0.947	1.262	2.824	0.086	0.647	0.863	1.931
105	0.127	0.951	1.268	2.839	0.086	0.646	0.862	1.929
110 (M2)	0.129	0.968	1.291	2.889	0.086	0.648	0.864	1.934

Table 9: Median values of damage state thresholds in terms of peak ground acceleration A_g for Kosynthos bridge, for all excitation angles

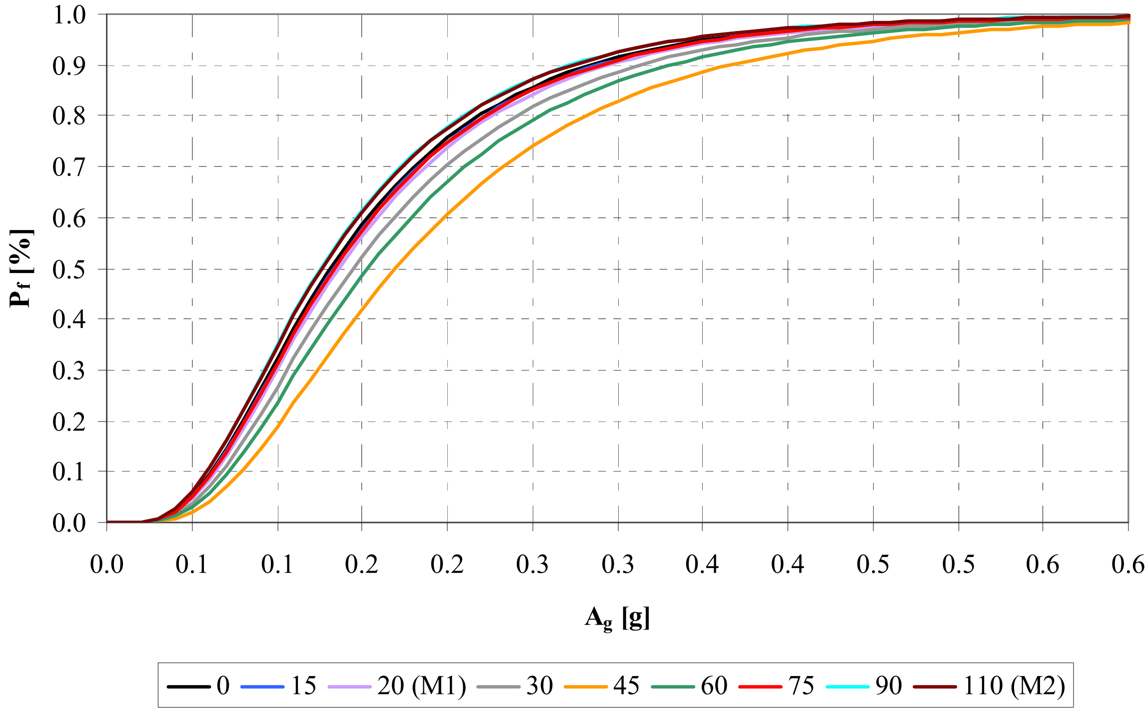

Figure 19: Generalized fragility curves of Kosynthos bridge for single-component seismic action, DS1: Minor/Slight Damage.

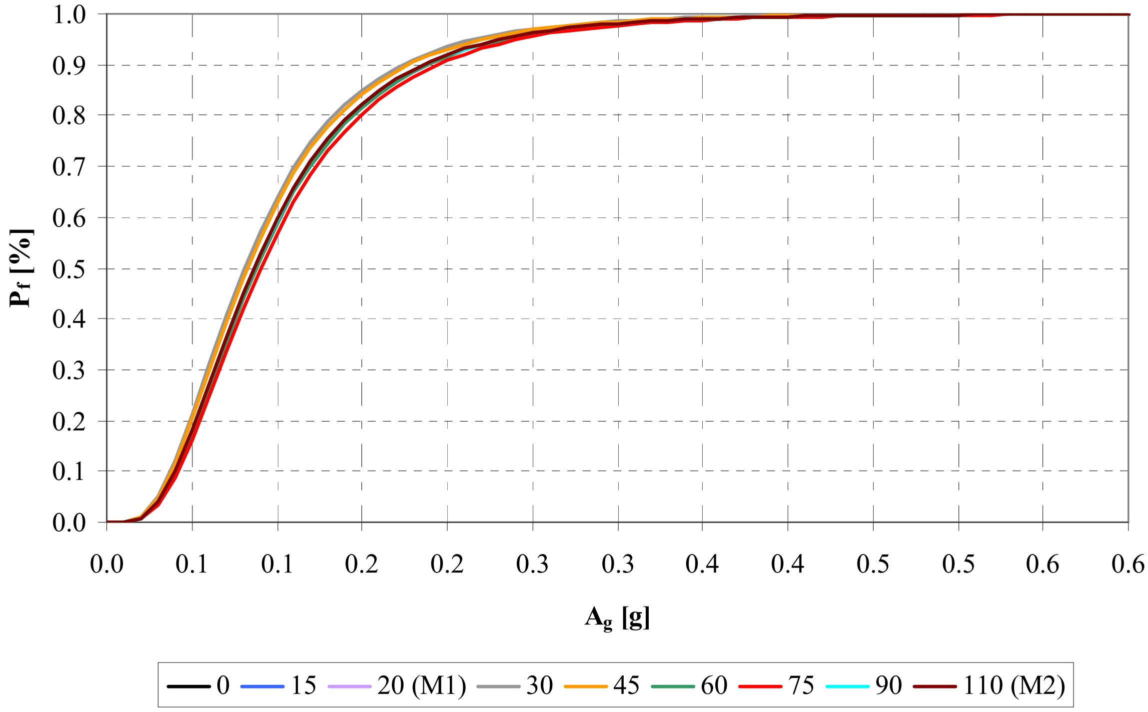

Figure 20: Generalized fragility curves of Kosynthos bridge for dual-component seismic action, DS1: Minor/Slight Damage.

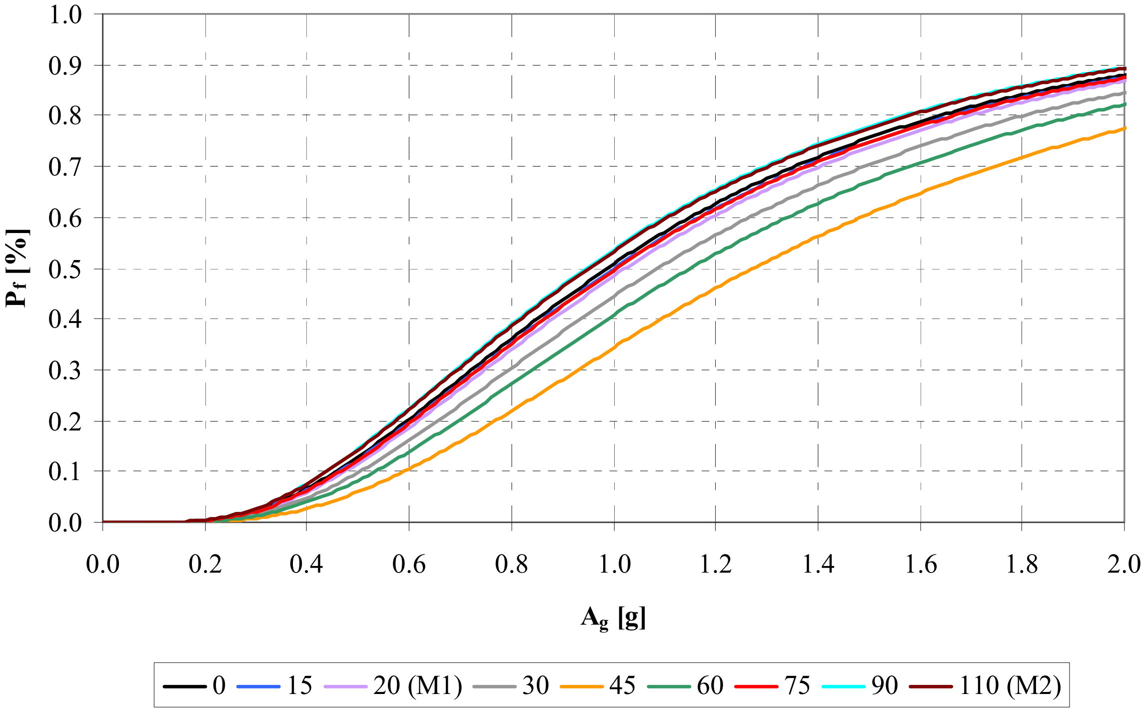

Figure 21: Generalized fragility curves of Kosynthos bridge for single-component seismic action, DS2: Moderate Damage.

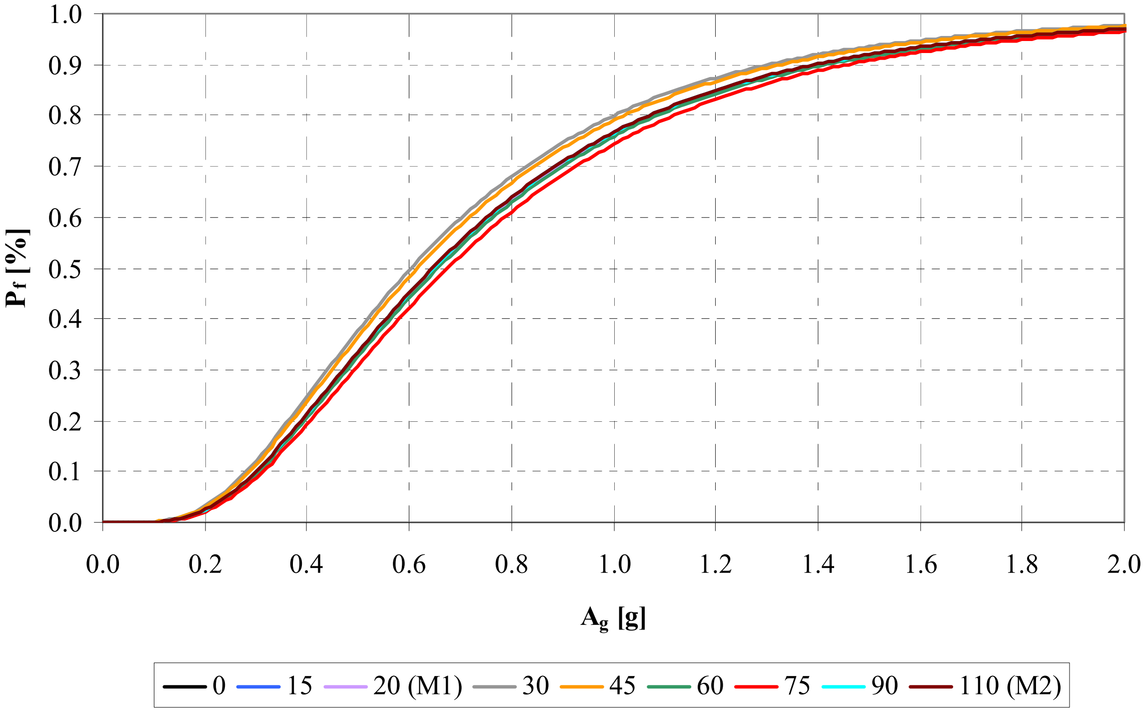

Figure 22: Generalized fragility curves of Kosynthos bridge for dual-component seismic action, DS2: Moderate Damage.

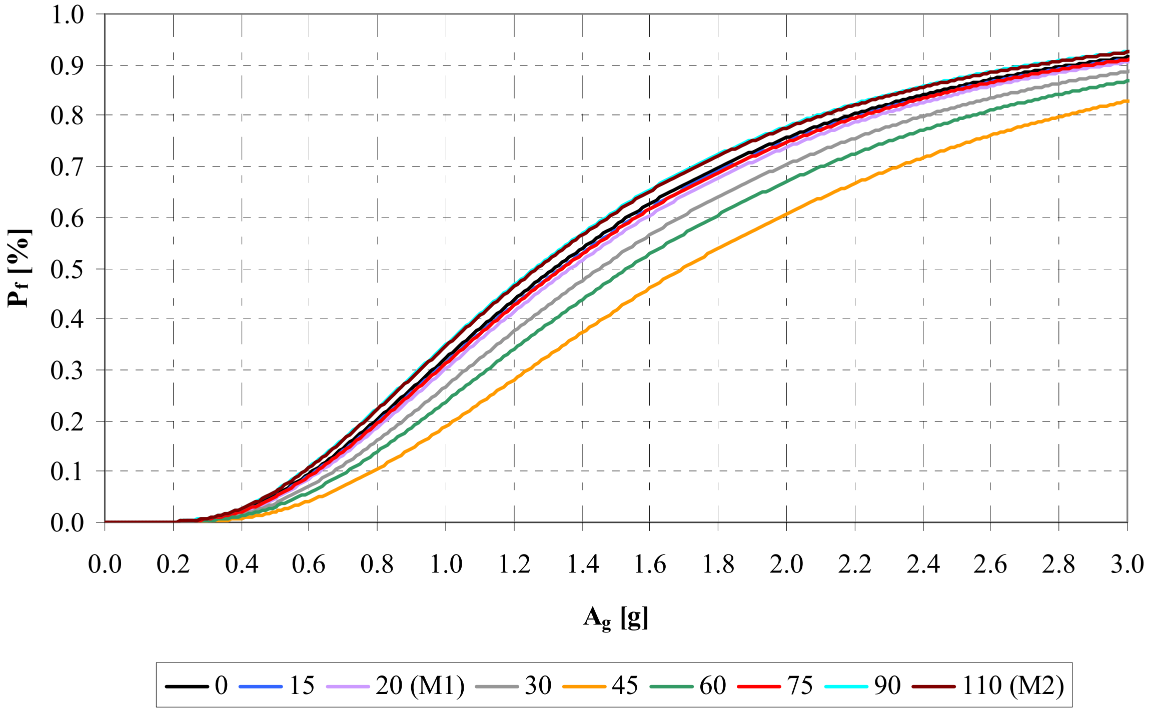

Figure 23: Generalized fragility curves of Kosynthos bridge for single-component seismic action, DS3: Major/Extensive Damage.

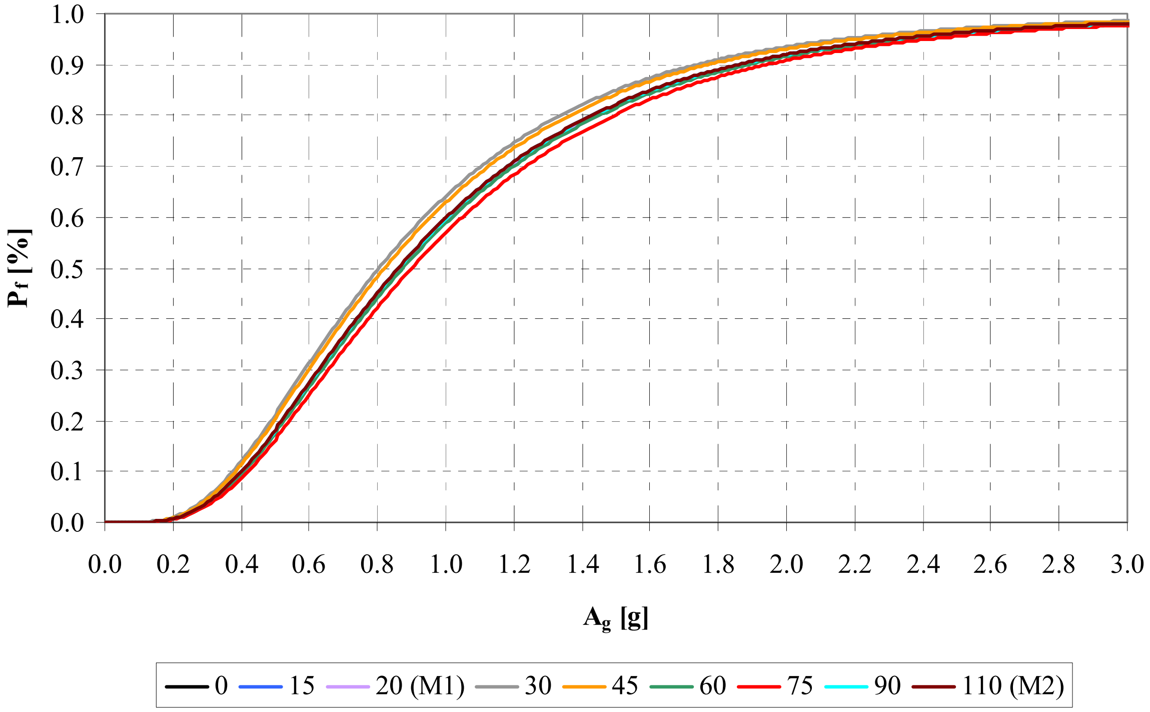

Figure 24: Generalized fragility curves of Kosynthos bridge for dual-component seismic action, DS3: Major/Extensive Damage.

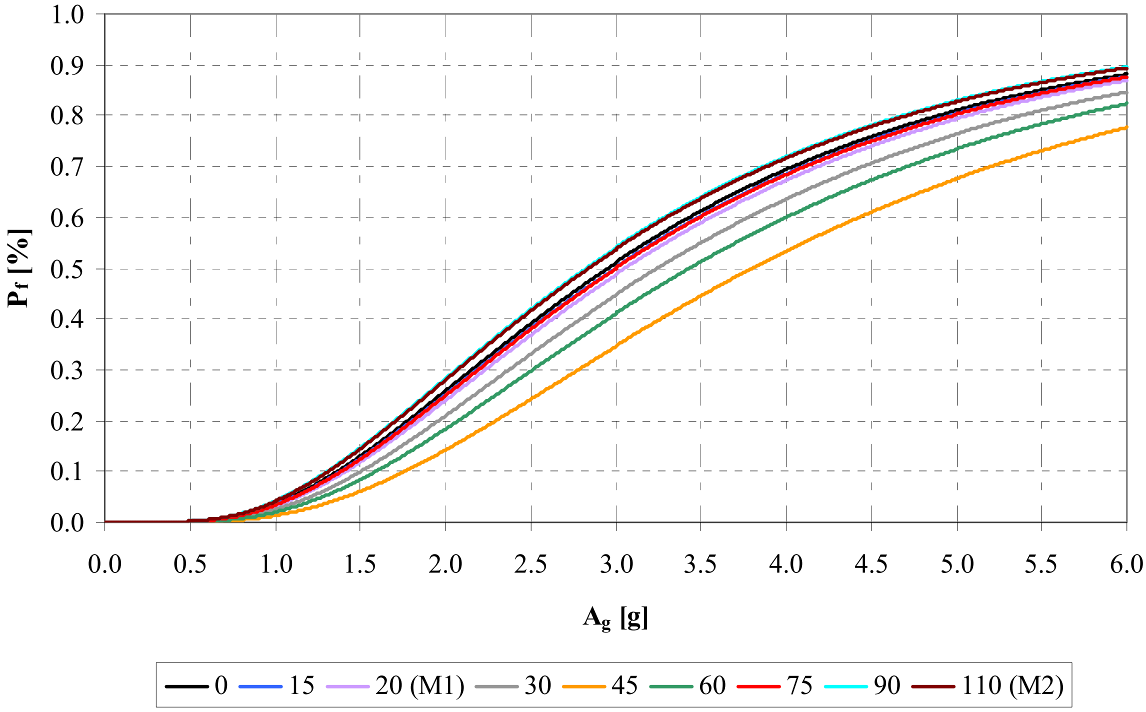

Figure 25: Generalized fragility curves of Kosynthos bridge for single-component seismic action, DS4: Failure/Collapse.

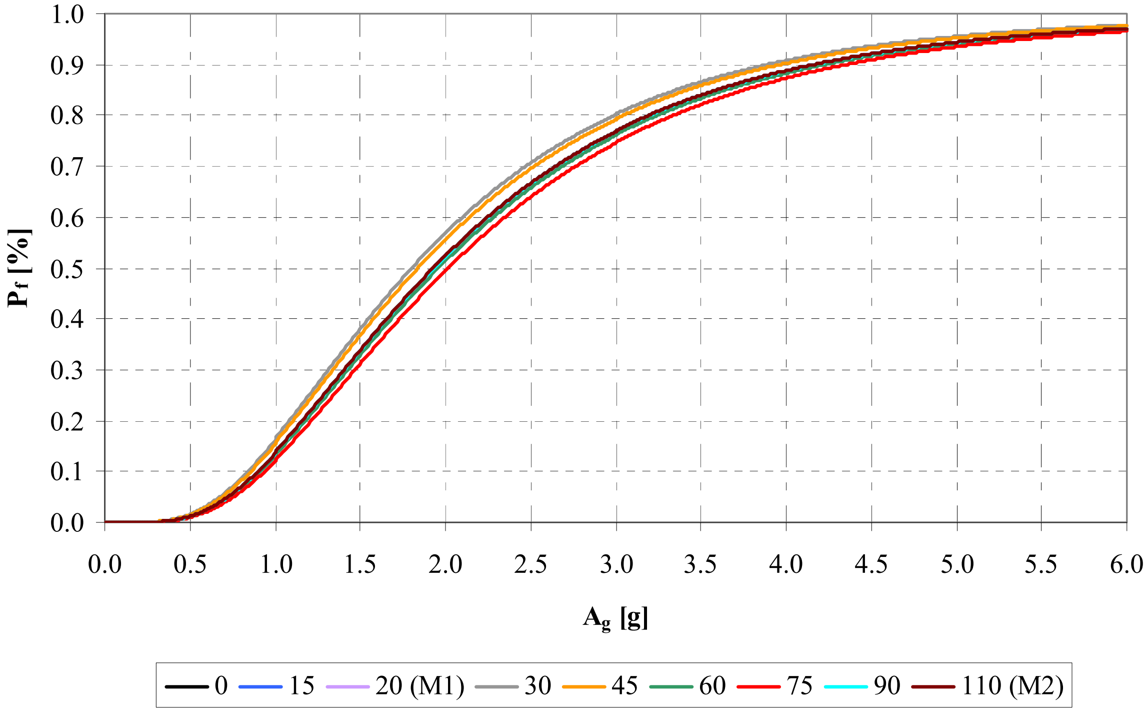

Figure 26: Generalized fragility curves of Kosynthos bridge for dual-component seismic action, DS4: Failure/Collapse.

It is important to point out that when the minor principal component is considered in the analysis, median threshold values of A_g are reduced by 41.6%, indicated a significant increase in bridge fragility, for all excitation angles. Finally, the maximum and the minimum median threshold values of A_g differ by 25.7% in the single-component case, while in the dual-component case the difference is reduced to 10.5%. This suggests that bridge fragility remains practically insensitive to the earthquake direction when the minor principal component of the earthquake is taken into account.

4 CONCLUDING REMARKS

A methodology for bridge fragility analysis under arbitrary angle of incidence of the earthquake, previously proposed by the authors [7], was extended here to take into account the minor principal horizontal component of the earthquake (dual-component seismic action). Furthermore, damage states for the case of bearing-supported bridges were redefined in a broader manner in order to take into account the interaction between biaxial shear and axial load, as well as all possible failure mechanisms, of the bearings. The proposed methodology was applied to an actual skew bridge for both single- and dual-component seismic action.

In skew bridges modal principal directions are not identical to geometric principal bridge directions, as in straight bridges, but they are rotated at a specific angle. According to the proposed methodology standard pushover analyses are performed for force distributions consistent with each of the prevailing bridge modes (longitudinal-transverse). Thus, modal principal bridge directions are used for the application of the proposed methodology. In the single-component case the CQC rule is used for the combination of the projections of the control point displacement and of the base shear, due to the significant correlation of modal responses in bearing-supported bridges. Conversely, in the dual-component case the SRSS rule is used, ignoring the correlation between the modal responses and also the earthquake components acting along the modal principal bridge directions. The expected differences in the range of excitation angles wherein the correlation between the earthquake components acting along modal principal direction is maximized are reasonably small (15%), showing the validity of the use of the SRSS rule in the dual-component case, for all excitation angles.

From the derived generalized fragility curves for arbitrary angle of incidence of seismic action it was seen that when the minor principal horizontal component is taken into account bridge fragility is significantly increased (more than 40% in the studied skew bridge), whereas it remains almost unaffected by the angle of incidence of the seismic action.

REFERENCES

[1] N.I. Basöz, A.S. Kiremidjian, *Evaluation of Bridge Damage Data from the Loma Prieta and Northridge, California Earthquakes. Technical Report MCEER-98-0004*, Multidisciplinary Center for Earthquake Engineering Research (MCEER), State University of New York at Buffalo, 1998.

[2] CSI, *CSI Analysis Reference Manual for SAP2000®, ETABS®, and SAFE®*, Computers & Structures Inc., Berkeley, California, USA, 2009.

[3] FEMA-NIBS, *Multi-Hazard Loss Estimation Methodology - HAZUS-MH MR4: Earthquake Model Technical Manual*, Federal Emergency Management Agency (under a contract with the National Institute of Building Sciences), Washington, D.C., 2003.

[4] K.R. Karim, F. Yamazaki, A simplified method of constructing fragility curves for highway bridges. *Earthquake Engineering & Structural Dynamics*, **32,** 1603-1626, 2003.

[5] O.A. López, J. J. Hernández, R. Bonilla, A. Fernández, Response spectra for multicomponent structural analysis. Earthquake Spectra, **22**, 85-113, 2006.

[6] K.R. Mackie, B. Stojadinović, R-factor parameterized bridge damage fragility curves. *Journal of Bridge Engineering*, *ASCE*, **12**, 500-510, 2007.

[7] I.F. Moschonas, A.J. Kappos, Generalized fragility curves for bridges, for arbitrary angle of incidence. *COMPDYN 2009*, CD-ROM Proceedings: Paper No. 186, Rhodes, Greece, June 22-24, 2009.

[8] I.F. Moschonas, A.J. Kappos, P. Panetsos, V. Papadopoulos, T. Makarios, P. Thanopoulos, Seismic fragility curves for greek bridges: methodology and case studies. *Bulletin of Earthquake Engineering*, **7**, 439-468, 2009.

[9] B.G. Nielson, R. DesRoches, Seismic fragility methodology for highway bridges using a component level approach. Earthquake *Engineering & Structural Dynamics*, **36**, 823-839, 2007.

[10] J.E. Padgett, R. DesRoches, Methodology for the development of analytical fragility curves for retrofitted bridges. *Earthquake Engineering & Structural Dynamics*, **37**, 1157-1174, 2008.

[11] G. Panagopoulos, A.J. Kappos, Bilinear idealization of force deformation diagrams. *16th Hellenic Conference on Concrete*, CD-ROM Proceedings: Paper No. 121105, Pafos, Cyprus, October 21-23, 2009 (*in Greek*).

[12] M. Shinozuka, S. Banerjee, S.H. Kim, *Statistical and Mechanistic Fragility Analysis of Concrete Bridges*. *Technical Report MCEER-07-0015*, Multidisciplinary Center for Earthquake Engineering Research (MCEER), State University of New York at Buffalo, 2007.

[13] M. Shinozuka, M.Q. Feng, H. Kim, S. Kim, Nonlinear Static Procedure for Fragility Curve Development. *Journal of Engineering Mechanics*, *ASCE*, **126**, 1287-1295, 2000.

[14] B. Song, J.S. Pan, Q. Liu, Study on critical angle to the seismic response of curved bridges based on pushover method. *14th World Conference on Earthquake Engineering*, CD-ROM Proceedings: Paper No. 14-0120, Beijing, China, October 12-17, 2008.

[15] B. Song, R. Yang, H. Shan, Determination of critical angle of seismic wave in safety evaluation of curved bridges. *International Symposium on Safety Science and Technology*, 2319-2324, Changsha, Hunan, China, October 12-17, 2006.

[16] E.L. Wilson, A. Der Kiureghian, E.P. Bayo. A replacement for the SRSS method in seismic analysis. *Earthquake Engineering & Structural Dynamics*, **9**, 187-192, 1981.

COMPDYN 2011
III ECCOMAS Thematic Conference on
Computational Methods in Structural Dynamics and Earthquake Engineering
M. Papadrakakis, M. Fragiadakis, V. Plevris (eds.)
Corfu, Greece, 25–28 May 2011

PRELIMINARY DESIGN OF SEISMICALLY ISOLATED R/C HIGHWAY OVERPASSES – FEATURES OF RELEVANT SOFTWARE AND EXPERIMENTAL TESTING OF ELASTOMERIC BEARINGS

George C. Manos[1], **Stergios A. Mitoulis**[2], **and Anastasios G. Sextos**[2]

[1] Laboratory of Experimental Strength of Materials, Department of Civil Engineering
Aristotle University of Thessaloniki
e-mail: gcmanos@civil.auth.gr

[2] Aristotle University of Thessaloniki
mitoulis@ civil.auth.gr

[2] Aristotle University of Thessaloniki
asextos@ civil.auth.gr

Keywords: bridges; seismic isolation; knowledge-based systems; software; preliminary design; testing of elastomeric bearings

Abstract. *The preliminary design of seismically isolated R/C highway overpasses is the target of a software based on the current design provisions of Eurocode 8 (Part 2) as well as on engineering decisions included in the expert system. The features of this expert system, which is aimed to facilitate the design of a highway overpass by isolating its deck with the inclusion of elastomeric bearings, are presented and discussed. For such an upgrade scheme a number of successive checks is necessary in order to select an optimum geometry of the bearings. The developed software includes a series of checks provided by Eurocode 8 (Part 2), in order to ensure the satisfactory seismic performance of the selected upgrade scheme. In doing so, the software accesses a specially created database of the geometrical and mechanical characteristics of either cylindrical or prismatic elastometallic bearings which are commercially available; this database can be easily enriched by relevant data from laboratory tests on isolation devices. The basic assumptions included in the software are (a) modeling the seismic response of the bridge overpass as a SDOF system, and (b) only the longitudinal direction response is considered; it is common practice for seismically isolated bridge systems to restrain the transverse movement of the deck by stoppers. Moreover, the results form a number of tests performed in the Laboratory of Strength of Materials and Structures of Aristotle University, verified the quality of the production process of a local producer of elastomeric bearings subjecting production samples to the sequence of tests specified by International Standard ISO 22762-1 (2005). Strain amplitudes larger than 250% resulted in the debonding of the elastomer from the steel plating. Artificial aging resulted in a small increase of the axial (vertical) stiffness and a small decrease of the shear (horizontal) stiffness of the tested bearings. More specimens must be tested to validate further these findings.*

1 INTRODUCTION

Seismic design of structures, in general, involves the conceptual, preliminary and final design [1], the latter being typically prescribed in detail, for most conventional structures, by the existing seismic code requirements. The conceptual design, however, is not, and cannot easily be, encapsulated in codes' provisions; hence, it relies heavily on engineering judgment, expertise and experience. It is therefore quite often the case that the final design, although completely covered by detailed seismic code provisions, is essentially driven by the choices initially made. The same design process described above is also followed in the case of bridge structures, independently of whether they are typical, short highway overpasses or more complex, long and/or curved bridges. Such bridges, although appearing to be relatively simple structures compared to some irregular buildings, may be designed with numerous different configurations depending on a set of performance (in terms of safety and serviceability), economic (including maintenance), constructability or even aesthetic criteria [2]. This gives the designer the flexibility to choose among various structural configurations, and especially among different strategies for the support of the deck on the abutments and piers; a decision related to the use of monolithic or bearing-type connections. On the other hand, the process to select the desired dimensions and the number of the bearings to be used at each support is often time consuming, as it commonly leads to iterative calculations and numerical analyses [3] and multiple design checks against target code-based criteria concerning both the maximum bearing strain and the overall performance of the bridge structure [4][5].

In general though, it can be claimed that no comprehensive procedure has been presented to this date for the optimal (i.e., cost-effective), preliminary design of seismically isolated highway overpasses and bridges. To this end, the present study aims to facilitate the designer of typical overpass configurations [6] in selecting from a smaller, filtered sample of "eligible" bearing sections, and quickly spot the preferable combination of bearing size, type, number, location and cost at minimal computational effort. The decision-making system developed is based on multiple code-based performance criteria [4][5], statistics arising from the construction of 40 km of bridges along the 680 km, newly built, Egnatia Highway in northern Greece [7], engineering judgment and recent research findings as well as ad-hoc laboratory testing, conducted for the purpose of this study. The particular process is also integrated and implemented in a user-friendly software, which permits the quick selection of the bearing scheme for given structural systems and seismic conditions. An effort was made to cover the majority of realistic overpass and simple bridge configurations, and a wide variety of steel laminated elastomeric bearing sections which are most commonly adopted for practical purposes [8][9][10]. The structure of both the Knowledge-Based Expert System (KBES) and the software developed for preliminary design of base-isolated overpasses, together with their validation against more rigorous numerical analysis procedures, is presented in the following.

2 PRINCIPLES OF SEISMIC ISOLATION OF BRIDGE SYSTEMS AND CURRENT CODE PROVISIONS

2.1 Preliminary design

In Europe, seismic isolation of bridges is performed according to the Eurocode 8 - Part 2 [4] and more specifically according to clause 7, which refers to the basic requirements and compliance criteria, analysis procedures and the verification of the isolating system. Annexes J and K of the Eurocode 8-Part 2 also make reference to the laboratory tests required in order to determine the variation of the design properties of the seismic isolator units and to verify the elastomeric bearings under seismic design situations. Similar provisions exist in the

United States. [5]. The Bridge Engineer is also given the choice between commercially available bearings or any other, experimentally tested, rubber bearing suitable for seismic isolation.

In most practical cases, the preliminary design of seismically isolated bridges can be performed using the response spectrum analysis framework prescribed by Eurocode 8, for a simple rigid deck finite element model which adequately provides a first estimate of the bearings' size, number and configuration. It is noted herein, that the rigid deck model is valid for most of the straight isolated bridges with continuous deck, at least in the longitudinal direction, in which the deck actually "floats" along the isolation pier-deck interface. In the transverse direction, however, the deck is in most cases restrained by stoppers (i.e., seismic links) which prevent excessive transverse deck displacements. In both cases though, as long as the displacements are kept below a prescribed magnitude, the system can be reliably assumed to be a single degree of freedom (SDOF).

The process for the design of the seismic isolation of the above bridges, considering a SDOF response, usually follows a series of simple steps, which are not prescribed by most codes [4][5] with the exception of the Indian code specifications [11], but results from fundamentals of the dynamics of structures:

a) calculation of the weight of the bridge per unit length according to the code provisions for the combination of the dead and permanent loading of the bridge (i.e., according to [12] and partly from the variable vertical loading (i.e., 0.2 for highway or 0.3 for railway bridges according to [4],

b) initial selection of the bearings' cross section, the total height of the elastomer and the number of the bearings per support,

c) calculation of the total effective stiffness K_{tot} of the isolation system in the longitudinal direction of the bridge,

d) calculation of the effective longitudinal period of the bridge as $T_{eff} = 2 \cdot \pi \cdot \sqrt{\frac{m_{tot}}{K_{tot}}}$, where m_{tot} is the total mass of the bridge,

e) calculation of the seismic displacement $d_{Ed,x}$ of the deck in the longitudinal direction, by using the elastic spectrum of the code, according to Eurocode 8 specific guidance for seismically isolated bridges and

f) performing a final check to judge the bearing adequacy according to code-based performance criteria.

The most common engineering practice for the final design of the aforementioned bridge systems is given in the following with emphasis on the commonly used Low Damping Rubber Bearings (LDRB).

2.2 Final design

The techno-economical selection of an LDRB bridge isolation system is made so as to satisfy all the design constraints arising from safety-oriented code provisions, but also to maximize performance at the lowest possible cost. This is a complicated problem, and depending on the structural configuration of the bridge, the designer has many design alternatives which require an iterative procedure, involving the repeated analysis and the design of the bridge isolation system until both criteria, i.e. code requirements that ensure both safety and cost-effectiveness, are simultaneously satisfied. Typically, the designer selects an acceptable isolation system for the bridge without considering all the possible combinations of bearing type, size and configuration, and without knowing whether the system selected was the best possible balance between cost and performance. Furthermore, most bridge isolation systems use bearings that are manufactured by international companies. In addition, due to the complexity of the above process and although permissible according to the codes, in most cases the designers are reluctant to use experimentally tested products of the local industry, hence, they lean primarily towards commercially manufactured products of the international market.

3 THE PROPOSED KNOWLEDGE-BASED DECISION MAKING SYSTEM

The methodology presented herein for the preliminary design of base isolated bridges is described in detail. The methodology applies to all bridges isolated with low damping steel laminated elastomeric bearings (LDRBs), with the exception of cases where monolithic pier-deck or abutment-deck connections are combined with bearing-type pier-deck connections. The verification of the methodology is given in section 6 of the paper and shows satisfactory results in straight bridges. The structure of the KBES can be summarized in the following three steps, which also conceptually comply with those proposed by [13].

3.1 Step 1: User Input

A database of commercially available and experimentally tested elastomeric bearings is first compiled consisting of bearings' properties, (i.e. shear stiffness G), shape (i.e., rectangular or circular), rubber and steel plate thickness, height, and width, overall area (A) and dimensions (B_x, B_y or D). Possible bridge structural systems, characterized by different number and length of middle and central spans (L_1 or L_2), that define the total bridge length (L_{tot}) and the mass per unit length (m), as well as initial configurations of n bearings are herein defined by the designer. Seismic hazard is also considered with the most commonly used parameters in mind, i.e. the design seismic acceleration (S_a), soil type and the importance factor of the bridge under study.

3.2 Step 2: Decision process

The second step of the methodology includes the necessary and basic calculations and checks for the seismically isolated bridge. The designer decides the acceptable range for bearing compression (σ_e) where a minimum of 2.0 MPa and a maximum value of 5.0 MPa are proposed by the system itself according to [14]. The limit for the bearing's compression ensures that friction will be adequate to avoid the sliding of the bearing during seismic shear loading, whereas the upper limit is given to ensure that the shear strain due to the interaction between the neoprene and the steel plates under compression will remain at acceptable limits (i.e., $\varepsilon c,d \leq 2.5$ according to Eurocode 8 Part 2). It is noted that this limitation is optional, in the sense that it is not explicitly imposed by the codes, however, it is good common practice. For instance, the vast majority of the bearings used in isolated bridges built along the Egnatia Highway have been designed not to exceed 5.0 MPa in compression. As such, the compression criterion is adopted as the first filter applied to all the bearings checked.

Based on the mass of the bridge, the compression stress (σ_e) is derived as a ratio of the total vertical load acting on each bearing (P_i) over its own area (A). The criterion proposed by Eurocode 8-Part 2 for the calculation of the maximum effective normal stress of the bearing is herein adopted:

$$\sigma_e \leq \frac{2 \cdot b_{min}}{3 \cdot t_t} \cdot G \cdot S_{min} \tag{1}$$

where σ_e is maximum effective normal stress of the bearing, b_{min} is the minimum dimension of the bearing, t_t is the total thickness of the elastomeric, G the shear modulus of the elastomer and S_{min} the minimum shape factor of the bearing layers.

It is noted that this criterion has to be applied to every single eligible bearing, in this case, stored in an external database as will be described in Section 4.1. All bearings that pass this filter are marked as “potentially eligible” and proceed to the next check.

By respecting the desired configuration of the bearings as set by the designer at the beginning of the process, for each bearing that has passed the previous check, the total isolation system stiffness (K_{tot}), its effective period (T_{eff}) and spectral displacement (d_{Ed}) are defined and each bearing is separately checked against seismic actions. The criterion used herein is strain-based, checking the horizontal shear deflections of the bearing given the computed level of vertical loading.

All the bearings that passed the above initial screening process are checked against a set of code-prescribed criteria, involving the normalized shear strain of the bearing due to (a) seismic loading, (b) vertical loading and (c) rotation. Herein, the criterion prescribed in Eurocode 8 is adopted, according to which the maximum total shear strain ε_{td} of the equivalent single degree of freedom system of the seismically isolated bridge should not exceed:

$$\varepsilon_{t,d} \leq 6.0 \tag{2}$$

where:

$$\varepsilon_{t,d} = \varepsilon_{s,d} + \varepsilon_{c,d} + \varepsilon_{a,d} \tag{3}$$

and $\varepsilon_{s,d}$ is the shear strain due to the total design seismic displacement, $\varepsilon_{c,d}$ is the shear strain due to compression and $\varepsilon_{a,d}$ is the shear strain due to angular rotation. The latter is clearly the less critical [4]. Shear strain due to the vertical load combination $\varepsilon_{c,d}$ is of the order of 0.70 for a maximum effective normal stress of the bearing that remains below 5.0 MPa as described above.

The second criterion [4] is that the seismically induced shear strain $\varepsilon_{s,d}$ should be limited to:

$$\varepsilon_{s,d} \leq 2.0 \tag{4}$$

The shear strain of the bearing due to seismic load is computed again for the equivalent single degree of freedom system of the isolated bridge based on its dynamic characteristics and seismic response. Equation (4) can be written in terms of the displacement d_{Ed} of the system under study as:

$$\varepsilon_{s,d} = \frac{d_{Ed}}{t_t} \tag{5}$$

where t_t is the total thickness of the elastomeric and $d_{Ed} = \sqrt{d^2_{Ed,x} + d^2_{Ed,y}}$ $d_{Ed} = \sqrt{d^2_{Ed,x} + d^2_{Ed,y}}$

the SRSS combination o the two horizontal components of seismic displacement. It is noted that, in many practical cases, $d_{Ed,y}$ is negligible, as the transverse movements of the deck are restrained by seismic links. Moreover, it was found that the shear strain due to the total design seismic displacement expressed in eq. (5) is more critical than the $\varepsilon_{t,d} \leq 6.0$ criterion of eq. (2) at least for cases where the compressive stress σ_e is kept within the proposed limits, (i.e., $2.0 < \sigma_e < 5.0$ MPa).

4 EXPERIMENTAL TESTING

An experimental investigation was carried out aiming at establishing the mechanical characteristics of elastomeric bearings locally produced. For this purpose a series of standard tests were performed at the Laboratory of Strength of Materials and Structures of Aristotle University according to the International Standard ISO 22762-1 (2005). Initially, these tests were used as qualification tests for the materials used in the production; that is the neoprene, the steel plates and the adhesion materials and processes. These tests are presented in a summary form and discussed in what follows. Next, in an effort to study the influence of certain parameters in the mechanical characteristics of these elastomeric bearings, the vulcanization process was investigated. Finally, compression and shear tests were also conducted with elastomeric bearings as will be presented in the following subsections.

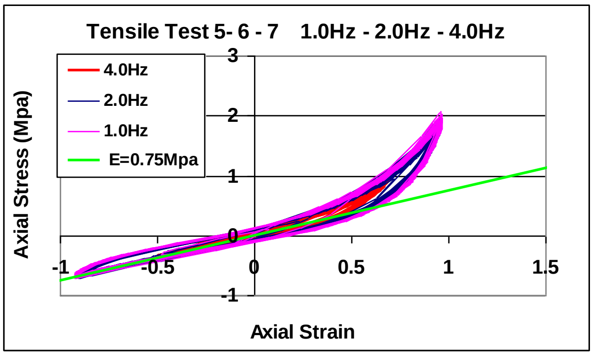

Figure 1a. Tensile cyclic tests with 200% strains

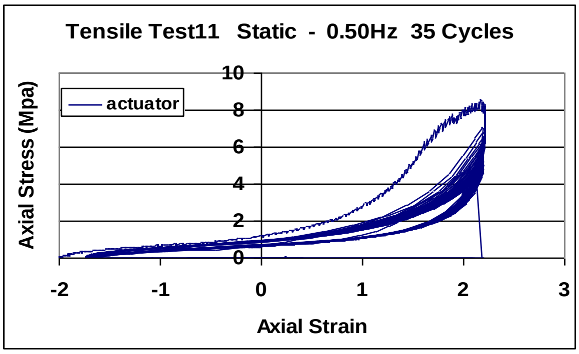

Figure 1b. Tensile cyclic tests with 400% strains that lead to the fracture of the specimen

4.1 Tensile cyclic tests of the neoprene

Eleven tests were performed with frequencies varying from 0.25Hz to 4.0Hz. At the end of the series the specimens failed at maximum axial strain 400% and maximum axial stress 8MPa. At fracture the specimen underwent approximately 500 cycles. The approximate Young’s modulus was found to be equal to 0.75MPa. At high levels of axial strain (more than 100%) this value was more than double. At even higher levels of strain this value was further increased. At the initial static load-unload cycles there was a considerable difference in the load-unload path that tended to become less pronounced when the loading cycles increased in numbers. There was no noticeable influence on the behavior of the specimen arising from the frequency of the loading. The cyclic loading was introduced from an initial condition that was the result of preloading it with 50% of the target maximum strain level. Figure 1a depicts the test results for maximum target strain 200% whereas figure 1b depicts similar results for maximum target strain 400% which resulted in the fracture of the test specimen.

4.2 Shear cyclic tests of unit slices of elastomeric bearings

Shear cyclic tests of a specimens made of two unit slices were performed according to the International Standard ISO 22762-1 (2005). For the prismatic specimens each unit slice included a layer of elastomer and two steel plates from a bearing with plan dimensions 200mm x 200mm. The dimensions of each slice of elastomer were 200mm x 200mm and 7.62mm thickness for the orthogonal specimens (figure 2a); for the cylindrical specimens the diameter of the elastomer was 250mm and its thickness 7.62mm (figure 2b) with the appropriate steel plating. Thus, the tested specimens were formed by two slices of elastomer and four steel plates. Each steel plate had a thickness of 2.94mm and sufficient dimensions in plan to have the elastomer attached and to provide enough room for the loading arrangement. Figure 2b and 3a depicts the used loading arrangement. The final slice-specimen was of relatively large dimensions as to be in plan a one to one representations of elastomeric bearings produced by the same process; that is employing identical unit slices and building it up at the desired height with the appropriate number of such unit slices [14]. A dynamic actuator of considerable displacement and force capability was utilized to introduce a series of cyclic shear strain imposed loading sequences to the specimens (see figures 3b). Initially, the series of tests did not exceed a maximum strain level of 100%. Next a series of similar tests introduced maximum shear strain levels larger than 100% up to the failure of the specimen that appeared in the form of debonding of the elastomer from the steel plating. In what follows typical tests results are presented in brief.

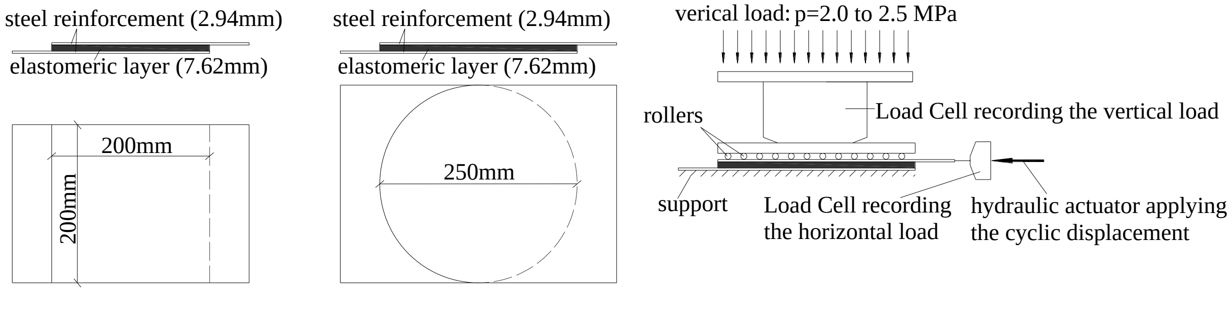

(a) (b) (c)

Figure 2: Cross sections and plan views of: (a) Rectangular specimens (200x200x13.5(7.62)mm) and (b) cylindrical specimens (Ø250x13.5(7.62)mm), (c) testing arrangement.

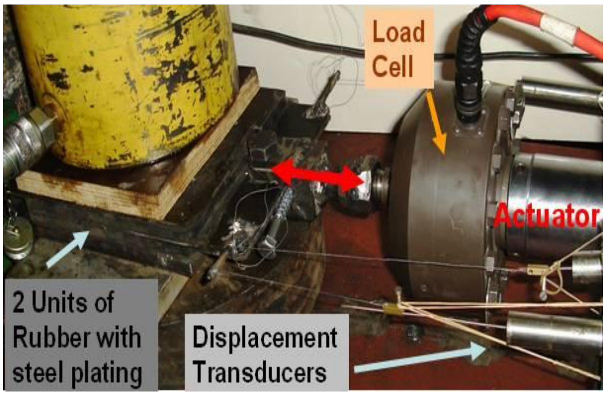

Figure 3a. Loading arrangement of a unit slice.

Figure 3b. Loading arrangement of a unit slice with the simultaneous application of a compressive stress field.

4.2.1. Shear cyclic tests with strain amplitude lower than 100%

Both orthogonal as well as cylindrical geometry elastomeric specimens were tested during this sequence. Throughout all the tests the applied load producing the shear strains was monitored together with the corresponding displacements of the specimen that were utilized to deduce the applied shear stress and shear strain levels to the specimen. At the same time the applied vertical load, normal to the slices of neoprene, was recorded and checked for any significant variations; the objective in this case being to keep the vertical load almost constant at the range of 2.0 to 2.5 MPa throughout all tests. These cyclic tests were performed for the following combinations: 3-11 cycles for each test, with temperature 23 degrees Celsius and cyclic loading varying with frequency 0.2Hz. The shear strain amplitude was varied from 5% to

75% in the following steps: 5% (0.38mm), 10% (0.76mm), 25% (1.91mm), 50% (3.81mm), and 75% (5.72mm). An increase in the shear stiffness was observed when the cyclic shear strain became larger than 75%. Subsequent tests that followed the initial tests with shear strain amplitudes varying again in the range from 5% to 75% exhibited an increase in the shear stiffness when they are compared with the results of the initial shear tests. Again, the specimen exhibited a stable performance throughout the increasing shear strain amplitude from 5% to 75% during these subsequent tests. Additional tests were also performed with the same specimens whereby the studied variable this time was the frequency of imposing the shear strain, keeping the maximum target strain amplitude constant and equal to 75%. The corresponding results are depicted in figure 4a. In this case the specimen's performance was examined for loading frequencies equal to 0.1Hz, 0.5Hz and 1.0Hz. As can be seen from this figure no significant variation in the performance of the specimen could be observed from the obtained response whereby the loading frequency was varied from 0.1Hz to 1.00Hz. An additional specimen of the same geometry and produced by the same process was tested by the loading arrangement shown in figure 3b. This time, apart from imposing the shear strain levels of continuously increasing amplitude, the specimen was placed under a constant compressive stress field normal to the horizontal plane of the elastomer. This stress field corresponded to an equivalent compressive stress equal to 2.4MPa. The frequency of the cyclic load was equal to 0.5Hz and the shear strain amplitude was continuously increasing from 10% to 75%. The summary results of this test are depicted in figure 4b. An increase in the stiffness and a decrease in the equivalent damping ratio is evident when the specimen is subjected to the previously described compressive stress field of 2.4MPMa equivalent uniform stress normal to the elastomer. However, this observation should not be generalized; as was shown from the measurements of another investigation (Ryan et. al. 2004, Manos et. al. 2007) further increase in this compressive stress field has the opposite effect.

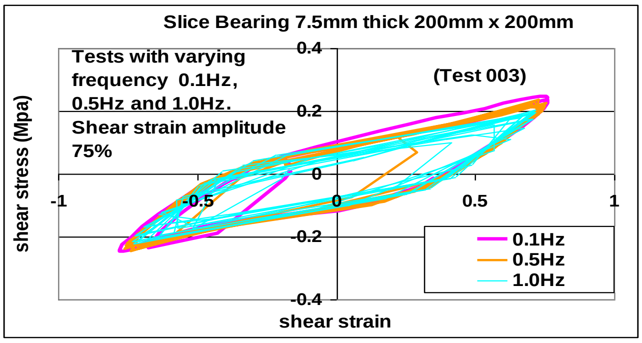

Figure 4a. Shear cyclic test results for shear strain amplitude 75% and frequencies 0.1Hz, 0.5Hz and 1.0Hz

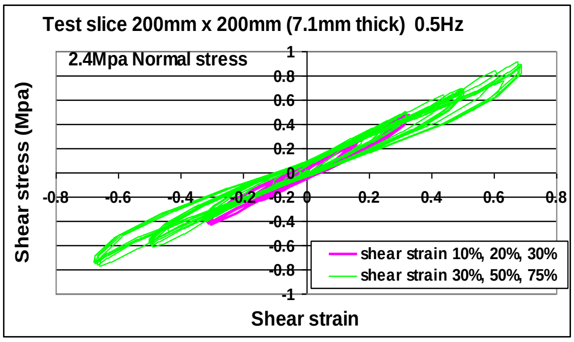

Figure 4b. Shear test results for frequency 0.5Hz and shear strain amplitude from 5% to 75% slice with the simultaneous application of a compressive stress field.

Similar observations can be drawn from the shear test results obtained from the cylindrical geometry specimens. Typical shear test results are depicted in figure 5 whereby a cylindrical bearing slice specimen d=250mm with a variation on the shear strain amplitude up to 90% and the normal stress amplitude (σ) from 0 to 2.0 MPa.

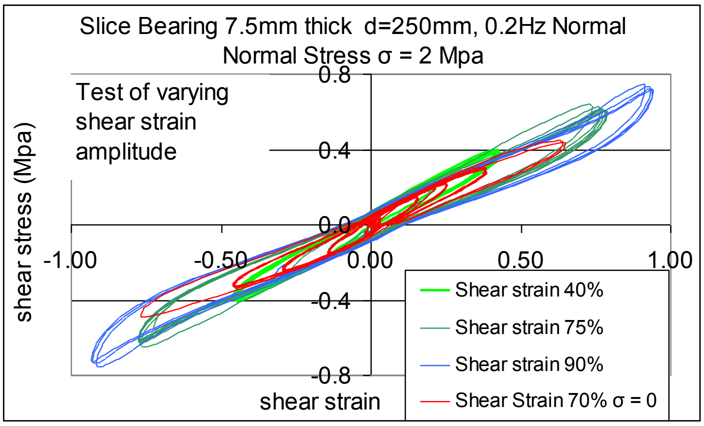

Figure 5: cylindrical bearing slice specimen d=250mm with a variation on the shear strain amplitude up to 90% and the normal stress amplitude (σ) from 0 to 2.0 MPa.

4.2.2. Shear cyclic tests with strain amplitude higher than 100%

The previously described loading sequences were repeated again with unit slice elastomeric specimens of the orthogonal and cylindrical geometry being loaded this time with shear strain amplitudes higher than 100% up to the failure of the specimen. Two distinct loading arrangements were again adopted. First, the shear strains were introduced without the application of compressive load normal to the horizontal plane of the elastomer (figures 2c and 6a) whereas in the second case a vertical load was applied and kept constant producing an equivalent uniform compressive stress normal to the plane of the elastomer in the range of 2.0 to 2.5 MPa (figure 2c and 3b). Figure 6b depicts a typical failing mode during this loading process without the presence of the compressive stress field. Figure 7a depicts the load-unload behavior of this test with large shear strains without the application of compressive normal stress; figure 7b shows the resulting debonding of the elastomer from the steel plating at the end of this loading sequence. The levels of shear strain ranged from 100% and gradually increased to 275%. It can be observed that for shear strain levels lower than 200% the specimen's behavior remains stable even for this demanding test that corresponds to an elastomeric bearing that does not have the beneficial stabilizing effect of the compressive stress field normal to the slices of the elastomer within the bearing.

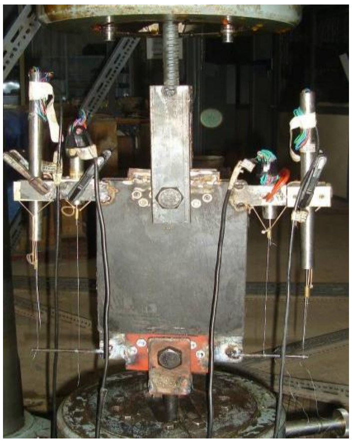

Figure 6a. Loading the unit slice specimen without the presence of the compressive stress field.

Figure 6b. Failing mode of the unit slice specimen without the presence of the compressive stress field.

The maximum shear stress capacity reached for this specimen a value equal to 1.7MPa; this occurred for a maximum strain level equal to 275%. The load-unload behavior of the specimen with the simultaneous application of continuously increasing shear strains and an imposed compressive stress field normal to the elastomer equal to 2.0MPa is shown in figure 7c; figure 7d shows the resulting debonding of the elastomer from the steel plating at the end of this loading sequence. When no compressive field was applied, the level of shear strain reached first a maximum strain equal to 250% whereby the maximum shear stress was observed equal to 1.6Mpa; then for larger shear strain amplitudes the bearing capacity degrades and the specimen reaches its debonding failure mode. The maximum shear stress, when the 2.0Mpa compressive field was applied, reached a maximum value equal to 2.4Mpa for a shear strain level equal to 275%. Then for higher shear strain levels the bearing capacity degrades and the specimen reaches its debonding failure mode. From the comparison of the performance of the specimens with and without the compressive stress field (figures 7c and 7a) it can be seen that the most severe test is that without the normal compressive stress field. It corresponds to an elastomeric bearing that does not have the beneficial stabilizing effect of the compressive stress field normal to the slices of the elastomer.

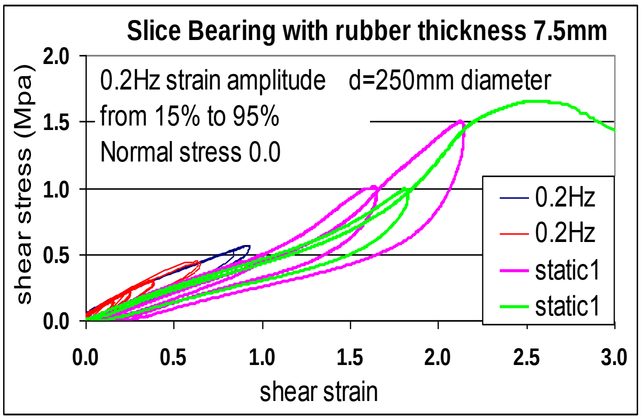

Figure 7a. Shear stress-strain response of the sliced elastomeric specimens up to failure for strains in the region of 300%. (σ=0.0 Mpa)

Figure 7b. The debonding of the elastomer from the steel plating at the end of this loading sequence.

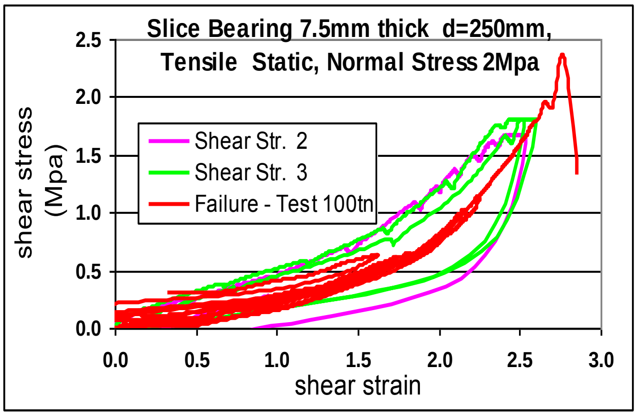

Figure 7c. Shear stress-strain response of the sliced elastomeric specimens up to failure for strains in the region of 300%. (σ=2.0 Mpa)

Figure 7d. Failing mode of the unit slice specimen with the presence of the compressive stress field.

4.3 Tests with elastomeric bearings

After completing an extensive sequence of tests with the slices of the elastomeric bearings, that tried to improve and validate the production process, another sequence of tests was conducted with elastomeric bearings of certain geometry as will be described in the following subsection. This series of tests had as an objective to study the compression and shear behavior of these elastomeric bearings in time and examine the influence on the behavior of an artificial aging process that these bearings were subjected to by keeping them in specific heating conditions for a certain time. Two different elastomeric bearings were examined; the fist was a square bearing with dimensions 150mm x 150mm in plan and a height of 95mm. The clear thickness of the elastomer was 70mm with two layers of elastomer and a thickness of the steel plating equal to 10mm for the outer plates and 5mm for the middle plate. The second elastomeric bearing was again of orthogonal geometry with dimensions 200mm x 250mm in plan having six layers of elastomer. All the steel plating was 3.5mm thick. Two specimens of this bearing were examined; the first had a thickness of the elastomer equal to 72mm (thick) whereas the second specimen had a thickness of the elastomer equal to 57mm. These specimens were subjected to vertical loading tests as well as to test that combined a vertical preloading condition, that resulted to an axial compressive field of approximately 2.0MPa, with a horizontal dynamic load, which produced the desired level of shear strain. The loading arrangement that was utilized is in accordance with the International Standard ISO 22762-1.

4.3.1. Tests with elastomeric bearings 150mm x 150mm

Initially, this elastomeric bearing specimen was tested in compression and then in combined pre-compression of 2.0 MPa and in shear without any artificial aging (23rd September 2008). Then the same specimen was heat treated for 20 days in a temperature equal to 80 C and after cooling it was subjected again to the same loading sequence; e.g. in combined pre-compression of 2.0 MPa and in shear (11th November 2008). During the shear tests, cyclic load was applied with varied frequencies in the range of 0.1 Hz to 1.0Hz. Figures 8a and 8c depict the vertical stress-strain diagram for this specimen before and after the heat treatment whereas figures 8b and 8d depict the shear stress-strain diagram for the same specimen that was first subjected to pre-compression of 2MPa and then to shear strain; again this test was conducted before (figure 8b) and after (figure 8d) the described heat treatment.

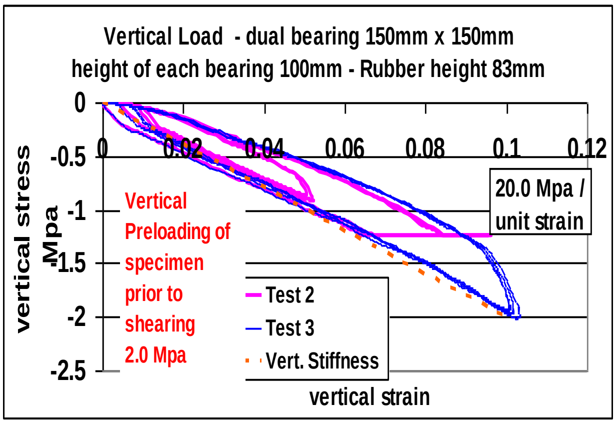

Figure 8a.

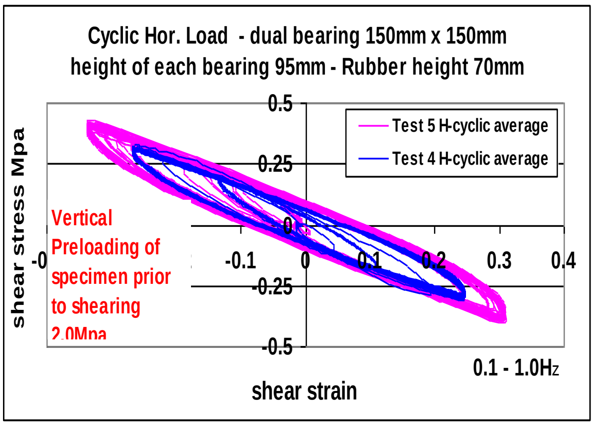

Figure 8b.

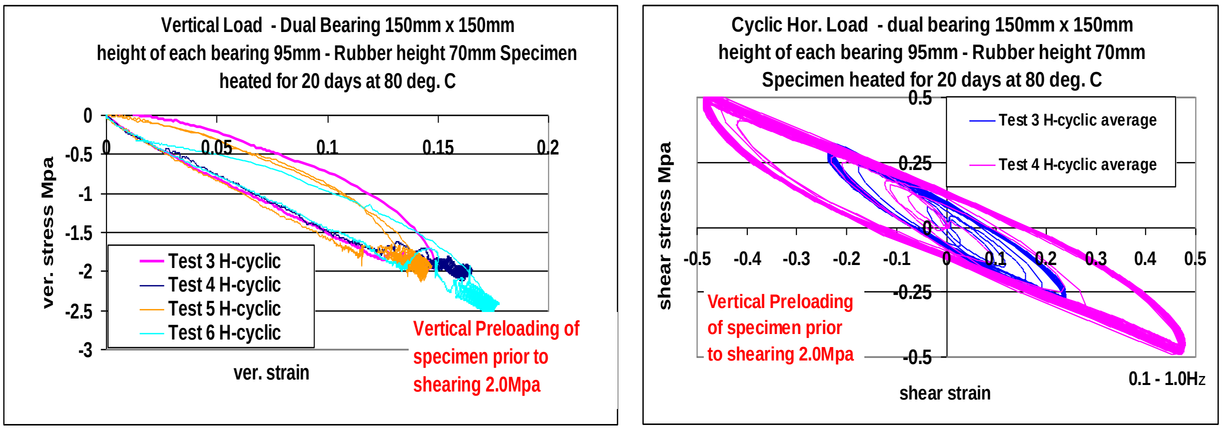

Figure 8c. Figure 8d.

Figure 8. Results from compression as well as from combined pre-compression and shear for the elastomeric specimen 150mm x 150mm before and after the artificial aging.

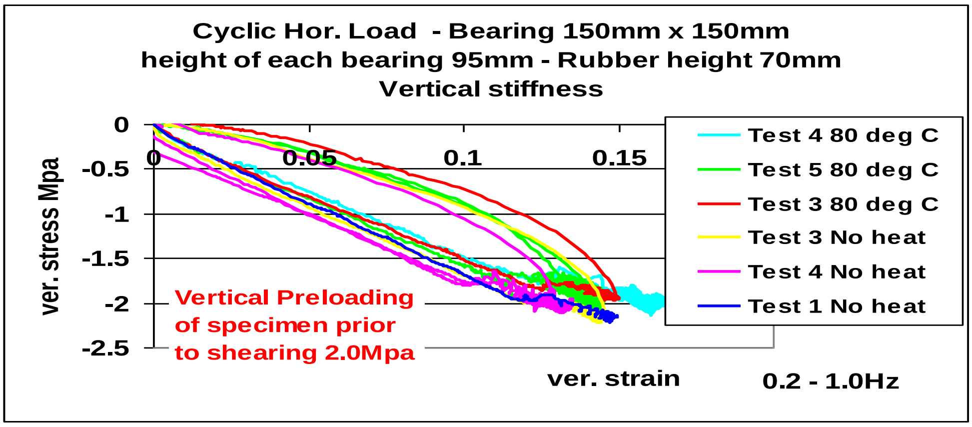

Figure 9. Comparison of the vertical stress-strain response before and after artificial aging.

In figure 9 the comparison of the vertical stress-strain response for this elastomeric bearing specimen before and after artificial aging is shown. As can be seen, this artificial aging process resulted in a small decrease in the vertical stiffness for this elastomeric bearing. In figure 10 the effect of the artificial aging is depicted by comparing the cyclic shear stress-strain response before and after the heat treatment. As can be seen in this figure, this artificial aging process resulted in a very small increase in the shear stiffness for this bearing.

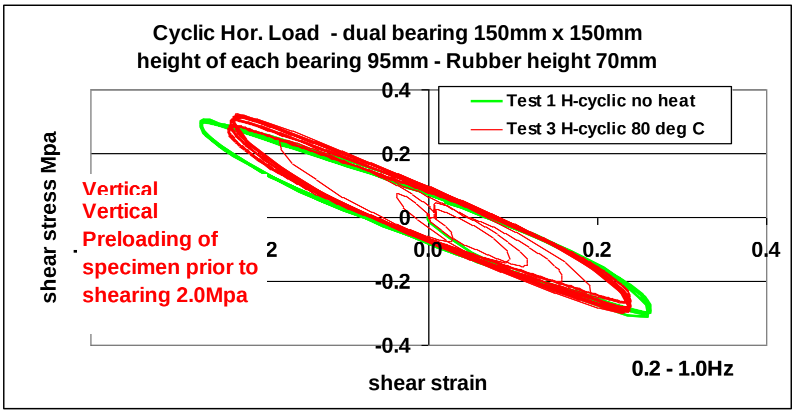

Figure 10. Comparison of the shear stress-strain response before and after artificial aging.

4.3.2. Tests with elastomeric bearings 250mm x 200mm

All the tests for this elastomeric bearing were conducted at the “new” strong reaction frame of the Laboratory of Strength of Materials and Structures of Aristotle University which houses a dynamic actuator with capabilities of ±1000KN in load and ±250mm in displacement and includes servo-electronic control in order to perform dynamic tests in real-time. Figure 11a illustrates a view of this strong reaction frame whereas figure 11b depicts the placement of the elastomeric bearing in this loading arrangement being supported by a special sliding device with very low coefficient of friction.

Figure 11a. The strong reaction frame of Aristotle University.

Figure 11b. The 250mm x 200m elastomeric bearing at the strong reaction frame

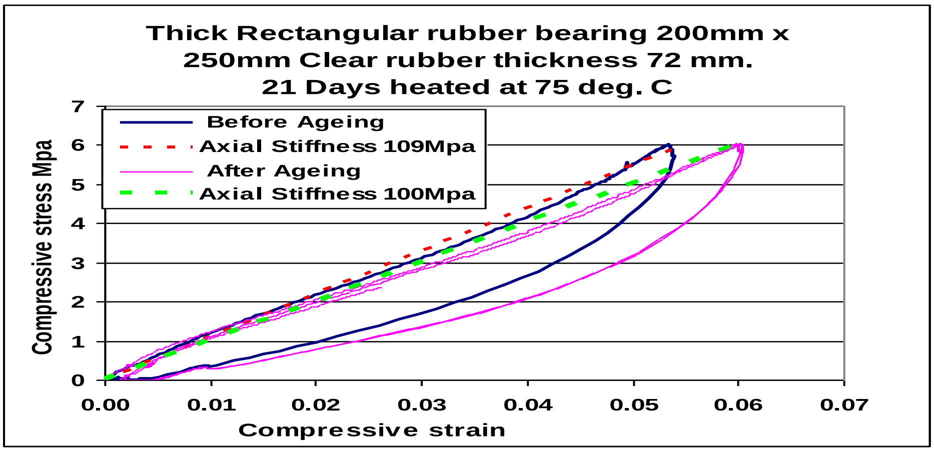

Figure 12. Comparison of the vertical stress-strain response before and after artificial aging.

Initially, this elastomeric bearing specimen was tested in compression and then in combined pre-compression of 6.0 MPa and in shear without any artificial aging. Then the same specimen was heat treated for 21 days in a temperature equal to 75 C and after cooling it was subjected again to the same loading sequence; e.g. in combined pre-compression of 6.0 MPa and in shear. During the shear tests, cyclic load was applied with varied frequencies in the range of 0.1Hz to 0.2Hz. Figures 12 and 13 include summary results of these tests for the specimen with the relatively thick layers of the elastomer (72mm total elastomer thickness). In figure 12 the comparison of the vertical stress-strain response for this elastomeric bearing specimen before and after artificial aging is shown. As can be seen, this artificial aging process resulted in a small decrease in the vertical stiffness for this bearing. In figure 13 the effect of the artificial aging is depicted by comparing the cyclic shear stress-strain response before and after the heat treatment. As can be seen in this figure, this artificial aging process resulted again in a small decrease in the shear stiffness for this bearing.

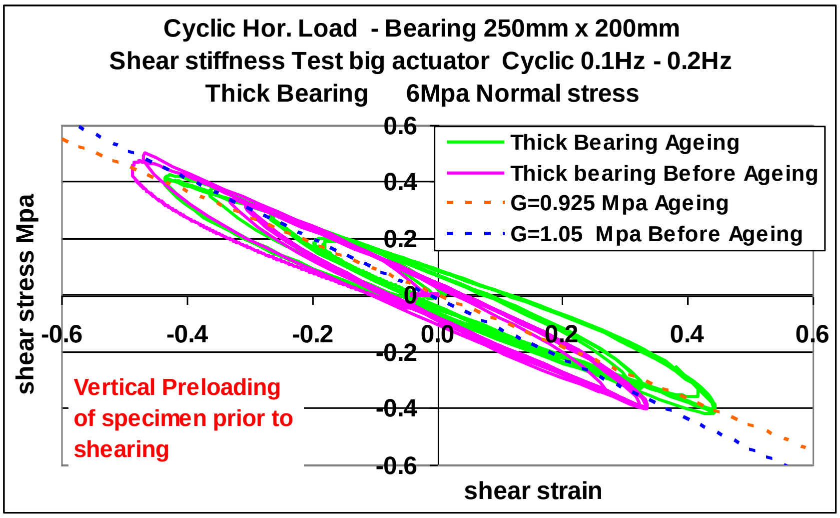

Figure 13. Comparison of the shear stress-strain response before and after artificial aging.

5 SOFTWARE STRUCTURE AND FLOW

5.1 Database structure

The above decision-making system was integrated and implemented in a computer software in order to facilitate the process and visualize the results in a way useful to the designer. As already mentioned, a database of 260 commercially available bearings is developed in Microsoft Access using three distinct relational tables containing the aforementioned necessary fields to describe the bearing geometry and capacity.

5.2 Embedment of non-commercial bearings after laboratory testing

It is noted that the database, which is part of the software, has the ability to be enriched by experimentally verified bearings. This was done for three additional bearings, produced by a local industry, which have been subjected to an extensive testing performed at the Laboratory of Strength of Materials of Aristotle University Thessaloniki. As already mentioned, the experimental study of the present investigation followed the specifications of the International Standards [15], which refer to the properties of the materials of which the elastomeric bearing are composed. These tests involved quality control, vulcanization procedures and construction guidelines and were performed with samples of elastomeric slices taken from the production process. Then, a sequence of prototype tests according to [4] were applied to a series of steel laminated elastomeric bearings produced by the local industry.

The influence of the normal stress level, shear strain amplitude, frequency of shear stress loading and artificial aging was investigated. From such tests the effective shear stiffness and the equivalent effective damping can be deduced together with their variation; the measured values can become input parameters for the developed software [14] [16] [17]. A complete set of the experimental campaign results can be found in [18] [19].

5.3 User input

The main input of the software refers to Step 1 of the proposed methodology and is made through a user-friendly interface which manages previous and new bridge seismic isolation alternative solutions as these are progressively created by the user. A new project, i.e. a new preliminary design of isolation system requires the following input parameters:

(a) **Selection of structural system and bearing type:** The software developed provides for four different bridge structural systems of up to four spans as is illustrated in Figure 6. The first system (Type 1) corresponds to a single span bridge with a length equal to L that is typical for a highway overpass. Type 2 corresponds to an overpass of a higher class of highway with two spans of equal lengths and a middle pier between the lanes of a two-way highway. Types 3 and 4 are alternatives of longer highway bridges. The weight of the superstructure, which essentially controls the vertical load on the bearings, is given by the designer as it is quite possible that the deck section has been selected prior to the selection of the isolation system. A commonly used value of 200 KN/m, is also proposed for cases for which more detailed geometrical data are not available.

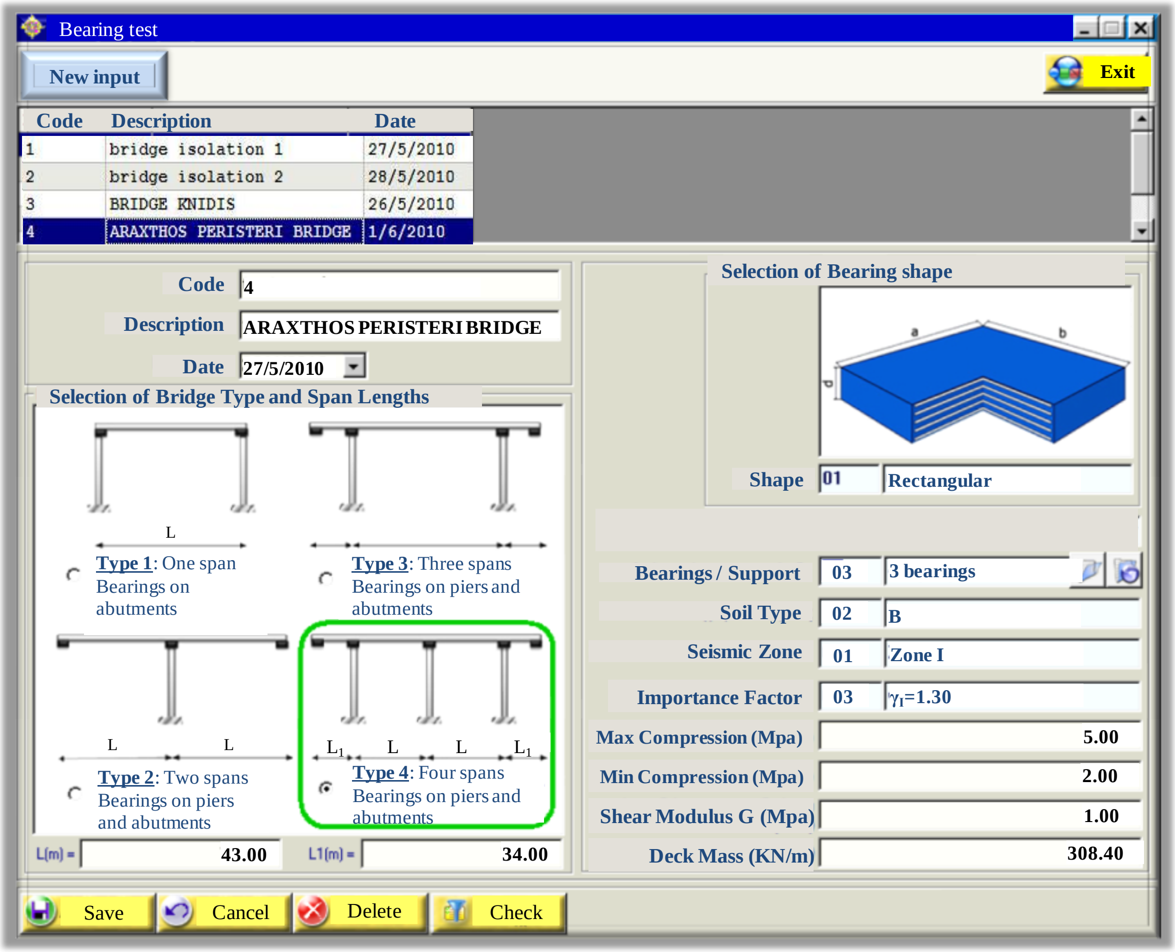

Code	Description	Date
1	bridge isolation 1	27/5/2010
2	bridge isolation 2	28/5/2010
3	BRIDGE KNIDIS	26/5/2010
4	ARAXTHOS PERISTERI BRIDGE	1/6/2010

Code: 4

Description: ARAXTHOS PERISTERI BRIDGE

Date: 27/5/2010

Selection of Bridge Type and Span Lengths

○ Type 1: One span Bearings on abutments

○ Type 3: Three spans Bearings on piers and abutments

○ Type 2: Two spans Bearings on piers and abutments

● Type 4: Four spans Bearings on piers and abutments

L(m) = 43.00

L1(m) = 34.00

Selection of Bearing shape

Shape: 01 Rectangular

Bearings / Support: 03 3 bearings

Soil Type: 02 B

Seismic Zone: 01 Zone I

Importance Factor: 03 γ_I=1.30

Max Compression (Mpa): 5.00

Min Compression (Mpa): 2.00

Shear Modulus G (Mpa): 1.00

Deck Mass (KN/m): 308.40

Figure 14: Typical overpass configurations supported by the software developed and overview of the user's interface of the software developed for the preliminary design of bridge isolation system.

(b) Desirable bearing type and configuration: The cross-section of the bearing (i.e., rectangular and/or circular) can also be selected at this stage. In case of pre-stressed and precast I-beam bridge decks, the number of bearings on each support (pier or abutment) is based on the number of the longitudinal beams. In the case of a cast-in-situ box girder or slab-type bridge deck, the number of bearings per support can be decided by the designer as a function of the dimensions of the pier's cap and the anticipated response of the isolated deck as well as making use of the software. As already mentioned, the user can define a minimum and a maximum value for the compression of the bearings or confirm the default range between 2.0 to 5.0MPa. The shear modulus of the bearings is automatically set by the program based on the manufacturer's specifications or any other experimentally justified value for the case of non-commercial bearings after appropriate testing, as described in section 4.2. It is noted that the value generally suggested by Eurocode 8 [4] is 1.0 MPa. However, Eurocode 8 also provides a lower limit of 0.9 MPa and upper limit of 1.5 MPa to be used in two successive analyses that can lead to the maximum displacements or the maximum forces of the isolating system and the bridge piers respectively.

(c) Level of seismic demand: The user defines the level of seismic demand, based on the elastic response spectrum of Eurocode 8-Part 1, the relevant soil classification and importance factor and a peak ground acceleration of 0.16, 0.24 and 0.36 that corresponds to the seismic zonation of Greece; the latter being an open parameter to potentially comply with different levels of seismic hazard in other countries.

5.4 Decision process

The system automatically checks all bearings stored in the database against compression (through the resulting shear strain in the bearing) and the shear strains produced by the earthquake loading based on the compression and shear strain criteria described in Sections 3.2.1 and 3.2.2 and then ranks all eligible bearings that have passed the above checks according to the Optimal Performance criterion. The results are illustrated in a graph, of the $OP_{(i)}$ ratios with the section geometry. The same graph also illustrates the individual safety criterion value ($SC_{(i)}$) and total costs ($CC_{(i)}$) in order to facilitate the designer when making selections based on purely safety or cost criteria. The software also provides in a tabular form the following summary results: (a) the maximum displacement of the deck subjected to the design seismic action, and (b) the aforementioned safety criterion values, cost ratios and optimal performance indicators. Apart from the graph and the table, the software provides an output interface for each eligible bearing, showing the main dynamic characteristics of the analyzed bridge system, i.e. the effective stiffness of the resulting isolating system, the total weight of the superstructure, the effective period of the bridge, the design acceleration at the specific period, the design seismic displacement and finally, a video representation illustrating the fundamental mode of the bridge along the longitudinal direction.

5.5 Assumptions and limitations

The simplified analysis performed in the software considering the rigid deck model for the bridge, is applicable when the total mass of the piers is less than 20% of the total bridge mass, as prescribed by Eurocode 8. The bridges under design should also be straight or have small curvature in plan and small longitudinal inclination. The developed software is not limited by the choice of the deck cross section. The user can employ a default vertical deck load value equal to 200 KN/m, considering that the used combination of loads includes earthquake loading. Otherwise, the user should input an appropriate vertical deck load value if the particular deck does not correspond to the default value. The software can be used in all isolated bridges with elastomeric bearings. However, the software cannot be used in cases when monolithic pier-deck or abutment-deck connections are combined with seismic isolation in the bridge. This structural scheme represents a design alternative implemented in case of long cast, in situ bridge decks or in irregular bridges, which have short piers and are usually protected from the deck's movements through isolation bearings.

As already mentioned, the software is designed for the preliminary design of the isolation of bridges with up to four spans. This restraint is not related with the seismic action, but mostly with the in-service induced movements of the deck, which become significant in bridges with total lengths greater than 150 m according to the limits imposed by various transportation agencies also described by [20]. It was finally decided that the work should be restricted to overpasses and typical small, and intermediate span continuous deck bridges, i.e. with a total length up to, say, 150m.

The bearings are assumed to be actually fixed in their feet, which means that the flexibility of the longitudinal seismic resisting system of the bridge is determined by the flexibility of the isolation. The piers with their foundations were considered to be quite stiff, as compared with the corresponding stiffness of the isolation interface. Therefore, the piers are not considered to participate in the seismic resisting system and they only receive the seismic actions of the bearings supporting the deck. It follows that the software is not recommended to be used in bridges with a flexible pier-foundation system, i.e. in bridges with slender and/or tall piers with flexible foundations. However, it can be underlined that seismic isolation with elastomeric, i.e. LDRB, bearings does not seem to be a design alternative for bridges with flexible pier-foundation systems.

Another assumption of the software concerns the bearings used for the support of the deck to the piers and abutments. The software has the ability to consider a number of bearings per support. This number does not have a restraint due to the calculation procedure used in the software. The software, however, considers that the number of bearings used for the isolation of the bridge deck is the same in all supports, and these bearings are all of the same type, e.g. they have the same cross section area and the same total thickness of the elastomer layers along deck. This assumption is considered to be rational as most bridge structures up to 150m, typically do not use an escalation of either bearings' areas or total thickness of the elastomer.

As far as the seismic action is concerned, the software considers that the isolation system is activated only during the longitudinal design earthquake. The response of the bridge in the transverse direction was assumed to be restrained by seismic links, which join the deck with the piers' heads. This assumption is deemed to be rational, since most bridges with isolated decks use seismic links [4] in the transverse direction, in which the in-service movements, due to creep and/or shrinkage [21] and pre-stressing [22], are negligible. Under the above assumptions, the longitudinal seismic action is transferred to the piers of the bridge through the isolating interface. In the transverse direction, capacity design stoppers transfer the total seismic action directly to the supporting piers without the interjection of the flexible isolation.

6 CONCLUSIVE REMARKS

The knowledge-based methodology developed for the preliminary design of the seismic isolation of bridges is presented in this paper. The proposed methodology is based on the current design provisions of Eurocode 8, but is also complemented by additional criteria set according to expert judgment, laboratory testing and recent research findings, while using a combined cost/performance criterion to select from a database of commercially available bearing products. It also offers the advantage that all possible selections of bearing sections can be considered as potential design solutions as opposed to the common preliminary design procedure, which due to time and complexity constraints investigates a limited number of design alternatives. The methodology is also implemented in a software whose efficiency is validated through more rigorous MDOF parametric numerical analyses as well as by using the case of a real bridge.

It is evident that the prediction success of the preliminary design process, that is proposed here, heavily relies on the extent of the contribution of the fundamental mode in the longitudinal direction, which, when dominant, yields the SDOF simplification as reasonable assumption. To sum up, it is believed that: a) the criteria imposed regarding compression stress limits, which are complementary to the ones prescribed in the codes, b) the automation of the process achieved though the developed software, which permits the investigation of hundreds of different bearing solutions, and c) the eligible bearing hierarchy provided through the proposed safety over cost (Optimal Performance) criterion, provide a significantly large number of potential design alternatives to be considered for the final selection. In this way, the proposed process can be seen as an effective preliminary design tool which is believed to lead to the quicker and more reliable estimate of the optimal bearing selection and seismic response of a highway overpass bridge either in the stage before its final design or when such an existing bridge is checked for upgrading its seismic performance utilizing such an isolation scheme.

The extensive experimental sequence verified the quality of the production process of a local producer of elastomeric bearings by subjecting slices of these bearings, being sampled during production, to the loading sequence specified by the International Standard ISO 22762-1 (2005). As can be concluded from these tests, for shear strain amplitudes lower than 250%, the variation of the frequency and shear strain amplitude did not influence the stiffness and strength properties of the tested specimens. For strain amplitudes larger than 250% the prevailing mode of failure was that of the debonding of the elastomer from the steel plating. Next, the experimental investigation examined the cyclic shear strain performance of locally produced prototype elastomeric bearings by subjecting samples of such bearings to the test sequence specified by the same International Standard ISO 22762-1. This time, the influence of aging was also investigated. As can be deduced from the measured behavior, aging resulted in a small increase of the axial (vertical) stiffness and a small decrease of the shear (horizontal) stiffness of the tested elastomeric bearings. More specimens must be tested to validate further these findings.

7 ACKNOWLEDGEMENTS

This research was conducted in the framework of the Regional Innovation Pole of the Region of Central Macedonia in northern Greece which was established in 2006, in the city of Thessaloniki. The project was funded by the General Secretariat of Research and Technology of the Greek Ministry of Development; its support is gratefully acknowledged. Ms. M. Geraki's contribution in the parametric validation of the software and the help of the personnel of the Laboratory of Strength of Materials and Structures of Aristotle University of Thessaloniki during the experimental tests are also acknowledged. The authors also wish to thank P. Skalkos for his contribution to the development of this specific software.

REFERENCES

[1] Pracasa R. A.V.N.S. BEAS: Expert system for the preliminary design of bearings. Technical Note. Advances in Engineering Software 1992; 14(2): 163-166.
[2] Gavaise E, Papaefthimiou K, Tzaveas T, Stylianidis K, Tegos J. The problem of minimum cost for structural members of earthquake resistant bridges. In Proc. of 5th International Conference of Earthquake Resistant Engineering Structures. Skiathos 2005.
[3] Naeim F, Kelly JM. Design of seismic isolated structures, From theory to practice. John Wiley and Sons, Inc; 1999.

[4] Eurocode 8 - Design of structures for earthquake resistance - Part 2: Bridges, DRAFT No 3. European Committee for Standardization; 2004.
[5] AASHTO. Recommended LRFD Guidelines for the Seismic Design of Highway Bridges. Based on: NCHRP 12-49, Comprehensive Specification for the Seismic Design of Bridges, Revised LRFD Design Specifications, (Seismic Provisions), Third draft of specifications and commentary; March 2001.
[6] Kappos A, Moschonas J. Documented classification of bridges in Greece. Technical Report, Aristotle University Thessaloniki, Greece; 2006.
[7] Konstantinidis D, Maravas A. Egnatia Motorway concrete bridges statistics. In Proc. of 31st ASECAP Study and Information Days, Portoroz, Slovenia 2003; 92-109.
[8] Hamzeh O, Tassoulas JT, Becker EB. Analysis of Elastomeric Bridge Bearings. Report No. 1304-5, Center for Transportation Research, University of Texas, Austin; August 1995: 139.
[9] Kunde MC, Jangid RS. Seismic behavior of isolated bridges: A-state-of-the-art review. Electronic Journal of Structural Engineering 2003; 3: 140-170.
[10] Faravelli L. Modelling the Response of an Elastomeric Base Isolator. Journal of Structural Control. 2001;8(1):17-31.
[11] Indian Railways Institute of Civil Engineering (IRICE), PUNE 411001, Bridge Bearings; 2006.
[12] Eurocode 8 - Design of structures for earthquake resistance - Part 1: General rules, seismic actions and rules for buildings, DRAFT No 3. European Committee for Standardization; 2004.
[13] Pham DT, Pham PTN. Expert Systems in Mechanical and Manufacturing Engineering. The International Journal of Advanced Manufacturing Technology 1998; 3(3):3-21.
[14] Abe M, Yoshida J, Fujino Y. Multi-axial Behaviors of Laminated Rubber Bearings and Their Modeling. I: Experimental Study. ASCE Journal of Structural Engineering 2004; 130(8): 1119-1132.
[15] International Standard ISO 22762-1. Elastomeric seismic protection isolators - Part1: Test methods; 2005.
[16] Kelly JM. Earthquake Resistant Design with rubber. Springer; 1997.
[17] Ryan KL, Kelly JM, Chopra AK. Experimental observation of axial load effects in isolation bearings. In Proc. of 13th World Conference on Earthquake Engineering, Vancouver, B.C., Canada; August 2004; No. 1707.
[18] Manos G, Mitoulis S, Kourtidis V, Sextos A, Tegos I. Study of the behavior of steel laminated rubber bearings under prescribed loads. In Proc. of 10th World Conference on Seismic Isolation, Energy Dissipation and Active Vibrations Control of Structures, Istanbul, Turkey; May 2007.
[19] Manos G, Sextos A, Mitoulis S, Kourtidis V, Geraki M. Tests and improvements of bridge elastomeric bearings and software development for their preliminary design. In Proc of 14th World Conference on Earthquake Engineering, Beijing, China; 2008.
[20] Dicleli M, Albhaisi SM. Estimation of Length Limits for Integral Bridges Built on Clay. ASCE Journal of Bridge Engineering 2004;9(6): 572-581.
[21] Arockiasamy M, Sivakumar M. Design Implications of Creep and Shrinkage in Integral Abutment Bridges. ACI Special Publication 2005; 227(5):85-106.
[22] PCI, Precast, prestressed concrete bridges, the high performance solution, Comprehensive Bridge Design Manual, Accessed online: 1 Dec 2008 (Available via DIALOG. ww.pci.org/publications/bridge).
[23] Mitoulis SA, Tegos IA, Stylianidis K-C. Cost-effectiveness related to the earthquake resisting system of multi-span bridges. Engineering Structures 2010; 32(9):2658-2671.

[24] Seidl G, Weizenegger M. Frame structures in bridge construction. Design, analysis and economic considerations. In Proc. of International Workshop on the Bridges with Integral Abutments. Topics of relevance for the INTAB project, Technical Report 2006:14.
[25] Hawk H. NCHRP 483. Bridge Life-Cycle Cost Analysis. Washington, DC; 2003.
[26] Computers and Structures INC. SAP 2000. Nonlinear Ver. 11.0.4. User's Reference Manual, Berkeley, California; 2002.

COMPDYN 2011
3rd ECCOMAS Thematic Conference on
Computational Methods in Structural Dynamics and Earthquake Engineering
M. Papadrakakis, M. Fragiadakis, V. Plevris (eds.)
Corfu, Greece, 25–28 May 2011

INVESTIGATION OF THE DYNAMIC RESPONSE OF THE EVRIPOS CABLE-STAYED BRIDGE IN GREECE, UNDER ASYNCHRONOUS GROUND MOTION RECORDS

Christos Karakostas[1*], Anastasios Sextos[2], Vassilios Lekidis[1] and Savvas Papadopoulos[2]

[1]Institute of Engineering Seismology & Earthquake Engineering (ITSAK)
5 Agiou Georgou Str., Patriarchika Pylaias, GR55535 Thessaloniki, Greece
christos@itsak.gr , lekidis@itsak.gr

[2]Department of Civil Engineering
Aristotle University of Thessaloniki, Greece
asextos@civil.auth.gr, savvaspp@civil.auth.gr

Keywords: Spatial variation, Cable-stayed bridge, Coherency, Higher modes excitation.

Abstract.

The Evripos bridge in central Greece, connects the island of Evia to the mainland. The cable-stayed section of the bridge is 395m in length, with a central span of 215m and side-spans of 90m each. The deck, 13.5m in width, is at 40m above sea-level, suspended by cables from two, 90m high pylons. A permanent accelerometer special array of 43 sensors was installed on the bridge in 1994 by the Institute of Engineering Seismology and Earthquake Engineering Two triaxial sensors have been monitoring the free-field (near pier M4) and pier M5 base response on the mainland (Boeotean) coast and two others the respective locations (pier base M6 and free-field near pier M7) on the Euboean coast. Since then the bridge's behaviour to seismic excitations has been continuously monitored and investigated. From various earthquake events recorded at the site, it became obvious that the excitation at each of the aforementioned locations differs, with the lowest peak acceleration values observed at site M7 for all three components, independently of magnitude, azimuth and epicentral distance of the earthquake, a fact that can be attributed to local site conditions. In the present research effort, an investigation of the dynamic response of the Evripos bridge due to the asynchronous base excitations along its supports is carried out. Comparisons are made with the conventional design procedure of assuming a common (synchronous) base excitation at all the supports and interesting conclusions are drawn regarding the impact of spatially variable ground motion on the seismic response of the particular bridge.

1 INTRODUCTION

During the last decade, time history analyses have become increasingly popular both for design and research purposes, especially for the case of complex and/or important bridges. This trend has significantly improved the analysis rigor and facilitated the consideration of various physical phenomena that were too complicated to be taken into account in the past. One of those issues, is the identification of a realistic, spatially variable earthquake ground motion (SVEGM) which can be used for the excitation of the bridge for design or assessment purposes. As it is well known, this phenomenon may affect the seismic response of long bridges, or of bridges crossing abruptly changing soil profiles; however, its potentiallly beneficial or detrimental impact on the final bridge performance cannot be easily assessed in advance ([1]-[5] among others).

One major difficulty in assessing the spatially variable patterns of earthquake ground motion is the complex wave reflections, refractions and superpositions that take place as seismic waves travel within inhomogeneous soil media. Different analytical formulations have been proposed in the past, but the inherent multi-parametric nature of wave propagation and soil-structure interaction makes it practically impossible to predict the spatially varying earthquake input along the bridge length in a deterministic manner. Dense seismograph arrays, primarily in Taiwan, Japan and the U.S., have contributed in shedding some light into this problem which can be primarily attributed to four major factors that take place simultaneously, i.e., wave passage effect, the extended source effect, wave scattering and attenuation effect [6]. The operation of these arrays, also led to the development of numerous empirical, semi-empirical and analytical coherency models, fit to represent the decaying signal correlation with distance and frequency.

Despite the significant impact of the aforementioned analytical approaches and experimental evidence, a reliable and simple methodology for the prediction of the effects of asynchronous motion on bridges is still lacking. Even modern seismic codes like Eurocode 8 deal with the problem through either simplified code-based calculations or indirect measures involving larger seating deck lengths [7].

An interesting case for the study of this phenomenon using recorded data is the Evripos cable-stayed bridge, which has been permanently monitored by an accelerometer network since 1994 [8], [9]. A series of minor to moderate intensity seismic events have been recorded by this network, providing a useful set of motions recorded both in the vicinity of the structure and on specific locations on the structure and its foundation. Scope of this study therefore, is to:

(a) Make use of the recorded data in order to investigate the nature of earthquake ground motion and the effects of its spatial variation on the dynamic response (in terms of forces and displacements) of the particular cable-stayed bridge.

(b) Attempt to correlate the beneficial or detrimental effect of asynchronous motion with the excitation of higher structural modes observed under multiple-support earthquake input.

The description of the bridge, its monitoring system as well as its response under various asynchronous ground motion records, is presented in the following.

2 DESCRIPTION OF EVRIPOS CABLE-STAYED BRIDGE

The Evripos bridge, a 694.5m R/C structure, connects the Euboean coast in the island of Evia to the Boeotean coast in continental central Greece (Figure 1). It is composed of three parts, the central cable stayed section and two side (approaching) parts made of pre-stressed R/C beams that rest on elastomeric bearings. The central section of the bridge is divided into three spans of length 90m, 215m and 90m respectively, while the deck (of 13.50m width) is suspended by the 90m height pylons M5 and M6 with cables. The displacements of the deck along the longitudinal direction are permitted in piers M4 and M7 while those in the transverse direction are blocked [8], [9]. In the present study, it is only the central cable-stayed section that is examined.

As already mentioned, the Evripos cable-stayed bridge behavior is constantly monitored through a special accelerometer array installed by the Institute of Engineering Seismology and Earthquake Engineering (ITSAK). The network is composed by four triaxial accelerometers installed at the base of the bridge, in particular, on the pile caps of piers M5 and M6 and on soil surface in areas adjacent to piers M4 and M7. There are also 31 additional uniaxial accelerometers installed on the superstructure, for system identification purposes. It is noted that all sensors have common time and common trigger settings [8],[9] thus permitting signal processing and correlation. The Finite Element model of the bridge is illustrated in Figure 2.

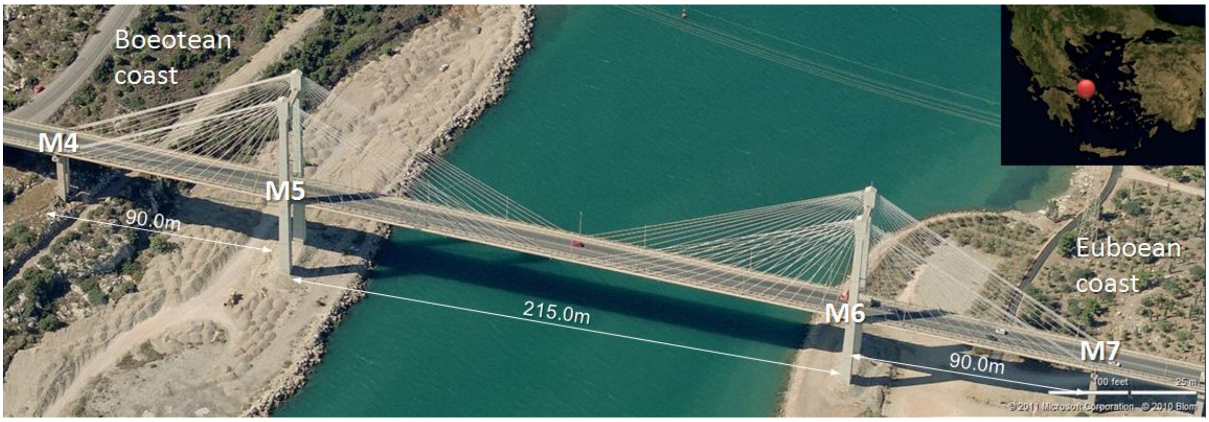

Figure 1: The central section of the Evripos cable-stayed bridge.

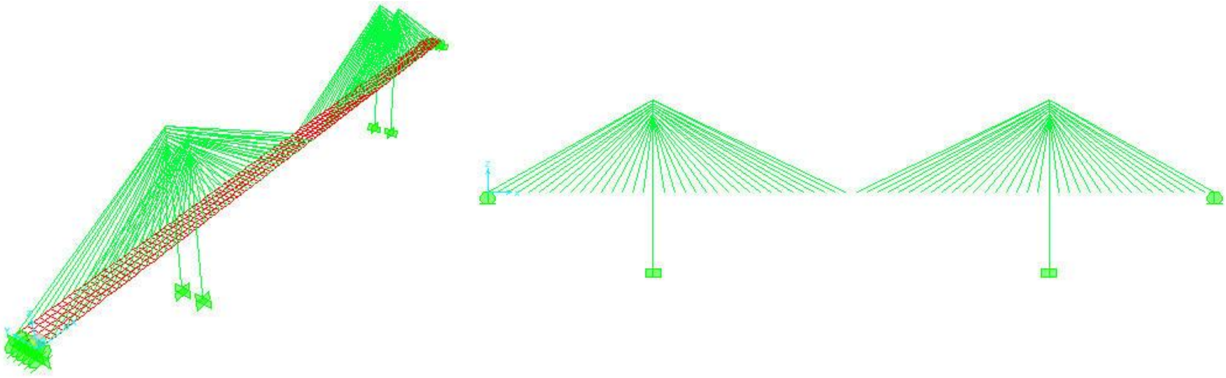

Figure 2: Finite model of the Evripos cable-stayed bridge.

3 EARTHQUAKE STRONG MOTION DATA AVAILABLE ON SITE

Due to the significant overall length of the central section of the bridge that is almost 400m in total, an effort is made to process specific groups of records available on-site in order to investigate the impact of spatial variability of seismic ground motion. For this purpose, a set of four ground motions was used, as recorded during the Athens earthquake, that occurred on 7/9/1999 at a source-to-site distance of approximately 50km with a surface Magnitude M_s=5.9. The recorded time histories are presented in Figure 3 where the longitudinal, transverse and vertical component is illustrated in different rows for each location. Having ensured that the common time and common trigger condition was fulfilled, the records were first filtered in the frequency range 0.65-25Hz in order to remove the influence of the vibration of the superstructure which was transmitting waves back to the soil due to inertial soil-structure interaction. Then, the coherency between all pairs of records was computed using a GUI-based, Matlab script written for this purpose. For each individual record, the power spectrum was computed after appropriate smoothing using an 11-point Hamming window as proposed by Abrahamson for 5% structural damping [10], [11]:

$$\bar{S}_{jj}(\omega_n) = \sum_{m=-M}^{+M} W(m\Delta\omega)\hat{S}_{jj}(\omega_n + m\Delta\omega) \tag{1}$$

where ω_n is the discrete frequency, W(mΔω) the (Hamming) spectral window and $\hat{S}_{jj}$ the unsmoothed power spectra.

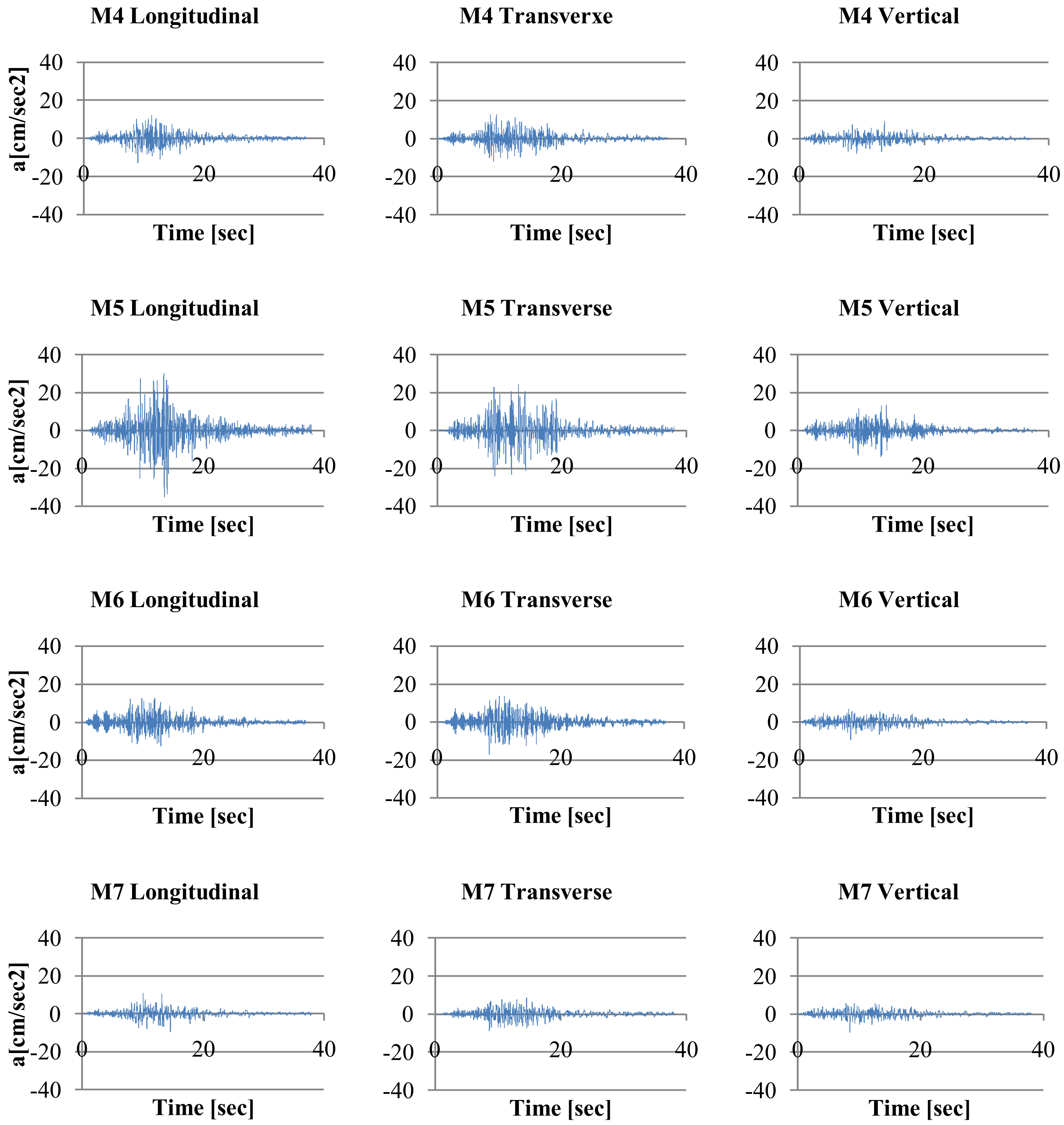

Figure 3: Horizontal and Vertical components of the strong ground motions recorded at the base of piers M4, M5, M6 and M7 due to the 1999 M_s=5.9 Athens earthquake.

Similarly, the smoothed cross spectral densities were calculated for all six pairs of records M_{jk} (i.e., M4-M5, M4-M6, M4-M7, M5-M6, M5-M7, M6-M7) according to the following expression:

$$\bar{S}_{jk}(\omega_n) = \frac{2\pi}{T}\sum_{m=-M}^{+M} W(m\Delta\omega)\Lambda_j(\omega_n + m\Delta\omega)\Lambda_k(\omega_n + m\Delta\omega)\exp\{i[\Phi_k(\omega_n + m\Delta\omega) - \Phi_j(\omega_n + m\Delta\omega)]\} \qquad (2)$$

where Λ_j and Λ_k is the Fourier amplitude in stations j and k respectively and Φ_j, Φ_k is the corresponding phase. The lagged coherency, expressing the correlation of the records among all stations, can then be calculated as:

$$\left|\bar{\gamma}_{jk}^{M}(\omega)\right| = \frac{\left|\bar{S}_{jk}^{M}(\omega)\right|}{\sqrt{\bar{S}_{jj}^{M}(\omega)\cdot\bar{S}_{kk}^{M}(\omega)}} \qquad (3)$$

The diagrams of lagged coherency in the frequency range 0-10Hz, where the frequencies of all significant modes of a structure are expected to be, computed individually for the longitudinal, transverse and vertical component of the recorded motions are illustrated in Figure 4 for pairs M4-M5, M4-M6 and M4-M7, in Figure 5 for pairs M5-M6 and M5-M7 and in Figure 6 for pair M6-M7. As anticipated, the coherency loss increases with increasing separation distance and frequency.

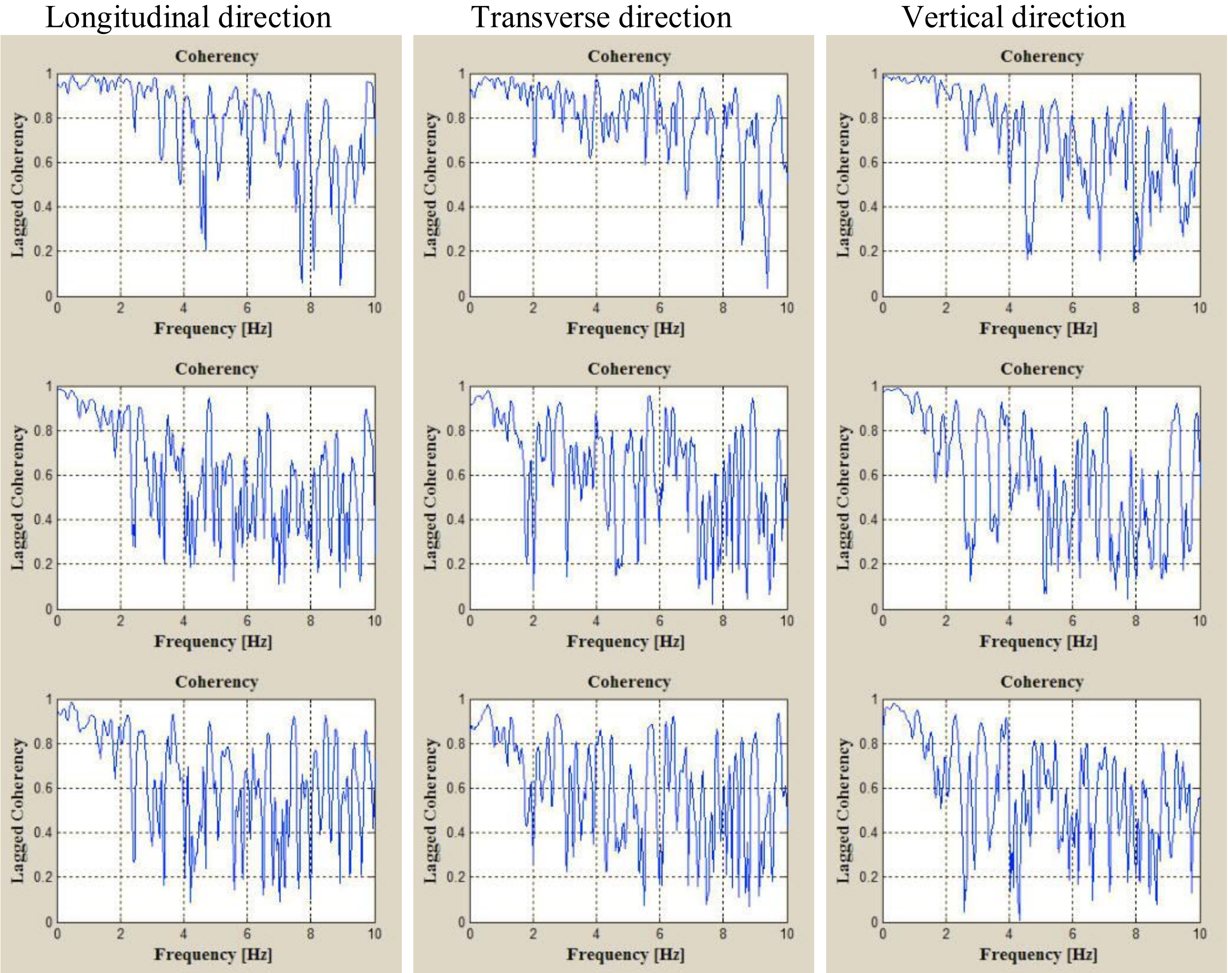

Figure 4: Lagged coherency of motions recorded between piers M4-M5 (at distance l=90m, top), M4-M6 (at distance l=305m, middle) and M4-M7 (at distance l=395m, bottom).

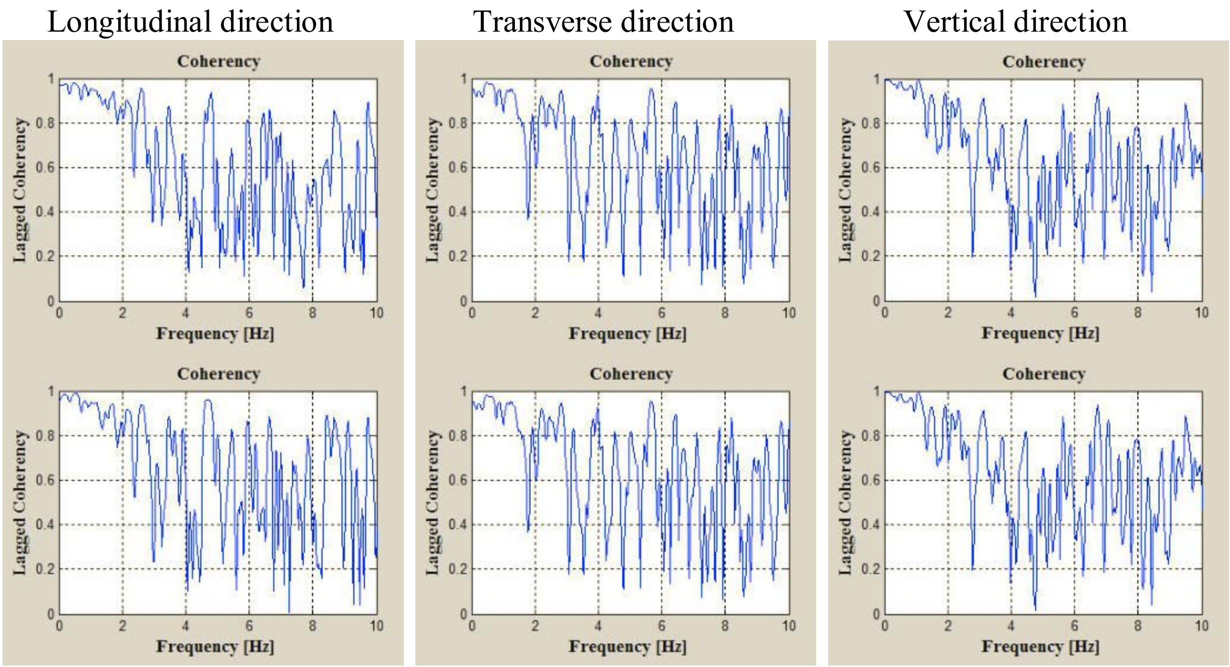

Figure 5: Lagged coherency of motions recorded between piers M5-M6 (at distance l=215m, top), and M5-M7 (at distance l=305m, bottom).

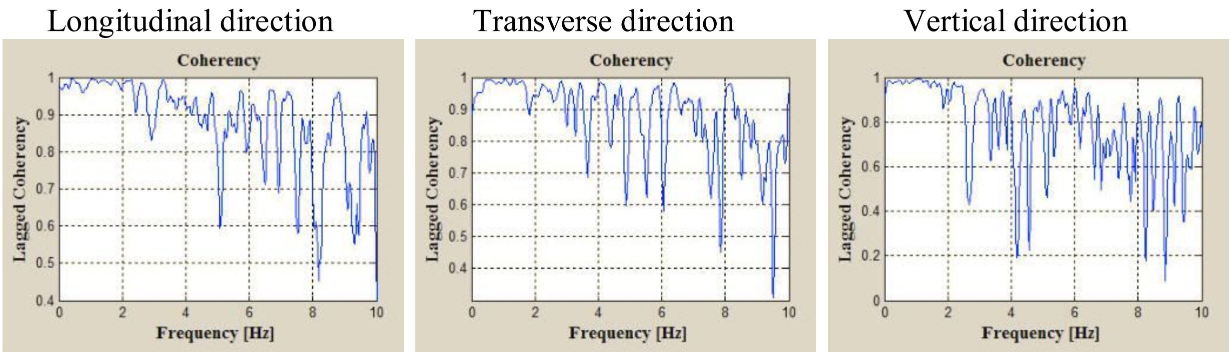

Figure 6: Lagged coherency of the motions recorded between piers M6-M7 (at distance l=90m).

The comparison of the computed incoherencies with one of the most commonly used patterns proposed by Luco and Wong [12] is made in Figure 7, where the lagged coherency is given by the following expression:

$$|\gamma(\xi,\omega)| = e^{-\left(\frac{v\omega\xi}{V_s}\right)^2} = e^{-a^2\omega^2\xi^2} \tag{4}$$

In eq. (4), the coherency drop parameter α controls the exponential decay and ξ is the distance between the two stations examined. Typically, α is taken equal to $2.5\text{x}10^{-4}$sec/m; however, comparison for the case of motions recorded along the longitudinal direction at the bases of the piers M4 and M7 (i.e., at separation distance ξ=395m) reveals that a value of α equal to $0.5\text{x}10^{-4}$sec/m leads to better matching with the observed incoherency.

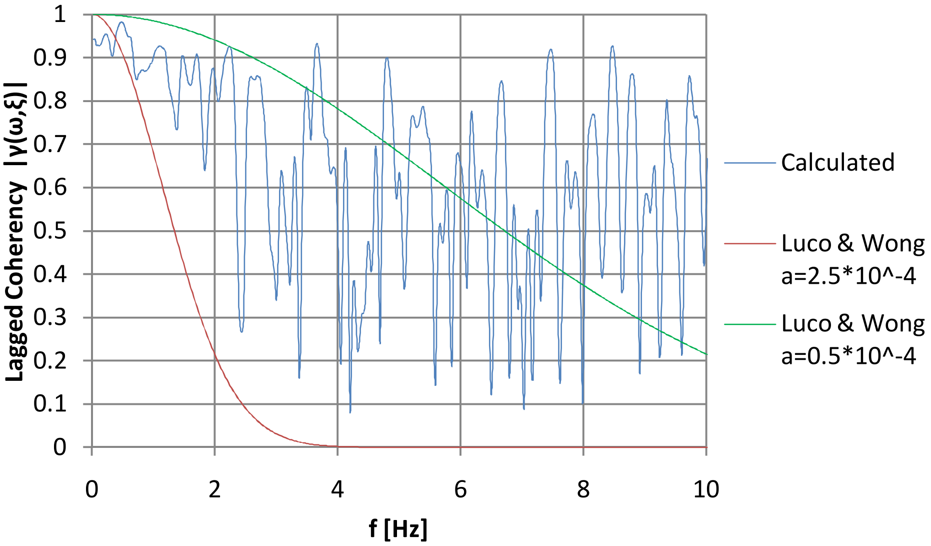

Figure 7: Comparison between observed and predicted coherency loss for different values of the Luco and Wong model [12].

4 ANALYSES PERFORMED

Most analytical or numerical studies investigating the effects of spatial variability of earthquake ground motion on the response of bridges compare the results of multiple-support excitation analysis with those of a reference condition which typically assumes synchronous excitation among all bridge supports. The comparison can then be made in terms of a ratio of the action effects (forces or displacements) of specific structural components over the response under synchronous conditions.

In the case examined herein though, the fact that the ground motions have been recorded at the bases of the four bridge piers leads to a realistic excitation scenario with respect to the actual seismo-tectonic and soil conditions of the site under study but at the same time makes it difficult to assume the corresponding compatible “synchronous” excitation conditions. One option would have been to pick one of the recorded motions and apply it synchronously at all pier supports; however, this option is limited by the fact that the available records show significant discrepancy in terms of both their PGA and spectral amplification, primarily due to local site effects at the location of pier M5 (Figure 8).

In order to overcome this difficulty, it was decided to adopt the following procedure: as the strongest component of the motions recorded is in the longitudinal direction, all records (in all components) are scaled (Table 1) to the average spectral acceleration of all records at period T=1.64sec, which is the period of the highest contributing mode, activating 76% of the mass in the longitudinal direction (Table 2). Then, four different “synchronous” excitation scenarios are developed, assuming each time that the scaled motions in piers M4, M5, M6 and M7 respectively, are applied uniformly at all supports. Given the aforementioned scaling, it is deemed that the four different versions of uniform excitation are compatible in terms of spectral amplification (at least at the period of vibration that is affected by the dominant earthquake component), while the fact that all the resulting scaling factors are close to unity, guarantees that the scaling-induced dispersion is limited.

Based on the above, five non-linear dynamic analyses of the Evripos cable-stayed bridge are performed using the computer program SAP2000 [13], that is one using the recorded set of motions and four considering the aforementioned compatible “synchronous” excitation scenarios. All three components of the motions were applied simultaneously. The geometrical non-linearity induced by the bridge cables was considered assuming tension-only capabilities and the initial cable stress state due to dead loading was applied through non-linear staged-construction static analysis.

Beam elements were used to model the piers, while the bridge deck was simulated by shell elements. Piers were assumed fixed at their bases while the supporting conditions at the two bridge edges were considered as rolled in the longitudinal direction and pined in the transverse.

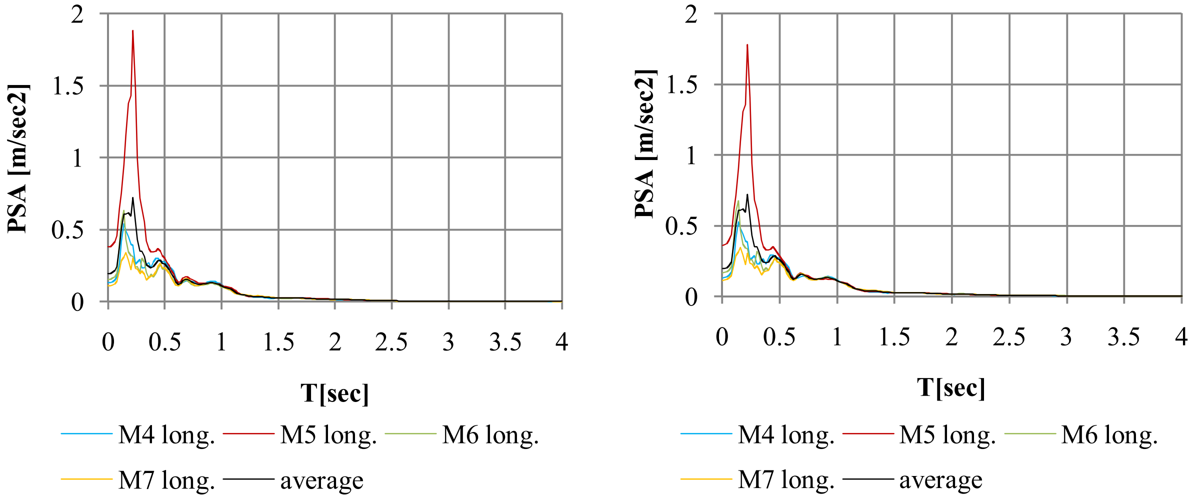

Figure 8: 5% damped elastic response spectra of the longitudinal components of the records at piers M4, M5, M6, M7 compared to the average response spectrum.

Pier	M4	M5	M6	M7
Scale factor	0.977	0.947	1.069	1.014

Table 1: The scaling factors for the records at M4, M5, M6 and M7 so as to their response spectra to have the PSA with the average response spectrum for T=1.64sec.

Mode ID	Period	UX	UY	UZ	RX	RY	RZ
#1	2.712	0	0	6.7	1.2	2.3	0
#2	2.385	20.2	0	0	0	0	0
#3	2.061	0	58.3	0	3.4	0	47.2
#4	1.645	76.3	0	0	0	0	0
#5	1.298	0	0	6.2	1.4	5.5	0
#9	1.065	0	0	37.4	7.3	28.8	0

Table 2: Dynamic characteristics (eigenfrequencies and corresponding modal contribution) of the Evripos cable-stayed bridge.

The amplitude of the seismic moments (i.e., the earthquake-induced bending moments at the bases of piers M4 and M7 and at one of the two columns at each pier M5 and M6), the displacements at the top of each pier and the displacements in the middle of the deck are examined for all asynchronous and synchronous excitation cases previously presented.

Figure 9 presents the comparison between the computed seismic moments at the base of pier M6 using the Athens 1999 (asynchronous) recorded motions, and those computed through the four "synchronous" excitation scenarios, that is, by the uniform application of records M4, M5, M6, and M7 respectively. The comparison of the maxima among all cases are summarized in Table 3. It can be seen that the moments M_2 developed at the base of pier M6 transversely to the bridge plane, due to the asynchronous recorded ground motions is systematically lower regardless of the "synchronous" excitation pattern adopted. As anticipated, this is more intense (approximately 32%) for the synchronous case involving the uniform application of record M5, which, despite of the scaling to a common level of spectral amplification, still corresponds to the highest PGA among the records at all locations. On the other hand, the situation reverses for the bending moments M_3 within the bridge plane and the asynchronous excitation results in higher levels of stress in all cases, reaching 43% increase in the extreme case of applying record M7 uniformly at all support points. The respective results for pier M5 are also summarized in Table 3. It can be seen that seismically-induced bending moments in both directions are decreased when assuming uniform excitation conditions independently of the scenario adopted.

As far as the displacements are concerned, the corresponding time histories are plotted in Figures 10, 11 and 12 for the middle of the central span and the top of the pylons M5 and M6 respectively, while the maximum in time displacements are compared in Tables 4, 5 and 6. More specifically, asynchronous excitation is systematically favorable for the span middle deck displacements which are decreased up to 36%, 45% and 63% along the three principal direction U_x, U_y and U_z. The same trend is also observed for the case of the top of the M5 pylon - though to a lesser degree - and with the exception of a minor (6%) increase in vertical displacements for one of the scenarios studied. In contrast to the above, the displacements at the top of pylon M6 derived under the asynchronous recorded ground motions are generally increased compared to the synchronous case and are almost double (increased by 82%) when compared to the uniform application of record M4. Vertical displacements are also increased up to 11% due to asynchronous motion.

Uniform excitation scenario	Case studied	Pier M5		Pier M6	
		M_2 [kNm]	M_3[kNm]	M_2[kNm]	M_3[kNm]
Synch M4	Synch	1350.70	798.54	1338.30	759.11
	Asynch	833.53	743.05	949.48	943.70
	Asyn/Sync-1	*-38%*	*-7%*	*-29%*	*+24%*
Synch M5	Synch	1510.39	1008.53	1403.31	919.10
	Asynch	833.53	743.05	949.48	943.70
	Asyn/Sync-1	*-45%*	*-26%*	*-32%*	*+3%*
Synch M6	Synch	1401.33	981.36	1345.28	815.00
	Asynch	833.53	743.05	949.48	943.70
	Asyn/Sync-1	*-41%*	*-24%*	*-29%*	*+16%*
Synch M7	Synch	1314.79	849.06	1335.77	658.05
	Asynch	833.53	743.05	949.48	943.70
	Asyn/Sync-1	*-37%*	*-13%*	*-29%*	*+43%*

Table 3: Comparison of maximum absolute earthquake-induced bending moments developed in pier M6 for synchronous and asynchronous excitation (cases M4, M5, M6, M7).

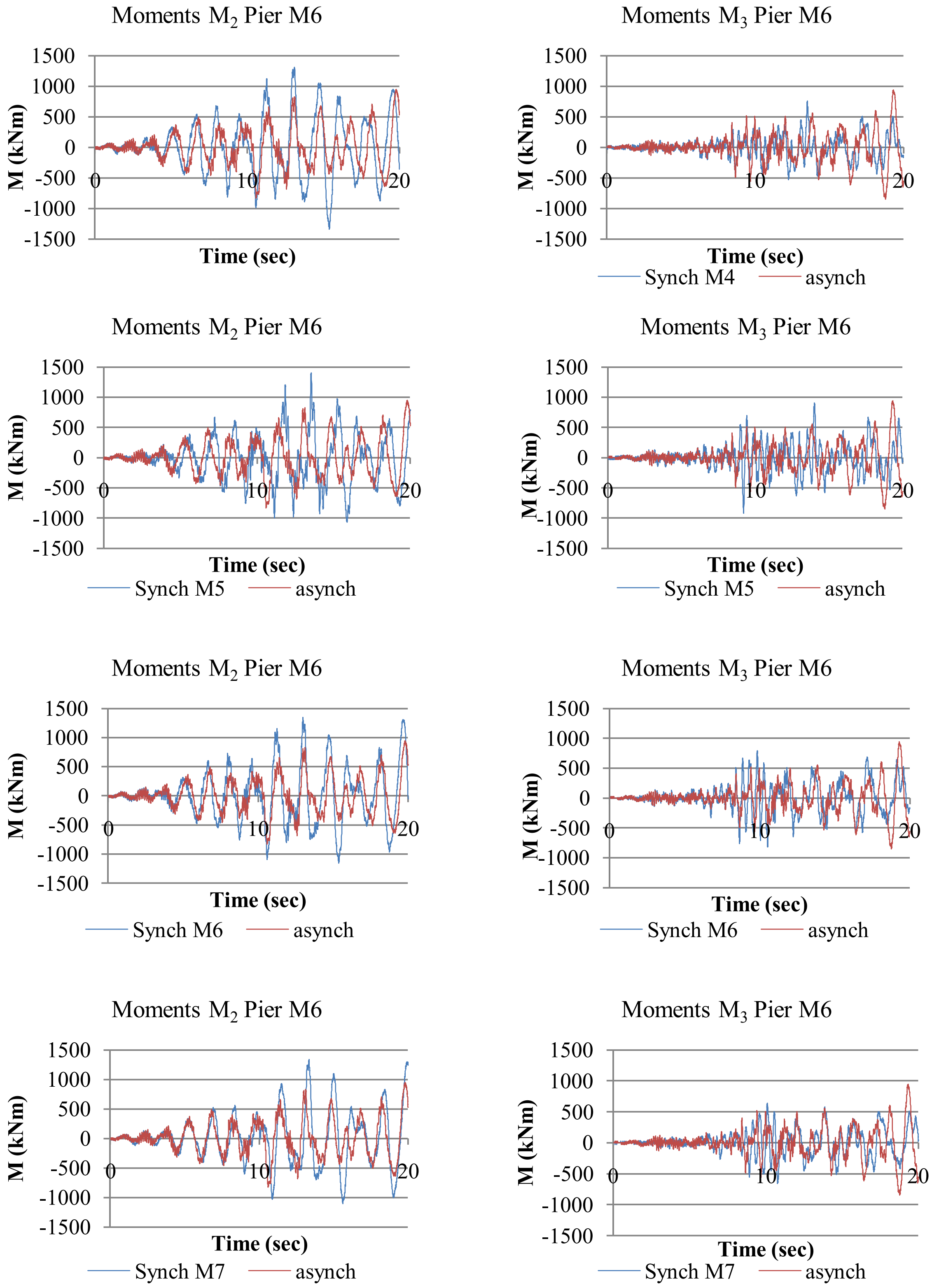

Figure 9: Comparison of the computed seismic moments at the base of pier M6 using the Athens 1999 (asynchronous) recorded motions, with those computed through the four “synchronous” excitation scenarios (uniform application of records M4, M5, M6, M7 respectively).

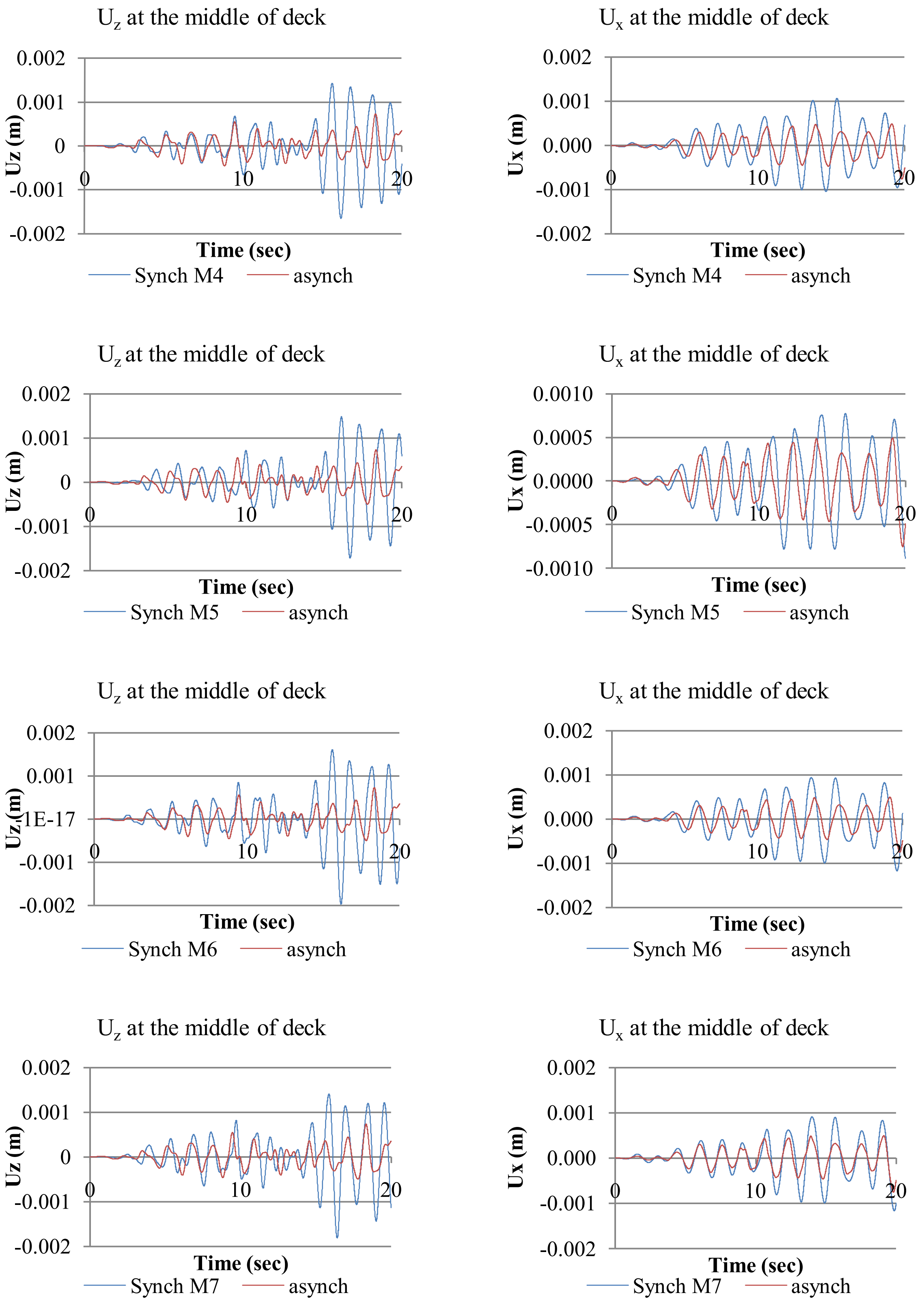

Figure 10: Comparison of the seismic deck displacements in the middle of the central span using the Athens 1999 (asynchronous) recorded motions, with those computed through the four “synchronous” excitation scenarios (uniform application of records M4, M5, M6, M7 respectively).

Displacements at the middle of the bridge deck (cm)				
Uniform excitation scenario	Case studied	U_x	U_y	U_z
Synch M4	Synch	0.11	0.14	0.16
	Asynch	0.08	0.10	0.07
	Asyn/Syn-1	*-28%*	*-25%*	*-56%*
Synch M5	Synch	0.09	0.14	0.17
	Asynch	0.08	0.10	0.07
	Asyn/Syn-1	*-15%*	*-29%*	*-58%*
Synch M6	Synch	0.12	0.18	0.20
	Asynch	0.08	0.10	0.07
	Asyn/Syn-1	*-36%*	*-45%*	*-63%*
Synch M7	Synch	0.12	0.16	0.18
	Asynch	0.08	0.10	0.07
	Asyn/Syn-1	*-36%*	*-41%*	*-60%*

Table 4: Maximum values of absolute displacements [cm] which developed due to asynchronous and synchronous (M4, M5, M6, M7) excitation scenarios at the middle of the bridge deck.

Displacements at the pier M5 top [cm]				
Uniform excitation scenario	Case studied	U_x	U_y	U_z
Synch M4	Synch	0.09	0.18	0.05
	Asynch	0.07	0.16	0.05
	Asyn/Syn-1	*-22%*	*-12%*	*+7%*
Synch M5	Synch	0.067	0.23	0.05
	Asynch	0.071	0.16	0.05
	Asyn/Syn-1	*+6%*	*-34%*	*0%*
Synch M6	Synch	0.09	0.27	0.06
	Asynch	0.07	0.16	0.05
	Asyn/Syn-1	*-20%*	*-42%*	*-14%*
Synch M7	Synch	0.09	0.25	0.05
	Asynch	0.07	0.16	0.05
	Asyn/Syn-1	*-23%*	*-37%*	*-6%*

Table 5: Maximum values of absolute displacements [cm] which developed due to asynchronous and synchronous (M4, M5, M6, M7) excitation scenarios at the top of pier M5.

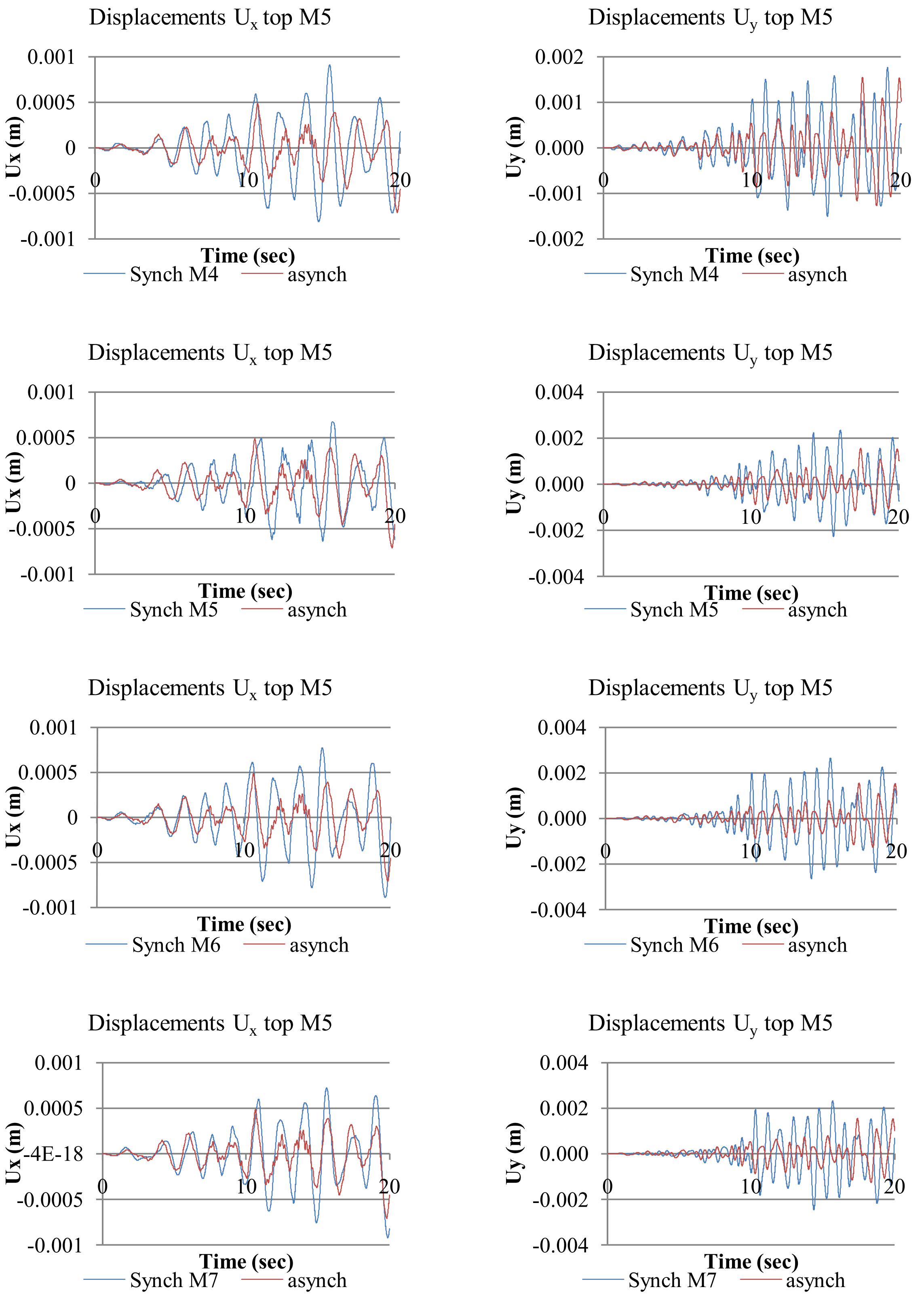

Figure 11: Comparison of the seismic displacements at the top of the pylon at the location of pier M5 using the Athens 1999 (asynchronous) recorded motions, with those computed through the four “synchronous” excitation scenarios (uniform application of records M4, M5, M6, M7 respectively).

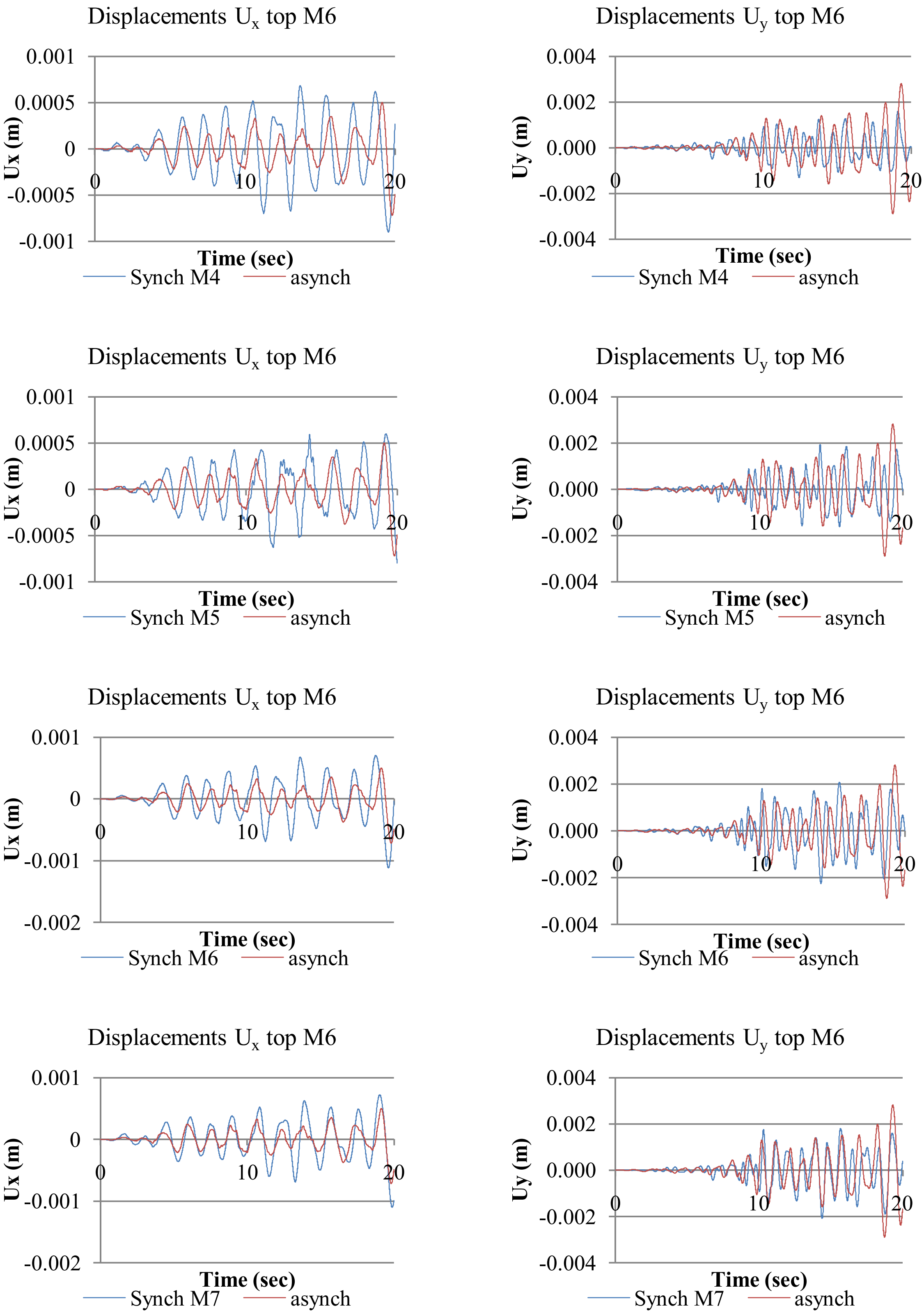

Figure 12: Comparison of the seismic displacements at the top of the pylon at the location of pier M6 using the Athens 1999 (asynchronous) recorded motions, with those computed through the four “synchronous” excitation scenarios (uniform application of records M4, M5, M6, M7 respectively).

Displacements at the pier M6 top [cm]				
Uniform excitation scenario	Case studied	U_x	U_y	U_z
Synch M4	Synch	0.09	0.16	0.04
	Asynch	0.07	0.29	0.05
	Asyn/Syn-1	*-20%*	*+82%*	*+11%*
Synch M5	Synch	0.08	0.19	0.047
	Asynch	0.07	0.29	0.049
	Asyn/Syn-1	*-10%*	*+49%*	*+4%*
Synch M6	Synch	0.11	0.23	0.054
	Asynch	0.07	0.29	0.049
	Asyn/Syn-1	*-36%*	*+28%*	*-9%*
Synch M7	Synch	0.11	0.21	0.050
	Asynch	0.07	0.29	0.049
	Asyn/Syn-1	*-35%*	*+38%*	*-2%*

Table 6: Maximum absolute values of displacements [cm] which developed due to asynchronous and synchronous (M4, M5, M6, M7) excitation at the pier M6 top. In last row is presented the rate of increase or decrease.

These results indicate that the complex inherent nature of ground motion incoherency are strongly correlated to the dynamic characteristics of the excited structure and do not systematically lead to uniform increase or decrease of the corresponding action effects. For this reason, it was deemed useful to investigate further the significance of the potential excitation of higher structural modes for which there are strong indications ([2], [7], [14]) that it is one of the key features of multiple support excitation.

It has to be noted that due to the cable suspension of the Evripos bridge, the associated geometrical non-linearities make it difficult to spot specific, load independent, modes of vibration. However, it was computationally verified that the low level of excitation of the event considered in this work (which does not exceed 0.032g) does not lead to any untensioning of the suspension cables, thus ensuring that at least for the particular earthquake intensity, the eigen-frequencies summarized in Table 2 still hold.

In order to examine the higher modes excitation, the Fourier spectra of the accelerations were plotted at the same points as for the displacements (Figures 13 and 14). As the analysis is in fact linear elastic, (since the dynamic characteristics remain constant during the studied excitation), the frequencies where the peaks of the Fourier spectra are observed coincide with the eigen-frequencies of the structure. In principle, one would expect that the decreased response due to asynchronous excitation observed in Figures 9-12 should correlate well with the decrease of the Fourier amplitudes at the corresponding frequencies of the associated modes.

Indeed, Figure 13 shows a clear reduction in the Fourier amplitudes of acceleration at the middle of the central span, at the period of 1.64 sec, which corresponds to the 4th mode activating 76% of mass in the longitudinal direction when the response under the recorded asynchronous excitation is compared to that of the uniform application of the M5 record. This is in good agreement with the decrease in both bending moments and displacements summarized in Table 4. The same correlation is observed with respect to the vertical direction where the Fourier amplitudes are decreased at periods 1.30 sec and 1.06 sec corresponding to the 5th mode (activating 6.5% of mass in the vertical direction) and 9th mode (activating 37% of mass in the vertical direction) respectively; a fact that is also in line with the favorable effect of asynchronous excitation in Table 4.

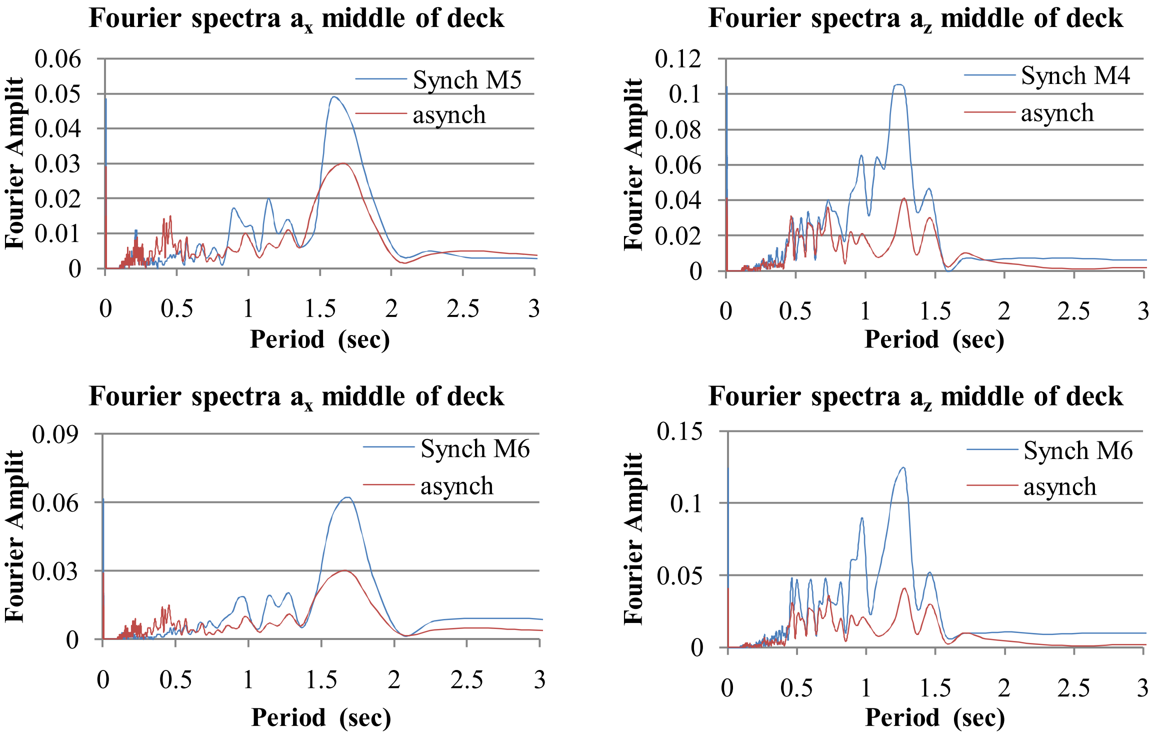

Figure 13: Comparison of the Fourier spectra of the accelerations computed in the longitudinal and vertical direction at the middle of the deck using the Athens 1999 (asynchronous) recorded motions, with those computed by the four “synchronous” excitation scenarios (uniform application of records M4, M5, M6, M7 respectively).

Similarly to the above, when the comparison is made on the basis of the uniform application of record M5, the reduction of the Fourier amplitudes at periods 2.38 sec (2nd mode-activating 20% in the longitudinal direction) and 1.64 sec (4th mode-activating 76% in the longitudinal direction) is confirmed with the response reduction in Table 4. Again, good correlation is observed for the vertical direction, where the reduction of the Fourier amplitudes takes place at periods 1.3 sec (5th mode-activating 6.5% in the vertical direction), 1.06 sec (9th mode-activating 37% in the vertical direction) and 0.82 sec (15th mode-activating 68% in the same direction) and the comparison of the maxima in the time domain depicted in Table 4. It is noted that the same trend is also observed in numerous locations of the bridge.

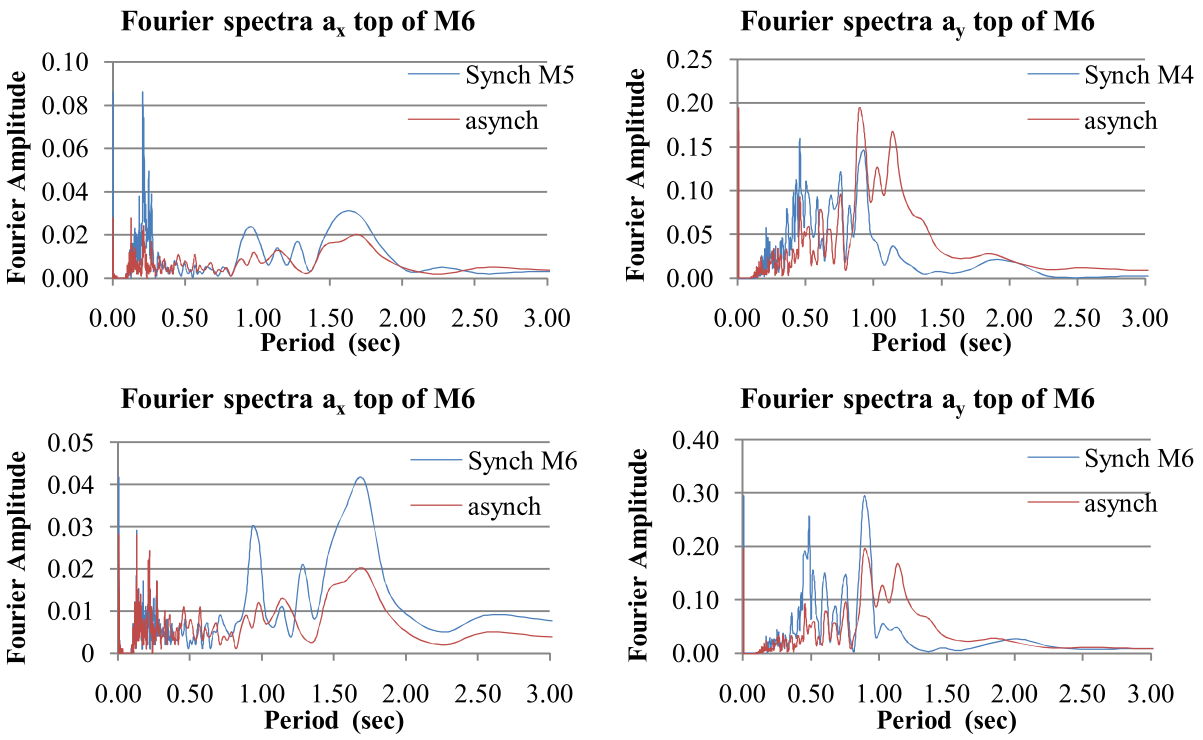

Figure 14: Comparison of the Fourier spectra of the accelerations computed in the longitudinal and vertical direction at the top of the pylon of M6 using the Athens 1999 (asynchronous) recorded motions, with those computed by the four “synchronous” excitation scenarios (uniform application of records M4, M5, M6, M7).

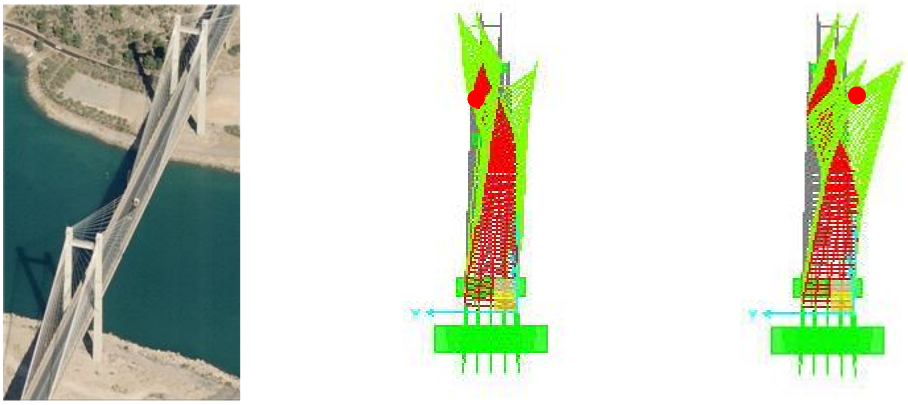

Figure 15: Characteristic antisymmetric (mode 8: T=1.11sec, R_z=10%, middle) and symmetric (mode 11: T=0.89, U_y=10.7%, left) mode shapes, excited due to asynchronous excitation.

Figure 14 presents the Fourier spectra of the accelerations in the longitudinal and transverse directions at the top of the M6 pylon. When the comparison is made on the basis of the uniform application of the M5 record, a reduction of the Fourier amplitudes is first observed at periods 2.38 sec (corresponding to the 2nd mode, activating 20% of the mass in the longitudinal direction) and 1.64 sec (4th mode, activating 76% of the mass in the same direction), which justifies the reduction of the displacements documented in Table 6. On the other hand, when the transverse direction is examined, a remarkable amplification is observed at period 0.89 sec corresponding to the symmetric 11th mode, activating 10.7% of the mass in the transverse direction, while significant amplification is also depicted at period T=1.11 sec which corresponds to the antisymmetric 8th mode (activating 9.8% of the mass around the z axis). Both mode shares are illustrated in Figure 15 where it is clearly seen that the transverse displacement of the top of the M6 pylon is very much affected by the excitation of the particular modes. As a result, the good correlation between the excited higher modes of vibration due to asynchronous earthquake motion and the corresponding impact of the latter on the overall bridge response is also confirmed for the case of the particular cable-stayed bridge. This observation is deemed interesting, especially bearing in mind that it has been made for the case of a real bridge using recorded earthquake ground motions.

5 CONCLUSIONS

The scope of this study was to examine the effects of asynchronous excitation on the Evripos cable-stayed bridge, utilizing the recorded response at four locations of the accelerometer network maintained by ITSAK, due to the M_s=5.9, 7/9/1999 Athens earthquake. The records were filtered to remove inertial interaction effects and their coherency was computed for all available record pairs. A detailed finite element model of the cable-stayed bridge was developed and its response was computed using both the recorded motions and four synchronous excitation scenarios. The comparative study of the results indicates that:

- For the particular bridge studied, spatial variability of seismic ground motion has a generally favorable effect, at least on the pier base bending moments and the displacements middle of the central span deck. Apparently, the extent of this beneficial phenomenon is very much dependent on the assumptions made regarding the definition of the “synchronous” excitation, which, in contrast to the actual, recorded asynchronous case, is not obvious.
- There are specific cases (i.e., out-of-plane bending moments and displacements at the top of the two bridge pylons) where the asynchronous excitation has a clearly critical effect.
- In all cases, the observed deamplification or amplification of the bridge displacements was verified by the reduced or increased amplitude of the Fourier spectra respectively, at selected frequencies, which correspond to specific modes that have a strong impact on the vibration of the structure along the directions examined. It is believed that, given the complexity of the problem studied, the potential excitation of higher modes due to asynchronous excitation may be a key tool for understanding the role of spatial variability of earthquake ground motion on the overall seismic response of bridges.

REFERENCES

[1] G. Deodatis, V. Saxena, and M. Shinozuka, “Effect of spatial variability of ground motion on bridge fragility curves,” *8th ASCE Specialty Conference on Probabilistic Mechanics and Structural Reliability*, 2000, pp. 1-6.

[2] A.G. Sextos, A.J. Kappos, and K.D. Pitilakis, “Inelastic dynamic analysis of RC bridges accounting for spatial variability of ground motion, site effects and soil-

structure interaction phenomena. Part 2: Parametric study," *Earthquake Engineering & Structural Dynamics*, vol. 32, 2003, pp. 629-652.

[3] A. Lupoi, P. Franchin, P.E. Pinto, and G. Monti, "Seismic design of bridges accounting for spatial variability of ground motion," *Earthquake Engineering and Structural Dynamics*, vol. 34, 2005, pp. 327-348.

[4] N.J. Burdette and A.S. Elnashai, "Effect of Asynchronous Earthquake Motion on Complex Bridges. II: Results and Implications on Assessment," *Journal of Bridge Engineering*, vol. 13(2), 2008, pp. 166-172.

[5] A.S. Nazmy and A.M. Abdeel-Ghaffar, "Effect of ground motion spatial variability on the response of cable-stayed bridges", Earthquake Engineering and Structural Dynamics, vol. 21, 1992, pp.1-20.

[6] N.A.Abrahamson, "Spatial variation of multiple support inputs," Proceedings of the 1st U.S. Seminar on Seismic Evaluation and Retrofit of Steel Bridges. A Caltrans and University of California at Berkeley Seminar, San Francisco, CA, 1993.

[7] A.G. Sextos and A.J. Kappos, "Evaluation of seismic response of bridges under asynchronous excitation and comparisons with Eurocode 8-2 provisions", *Bulletin of Earthquake Engineering*, vol. 7, 2009, pp. 519-545.

[8] V. Lekidis, M. Tsakiri, K. Makra, C. Karakostas, N. Klimis, and I. Sous, "Evaluation of dynamic response and local soil effects of the Evripos cable-stayed bridge using multi-sensor monitoring systems", *Engineering Geology*, vol. 79, 2005, pp. 43-59.

[9] V. Lekidis, "Investigation of the seismic response of the Evripos high bridge: Experimental and analytical approach", Technical Report, Institute of Engineering Seismology and Earthquake Engineering, Thessaloniki: 2003 (in Greek).

[10] N.A. Abrahamson, J.F. Schneider, and J.C. Stepp, "Empirical spatial coherency functions for applications to soil-structure interaction analyses", *Earthquake Spectra*, vol. 7, 1991, pp. 1-28.

[11] A. Zerva, *Spatial Variation of Seismic Ground Motions-Modelling and Engineering Applications*, CRC Press, Taylor & Francis Group, FL, 2009.

[12] J.E.Luco and H.L.Wong, "Response of a rigid foundation to a spatially random ground motion," Earthquake Engineering and Structural Dynamics, Vol. 14, 1986, pp.891-908.

[13] CSI, *SAP 2000* Nonlinear Ver. 10.01, *User's Reference Manual*, *Berkeley*, California, U.S.

[14] T.E. Price and M.O. Eberhard, "Effects of Spatially Varying Ground Motions on Short Bridges", *Journal of Structural Engineering*, vol. 124(8), 1998, pp. 948-955.

COMPDYN 2011
III ECCOMAS Thematic Conference on
Computational Methods in Structural Dynamics and Earthquake Engineering
M. Papadrakakis, M. Fragiadakis, V. Plevris (eds.)
Corfu, Greece, 25–28 May 2011

A NUMERICAL STUDY ON THE BEHAVIOR OF HIGH-PERFORMANCE BUCKLING-RESTRAINED BRACES

Tsutomu Usami[1], Chunlin Wang[2], and Jyunki Funayama[3]

[1] Department of Civil Engineering, Meijo University
1-501 Tempaku-ku, Nagoya, 468-8502, Japan
e-mail: usamit@meijo-u.ac.jp

[2] Department of Civil Engineering, Meijo University
1-501 Tempaku-ku, Nagoya, 468-8502, Japan
e-mail: wangmeijo@gmail.com

[3] Department of Civil Engineering, Meijo University
1-501 Tempaku-ku, Nagoya, 468-8502, Japan
e-mail: 103437009@ccalumni.meijo-u.ac.jp

Keywords: Analytical Study, Buckling-restrained Braces, Steel Bridges, Low-cycle Fatigue.

Abstract. *The paper presents experimental and analytical studies on developing high-performance (i.e., high-energy absorption) BRBs for steel bridge structures. Low-cycle fatigue tests of four BRB's specimens with different constant strain amplitudes and with different constraints on the core brace were conducted as benchmark experiments in order to evaluate the results of the simulations. Both half and whole models of beam elements are proposed with and without taking into account the symmetry of the brace member. Experimental and analytical results show that the BRB's specimens with the stoppers possess better low-cycle fatigue performance than the specimens without the stoppers. The CID performance of steel BRBs with the stoppers even under the strain amplitude, larger than 3%, can meet the requirements of High-performance BRBs but the CID performance of steel BRBs without the stoppers cannot meet the requirements of High-performance BRBs. The friction coefficient of 0.075 is regarded as the right value for the simulations and half and models can effectively simulate the mechanical behavior of the BRB with or without the stoppers.*

1 INTRODUCTION

In the last few decades, the recent trend of seismic design methodology for steel building structures is that the primary members of building structures almost remain elastic and most of the inelastic deformations are enforced to occur in some energy absorption members, such as bracing members. Residual deformations of building structures after a severe earthquake could be reduced based on this design philosophy because most of main members have not been damaged during the earthquake excitation.

This design philosophy has been gradually implemented and refined in steel bridge structures. Developing a reliable method of designing the energy absorption equipment is indispensable. One way is to utilize some lateral or diagonal bracing members in a bridge structure as energy absorption members. Members in the lateral bracing system will be performed under cyclic compression and tension so that they should have high energy absorption capacity. Therefore, in order to obtain a stable performance, the global buckling of bracing members must be restrained by restraining cover members. This is the buckling-restrained brace (BRB), which attracts more and more attentions, because it does not buckle in compression but yield in both tension and compression and represents an effective energy absorption mechanism for damping of engineering structures with low cost.

As an axial-type damping device, BRBs are widely studied on component behavior and system applications in building [1, 2] and bridge engineering [3]. Test results in references[4, 5] show that BRBs process good cumulative inelastic ductility capacity before failure of the core segment, larger than the minimum required value of 200 by AISC seismic provisions[6]. It has been indicated from recent research series by the authors[3, 7] that light weight BRBs were employed to replace insufficient lateral braces and cross diagonal braces for retrofitting an existing steel arch bridge, which leads to damage concentration in sacrificing damping devices and mitigates damage of main structures.

Based on authors' past researches, the concept of high-performance BRBs (HPBRBs) is proposed that no replacement is needed during the lifecycle of bridges and it is likely to suffer three times of strong earthquakes without severe damage[8]. Therefore, besides general performance requirements for BRBs used in building engineering, additional special performance requirements for HPSDs in bridge engineering are summarized as follows [8]: (1) Stable hysteretic characteristics and high energy dissipation capacity; (2) High deformation capacity; (3) High low-cycle fatigue strength; (4) Easy fabrication and construction with low cost; (5) High durability; (6) No need of replacement. Moreover, two performance indices for high-performance BRBs under strong earthquake excitations, the target maximum strain and cumulative inelastic strain, are recommended as 3% and 70%, respectively.

In order to meet the requirements of HPBRBs, series of low-cycle fatigue tests are performed to evaluate the light-weight bolt-assembled steel BRBs proposed by authors[9, 10]. During the experiment, the constraints of the flat core brace, such as the stopper pins used to prevent the relative displacement between the core brace and the restraining members, attracted our attentions and obviously affected the low-cycle fatigue performance verified by the contrastive low-cycle fatigue tests.

In this paper, the experiment, including four steel BRB's specimens looked as the benchmark tests, is firstly presented. These specimens are selected from a series of low-cycle fatigue tests[11] and used to validate both half and whole models of beam elements, considered with and without taking into account the symmetry of the brace member. Details of the experimental and analytical results are given as follows. All the tests were performed at the Advanced Research Center for Seismic Experiments and Computations (ARCSEC) at Meijo University.

2 TEST SPECIMENS AND PROGRAM

As shown in Figure 1, light-weight steel BRBs mainly consist of a steel plate brace member (BM), a pair of restraining members (RMs) connected by high-strength bolts through two filler members, and unbonding material stuck to the brace member as the isolation material in order to reduce the friction between the BM and RMs.

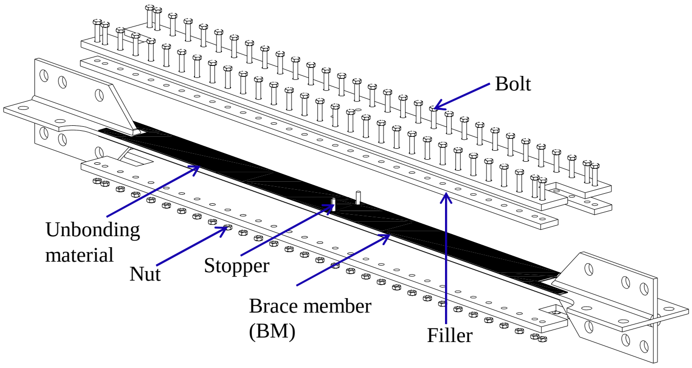

Figure 1: Assemblage of steel BRBs.

2.1 Brace member

The full view of the BM is shown in Figure 2, geometric dimensions and structural properties are listed in Table 1. A flat steel plate is used as the BM, and aiming at well connection to the test equipment, cruciform sections at both ends are expanded by welding 12mm thick rib stiffeners to each side of the plate. The BM is made of SM400A mild steel. Three JIS No.1-typed test pieces for each series are made from the same steel of the BM and average values tested as material constants are listed in Table 2, respectively. At the center of FE-4.0 and FT-3.5 specimens' BMs, two welded stoppers of 9 mm in diameter and 30 mm in height are used to prevent the relative movement between the BM and RMs in the longitudinal direction. But there are nothing at the center of FT-3.5(NS) and FT-4.0(NS) specimens.

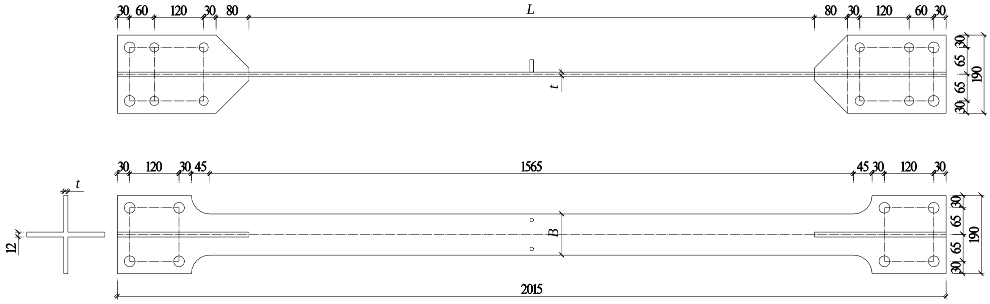

Figure 2: Dimensions of brace member.

Series	Specimen	Steel Type	L	B	t	A(mm^2)	λ	δ_y	Stopper
S-I	FE-4.0	SM400A	1375	99.8	10.3	1028	457	1.91	Yes
S-II	FT-3.5			100.2	10.6	1060	438	1.91	Yes
	FT-3.5(NS)			100.3	10.2	1026	461	1.91	No
	FT-4.0(NS)			100.0	10.6	1060	438	1.91	No

Note: L = length of brace member without cruciform part; B = width; t = thickness; A = sectional area; λ = slenderness ratio on weak axis; P_y = yield axial load; δ_y = Nominal axial yield displacement. Unit: mm.

Table 1: Geometric dimensions and structural properties of BMs.

2.2 Restraining member

Figure 3 gives cross-sectional details of the BRB. The BM is sandwiched by a pair of RMs, and small gaps, d and d_0, are provided between the BM and RMs or filler members. Geometric dimensions and structural properties of RMs are listed in Table 3. The same SM400A mild steel is used for RMs and filler members made of flat steel plates. Nominal values of gap widths are given in Table 3, together with measured material properties of RMs.

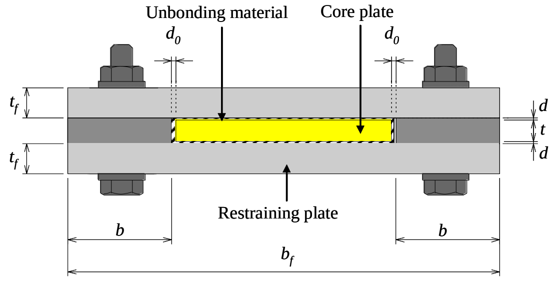

Figure 3: Cross-sectional details of BRB.

Series	Steel Type	E (GPa)	σ_y (Mpa)	ε_y (%)	σ_u (Mpa)	ε_u (%)	ν
S-I	SM400A	210	291	0.139	433	30.2	0.285
S-II		209	251	0.130	409	29.2	0.280

Note: E = Young's modulus; σ_y= yield stress; ε_y=yield strain; σ_u=tensile strength; ν=Poisson ratio.

Table 2: Material constants of brace members.

Series	Steel Type	E^R (Gpa)	σ_y^R (Mpa)	b_f (mm)	t_f (mm)	Gap width (mm)	
						d	d_0
S-I	SM400A	198	260	201	14.3	1	2
S-II		212	264	201	14.3	1	2

Note: E^R=Young's modulus; σ_y^R =yield stress; Notations of b_f, t_f, d and d_0 refer to Figure 3.

Table 3: Geometric dimensions and structural properties of restraining members.

2.3 Testing setup

As shown in Figure 4, the specimen is horizontally pinned by high-strength bolts between two rigid pillars while the BM is horizontally placed. The loading is applied by two jacks parallelly arranged in the vertical direction. The edge of specimens is well treated to avoid eccentric axis load. Before installing specimens, the initial deflection of the specimen is measured in the direction perpendicular to the plate plane so that the initial deflection could direct downward. During a typical experiment, axial displacements of the restrained yielding segment were monitored using eight displacement gauges. These gauges were mounted on both ends of the specimen and displacements were collected by a digital data acquisition system.

2.4 Loading patterns

In the present study, a tensile and compressive alternative cyclic loading controlled by the axial strain of specimens is illustrated in Figure 5. Two cycles of the axial loading of the yield strain amplitude are firstly imposed as an evaluated procedure for testing the specimen and system. For this reason, counting of the cycles starts subsequently. As shown in Figure 5, the constant strain amplitude specified in Table 4 is imposed cyclically until the failure of the BM in the tests. When the loading displacement becomes steady, the strain control equals to the displacement control. Therefore, we conducted the present fatigue tests by controlling the axial displacement.

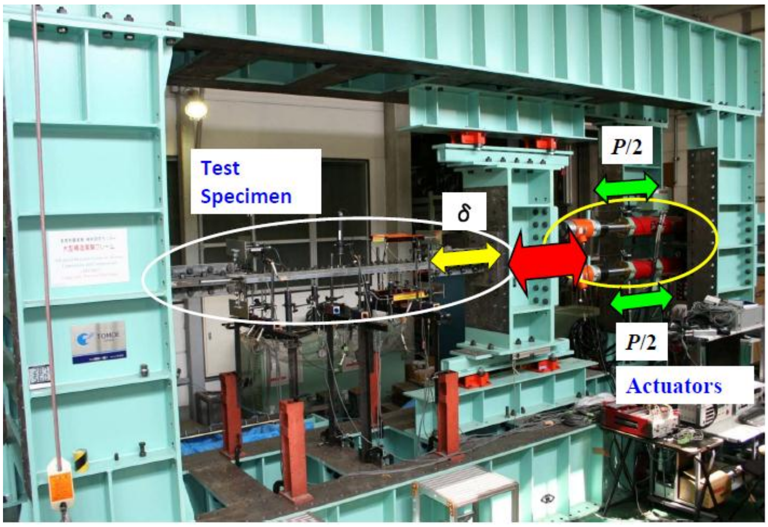

Figure 4: Testing setup

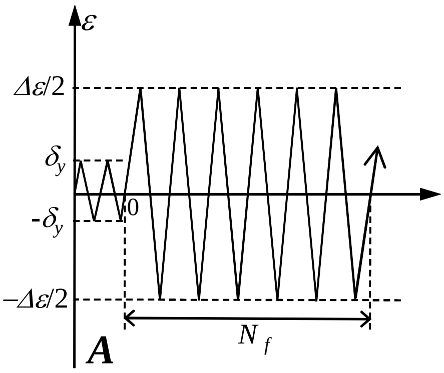

Figure 5: Strain-controlled loading pattern

Series	Test specimen	$\Delta\varepsilon/2$	$\Delta\varepsilon$	$\Delta\varepsilon_e$	$\Delta\varepsilon_p$	N_f	*CID*	Failure position
S-I	FE-4.0	0.040	0.08	0.006	0.074	7	0.96	Mid-span
	FT-3.5	0.035	0.07	0.005	0.065	9	1.18	Mid-span
S-II	FT-3.5(NS)	0.035	0.07	0.005	0.065	5	0.65	Mid-span
	FT-4.0(NS)	0.040	0.08	0.006	0.074	4	0.59	Mid-span

Note: $\Delta\varepsilon/2$ = strain amplitude; $\Delta\varepsilon$ =strain range; $\Delta\varepsilon_e$ = elastic strain range; $\Delta\varepsilon_p$ = plastic strain range; N_f = number of failure cycles; *CID* = cumulative inelastic deformation.

Table 4: Test results of BRB's specimens.

3 TEST RESULTS

3.1 Experimental stress-strain relations

Overall experimental stress-strain curves of the BRBs' specimens are given in Figure 6. The tensile state of BRBs is displayed in the positive direction. The abscissa is the engineering strain, ε, defined as the relative displacement divided by the original length of both ends of the core plate, while the ordinate is the engineering stress, σ, defined as the axial force divided by the original cross-sectional area of the core plate. The core plate indicates the portion of the BM where it behaves plastically. Test results of all the specimens are summarized in Table 4. In addition, stable stress-strain curves were obtained without overall buckling occurrence in the whole loading history of all the specimens even though the maximum strain amplitude was as large as 4%.

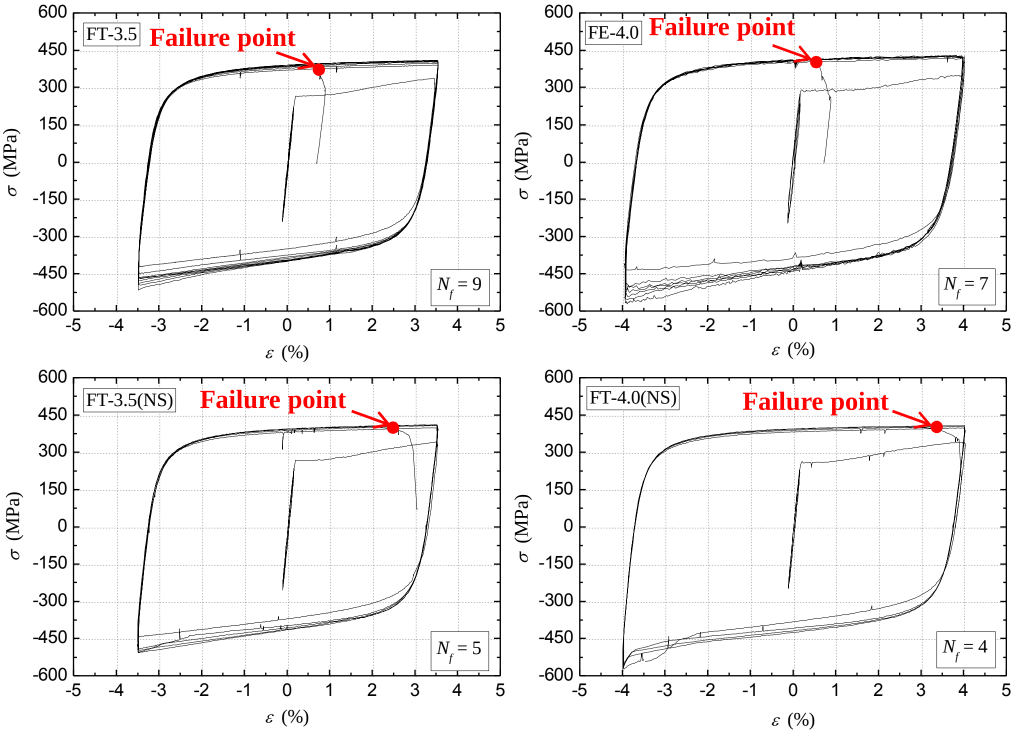

Figure 6: Stress-strain relations.

It is shown in the hysteretic curve of the FT-3.5 specimen with the constant strain amplitude that the first loop is hardly affected by the strain hardening effect while the others are remarkably influenced by the strain hardening effect. At the last loop, the strength decreases rapidly in the tensile state of the BM and then unloading is applied when the axial force fells down by over 10% of the maximum axial force. The same results can be observed in other specimens with the constant strain amplitude.

Hysteretic behaviors of BRB's specimens are unsymmetric in tension and compression, and the maximum absolute compressive stress is 21% to 37% larger than the maximum tensile stress. The reason for this behavior is explained as follows: with the strain amplitude increasing in the compressive state, the contact force and the friction between RMs and the BM increased under the multi-wave deformation.

As listed in Table 4, the failure cycle number N_f of the FT-3.5 specimen with the stopper under the same 3.5% strain amplitude decreased from 9 to 5 in contrast with the FT-3.5(NS) specimen without the stopper, while N_f of the FE-4.0 specimen with the stopper under the same 4.0% strain amplitude decreased from 7 to 4 in contrast with the FT-4.0(NS) specimen without the stopper. It is concluded that the stopper used to prevent the relative displacement obviously affects the low-cycle fatigue performance of steel BRBs.

3.2 Failure mode

Failure modes of the BMs are presented in Figure 7, while failure positions of all the test specimens are sketched out in Figure 7(e). It is clear that crack initiating from the mid-span of the BMs induced the failure of specimens. From the failure modes of the FT-3.5 and FE-4.0 specimens with the stoppers, crack began to appear on the side of the BM and propagate in the transversal direction, but from the failure modes of the FT-3.5(NS) and FT-4.0(NS) specimens without the stoppers, crack began to develop in the middle of the BM and the fold deformations were observed after the failure of the BRB's specimens. So, it is concluded that the stoppers have a noticeable impact on the failure of the BRB, and then the analytical models are proposed to simulate the behaviors of the BRB with or without the stoppers.

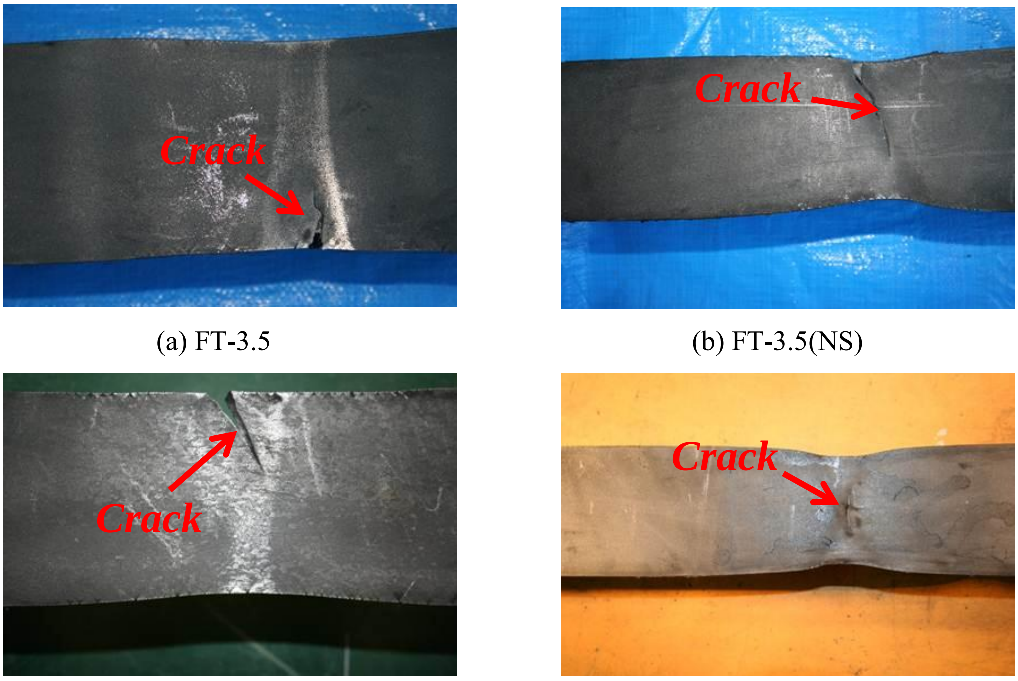

(a) FT-3.5

(b) FT-3.5(NS)

(c) FE-4.0

(d) FT-4.0(NS)

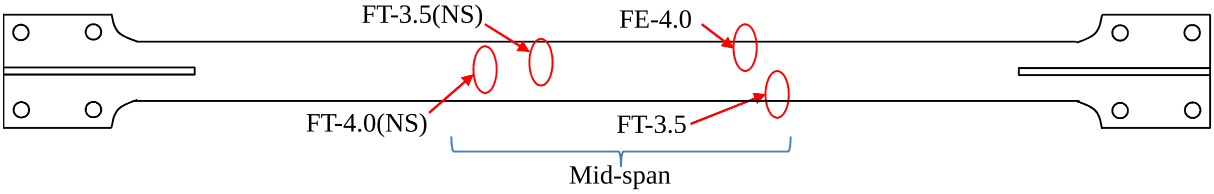

(e) Failure position.

Figure 7: Failure modes of BRB's specimens

3.3 Cumulative inelastic deformation

A measure used in practice to describe the plastic demand on a BRB element is the cumulative inelastic strain, or alternatively, the cumulative inelastic deformation (*CID*). The *CID*, which is expression of the cumulative plastic deformation, is defined by

$$CID = \sum_i \Delta\beta_p^i \tag{1}$$

where, $\Delta\varepsilon_p^i$ = plastic strain during each visit i into the inelastic range, as shown in Figure 8.

The *CID* values of all test specimens are summarized in Table 4. The calculation of the *CID* was achieved with an algorithm that detects local peaks and valleys in the strain history. *CID* values indicate that the *CID* performance of steel BRBs with the stoppers even under the strain amplitude, larger than 3%, can meet the requirements of high-performance BRBs but *CID* performance of steel BRBs without the stoppers cannot meet the requirements of high-performance BRBs.

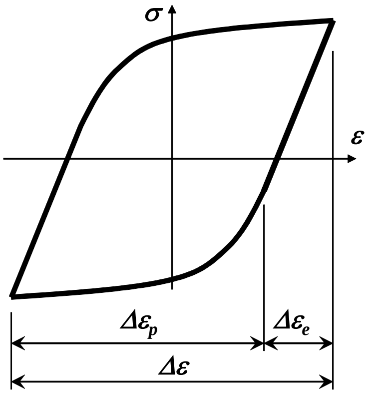

Figure 8: Stress-strain loop.

4 PROPOSED MODELS

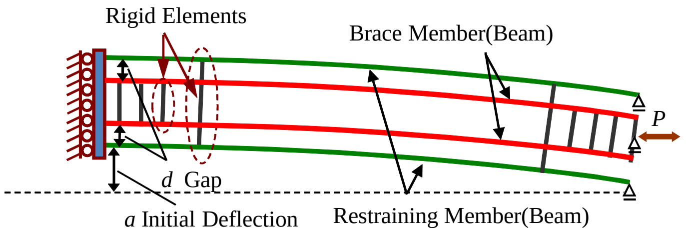

(a) *Half Model*

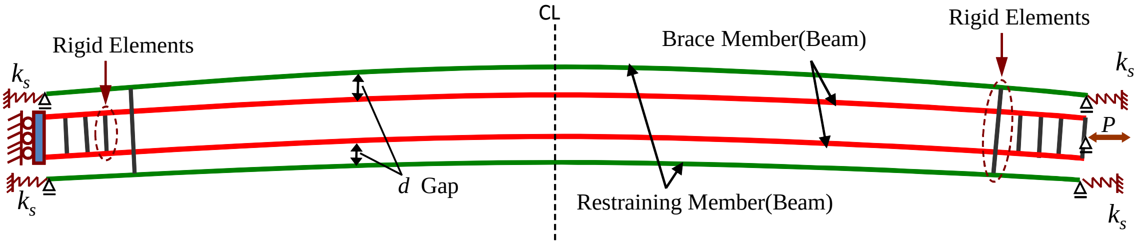

(b) *Whole Model*

Figure 9: Analytical models based on beam element.

In order to simulate the mechanical behaviors of the BRBs with or without stoppers, two analytical models built in ABAQUS[12] are given as follows.

Considering that stoppers are welded on the BM, the mechanical behavior of the BRB is symmetric. So an elastic-plastic 2D model simulating the BRB with the stoppers is proposed and illustrated in Figure 9(a), where half a BRB is modeled under the symmetry condition. A pair of RMs is simulated as two 2D beams equably divided into 54 segments and the BM is also simulated using two 2D beams considering that it is easy to accurately simulate the contact between the BM and RMs. A number of rigid elements between the BM beams are used to satisfy the linear plane assumption. The same elements are applied between the RMs to simulate high-strength bolts. Initial deflection of a sinusoidal pattern is considered with the maximum value of a, which is set to one thousandth of the length of the BM without cruciform part. The constant gap d between the RMs and the BM is assumed.

The unbonding material was stuck to the BM as the isolation material in order to reduce the friction between the BM and RMs. So, the rigidity of the unbonding material is neglected in this model. However, when one of the BM beams comes into contact with a RM beam, friction effects will exist between them. As shown in Fig. 6, the compressive force is over 20% larger than the tensile force, and therefore the static friction coefficient μ is considered in the model.

Moreover, the horizontal displacement and the rotation are restrained at the mid-span nodes due to symmetry conditions, the vertical displacement is restrained at the right end nodes and the rotation is restrained at the BM's end where the force is applied. A general purpose finite element analysis software ABAQUS is used with 2D Timoshenko beam element (B21) considering shear deformation[12]. The modified two surface model developed by the authors [13] is used for the constitutive law in the analysis.

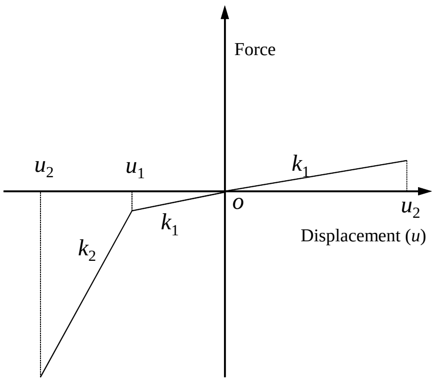

Figure 9: Nonlinear spring force-relative displacement relation.

Because the stoppers were not welded in the FT-3.5(NS) and FT-4.0(NS) specimens' tests, the RMs of the steel BRB, were driven by the friction at the beginning of low-cycle fatigue tests, and were stopped because of the interaction between the RMs and the cruciform section part of the BM in the axial direction. Therefore, the second elastic-plastic model of a whole BRB is presented in Figure 9(b) and the different boundary conditions of the RMs are given. The four nonlinear springs are used to simulate this movement and the force-relative displacement relation of nonlinear springs is given in Figure 9. As shown in Figure 9, the nonlinear spring behavior is defined by a group of the stiffness coefficient and the displacement. The value of k_1, about one thousandth of the axial stiffness of the RM, makes the RM free and the value of k_2, equal to the axial stiffness of the RM, prevents the RM's movement. The displacement u_1 is decided by the gap between the RM and the cruciform section part of the BM, so u_1 is set to 32.5mm. The elements, initial deflection, friction coefficient and material constants are same to the first elastic-plastic model. In order to compare with each other conveniently, the first model is called *Half Model*, and the second model is called *Whole Model*.

5 COMPARISON WITH TEST RESULTS

5.1 Experimental data

In this section, low-cycle fatigue test results of the FT-3.5 and FT-3.5(NS) specimens will be conducted to evaluate the proposed analytical models. As shown in Figure 10, the maximum absolute compressive stress at the first loop of the FT-3.5(NS) specimen is about 5% larger than the FT-3.5 specimen, but it is nearly the same as the FT-3.5 specimen. It is considered that the difference of the first loop is affected by the constraint of the RM. However, the indifference of the last loop is considered to affect by two factors: one is that the stoppers of the FT-3.5 specimen had broken at last, and another is that the residual deformation of the previous loops had an effect on the last loop. So in the next section, we will only use the data of the first loop as the criteria to check the analytical results.

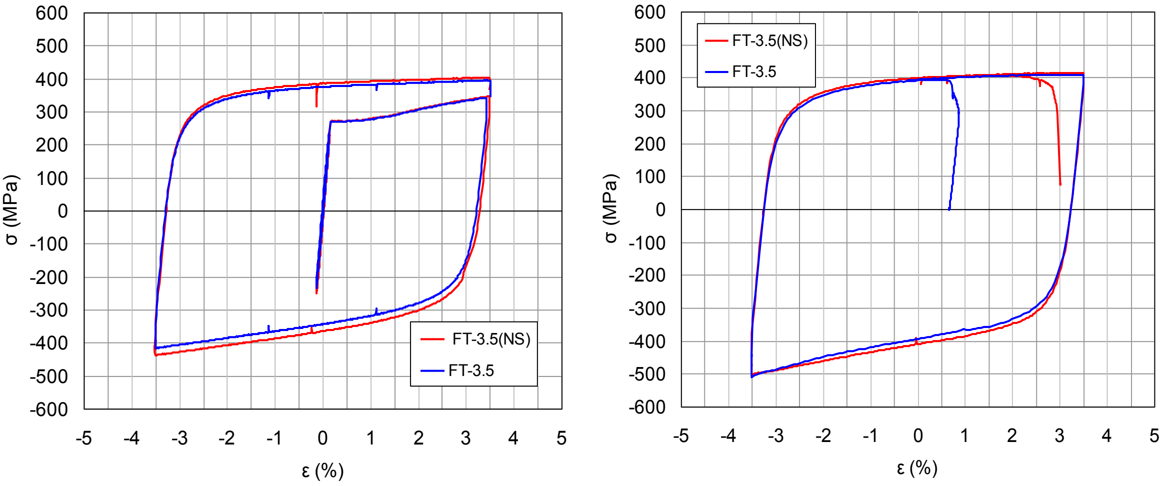

(a) First loop

(b) Last loop

Figure 10: Stress-strain relations (μ=0.0).

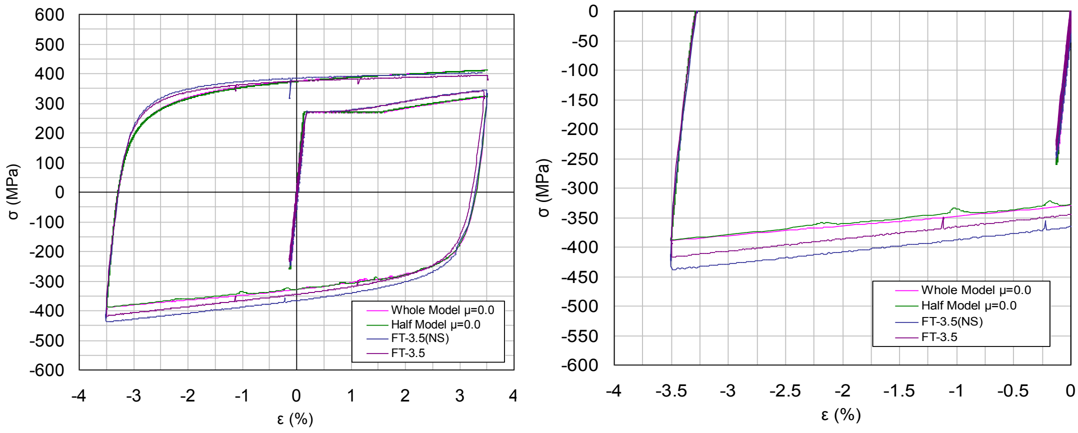

(a) Overall view

(b) Partial view

Figure 11: Stress-strain relations (μ=0.0).

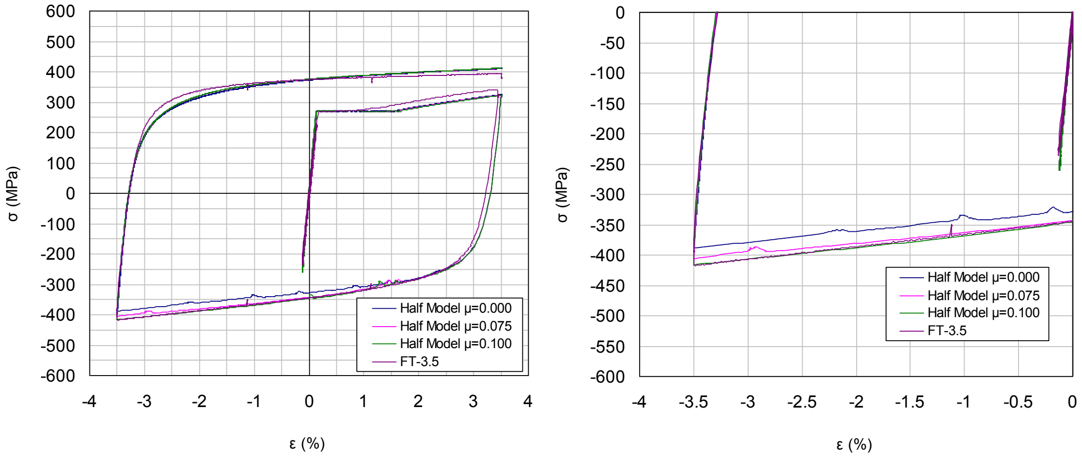

(a) Overall view (b) Partial view

Figure 12: Stress-strain relations of *Half Models* (μ=0.0, 0.075, 0.1).

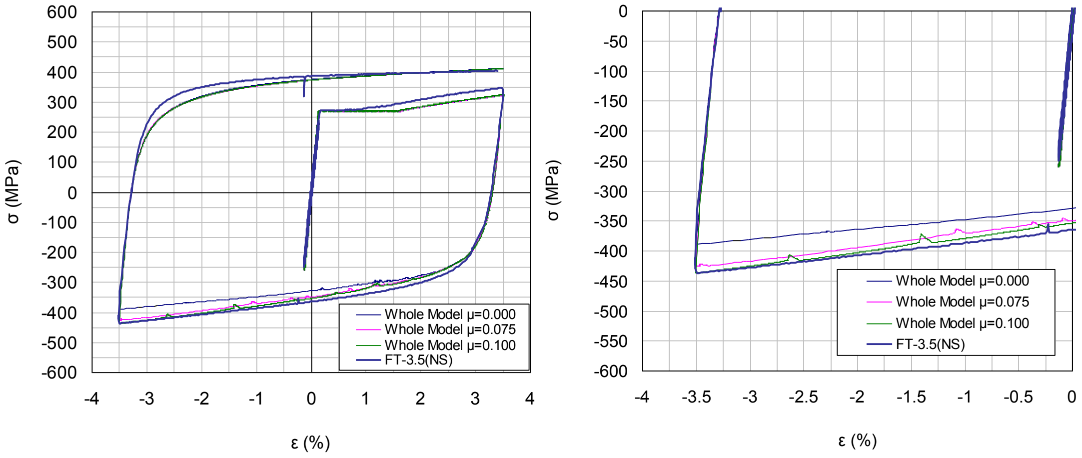

(a) Overall view (b) Partial view

Figure 13: Stress-strain relations of *Whole Models* (μ=0.0, 0.075, 0.1).

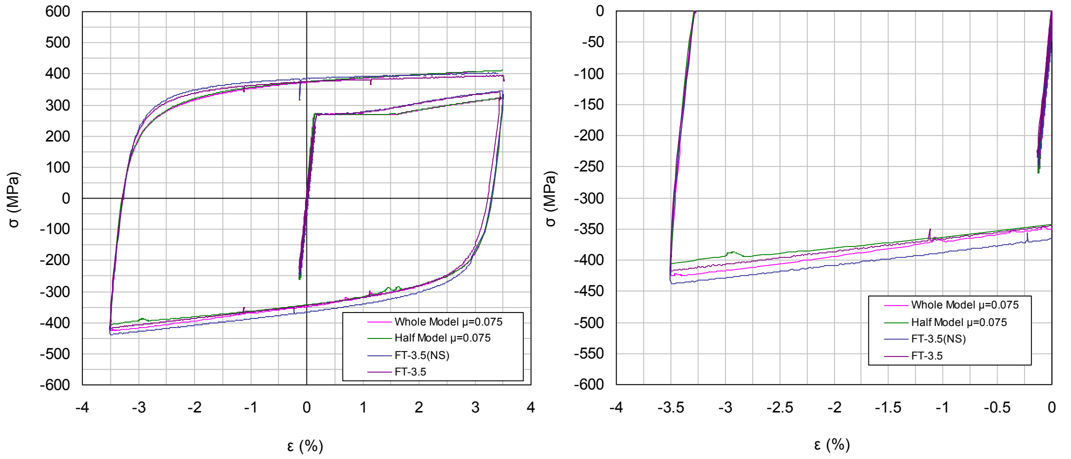

(a) Overall view (b) Partial view

Figure 14: Stress-strain relations (μ=0.075).

5.2 Stress-strain relation

Stress-strain relations of *Half Model* and *Whole Model* are given together with the experimental data in Figure 11. Stress-strain relations of two analytical models are identical and symmetric in tension and compression when the friction between the BMs and the RM is neglected. However, the maximum absolute compressive stress of the first loop of the FT-3.5(NS) specimen is about 13% larger than the results of *Half Model* or *Whole Model*. It can be seen that if the friction is neglected in the analytical model, *Half Model* and *Whole Model* cannot simulate the experiment accurately, but from nearly the same hysteretic behavior, *Half Model* and *Whole Model* are proper.

Stress-strain relations of *Half Model* and *Whole Model* with different friction coefficients are given together with the experimental data in Figures 12 and 13. It is clear that with the friction coefficient increasing, *Half Model* and *Whole Model* can effectively simulate the mechanical behavior of the FT-3.5 and FT-3.5(NS) specimens. As shown in Figure 14, the friction coefficient of 0.075 is regarded as the right value for the following simulations.

5.3 Deformation of BM

The BM's deformations of *Half Model* and *Whole Model* with the same 3.5% compressive strain amplitude are compared in Figure 15. The multi-wave deformation of the *Half Model* is symmetric because of the symmetry conditions. It can be seen that the BM of *Half Model* has fifteen peaks and fifteen valleys, while the BM of *Whole Model* has seventeen peaks and seventeen valleys. So, some of wave peaks of *Whole Model* is sharper than the peaks of *Half Model*. It is considered to be one of the reasons why the failure life of the FT-3.5(NS) specimen is shorter than the failure life of the FT-3.5 specimen.

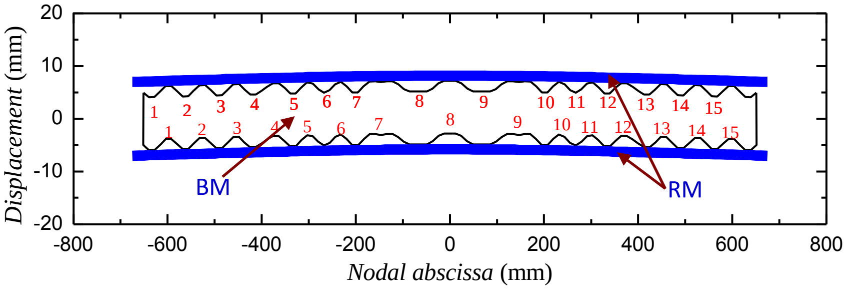

(a) *Half Model*

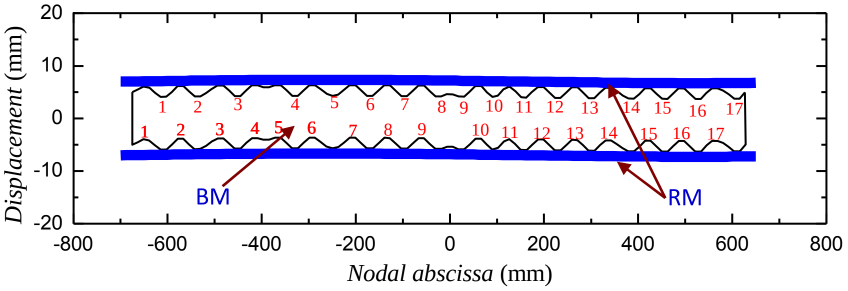

(b) *Whole Model*

Figure 15: Deformation of brace member.

6 CONCLUSION

In this study, low-cycle fatigue tests of benchmark specimens with or without the stoppers were carried out to evaluate the proposed analytical models. The main results are summarized as follows:

1) Low-cycle fatigue tests were conducted to verify that the BRB's specimens with the stoppers possess better low-cycle fatigue performance than the specimens without the stoppers.

2) It was experimentally indicated that the *CID* performance of steel BRBs with the stoppers even under the strain amplitude, larger than 3%, can meet the requirements of HPBRBs but the *CID* performance of steel BRBs without the stoppers cannot meet the requirements of HPBRBs.

3) It is clear that the friction coefficient of 0.075 is regarded as the right value for the simulations and *Half Model* and *Whole Model* can effectively simulate the mechanical behavior of the BRB with or without the stoppers.

REFERENCES

[1] M. Iwata, M. Murai. Buckling-restrained brace using steel mortar planks; performance evaluation as a hysteretic damper. *Earthquake Engineering & Structural Dynamics*, **35**, 1807-1826, 2006.

[2] L.A. Fahnestock, J.M. Ricles, R. Sause. Experimental evaluation of a large-scale buckling-restrained braced frame. *Journal of Structural Engineering (ASCE)*, **133**, 1205-1214, 2007.

[3] T. Usami, Z.H. Lu, H.B. Ge. A seismic upgrading method for steel arch bridges using buckling-restrained braces. *Earthquake Engineering & Structural Dynamics*, **34**, 471-496, 2005.

[4] C.C. Chou, S.Y. Chen. Subassemblage tests and finite element analyses of sandwiched buckling-restrained braces. *Engineering Structures*, **32**, 2108-2121, 2010.

[5] H. Nakamura, T. Takeuchi, Y. Maeda *et al.* Fatigue properties of practical-scale unbonded braces. *Nippon Steel Technical Report*, 2000.

[6] AISC, 2005. Seismic provisions for structural steel buildings, Chicago, Illinois.

[7] T. Usami, H.B. Ge, A. Kasai. Overall buckling prevention condition of buckling-restrained braces as a structural control damper. *Proceedings of the 14th World Conference on Earthquake Engineering*, Beijing, China, 2008.

[8] T. Usami. Developing high-performance damage control seismic dampers. *Proceedings of the 10th symposium on ductile design method for bridges (Special Lecture)*, Tokyo, Japan, 2007.

[9] T. Usami, T. Sato. Low-cycle fatigue tests and verification method for a steel buckling-restrained brace. *Journal of Structural Engineering, JSCE*, **56A**, 486-498, 2010(in Japanese).

[10] T. Usami, C.L. Wang, J. Funayama. Low-cycle fatigue tests of a type of buckling restrained braces. *Proceedings of 12th East Asia-Pacific Conference on Structural Engineering and Construction*, HongKong, 2011.

[11] J. Funayama, C.L. Wang, T. Usami. Improving low-cycle fatigue performance of a type of steel brbs by weld toe-finishing. *Journal of Structural Engineering, JSCE*, **57A**, (in Japanese), 2011.

[12] ABAQUS, 2008. Analysis user's manual(version 6.8). ABAQUS Inc., Pawtucket, R.I.

[13] C. Shen, I. Mamaghani, E. Mizuno *et al.* Cyclic behavior of structural steels. Ii: Theory. *Journal of Engineering Mechanics*, **121**, 1165-1172, 1995.

COMPDYN 2011
3rd ECCOMAS Thematic Conference on
Computational Methods in Structural Dynamics and Earthquake Engineering
M. Papadrakakis, M. Fragiadakis, V. Plevris (eds.)
Corfu, Greece, 25–28 May 2011

NUMERICAL SIMULATIONS OF THE WARTH BRIDGE SEISMIC RESPONSE

Pedro Delgado[1], **Nelson Vila Pouca**[2], **António Arêde**[2], **Rui Faria**[2], **Raimundo Delgado**[2]

[1] Polytechnic Institute of Viana do Castelo, Portugal
Avenida do Atlântico, 4900-348 Viana do Castelo
pdelgado@estg.ipvc.pt

[2] University of Porto, Civil Engineering Department
Rua Dr. Roberto Frias, s/n, 4200-465 Porto, Portugal
nelsonvp@fe.up.pt, aarede@fe.up.pt, rfaria@fe.up.pt, rdelgado@fe.up.pt

Keywords: Numerical structural modeling, Non-linear behavior, Seismic response, Bridge piers, asynchronous, synchronous

Abstract. *This work consists on the seismic analysis of the Talübergang Warth bridge studied within the framework of the European research project entitled VAB - Vulnerability Assessment of Bridges [1]. This case-study bridge was built in Austria during the 70's, designed to a very low seismic level, consisting of a seven span continuous deck supported on two abutments and six rectangular hollow section piers, the latter with some peculiar characteristics concerning the reinforcement detailing whose modeling is quite demanding for cyclic response simulation. Still in the VAB project context, a physical scaled model of the bridge was also experimental tested under pseudo-dynamic conditions at the JRC-Ispra [2] and the results were compared against numerical simulations carried out by the FEUP team involved in the project.*

The non-linear behavior is considered concentrated in the piers, which are discretized with (i) a refined constitutive model or (ii) a Plastic hinge type model for the nonlinear material behavior simulation. For the numerical prediction of the seismic performance of the Talübergang Warth bridge these methodologies were adopted with the seismic action taken as an asynchronous and synchronous ground motion induced along the transverse direction only.

The main results of the seismic analyses will be presented focusing on the essential role that the longitudinal reinforcement curtailment plays on macro-crack localization, which leads to a shift of the plastic hinge (usually at the base of piers) up to the elevation where a significant reduction of the longitudinal reinforcement takes place. From the comparison of the numerical predictions with the experimental results, as recorded during the pseudo-dynamic tests performed at the JRC, the capability from the damage model to provide accurate simulations of the seismic performance of the bridge was brought into evidence, even when the piers are difficult to simulate due to the concrete hollow section geometry and to the unusual reinforcement layout adopted in the design (as in this case).

1 INTRODUCTION

Recent earthquake effects on reinforced concrete bridges have shown that many behave poorly and some possess very low levels of safety, to the extent that they are at risk of collapse, especially those built according to outdated seismic codes. Thus, efforts must be made to develop and apply accurate bridge assessment methodologies that will assist in the determination of failure probability in order to evaluate the need for retrofitting and to improve seismic safety levels.

The difficulties of carry out analyses with methodologies that adopt hysteretic non-linear material behavior increase significantly with the complexity degree of the model, involving a compromise between the accuracy and time computer consuming, and with the several parameters that is necessary to define. In the current work a comparative study with several strategies to evaluate the seismic behavior of bridges was intended to carry out. Therefore, two numerical models were used:

(i) PNL [3] –non-linear behavior lumped in plastic hinges.

(ii) Damage Model [4] – refined constitutive model for the nonlinear material behavior.

The numerical prediction of the seismic performance of this bridge adopts a peculiar two-dimensional modeling of the entire bridge [3, 5] consisting of a simplified plane model with easy practical application and involving reduced calculation efforts while maintaining adequate accuracy. The bridge structural modeling is carried out with plane elements, bars or 2D finite elements, maintaining the essential features of the 3D transverse response through an appropriate plane structural simulation. This is achieved by considering the deck and piers in the same plane, while the top pier horizontal displacement and the correspondent horizontal transversal deck displacement are constrained by uniaxial tie elements in order to have the same value. The comparative analyses were carried out with increasing seismic action level, in order to show the sensibility of the results with the different non-linear levels. Finally, the performances and solutions of the different methodologies are compared and discussed.

2 DESCRIPTION OF STUDIED BRIDGE

The Talübergang Warth bridge was studied within the framework of the European research project entitled VAB - Vulnerability Assessment of Bridges [1, 2], and is illustrated in Figure 1. This bridge, at about 63 km to the south of Vienna, is formed by a deck with 7 spans and a total length of 459m, and it is supported by 6 piers and 2 abutments. Piers’ nomenclature is also indicated in Figure 4, to ensure a clear identification.

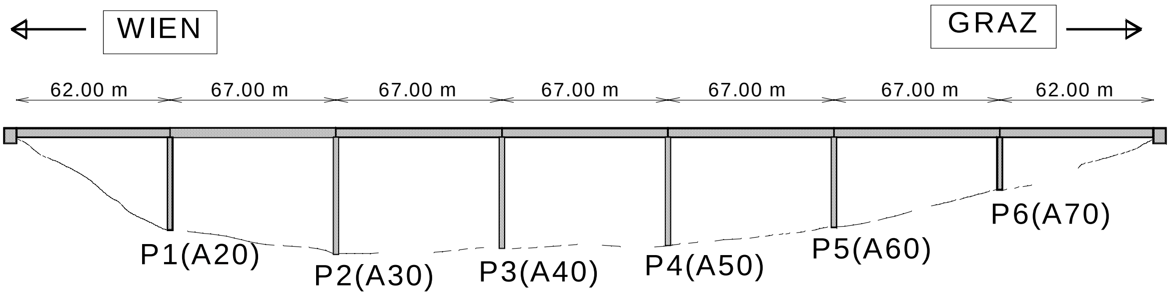

Figure 1: Talübergang Warth bridge and piers’ nomenclature.

The geometry of the bridge piers was defined on the basis of the design drawings documented in Talübergang Warth Bridge Drawings (1975). Figure 2 and Table 1 reproduce the basic geometry of the piers, both for the concrete section and for the footings (piers height L refers to the distance between the top of the footing and the base of the deck bearings.). All the piers have 6.8×2.5m^2 concrete hollow sections.

In what concerns the curtailment of the longitudinal reinforcement, involving bars of different diameters, 4 regions are depicted in Figure 2. Details about the reinforcement layout are referred in previous publications [1, 6]. For piers P2, P3 and P4 the first interruption of the longitudinal rebars occurs close to the foundation, leading to a reduction of about 50% on the amount of steel reinforcement.

Transversal reinforcement is provided by a single rectangular stirrup on each wall of the hollow section [1, 6], according to the following distribution: *(i)* $A_{sw} = \phi 12//0.20$m on the first 1m layer close to the piers footing, and *(ii)* $A_{sw} = \phi 8//0.20$m elsewhere.

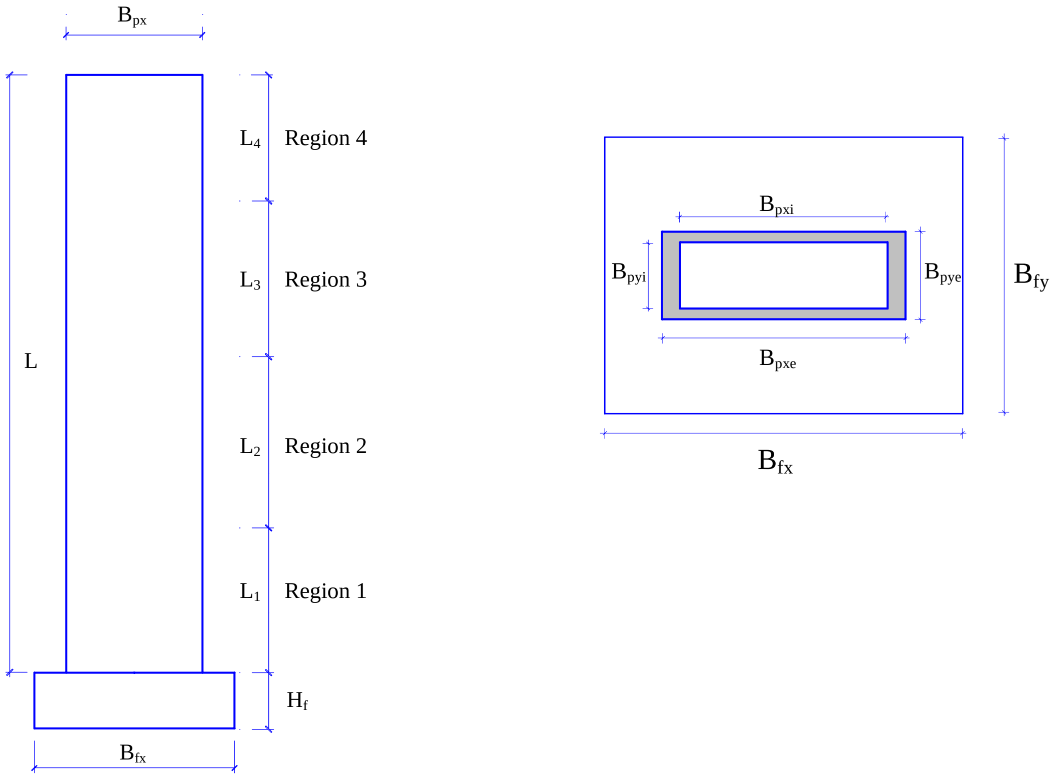

Figure 2: Basic geometry nomenclature.

Pier	L (m)	L/B_{pxe}	L/B_{pye}	Hollow section	Foundation		
					B_{fx}	B_{fy}	H_f
P1 (A20)	29.8	4.4	11.9	B_{pxe} = 6.8m B_{pxi} = 5.8m B_{pye} = 2.5m B_{pyi} = 1.9m	10.8	10.1	3.45
P2 (A30)	38.9	5.7	15.6		10.2	8.0	2.80
P3 (A40)	37.8	5.6	15.1		10.2	8.0	2.80
P4 (A50)	36.0	5.3	14.4		10.2	8.0	2.80
P5 (A60)	30.0	4.4	12.0		10.5	9.0	3.20
P6 (A70)	16.9	2.5	6.8		10.4	9.5	3.20

Table 1: Basic geometry.

Taking into consideration the stirrup arrangement documented in the design drawings, it is doubtful that concrete could benefit from any significant effect of confinement. Accordingly, for Talübergang Warth bridge piers the class B400 concrete was assumed as under unconfined conditions, with the material properties reproduced in Table 2 (average values).

E (GPa)	f_{co} (MPa)	ε_{co}	f_o^+ (MPa)	f_{cm} (MPa)	ε_{cm}	Z
33.5	43.0	2.0‰	3.1	–	–	100

Table 2: Concrete properties (class B400, unconfined).

Table 3 resumes the average material properties assumed for the longitudinal and transversal rebars, defined as corresponding to a class RT50 steel.

f_{sy} (MPa)	f_{su} (MPa)	ε_{su}	ε_{sh}	E_h/E	R_o	a_1	a_2
545	611	100‰	5.0‰	0.0034	20	18.5	0.15
f_{su} and ε_{su} are the ultimate strength and strain for the steel.							

Table 3: Steel properties (class RT50).

3 SIMULATION OF THE PSD TEST (ASYNCHRONOUS MOTION)

The Talübergang Warth bridge was tested on the ELSA Laboratory (Joint Research Centre, at Ispra) under pseudo-dynamic conditions and asynchronous ground motion induced along the transverse direction only, being all the experimental results described in the reference Pinto et al. [2].

The non-linear behavior is considered concentrated in the piers, which are discretized with a refined constitutive model for the nonlinear material behavior simulation. The refined numerical model combines a 2D plane-stress finite element discretization for the concrete with 2-noded truss elements to include the steel reinforcement. The concrete behavior is simulated resorting to a constitutive model based on Continuum Damage Mechanics, involving two independent scalar damage variables to account for degradation under tensile and compressive stress conditions. The cyclic response of steel is simulated via the Giuffré-Menegotto-Pinto model [7].

The numerical analysis were performed in a sequential way, where the accelerograms were inputted according to increasing intensities, in order to better reproduce the experimental tests; when a given seismic action is considered the structure has already been modified due to the non-linear effects induced by the previous one.

Figure 3 illustrates the comparison of the pier P3 top displacement responses obtained numerically (using the Damage Model) and experimentally (pseudo-dynamic test performed at the JRC), for three different intensity level earthquakes. These three responses are in general very close as much in frequency as in maximum values, except for the high level earthquake where some differences can be found on the response last part.

From the comparison of the numerical simulations with the experimental results, the capability from the damage model to provide accurate simulations of the seismic performance of the bridge was brought into evidence, even when the piers are difficult to simulate due to the concrete hollow section geometry and to the unusual reinforcement layout adopted in the design. In fact, the longitudinal reinforcement curtailment represents an important influence on macro-crack localization, which leads to a shift of the plastic hinge up to the elevation where a significant reduction of the longitudinal reinforcement takes place.

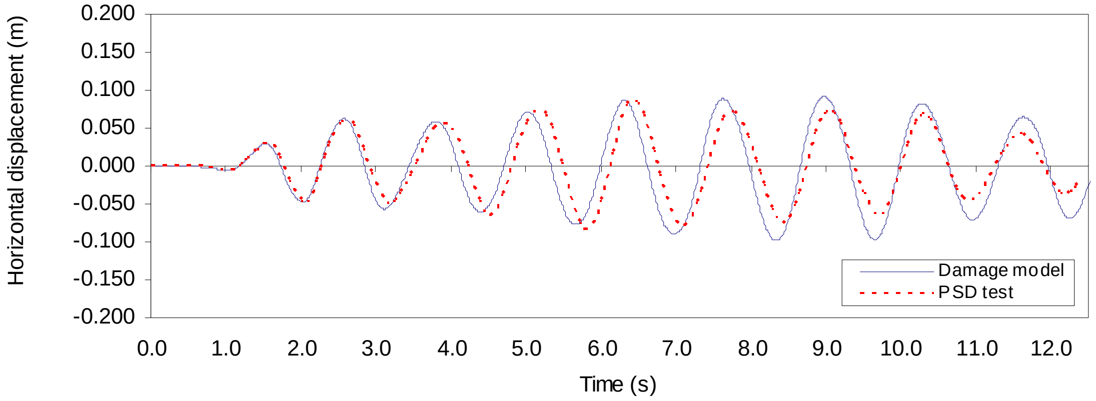

a) Low level earthquake

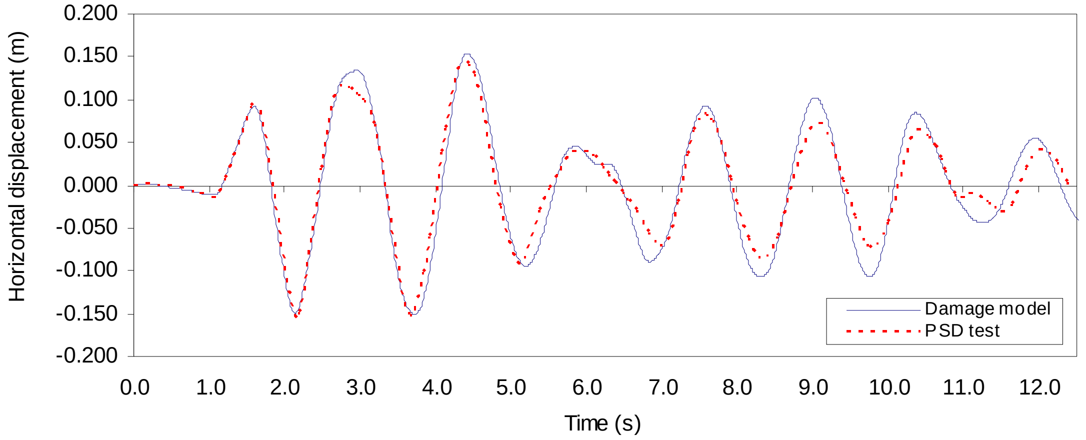

b) Moderate level earthquake

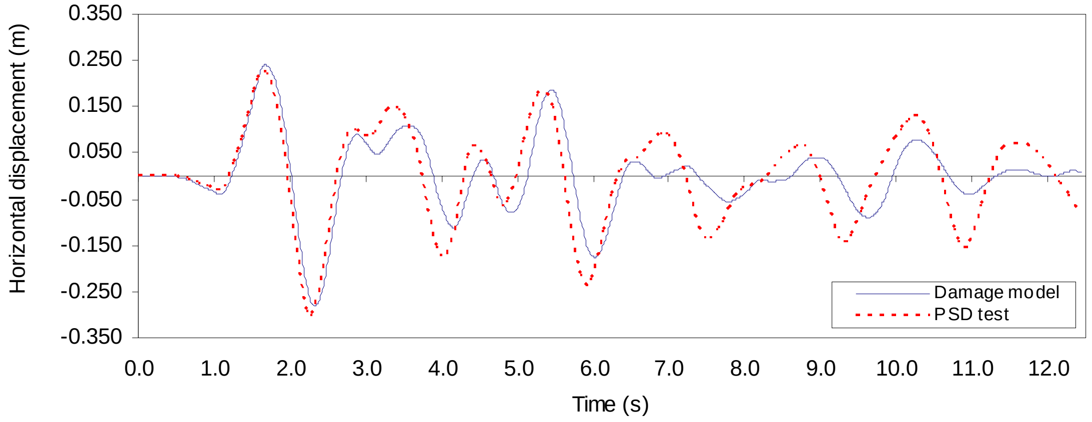

c) High level earthquake

Figure 3: Top horizontal displacement history of pier P3.

4 SYNCHRONOUS NUMERICAL ANALYSIS

In this section, the numerical analyses were carried out assuming synchronous ground motion in the transverse direction, being considered the pier P3 accelerogram as the reference.

Again the numerical analysis were performed in a sequential way, where the accelerograms were inputted according to increasing intensities, therefore; when a given seismic action is considered the structure has already been modified due to the non-linear effects induced by the previous one. The non-linear behavior was considered concentrated in the piers, which are discretized with (i) the Damage model, a refined constitutive model or (ii) the PNL model [3, 8], a plastic hinge type model for the nonlinear material behavior simulation.

Once the capability from the damage model to provide accurate simulations of the bridge seismic performance was brought into evidence from previous asynchronous responses, it is reasonable to assume that accurate response simulations are expected for synchronous input motion.

Figure 4 illustrates the comparison of the pier P3 top displacement responses obtained numerically, using the Damage Model and the plastic hinge model, for three different intensity level earthquakes. The first response, for low level earthquake, has similar results for both models in the initial seconds, but after half time the frequencies become different and higher maximum displacement values were achieved for the plastic hinge model. For subsequence responses of the numerical simulations, it was difficult to achieve accurate results for the plastic hinge model due to the unusual reinforcement layout adopted in the design, the longitudinal reinforcement curtailment represents an important influence on crack localization and plastic hinge formation, which leads to a shift of the plastic hinge up to the elevation where a significant reduction of the longitudinal reinforcement takes place.

For this assumption of consider the bridge synchronous ground motion as the pier P3 accelerogram (used in asynchronous analysis), the comparison between the asynchronous and synchronous response obtained with the damage model, Figure 3 and Figure 4, allows to verify that maximum peak displacement is reasonable similar, for moderate and high level earthquake. Both responses are similar for initial seconds, however with some differences for final seconds of the accelerograms.

After these first results and conclusions obtained with the plastic hinge modeling, a second set of simulations was carried out assuming the longitudinal reinforcement reduction at the pier base and therefore the corresponding decrease on the yielding moment, but keeping the plastic hinges in the same place (near the foundation), although the referred longitudinal reinforcement curtailment takes place in region 2 (see Figure 2). Figure 5 illustrates the comparison of the pier P3 top displacement responses obtained numerically with the referred plastic hinge model modifications, for three different intensity level earthquakes.

Generically, as is possible to see from Figure 5, the results for the plastic hinge model considering the longitudinal reinforcement reduction improve the quality of the responses, once both damage model and PNL model are now more similar responses. In fact, regarding frequencies and maximum displacement values, both responses are now significantly closer.

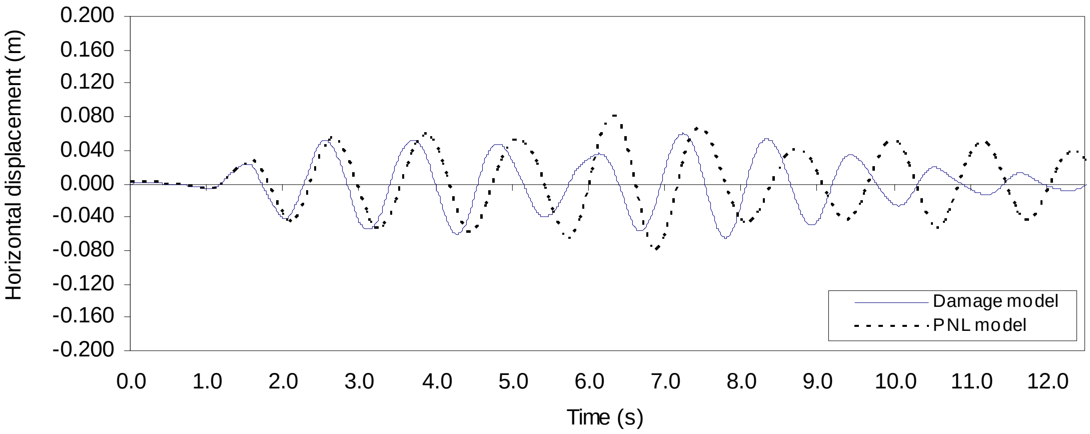

a) Low level earthquake

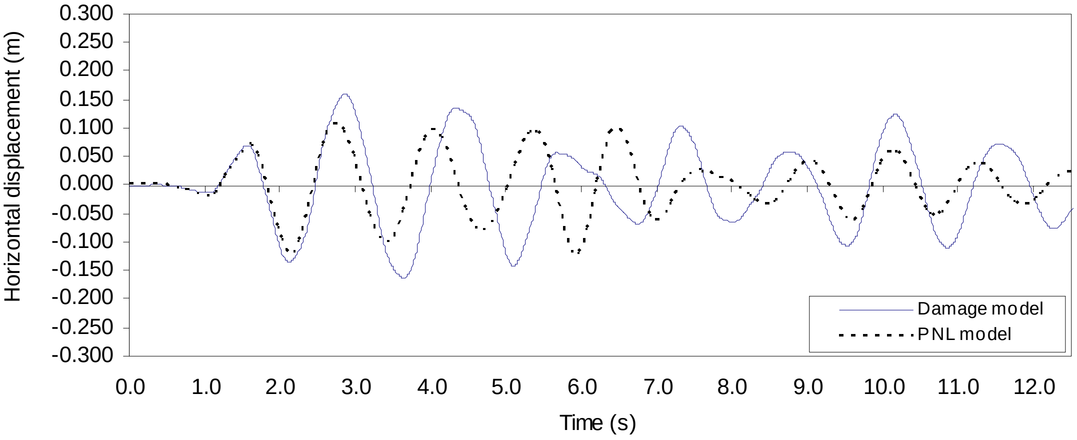

b) Moderate level earthquake

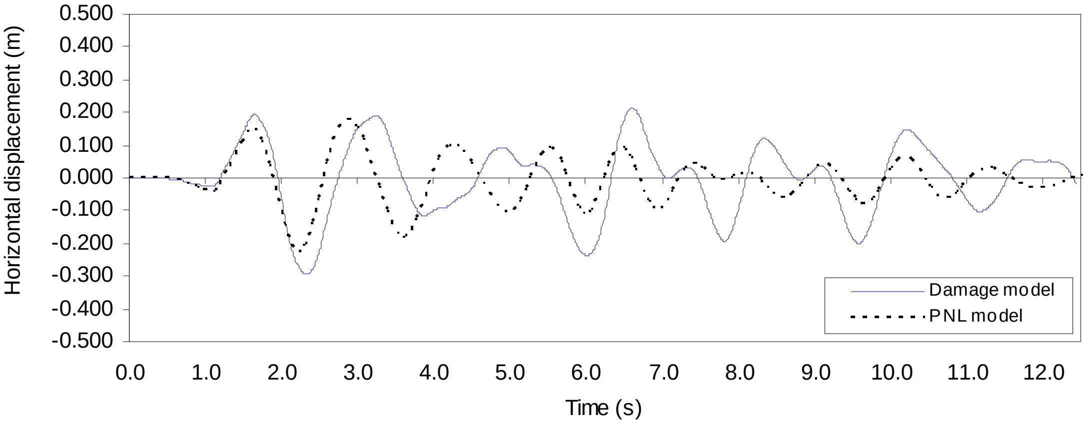

c) High level earthquake

Figure 4: Top horizontal displacement history of pier P3.

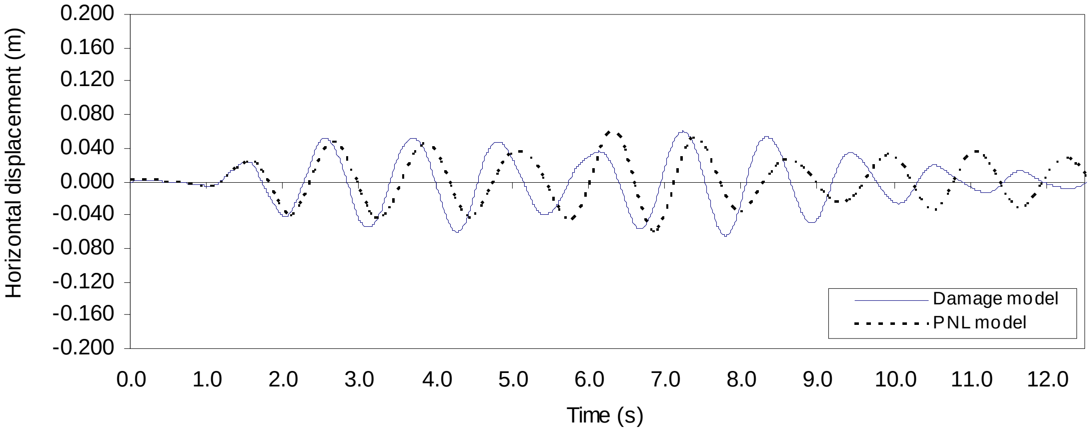

a) Low level earthquake

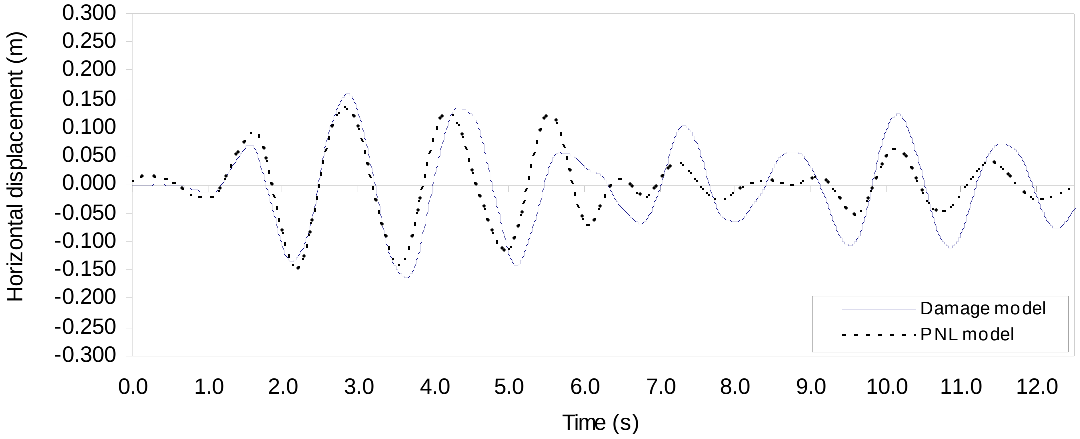

b) Moderate level earthquake

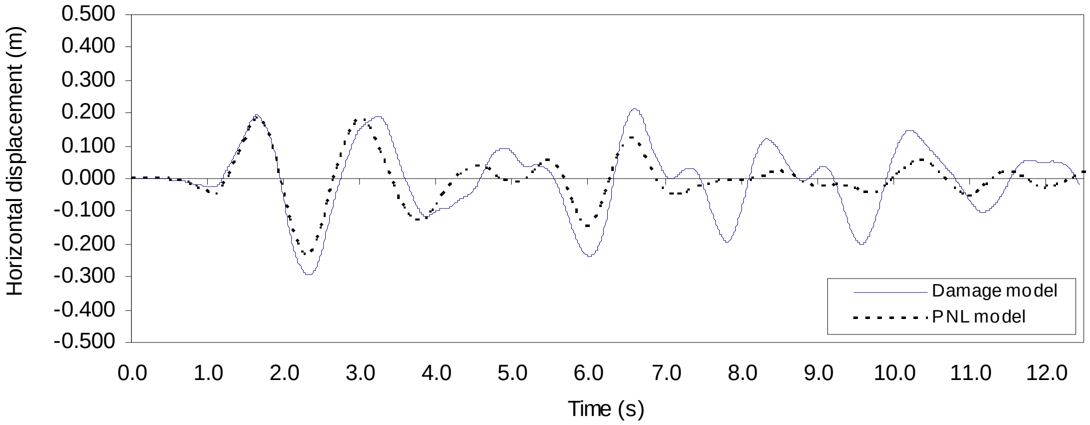

c) High level earthquake

Figure 5: Top horizontal displacement history of pier P3 (with long. reinf. reduction).

5 CONCLUSIONS

- The Talübergang Warth bridge, studied in the VAB project context, was experimental tested under asynchronous pseudo-dynamic conditions at the JRC and the results were compared against numerical simulations carried out with the damage model.
- Displacement responses obtained numerically and experimentally, for three different intensity level earthquakes, are in general very close as much in frequency as in maximum values, being highlighted the capability from the damage model to provide accurate simulations of the seismic performance of the bridge even when the longitudinal reinforcement curtailment represents an important influence on macro-crack localization.
- Once the capability from the damage model to provide accurate simulations of the bridge seismic performance was brought into evidence from asynchronous responses, it is reasonable to assume that accurate response simulations are expected for synchronous input motion.
- The comparison between the asynchronous and synchronous response obtained with the damage model allows to conclude that maximum peak displacement is reasonable similar, for moderate and high level earthquake.
- For the synchronous numerical simulations with damage model and a plastic hinge model, it was difficult to achieve accurate results for the plastic hinge model due to the longitudinal reinforcement curtailment, which leads to a shift of the plastic hinge up to the elevation where a significant reduction of the longitudinal reinforcement takes place.
- The results for the plastic hinge model considering the longitudinal reinforcement reduction improve the quality of the responses, once both damage model and PNL model are now closer responses. Therefore, a significant importance must be given to the simulations with plastic hinge model regarding the aspects and singularities of the structures that are likely to affect the seismic response.

REFERENCES

[1] Faria R, Vila Pouca N, Delgado R., Numerical Models to Predict the Nonlinear Behaviour of Bridge Piers Under Severe Earthquake Loading, Deliverable N. 6, Task 3, Report N. 3/2 (VAB Project), FEUP, Porto, 2001.

[2] Pinto A., Pegon P., Magonette G., Molina J., Buchet P., Tsionis G., Pseudodynamic tests on a large-scale model of an existing RC bridge using non-linear substructuring and asynchronous motion, EUR 20525 EN, EC, Joint Research Centre, ISIS, 2002.

[3] Delgado, P., Costa, A., Delgado, R., A Simple Methodology For Seismic Safety Assessment Of Bridges, *Proceedings of the 12th ECEE*, London, 2002.

[4] Faria, R., Oliver, J., Cervera, M. A strain based plastic viscous damage model for massive concrete structures, *International Journal of Solids and Structures* 35(14), 1533-1558, 1998.

[5] Vila Pouca, N., Faria, R., Delgado, R., Numerical Simulation of the Seismic Behaviour of Talübergang Warth Bridge, *Proceedings of the 12th ECEE*, London, 2002.

[6] Vila Pouca, N. Simulação Numérica da Resposta Sísmica de Elementos Laminares em Betão Armado, *Ph.D. thesis*, FEUP, 2001 (in Portuguese), (http://ncrep.fe.up.pt/web/artigos/NVilaPouca_PhD_Thesis.pdf).

[7] Giuffrè, A., Pinto, P. Il comportamento del cemento armato per sollecitazione ciclice di forte intensitá, *Giornale del Genio Civile,* 1970.

[8] Delgado, P., Costa, A., Pinho, R., Delgado, R. Different Strategies for Seismic Assessment of Bridges – Comparative studies, *Proceedings of the 13th World Conference on Earthquake Engineering* – 13WCEE, Vancouver, Canada, 2004.

COMPDYN 2011
3rd ECCOMAS Thematic Conference on
Computational Methods in Structural Dynamics and Earthquake Engineering
M. Papadrakakis, M. Fragiadakis, V. Plevris (eds.)
Corfu, Greece, 25–28 May 2011

SIMPLIFIED SEISMIC PERFORMANCE ASSESMENT OVER THE LIFETIME OF A HIGHWAY BRIDGE SUBJECT TO PIER REINFORCEMENT CORROSION

Christos Giannelos[1*], Dimitrios Vamvatsikos[2]

[1]Kalliergos Omilos Technikon Meleton
6 Koumarianou Str, 11473 Athens, Greece
cgiannelos@gmail.com

[2]National Technical University of Athens
9 Heroon Polytechneiou, 157 80 Athens, Greece
divamva@mail.ntua.gr

Keywords: Bridges, Corrosion, Reinforced Concrete, Static Pushover Analysis, Incremental Dynamic Analysis, Equivalent Single-Degree-Of-Freedom Model, Performance-Based Earthquake Engineering.

Abstract. *The lifetime seismic performance of a typical segmental three-span (75+120+75) Egnatia Odos Highway bridge is assessed, considering the corrosive action of chloride ions that leads to pier strength degradation over time. The aim is to show the influence of corrosion on the seismic demand and capacity over the entire design life of the bridge, as well as the usefulness of simplified single-degree-of-freedom (SDOF) models to minimize the computational cost to non-prohibitive levels for contemporary capabilities. Five different time instants are chosen within the 120 year design life of the bridge. For each instant, the piers' reinforcement steel loss is calculated via a probabilistic model using Monte Carlo simulation to account for the uncertainty in the factors that affect the corrosion. While incremental dynamic analysis (IDA) of the complex model would be the method of choice for a comprehensive evaluation, we employ instead approximate IDA of equivalent SDOF systems with capacity curves derived by static pushover analysis. Such analyses are efficiently executed for different time moments of the design life of the bridge, taking into account the active pier rebar diameter due to corrosion effects. Thus, the usefulness of the equivalent SDOF system concept combined with nonlinear dynamic analysis or a powerful R-μ-T relationship such as SPO2IDA is shown. This usefulness turns to a necessity when more factors of epistemic uncertainty beyond the corrosion process are added in this already complex problem, disproportionately magnifying the required computational load.*

1 INTRODUCTION

In bridge design, the seismic load often constitutes the most critical loading case. Still, even though there is a relatively long inventory of bridges in Greece designed according to older guidelines, no significant damages have ever appeared due to earthquakes. On the contrary, the most common damage found can be attributed to the environmental conditions. Moisture, chlorides and CO_2 can impact the mechanical properties of structural materials, most importantly of structural steel, through the process of corrosion. Thus, the topic of ageing bridges subject to corrosion is a potentially dangerous situation in a seismically active region. The main question is whether, and at to extent, corrosion influences the seismic performance over the lifetime of a bridge.

Corrosion is a complex process that may affect a concrete bridge in a variety of ways, including, among others, cover spalling, loss of prestress, loss of steel-concrete bond strength and loss of steel itself. Since the seismic response is our topic of interest, we will focus exclusively on the effect of steel loss for the longitudinal and transverse pier reinforcement, while ignoring the potentially important impact of debonding. The reinforcement area losses lead to a direct decrease in the shear and moment capacity and secondarily in a reduction of the stiffness of piers. All the above contribute to a degradation of the bridge seismic performance. We aim to calculate this degradation over the 120 year lifetime of a well-designed modern bridge.

The corrosion in the case of reinforced concrete (RC) structures is a phenomenon that has received wide attention. Of immediate interest for the present study is the work of Stewart and Rosowsky [1] and Vu and Stewart [2] who have calculated RC bridge deck strength degradation against static loads as a function of time and distance from sea. More recently, Celarec et al. [3] have employed simplified single-degree-of-freedom models to calculate the increase of seismic risk in RC buildings due to corrosion. Finally, Ghosh and Padgett [4] have offered a holistic picture of ageing effects on the seismic fragility curves of bridges through time. Most importantly, researchers tend to agree that corrosion phenomena are subject to severe uncertainties thus necessitating the use of probabilistic models.

2 CASE STUDY BRIDGE

The G7 bridge is part of the Egnatia highway. It has a total length of 270m (Figure 1). The longitudinal axis of the bridge is shaped as a circular arc both in the horizontal and in the vertical plane, having radii of curvature equal to +320m and –1000m, respectively. For the construction of the bridge the segmental cantilever method has been chosen, where the piers function temporarily as pure cantilevers. These support the construction of the deck, short segments of which are extended in alternation or simultaneously from the two opposite sides of the piers to maintain a balanced load. Due to the specifics of the construction method, it is often the case that earthquakes do not constitute the critical loading for such bridges. Combined with the curvature of the bridge and the height of the piers which favor non-seismic loading cases, we do not expect to see integrity-threatening situations due to the combined corrosion and earthquake effect. Nevertheless, the relative change in the performance will help us understand the effect of corrosion for bridges where earthquake loads are dominant.

The bridge deck has a heavily post-tensioned single-cell box section (Figure 2a). The two piers M1 and M2 have box cross sections of 4.0x7.35m (Figure 2b) with a height of 41.70m and 49.50m, respectively. They are connected monolithically with the superstructure. At the abutments A1 and A2 the deck is supported on bearings of the elastic single-point type (pot bearings) moving freely. The mobility of the deck in the transverse direction is restrained by shear keys up to the point of the earthquake design loads (Figure 3). The pier foundations are deep, situated within the rocky substrate.

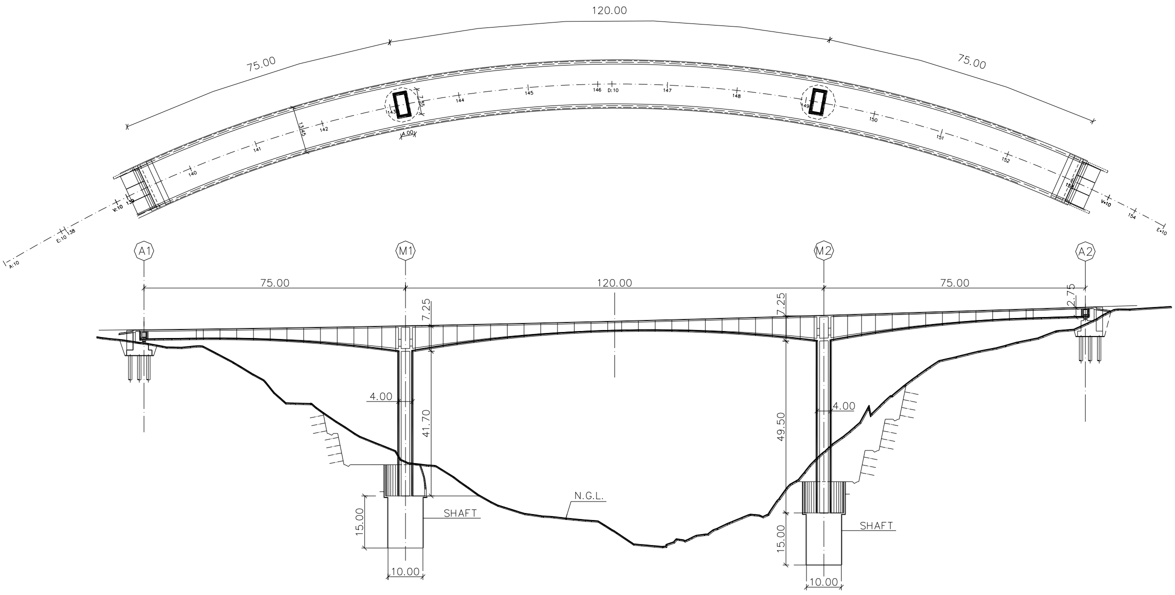

Figure 1. (a) plan view and (b) Longitudinal section.

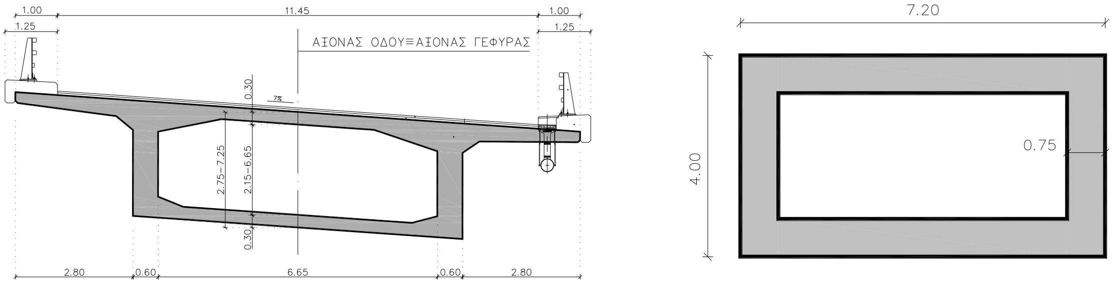

Figure 2. (a) Deck cross section and (b) Pier cross section.

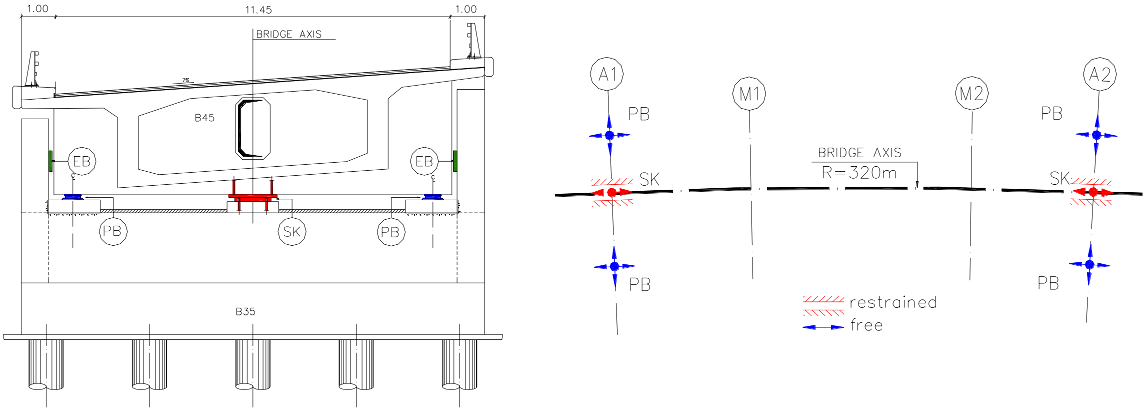

Figure 3. Deck support conditions.

A three dimensional finite-element model (Figure 4a) has been developed using the Opensees platform [5]. It is a powerful program that offers the possibility to create realistic nonlinear models with elements that approach with accuracy the real behavior of reinforced concrete structures. In addition it allows reliable analyses even under numerically unstable conditions that approach global collapse.

The bridge deck has been modeled with linear beam-column elements, closely following the centroidal axis of the tapering cross sections. The superstructure and the abutments are connected to the bearings via stiff zero-mass elements. The piers are modeled using force-based beam-column elements with fiber sections. Therein, different material properties have been used (Figure 4b) to distinguish the confined core concrete from the unconfined cover and the steel reinforcement. The effect of confinement allows higher strength and ductility at the core, an effect that is taken into account according to the Mander et al. [6] model.

For the pot bearings, a set of one-dimensional non-interacting springs have been grouped into a single macroelement. They simulate accurately the freedom of the horizontal movement under friction and the transverse connection of the bridge with the central shear key up to the load of 250 tn by employing a bilinear force-deformation relationship. Still, they do not take into account the possibility of a contact with the side walls of the abutments when the shear key collapses. At the two outer bearings of each abutment, a link with stiffness of 1MN/m has been used in the vertical direction to reduce the deck uplift during earthquake loading.

The first two mode shapes of the bridge are mainly translational for the deck (Figure 5). The first is a displacement along the longitudinal axis; the second is a displacement along the transverse axis; the third is a symmetric deformation in the vertical direction. The corresponding periods are T_1=1.59s, T_2= 1.48s and T_3= 0.85s. It must be noted that due to the curvature of the bridge and the existence of transverse links at the abutments, the transverse and longitudinal displacements are partially interacting [7]. As a result, the two prime mode shapes combine both transverse and longitudinal displacement of the piers.

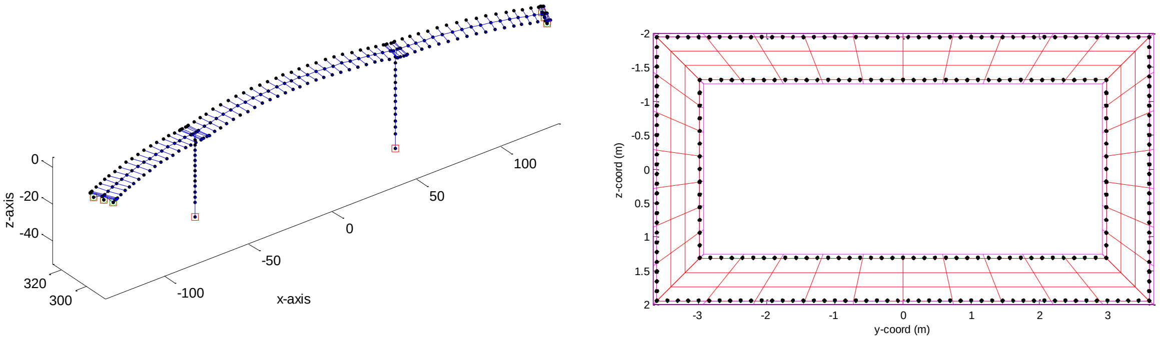

Figure 4. (a) finite-element model and (b) fiber model of the pier section.

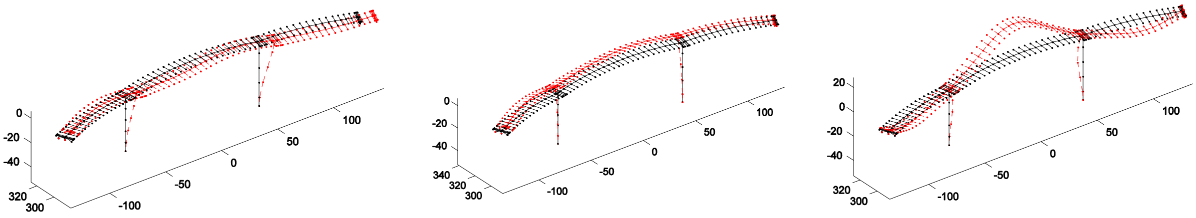

Figure 5. (a) first mode shape, (b) second mode shape and (c) third mode shape.

3 PIER DEGRADATION DUE TO CORROSION

Corrosion may be initiated either due to carbonation in dry-air conditions or due to the action of chlorides and moisture. The latter constitute the main corrosive hazard for this bridge, arising from the application of de-icing salts and due to sea spray exposure in a coastal environment. Reinforcement corrosion is a complex process that can attack the pier integrity via multiple vectors, e.g. spalling, debonding and steel material loss. In our case, we will only focus on the latter and will assume that corrosion leads to a uniform reduction in reinforcing steel along the pier height, equally affecting the entire external row of longitudinal and transverse reinforcement bars. A probabilistic model is used to take into account the aleatory and epistemic uncertainty inherent in the process while Monte Carlo simulation is performed to propagate the effects to the estimated structural performance.

3.1 Corrosion Model

The aim is to estimate the corrosion initiation time T_i and the respective rebar diameter loss ΔD_b for every time instant. The corrosion deterioration model proposed by Stewart and Rosowsky [1], as amended later by Vu and Stewart [2], is used as our basis. It leads to a uniform reduction in the bar diameter of the reinforcing steel due to general (non-pitting) corrosion. For reasons of completeness, the fundamentals of the model are repeated here.

First of all, chloride content $C(x,t)$ at a distance x from the concrete surface at time t follows Fick's second law:

$$C(x,t) = C_o\left[1 - \operatorname{erf}\left(\frac{x}{2\sqrt{tD}}\right)\right] \tag{1}$$

where C_o is the surface chloride content (kg/m^3), D is the chloride diffusion coefficient (cm^2 /sec) and erf is the error function. The surface chloride concentration C_o is the sum due to the application of de-icing salts C_{oi} = 3.5 and air-born chlorides C_{od}. The latter is assumed to depend only on the distance from the coastline:

$$C_o = C_{oi} + C_{od} \tag{2}$$

The surface chloride concentration C_{od} as a function of distance from the coast (d in km) is:

$$C_{od} = \begin{cases} 2.95 & d \le 0{,}1\text{km} \\ 1.15 - 1.81\log_{10}(d) & 0.1\text{km} < d \le 2.84\text{km} \\ 0.03 & d > 2.84\text{km} \end{cases} \tag{3}$$

The chloride diffusion coefficient (D) is influenced mainly by the mix proportions (water-cement ratio):

$$D = D_{H_2O}\,0.15\,\frac{1+\rho_c\dfrac{c}{w}}{1+\rho_c\dfrac{w}{c}+\dfrac{\rho_c}{\rho_a}\dfrac{a}{c}}\left(\frac{\rho_c\dfrac{w}{c}-0.85}{1+\rho_c\dfrac{w}{c}}\right)^3 \ (cm^2/\text{sec}) \tag{4}$$

The terms ρ_a = 2.7g/cm^3 and ρ_c = 3.12g/cm^3 are the mass densities of cement and limestone aggregates, respectively. The ratio a/c = 0.66/0.11 is the aggregate-cement ratio, D_{H2O} =1.6x10^{-5} cm^2/sec is the chloride diffusion coefficient in an infinite solution and the water-cement ratio is estimated as

$$w/c = \frac{27}{f'_{cyl} + 13.5} \tag{5}$$

where f'_{cyl} is the mean concrete compressive strength in MPa, assumed to be approximately 7.5MPa above the characteristic strength.

The corrosion rate is a function of concrete quality, cover thickness and time. The time-dependency appears due to the formation of rust on the steel surface, which tends to reduce the corrosion rate:

$$i_{corr}(t_p) = \frac{32.13}{b}\left(1 - w/c\right)^{-1.64} t_p^{-0.29} \qquad (\mu\mathrm{A}/cm^2) \tag{6}$$

where the concrete cover b is given in cm and t_p is the time since corrosion initiation.

The corrosion initiation time T_i is calculated from Equation (1) to coincide with the time that the chloride concentration reaches a critical value C_r of 0.9kg/m^3 on average. Thus, if the inverse of the error function is erf^{-1}, we have:

$$T_i = \frac{b^2}{4D}\left[\mathrm{erf}^{-1}(1 - C_r / C_0)\right]^{-2}. \tag{7}$$

Finally the deterioration process caused by reinforcement corrosion will lead to a uniform reduction $\Delta D_b(t_p)$ in the bar diameter of the reinforcing steel as follows:

$$\Delta D_b(t_p) = \min\left(0.0232 \int_{T_i}^{t_p} i_{corr}(\tau)\mathrm{d}\tau \, , \, D_{b0} \right). \tag{8}$$

The reduction is zero for times earlier than T_i, D_{b0} is the initial bar diameter and the instantaneous corrosion rate (at the surface) in mm/yr is taken as $\lambda(\tau)=0.0116 \cdot R \cdot i_{corr}(\tau)$, where R=1 for general corrosion. The parameters f'_{cyl}, C_{od}, C_{oi}, C_r, D and i_{corr} are randomly distributed as described in [2]. The latter two quantities, in addition to the randomness induced by their parameters, also incorporate model epistemic uncertainty.

3.2 Impact of corrosion on the longitudinal pier reinforcement

The effects of corrosion on the longitudinal reinforcement are presented in Figure 6. The rebar diameter decreases throughout the lifetime of bridge from 25 mm to a median value of 22.7 mm which corresponds to a 9% reduction. At each of the five time instants selected, Monte Carlo simulation is performed for 100 realizations of the bridge. Since nonlinear dynamic analysis is prohibitive for such numbers, we instead chose to employ static pushover analysis (SPO). Thus, the bridge is pushed along its longitudinal axis where it is most vulnerable to collapse. Figure 7 shows the resulting 500 SPO curves together with their corresponding medians. Although the effect is not overwhelming, there is still a 10% median reduction in terms of the maximum base shear capacity after 120 years; it drops from 17720 kN to 15880 kN. The low impact of corrosion is mainly attributed to the large diameter bars, the sufficient concrete cover and the good quality of the concrete. While the latter two factors are intuitive, the former is perhaps slightly more difficult to understand. The reason is that corrosion uniformly attacks the entire surface area of the rebars. At least for general corrosion, the diameter reduction is the same under the same conditions, regardless of the bar size. Thus, if the same amount of steel is distributed among few large diameter bars or many small diameter ones, corrosion will always impact more heavily the latter configuration. For the above reasons, the longitudinal reinforcement will not suffer much from the chloride attack.

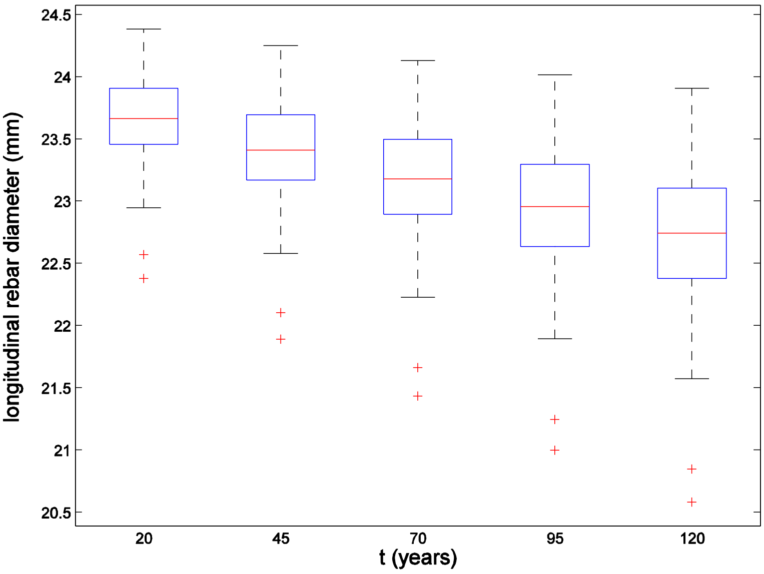

Figure 6. Boxplots of the longitudinal rebar diameter at 25 year intervals. The three horizontal lines defining each box represent the 25, 50 and 75% values of the sample while the whiskers show the gross extent of the sample distribution, out of which the outliers (red crosses) are.

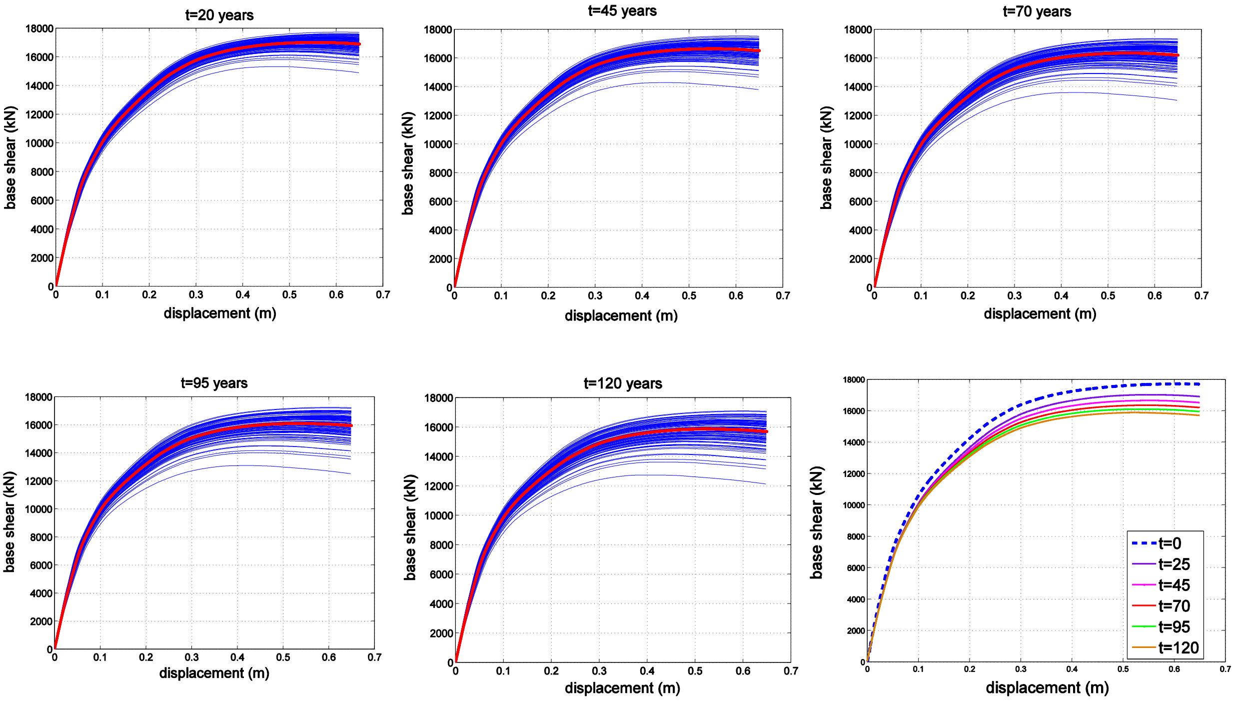

Figure 7. (a),(b),(c),(d),(e) SPOs of 100 samples (blue) at 25 year intervals together with their median (red); (f) the median SPOs for every time instant.

3.3 Impact of corrosion on the transverse pier reinforcement

While longitudinal reinforcement is well protected from corrosion, the same is not true for transverse reinforcement. Actually, the shorter distance to the surface and the significantly smaller bar diameter are both heavily aggravating factors that work against the integrity of the stirrups.

The shear strength of concrete members is given by

$$V_R = V_s + V_c \tag{9}$$

where V_c and V_s are the nominal strength of concrete and transverse reinforcement shear-resisting mechanisms, respectively. According to Directive E39/99 [8], within the plastic end regions the concrete contribution is removed from the shear strength. The reinforcement contribution (truss mechanism) according to DIN1072 is given by

$$V_s = \frac{A_{sv}}{s} f_y \frac{7}{8} d \tag{10}$$

where A_{sv} is the total area of transverse reinforcement in a layer in the direction of the shear force, s is the spacing along the member axis of the layers of stirrups or hoops, and d the effective depth of the section.

The results of corrosion impact to the transverse reinforcement and finally to the piers' shear strength are presented in Figure 8. The base shear strength throughout the lifetime of the bridge decreases from 21770 kN to 17140 kN. This corresponds to a 21% reduction in the median value, most of which happens at an early stage: After the first 20 years of the bridge's life, shear strength decreases from 21770 kN to 18950 kN, having a 13% median reduction. While still not threatening for the bridge, which retains enormous amounts of shear capacity due to the overdesign mandated by the code minima for reinforcement, such reductions are not to be ignored.

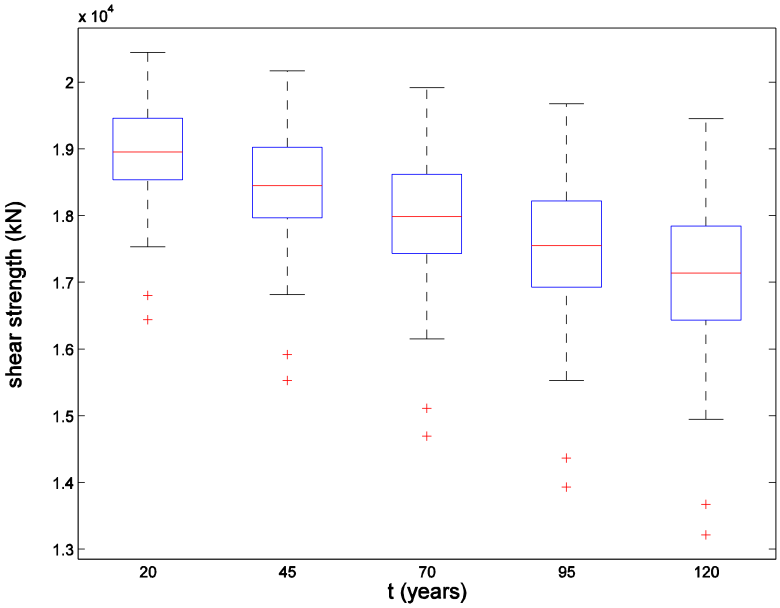

Figure 8. Boxplots of the pier shear strength at 25 year intervals. The three horizontal lines defining each box represent the 25, 50 and 75% values of the sample while the whiskers show the gross extent of the sample distribution, out of which the outliers (red crosses) are.

4 DYNAMIC PERFORMANCE OF CORRODED BRIDGE

Perhaps the most comprehensive method for estimating seismic performance is Incremental Dynamic Analysis (IDA) [9]. It utilizes numerous nonlinear time-history analyses of the system under a suite of multiply-scaled ground motion records. In our case the aim is to produce the distribution of seismic demand and capacity, ideally represented by summarized 16, 50 and 84% IDA curves, for each of the five time instants (20, 45, 70, 95 and 120 years) within the 120 years design life of the bridge. The seismic performance of the bridge is investigated for loads mainly along its longitudinal axis, where it is most vulnerable to collapse. In this direction, the bridge has a general elastoplastic response as shown by the SPO curve (Figure 7). For every time instant 100 model realizations are used in a Monte Carlo simulation in order to take into account the epistemic uncertainty inherent in corrosion.

Assuming that 30 records are used at seven intensity levels for IDA for each corroded bridge realization, then 30x7x5x100=105.000 dynamic time-history analyses should be executed on a multi-degree-of-freedom (MDOF) model, requiring unreasonable computational resources. In order to reduce the computational load to realistic levels, simplified methods must be employed. Thus, following the example of Celarec et al. [3], we will use a suitable equivalent SDOF instead of the MDOF model, and replace the expensive IDA with an SPO analysis together with SPO2IDA [10,11]. The latter is a powerful R-μ-T (reduction factor-ductility-period) relationship which allows instantaneous estimation of summarized IDA curves of SDOF systems, offering significant savings in computations at the cost of a small error. Thus, weeks of analysis are reduced to less than 48hrs on a single computer.

4.1 Simplified single-degree-of-freedom (SDOF) models

The applicability of equivalent SDOF models to estimate the MDOF response largely depends on the regularity of the structure (Isakovic et al. [12]). In irregular structures such a substitution may underestimate significantly the seismic response. According to the eigenvalue analysis, the studied bridge responds in each direction predominantly in a single mode. Moreover the primary mode shapes are mainly translational with only low coupling between them. On the contrary the rotational mode shapes are of secondary importance. Thus, the bridge can be characterized as regular and the use of equivalent SDOF models is appropriate.

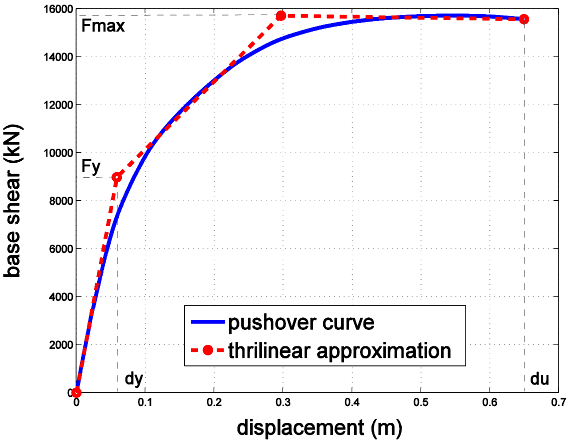

Figure 9. The SPO curve and its trilinear approximation.

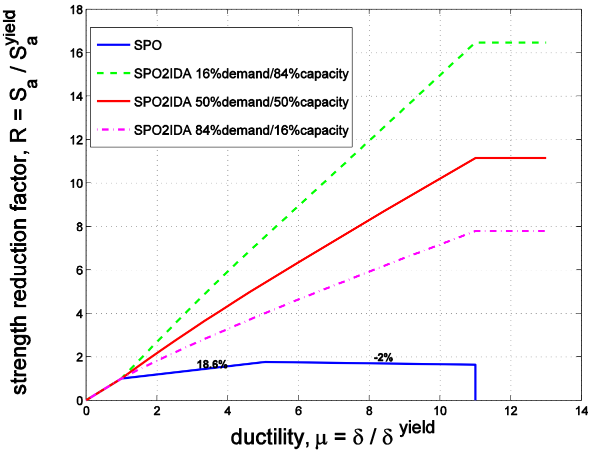

Figure 10. The summarized IDA curves as predicted by SPO2IDA for the adopted trilinear fit to the SPO.

4.2 Approximate Incremental Dynamic Analysis via SPO2IDA

The Static Pushover to IDA (SPO2IDA) software [10,11] is used to approximate the IDA 16, 50 and 84% curves by taking advantage of the results of the static pushover (SPO). In our case, the capacity curves are closely approximated with a trilinear shape. This starts elastically, followed by a hardening positive-stiffness part and then by a lightly negative-stiffness segment that we choose to terminate at a reasonable maximum attainable displacement dictated by the abutment geometry (Figure 9).

The SPO2IDA software is based on the fitted response of multiple SDOF systems with a wide range of periods, moderately pinching hysteresis and 5% viscous damping. It can effortlessly generate the statistics of the normalized intensity R versus normalized response μ curves (Figure 10) for complex quadrilinear force-deformation backbone shapes, unlike simpler R-μ-T relationships that are restricted to the simplest of shapes and just the mean response. R is the reduction factor, defined as the ratio $S_a(T_1,5\%)/S_a^{\text{yield}}(T_1,5\%)$ of the spectral acceleration over its value at yield. Similarly, μ is the ductility, i.e., the ratio of displacement response over the displacement at yield δ/δ^y

To obtain proper IDA curves in terms of $S_a(T_1,5\%)$ and for any desired structural response, a denormalization must take place. We employ the procedure described by Vamvatsikos and Cornell [12] but allowing for the simplifications of Fragiadakis and Vamvatsikos [13]. Thus, the initial elastic slope of the IDA fractile curves for the deck displacement is set to $4\pi^2/(C_0T_1^2g)$, where C_0 is the first-mode participation factor, e.g., as defined by FEMA-356 [14]. The approximate 16, 50 and 84% IDA curves are then produced for every realization of the bridge and every time instant considered, shown in Figure 11. According to the results, the corrosion causes the displacement of bridge deck to increase by 10% on average for any given level of $S_a(T_1,5\%)$, closely following our earlier SPO-based conclusions for this simple SPO shape. While not a threatening condition for this bridge, where seismic loads were not critical for design, it still provides a useful standard of comparison for other, less-protected cases.

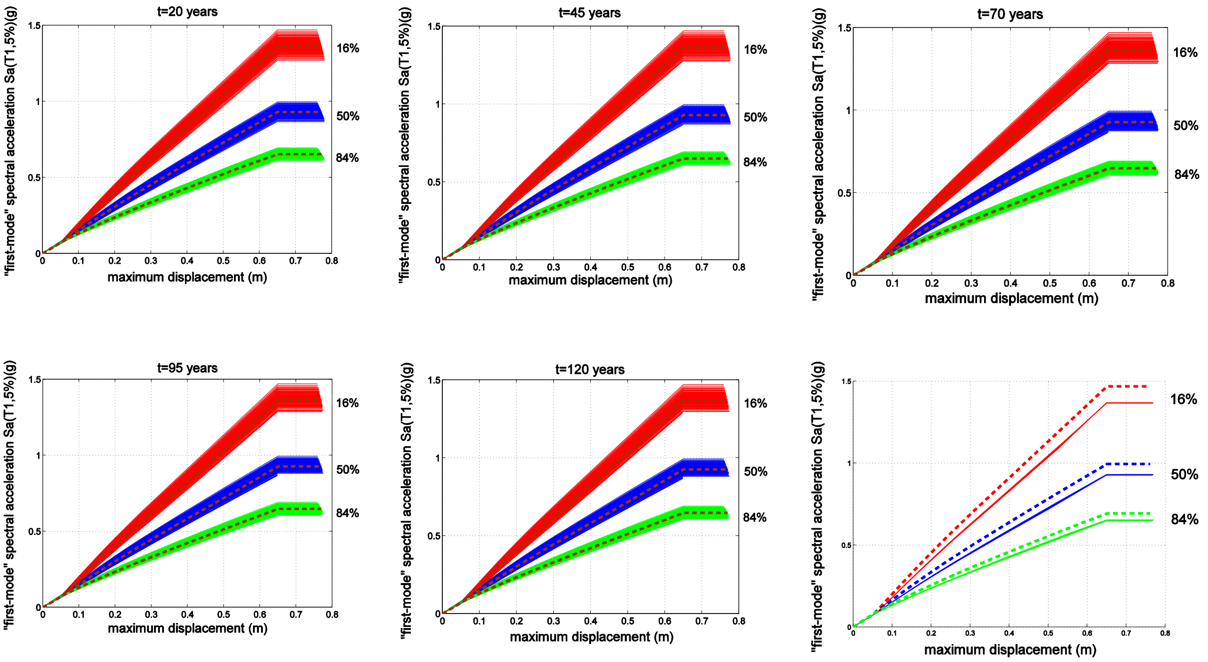

Figure 11. (a),(b),(c),(d),(e) 16, 50 and 84% fractile IDA curves for 100 samples together with the overall median curve for each fractile (in black) ; (f) the overall median IDA curves for all time instants and each fractile.

5 CONCLUSIONS

The seismic performance of a typical cantilever-construction three-span bridge under the effect of corrosion has been examined. Instead of performing IDA on the MDOF bridge model, we produce instead the 16, 50 and 84% IDA capacity curves approximately, for each of the five time instants within the 120 years design life of the bridge, using the SPO2IDA software on the equivalent SDOF bridge model. The latest simplification is generally applicable as the examined structure is a first-mode dominated system as most similar bridges tend to be. Thus, the equivalent of almost 100,000 dynamic time-history analyses can be executed in less than two days rather than several weeks. This allows us to consider a fully probabilistic model of steel reinforcement corrosion and accurately assess its effects on the seismic response of the bridge. It is a general method that can be efficiently applied to reinforced concrete structures and leads to useful, quantifiable results.

In the case examined, since only the external layer of pier reinforcement is exposed to corrosion, a median degradation of 10% for flexural capacity and 20% for shear capacity is expected to occur within the design life of 120 years. In both cases, the degradation rate is at its highest at the initiation of corrosion and it slowly declines with time. Thus, more than half of the reduction is typically reached within the first twenty years. Still, the effects are not overwhelming for this bridge. For example, although the shear capacity loss seems substantial, it poses no threat for the bridge as the code-minimum transverse reinforcement has led to large amounts of reserve shear capacity.

Bridge G7 is a contemporary bridge designed by the latest codes. It enjoys good quality concrete and a thick reinforcement cover which are the principal factors acting against corrosion. Added to the fact that earthquakes are not the critical loading case, it becomes clear that corrosion will never be catastrophical for the piers. This conclusion might be very different for older or contemporary bridges where earthquake loads are dominant. In such cases, performing assessment or design while neglecting the substantial effect of corrosion may not be a wise choice.

REFERENCES

[1] M.G. Stewart, D.V. Rosowsky, Time-dependent reliability of deterioration reinforced concrete bridge decks, *Structural Safety*, **20**, 91–109, 1998.

[2] K.A.T. Vu, M.G. Stewart, Structural reliability of concrete bridges including improved chloride-induced corrosion models, *Structural Safety*, **22**, 313–333, 2000.

[3] D. Celarec, D. Vamvatsikos, M. Dolsek, Estimation of the seismic risk with consideration of capacity degradation over time for RC buildings, *Bulleting of Earthquake Engineering*, 2011 (to appear).

[4] J. Ghosh, J.E. Padgett, Aging Consideration in the Development of time-dependent seismic fragility curves, *ASECE Journal of structural engineering,* **136**(12),1497-1511, 2010.

[5] F. McKenna, G. Fenves, *Open system for earthquake engineering simulation,* Pacific Earthquake Engineering research Center, Berkley, California.

[6] J.B. Mander, M.J.N. Priestley, R. Park, Theoretical stress-strain model for confined concrete, *ASCE Journal of structural engineering,* **114**(8), 1804-1826, 1988.

[7] C. Giannelos, D. Vamvatsikos, Simplified Methods of Nonlinear Dynamic Analysis of a Bridge under Bi-Directional Seismic Load, *Proceedings of the* 3*th* *Greek Conference on Earthquake Engineering and Engineering Seismology*, Athens, November 5-7, 2008.

[8] Greek Ministry for the Environment, Physical Planning and Public Works, Guidelines for the seismic design of bridges, Directive 39, 1999.

[9] D. Vamvatsikos, C.A. Cornell, Incremental Dynamic Analysis. *Earthquake Engineering and Structural Dynamics*, **31**(3), 491–514, 2002.

[10] D. Vamvatsikos, *SPO2IDA software for short, moderate and long periods*, 2002. http://users.ntua.gr/divamva/software/spo2ida-allt.xls.

[11] D. Vamvatsikos, C.A. Cornell, Direct estimation of the seismic demand and capacity of MDOF systems through Incremental Dynamic Analysis of an SDOF Approximation. *ASCE Journal of Structural Engineering*, **131**(4), 589–599, 2005.

[12] T. Isakovic, M. Fischinger, P. Kante, *Bridges: when is single mode seismic analysis adequate?*, Proceedings of the Institution of Civil Engineers-Structures and Buildings, 156(2), 165-173, 2003.

[13] M. Fragiadakis, D. Vamvatsikos, Fast performance uncertainty estimation via pushover and approximate IDA. *Earthquake Engineering and Structural Dynamics*, **39**(6), 683–703, 2010.

[14] FEMA-356. *Prestandard and Commentary for Seismic rehabilitation of buildings.* Federal Emergency management Agency: Washington, DC, 2000.

COMPDYN 2011
III ECCOMAS Thematic Conference on
Computational Methods in Structural Dynamics and Earthquake Engineering
M. Papadrakakis, M. Fragiadakis, V. Plevris (eds.)
Corfu, Greece, 25–28 May 2011

SEISMIC BRIDGE RESPONSE TO DIFFERENTIAL GROUND MOTION AND COMPARISON WITH ALGERIAN SEISMIC DESIGN RULE.

N. Benmansour[1], M. Djafour[1], A. Bekkouche[1], D. Zendagui[1].

[1] RISAM research laboratory,Departement of Civil Engineering ,University of Tlemcen, BP 230,
Tlemcen ALGERIA.
benmansournassima@yahoo.fr

Keywords: Bridges, Dynamic Analysis, Earthquake, Spatial variability, RPOA.

Abstract. *Seismic response of extended structures, such as bridges, must take into account spatial variability of earthquake ground motion (SVGM). Models that describe SVGM have been developed during last decades and structural analyses have been performed on numerous structures. Based on these studies, simplified approaches have been developed. The new Algerian bridge seismic regulation code proposes a simplified approach that takes into account SVGM. This paper aims at performing preliminarily studies on the accuracy of this method. This is performed through comparison with more refined approaches. Bridges, with different overall lengths and seating on different types of site conditions, are considered. The results show that this simplified method overestimates the response of the analyzed bridges* **.**

1 INTRODUCTION

Seismic analysis of extended structures, such as bridges, must take into account spatial variability of earthquake ground motion (SVGM) which can induce significant additional forces. In fact, it has been recognized that space-time variability of the seismic of ground motion is the results of three distinct effects [2]: (1) loss of coherence of the seismic movement due to multiple refractions and reflexions of the seismic waves along their paths, named incoherence effect, (2) difference in arrival times of the seismic waves at the various recording stations due to the variation of their apparent propagation velocity, named wave passage effect, (3) space variation of the geotechnical properties, named site effect.

During last decades, models that describe SVGM have been developed based on either empirical or analytical approach (as e.g., [3, 4]) and it is now widely accepted that the coherency function describes the SVGM. Using these models, structural analyses have been performed on numerous structures and show the importance of taking into account SVGM as, e.g., among many others, in references: [5, 6, 7, 8, 9, 10]. Based on these studies, simplified approaches have been introduced in regulation codes to take into account SVGM. The Algerian bridge seismic regulation code (RPOA) [1] has been recently lunched.

This paper aims at performing preliminarily studies on the accuracy of the simplified approach proposed by the RPOA. For the purpose of the study, seismic motion is simulated using time domain segmentation and the well-established method of Deodatis [11]; SVGM is described by the empirical model of Harichandran and Vanmarcke [3]. The simulated time histories are used as input excitations at bridge supports. The time-history analysis results are compared to those obtained by the simplified method of RPOA for different bridges. Results are presented in terms of internal forces.

2 SIMULATION OF SPATIALLY VARYING GROUND MOTIONS

In order to study the effect of SVGM on bridges responses, it is necessary to generate acceleration and displacement time-histories at several locations on the ground surface, corresponding to the bridge supports. In this study, the seismic ground motions are simulated as non stationary from predefined time history, using time domain segmentation method [12, 13, 14]. The predefined time histories are divided into nearly stationary segments with different durations. Then, each segment is used as a reference time series and stationary conditional simulations are carried out for each segment, using the simulation technique proposed by Deodatis [11]. The simulated segments are joined together to obtain the entire non stationary and spatially variable acceleration time-histories, after the incorporation of a time shift to account for the wave passage effect.

The generated acceleration time histories are further corrected and integrated in order to obtain the corresponding displacement time-histories. The properties of each set of simulated time-histories are the same in terms of target power spectral density function, peak of displacement and response spectrum compatibility.

3 OVERVIEW OF THE RPOA PROVISIONS REGARDING SVGM

RPOA [1] is the first Algerian code established for the seismic design of bridges. RPOA clearly recognizes that, since the differential ground motion induces significant internal forces, the seismic action cannot be based only on the characterization of uniform motion, and proposes a simplified approach to take into account SVGM effects. According to RPOA, the effects of differential displacements between supports are generally negligible for current structures, except when: (a) the structure crosses an active fault, (b) the soil properties vary along the bridge, (c) the length of the bridge is very important.

According to RPOA, designers must perform, firstly, a dynamic analysis of the structure under uniform seismic excitations, and secondly, a pseudo-static analysis based on pattern of prescribed differentials displacements at the bridge supports. Finally, the dynamic response is combined with the pseudo-static response using the SRSS rule.

On a ground site without significant mechanical discontinuity, the design differential displacement *d*, between two points separated by a distance X, is given by [1]:

$$d = \eta AgX;\ \text{for}\quad X < L_M \tag{1}$$

$$d = AgD_M\sqrt{2}\,;\text{for}\quad X \geq L_M \tag{2}$$

With:

$$\eta = \frac{D_M}{L_M}\sqrt{2} \tag{3}$$

Ag: is the design seismic acceleration; g is the acceleration of gravity.

L_M : is the distance beyond which the motions of the two supports can be regarded as independent.

D_M: are absolute displacements; they are given for unit acceleration (1m/s²).

The values of D_M and L_M are given in Table 1 for the four ground types in RPOA, S1 to S4, which are classified on the basis of the shear wave velocity V_s.

Ground Type	S1	S2	S3	S4
$V_s\ (m/s)$	$V_s \geq 800$	$400 \leq V_s \leq 800$	$200 \leq V_s \leq 400$	$V_s \leq 200$
$L_M\ (m)$	600	500	400	300
$D_M\ (m)$	0.03	0.05	0.07	0.09

Table 1. Values of L_M and D_M [1]

RPOA do consider two special situations. If two support points are located on both sides of a significant topographic discontinuity (valley), and in absence of a better approach, the value of *d* is raised by 50%. In case they are located on both sides of a mechanical discontinuity (fault), design differential displacement *d* is given by:

$$d = Ag\sqrt{D_{M,1}^2 + D_{M,2}^2} \tag{4}$$

Where:

$D_{M,1}$ and $D_{M,2}$ are the absolute displacements at points 1 and 2.

4 EVALUATION OF THE SIMPLIFIED APPROACH OF RPOA

4.1 Bridge model

In order to quantitatively assess the simplified method of RPOA, two bridges are selected (Bridge A and Bridge B). They have different overall lengths (i.e.400m and 600m, respectively); they have the same configuration (Figure 1) which is taken from design example No. 1 from the Federal Highway Administration seismic design examples [15]. The span length is constant and equal 50 m; the respective numbers of spans are 8 and 12.

The finite element models use six equal-length 3-D elastic beam elements per spans and four beam elements per pier. The superstructure and the columns are connected by rigid elements. The shear stiffness of the bearings is assumed to provide no restraint in the longitudinal direction. In the vertical direction, the bearings are considered fully restrained due to the gravity forces of the superstructure. The rigid element at each end of the bridge is restrained in the transverse direction by springs, which represent the effect of the girder stops at both ends of the bridge. The stiffness of each bent foundation is modeled by six springs at the lower end of the footing elements, which were determined using an elastic half-space approach [15]. Finally, 5% Rayleigh damping is utilized.

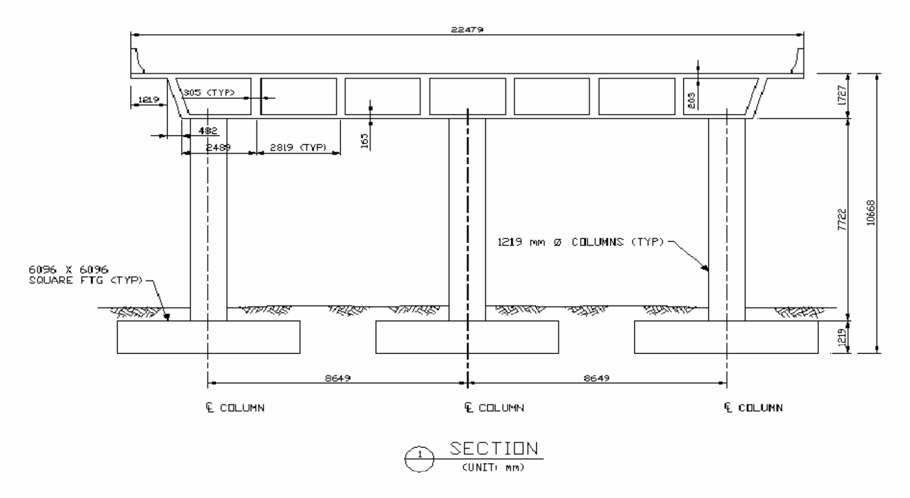

Figure 1. Girder cross-section.

4.2 Support motions

In this study, uniform soil conditions are assumed and only the longitudinal component of the excitation is considered. The accelerograms used for the conditional simulation of support motions are compatible with RPOA’s response spectrum. Two ground types S1 (firm soil) and S3 (soft soil), 5% damping and 0.4g peak ground acceleration are selected to describe the ground motion at piers. The Harichandran and Vanmarcke model [3] is chosen to model the coherence loss between pair of bridge supports:

$$\left|\gamma_{jk}\left(\omega, d_{jk}\right)\right| = A.exp\left(-\frac{2(1-A+\alpha A)\left|d_{jk}\right|}{\alpha\theta(\omega)}\right) + (1-A).exp\left(-\frac{2(1-A+\alpha A)\left|d_{jk}\right|}{\theta(\omega)}\right) \tag{5}$$

$$\theta(\omega) = k\left[1+\left(\frac{\omega}{2\pi\omega_0}\right)^b\right]^{-\frac{1}{2}} \tag{6}$$

The following parameters of the model are used: $A = 0.736$, $\alpha = 0.147$, $k = 5210\,m$, $\omega_0 = 6.85\ rad/s$ and b=2.78, which correspond to data recorded during Event 20 at the SMART-1 array, Lotung, Taiwan. Since the span length is the same for all bridges, it was decided to simulate stationary SVGM every 50 m. In this study, an apparent propagation velocity $v = 750\ m/s$ was used.

For Monte Carlo simulation needs, the procedure of simulation is repeated 10 times. Fig. 2 gives one set of non stationary SVGM displacements corresponding to ground types S1 and S3 which were simulated for the longest bridge (600 m, i.e., 13 support points).

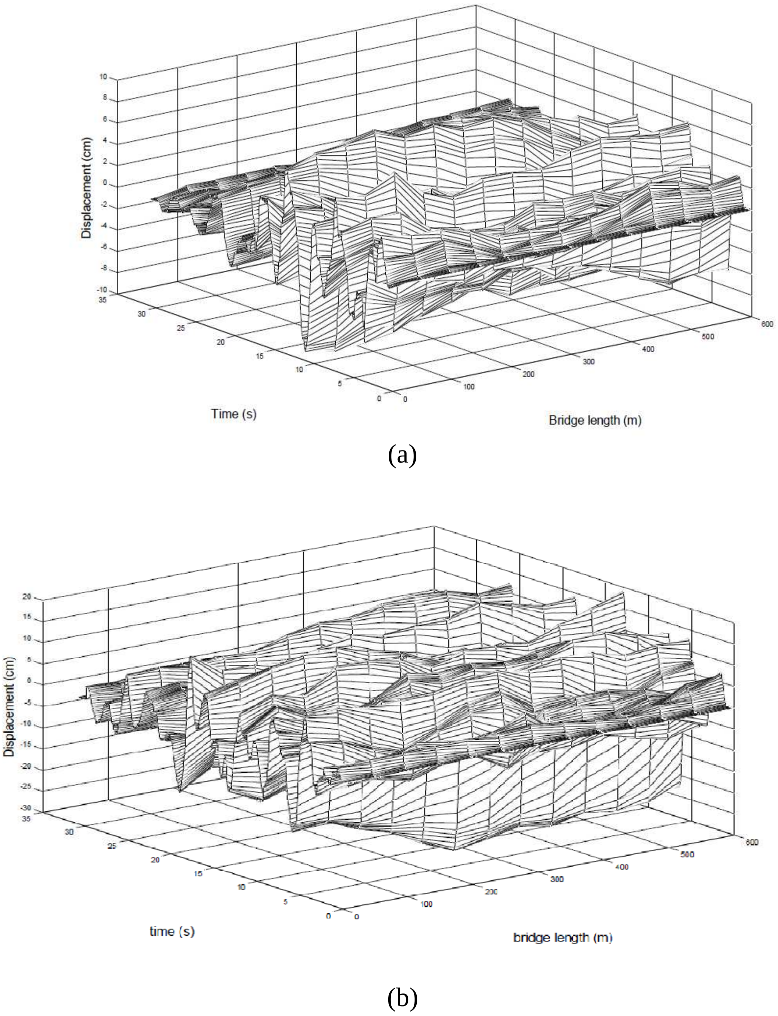

Figure 2. One sample of non stationary SVGM displacements
for ground types (a) S1 and (b) S3.

4.3 Analysis Results

In order to evaluate RPOA's simplified approach, the bridges presented in section 4.1 are analyzed three times, using the following three cases of analysis:

URSA: Conventional response spectrum analysis, i.e., which assumes uniform ground motion, using RPOA's response spectrum.

VTHA: Time-history analysis using the asynchronous displacements simulated in section 4.2.

VRPA: RPOA's simplified analysis for SVGM (see section 3) using RPOA's response spectrum. The prescribed differential displacements are calculated using Eqs. (1) to (3) and are presented in Table 2.

Tables 3 and 4 present comparisons of the bending moment demand envelopes at the extreme column of each bent of Bridge A. It should be noted that VTHA results are the mean values obtained from 10 time-history analyses. These tables show that VTHA results remain equal or lower than those obtained using conventional response spectrum analysis (URSA). Consequently, in this case, the effect of SVGM is negligible (i.e. lower than 5%), and to a certain degree, it is even beneficial (i.e. a reduction in the resulting bending moments is observed). The latter is an observation in agreement with the findings of previous studies [16], for the symmetric bridge configuration and uniform soil condition. However other studies as, e.g.,[17, 6, 8], observed that this findings cannot be generalized, and concluded that, depending on the characteristics of the SVGM, the bridge configuration and its boundary conditions, spatially variable ground motions can induce a higher or lower response in the structure than the response resulting from uniform ground motions.

Site		***S1***	***S3***
η		$0.7\mathrm{x}10^{-4}$	$2.5\ \mathrm{x}10^{-4}$
L_M		*600*	*400*
d **(m)**	Abut A X=0	0	0
	Pier 1 X=50m	0.013	0.049
	Pier 2 X=100m	0.027	0.098
	Pier 3 X=150m	0.041	0.147
	Pier 4 X=200m	0.055	0.196
	Pier 5 X=250m	0.068	0.245
	Pier 6 X=300m	0.082	0.294
	Pier 7 X=350m	0.096	0.343
	Pier8 X=400m	0.11	0.388
	Pier9 X=450m	0.123	0.388
	Pier10 X=500m	0.137	0.388
	Pier11 X=550m	0.151	0.388
	Abut BX=600m	0.165	0.388

Table 2. Differential displacements for Bridge A and Bridge B, according to RPOA.

In addition, tables 3 and 4 suggest that VRPA and VTHA give comparable results: they reduce the seismic demand in the central piers and increase it in piers close to abutments. However it is found that VRPA amplify the results and the differences are more pronounced in the lateral piers. VRPA can amplify the results by 20% for the firm soil and 50% for the soft one.

Table 5 presents ratios between pier top displacements given by VRPA and VTHA. It is found that VRPA displacement amplification is as high as 1.44 and 1.82, for ground types S1 and S3, respectively

The results for Bridge B are presented in Tables 6-7. Once again, it is observed that VRPA overestimates the seismic demand. It reaches 37% for the firm ground type and 55% for the soft one, which is higher than those observed for Bridge A.

Pier maximum bending moment (MN.m)	Pier 1	Pier 2	Pier 3	Pier 4	Pier 5	Pier 6	Pier 7
URSA	13.07	13.95	13.62	13.70	13.62	13.95	13.07
VTHA	13.75	12.74	12.70	09.87	09.75	10.13	11.84
VRPA	14.65	14.53	13.69	13.75	14.07	15.31	15.7
Ratio							
VTHA/URSA	1.05	0.91	0.93	0.72	0.71	0.72	0.90
VRPA/URSA	1.12	1.04	1.00	1.00	1.03	1.09	1.20

Table 3. Bending Moment demand envelopes: Bridge A- S1.

Piers maximum bending moment (MN.m)	Pier 1	Pier 2	Pier 3	Pier 4	Pier 5	Pier 6	Pier 7
URSA	24.75	26.22	25.64	25.85	25.64	26.22	24.75
VTHA	24.95	22.97	20.90	19.10	17.81	21.13	22.50
VRPA	32.38	34.02	26.02	26.11	28.25	33.39	37.53
Ratio							
VTHA/URSA	1.00	0.87	0.81	0.74	0.69	0.80	0.9
VRPA/URSA	1.30	1.48	1.01	1.01	1.10	1.27	1.51

Table 4. Bending Moment demand envelopes: Bridge A- S3.

Piers Top displacement Ratio	Pier 1	Pier 2	Pier 3	Pier 4	Pier 5	Pier 6	Pier 7
VRPA/VTHA (S1)	1.34	1.36	1.37	1.39	1.41	1.43	1.44
VRPA/VTHA (S3)	1.67	1.69	1.71	1.73	1.76	1.79	1.82

Table 5. Comparison of Pier Top Displacement: BridgeA-S1 and S3.

Pier maximum bending Moment (MN.m)	Pier1	Pier2	Pier3	Pier4	Pier5	Pier6	Pier7	Pier8	Pier9	Pier10	Pier11
URSA	13.12	14.01	13.65	13.70	13.69	13.66	13.69	13.70	13.65	14.01	13.12
VTHA	12.82	12.2	12.39	9.22	8.49	7.78	8.36	9.05	8.78	10.16	11.66
VRPA	16.59	16.03	14.67	14.05	13.74	13.69	14.04	14.7	15.57	17.33	18.01
Ratio											
VTHA/URSA	0.97	0.87	0.90	0.67	0.62	0.57	0.61	0.66	0.64	0.72	0.88
VRPA/URSA	1.26	1.14	1.07	1.02	1.00	1.00	1.02	1.07	1.14	1.23	1.37

Table 6. Absolute Moment demand envelopes of the bridge pier: Bridge B-S1.

Pier maximum bending Moment (MN.m)	Pier1	Pier2	Pier3	Pier4	Pier5	Pier6	Pier7	Pier8	Pier9	Pier10	Pier11
URSA	24.79	26.28	25.68	25.81	25.76	25.75	25.76	25.81	25.68	26.28	24.79
VTHA	22.71	22.54	21.29	18.52	14.98	15.42	14.4	16.09	18.27	20.94	23.41
VRPA	38.55	34.16	29.23	26.65	25.77	26.94	29.99	34.10	33.42	33.73	31.81
Ratio											
VTHA/URSA	0.91	0.85	0.82	0.71	0.58	0.59	0.56	0.62	0.71	0.79	0.94
VRPA/URSA	1.55	1.29	1.14	1.03	1.00	1.04	1.16	1.32	1.30	1.28	1.28

Table 7. Absolute Moment demand envelopes of the bridge pier: Bridge B- S3.

5 CONCLUSIONS

RPOA gives a simplified approach to introduce the effect of the SVGM in the design of bridges. In this paper, the accuracy of this method is evaluated through comparison with a more refined approach. Two bridges, having different lengths and seating on different types of ground conditions, are considered. For each bridge/site case, three types of linear analyses are conducted. Based on this study, the following conclusions can be done:

The spatial variability of earthquake ground motion can significantly change the structural response. SVGM increases seismic demand in some cases and reduces it in others. The present study clearly demonstrates that the simplified method does not give satisfactory results and overestimates the seismic demand, especially for laterals piers. In order to reduce those results it is suggested to decrease the differential displacement given by RPOA code.

It should be noted that the present analysis correspond only to one model of bridge with different overall lengths. However, additional research needs to be conducted in this area for enrichment of the presents study.

REFERENCES

[1] MTP. *Règles parasismiques applicables au domaine des ouvrages d'art.* Alger : Ministère des Travaux Publics, 2010.

[2] A. Der Kiureghian, A. Neuenhofer. Response spectrum method for multiple support excitations. *Earthquake engineering and structural dynamics.* Vol. 21, 713–740,1992.

[3] RS. Harichandran, E. Vanmarcke. Stochastic variation of earthquake ground motion in space and time. *Journal of Engineering Mechanics, ASCE.* Vol. 112, 154–174,1986.

[4] D. Zendagui, M.K. Berrah, E. Kasusel. Stochastic deamplification of spatially varying seismic. *Soil Dynamics and Earthquake Engineering.* Vol. 1, 409-421,1999.

[5] V. Saxena. *Spatial variation of earthquake ground motion and development of bridge fragility curves.* Princeton University, Princeton, NJ : Ph.D. Dissertation, Department of Civil Engineering and Operations Research, 2000.

[6] A. Lupoi, P. Franchin, P.E. Pinto, G. Monti. Seismic design of bridges accounting for spatial variability of ground motion. *Earthquake Engineering and Structural Dynamics.* Vol. 34,327-348,2005.

[7] L. Lou, A. Zerva. Effects of spatially variable ground motions on the seismic response of a skewed, multi-span bridge. *Soil Dynamics and Earthquake Engineering.* Vol. 25,729-740, 2005

[8] N. Burdette, A.S. Elnashai. The effect of asynchronous earthquake motion on complex bridges. Part 2:Results and implications on Assessment. *Journal Bridge Engineering.* Vol. 13(2),166-172,2007.

[9] A.G. Sextos, A.J. Kappos. Evaluation of seismic response of bridges under asynchronous excitation and comparisons with Eurocode 8-2 provisions. *Bull Earthquake Engineering.* Vol. 7, 519-547,2009.

[10] J. Wang, A.J. Carr, N. Cooke, P.J. Moss . The response of a 344 m long bridge to non-uniform earthquakeground motions. *Engineering Structures.* Vol. 31(11), 2554-2567,2009.

[11] G. Deodatis. *Simulation of Stochastic Processes and Fields to Model Loading and Material Uncertainties.* Vol. Chapter in book "Probabilistic methods for Structural Design" Klumer Academic Pub, Europe, 1997.

[12] S. Liao, A. Zerva. Physically-compliant, conditionally simulated spatially variable seismic ground motions for performance-based design. *Earthquake Engineering and Structural Dynamics.* Vol. 35, 891–919, 2006

[13] A. Ayman Shama. Simplified procedure for simulating spatially correlated earthquake ground motions. *Engineering Structures.* Vol. 29, 248–258, 2007

[14] A. Zerva. *Spatial variation of seismic ground motions: modeling and engineering applications,*. Boca Raton,Florida : CRC Press,Group, Taylor & Francis, 2009.

[15] FHWA. *Seismic design of bridges design example no. 1 – Two-span continuous CIP.* s.l. : Federal Highway Administration . FHWA-SA-97-006, 1996.

[16] G. Monti, C. Nuti, P.E. Pinto. Nonlinear response of bridges under multi-support excitation. *Journal of Structural Engineering, ASCE.* Vol. 122, 1147–1159, 1996.

[17] A.G. Sextos, K.D. Pitilakis, A.J. Kappos. Inelastic dynamic analysis of RC bridges accounting for spatial variability of ground motion, site effects and soil-structure interaction phenomena. Part 2: Parametric study. *Earthquake Engineering.*Vol. 32, 629–652, 2003.

COMPDYN 2011
3rd ECCOMAS Thematic Conference on
Computational Methods in Structural Dynamics and Earthquake Engineering
M. Papadrakakis, M. Fragiadakis, V. Plevris (eds.)
Corfu, Greece, 25–28 May 2011

NUMERICAL SIMULATION OF BRIDGE PIERS' SEISMIC BEHAVIOR: A BLIND PREDICTION METHODOLOGY

N. Vila – Pouca[1], A. Monteiro[1], A. Arêde[1], P. Delgado[2], R. Delgado[1]

[1] Departamento de Engenharia Civil, Faculdade de Engenharia, Universidade do Porto,
Rua Dr. Roberto Frias, s/n 4200-465 Porto, Portugal
e-mail: nelsonvp@fe.up.pt; abessa@fe.up.pt; aarede@fe.up.pt; rdelgado@fe.up.pt

[2] Escola Superior de Tecnologia e Gestão, Instituto Politécnico de Viana do Castelo.
Av. Atlântico, 4900-348 Viana do Castelo, Portugal
e-mail: pdelgado@estg.ipvc.pt

Keywords: Blind prediction, Seismic Behavior, Numerical Simulation, Bridge Piers, CCBPC 2010.

Abstract. *During mid-2010, the PEER (Pacific Earthquake Engineering Research Center) and NEES (George E. Brown, Jr. Network for Earthquake Engineering Simulation) institutions co-sponsored a shaking table test on a full-scale reinforced concrete bridge pier that was carried out at the UCSD Large High-Performance Outdoor Shake Table. This experimental initiative was encompassed by a worldwide blind prediction contest (Concrete Column Blind Prediction Contest – CCBPC 2010) with over 40 participant teams seeking for the best numerical simulation results. The authors of this paper have participated in that contest and managed to achieve very good results as recognized by an "Award of Excellence" by the contest judges.*

The tested pier was included in a 10.50m high structure, comprising a 5.50m wide footing, a pier body 7.30m high with 1.20m diameter solid circular section. A 250ton reinforced concrete block was placed on the top of the pier in order to drive inertia forces large enough to mobilize the pier capacity, under increasing intensity uniaxial ground motions derived from real earthquake records. The blind numerical analyses were performed knowing only the specimen geometry, reinforcement detailing, material characteristics and the actual ground motions recorded during the testing.

In this context and, in view of the author's participation success, the present paper mainly aims at presenting several aspects of the adopted numerical methodology (and related difficulties) which proved to yield good results, while also providing some insight regarding key problems in numerical simulations of bridge pier seismic behavior. The main numerical and experimental results are compared and a brief discussion is included concerning the reasons for mismatching of some results.

1 INTRODUCTION

Understanding seismic performance of constructions, in general, has been a concern of the scientific community for quite long. That knowledge has met great advances over the last three decades but many problems of earthquake engineering are still difficult to assess in an easy and straightforward way. As an example, most code recommendations are based on reduced scale experimental validation, which for large structures such as bridges, is not easy to accomplish due to a need of considering heterogeneous multi-support excitation [1]. Aiming at providing ever more insight to this particular area, several methodologies and techniques were developed. Such example is the shaking table test, which allows imposing ground motions on structures, attempting to reproduce real earthquake-induced behaviour.

On that particular subject, notable cases can be referred such as the very large E-Defense [2] facility in Japan (some recent works related to it by Yu *et al.* [2010] or Chung *et al.* [2010], ([3,4])), or the NEES [5] equipment sites network of University of Buffalo, SUNY, University of California at San Diego and University of Nevada at Reno (most recent works from NEES@UCSD by Moaveni *et al.* [2010], or NEES@UNR by Johnson *et al.* [2009], ([6,7])). Other smaller scale equipments can be found for example in European facilities such as the Italian EUCENTRE [8], or the French CEA laboratory [9], and even the Portuguese LNEC [10]. Moreover, other relevant testing facilities have been in preparation in the last few years, such as the large shaking table array at Tongji University in Shanghai, China, the Korean laboratory network, and the advanced testing facility currently being developed in the European EFAST program [11].

In the context of scientific testing works carried out resorting to shaking tables, which usually happens with the objective of providing additional information not available from simpler experimental tests, blind numerical prediction initiatives have also been held in the past like SMART 2008 [12], UCSD Englekirk Structural Research Centre’s full scale 7 story RC building test [13], or the CAMUS International Benchmark [14,15], the later where some of this paper authors have also participated with great success [16,17,18]. Those simulations are always dependent on deep understanding of the phenomena associated with the seismic behavior of the structures at hand. Besides that, a well-thought methodology needs to be devised in order to adequately address modeling issues without a thorough experimental knowledge.

In light of the documented experience and taking into account the recent results at the Concrete Column Blind Prediction Contest 2010 [19], this paper aims at describing the adopted analysis strategy and, therefore, discussing a number of aspects which are both critical and difficult to evaluate, regarding a given bridge pier seismic behaviour and a correct assessment of its numerical simulation.

2 EXPERIMENTAL CAMPAIGN (CCBPC 2010)

The experimental program associated with the Concrete Column Blind Prediction Contest 2010 initiative was devised by PEER (Pacific Earthquake Engineering Research Center) and NEES (George E. Brown Jr. Network for Earthquake Engineering Simulation) and is briefly described in this chapter. It basically involved of a full-scale reinforced concrete column tested at the UCSD Large High-Performance Outdoor Shake Table [20,21], under uniaxial ground motions with increasing intensity.

2.1 Specimen and material properties

The specimen was a large circular bridge column, bearing a massive concrete block (250 ton) on the top. Figure 1 illustrates its schematic layout and dimensions.

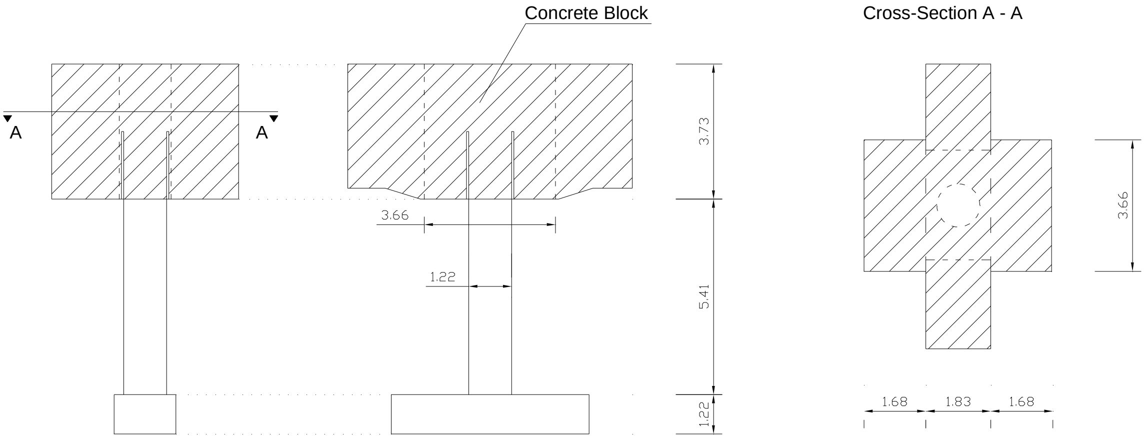

Figure 1 – Column model and dimensions (in meters)

The column was built on the UCSD shaking table, together with two steel-based restraint towers installed around it, in order to prevent excessive (and potentially dangerous) concrete block lateral movements, as depicted by Figure 2 .

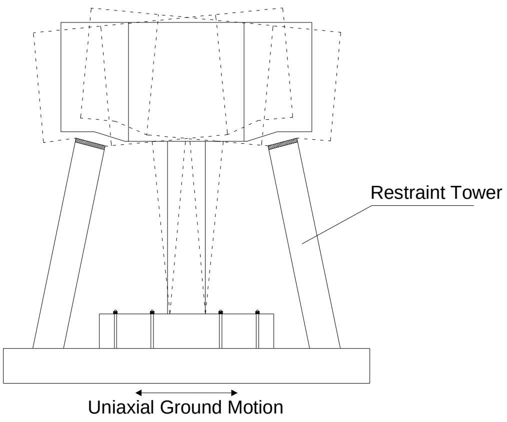

Figure 2 – Restraint towers

The pier's reinforcement steel layout was based on 18 equally spaced No. 11 continuous bars ($\phi \approx 36\,(35.81mm)$). The transverse reinforcement consisted of butt-welded double No. 5 ($\phi \approx 16\,(15.875mm)$) hoops, roughly spaced at 0.15m. The longitudinal bars and circular stirrups development is constant throughout the pier height, both of them penetrating inside the column footing. The properties of the construction materials used in the aforementioned test column were available to all the participant teams and are briefly addressed in the Table 1.

Concrete		Longitudinal Steel		Transverse Steel	
$\sigma_{c\ (21\ days)}$	36.96 MPa	σ_{sy}	518.5 MPa	σ_{sy}	453.7 MPa
$\sigma_{c\ (29\ days)*}$	40.33 MPa	σ_{su}	706.0 Mpa	σ_{su}	592.0 Mpa
$\sigma_{c\ (45\ days)}$	41.85 Mpa				

* - Tests started more than 28 days after concrete casting.

Table 1 – Material Properties

2.2 Instrumentation and Result Demands

The prototype column was densely instrumented in order to obtain good quality results. Specifically, several Linear Voltage Displacement Transducers (LVDTs) were mounted on rods that were rigidly fixed to the concrete column at multiple height levels and accelerations were recorded, using a 16-bit data acquisition system. All the quantities requested in the contest were taken from the resulting data, by direct measurement or implied calculation. Figure 3 describes the aforementioned quantities and the instrumentation layout as used in the tests.

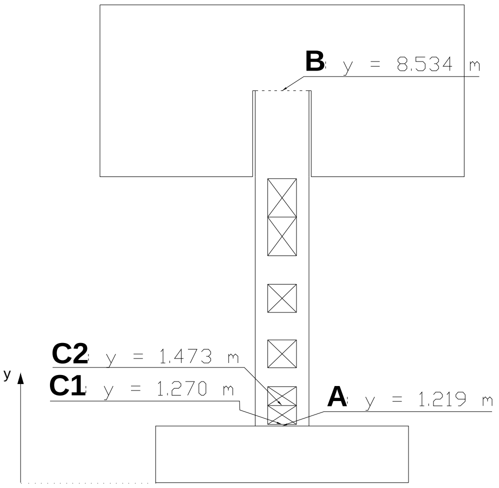

Requested quantities (Maximum values)

1 – Horizontal displacement at level B relative to A
2 – Total horizontal acceleration at level B
3 – Bending Moment at level A (column base)
4 – Shear Force at level A
5 – Average curvature between C1 and C2
6 – Average axial strain between C1 and C2
7 – Residual displacement at level B relative to A
8 – Largest column compressive axial force at level A
9 – Failure Mode

Figure 3 – Instrumentation layout and Contest requested response parameters

2.3 Ground Motions and Test Sequence

Since the experimental programme aimed at assessing the adequacy of design procedures developed by Caltrans to deal with seismic-based structural problems, real earthquake records were used to test the prototype column. Four different acceleration time histories were chosen from Loma Prieta (3 records) and Kobe (1 record) seismic events.

The complete test sequence was performed as described in Table 2, where the really applied seismic events are numbered by even numbers; before each of these six events, a white noise ground motion was applied in order to perform dynamic identification of the system throughout the whole response range.

Event	Ground Motion	Earthquake	Station Name	Scale	Target drift
2	*EQ1*	*Loma Prieta*	*Agnews State Hospital*	1.0 (PGA=4.00 m/s^2)	1%
4	*EQ2*	*Loma Prieta*	*Corralitos*	1.0 (PGA=4.38 m/s^2)	2%
6	*EQ3*	*Loma Prieta*	*LGPC*	1.0 (PGA=4.99 m/s^2)	4%
8	*EQ4 = EQ2*	*Loma Prieta*	*Corralitos*	1.0 (PGA=4.38 m/s^2)	2%
10	*EQ5*	*Kobe*	*Takatori*	0.8 (PGA=5.27 m/s^2)	N/A
12	*EQ6 = EQ3*	*Loma Prieta*	*LGPC*	1.0 (PGA=4.99 m/s^2)	4%

Table 2 – Testing Sequence covering only recorded seismic events

3 MODELLING STRATEGY

This participation in the CCBPC 2010 contest was based in numerical modeling carried out with the Seismostruct analysis software [22]. Since the behavior of the column (due to the uniaxial nature of the table movements) was expected to be dominated by its first vibration mode (because no other significant mass is involved apart from the concrete block), the column was modeled as a simple cantilever structure built upon a sequence of beam elements. Although inelastic force-based elements were used (which helps on reducing the need of a very refined mesh for this type of motion) several finite elements were adopted in order to facilitate the result analysis process, by choosing control sections at appropriate height levels.

The massive concrete block on top of the full-scale column was modeled as a simple lumped mass element at the height level B (y = 8.534m), with corresponding translational mass of 236.15 ton and zero rotational mass moments of inertia.

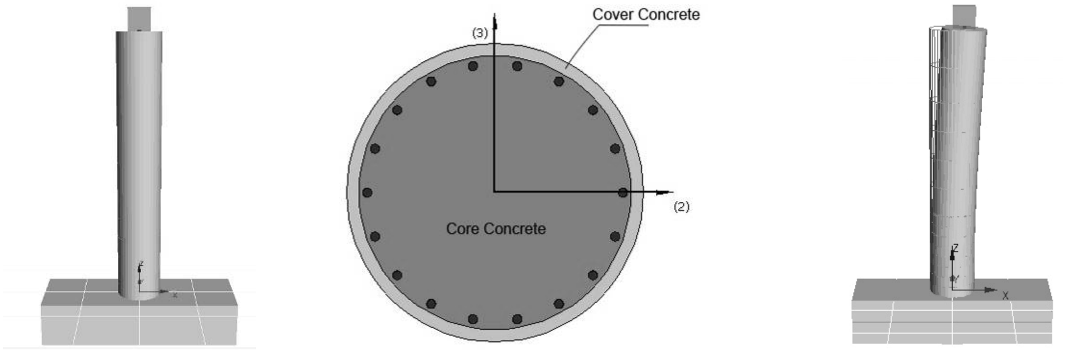

a) Global model illustration

b) Cross-section

c) First vibration mode (*f=1.46 Hz*) representation

Figure 4 – Numerical finite element model representation

The column cross-section was considered with two distinct zones having different characteristics that were taken into account resorting to the fiber model implemented in Seismostruct. Table 3 includes the parameters used to describe the column behavior of the different types of fibers, while elastic behavior was assumed for the column footing.

A cover band was defined for the peripherical concrete ring, with the remaining cross-section area associated with confined core behavior. Material properties of both zones were defined according to the compressive test results, but an improved scheme was used to simulate the beneficial effect of transverse reinforcement on the core concrete confinement. Thus, Mander's constitutive relations and confinement effects simulation rules [23] were adopted, coupled with cyclic rules proposed by Martinez-Rueda and Elnashai [1997] ([24]), as documented in the adopted software manual.

Cover concrete		Confined Concrete		Longitudinal Steel	
Compressive strength (f_c)	41 MPa	Compressive strength (f_c)	41 MPa	Elastic Modulus (E_s)	200 GPa
Tensile strength (f_t)	3 MPa	Tensile strength (f_t)	3 MPa	Yield Strength (f_y)	520 MPa
Strain at peak stress (ε_c)	0.0028	Strain at peak stress (ε_c)	0.0028	Strain hardening parameter (μ)	0.011
Confinement factor (k_c)	1.0	Confinement factor (k_c)	1.296	R_0 *	20
Unit weight (γ) (kN/m^3)	23.6	Unit weight (γ)	23.6	Unit weight (γ)	77 kN/m^3

Table 3 – Model Properties (*: notation as adopted in [22])

Steel was simulated using the Menegotto-Pinto model [25] implemented in Seismostruct, which also considers isotropic hardening [26]. Default code parameters were used for that purpose, as well as for describing the transition curve.

The above referred modeling aspects are associated with either geometrical or material behavior description issues of an experimental test numerical simulation. However, the most important modeling decisions are strongly related with the seismic loading applied to the structure and to an accurate representation of its effects on the column, because they reflect the dynamic nature of the interaction between the inertia forces (generated by the imposed ground motions) and the non-linear material behavior associated with the accommodation of the developed deformations. Thus, an accurate simulation requires thorough evaluation of the characteristics of both the loading and the structure, in order to understand the influence of some phenomena on the overall column behavior (crack development, stiffness reduction, resonance effects, etc).

The modal analysis of the structural model showed a first vibration mode frequency of 1.46 Hz which is inherently associated with an undeformed state. When drift movements reach a certain level and pier cracks start to develop, the column stiffness drops. This means that the interaction between the loading pattern and the structural response is not constant and can change over time, according to the increasing damage imposed to the column.

The second step in this process consisted on the evaluation of the frequency content of the ground motion signals by means of FFT analyses. Figure 5 displays the FFT amplitude results obtained for each ground motion and a vertical line represents the aforementioned first mode frequency of the structure. Horizontal lines refer to the PGA level of each record adopted.

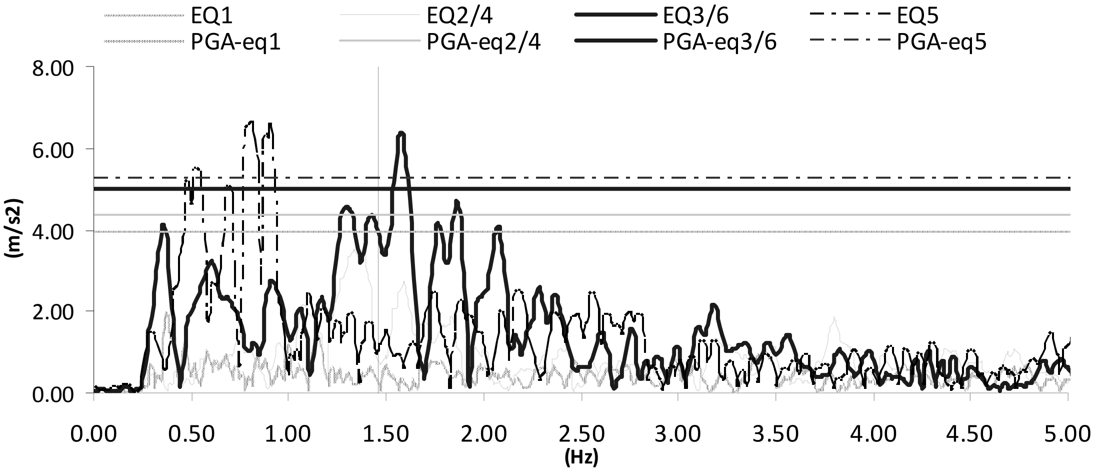

Figure 5 – FFT results for the testing ground motions.

In the previous figure it can be seen that ground motions 2 and 3 have more significant frequency contents around 1.50 Hz (i.e., near the structural frequency). However, once the frequency drops to values slightly smaller than 1.00 Hz, EQ5 can be seen also to have larger significance. In order to better evaluate the inherent consequences, elastic displacement spectra regarding each of the four ground motions were developed for a damping range of 0-2% of the corresponding critical damping. A sound interpretation of such results shown in Figure 6, regarding the experimental sequence which is known beforehand, is very important to understand how the column is likely to perform.

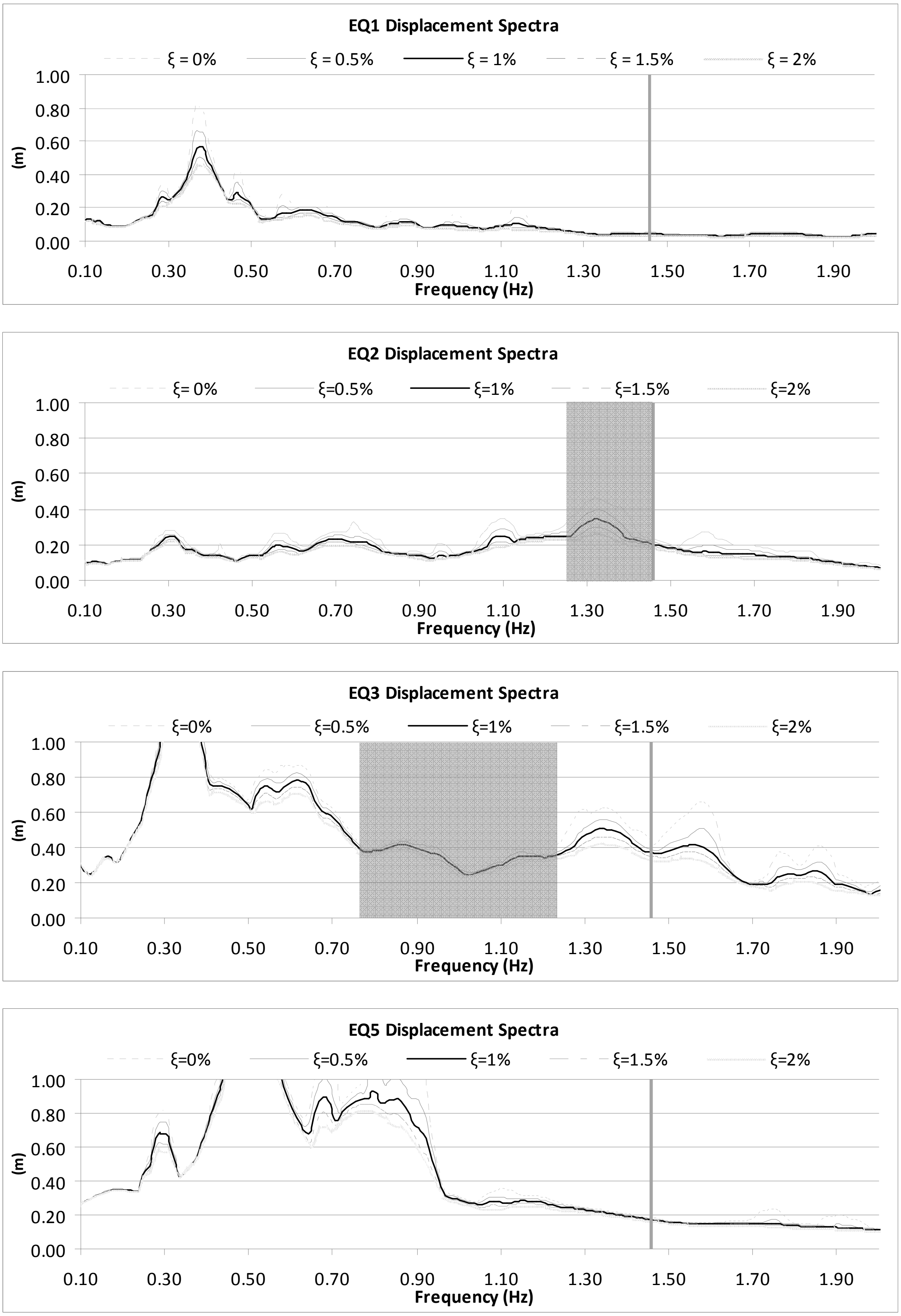

Figure 6 – Elastic displacement spectra due to the imposed ground motions, for several damping ratios

According to Figure 6, the displacement spectra for EQ1 shows low impact for the first vibration mode frequency and also no severe displacement peak in the near range; therefore, it sounds reasonable to assume that the damage imposed to the column during that event was minimal. However, due to low tensile strength of concrete, the column was expected to exhibit cracking on early stages (during EQ2 or even EQ1) leading to stiffness reduction which shifts down the fundamental frequency whose exact range is hard to predict (for that reason, shadow bands are included in the displacement spectra to provide an estimate of the frequency range for the damaged structure). That reduction increases as the concrete cracks develop in size and number, which is consistent with a damage state indicative of moderate non-linear incursion.

As shown in Figure 6, EQ3 ground motion displacement spectra shows relatively uniform values for a wide range of frequencies (within the shadow band) onto which the fundamental frequency is likely to drop. Thus, it is reasonable to assume that important drift values could be reached (say between 200mm and 400mm), regardless of the actually observed column stiffness despite its progressive reduction due to accumulated damage. If the ground motion was shown to be strong enough to induce yielding of the longitudinal rebars, a plastic-hinge mechanism would be due to form, which was further likely to occur because the peak ground acceleration (PGA) was higher for EQ3 than for EQ2.

This reasoning also raises another important point relative to the adopted damping scheme. It is known that viscous damping is especially relevant until the development of a clear hysteretic mechanism, after which the energy dissipation due to hysteretic behavior is much larger than that assumed from viscous damping alone. Therefore, accurate calibration of a numerical model for earthquake simulation requires good viscous damping representation until the plastic-hinge formation and, essentially, good non-linear material behavior description from then onwards. With that in mind, and attempting to reduce the viscous damping impact on the column response after EQ3, the methodology herein adopted was the consideration of a Rayleigh damping matrix matching $\xi = 1\%$ for target frequencies of 1.46 Hz and 0.67 Hz using the tangent stiffness instead of the initial elastic one.

Finally, beyond an effective representation of the interaction between loading, structural properties, viscous damping and hysteretic mechanisms, the time-history analyses of structures subjected to earthquake motions require also an adequate time-step. Thus, in order to correctly represent the loading and to capture its effects on the structure, the time-step of 0.05s was used, which allows vibration components to be adequately described for frequencies of up to 2 Hz.

It should be mentioned that, unlike the experimental activity, no white-noise simulations were made in this work; the ground motions were applied sequentially from EQ1 to EQ6.

4 NUMERICAL SIMULATION RESULTS

The results achieved with the modeling strategy herein presented were generally very good. Although depending on the testing stage, some very significant quantities like top displacement, acceleration or base shear were quite accurately captured, while mainly strains and curvatures exhibited clear deviations from the experimental results. Some of the numerical results are shown in the next paragraphs, generally plotted together with the corresponding experimental results for comparison purposes.

One first issue to be addressed relates to residual displacements that can reach important figures but may not be easily captured in numerical analyses. In order to identify the performance of numerical simulations on this particular issue, shows the complete sequential response of the numerical model in terms of top displacement; horizontal lines corresponding to the numerical and experimental residual displacements are also included in order to compare permanent deformation levels captured with this modeling strategy and those recorded in the experimental test.

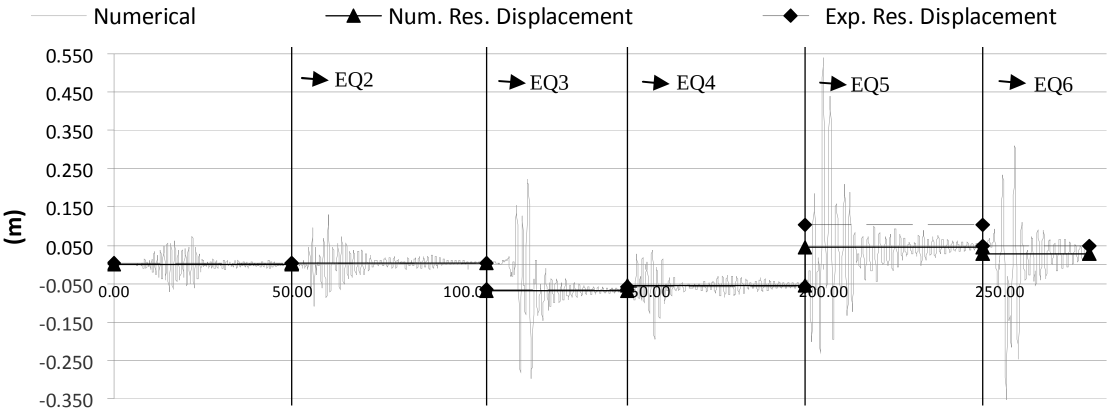

Figure 7 – Complete series of numerical top displacement time-histories with residual displacements (numerical and experimental).

Results show that residual deformations were quite accurately captured except for EQ5, where the difference was larger. It indicates that the overall column stiffness level and material properties were adequately simulated, since each ground motion was able to reproduce the same deformation levels on both the experiment and its numerical model. Non-linear progression might have been similar, although this argument needs further support in view of the difference shown for EQ5 where plastic hinging was due to be established.

A more in-depth, motion by motion, analysis can provide additional information regarding this modeling strategy's adequacy to the blind prediction problem.

Taking for example the horizontal acceleration time histories represented in -a) for the first stage (EQ1), both experimental and numerical curves seem to be in good agreement, with slight numerical overestimation of peak values, until approximately 23s. From then on, i.e., after the peak displacement values, the experimental period elongation was more evidenced than in the numerical response, which might have been due to more damage in the real test. This effect contributes, not only for the period elongation, but also to the increase of damping which is reflected in lower experimental displacements (than the numerical ones) around the 30s time instant.

Similar conclusions are drawn for the corresponding displacement time histories -b) and it is worth mentioning that, by the end of this test (EQ1) when displacements become smaller, the numerical response shows lower values than the experimental one. This modification of the relative magnitude of experimental and numerical response might be explained by the difficulties on achieving a robust simulation of damping that is able to follow adequately the response both in the large and small amplitude cycles.

This issue was also observed for other earthquake motions but, unlike EQ1 where the post-peak differences were mild, larger discrepancies were observed between numerical and experimental curves for the other earthquakes, on the post-peak range, as shown for instance in the top horizontal acceleration time-history for EQ2 (see Figure 9).

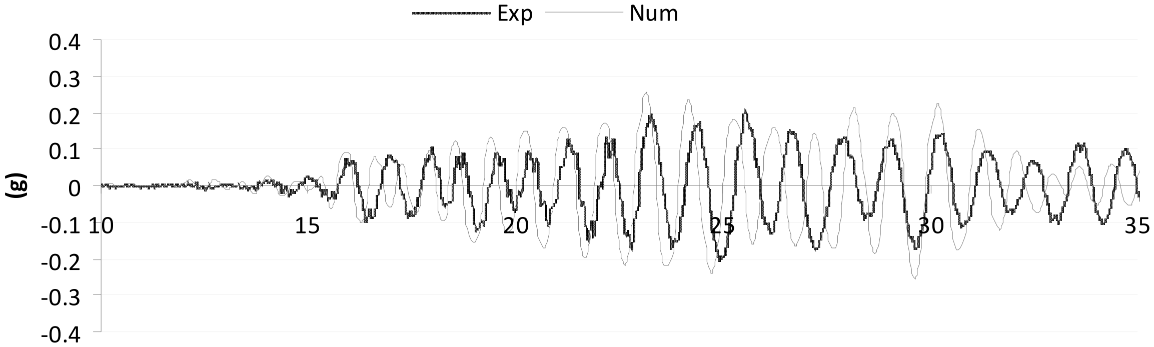

a)

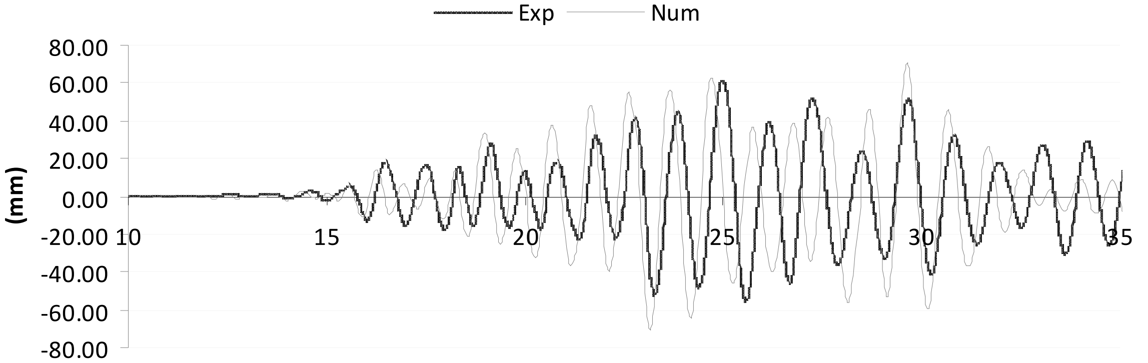

b)

Figure 8 – Numerical vs. Experimental time histories of horizontal a) acceleration and b) displacements (EQ1).

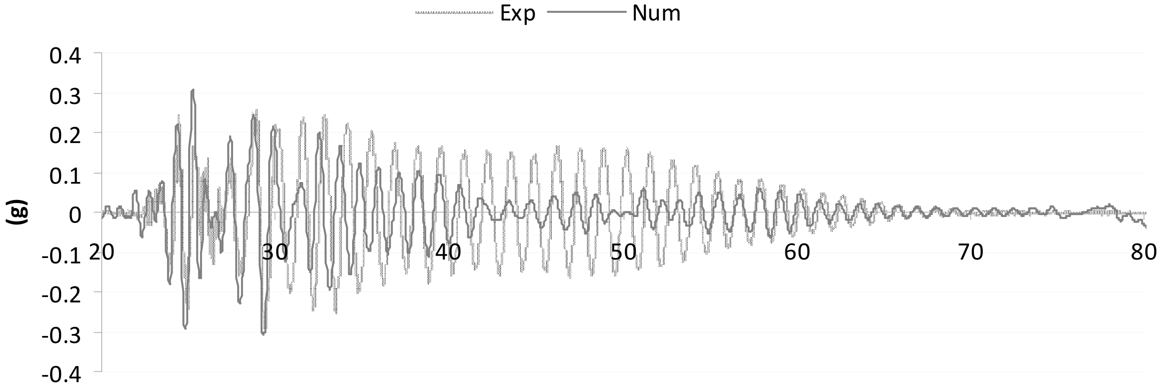

Figure 9 – Numerical vs. Experimental horizontal acceleration time-history (EQ2).

In contrast however, EQ3 showed remarkable results for a blind prediction, with almost all parameters simulated with quite good accuracy (as globally depicted in Figure 10).

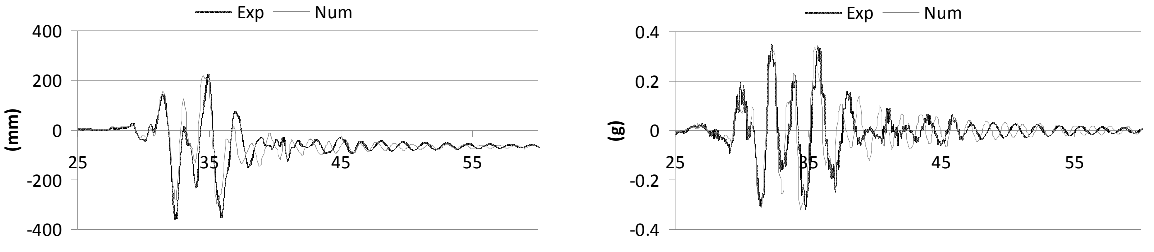

a) Horizontal displacement

b) Horizontal acceleration

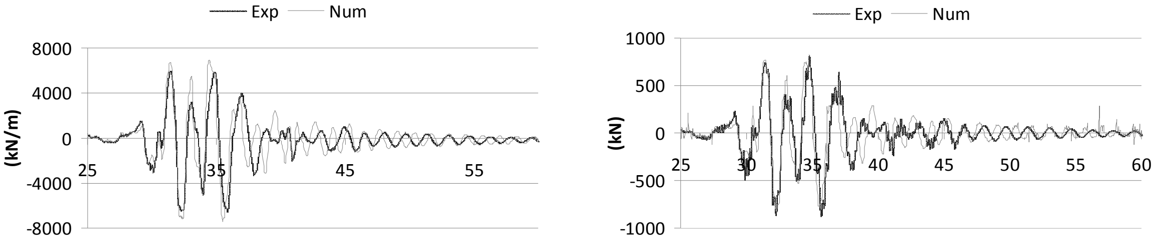

c) Base Moment

d) Base Shear

Figure 10 – Numerical vs. Experimental horizontal results (EQ3).

This was especially important because EQ3 was the first ground motion to clearly push the column into plastic behavior of the longitudinal reinforcement as it was predicted (see Figure 11, where the complete time history of longitudinal reinforcement stress is compared against the yielding threshold). Therefore, the plastic hinge formation was adequately captured by the numerical model.

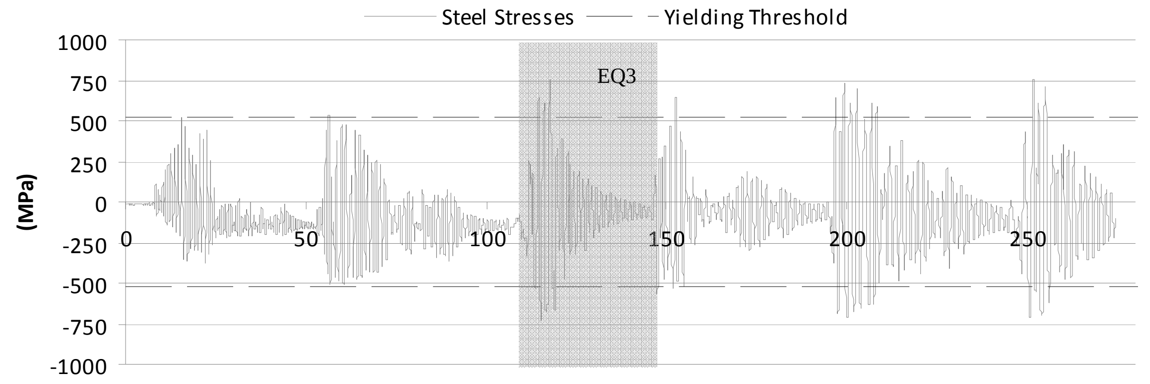

Figure 11 – Complete longitudinal reinforcement stress time-history.

Since the numerical simulation was so similar to the experimental results for this specific ground motion, it follows that the adopted damping was probably accurate enough to provide a good balance between viscous damping during EQ1 and EQ2 (especially concerning peak response values), while making sure the plastic hinge contribution was the main dissipation mechanism once it formed.

It is noteworthy that, for plastic behavior clearly installed (as for EQ3), the influence of viscous damping, adopted to simulate (essentially) the cracking stage preceding the yielding threshold, becomes less important in global response, particularly in what concerns peak values.

This is further confirmed with the response simulation for EQ5earthquake, which has exhibited quite satisfactory agreement between numerical and experimental results (Figure 12) for the same parameters as for EQ3, notwithstanding the fact (already stated before) that deformation measures (axial strain and curvature) were not accurately simulated in the post-peak behavior.

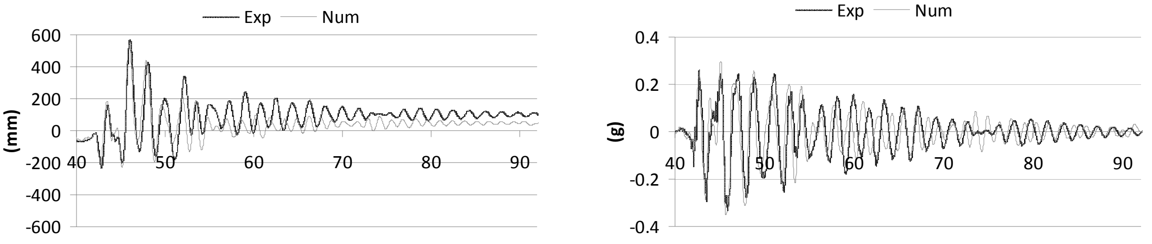

a) Horizontal displacement b) Horizontal acceleration

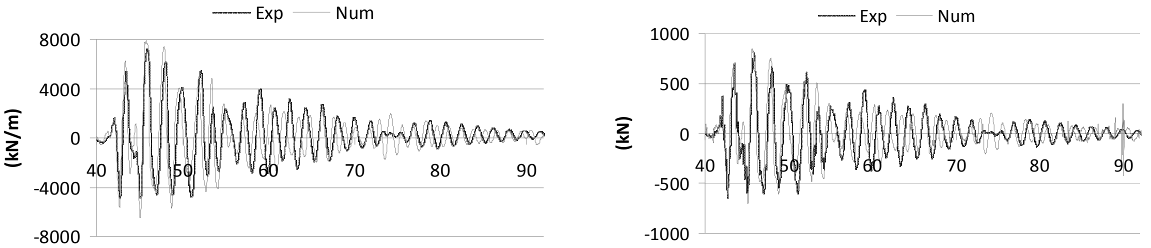

c) Base Moment d) Base Shear

Figure 12 – Numerical vs. Experimental horizontal results (EQ5).

From the above described, an overall observation allows confirming that very satisfactory results were obtained. Differences focused mainly on the column post-peak behavior for each time-history, encompassed by slight out-of-phase response records due to difficulties on simulating accurately the cracking (thus affecting the fundamental period of vibration). Inaccurate residual deformations in the numerical modeling were also identified, although mainly for the EQ5 motion.

5 CONCLUSIONS

This paper described the work carried out by the authors in the framework of their participation in the Concrete Column Blind Prediction Contest 2010 sponsored by PEER and NEES. The blind numerical analyses were presented, preceded by a brief description of the strategy upon which the modeling decisions were made. That was based in simple procedures to evaluate the impact of the seismic loading (such as FFT analyses) and a refined characterization of the structural model using well proven constitutive relations, wherein confinement effects were also considered. The interaction between the seismic loading and the resulting structural degradation was addressed as being of key importance. The former directly increases the latter which, in turn, influences the intensity of the structural response. An adequate representation of the energy dissipation mechanisms was devised for this case, namely by adopting a suitable compromise between structural viscous damping and non-linear material behavior. As expected, the influence of the former was found of greater importance up to the plastic-hinge formation point.

The six ground motions were applied to the numerical model and the results obtained were compared against the test recorded values. The scenario was globally very good. Peak values were simulated with little difference relative to their experimental counterparts (like horizontal displacement and acceleration, base shear, etc) and overall time-history responses exhibited similar behavior. The main negative aspects of this modeling strategy consisted on the difficulties to reproduce adequately the strain and curvature values (probably related to the way they are recorded in the test and read in the numerical simulation), as well as mismatching the post-peak vibration period and the residual deformation from ground motion EQ5. Nonetheless, the plastic-hinge formation was quite accurately predicted.

However, perhaps the most important issue of this work was the development of a good perception of the evolution of the column non-linear response in order to enable and control the model for addressing the involved and relevant phenomena. Without a clear understanding of such phenomena, as well as the overall reinforced concrete cyclic behavior, simulation would be hardly feasible because any modeling could have many shortcomings and lead to considerable differences. Therefore, successful results within a blind prediction process reflect, not only the quality of the tools used in the work, but also the analysts ability to predict the key issues of the structural response.

REFERENCES

[1] Marazzi, F., Politopoulos, I. and Pavese, A., An overview of seismic testing needs in Europe: towards a new advanced experimental facility. *Bulletin of Earthquake Engineering* DOI 10.1007/s10518-010-9212-8, 2010.

[2] http://www.bosai.go.jp/hyogo/ehyogo/

[3] Yu, Y., Tsai, K., Weng, Y., Lin, B. and Lin, J., Analytical studies of a full-scale steel building shaken to collapse. *Engineering Structures*, **32**, 3418-3430, 2010.

[4] Chung, Y., Nagae, T., Hitaka, T. and Nakashima, M., Seismic Resistance Capacity of High-Rise Buildings Subjected to Long-Period Ground Motions: E-Defense Shaking Table Test. *Journal of Structural Engineering*, ASCE, **136** (6), 637-644, 2010.

[5] http://nees.org/sites-mainpage/shaketablelabs/

[6] Moaveni, B., He, X., Conte, J. and Restrepo, J., Damage identification study of a seven-story full-scale building slice tested on the UCSD-NEES shake table. *Structural Safety*, **32**, 347-356, 2010.

[7] Johnson, N., Saiidi, M. and Sanders, D., Nonlinear Earthquake Response Modeling of a Large-Scale Two-Span Concrete Bridge. *Journal of Bridge Engineering*, ASCE, **14** (6), 460-471, 2009.

[8] http://www.series.upatras.gr/EUCENTRE

[9] http://www-tamaris.cea.fr/html/en/tests/azalee.php

[10] http://www.series.upatras.gr/LNEC

[11] Marazzi, F. and Molina, F., 1st EFAST workshop—challenges, needs and open questions. *EUR 23822 EN*. Luxembourg: Publications Office of the European Union. JRC5 51632, 2009.

[12] Varpasuo, P. and Kâhkönen, J., Blind prediction of smart 2008 seismic structural response test results. *Proceedings of the International Conference on Nuclear Engineering, ICONE*, **4**, 131-137, 2008.

[13] Kelly, T., A blind prediction test of nonlinear analysis procedures for reinforced concrete shear walls. *Bulletin of the New Zealand Society for Earthquake Engineering*, **40** (3), 142-159, 2007.

[14] CIB-RI, CAMUS International Benchmark - Report I, Mock-Up and Loading Characteristics. Specifications for the Participants Report. *Report SEMT/EMSI/RT/98-066A*, CEA, France, 1998.

[15] CIB-RI, CAMUS International Benchmark - Experimental Results. Synthesis of the Participants Reports, *Report SEMT/EMSI/RT/98-067A*, CEA, France, 1998.

[16] Faria, R., Vila-Pouca, N. and Delgado, R., Seismic Behaviour of a RC Wall: Numerical Simulation and Experimental Validation. *Proceedings of the IV Congreso de Métodos Numéricos en Ingeniería* (CD-ROM), Seville, Spain, 1999.

[17] Vila-Pouca, N., Faria, R. and Delgado, R. Prediction Analysis of a Reduced Scale Wall Building. *Relatório sobre a Participação da FEUP no "CAMUS 1 International Benchmark"*, Faculdade de Engenharia da Universidade do Porto, Porto, Portugal, 1998.

[18] Vila-Pouca, N., Faria, R. and Delgado, R., Numerical Simulation of the Seismic Behaviour of a Reduced Scale RC Wall Building. *Relatório sobre a Participação da FEUP no "CAMUS 3 International Benchmark"*, Faculdade de Engenharia da Universidade do Porto, Porto, Portugal, 2000.

[19] http://nisee2.berkeley.edu/peer/prediction_contest/

[20] Restrepo, J., Conte, J., Luco, J., Seible, F. and Van den Einde, L., The NEES@UCSD large high performance outdoor shake table. *Geotechnical Special Publication*, (130-142), 931-946, 2005.

[21] Ozcelik, O., Luco, J., Conte, J., Trombetti, T. and Restrepo, J., Experimental characterization, modeling and identification of the NEES-UCSD shake table mechanical system. *Earthquake Engineering and Structural Dynamics*, **37**, 243-264, 2008.

[22] www.seismosoft.com

[23] Mander, J., Priestley, M. and Park, R., Theoretical Stress-Strain Model for Confined Concrete. *Journal of Structural Engineering*, ASCE, **114** (8), 1804-1826, 1988.

[24] Martinez-Rueda, J. and Elnashai, A., Confined concrete model under cyclic load. *Materials and Structures*, **30** (197), 139-147, 1997.

[25] Menegotto, M. and Pinto, P., Method of analysis for cyclically loaded reinforced concrete plane frames including changes in geometry and non-elastic behaviour of elements under combined normal force and bending. *IABSE Symposium on Resistance and Ultimate Deformation of Structures Acted on by Well-Defined Repeated Loads*, Final Report, Lisbon, 1973.

[26] Filippou, F., Popov, E. and Bertero, V., Modelling of R/C joints under cyclic excitations. *Journal of Structural Engineering*, ASCE, **109** (11), 2666-2684, 1983.

COMPDYN 2011
III ECCOMAS Thematic Conference on
Computational Methods in Structural Dynamics and Earthquake Engineering
M. Papadrakakis, M. Fragiadakis, V. Plevris (eds.)
Corfu, Greece, 25–28 May 2011

INTEGRATION OF GEOMETRY AND FINITE ELEMENTS IN THE ANALYSIS OF NONLINEAR SYSTEMS

Ahmed A. Shabana[1], **Ashraf M. Hamed**[1], **Paramsothy Jayakumar**[2], **and Michael D. Letherwood**[2]

[1] Department of Mechanical and Industrial Engineering
University of Illinois at Chicago
842 West Taylor Street
Chicago, Illinois 60607, U.S.A.
e-mail: {shabana, aabdal5}@uic.edu

[2] U.S. Army RDECOM-TARDEC
6501 E. 11 Mile Road
Warren, MI 48397-5000, U.S.A.
e-mail: {paramsothy.jayakumar, mike.letherwood}@ us.army.mil

Keywords: Geometric discontinuities; Finite element; Multibody systems; B-spline; NURBS.

Abstract. *In this paper, a method for the* ***i****ntegration of* ***c****omputer* ***a****ided* ***d****esign and* ***a****nalysis (I-CAD-A) is discussed. The method is based on using a finite element formulation that employs a kinematic description that is consistent with computational geometry methods. This allows for the development of an efficient interface between CAD systems and finite element (FE) and multibody system (MBS) software using simple linear coordinate transformation. The finite element absolute nodal coordinate formulation (ANCF) is used to successfully achieve this integration. ANCF structural finite elements, such as beams, plates, and shells, define shapes that are invariant under arbitrary rigid body displacements. It is shown in this paper that B-spline geometry can always be converted to ANCF geometry. The converse, however, is not true. ANCF provides the flexibility of selecting the basis functions, allowing for the development of finite elements with less number of degrees of freedom as compared to the B-spline counterparts. It is also demonstrated that the B-spline representation fails to capture certain type of discontinuities. To this end,* C^0 *discontinuities are classified as structural and non-structural discontinuities. Structural discontinuities do not allow for rigid body displacement between the finite elements, while non-structural discontinuities allow for such a rigid body displacement. Using ANCF finite elements, new FE/MBS meshes can be developed. These new FE meshes allow for describing mechanical joints that permit relative rigid body rotations using linear connectivity conditions. Furthermore, the new FE meshes have constant mass matrix and zero Coriolis and centrifugal forces despite the large relative rotation between the finite elements of the structure. Numerical results are presented in order to demonstrate the integration of CAD and FE/MBS analysis.*

1 INTRODUCTION

The geometry description used in many of the existing finite element (FE) formulations cannot be exactly converted to the geometry developed by computational geometry methods such as B-spline and NURBS (**N**on-**U**niform **R**ational **B**-**S**plines) representations. This fact has motivated researchers in the mechanics community to adopt the methods of computational geometry as analysis tools instead of using conventional FE formulations. While the methods of computational geometry, such as B-spline, have several desirable analysis features; these methods have serious limitations when used as analysis tools. The B-spline recurrence formula and the rigid definition of the knot vector make B-spline less attractive as compared to the *absolute nodal coordinate formulation* (ANCF) geometry description. While B-spline geometry can always be converted exactly to ANCF geometry [1-3], the converse is not always true. ANCF geometry does not restrict the order of the parameters or the number of basis functions used in the interpolating polynomials [4-14]. This advantage, as will be demonstrated in this paper, allows for developing finite elements with less number of degrees of freedom as compared to those developed using the B-spline geometry. Another fundamental difference between B-spline and ANCF geometric descriptions lies in modeling discontinuities. There are two types of discontinuities when chain systems are considered [15]. The first is *structural discontinuity* which does not allow rigid body displacement between two elements connected at the joint definition point. This joint allows only for deformation degrees of freedom. The second type of discontinuity is called *non-structural discontinuity* which allows for rigid body displacement at the joint definition point. Figure 1 shows a chain which has a structural discontinuity at point C and non-structural discontinuity at point O. At the junction at C, only deformation degrees of freedom are allowed, while at point O, relative rigid body rotation is permitted. Nonetheless, the degree of continuity at both points is C^0. B-spline can be used as an analysis tool to describe the non-structural C^0 discontinuity at point O, but because of its rigid recurrence structure and the definition of its knot vector and knot multiplicity, B-spline cannot be used in the motion analysis of structural C^0 continuity at point C since B-spline C^0 description leads to a rigid body mode; that is, the elimination of one control point by reducing the knot multiplicity by one is not sufficient for eliminating the modes of rigid body rotations between two B-spline segments. ANCF geometry, on the other hand, can be used in the analysis of both structural and non-structural discontinuities [15].

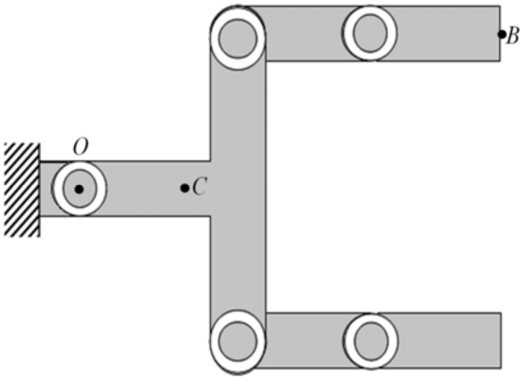

Figure 1 System with structural and non-structural discontinuities

Example of *Non-structural discontinuities* that characterize the motion of MBS applications is chain of links connected by pin joints as the one shown in Fig. 2. Each link is permitted to undergo an independent rigid body rotation. If the links are considered to be flexible bodies, the relative motion between the links is a combination of rigid body and deformation displacements. Nonetheless, the dynamics of a simple planar rigid-link chain is governed by highly nonlinear equations as the result of the geometric nonlinearities due to the finite relative rotations. Existing FE algorithms and computer programs, however, do not allow for generating a FE mesh for such chains using linear connectivity conditions. One of the main goals of this investigation is to develop a new three-dimensional flexible-link chain model using fully parameterized ANCF finite elements. This chain model is based on a new FE mesh defined using linear connectivity conditions. The FE mesh allows for relative rigid body rotations between its elements and has a constant inertia matrix and zero Coriolis and centrifugal forces. In order to develop the new flexible-link chain model presented in this paper, a new pin joint model is introduced. At the joint definition point, different degrees of continuity are used with different parameters; leading to some strain components to be continuous while the others are discontinuous. The modes of deformation at the joint definition points are discussed in order to shed light on the nature of the new joint and kinematic constraints developed in this paper.

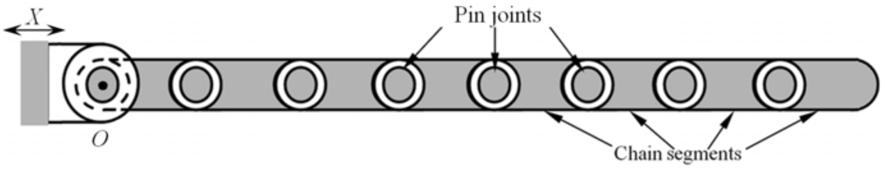

Figure 2 Eight-link chain system

The second main contribution of this paper is to demonstrate the fundamental differences between B-spline and ANCF geometries. It is shown that while B-spline geometry can always be converted to ANCF geometry, the converse is not true because of the rigid B-spline recurrence structure. It is also shown that B-spline representation can be used only in the analysis of one type of C^0 continuity; while such a B-spline representation cannot be used in the analysis of another type of C^0 continuity referred to as structural discontinuity. It is shown that ANCF finite elements which have degrees of freedom less than their B-spline counterparts can be developed since ANCF does not have specific requirements on the order of the parameterization variables or the number of basis functions used in the interpolating polynomials.

2 CONSTRAINT NONLINEARITIES

Existing FE algorithms and computer codes allow for developing meshes in which the finite elements are rigidly connected. In the case of arbitrarily large relative rigid body rotations between the finite elements of one mesh, an incremental solution procedure based on a co-rotational formulation is used. This FE solution procedure leads to a highly nonlinear inertia matrix and due to the nature of the incremental approach used and the set of coordinates employed, existing FE algorithms and computer programs are not suited for the analysis of complex multibody systems that are characterized by geometric nonlinearities that result from the independent rigid body rotations of the finite elements. In most formulations, including rigid body dynamics formulations, such non-structural geometric discontinuities are governed by nonlinear algebraic constraint equations which lead to highly nonlinear inertia matrix. For such articulated systems, components which are not rigidly connected are treated as separate bodies when MBS algorithms are used. Consider, for example, the simple planar double-pendulum example shown in Fig. 3. The pendulum consists of two rigid bodies, i and j, connected by a pin (revolute) joint at point P whose local position vector is defined in the two body coordinate systems by the vectors $\bar{\mathbf{u}}_P^i$ and $\bar{\mathbf{u}}_P^j$, respectively. The global position vector of this point in terms of the coordinates of bodies i and j are denoted as $\mathbf{r}_P^i$ and $\mathbf{r}_P^j$, respectively.

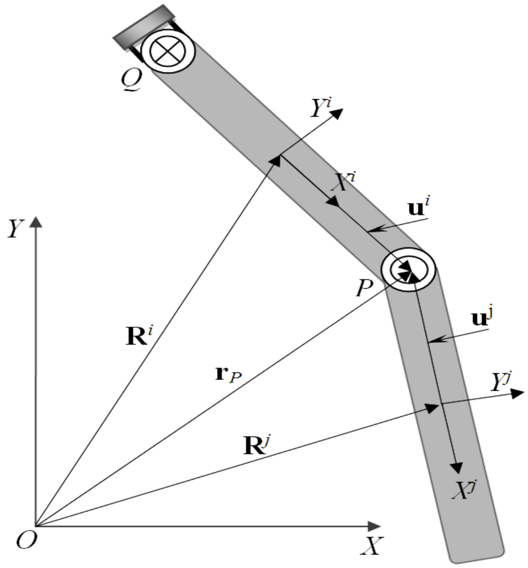

Figure 3 Double pendulum example

In this simple planar rigid body example, the kinematic constraint conditions of the pin joint can be written as $\mathbf{r}_P^i = \mathbf{r}_P^j$. This equation can be written more explicitly in terms of the co-ordinates of bodies i and j, as

$$\mathbf{R}^i + \mathbf{A}^i \bar{\mathbf{u}}_P^i = \mathbf{R}^j + \mathbf{A}^j \bar{\mathbf{u}}_P^j \tag{1}$$

where $\mathbf{R}^i$ and $\mathbf{R}^j$ define the global position vector of the origins of the coordinates systems of the two bodies, and $\mathbf{A}^i$ and $\mathbf{A}^j$ are the transformation matrices that define the orientations of the two bodies. In the planar analysis, the vectors and matrices that appear in Eq. 1 can be written as

$$\left.\begin{aligned} &\bar{\mathbf{u}}_P^k = [\bar{x}^k \quad \bar{\mathrm{y}}^k], \qquad \mathbf{R}^k = [R_{\mathrm{x}}^k \quad R_y^k] \\ &\mathbf{A}^k = \begin{bmatrix} \cos(\theta^k) & \text{-}\sin(\theta^k) \\ \sin(\theta^k) & \cos(\theta^k) \end{bmatrix}, \quad k = i, j \end{aligned}\right\} \tag{2}$$

The geometric nonlinearities of the connectivity condition of Eq.1 characterize all MBS formulations including the augmented and embedding techniques. Using the embedding technique, one can show that the two equations of motion of the planar rigid body double pendulum shown in Fig. 3 can be written as

$$\left.\begin{aligned}&\left(m^i(l^i)^2+J^i+m^j(l^i)^2\right)\ddot{\theta}^i+\left(2m^jl^il^j\cos\theta^{ij}\right)\ddot{\theta}^j=\\&\qquad-2m^igl^i\cos\theta^i-m^jgl^i\cos\theta^i-2m^jl^il^j\left(\dot{\theta}^j\right)^2\sin\theta^{ij}\\&\left(2m^jl^il^j\cos\theta^{ij}\right)\ddot{\theta}^i+\left(m^j(l^j)^2+J^j\right)\ddot{\theta}^j=\\&\qquad-2m^jgl^j\cos\theta^j+m^jl^il^j\left(\dot{\theta}^i\right)^2\sin\theta^{ij}\end{aligned}\right\}\qquad(3)$$

In this equation, m^k and l^k are, respectively, the mass and length of link $k, k=i, j$, $\ddot{\theta}^k$ is the angular acceleration of link k, $\theta^{ij}=\theta^i-\theta^j$ and g is the gravity constant. It is clear from Eq. 3 that the equations of motion for a simple planar rigid body double pendulum are highly nonlinear as the result of the nonlinear connectivity conditions. The resulting inertia coefficients are also highly nonlinear because of the geometric nonlinearities that result from the non-structural discontinuities. Such non-structural geometric discontinuities also lead to more geometric nonlinearities when the deformation of the links are considered using the FE/FFR formulation due to the dynamic coupling between the reference motion and the elastic deformations. In the FFR formulation, $\bar{\mathbf{u}}_P^k$ is expressed in terms of the elastic coordinates and the number of equations of motion increases by the number of these elastic coordinates.

3 B-SPLINE CURVES AND SURFACES

In B-spline representation, any curve can be represented as a combination of several polynomial segments. Generally, B-spline curves can be defined using following equation [1, 18]:

$$\mathbf{r}(u)=N_{0,p}(u)\mathbf{P}_0+N_{1,p}(u)\mathbf{P}_1+......+N_{n,p}(u)\mathbf{P}_n=\sum_{i=0}^{n}N_{i,p}(u)\mathbf{P}_i\qquad(4)$$

where $N_{i,p}(u)$ are the B-spline basis functions of degree p, u is the parameter, and $\mathbf{P}_i$ are the control points that define the control polygon. The basis functions can be defined as

$$\left.\begin{aligned}&N_{i,0}(u)=\begin{cases}1 & \text{if } u_i\le u<u_{i+1}\\0 & \text{otherwise}\end{cases}\\&N_{i,j}(u)=\frac{u-u_i}{u_{i+j}-u_i}N_{i,j-1}(u)+\frac{u_{i+j+1}-u}{u_{i+j+1}-u_{i+1}}N_{i+1,j-1}(u)\end{aligned}\right\}\qquad(5)$$

where $u_i\le u_{i+1}$, and U= $\{u_0\ u_1\ \ldots.u_{n+p+1}\}$ is called the knot vector. The elements of the knot vector need not be distinct. Each nonzero span corresponds to a B-spline segment defined by two knot points called in this case breakpoints that represent distinct knot values. The number of equal knots at a point is referred to as the knot multiplicity.

B-spline surfaces can also be defined using the product of B-spline base functions, two parameters, and two knot vectors. B-spline surfaces can be defined in the following parametric form [1, 18]:

$$\mathbf{r}(u,v)=\sum_{i=0}^{n}\sum_{j=0}^{m}N_{i,p}(u)N_{j,q}(v)\mathbf{P}_{i,j} \tag{6}$$

where u and v are the parameters; $N_{i,p}(u)$ and $N_{j,q}(v)$ are B-spline basis functions of degree p and q, respectively; and $\mathbf{P}_{i,j}$ are a set of bidirectional net of control points. $N_{j,q}(v)$ can be defined similar to the definition introduced for $N_{i,p}(u)$ with another knot vector $\mathbf{V}=\{v_0 \quad v_1 \quad \cdots \quad v_{m+q+1}\}$. Note that the orders of the polynomials in the u and v directions can be different; for example, a cubic interpolation can be used along u while a linear interpolation can be used along v. As in the case of B-spline curves, the knots of B-spline surfaces do not have to be distinct; distinct knots are called breakpoints and define surface segments with non-zero dimensions. The number of the non-distinct knots in $\mathbf{U}$ and $\mathbf{V}$ at a point is referred to as the knot multiplicity associated, respectively, with the parameters u and v at this point. At a given breakpoint, the multiplicity associated with u can be different from the multiplicity associated with v; allowing for different degrees of continuity for the derivatives with respect to u and v. For cubic $N_{i,p}$ ($p=3$), C^0, C^1, or C^2 conditions correspond, respectively, to knot multiplicity of three, two, and one; while in the case of linear interpolation of $N_{j,q}$, the highest continuity degree that can be demanded is continuity of the gradients.

In B-spline surface representation, there is a relationship between the polynomial degree, the number of knots, and the number of control points. This relationship must be fully understood if B-spline geometry will be used as an analysis tool. If $r+1$ is the number of knots in $\mathbf{U}$ and $s+1$ is the number of knots in $\mathbf{V}$, then in B-spline geometry, one must have

$$r=n+p+1, \quad s=m+q+1 \tag{7}$$

These formulas imply that, for a given polynomial order, if the number of knots decreases, the number of control points (degrees of freedom used in the analysis) must also decrease. A decrease in the knot multiplicity by one is equivalent to eliminating one control point. This can also be equivalent to increasing the degree of continuity since eliminating a control point can be the result of imposing algebraic equations that relates the derivatives at a certain breakpoint. From the bidirectional structure used in Eq. 6, a surface segment which has cubic interpolation along u ($p=3, n=3, r+1=8$) and a linear interpolation along v ($q=1, m=1, s+1=4$), should have $(n+1)\times(m+1)=8$ control points; this is regardless of whether the surface is two- or three-dimensional. Manipulation of the B-spline surface of Eq.6 shows that these eight control points are the result of using the alternate basis set $1,u,v,uv,u^2,u^2v,u^3,u^3v$. That is, B-spline representation and the formulas of Eq. 7 do not allow for the use of the basis set $1,u,v,uv,u^2,u^3$ which can be effectively used to develop a shear deformable beam model. If a cubic interpolation is used for both u and v (thin plate), the B-spline representation will require 16 control points because the expansion must include all terms $u^k v^l$; $k,l=0,1,2,3$ regardless of whether the shape of deformation of the plate is simple or complex; one must strictly follow the B-spline rigid structure. This can be of disadvantage in the analysis since such a geometric representation can unnecessarily increase the dimension of the analysis model and leads to the loss of the flexibility offered by the FE method or modal analysis techniques. As the degree of the polynomial interpolation increases, the problem gets even worse.

4 ANCF FINITE ELEMENT GEOMETRY

In the absolute nodal coordinate formulation, the position vector of any arbitrary point of the finite element with respect to the fixed global reference frame can be generally written as follows

$$\mathbf{r}(x,y)=\mathbf{S}(x,y)\mathbf{e}(t) \tag{8}$$

where x and y are the element spatial coordinates, t is time, $\mathbf{S}$ is the element shape function matrix, and $\mathbf{e}$ is the vector of the element nodal coordinates. An example of ANCF elements can be planar two-node shear deformable beam element. The shape function matrix for this element is defined as

$$\mathbf{S}=\begin{bmatrix} s_1\mathbf{I} & s_2\mathbf{I} & s_3\mathbf{I} & s_4\mathbf{I} & s_5\mathbf{I} & s_6\mathbf{I} \end{bmatrix} \tag{9}$$

In this equation, $\mathbf{I}$ is the identity matrix, and $\mathrm{s}_i, i=1,2,\ldots,6$ are shape functions defined as [16]:

$$\left.\begin{aligned} &s_1=1-3\xi^2+2\xi^3, \quad s_2=l\left(\xi-2\xi^2+\xi^3\right), \quad s_3=l\eta\left(1-\xi\right), \\ &s_4=3\xi^2-2\xi^3, \quad s_5=l\left(-\xi^2+\xi^3\right), \quad s_6=l\xi\eta \end{aligned}\right\} \tag{10}$$

where l is the element length, $\xi=\dfrac{x}{l}$ and $\eta=\dfrac{y}{l}$.

Each of the element nodes has six degrees of freedom; two translational coordinates defined by the two-dimensional vector $\mathbf{r}=\begin{bmatrix} r_1 & r_2 \end{bmatrix}^{\mathbf{T}}$, and four gradient coordinates defined by the two vectors $\mathbf{r}_x=\begin{bmatrix} r_{x1} & r_{\mathbf{x2}} \end{bmatrix}^{\mathbf{T}}$ and $\mathbf{r}_y=\begin{bmatrix} r_{y1} & r_{y2} \end{bmatrix}^{\mathrm{T}}$. The vector of nodal coordinates $\mathbf{e}$ can then be written as

$$\mathbf{e}=\begin{bmatrix} \mathbf{r}^{A\mathrm{T}} & \mathbf{r}_x^{\ A\mathrm{T}} & \mathbf{r}_y^{\ A\mathrm{T}} & \mathbf{r}^{B\mathrm{T}} & \mathbf{r}_x^{\ B\mathrm{T}} & \mathbf{r}_y^{\ B\mathrm{T}} \end{bmatrix}^{\mathrm{T}} \tag{11}$$

In this equation, A and B refer to the end points of the finite element. Note that the element defined by the preceding equations is based on a cubic interpolation for x and a linear interpolation for y. This element has been widely used in the analysis of large deformation problems. The standard ANCF assembly process ensures continuity of both position and gradient coordinates when two finite elements are rigidly connected.

Structural discontinuities can be systematically modeled using ANCF finite elements by using the proper gradient transformations. The gradient transformations, which are different from vector transformations, enter into the formulation of the element dynamic equations. Furthermore, constraints on higher derivatives can also be imposed at a preprocessing stage using linear algebraic equations; allowing for having a higher degree of continuity.

5 ANCF VS B-SPLINE CURVES AS ANALYSIS TOOLS

While B-spline geometry can always be converted to ANCF geometry, the converse is not true. ANCF geometry does not impose restriction on the basis functions that must be included in the interpolating polynomials. This allows for developing finite elements that have less co-ordinates as compared to those developed using the B-spline representation. Furthermore, ANCF geometry can be used to model both structural and non-structural discontinuities [13, 15, 17, and 18], while the rigid recurrence formula for B-spline representation cannot be used to model structural discontinuities in a straight forward manner. The basic differences between ANCF and B-spline geometries are demonstrated in this section using a planar beam example. This element is an example of ANCF elements that cannot be converted to B-spline representation. This element is based on a polynomial expansion that does not have the two basis functions x^2y and x^3y. These terms can be included in ANCF geometry by adding nodal coordinates allowing for converting B-spline representation to ANCF representation. Similar comments apply to ANCF thin plate elements that do not have to include all the basis functions $x^k y^l; k, l = 0,1,2,3$. This flexibility offered by ANCF geometry allows for developing finite elements that have smaller number of coordinates compared to those elements developed by B-spline geometry.

One can also show that ANCF finite elements can describe structural and non-structural discontinuities. Non-structural discontinuities that allow for large rigid body rotations can be described using a C^0 model obtained by imposing constraints on the position coordinates only. For example if two elements i and j are connected by pin joint at a node, one can apply the algebraic equations $\mathbf{r}^i = \mathbf{r}^j$ at this node. These algebraic equations can be imposed at a preprocessing stage to eliminate the dependent variables and define FE mesh that has a constant mass matrix and zero Coriolis and centrifugal forces despite the finite rotations allowed between the finite elements of the mesh. Non-structural discontinuities can also be described using B-spline geometry by reducing the knot multiplicity at the joint node by one. Note that in the case of non-structural discontinuities no constraints are imposed on the gradient vectors, and therefore, the state of strain is not unique at the joint node. Each of the Lagrangian strains $\varepsilon_{xx} = \left(\mathbf{r}_x^T \mathbf{r}_x - 1\right)/2$, $\varepsilon_{yy} = \left(\mathbf{r}_y^T \mathbf{r}_y - 1\right)/2$, and $\varepsilon_{xy} = \mathbf{r}_x^T \mathbf{r}_y / 2$ have two values at the joint node; one defined on element i and the other is defined on element j. Here $\mathbf{r}_x = \partial \mathbf{r}/\partial x,\ \mathbf{r}_y = \partial \mathbf{r}/\partial y,\ \mathbf{r}_z = \partial \mathbf{r}/\partial z$.

The concept of degrees of freedom widely used in mechanics is not considered in developing the recurrence relationships on which B-spline and NURBS geometry are based. This represents another serious limitation when these computational geometry methods are used as analysis tools; as evident by the fact that B-spline geometry cannot describe structural discontinuities. This type of discontinuities, while it remains of the C^0 continuity type, requires imposing additional constraints on the gradients; these constraints cannot be captured by the B-spline recurrence formula since they require the elimination of additional vectors. In the case of B-spline, C^0 continuity is achieved by reducing the knot multiplicity by one, and this eliminates one control point leading to the definition of a pin joint (non-structural discontinuity). ANCF geometry, on the other hand, allows for imposing constraints on the gradients using the tensor transformation $\left(\partial \mathbf{r}/\partial \mathbf{x}_1\right) = \left(\partial \mathbf{r}/\partial \mathbf{x}_2\right)\mathbf{A}$, where $\mathbf{x}_1 = \begin{bmatrix} x_1 & y_1 \end{bmatrix}^T$ and $\mathbf{x}_2 = \begin{bmatrix} x_2 & y_2 \end{bmatrix}^T$ are two sets of coordinate lines, and $\mathbf{A}$ is the matrix of coordinate line transformation. Using this tensor gradient transformation, the structural discontinuities can be systematically modeled using ANCF finite elements [13, 17].

6 NEW ANCF FINITE ELEMENT MESH

In this section, it is shown how fully parameterized ANCF three-dimensional finite elements can be used to develop spatial joint models that allow large relative rigid body rotation between the finite elements. ANCF finite elements connected by this joint can be assembled using linear connectivity conditions leading to FE mesh that has a constant mass matrix and zero Coriolis and centrifugal forces. The fully parameterized three-dimensional ANCF beam element is used in this investigation to demonstrate the development of such joint models. The displacement field of the element can be written as $\mathbf{r}(x, y, z) = \mathbf{S}(x, y, z)\mathbf{e}(t)$ where x, y, and z are the element spatial coordinates [12, 19]. The element has two nodes; each node has 12 nodal coordinates defined by the vector $\mathbf{e}^k = \begin{bmatrix} \mathbf{r}^{kT} & \mathbf{r}_x^{kT} & \mathbf{r}_y^{kT} & \mathbf{r}_z^{kT} \end{bmatrix}^T$, where k is the node number. This ANCF finite element captures the cross section deformation and its coupling with extension and bending. Therefore, this element can be used to develop general models for belt drives and rubber tracked vehicles. Furthermore, this three-dimensional beam element is another example that can be used to demonstrate the generality of the ANCF geometry. This element is based on cubic interpolation in x and linear interpolation in y and z. Nonetheless, one can show that the four basis functions x^2y, x^3y, x^2z, x^3z are not used in developing the displacement field of this widely used ANCF beam element. Therefore, the geometry of this element cannot be converted to B-spline volume geometry. These missing basis functions can be systematically included in the development of another ANCF finite element that can be converted to B-spline volume geometry. However, such an element will lead to 50% increase in the number of the element nodal coordinates.

A planar pin joint between rigid or flexible bodies is an example of C^0 continuity, as previously discussed. A pin joint between two rigid bodies in the spatial analysis also allows for only one degree of freedom, which is a relative rotation about the joint axis. Since the pin joint eliminates five degrees of freedom in the rigid body analysis, its formulation requires five algebraic constraint equations that eliminate three relative translation displacements and two relative rotations between the two bodies. In the case of flexible bodies, an infinitesimal volume can have 12 modes of displacements; three rigid body translations, three rotations, and six deformation modes. In this section, a new model of pin joint between ANCF finite elements is introduced. The formulation of this pin joint between elements i and j employs the following six scalar equations defined at the joint node:

$$\mathbf{r}^i = \mathbf{r}^j, \qquad \mathbf{r}_\alpha^i = \mathbf{r}_\alpha^j \tag{12}$$

Here α is the coordinate line that defines the joint axis; α can be x, y, z or any other coordinate line as discussed later in this section. The six scalar equations of Eq. 12 eliminate six degrees of freedom; three translations, two rotations, and one deformation mode. This joint model ensures C^1 continuity with respect to the coordinate line α and C^0 continuity with respect to the other two parameters. It follows that the Lagrangian strain component $\varepsilon_{\alpha\alpha} = \left(\mathbf{r}_\alpha^T\mathbf{r}_\alpha - 1\right)/2$ is continuous at the joint definition point, while the other five strain components can be discontinuous.

While the algebraic constraint equations of a pin joint between two rigid bodies are highly nonlinear. The algebraic constraint equations of Eq. 12 are linear. Therefore, these equations can be applied at a preprocessing stage to systematically eliminate the dependent variables. Using these equations, one can develop a new kinematically linear FE mesh for flexible-link chains in which the links can have arbitrarily large relative rotations. The use of this pin joint model with ANCF finite elements leads to a constant mass matrix and zero Coriolis and centrifugal forces.

As previously mentioned in this paper, B-spline geometry can describe the type of non-structural discontinuity discussed in this section. Nonetheless, if an arbitrary axis of a pin joint is to be used in the analysis, the use of B-spline geometry can be difficult given the rigid structure of the B-spline recurrence formula. In order to be able to choose an arbitrary axis of rotation for the pin joint, one must be able to define the gradient vector in the direction of a coordinate line along this axis of rotation. Such a definition can be easily made using ANCF geometry using the gradient tensor transformation. Let u, v, and w be another set of parameters; one of them can be used to define the joint axis. It follows that $\begin{bmatrix}\mathbf{r}_u & \mathbf{r}_v & \mathbf{r}_w\end{bmatrix} = \begin{bmatrix}\mathbf{r}_x & \mathbf{r}_y & \mathbf{r}_z\end{bmatrix}\mathbf{A}$, where $\mathbf{A}$ is the constant matrix of coordinate transformation defined as

$$\mathbf{A} = \begin{bmatrix} \frac{\partial x}{\partial u} & \frac{\partial x}{\partial v} & \frac{\partial x}{\partial w} \\ \frac{\partial y}{\partial u} & \frac{\partial y}{\partial v} & \frac{\partial y}{\partial w} \\ \frac{\partial z}{\partial u} & \frac{\partial z}{\partial v} & \frac{\partial z}{\partial w} \end{bmatrix} \tag{13}$$

The fact that this matrix is constant allows having linear pin joint connectivity conditions when ANCF finite elements are used [13, 17].

7 NUMERICAL RESULTS

It will be demonstrated in this section that ANCF meshes that allow relative motion between the finite elements can be developed. In these ANCF meshes, the finite elements are connected using linear algebraic equations and the mesh mass matrix remains constant. Chain example characterized by non-structural discontinuities is considered in this section. The links of the chain used in this section are assumed to be flexible with mass density of 7200 kg/m^3, and a Poisson ratio of 0.3. Two different values of the modulus of elasticity, 2×10^8 and 2×10^{11} N/m^2, are used in the simulations. The elastic forces of the ANCF elements are formulated using a general continuum mechanics approach that employs a Hookean constitutive model. The system is represented by one FE mesh (one flexible body).

The chain used is a multi-link chain that has an overall length of 1 m (Fig. 2). It consists of 8 links that are connected by pin joints. These pin joints ensure C^0 continuity and allow for independent relative rotations and deformation modes at the joint nodes. In computational geometry, this case of non-structural discontinuities at the joint nodes corresponds to knot multiplicity of 3 when cubic polynomials are used for the finite elements. Each link in this chain is represented by one planar shear deformable beam element. Therefore, the chain has 80 degrees of freedom; 8 degrees of freedom represent rigid body relative rotations, and the remaining 72 degrees of freedom represent deformation modes; with 9 deformation modes for each link. The chain is subjected to a base excitation defined by the function $X = -0.01\sin(0.1\pi\ t)$. All the links of the chain are assumed to be initially horizontal. The effect of the link gravity is considered.

In order to verify the obtained results, a simulation of a very stiff pendulum is carried out first, and the results are compared with the results of a rigid link chain model. For the very stiff chain, a modulus of elasticity of 2×10^{11} N/m^2 is used for the finite elements. Figure 4 shows the vertical position of the center of the last link as function of time for both cases of the rigid and stiff chains.

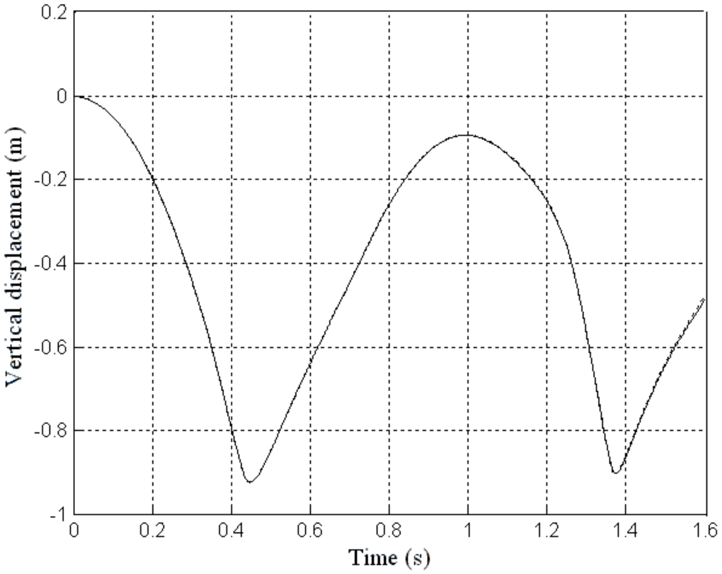

Figure 4 Vertical displacement of the center of link 8

(—— Flexible link chain, ---- Rigid link chain)

Figure 5 shows the absolute rotation of the last link of the chain about an axis parallel to the pin join axes. The results presented in Figs. 4 and 5 show a good agreement between the results obtained using the rigid and very stiff link chain models. For the rigid link chain model, nonlinear algebraic equations are used to define the pin joints and the resulting generalized mass matrix associated with the system degrees of freedom is highly nonlinear. For the flexible ANCF chain model, the chain is represented by one FE mesh (one flexible body), the pin joint constraints are linear, and the mass matrix is constant. Figure 6 shows the vertical displacement of the tip point of link 8 of the chain when the modulus of elasticity is reduced to 2×10^{8} N/m^2. Figure 7 shows the relative rotation between links 7 and 8 of the flexible chain as function of time.

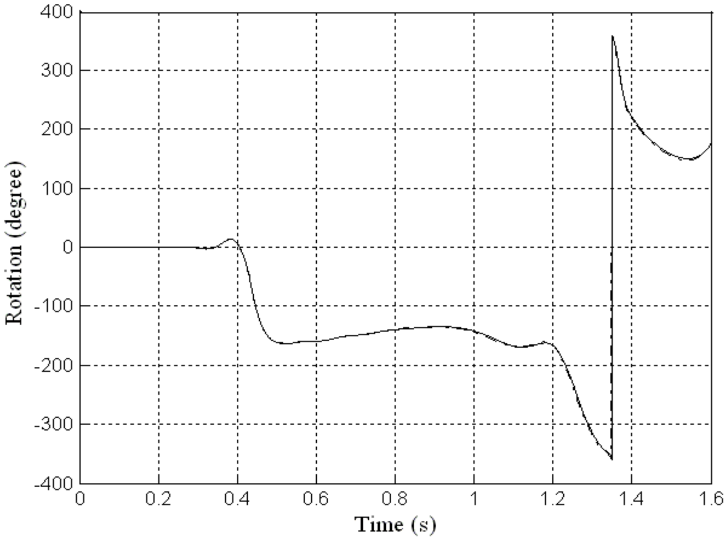

Figure 5 Rotation of link 8 (—— Flexible link chain, ---- Rigid link chain)

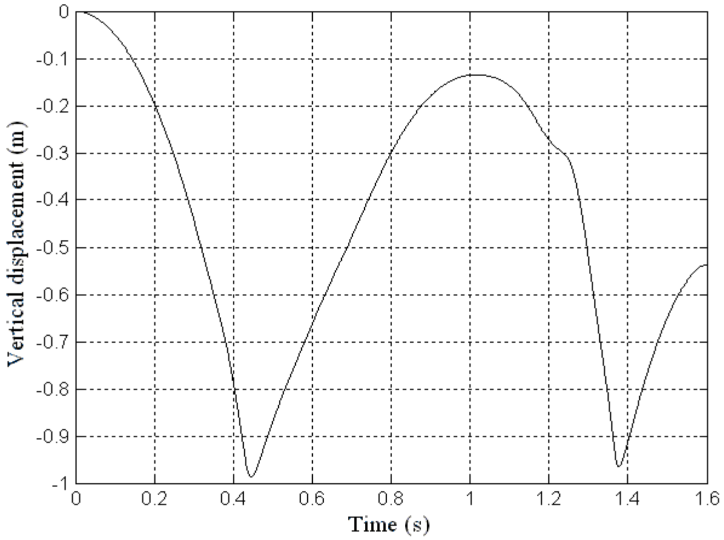

Figure 6 Vertical displacement of the tip point of link 8 of the flexible chain

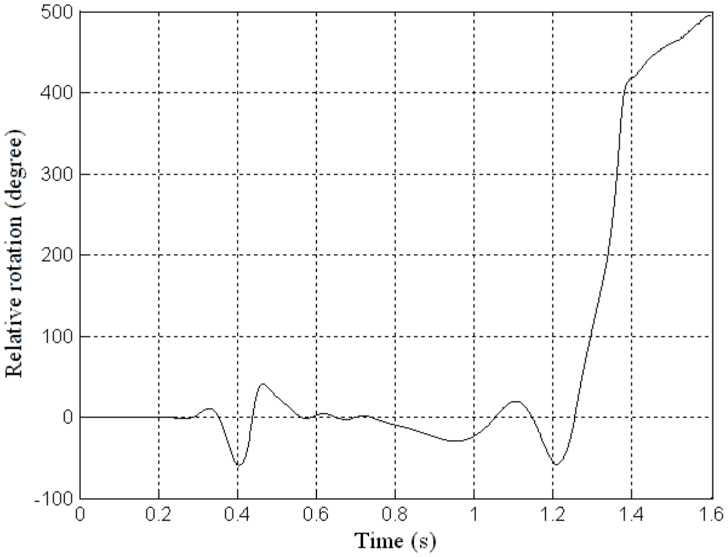

Figure 7 Relative rotation between last two chain links

Figures 8 and 9 show the distribution of the normal strain components ε_{xx} and ε_{yy}. It is clear from the results presented in these figures that the strains are discontinuous as the result of the non-structural discontinuities at the joints; the strains are continuous within the elements, and ε_{xx} decreases since the links at the beginning of the chain are subjected to higher gravity forces as compared to the links at the end of the chain. It is important, however, to point out that for fully parameterized ANCF finite elements one can always define at an arbitrary point inside the element, coordinate lines in which there are continuous strain components regardless of the shape of the structure.

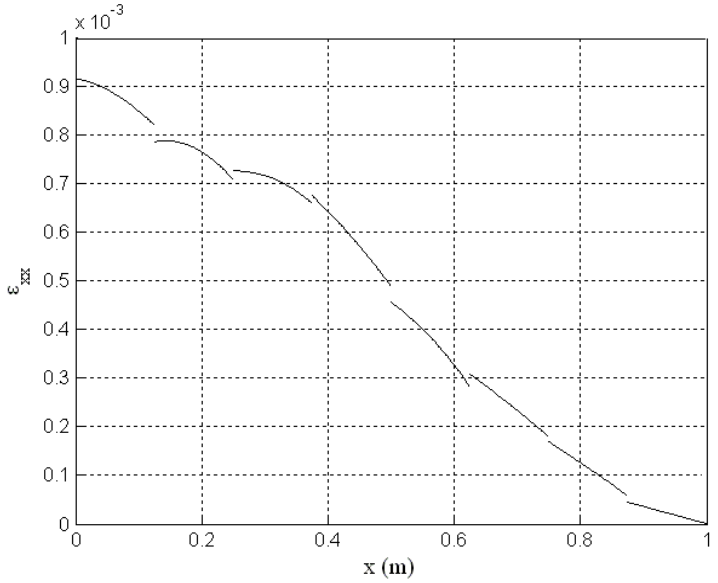

Figure 8 Distribution of the normal strain ε_{xx}

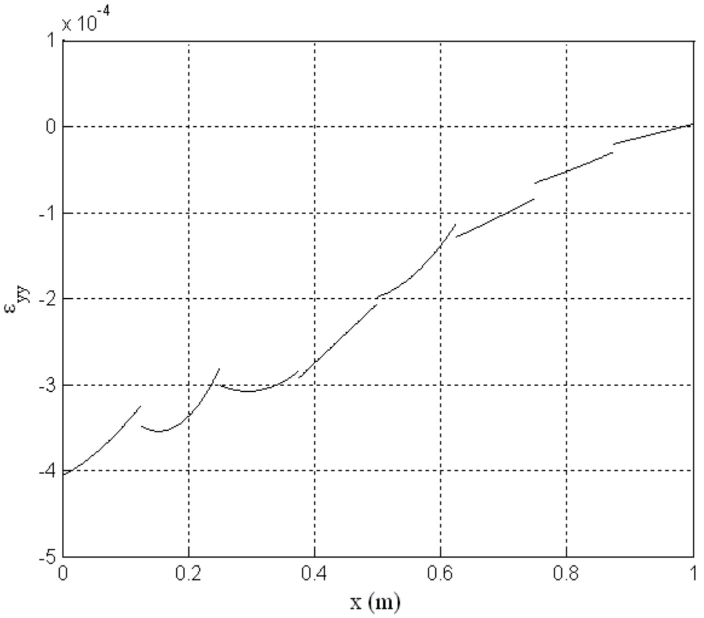

Figure 9 Distribution of the normal strain ε_{yy}

8 CONCLUSIONS

This paper addresses the important issue of using computational geometry methods such as B-spline and NURBS as analysis tools. B-spline and NURBS employ recurrence formulas that allow changing the degree of continuity at a breakpoint by adjusting the knot multiplicity at this point. As demonstrated in this paper, the recurrence formula has several drawbacks when B-spline representation is used as an analysis tool. Because the recurrence formula does not provide flexibility for choosing the basis functions, B-spline representation can lead to significantly larger number of coordinates and a higher dimensional model. This fact was used to demonstrate the generality of the ANCF geometry. While B-spline geometry can always be converted to ANCF geometry, the converse is not true. It is also shown that the B-spline recurrence formula cannot be used to model structural discontinuity in a straight forward manner. While structural discontinuities are of the C^0 type, they cannot be captured in the B-spline representation by reducing the knot multiplicity by one. This reduction of the knot multiplicity is equivalent to elimination of the relative translation only; and such a reduction in the knot multiplicity leads to a rigid body mode that defines the conditions of a pin joint. In the case of structural discontinuities, on the other hand, the C^0 B-spline representation does not eliminate the rigid body mode since additional algebraic constraint equations are required in order to eliminate the relative rotations between two segments. The paper also presents a new three-dimensional pin joint model that leads to linear connectivity conditions and constant mass matrix when used with ANCF finite elements. The limitations identified in this paper when B-spline geometry is used as analysis tool suggest the use of the I-CAD-A approach in which a constant transformation can be developed to convert CAD geometry to FE mesh.

REFERENCES

[1] L. Piegl, W. Tiller, *The NURBS Book*. 2nd edn. Springer, New York, 1997.

[2] G.G. Sanborn, A.A. Shabana, On The Integration of Computer Aided Design and Analysis Using The Finite Element Absolute Nodal Coordinate Formulation. *Multibody System Dynamics,* Vol. 22, pp. 181–197, 2009.

[3] P. Lan, A.A. Shabana, Integration of B-spline Geometry and ANCF Finite Element Analysis. *Nonlinear Dynamics*, DOI 10.1007/s11071-009-9641-6, 2010.

[4] O. N. Dmitrochenko, D.Y. Pogorelov, Generalization of Plate Finite Elements for Absolute Nodal Coordinate Formulatio. *Multibody System Dynamics*, Vol. 10, no. 1: 17-43, 2003.

[5] K.E. Dufva, J.T. Sopanen, A.M. Mikkola, A Two-Dimensional Shear Deformable Beam Element Based on the Absolute Nodal Coordinate Formulation. *Sound and Vibration,* Vol. 280, pp. 719-738, 2005.

[6] D. Garcia-Vallejo, J. Mayo, J. L. Escalona, Three-Dimensional Formulation of Rigid-Flexible Multibody Systems with Flexible Beam Elements. *Multibody System Dynamics*, Vol. 20 (1), pp. 1-28, 2008.

[7] K.S. Kerkkänen, D. García-Vallejo, A.M. Mikkola, Modeling of Belt-Drives using a Large Deformation Finite Element Formulation. *Nonlinear Dynamics*, Vol.43, pp. 239-256, 2006.

[8] A.L. Schwab, J.P .Meijaard, Comparison of Three-Dimensional Flexible Beam Elements for Dynamic Analysis: Classical Finite Element Formulation and Absolute Nodal Coordinate Formulation. *Journal of Computational and Nonlinear Dynamics,* Vol. 5 (1), 011010-1 – 011010-10, 2010.

[9] Q. Tian, L.P. Chen, Y.Q. Zhang, J.Z. Yang, An Efficient Hybrid Method for Multibody Dynamics Simulation Based on Absolute Nodal Coordinate Formulation. *ASME Journal of Computational and Nonlinear Dynamics*, Vol. 4, pp. 021009-1 - 021009-14 , 2009.

[10] Q. Tian, Y. Zhang, L. Chen, J. Yang, Simulation of Planar Flexible Multibody Systems with Clearance and Lubricated Revolute Joints. *Nonlinear Dynamics*, Vol. 60, pp. 489-511, 2010.

[11] W.S. Yoo, J.H. Lee, S.J. Park, J.H. Sohn, D.Pogorelov, O. Dimitrochenko, Large Deflection Analysis of a Thin Plate: Computer Simulation and Experiment. *Multibody System Dynamics*, Vol. 11, pp. 185-208, 2004.

[12] R.Y. Yakoub, A.A. Shabana, Three Dimensional Absolute Nodal Coordinate Formulation for Beam Elements: Implementation and Application. *ASME Journal for Mechanical Design*, Vol. 123, pp. 614–621, 2001.

[13] A.A. Shabana, A.M. Mikkola, Use of the Finite Element Absolute Nodal Coordinate Formulation in Modeling Slope Discontinuity. *ASME Journal for* Mechanical *Design*, Vol. 125(2), pp. 342–350, 2003.

[14] L.K. Abbas, X. Rui, Z.S. Hammoudi, Plate/Shell Element of Variable Thickness Based on the Absolute Nodal Coordinate Formulation. *IMechE Journal of Multibody Dynamics*, Vol. 224, Part K, pp. 127-141, 2010.

[15] A.M. Hamed, A.A. Shabana, P. Jayakumar, M.D. Letherwood, Non-Structural Geometric Discontinuities in Finite Element/Multibody System Analysis. *Nonlinear Dynamics*, 2011, in press.

[16] M.A. Omar, A.A. Shabana, A Two-Dimensional Shear Deformation Beam for Large Rotation and Deformation. *Journal of Sound and Vibration*, Vol. 243(3), pp. 565–576, 2001.

[17] A.A. Shabana, General Method for Modeling Slope Discontinuities and T-Sections using ANCF Gradient Deficient Finite Elements. *ASME Journal of Computational and Nonlinear Dynamics*, 2010, in press.

[18] A.A. Shabana, A.M. Hamed, A.A Mohamed, P. Jayakumar, M.D. Letherwood, Development of New Three-Dimensional Flexible-Link Chain Model Using ANCF Geometry. Technical Report # MBS2011-1-UIC, Department of Mechanical Engineering, University of Illinois at Chicago, Chicago, 2011.

[19] A.A. Shabana, *Computational Continuum Mechanics*. Cambridge University Press, Cambridge, 2008.

COMPDYN 2011
III ECCOMAS Thematic Conference on
Computational Methods in Structural Dynamics and Earthquake Engineering
M. Papadrakakis, M. Fragiadakis, V. Plevris (eds.)
Corfu, Greece, 25–28 May 2011

INVESTIGATION OF COUPLING BETWEEN EXTERNAL AND PARAMETRIC RESONANCES IN SMALL SAGGED INCLINED CABLES

Cyril E. Douthe[1,2], Charis J. Gantes[1]

[1] National Technical University of Athens
Metal Structures Laboratory, 9 Heroon Polytechniou, 15780 Zographou, Greece
e-mail: chgantes@central.ntua.gr

[2] Université Paris-Est
IFSTTAR, Dép. Structures et Ouvrages d'Art (Pt 34), 58, Bd Lefebvre, 75732 Paris Cedex 15, France
e-mail: cyril.douthe@ifsttar.fr

Keywords: Stay cable, modal interaction, method of harmonic balance, instability zone, threshold amplitude.

Abstract: *The coupling between parametric and external resonances in inclined cables subjected to a motion of an anchorage with components both along and perpendicular to their axis is investigated. Besides posing theoretical challenges, this problem is of practical interest for inclined cables of cable-stayed bridges and guyed towers. First, the state of the art on the subject of multi-modal interactions of cables with moving anchorages is summarized. Then, the proposed analytical model is presented, which is selected to be as simple as possible, but still suitable for capturing the coupling between the first and second eigenmodes, hence between parametric and external resonances. Next, two specific cases of the general model, in which no coupling appears, are studied in order to identify the intrinsic characteristics of external and parametric resonance, respectively. Finally, the coupling between the two instabilities is investigated, aiming at a better understanding of the interaction phenomenon and at formulating practical engineering guidelines.*

1 STATE-OF-ART ON MULTI-MODAL VIBRATIONS OF CABLES

In cable stayed bridges or guyed towers, indirect excitation through the vibrations of the neighboring structural elements, the bridge deck and the tower respectively, can lead to oscillations with high amplitudes in case resonance takes place. This resonance may be external, parametric or a combination of both. External resonance is induced by a motion of the anchorage perpendicular to the cable axis and occurs when the exciting frequency is equal to any eigenfrequency of the cable. Parametric resonance describes the dynamic instability which is induced by a motion of the anchorage along the axis of the cable and is observed when the ratio between the exciting frequency and some eigenfrequency takes specific values like 2:1, 3:1, 1:2 or 1:3.

The phenomenon of external resonance is well known among bridge designers and many design guidelines of cable stayed bridges provide a description of it and propose measures to prevent its effects [1, 2]. Most current models are linear [1, 2], but models including cubic non-linearities exist, like Irvine's solution for undamped motion (chapter 3.4 of [3]) or that of Caetano including damping [4]. The phenomenon of parametric resonance has entered the structural engineers' culture more recently with the development of the new generation of cable stayed bridges [5], it is hence detailed in [2] but only mentioned in [1]. It has been described first by Kovacs [6]. Then, Uhrig [7] proposed the first expressions of the main instability zones for the excitation frequencies in which the response diverges. Lilien and Pinto da Costa [8], in parallel with Cai and Chen [9], established the first values of the amplitude of the non-linear response in the main instability zone, the so-called two to one (2:1) resonance. These results were confirmed by Clément and Crémona using the harmonic balance method [10] and by Berlioz and Lamarque using the multiple scales method [11]. Takahashi [12] has shown that there were many instability zones around the multiples of the cable eigenfrequencies but also in the neighborhood of combinations of those, the so-called combination resonances.

The interaction between external and parametric resonance has been studied using different approximations depending on the sag of the cable, as outlined in Rega's bibliographical report [13]. A detailed literature review for coupled external-parametric resonances for taut strings can be found in Nayfeh and Mook [14]. The first studies of modal interaction in sagged cables concern internal resonances [15] or the coupled response to distributed load [16, 17, 18]. Luongo *et al.* have shown that, when the sag is significant, quadratic non-linearities govern the response while cubic non-linearities dominate when the sag is small [15, 19]. For instance, the publications on uncoupled parametric resonance cited above [6, 12, 7, 8, 9, 10, 11] concern only small sagged cables and include only cubic non-linearities.

A two degrees of freedom model for in-plane external resonance / out-of-plane parametric resonance interaction of large sagged cables was proposed by Perkins [20]. He observed that, like for taut strings, for small exciting amplitudes the system is uncoupled but, when the amplitude exceeds a certain value, parametric resonance occurs and the system becomes coupled. Gonzalez-Buelga *et al.* extended this model by taking into account the second out-of-plane mode in the response, but they limited themselves to small sagged cables [21]. Two mode planar interaction was also studied by Chatjigeorgiou and Mavrakos in a marine context [22], including small bending stiffness and quadratic damping due to fluid drag forces. A four degrees of freedom model for a large sagged cable was studied by Benedettini and Rega [23]. Zhang and Tang investigated also multi-modal interaction, focusing on the bifurcation type and on the response to chaotic excitation [24]. Multi-modal interaction was also studied by Srinil and Rega who compared finite differences numerical results with multiple scales analytical results (with up to 15 modes), in order to check if simulations can capture the richness of the cable's behavior near the first cross-over region undergoing 1:1 or 2:1

resonance [25]. Srinil and Rega also investigated the accuracy of reduced order models for the modeling of 2:1 resonance in horizontal and inclined cables. They showed that “the minimal (two-degrees-of-freedom) model” involving only the resonant modes seems capable of providing reliable results only for very low-sagged cables [26].

Advanced multi-modal models are thus nowadays available for researchers studying the dynamic interaction of sagged cables excited parametrically. These models try to take into account the whole complexity of the problem (generally in a relatively theoretical manner), the problem of coupled external/parametric resonance of small sagged cables being treated as a simple specific case. There is, however, need for a coupled model of small sagged cables for structural design of stay cables in engineering practice, in order to identify clearly the instability regions and the amplitude of responses. Gonzalez-Buelga *et al.* made a first step in this direction using the multiple scales method for out-of-plane parametric resonance [21]. For small sag however, the frequencies of in-plane and out-of-plane symmetric modes are very close, so that there might be internal resonance. It is thus proposed here to study the relative influence of in-plane and out-of-plane parametric resonance and its coupling with in-plane external resonance. In section 2 an analytical model is developed based on the harmonic balance method and compared with finite element numerical results. Uncoupled external and parametric resonances are studied in the third and fourth section, respectively, in order to identify their characteristics. The fifth section is dedicated to the study of the coupled problem.

2 DEVELOPMENT OF THE ANALYTICAL MODEL

2.1 Presentation of the problem

The analytical model presented here is dedicated to the study of multi-modal non-linear vibrations of inclined cables subjected to coupled external/parametric resonance. One end of the cable is fixed while the other end is subjected to an imposed motion (figure 1). This situation could correspond to a cable of a cable stayed bridge with the upper end fixed on a stiff pylon and the lower end supporting a flexible deck. The imposed motion of the lower end could be due to wind or traffic induced vibration of the deck. The cable is assumed to have small sag, which is a realistic assumption for bridge cables.

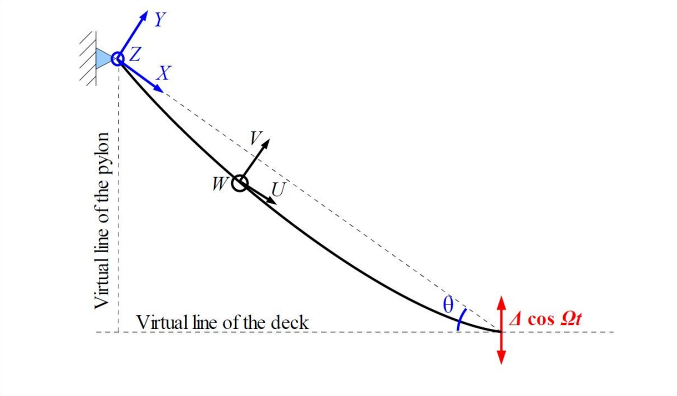

Figure 1: Inclined cable submitted to harmonic excitation at one end.

The plane of the cable is described by coordinates X, along the line joining the two ends of the cable and Y, perpendicular to this line, with the origin located at the fixed end. The out-of-plane coordinates are represented by Z. The inclination of the cable axis with respect to the virtual line of the deck (which is here supposed to be horizontal) is denoted by the angle θ. Without loss of generality, the imposed motion is supposed to be vertical and harmonic with amplitude Δ and frequency Ω, called respectively exciting amplitude and exciting frequency. All other forces except gravity are neglected. As noted above, it is further assumed that the sag of the cable is small, so that the difference between the abscissa along the cable and the abscissa along the chord can be neglected. Another consequence of the small sag is that the static equilibrium shape of the cable, which is in reality a catenary, can be assumed as parabolic [5].

2.2 Derivation of equations of motion

For common stay cables, axial displacements are much smaller than transverse displacements, so that here only displacements in the *Y* and *Z* directions will be considered and denoted as $V(X,t)$ and $W(X,t)$, respectively. The equations of motion being non-linear, their solutions are generally derived using Galerkin's method [20, 23, 10, 24, 11, 21]. Considering previous investigations by Gonzalvez Buena *et al.* [21] and the targeted field of application (small sagged stay cables), the present study is limited to the first out-of-plane mode, the first in-plane mode and the second in-plane mode. The approximate displacements are thus expressed as:

$$v(x,t)=p_1(t)\sin(\pi x)+p_2(t)\sin(2\pi x)+\delta\cos(\Omega t)x\cos\theta \tag{1a}$$

$$w(x,t)=q_1(t)\sin(\pi x) \tag{1b}$$

where p_1 and p_2 are time functions corresponding to the first and second in-plane mode, and q_1 that of the first out-of-plane mode. Note that in the previous expressions, the various parameters have been expressed in a dimensionless form with respect to the length of the cable:

$$x=\frac{X}{L}\quad,\quad\delta=\frac{\Delta}{L}\quad,\quad v=\frac{V(X,t)}{L}\quad\text{and}\quad w=\frac{W(X,t)}{L} \tag{2}$$

Considering the small sag of the cable, the eigenfrequencies are obtained following the approximation proposed by Gonzalvez Buena *et al.* [21] and are given by:

$$\omega_i^{\text{in}} = \frac{\pi i}{L}\sqrt{\frac{T}{\rho}}\sqrt{1+\frac{2\lambda^2}{i^4\pi^4}\left[1+(-1)^{i+1}\right]^2}\ ,\ \omega_j^{\text{out}} = \frac{\pi j}{L}\sqrt{\frac{T}{\rho}} \tag{3}$$

where T is the tension in the cable (which is assumed constant along the length), ρ its mass per unit length and λ the so-called Irvine's parameter, which is generally smaller than 1, except for very large cable stayed bridges; it is given in terms of the elastic modulus E of the cable, its cross-sectional area S and the gravity acceleration g:

$$\lambda^2 = \frac{ES}{T}\cdot\left(\frac{\rho L g\cos\theta}{T}\right)^2 \tag{4}$$

Following then the procedure proposed by Luongo *et al.* [15], the quadratic terms in the equations of motion are neglected. Looking at the remaining equations, one observes that the roles played by the first in-plane mode p_1 and by the first out-of-plane mode q_1 are identical. Moreover, previous experiments on taut cables have shown that only one of the two modes has a nonzero amplitude [11, 20, 21] (in general only the out-of-plane mode occurs). So, for simplicity reasons, only one of the two modes will be considered. The equations of motion reduce hence to:

$$\ddot{p}_1+2\xi\omega_1\dot{p}_1+\omega_1^2(1+2a\cos\Omega t)p_1+c_3p_1(p_1^2+4p_2^2) = 0 \tag{5a}$$

$$\ddot{p}_2+\xi\omega_2\dot{p}_2+\omega_2^2(1+2a\cos\Omega t)p_2+4c_3p_2(p_1^2+4p_2^2) = F_2(t) \tag{5b}$$

where ω_1 denotes, indifferently, the frequency of the first out-of-plane mode ω_1^{out} or that of the first in-plane mode ω_1^{in}. ξ is the modal damping ratio of the first out-of-plane mode which is assumed identical to that of the first in-plane mode and equal to twice that of the second mode. The dimensionless amplitude a of parametric excitation, the coefficient of the cubic terms c_3 and that of external excitation in-plane F_2 are given respectively by:

$$a = \frac{E\,S}{2T}\delta\sin\theta\ ,\ c_3 = \frac{\pi^2}{4}\frac{E\,S}{T}\omega_1^2 \ \text{ and } \ F_2(t) = -\frac{\delta\cos\theta\,\Omega^2}{\pi}\cos(\Omega\,t) \tag{6}$$

2.3 Method of harmonic balance

In equations (5a) and (5b), the coupling is limited to the non-linear terms. For this reason, the coupling will have an influence only near resonance conditions. Previous research [20, 23, 27] has indeed shown that the instability regions were only marginally affected by the coupling. Thus, the exciting frequencies, which might cause instability of the cable, are:

- $\Omega \approx 2\,\omega_1$ for the first in-plane or out-of-plane mode (parametric resonance);
- $\Omega \approx \omega_2$ for the second in-plane mode (external resonance).

As, for small sagged cables, these three frequencies are close to each other, interactions between parametric resonance in-plane or out-of-plane and external resonance in-plane might appear. The present study will thus be limited to a frequency region in the vicinity of the frequency of the second in-plane mode. In this region, it can be assumed that the time functions p_1 and p_2 are of the following form [10]:

$$p_1(t) = p_{11}\sin(\Omega\,t/2) + p_{12}\cos(\Omega\,t/2) \tag{7a}$$

$$p_2(t) = p_{21}\sin(\Omega\,t) + p_{22}\cos(\Omega\,t) \tag{7b}$$

where p_{11}, p_{12}, p_{21}, and p_{22} are real numbers, which will be determined later.

Introducing these terms into (5a) and (5b) and using the method of harmonic balance (which allows us to neglect the terms of high frequencies), leads finally to a system of four equations with four unknowns (p_{11}, p_{12}, p_{21} and p_{22}). This system can be separated into two matrix equations, which are characteristic of the coupled problem of inclined cables submitted to a harmonic motion at one end:

$$\begin{bmatrix} \frac{3}{4}c_3A^2 + 2c_3B^2 + \omega_1^2 a + \omega_1^2 - \frac{\Omega^2}{4} & -\xi\,\omega_1\Omega \\ \xi\,\omega_1\Omega & \frac{3}{4}c_3A^2 + 2c_3B^2 - \omega_1^2 a + \omega_1^2 - \frac{\Omega^2}{4} \end{bmatrix} \cdot \begin{bmatrix} p_{11} \\ p_{12} \end{bmatrix} = \begin{bmatrix} 0 \\ 0 \end{bmatrix} \tag{8a}$$

$$\begin{bmatrix} 2\,c_3A^2 + 12\,c_3B^2 + \omega_2^2 - \Omega^2 & -\xi\,\omega_2\Omega \\ \xi\,\omega_2\Omega & 2\,c_3A^2 + 12\,c_3B^2 + \omega_2^2 - \Omega^2 \end{bmatrix} \cdot \begin{bmatrix} p_{21} \\ p_{22} \end{bmatrix} = \begin{bmatrix} 0 \\ -\delta\cos\theta\,\Omega^2/\pi \end{bmatrix} \tag{8b}$$

where $A^2 = p^2_{11} + p^2_{12}$ and $B^2 = p^2_{21} + p^2_{22}$.

3 UNCOUPLED EXTERNAL RESONANCE

3.1 Characteristic equation of uncoupled external resonance

Before studying the coupled system, the problems of external resonance and parametric resonance are treated separately, in order to understand better their characteristics. The study of external resonance is generally concerned with the response to an excitation according to the first mode of vibration, while here focus will be on the second in-plane mode of vibration, which is susceptible to interact with parametric resonance terms when coupling is considered. Thus, considering a horizontal cable subjected to a vertical excitation at one end, the amplitude of the first mode vanishes in expression (8b) ($A = 0$) and one obtains the following system of equations, which is characteristic of the uncoupled external resonance:

$$\begin{bmatrix} 12c_3B^2+\omega_2^2-\Omega^2 & -\xi\,\omega_2\Omega \\ \xi\,\omega_2\Omega & 12c_3B^2+\omega_2^2-\Omega^2 \end{bmatrix} \cdot \begin{bmatrix} p_{21} \\ p_{22} \end{bmatrix} = \begin{bmatrix} 0 \\ -\delta\cos\theta\,\Omega^2/\pi \end{bmatrix} \tag{9}$$

To solve the above equation, it is necessary to check under what conditions the determinant of the matrix is different from zero:

$$144\,c_3^2B^4+24\,c_3(\omega_2^2-\Omega^2)B^2+(\omega_2^2-\Omega^2)^2+\xi^2\omega_2^2\Omega^2 = 0 \tag{10}$$

This is a bi-quadratic equation which has real solutions if and only if its discriminant is positive. As it is always negative, the matrix in (9) can be inverted and a third degree polynomial equation linking the square amplitude of the response B^2 with the amplitude of the excitation δ is obtained:

$$144\,c_3^2B^6+24\,c_3(\omega_2^2-\Omega^2)B^4+\left[(\omega_2^2-\Omega^2)^2+\xi^2\omega_2^2\Omega^2\right]B^2-\delta^2\cos^2\theta\frac{\Omega^4}{\pi^2} = 0 \tag{11}$$

The real roots of (11) can be calculated with the method of Cardan. Depending on the value of the parameters, equation (11) might have one or three real roots, out of which only two are stable amplitudes of response.

3.2 Characteristics of the hysteresis region

The interval of exciting amplitudes for which two stable amplitudes exist is called hysteresis region, because of the role played by the state of the cable at the preceding time in the determination of the actual amplitude. The limits of the hysteresis region can be determined from the characteristic equation of external resonance (11), which can be rewritten in a more concise manner:

$$k_1Y^3+k_2Y^2+k_3Y+k_4=0 \tag{12}$$

where:

$$k_1 = 144\,c_3^2\,,\ k_2 = 24\,c_3(\omega_2^2-\Omega^2)\,,\ k_3=(\omega_2^2-\Omega^2)^2+\xi^2\omega_2^2\Omega^2 \text{ and } k_4=-\delta^2\cos^2\theta\,\Omega^4/\pi^2 \tag{13}$$

Equation (12) has three real solutions if and only if its discriminant is positive. The borders of the hysteresis region are thus given by the parameters which nullify this discriminant. After some standard algebraic manipulations, one finally finds the expressions of the two critical exciting amplitudes, which limit the hysteresis region:

$$\delta_1 = \frac{\pi}{\cos\theta\,\Omega^2}\sqrt{\frac{1}{27}k_2\left[2\left(\frac{k_2}{k_1}\right)^2-9\frac{k_3}{k_1}\right]-\frac{k_1}{\sqrt{2}}\left[\frac{2}{9}\left(\frac{k_2}{k_1}\right)^2-\frac{2k_3}{3k_1}\right]^{\frac{3}{2}}} \tag{14a}$$

$$\delta_2 = \frac{\pi}{\cos\theta\,\Omega^2}\sqrt{\frac{1}{27}k_2\left[2\left(\frac{k_2}{k_1}\right)^2-9\frac{k_3}{k_1}\right]+\frac{k_1}{\sqrt{2}}\left[\frac{2}{9}\left(\frac{k_2}{k_1}\right)^2-\frac{2k_3}{3k_1}\right]^{\frac{3}{2}}} \tag{14b}$$

The critical frequency Ω_{cr} for which more than one solutions exist, is given by the intersection of the two curves resulting from (14a) and (14b). This frequency, which is higher than the frequency of the second eigenmode ($\Omega_{cr} > \omega_2$), can be evaluated using (13), (14a) and (14b):

$$\Omega_{cr} = \omega_2\sqrt{1+\frac{3}{2}\xi^2+\frac{\xi}{2}\sqrt{12+9\xi^2}} \tag{15}$$

Expressions (14a), (14b) and (15) allow us to define four regions, each corresponding to a different nature of the response to external resonance. These regions are represented in figure 2 for excitation parameters in dimensionless forms:

- $\Omega < \Omega_{cr}$: The response is undifferentiated, the highest the frequency and the amplitude of excitation, the higher the amplitude of the response;
- $\Omega > \Omega_{cr}$ and $\delta < \delta_1$: Low external resonance occurs, small amplitude response;
- $\Omega > \Omega_{cr}$ and $\delta > \delta_2$: High external resonance occurs, large amplitude response;
- $\Omega > \Omega_{cr}$ and $\delta_1 < \delta < \delta_2$: Hysteresis region, high external resonance might occur, depending on the time history of the excitation; two amplitudes, one small and one large, are thus possible.

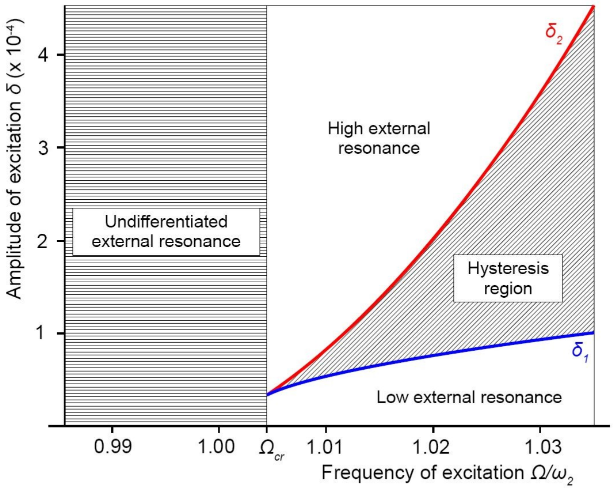

Figure 2: Nature of the response to external resonance.

3.3 Practical example: a cable of the Ben-Ahin Bridge

To illustrate the expressions found in the previous sub-section, some results are shown based on the geometric and mechanical properties of a cable of the Ben-Ahin Bridge in Belgium, which was abundantly studied by Da Caetano [5]. Its main characteristics are all supposed constant along its length and are the following:

- Length: $L = 110.505$ m (distance between the anchorages);
- Mass per unit length: $\rho = 64.841$ kg/m;
- Cross-sectional area: $S = 82.6$ cm^2;
- Young Modulus: $E = 210$ GPa ;
- Prestress: $T = 4902.7$ kN (actually the prestress is not exactly constant in the numerical model due to gravity; the value given here is that at the lower anchorage).

From those values, the parameters characterizing the vibrations of the horizontal cable can be evaluated: Irvine's parameter $\lambda^2 = 0.0727$, the frequency of the 1st out-of-plane mode $\omega_1^{out} = 7.82$ rad/s, the frequency of the first in-plane mode $\omega_1^{in} = 7.84$ rad/s. One remarks that the value of Irvine's parameter of this cable is very low, therefore, the cable is small sagged.

The finite element software used to validate the analytical model and its hypotheses is ADINA, a software which has already been successfully used for the calculation of cable structures [27, 28]. A convergence study in time and space was first conducted for a horizontal cable subjected to gravity and to an excitation perpendicular to its axis with a frequency equal to that of the second in-plane eigenmode and an amplitude of 10 mm. Rayleigh damping proportional to the mass is chosen, because this is what is generally used for the modeling of cables and because it is the numerical damping which is the closest to the analytical model (in the present example $\xi = 0.5$ %). Geometrical non-linearities are taken into account and the default implicit dynamic algorithm based on Newmark integration method is used with a consistent mass matrix. The time step is varied from 1 ms to 10 ms and the number of elements from 30 to 100. The calculations are separated into two parts: the transient period, from 0 s to 300 s, and the steady state, from 300 s and 340 s. From the variations of the amplitude of the steady state response, 40 truss elements and $\Delta t = 5$ ms was chosen as the best compromise between computation time and accuracy.

Then the results of the numerical model were compared with those of the analytical model for an excitation of $\Delta = 20$ mm. They globally showed very good agreement and the differences in the steady state amplitude varied from 1.5 % for $\Omega = \omega_2$ to 5 % for $\Omega = 1.05\,\omega_2$.

4. UNCOUPLED PARAMETRIC RESONANCE

The phenomenon of parametric resonance is relatively well known from the literature but it is often not distinguished between in-plane and out-of-plane resonance. As, for small sagged cables, the frequency of the first out-of-plane mode is very close to that of the first in-plane mode (a few percentage points in cables of cable stayed bridges), they might often be confused. Therefore, it is meaningful to study the phenomenon and to look for a possible internal resonance between the first in-plane and out-of-plane modes.

4.1 Analytical expression of the amplitude and the threshold

The equations of uncoupled parametric resonance are often found by taking into account only the first in-plane mode in the general equations of motion [8], [10]. Here, the first in-plane and first out-of-plane modes will be considered alternatively (ω_1 representing either the frequency of the first in-plane or first out-of-plane mode) and the characteristic equation of parametric resonance is deduced from (8a) by considering that the cable is horizontal and submitted to a horizontal motion ($B = 0$):

$$\begin{bmatrix} \frac{3}{4}c_3A^2-\omega_1^2a+\omega_1^2-\frac{\Omega^2}{4} & -\xi\,\omega_1\Omega \\ \xi\,\omega_1\Omega & \frac{3}{4}c_3A^2+\omega_1^2a+\omega_1^2-\frac{\Omega^2}{4} \end{bmatrix} \cdot \begin{bmatrix} p_{11} \\ p_{12} \end{bmatrix} = \begin{bmatrix} 0 \\ 0 \end{bmatrix} \tag{16}$$

This problem has a nonzero solution, if the determinant of the matrix is equal to zero:

$$\frac{9}{16}c_3^2A^4+\frac{3}{2}c_3(\omega_1^2-\frac{\Omega^2}{4})A^2+\xi^2\omega_1^2\Omega^2-\omega_1^4a^2+\left(\omega_1^2-\frac{\Omega^2}{4}\right)^2 = 0 \tag{17}$$

One recognizes in (17) a bi-quadratic equation in A. It has real solutions if and only if its discriminant is larger than or equal to zero, which is equivalent to the following condition:

$$a^2\omega_1^2-\xi^2\Omega^2 \geqslant 0 \tag{18}$$

Equation (18) determines a first condition on the instability zone: for a given exciting frequency Ω, as long as the dimensionless amplitude of the excitation is below a certain threshold $a^2 < \xi^2\Omega^2/\omega_1^2$, there is no instability and the only solution of the problem of parametric excitation is zero ($p_{11} = p_{12} = 0$); on the contrary, when the exciting amplitude reaches the limit amplitude $a^2 \geqslant \xi^2\Omega^2/\omega_1^2$, equation (17) has two solutions and the characteristic amplitudes of uncoupled parametric resonance A_U are given by:

$$A_U = \sqrt{\frac{4}{3}\frac{\omega_1^2}{c_3}} \cdot \sqrt{\left(\frac{\Omega}{2\omega_1}\right)^2 - 1 \pm \sqrt{a^2 - 4\xi^2\left(\frac{\Omega}{2\omega_1}\right)^2}} \tag{19}$$

One remarks that the limit case $a^2 = \xi^2\Omega^2/\omega_1^2$ corresponds to the pair "exciting amplitude/ exciting frequency" for which the two characteristic amplitudes of uncoupled parametric resonance (19) are equal. For a given exciting amplitude, this frequency is the highest frequency for which parametric resonance may occur. It is also the frequency for which the amplitude of parametric resonance is the highest. It is noted also that condition (18) is not sufficient for appearance of parametric resonance: the expression under the square root in (19) has to be positive. It is, thus, necessary for the dimensionless amplitude of parametric excitation to be higher than a certain critical value a_U which is often called the threshold of parametric excitation:

$$a_U = \sqrt{\left[\left(\frac{\Omega}{2\omega_1}\right)^2 - 1\right]^2 + 4\xi^2\left(\frac{\Omega}{2\omega_1}\right)^2} \tag{20}$$

Another way to look at this condition, on the dimensionless amplitude of excitation, is to rewrite (20) as a condition on the exciting frequency:

$$\Omega \in \left[2\omega_1\sqrt{1-2\xi^2-\sqrt{a^2-4\xi^2(1-\xi^2)}}\ ,\ 2\omega_1\sqrt{1-2\xi^2+\sqrt{a^2-4\xi^2(1-\xi^2)}}\right] \tag{21}$$

4.2 Numerical study of amplitudes and thresholds

As the influences of damping ratio, frequency and exciting amplitude have been studied abundantly in the past (for example in [10]), it is here focused on the interaction between in-plane and out-of-plane parametric resonance. A first model, in which a horizontal cable identical to the one in section 3.3 has an anchorage moving horizontally, is hence considered. It is then modified for the out-of-plane instability by introducing at time zero an out-of-plane perturbation in the form of a small vanishing wind gust, uniformly distributed along the cable. The variations of the amplitude of both responses with the frequency of the excitation are shown in figure 3a for $\Delta = 20$ mm and $\xi = 0.08$ %. The amplitudes of the response plotted in this figure are steady state amplitudes obtained after a transient period of 1000 cycles. It is observed that there is very good agreement between numerical and analytical results for both in-plane and out-of-plane response for the stable branches (corresponding to growing frequencies). There is also good agreement of the frequency of the jump phenomenon (obtained with a decreasing frequency) for the in-plane numerical simulations; but, numerically, the frequency of the out-of-plane jump coincides with the frequency of the in-plane jump.

From this last observation, one may suppose that the in-plane vibration is not stable and turns into out-of-plane vibration when it is disturbed. Indeed, every time that a small out-of-plane perturbation is introduced in a plane model where in-plane parametric resonance is installed, out-of-plane resonance appears and then gradually dominates the whole response and the in-plane vibration vanishes.

These results are confirmed when investigating more specifically the threshold amplitudes of the out-of-plane mode (figure 3b). Two damping factors are tested ($\xi = 0.1$ % and $\xi = 0.5$ %) and both sets of simulations lead to similar results. Figure 3b represents the threshold amplitudes for $\xi = 0.5$ %. For low frequencies, there is very good agreement between analytical and numerical results for both the in-plane and the out-of-plane threshold. For high frequencies, numerical results for the in-plane and out-of-plane threshold coincide and are in very good agreement with the analytical values of the in-plane mode. The in-plane mode of vibration is unstable and turns into out-of-plane vibration. These results should be confirmed for other values of Irvine's parameter, thus, with other ratios between in-plane and out-of-plane frequencies. Yet, it seems that the amplitude of the response which should be taken into account is that of the out-of-plane mode and that the following bandwidth of parametric resonance has to be considered:

$$\Omega \in I^{\text{in}} \cup I^{\text{out}} \text{ where } \begin{array}{l} I^{\text{in}} = \left[2\,\omega_1^{\text{in}}\sqrt{1-2\,\xi^2-\sqrt{a^2-4\,\xi^2}}\,,\,2\,\omega_1^{\text{in}}\sqrt{1-2\,\xi^2+\sqrt{a^2-4\,\xi^2}}\right] \\ I^{\text{out}} = \left[2\,\omega_1^{\text{out}}\sqrt{1-2\,\xi^2-\sqrt{a^2-4\,\xi^2}}\,,\,2\,\omega_1^{\text{out}}\sqrt{1-2\,\xi^2+\sqrt{a^2-4\,\xi^2}}\right] \end{array} \qquad (22)$$

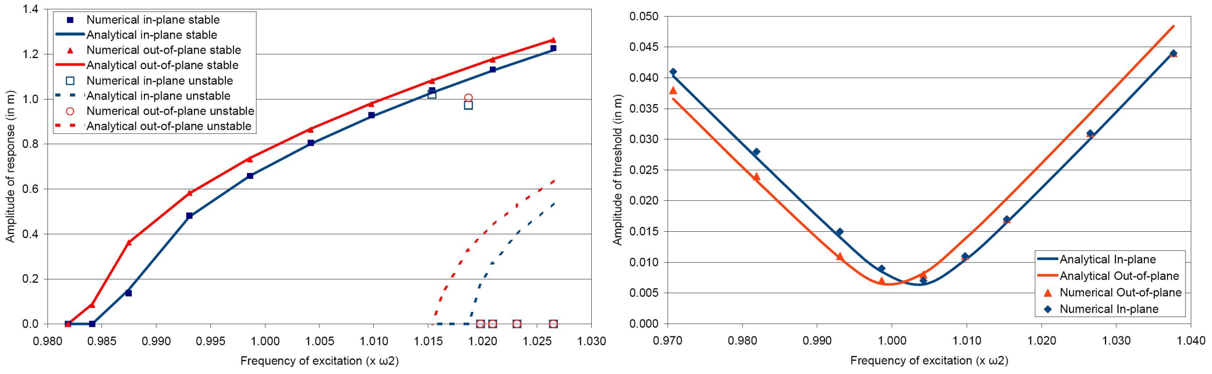

Figure 3: Influence of the excitation frequency
a) on the amplitude of in-plane and out-of-plane parametric resonance, b) on the corresponding thresholds.

5. COUPLED EXTERNAL/PARAMETRIC RESONANCE

5.1 Coupled threshold of parametric resonance

5.1.1 Analytical expression

Considering now the coupled system of equations (8a) and (8b), equation (8a) will be studied first. This system of equations is homogeneous, so that it has nonzero solutions if and only if the determinant of the matrix is equal to zero, which is equivalent to requiring that solutions of the following equation can be found:

$$\frac{9}{16}c_3^2A^4+3\frac{c_3}{2}\left[2\,c_3\,B^2+\left(\omega_1^2-\frac{\Omega^2}{4}\right)\right]A^2+\left[\omega_1^2-\frac{\Omega^2}{4}+2\,c_3\,B^2\right]^2-\omega_1^4a^2+\xi^2\omega_1^2\Omega^2 \;=\; 0 \qquad (23)$$

A bi-quadratic equation in A can be recognized in (23) and thus, the first condition for the existence of real roots to this equation is that its discriminant is equal to zero:

$$a^2\omega_1^2-\xi^2\Omega^2 \;>\; 0 \qquad (24)$$

It is noteworthy that this condition is identical to the one obtained for the uncoupled problem (18): the highest frequency for which parametric resonance may appear is thus identical for the coupled and the uncoupled problem. As previously, if the non-dimensional amplitude of parametric excitation is higher than a certain threshold ($a > \xi\,\Omega/\omega_1$), then the solution of (23) can be written:

$$A=\sqrt{-\frac{8}{3}B^2+\frac{4}{3}\frac{\omega_1^2}{c_3}\left[\left(\frac{\Omega}{2\omega_1}\right)^2-1\pm\sqrt{a^2-4\,\xi^2\left(\frac{\Omega}{2\omega_1}\right)^2}\right]}\;\left(=\sqrt{A_U^2-\frac{8}{3}B^2}\right) \qquad (25)$$

Considering (25), one remarks that like for uncoupled parametric resonance, the problem of coupled parametric resonance has two solutions: one stable (with the positive sign under the square root) and one unstable. Like for uncoupled parametric resonance, the non-dimensional amplitude of parametric excitation has to be higher than a certain value, called threshold of coupled parametric resonance a_C. Below the threshold, no parametric resonance appears: the system is uncoupled and external resonance only may occur. Above this threshold, coupled external-parametric resonance may occur and the amplitude of the coupled parametric resonance is always smaller than that of uncoupled parametric resonance (the amplitude of the second mode reduces the amplitude of the first mode).

The value of the threshold amplitude depends thus on the history of the vibration of the cable. If the vibration starts from a non-coupled state where only external resonance exists, then when the threshold of coupled parametric resonance is just reached, the amplitude of external resonance is still the uncoupled one ($B_C = B_U$ given by (11)). On the contrary, if the vibration starts from a coupled state where both resonances exist, then, when the threshold is reached, the amplitude of external resonance is still the coupled one.

In the first case, the coupled threshold amplitude δ_{CU} can be found without solving the coupled system of equations. Its value is obtained by solving the following non-linear equation resulting from (26) with $A = 0$ and $B = B_U$ which is a stable solution of (11):

$$\delta_{CU} = \frac{2T}{ES\sin\theta}\sqrt{\left[\left(\left(\frac{\Omega}{2\omega_1}\right)^2 - 1\right) - \frac{2c_3}{\omega_1^2}B_U^2(\delta_{CU})\right]^2 + 4\xi^2\left(\frac{\Omega}{2\omega_1}\right)^2} \tag{26a}$$

In the second case, it is necessary to solve the coupled system of equations and to obtain the value of the coupled amplitude B_C in order to introduce it in the expression of the threshold amplitude which is then given by:

$$\delta_{CC} = \frac{2T}{ES\sin\theta}\sqrt{\left[\left(\left(\frac{\Omega}{2\omega_1}\right)^2 - 1\right) - \frac{2c_3}{\omega_1^2}B_C^2(\delta_{CC})\right]^2 + 4\xi^2\left(\frac{\Omega}{2\omega_1}\right)^2} \tag{26b}$$

5.1.2 Nature of the coupled response

The exciting frequencies and exciting amplitudes, for which external resonance occurs, are known from section 3, so that the nature of the coupled response can be deduced by adding the curve corresponding to the threshold of coupled parametric resonance (26a) and (26b) into the diagram of external resonance (figure 2). Such a diagram is shown in figure 4 for the cable of the Ben Ahin Bridge studied previously (section 3.3), with an inclination of 30° and a damping ratio of 0.5 %. For this angle, Irvine's parameter becomes $\lambda^2 = 0.0544$ and the frequency of the first in-plane mode becomes $\omega_1^{\text{in}} = 7.84$ rad/s. The curve δ_{CU} represents the amplitude of the coupled threshold when coming from an uncoupled situation (26a), while the curve δ_{CC} represents the amplitude of the coupled threshold when coming from a coupled situation (26b). The curve δ_1 is the amplitude below which no external resonance occurs (14a) and below which the amplitude of the response is that of the lower branch of external resonance. The curve δ_2 indicates the amplitude above which external resonance occurs with certainty (14b) and above which the amplitude of the response is that of the upper branch of external resonance.

In figure 4, seven different regions can be distinguished:

- $\Omega < \Omega_{cr}$ and $\delta < \delta_{CU}$: The response is undifferentiated, the higher the frequency and the amplitude of excitation, the higher the amplitude of the response (region 1).
- $\Omega > \Omega_{cr}$ and $\delta < \delta_1$: No external resonance occurs, the response has a small amplitude (region 2).
- $\Omega > \Omega_{cr}$ and $\delta_2 < \delta < \delta_{CU}$: Only external resonance occurs with large amplitude

(region 3).

- $\Omega > \Omega_{cr}$ and $\delta_2 < \delta < \min(\delta_{CC}, \delta_2)$: Uncoupled hysteresis region. External resonance might occur alone, depending on the time history of the excitation; two amplitudes, one small and one large are possible for the response (region 4).
- $\Omega > \Omega_{cr}$ and $\delta_{CU} < \delta < \delta_2$: Coupled hysteresis region I. Coupled resonance might occur depending on the time history of the excitation. Two sets of amplitudes are possible: one uncoupled external resonance with low amplitude, coupled external and parametric resonances, both with high amplitudes (region 5).
- $\Omega > \Omega_{cr}$ and $\delta_{CC} < \delta < \delta_{CU}$: Coupled hysteresis region II. Coupled resonance might occur depending on the time history of the excitation (oscillation must come from an initial coupled situation). Two sets of amplitudes are possible and identical to those of the coupled hysteresis region I (region 6).
- $\Omega > \Omega_{cr}$ and $\max(\delta_{CU}, \delta_2) < \delta$: Coupled external/parametric resonance occurs with high amplitudes of the response of the first and second modes (region 7).

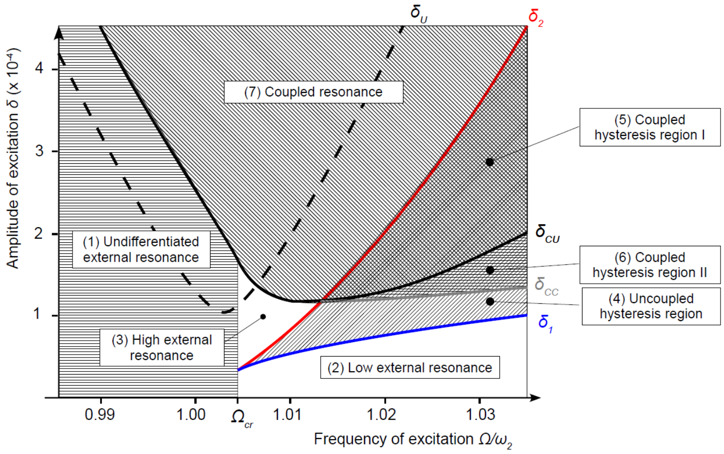

Figure 4: Nature of the response to coupled external/parametric resonance ($\xi = 0.5$ %).

Comparing then the amplitude of the uncoupled threshold δ_U (20) (dotted curve on figure 4) with the characteristic curves of the coupled thresholds δ_{CU} (26a) and δ_{CC} (26b) and those of the uncoupled hysteresis region δ_1 (14a) and δ_2 (14b), it is observed that the coupling causes a shift toward the high frequencies of the instability region, as well as a widening of this instability region. This widening is reduced by the hysteresis region but still, the coupled instability region remains wider than the uncoupled one. Taking the coupling into account seems, thus, necessary.

5.1.3 In-plane/out-of-plane interaction and numerical validation

To investigate the different thresholds, three different schemes are used for the time history of the excitation because of the hysteresis region:

- the "increasing low" scheme used to get the lower branch of external resonance: the amplitude grows slowly until it reaches the desired value, and then it remains constant until steady state.
- the "increasing high" scheme used to get the higher branch of external resonance before coupling appears: calculations start from a first run in which the frequency is out-of the hysteresis region and for which the exciting amplitude is below that of the threshold of coupled parametric resonance, the exciting frequency is increased until the desired one and then the amplitude until parametric resonance appears.
- the "decreasing coupled" scheme used to get the upper branch of external resonance with coupled external/parametric resonance: the amplitude starts from a high value

which is out-of the hysteresis range of coupled external/parametric resonance and remains constant until steady state takes place, then it is decreased slowly until it reaches the desired amplitude of excitation and remains constant until steady state.

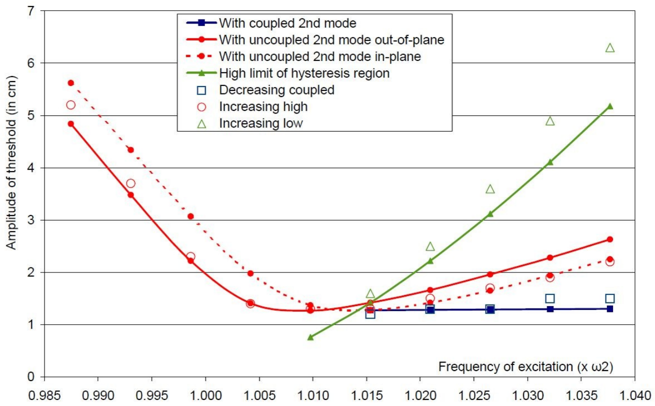

Figure 5: Thresholds of coupled external-parametric resonance out-of-plane.

Using these three time histories numerical values for the threshold have been determined and compared to analytical values obtained by expressions (26a), (26b) and (20). For the plane model, very good agreement of the various thresholds was found. The results for out-of-plane model are presented in figure 5 for the out-of-plane model. One observed that there is good agreement of the two thresholds and a slight underestimation of the amplitude of the high limit of the hysteresis region. It is however remarkable that, like for the horizontal cable, when the analytical value of the threshold of coupled in-plane parametric resonance is below that of coupled out-of-plane resonance, the numerical value of the out-of-plane threshold follows that of the in-plane threshold. In other terms, like for the horizontal cable, the first in-plane mode is unstable and almost vanishes when an out-of-plane perturbation is introduced. This time however, when the out-of-plane perturbation is introduced, the first out-of-plane mode settles slowly and finally dominates the response, but the first in-plane mode does not vanish completely. The second out-of-plane mode also accompanies the first out-of-plane mode, and indeed, develops more quickly (the interaction of these four modes is further discussed in section 5.3.2).

5.2 Coupled amplitudes and phases

5.2.1 Influence of the exciting amplitude

It is supposed now that the dimensionless amplitude of parametric excitation is above that of the threshold (26a) or (26b), which means that parametric resonance appears and that there is actually coupling between the first and second mode of vibration. The purpose of this subsection is to determine the amplitudes of coupled external and parametric resonance by solving simultaneously (8a) and (8b). The expression of parametric resonance (30) resulting from (8a) is introduced into (8b):

$$\begin{bmatrix} \frac{20}{3}c_3B^2+\omega_2^2-\Omega^2+2c_3A_U^2 & -\xi\omega_2\Omega \\ \xi\omega_2\Omega & \frac{20}{3}c_3B^2+\omega_2^2-\Omega^2+2c_3A_U^2 \end{bmatrix} \cdot \begin{bmatrix} p_{21} \\ p_{22} \end{bmatrix} = \begin{bmatrix} 0 \\ -\frac{\delta\cos\theta\Omega^2}{\pi} \end{bmatrix} \qquad (27)$$

The above matrix can always be inverted. The coupled equations (27) are thus solved and combined, writing that $B^2=p_{21}^2+p_{22}^2$, in order to find the value of the amplitude of the vibration of the second mode:

$$\frac{400}{9}c_3^2B^6+\frac{40}{3}c_3\left(\omega_2^2-\Omega^2+2c_3A_U^2\right)B^4+\left[\left(\omega_2^2-\Omega^2+2c_3A_U^2\right)^2+\xi^2\omega_2^2\Omega^2\right]B^2=\frac{\delta^2\cos^2\theta\,\Omega^4}{\pi^2} \qquad (28)$$

This equation differs a lot from that of the uncoupled problem (equation (11)). Again, it can be solved analytically by using Cardan's method, but developing it here is not meaningful, and it is used only for numerical analysis. Figure 6a, for example, shows the variations of the amplitude of the response with the amplitude of the excitation for an exciting frequency of $\Omega = \omega_2$. The damping ratio is 0.5 %. One notes that the exciting frequency is smaller than the critical frequency of external resonance, reducing the hysteresis region ($\Omega = \omega_2 < \Omega_{cr}$). Thus, it is verified that, below the threshold amplitude of coupled parametric resonance δ_{CU} (26a), the response is uncoupled and only the second mode is excited. Above this threshold, parametric resonance appears and the response is coupled. The amplitude of the second mode is lower than in the uncoupled situation (dotted line), which is reasonable because the second mode competes with the first mode.

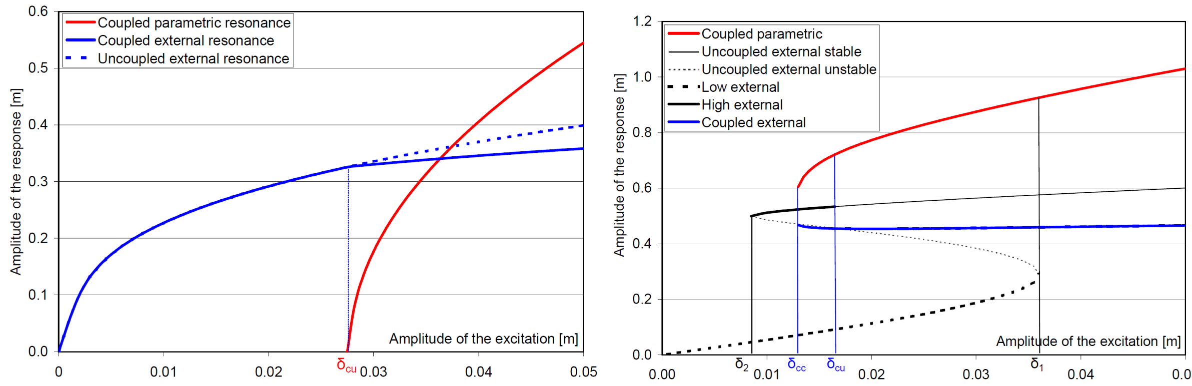

Figure 6: Influence of the exciting amplitude on the amplitude of coupled response, a) $\Omega = \omega_2$, b) $\Omega = 1.026\ \omega_2$.

When the frequency is higher than the critical frequency of external resonance, hysteresis phenomena appear and, for a given amplitude of excitation, many states of vibration can exist, depending on the time history of the vibration, as illustrated in figure 6b for $\Omega = 1.026\ \omega_2 > \Omega_{cr}$. It is noted that:

- $0 < \delta < \delta_2$: only low amplitude external resonance occurs (heavy dotted black curve).
- $\delta_2 < \delta < \delta_{CC}$: only external resonance occurs but it might have high (heavy full black curve) or low (heavy dotted black curve) amplitude.
- $\delta_{CC} < \delta < \delta_{CU}$: the response might be coupled external-parametric resonance (blue and red curves) if it is coming from a coupled situation or, otherwise, uncoupled with external resonance only, either high or low amplitude (heavy full and dotted black curve respectively).
- $\delta_{CU} < \delta < \delta_1$: the response might be coupled (blue and red curves) if coming from a coupled situation or from a situation with high amplitude of the second mode or, otherwise, it might be uncoupled with low amplitude external resonance only (heavy dotted black curve).
- $\delta_1 < \delta$: only coupled external-parametric response occurs.

5.3. Numerical validation with ADINA

5.3.1 Influence of the amplitude of excitation

To validate the analytical results presented above, purely plane simulations are conducted, as well as three dimensional simulations by introducing a small out-of-plane perturbation into the plane model. Figures 7a and 7b show the amplitude of external resonance and the amplitude of parametric resonance, respectively. The exciting frequency is here $\Omega = 1.004\ \omega_2$. Before parametric resonance occurs, the system is uncoupled and there is excellent agreement between the numerical simulations and the analytical model (figure 7a). In figure 7b, it is observed that the threshold amplitudes of parametric resonances almost coincide for the in-plane model as well as for the out-of-plane model. The numerical threshold out-of-plane is between 14 mm and 15 mm while the analytical model gives $\Delta^{thr} = 14.0$ mm, and the threshold in-plane is between 20 mm and 21 mm while analytically $\Delta^{thr} = 19.7$ mm.

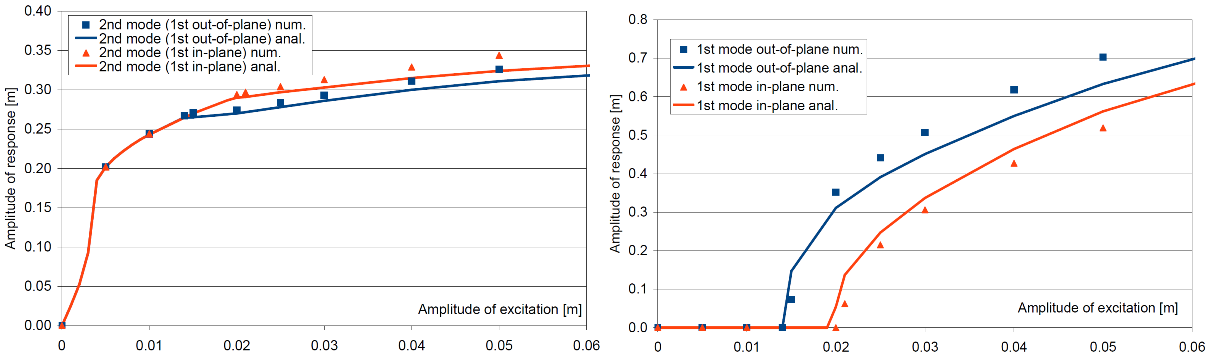

Figure 7: Comparison of analytical and numerical amplitudes of a) external resonance, b) parametric resonance.

Looking now at the amplitudes of response, once parametric resonance has appeared, the numerical in-plane parametric resonance response values are slightly below the analytical ones, contrary to the numerical out-of-plane amplitudes, which are slightly higher than the analytical ones. This is in accordance with the facts that the numerical threshold in-plane is higher than the analytical threshold, and that the numerical threshold out-of-plane is smaller than the analytical one. Moreover, in figure 7a, it is observed that the analytical model slightly underestimates the amplitude of coupled external resonance (about 2 % for $\Delta = 20$ mm and 5 % for $\Delta = 100$ mm). In these two figures the agreement of the analytical and numerical results can be described as very good for small exciting amplitudes and as satisfactory for higher amplitudes.

5.3.2 Influence of the frequency of the excitation

Another set of numerical experiments is conducted to study the influence of the exciting frequency for a fixed exciting amplitude, here $\Delta = 20$ mm. The exciting frequency was increased from $0.98\ \omega_2$ to $1.04\ \omega_2$ and decreased from $1.04\ \omega_2$ to $1.01\ \omega_2$ with a step of $0.005\ \omega_2$, each frequency being kept constant during 1000 cycles for the steady state to install. The results are presented in figure 8a. The curves (analytical model) and dots (numerical simulations) fit remarkably well for growing and decreasing exciting frequency.

A similar set of experiments with $\Delta = 20$ mm and $\xi = 0.5$ % is then conducted numerically for the out-of-plane response for both increasing and decreasing frequencies from $0.98\ \omega_2$ to $1.04\ \omega_2$ introducing again a small out-of-plane perturbation at time zero (see figure 8b and figure 9). One remarks first that, like for the horizontal cable (section 4.2.2), the out-of-plane perturbation causes an instability of the in-plane mode, so that the first in-plane mode vanishes and the first out-of-plane mode dominates the steady state response. However, for high frequencies, the coupled out-of-plane response becomes more complex and may have nonzero components for up to four eigenmodes (see figure 9). Depending on the frequency and on the history of excitation different states might exist:

- The first one corresponds to low frequencies below that of resonance ($\Omega < \omega_2$), where response of the cable is purely external in-plane resonance.
- The second one is a bi-modal vibration state where out-of-plane parametric resonance is coupled with in-plane external resonance. It occurs for a relatively reduced

bandwidth ($\omega_2 < \Omega < 1.01\ \omega_2$).

- The third one involves the first four eigenmodes and occurs also for a reduced bandwidth ($1.01\ \omega_2 < \Omega < 1.02\ \omega_2$).
- The fourth one corresponds to the hysteresis region ($\Omega > 1.02\ \omega_2$) where the response might be either that of purely uncoupled in-plane resonance (dotted lines in figure 9), or a four modes coupled response, in which the coupling between the four modes is very strong.

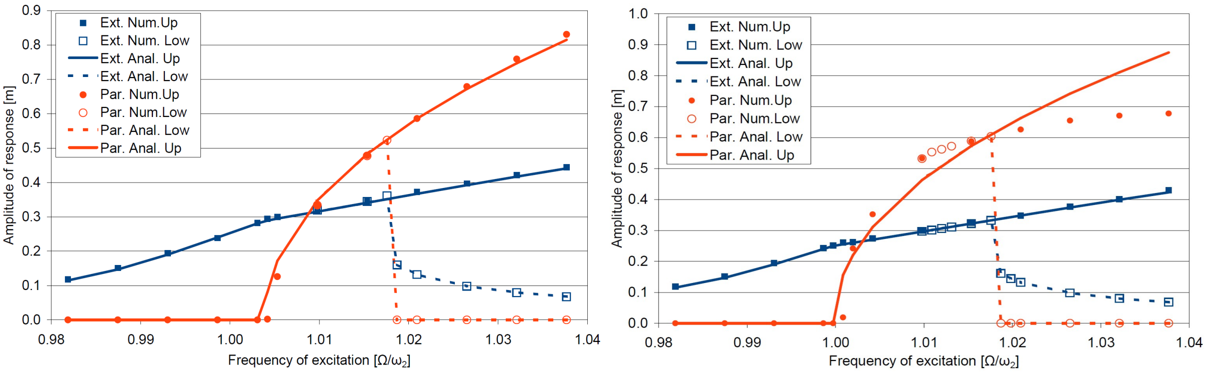

Figure 8: Influence of the excitation frequency on a) the in-plane coupled response, b) the out-of-plane response.

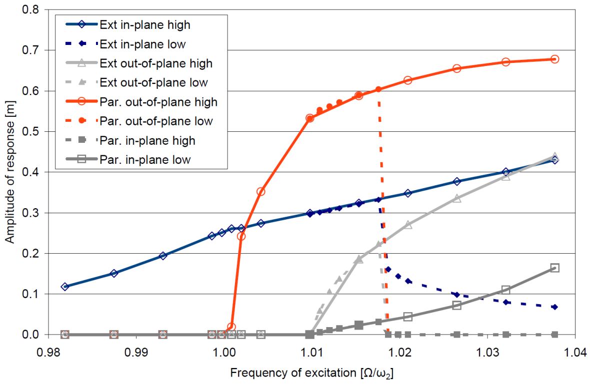

Figure 9: Influence of the excitation frequency on the number of modes in the out-of-plane coupled response.

It is hence clear that the two modes interaction analytical model presented here can not capture the whole response of the inclined cable because it involves up to four modes. However, it is noted in figure 8b that there is very good agreement between the amplitudes of the analytical model and the numerical simulations for the second in-plane mode. One thus deduces that in-plane external resonance is not affected by the presence of the first in-plane and second out-of plane modes, so that, practically, the two modes interaction is valid for external resonance. One observes then that the threshold of coupled out-of-plane parametric resonance is correctly predicted by the analytical model as well as the threshold of the hysteresis region. Moreover, in the regions where the response has only two non-zero components or a small contribution of the second out-of-plane mode ($\omega_2 < \Omega < 1.02\ \omega_2$), the analytical model fits relatively well with numerical results.

It is therefore considered that the two modes interaction model captures the main characteristics of the response and is sufficient for practical structural design purposes. Considering the fact that for $1.01\ \omega_2 < \Omega < 1.02\ \omega_2$, the amplitude of the first in-plane mode is small when compared to that of the other eigenmodes, the three modes interaction model of Gonzalvez-Buena *et al.* [21] is satisfactory and it can be used to determine the value of the threshold of the second out-of-plane mode. For higher frequencies, it is necessary to refer to the general four modes interaction of Rega [23].

6. CONCLUSION

The objective of the present work was to propose the simplest possible analytical model for the proper investigation of coupled external/parametric resonance in order to bridge the gap between complex mathematical interaction models and practical design of cables in structural engineering. To this end, abundant numerical applications and simulations were conducted for realistic values, based on actual bridge cables. Two specific cases were first investigated to gain better understanding of the two resonance phenomena separately. The first one was dedicated to external resonance and dealt with a horizontal cable submitted to a vertical harmonic motion at one end. Most of the existing results on the phenomenon were re-established analytically (in particular the limits of the hysteresis region) and confirmed numerically. The second specific case was dedicated to parametric resonance and dealt with a horizontal cable submitted to a horizontal harmonic motion at one end. Again, most of the existing results on parametric resonance were re-established analytically and confirmed numerically. Moreover it was observed that, when disturbed out-of-plane, the in-plane parametric resonance was unstable and turned into out-of-plane parametric resonance, so that only out-of-plane parametric resonance is stable and its bandwidth is formed by the disjunction of the in-plane and out-of-plane bandwidth.

Then, the coupling phenomenon strictly speaking was investigated, focusing on a cable with a 30° inclination. Analytical expressions for the coupled amplitudes were developed and their comparison with numerical simulations showed very good agreement. The study has proved that the coupling shifts the bandwidth of parametric resonance toward the higher frequencies and diminishes the value of the threshold when the frequency is above that of resonance. However, very strong interaction between the hysteresis regions of the two resonances has been found. Indeed, parametric resonance requires a high amplitude of external resonance to take place, so that one could say that it is necessary that external resonance appears first to cause parametric resonance. Concerning amplitudes, when coupling appears, it diminishes both, the amplitude of external and parametric resonance.

Moreover, numerical simulations showed that the introduction of an out-of-plane perturbation led to coupled out-of-plane vibrations so that, like for the horizontal cable, the only stable parametric resonance is the out-of plane of which the instability bandwidth might be considered in a first approximation as formed by the disjunction of the in-plane and out-of-plane bandwidth. However, it has been shown that, under certain conditions, the coupling phenomenon might involve up to four eigenmodes: the first in-plane and out-plane and second in-plane and out-of-plane modes. It has been also shown that the additional vibration modes only partially affect the amplitude of the main eigenmodes in the frequency domain useful for the engineer, for frequencies out-of the hysteresis range.

REFERENCES

[1] Kumarasena S., Jones N.P., Irwin P., Taylor P., Wind-Induced Vibration of Stay Cables, Office of Infrastructure R&D, Fed. Highway Adm., FHWA-RD-05-083, 284 pages, 2007.

[2] SETRA, Haubans, Recommandations de la commission interministérielle de la précontrainte, 200 pages, 2001.

[3] Irvine M., Cable structures, The MIT press, 1981.

[4] Caetano E., Indirect excitation of stays on cable-stayed bridges, in Proceedings of the 4th international symposium on cable dynamics, Montréal, Canada, 2001, 129-136.

[5] Caetano E., Cable vibrations in cable-stayed bridges, IABSE, 188 pages, 2007.

[6] Kovacs I., Zur Frage der Seilschwingungen und der Seildämpfung, Die Bautechnik 1982; 325-332.

[7] Uhrig R., On kinetic response of cable of cable-stayed bridges due to combined parametric and forced excitation, Journal of sound and vibration (JSV) 1993; 165(1): 185-192.

[8] Lilien J., Pinto da Costa A., Vibrations amplitude caused by parametric excitation of cables stayed structures, JSV 1994, 174(1): 69-90.

[9] Cai Y., Chen S., Dynamic of elastic cable under parametric external resonances, Journal of engineering mechanics 1994; 120(8): 1786-1802.

[10] Clément H., Crémona, C.: Étude mathématique du phénomène d'excitation paramétrique appliquée aux haubans de pont, in Études et recherches des laboratoires des ponts et chaussées, OA18, LCPC, Paris, 1996.

[11] Berlioz A. and Lamarque C.H., A non-linear model for the dynamics of an inclined cable, JSV 2005; 279: 619-639.

[12] Takahashi K., Dynamic stability of cables subjected to axial periodic load, JSV 1991, vol. 144, n 2, 323-330.

[13] Rega G.,Nonlinear vibrations of suspended cables - Part I: Modeling and analysis, Applied Mechanics Reviews (ASME) 2004; 57(6): 443-478.

[14] Nayfey A., Mook D., Non linear oscillations, ed. John Wiley and sons, USA, 1979.

[15] Luongo A, Rega G., Vestroni F., Monofrequent oscillations of a non-linear model of a suspended cable, JSV 1982; 82: 247-259.

[16] Al-Noury S.I., Ali S.A., Large amplitude vibrations of parabolic cables, JSV 1985; 101: 451-462.

[17] Takahashi K., Konishi Y., Nonlinear vibrations of cables in three dimensions. Part II: out-of-plane vibration under in-plane sinusoidally time varying loading, JSV 1987; 118: 85-97.

[18] Visweswara Rao G., Iyengar R. N., Internal resonance and non-linear response of a cable under periodic excitation, JSV 1991; 149(1): 25-41.

[19] Benedettini F., Rega G., Non-linear dynamics of an elastic cable under planar excitation. International Journal of non-linear mechanics 1987; 22: 497.

[20] Perkins N.C., Modal interactions in the non-linear response of elastic cables under parametric/external excitation, Journal of non-linear mechanics 1992; 27(2): 233-250.

[21] Gonzalez-Buelga A., Neidl S.A., Wagg D.J., Macdonald S.H.G, Modal stability of inclined cables subjected to vertical support excitation, JSV 2008; 318: 565-579.

[22] Chatjigeorgiou I.K., Mavrakos S.A., Nonlinear resonances of parametrically excited risers, numerical and analytic investigation for $\Omega = 2\omega_1$, Comp. & Str. 2005; 83: 560–573.

[23] Benedettini F., Rega G., Alaggio R., Non-linear oscillations of a four degrees of freedom model of a suspended cable under multiple internal resonance conditions, JSV 1995; 182(5): 775-798.

[24] Zhang W., Tang Y., Global dynamics of the cable under combined parametric and external excitations, International Journal of Non linear mechanics 2002; 37: 505-526.

[25] Srinil N., Rega G., Space-time numerical simulation and validation of analytical predictions for nonlinear forced dynamics of suspended cables, JSV 2008; 315: 394–413.

[26] Srinil N., Rega G., Two-to-one resonant multi-modal dynamics of horizontal/inclined cables: Part II: Internal resonance activation, reduced-order models and non-linear normal modes. Nonlinear Dynamics 2008; 48: 253-274.

[27] McClure G., Lapointe M., Modeling the structural dynamic response of overhead transmission lines, Computers and Structures 2003; 81: 825–834.

[28] Vassilopoulou I., Gantes C. J., Vibration modes and natural frequencies of saddle form cable nets, Computers and Structures 2010; 88 (1-2): 105-119.

COMPDYN 2011
III ECCOMAS Thematic Conference on
Computational Methods in Structural Dynamics and Earthquake Engineering
M. Papadrakakis, M. Fragiadakis, V. Plevris (eds.)
Corfu, Greece, 25–28 May 2011

AN EFFICIENT USE OF THE SYMBOLIC SPLINE-BASED DIFFERENTIAL QUADRATURE METHOD IN VIBRATION ANALYSIS OF SHELLS

Artur Krowiak

Institute of Computing Science, Cracow University of Technology
Al. Jana Pawła II 37, 31-864 Kraków
e-mail: krowiak@mech.pk.edu.pl

Keywords: differential quadrature, spline interpolation, free vibration, composite shell.

Abstract. *The paper presents the differential quadrature method (DQM) based on a modified spline interpolation and the application of the method in vibration analysis of laminated, composite shells. The goal of the modification of the spline interpolation is to improve the rate of convergence and preserve the stability of the method. The modification changes the definition of the end conditions for the spline interpolation. Two types of the end conditions are combined and appropriately applied at the stage of the determination of the weighting coefficients for the DQM. With the aid of the symbolic computation the weighting coefficients can be successfully determined for any spline degree. The efficiency of the method is examined by the example of the free vibration of composite, conical shells. The influence of the modified end conditions, number of nodes and spline degree on the convergence and accuracy is studied. The achieved results are compared with the results obtained using conventional DQM and using other numerical techniques.*

1 INTRODUCTION

More and more advanced mechanical structures as well as new construction materials require to develop computational methods that allow efficiently to estimate mechanical properties. Some of the mechanical structures can be efficiently analyzed by analytical methods but usually numerical methods give more versatility. Among the latter, the finite element method seems to be the most common and it is applied to many challenging problems. This method belongs to low order numerical techniques, what means that accurate numerical results can be achieved using large number of nodes. It requires much computational effort. In the case of eigenvalue problem, where the number of nodes corresponds to the number of obtained eigenpairs, only the lowest eigenpairs are of the much interest in mechanical problems. However, to compute these eigenpairs with acceptable accuracy using low order techniques, one has to aggregate and solve large sets of equations, unlike applying methods that use high order approximation. One of them is differential quadrature method (DQM) [1], which allows to obtain very accurate results using few discrete points. This feature as well as simple formulation cause the DQM to be applied in many fields of mathematics and mechanics [2].

However, the DQM has some drawbacks resulting from the assumed approximation of the sought solution. One of these drawbacks is computational instability. To overcome the problem, new approaches have been developed. In one of them, only some neighbouring nodes are used to approximate a derivative [3]. In others, variable order approach is applied [4] or B-Spline interpolation is used [5,6] instead of conventional polynomial. The latest advances in the DQM are presented in [7].

In [8] another idea to improve the stability of the method is proposed. In this idea, spline functions, considered as *n* degree polynomials, defined separately in each subinterval of the domain are used. In this manner, the solution is approximated. The developed algorithm requires to use symbolic manipulations at a initial step of computation, therefore in present paper the method is referred to Symbolic Spline-based Differential Quadrature Method (SSDQM). This algorithm allows to determine the weighting coefficients for the derivative approximation in the DQM with the use of any spline degree, unlike the technique that uses B-Spline functions [5,6]. In the latter, the formulas based on quintic and sextic B-Splines are developed so far. Obtained results indicate that the SSDQM provides a balance between low order methods and high order ones. It is characterized by less rate of convergence then the conventional DQM, but ensures computational stability, what is clearly seen in dynamic problems [9]. The SSDQM gives also reasonable results using uniform point distribution, what is usually impossible in the case of the conventional DQM. Accurate results are also obtained for problems, where the DQM fails [10].

In order to improve the rate of convergence of the SSDQM a modification is proposed in this paper. This modification changes the formulation of the end conditions for the spline interpolation. The improvement is shown by the example of the free vibration of laminated, orthotropic, conical shells.

The layout of the paper is as follows. In section 2, the short description of the DQM and the SSDQM is presented. In the latter, the way of the determination of the weighting coefficients is shown. In section 3, the approach to improve the SSDQM is proposed. In section 4, the presented idea is tested on the example of the free vibration analysis of the conical shells. On the basis of the results some concluding remarks on the convergence and accuracy are drawn.

2 SYMBOLIC SPLINE-BASED DIFFERENTIAL QUADRATURE METHOD

The basic idea of the DQM lies in the fact that the spatial derivative of a function at a given point is approximated by a linear weighted sum of the function values at all discrete points in the domain along the coordinate lines. It can be put as follows

$$\frac{d^r f(x)}{dx^r}\Big|_{x=x_i} = \sum_{j=1}^{N} a_j^{(r)}(x_i) f(x_j) = \sum_{j=1}^{N} a_{ij}^{(r)} f_j \qquad i=1,...,N \tag{1}$$

where N denotes the number of grid points and $a_{ij}^{(r)}$ are the weighting coefficients of the rth order derivative.

In the case of the multidimensional problem, the derivatives with respect to other spatial variables are approximated in the similar manner and the approximation of the mixed derivatives is done with the use of the weighting coefficients determined separately for derivatives with respect to appropriate variables.

Applying the governing equation with the derivatives described by Eq. (1) at each interior point of the domain and implementing boundary conditions, one obtains a set of algebraic equations. A key stage of the method is to determine the weighting coefficients. These coefficients depend on the way the sought solution is approximated. Therefore, they influence the convergence, accuracy and stability of the method.

In the conventional approach, the solution is approximated by the interpolation polynomial. The use of the Lagrange base functions and the recurrence relationships [11] allows efficiently to determine the weighting coefficients in this approach. The method provides very high rate of convergence and accuracy, when appropriate point distribution is applied. When the number of points is too large or the points are uniformly distributed then the method fails.

2.1 Spline interpolation in the DQM

The definition of the interpolation function depends on whether the spline degree n is odd or even. If the spline degree is odd then the interpolation function has the following form

$$f(x) \approx \left\{ s_i(x),\, x \in \left[x_i, x_{i+1}\right],\ i=1,...,N-1 \right\} \tag{2}$$

where N is the number of nodes and the ith spline section $s_i(x)$ can be written as

$$s_i(x) = \sum_{j=0}^{n} c_{ij}(x-x_i)^j \tag{3}$$

In order to determine the interpolation function, the $(n+1)\cdot(N-1)$ coefficients c_{ij} in Eq. (3) have to be calculated. To this end, the interpolation conditions and the derivative continuity conditions at the nodes are used. They constitute the set of $(n+1)\cdot N-2n$ equations. The detailed description of these equations is presented in [8]. To complete the set of equations, the n-1 end conditions have to be introduced. They can be defined in different forms. The most common form is obtained by equating some high order derivatives to zero at the end points – so-called the natural end conditions

$$s_1^{(k)}(x_1)=0,\ s_{N-1}^{(k)}(x_N)=0,\ \ k=\frac{n+1}{2},..,n-1 \tag{4}$$

or by requiring the nth order derivative to be continuous at some nodes at the left and right end of the domain – so-called the not-a-knot end conditions

$$s_i^{(n)}(x_{i+1}) = s_{i+1}^{(n)}(x_{i+1}), \quad s_{N-1-i}^{(n)}(x_{N-i}) = s_{N-i}^{(n)}(x_{N-i}), \quad i = 1,\dots,\frac{n-1}{2} \tag{5}$$

If the spline degree is even, the auxiliary spline knots have to be introduced in order to define the sufficient number of conditions. The spline knots are introduced at the midpoints of the existing nodes as follows

$$z_1 = x_1, \; z_{i+1} = \frac{1}{2}\left[x_i + x_{i+1}\right], \; i = 1,..,N-1, \; z_{N+1} = x_N \tag{6}$$

The interpolation function is defined between these auxiliary points by the formula

$$f(x) \approx \left\{ s_i(x), \; x \in \left[z_i, z_{i+1}\right], \; i = 1,..,N \right\} \tag{7}$$

Each spline segment $s_i(x)$ is expressed by Eq. (3). In order to calculate the $(n+1)\cdot N$ spline coefficients c_{ij} in Eq. (3) one uses the interpolation conditions at the nodes as well as at the spline knots and the derivative continuity conditions at the spline knots. It gives $(n+1)\cdot N - n$ equations. To complete the set of equations, the n end conditions are introduced in two different forms, similarly to Eqs. (4) or (5)

$$s_1^{(k)}(x_1) = 0, \; s_N^{(k)}(x_N) = 0, \quad k = \frac{n}{2},\dots,n-1 \tag{8}$$

$$s_i^{(n)}(z_{i+1}) = s_{i+1}^{(n)}(z_{i+1}), \quad s_{N-i}^{(n)}(z_{N+1-i}) = s_{N+1-i}^{(n)}(z_{N+1-i}), \quad i = 1,\dots,\frac{n}{2} \tag{9}$$

Equation (8) represents the natural end conditions and Eq. (9) – the not-a-knot end conditions.

2.2 Weighting coefficients in the SSDQM

Using equations discussed in section 2.1 one can express the spline coefficients c_{ij} as a function of node distribution and unknown values of the solution f_i at the nodes. It can be put in general form as

$$c_{ij} = \sum_{k=1}^{N} C_{ijk}(x_1,\dots,x_N)\cdot f_k, \quad i = 1,\dots,\overline{N}, j = 0,\dots,n \tag{10}$$

where $\overline{N} = N-1$ when n is odd and $\overline{N} = N$ when n is even.

In order to determine the weighting coefficients for the SSDQM one should calculate an appropriate order derivative of the interpolation function (2) or (7)

$$f^{(r)}(x) \approx \left\{ s_i^{(r)}(x), \, i = 1,..,\overline{N} \right\} \tag{11}$$

where

$$s_i^{(r)}(x) = \sum_{j=r}^{n}\left(c_{ij}\cdot(x-x_i)^{j-r}\cdot\frac{j!}{(j-r)!}\right) \tag{12}$$

and evaluate it at each node, what yields

$$
\begin{aligned}
&s_i^{(r)}(x_i) = c_{ir} \cdot r!, \quad i = 1,\dots,\bar{N} \\
&s_{N-1}^{(r)}(x_N) = \sum_{j=r}^{n} \left(c_{N-1j} \cdot (x_N - x_{N-1})^{j-r} \cdot \frac{j!}{(j-r)!} \right), \quad \text{when } n \text{ is odd}
\end{aligned} \tag{13}
$$

Taking into account Eq. (10), the derivatives $s_i^{(r)}(x_i)$ and $s_{N-1}^{(r)}(x_N)$ in Eq. (13), after some algebraic manipulations, can be written as

$$
\begin{aligned}
&s_i^{(r)}(x_i) = \sum_{k=1}^{N} \left[C_{irk} \cdot r! \right] f_k, \quad i = 1,\dots,\bar{N} \\
&s_{N-1}^{(r)}(x_N) = \sum_{k=1}^{N} \left[\sum_{j=r}^{n} \left(C_{N-1jk} \cdot (x_N - x_{N-1})^{j-r} \cdot \frac{j!}{(j-r)!} \right) \right] f_k
\end{aligned} \tag{14}
$$

Comparing with Eq. (1), it is easy to notice that the expressions in the square brackets in Eq. (14) are the weighting coefficients $a_{ij}^{(r)}$ for the *r*th order derivative in the DQM based on the spline interpolation.

The assumed spline segments are not typical base functions, what makes impossible to determine the weighting coefficients in pure numeric approach, especially deriving explicit formulas. These coefficients can be determined with the use of symbolic-numeric manipulations, where the unknown function values are noted as symbols. Equations discussed in section 2.1 allow to obtain spline coefficients (10) in symbolic-numeric form. Then, coefficients C_{ijk} in Eq. (10) can be determined by separating numbers from appropriate symbols f_k, what allows easily to compute the weighting coefficients contained in Eq. (14). This algorithm has been implemented in Computer Algebra System – Maple [12].

3 MODIFIED SSDQM – COMBINING OF THE END CONDITIONS

The research done so far indicates that the use of different forms of the end conditions (Eqs. (4) or (5) and (8) or (9)) significantly influences the quality of the solution. The use of the not-a-knot end conditions (Eqs. (5) or (9)) rapidly improves the convergence of the method but leads to the computational instability, especially when the spline degree is high. The use of the natural end conditions (Eqs. (4) or (8)) gives stable results, however the rate of convergence is significantly weaker in this case. Therefore in this paper a modification is proposed. In this approach the assumed, small number of the not-a-knot end conditions is completed by the appropriate number of the natural end conditions. These equations form the set of the combined end conditions used for computing the spline coefficients (10) and finally the weighting coefficients.

Assuming that N_{nak} denotes the assumed number of the not-a-knot end conditions, the combined end conditions take the form

$$
\begin{aligned}
&s_i^{(n)}(x_{i+1}) = s_{i+1}^{(n)}(x_{i+1}), \quad s_{N-1-i}^{(n)}(x_{N-i}) = s_{N-i}^{(n)}(x_{N-i}), \quad i = 1,\dots,N_{nak} \\
&s_1^{(k)}(x_1) = 0, \; s_{N-1}^{(k)}(x_N) = 0, \; k = \frac{n+1}{2} + N_{nak},..,n-1
\end{aligned} \tag{15}
$$

for odd spline degree and

$$
\begin{aligned}
&s_i^{(n)}(z_{i+1}) = s_{i+1}^{(n)}(z_{i+1}), \quad s_{N-i}^{(n)}(z_{N+1-i}) = s_{N+1-i}^{(n)}(z_{N+1-i}), \quad i = 1,\dots,N_{nak} \\
&s_1^{(k)}(x_1) = 0, \; s_N^{(k)}(x_N) = 0, \; k = \frac{n}{2} + N_{nak},\dots,n-1
\end{aligned} \tag{16}
$$

for even spline degree.

Equation (15) is introduced into the algorithm presented in section 2 instead of Eq. (4) or (5) and Eq. (16) – instead of Eq. (8) or (9). The presented formulation makes a balance between rapid convergence and the stability of the method.

4 FREE VIBRATION ANALYSIS OF CONICAL SHELLS

The presented modification is tested in the problem of the free vibration of thin, composite, orthotropic shells. The governing equations that follow from classical shell theory are taken under consideration.

Shell structures are commonly used in civil, mechanical and aerospace engineering. Various analytical [13-16] and numerical [17-20] methods have been used to analyze mechanical properties of these structures or to test novel computational procedures. The DQM has been also applied to these ends [21,22]. The known results enable to estimate the effectiveness of the approach presented in the paper in this type of mechanical problems.

In Fig. 1, the analyzed conical shell with the reference coordinate system (x, θ, z) and the components of the displacement field in appropriate directions (u, v, w) are shown.

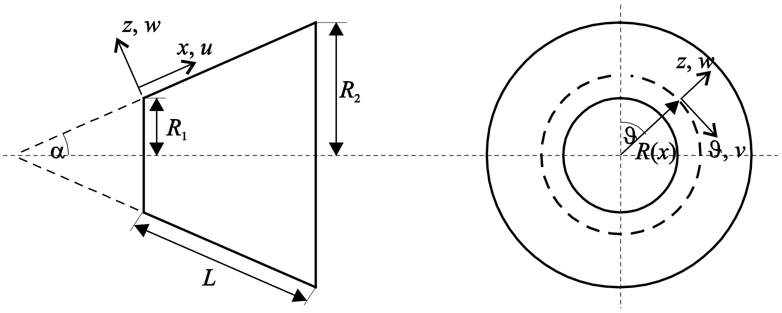

Figure 1: Geometry of truncated conical shell.

The derivation of the governing equations for the thin, composite, conical shell based on classical shell theory is presented in several papers, e.g. [21].

Taking into account that the field of displacement, in the case of the free vibration of this structure, can be expressed as

$$u = U(x)\cos(m\theta)\cos(\omega t),\ v = V(x)\sin(m\theta)\cos(\omega t),\ w = W(x)\cos(m\theta)\cos(\omega t) \quad (17)$$

where m is the wave number in the circumferential direction and ω is the circular frequency, mathematical model of the shell can be written in a compact matrix form as follows

$$\begin{bmatrix} L_{11} & L_{12} & L_{13} \\ L_{21} & L_{22} & L_{23} \\ L_{31} & L_{32} & L_{33} \end{bmatrix} \begin{bmatrix} U \\ V \\ W \end{bmatrix} = -\rho h \omega^2 \begin{bmatrix} U \\ V \\ W \end{bmatrix} \quad (18)$$

In Equation (18), L_{ij} are differential operators, e.g.

$$L_{22}=\left(\frac{A_{66}\sin(\alpha)}{R}-\frac{B_{66}\sin(\alpha)\cos(\alpha)}{R^2}-\frac{4D_{66}\sin(\alpha)\cos^2(\alpha)}{R^3}\right)\frac{d}{dx}$$
$$+\left(A_{66}+\frac{3B_{66}\cos(\alpha)}{R}+\frac{2D_{66}\cos^2(\alpha)}{R^2}\right)\frac{d^2}{dx^2}-\frac{A_{22}m^2+A_{66}\sin^2(\alpha)}{R^2}$$
$$-\frac{(2m^2B_{22}-B_{66}\sin^2(\alpha))\cos(\alpha)}{R^3}-\frac{(D_{22}m^2-4D_{66}\sin^2(\alpha))\cos^2(\alpha)}{R^4},$$

These operators contain constants A_{ij}, B_{ij} and D_{ij} that denote extensional, coupling and bending stiffnesses. For a shell that is composed of different layers of orthotropic materials, these stiffnesses can be expressed as

$$A_{ij}=\sum_{k=1}^{N_l}\overline{Q}_{ij}^{k}(h_k-h_{k-1}),\ B_{ij}=\frac{1}{2}\sum_{k=1}^{N_l}\overline{Q}_{ij}^{k}(h_k^2-h_{k-1}^2),\ D_{ij}=\frac{1}{3}\sum_{k=1}^{N_l}\overline{Q}_{ij}^{k}(h_k^3-h_{k-1}^3) \tag{19}$$

where N_l denotes the number of layers in the shell and h_k i h_{k-1} are the distances from the shell reference surface to the outer and inner surfaces of the kth layer, respectively. $\overline{Q}_{ij}^{k}$ are elements of the transformed, reduced, elasticity matrix of the kth layer.

For a given layer of orthotropic material, the $\overline{\mathbf{Q}}$ matrix is a result of the transformation of the elasticity matrix $\mathbf{Q}$ between the principal material coordinates and the shell's coordinates according to the formula

$$\overline{\mathbf{Q}}=\mathbf{T}\mathbf{Q}\mathbf{T}^T \tag{20}$$

The transformation matrix $\mathbf{T}$ can be expressed as

$$\mathbf{T}=\begin{bmatrix}\cos^2(\phi) & \sin^2(\phi) & -2\sin(\phi)\cos(\phi)\\ \sin^2(\phi) & \cos^2(\phi) & 2\sin(\phi)\cos(\phi)\\ \sin(\phi)\cos(\phi) & -\sin(\phi)\cos(\phi) & \cos^2(\phi)-\sin^2(\phi)\end{bmatrix} \tag{21}$$

where ϕ is the angular orientation of the fibers.

The material constants in $\mathbf{Q}$ are defined by Young's moduli: E_1, E_2, the shear moduli G_{12} and the Poisson's ratios: ν_{12}, ν_{21} with the following formulas

$$Q_{11}=\frac{E_1}{1-\nu_{12}\nu_{21}},\ Q_{12}=\frac{\nu_{12}E_2}{1-\nu_{12}\nu_{21}},\ Q_{22}=\frac{E_2}{1-\nu_{12}\nu_{21}},\ Q_{66}=G_{12} \tag{22}$$

In the paper, the shell, which is simply supported at both edges ($R=R_1, R=R_2$) is considered. At these edges, appropriate displacement functions V, W as well as force N_x and moment M_x have to be zero, what can be put as

$$V=0,\ W=0 \tag{23}$$

$$U^{(1)}+a_1U+a_2V+a_3W+a_4W^{(1)}+a_5W^{(2)}=0 \tag{24}$$

$$W^{(2)}+b_1U+b_2U^{(1)}+b_3V+b_4W+b_5W^{(1)}=0 \tag{25}$$

where constants a_i and b_i are as follows

$$
\begin{aligned}
&a_1 = A_{12}\sin(\alpha)/A_{11}R,\; a_2 = B_{12}m\cos(\alpha)/A_{11}R^2 + A_{12}m/A_{11}R,\\
&a_3 = A_{12}\cos(\alpha)/A_{11}R + B_{12}m^2/A_{11}R^2,\; a_4 = -B_{12}\sin(\alpha)/A_{11}R,\\
&a_5 = -B_{11}/A_{11},\; b_1 = -B_{12}\sin(\alpha)/D_{11}R,\; b_2 = -B_{11}/D_{11},\\
&b_3 = -D_{12}m\cos(\alpha)/D_{11}R^2 - B_{12}m/D_{11}R,\\
&b_4 = -B_{12}\cos(\alpha)/D_{11}R - D_{12}m^2/D_{11}R^2,\; b_5 = D_{12}\sin(\alpha)/D_{11}R
\end{aligned}
$$

Taking advantage of the algorithm discussed in section 2, where the modification based on combining of the end conditions is introduced, the weighting coefficients $a_{ij}^{(r)}$ for the *r*th order derivative are computed. This approach is characterized by the number N_{nak}, that denotes the number of the not-a-knot type conditions contained in the set of the end conditions.
Equation (18), which is discretized using differential quadrature rules, takes the form

$$
\begin{bmatrix} \mathbf{P}_{11} & \mathbf{P}_{12} & \mathbf{P}_{13} \\ \mathbf{P}_{21} & \mathbf{P}_{22} & \mathbf{P}_{23} \\ \mathbf{P}_{31} & \mathbf{P}_{32} & \mathbf{P}_{33} \end{bmatrix} \begin{bmatrix} \mathbf{U} \\ \mathbf{V} \\ \mathbf{W} \end{bmatrix} = -\rho h \omega^2 \begin{bmatrix} \mathbf{U} \\ \mathbf{V} \\ \mathbf{W} \end{bmatrix} \tag{26}
$$

where vectors **U**, **V**, **W** contain nodal function values and elements of matrices $\mathbf{P}_{lk}$ contain appropriate weighting coefficients $a_{ij}^{(r)}$, $i, j = 1,\ldots,N$, for example

$$
\begin{aligned}
P_{22_{ij}} = &\left(\frac{A_{66}\sin(\alpha)}{R_i} - \frac{B_{66}\sin(\alpha)\cos(\alpha)}{R_i^2} - \frac{4D_{66}\sin(\alpha)\cos^2(\alpha)}{R_i^3} \right) a_{ij}^{(1)} \\
&+ \left(A_{66} + \frac{3B_{66}\cos(\alpha)}{R_i} + \frac{2D_{66}\cos^2(\alpha)}{R_i^2} \right) a_{ij}^{(2)} - \left(\frac{A_{22}m^2 + A_{66}\sin^2(\alpha)}{R_i^2} \right. \\
&\left. + \frac{(2m^2B_{22} - B_{66}\sin^2(\alpha))\cos(\alpha)}{R_i^3} + \frac{(D_{22}m^2 - 4D_{66}\sin^2(\alpha))\cos^2(\alpha)}{R_i^4} \right) \delta_{ij},
\end{aligned}
$$

To implement boundary conditions, Eqs. (23)-(25) are discretized at both edges

$$
V_k = 0,\; W_k = 0 \tag{27}
$$

$$
\sum_{j=1}^{N} a_{kj}^{(1)} U_j + a_1 U_k + a_2 V_k + a_3 W_k + a_4 \sum_{j=1}^{N} a_{kj}^{(1)} W_j + a_5 \sum_{j=1}^{N} a_{kj}^{(2)} W_j = 0 \tag{28}
$$

$$
\sum_{j=1}^{N} a_{kj}^{(2)} W_j + b_1 U_k + b_2 \sum_{j=1}^{N} a_{kj}^{(1)} U_j + b_3 V_k + b_4 W_k + b_5 \sum_{j=1}^{N} a_{kj}^{(1)} W_j = 0 \tag{29}
$$

where $k = 1$ at the small edge (R_1) and $k = N$ at the large one (R_2).

Following the general approach to implement boundary conditions in the DQM [23], Eqs. (26)-(29) can be put as the final eigenvalue equation

$$
\mathbf{A} \cdot \mathbf{Z} = -\rho h \omega^2 \cdot \mathbf{Z} \tag{30}
$$

where vector **Z** contains nodal function values at the inner points
$\mathbf{Z} = [U_2,\ldots,U_{N-1},V_2,\ldots,V_{N-1},W_3,\ldots,W_{N-2}]$.

The calculations are carried out for the antisymmetric cross-ply conical shell. The elementary material parameters of each layer are given as

$$
E_1/E_2 = 15,\; \nu_{12} = 0.25,\; G_{12}/E_2 = 0.5 \tag{31}
$$

As the result, the coefficients in Eq. (19) can be simplified as [15]

$$\begin{aligned} &A_{11} = A_{22} = h/2(Q_{11} + Q_{22}), \quad A_{12} = Q_{12}h, \quad A_{66} = Q_{66}h, \\ &B_{11} = -B_{22} = (h^2/4N_l)(Q_{11} - Q_{22}), \quad B_{12} = B_{66} = 0, \\ &D_{11} = D_{22} = (h^3/24)(Q_{11} + Q_{22}), \quad D_{12} = \tfrac{1}{12}Q_{12}h^3, \quad D_{66} = \tfrac{1}{12}Q_{66}h^3 \end{aligned} \tag{32}$$

where N_l is the number of plies.

The calculations are carried out using uniform node distribution as well as Chebyshev-Gauss-Lobatto pattern. The results are presented in the form of dimensionless frequency parameter

$$\lambda = R_2\sqrt{\rho h/A_{11}}\,\omega \tag{33}$$

The dependence on the combined end conditions (N_{nak}), spline degree (n) and the number of nodes (N) is presented in Fig. 2 (Chebyshev-Gauss-Lobatto pattern) and Fig. 3 (uniform grid). These figures show the percentage relative error $\delta = (\lambda_{SSDQM} - \lambda_{DQM})/\lambda_{DQM} \cdot 100\%$ between the results from the SSDQM and the reference value taken as the result from the DQM ($\lambda_{DQM} = 0.1779$) obtained in present work.

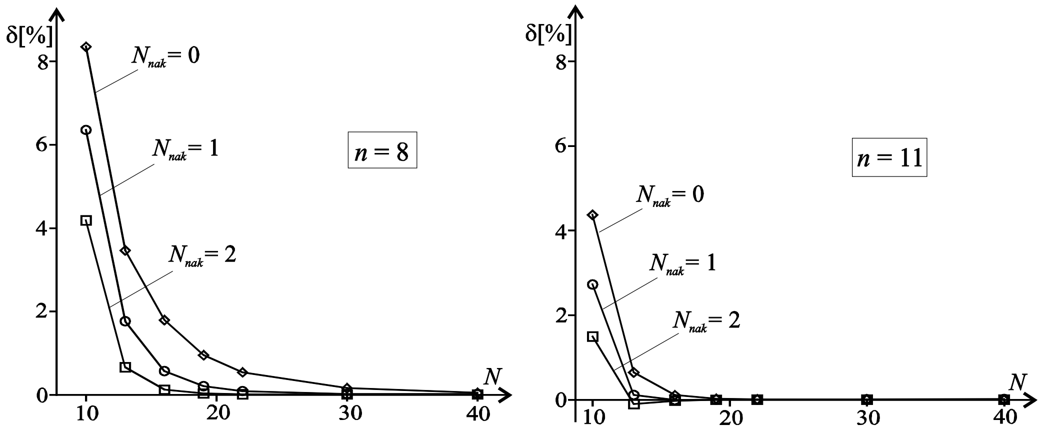

Figure 2: Error of fundamental frequency parameter λ for antisymmetric cross-plied laminated conical shell ($N_l = 2$, $h/R_2 = 0.01$, $\alpha = 30°$, $L\sin\alpha/R_2 = 0.25$, $m = 0$) – Chebyshev-Gauss-Lobatto grid.

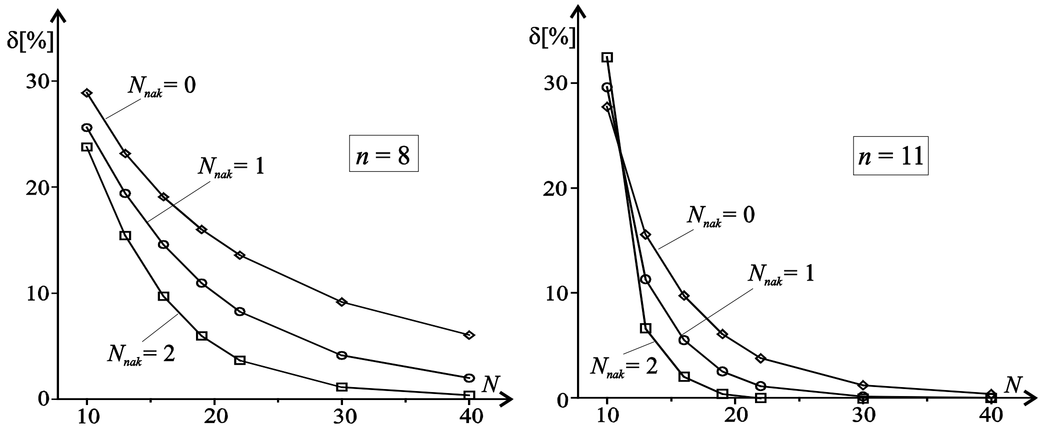

Figure 3: Error of fundamental frequency parameter λ for antisymmetric cross-plied laminated conical shell ($N_l = 2$, $h/R_2 = 0.01$, $\alpha = 30°$, $L\sin\alpha/R_2 = 0.25$, $m = 0$) – uniform grid distribution.

Presented results indicate that the use of the combined end conditions significantly improves the rate of convergence. When one spline segment covers more intervals at each end of the domain ($N_{nak} > 0$) then more accurate results are obtained. The results can be improved also using higher spline degree. It should be noted that the SSDQM converges, when the uniform node distribution is applied, unlike the conventional DQM.

Table 1 shows the fundamental frequency parameters (33) for different number of layers and various shell thickness. These results are obtained with the SSDQM based on the eleventh spline degree, imposing $N = 16$ nodes according to the Chebyshev-Gauss-Lobatto pattern and using the modification ($N_{nak} = 2$) discussed in section 3. As Fig. 2 reports, these computational parameters ensure fast convergence and high accuracy.

In the theoretical case, when the number of layers N_l approaches to infinity, coupling stiffnesses B_{11}, B_{22}, contained in Eq. (32), approach to zeros, unlike the case, when the number $N_l = 2$. Then the mentioned stiffnesses achieve maximum value.

h/R_2	Number of layers N_l					
	2	4	6	10	20	∞
0.01	0.1779 (0.1769)	0.1941	0.1962	0.1972	0.1976	0.1978 (0.1978)
0.02	0.2116 (0.2119)	0.2305	0.2332	0.2346	0.2352	0.2355 (0.2355)
0.03	0.2341 (0.2360)	0.2596	0.2637	0.2658	0.2667	0.2671 (0.2671)
0.04	0.2546 (0.2578)	0.2891	0.2947	0.2975	0.2987	0.2992 (0.2992)
0.05	0.2755 (0.2794)	0.3188	0.3254	0.3288	0.3302	0.3308 (0.3308)
0.06	0.2967 (0.3010)	0.3473	0.3548	0.3585	0.3600	0.3606 (0.3606)
0.07	0.3179 (0.3222)	0.3738	0.3817	0.3855	0.3871	0.3877 (0.3877)
0.08	0.3386 (0.3426)	0.3978	0.4057	0.4096	0.4111	0.4117 (0.4117)
0.09	0.3584 (0.3620)	0.4190	0.4268	0.4305	0.4320	0.4325 (0.4325)
0.10	0.3770 (0.3801)	0.4376	0.4450	0.4485	0.4500	0.4504 (0.4504)

Table 1: Fundamental frequency parameters λ for antisymmetric cross-plied laminated conical shells ($\alpha = 30°$, $L \sin\alpha / R_2 = 0.25$, $m = 0$).

In Tab. 1, for two extreme cases, the results obtained in [15] (values in parenthesis) are also presented for comparison. As one can notice, very good agreement is achieved, when the coupling stiffnesses vanish ($N_l = \infty$), while some differences occur, when these stiffnesses take maximum value ($N_l = 2$). The reason may lie in the use of various shell theories. In present paper Love's shell theory is taken under consideration, while in [15] Donnell's theory is used.

5 CONCLUSION

In the paper, the method based on the differential quadrature is presented and applied to vibration analysis of shells. These type methods belong to high order approximation techniques and provide high convergence and accuracy. In order to ensures the computational stability, the weighting coefficients in present method are computed using spline functions and the modification proposed in the paper improves the rate of convergence of the method under this conditions.

The effectiveness of this modification is shown by the example of the free vibration of the composite, conical shell. The results indicate that the combined end conditions, where the small number of not-a-knot end conditions are used, can significantly improve the results.

REFERENCES

[1] R. Bellman, J. Casti, Differential quadrature and long term integration, *Journal of Mathematical Analysis and Application,* **34**, 235–238, 1971.

[2] C.W. Bert, M. Malik, Differential quadrature method in computational mechanics, *Applied Mechanics Reviews*, **49**, 1-28, 1996.

[3] Z. Zong, K.Y. Lam, A localized differential quadrature method and it application to 2D wave equations, *Computational Mechanics*, **29**, 382-391, 2002.

[4] Z. Zong, A variable order approach to improve differential quadrature accuracy in dynamic analysis, *Journal of Sound and Vibration*, **266**, 307-323, 2003.

[5] H. Zhong, Spline-based differential quadrature for fourth order differential equations and its application to Kirchhoff plates, *Applied Mathematical Modelling*, 28, 353–366, 2004.

[6] Q. Guo, H. Zhong, Non-linear vibration analysis of beams by a spline-based differential quadrature method, *Journal of Sound and Vibration*, **269**, 413-420, 2004.

[7] Z. Zong, Y. Zhang, *Advanced Differential Quadrature Methods*, Chapman & Hall/CRC, 2009.

[8] A. Krowiak, Symbolic computing in spline-based differential quadrature method, *Communications in Numerical Methods in Engineering*, **22**, 1097-1107, 2006.

[9] A. Krowiak, The application of the differential quadrature method based on a piecewise polynomial to the vibration analysis of geometrically nonlinear beams, *Computer Assisted Mechanics and Engineering Sciences*, **15**, 1-13, 2008.

[10] A. Krowiak, The convergence and stability of the spline-based differential quadrature method applied to the vibration analysis of rectangular plates with free corners, *Vibration in Physical Systems*, **22**, 197-202, 2006.

[11] C. Shu, B.E. Richards, Application of generalized differential quadrature to solve two-dimensional incompressible Nanier-Stokes equations, *International Journal for Numerical Methods in Fluids*, **15**, 791-798, 1992.

[12] M.B. Monagan, K.O. Geddes, K.M. Heal, G. Labahm, S.M. Vorkoetter, J. McCarron, P. DeMarco, *Maple 14 – Advanced programming guide*, Maplesoft, Canada, 2010.

[13] H. Saunders, E.J. Wisniewski, P.R. Pasley, Vibration of conical shells, *J. Acoust. Soc. Am.* **32**, 765-772, 1960.

[14] H. Garnet, J. Kemper, Axisymmetric free vibration of conical shells, *Journal of Applied Mechanics*, **31**, 458-466, 1964.

[15] L. Tong, Free vibration of laminated conical shells including transverse shear deformaton, *International Journal of Solids and Structures*, **31**, 443-456, 1994.

[16] T. Irie, G. Yamada, Y. Kaneko, Natural frequencies of truncated conical shells, *Journal of Sound and Vibration*, **92**, 447-453, 1984.

[17] S.K. Sen, P.L. Gould, Free vibration of shells of revolution using FEM, *Journal of Engineering Mechanics Division, ASCE*, **100**, 283-303, 1974.

[18] K.R. Sivadas, N. Ganesan, Vibration analysis of laminated conical shells with variable thickness, *Journal of Sound and Vibration*, **148**, 477-481, 1991.

[19] Ö. Civalek, Frequency analysis of isotropic conical shells by discrete singular convolution (DSC), *International Journal of Structural Engineering and Mechanics*, **25**, 127-131, 2007.

[20] Ö. Civalek, The determination of frequencies of laminated conical shells via the discrete singular convolution method, *Journal of Mechanics of Material and Structures*, **1**, 165-192, 2006.

[21] C. Shu, Free vibration analysis of composite laminated conical shells by generalized differential quadrature, *Journal of Sound and Vibration*, **194**, 587-604, 1996.

[22] C. Shu, An efficient approach for free vibration analysis of conical shells, *International Journal of Mechanical Sciences*, **38**, 935-949, 1996.

[23] C. Shu, H. Du, A generalized approach for implementing general boundary conditions in the GDQ free vibration analysis of plates, *International Journal of Solids and Structures*, **34**, 837-864, 1997.

COMPDYN 2011
III ECCOMAS Thematic Conference on
Computational Methods in Structural Dynamics and Earthquake Engineering
M. Papadrakakis, M. Fragiadakis, V. Plevris (eds.)
Corfu, Greece, 25–28 May 2011

IMPLEMENTATION OF FRACTURE MECHANICS CONCEPTS IN DYNAMIC PROGRESSIVE COLLAPSE PREDICTION USING AN OPTIMIZATION BASED ALGORITHM

David Tubul[1], **and Oren Lavan**[2]
[1]Technion-Israel institute of Technology
Haifa 32000, Israel
e-mail: tubul@tx.technion.ac.il
[2]Technion-Israel institute of Technology
Haifa 32000, Israel
e-mail: lavan@tx.technion.ac.il

Keywords: Progressive collapse, disproportionate collapse, Lagrangian dynamics, Fracture, Strength degradation, Mixed Lagrangian Formulation (MLF).

Abstract. *Prediction of progressive collapse of buildings under extreme events is one of the challenges that the civil engineering community must face. The ability to predict progressive collapse would enable the identification of deficiencies in the common practice of structural design without having to wait for the next extreme event to occur. With such ability, new design strategies and technologies for progressive collapse prevention could be addressed.*

Progressive collapse prediction, where the capacity of structures for progressive collapse is assessed, faces a great number of challenges. In terms of feasibility, it should address the challenge of analyzing large scale buildings in all stages of collapse. The complex behavior of buildings during collapse often leads to issues of stability of the numerical scheme, hence to the collapse of the analysis prior to the actual analysis of collapse. Indeed, the area of dynamics of structures including phenomena expected during progressive collapse (e.g. contact, fracture) has been developed to a high level. Nevertheless, there is no theory and computational tool that can efficiently predict all stages of progressive collapse of large scale structures.

The Mixed Lagrangian Formulation (MLF) could potentially provide such a theory as well as an accompanied efficient, robust and stable numerical scheme. It also considers almost all stages of collapse in a unified manner, thus, almost completes the puzzle of Progressive collapse prediction. The missing part of the puzzle, considering fracture in a unified manner, is the aim of this paper. This is developed using concepts from Fracture Mechanics for brittle material by using Griffith's theory. This, in turn, will lay the foundation for considering more complex models in the future. Additional state variables required to model fracture using fracture mechanics concepts are identified. Subsequently, appropriate stored energy and dissipation functions, which lead to Griffith's theory, are formulated. Once the stored energy and dissipation functions are formulated, Hamilton's principle is discretized in time to lead to an optimization problem at each time step. The solution of the optimization problem supplies with the states at the end of the time step. This results in a sound theory as well as an efficient, robust and stable numerical scheme for progressive collapse prediction, as supported by the examples.

1 INTRODUCTION

Prediction of progressive collapse of large scale buildings due to natural or man-made extreme events is a major challenge in structural engineering. The main challenge stems from the various complex and sudden phenomena that structures experience during collapse. Those often lead to the collapse of the analysis prior to the actual analysis of collapse. With theory and tools for Progressive Collapse Prediction (PCP), deficiencies in the common practice of structural design, in the context of progressive collapse, could be identified without having to wait for the next extreme event to occur. With such theory and tools, the efficiency of existing design strategies for progressive collapse prevention (e.g. [1] and references therein) could be rigorously assessed, and the development of new strategies and technologies could be addressed. In addition, those tools could be used in forensic engineering or for the design of demolition.

The progressive collapse of the Ronan Point apartment building (England, 1968) and the terrorist attacks on the Murrah building (Oklahoma, 1995) and the WTC (New-York city, 2001) revealed the drawbacks of the traditional philosophy behind the design of structures: Buildings are designed to withstand the expected loads with a given performance level, while their capacity to withstand collapse due to extreme events remains unknown. This recognition has led to the new field of PCP in structural engineering. This field addresses the modeling and simulation of buildings up to the prediction of total collapse, where a progressive creation of "rubble" of structural mass is expected. This can be initiated by a rather local damage in a limited number of structural components. This local damage eventually causes a sequential failure of additional components, or a chain reaction, up to collapse. Several phases of behavior can be identified during the progress of collapse. These are elastic behavior, plastic behavior, stiffness and strength degradation, buckling and other geometric nonlinear phenomena, fracture, detachment of objects from the structure and impact or contact of structural elements with each other.

Pretlov et al. [2] pointed out that static analysis cannot capture important effects in progressive collapse. This statement has been verified in numerous occasions (e.g. [3, 4] and references therein). Hence, a dynamic approach should be considered. Here, the modeling for prediction of progressive collapse can be done at several levels. At the finest level, one can adopt micro-modeling, where each of the structural components (beams, columns, etc.) is modeled by a large number of solid elements. The Finite Elements Method (e.g. [5]) or the Distinct Element Method (e.g. [6]) have been adopted in that context. At the other limit, macro-modeling of large structural systems, each story or even the whole structure can be used (e.g. [7, 8]). Recently, an intermediate approach seems to gain attention in the context of PCP. This approach makes use of macro-modeling of different structural components (e.g. [3, 9, 10, 11 ,12 ,13 ,14]). It combines advantages from the two previous approaches as it is general enough to be used for a large spectrum of types of buildings, collapse modes and extreme events, while is potentially feasible for large scale structures. Another advanced approach combines various scales of elements and is based on multibody models [15]. This efficient approach was used for the simulation of collapse considering uncertainty, where a large number of deterministic analyses is required.

A crucial issue in most approaches presented above is the time integration schemes they adopt. The theoretical basis of those methods cannot provide answers regarding the existence or uniqueness of the solutions. Those may be very important in PCP as the complex behavior may lead to bifurcations where more than a single solution may exist. In addition, those numerical schemes require very small time steps. This is due to the sudden changes in the response of structures expected when fracture or contact occur. In case where those numerical schemes do converge to a solution, it is also not clear whether it is the true physical solution of the problem. If the problem does possess bifurcations, it is not clear what solution those schemes would follow. Additionally, no approach seems to efficiently cover all stages of progressive collapse and enable a feasible prediction for large scale structures.

A new approach for nonlinear dynamic structural analysis, namely the Mixed Lagrangian Formulation (MLF), has recently been proposed [16]. MLF was originally developed for the analysis of elastic-plastic response while considering geometric nonlinearity. This approach lays on a sound theory that may enable the investigation of existence and uniqueness of solutions. It is based on time discretization of Hamilton's principle [17]. Hence, the computation of the response quantities in each time step reduces to the solution of an optimization problem. This weak formulation in time leads to a very stable and accurate numerical scheme that allows for large time step sizes, while allowing for sharp changes in its variables. It also requires a small number of iterations within each time step. In much similarity to the generalized standard material framework [18], MLF is also based on two scalar functions: The stored energy function and the dissipation function.

MLF has been modified to enable an efficient analysis of large scale 3D buildings [19]. It was shown to scale very well with the size of the system analyzed. The theory of MLF and the numerical tool have been successfully extended to account for contact analysis by a carefull formulation of an appropriate stored energy function [20]. The capabilities of this framework have been also extended to account for strength degradation and fracture [21]. This was achieved, however, by somewhat deviating from the rigorous MLF and formulating a new hybrid implicit-explicit approach. MLF can potentially present a unified approach with a strong theoretical background that accounts for all stages of collapse. A more unified approach to include fracture in MLF, which is the aim of this paper, is the missing part of this puzzle.

Development of such a strong theory that includes all stages of collapse in a unified manner would possibly enable finding the answers to some very important questions regarding existence of solutions, their uniqueness, and the sensitivity to perturbations. In addition, the numerical schemes stemming from such theory could be provided with assurance regarding their convergence and the quality of their numerical solutions. Those numerical simulation tools are expected to be efficient, robust and stable while efficiently analyzing large scale structures for all stages of collapse.

The purpose of this paper is to lay the foundations for accounting for fracture in MLF. The analysis of large scale structures in all stages of collapse requires a focus on the scale of the structural elements (beams, columns, etc.). Thus, macro-modeling is used to avoid infeasible computational effort. In this paper, a uni-dimensional brittle element is formulated. This lays the foundations to account for fracture in MLF. Formulations of more complex macro-elements and behavior could then follow, in future research. For that purpose, additional state variables are first identified and added to the formulation. In turn, appropriate Lagrangian and Dissipation functions are formulated. Those are then used with a discretized version of Hamilton's principal to result an optimization problem in each time step. The solution of the optimization problem leads to the values of the state variables at the end of the time step.

2 PROPOSED FORMULATION

In this section it will be shown that appropriate Lagrangian and Dissipation functions could be formulated such that upon their use with the Euler-Lagrange equations, the known governing equations could be attained. The proposed Lagrangian and Dissipation functions would be used in the next section to form a robust numerical scheme. In order to present the concept of the proposed formulation the simplest case of a SDOF system with equal damage in tension and compression will be considered first. More general cases will then follow.

As discussed above, macro-modeling is used to avoid infeasible computational effort. At this stage of research, a uni-dimensional brittle element is formulated to lay the foundations to account for fracture in MLF. Being an energy based approach, MLF could strongly benefit from adopting energy based criteria for fracture. A well-known criterion for fracture of brittle materials, for example, is based on Griffith's theory (e.g. [22, 23]). This criterion states that a crack would propagate if the energy to be released by the incremental growth of the crack, or energy release rate, is larger than the surface energy of the material. This criterion is incorporated to MLF by adopting the crack area as an additional state variable in MLF. In turn, appropriate Lagrangian and Dissipation functions are carefully formulated. It should be noted that as the purpose of this paper is to lay the foundations for incorporating fracture and damage mechanics concepts in MLF, Griffith's theory is applied here to model damage in both tension and compression.

2.1 SDOF system with equal damage in tension and compression

In order to account for fracture, this section makes use of a uni-dimensional macro-element whose stiffness in both tension and compression depends on a "crack area" variable, *a*. Modifications will be done in the following sections to account for different behavior in tension and compression and MDOF systems.

Let us consider the SDOF system presented in Figure 1. It is comprised of a mass, *m*, a dashpot having a damping coefficient *c* and a spring whose stiffness *k*(*a*) depends on a "crack area" variable, *a*, in an appropriate manner. Let us also assume that the evolution of the crack propagation obeys Griffith's theory. The aim of this section is to formulate appropriate Lagrangian and Dissipation function such that upon their substitution to Euler-Lagrange equations one could attain the known governing equations (the equilibrium equation and an equation to reflect Griffith's theory)

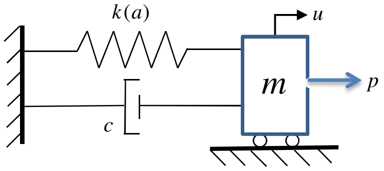

Figure 1: SDOF system with equal damage in tension and compression.

The proposed Lagrangian and Dissipation functions take the form:

$$L(u,\dot{u},a)=\frac{1}{2}m\dot{u}^2-\frac{1}{2}\cdot k(a)\cdot u^2+p^Tu-g(a) \tag{1}$$

$$\bar{\varphi}(\dot{u},\dot{a})=\frac{1}{2}c\dot{u}^2+\varphi(\dot{a})+2\gamma\dot{a} \tag{2}$$

Where L is the Lagrangian function, $\bar{\varphi}$ is the Dissipation function, *m* is the mass of the system, *c* is the damping coefficient of the dashpot, *k*(*a*) is the stiffness of the spring , *a* is the fracture area or damage parameter, *u*(*t*) is the displacement of the mass, γ is the surface energy, *p*(*t*) is the external force exerted on the mass, *t* is time, a dot represents a derivative w.r.t time and $\varphi(\cdot)$ and $g(\cdot)$ convex index functions. Figure 2a presents the function $g(\cdot)$ and Figure 2c presents the function $\varphi(\cdot)$. In these figures a_0 is the total cross section area. Their derivatives $\partial g(a)/\partial a$ and $\partial\varphi(\dot{a})/\partial\dot{a}$ are presented in Figures 2b and 2d, respectively. Those will be used later on. As can be seen, the function $g(\cdot)$ is zero for values of $a<a_0$ and can take any positive value when $a=a_0$. This will later lead to a constraint on a such that $a\leq a_0$. The function $\varphi(\cdot)$, on the other hand, is assigned with a zero value for $\dot{a}>0$ and can take any positive value when $\dot{a}=0$. This will be required for controlling the propagation of fracture.

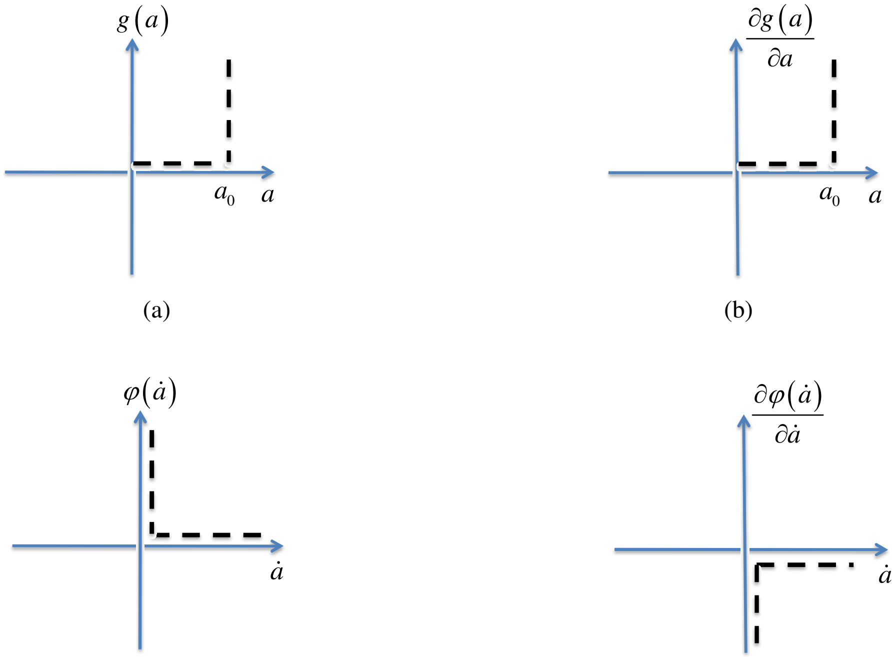

(a) (b)

(c) (d)

Figure 2: Index functions for the SDOF system with equal damage in tension and compression.

For the problem at hand, with both the displacement and the crack area as state variables, the Euler-Lagrange equations in terms of the Lagrangian and Dissipation functions are given as follows:

$$\frac{d}{dt}\left(\frac{\partial L}{\partial\dot{u}}\right)-\frac{\partial L}{\partial u}+\frac{\partial\bar{\varphi}}{\partial\dot{u}}=0 \tag{3}$$

$$\frac{d}{dt}\left(\frac{\partial L}{\partial\dot{a}}\right)-\frac{\partial L}{\partial a}+\frac{\partial\bar{\varphi}}{\partial\dot{a}}=0 \tag{4}$$

Upon substitution of the proposed Lagrangian and Dissipation functions to the first of Euler-Lagrange equations (Equation 3) one could attain the first governing equation as follows:

$$m\ddot{u}+k(a)\cdot u+c\dot{u}=p \tag{5}$$

This equation is, obviously, the equation of motion of the system. Substitution of the proposed Lagrangian and Dissipation functions to the second of Euler-Lagrange equations (Equation 4) leads to:

$$\frac{1}{2}\frac{\partial k(a)}{\partial a}u^2+\frac{\partial\varphi(\dot{a})}{\partial\dot{a}}+\frac{\partial g(a)}{\partial a}+2\gamma=0 \tag{6}$$

This equation could be brought to the form:

$$-\frac{\partial \Pi}{\partial a}-\frac{\partial \varphi(\dot{a})}{\partial \dot{a}}-\frac{\partial g(a)}{\partial a}=2\gamma \tag{7}$$

where $\Pi = U_E - W$, U_E is the elastic energy and W is the work performed by the applied loads. That is, $-\Pi$ is the complementary energy. This equation controls the crack propagation. It is, actually, equivalent to Griffiths theory where in order to increase the length of the crack the negative of the derivative of the potential energy, $\Pi = U_E - W$, w.r.t the crack length, should be equal to 2γ as will now be demonstrated.

Let us first consider the case where $a<a_0$. In this case, as can be seen from Figure 2b, a value of zero is assigned to $\partial g(a)/\partial a$. Hence, the value of $\partial\varphi(\dot{a})/\partial\dot{a}$ (from Equation 7) depends on the value of $-\partial\Pi/\partial a$ as well as on the value of 2γ. As can be seen by Equation 7, when $-\partial\Pi/\partial a = 2\gamma$ (and $a<a_0$) a value of zero is assigned to $\partial\varphi(\dot{a})/\partial\dot{a}$. Hence, from Figure 2d, $\dot{a}$ can be equal or larger than zero and fracture can take place. If, on the contrary, $-\partial\Pi/\partial a < 2\gamma$ (and $a<a_0$) a negative value is required for $\partial\varphi(\dot{a})/\partial\dot{a}$ so as to satisfy Equation 7. Hence, from Figure 2d, $\dot{a}=0$ and fracture cannot propagate. The case where $-\partial\Pi/\partial a > 2\gamma$ (and $a<a_0$) cannot be attained since in that case fracture already would have occurred earlier.

In the case where $a=a_0$ the spring is fully fractured and fracture can no longer propagate. This is accounted for in the formulation by using the function $g(a)$ that penalizes values of a larger than a_0. This is reflected in Equation 7 as $\partial g(a)/\partial a$ can take any non-negative value (Figure 2b) while $\partial\varphi(\dot{a})/\partial\dot{a}$ can be assigned with any non-positive value. Hence, Equation 7 indicates that fracture can no longer propagate. In this case, the spring loses its stiffness. Although not necessary, the spring could be removed manually at the end of the time step where a reached a_0. Note that fracture (or damage) evolution is enabled by considering the term $\varphi(\cdot)$. Appearing in the Dissipation function, this term leads to an irreversible process. Hence, fracture (or damage) that is created by increase of area crack cannot reduce even if the force is reversed. That is, the crack area variable can only increase.

2.2 SDOF system with different damage in tension and compression

The model presented in the previous section is now extended to account for different behavior in tension and in compression. For that purpose, a tension-only element and a compression-only element are introduced. The former can take only tension forces when the relative displacement at its edges is zero while its internal force is zero when the relative displacement is negative (i.e. the element is shortens). The latter can take only compression forces when the relative displacement at its edges is zero while its internal force is zero when the relative displacement is positive (i.e. the element elongates). The assembly of the system is presented in Figure 3. It is comprised of a mass, a dashpot and two springs in parallel. The first spring is connected in series to a tension-only element while the second spring is connected in series to a compression-only element. Thus, different behavior could be modeled for tension and compression. Both springs are assumed to depend on “crack area” or damage variables. Although Griffith’s theory was originally proposed for the propagation of cracks due to tension, both “crack area” variables in tension and in compression are assumed here to evolve obeying Griffith’s theory.

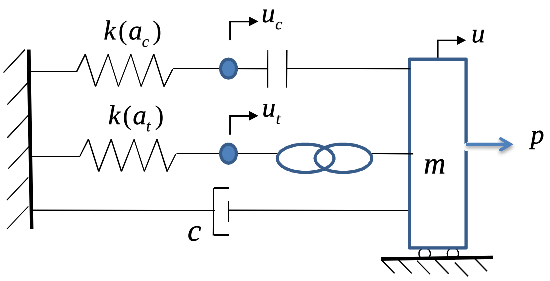

Figure 3: SDOF system with different damage in tension and compression.

The proposed Lagrangian and Dissipation functions take the form:

$$\begin{aligned} L &= \frac{1}{2}m\dot{u}^2 - \frac{1}{2}k_t(a_t)u_t^2 - \frac{1}{2}k_c(a_c)u_c^2 - g(a_t) - g(a_c) - \eta_t(u-u_t) - \eta_c(u-u_c) + pu \\ \varphi &= \frac{1}{2}c\dot{u}^2 + \varphi(\dot{a}_t) + 2\gamma_t\dot{a}_t + \varphi(\dot{a}_c) + 2\gamma_c\dot{a}_c \end{aligned} \tag{8}$$

where the subscript *t* represents variables related to the tension-only system, the subscript *c* represents variables related to the compression-only system, and the convex functions η_t and η_c are presented in Figure 4 with their partial derivatives w.r.t their arguments. Those functions would later lead to the tension-only and compression-only behavior.

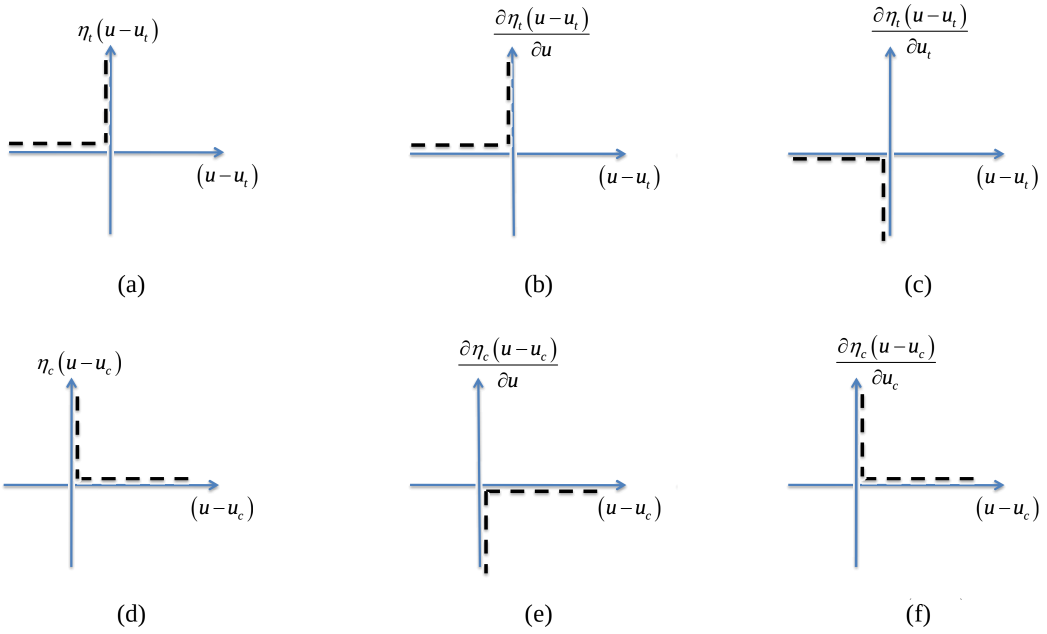

(a) (b) (c)

(d) (e) (f)

Figure 4: Index functions for the SDOF system with different damage in tension and compression.

For the problem at hand, with the displacements u, u_t and u_c, as well as the “crack area” variables a_t and a_c, as state variables, the Euler-Lagrange equations are given as follows:

$$\begin{cases} u: & m\ddot{u}+\dfrac{\partial\eta_t\left(u-u_t\right)}{\partial u}+\dfrac{\partial\eta_c\left(u-u_c\right)}{\partial u}+c\dot{u}=p \\ u_t: & k_t\left(a_t\right)u_t+\dfrac{\partial\eta_t\left(u-u_t\right)}{\partial u_t}=0 \\ u_c: & k_c\left(a_c\right)u_c+\dfrac{\partial\eta_c\left(u-u_c\right)}{\partial u_c}=0 \\ a_t: & \dfrac{1}{2}\dfrac{\partial k_t\left(a_t\right)}{\partial a_t}u_t^2+\dfrac{\partial g\left(a_t\right)}{\partial a_t}+\dfrac{\partial\varphi\left(\dot{a}_t\right)}{\partial\dot{a}_t}+2\gamma_t=0 \;\rightarrow\; -\dfrac{1}{2}\dfrac{\partial k_t\left(a_t\right)}{\partial a_t}u_t^2-\dfrac{\partial g\left(a_t\right)}{\partial a_t}-\dfrac{\partial\varphi\left(\dot{a}_t\right)}{\partial\dot{a}_t}=2\gamma_t \\ a_c: & \dfrac{1}{2}\dfrac{\partial k_c\left(a_c\right)}{\partial a_c}u_c^2+\dfrac{\partial g\left(a_c\right)}{\partial a_c}+\dfrac{\partial\varphi\left(\dot{a}_c\right)}{\partial\dot{a}_c}+2\gamma_c=0 \;\rightarrow\; -\dfrac{1}{2}\dfrac{\partial k_c\left(a_t\right)}{\partial a_c}u_c^2-\dfrac{\partial g\left(a_c\right)}{\partial a_c}-\dfrac{\partial\varphi\left(\dot{a}_c\right)}{\partial\dot{a}_c}=2\gamma_c \end{cases} \tag{9}$$

Here the first equation is the equation of motion while the fourth and fifth equations dictate the evolution of the "crack area" variables for the tension and compression springs, respectively. The second and third equations enforce tension-only and compression-only behavior on the springs connected to the tension-only and compression-only elements, respectively, as will now be demonstrated.

Let us first note that $\partial\eta_t\left(u-u_t\right)/\partial u=-\partial\eta_t\left(u-u_t\right)/\partial u_t$. Hence, from the second of Equation 9 one could write $\partial\eta_t\left(u-u_t\right)/\partial u=k_t\left(a_t\right)u_t$. That is, in the first of Equation 9 one could replace $\partial\eta_t\left(u-u_t\right)/\partial u$ with $k_t\left(a_t\right)u_t$. Let us now focus on the second of Equation 9 with Figure 4c. As can be seen from Figure 4c, when $u<u_t$ a zero value is assigned to $\partial\eta_t\left(u-u_t\right)/\partial u_t$. Hence, from the second of Equation 9, $k_t\left(a_t\right)u_t=0$ and the spring force is zero. It could also be seen that in that case $u_t=0$ thus $u<0$. If, on the other hand, $u=u_t$, a non-positive value is assigned to $\partial\eta_t\left(u-u_t\right)/\partial u_t$. Hence, from the second of Equation 9, $k_t\left(a_t\right)u_t\geq 0$ and the spring force is non-negative. It could also be seen that in that case $u_t\geq 0$. A similar argument holds for the compression only system.

2.3 MDOF system with contact

The formulation of the previous section is now generalized to MDOF systems. Here, the Lagrangian and Dissipation functions are formulated in terms of vectors representing the displacements of the various degrees-of-freedom (DOFs), $\boldsymbol{u}$, the displacements of the tension-only and compression-only elements, $\boldsymbol{u}_t$ and $\boldsymbol{u}_c$, and the "crack area" variables for the tension-only and compression-only systems, $\boldsymbol{a}_t$ and $\boldsymbol{a}_c$, respectively. The proposed Lagrangian and Dissipation functions take the form:

$$\begin{aligned} L(\boldsymbol{u},\dot{\boldsymbol{u}},\boldsymbol{a}) &= \frac{1}{2}\dot{\boldsymbol{u}}^T\mathbf{M}\dot{\boldsymbol{u}}-\frac{1}{2}\boldsymbol{u}_t^T\mathbf{K}_t(\boldsymbol{a}_t)\boldsymbol{u}_t-\frac{1}{2}\boldsymbol{u}_c^T\mathbf{K}_c(\boldsymbol{a}_c)\boldsymbol{u}_c \\ &\quad -g(\boldsymbol{a}_t)-g(\boldsymbol{a}_c)-\eta\left(\boldsymbol{B}^T\boldsymbol{u}-\boldsymbol{u}_t\right)-\eta\left(\boldsymbol{B}^T\boldsymbol{u}-\boldsymbol{u}_c\right)+\boldsymbol{p}^T\boldsymbol{u} \end{aligned} \tag{10}$$

$$\varphi(\dot{\boldsymbol{u}},\dot{\boldsymbol{a}})=\frac{1}{2}\dot{\boldsymbol{u}}^T\mathbf{C}\dot{\boldsymbol{u}}+\varphi\left(\dot{\boldsymbol{a}}_t\right)+2\boldsymbol{\gamma}_t^T\dot{\boldsymbol{a}}+\varphi\left(\dot{\boldsymbol{a}}_c\right)+2\boldsymbol{\gamma}_t^T\dot{\boldsymbol{a}} \tag{11}$$

where $\mathbf{M}$ is the mass matrix, $\mathbf{K}_t$ and $\mathbf{K}_c$ are the stiffness matrices of the tension and the compression springs in their local coordinate systems, respectively, $\boldsymbol{B}^T$ is the compatibility matrix , **C** is the damping matrix , **p** is the external force vector on the DOFs , γ_t and γ_c are the surface energy vectors (energy threshold values for damage propagation) for the tension and the compression respectively, The scalar functions g, η and φ were defined in previous sections for scalar arguments. In the case of vector arguments the sum of the values attained for each entry of the vector as the argument is taken (e.g. $g(\boldsymbol{a}_t) = g(a_{t,1})+g(a_{t,2})+\cdots+g(a_{t,n})$).

It should be noted that the displacements of the DOFs are sufficient to define the state of all masses. The mass matrix, the damping matrix and the external force vector are defined in this coordinate system. Displacements of additional DOFs, however, are required to define the state of the system. Those are the displacements of the tension-only and compression-only elements. The stiffness matrices are defined in this coordinate system. The functions η, required to account for tension-only and compression-only elements, compare displacements from the two different coordinate systems. Hence, the compatibility matrix, $\boldsymbol{B}^T$, transforms displacements from one coordinate system to the other, is required (can be seen in example 4.2).

As the displacements $\boldsymbol{u}$, $\boldsymbol{u}_t$ and $\boldsymbol{u}_c$, and the “crack area” variables $\boldsymbol{a}_t$ and $\boldsymbol{a}_c$, are adopted here as state variables, the Euler-Lagrange equations take the following form:

$$
\left\{
\begin{array}{ll}
\boldsymbol{u}: & \mathbf{M}\ddot{\boldsymbol{u}} + \dfrac{\partial \eta_t\left(\boldsymbol{B}^T\boldsymbol{u}-\boldsymbol{u}_t\right)}{\partial \boldsymbol{u}} + \dfrac{\partial \eta_c\left(\boldsymbol{B}^T\boldsymbol{u}-\boldsymbol{u}_c\right)}{\partial \boldsymbol{u}} + \mathbf{C}\dot{\boldsymbol{u}} = \boldsymbol{p} \\
\boldsymbol{u}_t: & \mathbf{K}_t(\boldsymbol{a}_t)\boldsymbol{u}_t + \dfrac{\partial \eta_t\left(\boldsymbol{B}^T\boldsymbol{u}-\boldsymbol{u}_t\right)}{\partial \boldsymbol{u}_t} = 0 \\
\boldsymbol{u}_c: & \mathbf{K}_c(\boldsymbol{a}_c)\boldsymbol{u}_c + \dfrac{\partial \eta_c\left(\boldsymbol{B}^T\boldsymbol{u}-\boldsymbol{u}_c\right)}{\partial \boldsymbol{u}_c} = 0 \\
\boldsymbol{a}_t: & \dfrac{1}{2}\boldsymbol{u}_t^T\dfrac{\partial \mathbf{K}_t(\boldsymbol{a}_t)}{\partial \boldsymbol{a}_t}\boldsymbol{u}_t + \dfrac{\partial g\left(\boldsymbol{a}_t\right)}{\partial \boldsymbol{a}_t} + \dfrac{\partial \varphi\left(\dot{\boldsymbol{a}}_t\right)}{\partial \dot{\boldsymbol{a}}_t} + 2\boldsymbol{\gamma}_t = 0 \\
\boldsymbol{a}_c: & \dfrac{1}{2}\boldsymbol{u}_c^T\dfrac{\partial \mathbf{K}_c(\boldsymbol{a}_c)}{\partial \boldsymbol{a}_c}\boldsymbol{u}_c + \dfrac{\partial g\left(\boldsymbol{a}_c\right)}{\partial \boldsymbol{a}_c} + \dfrac{\partial \varphi\left(\dot{\boldsymbol{a}}_c\right)}{\partial \dot{\boldsymbol{a}}_c} + 2\boldsymbol{\gamma}_c = 0
\end{array}
\right. \tag{12}
$$

As in the previous section, here the first equation is the equation of motion. The second and third equations enforce tension-only and compression-only behavior on the springs connected to the tension-only and compression-only elements, respectively. And the fourth and fifth equations dictate the evolution of the “crack area” variables for the tension and compression springs, respectively.

3 PROPOSED NUMERICAL SCHEME

In the previous section, appropriate Lagrangian and Dissipation functions have been formulated. It was shown that use of those functions with the Euler-Lagrange equations leads to the expected governing equations. Those include the equations of motion as well as the equations for the evolution of the crack area. The traditional approach would make use of advanced time discretization schemes to integrate those equations in time at their strong form. With those Lagrangian and Dissipation functions at hand, however, another approach could be taken using the weak form (in time). That is, those functions could be used with Hamilton’s principal. By discretizing the action integral in time, the value of the state variables at the end of the time step may be attained by finding a stationary point of a discrete functional.

In some cases, the stationary point is actually a minimum, hence, an optimization problem could be attained. This leads to a very robust numerical scheme that allows for sharp gradients of the state variables in time. The derivations to follow do not directly apply Hamilton's principal. For the case of an elastic-plastic behavior, however, it was shown [16] that those are equivalent to directly applying Hamilton's principal.

Let us first write Equations 12 at time ***i***+½ using the central difference approximation:

$$\begin{gathered}
\mathbf{M}\left(\frac{\boldsymbol{v}_{i+1}-\boldsymbol{v}_i}{h}\right)+\mathbf{C}\left(\frac{\boldsymbol{v}_{i+1}+\boldsymbol{v}_i}{2}\right)+\frac{1}{2}\left[\left.\frac{\partial\eta_t\left(\boldsymbol{B}^T\boldsymbol{u}-\boldsymbol{u}_t\right)}{\partial\boldsymbol{u}}\right|_{i+1}+\left.\frac{\partial\eta_t\left(\boldsymbol{B}^T\boldsymbol{u}-\boldsymbol{u}_t\right)}{\partial\boldsymbol{u}}\right|_{i}\right]\\
+\frac{1}{2}\left[\left.\frac{\partial\eta_c\left(\boldsymbol{B}^T\boldsymbol{u}-\boldsymbol{u}_c\right)}{\partial\boldsymbol{u}}\right|_{i+1}+\left.\frac{\partial\eta_c\left(\boldsymbol{B}^T\boldsymbol{u}-\boldsymbol{u}_c\right)}{\partial\boldsymbol{u}}\right|_{i}\right]-\frac{\boldsymbol{p}_{i+1}+\boldsymbol{p}_i}{2}=0\\
\frac{1}{2}\left[\mathbf{K}_t(\boldsymbol{a}_{t,i+1})\boldsymbol{u}_{t,i+1}+\mathbf{K}_t(\boldsymbol{a}_{t,i})\boldsymbol{u}_{t,i}\right]+\frac{1}{2}\left[\left.\frac{\partial\eta_t\left(\boldsymbol{B}^T\boldsymbol{u}-\boldsymbol{u}_t\right)}{\partial\boldsymbol{u}_t}\right|_{i+1}+\left.\frac{\partial\eta_t\left(\boldsymbol{B}^T\boldsymbol{u}-\boldsymbol{u}_t\right)}{\partial\boldsymbol{u}_t}\right|_{i}\right]=0\\
\frac{1}{2}\left[\mathbf{K}_c(\boldsymbol{a}_{c,i+1})\boldsymbol{u}_{c,i+1}+\mathbf{K}_c(\boldsymbol{a}_{c,i})\boldsymbol{u}_{c,i}\right]+\frac{1}{2}\left[\left.\frac{\partial\eta_c\left(\boldsymbol{B}^T\boldsymbol{u}-\boldsymbol{u}_c\right)}{\partial\boldsymbol{u}_c}\right|_{i+1}+\left.\frac{\partial\eta_c\left(\boldsymbol{B}^T\boldsymbol{u}-\boldsymbol{u}_c\right)}{\partial\boldsymbol{u}_c}\right|_{i}\right]=0\\
\frac{1}{2}\left[\frac{1}{2}\boldsymbol{u}_{t,i+1}^T\frac{\partial\mathbf{K}_t(\boldsymbol{a}_{t,i+1})}{\partial\boldsymbol{a}_{t,i+1}}\boldsymbol{u}_{t,i+1}+\frac{1}{2}\boldsymbol{u}_{t,i}^T\frac{\partial\mathbf{K}_t(\boldsymbol{a}_{t,i})}{\partial\boldsymbol{a}_{t,i}}\boldsymbol{u}_{t,i}\right]+\frac{1}{2}\left[\left.\frac{\partial g(\boldsymbol{a}_t)}{\partial\boldsymbol{a}_t}\right|_{i+1}+\left.\frac{\partial g(\boldsymbol{a}_t)}{\partial\boldsymbol{a}_t}\right|_{i}\right]+\frac{1}{2}\left[\left.\frac{\partial\varphi(\dot{\boldsymbol{a}}_t)}{\partial\dot{\boldsymbol{a}}_t}\right|_{i+1}+\left.\frac{\partial\varphi(\dot{\boldsymbol{a}}_t)}{\partial\dot{\boldsymbol{a}}_t}\right|_{i}\right]+2\boldsymbol{\gamma}_t=0\\
\frac{1}{2}\left[\frac{1}{2}\boldsymbol{u}_{c,i+1}^T\frac{\partial\mathbf{K}_c(\boldsymbol{a}_{c,i+1})}{\partial\boldsymbol{a}_{c,i+1}}\boldsymbol{u}_{c,i+1}+\frac{1}{2}\boldsymbol{u}_{c,i}^T\frac{\partial\mathbf{K}_c(\boldsymbol{a}_{c,i})}{\partial\boldsymbol{a}_{c,i}}\boldsymbol{u}_{c,i}\right]+\frac{1}{2}\left[\left.\frac{\partial g(\boldsymbol{a}_c)}{\partial\boldsymbol{a}_c}\right|_{i+1}+\left.\frac{\partial g(\boldsymbol{a}_c)}{\partial\boldsymbol{a}_c}\right|_{i}\right]+\frac{1}{2}\left[\left.\frac{\partial\varphi(\dot{\boldsymbol{a}}_c)}{\partial\dot{\boldsymbol{a}}_c}\right|_{i+1}+\left.\frac{\partial\varphi(\dot{\boldsymbol{a}}_c)}{\partial\dot{\boldsymbol{a}}_c}\right|_{i}\right]+2\boldsymbol{\gamma}_c=0
\end{gathered}\tag{13}$$

Using the approximation $\boldsymbol{u}_{j,i+1}=\boldsymbol{u}_{j,i}+\frac{h}{2}\left(\boldsymbol{v}_{j,i+1}+\boldsymbol{v}_{j,i}\right)$ one could obtain:

$$\begin{gathered}
\frac{1}{h}\mathbf{M}\boldsymbol{v}_{i+1}-\frac{1}{h}\mathbf{M}\boldsymbol{v}_i+\frac{1}{2}\mathbf{C}\boldsymbol{v}_{i+1}+\frac{1}{2}\mathbf{C}\boldsymbol{v}_i+\frac{1}{2}\left[\left.\frac{\partial\eta_t\left(\boldsymbol{B}^T\boldsymbol{u}-\boldsymbol{u}_t\right)}{\partial\boldsymbol{u}}\right|_{i+1}+\left.\frac{\partial\eta_t\left(\boldsymbol{B}^T\boldsymbol{u}-\boldsymbol{u}_t\right)}{\partial\boldsymbol{u}}\right|_{i}\right]\\
+\frac{1}{2}\left[\left.\frac{\partial\eta_c\left(\boldsymbol{B}^T\boldsymbol{u}-\boldsymbol{u}_c\right)}{\partial\boldsymbol{u}}\right|_{i+1}+\left.\frac{\partial\eta_c\left(\boldsymbol{B}^T\boldsymbol{u}-\boldsymbol{u}_c\right)}{\partial\boldsymbol{u}}\right|_{i}\right]-\frac{\boldsymbol{p}_{i+1}+\boldsymbol{p}_i}{2}=0\\
\frac{1}{2}\mathbf{K}_t(\boldsymbol{a}_{t,i+1})\boldsymbol{u}_{t,i}+\frac{h}{4}\mathbf{K}_t(\boldsymbol{a}_{t,i+1})\boldsymbol{v}_{t,i+1}+\frac{h}{4}\mathbf{K}_t(\boldsymbol{a}_{t,i+1})\boldsymbol{v}_{t,i}+\frac{1}{2}\mathbf{K}_t(\boldsymbol{a}_{t,i})\boldsymbol{u}_{t,i}+\frac{1}{2}\left[\left.\frac{\partial\eta_t\left(\boldsymbol{B}^T\boldsymbol{u}-\boldsymbol{u}_t\right)}{\partial\boldsymbol{u}_t}\right|_{i+1}+\left.\frac{\partial\eta_t\left(\boldsymbol{B}^T\boldsymbol{u}-\boldsymbol{u}_t\right)}{\partial\boldsymbol{u}_t}\right|_{i}\right]=0\\
\frac{1}{2}\mathbf{K}_c(\boldsymbol{a}_{c,i+1})\boldsymbol{u}_{c,i}+\frac{h}{4}\mathbf{K}_c(\boldsymbol{a}_{c,i+1})\boldsymbol{v}_{c,i+1}+\frac{h}{4}\mathbf{K}_c(\boldsymbol{a}_{c,i+1})\boldsymbol{v}_{c,i}+\frac{1}{2}\mathbf{K}_c(\boldsymbol{a}_{c,i})\boldsymbol{u}_{c,i}+\frac{1}{2}\left[\left.\frac{\partial\eta_c\left(\boldsymbol{B}^T\boldsymbol{u}-\boldsymbol{u}_c\right)}{\partial\boldsymbol{u}_c}\right|_{i+1}+\left.\frac{\partial\eta_c\left(\boldsymbol{B}^T\boldsymbol{u}-\boldsymbol{u}_c\right)}{\partial\boldsymbol{u}_c}\right|_{i}\right]=0\\
\frac{1}{2}\left[\frac{1}{2}\left(\boldsymbol{u}_{t,i}+\frac{h}{2}\left(\boldsymbol{v}_{t,i+1}+\boldsymbol{v}_{t,i}\right)\right)^T\frac{\partial\mathbf{K}_t(\boldsymbol{a}_{t,i+1})}{\partial\boldsymbol{a}_{t,i+1}}\left(\boldsymbol{u}_{t,i}+\frac{h}{2}\left(\boldsymbol{v}_{t,i+1}+\boldsymbol{v}_{t,i}\right)\right)+\frac{1}{2}\boldsymbol{u}_{t,i}^T\frac{\partial\mathbf{K}_t(\boldsymbol{a}_{t,i})}{\partial\boldsymbol{a}_{t,i}}\boldsymbol{u}_{t,i}\right]\\
+\frac{1}{2}\left[\left.\frac{\partial g(\boldsymbol{a}_t)}{\partial\boldsymbol{a}_t}\right|_{i+1}+\left.\frac{\partial g(\boldsymbol{a}_t)}{\partial\boldsymbol{a}_t}\right|_{i}\right]+\frac{1}{2}\left[\left.\frac{\partial\varphi(\dot{\boldsymbol{a}}_t)}{\partial\dot{\boldsymbol{a}}_t}\right|_{i+1}+\left.\frac{\partial\varphi(\dot{\boldsymbol{a}}_t)}{\partial\dot{\boldsymbol{a}}_t}\right|_{i}\right]+2\boldsymbol{\gamma}_t=0\\
\frac{1}{2}\left[\frac{1}{2}\left(\boldsymbol{u}_{c,i}+\frac{h}{2}\left(\boldsymbol{v}_{c,i+1}+\boldsymbol{v}_{c,i}\right)\right)^T\frac{\partial\mathbf{K}_c(\boldsymbol{a}_{c,i+1})}{\partial\boldsymbol{a}_{c,i+1}}\left(\boldsymbol{u}_{c,i}+\frac{h}{2}\left(\boldsymbol{v}_{c,i+1}+\boldsymbol{v}_{c,i}\right)\right)+\frac{1}{2}\boldsymbol{u}_{c,i}^T\frac{\partial\mathbf{K}_c(\boldsymbol{a}_{c,i})}{\partial\boldsymbol{a}_{c,i}}\boldsymbol{u}_{c,i}\right]\\
+\frac{1}{2}\left[\left.\frac{\partial g(\boldsymbol{a}_c)}{\partial\boldsymbol{a}_c}\right|_{i+1}+\left.\frac{\partial g(\boldsymbol{a}_c)}{\partial\boldsymbol{a}_c}\right|_{i}\right]+\frac{1}{2}\left[\left.\frac{\partial\varphi(\dot{\boldsymbol{a}}_c)}{\partial\dot{\boldsymbol{a}}_c}\right|_{i+1}+\left.\frac{\partial\varphi(\dot{\boldsymbol{a}}_c)}{\partial\dot{\boldsymbol{a}}_c}\right|_{i}\right]+2\boldsymbol{\gamma}_c=0
\end{gathered}\tag{14}$$

It could be shown that the set of equations 14 is equivalent to the stationarity conditions on the following potential function:

$$\begin{aligned}&\frac{1}{2h}\boldsymbol{v}_{i+1}^T\mathbf{M}\boldsymbol{v}_{i+1}+\frac{1}{4}\boldsymbol{v}_{i+1}^T\mathbf{C}\boldsymbol{v}_{i+1}-\frac{1}{h}\boldsymbol{v}_{i+1}^T\mathbf{M}\boldsymbol{v}_i-\frac{1}{2}\boldsymbol{v}_{i+1}\mathbf{M}\ddot{\boldsymbol{u}}_i-\frac{1}{2}\boldsymbol{v}_{i+1}^T\boldsymbol{p}_{i+1}+\frac{1}{2h}\boldsymbol{u}_{t,i}^T\mathbf{K}_t(\boldsymbol{a}_{t,i+1})\boldsymbol{u}_{t,i}+\frac{1}{2}\boldsymbol{v}_{t,i+1}^T\mathbf{K}_t(\boldsymbol{a}_{t,i+1})\left(\boldsymbol{u}_{t,i}+\frac{h}{4}\boldsymbol{v}_{t,i+1}+\frac{h}{2}\boldsymbol{v}_{t,i}\right)+\\&\frac{1}{2}\boldsymbol{v}_{t,i}^T\mathbf{K}_t(\boldsymbol{a}_{t,i+1})\left(\boldsymbol{u}_{t,i}+\frac{h}{4}\boldsymbol{v}_{t,i}\right)+\frac{1}{2h}\boldsymbol{u}_{c,i}^T\mathbf{K}_c(\boldsymbol{a}_{c,i+1})\boldsymbol{u}_{c,i}+\frac{1}{2}\boldsymbol{v}_{c,i+1}^T\mathbf{K}_t(\boldsymbol{a}_{c,i+1})\left(\boldsymbol{u}_{c,i}+\frac{h}{4}\boldsymbol{v}_{c,i+1}+\frac{h}{2}\boldsymbol{v}_{c,i}\right)+\\&\frac{1}{2}\boldsymbol{v}_{c,i}^T\mathbf{K}_c(\boldsymbol{a}_{c,i+1})\left(\boldsymbol{u}_{c,i}+\frac{h}{4}\boldsymbol{v}_{c,i}\right)+\dot{\boldsymbol{a}}_{t,i+1}^T\boldsymbol{\gamma}_t+\dot{\boldsymbol{a}}_{c,i+1}^T\boldsymbol{\gamma}_c+\frac{1}{h}\left(\eta_t\left(\boldsymbol{B}^T\boldsymbol{u}-\boldsymbol{u}_t\right)\Big|_{i+1}+\eta_c\left(\boldsymbol{B}^T\boldsymbol{u}-\boldsymbol{u}_c\right)\Big|_{i+1}+g(\boldsymbol{a}_t)\big|_{i+1}+g(\boldsymbol{a}_c)\big|_{i+1}\right)+\frac{1}{2}\left(\varphi(\dot{\boldsymbol{a}}_t)\big|_{i+1}+\varphi(\dot{\boldsymbol{a}}_c)\big|_{i+1}\right)\end{aligned}\tag{15}$$

Or, equivalently, to the following constrained optimization problem:

$$\begin{aligned}\min\quad&\frac{1}{2h}\boldsymbol{v}_{i+1}^T\mathbf{M}\boldsymbol{v}_{i+1}+\frac{1}{4}\boldsymbol{v}_{i+1}^T\mathbf{C}\boldsymbol{v}_{i+1}-\frac{1}{h}\boldsymbol{v}_{i+1}^T\mathbf{M}\boldsymbol{v}_i-\frac{1}{2}\boldsymbol{v}_{i+1}\mathbf{M}\ddot{\boldsymbol{u}}_i-\frac{1}{2}\boldsymbol{v}_{i+1}^T\boldsymbol{p}_{i+1}+\\&\frac{1}{2}\boldsymbol{v}_{c,i}^T\mathbf{K}_c(\boldsymbol{a}_{c,i+1})\left(\boldsymbol{u}_{c,i}+\frac{h}{4}\boldsymbol{v}_{c,i}\right)+\frac{1}{2h}\boldsymbol{u}_{c,i}^T\mathbf{K}_c(\boldsymbol{a}_{c,i+1})\boldsymbol{u}_{c,i}+\frac{1}{2}\boldsymbol{v}_{c,i+1}^T\mathbf{K}_c(\boldsymbol{a}_{c,i+1})\left(\boldsymbol{u}_{c,i}+\frac{h}{4}\boldsymbol{v}_{c,i+1}+\frac{h}{2}\boldsymbol{v}_{c,i}\right)+\dot{\boldsymbol{a}}_{c,i+1}^T\boldsymbol{\gamma}_c+\\&\frac{1}{2}\boldsymbol{v}_{t,i}^T\mathbf{K}_t(\boldsymbol{a}_{t,i+1})\left(\boldsymbol{u}_{t,i}+\frac{h}{4}\boldsymbol{v}_{t,i}\right)+\frac{1}{2h}\boldsymbol{u}_{t,i}^T\mathbf{K}_t(\boldsymbol{a}_{t,i+1})\boldsymbol{u}_{t,i}+\frac{1}{2}\boldsymbol{v}_{t,i+1}^T\mathbf{K}_t(\boldsymbol{a}_{t,i+1})\left(\boldsymbol{u}_{t,i}+\frac{h}{4}\boldsymbol{v}_{t,i+1}+\frac{h}{2}\boldsymbol{v}_{t,i}\right)+\dot{\boldsymbol{a}}_{t,i+1}^T\boldsymbol{\gamma}_t\\ s.t\quad&\\&-\dot{\boldsymbol{a}}_{t,i+1}\le 0\\&\dot{\boldsymbol{a}}_{t,i+1}\le\max\left(\frac{2}{h}\left(\boldsymbol{a}_0-\boldsymbol{a}_{t,i}\right)-\dot{\boldsymbol{a}}_{t,i},0\right)\\&-\dot{\boldsymbol{a}}_{c,i+1}\le 0\\&\dot{\boldsymbol{a}}_{c,i+1}\le\max\left(\frac{2}{h}\left(\boldsymbol{a}_0-\boldsymbol{a}_{c,i}\right)-\dot{\boldsymbol{a}}_{c,i},0\right)\\&\boldsymbol{B}^T\left(\boldsymbol{u}_{i+1}\right)-\boldsymbol{u}_{c,i+1}\ge 0\rightarrow\left(\boldsymbol{v}_{c,i+1}-\boldsymbol{B}^T\boldsymbol{v}_{i+1}\right)\le\left[\frac{2}{h}\left(\boldsymbol{B}^T\boldsymbol{u}_i-\boldsymbol{u}_{c,i}\right)+\left(\boldsymbol{B}^T\boldsymbol{v}_i-\boldsymbol{v}_{c,i}\right)\right]\\&\boldsymbol{B}^T\left(\boldsymbol{u}_{i+1}\right)-\boldsymbol{u}_{t,i+1}\le 0\rightarrow\left(\boldsymbol{B}^T\boldsymbol{v}_{i+1}-\boldsymbol{v}_{t,i+1}\right)\le\left[\frac{2}{h}\left(\boldsymbol{u}_{t,i}-\boldsymbol{B}^T\boldsymbol{u}_i\right)+\left(\boldsymbol{v}_{t,i}-\boldsymbol{B}^T\boldsymbol{v}_i\right)\right]\end{aligned}\tag{16}$$

The solution of the optimization problem 16 in each time step results the values of the state variables at the end of the time step.

It should be noted that the attained optimization problem may not be convex thus a single local minimum is not guaranteed. Hence, in case of bifurcations the question "which minimum is the one reflecting the behavior of the physical system?" may arise. Here, the insight from the physics of the problem is accounted for. Griffith's theory is based on the partial derivatives of energy quantities w.r.t the crack area. That is, Griffith's theory sets a criterion that is based on first order conditions at the current state. Hence, the correct solution is the local minimum near the current state. For the purpose of finding the solution, a gradient based approach is to be adopted. In addition, the state at the beginning of each time step should be adopted as the initial guess for the solution of the optimization problem at that time step. Moreover, a relatively small limit should be adopted to the change in the state vector in each iteration of the optimization problem.

4 EXAMPLES

4.1 SDOF system

This example considers the SDOF system presented in Figure 3. The tension spring stiffness is taken here as $k_t(a_t)=k_{0t}(a_0-a_t)^n$ while the compression spring stiffness is taken here as $k_c(a_c)=k_{0c}(a_0-a_c)^n$. The following values are assigned to the various parameters: $m=1$, $k_{0t}=k_{0c}=2000$, $a_0=1.2$, $2\gamma_t=2\gamma_c=80$, $c=0$. No external load was considered, however an initial velocity of 15 was accounted for. The example was executed for various values of *n*, namely *n=1, 2, 3, 4, 5, 10* and *20*, to explore the behavior and the stability of the algorithm. The problem is solved for a time increment of 10^{-3} and the results are summarized in Figures 5-7. Figure 5a presents the displacements of the system with various values of the exponent versus time while Figure 5b presents the velocities. The crack area and tension stiffness versus time are presented in Figures 6a and 6b, respectively. Finally, Figure 7a presents the force-displacement relation for various values of the exponent while Figure 7b zooms on the first 1.5 time units.

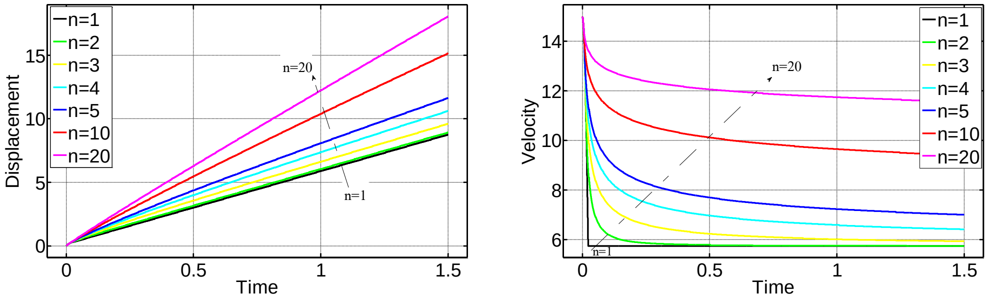

(a) (b)

Figure 5: (a) Displacement and (b) Velocity of the mass versus time.

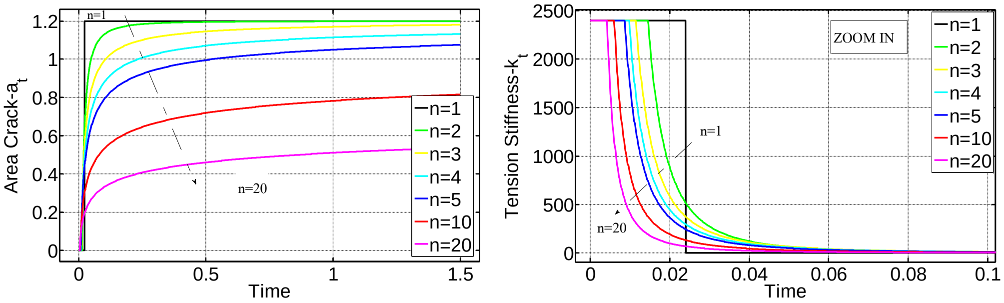

(a) (b)

Figure 6: (a) Crack Area in tension a_t and (b) “zoom in” of Tension Stiffness k_t versus time.

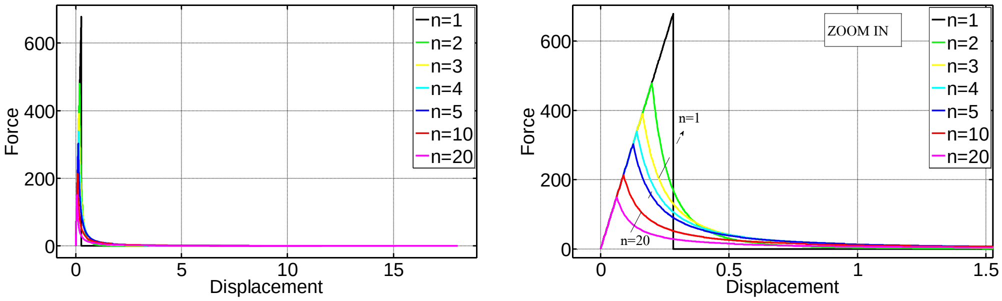

(a) (b)

Figure 7: (a) Force-Displacement and (b) “zoom in”.

It should be noted that, as expected, the area under each of the force-displacement graphs (Figure 7), that represents the spring energy, approaches $2\gamma_t \cdot a_0 = 80\cdot 1.2 = 96$ as the crack area approaches a_0.

4.2 MDOF system

This example considers the 2 DOF system presented in Figure 8. This system is comprised of a rigid beam of mass *m*=1 and moment of inertia *I*=1 mounted on 7 systems of springs. The characteristics of all spring systems are identical. Those include a tension spring of stiffness

$k_t(a_t)=k_{0t}(a_0 - a_t)$ and surface energy $2\gamma_t$, a compression spring of stiffness $k_c(a_c)=k_{0c}(a_0 - a_c)$ and surface energy $2\gamma_c$, and a linear dashpot with a damping coefficient c. Here, $k_{0t}=k_{0c}=2000$, $a_0=1.2$, $2\gamma_t=2\gamma_c=80$, $c=0$ and $l=0.2$. No external load was considered, however an initial angular velocity of 30 was accounted for.

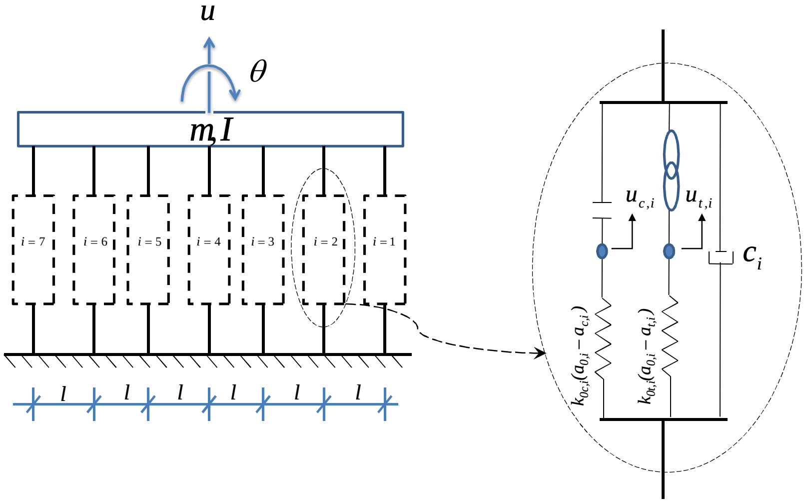

Figure 8: Two DOF system for Example 2.

The stiffness matrices for the tension-only and compression-only systems are given by:

$$\mathbf{K}_t = \begin{bmatrix} 2000\left(1.2 - a_{t,1}\right) & & 0 \\ & \ddots & \\ 0 & & 2000\left(1.2 - a_{t,7}\right) \end{bmatrix}$$

$$\mathbf{K}_c = \begin{bmatrix} 2000\left(1.2 - a_{c,1}\right) & & 0 \\ & \ddots & \\ 0 & & 2000\left(1.2 - a_{c,7}\right) \end{bmatrix}$$

Note that while those matrices look similar, they differ in the crack area variables considered. The mass and damping matrices, as well as the compatibility matrix, $\boldsymbol{B}^T$, are given by:

$$\mathbf{M} = \mathbf{I}_{2x2}$$

$$\mathbf{C} = \mathbf{0}_{2x2}$$

$$\mathbf{B}^T = \begin{bmatrix} 1 & 1 & 1 & 1 & 1 & 1 & 1 \\ -0.6 & -0.4 & -0.2 & 0 & 0.2 & 0.4 & 0.6 \end{bmatrix}^T$$

The problem is first solved for a time increment of 10^{-3} and the results are summarized in Figures 9-12. Figure 9a presents the displacements of the DOFs while Figure 9b presents their velocities. Also presented (Figures 10a and 10b, respectively) are the displacements and velocities of the connections of the springs to the beam. In addition, the tension and compression stiffnesses of the various systems are presented versus time in Figures 11a and 11b, respectively. As can be seen, during the first quarter of cycle, two pairs of springs are fractured, two in tension and two in compression. As some energy was required to result fracture, it was dissipated from the system. Hence, the total energy of the system reduced to a level such that when the direction of the angle was reversed, the potential energy was not sufficient to result fracture. Thus, the resulted system behaves asymmetrically with reduced stiffness for rotation in one direction and full stiffness in the other. This is also reflected from Figure 10a where the time required to complete a half cycle is different in each direction.

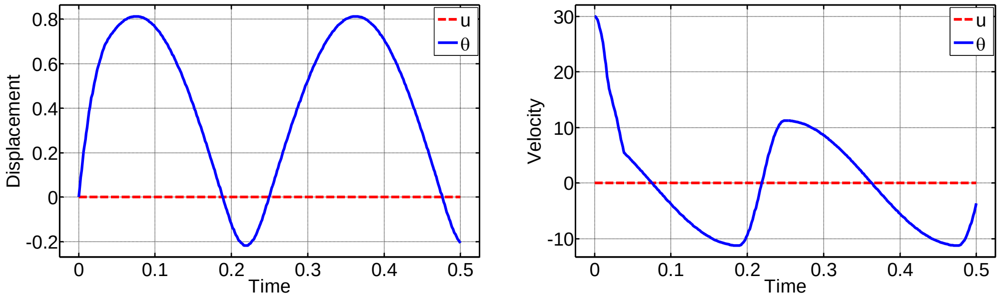

(b) (b)

Figure 9: (a) Displacement and (b) Velocity at DOFs versus time.

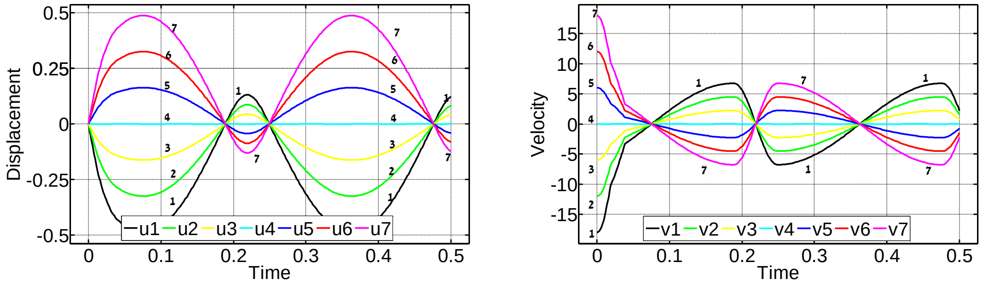

(a) (b)

Figure 10: (a) Displacement and (b) Velocity at system points (see Fig. 8) versus time.

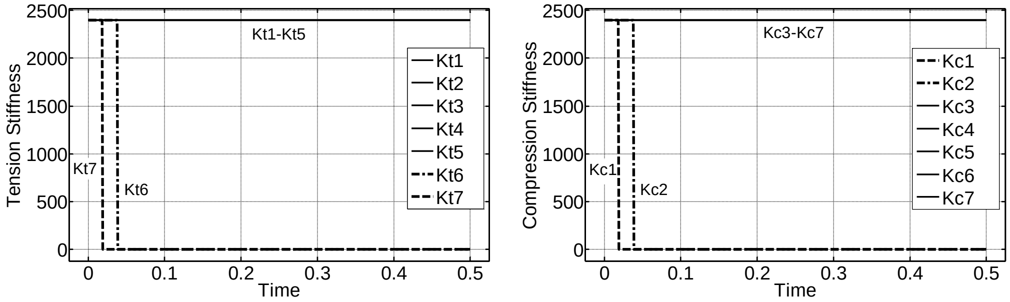

(a) (b)

Figure 11: Stiffness at (a) tension and (b) compression springs versus time.

Figures 12a and 2b present the force-displacement behavior of system 1 and 2, respectively. As can be seen, both spring present a linear relation in compression up to fracture that occurs in an instant as expected. Spring 1 fractures at time 0.019 while spring 2 fractures at time0.039 The behavior in tension remains linear as those spring systems did not fracture in tension.

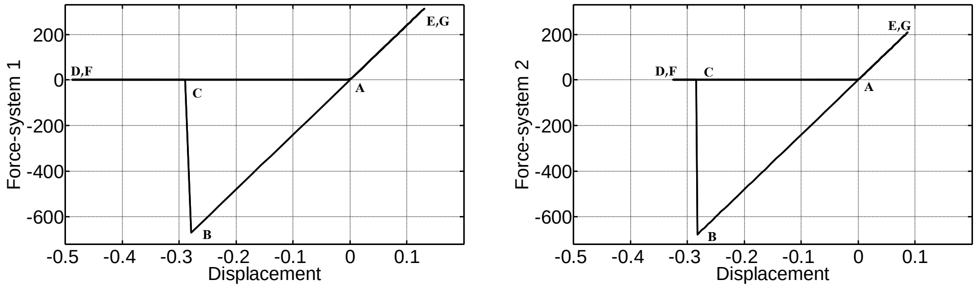

(a) (b)

Figure 12: Force-Displacement at (a) system 1 and (b) system 2

Finally, a convergence test was conducted. The problem was solved for various time increment values and the displacements and velocities of the DOFs versus time are presented in Figures 13a and 10b, respectively. Additionally, the force displacements behavior of system 1 and 2 in compression are presented in Figures 14a and 14b, respectively. As can be seen, the time increment of 10^{-3} is sufficient for convergence. This is very encouraging as the state variables of this problem show very sharp gradients in time. Those usually lead to large sensitivities. It should also be noted that while the use of a time increment of 10^{-2} leads to inaccuracy, the important phenomena are captured by the algorithm. Note also that the theoretical force and displacements of each spring at fracture are 678.82 and 0.28284, respectively. Those are traced by the algorithm with good accuracy using a time increment of 10^{-3} or smaller.

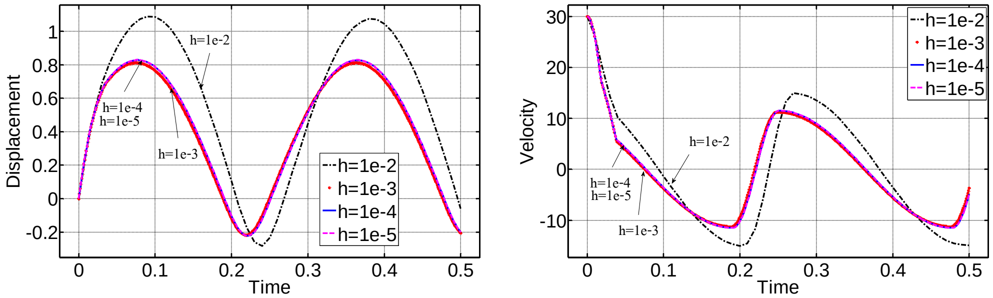

(a) (b)

Figure 13: (a) Displacements and (b) Velocities at DOFs versus time for various time increments.

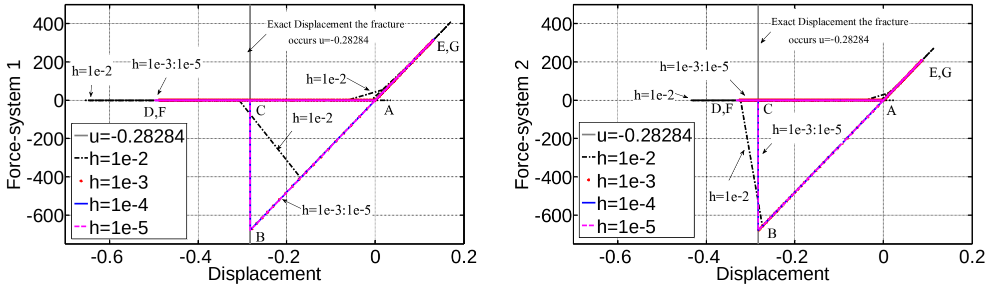

(a) (b)

Figure 14: Force-Displacement at (a) system 1 and (b) system 2 for various time increments.

5 CONCLUSIONS

- This paper presented a first step towards accounting for fracture in MLF in a unified manner through energy based fracture mechanics criteria. This important step shows feasibility of accounting for damage and fracture mechanics concepts in MLF.
- It was shown that although problems related to damage and fracture may reach bifurcation points, gained insight from the physics of the problem may assist in choosing the right path for the evolution of the state variables in time. In the problem at hand, for example, the optimization problem attained in each time step may not be convex. Nevertheless, insight from the nature of Griffith's criteria assisted in identifying the correct local minimum that, in turn, leads to the right path of the evolution in time.
- Finally, the example problems revealed that relatively large time increments were sufficient for convergence even when sudden fracture (n=1) was considered. This is very encouraging and is attributed to the weak formulation in time.

6 ACKNOWLEDGEMENT

This research was supported by a Grant from the G.I.F., the German-Israeli Foundation for Scientific Research and Development. The authors gratefully acknowledge this support.

REFERENCES

[1] U. Starossek, *Progressive Collapse of Structures.* Thomas Telford Publishing, 2009.

[2] A. J. Pretlove, M. Ramsden, A.G. Atkins, Dynamic effects in progressive failure of structures. *International Journal of Impact Engineering* **11**(4): 539-546, 1991.

[3] G. Kaewkulchai, and E.B. Williamson, Beam element formulation and solution procedure for dynamic progressive collapse analysis. *Computers and Structures* **82**: 639-651, 2004.

[4] R. Villaverde, Methods to assess the seismic collapse capacity of building structures: State of the art. *Journal of Structural Engineering* **133**(1): 57-66, 2007.

[5] D. Isobe, and M. Tsuda, Seismic collapse analysis of reinforced concrete framed structures using the finite element method. *Earthquake Engineering & Structural Dynamics* **32**: 2027–2046, 2003.

[6] M. Hakuno, K. Meguro, Simulation of Concrete-Frame Collapse due to Dynamic Loading. *Journal of Engineering Mechanics* **119**(9): 1709-1723, 1993.

[7] Z.P. Bazant, and M. Verdure, Mechanics of progressive collapse: learning from world trade center and building demolitions. *Journal of Engineering Mechanics, ASCE,* **133**(3), 308-319, 2007.

[8] B.A. Izzuddin, A.G. Vlassis, A.Y. Elghazouli, D.A. Nethercot, Progressive collapse of multi-storey buildings due to sudden column loss -Part I: Simplified assessment framework. *Engineering Structures,* **30** :1308–1318, 2008.

[9] S.K. Kunnath, A.M. Reinhorn, J.F. Abel, A Macromodel Approach to Practical Analysis of R/C Buildings under Seismic Excitation, *in Computer Aided Analysis and Design of Concrete Structures, N. Bicanic and H. Mang (Eds.), Pineridge Press, Vol. 2*, 1155-1167, 1990.

[10] Y. Bao, S.K. Kunnath, S. EL-Tawil, H.S. Leo, Macromodel-based simulation of progressive collapse: RC frame structures. *Journal of Structural Engineering, ASCE,* **134** (7): 1079-1091, 2008.

[11] L.F. Ibarra, R.A. Medina, H. Krawinkler, Hysteretic models that incorporate strength and stiffness deterioration. *Earthquake Engineering and Structural Dynamics*, **34**(12), 1489-1511, 2005.

[12] K.J. Elwood and J.P. Moehle, Dynamic collapse analysis for a reinforced concrete frame sustaining shear and axial failures. *Earthquake Engineering and Structural Dynamics*, **37**(7), 991-1012, 2008.

[13] J.E. Rodgers, S.A. Mahin, Effects of Connection Fractures on Global Behavior of Steel Moment Frames Subjected to Earthquakes*.* *Journal of Structural Engineering*, **132**(1), 78-88, 2006.

[14] D.E. Grierson, L. Xu, Y. Liu, Progressive-Failure Analysis of Buildings Subjected to Abnormal Loading. *Computer-Aided Civil and Infrastructure Engineering,* **20**(3), 155-171, 2005.

[15] D. Hartmann, M. Breidt, V.V. Nguyen, F. Stangenberg, S. Hohler, K. Schweizerhof, S. Mattern, G. Blankenhorn, B. Moller, M. Liebscher, Structural collapse simulation under consideration of uncertainty - Fundamental concept and results*.* *Computers & Structures* **86**(21-22): 2064-2078, 2008.

[16] M.V. Sivaselvan, A.M. Reinhorn, Lagrangian approach to structural collapse simulation. *Journal of Engineering Mechanics, ASCE*, **132** (8): 795-805, 2006.

[17] L. Meirovitch, *Methods of analytical dynamics*. McGraw-Hill, 1970.

[18] B. Halphen, Q.S. Nguyen, Sur les materiaux standard generalizes. *Journal de Mecanique* **14**(1): 39, 1975.

[19] M.V. Sivaselvan, O. Lavan, G.F. Dargush, H. Kurino, Y. Hyodo, R. Fukuda, K. Sato, G. Apostolakis, A.M. Reinhorn, Numerical collapse simulation of large-scale structural systems using an optimization-based algorithm. *Earthquake Engineering & Structural Dynamics*, **38**(5): 655-677, 2009.

[20] O. Lavan, Dynamic analysis of gap closing and contact in the Mixed Lagrangian Framework – towards progressive collapse prediction. *Journal of Engineering Mechanics, ASCE*, **136**(8), 979-986, 2010.

[21] O. Lavan, M.V. Sivaselvan, G.F. Dargush, Progressive collapse analysis through

strength degradation and fracture in the Mixed Lagrangian Framework. *Earthquake Engineering & Structural Dynamics*, **38**(13): 1483-1504, 2009.

[22] T.L. Anderson, *Fracture Mechanics: Fundamentals and Applications*. CRC Press, 1995.

[23] A.A. Griffith, The phenomena of rupture and flow in solids. *Philosophical Transactions of the Royal Society of London,* **A221**: 163–198, 1921.

COMPDYN 2011
III ECCOMAS Thematic Conference on
Computational Methods in Structural Dynamics and Earthquake Engineering
M. Papadrakakis, M. Fragiadakis, V. Plevris (eds.)
Corfu, Greece, 25–28 May 2011

STABILIZATION EFFECT OF SHOCK NON-LINEARITY ON THE DYNAMICS OF A STEAM GENERATOR TUBE

T. Thénint[1], E. Balmes[2] and M. Corus[1]

[1] LaMSID UMR EDF/CNRS/CEA 2832
1, avenue du général de Gaulle. 92140 Clamart. France
{thibaud.thenint, mathieu.corus}@edf.com

[2] Arts et Métiers Paris Tech
151, boulevard de l'Hôpital. 75013 Paris. France
balmes@sdtools.com

Keywords: dynamics, shock, stability.

Abstract. *In Pressurized Water Reactors of nuclear power plants, steam generators act as heat exchangers between primary and secondary coolant fluids. They consist of a bundle of U-tubes in which flows the primary coolant fluid. Several support plates guide these tubes vertically. Secondary coolant fluid flows along the U-tubes and passes through the space between tubes and plates. This space, initially of a foliate shape, is filled with sludge deposits. Consequently, fluid flow is accelerated and the tubes are more excited. Moreover, the mechanical bonding between tube and plate is changed. The combination of these two phenomena can lead to dynamic instabilities and tube cracks. This paper focuses on the effects of shocks on tube instability. As we concentrate on a mechanical point of view, the study of the nonlinear dynamics is made in the following specific conditions: the tube is in air with no flowing fluid; an instability is generated by injecting a force proportional to the velocity of a point of the leg of the tube. The tube is modeled as an Euler-Bernoulli beam. The contact between tube and plate is computed assuming circular obstacles and a contact force that is linear with a gap. A reduced model is generated to represent the bandwidth of interest and the effect of contact forces. Time evolution is then computed using a nonlinear Newmark scheme. Numerical simulations show the effect of shock nonlinearities on the dynamics. Cases of unstable unconstrained tubes leading to bounded stable dynamics when shocks occur are analyzed. The instability in the unconstrained condition does not imply that the bilateral contact condition is unstable. Areas of the contact stiffness/feedback gain plane are shown to lead to stable modes of the bilateral model. The work then presents results on an experimental bench that includes the curved part of a tube and one Support Plate. The instability is generated by feeding back to a shaker the amplified signal of a velocity measurement performed with an integrated accelerometer. For great enough feedback gains, the vibration amplitudes grow until shocks occur. The permanent regime eventually found is analyzed. A good similarity between test and analysis is found.*

1 INTRODUCTION

In Pressurized Water Reactor (PWR) of nuclear power plants, steam generators exchange heat between primary coolant fluid and secondary coolant fluid (Figure 1). They consist of a bundle of inversed U-tubes in which flows the primary coolant fluid. These tubes are clamped at the bottom of their legs. Several support plates maintain them vertically. Secondary coolant fluid flows along the tubes and through the holes made on the support plates.

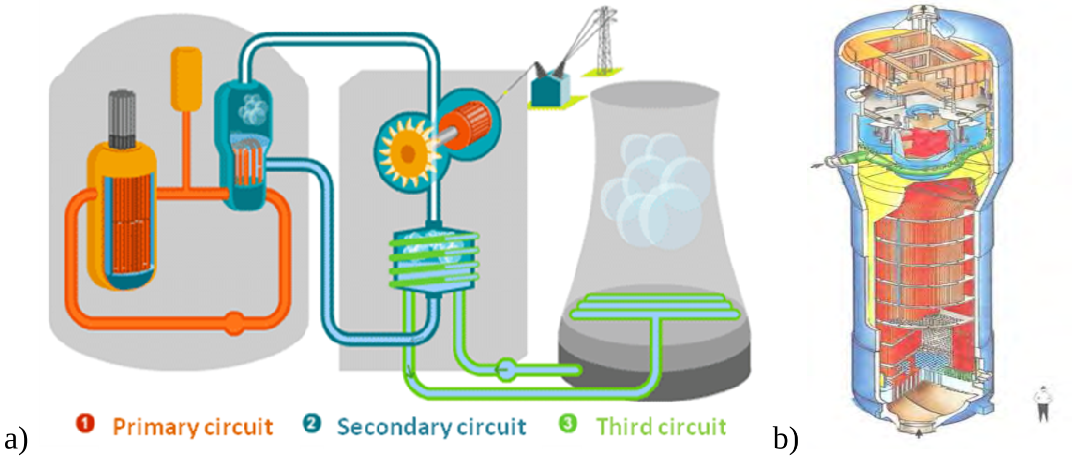

Figure 1 a) Scheme of a PWR nuclear plant. Three fluid circuits are described: primary circuit (red), secondary circuit (blue) and a cooling circuit (green). b) Scheme of a steam generator. The bundle of U-tubes and support plates are shown.

The space between the tubes and the support plates, initially of a foliate shape, is filled with sludge deposits. Consequently, fluid flow is accelerated and the tubes are more excited. Moreover, the mechanical bonding between tube and plate is changed, from free gap to clamping. The combination of these two phenomena can lead to dynamic instabilities and tube cracks.

Different methods are available to predict tube instability in regard with external fluid flow. The method developed by EDF uses linear boundary conditions to model the interaction between the tube and the support plates, typically clamping or supporting. Investigations have been made to get better understanding of the role played by shock non-linearity in respect with tube instability.

Piteau et al. [1] have made experiments and computations of a vibro-impacting straight tube subjected to fluid-elastic forces and planar displacements. Shocks modify the instantaneous response frequency and thus modify the fluid-elastic forces, explaining how shocks can stabilize this unstable dynamics. Here, we investigate the stabilization effect of shock non-linearity by itself. The study of the nonlinear dynamics is made in the following conditions: the U-tube is in air with no flowing fluid; instability is generated by injecting a force proportional to the velocity of a point of the leg of the tube.

Section 2 presents the experimental setup. Contact model and reduced basis used for numerical simulations are presented in section 3. The stability of a tube with linear contact stiffness is studied in section 4. Finally, numerical and experimental non-linear simulations are presented in section 5.

2 EXPERIMENTAL BENCH

The experimental bench consists of a portion of a U-tube (Figure 2), constrained at its basis to be as near as possible to a clamped condition. The two legs of the tube are inserted in foliated obstacles, whose geometry reproduces real support plates. These obstacles have been machined with different radius, the gap between the plate and the tube approximating the quantity of sludge deposits. The maximum gap available is around one percent of the external diameter of the tube. The thickness of a support plate is about 1.5 times the external diameter of the tube.

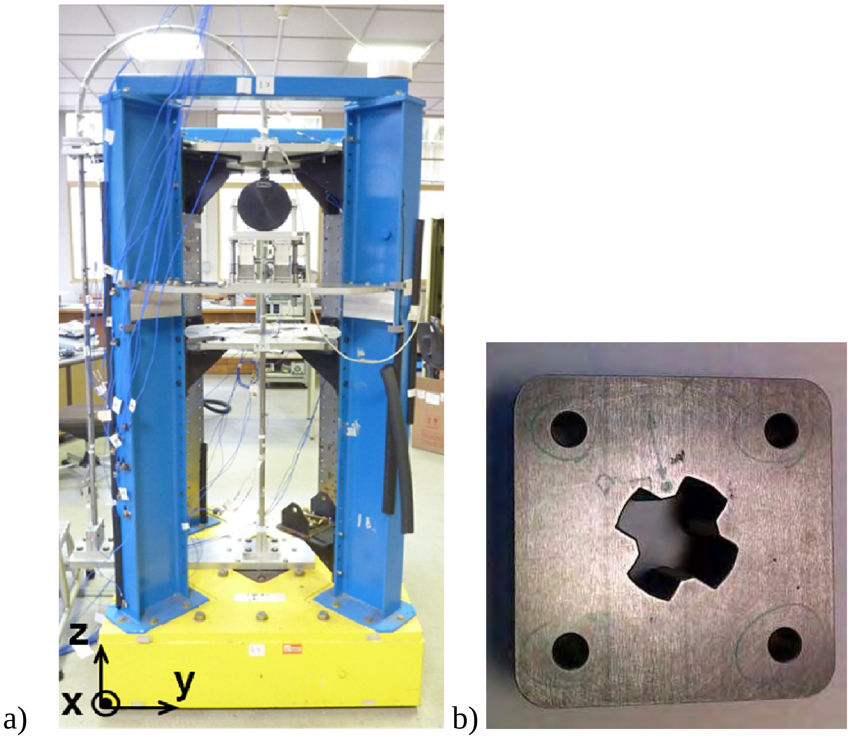

Figure 2 a) Global view of the experimental bench. We distinguish the two foliated obstacles right under the curved part and the shaker on the right leg. b) Detailed view of a foliated obstacle.

A shaker excites the leg in the out-of-plane *x* direction (*z* is the vertical and *y* is an in-plane direction). The shaker is fixed on a lift table, so as to adjust the height of the destabilizing force. Twenty-two B&K 4375 sensors measure accelerations at different points of the structure. A B&K 2635 charge amplifier integrates the acceleration and feeds an electrical voltage proportional to the velocity of the excitation point. Measurements are sampled using LMS Scadas III Front-end, driven by LMS Test.Lab software.

3 NUMERICAL MODEL

A reduced model has been built to perform non-linear numerical simulations. An updated numerical model of the experimental bench is created in section 3.1. The contact model between tube and plate is presented in section 3.2. Reduced basis is built in section 3.3. Numerical simulations are compared with test results in section 3.4.

3.1 Beam model

The tube is modeled as a curved beam. The length of the elements is compatible with a maximum frequency of interest linked to the spectrum of the contact loads. A preliminary study of the kinematic in the contact area has led us to consider an Euler-Bernoulli formulation rather than a Timoshenko formulation.

The mechanical connection between the tube and the frame is quite stiff but is far from clamped conditions. We represent this bind with six discrete springs, three affecting the translation degrees of freedom and three affecting the rotation degrees of freedom. A modal analysis gave us twelve modes under 200Hz. The tube material parameters and the stiffness of the discrete springs were updated taking into account the frequency of the modes 4, 7, 9 and 11, out-of-plane bending or torsion modes.

The frequencies smaller than 100Hz are quite well correlated (Table 1). The MAC (Modal Assurance Criterion), normalized scalar product between two vectors, is very close to 1, indicating a linear relation between experimental mode shapes and updated numerical mode shapes. Mode shapes are quite close to the ones of a base-clamped tube (Figure 3). A double mode around 85Hz has been badly identified experimentally and the updated numerical frequencies and deformed shapes are not consistent.

Mode number	Measured frequency (Hz)	Measured damping ratio (%)	Updated frequency (Hz)	MAC
1	4.9	1.5	4.9	0.97
2	8.5	1.5	8.4	0.97
3	16.5	0.4	16.7	0.99
4	31.8	0.2	31.7	0.98
5	32.2	0.2	32.1	0.97
6	47.8	0.2	47.5	0.99
7	49.9	0.2	49.6	0.98
8	88.5	0.2	87.7	0.80
9	88.9	0.2	88.4	0.66

Table 1 Comparison between measured and updated frequencies. Damping ratio and MAC.

As the mode frequencies are well separated and providing that the damping is small, we make the modal damping assumption. The few well identified damping values will be used, typically 1.5% for the two first modes and 0.4% for the third mode. The other modes will be affected with 0.2%, common value for the metallic structures cast in one piece. The high frequency modes above 7500Hz (this limit is derived from measured contact forces) will be arbitrary affected of a 2% damping ratio.

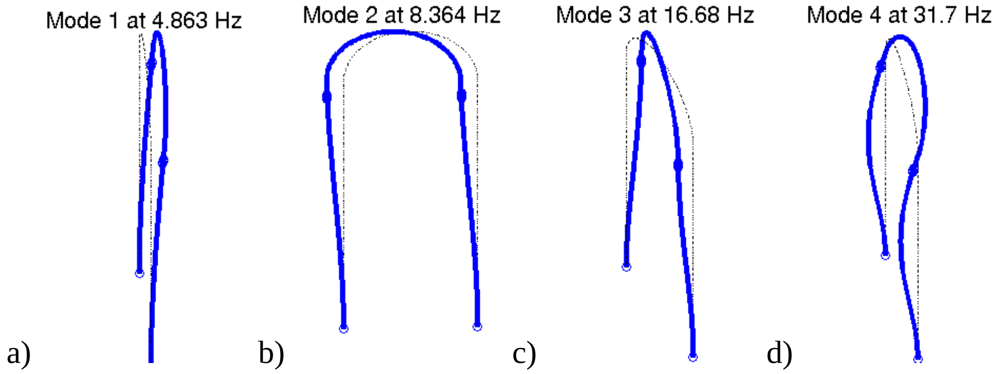

Figure 3 First four modal shapes of the updated numerical model: out-of-plane bending (a), in-plane bending (b), torsion (c), out-of-plane bending (d).

3.2 Contact model

The contact between tube and plates is solved using a functional representation of contact forces: if the displacement is smaller than a defined gap, then the contact force is null; else, the contact force applied to the node is proportional to the penetration and normal to the surface of the obstacle. The global stiffness of the contact between tube and plate has been experimentally measured at 4.10^6N/m, which is of the same order than the ovalization stiffness of a pipe presented in [2] or than the stiffness used in [1].

The geometry of the obstacle has been simplified, assuming that circles would be a good approximation of the foliated holes. The stiffness has to be distributed over the height of the support plate only using a few planar obstacles (Figure 4). This is done degrading the initial contact where both the plate and the tube are modeled as solids. The contact between a beam and the plate would be modeled as the interaction between a neutral fiber and a contact stiffness density. Here, contact conditions are assigned to nodes interacting with discrete springs whose value is the global stiffness divided by the number of planar obstacles.

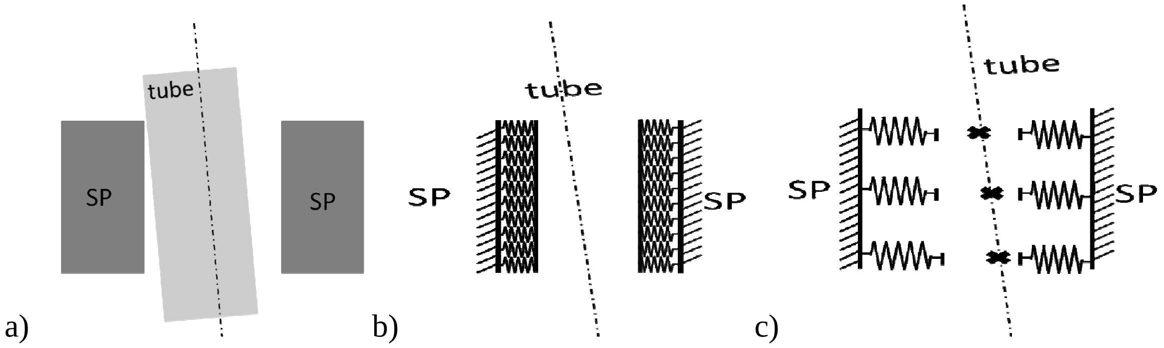

Figure 4 Different contact models: a) solid-solid, b) neutral fiber-stiffness density, c) beam nodes-discrete springs.

When the gap between tube and plate reduces to zero, the translations along *x* and *y* are blocked. Due to the support plate thickness, the corresponding rotations are also blocked. To block the rotations, at least two levels of obstacles must be considered. When the gap is zero, the tube is connected to the discrete springs. The evolution of the eigen modes with respect to the contact stiffness is compared for different number of discrete obstacles. There are twenty-one nodes along the plate thickness so at most twenty-one obstacles can be considered. Five levels of obstacles imply very limited errors on frequencies compared to those found with twenty-one obstacles.

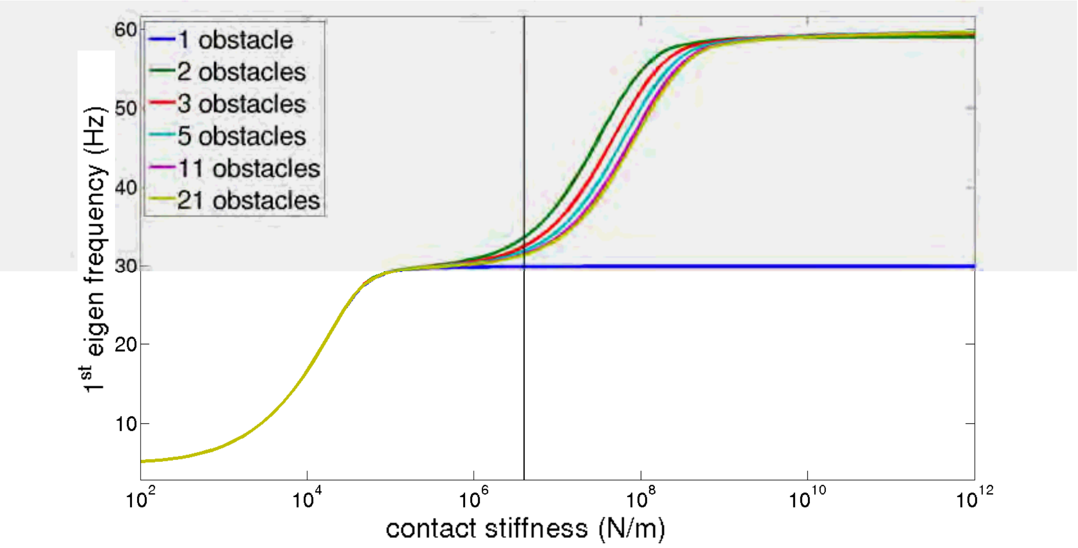

Figure 5 Evolution of the first eigen frequency with respect to the global contact stiffness. The modes go from unconstrained boundary conditions to supported and then clamped ones.

No shock damping was used as no physical value has been identified. Friction was not taken into account. We consider that the dissipation induced by the modal damping stands for all the physical dissipation.

3.3 Reduced basis

The tube non-linear dynamics are computed solving the discretized equation:

$$M\ddot{X} + C\dot{X} + KX = F_{\text{shaker}}(t) + F_{\text{shock}}^{NL}(X) \tag{1}$$

where *M*, *C* and *K* are the mass, damping and stiffness matrices of the unconstrained tube. The external excitation field has been separated between the excitation term that stems from the shaker and the contact/impact forces located at five nodes per support plate. To reduce the size of this system, we project (1) on a reduced basis *T*. The degrees of freedom *q* are solution of (2), with $X = Tq$:

$$M_r\ddot{q} + C_r\dot{q} + K_r q = T^T F_{\text{shaker}} + T^T F_{\text{shock}}^{NL}(cTq) = f_{\text{shaker}}(t) + f_{\text{shock}}^{NL}(q) \tag{2}$$

and *[c]* is an observation matrix used to express the penetration as a linear combination of the degrees of freedom.

We now detail the reduction basis building procedure. The basis must be rich enough to solve precisely the non-linear dynamics but should be as reduced as possible to allow quick computations. The basis must describe tube displacements when the gap is large, i.e. the tube is unconstrained, and when the gap is close to zero, i.e. when the tube is constrained. Moreover, shock forces applied at a few nodes must be well projected. Finally, the induced spectral bandwidth must include the high frequencies excited by contact/impact forces (around 7500Hz).

The quality of the reduced basis is first based on the computation of the eigen modes of the tube with bilateral contact conditions. We compare frequencies and deformed shapes found solving the reduced problem or solving the un-projected problem. The error is not significant for a wide range of bilateral contact stiffness if the reduced basis is built concatenating deformed shapes of:

- the unconstrained tube,
- the tube with *x* and *y* translation degrees of freedom blocked over the thickness of the support plate,
- the tube with *x* and *y* translation degrees of freedom blocked at middle node of the support plate,
- static corrections which correspond to unitary force imposed on each degree of freedom of the obstacles ($KX=b_i$).

Family of vectors *T* is no more orthogonal with respect to *M* and *K*. That is, some vectors are nearly collinear. For example, the static corrections are nearly collinear one to each other and nearly collinear to the first in-plane and out-of-plane bending modes. Collinear vectors are eliminated and the remaining family is orthonormalized with respect to *M* and *K*, as presented for example in [3]. The first deformed shapes, corresponding to the unconstrained tube, are not changed. In fact, only the information (frequency and deformed shapes) about high frequencies has been modified. As C_r is assumed diagonal by hypothesis (modal damping), all the matrices appearing in (2) are diagonal. Thus, the numerical computations are accelerated.

The choice of the reduced basis, presented in Table 2, has been validated with non-linear numerical simulations. “Blocked modes” and static corrections are really useful: the same quality of results is obtained but using fewer modes.

Type of basis	Number of modes	Minimal frequency (Hz)	Maximal frequency (Hz)
Unconstrained modes	130	4.9	7430
Clamped modes	126	59.7	7490
Supported modes	126	30.0	7430
Static corrections	20	-	-
Concatenated	402	-	-
Orthonormalized	199	4.9	$1.8.10^5$

Table 2 Comparison of different projection basis. Orthonormalisation has eliminated half of the vectors and affected high frequencies to static corrections and blocked modes.

3.4 Comparison of numerical simulations with test results

Numerical simulations have been computed for different gaps and different imposed excitations, without velocity feedback. A non-linear Newmark average acceleration scheme [4] is used, with a time-step of 2.10^{-5}s, small enough to avoid energy errors during non-linear time integration. No numerical dissipation is introduced. Measurements are performed at a sampling frequency of 2048Hz. Power Spectral Densities (PSD) (see [5] for example), are computed. The PSD estimator is normalized to compare signals with different time-steps:

$$S_{xx}(f_k) = \frac{2dt^2}{M}\sum_{m=1}^{M}\left|X_{m,k}\right|^2 \tag{3}$$

M windowed signals are extracted using overlap and a Hann window leading to *M* Discrete Fourier Transform (DFT) $X_{m,k}$. At each frequency, to take into account the variability of each windowed signal, we store the maximal and minimal value over these *M* DFT and compute the mean value.

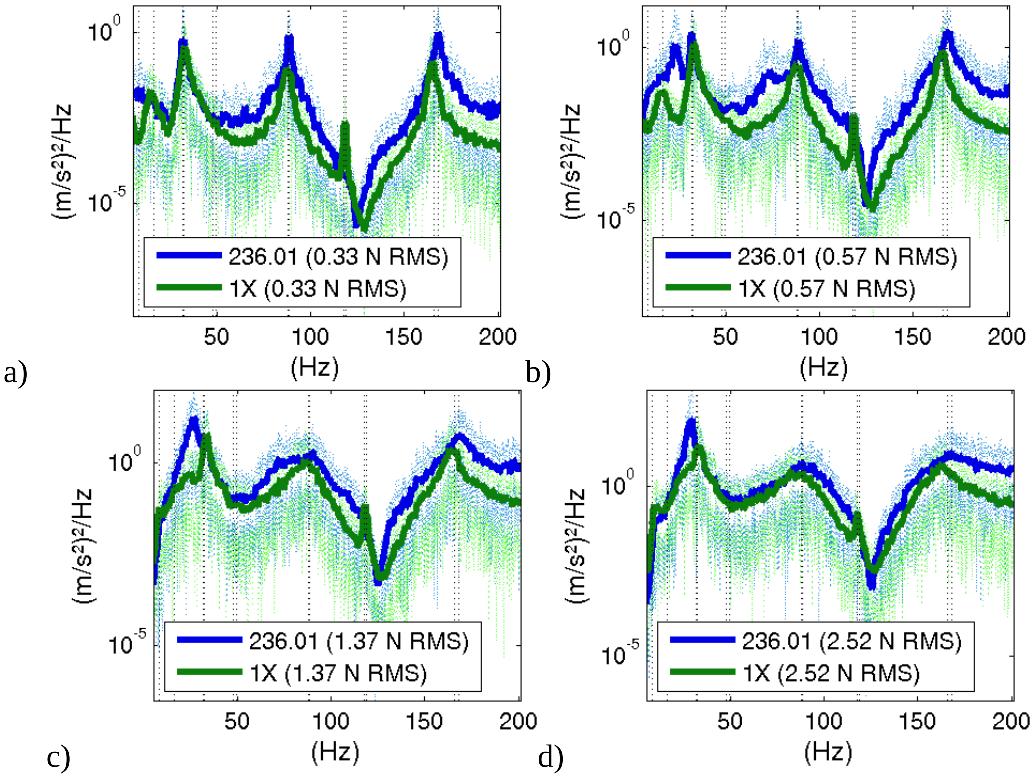

a) b) c) d)

Figure 6 PSD of the out-of-plane apex acceleration measured (green) or simulated (blue), for increasing RMS value of the excitation (a to d). Vertical lines indicate unconstrained modes of the tube.

A random voltage filtered between 10 and 40Hz is fed to the shaker; the injected force is modulated by the interaction between the tube and the shaker. This force is measured and used as excitation in the numerical simulations. Accelerations are computed or measured at the tube apex, in the out-of-plane direction (Figure 6). Test-analysis correlation is correct over the frequency band [10Hz, 200Hz]. For most peaks and most levels of excitation, amplitudes and frequencies match. The spread of the peaks around 90Hz and 170 Hz is well represented. The anti-resonance around 120Hz is both measured and computed. But the emerging peaks around 28-30Hz and 70Hz are not well reproduced numerically, with the response over-estimated and frequencies that not really match.

The satisfactory correlation between test results and numerical simulations validate the construction of the numerical model. A beam model, a contact model, a reduced basis and an integration scheme have been chosen to accurately and quickly compute the non-linear dynamics of a U-tube impacting support plates.

4 EFFECT OF BILATERAL CONTACT ON COMPLEX POLES

An apparent contact stiffness can be derived from the retained shock model by dividing the contact force with the node displacement. This apparent contact stiffness is null when the contact force is null and tends to the contact stiffness when the force goes to infinity. At every time instant, depending on contact conditions, an underlying linear system exists. In this part, we consider a very simple underlying linear system: each contact node is affected bilateral contact conditions with equal contact stiffness, varying from 0 to 10^8N/m, as if the gap was null.

Assuming that a feedback loop makes the shaker inject a collocated force proportional to the out-of-plane velocity of a tube leg point and replacing contact/impact forces with bilateral contact conditions, the dynamics (2) is now solution of:

$$M_r\ddot{q}+C_r\dot{q}+K_r q = g\ T^T\left[c\right]^T\left[c\right]T\dot{q}-k\ K_{bil}q = g\ C_{loop}\dot{q}-k\ K_{bil}q \tag{4}$$

with *[c]* the observation matrix of the degree of freedom whose velocity is measured and *g* the gain of the feedback loop; K_{bil} is the unitary bilateral contact stiffness matrix and *k* is the apparent contact stiffness. It is worth noting that C_{loop} and K_{bil} are not diagonal matrices. We study the stability of this linear system with respect to the position *[c]*, gain *g* and stiffness *k*. To do this, we compute the complex eigenmodes of the following system:

$$\left[\lambda_i^2 M_r+\lambda_i\left(C_r-g\ C_{loop}\right)+\left(K_r+k\ K_{bil}\right)\right]\left\{\psi_i\right\}=\left\{0\right\} \tag{5}$$

The complex poles are expressed in terms of frequency ω_i and damping ratio ζ_i (6). They are arbitrary sorted by increasing frequency, which is a convenient but delusive choice.

$$\lambda_i=-\zeta_i\omega_i+j\omega_i\sqrt{1-\zeta_i^2} \tag{6}$$

We are interested in destabilizing low frequency modes. This is done choosing the point where to inject the feedback force, about 20cm below the support plate. The modes which can be easily observed, i.e. with high *[cT$_i$]*, are the ones whose damping ratio is changed. Every mode with large out-of-plane components becomes unstable except for the second torsion mode and the third out-of-plane bending mode (Figure 7): a vibration node is located near the shaker. We remark that frequencies are not modified when *g* increases. Damping ratio is a linear function of *g*. Even if the damping ratio is quite high (-10% for the first mode and *g*=20), mode shapes are very correlated to the mode shapes of the unconstrained model.

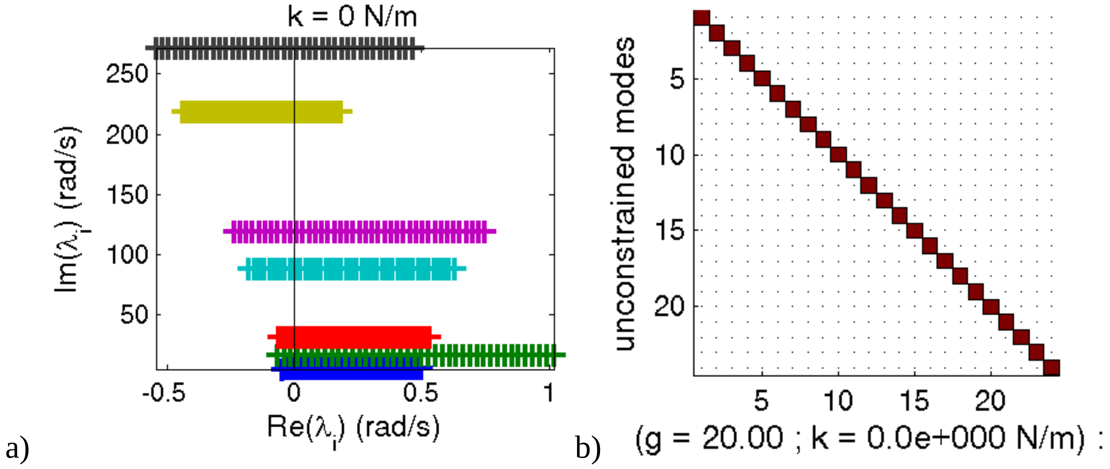

Figure 7 a) Evolution of the complex poles with respect to the feedback parameter. If the real part is positive, the mode is unstable. b) MAC-M between the unconstrained modes and the complex modes obtained for *g*=20.

Pole evolution in the complex plane with respect to the apparent contact stiffness is much more complex, with many crossings. In the meantime, deformed shapes are continuously transformed. For large enough apparent contact stiffness, the deformed shapes are no longer correlated to those of the unconstrained model. The MAC matrix between these two sets of deformed shapes is not diagonal (Figure 8). We focus on the evolution of frequencies and damping ratios (Figure 8), for a given feedback parameter (here, *g*=5). Frequencies increase with respect to the apparent contact stiffness. Damping ratio evolution is more complex. For some modes, damping ratio is not affected by the apparent contact stiffness. These modes were stable and stay stable. The first in-plane flexion mode has an initial damping ratio of 1% which decreases to 0.2%. Initially unstable modes become stable, their damping ratio increasing with respect to the apparent contact stiffness. The mechanical system is stabilized for apparent contact stiffness greater than 10^6N/m: every damping ratio is positive.

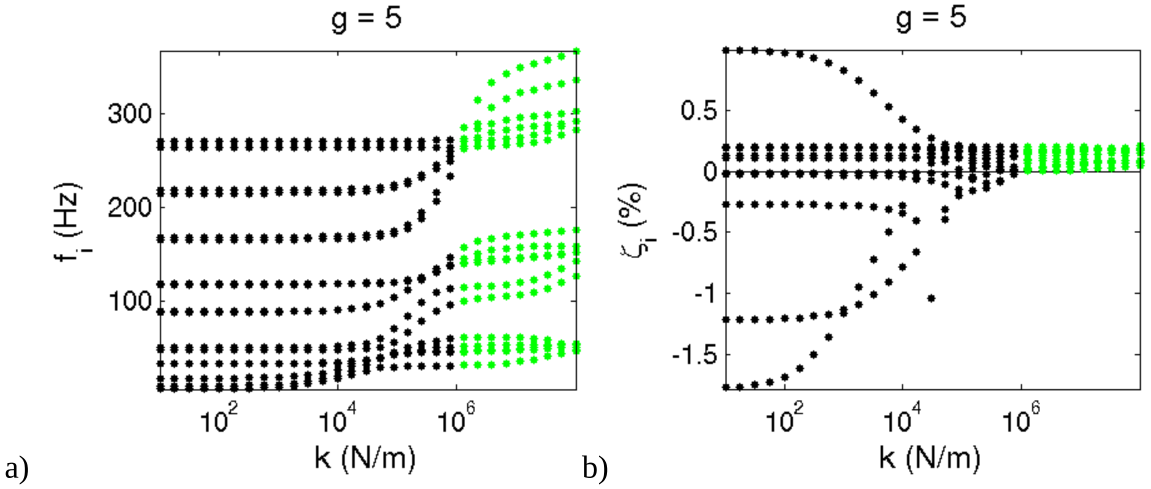

Figure 8 Evolution of the frequency (a) and the damping ratio (b) with respect to the apparent contact stiffness. Green points denote stable systems, with no negative damping ratio.

For a given feedback parameter, adding bilateral contact conditions leads to pole modifications and unstable modes are transformed to stable ones. The stability of the mechanical system has been studied for a wide range of feedback parameter and apparent contact stiffness (Figure 9). If *g* is small enough, the system is stable. If *g* is large enough, the system is unstable. If not, the system is unstable unless *k* is greater than a given value, which increases as *g* increases.

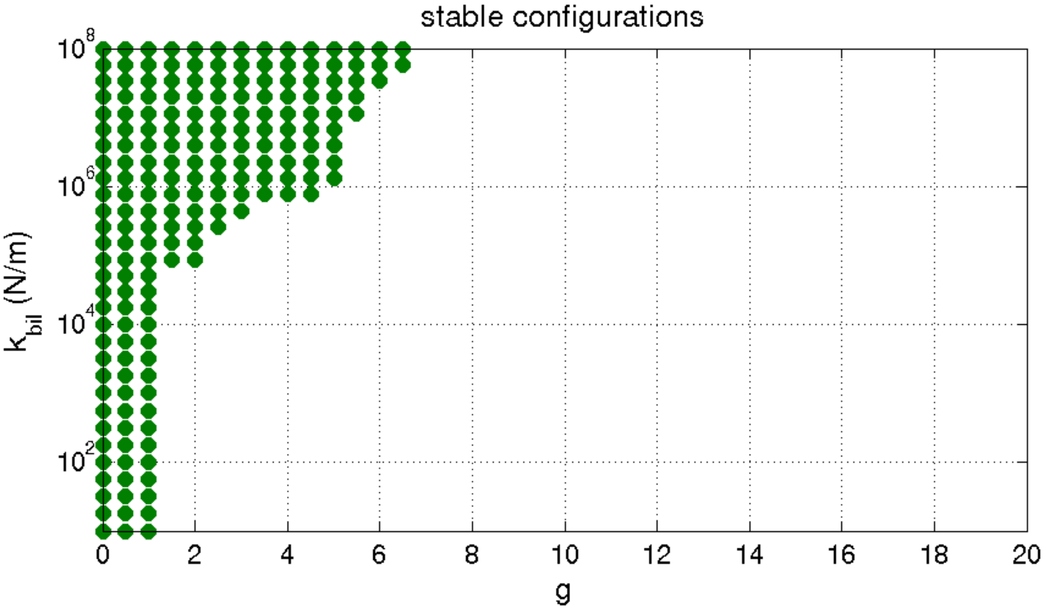

Figure 9 Stable configurations with respect to the feedback parameter and the apparent contact stiffness.

5 NON-LINEAR SIMULATIONS

Adding bilateral contact conditions to the destabilized tube can lead to stable mechanical system. In this part, we investigate the effect of shocks on the stability of the tube, subjected to a positive feedback loop on the velocity. Numerical and experimental results are presented. Computed out-of-plane displacements and measured accelerations are observed (Figure 10). Support plates are between P3 and P4 and between P8 and P9, i.e. close to the top of the legs. The shaker is right under P3.

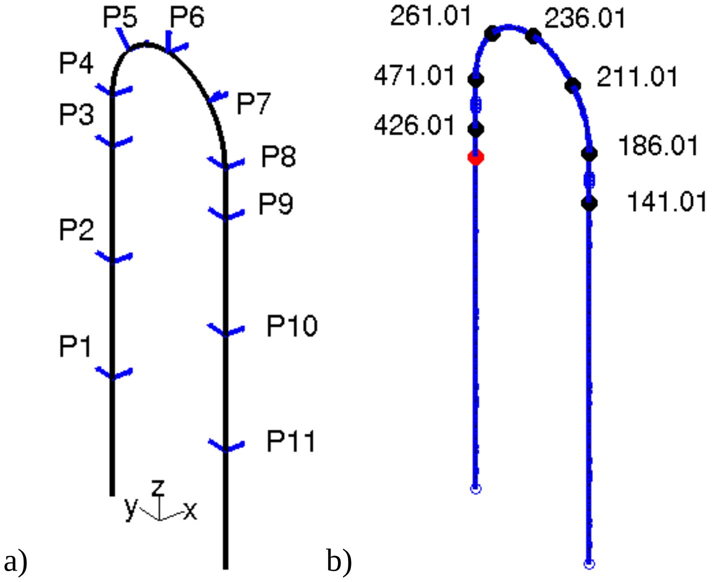

Figure 10 a) Sensor location. b) Corresponding out-of-plane translation degrees of freedom. For example, P4X corresponds to 471.01. The shaker is indicated with a red point.

5.1 Numerical results

Initial conditions are null. Tube is excited at its apex by an impact or by a low-pass filtered noise. Non-linear simulations are made over 30s, with a time-step of 2.10^{-5}s.

For low values of *g*, displacements are bounded (Figure 11). For *g*=0, free vibrations of a damped mechanical system are observed. *g*=6 should imply an unstable dynamics, as the apparent contact stiffness stabilizing it is greater than the contact stiffness used in the contact model. Feedback loop brings energy to the tube, which is dissipated during contact phases and in high-frequency modes. The vibration regime is stationary.

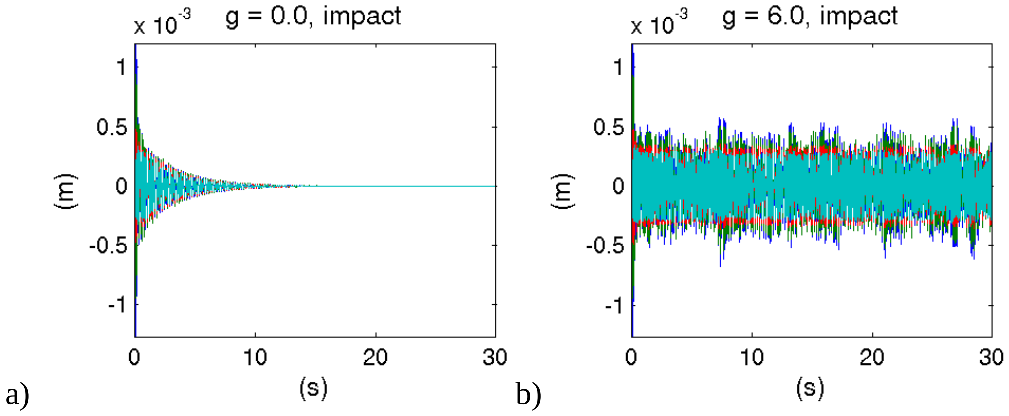

Figure 11 Computed displacements (blue: 236.01; green: 261.01; red: 471.01; cyan: 426.01) for different values of *g*. a) Damped vibrations. b) Stationary vibrations: displacements are bounded.

When displacements grow, penetrations and contact forces grow. This can define a criterion describing the stability of a computed non-linear dynamics: if contact forces exceed 1000N, which corresponds to a penetration equal to the tube thickness, the simulation is described as unstable. Non-linear contact forces computed in section (3.4) were less than 50N. For greater values of *g*, displacement amplitude increases (Figure 12). Even if crest-to-crest out-of-plane apex displacement reaches 8mm, which is quite high, simulated dynamics with *g*=12, seems stable. When displacements are big enough, contact forces grow and energy is dissipated. Unstable dynamics is exhibited for *g*=12.1. Contact forces do not stabilize the system, damping stays negative and amplitude of displacements grows until maximum contact force criterion is met.

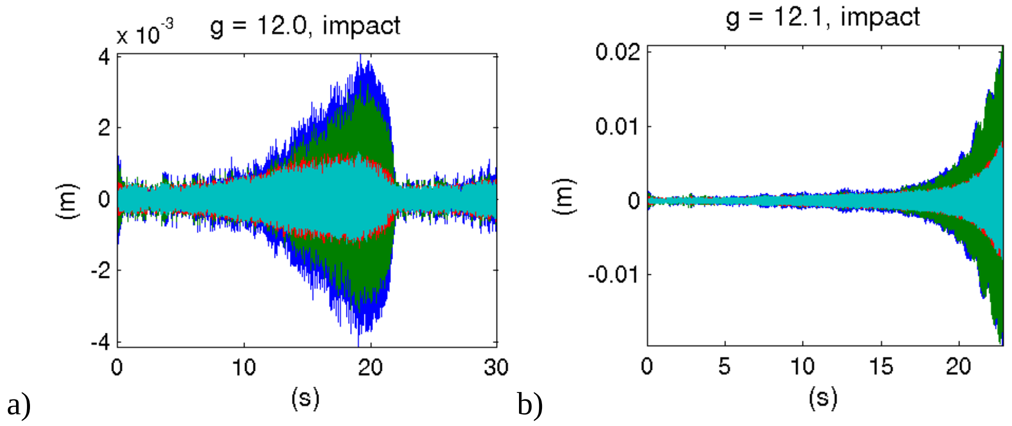

Figure 12 Computed displacements (blue: 236.01; green: 261.01; red: 471.01; cyan: 426.01) for different values of *g*. Tube is initially excited by an impact. a) displacements grow but remain bounded and eventually decrease; b) unstable regime: contact forces do not stabilize growing displacements

The same behavior has been observed when the impact excitation was replaced by a low-pass filtered noise. Feedback parameters lower than g=12.6 lead to stable dynamics. Contact forces can numerically stabilize unstable dynamics, and for a wider range of feedback parameter g than a bilateral contact model.

The apparent contact stiffness distribution drives the maximal stable value of g. For nominal value of gap between tube and support plates, bilateral contact model with equal stiffness affected at each discrete obstacle is a bad approximation of the real distribution of apparent contact stiffness (Figure 13). Apparent contact stiffness is not uniformly distributed over the different obstacles. Superior obstacles apparent stiffness is globally higher than this of inferior obstacles. The apparent stiffness of the left leg obstacles is totally linearly uncorrelated to apparent stiffness of the right leg obstacles. The apparent stiffness of neighbour contact points is highly correlated and decreases with the distance.

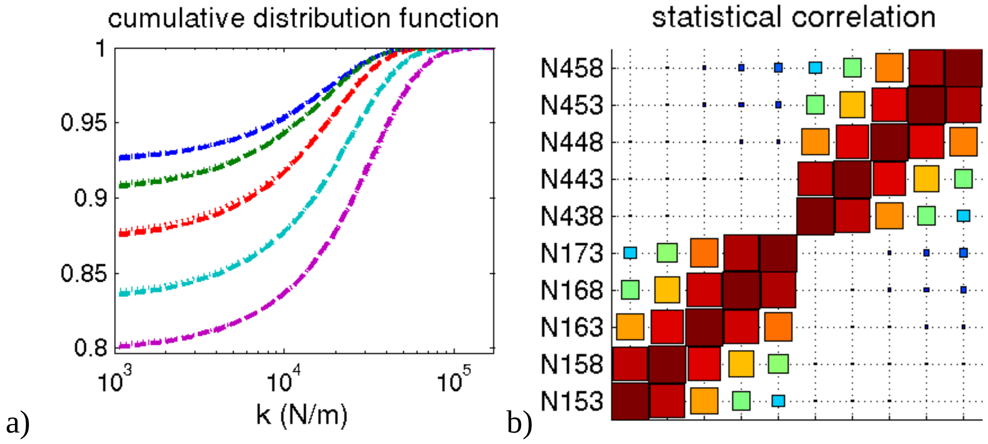

Figure 13 a) Cumulative distribution function of apparent contact stiffness. Contact nodes from bottom to top of the support plate: N153 and N438 (blue), N158 and N443 (green), N163 and N448 (red), N168 and N453 (cyan), N173 and N458 (magenta). b) Statistical correlation of apparent contact stiffness.

5.2 Experimental results

The destabilization is achieved by feeding to the shaker a velocity signal obtained by integrating measured acceleration. The feedback parameter g is fixed using a voltage amplifier. Due to the coupling between tube and shaker, the injected force is not simply proportional to the velocity: peak amplifications and differences of phase are observed. To impose null initial conditions, shaker rod and tube are manually stopped and then let free. Measurement noise is thus amplified by the feedback loop and excites the tube. If g is large enough, vibration amplitude grows. Shocks occur and vibration amplitude remains bounded.

Different regimes can be distinguished in Figure 14. The initial amplitude growth clearly appears on all measurement channels. A stabilized shock regime lasted for about one minute. Then, three different regimes where observed. They differ by their spectral repartition of energy, peak frequencies not being modified.

Operating Deflection Shapes (ODS) can be exhibited. They have vibration nodes located at nodes close to the support plates. They differ from mode shapes of the unconstrained model. They look like mode shapes of the bilateral contact model: ODS are combinations of different shapes, with phase difference, for example a torsion mode combined with an in-plane bending mode. In-plane movements are of the same amplitude as the out-of-plane movements: the specific shape of the foliate hole couples these directions.

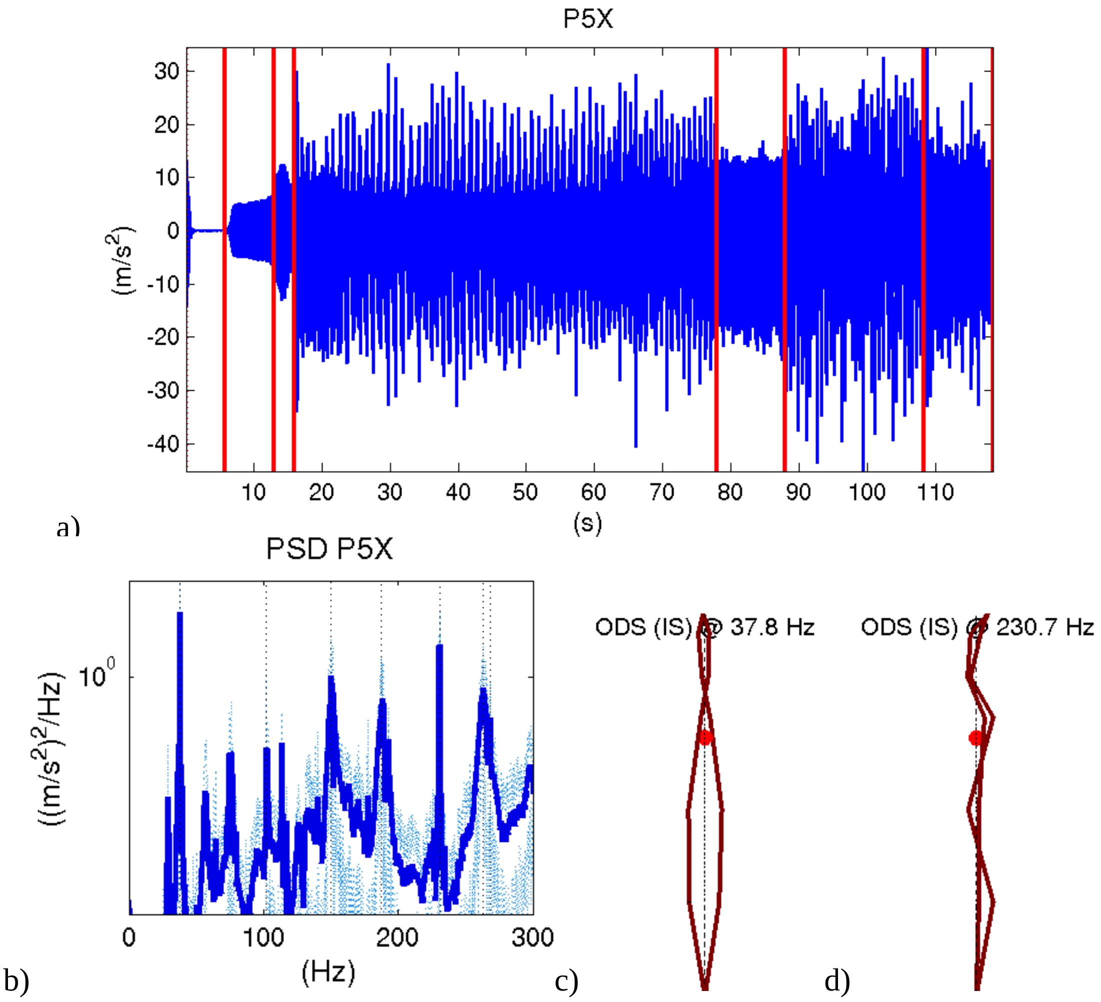

Figure 14 a) Measured acceleration signals. Red lines separate the different observed regimes. b) PSD of the stabilized regime (16s to 78s). c) ODS at 37.8 Hz for the stabilized regime: torsion mode. d) ODS at 230.7 Hz for the stabilized regime: out-of-plane bending.

Despite drawbacks on velocity measurement and on injection of a proportional force, the tube has been destabilized, and it has been shown that contact forces kept vibration amplitude bounded.

6 CONCLUSIONS

This paper presents the stabilization effect of shocks on an unstable mechanical system. An experimental bench consists of a portion of steam generator U-tube. A feedback loop injects a force proportional to a measured velocity. The tube is destabilized by this “negative damping”. Foliate obstacles stop the growth of vibration amplitudes, which remain bounded. A numerical model has been built. The choice of a beam model, a simplified contact model and a reduced basis has been presented. Numerical simulations are quick and correlated to measurements, in the absence of feedback loop. Feedback loop is idealized for numerical simulations: injected force is proportional to the velocity. Unstable free systems are kept bounded by shocks. A possible explanation of the stabilization effect is given studying a linear bilateral contact system: contact stiffness modifies the complex poles.

Some work has still to be done to make the three approaches converge and predict the same feedback parameter leading to global instability and dynamical divergence. The contact model should be more complex, the specific foliate shape coupling in in-plane and out-of-plane motions. The feedback loop from measured velocity to injected force should be modeled and affected to numerical simulations. Finally, bilateral contact is a too rough linear model: apparent contact stiffness is not uniformly distributed over the obstacles.

ACKNOWLEGEMENTS

The authors want to thank I. Negreanu (EDF R&D) for his valuable contribution on experimental setup and tests.

REFERENCES

[1] P. Piteau, X. Delaune, J. Antunes, L. Borsoi, Vibro-impact experiments and computations of a gap-supported tube subjected to single-phase fluid-elastic coupling forces. *Proceedings of the 7th International Symposium on Fluid-Structure Interaction, Flow-Sound Interaction, Flow-Induced Vibration and Noise (IASS-IACM 2000),* Montreal, Québec, Canada, August 1-4, 2010.

[2] J. Antunes, F. Axisa, H. Bung, F. Doveil, E. de Langre, Méthodes d'analyse en dynamique non-linéaire des structures. *Cours IPSI*. May 28-30, 1991.

[3] A. Sternchüss. *Multi-level parametric reduced models of rotating bladed disk assemblies*. PhD thesis, École Centrale de Paris, 2009.

[4] M. Gérardin, D. Rixen. *Théorie des vibrations. Application à la dynamique des structures, 2ème édition*. Éditions Masson, 1996.

[5] Kenneth G. McConnell. *Vibration testing: theory and practice.* John Wiley & Sons Edition, 1995.

COMPDYN 2011
3^{rd} ECCOMAS Thematic Conference on
Computational Methods in Structural Dynamics and Earthquake Engineering
M. Papadrakakis, M. Fragiadakis, V. Plevris (eds.)
Corfu, Greece, 25-28 May 2011

IMPACT AND EXPLOSIVE LOADS ON CONCRETE BUILDINGS USING SHELL AND BEAM TYPE ELEMENTS

Mario Bermejo[1], **José M. Goicolea**[1], **Felipe Gabaldón**[1] **and Anastasio Santos**[2]

[1]Dept. of Mechanics and Structures, School of Civil Engineering, Technical University of Madrid
C/ Profesor Aranguren s/n, 28040, Madrid, Spain
e-mail: {mario.bermejo,jose.goicolea,felipe.gabaldon}@upm.es

[2] Dept. of Materials Engineering, School of Mines, Technical University of Madrid
C/ Ríos Rosas 21, 28003, Madrid, Spain
e-mail: tasio.santos@upm.es

Keywords: Blast, Bombing, Reinforcement Concrete, Waffle Slab, Frame-type Building, Progressive Colapse.

Abstract. *The threat of impact or explosive loads is regrettably a scenario to be taken into account in the design of lifeline or critical civilian buildings. These are often made of concrete and not specifically designed for military threats. Numerical simulation of such cases may be undertaken with the aid of state of the art explicit dynamic codes, however several difficult challenges are inherent to such models: the material modeling for the concrete anisotropic failure, consideration of reinforcement bars and important structural details, adequate modeling of pressure waves from explosions in complex geometries, and efficient solution to models of complete buildings which can realistically assess failure modes.*

In this work we employ LS-Dyna for calculation, with Lagrangian finite elements and explicit time integration. Reinforced concrete may be represented in a fairly accurate fashion with recent models such as CSCM model [1] and segregated rebars constrained within the continuum mesh. However, such models cannot be realistically employed for complete models of large buildings, due to limitations of time and computer resources. The use of structural beam and shell elements for this purpose would be the obvious solution, with much lower computational cost. However, this modeling requires careful calibration in order to reproduce adequately the highly nonlinear response of structural concrete members, including bending with and without compression, cracking or plastic crushing, plastic deformation of reinforcement, erosion of vanished elements etc.

The main objective of this work is to provide a strategy for modeling such scenarios based on structural elements, using available material models for structural elements [2] and techniques to include the reinforcement in a realistic way. These models are calibrated against fully three-dimensional models and shown to be accurate enough. At the same time they provide the basis for realistic simulation of impact and explosion on full-scale buildings.

1 INTRODUCTION AND MOTIVATION

The threat of impact or explosive loads is regrettably a scenario to be taken into account in the design of lifeline of critical civilian buildings. These are often made of concrete and not specifically designed for military threats. In the last years there were several cases in which civil buildings were the target of terrorism attacks.

Oklahoma City bombing [?] on April 19, 1995 in USA can show the destruction that can be caused by bombing attack. In this case 2300 kilograms of ANFO were used; The blast claimed 168 lives and injured more than 680 people; the blast destroyed or damaged 324 buildings within a sixteen-block radius. The Alfred P. Murrah Federal Building was the target; the building suffered several/enormous damages although it didn't collapse.

The Asociación Mutual Israelita Argentina (AMIA; Argentine Israelite Mutual Association) building in Buenos Aires was attack on July 18, 1994. In this attack 85 people were killed and hundreds were injured. 275 kilograms of ammonium nitrate fertilizer and fuel oil explosive mixture were used in this attack. The blast totally destroyed the exposed load-bearing walls, led to progressive failure of the floor slabs and collapse of the building.

The parking of the Terminal 4 of the Madrid-Barajas Airport in Spain was attacked on December 30, when a van bomb exploded in, killing two and injuring 52 people; 500 to 800 kilograms of an unknown kind of explosive, probably a mix of ammonium nitrate and hexogen cause the explosion that demolished almost all of the five floors of the car park and produced around 40 tones of debris [4].

The 2009 Burgos bombing occurred on July 29, 2009, when at least 65 people were injured after a van bomb carrying more than 300 kg of explosive went off outside a Civil Guard barracks in the northern city of Burgos, Spain.

This four examples shows the importance of the blast loads in order to design critical civilian buildings. In general, the measures taken to avoid those threats focus on prevent that a significative quantity of explosives could be close of those buildings. Recently several research was made in order to modeling the past terrorism attacks [3], simulate blast on concrete structures [5] and to explain the progressive collapse of civil structures [6].

With this orientation this work present a strategy for modeling frame-buildings subject to blast loads, in order to provide sufficient accuracy results for choose between structural designs and to estimate the amount of explosive that one building can resist without collapse.

1.1 Numerical models for simulation and allow evaluation of structural alternatives

Numerical simulation of such cases may be undertaken with the aid of state of the art explicit dynamic codes. This codes, like LS-Dyna [2] used in this work, are available methods to study blast loads through very short times in witch they apply. LS-Dyna use a lagrangian finite element method with explicit time integration, that can be used to model, in this case, complete concrete structures.

The computational cost of this method depends essentially on the minimum size of the model elements, number of elements and on time simulation. It is possible, in computational costs, analyze a small part of one building with very accuracy lagrangian finite element method using non-linear continuum elements for concrete modeling and non-linear beam elements for steel reinforcement modeling, constrained in concrete continuum elements, in a model with geometries of each part (columns, beams and slabs) very close to real. But the computational cost is excessive in the case of full building analysis. In the way of full building analysis it's necessary other approximation. This work propose use structural elements (shells and beams) for concrete and reinforcement in segregate way for a low computation cost model that have approximately the same structural behaviour.

1.2 Requirements for modeling

However several difficult challenges are inherent to such models: the material modeling for the concrete anisotropic failure, consideration of reinforcement bars and important structural details, adequate modeling of pressure waves from explosions in complex geometries, and efficient solution to models of complete buildings which can realistically assess failure modes.

The model must be able to represent accuracy the global structure behaviour. This include the wave transmission through columns and slabs, the stress redistribution when any element reach the elastic limit and plastify, the stress redistribution and the appearance of new action due to the erosion of structural elements or parts of them, and the process of progressive collapse of the complete building.

The model must be able to evaluate the action of different quantities of explosive the must be applied in different positions in the building. The blast is a short action (the application time range is in 0.01 to 0.1 milliseconds) and, depends of quantity and distance, high values of applied pressure can be reached.

The reinforcement concrete have a heterogeneous behaviour, caused by two different material working together. So the model must represent properly this behaviour. Using an homogeneous model is more limited the using segregated elements. In the other hand, modeling concrete and steel in segregated elements needs an interface in order to work together.

Concrete has complex behaviour, it is a no-linear material with different behaviour in tension and compression, plastic deformation with softening in compression and damage due to cracking in tension. Additionally there is an increment of elastic limit due to strain rate, and the fail of concrete can be controlled in model by element erosion. Concrete has other properties like fatigue and retraction but those are not important for our application.

And steel is a no-linear material too, with same behaviour in tension and compression and with increment of elastic limit due to strain rate. It plastify when the elastic limit is reached and when the strain is enough it fail.

The material models must represent accuracy the behaviour described above and there must be an model interface to make both materials work together.

2 MATERIAL BEHAVIOR AND ELEMENT FORMULATION

This chapter is dedicated to describe the models and formulation we use to obtain a sufficient approximate behaviour in reinforcement concrete on blast actions.

2.1 Concrete

For concrete we use two different materials models. The first one is used for continuum elements and the second one is used for structural elements (shells and beams).

Continuum element model: The model used for continuum elements is the CSCM LS-Dyna model [1]. This material is able to represent the complex behaviour described above (figure 1). It can be used only in continuum elements.

- Isotropic behaviour.
- Different behaviour in tension and compression.

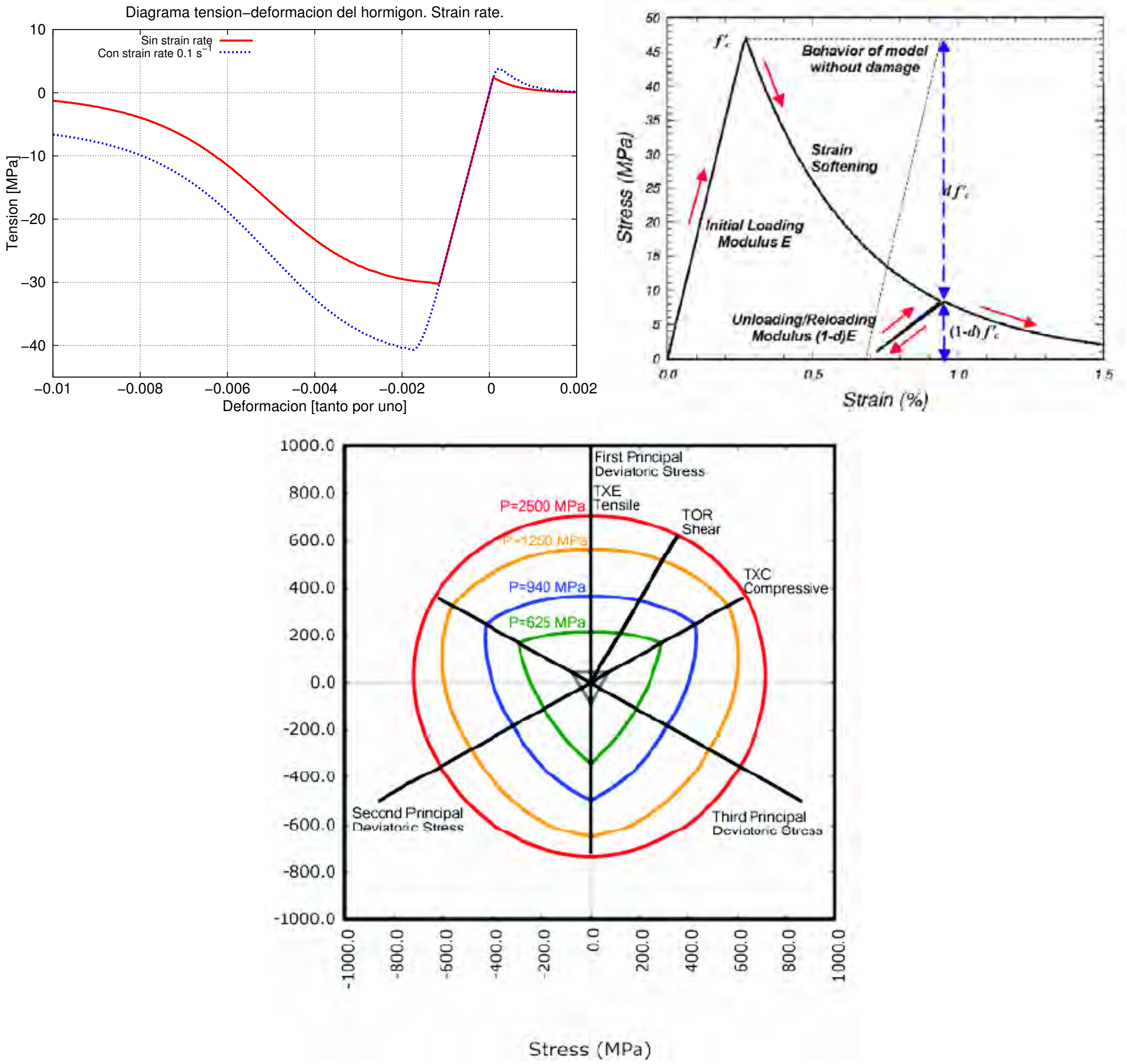

Figure 1: Properties of CSCM concrete model [7]

- Plastity surfaces (TXE Tensile, TOR Shear, TXC Compressive).
- Softening in compression.
- Damage in tension.
- strain rate effects.
- Erosion

Structural element model. Shell and beam model: The model used for structural elements is the EC2 LS-Dyna model [7]. It can be used in shell and beam type elements. Figure 2 show the tension-deformation diagram.

- Softening in compression.
- Damage in tension.

- Erosion with mat add erosion formulation (not by itself).
- No strain rate effects.
- Plastify surfaces.
- Quantities of steel reinforcement cam be included in material homogeneously.

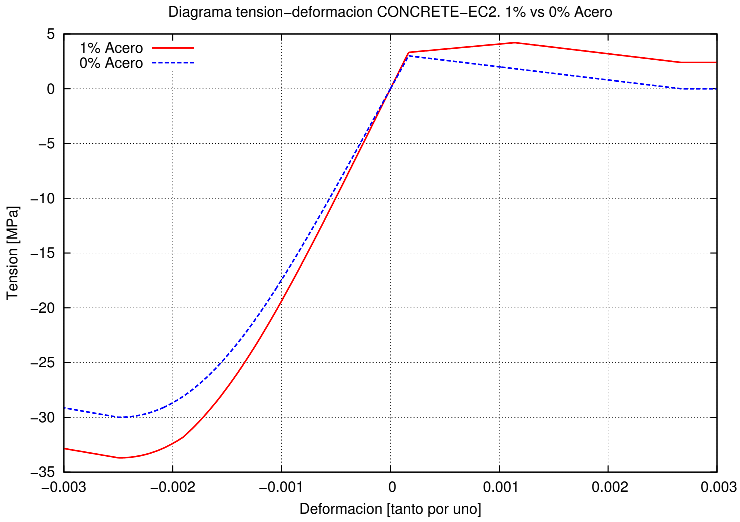

Figure 2: Properties of EC2 concrete model

2.2 Steel reinforcement:

We use the piecewise linear plasticity LS-Dyna model [7] to represent rebar in concrete. This model represents perfectly the behaviour we need for steel reinforcement, with plastic deformation, strain rate effects and fail. We use it in beam elements.

2.3 Concrete/steel interface:

We use two options to model the interface. The first one is merge common nodes between steel and concrete elements, and the second one is use the constrain lagrange in solid [7] formulation implemented in LS-Dyna.

The constrain lagrange in solid option has one advantage: no coincident modes of concrete and steel are needed. This implies that the size of concrete continuum elements are no limited by the rebar geometry and position, that cause low computation cost. In the other hand this option can not be applied for concrete structural elements.

The figure 3 shows the mesh of validation example for the evaluation of proper behaviour of constrain lagrange is solid formulation. Rebar is model with beams elements and concrete is model with continuum elements. We check the global behaviour is correct.

In this way we use the constrain lagrange in solid formulation for continuum models and the mode merge option for structural models.

There are a limitation in both methods: the adherence is not modelized but we assume this limitation.

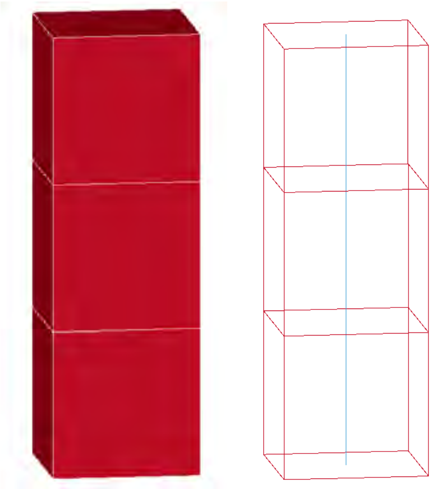

Figure 3: Constrain lagrange in solid

2.4 Offset formulation

In structural models the reinforcement steel beam elements are linked with the concrete shells elements by nodes. It is a problem because all elements are in the same plane, and the influence of reinforcement eccentricity can not be included. To avoid this problem we use a Ls-Dyna beam offset formulation [7] to take account this influence. With beam offset is possible to define a offset distance from the plane in order to correct the position of rebar in model to simulate the real position. The table 1 shows the check of this formulation in a simple beam test model.

Eccentric Reinforcement		
Case	Reaction	Description
Theory B	25.9 kN	Bernouilli beam
Theory T	22.1 kN	Timoshenko beam
Beams	26.9 kN	Beams elements
Shells	25.5 kN	Shell and beam elements

Table 1: Validation offset beam formulation.

2.5 Blast formulation

The blast load is defined with a pressure law that depend on time and position for each quantity of explosive.

In this work we use the blast LS-Dyna formulation [8] that it is the implementation of CONWEP formulation of TM-855-1 manual from U.S. Department of the Army [9].

3 APPLICATION: EXPLOSIVE LOADS ON STRUCTURAL ELEMENTS

Material and element formulation make possible to analyze structural elements of a real frame-type building. The objective of this section is to analyze structural elements of frame-type buildings and check the viability of use structural finite elements with the same structural response.

There are three main structural elements forming part of a frame-type building: columns, beams and slabs.

In order to analyze this structural elements two models were develop. In first place, continuum elements model was develop, which represents the better characterization of the real quasi-static and dynamic behaviour, and in second place a structural finite elements model was develop, which have the similar structural behaviour and low computational cost. Similar structural behaviour for second model is achieved with properly geometry and materials models parameter adjustment.

3.1 Column

In order to analyze columns on frame-type buildings we choose a representative one which is testing in two ways: quasi-static an dynamic. Bending perform the quasi-static analysis and three different cases with two quantities of explosive perform the dynamic analysis.

We use a simply supported $40\,\mathrm{MPa}$ concrete column with twelve longitudinal reinforcement bars of $20\,\mathrm{mm}$ diameter and transversal reinforcement of $8\,\mathrm{mm}$, and steel is type B500S. The column is 3.15 meters length and 45×45 centimeters section Column mesh and reinforcement for continuum elements model are showed in figure 4.

We develop two models of continuum model using CSCM concrete material for continuum elements and piecewise linear plasticity for reinforcement beam elements: the first one with the constrain lagrange in solid formulation to model the interface, with bigger elements in the mesh, and the second one with merge nodes of common elements, with the necessary smaller elements. We check both models to be ensure the constrain lagrange in solid formulation model has the same structural response than the merge nodes model. In the successive we use the constrain lagrange in solid model due to its low computational cost.

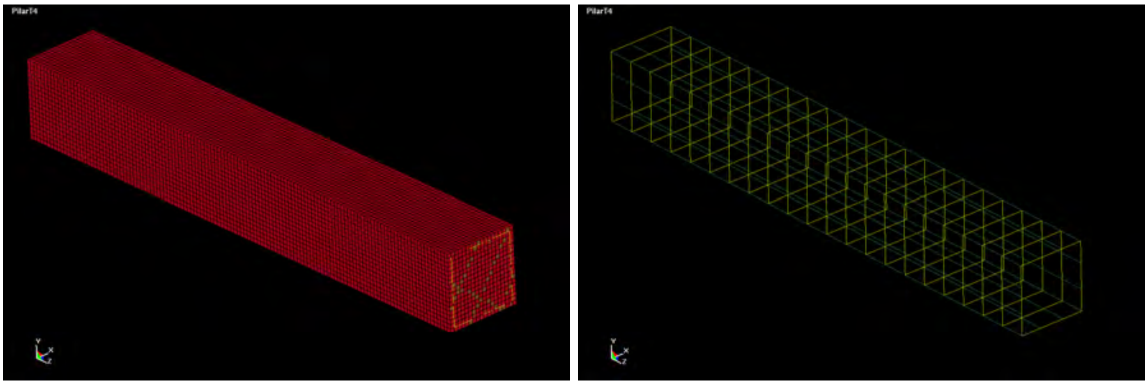

Figure 4: Column mesh and reinforcement for continuum elements model

For the structural model we develop a concrete shell model with offset beams witch nodes are merged in the cross node shells (figure 5a). The geometry properties of the shell elements are adjustment to have the same mass and inertia than the continuum model, and the longitudinal reinforcement is model in the real position with the aid of offset beam formulation. The transversal reinforcement are not model, but it is possible to include it in the EC2 concrete material model like a fraction of steel reinforcement. It is possible too develop a model with concrete beam elements, but this model, only with beam elements are unable to recibe the blast action. This is the reason to use shell elements for the structural model.

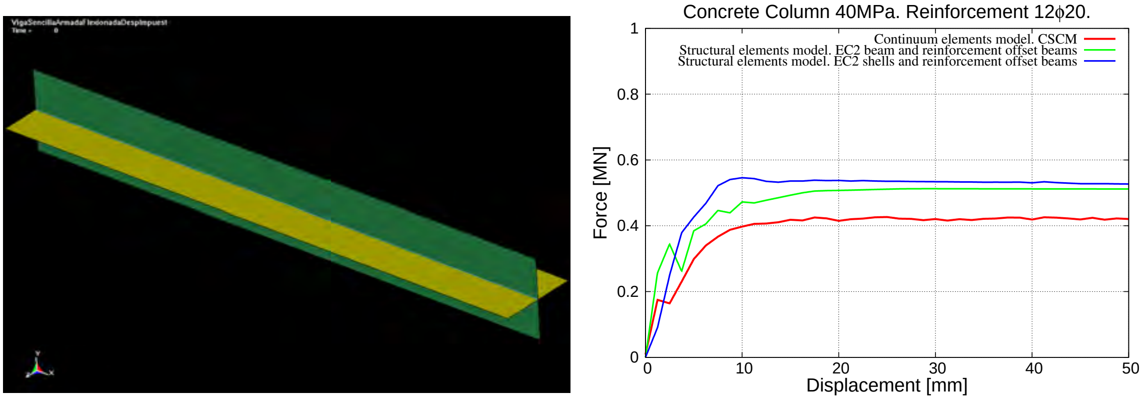

Figure 5: Column mesh for structural elements model and bending comparison column models

Quasi-static bending comparison: The figure 5b shows the response of continuum element model (red line) and structural shell element model (blue line) for a prescribed motion that produce the bending in the column. In this graphic we see that there is a good correlation between models. The structural model is more rigid than the continuum model despite it have not the transversal reinforcement. It is due to in the progressive plastify of continuum elements through the column section in continuum model, whereas the structural model with less elements in section become more rigid until the elements plastify.

Blast action. Dynamic response comparison: We must check the dynamic response to blast action in both models like the quasi-static response. In this case, we compare the response to different quantities of explosive and distances. The structural response is quite different depends on explosive quantity and distance: For incremental quantities of explosive the column have more and more damage, in first place the concrete in the rear of blast impact face plastify, then some elements of this concrete are erosioned, then the rear reinforcement plastify and the concrete plastify is extended to all the column section and finally the column collapse due to full section erosion of concrete and plastify and erosion of rebar.

The figure 6 show the response comparison of continuum and structural models for a quantity of $400\,$kg of TNT at four meters distance. In this case the rear concrete plastify but it is not eroded. The center column displacement are measure in time and compare in both models. The displacement of structural model is minor than continuum model due to more transversal flexibility but is a good correlation.

The figure 7 show the response comparison of continuum and structural models for a cuantity of $400\,$kg of TNT at four meters distance. In this case the concrete plastify but it is not eroded. The center column displacement are measure in time and compare in both models. The displacement of structural model is minor than continuum model due to the full erosion of the shells elements whereas in the continuum model remains some concrete elements. We take account of this behaviour and assume less displacement but more damage in structural column model.

3.2 Beam

In the same way column is analyzed we analyze a beam, to ensure there is not differences when the reinforcement is asymmetric. In this case we use a simply supported $40\,$MPa concrete

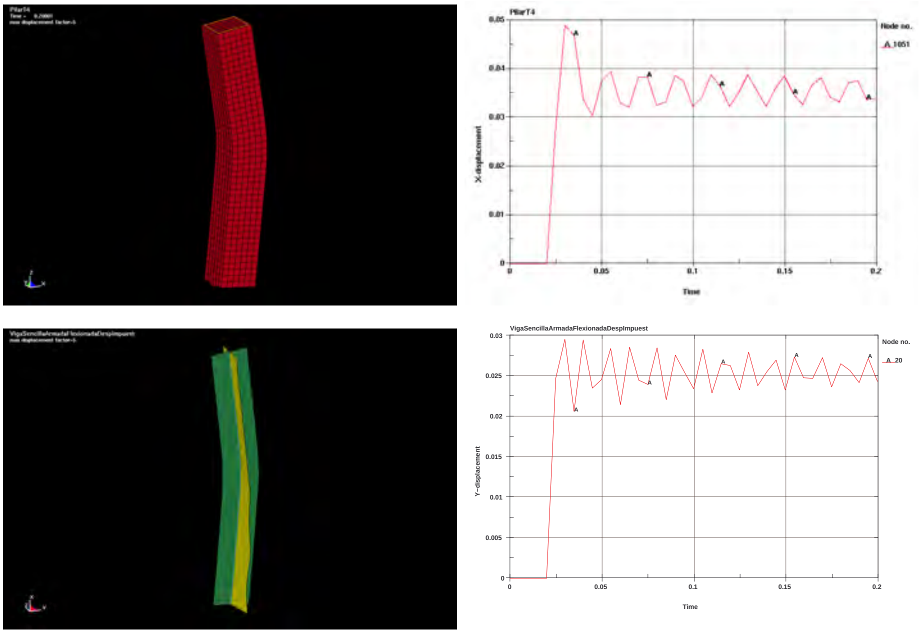

Figure 6: Column deformed mesh and displacement (x5 scaled) in center of column. Continuum and structural models.

column with five longitudinal reinforcement bars of 16 mm diameter in the rear face and five longitudinal reinforcement bars of 12 mm diameter in the front face.

Figure 8 show the comparison of this case for quasi-static bending. It is similar than the column one. The blast results on similar behaviour, with more damage and less displacement.

3.3 Slab

The are some types of slabs that can be used in frame-type buildings, we study the waffle slab case. This type of slab uses prefabricated hollow sheet metal or plastic domes to create a grid pattern of voids in a solid floor slab. It have several reinforcement bars, with various sections, in different positions, both sides. This case is complex due to complex reinforcement layout and the concrete geometry.

The case we study use 30 MPa concrete and B500S steel reinforcement in a 8×8 meters waffle slab with 80×80 centimeters hollow sheet domes and 38 centimeters thickness. It have complex reinforcement layout, superior grid, superior and inferior reinforcement in joists.

We develop two models for waffle slab, like in the column case, the continuum model using CSCM concrete material model in continuum elements and piecewise linear plasticity material model in beams elements using constrain lagrange in solid to get work together, and the structural model using EC2 concrete material model in shell elements and piecewise linear plasticity material model in offset beams elements using merge nodes option to get work together.

The continuum model show in figure 9 has detailed mesh. All reinforcement bars of real waffle slab are model with beam elements and the hollows geometry of concrete are model with continuum elements. The continuum model use constrain lagrange in solid formulation. In this model is not possible use the node merge option for model the interface between steel and concrete. The complex geometry of the model and the amount of reinforcement bars and their positions led to very small size and elevated number of continuum concrete elements, producing excessive computational cost.

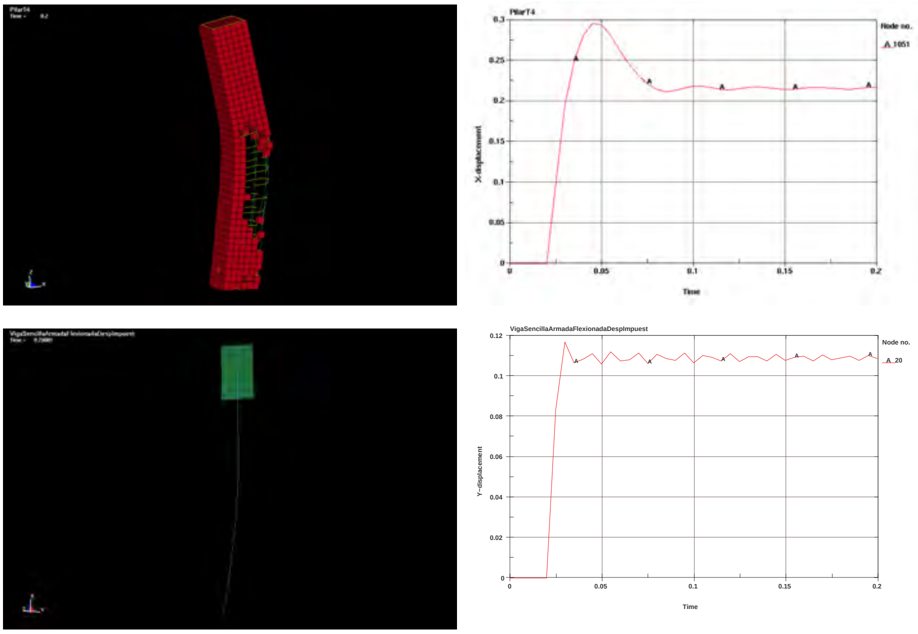

Figure 7: Column deformed mesh and displacement in center of column. Continuum and structural models.

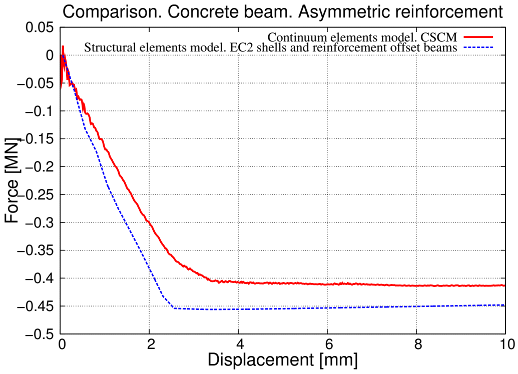

Figure 8: Bending comparison beams models with asymmetric reinforcement

The structural model show in figure 9 has very few elements than continuum model. The concrete is model with shells elements without joists. The thickness of shell elements is calculated to obtain the same mass in continuum and structural models. The reinforcement are model for each dome with a fictional rebar section that represent the total quantities of reinforcement in each direction and differentiate between superior and inferior reinforcement. This fictional rebar are model with offset beams to represent properly the eccentricity of the rebar.

Quasi-static bending comparison: The figure 10 shows the response of continuum element model (red line) and structural shell element model (blue line) for a prescribed motion in the slab center that produce bending. In this graphic we see that there is a rough correlation between models. Both models have peaks in the graphic line of resultant force due to the successive plastify of slab parts. It is difficult obtain the same results in structural model and continuum model. But this rough approximation can provide a range to study the slab behaviour with one

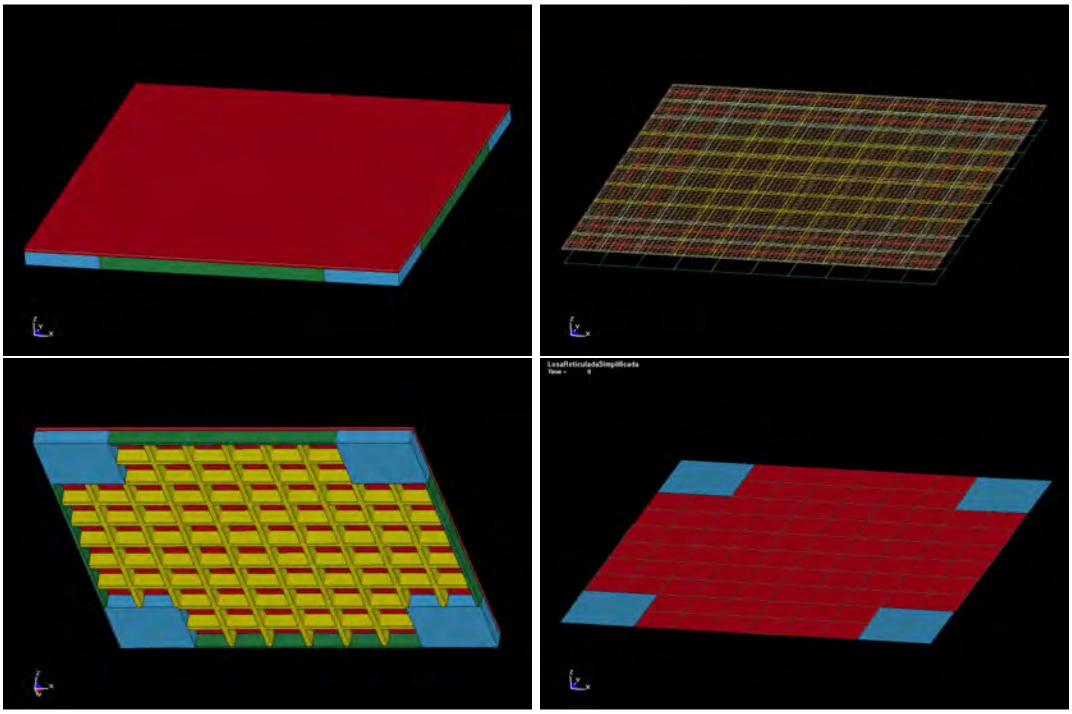

Figure 9: Top left: Mesh of continuum elements waffle slab (top view); Top right: Reinforcement of continuum elements waffle slab; Bottom left: Mesh of continuum elements waffle slab (bottom view). Mesh of structural elements waffle slab (top view)

structural model.

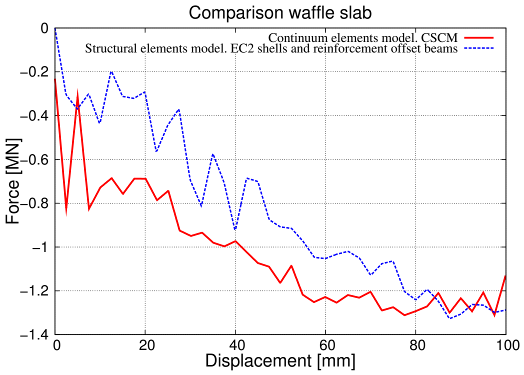

Figure 10: Bending comparison waffle slabs models

Blast action. Dynamic response comparison: We must check the dynamic response to blast action in both models like the quasi-static response. We compare the response to different quantities of explosive and distances. We compare the damage and erosion that is produced in both models.

The figure 11 show the comparison of continuum and structural models for a cuantity of 200 kg of TNT at 2 meters distance from the center of the slab in the inferior side. There is

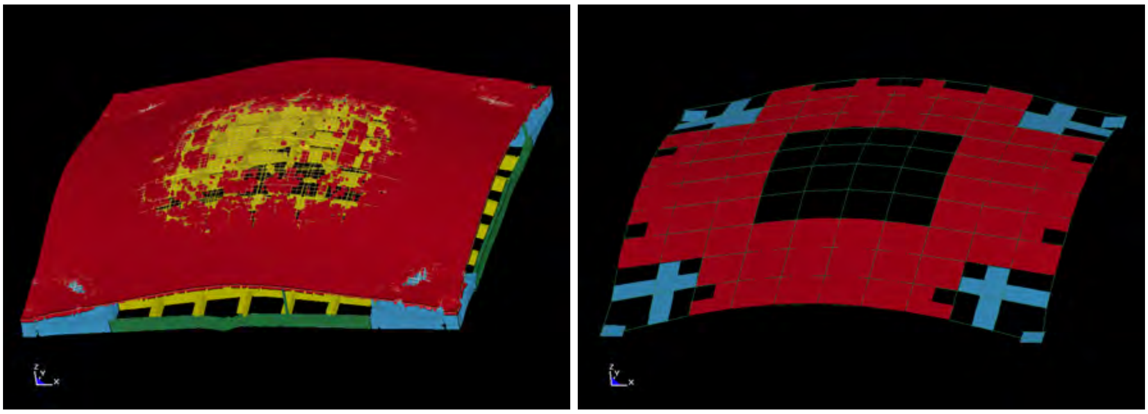

Figure 11: Comparison: deformed mesh in continuum elements model and structural elements model. 200 kg TNT

a good correlation between both models, and we can use the structural model to evaluate the damage produced in a waffle slab from a frame-type building.

4 APPLICATION: FRAME-TYPE BUILDINGS

The final application of this work is evaluate the response of a frame-type building subject to blast action.

Column and slab models are being developed, and it can be use together in the develop of a frame-type complete building. The figure 12 show the model developed for a 3 floors building, with 4×4 waffle slabs in each floor. This model provide us a tool to evaluate the damage caused in a building by blast. In this case a 400 kg of TNT in the first floor center in one slab at 1 meter from the first floor cause the damage show in the figure.

This case can be resolved with moderate computational cost. For this application model calculation time are in the range of 0.1 to 0.5 seconds, sufficient time to evaluate the action of blast in the structure.

There are limitations on the application of this strategy. One of them is that is not possible to evaluate pressure of the blast in a second floor when a previous floor is damaged and the blast wave pass trough it. The blast energy loss in the process of breaking the previous slab is difficult to be evaluated. To avoid this problem it is necessary to use an ALE mesh [11] to evaluate the propagation of the wave trough an air mesh. Other of this problems is that there are some parts of concrete slabs that become projectiles and impact on the structure. The erosion in the shells elements needed to simulate the damage in the structure make few projectiles than be in reality.

This model can be used too to evaluate the possible progressive collapse of the structure, with the inconvenient of more model calculation time, in the range of 3 to 10 seconds for a tree floors building. This causes the CPU calculation time increases, but it can be calculated. Progressive collapse and multiple floor blast analysis are current in develop in the research project we are involved.

5 CONCLUDING REMARKS

We present a strategy for modeling such scenarios based on structural elements, using available material models for structural elements and techniques to include the reinforcement in a realistic way. These models are calibrated against fully three-dimensional models and shown to be accurate enough. At the same time they provide the basis for realistic simulation of impact

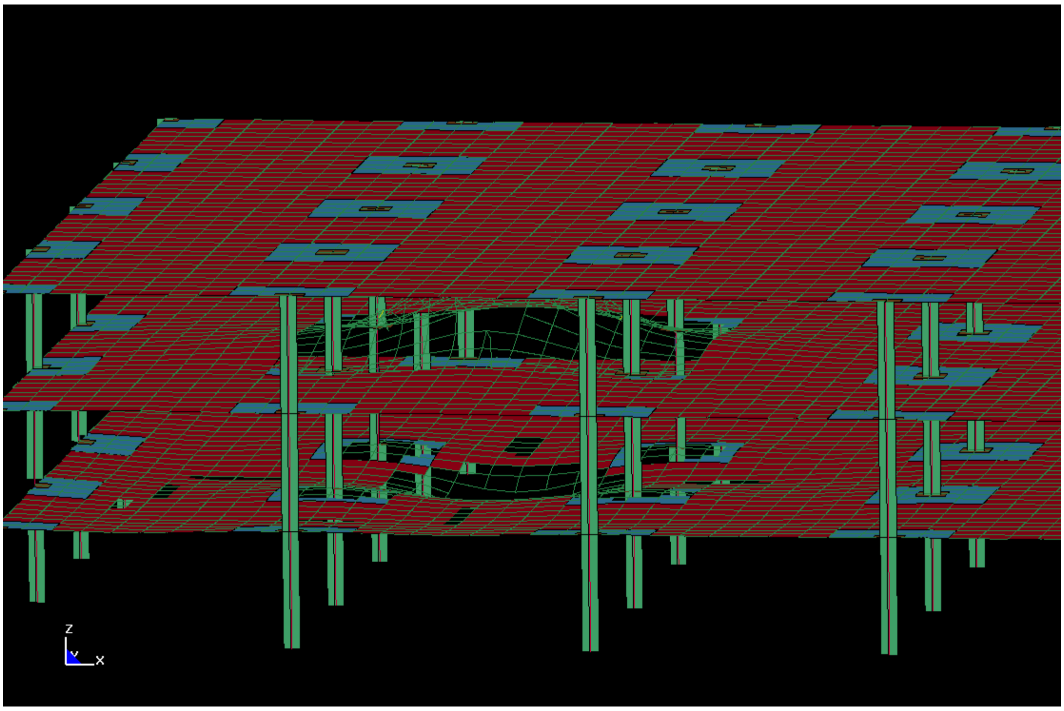

Figure 12: Blast into a frame-type building. 400 kg TNT

and explosion on full-scale buildings.

- Structural elements are needed for full frame-type building analysis due to computational cost.
- Structural elements models must be calibrated against fully three-dimensional models to obtain accurate enough.
- The strategy provide an approximate problem solution, for detailed analysis of structure parts three-dimensional model must be used.
- This strategy has limitations like action evaluation in successive floors and projectile considerations that need further develop. Structure collapse require additional adjustment of models.
- This strategy can be used to evaluate damage in building for blast loading and to test design improves on future buildings.

The studies which are presented herein have been carried out as part of a research project involving the Polytechnic University of Madrid and FHECOR Consulting Engineers, with the financial support of the Spanish Airport Authority (AENA) with the aim of modeling explosion hazards and improving robustness in the design of new structures. The work presented in this paper is but a small part of the research project whose scheduled time duration is 3 years.

REFERENCES

[1] Y. D. Murray, A.Abu-Odeh, R. Bligh, *Evaluation of LS-DYNA concrete material model 159*. U.S. Department of Transportation Federal Highway Administration, 2007.

[2] J.O. Hallquist, *LS-DYNA theory manual*. Livermore Software Technology Corporation, 2006.

[3] B. M. Luccioni, D. Ambrosini, R. Danesi, Colapso estructural bajo cargas explosivas, *Mecánica Computacional*, **XXII**, 957-970, 2003.

[4] H. Corres, E. Romero, *Reconstrucción ”módulo D” aparcamiento Madrid Barajas T-4*, Fhecor report.

[5] J. Leppänen, *Dynamic Behaviour of Concrete Structures subjected to Blast and Fragment Impacts*, Department of Structural Engineering Concrete Structures, Chalmers University of Technology, Gteborg, Sweden, 2002.

[6] B. Luccioni, R. Ambrosini, R. Danesi, Analysis of building collapse under blast loads, *Engineering Structures*, 2004, **26**, 63-71.

[7] *LS-DYNA keyword user manual*. Livermore Software Technology Corporation, 2010.

[8] G. Randers-Pehrson, K. A. Bannister, *Airblast Loading Model for DYNA2D and DYNA3D*. ARMY RESEARCH LABORATORY, 1997.

[9] *TM5-855-1. Fundamentals of protective design for conventional wepons*. U.S. Department of the Army Technical Manual, 1978.

[10] D. Hao, L. Zhongxian, Numerical Analysis of Dynamic Behavior of RC Slabs Under Blast Loading, *Trans. Tianjin Univ*, 2009, 15: 061-064. 2009

[11] T. P. Slavik, A Coupling of Empirical Explosive Blast Loads to ALE Air Domains in LS-DYNA, *7th European LS-DYNA Conference*, 2009

COMPDYN 2011
3rd ECCOMAS Thematic Conference on
Computational Methods in Structural Dynamics and Earthquake Engineering
M. Papadrakakis, M. Fragiadakis, V. Plevris (eds.)
Corfu, Greece, 25–28 May 2011

INFLUENCE OF THE FLUID-STRUCTURE INTERACTION ON THE MODAL ANALYSIS, AND ON THE DYNAMICS OF COMPOSITE MONOFIN : OPTIMIZATION OF PROPULSION

B. Mahiou, F. Razafimahery and L. R. Rakotomanana

IRMAR, UMR 6625, CNRS & Université de Rennes 1, Equipe de Mécanique
Campus de Beaulieu, 35042, Rennes Cédex
Email : benjamin.mahiou@free.fr
Email : fulgence.razafimahery@univ-rennes1.fr
Email : lalaonirina.rakotomanana-ravelonarivo@univ-rennes1.fr

Keywords: Fluid-structure interaction, modal analysis, thrust, finite element method.

Abstract. *This study aims to analyze the propulsive efficiency of a swimming multi-layers fin. For this purpose, we develop a finite element model accounting for the fluid-structure interaction and the structural anisotropy of each layer. Two types of fins have been tested by comparing their eigenfrequencies. A dynamical situation has been simulated by imposing a translation (heaving) and a rotation (pitching) motions at the end of the fin, using in some sense a relative frame attached to the ankle joint. Thrust, lift and pitching moment are evaluated and compared for the two types of fins.*

1 INTRODUCTION

The aquatic locomotion of animal constitutes a fascinating research domain in biomechanics. The search for performance of aquatic propulsion generated by a foil undergoing harmonic flapping, including translation (heaving) and rotation (pitching) motions, has stimulated numerous works during these last years e.g. [4], [10], [13], [17] . In the case of swimming with fins, the propulsive efficiency depends on several factors. Most previous models evaluate the dynamic performances, including drag and lift which are the two parameters usually considered as relevant to quantify the propulsive efficiency of a fin e.g. [12]. Some models are essentially of discrete type[11], [8], while others, inspired from propulsion of marine cetaceans, use continuous models [1], [18]. Most of these authors do not always demonstrate the highly coupled nature of the problem. In fact, for range of stresses observed in actual swimming, the coupling between the fluid and the fin cannot be neglected. Another aspect is the accounting of the ankle muscle for the propulsion. The frequency determination is deemed necessary since the muscle activity during fin swimming has important correlation with the oscillating flapping frequency e.g. [9]. The activation of muscles increases up to $25\ \%$ when the swimming frequency increases from $0.8\ [Hz]$ to $1\ [Hz]$. In order to improve the adequation of fin with muscle activities, previous studies highlight the role of structural composites and their arrangement for optimizing the propulsion of fin. The static deformation together with the eigenfrequencies of the fin are considered as basic parameters for optimization e.g. [7]. Unfortunately most of them do not account for the water interaction with the fin.

This work is mainly numerical and develops a continuous model in the framework of the fluid-structure interaction approach and constitutes a continuation of a previous study in [2]. The goal is to undertake a parametric analysis of two different designs of multi-layers fin by comparing their eigenfrequencies by accounting for the water interaction. We simulate the evolution of thrust and lift forces, together with the moment (torque about the pitch axis) during a steady propulsion. This approach enables a parametric study, where we can vary some data related to the geometrical, physical and kinematic model. The study consists of three parts. The first part sets out the different assumptions underlying, the development of the theoretical basic model. In the second part, we focus on the modal analysis. To this end, we analyze the changes of eigenfrequencies when varying the physical characteristics of the fin. We are interested on the influence of the layers arrangement and on the influence of the interacting water on the fin eigenmodes. The third part deals with the dynamics. For this purpose, we consider a frame attached to the fin, or more precisely at the foot of the swimmer, and impose a translational (heaving) and rotational (pitching) motions. Two types of multi-layers fins are also studied.

2 Theoretical model of the multi-layers fin

We assume an amateur swimmer, where the range of velocity U_0 is assumed to be small compared to the compression wave celerity c_L within the material of the fin. The ratio $\varepsilon = U_0/c_L << 1$, called displacement parameter, allows to characterize the nature of the coupling considered in this work. It has been shown in [3] that the adapted model is the inertial coupling.

The model is bidimensional (since we are mainly interested in the first bending modes in this preliminary analysis) and the (thin) fin is immersed in a large swimming pool. The fin is modeled by a multilayer linear elastic transverse anisotropic material. The fluid domain is denoted Ω_f, while each layer constituting the fin is denoted by Ω_i and has the density ρ_i.

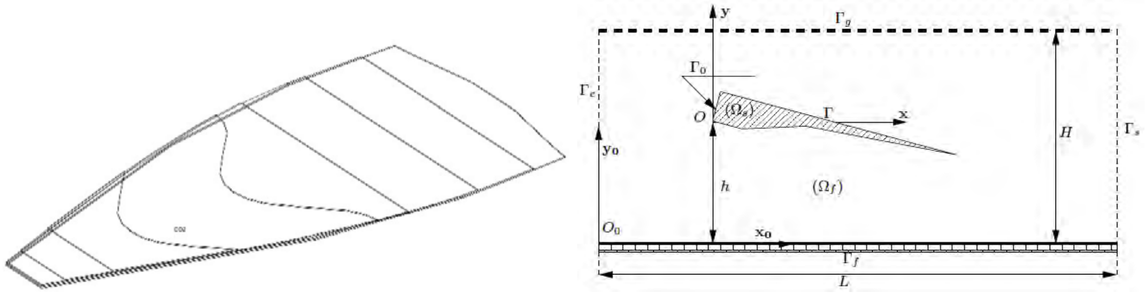

Figure 1: Geometry of 3D fin (dimensions are given below) and scheme of the computational domain (Dimensions of the swimming pool : length $5\ [m]$, depth $2\ [m]$).

2.1 Basic equations

We denote $\mathbf{u}_i$ the displacement field in the fin and p the pressure field in the water, which is considered as non viscous compressible fluid. The quantities c_0 and ρ_0 denote the sound velocity and density of the water respectively. We accordingly remain in the framework of vibro-acoustic problems. The longitudinal axis of the fin is denoted $\mathbf{x}$. Use of the ALE method is not necessary in this study because the material is assumed linear and the deformation is assumed small. In the frame attached to the fin, the problem is to find $(\mathbf{u}_i, p)$ solutions

$$\left\{\begin{array}{ccccc}
\rho_i \dfrac{\partial^2 \mathbf{u}_i}{\partial t^2} & = & \nabla \cdot \sigma(\mathbf{u}_i) + \rho_i \mathbf{F} & (\Omega_i) \\
\dfrac{1}{\rho_0 c_0^2} \dfrac{\partial^2 p}{\partial t^2} & = & \nabla \cdot \left[\dfrac{1}{\rho_0} \left(\nabla p - \rho_0 \mathbf{F} \right) \right] & (\Omega_f) \\
\mathbf{u} & = & \mathbf{0} & (\Gamma_0) \\
\sigma(\mathbf{u})\mathbf{n} & = & -p\mathbf{n} & (\Gamma) \\
[\nabla p - \mathbf{q}] \cdot \mathbf{n} & = & -\rho_0 \dfrac{\partial^2 \mathbf{u}}{\partial t^2} \cdot \mathbf{n} & (\Gamma) \\
[\nabla p - \mathbf{q}] \cdot \mathbf{n} & = & 0 & (\Gamma_1) \\
p & = & 0 & (\Gamma_L) \\
\sigma(\mathbf{u}_i) & = & \mathbb{K}(\theta_i) \varepsilon(\mathbf{u}_i) & (\Omega_i)
\end{array}\right. \tag{1}$$

where $\mathbf{F}$ is the relative and Coriolis force induced by the heaving and pitching motions (relative frame concept) of the fin. The angle θ_i denotes the orientation of fibers relative to the longitudinal axis $\mathbf{x}$ on the fin. In our case, each layer is made of matrix and carbon fibers. The orientation of fibers is usually $0°$ or $90°$ relative to the axis of the fin. The physical properties of each layer defined by the tangent stiffness $\mathbb{K}(\theta_i)$ are well defined for anisotropic componenet e.g. [14]. However, some characteristic values are not displayed for industrial confidentiality reason. In this study, each layer has the same properties, only the fiber orientation is different for each layer as indicated below.

2.2 Modal analysis of coupled problem

For the modal analysis, we search for the eigenfrequencies and modal shapes of the fin in vacuum and in water. Indeed, to test the quality of a fin, it is usual to determine its quasi-static deformed shape and dynamic response in air (approximately as in vacuum). The objective here is to test if the presence of the surrounding fluid can or cannot be quantitavely neglected. The frequencies provide key information for the dynamic behavior of the fin e.g. [8]. The modal problem associated with the system (1) is to find the displacement, the pressure and the eigenfrequencies $(\mathbf{u}_i, p, \omega)$ solutions

$$\left\{\begin{array}{rcll} -\rho_i\omega^2\mathbf{u}_i & = & \nabla\cdot\sigma(\mathbf{u}_i) & (\Omega_i) \\ -\dfrac{p}{\rho_0 c_0^2}\omega^2 & = & \nabla\cdot\left[\dfrac{1}{\rho_0}\nabla p\right] & (\Omega_f) \\ \mathbf{u} & = & \mathbf{0} & (\Gamma_0) \\ \sigma(\mathbf{u})\mathbf{n} & = & -p\mathbf{n} & (\Gamma) \\ \nabla p\cdot\mathbf{n} & = & \rho_0\omega^2\mathbf{u}\cdot\mathbf{n} & (\Gamma) \\ \nabla p\cdot\mathbf{n} & = & 0 & (\Gamma_1) \\ p & = & 0 & (\Gamma_L) \\ \sigma(\mathbf{u}_i) & = & \mathbb{K}(\theta_i)\varepsilon(\mathbf{u}_i) & (\Omega_i) \end{array}\right. \tag{2}$$

By introducing the spaces of test functions $\mathbf{V} = \{\mathbf{v}\in\mathbf{H}^1(\Omega_1),\ \mathbf{v} = \mathbf{0}\ (\Gamma_0)\}$ for displacement and $Q = H^1(\Omega)$ for pressure, the variational formulation of boundary value problem (2) holds

$$\left\{\begin{array}{lcl} \dfrac{d^2}{dt^2}\displaystyle\int_{\Omega_s}\rho\mathbf{u}\cdot\mathbf{v}dx + \int_{\Omega_s}\sigma(\mathbf{u}):\varepsilon(\mathbf{v})dx + \int_{\Gamma_1}p\mathbf{v}\cdot\mathbf{n}d\Gamma & = & 0 \\ \dfrac{d^2}{dt^2}\left(\displaystyle\int_{\Omega_f}\frac{p\phi}{\rho_0 c_0^2}dx + \int_{\Gamma_1}\mathbf{u}\cdot\mathbf{n}\phi d\Gamma\right) + \displaystyle\int_{\Omega_f}\frac{1}{\rho_0}\nabla p\cdot\nabla\phi dx & = & 0 \end{array}\right. \quad \forall(\mathbf{v},\phi)\in\mathbf{V}\times Q \tag{3}$$

with $\displaystyle\int_{\Omega_s}\rho\mathbf{u}\cdot\mathbf{v}dx = \sum_{i=1}^{N_L}\int_{\Omega_i}\rho_i\mathbf{u}_i\cdot\mathbf{v}_i dx$ and $\displaystyle\int_{\Omega_s}\sigma(\mathbf{u}):\varepsilon(\mathbf{v})dx = \sum_{i=1}^{N_L}\int_{\Omega_i}\sigma(\mathbf{u}_i):\varepsilon(\mathbf{v}_i)dx$, where N_L is a number of layers. Using Lagrange finite elements, where $\mathbf{u}_h\in\mathbb{P}_2\times\mathbb{P}_2$ and $p_h\in\mathbb{P}_1$, discretization of the variational problem (3) leads to the system

$$\left\{\left[\begin{array}{cc}\mathbb{K}_1 & \mathbb{B}_1 \\ \mathbb{O} & \mathbb{K}_p\end{array}\right] - \omega^2\left[\begin{array}{cc}\mathbb{M}_1 & \mathbb{O} \\ \mathbb{M}_{1a} & \mathbb{M}_p\end{array}\right]\right\}\mathbf{X} = \mathbf{0} \tag{4}$$

This non symetric system is solved using the commercial software Comsol Multiphysics. Two types of calculations were carried out. The first is when the fin is plunged into a vacuum and the second interacting with water. We give below the results for a model up to five layers ($N_L = 5$) and the eigenfrequencies in vacuum (V) and in the water (W).

3 Numerical results

Two designs of multi-layers fins are compared in this section. Both of them are analyzed first in a vacuum and second in the swimming pool, and then interacting with water. Each layer is a biphasic composite and the matrix (m) and fiber (f) have the following properties respectively: Volume fraction $V_m = 0.4$ and $V_f = 0.6$, Young's modulus : $E_m = 3.45E9[GPa]$, and $38E9[GPa]$; Density $\rho_m = 1200[kg/m^3]$, and $\rho_f = 1950[kg/m^3]$; Poisson's ratio : $\nu_m = 0.3$, and $\nu_f = 0.22$.

3.1 Fin with Oriented fibers : $0°/90°/0°/90°/0°$

The fibers of each layer are arranged alternately along the two directions orthogonal axis **x** and **y** of the mean plane of the fin.

For this first fin, the first layer is oriented along x. The length of each layer is not the same. Lengths of layers are respectively $\ell := \ell_1 = 0.8[m]$, $\ell_2 = 0.6[m]$, $\ell_3 = 0.5[m]$, $\ell_4 = 0.4[m]$, and $\ell_5 = 0.3[m]$. Layer's length corresponds to the ply drop in [7]. The total thickness of the fin is maintained constant $e = 5.8[mm]$, and it is not depending on the number of layers. The fin is clamped at the end $x = 0$ and free of stress at end $x = \ell$.

1. Eigenfrequencies of fin in the vacuum

   The three-layers fin presents the highest eigenfrequencies in either a vacuum or in the water (see table 1), at least for the first frequencies.

	f_1	f_2	f_3	f_4	f_5	f_6	f_7	f_8
$2L$(V)	12.62	76.02	205.33	389.27	628.95	929.39	1293.32	1717.79
$3L$(V)	29.38	122.99	265.07	555.85	825.17	1326.14	1764.36	2321.13
$4L$(V)	22.68	90.16	192.04	404.72	600.38	958.85	1303.21	1692.38
$5L$(V)	28.82	79.74	185.16	373.97	560.99	904.69	1185.87	1632.83

Table 1: Eigenfrequencies f_n $[Hz]$ of the multi-layers fin in vacuum. Row $2L$ up to $5L$ indicates the number of layers of the fin.

2. Eigenfrequencies of fin interacting with water

	f_1	f_2	f_3	f_4	f_5	f_6	f_7	f_8
$2L$(W)	1.71	46.06	103.15	180.88	186.73	232.08	297.77	342.08
$3L$(W)	3.52	21.72	55.17	136.63	181.29	222.63	232.10	341.95
$4L$(W)	2.42	14.56	37.35	92.22	150.82	181.27	232.08	263.14
$5L$(W)	2.77	11.85	33.49	78.53	128.93	181.22	227.74	232.11

Table 2: Eigenfrequencies f_n $[Hz]$ of the multi-layers fin interacting with water. Row $2L$ up to $5L$ indicates the number of layers of the fin.

The fundamental eigenfrequency f_1 (and the others) depends on the arrangement of the layers. The two-layers fin has mostly the lowest fundamental frequency either in the vaccum or in the water (see table 2). There is systematically a peak of frequencies for the three-layers fin, not depending on the environnement (vacuum or water). This means that this arrangement induces the stiffest fin, at least for a dynamics point of view. The fundamental eigenfrequency of the coupled fin-water is far lower than of the fin in vacuum. This observation does not depend on the number of layers. To give an idea of the eigenmodes, we display on figure 2 the first six modal shapes of the fin interacting with the water for a five-layers case ($5L(W)$).

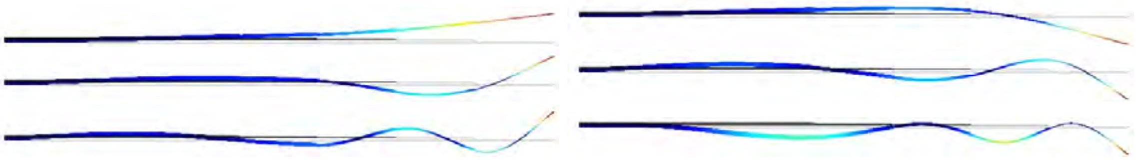

Figure 2: The first six mode shapes of the five-layers fin ($5L(W)$).

These are mainly bending modes for this 2D model. Due to the clamping at $x = 0$, and due to the progressive ply drop, the largest deformation is mainly located at the free end of the fin. For the terminolgy, if the first and second modes are involved for the propulsion, the fin swimming could be considered as undulatory type (anguilliform), whereas if the higher mode ranks are involved (oscillation of posterior part of the fin) then the fin swimming could be considered as carangiform e.g. [17].

3.2 Fin with Oriented fibers : $90°/0°/90°/0°/90°$

As for previous fin, fibers of each layer are arranged alternately along the two directions orthogonal axis **x** and **y** of the mean plane of the fin. However for this second fin, the first layer is oriented along $\mathbf{y}$. The length of each layer is not the same. Lengths of layers are respectively $\ell := \ell_1 = 0.8[m]$, $\ell_2 = 0.6[m]$, $\ell_3 = 0.5[m]$, $\ell_4 = 0.4[m]$, and $\ell_5 = 0.3[m]$. The total thickness of the fin is also maintained constant $e = 5.8[mm]$, and it is not depending on the number of layers. The fin is also clamped at the end $x = 0$ and free of stress at $x = \ell$.

1. Eigenfreqncies of fin in a vacuum

	f_1	f_2	f_3	f_4	f_5	f_6	f_7	f_8
$2L$(V)	12.61	73.51	158.46	273.94	488.33	757.90	997.37	1284.11
$3L$(V)	9.52	51.39	105.50	186.01	327.05	507.18	670.71	861.59
$4L$(V)	21.21	56.23	115.59	237.62	395.78	560.89	773.54	1093.47
$5L$(V)	17.44	44.84	91.62	186.19	313.60	444.60	606.69	867.88

Table 3: Eigenfrequencies f_n $[Hz]$ of the multi-layers fin in the vacuum. Row $2L$ up to $5L$ indicates the number of layers of the fin.

2. Eigenfrequencies of fin interacting with water

	f_1	f_2	f_3	f_4	f_5	f_6	f_7	f_8
$2L$(W)	1.71	13.30	39.45	72.24	136.51	181.24	232.04	235.54
$3L$(W)	1.14	8.74	23.87	45.06	86.89	147.57	181.24	215.08
$4L$(W)	2.28	9.53	23.83	50.30	97.46	156.71	181.22	219.41
$5L$(W)	1.68	6.89	17.23	36.93	70.87	113.85	161.15	181.31

Table 4: Eigenfrequencies f_n $[Hz]$ of the multi-layers fin interacting with water. Row $2L$ up to $5L$ indicates the number of layers of the fin.

Contrarily to the first type, the three-layers fin presents the lowest eigenfrequencies, and it is depending neither on the environnement vacuum or water, nor on the mode rank. Highest eigenfrequencies mostly correspond to the two-layers fin. Again, the influence of the fin-water interaction is pointed out, the presence of water, which is more realistic, in the model drastically decreases the eigenfrequencies of the fin.

Comparing the two types of multi-layers fins, we may observe that : the eigenfrequencies value depends strongly on the arrangement of layers, and such is the case either in a vacuum or in water. Fibers of the first layer along $\mathbf{x}$ seems to give highest fundamental eigenfrequency when there are several layers in the fin. The frequencies of the coupled model are always lower. It is quite understandable due to the effect of added mass from water interaction. Anticipating a study in progress in our team, it should also be observed that accounting the 3D effects decreased the fundamental frequency, which also corresponds to a bending modes, for instance the four-layers fin gives in vacuum $f_1 \simeq 7.74$ $[Hz]$, and in water $f_1 \simeq 1.13$ $[Hz]$ as fundamental eigenfrequency.

4 The dynamic problem

The dynamic problem was conducted using data in [15]. For this purpose, the fin is immersed in water, and is subjected to a combined heaving and pitching motions, mimicking the ankle joint motion. This motion is imposed at the end $x = 0$, the other end $x = \ell$ remains free. In this case, the force $\mathbf{F}$ induced by the relative frame motion introduced in the equation (1) has the expression :

$$\mathbf{F}(t) = -\left[\begin{array}{c} \ddot{h}(t)\sin[\omega(t)] - y\ddot{\omega}(t) - x\dot{\omega}^2(t) \\ \ddot{h}(t)\cos[\omega(t)] + x\ddot{\omega}(t) - y\dot{\omega}^2(t) \end{array}\right] \tag{5}$$

in which we have defined the imposed translation and rotation e.g. [15] :

$$\left\{\begin{array}{l} \omega(t) = \theta_0 \sin(2\pi f t)\ ;\ h(t) = h_0 \sin(2\pi f t - \psi) \\ \theta_0 = 40^\circ\ ;\ \psi = \dfrac{\pi}{2}\ ;\ h_0 = 1c\ ;\ f = 0.225Hz \end{array}\right. \tag{6}$$

where $c = 0.7$ is the chord of the profile, that is to say, the length of the fin. The phase ψ is introduced to model the muscle dissymmetry. To avoid a resonance phenomenon, the excitation frequency is imposed small enough compared to the first natural frequency of the coupled system. The most relevant hydrodynamic parameters are the total force $\mathbf{R}$ and moment $\mathbf{M}$ exerted on the fin during the movement. Notice that these forces and moment are solely due to the water reaction. These quantities are defined by

$$\mathbf{R} = \int_\Gamma \sigma(\mathbf{u})\mathbf{n}d\Gamma\ ;\ \mathbf{M} = \int_\Gamma \mathbf{OM} \wedge \sigma(\mathbf{u})\mathbf{n}d\Gamma \tag{7}$$

The two components of D and L onto the axes $\mathbf{x}$ and $\mathbf{y}$, are respectively the drag and lift of the fin. The quantity $T(t) = -X(t)$ is called thrust. Different types of layers exist in the manufacture of fins, where the thickness is mostly fixed in advance. We test the same fins as in the modal analysis. Using the same notation as before, the variational formulation of boundary value problem (1) is then written

$$\left\{\begin{array}{lcl} \dfrac{d^2}{dt^2}\displaystyle\int_{\Omega_s} \rho\mathbf{u}\cdot\mathbf{v}dx + \int_{\Omega_s} \sigma(\mathbf{u}) : \varepsilon(\mathbf{v})dx + \int_{\Gamma_1} p\mathbf{v}\cdot\mathbf{n}d\Gamma & = & -\displaystyle\int_{\Omega_s} \rho\mathbf{F}\cdot\mathbf{v}dx \\ \dfrac{d^2}{dt^2}\left(\displaystyle\int_{\Omega_f} \frac{p\phi}{\rho_0 c_0^2}dx + \int_{\Gamma_1} \mathbf{u}\cdot\mathbf{n}\phi d\Gamma\right) + \displaystyle\int_{\Omega_f} \frac{1}{\rho_0}\nabla p\cdot\nabla\phi dx & = & \displaystyle\int_{\Omega_f} \frac{1}{\rho_0}\mathbf{q}\cdot\nabla\phi dx \end{array}\right. \tag{8}$$

forall $(\mathbf{v}, \phi) \in \mathbf{V} \times Q$, with $\mathbf{V} = \{\mathbf{v} \in \mathbf{H}^1(\Omega_1),\ \mathbf{v} = \mathbf{0}\ (\Gamma_0)\}$ and $Q = H^1(\Omega)$.

Using Lagrange finite elements, where $\mathbf{u}_h \in \mathbb{P}_2 \times \mathbb{P}_2$ et $p_h \in \mathbb{P}_1$, discretization of the variational problem (8) leads to the semi-discretized system

$$\left[\begin{array}{cc} \mathbb{M}_1 & \mathbb{O} \\ \mathbb{M}_{1a} & \mathbb{M}_p \end{array}\right]\frac{d^2\mathbf{X}}{dt^2} + \left[\begin{array}{cc} \mathbb{K}_1 & \mathbb{B}_1 \\ \mathbb{O} & \mathbb{K}_p \end{array}\right]\mathbf{X} = \mathbf{F} \tag{9}$$

with $\mathbf{X} = [\mathbf{U}, \mathbf{P}]^T$ and $\mathbf{F} = [\mathbf{F}_1, \mathbf{F}_2]^T$. In this section, we use a particular kinematics proposed in [15]-[16], even if our models are not exactly similar. Indeed, the kinematics will allow us in future to develop a new experimental protocol for measuring various hydrodynamic parameters of a fin.

4.1 Dynamic response to the fin

To better define a reasonable perfomance of the fin, we take the total expression of the excitation force $\mathbf{F}(t)$ resulting from (6). We then obtain the different response curves where the end $x = 0$ is constrained to a combined translational and rotation motions.

4.1.1 Oriented fibers : $0°/90°/0°/90°/0°$

As a recall, fibers of each layer are arranged alternately along the two directions orthogonal axis **x** and **y** of the mean plane of the fin. For this first fin, the first layer is oriented along **x**. The length of each layer is not the same. Lengths of layers are respectively $\ell := \ell_1 = 0.8[m]$, $\ell_2 = 0.6[m]$, $\ell_3 = 0.5[m]$, $\ell_4 = 0.4[m]$, and $\ell_5 = 0.3[m]$. The total thickness of the fin is maintained constant $e = 5.8[mm]$, and it is not depending on the number of layers.

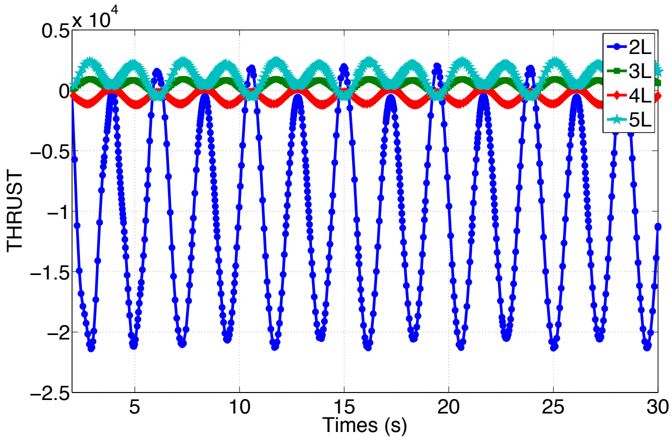

Figure 3: Thrust force $[N]$ during the course of time $[s]$ for the $2L$, $3L$, $4L$, and $5L$ models.

The magnitude of thrust force induced by the two-layers fin is greater than the other fins, although its value is mosty negative. Remind that the eigenfrequency of this fin is the lowest. This nevertheless seems abnormal and requires further close analysis. The behaviours of the other three fins are quite similar.

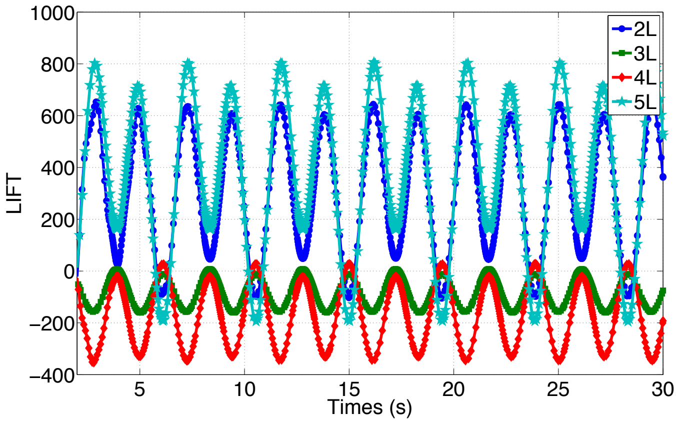

Figure 4: Lift force $[N]$ during the course of time $[s]$ for the $2L$, $3L$, $4L$, and $5L$ models.

We remark that the lift force for the two-layers and the five-layers fins behaves similarly (they are mostly positive), whereas the three and four-layers are quite comparable (they are mostly negative). Magnitude of lift force is greater for the two-layers and the five-layers fins. By the way, they are mostly positive.

The moment magnitude is lowest for the two-layers models, compared to the other fins. Again the two- and five-layers fins have similar behaviour (positive moment), although with

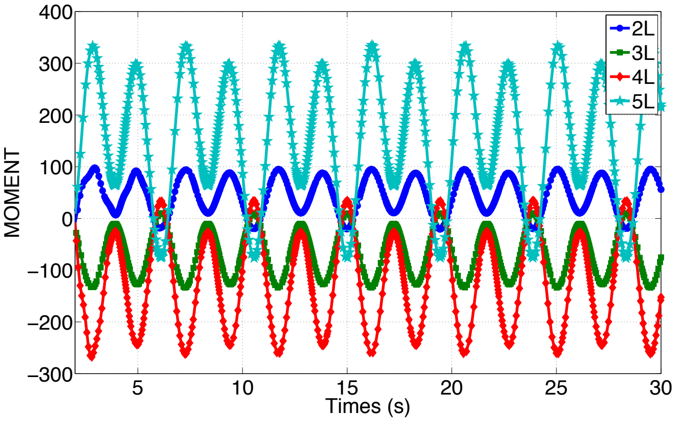

Figure 5: Moment $[m\ N]$ during the course of time $[s]$ for the $2L$, $3L$, $4L$, and $5L$ models.

different magnitude; whereas the three- and four-layers fins have negative moment.

4.1.2 Oriented fibers : $90°/0°/90°/0°/90°$

Recall also that fibers of each layer are arranged alternately along the two directions orthogonal axis **x** and **y** of the mean plane of the fin. However for this second fin, the first layer is oriented along $\mathbf{y}$. The length of each layer is not the same. Lengths of layers are respectively $\ell := \ell_1 = 0.8[m]$, $\ell_2 = 0.6[m]$, $\ell_3 = 0.5[m]$, $\ell_4 = 0.4[m]$, and $\ell_5 = 0.3[m]$. The total thickness of the fin is maintained constant $e = 5.8[mm]$, and it is not depending on the number of layers.

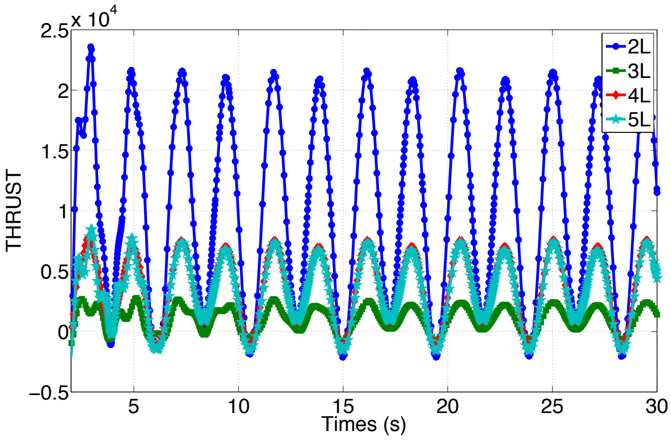

Figure 6: Thrust force $[N]$ during the course of time $[s]$ for the $2L$, $3L$, $4L$, and $5L$ models.

Again, the magnitude of thrust force induced by the two-layers fin is greater than the other fins, although its value is mosty now positive. Remind also that the eigenfrequency of this fin is the lowest. The behaviours of the other three fins are quite similar, with a positive thrust force for all of them (Figure 6).

The four-layers fin present the lowest magnitude for the lift force (mostly negative values), whereas the three-layers fin has the greatest amplitude. The other three models have positive lift force (Figure 7).

The five-layers fin induces very low moment magnitude compared to the other fins. Again

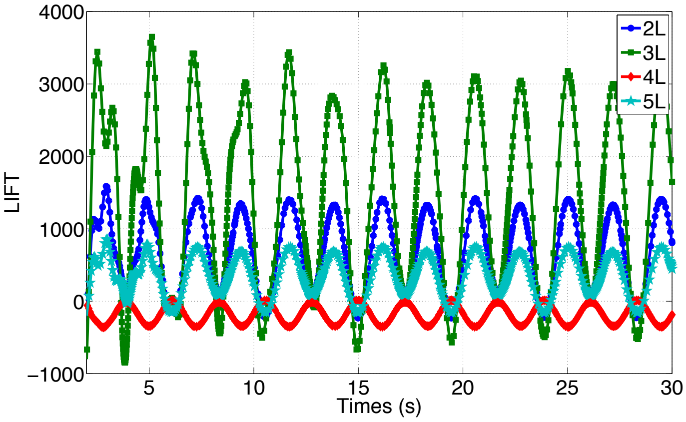

Figure 7: Lift force $[N]$ during the course of time $[s]$ for the $2L$, $3L$, $4L$, and $5L$ models.

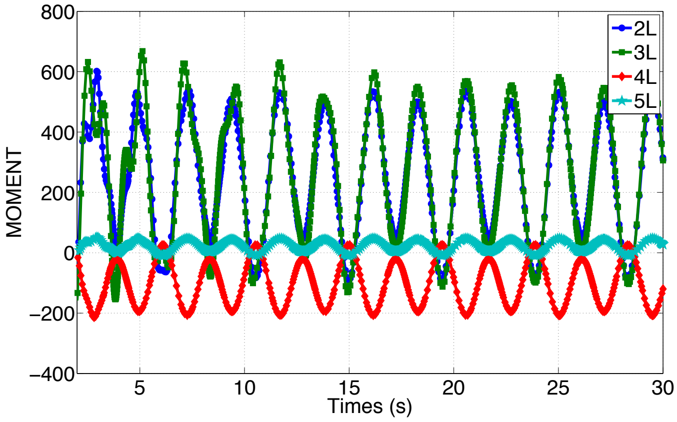

Figure 8: Moment $[m\ N]$ during the course of time $[s]$ for the $2L$, $3L$, $4L$, and $5L$ models.

the four-layers fin has mostly negative moment (Figure 8). Such is not the case for the other models.

Again comparing the two types of multi-layers fins, we may draw some remarks. The two-layers model always gives a greater thrust than the other models. It should be however pointed out that the fibers arrangement may induce negative or positive thrust for this fin. If we eliminate this case, we may see that the five-layers fin gives the best performance.

In a general manner, the three-layers fin seems to give a better compromise. Indeed, its thrust remains positive all the time, while its lift has negative value and nevertheless less of lower importance than other fins. The moment magnitude associated to the three-layers model is also the lowest. In sum, it is then shown that by varying some physical parameters, we can significantly reduce or increase hydrodynamic quantities, such as the thrust, the moment, and the lift.

4.1.3 Water pressure for fin with Oriented fibers : $0°/90°/0°/90°/0°$

To see how the overall response of the coupled system evolves, we display in the figures below (Figure 9) and at different times $t = 2, 4, 6, 8\ [s]$ the pressure field within water, and the iso-acceleration lines. We also display the deformed shapes of the fin (first layer parallel to x) at the associated times. The present model uses an acoustic model of the water, and neglects the viscosity, although the thrust production is thought to be strongly correlated with the formation and shedding of leading edge vortices. In a viscous situation, the wake formed behind the fin is affected by the interaction of the leading edge vortex with the fin and with the training vortex. This could captured in our model. In the present study, the evolution of the field pressure $p\left(\mathbf{x},t\right)$ in the course of time shows the influence of the swimming pool dimensions on the result. Accuracy of results may be improved by considering much larger dimensions of the pool.

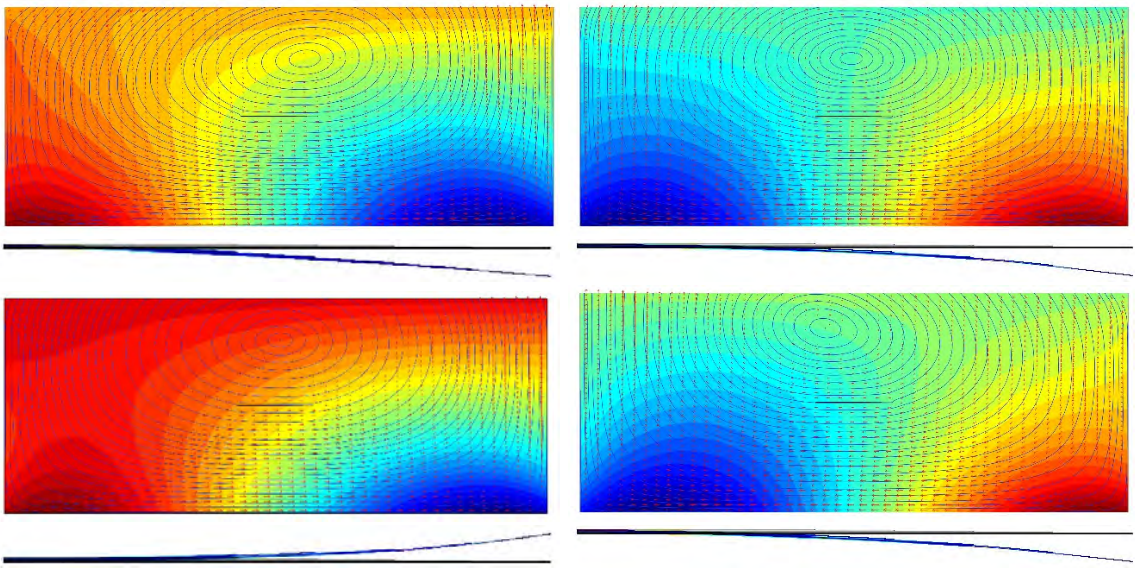

Figure 9: Pressure contour plot $p\left(\mathbf{x},t\right)$, iso-acceleration lines, and associated deformed shapes of the five-layers fin, at different times $t = 2, 4, 6, 8$ $[s]$. Remind that the fundamental frequency of this fin is $f_1 = 2.77$ $[Hz]$, and the excitation frequency $f_{exc} = 0.225$ $[Hz]$. The fin is displayed in the middle region of the pool.

5 CONCLUDING REMARKS

A parametric analysis of eigenfrequencies of multilayers composite fin has been done by considering the influence of the surrounding water. The fluid flow, and more precisely the evolution of water pressure around a 2D deformable fin, and the deformation of the fin itself in a steady motion due to a harmonic heaving and pitching motions, have been simulated by accounting the mutual interaction of the water and the fin. From the present results, we may draw some concluding remarks.

- The presence of layers provides some flexibility for the fin design as indicated by the results of modal analysis. The first mode is bending type, which justifies the use of models proposed in [11].
- Fins with anisotropic material structures allow to develop a method of layers parametrization to improve performance. It is quite possible now to bring special attention to the structure of the layers, and types of constituent materials thereof.
- The present study points out the sensitivity of the dynamic behavior of the fin with respect to the constitute materials, and also the influence of the boundary conditions for the fluid

domain. Indeed, the presence of rigid walls alters significantly the eigenmodes and frequencies of the coupled system. Accordingly, the dynamic behavior of a swimmer may depend on this location at each time in the pool.

- Finally, to obtain a better thrust, the fin has to be elastic at least in rotation. The amplitude of the vertical translation must be controlled to avoid a too great lift, which may lead to an expenditure of extra energy of the swimmer to remain at a constant depth. The use of multilayer fins allows to control the non desirable excessive variation of lift.

Extension of the present study to 3D fins together with viscous fluid is ongoing.

Acknowledgments.

B.M. was partially supported by the Breier Fin Company, France (CIFRE grants).

REFERENCES

[1] I. Akhtar, R. Mittal, G. V. Lauder and E. Drucker. Hydrodynamic of biologically inspired tandem flapping foil configuration. *Theor. Comput. Fluid Dyn.*, 21, 155-170, 2007.

[2] N. Bideau, B. Mahiou, L. Monier, B. Bideau, G. Nicolas, F. Razafimahery, L. Rakotomanana. Dynamique couplée 2D d'un modèle de palme. *Proceedings, 4èmes journées spécialisées de Natation*, p. 119-120, 27-28 mai 2008, Lille.

[3] A. El-Baroudi, F. Razamahery, N. Bideau, L. Rakotomanana. Inuence of fluid-structure interaction in biomechanics : Application to parametric modal analysis and dynamics of the aorta under a shock, *International Journal in Biomedical Engineering and Technology*, To appear, 2011.

[4] T.Y. Hou, V.G. Stredie, T.Y. Wu. Mathematical modeling and simulation of aquatic and aerial animal locomotion. *Journal of Computational Physics*, 225, 1603-1631, 2007.

[5] W-R. Hu. A numerical study on mechanism of S-Starts of Northern Pike (Esox Lucius). *Journal of Hydrodynamics*, Ser. B, 19(2), 135-142, 2007.

[6] W. Kowalczyk and A. Delgado. Simulation of Fluid Flow in a Chanel Induced by Three Types of Fin-Like Motion. *Journal of Bionic Engineering*, 4, 165-176, 2007.

[7] M. A. Luersen, R. Le Riche. Adapting ply drop positions for compensating fabric changes - Applications to swimming monofins. *Finite Elements in Analysis and Design*, 46, 930-935, 2010.

[8] M. A. Luersen, R. Le Riche, D. Lemosse and O. Le Maître. A computationally efficient approach to swimming monofin optimization. *Struct. Multidisc. Optim.*, 31, 488-496, 2006.

[9] M. Koch, G. Gouvernet, P. Chavet, C. Barla, A. Sabo. Muscle activity during fin swimming. *Procedia Engineering*, 2, 3029-3034, 2010.

[10] J.-M. Miao and M.-H. Ho. Effects of flexure on aerodynamic propulsive efficiency of flapping flexible. *Journal of Fluids and Structures*, 22, 401-419, 2006.

[11] J. C. Mollendorf, J. D. Felske and S. Samimy. A Fluid/Solide Model for Predicting Slender Body Deflection in a Moving Fluid. *Transactions of ASME.*, 346, Vol. 70, May 2003.

[12] G. Nicolas, B. Bideau, B. Colobert and E. Berton. How are Strouhal number, drag, and efficiency adjusted in high level underwater monofin-swimming ? *Human Movement Science*, 26, 426-442, 2007.

[13] G. Pedro, A. Suleman and N. Djilali. A numerical study of the propulsive efficiency of a flapping hydrofoil. *International Journal for Numerical Methods in Fluids*, 42, 493-526, 2003.

[14] L.R. Rakotomanana. *Eléments de dynamique des solides et structures déformables*, Presses Polytechniques et Universitaires Romandes, Lausanne, 2009.

[15] D. A. Read, F. S. Hover and M. S. Triantafyllou. Forces on oscillating foils for propulsion and maneuvering. *Journal of Fluids and Structures*, 17, 163-183, 2003.

[16] S. Shin, S. Y. Bae, I. C. Kim and Y. J. Kim. Effects of flexibility on propulsive force acting on a heaving foil. *Ocean Engineering*, 36, 285-294, 2009.

[17] Schouveiler L., Hover F. S., Triantafyllou M.S. Peformance of flapping foil propulsion. *Journal of Fluids and Structures*, 20, 049-959, 2005.

[18] Y. Yadykin, V. Tenetov and D. Levin. The added mass of a flexible plate oscillating in a fluid. *Journal of Fluids and Structures*, 17, 115-123, 2003.

[19] C. Zhang, L-X. Zhuang and X-Y. Lu. Analysis for hydrodynamics for two-dimensional flow around waving plates. *Journal of Hydrodynamics*, Ser. B, 19(1), 18-22, 2007.

COMPDYN 2011
III ECCOMAS Thematic Conference on
Computational Methods in Structural Dynamics and Earthquake Engineering
M. Papadrakakis, M. Fragiadakis, V. Plevris (eds.)
Corfu, Greece, 25–28 May 2011

COUPLED DAMAGE-PLASTICITY BASED CONSTITUTIVE MODELING OF METALLIC MEMBRANE ELEMENT UNDER CYCLIC LOADING

Bahar Ayhan Tezer[1, 2*], **Pierre Jehel**[3], **Adnan Ibrahimbegovic**[1], **Hasan Engin**[2]

[1] Ecole Normale Supérieure de Cachan, LMT-Cachan
61, Avenue du Président Wilson, 94235, Cachan, France
ayhan@lmt.ens-cachan.fr, ai@lmt.ens-cachan.fr

[2] Istanbul Technical University, Department of Civil Engineering
34469, Istanbul, Turkey
ayhanb@itu.edu.tr, enginh@itu.edu.tr

[3] Ecole Centrale Paris, LMSSMat
Grande Voie des Vignes, 92296, Châtenay-Malabry, France
pierre.jehel@ecp.fr

Keywords: Plasticity, Damage, Cyclic Loading, FEM.

Abstract. *Micromechanics is employed in order to define the whole nonlinear inelastic behavior of a structure at meso/macro scale level where the presence of the inelastic phenomena (plasticity and/or damage) affects the material constitutive response depending on the loading conditions. This concept is important in the design of civil and mechanical engineering applications. This study illustrates a comprehensive theoretical formulation for a coupled damage-plasticity model and its numerical implementation under an extreme loading type such as an earthquake, which causes cyclic response and can lead to failure. Irreversible plastic deformation by plasticity, elastic response modification by the damage and the cyclic accumulation of deformation are modeled. A couple of numerical examples are presented in order to show the capability and efficiency of the proposed model for 2D membrane element, by using the operator split methodology.*

1 INTRODUCTION

Materials, which are used in the different domains of civil and mechanical engineering, can most probably be heterogeneous at a micro-scale. It may be difficult to predict the response of the whole structure to different kinds of loading due to the material characteristics.

Simo et al. [1] employed the stress-based formulation, which is the core of the numerical part of this current study for the elasto-plastic material behavior by using the classical finite element method [2]. Here, this type of formulation is constructed in order to couple both plasticity and damage [3]. The dependent Gauss point equations, which represent the evolution equations of the internal variables for both inelastic behaviors just mentioned, are solved simultaneously, so as to provide a single return mapping algorithm per element to control the equilibrium equations at macro scale. We use the operator split method to simplify the details of the numerical implementation, concerning the calculation of internal variables and equilibrium equations resulting with finite element approach at the structural state.

Study realized by Drucker and Palgen [4] stated that the material behavior under cyclic loading are much more complex than monotonic loading and cannot be modeled by isotropy alone. Therefore, the purpose of the present research is to present a plasticity model, in which both isotropic and kinematic hardening is taken into account. This will also be coupled with the damage model, which is defined in an analogous way as the plasticity model.

There are some important notifications based on researches [5, 6] for cyclic inelastic models; (i) symmetric stress and strain cycles occur with a well defined kinematic hardening, (ii) unsymmetrical stress cycles cause the ratcheting effect and (iii) unsymmetrical strain cycles cause the progressive relaxation.

This paper is organized as follows. In section 2, we describe basic concepts of inelastic behavior of the model. In section 3, the computational algorithm is presented. Section 4 is devoted to numerical examples for illustrating the proposed model. Finally, a brief conclusion is presented in section 5.

2 MODEL FORMULATION

2.1 Basic concepts of internal variables

State variables defining the inelastic behavior of the material, which are composed of the plastic strain ($\boldsymbol{\varepsilon}^p$), damage compliance ($\mathbf{D}$), the internal variables ($\xi^p, \boldsymbol{\kappa}^p$), which control isotropic and kinematic hardening of the plasticity, and the internal variable (ξ^d) of damage, are obtained by using the standard thermodynamic consideration

$$0 \le \dot{\mathcal{D}} = \sigma : \dot{\boldsymbol{\varepsilon}} - \dot{\psi} \tag{1}$$

and the principle of maximum plastic and damage dissipations, which are decomposed from total inelastic dissipation $\mathcal{D}$, with these three fundamental equations firstly defining;

- the decomposition of the total strain

$$\boldsymbol{\varepsilon} = \boldsymbol{\varepsilon}^e + \boldsymbol{\varepsilon}^p + \boldsymbol{\varepsilon}^d \tag{2}$$

- the total strain energy

$$\psi(\boldsymbol{\varepsilon}, \boldsymbol{\varepsilon}^d, \mathbf{D}, \xi^d, \boldsymbol{\varepsilon}^p, \xi^p, \boldsymbol{\kappa}^p) = \psi^e(\boldsymbol{\varepsilon}^e) + \psi^d(\boldsymbol{\varepsilon}^e, \mathbf{D}) + \Xi^p(\xi^p) + \Xi^d(\xi^d) + \Lambda^p(\boldsymbol{\kappa}^p) \tag{3}$$

- the yield criteria of plasticity and damage

$$\begin{aligned}
&\phi^p(\boldsymbol{\sigma}, q^p, \boldsymbol{\alpha}) = \left\|\mathbf{Dev}\boldsymbol{\sigma} + \boldsymbol{\alpha}\right\| - \sqrt{\frac{2}{3}}\left(\sigma_y - q^p\right) \leq 0 \\
&\phi^d(\boldsymbol{\sigma}, q^d) = \frac{1}{3}\mathbf{Tr}(\boldsymbol{\sigma}) - \left(\sigma_f - q^d\right) \leq 0
\end{aligned} \tag{4}$$

where q^p, q^d are the stress-like variables describing the hardening phenomena, $\boldsymbol{\alpha}$ is the deviatoric back stress representing the kinematic hardening behavior and σ_y, σ_f are the yield and fracture stresses, respectively.

The principle of maximum inelastic (plastic and damage) dissipation states that among all the admissible values of dual variables $(\boldsymbol{\sigma}, q^p, \boldsymbol{\alpha}, q^d)$, those, which maximize the plastic and damage dissipation, must be selected. This maximization problem is presented as a minimization problem by introducing Lagrange multiplier. We obtain the evolution equations of internal variables for plasticity and damage phenomenon separately by using the Kuhn-Tucker optimality conditions. Once the suitable values of internal variables are obtained, we can go through the finite element calculation.

2.2 Variational formulation

We use the mixed variational formulation of the Hellinger-Reissner type in order to couple both plastic and damage behaviors for fixed given values of internal variables.

$$\Pi(\boldsymbol{\sigma}, \mathbf{u}) = \int_V \left(\psi^e(\boldsymbol{\varepsilon}^e) + \psi^d(\boldsymbol{\varepsilon}^d, \mathbf{D})\right) dV - \int_{\partial V} \bar{\mathbf{t}}.\mathbf{u} dS \tag{5}$$

where we can rewrite the same functional by using the complementary energies instead of the strain energies.

$$\Pi(\boldsymbol{\sigma}, \mathbf{u}) = \int_V \left(\sigma : \boldsymbol{\varepsilon}^e - \chi^e(\boldsymbol{\sigma}) + \boldsymbol{\sigma} : \boldsymbol{\varepsilon}^d - \chi^d(\boldsymbol{\sigma}, \mathbf{D})\right) dV - \int_{\partial V} \bar{\mathbf{t}}.\mathbf{u} dS \tag{6}$$

The stationary conditions of the functional for each independent displacement and stress fields are taken into account as follows.

$$\begin{aligned}
&G_u(\mathbf{u}, \boldsymbol{\sigma}, \boldsymbol{\delta}\mathbf{u}) = \int_\Omega \nabla^s \boldsymbol{\delta}\mathbf{u}\boldsymbol{\sigma} dV - \int_{\Gamma_\sigma} \boldsymbol{\delta}\mathbf{u}\bar{\mathbf{t}} dS \\
&G_\sigma(\mathbf{u}, \boldsymbol{\sigma}, \boldsymbol{\delta\sigma}) = \int_\Omega \boldsymbol{\delta\sigma}(\nabla^s \mathbf{u} - \boldsymbol{\varepsilon}^p - \frac{\partial \chi^e}{\partial \boldsymbol{\sigma}} - \frac{\partial \chi^d}{\partial \boldsymbol{\sigma}}) dV
\end{aligned} \tag{7}$$

The first equation is the weak form the local equilibrium equation based on Euler-Lagrange equation and the second one is the weak form of the additive decomposition field.

The discretized model is constructed from the weak formulations (7) by using the interpolation functions for the stress (**S)** and the displacement (**N)** fields.

$$\begin{aligned}
&\mathbf{u} = \mathbf{NU} \\
&\boldsymbol{\sigma} = \mathbf{S}\boldsymbol{\beta}
\end{aligned} \tag{8}$$

Next, we implement into the equation (7) the internal variables considering with the time integration and then define the residuals, which is commonly used for the finite element method.

3 COMPUTATIONAL ALGORITHM

We define three levels of computations; (i) local level computation at each Gauss quadrature point for plastic and damage internal variables, for which the implicit backward Euler time integration is used, (ii) element level computation, which is characterized by the stress field, (iii) global level computation of the set of equilibrium equations from which we obtain the displacement values. We verify the convergence of the result at a given level in the spirit of operator-split approach before going through the subsequent level. Newton method is used in order to solve the nonlinear equations, for which 3 to 10 iterations are sufficient at each level. This computational model is implemented into FEAP [7] for numerical examples.

4 NUMERICAL EXAMPLES

In this part, three numerical simulations are presented for a quadrilateral element, which is fixed at one side with displacements or forces imposed at the other side. It is shown that different kinds of cyclic response can be obtained due to the loading types. A comparison is made between the plasticity versus coupled plasticity-damage phenomenon for the same material. The characteristic of the material, which is stainless steel 304, is given in Table 1.

Elasticity Modulus E (MPa)	Poisson ratio ν	Yield stress σ_y (MPa)	Saturation stress σ_∞ (MPa)	Fracture stress σ_f (MPa)
1,93*10^5	0,29	241	579	300

Table 1: Characteristics of the stainless steel 304

4.1 Cyclic response for symmetric imposed displacement

In this example displacement is imposed at the right side of the membrane, which value is between 0.05 and -0.05 in the direction of x-axis for a time interval 0 to 25 seconds, defining as “loading condition 1” in Fig.1.

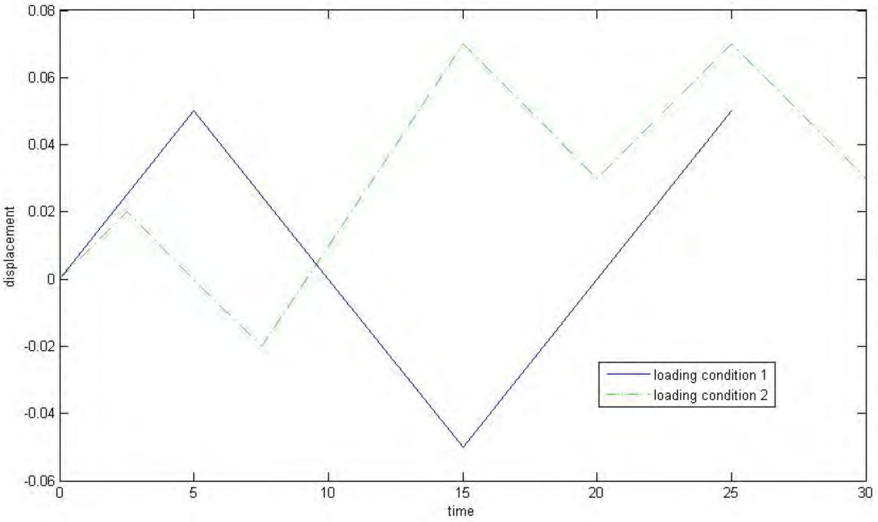

Figure 1: Comparison of the plasticity and coupled plasticity-damage behavior

The diagram obtained from this type of loading shows the coupled plasticity-damage effect over the plasticity phenomenon. It can be seen that the stress values decrease in the same imposed displacement by taking into account damage and plasticity together. Besides, the slope, which gives an idea about the tangent modulus of the material, is reduced for the coupled phenomenon.

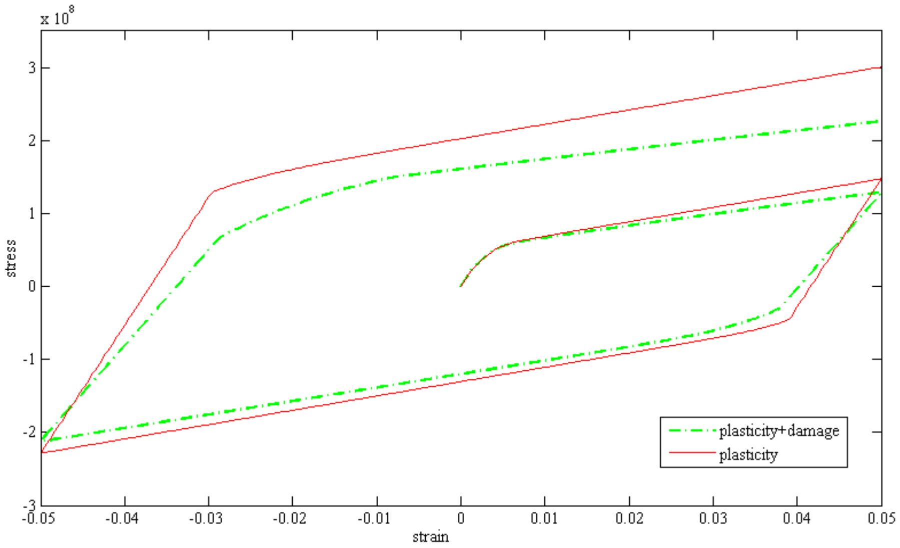

Figure 2: Comparison of the plasticity and coupled plasticity-damage behavior

4.2 Progressive relaxation effect

This response of the material is caused by the strain cycling between any two fixed values. We should define the cyclic loading condition in two parts. At the beginning, it takes the values between [-0.02, 0.02] in the time interval T [0, 7.5s] and then jumps to the value of 0.07. This type of imposed displacement is presented with the name “loading condition 2” in Fig.1. We can see from Fig.3 that stress attained by the element increase with these increasing levels of such imposed displacement.

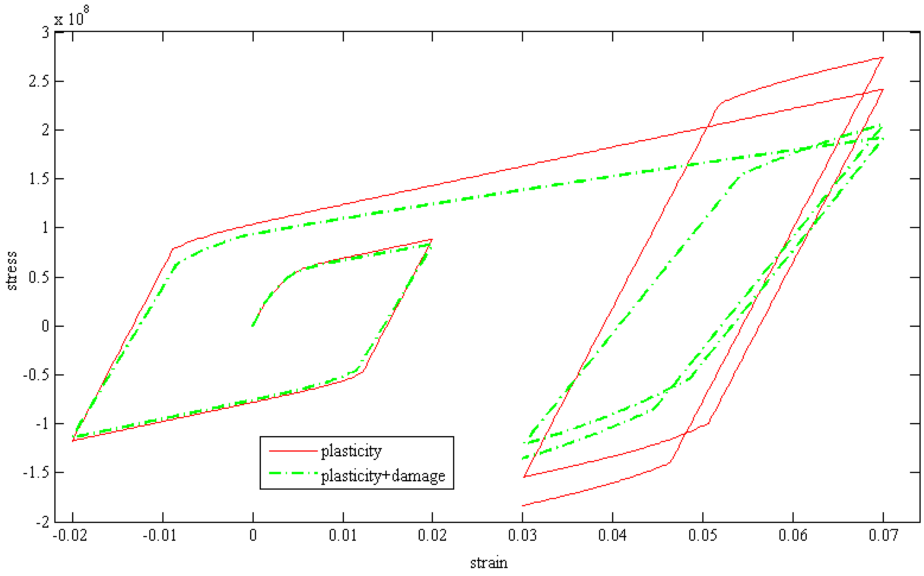

Figure 3: Strain-stress response showing the progressive relaxation phenomenon

4.3 Ratcheting effect

A cyclic loading program in tension and compression between fixed values of stress as seen in Fig.4 has been performed in order to simulate the ratcheting effect of the constitutive material behavior.

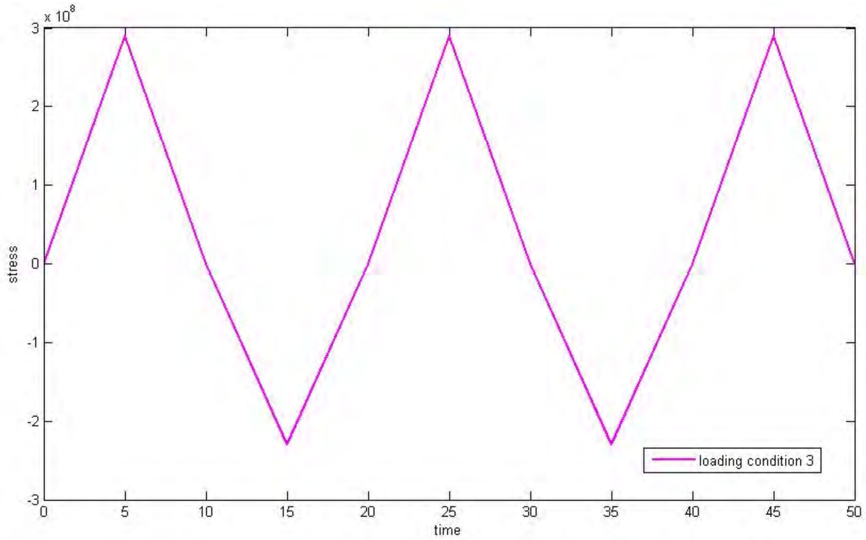

Figure 4: Stress-strain response to cyclic loading resulting in ratcheting of strain

Ratcheting, which is one of the characteristic of the material, is presented here for the asymmetrical stress cycling. The ratcheting deformation accumulates continuously with the applied number of cycles. It can be inferred that the strain limits of the cycles are displaced progressively along the strain axis from one cycle to the next one.

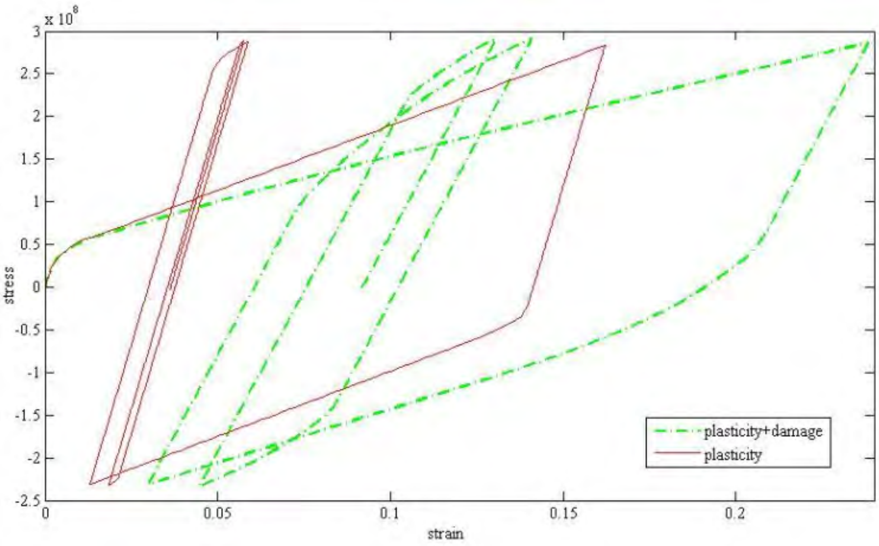

Figure 5: Stress-strain response to cyclic loading resulting in ratcheting of strain.

5 CONCLUSION

In this study, we have presented the phenomenological model of classical plasticity, which is capable of accounting for both isotropic and kinematic hardening effects, and damage model, which is described in an analogous way to the classical plasticity model. The coupled plasticity-damage model points out the irreversible deformation and change of elastic response. The defined elasto-plastic damage model is adapted to the stress based formulation. The mechanism of damage and elasto-plasticity behavior depends on the stress field. For that purpose, the mixed variational type of Hellinger-Reissner is used to develop the finite element approach.

Numerical computations and results are shown in order to illustrate the effectiveness of the algorithmic procedure. The performed analysis allows to have better understanding on the inelastic behavior, which depend on the cyclic loading conditions.

REFERENCES

[1] J.C. Simo, J.G. Kennedy, R.L. Taylor, Complementary mixed finite element formulations for elastoplasticity. *Computer Methods in Applied Mechanics and Engineering*, **74**, 177-206, 1989.

[2] O.C. Zienkiewicz, R.L. Taylor, *The finite element method, Vol.I, 4th Edition*. McGraw Hill. 1989.

[3] A. Ibrahimbegovic, Nonlinear solid mechanics: theoretical formulation and finite element solution methods, Springer, 2009.

[4] D.C. Drucker, L. Palgen, On stress-strain relations suitable for cyclic and other loadings. *Journal of Applied Mechanics*, **48**, 479-485, 1981.

[5] P.M. Naghdi, D.J. Nikkel, Jr., Calculations for uniaxial stress and strain cycling in plasticity. *Journal of Applied Mechanics*, **51**, 487-493,1984

[6] Y.F. Daflias, Bounding surface plasticity; mathematical foundation and hypo-plasticity. *ASCE J. Eng. Mech.*, **112**, 966-987, 1986.

[7] R.L. Taylor, http://www.ce.berkeley.edu/~rlt/feap/

COMPDYN 2011
III ECCOMAS Thematic Conference on
Computational Methods in Structural Dynamics and Earthquake Engineering
M. Papadrakakis, M. Fragiadakis, V. Plevris (eds.)
Corfu, Greece, 25–28 May 2011

EXPERIMENTAL AND NUMERICAL SIMULATION OF DROP TESTS OF CORRUGATED CARDBAORD PACKAGING USING AN ANALYTICAL HOMOGENIZED MODEL

Abdelkader D. Hammou[1,2], Boussad Abbès[1], Ying-Qiao Guo[1], Mohammed Makhlouf[3]

[1] GRESPI/Materials, Processes and Packaging Systems, University of Reims Champagne-Ardenne
UFR Sciences, Moulin de la Housse, BP1039, 51687 Reims, France
boussad.abbes@univ-reims.fr, yq.guo@univ-reims.fr

[2] University of Laghouat, Process Engineering Laboratory
03000 Laghouat, Algeria
hammouad@gmail.com

[3] Djillali Liabès University of Sidi-Bel-Abbès
B.P. N° 89, 22000 Sidi-Bel-Abbès, Algeria
md.makhlouf@yahoo.fr

Keywords: Drop-test, Shock, Corrugated cardboard, Finite element, Homogenization model, Crushable foam model.

Abstract. *This paper presents experimental and numerical studies of drop tests of corrugated cardboard packaging containing different foam inserts. An efficient homogenization model for the corrugated cardboard has been developed. In our H-model, the corrugated cardboard is represented by a 2D plate. Instead of using a local constitutive law (relating the strains to the stresses) at each material point, the homogenization process leads to a generalized constitutive law (relating the generalized strains to the resultant forces) for the equivalent homogeneous plate. Our H-model was implemented into the finite element software ABAQUS. The foam behaviour was experimentally determined and modeled with a crushable foam model of ABAQUS. The drop tests were performed as a free fall from a given height onto a rigid floor. The acceleration of the packed product was recorded using a triaxial accelerometer. The numerical results obtained using the FE simulation with our H-model agree very well with the experimental results. We have also shown that the contribution of the corrugated cardboard box to the shock response is very important.*

1 INTRODUCTION

During storage and transportation, products can accidentally fall onto the floor causing some damages on the products. The corrugated cardboard packages and the foam inserts are designed to protect the product from the shock it can undergo. As the product design always tends towards light, a high impact performance becomes extremely critical for product design issues [1-2]. Conventionally, a product reliability test to prevent impact-induced damage is carried out by a procedure of "design – prototype – test – redesign" which is highly cost and time consuming. A numerical modelling of the product and its packaging provides an efficient methodology to predict the structural strength during impact [3]. Moreover, the finite element simulation allows to avoid numerous experimental drop tests and to predict possible failures during the design stage. This study deals with the drop impact problem of product-packaging systems using both numerical and experimental methods. Different packaging systems, using corrugated cardboard box and different foam inserts, are studied to analyse the influence of corrugated cardboard and the foam inserts configurations.

Firstly, we present the experimental setups and results. Then, we describe the homogenization model for the corrugated cardboard and its implementation in the finite element code ABAQUS. Finally, the accelerations measured during the shock using the data acquisition system of drop test platform are compared with the results obtained from ABAQUS simulations.

2 EXPERIMENTAL TESTS

2.1 Materials and products

The corrugated cardboard boxes with interior dimensions of 150×150×90 mm^3 are used for the experimental drop tests (figure 1). The product in the box is a thick steel plate of 87×87×30 mm^3, with a total mass of 1.686 kg. The boxes are made with a corrugated C flute cardboard. The insert between the boxes and the product is the Ethafoam 400 extruded polyethylene (PE) foam produced by DOW, with a density of 58 kg/m^3. In this study, we have used two configurations shown in figure 2: the foam surrounds the product (figure 2.a), or it is only placed in the corners of the product (figure 2.b).

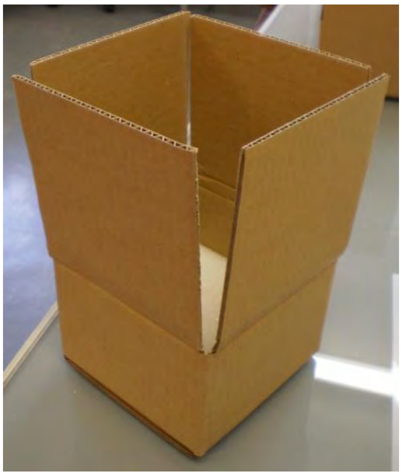

Figure 1: Corrugated cardboard box.


(a) (b)

Figure 2: Two types of foam configurations.

2.2 Characterization of corrugated cardboard constituents

The procedure to determine the elastic parameters of the corrugated cardboard constituents is described below. The corrugated cardboard consists of two flat layers and a flute (figure 3). These constituents are separated according to the French norm NFQ03-043 in order to determine the material parameters of each layer. The tensile test samples are cut using the ELCEDE MFT20 cutting table. The tensile tests are performed on the 3 layers in the Machine Direction (MD), Cross Direction (CD) and 45° Direction. We observe that the paperboards have a higher strength in the MD direction (figure 4).

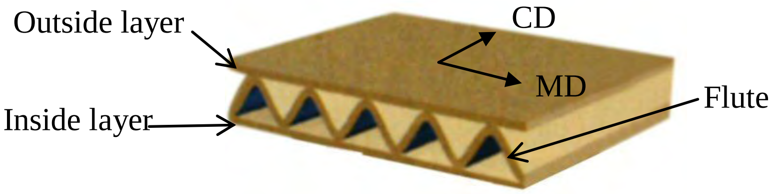

Figure 3: Corrugated cardboard constituents.

The orthotropic constitutive relation between the stresses and strains is defined as follows:

$$\{\sigma\} = \begin{Bmatrix} \sigma_1 \\ \sigma_2 \\ \sigma_{12} \end{Bmatrix} = [D]\{\varepsilon\} = \begin{bmatrix} \frac{E_1}{1-\upsilon_{12}\upsilon_{21}} & \frac{\upsilon_{12}E_2}{1-\upsilon_{12}\upsilon_{21}} & 0 \\ \frac{\upsilon_{21}E_1}{1-\upsilon_{12}\upsilon_{21}} & \frac{E_2}{1-\upsilon_{12}\upsilon_{21}} & 0 \\ 0 & 0 & G_{12} \end{bmatrix} \begin{Bmatrix} \varepsilon_1 \\ \varepsilon_2 \\ \gamma_{12} \end{Bmatrix} \tag{1}$$

where the subscripts 1 and 2 refer to the MD and CD directions respectively.

The Young's moduli are obtained by calculating the slopes of the tensile curves in the elastic zones. The empirical relations established by Baum *et al.* [4] are used to determine the Poisson ratios and the in-plane shear modulus:

$$\begin{cases} \sqrt{\nu_{12}\nu_{21}} \approx 0.293 \\ G_{12} \approx 0.387\sqrt{E_1 E_2} \end{cases} \quad \text{with:} \quad \frac{\upsilon_{12}}{E_1} = \frac{\upsilon_{21}}{E_2} \tag{2}$$

The above characterization procedure allows obtaining the elastic properties of the three cardboard layers (Table 1).

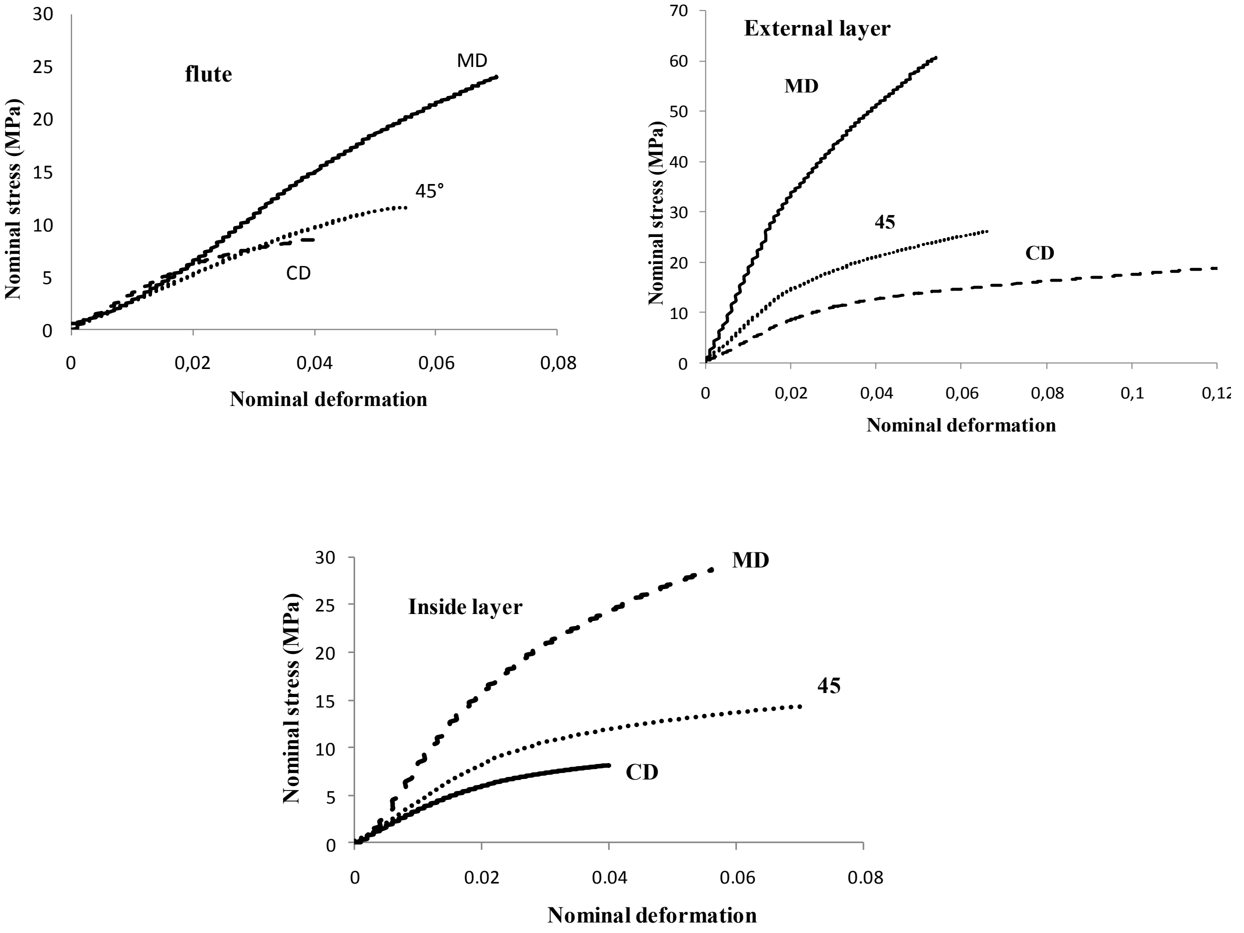

Figure 4: Tensile test on the corrugated cardboard constituents.

Layers	E_1 (MPa)	E_2 (MPa)	ν_{12}	G_{12} (MPa)	Thickness (µm)
Outside layer	1913.7	526.2	0.56	322.0	216.5
Flute	464.3	355.9	0.33	93.0	191.0
Inside layer	1006.8	279.8	0.56	214.0	282.4

Table 1: Material characteristics of the corrugated cardboard constituents.

2.3 Characterization of the foam

Uniaxial and hydrostatic compression tests are performed to characterize the foam. The nominal stresses versus nominal strains are plotted in figure 5. These curves are used to determine the elastic modulus ($E_{foam} = 1.5\,MPa$) and the hardening curve needed for the crushable foam model of ABAQUS.

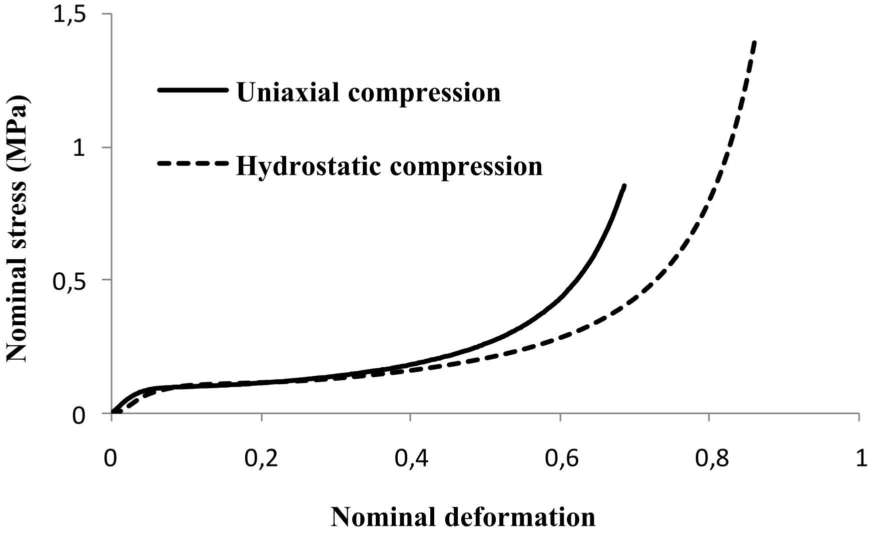

Figure 5. Uniaxial and hydrostatic compression curves of Ethafoam 400.

2.4 Drop tests

The drop test is a simple test method and corresponds well to the reality. The impact velocity of the package is a crucial parameter since great forces affect the package during a short time. This velocity depends on the drop height. The package is placed on a fork at a given height. The fork is withdrawn very fast and the package falls to the ground.

The drop test equipment used here is an AccruDrop Tester from L.A.B. Equipment Inc. (figure 6). The drop height is fixed to $H_{drop} = 1.05\,m$. To record the acceleration of the product, a triaxial accelerometer (Andevco Isotron 2258A-10) is glued to its horizontal top face as shown in figure 2. The analysis and the visualisation of the measurements are done with Lansmont Test Partner 3 software.

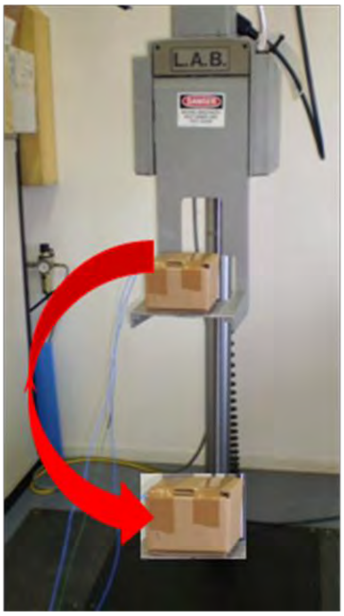

Figure 6: Drop test equipment.

Two types of tests are carried out to study the influence of the packaging for the product protection. In the first one, the product is protected only by the foam. In the second one, the product is protected by the foam and the corrugated cardboard box. Figure 7 shows typical curves of acceleration versus time corresponding to the shock of the box on the floor. We observe that the protection by the foam insert alone gives the maximum acceleration, which is about 20% higher than the acceleration recorded when using both the foam insert and the corrugated cardboard. Tow configurations are studied, one with the foam inserts surrounding the product and the other with the foam inserts on the corners of product.

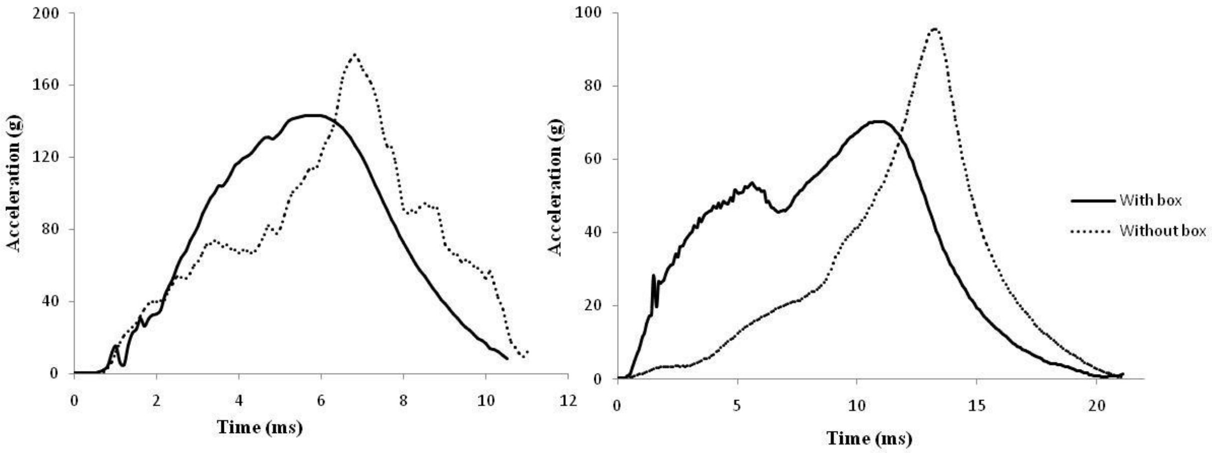

Figure 7: Drop tests with/without corrugated cardboard box using the foam surrounding product (left) or only on the corner of the product (right).

3 MATERIAL MODELS

The material models in the FE simulation are presented in this section. The 3D corrugated cardboard structure is homogenised and replaced by an orthotropic elastic shell. The H-model is then implemented into ABAQUS using UGENS subroutine [5]. The crushable foam model of ABAQUS is used for the foam which is considered as an isotropic material, whose hardening behaviour is a function of the volume change [6].

3.1 Homogenization model of the corrugated cardboard

A 3D geometrical modelling of the three layers of the corrugated cardboard is very tedious and time consuming. In our homogenization model, the corrugated cardboard is represented by a 2D plate. Instead of using a local constitutive law (relating the strains to the stresses) at each material point, the homogenisation leads to a generalised constitutive law (relating the generalised strains to the resultant forces) for the equivalent homogeneous plate. The integrations through the thickness and the machine directions MD are required.

After the integrations or other calculations based on the beam theories [7-8], we obtain the generalised constitutive law in a matrix form:

$$\begin{Bmatrix} \{N\} \\ \{M\} \\ \{Q\} \end{Bmatrix} = \begin{bmatrix} [A] & [B] & 0 \\ [B] & [D] & 0 \\ 0 & 0 & [F] \end{bmatrix} \begin{Bmatrix} \{\varepsilon_m\} \\ \{\kappa\} \\ \{\gamma\} \end{Bmatrix} \tag{3}$$

where $\{N\}$, $\{T\}$ and $\{M\}$ are the internal forces and moments obtained by integrating the local constitutive laws through the thickness of the corrugated cardboard, $[A]$ is the membrane rigidity matrix, $[D]$ is the bending-torsion rigidity matrix, $[F]$ is the transverse shear rigidity matrix and $[B]$ is the membrane-bending coupling matrix.

The corrugated cardboard is more complex than a laminated plate because of the fluting core and the cavities between the two flat layers. In the above matrix, some global effective rigidities obtained by the theory of laminated plates should be modified, such as the rigidities related to the membrane forces and bending moments on the MD section, the transverse shear forces and the torsion moments.

In this paper, the corrugated cardboard is modelled by shell elements, the strains and stresses at every integration point of an element are calculated incrementally. Let $\{dN\}$ the external forces and moments per unit length, they have the following relationship with the increments of the membrane strains and bending curvatures:

$$\{dN\} = [Q]\{d\varepsilon\} \tag{4}$$

The resultant forces and generalized strains at a given point are updated as follows:

$$\{N\} = \{N\} + \{dN\}\,;\, \{\varepsilon\} = \{\varepsilon\} + \{d\varepsilon\} \tag{5}$$

The above homogenization model is implemented into ABAQUS using a user subroutine UGENS. The main purpose of this subroutine is to compute the element material stiffness matrix $[Q]$ defined in equation (4), which is used to define the elemental stiffness matrix.

3.2 Model of the foam plastic behaviour

The foam materials have a cellular structure and hence behave in a complex manner, especially under crush conditions [9]. A usual stress–strain curve of polymeric foam has distinct major regions, which are caused by different mechanisms. A linear elastic region, followed by an almost horizontal plateau; this plateau is caused by the cells’ collapsing; they buckle elastically and recover completely when the foam is unloaded. When the cells collapse completely, the stress rises steeply (densification) [9-11]. In this section a phenomenological plasticity model, based on the models presented, is proposed for isotropic crushable foam materials. It consists of a modified plasticity model that accounts for a different response in compression or tension, which incorporates uniaxial and hydrostatic compressive hardening laws.

This model with volumetric hardening uses a yield surface with an elliptical dependence of the deviatoric stress $[s]$ on the pressure p in the meridional plane. The elastic behaviour of the foam can be considered as isotropic and linear. The yield surface and the flow potential for the crushable foam model is defined in terms of the pressure p $-\frac{1}{3}trace[\sigma]$ and the von Mises stress $q=\sqrt{\frac{3}{2}[s]:[s]}$. The yield surface is defined as follows:

$$F = \sqrt{q^2 + \alpha^2(p - p_0)^2} - B = 0 \tag{6}$$

where the parameter α represents the shape of the yield ellipse in the p-q stress plane; α can be calculated from the initial yield strength in an uniaxial compression (σ_c^0 taken as a positive value), the initial yield strength in hydrostatic compression (p_c^0) and the yield strength in hydrostatic tension (p_t):

$$\alpha=\frac{3k}{\sqrt{(3k_t+k)(3\text{-}k)}} \quad \text{with } k=\frac{\sigma_c^0}{p_c^0} \quad \text{and} \quad \sigma_t=\frac{p_t}{p_c^0} \tag{7}$$

The plastic flow potential G is given by:

$$G = \sqrt{q^2 + \beta^2 p^2} \tag{8}$$

where β is related to the plastic Poisson’s ratio ν_p as:

$$\beta = \frac{3}{\sqrt{2}}\sqrt{\frac{1-2\nu_P}{1+\nu_p}} \tag{9}$$

The plastic Poisson's ratio, which is the ratio between the transverse and the longitudinal plastic strains under uniaxial compression, must be in the range of -1 and 0.5.

4 RESULTS AND DISCUSSION

The product is considered as a rigid body. The corrugated cardboard box is modelled with a 1024 S4R linear quadrilateral shell elements. The foam is modelled with a 4892 C3D4 tetrahedral elements. The ground is considered as a flat rigid body and fixed in the space. A frictionless contact is assumed between the ground-box, box-foam and foam-product.

The box is positioned 2 mm from the ground and has an initial velocity $V = \sqrt{2gH_{drop}}$, with $H_{drop} = 1.05m$.

The comparisons of experimental and simulated curves of acceleration versus time for three configuration tests are shown in figures 8, 9 and 10. We can see that the finite element simulation results agree well with the experimental results. In table 2, we present the maximum acceleration and the duration of the shock for different configurations. Between the experimental and the numerical results, we have an error of 2.8% for the case with the foam around the product, 9.7% for the case with the foam on the corners of the product and 7.7% for the same case but for the shock in the lateral direction.

It can be noted that the corrugated cardboard box contribute about 20% to the shock absorption. We observe that the corrugated cardboard box undergoes higher von Mises stresses than the foam as shown in figure 11. The comparison between figures 8 and 9 shows also that the surrounding foam gives a more rigid support to the product, leading to a shorter shock so a much stronger impact to the product with respect to the corner foams.

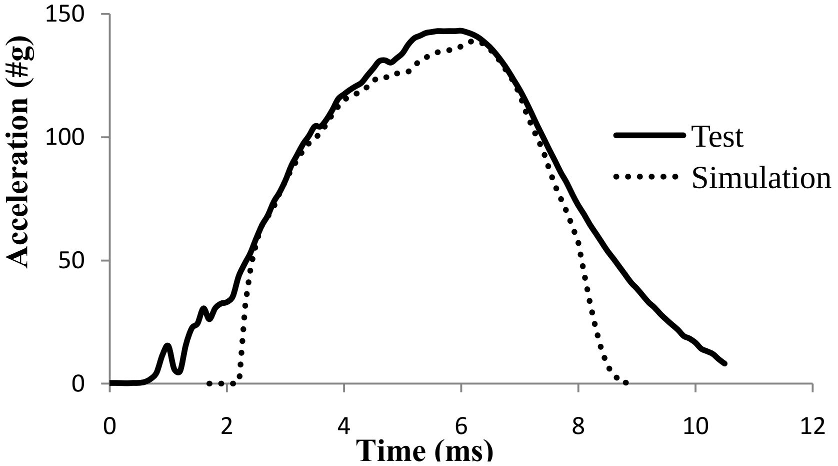

Figure 8: Experimental and numerical curves of acceleration vs. time in the case of surrounding foam.

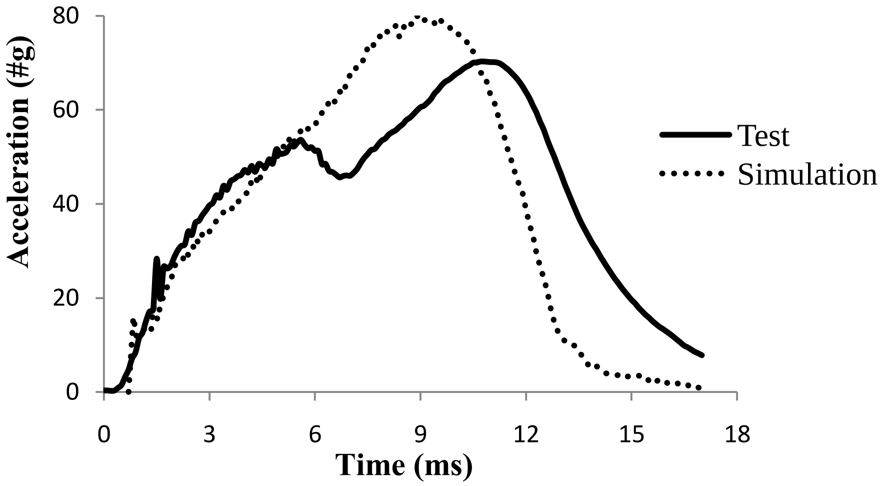

Figure 9: Experimental and numerical curves of acceleration vs. time in the case of corner foams.

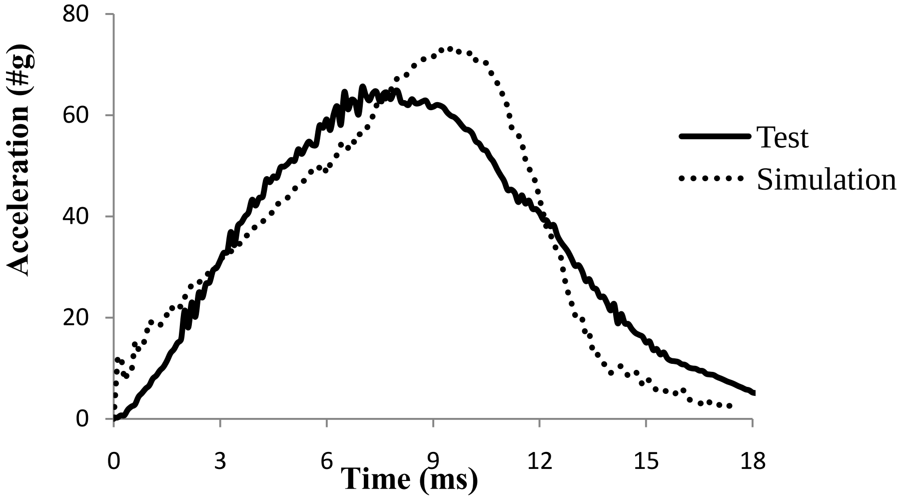

Figure 10: Experimental and numerical curves of acceleration vs. time in the case of corner foams with the shock in lateral direction.

	Foam around product		Foam on the corners		Foam on the corners under lateral shock	
	Simulation	Test	Simulation	Test	Simulation	test
Maximum acceleration (#g)	139	143.12	80	70.2	73.2	65.5
Duration of shock (ms)	6.5	9.3	16.2	19.5	17.3	19.1

Table 2: Comparison of the results obtained by the drop test and the FE simulation.

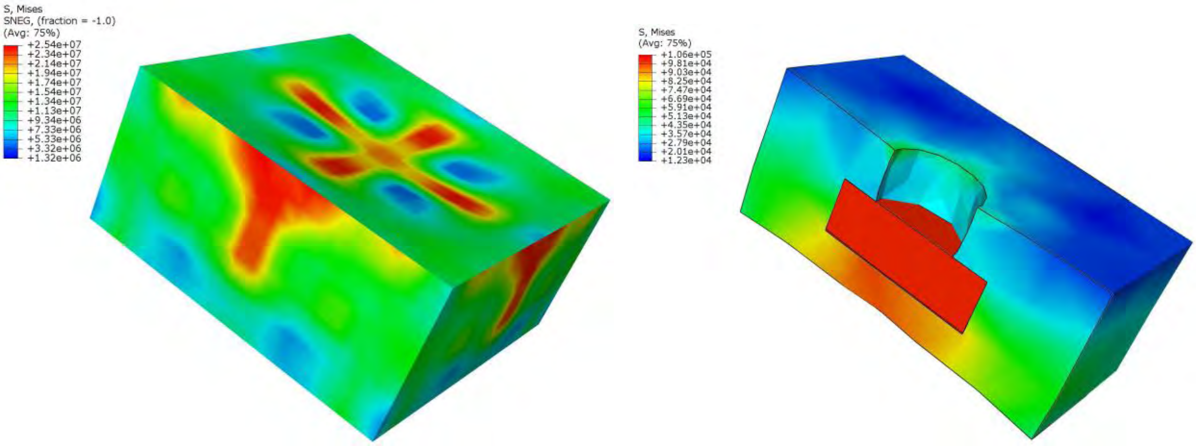

Figure 11: Von Mises stresses on the corrugated cardboard box and on the foam insert.

5 CONCLUSION

In the design stage of packaging systems, we need to simulate the contributions of both the corrugated cardboard box and the foam. According to the drop tests, it is evident that one cannot neglect the corrugated cardboard contribution in the protection of the product. An efficient homogenization model for the corrugated cardboard is developed and implemented into the FE software ABAQUS through the user subroutine UGENS. This model has been used to simulate the drop test of corrugated cardboard box containing different foam inserts and a rigid product. The drop test is instrumented, giving the curves of acceleration vs. time. The FE simulation results agree well with the experimental results. We have also shown that the corrugated cardboard box with supple foams gives a more damping effect to the shock response of the product.

REFERENCES

[1] S. Goyal, S. Upasani, and D.M. Patel, Improving Impact Tolerance of Portable Electric Products: Case Study of Cellular Phones, *Experimental Mechanics*, **39**, 43-52, 1999.

[2] S. Goyal, Methods for realistic Drop-Testing, *International Journal of Microcircuits and Electronic Packaging*, **23**, 45-52, 2000.

[3] A.D. Hammou, B. Abbès, Y.Q. Guo, D. Erre, J.B. Nolot, Drop impact of a packaging with corrugated cardboard and foam: Experimental tests and finite element analysis. *1st International Colloquium IMPACT 2010*, Djerba, Tunisia, March 22-24, 2010.

[4] G.A. Baum, D.C. Brennan, C.C. Habeger, Orthotropic elastic constants of papers, *Tappi Journal*, **64**, 97-101, 1981.

[5] Abaqus user subroutine reference manual v6.7. *Simulia*, 2007.

[6] Abaqus theory manual v6.7. *Simulia*, 2007.

[7] N. Talbi, A. Batti, R. Ayad and Y.Q. Guo, An analytical homogenization model for finite element modelling of corrugated cardboard. *Composite Structures*, **88**, 280-289, 2009.

[8] B. Abbès, Y.Q. Guo, Analytic homogenization for torsion of orthotropic sandwich plates: Application to corrugated cardboard. *Composite Structures*, **92**, 699-706, 2010.

[9] Q. M. Li, R. A. W. Mines, Strain measures for rigid crushable foam in uniaxial compression. *Strain*, **38**, 132–140, 2002.

[10] L. J. Gibson, M. F. Ashby, The mechanics of three-dimensional cellular materials. *Proceeding of the Royal Society A: Mathematical, Physical and Engineering Sciences,* **382**, 43-59, 1982.

[11] G.C. Machado, M.K. Alves, R. Rossi, C.R.A. Silva Jr, Numerical modeling of large strain behavior of polymeric crushable foams. *Applied Mathematical Modelling*, **35**, 1271–1281, 2011.

COMPDYN 2011
3^{rd} ECCOMAS Thematic Conference on
Computational Methods in Structural Dynamics and Earthquake Engineering
M. Papadrakakis, M. Fragiadakis, V. Plevris (eds.)
Corfu, Greece, 25-28 May 2011

ARLEQUIN FRAMEWORK FOR STRUCTURAL TRANSIENT DYNAMICS

Assaf Ghanem[1 2], **Thouraya Nouri Baranger**[2], **Najib Mahjoubi**[1],
and Mohamed Torkhani[1]

[1]LAMSID, CNRS: UMR2832, EDF R&D,
1, avenue du Général de Gaulle 92141 Clamart Cedex, France
e-mail:{assaf.ghanem, mohamed.torkhani, najib-externe.mahjoubi}@edf.fr

[2]Université de Lyon, CNRS, Université Lyon1, LAMCOS UMR5259 INSA-Lyon,
18-20 rue des sciences, F69621 Villeurbanne cedex
thouraya.baranger@univ-lyon1.fr

Keywords: Arlequin method, Structural dynamics, Multiscale, Multimodel, Heterogeneous time integrators.

Abstract. *Arlequin method is a modeling framework based on the combination of concurrent multiscale and multi mechanical models. It is a general application of overlapping domain decomposition. The choice of the coupling operators written in common areas between different models provide the main key to ensure the continuity of displacement, velocity, and equilibrium of forces. Using overlap coupling methods in the context of structural dynamics is advantageous when treating dissimilar domains, mainly when wave propagation between the different models is taken into consideration. In this paper we propose to couple and analyze different numerical time schemes using the Arlequin method. Numerical studies, based on multiscale and multimodel space coupling are used to exemplify the efficiency of our approach.*

1 INTRODUCTION

Performing numerical simulations of the dynamic response in rotating machinery is mostly based on beam structures representing the coarse model.
Taking into consideration local physical phenomena occurring at microscopic levels such as crack propagation or contact requires a fine three dimensional modeling of the structure. On the other side, carrying out calculations on very finely meshed models can be very expensive in computational terms.

Many adaptive methods [1] proposing solutions for this kind of multiscale studies have been developed in order to enhance the accuracy of the numerical approximations and also reduce CPU (Central Processing Unit) and memory problems. But in spite of their main advantage, these multi-meshes methods are considered very expensive to implement in practical computations.

An other approach is offered by multiscale methods. The main idea is to have one global domain with a coarse mesh, including a zone of interest where a very fine mesh is super-imposed. These methods are to divide into two major classes: the first one is based on coupling domains at discrete interface [2], and the second consists on using an overlapping zone [3] where the two interfaces are superposed.

Arlequin method [4] is developed in the context of multiscale overlapping methods. Using a partition of models, this approach provides a progressive passage between different models with enhanced flexibility by means of multiple parameters [5]. In static and dynamic cases, Arlequin method gives the possibility of coupling dissimilar models with concurrent scales such as 2D-1D and 3D-1D models. In dynamic studies, it presents an important ability to treat problems where aspects like wave propagation are taken into consideration. It has been shown in [6], that if the coupling parameters of this method are correctly used, wave transition is guaranteed and problems of spurious reflections are avoided while transiting between models.

Moreove, being capable of coupling different models where each one has its own time integration scheme is a very important aspect. It can be considered as a first step for introducing different time discretizations, as well as a main key for coupling multiple finite element codes. Extending the Arlequin method to such application can be very advantageous.

In this study, we will visit energy conservation aspects for continuous and discrete Arlequin formulations. Then we will analyze the energy balance of the Newmark [10] algorithm while coupling different Newmark schemes, and propose a formalism for coupling different time integration schemes in the Arlequin framework.

Based on this formalism, two numerical applications are presented. The first one considers a multiscale coupling of two bar models. The second concerns a multimodel coupling of continuous 2D and beam structures. Future industrial applications of this work will mainly be used in the domain of rotor dynamics where multimodel coupling authorizing multiscale time integration is believed to be useful for such studies.

Figure 1: 1D-1D mesh coupling.

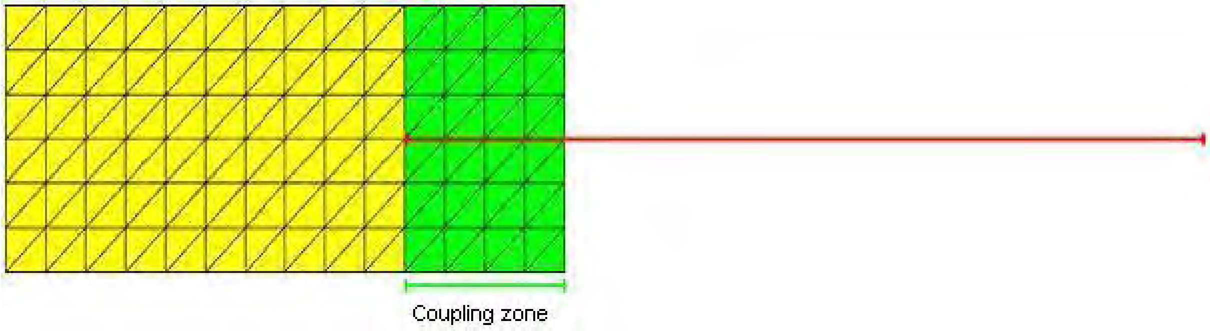

Figure 2: 2D-1D mesh coupling.

2 ARLEQUIN CONTINUOUS FORMULATION IN DYNAMIC REGIMES

An Arlequin-based mechanical study consists in dividing a global model Ω into two or more sub-domains Ω_i. These sub-domains have a common overlap area S.
Considering two domains Ω_1 and Ω_2, the overlap is equivalent to their intersection $S = S_1 \cap S_2$.

In general terms, the Arlequin formulations are obtained by three main steps:

- super-imposing a local model Ω_2 to a global one Ω_1 in a zone of interest S.
- distributing the mechanical energies between the overlapping sub-systems by means of partition of unity functions.
- gluing the models in a part S_g of S.

We note that for the numerical applications presented in this paper, the gluing area S_g is equal to the overlapping zone S (external junction).
We consider a time dependent problem, where Ω_1 and Ω_2 are subjected to a field of volume density of forces f_i $(i = 1, 2)$ and clamped in a non zero measured part Γ_1 of its boundary $d\Omega_1$.
We denote W_1 and W_2 as the spaces of kinematical admissible fields related to Ω_1 and Ω_2, and M the Lagrange multiplier space called the mediator space (for more details on these definitions we refer to [7]):

$$W_1 = \left\{ v_1 \in H^1(\Omega_1);\; v_1 = 0 \, on \, \Gamma_1 \right\} \tag{1}$$

$$W_2 = H^1(\Omega_2) \tag{2}$$

Based on the Virtual Work Principle (VWP), the classical continuous Arlequin formulation consists in finding the admissible displacement fields u_1 and u_2, as well as the Lagrange multipliers fields λ.
It can be written as follows:

$$Find\ (u_1,\ u_2,\ \lambda) \in W_1 \times W_2 \times M; \tag{3}$$

$$\forall(w_1,\ w_2,\ \mu) \in W_1 \times W_2 \times M, \tag{4}$$

$$G_{dyn}(u_1, w_1, u_2, w_2, \alpha) + G_{int}(u_1, w_1, u_2, w_2, \beta) + G_{arl}(\lambda, w_1, w_2) = G_{ext}(w_1, w_2, \varphi) \tag{5}$$

$$G_{arl}(\mu, u_1, u_2) = 0 \tag{6}$$

Weight parameters $\alpha, \beta,$ and $\varphi \in [0\ 1]$ used to distribute energy between different models are defined by two main properties:

- $\alpha = \beta = \varphi = 1$ in $\Omega | S_g$
- $0 < \alpha, \beta, \varphi < 1$ in S_g

We note:

- $\alpha_2 = 1 - \alpha_1$
- $\beta_2 = 1 - \beta_1$
- $\varphi_2 = 1 - \varphi_1$

G_{dyn} , G_{int} , G_{arl} , G_{ext} represent respectively the work of inertial forces, the work of the internal forces, the work of the Arlequin forces, and finally the work of the external forces applied on the different models. They are defined by:

$$G_{dyn}(u_1, w_1, u_2, w_2, \alpha) = \int_{\Omega_1} \alpha_1 \rho_1 \ddot{u}_1 w_1 d\Omega_1 + \int_{\Omega_2} \alpha_2 \rho_2 \ddot{u}_2 w_2 d\Omega_2 \tag{7}$$

$$G_{int}(u_1, w_1, u_2, w_2, \beta) = \int_{\Omega_1} \beta_1 \sigma(u_1) : \varepsilon(w_1) d\Omega_1 + \int_{\Omega_2} \beta_2 \sigma(u_2) : \varepsilon(w_2) d\Omega_2 \tag{8}$$

$$G_{ext}(\varphi, w_1, w_2) = f_1(w_1) + f_2(w_2) = \int_{\Omega_1} \varphi_1 f.w_1 d\Omega_1 + \int_{\Omega_2} \varphi_2 f.w_2 d\Omega_2 \tag{9}$$

$$G_{arl}(\lambda, w_1, w_2) = < \lambda, w_1 - w_2 > where\ \ <,> represent\ a\ coupling\ operator \tag{10}$$

Where $\sigma(u)$ and $\varepsilon(u)$ respectively denote the strain and stress tensors associated to the displacement field u.

2.1 COUPLING OPERATORS

Constructing the coupling matrix is a main step in the application of the Arlequin method especially when a multimodel coupling is taken into consideration (2D or 3D models coupled with 1D models). The gluing volume of displacement field is treated in a natural way by introducing the Lagrange multiplier field.

Several operators are proposed for coupling models in the context of the Arlequin framework [4], [5], [7], [8]. We define u as the general displacement vector formed of u_1 and u_2. The three main operators are presented as follows:

$$L^2\, coupling\ G_{arl} = \int_{S_g} \lambda.u \, dS_g \tag{11}$$

$$H^1\, coupling\ G_{arl} = \int_{S_g} \left[\lambda.u + l^2 \varepsilon(\lambda) : \varepsilon(u)\right]\, dS_g \tag{12}$$

where l is a strictly positive parameter homogeneous to a length.

$$Energy\,coupling\ G_{arl} = \int_{S_g} \sigma(\lambda) : \varepsilon(u)\, dS_g \tag{13}$$

Depending on the application, L^2 coupling may introduce ill conditioning of the global stiffness matrix. This can be treated in an artificial manner by introducing an homogenous parameter (H^1 coupling), or in a more natural way by using the energy coupling.
The three operators listed above are tested in the context of our applications (2D-1D an 1D-1D coupling). In general terms, they all present similar results.

3 ENERGY CONSERVATION: CONTINUOUS ARLEQUIN FORMULATION

In this section we will write the energy conservation in a transient dynamic regime while using the Arlequin continuous framework.

Considering the same problem presented in the section 2 but with no external loads, the expression of total mechanical energy (E_{tot}) of the system is given by:

$$E_{tot} = E_{kinetic} + E_{potential} \tag{14}$$

where kinetic and potential energies are respectively defined as:

$$E_{kinetic} = \int_{\Omega_1} \frac{1}{2}\alpha_1\rho_1(\dot{u}_1)^2 d\Omega_1 + \int_{\Omega_2} \frac{1}{2}\alpha_2\rho_2(\dot{u}_2)^2 d\Omega_2 \tag{15}$$

$$E_{potential} = \int_{\Omega_1} \frac{1}{2}\rho_1\sigma(u_1) : \varepsilon(u_1) d\Omega_1 + \int_{\Omega_2} \frac{1}{2}\rho_2\sigma(u_2) : \varepsilon(u_2) d\Omega_2 \tag{16}$$

We assume that the constitutive material follows a hooke's law:

$$\sigma_i = \mathbf{D}\varepsilon(u_i) \tag{17}$$

with $\mathbf{D}$ the elastic constant matrix.
The derivative of the total energy formula with respect to time gives:

$$\frac{dE_{tot}}{dt} = \int_{\Omega_1} \alpha_1\rho_1\dot{u}_1\ddot{u}_1 d\Omega_1 + \int_{\Omega_2} \alpha_2\rho_2\dot{u}_2\ddot{u}_2 d\Omega_2 + \int_{\Omega_1} \rho_1\sigma(u_1) : \varepsilon(\dot{u}_1) d\Omega_1 + \int_{\Omega_2} \rho_2\sigma(u_2) : \varepsilon(\dot{u}_2) d\Omega_2 \tag{18}$$

We assume that virtual fields are equivalent to velocity fields $w_1 = \dot{u}_1$ and $w_2 = \dot{u}_2$.
Comparing (18) and (5) enables us to write:

$$\frac{dE_{tot}}{dt} = - < \lambda, \dot{u}_1 - \dot{u}_2 > \tag{19}$$

For $\lambda = \mu$, the derivative of (6) gives:

$$\frac{dG_{arl}}{dt} = < \lambda, \dot{u}_1 - \dot{u}_2 > + < \frac{d\lambda}{dt}, u_1 - u_2 > \tag{20}$$

Assuming λ as a time independent field, the second term of 20 is reduced to zero, and we are capable to write the energy conservation as:

$$\frac{dE_{tot}}{dt} = < \lambda, \dot{u}_1 - \dot{u}_2 > = 0 \tag{21}$$

Based on (21), we proved that in a general case, when the Lagrange multiplier field is time independent, the Arlequin framework provides an energy conservation of the global problem.

4 DISCRETIZED PROBLEM

In the following sections, we consider the energy coupling (13). This choice is based on several study results realized in the context of our 2D-1D and 1D-1D applications, and on the homogeneity between the ingredients of this operator and the quantities evaluated in (8).
We now introduce the spatio-temporal discretizations corresponding to (5) and (6). We take into consideration the effect of the damping matrix:

$$M_1\ddot{u}^1_{n+1} + C_1\dot{u}^1_{n+1} + K_1 u^1_{n+1} + L^t_1\lambda_{n+1} = f^1_{n+1/ext} \tag{22}$$

$$M_2\ddot{u}^2_{n+1} + C_2\dot{u}^2_{n+1} + K_2 u^2_{n+1} + L^t_2\lambda_{n+1} = f^2_{n+1/ext} \tag{23}$$

$$L_1 u^1_{n+1} + L_2 u^2_{n+1} = 0 \tag{24}$$

In this discretized equation system, M_i, C_i, and K_i are the mass, damping, and stiffness matrices of the system, and $f^i_{n+1/ext}$ is the external load vector. L_i matrices are the Arlequin coupling matrices (24) acting on the displacement fields in this case.

We note that the different matrices figuring in (22) and (23), with the exception of the L_i matrices, are weighted by the mean of the weight parameters defined in section 2. C_i matrix has a special importance in the rotor dynamics domain since it can contain the gyroscopic terms essential for such studies.

5 NUMERICAL INTEGRATION

For our two applications we apply the Gravouil-Combescure [14] method for coupling two sub-domains with different Newmark integration schemes and the same time scale.

5.1 Problem statement

Tests realized on the 2D-1D and 1D-1D couplings show coherent results and balanced energy Newmark algorithm when the average acceleration method is applied or when the same scheme is used for both models. However, when different Newmark schemes are involved, the energy balance is no more respected and differences caused by the work of the gluing forces appear.

5.2 Energy balance of the Newmark algorithm

Ideally, a single-step time integration algorithm should lead to a similar energy balance equation for finite increments. Using ([11]), we will establish the energy balance for multi-Newmark scheme coupling. Our main goal is to focus the contribution of the Arlequin forces in this equilibrium equation.

The work of these forces at the interface between the overlapping domains leads to undesirable energy dissipation effects. The discrete form of the energy balance equation involves the increment of the mechanical energy over the time interval from t_n to t_{n+1}. This increment can be expressed in terms of mean values and increments of the displacement and velocity as follows:

$$\sum\nolimits_{i=1,2}\Big[E_c^i + E_p^i\Big]_n^{n+1} = \sum\nolimits_{i=1,2}\Big[\frac{1}{2}(\dot{u}^i)^t M_i(\dot{u}_n^i) + \frac{1}{2}(u^i)^t K_i(u^i)\Big]_n^{n+1} \tag{25}$$

$$= \sum\nolimits_{i=1,2}\left[(\frac{1}{2}(\dot{u}^i_{n+1} + \dot{u}^i_n)^t M_i(\dot{u}^i_n - \dot{u}^i_{n+1}) + \frac{1}{2}(u^i_{n+1} + u^i_n)^t K_i(u^i_n - u^i_{n+1})\right] \tag{26}$$

Using different ingredient of the Newmark scheme, the energy balance equation taking into consideration the contribution of the gluing forces at the interface can be written as following:

$$\sum\nolimits_{i=1,2}\Big[\frac{1}{2}(\dot{u}^i)^t M_i(\dot{u}^i_n) + \frac{1}{2}(u^i)^t K_i(u^i) + (\beta^i - \frac{1}{2}\gamma^i)\frac{1}{2}(\triangle t)^2(\ddot{u}^i)^t M_i(\ddot{u}^i)\Big]_n^{n+1} \tag{27}$$

$$= \sum\nolimits_{i=1,2}(\triangle u^i)^t \Big[\Big(\bar{f}^i + (\gamma^i - \frac{1}{2})\triangle f^i\Big) \tag{28}$$

$$- \sum\nolimits_{i=1,2}(\triangle u^i)^t \Big(L_i^t\bar{\lambda} + (\gamma^i - \frac{1}{2})L_i^t\triangle(\lambda)\Big) \tag{29}$$

$$- \sum\nolimits_{i=1,2}(\gamma^i - \frac{1}{2})\Big\{(\triangle u^i)^t K_i \triangle u^i + (\beta^i - \frac{1}{2}\gamma^i)(\triangle t)^2(\triangle\ddot{u}^i)^t M_i(\triangle\ddot{u}^i)\Big) \tag{30}$$

$$- \sum\nolimits_{i=1,2}(\triangle u^i)^t C_i \Big\{\frac{1}{2}(\dot{u}^i_{n+1} + \dot{u}^i_n) + (\gamma^i - \frac{1}{2})\triangle\dot{u}^i\Big\} \tag{31}$$

where
$\triangle f^i = f^i_{n+1} - f^i_n$
$\triangle\lambda = \lambda_{n+1} - \lambda_n$
$\triangle u = u_{n+1} - u_n$
$\bar{f}^i = \frac{1}{2}(f^i_{n+1} + f^i_n)$
$\bar{\lambda} = \frac{1}{2}(\lambda_{n+1} + \lambda_n)$

Terms in (27) are the total mechanical energy plus a conservative Newmark term. In (28) and (29) , we respectively have the work of the external forces and the work of gluing forces. In (30) we have a Newmark dissipative term, and in (31) the contribution of the damping matrix. We are mainly interested in (29). It represents the Arlequin contribution and it will be studied in details in the next section.

In order to show conservative terms on the left side of Newmark's energy balance, and dissipative terms on the right side, we can express (30) with quadratic terms.
If the mass matrix M_i is replaced with an equivalent mass matrix M_i^* defined by:

$$M_i^* = M_i + (\gamma - \frac{1}{2})hC \tag{32}$$

Equations (27) to (31) can be written as:

$$\sum\nolimits_{i=1,2}\Big[\frac{1}{2}(\dot{u}^i)^t M_i^*(\dot{u}^i_n) + \frac{1}{2}(u^i)^t K_i(u^i) + (\beta^i - \frac{1}{2}\gamma^i)\frac{1}{2}(\triangle t)^2(\ddot{u}^i)^t M_i^*(\ddot{u}^i)\Big]_n^{n+1} \tag{33}$$

$$= \sum\nolimits_{i=1,2} (\triangle u^i)^t \left[\left(\bar{f}^i + (\gamma^i - \frac{1}{2}) \triangle f^i \right)\right. \tag{34}$$

$$- \sum\nolimits_{i=1,2} (\triangle u^i)^t \left(L_i^t \overline{\lambda} + (\gamma^i - \frac{1}{2}) L_i^t \triangle(\lambda) \right) \tag{35}$$

$$- \sum\nolimits_{i=1,2} (\gamma^i - \frac{1}{2}) \left\{ (\triangle u^i)^t K_i \triangle u^i + (\beta^i - \frac{1}{2}\gamma^i)(\triangle t)^2 (\triangle \ddot{u}^i)^t M_i^* (\triangle \ddot{u}^i) \right) \tag{36}$$

$$\frac{1}{2} \Delta t \left\{ \Delta t^{-2} \Delta u^t C \Delta u + \frac{1}{4} (\dot{u}_{n+1} + \dot{u}_n)^t C (\dot{u}_{n+1} + \dot{u}_n) \right\} \tag{37}$$

$$- \frac{1}{2} (\beta^i - \frac{1}{2}\gamma^i) \left\{ (\gamma^i - \frac{1}{2})^2 - \frac{1}{2} (\beta^i - \frac{1}{2}\gamma^i) \right\} \Delta t^3 \Delta \ddot{u}^t C \Delta \ddot{u} \tag{38}$$

Now we have a Newmark energy balance system with conservative and dissipative terms respectively on the left and right side of the equation.

6 ARLEQUIN INTERFACE WORK

The contribution of the Arlequin gluing forces at the interface appear in the Newmark energy balance equation and it is given by:

$$W_{inter}^{arl} = \sum_{i=1,2} (\triangle u^i)^t \left(L_i^t \overline{\lambda} + (\gamma^i - \frac{1}{2}) L_i^t \triangle \lambda \right) \tag{39}$$

We can re-write this term as an interpolation of λ between n and $n+1$ as follows:

$$W_{inter}^{arl} = \sum_{i=1,2} (\triangle u^i)^t \left(L_i^t \overline{\lambda} + (\gamma^i - \frac{1}{2}) L_i^t \triangle \lambda \right) = \sum_{i=1,2} (\triangle u^i)^t L_i^t \left(\gamma^i \lambda_{n+1} + (1 - \gamma^i) \lambda_n \right)$$

$$= (\triangle u^1)^t L_1^t \left(\gamma^1 \lambda_{n+1} + (1 - \gamma^1) \lambda_n \right) + (\triangle u^2)^t L_2^t \left(\gamma^2 \lambda_{n+1} + (1 - \gamma^2) \lambda_n \right) \tag{40}$$

$$= \left((\triangle u^1)^t L_1^t \gamma^1 + (\triangle u^2)^t L_2^t \gamma^2 \right) \lambda_{n+1} + \left((\triangle u^1)^t L_1^t (1 - \gamma^1) + (\triangle u^2)^t L_2^t (1 - \gamma^2) \right) \lambda_n \tag{41}$$

In order to find a solution to the problem statement (5.1) we have to be able to use the Arlequin condition (24).
In (41) we can notice that the presence of γ^1 and γ^2 makes the factorization unrealizable and the use of the Arlequin condition impossible.
Based on [13], we propose to introduce **a time independent Lagrange multiplier field** $\lambda_{n+\gamma}$**.**
In other terms, between two successful time steps, $\lambda_{n+\gamma}$ is a constant field.
Equation (39) can now be written as:

$$W_{inter}^{arl} = \sum_{i=1,2} (\triangle u^i)^t L_i^t \lambda_{n+\gamma} \tag{42}$$

If the numerical integration conditions are well respected, between two successive time steps, Arlequin condition (24) gives:

$$\sum_{i=1,2} (L_i u_{n+1}) = 0 \ and \sum_{i=1,2} (L_i u_n) = 0 \tag{43}$$

Now we have (42) equivalent to zero.
In this section we have demonstrated that by the mean of a time independent Lagrange multiplier field, the work of the Arlequin gluing forces is reduced to zero while using two different Newmark schemes and a space recovering method.

6.1 A PRACTICAL WAY TO ENFORCE THE INTERPOLATION OF $\lambda_{n+\gamma}$

The idea proposed in the last section, is a theorical framework permitting the suppression of undesirable interface effects. But no indications concerning constant value of the time independent field $\lambda_{n+\gamma}$ are presented.
We will now suggest a method which aims to determine a general form of $\lambda_{n+\gamma}$. This form should be applicable on both models and on the gluing zone.

Based on (41),

$$\lambda_{n+\gamma} = (\gamma^i \lambda_{n+1} + (1-\gamma^i)\lambda_n) \tag{44}$$

we define $\lambda_{n+\gamma}$ as follows:

$$\lambda_{n+\gamma} = (\gamma^* \lambda_{n+1} + (1-\gamma^*)\lambda_n) \tag{45}$$

One can notice that with this definition, according a value to $\lambda_{n+\gamma}$ is equivalent to according a value to γ^*.
In order to stay coherent with the partition of unity used for spatial gluing part, we propose to weight the Newmark parameters γ^1 and γ^2 with a weight parameter ξ.

By means of this approach we will have:

- $\gamma^* = \gamma^1 \; in \; \Omega_1 | S_c$;
- $\gamma^* = \gamma^2 \; in \; \Omega_2 | S_c$;
- $\gamma^* = \xi\gamma^1 + (1-\xi)\gamma^2 \; in \; S_c$;

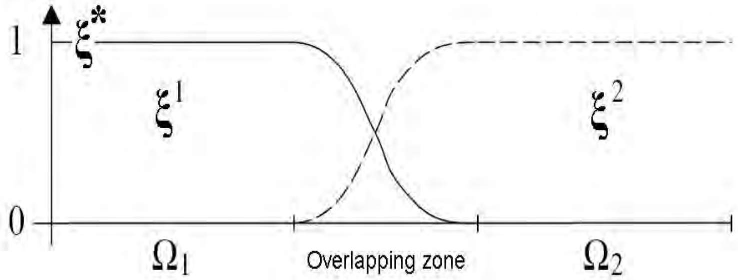

Figure 3: Wave propagation.

We are now able to write (42) as:

$$W^{arl}_{inter} = \left(L_1(\triangle u^1) + L_2(\triangle u^2)\right)\gamma^*\lambda_{n+1} + \left(L_1(\triangle u^1) + L_2(\triangle u^2)\right)(1-\gamma^*)\lambda_n \tag{46}$$

We can notice that (46) is very similar to (41). The main difference is that in 46 the Arlequin conditions can take effect and suppress the undesirable energy dissipation introduced at the interface.

7 NUMERICAL APPLICATION

The proposed methodology here below, is applied for both 2D-1D and 1D-1D couplings. We used two different dissipative Newmark schemes, and a unique time scale. Results were validated by comparison with an analytic solution [9] of a free climbed bar model, undergoing a constant concentrated effort at its free edge. The same work was realized with sinusoidal loading.

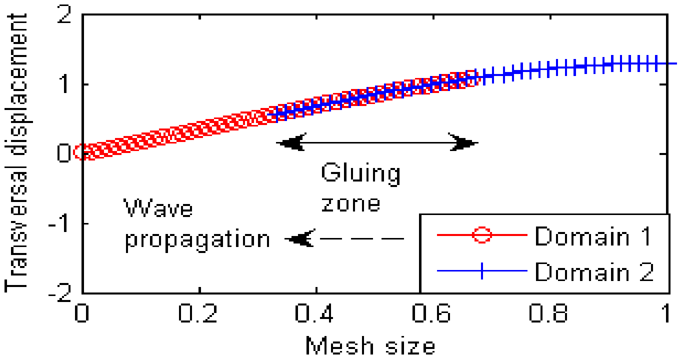

Figure 4: Wave propagation.

In figure 5, the left graph shows the work of the gluing forces at the interface while using two different Newmark schemes on the 1D-1D bar coupling. The right one represents the same work but here we use the $\lambda_{n+\gamma}$ introduced in section 5.1. We can clearly see that the numerical dissipation disappear, and the contribution of the gluing forces at the interface is reduced to zero. We can find the corresponding energy balance of the Newmark algorithm (figure7).

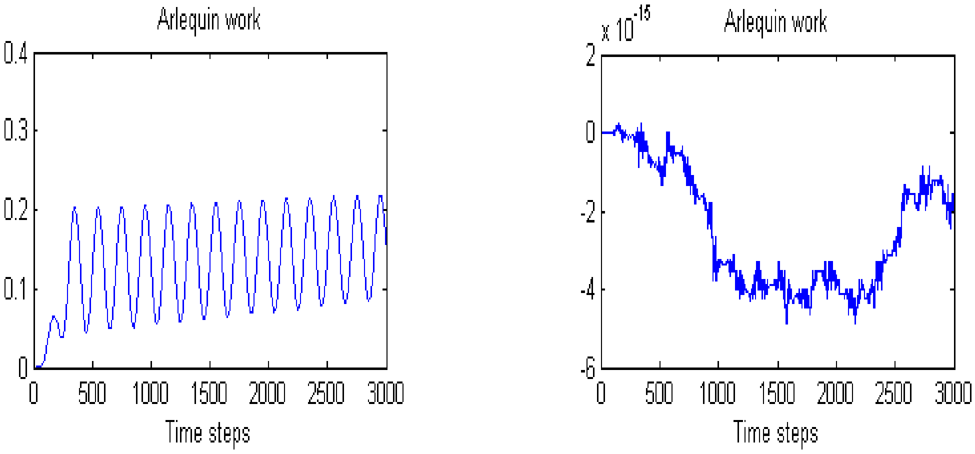

Figure 5: Arlequin interface work ; $\lambda_{n+\gamma}$ Effect.

Graphs in figure 5 are generated for compatible bar meshes. Next results (figure 6) are obtained when bar models presenting incompatible mesh are coupled. For both cases the contribution of the Arlequin forces at the interface is negligible. But we can notice a degradation of the results when incompatible mesh are used. Properly treating the numerical integration issue is the main clue to address this kind of difficulties.

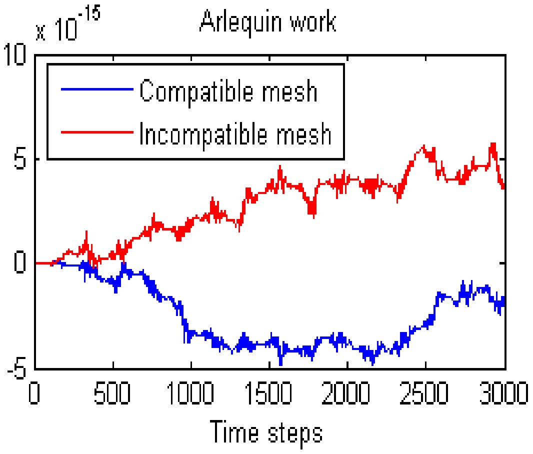

Figure 6: Arlequin interface work - Mesh compatibility effect.

Energy balance equation (27) to (31) is represented in the figure 7. Both cases described in figure 5 are reviewed in the global energy balance system. (Left term holds for (27) and right term holds for (28) to (30)). The contribution of the gluing forces disappear on the right side graph. On the other side, one can notice coherent kinetic and potential energy profiles. The proposed method present satisfying results.

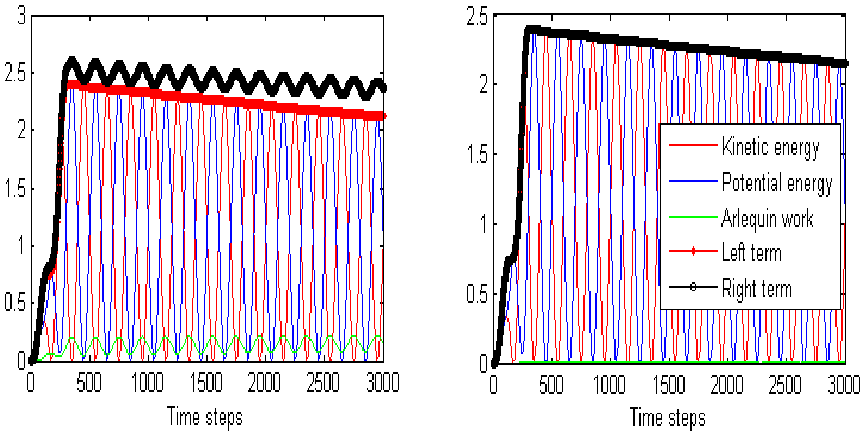

Figure 7: Newmark energy balance - 1D-1D coupling.

Other interesting aspects are currently being investigated. For instance, we are evaluating the model's response to high frequency solicitations and studying how do high frequency waves transit between the different mesh scales.

The study was reviewed in the context of a multimodel 2D-1D coupling (Figure 8), and we obtained similar results.

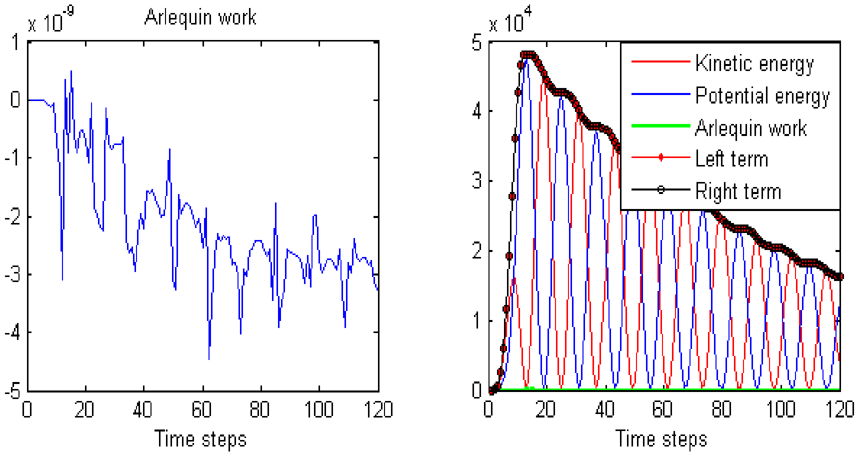

Figure 8: Newmark energy balance - 2D-1D coupling.

8 CONCLUSION

In this article we propose a general formalism to couple different time schemes without introducing undesirable numerical dissipation due to the gluing forces work effects at the interface. This formalism authorizes multiscale/multimodel coupling since it is based on the Arlequin method. Two applications (1D-1D and 2D-1D) were presented in order to exemplify the relevance of the method. An extension to a 3D-1D coupling is planned to be developed. Our main goal is to formulate a generale formalism leading to a space-time multimodel-multiscale/multischeme coupling which guaranties a global energy balance of the system during the resolution, in the context of the Arlequin method.
More elaborated applications are under progress and will be presented during the conference.

REFERENCES

[1] R. Li, On Multi-Mesh H-Adaptive Methods. *Journal of Scientific Computing*, **24**, No. 3, 2005.

[2] P. Le Tallec, Domain decomposition methods in computational mechanics. *Computational Mechanics Advances*, **1**, 121-220, 1994.

[3] H.A. Schwarz. Über einige Abbildungsaufgaben. *IGes. Math. Abh.*, **11**, 65-83, 1869.

[4] H. Ben Dhia, G. Rateau, The Arlequin method as flexible engineering design tool. *Int. J. Num. Meth. Eng*, **62**, 1442-1462, 2005.

[5] H. Ben Dhia, Further Insights by Theoretical Investigations of the Multiscale Arlequin Method. *International Journal for Multiscale Computational Engineering*, **6**, 215-232, 2008.

[6] P. Aubertin, J. Rethoré and R. Borst, Energy conservation of atomistic/continuum coupling. *Int. J. Num. Meth. Eng*, **78**, 1365-1386, 2009.

[7] G. Rateau, Méthode Arlequin pour les problèmes mécaniques multi-échelles. PhD Thesis, 2003.

[8] T. N. Baranger and S. Andrieux, Energy methods for Cauchy problems of evolutions equations. *6th International Conference on Inverse Problems in Engineering : Theory and Prac- tice, Journal of physics : Conference Series* , **135**, 2008.

[9] M. Bonnet and A. Frangi. *Analyse des solides déformables par la méthode des éléments finis.* 2006.

[10] NM. Newmark, A method of computation for structural dynamics. *Journal of the Engineering Mechanics Division (ASCE)*, **85**, 67-94, 1959.

[11] S. Krenk, Energy conservation in Newmark based time integration algorithms. *Computer Methods in Applied Mechanics and Engineering*, **195**, 6110-6124, 2006.

[12] Contribution à la modélisation en mécanique et dynamique des structures sous contact. PhD Thesis, 2005.

[13] N. Mahjoubi. A monolithic energy conserving method to couple heterogeneous time integrators with incompatible time steps in structural dynamics. *Computer Methods in Applied Mechanics and Engineering*, **200**, 1069-1086, 2011.

[14] A. Combescure and A. Gravouil. A numerical scheme to couple subdomains with different time-steps for predominantly linear transient analyses. *Computer Methods in Applied Mechanics and Engineering*, **191**, 1129-1157, 2002.

COMPDYN 2011
3rd ECCOMAS Thematic Conference on
Computational Methods in Structural Dynamics and Earthquake Engineering
M. Papadrakakis, M. Fragiadakis, V. Plevris (eds.)
Corfu, Greece, 25–28 May 2011

VIBRATIONS IN NEIGHBORHOOD BUILDINGS DUE TO ROCK CONCERT IN STADIUMS

Raul D. Bertero[1], Alejandro Lehmann[1], Juan Mussat[1] and Sebastian Vaquero[1]

[1] Universidad de Buenos Aires
Larrea 1142 – Buenos Aires - Argentina
e-mail: rbertero@freyreyasoc.com.ar

Keywords: Ground vibrations, rock concert vibrations, building vibrations, crowd induced rhythmic vibrations.

Abstract. *Rock concerts events in the River Plate Stadium in Buenos Aires (and other stadiums) has raised neighborhood complains due to molest vibrations felt by the inhabitants of some buildings at distances up to 3 km. In this paper are described the results of the studies conducted to determine the origin and the effects on buildings of vibrations generated during rock concerts in stadiums. First, are presented the equations for modeling: a) the coordinate jump of the public on the field and the generated load; b) the acceleration wave propagation over the surface of an elastic solid and c) the response of buildings at different distances from the stadium. The resulting equations are used to estimate the accelerations at top of buildings at distances inside a 3 km radio from the stadium. Then, the planned and obtained measurements during the concerts are shown and evaluated. Finally the conclusions and recommendations in relation with the effects of the coordinate jump of the public on the field, the properties of the affected buildings, their distance to the stadium and the effects on the structures, contents and inhabitants are presented. It is shown that for buildings in resonance with the spectator jumps (2 Hz of natural frequency, i.e. buildings around 10 to 12 stories at Buenos Aires), the acceleration level at the upper stories is sever to persons (even is not high enough to produce structural and non structural damage) to distances of more than 3 km from the stadium.*

1. INTRODUCTION

This paper summarize the studies carried out at University of Buenos Aires (UBA) to establish the causes and effects of building vibrations generated by rock concerts at River Plate stadium at Buenos Aires city.

The research activities were developed in the framework of a Cooperation Agreement between the UBA College of Engineering and the Enviromental Protection Agency (APRA) of Buenos Aires City due to vibration claims from owners of multistory buildings during rock concert events in the River Plate Stadium. The buildings (in general, 10 and 11 levels) were 600 to 2000m away from the Stadium (Fig. 1).

Fig. 1. Vibrations claims during rock concert events at River Plate Stadium in Buenos Aires

Due to the lack of an analytical model generally accepted and a systematic and planned set of acceleration records, there is a broad controversy regarding the causes, the intensity and the effects of stadium field crowd-induced vibrations during rock concerts on neighborhood buildings.

In order to have a correct diagnosis about the level of annoyance and the possible solutions to the problem is needed a physical model capable of predict the building vibrations due to the actions generated by the spectacle. To satisfy this objective it was necessary to develop: a) an analytical model capable of representing the building responses, b) a planned set of acceleration records at soil and building floors at different distances of stadium during the rock concerts and c) the adjustment of the model according to the experimental results.

In this paper, are first summarized the limits of the vibrations human sensitivity. Then, the dynamic loads generated by the public during a rock concert, and in particular, the action on the environmental generated by the coordinated crowd jumping at the rhythm of the music at the field of the stadium are presented.

After that, it is developed an acceleration wave propagation model with origin at the periodic type of loading generated by the coordinated crowd jumping. The soil is represented by a semi-infinite isotropic elastic solid where the energy is propagated through volumetric waves (compression waves P and shear waves S) and surface Rayleigh waves R as shown in Fig. 2.

On turn, the acceleration waves reach the building foundations so that the accelerations at the different levels of the buildings can increase or decrease according to the dynamical structural properties. In particular, if the natural frequency of the building coincides with the excitation frequency, the resonance effect produces a large amplification of accelerations at uppers floors.

Finally, from the equations describing the above behavior and the results obtained in the planned measurements, conclusions regarding the effects on the structural, non-structural components and inhabitants of buildings are presented.

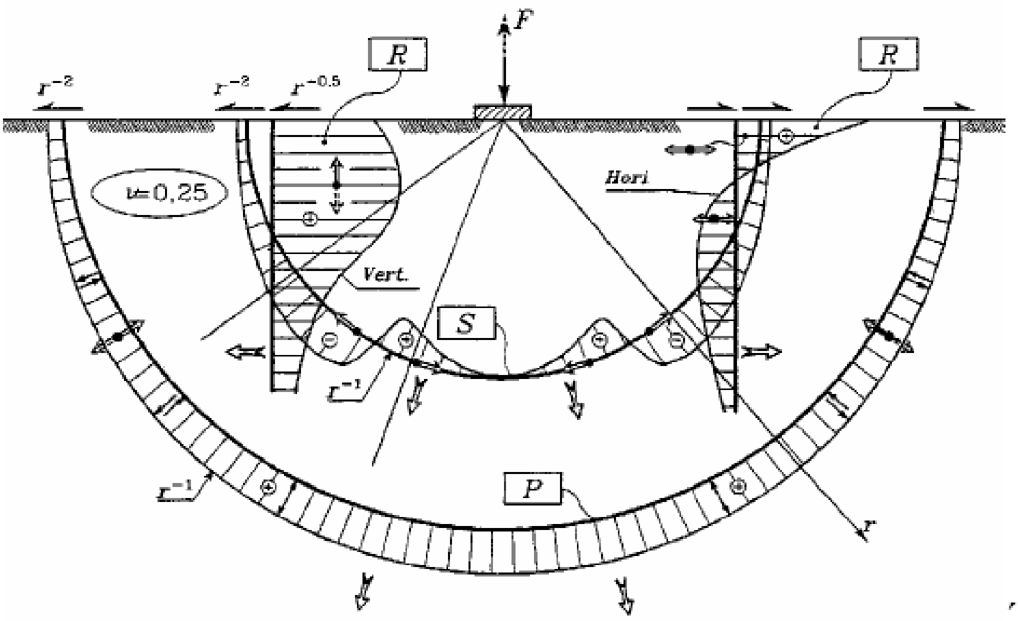

Fig. 2. Wave propagations in a semi-infinite isotropic elastic solid

2. HUMAN SENSIVITY TO VIBRATIONS

In Argentina, the human exposure to vibrations in buildings (frequency between 1 Hz to 80 Hz) is regulated by the norm IRAM 4078 Parte II (December 1990) based on the ISO Standard 2631/1985 "Evaluation of Human Exposure to whole-body Vibration".

According to that norm, the experience in several countries has shown that it is usual that the vibration claims in dwelling buildings start as soon as the vibrations reach the perception threshold. Therefore the allowable levels of vibrations are established in the norm mainly to minimize inhabitant complains than to other factors like health risk or work difficulties.

The norm defines basic curves representing constant levels of human response to vibrations considering the human perceptions or complaints. These curves are acceleration levels as a function of the excitation frequency. The allowable acceleration levels for different building uses and event hours are established as a multiple of these basic curves. For acceleration of velocity levels below these basic curves it is expected no comments or complain due to vibrations.

The primary magnitude used in the norm to describe the vibration intensity is the root mean square (RMS) of the accelerations. Given an acceleration history $a(t)$, the acceleration RMS (σ_a) for a period of time T is computed as

$$\sigma_a = \sqrt{\frac{1}{T}\cdot\left(\int_0^T a(t)^2\,dt\right)} \tag{1}$$

Thus, in the particular case of an harmonic excitation, $a(t) = A\sin\left(\frac{2\pi t}{T}\right)$, the amplitude A, satisfy the following equation

$$\sigma_a = \frac{A}{\sqrt{2}} \tag{2}$$

Fig. 3 shows the basic curves defined by the norm for accelerations $a_x(f)$ and $a_z(f)$ (m/s^2) as a function of frequency f in the directions of the axis x (horizontal accelerations) and z (vertical accelerations).

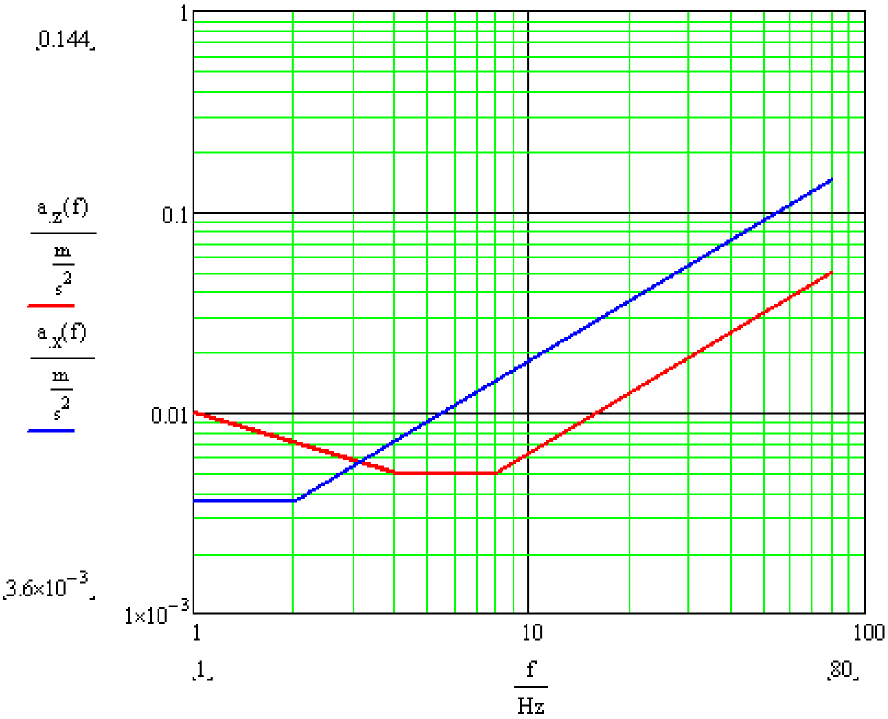

Fig. 3. Curvas básicas de respuesta humana constante a las vibraciones en las direcciones X y Z

For dwellings, the norm establishes the following multiplication factors for the allowable levels of vibration: a) During day hours: (2.0 to 4.0) and b) at night: (1.40). Since most of the musical events are at night, the last factor is used in this paper as a multiplication factor of the basic curves of Fig. 3 to obtain the acceleration limits.

If it is considered an excitation frequency of 130 beats/minute, $f_b = 130.\frac{1}{\min} = 2.167\frac{1}{s}$ (corresponding to the music rhythm in a rock concert), the allowable continous acceleration RMS in the vertical and horizontal directions are respectively $A_Z(f_b) = 0.097.\%.g$ and

$A_X(f_b) = 0.056.\%.g$, where g is the gravity acceleration. Note that for the frequency of the music beat in a rock concert, the human body is more sensitive to the horizontal than to the vertical vibrations.

It is important to take into account that in residential areas the tolerable vibrations can vary in a wide range. The specific values depend on cultural and social factors as well as psychological predisposition of building occupants.

Considering the international recommendations and the observations obtained in this study, it is assumed in this paper that the level of the acceleration RMS above what intermittent vibrations are clearly noticed for most of the people at buildings away of the stadium - where the vibrations are generated by the coordinate crowd jumping on the field following the rhythm of the music of a rock concert - is $A_1 = 0.1\%g$ $(0.01 m/s^2)$.

On the other hand, for ten times larger values, about $1\%g$ $(0.10\, m/s^2)$, the accelerations are molest for persons, the hanging objects (lamps, flower-pots) can oscillate few millimeters and persons can feel alarmed by the movement.

3. DYNAMIC LOADS GENERATED BY THE CROWD DURING A ROCK CONCERT

3.1. Experimental studies and analytical representation of loads

During a rock concert, the music has the effect of synchronizing the movement of the spectators. Thousands of people, particularly, on the field jump exactly at the same time due to auditive and, specially, visual impact. For people on the stadium tribunes' exact synchronization for so many people is much more difficult.

In this paper the action of the crowd is modeled following the experimental studies carried out in the University of Surrey, UK [1]. In these studies it was examined thoroughly the statistical nature of crowd loading by measuring the individual performance of 100 people jumping and bobbing (oscillating vertically with feet in permanent contact with the ground) to four different tempos (frequencies of 1.5, 2.0, 2.67 y 3.5 Hz) in such a way as to allow the loading from very large crowds to be estimated by summing the individual force histories of the participants. They were encouraged to move as if they were enjoying a lively rock concert (Fig. 4).

From the studies of the University of Surrey it was recommended a synchronized load representing the crowd action given by eq.(3), where W is the weight of the crowd, f is the frequency of the beat, DLF_n is the dynamic load factor for each harmonic n y φ_n is the phase lag of each harmonic.

$$P(t) = W.\left[1 + \sum_{n=1}^{\infty}\left(DLF_n.\cos(2.\pi.n.f.t - \varphi_n)\right)\right] \tag{3}$$

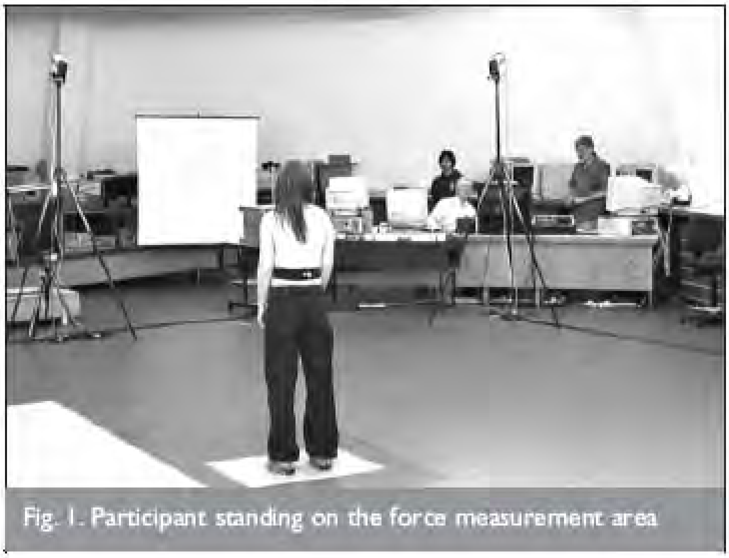

Fig. 4. Studies of Crowd-induced rhythmic loading at University of Surrey [1]

In **Fig. 5** it is shown the normalized force of people jumping following a beat of 2 Hz [1].

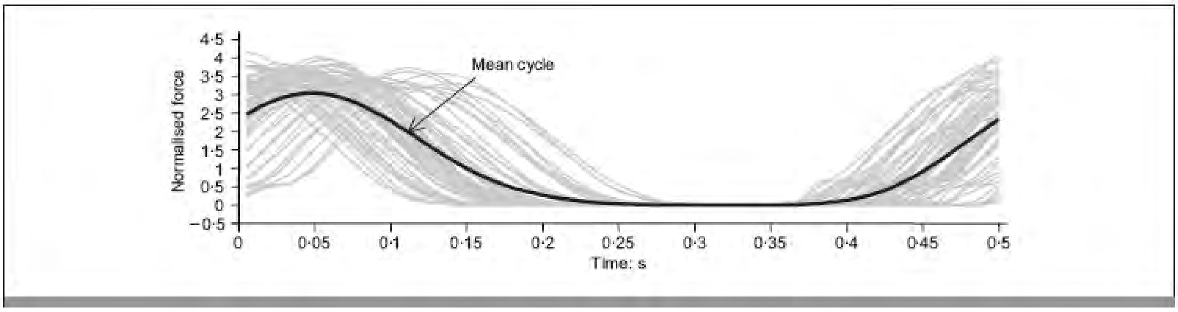

Fig. 5. Segment superposition of 29 s of force history and their mean [1]

In Fig. 6 it is shown the variation of dynamic load factors with crowd size for the first three harmonics.

The loads in the study of the University of Surrey have been measured on a rigid base. Considering that the crowd jumping on grass maintains the feet in permanent contact with the ground, the bobbing values have been used in this paper.

Therefore, from the values recommended in the study of the University of Surry and considering a frequency of 120 beats/minute (2 Hz) coincident with the experimental values obtained around the River Plate Stadium, the following dynamic loads factors were used in this paper for the first three harmonics $DLF = \begin{pmatrix} 0.321 \\ 0.080 \\ 0.010 \end{pmatrix}$, with a beat frequency, $f_b = 120 . \frac{1}{\min} = 2 . \frac{1}{s}$

.

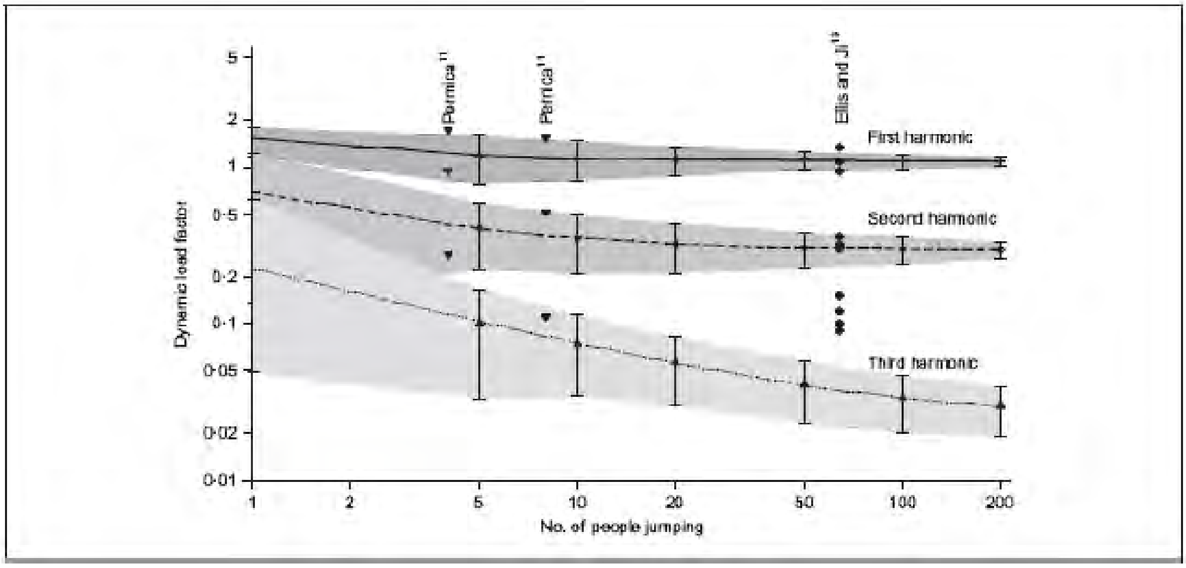

Fig. 6. Variation of dynamic load factors with crowd size [1]

3.2. Crowd-induced rhythmic loading on the stadium field

Assuming the synchronized jumping of 35,000 people on the field and an average weight of 62.4 kgf for the assistants to a rock concert a total weight of $W_t = W_0 . N_{esp} = 2.204.10^4 .kN$ is obtained. Considering eq. (3), it is possible to compute the power spectral density for the first three harmonics of the crowd-induced rhythmic loading as

$$S_{esp_i} = \frac{1}{2} . \left[(DLF_i . W_t)^2 \right] = \begin{pmatrix} 2.502.10^7 \\ 1.554.10^6 \\ 2.428.10^4 \end{pmatrix} .kN^2 \tag{4}$$

with the following frequencies for each harmonic:

$$F_{b_i} = f_b . i = \begin{pmatrix} 2 \\ 4 \\ 6 \end{pmatrix} .Hz \tag{5}$$

$$\omega_b = 2.\pi.F_b = \begin{pmatrix} 12.566 \\ 25.133 \\ 37.699 \end{pmatrix} \frac{1}{s} \tag{6}$$

4. WAVE PROPAGATION FROM THE STADIUM TO THE NEIGHBORHOOD

4.1. Dynamic soil properties at the stadium neighborhood

Considering the average soil properties in a depth according to the length of the Rayleigh waves corresponding to the 2 Hz frequency of the crowd jumping, the following values are obtained from soils studies around the stadium:: shear modulus $G = 60.3MPa$, soil density, $\rho = 1900.\frac{kg}{m^3}$, Poisson modulus $\nu = 0.35$, soil damping factor $\varsigma = 0.005$, elasticity modulus,

$\mathrm{E}=2.(1+\nu).G=162.795.MPa$, Lamé constant $\lambda=\dfrac{\nu.\mathrm{E}}{(1+\nu).(1-2.\nu)}=140.687.MPa$, P wave propagation velocity P, $Cp=\sqrt{\dfrac{\lambda+2.G}{\rho}}=370.828\dfrac{m}{s}$, S wave propagation velocity $C_S=\sqrt{\dfrac{G}{\rho}}=178.14\dfrac{m}{s}$, R wave propagation velocity for $\nu=0.35$, $C_R=\sqrt{c_{R_1}}.C_S=166.563\dfrac{m}{s}$, with a wave propagation velocity ratio, $\dfrac{C_R}{C_S}=0.935$.

4.2. Wave propagation on the surface of a semi-infinite isotropic elastic solid

In 1904, assuming that most of the vibration energy is transported by the Rayleigh waves, Lamb [2] obtained analytically the displacements $u(t)$ at any point of a semi-infinite isotropic elastic solid located at a distance r from an harmonic load $Pe^{i\omega t}$ of frequency ω. The Lamb solution can be written as [3]:

$$u(t)=U(\omega,\varsigma,r)e^{i\omega t}=-\frac{\omega H}{2\rho C_R{}^3}e^{-\frac{\varsigma\omega r}{2C_R}}H1^{(2)}\left(\frac{\omega\, r}{C_R}\right)Pe^{i\omega t}=H_u(\omega,\varsigma,r)Pe^{i\omega t} \tag{7}$$

where $H1^{(2)}(\cdot)$ is the Hankel function of second kind and first order . H is a constant that depends on the Poisson modulus only ($H=0.095$ for $\nu=0.35$). Therefore, $H_u(\omega,\varsigma,r)$ is the transfer function representing the displacement soil response.

By double differentiation of eq. (7) respect of time, the acceleration response $\ddot{u}(t)$ in any point of the semi-infinite space can be computed as

$$\ddot{u}(t)=\ddot{U}(\omega,\varsigma,r)e^{i\omega t}=-\omega^2H_u(\omega,\varsigma,r)Pe^{i\omega t}=H_{\ddot{u}}(\omega,\varsigma,r)Pe^{i\omega t} \tag{8}$$

4.3. Soil accelerations away the stadium due to crowd-induced rhythmic loading on the field

Using the random vibrations theory [4], the transfer function of eq.(8) $H_{\ddot{u}}(\omega,\varsigma,r)$ and the power spectral density of the crowd-induced rhythmic loading S_{esp_i} [eq.(4)] it is possible to obtain the power spectral density of the horizontal acceleration at different distances from the stadium r for each harmonic i as

$$S_{\ddot{u}}(i,\zeta,r)=S_{esp_i}.\left(\left|H_{\ddot{u}}(2\pi f_b i,\zeta,r)\right|\right)^2 \tag{9}$$

Thus, the RMS horizontal accelerations can be computed as

$$\sigma_{\ddot{u}}(\zeta,r)=\left(\sum_{i=1}^{3}S_{\ddot{u}}\left(i,\zeta,r\right)\right)^{\frac{1}{2}} \tag{10}$$

In Fig. 7 are shown the RMS horizontal accelerations obtained on soil at 500, 1000 and 1500 m distance from the River Plate stadium (0.081 %g, 0.042 %g and 0.026 %g respectively) using eq. (10).

These small values explain why the vibrations are practically no felt at the one or two story dwellings, even at those located closest to the River Plate stadium. In Section 2, it was shown that the limit above what intermittent vibrations are clearly noticed for most of the people is around 0.1 %g.

Fig. 7. RMS horizontal acceleration on soil at 500, 1000 y 1500 m from River Plate stadium

4.4. Building accelerations away the stadium due to crowd-induced rhythmic loading on the field

As shown in Fig. 7, the accelerations on soil and at rigid dwellings (no amplification) are just perceptible, even for those in the closest zone near the River Plate stadium.

However, when the low frequency horizontal accelerations reach the foundations of multi-story buildings the accelerations can be amplified or reduced at the different floors depending on the dynamic building properties. In particular, when the excitation frequency coincides with the building natural frequency, a large amplification is obtained at the upper stories due to the resonance condition.

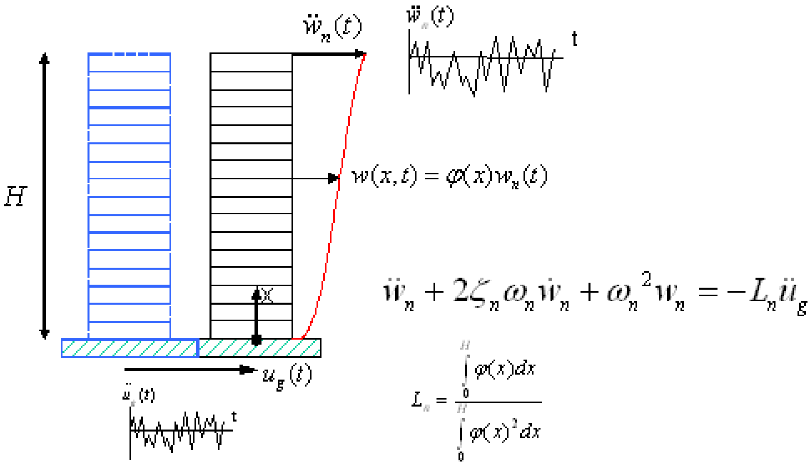

Fig. 8. Building vibrations due to base accelerations. Generalized single degree of freedom system model.

Fig. 8 shows the response to base accelerations of a multi-story building using a generalized single degree of freedom system [5]. The equation of motion is

$$\ddot{w}_n(t) + 2\xi_n\omega_n\dot{w}_n(t) + \omega_n^2 w_n(t) = -L_n\ddot{u}(t) \tag{11}$$

where w_n is the displacement of the top of the building, ξ_n is the building damping factor, ω_n is the building natural vibration frequency, $L_n = \dfrac{\int_0^H m(x)\varphi(x)dx}{\int_0^H m(x)\varphi(x)^2 dx} = 1.50 \; for \; \varphi(x) = \dfrac{x}{H}$ is the generalized participation factor, $m(x)$ is the mass along the building height assumed constant in this paper, H is the building height, $\varphi(x)$ is the shape function that define the form of deflections (assumed linear in this paper) and $\ddot{u}(t)$ is the soil acceleration as described in the previous section.

By applying the Fourier transform to eq.(11), the response in the frequency domain is obtained as

$$W_n(\omega,\omega_n,\xi) = -\frac{L_n}{\omega_n^2 - \omega^2 + 2\xi_n\omega_n\omega\, i}\ddot{U}(\omega) = H_n(\omega,\omega_n,\xi_n)\ddot{U}(\omega) \tag{12}$$

where $H_n(\omega,\omega_n,\xi_n)$ is the transfer function representing the building top displacement response for a building of frequency ω_n and damping factor ξ_n, $\ddot{U}(\omega)$ is the Fourier transform of $\ddot{u}(t)$ and $W_n(\omega,\omega_n,\xi)$ is the Fourier transform of the top building displacement $w(t)$.

Using eq. (12), the Fourier transform of the top building acceleration $\ddot{w}(t)$ can be computed as

$$\ddot{W}_n(\omega,\omega_n,\xi) = \frac{\omega^2 \; L_n}{\omega_n^2 - \omega^2 + 2\xi_n\omega_n\omega\, i}\ddot{U}(\omega) = \omega^2 H_n(\omega,\omega_n,\xi_n)\ddot{U}(\omega) = H_{\ddot{w}}(\omega,\omega_n,\xi_n)\ddot{U}(\omega) \tag{13}$$

Therefore, the power spectral density of top building accelerations for each excitation frequency ω_i can be computed as

$$S_{\ddot{w}_n}(\omega_n,\xi_n,\omega_i,\zeta,r) = \left(\left|H_{\ddot{w}}(\omega_i,\omega_n,\xi_n)\right|\right)^2 S_{\ddot{u}}(\omega_i,\zeta,r) \tag{14}$$

Thus, the RMS top building acceleration can be computed for the first three harmonics as

$$\sigma_{\ddot{w}_n}(\omega_n,\xi_n,\zeta,r) = \left(\sum_{i=1}^{3} S_{\ddot{w}_n}\left(\omega_n,\xi_n,\omega_i,\zeta,r\right)\right)^{\frac{1}{2}} \tag{15}$$

Fig. 9 shows the RMS top building accelerations (building damping factor $\xi_n = 0.02$) as a function of the period of the first vibration mode $T_n = \dfrac{2\pi}{\omega_n}$ obtained using eq.(15) at distances of 1000, 1500 and 2000 m away of River Plate stadium.

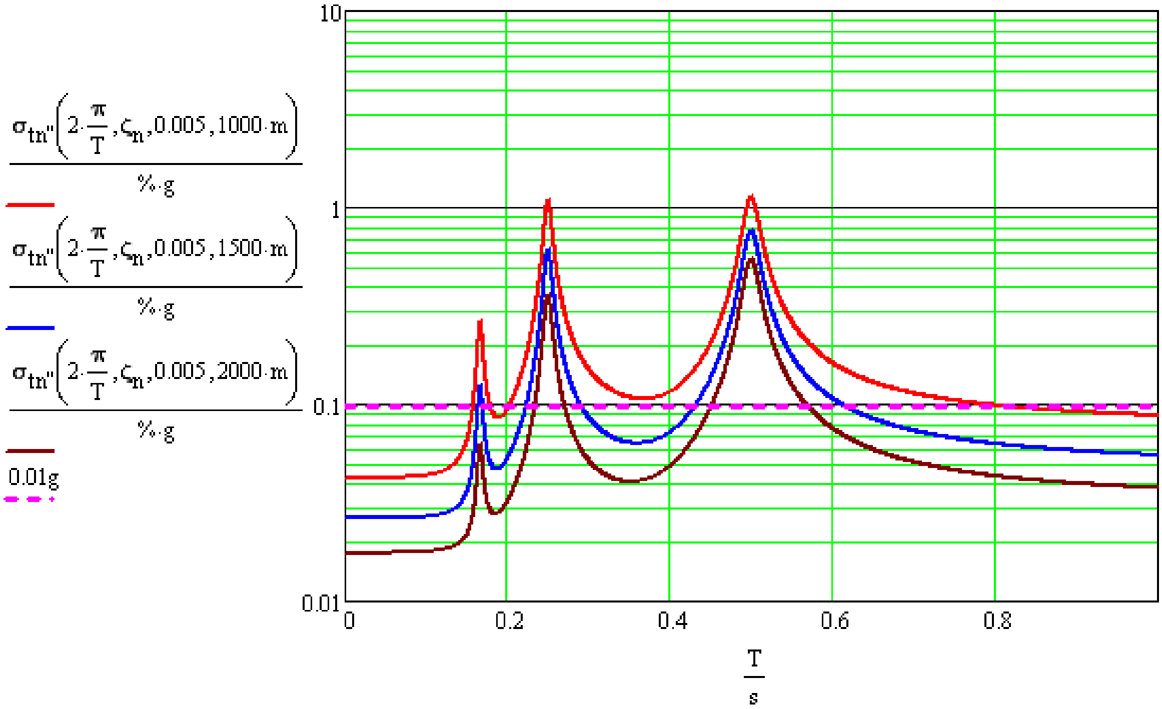

Fig. 9 RMS building top accelerations [%g] for natural periods between 0 to 1 sec

Fig. 9 clearly shows the resonance with the first and second harmonic of the crowd-induced rhythmic loading [eq. (5)] at frequency of 2 and 4 Hz (Periods of 0.5 and 0.25 s respectively).

Although in most of the cases, the building top accelerations are below the perception threshold of 0.1%g, they reach values near 1% g, even for distances larger than 1500m from the stadium, for buildings whose natural frequencies coincide with the crowd jumping frequencies.

In Fig. 10 are shown the RMS building top accelerations for buildings with 2 Hz of natural frequency obtained at 500, 1000, 1500 and 2000 m distance from the River Plate stadium (1.93 %g, 1.13 %g, 0.76 %g and 0.55 %g respectively) using eq.(15).

The period of the building first mode of vibration is strongly correlated to the building height. From experimental data on reinforced concrete shear wall buildings (the usual structural construction for multi-story buildings in Buenos Aires), Satake et al [6] proposed in 2003 the following relationship,

$$T_n = 0.015\frac{H}{m} \tag{16}$$

Considering an average inter-story height of 3 m and using eq.(16), the resonance frequencies of 2 and 4 Hz would correspond to buildings between 11 and 12 stories and 6 stories respectively, depending on the specific values of the dynamic building parameters (stiffness, mass and damping).

The analytical results clearly explain why the vibrations are mostly felt at buildings of that number of stories, even to long distances away the stadium (3000 m), meanwhile the inhabitants of lower and taller buildings do not feel vibrations even if they are located closer the River Plate stadium.

Fig. 10. RMS building top accelerations for buildings with 2 Hz of natural frequency computed at 500, 1000, 1500 and 2000 m distance from the River Plate stadium

5. STRUCTURAL AND NON-STRUCTURAL DAMAGE RISK

For accelerations smaller than 2% g at the building top, the influence of the acceleration on damage is neglectful. The structural and non-structural building damage is more related with the level of displacements, particularly the inter-story relative displacements as considered for wind and earthquake building codes.

Considering that the maximum building horizontal acceleration, A, happens at resonance with the first harmonic of the spectators jumping ($f_b = 2Hz$), it is possible to compute the maximum displacement at the building top, X , as

$$X(A) = \frac{A}{\left(2\pi f_b\right)^2} \tag{17}$$

The buildings closest to the River Plate stadium with a height susceptible of reaching the resonance condition are located about 800 m away from the stadium. Using the RMS building top acceleration $\sigma_{\ddot{w}_n}$ [eq. (15)] and eq. (2), the acceleration amplitude can be computed as

$$A = \sqrt{2} . \sigma_{\ddot{w}_n}\left(2\pi f_b, \zeta_n, 0.005, 800\, m\right) = 1.927\ \%\ g \tag{18}$$

Although this acceleration level is very molest for building inhabitants, the corresponding maximum displacement is only

$$X(A) = 1.2\ mm \tag{19}$$

Considering that the approximate height of a building in resonance with the crowd jumping is [eq.(16)], $H = \dfrac{T_b}{0.015} m = \dfrac{0.5}{0.015} m = 33.33 m$, the ratio displacement/height can be computed as

$$\frac{X(A)}{H}=\frac{1.2\,10^{-3}m}{33.33m}=\frac{1}{1000}\frac{1}{28} \tag{20}$$

That means that the maximum displacement of the closest buildings near the River Plate stadium due to the crowd-induced rhythmic loading on the stadium field is about 30 times smaller than the serviceability allowable displacement for wind action established by most of the structural codes (H/1000).

Therefore, this level of relative displacement is much smaller than the required to produce damage to structural and non-structural elements.

6. ACCELERATION RECORDS OBTAINED DURING THE CONCERTS

In order to validate the analytical model a measurement plan was developed. The ground accelerations and the building responses were measured during the concerts of ACDC (4th and 6th of December, 2009), Metallica (21st and 22nd of January, 2010) and Cold Play (26th of February, 2010) at the River Plate Stadium. Measures were also taken during the Gustavo Cerati concert (20th of December, 2009) at Club Ciudad. In Fig. 11 it is shown where the measures were obtained during the concerts. The coordinate jump of the spectators was caught on video during the Metallica and Cold Play concerts.

Fig. 11. Locations were the ground accelerations and the building response were obtained

The ground accelerations obtained at 450 m away from the stadium show that the frequency content matches the spectator's movement during rock concerts (Fig. 12). The acceleration levels measured at the ground were below the human perception threshold (0.06% g).

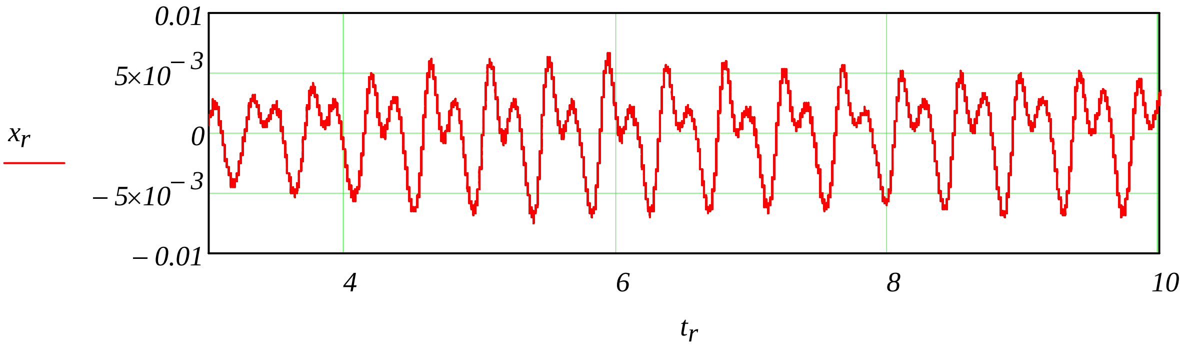

Fig. 12. Acceleration record obtained on ground 450m away from the stadium during the coordinate crowd jumping at stadium field – Metallica concert (sample duration 7sec)

On the other hand, during the concerts, the recorded accelerations at buildings inside a 1000m radius were well above the comfort limits. The buildings having natural frequencies around 2-2.5 Hz were the most affected by the Rayleigh wave's transmitted trough the foundations. The maximum measured accelerations reached up to 1.5% g (RMS 1.1% g) at the top of an 11-story building located 850m away from the stadium (Fig. 13).

Fig. 13. Accelerations recorded at the top of an 11-story building located 850m away from the stadium during the ACDC concert (sample duration 20 minutes)

7. CONCLUSIONS

7.1. Conclusions from the obtained measures

As a result of the obtained measured the following conclusions were reached:

- From the acceleration records and the simultaneous crowd jumps caught on video, it was established that the Rayleigh waves were the result of the coordinate jump of the spectators during some segments of the rock concerts. The obtained accelerations and the radius where the vibrations are felt by the building inhabitants are related to the number of spectators coordinately jumping following the rhythm of the music.

- The recorded ground and building accelerations matched reasonably with the results of the analytical model of wave propagation and building response.

- The recorded accelerations and displacements are below the levels required to produce structural and/or non-structural damage on buildings. However the accelerations on 10 to 12 story buildings located about1000m away the stadium produced alarm in the inhabitants of the upper floors.

7.2. Conclusions from the analytical model

This paper studies the vibration transmitted from the ground to the buildings (and the people living in them) due to the coordinated jump of 35,000 spectators during rock concerts developed at River Plate Stadium, in Buenos Aires. The main conclusions are:

- The coordinated movement of the spectators jumping to rhythm of the music generates acceleration waves with a frequency of 2 and 4 Hz. These waves (mainly Rayleigh waves) are propagated over the ground reaching the buildings foundations in the surrounding area of the stadium.

- At the ground level of dwellings some occupant could perceive the vibrations inside approximately 380m radius from the stadium (Fig. 14).

Fig. 14.Area where some people could feel vibrations on ground level

- The horizontal vibrations are magnified by buildings whose natural frequency matches the frequency of the spectator's movement.

- The RMS accelerations could reach values between 0.6% g and 1.1% g at the top level of buildings about 10-12 stories (at resonance with the first harmonic of the spectators movement) and at the top level of buildings about 6 stories (at resonance with the second harmonic of the spectators movement) inside a 3000m radius away from the stadium (Fig. 15). The number of stories to get resonance can slightly change as a function of the characteristics of the structural system, the foundation type, the quantity of the non-structural walls and the spectator's movement.

- For RMS values larger than 0.6% g, the accelerations are very molesting for persons. The hanging objects (lamps, flower-pots) can oscillate few millimeters, the water in fishbowls can move clearly and inhabitants can alarm by the movement.

- The calculated drifts and accelerations on buildings in the surrounding areas of the stadium are not high enough to produce structural and/or non-structural damage.

- This study was conducted assuming the simultaneous jump of 35,000 spectators at the stadium field. The ground and building accelerations are directly proportional to the number of spectators jumping in a coordinated manner with the music.

- As a result of the low frequency of the vibration it is not possible to use the traditional vibration control methods such as digging a shallow trench around the source (because of the depth of the Raleigh waves).

Fig. 15. Area where people at the upper floors could feel vibrations on buildings at resonance with the spectators movement

8. REFERENCES

[1] Parkhouse, J.G. and Ewins, D.J.. (2006). "Crowd-induced rhythmic loading". Structures & Buildings 159, October 2006, pag. 247-259

[2] Lamb, H. (1904). “On the propagation of tremors over the surface of an elastic solid”. Philosophical Transactions of the Royal Society (London) A203, l-42.

[3] Hunt, H.E.M. (1991) “Stochastic Modelling Of Traffic-Induced Ground Vibration” Journal of Sound and Vibration 144(l), pag. 53-70

[4] Ray W. Clough and Joseph Penzien (1995). “Dynamics of Structures”. Third Edition. Computers & Structures, Inc. University Ave. Berkeley, CA 94704. USA

[5] Anil K. Chopra (1995). “Dynamic of Structures: Theory and applications to earthquake engineering”. Prentice Hall. Englewood Cliffs. New Jersey. USA.

[6] Naoki Satake et al, (2003), "Damping Evaluation Using Full-Scale Data of Buildings in Japan", Journal of Structural Engineering, Vol. 129, No. 4, April 1, 2003.

COMPDYN 2011
III ECCOMAS Thematic Conference on
Computational Methods in Structural Dynamics and Earthquake Engineering
M. Papadrakakis, M. Fragiadakis, V. Plevris (eds.)
Corfu, Greece, 25–28 May 2011

NONLINEAR ANALYSIS OF R/C PANELS BY A TWO PARAMETER CONCRETE DAMAGE MODEL

L. Tesser[1], F.C. Filippou[2], D.A. Talledo[3], R. Scotta[1], R. Vitaliani[1]

[1] University of Padua – Dept. of Structural and Transportation Engineering
Via Marzolo, 9 – 35131 Padua, ITALY
tesser@dic.unipd.it

[2] University of California at Berkeley – Dept. of Civil and Environmental Engineering
760 Davis Hall – 94720 Berkeley CA, USA
filippou@ce.berkeley.edu

[3] University IUAV of Venice
Terese – Dorsoduro 2206 – 30123 Venice, ITALY
talledo.diego@gmail.com

Keywords: reinforced concrete panel, membrane model, nonlinear analysis, damage model

Abstract. *The paper prosents an efficient numerical model for the inelastic response analysis of R/C panels under cyclic excitations. A plane stress 2d membrane model has been developed that accounts for the concrete and reinforcing steel interaction. The reinforcing bars are modeled as multiple smeared steel layers with an uniaxial stress-strain relation in the bar direction following the Menegotto-Pinto constitutive model with isotropic hardening. The concrete material model is based on damage mechanics with an efficient two parameter damage law. At this stage of the research the bond-slip between concrete and rebars is not taken into account.*

The new model is validated by comparison with several experimental results on reinforced concrete panels from the literature. The tests are carried out under quasi-static conditions. The accuracy of the model in reproducing the cyclic behavior of reinforced concrete panels with different reinforcement ratio and bar inclination is excellent.

1 INTRODUCTION

Reinforced concrete (R/C) panels are commonly used in the lateral force resisting system of structures in seismic risk zones for serviceability, ultimate strength and ductility considerations. They are either used alone or are coupled with moment resisting frames to resist the lateral forces.

The assessment of the behavior of R/C panels have been the focus of important analytical and experimental investigations aiming to evaluate the strength and particularly the shear transfer across the cracks [1–4].

The necessity of assessing advanced performance levels in high seismic zones has encouraged the research towards a deeper understanding on the nonlinear cyclic behavior of the R/C panels [5–9].

All the while many investigations on nonlinear analysis of R/C panels by finite element methods have been carried out. The available studies are not reviewed here in details, nonetheless, in the opinion of the authors, they can be subdivided into two categories: some researchers developed very sophisticated models while others searched for simplified ones as it is clarified below.

The works of the first category focus their attention on addressing the general two-dimensional problem, by means of R/C nonlinear constitutive models belonging to the different frameworks; i.e. elasto/viscoplasticity [10–12], fracture theory [13, 14], continuum damage mechanics [15–17], smeared crack models [18], modified compression field theory [19–21], softened membrane models [22].

Some of the cited works found their way into modern computer codes, but they often turn out to be rather complex or excessively expensive from the computational point of view, especially if applied to large scale structures.

The models in the second category are less general and they are addressing specific problems as beam-column joint panel [23], macroscopic fiber based model for shear walls [24, 25] or enhanced beam model [26, 27]. These models are suitable for large scale structures but they can be applied only for moderate shear demand since they do not address all the physical issues in the case of significant biaxial membrane stresses. Because of these limitations, the use of such nonlinear methods for the R/C panel design and assessment do not seem to meet the challenges of the earthquake engineering practice.

The purpose of the present study is the development of a membrane model for R/C panels addressing the evaluation of strength and ductility under cyclic loading. The proposed model belongs to the first model category while being suitable for the analysis of large scale structures. The membrane under plane stress state conditions is defined by superposition of distinct concrete and reinforcing steel material models. The model takes into account only the axial response of the reinforcing bars [28]. The bond slip effects are not taken into account at the present stage as well as the stiffness and strength of the bars perpendicularly to their alignment. The selection of the damage mechanics as framework for the concrete constitutive law comes from its ability in describing concrete behaviors avoiding excessive complications in the numerical procedure for the material state determination. In order to study the cyclic behavior of concrete panels subjected to shear loading, it is necessary to introduce two damage parameters, that account for the two different concrete failure modes in tension and in compression [16, 28]. The model of Faria et al. [29], although notably efficient, was developed for massive concrete structure such as dams in which the influence of the plastic strain in tension is supposed to be very low. Thus the simplified plastic evolution law, that disregards the plastic strains for tensile stresses, cannot capture the progressive crack opening typical of a cyclic loading of R/C panels. A more general plastic evolution law, that is more accurate for plane stress state problem, is proposed to reproduce the plastic strains for general stress configurations.

For what concerns the reinforcing steel material, the simulation of the Baushinger effect is important to estimate the dissipated energy in hysteretic cycles precisely. Thus the model of Menegotto-Pinto with isotropic hardening developed by Filippou et al. [30] is profitably used.

2 CONCRETE DAMAGE MODEL

2.1 The model fundamentals

The proposed concrete constitutive law belongs to the class of energy-based isotropic continuum damage models. The model presented in this work takes into account both tensile and compressive concrete failure modes, by means of two damage parameters, and also the micro-crack opening and closing, by considering the spectral decomposition of the stress tensor.

The damage and plastic unloading processes are assumed to be elastic. Reference is made to the paper of Ju [31] for the detailed explanation of the elastoplastic damage model framework and the adopted notations.

The split of the total strain tensor into “elastic-damage” and “plastic-damage” parts is assumed:

$$\boldsymbol{\varepsilon} = \boldsymbol{\varepsilon}^e + \boldsymbol{\varepsilon}^p \tag{1}$$

The locally averaged free energy potential is postulated according to the work of Faria et al. [29]:

$$\begin{aligned}\Psi(\boldsymbol{\varepsilon}, \boldsymbol{\varepsilon}^p, d^+, d^-) &= (1-d^+)\Psi_0^+(\boldsymbol{\varepsilon}, \boldsymbol{\varepsilon}^p) + (1-d^-)\Psi_0^-(\boldsymbol{\varepsilon}, \boldsymbol{\varepsilon}^p) = \\ &= (1-d^+)\frac{1}{2}\bar{\boldsymbol{\sigma}}^+ : \boldsymbol{\varepsilon}^e + (1-d^-)\frac{1}{2}\bar{\boldsymbol{\sigma}}^- : \boldsymbol{\varepsilon}^e\end{aligned} \tag{2}$$

where d^+, d^- represent the positive and negative damage parameters respectively and $\bar{\boldsymbol{\sigma}}^+$, and $\bar{\boldsymbol{\sigma}}^-$ are the positive and negative part of the effective stress tensor defined by:

$$\bar{\boldsymbol{\sigma}} \equiv \mathbf{C}^0 : \boldsymbol{\varepsilon}^e \tag{3}$$

where $\mathbf{C}^0$ is the fourth-order elastic stiffness tensor.

During any physical process the energy dissipation shall be always non-negative in agreement with the first thermodynamic principle. This condition is expressed by the following Clausius-Duhem inequality that holds for any admissible process:

$$\dot{\boldsymbol{\varepsilon}} : \left[\boldsymbol{\sigma} - \frac{\partial \Psi}{\partial \boldsymbol{\varepsilon}}\right] - \left[\frac{\partial \Psi}{\partial d^+} : \dot{d}^+ + \frac{\partial \Psi}{\partial d^-} : \dot{d}^-\right] - \frac{\partial \Psi}{\partial \boldsymbol{\varepsilon}^p} : \dot{\boldsymbol{\varepsilon}}^p \geq 0 \tag{4}$$

With the total strain a free variable, the term within the first square brackets shall be always zero. Thus the definition of the relation between the Cauchy stress tensor and the effective stress tensor can be obtained:

$$\begin{aligned}\boldsymbol{\sigma} = \frac{\partial \Psi}{\partial \boldsymbol{\varepsilon}} = \frac{\partial \Psi}{\partial \boldsymbol{\varepsilon}^e} = (1-d^+)\frac{\partial \Psi_0^+}{\partial \boldsymbol{\varepsilon}^e} + (1-d^-)\frac{\partial \Psi_0^-}{\partial \boldsymbol{\varepsilon}^e} = (1-d^+)\bar{\boldsymbol{\sigma}}^+ + (1-d^-)\bar{\boldsymbol{\sigma}}^- = \\ = (\mathbf{I} - \mathbf{D}) : \bar{\boldsymbol{\sigma}}\end{aligned} \tag{5}$$

The second and the third terms of the Equation (4) provide the damage and the plastic dissipation inequalities:

$$-\frac{\partial \Psi}{\partial d^+} : \dot{d}^+ - \frac{\partial \Psi}{\partial d^-} : \dot{d}^- = -\frac{\partial \Psi}{\partial \boldsymbol{d}} : \dot{\mathbf{d}} \geq 0 \tag{6}$$

$$-\frac{\partial \Psi}{\partial \boldsymbol{\varepsilon}^p} : \dot{\boldsymbol{\varepsilon}}^p \geq 0 \tag{7}$$

The reader is referred to the work of Faria et al. [29] that contains the demonstration of the validity of these inequalities.

Starting from the stress-strain relation of Equation (5), the fourth-order damage tensor $\mathbf{D}$ can be defined by the following expression [32]:

$$\mathbf{D} = \mathrm{d}^+ \mathbf{P}^+ + \mathrm{d}^- \mathbf{P}^- \tag{8}$$

with $\mathbf{P}^+$ and $\mathbf{P}^-$ standing for the fourth-order projection tensors, positive and negative respectively, that have the following definitions:

$$\boldsymbol{P}^+ = \sum_i H(\bar{\sigma}_i)\, \boldsymbol{p}_i \otimes \boldsymbol{p}_i \tag{9}$$

$$\boldsymbol{P}^- = \boldsymbol{I} - \boldsymbol{P}^+ \tag{10}$$

where H is the Heaviside step function, $\bar{\sigma}_i$ is the i-th principal stress of the effective stress tensor $\bar{\boldsymbol{\sigma}}$ and $\boldsymbol{p}_i$ stands for the associated principal direction.

Then developing the Equation (6), the energy dissipated by the damage process shall be defined. The thermodynamic force, also called damage energy released rate, is expressed as:

$$-\boldsymbol{Y} = \frac{\partial \Psi}{\partial \boldsymbol{d}} \tag{11}$$

The damage energy release rate characterizes the damage evolution taking into account the progressive degradation of the mechanical properties of the material.

For the damage criteria, the damage energy release rate functions are defined with the following formulas:

$$Y^+ = \sqrt{E^0 \bar{\boldsymbol{\sigma}}^+ : \mathbf{C}^{0^{-1}} : \bar{\boldsymbol{\sigma}}^+} \tag{12}$$

$$Y^- = \sqrt{3}(K\bar{\sigma}_{oct}^- + \bar{\tau}_{oct}^-) \quad or \quad Y^- = \sqrt{3}\left(KI_1 + \sqrt{J_2}\right) \tag{13}$$

where $\bar{\sigma}_{oct}^-$ and $\bar{\tau}_{oct}^-$ are the octahedral normal and shear stresses respectively (while I_1 and J_2 are the first invariant of the effective stress tensor and the second invariant of the deviatoric effective stress tensor), E^0 is the concrete Young modulus and K is a material property that accounts for the increase of compressive strength due to biaxial compression [29].

The energy release rate functions have also been called equivalent effective stresses $\bar{\tau}^+$ and $\bar{\tau}^-$ since they provide two scalar measures of the effective stress tensor [29].

With respect to the work in [29], the negative equivalent stress is defined slightly different so as to be homogeneous to the positive equivalent stress. As a result both the equivalent stresses have the same dimension of a stress component.

The damage threshold in uniaxial tension and uniaxial compression is described by variable r^+ and r^-, respectively, and they monitor the size of the expanding damage surface.

The numerical applications, carried out by the same authors, showed that the original damage criteria proposed by Faria et al. [29] agrees quite well with the experimental results for uniaxial, biaxial tension and biaxial compression stress states, whereas it has been demonstrated that improvements were necessary to better fit the experimental information for biaxial tension-compression states (see Figure 1).

A substantial improvement can be obtained by defining a unique damage criterion instead of two distinct ones in the earlier studies [29, 32].

Taking advantage from the homogeneity of the equivalent stresses, the following unique expression can adequately account for the interaction between tensile and compressive damage evolutions [36]:

$$g(Y^+, Y^-, r^+, r^-) = \left(\frac{Y^+}{r^+}\right)^2 + \left(\frac{Y^-}{r^-}\right)^2 - 1 \leq 0 \tag{14}$$

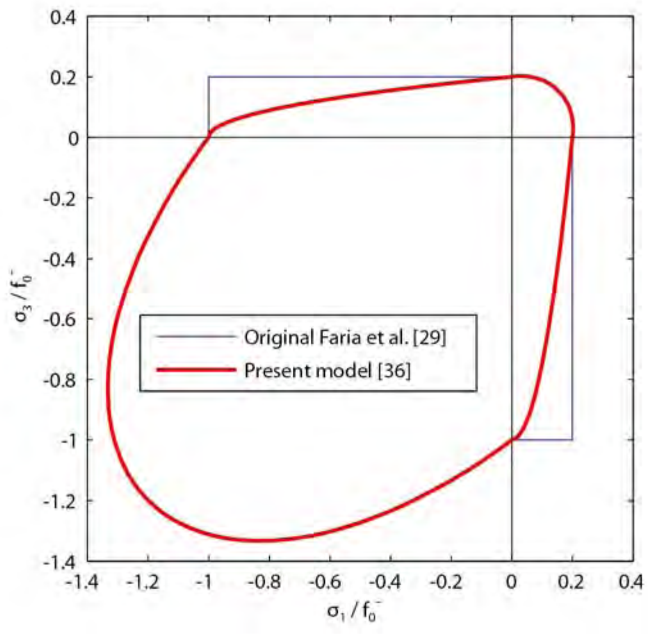

Figure 1: Initial elastic domain for plane stress states

The new damage criterion, that constitutes the damage surface, is superimposed to Faria's proposal in Figure 1.

It can be easily verified that, in the compression field ($Y^+ = 0$), the damage criterion becomes the modified Drucker-Pruger criterion and its suitability in representing biaxial stresses has been demonstrated by several studies [17, 29, 32].

In addition to the damage criterion the evolution of the damage threshold is determined by the following flow rule:

$$\dot{\boldsymbol{r}} = \dot{\gamma} \frac{\partial g(\boldsymbol{Y}, \boldsymbol{r})}{\partial \boldsymbol{Y}} \tag{15}$$

where γ is the damage consistency parameter. The relative Khun-Tucker conditions give:

$$g(\boldsymbol{Y}, \boldsymbol{r}) \leq 0 \qquad \dot{\gamma} \geq 0 \qquad \dot{\gamma} g(\boldsymbol{Y}, \boldsymbol{r}) = 0 \tag{16}$$

while the consistency condition is

$$\dot{\gamma} \dot{g}(\boldsymbol{Y}, \boldsymbol{r}) = 0 \tag{17}$$

The new damage threshold variables r can be computed with the Newton-Raphson method assuring the quadratic convergence of the material state determination.

It can be underlined that the elliptical shape of the damage criteria assures independent evolution of the positive and negative damage threshold for uniaxial tensile and compressive tests respectively.

In fact the tangent of the damage criteria is orthogonal to the normal vector when one of the thermodynamic forces is null.

Four parameters are needed to determine the initial damage surface: r_0^+ and r_0^- are the initial elastic damage thresholds for uniaxial tension and compression loadings respectively, K takes into account the additional strength under condition of biaxial compression and ν is the Poisson modulus.

Three common lab tests are necessary to compute the value of those parameters [29]: an uniaxial tension experiment, an uniaxial and a biaxial compression ones.

Using the Equation (12), the positive damage initial threshold is exactly equal to the concrete tensile strength, that is assumed to characterized the end of the elastic domain in the constitutive stress-strain relationship:

$$r_0^+ = f_0^+ = f_{ct} \tag{18}$$

Since the compressive constitutive law ends the linearity before reaching the peak strength, the uniaxial initial elastic limit f_0^- shall be evaluated from the uniaxial compression test leading to the corresponding negative damage threshold from the Equation (13):

$$r_0^- = \frac{\sqrt{3}}{3}\left(K - \sqrt{2}\right) f_0^- \tag{19}$$

From the results of a biaxial compression test, the biaxial compression elastic limit $f_{0,2D}^-$ can be obtained. Thus the parameter K, accounting for the increase of compressive strength due to biaxial compression, can be computed as

$$K = \sqrt{2}\,\frac{\left(f_{0,2D}^- - f_0^-\right)}{2f_{0,2D}^- - f_0^-} \tag{20}$$

The present constitutive model considers that damage criteria describes also the plastic surface so that the development of material damaging is simultaneous to the accumulation of irreversible strains for all the stress states.

Recalling the considerations of the work by Faria et al. [29] the following plastic evolution law is defined:

$$\dot{\boldsymbol{\varepsilon}}^p = \beta E^0 \frac{\langle \bar{\boldsymbol{\sigma}} : \dot{\boldsymbol{\varepsilon}} \rangle}{\bar{\boldsymbol{\sigma}} : \bar{\boldsymbol{\sigma}}} \mathbf{C}^{0^{-1}} : \bar{\boldsymbol{\sigma}} \tag{21}$$

having introduced β for the plastic strain coefficient.

It is clear that the plastic strain evolution proposes several simplifications with respect to the “effective stress space plasticity” [31] used to couple the damage evolution and the plastic flows in the spirit of obtaining a powerful tool for large time consuming seismic analyses.

In fact the adopted law determines the efficiency of the procedure. The presented choice leads to have the direction of the plastic strain rate parallel to those of the total strain rate. The effect is to introduce a simplification in the coupling between damage and plasticity and thus eliminating the additional iterative cycles inside the material state determination procedure. A consequent accepted limitation is a low efficacy in predicting the dilatancy of the concrete. In the cases in which the dilatancy plays an important role, the proposed model can be suitably applied taking care of choosing a different plastic potential.

The damage parameter evolution laws can be defined and they shape the concrete constitutive behavior. The analyses presented in this paper have been carried out using the laws proposed by Wu et al. [32].

The elastoplastic damage tangent modulus in the effective stress space can be derived from the previous expressions

$$\bar{\mathbf{C}}^{\mathrm{ep}} = \mathbf{C}^0 - \frac{\left(\mathbf{C}^0 : \boldsymbol{l}(\bar{\boldsymbol{\sigma}})\right) \otimes \left(\mathbf{C}^0 : \frac{\partial g}{\partial \bar{\boldsymbol{\sigma}}}\right)}{\frac{\partial g}{\partial \bar{\boldsymbol{\sigma}}} : \mathbf{C}^0 : \boldsymbol{l}(\bar{\boldsymbol{\sigma}}) - \frac{\partial g}{\partial \mathbf{r}} \cdot \frac{\partial \mathbf{r}}{\partial \boldsymbol{Y}}} \tag{22}$$

in which the following symbol

$$\boldsymbol{l}(\bar{\boldsymbol{\sigma}}) = \frac{\bar{\boldsymbol{\sigma}}}{\sqrt{\bar{\boldsymbol{\sigma}} : \bar{\boldsymbol{\sigma}}}} \tag{23}$$

has the physical meaning of the unit tensor parallel to the effective stress tensor.

2.2 Notes on integration algorithm

The concrete material state determination presents similarities to the classical plasticity return-mapping algorithm and it is quite straightforward.

The total strain is updated by the given incremental displacement field:

$$\boldsymbol{\varepsilon}_{n+1} = \boldsymbol{\varepsilon}_n + \nabla^{\mathrm{s}}(\Delta \mathbf{u}) \tag{24}$$

And the trial elastic state is computed as

$$\bar{\boldsymbol{\sigma}}_{n+1}^{trial} = \boldsymbol{C}^0 : (\boldsymbol{\varepsilon}_{n+1} - \boldsymbol{\varepsilon}_n^p) \tag{25}$$

If the plastic-damage criteria is respected there is evolution neither of the plastic strain, nor of the damage thresholds, nor of the damage parameters:

$$\boldsymbol{\varepsilon}_{n+1}^p = \boldsymbol{\varepsilon}_n^p \tag{26}$$

$$\boldsymbol{r}_{n+1} = \boldsymbol{r}_n \tag{27}$$

$$\boldsymbol{d}_{n+1} = \boldsymbol{d}_n \tag{28}$$

and therefore the trial effective stress can be confirmed

$$\bar{\boldsymbol{\sigma}}_{\boldsymbol{n+1}} = \bar{\boldsymbol{\sigma}}_{n+1}^{trial} \tag{29}$$

If the plastic-damage criteria is not respected it is necessary to use a return-mapping algorithm to update effective stress, plastic strain and plastic-damage thresholds such that the following equalities hold:

$$\bar{\boldsymbol{\sigma}}_{\boldsymbol{n+1}} = \boldsymbol{C}^0 : (\boldsymbol{\varepsilon}_{n+1} - \boldsymbol{\varepsilon}_{n+1}^p) \tag{30}$$

$$\boldsymbol{\varepsilon}_{n+1}^p = \boldsymbol{\varepsilon}_n^p + \beta E \frac{\langle \bar{\boldsymbol{\sigma}}_{\boldsymbol{n+1}} : \Delta \boldsymbol{\varepsilon} \rangle}{\bar{\boldsymbol{\sigma}}_{\boldsymbol{n+1}} : \bar{\boldsymbol{\sigma}}_{\boldsymbol{n+1}}} {\boldsymbol{C}^0}^{-1} : \bar{\boldsymbol{\sigma}}_{\boldsymbol{n+1}} \tag{31}$$

$$g(Y_{n+1}^+, Y_{n+1}^-, r_{n+1}^+, r_{n+1}^-) = \left(\frac{Y_{n+1}^+}{r_{n+1}^+}\right)^2 + \left(\frac{Y_{n+1}^-}{r_{n+1}^-}\right)^2 - 1 = 0 \tag{32}$$

The solution of the previous nonlinear equations requires an iterative scheme that can be solved by the Newton method using the elastoplastic damage tangent modulus of the Equation (22).

As a consequence the damage parameters can be calculated directly

$$\boldsymbol{d}_{n+1} = \boldsymbol{d}_{n+1}(\boldsymbol{r}_{n+1}, \boldsymbol{r}_0) \tag{33}$$

When the two alternative branches of the integration have been completed, the Cauchy stress is obtained from the following equation

$$\boldsymbol{\sigma}_{n+1} = (1 - \boldsymbol{d}_{n+1}) : \boldsymbol{\bar{\sigma}_{n+1}} \tag{34}$$

3 VALIDATION EXAMPLE FOR CONCRETE MATERIAL

Two simple numerical examples are reported in order to show the ability of the concrete damage model in reproducing the typical concrete behavior for 1D cyclic tests under tensile and compressive solicitations.

3.1 Cyclic uniaxial compressive loading test

In Figure 2 the experimental results, taken from Sinha et al. [33], are plotted against the numerical results. This experiment was already selected by Faria et al. [29], among others, to validate their model. The concrete material properties assumed for the model are derived from those reported by the authors of the experimental study: the compressive peak strength f_c^- = 32 MPa, the Young modulus E = 26 GPa, the compressive uniaxial initial elastic threshold f_0^- = 15 MPa, the plastic strain coefficient β = 0.590. The numerical model is very capable in reproducing the concrete nonlinear behavior. When the initial elastic limit is passed, the plastic strain and the damage parameter increase. The hysteresis of the reloading loop cannot be simulated by the model because of the rate-independent elastic loading/unloading assumption but the progressive degradation of the secant modulus fits the loading/unloading test curves on average very well.

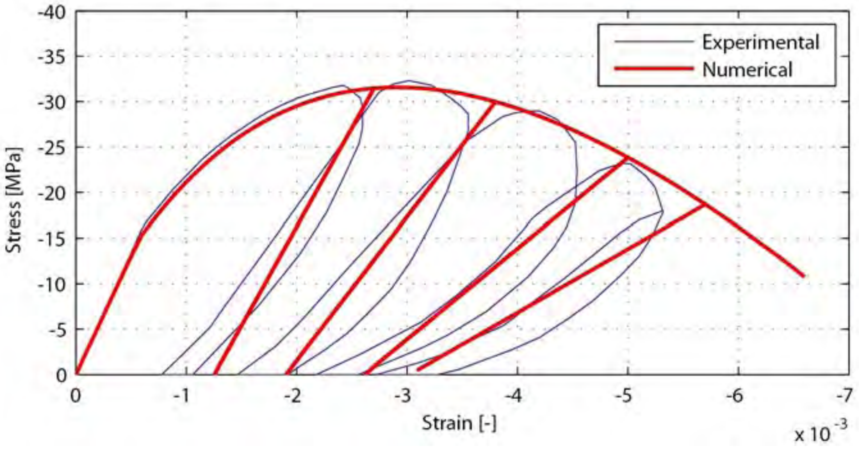

Figure 2: Cyclic uniaxial compressive loading test

The values reached by the negative damage parameter at the maximum strain of each cycle are depicted in Figure 3. In can be noted that its value is about 0.2 when the compressive peak strength is achieved. After a strength decay of about 25%, the damage parameter approaches 0.6. A damage value equal to 1.0 means that the strength and stiffness of the material are completely lost. It should be underlined that the damage parameters are positive scalar values that cannot decrease since they depend on the maximum recorded damage threshold. This implies that a damage parameter remains constant during an unloading/reloading cycle until the maximum effective stress is exceeded again.

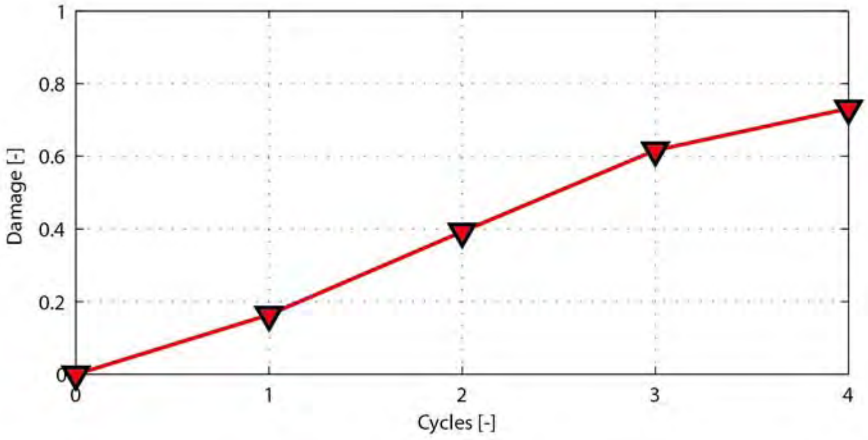

Figure 3: Negative damage index evolution

3.2 Cyclic uniaxial tensile loading test

The comparison between the experimental data (Gopalaratnam and Shah [34]) and the numerical results by means of a simple element patch, 82.6 x 82.6 mm, is illustrated in Figure 4. Also Lee and Fenves [17] chose this test to showcase their plastic-damage model. The degradation of stiffness is simulated at each unloading/reloading cycle as well as the softening behavior.

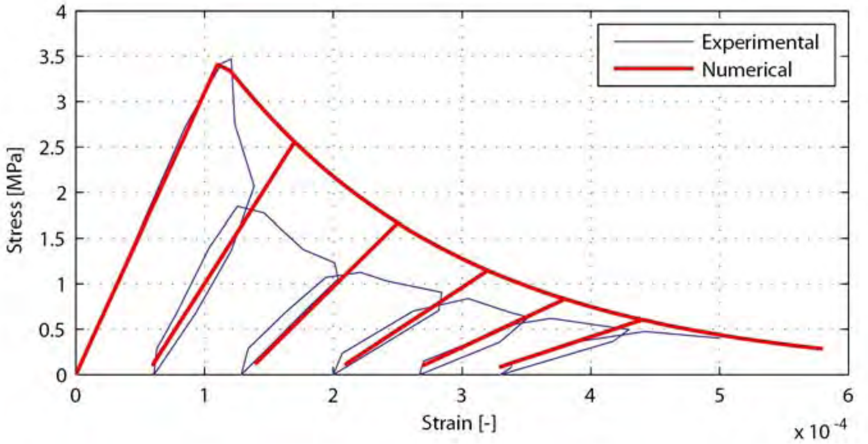

Figure 4: Cyclic uniaxial tensile loading test

Attention should be focused on the residual strain after complete unloading. In fact the residual strain consistently increases even for relatively high strain and very low residual tensile concrete strength. The numerical model can capture very effectively this effect though the plasticity extended in the present work also for tensile concrete stresses. The residual strains in tension are quite important because they affect crack closure state at loading reversals and they becomes particularly evident for cyclic shear tests of reinforced concrete membranes.

On the contrary, the gap between the experimental curve and the numerical one immediately after the peak strength does not condition the effectiveness of the model for the purposes of the present work because of two reasons: the difference of the two curves is relatively insignificant in terms of dissipated energy having the concrete material a very low tensile peak strength compared to the compressive one; the post crack behavior for reinforced concrete elements subjected to tension is characterized by the steel response and by the narrow tension stiffening effect.

The evolution of the positive damage parameter is shown in Figure 5. The damage parameter increases drastically at the beginning of the softening branch and then it approaches the unit asymptotically since the depletion of the fracture energy take place at strains much larger than the elastic limit.

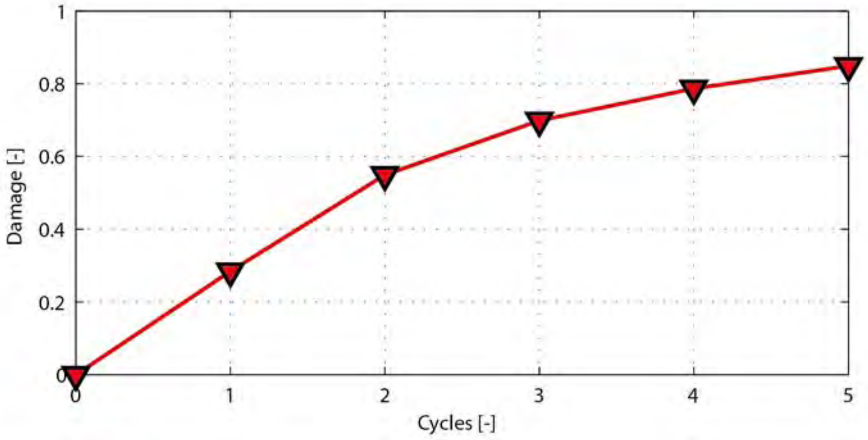

Figure 5: Positive damage index evolution

4 R/C MEMBRANE MODEL

The general three-dimensional concrete model has been developed in a plane stress state to represent the behavior of concrete panels.

Several choices are possible in order to reproduce the reinforcements. The simplest model considers the use of different finite elements for the reinforcing bars joining the concrete panels at the nodes (discrete approach). The main drawbacks of this choice are the need of introducing a steel element for each reinforcement position and the difficulty of introducing bars inclined differently respect to the panel mesh.

The proposed model considers the superposition of different material models to create the membrane model (embedded approach). Thus the reinforcements shall be represented as smeared since the overall behavior of the membrane shall comply with the panel kinematic. As a result the equivalence of the total strains of the different material is imposed. From the physical point of view this is equal to assume a perfect bond between concrete and reinforcing steel. Each steel layer can reproduce the behavior of a set of bars aligned to a generic direction respect to the element principal axis. As a simple generalization a steel layer can simulate the response of a reinforcement net with bars disposed in two orthogonal directions.

An important benefit of the membrane model is the possibility to reproduce all possible reinforcement configurations by simply adding the appropriate number of layers.

The model could be further extended to take into account the bond slip between the two materials at the cost of additional computational effort.

If a steel layer represents one set of parallel rebars, it has an uniaxial stress response in the direction of the bars. On the contrary, a net with bars in two orthogonal directions is simulated by a biaxial orthotropic stress response.

In the first case, the reinforcing layer state determination starts with the projection of the generic total strain tensor in the direction of the bars. Without losing in generality that direction is denoted by its cosine directors $\boldsymbol{u}$.

The total strain along the steel bar is easily obtained as:

$$\varepsilon_\varphi = \boldsymbol{\varepsilon}\,\boldsymbol{u}\cdot\boldsymbol{u} \tag{35}$$

that is used to compute the uniaxial steel material state determination by using the reinforcement constitutive law. In the present work the Menegotto-Pinto law with the isotropic hardening introduced by Filippou et al. [30] has been profitably selected for its ability to evaluate precisely the hysteretic behavior of the reinforcing steel.

The material state in terms of steel stress and tangent modulus are therefore re-projected in the original element reference frame:

$$\boldsymbol{\sigma}_s = \sigma_\varphi(\boldsymbol{u}\otimes\boldsymbol{u}) \tag{36}$$

$$\boldsymbol{C}_s = C_{s,\varphi}(\boldsymbol{u}\otimes\boldsymbol{u}\otimes\boldsymbol{u}\otimes\boldsymbol{u}) \tag{37}$$

These layer responses are added to those coming from the other concrete and steel layers. It can be underlined that the membrane model can be applied to any two-dimensional finite element. The authors have carried out several analyses running different elements i.e. four-node and nine-node quadrilateral and six-node triangular.

5 QUASI-STATIC EXAMPLES FOR THE R/C MEMBRANE MODEL

5.1 Examples of deep beams

The well known reinforced concrete beams tested by Leonhardt and Walther [35] are selected to validate the proposed model. Table 1 summarizes their geometry and the reinforcing steel. They are simply supported beams with two concentrated vertical loads symmetric respect to the beam midspan. The beams are characterized by the absence of shear reinforcement and a constant longitudinal reinforcement ratio of $\rho = 2.0\%$.

Beam ID	*L* (mm)	*a* (mm)	*h* (mm)	*b* (mm)	*a/d*	ρ (%)
T4	1700	670	320	190	2.5	2.0
T5	1950	810	320	190	3.0	2.0
T6	2350	1080	320	190	4.0	2.0
T7	3100	1350	320	190	5.0	2.0
T8	3600	1620	320	190	6.0	2.0
T9	5800	1890	320	190	7.0	2.0
T10	4700	2160	320	190	8.0	2.0

Table 1: geometry and reinforcement of the beams

The shear span-to-depth ratio a/d conditioned the experimental failure mode: flexural failure took place for high ratios while shear failure occurred for low ratios. In particular the transition from flexural to shear failure can be distinguished for $a/d = 6$.

The experimental setup has been numerically simulated. The constitutive laws of the concrete and steel have been calibrated using the parameters of Table 2, starting from the material mechanical properties of the specimens [35].

In Figure 6 the experimental failure loads are compared with the one related to the theoretical flexural strength and with those obtained by the numerical membrane model. The good agreement between the experimental and the numerical values confirms the accuracy of the non linear model.

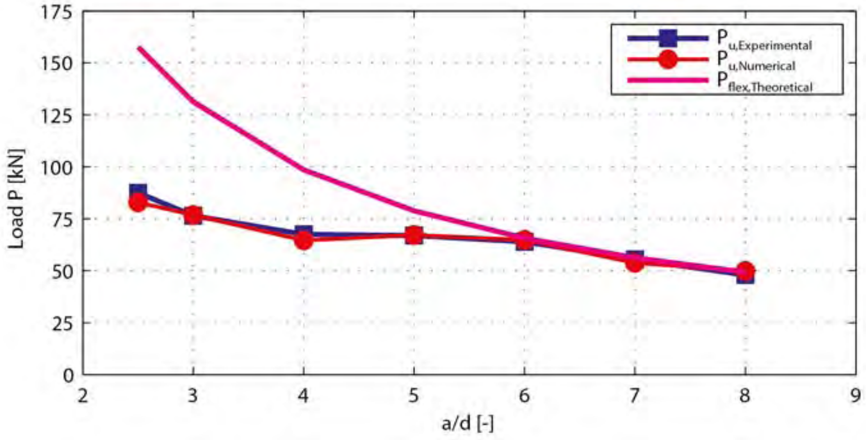

Figure 6: Comparison between experimental and numerical results for the failure load vs. span to depth ratio

Concrete		Reinforcing steel	
Young modulus	36 GPa	Young modulus	190 GPa
Poisson coefficient	0.15	Yielding strength	360 MPa
1D compr. strength	28.0 MPa	Hardening modulus	3 GPa
2D compr. strength	33.6 MPa		
1D compr. elastic threshold	18.2 MPa		
1D tensile strength	2.0 MPa		

Table 2: material model parameters used for the numerical analysis

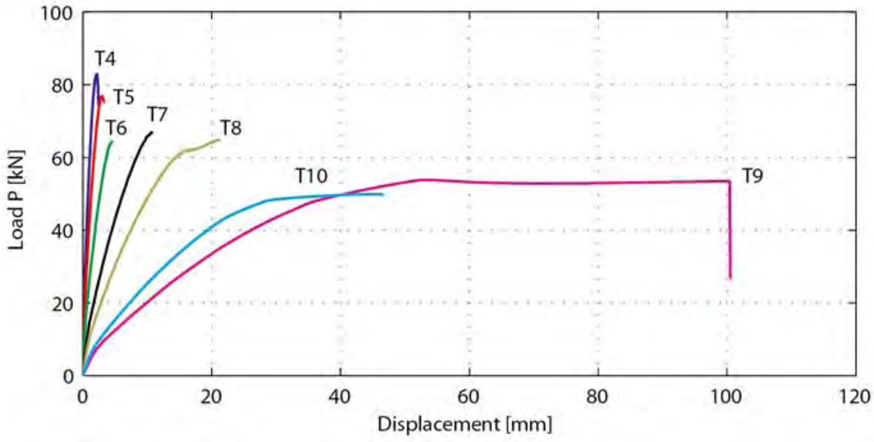

Figure 7: Numerical load vs. displacement curves of the beams

Figure 7 shows the load vs. displacement curves obtained by the numerical models. The corresponding experimental curves were not reported by the test authors.

The curves for the beam T9 and T10 show high plastic deformations, after the longitudinal bar yielding characteristic of a flexural failure mode, whereas the remaining beams with lower span-to-depth ratios suffered shear failure as the abrupt termination of their curves demonstrates.

The specimen T4, with the lowest a/d =2.5, showed a so-called "shear compression failure" that is the crushing of upper compressed concrete area due to the progressive development of the diagonal cracks induced by shear stresses under the point of load application. The experimental failure occurred at the load of 87.5 kN, while the numerical simulation provides a corresponding value of 83 kN. This beam characterizes the deepest point for the "shear valley" of the specimen set having a reduction of the failure moment equal to the 53% of the theoretical flexural value.

5.2 Example of R/C panels

The new model has been validated by comparison with several experimental results on reinforced concrete panels from the literature.

In particular all the specimens presented by Mansour and Hsu [8] have been considered. The comparison has been even more significant thanks to the kind availability of Professor Hsu to produce the experimental measured data upon request.

These R/C panels were submitted to increasing amplitude cyclic load reversals of pure shear solicitations in their mid-plane by means of the "Universal Panel Tester" at the University of Huston (Texas, USA). The loads had been applied uniformly on the panels edges.

The reinforcement had been placed in different directions respect to the solicitation principal axes and with variable ratios for each panels.

Table 3 recalls the main panel properties while the exhaustive specimen description can be found in the work of the test authors [8]. The symbols assume the following meanings:

f'_c	compressive strength of cylindrical concrete specimen;
α_2	angle between the vertical specimen direction and the l reinforcing bar one;
ρ_l	reinforcement ratio in l direction;
f_{ly}	tensile yielding strength of reinforcing bar in l direction;
ρ_t	reinforcement ratio in t direction (at 90° respect to l direction);
f_{ty}	tensile yielding strength of reinforcing bar in t direction.

The specimens had been loaded through cyclic load reversals under load control before the yielding strength and under displacement control for further cycles. During this last part the shear deformation has been used as controlling parameter and the shear strain values are multiple of the yield shear strain.

Panel ID	f'_c	α_2	ρ_l	f_{ly}	ρ_t	f_{ty}
CA2	45.0	45.0°	0.0077	424.1	0.0077	424.1
CB3	48.0	45.0°	0.0170	425.4	0.0077	424.1
CD3	47.0	68.2°	0.0130	425.3	0.0130	425.4
CF2	44.0	79.8°	0.0056	424.1	0.0056	424.1
CE3	50.0	90.0°	0.0120	425.4	0.0120	425.4

Table 3: Mechanical properties of the panel materials

The pure shear solicitation had been applied by imposing normal stresses equal in absolute value but opposite in sign along the vertical and the horizontal directions of the specimens.

The applied loads and the panel averaged strains had been measured by load cells placed on each jack and by displacement transducers over a length traversing several cracks.

In order to verify the accuracy of the numerical model and thanks to the availability of the experimental data, the numerical results are compared to the specimen ones.

In sake of brevity the results of one panel for each series of bar inclination are presented in terms of shear stress vs. shear strain response (see from Figure 8 to Figure 12).

The specimens identified by CA2, CB3, CD3, CF2, CE3 are considered in decreasing order of angle amplitude between the rebar directions and the principal stress ones.

The letter A stands for an angle between the steel bar orientation and the vertical principal stresses equal to 45°. The specimen CA2 has equal reinforcement ratios of 0.0077 in both the net directions. The experiment authors have reported that an “out of stroke” happened at the end of the test. That inconvenience had inevitably conditioned the data recorded in the last load cycles both for positive and negative shear stresses (see Figure 8). Thus the strength decay, in the last cycles, was not caused by the panel failure but rather by the insufficient push of the jacks. It is confirmed by the same authors when they admit that the ductility of the panel CA2 shall be considered higher than that recorded because the collapse of the panel was not reached due to “equipment limitations”.

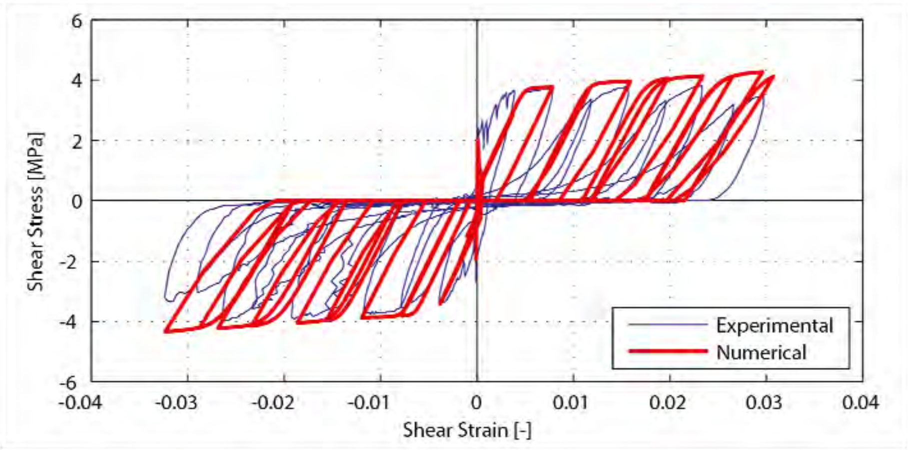

Figure 8: Comparison between experimental and numerical results of the specimen CA2 for shear stress vs. shear strain response

The behavior of the specimen has been rather correctly simulated in terms of fracture load, shear strength, ductility of the panel, pinching effect of the hysteretic curve.

Since the bar net is inclined of 45° respect to the principal stress directions, all the reinforcements bear the tensile loads in both the principal directions with equal stresses. This leads to a progressive delay in recovering the stiffness and the strength at load reversals as far as the plastic strain increases. Even if the numerical model cannot account for the crack interlocking and the progressive stiffness recovering of the specimen, nonetheless it can fairly simulate the stiffness recovering in the average.

The tension stiffening effect does not seem to be captured by the numerical model, but also the experimental data appear to be definitely unstable.

The unloading stiffness of the model is lower than the specimen one after the yielding conditions. This evidence is likely due to the inability of the model to account for bar bond slip and bar dowel action effects.

The specimen CB3 has reinforcement ratios equal to 0.0077 and 0.0170 in the two rebar directions aligned again at 45° respect to the principal stress ones. The experiment authors did not have reported any inconvenience occurred during the test. The numerical model shows good results referring in particular to the cyclic response envelope that includes (see Figure 9): the initial stiffness, the yielding load, the peak strength and the compressive concrete failure. The unloading stiffness seems underestimated especially after the concrete crushing as for the previous example.

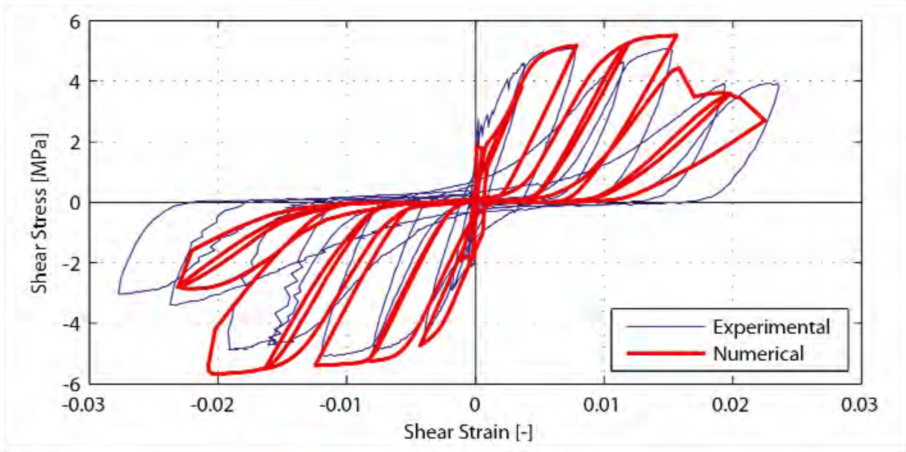

Figure 9: Comparison between experimental and numerical results of the specimen CB3 for shear stress vs. shear strain response

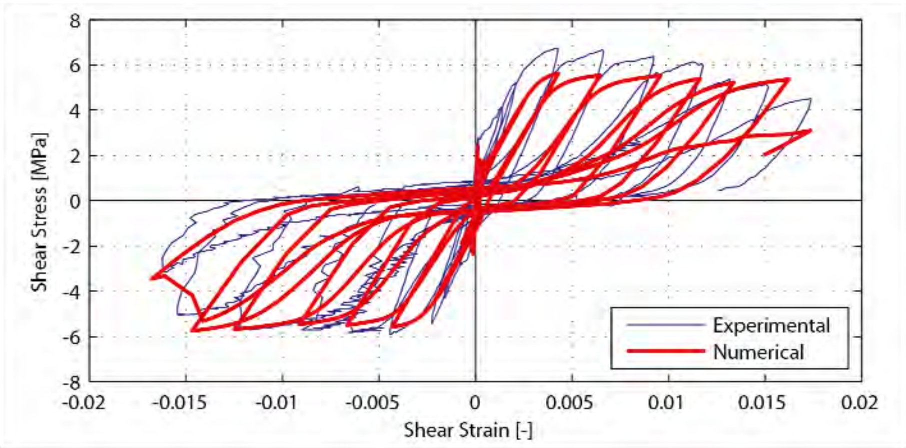

Figure 10: Comparison between experimental and numerical results of the specimen CD3 for shear stress vs. shear strain response

The specimen CD3 has the bar inclination angle equal to 68.2° and a reinforcement ratio of 0.0130 in both the net directions. The strength reduction of the specimen in the cycles can be attributed to the panel failure and the panel ductility had been accurately described. No comment was pointed out by the experimenters on the equipment functioning even though the strain transducers show a certain instability both in the loading and unloading cycle branches. The measured strength turned out to be markedly non symmetric for the positive and negative shear values. Such evidence is not justified by any specimen theoretical asymmetry and it can be caused by an unknown realization fault in the test geometrical configuration. The response of the numerical model is necessarily symmetric and it fits very well the envelope for the negative shear stresses being able to simulate the concrete cracking, the post-cracking loading stiffness, the yielding strength, the maximum ductility determined by the compressive concrete crushing and the pinching effects of the hysteretic curve. The panel progressive cracking phase does not seem to be fully captured even if the experimental data look quite asymmetric and partially unstable.

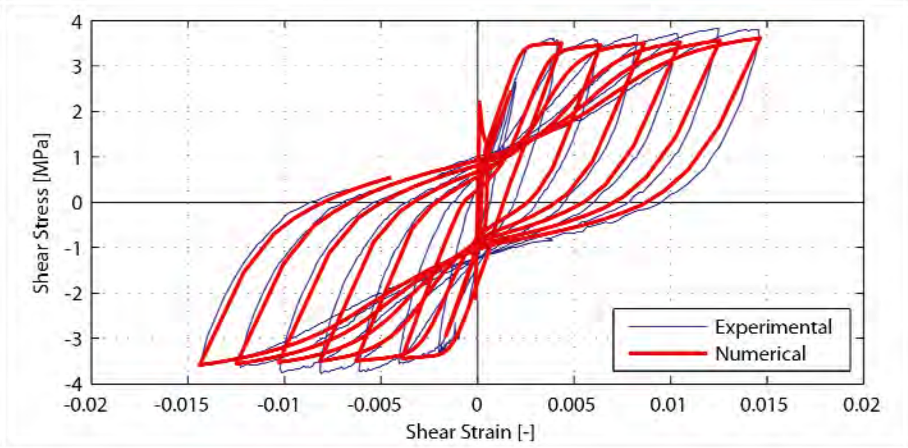

Figure 11: Comparison between experimental and numerical results of the specimen CF2 for shear stress vs. shear strain response

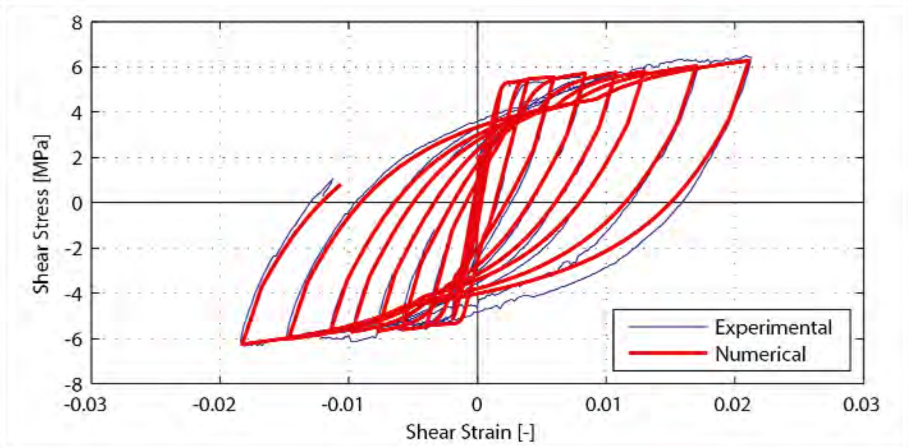

Figure 12: Comparison between experimental and numerical results of the specimen CE3 for shear stress vs. shear strain response

The CF2 panel is the only panel with an angle of 79.8° between the steel net and the principal stress axes and the reinforcement ratio is 0.0056 in both the directions. The numerical model describes accurately the specimen behavior being able to catch the cracking load, the yielding strength, the ductility and the dissipation capacity (see Figure 11). As it is shown by the present example, but it can be noted in general, the proposed model provide an estimation of the dissipated energy that is lightly less than the real one. This fact might be caused by the hypothesis of disregarding the bond slip phenomenon and by considering only the axial response of the reinforcing bars. In compensation the numerical procedure is quite efficient and it is suitable for application to large scale structures. Furthermore a light underestimation of the dissipated energy is pro-safety in executing nonlinear seismic analyses.

The example of the last series is the panel CE3 which has the reinforcing bars parallel to the applied principal stresses and a symmetric reinforcement ratio equal to 0.0120. The test authors reported that the ductility of the specimen could not have completely exploited since the maximum lengthening of the jacks was reached. The experimental data show an unexplained minor asymmetry concerning the last two reloading negative braches of the global response as it can be seen from Figure 12. Nonetheless the example show clearly how the numerical model can reproduce precisely the recorded panel behavior in all its features such as, for instance, the yielding strength and the following hardening behavior, the unloading stiffness and the residual deformation at load reversals and energy dissipation capacity.

In order to further investigate in the response of the numerical model for the last example, other two responses are herein presented: the vertical strain vs. horizontal strain curve and the vertical normal stress vs. the corresponding vertical strain one (see. Figure 13 and Figure 14).

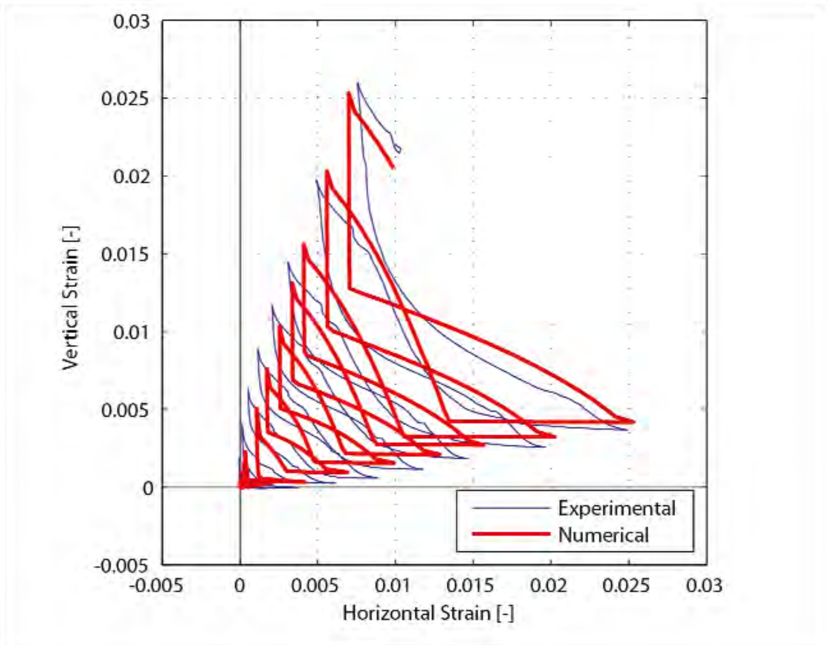

Figure 13: Comparison between experimental and numerical results of the specimen CE3 for vertical strain vs. horizontal strain response

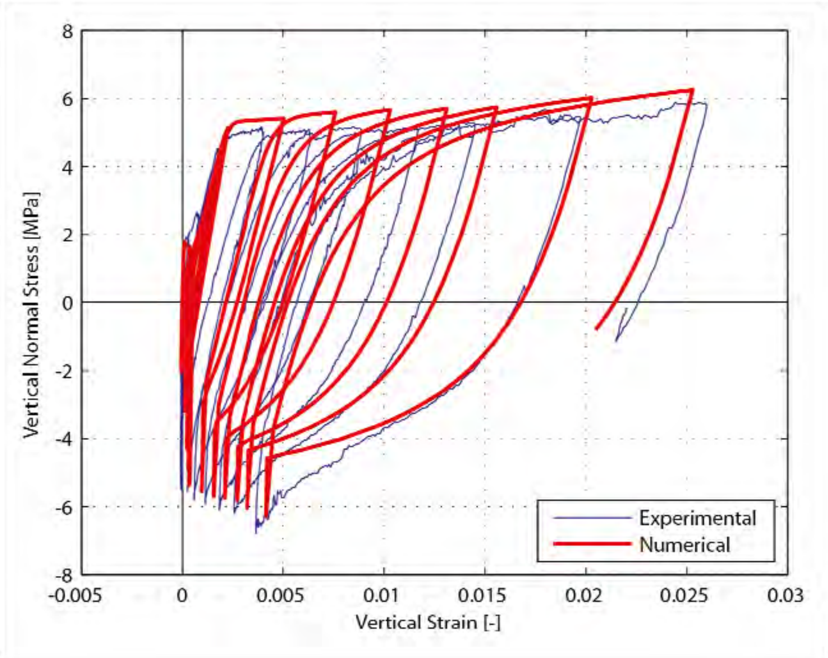

Figure 14: Comparison between experimental and numerical results of the specimen CE3 for vertical normal stress vs. vertical strain response

It can be noted that the axial strains are evaluated with high accuracy. This shall not be considered an automatic consequence of imposing the shear strain in the cycles after the panel yielding. In fact the shear strain compels only the difference between the positive and the negative axial strains but not their values separately.

The progressive expansion of the panel due to the accumulation of plastic strain is correctly captured by the proposed model. The gap between the two curves visible in the central part between following tips is explained by the sudden closure of the cracks in the numerical model, whereas the experiment exhibits a progressive stiffness recovery due to local effects occurring when the opposite irregular surfaces of a crack move close again. This fact is evident also comparing the vertical stress-strain response depicted in Fig. 14.

It is important to notice that the strain data are computed from dilatation measures over several crack distances leading to averaged values while the numerical response is punctual and would properly represent the behavior of a cracked section.

6 CONCLUSIONS

- An efficient two parameter concrete plastic damage model has been developed that is suitable for the simulation of large scale structural models with RC panels.
- The validation examples have confirmed the ability of the concrete material to simulate the nonlinear cyclic behavior of concrete under tensile and compressive strains.
- A straightforward formulation of a R/C membrane model has been proposed by superimposing different materials, concrete and reinforcing steel, to create a single membrane model with smeared reinforcement of general orientation.
- The well-known Leonhardt beams are simulated to point out the efficiency of the model in reproducing the transition from flexural to shear failure mode for deep beams. The membrane model has been able to correctly predict the “shear valley”.
- A second set of simulation of R/C panel is carried out. The examples show clearly the ability of the proposed model to reproduce the main features of the experimental panel behavior such as: the yield strength, the subsequent hardening/softening behavior, the residual deformation at load reversals and energy dissipation capacity.

ACKNOWLEDGEMENT

The authors warmly thank Professor T.T.C. Hsu for making available the experimental data obtained in the Structural Research Laboratory at the University of Houston (Texas, USA).

REFERENCES

[1] F. Leonhardt, E. Mönnig, *Vorlesungen über Massivbau. Teil 2: Sonderfälle der Bemessung im Stahlbetonbau*. Springer Verlag, 1975.

[2] Z.P. Bazant, T. Tsubaki, T.B. Belytschko, Concrete reinforcing net - safe design. *Journal of the Structural Division ASCE*, **106**, 1899-1906, 1980.

[3] F. Vecchio, M.P. Collins, *Response of reinforced concrete to in-plane shear and normal stresses*. Department of Civil Engineering, University of Toronto, 1982.

[4] S.B. Bhide, M.P. Collins, *Reinforced concrete elements in shear and tension*. Department of Civil Engineering, University of Toronto, 1987.

[5] N. Ohomori, H. Tsubota, N. Inoue, K. Kurihara, S. Watanabe, Reinforced concrete membrane elements subjected to reversed cyclic in-plane shear stress. *Nuclear Engineering and Design*, **115**, 61-72, 1989.

[6] T.N. Salonikios, A.J. Kappos, I.A. Tegos, G.G. Penelis, Cyclic load behavior of low-slenderness reinforced concrete walls: Design basis and test results. *ACI Structural Journal*, **96**, 649-660, 1999.

[7] J.H. Thomsen, J.W. Wallace, Displacement-based design of slender reinforced concrete structural walls - experimental verification, *Journal of Structural Engineering ASCE,* **130**, 618-630, 2004.

[8] M. Mansour, T.T.C. Hsu, Behavior of reinforced concrete elements under cyclic shear. I: experiments. *Journal of Structural Engineering ASCE*, **131**, 44-53, 2005.

[9] C. Greifenhagen, P. Lestuzzi, Static cyclic tests on lightly reinforced concrete shear walls. *Engineering Structures,* **27**, 1073-1712, 2005.

[10] D. Darwin, D. Pechnold, Analysis of RC shear panels under cyclic loading. *Journal of the Structural Division ASCE*, **102**, 355-369, 1976.

[11] N. Bicanic, O.C. Zienkiewicz, Constructive model for concrete under dynamic loading. *Earthquake Engineering and Structural Dynamics*, **11**, 689-710, 1983.

[12] Y. Ohtani, W.F. Chen, Multiple hardening plasticity for concrete materials. *Journal of Engineering Mechanics ASCE,* **114**, 1890-1910, 1988.

[13] Z.P. Bazant, B. Oh, Crack band theory for fracture of concrete. *Materials and Structures,* **16**, 155-177, 1983.

[14] J. Cervenka, V.K. Papanikolaou, Three dimensional combined fracture-plastic material model for concrete. *International Journal of Plasticity,* **24**, 2192-2220, 2008.

[15] L.M. Kachanov, *Introduction to continuum damage mechanics*. Martinus Nijhoff Publisher, 1986.

[16] J. Mazars, G. Pijaudier-Cabot, Continuum damage theory - application to concrete. *Journal of Engineering Mechanics ASCE*, **115**, 345-365, 1989.

[17] J. Lee, G. Fenves, Plastic-damage model for cyclic loading of concrete structures. *Journal of Engineering Mechanics ASCE,* **124**, 892-900, 1998.

[18] R.H. Graves, K.N. Derucher, Interface smeared crack model analysis of concrete dams in earthquakes. *Journal of Engineering Mechanics ASCE*, **113**, 1678-1693,1987.

[19] F.J. Vecchio, M.P. Collins, The modified compression-field theory for reinforced-concrete elements subjected to shear. *ACI Structural Journal*, **83**, 219-231, 1986.

[20] F.J. Vecchio, Reinforced concrete membrane element formulations. *Journal of Structural Engineering ASCE,* **116**, 730-750, 1990.

[21] M.A. Polak, F.J. Vecchio, Reinforced-concrete shell elements subjected to bending and membrane loads. *ACI Structural Journal*, **91**, 261-268, 1994.

[22] M. Mansour, T.T.C. Hsu, Behavior of reinforced concrete elements under cyclic shear. II: Theoretical model. *Journal of Structural Engineering ASCE,* **131**, 54-65, 2005.

[23] L.N. Lowes, A. Altoontash, Modeling reinforced-concrete beam-column joints subjected to cyclic loading. *Journal of Structural Engineering ASCE*, **129**, 1686-1697, 2003.

[24] L.M. Massone, J.W. Wallace, Load – deformation responses of slender reinforced concrete walls. *ACI Structural Journal*, **101**, 103-113, 2004.

[25] L.M. Massone, K. Orakcal, J.W. Wallace, Shear - flexure interaction for structural walls. *ACI Special Publication SP-236: Deformation Capacity and Shear Strength of Reinforced Concrete Members Under Cyclic Loading,* Editor Adolfo Matamoros & Kenneth Elwood, 127-150, 2006.

[26] A. Saritas, F.C. Filippou, Inelastic axial-flexural-shear coupling in a mixed formulation beam finite element. *International Journal of Non-Linear Mechanics*, **44**, 913-922, 2009.

[27] P. Martinelli, F.C. Filippou, Simulation of the shaking table test of a seven-story shear wall building. *Earthquake Engineering and Structural Dynamics*, **38**, 587-607, 2009.

[28] R. Scotta, R. Vitaliani, A. Saetta, E. Oñate, A. Hanganu, A scalar damage model with a shear retention factor for the analysis of reinforced concrete structures: theory and validation. *Journal of Computer and Structures,* **79**, 737-755, 2001.

[29] R. Faria, J. Oliver, M. Cervera, A strain-based plastic viscous-damage model for massive concrete structures. *International Journal of Solids and Structures,* **35**, 1533-1558, 1998.

[30] F.C. Filippou, E.P. Popov, V.V. Bertero, *Effects of Bond Deterioration on Hysteretic Behavior of Reinforced Concrete Joints*. Earthquake Engineering Research Center, University of California, Berkeley, 1983.

[31] J.W. Ju, On energy-based coupled elastoplastic damage theories: constitutive modeling and computational aspects. *International Journal of Solids and Structures,* **25**, 803-833, 1989.

[32] J.Y. Wu, J. Li, R. Faria, An energy release rate-based plastic-damage model for concrete. *International Journal of Solids and Structures,* **43**, 583-612, 2006.

[33] E. Sinha, K. Gerstle, L. Tulin, Stress-strain relations for concrete under cyclic loading. *Journal of the ACI*, **62**, 195-210, 1964.

[34] V.S. Gopalaratnam, S.P. Shah, Softening response of plain concrete in direct tension. *Journal of the ACI*, **82**, 310-323, 1985.

[35] F. Leonhardt, R. Walther, Einfluss des Momenten-Schub-Verhältnises auf die Schubtragfähigkeit bei Rechtenbalken ohne Schubbewehrung unter Einzel- und Gleichlast. *Beton und Stahlbeton,* **2**, 1962.

[36] R. Scotta, D.A. Talledo, L. Tesser, R. Vitaliani, Non-Linear Behaviour Modelling of RC Panels Subjected to In-Plane Loads. *IV European Conference on Computational Mechanics*, paper n. 1065, Paris, May 16-21, 2010.

COMPDYN 2011
3rd ECCOMAS Thematic Conference on
Computational Methods in Structural Dynamics and Earthquake Engineering
M. Papadrakakis, M. Fragiadakis, V. Plevris (eds.)
Corfu, Greece, 25–28 May 2011

INELASTIC SEISMIC SHEAR IN MULTI-STOREY CANTILEVER COLUMNS

Matej Fischinger[1], Marianna Ercolino[2], Miha Kramar[1], Crescenzo Petrone[2], Tatjana Isakovic[1]

[1]University of Ljubljana, FGG
Jamova 2, 1000 Ljubljana, Slovenia
matej.fischinger@ikpir.fgg.uni-lj.si

[2]University of Napoli Federico II
Via Claudio, 21-80125 Naples
crescenzopetrone@hotmail.com

Key words: Seismic shear forces, Shear magnification factor, Multi-storey precast structures, Multi-storey cantilever columns, Eurocode 8.

Abstract. *Seismic shear force magnification in the columns of multi-storey precast structures entering far into inelastic domain is addressed in the paper. Such structures consist of an assemblage of cantilever columns connected with ties. Considering analogy with cantilever walls, it has been expected that during inelastic response the actual shear forces in multi-storey cantilever columns could be considerably higher than the forces foreseen by traditional equivalent elastic analytical procedures (equivalent lateral force or modal spectrum).*

A parametric study of a set of realistic three-storey structures/columns was performed. These structures were designed according to Eurocodes and shear forces were determined by the equivalent elastic (modal spectrum) analysis. Average values of the shear forces obtained by the inelastic response analysis were compared to those of the traditional (modal spectrum) procedure. They were also compared to magnified shear forces predicted using the shear magnification factor ε suggested in Eurocode 8 for RC ductile walls. In parallel, modelling issues related to the inelastic response analysis of multi-storey cantilever columns were also discussed.

Very large seismic shear force magnifications (up to 3 times and more) were observed. Therefore it is essential to account for this phenomenon in the seismic (capacity) design of cantilever columns in multi-storey precast buildings. It was demonstrated that for this purpose the expression given in Eurocode 8 to account for seismic shear force magnification in ductile cantilever walls could be used with some minor modifications.

1 INTRODUCTION

Precast buildings house a predominant share of industrial facilities in many European countries. The most common precast system in Europe has been using dowel joints providing hinged connection between the beams and columns. Therefore such structures behave essentially as an assemblage of cantilever columns with ties. Up to now many precast industrial buildings have been one-storey structures. In such structures the capacity design for shear in the columns and joints is straightforward. However, recently the multi-storey structures are emerging as competitive market potential in the reinforced concrete construction sector. Question arises how to perform seismic (shear) design of multi-storey cantilever columns entering far into inelastic domain. Indeed, considering analogy with cantilever walls [1 – 6] and the results of the PRECAST [7] and SAFECAST 7th EU Framework research projects, a considerable dynamic magnification of shear forces during inelastic response has been expected. The main reasons for the shear magnification are the following:

- Overstrength: a consideration of simple equilibrium shows that the design seismic shear forces increase proportionally to the flexural overstrength.
- Period shift: Due to the softening of the structure in the inelastic range, the first mode spectral acceleration value typically diminishes, whereas the spectrum values for the higher modes (having the natural period at least 6 times lower than that of the first mode) usually remain in the plateau of the spectrum. The relative influence of the higher modes therefore increases in the inelastic range.
- Amplified influence of higher modes: The first mode seismic forces contribute most of the overall seismic moment at the base of the cantilever, which is limited by its flexural resistance. Energy dissipation is therefore predominantly limited to the flexural response in the first mode. Consequently, the first mode shear forces are reduced due to the energy dissipating mechanism, whereas the shear forces due to the higher modes are not. This significantly increases the relative contribution of the higher modes to the shear force which occurs during the inelastic response.

The increased relative importance of higher modes lowers the position of the resultant of the seismic forces closer to the base of the wall (Figure 1). With the given bending moment at the base, which is equal to the flexural capacity of the column, it is obvious that the resultant seismic force (shear force) should increase.

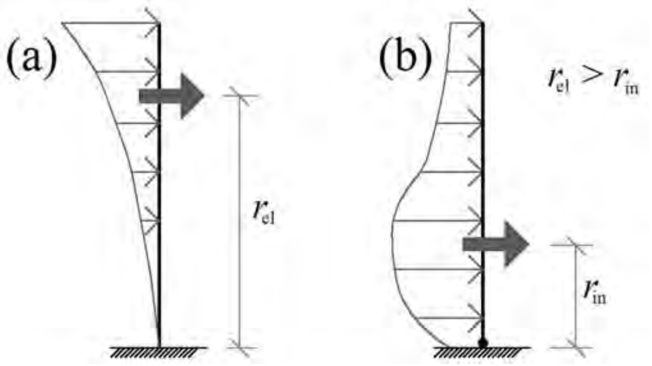

Figure 1 - Higher modes effects on the distribution of lateral forces and base shear

Since in the present design practice this increase in shear forces is frequently not considered properly, there is a danger of brittle shear failure, both in the column and in the connections at each storey.

The capacity design for shear in single storey cantilever columns is straightforward. Since there is no influence of the higher modes, only overstrength has to be considered. The maximum expected shear force is therefore simply obtained by dividing flexural moment capacity at the base by the height of the column. However, in the case of multi-storey cantilevers, the distribution of the moment over the height of the column is not known and it also changes during the response (see Figure 2(a) and 2(b)).

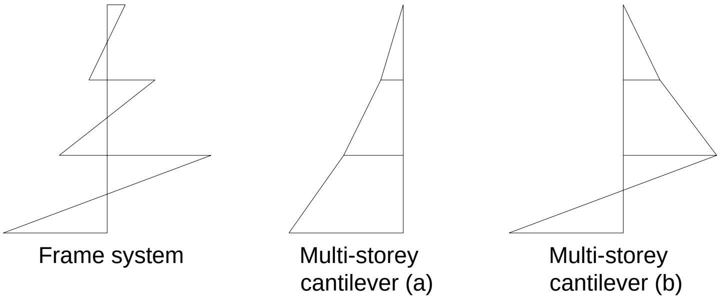

Figure 2 – Typical moment diagram shape in frame and cantilever multi-storey column

So designers are facing serious problem how to perform the capacity design of columns and connections required by Eurocode 8 [8] in order to preclude the brittle failure of these key components of the structural system. Contrary to the case of RC structural walls, the problem of the shear magnification in the multi-storey cantilever columns in RC precast structures has not been explicitly addressed in the current version of the Eurocode 8. It has been believed by the authors that appropriately modified shear magnification factors defined in Eurocode for structural walls could be also used for multi-storey cantilever columns in precast buildings.

To address the problems mentioned in the previous paragraph, a parametric study of the inelastic response of realistic three-storey cantilevered multi–storey precast buildings, designed according to Eurocode 8, was made [9]. The configuration of the building was defined by the three-storey building prototype which is being pseudo-dynamically tested in the European Laboratory for Structural Assessment in Ispra within the frame of the SAFECAST research project (coordinated by the Association of the precast producers in Italy ASSOBETON). Shear forces obtained during the inelastic response were compared to those predicted by traditional equivalent elastic design procedures to evaluate the expected shear magnification. Finally the shear magnification factor (ε) used in Eurocode for shear walls was tested in the case of multi-storey cantilever columns in precast structures.

2 MODELLING ISSUES

As shown before (see cases “a” and “b” in Figure 2), moment diagram shape can vary considerably during the response of the analysed structural systems. Since in lumped plasticity models it is assumed that the moment distribution along the element does not change during the time, the use of only one lumped plasticity element per storey is precluded or at least questionable. Several models were studied to overcome this problem. Two relatively simple models could yield appropriate solution. One is using several lumped plasticity elements per storey (Figure 3) and the other is based on the fiber approach.

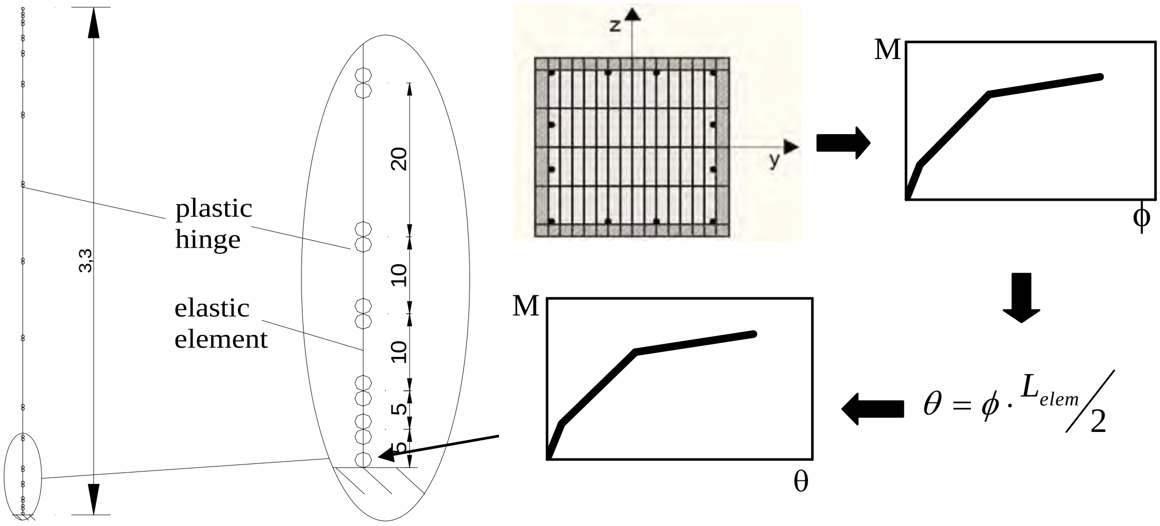

Figure 3 – Analytical model with several lumped plasticity elements per storey (bending in x – y plane is considered only)

Both models were extensively tested to check their efficiency and first of all their numerical stability. Finally the model with several short lumped plasticity elements per storey was chosen. This model did not exhibit larger problems with numerical stability opposed to the fiber element which was strongly dependent on the number of the integration points and the influence of the second order theory effects. In addition to the pure flexural behaviour (described by both models) some other phenomena (like slip of the reinforcement and deformability due to the shear cracking) can be approximately (empirically) included into the hysteretic rules used in the lumped plasticity model.

3 PARAMETRIC STUDY

3.1 Description of the analyzed structures

The actual shear magnification factors were determined by inelastic response analyses on five three–storey cantilevered structures, typical for the construction practice in Europe. The height of the typical storey was $3.2m$.

Due to the hinged beam-column connections and assuming floors being rigid in their own plane, buildings were modelled as single multi-storey columns. To each of the five buildings/columns different value of the normalized axial force ν_d (0,05≤ν_d≤ 0,20) was assigned to reflect actual spans and loads used in practice (Table 1). Only the highest value (0,20) tends to be unrealistic due to the drift limitations. However it was included in the research just to study the general trends of the results. Square section $80 \times 80cm$ was chosen for the column, while masses (assumed to be the same at each floor) and fundamental periods depended on the level of normalized axial forces.

The buildings were designed according to Eurocode 8, using standard design procedures based on the results of the equivalent elastic spectrum modal analysis ($a_{g,\max} = 0.25g$ and Soil Type B) considering one half of the inertia characteristics of the uncracked sections. The same reduction as for DCH cast-in-situ frames $(q = 4.5)$ was assumed [10]. Concrete C45/55 and steel B450C was used in the design.

ν_d [-]	m [t]	A_{inf} [m^2]
0.05	32.6	45.7
0.075	48.9	68.6
0.10	65.2	91.4
0.125	81.6	114.3
0.20	130.5	182.9

Table 1 – Normalized axial force, floor mass and influence area (assuming distributed storey weight of w=7kN/m^2) of the five analyzed buildings

The response history analyses were performed using OpenSees [11] with a set of 9 accelerograms, matching the EC8 spectrum for $a_g = 0.25g$ and Soil Type B (Figure 5). These accelerograms were obtained by the modification of the actual accelerograms recorded in Europe. Again the mean spectrum of these recorded accelerograms matched the EC8 spectrum (Figure 4). Five percent mass and current stiffness proportional Rayleigh damping was considered in the first and second modes.

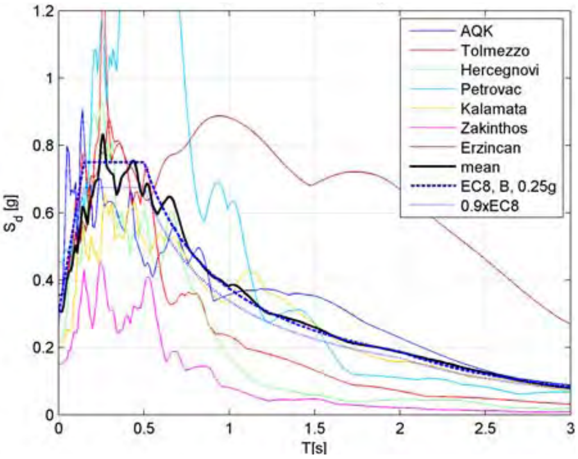

Figure 4 - Spectra of the recorded accelerograms (note that the mean spectrum matches the EC8 spectrum very well)

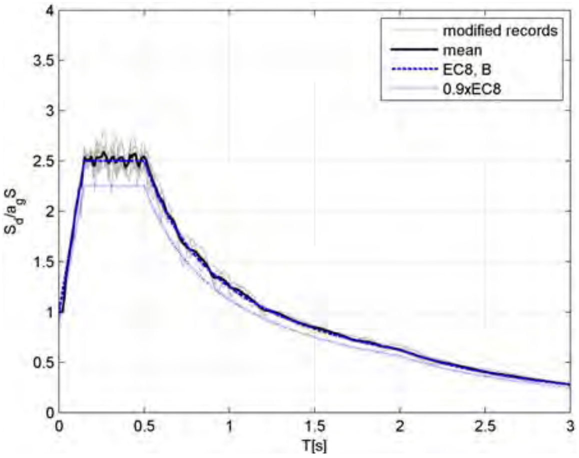

Figure 5 – Normalized spectra of the modified accelerograms matching EC8 – Soil B spectrum

3.2 Results for the shear magnification factors

Figure 6 shows the shear magnification factor (the ratio between the shear forces obtained by the inelastic analyses and those obtained by the equivalent elastic spectrum modal analysis) for the five investigated structures, which are denoted using the corresponding normalized axial force value ν_d.

For each structure, three different assumptions regarding stiffness of the columns and overstrength were considered in the inelastic response analyses. In Figure 6 the circles denote results of the model based on the actual stiffness during response (model 1). Squares indicate the results obtained with the inelastic analysis using the bilinear model having the same initial stiffness as it had been used in the design – model 2 (one half of the inertia characteristics based on the uncracked section were used). Model 3 (triangles) is basically the same as Model 2, except for the overstrength, which is not considered.

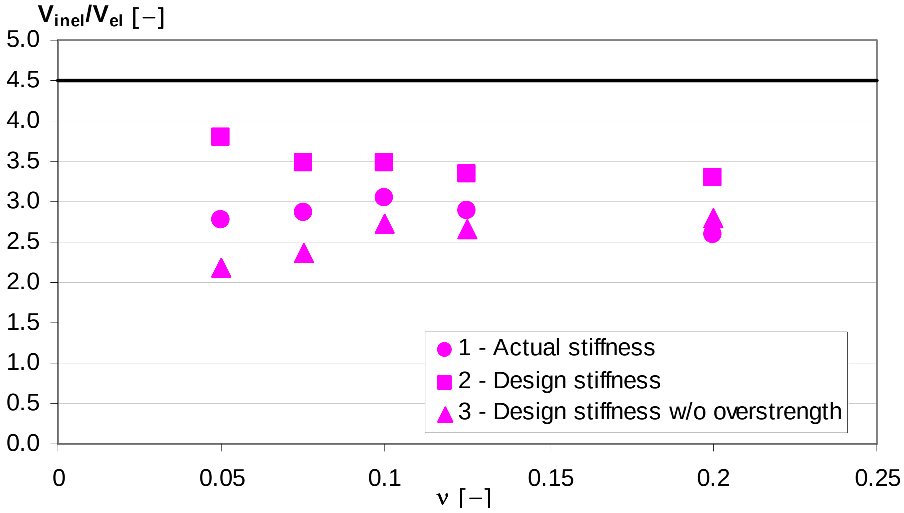

Figure 6 - Shear magnification ratios evaluation for the five analyzed structures using different stiffness/overstrength models

As clearly shown in Figure 6, the actual shear forces induced during the inelastic response of multi-storey columns in typical precast industrial buildings are much higher (2 to 4 times) of those predicted with equivalent elastic procedures commonly used by the design engineers! So the shear forces provided by standard computer design programs, using the reduced seismic forces, grossly underestimate actual shear demand if they are not appropriately corrected. Fortunately in these slender columns the absolute value of the shear forces predicted by traditional methods is typically quite low. However, when multiplied with a factor up to 4 to obtain the actual level of shear forces, it becomes clear that this problem calls for serious attention. Therefore, to avoid brittle failure of the columns and/or in the beam-to-column connections it is essential to account for this phenomenon in the capacity design of cantilever columns in multi–storey precast buildings.

It can be further observed that:

- The shear force magnification is much larger if the same initial stiffness as in the case of design (one half of that obtained for the uncracked gross section – squares in Figure 6) is used also in the inelastic analysis. Considering the actual/realistic stiffness degradation due to cracking (up to 4 times in the case of elements with small to moderate compressive axial force) the shear increase is smaller (circles in Figure 6).
- If the effect of overstrength is eliminated (Model 3; triangles in the Figure 6) the magnification is still high (over 2). This demonstrates that, at least in the case of the analyzed buildings, the effect of higher modes on the shear magnification is predominant.

4 PROPOSAL OF THE DESIGN SHEAR MAGNIFICATION FACTOR

Eurocodes [8] already provide a shear magnification factor ε for RC ductile walls, while for multi-storey precast structures this problem is not properly addressed in the current codes as well as in the literature.

The ε factor for walls is used in Eurocode to multiply the values obtained by the linear-elastic lateral force or modal response spectrum analysis. For walls which enter far into the inelastic range (ductility class “high”), large shear magnifications are expected, and the factor ε should be calculated using the expression proposed by Keintzel [2], which explicitly takes into account the effects of higher modes in the inelastic range as well as flexural overstrength:

$$\varepsilon = q \cdot \sqrt{\left(\frac{\gamma_{Rd}}{q} \cdot \frac{M_{Rd}}{M_{Ed}}\right)^2 + 0.1 \cdot \left(\frac{S_e(T_C)}{S_e(T_1)}\right)^2} \begin{cases} \leq q \\ \geq 1.5 \end{cases} \tag{1}$$

where:

q is the behaviour (seismic force reduction) factor used in the design;

M_{Ed} is the design bending moment at the base of the wall;

M_{Rd} is the design flexural resistance at the base of the wall;

γ_{Rd} is the model uncertainty factor on design value of resistances accounting for various sources of overstrength;

T_1 is the fundamental period of vibration of the building in the direction of shear forces;

T_C is the upper limit period of the constant spectral acceleration region of the spectrum;

$S_e(T)$ is the ordinate of the elastic response spectrum.

Although Keintzel's expression for the shear magnification factor in RC structural walls has been based on a series of quite crude assumptions and approximations, like superposition principles in inelastic range, it was demonstrated by numerical tests that it has been working fine [6, 12]. It has been believed by the authors that a similar modified expression for the ε factor could be used also in the case of RC multi-storey columns in precast structures.

In the study, the values of the seismic design shear forces (denoted as V_{Ed}), evaluated by applying ε to the base shear resulting from the SRSS analysis, are compared with those obtained by inelastic response history analysis (denoted as V_{an}). The ratios $V_{\mathrm{Ed}}/V_{\mathrm{an}}$ are illustrated in Figure 7.

If ε is applied to the base shear determined by the contribution of the first mode only (white dots in Figure 7), as originally intended by Keintzel, the magnification is very well estimated (note that ν_{d} = 0,20 is not realistic in practical design). The proposed factor is slightly conservative, which makes it suitable for design purposes.

Most computer programs would, however, output the total base shear based on the contribution of all the considered modes. It is therefore most likely that designers will tend to apply ε to the total shear forces. This would be somewhat (up to 1,5 times) conservative (see black dots in Figure 7). An alternative solution is to propose a modified magnification factor, which is still under investigation.

It should be also noted that:

- The equivalent elastic shear forces were calculated based on the inertia of the cracked concrete sections equal to one half of the uncracked gross section. In this way the actual stiffness of the typical precast columns is overestimated. Therefore if the designer opts to use realistic (calculated) yielding stiffness in design, the proposed ε factor may be unconservative.
- It is suggested in Eurocode 8 that the overstrength factor $\gamma_{Rd} = 1.2$ should be used in Keintzel's formula for structural walls. In the presented study the actual overstrength factor for the analysed columns was closer to 1,3. If considered, the proposed factor will be slightly more conservative.

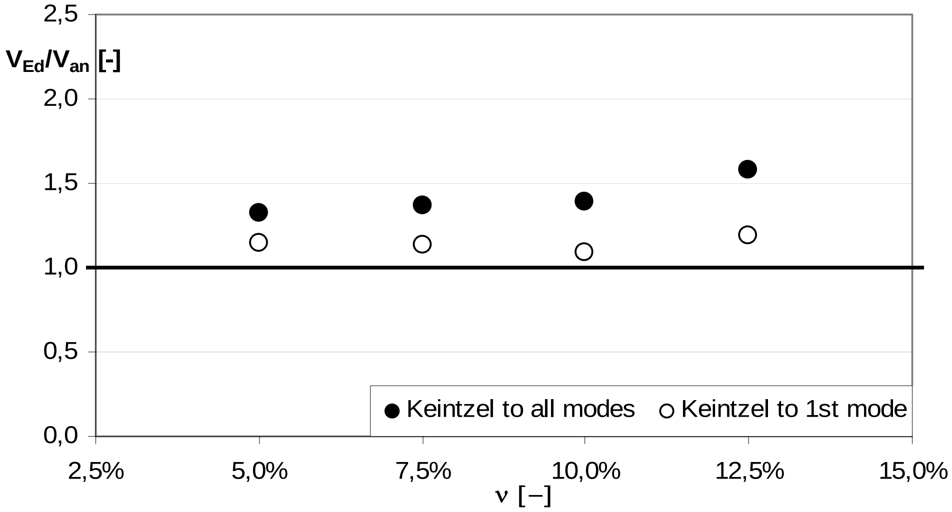

Figure 7 – Design base shear evaluated according to Keintzel's factor compared to actual base shear resulting from dynamic analysis

5 SELECTED IMPORTANT RESULTS OF THE RELEVANT AND/OR ONGOING RESEARCH

Some other relevant conclusions of the research, which are not discussed in detail in this paper include (see [9] for additional information):

- A short study on a hypothetical 10-storey building suggested that the same base shear magnification factor could be used also for buildings higher than 3-storeys.
- ε factor was originally proposed for the base shear and all the above conclusions and discussions apply for the base shear. However, it was demonstrated (though by the study, which was limited in scope) that the same factor could be used over the entire height of the column (at least in the case of 3-storey buildings).
- Local shear magnification can be very critical for the design of the dowel beam-to-column connections. In particular in the first storey the design force on the connection could be underestimated up to 10-times if proper magnification was not considered.

6 CONCLUSIONS

The actual shear forces in multi storey cantilevered structures due to seismic loads are considerably higher than the forces foreseen by the equivalent linear-elastic lateral force analysis, or by the modal response spectrum analysis specified in the codes. Simply said, this magnification occurs due to flexural overstrength and the amplified effect of the higher modes in the inelastic range.

In this study five realistic three–storey cantilevered structures, typical for the construction practice in Europe and designed according to Eurocode provisions were tested. The actual shear magnifications were determined by the inelastic response analyses as well as compared with the values obtained by the EC8 (Keintzel's) shear magnification factor, valid for RC structural walls.

Two main conclusions have been made:

1) It has been demonstrated that the actual shear forces induced during the inelastic response of multi-storey cantilever columns in typical precast industrial buildings are much higher (2 to 4 times) of those predicted with equivalent elastic procedures commonly used by the design engineers. So the shear forces provided by standard computer design programs using the reduced seismic forces grossly underestimate actual

shear demand if they are not appropriately corrected. Therefore to avoid brittle failure of the columns and/or in the connections, it is essential to account for this phenomenon in the capacity design of the cantilever columns in multi–storey precast buildings. However, neither Eurocodes, nor national seismic codes explicitly require appropriate seismic shear magnification for such columns. Related capacity design procedures are also not defined.

2) It has been demonstrated that the similar shear magnification factor as proposed in Eurocode 8 for ductile (DCH) RC structural walls can be used also in the case of multi-storey cantilever columns in precast buildings:

$$\varepsilon = q \cdot \sqrt{\left(\frac{\gamma_{Rd}}{q} \cdot \frac{M_{Rd}}{M_{Ed}}\right)^2 + 0.1 \cdot \left(\frac{S_e(T_C)}{S_e(T_1)}\right)^2} \begin{cases} \leq q \\ \geq 1.5 \end{cases} \tag{2}$$

This factor primarily depends on (a) the flexural overstrength and (b) the magnified contribution of the higher modes during inelastic response.

The above results strictly apply for the base of the analyzed 3-storey structures. However, in parallel research the conclusions were generalized also to higher buildings as well as for the shear forces along the entire height of the column.

ACKNOWLEDGEMENT

Part of the Graduation dissertation of Crescenzo Petrone, done in the frame of the research collaboration of the University of Ljubljana and the University of Napoli "Federico II" is presented in this paper. The structures analyzed in the numerical study are based on the prototype structure being tested in ELSA in Italy in the frame of the EU research project SAFECAST coordinated by ASSOBETON. The advice provided by Klemen Rejec, Ph.D. student at the University of Ljubljana is gratefully acknowledged.

REFERENCES

[1] R.W.G. Blakeley, R.C. Cooney, L.M. Megget, Seismic shear loading at flexural capacity in cantilever wall structures. Bull New Zeal Natl Soc Earthquake Eng 8(4):278–290, 1975.

[2] E. Keintzel, Seismic design shear forces in RC cantilever shear wall structures. Eur Earthquake Eng 3:7-16, 1990.

[3] M.N. Fardis, Seismic Seismic design, assessment and retrofitting of concrete buildings based on EN-Eurocode 8, Springer Dordrecht, Heidelberg, London, New York. doi: 10.1007/978-1-4020-9842-0, 2009.

[4] A. Rutenberg, E. Nsieri, The seismic shear demand in ductile cantilever wall systems and the EC8 provisions. Bulletin of Earthquake Engineering, 4:1-21, 2006.

[5] K. Rejec, Personal communication, 2010.

[6] K. Rejec, T. Isakovic, M. Fischinger, Seismic shear force magnification in RC cantilever structural walls, designed according to Eurocode 8, submitted for possible publication in Bulletin of Earthquake Engineering.

[7] M. Fischinger, M. Kramar, T. Isakovic, P. Kante, M.N. Popeyo Lazaro, M. Kreslin, K. Rejec, Z. Vidrih, M. Peljhan, Precast structures EC8, 111 pp. In G. Toniolo (Ed.), Seismic behaviour of precast structures with respect to Eurocode 8 (co-normative research), Final Technical report, Politechnico di Milano, 2007.

[8] CEN Eurocode 8 – design of structures for earthquake resistance. Part 1: General rules, seismic actions and rules for buildings. European standard EN 1998-1, December 2004, Europenan Committee for Standardization, Brussels.

[9] C. Petrone, Inelastic seismic response and risk analysis of multi-storey precast building, Graduation Thesis, Naples, 2010.

[10] G. Toniolo, Progetto agli stati limite delle strutture di calcestruzzo in zona sismica-Parte1: criteri di base delle progettazione sismica, 2007.

[11] OpenSees, Pacific Earthquake Engineering Research Center, University of California, Berkeley. http://opensees.berkeley.edu. Cited 8 Jul 2010, 2008.

[12] M. Fischinger, K. Rejec, T. Isakovic, Shear magnification factors for RC structural walls in Eurocode 8. 14th ECEE, Ohrid, 2010.

COMPDYN 2011
III ECCOMAS Thematic Conference on
Computational Methods in Structural Dynamics and Earthquake Engineering
M. Papadrakakis, M. Fragiadakis, V. Plevris (eds.)
Corfu, Greece, 25–28 May 2011

MODELING THE BOND-SLIP BEHAVIOR OF CONFINED LARGE-DIAMETER REINFORCING BARS

Juan Murcia-Delso[1], **Andreas Stavridis**[1], **and Benson Shing**[1]
[1] University of California San Diego, Department of Structural Engineering
9500 Gilman Drive, La Jolla, CA 92093-0085
jmurciad@ucsd.edu, andreas@ucsd.edu, pshing@ucsd.edu

Keywords: Bond Slip, Bond Strength, Reinforcement, Large-Diameter Bars, Reinforced Concrete, Pull-out Tests, Cyclic Loading

Abstract. *The performance of reinforced concrete structures depends on the bond strength and bond-slip behavior between the concrete and reinforcing steel. Although the bond behavior of deformed bars has been extensively studied, there is little data available for large-diameter reinforcing bars under cyclic load reversals. As a result, current code specifications for the development lengths of reinforcing bars are largely based on experimental data obtained for bars with diameters of 36 mm or smaller. This paper presents an analytical model to describe the bond-slip behavior of reinforcing bars in well-confined concrete under monotonic and low-cycle fatigue loads. The model has been validated and calibrated with recently obtained experimental data from pull-out tests conducted on reinforcing bars with diameters of 36, 43, and 57 mm. It is successful in predicting the bond-slip behavior including the degradation of the bond strength and stiffness under monotonic as well as different cyclic load histories. This model has been implemented in an interface element in a finite element program. Analyses have been conducted with finite element models to estimate the minimum development length required for these large-diameter bars under a well-confined situation.*

1 INTRODUCTION

The performance of reinforced concrete (RC) structures depends on the composite action of the concrete and reinforcing steel, which relies on the bond between the two materials. When RC structures are subjected to earthquake loads, they may experience severe bond demands in regions where the reinforcement is anchored, e.g., in the foundation of a bridge column. Inadequate embedment lengths in these regions can lead to bond failures like those observed in bridge columns during the San Fernando (1971) earthquake, where the longitudinal reinforcement was pulled out from the foundation, as shown in Figure 1.

Figure 1: Pull-out of longitudinal reinforcement in bridge columns from foundations during the San Fernando (1971) earthquake [1]

For very large structural components, such as large bridge columns and piles, the use of reinforcing bars with diameters larger than 25 mm is common. This can avoid too close a bar spacing and allows the ease in concrete placement. However, despite the extensive studies carried out on the bond behavior of deformed bars, there is little data available on the bond strength and bond-slip behavior of large-diameter bars under cyclic load reversals. As a result, current code specifications in the United States for the development lengths of reinforcing bars are largely based on experimental data obtained for bar sizes of 36 mm or smaller, and they do not allow lap-splicing of bars with diameters larger than 36 mm because of the lack of experimental data [2].

This paper presents an analytical model to describe the bond-slip behavior of reinforcing bars embedded in well-confined concrete under monotonic and low-cycle fatigue loads. This model has been validated and calibrated with data obtained from pull-out tests recently conducted on bars with diameters of 36, 43 and 57 mm, which correspond to sizes #11, #14 and #18, respectively, in the United States. This study is part of an experimental and analytical investigation aimed to produce basic bond data and improved specifications on the required embedment length of column reinforcement extended into drilled shaft foundations.

2 BOND OF REINFORCEMENT

With numerous studies carried out in the last 40 years [3], the bond-slip behavior and mechanisms between a reinforcing bar and concrete are well understood. The bond force between a deformed bar and the surrounding concrete can be attributed to several sources: a) chemical adhesion between the bar and the concrete; b) frictional forces at the interface; and c) bearing of the ribs against the concrete surface.

The source and magnitude of the bond resistance between the steel and concrete depends on the relative displacement (slip) between the two. There are many factors that have been found to affect the bond strength: the bar size and deformation pattern, the compressive and tensile strengths of concrete, the aggregate size, the concrete cover, the transverse reinforcement, the casting position, the bar corrosion level, etc. [4]. A detailed explanation of bond-slip mechanisms can be found in [3] and [4]. They are briefly summarized below.

At very low level of bond stress, bond is assured mostly by chemical adhesion. After the initial slip of the bar with respect to the concrete, chemical adhesion is lost, and friction forces at the surface of the bar and bearing forces at the ribs caused by the interlocking action are mobilized. Transverse micro-cracks originate at the tips of the ribs, allowing the bar to slip as shown in Figure 2a. As slip increases, concrete in front of the ribs starts to crush, which in turns induces a wedging action that increases the normal component of the bearing forces. This normal component is resisted by hoop stresses in the concrete, which cause splitting cracks to develop at the contact with the bar and to propagate radially, as shown in Figure 2b. At this stage, the bond resistance is provided by an interlocking mechanism from the concrete struts confined by the undamaged outer concrete ring as well as the confining reinforcement if any. Depending on the level of the confinement, bond can fail by the splitting of the concrete or pull-out of the bar. For low confinement conditions, splitting cracks can propagate radially through the concrete cover and the bond fails abruptly, as shown in Figure 3. When the concrete is well confined, the splitting failure mode is precluded and higher bond strengths can be achieved, as shown in Figure 3. In this case, the bond fails due to the crushing and shearing of the concrete keys between the ribs, diminishing the interlocking action. Finally, the bar is pulled-out from the concrete, which eventually provides only a residual frictional resistance.

Bond deterioration under low-cycle fatigue (e.g., caused by earthquake loads) was studied by Eligehausen et al. [5] for bars with a diameter of 25 mm. They conducted an extensive experimental program of pull-out tests with specimens representing the confined region of a beam-column joint, and proposed a relatively simple analytical cyclic bond-slip law based on the experimental observations.

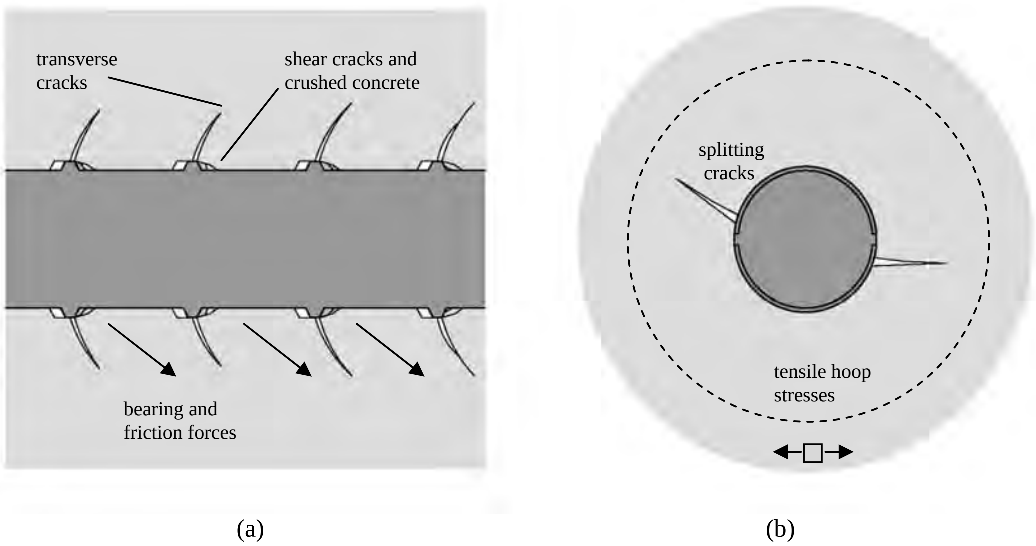

(a) (b)

Figure 2: (a) Transverse cracks; and (b) radial splitting cracks

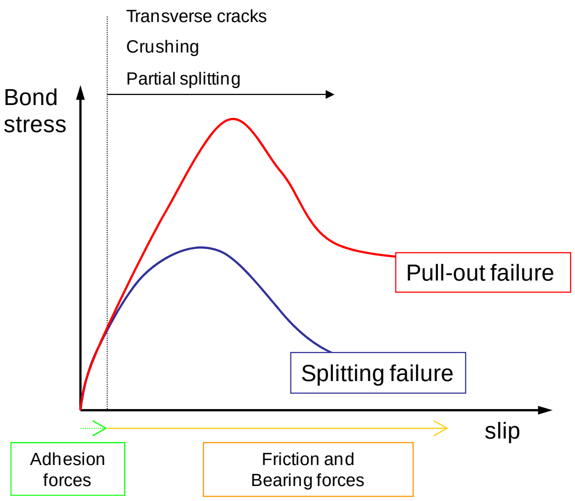

Figure 3: Bond stress vs. slip behavior of deformed bars

3 BOND-SLIP TESTS ON LARGE-DIAMETER BARS

As part of the study reported here, pull-out tests were conducted on large-diameter reinforcing bars embedded in well-confined concrete to obtain their local bond-slip behavior. These tests tried to reproduce the confinement conditions of a vertical bridge column rebar that is embedded in a foundation shaft, where no splitting failure is expected. Four series of tests were carried out: three to study the bond-slip behavior for each of the 35, 43 and 57-mm bar sizes; and the fourth to study the influence of the compressive strength of concrete on the bond strength. A total of 22 specimens were tested, of which 8 were subjected to monotonic loading and 14 to cyclic loading.

3.1 Specimens and test set up

A typical test specimen and the test setup are shown in Figure 4. Each specimen consisted of a reinforcing bar embedded in a 3-ft.-diameter concrete cylinder with an embedment length equal to 5 times the bar diameter (D_b). The bar was bonded only in the central portion of the cylinder, and ungrouted PVC tubes were used to create unbonded zones in the upper and lower regions of the concrete cylinder to minimize any local disturbance to the bonded zone during the loading process. The test setup was designed to allow the bar to be pulled upwards or downwards using two center-hole hydraulic jacks, one at each end. A threaded T-head was used to anchor the bar at each end. The bar was pulled out from the concrete cylinder when one of the hydraulic jacks pushed against the adjacent anchor head. This was a self-reacting system; thus, the concrete was subjected to compression while the bar was being pulled out. During the test, the pull-out force was measured with a load cell and confirmed with strain gages attached to two opposite sides of the bar near each end of the concrete cylinder; and bar slips were measured at both ends by two linear potentiometers at each end mounted on two opposite sides of the bar. The local bond stress (τ) vs. slip (s) relation was obtained as the average bond stress vs. the average of the slip at the two ends of the bonded portion, s_{top} and s_{bottom}. These slip values are calculated as the average of the slips measured at the two linear potentiometers with the bar deformation on the loaded side between the attachment point of the pair of linear potentiometers and the end of bonded zone taken out. The bar deformation was calculated from strain-gage readings.

$$\tau = \frac{F}{5\pi D_b^2} \qquad s = 0.5\left(s_{top} + s_{bottom}\right) \tag{1}$$

The tests were started once the concrete reached the targeted strength. Test Series 1 through 3 had a targeted concrete compressive strength of 35 MPa, while Series 4 had a minimum targeted strength of 55 MPa.

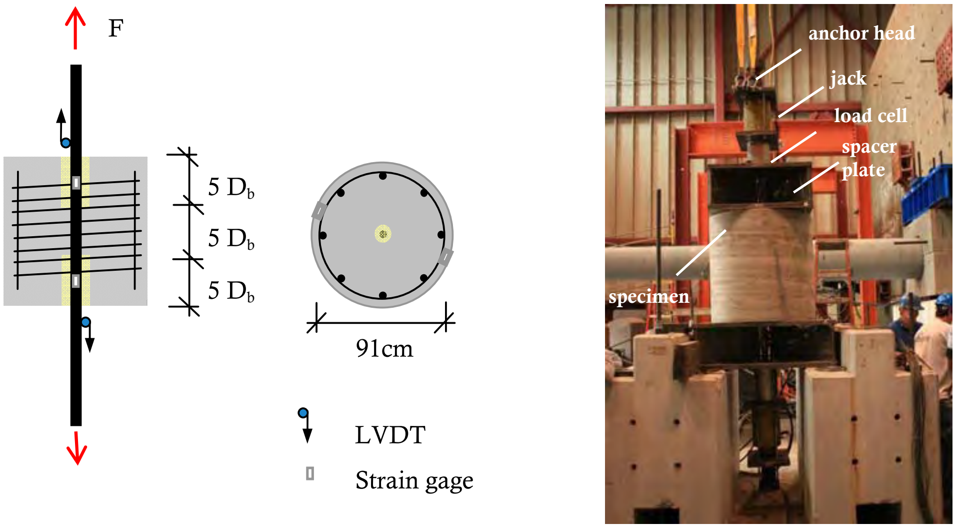

(a) (b)

Figure 4 : (a) Test specimen; and (b) test setup

3.2 Test results

The bond strengths, τ_{max}, obtained from the experiments are summarized in Table 1. The values are the average of the bond strengths obtained from monotonic pull-out tests in which the bars were pulled up. Results from the first three series, which had a concrete compressive strength of 35 MPa, have shown that τ_{max} increased with the bar diameter from 15.2 MPa for 36-mm bars to 17.6 MPa for 57-mm bars. The tests conducted by Eligehausen et al. [5] for 25-mm bars obtained an average bond strength of 13.9 MPa; but the concrete used in their tests had a slightly lower compressive strength of 30 MPa and lower level of confinement. Results from Series 4, which had 55-MPa concrete and 43-mm bars, have shown a 45% increase of the average bond strength as compared to that obtained from Series 2, which had the same bar size but 35-MPa concrete. Based on the data from these tests, the bond strength is more or less proportional to $f_c'^{0.75}$ rather than $f_c'^{0.5}$, which has been often reported in the literature [4], [5]. Finally, the tests have shown that the bond strength could decrease by 10 to 20% when the bar was pulled downward instead of upward. This observation is consistent with results from previous studies [3].

The averaged bond stress vs. slip relations obtained from monotonic pull-out tests for series 1, 2 and 3 are plotted in Figure 5. The shape of the curves is similar to the one obtained for 25-mm bars by Eligehausen et al. [5]. In all cases, a practically constant residual bond resistance is attained when the slip equals the clear rib spacing of the bar. Since the clear rib spacing is usually proportional to the bar diameter, this slip level is larger for larger bars. On the contrary, the value of the slip at the peak strength does not show a clear relation with the bar size. It is around 1.5 mm for 25 mm bars [5], and remains at about 3.0 mm for 35-mm, 43-

mm, and 57-mm bars. The concrete characteristics and test set up may also have an influence in the slip level at which the peak strength is reached.

Series	Series 1	Series 2	Series 3	Series 4	Tested by [5]
D_b (mm)	36	43	57	43	25
$f_c^{'}$ (MPa)	35	35	35	55	30
τ_{max} (MPa)	15.2	16.2	17.6	23.7	13.9

Table 1: Average bond strength obtained from pull-out tests

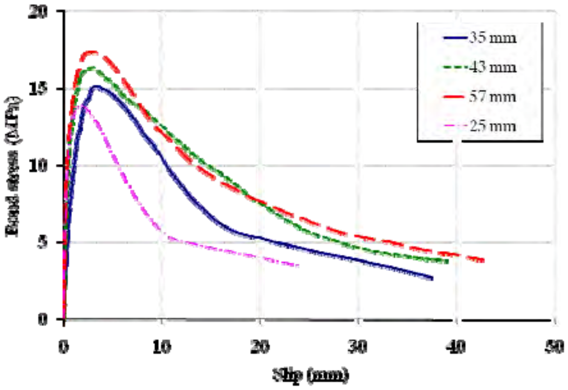

Figure 5: Monotonic bond stress vs. slip relations obtained from tests
(the curve for 25-mm bars was from Eligehausen et al. [5])

Several load histories were used for the cyclic tests, with variables including the increment of the slip amplitude in each loading cycle, the number of cycles per amplitude, and the type of cyclic reversals. Two types of cyclic reversals were considered: (a) full cycles with the same slip amplitudes in both directions for each cycle; and (b) half cycles with slips mainly in one direction and slightly passing the origin in the other. Figure 6 shows the bond stress vs. slip relations for four cyclic tests carried out in Series 2 and 3. The comparison of the results from different cyclic load histories has indicated that the bond strength started to deteriorate when a load cycle went beyond 70% of the peak strength. Moreover, it has been observed that full cycles induce a faster degradation than half cycles. In general, the large-diameter bars show a similar hysteretic bond-slip behavior as the 25-mm bars tested by Eligehausen et al. [5].

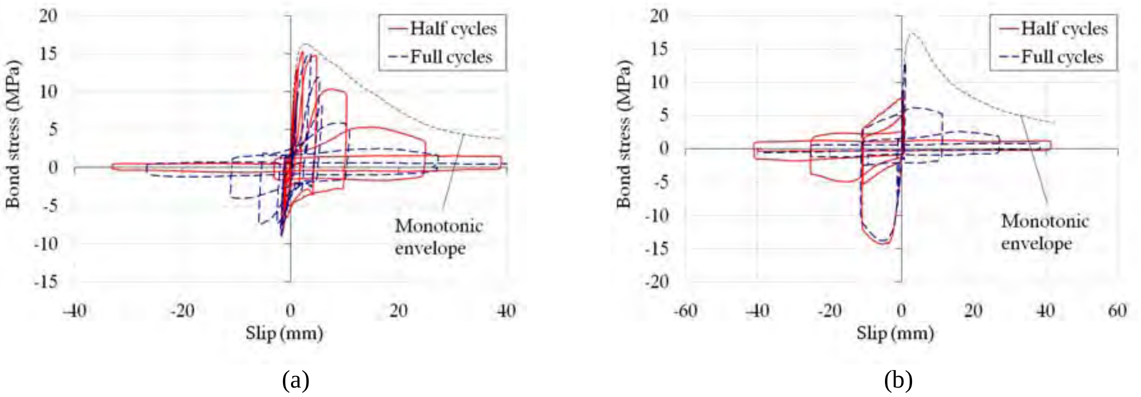

(a) (b)

Figure 6: Cyclic bond stress vs. slip relations obtained from tests;
(a) 43-mm bars and 35-MPa concrete, and (b) 57-mm bars and 35-MPa concrete

4 BOND-SLIP LAW FOR CONFINED BARS

A phenomenological bond-slip model for bars embedded in well-confined concrete has been developed based on the experimental data presented in the previous section. The model is similar to the ones proposed in [5] and [6] but has a more general bond-slip law. For monotonic loading, the bond stress is defined as a function of the slip by means of simple polynomial functions. This law is extended to cyclic loading by scaling down the monotonic envelope using damage parameters that depend on the slip history to account for cyclic bond degradation. The main difference with previous models is that the degradation of the envelope curve is governed by two damage parameters presenting the degradations of the bearing resistance and friction resistance, respectively. In addition, the model is more general in that it can be used for different bar sizes and concrete types with the calibration of only three parameters.

4.1 Bond-slip law for monotonic loading

The bond stress (τ) vs. slip (s) relation for monotonic loading is defined piecewise by a set of five polynomial functions, as shown in Figure 7, based on experimental observations. Up to 40% of the peak strength (τ_{max}), the bond stress increases linearly with the slip. The nonlinear hardening behavior is represented by a fourth-order polynomial, followed by a plateau at τ_{max}. The bond strength degradation is described by a linear descending branch. When the slip equals the clear rib spacing of the bar (s_R), a residual bond stress equal to 25% of τ_{max} is assumed, and this value remains constant for further slip.

The expression for the monotonic envelope is provided in Equation 2 in terms of three parameters: the maximum bond strength (τ_{max}), the slip at which τ_{max} is attained (s_{peak}), and the clear spacing between the ribs (s_R). The details are shown in Figure 7.

$$\tau(s)=\begin{cases} 4\dfrac{\tau_{\max}}{s_{peak}}s & s<0.1s_{peak} \\ \tau_{\max}\left[1-0.6\left(\dfrac{s-s_{peak}}{0.9s_{peak}}\right)^4\right] & 0.1s_{peak}\le s<s_{peak} \\ \tau_{\max} & s_{peak}\le s<1.1s_{peak} \\ \tau_{\max}\left[1-0.75\dfrac{s-1.1s_{peak}}{s_R-s_{peak}}\right] & 1.1s_{peak}\le s<s_R \\ 0.25\tau_{\max} & s\ge s_R \end{cases} \tag{2}$$

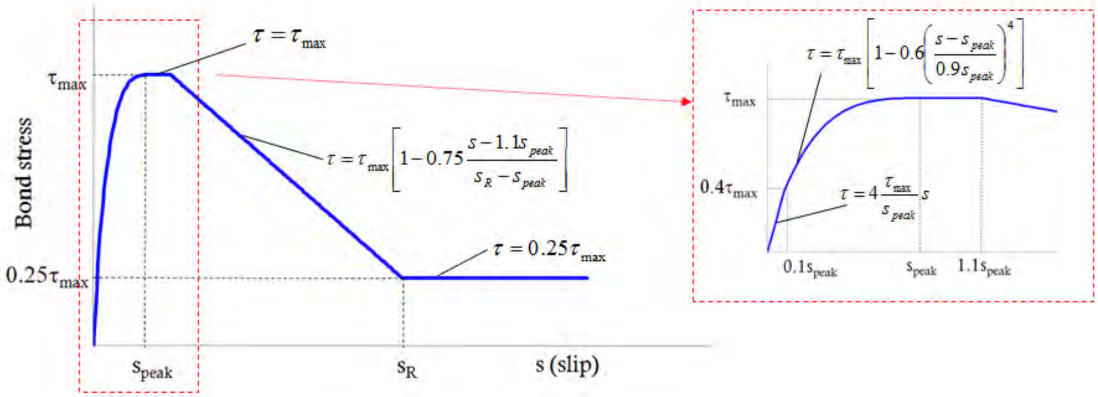

Figure 7: Analytical bond stress - slip law for monotonic loading

The values of s_R , τ_{max}, and s_{peak} determined for the bars tested here are presented in Table 2. The analytical and experimental curves for monotonic pull-out tests from Series 2 and 3 are compared in Figure 8. The same analytical law has been used to model the bond-slip behavior of smaller bars by changing the values of the three governing parameters (see Table 2). Figure 9 shows that the model matches the experimental results ([5] and [7]) for the smaller bars well.

Bar size	36 mm	43 mm	57 mm	43 mm	25 mm [5]	16 mm [7]
s_R (mm)	19.0	25.0	24.5	25.0	11.5	8
τ_{max} (MPa)	15.2	16.2	17.6	23.7	13.9	20.9
s_{peak} (mm)	3.0	3.0	3.0	3.0	1.5	1.2

Table 2: Modeling parameters

The clear rib spacing (s_R) is a measured geometric property of the rebar, and it is usually between 40 to 60% of the bar diameter. Since the bond strength depends on many factors, no theoretical formulas are available to accurately determine τ_{max} and s_{peak} . Therefore, they have to be determined experimentally. When no experimental data are available, the following empirical rules are suggested to estimate these values. The slip at the peak strength, $s_{peak,}$ can be taken to be 7 % of the bar diameter, which is the average of the values presented in Table 2. The bond strength, τ_{max}, can be assumed to be equal to 16.3 MPa, which is the average from the values shown in Table 2 for 36-mm, 43-mm, and 57-mm bars and 35-MPa concrete, and scaled by a factor of $f_c^{\prime 0.75}$, if necessary.

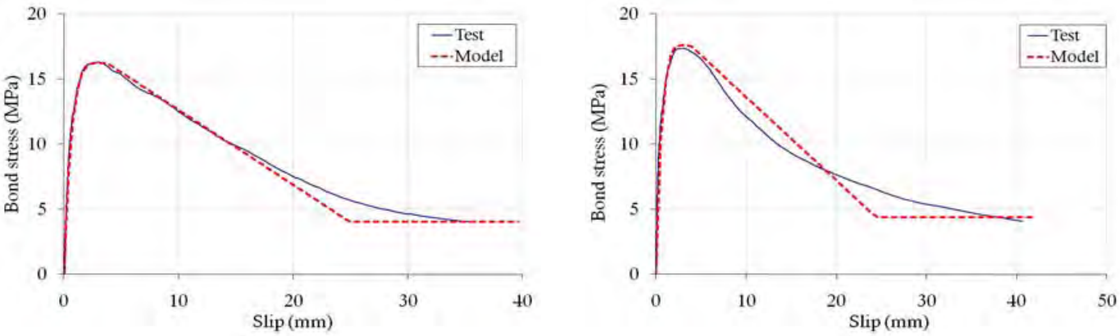

(a) (b)

Figure 8: Comparison of experimental and analytical bond stress – slip relations for monotonic tests on large-diameter bars;(a) 43-mm bars and 35-MPa concrete, (b) 57-mm bars and 35-MPa concrete

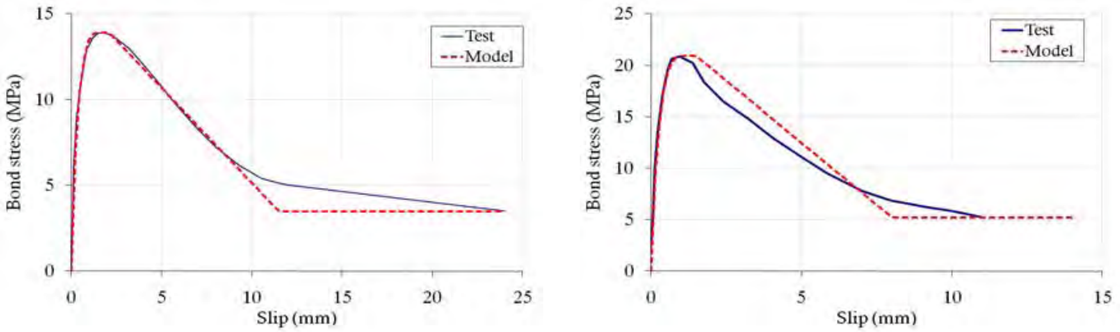

(a) (b)

Figure 9: Comparison of experimental and analytical bond stress – slip relations for monotonic tests on smaller bars; (a) 25-mm bars and 30-MPa concrete [5], (b) 16-mm bars and 36-MPa concrete [7]

4.2 Bond-slip law for cyclic loading

Under cyclic loading, bond stress is defined as a function of the current slip and the slip history. Similar to that suggested in [5], the cyclic bond-slip law proposed here assumes that cyclic bond degradation can be represented by the degradation of a bond stress-slip envelope curve governed by damage parameters that depend on the slip history. The initial envelop curve corresponds to the monotonic bond stress – slip curve. However, while [5] uses a single damage parameter related to the energy dissipated, the model proposed here distinguishes between the cyclic deterioration of the bearing forces and the cyclic deterioration of the friction forces. This is based on the observation from tests that the cyclic deterioration for the peak bond strength, which is provided by bearing and friction forces, and that of the residual bond strength, which is provided by friction forces only, are different. Based on this observation, the total bond stress is decomposed into bearing and friction contributions as represented in Figure 10. The maximum frictional resistance $\tau_{f,max}$ is assumed to be equal to 25% of τ_{max}, which is the same value as the residual bond strength observed in typical monotonic bond stress – slip curves. This resistance is fully developed at s_{peak}, and remains constant for higher slip levels. The maximum bearing resistance $\tau_{b,max}$ is considered to be equal to 75% of τ_{max}. It is fully developed at s_{peak}, and decays linearly to zero at a slip equal to s_R. The aforementioned relations for the initial monotonic bond stress – slip curve are shown in Equation 3.

$$\begin{aligned} \tau &= \tau_b + \tau_f \\ \tau_{b,\max} &= 0.75\tau_{\max} \\ \tau_{f,\max} &= 0.25\tau_{\max} \end{aligned} \tag{3}$$

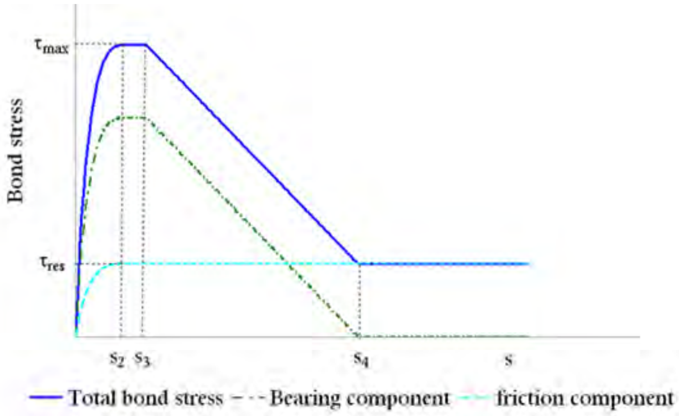

Figure 10: Analytical decomposition of bond stress into bearing and friction

Figure 11 shows a sketch of the analytical bond-slip law for cyclic loading including the initial monotonic bond stress – slip curve and a deteriorated envelope (labeled as curve 1). The total deteriorated resistance τ_{red} at any time is assumed to be the sum of the deteriorated bearing resistance, $\tau_{b,red}$, and the deteriorated friction resistance, $\tau_{f,red}$. The reduction of the two resistance components is controlled by two damage parameters that depend on the loading history and are updated every time the load is reversed. These relations are shown in Equation 4.

$$\begin{aligned} \tau_{red} &= \tau_{b,red} + \tau_{f,red} \\ \tau_{b,red} &= (1-d_b)\tau_b \\ \tau_{f,red} &= (1-d_f)\tau_f \end{aligned} \tag{4}$$

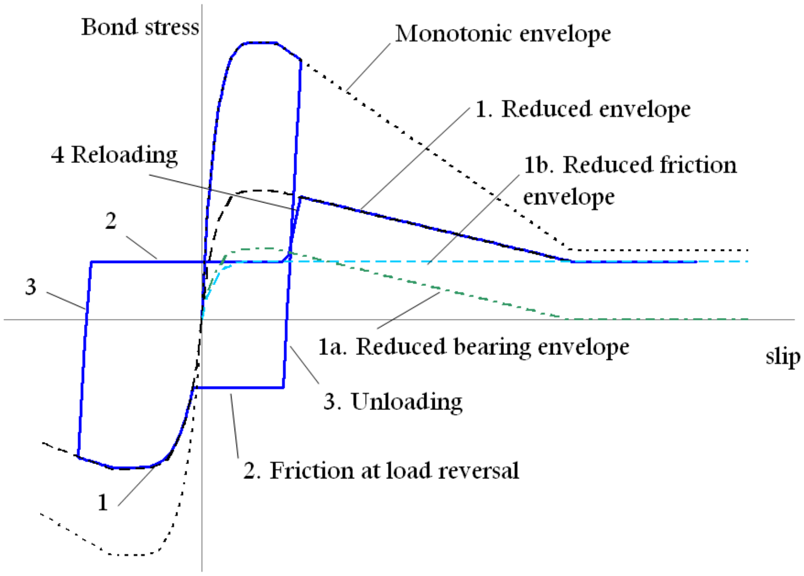

Figure 11: Analytical bond-slip law for cyclic loading

The damage factor for the bearing resistance, $d_{b,}$ is assumed to be a function of the maximum slip. Since full cycles have shown to produce more damage than half cycles, the maximum slip considered here is a weighted average of the absolute maximum slip reached in any of the two directions and the average of the maximum slips in the two directions, $s^{+}_{\max}$ and $s^{-}_{\max}$. This damage parameter is defined in Equation 5.

$$d_b(\hat{s}_{\max}) = 1 - e^{2.5\left(\frac{\hat{s}_{\max}}{s_R}\right)^{0.8}}$$
$$\hat{s}_{\max} = 0.75\max(s^{+}_{\max}, s^{-}_{\max}) + 0.125(s^{+}_{\max} + s^{-}_{\max}) \tag{5}$$

The damage parameter for the friction resistance, d_b, is assumed to be a function of both the maximum slip in each direction and the total accumulated slip s_{acc}, shown in Equation 6. The frictional resistance is reduced progressively due to the smoothening of the interface.

$$d_f(s_{acc}, s^{+}_{\max}, s^{-}_{\max}) = \frac{s^{+}_{\max} + s^{-}_{\max}}{s_R}\left(1 - e^{0.4\left(\frac{s_{acc}}{s_R}\right)^{0.75}}\right) \tag{6}$$

When sliding is between the levels of slip achieved previously, there is no contact between the ribs and the concrete, and the bond stress developed is entirely contributed by the friction generated at the bar barrel. This frictional resistance generated at slip reversal, τ_{rev} , is defined as a function of the reduced residual friction and the maximum slip achieved. This branch of the bond-slip law is labeled as curve 2 in Figure 11.

$$\tau_{rev} = k_{rev}\tau_{f,red}$$
$$k_{rev} = \frac{\max(s^{+}_{\max}, s^{-}_{\max})}{s_{peak}} \leq 1 \tag{7}$$

With the above considerations, cycling between previously achieved slip levels induces additional deterioration to the friction forces but not to the bearing forces, which is consistent mechanical considerations. Bearing forces are only activated when concrete is in contact with the ribs, and this happens for slip levels exceeding previously reached values. Deterioration of the bearing forces is caused by crushing and shearing of concrete in front of the ribs.

To fully define the cyclic law, unloading and reloading rules need to be specified. Upon slip reversal, bond stress decreases linearly until τ_{rev} is achieved. This branch of the bond-slip law is labeled as curve 3 in Figure 11. For the reloading branch, labeled as curve 4 in Figure 11, the stress increases linearly from τ_{rev} until the reduced envelope is reached. Both unloading and reloading stiffnesses are equal to the initial stiffness of the monotonic bond stress - slip curve: $k = 4\frac{\tau_{\max}}{s_{peak}}$.

The aforementioned damage law has been calibrated using the experimental data from the test series 1, 2 and 3. The experimental and analytical bond-slip laws for a cyclic test in Series 1 are compared in Figure 12a. The analytical model reproduces very well the cyclic bond deterioration, the resistance right after slip reversal, and the unloading and reloading branches. The model is compared to a test in Series 4 in Figure 12b, which also shows a good match between the experiment and the analytical results. The cyclic deterioration rules obtained for large-diameter bars are also applicable to smaller bars, as demonstrated by the good match between the experiments and analytical results shown in Figure 13.

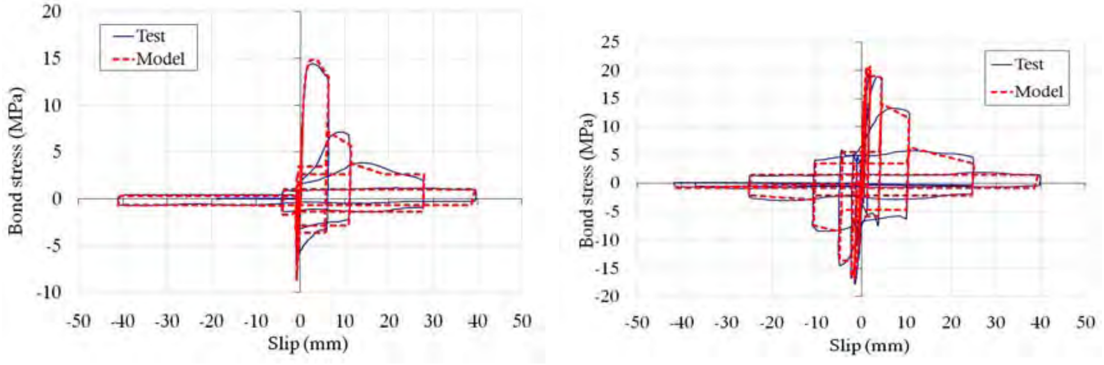

(a) (b)

Figure 12: Comparison of experimental and analytical bond stress – slip relations for cyclic tests on large-diameter bars; (a) 36-mm bars and 35-MPa concrete, (b) 43-mm bars and 55-MPa concrete

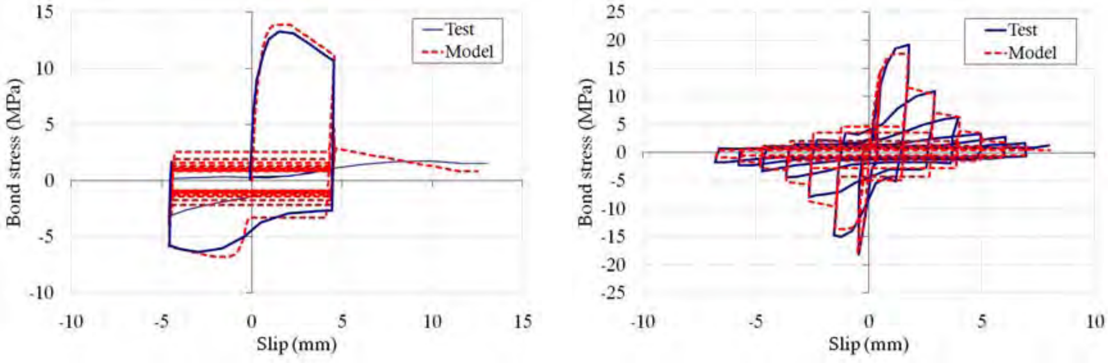

(a) (b)

Figure 13: Comparison of experimental and analytical bond stress – slip relations for cyclic tests on smaller bars; (a) 25-mm bars and 30-MPa concrete, tested by [5], (b) 16-mm bars and 36-MPa concrete, tested by [7]

5 FINITE ELEMENT ANALYSIS APPLICATION

The bond-slip law described above has been implemented in an interface element in ABAQUS [8], and finite element analyses have been conducted on large-diameter bars to determine the minimum development lengths required to prevent pull-out failure. The results are compared to those required by the AASHTO LRFD Specifications [2]. Figure 14 shows a 2-dimensional axi-symmetric model of a bar embedded in concrete developed for these analyses. The concrete is modeled using a damaged-plasticity law based on [9] and [10], and the steel is modeled with a von Mises plasticity law with linear hardening. Both material laws are available in ABAQUS. The steel bar is connected to the concrete elements using interface elements with the proposed bond-slip law. The compressive strength of concrete is taken as 35MPa. The nominal yield strength of the steel is 414 MPa, but in the analyses the actual yield strengths obtained from material tests have been used: 510 MPa for 35-mm bars, 490 MPa for 43-mm bars, and 450 MPa for 57-mm bars. The tensile strength of the steel is 680 MPa for 35-mm bars, 655 MPa for 43-mm bars, and 620 MPa for 57-mm bars.

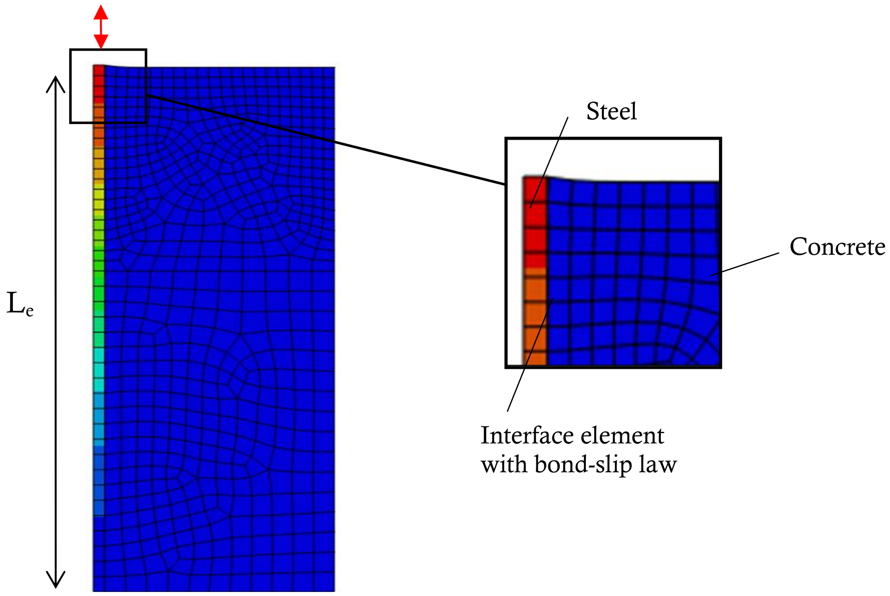

Figure 14: FE model of the pull-out simulation of a reinforcing bar

Analyses have been carried out with the embedment length of the bar, L_e , gradually reduced until pull-out failure occurs. Figure 15 presents the results of a pull-out simulation of a 43-mm rebar using four different values for L_e. It can be concluded from these results that the minimum embedment length necessary to reach the ultimate strength of the steel is equal to 12 times the bar diameter, D_b. This value is less than half of the development length required by the AASHTO Specifications [2], which in this case is equal to $26D_b$. Moreover, the responses with L_e=12D_b and L_e=26D_b are very similar, showing no substantial loss of stiffness by using a significantly shorter length. The results also show that for L_e=10D_b, yielding of the bar can occur, but it can be followed by a pull-out failure before the bar could rupture; and for L_e=8D_b, a pull-out failure can take place without yielding the bar.

Results have also been obtained for 36-mm and 57-mm bars. The values of the development lengths required by [2] for well confined bars, $L_{e,AASHTO}$, and the minimum required values obtained from the analyses, $L_{e,min}$, are presented in Table 3. The minimum required development lengths shown by the analyses are about half of the values required by the

AASHTO Specifications. In addition, it is interesting to note that the AASHTO requirements and the numerical results show opposite trends with respect to the relation between the required development length and the bar size. According to AASHTO, the L_e/D_b ratio is higher for larger-diameter bars, while the numerical results show that the required L_e/D_b ratio decreases with the bar size.

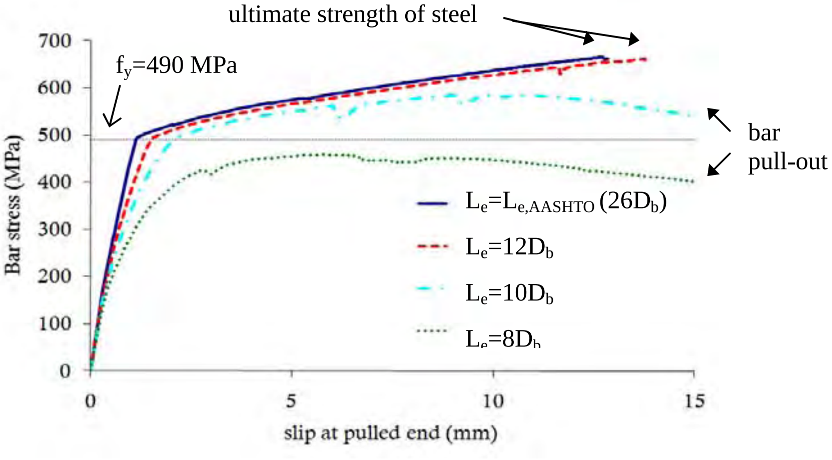

Figure 15: Bar stress vs. slip at pulled end for different embedment lengths (D_b=43 mm and f_c'=35 MPa)

Bar size	$L_{e,AASHTO}$	$L_{e,min}$
36 mm (US #11)	22D_b	14D_b
43 mm (US #14)	26D_b	12D_b
57 mm (US #18)	25D_b	11D_b

Table 3: Minimum embedment lengths

6 CONCLUSIONS

An analytical model to predict the cyclic bond-slip behavior of reinforcing bars embedded in well-confined concrete has been presented. The model has been calibrated with recent monotonic and cyclic pull-out tests conducted on bars with diameters of 36, 43 and 57 mm. The model successfully reproduces the bond-slip behavior of these bars as well as that of smaller bars, including the degradation of the bond strength and bond stiffness under different load histories.

The bond-slip law proposed has been implemented in an interface element in a finite element program. Finite element analyses have been carried out to obtain the minimum development length required of large-diameter bars (35, 43, and 57 mm). The results show that the development length requirements in the current AASHTO Specifications for bridge structures in the U.S. are very conservative.

REFERENCES

[1] M.Yashinsky, Earthquake Damage to Structures. *Structural Engineering Handbook,* Ed. Lian Duan, CRC Press LLC, 2001.

[2] American Association of State Highway and Transportation Officials (AASHTO), *LRFD Bridge Design Specifications, 5th Edition*, 2010.

[3] Fédération internationale du béton (fib), *fib bulletin 10: Bond of reinforcement in concrete*, Task group bond model, Lausanne, 2000.

[4] American Concrete Institute (ACI) Committee 408, *Bond and Development of Straight Reinforcing Bars in Tension*, ACI-408R-03, 2003.

[5] R. Eligehausen, E.G. Popov, V.V. Bertero, *Local bond stress - slip relationships of deformed bars under generalized excitations*, UCB-EERC, 1983.

[6] L.N., Lowes, J.P. Moehle, S. Govindjee, Concrete-Steel Bond Model for Use in Finite Element Modeling of Reinforced Concrete Structures. *ACI Structural Journal*, 101-S50, 2004.

[7] K. Lundgren, Pull-out tests of steel-encased specimens subjected to reversed cyclic loading. *Materials and Structures*, **33-231**, 450-456, 2000.

[8] Dassault Systemes, *Abaqus Analysis User's Manual Version 6.9*, 2009.

[9] J. Lubliner, J. Oliver, S. Oller, E. Oñate, A plastic-damage model for concrete. *Int. J. Solids Structures*, **25**, 299-326, 1989.

[10] J. Lee, G.L. Fenves, A plastic-damage concrete model for earthquake analysis of dams. *Earthquake Engineering and Structural Dynamics*, **27**, 937-956, 1998.

COMPDYN 2011
III ECCOMAS Thematic Conference on
Computational Methods in Structural Dynamics and Earthquake Engineering
M. Papadrakakis, M. Fragiadakis, V. Plevris (eds.)
Corfu, Greece, 26–28 May 2011

SEISMIC STRENGTH EVALUATION OF REINFORCED CONCRETE SHEAR WALLS WITH CRACKS, USING THE NOTION OF FRACTAL GEOMETRY

O. Panagouli, E. Mistakidis and K. Iordanidou

Laboratory of Structural Analysis and Design, Dept. of Civil Engineering, University of Thessaly,
Pedion Areos, 38334 Volos, Greece
{olpanag,emistaki}@uth.gr

Keywords: Cracked shear walls, rough interfaces, fractal geometry, fractal resolution, unilateral contact, variational formulation

Abstract. *Shear walls play an important role to the seismic strength of modern seismic resistant structures. They are designed so that they have significant bending and shear strengths and ductility. However, existing structures have lightly reinforced shear walls. In most cases, especially under cycling loading, shear cracks appear reducing the shear capacity of the wall. Here, a typical shear wall of an existing structure is examined in which it is assumed that a crack has been formed. For the modeling of the geometry of the crack a new approach is applied, using the notion of fractal geometry. The aim of the paper is the estimation of the post-cracking strength of the wall, taking into account the geometry of the cracks and the mixed friction-plastification mechanisms that develop in the vicinity of the crack. Due to the significance of the crack geometry a multi-resolution analysis is performed. The materials (steel and concrete) are assumed to have elastic-plastic behaviour. For concrete both cracking and crushing are taken into account in an accurate manner. On the interface unilateral contact and friction conditions are assumed to hold. For every structure resulting for each resolution of the interface, a classical Euclidean problem is solved. The obtained results lead to interesting conclusions concerning the post-cracking strength of lightly reinforced shear walls.*

1 INTRODUCTION

Shear walls play a significant role to the seismic strength of structures built in seismic prone areas. Shear walls in modern structures are designed to have significant bending and shear strengths and ductility. However, shear walls in old, existing buildings have been constructed using poor materials and usually have inadequate shear strength. In such elements, shear cracks appear reducing their overall capacity. The aim of this paper is to apply, a new approach in order to estimate the post-cracking strength of a shear wall which is part of an existing structure, taking into account the geometry of the formed cracks. To this end, the notion of fractal geometry is applied in order to approximate the geometry of the crack.

It is well known that the geometry and structure of the interface between two solid surfaces in contact is of fundamental importance to the study of friction, wear, lubrication and also strength evaluation. Experimental studies [1], [2], [3], [4] have shown that the fracture interfaces have irregularities of all scales, and require advanced mathematical models for their description. In general, the actual contact between two real interfaces is realized only over a small fraction in a discrete number of areas. Consequently, the real area of contact is only a fraction of the apparent area [5], [6] and the parameters of the actual contact regions are strongly influenced by the roughness of the contacting surfaces. For that, fractal contact models are suitable for the simulation of contact.

The fractal approach adopted here for the simulation of the geometry of the cracks formed in the shear wall, uses computer generated self-affine curves for the modelling of the interface roughness, which is strongly dependent on the values of the structural parameters of these curves. The computer generated interfaces, which are characterized by a precise value of the resolution δ of the fractal curve, permit the study of the interface roughness on iteratively generated rough profiles. This fact makes this approach suitable for engineering problems, since it permits the satisfactory study of the whole problem with reliable numerical calculations.

Among the aims of this paper is to study how the resolution of a fractal interface F affects the strength of a reinforced concrete shear wall element, in which it is assumed that a crack has been developed. The geometry of the crack is modelled through the application of the principles of fractal geometry. On the interface between the two cracked surfaces, unilateral contact and friction conditions are assumed to hold. The applied approach takes into account the nonlinear behaviour of the materials, including the limited strength of the concrete under tension. The shear wall is applied to shear loading. As a result of the applied approach, the contribution of the friction between the cracked surfaces is taken into account, as well as the additional strength coming from the mechanical interlock between the two faces of the crack. For every structure resulting for each resolution of the interface, a classical Euclidean problem is solved by using a variational formulation [7].

2 FRACTAL REPRESENTATION OF ROUGH INTERFACES

The fractal nature of material damage has been a matter of a very intense research during the last three decades. The fractal nature of fracture surfaces in metals was shown more than 20 years ago by Mandelbrot et. al. [1]. In this paper the authors studied the fracture of cracked surfaces in metals fractured either by tensile or impact loading, which were shown to develop fractal structure over more than three orders of magnitude. In quasi-brittle materials observations have shown that fracture surfaces display self-affine scale properties in a certain range of scales which is in most cases very large and which greatly depends on the material microstructure. This is true for a large variety of quasi-brittle materials such as rock, concrete, wood and ceramics [8], [9].

Fractal sets are characterized by non-integer dimensions [10]. The dimension of a fractal set in plane can vary from 0 to 2. Accordingly, by increasing the resolution of a fractal set, its length tends to 0 if its dimension is smaller than 1 (totally disconnected set), or tends to infinity if it is larger than 1. In these cases the length is a nominal, useless quantity, since it changes as the resolution increases. Conversely, the fractal dimension of a fractal set is a parameter of great importance because of its scale-independent character.

Many methods which are based on experimental or numerical calculations, such as the Richardson method [10], have been developed for the estimation of the fractal dimension of a curve. According to this method, dividers, which are set to a prescribed opening δ, are used. Moving with these dividers along the curve so that each new step starts where the previous step leaves off, one obtains the number of steps $N(\delta)$. The curve is said to be of fractal nature if by repeating this procedure for different values of δ the relation

$$N(\delta) \sim \delta^{-D} \tag{1}$$

is obtained in some interval $\delta^{(*)} < \delta < \Delta^{(*)}$. The power D denotes the fractal dimension of the profile, which is in the range $1 \le D < 2$. The relation between the fractal dimension D of this profile and the dimension of the corresponding surface is $D_s = D + 1$ [10].

The idea of self-affinity is very popular in studying surface roughness because experimental studies have shown that usually, under repeated magnifications, the profiles of real surfaces are statistically self-affine to themselves [1], [11]. The self-affine fractals were used in a number of papers as a tool for the description of rough surfaces [12]-[17]. Typically, such a profile can be measured by taking height data y_i with respect to an arbitrary datum at N equidistant discrete points x_i and following the procedure presented in [18]. Here, fractal interpolation functions are used for the passage from this discrete set of data $\{(x_i, y_i), i = 0,1,2,...,N\}$ to a continuous model, where $\mathrm{F}\,(x_i) = y_i$, $i = 0,1,...,N$. It has been proved [18] that there is a sequence of functions $\mathrm{F}_{n+1}(x) = (T\mathrm{F}_n\ )(x)$, where $T: C^0 \to C^0$ is an operator defined by:

$$\mathrm{F}_{n+1}(x) = (T\mathrm{F}_n)(x) = c_i l_i^{-1}(x) + d_i \mathrm{F}_n\left(l_i^{-1}(x)\right) + g_i \tag{2}$$

for $x \in [x_{i-1}, x_i], i = 1,2,...,N$. The operator T converges to a fractal curve F , as $n \to \infty$. The transformation l_i transforms $[x_0, x_N]$ to $[x_{i-1}, x_i]$ and it is defined by the relation

$$l_i(x) = a_i x + b_i. \tag{3}$$

The factors d_i are the hidden variables of the transformations and they have to satisfy $0 \le d_i < 1$ in order for $T: C^0 \to C^0$ to have a unique fixed point. Moreover, the remaining parameters are given by the following equations:

$$a_i = (x_i - x_{i-1}) / (x_N - x_0) \tag{4}$$

$$c_i = (y_i - y_{i-1}) / (x_N - x_0) - d_i (y_N - y_0) / (x_N - x_0) \tag{5}$$

$$b_i = (x_N x_{i-1} - x_0 x_i) / (x_N - x_0) \tag{6}$$

$$g_i = \left(x_N y_{i-1} - x_0 y_i\right) / \left(x_N - x_0\right) - d_i \left(x_N y_0 - x_0 y_N\right) / \left(x_N - x_0\right). \tag{7}$$

The fractal interpolation functions give profiles which look quite attractive from the viewpoint of a graphic roughness simulation. In higher approximations these profiles appear rougher as it is shown in the next section where the first to fourth approximations of a fractal interpolation function are presented. Moreover, the roughness of the profile is strongly affected by the free parameters $d_i, i = 1, \ldots, N$ of the interpolation functions. As these parameters take larger values, the resulting profiles appear rougher.

It must be mentioned here that an important advantage of the fractal interpolation functions presented here is that their fractal dimension can be obtained numerically [18] and is given by the relation:

$$\delta^{-D} \approx \sum_{i=1}^{N} |d_i|\, a_i^{D-1} \delta^{-D} \Leftrightarrow \sum_{i=1}^{N} |d_i|\, a_i^{D-1} = 1. \tag{8}$$

3 DESCRIPTION OF THE CONSIDERED PROBLEM

In Figure 1 a reinforced concrete shear wall element is presented which is assumed to be part of a typical existing structure built during the 60s or 70s. The wall is reinforced by a double steel mesh consisting of horizontal and vertical rebars having a diameter of 8mm and a spacing of 200mm. The quality of the steel mesh is assumed to be S220 (typical for buildings of that age). At the two ends of the wall the amount of reinforcement is higher. Four 20mm rebars of higher quality (S400) are used, without specific provisions to increase the confinement. The thickness of the wall is 200mm and the quality of concrete is assumed to be C16, typical for this kind of constructions. The wall is fixed on the lower horizontal boundary.

The considered shear wall is divided into two parts by a crack which is assumed that has been formed as a result of the action of an earthquake. Obviously, the depicted crack has been formed due to shear failure of concrete. For the description of the geometry of the crack, the notion of fractals is used. More specifically, the crack is assumed to be a fractal interface, described by the fixed point of a fractal interpolation function interpolating the set of data $\left\{(-1.0, 2.95), (0.4, 2.0)(1.8, 1.0)(3.2, 0.5)\right\}$. The free parameters of the fractal interpolation function are taken to have the values $d_1 = d_2 = d_3 = 0.50$.

The objective here is to estimate the capacity of the shear wall under an action similar to the one that has created the crack. For this reason, a horizontal displacement of 20mm is applied on the upper side of the wall (see Fig. 1). Moreover, a vertical distributed loading q_N is applied on the upper horizontal boundary, creating a compressive axial loading. The resultant of this loading is denoted by N. For N, six different values will be considered from 0 to 2.500 kN with a step of 500 kN.

As it was mentioned in the previous section, self-affine interfaces are adopted for the interface simulation. The computer generated interfaces $\mathrm{F}_n, n = 1, 2, \ldots$ are only images “pre-fractals” characterized by a precise value of the resolution $\delta^{(n)}$ of the fractal set. The resolution $\delta^{(n)}$ is related to the (n)-th iteration of the fractal interpolation function and represents the characteristic linear size of the interface. As it is shown in Fig. 2 where four iterations of a fractal interface are given, the linear size of the interface changes rapidly when higher order approximations are taken into account. It is assumed that the opposite sides of the fracture are perfectly matching surfaces, so only one side of the fracture was generated by using the described fractal interpolation function. By applying relation (8) the fractal dimension D of the interface studied here results to be equal to 1.369.

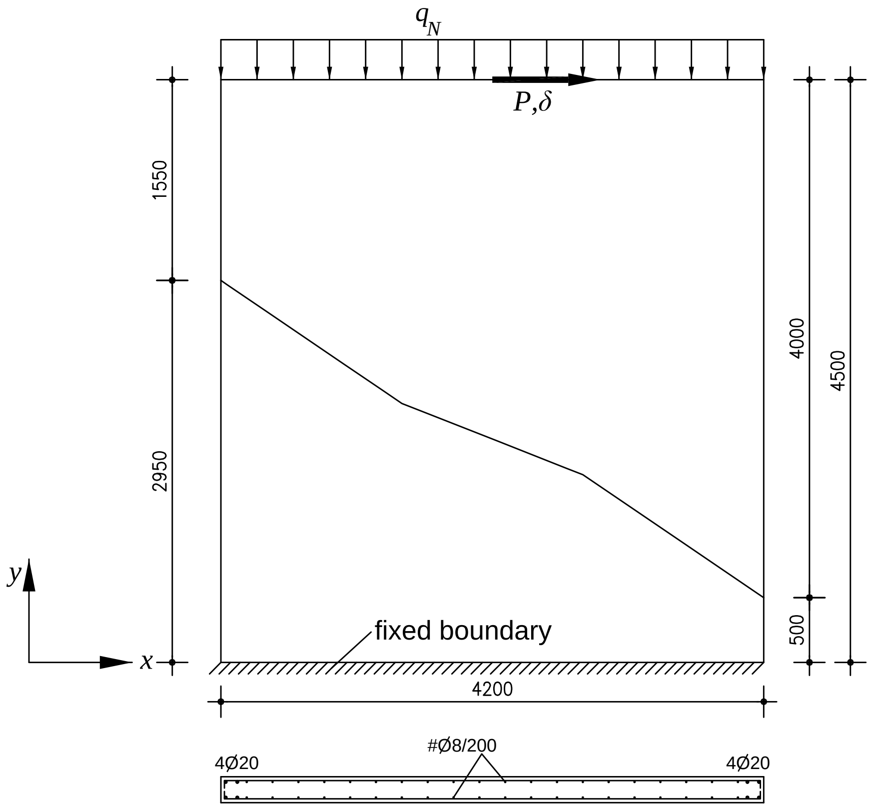

Figure 1: The considered shear wall.

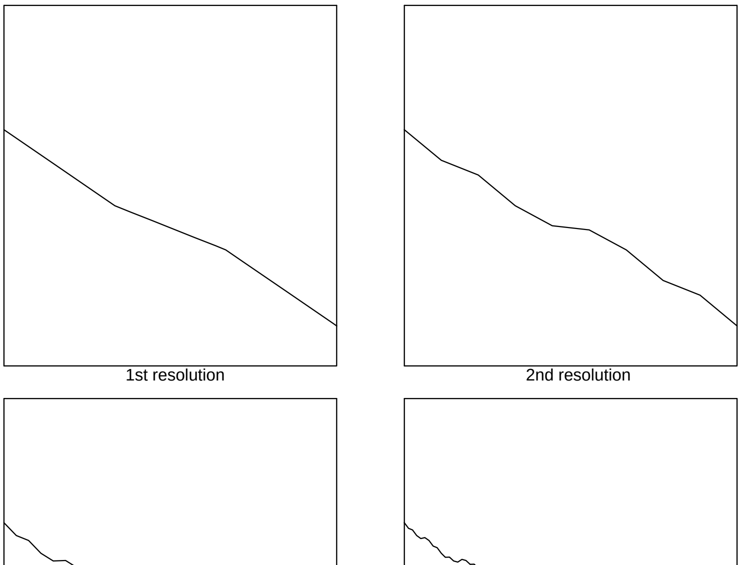

Figure 2: The first four resolutions of the fractal crack.

In Table 1 the characteristics of each resolution are presented. The resolution $\delta^{(n)}$ for each iteration (n) is given in the second column of Table 1. The last column of this table presents the total crack lengths $L^{(n)}$ in m.

Iteration (n)	Resolution $\delta^{(n)}$ (m)	Interface length $L^{(n)}$ (m)
1st	1.404	4.888
2nd	0.468	4.946
3rd	0.156	5.080
4th	0.052	5.373

Table 1: Characteristics of the considered structures

For the modelling of the above problem the finite element method is used. In order to avoid a much more complicated three-dimensional analysis, two-dimensional finite elements were employed, however, special consideration was given to the incorporation of the nonlinearities that govern the response of the wall. More specifically, the mass of the concrete was modelled through quadrilateral and triangular plain stress elements. The finite element discretization density is similar for all the considered problems [19]. This rule ensures that the discretization density will not affect the comparison between the results of the various analyses that were performed.

The modulus of elasticity for the elements representing the mass of concrete was taken equal to $E = 21\text{MPa}$ and the Poisson's coefficient equal to $\nu = 0.16$. The material was assumed to follow the nonlinear law depicted in Fig. 3a. Under compression, the material behaves elastoplastically, until a total strain of 0.004. After this strain value crushing develops in the concrete, leading its strength to zero. A more complicated behaviour is considered under tension. More specifically, after the exhaustion of the tension strength of concrete, a softening branch follows, having a slope $k_s = 10^7\,\text{MPa}$. Progressively the tension strength of concrete is also zeroed. The above uni-directional nonlinear law is complemented by an appropriate yield criterion (Tresca) which takes into account the two-dimensional stress fields that develop in the considered problem. For the simulation of cracking a smeared crack algorithm is used, in which the cracks are evenly distributed over the area of each finite element [20].

The steel rebars were modelled through two-dimensional beam elements, which were connected to the same grid of nodes as the plain stress elements simulating the concrete. At each position, the properties that were given to the steel rebars take into account the reinforcement that exists in the whole depth of the wall. For example, the horizontal and vertical elements that simulate the steel mesh are assigned an area of 100.5 mm^2 that corresponds to the cross-sectional area of two 8mm steel rebars. For simplicity, the edge reinforcements were simulated by a single row of beam elements that have an area of 1256mm^2 (i.e. $4\times314\text{mm}^2$). For the steel rebars, a modulus of elasticity $E = 210\,\text{MPa}$ was assumed. Moreover, the nonlinear laws of Fig. 3b,c were considered for the S220 and S400 steel qualities respectively. These laws exhibit a hardening branch, after the yield stress of the material is attained.

Figure 4 depicts the finite element discretizations for the structures that correspond to the third and fourth iterations of the fractal interface. The grey lines in the finite element meshes correspond to the positions of the steel rebars. The distance between the two facing parts of the interface is only 0.1mm. Special attention was given in the modelling so that the steel rebars retain their initial horizontal and vertical positions, i.e. no eccentricity exists between the corresponding rows of beam finite elements due to the formation of the crack.

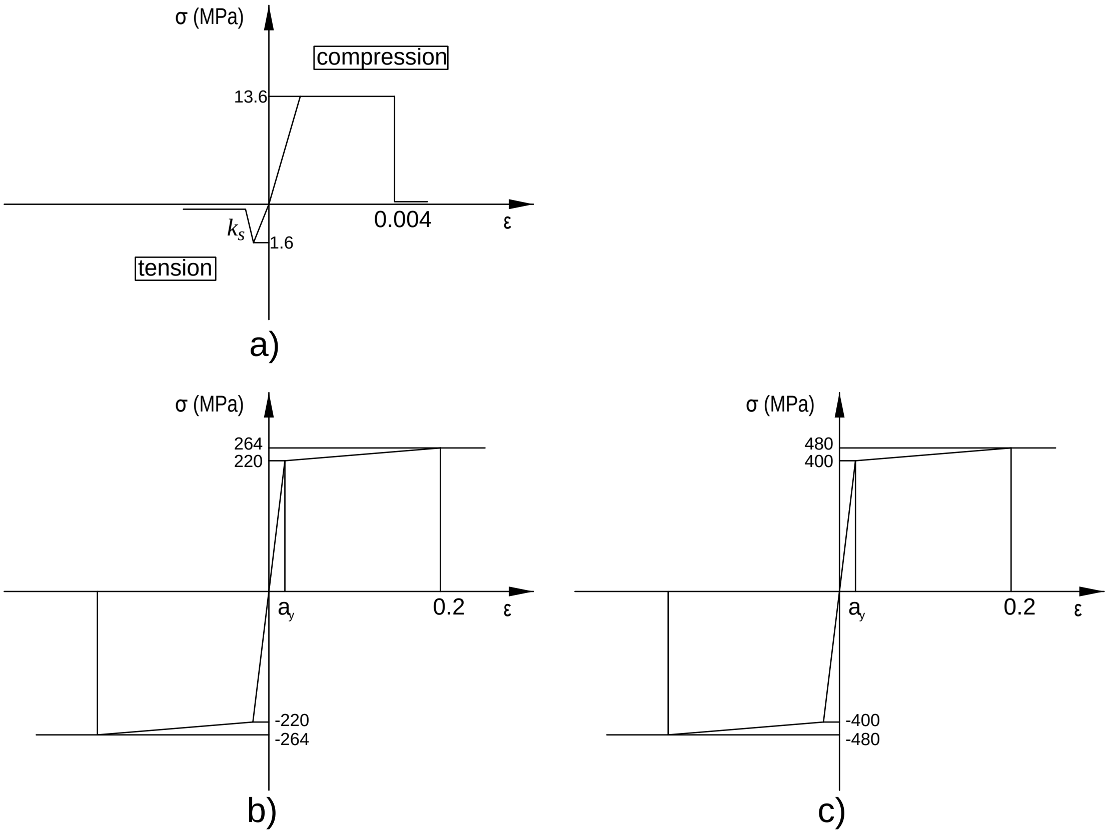

Figure 3: The adopted materials laws a) C16 concrete, b) S220 steel, c) S400 steel.

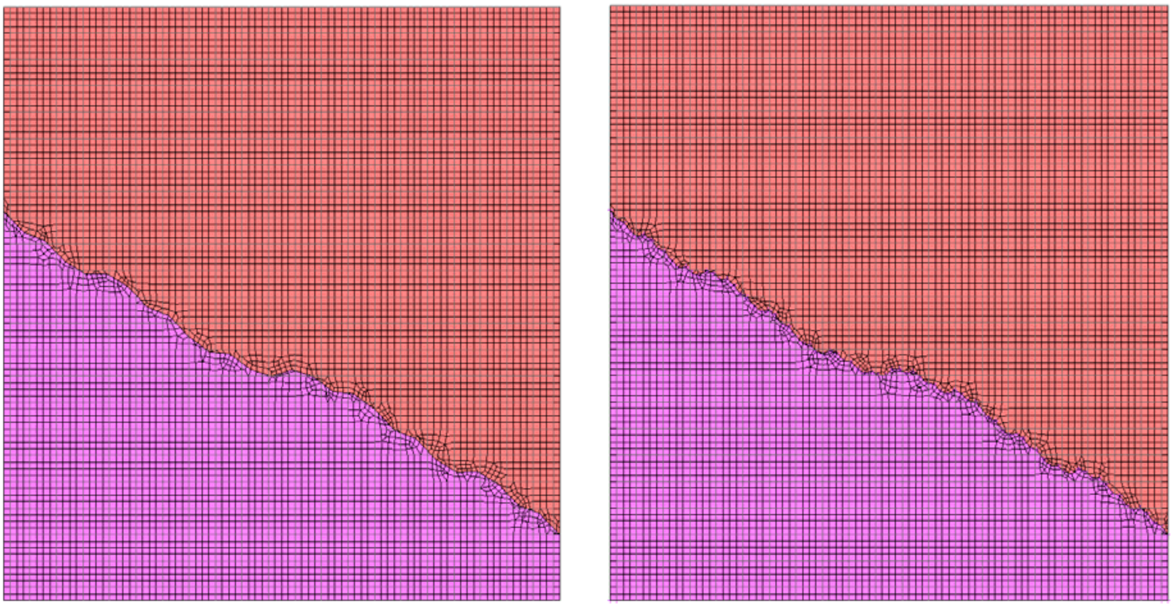

Figure 4: F.E. discretizations for third and fourth approximations of the fractal interface.

In this paper, only the finite element models corresponding to the 3rd and 4th approximations of the fractal crack were considered, because 1st and 2nd approximations don’t have meaning from the engineering point of view.

At the interfaces, unilateral contact and friction conditions were assumed to hold. The Coulomb's friction model was followed with a coefficient equal to 0.6 At each scale, where a classical Euclidean problem is solved, a variational formulation [7] was used in order to describe the contact between the two parts of the crack.

For every value of the vertical loading N, a solution is taken in terms of shear forces and horizontal displacements at the interface, for different values of the resolution of the cracked wall and for the case of the uncracked wall. The aim of this work is to study the behaviour of the shear wall, i.e. the behaviour of the concrete and the forces in the rods, as the vertical loading and the resolution of the interface change.

Two cases are considered:

- In the first case the wall is uncracked.
- In the second case, where a fractal crack F has been developed in the wall, different resolutions are taken into account in order to examine how the resolution of a fractal interface F affects the strength of a reinforced concrete shear wall element.

The solution of the above problems is obtained through the application of the Newton-Raphson iterative method. Due to the highly nonlinear nature of the problem, a very fine load incrementation was used. The maximum value of the horizontal displacement (20mm) was applied in 2000 loading steps, while the total vertical loading was applied in the 1st load step and was assumed as constant in the subsequent steps.

4 EXPERIMENTAL AND NUMERICAL RESULTS

Figure 5 presents the applied horizontal load verse the corresponding displacement ($P-\delta$ curves) for the different values of the vertical loading N. It has to be noticed, starting from the case of the uncracked wall, that the value of the vertical loading plays a significant role. As the value of the vertical loading increases, the capacity of the wall to undertake horizontal loading increases as well. However, for the higher load values (for N=2.000 and 2.500 kN), strength degradations are noticed. As it will be explained later, these degradations have their nature to the exhaustion of the shear strength of concrete. However, after this strength degradation, the resistance of the wall increases again as a result of the transfer of the loading from the concrete to the horizontal steel rebars.

Coming now to the cases of the cracked walls, the beneficial effect of the normal compressive loading is once more verified. This result holds for both the 3rd and the 4th approximations of the fractal crack but for small displacement values only. For larger displacement values, the two variants of the cracked wall behave differently. The 4th approximation appears to have a stable behaviour without strength degradations. However, it is noticed that in the case of the 3rd approximation and for heavy axial loading, significant strength degradation takes place.

The above results can be more easily understood if we compare in the same diagram the curves obtained for the three different structures studied here (uncracked, 3rd iteration, 4th itration) for specific load levels. Figure 6 gives the *P-δ* curves for three cases of axial loading, namely for N=0, N=1500kN and N=2.500 kN. It is noticed that for low values of the compressive axial loading, there is actually no difference between the uncracked and the cracked walls. In all the cases the horizontal loading is easily transferred and no signs of strength degradation are noticed. That means that the wall works mainly in bending and the shear forces are well below the shear strength of the wall. For moderate axial loading values (i.e. for N=1.500 kN), it is noticed that the uncracked wall appears to have greater strength that the cracked variants examined here. It is also noticed that the 4th iteration of the fractal crack leads to greater ultimate strength. This fact can be primarily attributed to the fact that the 4th iteration seems to lead to a greater degree of interlocking between the two parts of the crack.

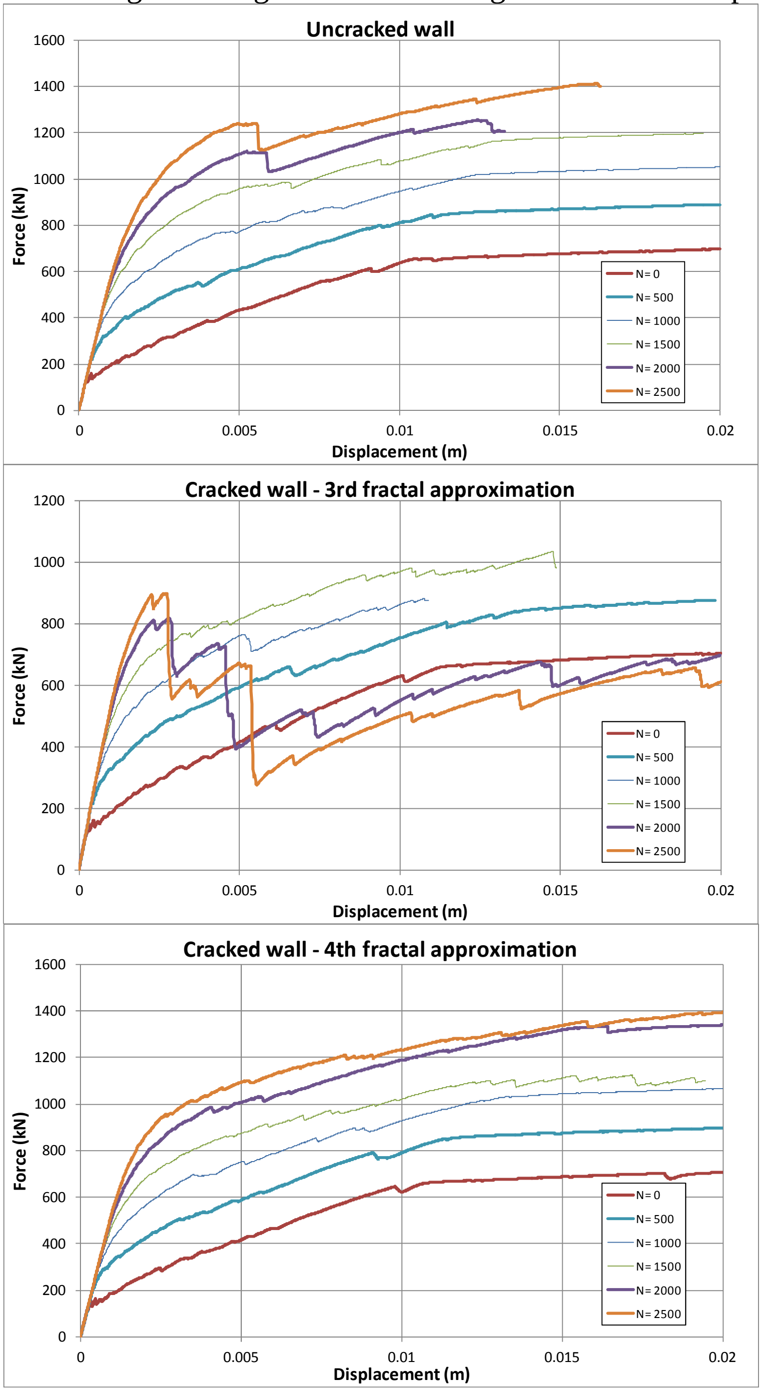

Figure 5: Load-displacement (P-δ) curves for the cases of the uncracked and cracked walls.

However, the most interesting case is that of the heave axial loading (N=2.500 kN). First, it can be noticed that the behavior of the 4th approximation of the fractal crack leads to results that are close enough to those of the uncracked wall. There exist some differences for horizontal displacements in the range of 2-6mm. In this range the uncracked wall exhibit greater resistance. However, for 6mm, the uncracked wall appears strength degradation and after this displacement value the results of the 4th approximation of the fractal crack are again very close to those of the initially uncracked wall.

Significantly different is the case of the 3rd approximation of the fractal crack. It is noticed that although in the first loading steps the results follow closely those of the 4th approximation, after a displacement value of 3mm significant strength degradation appears, having the form of successive vertical branches. The ultimate strength of this wall is significantly lower than the other variants.

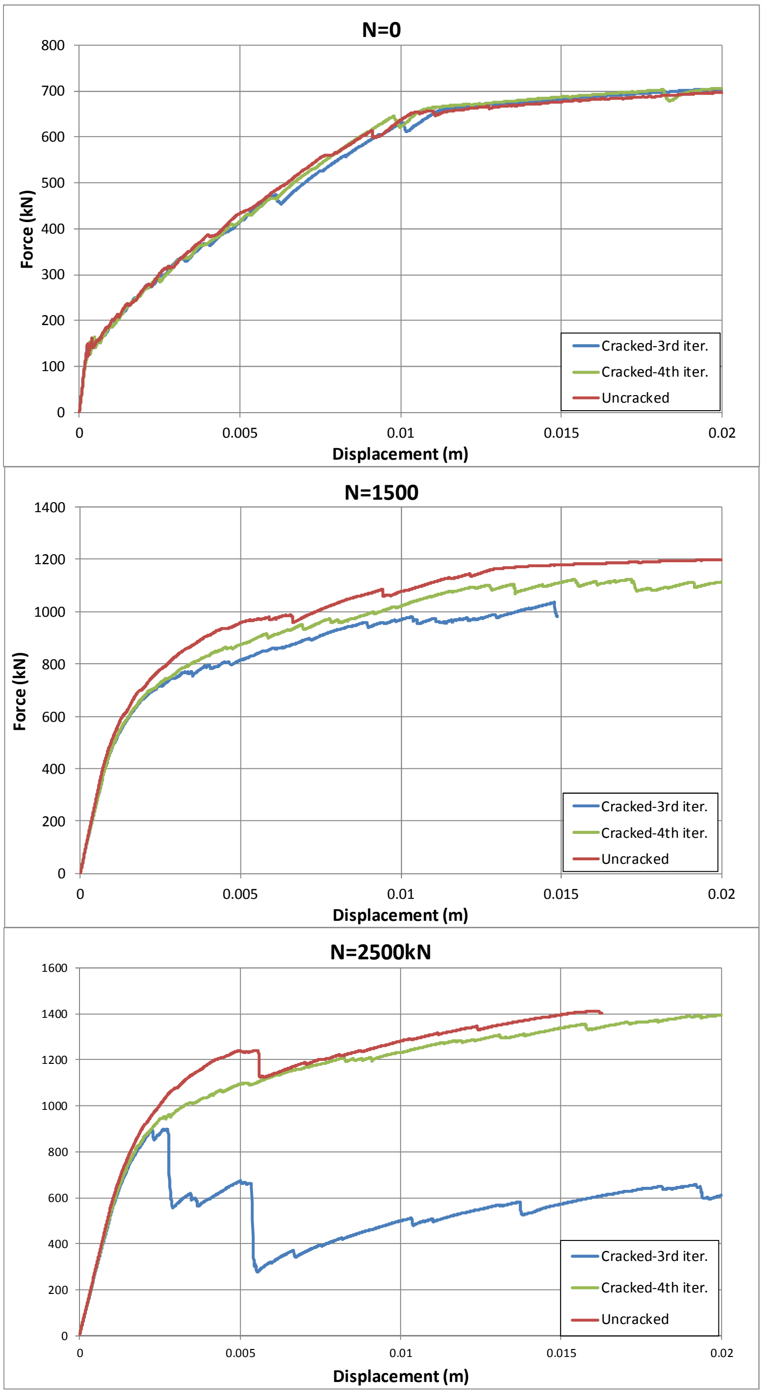

Figure 6: Comparison of the behaviour of the three variants of the examined wall for specific values of the compressive axial loading.

It is interesting to try to explain this significantly different behaviour that appears between the walls corresponding to the 3rd and 4th approximations of the fractal crack. For this reason, all the parameters affecting the behaviour of the wall will be comparatively studied in the sequel.

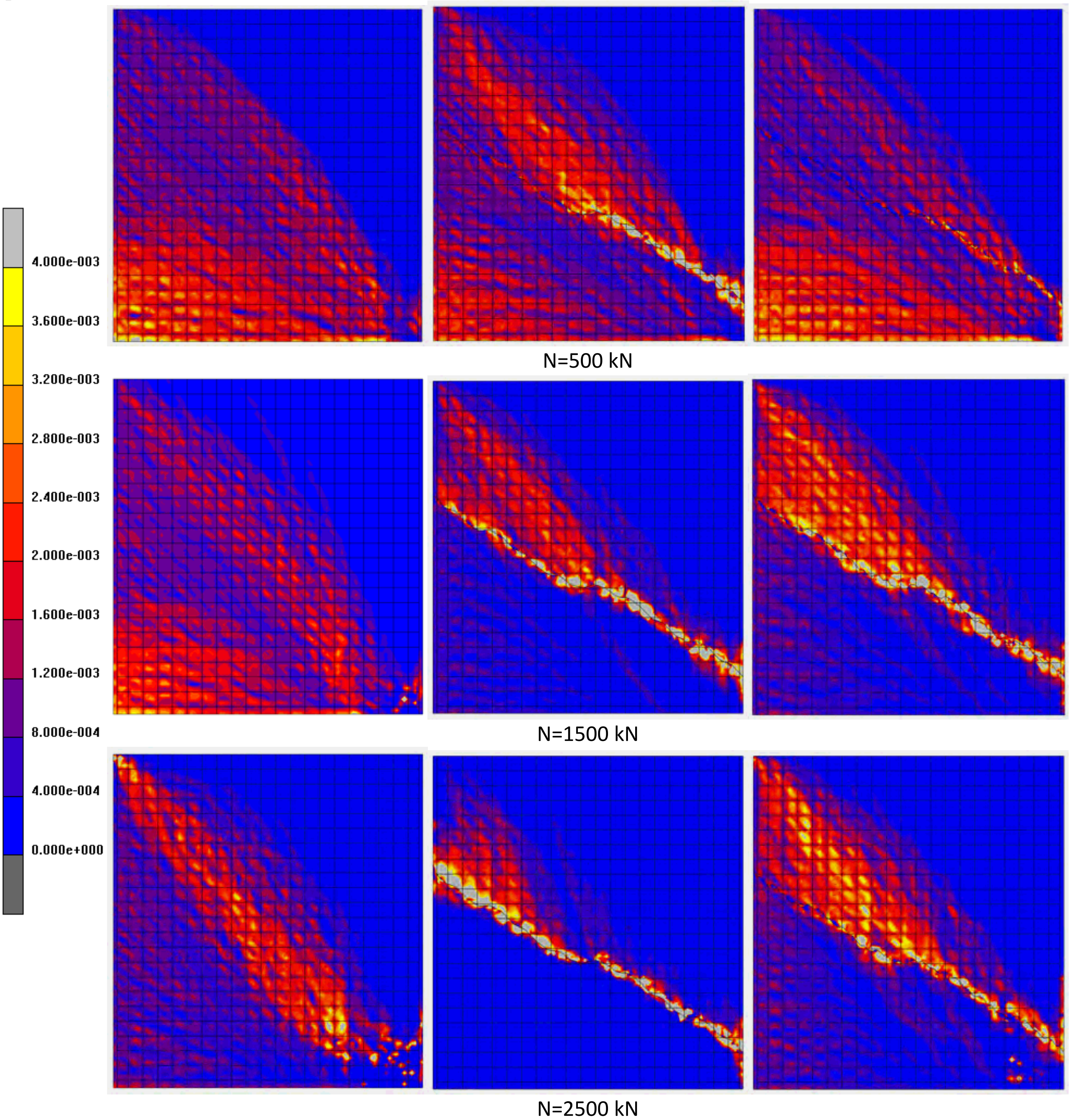

Figure 7: Cracking strains for various values of the vertical loading, for the cases of the uncracked wall (left column) and the cracked walls (3rd approximation- middle column and 4th approximation – right column).

Figure 7 depicts the cracking strains of concrete for specific values of the axial loading. All the depicted results correspond to the end of the analysis, i.e. they have been obtained for an applied horizontal displacement of 20mm. First of all, it can be noticed that for low values of the axial loading, the cracking patterns that have been developed in all the studied walls are rather similar. The larger cracking strain values (yellow and grey colours) have their nature in the bending deformation of the wall. For moderate axial loading, the cracking patterns are quite different. The uncracked wall has again a bending type cracking pattern. The cracked walls seem to behave differently. Both of them exhibit significant cracking in the vicinity of the crack (grey colors). Apart from this, shear type cracking patterns develop at the upper parts of the walls.

The above results alone cannot explain the significantly different responses that the two cracked variants of the wall exhibit. For this reason, the plastic strains of concrete are examined in the following. Figure 8 depicts the plastic concrete strains for the three different variants of the wall and for specific values of axial loading. The upper value of the presented scale corresponds actually to the crushing limit (grey values). Therefore, it can be considered that the concrete stresses in these areas are actually zero. For the uncracked wall (left column of Fig. 8) it can be noticed that the more heavily deformed region is the lower right corner. It is clear that in this case the wall exhibits a typical bending type deformation behaviour (cracking at the lower left region, crushing at the lower right corner).

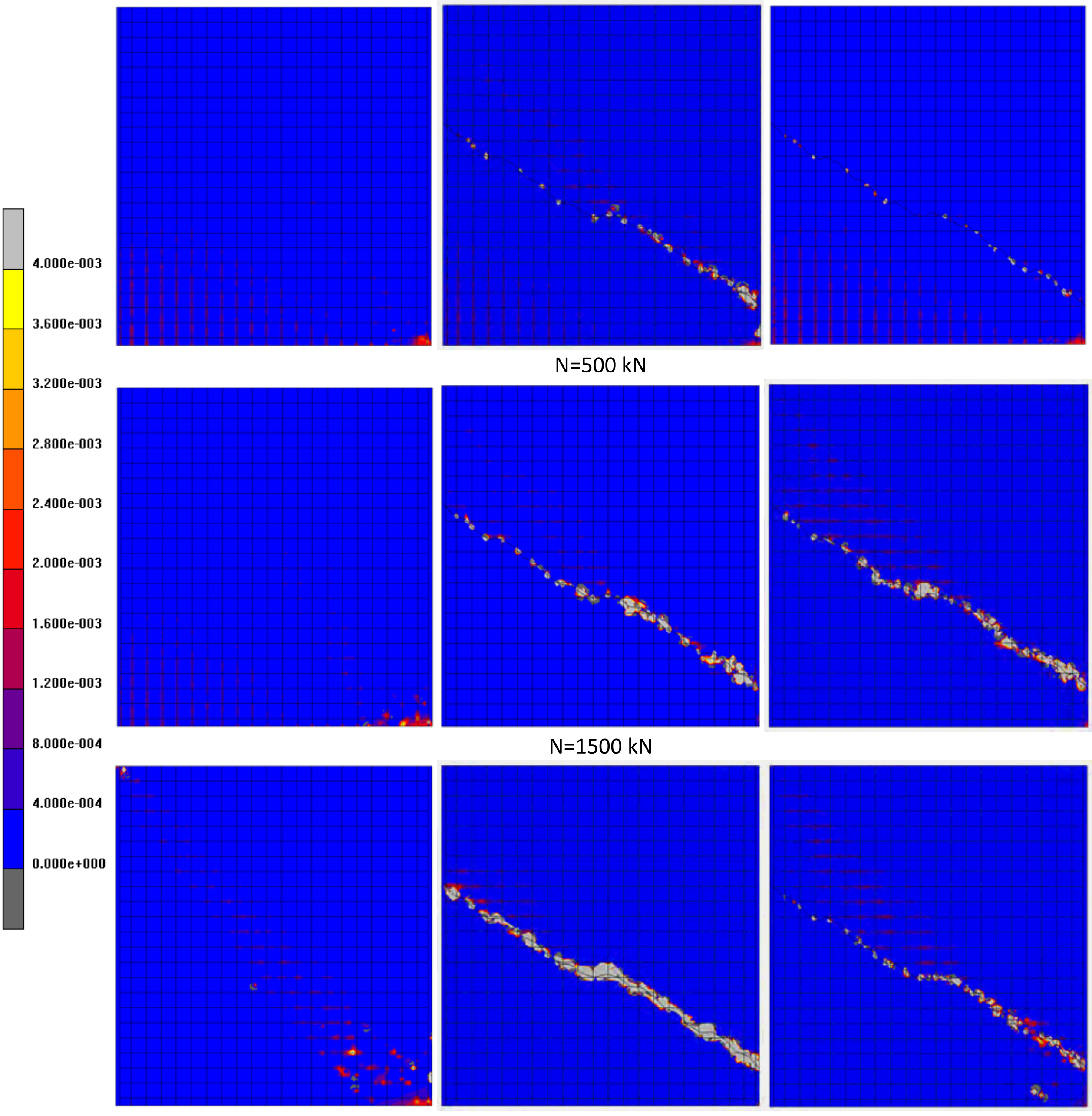

N=500 kN

N=1500 kN

N=2000 kN

Figure 8: Plastic strains for various values of the vertical loading, for the cases of the uncracked wall (left column) and the cracked walls (3rd approximation- middle column and 4th approximation – right column)

On the other hand, the cracked walls seem to deform significantly in the vicinity of the crack. This phenomenon is more pronounced in the case of the 3rd approximation of the fractal wall. Especially in the case of heavy axial loading, it can be noticed that the vicinity of the crack is in crushed state, i.e. in this region the forces are transmitted solely by the steel mesh (the concrete has no ability to transfer any kind of forces). For the case of the 4th approximation, this phenomenon is rather limited, i.e. it can be concluded that in this case the crack retains partial its ability to transfer shear and compressive forces through the contact and friction phenomena that develop in the interface and through the mechanical interlocking that occurs between the two interface parts.

It is now interesting to examine the deformations that have occurred at the steel mesh. Figure 9 displays the steel mesh for the three variants of the considered wall and for different values of the vertical loading. The presented deformations correspond to the last load step and have been magnified by a factor of 10 so that the differences between the examined cases visible.

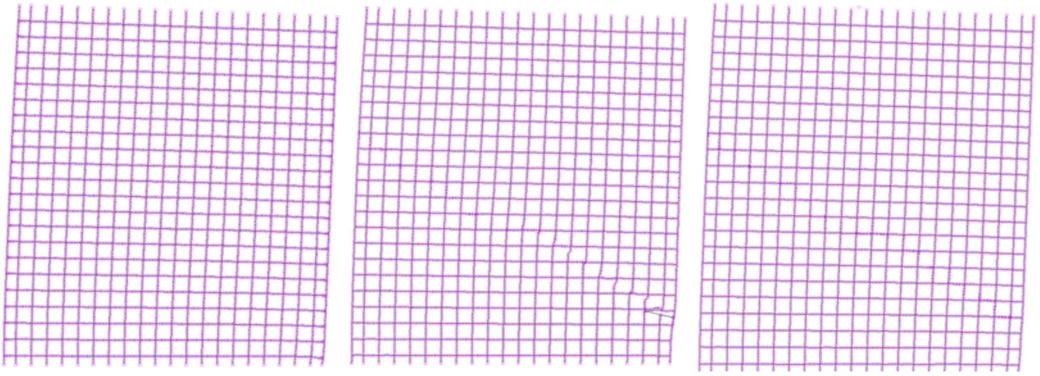

N=500 kN

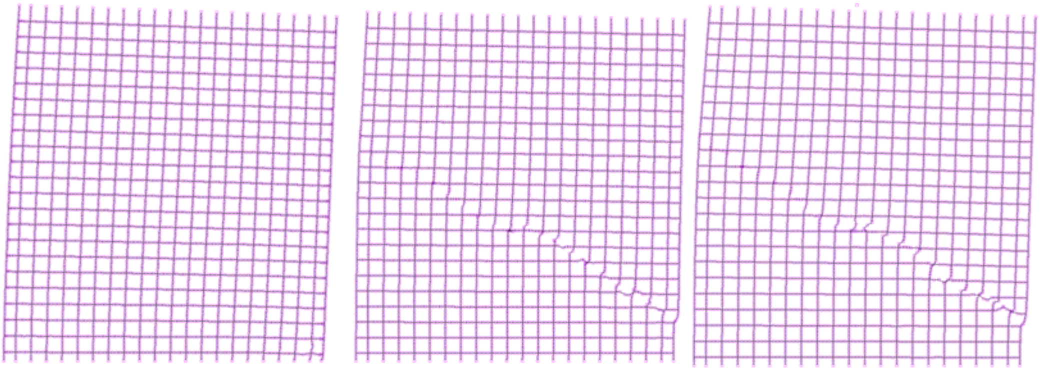

N=1500 kN

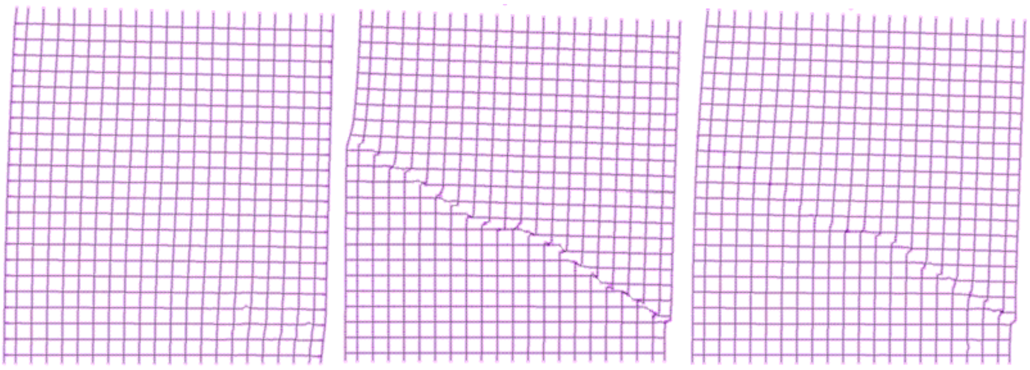

N=2500 kN

Figure 9: Deformation of the steel mesh for various values of the vertical loading, for the cases of the uncracked wall (left column) and the cracked walls (3rd approximation- middle column and 4th approximation – right column).

For low vertical loading values, the deformations of the steel meshes are actually very similar. However, for moderate values of the vertical loading (N=1.000kN) there exist some differences. The steel meshes of the cracked walls seem to be distorted in the vicinity of the right part of the formed crack. In this region the vertical rebars above and below the crack present an offset which can be attributed to the inability of the interface to transfer shear forces. For the case of heavy vertical loading, the situation is different again. The wall corresponding to the 4th resolution of the fractal crack has a deformation similar to that of the case of the moderate loading. However, the steel mesh of the wall corresponding to the 3rd resolution of the fractal crack exhibits significant deformations all along the crack. All the upper vertical rebars present a significant horizontal offset with respect to the lower ones. This horizontal offset is obvious even in the leftmost part of the wall. Moreover, the horizontal rebars of the upper part present a vertical offset with respect to the ones of the lower part. This deformation pattern verifies the findings that were noticed in Fig. 8 concerning the excessive strains in the vicinity of the crack (which had values well above the crushing strain limit). This deformation type of the steel mesh has its nature to the inability of the concrete to transfer any loading in this case.

In the sequel, the difference in the response between the 3rd and the 4th approximations of the fractal crack for the case of the heavy vertical loading will be explained. First of all, it has to be noticed that the higher vertical loading leads also to higher values of the horizontal loading, as it has been explained for the case of the uncracked wall. These increased horizontal forces have to be transferred from the upper part of the cracked wall to its lower part. In this respect, three mechanisms develop in order to facilitate the horizontal load transfer:

- Exploitation of the tensile strength of the horizontal rebars;
- Development of friction on the part of the crack where contact forces occur;
- Mechanical interlock between the two faces of the crack.

The first two mechanisms are almost similar in both cracked walls. However, it is obvious from Fig. 6 that the higher resolution approximations of the fractal crack have improved capacity to transfer forces through the mechanical interlock mechanism. To the authors’ opinion, this is the most important reason for the difference in the response between the walls corresponding to the 3rd and the 4th approximation of the fractal crack. For lower vertical load values the differences are rather limited, however, as the vertical loading increases, the response is completely different because the increased vertical forces are combined with the increased horizontal forces and “destroy” completely the vicinity of the interface.

Figures 10,11 and 12 display the forces that develop at the horizontal and vertical rebars of the steel mesh for the three variants of the wall examined here (uncracked, 3rd approximation, 4th approximation respectively) for displacements of 5 and 20mm. The left column of each figure corresponds to lower values of the axial loading (N=500kN), the middle column to moderate loading values (N=1500 kN) and the right column to heavy axial loading (N=2.500 kN).

For the case of the uncracked wall (Fig. 10) it is noticed that in the early horizontal loading steps (δ=5mm), only the vertical rebars are significantly loaded. The rebars in the left side of the wall have tensile forces while the rebars in the right side develop compressive forces, as a result of the bending of the wall. For δ=20mm, after the development of cracking in various parts of the initially uncracked wall, the horizontal rebars are also stressed, mainly in the areas where the corresponding cracks have reduced or zeroed the ability of concrete to transfer shear forces.

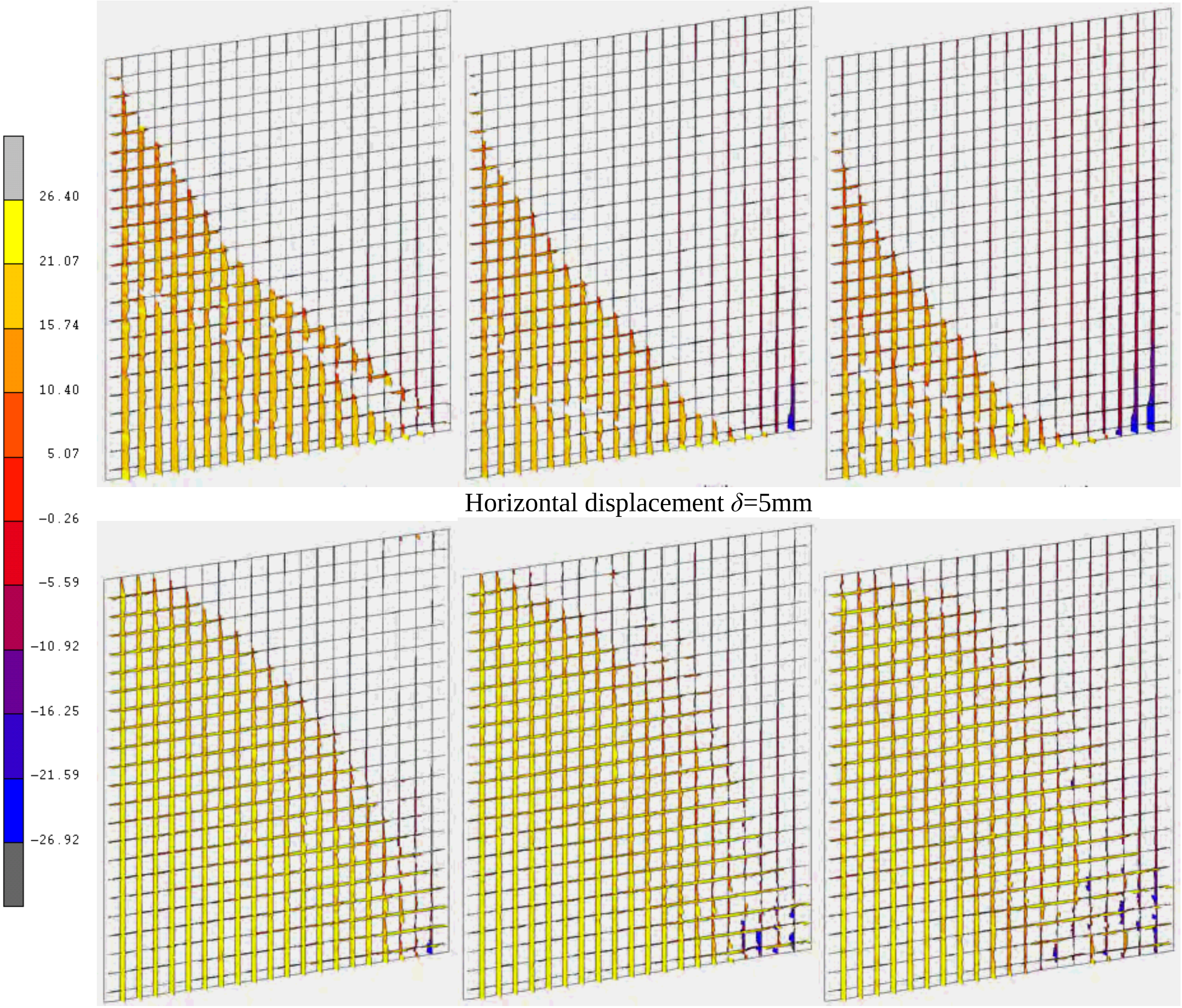

Horizontal displacement δ=5mm

Horizontal displacement δ=20mm

Figure 10: Forces developed in the steel mesh for various values of the vertical loading for the uncracked wall (left column: N=500 kN, middle column: N=1500 kN, right column: N=2500 kN).

For the case of the 3rd approximation of the crack, it is noticed that the vertical rebars are stressed only for small axial loading values. For moderate and heavy axial loading, the vertical rebars are only partial stressed. It deserves to be noticed that the rebar stresses are negative in the vicinity of the crack, a fact that verifies that the concrete is unable to transfer even compressive loading. Moreover, it is noticed that the rebars of the right side of the wall do not develop compressive stresses any more, due to the fact that the magnitude of bending that develops in this case is significantly smaller than that in the case of the uncracked wall. The horizontal rebars are stressed only in specific areas, near the crack and in the regions where cracking strains have been developed. In any case, a closer look in the forces that have been developed in the rebars verifies the significantly decreased bending capacity of the specific wall.

The situation is rather different for the case of the 4th approximation of the fractal crack. The corresponding rebar forces are depicted in Fig. 12. It can easily be verified that for small values of the axial loading, the picture of the forces of the vertical rebars is quite similar to that of the uncracked wall. The same holds also for the forces of the horizontal rebars. For moderate axial load values, the forces of the vertical rebars appear discontinuities. At the right part of the crack it can be noticed that in some rebars the forces are compressive, indicating again the partial inability of the concrete in this region to transfer compressive loading. The horizontal rebars are mainly stressed in the upper part of the cracked wall and in the vicinity of the crack. Notice that this result is absolutely compatible with the remarks given for the cracked areas in Fig. 7.

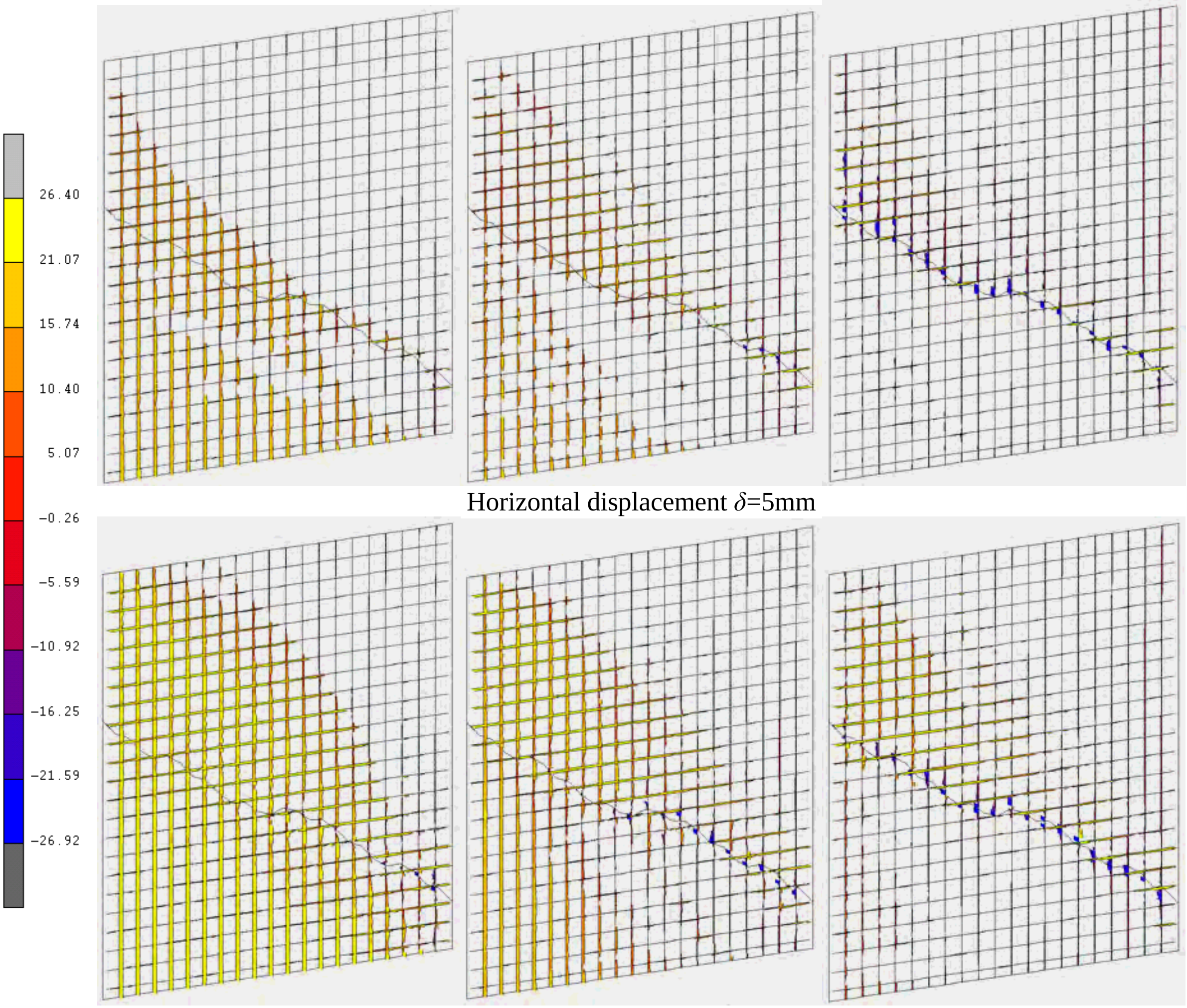

Horizontal displacement δ=5mm

Horizontal displacement δ=20mm

Figure 11: Forces developed in the steel mesh for various values of the vertical loading for the 3rd approximation (left column: N=500 kN, middle column: N=1500 kN, right column: N=2500 kN).

5 CONCLUSIONS

In the paper, the finite element analysis of a typical wall element was presented assuming that a certain crack has been developed as a result of an earthquake action. The crack was modelled following tools from the theory of fractals. Two different resolutions of the fractal curve were considered and their results were compared to those of the initially uncracked wall. The main finding of the paper is that the cracked wall still has the capacity to sustain monotonic horizontal loading. For small axial loading values, this capacity is similar to that of the initially uncracked wall. However, for larger axial loading values, the demands increase. In this case, it seems that a more accurate modelling of the fractal crack (i.e. considering higher values of the resolution) leads to better result. Using lower resolution values, the mechanical interlock between the two faces of the crack is rather limited, leading the concrete in vicinity of the crack to overstressing and gradually to a complete loss of its capacity to sustain any kind of forces. In this case the bending capacity of the wall is significantly limited with respect to that of the uncracked concrete.

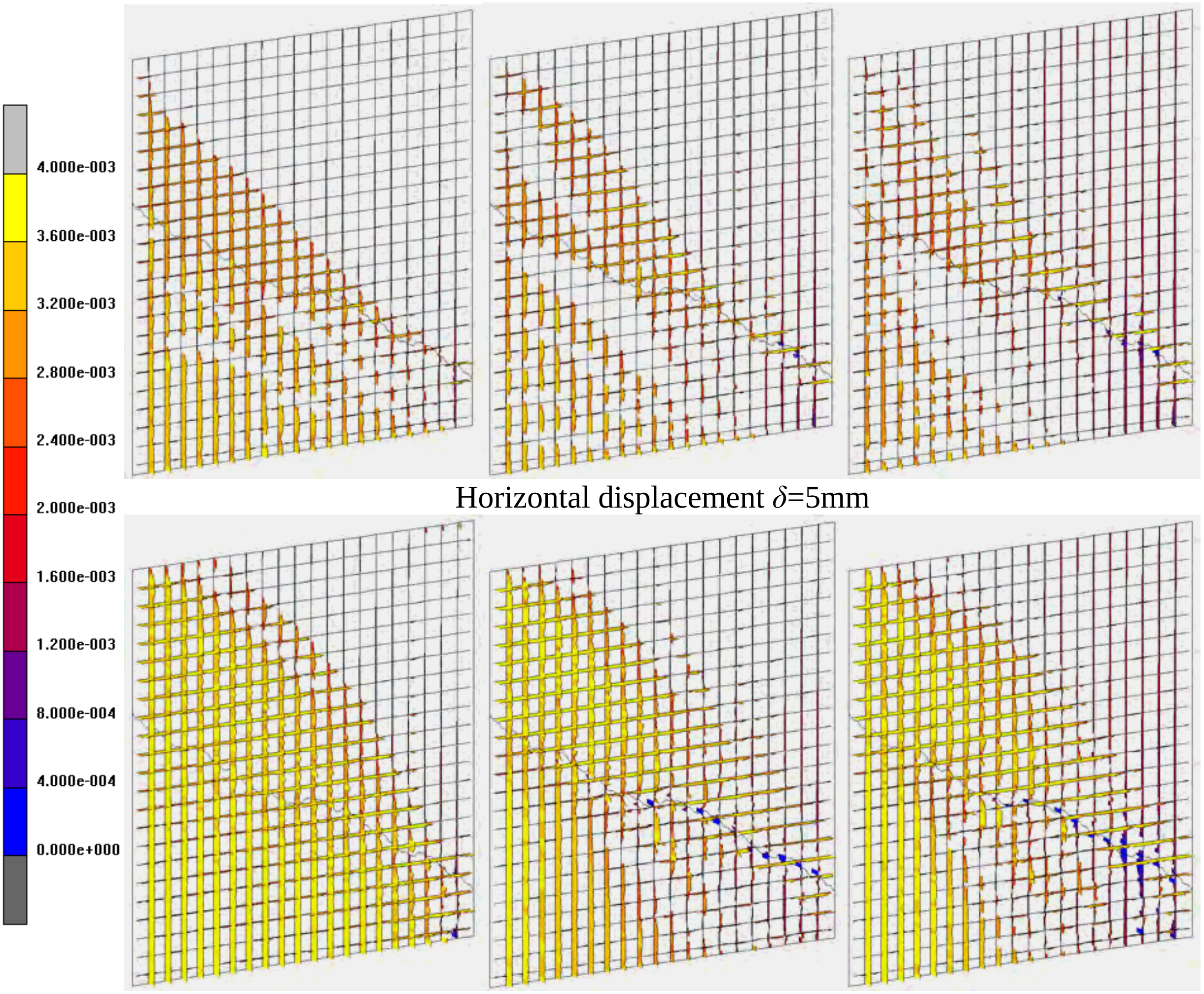

Horizontal displacement δ=5mm

Horizontal displacement δ=20mm

Figure 12: Forces developed in the steel mesh for various values of the vertical loading for the 4th approximation (left column: N=500 kN, middle column: N=1500 kN, right column: N=2500 kN).

REFERENCES

[1] B. Mandelbrot, D. Passoja, A. Paullay, Fractal character of fractured surfaces of metals. *Nature*, **308**, 721-723, 1984.

[2] V.C.B. Saouma, C. Barton, N. Gamaleldin, Fractal characterization of fracture surfaces in concrete. *Eng. Fract. Mech*., **35**, 47-53, 1990.

[3] F.M. Borodich, A.B. Mosolov, Fractal roufhness in contact problems. *Journal of Applied Mathematics and Mechanics*, **56**, 681-690, 1992.

[4] A. Majumdar, C.L. Tien, Fractal characterization and simulation of roufh surfaces, *Wear*, **136**, 313-327, 1990.

[5] Borri-Brunetto, M., Carpinteri, A., and Chiaia, B. (1999), "Scaling phenomena due to fractal contact in concrete and rock fractures", *Int. J. Fracture,* **95**, 221-238, 1999.

[6] O. K. Panagouli, E.S. Mistakidis, Dependence of contact area on the resolution of fractal interfaces in elastic and inelastic problems, *Engineering Computations*, 2010 (in press).

[7] E. Mistakidis and G. Stavroulakis, Nonconvex optimization in Mechanics. Algorithms, heuristic and engineering applications by the FEM, Kluwer, Boston, 1997.

[8] G. Mourot, S. Morel, E. Bouchaud and G. Valentin, "Anomalous scaling of mortar fracture surfaces, *Phys Rev E*, **71**, 2005.

[9] A. Carpinteri, B. Chiaia, S. Invernizzi, Three-dimensional fractal analysis of concrete fracture at the meso-level*, Theor Appl Fract Mech*, **31**, 163-172, 1999.

[10] B. Mandelbrot, The Fractal Geometry of Nature, W.H. Freemann & Company, New York, 1982.

[11] Måloy, K.J., Hansen A., Hinrichsen E.L. and Eoux S., "Experimental measurements of the roughness of brittle cracks", *Phys Rev Lett*, **68**, 213-215, 1992.

[12] A. Majumdar, and B. Buhushan, "Role of fractal geometry in roughness characterization and contact mechanics of surfaces", *Trans ASME J. Tribology*, **112**, 205-216, 1990.

[13] P.D. Panagiotopoulos and O.K. Panagouli, "Fractal geometry in contact mechanics and numerical applications", in Carpintieri, A. and Mainardi, F. (Ed.), *CISM-Book on Scaling, Fractals and Fractional Calculus in Continum Mechanics*, Springer Verlag, 109-171, 1997.

[14] F.M. Borodich and D.A. Onishchenko, "Similarity and fractality in the modeling of roufhness by a multilevel profile with hierarchical structure" *Solids and Structures*, **36**(17), 2585-2612.

[15] E.S. Mistakidis and O.K. Panagouli, (2002), "Strength evalution of retrofit shear wall elements with interfaces of fractal geometry", *Engineering Structures*, **24**, 649-659, 2002.

[16] Mistakidis, E.S. and Panagouli, O.K., "Friction evolution as a result of roughness in fractal interfaces", *Engineering Computations*, **20(**1), 40-57, 2003.

[17] Ching-Ju Chen, Tzong-Yeang Lee, Y. M. Huang, and Fu-Jou Lai, "Extraction of characteristic points and its fractal reconstruction for terrain profile data",*Chaos, Solitons& Fractals*, **39,** 1732-1743, 2009.

[18] M. Barnsley, Fractals Everywhere, Academic Press, Boston- New York, 1988.

[19] Hu, Guang-Di, P.D. Panagiotopoulos, O.K. Panagouli, O. Scherf and P. Wriggers, "Adaptive finite element analysis of fractal interfaces in contact problems", *Comp. Methods Appl. Mech. Engrg*., **182,** 17-37, 2000.

[20] R. deBorst, J. Remmers, A. Needleman, and M-A Abellan, "Discrete vs smeared crack models for concrete fracture: bridging the gap", *Int J Numer Anal Met*, **28**(7-8), 583-607, 2004.

COMPDYN 2011
III ECCOMAS Thematic Conference on
Computational Methods in Structural Dynamics and Earthquake Engineering
M. Papadrakakis, M. Fragiadakis, V. Plevris (eds.)
Corfu, Greece, 25–28 May 2011

GRAVITY LOAD-DESIGNED CONCEALED WIDE BEAM-NARROW COLUMN CONNECTIONS: EXPERIMENTAL ASSESSMENT OF SEISMIC RESPONSE

Amer M. Elsouri[1*], **Mohamed H. Harajli**[2]

[1]American University of Beirut, Beirut-Lebanon
e-mail: ame58@aub.edu.lb

[2]American University of Beirut, Beirut-Lebanon
e-mail: mharajli@aub.edu.lb

Keywords: Concealed beam-column connection, connection, cyclic load, joints, seismic.

Abstract. *Reinforced concrete (RC) wide concealed beam-narrow column connections represent the predominant structural system of building structures in Lebanon and the region. For a long time, engineers have paid little attention to the seismic design of these connections, despite their critical role in transferring internal forces when subjected to lateral earthquake load. A two-part experimental study is carried out for evaluating the seismic behaviour of these connections. The first part concentrates on the seismic performance of the connections when designed and detailed for gravity loads (as built) in accordance with local design and construction practices, while the second part focus on the seismic behaviour of the same connections when the reinforcement is detailed more properly against earthquake loads. This paper presents the results of two as built full-scale concealed beam-narrow column connections tested in the first part of the investigation. The connections experienced shear failure within the joint core at relatively small drift ratios varying between 1.5% and 2.0%, and before yielding of the beam or column reinforcement. At drift ratios of about 4.0%, corresponding to drift demands of building structures in regions of high seismic hazard, the connections experienced excessive and un-reparable damage within the joint core. The findings of this first part of the investigation guided the second part for introducing more adequate reinforcement detailing for improving the seismic performance of such type of connections.*

1 INTRODUCTION

The predominant building structural system in Lebanon and neighbouring countries is composed of a monolithic flexible ribbed (joist) one-way slab supported on wide concealed (shallow) beams. The beams frame into narrow columns having section aspect ratio between two to four so as to be merged with the infill masonry block walls. The long side of the column could be either parallel or normal to the axis of the beam. Being shallow or concealed the beams have to be quite wide for resisting the shear forces and bending moments produced by the applied loads. The corresponding structural system offers several advantages over the conventional slab-drop beam system in that the concealed beams and narrow columns are preferred by architects and interior designers as they are less obstructing and provide more flexible space. Also, concealed beams (having the same depth as the slab) lead to a more economical formwork, they minimize story heights, and, being wide, they reduce reinforcing steel congestions.

Unfortunately, despite being a region of moderate to high seismic hazard, [1, 2], the majority of building structures in this part of the world, particularly those between 5 and 12 stories in height, are designed with no regards to the seismic activities in the region. Accordingly, the concealed beam–narrow column connections, which constitute an important part of the building structural system, are designed to resist gravity load only. That is, the columns in these connections are designed to resist pure axial compression, with little or no attention to the moment transfer between the floor beams and the columns, and at each floor level, the column reinforcement is spliced with the reinforcement extending from the column below and tied with minimum ties required for gravity load design only. Also, the concealed beams in these connections are designed to resist flexure induced by gravity loads, where the beam positive (bottom) reinforcement on either side of the connection is terminated within a very short length inside the joint core or beyond the beam-column interface section. Furthermore, the core of these joints is constructed with no confinement reinforcement usually required in seismic design.

Little research has been conducted on shallow or wide beam - narrow column connections, [3, 4]. Consequently, most design codes place restrictions on the use of wide beam framing systems in seismic regions because there are insufficient information about their behaviour under the effects of earthquake loadings. A limited number of studies have been carried out on wide shallow beam-column connections, [5, 6, 7, 8], but most of these studies have concentrated on connections that are already designed for earthquake loads and which to a large extent satisfy the dimensions limitations set forth in recognized codes of practice. Consequently the experimental observations and conclusions reported in these studies may not be applicable to the connections under investigation.

A two-part experimental research program is being carried out at the American University of Beirut for evaluating the seismic response of concealed wide beam-narrow column connections. The first part deals with joints that were designed and constructed for gravity load (as built) in accordance with local design and construction practices. The second part, the testing of which is still underway, focus on the seismic behaviour of the same connections when detailed more properly for lateral earthquake loads. In the first part of the investigation, two types of as built beam-column sub-assemblages, representing local construction practices, were tested under lateral earthquake loads. One type in which the long dimension of the narrow column is normal to the direction of lateral load (or beam axis), while the second type is when the long dimension of the column is oriented parallel to the direction of lateral load (or beam axis). This paper presents the experimental results of the first type.

2 EXPERIMENTAL PROGRAM

The dimensions and reinforcement details of two joint specimens, one interior (IJ-F2) and one exterior (EJ-F2), tested in this investigation, are provided in Fig. 1 and are summarized for convenience in Table 1. The connections are composed of 800 mm wide by 250 mm deep beams framing into 700 mm wide by 250 mm deep column for Specimen IJ-F2 and 650 mm wide by 200 mm deep column for Specimen EJ-F2. The connections represent the frame of actual building structures that were designed for gravity load and detailed in accordance with local construction practices.

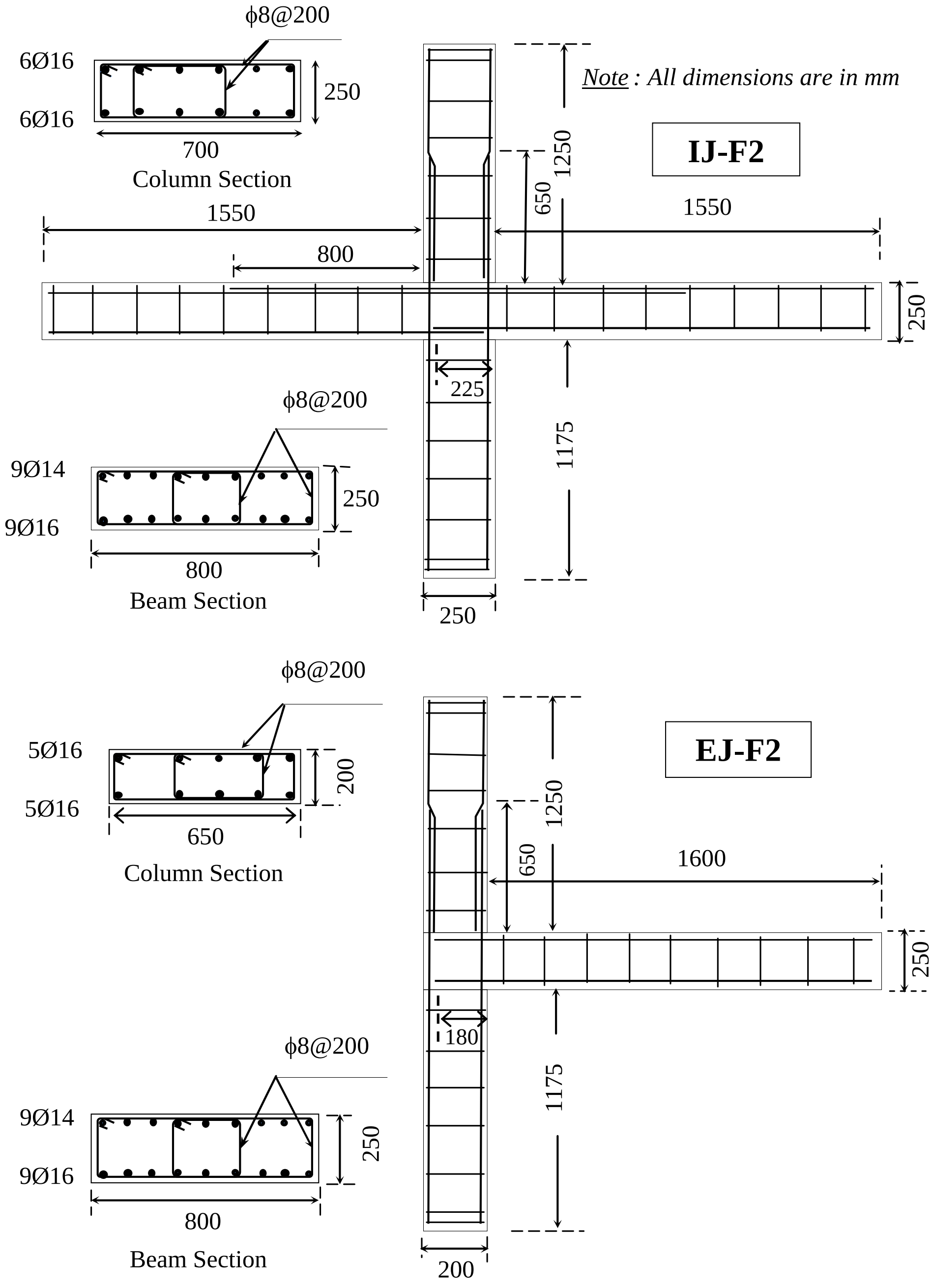

Figure 1: Dimensions and reinforcement details of the specimens

Joint Component	Dimension and steel reinforcement	**IJ-F2**	**EJ-F2**
Column	Size ($b_c x h_c$) mm	700x250	650x200
	Reinforcement & Reinforcement ratio (%)	12ϕ16 (1.37%)	10ϕ16 (1.53%)
	Transverse reinforcement	4 legs ϕ8@200	4legs ϕ8@200
Beam	Size($b_w x h_b$) mm	800x250	800x250
	Top reinforcement & Reinforcement ratio	2x9ϕ14 (1.65%)	9ϕ14 (0.83%)
	Bottom reinforcement & Reinforcement ratio (%)	9ϕ16 (1.08%)	9ϕ16 (1.08%)
	Transverse reinforcement	4 legs ϕ8@200	4 legs ϕ8@200
Joint	Shear reinforcement	None	None

$b = \sec tion\ \ width, h = \sec tion\ \ depth$

Table 1: Dimensions and reinforcement of the joint specimens

Some of the specific reinforcement details that are pertinent to local construction practices include: (i) the lap splice length (of 650 mm) at which the column reinforcement is spliced above the floor level; (ii) the embedment length of the beam bottom reinforcement inside the joint core of 225 mm for the interior and 180 mm for the exterior joint, respectively; (iii) the distance at which the beam top reinforcement is extended on either side of the interior connection beyond the beam-column interface (of 800 mm); and (iv) the anchorage length (of 180 mm) of the beam top and bottom reinforcement inside the exterior connection core beyond the beam-column interface section.

Commercially available Grade 60 steel bars (design yield strength of 415 MPa) having 14 mm and 16 mm diameter were used as the main beam and column longitudinal reinforcement. The measured yield strengths of the steel bars were 627 MPa for the 14 mm and 545 MPa for the 16 mm bars, respectively. The transverse steel reinforcement in both the beams and the columns consisted of plain 8 mm diameter bars having yield strength of 284 MPa.

Both specimens were cast using one batch of Ready Mix concrete. The concrete mix was prepared using Portland cement type I, coarse aggregate with maximum aggregate size of 19 mm and natural sand. The mix was designed for producing a target 28-day cylindrical concrete compressive strength of 20 MPa. The actual compressive strength, measured using standard 150 x 300 mm cylinders, was 21.0 MPa.

2.1 Testing setup and measurements

A schematic view of the test setup is given in Fig. 2. Each connection sub-assemblage was supported on steel fixtures to simulate a statically determinate structure with hinge points to represent points of inflection for the actual building structure when subjected to lateral loads. A 500 kN capacity hydraulic actuator with a maximum stroke of ±127 mm in tension and compression was used to generate cyclic displacements. Axial force was applied at the top of the column using a hydraulic jack. The jack force was transmitted to the column through four steel rods tied to steel plates at the top and bottom of the column. The magnitude of the column axial force was approximately $0.1 f'_c A_g$ for Specimen IJ-F2 and $0.15 f'_c A_g$ for Specimen EJ-F2 where A_g is the gross area of the column section. The loading history for all specimens was composed of a sequence of displacement-controlled cycles as shown in Fig. 3, given in *percent* of story drift or drift ratio *DR*. The drift ratio *DR* is expressed as $DR, \% = \frac{\Delta_\ell}{h_o} x100$ where Δ_ℓ is the lateral drift at the point where the actuator load is applied, and h_o is the story height or height of the column (measured from the point where the lateral load is applied to the bottom pin support of the column) which is equal to 2.8 m for both specimens. The loading history is composed of two cycles at each drift ratio which varied between 0.5% and 4.5%. Notice that while a maximum drift ratio of 4.5% is considered as a satisfactory story drift in regions of high seismic hazard, the stroke limit of ±127 mm of the hydraulic actuator used to apply the lateral load and the size of the specimens (column or story height) did not allow symmetrical drift history beyond 4.5%. Nevertheless, specimen IJ-F2 was tested beyond 4.5% using two stages of applied load: in the first stage (Stage 1), the specimen was subjected to cyclic displacements up to a maximum drift ratio of 4.5% (lateral drift of ±127 mm) in accordance with loading history of Fig. 3. In the second stage (Stage 2), the specimen was subjected to half-cycle displacement protocol ranging between a drift ratio of 5.0% (lateral drift of 140 mm) and a drift ratio of 8.5% (lateral drift of 240 mm). This was achieved by readjusting (retracting) the position of the actuator for utilizing its full stroke capacity in one direction.

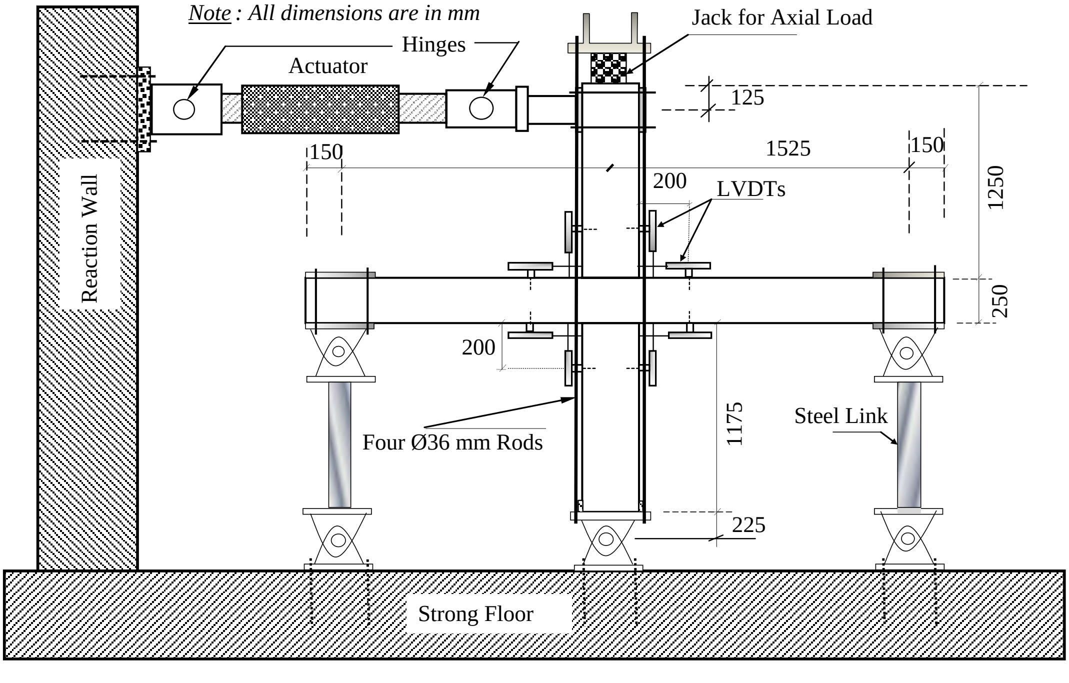

Fig. 2: Test setup

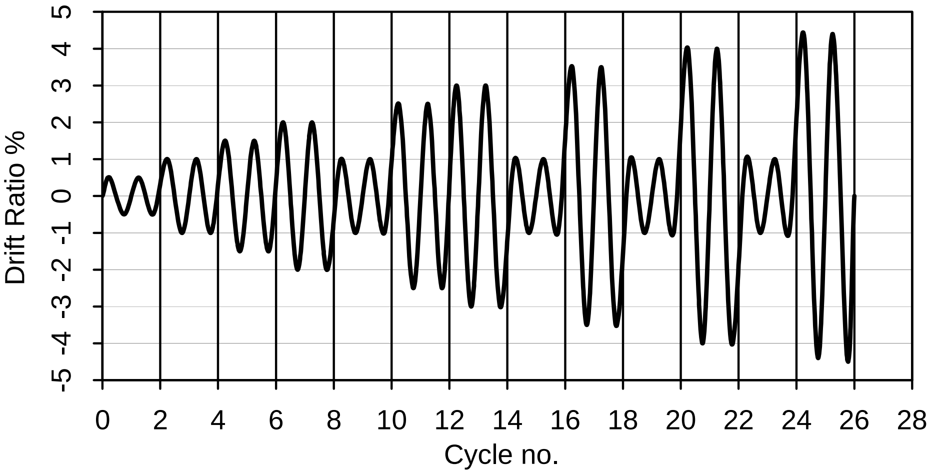

Fig. 3: Loading history

Test measurements included applied load and lateral drift, strain in the outermost column reinforcement (starter bars) at the column-beam interface, strain in the top and bottom longitudinal bars of the beams, and average curvature or rotation in the end zones of the columns and beams. The strains were measured using electric strain gauges, while curvatures were measured using Linear Variable Differential Transducers (LVDTs). The test data was recorded using a data acquisition and control system.

Figure 4: Failure mode of the joint specimens

3 TEST RESULTS

3.1 General behaviour and mode of failure

(i) Specimen IJ-F2

A typical photo of the specimen taken at the conclusion of the test is shown in Fig. 4. As indicated earlier, this specimen was subjected to two stages of load application (Stages 1 and 2). The first flexural crack in this specimen developed in the beam at the joint interface section at a drift ratio of 1.0%. As the lateral drift increased to somewhere between 1.5% and 2.0% diagonal shear cracks started to develop mainly in the joint core indicating the initiation of a joint shear failure. These diagonal cracks continued to spread and widen as the lateral drift increased and to propagate outside the joint core a distance equal approximately a beam depth away from the beam-column interface section (Fig. 4). However, at the end of Stage 1 of the test, corresponding to a maximum drift ratio of 4.5%, despite the development of shear cracks, the specimen did not show signs of strength degradation. In fact, during Stage 2 of the test, the specimen continued to resist lateral load steadily until a drift ratio of 7.0%, beyond which the specimen started experiencing gradual strength degradation. The width of the shear cracks at the maximum drift ratio in Stage 2 of load application reached 6 mm, causing considerable concrete damage.

During the first stage of load application, bond splitting cracks appeared along one of the outermost bottom beam bars on one side of the beam at a drift ratio of about 4.0%. During the second stage, splitting cracks developed as well along the outermost bottom bar on the other side of the beam. At the end of the test in Stage 2, these splitting cracks widened leading to concrete spalling at the bottom corners of the beam (Fig. 4).

(ii) Specimen EJ-F2

The first flexural cracks in specimen EJ-F2 appeared in the beam at the beam-column interface sections at drift ratios of about 1.0%. As the drift increased between 1.0% and 1.5%, the lateral applied load increased gradually, and at the same time, diagonal shear cracks started to develop within the joint core indicating the start of joint shear failure. These diagonal cracks continued to spread and widen as the lateral load increased until the development of a complete joint shear failure which occurred in this specimen at a drift ratio of approximately 1.75% to 2%. The width of the shear cracks at this stage reached between 2 to 3 mm. Beyond a drift ratio of 2%, the specimens experienced progressive strength degradation towards the end of the test. At maximum drift ratios of about 4.5%, the width of the shear cracks increased to about 6 mm, leading to a substantial concrete damage within the joint core (Fig. 4).

While the shear cracks concentrated mainly within the joint core, beyond a drift ratio of 2.0% the cracks tended to propagate outside the joint core similar to Specimen IJ-F2. Although few flexural cracks developed in the beam close to the beam-column interface, the number and width of these cracks stabilized as soon as the diagonal cracks in the joint core started to prevail.

During the tests, at drift levels of 3.0%, bond splitting cracks developed along the beam bottom longitudinal reinforcement outside the column core (one corner bar from each side). These cracks propagated along the full embedment length of the bars beyond the beam-column interface section, of 180 mm (Figs. 3). Eventually these cracks led to spalling of the concrete at the bottom face of the beam indicating bond splitting failure in localized regions of the specimens. This was regarded however as a secondary mode of failure as the development of these cracks did not affect the overall response of the specimens

3.2 Column shear-drift response

The hysteresis response of applied lateral load (column shear force) versus drift ratio are presented in Fig. 5 for both the interior and exterior specimens, and compared with the estimated maximum lateral load capacities $H_{\max}$ of the connections. The estimated capacities $H_{\max}$ were obtained using force equilibrium of the whole connection sub-assemblages calculated as the minimum lateral force required for developing the nominal positive or nominal negative flexural strength of the beam, respectively, or nominal flexural strength of the column. As indicated earlier, the specimens experienced connection shear failure at drift ratios varying between 1.75% and 2.0%.

For Specimen IJ-F2, despite the development of joint shear cracks at a drift ratio of 2.0%, the specimen continued to resist lateral loads at a small rate reaching a load of 72.0kN at a drift ratio of 4.5% (end of the test in the first loading stage). The corresponding lateral load resistance is 59% of the estimated static lateral load capacity $H_{\max}$ of the specimen of 122 kN. It is interesting to observe in Fig. 5 that even subjecting the specimen to 8.5% lateral drift in a half-cycle mode, it did not lead to significant strength degradation. The low strength degradation of this specimen below the load at which shear failure occurred may be attributed to the relatively low lateral load at which the specimen failed in shear (of about 56 kN) combined with relatively low shear decay associated with stabilization of the shear cracks within the joint core. The stiffness of the specimen (defined as the slope of the line that passes from the origin to the point on the envelope response) decreased to about 50% of the initial stiffness (stiffness at initial loading) at drift ratio of 4.5% (Stage 1) and 25% of the initial stiffness at drift ratio of 8.0% (Stage 2), respectively.

After the initiation of shear cracks at a drift ratio of about 1.75%, Specimen EJ-F2 displayed a stable behaviour without loss in load resistance until reaching a drift ratio of 2.5%. The peak lateral load developed in this specimen was approximately 20.0 kN which is only 35% of the estimated static lateral load resistance $H_{\max}$ of 54 kN. Beyond a drift of 2.5%, the lateral load resistance degraded gradually, reaching at 4.0% drift about 50% of the peak load. Also, at a drift ratio of 4.0%, the stiffness of the specimen decreased to about 17.0% of the initial stiffness.

3.3 Reinforcement strains/stresses and bond performance

3.3.1 Beam reinforcement

Cyclic response of the beam reinforcement strain with lateral drift of the specimens is presented in Fig. 6. As a result of the premature connection shear failure, the strains developed in the steel reinforcement were well below yield. The maximum tension strains of the beam bottom and top bars at peak lateral load were 1536 $\mu\varepsilon$ and 1847 $\mu\varepsilon$ for Specimen IJ-F2; and 1435 $\mu\varepsilon$ and 1670 $\mu\varepsilon$ for Specimen EJ-F2, respectively.

As indicated earlier, both of Specimens IJ-F2 and EJ-F2 developed localized bond splitting cracks in the outermost beam bottom bars outside the column core. Some of the main reasons for the localized bond splitting failure are the short development length provided for the beam bottom bars beyond the beam-column interface section, and the lack of concrete or steel confinement for the bars outside the column core. Notice that the development

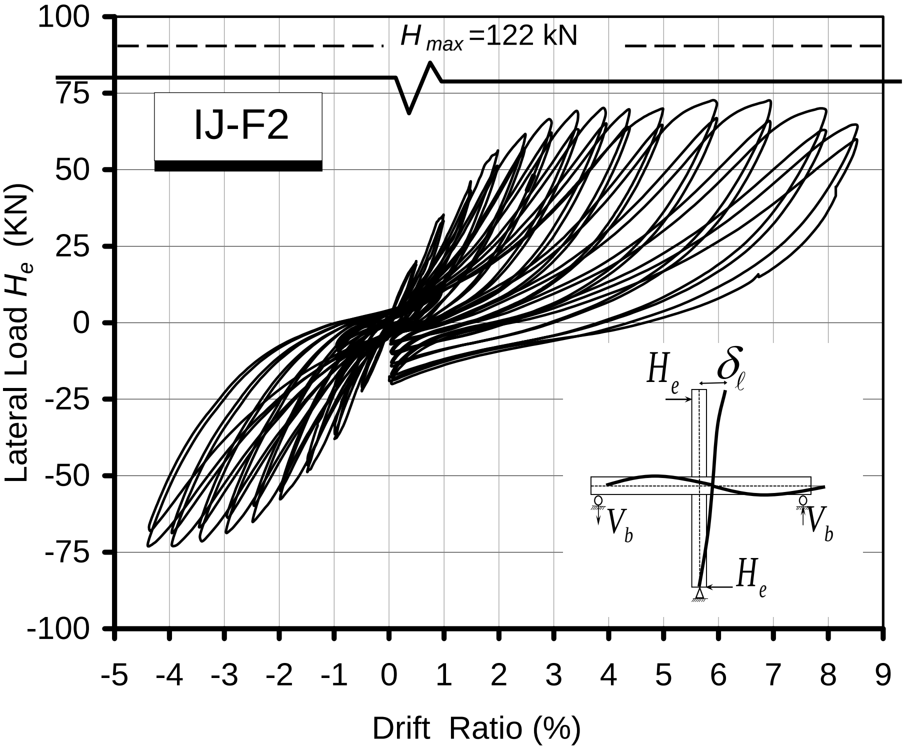

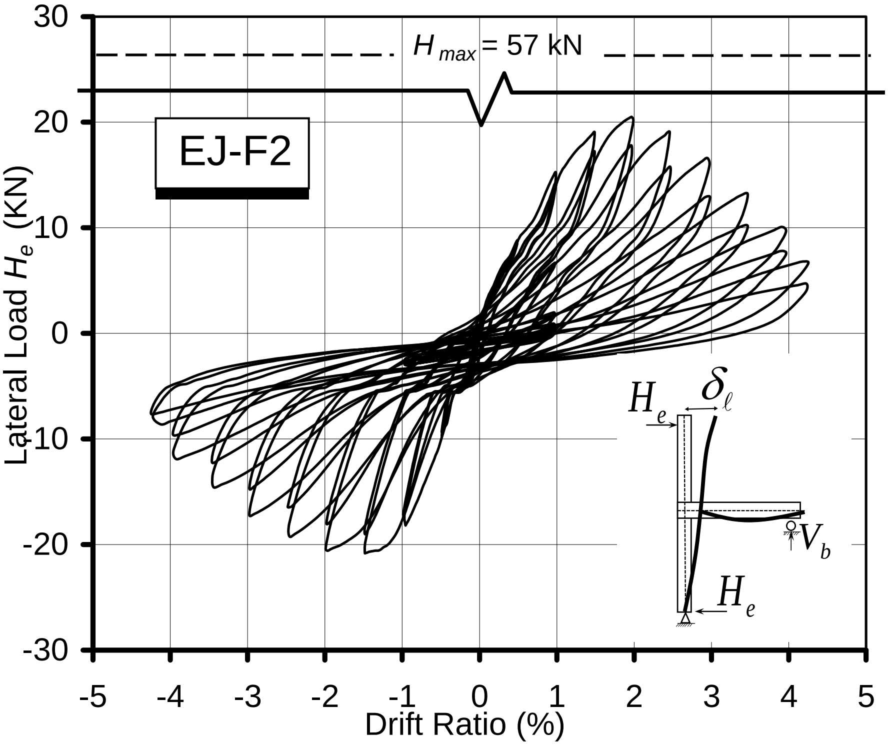

Figure 5: Lateral load-drift ratio response of the specimens

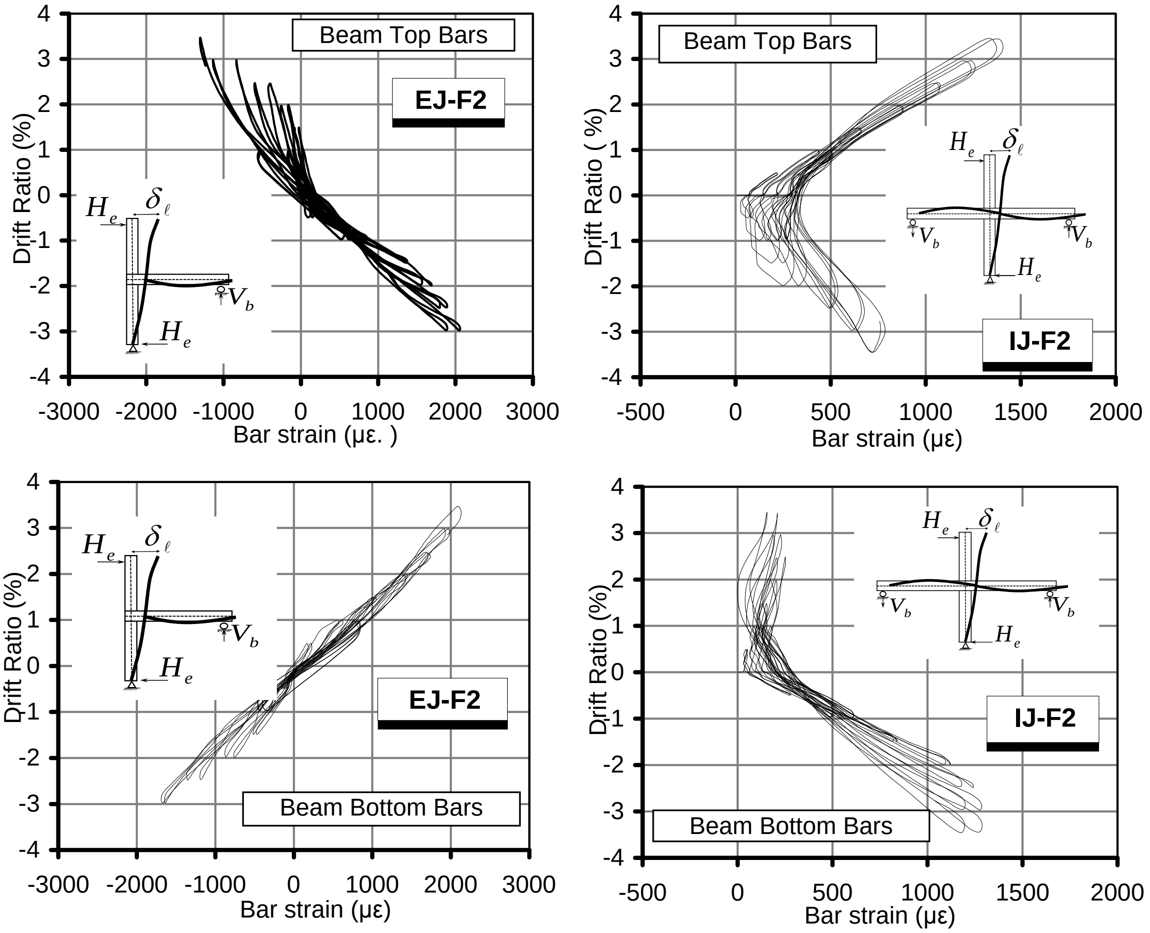

Fig. 6: Variation of beam reinforcement strain with drift ratio

lengths provided for the beam bottom bars were 225 mm or $14.0d_b$ for Specimen IJ-F2, and 180 mm or $11.3d_b$ for EJ-F2, respectively. These development lengths are less than the minimum of $27d_b$ required by ACI 318-08 for $f'_c = 21$ MPa.

3.3.2 Column reinforcement

The maximum strain developed in the column reinforcement of Specimen EJ-F2 was 2630 $\mu\varepsilon$, which is below yield. However, during the second stage of loading, the outermost left column bar in Specimen IJ-F2 did indeed develop yielding and attained a measured strain of 4545 $\mu\varepsilon$ at a drift ratio of 5.0%.

It should be mentioned that, based on test observations, all of the column reinforcement for Specimen EJ-F2 did not exhibit bond deterioration associated with bond splitting and/or excessive bond slip. However, during the second stage of loading for Specimen IJ-F2, a bond splitting crack was observed along one the corner column bars, but it was not critical as it did not result in a noticeable change of the specimen behaviour. Notice that the ACI Building code prohibits splicing of column reinforcement at the base of the column in regions of high seismic hazard so as to avoid possible bond failure at the column base where plastic hinging is likely to develop. However, because of the premature joint shear failure and the consequent development of relatively small stresses in the column reinforcement at nominal lateral load capacities of the specimens, no conclusions can be drawn regarding this requirement in relation to the beam-column connections under investigation. A conclusion regarding this requirement is addressed during the second part of this investigation dealing with the seismic response of the same beam-column connections after being detailed more properly for avoiding joint shear failure.

4 CONCLUSIONS

The following conclusions can be drawn from this investigation:

- When subjected to drift reversals induced by even moderate earthquakes, gravity load designed concealed wide beam-narrow column connections of the type under investigation will develop sizable diagonal shear cracks and consequently joint shear failure at drift ratios varying between 1.5 and 2.0%. These connections are expected to experience large damage beyond repair and possibly structural collapse when subjected to large drift reversals induced by strong earthquakes.
- As a result of the premature joint shear failure, the strains in the beam and column reinforcement developed at maximum lateral load capacity were well below yield. The lateral load capacities reached by the specimens in percent of the estimated capacities should the beams or columns acquire their nominal flexural strength were 59% for the interior and 35% for the exterior connection, respectively.
- Bond splitting cracks did develop around the outermost beam bars outside the column core due to the short embedment length beyond the beam-column interface section and the lack of concrete or steel confinement, but these cracks were not as critical in controlling the performance of the joints when compared with the joint diagonal shear cracks.
- Even in regions of moderate seismic hazard, unless designed and detailed to prevent joint shear failure, the connections under investigation are significantly weak to be considered as part of the earthquake lateral load resisting system.

ACKNOWLEDMENTS

The authors are most grateful for the support of the Faculty of Engineering and Architecture at the American University of Beirut (AUB) for providing the test facilities.

RERFERENCES

[1] M. Harajli, S. Sadek, R. Asbahan, Evaluation of seismic hazard of Lebanon: implications of recent earthquakes and new technical developments. *Journal of Seismology*, Kluwer Academic Publishers, 6(2), 257-27, 2002.

[2] C. Huijer, M. Harajli, S. Sadek, *Implications of the recent mapping of the offshore thrust fault system on the seismic hazard of Lebanon*, Research Report submitted to the Lebanese National Council for Scientific Research (LNCSR), October 2010. Also, MS Thesis presented by the first author to the CEE Dept. at the American University of Beirut (AUB), Beirut, Lebanon, 100 pp.

[3] ACI Committee 318, *Building Code Requirements for Reinforced Concrete and Commentary,* American Concrete Institute, Farmington Hills, Mich., 2008.

[4] ACI-ASCE Committee 352R-02, *Recommendation for Design of Beam-Column Connections in Monolithic Reinforced Concrete Structures*, American Concrete Institute, Farmington Hills, Mich., 2002.

[5] J.M. Lafave, J.K. Wight, Reinforced concrete exterior wide beam-column-slab connections subjected to lateral earthquake loading. *ACI Structural Journal*, 96(3), 577-586, 1999.

[6] J.M. Lafave, J.K. Wight, Reinforced concrete wide-beam construction vs. conventional construction: resistance to lateral earthquake loads. *Earthquake Spectra*, 17(3), 2001.

[7] B. Li, S.A. Kulkarni, Seismic behaviour of reinforced concrete exterior wide beam-column connections. *Journal of Structural Engineering*, ASCE, 136(1), 26-36, 2010.

[8] C.G. Quintero-Febres, J.K. Wight, Experimental study of reinforced concrete interior wide beam-Column connections subjected to lateral earthquake loading. *ACI Structural Journal*, 98(4), 572-582, 2001.

COMPDYN 2011
III ECCOMAS Thematic Conference on
Computational Methods in Structural Dynamics and Earthquake Engineering
M. Papadrakakis, M. Fragiadakis, V. Plevris (eds.)
Corfu, Greece, 25–28 May 2011

CUTOFF WAVE NUMBERS FOR ENERGY-ORTHOGONAL TWENTY-NODE HEXAHEDRAL ELEMENTS

Francisco José Brito Castro

Departamento de Física Fundamental y Experimental, Universidad de La Laguna
Calle Mendez Nuñez 67- 2C, Santa Cruz de Tenerife 38001, SPAIN
fjbrito@ull.es

Key words: wave propagation, modal analysis, energy-orthogonal stiffness.

Abstract. *This paper studies the propagation of plane harmonic waves in unbounded media discretized by the standard twenty-node hexahedral finite element. The element stiffness matrix is split into basic and higher order components which are obtained from mean and deviatoric strain fields, respectively. This decomposition is applied to the elastic energy. Based on the properties of the higher order energy, two values of the wave number are selected. Depending on the desired precision one of those values can be used as optimum cutoff wave number to properly capture a wave field.*

1 INTRODUCTION

The wave propagation in solids is a so broad scientific subject that analytical solutions to the governing equation of motion exist for just the simplest cases and only approximate solutions are feasible for the others. One method for obtaining approximate solutions is to use numerical procedures, such as the finite element method, which often introduce phenomena that are not present in the physical system [1]. In references [2, 3] the wave propagation in solids is analyzed through.

The governing equation of motion for a homogeneous isotropic elastic solid may be summarized as

$$(\lambda+\mu)\nabla\nabla\cdot\mathbf{u}+\mu\nabla^2\mathbf{u}+\rho\mathbf{f}=\rho\ddot{\mathbf{u}} \tag{1}$$

where: the elastic constants for the material are λ and μ, the Lamé constants; ρ, the mass density per unit volume of the material; **u**, the displacement vector; **f**, the body force per unit mass of material.

The Lamé constants can be expressed as

$$\lambda=\frac{E\nu}{(1+\nu)(1-2\nu)},\quad \mu=\frac{E}{2(1+\nu)} \tag{2}$$

where: E, Young´s modulus; ν, Poisson´s ratio for the material.

Let us consider the Helmholtz decomposition of the displacement vector as the gradient of a scalar and the curl of a zero divergence vector,

$$\mathbf{u}=\nabla\Phi+\nabla\times\mathbf{H},\quad \nabla\cdot\mathbf{H}=0 \tag{3}$$

The scalar potential Φ is associated with the dilatational part of the disturbance, and the vector potential **H** with the rotational part.

By considering Eq. (3), the governing equation of motion Eq. (1) is decomposed as two simplified wave equations, in the absence of body forces,

$$\nabla^2\Phi=\frac{1}{c_L^2}\frac{\partial^2\Phi}{\partial t^2},\quad \nabla^2\mathbf{H}=\frac{1}{c_T^2}\frac{\partial^2\mathbf{H}}{\partial t^2} \tag{4}$$

where:

$$c_L=\left(\frac{\lambda+2\mu}{\rho}\right)^{1/2},\quad c_T=\left(\frac{\mu}{\rho}\right)^{1/2} \tag{5}$$

Bulk wave propagation refers to wave propagation in unbounded media; guided waves are those that require a boundary for their existence, such as surface waves, Lamb waves, and interface waves. This paper will focus on bulk wave propagation in unbounded media. By considering Eq. (4) we deduce that the dilatational and rotational bulk waves propagate without interaction in unbounded media with the velocities c_L and c_T, respectively. These two types of waves are coupled only on the boundary of the elastic solid, an obvious consequence of satisfying the boundary conditions. The dilatational and rotational bulk waves are also called primary (P) and secondary (S) waves, respectively.

In this paper we consider the propagation of uniform plane harmonic waves,

$$\mathbf{u}=A\hat{\mathbf{a}}\exp[i(\kappa\mathbf{n}\cdot\mathbf{r}-\omega t)] \tag{6}$$

where: A, amplitude of the wave; ω, radial frequency; κ, wave number; $\hat{\mathbf{a}}$, polarization vector, unit vector indicating the direction of the particle displacement; **n**, wave normal, unit vector indicating the direction of the wave propagation; **r**, position vector.

The wave number and the radial frequency will be

$$\kappa = \frac{2\pi}{\lambda} = \frac{\omega}{c}, \quad \omega = \frac{2\pi}{T} = 2\pi f \tag{7}$$

where: λ, wavelength; c, phase speed of the continuum; T, period of wave; f, cyclic frequency.

The longitudinal plane waves, where the displacements are in the direction of the wave normal and only normal stresses are acting along the wave front, are dilatational waves; nevertheless, the transverse plane waves, where the displacements are perpendicular to the wave normal and only shearing stresses are acting along the wave front, are rotational waves.

For isotropic elastic material, the relationship between strains and stresses, in the absence of initial strains and stresses, can be expressed in matrix form as

$$\{\sigma_x \quad \sigma_y \quad \sigma_z \quad \tau_{xy} \quad \tau_{xz} \quad \tau_{yz}\}^t = \mathbf{E}\{\varepsilon_x \quad \varepsilon_y \quad \varepsilon_z \quad \gamma_{xy} \quad \gamma_{xz} \quad \gamma_{yz}\}^t \tag{8}$$

where **E** is the elasticity matrix,

$$\mathbf{E} = \begin{bmatrix} \lambda+2\mu & \lambda & \lambda & 0 & 0 & 0 \\ \lambda & \lambda+2\mu & \lambda & 0 & 0 & 0 \\ \lambda & \lambda & \lambda+2\mu & 0 & 0 & 0 \\ 0 & 0 & 0 & \mu & 0 & 0 \\ 0 & 0 & 0 & 0 & \mu & 0 \\ 0 & 0 & 0 & 0 & 0 & \mu \end{bmatrix} \tag{9}$$

By considering Eq. (5), the elasticity matrix also can be expressed in the forms

$$\mathbf{E}_L = \rho c_L^2 \begin{bmatrix} 1 & p & p & 0 & 0 & 0 \\ p & 1 & p & 0 & 0 & 0 \\ p & p & 1 & 0 & 0 & 0 \\ 0 & 0 & 0 & q & 0 & 0 \\ 0 & 0 & 0 & 0 & q & 0 \\ 0 & 0 & 0 & 0 & 0 & q \end{bmatrix}, \quad \mathbf{E}_T = \rho c_T^2 \begin{bmatrix} \varepsilon & r & r & 0 & 0 & 0 \\ r & \varepsilon & r & 0 & 0 & 0 \\ r & r & \varepsilon & 0 & 0 & 0 \\ 0 & 0 & 0 & 1 & 0 & 0 \\ 0 & 0 & 0 & 0 & 1 & 0 \\ 0 & 0 & 0 & 0 & 0 & 1 \end{bmatrix} \tag{10}$$

where: $p = 1 - 2/\varepsilon$, $q = 1/\varepsilon$, $r = \varepsilon - 2$ and $\varepsilon = c_L^2/c_T^2 = (\lambda+2\mu)/\mu = (2-2\nu)/(1-2\nu)$. Since $0 \le \nu \le 1/2$ always, we deduce the inequality $c_L > c_T$.

The forms of the elasticity matrix given by the Eq. (10) will be useful to analyze the propagation of longitudinal and transverse waves, respectively.

This work essentially extends the author′s previous work on the eight-node quadrilateral and the six-node triangle [4, 5]. The elastic media is discretized by the standard twenty-node hexahedral finite element [6] with consistent mass matrix [7]. By splitting the strain-nodal displacements matrix into mean and deviatoric components

$$\mathbf{e}^e = \mathbf{B}^e\mathbf{x}^e = (\overline{\mathbf{B}}^e + \mathbf{B}_d^e)\mathbf{x}^e \tag{11}$$

$$\overline{\mathbf{B}}^e V^e = \int_V \mathbf{B}^e dV, \quad \mathbf{B}_d^e = \mathbf{B}^e - \overline{\mathbf{B}}^e \tag{12}$$

the element stiffness matrix will be

$$\mathbf{K}^e = \mathbf{K}_b^e + \mathbf{K}_h^e \tag{13}$$

$$\mathbf{K}_b^e = \int_V (\overline{\mathbf{B}}^e)^t \mathbf{E} \overline{\mathbf{B}}^e dV \tag{14}$$

$$\mathbf{K}_h^e = \int_V (\mathbf{B}_d^e)^t \mathbf{E} \mathbf{B}_d^e dV \tag{15}$$

where: $\mathbf{K}_b^e$, basic stiffness matrix; and $\mathbf{K}_h^e$, higher order stiffness matrix.

In this case the element stiffness matrix is decomposed in energy-orthogonal form [8]. The basic and higher order matrices are related to the mean and deviatoric strain fields,

$$\overline{\mathbf{e}}^e = \overline{\mathbf{B}}^e \mathbf{x}^e, \quad \mathbf{e}_d^e = \mathbf{B}_d^e \mathbf{x}^e \tag{16}$$

respectively.

The concept of energy-orthogonal stiffness matrix used in this paper was explicitly introduced by Bergan and Nygärd in the context of the Free Formulation [9], and by Felippa within the framework of the Parametrized Variational Principles [10].

The decomposition Eq. (13) holds for the complete model whenever $\mathbf{K}_b^e$ and $\mathbf{K}_h^e$ are independently assembled,

$$\mathbf{K} = \mathbf{K}_b + \mathbf{K}_h \tag{17}$$

This decomposition is also applied to the elastic energy of the finite element assemblage,

$$U = U_b + U_h \tag{18}$$

$$U_b = \tfrac{1}{2}\mathbf{x}^t \mathbf{F}_b, \quad \mathbf{F}_b = \mathbf{K}_b \mathbf{x} \tag{19}$$

$$U_h = \tfrac{1}{2}\mathbf{x}^t \mathbf{F}_h, \quad \mathbf{F}_h = \mathbf{K}_h \mathbf{x} \tag{20}$$

where: U_b, basic elastic energy; U_h, higher order elastic energy; $\mathbf{F}_b$ and $\mathbf{F}_h$, basic and higher order forces vector, respectively.

In this paper the dispersion properties and the elastic energy of both longitudinal and transverse waves are computed for the unbounded media discretized by regular meshes. If the exact solution of the problem consists of a constant stress state, the higher order elastic energy vanishes over each element. Similarly, as the solution converges on account of mesh refinement, the element energy is increasingly dominated by the basic energy. This behavior has been numerically verified for the standard twenty-node hexahedral finite element in the context of modal analysis [11].

The above heuristic argument shows that the higher order elastic energy may be regarded as a local error indicator [10]. Although this assumption is based largely on numerical experiments motivates to explore the relationship between the higher order elastic energy and the numerical dispersion introduced by the finite element method.

In this paper the behavior of the higher order elastic energy is investigated and based on its properties two values of the wave number are selected as reference values. The use of one of those values as optimum cutoff wave number to properly capture a wave field is investigated. The concept is extended to define an optimum cutoff frequency to properly capture the natural modes of a solid.

The distinctive contributions of this paper over the author´s previous works [4, 5] are related to the consideration of hexahedral elements both moderately and highly distorted. These ones could be useful for the 3D modelling of structural elements.

2 WAVES IN UNBOUNDED MEDIA

2.1 Characteristic equations

In a solid discretized by the finite element method the equations of equilibrium governing its linear dynamic response may be cast in matrix form

$$\mathbf{M}\ddot{\mathbf{x}} + \mathbf{C}\dot{\mathbf{x}} + \mathbf{K}\mathbf{x} = \mathbf{f} \tag{21}$$

where **M**, **C** and **K** are the mass, damping, and stiffness matrices; **f** is the external load vector; and **x** is the displacement vector of the finite element assemblage [12].

The homogeneous and isotropic unbounded media is discretized by a regular mesh of standard twenty-node hexahedral elements, Figure 1. The nodal lattice has four nodes per unit cell which are labeled *A*, *B, C* and *D*, respectively. The node *A* is a corner one, whereas the nodes *B, C* and *D* are mid-side ones. Specifically, the elements analyzed are of brick geometry. Different meshes with the same element volume can be obtained by changing the aspect ratio parameter, γ; where, $1 \geq \gamma > 0$. The finite element analysis will be performed by using the rectangular coordinate system Σ: XYZ.

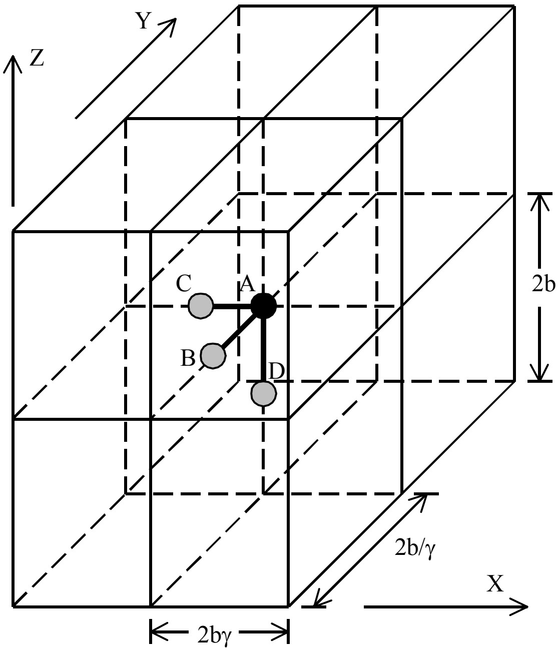

Figure 1: Regular mesh of standard twenty-node hexahedral elements and unit cell.

The characteristic equations can be found assuming uniform plane harmonic waves with different amplitudes in each node of the unit cell,

$$\mathbf{u} = A_i \hat{\mathbf{a}} \cos[\kappa \mathbf{n} \cdot \mathbf{r} - \omega t], \quad i = 1,2,3,4 \tag{22}$$

where: A_1, A_2, A_3 and A_4, wave amplitudes in the nodes *A*, *C, B* and *D*, respectively.

The wave normal **n** and the assumed polarization vector $\hat{\mathbf{a}}$ are related to the rectangular coordinate system Σp, obtained from Σ by three successive rotations defined by the Euler angles, Figure 2. For longitudinal waves, $\mathbf{n} = \hat{\mathbf{a}} = \mathbf{i}_{\mathrm{p}}$; for transverse waves, $\hat{\mathbf{a}} = \mathbf{j}_{\mathrm{p}}$ or $\hat{\mathbf{a}} = \mathbf{k}_{\mathrm{p}}$.

The components of the displacement vector **u** with respect to the coordinate system Σ are obtained from the ones respect to the coordinate system Σp by

$$\{u \quad v \quad w\}^t = \mathbf{R}^t \{u_p \quad v_p \quad w_p\}^t \tag{23}$$

The transformation matrix will be

$$\mathbf{R} = \mathbf{CBA} \tag{24}$$

where

$$\mathbf{A} = \begin{bmatrix} \cos\phi & \sin\phi & 0 \\ -\sin\phi & \cos\phi & 0 \\ 0 & 0 & 1 \end{bmatrix}, \quad \mathbf{B} = \begin{bmatrix} 1 & 0 & 0 \\ 0 & \cos\theta & \sin\theta \\ 0 & -\sin\theta & \cos\theta \end{bmatrix}, \quad \mathbf{C} = \begin{bmatrix} \cos\psi & \sin\psi & 0 \\ -\sin\psi & \cos\psi & 0 \\ 0 & 0 & 1 \end{bmatrix} \tag{25}$$

are the transformation matrices for the rotations Σ → Σa, Σa → Σb and Σb → Σp, respectively. The three Euler angles are called the precession ϕ, the nutation θ, and the spin ψ [13].

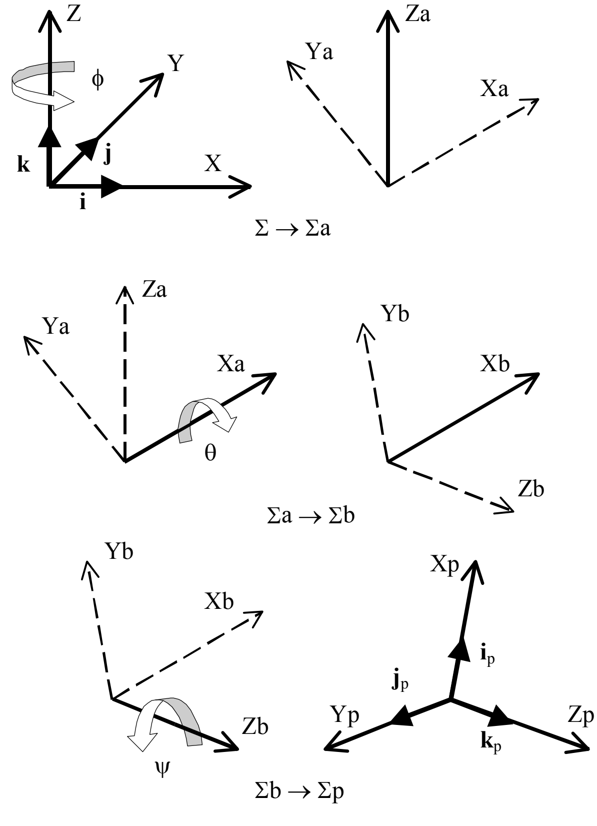

Figure 2: Rectangular coordinate transformation corresponding to three successive rotations defined by the Euler angles.

By considering the homogeneous part of Eq. (21) with damping neglected and substituting the assumed harmonic solutions we obtain the characteristic equation for each node of the unit cell by the equilibrium of nodal forces into the direction of the particle displacement [14].

The four characteristic equations form a system of homogeneous algebraic equations,

$$\mathbf{ZA} = \begin{bmatrix} z_{11} & z_{12} & z_{13} & z_{14} \\ z_{21} & z_{22} & z_{23} & z_{24} \\ z_{31} & z_{32} & z_{33} & z_{34} \\ z_{41} & z_{42} & z_{43} & z_{44} \end{bmatrix} \begin{Bmatrix} A_1 \\ A_2 \\ A_3 \\ A_4 \end{Bmatrix} = \begin{Bmatrix} 0 \\ 0 \\ 0 \\ 0 \end{Bmatrix} \tag{26}$$

$$z_{ij} = a_{ij}(m,\phi,\theta,\psi,\nu,\gamma) + \varpi^2 b_{ij}(m,\phi,\theta,\psi,\nu,\gamma) \tag{27}$$

$$m = \frac{b\kappa}{\pi} = \frac{2b}{\lambda}, \quad \varpi = \frac{2b}{c}\omega \tag{28}$$

where: m, dimensionless wave number; b, half of the cubic element size; ϖ, dimensionless frequency of the discretized media.

The dimensionless wave number will be $m_L = b\kappa_L/\pi$ and $m_T = b\kappa_T/\pi$ for longitudinal and transverse waves, respectively. From the continuum frequencies and Eq. (7) we obtain the relationship $m_T/m_L = c_L/c_T$. From $c_L > c_T$ we deduce the inequality $m_L < m_T$.

2.2 Dispersion equations

The system of homogeneous algebraic equations given in Eq. (26) has a non-trivial solution only if the matrix **Z** is singular; that is,

$$\det[\mathbf{Z}(m,\phi,\theta,\psi,\nu,\gamma,\varpi)] = 0 \tag{29}$$

By considering Eq. (27), from Eq. (29) we obtain the quartic equation

$$q^4 + d_3 q^3 + d_2 q^2 + d_1 q + d_0 = 0 \tag{30}$$

where: $q = \varpi^2$; $d_i(m,\phi,\theta,\psi,\nu,\gamma)$, coefficients obtained from a_{ij} and b_{ij}.

Either of Eq. (29) and (30) is called a characteristic frequency equation for plane wave propagation.

It is an important fact that the n zeroes of a polynomial of degree $n \geq 1$ with complex coefficients depend continuously upon the coefficients [15]. Thus, sufficiently small changes in the coefficients of a polynomial can lead only to small changes in any zero. However there is no simple way to define a function which takes the n coefficients (all but the leading 1) of a monic polynomial of degree n to the n zeroes of the polynomial, since there is no natural way to define an ordering among the n zeroes. In the case of the quartic polynomial Eq. (30), this problem has been solved by obtaining the zeroes in closed form. Then, the components

$$q_i = q_i(d_0,d_1,d_2,d_3), \quad i = 1,2,3,4 \tag{31}$$

or, alternatively,

$$\varpi_i = \varpi_i(m,\phi,\theta,\psi,\nu,\gamma), \quad i = 1,2,3,4 \tag{32}$$

will be continuous functions precisely defined. They are called dispersion equations. Obviously, we suppose that the coefficients $d_i(m,\phi,\theta,\psi,\nu,\gamma)$ are also continuous functions.

Substituting Eq. (32) into Eq. (26), the wave amplitudes for each dispersion equation are produced. In this work, each set of linear algebraic equations is numerically solved by using the singular value decomposition method SVD [16].

The range of dimensionless wave number values where each dispersion equation represents the propagation of acoustic waves in the discretized media will be called the acoustical branch of the dispersion equation. In order to determine the acoustical branches, a preliminary constraint condition over the dimension of the null space of **Z** must be imposed,

$$\dim\left[\mathbf{N}(\mathbf{Z})\right]=1 \tag{33}$$

The constraint condition Eq. (33) implies that the subspace of solutions to Eq. (26) must be one-dimensional. In this case the vector of wave amplitudes **A** is arbitrary to the extent that a scalar multiple of it is also a solution. Then the following constraint conditions are imposed,

$$A_{1,i}=1,\quad \begin{cases} A_{2,i}(m,\phi,\theta,\psi,\nu,\gamma)>0 \\ A_{3,i}(m,\phi,\theta,\psi,\nu,\gamma)>0, \quad i=1,2,3,4 \\ A_{4,i}(m,\phi,\theta,\psi,\nu,\gamma)>0 \end{cases} \tag{34}$$

$$\left(\frac{\partial \varpi_i}{\partial m}\right)_{\phi,\theta,\psi,\nu,\gamma}>0, \quad i=1,2,3,4 \tag{35}$$

The constraint condition Eq. (34) implies that the four nodes on the unit cell vibrate along the same direction. In molecular physics, condition Eq. (34) is called the restriction of the lattice spectrum to the acoustical branch [17]. Obviously, if the constraint condition Eq. (33) is not imposed, the constraint condition Eq. (34) is meaningless.

From Eq. (28) we obtain both the phase velocity and group velocity of the discretized media,

$$c_d=\frac{c}{2\pi}\frac{\varpi}{m}, \quad c_{g,d}=\frac{\partial\omega}{\partial\kappa}=\frac{c}{2\pi}\frac{\partial\varpi}{\partial m} \tag{36}$$

Therefore, the constraint condition Eq. (35) is equivalent to

$$c_{g,d}>0 \tag{37}$$

It can be proven that for general periodic motion in lossless or low loss media the energy propagates with the group velocity [2]; therefore, the constraint condition Eq. (37) imposes that the energy propagates into the wave direction.

From this point, for each dispersion equation only the acoustical branch will be considered. This one represents the physically admissible solution for mechanical wave propagation.

It must be recall that the group velocity of the continuum will be equal to the phase velocity because the waves propagate non-dispersively. Nevertheless, for the dispersive discretized media the group velocity will be different from the phase velocity; therefore, the velocity of energy transport will be different from the phase velocity. As a consequence, when we consider the numerical dispersion associated with the finite element spatial discretization, not only the effect over the phase velocity must be analyzed but also the effect over the group velocity or velocity of energy transport.

2.3 Indicators of dispersion

By considering Eq. (36), the indicators of the dispersion associated with spatial discretization that is introduced by the finite element model are defined as

$$e_d=\frac{c_d}{c}=\frac{\varpi}{2m\pi}, \quad e_d=e_d(m,\phi,\theta,\psi,\nu,\gamma) \tag{38}$$

$$e_{g,d} = \frac{c_{g,d}}{c} = \frac{1}{2\pi}\frac{\partial \varpi}{\partial m}, \quad e_{g,d} = e_{g,d}(m,\phi,\theta,\psi,\nu,\gamma) \tag{39}$$

These indicators consider the effect of the spatial discretization over the wave velocity and the velocity of energy transport, respectively. The indicators of spatial dispersion Eq. (38) and Eq. (39) are computed versus the dimensionless wave number both for longitudinal and transverse waves. Specifically, three test problems are analyzed in this paper, Figure 3.

For the Test A, the wave normal has direction parallel to two faces of the brick, and the polarization vector has direction either parallel to or perpendicular to those faces. Depending on the selected faces it can be distinguish three different cases:

$$\begin{aligned} &TEST \quad A-XY: \quad \phi = 0^{o}, \quad \theta = 0^{o}; \quad 0 \le \psi \le 90^{o}. \\ &TEST \quad A-XZ: \quad \phi = 0^{o}, \quad \theta = 90^{o}; \quad 0 \le \psi \le 90^{o}. \\ &TEST \quad A-YZ: \quad \phi = 90^{o}, \quad \theta = 90^{o}; \quad 0 \le \psi \le 90^{o}. \end{aligned} \tag{40}$$

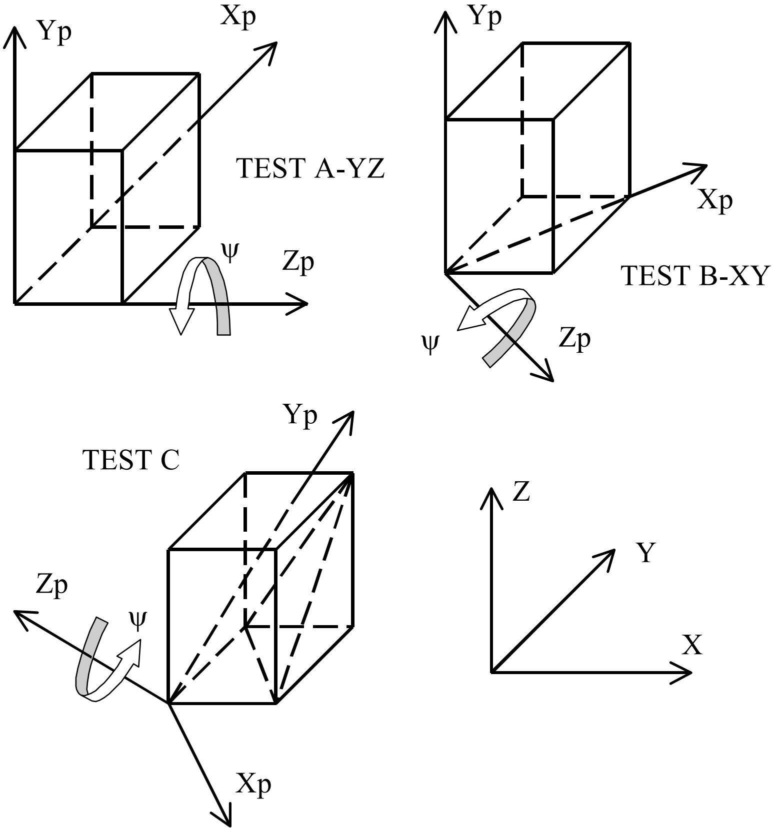

Figure 3: Test problems to evaluate the numerical dispersion.

For the Test B, the wave normal has direction parallel to a plane that diagonally intesects two opposite faces of the brick, and the polarization vector has direction either parallel to or perpendicular to that plane. Depending on the selected faces it can be distinguish three different cases:

$$\begin{aligned} &TEST \quad B-XY: \quad tg\phi = \frac{1}{\gamma^2}, \quad \theta = 90^{\circ}; \quad 0 \le \psi \le 90^{\circ}. \\ &TEST \quad B-XZ: \quad \phi = 90^{\circ}, \quad tg\theta = \frac{1}{\gamma}; \quad 0 \le \psi \le 90^{\circ}. \\ &TEST \quad B-YZ: \quad \phi = 0^{\circ}, \quad tg\theta = \gamma; \quad 0 \le \psi \le 90^{\circ}. \end{aligned} \tag{41}$$

For the Test C, the wave normal has direction parallel to a plane that diagonally intesects three faces of the brick, and the polarization vector has direction either parallel to or perpendicular to that plane,

$$TEST \quad C: \quad tg\phi = -\frac{1}{\gamma^2}, \quad tg\theta = \sqrt{\gamma^2 + \frac{1}{\gamma^2}}; \quad 0 \le \psi < 180^{\circ}. \tag{42}$$

For the Test C, a particular case of Eq. (38) is plotted in Figure 4. Three values of the angle of wave propagation are considered in order to represent the anisotropy induced by the spatial discretization. The dispersion associated with spatial discretization is clearly displayed as the dimensionless wave number increases.

It must be remarked that for the Test A and γ = 1, the values of Eq. (38) and Eq. (39) obtained both for longitudinal waves $\mathbf{n} = \hat{\mathbf{a}} = \mathbf{i}_{\mathrm{p}}$ and transverse waves $\hat{\mathbf{a}} = \mathbf{j}_{\mathrm{p}}$ are coincident with the ones obtained for the eight-node square element [4].

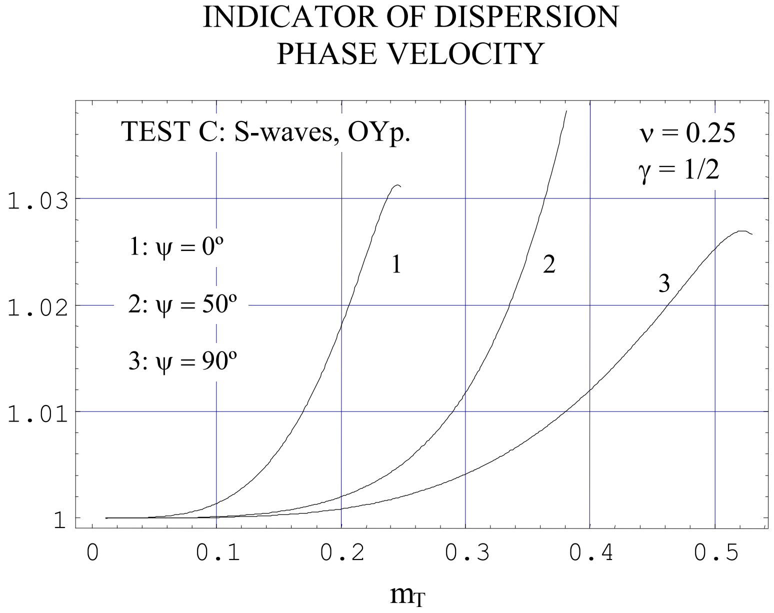

Figure 4: Test C. Indicator of spatial dispersion associated to the phase velocity versus dimensionless wave number for three values of the angle of wave propagation.

2.4 Higher order elastic energy at the unit cell

By considering the decomposition Eq. (18), in this paper we explore the relationship between the higher order elastic energy at the unit cell and the discretization error introduced by the finite element method. Assuming the harmonic waves Eq. (22), we obtain the higher order energy at the unit cell as the sum of the component associated with the corner node *A*,

$$U_h^A = \rho c^2 (2b) F_h^A (m, \phi, \theta, \psi, \nu, \gamma, \tau) \tag{43}$$

and the component associated with the mid-side nodes B, C and D,

$$U_h^M = \rho c^2 (2b) F_h^M (m,\phi,\theta,\psi,\nu,\gamma,\tau) \tag{44}$$

where: $\tau = t/T$, dimensionless time.

The period-averaged values,

$$\overline{F}_h^A (m,\phi,\theta,\psi,\nu,\gamma) = \int_0^1 F_h^A (m,\phi,\theta,\psi,\nu,\gamma,\tau) d\tau \tag{45}$$

$$\overline{F}_h^M (m,\phi,\theta,\psi,\nu,\gamma) = \int_0^1 F_h^M (m,\phi,\theta,\psi,\nu,\gamma,\tau) d\tau \tag{46}$$

are defined as the specific higher order corner energy and the specific higher order mid-side energy, respectively. The sum of these two components is the specific higher order energy at the unit cell.

The specific higher order corner and mid-side energies are computed versus the dimensionless wave number both for longitudinal and transverse waves. For the Test C, a particular case is plotted in Figures 5 and 6.

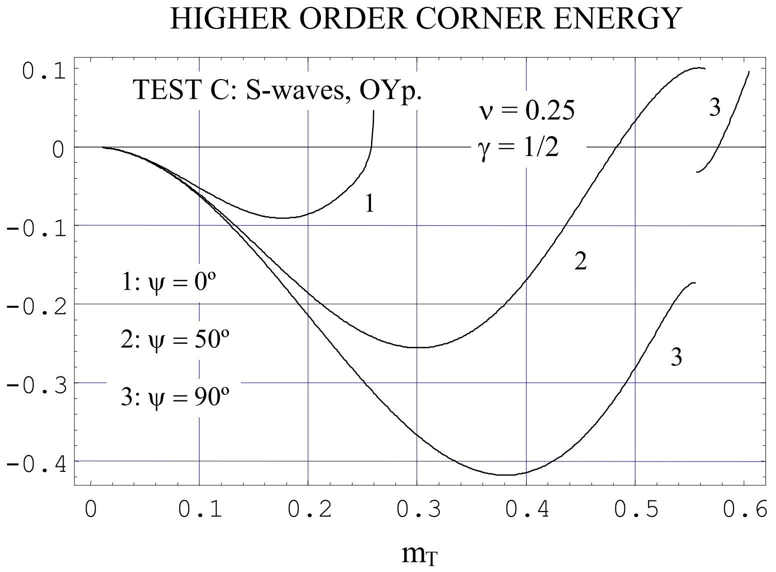

Figure 5: Test C. Specific higher order corner energy versus the dimensionless wave number.

We focus on the specific higher order corner energy. It is observed that the computed value decreases from zero as the dimensionless wave number increases until it reaches a minimum, then increases and eventually becomes positive. The sign-reversal value depends on the three Euler angles, the Poisson´s ratio and the aspect ratio parameter,

$$m_{L0}(\phi,\theta,\psi,\nu,\gamma), \quad m_{TY0}(\phi,\theta,\psi,\nu,\gamma), \quad m_{TZ0}(\phi,\theta,\psi,\nu,\gamma) \tag{47}$$

The first derivative of the specific higher order corner energy with respect to the dimensionless wave number is also computed. For the Tests C, a particular case is plotted in Figure 7. It is observed that the computed value decreases from zero as the dimensionless wave number increases until it reaches a minimum, then increases and eventually becomes positive. Obviously, the second derivative changes from negative to positive when the first derivative reaches its local minimum. The sign-reversal value depends on the three Euler angles, the Poisson´s ratio and the aspect ratio parameter,

$$m_{L1}(\phi,\theta,\psi,\nu,\gamma), \quad m_{TY1}(\phi,\theta,\psi,\nu,\gamma), \quad m_{TZ1}(\phi,\theta,\psi,\nu,\gamma) \tag{48}$$

$$m_{L2}(\phi,\theta,\psi,\nu,\gamma), \quad m_{TY2}(\phi,\theta,\psi,\nu,\gamma), \quad m_{TZ2}(\phi,\theta,\psi,\nu,\gamma) \tag{49}$$

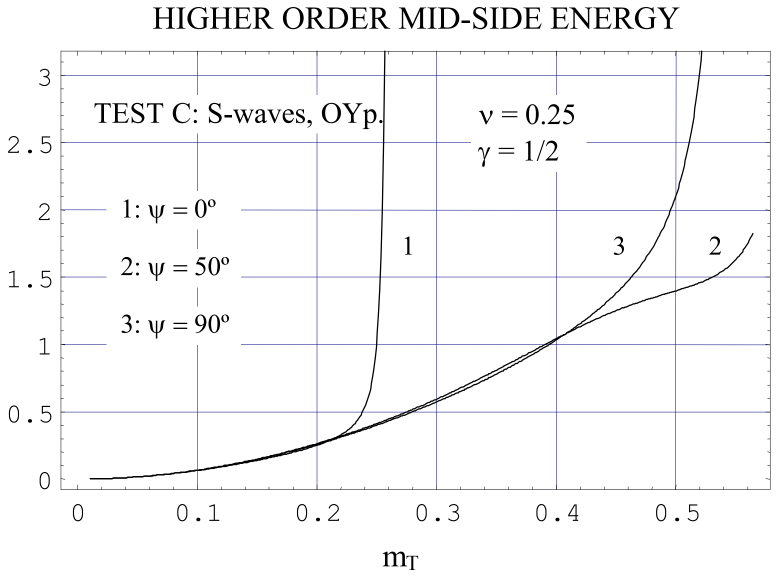

Figure 6: Test C. Specific higher order mid-side energy versus the dimensionless wave number.

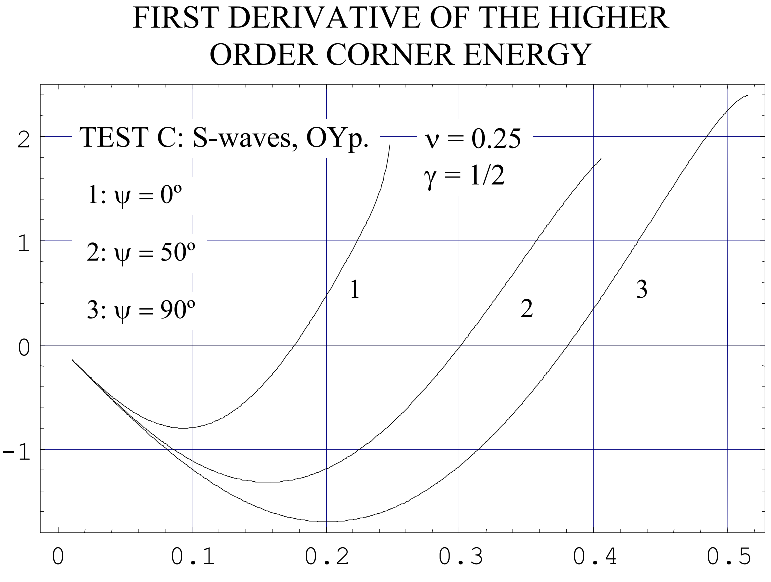

Figure 7: Test C. First derivative of the specific higher order corner energy versus the dimensionless wave number.

By also considering the behavior of the specific higher order mid-side energy, we can conclude that the components of the specific higher order energy at the unit cell satisfy the inequalities,

$$\overline{F}_h^A < 0, \quad \overline{F}_h^M > 0 \quad if \quad 0 < m < m_0 \tag{50}$$

$$\frac{\partial}{\partial m}\overline{F}_h^A < 0, \quad \frac{\partial}{\partial m}\overline{F}_h^M > 0 \quad if \quad 0 < m < m_1 \tag{51}$$

$$\frac{\partial^2}{\partial m^2}\overline{F}_h^A < 0, \quad \frac{\partial^2}{\partial m^2}\overline{F}_h^M > 0 \quad if \quad 0 < m < m_2 \tag{52}$$

where m_0, m_1 and m_2 are the values defined in Eq. (47)-(49).

Obviously, the specific higher order energy is always positive; nevertheless, as the discretization error decreases with the dimensionless wave number, it vanishes as a cancellation of two components, the positive mid-side energy and the negative corner energy. This behavior, which is called the cancellation property of the higher order energy at the unit cell, already has been observed by the author for the eight-node quadrilateral and the six-node triangle [4, 5]. Therefore, as the discretization error decreases, the higher order energy components tend to be equal but opposite in sign. By considering this evolution to the symmetry and the inequalities Eq. (50)-(52) we can conclude that the dimensionless wave numbers Eq. (47)-(49) determine behavioral ranges for the specific higher order energy. By considering this behavior, in this paper we propose to define Eq. (48) as the first reference wave number, and Eq. (49) as the second reference wave number. Both reference wave numbers basically depend on the three Euler angles and the aspect ratio parameter, and they exhibit a weak dependence respect to the Poisson´s ratio.

For a brick with cubic geometry, and for the Test A, in Tables 1 and 2 some computed values of the first and the second reference wave number are presented.

TEST A	$\gamma = 1$	$\nu = 0.45$	$\nu = 0.33$	$\nu = 0.25$	$\nu = 0.05$
$\psi = 0°$	P, OXp	0.3411	0.3411	0.3411	0.3411
	S, OYp	0.3411	0.3411	0.3411	0.3411
	S, OZp	0.3411	0.3411	0.3411	0.3411
$\psi = 25°$	P, OXp	0.3669	0.3738	0.3738	0.3728
	S, OYp	0.3689	0.3629	0.3629	0.3639
	S, OZp	0.3679	0.3679	0.3679	0.3679
$\psi = 37.5°$	P, OXp	0.3877	0.3897	0.3887	0.3877
	S, OYp	0.4154	0.3916	0.3887	0.3867
	S, OZp	0.3857	0.3857	0.3857	0.3857
$\psi = 45°$	P, OXp	0.3976	0.3906	0.3897	0.3887
	S, OYp	0.4273	0.3996	0.3966	0.3926
	S, OZp	0.3897	0.3897	0.3897	0.3897

Table 1: Test A. Dimensionless wave number for which the sign of the first derivative of the specific higher order corner energy changes from negative to positive.

For non-cubic brick, and for each of the test problems, some computed values of the first and the second reference wave number are plotted in Figures 8-10. It must be remarked that the strong numerical anisotropy induced by the non-cubic brick results in broad variations of both reference wave numbers versus the angle of wave propagation. Clearly, the numerical anisotropy increases as the aspect ratio parameter decreases.

TEST A	$\gamma = 1$	$\nu = 0.45$	$\nu = 0.33$	$\nu = 0.25$	$\nu = 0.05$
$\psi = 0^{o}$	P, OXp	0.1813	0.1813	0.1813	0.1813
	S, OYp	0.1813	0.1813	0.1813	0.1813
	S, OZp	0.1813	0.1813	0.1813	0.1813
$\psi = 25^{o}$	P, OXp	0.1951	0.1951	0.1941	0.1941
	S, OYp	0.1931	0.1912	0.1922	0.1922
	S, OZp	0.1931	0.1931	0.1931	0.1931
$\psi = 37.5^{o}$	P, OXp	0.2100	0.2060	0.2050	0.2040
	S, OYp	0.2050	0.2001	0.2001	0.2001
	S, OZp	0.2021	0.2021	0.2021	0.2021
$\psi = 45^{o}$	P, OXp	0.2129	0.2090	0.2080	0.2060
	S, OYp	0.2080	0.2021	0.2021	0.2021
	S, OZp	0.2030	0.2030	0.2030	0.2030

Table 2: Test A. Dimensionless wave number for which the sign of the second derivative of the specific higher order corner energy changes from negative to positive.

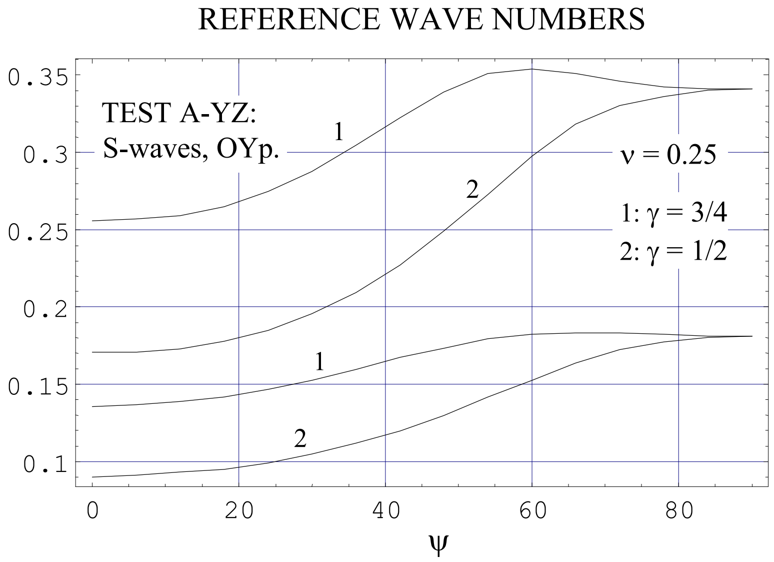

Figure 8: Test A-YZ. Reference wave numbers versus the angle of wave propagation.

Both reference wave numbers decrease as the angle of wave propagation exhibits a higher numerical dispersion, as it is observed for the Test C in Figures 4, 5 and 7. By considering this property, we investigate the use of one of the reference wave numbers as optimum cutoff wave number to properly capture the harmonic wave.

For the Test C, in Figures 11 and 12 we compute the maximum of Eq. (38) and the maximum of Eq. (39), respectively, for dimensionless wave number up to reach the first reference value. In this case, we consider that the harmonic wave is only properly captured from the wave velocity standpoint. In Figure 13 we compute the maximum of Eq. (39) for dimensionless wave number up to reach the second reference value. In this case, we consider that the harmonic wave is properly captured also from the velocity of energy transport standpoint. Similar results have been obtained for the Test A and the Test B.

We can conclude that, depending on the desired precision, the reference wave numbers could be used as optimum cutoff wave numbers tuned to taking into account the effect of the numerical anisotropy induced by the spatial discretization. The tuning effect can be clearly observed for the Test C by considering Figures 4, 5 and 7.

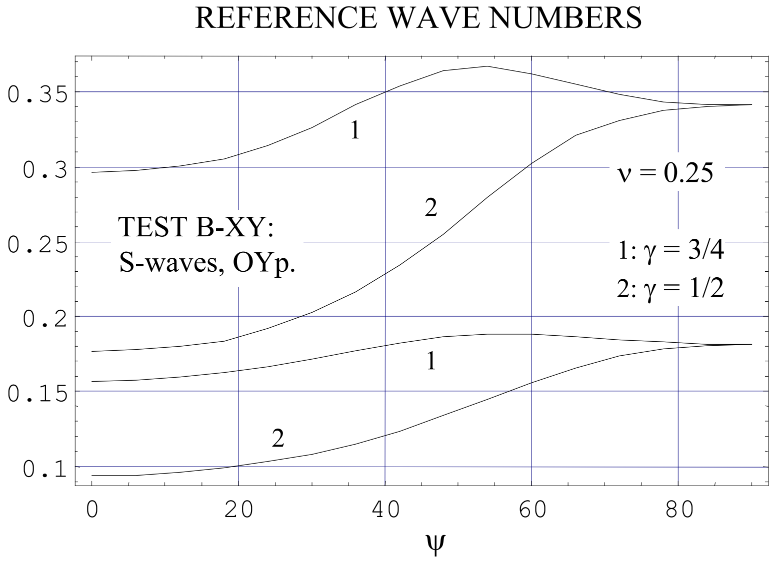

Figure 9: Test B-XY. Reference wave numbers versus the angle of wave propagation.

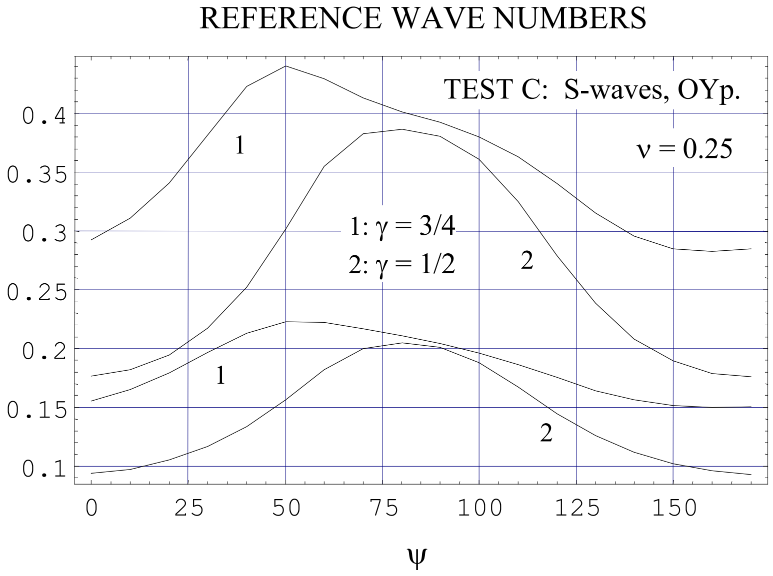

Figure 10: Test C. Reference wave numbers versus the angle of wave propagation.

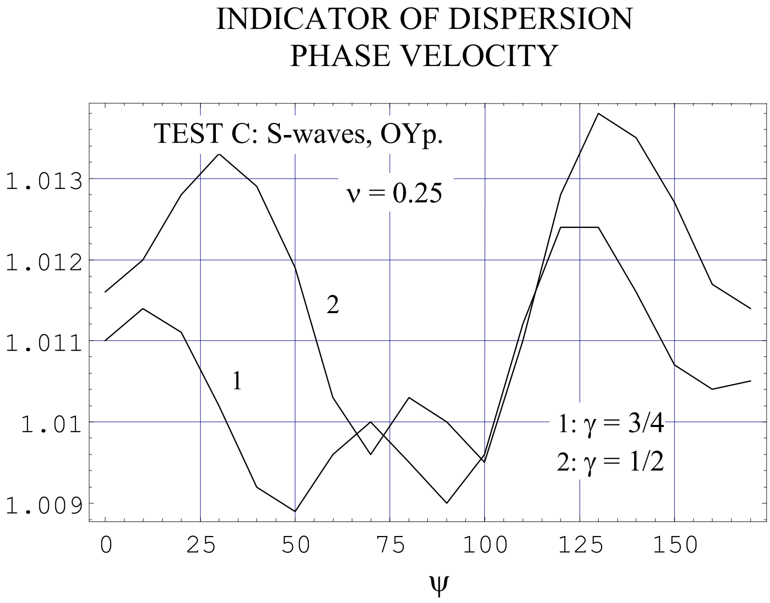

Figure 11: Test C. Maximum of the indicator of spatial dispersion associated to the phase velocity for dimensionless wave number up to reach the first reference value versus the angle of wave propagation.

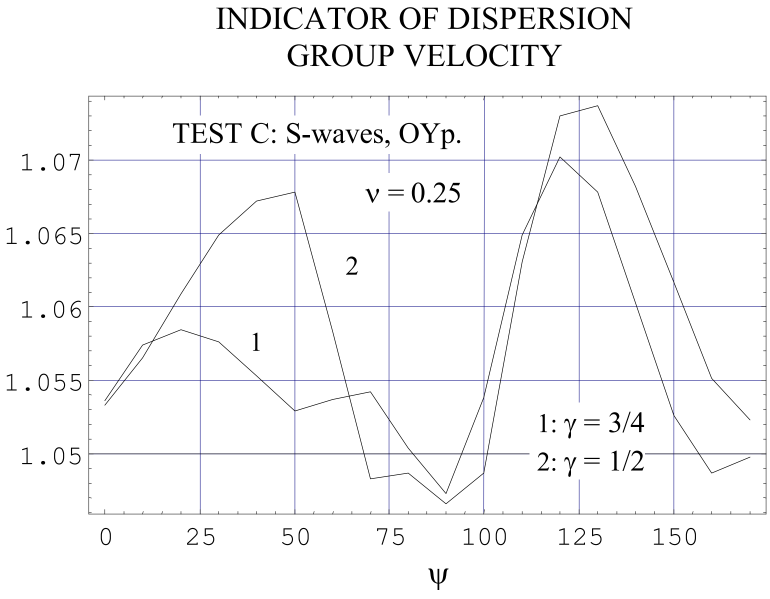

Figure 12: Test C. Maximum of the indicator of spatial dispersion associated to the group velocity for dimensionless wave number up to reach the first reference value versus the angle of wave propagation.

The mean values of the first reference wave number and the ones of the second reference wave number are computed in Tables 3 and 4, respectively, for each of the test problems. By considering the minimum mean values computed for the tests A and B, which are obtained for the cases Test A-YZ and Test B-XY, and the mean values computed for the Test C, we propose to select the values,

$$\gamma = 1: \quad m_1 = 0.38, \quad m_2 = 0.2 \tag{53}$$

$$\gamma = 0.75: \quad m_1 = 0.33, \quad m_2 = 0.17 \tag{54}$$

$$\gamma = 0.5: \quad m_1 = 0.25, \quad m_2 = 0.13 \tag{55}$$

as the first and the second standard reference wave number, respectively. Both standard reference wave numbers decrease as the distortion of the regular mesh increases.

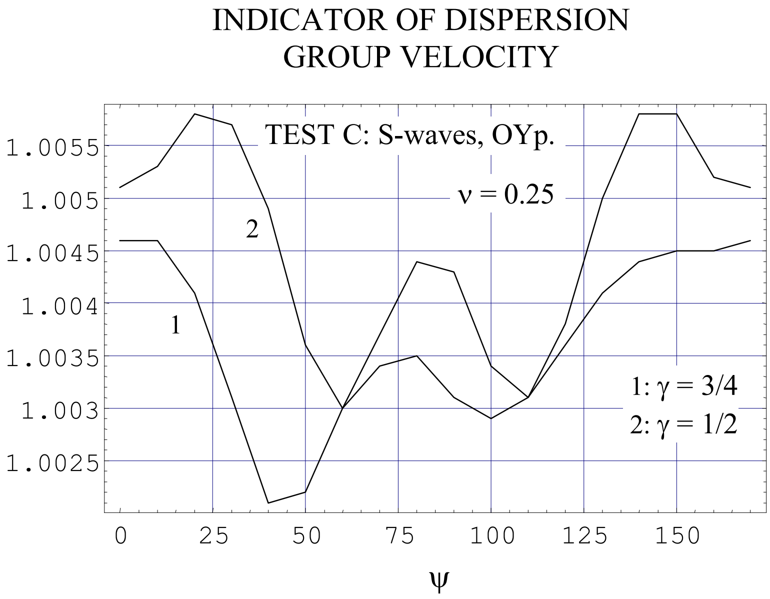

Figure 13: Test C. Maximum of the indicator of spatial dispersion associated to the group velocity for dimensionless wave number up to reach the second reference value versus the angle of wave propagation.

	ν = 0.25	γ = 1	γ = 3/4	γ = 1/2
TEST A				
XY	S, OYp	0.3723	0.3559	0.3293
	S, OZp	0.3711	0.3558	0.3262
XZ	S, OYp	0.3723	0.4159	0.4993
	S, OZp	0.3711	0.4171	0.4989
YZ	S, OYp	0.3723	0.3120	0.2497
	S, OZp	0.3711	0.3127	0.2494
TEST B				
XY	S, OYp	0.3842	0.3348	0.2544
	S, OZp	0.3875	0.3333	0.2531
XZ	S, OYp	0.3842	0.3395	0.2630
	S, OZp	0.3875	0.3372	0.2591
YZ	S, OYp	0.3842	0.3901	0.3514
	S, OZp	0.3875	0.3917	0.3481
TEST C				
	S, OYp	0.3914	0.3541	0.2658
	S, OZp	0.3916	0.3507	0.2615

Table 3: Mean values of the dimensionless wave number for which the sign of the first derivative of the specific higher order corner energy changes from negative to positive.

The use of one of the standard reference wave numbers as optimum cutoff wave number to properly capture an arbitrary interference field composed of both longitudinal and transverse harmonic waves is also investigated. To approach this question, the computation of natural modes when a solid is discretized by a regular mesh will be analyzed.

	$\nu = 0.25$	$\gamma = 1$	$\gamma = 3/4$	$\gamma = 1/2$
TEST A				
XY	S, OYp	0.1939	0.1875	0.1750
	S, OZp	0.1949	0.1883	0.1755
XZ	S, OYp	0.1939	0.2186	0.2633
	S, OZp	0.1949	0.2199	0.2645
YZ	S, OYp	0.1939	0.1641	0.1315
	S, OZp	0.1949	0.1648	0.1323
TEST B				
XY	S, OYp	0.1998	0.1758	0.1341
	S, OZp	0.1998	0.1758	0.1345
XZ	S, OYp	0.1998	0.1773	0.1385
	S, OZp	0.1998	0.1772	0.1386
YZ	S, OYp	0.1998	0.2042	0.1866
	S, OZp	0.1998	0.2042	0.1865
TEST C				
	S, OYp	0.2025	0.1843	0.1401
	S, OZp	0.2021	0.1838	0.1400

Table 4: Mean values of the dimensionless wave number for which the sign of the second derivative of the specific higher order corner energy changes from negative to positive.

3 MODAL ANALYSIS

In order to properly capture a natural mode, a discretized solid must properly capture both the longitudinal and transverse waves with frequency equal to the associated natural frequency. From the inequality $m_L < m_T$ we deduce that if the solid discretized by a regular mesh properly captures the transverse waves also properly captures the longitudinal waves; obviously, the inverse is not true.

From Eq. (7) and Eq. (28), given the dimensionless wave number based on the transverse wave, we obtain the associated frequency at the continuum, for the solid discretized by a regular mesh,

$$f_T = \frac{c_T}{2b} m_T \tag{56}$$

From Eq. (56) and Eq. (53)-(55) we obtain the first and the second reference frequency. Both reference frequencies depend on the aspect ratio parameter.

Two test problems will be analyzed: the clamped block and the cantilever beam [18], which are discretized by the regular meshes represented in Figure 14. The clamped block is a relatively bulk solid which is discretized by a moderately distorted mesh. The cantilever beam is a slender structural element which is discretized by a highly distorted mesh. For the clamped block: Young´s modulus, $E = 68.95 \times 10^9$ Pa; Poisson´s ratio, $\nu = 0.3$; mass density per unit volume of the material, $\rho = 2560$ kg/m^3; aspect ratio parameter, $\gamma = 3/4$. For the cantilever beam: Young´s modulus, $E = 2.068 \times 10^{11}$ Pa; Poisson´s ratio, $\nu = 0.3$; mass density per unit volume of the material, $\rho = 8058$ kg/m^3; aspect ratio parameter, $\gamma = 1/2$.

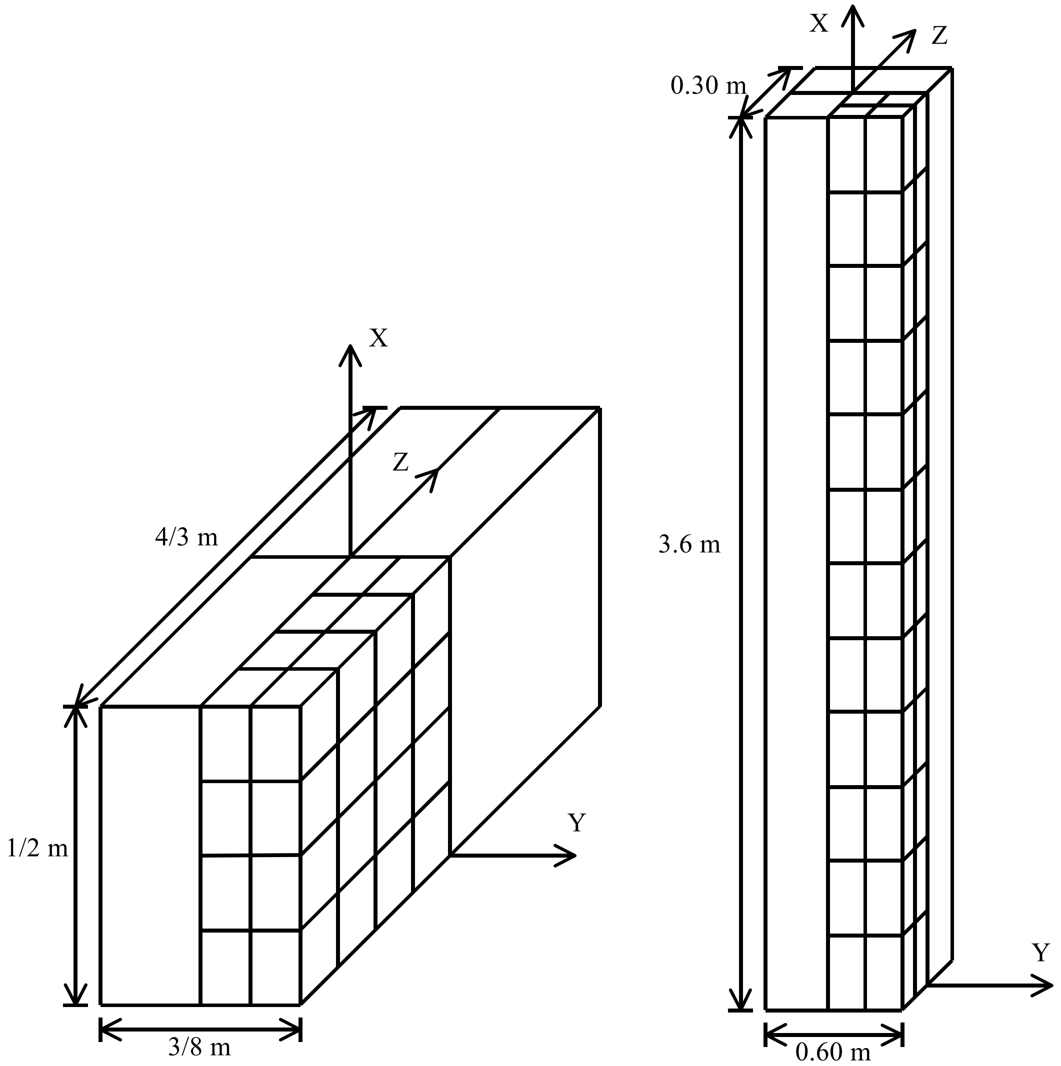

Figure 14: Clamped block and cantilever beam.

The reference frequencies for the clamped block and the cantilever beam are, respectively,

$$f_{T1} = 8496.98 \quad Hz, \quad f_{T2} = 4377.23 \quad Hz \tag{57}$$

and

$$f_{T1} = 5236.29 \quad Hz \quad f_{T2} = 2722.87 \quad Hz \tag{58}$$

An estimation of the error for the natural frequencies and modes obtained with the discretized solid is presented. In each case the reference model is obtained by dividing each element of the actual mesh into eight elements. The natural frequencies and the modal displacements obtained with the actual model and the ones obtained with the reference model are compared by the frequency error and the correlated coefficient for modal vector [19], respectively,

$$FE = \frac{\omega - \omega_{ref}}{\omega_{ref}} x100 \tag{59}$$

$$CCFMV = \frac{\left| \varphi^t \cdot \varphi_{ref} \right|}{(\varphi^t \cdot \varphi)^{1/2} (\varphi^t_{ref} \cdot \varphi_{ref})^{1/2}} \tag{60}$$

The vectors in Eq. (60) are obtained by computing each modal displacement at the nodes of the reference mesh. A value of *CCFMV* close to 1 suggests that the two vectors are well correlated, and a value close to 0 indicates uncorrelated vectors. A poor correlation between the results obtained with the actual model and the ones obtained with the reference model is indicated by frequency error greater than 5, and by *CCFMV* less than 0.90 [20].

For the test problems, in Tables 5-8 we present the evolution of Eq. (59) and Eq. (60) versus the natural frequency computed by the actual model.

MODE	FR (Hz)	FE	CCFMV	MODE	FR (Hz)	FE	CCFMV
SS				SA			
1	2199.821	0.179	1.000	1	971.640	0.534	1.000
2	2727.118	0.185	1.000	2	1613.714	0.274	1.000
3	3042.302	0.133	1.000	3	2950.334	0.440	1.000
4	4056.529	0.430	1.000	4	3344.607	0.374	1.000
5	5346.486	0.817	0.999	5	3763.871	0.425	1.000
6	5590.840	0.238	1.000	6	4901.894	0.575	1.000
7	6065.390	0.790	0.996	7	5164.174	0.725	1.000
8	6346.069	0.361	0.984	8	5483.621	0.544	0.999
9	6426.352	0.573	0.975	9	5613.046	0.618	0.999
10	6645.206	0.744	0.971	10	5963.634	0.511	0.999
11	6746.201	0.410	0.967	11	6288.133	1.725	0.997
12	6817.067	0.821	0.956	12	6863.180	1.421	0.997
13	7172.877	0.741	0.983	13	7036.543	1.216	0.993
14	7297.092	1.656	0.978	14	7211.806	1.071	0.540
15	7433.359	1.183	0.996	15	7275.739	1.850	0.558
16	7797.719	1.442	0.990	16	7585.119	1.276	0.988
17	8070.746	1.607	0.981	17	7867.853	1.356	0.989
18	8169.500	1.548	0.971	18	8201.079	1.961	0.981
19	8424.037	1.451	0.941	19	8329.689	1.378	0.987
20	8557.213	1.191	0.976	20	8827.818	3.605	0.038
21	8671.875	1.517	0.896	21	8987.235	3.102	0.183
22	8850.724	2.430	0.190	22	9085.131	2.468	0.097
23	8974.079	2.743	0.145	23	9259.918	2.966	0.007
24	9170.113	2.203	0.134	24	9617.571	3.690	0.396
25	9371.654	3.674	0.258	25	9827.690	4.762	0.031
26	9458.243	3.038	0.414	26	10057.981	5.405	0.082
27	9538.228	2.566	0.179	27	10269.557	5.395	0.415
28	9675.288	3.585	0.565	28	10296.553	4.117	0.096
29	9842.971	2.247	0.851	29	10403.791	4.255	0.314
30	9891.466	2.295	0.861	30	10515.302	3.554	0.588

Table 5: Clamped block. Frequency error and correlated coefficient for modal vector versus the computed natural frequency. Modes SS and SA.

For the clamped block is observed that whenever the computed natural frequency is less than the second reference frequency the results obtained with the actual model and the ones obtained with the reference model exhibit a high correlation. The results in the range between the second reference frequency and the first one are generally well correlated; nevertheless, if the first reference frequency is gone through the results clearly exhibit a poor correlation.

For the cantilever beam is observed that whenever the computed natural frequency is less than the second reference frequency the results obtained with the actual model and the ones obtained with the reference model exhibit a high correlation or, alternatively, a good correlation; nevertheless, in the range between the second reference frequency and the first one a non-negligible number of modes exhibit a poor correlation.

MODE	FR (Hz)	FE	CCFMV	MODE	FR (Hz)	FE	CCFMV
AS				AA			
1	1425.965	0.267	1.000	1	1131.355	0.418	1.000
2	2742.309	0.124	1.000	2	2399.369	0.275	1.000
3	3298.543	0.206	1.000	3	3143.737	0.402	1.000
4	4115.889	0.138	1.000	4	4145.977	0.425	1.000
5	4670.003	0.594	1.000	5	4551.929	0.489	1.000
6	5347.425	0.600	0.999	6	5097.987	0.618	0.993
7	6138.249	0.698	0.981	7	5193.445	0.593	0.996
8	6201.578	0.568	0.984	8	5589.388	0.491	1.000
9	6447.421	0.321	0.999	9	6061.990	0.964	0.998
10	6702.224	0.370	0.991	10	6420.540	1.052	0.997
11	6759.073	0.611	0.991	11	6489.071	0.614	0.998
12	6973.841	0.962	0.964	12	6907.589	1.205	0.966
13	7132.266	1.647	0.953	13	7003.408	0.687	0.966
14	7339.887	1.116	0.966	14	7453.756	2.415	0.957
15	7696.521	1.236	0.980	15	7788.464	2.590	0.956
16	7962.018	2.898	0.959	16	7959.445	1.579	0.942
17	8065.381	1.591	0.965	17	8068.548	1.748	0.948
18	8125.485	0.861	0.967	18	8597.211	2.834	0.359
19	8411.192	1.882	0.802	19	8650.454	1.667	0.281
20	8461.104	1.145	0.813	20	8824.951	0.859	0.984
21	8781.663	1.964	0.992	21	9012.522	1.964	0.968
22	8852.156	1.780	0.989	22	9158.781	2.621	0.970
23	9167.227	1.706	0.968	23	9431.149	1.110	0.982
24	9250.645	1.851	0.970	24	9624.671	1.708	0.386
25	9427.560	1.937	0.950	25	9947.605	4.385	0.240
26	9522.444	2.017	0.547	26	10081.541	3.585	0.361
27	9599.327	2.587	0.555	27	10318.279	4.558	0.588
28	9772.311	2.631	0.695	28	10399.856	3.357	0.513
29	9890.698	2.122	0.409	29	10720.404	4.805	0.862
30	10066.772	3.013	0.253	30	10908.133	4.860	0.043

Table 6: Clamped block. Frequency error and correlated coefficient for modal vector versus the computed natural frequency. Modes AS and AA.

4 CONCLUSIONS

This paper studies the propagation of plane harmonic waves in unbounded media discretized by the standard twenty-node hexahedral finite element. The element stiffness matrix is split into basic and higher order components which are obtained from mean and deviatoric strain fields, respectively. This decomposition is applied to the elastic energy. The research is focused on the properties of the higher order elastic energy versus the wave number. Based on the properties of the higher order energy, two values of the wave number are selected as reference values. The noteworthy conclusions of this paper are:

MODE	FR (Hz)	FE	CCFMV	MODE	FR (Hz)	FE	CCFMV
SS				SA			
1	353.417	0.082	1.000	1	37.380	0.218	1.000
2	1057.604	0.087	1.000	2	209.804	0.225	1.000
3	1752.870	0.106	1.000	3	516.261	0.249	1.000
4	2428.493	0.155	1.000	4	881.088	0.312	1.000
5	3058.068	0.256	1.000	5	1279.072	0.443	1.000
6	3569.675	0.425	0.999	6	1693.375	0.662	1.000
7	3701.198	0.336	1.000	7	2114.270	0.978	1.000
8	3899.181	0.686	0.999	8	2514.574	1.216	0.998
9	4129.715	0.984	0.990	9	2740.195	0.360	0.994
10	4166.233	0.160	0.992	10	2866.200	1.003	0.991
11	4175.800	0.136	0.998	11	3120.875	1.247	0.985
12	4264.840	0.214	0.988	12	3263.999	1.205	0.983
13	4286.941	0.456	0.939	13	3595.522	2.209	0.960
14	4385.815	1.182	0.891	14	3713.496	1.487	0.951
15	4405.419	0.414	0.937	15	4103.630	3.509	0.919
16	4624.747	2.380	0.985	16	4191.904	1.596	0.899
17	4837.400	2.416	0.774	17	4634.283	5.162	0.935
18	4955.171	2.304	0.761	18	4668.742	1.214	0.965
19	5259.268	5.054	0.886	19	5130.796	5.919	0.702
20	5371.512	1.860	0.146	20	5303.737	3.959	0.468

Table 7: Cantilever beam. Frequency error and correlated coefficient for modal vector versus the computed natural frequency. Modes SS and SA.

- The numerical research reveals that the first reference wave number could be used as an optimum cutoff wave number to properly capture an harmonic wave from the wave velocity standpoint. For dimensionless wave number less than the second reference wave number the harmonic wave would be properly captured also from the velocity of energy transport standpoint.
- The strong numerical anisotropy induced by the non-cubic meshes results in broad variations of both reference wave numbers versus the direction of wave propagation; nevertheless, by considering the mean values, the first and the second standard reference wave number can be defined. These ones depend on the aspect ratio parameter. Given the standard reference wave numbers based on the transverse wave, the first and the second reference frequency are defined.
- The numerical research reveals that a finite element natural mode exhibits a high precision or, alternatively, a good precision whenever the natural frequency is less than

the second reference frequency; nevertheless, in the range between the second reference frequency and the first one, the precision of the natural modes is clearly depending on the problem. Generally, it could be regarded that, in the range between the second reference frequency and the first one, the finite element model has an intermediate precision.

The consideration of more complex waves and media is subject of research.

MODE	FR (Hz)	FE	CCFMV	MODE	FR (Hz)	FE	CCFMV
AS				AA			
1	19.041	0.239	1.000	1	164.960	0.217	1.000
2	115.702	0.283	1.000	2	496.209	0.230	1.000
3	310.034	0.372	1.000	3	831.344	0.266	1.000
4	574.523	0.532	1.000	4	1172.703	0.344	1.000
5	893.127	0.788	1.000	5	1522.456	0.491	1.000
6	1252.357	1.171	1.000	6	1882.767	0.740	1.000
7	1643.297	1.714	1.000	7	2255.951	1.128	1.000
8	2060.514	2.448	0.999	8	2644.537	1.700	0.999
9	2499.275	3.367	0.998	9	3051.184	2.495	0.998
10	2849.359	1.745	0.870	10	3478.099	3.545	0.997
11	2909.888	1.099	0.717	11	3924.298	4.820	0.992
12	2990.308	2.269	0.699	12	4366.385	5.878	0.950
13	3034.928	0.675	0.929	13	4579.422	2.468	0.976
14	3180.253	0.504	0.992	14	4708.509	0.975	0.755
15	3365.136	2.755	0.514	15	4733.350	0.914	0.616
16	3491.702	3.746	0.506	16	4778.153	1.256	0.558
17	3606.540	0.696	0.989	17	4856.998	1.590	0.508
18	3873.630	4.370	0.204	18	4955.099	2.154	0.423
19	4022.877	4.693	0.198	19	5086.594	2.591	0.320
20	4179.955	1.586	0.927	20	5231.727	3.745	0.118
21	4382.056	5.620	0.878	21	5400.464	4.503	0.062
22	4521.035	2.244	0.979				
23	4885.734	6.862	0.175				
24	5135.984	8.367	0.155				
25	5294.493	6.096	0.253				

Table 8: Cantilever beam. Frequency error and correlated coefficient for modal vector versus the computed natural frequency. Modes AS and AA.

REFERENCES

[1] H.L. Schreyer, Dispersion of semidiscretized and fully discretized systems. T. Belytschko, T.J.R. Hughes eds. *Computational methods for transient analysis*. Elsevier Science, 1983.

[2] J.D. Achenbach, *Wave propagation in elastic solids*. Elsevier, 1975.

[3] K.F. Graff, *Wave motion in elastic solids*. Dover Publications, 1991.

[4] F.J. Brito Castro, Cutoff wave numbers for energy-orthogonal eight-node quadrilateral plane-strain elements. *Computers and Structures*, **84**, 230-242, 2006.

[5] F.J. Brito Castro, Cutoff wave numbers for energy-orthogonal six-node triangular plane-strain elements. *Computers and Structures*, **87**, 395-406, 2009.

[6] O.C. Zienkiewicz, R.L. Taylor, *The finite element method, Vol. 1*. Butterworth-Heinemann, 2000.

[7] R.D. Cook, D.S. Malkus, M.E. Plesha, *Concepts and applications of finite element analysis*. John Wiley & Sons, 1989.

[8] C.A. Felippa, B. Haugen, C. Militello, From the individual element test to finite element templates: evolution of the Patch Test. *International Journal for Numerical Methods in Engineering*, **38**, 199-229, 1995.

[9] P.G. Bergan, M.K. Nygärd, Finite elements with increased freedom in choosing shape functions. *International Journal for Numerical Methods in Engineering*, **20**, 643-664, 1984.

[10] C.A. Felippa, A survey of parametrized variational principles and applications to computational mechanics. *Computer Methods in Applied Mechanics and Engineering*, **113**, 109-139, 1994.

[11] F.J. Brito Castro, A modal error indicator based on a work-cancellation property of energy-orthogonal quadrilateral and hexahedral finite elements. *International Journal for Computational Methods in Engineering Science and Mechanics*, **6**, 127-135, 2005.

[12] K.J. Bathe, *Finite element procedures*. Prentice Hall, 1996.

[13] A.A. Shabana, *Computational dynamics*. John Wiley & Sons, 1994.

[14] M. Okrouhlík, C. Höschl, A contribution to the study of dispersive properties of one-dimensional lagrangian and hermitian elements. *Computers and Structures*, **49**, 779-795, 1993.

[15] R.A. Horn, C.R. Johnson, *Matrix analysis*. Cambridge University Press, 1992.

[16] W.H. Press, S.A. Teukolsky, W.T. Vetterling, B.P. Flannery, *Numerical recipes in fortran*. Cambridge University Press, 1992.

[17] L. Brillouin, *Wave propagation in periodic structures*. McGraw-Hill, 1946.

[18] M. Petyt, *Introduction to finite element vibration analysis*. Cambridge University Press, 1990.

[19] Z-Q. Qu, *Model order reduction techniques: with applications in finite element analysis*. Springer, 2004.

[20] F.M. Hemez, *Theoretical and experimental correlation between finite element models and modal tests in the context of large flexible space structures*, Ph.D. Thesis. University of Colorado, 1993.

COMPDYN 2011
III ECCOMAS Thematic Conference on
Computational Methods in Structural Dynamics and Earthquake Engineering
M. Papadrakakis, M. Fragiadakis, V. Plevris (eds.)
Corfu, Greece, 25–28 May 2011

DETECTION OF INTERLAMINAR CRACKS IN COMPOSITE STRUCTURES WITH THE USE OF PIEZOELECTRIC SENSORS AND THERMOGRAPHY

Piotr Kędziora

Cracow University of Technology
31-155 Kraków, ul. Warszawska 24, Poland
kedziora@mech.pk.edu.pl

Keywords: Delaminations, Thermography, Piezoelectric Sensors and Actuators, Lamb Wave, Composite Laminate.

Abstract. *Delaminations are one of the most severe defects associated with multilayered laminated composite structures. Initiation of delamination and numerical analysis of delamination growth are presented. Results of damage detection in composite laminated panels are demonstrated with use of piezoelectric patches and thermography. Thermography is utilized to detect and visualize the size of delaminations. Damage detection in fiber-reinforced composite laminated panels using Lamb waves (wave propagation) is demonstrated with the use of a sensor array. Experiments are conducted to empirically characterize the wave propagation behavior in a manufactured laminate. Piezoelectric patches are used as sensors and actuators in the experiments. Composite laminates are manufactured with an embedded defect to simulate inter-ply delamination.*

1 INTRODUCTION

Delaminations are one of the most severe defects associated with multilayered laminated composite structures. They may be caused by imperfections such as air entrapment and insufficient resin during fabrication or by impact and fatigue loads during services. Delaminations may lead to the severe degradation of the mechanical behavior of structures due to the loss of structural integrity. The detection of delaminations and the study of their effects on the mechanical behavior of delaminated composite structures become important practical issues.

Damage modeling in composite structures has been attempted by various researchers in the past. The latest effort includes a generalized laminate model featuring both weak interfacial bonding and local delamination by Shu [1]; a plasticity model coupled with the damage and identification for carbon fibre composite laminates by Boutaous et al. [2].

There have been many works on wave propagation problems related to composite shells. The first work (Lord-Rayleigh [3]) of this field dealt with wave propagation in a semi-infinite solid. In 1917 Lamb published the first work [4] of dealing with guided wave propagation in thin elastic specimens. Mirsky [5] and Nowinski [6] solved for axially symmetric waves in orthotropic shells. Chou and Achenbach [7] provided a three-dimensional solution for orthotropic shell as well. Nayfeh [8] discussed scattering of horizontally polarized elastic waves from multilayered anisotropic cylinders embedded in isotropic solids. Yuan and Hsieh [9] proposed an analytical method for the investigation of free harmonic wave propagation in laminated shells. The numerical description of the waves traveling into waveguides and slender structures has also raised many interests – information about those problems is discussed in Refs [10].

The first introduction of Lamb waves as a means of damage detection was made by Worlton [11] in 1961. He noticed that distinguish characteristics of the various modes of Lamb waves can be useful in nondestructive testing applications. Prosser et al. [12] used acoustic emission to identify cracking of thin composite specimens; also outlined the difficulties associated with acoustic emission. Wevers [13] outlined the advantages of acoustic emission techniques over other NDE methods for identifying damage in a loaded composite component. Lakshmanan and Pines [14] used and developed a wave propagation method to identify delaminations and transverse cracks in Gr/Ep composite rotorcraft. Ihn and Chang [15] used spectrograms to process guided wave signals obtained from an array of piezoelectric transducers to detect and monitor fatigue crack growth.

In this paper, we intend in order to assess the effect of delamination on the global characteristics of composite laminated cylindrical shells. Theoretical and numerical analysis of deformation initiation and growth is presented by Muc and Kędziora [16] and Muc [17]. Thermography is used to detect and visualize the size of delaminations. Results of damage detection in composite laminated panels are demonstrated with use of a piezoelectric sensor and thermography. Damage detection in fiber-reinforced composite laminated panels using Lamb waves (wave propagation) is demonstrated with the use of a sensor array. Experiments were conducted to empirically characterize the wave propagation behavior in a manufactured laminate. Piezoelectric patches were used as sensors and actuators in the experiments. Sensor arrays and associated processing were used for wave number decomposition and filtering of the Lamb wave modes. Composite laminates were manufactured with an embedded defect to simulate inter-ply delamination. Experiments were conducted to detect the presence of delamination damage in a composite laminate.

Comparisons were made between analytical predictions and experimental results, which demonstrate that the model captured essential wave propagation behavior at frequencies of interest.

2 INITIATION OF DELAMINATIONS – LINEAR FRACTURE MECHANICS

Using the continuum fracture (damage) mechanics concept it is possible to model fatigue phenomena taking into account macroscopic degradation models in the evaluation of an individual finite element (or group of them) mechanical properties – see e.g. Muc et al. [18]. However, in the distinction to the continuum fracture mechanics approach, the damage behavior of composites is represented here in the differential (incremental – not global, integral) form but in general, the method of the description is almost identical.

Employing formulations introduced in classical fracture mechanics several models for delamination growth in laminates may be proposed. Early experimental works point to strong correlation between the growth of cracks and the strain energy release rate G. The approximate size of delamination area A is governed by the following equation:

$$\frac{dA}{dN} = f\left(G_{\max}, \xi, \psi\right), \quad \xi = \frac{G_{\min}}{G_{\max}}, \quad \psi = a\tan\left(\frac{K_{II}}{K_{I}}\right) \tag{1}$$

where N is a number of cycles, and f denotes a function.

The parameter ξ expresses the ratio of minimum to maximum loading, and ψ denotes the relative amount of mode I (opening) and mode II (shearing). However, the mode dependence of the delamination growth is not yet fully understood and is a subject of considerable research.

For constant amplitude loading and a stable delamination growth, a power law relation has been first developed by Paris et al. [19]:

$$f\left(G_{\max}, \xi, \psi\right) = c\left(\Delta G\right)^{n}, \quad \Delta G = G_{\max} - G_{\min} \tag{2}$$

where c and n are material constants.

In the high stress intensity factor (SIF) range, the curve obtained from Eqs (1) and (2) is very steep indicating unstable crack propagation and hence the region does not contribute much to the propagation life of a component. Therefore, Forman et al. [20] improved the crack growth rate equation and proposed to apply the function f in the following form:

$$f\left(G_{\max}, \xi, \psi\right) = \frac{c\left(\Delta G\right)^{n}}{\left(1-R\right)K_{c} - \Delta G} \tag{3}$$

where R is the stress ratio, and K_c means the fracture toughness.

Since the delamination growth can be attributed to a mixed mode of fracture, the criterion for determining the initiation of the delamination growth was selected as [21]:

$$RB = g_{1}^{\delta} + g_{2}^{\gamma}, \quad g_{1} = \frac{G_{I}}{G_{Ic}}, \quad g_{2} = \frac{G_{II}}{G_{IIc}} \tag{4}$$

where RB is the failure index, G_{Ic} and G_{IIc} are the critical strain energy release rates corresponding to mode I and mode II fracture, respectively. δ and γ are coefficients – it was found that $\delta=\gamma=1$ provides the best fit to the experimental results (see [21]). A delamination would start to propagate when $RB \geq 1$.

3 NUMERICAL ANALYSIS OF DELAMINATION GROWTH

For instance let us consider the cross-ply laminate $[0^0,90^0{}_n]_S$, loaded in a tension (equal to 1 MPa) along the x direction. The thickness of each individual ply is equal to t, so that the total thickness of the laminate is equal to 2(n+2)t. The crack is described by its size a in the y direction and the position of its center x_a. The geometrical parameters of the laminate and of the crack are shown in Fig.1.

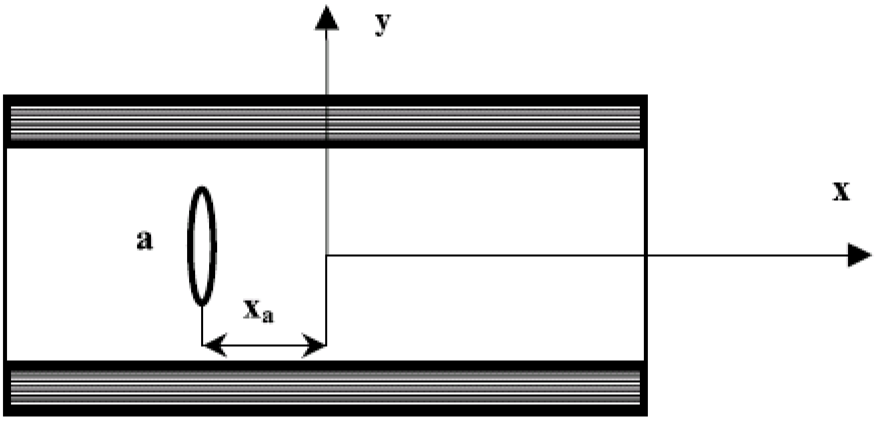

Figure 1: The geometrical parameters of the laminate with the crack.

The crack is always symmetric with respect to the x axis. Thus, only a half of the laminate is discretised with the use of finite elements. The plate have been modeled using 1536 2-D eight node isoparametric plane stress element. In the model crack face nodes are left free. The thickness of the laminate in the z direction is assumed to be equal to one. All geometrical quantities are given in mm.

With the aid of the presented finite element model the J-integral have been computed. In terms of stresses and strains it is defined as follows:

$$J = \int_{\Gamma} (Wn_1 - t_i u_{i,1}) ds \tag{5}$$

where W is the strain energy, u is displacement vector at any point on the contour, n_1 is the normal vector component, $u_{i,1}$ is the derivative of the displacement and t_i is the traction vector at the same point at the contour Γ. Γ is the contour starting from the crack face and going round the crack tip in an anti-clock wise direction and ending on the other crack face. This J-integral is seen to be the rate of change of potential energy with respect to the crack length a. For the linear elastic material the J-integral is equal to the energy release rate G. Since the laminate is subjected to the remote tension the first mode only is analyzed herein. In the evaluation of the J-integral, contour path is taken along the finite element edge and values and quantities in Eqn (5) are computed at the element level.

In the numerical analysis each ply is assumed to be made of carbon/epoxy resin having the following material properties (treated as it will be explained later as mean values): E_1= 200 [GPa], E_2= 12 [GPa], G_{12}= 8 [GPa], G_{23}= G_{12}= 8 [GPa], G_{13}= 0.6·G_{12}= 4.8 [GPa], $\nu_{12} = 0.3$. In order to verify the effectiveness of the proposed method of the numerical computations the analytical example dealing with the fracture analysis of a square isotropic homogeneous plate with central crack subjected to tension have been solved – see Broek [22]. Due to the central symmetry one quarter of the plate have been analyzed and discretised with the use of 768 finite elements. In the evaluation of the J-integral two contour paths are taken to compare the results. Each contour paths runs around the crack tip from lower crack face up to the top crack surface along the finite element edges – it is drawn schematically in Fig. 2.

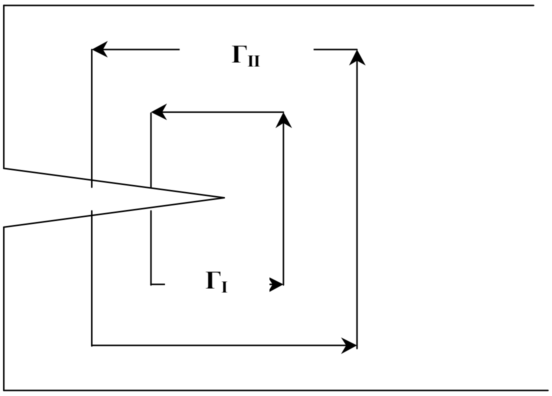

Figure 2: Contour paths Γ definitions.

The results of computations are presented in Table 1 together with the analytical results. The agreement between them seems to be very good. In further computations two different contour paths are always taken into considerations in order to eliminate possible errors in modeling of the path.

Path I	Path II	Analytical [22]
0.14374 E-04	0.15189 E-04	0.15122 E-04

Table 1: Comparison of analytical and numerical values of the J-integral.

4 EXPERIMENTAL ANALYSIS DAMAGE IDENTIFICATION

4.1 Detection of delamination via thermography

Thermography is a measurement technique which provides an image of the distribution of the temperature on the surface of the examined object. Thermography proceeds by decoding, using an adapted detector, information ‘‘temperature’’ resulting from the infra-red radiation emitted by any object. The principal advantage of infra-red thermography is its non-intrusive character. Indeed, it forms part of the techniques of non-destructive testing and can be carried out on installations in service. The deformation of solid materials is almost always accompanied by releases of heat. When the material becomes deformed or is damaged and fissured, a part of energy necessary to starting and the propagation of the damage is transformed in an irreversible way into heat [23].

During low frequency mechanical excitation, the average temperature in the gage section of the specimen increased with cycles. The small amplitude oscillatory temperature variation is due to the reversible thermal heating and cooling during each loading cycle. The objective in this study was to make a correlation between the increase in the temperature of specimen and the evolution of the damage [24].

The experimental analysis was conducted with the use of the thermovision camera Flir joined with the system IRNDT. The tested cylindrical panel was made of 8 layers and had the following geometrical parameters: L=298 [mm], R=92 [mm], t=1.8 [mm] – see Fig. 3. The thermal excitation was obtained from halogen lamps. During tests the temperature on the surface does not exceeded 40 [^{o}C] and the time of heating was equal to 20 [s].

In the tested specimen delaminations were inserted at the shell mid-surface. They have different dimensions as it may be seen in Fig. 4. The plotted results demonstrate that the sensitivity of detection depends on the distance of the camera to the cylinder and on the lens diameter. It shows that those values have to be carefully chosen for each individual experimental case.

Figure 3: Experimented setup – an overview.

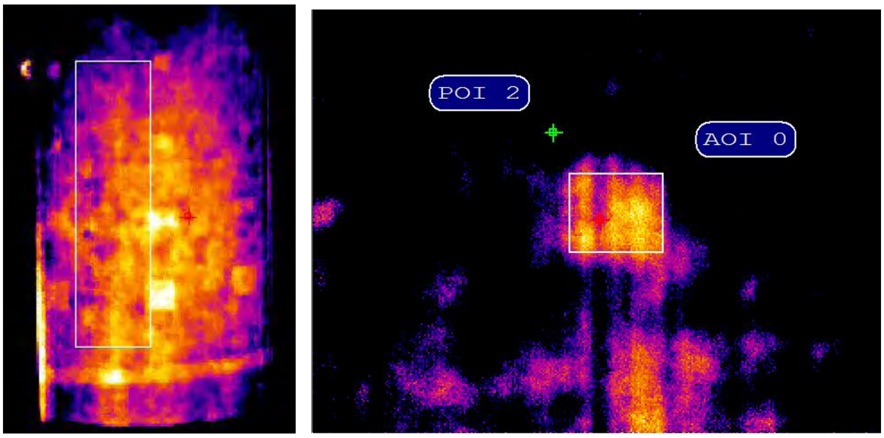

a) lens 18 [mm], distance 88 [cm]

b) lens 18 [mm], distance 16 [cm]

c) lens 10 [mm-, distance 30 [cm]

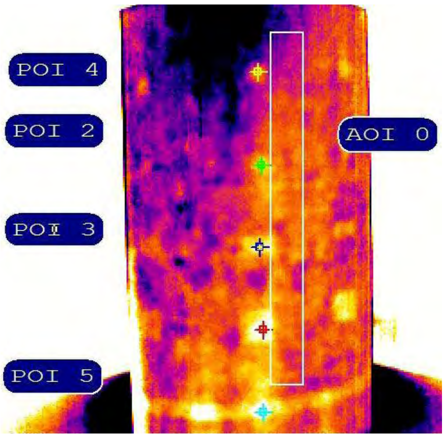

Figure 4: Effects of lens diameter and of distance to the specimen on the sensitivity of results.

Figure 5 represents the decrease of temperature with time for selected points at the panel. These values are particularly attributed to the location of delaminations.

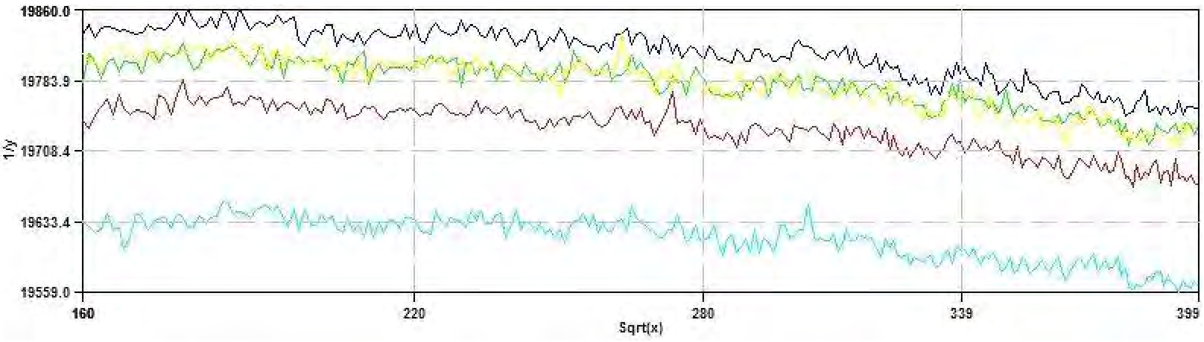

Figure 5: Graph of thermal response at selected locations.

4.2 Piezoelectric sensors

Damage detection in composite laminated panels using Lamb waves is demonstrated with use of a sensor array. Experiments were conducted to characterize empirically the wave propagation behavior in a manufactured laminate. Piezoelectric patches were used as sensors and actuators in the experiments. Sensor arrays and associated processing were used for wave number decomposition and filtering of the Lamb wave modes. Composite laminates were manufactured with an embedded defect to simulate inter-ply delamination. Experiments were conducted to detect the presence of delamination damage in a composite laminate.

A cylindrical panel made of glass woven roving having the mechanical and geometrical parameters identical to those mentioned in section 4.1 – Fig.6. An excitation signal took the form of sine wave function was modulated with the Hanning window and was applied at the left piezoelectric actuator in Fig.6; its frequency is varies from 100÷500 [kHz]. The piezoelectric sensor (on the right side in Fig.6) was placed close to the local square delamination having the size 10 [mm] and being in the middle of the laminate.

Figure 6: General configuration of the cylindrical panel with one sensor and one actuator – they are located parallel to the delaminated area.

The wave propagation in the panel with local delamination was analyzed experimentally. The excitation signal and the response signal were generated and collected by the analyzer and then those signals were converted to digital ones with the use of MATLAB package.

Figure 7 demonstrates the response signals obtained experimentally for the perfect and imperfect (with the single delamination) cylindrical panel. As it may be seen there is a visible difference between response signals for perfect and imperfect shells for each excitation signal frequency considered.

a) excitation signal frequency 100 [kHz]

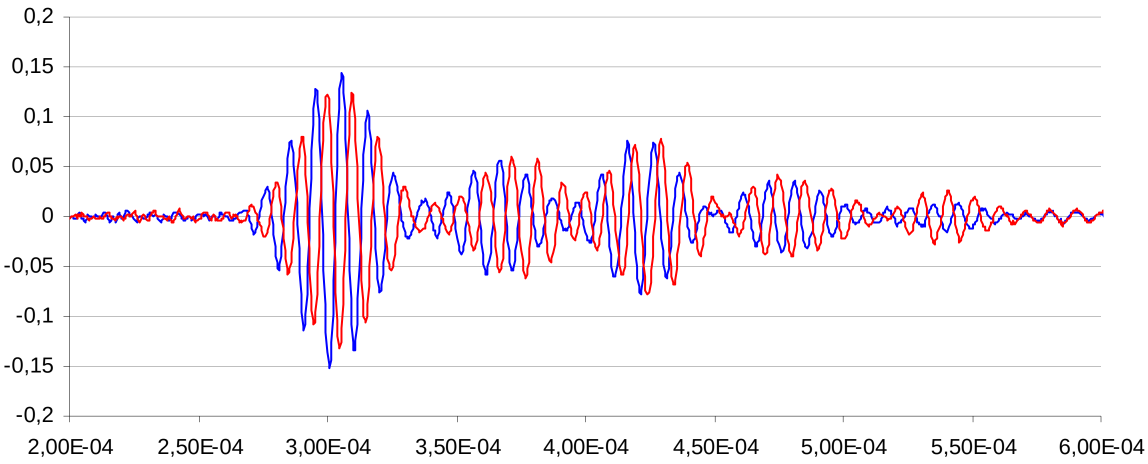

b) excitation signal frequency 200 [kHz]

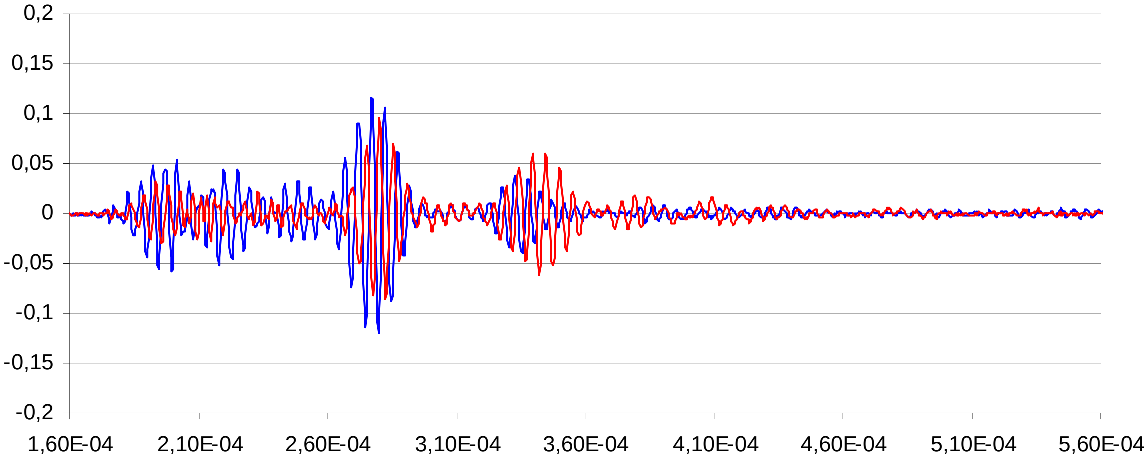

c) excitation signal frequency 300 [kHz]

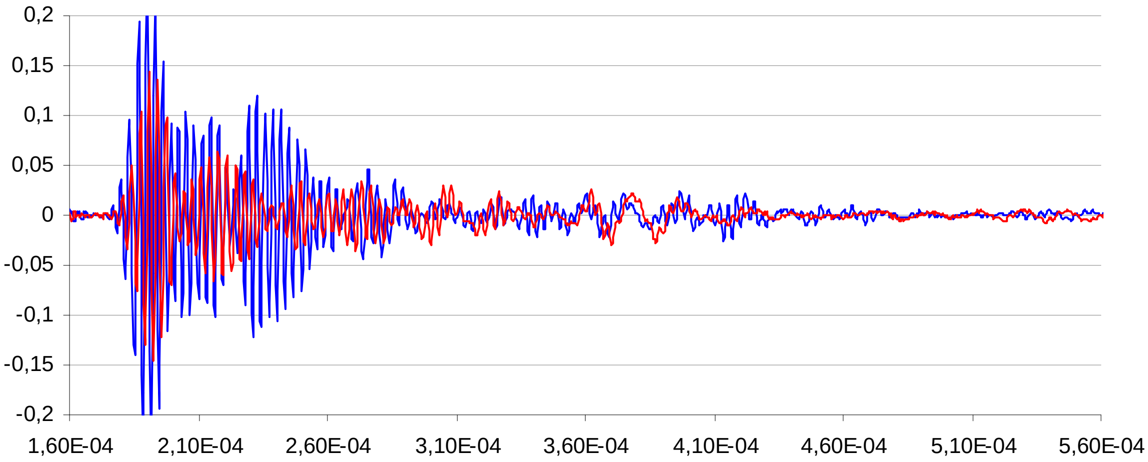

Figure 7: Experimental wave propagation results (blue line – without delamination, red line – with delamination); for various frequencies.

However, the reasonable detection of the size and the location of delamination require the careful analysis and optimal design of the location and number of piezoelectric sensors and actuator. In addition, in the delaminated region the interference between generated and reflected waves is observed that affects the signal collected by the sensor (see Figs 7a, b and c). In order to obtain better experimental results it is necessary to conduct further work dealing particularly with the optimal design of sensors number, locations and the frequency of the excitation signal.

The locations of piezoelectric sensor and actuator have significant effects on the displacement response. Different locations are presented in Figs 8 and 10. The response result (Figs 9 and 11) are plotted for one value of the signal excitation frequency equal to 100 [kHz]. The amplitude of response displacement is strongly affected by the distance between sensor and actuator – compare results plotted in Figs 7a and 11. The growth of the distance reduces the amplitudes. For the sensor and actuator located in the parallel direction to the delamination the amplitude for imperfect shell is lower than for perfect one, whereas for other locations the amplitude is higher – compare the results presented in Figs 7a and 9, 11.

Figure 8: Configuration of the cylindrical panel with the sensor and actuator – they are located below delaminated area 5 [cm] from the panel edge.

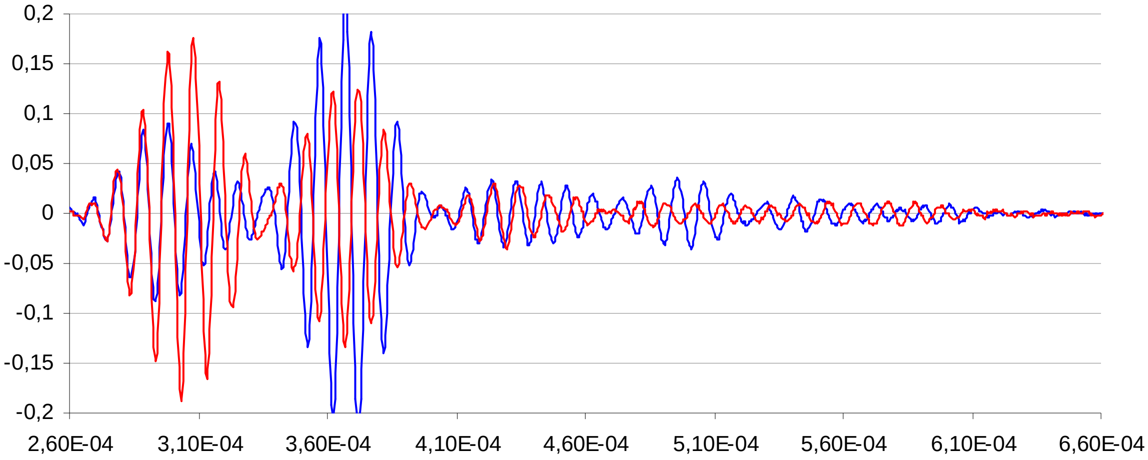

Figure 9: Experimental wave propagation results (blue line – without delamination, red line – with delamination); frequency is equal to 100 [kHz].

Figure 10: Configuration of the cylindrical panel with the sensor and actuator – the actuator is located above delaminated area 5 [cm] from the upper panel edge and the sensor 5 [cm] from lower panel edge.

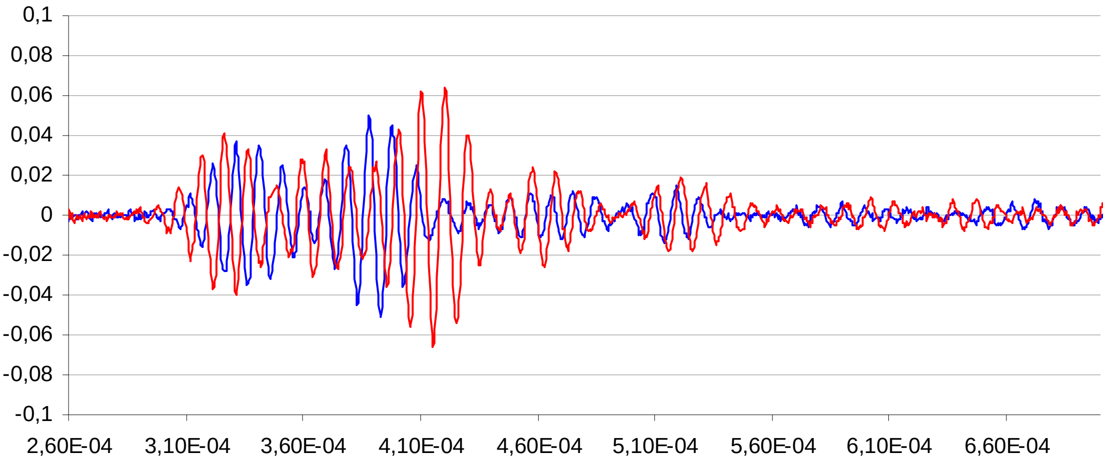

Figure 11: Experimental wave propagation results (blue line – without delamination, red line – with delamination); frequency is equal to 100 [kHz].

5 CONCLUSIONS

- This study is intended to show the relation between the dissipation of heat and the damage of the composites.
- These techniques propose to pass from temperature information given by the infrared camera to a distribution of heat sources on surface of the composites.
- The amplitude of the response is strongly affected by the excitation signal frequency and location of sensor and actuator; therefore, the optimization of they location and number is required.

ACKNOWLEDEGEMENT

The Polish Research Foundation PB 174/B/T02/2009/36 is gratefully acknowledged for financial support.

REFERENCES

[1] X.P. Shu, A generalised model of laminated composite plates with interfacial damage. *Compos. Struct.*, **74**, 237-246, 2006.

[2] A. Boutaous, B. Peseux, L. Gornet, A. Bélaidi. A new modeling of plasticity coupled with the damage and identification for carbon fibre composite laminates. *Compos. Struct.*, **74**, 1–9, 2006.

[3] Lord-Rayleigh, On the Free Vibrations of an Infinite Plate of Homogeneous Isotropic Matter. *Proc. of the London Mathematical Society*, **20**, 225-234, 1889.

[4] H. Lamb, On Waves in an Elastic Plate. *Proc. of the Royal Society*, London, **93**, 114–128, 1917.

[5] I. Mirsky, Axisymmetric vibrations of orthotropic cylinders. *J. Acoust. Soc. Am.*, **36**, 2106, 1964.

[6] J.L. Nowinski, Propagation of longitudinal waves in circular cylindrical orthotropic bars. *J. Engng. Ind.*, **89**, 408, 1967.

[7] F.H. Chou, J.D. Achenbach, Three-dimensional vibrations of orthotropic cylinders. *ASCE J. Engng. Mech.*, **98**, 813, 1981.

[8] A.H. Nayfeh, *Wave propagation in layered anisotropic media with applications to composites*. Elsevier, Amsterdam, 1995.

[9] F.G. Yuan, C.C. Hsieh, Three-dimensional wale propagation in composite cylindrical shells, *Compos. Str.*, **42**, 153, 1998.

[10] M.N. Ichchou. J.L. Mencik, W. Zhou, Wave finite elements for low and mid-frequency description of coupled structures with damage. *Comput. Methods Appl. Mech. Engrg.*, **198**, 1311, 2009.

[11] D.C. Worlton, Experimental Confirmation of Lamb Waves at Megacycle Frequencies. *J. Appl. Ph.*, **32**, 967, 1961.

[12] W.H. Prosser, K.E. Jackson, S. Kellas, B.T. Smith, J. McKeon, A. Friedman, Advanced, waveform based acoustic emission detection of matrix cracking in composites. *Materials Evaluation*, **53**, No. 9, 1052-1058, 1995.

[13] M. Wevers, Listening to the sound of materials: acoustic emission for the analysis of material behavior. *NDT&E International*, **30**, No. 2, 99-106, 1997.

[14] K.A. Lakshmanan, D.J. Pines, Modeling damage in rotorcraft flex beams using wave mechanics. *Smart Materials and Structures*, **6**, 383-392, 1997.

[15] J.B. Ihn, F.K. Chang, Detection and monitoring of hidden fatigue crack growth using a built-in piezoelectric sensor/actuator network: I. Diagnostics. *Smart Materials and Structures*, **13**, 609-620, 2004.

[16] A. Muc, P. Kędziora, A fuzzy set analysis for a fracture and fatigue damage response of composite materials. *Compos. Str.*, **54**, 283-287, 2001

[17] A. Muc, A fuzzy set approach to interlaminar cracks simulation problems. *International Journal of Fatigue*, **24**, 419–427, 2002.

[18] A. Muc, Z. Krawiec, FE modelling of laminates degradation in thin walled structures due to fatigue loads. *In: Proceedings WCCM-IV*, Buenos Aires, CD-Rom, I-588, 1998.

[19] P.C. Paris, F. Erdogan, A critical analysis of crack propagation laws. *J. Basic Engng.*, Trans ASME, **85**, 528–534, 1963.

[20] R.G. Forman, V.E. Keamey, R.M. Engle, Analysis of crack propagation in cyclic-loaded structures. *J. Basic Engng*., Trans ASME, **87**, 459–464, 1967.

[21] M.F. Kanninen, C.H. Popelar, *Advanced fracture mechanics*. Oxford engineering science series 15. Oxford University Press, 1985.

[22] D. Broek, *Elementary engineering fracture mechanics*. Nijhoff, Hague, 1982.

[23] A. Chrysochoos, Infrared thermography, a potential tool for analyzing the material behaviour. *Meca Indus*, **3**, 3-14, 2002.

[24] L. Toubal, Analytical and experimental approaches of damage by fatigue of a carbon/epoxy composite. *Ph.D. thesis,* University Paul Sabatier, Toulouse III; 2004.

COMPDYN 2011
III ECCOMAS Thematic Conference on
Computational Methods in Structural Dynamics and Earthquake Engineering
M. Papadrakakis, M. Fragiadakis, V. Plevris (eds.)
Corfu, Greece, 25–28 May 2011

AN EFFICIENT BEAM-COLUMN ELEMENT FOR NONLINEAR 3D FRAME ANALYSIS

Svetlana M. Kostic[1], **Prof. Filip C. Filippou**[2] **and Chin-Long Lee**[3]

[1] Faculty of Civil Engineering, University of Belgrade
Bulevar Kralja Aleksandra 73, Belgrade, Serbia
svetlana@grf.bg.ac.rs

[2] Department of Civil and Env. Engineering, University of California
Berkeley, CA 94720 - 1710
filippou@ce.berkeley.edu

[3] Simpson Gumpertz & Heger Inc, 41 Seyon Street
Waltham, MA 02453
clee@sgh.com

Keywords: Nonlinear Analysis, Beam-Column Element, Resultant Plasticity, Generalized Plasticity.

Abstract. *A three-dimensional nonlinear beam-column element for the simulation of the global and local response of frames under monotonic and cyclic loading conditions is presented. The element belongs to the group of concentrated plasticity models, with plastic hinges located at the ends of the element and described with yield and limit surfaces. The concept of generalized plasticity, originally developed for material plasticity, is extended to force resultants in the element formulation. The element takes into account the interaction of the axial force and the bending moments about the principal axes of the cross section and the hardening behavior. The gradual yielding of the cross section is described by the asymptotical approaching of the limit surface.*

1 INTRODUCTION

The adoption of performance-based guidelines for the earthquake resistant design of structures encourages the use of nonlinear analysis methods in professional engineering practice, since it provides more detailed information about the structural response, such as inelastic deformations, than traditional design procedures. Besides the need for a more accurate evaluation method, it is equally important to assess the efficiency and cost of the analysis, which directly, depends on the efficiency and cost of the deployed nonlinear elements. Because of the good compromise between accuracy and computational efficiency, frame elements are commonly used in earthquake engineering practice. In this context distributed inelasticity beam-column elements with integration of the inelastic material response over the cross-section, commonly called fiber beam-column elements, offer a high level of accuracy and flexibility in modeling the 3d inelastic response of structural members, but are computationally expensive, and put high demands on computer storage and memory. Consequently, more economical point hinge models are still widely used for the simulation of the hysteretic response of frames.

To date, many studies have been conducted on concentrated plasticity (or point hinge) beam-column elements [1-6]. The resultant plasticity beam-column elements use concepts of plasticity theory to describe the relation between basic element forces and deformations. The interaction of the axial force and bending moments about the principal axes of the cross section is described by a stress-resultant yield surface, which will be called yield surface in the following presentation. Yield surface equations for different types of cross sections are available [1, 7-9]. Also, different strategies have been proposed for approaching the yield surface and preventing the element force path from drifting away from it. Orbison [1] used a single polynomial expression for the yield surface and developed a five step procedure for mapping the element forces onto the yield surface. The algorithm has some limitations such as the need to subdivide each increment into several sub-increments in order to prevent large errors. Also, the element response can represent an elastic-perfectly plastic material, but not a material with hardening and it does not account for gradual yielding, since the element ends are either fully elastic or fully plastic.

Several models that improve the shortcomings of Orbison's model were proposed in the last 15 years. The idea of loading and bounding surfaces, introduced by Dafalias and Popov [10] for material plasticity, has been successfully applied to the concentrated and distributed plasticity beam-column elements [4, 5, 11-13]. In these models, the loading and bounding surfaces have the same shape, in order to prevent the two surfaces from overlapping. Once the force point touches the bounding surface (at point A), with continued plastic loading, the force point moves along the line that connects the point A and its conjugate point A' that lies on the bounding surface.

A different algorithm for the gradual, asymptotical approach of the bounding surface for the material plasticity was proposed in the generalized plasticity model by Lubliner and Aurichio [14-16]. The model is simple, does not require an expression for the bounding surface and has a straightforward implementation. It introduces two parameters with clear physical meaning β and δ. With the implementation of the return mapping algorithm, it is computationally very efficient.

The element in this paper adopts the idea of the generalized plasticity material model. The backward-Euler algorithm with general closest point projection [17] is modified to suit the element-based force-deformation relationship. Isotropic and kinematic hardening (or softening) is possible. Because of its quadratic convergence and simplicity, the element is computationally very efficient and overcomes shortcoming of elastic-perfectly plastic elements.

2 ELEMENT FORMULATION

2.1 Basic Framework

The underlying assumption of the generalized plasticity theory is the existence of two continuous real valued functions, the limit function F and yield function f [15, 16]. The yield function f encloses the region with elastic behavior forming the boundary between elastic and inelastic region:

$$\begin{aligned} f < 0 &\quad \Rightarrow \quad \text{elastic state} - \text{no inelastic effects} \\ f \geq 0 &\quad \Rightarrow \quad \text{inelastic state} - \text{inelastic effects may or may not occur} \\ &\qquad\quad\;\; \text{depending on loading or unloading} \end{aligned}$$

The basic forces **q** of a three-dimensional (3d) frame element without rigid body modes are shown in Figure 1. The corresponding deformations are denoted with **v**. Zero-length plastic hinges may form at one or both element ends, while the rest of the element is elastic.

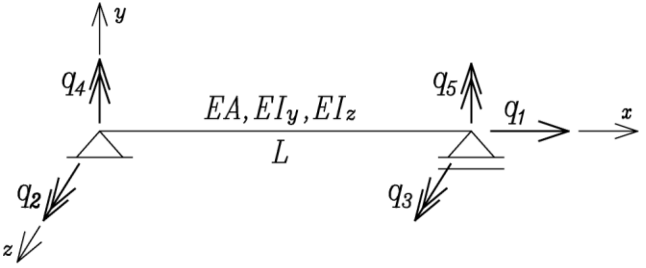

Figure 1: Basic element forces **q**.

In beam-column stress-resultant plasticity elements the classical material plasticity rules are modified to represent the axial force, bending moment interaction under inelastic behavior. Therefore, the following equations, that govern the element behavior, are assumed:

1. The element deformations **v** are decomposed into the linear elastic contribution $\mathbf{v}^{\mathbf{e}}$ and the plastic contribution $\mathbf{v}^{\mathbf{p}}$:

$$\mathbf{v} = \mathbf{v}^{\mathbf{e}} + \mathbf{v}^{\mathbf{p}} \tag{1}$$

2. There is a linear elastic relation between basic forces and elastic element deformations:

$$\mathbf{q} = \mathbf{k}_{\mathbf{e}} \mathbf{v}^{\mathbf{e}} = \mathbf{k}_{\mathbf{e}} \left(\mathbf{v} - \mathbf{v}^{\mathbf{p}} \right) \tag{2}$$

where $\mathbf{k}_{\mathbf{e}}$ is the elastic element stiffness matrix.

3. The yield function f is expressed in terms of the basic element forces **q**, of vector **a** which defines the position of the center of the surface and a hardening variable α which models isotropic hardening. H_{iso} and H_{kin} are the isotropic and kinematic plastic hardening (or softening) non-dimensional parameters, respectively. The yield function f distinguishes between elastic and inelastic states.

$$f(\mathbf{q}, \mathbf{a}, \alpha) = \Phi(\mathbf{q} - \mathbf{a}) - H_{iso} \alpha \tag{3}$$

4. The limit function F depends on the nonnegative consistency parameter λ and has the following form proposed for generalized plasticity models:

$$F = h(f) \frac{d}{dt}(\Phi) - \lambda \tag{4}$$

$$h(f) = \frac{f}{\delta(\beta - f) + (H_{iso} + H_{kin})\beta} \tag{5}$$

where δ and β are two non dimensional positive constants (δ measures the speed of approach of the model to the asymptotic behavior, and β measures the distance between the current and the asymptotic yield function). The meaning of surfaces and parameters δ and β is shown in Fig.2.

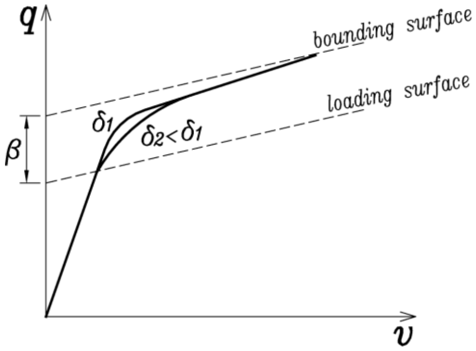

Figure 2: Basic force **q** versus generalized element deformation **v**.

5. An associative plastic flow rule is assumed that is described with the following equation:

$$\dot{\mathbf{v}}^{\mathbf{p}} = \lambda \frac{\partial f}{\partial \mathbf{q}}. \tag{6}$$

6. The surface motion (kinematic hardening mechanism) is defined by Ziegler's rule:

$$\dot{\mathbf{a}} = H_{kin}\mathbf{\Pi}\dot{\mathbf{v}}^{\mathbf{p}} = H_{kin}\mathbf{\Pi}\lambda \frac{\partial f}{\partial \mathbf{q}}. \tag{7}$$

where $\mathbf{\Pi}$ is a scaling matrix, that accounts for the different dimensions between $\mathbf{a}$ and $\mathbf{v}^{\mathbf{p}}$ and is adopted here equal to:

$$\mathbf{\Pi} = diag\left\{\frac{EA}{L}, \frac{EI_z}{L}, \frac{EI_z}{L}, \frac{EI_y}{L}, \frac{EI_y}{L}\right\}. \tag{8}$$

7. The simplest evolutionary equation for α is adopted corresponding to equivalent plastic strain:

$$\dot{\alpha} = \left\|\dot{\mathbf{v}}^{\mathbf{p}}\right\| = \lambda \left\|\frac{\partial f}{\partial \mathbf{q}}\right\|, \tag{9}$$

where:

$$\left\|\frac{\partial f}{\partial \mathbf{q}}\right\| = \left[\left(\frac{\partial f}{\partial \mathbf{q}}\right)^T \mathbf{\Lambda} \frac{\partial f}{\partial \mathbf{q}}\right]^{1/2}, \tag{10}$$

with a scaling matrix $\mathbf{\Lambda}$ defined as:

$$\mathbf{\Lambda} = diag\left\{\frac{1}{L^2}, \mathbf{I_4}\right\}. \tag{11}$$

Matrix $\mathbf{I_4}$ is the 4x4 identity matrix.

8. The Kuhn-Tucker complementarity conditions are:

$$\lambda \geq 0, \quad F \leq 0, \quad \lambda F = 0. \tag{12}$$

These conditions reduce the plastic problem to a constrained optimization problem.

9. The limit equation can be written in the following form, $-F=0$:

$$\lambda - h(f)\frac{d}{dt}(\Phi) = 0. \tag{13}$$

Integrating this equation over the time interval $[t_n, t_{n+1}]$, we obtain the discrete limit condition:

$$\Delta\lambda - h(f)(\Phi_{n+1} - \Phi_n) = 0. \tag{14}$$

2.2 Integration Algorithm

The model in the previous section can be transformed into a discrete constrained optimization problem by applying the backward (implicit) Euler numerical integration scheme.

Assuming that the state of the element is known at time step t_n, means that the values $\{\mathbf{v_n}, \mathbf{v_n^p}, \mathbf{a_n}, \boldsymbol{\alpha_n}\}$ are available. The basic forces are also known since they can be found from equation (2):

$$\mathbf{q_n} = \mathbf{k_e}(\mathbf{v_n} - \mathbf{v_n^p}). \tag{15}$$

Suppose that we know an increment in total element deformations $\mathbf{\Delta v}$ at the time step t_{n+1}, so that $\mathbf{v_{n+1}} = \mathbf{v_n} + \mathbf{\Delta v}$. Other state variables $\mathbf{v_{n+1}^p}$, $\mathbf{a_{n+1}}$ and α_{n+1} should be updated, as well, and this is the problem to be solved.

By applying the backward-Euler method we have:

$$\mathbf{v_{n+1}^p} = \mathbf{v_n^p} + \mathbf{g}_{n+1}(\mathbf{q}_{n+1}, \mathbf{a}_{n+1})\Delta\lambda. \tag{16}$$

$$\mathbf{a}_{n+1} = \mathbf{a}_n + H_{kin}\mathbf{\Pi g}_{n+1}(\mathbf{q}_{n+1}, \mathbf{a}_{n+1})\Delta\lambda. \tag{17}$$

$$\alpha_{n+1} = \alpha_n + \left\|\mathbf{g}_{n+1}(\mathbf{q}_{n+1}, \mathbf{a}_{n+1})\right\|\Delta\lambda. \tag{18}$$

where $\Delta\lambda = \int_{t_n}^{t_{n+1}} \lambda dt$ and $\mathbf{g} = \frac{\partial f}{\partial \mathbf{q}}$. The discrete version of the Kuhn-Tucker conditions (12) is:

$$\Delta\lambda \geq 0, \quad F_{n+1} \leq 0, \quad \Delta\lambda F_{n+1} = 0. \tag{19}$$

The discrete system of equations will be solved by the two-step predictor-corrector return mapping algorithm.

2.3 Return Mapping Algorithm

The return mapping algorithm is an efficient and robust integration scheme, which belongs to the family of elastic predictor - plastic corrector algorithms. In the first, predictor step, a purely elastic (trial) state is computed ($\mathbf{q_{n+1}^{trial}}$). If this trial state violates the integrated limit inequality *F≤0*, the element forces are corrected in the second, corrector, step using the trial state as an initial condition. Otherwise, the second step is skipped and the trial solution represents the solution at t_{n+1}.

Since the element has two nodes, and plastic deformations can occur at both of them, the yield functions f_1 and f_2, limit functions F_1 and F_2, consistency parameters $\Delta\lambda_1$ and $\Delta\lambda_2$ and hardening variables α_1 and α_2 are lumped into vectors **f**, **F**, **Δλ** and **α**, respectively. The diagonal 2x2 matrix that has nonzero values on the main diagonal, equal to f_1 and f_2 is denoted as *diag*(**f**), and similarly for others: *diag*(**F**), *diag*(**Δλ**), etc.

When both plastic hinges form at element ends, **g** is a 3x2 matrix, with the first column equal to $\partial_{\mathbf{q}} f_1 = \mathbf{g}_1$ and the second equal to $\partial_{\mathbf{q}} f_2 = \mathbf{g}_2$. If only one node yields, **g** is a 3x1 vector and is equal to $\mathbf{g}_1$ or $\mathbf{g}_2$, depending on which node yields. The parameter **ΔΔλ** for the non-yielding node is zero.

1. Predictor step: We consider a purely elastic step obtained by freezing the plastic flow, so that Δλ=0.

$$\mathbf{q}_{\mathbf{n+1}}^{trial} = \mathbf{k}_e(\mathbf{v}_{n+1} - \mathbf{v}_n^p) \tag{20}$$

$$\mathbf{v}_{n+1}^{p,\,trial} = \mathbf{v}_n^p \tag{21}$$

$$\mathbf{a}_{n+1}^{trial} = \mathbf{a}_n \tag{22}$$

$$\boldsymbol{\alpha}_{n+1}^{trial} = \boldsymbol{\alpha}_n \tag{23}$$

$$\mathbf{f}_{n+1}^{trial} = \mathbf{f}(\mathbf{q}_{n+1}^{trial}, \mathbf{a}_{n+1}^{trial}, \boldsymbol{\alpha}_{n+1}^{trial}) = \boldsymbol{\Phi}_{n+1}^{trial} - H_{iso}\boldsymbol{\alpha}_{n+1}^{trial} \tag{24}$$

$$\boldsymbol{\Phi}_{n+1}^{trial} = \boldsymbol{\Phi}(\mathbf{q}_{n+1}^{trial} - \mathbf{a}_{n+1}^{trial}) \tag{25}$$

Once the trial state is computed, we check the limit condition *F≤0*, which due to Δλ=0, reduces to the condition $\mathbf{f}_{n+1}^{trial}(\boldsymbol{\Phi}_{n+1}^{trial} - \boldsymbol{\Phi}_n) \leq 0$.

If this condition is not violated, the trial state is admissible state and:

$$\mathbf{v}_{n+1}^p = \mathbf{v}_n^p \tag{26}$$

$$\mathbf{a}_{n+1} = \mathbf{a}_n \tag{27}$$

$$\boldsymbol{\alpha}_{n+1} = \boldsymbol{\alpha}_n \tag{28}$$

$$\mathbf{q}_{n+1} = \mathbf{q}_{n+1}^{trial} \tag{29}$$

$$\mathbf{k} = \mathbf{k}_e \tag{30}$$

If the condition $\mathbf{f}_{n+1}^{trial}(\boldsymbol{\Phi}_{n+1}^{trial} - \boldsymbol{\Phi}_n) \leq 0$ is not satisfied, the trial state is nonadmissible state and the correction should be done in the corrector step.

2. Corrector step: We require the residuals $\mathbf{R}_{\mathbf{1,n+1}}$, $\mathbf{R}_{\mathbf{2,n+1}}$ and $\mathbf{R}_{\mathbf{3,n+1}}$ and the limit condition (14) to be zero.

$$\mathbf{R}_{\mathbf{1,n+1}} = -\mathbf{v}_{\mathbf{n+1}}^{\mathbf{p}} + \mathbf{v}_{\mathbf{n}}^{\mathbf{p}} + \mathbf{g}_{\mathbf{n+1}}\boldsymbol{\Delta\lambda} \tag{31}$$

$$\mathbf{R}_{\mathbf{2,n+1}} = -\mathbf{a}_{\mathbf{n+1}} + \mathbf{a}_{\mathbf{n}} + H_{kin}\boldsymbol{\Pi}\mathbf{g}_{\mathbf{n+1}}\boldsymbol{\Delta\lambda}_{\mathbf{n+1}} \tag{32}$$

$$\mathbf{R}_{\mathbf{3,n+1}} = -\boldsymbol{\alpha}_{\mathbf{n+1}} + \boldsymbol{\alpha}_{\mathbf{n}} + \left\|\mathbf{g}_{\mathbf{n+1}}\right\|\boldsymbol{\Delta\lambda}_{\mathbf{n+1}} \tag{33}$$

After linearization of equations (31)-(34) and the limit equation (14) and after some numerical manipulations, we get the following nonlinear system of equations for determining the parameter $\boldsymbol{\Delta\Delta\lambda}$:

$$(\mathbf{a}\boldsymbol{\Delta\Delta\lambda})(\mathbf{b}\boldsymbol{\Delta\Delta\lambda}) + \mathbf{c}\boldsymbol{\Delta\Delta\lambda} + \mathbf{d} = \mathbf{0} \tag{34}$$

The smallest positive solution $\boldsymbol{\Delta\Delta\lambda}$ (the increment of the consistency parameter in the *k*-th iteration) corresponds to the physically correct solution.

The system can be solved, for example, with the Newton method or another algorithm for a nonlinear equation system. The solution of the linear equation system $\mathbf{c}\boldsymbol{\Delta\Delta\lambda}$ +**d** =0 can be used as initial value. The coefficients **a**, **b**, **c** and **d** are:

$$\mathbf{a} = diag(\boldsymbol{\delta}) - \boldsymbol{\Phi}\mathbf{2} \tag{35}$$

$$\mathbf{b} = \mathbf{f2} \tag{36}$$

$$\begin{aligned}\mathbf{c} = {} & diag(\boldsymbol{\Delta\lambda\delta})\mathbf{f2} + diag(\boldsymbol{\delta}(\boldsymbol{\beta} - \mathbf{f1}) + (H_{iso} + H_{kin})\boldsymbol{\beta}) + diag(\mathbf{f1})\boldsymbol{\Phi}\mathbf{2} + \\ & + diag(\boldsymbol{\Phi}\mathbf{1} - \boldsymbol{\Phi}_{\mathbf{n}})\mathbf{f2}\end{aligned} \tag{37}$$

$$\mathbf{d} = diag(\boldsymbol{\Delta\lambda}(\boldsymbol{\delta}(\boldsymbol{\beta} - \mathbf{f1}) + (H_{iso} + H_{kin})\boldsymbol{\beta})) - \mathbf{f1}(\boldsymbol{\Phi}\mathbf{1} - \boldsymbol{\Phi}_{n}) \tag{38}$$

where

$$\mathbf{f1} = \mathbf{f}^{trial} + \mathbf{g}^{T}(\mathbf{M} - \mathbf{P}) - H_{iso}\mathbf{T} \tag{39}$$

$$\mathbf{f2} = \mathbf{g}^{T}(\mathbf{N} - \mathbf{S}) - H_{iso}\mathbf{L} \tag{40}$$

$$\boldsymbol{\Phi}\mathbf{1} = \boldsymbol{\Phi}^{trial} + \mathbf{g}^{T}(\mathbf{M} - \mathbf{P}) \tag{41}$$

$$\boldsymbol{\Phi}\mathbf{2} \ = \mathbf{g}^{T}(\mathbf{N} - \mathbf{S}) \tag{42}$$

$$\mathbf{M} = \mathbf{C}(-\mathbf{R}_{1} + \mathbf{Q}\boldsymbol{\Delta\Delta\lambda}\mathbf{B}\mathbf{R}_{\mathbf{2}}) \tag{43}$$

$$\mathbf{N} = \mathbf{C}(\mathbf{g} - \mathbf{Q}\boldsymbol{\Delta\Delta\lambda}H_{kin}\boldsymbol{\Pi}\mathbf{g}) \tag{44}$$

$$\mathbf{P} = \mathbf{B}(\mathbf{R}_{2} + H_{kin}\boldsymbol{\Pi}\mathbf{Q}\boldsymbol{\Delta\lambda}\mathbf{M}) \tag{45}$$

$$\mathbf{S} = \mathbf{B}H_{kin}\boldsymbol{\Pi}(\mathbf{Q}\boldsymbol{\Delta\Delta\lambda} - \mathbf{g}) \tag{46}$$

$$\mathbf{T} = \mathbf{R}_{3} + \boldsymbol{\Delta\lambda}(\mathbf{Qn})^{T}(\mathbf{M} - \mathbf{P}) \tag{47}$$

$$\mathbf{L} = \boldsymbol{\Delta\lambda}(\mathbf{Qn})^{T}(\mathbf{N} - \mathbf{S}) - \|\mathbf{g}\| \tag{48}$$

with

$\mathbf{A} = (\mathbf{k}_{e}^{-1} + \mathbf{Q}\boldsymbol{\Delta\Delta})^{-1}, \mathbf{Q} = \partial^{2}_{\mathbf{qq}}\mathbf{f}\,,\ \mathbf{B} = (\mathbf{1} + H_{kin}\boldsymbol{\Pi}\mathbf{Q}\boldsymbol{\Delta\lambda})^{-1},\ \mathbf{n} = \dfrac{\boldsymbol{\Lambda}\mathbf{g}}{\|\mathbf{g}\|}$ and

$\mathbf{C} = (\mathbf{A}^{-1} - \mathbf{Q}\boldsymbol{\Delta\Delta\lambda}H_{kin}\boldsymbol{\Pi}\mathbf{Q}\boldsymbol{\Delta\lambda})^{-1}$. In the equations (34) to (48) the superscript *k*, denoting the iteration, and subscript *n+1*, denoting the value at t_{n+1}, are omitted for simplicity.

For **δ=0** and H_{iso} =H_{kin} =0 the model reduces to elastic-perfectly plastic behavior with the solution:

$$\boldsymbol{\Delta\Delta\lambda}_{n+1}^{(k)} = \left(\left(\mathbf{g}_{n+1}^{(k)}\right)^{T}\mathbf{A}_{n+1}^{(k)}\mathbf{g}_{n+1}^{(k)}\right)^{-1}\left(\mathbf{f}_{n+1}^{(k)} - \left(\mathbf{g}_{n+1}^{(k)}\right)^{T}\mathbf{A}_{n+1}^{(k)}\mathbf{R}_{1,n+1}^{(k)}\right) \tag{49}$$

The elastic-perfectly plastic solution is also recovered when **β=0** and $H_{iso}=H_{kin}=0$. In the case when only one node yields, the system of nonlinear equations transforms into a single quadratic equation.

After finding the increment **ΔΔλ**, either as a solution of a system of nonlinear equations or a single equation, the consistency parameter is updated:

$$\boldsymbol{\Delta\Delta\lambda}_{n+1}^{(k+1)} = \boldsymbol{\Delta\lambda}_{n+1}^{(k)} + \boldsymbol{\Delta\Delta\lambda}_{n+1}^{(k)} \tag{50}$$

2.4 Tangent Stiffness Matrix

The tangent stiffness can be obtained by enforcing the satisfaction of the linearized discrete limit condition. After some manipulation the following expression for the tangent stiffness matrix $\mathbf{k}_{n+1}$ results

$$\begin{aligned}
\mathbf{k}_{n+1} &= \frac{d\mathbf{q}}{d\mathbf{v}}\Big|_{n+1} = \mathbf{C}_{n+1} - \mathbf{N}_{n+1}\left(\mathbf{Y}_{n+1}\right)^{-1}\mathbf{Z}_{n+1} \\
\mathbf{Y}_{n+1} &= diag(\boldsymbol{\delta}\left(\boldsymbol{\beta} - \mathbf{f}_{n+1}\right) + \left(H_{iso} + H_{kin}\right)\boldsymbol{\beta}) + diag(\mathbf{f}_{n+1} + \boldsymbol{\Phi}_{n+1} - \boldsymbol{\Phi}_{n} + \boldsymbol{\Delta\lambda}_{n+1}\boldsymbol{\delta})\mathbf{g}_{n+1}^{T}\mathbf{X}_2 - \\
&\quad - diag(H_{iso}(\boldsymbol{\Phi}_{n+1} - \boldsymbol{\Phi}_{n} + \boldsymbol{\Delta\lambda}_{n+1}\boldsymbol{\delta}))\mathbf{L}_{n+1} \\
\mathbf{Z}_{n+1} &= diag(\mathbf{f}_{n+1} + \boldsymbol{\Phi}_{n+1} - \boldsymbol{\Phi}_{n} + \boldsymbol{\Delta\lambda}_{n+1}\boldsymbol{\delta})\mathbf{g}_{n+1}^{T}\mathbf{X}_1 - diag\left(H_{iso}\boldsymbol{\Delta\lambda}_{n+1}\boldsymbol{\delta}\right)\boldsymbol{\Delta\lambda}_{n+1}\left(\mathbf{Q}_{n+1}\mathbf{n}_{n+1}\right)^{T}\mathbf{X}_1 - \\
&\quad - diag(H_{iso}(\boldsymbol{\Phi}_{n+1} - \boldsymbol{\Phi}_{n}))\boldsymbol{\Delta\lambda}_{n+1}\left(\mathbf{Q}_{n+1}\mathbf{n}_{n+1}\right)^{T}\mathbf{X}_1
\end{aligned} \tag{51}$$

We used the substitutions $\mathbf{X_1}$ and $\mathbf{X_2}$ with the following definition

$$\begin{aligned}
\mathbf{X}_1 &= \mathbf{C}_{n+1} - \mathbf{B}_{n+1}H_{kin}\boldsymbol{\Pi}\mathbf{Q}_{n+1}\boldsymbol{\Delta\lambda}_{n+1}\mathbf{C}_{n+1} \\
\mathbf{X}_2 &= \mathbf{N}_{n+1} - \mathbf{S}_{n+1}
\end{aligned} \tag{52}$$

As for the consistency parameter **ΔΔλ**, for parameters **δ=0** and $H_{iso}=H_{kin}=0$ or **β=0** and $H_{iso}=H_{kin}=0$, the consistent tangent stiffness matrix reduces to the expression for the elastic-perfectly plastic case:

$$\mathbf{k}_{n+1} = \mathbf{A}_{n+1} - \mathbf{A}_{n+1}\mathbf{g}_{n+1}\left(\mathbf{g}_{n+1}^{T}\mathbf{A}_{n+1}\mathbf{g}_{n+1}\right)^{-1}\mathbf{g}_{n+1}^{T}\mathbf{A}_{n+1} \tag{53}$$

3 NUMERICAL EXAMPLES

To verify the capabilities of the new element, two simple examples are studied. The response of the new element, named GPMNYS element (from Generalized Plasticity N-M Yield Surface), is compared with the solution of the elastic-perfectly plastic concentrated plasticity element (EPPNMYS element) [18] and the fiber hinge element [19] whose solution is denoted as FIBER and represents the benchmark solution. FEDEASLab, a Matlab toolbox for nonlinear static and dynamic analysis [20], was used for the simulation.

3.1 Cantilever Column

The first example refers to the cantilever column shown in Figure 3(a) which is used before in a study of efficient cross section discretization of fiber beam-column element [21]. In tests B6 and B8_7, the column was subjected to uniaxial and biaxial tip translation history with variable axial force (Figure 3(b-c)). In Test B6, the column tip is subjected to lateral displacements in the strong axis direction, with variation of axial force between -0.05Np and -0.45Np. In Test B8_7, the column tip is subjected to displacements in the Y and Z directions so that normalized bending moments about strong and weak axis are in the ratio 0.5, with variation of axial force between -0.05Np and -0.45Np.

The response of a homogeneous column with elastic perfectly plastic material, obtained with the distributed inelasticity fiber model with fine section discretization (108 fibers) and five Gauss-Lobatto integration points along its length, is compared with the response of the two concentrated plasticity elements, GPNMYS and EPPNMYS elements.

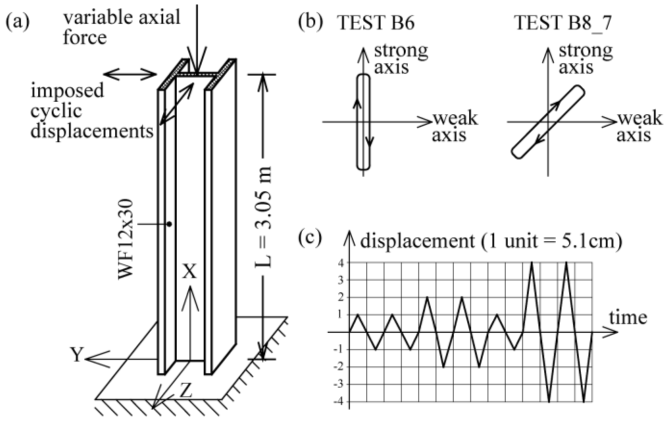

Figure 3: (a) Cantilever column; (b) B6 and B8_7 tip displacement pattern; (c) tip displacement history.

The assumed yield function, i.e. N-M_z-M_y interaction curve, for each end of the beam is:

$$f(p,m_z,m_y)=1.15p^2+m_z^2+m_y^4+3.67p^2m_z^2+3p^6m_y^2+4.65m_z^4m_y^2-c \qquad (54)$$

Where p is the normalized axial force $p=(N-a_p)/N_p$ and $m_z=(M_z-a_z)/M_{pz}$ and $m_y=(M_y-a_y)/M_{py}$, respectively, are the normalized bending moment about strong and weak axis. The variables a_p, a_z and a_y are components of the vector that describes the dispacement of the yield surface in the N-M_z-M_y space due to kinematic hardening mechanism. The variable c determines dimensions of the yield surface. Coefficients in the equation (54) are determined to fit the best yield surface for W12x30 US steel cross section with $c=1.0$ [1]. In GPNMYS and EPPNMYS models, both nodes are assumed to have the same properties. The coefficient c is taken equal to 0.3 in GPNMYS and 1.0 in EPPNMYS model. Additional parameters of the GPNMYS model are: $\delta=0.15$, $\beta=0.70$ and $H_{iso}=H_{kin}=0$. The results are shown in Figures 4-5 for Test B6 and in Figures 6-9 for Test B8_7.

It should be emphasized that the elapsed time during these tests were, approximately, in the ratio 1:1.15:21 for EPPNMYS: GPNMYS: FIBER element, respectively.

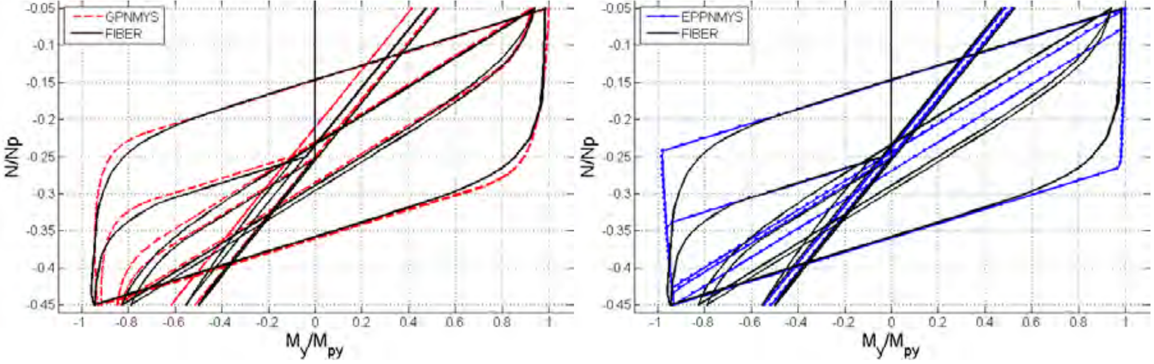

Figure 4: Test B6: normalized bending moment – normalized axial force path
(a) GPNMYS and FIBER; (b) EPPNMYS and FIBER element.

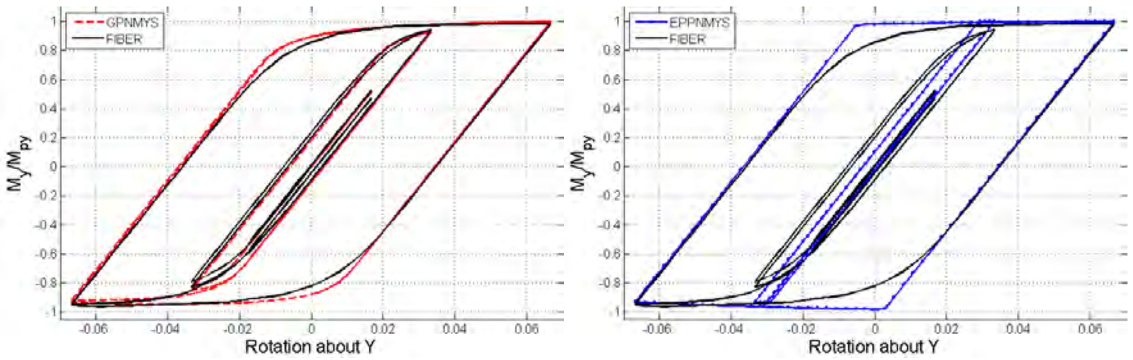

Figure 5: Test B6: normalized bending moment – rotation relation
(a) GPNMYS and FIBER; (b) EPPNMYS and FIBER element.

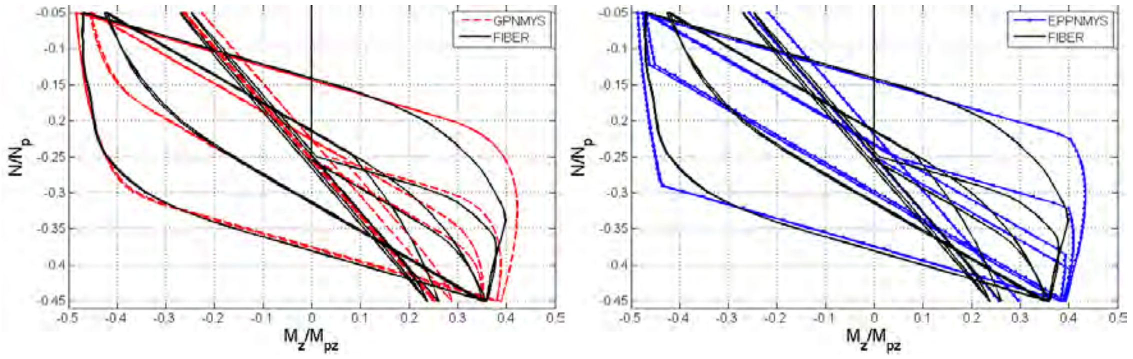

Figure 6: Test B8_7: normalized bending moment about Z – normalized axial force path
(a) GPNMYS and FIBER; (b) EPPNMYS and FIBER element.

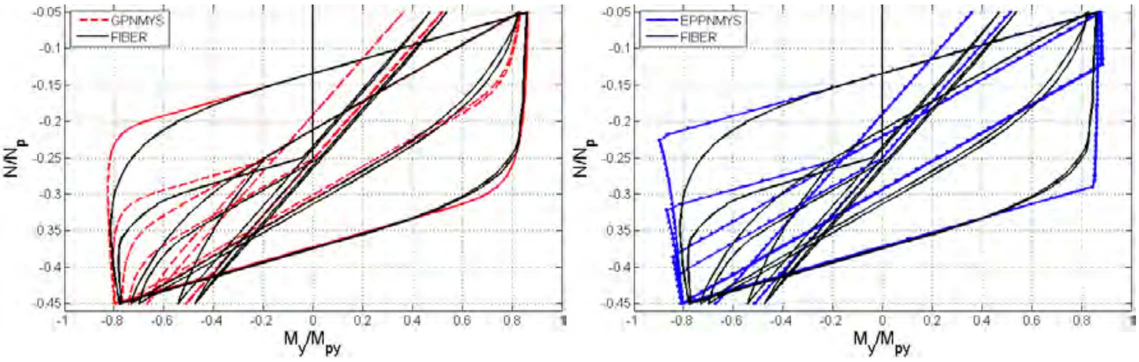

Figure 7: Test B8_7: normalized bending moment about Y – normalized axial force path
(a) GPNMYS and FIBER; (b) EPPNMYS and FIBER element.

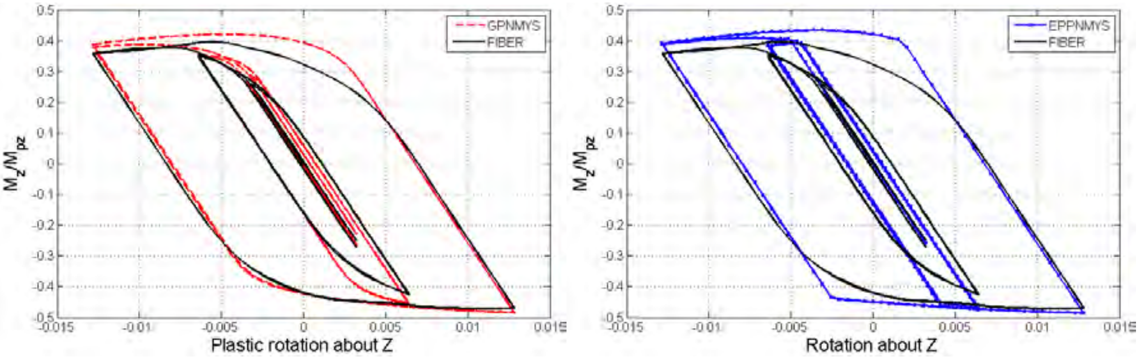

Figure 8: Test B8_7: normalized bending moment about Z – rotation relation
(a) GPNMYS and FIBER; (b) EPPNMYS and FIBER element.

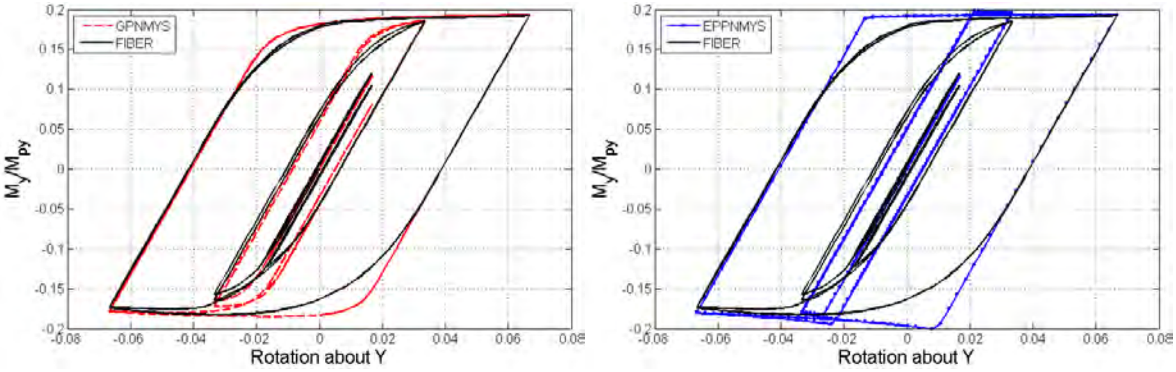

Figure 9: Test B8_7: normalized bending moment about Y – rotation relation
(a) GPNMYS and FIBER; (b) EPPNMYS and FIBER element.

To verify the capabilities of the GPNMYS element to simulate hardening behavior, the Test B6 is conducted again. The material is assumed to have 3% kinematic hardening in FIBER model. Parameter H_{kin} of the GPNMYS model is taken equal to *0.08*, while other parameters are the same as in the Test B6 without hardening. Results are shown in Figure 10.

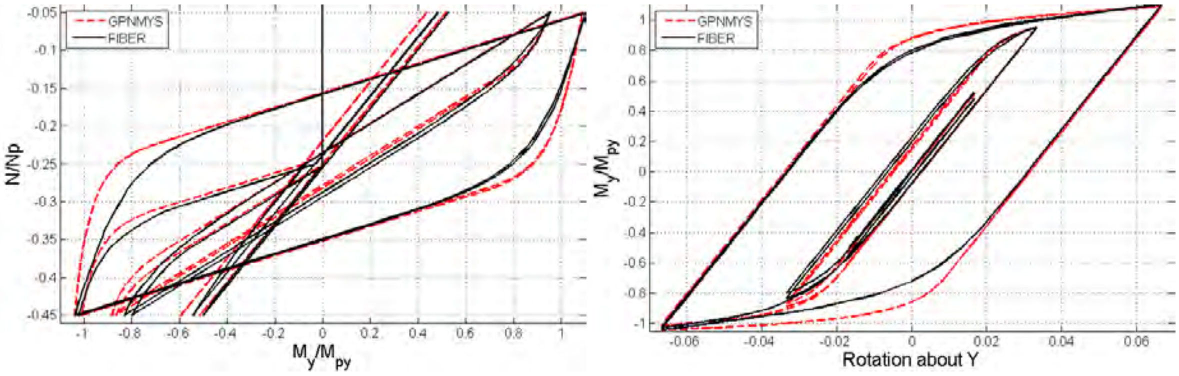

Figure 10: Test B6 with hardening - GPNMYS and FIBER element: (a) normalized bending moment – normalized axial force path; (b) normalized bending moment about Y – rotation relation.

3.2 Portal frame example

The second example refers to the portal frame shown in Figure 11, previously studied by El-Zanaty [22]. Gravity loads are applied first and then kept constant wile lateral load is gradually increasing. The residual stresses are not considered since this effect cannot be captured with the EPPNMYS element. In the GPNMYS element this effect can be included by specifying the size of the elastic domain (loading surface) [23].

The nonlinear geometry under large displacements is accounted for with the corotational formulation [24]. In each of the three models (GPNMYS, EPPNMYS and fiber) each member of the portal frame is represented with one element. The material model is assumed elastic-perfectly plastic. Three different levels of vertical load are studied: 20%, 40% and 60% of the ultimate vertical load of the frame and results for bending about the major axis are given in Figure 12.

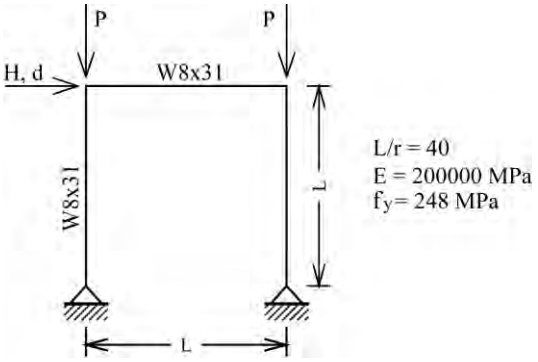

Figure 11: El-Zanaty portal frame.

The following yield function is used:

$$f(p,m_z) = p^2 + m_z^2 + 3.5p^2m_z^2 - c \tag{55}$$

Where p and m_z are as defined before. The parameter c equal to 1.0 is used in EPPNMYS element, and $c=0.71$ for GPNMYS element. Additional parameters of the GPNMYS model are: $\delta=0.1$, $\beta=0.27$.

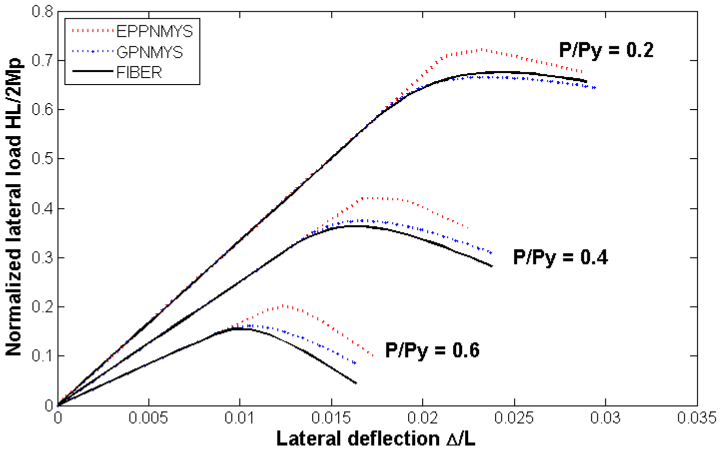

Figure 13: Load-displacement response of El-Zanaty frame.

As can be seen from the results, the response of the GPNMYS element is closer to the exact – FIBER solution due to its capability to describe the gradual yielding of the cross section.

4 CONCLUSION

In the paper, a new three-dimensional nonlinear beam-column element, called GPNMYS, for the simulation of the global and local response of frames under monotonic and cyclic loading conditions is presented. The element belongs to the family of concentrated plasticity elements, with plastic hinges located at the ends of the element and described with yield and limit surfaces. The concepts of generalized material plasticity are extended to force resultants and used in the element formulation. The element takes into account the interaction of the axial force and the bending moments about the principal axes of the cross section and the hardening behavior. The gradual yielding of the cross section is described by the asymptotical approach to the limit surface. The model is relatively simple and introduces parameters with clear physical meaning. With the implementation of the return mapping algorithm and quadratic convergence it is, also, computationally very efficient.

The capability of the new GPNMYS element is verified with two examples by comparing its response with that of an elastic perfectly plastic element resultant plasticity element, which is also based on the return map algorithm, and with the results of a fiber beam-column element. In comparison with perfectly-plastic element, the GPNMYS element proves significantly more versatile in the simulation of frame response under complex loading conditions without significant increase in calculation time, which remains equal to approximately 15% of the time required by the fiber beam-column with an adequate level of discretization.

ACKNOWLEDGEMENTS

The first author thanks the Ministry of Science of the Republic of Serbia for financial support under project TR36046.

REFERENCES

[1] J. G. Orbison*, et al.*, "Yield surface applications in nonlinear steel frame analysis," *Computer Methods in Applied Mechanics and Engineering,* vol. 33, pp. 557-573, 1982.
[2] S. I. Hilmy and J. F. Abel, "Material and geometric nonlinear dynamic analysis of steel frames using computer graphics," *Computers & Structures,* vol. 21, pp. 825-840, 1985.
[3] G. H. Powell and P. F.-S. Chen, "3D Beam-Column Element with Generalized Plastic Hinges," *Journal of Engineering Mechanics,* vol. 112, pp. 627-641, 1986.
[4] J. F. Hajjar and B. C. Gourley, "A cyclic nonlinear model for concrete-filled tubes. I: Formulation," *Journal of Structural Engineering,* vol. 123, p. 736, 1997.
[5] J. F. Hajjar and B. C. Gourley, "A cyclic nonlinear model for concrete-filled tubes. II: Verification," *Journal of Structural Engineering,* vol. 123, p. 745, 1997.
[6] C. K. Iu*, et al.*, "Second-order inelastic analysis of composite framed structures based on the refined plastic hinge method," *Engineering Structures,* vol. 31, pp. 799-813, 2009.
[7] S. Kitipornchai*, et al.*, "Single-equation yield surfaces for monosymmetric and asymmetric sections," *Engineering Structures,* vol. 13, pp. 366-370, 1991.
[8] B. Skallerud, "Yield surface formulations for eccentrically loaded planar bolted or welded connections," *Computers & Structures,* vol. 48, pp. 811-818, 1993.
[9] W. F. Chen and T. Atsuta, *Theory of Beam-Columns*. New York: McGraw Hill, 1977.
[10] Y. F. Dafalias and E. P. Popov, "Cyclic loading for materials with a vanishing elastic region," *Nuclear Engineering and Design,* vol. 41, pp. 293-302, 1977.
[11] S. El-Tawil and G. G. Deierlein, "NONLINEAR ANALYSIS OF MIXED STEEL-CONCRETE FRAMES. II: IMPLEMENTATION AND VERIFICATION," *Journal of Structural Engineering,* vol. 127, p. 656, 2001.
[12] S. El-Tawil and G. G. Deierlein, "NONLINEAR ANALYSIS OF MIXED STEEL-CONCRETE FRAMES. I: ELEMENT FORMULATION," *Journal of Structural Engineering,* vol. 127, p. 647, 2001.
[13] J. Jin and S. El-Tawil, "Inelastic Cyclic Model for Steel Braces," *Journal of Engineering Mechanics, ASCE,* vol. 129, pp. 548-557, May 2003 2003.
[14] J. Lubliner*, et al.*, "A New Model of Generalized Plasticity and Its Numerical Implementation," *International Journal of Solids and Structures,* vol. 30, pp. 3171-3184, 1993.

[15] F. Auricchio and R. L. Taylor, "2 Material Models for Cyclic Plasticity - Nonlinear Kinematic Hardening and Generalized Plasticity," *International Journal of Plasticity,* vol. 11, pp. 65-98, 1995.

[16] F. Auricchio and R. L. Taylor, "A generalized elastoplastic plate theory and its algorithmic implementation," *International Journal for Numerical Methods in Engineering,* vol. 37, pp. 2583-2608, 1994.

[17] J. C. Simo and T. J. Hughes, *Computational Inelasticity*. Secaucus, NJ, USA: Springer-Verlag New York, Incorporated, 1998.

[18] S. M. Kostic*, et al.*, "Evaluation of Resultant Plasticity and Fiber Beam-Column Elements for the Simulation of the 3D Nonlinear Response of Steel Structures," in *2nd International Conference on Computational Methods in Structural Dynamics and Earthquake Engineering - COMPDYN*, Island of Rhodes, Greece, 2009.

[19] F. C. Filippou and G. L. Fenves, "Methods of Analysis for Earthquake-Resistant Structures," in *Earthquake Engineering: From Engineering Seismology to Performance-Based Engineering*, Y. Bozorgnia and V. V. Bertero, Eds., ed: CRC Press, 2004.

[20] F. C. Filippou and M. Constantinides, "FEDEASLab Getting Started Guide and Simulation Examples," University of California, Berkeley, Technical Report2004.

[21] S. M. Kostic and F. C. Filippou, "Section Discretization Considerations in Fiber Beam-Column Elements for Nonlinear Frame Analysis," Pacific Earthquake Engineering Research Center, College of Engineering, University of California, Berkeley (to be published)2010.

[22] M. H. El-Zanaty*, et al.*, "Inelastic behavior of multistory steel frames," Univ. of Alberta, Edmonton, Alberta, Canada Struct. Engrg. Rep. No. 83, 1980.

[23] W. S. King and W. F. Chen, "Practical second-order inelastic analysis of semirigid frames," *J. Struct. Engrg., ASCE,* vol. 120, pp. 2156-2175, 1994.

[24] M. A. Crisfield, *Non-linear finite element analysis of solids and structures*. West Sussex: John Wiley & Sons, 1991.

COMPDYN 2011
III ECCOMAS Thematic Conference on
Computational Methods in Structural Dynamics and Earthquake Engineering
M. Papadrakakis, M. Fragiadakis, V. Plevris (eds.)
Corfu, Greece, 25–28 May 2011

FINITE ELEMENT MODELLING OF YIELDING SHEAR PANEL DEVICE FOR PASSIVE ENERGY DISSIPATION

Md Raquibul Hossain [1], **Mahmud Ashraf** [2], **and Faris Albermani** [3]

[1] School of Civil Engineering, The University of Queensland
St Lucia, QLD 4072, Australia
md.hossain@uqconnect.edu.au

[2] School of Civil Engineering, The University of Queensland
St Lucia, QLD 4072, Australia
m.ashraf@uq.edu.au

[3] School of Civil Engineering, The University of Queensland
St Lucia, QLD 4072, Australia
f.albermani@uq.edu.au

Keywords: Earthquake, Finite Element Method, Shear deformation, Passive Energy Dissipation, Yielding Shear Panel Device.

Abstract. *Yielding Shear Panel Device (YSPD) is a newly proposed passive energy dissipation device to make structures more sustainable against earthquakes by exploiting the shear deformation capacity of metallic plates. YSPD is easy to install using simple bolted connections and is significantly less expensive than currently available passive energy dissipation devices. If required, damaged YSPDs could be replaced easily after an earthquake causing minimum disruption to a structure. The current research explains the development of finite element models for the pilot experiments carried out on YSPD. The developed FE models include both material and geometric nonlinearities and use nonlinear spring elements to model appropriate support conditions observed in the experiments. Overall, good agreement is noticed between the FE models and the test results in regards to force displacement response and energy absorption. The developed FE models are validated for both monotonic and cyclic loading. This verification paves the way for generating further reliable set of data to develop appropriate design rules for YSPD.*

1 INTRODUCTION

Recent catastrophic earthquakes occurring in different parts of the world demonstrate the severity of this natural phenomenon on human civilization and points out the significance of further research to develop efficient cost-effective tools to minimise the resulting loss. Minimization of structural damages due to earthquake is a major area of research which contributed to the development of a number of active, semi-active and passive control mechanisms during the last few decades. The current research investigates the structural performance of a newly proposed yielding shear panel device (YSPD) for passive energy dissipation. YSPD is very simple to manufacture and is economical when compared against currently available devices. Pilot tests carried out on the device demonstrates its potential for considerable energy absorption [1]. Appropriate design rules for YSPD would require more understanding of its structural response when subjected to different types of loading. Finite element models are developed herein and verified against available monotonic and cyclic test results to pave the way for thorough parametric analysis leading to design rules. The scope of this paper covers details of the FE modelling technique using the general purpose FE package ANSYS.

2 YIELDING SHEAR PANEL DEVICE (YSPD)

Diagonal tension field that develops in the post-buckling regime of a thin steel plate under shear, which offers significant strength and ductility, can be utilized to dissipate energy. This concept led to the development of a new metallic passive energy dissipating device ‘Yielding Shear Panel Device’ (YSPD). YSPD was introduced by Williams and Albermani [2] based on the proposed design by U. Dorka at the University of Kassel, Germany to exploit the energy dissipative capability of steel plates through in-plane shear deformation and the concept was further explored by Schmidt et.al. [3] and Williams and Albermani [4]. YSPD relies on the in-plane shear deformation of a thin diaphragm steel plate welded inside a square hollow section (SHS). This device can be placed below a structural beam using a V-brace, as shown in Figure 1, so that it automatically comes into play in the event of any horizontal excitation.

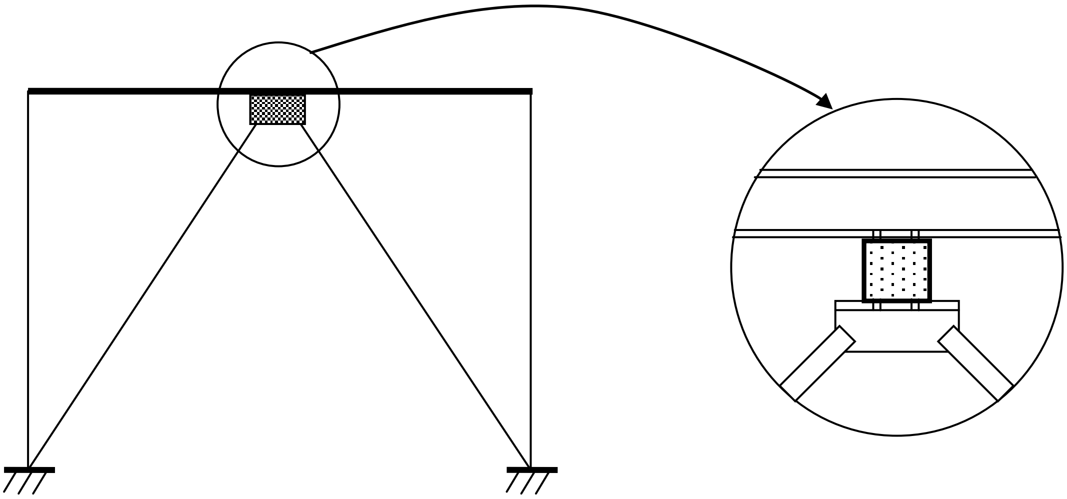

Figure 1: Typical YSPD-brace assembly.

Chan et. al. [1] conducted a series of monotonic and cyclic tests using various plate thicknesses and device configurations for YSPD. The tested specimens were fabricated using a short segment of a square hollow section (SHS) with a steel diaphragm plate welded inside it as shown in Figure 2. Four bolt holes spaced at a centre-to-centre distance ‘s’ were drilled on each of the two opposite SHS flanges for connecting the device to the test setup; this connection is analogous to the practical assembly where YSPDs are proposed to be connected using bolts to ensure easy installation and replacement. The SHS provides a boundary to the diaphragm plate so that shear forces can be applied to the plate, in addition to providing necessary detail for connections to the parent structural frame. Most importantly, the SHS serves as a boundary element allowing the tensile strips to be formed and the tension field to be developed following the post-buckling of the thin diaphragm plate. As a result of sufficiently large displacements occurring in the diaphragm plate, the input energy originating from an earthquake could be dissipated through plastic deformation.

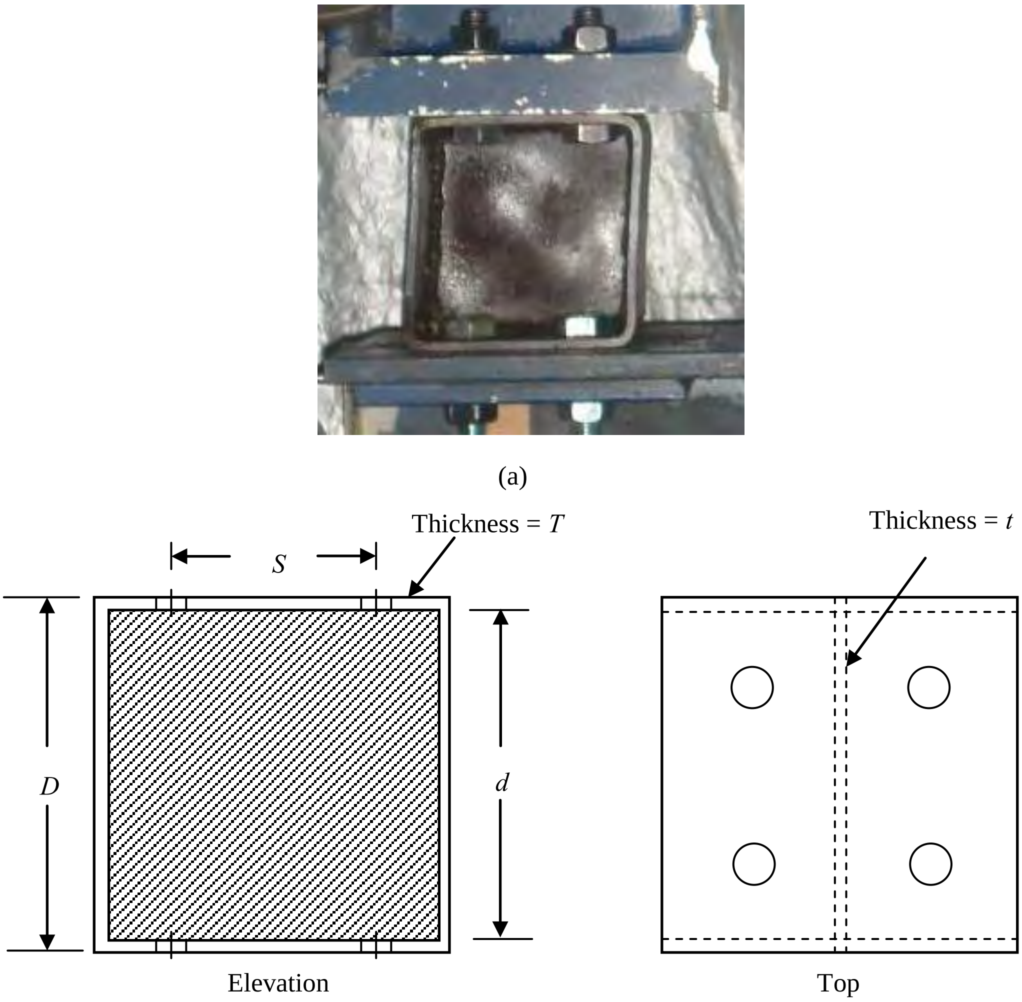

(a)

(b)

Figure 2: (a) Yielding shear panel device (YSPD) (b) Schematic diagram showing the geometric parameters of YSPD [5].

Chan et. al. [1] tested two different sizes of YSPD, 100mm × 100mm and 120mm × 120mm, with three different thickness of 2 mm, 3 mm and 4 mm for the diaphragm plate. Bolt spacing of 50 mm was used for four M16 bolts on each side of the SHS to install the test specimen between a ground beam and L-beam. Geometric dimensions of the test specimens are given in Table 1 and reported material properties are summarized in Table 2.

YSPD Designation (D × D × t)	Diaphragm Thickness, t (mm)	SHS Size, D (mm)	SHS Thickness, T (mm)	Bolt Spacing, S (mm)
100×100×2	1.86	100	3.76	50
100×100×3	2.83	100	3.76	50
100×100×4	3.78	100	3.76	50
120×120×2	1.86	120	4.91	50
120×120×3	2.83	120	4.91	50
120×120×4	3.78	120	4.91	50

Table 1: Geometric details of YSPD test specimens [1]

YSPD Designation	Tensile Yield Strength (MPa)	
(D × D × t)	Diaphragm Plate	SHS
100×100×2	211.3	414.9
100×100×3	321.3	414.9
100×100×4	351.2	414.9
120×120×2	211.3	333.3
120×120×3	321.3	333.3
120×120×4	351.2	333.3

Table 2: Material properties of the test specimens [1]

3 FINITE ELEMENT MODELLING OF YSPD

3.1 Material modelling

An appropriate material model is a prerequisite to obtain accurate predictions from a finite element model. Williams and Albermani [4] and Chan et. al. [1] used ordinary carbon steel plates and steel SHS sections to manufacture the tested YSPD specimens. Stress-strain response of ordinary steel shows a steep initial elastic response followed by strain hardening up to the ultimate stress followed by strain softening before failure. Most widely adopted material modelling technique for carbon steel is, however, the bilinear elastic, perfectly-plastic idealization. Alinia et. al. [6] recently used bilinear hardening model to analyze the plastic shear buckling capacity of unstiffened steel plates. Eurocode 3 [7] provides the following guideline for assuming the bilinear material behaviour – material behaviour can be modelled without strain hardening, with a nominal plateau slope or with linear strain hardening depending on the accuracy and the allowable strain required. The Code suggests that the tangent modulus after yielding can be reasonably assumed as 1% of the Young’s modulus of elasticity for a bilinear idealization to include the effects of strain hardening. Chan [5] reported two coupon tests for the 100×100×4 SHS. Figure 3 compares the reported coupon test results and the idealized bilinear material model. Young's modulus of elasticity E = 200 GPa and Poission's ratio ν = 0.3 for mild steel is used in material modelling.

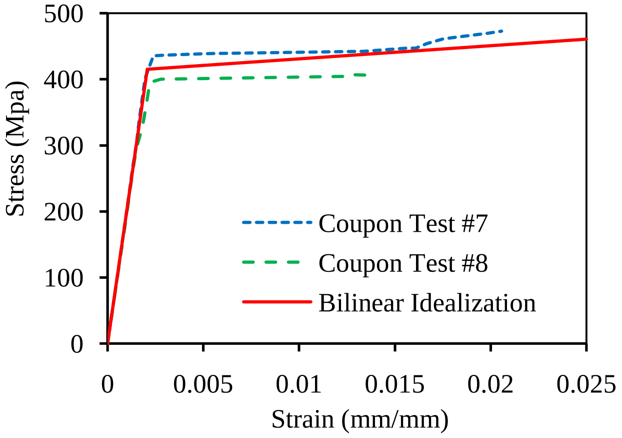

Figure 3. Material properties of the SHS plate of YSPD 100x100x4 [5]

An isotropic hardening model may be used to simulate the material behaviour only for monotonic loading, whilst cyclic behaviour would require a kinematic hardening model as the yield surface can translate in the direction of loading. A bilinear kinematic hardening model available in ANSYS assumes that the total stress range as twice the yield stress which eventually results in von Mises yield criteria with an associative flow rule. The yield surface is assumed to have a cylindrical shape in three-dimensional stress space as shown in Figure 4. This model represents the stress-stain response in two stages – the initial linear elastic part where the material follows the Hook's law and in the following linear plastic part where the material exhibits a constant strain hardening behaviour. The bilinear kinematic hardening model is used in the current study as the constitutive model for the steel plates used in the diaphragm plate as well as the SHS of YSPD for both monotonic and cyclic loading.

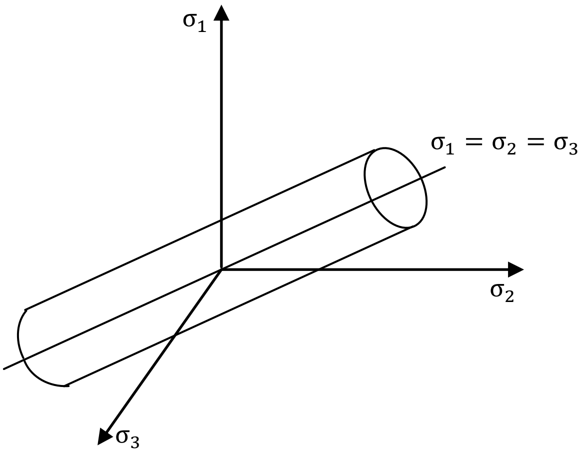

Figure 4: von Mises yield surface in the three-dimensional stress space.

3.2 Analysis technique and selection of element type

Developed FE models were analysed elastically to obtain appropriate Eigenmodes, which were used to model initial geometric imperfections in the subsequent nonlinear analysis. The 'BUCKLE' option available in ANSYS was used to obtain the required Eigenmodes followed by a nonlinear ‘STATIC’ analysis to simulate the force-displacement response of YSPD. To take appropriate account of the geometric nonlinearity effects arising as a result of excessive deformation of the thin diaphragm plate, the ‘NLGEOM’ option was adopted.

A number of techniques for solving the global system of simultaneous equations are available in the ANSYS program such as sparse direct, preconditioned conjugate gradient (PCG), Jacobi conjugate gradient (JCG), frontal direct etc. Among these available options, PCG solver is an iterative equation solver that can handle ill-conditioned problems and provide faster solution for large models when compared against the performance of sparse and frontal solvers. Line search option, accessed with ‘LNSRCH’ command, can further improve the performance of the solution technique [8]. The current FE modelling uses PCG solver with the line search option to obtain an accurate response of YSPD, whilst minimising computational time.

Shell elements are widely used to model thin-walled structures. In recent times, Alinia et. al [6] used four noded quadrilateral shell elements to investigate the plastic shear buckling capacity of unstiffened steel plates, whilst De Matteis et. al. [9] employed shell elements to model stiffened aluminium shear panels. Soo Kim and Kuwamura [10], Ashraf et. al. [11], Ellobody and Young [12] used general purpose shell elements to analyze the behaviour of thin-walled stainless steel members. ANSYS offers a range of shell elements including both general purpose and special purpose elements. ‘SHELL43’ and ‘SHELL181’ are two general purpose shell elements suitable for thin to moderately thick shell structures incorporating nonlinear, large deflection and large strain capabilities. Special purpose shell element ‘SHELL41’ is a membrane only element having only membrane stiffness, whilst ‘SHELL63’ is an elastic shell element. General purpose shell element ‘SHELL181’ is used in the current research to model both the diaphragm plate and the SHS. ‘SHELL181’ is a four-noded full integration quadrilateral shell element with six degrees of freedom at each node, which is well-suited for linear, large rotation, and/or large strain nonlinear applications [8]. It includes both bending and membrane stiffnesses.

3.3 Support conditions for YSPD

Modelling appropriate support conditions for YSPD has been one of the challenging tasks in the current research as it significantly affects the overall load-deformation response and the amount of dissipated energy. The current proposal is to connect YSPD to the parent structure using bolts to ensure easy installation and to facilitate replacement of damaged devices after an earthquake, if required.

3.3.1. Stiffness of the SHS

Chan et al. [1, 5] installed the test specimens between a ground beam and an L-beam, securely fastened by four M16 bolts on each side.. The left flange of the YSPD was connected to the ground beam, whilst the right flange was connected to the L beam. Forced displacements were applied using a 100kN capacity MTS actuator to the YSPD through the L-beam, which moved vertically downward and upward to simulate the horizontal displacement that would occur in a V-brace assembly due to an earthquake excitation.

Displacement measurements obtained from LVDT 2 and LVDT 3 showed some initial in-plane rotation of the L-beam (Figure 5a). Considerable deformations were observed in YSPD specimens. The upper flange of the YSPD moved rightward, whilst the lower flange moved leftward due to this in-plane rotation of the L-beam caused by the downward movement of the actuator. These movements caused the support end flange (left flange) and the loading end flange (right flange) to experience bending in upper and lower portions respectively. The upper two bolts of support end and the lower two bolts of loading end experienced minor deformations due to this bending. Opposite movements and deformations were observed when the actuator moved upwards. Figure 5(b) shows the deformed shape for YSPD 100×100×3 after the monotonic test. Noticeable bending observed at the flanges is highlighted by circles.

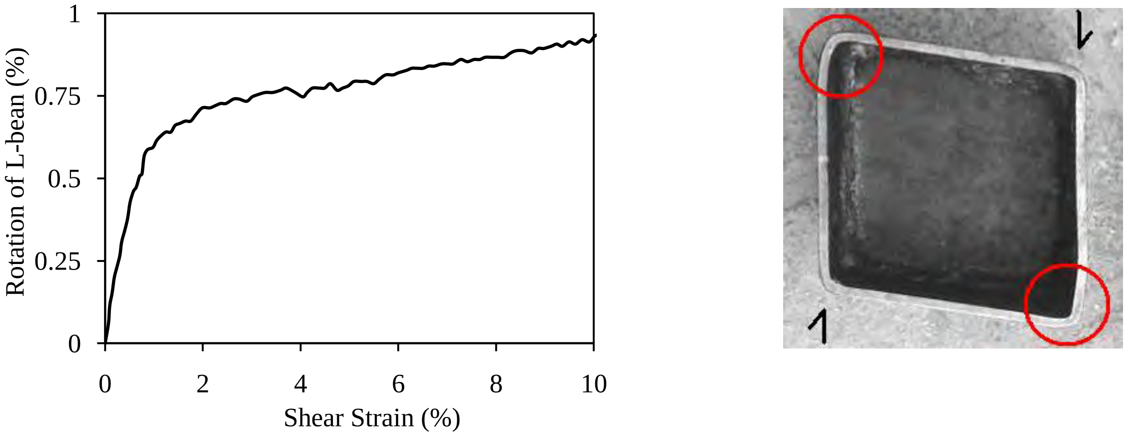

(a) (b)

Figure 5: (a) In-plane rotation of the L-beam of YSPD 100X100X3 under monotonic loading (b) Deformed shape of YSPD 100X100X3 under monotonic loading [5]

3.3.2. FE modelling of the boundary conditions

The developed FF models of the YSPD have the same orientation that would occur when YSPD will be placed in a V-brace assembly (Figure 6). In actual practice the upper flange will be connected to the beam, whilst the bottom flange will be connected to the V-brace. Both the upper and the lower bolted flanges will experience bending due the horizontal movement of the V-brace, which is simulated by applying horizontal nodal displacements to the nodes around the bolt holes of the lower flange. Bolts nearer to the bent flange plates will experience minor deformations due to bending effects originating from these movements. The other two edge lines are supported by the beam and the V-brace end plate.

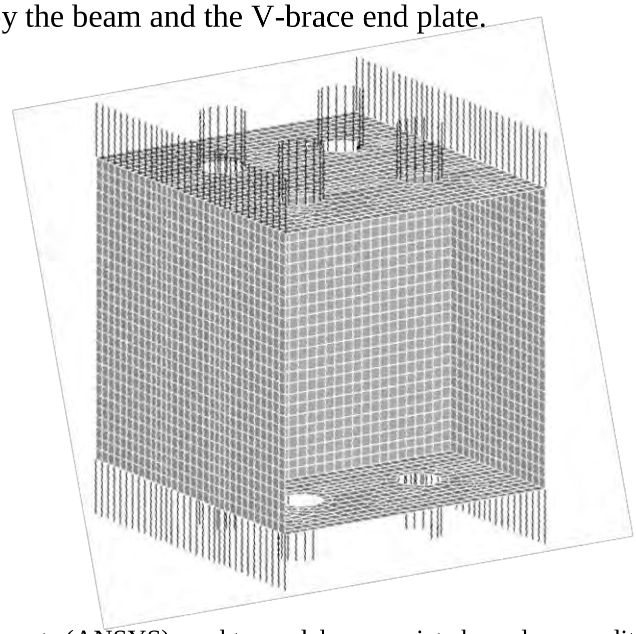

Figure 6: Spring elements (ANSYS) used to model appropriate boundary conditions for YSPD.

The deformations and movements observed in the bolts and the edges of YSPD were modelled using a combination of hinge and spring supports as shown in Figure 6. All nodes along four edge lines are supported by 'COMBIN39' spring elements, which act as a tension-compression element. Both tension and compression will occur due to the bending effects resulting from horizontal movements. Tension and compression stiffnesses are defined separately to allow the elements exhibit different force-displacement responses in tension and compression. The compression stiffness K_{ec} of the edge springs are taken equal to the stiffness of the flange plate. The cross-sectional area between two nodes constitutes the stiffness for a single spring. These springs resist the edge nodes to move beyond the support and the loading planes. The stiffness for the edge springs at the loading side is reduced by multiplying with a reduction factor λ to incorporate the effects of in-plane rotation observed at the loading side. The tension stiffness K_{et} is taken as a very small positive magnitude to eliminate the numerical singularity that allows the edge nodes to move freely in both directions but resists them to go away from the support and the loading planes.

Bolted connections are simulated using circular holes with appropriate boundary conditions around the perimeter. The nodes around the circular hole are divided into two categories - inner nodes and outer nodes as shown in Figure 7. At the support end, the translational degrees of freedom for the inner nodes are fully restrained, whilst the outer nodes are restrained only against the in-plane movements. To simulate the out of plane displacements, these nodes are supported by 'COMBIN39' spring elements with stiffness (K_b) whose combined stiffness is equal to the stiffness of the M16 bolts as used in the experiment. At the loading end, both the inner and the outer nodes are supported by 'COMBIN39' spring elements with stiffness equal to a fraction of the stiffness of M16 bolts λK_b. These nodes are free against in-plane displacements to simulate the observed horizontal movement of the V-brace end plate during testing. Table 3 presents a summary of the magnitudes of appropriate stiffness for spring supports used at the support and at the loading end.

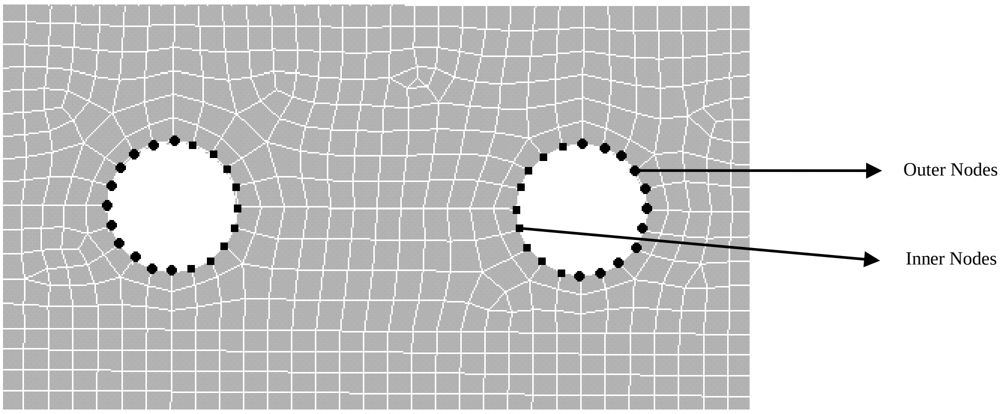

Figure 7: Definition of inner and outer nodes around the bolt hole.

	Stiffness
Tensile stiffness of the edge springs, K_{et}	0.0001
Compressive stiffness of the edge springs, K_{ec}	$T \times S_n \times E_{SHS}$
Stiffness of the springs at bolt holes, K_b	$\frac{A_b \times E_b}{N_b}$

Table 3: Spring stiffness values used for modelling boundary conditions of YSPD.

Where,

T = Thickness of the SHS plate
S_n = Nodal spacing in the SHS plate
E_{SHS} = Modulus of elasticity of SHS plate
A_b = Cross section area of bolt
E_b = Modulus of elasticity of bolt
N_b = Number of nodes per bolt hole

The reduction factor λ allows the in-plane rotation and degradation of the initial stiffness of YSPD, which are inevitable phenomenon as observed during testing (Figure 5a). The rotation at the loading end is significantly affected by the value of λ; a higher value of λ contributes to a smaller rotation. The support end and the loading end will be parallel if λ is taken as 1.0; this will eventually make the initial stiffness of the YSPD equal to that proposed by Chan et. al. [1]. The test results, however, show a significantly lower initial stiffness as a result of the observed rotation at the loading end.Test results showed noticeable in-plane rotation of the L beam despite its high stiffness. A parametric study was conducted to find an appropriate value for λ. Figure 8 shows the load-deformation responses of YSPD for different values of λ against test results. Comparisons show that only a small fraction of K_b and K_{ec} produces good agreement with test results and hence a value of λ = 0.002% has been adopted in the current research to allow for the in plane rotation.

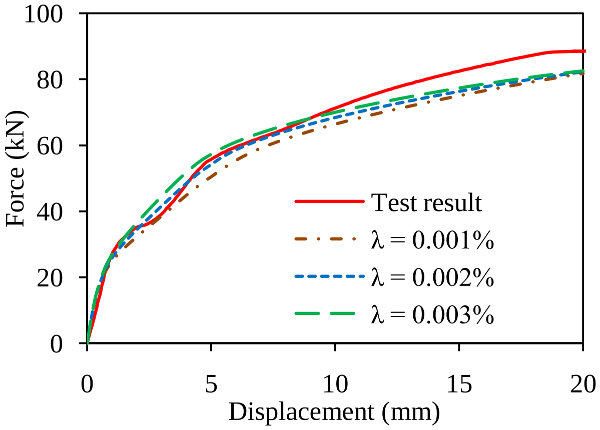

Figure 8: Load-deformation response of YSPD 100×100×4 with different values for λ.

3.4 Convergence study – selecting a suitable mesh

Selecting an appropriate mesh is one of the most important aspects of FE modelling. No general guidelines are available to choose a suitable mesh as it largely depends on the type of structure and the corresponding analysis involved. Finer mesh generally provides better predictions but require higher computational time. A convergence study was carried out to choose a suitable mesh to obtain an optimum balance between accuracy and computational time.

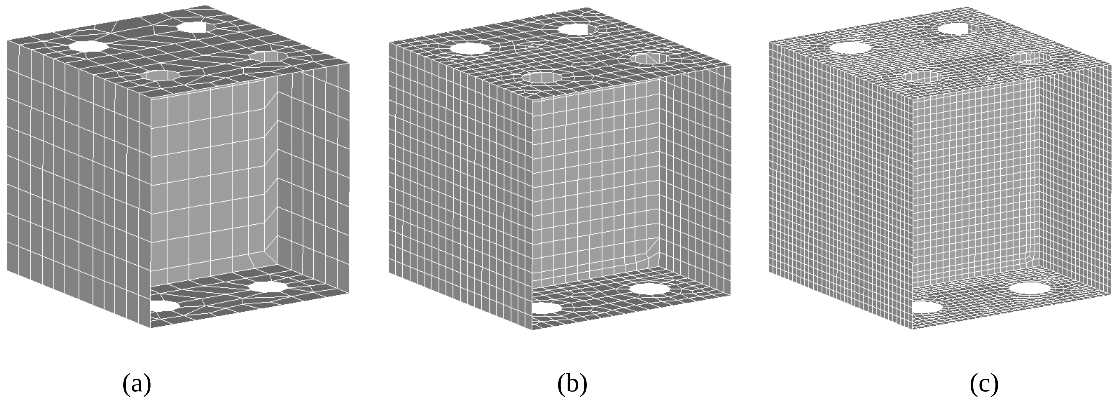

Figure 9. Convergence study of YSPD (100×100×4). (a) Coarse mesh (492 shell elements), (b) Medium mesh (1516 shell elements), (c) Fine Mesh (5238 shell elements)

Three different mesh sizes were used to simulate the load-deformation response of YSPD as shown in Figure 9. The size of element in the finer mesh was half of the size of medium mesh and one-fourth of the size of coarse mesh. Fig 10 shows a typical force-displacement response for different mesh densities. Results showed that both the finer mesh and the medium mesh give reasonable agreement with test result. No further refinement was attempted since the predictions were found to be in line with the test results and the finer mesh has been adopted in subsequent finite element models to ensure better accuracy.

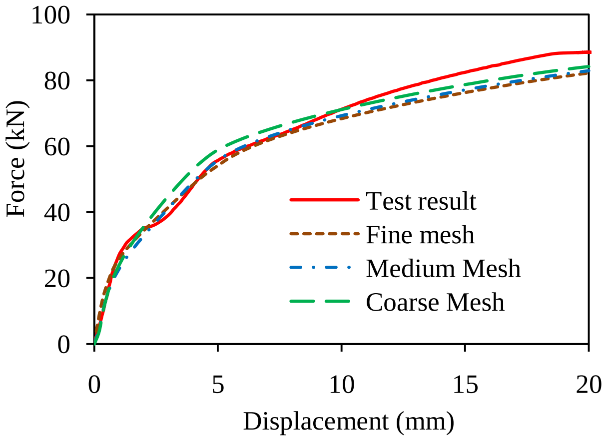

Figure 10: Typical force-displacement response due to different mesh sizes (YSPD 100×100×4)

3.5 Initial Imperfections

Yielding shear panel device consists of two main parts – a steel diaphragm plate and a square hollow section (SHS). The diaphragm plate is placed inside the SHS at mid depth and welded along the four sides of the diaphragm plate; this process induces residual stresses. In addition, the steel plates used to fabricate YSPD are not perfectly plane as they always inherit some geometric imperfections i.e. out-of-plane deformations. Effects of geometric imperfections and residual stresses are, therefore, investigated in this section as part of the FE modelling of YSPD.

3.5.1. Geometric Imperfections

Initial geometric imperfections are an inevitable property of steel structures because of the typically high width-to-thickness ratio, which influences their structural response. The importance of modelling initial imperfections attracted attention amongst researchers during the last few decades. In spite of its observed significance, there is no general guideline to model the magnitude and distribution of the initial geometric imperfections, largely due to the high degree of uncertainty associated with its formation process. Generally, an assumed shape and magnitude for the out-of-plane deformation is incorporated or an assumed transverse force is applied to simulate the effects of initial geometric imperfections. In recent times, the most commonly used technique for modelling imperfection distributions is either to adopt a sinusoidal wave or to use one of the Eigenmodes obtained from elastic buckling analysis; a number of recent approaches adopted for modelling thin-walled structural elements are discussed below.

Dawson and Walker [13] studied the geometric imperfections of cold-formed steel cross-sections and proposed the following relationships for geometrically imperfect plates with free edges under compression and bending,

$$\omega_0 = \alpha t \tag{1}$$

$$\frac{\omega_0}{t} = \beta \left(\frac{\sigma_y}{\sigma_{cr}}\right)^{0.5} \tag{2}$$

$$\frac{\omega_0}{t} = \gamma \left(\frac{\sigma_y}{\sigma_{cr}}\right) \tag{3}$$

Where, ω_0 is the amplitude of initial imperfection, t is the thickness of the plate, σ_y is the material yield stress, σ_{cr} is the critical plate buckling stress, whilst α, β and γ are constants. In addition, a conservative fit of the maximum imperfection amplitude was reported to be equal to 0.2t. Gardner [14] adopted Equation 7 with a proposed value of $\gamma = 0.023$ for roll-formed stainless steel hollow sections under compression and used the 1st Eigenmode for imperfection distribution.

Schafer and Pekoz [15] proposed the following two simplified regression based relationships to determine the imperfection amplitude ω_0 for cold formed steel lipped channel sections and assumed that the magnitude of imperfections in the lowest Eigenmode is sufficient to characterize the influence of imperfections. In the first formulation, the imperfection amplitude is linearly varied with the width (w) as follows,

$$\omega_0 = 0.006w \tag{4}$$

The second formulation is based on an exponential curve fit to the plate thickness as,

$$\omega_0 = 6te^{-2t} \tag{5}$$

EN 1993-1-5 [7] recommends to apply the equivalent local geometric imperfection for finite element models panels or sub panels based on the shape of the critical plate buckling modes with amplitude of w/200, which is linearly proportional to the minimum dimension of the panel. It gives lower imperfection magnitudes than Schafer and Pekoz's [15] proposed Equation 8.

Zhang et.al. [16] measured the maximum imperfections observed in cold formed steel channel columns and the obtained magnitudes varied from 0.03t to 0.25t, whilst the distribution of imperfections showed reasonable resemblance with the 1st Eigenmode. Sun and Butterworth [17] used imperfection magnitude of 0.167t, 0.333t, 0.5t and 0.667t to model the behaviour of steel single angle compression members eccentrically loaded through one leg; the use of amplitude 0.333t produced best predictions. Pokharel and Mahendran [18] investigated the sensitivity of imperfection for sandwich panels by varying the amplitude between 0.1t and 0.4t. The 1st Eigenmode was used to model imperfection distribution in all cases; the overall effect on the ultimate compressive strength was observed to be insignificant. Pavlovcic et.al. [19] investigated the reduction in shear resistance of longitudinally stiffened panels due to a range of local and global geometric imperfections within the prescribed limit according to EN 1993-1-5 [7]. Global imperfections were defined using the stiffener out-of-plane deflections in half-sine wave, whilst local imperfections in sub panels were modelled with critical local buckling modes for panels with trapezoidal stiffeners. Results obtained using combined imperfections showed that the reduction in panel shear resistance capacity has a small influence due to imperfections. Ashraf et.al. [11] reported a detailed review of different techniques adopted for modelling geometric imperfections observed in thin-walled structural components. The degree of uncertainty associated with geometric imperfections make it almost impossible to come up with a generalised formulation which can be adopted directly in FE modelling.

The current research adopts the most commonly used technique of obtaining Eigenmodes through elastic buckling analysis of the developed FE model, which are subsequently used as the initial shape in nonlinear analysis. Figure 11 shows some typical Eigenmodes of YSPD obtained through elastic buckling analysis. The distribution of the initial geometric imperfections is assumed to have the same shape as one of the obtained Eigenmodes. In ANSYS, the nodal displacements of an Eigenmode are normalised using the maximum displacement that occurs within a structure and thus the maximum displacement is set equal to unity. By specifying an appropriate multiplying factor, which is the maximum magnitude of imperfection, the nodal co-ordinates are scaled accordingly. This magnitude of the maximum initial geometric imperfection, commonly known as amplitude, is generally taken as a fraction of the plate thickness. A parametric study has been conducted to identify a suitable distribution and the corresponding amplitude of initial geometric imperfection. Figure 12 shows typical force-displacement response for variation in imperfection amplitude and distribution. Obtained results showed insignificant effect of initial geometric imperfections on the force-displacement response of YSPD. Diagonal tension in the diaphragm plate makes the incorporated initial imperfections less effective when compared to its significance in other types of loading e.g. members subjected to longitudinal compression. In the current research, the 1st Eigenmode is used to define the distribution of initial imperfections as this normally represents the lowest buckling capacity. An amplitude of 0.2t, where t is the thickness of the diaphragm plate, has been used to obtain a reasonable imperfection distribution for YSPD.

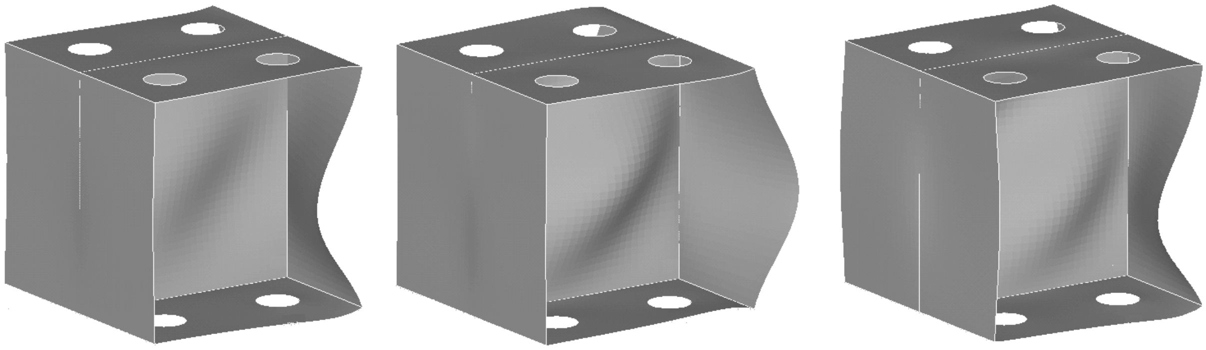

Figure 11: Eigenmodes 1, 2, and 3 for YSPD 100×100×4 obtained through elastic buckling analysis.

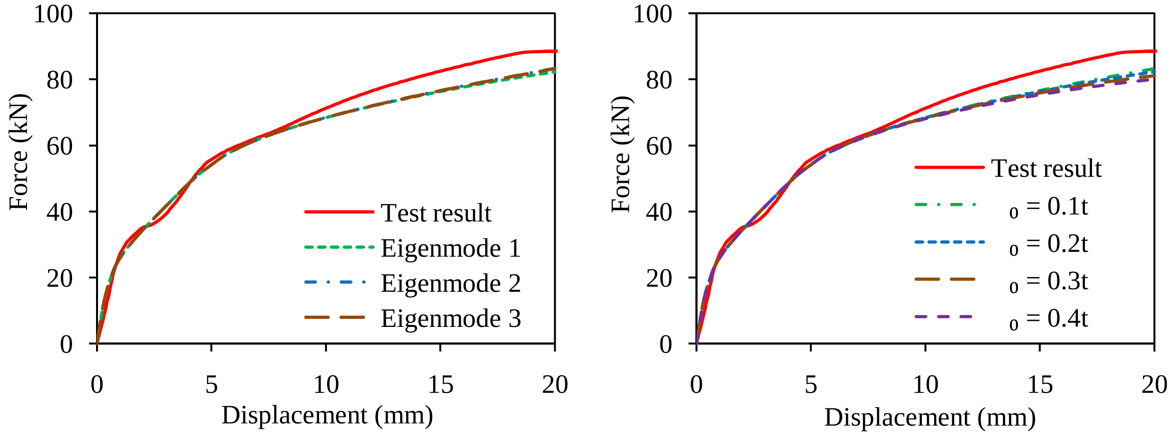

(a) (b)

Figure 12: (a) Typical force-displacement responses of YSPD (100×100×4) as a result of using different imperfection distributions (Eigenmodes) for imperfection amplitude, $_0 = 0.2t$, (b) Typical force-displacement responses due to different imperfection magnitude ($_0$) for the 1st Eigenmode.

3.5.2. Residual stresses

High thermal gradient involved in the welding process induces residual stresses; the magnitude and distribution of residual stresses are, however, quite complex in nature. Masubuchi [20] reported an extensive review on the distribution of residual stresses in different welded shapes. Odar et.al. [21] investigated the magnitude and distribution of residual stresses due to welding process on H and T sections using a method of sectioning, whilst Murugan et.al. [22] measured residual stresses in welded Tee-joint using contour method. Cruise and Gardner [23] conducted experiments for determining imperfections in long austenitic stainless steel sections and proposed simple predictive tools for both local and global imperfections. All experimental results show that tensile residual stress is induced nearer to the welded region, whilst compressive residual stresses are present in the remaining part of the cross-section.

Although the actual distribution of residual stresses is somewhat complicated, a number of simplified guide lines have been proposed by researchers. ECCS publication no. 33 [24] presents a simplified method to model thermally induced residual stresses for welded I sections – the tensile stresses nearer to the welded region and the compression stresses in the other part of the plate are assumed to have trapezoidal distributions. The magnitude of the tensile stress is assumed equal to the yield strength, whilst that for the compressive stress is equal to 25% of the yield strength; the resultant of the tensile and compressive stresses is self-balanced. Ueda et.al. [25] proposed a more simplified rectangular distribution for residual stresses in welded square plates. Liang et.al. [26] adopted the rectangular stress block approach to model residual stresses in concrete-filled welded steel box columns.

In the case of YSPD, a thin diaphragm steel plate is welded inside a square hollow section (SHS). The welding process induces residual stresses both in the diaphragm plate and the square hollow section. To investigate the effects of this residual stress, a simplified rectangular stress distribution is assumed with the magnitudes taken following ECCS specification i.e. the tensile stress is set equal to the yield strength, whilst the compressive stress is taken as 25% of the yield strength. The details are given in Figure 13. The force-displacement responses obtained for YSPDs with and without residual stresses are compared in Figure 14, which shows that residual stresses have negligible effect on the force-displacement response. Residual stress is incorporated for the exact finite element modelling of YSPD though it has an insignificant effect.

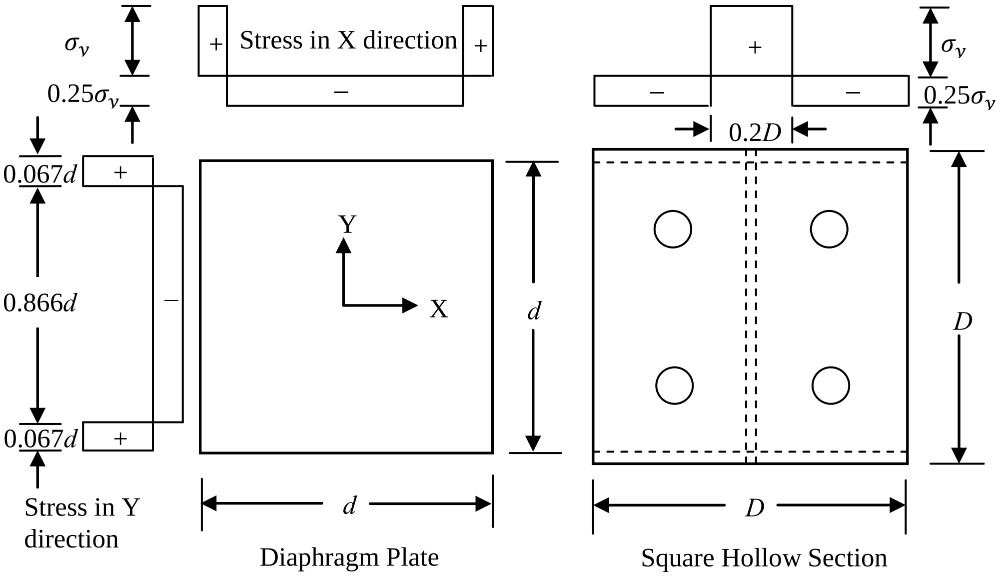

Figure 13: Residual stress Distribution in YSPD

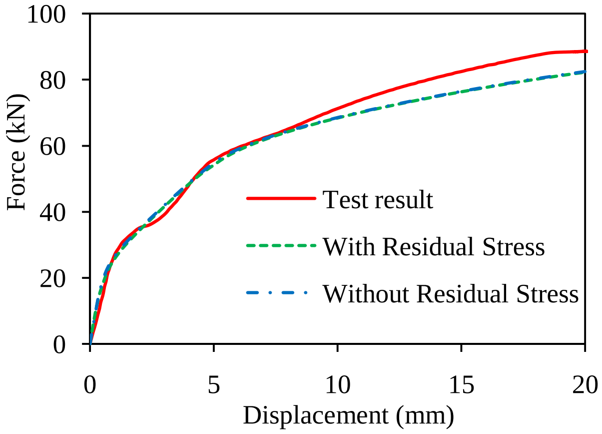

Figure 14: Typical force-displacement response with and without residual stress (YSPD 100×100×4)

4 LOAD-DEFORMATION RESPONSE OF YSPD UNDER MONOTONIC LOADING

A finite element model is developed for yielding shear panel device. Figure 15 compares the force-deformation response of YSPDs obtained from test results to those obtained from FE simulation. The devloped FE model with 2 mm diaphragm plate significantly underpredicts the test behaviour; this discrepancy is due to a higher strength shown by the material after a low yield strength (211.3 N/mm^2).

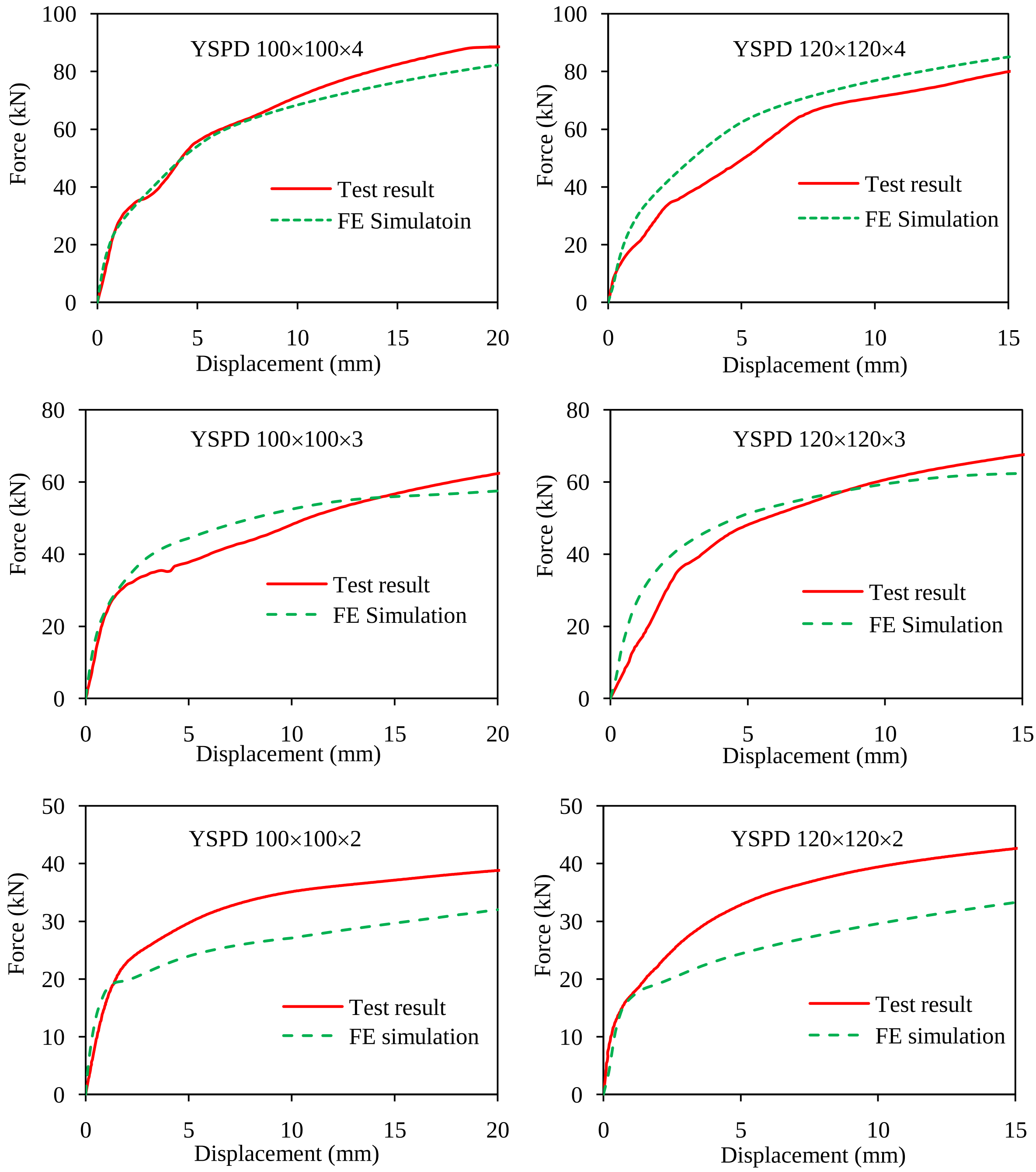

Figure 15. Force-displacement responce of YSPDs.

Table 4 compares the amount of energy required to achieve specified displacements during the monotonic loading tests of YSPDs to those obtained from finite element simulation. The ratio of energy required for different displacements indicates that the developed finite element models can predict the required energy with reasonable accuracy.

YSPD Designation	Ratio of Energy for different displacements (FE/Test)			
(D ×D×t)	5 mm	10 mm	15 mm	20 mm
100×100×2	0.89	0.83	0.81	0.81
100×100×3	1.13	1.14	1.09	1.05
100×100×4	1.01	0.99	0.97	0.95
120×120×2	0.81	0.77	0.77	-
120×120×3	1.22	1.09	1.03	-
120×120×4	1.29	1.17	1.13	-

Table 4: Comparison of energy required in monotonic loading.

5 LOAD-DEFORMATION RESPONSE OF YSPD UNDER CYCLIC LOADING

Developed FE models were subjected to cyclic loading to validate their accuracy so that reliable results could be generated to develop design rules for YSPD. Figure 16 shows the force-displacement response of YSPDs when subjected to a displacement controlled cyclic loading. Cyclic response, overall, shows a good correlation between the test results and finite element simulation.

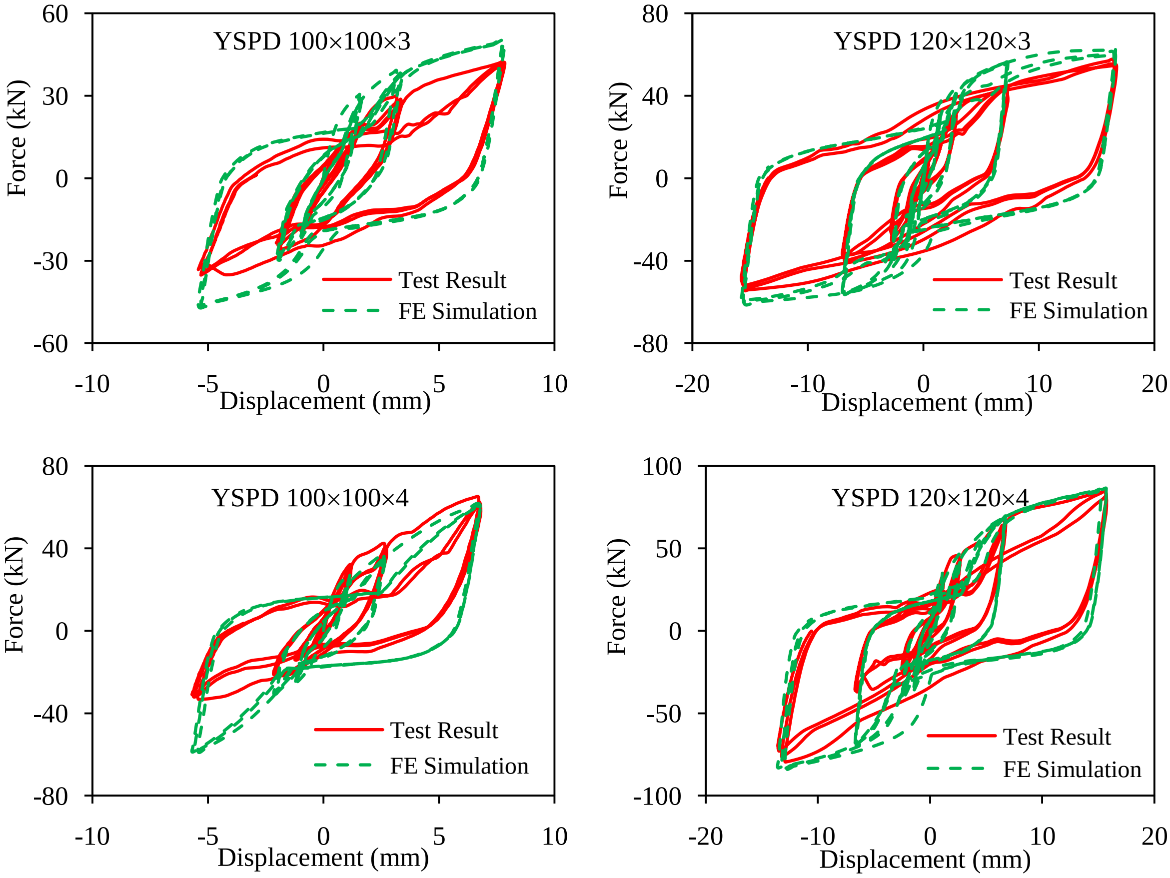

Figure 16. Cyclic responce of YSPDs

The energy dissipated in one cycle can be measured by calculating the area bounded by the cyclic response. Total energy dissipation for both test results and finite element simulation are calculated. Comparisons of energy dissipation with the cumulative number of cycles are plotted in Figure 17. The comparison shows that the developed FE models are able to predict the amount of energy absorbed with reasonable accuracy.

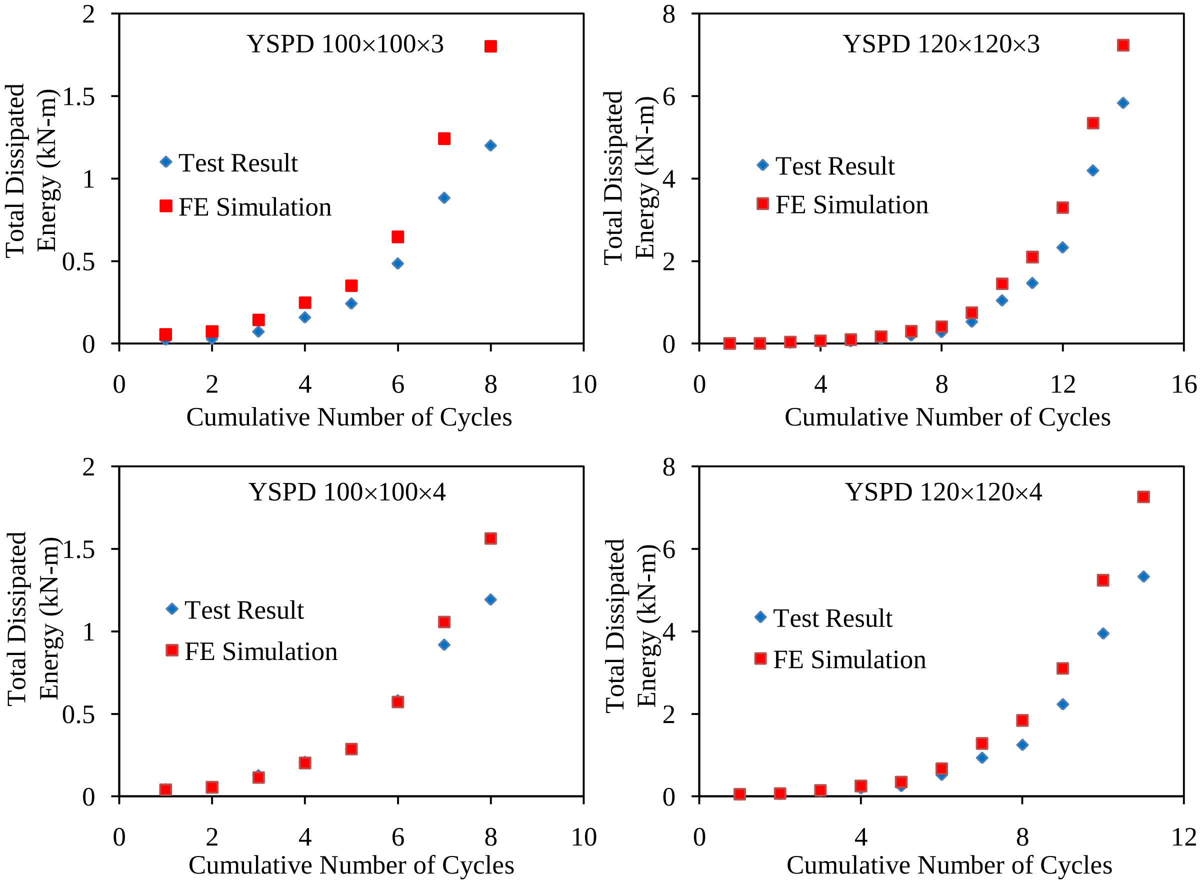

Figure 17. Comparison of hysteretic energy dissipation due to cyclic loading of YSPDs

6 CONCLUSION

Numerical modelling techniques for a newly proposed passive energy dissipation device YSPD is explained in detail, giving special significance of appropriate support conditions, initial geometric imperfections and residual stresses. Modelling of support conditions requires use of nonlinear spring elements with appropriate linear stiffness in both tension and compression. The out-of-plane rotation of the loading beam is observed to play a significant role in determining the initial slope of the load-deformation behaviour. Developed FE models were subjected to both monotonic and cyclic loading and the obtained results showed good agreement with the test results.

REFERENCES

[1] Chan, R. W. K., Albermani, F., and Williams, M. S., 2009, "Evaluation of Yielding Shear Panel Device for Passive Energy Dissipation," Journal of Constructional Steel Research, 65(2), pp. 260-268.

[2] Williams, M., and Albermani, F., 2003, "Monotonic and Cyclic Tests on Shear Diaphragm Dissipators for Steel Frames," Civil Engineering Bulletin No. 23, Department of Civil Engineering, University of Queensland, Australia.

[3] Schmidt, K., Dorka, U. E., Taucer, F., and Magnonette, G., 2004, "Seismic Retrofit of a Steel Frame and an Rc Frame with Hyde Systems," Institute for the Protection and the Security of the Citizen European Laboratory for Structural Assessment, European Commission Joint Research Centre.

[4] Williams, M., and Albermani, F., 2006, "Monotonic and Cyclic Tests on Shear Diaphragm Dissipators for Steel Frames," Advanced Steel Construction, 2(1), pp. 1-21.

[5] Chan, R. W. K., 2008, "Metallic Yielding Devices for Passive Dissipation of Seismic Energy," PhD Thesis, University of Queensland.

[6] Alinia, M. M., Gheitasi, A., and Erfani, S., 2009, "Plastic Shear Buckling of Unstiffened Stocky Plates," Journal of Constructional Steel Research, doi: 10.1016/j.jcsr.2009.04.001(

[7] Cen - European Committee for Standardization, 2006, "En 1993-1-5. Eurocode 3: Design of Steel Structures, Part 1.5: Plated Structural Elements."

[8] Ansys, "Ansys 11.0 Documentation," ANSYS Inc., Southpointe, 275 Technology Drive, Canonsburg, PA 15317.

[9] De Matteis, G., Formisano, A., Panico, S., and Mazzolani, F. M., 2008, "Numerical and Experimental Analysis of Pure Aluminium Shear Panels with Welded Stiffeners," Computers & Structures, 86(6), pp. 545-555.

[10] Soo Kim, T., and Kuwamura, H., 2007, "Finite Element Modeling of Bolted Connections in Thin-Walled Stainless Steel Plates under Static Shear," Thin-Walled Structures, 45(4), pp. 407-421.

[11] Ashraf, M., Gardner, L., and Nethercot, D. A., 2006, "Finite Element Modelling of Structural Stainless Steel Cross-Sections," Thin-Walled Structures, 44(10), pp. 1048-1062.

[12] Ellobody, E., and Young, B., 2005, "Structural Performance of Cold-Formed High Strength Stainless Steel Columns," Journal of Constructional Steel Research, 61(12), pp. 1631-1649.

[13] Dawson, R., and Walker, A., 1972, "Post-Buckling of Geometrically Imperfect Plates," Journal of the Structural Division, 98(1), pp. 75-94.

[14] Gardner, L., 2002, "A New Approach to Structural Stainless Steel Design," PhD. thesis. Structures Section, Department of Civil and Environmental Engineering. Imperial College London, UK.

[15] Schafer, B., and Pekoz, T., 1998, "Computational Modeling of Cold-Formed Steel: Characterizing Geometric Imperfections and Residual Stresses," Journal of Constructional Steel Research, 47(3), pp. 193-210.

[16] Zhang, Y. C., Wang, C. G., and Zhang, Z. N., 2007, "Tests and Finite Element Analysis of Pin-Ended Channel Columns with Inclined Simple Edge Stiffeners," Journal of Constructional Steel Research, 63(3), pp. 383-395.

[17] Sun, J., and Butterworth, J., 1998, "Behaviour of Steel Single Angle Compression Members Axially Loaded through One Leg," In: Proceedings of the Australian structural engineering conference, Auckland, pp. 859-66.

[18] Pokharel, N., and Mahendran, M., 2004, "Finite Element Analysis and Design of Sandwich Panels Subject to Local Buckling Effects," Thin-Walled Structures, 42(4), pp. 589-611.

[19] Pavlovcic, L., Detzel, A., Kuhlmann, U., and Beg, D., 2007, "Shear Resistance of Longitudinally Stiffened Panels - Part 1: Tests and Numerical Analysis of Imperfections," Journal of Constructional Steel Research, 63(3), pp. 337-350.

[20] Masubuchi, K., 1980, Analysis of Welded Structures : Residual Stresses, Distortion, and Their Consequences, Pergamon Press, Oxford ; New York.

[21] Odar, E., Nishino, F., and Tall, L., 1967, "Residual Stresses in Welded Built-Up "T-1" Shapes," WRC Bulletin, 121(April), pp. 22-29.

[22] Murugan, N., and Narayanan, R., 2009, "Finite Element Simulation of Residual Stresses and Their Measurement by Contour Method," Materials and Design, 30(6), pp. 2067-2071.

[23] Cruise, R., and Gardner, L., 2006, "Measurement and Prediction of Geometric Imperfections in Structural Stainless Steel Members," Structural Engineering and Mechanics, 24(1), pp. 63-89.

[24] European Convention for Constructional Steelwork, E., 1984, "Ultimate Limit State Calculation of Sway Frames with Rigid Joints," Technical Committee 8 - Structural Stability Technical Working Group 8.2 - System.

[25] Ueda, Y., Yasukawa, W., Yao, T., Ikegami, H., and Ohminami, R., 1975, "Effect of Welding Residual Stresses and Initial Deflection on Rigidity and Strength of Square Plates Subjected to Compression (Report I)," Trans, of JWRI, 4(2), pp. 29-43.

[26] Liang, Q., and Uy, B., 2000, "Theoretical Study on the Post-Local Buckling of Steel Plates in Concrete-Filled Box Columns," Computers and Structures, 75(5), pp. 479-490.

COMPDYN 2011
ECCOMAS Thematic Conference on
Computational Methods in Structural Dynamics and Earthquake Engineering
M. Papadrakakis, M. Fragiadakis, V. Plevris (eds.)
Corfu, Greece, 25-28 May 2011

DAMAGE ASSESSMENT OF HYPERBOLIC PARABOLOIDAL SHELLS USING FINITE ELEMENT UPDATING

Rafael Castro[1], Demosthenes Talaslidis[2], Rafael Gallego[3] and Guillermo Rus[3]

[1]University of Cordoba
Department of Mechanics, Campus de Rabanales, 14071 Cordoba, Spain
e-mail: me1catrr@uco.es

[2] Aristotle University Thessaloniki
Department of Civil Engineering, Mail Stop 502, 54124 Thessaloniki, Greece
e-mail: talaslid@civil.auth.gr

[3] University of Granada
Department of Structural Mechanics, Campus de Fuentenueva, 18071 Granada, Spain
e-mail: {gallego,grus}@ugr.es

Keywords: Finite Element Updating, Structural Damage, Structural Dynamics, Hyperbolic Paraboloidal Shells.

Abstract. *Assessment of the structural and functional integrity of civil engineering structures is an essential design issue and of continuous concern during the process of maintenance, repair and upgrading of such structures. The concept of Structural Health Monitoring (SHM) offers means to predict the structural behavior of a particular structure under operating conditions that differ from those taken into consideration in the initial design cycle. Employment of the aforementioned concept requires computational models that are verified, refined and adjusted with respect to actual measurements. In this paper, a finite element updating methodology is presented, which aims to reduce the discrepancies between the dynamic model parameters of the structure and the measurements. A sucessful finite element updating approach must rely on physically meaningful criteria for selecting the updating parameters and the most suitable method in order to modify the mass and stiffness matrices of the computational model. The proposed iterative method is based on a generalized variational principle, a modified version of the Hu-Washizu principle of elastodynamics, which treats displacements, rotations, strains and stresses as independent variables that can be treated as updating parameters. Thus, a more efficient and direct implementation of measurements is possible. Furthermore, the discretization yields simple and effective finite elements especially suited to repetitious computations required in dynamic finite element updating. Different parameter sensitivities are studied. Single and multi-objective optimization processes are carried out using objective functions that include the eigenfrequencies and the strain modal energy of the structure. Finally, some alternative damage scenarios are presented in order to validate the proposed formulation for the case of hyperbolic paraboloidal shell structures.*

1 INTRODUCTION

Assessment of the structural and functional integrity of civil engineering structures is an essential design issue and of continuous concern during the process of maintenance, repair and upgrading of such structures. The concept of Structural Predictive Maintenance (SPM) offers means to predict the structural behavior of a particular structure under operating conditions that differ from those taken into consideration in the initial design cycle. Employment of the aforementioned concept requires computational models that are verified, refined and adjusted with respect to actual measurements. The finite element updating method is employed to minimize those differences. Over the past decades, significant research has been performed in this area [1]. The monograph by Friswell [2] and the review article [3] mainly deal with the different steps in the updating procedure. Furthermore, Brownjohn *et al.* [4] focus on those steps by using a controlled laboratory-based study of a simple structure. Finite element modelling for updating is the first phase. In case of an updating process, the development of a finite element model for a civil engineering structure, differs from the finite element models used for common structural analysis purposes. Some important issues must be taken into consideration [5]: type of elements, boundary conditions and the presence of damage. Civil engineering structures are modelled by beam, plate, shell, and solid elements with thousands of degrees of freedom (displacements and rotations). An important issue is that not all degrees of freedom can be measured; also rotations are difficult to assess. Therefore, it is vital to employ finite elements that restrict the number of rotational degrees of freedom to a minimum. Furthermore, the element formulation should contain physically meaningful updating parameters. Selection of the appropriate updating parameters is crucial to the finite element updating process. A small perturbation of some parameters may affect the behavior of the structure, while other parameters not. The former may not necessarily be the ideal candidates for an updating process. Therefore, it is necessary to develop a sensitivity analysis preceded by an error localisation investigation. If some damage is present, the model has to take it also into account in order to realistically model the structure. The Force Balance Method [6] calculates a residual force vector, that if plotted can represent the non-equilibrated forces/moments in direction of the degrees of freedom; a fact that points to an error in the modelling phase. Sensitivity analysis represents the variation of an objective function with respect to structural parameters [7, 8]. The derivation of the objective functions can be performed by four different methodologies [9]: overall finite differences, discrete derivatives, continuum derivatives, and computational or automatic differentitation. The selection of a proper objective function can ensure an efficient sensitivity analysis [10]. The objective function establishes a relationship between the measurement results and the numerical predictions. Modal properties such as eigenfrequencies and mode shapes of a structure are normally employed in these objective functions. An optimization process serves to minimize the differences between experimental and numerical results [11–14]. Finally, to ensure the agreement of the updating results it is necessary to validate them. Towards this aim, some validation techniques are employed (e.g., Modal Assurance Criterion [15]).

In this paper, a finite element updating methodology is presented, which aims to reduce the discrepancies between the dynamic model parameters of the structure and the measurements. An effective finite element updating approach must rely on physically meaningful criteria for selecting the updating parameters and the most suitable method in order to modify the mass and stiffness matrices of the computational model. The proposed iterative method employs finite elements that are derived using a generalized variational principle, a version of the Hu-Washizu principle of elastodynamics. This variational principle treats displacements, rotations, strains, and stresses as independent variables that can be selected in a direct manner as updating parameters. The changes of these parameters are estimated by employing both single- and multi-objective optimisation processes. The application of the method is illustrated by employing four-noded doubly-curved shell elements with a total number of twenty degrees of freedom to study different cases such as damaged or undamaged models. Numerical examples demonstrate that the proposed approach is stable and produces accurate results.

2 FINITE ELEMENT MODELLING

2.1 Hyperbolic Paraboloidal shell

The accuracy of the method is demonstrated for the case of a homogeneous, isotropic, and thin hyperbolic paraboloidal shell (hypar shell) of rectangular planform with length a, width b, thickness h, and radii of curvature R_x and R_y, (see figure 1). The dimensions of the hypar shell are:

$$a = 20\,m \quad b = 20\,m \quad R_y = \frac{b}{0.1} \quad R_x = -R_y \quad h = 0.2\,m \tag{1}$$

Young's modulus and Poisson's ratio are taken as $2 \cdot 10^{10}\ N/mm^2$ and 0.3, respectively.

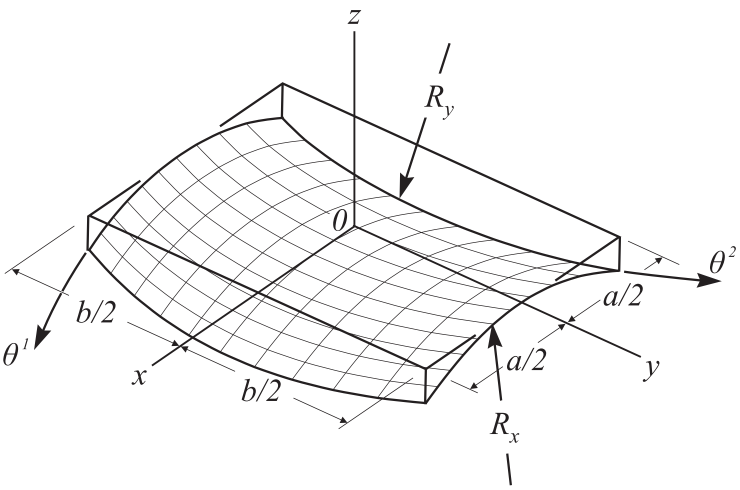

Figure 1: Hyperbolic paraboloidal shell with rectangular planform.

A damage scenario is considered with a stiffness reduction in two parts of the hypar (see figure 2). A uniform mesh with 8×8 elements is used. Eigenfrequencies and mode shapes obtained from computational methods for the damaged model of this hypar shell are condisered to be the experimental results to be validated.

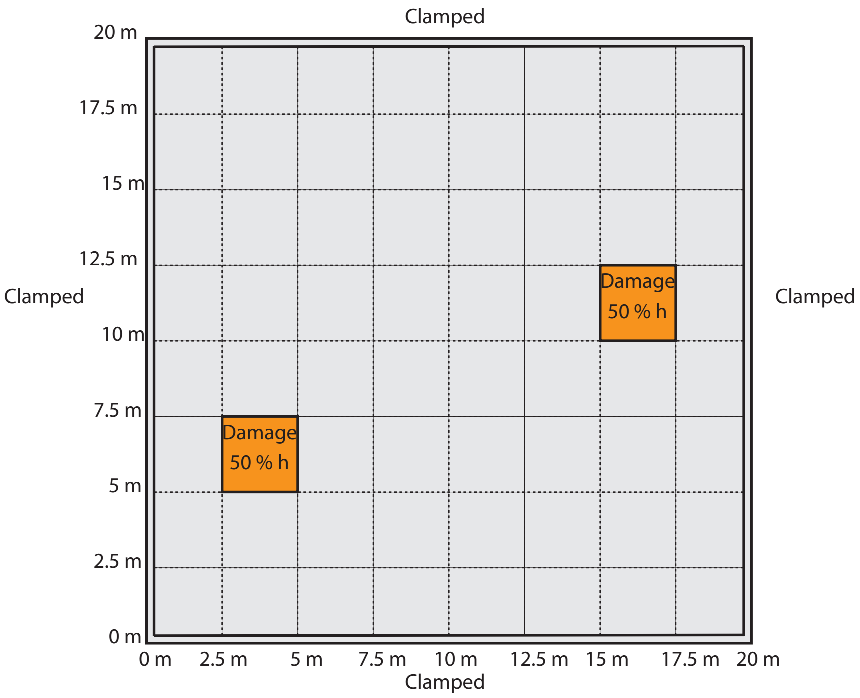

Figure 2: Damage scenario for the hyperbolic paraboloidal shell.

2.2 Finite element formulation

The shell element derived in the present study is a four-noded, doubly-curved isoparametric finite element with five degrees of freedom at each node: three physical components of the displacements u_1, u_2, u_3 and two components of the rotations φ_1, φ_2. Bilinear shape functions N_k are chosen for the physical components of the displacements and rotations:

$$\begin{aligned} &u_i = \sum_{k=1}^{4} u_i^k \, N_k \qquad \varphi_\alpha = \sum_{k=1}^{4} \varphi_\alpha^k \, N_k \\ \text{with} \quad &N_k = \frac{1}{4}\,(1+\xi_k\,\xi)\,(1+\eta_k\,\eta) \quad i=1,2,3 \quad \alpha=1,2 \end{aligned} \tag{2}$$

Denoting by $\mathcal{U}(\boldsymbol{\gamma})$ the strain energy and by $\boldsymbol{\gamma}$ and $\boldsymbol{\sigma}$ the vectors containing the strain and stress components, respectively, a version of the generalized Hu-Washizu principle assumes the form [16]:

$$\Pi_{HW}\left[\mathbf{v},\boldsymbol{\gamma},\boldsymbol{\sigma}\right] = \int_V \left[\mathcal{U}(\boldsymbol{\gamma}) - \boldsymbol{\sigma}^T\left(\boldsymbol{\gamma}-\mathbf{D}\,\mathbf{v}\right) - \Pi_b\right] dV - \int_{S_{\hat{v}}} \left(\mathbf{v}-\hat{\mathbf{v}}\right)\boldsymbol{\sigma}\,\mathbf{n}\,dS - \int_{S_t} \Pi_t\,dS \tag{3}$$

In the variational principle (3), $\mathbf{v}$ represents the displacement vector and the index b refers to the body forces. The vector $\hat{\mathbf{v}}$ denotes prescribed displacements on the part of the boundary, where displacements are prescribed $(S_{\hat{v}})$. If the body forces in V and surface tractions on S_t are conservative, then Π_b and Π_t denote the corresponding potentials.

As mentioned before, the use of the Hu-Washizu principle and the independent approximation of strain and stress yields a series of desirable features important for the reliability, convergence behavior, and efficiency of the elemental formulation, e.g., avoidance of superfluous energy and zero energy modes. Furthermore, the discrete approximation is drawn in a consistent manner from the general theory of the continuum and the mechanical behavior of the finite element, without resource to special manipulations or computational procedures. Also, it has been shown (see [16, 17]) that essential prerequisites for the achievement of these goals are: The identification of the constant and higher-order deformational modes that are contained in the displacement/rotation assumptions, the realization that constant terms are neccesary for convergence and that higher-order terms reappear in different strain components. Therefore, our approximations need not retain the higher-order terms in two different strain components (they are needed only to inhibit a mode). Suppressing such terms serves to reduce excessive internal energy and to improve convergence. As an example, the following assumptions for the extensional strains have been shown to serve the aforementioned goals:

$$\begin{aligned} \varepsilon_{11} &= \bar{\varepsilon}_{11} + \bar{\bar{\varepsilon}}_{11}\,\eta \\ \varepsilon_{22} &= \bar{\varepsilon}_{22} + \bar{\bar{\varepsilon}}_{22}\,\xi \\ \varepsilon_{12} &= \bar{\varepsilon}_{12} + \underline{\bar{\bar{\varepsilon}}_{11}\,\xi} + \underline{\bar{\bar{\varepsilon}}_{22}\,\eta} \end{aligned} \tag{4}$$

The higher order modes $(\bar{\bar{\varepsilon}}_{11}, \bar{\bar{\varepsilon}}_{22})$ in the expression for the shear strain ε_{12} appear also in the expressions for the strains ε_{11} and ε_{22}. In order to avoid succesive energy, the assumption for the shear strain should not contain the underlined terms.

The eigenvalue problem for the undamped free vibration problem takes the well-known form:

$$\mathbf{K}\,\mathbf{u_i} = \omega_i^2\,\mathbf{M}\,\mathbf{u_i} \tag{5}$$

where $\mathbf{K}$ is the stiffness matrix of the system, ω_i is the natural frequency in radians of mode i, $\mathbf{u_i}$ represent the corresponding eigenvector, and M is the mass matrix of the structure. The consistent element mass matrix is derived by discretizing the kinetic energy:

$$\delta\mathcal{U}_K = \frac{1}{2}\int_V \rho\,2\,\mathbf{v}\,\delta\ddot{\mathbf{v}}dV \tag{6}$$

$$\tag{7}$$

In table 1, numerical results are presented for the nondimensional frequency parameter λ given by:

$$\lambda = \omega\,a\,b\sqrt{\frac{\rho\,h}{D}} \qquad D = \frac{E\,h^3}{12\,(1-\nu^2)} \tag{8}$$

that demonstrate the convergence behavior for different meshes.

Damage identification based on changes in vibration characteristics requires that those changes are reliable. In table 2, the variation of λ for various ratios b/h is presented. These results are illustrated graphically by figure 3. From these results it can be concluded that the frequency vibration characteristic could not be used alone in a damage identification process due to its relatively low variation with thickness changes.

Mode	Mesh 6×6	Mesh 8×8	Mesh 10×10	Mesh 12×12
1	52.76	51.817	51.39	51.17
2	94.41	86.72	83.69	82.16
3	94.41	86.72	83.69	82.16
4	132.73	121.84	117.41	115.13
5	215.96	170.22	155.32	148.33
6	216.86	170.92	155.94	148.91
7	243.54	200.88	186.51	179.64
8	243.54	200.88	186.51	179.64
9	326.76	269.19	249.10	239.35
10	579.75	329.97	275.19	252.20

Table 1: Convergence behavior of frequency parameter ($\lambda = \omega ab\sqrt{\rho h/D}$) for the clamped (CCCC) thin hyperbolic paraboloidal shell of figure 1.

Mode	$b/h = 200$	175	150	125	100	75	50	25	10
1	80.77	73.02	65.53	58.40	51.81	46.01	41.28	37.72	33.78
2	100.91	96.74	92.96	89.61	86.72	84.31	82.22	78.99	67.37
3	100.91	96.74	92.96	89.61	86.72	84.31	82.22	78.99	67.37
4	129.04	126.90	124.99	123.31	121.84	120.48	118.85	114.00	93.63
5	179.26	176.61	174.24	172.13	170.22	168.31	165.61	156.38	120.29
6	179.64	177.08	174.79	172.76	170.92	169.08	166.44	157.32	121.51

Table 2: Variation of frequency parameter ($\lambda = \omega ab\sqrt{\rho h/D}$) with respect to thickness for the clamped (CCCC) thin hyperbolic paraboloidal shell of figure 1.

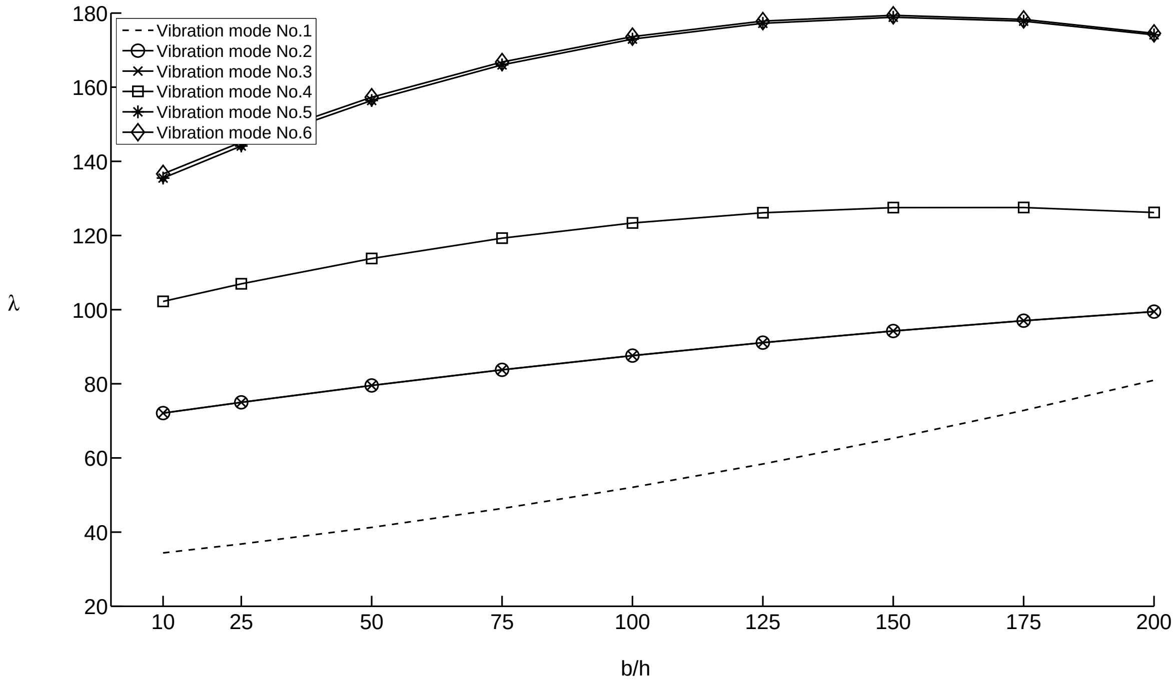

Figure 3: Graphical representation of the variation of frequency parameter ($\lambda = \omega ab\sqrt{\rho h/D}$) with respect to the thickness

3 CORRELATION

Analytical results from a finite element model must be validated with respect to those obtained by experimental measurements. Towards this aim, several techniques may be employed [19]. One of the simplest methods for data correlation is to calculate the percentage differences between the natural frequencies obtained by analytical and experimental techniques (see fourth column of table 3 and figure 4).

Mode	Undamaged hypar (Hz)	Damaged hypar (Hz)	Differences $(\%)$	MAC (%)
1	3.60	3.59	0.28	0.99
2	6.02	5.98	0.73	0.008
3	6.02	6.02	-0.01	0.008
4	8.47	8.38	1.01	0.99
5	11.83	11.54	2.45	0.64
6	11.88	11.78	0.78	0.64
7	13.96	13.69	1.91	0.11
8	13.96	13.80	1.17	0.11
9	18.71	18.45	1.38	0.97
10	22.93	22.06	3.83	0.71

Table 3: Differences in the first ten natural frequencies between the undamaged and damaged model for the CCCC hypar (8×8 mesh) of figure 1.

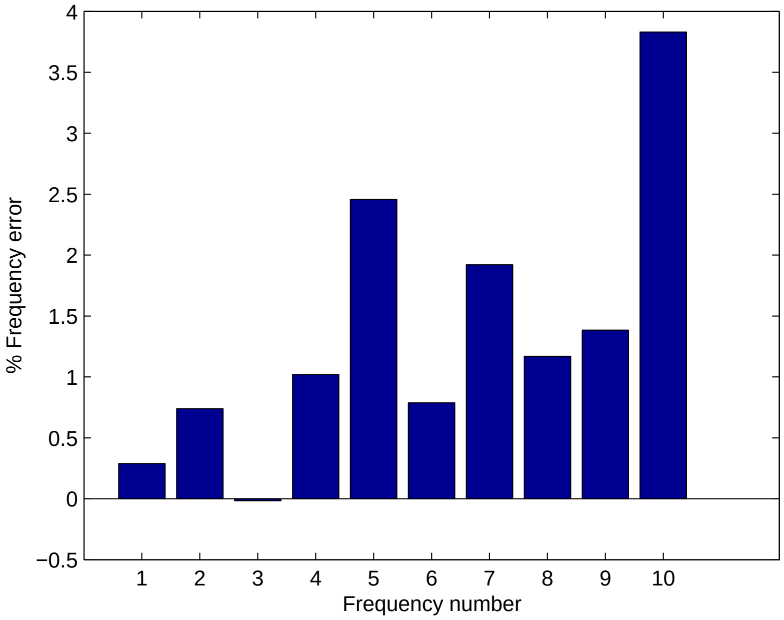

Figure 4: Percentage differences between analytically and experimentally obtained natural frequencies.

The modal assurance criterion (MAC) is another commonly used method to establish a correlation factor for each pair of analytical and experimental mode shapes:

$$MAC_{ij} = \frac{\left|\boldsymbol{\phi}_{a_i}^T \boldsymbol{\phi}_{e_j}\right|^2}{\left(\boldsymbol{\phi}_{a_i}^T \boldsymbol{\phi}_{a_i}^T\right)\left(\boldsymbol{\phi}_{e_j}^T \boldsymbol{\phi}_{e_j}^T\right)} \tag{9}$$

A high correlation yields a MAC value close to 1, whereas a low correlation assumes values near 0. The fifth colum of table 3 presents MAC values for the undamaged model of the hypar (analysis using doubly-curved shell elements) and those for the damaged hypar scenario (considered as experimental data). Furthermore, figure 5 represents the MAC-matrix for the first ten mode shapes.

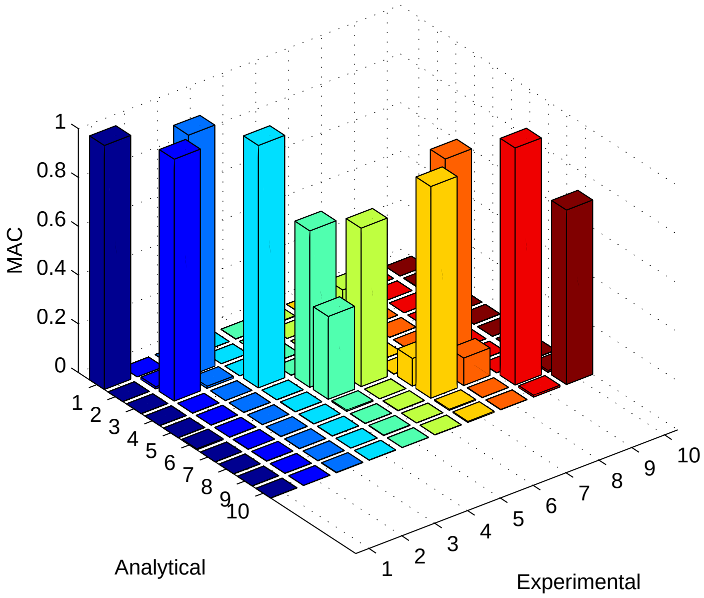

Figure 5: Representation of Modal Assurance Criterion (MAC) matrix between the undamaged and damaged models for the CCCC hypar.

4 OBJECTIVE FUNCTIONS AND SENSITIVITY ANALYSIS

Jaishi [11] proposed the use of two objective functions comprised of the discrepancies between experimental and numerical results. The modal strain energy residual function (Π_1) and the eigenfrequency residual function (Π_2) are defined as:

$$\Pi_1(p) = \frac{1}{\Pi_1(p_0)} \sum_{i=1}^{m} \left(\frac{\boldsymbol{\phi}_{ai}^T \mathbf{K} \boldsymbol{\phi}_{ai}}{\boldsymbol{\phi}_{ei}^T \mathbf{K} \boldsymbol{\phi}_{ei}} - 1 \right)^2 \qquad \Pi_2(p) = \frac{1}{\Pi_2(p_0)} \sum_{i=1}^{m} \left(\frac{\lambda_{ai}}{\lambda_{ei}} - 1 \right)^2 \tag{10}$$

where λ and $\boldsymbol{\phi}$ denote the m eigenfrequencies and modal vectors of the eigenvalue problem, the subindices ai and ei refer to the analytical and experimental results that in this case correspond to the undamaged and damaged models. Matrix $\mathbf{K}$ represents the stiffness matrix of the system and the variable p is defined as a normalization of model parameters (i.e., the thickness h of the bridge) between the initial (h_0) and updated values (h):

$$p_h = -\frac{h-h_0}{h_0} \qquad h = h_0(1-p_h) \tag{11}$$

Sensitivity analysis of these objective functions with respect to the model parameters is carried out by forming the gradients of the objective functions Π_1 and Π_2, respectively (derivatives of Π_1 and Π_2 with respect to the parameter p_j):

$$\frac{\partial \Pi_1}{\partial p_j} = \frac{1}{\Pi_1(p_0)} \sum_{i=1}^{m} \left[2\frac{A}{(\boldsymbol{\phi}_{ei}^T \mathbf{K} \boldsymbol{\phi}_{ei})^2} \left(\frac{\boldsymbol{\phi}_{ai}^T \mathbf{K} \boldsymbol{\phi}_{ai}}{\boldsymbol{\phi}_{ei}^T \mathbf{K} \boldsymbol{\phi}_{ei}} - 1 \right) \right] \tag{12}$$

$$A = \left[\left\{ \left(\boldsymbol{\phi}_{ei}^T \mathbf{K} \boldsymbol{\phi}_{ei} \right) \left[2\frac{\partial \boldsymbol{\phi}_{ai}^T}{\partial p_j} \mathbf{K} \boldsymbol{\phi}_{ai} + \boldsymbol{\phi}_{ai}^T \frac{\partial \mathbf{K}}{\partial p_j} \boldsymbol{\phi}_{ai} \right] \right\} - \left\{ \left(\boldsymbol{\phi}_{ai}^T \mathbf{K} \boldsymbol{\phi}_{ai} \right) \left(\boldsymbol{\phi}_{ai}^T \frac{\partial \mathbf{K}}{\partial p_j} \boldsymbol{\phi}_{ai} \right) \right\} \right] \tag{13}$$

$$\frac{\partial \Pi_2}{\partial p_j} = \frac{1}{\Pi_2(p_0)} \sum_{i=1}^{m} \left[2 \left(\frac{\lambda_{ai}}{\lambda_{ei}^2} - \frac{1}{\lambda_{ei}} \right) \frac{\partial \lambda_{ai}}{\partial p_j} \right] \tag{14}$$

For the derivatives:

$$\frac{\partial \lambda_i}{\partial p_j} \qquad \frac{\partial \boldsymbol{\phi}_i}{\partial p_j} \tag{15}$$

in equations (13) and (14), the expressions derived by Fox and Kapoor [18] are employed:

$$\frac{\partial \lambda_i}{\partial p_j} = \boldsymbol{\phi}_i^T \left[\frac{\partial \mathbf{K}}{\partial p_j} - \lambda_i \frac{\partial \mathbf{M}}{\partial p_j} \right] \boldsymbol{\phi}_i \tag{16}$$

$$\frac{\partial \boldsymbol{\phi}_i}{\partial p_j} = \sum_{q=1}^{d} \beta_{jiq} \boldsymbol{\phi}_q \qquad \beta_{jiq} = \begin{cases} \boldsymbol{\phi}_q^T \left[\left(\frac{\partial \mathbf{K}}{\partial p_i} - \lambda_j \frac{\partial \mathbf{M}}{\partial p_i} \right) / (\lambda_j - \lambda_q) \right] \boldsymbol{\phi}_j & q \neq j \\ -\frac{1}{2} \boldsymbol{\phi}_j^T \frac{\partial \mathbf{M}}{\partial p_i} \boldsymbol{\phi}_j & q = j \end{cases} \tag{17}$$

where d denotes the number of modes that will be considered in the evaluation. Since in a hypar model only few of the modes can be computed and the lower modes are of importance, it is reasonable to consider here only the first ten modes ($m = d = 10$). Furthermore, the derivatives of the stiffness and mass matrix, appearing in equations (16) and (17) are formed rather analytically than numerically using finite differences. This yields a series of advantages in the optimization process.

Figure 6(a) and figure 6(b) illustrate the sensitivity of the objective functions Π_1 and Π_2 with respect to variations of the thickness parameter. It can be observed that the strain modal energy function easily detects both damages. On the other hand, sensitivity of the objective function Π_2, which is related to the eigenfrequencies, assumes a symmetrical form that can not identify the position of the damages. Nevertheless, eigenfrequencies can be accurately measured by operational modal analysis and therefore are considered useful in the optimization process.

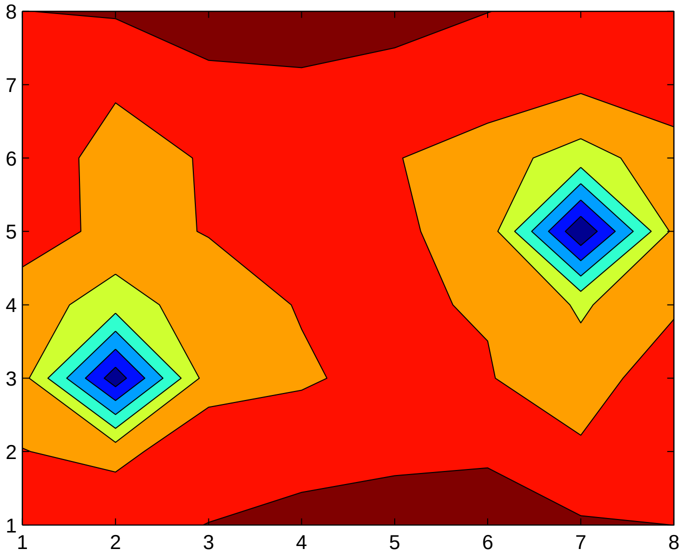

(a) Sensitivity of the objective function Π_1 with respect to thickness.

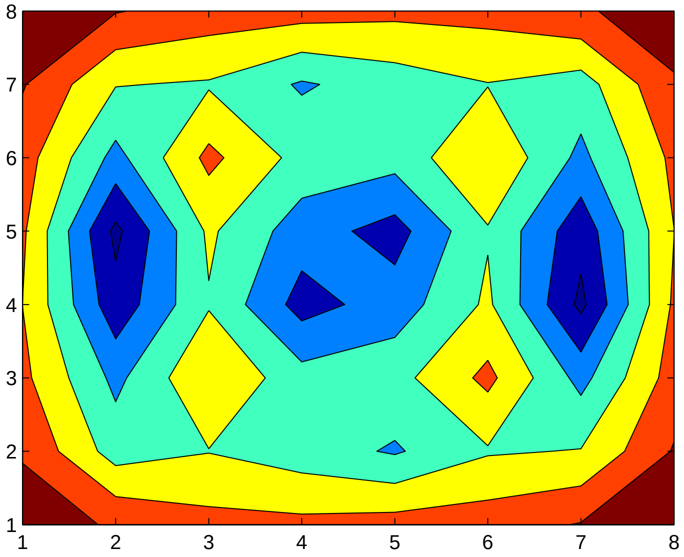

(b) Sensitivity of the objective function Π_2 with respect to thickness.

Figure 6: Sensitivity analysis of objective functions with respect to thickness.

5 SELECTION OF UPDATING PARAMETERS

As mentioned before, selection of the updating parameters is the most difficult step in an updating process and the accuracy of the results strongly depends upon this election. Finite element models with fine mesh configurations may lead to thousands of degrees of freedom. Furthermore, considering material properties of individual elements may lead to a very large number of updated parameters related to Young's modules, thickness, etc. Also, selection of updating parameters would be more difficult, if some damage scenario is considered. For these reasons, an error localisation approach and substructuring techniques are needed.

5.1 Error localisation

In view of possible damage scenarios, the optimization process would become more effective if a method is established for updating parameters that considers this particular case. The Force Balance Method (FBM) calculates a residual vector [6, 19]:

$$\mathbf{F}_r = (\mathbf{K}_a - \lambda_{e_r}\mathbf{M}_a)\,\boldsymbol{\phi}_{e_r} \tag{18}$$

that represents for each mode r the inaccuracies of the finite element model by plotting the degrees of freedom that are not in equilibrium. For illustrative purposes, non-balanced forces (moments) corresponding to the degrees of freedom of the finite element model for the damaged bridge are represented in figure 7.

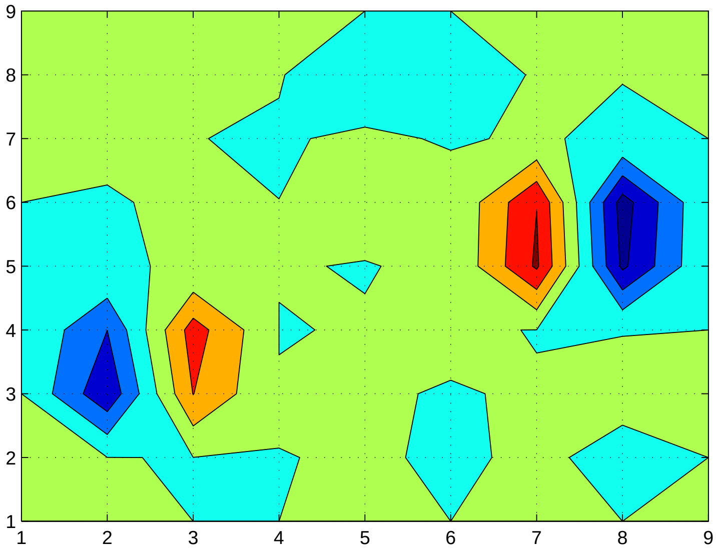

Figure 7: Error localisation based on Force Balance Method plotted for the first mode.

5.2 Substructure method for parameter selection

Model updating is a process that could lead to ill-conditioned problems, if the same number of updating parameters with respect to each finite element of the model is selected. A common and physically meaningful approach, the so-called “substructure method,” is to establish updating parameters for different groups of finite elements. Kim and Park [20, 21] proposed an automated parameter selection procedure for multi-objective optimisation problems. This method relies on the fact that two neighboring parameters p_i and p_j can be merged into one updating parameter, if the sensitivity with respect to the objective functions has the same sign. This yields a map in the structure with different areas associated with identical parameters.

In the present work, a new method to implement substructure divisions of the finite element model has been developed. By assuming that high sensitivities are associated with damaged zones, a priorization selection procedure is established. The sensitivity vector, that stores in each row the sensitivity of each element with respect to the objective function is classified by zones. These zones correspond to multiples of the semi-difference sensitivity extreme (maximum and minimum) absolut values, called step. To illustrate the method, figure 8 shows a substructure division for ten zones.

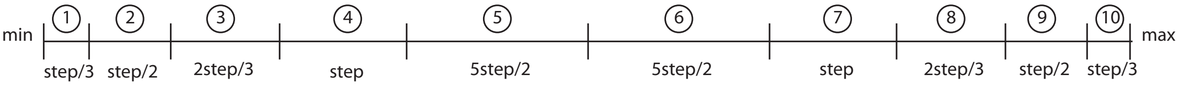

Figure 8: Substructure method.

In the case of the current hypar shell, the relationship between the element thickness and the updating parameters assumes the form:

$$\mathbf{H} = \mathbf{H_0} - h_0 \mathbf{S_b} \mathbf{P_h} \tag{19}$$

where $\mathbf{H}$ is a column vector that contains the hypar element thicknesses, vector $\mathbf{H_0}$ stores the reference thickness taken as h_0. Matrix $\mathbf{S_b}$, called *substructure-matrix*, is defined by the method explained before and assumes the following form:

$$\mathbf{S_b} = \begin{bmatrix} 1 & 0 & \dots & 0 & 0 \\ 1 & 0 & \dots & 0 & 0 \\ 0 & 0 & \dots & 0 & 1 \\ 0 & 1 & \dots & 0 & 0 \\ \vdots & \vdots & \vdots & \vdots & \vdots \\ 1 & 0 & 0 & \dots & 0 \end{bmatrix} \tag{20}$$

with the number of rows equal to the number of finite elements in the model and with the total number of columns equal to the number of non-dimensional updating variables, p_{h_i}. According to the matrix (20), every row consists of zeros except for a single element equal to one.

6 COMPUTATIONAL PROCEDURE

The computational work, related to the present finite element updating methodology, has been developed by programing several subroutines using MATLAB. Furthermore, “fmincon” and “fgoalattain” gradient-based MATLAB optimization algorithms are employed for single-objective and multi-objective optimization, respectively.

7 NUMERICAL EXAMPLES

In order to demonstrate the applicability of the proposed method, some numerical results are presented for the case of the damaged hypar of figure 2. Two different updating processes are studied, the first one considers a single-objective optimization by using a linear combination of objective functions $\Pi_1(p)$ and $\Pi_2(p)$ defined as follows:

$$\Pi_3(p) = \frac{1}{\Pi_1(p_0)} \sum_{i=1}^{m} \left(\frac{\boldsymbol{\phi}_{ai}^T \mathbf{K} \boldsymbol{\phi}_{ai}}{\boldsymbol{\phi}_{ei}^T \mathbf{K} \boldsymbol{\phi}_{ei}} - 1 \right)^2 + \frac{1}{\Pi_2(p_0)} \sum_{i=1}^{m} \left(\frac{\lambda_{ai}}{\lambda_{ei}} - 1 \right)^2 \tag{21}$$

and the second one considers a multi-objective optimisation process using the same objective functions but separately.

The convergence plots (figure 9(a) and figure 9(b)) show that for both, single-objective and multi-objective optimization, convergence is achieved in a similar way after ten iterations. The multi-objective optimization process shows that the results fluctuate in the first iterations due to the particular optimization process of the objective functions Π_1 and Π_2 to find a Pareto optimal. Furthermore, the objective function Π_2 is more difficult to optimize. The reason for such complication is the low sensitivity with respect to damage, as it was shown in figure 6(b).

Figures 10(a)-10(b) and tables 4-5 demonstrate that the proposed method is capable to localize all damaged elements. Additionally, correlation of modal shapes is high since the MAC factor is nearly 1.

Mode	Undamaged hypar (Hz)	Damaged hypar (Hz)	After updating (Hz)	Differences (%)	MAC (%)
1	3.6	3.59	3.59	0.15	100
2	6.02	5.98	5.98	0.14	100
3	6.02	6.02	6.02	-0.63	99.99
4	8.47	8.38	8.38	-0.30	99.99
5	11.83	11.54	11.54	-0.57	99.89
6	11.88	11.78	11.78	-0.003	99.98
7	13.96	13.69	13.69	-0.41	99.74
8	13.96	13.80	13.80	-0.15	99.68
9	18.71	18.45	18.45	-0.33	99.92
10	22.93	22.06	22.06	-0.16	99.67

Table 4: Frequency differences and MAC between the damaged and updated model for single-objective optimization of function Π_3

Mode	Undamaged hypar (Hz)	Damaged hypar (Hz)	After updating (Hz)	Differences (%)	MAC (%)
1	3.60	3.59	3.59	0.15	100
2	6.02	5.98	5.98	0.14	99.99
3	6.02	6.02	6.02	-0.63	99.98
4	8.47	8.38	8.38	-0.30	99.98
5	11.83	11.54	11.54	-0.59	99.89
6	11.88	11.78	11.79	-0.006	99.98
7	13.96	13.69	13.69	-0.41	99.88
8	13.96	13.80	13.80	-0.16	99.85
9	18.71	18.45	18.46	-0.34	99.92
10	22.93	22.06	22.08	-0.18	99.64

Table 5: Frequency differences and MAC between the damaged and updated model for multi-objective optimization of functions Π_1 and Π_2

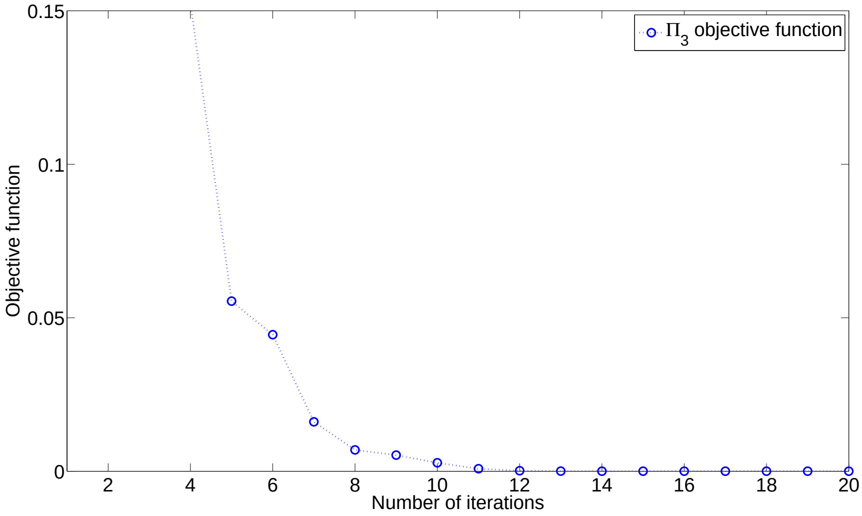

(a) Convergence behavior of the single-optimization process for objective function Π_3.

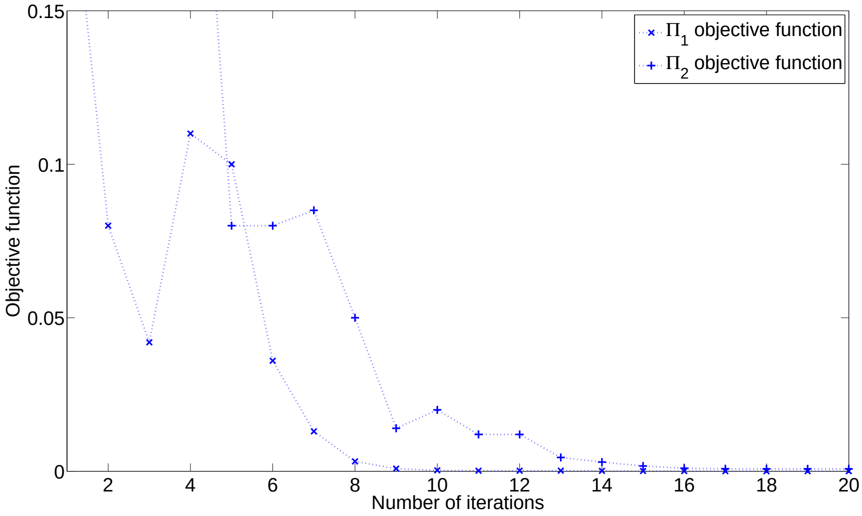

(b) Convergence behavior of the multi-objective optimization process for objective function Π_1 and Π_2.

Figure 9: Optimization convergence behavior.

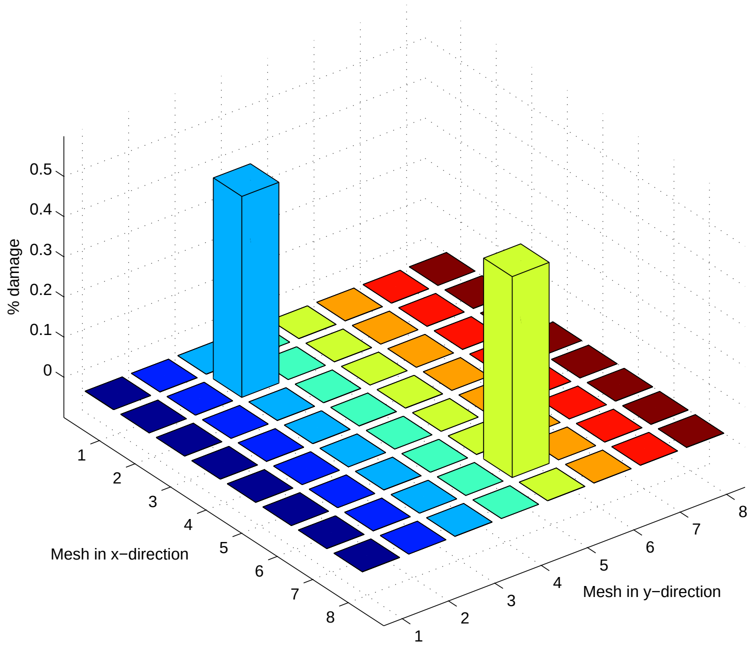

(a) Damage localization and severity after updating by single-objective optimization of function Π_3.

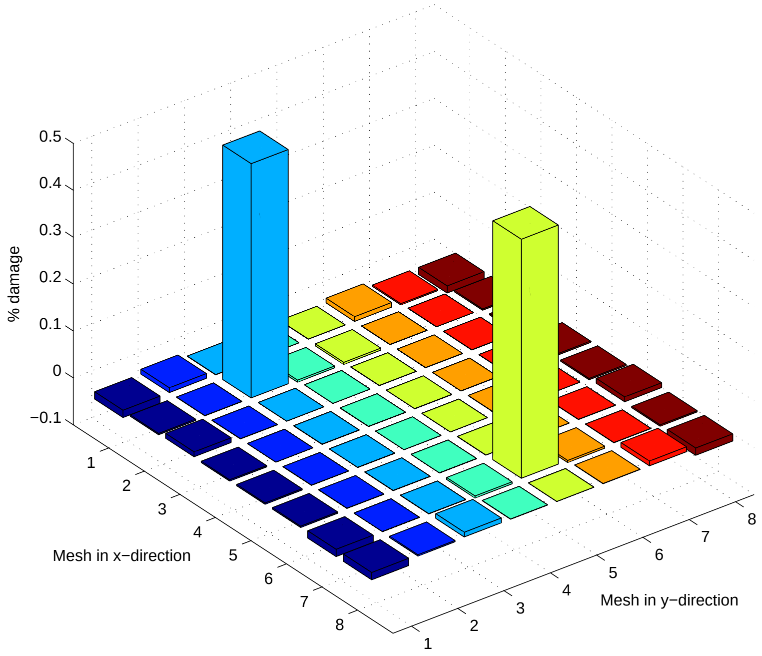

(b) Damage localization and severity after updating by multi-objective optimization of function Π_1 and Π_2.

Figure 10: Damage localization and severity.

7.1 Noisy vibration measurements

Vibration measurements are often contaminated by noise. It could be originated by the wind, the traffic, and also due to the cables that are connected to the accelerometers. This uncertainty can be simulated by adding some noisy-terms to the experimental modal shapes [22]:

$$\boldsymbol{\phi}_{e_j}^{noisy} = \boldsymbol{\phi}_{e_j} + \boldsymbol{\alpha}_j \, RMS(\boldsymbol{\phi}_{e_j}) \, \psi \tag{22}$$

where $\boldsymbol{\alpha}_j$ is a random matrix generated by a Gaussian distribution of mean 0 and standard deviation 1, ψ is an scalar that represents the noise level and RMS is the root mean square given by:

$$RMS(\boldsymbol{\phi}_{e_j}) = \sqrt{\frac{1}{N_j} \sum_{j=1}^{N_j} (\boldsymbol{\phi}_{e_j})^2} \tag{23}$$

For illustrative purposes, this methodology is followed for the case of the damaged hypar of figure 2 with a noise level of $0.5\,\%$. In this case, only single-objective optimization is employed (objective function Π_3). The optimization convergence is illustrated in figure 11. Table 6 shows the differences before and after updating the model . Frequency differences are plotted in figure 12. The damage localization, see figure 13, illustrates differences in the percentage of damage severity due to the effect of the noise.

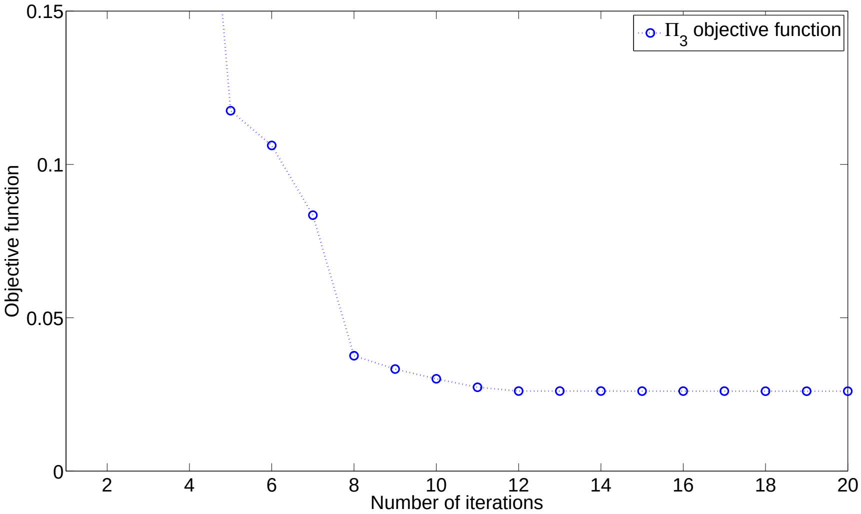

Figure 11: Convergence behavior of the single-optimization process for objective function Π_3 with noisy data.

Mode	Undamaged hypar (Hz)	Damaged hypar (Hz)	After updating (Hz)	Differences (%)	MAC (%)
1	3.60	3.59	3.59	0.14	100
2	6.02	5.98	5.97	-0.02	88.98
3	6.02	6.02	6.02	-0.44	89.02
4	8.47	8.38	8.40	-0.28	99.96
5	11.83	11.54	11.53	-0.64	99.85
6	11.88	11.78	11.77	-0.02	99.93
7	13.96	13.69	13.68	-0.34	99.88
8	13.96	13.80	13.79	-0.20	99.87
9	18.71	18.45	18.44	-0.43	99.91
10	22.93	22.06	22.05	-0.24	99.24

Table 6: Frequency differences and MAC between the damaged and updated model for single-objective optimization of function Π_3 with noisy data.

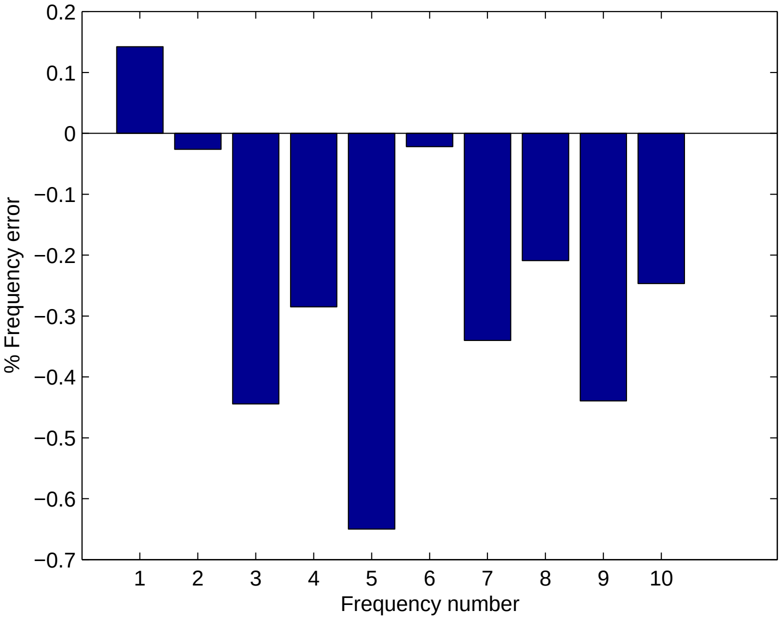

Figure 12: Percentage differences between analytical and noisy natural frequencies.

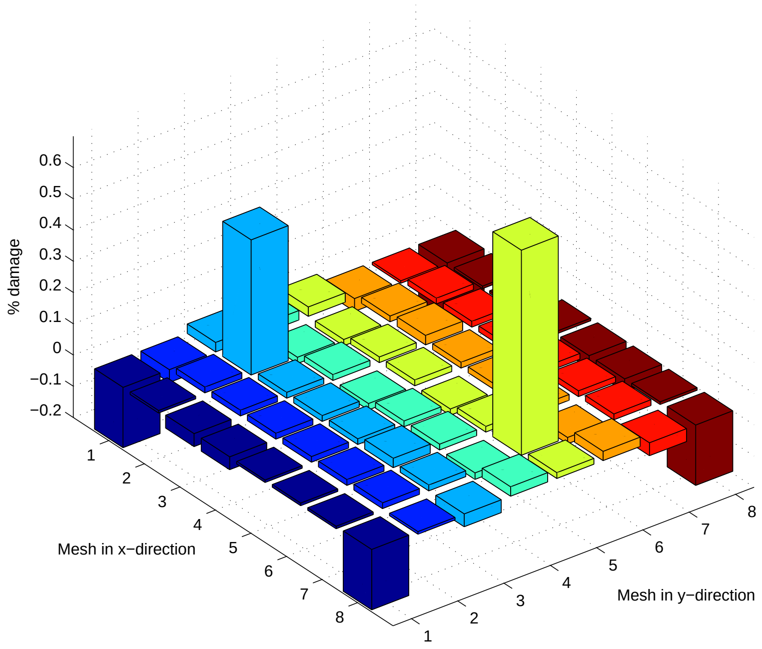

Figure 13: Damage localization and severity after updating the single-objective optimization of function Π_3 with noisy data.

8 CONCLUSIONS

In this paper, a finite element updating methodology is presented. Finite element modelling is carried out by using doubly-curved shell elements based on the variational principal of Hu-Washizu. The formulation possesses some important features that ensure low computational effort and reliable results. A hypar model with different damages is employed to test the accuracy of the proposed methodology. Eigenfrequencies and mode shapes of the damaged model are considered as experimental data that are used in the updating process of the numerical model. In order to study the confidence between the numerical and experimental results, several correlation techniques are employed.

The present methodology makes use of sensitivity for updating parameter selection. Two different objective functions are employed to determine the sensitivity of the model: modal strain energy residual and eigenfrequencies residual. High sensitivity zones are associated with possible damaged elements and are classified by the use of a simple-priorization technique. In order to establish the correspondence between the element parameters in the numerical model and the updating parameters, some matrix operations have been developed.

The performance of the method is demonstrated by presenting case studies for single-objective and multi-objective optimization. In the first case study, a linear combination of modal strain energy and eigenfrequencies residual functions was selected as objective function. On the contrary, in the case of multi-objective optimization process, both objective functions were independently employed. The results with respect to localization and severity of the damage are in good agreement with the damaged model. Furthermore, the convergence of the optimization process is achieved in both cases after a few iterations, thus revealing that the proposed approach produces an efficient and accurate computational tool suitable for complicated structural systems.

REFERENCES

[1] P. Avitabile, Model updating - Endless possibilities, *Sound and Vibration*, 2000.

[2] M.I. Friswell, J.E. Mottershead, *Finite element model updating in structural dynamics*, Kluwer Academic Publishers, 1995.

[3] J.E. Mottershead, M.I. Friswell, Model updating in structural dynamics: A survey, *Journal of Sound and Vibration*, **167**, 347–375, 1993.

[4] J.M.W. Brownjohn, Pin-Qi Xia, Hong Hao, Yong Xia, Civil structure condition assessment by FE model updating: Methodology and case studies, *Finite Elements in Analysis and Design*, **37**, 761–775, 2001.

[5] H.G. Natke, Problems of model updating procedures: A perspective resumption, *Mechanical Systems and Signal Processing*, **12**, 65–74, 1998.

[6] E. Fissette, S. Ibrahim, C. Stavrinidis, Error location and updating of analytical dynamic models using a force balance method, *Proceedings of the 6th International Modal Analysis Conference*, Kissimmee, Florida, 1998.

[7] L. Gil Espert, *Análisis de sensibilidad con comportamiento no lineal del material y su aplicación en el diseño asistido de estructuras*. PhD Thesis, Universidad Politécnica de Cataluña, Spain ,1997.

[8] S. Hernández, Del diseño convencional al diseño óptimo. Posibilidades y variantes. Part I: Análisis de sensibilidad y optimización local y global, *Revista Internacional de Métodos Numéricos para Cálculo y Diseño en Ingeniería*, **9**, 91–110, 1993.

[9] F. van Keulen, R.T. Haftka, N.H. Kim, Review of options for structural design sensitivity analysis. Part 1: Linear systems, *Computer Methods in Applied Mechanics and Engineering*, **194**, 3213–3243, 2005.

[10] Bijaya Jaishi, Wei-Xin Ren Structural finite element model updating using ambient vibration test results, *Journal of Structural Engineering*, **131**, 617–628, 2005.

[11] Bijaya Jaishi, Wei-Xin Ren, Finite element model updating based on eigenvalue and strain energy residuals using multiobjective optimisation technique, *Mechanical Systems and Signal Processing*, **21**, 2295–2317, 2007.

[12] R.T. Haftka, Z. Gurdal, *Elements of Structural Optimization*, Kluwer Academic Publishers, 1992.

[13] Kyung K. Choi, Nam-Ho Kim, *Structural Sensitivity Analysis and Optimization 1. Linear Systems*. Springer, 2005.

[14] S. Hernández, Del diseño convencional al diseño óptimo. Posibilidades y variantes. Part II: Optimización multiobjectivo y sensibilidad de la solución óptima, *Revista Internacional de Métodos Numéricos para Cálculo y Diseño en Ingeniería*, **9**, 259–270, 1993.

[15] R.J. Allemang, The modal assurance criterion-Twenty years of use and abuse, *Sound and Vibration*, 2003.

[16] G. Wempner, D. Talaslidis, *Mechanics of Solids and Shells*. CRC Press, 2003.

[17] G. Wempner, D. Talaslidis, C. Hwang, A simple and efficient approximation of shells via quadrilateral elements, *Journal of Applied Mechanics*, **49**, 115–120, 1982.

[18] R.L. Fox, M.P. Kapoor, Rates of change of eigenvalues and eigenvectors, *AIAA Journal*, **6**, 2426–2429, 1968.

[19] W. Heylen, S. Lammens, P. Sas, *Modal Analysis Theory and Testing*. Katholieke Universiteit Leuven, Departement Werktuigkunde, Leuven, 1997.

[20] Gyenong-Ho Kim, Youn-Sik Park, An improved updating parameter selection method and finite element model update using multiobjective optimisation technique, *Mechanical Systems and Signal Processing*, **18**, 59–78, 2004.

[21] Gyenong-Ho Kim, Youn-Sik Park, An improved updating parameter selection method and finite element model update using multiobjective optimisation technique, *Journal of Sound and Vibration*, **309**, 778–793, 2008.

[22] R. Palma, G. Rus, R. Gallego, Probabilistic inverse problem and system uncertainties for damage detection in piezoelectrics. *Mechanics of Materials*, **41**, 1000–1016, 2009.

COMPDYN 2011
3rdECCOMAS Thematic Conference on
Computational Methods in Structural Dynamics and Earthquake Engineering
M. Papadrakakis, M. Fragiadakis, V. Plevris (eds.)
Corfu, Greece, 25-28 May 2011

ENHANCED 3D FIBER BEAM-COLUMN ELEMENT WITH WARPING DISPLACEMENTS

V. Le Corvec[1], **F.C. Filippou**[2]

[1] University of California, Berkeley- Dept of Civil and Environmental Engineering
760 Davis Hall - 94720 Berkeley CA, USA
e-mail: lecorvec@berkeley.edu

[2] University of California, Berkeley- Dept of Civil and Environmental Engineering
760 Davis Hall - 94720 Berkeley CA, USA
e-mail: filippou@berkeley.edu

Keywords: fiber beam, mixed formulation, shear, torsion, shear lag

Abstract. *Beam elements are commonly used in the analysis of steel and reinforced concrete structures in earthquake engineering practice. These elements reproduce the global behavior of these structures at a reasonable computational cost. For this type of analysis the force-based fiber beam element has proven an excellent compromise between accuracy and computational cost for the simulation of the inelastic response of structural models of significant size. Recent studies have proposed extensions of the model to account for the effect of shear and torsion under fixed shear strain or stress distributions. These assumptions suffer from shortcomings for the representation of the coupling between shear and torsion, and are not suitable for the representation of local stress and strain distributions at critical sections. To describe such complex stress states, shell finite element models are often used with a significant increase in computational cost. This paper presents the mixed formulation of an enhanced 3d fiber beam element that represents accurately the global and local response of structural members under axial force, flexure, shear and torsion interaction. The proposed 3d fiber beam element determines the shear strain distribution at a section from the satisfaction of local equilibrium equations with the section warping displacements as local parameters. Unlike existing models, the coupling between sections is taken in account. Hence the enhanced fiber beam-column is able to capture the local effects due to constrained warping of the section, such as the flange shear lag effect. The model is also capable of representing accurately the maximum local stress at element boundaries, and of simulating the torsional response of beams under warping constraints.*

The element is validated with several examples involving inelastic response of steel members under high shear force, such as shear links. The simulations are conducted under monotonic and cyclic load conditions for specimens with wide flange and box sections. The accuracy and computational efficiency of the proposed element is demonstrated by comparing the results with experimental values and with local response estimates of shell finite element models.

1 INTRODUCTION

Nonlinear analysis is used increasingly for the evaluation of structures under extreme loading conditions. This type of loads induces high inelastic strains at critical sections and large node displacements. Recent studies have shown that the corotational formulation is a suitable framework for the description of large displacements allowing the nonlinear material response of the basic element to be limited to small deformations. For frame elements the force-based fiber beam element by Ciampi and Carlesimo [4] with its subsequent embedment in a consistent variational framework by Taylor [11] and Lee [7] has proven an excellent choice for describing the interaction between axial force and flexure under inelastic material response.

Recently, research interest has focused on the extension of the force-based beam element to the effect of shear and torsion. In older structures and short span elements the shear affects the failure mode and the member capacity. The first formulation of a beam element with shear was based on Timonshenko beam theory with the assumption of a constant shear stress distribution over the cross-section [12]. Subsequent models by A. Saritas [10], N. Gregori [5] and A. Papachristidis [9], postulate a strain or stress field distribution based on the analytical result for a homogeneous section. These models were used to simulate the inelastic response of shear links and shear walls with success. However, the assumption of a fixed shear distribution is not justified when inelastic deformations spread through the section and render the response inhomogeneous. The model of J.M. Bairan [1] and S. Mohr [8] overcomes this limitation with the addition of degrees of the freedom at the section level to represent the shear distribution while also accounting for section warping. Equations of local equilibrium are used to determine the response parameters at these degrees of freedom.

The model of A.Saritas [10] is limited to 2d applications, whereas the element proposed by N. Gregori [5] and A. Papachristidis [9] apply to 3d response without, however, accounting for the shear distribution due to torsion and the effect of warping. The model of J.M. Bairan [1] accounts for section warping and is thus able to represent the torsional response with accuracy. The model also accounts for the in-plane section deformation, which increases computational cost significantly.

Even though existing models account for a variable shear distribution and section warping, the interaction between sections of the beam element is not directly taken into account. In particular the effect of warping on axial deformation is neglected resulting in the incorrect representation of the local response near boundaries and other important local response phenomena such as shear-lag [13]. While neglecting this effect and decoupling the response of different beam sections has the advantage of maintaining the number of element degrees of freedom and reducing the element computational cost, the inability of representing the local stresses under warping constraints and at element boundaries is a serious limitation.

The proposed 3d enhanced fiber beam element model sets out to address some limitations of earlier formulations by allowing for arbitrary section warping under shear and torsion and by including the effect of boundaries on the warping distribution. This objective is met first with the introduction of warping degrees of freedom at each section, and secondly by imposing equilibrium on the entire element, so as to account for section interaction and thus incorporate the effect of boundary conditions. For simplicity only out-of-plane section displacements are represented by assuming that the section is rigid in its plane.

The paper presents a brief description of the theory of the proposed 3d enhanced fiber beam element and concludes with a few examples that demonstrate its capability for representing the shear stress distribution under combined loadings and the shear lag effect. In these examples

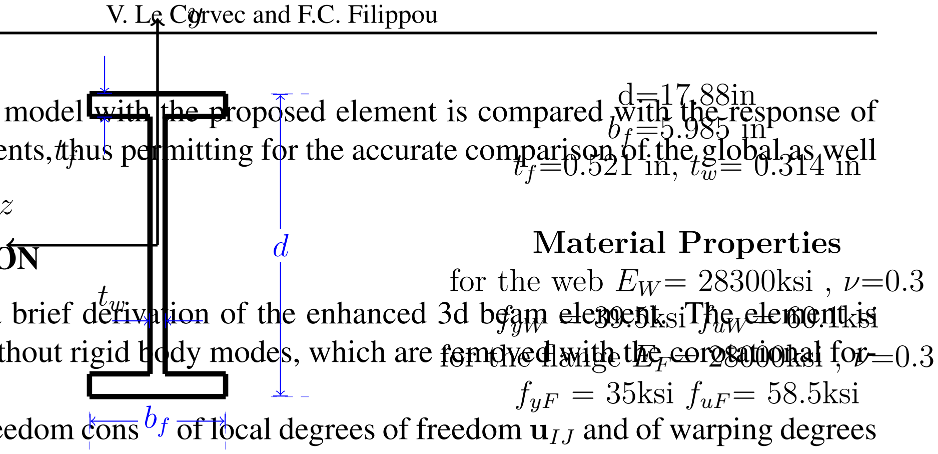

the response of structural model with the proposed element is compared with the response of the model with shell elements, thus permitting for the accurate comparison of the global as well as the local response.

2 BEAM DESCRIPTION

This section presents a brief derivation of the enhanced 3d beam element. The element is formulated in a system without rigid body modes, which are removed with the corotational formulation.
The element degrees of freedom consist of local degrees of freedom $\mathbf{u}_{IJ}$ and of warping degrees of freedom $\mathbf{u}^w_{IJ}$. The warping degrees of freedom describe the out-of-plane displacements of the section. The number of these degrees of freedom for each section is n_w. These are local degrees of freedom associated with local equilibrium equations. To satisfy displacement compatibility between adjacent elements, the warping displacements of the end sections are retained as element variables.

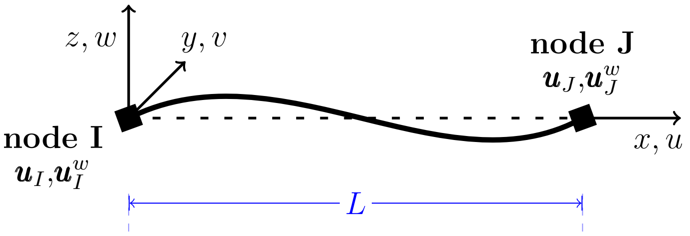

Figure 1: Basic element kinematics

$$\mathbf{u}^w_{IJ} = \begin{bmatrix} \mathbf{u}^w_I & \mathbf{u}^w_J \end{bmatrix} \tag{1}$$

In the local reference system the element deformations are denoted by $\mathbf{v}$ and consist of the axial deformation, of the rotations θ_y and θ_z at the element ends, and of the angle of twist ϕ. The associated forces $\mathbf{q}$ are the axial force, the bending moments about the y and z axis, and the torsional moment. The deformations are related to the local displacements with the compatibility matrix $\mathbf{a}_g$:

$$\mathbf{v} = \mathbf{a}_g \mathbf{u}_{IJ} \tag{2}$$

2.1 Section Kinematics

The displacements of any point (y,z) of a section, defined by its x along the element axis, are decomposed as follows:

$$\mathbf{u}_{total} = \mathbf{u}^r + \mathbf{u}^w \tag{3}$$

The rigid displacement of the section is denoted by $\mathbf{u}^r$ and is expressed in terms of the cross-section generalized displacements

$$\mathbf{u}(x) = \begin{bmatrix} u & v & w & \theta_z & \theta_y & \phi \end{bmatrix}^T (x) \tag{4}$$

The warping displacements $\mathbf{u}^w(x,y,z)$ are defined everywhere in the beam element by interpolation functions

$$\mathbf{u}^w(x,y,z) = \sum_{ij} M_i(x)N_j(y,z)\mathbf{u}^w(x_i,y_j,z_j) \tag{5}$$

In contrast to the formulation by J.M. Bairan [1], only the axial component of the warping displacement is taken into account by neglecting the in-plane section deformation.

The warping displacements are orthogonal to the section rigid body displacements $\mathbf{u}^r$. This condition is enforced by removing the rigid body modes from the displacements $\mathbf{u}^w$ with the use of a projection matrix. The details of this matrix are not presented here for the sake of brevity.

The displacement of any material point (y,z) of the cross section at position x along the axis is given by

$$u_x(x,y,z) = u(x) - y\theta_z(x) + z\theta_y(x) + u^w(x,y,z) \tag{6}$$
$$u_y(x,y,z) = v(x) - z\phi(x) \tag{7}$$
$$u_z(x,y,z) = w(x) + y\phi(x) \tag{8}$$

The strains are derived from the definition of the displacements and are expressed in the compact form:

$$\boldsymbol{\epsilon}(\mathbf{u}^r,\mathbf{u}^w) = \begin{bmatrix}\epsilon_{xx}\\ 2\epsilon_{xy}\\ 2\epsilon_{xz}\end{bmatrix} = \begin{bmatrix}1 & -y & 0 & 0 & z & 0\\ 0 & 0 & 1 & -z & 0 & 0\\ 0 & 0 & 0 & y & 0 & 1\end{bmatrix}\begin{bmatrix}u'\\ \theta'_z\\ v'-\theta_z\\ \phi'\\ \theta'_y\\ w'-\theta_y\end{bmatrix} + \begin{bmatrix}\epsilon_{xx}(\mathbf{u}^w)\\ 2\epsilon_{xy}(\mathbf{u}^w)\\ 2\epsilon_{xz}(\mathbf{u}^w)\end{bmatrix} \tag{9}$$

$$= \mathbf{a}_s\mathbf{e}(\mathbf{u}) + \boldsymbol{\epsilon}(\mathbf{u}^w) \tag{10}$$

where the notation $'$ denotes the derivative of the variable with respect to coordinate x.
The notation $\mathbf{e}$ for the generalized section deformations is introduced

$$\mathbf{e} = \begin{bmatrix}\epsilon_0 & \kappa_z & \gamma_y & \kappa_x & \kappa_y & \gamma_z\end{bmatrix}^T \tag{11}$$

where ϵ_0 is the axial strain, κ_z and κ_y the two curvatures and γ_y and γ_z the shear strains.
According to equation (10), the warping displacement contributes to the axial strain and to the shear strain. This fact is critical in the description of the effect of boundary conditions and the additional stresses due to warping constraints.

2.2 Variational principle

The element formulation is based on the Hu-Washizu variational principle [7]. The potential function of displacements $\mathbf{u}$ and $\mathbf{u}^w$, section deformations $\mathbf{e}$ and stresses $\boldsymbol{\sigma}$ is defined over the element volume V by

$$\Pi(\mathbf{u},\mathbf{u}^w,\mathbf{e},\boldsymbol{\sigma}) = \int_V \boldsymbol{\sigma}^T(\mathbf{a}_s\mathbf{e}(\mathbf{u}) - \mathbf{a}_s\mathbf{e})\,dV + \int_V W(\mathbf{e},\mathbf{u}^w)dV + \Pi_{ext}(\mathbf{u}_{IJ},\mathbf{u}^w_{IJ}) \tag{12}$$

where W is the internal potential energy. In the form of (12), the element formulation is mixed: the warping strain is derived from the warping displacements, while the section deformations

are imposed in weak form.
The external load is defined by

$$\Pi_{ext} = -\mathbf{u}_{IJ}^T \bar{\mathbf{p}} - \mathbf{u}_{IJ}^{wT} \bar{\mathbf{p}}^w \tag{13}$$

The forces $\bar{\mathbf{p}}$ and $\bar{\mathbf{p}}^w$ are the applied forces at the end nodes of the element. If the end sections are free to warp, the applied warping force is $\bar{\mathbf{p}}^w = \mathbf{0}$. Otherwise, warping displacements $\mathbf{u}_{IJ}^w$ are imposed. The case of element loading is not included for the sake of simplicity.

The variation of potential Π leads to the definition of the associative section forces by integration over the cross-section area A:

$$\mathbf{s} = \int_A \mathbf{a}_s^T \boldsymbol{\sigma} dA \ , \ s_x^{wj} = \int_A N_j \sigma_{xx} dA \ , \ s_{yz}^{wj} = \int_A \frac{\partial N_j}{\partial y}\sigma_{xy} + \frac{\partial N_j}{\partial z}\sigma_{xz} dA \tag{14}$$

By minimization of the potential Π, we obtain a set of equations:

$$\begin{aligned}
\bar{\mathbf{p}} &= \mathbf{a}_g \mathbf{q} && (15)\\
\mathbf{s}_i &= \mathbf{b}(x_i)\mathbf{q} && (16)\\
\mathbf{v} &= \int_0^L \mathbf{b}^T \mathbf{e} dx && (17)\\
\boldsymbol{\sigma} &= \frac{\partial W}{\partial \boldsymbol{\epsilon}} && (18)\\
p_i^{wj} &= \int_0^L \frac{\partial M_i}{\partial x} s_x^{wj} dx + \int_0^L M_i s_{yz}^{wj} dx && (19)
\end{aligned}$$

where $\mathbf{b}$ is a linear interpolation matrix given by

$$\mathbf{b}(x) = \begin{bmatrix} 1 & 0 & 0 & 0 & 0 & 0 \\ 0 & x/L & 1-x/L & 0 & 0 & 0 \\ 0 & 1/L & 1/L & 0 & 0 & 0 \\ 0 & 0 & 0 & 1 & 0 & 0 \\ 0 & 0 & 0 & 0 & x/L & 1-x/L \\ 0 & 0 & 0 & 0 & 1/L & 1/L \end{bmatrix} \tag{20}$$

The first four equations correspond to the mixed formulation equations for the beam: the equilibrium equations (15-16), the compatibility equation (17) and the constitutive law (18). The additional equations (19) correspond to the equilibrium conditions that need to be satisfied by the warping section forces $\mathbf{s}_x^w$ and $\mathbf{s}_{yz}^w$. These equilibrium equations are imposed at each section x_i with warping displacements $\mathbf{u}^w(x_i, ., .)$ as the unknowns (5). The section deformations and the warping displacements are determined during the element state determination by satisfying the equilibrium and compatibility equations.
The tangent stiffness associated with the set of equations (15-19) ensures optimal convergence of the element state determination algorithm.

2.3 Interpolations

The section warping is described by warping parameters denoted with $\mathbf{u}_{ij}^w$. The warping is then described over the section with the functions $N_j(y, z)$ in equation (5). With Lagrange polynomials for the functions N_j the warping parameters $\mathbf{u}_{ij}^w$ can be interpreted as local warping values. This approach differs from the fixed strain distribution assumed in earlier studies [10]. The enforcement of the warping equilibrium equations results in an accurate strain distribution. This formulation can be applied to any section geometry and does not require a shear correction factor, as is the case with earlier studies [10] and [9]. To reduce the number of warping parameters, advantage can be taken of the geometric characteristics of the section, such as symmetry and double-symmetry, in the choice of interpolation functions $N_j(y, z)$, as proposed in the report by Setec-Tpi [6].

The determination of the warping distribution over the element length is accomplished with the interpolation functions $M(x)$. For constrained warping, the choice of interpolation functions is critical. Under linear elastic response, the analytical solution consists of an exponential distribution of warping displacements along the element axis. Among the different choices for interpolation functions M are exponential functions, Lagrange polynomials, and quadratic spline functions. In the examples of the following section Lagrange polynomials are used.

3 EXAMPLES

The examples presented below demonstrate the capabilities of the enhanced 3d element. The element is tested on two shear links. Its response is compared to the response of the beam element by A.Saritas[10], which is extended to 3d with the assumption of a fixed shear strain distribution. The link response is also compared with the response of a model consisting of MITC shell elements [2]. The nonlinear material response of structural steel is described with the J2 plasticity model. The studies compare the global force-displacement response as well as the local stress distributions with focus on the axial stress σ_{xx} associated with the warping constraints.

The test configuration for the two shear links is shown in figure 2. Warping is assumed to be constrained at both ends. To demonstrate the coupling between shear and torsion, the element is allowed to twist at one end when the shear force is applied with an eccentricity. The shear link is modeled with one 3d beam element with 5 Gauss-Lobatto integration points along its axis.

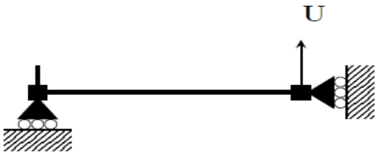

Figure 2: Shear Link Configuration

3.1 Example 1

The cross-section of the shear link is shown in figure 3. The length of the shear link is L= 456 mm. This example is part of the experimental campaign by Berman and Bruneau [3]. The analysis with beam elements is compared with the experimental results and the results with a shell model by limiting attention to the first three load cycles. The enhanced 3d beam element uses n_w=12 parameters in each section to describe the section warping. Figure 4 shows that the response of the three models is very close in terms of the shear reaction force for an imposed vertical displacement (or shear link rotation) and agrees very well with experimental measurements.

The local stress results are plotted for a link rotation $\gamma = U/L =$ 0.006 in the transition to

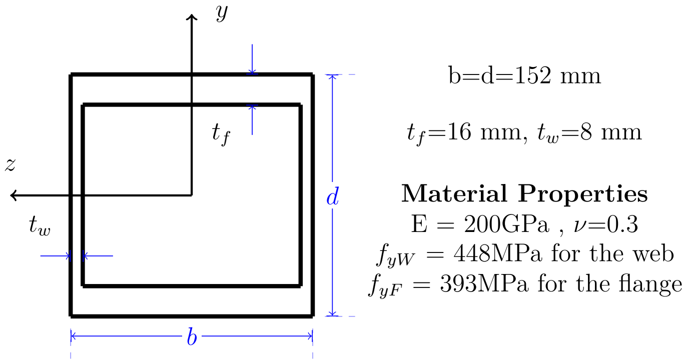

Figure 3: Cross section properties

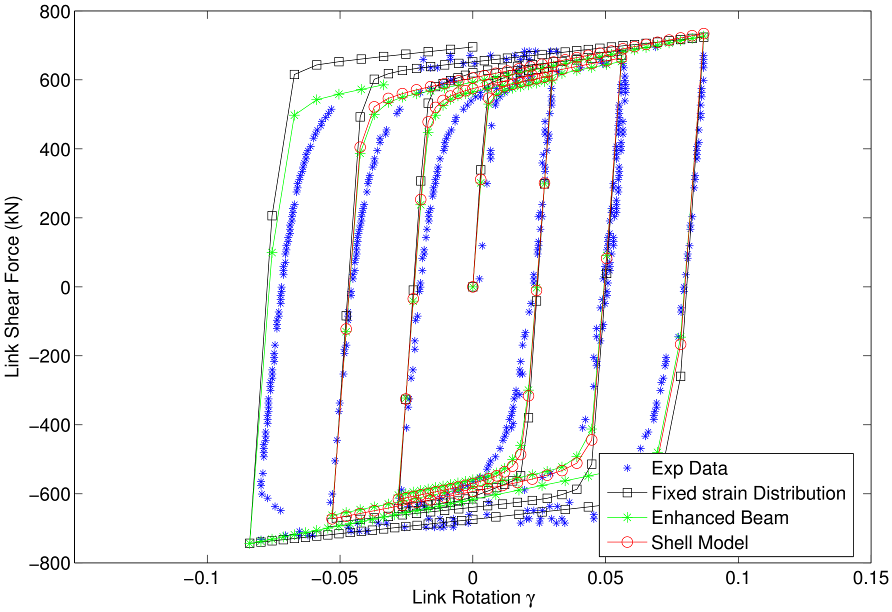

Figure 4: Shear link rotation vs. Shear Force

the plastic range. The figures 5 and 6 present the shear stresses of the middle section of the element, where warping is free. The results confirm that the enhanced 3d beam reproduces the shear stress distribution postulated by the fixed shear strain assumption of A. Saritas [10]. The distribution of the shear stresses σ_{xz} in the upper flange is also represented accurately.

The shear lag effect takes place at the boundary of the beam and at the load application points. At this boundary section, the warping constraint creates additional axial stresses. The comparison of the axial stresses in the web and in the flange is presented in figures 7 and 8. The enhanced 3d beam element gives a correct estimation of the maximum axial stress in the web, which is 30% higher than the value predicted by the beam with a fixed shear strain distribution.

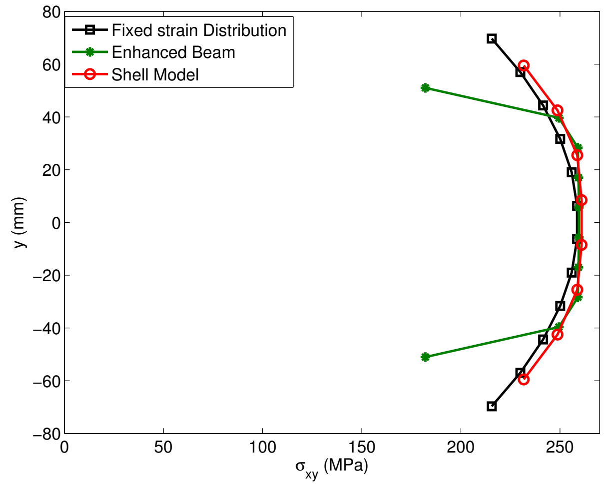

Figure 5: Shear stresses in the left web

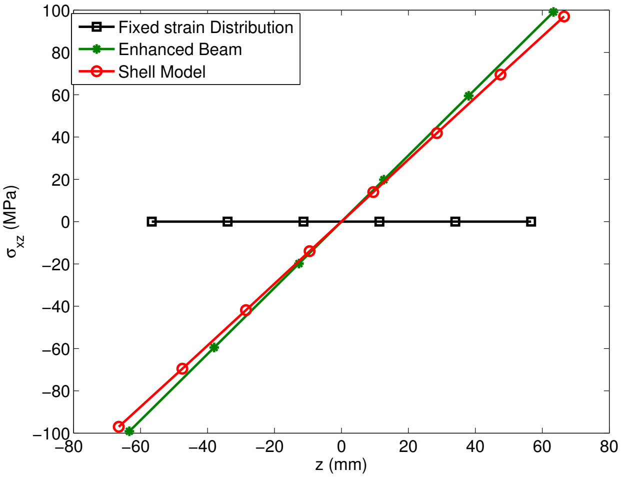

Figure 6: Shear stresses in the lower flange

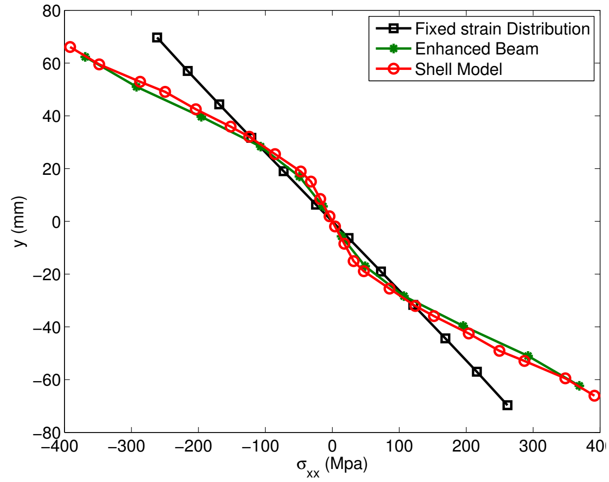

Figure 7: Axial stresses in the web

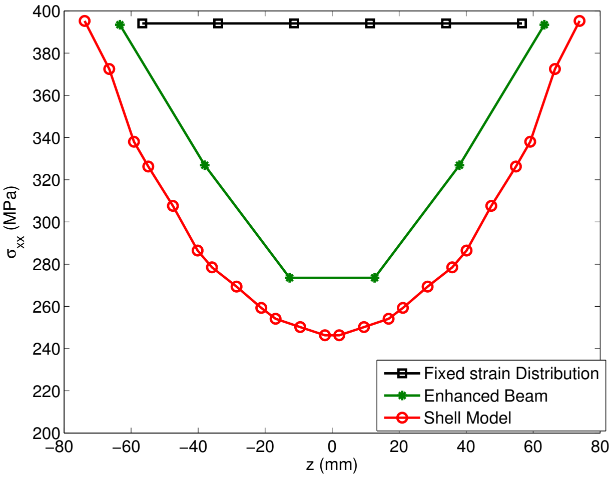

Figure 8: Axial stresses in the lower flange

3.2 Example 2

The dimensions of the I cross-section of the shear link are presented in figure 9. The length of the shear link is L =28in. The steel material is described by a generalized J2 plasticity Model, as presented in [10].

A shear force is applied on the shear link. To model the effect of torsion, the force is applied with an eccentricity of e_c =2 in from the centroid to create a torsional moment proportional to the shear force. The enhanced 3d beam describes the section warping with n_w=28 parameters. The figures 10 and 11 present the force-displacement response of the shear link: the shear force is plotted against the vertical displacement and the torsion force against the angle of twist ϕ. The enhanced beam model is able to represent with accuracy the lateral and torsional stiffness as well as the yielding force. In comparison, the beam with a fixed shear strain distribution cannot represent the exact elastic torsional stiffness, since warping is not taken into account. The interaction between shear and torsion is demonstrated in 10.

In addition to the global response, the proposed element describes with accuracy the local

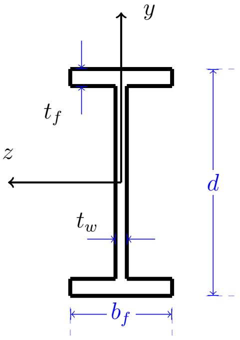

d=17.88in
b_f=5.985 in
t_f=0.521 in, t_w= 0.314 in

Material Properties
for the web E_W= 28300ksi , ν=0.3
f_{yW} = 39.5ksi f_{uW}= 60.1ksi
for the flange E_F= 28000ksi , ν=0.3
f_{yF} = 35ksi f_{uF}= 58.5ksi

Figure 9: Cross section properties

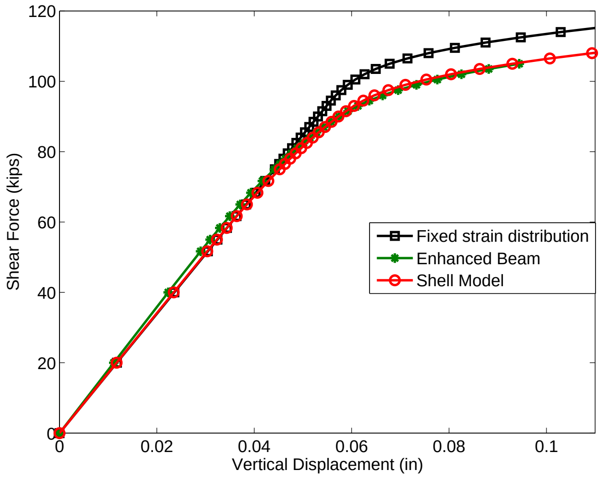

Figure 10: Shear Force vs. Vertical Displacement

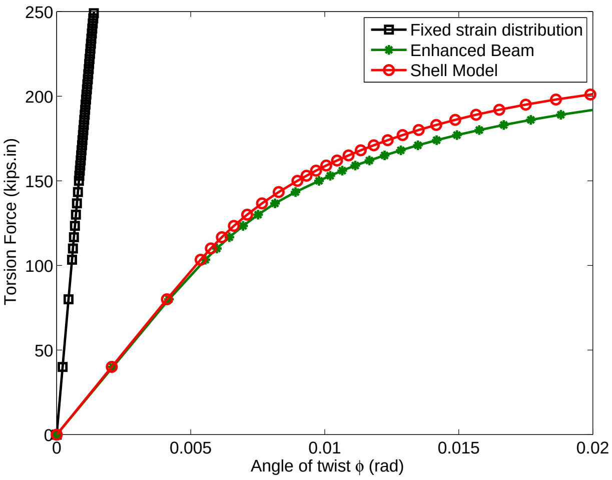

Figure 11: Torsion Force vs. Twist Angle

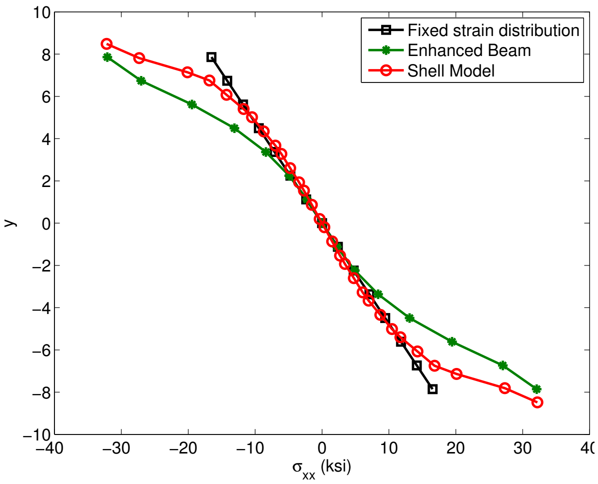

Figure 12: Axial stresses in the web

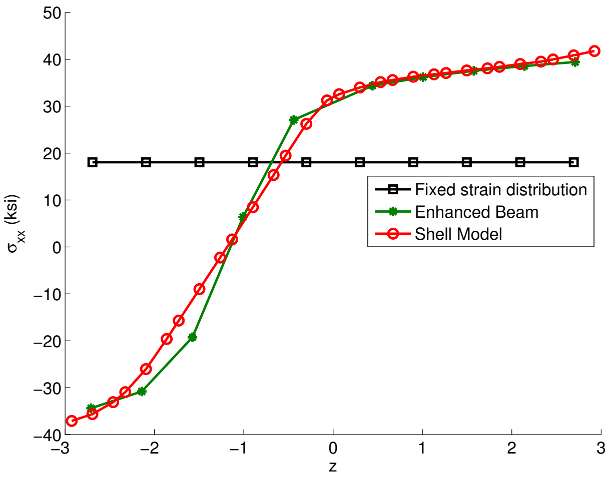

Figure 13: Axial stresses in the lower flange

response in the plastic range. For a shear force of 88.5 kips, the axial stresses at the boundary section are plotted for the web 12 and the lower flange 13 respectively.

4 CONCLUSIONS

The paper presents a 3d enhanced fiber beam element formulation that includes warping degrees of freedom so as to represent the effect of shear and torsion. No shear correction factor is required with the shear strain distribution determined directly from the section warping. The element is capable of representing accurately the local response of beams under different constraints for which a shell element is usually required. It is also capable of describing accurately the shear lag effect at a significantly lower computational cost than a shell model.
A few examples demonstrate the capabilities of the element for simulating inelastic response of steel structures under flexure, shear and torsion. Studies are under way to extend the element formulation to reinforced concrete frames, for which existing studies demonstrate the importance of shear modeling [8]. Further studies to optimize the element performance for earthquake engineering applications by reducing the number of warping degrees of freedom are under way.

5 ACKNOWLEDGEMENTS

The present work was sponsored by Setec TPI. The authors are grateful for the financial support and thank Dr Michel Kahan and Xavier Cespedes for their support and encouragement during the course of the study. The authors are also grateful for the exchange of information about the problem of torsion with warping constraints with Xavier Cespedes and his team. (www.tpi.setec.fr)

REFERENCES

[1] J M. Bairan, A non-linear totally-coupled model for RC sections under 3D bending, shear, torsion and axial loading. *PhD thesis* Technical University of Catalonia. Barcelona, 2005.

[2] K.-J. Bathe, E.N Dvorkin, A formulation of general shell elements- The use of mixed interpolation of tensorial components. *International Journal of Numerical Methods in Engineering* **22**, 697-722,1986.

[3] J.W. Berman, M. Bruneau, Experimental and analytical investigation of tubular links for eccentrically braced frames. *Engineering Structures* **8**, 1929–1938, 2007.

[4] V. Ciampi, L. Carlesimo, A Nonlinear Beam Element for Seismic Analysis of Structures. *8th European Conference on Earthquake Engineering, Lisbon, Laboratorio Nacional de Engenharia Civil* 1986

[5] J. N. Gregori, P. M. Sosa, M.A. F. Prada, F. C. Filippou, A 3D numerical model for reinforced and prestressed concrete elements subjected to combined axial, bending, shear and torsion loading. *Engineering Structures* **29**, 3404–3419, 2007.

[6] K. Ferradi, Etude du gauchissement et modelisation en element fini *Setec Report* 2010

[7] C.-L. Lee, F.C. Filippou, Frame elements with mixed formulation for singular section response. *International Journal for Numerical Methods in Engineering* **78**, 1320-1344, 2009.

[8] S. Mohr, J.M. Bairan, A. R. Mari, A frame element model for the analysis of reinforced concrete structures under shear and bending. *Engineering Structures* **12**, 3936–3954, 2010.

[9] A. Papachristidis, M. Fragiadakis, Manolis Papadrakakis, A 3D fibre beam-column element with shear modelling for the inelastic analysis of steel structures. *Computational Mechanics* **6**, 553–572, 2010.

[10] A. Saritas, Mixed formulation frame element for shear critical steel and reinforced concrete members. *PhD thesis* University of California, Berkeley, 2006.

[11] R.L. Taylor, F.C. Filippou, A. Saritas, F. Auricchio, A mixed finite element method for beam and frame problems. *Computational Mechanics* **31**, 192–203, 2003.

[12] S.P. Timoshenko, J.M. Gere, Theory of Elastic Stability. *McGraw-Hill New York* 1961

[13] S. Zhou, Finite Beam Element Considering Shear-Lag Effect in Box Girder. *Journal of Engineering Mechanics* **136**, 1115–1122, 2010

COMPDYN 2011
III ECCOMAS Thematic Conference on
Computational Methods in Structural Dynamics and Earthquake Engineering
M. Papadrakakis, M. Fragiadakis, V. Plevris (eds.)
Corfu, Greece, 25–28 May 2011

ADAPTIVE FORCE-BASED FRAME ELEMENT FOR REGULARIZED RESPONSE

João P. Almeida[1], Sandip Das[1], and Rui Pinho[2]

[1] EUCENTRE – European Centre for Training and Research in Earthquake Engineering
Via Ferrata 1, 27100 Pavia, Italy
{joao.pacheco, sandip.das}@eucentre.it

[2] University of Pavia
Via Ferrata 1, 2700 Pavia, Italy
rui.pinho@unipv.it

Keywords: regularization; force-based; distributed plasticity; frame; numerical integration; interpolatory quadrature; Gauss-Lobatto

Abstract. *Distributed inelasticity force-based elements, widely used in earthquake engineering modeling, lose objectivity at local and global level of response in the softening range of sectional behaviour. This motivated many researchers in the past to propose various regularization techniques to trace a physically meaningful post-peak curve. However, elements that give regularized response under softening behaviour are too flexible to be used for the hardening branch.*

The present work presents a new adaptive force-based plane element that overcomes the aforementioned limitations. As the name suggests, the element is capable of providing solutions for both hardening and softening response by automatically adjusting the element integration weights when a section undergoes into softening. The latter are computed with theoretically derived closed-form expressions from interpolatory quadrature. The 'adaptive' nature of the integration scheme renders it numerically very efficient. Furthermore, the proposed element can directly account for the value of axial force installed on the element in the estimation of the corresponding length of plastification, thus creating a physically sound regularization scheme.

The performance of the proposed adaptive element is first evaluated by comparing its results with those obtained by the standard numerical integration scheme under otherwise similar conditions. It is found that for both monotonic and cyclic response the adaptive model gives good matching at a little computational effort. Moreover, the results from the current model compare well against experimental data, both in the hardening and softening ranges of behaviour.

1 INTRODUCTION

In quasibrittle materials like concrete and rock relatively large fracture zones can occur resulting from progressive growth and coalescence of microcracks, which are usually described by softening laws. Softening behaviour of constitutive law, in general, refers to the descending branch of stress with increasing strain in the stress-strain curve. In continuum mechanics, softening behaviour poses complex mathematical difficulties as the problem becomes ill-posed and the finite element (FE) results become mesh size-dependent – a phenomenon called localization. Localization precludes achieving convergence by refining the mesh size (objectivity). The present study focuses on reinforced concrete (RC) beam elements, which also exhibit similar type of numerical difficulties.

Irrespective of the type of beam formulation, force-based (FB) or displacement-based (DB), the objectivity in response is sought by adopting pre-defined characteristic mesh size within the softening zone, which is widely known as regularization. The vast majority of regularization techniques that can be found in literature for continuum finite elements – of which are particularly relevant those based on integral non-local procedures [1, 2] and gradient models [3] – are generally applied with DB FE formulations. The first proposal applicable to FB fibre-section models was based on ensuring a constant fracture energy release [4]. However, it requires a laborious member-by-member modification of the uniaxial stress-strain relationship of each fibre based on the number of integration points (IPs) and the knowledge of the compressive fracture energy, which may not be easily available. Further, the global force-displacement response needs to be post-processed, using the physical characteristic length, to warrant an objective prediction of the curvature demand in the localized damage zone. On the other hand, the more straightforward regularization proposals by Scott and Fenves [5] and Addessi and Ciampi [6] are likely to produce too flexible solutions for the simulation of the hardening phase of behaviour.

Scott and Hamutçuoglu [7] recently proposed a numerically consistent regularization method that is able to accurately model both hardening and softening ranges of sectional behaviour. This is achieved by adding two additional IPs very close to the element ends, their weights being selected to ensure convergence for both types of sectional behaviours. However, the order of accuracy of their scheme is only of $N - 5$, N being the total number of IPs (including those close to the extremities), which means that for the solution of linear-elastic frame elements at least seven IPs should always be used. Additionally, the element performance is highly sensitive to the position of the two extra IPs.

The present study proposes a novel beam element featuring an adaptive integration method that has the ability of continuously controlling the IP weights, while preserving their positions, in order to maximize accuracy for strain-hardening sectional behaviour and maintain objectivity for strain-softening response. The central idea of the formulation is presented and several numerical verification examples are shown along with pertinent discussion.

2 PROPOSED REGULARIZATION TECHNIQUE

In FB elements, in order to control the beam end sections subjected to larger bending moments, Gauss-Lobatto (GL) quadrature (that includes IPs in the extremities of the integration interval) is commonly used. It has a high order of accuracy of degree $2N - 3$, where N is the number of IPs. On the other hand, the typical regularized integration schemes, restrained by the imposition of some pre-defined weights, have less order of accuracy.

The main idea of the present proposal is to allow the commutation, automatically during the loading history, between different numerical integration schemes in order to ensure high accuracy during hardening and also objective solution during softening response.

In order to monitor the history of section forces and deformations during the analysis, IP positions should not be varied and, consequently, only the corresponding weights are adaptively adjusted. Additionally, in order to pass a patch test, the element has to provide at least the linear-elastic solution; i.e. 2nd degree polynomials need to be integrated exactly.

In the present study, the IP positions considered are same as those of the GL integration scheme. Consequently, throughout the hardening branches, the weights of the several IPs are also defined as those of the standard GL quadrature. The full hardening case is denoted as case (a), for future reference. Whenever a section is softening, the associated integration weight of that section is adjusted to match the appropriate normalized characteristic length. Further, it is assumed that softening can only occur in one or both extremity sections. Once the element starts to soften, the integration weights of the several IPs are recomputed under the condition that the extreme integration weights match λ_{pI} or/and λ_{pJ} (respectively the normalized characteristic lengths of the initial and final sections). In the earthquake engineering modelling context, the characteristic length of a certain IP, L_p, can be assumed to be equal to the plastic hinge length (this term is adopted in the current manuscript, although the correct expression would be 'length of plastification'). The corresponding integration weight λ_p (i.e. the normalized characteristic length) can thus be computed as $(b - a)\, L_p / L_0$, where L_0 is the length of the element. In case of softening, one of the following three cases is bound to happen (typically, cases (b) or (c) will occur first, then (d) will follow for larger inelastic demands):

- Case (b): Softening of the initial IP. In this case, the integration weight of the initial IP matches the normalized characteristic length λ_{pI} ($w_1^* = \lambda_{pI}$). The computation of the integration weights of the remaining IPs can be achieved through interpolatory quadrature [8, 9], the goal of which is to select the weights $w_2^*, w_3^*, ..., w_N^*$ such that the error

$$E(f) = \int_a^b f(x)\,dx - \sum_{j=1}^{N} w_j^* f(x_j) \underset{w_1^*=\lambda_{pI}}{=} \int_a^b f(x)\,dx - \lambda_{pI} f(x_1) - \sum_{j=2}^{N} w_j^* f(x_j) \tag{1}$$

is zero for $f(x) = 1, x, ..., x^{N-2}$. It is noted that a general integration interval $[a,b]$ was used. Considering the positions of the GL integration scheme, the following linear system of $N-1$ equations and $N-1$ unknown weights $w_2^*, w_3^*, ..., w_N^*$ is obtained:

$$\begin{gathered} \lambda_{pI} + w_2^* + w_3^* + ... + w_N^* = \int_a^b dx \\ \lambda_{pI} a + w_2^* x_2 + w_3^* x_3 + ... + w_N^* b = \int_a^b x\,dx \\ \vdots \\ \lambda_{pI} a^{N-2} + w_2^* x_2^{N-2} + w_3^* x_3^{N-2} + ... + w_N^* b^{N-2} = \int_a^b x^{N-2}\,dx \end{gathered} \tag{2}$$

or, equivalently:

$$\begin{bmatrix} 1 & 1 & \dots & 1 \\ x_2 & x_3 & \dots & b \\ \vdots & \vdots & & \vdots \\ x_2^{N-2} & x_3^{N-2} & \dots & b^{N-2} \end{bmatrix} \begin{bmatrix} w_2^* \\ w_3^* \\ \vdots \\ w_N^* \end{bmatrix} = \begin{bmatrix} b-a-\lambda_{pI} \\ \left(b^2-a^2\right)/2-\lambda_{pI}a \\ \vdots \\ \left(b^{N-1}-a^{N-1}\right)/\left(N-1\right)-\lambda_{pI}a^{N-2} \end{bmatrix} \tag{3}$$

- Case (c): Softening of the final IP. In this case, the integration weight of the final IP matches the normalized characteristic length λ_{pJ} ($w_N^{**}=\lambda_{pJ}$). An analogous rationale to case (b) can be applied and the unknown weights $w_1^{**}, w_2^{**}, ..., w_{N-1}^{**}$ obtained through the next system of equations:

$$\begin{bmatrix} 1 & 1 & \dots & 1 \\ a & x_2 & \dots & x_{N-1} \\ \vdots & \vdots & & \vdots \\ a^{N-2} & x_2^{N-2} & \dots & x_{N-1}^{N-2} \end{bmatrix} \begin{bmatrix} w_1^{**} \\ w_2^{**} \\ \vdots \\ w_{N-1}^{**} \end{bmatrix} = \begin{bmatrix} b-a-\lambda_{pJ} \\ \left(b^2-a^2\right)/2-\lambda_{pJ}b \\ \vdots \\ \left(b^{N-1}-a^{N-1}\right)/\left(N-1\right)-\lambda_{pJ}b^{N-2} \end{bmatrix} \tag{4}$$

- Case (d): Softening of both end IPs. The numerical weights of the initial and final end IPs should match λ_{pI} and λ_{pJ} ($w_1^{***}=\lambda_{pI}$ and $w_N^{***}=\lambda_{pJ}$) respectively. Again, interpolatory quadrature can be used to compute the intermediate integration weights:

$$\begin{bmatrix} 1 & 1 & \dots & 1 \\ x_2 & x_3 & \dots & x_{N-1} \\ \vdots & \vdots & & \vdots \\ x_2^{N-3} & x_3^{N-3} & x_4^{N-3} & x_5^{N-3} \end{bmatrix} \begin{bmatrix} w_2^{***} \\ w_3^{***} \\ \vdots \\ w_{N-1}^{***} \end{bmatrix} = \begin{bmatrix} b-a-\lambda_{pI}-\lambda_{pJ} \\ \left(b^2-a^2\right)/2-a\lambda_{pI}-b\lambda_{pJ} \\ \vdots \\ \left(b^{N-2}-a^{N-2}\right)/\left(N-2\right)-a^{N-3}\lambda_{pI}-b^{N-3}\lambda_{pJ} \end{bmatrix} \tag{5}$$

The order of accuracy for cases (b) and (c) is of $N-2$, while for case (d) is of $N-3$. This implies that the minimum number of integration points to be used in the present adaptive element is five, which matches the approximate minimum number of IPs for objective strain-hardening response. It is recalled that the integration weights are used for the numerical integration required to compute the vector of basic displacements and the tangent flexibility matrix of the element.

The calculation of the IP weights for cases (b), (c) and (d) has to be performed continuously throughout the softening branch(es) if the characteristic length depends on the sectional force. This is however an inexpensive operation from the numerical viewpoint, since closed-form solutions can be easily derived. For example, the closed-form solution for 5 IPs and cases (b), (c) and (d) (taking $a=-1$ and $b=1$) is, respectively:

$$\begin{bmatrix} w_2^* \\ w_3^* \\ w_4^* \\ w_5^* \end{bmatrix} = \begin{bmatrix} \frac{7}{9}-\frac{7}{3}\lambda_{pI} \\ \frac{4}{9}+\frac{8}{3}\lambda_{pI} \\ \frac{7}{9}-\frac{7}{3}\lambda_{pI} \\ \lambda_{pI} \end{bmatrix}, \quad \begin{bmatrix} w_1^{**} \\ w_2^{**} \\ w_3^{**} \\ w_4^{**} \end{bmatrix} = \begin{bmatrix} \lambda_{pJ} \\ \frac{7}{9}-\frac{7}{3}\lambda_{pJ} \\ \frac{4}{9}+\frac{8}{3}\lambda_{pJ} \\ \frac{7}{9}-\frac{7}{3}\lambda_{pJ} \end{bmatrix}, \quad \begin{bmatrix} w_2^{***} \\ w_3^{***} \\ w_4^{***} \end{bmatrix} = \begin{bmatrix} \frac{7}{9}-\frac{\sqrt{21}}{6}\left(\lambda_{pI}-\lambda_{pJ}\right)-\frac{7}{6}\left(\lambda_{pI}+\lambda_{pJ}\right) \\ \frac{4}{3}\left(\frac{1}{3}+\lambda_{pI}+\lambda_{pJ}\right) \\ \frac{7}{9}+\frac{\sqrt{21}}{6}\left(\lambda_{pI}-\lambda_{pJ}\right)-\frac{7}{6}\left(\lambda_{pI}+\lambda_{pJ}\right) \end{bmatrix} \tag{6}$$

Figure 1 schematically describes the representation of a computed distribution of integration weights for the previous cases, considering arbitrary values of λ_{pI} and λ_{pJ}. It should be mentioned that the success of the current adaptive element is dependent on the correct identification of the sectional behaviour (hardening or softening). The description of the technique developed for such purpose, and implemented in an *ad hoc* computer code, as well as the associated state determination algorithm, falls out of the scope of this document. Nevertheless, the interested reader can find it in Almeida *et al.* [10]. Finally, it is noted that linear geometry is assumed.

3 NUMERICAL EXAMPLES

3.1 Laterally loaded cantilever

The performance of the proposed adaptive element is first demonstrated with the help of an idealized multi-linear moment-curvature relationship with initial post-yield hardening followed by a softening branch. Figure 2 shows the normalized moment-curvature relationship, where moment and curvatures are normalized by the ultimate moment (M_u) and the corresponding curvature (χ_u) respectively. Elastic unloading behaviour is considered. Furthermore, it is assumed that the softening branch will continue with the same slope for a higher demand of normalized curvature beyond two.

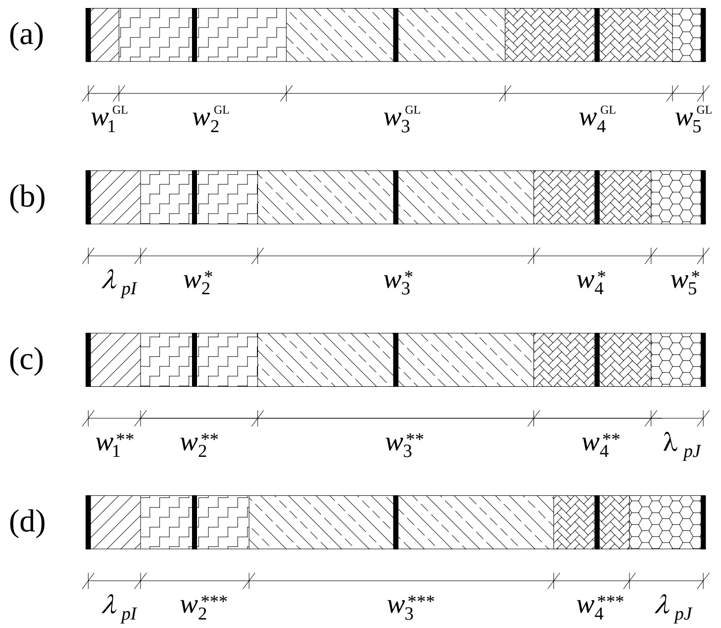

Figure 1: Illustrative example of weight computation: (a) Gauss-Lobatto; (b) softening of initial section; (c) softening of final section; (d) softening of both end sections.

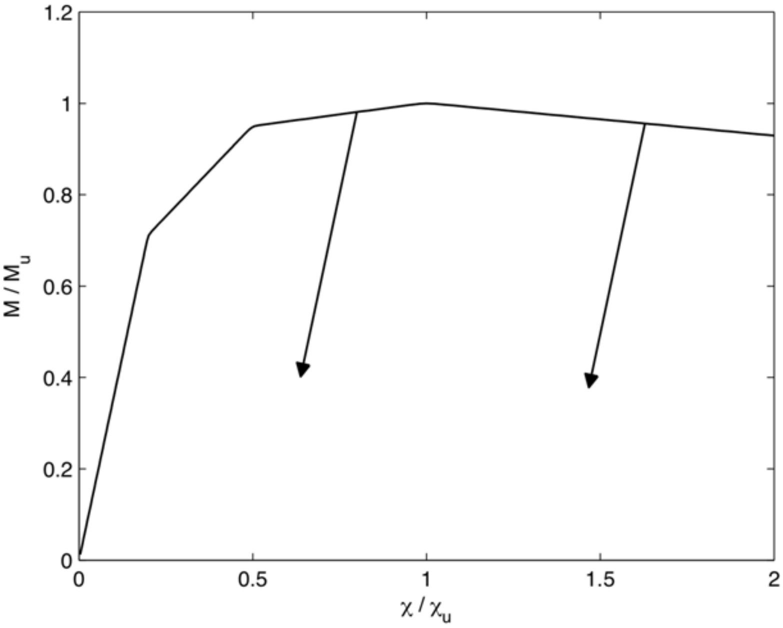

Figure 2: Idealized normalized multi-linear moment-curvature relationship.

Figure 3 shows the top lateral force, normalized by its ultimate value, versus top lateral drift (Δ) ratio of a cantilever column (modelled by a single element). Results for standard GL and for the new adaptive integration schemes with different numbers of IPs are compared. The characteristic length L_p is arbitrarily assumed to be $0.15L$, where L is the shear span associated to the bottom critical section (in the present case it corresponds to the full element length L_0).

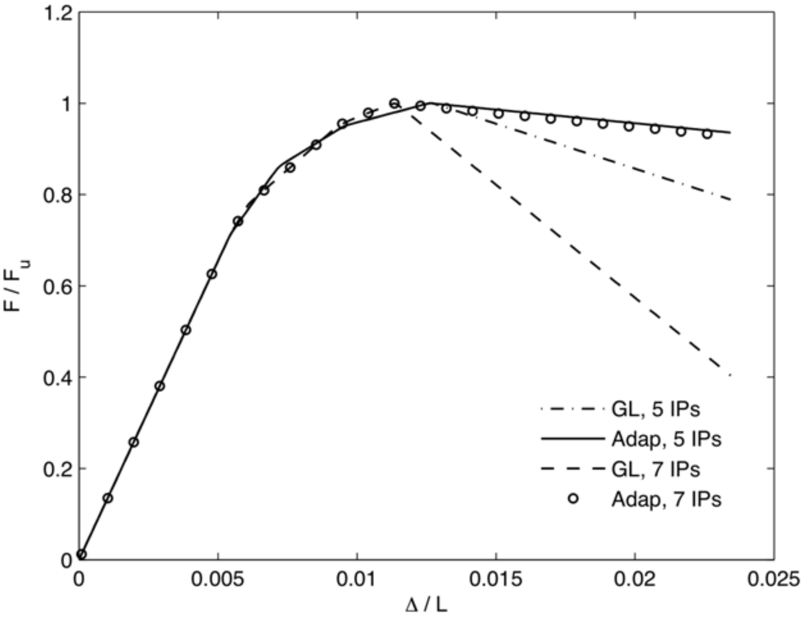

Figure 3: Normalized top lateral force versus top lateral drift ratio of the cantilever column in the cases of standard GL and adaptive schemes, for different number of IPs.

It can be observed, as expected, that during the hardening phase of response the new adaptive and the standard GL schemes yield identical results for the same number of IPs because there is a continuous correspondence between the integration weights employed. The difference in responses during the hardening phase is due to the number of IP-dependent spreading of inelasticity within the element, which is however objective. This is also the reason why the peak lateral loads correspond to different values of lateral drift for five and seven IPs. However, for the softening branch, a clear non-objective response is apparent for the standard GL scheme with different number of IPs, while the adaptive scheme produces an objective output.

Figure 4 shows the distribution of curvature at the end of the loading phase along the normalized length of the element. It is clear from the figure that for standard GL scheme the curvature demand at the initial section increases with increasing number of IPs because, during the softening branch, spreading of inelasticity is not possible. However, for the adaptive scheme the curvature demand is objective because it uses regularized integration weight for the initial section.

The ability of the adaptive element to switch the integration weights from those of standard GL to those of interpolatory quadrature, by identifying the type of sectional behaviour, is shown in Figure 5. The variations of the weights for the initial section during the entire loading history and different numbers of IPs are shown for this purpose. It should be noted that the sum of all IP weights adds up to 2, i.e. in equation (1) it is assumed $a = -1$ and $b = 1$.

The previous numerical cases show the results when the column is loaded monotonically. It will also be interesting to see the behaviour under cyclic loading since this will imply a cyclic commutation between the integration weights of standard GL and interpolatory quadrature. Figure 6 shows the general cyclic behaviour of the multi-linear moment-curvature relationship, which has the same monotonic behaviour as that of Figure 2.

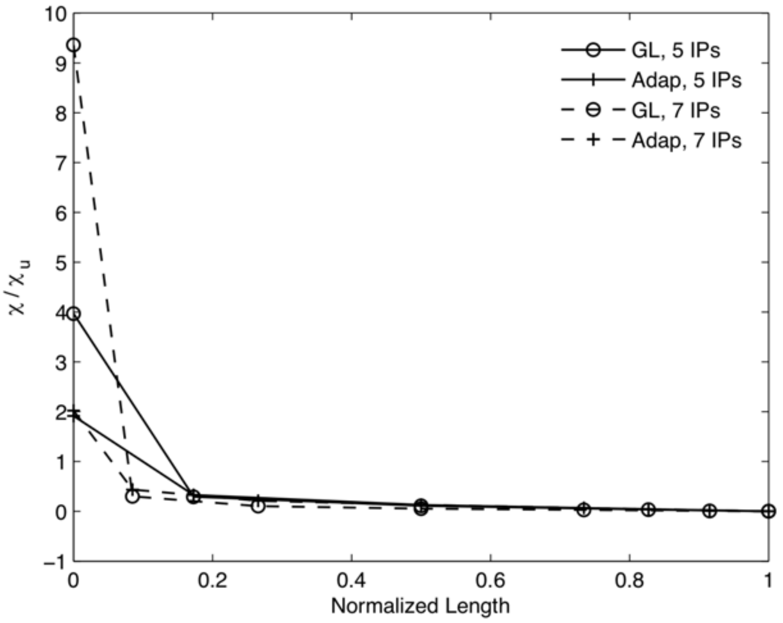

Figure 4: Normalized curvatures at the end of loading phase along the normalized length of the element, in the cases of GL and adaptive schemes for different number of IPs.

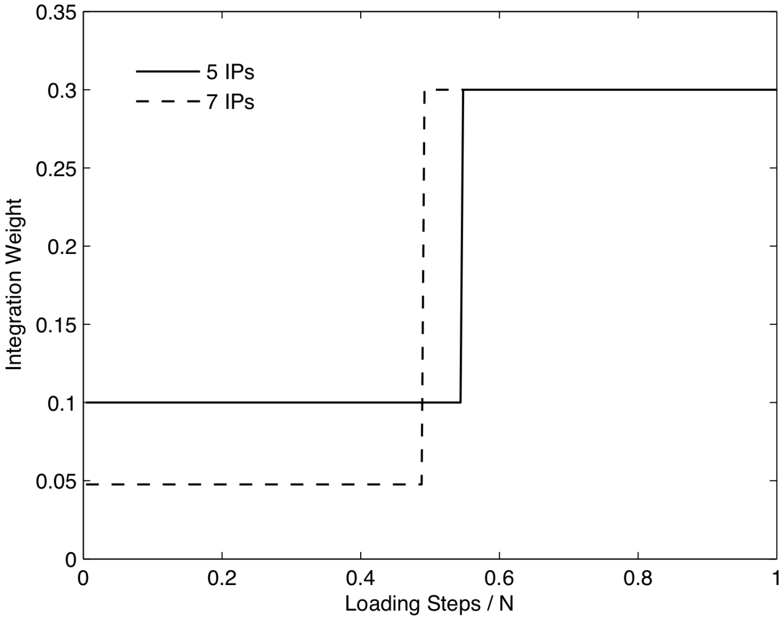

Figure 5: Variation of integration weight at the initial IP along normalized loading steps (N = total number of loading steps) in the case of adaptive element with different IPs.

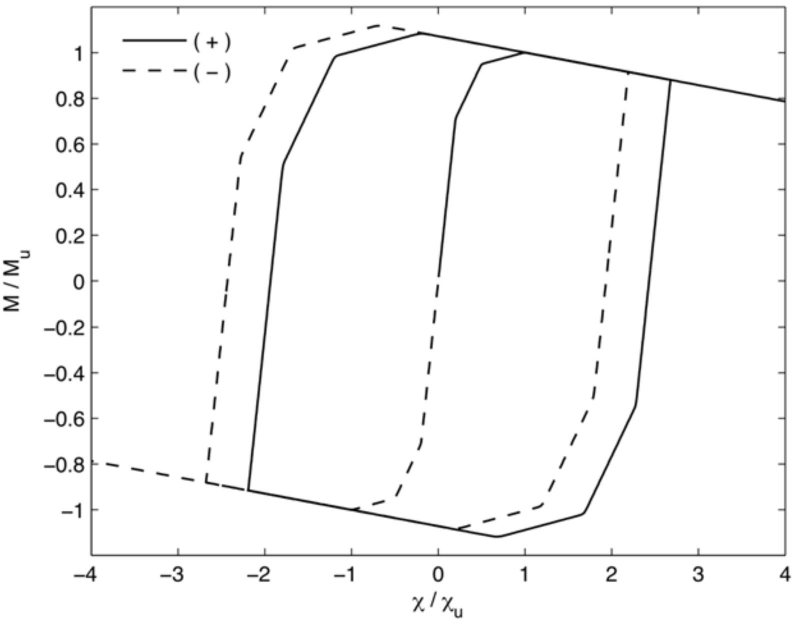

Figure 6: Multi-linear cyclic moment-curvature rule for positive and negative initial elastic loadings.

Figure 7 depicts the normalized top lateral force versus top lateral drift ratio for different integration schemes, with five and seven IPs, under cyclic loading. The entire loading phase has three salient parts chronologically, viz., the loading phase (increasing drift ratio), the unloading phase (decreasing drift ratio) and the reloading phase (again increasing drift ratio). At the end of the loading phase the results are identical to the previous monotonic case. When the unloading starts, the sectional response becomes of the hardening type and thus the integration weights for the adaptive scheme change back to those of the standard GL. At the initiation of softening towards the end of the unloading phase they again commute to those of the interpolatory quadrature, and so on. Consequently, the adaptive scheme yields an objective response for the entire cyclic load history. The commutation of integration weights for the initial section is shown in Figure 8. One thing to be noticed in Figure 7 is that the softening for standard GL with seven IPs is less pronounced in the unloading phase and also the final force level is much lower. This is due to the shift of localization from the extremity section to the adjacent one, a phenomenon that can happen during cyclic behaviour for elements with large number of IPs, and that was observed and explained by Almeida *et al.* [10].

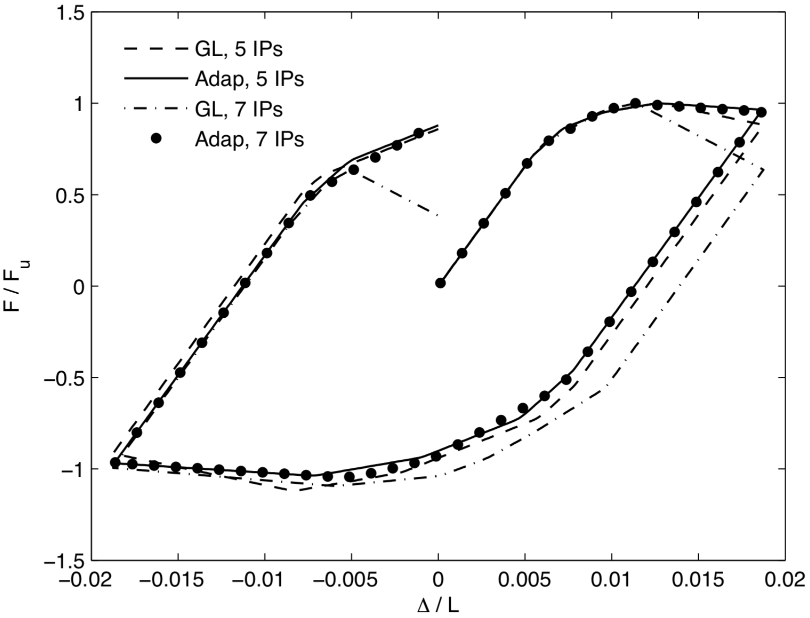

Figure 7: Normalized top lateral force versus top lateral drift ratio for adaptive and standard GL schemes with five and seven IPs.

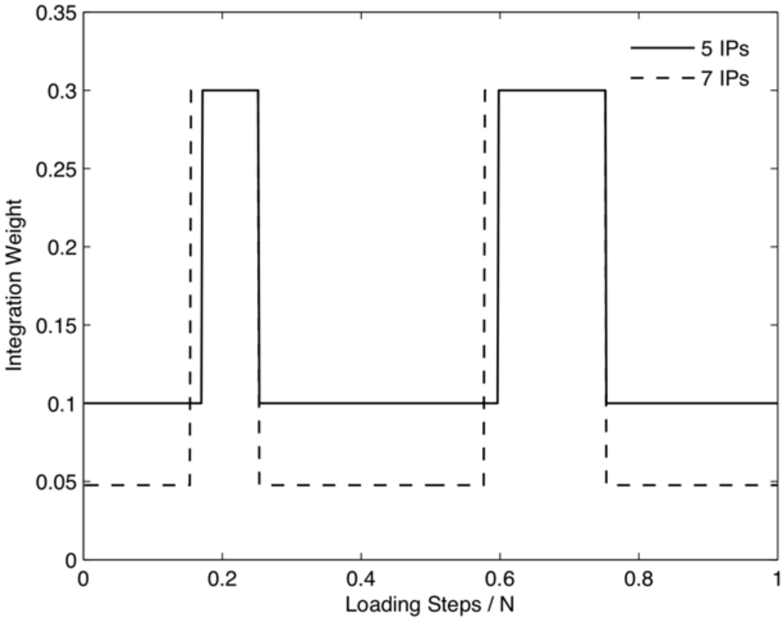

Figure 8: Variation of integration weights for the initial section during the entire load history in the cases of adaptive element with five and seven IPs.

The effects of such shift can be observed in Figure 9, which shows the curvature distributions along the normalized length of the element at the end of the cyclic loading phase. It is apparent that for GL with 7 IPs, unlike for the 5-IPs' GL case, there is a curvature reversal throughout the element length, which is attributable to the previous numerical occurrence.

3.2 Columns subjected to varying axial loads

The adaptive scheme's ability to continuously adjust the characteristic length can be best utilized by considering response-dependent characteristic length. This feature can be of relevance in real applications, e.g. columns located at the boundary of frame structures subjected to earthquake loading, where the axial load (due to global overturning moment) is expected to fluctuate. For this case-study, two cantilever columns of length *L*, viz. Column 1 and Column 2, are modelled by one element. A maximum lateral displacement (Δ) of 0.04*L* (4% drift) is imposed, as well as two different axial load ratios that vary during lateral displacement according to Figure 10. The axial load ratio, ρ_A, is defined as the ratio of the axial load to the ultimate axial load capacity of the section. From the figure it is clear that the gravity load and the maximum plus/minus variation correspond to ρ_A of 0.25.

The monotonic moment-curvature relationship with origin-oriented linear unloading, as shown in Figure 11, is adopted for the present case. An elastic constitutive law is assumed for the axial behaviour, which is uncoupled from the flexural response.

Since the characteristic length can depend on the level of axial force (e.g., [11]), a purely illustrative law is considered for the characteristic length. It is a function of ρ_A as:

$$L_p / L = \max[0.5\rho_A, 0.15] \tag{7}$$

where max[.] indicates the maximum of the two arguments.

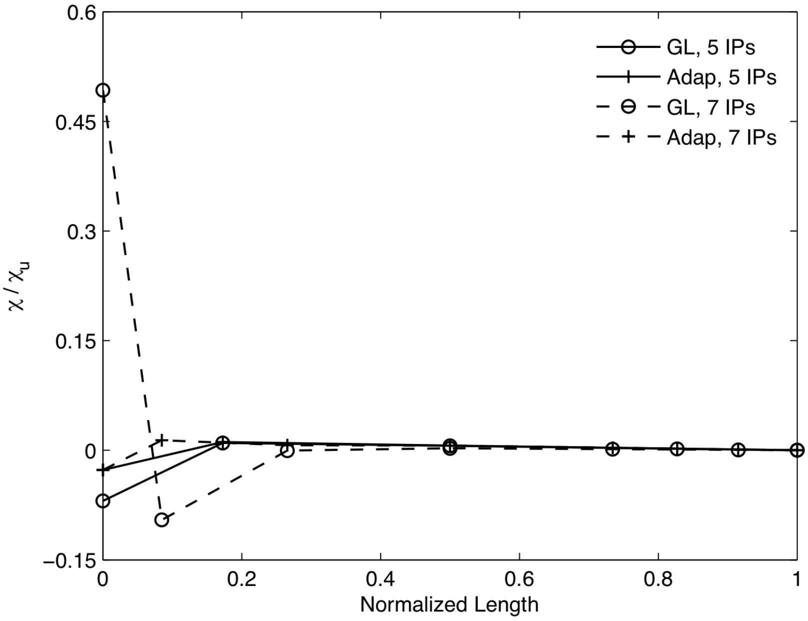

Figure 9: Normalized curvatures at the end of cyclic loading phase along the normalized length of the element, in the cases of GL and adaptive schemes for different number of IPs

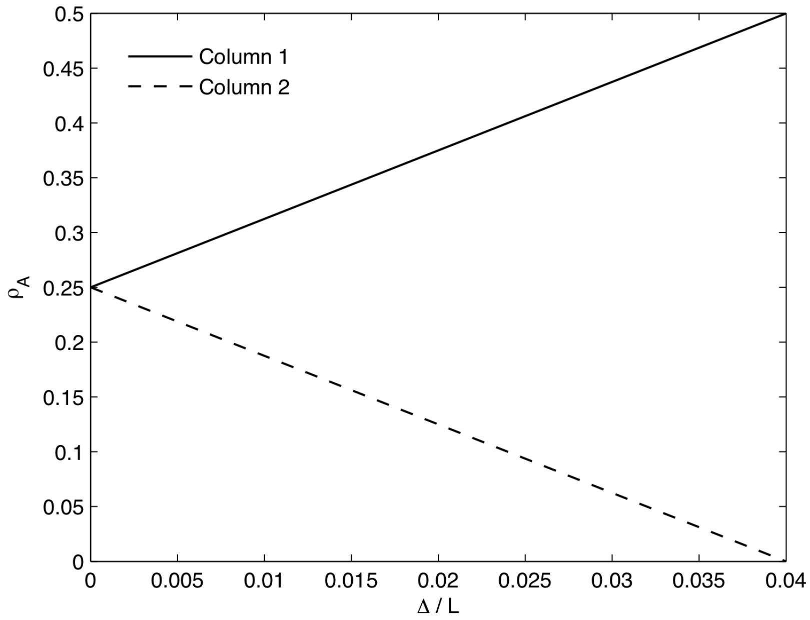

Figure 10: Variation of axial load ratio in Columns 1 and 2 with lateral drift.

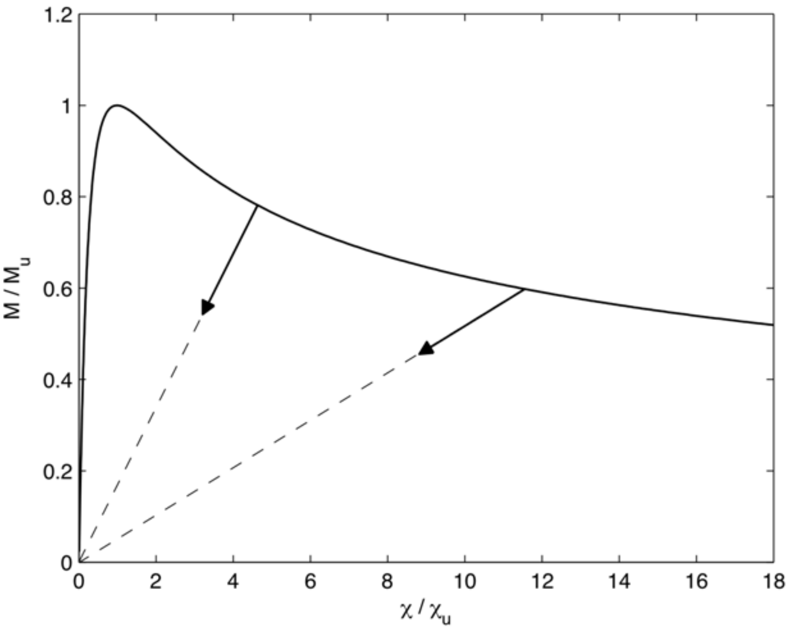

Figure 11: Idealized moment-curvature relationship.

The responses of Column 1 and Column 2 for standard GL and adaptive integration schemes with five and seven IPs are shown in Figure 12. It can be noticed that, once again, the present adaptive element provides objective response for each column and different number of IPs. The difference between both columns depicts obviously the influence of the varying axial force in the computation of the applicable characteristic length, as given by equation (7). Figure 13 shows the evolution of the initial integration weight, for the case of 5 IPs, remaining clear that for Column 2 it is less than for Column 1, due to the lower axial load ratio. It should be mentioned that the integration weight for Column 2 during softening is governed by the minimum criterion of $L_p = 0.15L$. On the other hand, the integration weight for Column 1 increases in proportion to the increasing axial load. The behaviour of the element with non-regularized GL scheme shows (see Figure 12) not only the typical localization phenomena associated to distinct number of IPs but also the expected insensitivity to the varying values of the axial force.

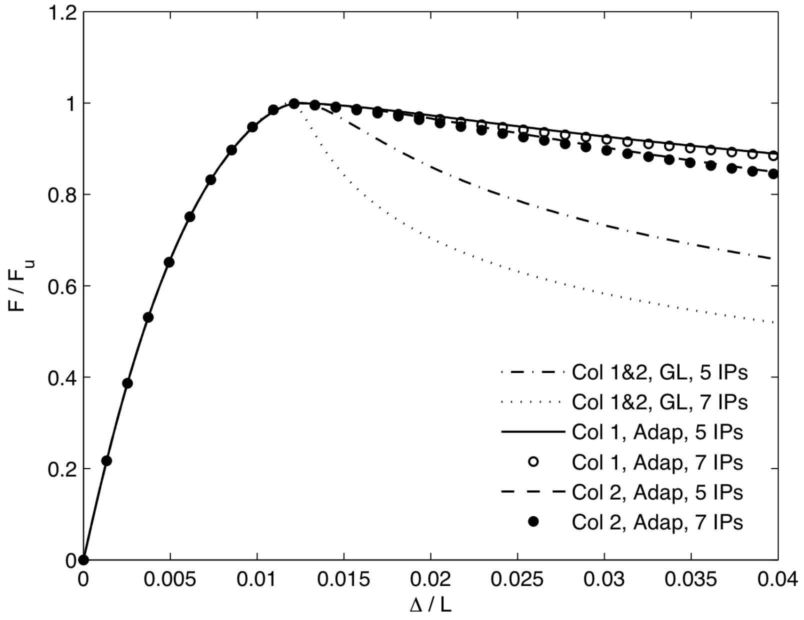

Figure 12: Responses of Column 1 and Column 2 at different levels of drift, for GL and adaptive integration schemes with different number of IPs.

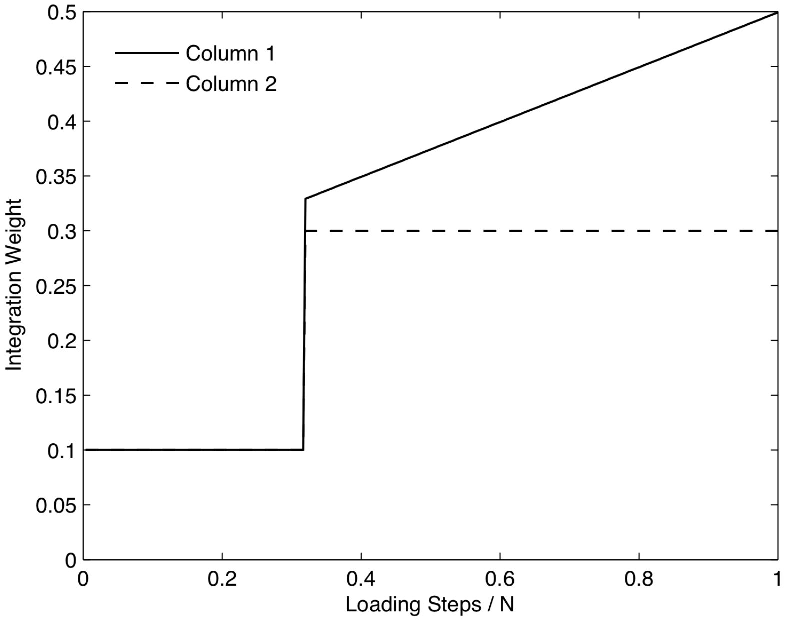

Figure 13: Variation of integration weight at initial IP for adaptive element with five IPs.

3.3 Experimentally tested column

The previous numerical examples intend to highlight the theoretical aspects of the proposed adaptive numerical scheme. Its application to model reinforced concrete member behaviour is now briefly addressed.

The test specimen U-5 of Watson and Park [12] has been used for experimental verification. The equivalent cantilever length of the column specimen is 1.6 m, where the cross section is 400 by 400 mm. The uniaxial concrete properties are f_{c0} = 41 MPa, f_{cc} = 53.3 MPa, ε_{c0} = 0.0027 and ε_{cc} = 0.00675 and the yield stress for longitudinal steel is 474 MPa. The column is subjected to a constant axial force of 3280 kN (axial load ratio of 0.5).

The cantilever is modelled by a single FB element and the sectional response is given by a classical concrete/steel fibre discretization approach. The uniaxial laws considered for concrete and steel are due to Martinez-Rueda and Elnashai [13] and Menegotto and Pinto [14] respectively. For concrete in traction an exponential decay was used to account for tension-stiffening effects. Moreover, two different formulae for plastic hinge length, representative of the characteristic length, due to Paulay and Priestley [15] and Bae and Bayrak [11] have been considered.

Figure 14 shows the monotonic envelopes predicted by the standard GL scheme with five and seven IPs, by the adaptive scheme with five IPs and different formulae for the plastic hinge length, as well as the experimental cyclic curves. The lateral force that equates the moment due to P-Δ effect is added to the experimentally applied horizontal force at each step for comparison with numerical results. It is clear from the figure that the adaptive schemes predict the monotonic backbone curve quite accurately while those predicted by the standard GL scheme are not acceptable (in the softening range). It is recalled that in the case of standard GL scheme, a steeper softening slope is due to an unrealistic concentration of curvature demand at the base for a specified lateral displacement at the column top.

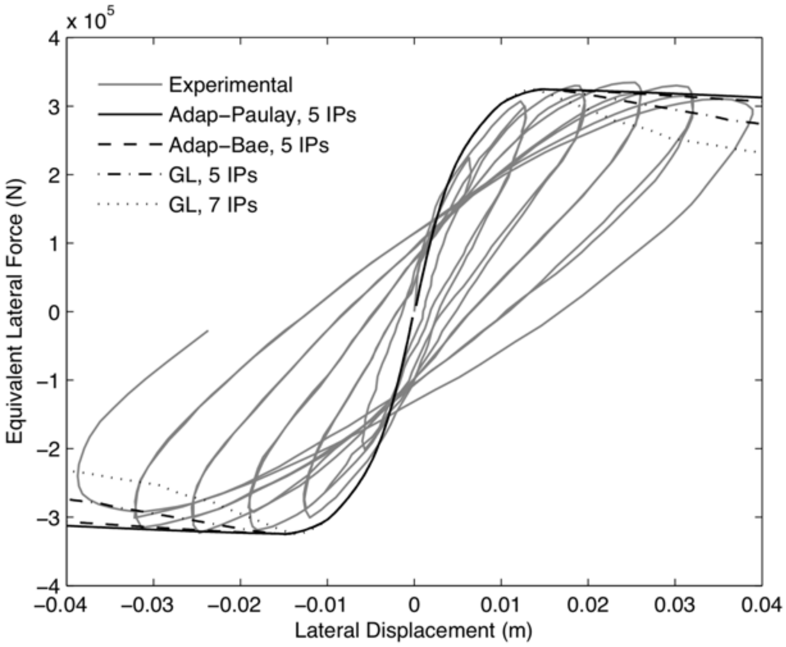

Figure 14: Comparison of experimental (cyclic) and numerical (monotonic) curves in the cases of standard GL and adaptive scheme (with different formulae of plastic hinge length), for different number of IPs.

The values of curvature demand along the length for the different cases are shown in Figure 15. For the GL scheme with five and seven IPs the curvature is unrealistically high (respectively around three and six times the objective value provided by the adaptive scheme). Figure 16 shows the moment-curvature demands for the adaptive scheme (with Bae and Bayrak's formula for plastic hinge length) and the standard GL scheme, with five IPs. Only the results corresponding to regular increments of the top node lateral displacement are depicted. As expected, it can be seen that the demands are identical up to the onset of softening, after which the rate of curvature increase is higher for the GL scheme than for the adaptive one.

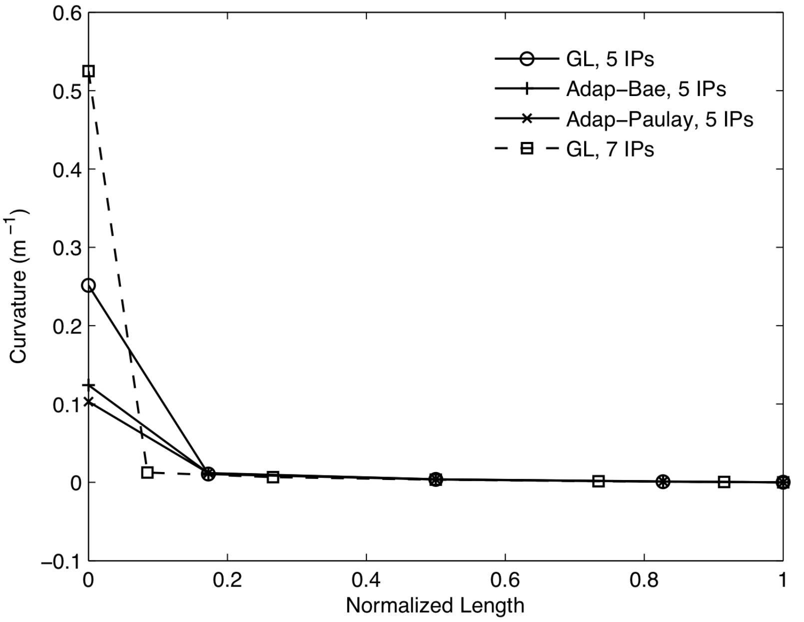

Figure 15: Curvature distribution along the normalized column length at the end of the loading phase, in the cases of standard GL and adaptive scheme (with different formulae of plastic hinge length).

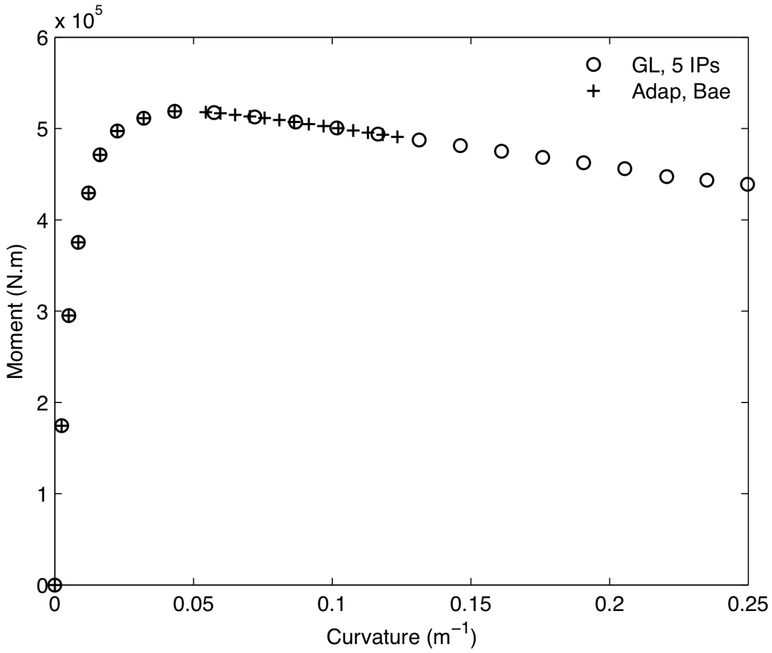

Figure 16: Comparison of monotonic curvature demands for Watson and Park's test specimen in the cases of standard GL and adaptive scheme (using Bae and Bayrak's formula for plastic hinge length) with 5 IPs.

4 CONCLUSIONS

A new load adaptive FB frame element was proposed, the integration scheme of which can automatically commute between the integration weights of standard GL and characteristic length-based interpolatory quadrature, depending on the type of sectional behavior (hardening or softening). This enables the element's integration scheme to maintain the high order of accuracy of the standard GL scheme during the hardening phase(s), while guaranteeing objective response during the softening part(s) of the response.

A number of numerical applications have been carried out to show the different features of the newly developed adaptive element and to emphasize its advantages over the standard GL integration scheme. It has been found that, although being computationally light, the proposed element can produce objective responses for distinct number of IPs. Additionally, this regularization technique also accounts directly for the axial load variation during softening response – an aspect that cannot be addressed by the currently existing regularization methods, based on pre-defined integration schemes. Finally, the current proposal was also verified against an experimental test, where it proved to yield accurate and realistic results.

REFERENCES

[1] G. Pijaudier-Cabot, Z.P. Bazant, Nonlocal damage theory. *Journal of Engineering Mechanics* (ASCE), **113**, 1512-1533, 1987.

[2] M. Jirásek, S. Rolshoven, Comparison of integral-type nonlocal plasticity models for strain-softening materials. *International Journal of Engineering Science*, **41**, 1553-1602, 2003.

[3] R.H.J. Peerlings, M.G.D. Geers, R. de Borst, W.A.M. Brekelmans, A critical comparison of nonlocal and gradient-enhanced softening continua. *International Journal of Solids and Structures*, **38**, 7723-7746, 2001.

[4] J. Coleman, E. Spacone, Localization issues in force-based frame elements. *Journal of Structural Engineering* (ASCE), **127**, 1257-1265, 2001.

[5] M.H. Scott, G.L. Fenves, Plastic hinge integration methods for force-based beam-column elements. *Journal of Structural Engineering* (ASCE), **132**, 244-252, 2006.

[6] D. Addessi, V. Ciampi, A regularized force-based beam element with a damage-plastic section constitutive law. *International Journal for Numerical Methods in Engineering*, **70**, 610-629, 2007.

[7] M.H. Scott, O.M. Hamutçuoglu, Numerically consistent regularization of force-based frame elements. *International Journal for Numerical Methods in Engineering*, **76**, 1612-1631, 2008.

[8] P.J. Davis, P. Rabinowitz, *Methods of numerical integration, 2nd Edition*. Dover Publications, 1975.

[9] P.K. Kythe, M.R. Schaferkotter, *Handbook of computational methods for integration*. CRC Press, 2004

[10] J.P. Almeida, S. Das, R. Pinho, Adaptive force-based frame element for regularized monotonic and cyclic response. *Computers and Structures* (under review).

[11] S. Bae, O. Bayrak, Plastic hinge length of reinforced concrete columns. *ACI Structural Journal*, **105**, 290-300, 2008.

[12] S. Watson, R. Park, Design of reinforced concrete frames of limited ductility. *Report 89-4, Department of Civil Engineering, University of Canterbury, Christ Church, New Zealand*, 1989.

[13] J.E. Martinez-Rueda, A.S. Elnashai, Confined concrete model under cyclic load. *Materials and Structures*, **30**, 139-147, 1997.

[14] M. Menegotto, P.E. Pinto, Method of analysis of cyclically loaded RC plane frames including changes in geometry and non-elastic behaviour of elements under normal force and bending. *Preliminary Report, IABSE*, **13**, 15-22, 1973.

[15] T. Paulay, M.J.N. Priestley, *Seismic design of reinforced concrete and masonry buildings*. John Wiley and Sons, 1992.

COMPDYN 2011
3rd ECCOMAS Thematic Conference on
Computational Methods in Structural Dynamics and Earthquake Engineering
M. Papadrakakis, M. Fragiadakis, V. Plevris (eds.)
Corfu, Greece, 25–28 May 2011

DETAILED FEM MODELLING OF STONE MASONRY ARCH BRIDGES UNDER ROAD TRAFFIC MOVING LOADS

Cristina Costa[1], **António Arêde**[2], **and Aníbal Costa**[3]

[1] Polytechnic Institute of Tomar / CEC - FEUP
Quinta do Contador 2300-313 Tomar / Rua Dr. Roberto Frias s/n 4200-465 Porto
e-mail: c.costa@ipt.pt

[2] Faculty of Engineering University of Porto / CEC - FEUP
Rua Dr. Roberto Frias s/n 4200-465 Porto
aarede @fe.up.pt

[3] University of Aveiro / CEC - FEUP
Campus Universitário de Santiago 3810-193 Aveiro / Rua Dr. Roberto Frias s/n 4200-465 Porto
email: agc@ua.pt

Keywords: Instructions, Masonry arch bridges; Moving loads; Pavement irregularities.

Abstract. *This paper aims at identifying suitable approaches for the numerical modelling of stone masonry arch bridges with the purpose of estimating the traffic effects by means of moving loads and taking in account the surface roughness of the pavement. For this purpose two ancient stone masonry arch bridges located near Porto are addressed. The bridge numerical analyses are performed based on detailed finite element models. Suitable nonlinear constitutive models are considered for the joints elements, while the Drucker Prager model is adopted for the infill. The interaction between the wheel and the pavement is considered through a simplified methodology comprising three phases of analysis where the bridge and the vehicle are studied separately. The bridge response shows that the activation of the material nonlinear behaviour has significant influence on the bridge effects (increase), however comparing the results with irregularities and without less influence is shown.*

1 INTRODUCTION

The study presented in this paper is included within the analysis framework of Portuguese masonry arch bridges, particularly for the S. Lázaro bridge and the Lagoncinha bridge herein addressed, aiming at calibrating analysis procedures for this type of structures, specifically by considering different types of materials and strategies for traffic load modelling.

3D and 2D structural numerical models, including the contribution of the backfill and the spandrel walls, were adopted resorting to the computer code CAST3M [1], based on the finite element method. Nonlinear constitutive models were considered both for the joint elements of the masonry structure and for the infill material.

The study included in-situ and laboratory tests on material samples for parameterization and calibration of numerical models fully presented elsewhere [2]. Additionally, ambient vibration tests on the bridge and its numerical modelling allowed for the model calibration, supported also by material calibration tests according to the adopted types of numerical models.

2 GENERAL DESCRIPTION OF THE CASE STUDIES

The S. Lázaro Bridge crosses the Leça river in Alfena, Valongo (nearby Porto) and it is a granite stone masonry bridge supposedly built in the Middle Age [3]. The bridge is about 28m long with two different perfect arches, one with 7.5m span and a smaller one with 2.3m. The deck is about 3.3m wide and the pavement is made of granite slabs (see Figure 1). During the year 2008 the bridge was consolidated by cement grout injection in the backfill as well as by injecting and repointing the masonry joints with appropriate mortar.

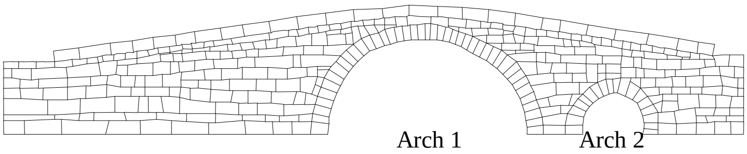

Figure 1: S. Lázaro bridge.

The granite masonry arch bridge of Lagoncinha, Lousado (nearby Porto), is classified as a National Monument and its construction dates back to the medieval period [4]. The bridge with about 150 m long and 3.5 m wide consists of six arches, three full turn and the others slightly ogival, as shown in Figure 2.

Figure 2: Lagoncinha bridge.

3 CHARACTERIZATION OF THE BRIDGES NUMERICAL MODELS

3.1 FEM mesh

As aforementioned, the FEM modelling was made in the CAST3M [1] computer code considering the stone masonry blocks (arches, spandrel walls and pavement) discretized using solid finite elements individualized from the adjacent blocks by considering zero thickness joint elements at their interfaces (stone-to-stone joint type). The backfill material was also modelled with solid finite elements connected to zero thickness joint elements in the interfaces between the infill and blocks of arches, spandrel walls and pavement; in this case, different characteristics were used for this infill-to-stone joint type.

The simulation of the bridges behaviour under the traffic loading was based on 2D and 3D models. The 3D modelling allowed simulating the structural behaviour in both bridge directions (longitudinal and transversal) whereas the 2D modelling aimed at representing the bridge behaviour in the longitudinal direction considering the arch zone under the backfill (central zone, along the bridge longitudinal axis.

3D and 2D finite element meshes of S. Lázaro bridge are illustrated in Figures 3 and 4. The Lagoncinha bridge 3D finite element model is shown in Figure 5.

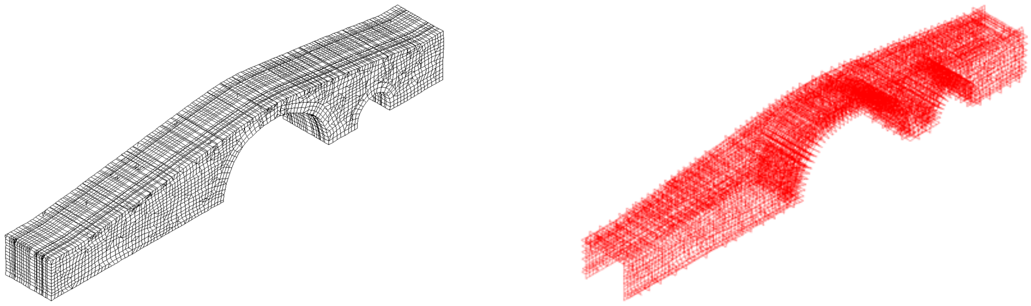
a) b)

Figure 3: 3D model of the S. Lázaro bridge. a) Solid and b) joint finite elements.

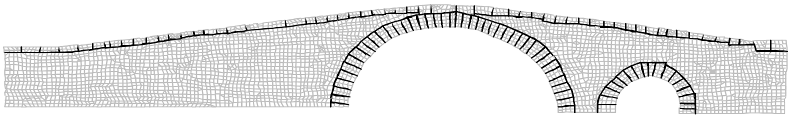

Figure 4: 2D model of the S. Lázaro bridge. Plane (2D) elements (gray) and joint elements (black).

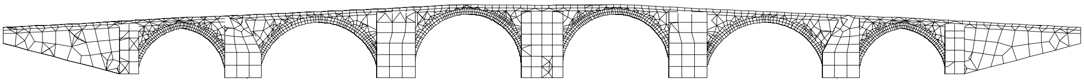

Figure 5: 3D model of the Lagoncinha bridge.

The boundary conditions were set using rigid support to fix the displacements at the bridges base in contact with the riverbed. The horizontal displacements were blocked in the vertical boundary of the abutments.

3.2 Material properties and constitutive models

The S. Lázaro bridge study aimed at calibrating analysis procedures for this type of structures, particularly by considering different types of materials and strategies for traffic load modelling. In this context, three scenarios were considered for the structural materials' constitution in terms of the type of joints and backfill materials. For one of the scenarios (scenario 1), the analysis aimed at simulating the bridge behaviour after rehabilitation, thus considering the stone block interfaces with filling mortar and the backfill (supposedly) composed by the initially existent granular material and by the added material through cement grout injection. The second scenario (scenario 2) intended to approximate the bridge conditions before a recently made rehabilitation intervention considering the stone block interfaces without filling mortar and the backfill (supposedly) composed by granular material. As for the third scenario (scenario 3), it was intended to simulate the bridge behaviour considering the material constitution with degradation.

Since no specific laboratory tests were carried out for the S. Lázaro bridge materials, the definition of numerical model parameters, including the mechanical properties of the materials, was based on the results of the laboratory tests performed on samples of materials used in other granite stone masonry constructions also from the North of Portugal as found in LNEC [5] and Costa [2]. These parameters were however adjusted to reach a suitable agreement between the in-situ measured frequencies and vibration modes and those numerically calculated through linear modal analysis of the bridge; such values were also compared with other results of materials tests existing in the literature. Observations recorded from visual inspections carried out before and after intervention were also taken in account.

In accordance with the scenarios' definition, Table 1 lists the physical and mechanical parameters assigned to the solid and the joint elements for the three above mentioned scenarios, namely the unit weight (γ), elastic modulus (E) and Poisson ratio (ν) for the solid elements and normal and shear stiffness (k_n and k_s, respectively) for the joints.

Material	γ (kN/m^3)	E (GPa)	ν	Material	k_n (MPa/mm)	k_s (MPa/mm)
Scenario 1 (after rehabilitation)						
Stone blocks	26.0	35.0	0.20	Stone-to-stone joints	6.24	0.56
Infill	21.5	0.03	0.33	Stone-to-infill joints	6.24	0.56
Scenario 2 (before rehabilitation)						
Stone blocks	26.0	35.0	0.20	Stone-to-stone joints	7.20	0.56
Infill	21.5	0.03	0.33	Stone-to-infill joints	0.53	0.28
Scenario 3 (before rehabilitation with material degradation)						
Stone blocks	26.0	15.5	0.20	Stone-to-stone joints	6.24	0.56
Infill	18.0	0.003	0.33	Stone-to-infill joints	0.53	0.28

Table 1: Physical and elastic properties of the materials of the S. Lázaro bridge.

Parameters' definition of Lagoncinha bridge materials were based on results of laboratory tests on stone and infill samples collected from the bridge, as well on the observations recorded during visual inspections, then adjusted to obtain good agreement between the frequencies and vibration modes in-situ measured and numerically determined through linear modal analysis [6]. Table 2 include the material parameters assigned to the solid and joints elements of the Lagoncinha bridge model.

Note that in S. Lázaro bridge all masonry structural elements (arches, spandrels, pavement) were defined as a micro-mechanical material, while for the Lagoncinha bridge the spandrel walls and the infill were considered as a macro-element with homogeneous properties; therefore higher values of E and γ were assigned in this bridge zone.

Material	γ (kN/m^3)	E (GPa)	ν	Material	k_n (MPa/mm)	k_s (MPa/mm)
Stone blocks of the arches	25-35	26	0.2	Stone-to-stone joints	4.46-6.24	0.48-0.69
Infill and spandrel walls	0.4-6.5	18-21	0.2-0.33	Stone-to-infill joints	4.00-65.0	1.67-27.1

Table 2: Physical and elastic properties of the materials of the Lagoncinha bridge.

The solid elements simulating the blocks of the masonry structure of the both bridges were considered linear elastic with the parameters included in Table 1 and Table 2. For the infill material it was used the Drucker Prager model with dilatancy available in CAST3M [1] considering the elastic parameters also included in Table 1 and Table 2. The yield surface was defined in correspondence with the parameters measured by triaxial tests [2] on a granular type material used in the Vila Fria bridge [7] which exhibited values of 30º for the friction angle, 13kPa for the cohesion and 6° for the dilatancy angle. Constitutive parameters assigned of the infill materials of the S. Lázaro and Lagoncinha bridges are shown in Table 3.

Material	ϕ (°)	c (kPa)	ψ (°)
S. Lázaro bridge			
Granular material with grout injections after rehabilitation (scenario 1)	33	50	33
Granular material before rehabilitation (scenario 2)	30	13	6
Granular material before rehabilitation with material degradation (scenario 3)	30	0	6
Lagoncinha bridge			
Granular material	35.5	9.4	6

Table 3: Constitutive parameters of the infill materials of the S. Lázaro and Lagoncinha bridges.

The joint element behaviour was modelled by a nonlinear Coulomb friction model without dilatancy called JOINT_SOFT_CY_T and implemented in the CAST3M package within the context of a previous work [2]. The values considered for the normal stiffness (k_n) and tangential stiffness (k_s) of the joint elements are also included in Table 1 and Table 2.

Regarding the hardening laws of the joint model, a perfect elastic-plastic law was defined in the shear direction because dry joins were considered for the S. Lázaro bridge scenarios 1 and 2 and for the Lagoncinha bridge. The shear strength is computed according to the yield surface defined by the slope $tan\phi$=0.72 and no cohesion according the behaviour recorded in laboratorial shear tests performed on samples of dry joints of the Vila Fria bridge [7]. In the normal direction the loading curve is defined by a constant stiffness k_n and bilinear curves were adopted for unloading/reloading laws according to the pattern observed also in cyclic compressive laboratory tests of stone-to-stone block joints.

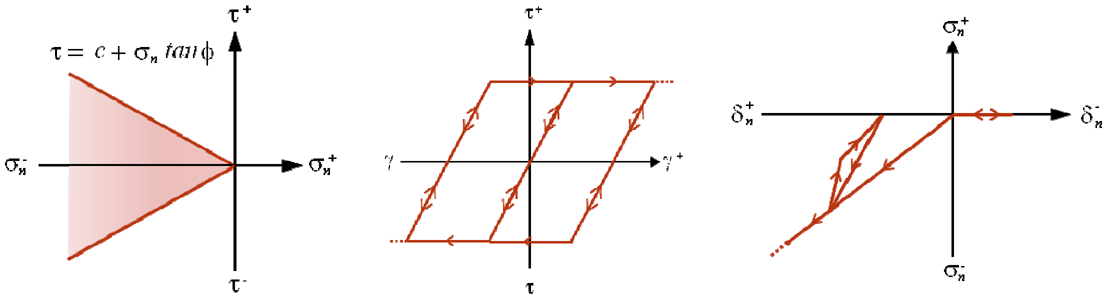

a) b) c)

Figure 6: JOINT_SOFT_CY_T model. a) Yield surface, b) shear and c) normal behaviour laws for dry joints.

For the S. Lázaro bridge scenario 3 (after rehabilitation) the parameter definition has also taken in account the experimental results observed in laboratory tests of mortared block joints. However, the behaviour of joints after repointing showed insignificant increase of cohesion and, therefore, elastic-plastic behaviour was considered also for these joints.

3.3 Dynamic Characteristics

Table 4 includes the values for the first five frequencies and the types of vibration modes calculated and experimentally identified for scenario 1 (after the rehabilitation). Concerning the experimental measurements, the frequency figures are given in terms of range of values, because modal identification was made using more than one method as reported elsewhere [2].

However, it is quite apparent that boundary values for each frequency are very close, thus supporting the validity of experimental findings.

The numerical dynamic characteristics were calculated through the detailed 3D model included in Figure 3.

The dynamic characteristics' results calculated for the scenario 2 (before the rehabilitation) model are also included in Table 4. These results were obtained by the simpler 2D finite element model (Figure 4), therefore not allowing computing transversal modes, but it is clear the frequency drop from scenarios 1 (after the rehabilitation) to 2 (before the rehabilitation).

Table 5 includes the dynamic characteristics' results in-situ measured and numerically calculated for the Lagoncinha bridge.

Identified Frequencies (Hz)	Numerical Frequencies (Hz)		Type of vibration mode
	Scenario 1	Scenario 2	
7.70 – 7.80	7.7	-	1st mode (transversal)
10.47 – 10.60	11.7	-	2nd mode (transversal)
12.70 – 12.96	12.9	8.3	3rd mode (longitudinal)
14.20 – 14.47	14.1	-	4th mode (transversal + torsion)
15.37 – 15.71	15.5	11.8	5th mode (vertical)

Table 4: In-situ measured and numerically calculated dynamic characteristics of the S. Lázaro bridge.

Identified Frequencies (Hz)	Numerical Frequencies (Hz)	Type of vibration mode
3.81	3.92	1st mode (transversal)
4.78	4.69	2nd mode (transversal)
5.48	5.33	3th mode (transversal)

Table 5: In-situ measured and numerically calculated dynamic characteristics of the Lagoncinha bridge.

4 MODELLING OF ROAD TRAFFIC MOVING LOADS

The loads transmitted by vehicles to a bridge consist of moving vertical loads corresponding to each vehicle axel. These loads should be considered as dynamic actions, since, on the one hand, the vehicle traffic with a specific speed on the bridge deck is likely to introduce potentially larger effects than those due to an equal intensity statically applied load (dynamic amplification effects) and, on the other hand, the pavement surface irregularities might trigger impacts on the deck which can further amplify the traffic dynamic effects.

One of the strategies for modelling vehicle loads in the dynamic behaviour of bridges consists on the application of a sequence of vertical concentrated forces. In this case, the vehicle mass is not involved in the numerical model. This load modelling simplification is valid when the vehicle mass is much lower than the total bridge mass and when the speed is not very high. These two conditions are generally met for stone masonry arch bridges but, when this is not the case, the vehicle load model has to be represented by a set of concentrated masses. This procedure implies the system mass updating at each time step of the analysis [8], which renders the numerical simulation more time consuming.

Within the analysis of S. Lázaro and Lagoncinha bridges, the first above mentioned strategy was adopted for studying the dynamic behaviour due to the moving loads. A set of vertical concentrated forces was therefore imposed including the effects of interaction between vehicle wheels and the bridge caused by the pavement surface irregularities and by the vehicle dynamic behaviour.

4.1.1. Bridge-vehicle interaction

The interaction between the wheel and the pavement is considered through a simplified methodology comprising three phases of analysis where the two systems (bridge and vehicle) are studied separately. The first phase consist on the bridge numerical modelling to simulate the vehicle action through a series of concentrated loads applied on the pavement (phase 1). This phase allows evaluating the time history of pavement settlements in accordance with the moving load application points. In the subsequent phase (phase 2), the dynamic analysis of the vehicle is carried out to determine the influence of the pavement irregularities added-up with the previous pavement settlement on the vehicle dynamic behaviour. Therefore, new values of the moving loads are obtained in phase 2, corresponding to the forces (reactions) in the contact wheel/deck surface to be used in the subsequent bridge analysis. Finally, phase 3 consists on a recalculation of the bridge considering the moving load values amplified due to the dynamic behaviour of the vehicle, thereby involving both the interaction vehicles/bridge and the effect of pavement irregularities [9].

4.1.2. Irregularities of the pavement

The pavement irregularities of S. Lázaro and Lagoncinha bridges (see Figures 7a and 7b) were recorded along two parallel axes in the deck longitudinal direction by performing a scan with a laser profilograph installed in a commercial vehicle as illustrated in Figure 7c. The scan sampling interval was taken as 0.025m and the acquisition was made during the vehicle ride centred in the deck at an approximately constant speed of 20km/h. A low-pass filter was applied during the acquisition with cut-off frequency corresponding to a wavelength of 100m. The measured signals were corrected adopting usual procedures for such applications [9]. The obtained upstream irregularity profiles in the S. Lázaro and Lagoncinha bridges are shown in Figure 8a and b.

The characterization of the profile amplitude of irregularities in the pavement along the deck of the bridges allowed observing the presence of amplitudes with about 0.015m.

a) b) c)

Figure 7: Pavement surface of a) S. Lázaro and b) Lagoncinha bridges. a) Equipment for measuring the irregularity profile.

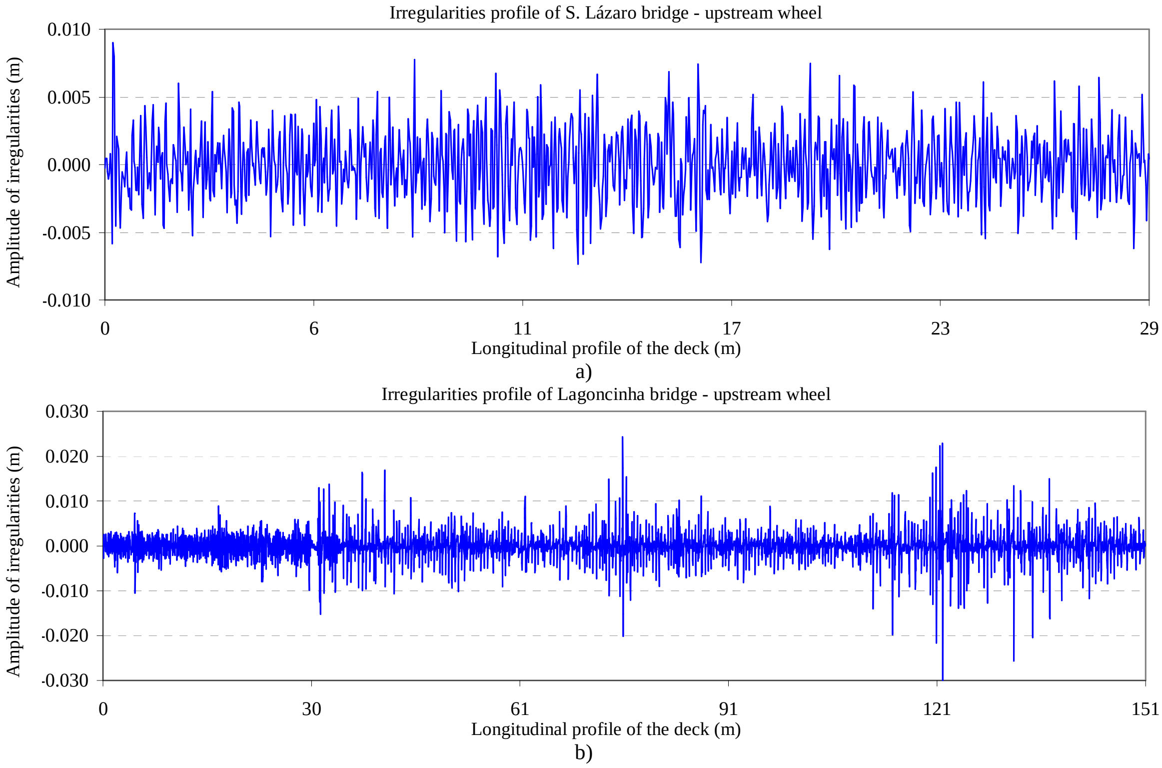

Figure 8: Profile of in-situ irregularities of a) S. Lázaro and b) Lagoncinha bridges.

4.1.1. Vehicle model

The vehicle modelling was carried out resorting to the CAST3M computer software by using 3D bar elements to discretize the axles of the vehicle (tires and suspension) and the corresponding masses were concentrated in the respective nodes. Thus, the springs corresponding to the vehicle suspensions and the contact between wheels and pavement were replaced by beams with no mass and axial stiffness and damping in accordance with the characteristics of these elements and considering a negligible bending stiffness. The rigid body, composed by the tractor and trailer, was simulated by horizontal plan elements with distributed mass and inertia and high bending stiffness. The connection points between the vehicle body and the axles were simulated by vertical bars with negligible bending stiffness and large axial stiffness.

The dynamic characteristics of the vehicle numerical model correspond to global modes for the first three frequencies: the 1st and 2nd are longitudinal modes while the 3rd is a transverse one, with natural frequencies of 1.6, 2.5 and 3.3Hz, respectively. The remaining modes are local ones involving the vehicle axles with frequencies between 12.7 and 14.4Hz for the 4th and 10th modes, respectively.

Taking into account that higher dynamic effects tend to occur when there is coincidence between natural frequencies of the bridge and vehicles ([10] cited by [8]), Table 6 includes the comparison between the vehicle natural frequencies and the bridge frequencies associated with the first transverse and vertical modes determined by ambient vibration tests.

It is observed that frequencies relevant to the vehicles (between 1.6 and 3.2Hz, associated with vehicle body motions) are lower than those estimated for the natural frequencies of bridges associated with the transverse components of bridge movements.

The range of vehicle higher frequencies (between 12.6 and 14.4Hz, concerning the vibration modes related to vehicle axles motions) is closer to the range of bridge frequencies relative to vertical modes, but the vehicle response has less energy content for this range of frequencies, which means that the higher energy content recorded in the vehicle response deviates from resonance with the bridge structure.

Mode type:	1st long.	2nd long.	1st trans.	1st vert.	7th vert.	Mode type:	1st trans.	1st vert.
4-axle truck	1.6	2.5	3.3	12.7	14.4	Lagoncinha bridge	3.9	11.3
						S. Lázaro bridge	7.7	15.5

Table 6: Frequency (Hz) and mode types of vehicles and masonry arch bridges

Considering the measured roughness distribution, the range of irregularities' wavelengths (λ) likely to contribute for the vehicle excitation in the frequency (*f*) interval from 1.6 to 14.4 Hz and assuming vehicle speed (ν), between 12 and 90 km/h, corresponds to λ within 0.23m and 6.15m as obtained by the expression $\lambda = v / f$).

The observation of the spectral densities determined by Fast Fourier Transform (FFT) of the roughness profile showed that the largest amplitude of the spectra occurs in the range of wavelengths between 0.08m and 0.2m, thus shifted away from the range of wavelengths most significant for the vehicle excitation.

5 RESULTS ANALYSIS OF THE BRIDGES BEHAVIOUR UNDER THE ROAD TRAFFIC CONSIDERING DIFFERENT APPROACHES

5.1 Bridge behaviour under road traffic moving loads

In order to evaluate the result sensitivity of the bridge response to the vehicle speed, effects of irregularities and type of calculation considered in the bridge numerical simulation, particularly concerning static vs. dynamic and linear vs. nonlinear analysis, several analysis were performed to study the influence of moving loads on the bridges.

For the S. Lázaro bridge, in case I linear static analysis was performed in two phases (1 and 3) of the structural calculation. In case II, the dynamic behaviour was activated in both phases, but assuming a linear material. In cases III and IV the material nonlinear behaviour was taken into account, case III involving static calculations and case IV including also the activation of the dynamic behaviour. For each case, the following four speed values were considered: 13, 30, 60 and 90km/h.

For the Lagoncinha bridge in the first calculation phase (phase 1) dynamic analyses were carried out considering the linear velocities of 20, 30, 60 and 90km/h.

In the analyses including the roughness effects (phase 3) three calculation options were considered. One of the options held also linear dynamic analysis. In two cases, the nonlinear behaviour of materials was considered, in one case, performing nonlinear dynamic analysis and, on the other, non-linear static analysis. The speed of 90km/h was considered in the cases where the dynamic behaviour was activated in phase 3. The option for this speed value drive from the fact that a smaller number of steps is needed for the load history and, consequently, the required time for the 3D bridge analysis decreased.

In all cases the study of vehicle response (phase 2) was based on linear dynamic analysis.

Numerical integration of dynamic equations was made resorting to the Newmark scheme and the non-linearity was solved using the classical Newton-Raphson method.

Figure 9 shows the results in terms of the influence lines of de vertical displacement on the principal arch of the S. Lázaro bridge (at the node P1 for which the maximum arch vertical displacement was found). Dynamic linear and nonlinear analyses were performed in the two calculation phases (phase 1 - without irregularities and phase 3 - with irregularities) considering the 2D bridge model shown in Figure 4.

The influence lines show that the maximum arch displacement occurs considering the speed of 30km/h when the vehicle front axle is placed on the section at 22.6m (from the left abutment) which corresponds to a step after the first three axles of the vehicle had passed over the crown section.

Aggravation coefficients were evaluated between the results obtained in phase 1 (without irregularities) and in phase 3 (with irregularities) concerning the maximum displacement in arch 1 for 30km/h speed. Adopting the same analysis type in the two phases and considering the irregularity effects (phase 3), displacements are 1.6 to 6.7% larger than those obtained in the analysis without irregularity effects (phase 1). This aggravation trend observed in the arch occurs also in other bridge elements.

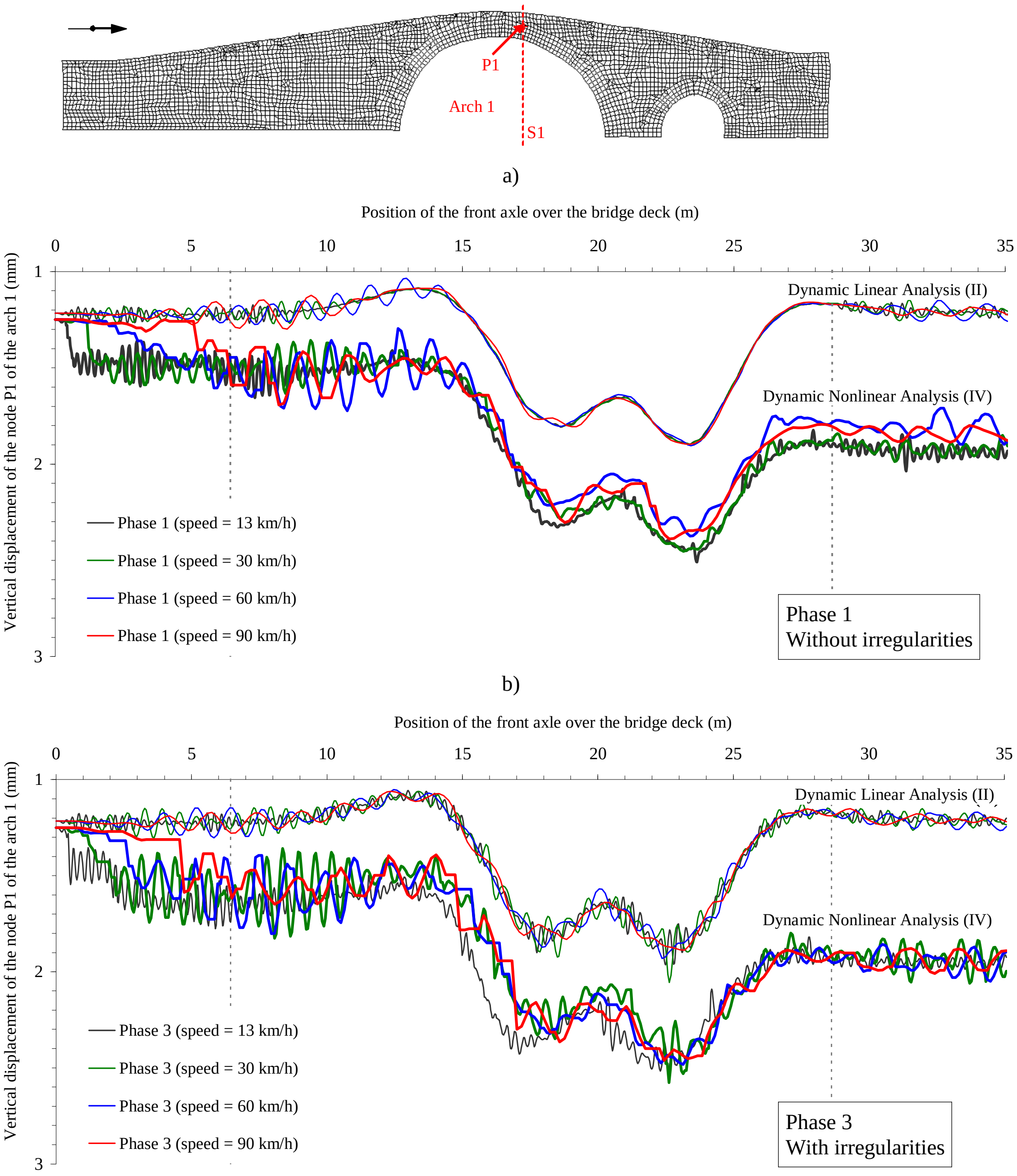

a)

b)

c)

Figure 9: Influence lines of the vertical displacement at the node P1 at Arch 1 (a) for the speed of 13, 30, 60 and 90 km/h, results from cases II and IV of phase 1 (b) and phase 3 (c).

The maximum displacement of 2.6 mm was obtained in phase 3 (with irregularities) considering the analysis where the nonlinear behaviour of materials is activated in the two phases. Comparing the maximum displacement obtained in the nonlinear static analysis with the effects of irregularities (phase 3) and the displacement obtained in the linear static analysis without the effects of irregularities (phase 1) it was found an aggravation of about 37.4%.

The comparison of the influence line obtained from nonlinear dynamic analysis with that obtained from nonlinear static analysis shows that the displacement of node P1 is lower in the latter case only when loads are at the bridge entrance. By contrast, in the remaining path, the results are quite similar to those obtained considering dynamic behaviour, thus showing that the consideration of the dynamic calculation has little influence on the response of this bridge.

The results show also greater dynamic component in the vertical displacement of the node P1 when the moving loads are in the entry and exit zones of the bridge, rather than in the arch neighbourhood. Therefore, considering the position of the moving loads in relation to the node P1, it is concluded that the vibration recorded on the arch follows the vibration transmitted by the infill.

The study of the Lagoncinha bridge behaviour showed that the linear dynamic response of the bridge under the moving loads without including the irregularities in the pavement (phase 1) exhibits very low dynamic components, therefore, the maximum displacement of the arch (at the node P1 where the maximum displacement on that arch is found, see Figure 10) is almost independent of the speed. When the roughness profile is considered in the contact wheel-pavement (phase 3), oscillations appear in the influence line of the vertical displacement denoting the presence of more significant dynamic components, however the aggravation caused by adding the irregularities to the settlements' profile is not significant, increasing only by 2% the vertical displacement for 20 km/h speed (see Figure 10).

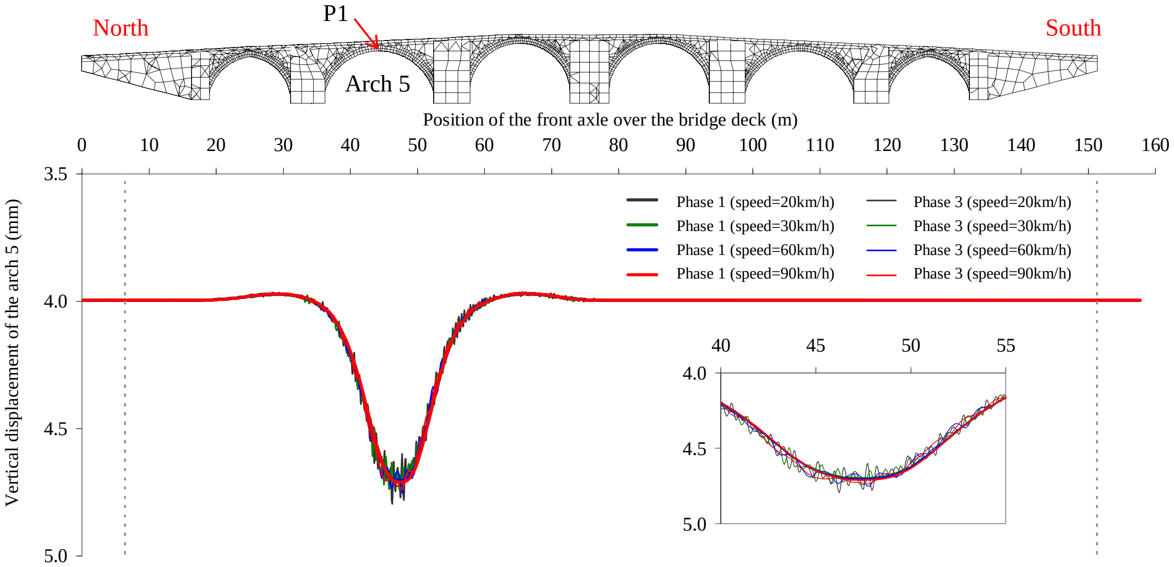

Figure 10: Influence lines of the vertical displacement. Linear dynamic response of the bridge for moving loads with and without the effect of irregularities (Phase 1 and phase 3, respectively).

In the case of nonlinear dynamic response for 90 km/h speed with irregularities, it was found that the value of the maximum vertical arch displacement (7.57 mm) increases about 60% when compared with the value (4.74 mm) obtained from linear dynamic calculation. Through the static nonlinear analysis it was found also that the maximum vertical displacement obtained (7.54 mm) is 0.4% lower than the maximum displacement resulting from the nonlinear dynamic calculation. As in the case study of S. Lázaro bridge, it is observed that the consideration of material nonlinear behaviour produces a significant effect on the maximum displacement of the bridge main arch and less influence is found when the bridge dynamic behaviour is taken in account.

In order to evaluate the influence of the loading history on the response of the two bridges, the maximum vertical displacement of the arches obtained from the nonlinear dynamic calculation with irregularities $d_v^{dy\,nl}$ are compared in Table 7 with similar results obtained from a nonlinear static analysis $d_v^{est\,nl}$, but considering identical positions and values for the static loads. It is verified that the vertical displacement obtained considering the load history is 22% and 12% larger than that determined by static analysis of the S. Lázaro and Lagoncinha bridges, respectively, allowing the conclude that the entire history of loading is important to evaluate the structural response.

	$d_v^{est\,nl}$	$d_v^{dy\,nl}$	
S. Lázaro bridge (arch 1)	2.11	2.58	(+22%)
Lagoncinha bridge (arch 5)	6.70	7.57	(+12%)

Table 7: Maximum vertical displacement of the arch (mm). Static load position *vs.* moving loading model.

5.2 Bridge behaviour under incremental static loads

Considering the vehicle at the most unfavourable load position for the arch identified previously from the analysis of the bridge considering the moving loading, this section focuses on the relevant aspects of the bridge response considering the nonlinear behaviour of joints and infill and intensity load levels (multipliers) of one and twice the nominal vehicle load.

The evolution of the response parameters in terms of maximum vertical displacement and principal stresses on the arch blocks, concerning the effect of the bridge weight and the intensity levels of the vehicle load of 1P and 2P, can be evaluated through the results included in Table 8. For these load levels, Table 8 includes the response parameters of the joints of the arch in terms of normal and shear stresses (maximum) and the corresponding maximum values of the normal and tangential deformations.

Comparing the results of 2D and 3D simulations, good agreement is observed in the longitudinal direction behaviour parameters. Given the effects of the dead load, it is verified that opening of transverse joints between the arch blocks does not occur. This also means that no incursions occur in the nonlinear range for the normal direction; since these joints have zero tensile strength, shear yielding is not triggered as well.

In the longitudinal joints of the arch (modelled only in 3D models) there were opening deformations. In the bridge transverse direction, that fact indicates the effect on the arch which induces impulses in the spandrels, leading to opening movements and decompression in the transverse direction. This aspect is not represented in 2D modelling and is not well reproduced in 3D linear calculation, because in the latter the stress transmission is kept even when separation occurs at the interfaces between the bridge elements. In the longitudinal arch joints, plastic components of the sliding joint deformation (shear yielding) are also observed.

The inclusion of the vehicle action shows that, in the arch transverse joints, normal opening deformations occur in tensioned areas but without forming a hinge mechanism, which is consistent with the smooth functioning of the arch in this scenario.

The existence of plastic deformations in the infill, only in a limited area under the loading in both 3D and 2D modelling, also adds to the confirmation of the smoothening effect of the infill.

Loads	3D σ_1^+	3D σ_3^-	3D d_v	2D σ_1^+	2D σ_2^-	2D d_v		3D $\sigma_n^{máx}$	3D σ_n^{min}	3D $\delta_n^{máx}$	2D $\sigma_n^{máx}$	2D σ_n^{min}	2D $\delta_n^{máx}$
DL	0.12	-0.48	1.35	0.04	-0.57	1.48	(t)	-0.03	-0.40	0.00	-0.01	-0.43	0.00
							(l)	0.00	-0.02	0.08	-	-	-
DL+1 x 4-axles truck	0.20	-0.65	2.42	0.07	-0.69	2.50	(t)	0.00	-0.61	0.04	0.00	-0.59	0.05
							(l)	0.00	-0.05	0.11	-	-	-
DL+2 x 4-axles truck	0.31	-0.94	3.61	0.12	-0.90	3.70	(t)	0.00	-0.86	0.09	0.00	-0.85	-0.06
							(l)	0.00	-0.09	0.02	-	-	-

DL – Dead load; (t) Transversal joints; (l) Longitudinal joints; - joints not considered in the 2D model

Table 8: Principal stresses in blocks and joints (MPa) and maximum displacement (mm) and deformations in joints of arch 1. Results from 3D and 2D models.

Figure 11 shows the distributions minimum principal stresses of the blocks in the deformed configurations corresponding to dead load plus the vehicle loading (at level 2P) considering behaviour scenarios 2 and 3 as reported before. In these conditions, it is possible to identify the formation of a four hinge mechanism when the infill consists of a weak material (scenario 3). The joints where the hinges are formed are identified in the figures with the letters A, B, C and D.

For the scenario 2 the identification of the nodes in which no contact occurs allows recognizing the (potential) location of the hinges corresponding to one mechanism; in this case, the nodes with no contact between blocks are located in the intrados of the arch under the loaded zone and near the abutment of the arch, and in the extrados around the ¼ to ¾ of the span. It should be noted, however, that the bridge exhibits a high load capacity for the conditions considered in scenario 1. It is noteworthy that the bridge analysis was continued by increasing the loading intensity of the vehicle up to 10P, for which no hinge was formed.

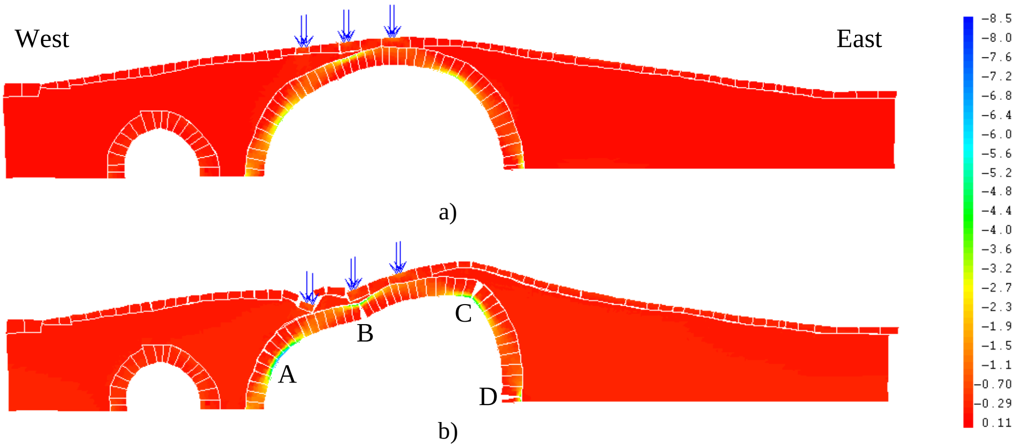

Amplification factor of the deformed = 4

Figure 11: Minimum principal stresses (MPa) and deformed configurations of the bridge under dead loads and vehicle loading for level 2P. a) Scenario 2 e b) scenario 3.

Finally, Figure 12 shows the distributions of the vertical components of the plastic deformation in the infill; the corresponding values of the maximum and minimum plastic strains and total deformations in the infill are included in Table 9.

As evidenced by the values of Table 9b (scenario 3), plastic deformations take place in the infill, for the three load levels. Taking in account the distribution of the vertical components of the plastic deformation shown in Figure 12b, it is verified that such fact influences the interaction between the arch and the infill material. In the arch extrados zone, near the hinges A and C, the filling material yields and, consequently, deformations increase which allows arch joint opening in that zone.

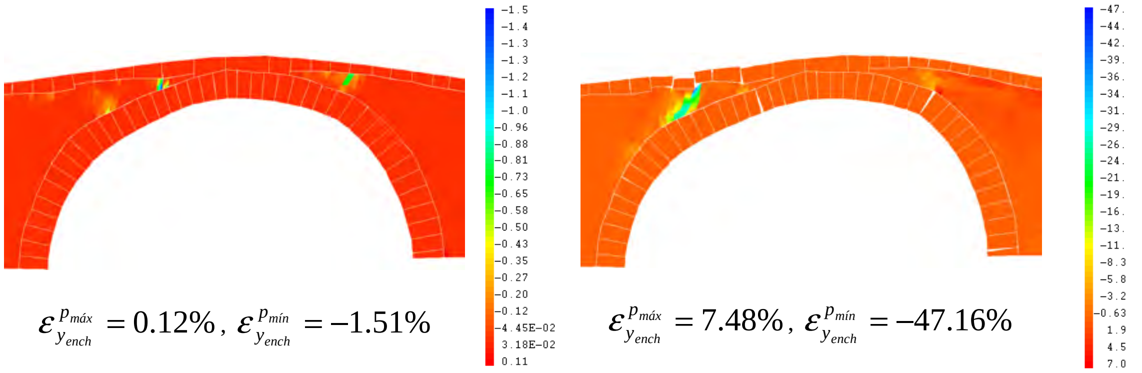

a) b)

Amplification factor of the deformed = 1

Figure 12: Plastic deformation (%) in the infill under dead loads and vehicle loading for load level of 2P. a) Scenario 2 e b) scenario 3.

Loads		a)				b)			
		ε_x^{tot} (%)	ε_y^{tot} (%)	ε_x^{p} (%)	ε_y^{p} (%)	ε_x^{tot} (%)	ε_y^{tot} (%)	ε_x^{p} (%)	ε_y^{p} (%)
DL	(máx.)	0.05	0.00	0.00	0.00	1.32	0.04	1.32	0.01
	(mín.)	-0.08	-0.15	0.00	0.00	-0.85	-1.93	-0.02	-0.93
DL +1 x RSA vehicle	(máx.)	1.40	0.04	1.38	0.00	15.76	0.96	15.61	0.78
	(mín.)	-0.12	-0.82	0.00	-0.74	-1.24	-20.08	-0.69	-11.43
DL +2 x RSA vehicle	(máx.)	3.99	0.14	3.98	0.12	65.00	7.48	64.27	7.48
	(mín.)	-0.28	-1.73	-0.06	-1.51	-4.58	-63.90	-3.90	-47.16

Table 9: Total deformation and plastic deformations in the infill under dead loads and vehicle loading. a) Scenario 2 e b) scenario 3.

Comparing the response of the bridge with weak infill material (scenario 1) with the bridge response in scenario 2 under identical conditions but with better filling material, it is observed that the presence of the infill material under better conditions restricts the formation of the hinge mechanism in the arch. By contrast, the infill plastic deformation in scenario 1, whose maximum and minimum values are included in the Table 9a and the corresponding distribution of the vertical components are illustrated in Figure 12a, shows that the infill material yielding occurs only in a very limited zone underneath the vehicle axles loading.

These facts explain the good behaviour of the bridge under the conditions considered in scenario 1, because the infill material prevents the formation of the hinges mechanism in the arch, restricting the joint opening in the arch extrados.

6 CONCLUSIONS

Throughout the previous sections some details were presented concerning the numerical simulation of a stone masonry arch bridge by finite element method modelling aiming at estimating the traffic effects due to moving loads and accounting for the pavement roughness.

In order to account for the interaction between the vehicle, the pavement roughness and the bridge, a simplified approach was followed comprising three distinct phases where the two systems (vehicle and bridge) were studied separately.

The bridge response shows that the activation of the material nonlinear behaviour has significant influence on the bridge effects (increase), however comparing the results with irregularities and without less influence is shown. The loading history produces also a significant effect on the maximum displacement of the main arch of the bridges (when comparing with the results from a static load position analysis).

The results show that the dynamic behaviour activation does not produce a significant effect on the maximum displacement of the main arch of the bridges. The study also allowed concluding that the dynamic effects are mainly due to the vehicle dynamic response, with negligible influence on the dynamic response of the bridge.

REFERENCES

[1] CEA, *Manuel d'utilisation de CAST3M*. by P. Pasquet, Commissariat à l'Énergie Atomique, 2003. http://www.cast3m.cea.fr .

[2] Costa, C., *Análise numérica e experimental do comportamento estrutural de pontes em arco de alvenaria de pedra*. PhD thesis, FEUP, 2009. (in Portuguese, available at site NCREP)

[3] IHRU, *Ponte de São Lázaro*. Sistema de Informação para o Património Arquitectónico - SIPA. Nº IPA: PT011315010002, 1998. http://www.monumentos.pt/Monumentos/.

[4] DGEMN, *Ponte da Lagoncinha*, Boletim da Direcção Geral dos Edifícios e Monumentos Nacionais, MOP, 1957. (in Portuguese)

[5] LNEC, *Ensaios de Mecânica das Rochas na Igreja do Mosteiro da Serra do Pilar*. Technical Report. Laboratório Nacional de Engenharia Civil, 2000. (in Portuguese)

[6] Costa, C., Arêde, A. and Costa, A., Dynamic Characterization of a Masonry Arch Bridge. 1st International Operational Modal Analysis Conference. AU-SVS-B&K, Copenhagen, 2005.

[7] Costa, C., Costa, P., Arêde, A. and Costa, A., *Structural design, modelling, material testing and construction of a new stone masonry arch bridge in Vila Fria, Portugal*. 5th International Conference on Arch Bridges (ARCH'07), 2007.

[8] Calçada, R, *Avaliação experimental e numérica de efeitos dinâmicos de cargas de tráfego em pontes rodoviárias*. PhD thesis, FEUP, 2001. (in Portuguese, available at http://aleph.fe.up.pt/)

[9] Costa, C., Arêde, A. and Costa, A., *Numerical simulation of stone masonry arch bridges behaviour under road traffic moving loads* 6th International Conference on Arch Bridges (ARCH'10), 2010

[10] OCDE, *Dynamic interaction between vehicles and infrastructure experiment (DIVINE)*. Paris, Organisation for Economic Co-operation and Development, 1998.

COMPDYN 2011
III ECCOMAS Thematic Conference on
Computational Methods in Structural Dynamics and Earthquake Engineering
M. Papadrakakis, M. Fragiadakis, V. Plevris (eds.)
Corfu, Greece, 25–28 May 2011

DAMAGE DETECTION IN PLATE USING GRADIENT SEARCH SENSITIVITY METHOD OF FE MODEL UPDATING

Rohan Soman[1], **Jyoti K. Sinha**[2]
[1] School of Civil Engineering and Geomatics,
Cyprus University of Technology, Limassol, Cyprus
e-mail: rohan.soman@cut.ac.cy

[2] School of MACE, The University of Manchester
Sackville Street, Manchester M13 9PL, UK
Email: Jyoti.Sinha@manchester.ac.uk

Keywords: Damage Detection, Finite Element Model, Modal Analysis, Model Updating Method.

Abstract. *Damage Detection in the structure is an active research area since decades. Number of the research studies has been done to meet this objective, particularly, the identification of the damage size and location. The finite element (FE) updating methods have also been used in the literature for the damage size and location identification. However, most of the studies are generally related to the beam type structures with the crack/damage. This concept has now been extended to the plate type structure with damage. Here again, the modal properties (natural frequencies and mode shapes) of the damaged plate have been used to estimate the damage size assuming the location of the damage was known. In the present study, the damage in the plate has been simulated in the FE model of the plate by the reduction in the plate thickness in the small portion of the plate and then the thickness of the plate has been chosen as the updating parameter. The Gradient Search based Sensitivity Model Updating method has then been applied to calculate the plate thickness for the damaged area from the FE model of the healthy plate (without damage). The proposed method has been examined on a simple simulated example of a steel plate. The paper presents the proposed method and the result from a simulated example.*

1 INTRODUCTION

Accurate condition assessment of engineering structures has become increasingly important. Current damage detection methods are either visual or localised experimental methods such as acoustic or ultrasonic methods, magnetic or thermal field methods, etc. [1]. All of these experimental techniques require that the vicinity of the damage is known a priori and that the portion of the structure being inspected is readily accessible. Furthermore, these tests are cumbersome and expensive. The need for quantitative global damage detection methods that can be applied to complex structures, has led to the development of methods that examine changes in vibration. Doebling et al. [2] give an extensive overview of vibration-based detection methods. The vibration characteristics of a structure are the function of its damping, stiffness and mass which in turn are a function of the condition of the structure. Among the various dynamic parameters which are used for damage detection, modal frequency and mode shape are the ones most commonly used. Salawu [3] presents a review on the use of modal frequency changes for damage diagnostics. It was later on confirmed that the modal frequencies are insensitive to the local condition of the structure and as such has limitations for damage isolation. In order to isolate the damage, mode shapes are necessary, which increase the data handling as well as increased instrumentation for accurate measurement. In order to overcome these shortcomings, several different parameters were studied, like the mode shape curvature [4-5], dynamically measured flexibility [6-7], damping [8-9] etc. All the monitored parameters have their set of advantages and disadvantages and the search of an elusive method which can overcome all the problems faced during damage detection is still on.

In recent years, sensitivity-based Finite Element (FE) model updating has been successfully used for damage assessment. In general, FE model updating aims at adjusting the dynamics of the mathematical model so that it becomes close to the experimental model. Many methods have been proposed for the updating of the mathematical model [10]. Some of the methods are direct while others are iterative. The direct methods compute a closed-form direct solution for the global stiffness and/or mass matrices using the structural equations of motion and the orthogonality equations. The changes made in the global matrix do not often make any physical sense. The iterative methods update the physical model variables like the Young’s modulus, density, thickness, etc. by minimising the differences between the numerical and experimental vibration data. This gradient based sensitivity approach is an iterative process making use of updating variables to alter the stiffness matrix so as to achieve matching dynamics of the mathematical and the experimental models.

The present paper deal with determination of the extent of damage in plates using the gradient search sensitivity based approach when the location of damage is assumed to be known. The FE model of the plate was developed in the commercial FE code ABAQUS. The computed modal parameters have then been integrated with the computational code developed in the MatLab to calculate the sensitivity matrix and the updating parameter (plate thickness) by minimising the error in the penalty function by the iterative process till the problem converges to the required solution. The proposed method has been examined on a simple simulated example of a steel plate. The paper presents the proposed method, results from a simulated example and possible extension of proposed method to identify damage location as well as its size to meet the requirement of Level 3 in Damage Detection.

2 THEOROTICAL BACKGROUND

The error function at *n*th iteration is given by [10]

$$\boldsymbol{\varepsilon}_n = \boldsymbol{\delta}\mathbf{z}_n - \mathbf{S}_n \boldsymbol{\delta\theta}_n \tag{1}$$

where, $\boldsymbol{\delta}\mathbf{z}_n$ is the vectors of the eigen values error between the calculated experimental natural frequencies and corresponding computed natural frequencies from the FE model assuming only modes are used for this purpose.

$\boldsymbol{S}_n$ is the sensitivity matrix which is the first derivative of the eigenvalues with respect to the updating parameters

$\boldsymbol{\delta\theta}_n$ is the change in the updating parameter at the n^{th} iteration.

The size of the sensitivity matrix depends on the number of updating parameters and number of modes used for this purpose. The penalty function (*J*) at the n^{th} iteration is given by

$$J(\boldsymbol{\delta\theta}) = \boldsymbol{\varepsilon}_n^T \mathbf{W} \boldsymbol{\varepsilon}_n \tag{2}$$

where ***W*** is the positive diagonal weighing matrix. The vector of the updating parameters can be calculated by minimizing *J* with respect to $\delta\theta$ which involves differentiating of *J* with respect to each element of $\delta\theta$ and setting the result equal to 0. The solution obtained at each step is a weighted least square solution. Finally this leads to the following equation for the vector of updating parameters at each iteration.

$$\boldsymbol{\theta}_{n+1} = \boldsymbol{\theta}_n + (\mathbf{S}_n^T \mathbf{W} \mathbf{S}_n)^{-1} \mathbf{S}_n^T \mathbf{W} (\boldsymbol{\delta}\mathbf{z}_n) \tag{3}$$

The iterative process will be carried out till the targeted accuracy is reached. The target accuracy determines the computational effort needed to be put in and the target should be optimal to ensure efficient computation. The elements of the sensitivity matrix can be computed as [10-12].

$$\mathbf{S}_{i,j} = \frac{\partial \lambda_{ci}}{\partial \theta_j} = \boldsymbol{\varphi}_i^T \left[\frac{\partial \mathbf{K}}{\partial \theta_j} - \lambda_{ci} \frac{\partial \mathbf{M}}{\partial \theta_j} \right] \boldsymbol{\varphi}_i \tag{4}$$

where, $\mathbf{S}_{i,j}$ is the element of the sensitivity matrix for the computed *i*th eigenvalue (λ_{ci}) w.r.to the *j*th updating parameter (θ_j). The system matrix, **K, M** are the stiffness and mass matrices respectively and $\boldsymbol{\varphi}_i$ is the normalized eigenvectors for the *i*th mode.

3 EXAMPLE

A test plate of 1.2 × 1.2 m and thickness of 1mm has been considered. The material of the plate was assumed to be steel with Young’s Modulus 210GPa, Poisson’s ratio 0.33 and density 7800kg/m^3. For the simulated example, the plate is divided into 9 elements as shown in Figure 1(a) and all the 4 edges of the plate were assumed to be fixed supports. It has also been assumed that the Nodes 1 to 4 are measured location for vibration during modal testing using tri-axial accelerometers. Hence the measured degree of freedoms (DoFs) at each measurement node is 3 (2 in plane and 1 out of plane). The thickness of the element 1 is assumed to be 0.8mm (20% less from the original thickness of 1mm) which represents the damage in the plate.

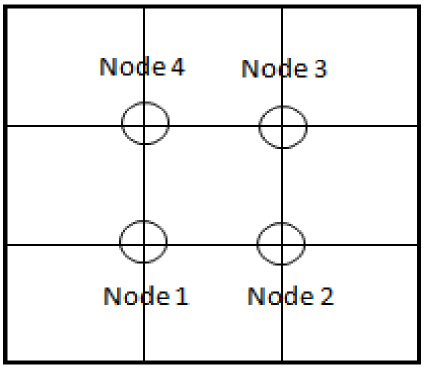

(a) Plate with 4 nodes for vibration measurement

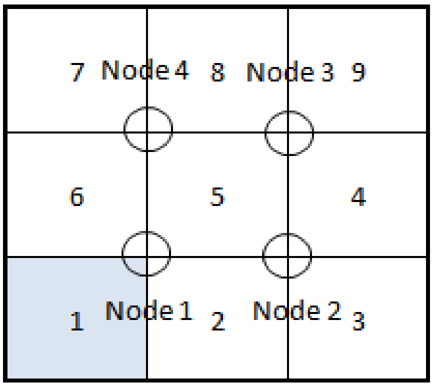

(b) Damage in Element 1 asuumed

Figure 1 Simulated example of a damage plate

An FE model of the simulated example of a damage plate shown in Figure 1 has also been constructed in the FE code ABAQUS which is shown in Figure 2. The FE model has then been used to calculate the natural frequencies and the mode shapes related to 12 DoFs at 4 measurement locations shown in Figure 1. The calculated natural frequencies are assumed as the experimental natural frequencies (Target data) which are listed in Table 1.

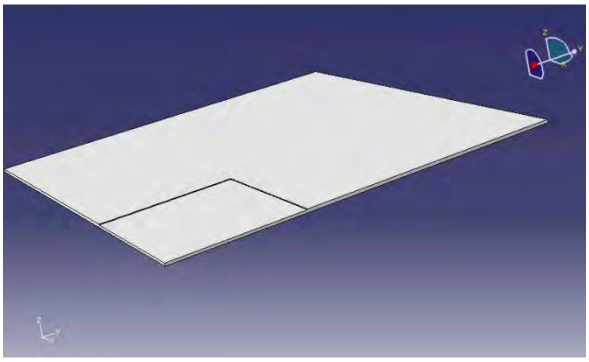

(a) Plate geometry in FE model

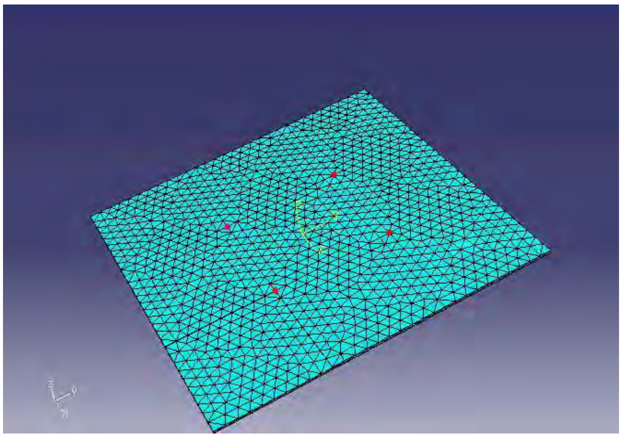

(b) FE mesh

Figure 2 An FE model of the plate shown in Figure 1

3.1. Damage Detection

Now it has been assumed that the damage location is known but the extent of the damage is unknown. Hence the flexural rigidity of the plate $\left(D = \frac{Et^3}{12(1-\nu^2)}\right)$ has been chosen as the updating parameter. It is because the flexural rigidity is nearly proportional to the plate stiffness matrix, **K**. A computation program has also been written the MatLab code to calculate the sensitivity matrix using Equation (4) based on the calculated natural frequencies and the modeshapes (eigenvalues) at the measured 12 DoFs and then iterative process as per Equation (3). Initial guess of the damage is assumed to be 0.7mm to start the iteration. The first 6 modes are used for this iterative process. The natural frequencies for initial guess are also listed in Table 1. At the end of each iteration, the change in the updating parameter, *dD,* is converted to the change in the plate thickness, *dt*, as

$$dt = \sqrt[3]{\frac{12dD(1-\nu^2)}{E}} \tag{5}$$

The calculated new thickness of the plate is then used into the FE model to estimate natural frequencies and mode shapes for the next iteration. The process is continued still convergence. Table 1 list the updated thickness and natural frequencies with iteration and the error at each mode with iterations in Table 2 and graphically in Figure 3 which confirms the success of the iterative technique proposed.

Table 1 Updating parameter and the natural frequencies with iterations

Iteration		1	2	3	4	5
Extent	0.8	0.7	0.73	0.75	0.77	0.8
Mode 1	280.411	281.343	281.618	280.703	280.755	280.523
Mode 2	589.161	590.495	591.287	589.201	589.186	589.159
Mode 3	597.970	601.914	603.244	599.809	598.957	597.796
Mode 4	846.398	851.671	854.073	848.879	848.099	847.038
Mode 5	1030.060	1034.770	1035.840	1032.180	1030.870	1030.670
Mode 6	1053.130	1060.240	1061.600	1057.020	1054.480	1053.880

Table 2 Error at each mode with iterations

Iteration	1	2	3	4	5
Extent	0.7	0.73	0.75	0.77	0.8
Mode 1	-0.332	-0.430	-0.104	-0.123	-0.040
Mode 2	-0.226	-0.361	-0.007	-0.004	0.000
Mode 3	-0.660	-0.882	-0.308	-0.165	0.029
Mode 4	-0.623	-0.907	-0.293	-0.201	-0.076
Mode 5	-0.457	-0.561	-0.206	-0.079	-0.059
Mode 6	-0.675	-0.804	-0.369	-0.128	-0.071

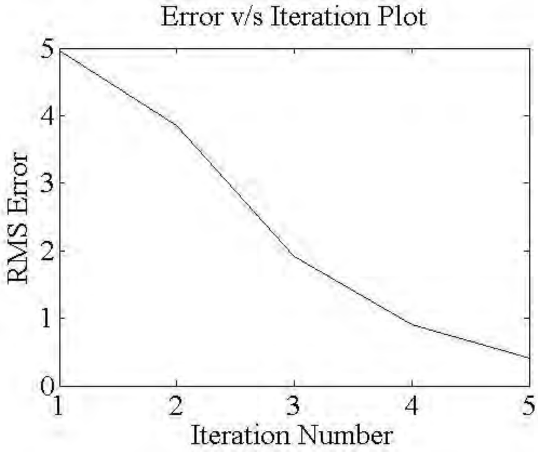

Figure 3 Iterative process showing convergence

4 CONCLUSION

The model updating method has been proposed to find the extent of damage in a plate type structure. The proposed method has been validated through a simple simulated example but it needs further validation through the experimental examples to enhance the confidence level in the proposed method. Currently just one updating parameter has been used but the proposed method can further be extended such that it can identify both location and size of damage in the plate.

REFERENCES

[1] Teughals, A, Maeck, J, Roecke, D. Damage Assessment by FE Model Updating using damage functions, *Computers and Structures 80 1869–1879,* 2002

[2] Doebling SW, Farrar CR, Prime MB. A summary review of vibration-based damage identification methods. *Shock Vibration Digest ;30(2):91–105.*1998

[3] Salawu OS. Detection of structural damage through changes in frequency: a review. *Engineering Structures;19(9):718–23,* 1997

[4] Pandey, A. K., Biswas, M., and Samman, M. M., Damage Detection From Changes In Curvature Mode Shapes, *Journal of Sound and Vibration*, *Vol. 145, No. 2, pp. 321–332,* 1997

[5] Chance, J., Tomlinson, G. R., and Worden, K., A Simplified Approach To The Numerical And Experimental Modelling Of The Dynamics Of A Cracked Beam, *Proc. of the 12th International Modal Analysis Conference, pp. 778–785,*.1994

[6] Pandey, A. K., and Biswas, M. Damage Detection In Structures Using Changes In Flexibility, *Journal of Sound and Vibration*, *Vol. 169, No. 1, pp. 3–17,* 1994

[7] Peterson, L. D., Alvin, K. F., Doebling, S. W., and Park, K. C. "Damage Detection Using Experimentally Measured Mass And Stiffness Matrices". *Proc. of 34th AIAA/ASME/ASCE/AHS/ASC Structures, Structural Dynamics, and Materials Conference, AIAA-93-1482-CP, pp. 1518-1528,*1993

[8] Zonta, D., Modena, C., and Bursi, O.S."Analysis of Dispersive Phenomena in Damaged Structures," *European COST F3 Conference on System Identification and Structural Health Monitoring, Madrid, Spain, pp. 801–810*, 2003

[9] Curadelli, R, Riera, J, Ambrosini, D, Amani, M,"Damage Detection by means of Structural Damping Identification", *Conf. Proceedings of Engineering Structures 30, pp 3497-3504.*2008

[10] Mottershead, J. E. and Friswell, M. I. Model Updating in Structural Dynamics: A survey. *Journal of Sound and Vibration, vol. 167, No. 2, pp 347-375*, 1993

[11] Sinha, J. K. and Friswell, M. I. The Use Of Model Updating For Reliable Finite Element Modelling And Fault Diagnosis Of Structural Components In Nuclear Power Plant. *Elsevier Science Publication,* 2003

[12] Sinha, J. K. , Mujumdar, P. M. and Moorthy, R. I. K. A Parameter Identification Technique For Detection Of Spacer Locations In An Assembly Of 2 Coaxial Flexible Tubes, *Elsevier Science Publication,* 2000

COMPDYN 2011
III ECCOMAS Thematic Conference on
Computational Methods in Structural Dynamics and Earthquake Engineering
M. Papadrakakis, M. Fragiadakis, V. Plevris (eds.)
Corfu, Greece, 25–28 May 2011

An investigation on the value-based evaluation: optimum rehabilitation process of the unreinforced masonry buildings

Behnam Mahzoun Azmoodeh[1], **A.S.Moghadam**[2]

[1] Msc. Graduate, University of Science and Technology of Mazandaran (USTMB)
No.7, Mohammadi alley, Nahid Street, Marzdaran Boulevard, Tehran, Iran
Behnamazmoodeh@yahoo.com

[2]Assistant Professor, International Institute of Earthquake Engineering and Seismology (IIEES)
No. 21, Arghavan St., North Dibajee, Farmanieh, Tehran, Iran
Moghadam@iiees.ac.ir

Keywords*:* The analytic hierarchy process, unreinforced masonry building, seismic rehabilitation alternatives

Abstract. *Nowadays, distinctive methods are being used for evaluation of alternatives in making-decision. Among them the analytic hierarchy process (AHP) is one of the most efficient one. The study is set up for the low-rise unreinforced masonry buildings and includes classification of the most important parameters in strengthening of masonry buildings, and the factor analysis is performed to make the preferences of the alternatives. Due to the existence of the large number of unreinforced masonry buildings, and also the great importance of process duration for clients, the application of the AHP method in order to optimize the process and reach to the best alternative of the masonry buildings strengthening are developed. Effective parameters in evaluation of the alternatives are classified and suitable alternatives for rehabilitation are evaluated. Finally, based on the binary concept the model of binary approach decision-making (BADM) is utilized to analyze the decision parameters. Therefore, each criterion is simulated by question texts which appraiser faces two possible answers; yes and no. The results illustrate preference of the strengthening the masonry walls with interior shear wall, compared to the other alternatives. Also, effectiveness of the method is compared to the expert judgment.*

1 INTRODUCTION

Earthquake is an unpredictable phenomenon that the probability of the occurrence can be sensed at any moment. Hence, the study of suitable techniques in earthquake management will be influential in keeping the society safe and declining the losses of this mortal event. The consideration has shown that most of the masonry buildings are vulnerable so in recent years the seismic rehabilitation of the existing buildings has been gained more careful attention. The duration of the theoretical phase is a key point for the decision makers; that is, long process will cause severe economical losses for the clients. That the procedure evaluates the alternatives in the shortened time will decrease the further losses. In this area, different methods as a multi-criteria decision making methods (MCDM), have been used by the decision makers: such as analytic hierarchy process (AHP) a quantitative decision model by using pair-wise comparison, analytic network process (ANP) which is a general form of the AHP method but the elements are not independent and have interaction as a network, multi-attribute utility theory (MAUT) used to combine dissimilar measures of costs, risks, and benefits along with stakeholder preferences, cost-benefit analysis (CBA) a systematic quantitative method of assessing the desirability of government projects or policies, Kepner-Tregoe (K-T decision analysis) in which a team of experts numerically score criteria and alternatives based on individual judgment/assessment [1]. As a matter of the applicability, efficiency, and uniqueness, the analytic hierarchy process (AHP) is used to depict an operative procedure for the decision makers in the optimum alternative selection of the rehabilitation a vulnerable masonry building.

The method has been the subject of many researchers who have tried to optimize the selection process. Among them, the establishment measurement for intangible properties [3], the benefits, opportunities, costs, and risks of a decision [4], the application of the method in risk management [5], a novel approach of cotton fiber selection [6], the result consolidation of the large nominal group of dispersed decision makers [7], the prioritization of road maintenance project [8], structuring remedial decision at contaminated site [9], making decision by using dynamic criteria [10] are appreciative studies in recent years. On the other hand, some papers are discussed about the disadvantages of the applied method [11, 12].

2 THE METHODOLOGY

Decision analysis is a logical process of the ideas, experiences, and information so that the justified decision is resulted from the reasonable procedure. In general, results are described in the qualified appraisal so that an AHP hierarchy provides a comprehensive and rational framework to organize a decision problem, for quantifying its elements. The method includes three main parts, the overall *goal*, a group of options as the *alternatives* for reaching the goal, and the *criteria* that relate the alternatives to the goal which in some cases the criteria can be further broken down into the *sub-criteria* and so on. The design of the hierarchical process depends on the nature of the problem and the appropriate model should be presented. The model consists of five steps which are illustrated in the figure 1. In the first step, based on the nature of the problem, the project objective is defined. The next step deals with the limited assumptions, interfaces, ambiguities, organizational boundaries, and any stakeholders' issues. Therefore, the policy of decision analysis with the circumstances is adopted. In the third step, the appropriate criteria and alternatives are identified. In this regard, the discriminating criteria are introduced and the associated ones are classified in the specific categories. Similarly, those alternatives that cover the principles are eligible for further consideration. Basically, alternatives vary in their ability to meet the requirements and goal and offer different approaches for changing the initial condition into the desired condition [1]. The next phase includes analyzing criteria and alternatives by using the systematic method in order to handle the information. This part is the main body of the assessment and within this part the weight is assigned to each criteria and alternatives. The optimum option is elicited from the accurate analysis and the level of the accuracy is related to the level of the experience which in this study the consistency ratio is used to restrict the deviation of the preciseness. Finally, the most efficient alternative is chosen with the highest score compared to the others, in the grading process.

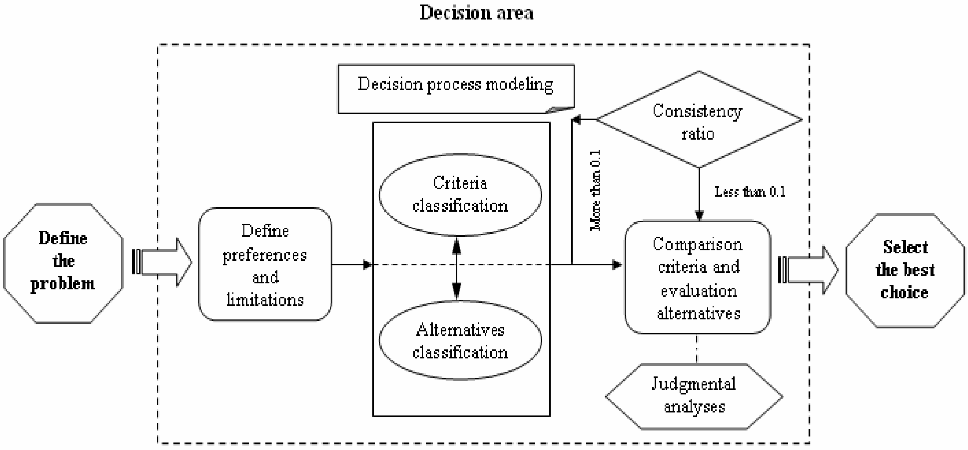

Figure 1: procedure of the decision optimization

2.1 The decision process

Once the hierarchy has been constructed, the pair-wise matrices are configured for each node of the process. The participants establish the two-by-two comparison of the priorities for all nodes, so that the intensity of the relative importance (table 1) is utilized to perform rational analysis of the decision elements. In the completion of each matrix, the array a_{ij} signifies the determinate priority of i-th item over the j-th item. By definition, the array a_{ji} points out the inverse preference of the compared item $(a_{ij} = \frac{w_i}{w_j} \Rightarrow a_{ij} = \frac{1}{a_{ji}})$. In this manner, if the group has N items then the decision-makers need to fulfill the $\frac{N(N-1)}{2}$ comparisons.

Importance scale	The intensity of relative importance
Equal importance	1
Significantly less importance	3
Somewhat more importance	5
Strong importance	7
Extremely importance	9
The intensity measurement of 2, 4, 6, and 8 are used to explicit the median bound of the importance	

Table 1: Relative scale for pair-wise comparison

A comparison matrix A is said to be consistent if $a_{ij}.a_{jk} = a_{ik}$ for all i, j and k. Mostly, in the multi-criteria problems, the matrices are inconsistent, so the rate which is called the consistency ratio is calculated. Consistency ratio of a matrix with the array $a_{ij} \neq \frac{w_i}{w_j}$ is a deviation that shows the variance of $(\lambda_{\max} - n)$ from the zero, and $\lambda_{\max}$ is achieved by solving the $A.W = \lambda_{\max}.W$ equation. The largest Eigen value is equal to the size of comparison matrix, or $\lambda_{\max} = n$. Following the equation 1 the consistency index and by using the equation 2 the consistency ratio is computed. If the value of consistency ratio is smaller or equal to 10%, the inconsistency is acceptable, and if the consistency ratio is greater than 10%, we need to revise the subjective judgment [14, 15].

$$C.I = \frac{\lambda_{\max} - n}{n-1} \tag{1}$$

$$C.R = \frac{I.I}{R.I} \leq 0.1 \tag{2}$$

Where

n : Number of elements

$\lambda_{\max}$: Maximum eigenvalue

$C.I$: Consistency index

$R.I$: Random consistency index (table 2)

$C.R$: Consistency ratio

The reciprocal matrix using scale, 1/9, 1/8, …,…, 8, 9 is randomly generated [3] (similar to the idea of Bootstrap) and get the random consistency index to see if it is about 10% or less. The average random consistency index of sample size 500 matrices is shown in the table below.

n	1	2	3	4	5	6	7	8	9	10
I.I.R	0	0	0.58	0.9	1.12	1.24	1.32	1.41	1.45	1.45

Table 2: random consistency index

To incorporate the results, the process is used to allocate the proportional weight factor for each item. In this regard, there are some mathematical-based methods which lead the process to the desired weight. The methods such as least logarithmic square, Eigen Values and the approximate methods which are the approaches of the Eigen Values are used to figure out the definite weights. By the way, the four approximate methods are evaluated and the result is shown (figure 2) the least deviation of the arithmetic average results; therefore, in this study the weighting factors are obtained by using this routine.

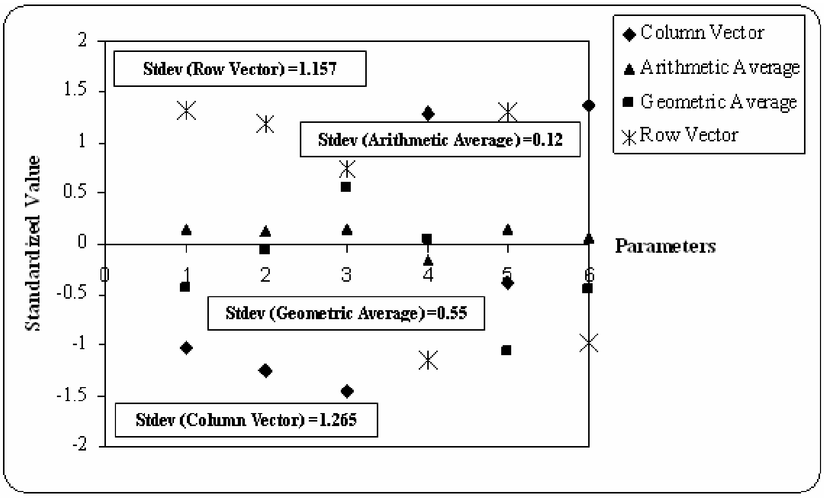

Figure 2: The comparison of approximate methods results

According to this procedure, the weight of the each criterion and also alternatives in every criterion which reveal the priority of the items is computed. Eventually, the final score of the each alternative is acquired using the following equation.

$$\Pr eferable(Alternativ\,e) = \max \sum_{i=1}^{n} w_{c(i)} . w_{a(i)} \qquad (3)$$

Where

$w_{c(i)}$: Indicates the decisive weight of i-th criterion

$w_{c(i)}$: Indicates the decisive weight of i-th alternative

Priorities are absolute numbers between zero and one and they represent the relative weights of the nodes in any group. Due to the different number of the items in the specific groups, the value of each group is normalized to express the same value of distinctive groups. Depends on the problem nature; the final weight refers to the importance, likelihood, capability or whatever factor is being considered by the decision makers.

Beside all the facts, there is a factor that has influence on the final decision and somewhat may change the result. The decision is developed basically on the expert judgment and the decision-makers use their knowledge and experiences to decide, thus, the decision conducted by the group with the more background, more realistic outcome will be concluded. Hence, a coefficient is defined here to take this subject into the consideration which is multiplied to the final result.

	Coefficient of the background
No background	0.9
Less than 3 years	1.0
More than 3 years	1.1

Table 3: proposed coefficient of proportionate study background

3 THE APPLICATION IN THE REHABILITATION OF A MASONRY BUILDING

3.1 Objective

Every year, large amount of money is spent for developing the infrastructural projects in which the allocation of the resources in the right order is the stakeholders' concern. Researches in this area demonstrate that study the optimization methods can bring significant outcome in the time-cost management and the decision-makers are capable to utilize a proper policy to save time and expenditures. Among them the consideration of the effective parameters in seismic rehabilitation [15], assessing the benefits and costs of earthquake mitigation [16], and also the study of affecting issues in the sustainability of buildings by the optimum design [17] can be mentioned. The unreinforced masonry buildings include the large part of the urban constructions and the researches have indicated the vulnerability of the majority numbers. In order to rehabilitate the structure and increase its seismic performance the retrofitting process is conducted, but the remarkable point for the clients is the process duration and the cost of the strengthening which the undesirable management will impose some losses to the project finance. Due to the aforementioned subject, the main purpose of this study is to demonstrate the applied procedure by the comparative algorithm to designate the optimum strengthening alternative with the assessment of the all related criteria in the selection process of unreinforced masonry buildings. As been stated before, to analyze the decision process, the criteria and alternatives are necessitated, so in the following part the appropriate criteria and possible alternatives are identified.

3.2 Criteria and sub-criteria

In the strengthening process of the masonry building, there are some parameters which affect the process and these parameters are identified and classified properly. These parameters are picked out by reviewing the related methodologies, codes, and provisions [18, 19, 20, 21, and 22]. The main criteria which are selected in the procedure include: *building characteristics*, *constructional aspects*, *economical aspects*, *technical aspects*, *architectural aspects*, and *mechanical and electrical equipment*. Each category has some sub-criteria which can be observed in the table 4.

3.3 Alternatives

The vulnerability of a building subjected to an earthquake is dependent on seismic deficiency of that building relative to a required performance objective [23]. Two possible ways are constructive, here. One is to demolish and rebuilt the building and the other one is to rehabilitate which can be the increasing the capacity of structure (add new elements, enhance existing elements; improve connections) or reduction the demand on the building. The rehabilitate techniques are used to enhance the seismic performance of the building and eliminate those deficiencies, subsequently. Different buildings types require different mitigation technique, and depend on the seismic deficiencies alternative recommendation are made to satisfy the performance objective of rehabilitation. In this study, six alternatives are proposed to improve the lateral performance of the unreinforced masonry building. The alternatives include: *strengthening with the shotcrete* (using the shotcrete overlay on the masonry wall), *strengthening with the interior shear wall* (adding the concrete shear wall inside the plan), *strengthening with the FRP* (using the FRP laminate on the masonry wall), *strengthening with the exterior steel frame* (adding the steel frame outside the plan), *strengthening with the exterior concrete frame* (adding the concrete frame outside the plan), *strengthening with the exterior shear wall* (adding the concrete shear wall outside the plan).

3.4 Concluding remarks

The parameters which affect the selection process of the masonry buildings are categorized. The sort is performed based on the different characteristic of the items and in the term which can be compared, simultaneously. More discussion is provided in detail in the subsequent parts.

3.4.1 Building characteristics

Building characteristics include: *plan dimension*, *design and construction quality*, *building area*, and *vulnerability intensity*. Due to load distribution, using the strengthening with shotcrete and FRP will be more desirable in the buildings with large-sized plan. Some buildings have low design and construction quality, so that the alternatives like the shear wall which absorb the large amount of seismic loads, is desirable.

In some projects, the client may need to increase the building area beside the retrofitting implementation, so the alternatives which are adjunct to the structure (exterior frame or shear wall) will be more effective, and like wise if the existing building has the high vulnerability index which is obtained by the defenselessness analysis, those alternatives such as added-frame or shear wall are more productive. In this case, for a poor quality building, sometimes it is better to employ a method that reduces the transferred seismic force to the building rather than designing a huge new system for it [15].

3.4.2 Constructional aspects

Constructional aspects include: *construction duration*, *construction difficulties*, *construction technology*, *availability of materials*, *automation possibility*, *availability of constructional guideline*, and *level of experience needed for contractors and labors*. Projects related to their occupancy demand a specific duration timeline. In this regard, experiences have indicated the effectiveness of the strengthening with the FRP in comparison with the other alternatives and it is more operable for those projects which have limited time.

Adding the reinforced elements to the existing building is executed with some difficulties (hard accessibility to the structural components, connections, or even foundation) and mostly, it may affect severe impact on the project fund. In execution of shear wall the most troublesome part is the strengthening the foundation and if the wall designed outer part, the excavation and also the construction of new foundation is needed, too. Those alternative in which are added from outside, the adequate connection to the storey diaphragm is so important. However, the interior shear wall and strengthening with shotcrete need some difficulties in connection to the storey diaphragm, if the diaphragm has rigid material. Therefore, the strengthening with the FRP is evaluated the more efficient one.

The mechanized scheme which the required materials and the construction technology are available is more impressive. The level of the experience for the construction team is another important item so that some schemes are more sensitive to the errors and the high-experienced team is needed. Also, the availability of constructional guideline can be useful for low-experienced contractors to be aware of the executing process.

3.4.3 Economical aspects

Economical aspects include: *effect on the loss reduction*, *cost of retrofitting*, *cost of required tools and machinery*, *cost of labors*, *current value of building*, and *presence of occupants in the time of rehabilitation*. The main goal of the rehabilitation process is to decrease the expected losses in the existing building. The losses have direct relation with the stiffness of the building, so the constant-ductile alternatives which increase the global stiffness such as shear wall will be more efficient.

One of the important parts of the evaluation is dedicated to the cost estimation, and it is among the most important parameters, specifically for the clients who should consider selecting the best retrofitting option. The cost of retrofitting comprises the destruction, strengthening, and repair cost which denote a series of items from the cost of removing some components to the cost of adding new material or elements and finally provide a new finishing. In fact, the value of retrofitting costs, including designers, labors, equipments and materials expenditure, compared with the benefit of performing the strengthening plan. The cost of the labors and tool/machinery will be added to the cost of retrofitting which are varying in different area.

According to the lifetime of the building, the retrofitting will increase the value of the building and the amount will be more significant for the older buildings. Also, those alternatives which are added from outside will increase the area and accordingly increase the building value. Some buildings have critical occupancy in which the interruption in the service will bring some losses to the occupants. In this regard, the alternatives which are adjunct to the structure will be preferable, because these approaches have no interference in the existing occupancy.

3.4.4 Technical aspects

Technical aspects include some parameters related to the structural and dynamic attributes such as: *effect on the building weight*, or increasing the global *stiffness* and *ductility*. Basically, the seismic load is received by the mass of the building. So, one way to resist the earthquake hazards is to decline the mass of building. Another way is to use an absorption mechanism of the earthquake energy by increasing the stiffness or the ductility of the building. Based on the behavior, the shear wall and frame highly increase the global stiffness of the building. Depend on the design parameters, the shear wall and frame are more ductile and can be more desirable, comparatively.

A discontinuity in the load distribution from diaphragm to the supporting soil brings about the local defect and prevents the seismic system to be effective. The irregularity (plan and vertical) feature has some negative effects on the building performance. The irregularity may place extraordinary demands on elements and the irregular building has more unknown behavior and different modes should be taking into the analysis so that codes are strongly recommended to avoid this feature. The solid movement of the building as grouped components is suggested in leading to the reliable behavior against applied loads. Some alternatives are preferable according to its effectiveness in completing the *load path*, improving the *irregularity*, increasing the overall *solidarity* and *torsional capacity*, like the shear wall, and added frame, respectively. On the contrary, the strengthening with the shotcrete and FRP are preferable in the *minimum strengthening in the foundation* and relative easiness in the *connection to the storey diaphragm*.

These two items are among the most difficult part of strengthening which the ignorance will cause increasing the costs. In supporting of the boundary conditions, the foundations of most masonry buildings are superficial and present noticeable settlements: they are far from the rigid foundations of the structural textbooks. They are unknown, and essentially unknowable, as slight changes of the soil conditions, the sudden action of loads (e.g., storms or earthquakes) could alter the response to the loads [24]. Also, the diaphragm deficiencies are described as inadequate restraints, in-plane strength, and insufficient local shear transfer to lateral-force resisting elements.

Masonry walls are the part of the lateral resisting system which is qualified to endure the seismic loads. Although, the alternatives such as shear wall and frame absorb the high rate of the earthquake energy, but they decrease the portion of masonry walls. If the *using of maximum structural capacity* is the purpose, the strengthening with the shotcrete and FRP are more operative. Diaphragm shall be designed to resist the effects of the seismic forces calculated by dynamic analysis [25]. *The rigidity of the diaphragm* is the key point in the lateral load distribution and reduces the three degree-of-freedom. In buildings with rigid diaphragm the load distribution is based on the stiffness of the elements, so the alternatives with high stiffness such as shear wall are not suitable for the building with flexible diaphragm. Moreover, due to stiffness of the shear walls, the load transmission between diaphragm and shear wall cause stress concentration and the connections are needed strengthen with the resistant materials.

The sensitivity of performance of each scheme *to the technical and constructional errors*, and also the availability of information on performance of such schemes in previous earthquakes is much useful. In all design codes there is a safety factor to consider the indispensable uncertainties in designing where in the rehabilitation process with limited structural information and knowledge factor is certainly much more. The error can be part of the process, but the avoidance or even reduction the errors should be taking into the consideration. The errors include design errors, constructional errors, experiments errors or even the lack of structural information. Conceptually, the shear wall and frame bear the major part of the force, so that they are more sensible to the expected errors. On the other hand, the shotcrete or FRP added-layers are linked to the masonry wall and the combination is assumed to endure the applied force, so the experiments errors and also the lack of structural information have a certain disposition towards the results. Also, in order to design each alternative and lateral capacity appraisal, a design code should be available.

Sometimes, the building under consideration has some weakness in *gravitational load-bearing* which added elements like the shear wall or frame are eligible for improving this deficiency. In using the exterior alternatives, the sufficient area is needed. Due to the strengthening with the shotcrete, interior shear wall, and FRP inside the building, they are evaluated more efficient. Beside the assessment of the structural elements, non structural components which are separated into the displacement-sensitive and acceleration-sensitive should be appraised. The alternative with more stiffness are more effective, so the shear wall, frame, shotcrete, and FRP are preferable, respectively. But the shear wall and somehow the frame increase the diaphragm acceleration, and in this manner the application are not justified.

Occasionally, the local renovation of the masonry walls is needed. In this case, the shotcrete overlay and also the FRP laminate would be preferable compared to the shear wall and frame. These renovations are enhancing the poor condition walls by removing some deteriorated masonries, repointing by using grout and epoxy injection to increase the shear strength. Thus the deformation-controlled action would be replaced with the force-controlled of the diagonal tension. Masonry wall with height-to-thickness ratio or out-of-plane stresses in excess of the permitted by codes need to be strengthen and the shotcrete and FRP can be proper. Also, the masonry walls are weak in the corner of the opening in which the shear cracks are extended, if the dimension exceeds the allowable values [26, 27, and 28]. Masonry walls with undesirable length or height can not behave properly in earthquake and the maximum value are limited in the related codes [25]. In this order, the application of the shotcrete and FRP are qualified in decreasing the length and height in using as a tie.

According to the resisting system, all connection should have the desirable anchorage. Adequate strength should be provided in the connection between walls, wall to diaphragm and wall to the partition to resist the transfer forces. For local renovations the local scheme can be made to improve the local performance, but either shotcrete overlay or FRP laminate can be applicable.

Finally*, Past experience* is relevant in proving that retrofitting URM buildings reduce damage and loss of life, but also that building configuration and the quality of the evaluation, design and construction makes a substantial difference in the degree of improvement [29].

3.4.5 Architectural aspects

Architectural aspects include: *effect on the building's façade*, *effect on the building spacing*, *effect on the building lighting*, and *changing rooms' occupancy*. In the architectural viewpoint, the optimum alternative is the one which has the least affect on the building architecture and the clients prefer an alternative which has less interference in the aesthetic. In this regard, the most efficient option is the one which does not need to change the spacing, reduce the lighting, or even cause changing some rooms' occupancy. These are some limitations that mostly the designers are faced and are requested to avoid them. Among the proposed alternatives, the adjunct components like the exterior frame or shear wall have significant impact on the façade, or even reduce the lighting. In addition, in many cases the interior shear wall cause changing in some occupancy. Thus, the strengthening with the FRP is more productive.

3.4.6 Mechanical and electrical equipment

The mechanical and electrical equipments are one of the important parts of the building which removing can impose extra costs to the project finance. The effective alternative is defined the less necessity to the equipment removal, and accessibility. The alternatives which are added from the outside, unaffectedly, do not interfere in the building equipments. Also, compared to the strengthening with the shotcrete and FRP, the less shear wall is needed to fulfill the capacity requirements.

3.4.7 Case study

As been mentioned in the prior part, some parameters are constant in comparative evaluation, but some others can be varying in different area, so that different result will be obtained. The study is localized the evaluation of the effective parameter in order to select the best alternative for the rehabilitation of the masonry buildings. The results which is illustrated in the table 4, is accomplished for a masonry building located in the Tehran city to give us a broader perspective of the procedure.

						Strengthening with the shotcrete	Strengthening with the Interior shear wall	Strengthening with the FRP	Strengthening with the exterior steel frame	Strengthening with the exterior concrete frame	Strengthening with the exterior shear wall	I.R
Building Characteristics	0.850	Plan Dimension			1.280	3.586	1.645	3.586	0.657	0.657	0.657	0.009
		Design and Construction Quality			2.372	1.307	8.720	0.784	4.784	2.195	2.195	0.055
		Building Area			0.659	0.185	0.185	0.185	1.667	1.667	1.667	0.000
		Vulnerability Intensity			5.688	2.768	5.501	1.487	12.721	12.721	12.721	0.023
	Section scores					0.931	1.905	0.717	2.354	2.046	2.046	
Constructional Aspects	1.395	Construction Duration			2.149	1.047	2.065	11.725	6.028	4.288	4.856	0.043
		Construction Difficulties			3.379	1.714	3.648	19.023	11.711	7.650	3.441	0.051
		Construction Technology			0.366	0.471	1.870	0.191	0.862	0.862	0.862	0.058
		Availability of Materials			0.334	0.898	0.898	0.180	0.898	0.898	0.898	0.000
		Automation Possibility			1.197	1.213	6.252	0.689	3.534	3.534	1.498	0.059
		Availability of Constructional Guideline			1.924	7.093	10.155	0.857	3.560	3.560	1.649	0.048
		Level of Experience needed for Contractors and Labors			0.650	2.157	3.483	0.312	1.254	1.254	0.618	0.053
	Section scores					1.045	2.032	2.362	1.995	1.579	0.990	
Economical Aspects	2.540	Effect on Loss Reduction			2.036	3.577	16.229	2.384	6.647	6.647	16.229	0.037
		Cost of Retrofitting	3.884	Destruction Cost	2.605	65.342	34.707	116.043	16.211	16.211	8.539	0.052
				Strengthening Cost	6.333	234.659	81.691	18.887	44.604	163.434	81.691	0.068
				Repair Cost	1.062	22.669	12.679	45.164	8.172	12.679	3.389	0.084
		Cost of required tools and machinery			1.044	4.068	5.814	11.525	2.074	2.074	0.969	0.055
		Cost of Labors			0.356	3.909	0.940	2.513	0.480	0.940	0.254	0.068
		Current Value of Building			0.337	0.356	0.356	0.356	2.495	2.495	2.495	0.000
		Presence of Occupants in Time of Rehabilitation			2.343	2.049	5.856	2.049	16.523	16.523	16.523	0.048
	Section scores					2.947	1.386	1.742	0.851	1.935	1.139	
Technical Aspects	4.463	Effects on building weight			0.277	3.264	0.640	4.649	1.584	1.584	0.640	0.035
		Using Maximum Structural Capacity			0.456	7.914	1.131	7.914	1.131	1.131	1.131	0.000
		Accordance to the diaphragm rigidity			0.641	10.351	1.192	10.351	2.764	2.764	1.192	0.021
		Load path			0.159	0.236	1.653	0.236	1.653	1.653	1.653	0.000
		Effect on the regularity of the building			0.796	2.642	11.257	1.224	4.775	4.775	10.834	0.058
		Effect on the torsion of the building			0.656	2.374	3.595	1.083	5.629	5.629	10.951	0.088
		Minimum Strengthening in Foundation			0.386	4.935	1.845	8.195	0.891	0.891	0.473	0.063
		Increase the solidarity of the building			1.003	2.004	6.414	1.128	14.400	14.400	6.414	0.037
		Increase the stiffness of the building			0.230	0.652	3.400	0.255	1.802	1.027	3.127	0.069
		Increase the ductility of the building			0.138	0.280	1.399	0.280	1.399	1.399	1.399	0.000
		Connect to the storye diaphragm			1.276	12.889	7.426	28.737	4.102	1.898	1.898	0.073
		Local renovation of the walls deficincies	0.468	Conditional improvement of the walls	0.263	0.250	1.250	0.250	1.250	1.250	1.250	0.000
				Repointing	0.902	0.856	4.281	0.856	4.281	4.281	4.281	0.000
				The ratio of the height to the tickness	2.333	24.430	5.536	2.164	5.536	5.536	5.536	0.011
				Wall length	1.200	12.569	2.848	1.113	2.848	2.848	2.848	0.011
				Wall height	1.580	16.538	3.748	1.465	3.748	3.748	3.748	0.011
				Wall out-of-plane strength	3.224	33.755	7.649	2.990	7.649	7.649	7.649	0.011
				Enlarged opening	0.497	5.208	1.180	0.461	1.180	1.180	1.180	0.011
		Walls connection renovation	0.165	Connection between walls	2.828	8.116	1.159	8.116	1.159	1.159	1.159	0.000
				Connection between wall and diaphragm	6.434	18.462	2.637	18.462	2.637	2.637	2.637	0.000
				Connection between wall and partition	0.738	2.117	0.302	2.117	0.302	0.302	0.302	0.000
		Access to the building different faces			0.132	1.715	1.715	1.715	0.245	0.245	0.245	0.000
		Effect on the gravitational load-bearing			0.088	0.198	1.986	0.198	0.513	0.513	0.513	0.016
		Effect on the displacement sensitive non-structural component			0.167	0.538	2.310	0.230	1.214	0.872	2.310	0.068
		Effect on the acceleration sensitive non-structural component			0.165	1.771	0.372	3.076	0.741	1.016	0.372	0.067

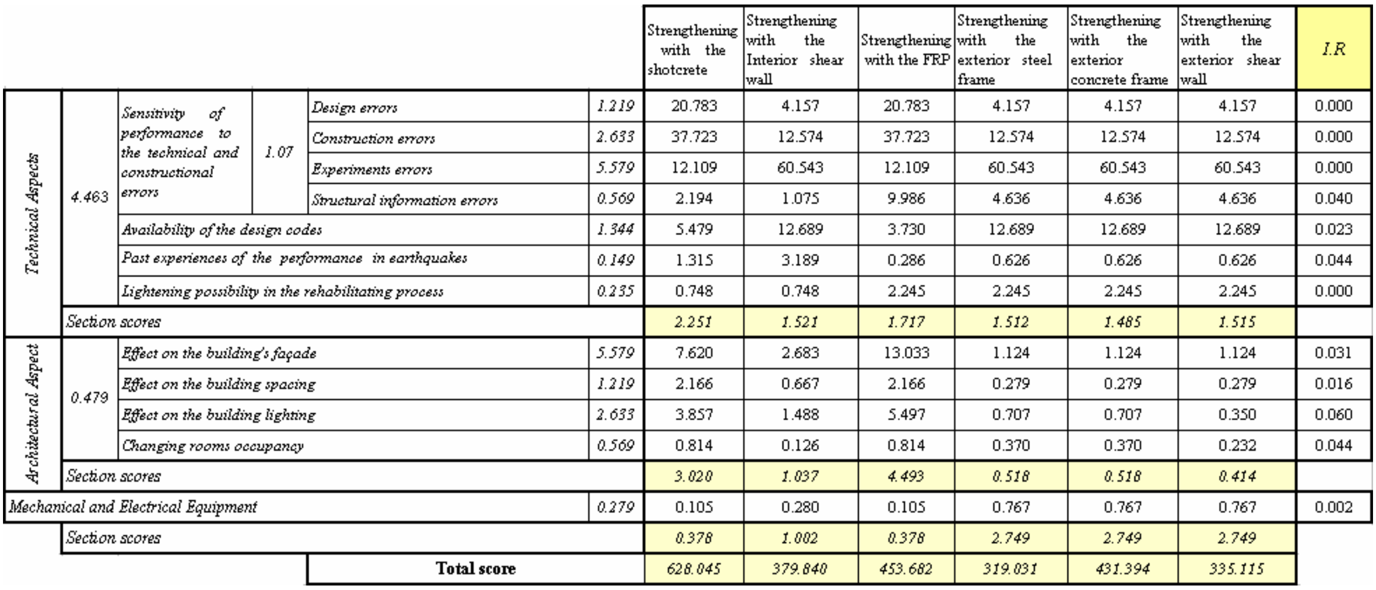

						Strengthening with the shotcrete	Strengthening with the Interior shear wall	Strengthening with the FRP	Strengthening with the exterior steel frame	Strengthening with the exterior concrete frame	Strengthening with the exterior shear wall	*I.R*
Technical Aspects	*4.463*	*Sensitivity of performance to the technical and constructional errors*	*1.07*	*Design errors*	*1.219*	20.783	4.157	20.783	4.157	4.157	4.157	0.000
				Construction errors	*2.633*	37.723	12.574	37.723	12.574	12.574	12.574	0.000
				Experiments errors	*5.579*	12.109	60.543	12.109	60.543	60.543	60.543	0.000
				Structural information errors	*0.569*	2.194	1.075	9.986	4.636	4.636	4.636	0.040
		Availability of the design codes			*1.344*	5.479	12.689	3.730	12.689	12.689	12.689	0.023
		Past experiences of the performance in earthquakes			*0.149*	1.315	3.189	0.286	0.626	0.626	0.626	0.044
		Lightening possibility in the rehabilitating process			*0.235*	0.748	0.748	2.245	2.245	2.245	2.245	0.000
	Section scores					*2.251*	*1.521*	*1.717*	*1.512*	*1.485*	*1.515*	
Architectural Aspect	*0.479*	*Effect on the building's façade*			*5.579*	7.620	2.683	13.033	1.124	1.124	1.124	0.031
		Effect on the building spacing			*1.219*	2.166	0.667	2.166	0.279	0.279	0.279	0.016
		Effect on the building lighting			*2.633*	3.857	1.488	5.497	0.707	0.707	0.350	0.060
		Changing rooms occupancy			*0.569*	0.814	0.126	0.814	0.370	0.370	0.232	0.044
	Section scores					*3.020*	*1.037*	*4.493*	*0.518*	*0.518*	*0.414*	
Mechanical and Electrical Equipment					*0.279*	0.105	0.280	0.105	0.767	0.767	0.767	0.002
	Section scores					*0.378*	*1.002*	*0.378*	*2.749*	*2.749*	*2.749*	
				Total score		*628.045*	*379.840*	*453.682*	*319.031*	*431.394*	*335.115*	

Table 4: relatively weighted criteria, sub-criteria and alternatives

According to the figure.1 the problem is designed in which the model include the goal as a rehabilitation the masonry building. By reviewing the preferences and limitation in the rehabilitation process, the appropriate criteria are explained in the section 3.2, and the qualified alternatives are proposed in the section 3.3 The pair-wise comparative matrices are established and in this order the 5 matrices with different size for the criteria and 56 matrices for alternatives are set up. Using the mathematical syntax of numerical judgments in the decision problem, the absolute weight for the criteria and also for the alternatives is obtained. The consistency of the judgments is checked and the equation 3 is used to gain the final score in determination of the best alternative.

The results are summarized in the table 4 in which the proposed alternatives in the case of each classified criteria are compared and the priority is obtained for each of them. In the analysis the building characteristics, the vulnerability intensity serve the highest rank so the application of those schemes like the shear wall or the frame which can absorb the high rate of the earthquake energy is evaluated more desirable. The assessment of the constructional aspects denotes the importance of the construction duration and the construction difficulties among the other criteria. Based on the experience in this area, the strengthening of the masonry walls with the FRP is judged as a preferable alternative. In proceeding the economical aspects, the cost of the retrofitting and also the presence of the occupants in the time of rehabilitation acquire more effectiveness and the strengthening of the masonry walls with the shotcrete overlay is deserved higher priority. Among all the designated criteria in introducing the technical aspect of the process, the availability of the design codes and then connecting to the storey diaphragm are evaluated the most influential one. In this regard, the outcome indicates the efficiency of the strengthening of the masonry walls with the shotcrete overlay. The analysis of the architectural aspects signifies the precedence of the effect on the building's façade and the strengthening of the masonry walls with the FRP is the privileged alternative. Finally, the three exterior alternatives include strengthening with the steel frame; concrete frame and the shear wall are tending to be more useful in the mechanical and electrical equipment aspect. Whereas, the study of the effectiveness of different alternatives needs to have the acceptable level of knowledge and experiences in leading to the authentic judgment, the presented study endeavors to be performed precisely. The results illustrate the preference of the strengthening the masonry walls with the shotcrete, compared to the other alternatives.

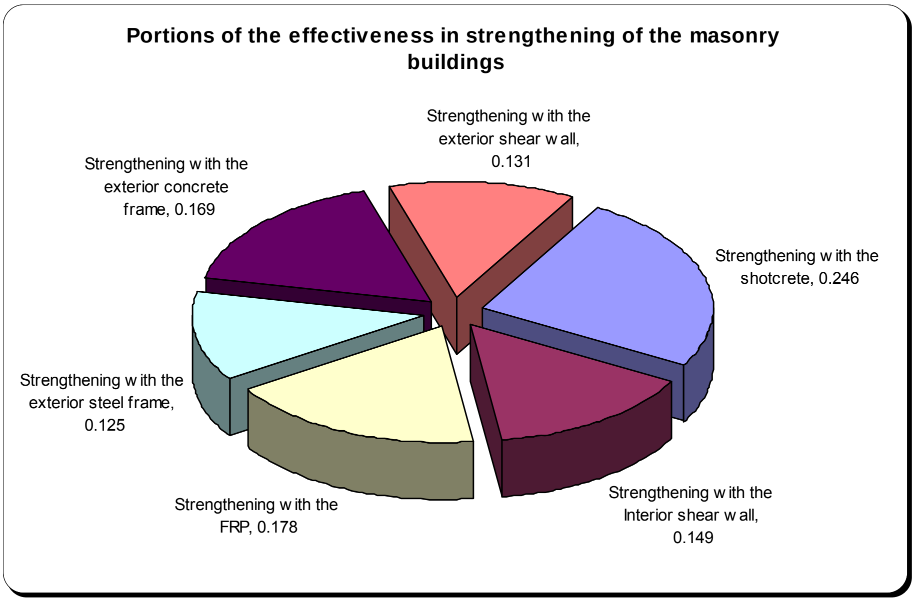

Figure 3: Final results of the proposed evaluation of the masonry buildings

4 VERIFICATION OF THE PREVIOUS STUDY

Several methods have been proposed in making-decision and in recent years various studies have been developed to analyze the decision problems. The authors presented a procedure to quantify the process for selecting the most advantageous technique, and also a practical method for specifying and prioritizing a criteria and goals for seismic retrofitting of a building [15]. A survey was conducted and some expert's opinions are gathered from some leading authorities, both from academia and profession, to calibrate the method. The aforementioned study was based on the experts' judgment and the criteria and alternatives were compared entirely in a group which it needed more concentration of its larger domain. The comparison of criteria and alternatives in this study is performed with this method again in consideration the final results. In spite of that the evaluation by the experts' judgment is expected to have divergent results but the result which is illustrated in figure 4, has shown the admissible level of outcomes. Due to close assessment, the variance of the combined results is calculated based on the equation 4.

$$\text{If } \mu = E(x) \text{ then } VAR(x) = E\left[(x-\mu)^2\right] \text{ or } VAR(x) = E\left(x^2\right) - \left[E(x)\right]^2 \qquad (4)$$

Where

x : Random variable

$p(x)$: The probability of the random variable (x_i)

$E(x)$: The expected value of the random variable (x_i)

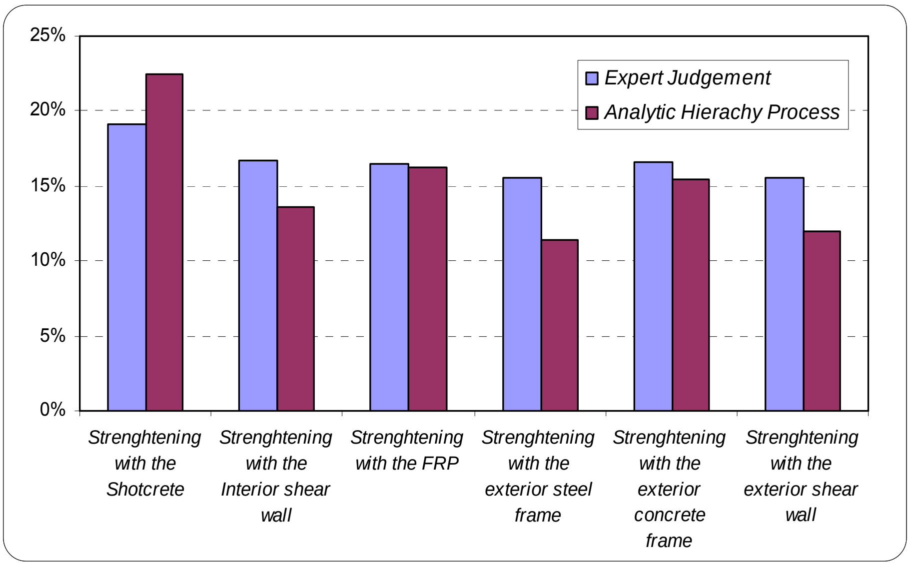

Figure 4: The results comparison of the AHP technique with the expert judgment procedure

x	p(x)	E(x)=xp(x)	x^2	$E(x^2)=x^2p(x)$
628.045	0.247	154.86	394440.76	97258.06
379.840	0.149	56.64	144278.12	21515.61
453.682	0.178	80.81	205827.04	36661.19
319.031	0.125	39.96	101781.05	12748.33
431.394	0.169	73.06	186100.67	31519.17
335.115	0.132	44.09	112301.77	14775.18
2547.106	1	449.42	1144729.40	214477.55
$Var(x)=E(x^2)-[E(x)]^2$		12496.073		

Table 5: the expected value and variance for the method-AHP

x	p(x)	xp(x)	x^2	$x^2p(x)$
402.890	0.192	77.17	162320.35	31092.83
350.540	0.167	58.42	122878.29	20479.23
346.610	0.165	57.12	120138.49	19798.13
327.290	0.156	50.93	107118.74	16668.60
349.130	0.166	57.95	121891.76	20233.10
326.830	0.155	50.79	106817.85	16598.41
2103.290	1	352.38	741165.49	124870.30
$Var(x)=E(x^2)-[E(x)]^2$		695.899		

Table 6: the expected value and variance for the method-Judgmental

The results presented in the figure 4 and the table 5 and 6 implicate the effectiveness of the experts' judgment and the variance of this method here is less than the AHP method, but the sequence of the priorities is changed. As been mentioned before, the accuracy of decision-makers in analyzing the process and making comparison has a direct relationship with the final result.

5 THE BINARY PROCESS

The productive criteria identified and properly classified and also according to the aforementioned process in the prior section, the relative weight is assigned to each criterion and also the method is used to compare the alternatives to make the preferences in each criterion. In this step, each criterion is simulated by a question tag which covers the intelligible concept of those criteria. In this regard, the only two possible answers are drawn here: “Yes” or “No” which *yes* points the 1 and *no* refers to 0 (eq.5). The main purpose of this study is to draw a simplified flexible procedure in optimization the proposed rehabilitation alternative with consideration the interaction of criteria and alternatives; hence a binary approach decision-making (BADM) is established in this regard. The applied model tries to make a rational conclusion based on the judgmental analysis and its binary utilization authorizes the decision-makers to omit those criteria that are irrelevant to the building under consideration by giving the *no* answer. Finally, the quick survey of building with considering the structural and non-structural components, gathering comprehensive information, limitations and also clients’ objective the alternatives are evaluated by completing the survey.

$$\textit{The}\text{ most efficient alternative} = \max \sum_{i=1}^{n} CW_i \times \varphi_{bi} \begin{Bmatrix} 0 \\ 1 \end{Bmatrix} \qquad (5)$$

Where

CW_i : Indicates the relative weight of i-th criterion

φ_{bi} : The binary coefficient of i-th alternative

The filled cells are those considered as the preferred alternative in the specific criteria, therefore each answer will be evaluated just for these alternatives and the final result will be achieved by summing up the grades. The applied form is presented in table 7 and the result is obtained for a particular building which is considered vulnerable.

Building name	Adab high school
Appraiser name	B.M.Azmoodeh
Survey date	September 17, 2009
Occupancy	Educational
Number of story	2
Number of occupants	350 persons
Year of built	1982
Building area	910 square meter
Objective performance level	Life safety for the BSE-1
Adjucent building	Not any hazards will impact the performance
Address	
N.33-Vahdati St.-Tehran	

Zone seismicity	Very High Risk ☑	High risk ☐	Moderate risk ☐	Low risk ☐
Type of diaphragm	One-way masonry slab ☐		Concrete slab ☑	Plywood ☐
Soil classification	Type I ☐	Type II ☐	Type III ☑	Type IV ☐
Type of foundation	Wall footing ☑	Single footing ☐	Strip footing ☐	Mat footing ☐
Bearing wall material	Solid brick ☑	Clay or shale brick ☐	Hollow brick ☐	Concrete block ☐
Regularity condition	Regular ☑		Irregular ☐	

Additional comment

It has many wide large openings-windows- which areas are more than 0.33 area of the walls

there were some partitin walls which the ratio of the height/thickness exceed the allowable ratio

there were some walls with the length of more than 5 meters

it is reqular in both plan and elevation with rigid floors with no discontinuty in load path

The quality of the mortar seems not in competent condition

Building photo

	main criteria weight			sub-criteria weight	cummulative weight			Strengthening with the shotcrete	Strengthening with the Interior shear wall	Strengthening with the FRP	Strengthening with the exterior steel frame	Strengthening with the exterior concrete frame	Strengthening with the exterior shear wall
Building Characteristics	0.846	**Plan Dimension**		1.280	1.083	whether the ratio of length/width of the building is more than 3?	Yes	1.0833					
		Design and Construction Quality		2.372	2.007	whether the quality of the construction is undesirable?	Yes		2.0068				
		Building Area		0.659	0.558	whether the increasing the building area is clients' objective?	No				0.0000	0.0000	0.0000
		Vulnerability Intensity		5.688	4.812	whether the vulnerability intensity of the building is more than 50 percent?	Yes				4.8120	4.8120	4.8120
Constructional Aspects	1.395	**Construction Duration**		2.149	2.998	whether the project has limited time for construct?	No			0.0000			
		Construction Difficulties		3.379	4.714	whether scheme with less difficulty in construction is preferable?	Yes			4.7135			
		Construction Technology		0.366	0.511	whether scheme with the available construction technology is needed?	Yes		0.5112				
		Availability of the Materials		0.334	0.466	whether scheme with available material is requested?	No	0.0000	0.0000		0.0000	0.0000	0.0000
		Automation Possibility		1.197	1.670	whether construction with the automation possibilities is required?	Yes		1.6700				
		Availability of the Constructional Guideline		1.924	2.685	whether the availability of the construction guidelines is necessary?	Yes		2.6845				
		Level of the Experience needed for the Contractors and Labors		0.650	0.907	whether the level of the contractors' experience is important?	Yes		0.9067				
Economical Aspects	2.538	**Effect on the Loss Reduction**		2.036	5.167	whether the expected loss reduction is important?	Yes		5.1667				5.1667
		Cost of the Retrofitting 3.884	**Destruction Cost**	1.011	2.565	whether scheme with the less destruction cost is preferable?	No			0.0000			
			Strengthening Cost	2.457	6.237	whether scheme with the less strengthening cost is preferable?	Yes	6.2368					
			Repair Cost	0.412	1.045	whether scheme with the less repair cost is preferable?	Yes			1.0454			
		Cost of the required tools and machinery		1.044	2.650	whether cost of the required tools and machinery is important?	No			0.0000			
		Cost of the Labors		0.356	0.903	whether cost of the labors is important?	No	0.0000					
		Current Value of the Building		0.337	0.855	whether increasing the current value of the building is requested?	No				0.0000	0.0000	0.0000
		Presence of the Occupants in the Time of Rehabilitation		2.343	5.947	whether the presence of the occupants in the time of rehabilitation is necessary?	No				0.0000	0.0000	0.0000

Technical Aspects	4.463	**Effects on building weight**			0.277	1.236	whether weight of the building is more than the usual?	No			0.0000			
		Using Maximum Structural Capacity			0.456	2.035	whether using maximum structural capacity is the purpose?	Yes	2.0352		2.0352			
		Accordance to the diaphragm rigidity			0.641	2.861	whether the storey diaphragm is rigid?	Yes	0.0000		0.0000			
		Load path			0.159	0.709	whether the load path is complete?	Yes		0.0000		0.0000	0.0000	0.0000
		Effect on the regularity of the building			0.796	3.551	whether the building is evaluated regular (in plan and height)?	Yes		0.0000				
		Effect on the torsion of the building			0.656	2.926	whether the building needs to increase its torsional strength?	No						0.0000
		Minimum Strengthening in Foundation			0.386	1.723	whether the amount of strengthening in foundation is important?	No			0.0000			
		Increase the solidarity of the building			1.003	4.476	whether the building fulfills the solidarity criteria? (Does it have masonry tie?)	Yes				0.0000	0.0000	
		Increase the stiffness of the building			0.230	1.026	whether the building need to be more stiffened?	Yes		1.0263				
		Increase the ductility of the building			0.138	0.615	whether the building needs to increase its ductility?	No		0.0000		0.0000	0.0000	0.0000
		Connect to the storey diaphragm			1.276	5.695	whether the easiness of connecting the added components to the storey diaphragm is important?	Yes			5.6952			
		Local renovation of the walls deficincies	0.468	**Conditional improvement of the walls**	0.012	0.055	whether the construction of the walls is evaluated in acceptable condition?	No		0.0550		0.0550	0.0550	0.0550
				Repointing	0.042	0.188	whether the walls are needs to be repointed with new mortar?	No		0.1883		0.1883	0.1883	0.1883
				The ratio of the height to the tickness	0.109	0.487	whether the ratio of the height to the tickness of the structural walls is more than 10?	Yes	0.4874					
				Wall length	0.056	0.251	whether length of structural walls is more than 5 meters?	Yes	0.2507					
				Wall height	0.074	0.330	whethe height of walls is more than 4 meters?	No	0.0000					
				Wall out-of-plane strength	0.151	0.673	whether the out-of-plane strength of the walls is adequate?	No	0.6734					
				Enlarged opening	0.023	0.104	whether the building has enlarged openings? (The area of the opening is more than 0.33 area of wall?)	Yes	0.1039					
		Walls connection renovation	0.165	**Connection between walls**	0.047	0.208	whether the connection between structural walls is appraised in fine condition?	No	0.2083		0.2083			
				Connection between wall and diaphragm	0.106	0.474	whether the connection between wall and diaphragm is appraised in fine condition?	No	0.4738		0.4738			
				Connection between wall and partition	0.012	0.054	whether the connection between wall and partition is appraised in fine condition?	No	0.0543		0.0543			
		Access to the building different faces			0.132	0.588	whether the building has enough space in each its four faces to add strengthened components?	Yes				0.5881	0.5881	0.5881
		Effect on the gravitational load-bearing			0.088	0.392	whether the building has deficiency in bearing the gravitational load?	No		0.0000				
		Effect on the displacement-sensitive non structural component			0.167	0.747	whether the building has displacement-sensitive non structural component?	Yes		0.7473				0.7473
		Effect on the acceleration-sensitive non structural component			0.165	0.735	whether the building has acceleration-sensitive non structural component?	No			0.0000			
		Sensitivity of performance to the technical and constructional errors	1.07	**Design errors**	0.130	0.582	whether the expected design errors is consequential?	Yes	0.5820		0.5820			
				Construction errors	0.282	1.258	whether the expected construction errors is consequential?	Yes	1.2576		1.2576			
				Experiments errors	0.597	2.664	whether the expected experiments errors is consequential?	Yes		2.6642		2.6642	2.6642	2.6642
				Structural information errors	0.061	0.272	whether the expected structural information errors is consequential?	No			0.0000			
		Availability of the design codes			1.344	5.997	whether the availability of the design codes is necessary?	Yes		5.9967		5.9967	5.9967	5.9967
		Past experiences of the performance in earthquakes			0.149	0.667	whether the past experiences of the alternative performance in earthquakes is important?	Yes		0.6668				
		Lightening possibility in the rehabilitating process			0.235	1.048	whether lightening the weight of the building in the rehabilitating process is needed?	No			0.0000	0.0000	0.0000	0.0000
Architectural Aspect	0.479	**Effect on the building's façade**			5.579	2.672	whether the functional interaction of the alternatives with the building's façade is authorized?	Yes			2.6723			
		Effect on the building spacing			1.219	0.584	whether the functional interaction of the alternatives with the building spacing is authorized?	No	0.0000		0.0000			
		Effect on the building lighting			2.633	1.261	whether the effect of the alternatives on the buildings' lighting is permitted?	Yes			1.2614			
		Changing the occupancy of rooms			0.569	0.273	whether the occupancy of rooms are changeable?	No	0.0000		0.0000			
Mechanical and Electrical Equipment					0.279	2.791	whether the functional interaction of the alternatives with the mechanical and electrical equipment is allowable?	No				2.7912	2.7912	2.7912
							(The most efficient alternative)= **Strengthening with the Interior shear wall**		**13.45**	**24.29**	**20.00**	**17.10**	**17.10**	**23.01**

Table 7: the applied criteria and evaluated alternatives

The consistency of the judgments is checked and the eq.5 is used to gain the final score in determination of the best alternative. The binary procedure is used as a complementary tool to cover the decision-making process. Depends on what is concluded from the classified criteria analyses by using the AHP method, the high ranked alternatives in each criterion are spotted (blue cells). The relative weights which are assigned in previous evaluation elicited and applied in this table. Based on client's circumstances and project's demand, provided questions; whether it is relevant and needed to consider or not; make a simplified point of view of the most appropriate alternative. Due to the distinctive specifications of different projects, the binary process is added to the decision analysis in order to help the decision makers to come up with their projects with an applicable tool incorporated with the basic concept of the masonry rehabilitation.

6 CONCLUSION

- Unreinforced masonry (URM) bearing wall buildings have shown poor performance in the past earthquakes and the reasons are the inherent brittleness, lack of tensile strength, and lack of ductility. Therefore, the rehabilitation is conducted for those buildings with inadequate capacity in order to improve its seismic performance. Whereas, the high amount of money that spend in this regard, stakeholders are so eager to complete the process in much less timeline and whatever the time duration of decision-making is less, the benefit of the process will be increase. Similar study was conducted by the authors in optimizing the selection process, but the method has a disadvantage that process was rigid model and can not be changeable for different projects in minimum time, so this study brings out the best usage of the model as a flexible model for different projects in a very simple way.
- The presented study helps decision-makers face complex problem with multiple conflicting and subjective criteria. However, explicit comparison of technical characteristics of the retrofitting options is usually conducted by performing linear or nonlinear analyses of the retrofitted building to check the acceptance criteria for structural, non structural and equipments, but the application will be useful in the preliminary evaluation of the alternatives and for buildings with less importance can be appropriate approach to decrease the process timeline.
- Based on the presented study, the method is developed to evaluate the optimum rehabilitation process of the unreinforced masonry buildings. The effective criteria and alternatives for the rehabilitation of these building are introduced and classified and according to the procedure they are evaluated comparatively. The final result indicates the effectiveness of the strengthening of the unreinforced masonry buildings with the shotcrete overlay.
- This paper presents a procedure in leading to select the best rehabilitation alternative of the unreinforced masonry (URM) buildings. The proposed method is carried out in three steps in which the effective criteria are classified and the hierarchical process is used to allot the weight to each criterion. Based on this process the proposed alternatives are compared to make the preferences of each one in different criteria. By using the binary concept the model is developed to select the optimum rehabilitation alternative of the specific unreinforced masonry buildings. The most remarkable characteristic of the applied model is its tendency to be done in minimum time and its simplified structure that will be useful for the decision-makers in this area to choose the optimum option by doing quick survey. The final result

indicates the effectiveness of the strengthening of the unreinforced masonry buildings with adding the interior shear wall.

7 ACKNOWLEDGEMENT

The study was carried out as a research project entitled “Development of the criterion for the vulnerability assessment and the rehabilitation process of the school buildings in Iran” awarded to the state organization of the schools renovation, development, and mobilization; and the support of the structural department of the international institute of earthquake engineering and seismology (IIEES) is appreciated.

8 REFERENCES

[1] Baker, D., Bridges, D., Hunter, R., Johnson, G., Krupa, J., Murphy, J., Sorenson, K., “*Guide to decision-making methods*”, developed for the department of energy, WSRC-IM-2002- 00002, 2002.

[2] Ghodsi poor, S., H., “*The discussion in multi-criteria decision-making, analytical hierarchy process (AHP)*”, Amir Kabir university press, 2000.

[3] Saaty, T.L., "*Relative measurement and its generalization in decision making why pair wise comparison are central in mathematics for the measurement of intangible factors the analytic hierarchy/network process*", RACSAM, statistics and operations research, vol 102(2), p.p 25-318, 2008.

[4] Saaty, T.L., “*Fundamental of the analytic network process-Multiple networks with benefits costs, opportunities, risks*”, journal of systems science and systems engineering, vol. 13, no. p.p 348-379, 2004.

[5] Ahmed, A., Kusumo, R., Savci, S., Kayis, B., Zhou, M., Khoo, Y.B., “*Application of analytical hierarchy process and Bayesian belief networks for risk analysis*”, complexity international, vol.12, 2005.

[6] Majumdar, A., Sarkar, B., Majumdar, P.K., “*Application of analytic hierarchy process for the selection of cotton fibers*”, fibers and polymers, vol.5, no.4, 297-302, 2004.

[7] Armacost, R.L., Hosseini, J.C., Pet-Edward J., “*Using the analytic hierarchy process as a two- phase integrated decision approach for large nominal group*”, group decision and negotiation 8: 535-555, 1999.

[8] Coulter, E., D., Coakley, J., “*The Analytic Hierarchy Process: a Tutorial for Use in Prioritizing Forest Road Investments to Minimize Environmental Effects*”, International journal of forest engineering, Volume 17 No. 2, July 2006.

[9] Linkov, I., Varghese, A., Jamil, S., Seager, T.P., Kiker, G., Bridges, T., “*Multi-criteria decision analysis: A framework for structuring remedial decisions at contaminated sites, comparative risk assessment and environmental decision making*”, kluwer, p.p 15-54, 2004.

[10] Khanmohammadi, S., Almeida Ribeiro, R., Jassbi, J., “*Multi-criteria decision making using dynamics criteria*”, 03C-MED-T3-013.

[11] Ishizaka, A., Labib, A., “*Analytic hierarchy process and expert choice: Benefit and limitation*”, ORInsight, 22(4), P.201-220, 2009.

[12] Chen, H., “*A research based on fuzzy AHP for multi-criteria supplier selection in supply chain*”, pc01.lib.ntust.edu.tw, (2005).

[13] McCaffrey, J., “The *Analytic Hierarchy Process, Test Run: The Analytic Hierarchy Process*”, MSDN Magazine, 2005.

[14] Saaty, T.L.," *The analytic hierarchy process*", McGraw Hill, New York, 1980.

[15] Azmoodeh, B., M., Moghadam, A.S., "*Optimum Seismic Retrofitting Technique for Buildings", civil engineering and environmental systems*, vol 28, issue 1, 2011.

[16] Grossi, P.A., "*Assessing the Benefits and Costs of Earthquake Mitigation*", Financial Institution Center, The Wharton school-University of Pennsylvania, 1998.

[17] Balcomb, J.D., Curtner, A., "*Multi-criteria decision-making process for buildings*", NREL/CP-550-28533, 2000.

[18] Azmoodeh, B., M., Moghadam, A.S., "*The effective parameters in the evaluation of the building seismic retrofitting”*, the conference of the new technologies in the seismic rehabilitation, the organization of the management and planning, 2006.

[19] *Design and construction of the masonry buildings (part 8)*, Iranian national provision of the building, ministry of building & urban development, 2005.

[20] *Iranian code of practice for seismic resistant design of buildings standard, no.2800-05,* building & house research center, permanent committee for revising the Iranian code of practice for seismic resistant design of buildings, 2005.

[21] *Code 376, seismic rehabilitation of the unreinforced masonry buildings,* International Institute of Earthquake Engineering and Seismology, Management and Planning Organization, Iranian building codes and standards, 2007.

[22] *Code 360, seismic rehabilitation of the existing buildings (SREB),* International Institute of Earthquake Engineering and Seismology, Management and Planning Organization, Iranian building codes and standards, 2002.

[23] *Seismic rehabilitation of existing buildings*, American society of civil engineers (ASCE 41- 06), 2007.

[24] Santiago, H., “*The analysis of masonry architecture: a historical approach*”, Architectural Science Review articles, the Gale Group, Farmington Hills, Michigan, 2008.

[25] *FEMA-356, Prestandard and commentary for the seismic rehabilitation of buildings,* Federal Emergency Management Agency, Washington DC, 2000.

[26] Anand, S., Agarwal, A. “*seismic assessment of brick masonry building*”, national disaster management division, ministry of home affairs, New Delhi.

[27] *New Zealand standard concrete masonry buildings not requiring specific engineering design*, NZS 4229:1999, Hutcheson Bowman & Stewart, 1999.

[28] *Acceptance criteria for dynamic seismic retrofit system for masonry structures*, ICC evaluation service, INC. 2006.

[29] Hess, R., L., "*unreinforced masonry (URM) buildings*", the shake out scenario (supplemental study), prepared for United States geological survey and California geological survey, 2008.

[30] T*echnologies for retrofitting of existing buildings and structures to make them earthquake resistant*- Retrofitting of masonry buildings, technology information, forecasting and assessment council (TIFAC), India, (www.tifac.org.in).

COMPDYN 2011
3rd ECCOMAS Thematic Conference on
Computational Methods in Structural Dynamics and Earthquake Engineering
M. Papadrakakis, M. Fragiadakis, V. Plevris (eds.)
Corfu, Greece, 25–28 May 2011

SEISMIC RESPONSE OF A STONE MASONRY SPIRE

Matthew J. DeJong[1], **Christopher Vibert**[1]

[1] University of Cambridge
Trumpington Street, Cambridge, CB2 1PZ, United Kingdom
mjd97@cam.ac.uk, cv257@cam.ac.uk

Keywords: masonry, spire, rocking, heritage structures, discrete element modeling.

Abstract. *Stone masonry spires are vulnerable to seismic loading. Computational methods are often used to predict the dynamic linear elastic response of masonry spires, but this approach is significantly limited to the point when the first masonry joint begins to open. In this paper, analytical and computational modeling methods are used to address the full dynamic response of masonry spires until collapse. An analytical framework is first presented, which addresses both the elastic oscillation response and the rigid rocking response of masonry spires. In this context, the seismic response of the spire of the church of St. Mary Magdalene in Waltham on the Wolds, United Kingdom, which was damaged in the 2008 Lincolnshire Earthquake, is addressed. Both analytical and computational discrete element modeling are applied to predict the response to a variety of base accelerations. Results of both methods are compared to evaluate their utility and to understand the seismic damage which occurred.*

1 INTRODUCTION

Large earthquakes are relatively rare in the United Kingdom, and ensuing damage is often limited to unreinforced masonry spires, chimneys and towers. As spires typically top significant heritage structures, there are numerous recorded examples of spire damage during historic seismic events [e.g. 1,2]. More recently, several stone masonry spires were badly damaged during the 2008 Lincolnshire Earthquake in the United Kingdom, despite the relatively small magnitude of earthquake ground motion. The damage to one such spire, which sat atop the 13th century parish church of St. Mary Magdalene in Waltham on the Wolds, provides the impetus for this research, and will be used as a case study herein.

The stability of masonry spires under static dead load and wind load was addressed by Heyman [3] in the context of ultimate load theory, assuming i) infinite compressive strength, ii) zero tensile strength, and iii) no sliding between masonry units. Heyman [3] assumes that octagonal spires can be modeled as conical shells, and demonstrates the importance of a solid spire tip to resist overturning during high winds.

The dynamic response and collapse of masonry spires has been given relatively little attention. Previous studies concentrate on the onset of cracking due to elastic response, rather than the prediction of post-damage response and complete collapse. In this study, dynamic response is also tackled in the context of rocking structures, for which the literature is extensive. Housner [4] provides the fundamental formulation for investigating the rocking response. Zhang and Makris [5] provide a critical contribution regarding the response of rocking objects to cycloidal pulses which can dominate earthquake ground motions and govern overturning collapse.

The dynamic response of masonry structures can be computationally predicted using Discrete Element Modeling (DEM), which models the contact and separation between individual stones within a masonry structure. In particular, DEM was used to model the dynamic rocking response of the masonry arches by De Lorenzis *et al.* [6], with a more in-depth sensitivity study of modeling parameters provided by DeJong *et al.* [7]. These studies demonstrate the utility of DEM to evaluate analytical models which capture the governing dynamic response.

The aim of this paper is to provide a general approach for evaluating the dynamic response of masonry spires under seismic loading, and then to evaluate that approach by assessment of the damage to the spire of the parish church of St. Mary Magdalene. The general approach is presented first, and makes use of an analytical formulation for predicting damage and rocking response. Subsequently, DEM is used to evaluate the analytical approach through an in-depth computational investigation of the spire in question.

2 ANALYTICAL FORMULATION

The analytical approach for modeling the dynamics of masonry spires will be broken down into three aspects. First, static analysis will be used to obtain a reference point for lateral stability. Second, the linear elastic dynamic response will be approximated. Finally, the rigid rocking response will be considered. A conical shell is assumed to be representative of the octagonal spire, and the three assumptions of ultimate load theory are taken [3].

2.1 Static Analysis

As a starting point, static analysis is useful to determine the minimum horizontal ground acceleration (if applied for infinite duration) necessary to cause overturning of a conical shell. For the geometry in Figure 1(a), the fraction (λ) of gravitational acceleration (g) required for overturning is:

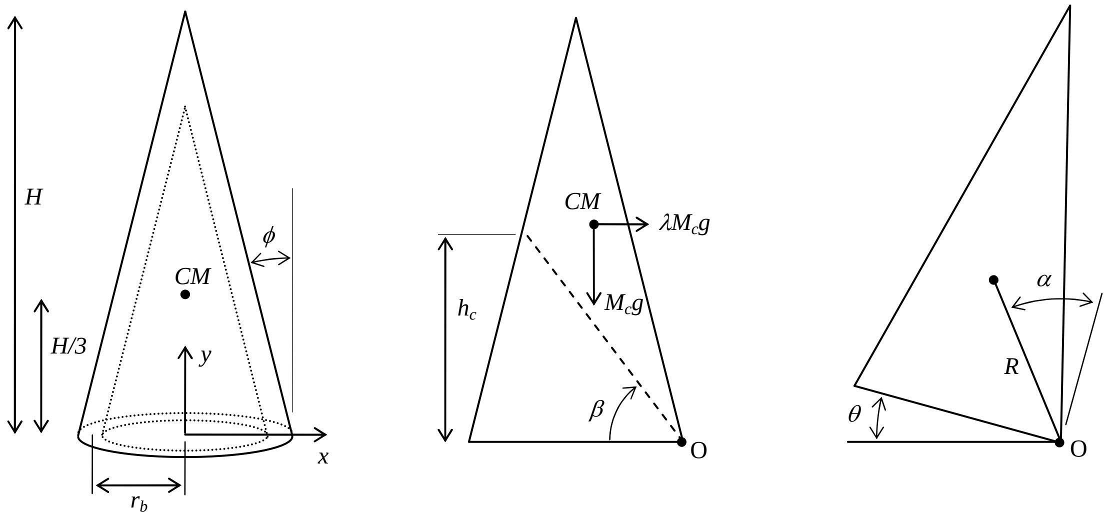

(a) (b) (c)

Figure 1: Definition of masonry spire geometry.

$$\lambda = \frac{3r_b}{H} \tag{1}$$

The conical shell has a relatively low center of gravity (H/3), and is therefore more resistant to overturning than a solid rectangular prism. However, assuming masonry structures have no tensile capacity, diagonal cracks may open when lateral loads are applied [8]. In reality, the location of these cracks may be limited by interlocking of blocks, but assuming that a diagonal crack can form at any angle β (Figure 1(b)), the fraction (λ) of gravitational acceleration (g) required for overturning is:

$$\lambda = \frac{3r_b}{H}\frac{\left(\frac{1}{\pi^2}h_c{}^3 - \left(\frac{2}{\pi^2}-\frac{2}{3}\right)h_c{}^2H - 2h_cH^2 + 2H^3\right)}{\left(h_c{}^3 - 2h_c{}^2H + 2H^3\right)} \tag{2}$$

where h_c is the crack height in Figure 1(b).

2.2 Dynamic Elastic Analysis

The dynamic response of masonry structures involves two stages: an initial elastic stage, during which the entire structure remains in compression, followed by a ‘rocking’ stage, during which masonry units separate and regain contact. The elastic stage will be addressed first, followed by the rocking stage in the next section.

Due to the slender nature of spires, Euler-Bernoulli beam theory can be used to estimate natural frequencies and mode shapes. The mass per unit height, *m(y)*, and bending stiffness, *EI*(y), of the spire can be written as:

$$\begin{aligned} m(y) &= \left(1-\frac{y}{H}\right)m_b \\ EI(y) &= \left(1-\frac{y}{H}\right)^3 EI_b \end{aligned} \tag{3}$$

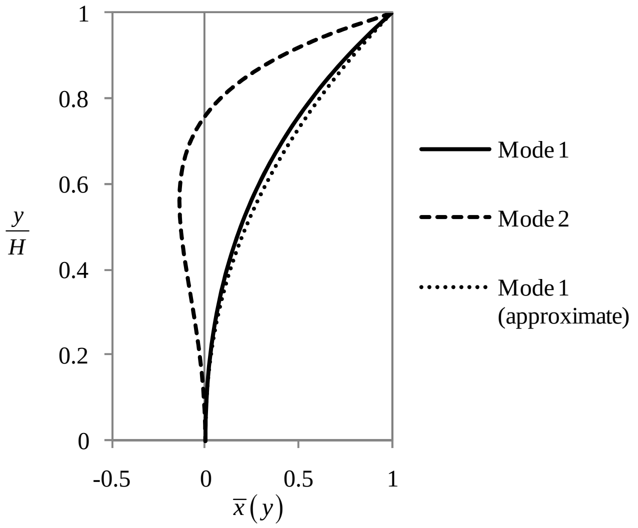

Figure 2: First two modes shapes of a conical shell [10], and the first mode shape from Equation (5) with *k* = 2.2.

where m_b is the mass per unit height at the base, I_b is the second moment of area at the base, and E is the Young's Modulus.

Therefore, the mass and bending stiffness vary similarly to the solid wedge beam analyzed by Naguleswaran [9], who determined the corresponding natural frequencies:

$$\omega_n = \sqrt{\frac{\Omega_n^{\,2} E I_b}{m_b H^4}} \tag{4}$$

where Ω_n = 5.315, 15.21, and 30.02 for the first three modes. The fundamental mode shapes for the first two modes are depicted in Figure 2.

Alternatively, Rayleigh's principle can be used to estimate the mode shape and compute the corresponding natural frequencies. Assume a mode shape of the form:

$$\bar{x}(y) = \left(\frac{y}{H}\right)^k \tag{5}$$

where $\bar{x}(y)$ is the modal translation at height *y*, and *k* is a constant. The fundamental natural frequency is approximated by:

$$\bar{\omega}_1 = \sqrt{\frac{\int_0^H EI(y)\left(\frac{d^2\bar{x}}{dy^2}\right)^2 dy}{\int_0^H m(y)\left(\bar{x}(y)\right)^2 dy}} \tag{6}$$

The minimum fundamental frequency $\bar{\omega}_1$ occurs for *k* = 2.2, and the corresponding mode shape compares reasonably well with the actual mode shape derived by Naguleswaran [9] (Figure 2). Modal analysis using equations (5) and (6) can now be applied to determine the point at which elastic oscillation would cause damage and initiate a rocking response.

2.3 Dynamic Rocking Analysis

If the earthquake loading induces a large enough response, the spire would begin to rock as it has no tensile capacity, and the elastic natural frequencies would be completely altered. To investigate whether rocking could cause collapse, consider a rigid conical shell on a rigid foundation.

The rigid conical shell will begin to rock (Figure 1(c)) when the overturning moment exceeds the resisting moment, which occurs at a maximum ground acceleration of $a_{crit} = \lambda g$, where λ is defined in Equation (1) above. Once rocking commences, the response can be treated in a similar fashion to Housner [4], assuming spinning of the cone about its vertical axis does not occur. The equations of motion are:

$$\begin{aligned} I_0\ddot{\theta} + MgR\sin\left(+\alpha-\theta\right) &= -M\ddot{u}_g R\cos\left(+\alpha-\theta\right) \quad \rightarrow \quad \theta > 0 \\ I_0\ddot{\theta} + MgR\sin\left(-\alpha-\theta\right) &= -M\ddot{u}_g R\cos\left(-\alpha-\theta\right) \quad \rightarrow \quad \theta < 0 \end{aligned} \tag{7}$$

where M is the total mass of the cone, R, α, and θ are defined in Figure 1(c), and I_O is the mass moment of inertia about point O in Figure 1(c):

$$I_0 = \frac{5}{4}Mr_b^{\,2} + \frac{1}{6}MH^2 \tag{8}$$

Assuming small angles, equation (7) can be rewritten in the form:

$$\begin{aligned} \ddot{\theta} - p^2\theta &= -p^2\left(\frac{\ddot{u}_g}{g} + \alpha\right) \quad \rightarrow \quad \theta > 0 \\ \ddot{\theta} - p^2\theta &= -p^2\left(\frac{\ddot{u}_g}{g} - \alpha\right) \quad \rightarrow \quad \theta < 0 \end{aligned} \tag{9}$$

where $p = \sqrt{MgR/I_O}$ is the frequency parameter of the block.

Still following the formulation of Housner [4], the impact can be modeled by a coefficient of restitution, c_v, defined as the ratio of the angular velocities before and after impact:

$$c_v = 1 - \frac{MR^2}{I_O}\left(1 - \cos 2\alpha\right) \tag{10}$$

Equations (9) and (10) now describe the response of the conical shell to horizontal ground motion in general. However, as ground motion impulses often govern overturning collapse, impulse collapse diagrams similar to those presented by Zhang and Makris [5] could directly be plotted.

Finally, the fact that the spire has no tensile capacity must again be considered. Diagonal cracking could result in the rocking response of the ‘cracked cone’ in Figure 2(b) about point O, where point O need not be located at the bottom corner. The crack could occur further up the spire. In this case, equations (7) and (9) could still be used to predict the dynamic response, but the impact formulation must be reconsidered.

3 DISCRETE ELEMENT MODELING

Discrete Element Modeling (DEM) is a tool which can predict the more detailed response of a spire which is actually comprised of numerous separate masonry units. DEM will be used to predict levels of damage and collapse to the spire, rather than to predict precise displacements, which is impossible. In this section, the modeling assumptions are first explained, followed by simulation of static, impulse, and earthquake loading. All simulations were carried out using 3DEC [10].

3.1 Spire Characteristics and Modeling Assumptions

The spire of the church of St. Mary Magdalene in Waltham on the Wolds, UK (Figure 3(a)), was badly damaged during the earthquake, after which the top half of the spire was reconstructed (Figure 3(b)). Construction and survey documents from the dismantling of the spire were used to develop an accurate model of the pre-earthquake spire, in which each stone is individually considered (Figure 3(c)). All earthquake damage was concentrated above the height of the top windows, so only the reconstructed section was modeled. The entire spire is 19.1 meters tall; the model consists of the top 9.4 meters (Figure 3(d)). The top 3.4 meters of spire is solid, with each course tied together by an interior metal rod. This section was modeled as a single rigid block. The average height of each masonry course is 0.3 meters, with an assumed average hydraulic lime mortar joint thickness of 1 cm.

The modeling parameters used for DEM simulations are presented in Table 1. Rigid blocks were specified to limit computational time. The joint stiffness k_j was calculated by lumping all of the stone and mortar deformation in the joints [11]. Stiffness proportional damping was specified to approximate inelastic impact between blocks and to limit unrealistic high frequency vibrations [11]. Mass proportional damping was not used.

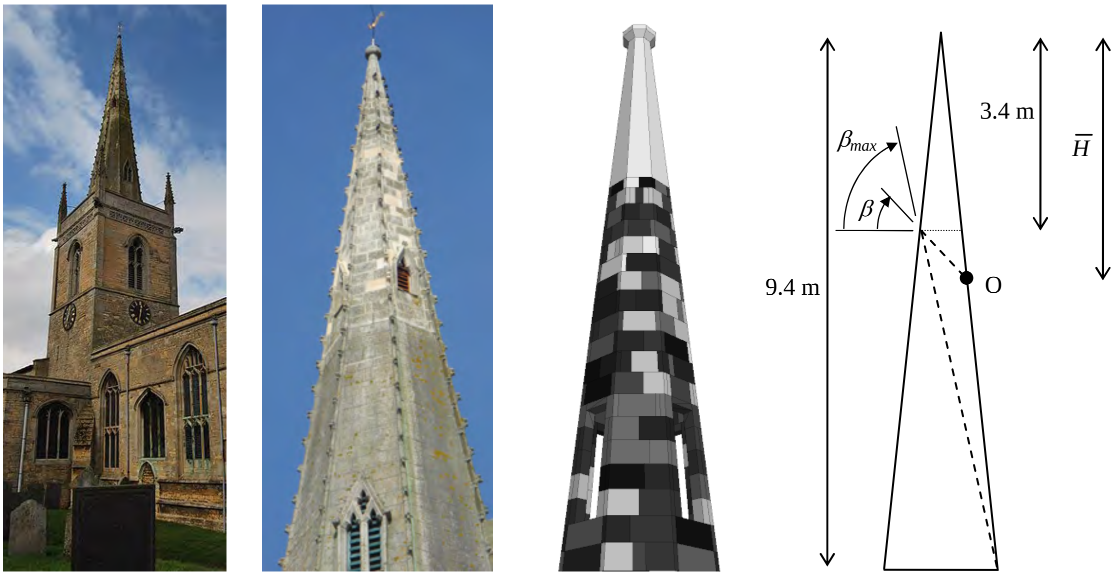

(a) (b) (c) (d)

Figure 3: (a) Church of St. Mary Magdalene, (b) repaired masonry spire, (c) DEM model of spire, and (d) model spire geometry.

E_{stone} [GPa]	E_{mortar} [GPa]	Density, ρ [kg/m^3]	k_{joint} [GPa/m]	Friction angle [degrees]	Stiffness proportional damping constant [-]
30	10	2600	98	30	$2.1\text{x}10^{-5}$

Table 1: Modeling parameters.

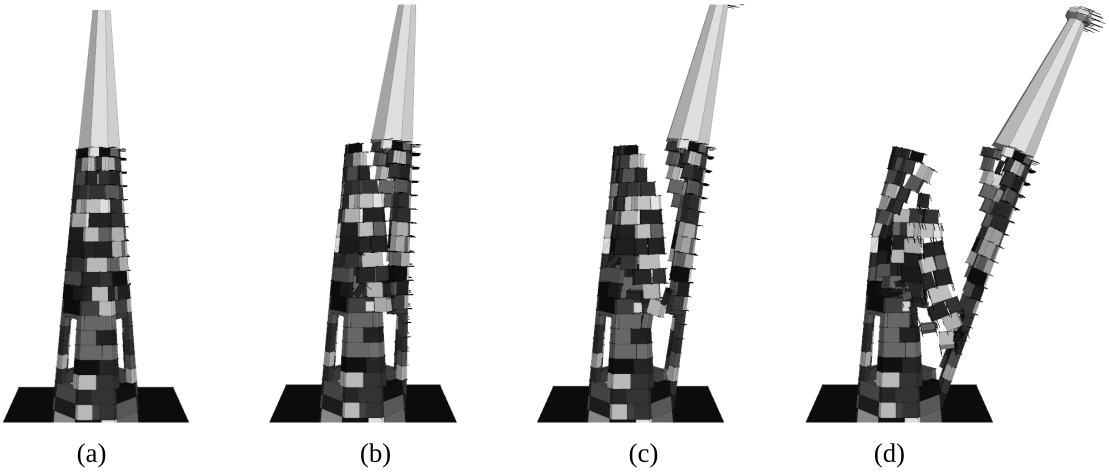

Figure 4: Progressive collapse under constant horizontal ground acceleration.

3.2 Constant acceleration results

To evaluate the minimum possible acceleration which could cause collapse, an increasing horizontal acceleration was applied until the overturning occurred. As expected, diagonal cracking of the spire occurred (Figure 4). The window openings and the lack of interlocking between blocks above the windows allowed a remarkably vertical crack to form. The collapse acceleration varied from 0.164g to 0.176g in the four horizontal directions, showing some effects of varying block interlock. In general, the spire collapsed with a crack angle of approximately $\beta_{\max}$ (Figure 3(d)). According to equation (2), $\lambda = 0.192$, which compares well considering the assumption of a perfect conical shell instead of a windowed octagonal spire with vertical joints. A refined analytical model including the solid tip and more precise geometry yields $\lambda = 0.168$.

It is worth noting that even this simple simulation indicates that the poor interlock between blocks limited the ability of the spire to withstand lateral acceleration. Friction due to better interlocking could significantly reduce β.

3.3 Single Impulse Results

The spire was also subjected to a suite of single cycle sinusoidal ground acceleration pulses of maximum amplitude a_p and of duration T_p. The response of the spire was repeatedly simulated to evaluate the pulse characteristics which cause damage (visible residual displacements) and complete collapse. The results are presented in Figure 5, in which the regions above the curves represent regions of damage and collapse respectively. A representative rocking response of the spire is depicted in Figure 6, where the ground moves to the right and the spire rocks to the left (Figure 6(a,b)), recovers and impacts (Figure 6(c)), and then collapses to the right (Figure 6(d)). This mode of collapse will be referred to as Mode I collapse; immediate collapse to the left without impact will be referred to as Mode II collapse (after [5]).

The analytical model presented in §2.3 enables the prediction of Mode I and Mode II rocking collapse. However, the response is sensitive to p. For two identical spires of different scale, the larger will be much more resistant to overturning. The collapse curve for the entire spire (9.4 meters tall), and for the solid spire tip alone (3.4 m tall), are also presented in Figure 5. The region inside the lower loop of the collapse curve represents Mode I collapse, while the region above the upper portion of the collapse curve represents mode II collapse. Clearly the tip alone is more vulnerable.

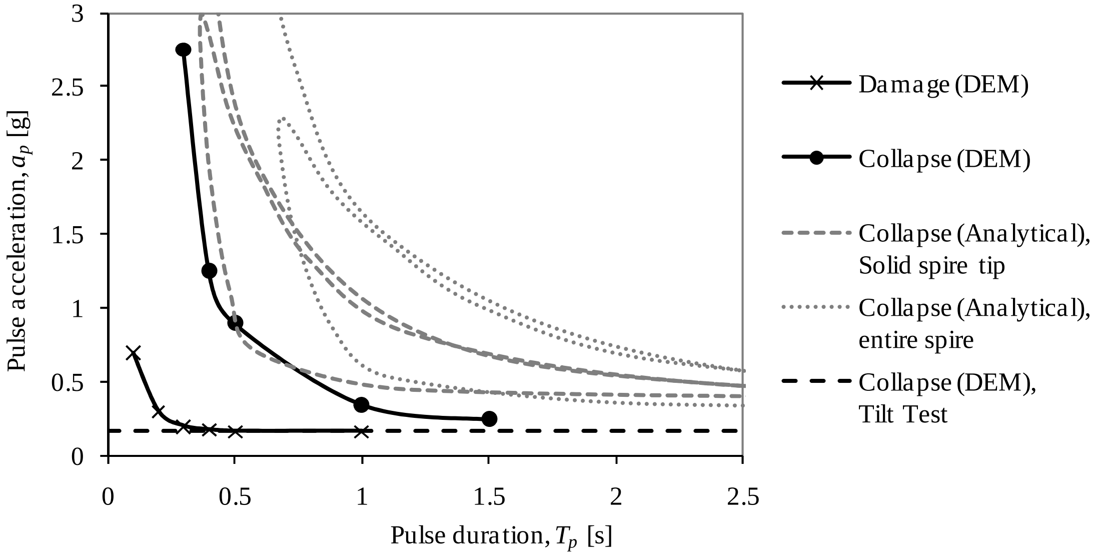

Figure 5: Damage and collapse diagram for a single sinusoidal base acceleration pulse.

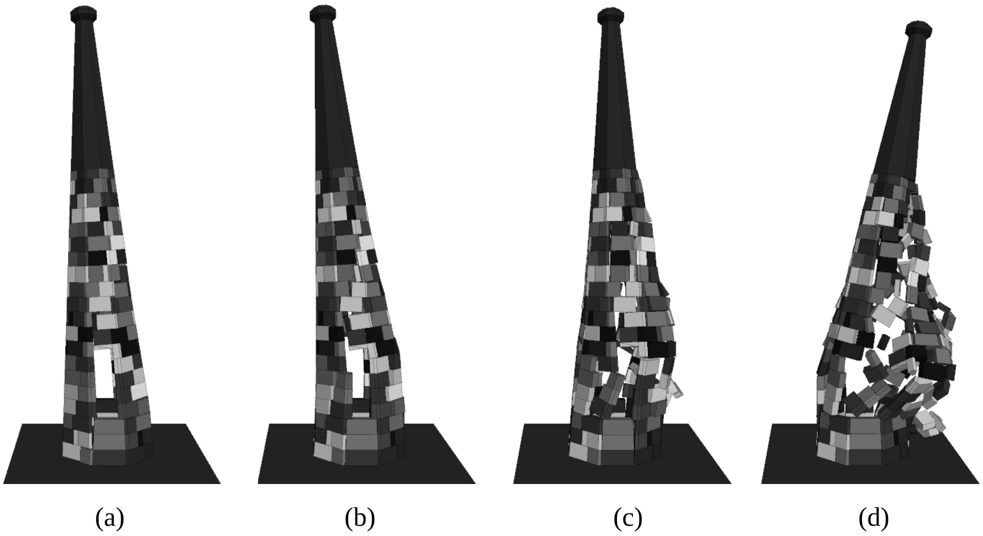

Figure 6: Progressive collapse under for a single sinusoidal base acceleration pulse with a_p = 1.0 g and T_p = 1.0 s (ground moves to the right).

In addition to considering the entire cracked cone and solely the cone tip, there may be a worse condition. Suppose the spire is allowed to crack, and the cracked portion begins rocking. For this case the maximum *p* value would shift the collapse curve furthest to the left. If the crack is assumed to initiate just below the solid tip, *p* is plotted as a function of the cracked height $\bar{H}$ in Figure 7(a). For the spire in question, the maximum value of *p* occurs for $\bar{H}$ = 4.1 meters, which would yield the collapse curve in Figure 7(b).

The results indicate that while rocking of the cracked spire tip is theoretically the worst condition, it may be slightly conservative. In fact, Mode I collapse due to this condition is unlikely due to the inability of the rocking mechanism to reflect without significant dissipation of energy. Instead, an alternate mode of failure may govern, in which the impulse is not large enough to cause Mode II collapse of the cracked spire, but the impulse is large enough to cause significant damage to the non-rocking portion of the spire, which then cannot sustain the impact resulting when the rocking portion of the spire recovers.

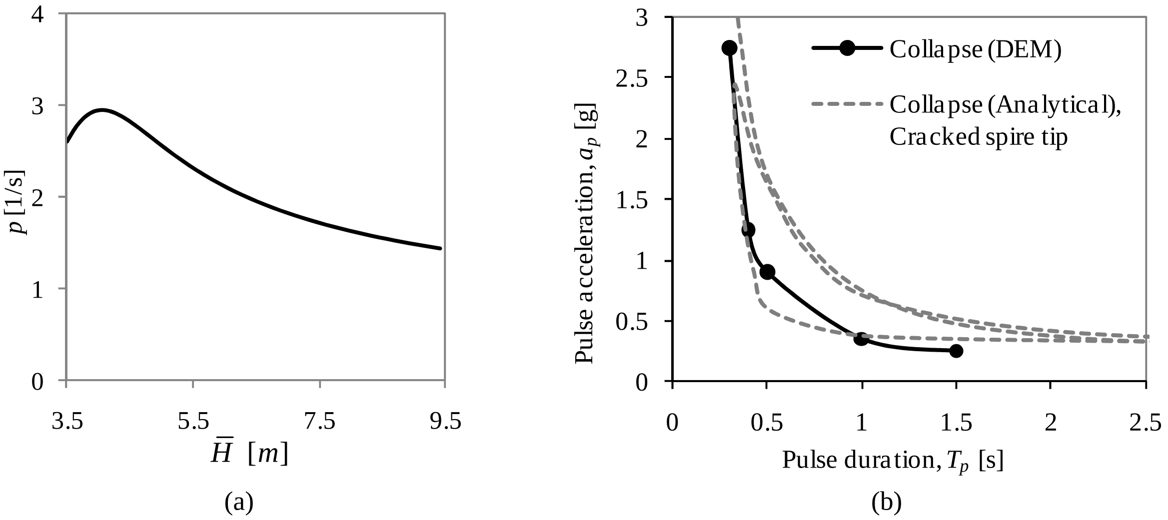

Figure 7: Progressive collapse under for a single sinusoidal horizontal base acceleration pulse.

Regardless, Figures 5 and 7(b) indicate that the primary impulse within the earthquake ground motion experienced by the spire was way too small for rocking damage or overturning collapse to occur.

3.4 Seismic Response Results

Unfortunately, ground motion acceleration data from the location of the earthquake was not available near the location of the spire. Instead, ground motion data from a similar epicentral distance was used. Unfortunately, this completely alters the effects of seismic wave directionality and local soil amplification. To compensate, the ground motion was scaled by a range of 2-6 times to account for local site amplification due to differences in soil conditions.

To determine the response of the spire, it is also necessary to consider the amplification of the ground motion by the structure itself. Using a procedure similar to that presented in §2.2, the natural frequency of the combined tower and spire was estimated to be ~ 6.8 Hz. The spectral earthquake data reached its maximum in a similar frequency range, so the fundamental mode was determined to dominate the response, and was used to approximate the horizontal motion at the base of the DEM model.

The DEM model was then used to simulate the seismic response. While assumptions are too numerous to be able to expect to exactly predict the spire response, a few conclusions can be drawn. Because the input acceleration was larger than 0.17g for very short durations, overturning mechanisms were repeatedly formed and closed almost immediately, causing the spire to very slightly walk apart, and leaving vertical gaps between stones (Figure 8(b)). Increased amplification of the ground motion input led to increased ‘walking’ and larger vertical gaps between stones. These same vertical gaps appeared above the windows of the actual spire (Figure 8(a)), and led to the need for reconstruction. The duration of the strong motion portion of the earthquake also appears to be critical to evaluate the level of ‘walking’. Generally, it is evident that earthquake ground accelerations must have been amplified locally, by both the soil and the structure, to have caused the observed damage.

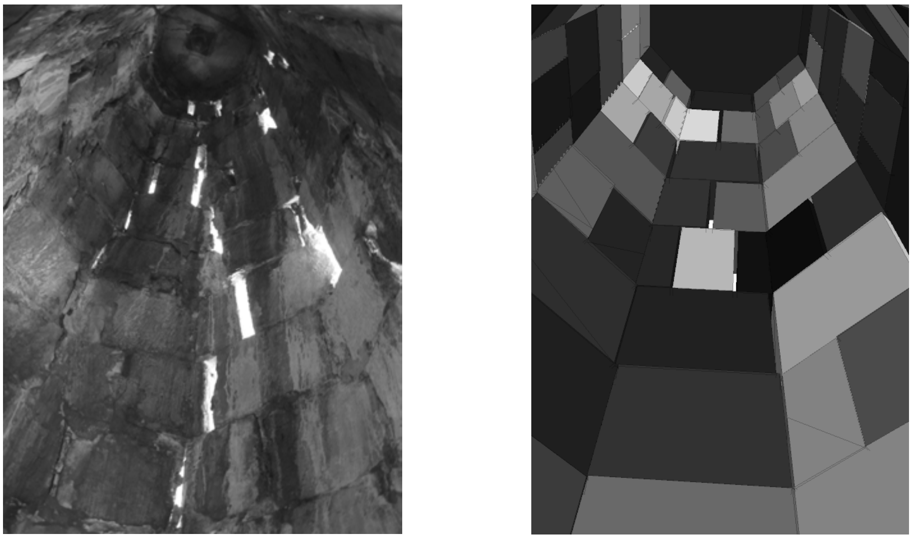
(a) (b)

Figure 8: Interior view of spire: (a) actual damage, (b) DEM simulation of damage.

4 CONCLUSIONS

The seismic collapse of unreinforced masonry spires is difficult to predict. There is clearly an initial elastic response which must be considered, followed by a rocking response which completely alters the dynamics of the system. The analytical approach presented herein provides a context for dealing with both of these aspects of the dynamic response. However, due to the number of simplifying assumptions involved in the analytical formulation, DEM is critical to evaluate the actual spire response.

Both the analytical and computational results indicate that the damage to the spire of the church of St. Mary Magdalene could not have been caused by the acceleration magnitudes recorded at a similar epicentral distance, or even the ground acceleration scaled due to local soil conditions. Additionally, it was not likely that the damage was caused by a single impulse within the ground motion. Instead, structural amplification seems to have caused large enough accelerations at the top of the spire to cause the spire to walk apart over a longer duration of time, producing the observed damage.

REFERENCES

[1] P. Hanning, *The Great English Earthquake*, Robert Hale Limited, 1976.

[2] S. Sargeant, R.M.W. Musson, Rotational earthquake effects in the United Kingdom. *Bulletin of the Seismological Society of America*, **99**(2B), 1475–1479, 2009.

[3] J. Heyman, *The stone skeleton*, Cambridge University Press, 1995.

[4] G.W. Housner, The behavior of inverted pendulum structures during earthquakes, *Bulletin of the Seismological Society of America*, **53**(2), 403-417.

[5] J. Zhang, N. Makris, Rocking response of free-standing blocks under cycloidal pulses, *ASCE Journal of Engineering Mechanics*, **127**(5), 473-483, 2001.

[6] L. De Lorenzis, M.J. DeJong, J. Ochsendorf, Failure of masonry arches under impulse base motion, *Earthquake Engineering and Structural Dynamics*, **36**(14), 2119-2136, 2007.

[7] M.J. DeJong, L. De Lorenzis, J. Ochsendorf, Numerical modeling of masonry arch stability under impulse base motion, M. Papadrakakis *et al.* (eds.), *Computational Methods in Structural Dynamics and Earthquake Engineering (COMPDYN2007),* Rethymno, Crete, Greece, June 13-16, 2007.

[8] J.A. Ochsendorf, J.I. Hernando, S. Huerta, Collapse of masonry buttresses, *ASCE Journal of Architectural Engineering*, **10**(3), 2004.

[9] S. Naguleswaran, A direct solutions for the transverse vibration of Euler-Bernoulli wedge beams and cones. *Journal of Sound and Vibration*, **172**(3), 289-304, 1992.

[10] Itasca Consulting Group, *3DEC Version 3.0: User's Guide*, Minneapolis, Minnesota, 2003.

[11] M.J. DeJong, *Seismic assessment strategies for masonry structures*, Ph.D. Dissertation, Massachusetts Institute of Technology, Cambridge, Massachusetts, 2009.

COMPDYN 2011
III ECCOMAS Thematic Conference on
Computational Methods in Structural Dynamics and Earthquake Engineering
M. Papadrakakis, M. Fragiadakis, V. Plevris (eds.)
Corfu, Greece, 25–28 May 2011

EARTHQUAKE RESISTANT DESIGN OF MASONRY STRUCTURAL SYSTEMS

I.P. Giannopoulos[1], P.G. Asteris[2]

[1] Research Associate, Computational Mechanics Laboratory, School of Pedagogical &Technological Education, Heraklion, GR 141 21, Athens, Greece
e-mail: igianno@cantab.net
[2] Asst. Professor, Computational Mechanics Laboratory, School of Pedagogical &Technological Education, Heraklion, GR 141 21, Athens, Greece
asteris@aspete.gr

Keywords: Masonry structures, earthquake resistance design, failure criterion, failure surface

Abstract. *Masonry structures are complicated structures and there is, currently, a lack of knowledge and information concerning the behaviour of their structural system under seismic loading. Successful modeling of a masonry structure is a prerequisite for a reliable earthquake resistant design. However, modeling a real structure to a robust quantitative (mathematical) representation is a very difficult and complicated task. This paper is presenting a contribution toward a solution of the problem. A new methodology for earthquake resistant design of masonry structural systems, either before or after their repair and/or strengthening is presented. The whole process is illustrated using the case study of a typical 4-storey masonry structure of the city of Patras in Greece.*

1 INTRODUCTION

The majority of the main structural systems for historical structures are masonry elements, composed of stone, bricks and mortar. For all types of old historical masonry structures (including monuments) erected in seismic zones of high seismicity, earthquake is always their number one “enemy” due to their very bad response to earthquakes [1]. The responsibility of protecting a historical structure falls mainly on the shoulders of the engineer. A successful intervention on a monument requires a good comprehension of its structural behaviour under static and dynamic (earthquake) loading. For an engineer, taking part to the restoration process of a historical structure, through the analysis of its structural system, means mainly to face the demanding task of equipping the historical structure with the capability to withstand future actions with the minimum possible amount of damage, while bearing in mind the characteristics and values which make this structure unique and worthy of special attention. This has to be carried out within the conditions imposed by current regulations and scientific Charters (e.g. the Athens Charter 1931 [2] the Venice Charter 1964 [3], etc.), which make the process of analysis more complicated.

Masonry structures are complicated structures and there is lack of knowledge and information concerning the behavior of their structural system under seismic loads. What can only be said is that typically these structures are more massive than today’s structures and that they usually carry their actions primarily in compression. It should be noted here that most of these historical structures were built with specific consideration given mainly to their geometry and aesthetic quality and less to their structural integrity.

Successful modeling of a masonry historical structure is a prerequisite for a reliable earthquake resistant design. Recent methods of analysis should be very carefully applied on masonry structures. For modern structures, with new industrial materials used (reinforced concrete, steel, etc.), the development of a reliable mathematical model is usually possible, due to the fact that, materials and member characteristics are uniform and mostly explicitly known. On the other hand, for the case of masonry, and especially for the traditional plain one, it seems that there is a lot to be done on that field, until engineers become confident about the accuracy of the modeling.

For the purpose of masonry analysis and design, an operationally simple strength criterion is essential. Masonry has a mechanical behavior, which has not yet been fully investigated. Systematic experimental and analytical investigations on the response of masonry and its failure modes have been conducted in the last decades. There have been numerous analytical criteria for masonry structures [4][5][6]. The main disadvantage of existing criteria is that they ignore the distinct anisotropic nature of masonry; even if they do not ignore that, they consist of more than one type of surface leading to additional effort in the analysis process of the masonry structures [7]. According to Zienkiewicz et. al [8] the computation of singular points on failure surfaces may be avoided by a suitable choice of a continuous surface, which usually can represent, with a good degree of accuracy, the real condition.

Since reliable experimental data in the combined-stress state are rising rapidly [9][10][11], it is, therefore, timely to examine the validity and utility of existing criteria, and to propose a failure surface of convex shape suitable for the anisotropic nature of masonry material. According to Hill [12] and Prager [13] the failure surface for a stable material must be convex. This, in mathematical terms, is valid if the total Gaussian curvature K of the failure surface is positive.

As can be concluded, various researchers have been working on the earthquake resistant design of masonry structural systems and especially determining a strength criterion, but there is still a lot ongoing research on that field.

2 EARTHQUAKE RESISTANT DESIGN OF MASONRY STRUCTURAL SYSTEMS

2.1 Methodology

The proposed methodology includes six steps for the structural analysis of a historical building. Detailed architectural and structural drawings, describing the existing status of the structure, are always prerequisites for the application of the proposed methodology.

(1) Material characteristics
The characteristics of materials composing the structure are basic input data for structural analysis. Namely, the compressive-tensile strength of the materials, their modulus of elasticity and Poisson ratio are of primary importance. For the estimation of those parameters, combination of analytical or semi-empirical methods and experimental data have to be used. For the determination of the masonry compressive and tensile strength, several semi-empirical expressions exist. Among them the formulae [14]:

$$f_{wc} = \xi\left[\left(\tfrac{2}{3}\sqrt{f_{bc}} - a\right) + \beta f_{mc}\right] \qquad f_{wt} = \frac{2}{3} f_{mt} \qquad (1)$$

(compressive strength) (tensile strength)

are combining all parameters affecting the value of f_w. These parameters are described elsewhere in detail [14].

(2) Structural model
A 3-D finite element model seems to be generally the most suitable for the analysis.

(3) Actions
Different loading cases have to be taken into consideration, including the seismic actions, especially for structures built in seismic areas. Combinations of dead loads, live loads and earthquake loads, is used, following the general rules provided by codes [18][19]. Earthquake has to be considered along all unfavorable directions for the building.

(4) Analysis
Using input data of the previous steps a Finite Element Analysis is performed and moments (normal-shear) - displacements at the joints of the mesh are calculated. Due to the actual behaviour of plain masonry and the high degree of uncertainty in the previous steps, elastic analysis seems to be the most realistic one for the analysis of such structures, especially before any repair and/or strengthening.

(5) Failure criterion
A failure criterion must be established for the definition of the failed regions of the structure. Taking into account the conclusions of step 1 concerning materials' characteristics, such a criterion is proposed, and will be used as an input to carry out the analysis.

(6) Repairing and/or strengthening decisions and reanalysis
According to the results of step 5, all the failed regions are repaired and/or strengthened. The method to be used, the extend of the interventions, the type of the materials, etc., are directly related to the results and are based on semi-empirical expressions for the final mechanical characteristics of masonry [14].

Last, a new structural analysis has to be performed, using the new materials, loadings and structural data. Results of the analysis have subsequently to be used in the process of step 5, leading to a final approval (or rejection) of the decisions already taken for repair or strengthening of the existing structure.

2.2 Failure criterion

The basic step of the proposed methodology is the quantitative damage evaluation of masonry, which is the basic material of historical and monumental structures. The damage is estimated by a cubic polynomial function that is used for composite materials. In this method, the failure surface in the stress space can be described by the equation [15][16].

$$\begin{aligned}&2.27\sigma_x + 9.87\sigma_y + 0.573\sigma_x^2 + 1.32\sigma_y^2 + 6.25\tau^2 - 0.30\sigma_x\sigma_y + \\ &+ 0.009585\sigma_x^2\sigma_y + 0.003135\sigma_x\sigma_y^2 + 0.28398\sigma_x\tau^2 + 0.4689\sigma_y\tau^2 = 1\end{aligned} \tag{2}$$

Their results showed a good correlation with data from the literature. However, this anisotropic failure criterion applies only to the specific masonry material that he was studying. This disadvantage could be reversed if this criterion is expressed in a non-dimensional form, and, as such, can be applied more generally to a plethora of masonry materials. This can be achieved by dividing and multiplying (at the same time) each term in Eq. 2 by one material monoaxial strength raised in the sum of the exponents of the variables σ_x, σ_y, τ (as appeared in each term). It is selected the uniaxial compressive strength Y' to be across the y-axis, which, in terms of the masonry material corresponds to the uniaxial compressive strength denoted with the symbol $f_{wc}^{90^\circ}$. This model was proposed by Asteris et al. [17].
Eq. 2 can thus take the following form:

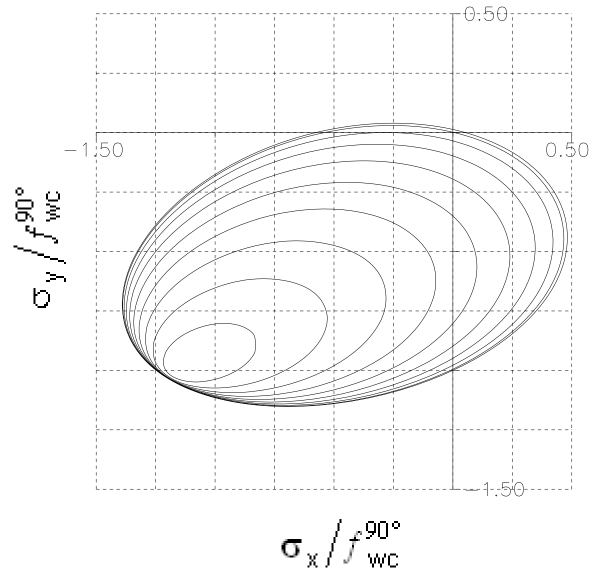

Figure 1: Non-Dimensional Failure Surface of Masonry in Normal Stress Terms ($\tau / f_{wc}^{90°}$ =0.00 up to 0.45 by step=0.05) [17]

$$F= 17.15\left(\frac{\sigma_x}{f_{wc}^{90°}}\right) + 74.57\left(\frac{\sigma_y}{f_{wc}^{90°}}\right) + 32.71\left(\frac{\sigma_x}{f_{wc}^{90°}}\right)^2 + 75.34\left(\frac{\sigma_y}{f_{wc}^{90°}}\right)^2 + 356.74\left(\frac{\tau}{f_{wc}^{90°}}\right)^2 - 17.12\left(\frac{\sigma_x}{f_{wc}^{90°}}\right)\left(\frac{\sigma_y}{f_{wc}^{90°}}\right) + \\ + 4.13\left(\frac{\sigma_x}{f_{wc}^{90°}}\right)^2\left(\frac{\sigma_y}{f_{wc}^{90°}}\right) + 1.35\left(\frac{\sigma_x}{f_{wc}^{90°}}\right)\left(\frac{\sigma_y}{f_{wc}^{90°}}\right)^2 + 122.46\left(\frac{\sigma_x}{f_{wc}^{90°}}\right)\left(\frac{\tau}{f_{wc}^{90°}}\right)^2 + 202.20\left(\frac{\sigma_y}{f_{wc}^{90°}}\right)\left(\frac{\tau}{f_{wc}^{90°}}\right)^2 = 1 \qquad (3)$$

Fig. 1 depicts the contour map of Eq. 3, that is the non-dimensional failure surface of masonry in normal stress terms (with $\tau / f_{wc}^{90°}$ taking values of 0 up to 0.45 by steps of 0.05).

The resulting F value denotes the type of failure (Table 1), e.g.:
$F<1$ no failure of the element (type 1)
$F\geq1$ failure of the element (type 2 to 5)

No	Type of masonry failure		Failure criterion
1	No failure	🟦	$F < 1$
2	Failure under biaxial tension/tension	🟦	$F \geq 1$ & $\sigma_x > 0$ & $\sigma_y > 0$
3	Failure under biaxial tension/compression	🟨	$F \geq 1$ & $\sigma_x > 0$ & $\sigma_y < 0$
4	Failure under biaxial compression/tension	🟩	$F \geq 1$ & $\sigma_x < 0$ & $\sigma_y > 0$
5	Failure under biaxial compression/compression	🟥	$F \geq 1$ & $\sigma_x < 0$ & $\sigma_y < 0$

Table 1: Non-dimensional masonry failure criterion under biaxial stress state

3 CASE STUDY

The methodology described before is illustrated in a comprehensive form, through the case-study of a 4-storey masonry structure of the city of Patras in Greece. The building was built at the beginning of the 20th century and has been characterized recently as a historical building. The structural system is composed by porous stones and mortar; the floor system is consisted by wooden boards mounted on wooden beams spanning one direction. The building has suffered several earthquakes during its service life, but has never been repaired or strengthened. A typical plan view is shown in Fig. 2.

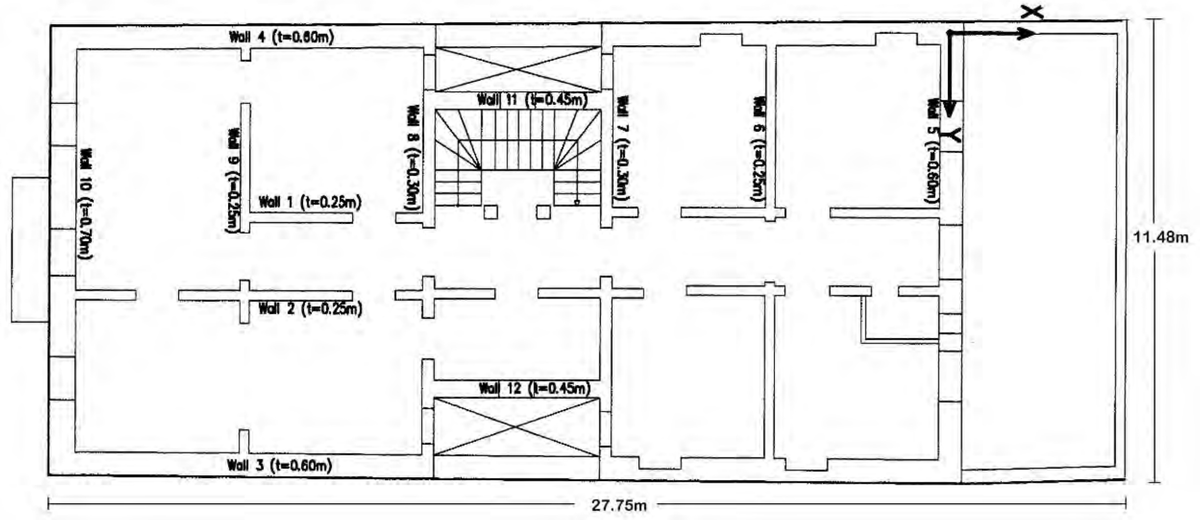

Figure 2: Typical plan view of the examined building

The new methodology for earthquake resistant design of masonry structural systems either before, or after their repair and/or strengthening is presented, by a short description of all steps.

1. In situ inspection showed that masonry stones were porous stones. Several experiments have been performed in the literature for the determination of the mechanical behavior of stone and mortar; the values shown in Table 2 have been used for the analysis. Taking into account these and using semi-empirical expressions [14], the values of masonry compressive and tensile strength, have been calculated.

Material	Strength		Elastic Modulus	Poisson ratio
	Compressive	Tensile		
porous stone (f_{bc})	10 MPa	-	-	-
mortar (f_{mc} & f_{mt})	0.75 MPa	0.15 MPa	-	-
masonry (f_{wc} & f_{wt})	1.13 MPa	0.20 MPa	1130 MPa	0.3

Table 2: Mechanical characteristics of all materials used

2. For the simulation of the structural characteristics, a 3-D finite element model was built, using the Sofistik design software package (Fig. 3). All masonry walls were model using a 4-noded shell element. About 7800 element were needed to model the structure. For the determination of the strains in each element, six degrees of freedom (6 DoF) were con-

sidered. This refers to the motion of a rigid body in three-dimensional space; translation in three perpendicular axes combined with rotation about three perpendicular axes.

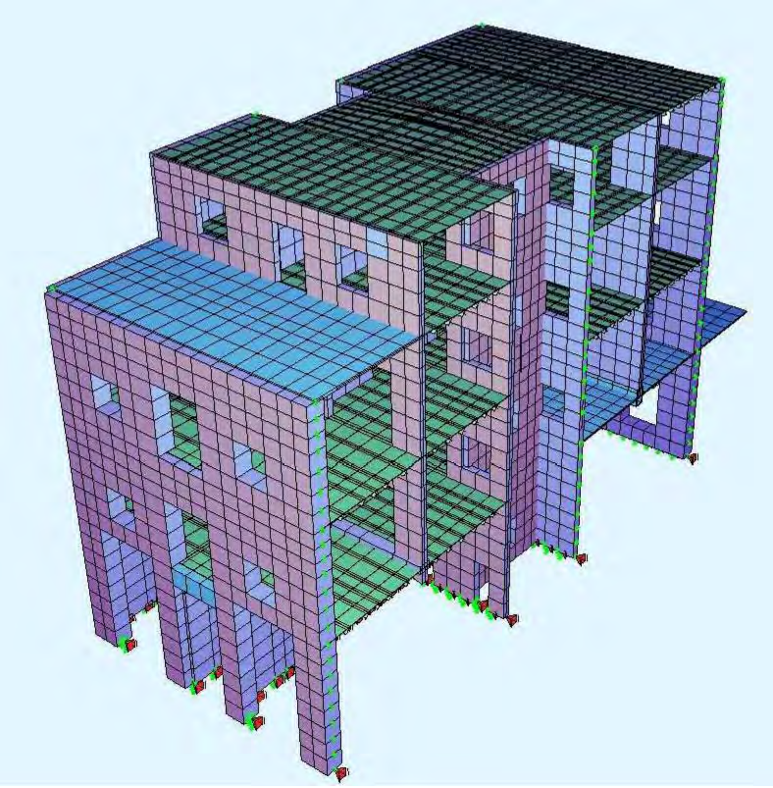

Figure 3: The 3-D FEM model of the building

3. Nominal values of dead and live loads were specified in the Greek Loading Codes [18], which are still in effect today. The seismic loads were also specified in the Greek Earthquake Code [19].

(a) Dead loads (G)
LC1: Self-weight of masonry walls, wooden floor and roof.
LC6: Additional dead load for the roof = 2 kN/m^2

(b) Live loads (Q)
LC2: 1st storey Live load = 3,5 kN/m^2
LC3: 2nd storey Live load = 3,5 kN/m^2
LC4: 3rd storey Live load = 3,5 kN/m^2
LC5: Roof Live load (snow & wind) = 1,0 kN/m^2

(c) Seismic loads (E)
The seismic action was examined at X & Y direction and at 45^o of X-direction.
LC7: Seismic load – X direction: ε_X= 0,08g / 0,12g / 0,16g
LC8: Seismic load – Y direction: ε_Y = 0,08g / 0,12g / 0,16g
LC9: Seismic load – 45^o of X direction: $\varepsilon_{45^o} = \varepsilon_X (\surd 2)/2 + \varepsilon_Y (\surd 2)/2$

According to the Greek Seismic Code, the seismic zone at the city of Patras is category B, which corresponds to a ground acceleration of 0.08g. However, in Paragraph 5 of the code is highlighted that for parapets and independent masonry walls, the stability and seismic analysis, must be carried out considering a value twice the one indicated; hence the ground acceleration is taken 0.16g for the analysis.

Based on the different loads the following combination actions have been used.

Combination with earthquake
LC21: G +Q = (LC1+LC6) + (LC2+LC4+LC4+LC5)

Combination with earthquake
LC31: G + Q + E_x = (LC1+LC6) + (LC2+LC4+LC4+LC5) + E_x
LC32: G + Q + E_y = (LC1+LC6) + (LC2+LC4+LC4+LC5) + E_y
LC33: G + Q + $E_{45}{}^{o}$ = (LC1+LC6) + (LC2+LC4+LC4+LC5) + $E_{45}{}^{o}$
LC41: G + Q - E_x = (LC1+LC6) + (LC2+LC4+LC4+LC5) – E_x
LC42: G + Q - E_y = (LC1+LC6) + (LC2+LC4+LC4+LC5) – E_y
LC43: G + Q - $E_{45}{}^{o}$ = (LC1+LC6) + (LC2+LC4+LC4+LC5) - $E_{45}{}^{o}$

X-direction is perpendicular to the front view of the building (longitudinal direction).
Y-direction is parallel to the front view of the building (transverse direction).

4. Carrying out the Finite Element Analysis, biaxial stresses σ_x and σ_y, shear stress τ_{xy}, as well as displacements and rotations have been calculated, using all the different load combinations described previously. The Sofistik software package provides numerical, as well as graphical, output of the results. The results for a typical masonry wall (Wall 6) is shown schematically in Fig. 4 for the biaxial stresses σ_x and σ_y and the shear stress τ_{xy}.

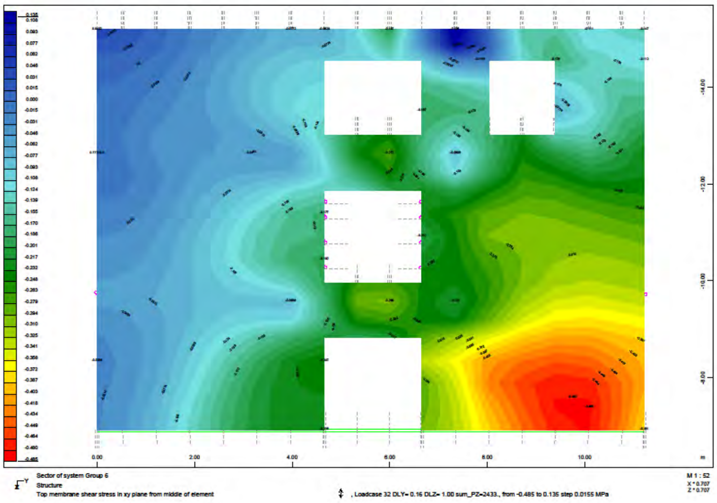

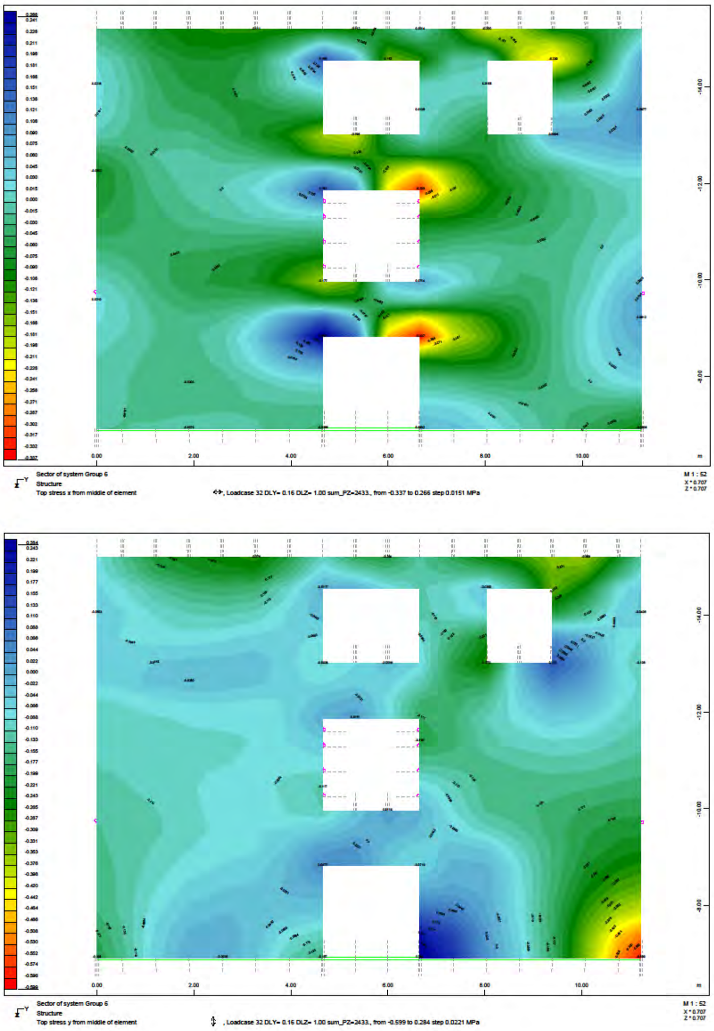

Figure 4: Typical graphical output for biaxial stresses σ_x and σ_y and shear stress τ_{xy} respectively before interventions

5. A spreadsheet has been established for the failure check of each element. 1st column denotes the number of element; 2nd – 9th columns are the internal forces and stress; 10th – 12th columns are the biaxial stresses σ_x and σ_y, shear stress τ_{xy}; last two columns show the application of the failure criterion proposed by Asteris et. al [17]. This spreadsheet gives also for each of the walls or for the whole structure and for each loading case, statistics for the number of failure points and the type of failure. This information provides a general view for the probable damage level and the main type of damages of the structure. This is shown in Table 3 for a typical masonry wall (Wall 6).

All the different types of failures have been inserted back to the Sofistik model and a corresponding illustration of the walls is obtained (Fig. 6). These diagrams have been proved very useful for the extraction of the required conclusions about the general type of the failures in the structure, as well as for decision making concerning the type and the extent of interventions.

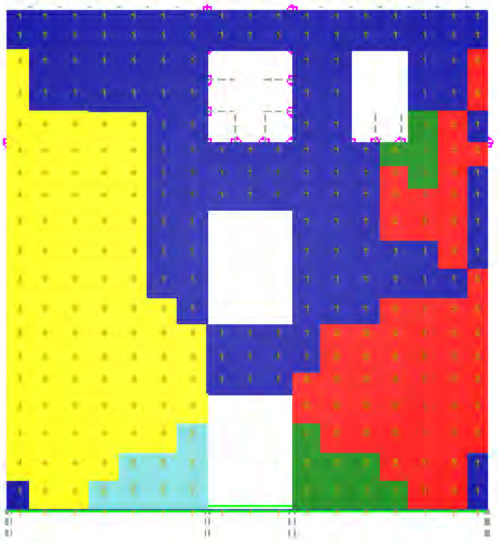

Figure 6: Illustration of failed elements and type of failure
for a typical masonry wall before interventions (Wall 6)

	Type of Failure				
	1	2	3	4	5
LC31	42.6	3.9	7.0	3.9	42.6
LC32	58.5	5.6	6.7	2.8	26.4
LC33	55.6	4.9	6.0	2.8	30.6
LC41	39.44	5.28	7.39	3.52	44.4
LC42	46.5	4.9	6.7	3.2	38.7
LC43	47.5	4.9	6.3	5.3	35.9

Table 3: Percentage (%) of failed elements and type of failure
for a typical masonry wall (Wall 6)

6. Following the last conclusion, appropriate decisions for the repair and/or strengthening process of the structure have been taken. It was decided to strengthen most of the walls by concrete jacketing the one side of the masonry walls with a thickness of 8 cm and provision of appropriate additional reinforcement (typically Φ10/15). For the reanalysis of the structure, the new data concerning values of material characteristics, loading and structural layout have been evaluated. The strengths of the new composite materials are modified as following: f_{wc}=1.51 Mpa, f_{wt}=0.35 Mpa. The results of the analysis after the proposed interventions have shown a significant decrease of the stress levels and thus a significant decrease of the failed elements within the wall.

4 CONCLUSIONS

In this paper, the earthquake resistant design of masonry structural system is discussed, in terms of finding an appropriate failure criterion and then applying an efficient strengthening strategy. A review of numerous failure criteria from various researchers are discussed. A non-dimensional anisotropic masonry failure criterion under biaxial stress state is presented and used in an real masonry structure. The results of the analysis have shown that this criterion is applied successfully and useful conclusions have been provided for the earthquake resistant of the structure. The graphical determination of all failed areas for each wall is important. Especially the categorization of those areas according to the type and intensity of stresses is particularly useful, because the designer can decide on the length and type of intervention. The reason is that some areas may fail due to biaxial compression and others due to biaxial tension and thus different treatment would be need for each case. The case study has shown that the decisions for strengthening each masonry wall separately, based on the failure criterion applied, is successful when comparing the two walls before and after intervention.

REFERENCES

[1] Asteris, P.G. (2008). On the Structural Analysis and Seismic Protection of Historical Masonry Structures, The Open Construction and Building Technology Journal, vol. 2, pp.124-133.

[2] ICOMOS 1931, “The Athens Charter for the Restoration of Historic Monuments”, Adopted at the First International Congress of Architects and Technicians of Historic Monuments, Athens, Greece, 1931, Available; http://www.icomos.org./athens_ charter.html.

[3] ICOMOS 1964, “The Venice Charter for the Restoration of Historic Monuments, Adopted at the Second International Congress of Architects and Technicians of Historic Monuments”, Venice, Italy, Available; http://www.icomos.org./e_venice.html

[4] Dhanasekar, M., Page, A. W., and Kleeman P. W. (1985) “The failure of brick masonry under biaxial stresses” Proceedings, The Institution of Civil Engineers, Part 2, 79, 295-313.

[5] Naraine, K., and Sinha, S. (1991) “Cyclic Behavior of Brick Masonry under Biaxial Compression” Journal of Structural Engineering, ASCE, Vol. 117, No. 5, 1336-1355.

[6] Bortolotti, L., Carta, S., and Cireddu, D. (2005) “Unified Yield Criterion for Masonry and Concrete in Multiaxial Stress States” Journal of Materials in Civil Engineering, ASCE, Vol. 17, No. 1, 54-62.

[7] Zienkiewicz, O. C. and Taylor, R. L. (1991) The finite element method , Volume 2, Solid and Fluid Mechanics, Dynamics and Non-Linearity, McGraw-Hill Book Company.

[8] Zienkiewicz, O. C., Valliapan, S., and King, I. P. (1969) “Elasto-plastic solutions of engineering problems; Initial stress finite element approach” Int. J. Num. Meth. Engng. 1, 75-100.

[9] Samarasinghe, W. (1980) “The in-plane failure of brickwork” PhD thesis, University of Edinburgh.

[10] Page, A. W. (1980) “A biaxial failure criterion for brick masonry in the tension-tension range” The International journal of Masonry Construction, Vol. 1, No. 1.

[11] Page, A. W. (1981) “The biaxial compressive strength of brick masonry” Proc. Instn Civ. Engrs, Part 2, Vol. 71, Sept., 893-906.

[12] Hill, R. (1950) The Mathematical Theory of Plasticity, Oxford University Press.

[13] Prager, W. (1959) An Introduction to Plasticity, Addison-Wesley.

[14] Tassios, T.P. & Chronopoulos, M.P. A seismic dimensioning of interventions (repairs/strengthening) on low-strength masonry building, Middle East and Mediterranean Re-

gional Conference on Earthen and low-strength masonry buildings in seismic areas, Ankara, Aug.-Sept., 1986.

[15] Syrmakezis, C.A., Asteris, P.G. (2001). Masonry Failure Criterion Under Biaxial Stress State, Journal Of Materials in Civil Engineering; American Society of Civil Engineers (ASCE), Vol. 13, Issue 1, pp. 58-64.

[16] Asteris, P.G. (2010). A simple heuristic algorithm to determine the set of closed surfaces of the cubic tensor polynomial, The Open Applied Mathematics Journal, vol. 4, pp.1-5.

[17] Asteris, P.G., Syrmakezis, C.A. (2009). Non-dimensional masonry failure criterion under biaxial stress state, CD Proceedings of the Eleventh Canadian Masonry Symposium, May 31 - June 3, 2009, Toronto, Ontario, Canada.

[18] LC45 [1945]. Ministry of Public Works, Greek Loadings Code, G.G. 325 A 31.12.45 (in Greek), Athens, Greece. (in Greek).

[19] EAK (2000). Greek Seismic Code. (in Greek).

COMPDYN 2011
III ECCOMAS Thematic Conference on
Computational Methods in Structural Dynamics and Earthquake Engineering
M. Papadrakakis, M. Fragiadakis, V. Plevris (eds.)
Corfu, Greece, 27–28 May 2011

NUMERICAL SIMULATION OF UNREINFORCED MASONRY WALLS SUBJECT TO DYNAMIC OUT-OF-PLANE LOADING

L. Reindl, C. Butenweg, and T. Kubalski

Department of Civil Engineering, RWTH Aachen
Chair of Structural Statics and Dynamics
Mies-van-der-Rohe-Str. 1, 52074 Aachen, Germany
e-mail: masonry@lbb.rwth-aachen.de

Keywords: unreinforced masonry, out-of-plane bending, seismic design, ABAQUS®.

Abstract. *Out-of-plane failure is a very common failure mode of unreinforced masonry walls. After earthquake events in Germany (Albstadt 1978, Roermond 1992) damage due to out-of-plane loading was one of the main problems observed. Especially the failure of infill walls and gables was dominated by out-of-plane instability. Since these walls have a relatively low vertical load level, the out-of-plane stability is mainly governed by the slenderness, the thickness of the wall and the bending stiffness parallel and orthogonal to the bed joints, which depend on the bending stiffness of the masonry units, the mortar used, the interconnection between the units as well as the unit geometry and the connection to adjacent constructional elements. In general, current codes only provide limit values for the wall slenderness that are based on experimental results and engineering experience, and simple design concepts based on traditional, force-based design procedures. However, recent research has shown, that masonry walls subject to dynamic out-of-plane loading have deformation reserves exceeding the deformation capacity calculated using traditional, force-based design.*

In order to further investigate the deformation capability of dynamically out-of-plane loaded unreinforced masonry walls, a detailed 3D numerical model on the meso-scale has been developed using the FE toolkit ABAQUS. The model is able to reproduce typical failure modes of single wall panels with different boundary conditions and varying vertical load levels. It is used to investigate and classify the different influence parameters. The results shall be used to define new and refine existing constructional rules. Also, a simplified concept for a dynamic stability check shall be derived.

The paper gives an overview of the current state of the research. It addresses typical problems that arise in the development of numerical models for out-of-plane loaded masonry walls for seismic loading. The numerical model and the results from static and dynamic calculations are presented and - where possible - compared to experimental data.

1 INTRODUCTION

The behavior of out-of-plane loaded, unreinforced masonry wall panels subject to dynamic excitation such as seismic loading is very complex and – up to today – not yet entirely investigated and understood. In 1992 Paulay and Priestly [1] already described this subject accurately with the words:

„one of the most complex and ill-understood areas of seismic analysis“

The out-of-plane failure often happens at earthquake intensities with amplitudes much lower than the ones that are necessary to produce significant in-plane damage. Knowledge about the stability and vulnerability in the out-of-plane direction is therefore absolutely necessary.

Documented experimental investigations in this area of research were carried out as soon as 1802 (Rondolet [2]). Recent observations after different earthquake events have shown that in many cases wall failures due to out-of-plane loading resulted in greater damage than in-plane failure mechanisms.

Especially walls with low vertical load levels are vulnerable to out-of-plane loading. Out-of-plane damage can hence often be found in the upper stories and for poorly braced gable walls as shown in Figure 1.

Figure 1: Out-of-plane failure after the earthquake in Albstadt, Germany, 1978 (Photos: Peter Doll)

Traditionally, masonry is regarded as a brittle material with little ductility and is therefore considered to be especially vulnerable to its peak load bearing capacity resulting from the peak ground acceleration. Nowadays it is generally known that the calculated force-based loading capacity plays a subordinate role when it comes to the investigation of the dynamic stability of out-of-plane loaded wall panels. Recent results from current research projects have shown that after the calculated, static, force-based load bearing capacity is achieved, there are still very considerable reserves resulting from the deformation capabilities of the wall ([3], [4], [5]). Dynamically loaded walls are able to withstand accelerations that cannot be achieved with static loading. This discrepancy clearly reveals that the mechanisms leading to out-of-plane wall collapse are not yet entirely investigated and understood.

2 NON-LINEAR WALL BEHAVIOR

The highly non-linear behavior of unreinforced, masonry wall panels subject to out-of-plane loading is mainly governed by stability mechanisms while the calculated static load-bearing capacity is of fewer relevancies. This complicates the description of the relevant failure modes and the associated kinematic model. Figure 2 shows a typical load-deflection curve of a one-way spanning out-of-plane loaded masonry wall panel.

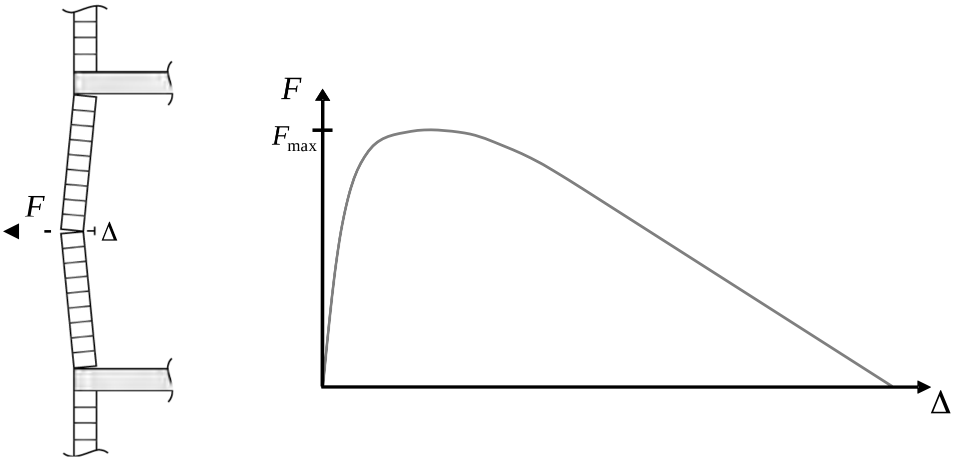

Figure 2: Qualitative load-deflection-curve of an out-of-plane loaded masonry wall panel

The wall panel exhibits a linear elastic behavior up to the point when the static force-based load bearing capacity is reached. The wall typically develops cracks around its mid-height as well as at its top and its base. It is split into single segments that rock around these pivot points which allows the wall to deform significantly until its point of instability.

It seems reasonable to take these apparently present non-linear reserves in the post-peak domain into account. Clearly, second order effects become more important due to the large deformations. A part from the physical nonlinearity, the geometric nonlinearity is increasingly important and has to be taken into account.

For now the ongoing challenge is the development of simple and feasible models that are able to reproduce this complex behavior and hence the derivation of a modern verification procedure.

3 STATE OF THE ART

The research focus of the past years in Germany was certainly put on the optimization and the determination of the behavior of masonry shear walls and accordingly on the development of a feasible concept for the approximation of in-plane capacity curves opening the way for a deformation based design concept. Consequently, usable verification concepts with a realistic depiction of the actual dynamic behavior of out-of-plane loaded masonry walls are missing until today.

Current design codes usually determine the bending capacity based only on the calculated, static load carrying capacity. E.g. in Eurocode 6 [6] two bending capacities parallel and orthogonal to the bed joints are calculated using the tensile capacity in each direction and the static moment. Beneficial influences of an existing vertical compression may be taken into account by increasing the tensile strength for bending parallel to the bed joints. It should be mentioned that Eurocode 6 [6] clearly excludes the use of this method for seismic design.

It is interesting to notice that Eurocode 8 [7] ignores the subject of the out-of-plane stability of load-bearing masonry walls. There are neither instructions for the determination of the seismic input onto the wall nor a concept for the approximation of the dynamic stability leaving it up to the structural engineer to find a practicable way for the seismic verification. Quite often the seismic input is hence determined by using the definition for non-structural components that may be an acceptable approximation in many cases. However, for very important non-structural components and for components that represent a potential risk, a seismic verification using a realistic model and realistic response spectra that take into account the filtering effects of the structure is required. Feasible guidelines for this kind of verification are not included in Eurocode 8 [7].

Some limit values for structural shear walls are included in Eurocode 8 0. In detail these are limits for the thickness, the slenderness and the aspect ratio that are defined in dependence on the seismic zone. Moreover, the national annex of Germany requires all gable walls to be properly braced by transversal walls or pilaster strips if they are not positively anchored to the roof structure. This directive is probably based on the observations after the earthquake in Albstadt in 1978 where these walls were identified to be especially vulnerable to out-of-plane loading.

This clearly shows that further research into this field of seismic engineering is inevitable. The outcome of the research should be a new verification concept that allows for a quick and easy verification based on limit values and also provides guidance for a more advanced investigation of the dynamic stability using displacement-based approaches.

4 NUMERICAL SIMULATIONS

In order to contribute to the development of a feasible deformation-based design concept for unreinforced masonry walls subject to out-of-plane seismic loading, numerical models have been developed. The most recent model was developed using the FEM code ABAQUS [8] which provides powerful material models out-of-the-box. For the current research a 3D model on the meso-scale was chosen. It uses the concrete damage plasticity constitutive law for the bricks and a cohesive contact law to represent the bond between the single bricks [9].

4.1 Assembly

In order to be able to use a 3D model and to fasten up the numerical computations, a few assumptions and simplifications had to be made. All the constraints such as walls or ceilings were reduced to simple concrete beams, which represent the boundary conditions given by adjacent components, with a simplified linear elastic material law. The concrete beam at the top is able to perform vertical movements ensuring a constant vertical load level within the wall. The dimensions of the thin bed mortar joints are neglected.

4.2 Material model

The developed model on the meso-scale consists of individual bricks, which are able to interact between each other and the surrounding concrete beams. Two different materials were used for the bricks in the simulation: calcium silicate and autoclaved aerated concrete. The damaged concrete plasticity material model (CDP), which is included in ABAQUS by default, was used for the material idealization. The masonry bricks are assumed to fail either due to tensile cracking or compressive crushing. The CDP also considers the degradation of the elastic stiffness due to damage and accounts for stiffness recovery effects. It is hence suitable for simulating cyclic loading conditions such as earthquakes.

4.3 Interactions

Each surface needs to be able to interact in every direction with its neighboring surfaces. While pressure and friction can be directly transferred between the surfaces, traction as well as shear forces are delegated through the adhesive effect of the mortar. Since modern high-performance masonry walls in Germany are usually built using precision blocks in combination with thin-bed mortar joints, there is no need to explicitly model the mortar joints. Consequently, the mechanical properties of the joints were defined as interactions properties between the surfaces. Several interaction forms were used to model contact in the different directions.

Pressure can be transferred directly by using the ‘hard contact’ formulation which propagates forces only when the surfaces are in contact and prevents the penetration of surfaces as ‘pressure overclosure’ is avoided. Shear forces and traction forces are transferred using cohesive interaction behavior. The underlying concept is a traction separation law, which allows the definition of stiffness for each direction. With this, a small elastic deformation of the mortar joint was defined in combination with the specification of maximum strain, damage evolution and failure of the joint.

During the investigations, friction wasn’t taken into account since friction failure is not considered relevant for the investigated walls.

4.4 Gravity

To obtain realistic results, gravity was applied to all models. When using gravity loads in explicit analyses, inertia effects must be taken into account. Otherwise it may occur that the wall bounces slightly, which can be shown by recording the vertical reaction forces at the bottom of the wall. The magnitude of the oscillations of the reaction forces varies depending on the walls’ boundary conditions as well as the used material definitions and the used contact interactions. Especially the use of the ‘hard contact’ formulation amplifies the effect since overclosure of the surfaces is prevented. In order to eliminate such disturbing phenomena induced by the wall’s inertia, the gravity load was applied in a separate analysis step where it was increased in small increments over a period of time.

4.5 Problems during numerical investigations

Within the scope of the of the FE-analysis 8-node-hexaeder elements type C3D8R were used for meshing the walls. During the calculations unrealistically large deformations occurred as shown in Figure 3.

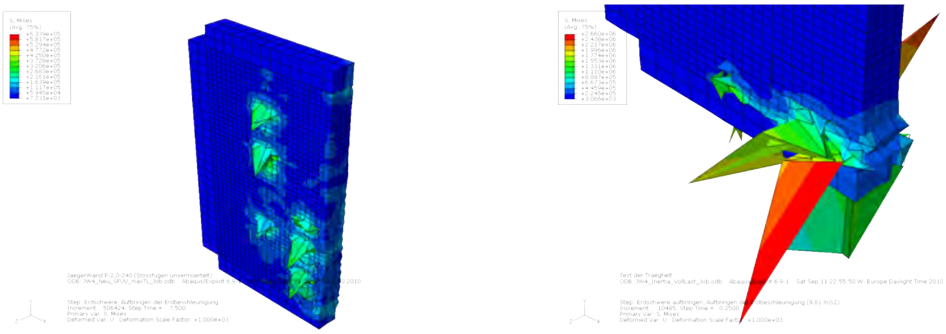

Figure 3: Hourglassing effects

These deformations were classified as hourglassing effects, which often happen when using plastic material behavior in dynamic response analysis combined with reduced integration in explicit analysis steps. Several measures for controlling the hourglassing effect were tested. As a result, a mesh refinement in combination with the use of ‘enhanced hourglass control’ was determined to be the most effective way to reduce such unrealistic deformations. Problems with the enhanced stiffness causing wrong results weren’t encountered.

5 SPECIMEN

5.1 Static specimen

In order to test the quality of the model, static tests were carried out and compared to real life specimen found in literature. In these tests a horizontal distributed load was applied to the wall's back while the wall's horizontal displacement was recorded. An example of the wall's geometry is shown in Figure 4 whereas Table 1 gives an overview of the tested walls' dimensions. All four walls are made of AAC precision blocks in combination with a thin-bed mortar.

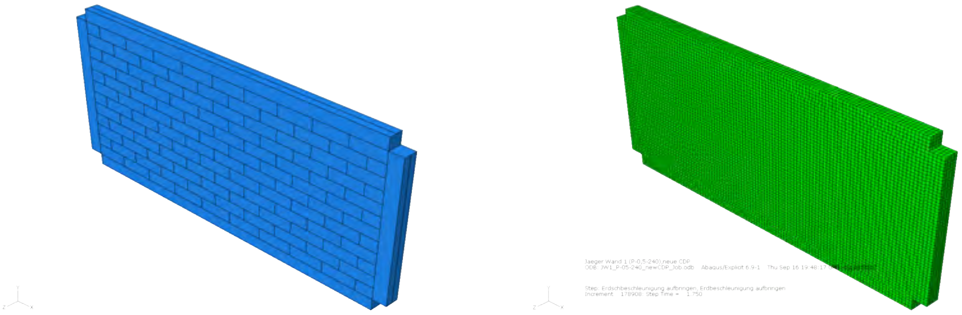

Figure 4: Example of unmeshed and meshed tested wall

	H/L	Height [m]	Thickness [mm]	Supports
JW1	0,5	3,0	240	4-sided
JW2	0,5	3,0	175	4-sided
JW3	1,0	3,0	240	3-sided
JW4	2,0	3,0	240	3-sided

Table 1: Overview of tested static walls

5.2 Dynamic / cyclic Specimen

	H/L	Height [m]	Thickness [mm]	Material	Supports	Acceleration
W1a	2,0	3,0	240	AAC	1-sided	ZVL 8
W1b	2,0	3,0	240	AAC	1-sided	El Centro
W1c	2,0	3,0	240	CS	1-sided	El Centro
W2a	1,5	1,5	110	CS	2-sided	El Centro
W2b	2,0	3,0	240	CS	2-sided	ZVL 8
W2c	2,0	3,0	240	CS	2-sided	ZVL 8
W3a	1,0	3,0	240	AAC	3-sided	ZVL 15
W3b	1,0	3,0	240	CS	3-sided	El Centro
W4a	1,0	3,0	240	AAC	4-sided	ZVL 8
W4b	1,0	3,0	240	CS	4-sided	ZVL 8

Table 2: Overview of tested dynamic walls

For research on the behavior of masonry walls subjected to dynamic loading, the geometry of the static walls was used while the distributed load was changed to a horizontal gravity load. The gravity was only distributed to the bricks in order to give conclusion to an equivalent distributed load. Two artificial accelerations (ZVL 8, ZVL 15: $a_{max} \approx 0,8m/s^2$) as well as the El Centro accelerogram record ($a_{max} \approx 3,0m/s^2$) were used to simulate different input motions. The geometries of the tested walls were derived from the static specimen. Different types of walls such as parapet walls or vertically spanned walls as well as 3-sided and 4-sided constraint walls were tested. A full list of the specimen tested under dynamic gravity load is given in Table 2. The dimension of the bricks as well as the properties of the mortar were chosen according to the experimental test results provided by [10] and [11].

6 RESULTS

6.1 Static specimen

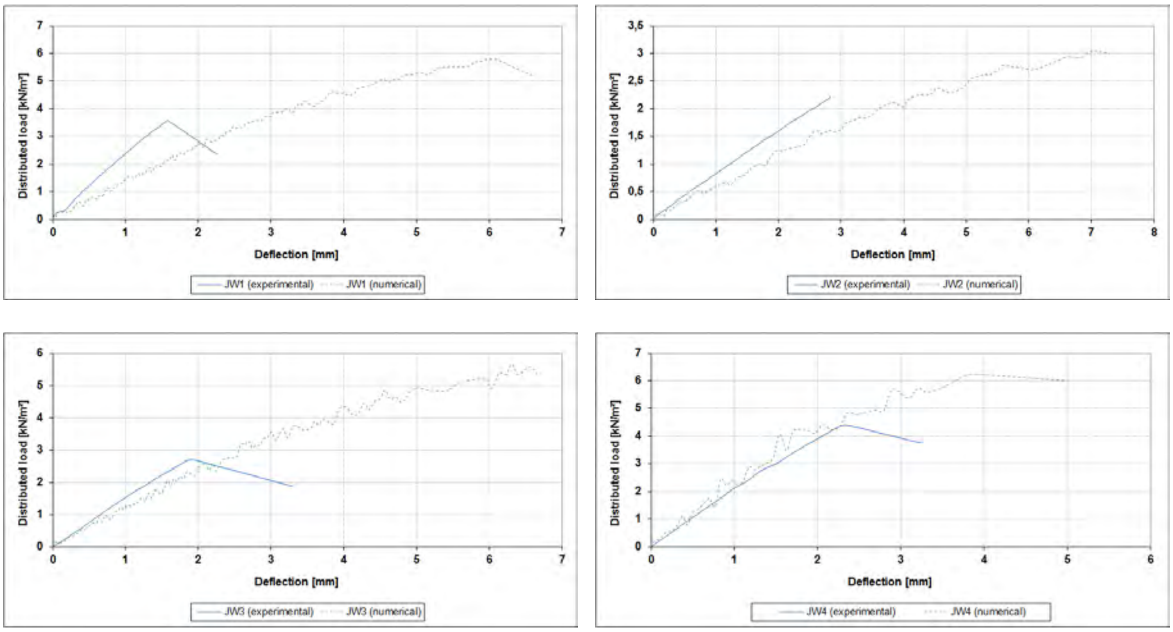

Figure 5: Results of static specimen

Figure 5 gives an overview of the numerical simulations compared to experimental tests found in [11]. In general the results show a good correlation considering the initial stiffness. However, big differences are present for the load bearing capacity and the deformation capability. This may be caused by several reasons. Firstly, the numerical model did not accurately reproduce the boundary conditions of the experimental tests, where the wall was built into a steel frame instead of being held by concrete beams. Moreover, there was no vertical load applied in the experiments while there was a concrete beam at the top charging the wall in the numerical simulations. It is also questionable whether or not the CDP constitutive law correctly described the material behavior since detailed information on the used bricks are not available. There is also a difference in the way the deflection was recorded. While the maximum displacement was used in the numerical model, the experimental testing setup had fixed reference points that did not necessarily provide the exact same deflections.

The failure mechanisms of the numerical walls give the expected results as shown for example in Figure 6. Failure at the 4-sided walls started about mid-height in the middle of the wall whereas the failure of the 3-sided walls started about mid-height of the free side. Crack propagation proceeded to the edges of the constraint sides.

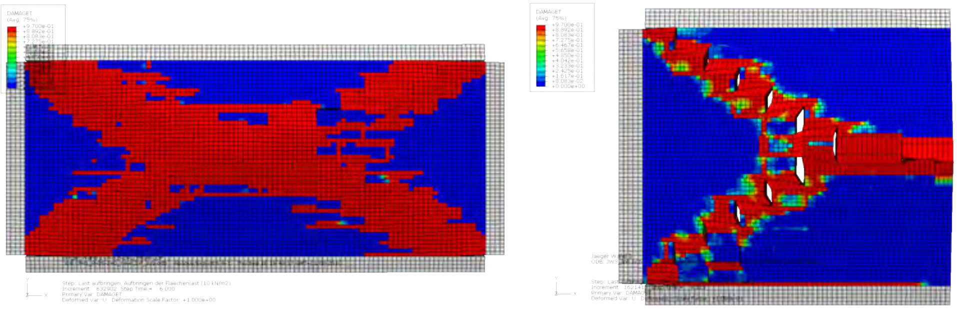

Figure 6: Failure of wall JW1 and wall JW3

6.2 Dynamic specimen

The different wall types showed specific buckling behavior resembling the typical behavior of such walls subjected to dynamic loadings. As an example the results of the parapet wall W1a and the results of the vertically spanned wall W2b are presented. These two walls were subjected to the same excitation. The parapet wall started quickly to buckle. The top of the wall deflected the most as shown in figure 5 while the joints at the bottom of the wall started to open slightly. Complete failure of the wall wasn't achieved, but small plastic strains occurred at about height of the bottom joints. The maximum deflection is about 4 mm as can be seen in Figure 7.

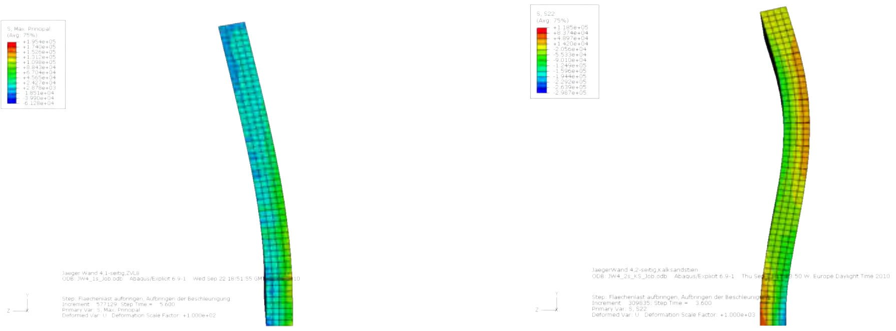

Figure 7: Comparison of (scaled) deformation of wall W1a (left) and wall W2b (right)

The vertically spanned wall has been supplied with an additional vertical load due to the top concrete beam. As a consequence of the added supply, the achieved deformations were smaller, just up to about 0,23 mm as shown in Figure 8. The biggest deflection occurred about mid-height of the wall. No plastic deformations were produced during this conducted test. The upper half of the wall bends due to the excitation.

Again, the results of the presented model show a good approximation of the overall behavior while the maximum deflections differ significantly when compared to experimental results found in [5]. In an attempt to verify the model, on of the walls tested in [5] was modeled. It showed maximum deformations significantly smaller than in the experiment. However, it has to be noted, that the construction type used in the experiments (general purpose mortar) is different from the one that the numerical model is intended for. It is therefore not surprising that the numerical model of the current German construction type with thin bed mortar and modern high performance masonry units has a greater stiffness and hence smaller deformations.

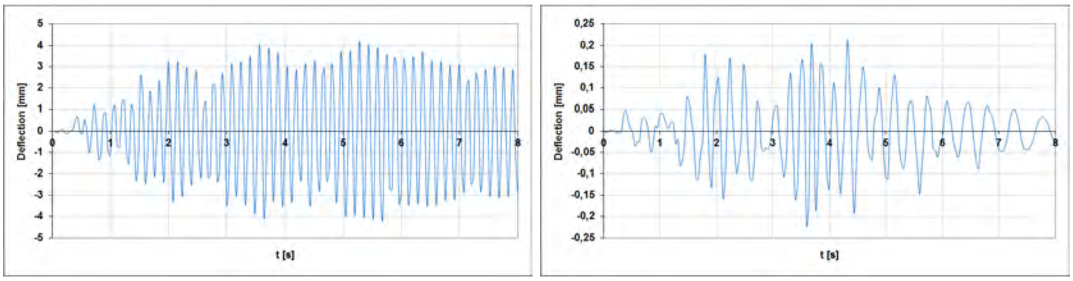

Figure 8: Comparison of deflection of wall W1a (left) and wall W2b (right)

In closing it can be said that the presented model is capable of modeling the failure modes and initial stiffness of an out-of-plane loaded wall made of modern high performance masonry sufficiently well. However, there are still great deficiencies when it comes to predicting the load bearing capacity and the deformation capability.

In its current state, the model cannot yet be used to do parametric tests in order to derive and verify e.g. load-deflection curves. It is already being used to study the typical cracking patterns as a function of the wall and unit geometries and hence the kinematics of cracked wall panels.

7 DISCUSSION

The presented numerical model is able to realistically simulate the typical failure modes of out-of-plane loaded unreinforced masonry walls. It provides a strong basis for comprehensive parametric studies on the influences of the wall geometry, brick dimensions and boundary conditions. Further enhancements are necessary to improve the quality of the results and hence the scope of the model.

The finite element code ABAQUS provides satisfactory results while providing sophisticated material models for brittle material and cohesive contact out of the box.

It is evident, that there is still a high demand for research in the field of seismic verification concepts for out-of-plane loaded unreinforced masonry walls. Basic simplified approaches are already available in European codes but they are very limited and cannot be applied to arbitrary wall configurations. A clear definition for walls not satisfying the provided limit values are still missing.

The development of practicable and efficient verification concepts should result in a mulit-stage verification concept.

A more detailed specification of limit values for thickness, slenderness, etc. in dependence on the seismic hazard should be provided along with detailed information on the design of the contact zone between walls and slabs. These values need to be defined for structural as well as non-structural components.

For walls exceeding the limits simplified approaches for a traditional force based design as well as for a typical dynamic stability check is necessary. This requires guidelines for definition of the seismic input as well as a concept for a simplified estimation of the kinematic equivalent system.

The presented numerical model along with future improvements will contribute to this development.

REFERENCES

[1] Paulay, T., Priestly, M., J., N., *Seismic Design of Reinforced Concrete and Masonry Buildings*, J. Wiley, 1992.

[2] Rondelet, J. B.: „Traité Théorique et Pratique de l'Art de Bâtir", Paris, 1802.

[3] Doherty, K. T.: „An Investigation of the Weak Links in the Seismic Load Path of Unreinforced Masonry Buildings", PhD Thesis, School of Civil and Environmental Engineering, Adelaide University, Australia, 2000.

[4] ABK – A Joint Venture: „Methodology for the Mitigation of Seismic Hazards in Existing Unreinforced Masonry Buildings: The Methodology", Topical Report, 1984.

[5] Doherty, K. T., Griffith, M. C., Lam, N., Wilson, J.: „Displacement-based Seismic Analysis for Out-of-plane Bending of Unreinforced Masonry Walls", Earthquake Engineering and Structural Dynamics, Vol. 31, pp 833-850, 2002.

[6] Comité Européen de Normalisation, Eurocode 6, Design of Masonry Structures, Brussels, 2006.

[7] Comité Européen de Normalisation, Eurocode 8, Design of Structures for Earthquake Resistance, Brussels, 2004.

[8] Dassault Systèmes, Abaqus 6.9 Documentation, 2010.

[9] Kubalski, T. Dynamische Untersuchung von aus der Ebene heraus belasteten Mauerwerksschalen mit ABAQUS. Bachelor Thesis, Baustatik und Baudynamik, RWTH Aachen, Germany, 2010.

[10] Brameshuber, W., Schmidt, U., Forschungsbericht F 7044/1. Untersuchungen zur Bestimmung von Stoffgesetzen von Kalksandsteinen und des Verbundes. Research report, RWTH Aachen, Germany, 2006.

[11] Jäger, W. Bemessung von drei- oder vierseitig gehaltenen, flächenbelasteten Mauerwerkswänden. Beitrag zum Mauerwerkskalender 2007, Ernst & Sohn, Germany, 2007.

COMPDYN 2011
3rd ECCOMAS Thematic Conference on
Computational Methods in Structural Dynamics and Earthquake Engineering
M. Papadrakakis, M. Fragiadakis, V. Plevris (eds.)
Corfu, Greece, 25–28 May 2011

IN-PLANE BEHAVIOR OF REIFORCED MASONRY WALLS: EXPERIMENTALLY BASED MODELLING

F. Mosele[1], G. Guidi[2], L. Nicolini[2] and F. da Porto[2]

[1] University of Padova, Dpt. Of Structural and Transportation Eng.
via Marzolo 9, 35131, Padova, ITALY
e-mail: mosele@dic.unipd.it

[2] University of Padova, Dpt. Of Structural and Transportation Eng.
via Marzolo 9, 35131, Padova, ITALY
{guidi,nicolini,daporto}@dic.unipd.it

Keywords: Reinforced masonry, Analytical Methods, Numerical Methods, Experimentally based modeling.

Abstract. *In the framework of a recent EU funded research project, innovative construction systems for clay unit reinforced masonry walls were developed. In particular, one system was developed for low-rise residential buildings. An extensive experimental program was mainly aimed to understand the cyclic in-plane behavior under shear and compression loads. The tests results were compared with code proposed formulations for the evaluation of shear strength, in order to check their reliability in predicting the ultimate load capacity of reinforced masonry walls. A new calibrated formulation is proposed. A FE continuum micro-model was calibrated on the experimental results and then used to carry out parametric analyses of the reinforced masonry system, to investigate the influence of the axial load level, the aspect ratio and the reinforcement ratio on the global in-plane behavior of the tested walls. A new analytical hysteretic model was also developed and used to carry out non-linear dynamic analyses of SDOF systems, to evaluate the reduction of the elastic response of reinforced walls, for a range of natural periods that characterize the elastic phase of load bearing masonry buildings.*

1 INTRODUCTION

Reinforced masonry (RM) was developed to exploit the strength potential of masonry and solve its lack of tensile strength [1] while significantly improving resistance, ductility and energy dissipation capacity with respect to unreinforced masonry (URM) [2, 3]. In the last few decades, a large variety of RM techniques have been made available. Many RM systems around the world are based on the use of hollow concrete [4, 5] and clay units [6], which are reinforced with steel bars and grouted with concrete. Other RM systems, traditionally developed in Europe, make use of perforated clay units combined with concentrated vertical reinforcement, [see, for example 7, 8, 9, 10].

Generally, RM systems are designed for low rise residential buildings in seismic areas, which resist horizontal earthquake actions with the walls parallel to the seismic actions, according to the box-type behavior [1]. Therefore, the main aim of any experimental and numerical study is to assess the behavior under in-plane cyclic actions. In the case that seismic design of this type of buildings is based on linear elastic methods of analysis, the evaluation of the strength capacity (ULS) and the numerical values of the seismic behavior factor (q-factor) to reduce the elastic design spectrum, are crucial. The shear strength of RM is generally evaluated as the sum of the contributions of unreinforced masonry and horizontal reinforcement [11, 12, 13, 14], where many issues regarding the evaluation of masonry strength and horizontal reinforcement efficiency are still open [15]. On the other hand, the q-factor has been recognized in the Italian code [12] to be implementing an “overstrength” ratio also in the case of masonry buildings [16, 17], and its values can be higher if capacity design principles are pursued, whereas the European code [18] does not provide these possibilities. Furthermore, more rational design methods, based on non-linear analyses, are being developed [see, for example 19]. Nevertheless, to adopt them, it is necessary to give deformation/drift limits that should be used, suitably revised on the basis of the more recent construction systems and available experimental information [20].

In this context, a RM systems for use in low rise were recently developed [21] and tested [22]. The main aims of the experimental and numerical work were to study the behavior in relation to the above mentioned issues.

2 STUDIED REINFORCED MASONRY SYSTEM

The RM system developed for low rise residential buildings is based on the use of concentrated vertical reinforcement, similar to confined masonry. Special clay units are laid with horizontal holes, with recesses for horizontal reinforcement on the bed faces (Figure 1 left). Vertically perforated units are used for the confining columns. Vertical reinforcement placed in the cavities of the confining columns is composed of steel bars (0.130%÷0.173%); horizontal reinforcement may be made of either steel bars or prefabricated steel trusses (0.045% and 0.040% respectively). The main advantages of the system are related to durability and construction process: placing the horizontal reinforcement inside mortared recesses improves reinforcement durability, makes reinforcement positioning easier and more precise, and allows good bond at the interface unit/ mortar and mortar/reinforcement. In addition, this technique is traditionally adopted in Mediterranean countries to improve thermal insulation. As regards mechanical behavior, this system is conceived to perform as RM, provided that units with horizontal holes are effective in bearing the horizontal loads and transferring them to the confining columns, without showing fragile behavior. More details about this system can be found elsewhere in [22] and [23].

Figure 1: RM system (left) and shear-compression test setup (right).

3 OVERVIEW OF THE MAIN EXPERIMENTAL RESULTS

The seismic performance of the proposed RM system was evaluated by means of in-plane cyclic shear compression tests (Figure 1 right), carried out with cantilever boundary conditions. Fourteen full-scale masonry specimens were tested differentiated by: presence or absence of vertical reinforced confining columns, use of steel bars or prefabricated trusses as horizontal reinforcement, aspect ratio and value of applied axial load, to force both shear and flexural failure modes.

The test results allowed evaluating the influence of the above aspects on the main seismic parameters of RM walls, such as strength and displacement capacity, energy dissipation, viscous damping, stiffness degradation [22, 24, 25].

In general, the failure mechanism strongly influenced all the measured seismic parameters. The tests showed that: the different types of horizontal reinforcement did not cause significant differences in global mechanical behavior, the horizontally perforated units are adequate in bearing the horizontal loads between the confining columns, and the interaction between the inner portion of the wall and the confining columns does not cause premature failure. The ultimate drift θ_u ranged from a minimum value of 0.7% for shear failures to values exceeding 1.7% for flexural failures. These values satisfy the limits associated to ULS for shear (0.6%) and flexural (1.2%) failures of RM walls, adopted by the Italian norms, but the European norms do not provide any drift limit for in-plane response of RM walls. The ductility ratio μ, moves from 2.5 to 4.0 for shear failures and from 3.5 to 6.0 for flexural failures, according to the axial load level. The ratio between dissipated and input energy was around 30%. The values of viscous damping were around 5%, and tended to increase in the post-peak phase.

4 EXPERIMENTALLY BASED MODELING

4.1 Shear strength evaluation

The shear capacity of RM walls is governed by several global and local resisting mechanisms. In general, the combination of vertical and horizontal reinforcement leads to the development of a global mechanism, which lies in between the arch-beam and truss mechanism [1, 26]. While the flexural strength of RM walls is relatively easy to calculate according to theoretical models, the shear strength, due to the complexity of the mechanism, is generally calculated as a sum of contributions, better than on the basis of theoretical models. Four main contributions are usually considered by formulations proposed to predict the nominal shear strength V_R of RM walls: V_m is the shear strength of URM, V_P is the contribution of axial load, V_s is the contribution due to horizontal reinforcement and V_{dw} is the contribution due to dowel-action of vertical reinforcement.

A crucial issue for the shear strength formulation is the efficiency of the horizontal reinforcement, which vary between 30% and 100% according to the various formulations available in literature [see for example 11, 12, 13, 14, 27, 28, 29, 30]. The shear reinforcement effectiveness, evaluated by means of strain gauges, was about 60%, in the present experimental tests, which is consistent with the values provided by codes such as the Italian and American standards [12, 13], and proposed by researchers such as Tomaževic and Anderson-Priestley [1, 28].

As a consequence of an extensive analyses of the shear strength formulations and the comparison with the present experimental data [22, 15], a calibrated formulation for shear strength evaluation has been proposed:

$$V_R = V_m + V_S = \left(\frac{f_t}{b} \cdot \sqrt{\frac{\sigma_0}{f_t} + 1} \right) \cdot td + 0.6 \cdot \frac{dA_{rh} f_y}{s} \tag{1}$$

The equation (1) is based on the Turnšek and Čačovic criterion [31] for evaluating V_m, which implicitly accounts for the contribution of axial load V_P, and which is consistent with the diagonal cracks experimentally observed. The contribution of horizontal reinforcement V_s, is calculated in equation (1) as for stirrups in reinforced concrete members [as in 12, 13], taking into account the number of stirrups, each of area A_{rh}, across the diagonal crack (with 45° slope, d is the effective length of the wall section and s the spacing of the stirrups). The 0.6 reduction coefficient corresponds to the shear reinforcement effectiveness experimentally evaluated.

The comparison between equation (1) and the experimental data is given in Figure 2.

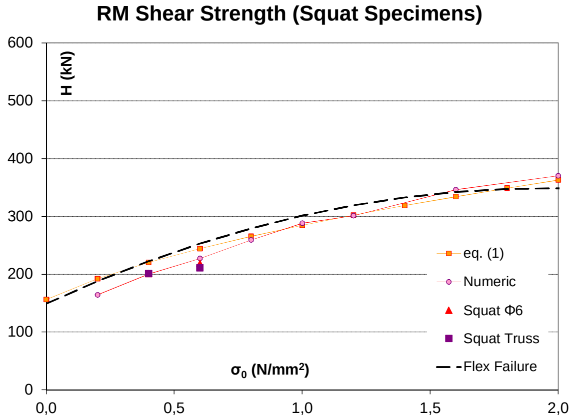

Figure 2: Shear equation and numerical trend vs experimental data.

4.2 Numerical modeling

A simplified micro-modeling strategy with continuum elements and no unit-mortar interface elements was adopted for modeling the envelope of cyclic behavior of the RM walls under study. The model properties were derived from experimental tests. The Total Strain Rotating Crack isotropic damage model [32] was adopted for mortar and blocks. The steel reinforcement was described by means of elasto-plastic Von Mises yield criterion, and had the shape of a line, full bonded and embedded in all the plane stress elements that define the wall geometry. Considering the type of model used, it was not possible to make a distinction between the truss and the bar reinforcement used. The analyses were carried out using the code DIANA. Eight-node isoparametric plane-stress elements with Gauss integration scheme were used in the models. The Newton-Raphson iteration procedure was used with a displacement control and an energetic convergence criterion. The values of fracture energy of masonry in tension (G_{ft}^{I}) and in compression (G_c) were found by means of extensive literature research, summarized into a database valid for masonry structures [33, 34]. Other parameters that were not directly available from the experimental tests carried out are the tensile strengths of the masonry components. The calibration process of the model was carried out starting from uniaxial compression tests, and aiming to solve some defects of the model such as the full-bonded hypothesis used for embedded reinforcement, which is not realistic.

Figure 3 compares the average of the experimental hysteresis loops envelope (H_{med} curve) obtained by the shear compression tests, and the numerical results (Numeric curve), for the specimens failed with shear and flexural mechanism, under axial load of 0.6 N/mm^2. The models slightly overestimate the initial stiffness and reproduce the maximum horizontal load with an average error of about ±5%. Displacements were generally underestimated, but the values of ultimate displacement (when a sudden drop of strength occurs), are in agreement with the experimental ones (average error ±15%), as can be seen in Figure 3.

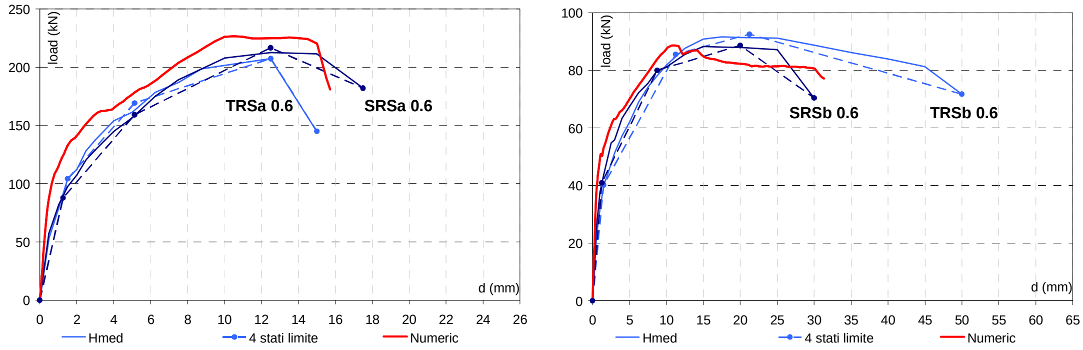

Figure 3: Experimental hysteretic envelopes and numerical pushover analysis: shear failure (left) flexural failure (right).

On the basis of calibrated models, we carried out an extensive parametric study [35, 22] to evaluate the influence of different parameters, such as axial load level, aspect ratio, and amount of vertical reinforcement, on the in-plane behavior of RM walls. The results gave indication about the reliability of the shear strength formulation proposed by equation (1), compared to other formulations available in codes and in the literature. It was possible to confirm the proposed relation between horizontal load and applied axial load, as reported in Figure 2.

In addition, it was found that the contribution of vertical reinforcement is essential for RM walls, since it changes the behavior from rocking mechanism, typical of URM wall, characterized by premature crushing of compressed toe with consequent numerical instability, to a flexural mechanism which leads to higher strength and displacement capacity. When the vertical reinforcement ratio was higher than 0.2%, the walls failed in shear with a limited ductility. This worsening of the wall behavior is more marked for slender rather than for squat specimens.

The parametric analysis on the aspect ratio allowed observing that the maximum shear stress presented a non-linear decrease with increase of H/L ratio.

4.3 Analytical modeling and dynamic analyses

To reproduce the experimental cyclic behaviour, a new hysteretic model was developed. The model was based on the quadri-linear envelope curves defined by the four limit states, and given in [36], and on energy considerations and stiffness degradation rules. Starting from some observation about the shape of the experimental hysteretic cycles [37], the cycles were modelled on the basis of four main points (A; B; C; D) and their symmetrical. These points were found on the basis of the parameters C_1 and C_2, which depend on the amount of the absorbed and dissipated energy during the cycle, and Z, which is a ductility parameter. Figure 4 (left) shows the geometrical scheme for the loops' construction. The slopes of the various loading and unloading phases are given by stiffness parameters, as in [38]. Other two parameters, R1 and R2, are used to model the repeated cycles on the basis of the ratio between input and dissipated energy in the first and, respectively, the second and the third cycle. Overall, the model uses four independent parameters, and the others are all based on those. A more detailed description of the model features is given in [39]. Figure 4 (right) shows the good agreement between the experimental hysteresis loops and those generated by the model.

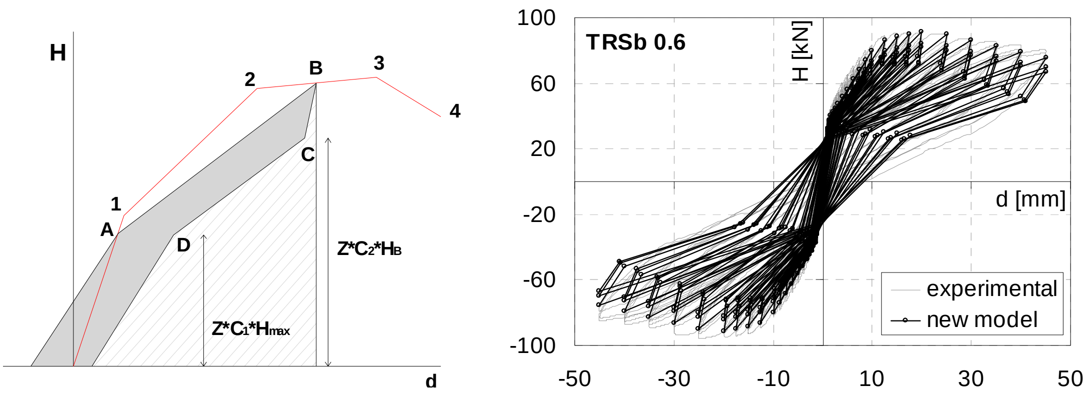

Figure 4: Scheme for the loops' construction (left) and experimental vs numerical hysteresis loops (right).

The developed analytical model was used to carry out non-linear dynamic analyses in order to evaluate the reduction of elastic response of RM walls due to their hysteretic behaviour. They were executed on a SDOF system, using a group of 10 synthetic time-histories, compatible with the spectra of national code. The analyses were carried out for a range of natural periods between 0.10 and 0.5 s, and they were repeated for each soil group classified by the Italian code [12]. Analyses were carried out on the basis of the given value of ultimate ductility factor μ, obtained during tests. The aim was to estimate load reduction factor R_μ due to energy dissipation and non-linear behaviour of the RM system, taking into account shear and flexural failure modes. 2160 analyses were carried out and the obtained values for R_μ were variable with the soil type, axial load level and failure mode. The study of the results, obtained from the dynamic analyses [37], allowed to observe that for natural period of 0.15÷0.20 s, characteristic of masonry buildings, the load reduction factors value is confirmed to be of 2.5 and 3.0 that the Italian norm suggests, respectively for RM failing in shear and in flexure, the latter being associated to the application of capacity design principles. It should be pointed out that the same range of values, regardless of the failure mode, is also given by [18], but as final values of q-factors to be adopted (i.e. neglecting overstrength).

5 CONCLUSIONS

- Extensive experimental and numerical investigations were carried out to improve the knowledge of seismic behavior of RM walls and the available design procedures
- New inputs were provided by the tests about the deformation capacity, to be adopted and implemented in non-linear analyses.
- A shear strength formulation derived from the analysis of the available formulations was in good agreement with the experimental results and consistent with the parametric analyses carried out with the developed numerical model
- The role of vertical reinforcement for RM walls was highlighted and a limitation for vertical reinforcement ratio was identified by means of the parametric analyses carried out with the calibrated numerical model.
- An analytical model derived from experimental results was able to account for the cyclic behavior of RM walls. Adopting this model into dynamic analyses, the capability of RM walls of reducing the dynamic response induced by earthquake, was quantified by the load reduction factor. The results confirmed the values reported in Italian code.
- However, taking into account the intrinsic limitation of the present design procedures [40], further analyses are in progress at University of Padova; mainly an analytical fibre model accounting for the shear/flexural interaction has been developed, to be used in direct displacement based design procedures for RM and URM masonry structures.

REFERENCES

[1] M. Tomaževič, *Earthquake-resistant design of masonry buildings*, Series on Innovation in Structures and Construction, Vol. 1, Imperial College Press, London, 1999.

[2] F. da Porto, M. Grendene, C. Modena, Estimation of load reduction factors for clay masonry walls. *Earthquake Engineering and Structural Dynamics*, **38**(10), 1155-1174, 2009.

[3] F. da Porto, G. Guidi, E. Garbin, C. Modena, In-plane behavior of clay masonry walls: experimental testing and finite element modeling. *Journal of Structural Engineering, ASCE*, **136**(11), 1-14, 2010.

[4] E. Minaie, M. Mota, F.L. Moon, A.A. Hamid, In-plane behavior of partially grouted reinforced concrete masonry shear walls. *Journal of Structural Engineering, ASCE*, 2010.

[5] K.C. Voon, J.M. Ingham, Experimental in-plane shear strength investigation of reinforced concrete masonry walls. *Journal of Structural Engineering, ASCE*, **132**(2), 400-408, 2006.

[6] K. Zilch, D. Schermer, W. Scheufler, Behaviour of reinforced masonry walls made of hollow clay units with concrete infill under combined loading. *14th Int. Brick and Block Masonry Conference*, Sydney, Australia, February 17-20, 2008. (CD-ROM)

[7] A. Bernardini, C. Modena, G. Lazzaro, M.R. Valluzzi, Cyclic behaviour and modelling of reinforced masonry panels. *11th Int. Brick and Block Masonry Conference*, Tongji University, Shangai, October 14-16, 1997.

[8] G. Magenes, In-plane cyclic testing of reinforced masonry shear walls. *11th European Conference on Earthquake Engineering*, Paris, France, 6-11 September 1998

[9] T.P. Tassios, N. Psilla, Reinforced masonry walls under seismic actions. *In: Implications of recent earthquakes on seismic risk. Series on 'Innovation in Structures and Construction', vol. 2*. Elnashai and Antoniou, eds. Imperial College Press, London. 215–228, 2000.

[10] M. Tomaževič, M. Lutman, V. Bosiljkov, Robustness of hollow clay masonry units and seismic behaviour of masonry walls. *Construction and Building Materials*, **20**(10), 1028–1039, 2006.

[11] European Committee for Standardization, *Eurocode 6 - Design of masonry structures. Part 1-1: General rules for reinforced and unreinforced masonry structures. EN1996-1-1*, Brussels, Belgium, 2005.

[12] Ministry of Infrastructures, *DM 14/01/08. Technical Standards for Constructions*. Rome, Italy, 2008. (In Italian)

[13] American Concrete Institute, *Building Code Requirements and Specification for Masonry Structures and Related Commentaries. ACI 530/530.1-08*, January 1, 2008.

[14] Standard Association of New Zeland – SANZ, *Design of reinforced concrete masonry structures. NZS 4230:2004*, January 29, 2004. (and following amendments).

[15] F. Mosele, F. da Porto, C. Modena, Reinforced clay masonry walls: effectiveness of reinforcement and shear equations. *11th Canadian Masonry Symposium*, Toronto, Canada, 31 May-3 June, 2009. (CD-ROM)

[16] G. Magenes, Masonry building design in seismic areas: recent experiences and prospects from a European standpoint. Keynote 9, *1st European Conference on Earthquake Engineering and Engineering Seismology*, Geneva, Switzerland, 3-8 September, 2006. (CD-ROM)

[17] G. Magenes, P. Morandi, Some issues on seismic design and assessment of masonry buildings based on linear elastic analysis. *Michael John Nigel Priestley Symposium, IUSS Press*, 83-94, Pavia, Italy, July, 2008.

[18] European Committee for Standardization, *Eurocode 8—Design of structures for earthquake resistance. Part 1: General rules, seismic actions and rules for buildings. EN1998-1*, Brussels, Belgium, 2004.

[19] G. Magenes, M. Remino, C. Manzini, P. Morandi, D. Bolognini, *SAM II, Software for the Simplified Seismic Analysis of Masonry buildings*. University of Pavia and EUCENTRE, 2006.

[20] G. Magenes, C. Modena, F. da Porto, P. Morandi, Seismic Behaviour and Design of New Masonry Buildings: Recent Developments and Consequent Effects on Design Codes, *Workshop: "Quali prospettive per l'Eurocodice 8 alla luce delle esperienze italiane"*, Università degli Studi di Napoli, Napoli, 3 Aprile, 2009.

[21] *DISWall, Developing innovative systems for Reinforced Masonry Walls*, COOP-CT-2005-018120, 2006-2008. (http://diswall.dic.unipd)

[22] F. Mosele, *In-plane and out-of-plane cyclic behaviour of reinforced masonry walls*. PhD Thesis, University of Trento, Trento, Italy, 2009.

[23] F. da Porto, F. Mosele, C. Modena, Compressive behaviour of a new reinforced masonry system, *RILEM Materials and Structures*, doi: 10.1617/s11527-010-9649-x, 2010.

[24] F. da Porto, F. Mosele, C. Modena, Reinforced clay masonry walls under shear-compression loads: experimental behavior. *11th Canadian Masonry Symposium*, Toronto, Canada, 31 May-3 June, 2009. (CD-ROM)

[25] F. da Porto, F. Mosele, C. Modena, In-plane cyclic behaviour of a new reinforced masonry system: Experimental results. *Engineering Structures, Elsevier,* accepted for publication, 2011.

[26] T.P. Tassios, *Meccanica delle murature*, Liguori Editore, Napoli, Italy, 1988. (in Italian).

[27] Standards Australia, *Masonry structures. AS 3700-2001*, January 1, 2001. (and following amendments)

[28] D.L. Anderson, M.J.N. Priestley, In plane shear strength of masonry walls, *6th Canadian Masonry Symposium*, Saskatoon, Canada, June 15-17, 1992.

[29] P.B. Shing, M. Schuller, V.S. Hoskere, In plane resistance of reinforced masonry shear walls, *Journal of Structural Engineering, ASCE*, **116**(3), 619-640, March 1990.

[30] M. Tomaževič, M. Lutman, Seismic resistance of reinforced masonry walls, *9th World Conference on Earthquake Engineering*, Tokyo-Kyoto, Japan, (Vol. VI), 97-102, August 2-9, 1988,.

[31] V. Turnšek, F. Čačovič, Some experimental results on the strength of brick masonry walls, *2nd Int. Brick Masonry Conference*, Stoke on Trent, British Ceramic Research Association, 149-156, London, UK, 1971.

[32] J.G. Rots, *Structural masonry an experimental/numerical basis for practical design rules*. Balkema: Rotterdam, The Netherlands, 1997.

[33] G. Guidi, *Sistemi di muratura portante in laterizio: calibrazione di modelli numerici sulla base di risultati sperimentali*. Graduation Thesis, Dept. of Structural and Transportation Engineering, University of Padova, Padova, Italy, 2006. (in Italian)

[34] F. da Porto, G. Guidi, E. Garbin, C. Modena, Modelling of in-plane loaded clay unit masonry walls. *14th International Brick and Block Masonry Conference,* Organized by: The University of Newcastle, Sydney, Australia, February 17-20, 2008. (CD-ROM)

[35] F. da Porto, G. Guidi, F. Mosele, C. Modena, Reinforced clay masonry walls under shear-compression loads: parametric analyses. *8th International Masonry Conference,* Dresden, Germany, 04-07 July, 2010.

[36] F. Mosele, F. da Porto, C. Modena, Experimental behaviour of newly developed systems for load bearing reinforced masonry walls. *14th International Brick and Block Masonry Conference*, Sydney, Australia, February 17-20, 2008. (CD-ROM)

[37] F. da Porto, M. Grendene, F. Mosele, C. Modena, In-plane cyclic testing and dynamic modelling of reinforced masonry walls. *14th World conference on Earthquake Engineering,* Bejing, China, 12-17 October, 2008.

[38] M. Tomaževič, M. Lutman, Seismic behaviour of masonry walls: modelling of hysteretic rules. *Journal of Structural Engineering, ASCE*, **122**(9),1048-1054, 1996.

[39] L. Nicolini, Sperimentazione e modellazione del comportamento ciclico nel piano di muratura armata per la definizione di fattori di riduzione delle forze. Graduation Thesis, Dept. of Structural and Transportation Engineering, University of Padova, Padova, Italy, 2008. (in Italian)

[40] M.J.N. Priestley, D.N. Grant, C.A. Blandon, Direct displacement-based seismic design, *New Zealand Society for Earthquake Engineering Conference*, 2005.

COMPDYN 2011
III ECCOMAS Thematic Conference on
Computational Methods in Structural Dynamics and Earthquake Engineering
M. Papadrakakis, M. Fragiadakis, V. Plevris (eds.)
Corfu, Greece, 25–28 May 2011

NUMERICAL SIMULATION OF ADJACENT BRIDGE STRUCTURES WITH NONLINEAR SFSI

Nawawi Chouw[1] **and Edwin M. Behrens**[2]

[1] University of Auckland
Department of Civil and Environmental Engineering,
Private Bag 92019, Auckland Mail Centre, Auckland 1142, New Zealand
n.chouw@auckland.ac.nz

[2] Universidad Catolica de la Santisima Conception
Alonso de Ribera 2850, Concepcion, Chile
ebehrens@ucsc.cl

Keywords: Nonlinear SFSI, Bridge, Earthquake, Adjacent Structures, Pounding, Relative Response.

Abstract. *Pounding between adjacent bridge structures in earthquakes have been investigated by many researchers in the past. However, most of works is performed with an assumption that the considered structures are fixed at their base. If soil-foundation-structure interaction (SFSI) is considered at all then linear soil behaviour is often assumed. Works including nonlinear SFSI is very limited. In this study the influence of non-uniform SFSI is considered. It is assumed that the left bridge structure is fixed at its base, while the soil of the right structure can behave nonlinearly. Each bridge structure with footing and subsoil is described by four degrees of freedom. A macro element is used to describe the dynamic behaviour of the footing and soil. The results show that nonlinear SFSI can have a beneficial effect on the activated forces in the structures. However, compared to bridge structure with linear SFSI more pounding occasions are observed and structural settlement can take place.*

1 INTRODUCTION

In the event of earthquakes seismic waves propagate and arrive at distant bridge support locations with a time delay. Because of the non-uniform development of soil along the bridge the arriving ground motions at adjacent bridge supports are incoherent. This time delay and coherency loss cause then a non-uniform support excitation. During an earthquake interaction between bridge structure, footing and supporting ground occurs. The local soil at adjacent bridge supports is normally not the same. Consequently, unequal soil-footing-structure interaction (SFSI) will take place. Also because of the different dynamic properties of adjacent bridge structures, strong relative movements between neighbouring bridge decks can occur. If the existing gap between the decks is insufficient to cope with the large closing relative movements, pounding will take place. Consequently, damage at girder ends occurs. If the seat length of the bridge deck is inadequately designed then collapse of bridge deck might take place due to insufficient seat length. Even if collapse does not occur, pounding damage can result in a bridge that is functionally disabled.

Bridge damages have been observed in almost all major earthquakes in the past decades, e.g. the 1989 Loma Prieta earthquake [1], the 1994 Northridge earthquake [2], the Kobe 1995 earthquake [3], the 1999 Chi-Chi earthquake [4], the 2008 Wenchuan earthquake [5] and the 2010 Chile earthquake [6]. Figure 1 shows clearly the consequence of strong relative movements at the girder support of the Llacolen Bridge that crosses the Bio-Bio River in Conception. The picture is taken by the authors in one of the field investigations of bridge damages due to the 2010 Chile earthquake.

Figure 1. Relative response induced damage of Puente Llacolen in the 2010 Chile earthquake

Researches on the consequence of relative movements for the seismic performance of bridges have been done mainly numerically. Most investigations have been performed under the assumption of uniform ground excitation [e.g. 7] and without considering the effect of SFSI [e.g. 8]. The significance of the influence of the spatial variation of ground excitations has been confirmed [8-14]. Experimental investigations of the effect of spatially non-uniform ground motions on the development of relative movements between adjacent bridge structures are still very limited [13, 14].

To prevent the occurrence of relative movements most of current design specifications, e.g. JRA [15], Part 2 of Eurocode 8 [16] and most recent CALTRANS [17] recommend that the adjacent bridge structures should have the same or at least similar fundamental frequencies so that the structures will respond to the ground motions mainly in phase. Consequently, relative response between the structures can be avoided or its influence significantly reduces. This is also currently the only suggested measure to prevent pounding damage at the same time to ensure the serviceability of the bridge due to the required small gap of a few centimetres.

Recently, investigations of a possible mitigation measure by installing the so-called modular expansion joints have shown that large relative movements between adjacent bridge structures can be accepted without causing damage to the bridge structures or hinder the functionality of the bridges [10-12].

The significance of nonlinear SFSI has been identified [18-21], however, only very limited works have been performed. This study addresses the influence of unequal SFSI, especially focuses on the consequence of nonlinear SFSI for the development of relative movements between two adjacent bridge structures.

2 SOIL-FOOTING-STRUCTURE SYSTEM AND GROUND EXCITATION

The bridge structures considered are assumed to have the same height of 9 m (Figure 2(a)). Figure 2(b) shows a simplified model of the bridge structures. The multiple bridge piers are described by a collective bridge pier. Each footing is assumed to be rigid with a size of 10 m. The mass of each bridge structure and its footing is assumed to be the same and has the values of 1000 t and 500 t, respectively. The fundamental frequency of the left and right bridge structures with an assumed fixed base is 1.5 Hz and 1 Hz, respectively. Both structures have the same material damping of 5 %.

In the considered cases the supporting ground can be uniform or non-uniform and can behave nonlinearly. The dynamic behaviour of the footing including plastic deformation of subsoil is described based on soil constitutive models as a macro element with a lumped mass and three degrees of freedom at the centre of the footing [18, 19]. The soil stiffness in the horizontal, vertical and rotational directions is 3.038E5 kN/m, 4.594E5 kN/m and 9.113E6 kNm/rad, respectively. The corresponding damping values are 1.35E4 kNs/m, 2.921E4 kNs/m and 2.44E4 kNms/rad. The soil bearing capacity is described by the strength surface which reflects the soil capability to bear the combined vertical, horizontal and moment loading. In this work a strain-hardening plasticity model for predicting the settlement of shallow foundation on sand proposed by Nova and Montrasio [22] is applied.

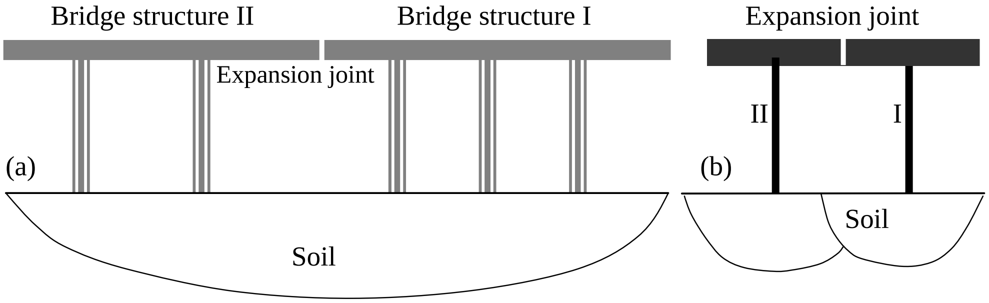

Figure 2. Adjacent bridge structures-foundation-soil system.
(a) MDOF systems and (b) simplified two four DOF systems

To limit the influence factors only linear pounding is considered. The pounding element has the stiffness of 5E6 kN/m. It is assumed that the bridge structures and their footings remain elastic during the entire earthquake loading and only uniform ground excitation is considered [Figure 3].

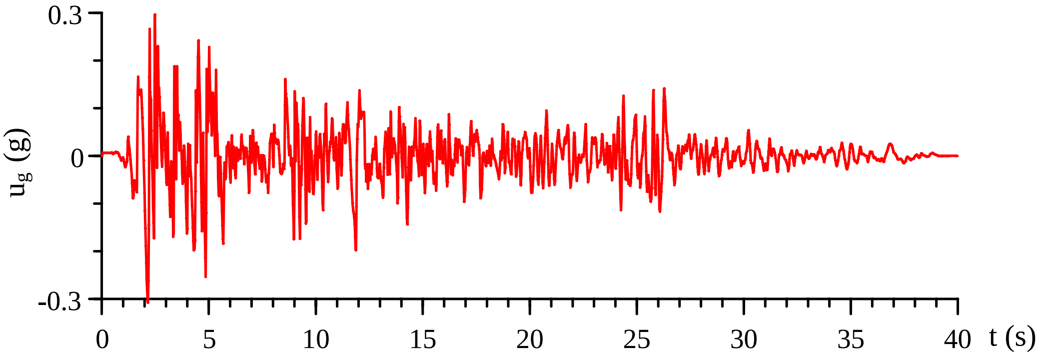

Figure 3. El-Centro ground motions

3 NUMERICAL RESULTS AND DISCUSSION

The effect of linear and nonlinear SFSI on the response of the two adjacent bridge structures can be observed from a comparison of the results with those without considering SFSI. It is assumed that both structures are supported by the same uniform ground. In the case without SFSI, both structures are fixed at their rigid base.

Figures 1(a) and (b) display the time histories of the displacement of the right (u_I) and left (u_{II}) bridge structures, respectively. The solid grey and dark lines are the displacement without SFSI and with linear SFSI effect while the dash line is the displacement with the influence of nonlinear SFSI.

As mentioned earlier the fundamental frequency of the right and left bridge structures with an assumed fixed base is 1 Hz and 1.5 Hz, respectively. As expected the flexible subsoil has stronger influence on the stiffer left bridge structure. The corresponding fundamental frequency of the structures with subsoil is reduced to 0.79 Hz and 1.16 Hz, respectively. In the considered case SFSI has a strong reduction effect on the displacement of the flexible right bridge structure. The maximum displacement without SFSI is 19.58 cm. The maximum displacement with linear and nonlinear SFSI effect reduces to 14.5 cm and 12.69 cm, respectively. In contrast, linear SFSI has an amplification effect on the left stiffer bridge structure. The maximum displacement without and with linear SFSI effect is 10.09 cm and 10.42 cm, respectively. Nonlinear SFSI has always reducing effect and causes a maximum displacement of only 5.97 cm.

From the displacement time histories one can expect that without a consideration of SFSI a realistic pounding potential of bridges cannot be properly predicted, since supporting ground can alter not only the fundamental frequencies of the adjacent soil-foundation-structure systems but also their response amplitudes and consequently the development of relative responses between the adjacent bridge structures.

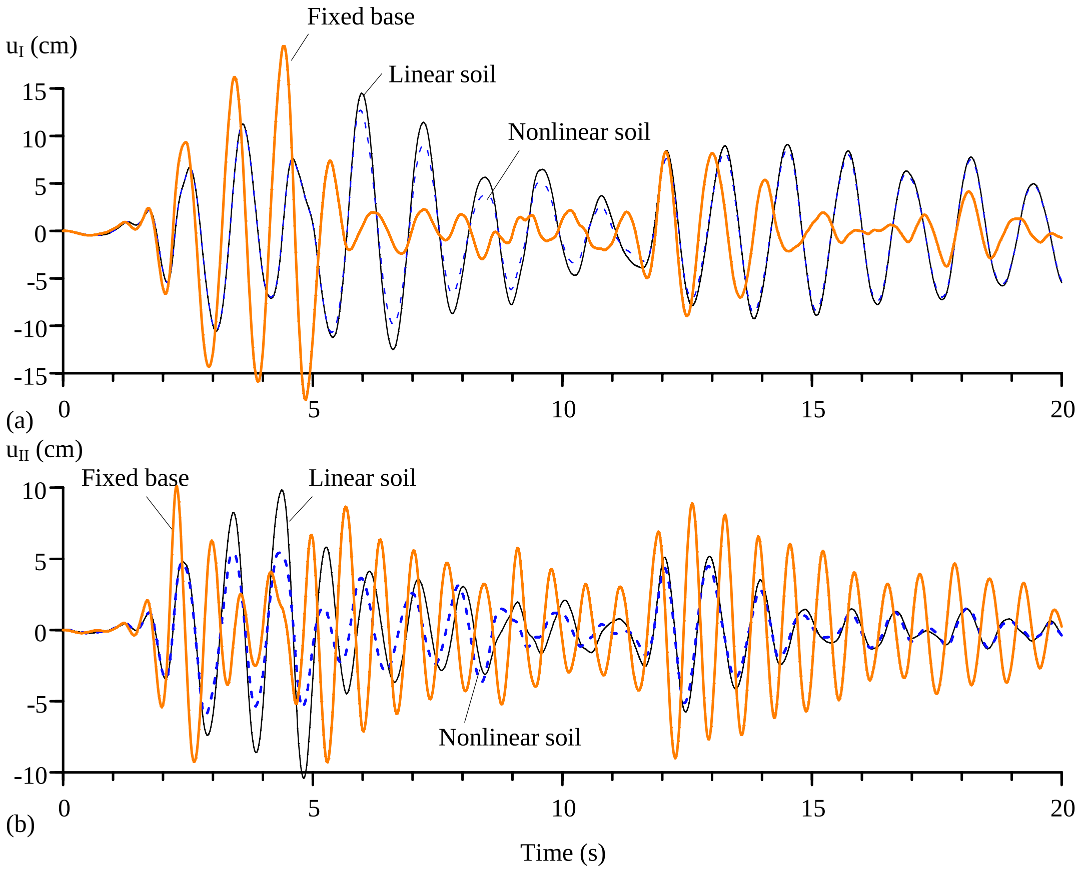

Figure 4. Influence of supporting ground condition on the displacement at (a) the right (u_I) and (b) left (u_{II}) bridge girders.

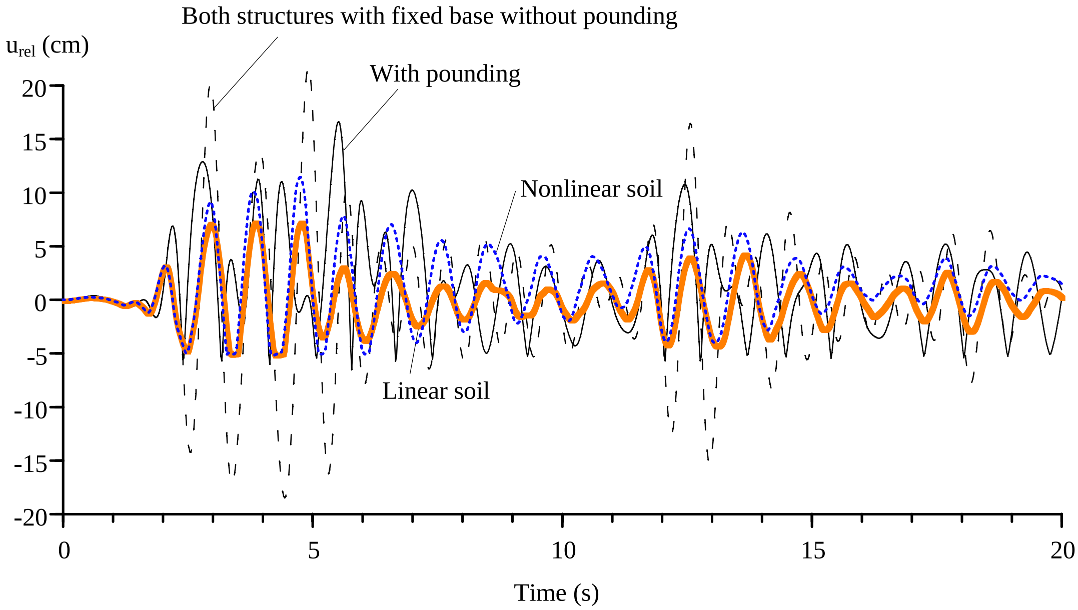

Figure 5. Influence of soil conditions on relative displacement

In Figure 5 the development of the relative displacement u_{rel} is presented. The dash and solid black lines are respectively the development of the relative displacement without and with a consideration of pounding when both bridge structures are assumed to be fixed at their base. The existing gap size of 5 cm can be clearly seen which restricts both girder movements when pounding is considered. The dotted and bold grey lines are respectively the relative displacement with considering nonlinear and linear SFSI effect at the right bridge segment while the left bridge segment is assumed be fixed at the base. Pounding is considered.

From a comparison of the dash and solid thin lines it is apparent that pounding between the adjacent bridge girders reduces the unseating potential of the bridge girders which is indicated by the opening or positive relative girder movement.

The consequence of different soil conditions of the right bridge site can be clearly seen in the pounding development. While an assumption of fixed base bridge structures causes poundings on 18 occasions, when the soil at the right bridge structure remains linear and behaves nonlinearly, poundings only occur on two and five occasions, respectively. It is well known that damage at girder ends is not only influenced by the strongness of the pounding but also by the number of strong poundings. In the considered case SFSI causes a further reduction of the unseating potential which is indicated by smaller positive relative displacement between the adjacent bridge girders. Compared to the linear SFSI case nonlinear soil causes a larger number of pounding occasions and also unseating potential.

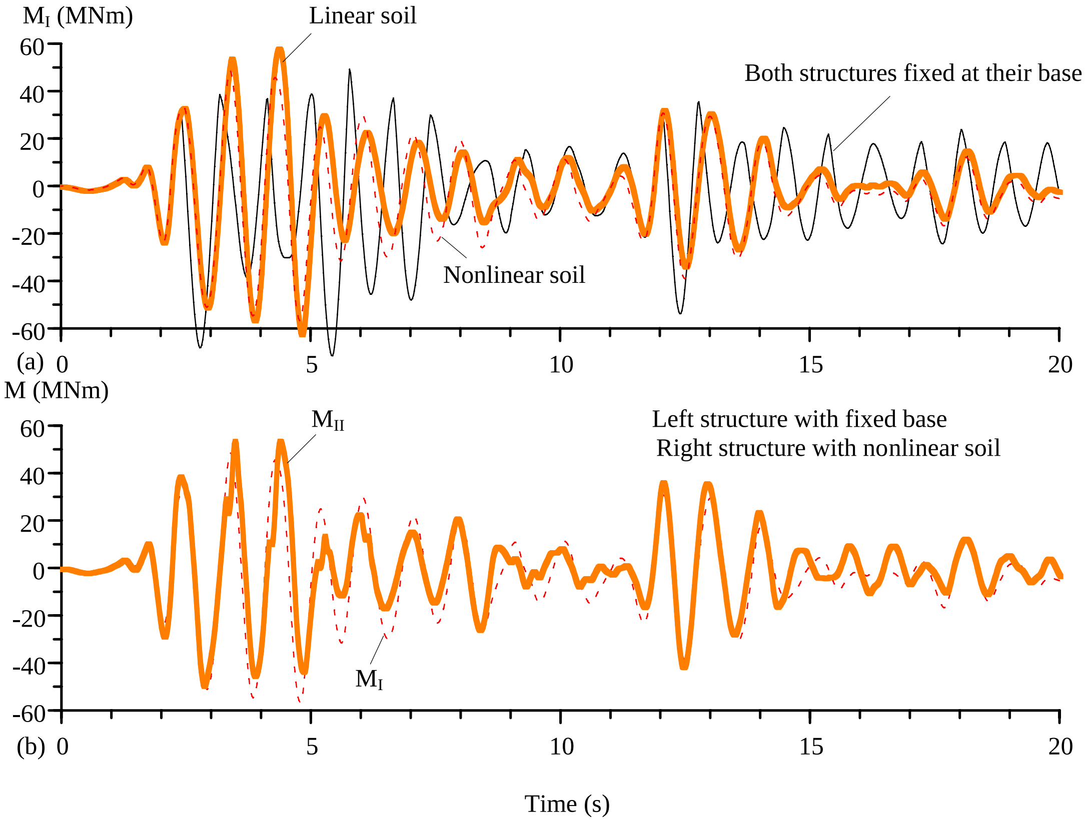

Figure 6. Influence of soil conditions on bending moment development.
(a) M_I and (b) M_I and M_{II} due to nonlinear soil

Figure 6(a) displays the influence of soil conditions of the right bridge structure on the bending moment development at the right bridge support. Pounding effect is considered, and it is assumed that the left bridge structure is fixed at the base. The solid thin line indicates the bending moment development when both adjacent structures are assumed to be fixed at their base. The maximum bending moment is 71.5 MNm. The bold grey and dashed lines are the bending moment when the soil at the right bridge site remains linear and can behave nonlinearly, respectively. The corresponding maximum bending moments are 62.08 MNm and 56.58 MNm. In the considered case the simultaneous influence of nonlinear soil and pounding causes the smallest maximum bending moment.

In Figure 6(b) the bending moment at both bridge supports is displayed. Pounding is considered. They have similar development. The maximum bending moment M_{II} at the left bridge support (bold grey line) is only slightly smaller and has the value of 53.9 MNm. However, the consequence of nonlinear soil deformation can be seen in the residual bending moment M_I (dashed line) at the end of the considered time window.

The results show that if the ground is permitted to behave nonlinearly the activated bending moment in the structures can be reduced significantly. In the considered case even though only one bridge site can have nonlinear soil, as long as a large residual settlement of the structures can be avoided, the nonlinear behaviour of soil can be used to reduce the impact of earthquakes on the structures.

4 CONCLUSIONS

In this work numerical analysis of the effect of soil-foundation-structure interaction (SFSI) on pounding behaviour of two adjacent bridge structures is addressed. Three cases are considered: 1) Both structures are fixed at their base; 2) the left bridge structure has a fixed base and the right structure has a linear soil and 3) the soil at the right bridge site can behave nonlinearly. The gap between the bridge girders is 5 cm. It is assumed that both bridge structures remain elastic during the whole spatially uniform earthquake loading. Each of the bridge structures and its supporting soil are described by four degrees of freedom. For the foundation and subsoil a macro element is used.

In the considered cases the study reveals:

- An analysis without considering SFSI effect will produce more conservative results.
- Even if SFSI is considered only on one of the bridge sites the activated forces in the structures can be reduced. This is also the case in terms of pounding occurrence.
- Nonlinear SFSI can further reduce the activated bending moment at the bridge support. However, the number of poundings is larger than that in the case of linear SFSI.

Additional investigations are necessary to have a better understanding of the interrelation between nonlinear SFSI, pounding behaviour and the characteristic of the bridge structures and loading.

ACKNOWNLEDGEMENTS

The authors would like to thank New Zealand Transport Agency for the support of this research under the grant TAR 08/32.

REFERENCES

[1] M. Yashinsky, M.J. Karshenas, *Fundamentals of seismic protection for bridges*, Earthquake Engineering Research Institute, 184 pages, 2003.

[2] F.J. Hall (Ed.) *Northridge earthquake, January 17, 1994*. Earthquake Engineering Research Institute, Preliminary reconnaissance report, EERI-94-01.

[3] K. Kawashima, S. Unjoh, Impact of Hanshin/Awaji earthquake on seismic design and seismic strengthening of highway bridges, *JSCE Structural Engineering/Earthquake Engineering*, **13(2)**, 211-240, 1996.

[4] Japan Society of Civil Engineers (JSCE), *The 1999 Ji-Ji earthquake, Taiwan-Investigation into damage to civil engineering structure*, Eds.: M. Hamada, S. Nakamura, T. Ohsumi, K. Megro, E. Wang, Tokyo, 160 pages.

[5] Q. Han, X. Du, J. Liu, Z. Li, L. Li, J. Zhao, Seismic damage of highway bridges during the 2008 Wenchuan earthquake, *Earthquake Engineering and Engineering Vibration*, **8(2)**, 263-373, 2009.

[6] A.S. Elnashai, B. Gencturk, A.-S. Kwon, I.L. Al-Qadi, Y. Hashash, J.R. Roesler, S.J. Kim, S.-H. Jeong, J. Duckes, A. Valdivia, *The Maule (Chile) earthquake of February 27, 2010: Consequence assessment and case studies*. Mid-America Earthquake Centre, Report No. 10-04, 190 pages, 2010.

[7] P. K. Malhotra, Dynamics of seismic pounding at expansion joints of concrete bridges, *ASCE Journal of Engineering Mechanics*, **124(7)**, 794-802, 1998.

[8] G. Zanardo, H. Hao, C. Modena, Seismic response of multi-span simply supported bridges to a spatially varying earthquake ground motion, *Earthquake Engineering and Structural Dynamics*, **31**, 1325-1345, 2002.

[9] N. Chouw, H. Hao, Significance of SSI and non-uniform near-fault ground motions in bridge response I: Effect on response with conventional expansion joint, *Engineering Structures*, **30(1)**, 141-153, 2008.

[10] N. Chouw, H. Hao, Significance of SSI and non-uniform near-fault ground motions in bridge response II: Effect on response with modular expansion joint, *Engineering Structures*, **30(1)**, 154-162, 2008.

[11] K. Bi, H. Hao, N. Chouw, Required separation distance between decks and at abutments of a bridge crossing a canyon site to avoid seismic pounding. *Earthquake Engineering and Structural Dynamics*, **39(3)**, 303-323, 2010.

[12] K. Bi, H. Hao, N. Chouw, Influence of ground motions spatial variation, site condition and SSI on the required separation distances of bridge structures to avoid seismic pounding, *Earthquake Engineering and Structural Dynamics*, published online, 2010.

[13] A. J. Crewe, J. A. Norman, Experimental modelling of multiple support excitation of long span bridges. *Proceedings of the 4th International Conference on Earthquake Engineering*, paper 127, Taipei, Taiwan, 2006.

[14] H. Sun, B. Li, K. Bi, N. Chouw, J.W. Butterworth, H. Hao, Shake table test of three-span bridge model, *Proceedings of the 9th Pacific Conference on Earthquake Engineering*, 14-16 April 2011, Auckland, New Zealand.

[15] Japan Road Association (JRA), *Specifications for highway bridges –Part V seismic design*, 5th ed., 406 p., 2004 (in Japanese)

[16] BS EN 1998-2, *Eurocode 8 - Design of structures for earthquake resistance*, British Standards Institution, London, 2005.

[17] California Department of Transportation (CALTRANS), *Seismic design criteria. Design manual –version 1.5,* Sacramento, California, USA, 2009.

[18] J. C.W. Toh, M. J. Pender, Design approaches and criteria for earthquake-resistant shallow foundation systems. In: *Soil-Foundation-Structure Interaction*, Eds.: R. Orense, N. Chouw, M. Pender, Leiden, CRC Press, 173-180, 2010.

[19] A. Pecker, C. T. Chatzigogos, Nonlinear soil structure interaction: impact on the seismic response structures, In: *Earthquake Engineering in Europe, Geotechnical, Geological and Earthquake Engineering*, **17**, Eds.: M. Garevski, A. Ansal, Heiderberg, Springer, 79-103, 2010.

[20] L. Deng, B. L. Kutter, S. Kunnath, T.B. Algie, Performance of bridge systems with nonlinear soil-footing-structure interactions. In: *Soil-Foundation-Structure Interaction*, Eds.: R. Orense, N. Chouw, M. Pender, Leiden, CRC Press, 49-56, 2010.

[21] E. M. Behrens Rincon, N. Chouw, Nonlinear SSI effect on adjacent bridge structures with pounding. *Proceedings of the 9th Pacific Conference on Earthquake Engineering*, Auckland, New Zealand, 14-16 April, 2011.

[22] R. Nova, L. Montrasio, Settlements of shallow foundations on sand, *Gèotechnique*, **41(2)**, 243-256, 1991.

COMPDYN 2011
III ECCOMAS Thematic Conference on
Computational Methods in Structural Dynamics and Earthquake Engineering
M. Papadrakakis, M. Fragiadakis, V. Plevris (eds.)
Corfu, Greece, 25–28 May 2011

THEORETICAL EVALUATION OF YIELDING SHEAR PANEL DEVICE FOR PASSIVE ENERGY DISSIPATION

Md Raquibul Hossain [1], Mahmud Ashraf [2] and Faris Albermani [3]

[1] School of Civil Engineering, The University of Queensland
St Lucia, QLD 4072, Australia
md.hossain@uqconnect.edu.au

[2] School of Civil Engineering, The University of Queensland
St Lucia, QLD 4072, Australia
m.ashraf@uq.edu.au

[3] School of Civil Engineering, The University of Queensland
St Lucia, QLD 4072, Australia
f.albermani@uq.edu.au

Keywords: Earthquake, Passive Energy Dissipation, Shear deformation, Tri-linear model, Yielding Shear Panel Device.

Abstract. *Metal yielding devices have been used in structures for decades to absorb earthquake energy whereby damages to the major structural components could be minimised. A recent technique to exploit the shear deformation of thin metal plates to dissipate energy has given rise to a new yielding shear panel device (YSPD); a thin steel plate is welded within steel a square hollow section (SHS)to form the device. Laboratory test results showed the potential of YSPD in energy dissipation. The behaviour of YSPD is determined by a complex interaction among the thin diaphragm plate, the surrounding SHS and the boundary conditions i.e. the structural elements that connect the device to the parent structure. This paper investigates the load-deformation response of YSPD and proposes a theoretical model to predict the experimental behaviour using the knowledge of the geometry of YSPD and the properties of the material. Previously proposed analytic method based only on the shear deformation of the diaphragm plate is revisited; appropriate modifications are proposed to include the effects of the deformations observed in the SHS and the obvious rotation of the loading plate. A tri-linear load-deformation model is proposed herein and the predictions obtained from the numerical models are compared with the available test results.*

1 INTRODUCTION

Earthquakes cause significant damages to structures resulting in either complete demolition or the affected structures require complex and expensive rehabilitation techniques to be serviceable. Minimization of structural damages due to earthquake is a major area of research which contributed to the development of a number of active, semi-active and passive control mechanisms during the last few decades. The current research investigates the structural performance of a newly proposed yielding shear panel device (YSPD) for passive energy dissipation. YSPD is simple to manufacture and is economical when compared against currently available devices. Tests carried out on the device demonstrate its potential for considerable energy absorption [1]. Hossain et. al. [2] developed finite element models and verified their performance against available monotonic and cyclic test results. An appropriate theoretical model for YSPD is required to understand the effects of this device by analysing structures including different YSPDs. Current paper proposes a tri-linear force-displacement model for YSPD, which is verified against the results obtained from tests and finite element simulation.

2 YIELDING SHEAR PANEL DEVICE (YSPD)

Diagonal tension field that develops in the post-buckling regime of a thin steel plate under shear offers significant strength and ductility and hence can be utilized to dissipate energy. This concept led to the development of a new metallic passive energy dissipating device ‘Yielding Shear Panel Device’ (YSPD). YSPD was introduced by Williams and Albermani [3] based on the design proposed by U. Dorka at the University of Kassel, Germany to exploit the energy dissipative capability of steel plates through in-plane shear deformation and the concept was further explored by Schmidt et.al. [4] and Williams and Albermani [5]. YSPD relies on the in-plane shear deformation of a thin diaphragm steel plate welded inside a square hollow section (SHS). This device can be placed beneath a structural beam using a V-braceso that it automatically comes into play in the event of any horizontal excitation. Figure 1 shows a typical assembly for YSPD.

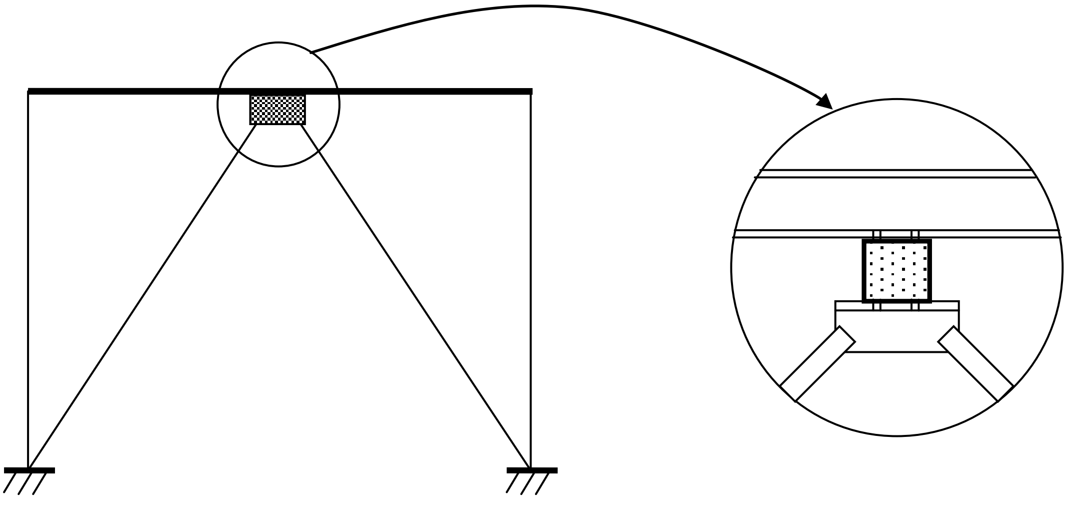

Figure 1: Typical YSPD-brace assembly.

Chan et. al. [1] conducted a series of monotonic and cyclic tests using various plate thicknesses and device configurations for YSPD. The tested specimens were fabricated using a short segment of a square hollow section (SHS) with a steel diaphragm plate welded inside, as shown in Figure 2. Four bolt holes spaced at a centre-to-centre distance ‘s’ were drilled on each of the two opposite SHS flanges for connecting the device to the test setup; this connection is analogous to the practical assembly where YSPDs are proposed to be connected using bolts to ensure easy installation and replacement. The SHS provides a boundary to the diaphragm plate so that shear forces can be applied to the plate, in addition to providing necessary detail for connections to the parent structural frame. Most importantly, the SHS serves as a boundary element allowing the tensile strips to be formed and the tension field to be developed following the post-buckling of the thin diaphragm plate. As a result of sufficiently large displacements occurring in the diaphragm plate, the input energy originating from an earthquake could be dissipated through plastic deformation.

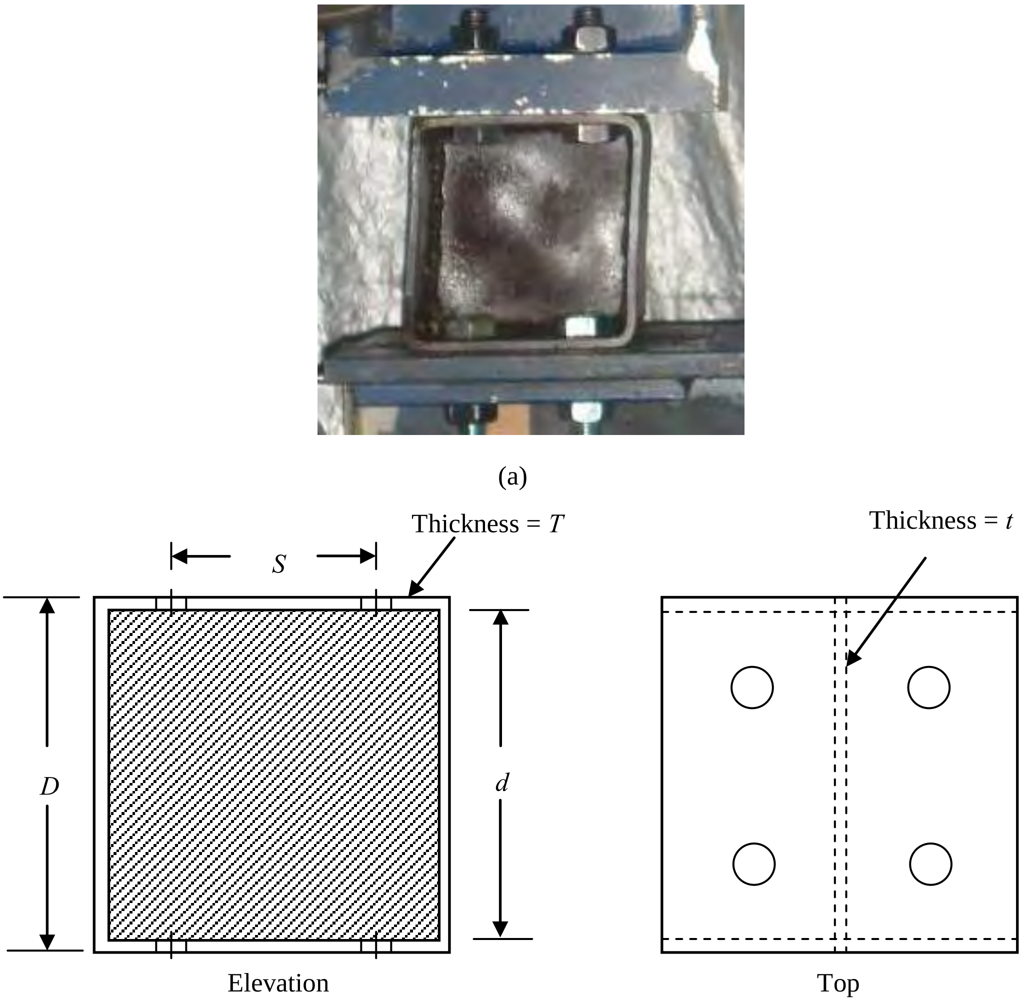

(b)

Figure 2: (a) Yielding shear panel device (YSPD) (b) Schematic diagram showing the geometric parameters of YSPD [6].

Chan et. al. [1] tested two different sizes of YSPD, 100mm × 100mm and 120mm × 120mm, with three different thickness of 2 mm, 3 mm and 4 mm for the diaphragm plate. Bolt spacing of 50 mm was used for four M16 bolts on each side of the SHS to install the test specimen between a ground beam and L-beam. The geometric dimensions of the test specimens are given in Table 1 and the reported material properties are summarized in Table 2.

YSPD Designation (D × D × t)	Diaphragm Thickness, t (mm)	SHS Size, D (mm)	SHS Thickness, T (mm)	Bolt Spacing, S (mm)
100×100×2	1.86	100	3.76	50
100×100×3	2.83	100	3.76	50
100×100×4	3.78	100	3.76	50
120×120×2	1.86	120	4.91	50
120×120×3	2.83	120	4.91	50
120×120×4	3.78	120	4.91	50

Table 1: Geometric details of YSPD test specimens [1]

YSPD Designation	Tensile Yield Strength (MPa)	
(D × D × t)	Diaphragm Plate	SHS
100×100×2	211.3	414.9
100×100×3	321.3	414.9
100×100×4	351.2	414.9
120×120×2	211.3	333.3
120×120×3	321.3	333.3
120×120×4	351.2	333.3

Table 2: Material properties of the test specimens [1]

3 ANALYTICAL EVALUATION OF YSPD BY CHAN ET. AL. [1]

Chan et. al. [1] classified YSPDs into two different categories based on the slenderness ratio of the diaphragm plate for theoretical evaluation. Material stress-strain response was considered elastic, perfectly-plastic with a von Mises yield criterion. Diaphragm plates were assumed to be simply supported by the SHS and were classified as either compact or slender depending on whether or not the critical shear buckling stress $_{cr}$ exceeds the material yielding stress. The critical shear stress for a simply supported plate is given by [7],

$$_{cr} = k_e \frac{^2E}{12(1- \ ^2)}\left(\frac{t}{d}\right)^2 \tag{1}$$

where k_e is a coefficient which depends on the aspect ratio and end restraints of the plate e.g. k_e is equal to 9.34 for square pates, whilst E and ν are Young’s modulus and Poisson’s ratio respectively. It is worth mentioning that the specimens used in the testing program fall within the category of YSPD with compact diaphragm plate.

Assuming an insignificant contribution from SHS, Chan et. al. [1] proposed the theoretical elastic in-plane lateral stiffness of the YSPD, k_{YSPD}as

$$k_{YSPD} = Gt \quad (2)$$

where G is the shear modulus of steel and t is the thickness of the diaphragm plate. For a device with compact diaphragm plate, the yield shear strength of YSPD is,

$$F_y = \frac{f_y}{\sqrt{3}} td \quad (3)$$

where d is the width of the steel plate and f_y is the yield strength in tension. Hence the yield displacement of the device becomes,

$$u_y = \frac{F_y}{k_{YSPD}} = \frac{f_y d}{\sqrt{3}G}$$
(4)

Figure 3 shows a comparison between the test result and the theoretical predictions proposed by Chan et al [1] for the load-deformation response of YSPD 100×100×4. This comparison clearly demonstrates that there is room for further modifications to the proposed theoretical model. The current research aims to develop FE models and to exploit the numerical results to propose more reliable analytic predictions for the load-deformation response of YSPD.

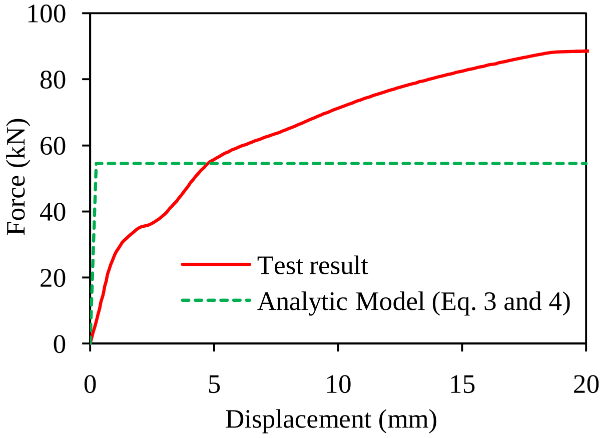

Figure 3. Comparison between the test result and the predicted force-displacement response of YSPD 100×100×4 based on the model proposed by Chan et al. [1].

4 ANALYTIC FORMULATION OF YSPD

YSPD specimens used in the laboratory testing had compact diaphragms and hence the current paper proposes analytic modelling techniques for such YSPDs so that the proposed model can be verified against test results. Size of the considered YSPDs varies within 100 to 120 mm to avoid the chance of developing large eccentric moment. Development of a tri-linear load-deformation model for YSPD is described in the following sections.

4.1 Evaluation of initial stiffness

When subjected to loading, the YSPD has to resist two equal and opposite forces acting through the bolted connections and hence its initial stiffness would be equal to the force required to produce unit horizontal displacement at the loaded flange. The diaphragm plate and the SHS deform simultaneously due to the applied deformation as shown in Figure 4.

The loading and the supporting ends are assumed to remain parallel for preliminary calculations. The resulting stiffness of YSPD can be obtained by combining the individual stiffness of two constituent elements i.e. the SHS and the diaphragm. Firstly the stiffness of the diaphragm plate is formulated assuming it to be simply supported by the SHS and the diaphragm plate is assumed to deform due to pure shear. In the next step, the stiffness of the SHS is calculated assuming that the diaphragm plate deforms due to in-plane compression. The vertical flanges are also compressed as a result of the flexural deformation of the bolted flanges. The overall stiffness of the YSPD may thus be obtained as follows,

$$\frac{1}{k_{YSPD}} = \frac{1}{k_{dia}} + \frac{1}{k_{shs}} \tag{5}$$

where, k_{YSPD} = Stiffness of YSPD
k_{dia} = Stiffness of the diaphragm
k_{shs} = Stiffness of the SHS

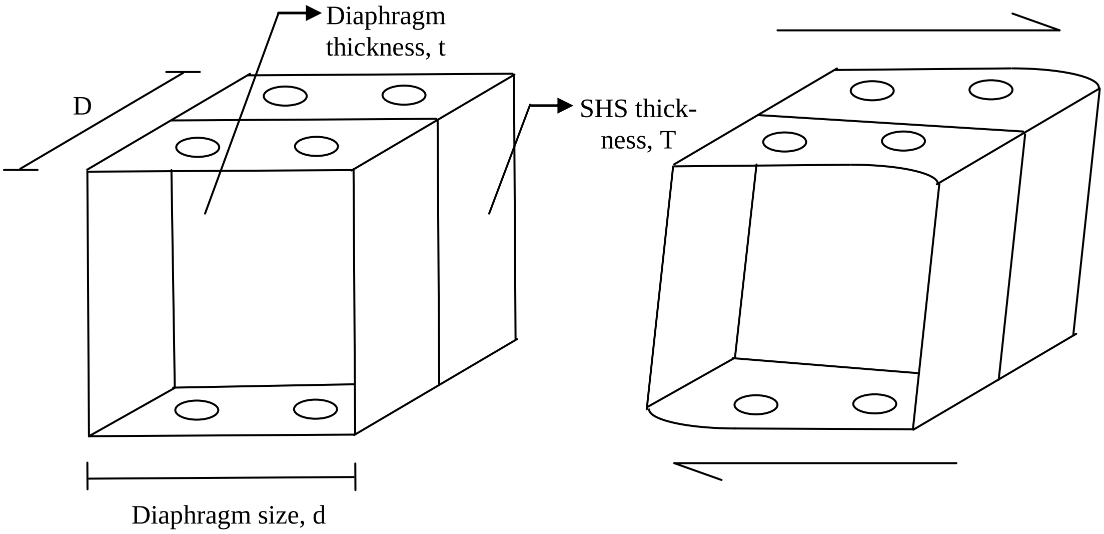

Figure 4. Undeformed and deformed shapes of a yielding shear panel device (YSPD).

4.1.1. Stiffness of the diaphragm plate

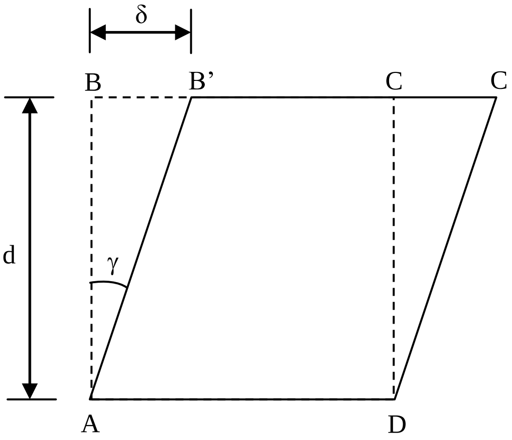

Figure 5. Undeformed Pure shear deformation of diaphragm plate.

For a unit displacement (δ = 1) of the diaphragm plate (Figure 5), B is displaced to B' and the shear stain is given by,

$$\tan \quad = \frac{\delta}{d} = \frac{1}{d} \qquad (6)$$

Considering small strain, it can be reduced to,

$$= \frac{\delta}{d} = \frac{1}{d} \qquad (7)$$

For elastic deformation, the shear stress,

$$= G \quad = \frac{G}{d} \qquad (8)$$

Hence the elastic stiffness of diaphragm plate in pure shear may be expressed as,

$$k_{dia} = \quad dt = Gt \qquad (9)$$

4.1.2. Stiffness of the SHS

The bolted flanges of the SHS undergo flexural deformation due to the in-plane compression of the diaphragm plate and the vertical flanges,. Figure 6 shows the details of assumed deformations with acting forces F_1 and F_2.

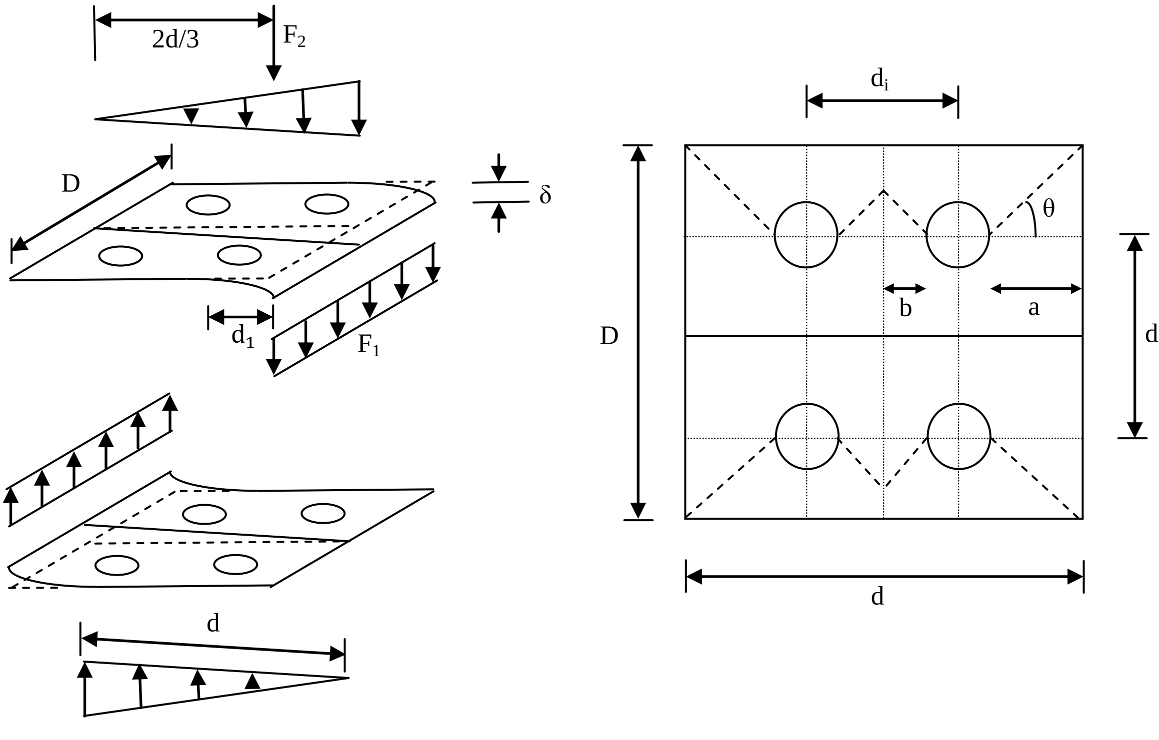

(a) (b)

Figure 6. (a) Deformation of bolted flanges, (b) Dimensions of bolted flange.

Bolted flanges experience bending about an axis perpendicular to the loading direction due to the force F_1. By assuming a zero rotation along the line passing through the centre of nearby bolts and ignoring the effects of bolt holes we can calculate,

$$F_1 = \frac{3EI_1}{{d_1}^3} = \frac{DT^3E}{4(a+r)^3} \tag{10}$$

where, $I_1 = \frac{DT^3}{12}$

r = Radius of the bolt hole

The compression at the diaphragm plate causes deformation along the line joining the flange and the diaphragm plate. . This deformation results in an additional bending to the flange about an axis parallel to the loading direction. The acting force F_2 responsible for this deformation is assumed to have a triangular distribution due to the large in-plane rigidity of the diaphragm plate. This force may be obtained by taking strips in the flange.

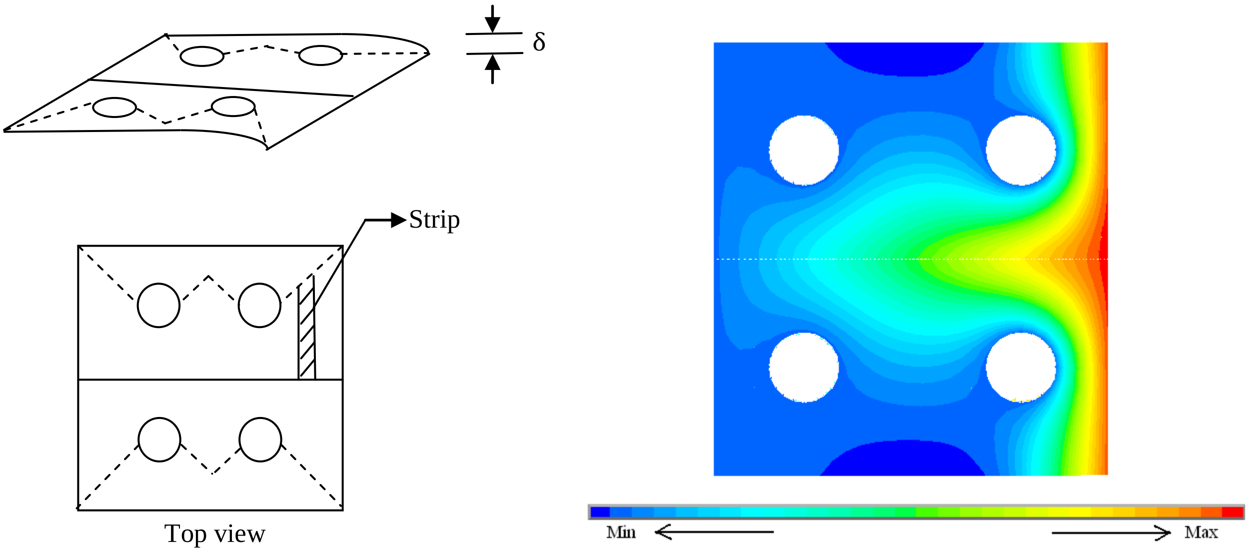

(a)

(b)

Figure 7. (a) Assumed zero rotation line on SHS flange. (b) Typical contour plot of the out of plane deformation of SHS flange

The zero rotation line is assumed as a zigzag dotted line as shown in Figure 7(a); this pattern is due to the boundary condition provided by the bolted connections. Each strip is considered to be fixed on both sides bounded by the dotted 'zero rotation' line and the line joining the diaphragm to the flange. Figure 7(b) shows a contour plot of the typical out of plane deformation of the SHS flange obtained from FE analysis [2]. The contour plot confirms that the deformation at the right part of the top flange is due to bending about both the orthogonal directions. The deformation pattern due to the compression of the diaphragm plate also verifies the assumed zigzag line for zero rotation.

The zero rotation line is assumed to make an angle of θ (Figure 6(b)) with a plane parallel to the diaphragm. The average distance (d_2) between the diaphragm line and zigzag support line can be calculated as follows,

$$d_2 = \left(\frac{d_0}{2} + \frac{a.\tan\theta}{2}\right) \times \frac{2a}{d} + \left(\frac{d_0}{2} + \frac{b.\tan\theta}{2}\right) \times \frac{2b}{d} + \left(\frac{d_0}{2} - \frac{r}{4}\right) \times \frac{4r}{d}$$

$$\text{or, } d_2 = \frac{d_0}{2} + \frac{a^2.\tan\theta + b^2.\tan\theta - r^2}{d} \tag{11}$$

The resultant of the triangular force considering a unit deformation at the end becomes,

$$F_2 = 2\times\left(\frac{6EI_2/d_2^3}{2}\right) = \frac{6EI_2}{d_2^3} = \frac{dT^3E}{2d_2^3} \tag{12}$$

where, $I_2 = \frac{dT^3}{12}$

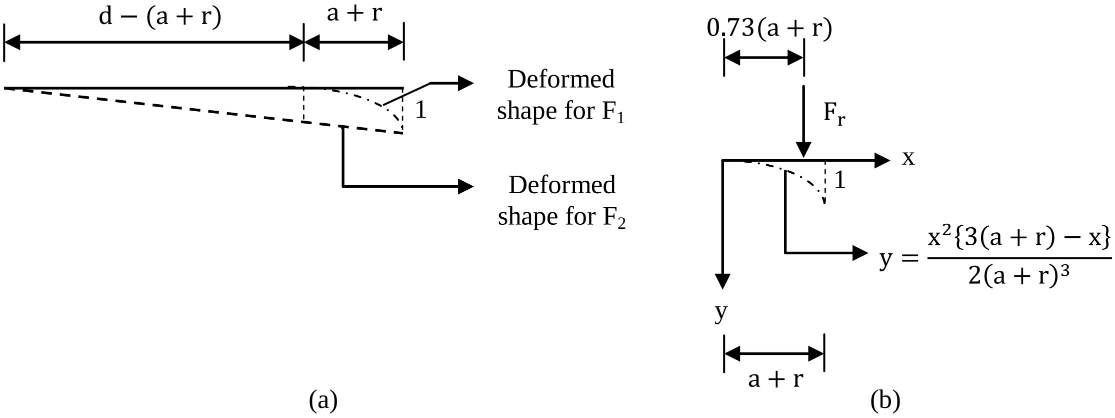

(a) (b)

Figure 8. (a) Deformed shapes due to force F_1 and F_2 of SHS flange (b) Equation of the deformed shape for the force F_1 and reduction force F_r

A reduction in the total calculated force is required for bending moments acting at orthogonal directions. Figure 8(b) shows the deformed shape with a unit deformation at the end for F_1. The average deformation becomes 3/8 by calculating the area and dividing it with the deformed length (a+r). The common deformation due to force F_1 and F_2 are calculated. Force required to produce this common deformation is the reduction force which can be calculated as,

$$F_r = 2\times\left(\frac{6EI_3}{d_2^3}\right)\times\frac{3}{8} = \frac{3E(a+r)T^3}{8d_2^3} \tag{13}$$

where, $I_3 = \frac{(a+r)T^3}{12}$

Force F_r acts at a distance of $d_r = \{d - 0.27(a + r)\}$ from the zero deformation end.

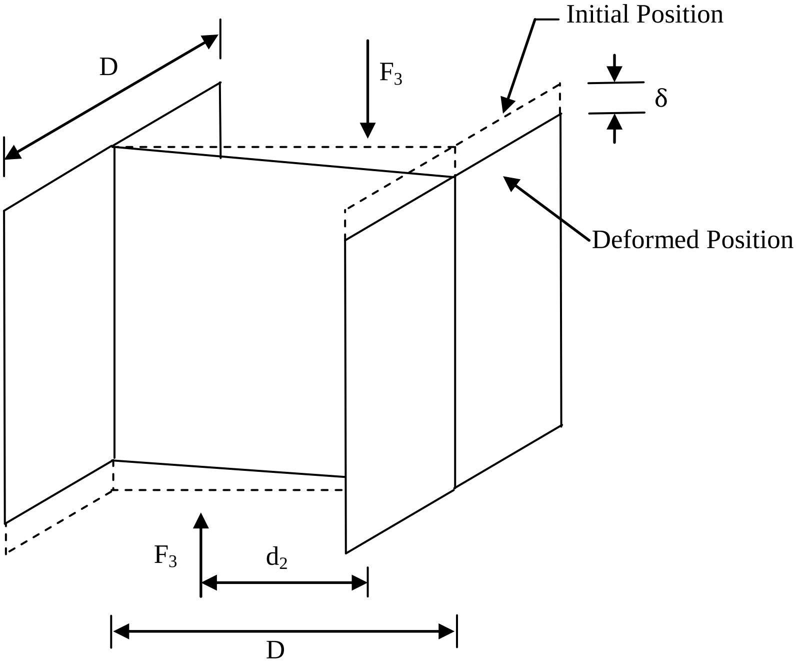

Figure 9. Compressive deformation of diaphragm plate and vertical flanges

The compression of the diaphragm plate and the vertical flanges in an YSPD is analogous to the deformation of an I-Section as shown in Figure 9. The force required to make a unit deformation i.e. strain = 1/d at the end of the flange,

$$\mathrm{F_3 = DT \times \frac{E}{d} + \frac{dt}{2} \times \frac{E}{d}} \tag{14}$$

The distance between the zero deformation and the line of action of the force,

$$\mathrm{d_3 = \frac{DTE + dtE/3}{F_3}} \tag{15}$$

The stiffness of the SHS can be calculated by the moment balance of these forces and thus may be expressed as follows

$$\mathrm{k_{SHS} = F_1 + \frac{F_2}{3} - \frac{F_r(2d_r - d)}{d} + \frac{F_3(2d_3 - d)}{d}} \tag{16}$$

Calculation showed that the contribution of force F_3 is more than 98.5%. The inclination of the zero deformation angle θ, thus, has negligible effect on the overall stiffness of the SHS and hence the angle θ may be taken as 45° whilst calculating the stiffness of SHS.

4.1.3. Combined Stiffness

Test results showed considerable rotation of the loading end within the elastic range [2], which causes the stiffness of the SHS to degrade. Hence the stiffness of the SHS may be taken as ϕk_{shs}, where ϕ is a reduction factor. The modifies stiffness of YSPD (k'_{YSPD}) is thus expressed as follows,

$$\mathrm{\frac{1}{k'_{YSPD}} = \frac{1}{k_{dia}} + \frac{1}{\phi k_{shs}}} \tag{17}$$

The value of ϕ can be determined using the initial stiffness of YSPDs obtained from the experimental investigation. Theoretical stiffness of the diaphragm plate and the SHS are calculated individually using Equations 9 and 16 ignoring the effects of rotation. Obtained stiffness magnitudes for the YSPDs and their corresponding diaphragm plates and SHS are used to plot Figure 10. The slope of the straight line is equal to $1/\phi$ according to Equation 17. The obtained value of ϕ is equal to 0.03 ignoring one outlier, which represents significantly low initial stiffness showed by YSPD 120×120×3 in the monotonic test.

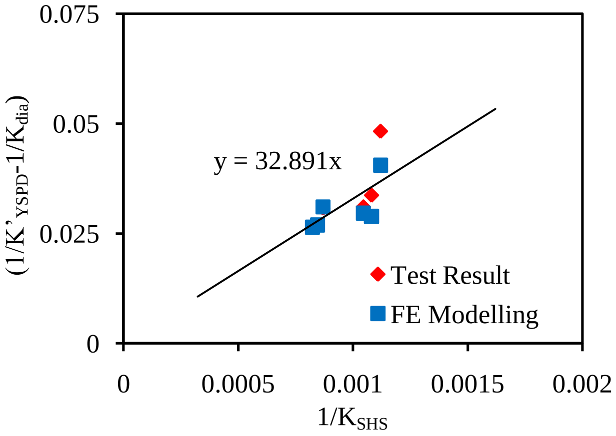

Figure 10. Stiffness plot of SHS to determine the reduction factor ϕ.

4.2 Yield Strength of YSPD

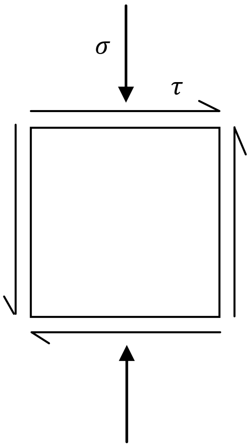

Figure 11. State of elastic stress of the diaphragm plate.

The yielding of YSPD occurs due to the combined action of axial compression and shear deformation of the diaphragm plate. The yield force and the corresponding deformation is initially calculated assuming the loading end and the support end remain parallel. The effect of support rotation is then incorporated to calculate the actual deformation. According to von Mises yield criterion,

$$\sigma_1^2 - \sigma_1\sigma_2 + \sigma_2^2 = \sigma_y^2 \tag{18}$$

where, σ_y is the tensile yield strength

Principal stresses, $\sigma_1, \sigma_2 = -\frac{\sigma}{2} \pm \sqrt{\frac{\sigma^2}{4} + \tau^2}$

The applied horizontal deformation δ can be divided into two components - $\delta_1$for the pure shear deformation of the diaphragm plate and δ_2 for the deformation of SHS. Thus,

$$\delta = \delta_1 + \delta_2 \tag{19}$$

$$\delta_1 = \frac{k_{YSPD}}{k_{dia}}\delta \tag{20}$$

$$\delta_2 = \frac{k_{YSPD}}{k_{SHS}}\delta \tag{21}$$

The resulting stresses become,

$$= \frac{\delta_1 G}{d} \tag{22}$$

$$= \frac{\delta_2 E}{d} \tag{23}$$

The yield deformation δ_y can be calculated by solving Equation 18. This yield displacement changes due to the rotation of the loading end. By incorporating the effect of end rotation, yield displacement becomes,

$$\delta_y^{'} = \delta_y \frac{k_{YSPD}}{k_{YSPD}^{'}} \tag{24}$$

The yield strength of YSPD can be calculated as,

$$F_y^{'} = k_{YSPD}^{'}\delta_y^{'} \tag{25}$$

Equation 25 gives the same yield strength as calculated by Chan et. al. [1], but the initial stiffness is modified by considering the deformation of the SHS in Equation 24.

The underlying assumption of this calculation is the diaphragm plate is simply supported by the SHS. Practically the diaphragm plate is welded inside the SHS. The thickness ration of diaphragm plate and the SHS plate (t/T) determines the support rigidity. The rigidity of the support increases with the decreasing t/T ratio. Consequently, the theoretical yield strength decreases with the increasing t/T ration. Figure 12 shows the variation of the ration of theoretical yield strength and actual yield strength with the varying td^2/T. The term d^2 is used to normalize the values with different diaphragm size. The graph shows a good correlation and indicates the yield strength reduces with the increasing t/T ration.

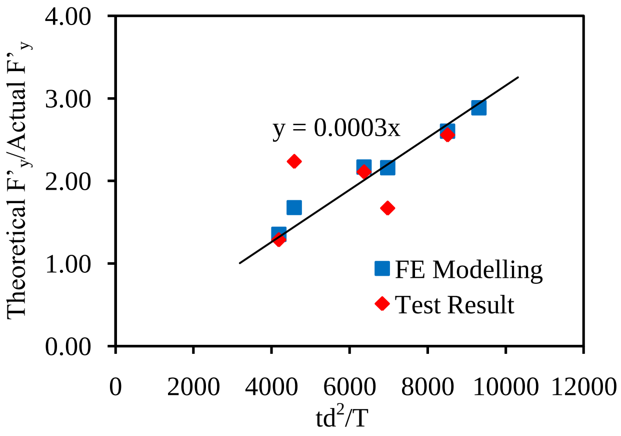

Figure 12. Correlation curve for theoretical and actual yield strength.

A strength reduction factor Ω_1 is calculated as follows,

$$\Omega_1=0.0003td^2/T \tag{26}$$

Reduced yield displacement and yield strength of YSPD becomes,

$$\delta_y' = \ _1\delta_y \frac{k_{YSPD}}{k_{YSPD}'} \tag{27}$$

$$F_y' = \ _1k_{YSPD}'\delta_y' \tag{28}$$

4.3 Plastic Buckling Strength in Shear

Early investigations into plastic plate shear buckling were reported by Gerard [8], Stowell [9] and Bijlaard [10]. Stowell [9] and Bijlaard [10] used deformation theory for the analysis of plastic buckling of plates, whilst Gerard [8] followed the secant modulus approach. Stowell [9] derived an expression using the deformation theory and finally suggested a simplified form depending on the secant modulus of elasticity for materials with nearly constant hardening behaviour in the plastic range. Gerard [8] suggested the critical shear stress is rather dependent on the secant shear modulus. Bleich [11] proposed a simplified approximation of Stowell's plastic reduction factor using the tangent modulus concept. Later, Inoue [12] used a Tresca yield criterion [12] based modified incremental theory to analyse the plastic shear buckling of thin plates. Tugcu [13] adopted bifurcation approach to determine the effect of tensile or compressive loading on the critical buckling stress for infinitely long shear plates. Wang and Aung [14] applied the p-Ritz method for the plastic buckling analysis of thick plates based on both deformation theory and incremental theory. Alinia et al. [15] showed that incremental theory based p-Ritz method provides upper bound solutions whereas deformation theory based method predicts lower bound solutions.

Stowell [16] derived a closed form solution for determining the critical shear stress for long plates using the deformation theory. Critical buckling stress may be expressed as,

$$_{cr} = k_e \frac{^2E}{12(1- \ ^2)}\left(\frac{t}{d}\right)^2 \tag{29}$$

where τ_{cr} is the critical shear stress, k_e is a coefficient which depends on the aspect ratio and the end restraints of the plate, E is the Young's modulus, ν is the Poisson's ratio and η is the coefficient allowing reduction in plastic range. The coefficient ηdepends on the secant modulus of elasticity, support restraint and the plasticity behaviour of the material. For a linear hardening material Stowell [16] suggested,

$$= \text{Constant}\frac{E_s}{E} \tag{30}$$

For 24S-O aluminium alloy, Stowell [16] found this constant as 0.89 for both simply supported edges and clamped edges. Bleich [11] proposed a simplified conservative approximation for the value of as

$$= \sqrt{\frac{E_t}{E}} \tag{31}$$

Gerard [8] approximated the value of η incorporating secant shear modulus G_s and shear modulus G as,

$$= \frac{G_s}{G} \tag{32}$$

Gerard [8] further advanced the theory by introducing the concept of critical shear strain γ_{cr}. Using Equation 34, the critical shear strain can be found as,

$${}_{cr} = k_e \frac{2(1+\ )\ ^2}{12(1-\ ^2)}\left(\frac{t}{b}\right)^2 \tag{33}$$

The expression for critical shear strain γ_{cr} is not dependent on coefficient η and hence γ_{cr} could be easily calculated using the knowledge of the size, the slenderness ratio and the support conditions of a thin plate.

Equation 29 and 33 are used to predict the critical bucking stress and strain for the diaphragm plate and used to calculate the buckling force of a YSPD.

Real et. al. [17] presented a method to identify the critical buckling stress for a metal plate subjected to shear using finite element analysis. The bucking occurs when the stress reversal takes place in the principal stress plot; the compressive principal stress suddenly decreases once the plate starts to buckle. Finite elemnt simulation of YSPD showed the critical buckling forceis over predicted. The redused strength is resulted by the axial compressive stress acting along with the shear stress. Buckling strain is found larger in the FE model. This excessive deformation is resulted from the support rotation. Figure 13(a) shows the variation of the ratio of theoretical critical buckling strength and actual buckling strength with varying slenderness ratio (d/t). The graph shows a good correlation and the buckling strength reduction factor is calculated as,

$$\Omega_2 = 1+0.011d/t \tag{34}$$

Critical plastic buckling strain calculated according to the equation 35 can be divided into elastic and plastic parts as follows,

$${}_{cr} = {}^{e}_{cr} + {}^{p}_{cr} \tag{35}$$

The multiplication factor for increasing the value of the plastic shear strain to include the effect of the support rotation depends on the plate area (td). Figure 13(b) shows the variation of the ratio of theoretical plastic shear buckling strain and actual plastic strain obtained from FE models with varying area of the diaphragm plate area (td). The graph showed a good correlation and the plastic strain multiplication factor is calculated as,

$$\Omega_3 = 0.0116td-1.81 \tag{36}$$

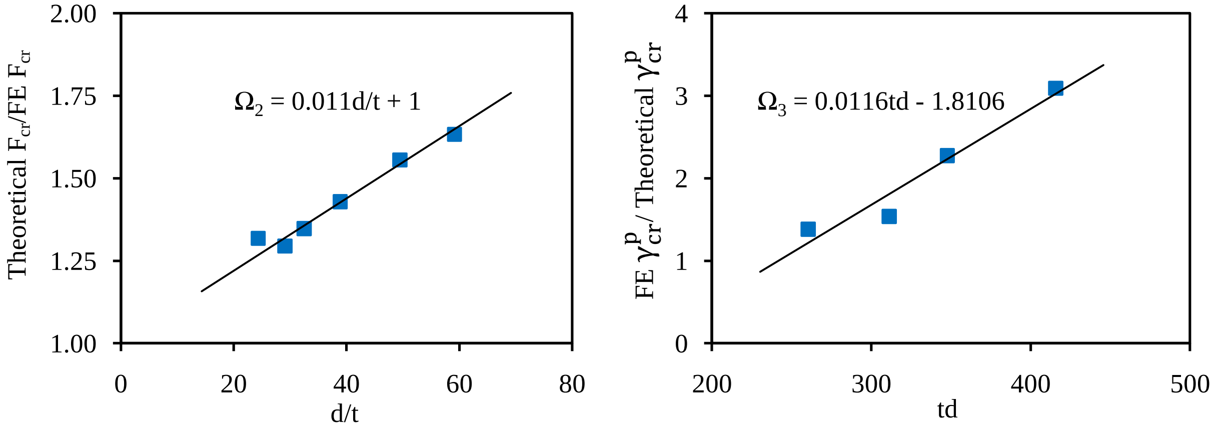

(a) (b)

Figure 13. (a) Correlation curve for theoretical and finite element critical plastic buckling strength. (b) Correlation curve for theoretical and finite element critical plastic buckling strain.

4.4 Post Buckling Stiffness

Force-displacement response of YSPD for large deflections after the buckling of the diaphragm plate is necessary to identify its energy dissipation characteristics. A tension field is developed after the shear buckling of diaphragm plate. A typical state of stress of the diaphragm plate with a tension field inclined at an angle α is shown in Figure 14.

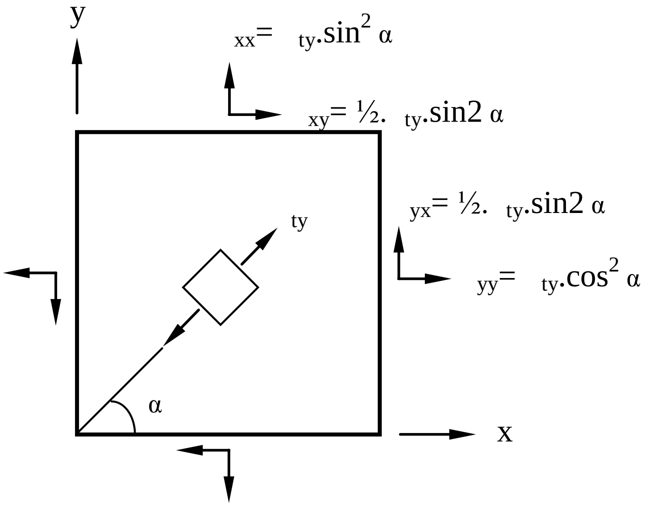

Figure 14. Tension field stresses in diaphragm plate after buckling.

The incremental shear strength of the YSPD after buckling becomes,

$$dF = ½.d\ _{ty}(\sin 2\alpha)td \tag{37}$$

Kharrazi [18] determined the elastic post bucking shear deformation by equating the work done by the post buckling component of the shear forces to the strain energy produced by the tension field. Kharrazi et. al. [19] extended the concept to consider hardening after reaching yield point by replacing the modulus of elasticity (E) with the tangent modulus of elasticity (E_t). Using the same technique, the incremental post buckling shear deformation becomes,

$$d\delta = 2d\ {}_{ty}.d/E_t\sin 2\alpha \qquad (38)$$

Thus, the post buckling stiffness of the YSPD may be expressed as,

$$k_t = ¼.E_t t\sin^2 2\alpha \qquad (39)$$

Equation 39 indicates that the shear deformation behaviour after buckling depends on the inclination angle α of the tension field. A number of research works have been conducted in the last few decades to identify the angle of inclination in tension field action; Shishkin et. al. [20] summarised all available literature relevant to inclination angle. CAN/CSA-S16-01 [21] suggests a limit varying between 38° and 45° for the inclination angle of pin ended strips in steel plate walls. Shishkin et. al. [22] reported that inclination angle values between 38° to 50° gave similar results for calculating the ultimate capacity of steel plate shear walls. An inclination angle of 45° can be reasonably assumed for the tension strips developed within the square diaphragm plate of YSPD. Considering an inclination angle of 45°, the post buckling stiffness may be expressed as follows

$$k_t = ¼.E_t t \qquad (40)$$

5 COMPARISON WITH TEST RESULTS AND FE MODELLING

The performance of the proposed tri-linear load deformation response is compared against those obtained from test and FE simulation. Figure 15 compares the load-deformation response for different YSPDs. The devloped FE model and analytic model with 2 mm diaphragm plate significantly underpredicts the test behaviour; this discrepancy is due to a higher strength shown by the material although the reported yield strength (211.3 N/mm^2) is unusually low.

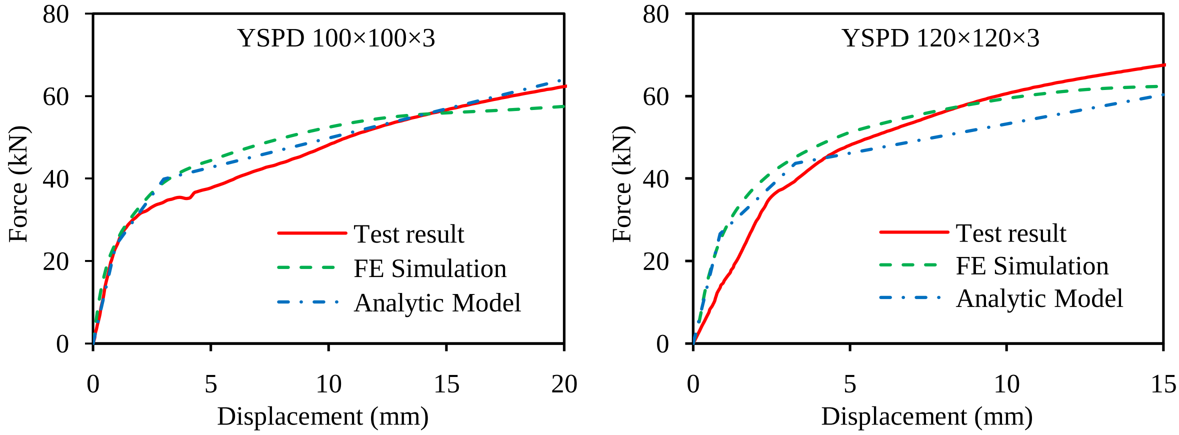

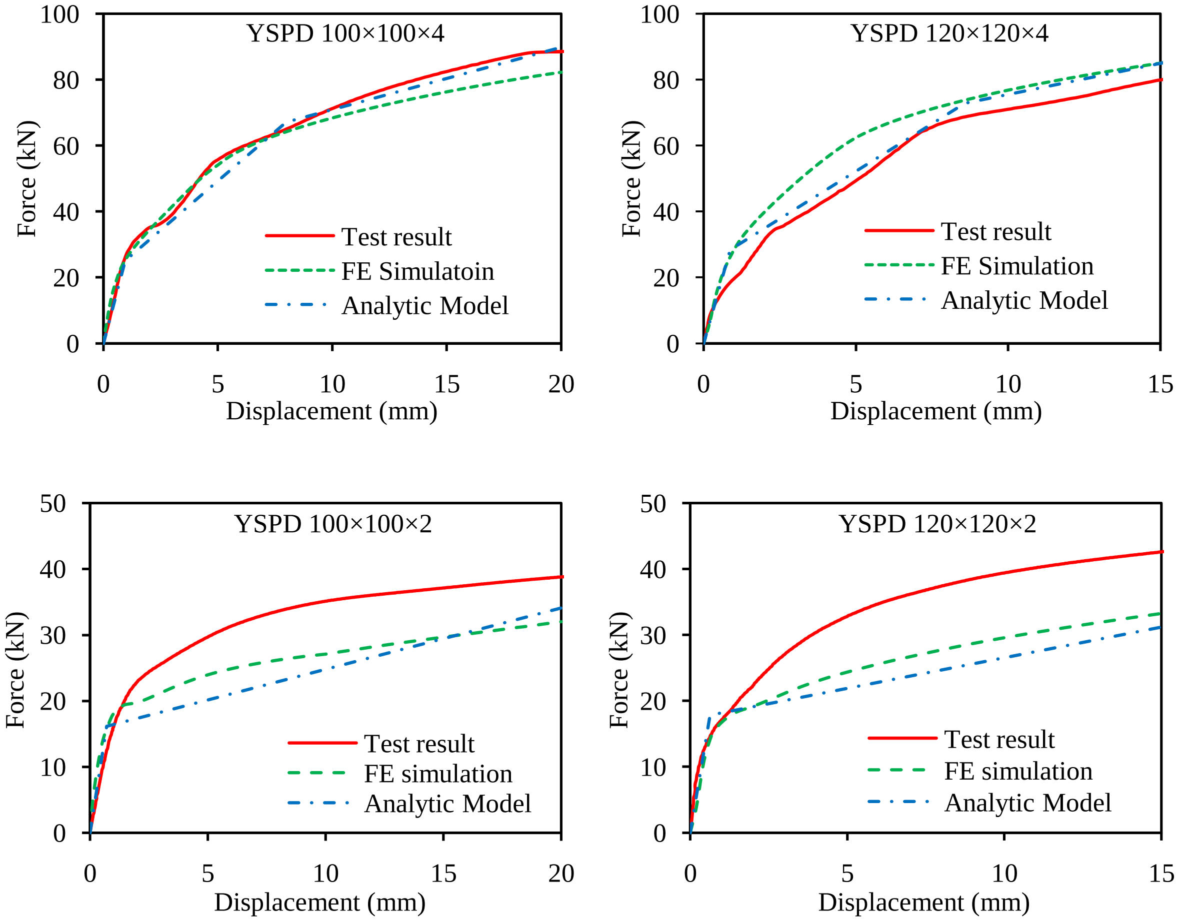

Figure 15. Force-displacement response of YSPDs.

Table 3 compares the amount of energy required to achieve specified displacements during the monotonic loading tests of YSPDs to those obtained from tri-linear models. The ratio of energy required for different displacements indicates that the developed tri-linear model can predict the required energy with reasonable accuracy.

YSPD Designation	Ratio of Energy for different displacements (Theoretical/Test)			
(D × D × t)	5 mm	10 mm	15 mm	20 mm
100×100×2	0.77	0.72	0.73	0.76
100×100×3	1.09	1.08	1.05	1.04
100×100×4	0.91	0.96	0.97	0.97
120×120×2	0.79	0.71	0.71	-
120×120×3	1.15	0.99	0.94	-
120×120X4	1.12	1.07	1.07	-

Table 3: Comparison of energy required in monotonic loading.

6 CONCLUSION

An analytic model for a newly proposed passive energy dissipation device YSPD has been presented in the current paper explaining all necessary theoretical derivations. The force-displacement response of YSPD has been idealized as a tri-linear curve. The first linear segment represents the elastic deformation; the slope of which depends on the individual stiffness of the diaphragm plate and that of the surrounding SHS in addition to the rotation of the support. Yield strength is calculated based on the yield capacity of the diaphragm plate, which is eventually reduced by introducing a yield strength reduction factor to consider the stiffness of the surrounding SHS. Second linear segment corresponds to the plastic deformation of the shear plate. Critical buckling strength is identified using Gerard's plastic buckling theory by calibrating the theoretical values using finite element results. Final linear segment represents the post buckling tension field response. Inclination of the tension field is observed not to play a significant role and hence an angle of 45^0 is adopted. Positive tangential stiffness (k_t) presents a hardening behaviour for post bucking response. The proposed theoretical model is compared with the available test results and the corresponding finite element simulations; overall, the comparisons showed good agreement. Developments of fully nonlinear theoretical formulations for YSPD are currently underway.

REFERENCES

[1] Chan, R. W. K., Albermani, F., and Williams, M. S., 2009, "Evaluation of Yielding Shear Panel Device for Passive Energy Dissipation," Journal of Constructional Steel Research, 65(2), pp. 260-268.

[2] Hossain, M. R., Ashraf, M., and Albermani, F., 2011, "Numerical Modelling of Yielding Shear Panel Device for Passive Energy Dissipation," Thin Walled Structures (Paper Submitted).

[3] Williams, M., and Albermani, F., 2003, "Monotonic and Cyclic Tests on Shear Diaphragm Dissipators for Steel Frames," Civil Engineering Bulletin No. 23, Department of Civil Engineering, University of Queensland, Australia.

[4] Schmidt, K., Dorka, U. E., Taucer, F., and Magnonette, G., 2004, "Seismic Retrofit of a Steel Frame and an Rc Frame with Hyde Systems," Institute for the Protection and the Security of the Citizen European Laboratory for Structural Assessment, European Commission Joint Research Centre.

[5] Williams, M., and Albermani, F., 2006, "Monotonic and Cyclic Tests on Shear Diaphragm Dissipators for Steel Frames," Advanced Steel Construction, 2(1), pp. 1-21.

[6] Chan, R. W. K., 2008, "Metallic Yielding Devices for Passive Dissipation of Seismic Energy," PhD Thesis, University of Queensland.

[7] Timoshenko, S., 1961, Theory of Elastic Stability, McGraw-Hill, New York.

[8] Gerard, G., 1948, "Critical Shear Stress of Plates above the Proportional Limit," Journal of Applied Mechanics-Transactions of the Asme, 15(1), pp. 7-12.

[9] Stowell, E. Z., 1948, "Critical Shear Stress of an Infinitely Long Plate in the Plastic Region," NACA Technical Note No. 1681.

[10] Bijlaard, P. P., 1949, "Theory and Tests on the Plastic Stability of Plates and Shells," Journal of the Aeronautical Sciences, 16(9), pp. 529-541.

[11] Bleich, F., 1952, Buckling Strength of Metal Structures, McGraw-Hill, New York ; London.

[12] Inoue, T., 1996, "Analysis of Plastic Buckling of Steel Plates in Shear Based on the Tresca Yield Criterion," International Journal of Solids and Structures, 33(26), pp. 3903-3923.

[13] Tugcu, P., 1998, "Effect of Axial Loading on Plastic Buckling of Long Strips under Pure Shear," Computers & Structures, 66(2-3), pp. 155-161.

[14] Wang, C. M., and Aung, T. M., 2007, "Plastic Buckling Analysis of Thick Plates Using P-Ritz Method," International Journal of Solids and Structures, 44(18-19), pp. 6239-6255.

[15] Alinia, M. M., Gheitasi, A., and Erfani, S., 2009, "Plastic Shear Buckling of Unstiffened Stocky Plates," Journal of Constructional Steel Research, doi: 10.1016/j.jcsr.2009.04.001(

[16] Stowell, E. Z., 1948, "Critical Shear Stress of an Infinitely Long Plate in the Plastic Region."

[17] Real, E., Estrada, I., and Mirambell, E., 2003, "Experimental and Numerical Investigation on Shear Response of Stainless Steel Plated Girders."

[18] Kharrazi, M., 2005, Rational Method for Analysis and Design of Steel Plate Walls, Ph.D. dissertation, University of British Columbia,Vancouver, B.C.

[19] Kharrazi, M., Ventura, C., and Prion, H., 2011, "Analysis and Design of Steel Plate Walls: Experimental Evaluation," Canadian Journal of Civil Engineering, 38(1), pp. 60-70.

[20] Shishkin, J. J., Driver, R. G., and Grondin, G. Y., 2005, Analysis of Steel Plate Shear Walls Using Modified Strip Method, Structural Engineering Rep. No. 261, Dept. of Civil Engineering, Univ. of Alberta, Alta.

[21] Can/Csa, 2001, "Csa-S16-01," Limit states design of steel structures, Canadian Standard Association, Rexdale (Ontario).

[22] Shishkin, J., Driver, R., and Grondin, G., 2009, "Analysis of Steel Plate Shear Walls Using the Modified Strip Model," Journal of Structural Engineering, 135(pp. 1357.

COMPDYN 2011
3rd ECCOMAS Thematic Conference on
Computational Methods in Structural Dynamics and Earthquake Engineering
M. Papadrakakis, M. Fragiadakis, V. Plevris (eds.)
Corfu, Greece, 25–28 May 2011

EVALUATION OF RESPONSE OF AN ISOLATED SYSTEM BASED ON DOUBLE CURVED SURFACE SLIDERS

Alberto Pavese[1], Chiara Casarotti[2], and Marco Furinghetti[2]

[1] University of Pavia, Structural Mechanics Department
via Ferrata 1, 27100 Pavia
e-mail: a.pavese@unipv.it

[2] European Centre for Training and Research in Earthquake Engineering
via Ferrata 1, 27100 Pavia
chiara.casarotti@eucentre.it, marco.furinghetti@eucentre.it

Keywords: DFPS, Curved Surface Sliders, Seismic Isolation, Double Friction Pendulum, Construction Defects, Variable Boundary Conditions

Abstract. *Nowadays, the use of seismic isolation within the Italian and European context is gaining more and more acknowledgement, thanks to the high level of protection which can be guaranteed to a structure from the earthquake damage. However, the installation of devices within complex structural systems may influence the actual response due to the random variation of the installation and operating conditions with respect to the theoretical structural scheme. It is then of paramount importance a proper assessment of the overall isolating system response, considering the variability of the construction conditions.*

The main objective of the present work is to study the response of a particular installation system for Double Curved Surface Sliders (DCSS) for buildings with large plan development in case of construction defects related to the non-perfect co-planarity of the devices. A case study is presented, in which the effects of randomly simulated construction defects are analyzed. Preliminary results showed that the simulated construction defects have only limited influence on the global hysteretic behavior of the system and that the contemporary loss of contact may occur only for a limited number of devices. On the other hand, the effects of the vertical and horizontal force redistribution may cause important increase of the actions locally induced in the base connecting slab and create an eccentricity of the resultant horizontal force.

1 INTRODUCTION

Nowadays, the use of seismic isolation within the Italian and European context is gaining more and more acknowledgement [1], [2]. The recent coming into force of the European Code for antiseismic devices [3] witnesses such increasing trend and highlights the importance of a major attention to all the aspects related to the response of installed isolators.

Concerning friction devices, a number of studies has been conducted first on curved surface sliders with single sliding surface ([4], [5], [6], [7], [8], among the others), and then on the most recent double / triple sliding surfaces sliders ([9], [10], [11]). Such studies highlighted features and advantages of such technology, from the theoretical, modeling and experimental point of view, at least for what concerns the single device.

However, complex isolation systems and the actual operating conditions of installed devices often differ from the ideal theoretical design conditions. In particular, when several devices are installed to work in parallel, the possibility of random variations in the installation conditions of each single device may arise issues regarding the response of the entire system.

The main objective of the present endeavor is to study a particular isolation scheme for buildings with large plan development (systems consisting of several isolators and a base connection slab upon which the building is constructed, Fig. 1), in order to evaluate the influence of defects related to non-parallel sliding surfaces. Such kind of defects can be generated by phenomena of deferred concrete creep or simply by construction errors: if isolators sliding plates are non perfectly horizontal, for a given slab displacement each device will encounter a differential vertical displacement, possibly leading some device to loose contact and inducing localized stress in the slab. This in turn causes a redistribution of the vertical reactions and consequently of the horizontal forces throughout the whole system.

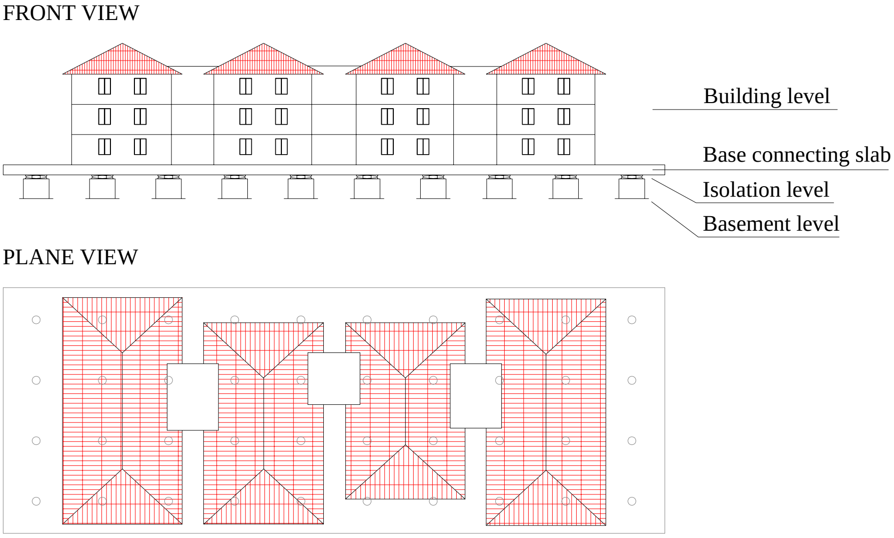

Fig. 1 . Schematic model of the isolated system consisting of isolators-base connection slab-building

The first step of the work has been to define the mechanical model of a single isolator, analyzing the geometry of each component, in order to obtain the value of the vertical displacement induced on the slab, for a given value of horizontal displacement. Subsequently, the interaction among the different devices and the base slab has been modeled, by developing a f.e.m. code able to simulate the varying conditions of the system (contact-no contact condition). Finally, a case study has been presented, in which construction defects have been simulated randomly on the different isolators for a large number of analysis, in order to evaluate the consequences at both global and local level.

Preliminary results showed that the simulated construction defects have only limited influence on the reduction of the global hysteretic behavior of the system, and that the simultaneous detachment during the motion may occur only for a limited number of devices. On the other hand, the effects of the vertical and horizontal force redistribution may cause an important increase of the actions locally induced in the slab (shears and moments) and create a global torsion effect on the system, due to the eccentricity of the horizontal resultant force.

2 THE DCSS MECHANICAL MODEL

The geometric model has been developed based on the general case of a DCSS isolator with articulated slider ([9], [10]). The DCSS isolator consists of two sliding surfaces, in general characterized by different values of curvature radius, separated by an articulated slider which allows differential rotations (Fig. 2), and may feature different dynamic friction coefficient at the interfaces with the two sliding surfaces.

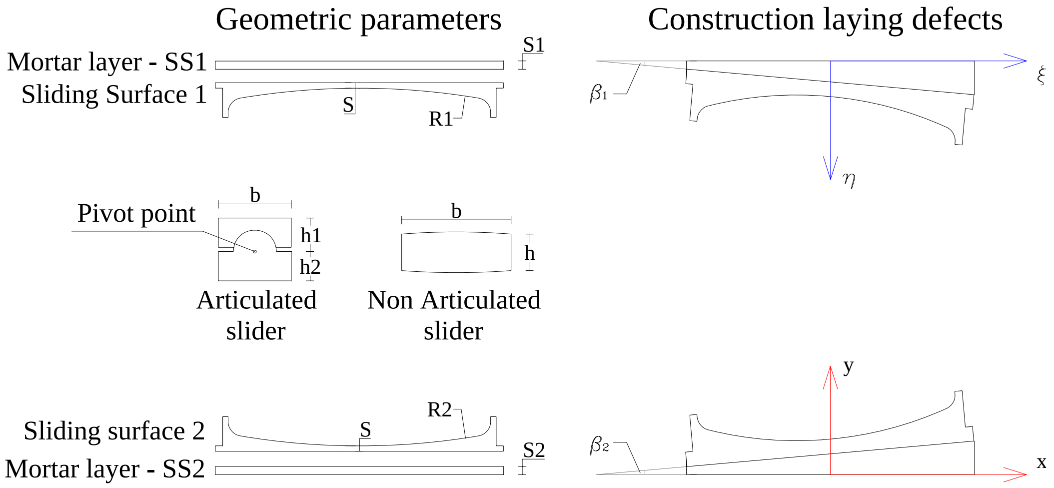

Fig. 2 . section of DCSS with non-articulated slider

The model ([9], [10]) allows to obtain the vertical displacement of the isolator upper surface as a function of the two horizontal displacements between the sliding surfaces and the pivot point of the articulated slider. The equivalent oscillation period of the device is:

$$T = 2\pi\sqrt{\frac{R_{eq}}{g}} = 2\pi\sqrt{\frac{R_1 + R_2 - h_1 - h_2}{g}} \tag{1}$$

When a device is installed, two layers of mortar constitute the interface between the device and the construction system in which it is installed. The construction laying defects can been modeled in terms of non-perfect planarity of such layers of mortar, i.e. as inclinations β_1 and β_2 of the sliding surfaces with respect to the horizontal direction (Fig. 2). The model is plane. In the present work, the model for a DCSS isolator with possible construction defects and with non-articulated slider has been obtained by considering the inclination of the upper and lower plates β_1 and β_2 and imposing no relative rotation between the two units of the slider, thus calculating the vertical displacement only as a function of the total horizontal displacement u between the two sliding surfaces and of the two angles. The inclinations of the sliding surfaces can be described in terms of change of coordinates of the respective center of curvature. Referring to Fig. 3, the angle θ_1 and θ_2 of the two units composing the slide with respect to the vertical axis are thus expressed as:

$$\vartheta_i = \arcsin\left(\frac{u_i - C_{ix}}{R_i - h_i}\right) \qquad i = 1,2 \tag{2}$$

Where C_{1x} and C_{2x} are the x- coordinates of the sliding surfaces centers, and u_1 and u_2 the relative horizontal displacement between the sliding surfaces and the pivot point (Fig. 3).

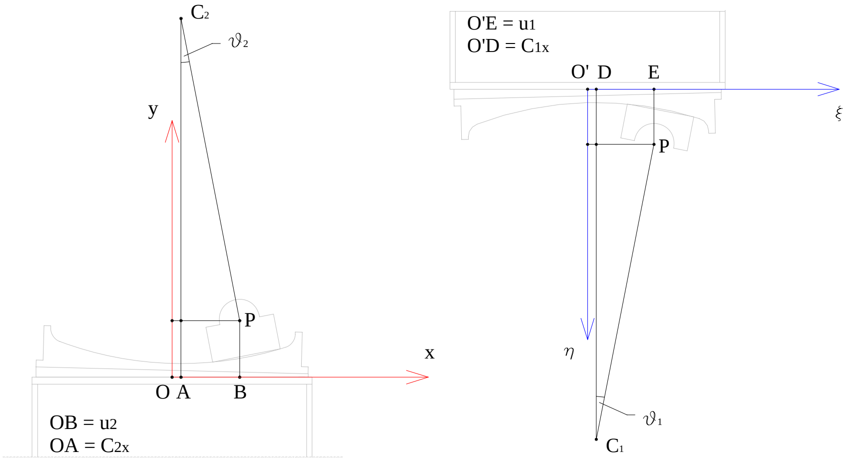

Fig. 3 . definition for the lower surface

By imposing equal to zero the relative rotation of the two axis of the units composing the slider (i.e. $\theta_1 = - \theta_2$), and with the relation among both the relative displacements u_1 and u_2 and the total horizontal displacement u_{TOT} ($u_2 - u_1 = u_{TOT}$), a linear system is obtained, which allows to express the values of u_1 and u_2 as a function of u_{TOT} and of the geometric characteristics of the device:

$$u_1 = \frac{C_{1x}(R_2 - h_2) + C_{2x}(R_1 - h_1)}{R_1 + R_2 - h_1 - h_2} - u_{TOT}\,\frac{R_1 - h_1}{R_1 + R_2 - h_1 - h_2} \tag{3}$$

$$u_2 = u_{TOT} + u_1 \tag{4}$$

Once obtained u_1 and u_2, the height of the extrados of the device can be calculated with the equations of the two sliding surfaces. Fig. 4 shows an example of the profiles of vertical displacement versus horizontal displacement for the device considered in the case study (with characteristics in Table 2), assuming only the upper surface with different inclinations (i.e. $\beta_1 \neq 0$ and $\beta_2 = 0$).

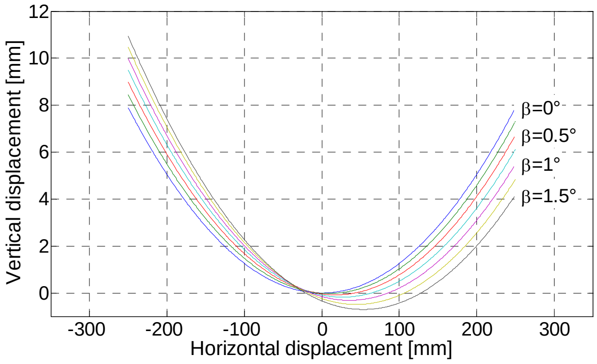

Fig. 4 . example of vertical displacements versus horizontal displacements for inclined upper plate

Regarding the sliding friction coefficient μ, it is well known that for common sliding materials μ is a decreasing function of the acting pressure [12]: a simplified relationship for the variability of the dynamic friction coefficient as a decreasing function of the vertical load is assumed (Fig. 5), based on the several tests carried out at the EUCENTRE TREES Lab (Pavia, Italy) on full scale devices. At this stage of the work, the curve has been assumed linear for sake of simplicity.

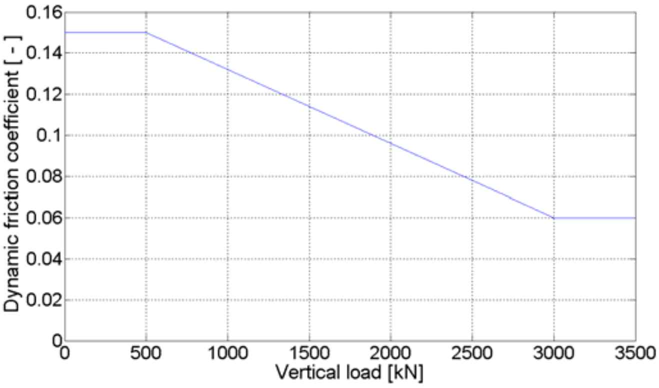

Fig. 5 . dynamic friction coefficient – vertical load variation curve

3 VARIABLE BOUNDARY CONDITIONS CODE

Subsequently, the interaction among the different devices and the base slab has been modeled, by developing a f.e.m. code able to simulate the varying contact-no contact conditions of isolators (Variable Boundary Conditions code, VBC).

The code flowchart is illustrated in Fig. 6: at each loading step, the program is able to identify devices still in contact and devices which have lost contact, updating the total system stiffness matrix at each new configuration.

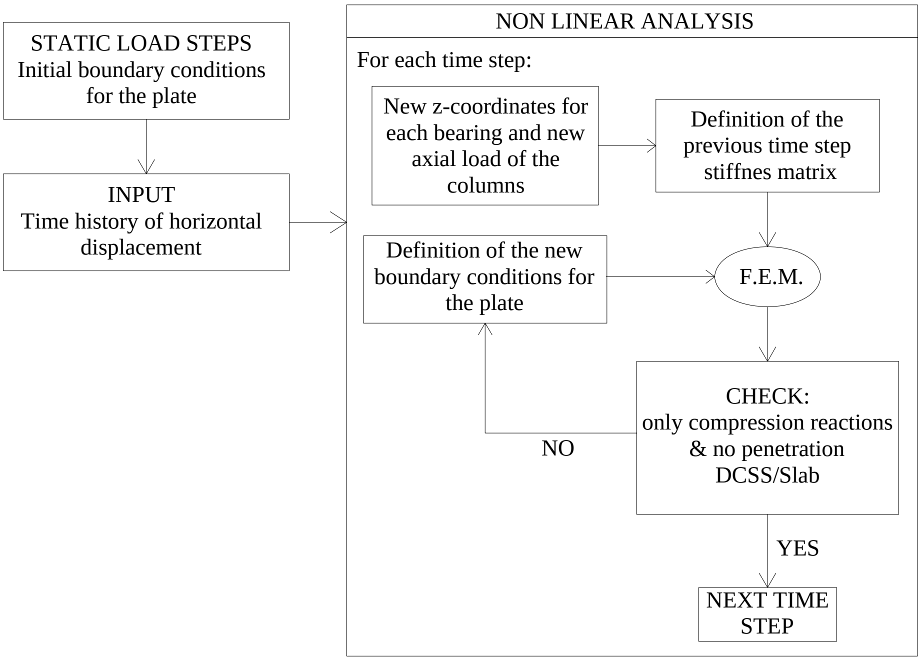

Fig. 6 . Flowchart of the VBC code

The first step of the program is the analysis of the system configuration corresponding to a zero horizontal displacement. The ideal situation of infinitely rigid slab is first studied, with an algorithm able to identify the plane determined by the three devices containing the vertical resultant application point, and with z-coordinate equal or greater than the other isolators (i.e. the three isolators bearing the infinitely rigid plate). Starting from the ideally rigid slab condition, the real deformation of the plate is then obtained by implementing the finite element problem: modeling the plate with its actual stiffness, the vertical load is applied by steps, checking that reactions are purely compressive that there is no penetration between the plate and the isolators. Once defined the zero-displacement deformed shape, the horizontal displacement is stepwise applied to the slab, considering the effects of the dynamic interaction of the building.

The weight of the plate is considered as evenly distributed over the entire surface, while the loads (static and dynamic) transmitted by the building are modeled in terms of concentrated vertical forces imposed on the isolated slab, according to the influence area of each building column. At this stage, the dynamic response of the system has been simulated in a simplified way, by imposing a sinusoidal displacement time history directly to the isolated plate, as during the dynamic testing of the system. The period of the input waveform is taken equal to the oscillation period of the isolation system, calculated as a function of the equivalent radius of the devices.

The dynamic interaction between the building and the isolation system has been simulated by considering the isolated building as an equivalent SDOF of given mass and period. The total base shear V_b is estimated by integrating the equation of motion of a SDOF oscillator. Assuming an equivalent height h_{eq} of the oscillator, the corresponding overturning moment M_{ovt} is computed, which in turn is used to obtain the axial load variation P_i of the building columns acting on the slab, for the x and y motion direction, respectively:

$$M_{ovt}(t) = V_b(t) h_{eq} \tag{5}$$

$$P_{i-X\_motion} = \frac{M_{ovt}(t)}{\sum x_j^2} x_i \tag{6}$$

$$P_{i-Y\_motion} = \frac{M_{cvt}(t)}{\sum y_j^2} y_i \tag{7}$$

Where x_i and y_i coordinates of isolators are measured with respect to the center of mass of the building columns. For each value of horizontal displacement and axial load variation, the new z_i coordinates of the isolators are calculated based on the DCSS model and imposed to the plate only for the isolators still in contact at the previous time step (compression reactions). Then boundary conditions are newly updated, considering at each iteration only the isolators still in contact.

According to the axial load acting on each isolator and to the actual position, the corresponding reaction force is step by step computed for each device.

4 CASE STUDY

The analyzed case study consists of a reinforced concrete frame structure, built on a slab of thickness 0.5 m, placed on a grid of 10 x 4 DCSS isolators with non-articulated slider. The plan view and a section of the system is shown in Fig. 7. The weight of the plate is 12.5 kN/m^2, while the building static vertical loads on the base slab are listed in Table 1, according to the position of the building columns. The geometric and mechanic characteristics of the DCSS are shown in Table 2 (geometric quantities refer to Fig. 2).

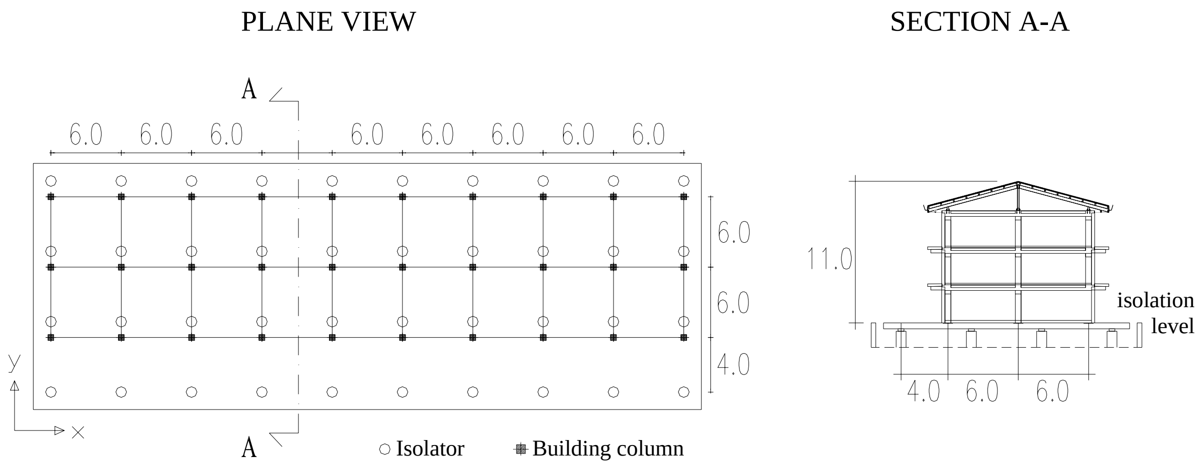

Fig. 7 . Schematic view of the studied isolating system

Table 1. static vertical load transmitted by the building columns on the base slab [kN]

Corner column	Edge column	Internal column
280.4	560.8	1121.6

Table 2. Geometric Characteristics of the isolator

$R_1 = R_2$	$s_1 = s_2$	B	h	S	$\mu_1 = \mu_2$
2024 mm	15 mm	335.44 mm	66.31 mm	20 mm	Variable with vertical force

The input for the analysis is a sinusoidal displacement waveform imposed to the plate (as during the dynamic testing of the system), with amplitude of 260 mm and period of 4 s, i.e. equal to the system design displacement and isolation period, respectively. For the dynamic interaction, the building has been modeled as a SDOF with period equal to 0.48 s, 5% damping, and h_{eq} of about 7 m (2/3 of the height).

The construction laying defects have been simulated by considering for each device the parameters β_1 and β_2 , randomly selected within an established range of variation, for a total of 135 and 125 configurations in the x and y direction of motion analysis, respectively. In order to maintain the maximum generality and to minimize the imposed a priori information, parameter distributions are assumed uniform and in general independent. Wide variation ranges are intentionally considered (±1.5°, much beyond the allowed installation tolerances) in order to evaluate the consequences in extreme conditions (an inclination of 1.5° corresponds to a total offset of 2 cm over a length of 80 cm).

Results are presented in comparison to the reference configuration, which is the ideal situation with isolators having perfectly horizontal sliding plates. At a global level, results are shown in terms of analysis of devices which loose contact, of global hysteretic response of the system and of eccentricity of the horizontal resultant force, while at a local level the variation of vertical loads and the moments induced in the slab are analyzed. The isolators labels and groups are illustrated in Fig. 8, according to their position with respect to the building projection. For the considered case study, it has been seen that isolators belonging to the same line (group 1 to 4, Fig. 8) feature similar response.

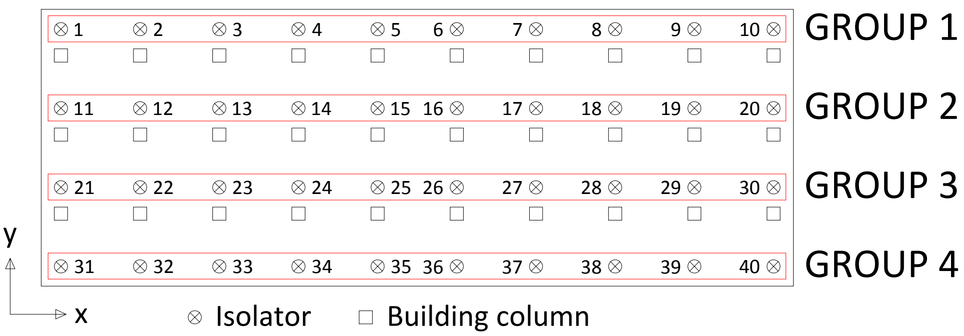

Fig. 8 . Nomenclature of the devices

4.1 Numerical results: global response

Fig. 9 and Fig. 10 show the number of devices which simultaneously lost contact at each value of horizontal displacement: averagely less than 5 DCSS out of 40 have lost the contact at the maximum displacement.

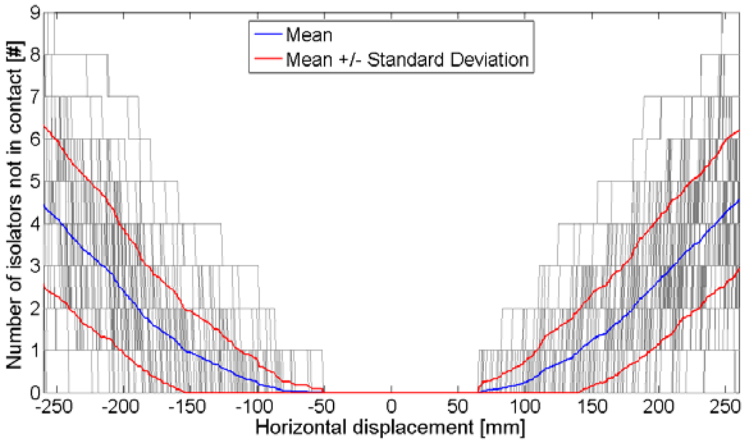

Fig. 9 . Number of isolators simultaneously not in contact (motion in the x direction)

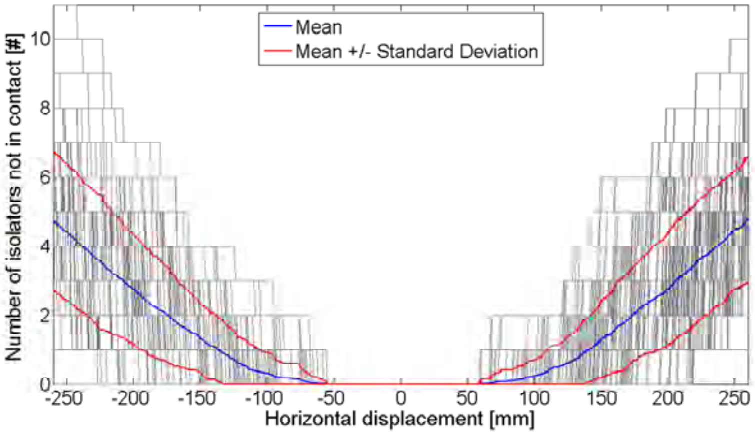

Fig. 10 . Number of isolators simultaneously loosing contact (motion in the y direction)

Fig. 11 and Fig. 12 show, for the motion in the x and y direction, the rate of contact loss for each device during the analyses, i.e. the rate of the cases in which an isolator looses contact at least once during motion: it is evident the similar response of isolators belonging to the same alignment. This is due to the position of the building with respect to the base slab. The most external line (group 4) has in fact the highest probability of detachment, while group 2, which is the closest line to the building center of mass, is the most stable. Table 3 shows the values of frequency of contact loss per group of isolators at the maximum displacement.

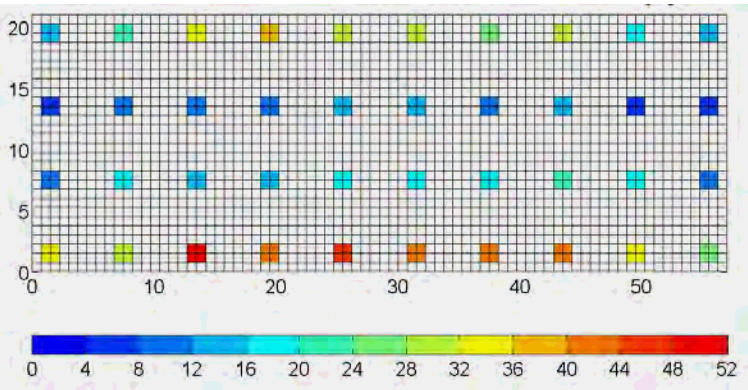

Fig. 11 . Rate of cases in which an isolator looses contact at least once during the motion (x direction)

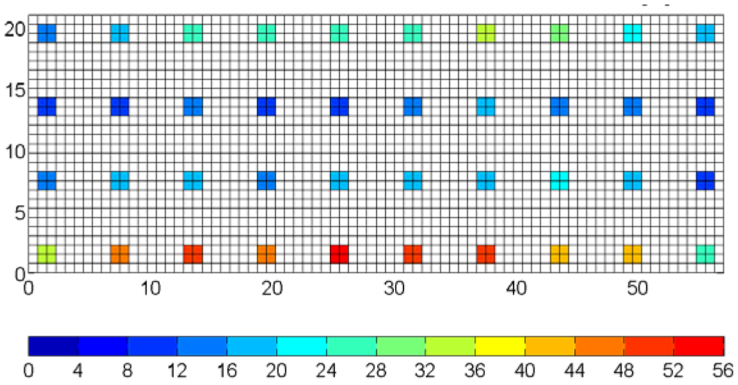

Fig. 12 . Rate of cases in which an isolator looses contact at least once during the motion (y direction)

Table 3. Frequency of no-contact across all the analyses, at the maximum displacement

	Motion x	Motion y
Group 1	14.48 %	13.56 %
Group 2	5.75 %	6.44 %
Group 3	9.18 %	9.28 %
Group 4	20.41 %	23.12 %

The total base shear as a function of the horizontal displacement is shown for both directions of motion in Fig. 13: the effects of the construction errors result in a limited reduction of the hysteresis loop. This is due to the redistribution of vertical loads among the isolators still in contact, which increase their reactions but not proportionally, due to the varying friction coefficient. Moreover, isolators not in contact do not contribute to the dissipative behavior.

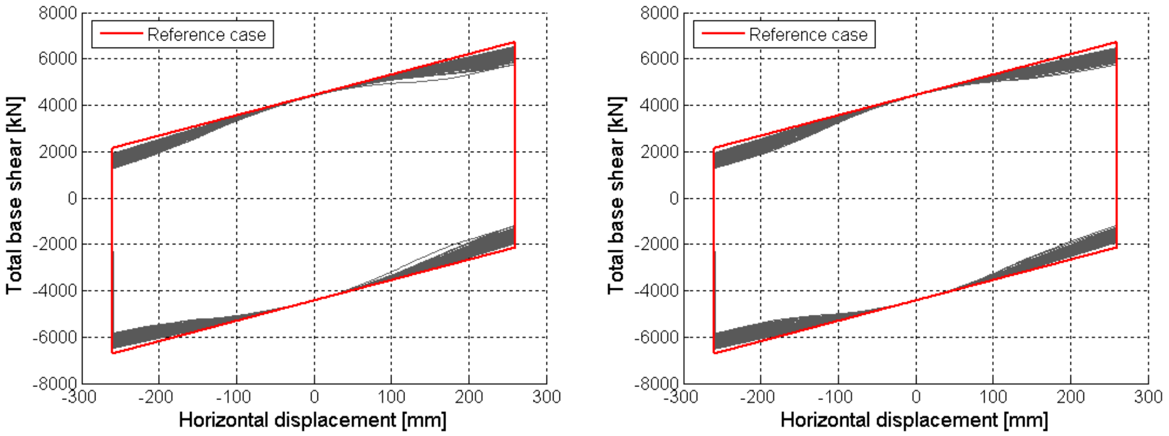

Fig. 13 . Global hysteresis cycles for the x (left) and y (right) direction of motion

Finally, the horizontal eccentricity of the DCSS resultant reaction with respect to the system center of mass has been evaluated. Fig. 14 illustrates the values of the eccentricity as a function of horizontal displacement. Values of eccentricity are normalized with respect to the correspondent plan dimensions of the base slab (L_x and L_y):

$$E_i = \frac{e_i}{L_i}[\%] \qquad (i = x, y) \tag{8}$$

For both directions of motion, at the maximum displacement, the normalized maximum eccentricity is about the 7%.

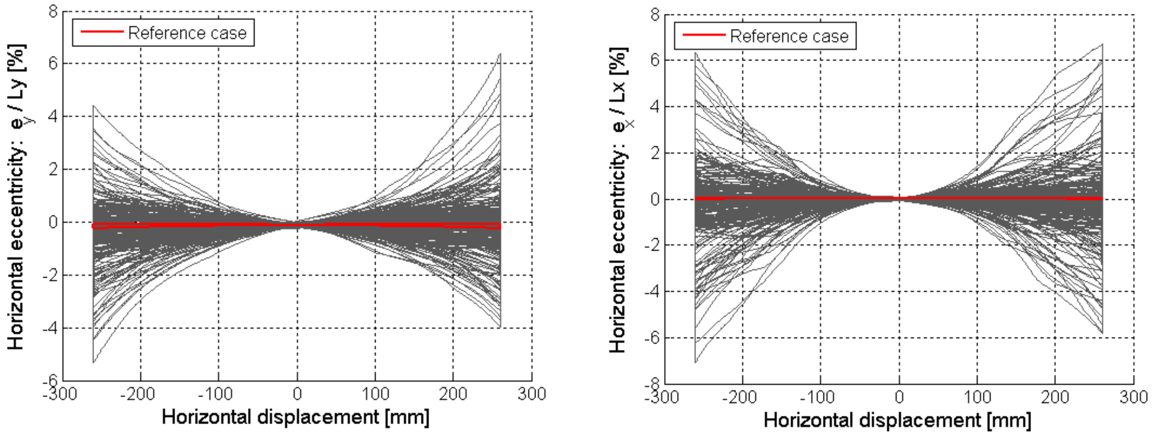

Fig. 14 . Horizontal eccentricity for the x (left) and y (right) direction of motion

4.2 Numerical results: local response

Fig. 15 and Fig. 16 show the distribution of the amount of the vertical load variation for each device at the maximum displacement, for the x and y motion respectively:

$$Var_j = \frac{R_j - R_0}{R_0}[\%] \tag{9}$$

Where R_0 represents the reaction of the reference case, and R_j is the reaction of the j-th analysis. The histograms representing the rate of variation of the vertical reactions with respect to the reference case confirm what already observed: the outer rows of isolators, in particular group 4, are characterized by more dispersed axial load variations, thus by the highest frequency of contact loss due to the considerable distance from application point of the vertical load resultant, whereas internal groups (e.g. group 2) are less susceptible to important axial load variation and thus to detachment. It is possible to see that compressive load can increase more than twice with respect to the reference situation.

Fig. 17 to Fig. 20 present at a local level, the range of variation of the bending moments induced in the base slab at the isolator locations: results are shown for both the main bending moments and for the two directions of motion. It can be seen that the mean value and the reference value approximately coincide, but the actual values are greatly dispersed, especially for the internal groups of isolators (from isolator #11 to isolator #30). This is due to the fact that, when an isolator looses contact, the plan dimensions of the corresponding slab field doubles, with immediate effects on the induced bending action. Such effect is increased for central devices since they are also subject to greater vertical loads, but are not aligned to the central columns of the building.

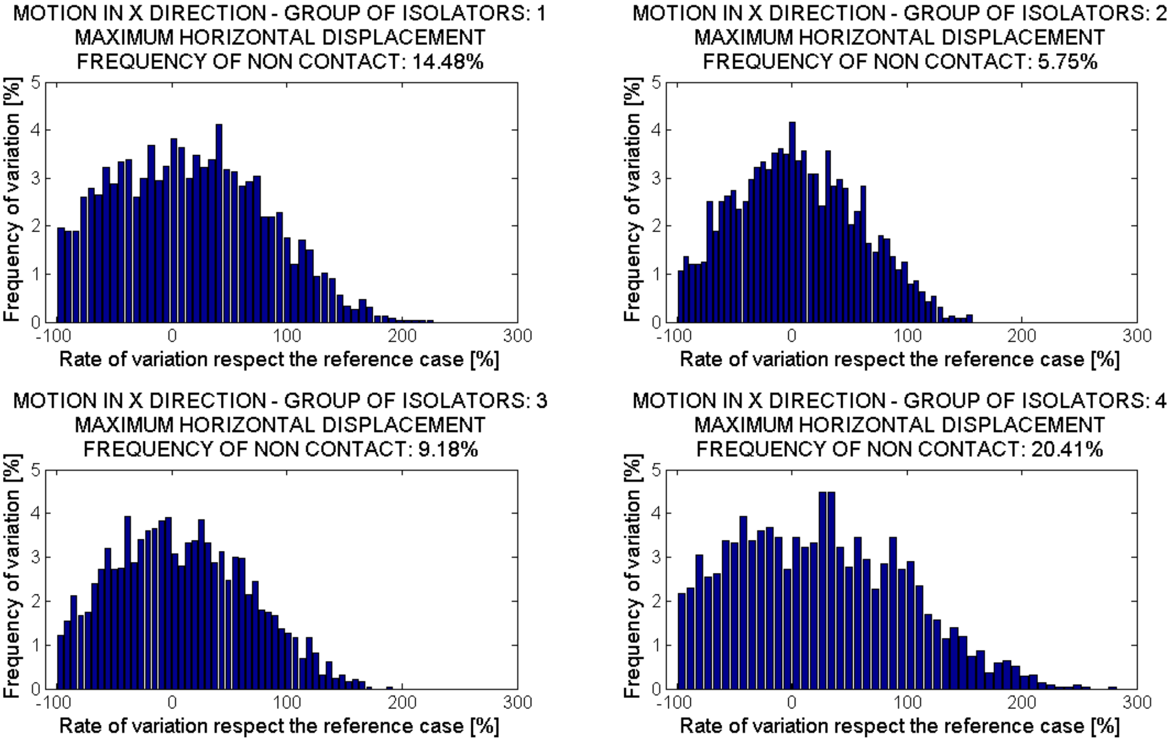

Fig. 15 . Rate of variation of the vertical reactions (motion in the x direction)

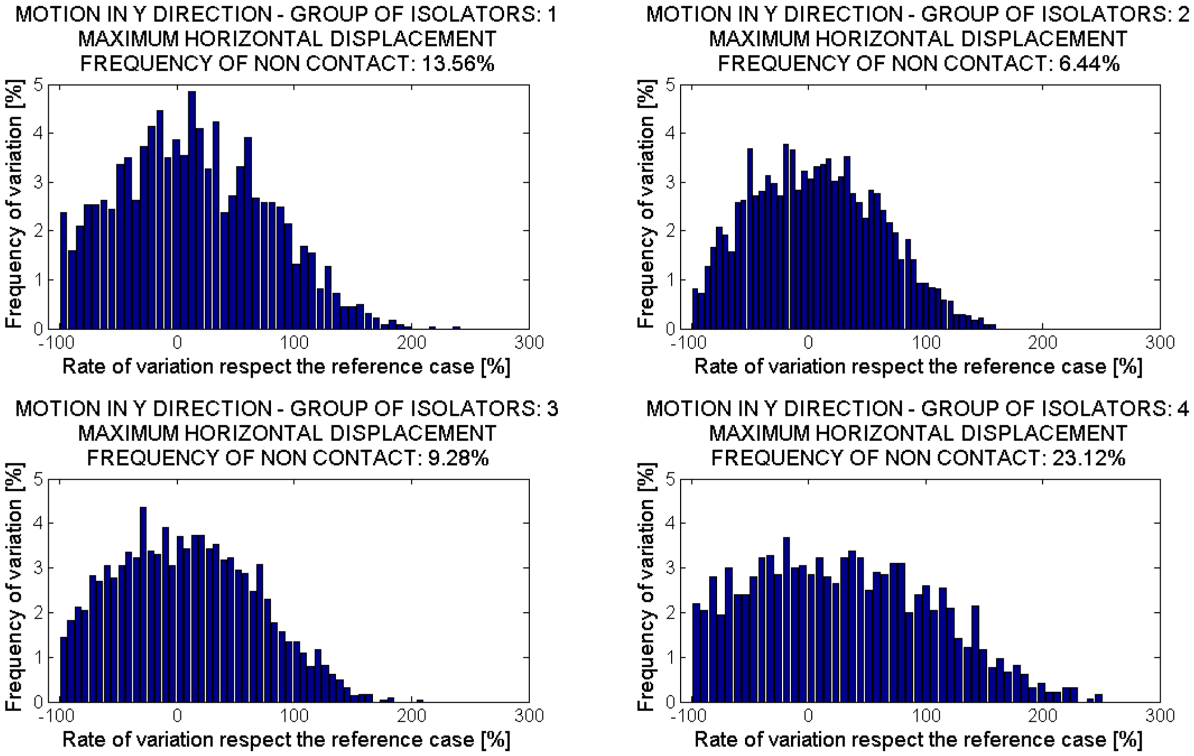

Fig. 16 . Rate of variation of the vertical reactions (motion in the y direction), at the maximum displacement

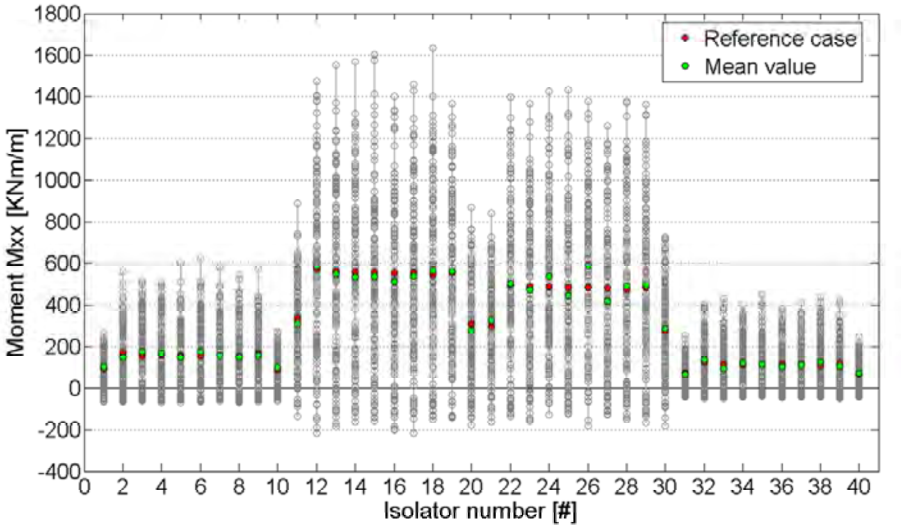

Fig. 17 . Moment M_{xx} for each isolator (motion in the x direction)

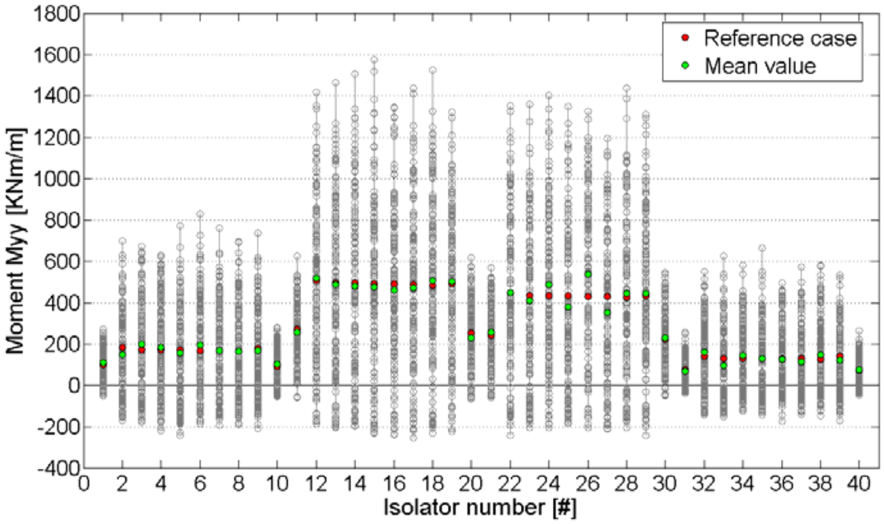

Fig. 18 . Moment M_{yy} for each isolator (motion in the x direction)

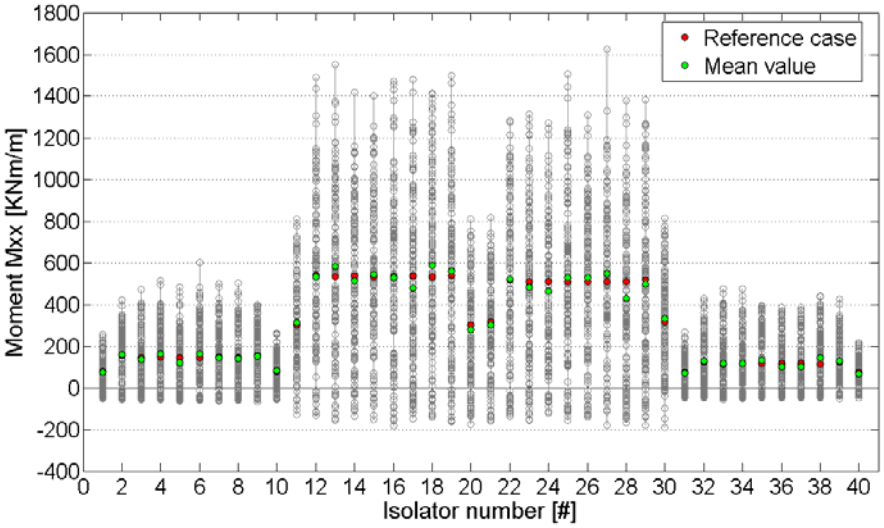

Fig. 19 . Moment M_{xx} for each isolator (motion in the y direction)

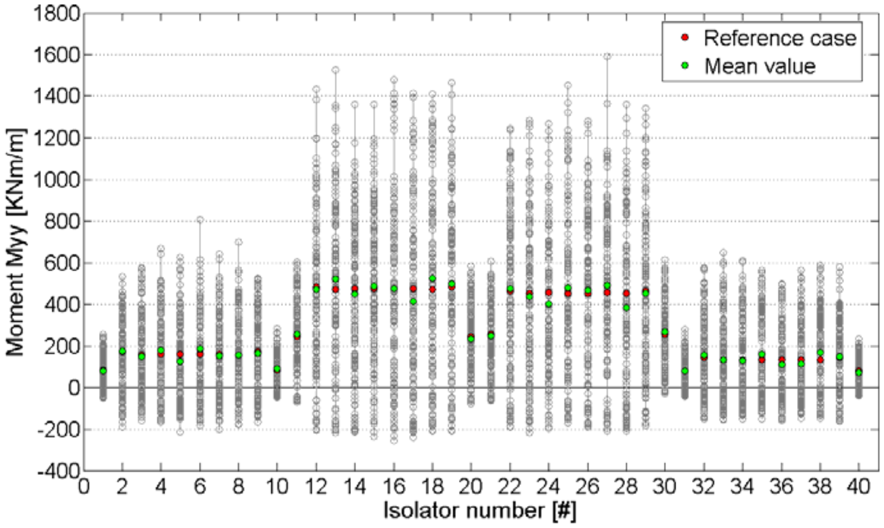

Fig. 20 . Moment M_{yy} for each isolator (motion in the y direction)

5 CONCUDING REMARKS AND FUTURE DEVELOPMENTS

In the present paper a particular isolation scheme for buildings with large plan development has been studied, consisting of a connecting base slab isolated by several DCSS devices upon which the structure is built. In particular, it is analyzed the problem of the possibility of construction laying defects of the isolators, in order to evaluate the influence on the system response of non-parallel sliding surfaces and to estimate the effects on the installed system with respect to the idealized configuration with perfectly horizontal sliding surfaces.

In order to study the problem, a plan geometric model of a single device has been first developed, considering the real geometry of each component, and modeling the defects in terms of inclination of the two sliding surfaces of the device. A f.e.m. code has been implemented, able to simulate the interaction between the devices and the base slab upon which the building is constructed, including the variability of the boundary conditions of the plate in case of isolators loosing the contact during the motion.

A case study has been finally analyzed, for which 260 analyses have been run, with different configurations simulating random defects in the isolators. The inclinations of the sliding surfaces of each device constituted the varying parameters of the analyses and were randomly selected within uniform distribution range. Such a range has been assumed intentionally large (±1.5°, much higher than admitted tolerances), in order to evaluate the consequences in extreme conditions.

The results of the numerical analyses showed that installation defects can influence the response of the isolated building more importantly at a local rather than at a global level. Results have been compared to the "ideal" reference case, corresponding to isolators with perfectly horizontal sliding surfaces.

From the global point of view it can be observed that:

- the dissipative behavior is only moderately affected, with a general reduction, due to the detachment of some device and to the redistribution of the vertical load among devices still in contact, considering the dependence of the friction coefficient on the vertical load.
- at the maximum displacement, the horizontal eccentricity of the system reaches values close to the 7%. The actual effects of such eccentricity have still to be evaluated, with a proper tridimensional model of the devices.
- the rate of devices loosing contact during the motion is a function of the relative position of the building with respect to the isolating base slab. As expected, the rows of isolators close to the centre of mass of the building have the lowest probability of loosing contact, while external rows are the most susceptible to detachment.
- For the considered case study, featuring some degree of asymmetry of the building location with respect to the plate, no more than 5 devices out of 40 loose contact simultaneously during the motion.

From the local point of view the analysis have shown that:

- the construction defects may result in localized concentration of vertical loads on occasion importantly higher than the reference situation.
- the loss of contact of some device may result in important increase of bending actions locally induced in the base slab.

From a merely structural point of view, the location of columns close to the devices would allow a more direct transmission of the vertical loads, thus reducing the risk of detachment of the isolators and the localization of high stress values in the slab.

AKNOLEDGEMENTS

Part of the current work has been carried out under the financial support Italian Civil Protection, within the framework of the Executive Project 2008–2011 (Project e2 – Bearings and isolation systems: characterization of existing typologies and development of innovative prototypes). Such support is gratefully acknowledged by the authors. The authors would also like to thank the Cariplo Foundation, for the contribution within the project 2008-2295.

REFERENCES

[1] M. Dolce, D. Cardone, F. C. Ponzo, A. Di Cesare, *Progetto di edifici con isolamento sismico*, Seconda Edizione. IUSS Press, 2010.

[2] G. M. Calvi, D. Pietra, M. Moratti, Criteri per la progettazione di dispositivi di isolamento a pendolo scorrevole. **3**: 7–30, 2010.

[3] CEN, European Code UNI EN 15129:2009 Anti-seismic devices. 2009.

[4] P. Tsopelas, M. C. Constantinou, Experimental study of FPS system in bridge seismic isolation. *Earthquake Engineering And Structural Dynamics*. **25**:65–78, 1996.

[5] J. L. Almazan, C. De La Llera, Analytical model of structures with frictional pendulum isolators. *Earthquake Engineering And Structural Dynamics.* **31**:305–332, 2002.

[6] J. L. Almazan, J. C. De La Llera, Physical model for dynamic analysis of structures with FPS isolators. *Earthquake Engineering And Structural Dynamics.* **32**:1157–1184, 2003.

[7] J. L. Almazan, J. C. De La Llera, An experimental study of nominally symmetric and asymmetric structures isolated with the FPS. *Earthquake Engineering And Structural Dynamics.* **32**:891–918, 2003.

[8] G. Benzoni, C. Casarotti, *Performance of Lead-Rubber and Sliding Bearings under Different Axial Load and velocity Conditions*. Report No.SRMD2006/05-rev3, Department of Structural Engineering University of California, San Diego, La Jolla, California 2008.

[9] D. Fenz, M. C. Constantinou, Behaviour of the double concave friction pendulum bearing. *Earthquake Engineering And Structural Dynamics.* **35**:1403–1424, 2006.

[10] M. C. Constantinou, Friction Pendulum double concave bearing. *NEES Report*, available at: http://nees.buffalo.edu/docs/dec304/FP-DC%20Report-DEMO.pdf, 2004.

[11] D. Fenz, M. C. Constantinou, Spherical sliding isolation bearings with adaptive behavior: Theory. *Earthquake Engineering And Structural Dynamics.* **37**:163–183, 2007.

[12] F. Khoshnondian, V. R. Hagdonst, Response of pure-friction sliding structures to three components of earthquake excitation considering variations in the coefficient of friction. *Scientia Iranica,* **16**:429–442, 2009.

COMPDYN 2011
3rd ECCOMAS Thematic Conference on
Computational Methods in Structural Dynamics and Earthquake Engineering
M. Papadrakakis, M. Fragiadakis, V. Plevris (eds.)
Corfu, Greece, 25–28 May 2011

A PARAMETRIC STUDY FOR THE INVESTIGATION OF THE EFFECTIVENESS OF RUBBER SHOCK-ABSORBERS AS A MITIGATION MEASURE FOR EARTHQUAKE-INDUCED STRUCTURAL POUNDINGS

Panayiotis C. Polycarpou[1] and Petros Komodromos[2]

Department of Civil and Environmental Engineering, University of Cyprus
75 Kallipoleos Str., P.O. Box 20537, 1678 Nicosia, Cyprus

[1]ppanikos@ucy.ac.cy, [2]komodromos@ucy.ac.cy

Keywords: Pounding, shock-absorber, bumper, earthquake, impacts, adjacent buildings.

Abstract. *Very often, especially in densely-resided areas and city centers, neighboring buildings are constructed very close to each other, without sufficient clearance between them. Thus, during strong earthquakes, structural poundings may occur between adjacent buildings due to deformations of their stories. The current study presents a simple but efficient methodology that can be used to numerically simulate the incorporation of rubber layers between neighboring buildings with relatively narrow seismic gaps in order to act as collision bumpers and mitigate the detrimental effects of earthquake-induced poundings. The efficiency of this potential impact mitigation measure is parametrically investigated considering the case of two neighboring multistory structures subjected to various earthquake excitations. The results indicate that under certain circumstances the incorporation of rubber bumpers in an excising seismic gap can reduce the amplifications of the peak responses of the structures due to pounding.*

1 INTRODUCTION

Very often, especially in densely-resided areas and city centers, neighboring buildings are constructed very close to each other without sufficient clearance between them. Therefore, during strong earthquakes, structural poundings may occur between adjacent buildings, due to deformations of their stories. Consequences of such pounding incidences, ranging from local light damage to severe structural damage or even collapse, have been observed and reported in past strong earthquakes [1-4]. In case of structural pounding, both floor accelerations and interstory deflections may be significantly amplified, threatening the functionality and the contents of the building [5-7]. The photograph in Figure 1 shows a pounding incidence between two neighboring buildings, as reported from an EERI/PEER reconnaissance team after the L'Aquila Earthquake, which hit Central Italy on April 2009 [8]. During that seismic event, the roof of a 2-story building hit an adjacent 4-story structure causing significant damage to the columns of the latter at that level. Nevertheless, the third and the fourth stories of the building experienced essentially no damage. The confinement of the damage of the 4-story building at the level of impact indicates the destructive effect of structural pounding.

Figure 1: Damage of a four-story conventional building due to pounding with its adjacent two-story building, during the L'Aquila earthquake in Italy, in April 2009

At the pounding floors, short-period impulses of high amplitude are observed in the acceleration response, while their amplitude is affected by the impact stiffness. The presence of high spikes in the acceleration response due to poundings is a very critical issue, especially for buildings that may house sensitive equipment. Therefore, it is very important to consider impact mitigation measures that could be employed in practice.

Certain mitigation measures have already been proposed, by various researchers who investigated this problem in buildings and bridge decks, in an effort to alleviate the detrimental effects of structural poundings [9]. One of the proposed measures is the incorporation of layers of soft material, such as rubber, on certain locations, where impact is likely to happen. Such elastomeric material could act as a shock-absorber. The effectiveness of such an impact mitigation measure is assessed in this paper, through numerical simulations and parametric studies.

2 IMPACT MODELING

Usually, in numerically simulated dynamic systems, such as multistory buildings under earthquake excitations, structural impact is considered using force-based methods, also known as “penalty” methods. These methods allow relatively small interpenetration between the colliding structures, which can be justified by the local deformability at the point of impact. The interpenetration depth is used along with an impact-stiffness coefficient, representing an impact spring, to calculate the impact forces that act on the colliding structures, pushing them apart. Based on the mathematic relation between the impact force and the interpenetration depth, the impact models can be classified as linear and non-linear models. Furthermore, some models assume that an impact dashpot acts in parallel to the contact spring in order to take into account the energy that is dissipated during an impact [10].

2.1 Concrete-to-concrete impacts

In the current study, impacts between concrete surfaces are simulated assuming a linear impact spring and an impact dashpot exerting, in parallel, impact forces to the colliding structures whenever their separation distances are exceeded. In particular, when a contact is detected, the impact force is estimated at each time-step using the following formulas [7]:

$$F_{imp}(t+\Delta t)=\begin{cases} k_{imp}\cdot\delta(t)+c_{imp}\cdot\dot{\delta}(t) & \text{when} \quad F_{imp}(t)>0 \\ 0 & \text{when} \quad F_{imp}(t)\leq 0 \end{cases} \tag{1}$$

where $\delta(t)$, is the interpenetration depth, $\dot{\delta}(t)$ is the relative velocity between the colliding bodies, k_{imp} is the impact spring’s stiffness and c_{imp} is the impact damping coefficient. The later is computed according to the following formulas, provided by Anagnostopoulos [6]:

$$c_{imp}=2\cdot\xi_{imp}\sqrt{k_{imp}\cdot\frac{m_1\cdot m_2}{m_1+m_2}} \tag{2}$$

$$\xi_{imp}=-\frac{ln(COR)}{\sqrt{\pi^2+\left(ln(COR)\right)^2}} \tag{3}$$

In the previous formulas, m_1, m_2 are the masses of the two bodies and *COR* is the coefficient of restitution, which is defined as the ratio of relative velocities after and before impact ($0<COR\leq 1$). In particular, the above impact model is a small variation of the classical linear viscoelastic impact model that had been initially proposed by Anagnostopoulos [1], in which the tensile forces that arise at the end of the restitution period are omitted and a small plastic deformation is introduced, which increases the available clearance between the buildings.

2.2 Simulation of rubber bumpers

A significant part of this numerical problem has to do with the simulation of the behavior of rubber bumpers under impact loading. Anagnostopoulos [6] simulated the usage of a soft material that acted as a shock absorber by simply considering a decreased impact stiffness value for the linear viscoelastic impact model that was used for the simulation of poundings of buildings in series. That research work demonstrated that the use of bumpers may reduce, in some cases, the response due to poundings, although the maximum response values remain higher than the corresponding case without poundings.

Jankowski et al [11] numerically simulated the use of several devises to mitigate structural pounding among bridge segments during earthquakes. That research work examined the case of using dampers and stiffeners, as connectors of the segments in series, or rubber bumpers to absorb impact energy between girders. The rubber bumpers in that case were simulated using a linear spring-dashpot element and the results showed that the incorporation of such devices may substantially reduce the overall response due to poundings.

However, the usage of linear impact models for simulating the response of rubber during impact loading does not seem to be the most suitable, considering the stress-strain curves obtained from experiments [12-15]. In particular, static and dynamic compressive tests of rubber reveal an exponential relationship between compressive load and displacement. Therefore, it would be more appropriate to simulate the incorporation of rubber-bumpers by using a non-linear impact model. Furthermore, since a rubber shock-absorber has a finite thickness, there is a possibility to reach its ultimate compressive strain during severe impacts, whereas the impact stiffness should represent the material behind the rubber (e.g. concrete) and not the rubber bumper, since the ultimate strain of the rubber is exceeded.

In a relevant research work [16, 17], regarding the usage of rubber bumpers as an impact mitigation measure for earthquake-induced poundings of seismically isolated buildings, a non-linear impact model with hysteretic damping has been proposed and verified. That simple and efficient impact model is also used in the simulations performed in the present research work. The impact force during the approaching phase is provided by the formula:

$$F_{imp}^{A} = \left\{ \begin{array}{ll} k_{imp} \cdot \delta^{n} & for \quad \delta < \delta_u \\ k_{imp} \cdot \delta_u^{n} + k_{imp\_PY} \cdot \left(\delta - \delta_u\right) & for \quad \delta > \delta_u \end{array} \right\} \text{ when } \dot{\delta} > 0 \tag{4}$$

While during the restitution phase the impact force is computed by the expression:

$$F_{imp}^{R} = k_{imp} \cdot \delta^{n} \cdot \left(1 + C_{imp} \cdot \dot{\delta}\right) \qquad for \quad \dot{\delta} < 0 \tag{5}$$

In Eq. (4), k_{imp} is the impact stiffness, δ is the indentation and n is the impact exponent ($n>1$). The impact stiffness is given by the following expression:

$$k_{imp} = \alpha \cdot k_{st} = \alpha \cdot \frac{A \cdot K_r}{d^n} \tag{6}$$

where k_{st} is the bumper's static stiffness and $\alpha > 1$ is a multiplier that ranges usually between the values of 2 to 2.5 as it was found from relevant experiments [15]. A is the contact area of the bumper, d is the bumper's thickness and K_r expresses the material stiffness. The unknown parameters that have to be determined in Eq. (6) is the material stiffness K_r and the exponent n. The values of both parameters depend on the material characteristics and, therefore, their evaluation can be done experimentally. In the current study, those values have been estimated [16-17], based on relevant experiments from the literature [15].

Eq. (4) takes into account the case of exceeding the ultimate compressive strain of the material, during the approach phase, as it is assumed that after a certain indentation, δ_u, which corresponds to the ultimate compressive capacity of the rubber bumper, the exponential trend becomes a linear trend with a linear post-yield stiffness, k_{imp_PY}.

The damping term C_{imp} in Eq. (5) is given by the formula:

$$C_{imp} = 1.55 \cdot \frac{1 - COR^2}{COR^{0.7076} \cdot \left(\dfrac{m_1 \cdot m_2}{m_1 + m_2}\right)^{0.0025} \cdot v_{imp}^{0.9755}} \tag{7}$$

where v_{imp} is the impact velocity, which is the relative velocity of the two bodies just before impact.

The force-time and force-displacement diagrams of the proposed non-linear model for simulating the response of rubber bumpers under impact loading are shown in Figure 2. Figure 3 demonstrates the same diagrams in the case of exceeding the ultimate compressive capacity of the bumper for three different values of the coefficient of restitution.

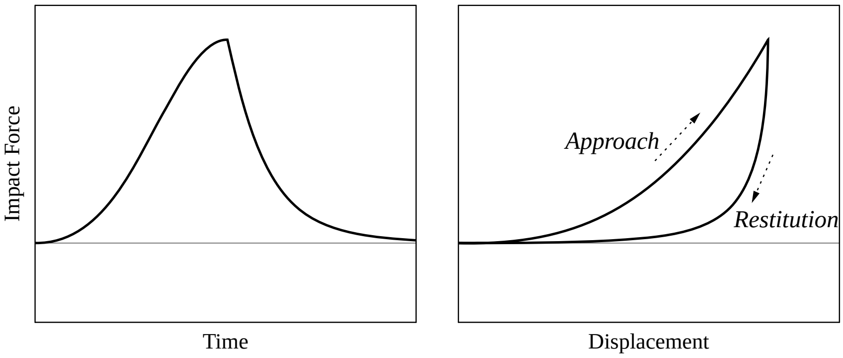

Figure 2. Force-displacement diagram of the non-linear impact model with hysteretic damping.

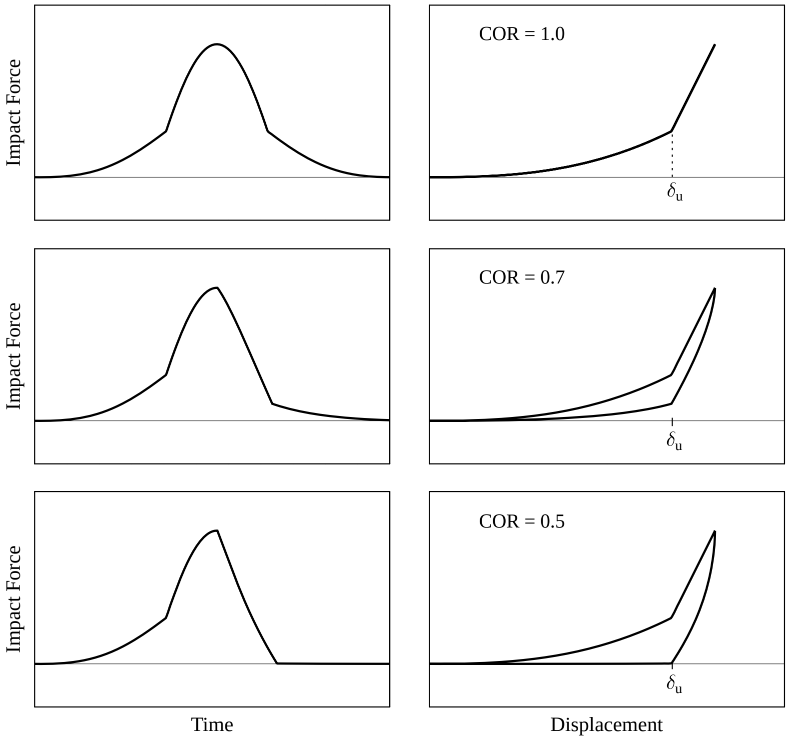

Figure 3: Impact force in terms of time and displacement in the case of exceeding the ultimate compressive strain capacity of the rubber bumper

3 NUMERICAL EXAMPLE CONSIDERING TWO RIGID BODIES

In order to examine the effect of using a rubber shock-absorber on the computed responses after impact, a simple numerical example of two free rigid bodies of equal masses that collide with a constant relative velocity has been performed. Two different circumstances were considered regarding the area of contact. In the first case, concrete-to-concrete impact was considered and the modified linear viscoelastic impact model was used (Eq. 1). In the second case a rubber bumper 5 cm thick was assumed to be incorporated at the area of contact, which is simulated using the non-linear impact model with hysteretic damping (Eq. 4 and 5). The impact parameters, used in both cases, are provided in Table 1. The masses of the two colliding rigid structures are assumed to be 320 tons each, while two different values of impact velocity were used, specifically 0.5 and 1.0 m/sec.

Property	**No Bumper**	**With Bumper**
Impact model	Linear	Non-linear
Exponent (n)	1.0	2.65
Impact stiffness (k_{imp})	2500 kN/mm	0.36 $\text{kN/mm}^{2.65}$
Coefficient of Restitution (COR)	0.6	0.5
Bumper thickness (d)	-	5 cm
Bumper's max strain (δ_u/d)	-	0.8
Post-yield impact stiffness (k_{imp_PY})	-	2500 kN/mm

Table 1: Impact parameters for the cases without and with rubber bumper.

Figure 4 demonstrates the load-displacement diagrams for the two cases of the impact velocity and for both cases of with and without the use of the rubber bumper. The results show that the indentation, which represents the local deformation at the vicinity of impact, is much larger in the case of having the rubber shock-absorber due to the reduced impact stiffness. Furthermore, in the case of the relatively high impact velocity of 1.0 m/sec, the deformation exceeds the maximum compressive capacity of the 5 cm thick rubber bumper and the impact force begins to rise rapidly, since the post-yield linear impact stiffness is used.

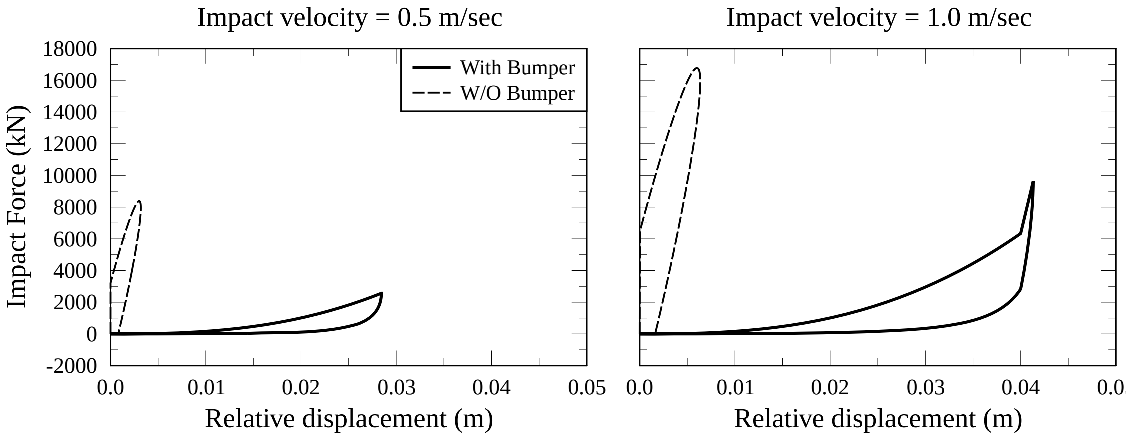

Figure 4: Impact force – displacement diagram for the cases of two impacting rigid bodies, with and without the incorporation of a rubber bumper and for two different values of the impact velocity.

The plots in Figure 5 show the impact force, relative velocity and acceleration time histories for the same cases. It is evident that the use of the rubber bumper elongates the duration of impact and reduces both the maximum impact force and the maximum acceleration. The ratio between the relative velocity after and before impact is equal to the coefficient of restitution used in the corresponding impact model, which verifies the correctness of the two impact models used in the simulations.

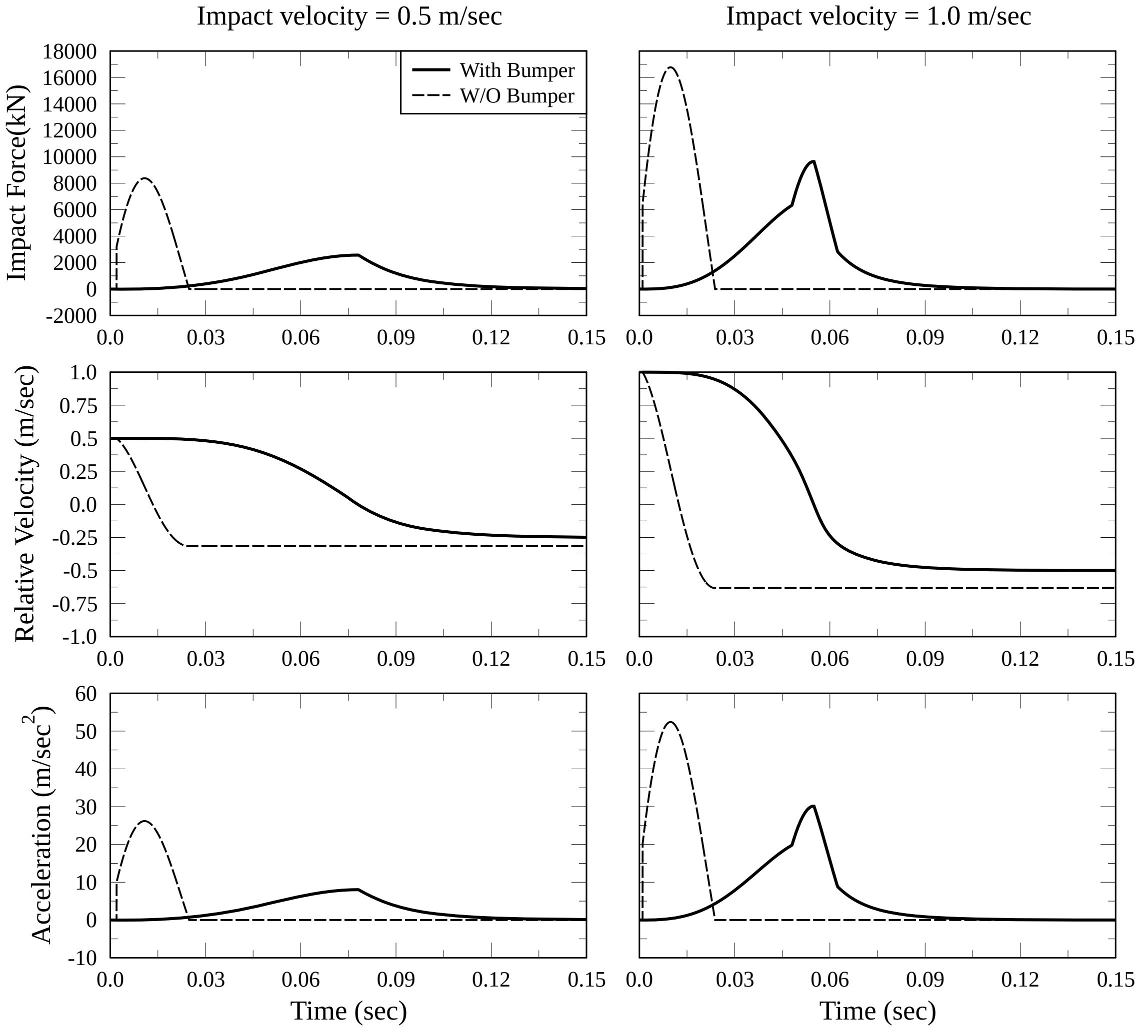

Figure 5: Impact force, relative velocity and acceleration time histories for the case of two impacting rigid bodies, with and without the incorporation of a rubber bumper and for two different cases of the impact velocity.

4 APPLICATION EXAMPLE AND PARAMETRIC ANALYSES

Next, a practical example is presented in order to assess the effectiveness of using rubber shock absorbers as an impact mitigation measure for cases of narrow seismic gap sizes between adjacent multistory buildings. For the numerical simulations, a specialized software application has been specifically developed using modern object-oriented programming in order to efficiently perform dynamic analyses of multistory buildings in two dimensions, modeling the consideration of potential structural pounding. The simulated buildings are modeled as multi-degree of freedom (MDOF) systems, with shear-beam behavior and the masses lumped at the floor levels, assuming linear elastic behavior during earthquake excitations.

A 4-story and a 6-story fixed-supported buildings were considered in series for the performed simulations, as shown in Figure 6. Each floor has a lamped mass of 320 tons, except of the top floor where a mass of 250 tons is considered. Each story has a horizontal stiffness of 600 MN, while a constant viscous damping ratio of 5% has been considered for both buildings. The floors of the neighboring buildings are assumed to be at the same levels.

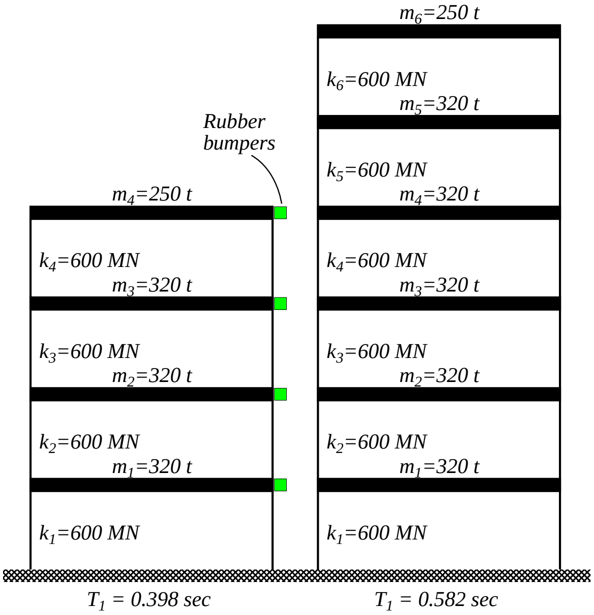

Figure 6: The two multistory buildings considered in the simulations and their structural properties.

For the particular structural system, the performed analysis examined whether the incorporation of rubber bumpers at the locations of potential impacts, which reduces the available seismic gap width, would be beneficial for the colliding buildings or not. For the performed simulations, 5 cm thick bumpers were assumed to be installed at all floor levels, as shown in Figure 6. Therefore, by applying the rubber shock-absorbers at the side of the one of the two buildings, the existing seismic gap size reduces by 5 cm, when compared with the case without the bumper. Consequently, the results obtained from the simulations considering the use of the rubber bumpers are compared with the corresponding results from the case without the bumpers but with a clearance that is 5 cm wider. In the performed parametric analyses, the available seismic gap was varied in the range of 5 to 25 cm, which corresponds to a clearance width of 0 to 20 cm in the case of incorporating rubber bumpers.

In order to investigate the effect of the earthquake characteristics, three different seismic records (Table 2) from relatively strong and widely-known earthquakes were selected as ground excitations.

Earthquake	**M_w**	**Station**	**PGA (g)**
Kobe, Japan 1995	6.9	0 KJMA	0.821
Northridge, USA 1994	6.7	74 Sylmar - Converter Station	0.897
San Fernando, USA 1971	6.6	Pacoima Dam, S16	1.170

Table 2: Earthquake records that were used in the simulations.

Plots in Figure 7 demonstrate the effect of using rubber bumpers on the computed response of the 4-story and the 6-story buildings, in terms of the size of the seismic gap for the Kobe earthquake record. In particular, the plots present the amplification of the peak floor accelerations and peak interstory deflections due to the implementation of the rubber shock-absorbers with a thickness of 5 cm, between the two buildings. The amplification of the response is defined as the ratio of the response obtained after the incorporation of rubber bumpers, which unavoidably reduce the available clearance, to the corresponding response, without the usage of bumpers. Therefore, the usage of rubber bumpers has beneficial effects on the corresponding response quantity when the amplification ratio value is smaller than 1.0.

The results indicate that the size of the seismic gap affects the effectiveness of the rubber bumper in a different manner on each floor and for each building. For example, the peak floor acceleration at the 4th floor of the 4-story building is reduced after the incorporation of the bumper almost for all seismic gap sizes, while at the same time the peak acceleration at the 2nd floor of the 6-story building amplifies up to 30%. Moreover, the maximum interstory deflections are not affected in the same way with the floor accelerations, since the later may be amplified after the use of the rubber bumper, while the former are reduced for a certain gap size. Nevertheless, peak floor accelerations seem to be more sensitive to the use of bumpers than interstory deflections, since the variations of the curves in the plots of Figure 7 are more pronounced in the former case.

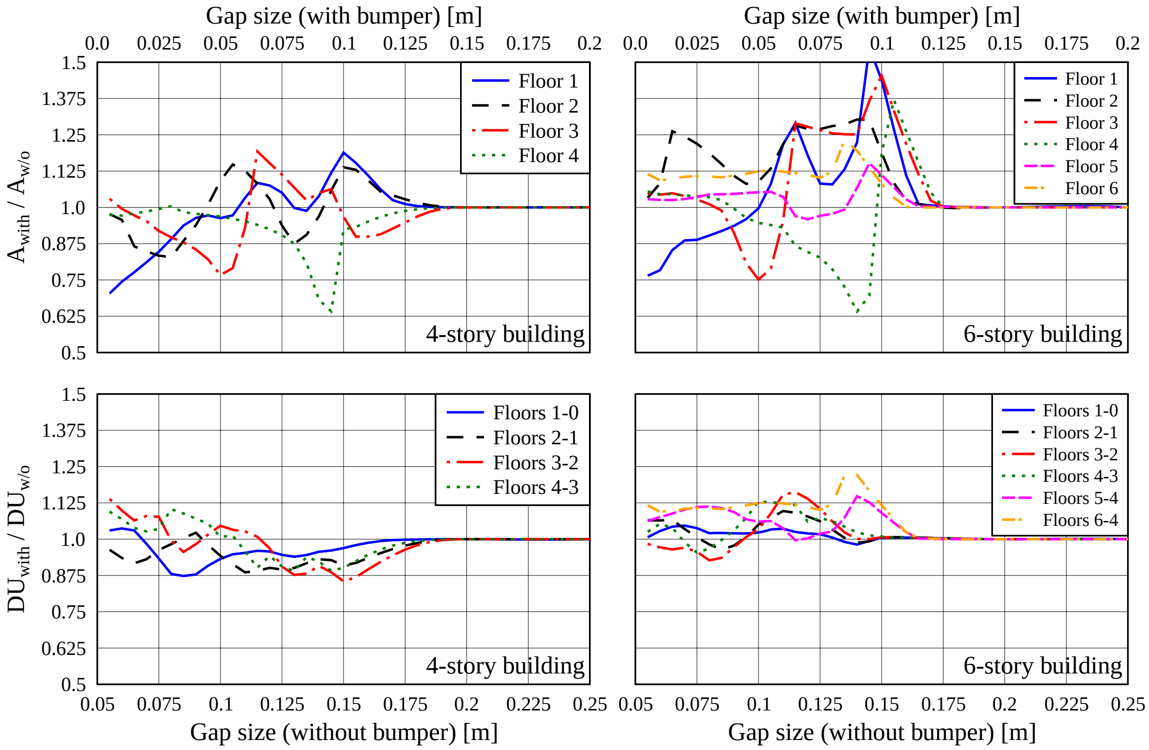

Figure 7: Amplification of the peak floor accelerations and interstory deflections of the 4-story and the 6-story buildings, due to the usage of rubber shock-absorbers, in terms of the width of the seismic gap, considering the Kobe earthquake record.

In order to be able to provide the computed results from all three earthquake records in the same plots, the mean peak responses among all floors of the buildings are computed and plotted in Figure 8. Specifically, these plots demonstrate, in a more general form, the effect of applying rubber bumpers of 5 cm thick inside the available gap on the overall seismic response of the two buildings. It is observed that the characteristics of the earthquake excitation affect the effectiveness of this kind of an impact mitigation measure, in combination with the size of the available clearance. It can be also observed that, under the considered circumstances, the incorporation of such a shock-absorber amplifies, in most of the times, the response, especially in the case of the 6-story building. However there are some cases of relatively narrow gap sizes in which the usage of rubber bumpers seems to be beneficial.

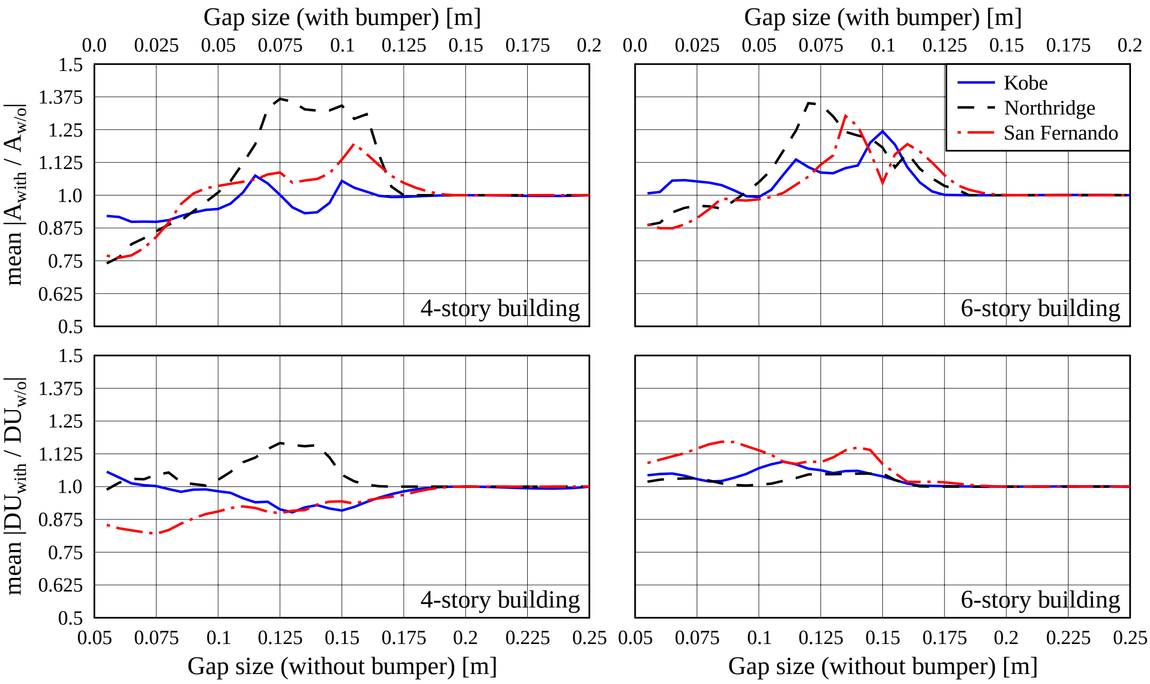

Figure 8: Mean values of the peak responses among all floors of the 4-story and the 6-story buildings, due to the usage of rubber shock-absorbers, in terms of the width of the seismic gap.

In the previously presented simulations, it has been assumed that, after the attachment of rubber bumpers on the side of the seismically isolated building, the reduction of the available clearance from the surrounding moat wall equals to the corresponding thickness of the bumpers. However, the rubber bumpers could be attached in small cavities on the buildings' walls, taking full advantage of the compressible width of the rubber, as shown in Figure 9, without unnecessarily decreasing further the width of the seismic gap. For example, if the thickness of a rubber bumper is 5 cm and its maximum compressive strain equals 0.8, then the compressible width δ_u of the bumper is 4 cm. Therefore, if the particular, 5 cm thick shock-absorber is attached in a cavity that is 1 cm deep, its effective width of 4 cm can be fully utilized, without unnecessarily decreasing further the width of the available seismic gap by 1 cm.

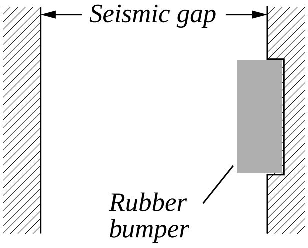

Figure 9: Attachment of a rubber shock-absorber in a cavity on the building's wall.

The above technique seems to be quite efficient since the corresponding amplification ratios due to the incorporation of the bumpers, shown in Figure 10, are substantially reduced in relation to those of Figure 8.

5 CONCLUSIONS

The performed simulations indicate that the incorporation of rubber shock-absorbers to an existing seismic clearance can reduce the peak responses of the pounding structures, under certain circumstances. The effectiveness of the bumpers depends on the existing gap size in combination with the earthquake characteristics and the structural properties (e.g number of stories). The attachment of the bumper in cavities on the building's wall, taking full advantage of the whole compressible width of the rubber, improves their efficiency.

Nevertheless, it has to be mentioned that the above observations concern only the specific earthquake excitations, structural properties and arrangement of buildings. There is a need for further investigation, performing numerous simulations considering different characteristics of the structures, more buildings and earthquake records, where the effectiveness of such impact mitigation measures will be more generally assessed.

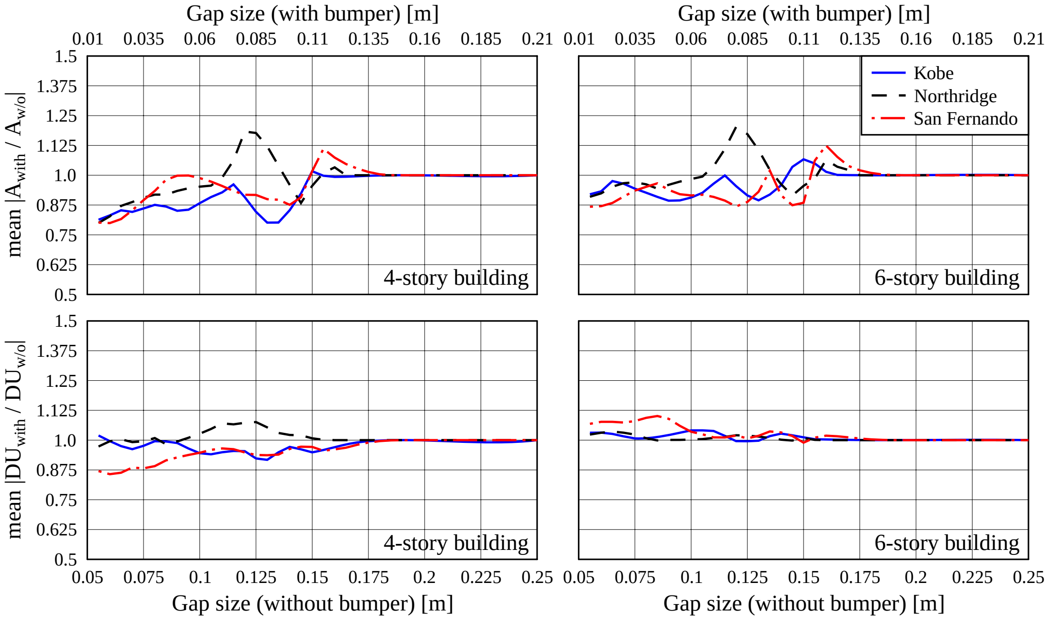

Figure 10: Mean values of the peak responses among all floors of the 4-story and the 6-story buildings, due to the usage of rubber shock-absorbers, in terms of the width of the seismic gap. with 1cm cavity (full advantage of bumper effective thickness, i.e. 4cm)

ACKNOWLEDGEMENT

This research is funded by the Cyprus Research Promotion Foundation grant ΔΙΔΑΚΤΩΡ/0609/39.

REFERENCES

[1] S.A. Anagnostopoulos, Earthquake induced poundings: State of the art. *10th European Conference on Earthquake Engineering*, Duma (Ed.), Balkema, Rotterdam, 1995.

[2] V.V. Bertero, Observations on Structural Pounding. *Proceedings International Conference on Mexico Earthquakes*, ASCE, 264-278, 1987.

[3] Earthquake Engineering Research Institute (EERI), Loma Prieta Earthquake Reconnaissance Report, Rep. No. 90-01, Benuska, L., ed., EERI, Oakland, CA, 1990.

[4] Earthquake Engineering Research Institute (EERI), Kocaeli, Turkey, Earthquake of August 17, 1999 Reconnaissance Report, Publ. No. 00-03, Youd, T. L., Bardet, J-P., Bray, J. D., ed., EERI, Oakland, CA, 2000.

[5] M. Papadrakakis and H. Mouzakis, Earthquake simulator testing of pounding between adjacent buildings. *Earthquake Engineering and Structural Dynamics*, **24**, 811–834, 1995.

[6] S.A. Anagnostopoulos, Pounding of buildings in series during earthquakes. *Earthquake Engineering and Structural Dynamics*, **16**, 443-456, 1988.

[7] P. Komodromos, P.C. Polycarpou, L. Papaloizou, MC. Phocas, Response of Seismically Isolated Buildings Considering Poundings. *Earthquake Engineering and Structural Dynamics*, **36**, 1605-1622, 2007.

[8] Earthquake Engineering Research Institute (EERI), L'Aquila, Italy Earthquake Clearinghouse - Observations from-EERI/PEER team, 2009 (*http://www.eqclearinghouse.org/italy-090406/*).

[9] V. Warnotte, D. Stoica, S. Majewski and M. Voiculescu, State of the art in the pounding mitigation techniques. *Intersections/Intersectii*, **4 (3)**, 102-117. ISSN: 1582-3024, 2007.

[10] P.C. Polycarpou and P. Komodromos, On the numerical simulation of impacts for the investigation of earthquake-induced pounding of buildings, *The Tenth International Conference on Computational Structures Technology (CST2010)*, 14 - 17 Sep., Valencia, Spain, 2010.

[11] R. Jankowski, K. Wilde, and Y. Fujino, Reduction of pounding effects in elevated bridges during earthquakes. *Earthquake Engineering and Structural Dynamics*, **29**, 195-212, 2000.

[12] Y. Kajita, Y. Nishimoto, N. Ishikawa and E. Watanabe, Energy Absorption Capacity of the Laminated Fiber Reinforced Rubber Installed at Girder Ends. *High Performance Materials in Bridges, International Conference on High Performance Materials in Bridges*, 122, 17, DOI:10.1061/40691(2003)17, Kona, Hawaii, USA, 2001.

[13] K. Kawashima, G. Shoji, M. Koshitoge, and S. Shimanoe, Design of an Earthquake-resistant Expansion Joint with Unseating Prevention System, *FIB Congress, E-282 (CD-ROM)*, Osaka, Japan, 2002.

[14] V.P.W. Shim, L.M. Yang, C.T. Lim, and P.H. Law, A Visco-Hyperelastic Constitu-tive Model to Characterize Both Tensile and Compressive Behavior of Rubber. *Journal of Applied Polymer Science*, **92**, 523–531, 2004.

[15] Y. Kajita, T. Kitahara, Y. Nishimoto, and H. Otsuka, Estimation of maximum impact force on natural rubber during collision of two steel bars. *First European Conference on Earthquake Engineering and Seismology (1st ECEES)*, Geneva, Switzerland, September 3-8, 2006.

[16] P.C. Polycarpou and P. Komodromos, Simulating the use of rubber shock absorbers for mitigating poundings of seismically isolated buildings during strong earthquakes, *2nd International Conference on Computational Methods in Structural Dynamics and Earthquake Engineering (COMPDYN 2009)*, Rhodes, Greece, 22–24 June 2009.

[17] P. Polycarpou and P. Komodromos, Numerical investigation of potential mitigation measures for poundings of seismically isolated buildings, *Journal of Earthquake and Structures*, **2(1)**, 1-24, 2011.

COMPDYN 2011
3rd ECCOMAS Thematic Conference on
Computational Methods in Structural Dynamics and Earthquake Engineering
M. Papadrakakis, M. Fragiadakis, V. Plevris (eds.)
Corfu, Greece, 25–28 May 2011

NEGATIVE STIFFNESS DEVICE FOR SEISMIC PROTECTION OF STRUCTURES – AN ANALYTICAL AND EXPERIMENTAL STUDY

Apostolos A. Sarlis[1], Dharma Theja R. Pasala[2], Michael C. Constantinou[1], Andrei M. Reinhorn[1], Satish Nagarajaiah[2] and Douglas Taylor[3]

[1]State University of New York at Buffalo, Buffalo, NY-14260, U.S.A
{aasarlis,constan1,reinhorn}@buffalo.edu

[2]Rice University, Houston, TX-77005, U.S.A
{drp1, Satish.Nagarajaiah}@rice.edu

[3]Taylor Devices Inc., North Tonawanda, NY-14120, U.S.A
TaylorDevi@aol.com

Keywords: Negative Stiffness Device, Apparent yielding, Passive, True Negative Stiffness

Abstract. *Structural weakening and damping is an approach previously proposed for the reduction of seismic forces and drifts in structures. While this approach is very efficient, it requires a reduction in strength, which will result in inelastic excursions and permanent deformation of the structural system during the seismic event. This paper describes a true Negative Stiffness Device (NSD) that can emulate weakening of the structural system without inelastic excursions and permanent deformations. The Negative Stiffness Device (NSD) is a self contained device that produces a force which is in the same direction as the imposed displacement, thus the name "negative stiffness". The device is inherently unstable but when installed in a structure transfers a force at its installation level which in turn reduces all forces, drifts and accelerations above that level. The NSD is therefore capable of limiting the forces developed in a structure without any yielding which could lead to permanent deformations. The NSD was developed at the University at Buffalo (UB), Rice University and Taylor Devices Inc. and tested on a shake table by authors in a three storied structural model isolated with elastomeric bearings. The NSD consists of a highly compressed spring in a double negative stiffness magnification mechanism. In order to ensure a considerable amount of positive stiffness of the global system around small displacements to minimize wind vibrations a so called gap spring assembly (GSA) mechanism is implemented which delays the engagement of the device by a prescribed displacement. Moreover, the device employs double containment chevron braces that contain the large vertical forces needed for the development of negative stiffness without transferring these forces to the structure. This paper describes the development of analytical and computational tools that describe the behavior of the device and presents results for the experimental verification of these tools.*

1 INTRODUCTION

Designing structures for ductile behavior and allowing for significant inelastic action in strong earthquakes results in reduction of inertia forces. However, this is accompanied by large drifts, permanent deformations and eventually loss of functionality of the structure after a seismic event. Reinhorn et al. (2005) [1] and Viti et al. (2006) [2] introduced the concept of weakening structures (reducing strength and implicitly stiffness), while introducing supplementary viscous damping to reduce simultaneously total accelerations and inter-story drifts. However, weakening also reduces strength and results in some permanent displacements. An alternative approach is to “simulate yielding” by introducing negative stiffness at predescribed displacements leading to the idea of “apparent weakening”.

The concept of true negative stiffness for structural applications was first introduced by Nagarajaiah et al [3]. True negative stiffness means the force must assist motion, not oppose it as it is in the case of a positive stiffness spring. Pseudo negative stiffness [4] can be accomplished using active or semiactive hydraulic device. True negative stiffness needs no external power supply. The Negative Stiffness Device (NSD) presented herein is entirely composed of springs and generates an elastic nonlinear true negative stiffness.

By engaging the NSD at an appropriate displacement (simulated yield displacement), which is well below the actual yield displacement of the structural system, the composite structure-device assembly, behaves like a yielding structure. The NSD has a re-centering mechanism thereby avoiding permanent deformation in the composite structure-device assembly unless, the main structure itself yields. However, the combined structural system with just the NSD develops increased structural deformations. Addition of passive dampers reduces and controls these deformations without any considerable increase in the base shear. The addition of dampers combined with the reduction of stiffness also lead to an increased damping ratio which presents an additional advantage in controlling the displacements.

In order to visualize the effect of adding true negative stiffness to a structure, consider the force displacement plots shown in Figure 1(a) (green line is structure, magenta is viscous damper and red is negative stiffness device). By adding NSD to the structure, schematically shown in Figure 1(b), the assembly stiffness reduces to $K_a = K_e - K_n$ beyond the displacement x_1 (shown as blue line in Figure 1(b)). If, F_2 and x_2 are the maximum restoring force and maximum displacement of a perfectly-linear system (green line in Figure 1(b)) then for the same load the maximum restoring force and maximum displacement of the assembly are F_3 and x_3 (blue line in Figure 1(b)), respectively. K_n is designed to achieve the desired reduction in base shear. Force exerted by the NSD is shown as red line in Figure 1(b). Although the reduction in base shear is achieved the maximum deformation of the adaptive system is substantially increased in the process when compared with an elastic system. Deformation of this assembly can be reduced by adding a passive damping device in parallel to the NSD, schematically shown in Figure 1(c).

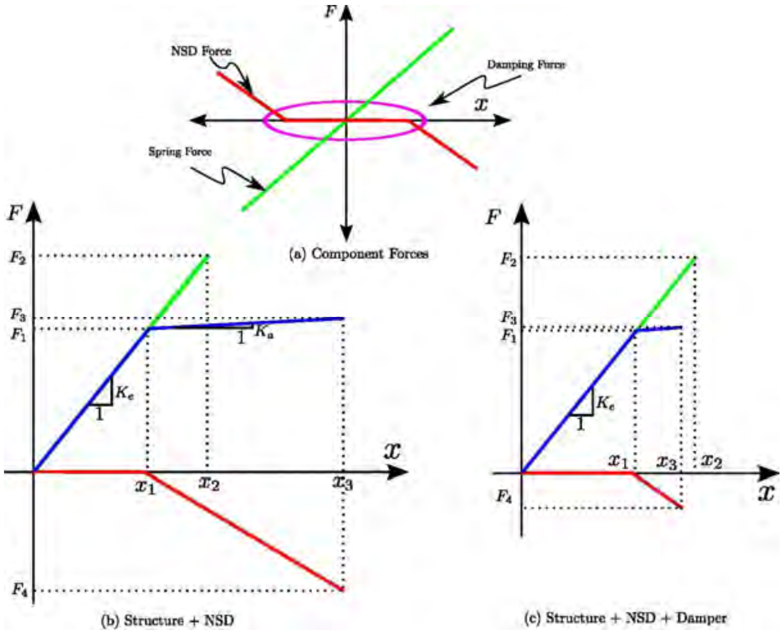

(a) Component Forces

(b) Structure + NSD

(c) Structure + NSD + Damper

Figure 1: Working Principle of NSD (Nagarajaiah et al 2010)

Photographs of the NSD are shown in Figure 2a (un-deformed) and Figure 2b (deformed). The device itself is inherently unstable. It can be installed in an isolated structure between the ground and the isolation level or in between the floors of any fixed and/ or isolated structure. Its effect is that it reduces the forces that are transferred above its installation level.

In order to ensure a considerable amount of positive stiffness around small displacements in order to minimize wind vibrations and account for some variability in structural and NSD properties, a so called gap spring assembly (GSA) mechanism is implemented which essentially makes the device engage at a larger displacement (displacement x_1 in Figure 1) rather than at the initial position of the structure.

The current paper focuses on the analytical framework and experimental validation of the NSD which uses only a part of the experimental NSD testing program. Complete details and additional analytical and computational issues, further experimental validation together with shake table testing and the verification of the true Negative Stiffness (NS) concept through shake table testing can be found in [5, 6].

2 NSD DESCRIPTION

2.1 NSD Operation

The NSD shown in Figure 2a is composed of a pre-compressed spring shown in the center of the device as well the gap spring assemblies on the bottom. A combination of frame elements and plates hold these pieces together. When the device deforms, the pre-compressed spring is the one that creates the force that assists the motion or the negative force and thus the name negative stiffness for the device. The bottom spring assemblies (gap spring assembly mechanism) provide the device inherently with a bilinear elastic positive stiffness in order to make the device engage at larger displacements (displacement x_1 in Figure 1). More specifically, around equilibrium, the positive stiffness caused by the gap spring assembly mechanism, cancels out the negative stiffness caused by the pre-compressed spring so that essentially the force/stiffness generated by the device is close to zero. After a prescribed displacement, the gap spring assembly softens drastically so that the pre-compressed spring acts essentially on its own creating the negative stiffness. It is noted that the operation of the gap spring assembly is achieved without any yielding so that there is no inherent permanent deformation in the device.

a) Un-deformed NSD b) Deformed NSD

Figure 2: View of Negative Stiffness Device tested at SUNY Buffalo

Schematic diagram of the device in its deformed configuration is shown in Figure 3 after imposing a displacement on the top of the device. The lever imposes a displacement on the top of the pivot plate (point B) making the pivot plate to rotate about point C. Due to the axial rigidity of the lever and its negligible rigid body rotation, the imposed displacement and the displacement of Point B are approximately equal. Since the pivot plate rotates about C, point D moves in the opposite direction from the imposed displacement. Point E is rigidly connected to the top of the device and therefore has a displacement equal to the one imposed. Due to the kinematics of points D and E, the pre-compressed spring rotates and its pre-compression force facilitates the motion rather than opposing it. Moreover since the "negative force" is generated by a spring whose deformation depends nonlinearly to the NSD imposed displacement, the NSD exhibits nonlinear elastic behavior.

The spring exhibits its minimum length when the device is un-deformed. As the device deforms, the spring extends thus its pre-compression force reduces while its inclination angle increases and the stiffness magnitude generated by the device reduces. This gradual stiffness reduction will eventually lead to positive stiffness at larger displacements and this is termed as "stiffening" throughout this paper. This stiffening part can be very important in the case the maximum considered earthquake has been exceeded since it limits the displacements of the structure or the isolators.

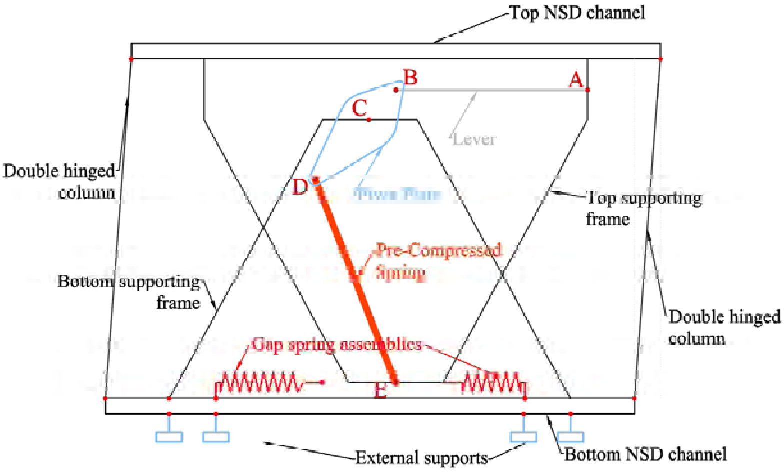

Figure 3: Terminology used for the elements of the Negative Stiffness Device

2.2 Advantages of NSD Tested at SUNY Buffalo

Negative Stiffness in applications other than earthquake has been proposed and used at small scale for the vibration isolation of equipment by Molyneaux (1957) [7], Platus [8-16], Carrella et al [17] and for car suspension systems [18]. It has also been proposed in base isolation [19] with the application of the convex pendulum bearings in parallel with elastomeric bearings. The NSD described in the current paper is a large scale novel design that passively generates negative stiffness and it is not restricted to only base isolation. The NSD presents the following advantages:

- The device changes the **apparent global lateral stiffness** of the structure, without changing the actual stiffness of the structure. The apparent stiffness is reduced to a very low level simulating global lateral yielding without actual yielding in the main structure.
- The device produces **true horizontal negative stiffness** by passively generating a force that assists the imposed displacement. No external power supply is needed since all the elements comprising the device are passive.
- The device is self contained and therefore when installed affects only the horizontal stiffness of the system while leaving the vertical stiffness intact. Stability and buckling limits of the structure are not affected. **The NSD does not participate in transferring the vertical loads.**
- There is no significant hysteresis in the device. The NSD is essentially elastic.
- The device provides variable stiffness which becomes positive at large deformations, therefore its global behavior is “elastic nonlinear”. This is a desired feature as it promotes stability.
- The device employs a double magnification mechanism that allows for easy adjustment of the negative stiffness value. The gap spring assembly (GSA) mechanism allows for adjustable gap opening.

3 OUTLINE OF THE EXPERIMENTAL PROGRAM

The experimental setup is shown in Figure 4a. The 3 story structure –used before as a six story structure [e.g., 20] - is sitting on top of four low damping elastomeric bearings used before in [20]. The elastomeric bearings were tested individually at the single bearing testing machine at UB described in [21]. Two NSD's were installed on the side of the shake table and were connected to the base of the superstructure with rollers in order to accommodate the height loss that they exhibit during deformation. The tests conducted at UB were divided in to two major categories: 1) Displacement controlled tests with and without the gap spring assembly and 2) Shake table tests involving various configurations of the NSD with and without viscous dampers. The displacement controlled tests were achieved by externally bracing the superstructure at the base-mat level through a reaction frame that was constructed on the side of the shake table and shown in Figure 4a on the right while the bracing system is shown in Figure 4b.

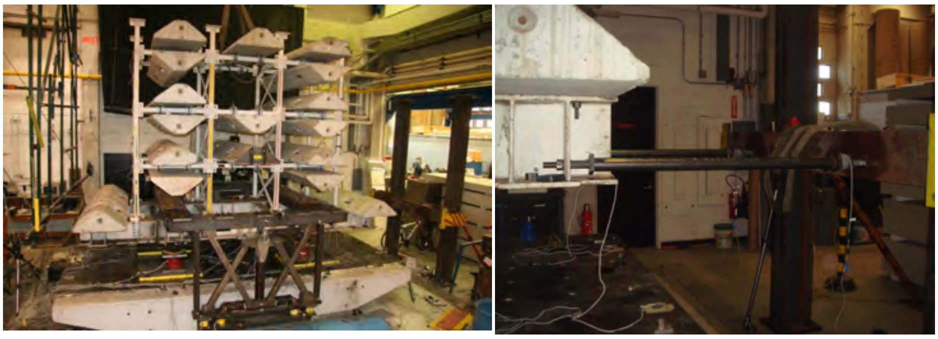

a) 3story structure tested at UB b) Bracing of superstructure

Figure 4: Experimental Setup

Each NSD is sitting on top of four load cells [22] and instrumented at points B,C,D,E with string pots and accelerometers. NSD East is also heavily instrumented with Krypton LED's. Krypton is an advanced camera coordinate tracking system described in [23].

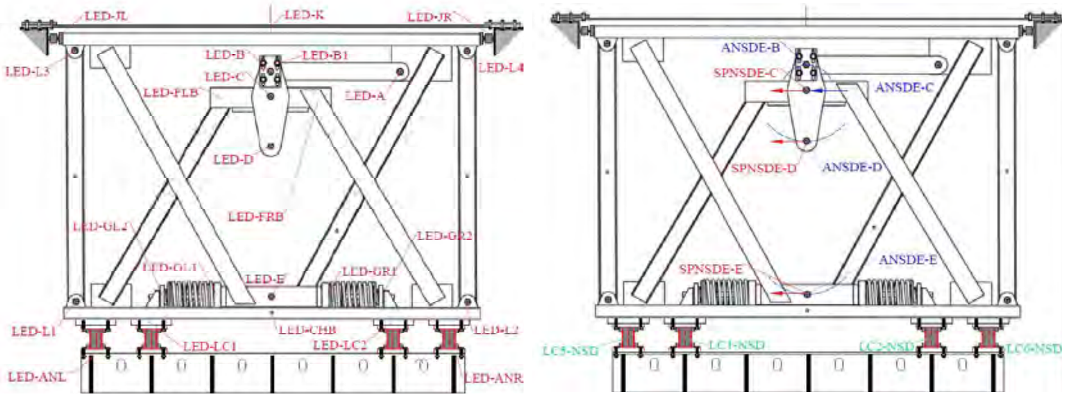

a) Position of LED's on NSD East b) Conventional Instrumentation of NSD East

Figure 5: Instrumentation for NSD East

4 ANALYTICAL EQUATIONS OF NEGATIVE STIFFNESS DEVICE

In order to derive the force displacement equations of the device, equilibrium at the deformed shape needs to be considered since essentially the operation of the device is based on geometric nonlinearity. Therefore one needs to consider the deformed shape and the device being supported horizontally on top by the application of a force which is essentially the negative force generated by the device. The forces acting on the pivot plate caused by the pre-compressed spring and the lever are shown in Figure 6. From geometry and considering the fact that point C is fixed, the displacements of other points of the device are:

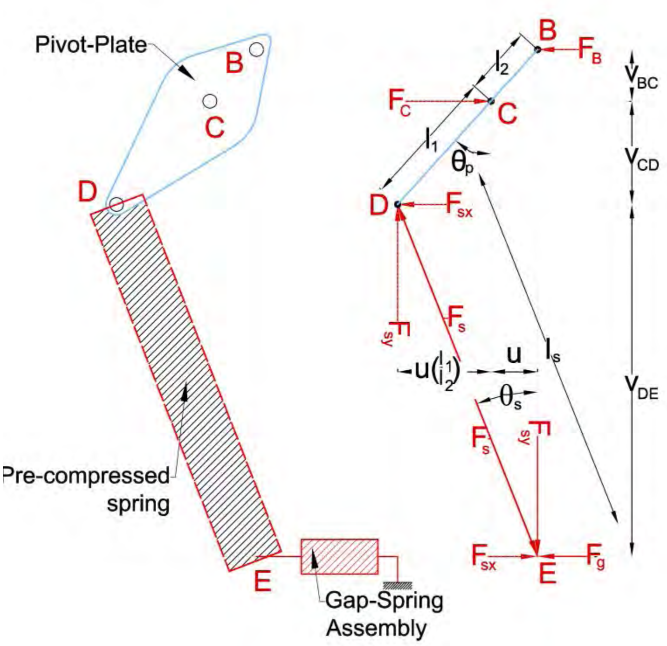

Figure 6: Forces acting on pivot plate

$$u_B = u_E = u_D \, {}^{l_2}\!/_{l_1} = u \tag{1}$$

In Figure 6, θ_s is the angle of the spring θ_p the angle of the pivot plate with respect to vertical. θ_s and θ_p are obtained from equation (2):

$$\begin{gathered} \theta_s = \arcsin \frac{1}{l_s} u \left(1 + \frac{l_1}{l_2}\right) \\ \theta_p(t) = \arcsin \frac{u}{l_2} \end{gathered} \tag{2}$$

The spring length at the deformed configuration is given by:

$$l_s = \sqrt{\left(l_p + l_1 - l_1\sqrt{1-\left(\frac{u}{l_2}\right)^2}\right)^2 + u^2\left(1+\frac{l_1}{l_2}\right)^2} \tag{3}$$

l_p is the length of the spring when the NSD is un-deformed and F_s is the force of the pre-compressed spring:

$$F_s = P_{in} - K_s\left(l_s - l_p\right) \tag{4}$$

P_{in}: is the pre-compression force of the spring and should have a positive value and K_s is the stiffness of the pre-compressed spring.

Writing the equilibrium equations for the pivot plate for the forces of Figure 6 and using equations (1)-(4) yields the horizontal force at point C. Then from Figure 3 one can see that the total NSD force is simply $F_{NSD} = F_C + F_g$. The final expression for the force generated by the NSD as a function of the imposed displacement is given in equation (5):

$$F_{NSD} = -\left(\frac{P_{in} + K_s l_p}{l_s} - K_s\right)\left(\frac{l_1}{l_2}\right)\left(2 + \frac{l_2}{l_1} + \frac{l_p + l_1}{\sqrt{l_2^{\,2} - u^2}}\right)u + F_g \tag{5}$$

The force displacement of the gap spring assembly for monotonic positive displacement is given by:

$$F_g = \left\{\begin{matrix} k_{g1}u, & 0 \le u \le d_{gap} \\ k_{g1}d_{gap} + k_{g2}\left(u - d_{gap}\right) & u > d_{gap} \end{matrix}\right\} \tag{6}$$

d_{gap} is a prescribed displacement at which the gap spring assembly softens and H is the Heaviside function

Quantity	**Value**
Distance from spring pin to fixed pin Distance from lever pin to fixed pin	$l_1 = 10in$ $l_2 = 5in$
Spring length Spring rate Preload	$l_p = 30in$ $K_s = 0.8\,{}^{kips}\!/_{in}$ $P_{in} = 3.7kips$
Gap opening Gap Spring Assembly Stiffness for $u < d_{gap}$ Secondary spring assembly stiffness $u > d_{gap}$	$d_{gap} = 0.65in$ $K_{g,1} = 2.81kips/in$ $K_{g,2} = 0.17kips/in$

Table 1: NSD Properties

The force displacement loops for the derivations above are generated in figure 7 for the properties shown in Table 1.

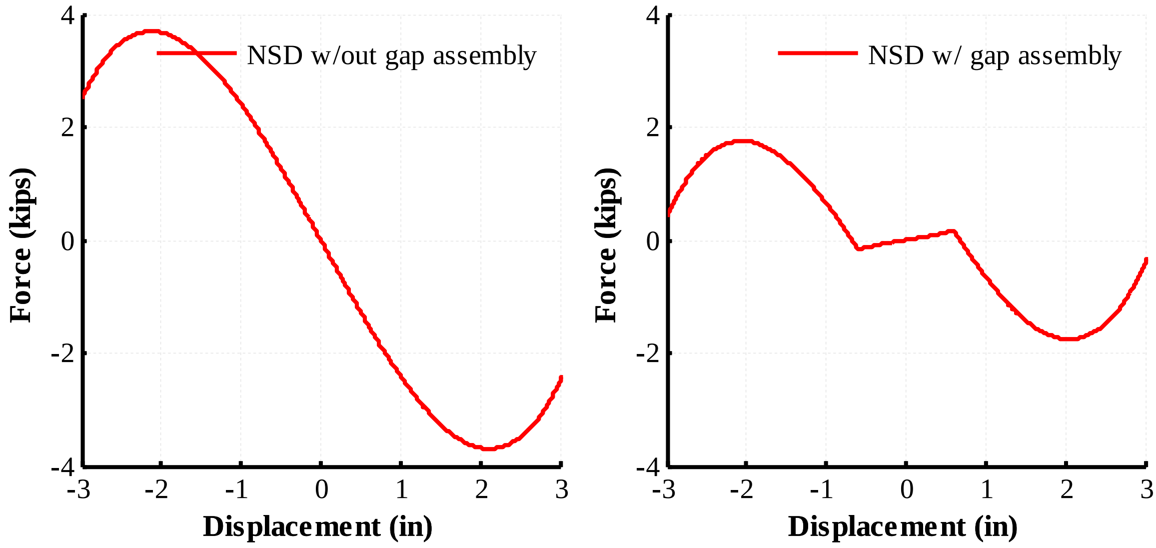

Figure 7: Force versus NSD imposed displacement plots for NSD with and without the gap spring assembly

5 MODELING OF NSD IN SAP2000

Modeling the NSD in user subroutines is straightforward by implementing equations (5) and (6). In SAP2000 [24], the NSD behavior can be modeled using the multi-linear elastic spring element. One can directly import the force displacement loop of the NSD into SAP2000. There is no restriction in SAP2000 for the sign of the stiffness and therefore negative springs can be implemented as well. The gap spring assembly can be also modeled using the same multi-linear element. The NSD model in SAP2000 is therefore a parallel arrangement of two elements 1) a multi- linear elastic element representing the negative nonlinear elastic component from equation (5) with $F_g=0$ and 2) a multi- linear elastic element representing the positive bilinear elastic component generated by the gap spring assembly and given by equation (6).

The configuration as implemented in SAP2000 is shown in Figure 8 on the left. Both elements ML1 and ML2 share the same joints on top and bottom. Comparisons of the results obtained in the SAP2000 model for a displacement controlled test are compared with the analytical equations in Figure 8 on the right. Results match identically.

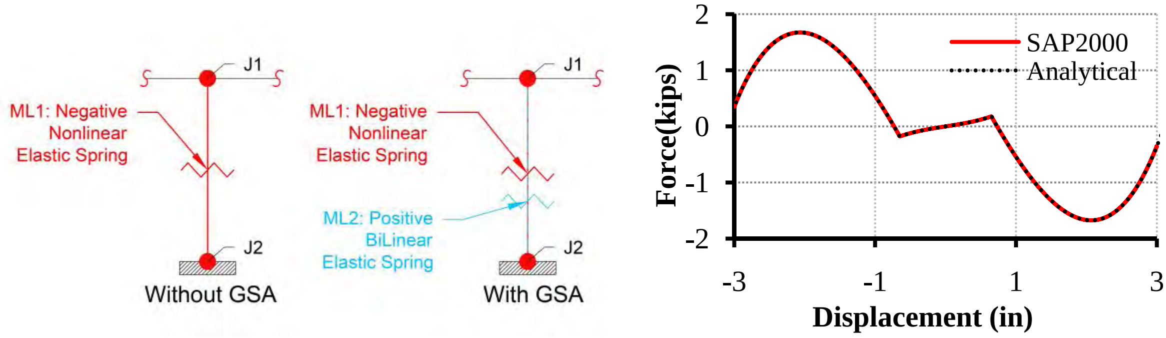

Figure 8: SAP2000 NSD elements for the cases with gap and without gap and comparisons of SAP2000 results with analytical results

6 ANALYTICAL INVESTIGATIONS AND MODELING OF THE DETAILED NSD BEHAVIOR

For most practical applications, the analytical equations and the modeling of sections 4 and 5 is sufficient to provide highly accurate results. The derivations of this section are intended to provide the reader with complete understanding of the detailed mechanics of the NSD. Understanding the complete mechanics of a system is essential in its practical implementation and later on use of the simplified models.

6.1 Analytical Derivations of NSD Dynamics

The rigid body dynamics of the Negative Stiffness are derived here using a Lagrangian formulation. The masses and moments of inertia in the actual device are shown in Figure 9. All frame elements connected to the top channel and the double hinged columns, undergo an inverted pendulum motion around the base and their moment of inertia is lumped at F and H respectively. At point C the mass moment of inertia of the pivot plate is lumped. The center of mass of the spring undergoes both translation and rotation. Its mass m_s is lumped at its center of mass located at point S. Its moment of inertia varies with displacement *u*.

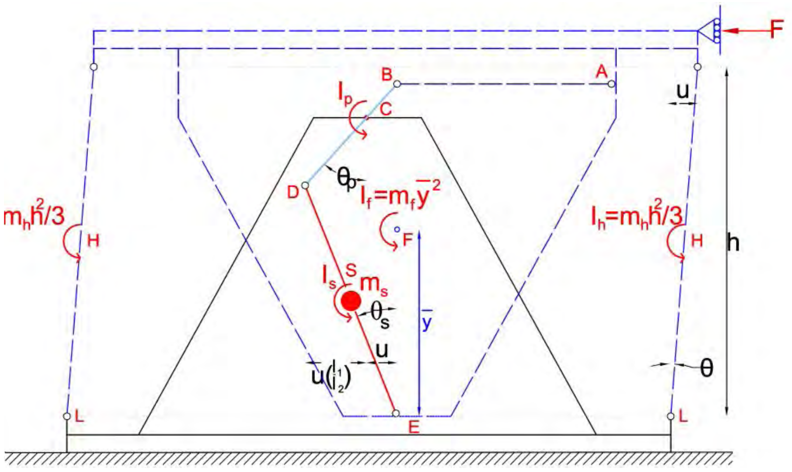

Figure 9: Discretization of the device

Considering the fact that the rotations of the individual components are coupled to the imposed displacement there is only one degree of freedom. The rotation of the pivot plate and spring is given by equation (2), the horizontal displacement of the center of mass of the spring is the average of the displacements of points D and E from equation (1) while the vertical displacement is half the vertical displacement of point D and can be easily calculated from geometry of Figures 3, 6 and 9 while angle θ can be calculated from the geometry of figure 9. All quantities above are functions of the imposed NSD displacement alone.

The Euler-Lagrange equation for the NSD is:

$$\frac{d}{dt}\left(\frac{\partial L}{\partial \dot{u}}\right)-\frac{\partial L}{\partial u}=0 \qquad (7)$$

$$L=K-V$$

Where K is the total kinetic energy of the system and V is the total potential energy of the system with respect to a reference coordinate system given as the sums of the kinetic and potential energies of the individual moving parts of the device. The total kinetic and potential energies (with reference to C) of the system are given from:

$$K=\frac{1}{2}I_p\dot{\theta}_p^{\,2}+\frac{1}{2}m_s\dot{u}_s^{\,2}+\frac{1}{2}m_s\dot{v}_s^{\,2}+\frac{1}{2}I_s\dot{\theta}_s^{\,2}+\frac{1}{2}I_h\dot{\theta}^2+\frac{1}{2}I_f\dot{\theta}^2$$
$$V=-m_f g\left(l_p+l_1-\bar{y}\cos\theta\right)-m_s g\left(l_1+\frac{v_{DE}}{2}\right)+m_c g\left(h-v_{LB}-\frac{h}{2}\cos\theta\right)+V_{el,s}+W \tag{8}$$

The potential energy coming from the deformation of the spring in equation (8) is:

$$V_{el,s}=\frac{1}{2}K_s\left[l_s-\left(l_p+\frac{P_{in}}{K_s}\right)\right]^2 \tag{9}$$

The external work done by a restraining force in (8) has to be expressed as a potential so:

$$W=-\int Fdu=-Fu+C \tag{10}$$

It is noted that the force above is the force needed to be applied at the top of device in order to hold the device in place and make it stable. Equivalently this is the force generated by the device.

Using equations (7)-(10), (1)- (4) and after performing some tedious algebra which involves the calculation of the derivatives involved in equations (7) and (8) we can get the equation of motion of the NSD which is given by:

$$M_a\ddot{u}+M_v\dot{u}^2+M_u u=F \tag{11}$$

The terms M_a, M_v and M_u, are given by complex expressions and final results are omitted for simplicity. The force displacement loops of the device for various driving frequencies are plotted in Figure 10 for the device properties of table 1. The effect of the inherent dynamics is that of increasing the negative stiffness and maximum force generated by the NSD while slightly delaying the initiation of stiffening. The driving frequencies of Figure 10 are only for demonstration purposes. The accelerations and velocities for the higher frequencies shown there are unrealistic and therefore the effect of the inherent dynamics is negligible.

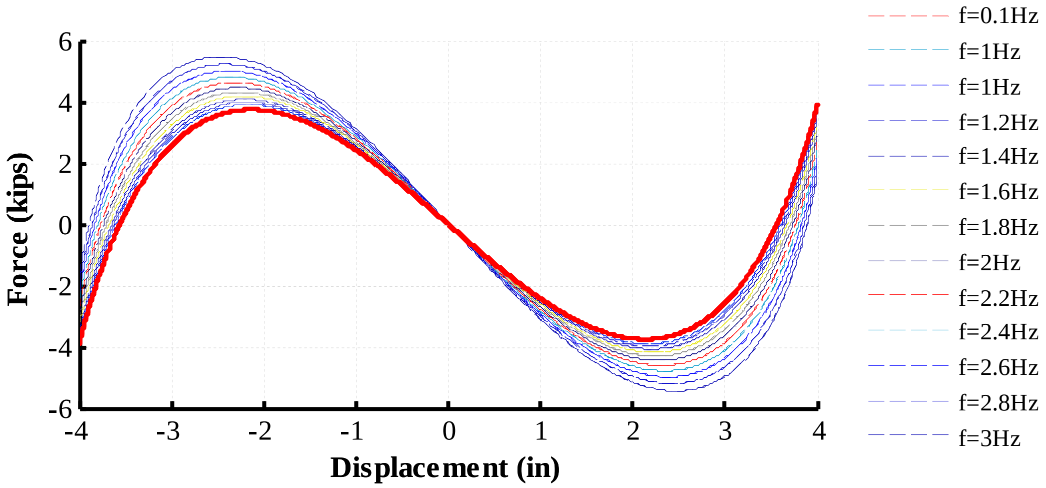

Figure 10: Force Displacement Loops of NSD for various excitation frequencies

6.2 Analytical Derivations of NSD Imperfections

Although the pins are typically assumed to be frictionless and dimensionless, in reality they are not. When a pin is connecting two members, in order for the member to start rotating relatively one to the other, a friction force must be overcome either between one member and the pin, or the other member and the pin, or both. For example consider the assembly shown in Figure 11a:

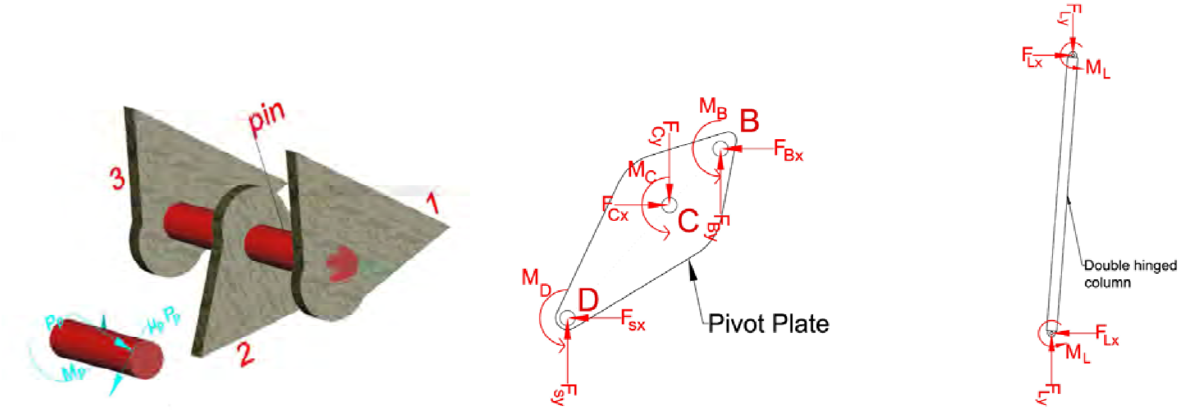

a) Pin Friction modeling FBD

b) Pivot Plate Free body Diagram

c) Double Hinged Column

Figure 11: Pin friction model

In Figure 11a, it is assumed that rotation of the pin occurs because connecting part 1 rotates relatively to the pin while the pin and part 2 are in sticking conditions. In order to have a relative rotation between one of the connecting parts and the pin, we need to apply a torque on the pin of magnitude:

$$M_p = r\mu_p |P_p| \tag{12}$$

r is the radius of the pin, P_p is the resultant force acting on the pin and μ_p is the friction coefficient.

Figure 11b shows the free body diagram of the pivot plate and 11c of the doubled hinged columns considering friction in the pins. Based on Figure 11b, due to the moment at points B and A, the lever now has a shear force equal to:

$$F_{By} = \frac{2M_B}{l_{lv}} \tag{13}$$

Writing the equilibrium equations for Figure 11b the unknown forces can be computed:

$$\begin{aligned}
F_{Bx} &= -\frac{F_s}{l_s}\frac{l_1}{l_2}\left[1+\frac{l_p+l_1}{\sqrt{l_2^{\,2}-u^2}}\right]u+\frac{M_D+M_B+M_C+\dfrac{2M_B}{l_{lv}}\left(l_2-\sqrt{l_2^{\,2}-u^2}\right)}{\sqrt{l_2^{\,2}-u^2}}\\
F_{Cx} &= F_{Bx}-\frac{F_s}{l_s}u\left(1+\frac{l_1}{l_2}\right)\\
F_{Cy} &= -F_s\,\frac{l_p+l_1-\dfrac{l_1}{l_2}\sqrt{l_2^{\,2}-u^2}}{l_s}+F_{By}
\end{aligned}\tag{14}$$

From Figure 11c, the end moments caused by the friction in the pins cause a shear force that is constant throughout the height of the double hinged columns:

$$F_{Lx}=\frac{2M_L}{h}\tag{15}$$

The total force of the NSD becomes:

$$F_{NSD}=F_{Cx}+2F_{Lx}+F_g\tag{16}$$

The equation above can be decomposed into a nonlinear elastic part and a hysteretic part, $F_{NSD}=F_{el}+F_{pl}$. We approximate the hysteretic moment by using the Sivaselvan-Reinhorn [25] hysteretic model:

$$dM=k_o\left\{1-\left|\frac{M}{M_y}\right|^2 sign(M)sign(d\theta)\right\}d\theta\tag{17}$$

$d\theta$ is the rotation increment of the pin being different for each pin, du is the increment of the imposed displacement while k_o elastic stiffness of the pin prior to slipping occurring.

According to equation (17), in order to calculate the moments of the pins, we need to calculate the resultant forces as well as the rotation increments of all the pins. The resultant forces can be calculated from the free body diagrams of Figure 11b, c. The pin rotation increments can be calculated by differentiating the pin rotations with respect to the imposed NSD displacement and then solving for the rotation differentials. The pin rotations are given from equation (2) for point C, similarly for point B if the negligible rotation of the lever is ignored, as $\theta_D=\theta_C+\theta_s$ for point D with the help of equation (2) for the spring angle and from the geometry of Figure 9 for the rotation θ of the double hinged columns.

The set of equations (12)-(15) and (17) written for each pin with its corresponding resultant forces and rotation increments represent a system of equations on the unknowns. Consider the unknown vector at time step $n+1$:

$$\mathbf{x}_{(n+1)}=\left\lfloor M_{Bn+1}\quad M_{Cn+1}\quad M_{Dn+1}\quad M_{Ln+1}\quad F_{(n+1)}\quad F_{Bx(n+1)}\quad F_{By(n+1)}\quad F_{Cx(n+1)}\quad F_{Cy(n+1)}\quad F_{Lx(n+1)}\right\rfloor^T\tag{18}$$

Collecting all terms of the equations on the left hand side and define $\mathbf{f}(\mathbf{x}_{n+1})=0$, using $\mathbf{x}_{n+1}{}^{(0)}=\mathbf{x}_n$ as the first iteration, then Newton Raphson iteration follows as:

$$\mathbf{x}_{n+1}{}^{(j+1)} = \mathbf{x}_{n+1}{}^{(j)} - D\mathbf{f}^{-1}\left(\mathbf{x}_{n+1}{}^{(j)}\right) f\left(\mathbf{x}_{n+1}{}^{(j)}\right) \tag{19}$$

Note that the initial conditions at the first step is $\mathbf{x}_0 = \lfloor 0 \quad 0 \quad 0 \quad 0 \quad 0 \quad 0 \quad 0 \quad 0 \quad P_{in} \quad 0 \rfloor$

Results are plotted in Figure 12 for the properties listed in table 1 for various friction coefficients. Hysteresis in the NSD is proportional to the horizontal force exerted by the NSD. At large displacements when the NSD force becomes zero so does the hysteretic force while after that it maintains the same sign.

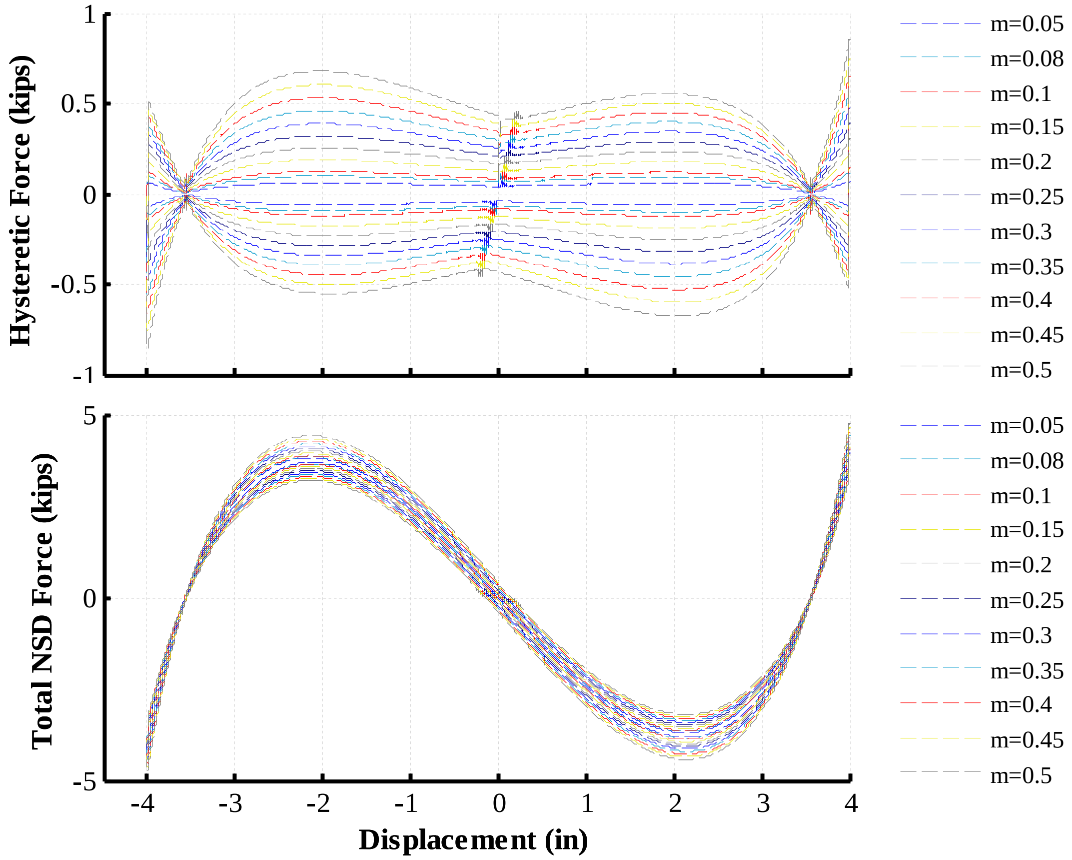

Figure 12: Force Displacement Loops of NSD for various friction coefficients

6.3 Analytical Derivations of NSD Inherent Flexibilities

All the equations up to this point have been derived based on the assumption that point C is fixed and point E undergoes only rigid body motion driven by the top channel of the device. This is only true if the connecting frame elements, namely, the top supporting and the bottom supporting frames are considered rigid. This in most cases is only approximately true.

In order to visualize the flexibility effects, consider an equivalent NSD model shown in Figure 13 in equivalence to the points of Figure 3. Now, at point C a spring k_b is added to approximately represent the flexibilities of the bottom frame together with the bottom supporting channel. Similarly for the top supporting frame, the rigid frame element is no longer assumed to be continuous since a spring k_t is added at its midpoint in order to approximate the flexibilities of the top supporting frame together with the top NSD channel.

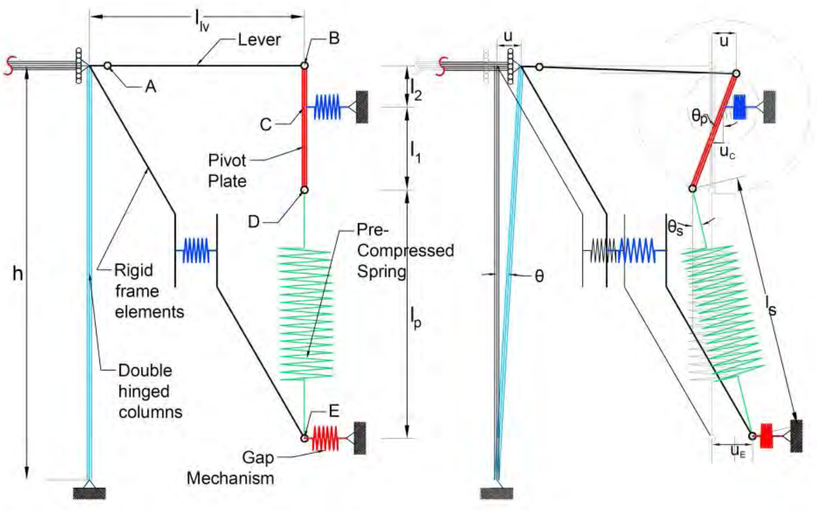

Figure 13: Flexibilities considered in the equivalent NSD model

Equilibrium equations and geometric equations need to be rewritten using equation (20) instead of equation (1):

$$u_{f,E} = u_E - u$$

$$u_D = (u - u_C)\frac{l_1}{l_2} - u_C \tag{20}$$

u_{fE}: Displacement of point E due to flexibilities of the top supporting frame

The spring length is now given from:

$$l_s = \sqrt{\left(l_p + l_1 - \sqrt{l_1^{\,2} - \left((u - u_C)\frac{l_1}{l_2}\right)^2}\right)^2 + \left[(u - u_C)\frac{l_1}{l_2} - u_C + u_E\right]^2} \tag{21}$$

The horizontal reaction at point C can be calculated from moment and force equilibrium of the pivot plate for the new geometry:

$$F_{Cx} = -\left(\frac{P_{in} - K_s l_p}{l_s} + K_s\right)\frac{l_1}{l_2}\left\{\left[\frac{(l_p + l_1)}{\sqrt{l_2^{\,2} - (u - u_C)^2}} + 1\right](u - u_C) + (u_E - u_C)\left(1 + \frac{l_2}{l_1}\right)\right\} \tag{22}$$

Moreover from equilibrium of forces at point C one gets:

$$F_{Cx} = k_b u_C \tag{23}$$

While from equilibrium of point E after substituting for the spring inclination angle:

$$-\left(\frac{P_{in} + K_s l_p}{l_s} - K_s\right)\left[(u - u_C)\left(\frac{l_1}{l_2}\right) - u_C + u_E\right] + F_g = k_t (u - u_E) \tag{24}$$

The force displacement of the GSA is related to the total displacement of point E and is given for positive displacements from equation (25):

$$F_g = \begin{cases} k_{g1}u_E, & 0 \le u_E \le d_{gap} \\ k_{g1}d_{gap} + k_{g2}\left(u_E - d_{gap}\right) & u_E > d_{gap} \end{cases} \tag{25}$$

Then the total NSD force is given from:

$$F_{NSD} = F_{Cx} + F_g \tag{26}$$

Equations (22)-(26) together with the help of (21) and (4) are a system of 5 nonlinear equations on 5 unknowns which are collected in the following vector $\mathbf{x} = \lfloor F_{Cx} \quad F_g \quad F_{NSD} \quad u_C \quad u_{fE} \rfloor^T$. Then similarly to the hysteresis derivations, all equations are brought on the left hand side, written at step $n+1$ and iterate based on equation (19).

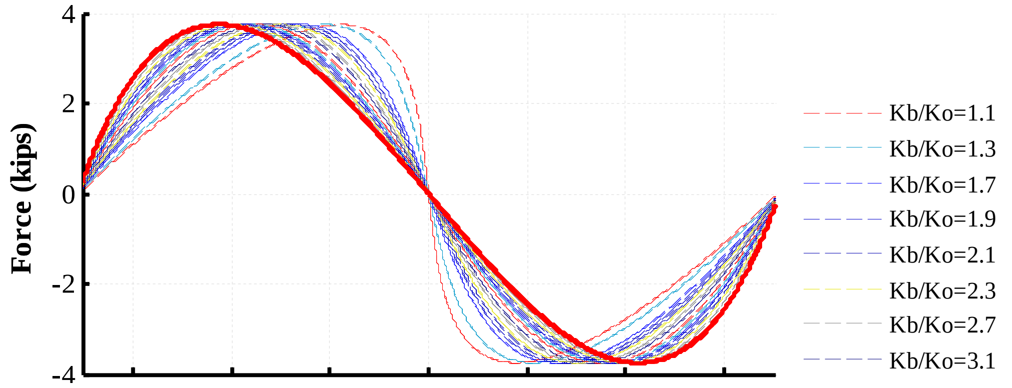

a) Force Displacement of NSD without Gap Spring Assembly

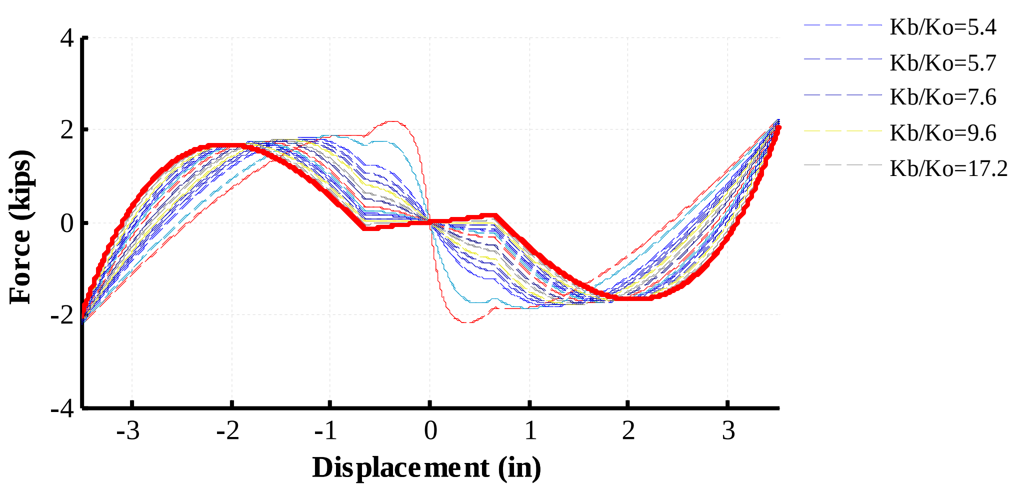

b) Force Displacement of NSD with Gap Spring Assembly

Figure 14: NSD force displacement loops assuming rigid top frame and flexible bottom supporting frame for various stiffness values of the bottom supporting frame

It is noted, that the flexibility of the bottom frame is equivalent to arranging a negative spring in series with a positive spring. Figure 14 shows the results assuming the top frame is rigid and considering various stiffness values for the bottom supporting frame. Legend values are given as ratios of the stiffness of the bottom supporting frame to the Negative NSD stiffness at zero displacement. Flexibility of the bottom frame leads to increased negative stiffness generated by the NSD while the peak force is unchanged and therefore stiffening of the NSD occurs faster than if the bottom frame was rigid. An additional effect of increasing the Negative Stiffness is the fact the gap spring assembly becomes ineffective since the imposed NSD displacements together with the NSD force becomes inconsistent as shown in Figure 14b.

Results assuming a rigid bottom frame and a flexible top frame are shown in Figure 15a. Due to this flexibility, this case affects the results only when the gap spring assembly is present since point E cannot follow the imposed NSD displacement. This is obvious in Figure 15b which is the force versus NSD imposed displacement of the gap spring assembly.

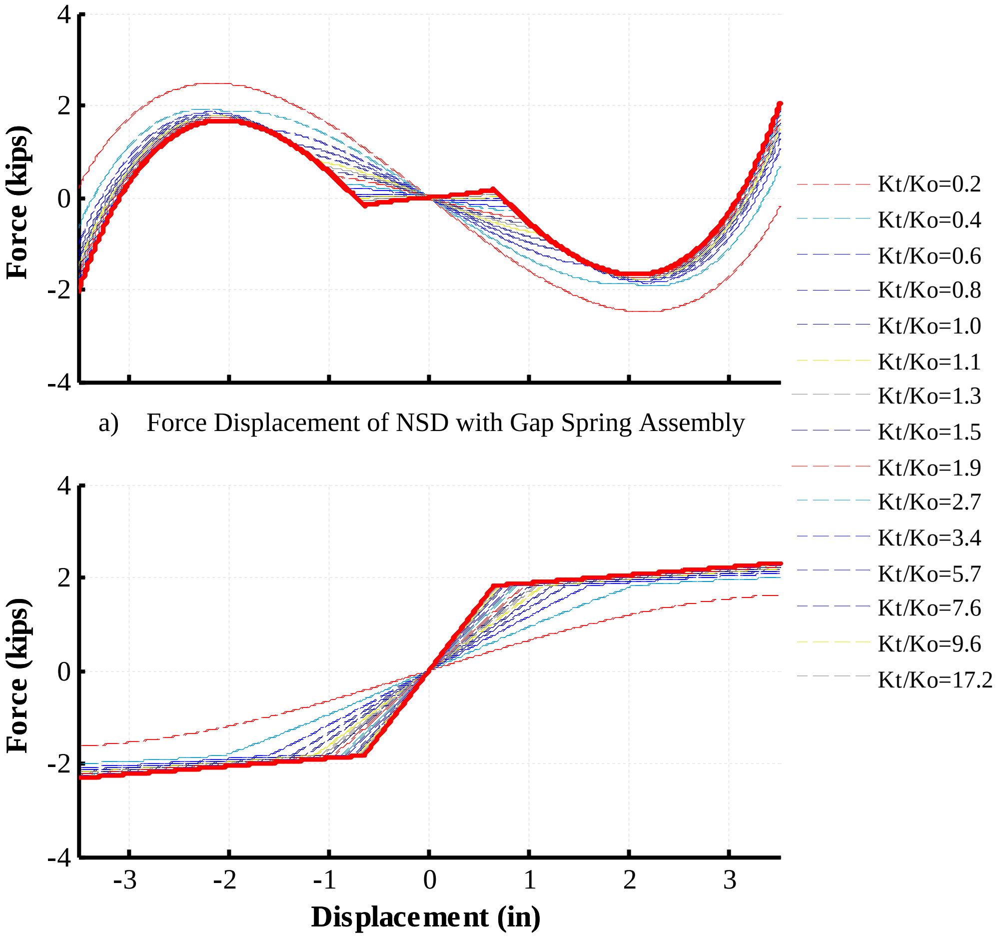

a) Force Displacement of NSD with Gap Spring Assembly

b) Force Displacement of NSD with Gap Spring Assembly

Figure 15: NSD and Gap Spring Assembly force displacement loops assuming rigid bottom and flexible top supporting frame for various stiffness values of the top supporting frame

7 EXPERIMENTAL RESULTS

Results from the experimental study conducted at UB are presented here for the displacement controlled tests. These results are only a minor portion of the complete experimental program. Complete details, additional analytical derivations and results are presented in [5 and 6]. Figure 16 shows the NSD force displacement loops obtained for displacement controlled tests conducted at *0.02Hz* as well as comparisons of the forces obtained from the elastomeric bearings, the NSD's and the total base shear. Installing the Negative stiffness device indeed reduces the total base shear and generates a "negative force" if one compares the red line with the blue line. The blue line represents what the base shear would have been in the absence of the NSD.

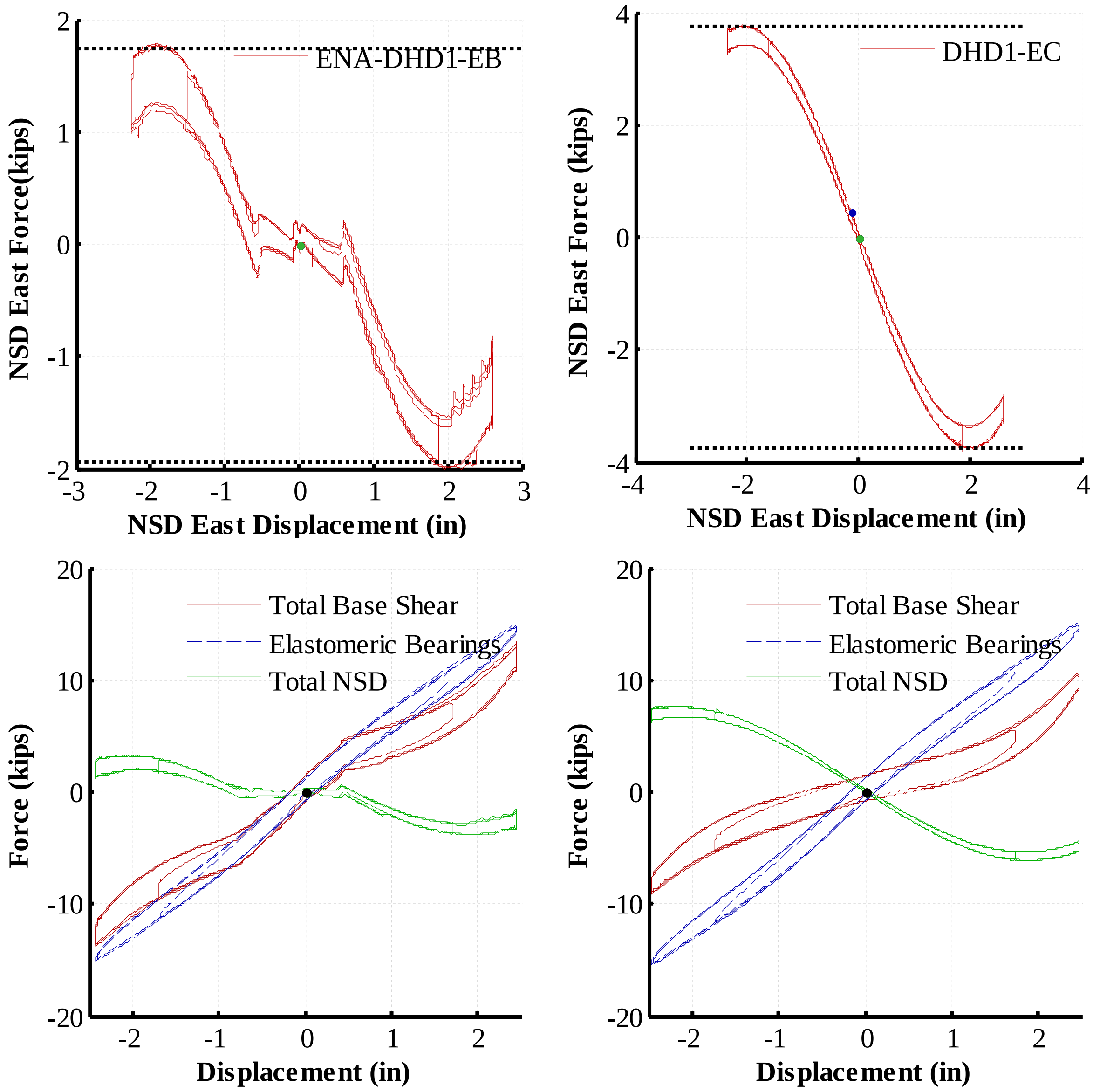

a) With Gap Spring Assembly b) Without Gap Spring Assembly

Figure 16: Experimental Results from Displacement Controlled Tests of NSD

Figure 17 shows the results obtained from Krypton for the most significant points of the NSD. As expected, point A which is the displacement imposed on the NSD, point B and point E have approximately equal displacements while point D is double in magnitude and opposite in sign from the displacement of point B. All displacements below are given as the relative displacements between their absolute displacements and the displacement of the shake table.

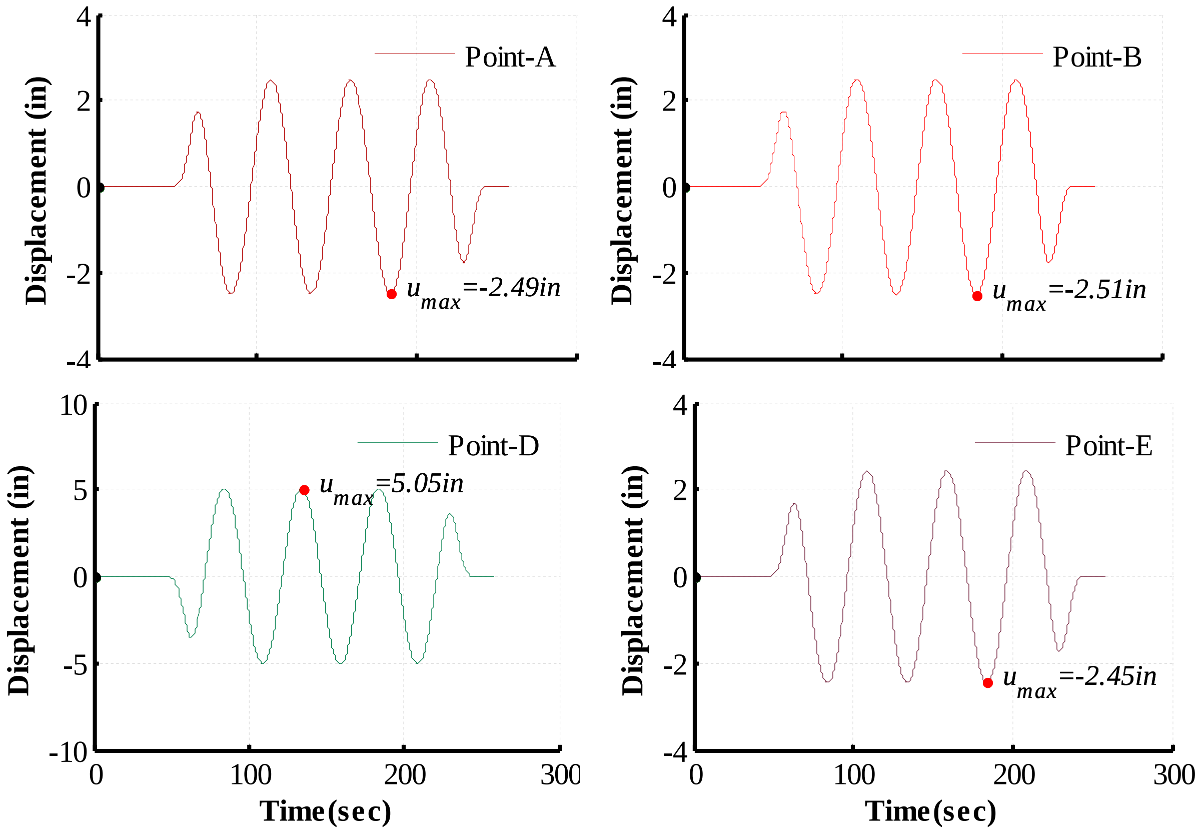

Figure 17: Experimental results from Krypton data acquisition system for displacement controlled tests

8 VERIFICATION OF ANALYTICAL EQUATIONS AND COMPUTATIONAL MODELS

Figure 18 compares all the analytical results described earlier with the results obtained from the experiments. With the exception of the dynamic model comparisons, all other results are shown for static tests conducted at *0.02Hz* frequency. Analytical results are plotted for the nominal properties of table 1 in order to demonstrate the additional advantage that the NSD exhibits of small variability of its properties. The absence of friction elements and the absolute dependence of the NSD behavior on the pre-loaded spring and geometry make the NSD behavior to be predictable at the design level. Note that inclusion of the flexibilities of the top frame explains the smaller stiffness in the gap spring assembly active region- observed in the experimental results- the dynamics explain the higher “negative force observed during the high frequency tests while the hysteretic element accurately follows the hysteresis trend observed in experiments. Based on these comparisons one can though conclude that the basic analytical equations derived in section 3 are sufficient for accurately capturing the NSD behavior assuming proper design was followed.

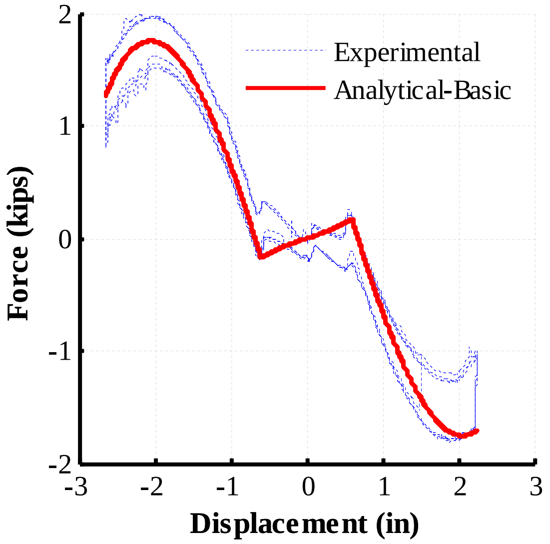
Experimental
Analytical-Basic
Force (kips)
Displacement (in)
2
1
0
-1
-2
-3
-2
-1
0
1
2
3

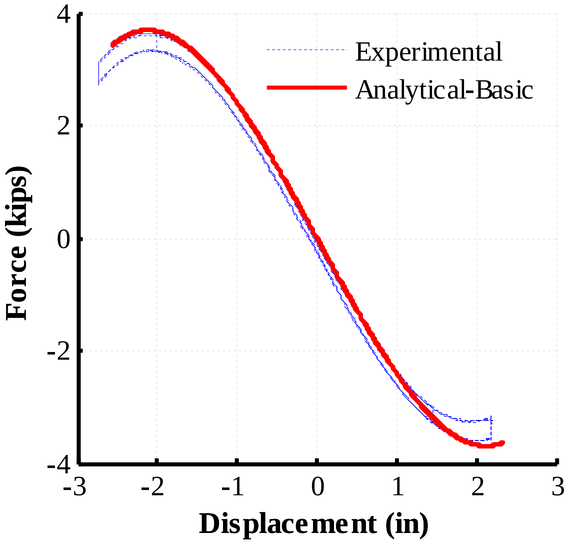
Experimental
Analytical-Basic
Force (kips)
Displacement (in)
4
2
0
-2
-4
-3
-2
-1
0
1
2
3

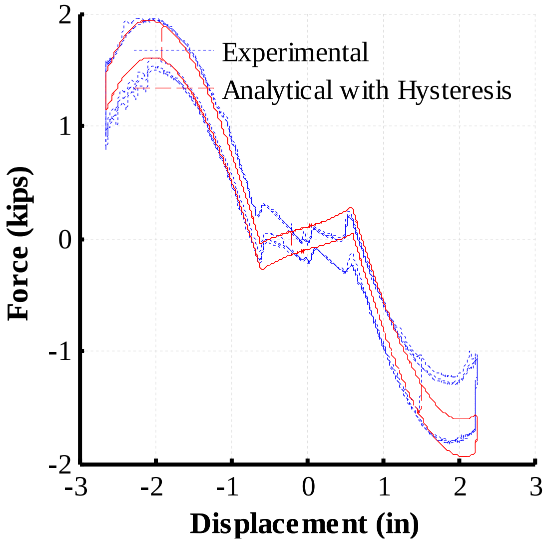
Experimental
Analytical with Hysteresis
Force (kips)
Displacement (in)
2
1
0
-1
-2
-3
-2
-1
0
1
2
3

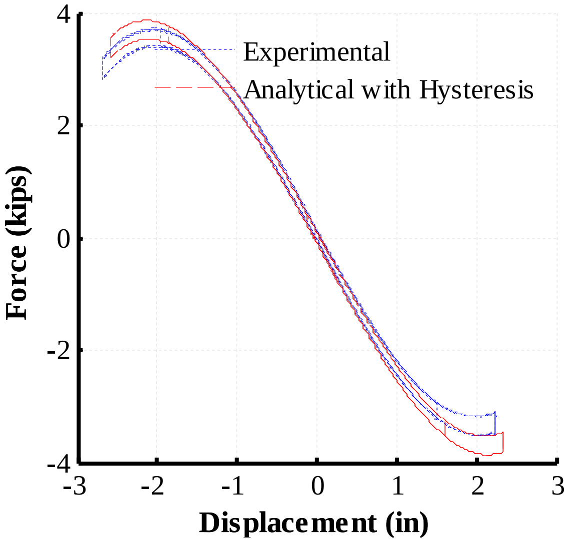
Experimental
Analytical with Hysteresis
Force (kips)
Displacement (in)
4
2
0
-2
-4
-3
-2
-1
0
1
2
3

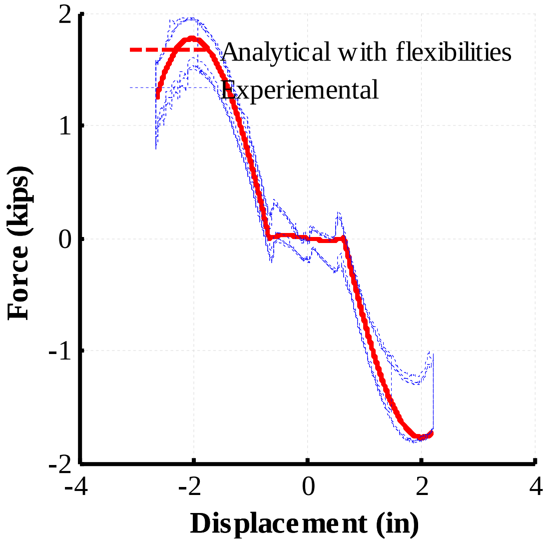
Analytical with flexibilities
Experiemental
Force (kips)
Displacement (in)
2
1
0
-1
-2
-4
-2
0
2
4

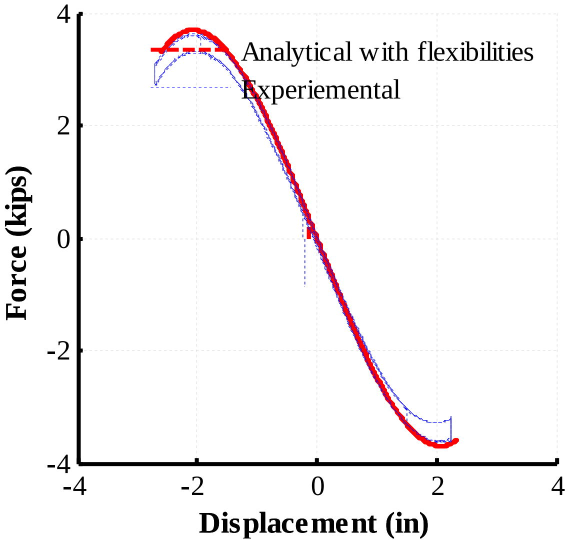
Analytical with flexibilities
Experiemental
Force (kips)
Displacement (in)
4
2
0
-2
-4
-4
-2
0
2
4

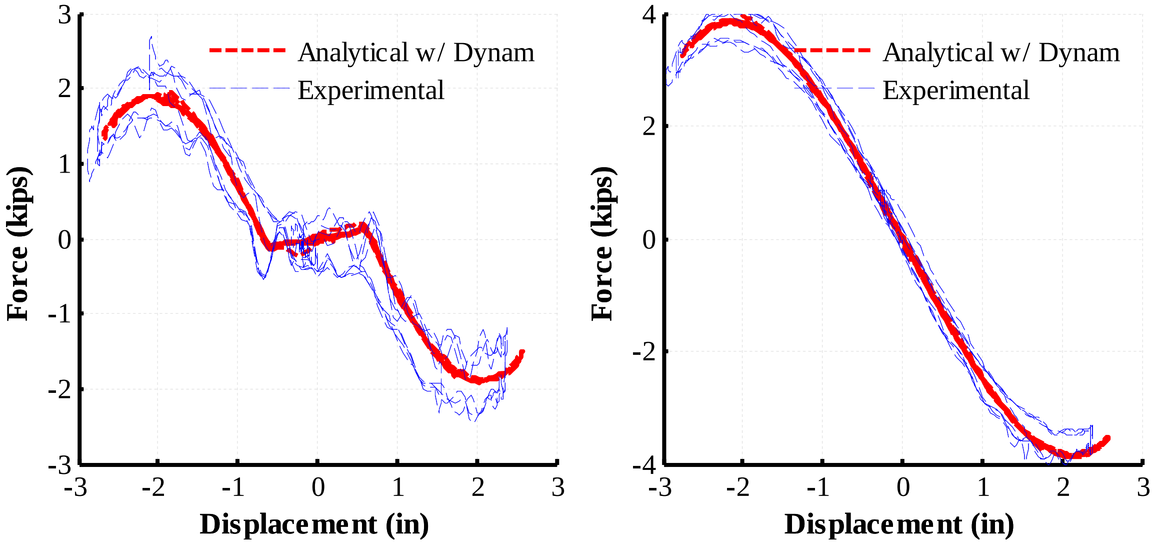

Figure 18: Verification of analytical derivations

9 CONCLUSIONS

Based on the material presented above the following may be concluded:

- A novel Negative Stiffness Device (NSD) has been developed. Proof of concept testing was performed at the NEES facility at the University at Buffalo. The NSD was shown to generate negative stiffness and reduce the base shear of a structure.
- Installing a Negative Stiffness Device is an efficient method of reducing the "apparent strength/stiffness" of a structure’s floor/story without affecting the vertical stiffness or stability limits of the structure.
- NSD operates with only minor energy dissipation and can be considered to be nonlinear "elastic". Any minor permanent deformations that the NSD might exhibit are eliminated by the gap-spring assembly.
- Basic NSD properties that determine its behavior are adjustable and therefore the NSD can generate a wide range of behaviors by simple adjustments that can be performed even after the installation of the device.
- NSD generates reliable and predictable behavior which can be accurately predicted. This is due to the mechanical nature of the device, consisting of links and springs of well known geometry and of predictable mechanical properties. Note that the comparisons of the analytical versus experimental results are done using the nominal spring properties in order to specifically demonstrate this advantage. No testing was conducted on the individual components (springs).
- Although the NSD behavior might be affected by many factors, the influence of those factors is minor. The NSD behavior can be very accurately predicted by the equations of section 3 and modeling of section 4. Additional complex derivations presented herein help in obtaining understanding of the complete mechanics of the system and provide the designer with additional confidence in using the NSD in practical applications.
- Complete details on the experimental program as well as further analytical and computational work will be enclosed in [5] and [6].

REFERENCES

[1] Reinhorn A.M., Viti S., and Cimellaro G.P. (2005), "Retrofit of Structures: Strength Reduction with damping enhancement.", Proceeding of the 37th UJNR Panel Meeting on Wind and Seismic Effects, Tsukuba, Japan.

[2] Viti S., Cimellaro G. P., and Reinhorn A. M. (2006), Retrofit of a Hospital through Strength Reduction and Enhanced Damping. Smart Structures and Systems, 2(4), 339-355.

[3] Nagarajaiah S., Reinhorn A. M., Constantinou M. C., Taylor D., Pasala, D. T. R. and Sarlis, A. A. (2010), "True Adaptive Negative Stiffness: A New Structural Modification Approach for Seismic Protection". 5th World Conference on Structural Control and Monitoring, Tokyo, Japan, July 12-14.

[4] Iemura H. and Pradono M.H. (2009), "Advances in the development of pseudo-negative-stiffness dampers for seismic response control," Structural Control and Health Monitoring, 16(7-8), 1545-2255.

[5] Sarlis A.A., Constantinou M.C, Reinhorn A.M, Pasala, D.T.R, Nagarajaiah S. and Taylor D. (2011), "Negative Stiffness Device- Part 1: Analytical Framework and Experimental Validation" - MCEER-11-XXXX, Multidisciplinary Center for Earthquake Engineering Research, Buffalo, NY.

[6] Sarlis A.A., Constantinou M.C, Reinhorn A.M, Pasala, D.T.R, Nagarajaiah S. and Taylor D. (2011) , Negative Stiffness Device- Part 2: Shake table testing and Proof of Negative Stiffness Concept" MCEER-11-XXXX, Multidisciplinary Center for Earthquake Engineering Research, Buffalo, NY.

[7] Molyneaux W. G. (1957), "Supports for vibration isolation", ARC/CP-322, Aeronautical Research Council, Great Britain.

[8] Platus D.L., Negative-stiffness-mechanism vibration isolation systems, Proceedings of SPIE—The International Society for Optical Engineering, Vibration Control in Microelectronics, Optics, and Metrology, San Jose, CA, USA, Vol. 1619, 1992, pp. 44–54.

[9] Platus D.L., Negative-stiffness-mechanism vibration isolation systems, Proceedings of the Opto-mechanical Engineering and Vibration Control Conference, SPIE—The International Society for Optical Engineering, Denver, CO, USA, Vol. 3786, 1999, pp. 98–105.

[10] Platus D.L. (1993), "Vibration Isolation System", US Patent No. 5178357, Washington DC: US Patent and Trademark Office.

[11] Platus D.L. (1994), "Vibration Isolation System", US Patent No. 5310157, Washington DC: US Patent and Trademark Office.

[12] Platus D.L. (1994), "Damped Vibration Isolation System", US Patent No. 5370352, Washington DC: US Patent and Trademark Office.

[13] Platus D.L. (1995), "Vibration Isolation System", US Patent No. 5390892, Washington DC: US Patent and Trademark Office.

[14] Platus D.L. and Cunningham P. J (1996), "Vibration Isolation System", US Patent No. 5549270, Washington DC: US Patent and Trademark Office.

[15] Platus D.L. and Durran D.A (1997), “Vibration Isolation System”, US Patent No. 5669594, Washington DC: US Patent and Trademark Office.

[16] Platus D.L. (2004), “Vibration Isolation System”, US Patent No. 6676101B2, Washington DC: US Patent and Trademark Office.

[17] Carrella A., Brennan M.J., Waters T.P. and Shin K. (2008) On the design of a high-static-low-dynamic stiffness isolator using linear mechanical springs and magnets, Journal of Sound and Vibration, 315(3), 712-720

[18] Lee C. M., V. Goverdovskiy and A. Temnikov (2007), “Design of springs with ‘negative’ stiffness to improve vehicle driver vibration isolation”, Journal of Sound and Vibration 302 (4-5) (2007) 865–874. URL http://dx.doi.org/10.1016/j.jsv.2006.12.024

[19] H. Iemura, O. Kouchiyama, A. Toyooka and I. Shimoda (2008). “Development of the Friction-Based Passive Negative Stiffness Damper and its Verification Tests using Shaking Table”.The 14th World Conference on Earthquake Engineering, October 12-17, 2008, Beijing, China

[20] Wolff E.D. and Constantinou M.C. (2004). “Experimental Study of Seismic Isolation Systems with Emphasis on Secondary System Response and Verification of Accuracy of Dynamic Response History Analysis Methods”, Technical Report MCEER-04-0001, Multidisciplinary Center for Earthquake Engineering Research, State University of New York at Buffalo, Buffalo, NY, USA.

[21] Kasalanati A. and Constantinou M.C. (1999). “Experimental Study of Bridge Elastomeric and Other Isolation and Energy Dissipation Systems with Emphasis on Uplift Prevention and High Velocity Near Source Seismic Excitation”, Technical Report MCEER-99-0004, Multidisciplinary Center for Earthquake Engineering Research, State University of New York at Buffalo, Buffalo, NY, USA

[22] Bracci J.M., Reinhorn A.M. and Mander J.B. (1992). “ Seismic Resistance of Reinforced Concrete Frame Structures Designed Only for Gravity Loads: Part I- Design and Properties of a One- Third Scale Model Structure”, Technical Report NCEER-92-0027, National Center for Earthquake Engineering Research, State University of New York at Buffalo, Buffalo, NY, USA

[23] Structural Engineering and Earthquake Simulation Laboratory (2004). “Laboratory Manual” SEESL, Buffalo, NY USA. Available online: htto://nees.buffalo.edu/docs/labmanual/html/

[24] Computers and Structures Inc. (2007).”SAP2000: Static and Dynamic Finite Element Analysis of Structures (Version 11.0.2) Analysis Reference Manual”, Computers and Structures, Inc., Berkeley

[25] Sivaselvan M.V. and Reinhorn A.M. (2001). “Hysteretic Models for Deteriorating Inelastic Structures”, ASCE Journal of Structural Engineering, 126(6) 633-640.

COMPDYN 2011
3rd ECCOMAS Thematic Conference on
Computational Methods in Structural Dynamics and Earthquake Engineering
M. Papadrakakis, M. Fragiadakis, V. Plevris (eds.)
Corfu, Greece, 25–28 May 2011

SEISMIC VIBRATION CONTROL OF IZADKHAST BRIDGE USING VISCOUS DAMPERS

H.R. Anajafi[1], A.K. Ghorbani-Tanha[1], and M. Rahimian[1]

[1] School of Civil Engineering, University of Tehran
P.O. Box 11155-4563, Tehran, Iran
e-mail: hra22_anajafi@yahoo.com, {ghtanha, rahimian}@ut.ac.ir

Keywords: Vibration control, Izadkhast Bridge, Viscous damper, Passive control, Earthquake

Abstract. *Present study addresses the effectiveness of viscous dampers (VDs) in reducing the response of Izadkhast Bridge under earthquake ground motions. With the length of 485 m, Izadkhast Bridge is the longest box girder bridge in Iran and is located in Isfahan-Shiraz railway. The bridge is installed with VDs at the two ends. The Finite element model of the bridge is developed. Five pairs of representative earthquake records are selected and scaled using the earthquake code and applied to the model. Nonlinear seismic analyses of the structure without and with VD's are performed and the results are reported. Comparison of the results clarifies VD's effectiveness on seismic response reduction of the bridge. Sensitivity analyses are performed to demonstrate the effects of damper parameters on structural response.*

1 INTRODUCTION

The basic function of passive energy dissipation devices when added to a structure is to absorb and dissipate a portion of the input energy, thereby reducing energy dissipation demand on primary structural members and minimizing possible structural damage. Serious efforts have been devoted to the development and utilization of passive energy dissipation devices [1]. Viscous dampers (VD's) are a kind of these devices which significant efforts have been directed toward their application for structural vibration control. In VDs, energy dissipation occurs via conversion of mechanical energy to heat as a piston deforms a thick, highly viscous substance [1]. In present study, the effectiveness of VD's on response reduction of Izadkhast Bridge under earthquake ground motions is investigated.

With the length of 485 m, Izadkhast Bridge is the longest box girder bridge in Iran. This bridge is located in the central part of Iran, spanning Izadkhast valley on the railway line between Isfahan and Shiraz. The bridge is composed of five 77 m spans in the middle, two side spans having the length of 20 m and 40 m, six piers and two abutments, as shown in Fig. 1. The cross section of piers is shown in Fig. 2. With the width of 6.6 m, the deck is composed of two 4.5 m high box girders (Fig. 3). Seismic considerations were considered in the design of the bridge due to its location. The bridge is equipped with four 100 t VDs (stroke 25 cm) longitudinally directed at both ends (Fig. 4). According to the manufacturer catalogs and design documents, the governing equation of the dampers is $f = cv^{\alpha}$, where f is force, c is the damping coefficient, v is the velocity, and α = 0.15 [2, 3]. Four 21.9×80×80 cm rubber bearings are placed at the top of each pier and two 35.7×80×80 cm rubber bearings at the top of each abutment (Fig. 5).

The Finite element model of the bridge is developed. Five pairs of representative earthquake records are selected and scaled using earthquake code and applied to the model. Nonlinear seismic analyses of the structure without and with VD's are performed and the results are reported. Comparison of the results clarifies VD's effectiveness on seismic response reduction of the structures.

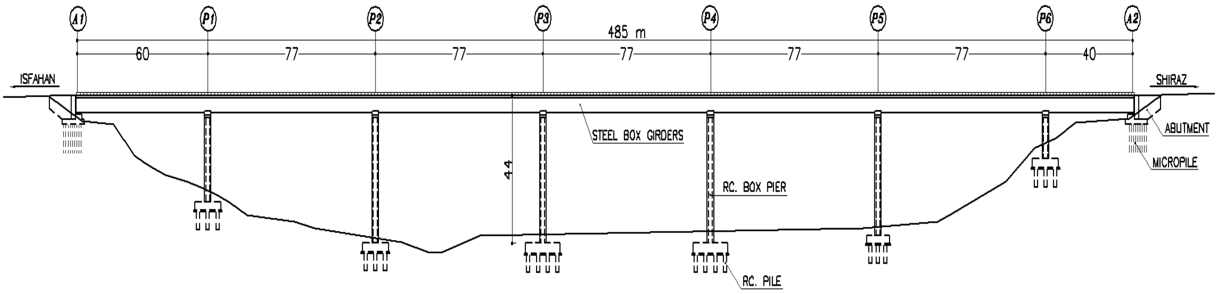

Figure 1: Izadkhast Bridge [2]

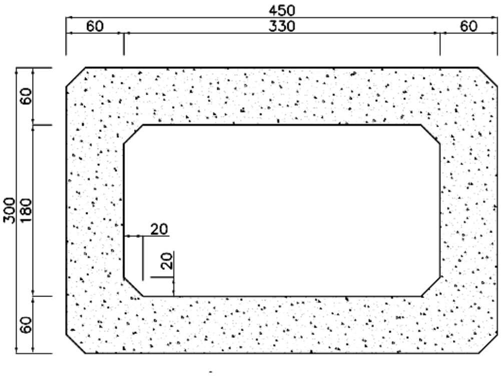

Figure 2: Cross section of piers [2]

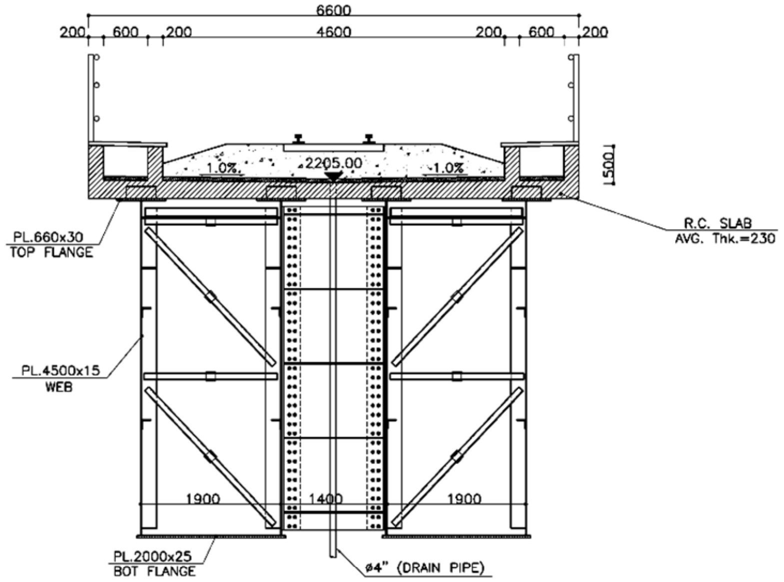

Figure 3: Cross section of bridge deck [2]

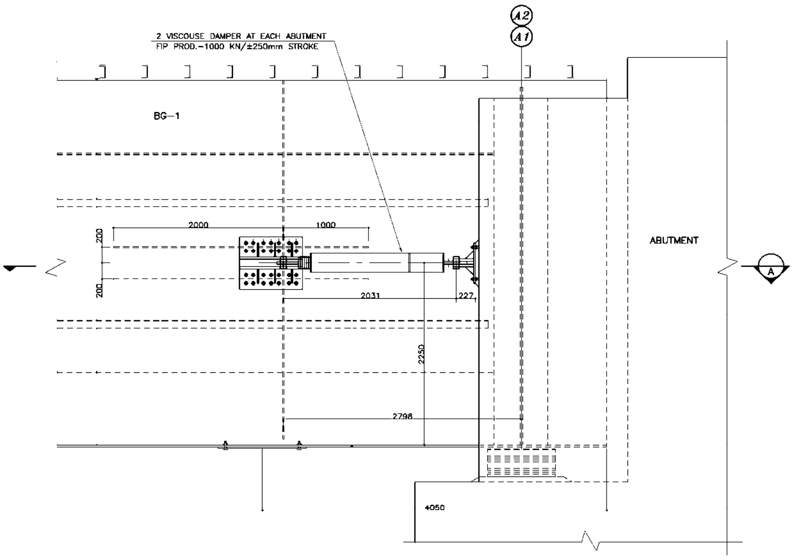

(a)

Figure 4: VDs placement [2]

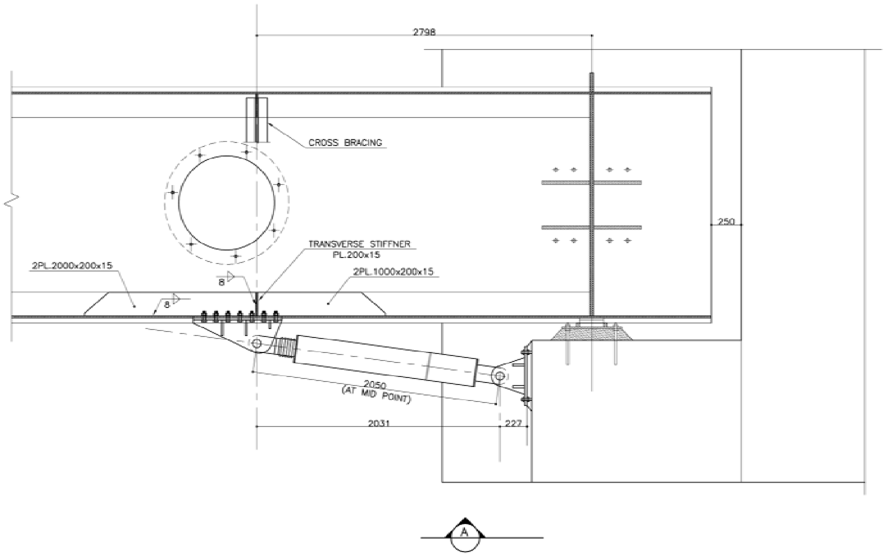

(b)

Figure 4: VDs placement [2]

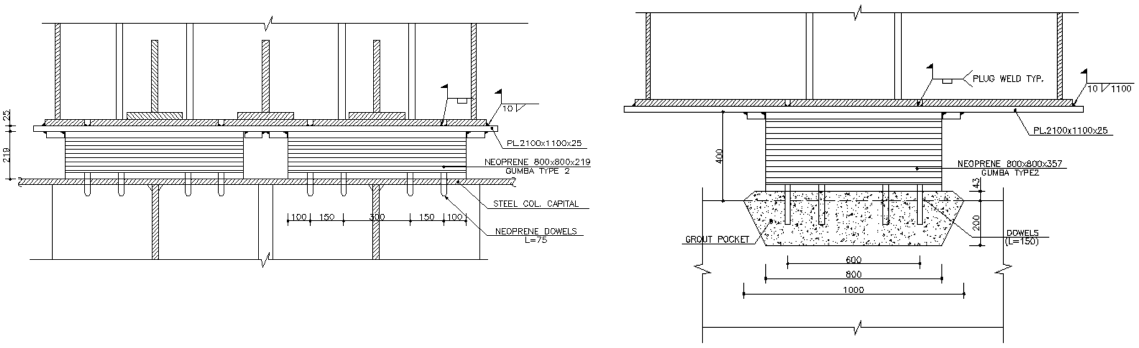

(a) (b)

Figure 5: Details of rubber bearings (a) at the top of piers, (b) at the top of abutments [2]

2 MODELLING AND ANALYSES

2.1 Finite element model of the bridge

A finite element model of the bridge is developed in PERFORM-3D [4]. Constraints are applied to restrict the deck from moving horizontally at Piers 2, 3, 4, and 5 and laterally at all piers. According to Caltrans [5], the displacement capacity of the rubber bearings are calculated as following

$$V_x = \mathrm{tg}\gamma\, T \tag{1a}$$

$$\frac{T}{a} \le 0.2\ : tg\gamma = 0.7 \quad ; \quad \frac{T}{a} \ge 0.2\ : tg\gamma = 0.9 - \frac{T}{a} \tag{2b}$$

where *T* is the effective thickness of the rubber bearing which according to the manufacturer catalogs is 14.4 cm for piers and 25.2 cm for abutments; and *a* is the minimum dimension of the cross section of rubber bearings. Under seismic loading, an increase of 50% should be applied to displacement capacity. As a result, the displacement capacity for the abutment bearings is 22 cm while this value for the pier bearings is 15 cm. The rubber bearing are modeled as non-linear springs whose initial stiffness are $k_s = GA/T$, where G is shear modulus, A is the area and T is the effective thickness of bearings. This leads to $k_s = 43600$ N/cm for piers and $k_s = 24914$ N/cm for abutments. An increase of 50% to the stiffness should be applied for seismic loading. For the definition of plastic hinge in piers, the famous available models are employed. The length of plastic hinge, Priestley relation is used [6]

$$L_p = 0.08L + 0.0022 f_y d_b \quad \text{(MPa)} \tag{2}$$

where L_p is the distance between critical section and inflection point of the member; d_b is the diameter of longitudinal bars and f_y is the yield stress.

According to design documents, the expansion joint between deck and abutments has a width of 25 cm which is taken into account in the model. If the longitudinal displacement of the deck is greater than this value, the deck knocks the abutments.

2.2 Earthquake records used

For the excitation of the bridge, five pairs of earthquake records are chosen (Table 1). These records are scaled according to UBC [7] and then applied to the structure.

Table 1: Earthquake records used

No.	Record Name	Date	PGA(g)
1	IZMIT 1	17/8/1999	0.2195
2	IZMIT 2	17/8/1999	0.1521
3	ELCENTRO 1	19/5/1940	0.2148
4	ELCENTRO 2	19/5/1940	0.3129
5	K0BE 1	16/1/1995	0.5985
6	K0BE 2	16/1/1995	0.8213
7	NORTHRIDGE 1	17/1/1994	0.493
8	NORTHRIDGE 2	17/1/1994	0.8283
9	SAN FRANCISCO 1	18/10/1989	0.056
10	SAN FRANCISCO 2	18/10/1989	0.105

3 RESULTS

3.1 Uncontrolled bridge

Dynamic analyses of the bridge without VD under scaled earthquake time histories are conducted. The first natural period of the bridge is 2.5 sec. The results show that the maximum longitudinal displacement of the deck occurs under scaled Izmit earthquake (PGA=0.546g) which is 51 cm. The time history of the longitudinal displacement response is shown in Fig. 6. The moment-curvature diagram for pier P6 is shown in Fig. 7. It is clear that the piers will exhibit nonlinear behavior. Fig. 8 shows the energy response of the bridge. A significant portion of the energy input to the structure is dissipated with both inelastic hysteretic mechanisms and viscous damping. In this case, the expansion joint will be closed and the deck will knock the abutments which can cause serious damages.

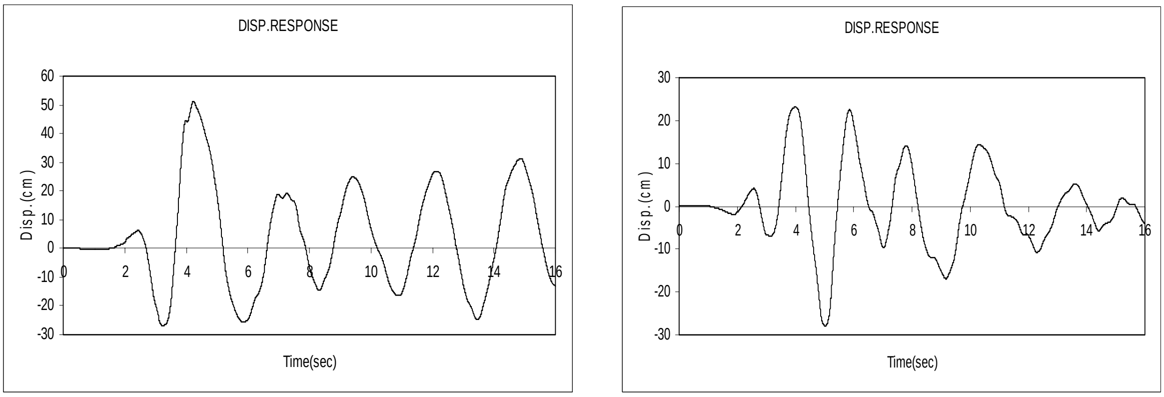

Figure 6: Longitudinal displacement response of the uncontrolled bridge under Izmit earthquake records

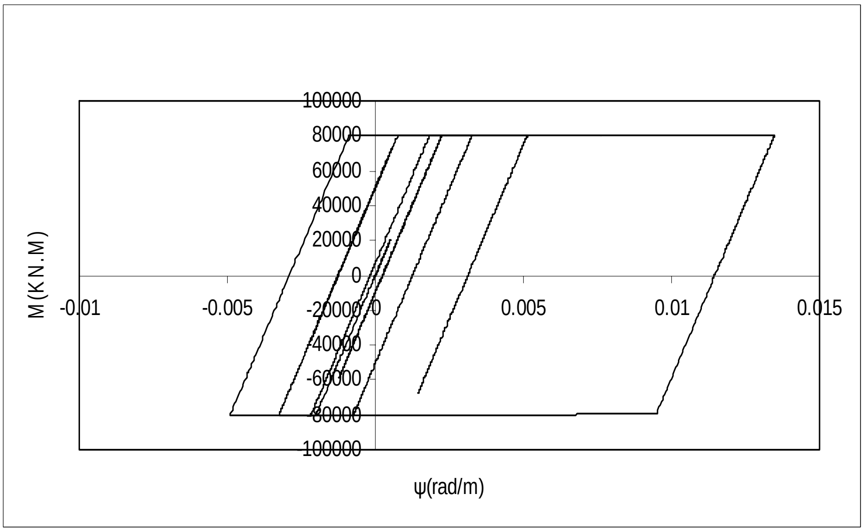

Figure 7: Moment-curvature diagram for pier P6 (shortest pier with the height of 11.9 m) for the uncontrolled bridge

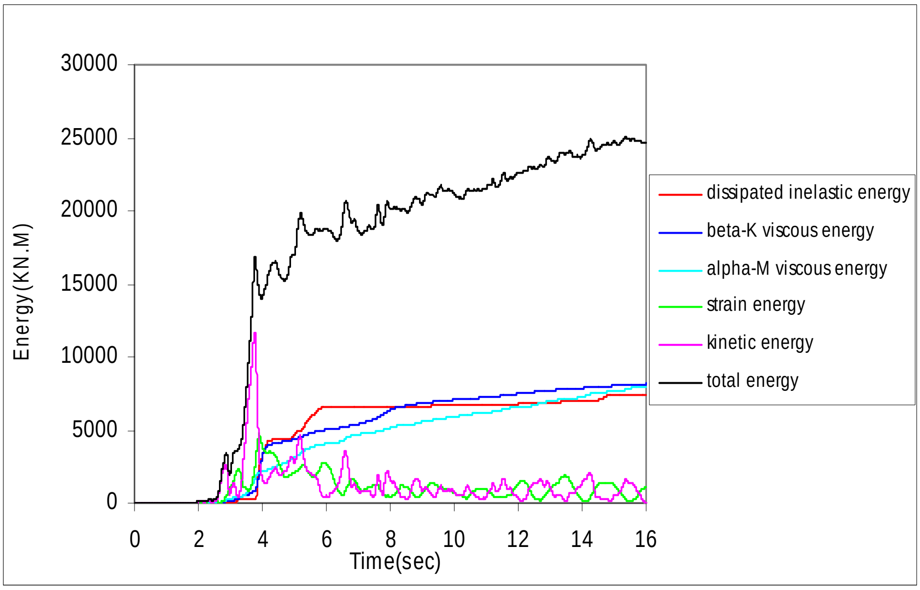

Figure 8: Energy response of the bridge under scaled Izmit earthquake

3.2 Controlled bridge

As mentioned before, the bridge is equipped with four 100 t VDs at both ends. Dynamic time-history analyses of the controlled bridge show that the maximum displacement of the bridge reduces to 38 cm but it is still greater than the width of expansion joint and the deck knocks the abutments (Fig. 9). However, a significant portion of the energy input is absorbed and dissipated by the dampers which reduces the nonlinear deformation of the structure. The moment-curvature diagram for pier P6 is shown in Fig. 10.

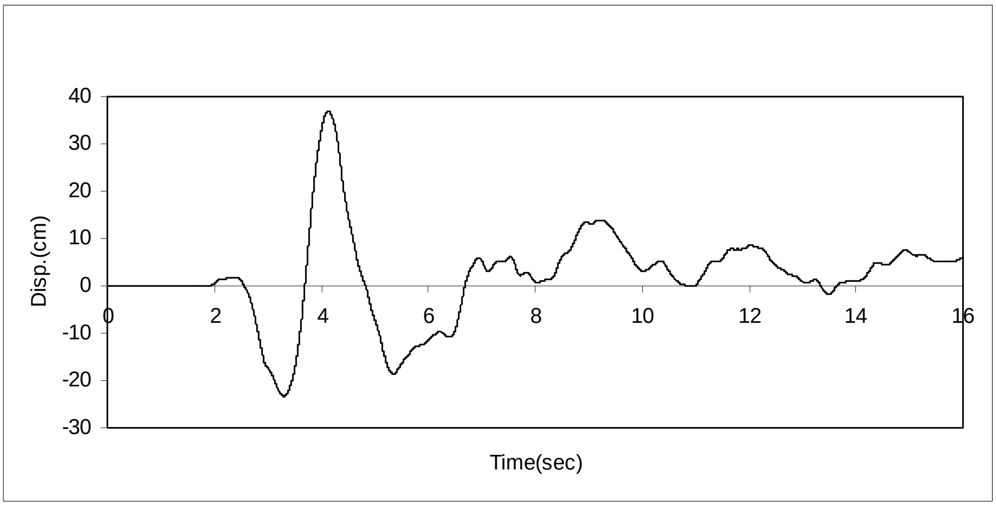

Figure 9: Longitudinal displacement response of the bridge fitted with four 100 t VDs under Izmit earthquake

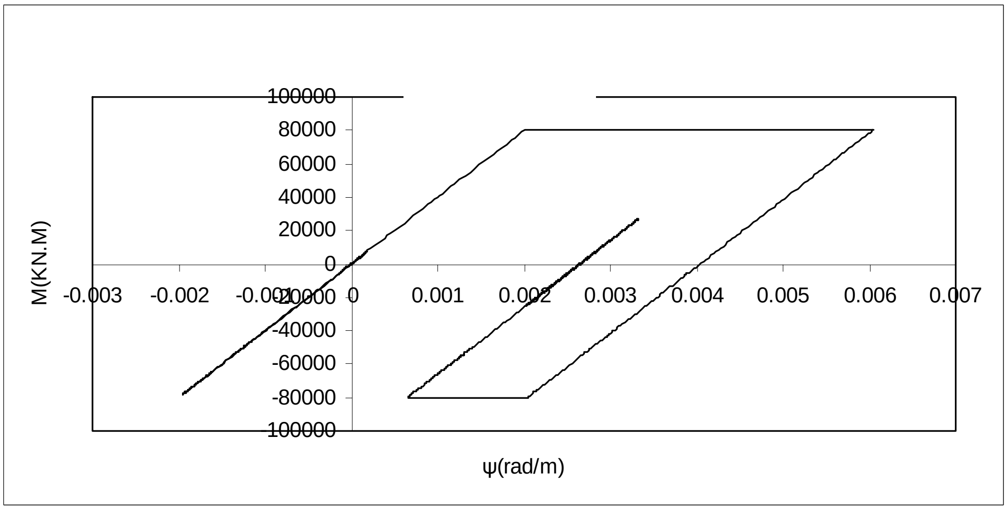

Figure 10: Moment-curvature diagram for pier P6 for the case that the bridge is equipped with four 100 t VDs

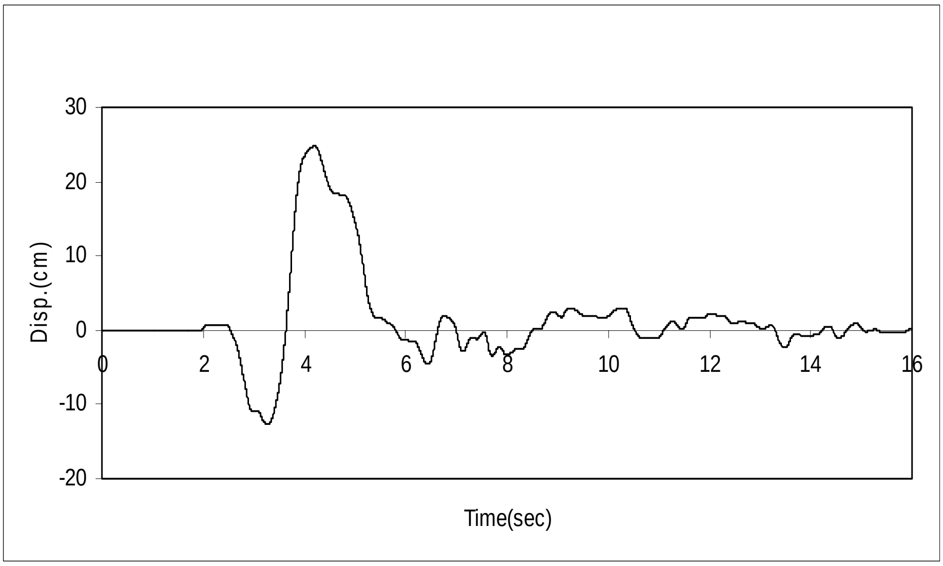

Figure 11: Longitudinal displacement response of the bridge fitted with four 250 t VDs under Izmit earthquake

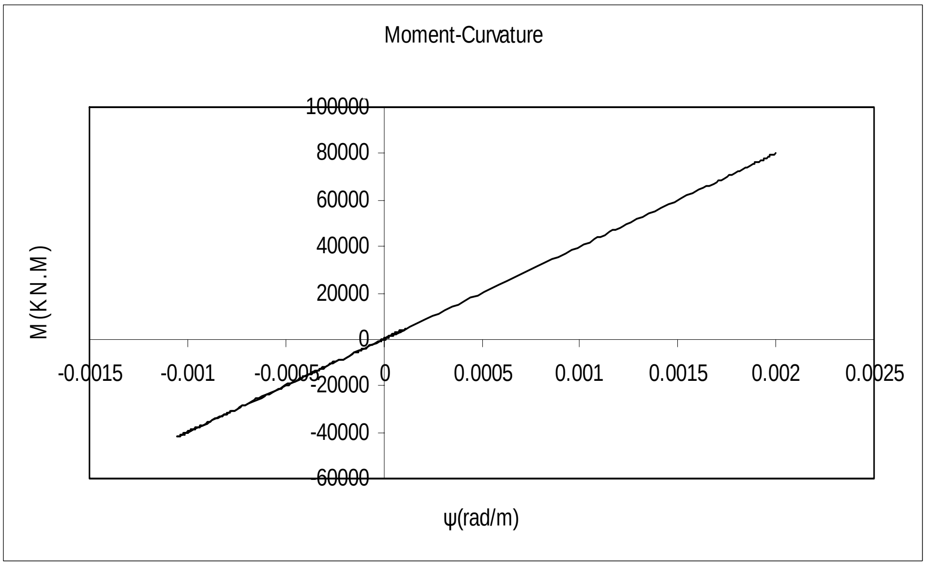

Figure 12: Moment-curvature diagram for pier P6 for the case that the bridge is equipped with four 250 t VDs

Proper VDs will prevent structural damages and does not let the deck knock the abutments. A trial and error procedure employed and finally it was concluded that if 100 t dampers are replaced by 250 t dampers, then the maximum longitudinal displacement reduces to 24 cm and piers will remain elastic (Figs. 11 and 12). These dampers are more expensive and off course apply higher values of reaction forces to the abutments which should be taken into consideration in design procedure.

4 SUMMARY AND CONCLUSIONS

- The inclusion of VDs enhances the seismic behavior of the bridge and the dampers dissipate a significant portion of the energy input to the bridge. This reduces the hysteretic energy dissipated by the sub-structural members and decreases damage to the structure and is favorable for earthquake resistant design.

- For the case that the bridge is fitted by 100 t VDs, the maximum longitudinal displacement under design earthquake is 38 cm which is more than the displacement capacity of the damper and expansion joint width and the deck knocks the abutments.
- To overcome the above-mentioned problems and improve aseismic performance of the bridge, 250 t dampers are recommended to be used. In this case the maximum displacement reduces to 24 cm.

ACKNOWLEDGEMENT

The authors are grateful to Tazand Co. for providing them with the bridge design documents and data.

REFERENCES

[1] T.T. Soong, G.F. Dargush, *Passive energy dissipation systems in structural engineering*, John Wiley & Sons, 1997

[2] Tazand Consulting Engineers, Design documents of Izadkhast Bridge, 2006 (In persian).

[3] http://www.fip-group.it

[4] CSI PERFORM-3D, V4.0.1, Computers and Structures Inc, Berkeley, California, Release 2006, Components and Elements.

[5] Caltrans, Seismic Design Criteria, V1.4, June 2006.

[6] T. Paulay, M.J.N. Priestley, *Seismic design of reinforced concrete and masonry buildings*, John Wiley & Sons, 1992.

[7] Unified Building Code, 2006.

COMPDYN 2011
III ECCOMAS Thematic Conference on
Computational Methods In Structural Dynamics and Earthquake Engineering
M. Papadrakakis, M. Fragiadakis, V. Prevris (eds.)
Corfu, Greece, 25-28 May 2011

MATHEMATICAL MODELING OF IRREVERSIBLE DEFORMING, MICRO- AND MACROFRACTURE OF ROCK IN THE VICINITY OF A BOREHOLE IN ITS DYNAMICAL UNLOADING

Alexey B. Kiselev and Pavel P. Zacharov

Mechanics and Mathematics Faculty of Moscow M.V. Lomonosov State University
Leninskie Gory, 1, MSU, Main Bldg, Moscow 119992, Russia
e-mail: akis@mech.math.msu.su

Key words: Computational Simulation, Damageable Thermoelastoviscoplastic Solids, Fracture

Abstract. *The rock formation at a depth of several thousand meters is exposed to a hydrostatic pressure. Drilling a borehole makes the drill experience same pressure from the walls of the borehole. On fast removing of the drill from the borehole the dynamical process of unloading borehole walls begins. The sharp decrease of normal pressure on the walls of the borehole brings to the increase of ring stresses. The waves of unloading propagate from the borehole, which could cause fragmentation of rock and blocking the borehole with fractured material. The goal of the present paper is to give the problem statement foe the dynamical process of unloading the internal walls of the borehole after removing the drill, and successive oil-bearing layer's fracturing. The layer is represented by the model of damageable thermoelastoplastic material with two parameters of damaging (by evolution of micropores and by shear microfracturing). The criterion of the beginning of new free surfaces within the material) uses the principle of the critical value of specific dissipated energy.The problem is treated as two-dimensional (plane deformed state). This task is solved numerical modeling on Lagrancian mesh by method similar to M.L. Wilkins one and on local reconstruction of the Lanrangian grid in the vicinity of the fracture origination.*

1 SETTING OF A PROBLEM

Description of process we will in cylindrical coordinate system which axis Oz is coincide with axis of a hole. Then all parameter of problem depend on space coordinate r, θ and the time t.

Write the mass, momentum and internal energy equations in cylindrical coordinate system r, θ:

$$\frac{\dot\rho}{\rho} = -\dot\varepsilon_r - \dot\varepsilon_\theta; \quad \rho\dot v_r = \frac{\partial\sigma_r}{\partial r} + \frac{1}{r}\frac{\partial\sigma_{r\theta}}{\partial\theta} + \frac{\sigma_r - \sigma_\theta}{r}, \quad \rho\dot v_\theta = \frac{\partial\sigma_{r\theta}}{\partial r} + \frac{1}{r}\frac{\partial\sigma_\theta}{\partial\theta} + 2\frac{\sigma_{r\theta}}{r}; \tag{1}$$

$$\rho c_\sigma \dot T + \alpha_v \dot\sigma T = S_r \dot\varepsilon_r^p + S_\theta \dot\varepsilon_\theta^p + S_z \dot\varepsilon_z^p + 2S_{r\theta}\dot\varepsilon_{r\theta}^p + A\dot\alpha^2 + \Lambda\dot\omega^2$$

Here and later point under symbol denote the material derivative with respect to time; ρ - density; v_r, v_θ - velocity components; σ_r, σ_θ, $\sigma_{r\theta}$ - stress tensor components (σ_θ – ring stress), which decompose on spherical $\sigma = (\sigma_r + \sigma_\theta + \sigma_z)/3$ and deviator parts $S_r, S_\theta, S_{r\theta} = \sigma_{r\theta}; S_r + S_z + S_\theta = 0;$ $\dot\varepsilon_r, \dot\varepsilon_\theta, \dot\varepsilon_{r\theta}$ - velocity strain tensor components; $\dot\varepsilon_r^p, \dot\varepsilon_\theta^p, \dot\varepsilon_z^p$, $\dot\varepsilon_{r\theta}^p$ - plastic components of velocity strain tensor; T - temperature; ω, α - scalar damage parameters; c_σ - is the heat conductivity at constant stress; α_v - is the coefficient of cubic expansion; Λ, A - constants of materials, connected with damage parameters ω and α; $\dot\varepsilon_r^p, \dot\varepsilon_\theta^p, \dot\varepsilon_z^p, \dot\varepsilon_{r\theta}^p$ - plastic components of velocity strain tensor; T - temperature; ω, α - scalar damage parameters of medium; c_σ - is the heat conductivity at constant stress; α_v - is the coefficient of cubic expansion; Λ, A - medium parameters connected thermal and damage processes.

Velocity strain tensor components are expressed over velocity components:

$$\dot\varepsilon_r = \frac{\partial v_r}{\partial r}, \quad \dot\varepsilon_\theta = \frac{1}{r}\frac{\partial v_\theta}{\partial\theta} + \frac{v_r}{r}, \quad \dot\varepsilon_{r\theta} = \frac{1}{2}\left(\frac{\partial v_\theta}{\partial r} + \frac{1}{r}\frac{\partial v_r}{\partial\theta} - \frac{v_\theta}{r}\right), \tag{2}$$

and decompose on elastic and plastic components:

$$\dot\varepsilon_r = \dot\varepsilon_r^e + \dot\varepsilon_r^p, \quad \dot\varepsilon_\theta = \dot\varepsilon_\theta^e + \dot\varepsilon_\theta^p, \quad \dot\varepsilon_{r\theta} = \dot\varepsilon_{r\theta}^e + \dot\varepsilon_{r\theta}^p, \quad \dot\varepsilon_z = \dot\varepsilon_z^e + \dot\varepsilon_z^p \equiv 0. \tag{3}$$

Plastic flow are incompressible: $\dot\varepsilon_r^p + \dot\varepsilon_\theta^p + \dot\varepsilon_z^p \equiv 0$.

The system of constitutive equation for a model of damageable thermoelastoviscoplastic medium is as follows [1-3]:

$$\begin{cases} \dot\sigma' = K_0\left(\dot\varepsilon_r + \dot\varepsilon_\theta - \alpha_v \dot T - \dfrac{\Lambda}{3}\dot\omega\dfrac{\partial\dot\omega}{\partial\sigma}\right) \\ \left(S'_{ij}\right)^\nabla + \lambda S'_{ij} = 2\mu_0 \dot e_{ij} - 2A\dot\alpha\dfrac{\partial\dot\alpha}{\partial S_{ij}} \\ S'_{ij}S'_{ij} \le \dfrac{2}{3}Y_0^2(\sigma) \\ Y_0 = c_1\sigma + c_2 \end{cases} . \tag{4}$$

Here symbol ∇ - Yaumann derivative of deviator components stress tensor; $\dot{e}_{ij}$ - deviator of velocity strain tensor; $\sigma' = \dfrac{\sigma}{(1-\omega)}$ $S'_{ij} = \dfrac{S_{ij}}{(1-\omega)(1-\alpha)}$; K_0 and μ_0 - volume and shear module for an undamaged material; ω_{ij} – tensor of rotation:

$$\omega_r = \omega_\theta = 0\,,\ \omega_{r\theta} = -\omega_{\theta r} = \frac{1}{2}\left(\frac{1}{r}\frac{\partial v_r}{\partial \theta} - \frac{v_\theta}{r} - \frac{\partial v_\theta}{\partial r}\right). \tag{5}$$

The last relation from (4) – Misses-Shlexer rule, connecting limit of elasticity under simple tension Y_0 and pressure in layer $(-\sigma)$; c_1, c_2 – material constants.

System of equations (1) - (5) close by kinetic equations for damage parameters ω, α:

$$\frac{\dot{\omega}}{\omega} = B\left(\frac{\sigma}{1-\omega} - \sigma_*\right)H\left(\frac{\sigma}{1-\omega} - \sigma_*\right) + \frac{\sigma - \sigma^+}{4\eta_0}H(\sigma - \sigma^+) + \frac{\sigma - \sigma^-}{4\eta_0}H(\sigma^+ - \sigma)\,, \tag{6}$$

$$\sigma^+ = -\frac{2}{3}Y_0 \ln\omega - p_0\left(\frac{\omega_0}{\omega}\right)^\gamma, \quad \sigma^- = +\frac{2}{3}Y_0 \ln\omega - p_0\left(\frac{\omega_0}{\omega}\right)^\gamma,$$

$$\dot{\alpha} = C\left(\frac{S_u}{(1-\omega)(1-\alpha)} - S_u^*\right)H\left(\frac{S_u}{(1-\omega)(1-\alpha)} - S_u^*\right).$$

Here η_0 - dynamic viscosity for an undamaged material; p_0 – initial pressure in pore («горное» pressure); γ - index of adiabatic curve for medium, filling pore; ω_0 - initial porosity; $S_u = \sqrt{S_{ij}S_{ij}}$ - intensity of stress deviator; S_u^*, σ_*, B, C - constants of material; $H(\mathrm{x})$ - Heaviside unit function.

From equations (6) we see that the first term describing the viscous growth in domains of tension of the material comes into play. The second term describes the viscoplastic flowing in pores when the material is compressed. Note that the equation for ω taken without the dynamical problem on a single spherical pore of inner radius a and other radius b in a viscoplastic incompressible material. Damage parameter α connect with intensity of stress deviator and describe fracture shear.

The evolution of the intensive plastic flow and accumulation of microstructure damages may be considered as a process of prefracture of the material. The entropy criterion of limiting specific dissipation [1, 3]:

$$D = \int_0^{t_*} \frac{1}{\rho}(d_M + d_F + d_T)dt = D_*\,, \tag{7}$$

$$d_M = S_{ij}\dot{\varepsilon}_{ij}^p\,,\ d_F = \Lambda\dot{\omega}^2 + A\dot{\alpha}^2\,,\ d_T = \kappa\frac{(grad\,T)^2}{T}$$

is proposed as the criterion of the beginning of macrofracture (i.e., the beginning of formation of cracks (new free surfaces) in material). Here t_* is the time of the beginning of fracture; D_* is a constant of the material (the limiting specific dissipation); d_M, d_F and d_T are mechanical dissipation, dissipation of continuum fracture and thermal dissipation. Similar model used for decision problem of hydraulic fracturing of oil layer ([2] etc.).

2 INITIAL AND BOUNDARY CONDITIONS

Initial rock layer be in rest: $v_r = v_\theta = 0$ in time $t = 0$. Additionally we must define initial description of stresses in layer σ_r, σ_θ, $\sigma_{r\theta}$, value of damage parameters ω and α as functions of space coordinates r and θ.

As initial distribution for stresses in rock layer we use decision of next static elasticity problem: consider infinite cylindrical solid with circular cut; on infinitum in two mutually perpendicular directions applied contractive stresses Σ_1 and Σ_2 corresponding known as “rock pressure”. In common case $\Sigma_1 \neq \Sigma_2$ that modeling no homogeneity stress state of rock layer. On surface of circular cut applied pressure $\Sigma_3 \geq 0$.

Distributions of initial stresses for this problem are [4]:

$$\begin{cases} \sigma_r = \dfrac{\Sigma_1 + \Sigma_2}{2} + \dfrac{\Sigma_1 - \Sigma_2}{2}\cos 2\theta + \dfrac{a^2}{r^2}\left(-\Sigma_3 - \dfrac{\Sigma_1 + \Sigma_2}{2} - 2\left(\Sigma_1 - \Sigma_2\right)\cos 2\theta \right) + \\ + \dfrac{a^4}{r^4}\left(\dfrac{3}{2}\left(\Sigma_1 - \Sigma_2\right)\cos 2\theta \right) \\ \sigma_\theta = \dfrac{\Sigma_1 + \Sigma_2}{2} - \dfrac{\Sigma_1 - \Sigma_2}{2}\cos 2\theta + \dfrac{a^2}{r^2}\left(\Sigma_3 + \dfrac{\Sigma_1 + \Sigma_2}{2} \right) + \dfrac{a^4}{r^4}\left(-\dfrac{3}{2}\left(\Sigma_1 - \Sigma_2\right)\cos 2\theta \right) \\ \sigma_z = \nu\left(\sigma_r + \sigma_\theta\right) \\ \sigma_{r\theta} = -\dfrac{\Sigma_1 - \Sigma_2}{2}\sin 2\theta - \dfrac{a^2}{r^2}\left(2\left(\Sigma_1 - \Sigma_2\right)\sin 2\theta \right) + \dfrac{a^4}{r^4}\left(\dfrac{3}{2}\left(\Sigma_1 - \Sigma_2\right)\sin 2\theta \right) \end{cases} \tag{8}$$

Here ν - Poisson coefficient, a - radius of hole.

At moment $t = 0$ happen sharply drop of pressure in hole from value Σ_3 to 0.

3 EXPLICIT SEPARATION OF MACRO FRACTURE ZONES

The entropy criterion of limiting specific dissipation is proposed as the criterion of the beginning of macro fracture (i.e., the beginning of formation of cracks (new free surfaces in material) (7). When criterion (7) is fulfilled at some point of material, a macro crack should be formed there, i.e., a new free surface that will spread over the body. In point where criterion of fracture fulfilled is realized explicit coasts of macro discontinuity. For this we construct separation of nodes of network on cells boundary – internal nodes and corresponding them edges of cells are boundary on this put condition of free surface or contact condition depending on situation [5]. Note that earlier we used procedure of bifurcation of Lagrangian network ([1, 3, 6, 7] et al).

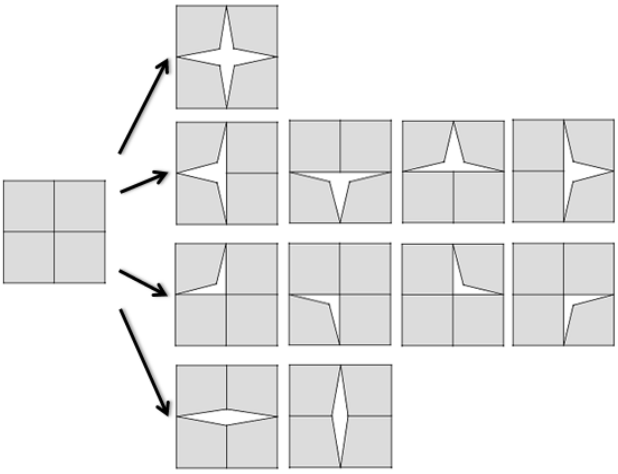

Figure 1: Types of “primary” cracks.

Procedure of decomposition for nodes of network consists of construction “primary” cracks for each node and their combination with already existing cracks. Interaction between “primary” cracks formation cracks biggest scale. On figure 1 show variants of construction “primary” cracks for internal node. Type of “primary” crack determine from analysis strain state on adjacent edges for present node.

4 RESULTS OF COMPUTATIONAL SIMULATION

This task is solved by numerical modeling on Lagrangian mesh by method similar to Wilkins one [18]. In calculation we used next value of parameters: ρ_0 =2000 kg/m^3; K_0=14000 MPa; μ_0=8400 MPA; η_0=100 Pa*c; Λ=1500 Pa*c; c_1=-0,09; c_2=40 MPa; γ=1,4; D^*=334,4 kJ/kg^3; $\omega_0 = 0{,}05$; A = 250 Pa*c; C = 0,00022(Pa*c)$^{-1}$; $B = 0$; $S_u^* = 32{,}5$ MPa. Radius of borehole is $a = 1m$, initial “rock” pressure, depending from coordinates r, θ, defined from formula (8) - $p_0 = -(\sigma_r + \sigma_\theta + \sigma_z)/3$.

Value of stresses, depending initial strain state are: $\Sigma_1 = -50$ MPa or $\Sigma_1 = -65$ MPa; $\Sigma_2 = -75$ MPa and $\Sigma_3 = 35$ MPa.

On figure 2 present dependence of velocities different borehole points, which position depended angle θ, from time t.

On figure 3 present process of origin and growth of cracks for different value of Σ_1. In left part of figure present sequential moments of time for $\Sigma_1 = -50$ MPa, in right part - for $\Sigma_1 = -65$ MPa. Intensity of grey color defines level of energy dissipation, white color correspondence limited dissipation in criteria of fracture (7) - $D_* = 334{,}4$ kJ/kg^3.

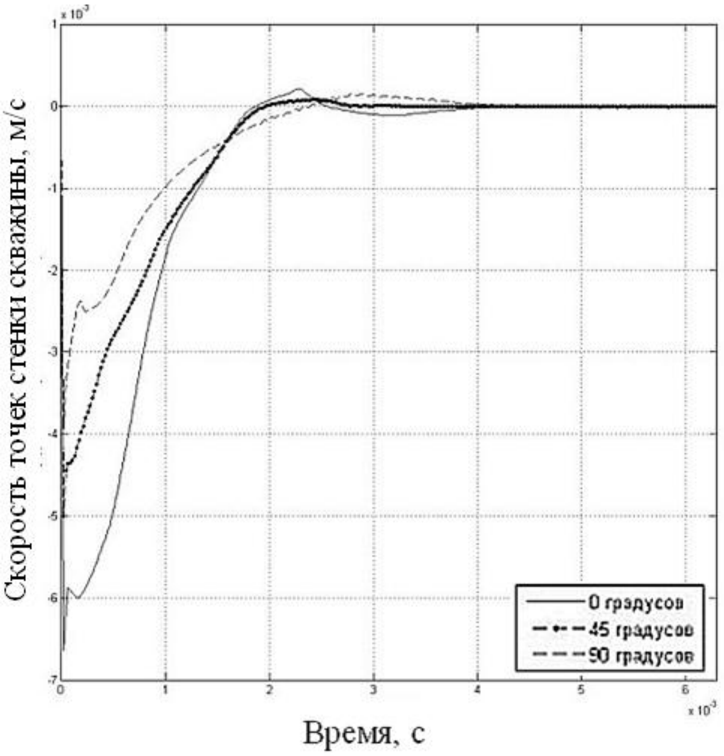

Figure 2: Velocity of different points of borehole.

As it show from figure 3, cracks in material origin and growth on internal surface of borehole and propagate deep into rock under angle near 45° to tangent of borehole contour. Further development of fracture process takes place on two scenarios: either crack continues your growth in initial direction or after some time moments it turns under angle near 90° to your initial moving. As it followed wait, in case $\Sigma_1 = \Sigma_2$ observed symmetrical not depended from angle θ situation of fracture shear type near surface of borehole with dispersion of rock fragments.

5 CONCLUSIONS

The authors would like to thank Russian Foundation of Basic Research (09-01-00144a) for financial support.

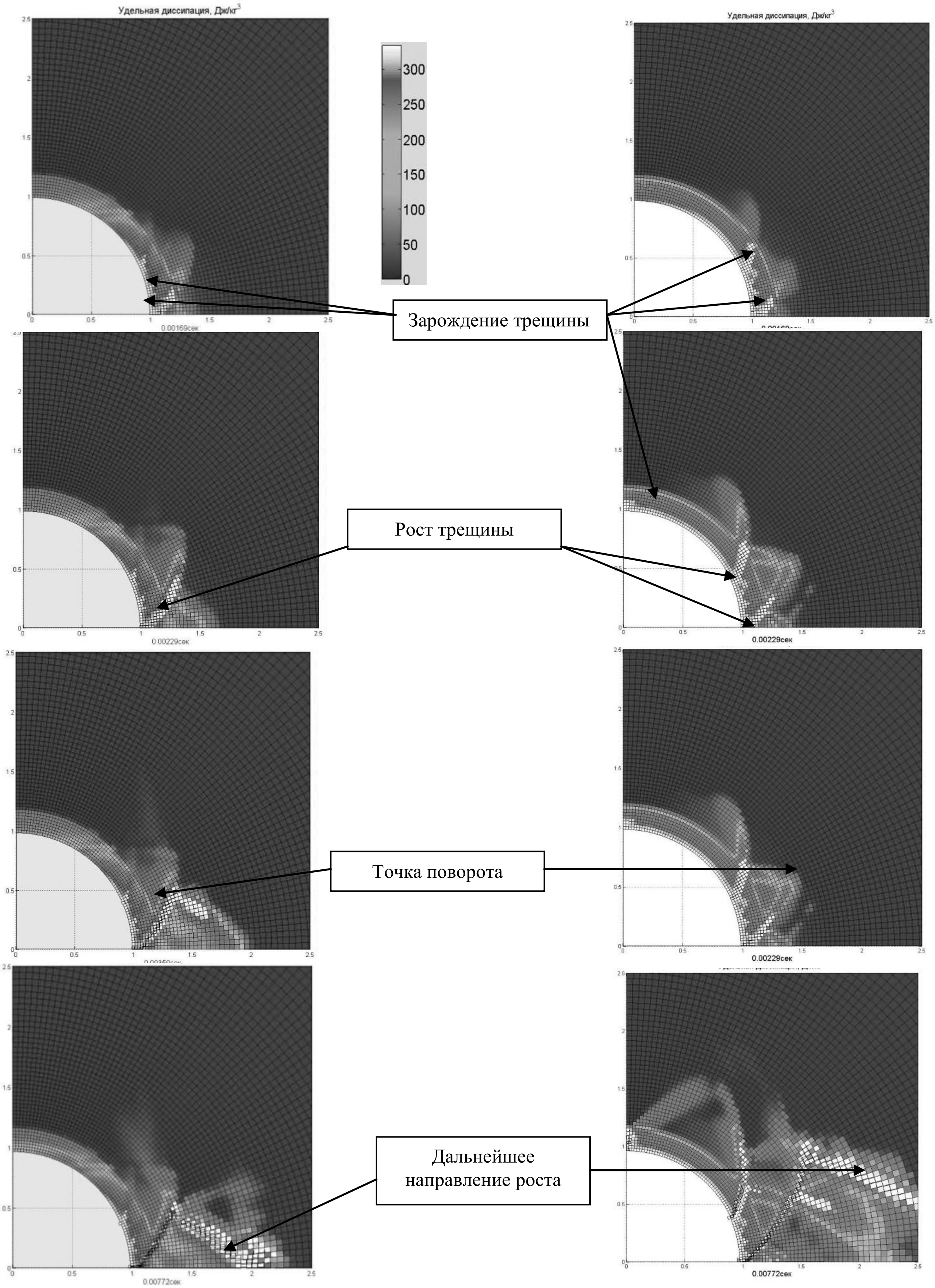

Figure 3: Process of cracks origin and growth.

REFERENCES

[1] A.B. Kiselev, M.V. Yumashev, Deforming and fracture under impact loading. The model of thermoelastoplastic medium. *J. Appl. Mech. Tech. Phys.,* **31,** no. 5, 116-123, 1990.

[2] A.B. Kiselev, Mathematical modeling of dynamical deformation and combined microfracture of a thermoelastoviscoplastic medium. *Moscow Univ. Mech. Bull.*, **53,** no. 6, 32-40, 1998.

[3] A.B. Kiselev, A.A. Lukyanov, M. Thiercelin, Numerical simulation of dynamic propagation of curvilinear cracks o hydraulic fracturing. *Moscow Univ. Mech. Bull.*, **59,** no. 1, 36-41, 2004.

[4] S.P. Timoshenko, J.N. Goodier, *Theory of Elasticity*. N.Y., McGraw-Hill, 1970.

[5] Yu.I. Stefanov, On some features of numerical simulation of the behavior of elastic-brittle-plastic materials. *Physical Mezomechanics,* **8,** no. 3, 129-142, 2005.

[6] V.M. Fomin, A.I. Gulidov, A.B. Kiselev, et al., *High-speed interaction of bodies.* Novosibirsk, Sibirian Branch of RAS, 1999.

[7] A.B. Kiselev, Numerical modeling in three-dimensional setting of inclined punching of thin obstacles, *Numerical solution of wave dynamics problems. Mathematical investigations, issue 108,* Kichinev, Chtiincha, 19-26, 1989.

[8] M.L. Wilkins, Modelling the behavior of materials. *Structural impact and crushworthiness: Proc. Int. Conf. ,* London, New York, 243-287, 1984.

COMPDYN 2011
III ECCOMAS Thematic Conference on
Computational Methods in Structural Dynamics and Earthquake Engineering
M. Papadrakakis, M. Fragiadakis, V. Plevris (eds.)
Corfu, Greece, 25–28 May 2011

NUMERICAL MODELLING OF A GEOSYNTHETIC REINFORCED STEEP SLOPE SUBJECTED TO SEISMIC LOADING

Castorina S. Vieira[1], M. Lurdes Lopes [1], and Laura Caldeira [2]

[1] University of Porto – Faculty of Engineering
R. Dr Roberto Frias, s/n 4200-465 Porto, Portugal
cvieira@fe.up.pt; lcosta@fe.up.pt

[2] National Laboratory of Civil Engineering
Av. do Brasil, 101, 1700-066 Lisbon, Portugal
laurac@lnec.pt

Keywords: Reinforced soil, Geosynthetics, Numerical modelling, Seismic loading.

Abstract. *In recent earthquakes the performance of reinforced soil retaining walls was diverse. The Hyogoken-Nambu (Kobe) Earthquake caused serious damage to conventional masonry retaining walls, unreinforced concrete gravity-type retaining walls and cantilever-type steel-reinforced concrete retaining walls, while geogrid-reinforced soil retaining walls, having a full-height concrete facing, performed very well during the earthquake [1]. On the other hand, the Chi-Chi earthquake, in Taiwan, caused serious damage to reinforced-soil retaining walls using keystones as facing [2].*

In this work the two-dimensional finite difference program Fast Lagrangian Analysis of Continua FLAC [3] was used to model the seismic response of a geogrid reinforced steep slope constructed in the North of Portugal. This structure was built in the Portuguese main itinerary, IP3, and is part of a reestablishment. The reinforced slope has an extension of about 206.2 m and the reinforced soil area reaches a maximum height of about 19.6 m. The slope behaviour was observed during 13 months, which includes three months of construction period.

The analysis of monitoring information of this geogrid reinforced steep slope and the numerical simulation of its construction are briefly presented. The seismic behaviour of this structure is analysed using FLAC program. Earthquake ground motions artificially generated with the program SIMQKE [4] were considered as seismic loading. The permanent displacements and reinforcement tensile forces are analysed and compared.

The numerical simulation of seismic loading showed a good performance of the reinforced steep slope. Since the structure is an overpass embankment, permanent vertical settlements can be the most disquieting factor. The residual reinforcement tensile forces remain smaller than the long term design strength of the geogrids.

1 INTRODUCTION

In recent earthquakes the performance of reinforced soil retaining walls was diverse. The Hyogoken-Nambu (Kobe) Earthquake caused serious damage to conventional masonry retaining walls, unreinforced concrete gravity-type retaining walls and cantilever-type steel-reinforced concrete retaining walls, while geogrid-reinforced soil retaining walls, having a full-height concrete facing, performed very well during the earthquake [1]. On the other hand, the Chi-Chi earthquake, in Taiwan, caused serious damage to reinforced-soil retaining walls using keystones as facing [2].

Usually reinforced soil retaining walls are designed using limit-equilibrium pseudo static methods. These methods are dependent only on peak ground acceleration, and disregard the effects due to duration of seismic action, frequency, foundation condition, stiffness of the reinforcement, facing type and others factors.

In this work the two-dimensional finite difference program *Fast Lagrangian Analysis of Continua* - FLAC [3] was used to investigate the seismic response of a geosynthetic reinforced steep slope. This code, suitable for modelling large distortions and dynamic response of earth structures, has also been used to investigate seismic response of reinforced soil retaining walls by other authors [5, 6].

2 BRIEF DESCRIPTION OF FLAC CODE AND SEISMIC LOADING

FLAC is an explicit finite difference program that performs a Lagrangian analysis. The finite difference method is perhaps the oldest numerical technique used for the solution of sets of differential equations, given initial values and/or boundary values [3]. For dynamic analyses the full equations of motion are solved using lumped gridpoint masses derived from the real density of surrounding zones (rather than fictitious masses used for static solution). Each triangular sub-zone contributes one-third of its mass (computed from zone density and area) to each of the three associated gridpoints. The final gridpoint mass is then divided by two in the case of a quadrilateral zone that contains two overlays. In finite-element terminology, FLAC uses lumped masses and a diagonal mass matrix [3].

In FLAC, the dynamic input can be applied as an acceleration history, as a velocity history, as a stress (or pressure) history or as a force history. Dynamic input can be applied either in the x or y directions corresponding to the xy axes for the model, or in the normal and shear directions to the model boundary.

Figure 1(a) presents one of the earthquake ground motions artificially generated [2] according to Portuguese National Annexes (PNA) of Eurocode 8 [7] for the greatest seismicity area of Portugal, considering seismic action type 2 (earthquake with moderate magnitude and small focal distance – close earthquake) and ground type B (deposits of very dense sand, gravel or very stiff clay). According to the PNA of Eurocode 8 [7], for the greatest seismicity area, the peak ground acceleration on type B ground is $2.5 m/s^2$ and $1.7 m/s^2$ for seismic action type 2 and type 1, respectively. The duration of the stationary part of the accelerograms are equal to 10 seconds and 30 seconds. The Fourier spectrum for the accelerogram presented in Figure 1(a) is plotted in Figure 1(b).

Figure 2 shows the horizontal displacements obtained by double integration of the earthquake ground motion presented in Figure 1(a). Without correction, significant residual displacements occur at the end of the motion. To avoid these unreal large displacements at the end of the dynamic action, a baseline correction should be performed. A low frequency wave is determined which, when added to the original history, produces a final displacement equal to zero (Figure 2). The velocity and acceleration time histories with and without baseline correction remain similar.

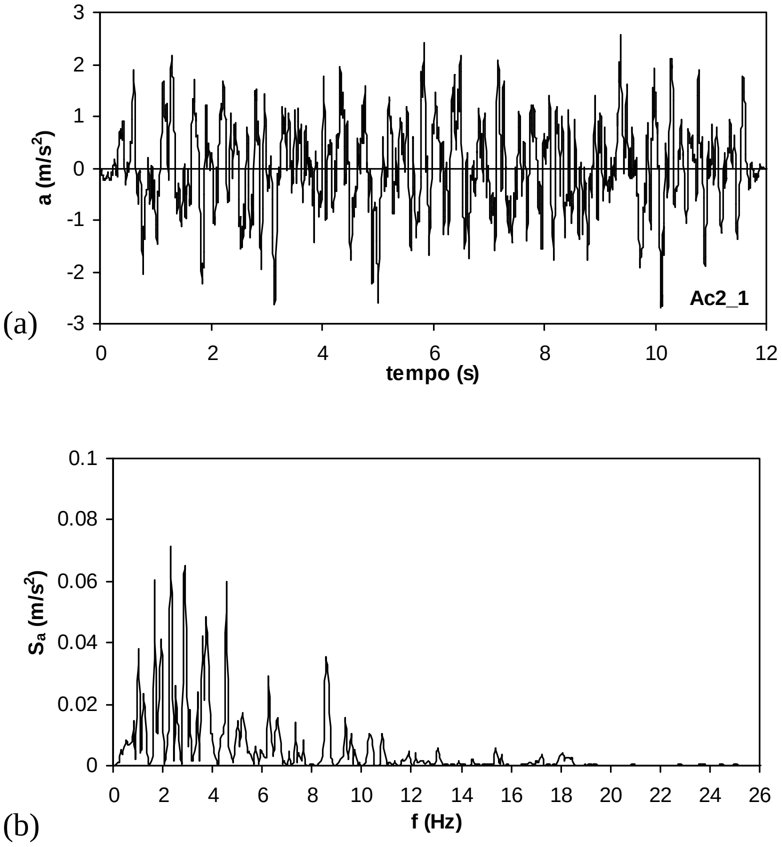

Figure 1: Example of one seismic action (type 2): a) artificial accelerogram [4]; b) Fourier spectrum.

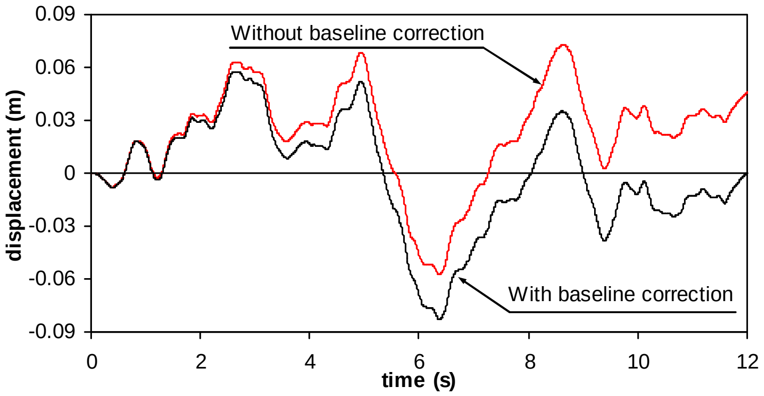

Figure 2: Effect of baseline correction on the imposed displacements.

To analyse the behaviour of this reinforced steep slope, earthquake ground motions artificially generated with the program SIMQKE [4] were considered as seismic loading. Two types of seismic action were considered: an earthquake with moderate magnitude and small focal distance - “close” earthquake (seismic action type 2) and an earthquake with greater magnitude and greater focal distance – “distant” earthquake (seismic action type 1). Although the embankment was constructed in the lower seismicity area (North of Portugal), the most adverse scenery in terms of seismicity was considered. Ten accelerograms were analysed for each seismic action type.

3 GENERAL OVERVIEW OF THE STRUCTURE

The geogrid-reinforced steep slope was built (in 1998) in the Portuguese main itinerary (IP3) and is part of a reestablishment. The embankment has an extension of about 206.2 m and the reinforced soil area reaches a maximum height of about 19.6 m. On sections higher than 10 m, a bench with variable width parallel to the road pavement was built. The inclination of the reinforced slope is about 60º (Figure 3).

Figure 3: Overview of the embankment at the end of construction [8].

The foundation of the structure is a natural compact granite residual soil. Due to the local morphology, a rockfill was executed. The backfill is, also, a residual soil from granite. The reinforcements are high density polyethylene (HDPE) uniaxial geogrids, placed horizontally and spaced 0.60 m on vertical direction. In the analysed cross section, 31 layers of HDPE geogrids with nominal tensile strength of 160 kN/m (7 layers), 120 kN/m (10 layers), 90 kN/m (4 layers) and 60 kN/m (10 layers) were placed. The geogrids length is about 12.8m. The face units were constructed using welded wire net with quadrangular openings (Figure 4). A biodegradable mat was placed inside the face elements to prevent surface erosion and promote the vegetation growth (Figure 4b).

The reinforcement strains were measured in three reinforcement layers using linear extensometers spaced of 0.50 m (20 extensometers per monitored geogrid). Vertical stresses were recorded using load cells placed near the three monitorized geogrids. The internal horizontal displacements were recorded using two inclinometer tubes [8, 9]. The inclinometer I_1, also called bench inclinometer, was placed at the middle of the bench width. The inclinometer I_2 was placed approximately at the middle of the higher bench (Figure 5). The displacements of the slope face were measured topographically. The analysed slope cross section, the monitoring devices and their positions are schematically represented in Figure 5.

The slope behaviour was observed during 13 months, which includes three months of construction period.

Figure 4: Detail of slope face: a) during the construction period [8]; b) August 2003 [9].

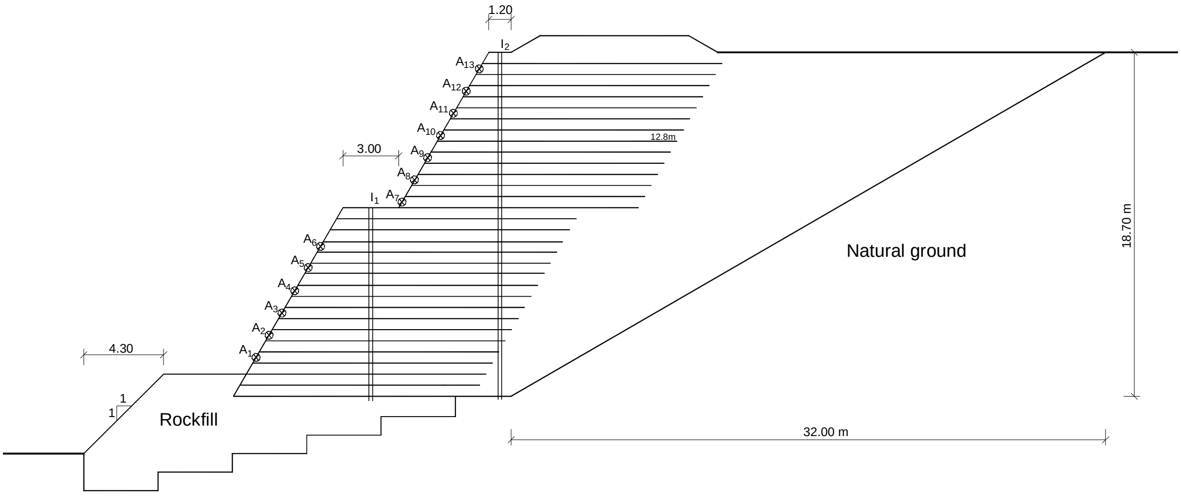

Figure 5: Analysed cross section and location of monitoring devices [9].

4 NUMERICAL MODELING OF THE CONSTRUCTION

4.1 Details of numerical modelling

The construction of an embankment is a progressive placement of soil layers. Consequently, the monitoring results are relative values. So, in order to compare the monitoring results with those obtained by the numerical analyses, the knowledge of the construction sequence is imperative. An estimate was made, based on data from the instrumentation and some photographs found in [8, 10].

The fill was modelled as a purely frictional elasto-plastic material, with a Mohr-Coulomb yield function and a non-associated flow rule. The friction angle of the soil was taken equal to 35º and the unit weight $\gamma = 21.5$ kN/m^3. Young modulus and Poisson ratio of the soil were taken equal to 30 MPa and 0.3, respectively. After conducting a parametric study [9], it was considered a value of 5 kPa for the soil cohesion. This value has not a great physical significance but improves the performance of the numerical model, eliminating some numerical instability, particularly in the slope face.

The reinforcement layers were modelled using linear elasto-plastic cable elements with negligible compressive strength. The linear elastic stiffness of the reinforcement layers depends on the reinforcement strength and strain level. So, it was considered the value for 2% of geogrids strain. The interface between the reinforcement and the soil was modelled by a grout material [3] with an interface friction angle of 19.5º and a bond stiffness of 3×10^3 kN/m/m. These values were achieved from the numerical simulation of an in-situ pullout test [9].

The wrap-around face was modelled with cable elements with compressive strength not null (equal to 20% of reinforcement tensile strength) and an interface friction angle equal to 35º.

After the clearing of natural ground, it was decided [8] to place a rockfill under and in front of the reinforced soil mass (see Figure 5). The foundation and the rockfill were modelled as elastic materials with Young modulus of 200 MPa. Over the rockfill foundation, it was considered a thin layer of soil, with similar properties to those of the backfill, which is the base for the first reinforcement layer.

In order to model, as closely as possible, the real construction sequence, the embankment was simulated by the placement of successive soil layers of 0.30 m thick. The pavement was simulated by a layer with increased density. When the position of the reinforcement layer "i" is achieved, the horizontal displacement of the face at this level is prevented, being allowed only in the next stage, ie the reinforcement layer "i" is only loaded in the following construction stage.

4.2 Comparison of numerical results with monitoring data

Taking into account the reference values of the topographic targets and the construction sequence, intermediate measurements of the face displacements were performed in the numerical analyses. With these intermediate values it was possible to obtain relative displacements comparable with those obtained with monitoring. To make possible the comparison between the internal displacements of the embankment obtained with the numerical analyses and the values recorded in the inclinometer tubes, intermediate measurements of the horizontal displacements along two vertical planes (coincident with the inclinometer tubes position - see Figure 5) were also performed.

Figure 6 compares the relative displacements of the slope face achieved in the numerical analyses with those from the topographic measurements. The analysis of this figure shows that the numerical model captures the real behaviour of the reinforced embankment. In the four targets placed nearest the top, the horizontal displacements of the model are very close to values recorded in-situ. In the remaining targets, the numerical model tends to overestimate the horizontal displacements of the slope face. The model reproduced very closely the vertical displacements of the slope face. Note that the targets were fixed to the welded wire net, which means, their movements may be related to a punctual displacement of the wire net and not to the behaviour of slope face. The numerical modelling of the real conditions of the slope face is not easy, since the system face is complex (geogrid+ biodegradable mat+ welded wire net).

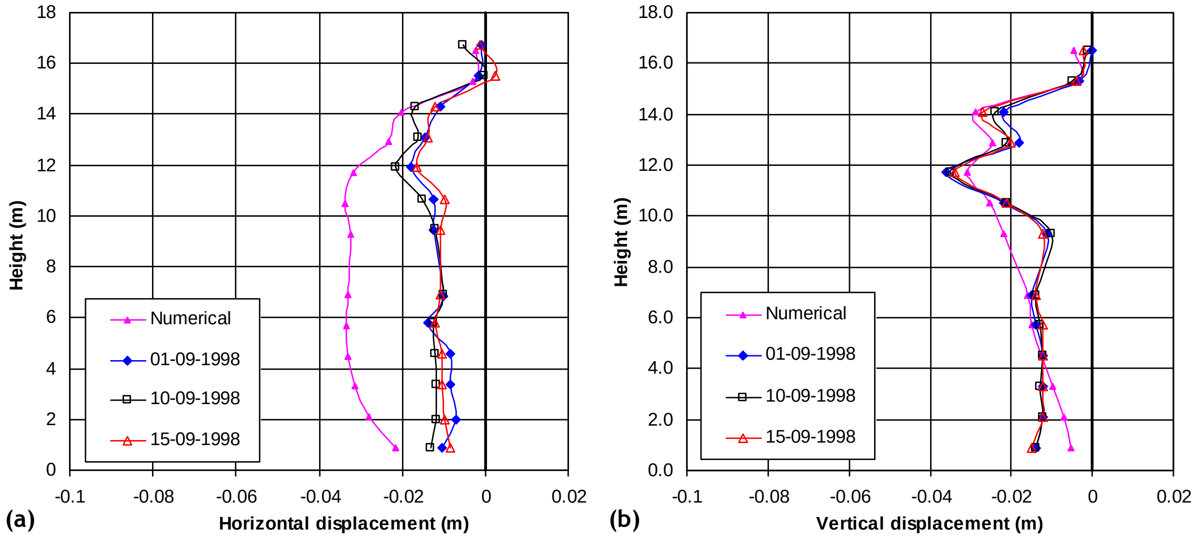

Figure 6: Comparison of numerical and monitoring results: a) horizontal displacements of the slope face; b) vertical displacements of the slope face.

Figure 7 presents the internal horizontal displacements along two vertical planes coincident with the inclinometer tubes position. The numerical results are compared with those obtained from the monitoring.

Figure 7 shows that the numerical analysis seems suitable for the internal horizontal displacements, particularly those relating to the inclinometer I_2 (Figure 7b). For the bench inclinometer (or inclinometer I_1), located near the slope face, the numerical analysis did not show the same effectiveness. For this inclinometer, the numerical model tends to overestimate the internal displacements in the upper part of the inclinometer. This may be partly justified by the influence of the complex face system.

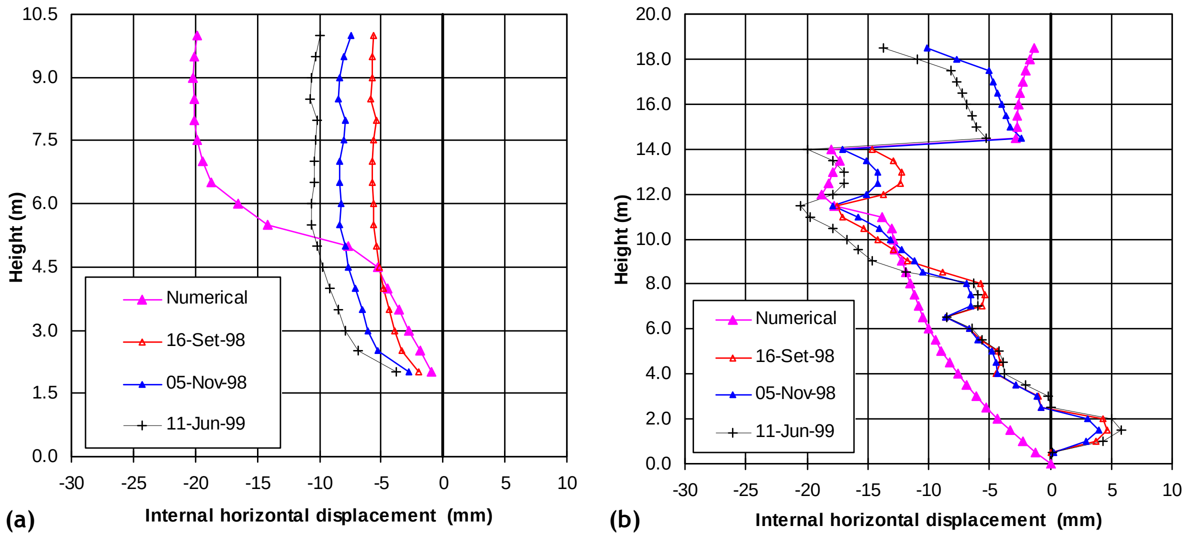

Figure 7: Comparison of internal horizontal displacements reached with numerical analyses and monitoring results: a) inclinometer I_1; b) inclinometer I_2.

5 SEISMIC BEHAVIOUR OF THE STRUCTURE

5.1 General

As mentioned, two types of seismic action were considered: an earthquake with moderate magnitude and small focal distance - “close” earthquake (seismic action type 2) and an earthquake with greater magnitude and greater focal distance - “distant” earthquake (seismic action type 1). In order to select 10 accelerograms representative of seismic action type 2 and 10 accelerograms representative of seismic action type 1, several series were artificially generated. Time increments of 0.01 seconds were considered. For seismic action type 2 and type 1, the duration of the stationary part of the accelerograms are equal to 10 seconds and 30s seconds and the duration of the transitory sections, before and after the stationary part, are equal to 1 second and 3 seconds, respectively.

To avoid the reflection of the waves back into the model, absorbing boundaries (free-field conditions [3]) were considered at the lateral limits of the mesh.

The hysteretic damping of the foundation and rockfill was represented by an equivalent Rayleigh damping with damping coefficient of 10%. In addition to the damping associated to the elasto-plastic behaviour of the backfill, no additional damping was considered.

5.2 Results for seismic action type 2 – “close” earthquake

Figure 8 presents time histories of horizontal displacements recorded at three points located at the slope face. The horizontal displacement at the base of reinforced slope (Point 1) follows closely the imposed displacement at the foundation. Note that, a rockfill was placed in front of the first reinforcement layers (up to 1.5 m high). The horizontal displacement at the crest of the upper slope (Point 3) in outside direction (negative values in Figure 8), tends to be smaller than those recorded at the crest of the lower slope (Point 2).

As an example, Figure 9 shows the geometry of the reinforced steep slope at the end of the seismic action Ac2_6. Note that the displacements were enlarged 10 times. It is evident some instability at the bench, including swelling of the soil. Vertical displacements with some significance are also shown at the top.

Figure 10 presents the reinforced load developed in a cable element of the 4th reinforcement layer. This element is located about 3 m from the slope face. The seismic horizontal displacement of one node of the same element is also plotted. In the time history of this reinforcement load, three sudden increases are visible. These increases occur when the accelerogram inverts the sign. In the horizontal displacement time history, positive values mean displacements inwards of reinforced slope.

Figure 11 shows the average curves of horizontal and vertical displacements of the slope face and those obtained by adding and subtracting the respective standard deviation, for the ten accelerograms considered (seismic action type 2). The analysis of this figure shows that, on the slope below the bench, the maximum horizontal displacement occurs in the upper half of the slope. In the slope above the bench the horizontal displacements in the upper half are lower. The maximum vertical displacement occurs at the crest of the embankment.

Figure 12 presents the average values of residual reinforcement tensile forces in all reinforcement layers and those obtained by adding and subtracting the respective standard deviation. To understand the sudden changes shown, it was included the reference to geogrids with distinct properties. Note that, geogrids with nominal strength of 160 kN/m and 120 kN/m

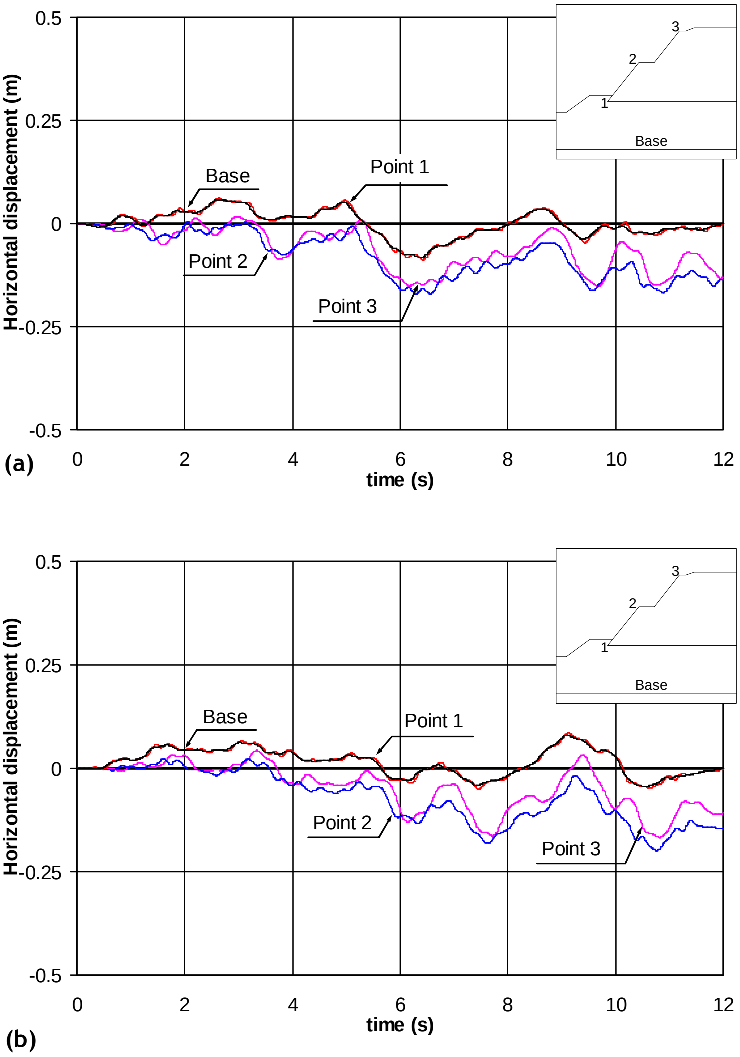

Figure 8: Horizontal displacements time histories of 3 points located at the slope face: a) accelerogram Ac2_1;.b) accelerogram Ac2_6.

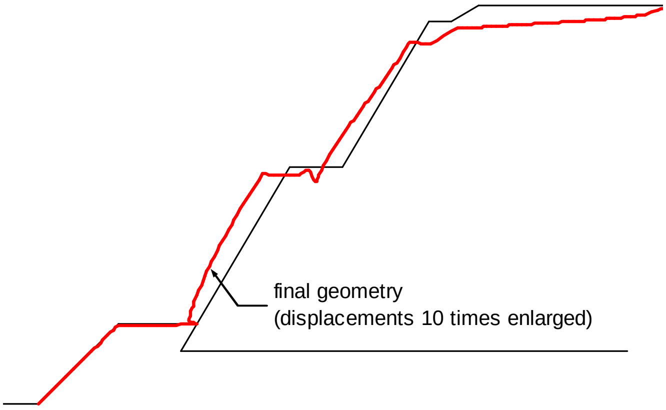

Figure 9: Deformed slope at the end of seismic action Ac2_6.

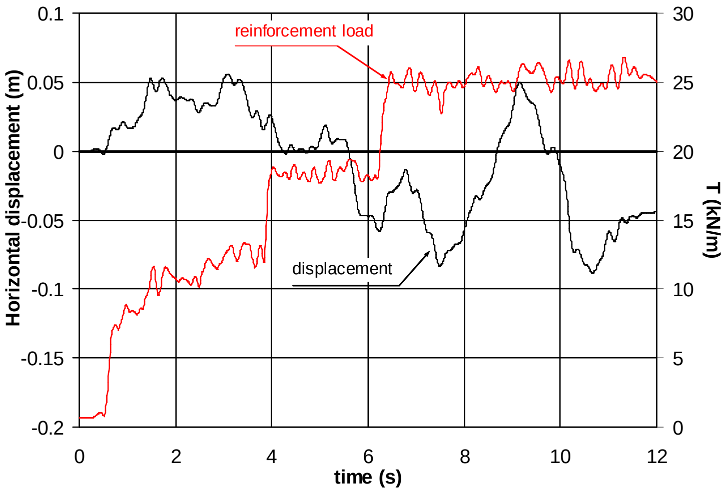

Figure 10: Time histories of reinforcement load and horizontal displacement recorded in one element of the 4th geogrid level (Ac2_6).

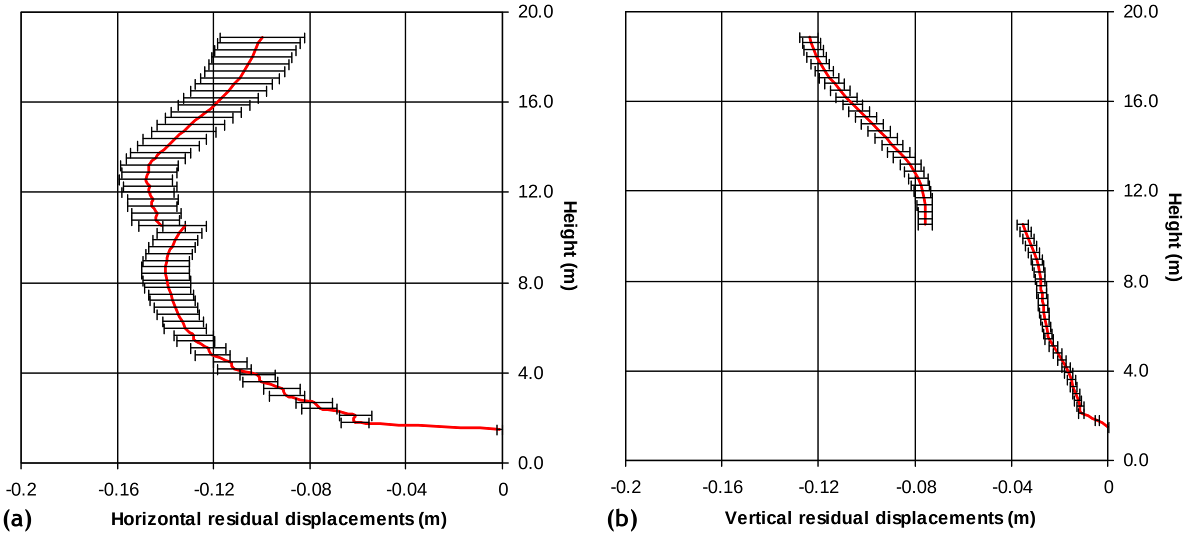

Figure 11: Pattern of mean residual displacements for seismic action Type 2: a) horizontal residual displacements of slope face; b) vertical residual displacements of slope face.

were placed on the embankment below the bench and geogrids with nominal strength of 90 kN/m and 60 kN/m were installed on the embankment above the bench. The presence of the rockfill in front of the lower reinforcement layers reduces, significantly, the tensile forces mobilized at these layers.

Although not presented in this work, it is important to mention that the maximum tensile loads recorded in the reinforcement elements located on the upper slope are very close to the residual values (at the end of motion). On the slope below the bench, the maximum tensile loads exceed the residual values, particularly in the 4th reinforcement layer (the first layer placed above the rockfill), where the difference can be substantial (around 50%).

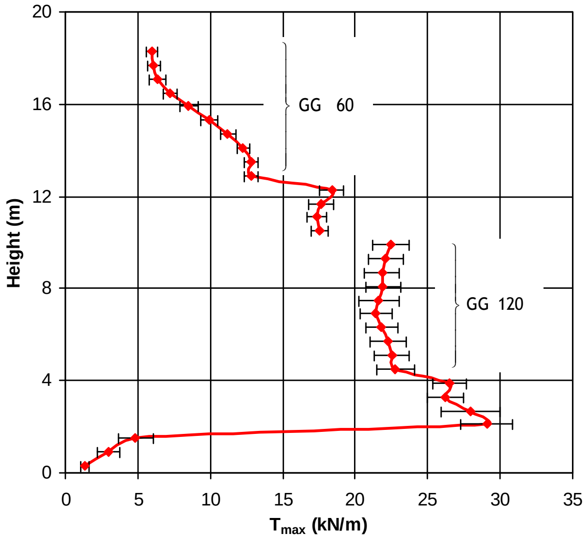

Figure 12: Pattern of mean residual reinforcement tensile forces for seismic action Type 2.

5.3 Results for seismic action type 1 – "distant" earthquake

Figure 13 shows time histories of horizontal displacements recorded at three points located at the slope face for the artificial accelerogram Ac1_9. As observed for the "close" earthquake, the horizontal displacement at the base of reinforced slope (Point 1) follows closely the imposed displacement at the foundation.

The horizontal displacements recorded during the simulated earthquakes are quite distinct (compare Figure 8 and Figure 13). Even so, the permanent horizontal displacements at the end of ground motion are not very different.

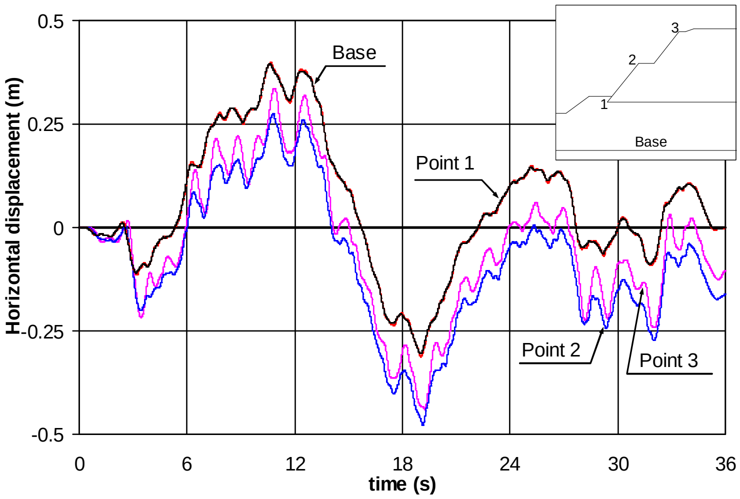

Figure 13: Horizontal displacements time histories of 3 points located at the slope face for the accelerogram Ac1_9.

Figure 14 illustrates the reinforced load recorded in a cable element of the 4th reinforcement layer during the numerical simulation relating to the accelerogram Ac1_9. The seismic horizontal displacement of one node of the same element is also plotted. As noted for the seismic action type 2, the reinforcement load tends to experience sudden increases. Although, for the accelerograms representative of seismic action type 1, after some seconds, the changes in the reinforcement load are very small (Figure 14).

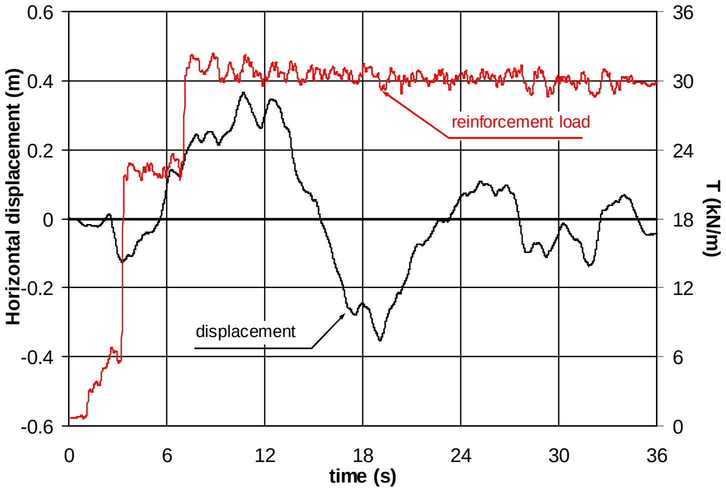

Figure 14: Time histories of reinforcement load and horizontal displacement recorded in one element of the 4th geogrid level (Ac1_9).

The average curves of horizontal and vertical displacements of the slope face, and those obtained by adding and subtracting the respective standard deviation, for the accelerograms representative of the seismic action type 1 are presented in Figure 15. As verified for the seismic action type 2 (Figure 11), the maximum horizontal displacements occur in the upper half of the slope below the bench and in the lower half of the slope above the bench. The maximum vertical displacement occurs at the crest of the embankment.

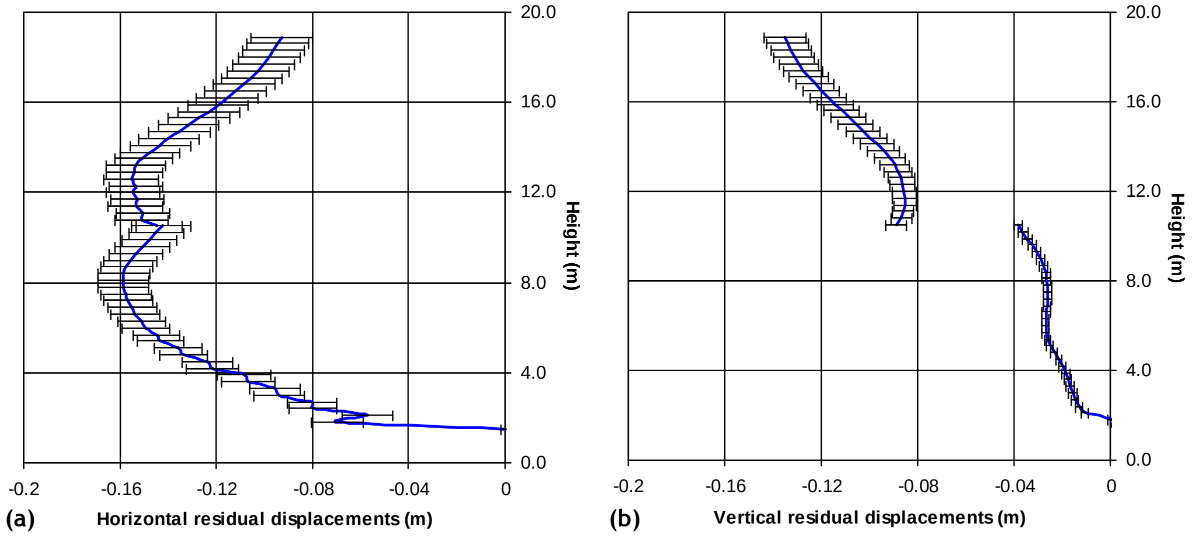

Figure 15: Pattern of mean residual displacements for seismic action Type 1: a) horizontal residual displacements of slope face; b) vertical residual displacements of slope face.

Figure 16 illustrates the average values of residual tensile forces in all reinforcement layers, and those obtained by adding and subtracting the respective standard deviation. The residual tensile forces distribution through the structure height is similar to that presented in Figure 12 for “close” earthquakes.

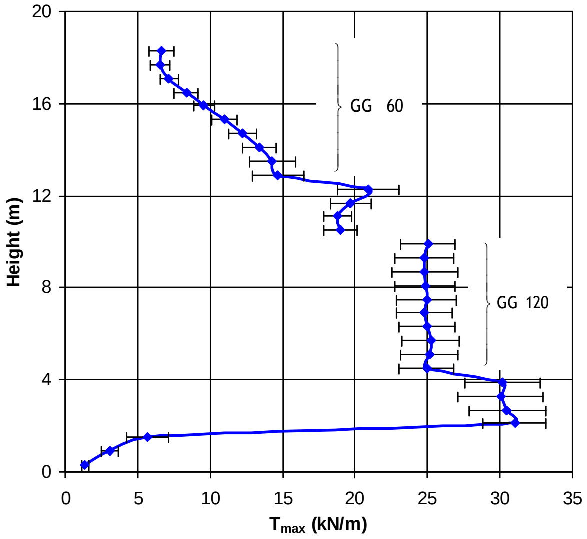

Figure 16: Pattern of mean residual reinforcement tensile forces for seismic action Type 1.

5.4 Influence of seismic action type

Figure 17 compares the average curves of horizontal and vertical displacements of the slope face for the two seismic actions considered. The first conclusion to be drawn, from the analysis of this figure, is that the “distant” earthquake is more adverse for the performance of this reinforced steep slope.

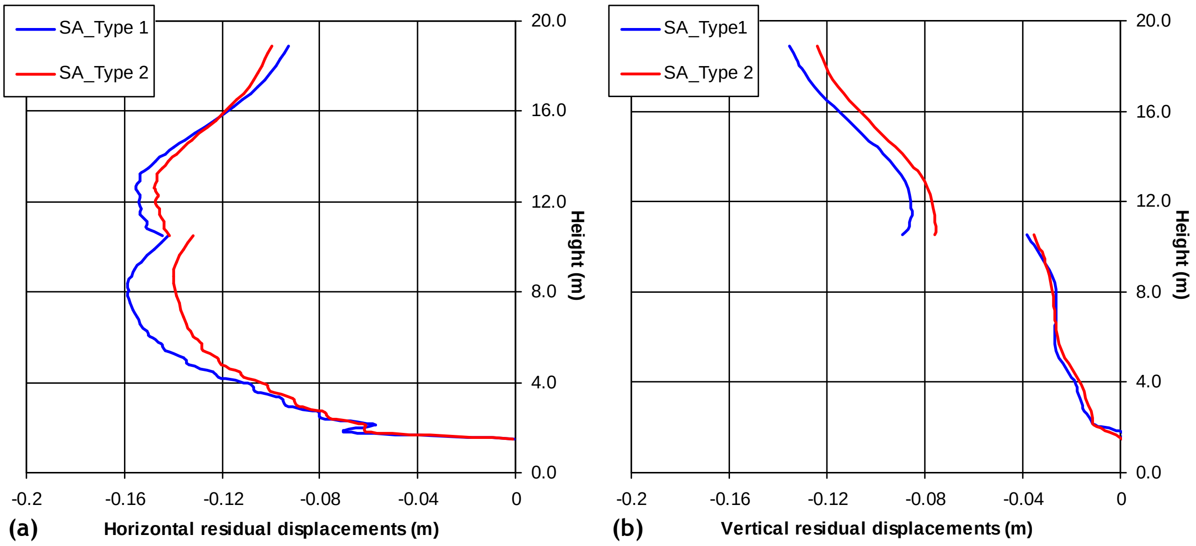

Figure 17: Influence of seismic action type on residual displacements of slope face: a) horizontal displacements; b) vertical displacements.

On average, the horizontal and vertical displacements recorded for “distant” earthquakes are, respectively, 7.1% and 9.1% greater than those recorded for “close” earthquakes. Even so, the horizontal displacements of the slope face near the top tend to be lower when the structure is subjected to distant earthquakes. The vertical displacements of the slope below the bench are quite small and they are not influenced by the seismic action type.

Figure 18 illustrates the average values of maximum reinforcement tensile loads at the end of ground motion (residual values) for the two seismic actions. The distribution of residual reinforcement tensile loads trough the structure height is similar. However the seismic action type 1 generates greater reinforcement loads.

The maximum values of the residual reinforcement tensile loads remain smaller than the long term design strength of the geogrids. These latter values are, according to [8], 46.1 kN/m, 35.0 kN/m, 25.9 kN/m and 17.5 kN/m for the geogrids GG160, GG120, GG90 and GG60, respectively.

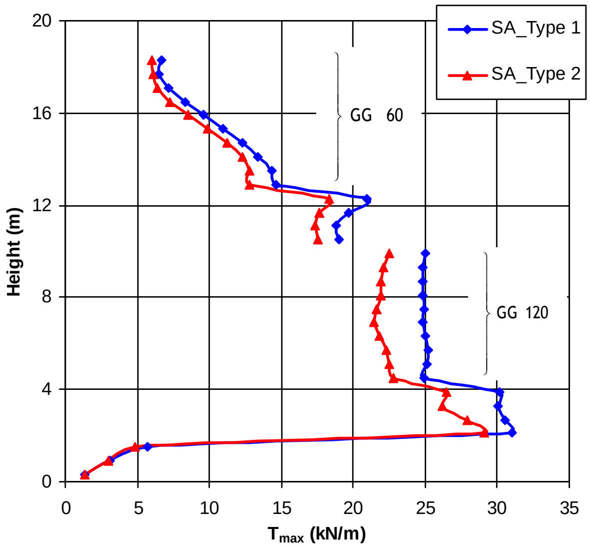

Figure 18: Influence of seismic action type on residual reinforcement tensile forces.

6 MAIN CONCLUSIONS

Despite some limitations related to the characterization and real progress of the embankment construction, resulting from the fact that the first author of this work did not follow the design and construction of the structure, the obtained results fit reasonably with the monitoring data. It was found that:

- with respect to distribution of slope face displacements through the structure height, either horizontal or vertical, the numerical model captures the real behaviour of the embankment;

- numerical modelling also seems appropriate for the internal horizontal displacements.

The numerical simulation of seismic loading showed a good performance of the reinforced steep slope. Since the structure is an overpass embankment, permanent vertical settlements can be the most disquieting factor. However, it should be noted that, according to the philosophy of safety codes, under the action of intense earthquakes, the occurrence of damages is allowed, provided they do not produce the rupture of the structure.

The residual reinforcement tensile forces remain smaller than the long term design strength of the geogrids.

The occurrence of a “distant” earthquake seems to be more adverse for the seismic performance of this structure. Nevertheless, numerical modelling of other geosynthetic reinforced soil structures has shown that “close” earthquakes can be critical. The fundamental frequencies of these structures will have, certainly, its influence.

ACKNOWLEDGMENTS

The authors would like to thank the financial support of FCT and FEDER, Research Project FCOMP-01-0124-FEDER-009750 - PTDC/ECM/100975/2008.

REFERENCES

[1] Tatsuoka, F., Koseki, J., Tateyama, M., and Horii, K.(1995). Performance of soil retaining walls during the Great Hanshin-Awaji Earthquake. *Bulletin of Earthquake Resistant Structures Research Center, University of Tokyo,* (28), pp. 3-12.

[2] Koseki, J. and Hayano, K.(2000). Preliminary Report on damage to retaining walls caused by the 1999 Chi-Chi earthquake. *Bulletin of Earthquake Resistant Structures Research Center, University of Tokyo,* (33), pp. 23-34.

[3] Itasca (2005). FLAC - Fast Lagrangian Analysis of Continua, in *Version 5.00, Itasca Consulting Group, Inc., USA.*

[4] Gasparini, D. and Vanmarcke, E. (1976). SIMQKE - A computer program for artificial motion generation, in *User's Manual and Documentation,* Department of Civil Engineering, Massachussets Institute of Technology.

[5] Bathurst, R.J. and Hatami, K.(1998). Seismic response analysis of a geosynthetic-reinforced soil retaining wall. *Geosynthetics International,* 5(1-2), pp. 127-166.

[6] El-Emam, M.M. (2003). Behaviour of reinforced soil walls under earthquake loading. PhD Thesis, Queen's University at Kingston, 411 p Behaviour of reinforced soil walls under earthquake loading.

[7] NP-ENV 1998-1-1 (2000). Eurocode 8: Design provisions for earthquake resistance of structures. Part 1-1: General rules – Seismic actions and general requirements for structures. *Portuguese NAD*, pp. 34.

[8] Lopes, M.L., Mendonça, A., Monteiro, B.P., Pais, M.J., and Caspurro, I.M. (1999). Geogrid reinforced embankment constructed in branch Régua-Reconcos of IP3 - Construction, in *Technical Report. Protocol JAE/FEUP (in Portuguese).*

[9] Vieira, C.S. (2008). Geosynthetic reinforced soil retaining walls and slopes. Seismic behaviour and design methodologies. PhD Thesis, Civil Engineering Department, University of Porto, 575 p (in Portuguese).

[10] Mendonça, A., Lopes, M.L., and Pinho Lopes, M.J.(2003). Construction and post-construction behaviour of a geogrid-reinforced steep slope. *Geotechnical and Geological Engineering,* 21, pp. 129–147.

COMPDYN 2011
3rd ECCOMAS Thematic Conference on
Computational Methods in Structural Dynamics and Earthquake Engineering
M. Papadrakakis, M. Fragiadakis, V. Plevris (eds.)
Corfu, Greece, 25–28 May 2011

FREE VIBRATION PROBLEM OF PRSI BRIDGES: ANALYTICAL SOLUTION AND PARAMETRIC ANALYSIS

E. Tubaldi[1], **A. Dall'Asta**[2]

[1] Dipartimento di Architettura Costruzione e Strutture, Marche Polytechnic University,
Via Brecce Bianche, 60131, Ancona (AN), Italy
etubaldi@libero.it

[2] Dipartimento di Progettazione e Costruzione dell'Ambiente, University of Camerino
Viale della Rimembranza, 63100, Ascoli Piceno (AP), Italy
a.asta@tin.it

Keywords: seismic isolation, bridge, partial restraint, free vibrations, non-classical damping.

Abstract. *This paper analyzes the dynamic behavior of partially restrained seismically isolated (PRSI) bridges. These are a particular class of multi-span seismically isolated bridges in which isolation bearings are posed only at the top of the piers, while seismic stoppers restrain the transverse motion of the superstructure at the abutments.*

The transverse dynamic behavior of these partially-restrained bridges is described analytically by considering a two-dimensional simply supported beam model, with intermediate visco-elastic restraints whose properties are calibrated to describe the substructures' behavior. Particular simplified configurations are considered which allow to identify a minimal set of characteristic problem parameters that completely describe the dynamic response. The properties of the dynamic systems are analyzed by considering separately the undamped and the damped case.

The results of the study contribute to improve the understanding of the dynamic behavior of partially restrained seismically isolated bridges and allow to draw some conclusions useful for their preliminary assessment and design.

1 INTRODUCTION

Seismic isolation in bridges has proven to be an effective method for the mitigation of the forces induced by the seismic actions ([1],[2]). It usually consists in the introduction of isolation/dissipation devices between the bridge substructures and the superstructure, in order to decouple their motion, shift the natural period of vibration away from the dominant period of earthquake excitation and introduce additional sources of damping.

Partially restrained seismically isolated (PRSI) bridges ([3]) are a particular class of isolated bridges in which isolation bearings are posed only at the top of the piers, with seismic stoppers restraining the transverse motion of the superstructure at the abutments. This restraint is usually introduced in order to avoid the use of bi-directional joints at the abutments and to exploit the abutment contribution in resisting the inertia forces, thus reducing the forces acting on the piers.

Recently, many authors have investigated the dynamic behavior of PRSI bridges ([3], [4], [5]). Tsai [3] evaluated the effectiveness of the partially restrained seismic isolation and describes the difference of the behavior of PRSI bridges with respect to fully isolated bridges. Analytical expressions were also proposed for estimating the transverse effective period and composite damping ratio of PRSI bridges. Makris et al. [4] examined the eigenvalues of PRSI bridges under transverse and longitudinal vibration, by considering the two cases of elastomeric bearings and friction-pendulum bearings. They concluded that regardless of the value of the isolation period along the longitudinal direction, there is a certain length beyond which the transverse period of the deck will exceed the longitudinal isolation period. Tubaldi and Dall'Asta [5] analyzed the dynamic problem of PRSI bridges in a variational form, in order to obtain a simplified solution based on assumed vibration shapes which coincide with the Fourier sine-only series terms. They also defined a design procedure for dimensioning the properties of the isolation system, with the objective of controlling the internal actions on the piers. The applications to realistic PRSI bridges allowed to highlight the following results: a) the response in terms of some quantities of interest in the seismic analysis (e.g., the abutment reactions and the superstructure transverse bending moments) can be strongly influenced by higher vibration modes, b) the response according to the higher modes of vibration is less affected by the pier-bearing restraint action and depends mostly on the superstructure properties, c) neglecting the non-classically damped nature of the problem may induce some inaccuracies in the assessment of the seismic response of this particular type of system.

In summary, PRSI bridges show a complex dynamic behavior in the transverse direction and many modal properties related to the seismic response, such as modal shapes and extent of non classical damping, significantly change by varying the properties and geometry of the deck and properties and location of the intermediate supports.

This study aims at providing some contribution to the further advancement in the understanding of the dynamic behavior of PRSI bridges. Under a qualitative point of view, the dynamic properties of a linear system, such as the ones analyzed in the present study, can be measured by solving the free vibrations problem. Thus, the focus of the paper is on the free-vibration response of PRSI bridges only.

The transverse dynamic behavior of PRSI bridges is described [5] by considering a model which consists in a continuous 2-dimensional simply supported beam resting on discrete visco-elastic supports. The properties of the intermediate supports can be calibrated to represent the behavior of the pier-bearing systems. Numerous studies are devoted to the analysis of the free vibration problem of continuous beams elastically restrained by intermediate linear springs ([6],[7],[8]) or dampers ([9],[10]). However, many of these studies analyze the problem from a purely mathematical perspective and are mostly focused on the influence of the restraint on the eigenvalues or in the observation of the transition condition in which multiple coincident eigenvalues are observed. Thus, there is a need for an engineering interpretation of the complex behavior of PRSI bridges in terms of physical quantities which can be of interest in the seismic analysis, e.g., displacement and bending moment shapes, participation factors, abutment reactions, vibration periods, damping properties and extent of non classical damping.

In this paper, the free vibration problem of a set of simplified PRSI bridges configuration is considered, assuming constant stiffness, mass and support spacing for the superstructure. This allows to identify a minimal set of characteristic problem parameters that completely describe the dynamic response of partially restrained bridges and to shed light on the relationship between these parameters and the response quantities of interest in the seismic analysis. Furthermore, the consideration of the simplified cases permits deriving an analytical solution of the free-vibrations problem and developing analytical relationships between the characteristic parameters and the system response.

The influence of the characteristic problem parameters on the free vibrations is analyzed through an extensive parametric analysis by considering separately the case of support systems without damping, and the case of support system with damping, thus generating a non-classical dynamical system. The results of the parametric analysis undertaken permit to draw important information which can be useful for the preliminary assessment and design of the particular class of bridges analyzed.

2 DYNAMIC BEHAVIOR OF PRSI BRIDGES

The continuous isolated bridge with partial restraint can be modeled as a 2-dimensional simply-supported beam resting on intermediate discrete visco-elastic supports that represent the pier-bearing systems (Fig. 1).

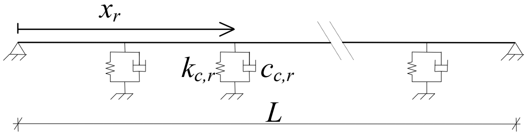

Fig. 1. Analytical 2-dimensional model for bridges with partial restraint.

Let $V=\left\{v(x)\in H^2[0,L]:v(0)=v(L)=0\right\}$ [1] be the space of displacement functions defined along the bridge length L and satisfying the kinematic (essential) boundary conditions and $u(x;t)\in U=C(V;[t_0,t_1])$ be the motion, defined in the time interval considered $[t_0, t_1]$.

The differential dynamic problem can be derived from the D'Alembert principle [11] and can be posed in the following form, $\forall\eta\in V;\forall t\in[t_0,t_1]$:

$$\begin{aligned}&\int_0^L m(x)\ddot{u}(x,t)\eta(x)dx+\int_0^L c_d(x)\dot{u}(x,t)\eta(x)dx+\sum_{r=1}^N c_{c,r}\dot{u}(x_r,t)\eta(x_r)+\\&+\int_0^L b(x)u''(x,t)\eta''(x)dx+\sum_{r=1}^N k_{c,r}u(x_r,t)\eta(x_{c,r})=-\int_0^L m(x)\ddot{u}_g(t)\eta(x)dx\end{aligned}\tag{1}$$

---

[1] The form $H^m(\Omega)$ denotes the space of functions defined on Ω for which the derivatives with respect to x of order less than or equal to m are on $L^m(\Omega)$.

The functions $m(x)$, $b(x)$ and $c_d(x)$ are piecewise continuous and denote the mass per unit length, the transverse stiffness per unit length and the distributed damping constant. The constants $k_{c,r}$ and $c_{c,r}$ are the stiffness and damping constant of the visco-elastic support located at the r-th position $x=x_r$. Finally, $\ddot{u}_g(t)$ denotes the ground motion input. It is noteworthy that although various models are available for describing the dissipation of energy in the deck [12],[13], in the present study the deck damping is simply described in terms of a force proportional to velocity. More cumbersome descriptions are avoided since the deck damping is usually smaller than the intermediate supports' damping and, moreover, the focus of the paper is on the influence of the intermediate supports on the response.

In the present work, particular simplified configurations of bridges are analyzed in order to identify the parameters which influence the most the bridges' dynamic properties. In these configurations, the mass per unit length, the beam transverse stiffness and the external damping coefficient are assumed constant and equal respectively to m_d, EI_d, c_d. Furthermore, the values of $k_{c,r}$ and $c_{c,r}$ at the N different intermediate supports are assumed constant and equal to $k_{c,r}=k_T/N$. Finally, the intermediate restraints are assumed equally spaced and the length of each span is set equal to $L/(N+1)$, where L is the total length of the bridge.

After these positions, the equation of motion can be expressed as:

$$\begin{aligned}&m_d\int_0^L \ddot{u}(x,t)\eta(x)\,dx + c_d\int_0^L \dot{u}(x,t)\eta(x)\,dx + \sum_{r=1}^{N}\frac{c_T}{N}\dot{u}(x_r,t)\eta(x_r) + EI_d\int_0^L u''(x,t)\eta''(x)\,dx + \\ &+\sum_{r=1}^{N}\frac{k_T}{N}u(x_r,t)\eta(x_r) = -m_d\int_0^L \ddot{u}_g(t)\eta(x)\,dx \qquad \forall\eta\in V;\forall t\in[t_0,t_1]\end{aligned} \tag{2}$$

Both the members of Eqn. (2) are divided by m_d, as usual, thus yielding:

$$\begin{aligned}&\int_0^L \ddot{u}(x,t)\eta(x)\,dx + 2\omega_d\gamma_d\int_0^L \dot{u}(x,t)\eta(x)\,dx + \sum_{r=1}^{N}\frac{c_T}{m_d N}\dot{u}(x_r,t)\eta(x_{c,r}) + \frac{\omega_d^2 L^4}{\pi^4}\int_0^L u''(x,t)\eta''(x)\,dx + \\ &+\sum_{r=1}^{N}\frac{k_T}{m_d N}u(x_r,t)\eta(x_{c,r}) = -\int_0^L \eta(x)\,dx\cdot\ddot{u}_g(t) \qquad \forall\eta\in V;\forall t\in[t_0,t_1]\end{aligned} \tag{3}$$

In deriving eqn.(3) the two following parameters have been introduced:

$$\begin{aligned}\omega_d &= \sqrt{\frac{\pi^4 EI_d}{m_d L^4}}\\ \gamma_d &= \frac{c_d}{2\omega_d m_d}\end{aligned} \tag{4}$$

The first one, ω_d, denotes the circular frequency of the first mode of vibration of the deck alone, i.e., the deck without intermediate supports [13]. The second one, γ_d, denotes the corresponding damping factor, i.e., the ratio between the energy dissipated by the external damping and the maximum strain energy attained due to deck bending, for an harmonic motion at the frequency ω_d, whose shape coincides with the first sinusoidal modal shape [13].

The properties of the system of visco-elastic intermediate supports can be conveniently described by introducing three non-dimensional parameters α, β and γ_c, defined as follows:

$$\begin{aligned}
\alpha^2 &= \frac{k_T L^3}{\pi^4 EI_d} = \frac{k_T}{\omega_d^2 L m_d} \\
\beta &= \frac{1}{N} \\
\gamma_c &= \frac{c_T}{2\alpha^2\omega_d m_d L} = \frac{c_T\omega_d}{2k_T}
\end{aligned} \tag{5}$$

The parameter *α* expresses the relative importance of the total spring stiffness with respect to a generalized measure of the global deck transverse stiffness. Low values of α^2 correspond to a stiff deck relative to the springs while high values correspond to a slender deck relative to the springs. The limit case $\alpha^2 = 0$ corresponds to the simply supported beam with no intermediate restraints.

The parameter *β* measures the degree of regularity of the total support stiffness' distribution along the bridge. It is inversely proportional to the number of intermediate springs and assumes values spanning from 0 to 1. The case $\beta = 1$ corresponds to the case of support stiffness concentrated at a single point while the limit case $\beta = 0$ ($N \to \infty$) corresponds to a beam resting on continuously distributed springs (Winkler beam).

The parameter γ_c describes the energy dissipation in the piers or the pier/bearing systems and it has the following physical interpretation: it is the ratio between the energy dissipated by the dampers and the maximum strain energy in the springs, for a rigid transverse harmonic motion of the deck with frequency ω_d.

After substituting eqn.(5) into eqn.(3) one obtains, $\forall \eta \in V; \forall t \in [t_0, t_1]$:

$$\begin{aligned}
&\int_0^L \ddot{u}(x,t)\eta(x)\,dx + 2\omega_d\gamma_d\int_0^L \dot{u}(x,t)\eta(x)\,dx + 2\alpha^2\beta\gamma_c\omega_d L\sum_{r=1}^{N}\dot{u}(x_r,t)\eta(x_r) + \\
&+\frac{\omega_d^2 L^4}{\pi^4}\int_0^L u''(x,t)\eta''(x)\,dx + \alpha^2\beta\omega_d^2 L\sum_{r=1}^{N} u(x_r,t)\eta(x_r) = -\int_0^L \eta(x)\,dx\cdot\ddot{u}_g(t)
\end{aligned} \tag{6}$$

In order to cut off also dimensional aspects related to the length, the variable $y=x/L$ can be introduced and accordingly the motion can be described by

$$\tilde{u}(y,t) = u(x,t) \tag{7}$$

Upon substitution in eqn.(6), one obtains:

$$\begin{aligned}
&\int_0^1 \ddot{\tilde{u}}(y,t)\tilde{\eta}(y)\,dy + 2\omega_d\gamma_d\int_0^1 \dot{\tilde{u}}(y,t)\tilde{\eta}(y)\,dy + 2\alpha^2\beta\gamma_c\omega_d\sum_{r=1}^{N}\dot{\tilde{u}}(y_r)\tilde{\eta}(y_r) + \frac{\omega_d^2}{\pi^4}\int_0^1 \tilde{u}''(y,t)\tilde{\eta}''(y)\,dy + \\
&+\alpha^2\beta\omega_d^2\sum_{r=1}^{N}\tilde{u}(y_r)\tilde{\eta}(y_r) = -\int_0^1 \tilde{\eta}(y)\,dy\cdot\ddot{u}_g \quad \forall\tilde{\eta}\in\tilde{V} = \left\{\tilde{v}(y)\in H^2[0,1] : \tilde{v}(0)=\tilde{v}(1)=0\right\}; \forall t\in[t_0,t_1]
\end{aligned} \tag{8}$$

The corresponding local form of the problem is obtained by integrating by parts and can be written as:

$$\begin{aligned}
&M\ddot{\tilde{u}}(y,t) + C\dot{\tilde{u}}(y,t) + K\tilde{u}(y,t) = -M\ddot{u}_g(t) \\
&\tilde{u}''(y,t)\tilde{\eta}'\Big|_0^1 = 0
\end{aligned} \tag{9}$$

where M, C, K are formal linear operator related to the mass, damping and stiffness:

$$
\begin{aligned}
M &= 1 \\
K &= \left[\frac{1}{\pi^4}\frac{\partial^4}{\partial x^4} + \alpha^2\beta\sum_{r=1}^{N}\delta\left(y-y_r\right)\right]\omega_d^2 = K_1\omega_d^2 \\
C &= 2\left[\gamma_d + \alpha^2\beta\gamma_c\sum_{r=1}^{N}\delta\left(y-y_r\right)\right]\omega_d = C_1\omega_d^2
\end{aligned}
\tag{10}
$$

and $\delta(\cdot)$ denotes the Dirac delta function.

3 FREE VIBRATIONS PROBLEM

3.1 Form of the characteristic equation

Under a qualitative point of view, the dynamic properties of a linear system, such as the ones analyzed in the present study, can be measured by solving the free vibrations problem that corresponds to eqn.(9) for $\ddot{u}_g = 0$. Thus, the study will proceed with the assessment of the influence of the parameters α, β, γ_d on the response in the most significant vibration modes. For this purpose, the differential boundary problem of eqn.(9) is reduced to an eigenvalue problem through the separation of variables technique. The transverse displacement $\tilde{u}$ is decomposed into the product of a spatial function and a time-dependent function, thus yielding:

$$\tilde{u}\left(y,t\right) = \psi\left(y\right)Z\left(t\right) \tag{11}$$

where $\psi(y)$ is a space-only dependent function while $Z(t)$ is a time function, whose expression is:

$$Z\left(t\right) = Z_0 e^{\lambda t} \tag{12}$$

After substituting eqns.(10), (11) and (12) into eqn.(9), one obtains the characteristic equation for the free-vibration problem:

$$\left\{\lambda^2 + 2\left[\gamma_d + \alpha^2\beta\gamma_c\sum_{r=1}^{N}\delta\left(y-y_r\right)\right]\omega_d\lambda + \left[\frac{1}{\pi^4}\frac{\partial^4}{\partial x^4} + \alpha^2\beta\sum_{r=1}^{N}\delta\left(y-y_r\right)\right]\omega_d^2\right\}\psi\left(y\right) = 0 \tag{13}$$

It is noteworthy that if λ_1 and $\psi(y)$ are solutions of eqn. (13) for a particular value of the deck circular frequency $\omega_d = \omega_{d1}$ then $\sigma\lambda_1$ and $\psi(y)$ are solution of eqn.(13) for $\omega_d = \sigma\omega_{d1}$. Thus, the particular choice of the characteristic parameters leads to a formulation such that the vibration shape $\psi(y)$ does not depend on the particular value of ω_d but it only varies by varying the parameters α, β, γ_d and γ_c. This makes it possible to obtain qualitative results that are not dependent on the deck stiffness or on the deck mass.

3.2 Analytical solution of the eigenvalue problem

In order to solve analytically the free vibrations problem it is convenient to divide the beam into a set of N_s segments, each bounded by two consecutive restraints (external or intermediate). The motion of the s-th segment is described by the function $\ddot{\tilde{u}}_s\left(z_s,t\right)$ as follows:

$$\ddot{\tilde{u}}_s\left(z_s,t\right) + 2\gamma_d\omega_d\dot{\tilde{u}}_r\left(z_s,t\right) + \frac{1}{\pi^4}\omega_d^2\tilde{u}_s\left(z_s,t\right) = 0 \quad \text{with} \quad z_s \in \left[0,1/N_s\right] \tag{14}$$

The transverse displacement $\tilde{u}_s$ is decomposed into the product of the spatial function $\psi_s(y)$ and the time-dependent function $Z(t)$ of eqn.(12), thus yielding the following equation of motion:

$$\left(\lambda^2+2\gamma_d\omega_d\lambda\right)\psi_s\left(y,t\right)+\frac{\omega_d^2}{\pi^4}\psi_s^{\;IV}\left(y,t\right)=0 \tag{15}$$

which is rewritten as:

$$\psi_s^{\;IV}\left(y,t\right)=\Omega^4\psi_s\left(y,t\right) \tag{16}$$

having posed $\Omega^4=-\dfrac{\pi^4\left(\lambda^2+2\gamma_d\omega_d\lambda\right)}{\omega_d^2}$, or $\lambda=-\gamma_d\omega_d+i\sqrt{\left(\dfrac{\Omega^4\omega_d^2}{\pi^4}\right)-\left(\gamma_d\omega_d\right)^2}$.

The solution to eqn.(15) is:

$$\psi_s\left(y\right)=C_{4s-3}\sin\left(\Omega y\right)+C_{4s-2}\cos\left(\Omega y\right)+C_{4s-1}\sinh\left(\Omega y\right)+C_{4s}\cosh\left(\Omega y\right) \tag{17}$$

with C_{4i-3} , C_{4i-2} , C_{4i-1} , C_{4i} to be determined based on the boundary conditions at the external supports and the continuity conditions at the intermediate restraints. This involves the calculation of higher order derivatives up to the third order.

In total, a set of $4N_\mathrm{s}$ conditions is required to determine the vibration shape along the whole beam. At the first span, i.e., for $s=1$, the conditions $\psi_1\left(0\right)=\psi_1\,''\left(0\right)=0$ apply while at the last span, i.e., for $s=N_\mathrm{s}$, the support conditions are $\psi_{N_s}\left(1/N_\mathrm{s}\right)=\psi''_{N_s}\left(1/N_\mathrm{s}\right)=0$. The boundary conditions expressing the continuity of the functions ψ_{i-1} and ψ_i at each of the N_s-1 spring locations can be expressed as:

$$\begin{aligned}
&\psi_{s-1}\left(1/N_\mathrm{s}\right)=\psi_s\left(0\right)\\
&\psi'_{s-1}\left(1/N_\mathrm{s}\right)=\psi'_s\left(0\right)\\
&\psi''_{s-1}\left(1/N_\mathrm{s}\right)=\psi''_s\left(0\right)\\
&\left[\psi'''_{s-1}\left(1/N_\mathrm{s}\right)-\psi'''_s\left(0\right)\right]-\beta\left(\pi^4\alpha^2+\frac{2\lambda\pi^4\alpha^2\gamma_c}{\omega_d}\right)\psi_s\left(0\right)=0
\end{aligned} \tag{18}$$

By substituting eqn. (17) into the boundary (supports and continuity) conditions, a system of $4N_s$ homogeneous equations in the constants $C_1,\ldots,C_{4N_S}$ is obtained. Since the system is homogeneous, the determinant of coefficients must be equal to zero for the existence of a nontrivial solution. This procedure yields the following frequency equation in the unknown Ω:

$$G\left(\Omega,\alpha^2,\beta,\gamma_d,\gamma_c\right)=0 \tag{19}$$

It is noteworthy that the particular choice of the set of characteristic adimensional parameters results in an function G which is independent from ω_d.

In the general case of non-zero damping, the solution of the equation must be sought in the complex domain. Since the system is continuous, an infinite set of Ω values satisfying eqn.(19) is obtained. However, only selected values of Ω are significant, because they correspond to the first vibration modes which are usually characterized by the highest participation factors. For a given value of Ω satisfying eqn. (19), the corresponding modal shape can be calculated, together with the corresponding circular frequency ω and damping factor ξ. It is remarked that the eigensolutions Ω are complex conjugate. Thus, if the couple $\Omega=\Omega_r+i\Omega_i$ and $\lambda=\lambda_r+i\lambda_i$ is a solution of eqn.(19), then the couple $\bar{\Omega}=\Omega_r-i\Omega_i$ and $\lambda=\lambda_r-i\lambda_i$ is a solution, too. The corresponding eigenvectors are complex conjugate, too. Finally, for zero-damping $\lambda=i\omega$ where $\omega=\Omega\sqrt{EI_d/m_d}$.

3.3 Generalized orthogonality conditions for vibration modes and modal properties

Eqn.(13) for mode *i* is multiplied by ψ_j and eqn.(13) for mode *j* is multiplied by ψ_i. After integrating over the entire length of the beam one obtains:

$$\begin{aligned}&\lambda_i^2\int_0^1\psi_i(y)\psi_j(y)dy+2\omega_d\lambda_i\left[\gamma_d\int_0^1\psi_i(y)\psi_j(y)dy+\alpha^2\beta\gamma_c\sum_{r=1}^{N}\psi_i(y_r)\psi_j(y_r)\right]+\\&+\frac{\omega_d^2}{\pi^4}\int_0^1\psi_i^{IV}(y)\psi_j(y)dy+\alpha^2\beta\omega_d^2\sum_{r=1}^{N}\psi_i(y_r)\psi_j(y_r)=0\end{aligned}\tag{20}$$

$$\begin{aligned}&\lambda_j^2\int_0^1\psi_j(y)\psi_i(y)dy+2\omega_d\lambda_j\left[\gamma_d\int_0^1\psi_j(y)\psi_i(y)dy+\alpha^2\beta\gamma_c\sum_{r=1}^{N}\psi_j(y_r)\psi_i(y_r)\right]+\\&+\frac{\omega_d^2}{\pi^4}\int_0^1\psi_j^{IV}(y)\psi_i(y)dy+\alpha^2\beta\omega_d^2\sum_{r=1}^{N}\psi_j(y_r)\psi_i(y_r)=0\end{aligned}\tag{21}$$

By integrating twice by parts the terms with the fourth order derivative and recalling the support boundary conditions, one finally obtains:

$$\begin{aligned}&\lambda_i^2\int_0^1\psi_i(y)\psi_j(y)dy+2\omega_d\lambda_i\left[\gamma_d\int_0^1\psi_i(y)\psi_j(y)dy+\alpha^2\beta\gamma_c\sum_{r=1}^{N}\psi_i(y_r)\psi_j(y_r)\right]+\\&+\frac{\omega_d^2}{\pi^4}\int_0^1\psi_i''(y)\psi_j''(y)dy+\alpha^2\beta\omega_d^2\sum_{r=1}^{N}\psi_i(y_r)\psi_j(y_r)=0\end{aligned}\tag{22}$$

$$\begin{aligned}&\lambda_j^2\int_0^1\psi_j(y)\psi_i(y)dy+2\omega_d\lambda_j\left[\gamma_d\int_0^1\psi_j(y)\psi_i(y)dy+\alpha^2\beta\gamma_c\sum_{r=1}^{N}\psi_j(y_r)\psi_i(y_r)\right]+\\&+\frac{\omega_d^2}{\pi^4}\int_0^1\psi_j''(y)\psi_i''(y)dy+\alpha^2\beta\omega_d^2\sum_{r=1}^{N}\psi_j(y_r)\psi_i(y_r)=0\end{aligned}\tag{23}$$

By subtracting eqn.(23) from eqn.(22), for $\lambda_i\neq\lambda_j$, one obtains the first orthogonality condition:

$$\left(\lambda_i+\lambda_j\right)\int_0^1\psi_i(y)\psi_j(y)dy+2\omega_d\gamma_d\int_0^1\psi_i(y)\psi_j(y)dy+2\alpha^2\beta\omega_d\gamma_c\sum_{r=1}^{N}\psi_i(y_r)\psi_j(y_r)=0\tag{24}$$

By subtracting eqn.(23) multiplied by λ_i from eqn.(22) multiplied by λ_j and dividing by $\left(\lambda_j-\lambda_i\right)$ one obtains the second orthogonality condition:

$$\frac{\omega_d^2}{\pi^4}\int_0^1 \psi_i''(y)\psi_j''(y)\,dy-\lambda_i\lambda_j\int_0^1 \psi_i(y)\psi_j(y)\,dy+2\alpha^2\beta\omega_d^2\sum_{r=1}^{N}\psi_i(y_r)\psi_k(y_r)=0 \tag{25}$$

which upon substitution of eqn.(24) may also read as follows:

$$\begin{gathered}\frac{\omega_d^2}{\pi^4}\left(\lambda_i+\lambda_j\right)\int_0^1 \psi_i''(y)\psi_j''(y)\,dy+2\omega_d\gamma_d\lambda_i\lambda_j\int_0^1 \psi_i(y)\psi_j(y)\,dy+\\ +2\alpha^2\omega_d\beta\gamma_c\sum_{r=1}^{N}\psi_i(y_r)\psi_j(y_r)+2\alpha^2\beta\omega_d^2\left(\lambda_i+\lambda_j\right)\sum_{r=1}^{N}\psi_i(y_r)\psi_j(y_r)=0\end{gathered} \tag{26}$$

For the case of zero damping, the two orthogonality conditions reduce to the well expression already derived in [8]:

$$\int_0^1 \psi_i(y)\psi_j(y)\,dy=0 \tag{27}$$

$$\frac{\omega_d^2}{\pi^4}\int_0^1 \psi_i''(y)\psi_j''(y)\,dy+2\alpha^2\beta\omega_d^2\sum_{r=1}^{N}\psi_i(y_r)\psi_j(y_r)=0 \tag{28}$$

Similarly to [14], the generalized orthogonality conditions are employed to derive the analytical expressions of the circular frequency of vibration ω_i and of the damping factor ξ_i for the *i*-th vibration mode. By setting $\lambda_j=\bar{\lambda}_i$ in eqn.(25) and in eqn.(24), and recalling that $\lambda_i\bar{\lambda}_i=\omega_i^2$ and $\lambda_i+\bar{\lambda}_i=-2\xi_i\,\omega_i$, one obtains:

$$\frac{\omega_i^2}{\omega_d^2}=\frac{\dfrac{1}{\pi^4}\displaystyle\int_0^1\left[\psi_i''(y)\right]^2 dy+2\alpha^2\beta\sum_{r=1}^{N}\psi_i^2(y_r)}{\displaystyle\int_0^1 \psi_i^2(y)\,dy} \tag{29}$$

$$\xi_i=\frac{\gamma_d\displaystyle\int_0^1 \psi_i^2(y)\,dy+\alpha^2\beta\gamma_c\sum_{r=1}^{N}\psi_i^2(y_r)}{\displaystyle\int_0^1 \psi_i^2(y)}\cdot\frac{\omega_d}{\omega_i} \tag{30}$$

The circular frequency ω_i, normalized in eqn.(29) with respect to ω_d, is simply expressed in terms of the ratio between the potential energy of the deck and the restraints, and the kinetic energy of the deck mass. It can be observed that the contribution to the potential energy of the deck is proportional to the deck curvature and becomes more and more important with respect to the other term when the number of the vibration mode increases.

The modal damping factor in eqn.(30) corresponds to the ratio between the energy dissipated by the deck and by the restraints and the kinetic energy of the deck. It should be stressed that the term of the dissipation related to the intermediate dampers qualitatively acts a mass-proportional similarly to the deck damping and, thus, the damping factor is expected to reduce significantly when the number of the vibration mode increases. Furthermore, damping factor ξ_i is not sensitive to ω_d.

4 PARAMETRIC ANALYSIS

4.1 Undamped free vibrations

This paragraph analyzes the free vibrations problem of the beam with intermediate restraints, disregarding the damping exerted by both the deck and the restraints. The values of γ_d and γ_c are assumed equal to zero at this stage, in order to describe the influence of the global stiffness of the supporting system, described by α^2, and the effects related to the distribution of its stiffness, described by β.

Different configurations of beams with intermediate restraints are considered which are representative of common short and medium span bridges (Fig. 2). They correspond to different values of the parameter β, i.e., β=1 (Fig. 2a), β=1/2 (Fig. 2b), β=1/3 (Fig. 2c). Moreover, the limit case of a beam simply supported at its extremes with no intermediate restraints (corresponding to $\alpha^2=0$) (Fig. 2d), and a beam resting on elastic continuous transverse restraints (corresponding to β=0) are also analyzed.

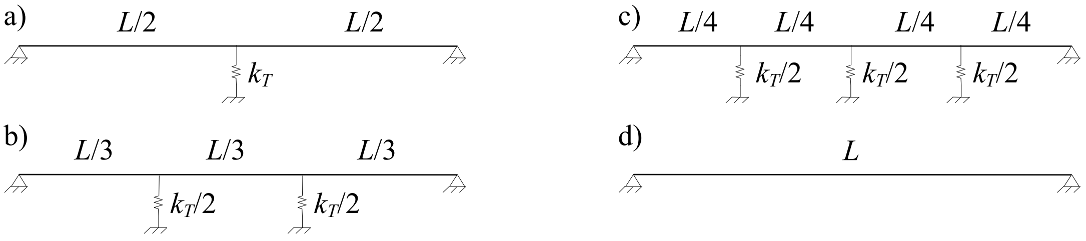

Fig. 2. Different configurations of beams with intermediate restraints analyzed.

The parameter α^2 is varied between about zero (stiff deck, flexible supports) and 10, that may be regarded as a realistic upper limit for slender superstructures on stiff supports. The results presented in the following include the modal shapes and periods of vibration. As previously shown, in the considered formulation the modal shapes depend on the parameters α and β only, and they are invariant with respect to the deck circular frequency ω_d. The vibration periods depend on the deck circular frequency, but they are divided by ω_d in order to make them independent from ω_d, too. Thus, the particular choice of the deck does not affect the following results. For the sake of completeness, the numerical results have been obtained by considering as reference the deck reported in [5], whose parameters are: L=200m, m_d=16.24t, EI_d=1100307114 kN/m^2, and ω_d=2.03Hz. Before discussing the results, it may be useful to recall that, in the limit case corresponding to β=0, the vibration modes are purely sinusoidal, irrespectively of the value of α^2 (see Appendix for the proof).

Fig. 3 reports the first three modal shapes for different values of α^2 and of β, normalized with respect to the L2 norm, i.e. $\|\psi_i\|_2 = \left(\int_0^1 |\psi_i(y)|^2 \, dy\right)^{1/2} = 1$. It is recalled that the even modes of vibration are characterized by an anti-symmetric shape and a participating factor equal to zero, and thus they do not affect the seismic response of the considered configurations.

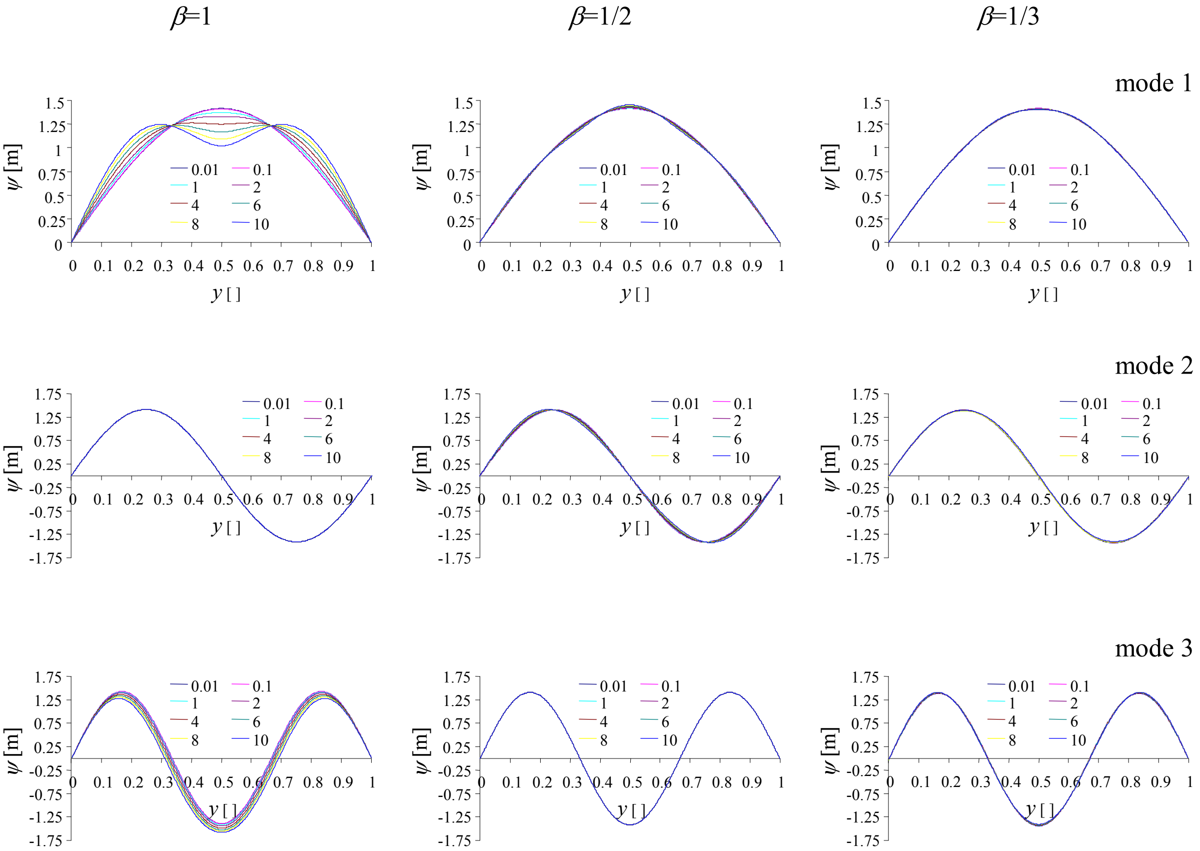

Fig. 3. Normalized first three modal shapes for different values of α^2 and for β.

The intermediate restraints have a remarkable influence on the first mode shape only for β=1. In this case, the first mode vibration shape significantly deviates from the shape of the deck vibrating alone (α^2=0), for high values of α^2. On the other hand, for β=1/2 and β=1/3, the vibration shape is very close to the shape of the deck vibrating alone, even for high values of α^2. This can be explained recalling that the vibration shape tends, for decreasing β values, to the sinusoidal shape of a simply-supported beam on continuous elastic restraints.

Globally, the influence of the restraints on the higher modes shapes is almost negligible, for any case of β, although a uniform trend is not observed, since the influence of the intermediate supports depend on their distance from the shape mode nodes.

In order to have a full insight into the influence of the restraints on the response along the deck, it is of interest to analyze the effects of the variation of the support properties on the second order derivative $\psi_i''(y)$ of the displacement shape, since this quantity is related to the deck's bending moments and strain energy distribution. Fig. 4 reports the normalized shape of $\psi_i''(y)$, for the first three vibration modes and for different values of the parameters α^2 and β.

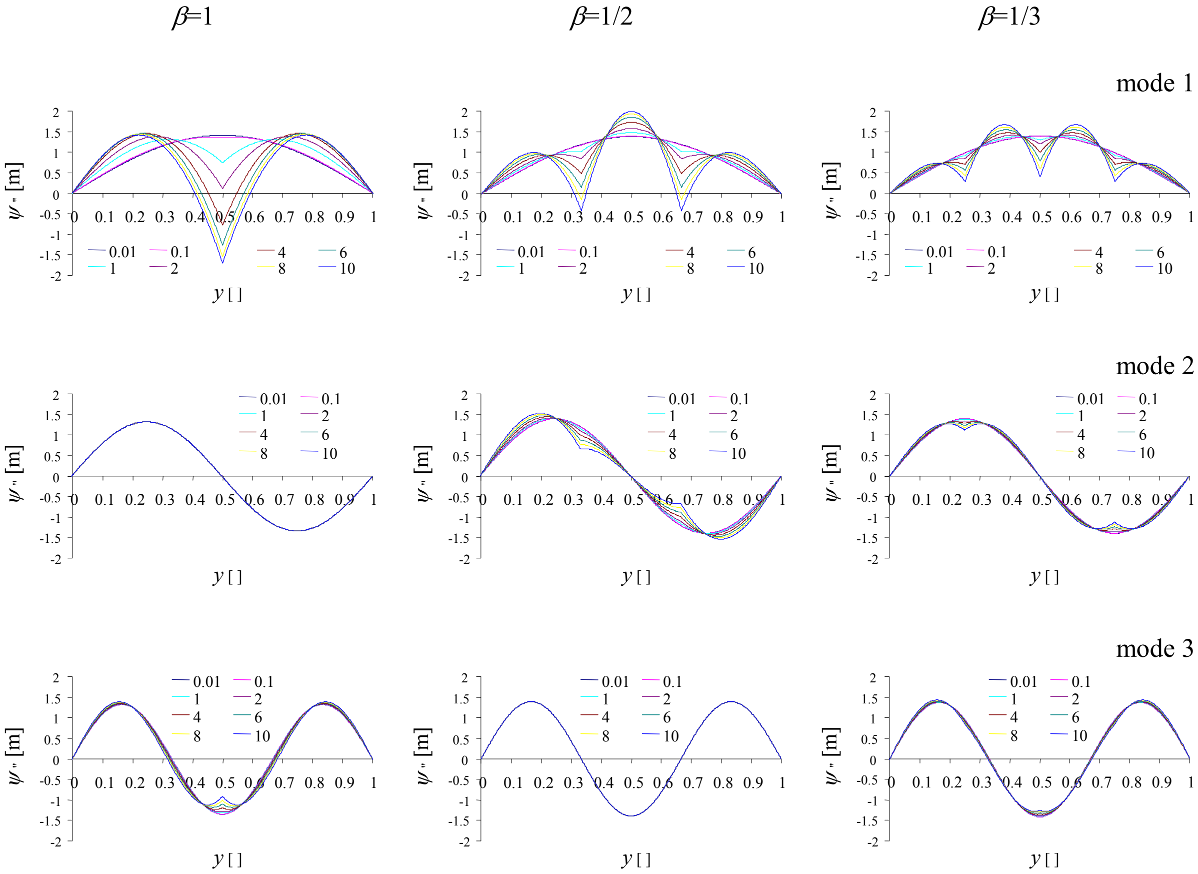

Fig. 4. Normalized second order derivatives of the first three modal shapes for different values of α^2 and β.

The intermediate supports influence more significantly the shape of the second order derivative than the displacement shape itself. Notable variations (with respect to the case corresponding to $\alpha^2=0$) are observed in the first mode shape, for all the three configurations considered. The variations in the higher modes are less significant and different from configuration to configuration.

In conclusion, the variation of the intermediate supports' properties induces minor variations in the distribution of the modal shapes, and thus in the distribution of the piers shear and inertia forces, directly related to them. Significant variations are limited to the first mode and to the configuration with a single support. On the other hand, the distribution of internal actions in the deck is strongly affected by the intermediate restraints, for the modes and configuration reported.

In order to describe synthetically the variation of the functions ψ_i and ψ_i'' defined along the bridge, the following scalar variation index is introduced:

$$\delta_{f_i} = \frac{\left\| f_i - f_{d,i} \right\|_2}{\left\| f_{d,i} \right\|_2} \quad \text{for } f_i = \psi_i, \psi_i'' \tag{31}$$

where the subscript "*i*" denotes the *i*-th vibration mode while the subscript "*d*" refers to the limit case corresponding to $\alpha^2=0$.

Other scalar quantities are of interest in the assessment of the system's seismic response and their variation due to the intermediate supports can be described synthetically in a similar way. In particular, the following results report the variation of the vibration periods T_i, of the participation factors ρ_i, and of the values of the third order derivative at the beam ends $R_i = \left|\psi_i'''(0)\right| = \left|\psi_i'''(L)\right|$, that is proportional to the transverse reaction at the abutments. The variation indexes for these quantities are defined as:

$$\delta_{f_i} = \frac{f_i - f_{d,i}}{f_{d,i}} \qquad \text{for } f_i = R_i, \rho_i, T_i \tag{32}$$

Fig. 5 shows the influence of parameters α^2 and β on the first-mode variation indexes. Fig. 5a highlights the different trend of the mode shape (displacement) and of its second order derivatives (bending moments). The variation index of the abutment reactions (Fig. 5b) assume positive and negative values spanning from -10% to around 40%-50%. Similar trends are observed for all the configuration considered. Finally, minor variations are observed for the participation factor while the vibration period strongly decreases with increasing α^2. Its sensitivity to α^2 is very high in the initial part of the range explored.

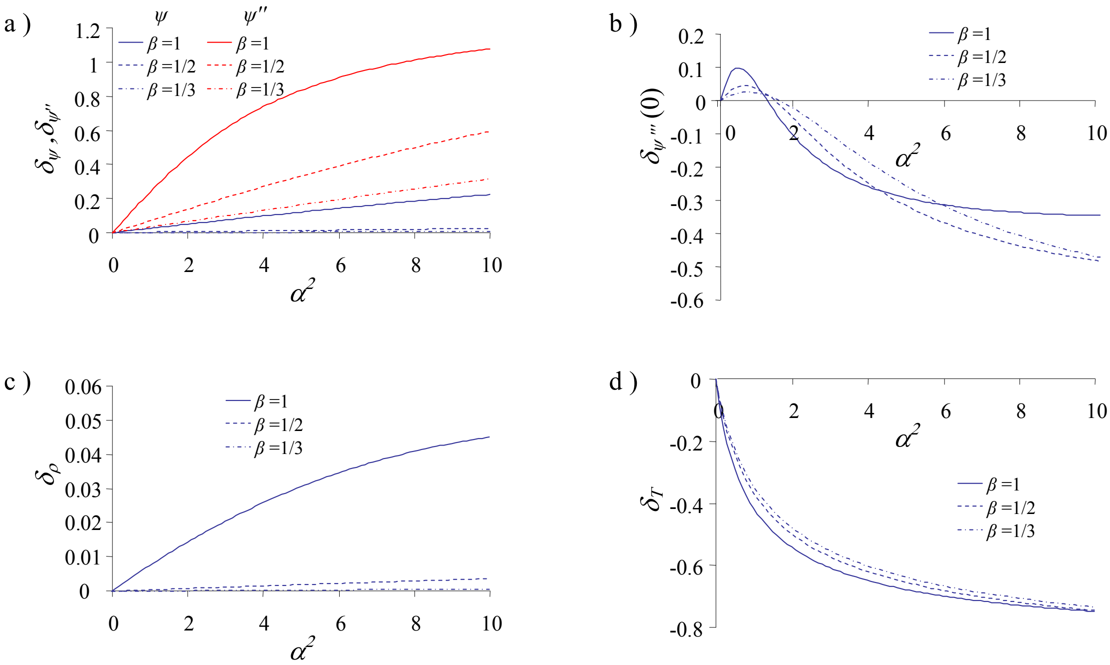

Fig. 5. Variation of δ with α^2 and β for mode 1 and relative to: a) displacements $\psi(y)$ and bending moments $\psi''(y)$, b) abutment shear $\psi'''(0)$, c) participation factor ρ, and d) vibration period T.

Fig. 6 and Fig. 7 show the influence of parameters α^2 and β on the variation indexes of the third and fifth mode. As previously noted, even modes are not of interest. Thus, the results concern odd terms only.

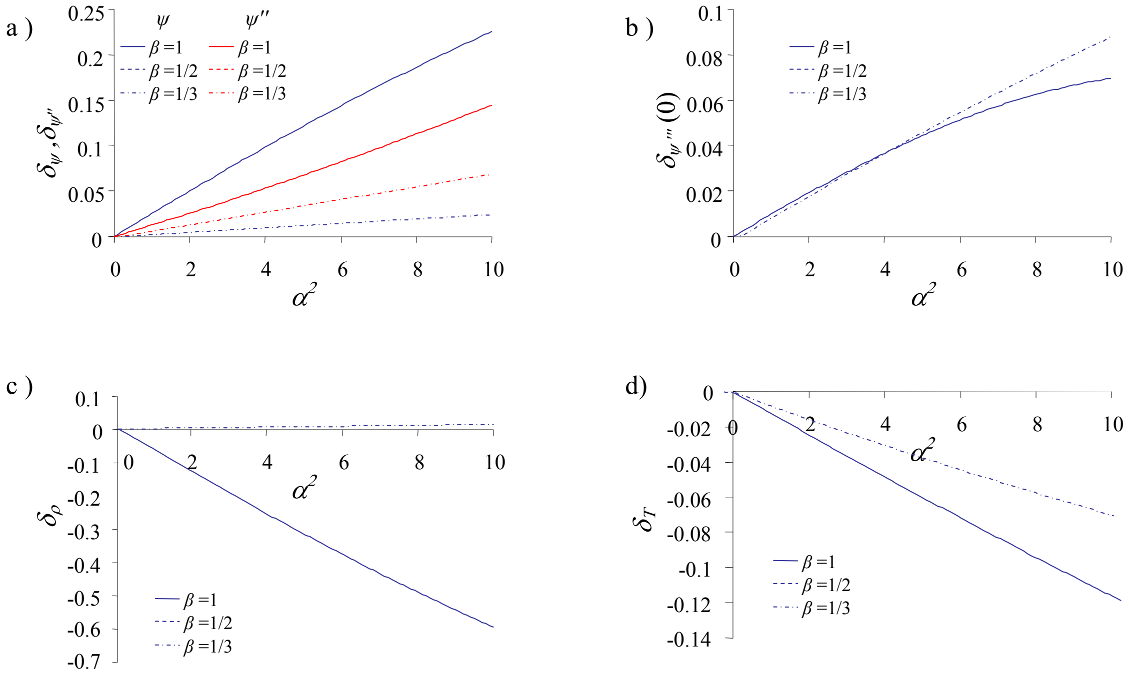

Fig. 6. Variation of δ with α^2 and β for mode 3 and relative to: a) displacements $\psi(y)$ and bending moments $\psi'''(y)$, b) abutment shear $\psi'''(0)$, c) participation factor ρ, and d) vibration period T.

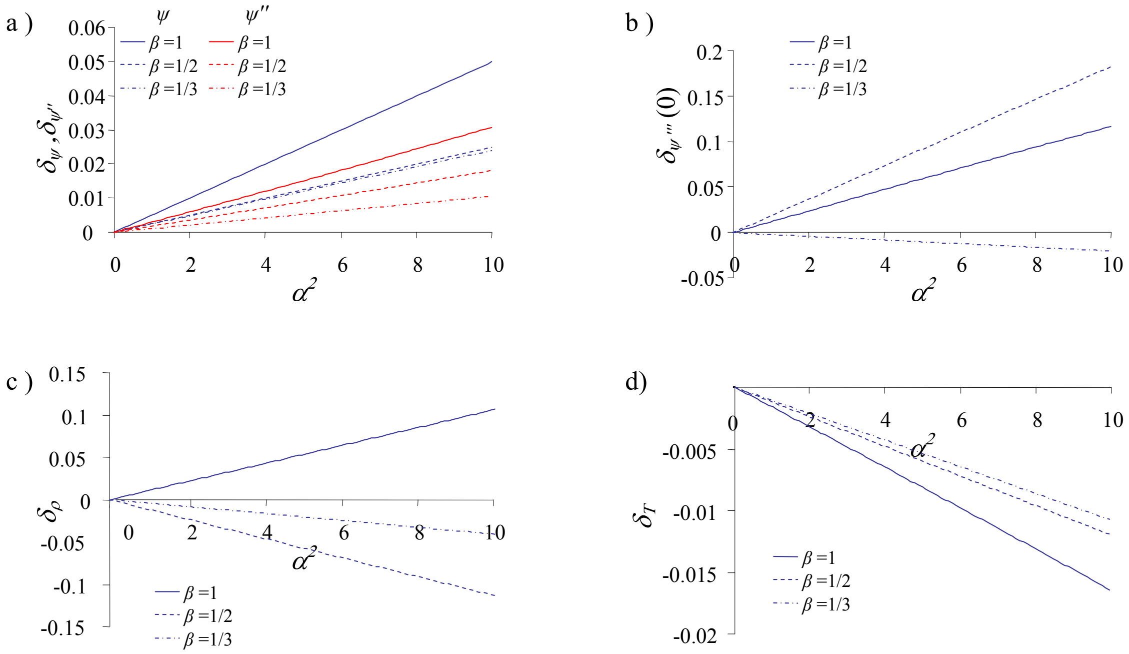

Fig. 7. Variation of δ with α^2 and β for mode 5 and relative to: a) displacements $\psi(y)$ and bending moments $\psi''(y)$, b) abutment shear $\psi'''(0)$, c) participation factor ρ, and d) vibration period T.

Generally, different trends can be observed in the higher-modes variation indexes. Variations in displacement and bending decrease for higher modes and higher number of supports. The reaction at the abutments, related to the third order derivative, is strongly influenced by the presence of intermediate supports, without distinction for the considered configurations, and it shows large variations with different sign. The intermediate supports in general reduce the vibration period but their influence is lower and lower for increasing order of modes. Finally, the participation factors are not significantly influenced by the intermediate restraints, with the exception of the second mode's participation factor, for β=1.

4.2 Non-classically damped free vibrations

This paragraph analyzes the damped free vibrations problem which corresponds to considering the deck damping and intermediate restraints with visco-elastic behavior. The solution to this problem is reported in Appendix A. A damping factor γ_d =0.02 is employed to describe the dissipation in the deck [5] while different values of γ_c from 0 to 0.25 are considered to describe the dissipation of the intermediate restraints. It is noteworthy that only the intermediate dampers are the cause of the non-classical damping, since the deck damping is assumed proportional to the mass. The most relevant effects of the variation of the intermediate dampers properties on the system free-vibration response are discussed below.

Fig. 8 shows the influence of the intermediate supports damping γ_c on the global dissipative properties, described by the damping factor ξ, for vibration modes 1, 3 and 5. The definition and the analytical expression of ξ are reported in Appendix A. Different values of the parameters describing the intermediate supports stiffness (α^2) and the bridge configuration (β) are considered.

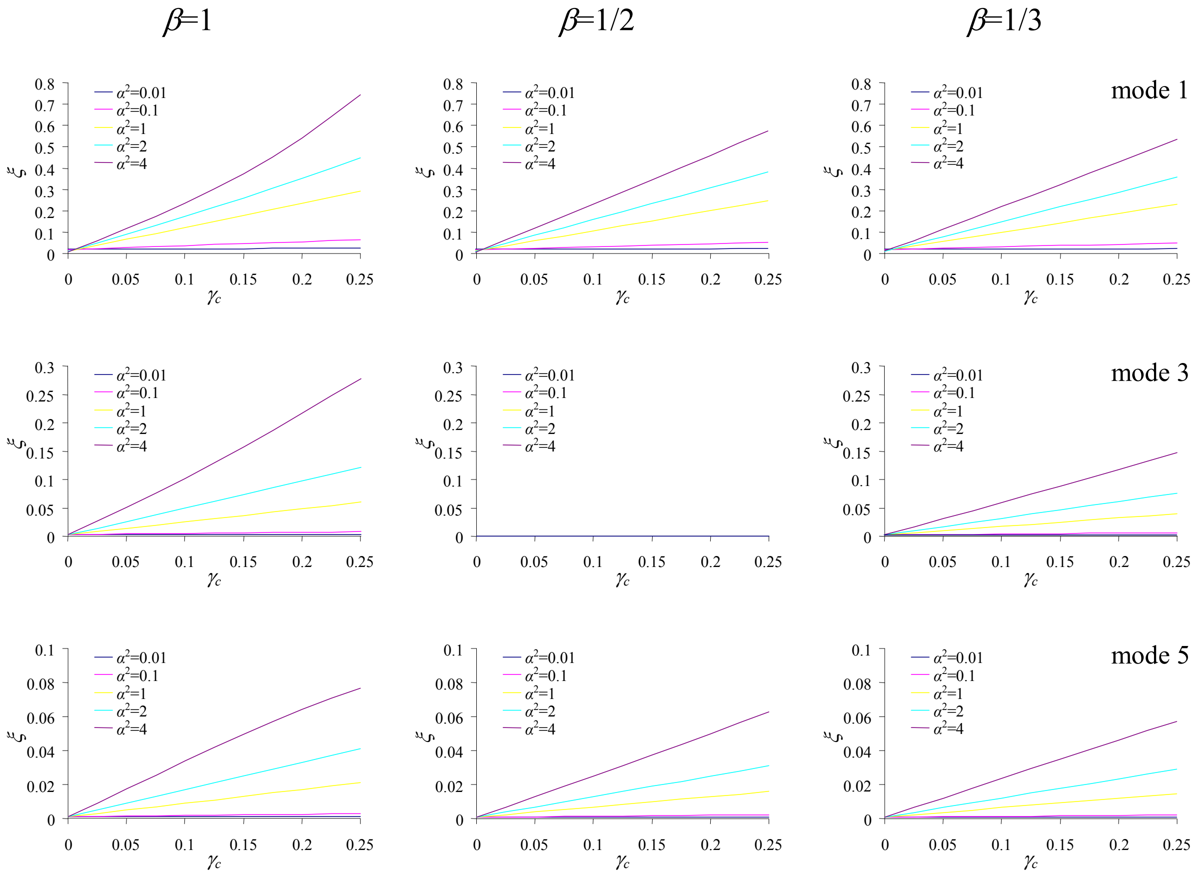

Fig. 8. Damping factor ξ vs. γ_c for different values of α^2 and β.

In general, the values of ξ corresponding to the first vibration mode (maximum value of 0.7 for γ_c =0.25) are significantly higher than those corresponding to the third (maximum value of 0.3 for γ_c=0.25) and the fifth vibration mode (maximum value of 0.08 for γ_c=0.25). It is also observed that the intermediate supports damping, which is proportional to the displacement, have a reduced efficiency in damping the higher modes and its decay rate is approximately proportional to $1/i^2$ (i denotes the mode index). Furthermore, the above figures demonstrate that the value of ξ increases almost linearly for increasing γ_c and for increasing α^2 while decreases slightly for decreasing β.

In a non-classically damped system such as those analyzed, the dampers may significantly affect the modal shape and the vibration motion may considerably vary with respect to the undamped case. In order to illustrate the modifications introduced by the intermediate dampers on the vibration shape with respect to the undamped case, a particular configuration is firstly analyzed which corresponds to the values of α^2=4, β=1 and γ_c=0.13, leading to ξ=0.3. Fig. 9 shows the real and imaginary part of the normalized first modal shape ($\psi_{1,ncd}^R$ and $\psi_{1,ncd}^I$) and of its second order derivative ($\psi''^R_{1,ncd}$ and $\psi''^I_{1,ncd}$) for the non-classically damped case. In the same figure, the normalized shape ($\psi_{1,cd}$) and its second order derivative ($\psi''_{1,cd}$) corresponding to the classically-damped case (γ_c=0) are also shown for comparison.

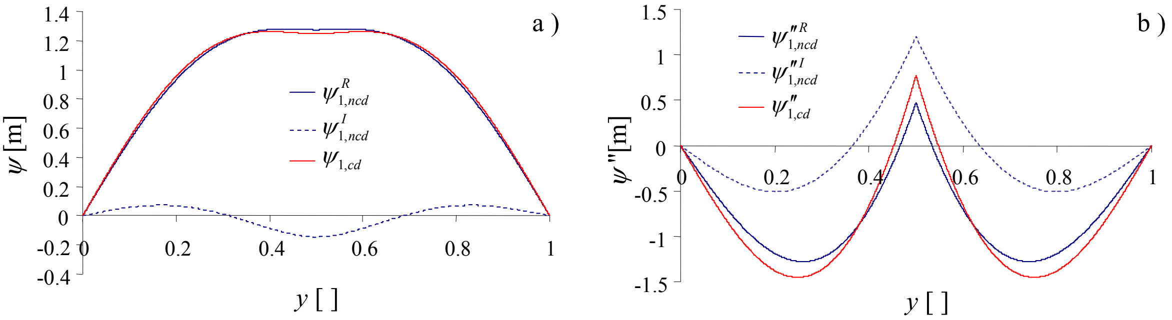

Fig. 9. (a) Real and imaginary part of the normalized first modal shape and (b) of the second order derivative for the non-classically damped case and for the classically-damped case (γ_c=0).

The intermediate dampers influence not only the imaginary part of the eigenvector and of its derivatives, but also, to a less extent, the real part. Furthermore, the imaginary part is quite small with respect to the corresponding real part in the displacement shape, but it assumes an high relevance in the moment shape.

For design purposes, it can be interesting to analyze the envelope of the free vibration response in the first classically ($\psi_{1,cd}$) and non-classically damped ($\psi_{1,ncd}$) modes obtained neglecting the amplitude decay term.

$$\psi_{1,ncd} = \max_t \left\{ \psi_1^R \cos(\omega_1 t) - \psi_1^I \sin(\omega_1 t) \right\} \tag{33}$$

Fig. 10a plots the envelope (acronym "env") of the modal shape. The envelope of the second-order derivative, derived in a similar manner, is also reported in Fig. 10b.

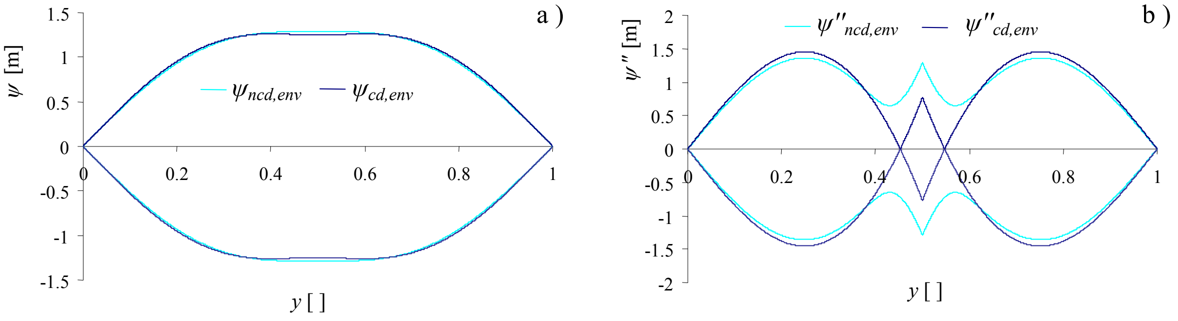

Fig. 10. Envelope of a) the first modal shape and b) of its second-order derivative for the non-classically damped case and the classically-damped case.

It is interesting to observe that the displacements envelopes accounting for and disregarding damping are very similar. On the other hand, the envelope of the curvatures for the non-proportionally damped case significantly differs from the corresponding envelope for the proportionally damped case. In conclusion, with reference to this case it is observed that neglecting the non proportionality of the damping yields sufficiently accurate estimates of the displacement shape but inadequate estimates of the maximum values of the internal actions attained during the vibration motion.

In order to provide information about the extent of non proportionality in the response, the following non-proportionality indexes are introduced for displacements, second order derivatives and end reactions:

$$\begin{aligned} \mu_{f_i} &= \frac{\left\| \mathrm{Im}\left(f_i\right) \right\|_2}{\left\| \mathrm{Re}\left(f_i\right) \right\|_2} \quad \text{with } f_i = \psi_i, \psi_i'' \\ \mu_{R_i} &= \frac{\mathrm{Im}\left(R_i\right)}{\mathrm{Re}\left(R_i\right)} \end{aligned} \tag{34}$$

The non-proportionality indexes generally increase for increasing α^2 and increase almost linearly for increasing γ_c ,except for the variation index of ψ in case β=1,mode 1. They also decrease for increasing β as expected, since when β tends to zero the system tends to a simply supported beam resting on continuously distributed visco-elastic restraints, whose damping is proportional and whose vibration modes are real.

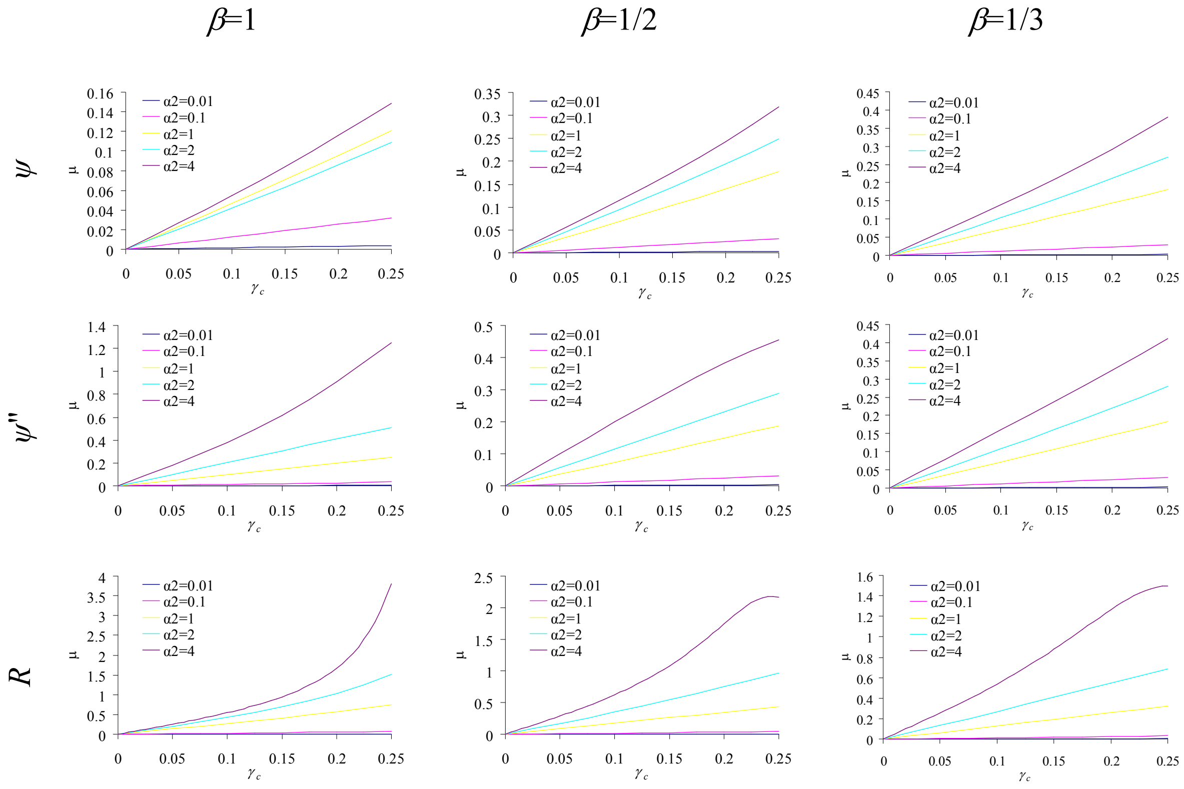

Fig. 11. Variation with γ_c of non-proportionality indexes relative to mode 1, for different values of α^2.

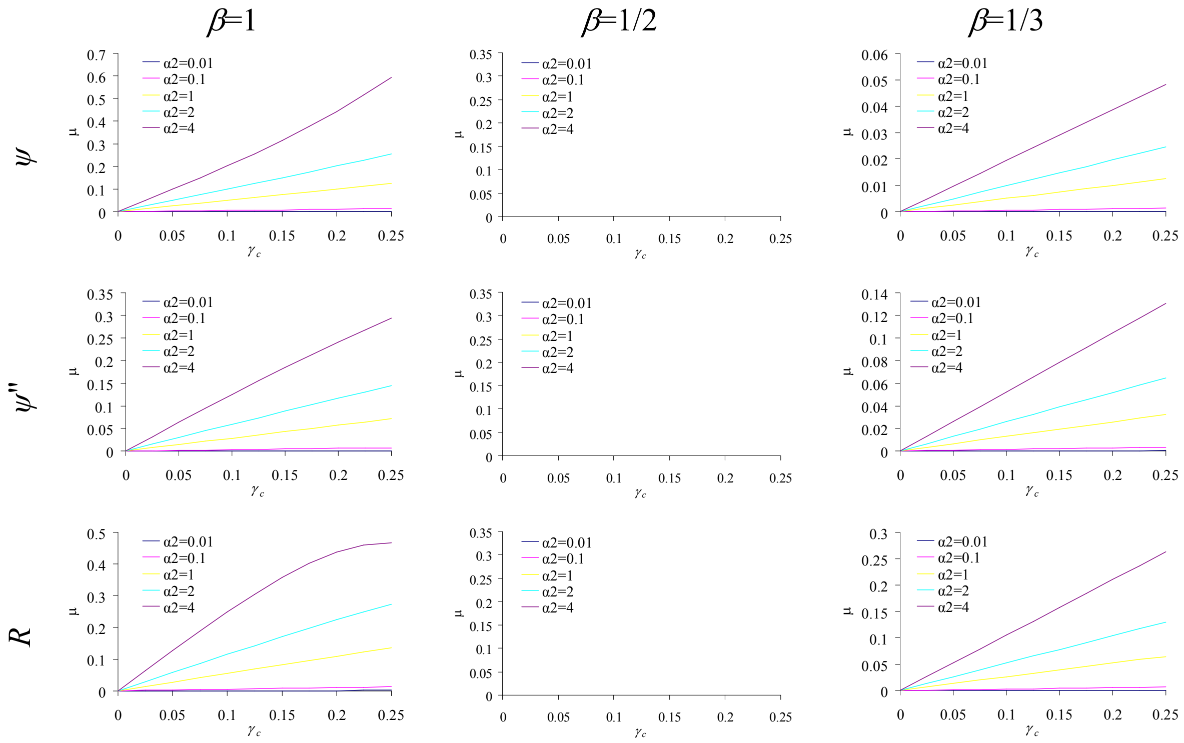

Fig. 12. Variation with γ_c of non-proportionality indexes relative to mode 3, for different values of α^2.

CONCLUSIONS

This paper examines the dynamic behavior of partially restrained seismically isolated bridges by studying the transverse free vibrations of a two-dimensional simply-supported beam model resting on intermediate visco-elastic supports.

Particular simplified configurations with constant deck properties and uniform equally spaced supports are considered, with two main aims: to seek a reduced set of characteristic parameters describing completely the dynamic system and to obtain analytical solutions useful to make explicit the relationship between the bridge properties and the dynamic response. Three parameters are identified that describe a) the global ratio between deck and supports stiffness (α), b) the regularity of the support stiffness distribution (β), and c) the global dissipative properties of the supports (γ_c).

A parametric analysis is carried out by varying the values assumed by these parameters, in order to highlight their influence on the dynamic properties of interest for the seismic response assessment. The reported results show that (a) variations in the distribution of displacements, related to the piers and inertia forces, are remarkable only for the first mode of the configuration with only one intermediate support, while minor variations are observed in the other cases; (b) variations in the curvatures' shape, related to the deck bending moments, are very significant and cannot be neglected for all the modes and configuration reported; (c) the abutment reactions are also strongly affected to the presence of intermediate supports, without distinction for the considered configurations; (d) the damping promoted by the intermediate supports is proportional to the displacements, and its effectiveness decreases rapidly with increasing mode order; (e) for certain values of the characteristic parameters the non classical damping induced by the intermediate supports can play an important role in the dynamic response and, thus, simplified approaches neglecting it can lead to not accurate estimates of the maximum values of the response parameters attained during the motion; (f) non-classical damping induces minor variations on the displacement shape and on related quantities rather than on higher order derivatives.

REFERENCES

[1] G.C. Lee, Y. Kitane, I.G. Buckle, Literature review of the observed performance of seismically isolated Bridges. *Report on Progress and Accomplishments: 2000-2001, MCEER Publications*, State University of New York, Buffalo, USA, 2001.

[2] M.C. Kunde, R.S. Jangid, Seismic behavior of isolated bridges: A state-of-the-art review. *Electronic Journal of Structural Engineering*, **3**, 140-170, 2003.

[3] M.H. Tsai, Transverse earthquake response analysis of a seismically isolated regular bridge with partial restraint. *Engineering structures*, **30**, 393-403, 2008.

[4] N. Makris, G. Kampas, D. Angelopoulou, The eigenvalues of isolated bridges with transverse restraints at the end-abutments. *Earthquake Engineering and Structural Dynamics*, **39**, 869-886, 2009.

[5] E. Tubaldi, A. Dall'Asta, A design method for seismically isolated bridges with abutment restraint. *Engineering Structures*, **33**, 786-795, 2011.

[6] C.M. Albarracín, L. Zannier, R.O. Grossi, Some observations in the dynamics of beams with intermediate supports, *Journal of Sound and Vibration*, **271**, 475-480, 2004.

[7] M.J. Maurizi, D.V. Bambilla, P.M. Bellès, M.A. De Rosa. Free vibration of Bernoulli Euler beams with intermediate elastic support: a concise thematic recension. *Journal of Sound and Vibration*, **281**, 1238-1239, 2005.

[8] P.A. Hassanpour, E. Esmailzadeh, W.L. Cleghorn, J.K. Mills, Generalized Orthogonality Condition for Beams with Intermediate Lumped Masses Subjected to Axial Force. *Journal of Vibration and Control*, **16**, 665-683, 2010.

[9] M. Gurgoze, On the eingenvalues of a viscously damped cantilever carrying heavy massed and restrained by linear and torsional spring. *Journal of Sound and Vibration*, **208**, 153-158, 1997.

[10] M.A. De Rosa, M. Lippiello, M.J. Maurizi, H.D. Martin, Free vibration of elastically restrained cantilever tapered beams with concentrated viscous damping and mass *Mechanics Research Communications*, **37**, 261-264, 2010.

[11] C.A. Truesdell, R.A. Toupin, *The Classical Field Theories*, Handbuch der Physik, vol. III-1, Springer-Verlag, Berlin, Germany, 1960.

[12] D.L. Russell, On mathematical models for the elastic beam with frequency-proportional damping. *Control and Estimation in Distributed Parameter Systems*, H.T. Banks, Editor, SIAM, Philadelphia, PA, 1992 .

[13] A.K. Chopra, *Dynamics of structures: Theory and Applications to earthquake engineering, 2nd Edition*, Prentice Hall, Englewood Cliffs, N.J, 2001.

[14] G. Oliveto, A. Santini. Complex modal analysis of a flexural vibrating beam with viscous end conditions. Journal of Sound and Vibration, **200**, 327-45, 1997.

COMPDYN 2011
III ECCOMAS Thematic Conference on
Computational Methods in Structural Dynamics and Earthquake Engineering
M. Papadrakakis, M. Fragiadakis, V. Plevris (eds.)
Corfu, Greece, 25–28 May 2011

A PROPOSAL FOR AN ALTERNATIVE TO SEISMIC ISOLATION PRACTICE: IMPLEMENTATION IN A SEISMIC ISOLATED RAILWAY BRIDGE

Sevasti D. Tegou[1] **and Ioannis A. Tegos**[2]

[1] Aristotle University of Thessaloniki
Department of Civil Engineering
e-mail: stegou@civil.auth.gr

[2] Aristotle University of Thessaloniki
Department of Civil Engineering
email: itegos@civil.auth.gr

Keywords: Bridge, Abutment, Earthquake Resistance, Restraining System, Steel Tube, Serviceability, Seismic Movement

Abstract. *The present study proposes an alternative to seismic isolation practice, which aims at the reduction in the bridge seismic actions mainly for the longitudinal design earthquake, which is more critical than the transverse one. The aforementioned purpose is achieved through the improved seismic participation of the bridge abutments. The deck slab is extended onto the embankments and is rigidly connected either with transversely directed RC walls or with transversely directed rows of hollow section steel tubes. This system is constructed into a concrete box-shaped substructure which replaces the conventional wing-walls. As a result the approach embankment does not affect the response of the proposed system. The efficiency of the proposed system was assessed by utilizing a conventional seismic isolated railway bridge. The analytical investigation was performed by means of non-linear dynamic time history analysis implemented with the FE commercial code SAP 2000. The bridge systems were subjected to artificial earthquake motion that is compatible to Eurocode 8 elastic spectra. The assessment of the efficiency was mainly carried out by comparing the response of the resulting modified bridge system with the response of the initial bridge system. The proposed system has the ability to accommodate the in-service movements of the deck, by means of the flexibility of the restraining members. The seismic response of the bridge is also enhanced. The displacements of the deck in the longitudinal direction of the bridge were found to be significantly reduced. The restraining effect also reflects on the seismic actions of the piers (shear actions and bending moments) leading to cost-effective bridge design.*

1 INTRODUCTION

Many countries around the world suffer from earthquakes and people expect that structural engineers will design structures so that they can survive the effects of these earthquakes. The basic requirement that the engineer work to meet during the design process is the ensuring that the capacity of the structure is greater than the demand [1,2]. The earthquake causes inertial forces proportional to the structure's mass and the earthquake ground accelerations. As the ground accelerations increase, the capacity of the structure must be increased to avoid structural damage. However it is not practical to continue to increase the strength of the structure indefinitely as this also increase the structural cost. So the Codes [3] allow engineers to use ductility to achieve the capacity. Ductility is a concept of allowing the structural elements to deform beyond the elastic limit in a controlled manner. Beyond this limit, the displacements increase with only a small increase in force.

Seismic isolation represents an opposite, to the aforementioned, approach, as it attempts to reduce the demand rather than increase the capacity of a structure [4-6]. In this framework, the effort on protection of bridges against earthquakes is mainly focused on minimizing the forces to be carried by the piers, in particular the shears. Isolation systems are basically typified into bearings and energy dissipation devices. Rubber bearings with high lateral flexibility are meant to shift the vibrational periods of the structures so as to avoid resonance with the excitations [7]. They are usually combined with high damping material and fluid dampers to increase the in-structure damping and to reduce the lateral movements of the bridge due to the seismic loading. Sliding bearings are introduced to filter out the imparting earthquake forces through the frictional interfaces. The support of the deck to the piers and abutments through bearings also accommodates the in-service induced movements of the deck due to shrinkage creep and thermal effects [8]. However, although seismic isolation is considered one of the most promising practices worldwide, the high purchase cost of the devices, which increases the total construction cost of the bridge constitutes a major disadvantage of this practice.

In this regard, concerning the reduction on the demand rather than the increase on the capacity of a structure, the seismic performance of bridges can also be enhanced by the abutment and backfill soil participation. Current research [9-11] focuses on the known problem of embankment-bridge interaction which can contribute to the enhancement of the seismic response of bridge structures. Specifically, recent studies have investigated the problem and came up to the conclusion that the dynamic participation of these elements results in significant displacement reductions [12]. Furthermore the seismic participation of the abutment was found to lead to cost- effective bridge design according to Nutt [13].

In the present study the seismic performance of bridges is enhanced through an external restraining system consisting of steel tubes which are arranged in rows behind the abutment's web. The efficiency of the proposed restraining system is examined by analyzing the seismic response of a railway bridge in Greece which is considered to be the "reference" bridge.

2 DESCRIPTION OF THE PROPOSED SYSTEM

The aim of the present study is the investigation on the efficiency of an external restrainer which has the ability to reduce the bridge seismic movements. The proposed restrainer is located behind the abutment's web and is consisted of transversely directed members which are either pairs of concrete walls or rows of pairs of steel tubes. The efficiency of the system consisting of pairs of concrete walls was extensively investigated in previous works [14]. In this study the investigation is extended in the field of the composite steel and concrete structures. The proposed system is given in Figure 1. Each pair of steel tubes is encased in the pile- cap while their heads are connected in the longitudinal and transverse direction through steel plates which are welded around their perimeter, see Detail 1 in Figure 1. The head of the pairs of the steel tubes is properly connected with the extension of the deck slab. As a result the in-service as well as the seismic loading causes the activation of the system. This system is constructed into a concrete box-shaped substructure which replaces the conventional wing-walls. Therefore the approach embankment does not affect the response of the proposed system.

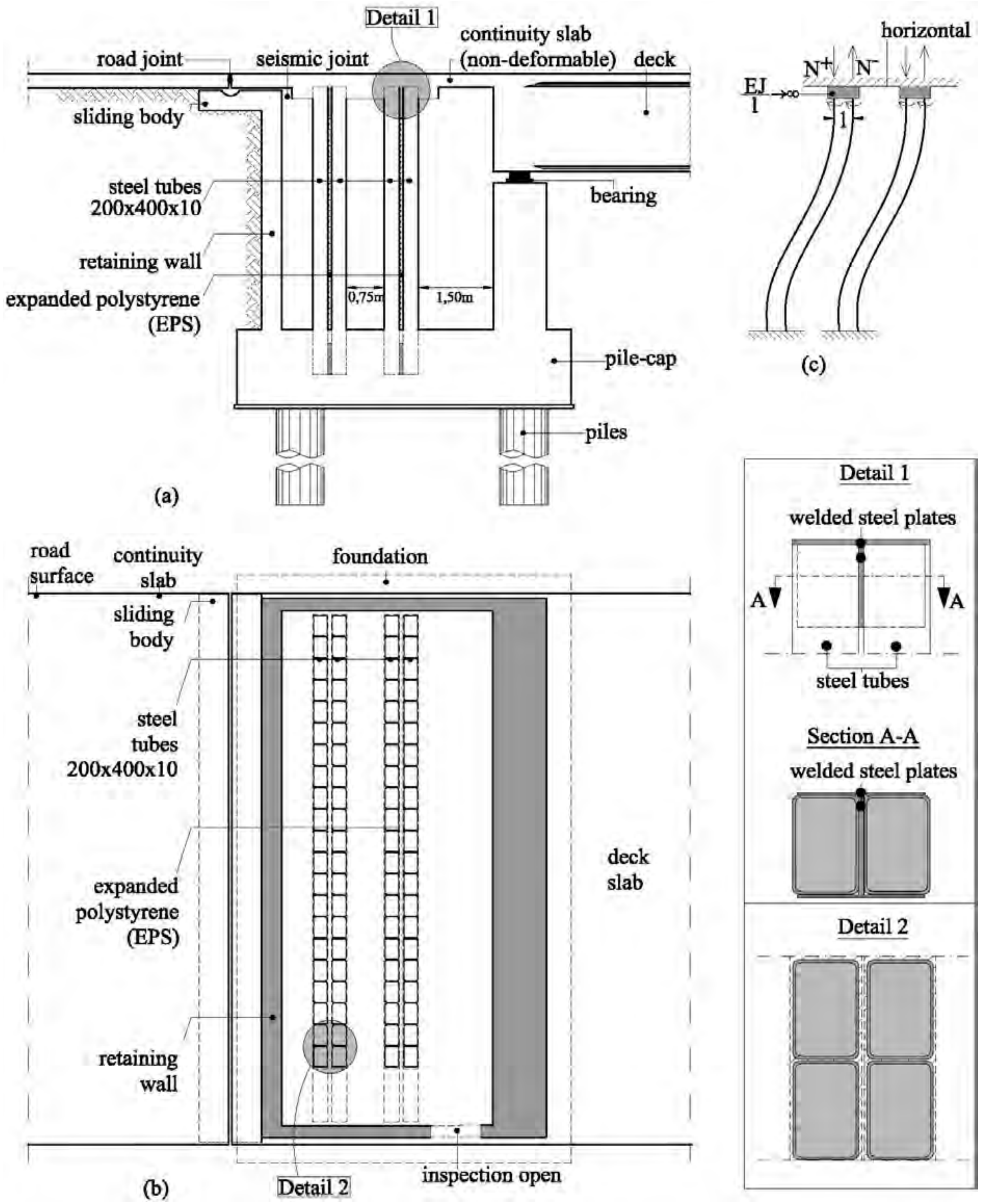

Figure 1:(a) Longitudinal section of the proposed restraining system, (b) Plan view of the proposed restraining system and (c) Restraining members’ model.

Any relevant movement between the tube's head and base causes (a) linear variant bending moments along the height of the tube (the zero point is at the middle of the height), (b) constant shear forces along the height of the tube which resist to the movement of the extension of the deck's slab, (c) tension and compression axial forces corresponding to the direction of the head's movement (every pair has one tensile and one compressive tube), (d) second-order effects due to the aforementioned axial loading. The additional bending moment due to these effects increases the initial bending moment at the base of the tensile member and decreases the bending moment at the base of the compressive one. It is also notable that the second-order effects affect the performance of the tube's pair and induce the synchronous yielding at the critical region of the tubes' bases. Otherwise the absence of the second-order effects causes the yielding at the base of the member subjected to tensile axial loading before the corresponding one at the compressive member. Although the aforementioned assumption cannot reasonably be made in the case of the members' heads, the inversion of the loading direction due to the cycling event leads to the acceptance of the asynchronous yielding at the members' heads. The aforementioned analysis regarding the behavior of the proposed restraining system rationalize the consideration of the restraining tubes as fixed members in the computational framework.

The steel tubes used in this system can either be rectangular or square cross-section [15]. The choice of the tube's cross-section determines the number of the steel tubes which can be used as the distance between the wing-walls is given. The response of the proposed system is strongly dependant on the dimensions of the aforementioned members which also affect the constructability of the system. The use of steel tubes with big dimensions complicates the constructability but increases the efficiency of the system. In this study has been chosen rectangular steel tubes whose dimensions are 200x400mm. Each row consists of 25 steel tubes whose weak axis is oriented parallel to the longitudinal direction of the bridge.

The proposed restraining system is rationally combined with sliding bearings which permit the free movement of the deck in the longitudinal direction of the bridge. The support of the deck to the piers through rubber bearings in bridge systems which develop the aforementioned system is in slight contrary to this proposal as on one hand the period of the system is reduced and on the other hand is attempted its increase through the flexibility of the system due to the presence of the bearings. However a solution with rubber bearings is quite interesting even for reasons concerning its economic efficiency and is presented in this study.

Finally, based on the aforementioned assumption concerning the static behavior of the restraining members, it is necessary to be mentioned an significant characteristic of the proposed system. The investigation on the efficiency of the system showed that two pairs of rows of steel tubes (one pair per abutment / 25 steel tubes per row) with a RHS cross-section 200x400x10mm and a height H_t=4.50m, have the same seismic resistance as five concrete piers monolithically connected to the deck. These piers have circular cross-section with a diameter d_c=1.5m and a height H_c=13.0m. The aforementioned conclusion derives from the equation of the resistances of the above members. The seismic resistance of a steel tube is calculated according to Equation (1). Equation (2) gives the seismic resistance of a pier. The resistance of two pairs of rows of steel tubes is 214 071 kN/m and is about five times the resistance of a pier with the above properties:

$$R_t = \frac{12E_s \cdot I}{H_t^3} \tag{1}$$

$$R_c = \frac{12E_c \cdot \pi \cdot d_c^4}{64H_c^3} \tag{2}$$

Respectively, 20 piers with the aforementioned properties, which are connected to the deck through bearings and their longitudinal movements are restrained through seismic links have the same resistance as two pairs of rows of steel tubes.

3 OVERVIEW OF THE BRIDGE STUDIED

In order to investigate the efficiency of the proposed practice a seismic isolated railway bridge located at Northern Greece was chosen as the case study. This bridge is straight, has four-spans and a total length equal to 168.0m, Figure 2. The end spans have a length equal to 39.0m, while the two intermediate spans are 45.,0m long. The prestressed deck, Figure 3(a), has a hollow T-beam-like section, is 13.60m wide and 3.60m high, is supported through LRB bearings placed on the two abutments and the three middle piers and is separated from the backwall through an expansion joint. Seismic forces are also resisted by the activation of stoppers (in the transverse direction) which are constructed at the seating of the abutments. Each abutment is equipped with two fluid dampers. The piers have a 3.00 x 5.50m hollow cross-section, 0.45m wall thickness and heights equal to 20.35m, 23.80m and 14.35m, Figure 3(b). The pier foundation consists of a 4x4 pile group of 15.0m long piles, connected with a 2.0x11.0x11.0m pile cap, while the abutments are supported on a 3x4 pile group of 12.0m long piles connected with a 2.0x7.5x11.0m pile cap. The axial spacing between all piles is 3.0m.

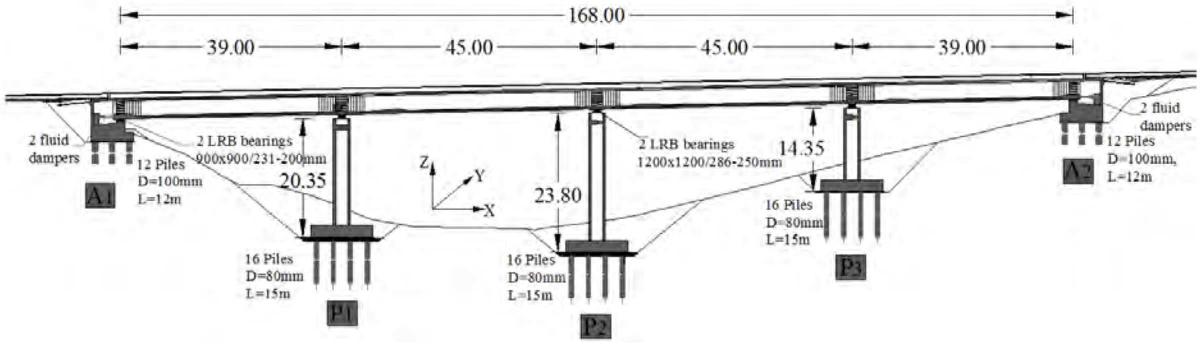

Figure 2: Longitudinal section of the seismic isolated bridge used for the purposes of the present study.

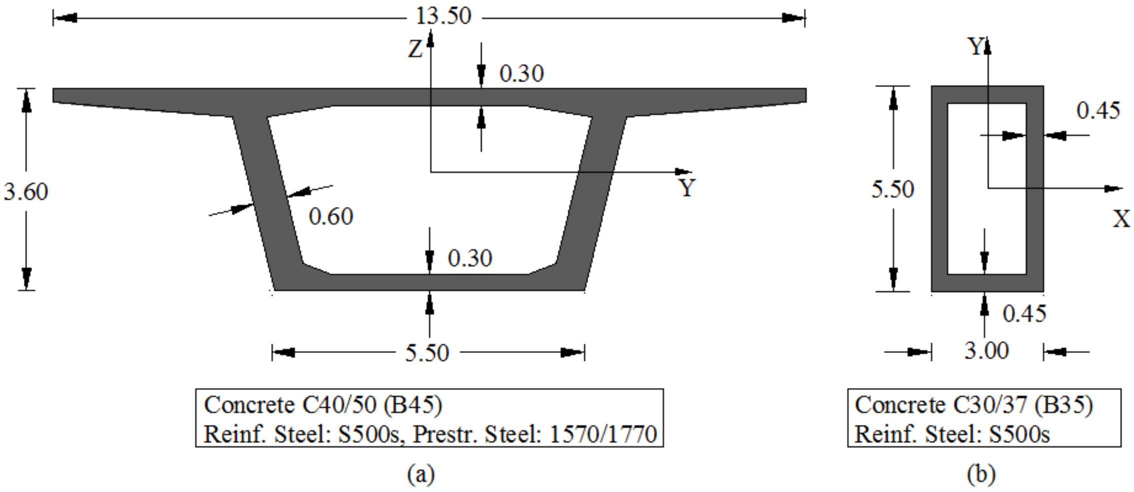

(a) (b)

Figure 3: (a) The cross-section of the deck in the middle and (b) the cross-section of the pier.

The bridge was designed for normal loads according to the German Norms [16] while the seismic design was carried out according to the Greek Seismic Code [17] and the relevant Greek standards [18] for the seismic design of bridges. The bridge is founded on a ground type B according to the Greek Seismic Code [17]. The corner periods of the spectrum used are 0.15s and 0.60s for ground type B. The site of the bridge belongs to Seismic Zone II according to the Greek Seismic Code, which is characterized by a Peak Ground Acceleration of 0.24g. The behavior factors of the system adopted for design according to the relevant Greek standards were $q_x=q_y=q_z=1.0$ for the response in the three principal directions, respectively.

4 COMPUTATIONAL FRAMEWORK

The proposed restraining system is implemented in the bridge described in the previous section. The modified bridge doesn't have hydraulic dampers and the LRB bearings are replaced by low-damping rubber bearings whose dimensions are calculated according to the Codes provisions [7]. The steel tubes are rectangular hollow sections 200x400mm with a wall thickness 10mm. Four rows of 25 steel tubes are considered per abutment as shows Figure 1. These tubes have a height equal to 4.5m and their weak axis is oriented parallel to the longitudinal direction of the bridge.

The numerical simulations of the two bridge systems (initial and modified) studied in the present investigation were carried out with the FE- Code SAP 2000 [19]. The aforementioned bridge systems were subjected to corresponding artificial Earthquake motions that are compatible to Eurocode 8 elastic spectra [3] and two different peak ground accelerations $a_g=0.24g$, $a_g=0.36g$ were considered. In Figure 4 are given the response spectra of the artificial earthquake motions used in the present investigation. Dynamic non-linear time history analysis was implemented and the direct integration, known as β-Newmark method, was used [20] as this method is the most robust to be used for the step-by-step dynamic analysis. The mass and stiffness proportional damping was chosen and critical damping ratios equal to 5% were considered for the first and the second period of the analyzed bridge systems [21].

Figure 5(a) gives the stick model of the initial bridge system. The deck of the bridge was modeled by frame elements, which have the section properties of the deck, Figure 3(a). The piers were also modeled by frame elements. The flexibility of their foundations was taken into account by assigning six spring elements -three translational and three rotational- whose stiffness values are given in Figure 5(a). These spring values were obtained by the in-situ geotechnical tests conducted for the design of the as-built bridge given in Figure 2. The LRB bearings which have a non-linear force-displacement relationship in the two horizontal directions were modeled by rubber isolator link elements. Their stiffness values were calculated according to Naeim and Kelly model [5]. Damper elements which are available in SAP 2000 were used for the modeling of the four fluid dampers of the bridge. These elements have a non-linear force-velocity relationship and their damping properties are based on the Maxwell model of viscoelasticity [22].

Figure 5(b) gives the stick model of the modified bridge system. The modeling of this bridge system developed the modeling of the initial bridge. The deck and the piers have the same cross-sections in the two bridge systems. As mentioned above the modified bridge doesn't have hydraulic dampers and the LRB bearings were replaced by low-damping rubber bearings. These bearings were modeled by link elements and their stiffness values were calculated according to Naeim and Kelly model [5]. The restraining system consists of two parts: (a) the extension of the deck slab, namely the continuity slab, which was modeled by frame elements. This slab has a width equal to 13,50m and a thickness equal to 0,40m and (b) the group of the steel tubes. The tubes were modeled by frame elements, which have an RHS cross-section 200x400x10mm. The steel tubes have a length equal to 4.5m and were considered to be fixed at the pile-cap of the foundation.

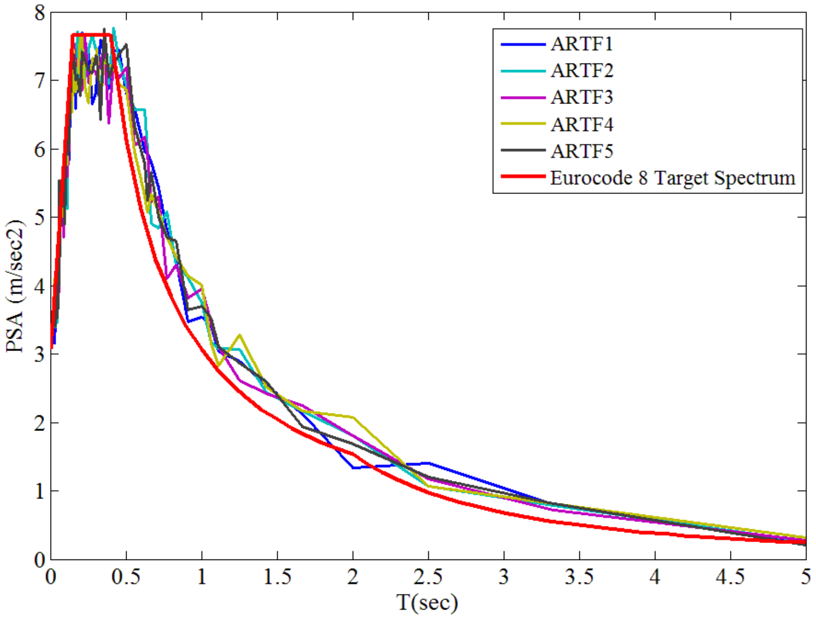

Figure 4: Response spectra of the artificial earthquake motions used in the present study and Eurocode 8 target spectrum (Soil Class B).

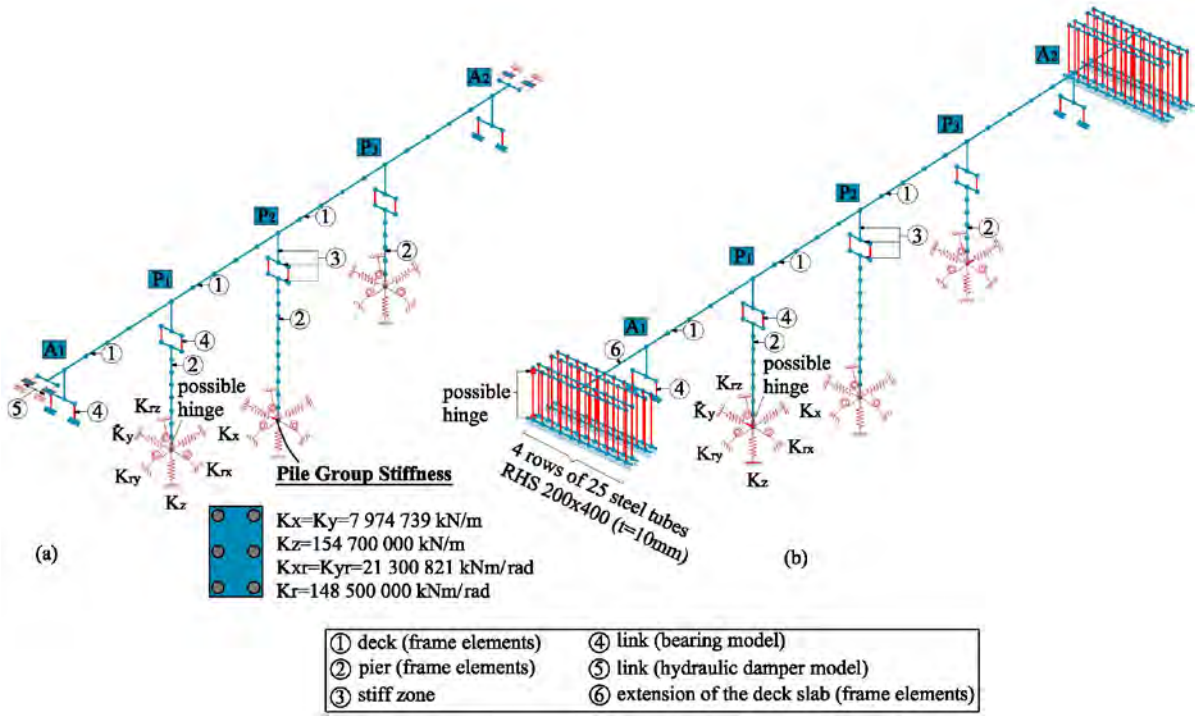

Figure 5: (a) Overview of the finite element models developed: (a) seismic isolated bridge system and (b) modified, according to the proposal of the present study, bridge system.

The possible plastic hinges at the piers' feet as well as at the restraining members' feet and heads were also modeled. The moment-curvature (M-φ) curves were calculated by means of RCCOLA-90 [23]. The model involves beam elements with inelastic springs located at their ends. Based on the members' geometry and the moment-curvature curves derived from the analysis of the cross- sections, the constants for the rotational springs are calculated. These springs are activated only whenever the developed bending moment exceeds the yield moment of the section and follows a non-linear force-rotation law that is a function of the cross-section properties.

5 EVALUATION ON THE EFFICIENCY OF THE PROPOSED SYSTEM

For the above two finite element models, non-linear dynamic analysis was performed using the 5 artificial earthquake motions. All analyses were conducted in the inelastic range and the excitation was performed in the longitudinal direction. As mentioned in the previous sections the proposed system is expected to dissipate part of the induced seismic energy through the flexural response of the restraining members. Figure 6(a) illustrates the hysteresis loop of a restraining member for a design ground acceleration a_g=0.24g. This figure shows that the restraining members respond in an inelastic manner. Consequently, the steel tubes are not only resisting with their stiffness, but also dissipate energy through hysteretic behavior. Figure 6(b) depicts the total input energy in the bridge system as well as the energy absorbed through the hysteretic behavior of the steel tubes for the same design ground acceleration. It can be deduced that a part of the input energy, about 35%, is absorbed through the hysteretic behavior of the restraining members.

The restrain of the bridge by the proposed system leads to an increase in the overall stiffness of the bridge. Specifically, the period of the first longitudinal mode shape is up to 73% reduced in the modified bridge system, in comparison to the period of the initial one. The reduction in the modal period of the modified bridge was found to lead in increases in its seismic loads, due to the fact that the modal periods are closer to the dominant periods of the elastic response spectrum. Despite this fact, the investigation showed that the movements of the deck of the modified bridge system are effectively reduced, in comparison to the corresponding ones of the initial bridge. Figure 7 shows the time histories of the longitudinal seismic displacements of the joint of the deck over the pier P_2 for the two bridge systems. From this figure it can be derived that the modified bridge system responds with smaller displacements in the longitudinal direction. The time histories also show that the overall resisting system of the modified bridge becomes stiffer. Both time histories given in Figure 7 correspond to an artificial accelerogramm, which is compatible to Eurocode's 8 [3] elastic spectrum for a ground acceleration equal to 0.24g.

The efficiency of the proposed practice was mainly determined by calculating the percentage reductions in the longitudinal movements and seismic actions of the initial bridge system, Figure 5(a), compared with the corresponding ones of the modified bridge system, Figure 5(b). The ratio of this percentage reduction (P.R.) is given in Equation (3). In this equation *P.R.* is the ratio of the percentage reduction of the movements of the deck or the seismic actions, $A_{,E1}$ is the seismic movement or the seismic action of the initial bridge system and $A_{,E2}$ is the seismic movement or the seismic action of the modified bridge system.

$$P.R. = \left[1 - \frac{A_{,E2}}{A_{,E1}}\right] \cdot 100 \tag{3}$$

In Figure 8 the percentage reductions in the longitudinal movements of the deck are illustrated for the two ground accelerations 0.24g and 0.36g. It is deduced that the proposed restraining system has the ability to reduce by up to 27% the longitudinal movements of the deck when the ground acceleration is 0.24g, while its efficiency is greater in higher ground acceleration (ag=0.36g) as the aforementioned reduction is 33%. This can be attributed to the energy dissipation through the hysteretic behavior of the restraining members.

In Figure 9 the percentage reduction in the bending moments M_{yy} at the base of the piers due to the longitudinal seismic action is illustrated for two different design ground accelerations 0.24g and 0.36g. The analysis showed that the M_{yy} moments were reduced up to 28% when the ground acceleration is 0.24g. The corresponding percentage reduction is greater when the bridge system is subjected to greater ground accelerations. Finally it seems that the restraining effect of the proposed restraining system is limited in the central pier of the bridge which is the tallest one.

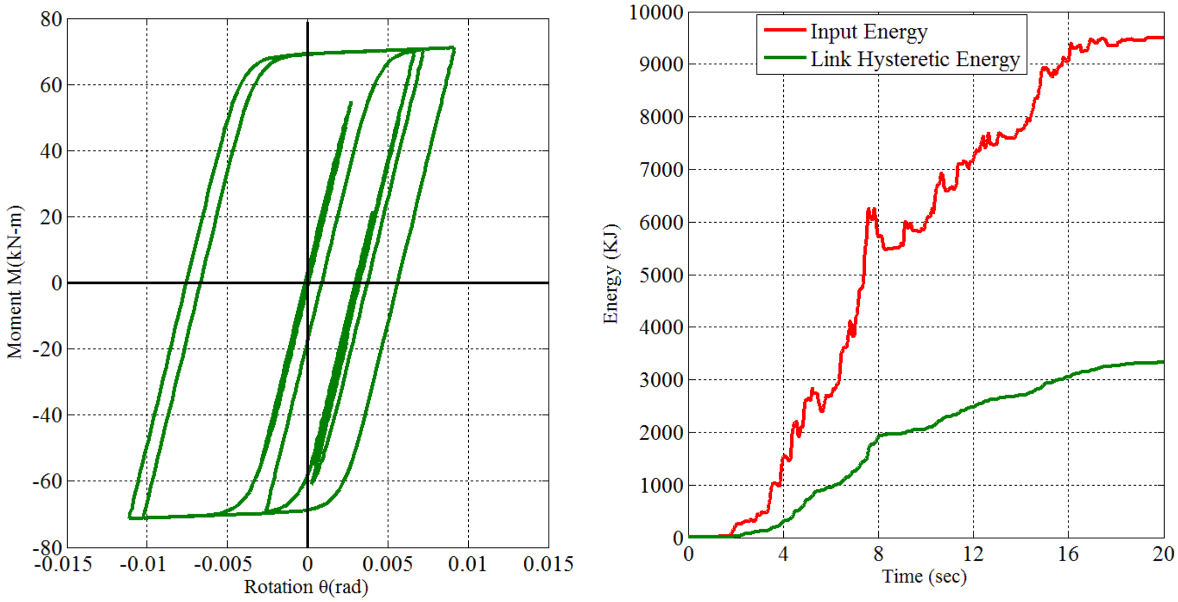

Figure 6: (a) The hysteresis loop of the steel tubes and (b) The input energy and the energy absorbed through the hysteretic flexural behavior of the steel tubes (Link Hysteretic Energy) for design ground acceleration a_g=0.24g.

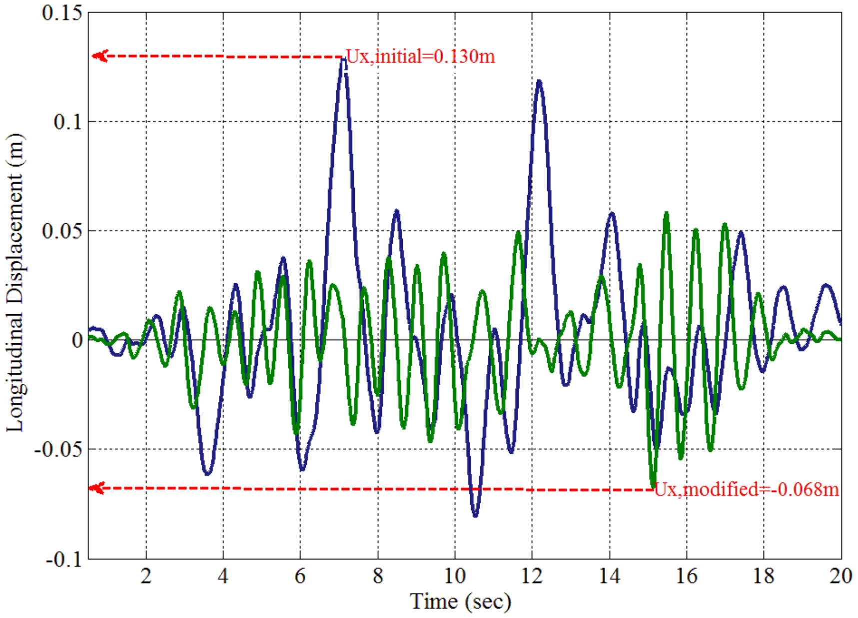

Figure 7: Longitudinal displacement time history (Joint of the deck over pier P2) for the initial and modified bridge system (soil class B, ground acceleration: 0.24g).

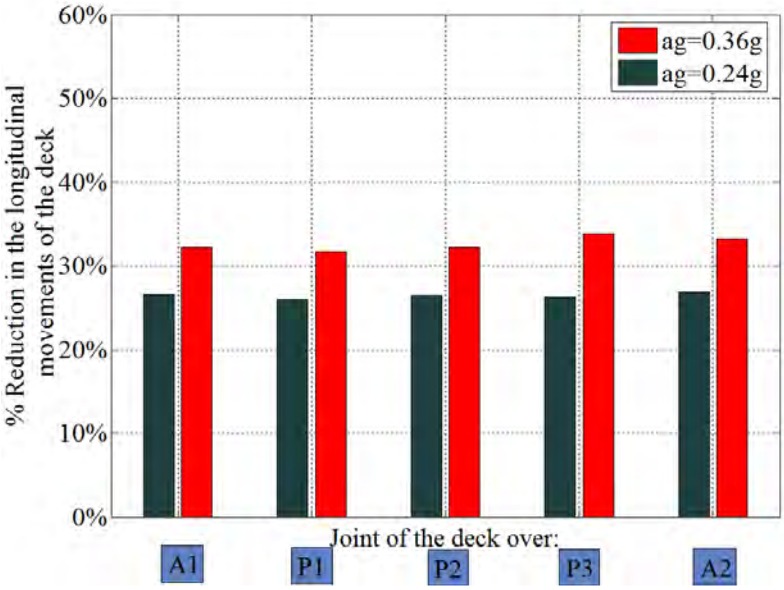

Figure 8: The percentage reductions in the longitudinal movements of the deck for two ground accelerations 0.24g and 0.36g.

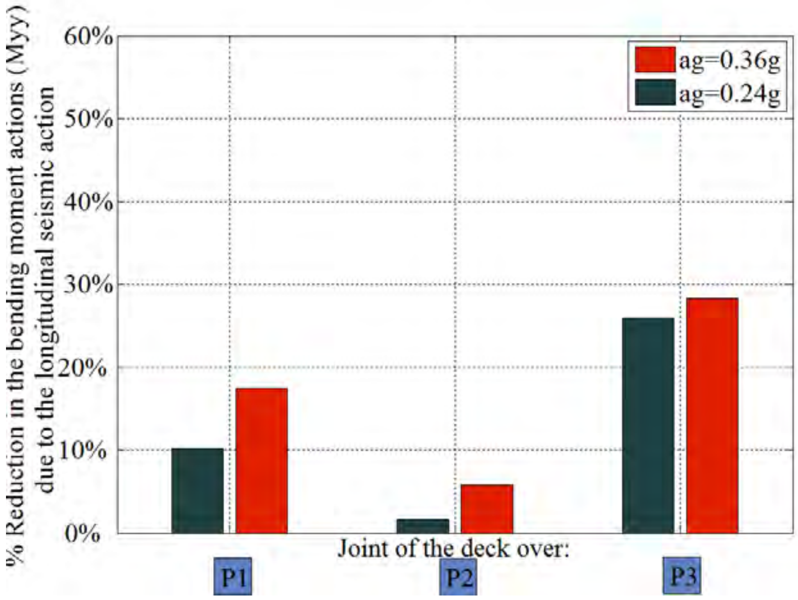

Figure 9: The percentage reductions in the bending moment actions M_{yy} at the base of the piers for two ground accelerations 0.24g and 0.36g.

6 CONCLUSIONS

In this study the seismic efficiency of an alternative to seismic isolation practice is investigated. The aforementioned purpose is achieved through the improved seismic participation of the bridge abutments. The deck slab is extended onto the embankments and is rigidly connected with transversely directed rows of hollow section steel tubes. Based on the results of this study, the following conclusions are drawn:

- The system is significantly efficient is seismic isolated bridge systems as a great part of the induced seismic energy is dissipated through the hysteretic behavior of the restraining members.
- The proposed seismic restrainer effectively reduces the movements of the deck and by extension the seismic actions of the piers, their foundations and the actions of the bearings. The aforementioned reduction is of the order of 27% for the longitudinal design earthquake.
- The ground acceleration influences the efficiency of the proposed restraining system as the restraining members dissipate greater part of the induced seismic energy through their hysteretic behavior.
- The restraining effect also reflects on the seismic actions of the piers (shear actions and bending moments) as well as on the bearings type and dimensions leading to cost-effective bridge design.
- The restraining effect of the proposed system is significant even in stiffer bridge resisting systems. The resulting bridge system is jointless, and has explicit advantages concerning durability and driving convenience.

ACKNOWLEDGEMENTS

This research is co-funded by the European Union (European Social Fund- ESF) and National Resources, in the framework of the program “HRAKLEITOS II” of the “Operational Program for Education and Initial Vocational Training”.

The authors wish also to thank METE SYSM S.A., for kindly providing the original study of the seismic isolated railway bridge used for the purposes of the present study.

REFERENCES

[1] A.H. Nilson, D. Darwin, C.W. Dolan, *Design of Concrete Structures.,* McGraw-Hill, New York 1991.

[2] M.J.N. Priestley. F. Seible, G.M. Calvi, *Seismic design and retrofit of bridges,* John Wiley, New York, 1996.

[3] CEN [Comité Européen de Normalisation] (2003). *Eurocode 8: Design of structures for earthquake resistance, Part 1: General rules, seismic actions and rules for buildings.*

[4] T.E. Kelly, *Base isolation of structures, Design guidelines.* S.E. Holmes Consulting Group Ltd, July 2001.

[5] F. Naeim, J.M. Kelly, *Design of seismic isolated structures, From theory to practice,* John Wiley and Sons, Inc 1999.

[6] T.E. Kelly, *In structure dumping and energy dissipation-Design Guidlines,* S.E. Holmes Consulting Group Ltd, July 2001.

[7] CEN [Comité Européen de Normalisation] (2003). *Eurocode 8: Design of structures for earthquake resistance, Part 2: Bridges*.

[8] CEN [Comité Européen de Normalisation] *Eurocode 1: Actions on structures - Part 1-5: General actions -Thermal actions*, 2003.

[9] G. Mylonakis, V.K. Simeonov, A.M. Reinhorn and I.G. Buckle, Implications of Spatial Variation of Ground Motion on the Seismic Response of Bridges: Case Study, *ACI International - Special Publication SP-187 (K. Krishnan Editor)*, 299-327, 1999.

[10] J. Zhang and N. Makris, Seismic Response Analysis of Highway Overcrossings Including Soil-Structure Interaction, *PEER Report 2001/02*, 2001.

[11] J. Zhang and N. Makris, Kinematic response functions and dynamic stiffnesses of bridge embankments, *Earthquake Eng. Struct. Dyn.*, 31, 1933–1966, 2002.

[12] S.A. Mitoulis and I.A. Tegos,"An unconventional restraining system for seismically isolated bridges", *Engineering Structures*, Vol. 32, Issue 4, pp. 1100-1112, 2010.

[13] R.V. Nutt and R.L. Mayes, *Comparison of Typical Bridge Columns Seismically Designed With and Without Abutment Participation Using AASHTO Division I-A and Proposed AASHTO LRFD Provisions*, Task F3-1(a),2000.

[14] S.D.Tegou, S.A. Mitoulis, I.A. Tegos, An unconventional earthquake resistant abutment with transversely directed R/C walls, *Engineering Structures*, Vol. 32, Issue 11, pp. 3801-3816, 2010.

[15] CEN [Comité Européen de Normalisation] *Cold Formed Welded Structural Hollow Sections of Non-Alloy and Fine Grain Steels – Part 2:Tolerances, Dimensions and Sectional Properties, EN 10219–2:2006(E)*, European Committee for Standardization, 2006.

[16] DIN 1075: Betonbrucken; Bemessung und Ausfuhrung. Ausgabe, April 1981.

[17] Ministry of Public Works, *Greek Seismic Code—EAK 2000*, Athens, 2000 (amended 2003, in Greek).

[18] Ministry of Environment, Physical Planning, and Public Works. *Circular 39/99: Guidelines for the Seismic Design of Bridges*, Athens, 1999 (in Greek).

[19] Computers and Structures Inc. *SAP 2000 Nonlinear Version 11.0.3, User's Reference Manual*, Berkeley, California, 2007.

[20] A.K. Chopra, *Dynamics of structures, Theory and applications to earthquake engineering*, Prentice Hall Inc, 1995.

[21] A. Aviram, K.R. Mackie, B. Stojadinovic *Guidelines for Nonlinear Analysis of Bridge Structures in California*, PEER 2008/03, 2008.

[22] L.E. Malvern, *Introduction to the Mechanics of a Continuous Medium*, Prentice- Hall, Englewood Cliffs, N.J., 1969.

[23] A.J. Kappos, RCCOLA-90: *A microcomputer program for the analysis of the inelastic response of reinforced concrete sections*", Dept. of Civ. Engin., Aristotle University of Thessaloniki, Thessaloniki, Greece, 2002.

COMPDYN 2011
3rd ECCOMAS Thematic Conference on
Computational Methods in Structural Dynamics and Earthquake Engineering
M. Papadrakakis, M. Fragiadakis, V. Plevris (eds.)
Corfu, Greece, 25–28 May 2011

THE IMPACT OF SUBWAY TUNNELS ON THE SEISMIC RESPONSE OF OVERLAYING STRUCTURES

C.C. Spyrakos [1], D.N. Vasileiou [2*]

[1]Professor, Dept. of Civil Engineering, Laboratory for Earthquake Engineering National Technical University, Athens, Greece
cspyrakos@central.ntua.gr

[2]Civil Engineering Student, Dept. of Civil Engineering, Laboratory for Earthquake Engineering National Technical University, Athens, Greece
vasileiou.dimitrios@gmail.com

Keywords : Subway, tunnels, metro stations, earthquake response

Abstract. The seismic response of structures overlaying soil strata has been extensively studied. Also, numerous studies can be found in the literature regarding the deformations imposed on structures during the excavation of tunnels in suburban areas. However, the impact of the presence of a tunnel on the seismic response of overlaying structures has drawn very limited attention.

The goal of this study is to examine the considerable influence that the existence of a tunnel has on ground acceleration, as well as to point out the limits of parameters, such as the tunnel depth and the horizontal distance of a structure from the axis of the tunnel, beyond which the difference in ground acceleration cannot be neglected.

The corrected accelerograms of the Athens(Greece), Kobe(Japan) and Duzce (Turkey) earthquakes are used in this investigation. The geotechnical data has been drawn from the drillings that took place during the construction of the subway in Athens. For the Athens earthquake two approaches were applied. In the first approach the soil stratum with the tunnel were modeled as a linear system with the finite element software called Plaxis. In the second approach the part of the soil stratum over the bedrock and up to a distance of 2.5 m below the lower part of the tunnel were modeled with software capable to account for nonlinear soil behavior, while the upper part including the tunnel were modeled as a linear system using Plaxis. The second approach is considered as more realistic especially for the latter two seismic excitation cases.

The results of this study showed that the presence of the shallow tunnels considerably modify the surface ground motion within a range that depends on their geometrical characteristics. Even though this is a limited study, the results clearly indicate that the phenomenon should be considered when : i) evaluating the anticipated seismic behavior of overlaying structures, ii) deciding on strengthening measures in order to protect structures with inferior strength, iii) specifying the design spectra of new buildings to be constructed in the vicinity of such tunnels and iv) making decisions regarding relocation of a tunnel to be constructed.

INTRODUCTION

In recent years there have been considerable advances on techniques of bored tunnel construction in any type of ground. This has led to a plethora of tunnelling projects being instigated, frequently in urban areas, in order to deal with increasing traffic congestion problems. As a consequence, there is respectable international interest in predicting the impact that tunnels have on the behaviour of overlaying and neighboring structures.

Even though the presence of tunnels in urban environments, such as low-depth subway tunnels is very common in countries with high seismicity, there are indeed very few studies reported in the literature on this topic. It should be noted that many of the overlaying structures are old and in many cases constructed without seismic provisions. The influence of the presence of a subway tunnel on the seismic response at the ground surface supporting a structure is investigated in this study.

This paper summarizes the methodology adopted to predict the critical area around a tunnel, depending on its depth, where the acceleration from an earthquake is increased due to the presence of the tunnel.

ANALYSIS PROCEDURE

Firstly, the soil profile is specified.

The soil profile has been obtained from the drillings during the construction of the metro at a location of central Athens. The soil profile with the corresponding characteristics is shown in *Figure 1*.

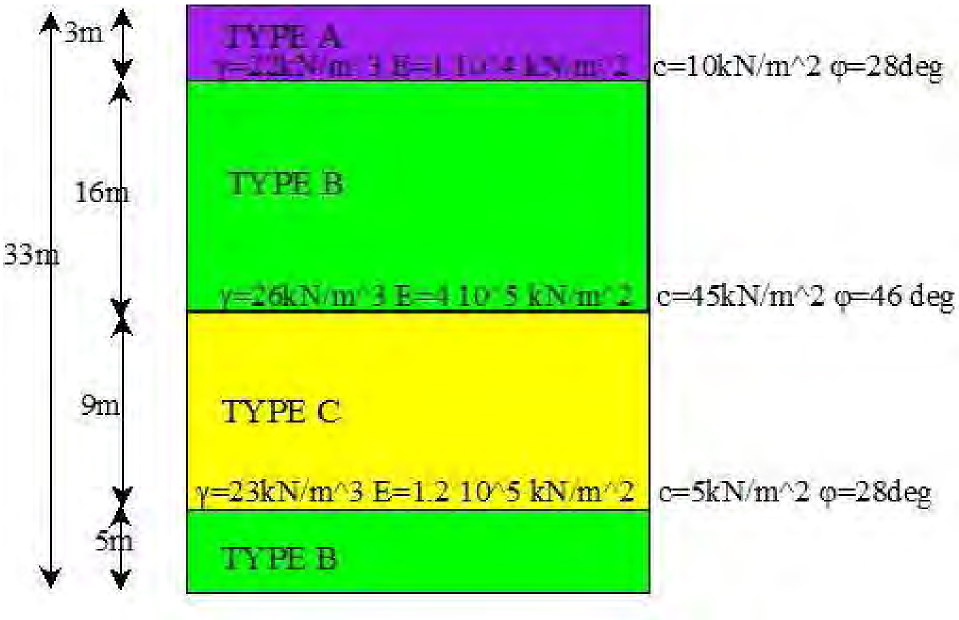

Figure 1 – The soil profile and characteristics

Where:

γ: bulk density, E: Young's modulus, c: effective cohesion, φ: effective internal angle of friction.

Ground motions for three well-known earthquake records were used, i.e. the Athens, the Kobe and the Duzce earthquakes. All records present near source directivity phenomena ([3], [4]). The earthquake records were used as is described in the following: For the Athens earthquake two approaches were applied. In the first approach the soil stratum with the tunnel were modeled as a linear system with the finite element software called Plaxis ([1], [5]). In the second approach the part of the soil stratum over the bedrock and up to a distance of 2.5 m below the lower part of the tunnel were modeled with software capable to account for nonlinear soil behavior, while the upper part including the tunnel were modeled as a linear system using Plaxis. The second approach is considered as more realistic. The models used in these approaches are dedicted in figures 2a, 2b and 3. Specifically, *figure 2a* :shows the model using Plaxis for the linear analysis of the soil stratification with the tunnel, *figure 2b* :shows the finite element mesh of the model using Plaxis, *figure 3:* shows the soil strata model using the Shake2000 ([2]) for the lower part and Plaxis for the upper part that includes the tunnel.

In all cases a tunnel with a diameter of 2.5 m is used.

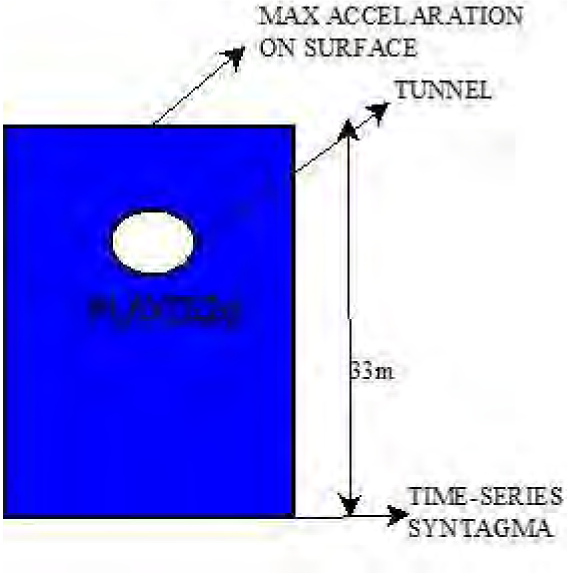

Figure 2a – Plaxis Model

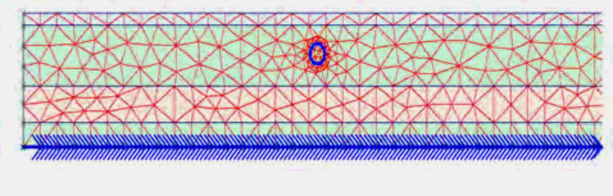

Figure 2b – The finite element mesh of Plaxis model

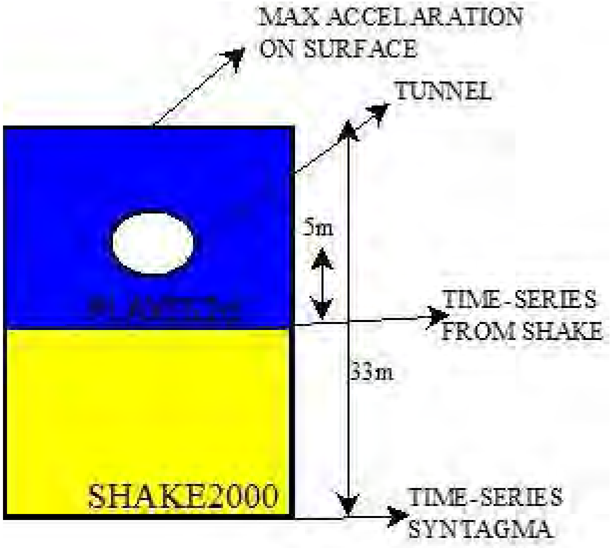

Figure 3 – Shake2000 & Plaxis model

Figures 4, 5, 6 show horizontal accelerations of the records at Syntagma (Athens) 1999, Kobe (Japan) 1995 and Duzce (Turkey) 1999 respectively.

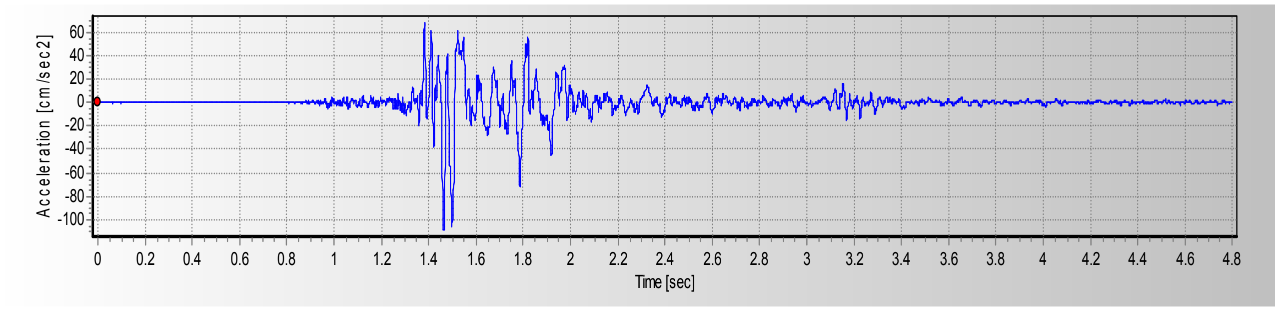

Figure 4 – Syntagma (Athens) 1999 earthquake record on the bedrock,

maximum acceleration : 1.08 (m/s^2) , estimated effective acceleration (EDA) : 0.37 (m/s^2)

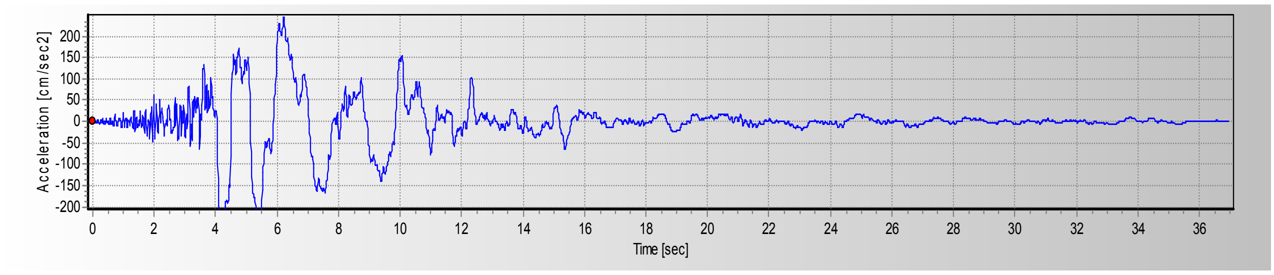

Figure 5 – Kobe (Japan) 1995 earthquake record on the bedrock,

maximum acceleration : 3.09 (m/s^2) , estimated effective acceleration (EDA) : 3.09 (m/s^2)

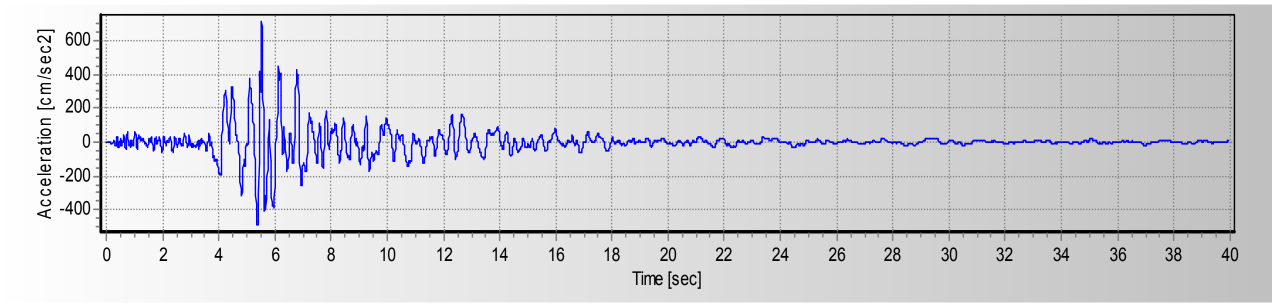

Figure 6 – Duzce (Turkey) 1999 earthquake record on the bedrock,

maximum acceleration : 7.14 (m/s^2) , estimated effective acceleration (EDA) : 5.99 (m/s^2)

The locations where the response of all analyses for the models of both approaches have been calculated are showed in *figure 7.*

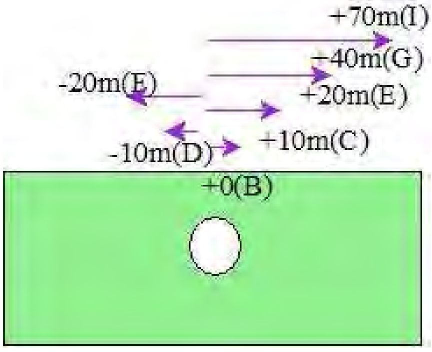

Figure 7 – Locations where ground acceleration values are calculated.

In the following all the results of the analyses are given in a table form for the locations presented in figure 7 and for each case of tunnel depth. In Tables 1a, 2a, 3a, 4a, 5a, 6a and 7a the results from the first method using Plaxis are showed, while in Tables 1b, 2b, 3b, 5b, 6b and 7b the results from the second method using Shake2000 & Plaxis are presented.
Red ink is used to point out when the increase of surface acceleration exceeds a limit of 5%.

POINT B	PLAXIS		Percentage
Dist.: 0	notunnel	**tunnel**	Increase (%)
depth=5	2.1708	3.054	40.69
depth=10	2.1708	2.515	15.86
depth=15	2.1708	2.411	11.07
depth=20	2.1708	2.39	10.10
depth=25	2.1708	2.34	7.79

Table 1a – Results from Plaxis model

POINT B	SHAKE		Percentage
Dist.: 0	notunnel	**tunnel**	Increase (%)
depth=5	1.44	1.66	15.47
depth=10	1.44	1.57	9.13
depth=15	1.44	1.456	1.46
depth=20	1.44	1.432	-0.21
depth=25	1.44	0.00	0.00

Table 1b – Results from Shake & Plaxis model

Athens earthquake 1999

The horizontal distance from the tunnel center is taken as 0 m.

POINT C	PLAXIS		Percentage
Dist.: 10	notunnel	tunnel	Increase (%)
depth=5	2.905	3.443	18.52
depth=10	2.905	3.229	11.15
depth=15	2.905	3.004	3.41
depth=20	2.905	3.002	3.34
depth=25	2.905	2.446	-15.80

Table 2a – Results from Plaxis model

POINT C	SHAKE		Percentage
Dist.: 10	notunnel	tunnel	Increase (%)
depth=5	1.88	2.12	13.01
depth=10	1.88	2.04	8.90
depth=15	1.88	1.865	-0.59
depth=20	1.88	1.801	-4.00
depth=25	1.88	0.00	0.00

Table 2b – Results from Shake & Plaxis model

Athens earthquake 1999

The horizontal distance from the tunnel center is taken as 10 m.

POINT E	PLAXIS		Percentage
Dist.: 20	notunnel	tunnel	Increase (%)
depth=5	3.3488	3.879	15.83
depth=10	3.3488	3.696	10.37
depth=15	3.3488	3.68	9.92
depth=20	3.3488	3.467	3.53
depth=25	3.3488	3.432	2.48

Table 3a – Results from Plaxis model

POINT E	SHAKE		Percentage
Dist.: 20	notunnel	tunnel	Increase (%)
depth=5	2.03	2.21	8.91
depth=10	2.03	2.15	5.56
depth=15	2.03	2.103	3.49
depth=20	2.03	2.096	3.15
depth=25	2.03	0.00	0.00

Table 3b – Results from Shake & Plaxis model

Athens earthquake 1999

The horizontal distance from the tunnel center is taken as 20 m.

POINT G	PLAXIS		Percentage
X.Θ.: 40	notunnel	tunnel	Increase (%)
depth=5	2.898	3.014	4.00
depth=10	2.898	3.021	4.24
depth=15	2.898	3.00	3.45
depth=20	2.898	3.054	5.38
depth=25	2.898	2.765	-4.59

Table 4a – Results from Plaxis model

POINT G	SHAKE		Percentage
X.Θ.: 40	notunnel	tunnel	Increase (%)
depth=5	1.77	1.81	2.66
depth=10	1.77	1.80	1.87
depth=15	1.77	1.698	-3.80
depth=20	1.77	1.805	2.27
depth=25	1.77	0.00	0.00

Table 4b – Results from Shake & Plaxis model

Athens earthquake 1999

The horizontal distance from the tunnel center is taken as 40 m.

POINT I	PLAXIS		Percentage
X.Θ.: 70	notunnel	tunnel	Increase (%)
depth=5	1.5423	1.675	8.60
depth=10	1.5423	1.678	8.80
depth=15	1.5423	1.60	3.94
depth=20	1.5423	1.607	4.20
depth=25	1.5423	1.467	-4.88

POINT I	SHAKE		Percentage
X.Θ.: 70	notunnel	tunnel	Increase (%)
depth=5	1.21	1.24	2.15
depth=10	1.21	1.20	-0.74
depth=15	1.21	1.209	-0.25
depth=20	1.21	1.211	-0.08
depth=25	1.21	0.00	0.00

Table 5a – Results from Plaxis model *Table 5b – Results from Shake & Plaxis model*

Athens earthquake 1999

The horizontal distance from the tunnel center is taken as 70 m.

Noticing the results showed in the tables above one could make the following remarks: In Table 1b (location B) it is observed that ground acceleration after the construction of a tunnel is increased by 15.5% : when the tunnel depth is 5m, by 9.1% : when the tunnel depth is 10m and less than 5% : when the tunnel depth is more than 10m. In Table 2b (location C) the increase is 13.0% when the tunnel depth is 5m, 8.9% when the tunnel depth is 10m and less than 5% when tunnel depth is more than 10m. In Table 3b (location E) the ground acceleration is increased because of the tunnel presence by 8.9% when the tunnel is located 5m below the surface, by 5.6% when it is located 10m below the surface and by less than 5% when it is located more than 10m below the surface. Finally, in Tables 4b (location G) and 5b (location I) the increase is less than 5% for any case of tunnel depth.

For the Kobe and Duzce earthquake records the combined method is used.

The results for the Kobe analysis are showed in a table form while red ink is used to point out when increase of surface acceleration exceeds the limit of 5% (Tables 6, 7, 8, 9).

POINT B	SHAKE		Percentage
Dist.: 0	notunnel	**tunnel**	Increase (%)
depth=5	1.56	1.90	22.24
depth=10	1.56	1.77	13.43
depth=15	1.56	1.654	6.30
depth=20	1.56	1.587	1.99
depth=25	1.56	0.00	0.00

POINT C	SHAKE		Percentage
Dist.: 10	notunnel	tunnel	Increase (%)
depth=5	1.72	2.10	22.13
depth=10	1.72	1.98	14.75
depth=15	1.72	1.865	8.30
depth=20	1.72	1.789	3.89
depth=25	1.72	0.00	0.00

Table 6 – Results from Shake&Plaxis model *Table 7 – Results from Shake&Plaxis model*

Kobe earthquake 1995

The horizontal distance from the tunnel center is taken as 0 m for Table 6 and 10m for Table 7.

POINT E	SHAKE		Percentage
Dist.: 20	notunnel	tunnel	Increase (%)
depth=5	2.03	2.21	8.91
depth=10	2.03	2.15	5.56
depth=15	2.03	2.103	3.49
depth=20	2.03	2.096	3.15
depth=25	2.03	0.00	0.00

POINT G	SHAKE		Percentage
X.Θ.: 40	notunnel	tunnel	Increase (%)
depth=5	1.77	1.81	2.66
depth=10	1.77	1.80	1.87
depth=15	1.77	1.698	-3.80
depth=20	1.77	1.805	2.27
depth=25	1.77	0.00	0.00

Table 8 – Results from Shake&Plaxis model Table 9 – Results from Shake&Plaxis model

Kobe earthquake 1995

The horizontal distance from the tunnel center is taken as 20 m for Table 8 and 40m for Table 9.

Table 6 (location B) shows that ground acceleration after the construction of a tunnel is increased by 22.2% when the tunnel depth is 5m, 13.4% when the tunnel depth is 10m, 6.3% when the tunnel depth is 15m and less than 5% when the tunnel depth is more than 15m. In Table 7 (location C) the increase is 22.1% when the tunnel depth is 5m, 14.7% when the tunnel depth is 10m, 8.3% when the tunnel depth is 15m and less than 5% when the tunnel depth is more than 15m. In Table 8 (location E) the ground acceleration is increased by 8.9% when the tunnel depth is 5m, by 5.6% when it is 10m and by less than 5% when it is more than 10m. Last, in Table 9 (location G) the increase is less than 5% regardless of the tunnel depth.

The results for the Duzce analysis are showed in a table form (Tables 10, 11, 12, 13), while red ink is used to point out when increase of surface acceleration exceeds the limit of 5%

POINT B	SHAKE		Percentage
Dist.: 0	notunnel	**tunnel**	Increase (%)
depth=5	1.79	2.13	19.06
depth=10	1.79	1.95	9.22
depth=15	1.79	1.821	1.79
depth=20	1.79	1.787	-0.11
depth=25	1.79	0.00	0.00

POINT C	SHAKE		Percentage
Dist.: 10	notunnel	tunnel	Increase (%)
depth=5	1.72	2.10	22.13
depth=10	1.72	1.92	11.73
depth=15	1.72	1.835	6.56
depth=20	1.72	1.789	3.89
depth=25	1.72	0.00	0.00

Table 10 – Results from Shake&Plaxis model Table 11 – Results from Shake&Plaxis model

Duzce earthquake 1999

The horizontal distance from the tunnel center is taken as 0 m for Table 10 and 10m for Table 11.

POINT E	SHAKE		Percentage
Dist.: 20	notunnel	tunnel	Increase (%)
depth=5	1.65	1.85	12.09
depth=10	1.65	1.77	6.83
depth=15	1.65	1.675	1.27
depth=20	1.65	1.664	0.60
depth=25	1.65	0.00	0.00

Table 12 – Results from Shake&Plaxis model

POINT G	SHAKE		Percentage
Χ.Θ.: 40	notunnel	tunnel	Increase (%)
depth=5	1.67	1.71	2.82
depth=10	1.67	1.70	1.98
depth=15	1.67	1.698	1.98
depth=20	1.67	1.705	2.40
depth=25	1.67	0.00	0.00

Table 13 – Results from Shake&Plaxis model

Kobe earthquake 1995

The horizontal distance from the tunnel center is taken as 20 m for Table 12 and 40m for Table 13.

In Table 10 (location B) the ground acceleration is increased because of the tunnel presence by 19.0% when the tunnel is located 5m below the surface, by 9.2% when it is located 10m below the surface and by less than 5% when it is located more than 10m below the surface. Table 11(location C) shows that increase of acceleration is 22.1% when the tunnel depth is 5m, 11.7% when the tunnel depth is 10m, 6.6% when the tunnel depth is 15m and less than 5% when the tunnel depth is more than 15m. In Table 12 (location E) the acceleration is increased by 12.1% when the tunnel depth is 5m, by 6.8% when the tunnel depth is 10m and by less than 5% when the tunnel depth is more than 10m. In table 13 (location G) the increase is less than 5% for any case of tunnel depth.

CONCLUSIONS

- In general, in Plaxis2d higher acceleration results were obtained in comparison with the ones from the combined Shake2000&Plaxis2d models. This difference is attributed to the fact that Shake accounts for nonlinear soil behavior
- The impact of the tunnel presence on the ground acceleration could be considerable, since the ground surface acceleration can be increased even by 22%.
- As the horizontal distance of the foundation of a structure from the tunnel center and the tunnel depth increase, the influence of the presence of the tunnel on the acceleration at the surface diminishes.
- When the horizontal distance from the tunnel center is 20m or less and the tunnel depth is 5m, the increase of the ground acceleration ranges from 7% to 22%. Furthermore, when the horizontal distance from the tunnel center is 20m or less and the tunnel depth is 10, the increase of the ground acceleration ranges from 5% to 15%.

The results indicate that the presence of the tunnel should be considered when the following two conditions are present:

- ***1st Condition***: Tunnel depth must be less than 10 meters.
- ***2nd Condition***: Horizontal distance from the tunnel center must be less than 20 meters.

Those conclusions were drawn from the analyses based on specific data (the soil profile from central Athens, Athens, Kobe and Duzce earthquakes, tunnel diameter 5.0 m).

Even though the conclusions are based on limited results, they clearly indicate that the impact of the tunnel presence on ground acceleration should be taken into consideration when:

i) specifying the design spectra of structures to be built at the area near the subway tunnel.
ii) selecting strengthening measures in order to strenghten structures that are vulnerable.
iii) deciding on the location of a tunnel to be constructed.
iv) evaluating the anticipated seismic behavior of overlaying structures.

REFERENCES

[1] Plaxis, Plaxis2d user's manual version 9

[2] Shake, Shake2000 user's manual, Ameritech engineering, 2000

[3] Spyrakos C.C., Maniatakis Ch.A. and Taflabas J. (2005) "Critical Evaluation of Near-Field Seismic Records in Greece", Earthquake Resistant Engineering Structures V, (ERES 2005), Skiathos, May 2005 pages 2-11.

[4] Spyrakos, C. C., Maniatakis , Ch. A. and Taflambas, J., Evaluation of Near-Source Seismic Records Based on Damage Potential Parameters. Case Study: Greece, Soil Dynamics and Earthquake Engineering, November 2007, pages 4-16

[5] Azadi, M. , Mir Mohammad Hosseini, The impact of Underground Tunnel on adjacent buildings. Case study : Shiraz Underground, Iran pages 2-6

COMPDYN 2011
3rd ECCOMAS Thematic Conference on
Computational Methods in Structural Dynamics and Earthquake Engineering
M. Papadrakakis, M. Fragiadakis, V. Plevris (eds.)
Corfu, Greece, 25–28 May 2011

COMPUTATIONAL EFFICIENCY OF PROGRESSIVE INCREMENTAL DYNAMIC ANALYSIS

Marko Brozovič[1] **and Matjaž Dolšek**[1]

[1] University of Ljubljana, Faculty of Civil and Geodetic Engineering
Jamova 2, 1000 Ljubljana, Slovenia
{mbrozovi, mdolsek}@ikpir.fgg.uni-lj.si

Keywords: Incremental dynamic analysis, Precedence list, Ground motion selection, Computational efficiency, PBEE toolbox.

Abstract. *Progressive incremental dynamic analysis involves precedence list of ground motion records aiming of selecting the most representative ground motions from a set of ground motions. The precedence list of ground motion records provides the advantage of a simple mathematical model, which is not computationally demanding, and it is defined as an optimization problem, which can be solved with sufficient accuracy by means of a simple procedure. Therefore, the seismic response parameters are computed progressively, starting from the first ground motion record in the precedence list. After an acceptable tolerance is achieved, the analysis can be terminated. Such approach facilitates practical application of incremental dynamic analysis (IDA), especially, if the number of ground motions in a set of ground motions is large, and its computational efficiency is higher than ordinary IDA. In the paper the precedence list of ground motion records is determined for three reinforced concrete frame structures in order to evaluate computational efficiency of the progressive IDA. The results indicate that 16th, 50th and 84th fractiles of seismic response parameters of frame structures can be determined with sufficient accuracy if about 12 to 15 records out of 30 are used in the analysis, this indicating that progressive IDA requires much less computational time than IDA.*

1 INTRODUCTION

Incremental dynamic analysis (IDA) [1] is widely used parametric analysis method for seismic performance assessment of structures. It enables direct evaluation of record-to-record variability in structural response through a set of ground motion records. If the set of ground motions is large, IDA becomes computationally demanding. In order to accommodate its practical application, precedence list of ground motions has been introduced [2, 3], aiming at selecting the most representative ground motion records for IDA analysis.

In progressive IDA the "selected" IDA curves are computed progressively from the first ground motion in the precedence list till the acceptable tolerance is attained. Therefore seismic response parameters are estimated by using the nonlinear dynamic analysis, which is performed for a limited number of records from a list. Such approach can significantly reduce computational efforts and consequently facilitate the use of nonlinear dynamic analysis for practical applications.

Since precedence list of ground motion records is based on dynamic response of equivalent SDOF model the computational efficiency of the progressive IDA varies from structure to structure and depends also on the set of ground motion records used in analysis. The objective of this study is to assess the computational efficiency of progressive IDA for different reinforced concrete frames, which were modeled by using the PBEE toolbox [4] in conjunction with OpenSees [5]. The toolbox was developed in Matlab [6] and provides functions for the rapid determination of simplified nonlinear structural models, performance assessment by employing different methods and the post-processing of analysis results. Since the PBEE toolbox is focused on simple nonlinear models, material nonlinearity is modeled only with the moment-rotation relationship in the plastic hinges of the columns and beams.

2 SUMMARY OF PROGRESSIVE INCREMENTAL DYNAMIC ANALYSIS

Progressive IDA was recently proposed [3] aiming at minimizing the computational time, which is required for prediction of seismic response parameters in the case if they are estimated with nonlinear dynamic analysis. For that reason a precedence list of ground motion records was introduced. The determination of such a list is an optimization problem and can be sufficiently solved by minimizing the defined fitness function, which is determined based on response of a simple model, e.g. the single-degree-of-freedom (SDOF) model.

The methodology was originally proposed for prediction of median seismic response (i.e. median IDA curve) [2]. However its use was extended for prediction of 16th, 50th and 84th fractile response [3]. In progressive IDA the so-called "selected" IDA curves are computed progressively starting from the first ground motion record in the precedence list. When the required tolerance in the prediction of seismic response is achieved, the analysis can be terminated. The benefit of progressive IDA, in comparison to the IDA, is the reduction of the computational effort. However, determination of the precedence list of ground motion records also requires some computational time, firstly, for IDA analysis of the simple model (e.g. SDOF system), which is needed in order to determine a precedence list, and secondly, for the optimization of the precedence list of ground motion records. Computational time needed for determination of precedence list is usually shorter than time needed for one IDA analysis of a structure.

The input data for determination of the precedence list of ground motion records are IDA curves for the simple (e.g. SDOF) model. The next step is definition of the so called fitness function, which incorporates IDA curves of the simple model, and it is defined in a way that its value changes if the position of the ground motions identification numbers (IDs) in a list are rearranged. The precedence list is determined when the ground motions IDs are arranged in the order that the fitness function takes on a minimum value.

In general, the fitness functions can be defined for different purposes. However, for the precedence list of ground motions aiming at predicting the fractile IDA curves, it was found [2, 3], that a good measure for defining the fitness function is the area between the "original" fractile IDA curve and the "selected" fractile IDA curve, where the term "original" is used for the case if fractile IDA curve is obtained from all the IDA curves while the term "selected" is used if the fractile IDA curve is determined only for the first *s* ground motions from the precedence list. If this area is normalized with the area defined by the "original" fractile IDA curve then the dimensionless measure for the error between the two types of the fractile IDA curves can be defined as follows [3]

$$Error(s,f) = 100 \times \frac{\displaystyle\int_{0}^{EDP_{\max}(s,f)} \left|\Delta IM\left(s,f\right)\right| dEDP}{\displaystyle\int_{0}^{EDP_{\max,or}(f)} IM_{or}\left(f\right) dEDP} \tag{1}$$

where *s* is the number of selected subsets of three ground motions, *IM* and *EDP* are usual notations for intensity measure and engineering demand parameter, respectively, $IM_{or}(f)$ is the intensity measure of the "original" *f*-th fractile IDA curve, $EDP_{\max,or}(f)$ is the engineering demand parameter corresponding to the capacity point of the "original" *f*-th fractile IDA curve, $\Delta IM(s,f)$ is the difference in the *IM* corresponding to the "original" and "selected" *f*-th fractile IDA curve, and $EDP_{max}(s,f)$ is the maximum of the engineering demand parameters corresponding to the capacity point of the "selected" and "original" *f*-th fractile IDA curves. The error as defined in the Eq. (1) is not yet the fitness function since it depends only on the first *s* selected number of records from the precedence list and on the selected *f*-th fractile IDA curve. In order to define the fitness function the sum of *Error(s,f)* over all values is required. In the case if the precedence list of ground motions is determined in order to predict the three fractile IDA curves it was found [3], that the best precedence list is obtained if the fitness function is defined in a way to give a preference to those ground motions, which IDA curves are close to the "original" fractile curves. Therefore, the fitness function *Z* is defined by sum of *Error(s,f)* over the *m* number of subsets of ground motion records and over all *f*-th fractile IDA curves

$$Z = \frac{1}{m}\sum_{s=1}^{m}\sum_{f=1}^{3} Error\left(s,f\right) \tag{2}$$

Different techniques can be used to minimize the fitness function. The simplest possible way, which actually does not require optimization method, is gradual minimization of *Error(s,f)*. It was proven that gradual minimization of *Error(s,f)* results in a value of the fitness function, which is close to the global minimum [3]. The first ground motion in the precedence list corresponds to the minimum value of errors (Eq. (1)) that are calculated for s=1, f=1 and for all *n* records in the given set of ground motion records. The second and third ground motion in the precedence list correspond to minimum error calculated for s=1, f=2 and f=3 for n-1 and n-2 records left to be placed in the precedence list, respectively. The following ground motion IDs in the precedence list are defined with repeating described procedure until all ground motion IDs are placed in the precedence list of ground motions.

Once the precedence list of ground motions is known, the difference between the fractile curve determined for s-1 and s subsets of ground motions can be obtained. This measure is called the tolerance function and is defined as follows [3]

$$Tolerance(s,f) = 100 \times \frac{\displaystyle\int_0^{Max\left[EDP_{\max}(s,f),EDP_{\max}(s-1,f)\right]} \left|IM(s,f) - IM(s-1,f)\right| dEDP}{\displaystyle\int_0^{EDP_{\max}(s-1,f)} IM(s-1,f)\, dEDP} \tag{3}$$

where $IM(s,f)$ and $IM(s-1,f)$ are the values of the intensity measures for the f-th fractile IDA curves, which are determined, respectively, on the basis of the first s and s-1 subsets of ground motion records. The additional parameters introduced into Eq. (3) are the engineering demand parameters $EDP_{\max}(s,f)$ and $EDP_{\max}(s-1,f)$, which correspond to the capacity point of the f-th fractile curve determined from first s and s-1 subsets of ground motion records.

In progressive IDA "selected" IDA curves are computed progressively starting from the first ground motion in the precedence list as long as required tolerance in the prediction of seismic response is achieved.

3 EXAMPLE: SEISMIC PERFORMANCE ASSESSMENT OF DIFFERENT REINFORCED CONCRETE FRAMES USING PROGRESSIVE IDA

Computational efficiency of progressive incremental analysis is studied by means of a seismic performance assessment of three reinforced concrete frame structures and a set of 30 ground motion records. The structural performance is assessed for two limit states, which were defined on the basis of the damage observed in the beams and columns. The peak ground acceleration and the maximum top displacement were adopted, respectively, as the intensity measure and the engineering demand parameter.

3.1 Description of the structures and the structural models

The eight-storey RC frame [7], six-storey building [8] and the eight storey building [9, 10] were selected from literature. Elevation and the plan views of the structures as well as typical reinforcement of columns and beams are shown in Figure 1. All the structures under consideration are symmetrical reinforced concrete frames, but there appear differences in the number of stories, height of the stories, position of columns, dimensions and reinforcement of columns and beams cross-sections, thickness of slabs, strength of concrete and reinforcement. In addition, these structures were designed according to different design requirements.

The first structure (S1), which was designed for gravity loads only, is eight-storey RC frame with constant storey height of 2.8 m. Typical cross-sections as shown in Figure 1a are equal for all beams and columns, except for inner two columns in lower two stories and outer two columns in the top storey, where for the longitudinal reinforcement 4Φ20 bars are used instead of 4Φ16 bars. Mean strength of the concrete is 25 MPa and the mean yield strength of the steel is 400 MPa.

The second structure (S2) is six-storey RC frame and is shown in Figure 1b. The bottom storey is 4 m high, while the height of other storeys is 3 m. The dimensions of cross-sections and steel reinforcement in the beams and columns do not change from element to element. The structure was probably design according to Eurocode 8 [11] provisions for high seismic hazard area, since the amount of longitudinal and shear reinforcement in the cross-sections of the columns and beams is high. The concrete strength class is C20/25, while the steel strength class is S500.

The third structure (S3), i.e. an eight-storey building (Figure 1c), was designed according to the European standard Eurocode 8. The building's height of the first or second storeys is 5 m, whereas the other storeys are 3.1 m high. The building has three bays in each horizontal direction and therefore the largest structure considered in the presented study. All the cross-sections of the columns and beams of the structure have dimensions of 60/60 cm and 40/60 cm, respectively. For the columns, the steel reinforcement is the same for all sections, except for the cross-sections at the base, where the density of the stirrups is greater (Φ8/5 cm and Φ10/5 cm). The steel reinforcement for the beams is the same for all cross-sections, except for the beams in first two storeys, where at the top of the beams there are 6 instead of 4Φ20 bars. The concrete strength class of the building is C30/37, and the steel strength class is B500.

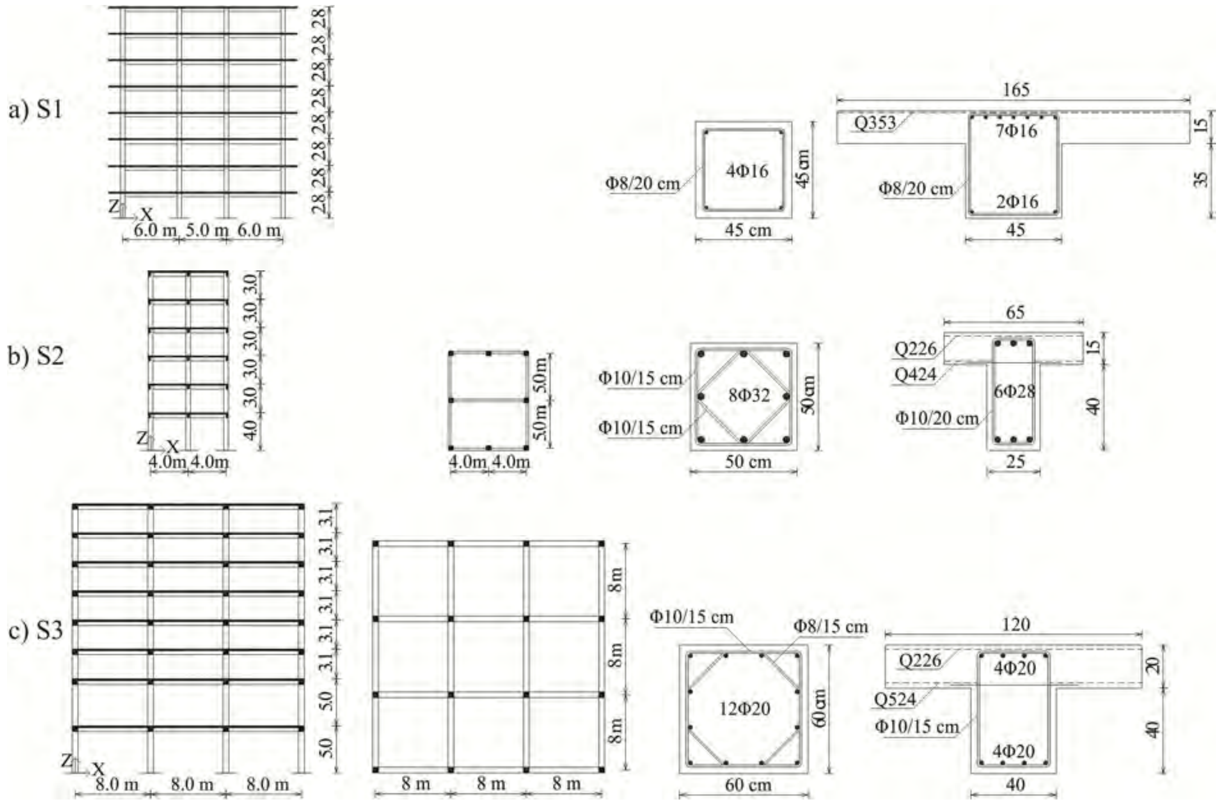

Figure 1: The elevation, plan view and the reinforcement in typical cross-sections of the columns and beams for a) eight storey frame, b) six-storey and c) eight-storey RC building.

Structural models of the buildings were prepared in the PBEE toolbox [4]. Structures S2 and S3 were modelled as 3D frame structures although they are symmetric. The height of the storeys was determined by the distance between the centrelines of the beams. The masses were concentrated at the storey levels, at the centre of gravity and the effective width of the beams was modelled as described in Eurocode 2 [12], assuming zero moment points at the midpoint of the beams. The effective width of all the beams in structure S1 was considered equal to 1.65 m, while the effective width of the beams of the structure S2 differed and amounted to 0.65 m, 0.75 m and 1.85 m. In the case of the structure S3, the effective width of the beams in the exterior and interior frames amounted 1.2 m and 2 m, respectively.

Beam and column flexural behaviour was modelled by one-component lumped plasticity elements, consisting of an elastic beam and two inelastic rotational hinges. The moment-rotation relationship before strength deterioration was modelled by a bi-linear relationship, whereas the post-capping stiffness was assumed to be linear, with a descending branch. The yield and maximum moment in the columns were calculated taking into account the axial forces due to the vertical loading. The ultimate rotation Θ_u in the columns at the near collapse (NC) limit state corresponded to 80% of the maximum moment measured in the post-capping range of the moment-rotation relationship. It was estimated by means of the Conditional Average Estimate (CAE) method [13]. For the beams, the EC8-3 [14] formulas were used to compute the ultimate rotations in the plastic hinges. In case of structure S1 ultimate rotations were multiplied by a factor of 0.85, because there was no seismic detailing considered in the design of the frame. The parameter β_u, which controls the unloading stiffness in the plastic hinges, was assumed to have a value of 0.8. Note, that computation of the moment-rotation envelopes in plastic hinges is embedded in the PBEE toolbox. Nonlinear dynamic analyses were performed by assuming 5 % damping proportional to mass.

3.2 Ground motion records

A set of 30 ground motion records [15] was used for seismic loading. The peak ground acceleration of the ground motions varies between 0.05 - 0.52 g. The records have been selected within events having a magnitude of between 6.5 and 6.9. All the ground motion records have been recorded on firm soil, with a distance range from the epicentre of 12 - 55 km. The acceleration spectra for each of the 30 ground motion records, and the corresponding 16th, 50th and 84th fractiles, are presented in Figure 2.

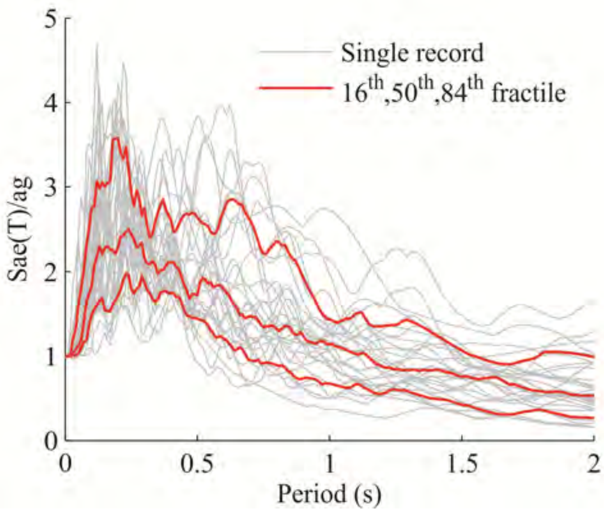

Figure 2: Acceleration spectra for all 30 ground motion records and corresponding 16th, 50th and 84th fractile.

3.3 Seismic performance assessment using progressive IDA

The seismic response parameters, the top displacement and the corresponding peak ground acceleration, were estimated for the significant damage (SD) and near collapse (NC) limit states (LS). It is considered that the SD limit state is violated at the structural level when the rotation in the plastic hinge of the first column or in all the beams in one of the storeys exceeds the rotation which corresponds to the maximum moment in the columns or beams, respectively. Similarly, it is considered that the NC limit state is violated when the rotation in the plastic hinge of the first column or all the beams in one of the storeys exceeds the ultimate rotation in the columns or beams, respectively. The NC limit state is also violated if the average residual top displacement in last five seconds of the analysis exceeds the height of a building by more than 1 %, or if global dynamic instability is reached before other conditions for near collapse limit state are violated.

In order to assess seismic performance of structure by using progressive IDA, a precedence list of ground motion records need to be determined based on the IDA, which is performed for a simple model, e.g. equivalent single-degree-of-freedom (SDOF) model. The equivalent SDOF models were therefore defined from results of pushover analyses. The pushover analyses were performed by assuming a modal distribution of the horizontal forces for all structures. The analysis is limited to horizontal direction X (Figure 1) since the structures are symmetric, pushover analyses were performed in positive X direction only. The pushover curves, together with the points which indicate the defined limit states, are presented in Figure 3. Pushover curves were idealized with the tri-linear force-displacement relationships as presented in Figure 3. The strength of the idealized force-displacement relationship was set equal to the maximum strength determined by the pushover analysis. In Table 1 mass of the equivalent SDOF model m^*, the transformation factor Γ, period of the equivalent SDOF model T^*, which is equal to fundamental period of MDOF structure in the analysed direction, and the ratio between the maximum base shear and weight of the structure F_b/W are presented for the three structures.

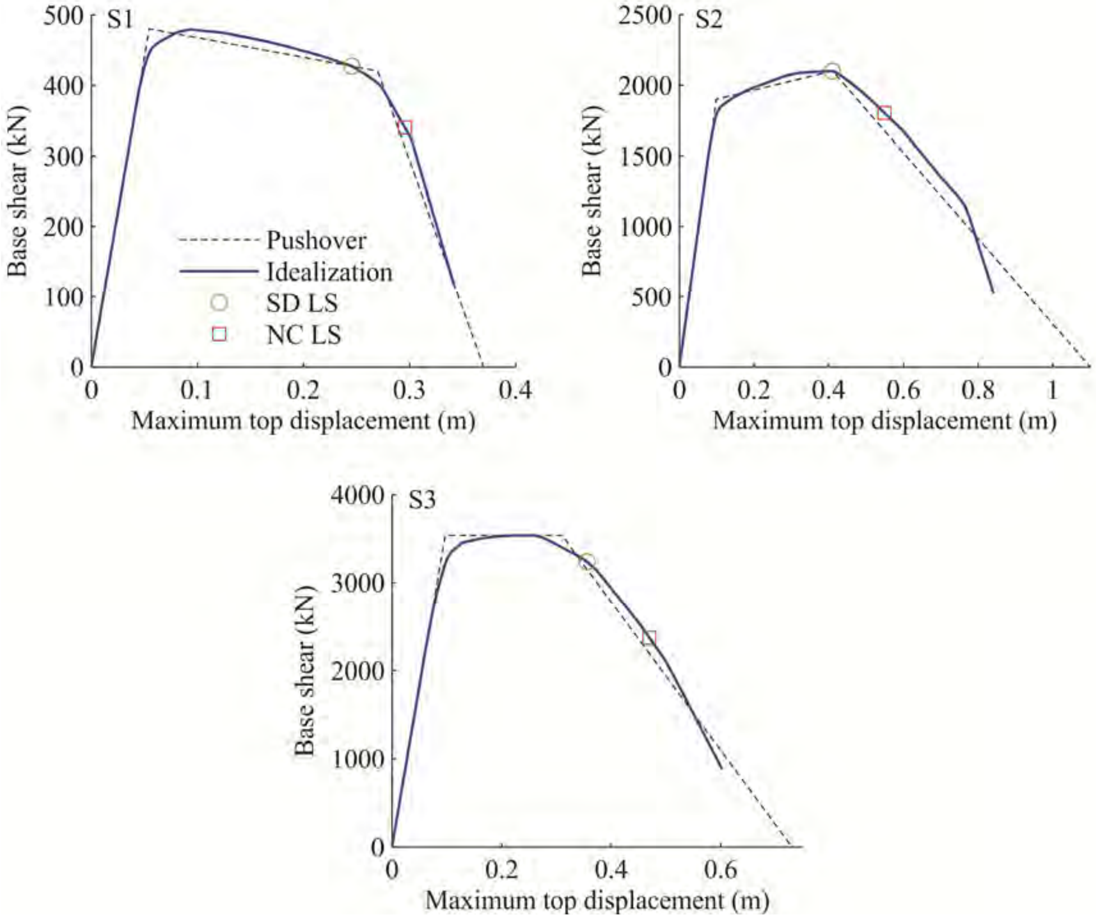

Figure 3: Pushover curves, showing the displacements which correspond to the SD limit state and NC limit state, and the idealized force-displacement relationships for structures S1, S2 and S3.

Table 1: Mass of the equivalent SDOF model m^*, the transformation factor Γ, period of equivalent SDOF model T^* and the ratio between the maximum base shear and weight of the structure F_b/W for structures S1, S2 and S3.

Structure	m^* (t)	Γ	T^* (s)	F_b/W
S1	606	1.27	1.65	0.05
S2	327	1.28	0.82	0.44
S3	2860	1.21	1.76	0.09

The damage at the plastic hinges of the beams and columns at NC limit state, which is obtained based on the pushover analysis, is presented in Figure 4. Note that, green, yellow and red colours represent, respectively, yielding of reinforcement, the state of exceeding the maximum moment, and the state of exceeding the ultimate rotation, whereas the grey part of the structure does not suffer any damage. The majority of the damage is concentrated in first and second storeys, while the upper stories remain almost undamaged.

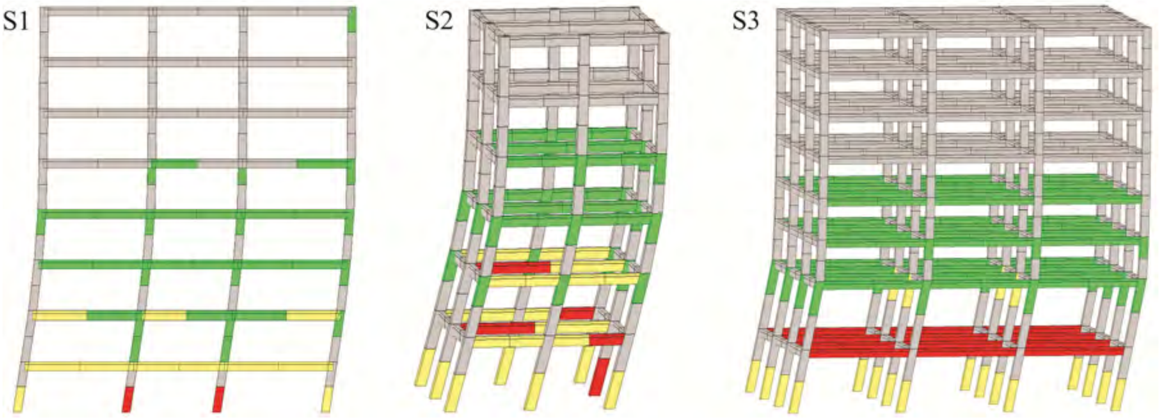

Figure 4: The distribution of damage for pushover analysis at NC limit state for structures S1, S2 and S3.

Precedence lists of ground motion records for all structures were determined from the IDA curves for the equivalent SDOF models by utilizing the simple optimization procedure [3]. Single record IDA curves were then computed progressively, starting from the first ground motion record in the precedence list for each structure. Progressive IDA was terminated after an acceptable tolerance for 16th, 50th and 84th fractile IDA curves was achieved. It was recognized the fractile IDA curves are predicted with sufficient accuracy with first 4, 5 and 4 subsets of ground motion records form the precedence list of records, respectively, for structure S1, S2 and S3. Note that each subset of ground motion records consists of three records.

The global dynamic instability of each computed IDA curves was estimated with a precision of 0.02 g. The largest interval between the peak ground acceleration, for which the seismic response parameters were computed, was defined as being equal to 0.05 g. However, if the peak ground acceleration, which corresponds to global dynamic instability, was large, the IDA curves were computed for only 20 points. Each nonlinear dynamic analysis within the IDA was calculated by employing the Newmark integration scheme, assuming $\gamma_n = 0.5$, $\beta_n = 0.25$ and an integration time interval of 0.005 s.

The "selected" IDA curves for the ground motion records from the precedence list of records and the corresponding 16th, 50th and 84th fractile response, with indication of the significant damage (SD) and near collapse (NC) limit states, are presented in figures 5a, 5c and 5e for all three structures.

In order to demonstrate the accuracy of results for 16th, 50th and 84th fractile response obtained with progressive IDA, IDA was performed for all 30 records. The comparison of fractile response obtained by progressive IDA and IDA is presented in figures 5b, 5d and 5f for all considered structures. The differences between the fractile IDA curves is practical negligible, even in the range close to the NC limit state, where the structures are already severely damaged. The indicated points in figures 5b, 5d and 5f represent the 16th, 50th and 84th fractiles of the peak ground acceleration, which cause the median top displacement corresponding to the SD or NC limit state for IDA and progressive IDA, and are also presented in Table 2. It can be observed that the error between the presented median estimates based on progressive IDA and IDA is always less than 10 % in all cases, while a mean error is only 3 %. Progressive IDA produces practically the same results as IDA. However, a bit larger errors are observed in the case of the prediction of global dynamic instability (figures 5b, 5d and 5f).

Table 2: The 16th, 50th and 84th fractiles of peak ground acceleration (PGA) causing the SD and NC limit states, and the corresponding median top displacement (MTD) for IDA and progressive IDA for all three structures. The values in brackets represent an error with respect to results of the IDA.

			SD limit state		NC limit state	
Structure	Method	Fractile	MTD (m)	PGA (g)	MTD (m)	PGA (g)
S1	IDA	16	0.24	1.01	0.34	1.24
		50		0.38		0.55
		84		0.18		0.27
	Progressive IDA	16	0.23 *(2%)*	0.97 *(3%)*	0.37 *(9%)*	1.28 *(3%)*
		50		0.37 *(3%)*		0.59 *(7%)*
		84		0.18 *(3%)*		0.27 *(0%)*
S2	IDA	16	0.40	1.99	0.53	2.32
		50		1.22		1.43
		84		0.82		0.91
	Progressive IDA	16	0.40 *(1%)*	2.02 *(2%)*	0.53 *(1%)*	2.29 *(2%)*
		50		1.26 *(3%)*		1.44 *(1%)*
		84		0.82 *(0%)*		0.90 *(1%)*
S3	IDA	16	0.32	1.23	0.45	1.87
		50		0.54		0.74
		84		0.24		0.32
	Progressive IDA	16	0.33 *(4%)*	1.26 *(2%)*	0.44 *(2%)*	1.82 *(3%)*
		50		0.55 *(2%)*		0.72 *(2%)*
		84		0.26 *(6%)*		0.33 *(3%)*

The seismic performance assessment by using progressive IDA requires significantly less computational time. It is shown that, by using progressive IDA, computational time can be reduced for about 50 % compared to that needed to perform IDA. It was proved, at least for the presented examples, that the seismic response parameters are sufficiently accurate when determined by progressive IDA, which requires only 12 to 15 IDA curves instead of 30, which was the number of records used in the IDA. Nevertheless there is some additional work with the preparation of the precedence list. Note that the method provided sufficiently accurate results, although it is based on response of an equivalent SDOF model.

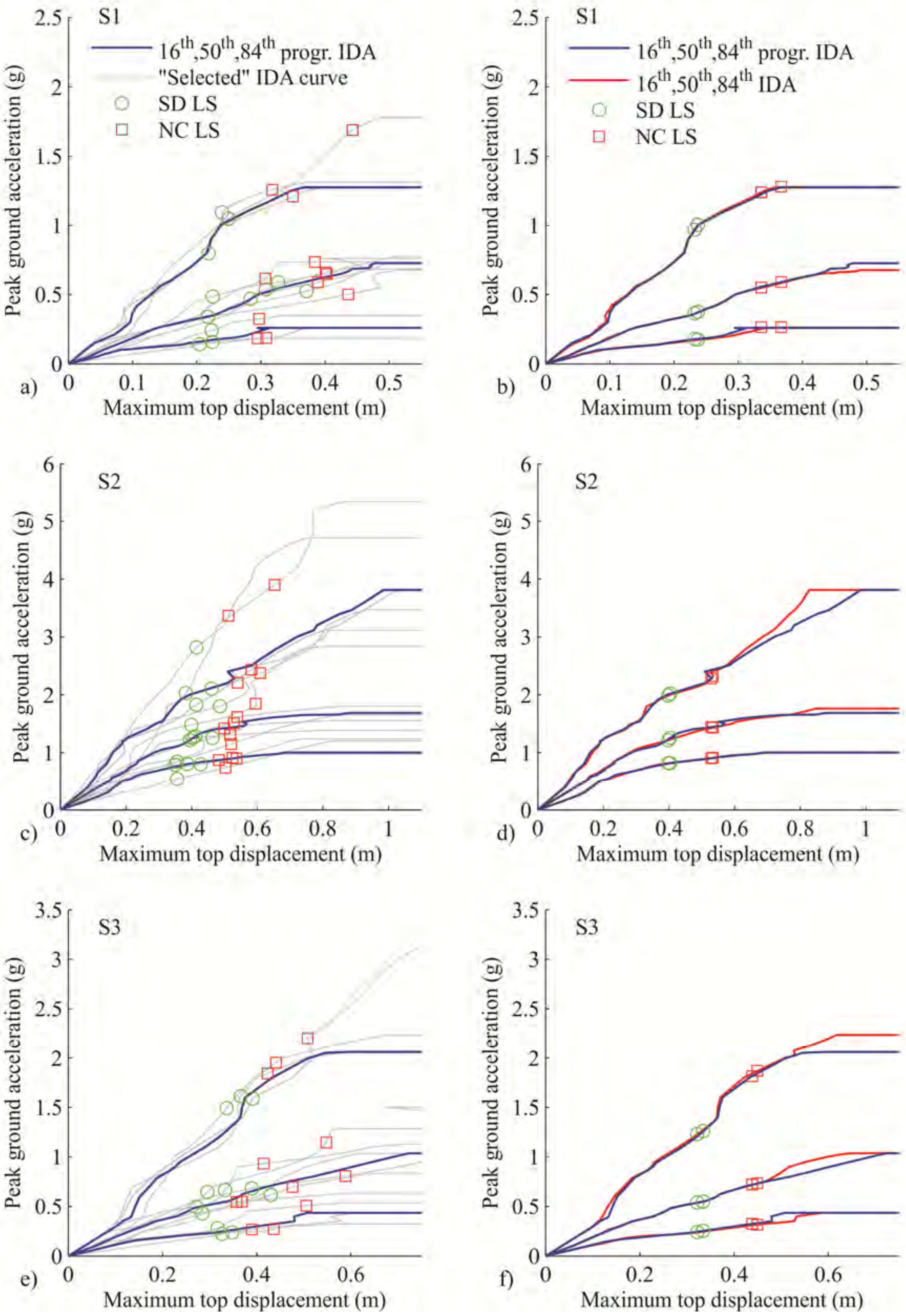

Figure 5: The “selected” IDA curves with the corresponding fractile response determined by progressive IDA and the comparison of the 16th, 50th and 84th fractile response determined by IDA and progressive IDA for structures S1, S2 and S3. Significant damage (SD) and near collapse (NC) limit states are indicated.

4 CONCLUSIONS

Computational efficiency of progressive IDA was assessed by means of seismic performance assessment of three symmetrical reinforced concrete frame structures. The considered structures differed in geometry, material, design requirements and consequently in period and ratio between the maximum base shear and weight of the structure significantly. However, it was shown that it is possible to predict the 16th, 50th and 84th fractiles of seismic response parameters for the significant damage and near collapse limit state by using the progressive IDA with minor errors in comparison to IDA for all three structures.

The differences in 16th, 50th and 84th fractiles of peak ground acceleration causing the significant damage and near collapse limit states, and in the corresponding median top displacement for progressive IDA and IDA are smaller than 10 %, for most cases only about 3 %. Progressive IDA produces practically the same results as IDA if compared in the range up to the near collapse limit state, although the results of progressive IDA are based on only 12 to 15 ground motion records. Therefore progressive IDA requires only about 50 % of computational time with respect to the computational time needed for the IDA. However, there is some additional work with determination of precedence list of ground motion.

ACKNOWLEDGMENTS

The results presented in this paper are based on work supported by the Slovenian Research Agency. This support is gratefully acknowledged.

REFERENCES

[1] D. Vamvatsikos, C.A. Cornell, Incremental Dynamic Analysis. *Earthquake Engineering and Structural Dynamics*, 31(3), 491-514, 2002.

[2] A. Azarbakht, M. Dolšek, Prediction of the median IDA curve by employing a limited number of ground motion records. *Earthquake Engineering and Structural Dynamics*, 36, 2401-2421, 2007.

[3] A. Azarbakht, M. Dolsek, Progressive Incremental Dynamic Analysis for First-Mode Dominated Structures. *Journal of Structural Engineering*, available on-line, doi:10.1061/(ASCE)ST.1943-541X.0000282, 2010.

[4] M. Dolsek, Development of computing environment for the seismic performance assessment of reinforced concrete frames by using simplified nonlinear models. *Bulletin of Earthquake Engineering* 8, 1309-1329, doi:10.1007/s10518-010-9184-8, 2010.

[5] F. McKenna, G.L. Fenves, Open system for earthquake engineering simulation. Pacific Earthquake Engineering Research Center, Berkeley, California, *http://opensees.berkeley.edu*, 2007.

[6] MathWorks, MATLAB the Language of Technical Computing, *http://www.mathworks.com/*, 2007.

[7] M. Dolsek, Estimation of Seismic Response Parameters Through Extended Incremental Dynamic Analysis. M. Papadrakakis, M. Michalis, N.D. Lagaros eds. *Computational Methods in Earthquake Engineering*. Springer, 2011.

[8] C.Ch. Mitropoulou, N.D. Lagaros, M. Papadrakakis, Advances in Life Cycle Cost Analysis of Structures. M. Papadrakakis, M. Michalis, N.D. Lagaros eds. *Computational Methods in Earthquake Engineering*. Springer, 2011.

[9] M. Causevic, S. Mitrovic, Comparison between non-linear dynamic and static seismic analysis of structures according to European and US provisions. *Bulletin of Earthquake Engineering*, doi:10.1007/s10518-010-9199-1, 2010.

[10] M. Kosič, Design of eight-storey reinforced concrete frame building according to European standard Eurocode 8. *Personal communication*, 15 December 2010.

[11] CEN, Eurocode 8: Design of structures for earthquake resistance, Part 1: General rules, seismic action and rules for buildings. *EN 1998-1*. European Committee for Standardisation, Brussels, December 2004.

[12] CEN, Eurocode 2: Design of concrete structures, Part 1-1: General rules and rules for buildings. *EN 1992-1-1*. European Committee for Standardisation, Brussels, December 2004.

[13] I. Peruš, K. Poljanšek, P. Fajfar, Flexural deformation capacity of rectangular RC columns determined by the CAE method. *Earthquake Engineering and Structural Dynamics* 35, 1453-1470, 2006.

[14] CEN, Eurocode 8: Design of structures for earthquake resistance, Part 3: Strengthening and repair of buildings. *EN 1998-3*. European Committee for Standardisation, Brussels, March 2005.

[15] D. Vamvatsikos, C.A. Cornell, Direct estimation of the seismic demand and capacity of oscillators with multi-linear static pushovers through IDA. *Earthquake Engineering and Structural Dynamics* 35, 1097-1117, 2006.

COMPDYN 2011
III ECCOMAS Thematic Conference on
Computational Methods in Structural Dynamics and Earthquake Engineering
M. Papadrakakis, M. Fragiadakis, V. Plevris (eds.)
Corfu, Greece, 25–28 May 2011

COMPARISON OF SEISMIC SCREENING METHODS FOR SCHOOLS IN A MODERATE SEISMIC ZONE

Helene Tischer[1], Denis Mitchell[2], and Ghyslaine McClure[2]

[1] Department of Civil Engineering and Applied Mechanics, McGill University
817 Sherbrooke Street West, Montréal, QC H3A 2K6, Canada
e-mail: helene.tischer@mail.mcgill.ca

[2] Department of Civil Engineering and Applied Mechanics, McGill University
817 Sherbrooke Street West, Montréal, QC H3A 2K6, Canada
denis.mitchell@mcgill.ca, ghyslaine.mcclure@mcgill.ca

Keywords: seismic screening methods, vulnerability, schools.

Abstract. *An ongoing project at McGill University is aimed at designing an adapted seismic screening method for schools in the province of Québec, Canada. As part of this project the "FEMA154 Rapid Visual Screening of Buildings for Potential Seismic Hazard" and the "NRC92 Manual for Screening of Buildings for Seismic Investigation" were used to assess the potential performance of 100 school buildings located in the city of Montréal. Results for both methods are in reasonable agreement, with 65% of the buildings requiring a detailed evaluation according to FEMA154 and 50% according to NRC92. The evaluation highlighted particular characteristics of the structures. School buildings are generally low-rise, of a limited number of structural types and have a high incidence of features that could affect seismic performance, such as steps in elevation and re-entrant corners. Findings were also used to identify advantages and shortcomings of each screening method. NRC92 is largely based on expert opinion, which makes the method difficult to update. FEMA154 uses a more rational methodology for calculating the vulnerability scores; however the nonlinear static seismic analysis procedure employed doesn't consider latest improvements in building codes. Updating the procedure increases the basic scores on average by 24%, with higher scores indicative of better performance. When using FEMA154 it has to be considered that seismicity and soil amplification factors were developed for the United States. NRC92, although conceived for the Canadian context, has to be updated to include latest findings in seismic hazard parameters and soil classification. Since schools typically have a high incidence of irregularities, accounting for them in the screening phase is essential. FEMA154 only considers vertical and plan irregularities and it was found that this is insufficient to capture the characteristics of the evaluated schools. NRC92 partially overcomes this shortcoming by specifying seven different types of irregularities. In conclusion it was recognized that the clear analytical procedure behind FEMA154 allows updating and adapting the method to its use outside its intended scope. Therefore the screening procedure currently under development is largely based on this method, incorporating key characteristics of NRC92.*

1 INTRODUCTION

Schools deserve special attention regarding earthquake performance because of their unique occupancy and important post-earthquake role. However experience in the past has demonstrated that they are especially vulnerable. This was illustrated by the effects of the 1997 Cariaco earthquake in Venezuela. Two out of five collapsed buildings were schools, and more than half the casualties were students [1]. There have been many other examples that have demonstrated that school buildings are especially vulnerable to damage in moderate to strong earthquakes (e.g. [2, 3]). Different reasons have been proposed to explain the observed poor performance, including the age of school buildings and that their complex structural features compromise seismic safety [4].

The protection of children is paramount in society because they provide for future generations and represent an especially vulnerable segment of society. It has also been argued that safe schools must be considered a basic right in countries where school attendance is obligatory [5]. In addition, school buildings play a key role in restoring the normal functioning of society after an earthquake. Immediately following a seismic event they can be used as shelters, and their operation permits parents to return to work. In 2005 the Organization for Economic Co-operation and Development, acknowledging these facts, published recommendations on the earthquake safety of schools. In this document, the organization suggests that "Member countries take steps to establish and implement programs of school seismic safety" [6]. The first step to ensure effective risk reduction in existing buildings is the assessment of this risk.

Seismic screening methods for schools are needed as the first phase in vulnerability assessment projects. One example of the successful application of the technique is the evaluation of all schools located in zones with high seismicity of the province of British Columbia, Canada. This study, conducted in 2004, found that 82% of the more than 850 evaluated schools were at moderate or high risk, and consequently a state of the art tool for the detailed evaluation and strengthening of the province's schools was developed [7]. Presently the schools identified to be the most critical are being reassessed and retrofitted [8, 9].

2 SEISMIC SCREENING METHODS

Seismic screening methods, more specifically rapid visual screening or score assignment procedures, are intended to be coarse screening procedures using little resources per building. This is achieved by evaluating a limited number of features that influence seismic performance and assigning an overall score to each building. An ideal screening method will identify all those buildings that are potentially seismically hazardous, while limiting the number of buildings that will pass a more detailed evaluation [10].

Seismic screening methods can be classified as observed or predicted vulnerability procedures, or hybrid methods, depending on the type of source information used. Observed vulnerability procedures use statistics of damages in past earthquakes, sometimes combined with expert opinion, to determine the probable behavior of structures under future seismic events. The main setback of this approach is the possible insufficiency of observational data, and the subjectivity in judging data. The method also lacks analytical justification. Predicted vulnerability methods try to overcome these shortages by using analytical procedures to determine the probable behavior of a structure subjected to earthquake loading. The limitation of this approach is the time and computational effort required by detailed analytical analyses. Therefore a balance between effort and precision has to be found [11].

The first comprehensive rapid visual screening method was developed in the United States by the Applied Technology Council under contract to the Federal Emergency Management Agency [12, 13]. This method, published as the FEMA154 report, *Rapid Visual Screening of*

Buildings for Potential Seismic Hazard, is probably the most widespread RVS tool, and there is considerable guidance on its application (e.g. [14, 15]). The method has served as a prototype for the development of screening tools in other countries, as for example in Switzerland [16] and Italy [17]. The current Canadian seismic screening method, *Manual for Screening of Buildings for Seismic Investigation* (NRC92) [18], is also largely based on the first edition of FEMA154. There are other methods, developed independently, such as the procedure of the New Zealand Society for Earthquake Engineering [10]. This method judges existing buildings by comparing them to current New Zealand standards. Another example is the Japanese Seismic Index Method, a multiphase screening procedure that estimates the vulnerability of an existing building by a seismic performance index calculated for every story in each main direction and based on key characteristics of the building. This method has been used to evaluate low- and mid-rise reinforced concrete buildings in Japan since 1975 [19].

For the present research FEMA154 and NCR92 were evaluated, due to their relevance at the global and national level, respectively. A more detailed description of the two methods follows.

2.1 FEMA154

FEMA154 was first published in 1988 [20, 21], but was significantly improved in 2002 with the release of its second edition. The screening is done by visual observation of the building, and can be completed by means of a sidewalk survey, although entering the building and consulting existing plans and other documentation is recommended. Based on this inspection a data collection form is completed. Initially the lateral load resisting system has to be identified and related to one of the 15 predefined building types. A basic structural hazard score is provided for each building type. To consider specific characteristics of the building that could affect its seismic performance, the score is then altered by adding or subtracting score modifiers to obtain the final structural score. Score modifiers related to building height, vertical and horizontal irregularities, year of construction and soil type are provided. Higher final structural scores correspond to a better seismic performance, and usually they range from 0 to around 6. It is recommended that buildings with a score of 2 or less should be evaluated in more detail.

The basic structural hazard score (*BSH*) for each building type is defined as the negative of the logarithm (base 10) of the probability of collapse (*P*) of the building, given a ground motion corresponding to the maximum considered earthquake (*MCE*), as shown in Equation 1.

$$BSH = -log_{10}[P(collapse\ given\ MCE)] \qquad (1)$$

The probability of collapse is the probability of the building being in complete damage state times the fraction of the buildings in complete damage state that collapse.

To determine the probability of being in complete damage state first the spectral displacement is calculated using a nonlinear static seismic analysis procedure. The technique used is the capacity spectrum method [22], depicted in Figure 1.a. The capacity spectrum method, an equivalent linearization technique, is based on the assumption that the maximum inelastic deformation of a nonlinear single degree of freedom system can be estimated from the maximum elastic deformation of a linear elastic single degree of freedom system which has natural period and damping values higher than the original one. The inputs of the method are the force-deformation relationship of the structure, commonly known as push-over curve, and the seismic demand. Both are plotted in acceleration-displacement response spectrum format. In this format periods can be represented by radial lines, and the equivalent period is assumed to be the secant period at the intersection of the capacity spectrum and the seismic demand spectrum reduced for equivalent damping. The equivalent damping is estimated based on the area under the capacity curve. Since both equivalent period and damping are dependent on the estimated maximum spectral displacement, an iterative process is followed for its calculation.

The estimated spectral displacement is used to determine the probability of complete damage state from a fragility curve corresponding to the building type, as can be seen in Figure 1.b. This value is multiplied by the fraction of buildings that will collapse being in complete damage state to obtain the probability of collapse and calculate the basic structural hazard scores. A similar procedure is used to calculate the score modifiers.

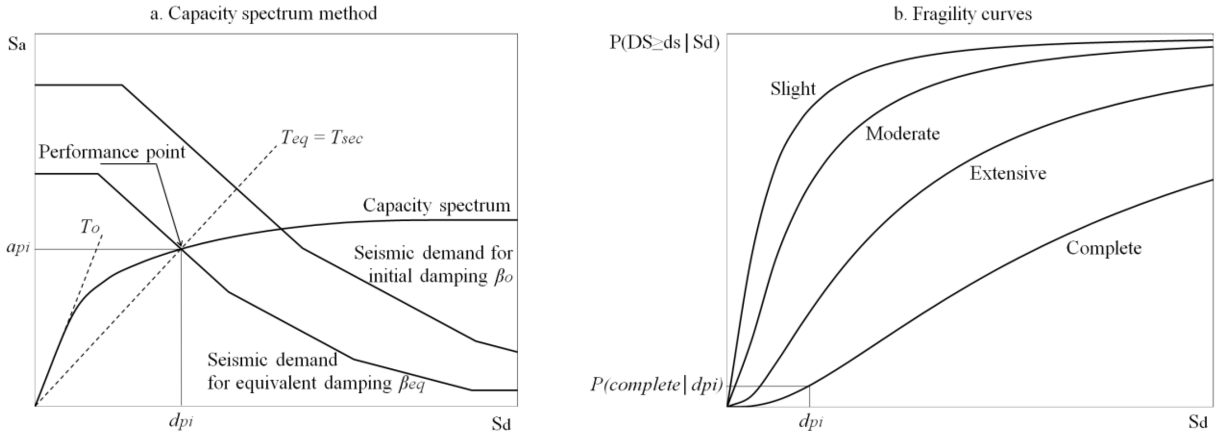
a. Capacity spectrum method

b. Fragility curves

Figure 1: Estimation of the probability of complete damage state of a building class [13].

2.2 NRC92

The NRC92 procedure was developed in Canada in 1992. Similar to FEMA154, the practical implementation of NRC92 relies on a data collection form that can be filled out by visual inspection of the building. It is expected that the exterior as well as the interior is evaluated, and recommended that building plans are considered. The user first has to identify the lateral load resisting system and correlate it to 15 different building types, very similar to those of FEMA154. High importance is given to the identification of building irregularities, differentiating between seven different types. Non-structural hazards also have to be identified.

A structural index is computed by multiplying five factors. They are related to local seismicity, soil conditions, lateral load resisting system, vertical and horizontal irregularities and building importance. A non-structural index is also computed, based on the observed non-structural hazards, the soil conditions and building importance. The final score, called the seismic priority index, is the sum of a structural index and a non-structural index. In contrast to FEMA154, a high final score indicates high priority for refined seismic vulnerability analysis of the building. It is suggested that buildings with a score less than 10 be treated as low priority, 10 to 20 as moderate priority, 20 to 30 as high priority and more than 30 as potentially hazardous requiring immediate attention.

NRC92 is largely based on the first edition of FEMA154. In this first edition the same types of scores and modifiers as the second edition are used, however calculations are mainly based on engineering expert opinion. The basic structural hazard scores were calculated as the negative of the logarithm (base10) of the probability of damage (D) exceeding 60% of the building value, given a ground motion represented by the NEHRP effective peak acceleration, as shown in Equation 2.

$$BSH = -log_{10}[P(D \geq 60\%)] \tag{2}$$

To determine the probability of occurrence of different levels of damage given a specified ground motion, expert opinion was used (ATC-13 report [23]). This report was concerned exclusively with buildings constructed according to Californian building practices, and again expert opinion was sought out to make the results applicable to other regions of different seismicity. The score modifiers were also calculated based on expert criteria.

To develop NRC92 the method was adapted to Canadian seismicity and building practice. The scoring system was also modified to consider structural and non-structural components in the evaluation, and the importance of the building, related to occupancy and use.

3 BACKGROUND: SCHOOLS IN QUÉBEC

The present study is conducted in the province of Québec, Canada, considered a moderate seismic zone. Most of the population is located in the St. Lawrence River valley, the province's most active seismic zone. The region with highest seismicity, LaMalbaie, has spectral accelerations response values of Sa(0.2s) = 2.3g for short periods and of Sa(1.0s) = 0.6g for long periods, with a probability of exceedence of 2% in 50 years. More typical values are those of the two largest cities of the province, Montréal with Sa(0.2s) = 0.69g and Sa(1.0s) = 0.14g, and Québec City, with Sa(0.2s) = 0.59g and Sa(1.0s) = 0.14g. These two cities account for half of the province's population.

In Québec moderate and strong earthquakes have occurred in the past, and they will most certainly occur in the future. The large events have a relatively long return period (several centuries) and hence the general population has the impression that earthquakes are not likely in the region. Although Québec's earthquakes in the past have not caused loss of human life, extensive property damage has been reported. Some examples are the 1935 Timiskaming earthquake (magnitude 6.2) and most recently the 1988 Saguenay earthquake (magnitude 6.0) [24].

Since experience in strong earthquakes is limited in Eastern Canada, reported seismic damage to schools has been mostly to non-structural elements. There was considerable damage reported to one Collegiate and Vocational School in Cornwall after the 1944 Cornwall-Massena earthquake [24]. The 1988 Saguenay earthquake produced architectural damage to 33 out of 42 public schools of the two most affected communities [25]. The site visit team also drew attention to the dangers of unreinforced masonry infill walls, and warned about the abundance of them particularly in schools and hospitals [26].

A school inventory report from the Québec Ministry of Education [26] has classified all the provincial public school buildings into five main structural/architectural categories and determined their general seismic vulnerability features relating the structural type to the construction year. The five categories and their province-wide occurrence are presented in Figure 2, totaling approximately 3600 schools. No distinction between different buildings at each location was made. About one half of the schools were built before 1960, i.e. before modern earthquake-resistant design procedures were introduced in the *National Building Code of Canada* (NBCC), and were therefore classified as the more vulnerable schools of the province. This inventory was a first step in the vulnerability assessment of schools in Québec and its results highlighted the need for more detailed studies. Clearly, a detailed school-by-school evaluation is not feasible on a large scale and the development of a screening method adapted to address the specific characteristics of the building inventory is necessary.

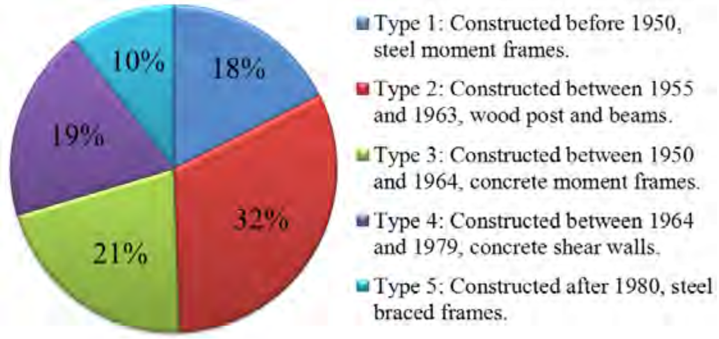

Figure 2: Initial classification of school buildings in Québec [26].

4 EVALUATION OF SCHOOL BUILDINGS

The goal of this research is to design such an adapted seismic screening method for school buildings of the province of Québec. As part of the study the seismic vulnerability of sixteen high schools (secondary education level) comprising a total of 102 individual buildings is being studied. These schools are designated as post-critical shelters on the island of Montréal, mostly based on their location and their capacity to shelter a large number of disaster victims. A detailed database of the characteristics of the school buildings was created. Information from plans, site visits and the city's seismic microzonation map [27] was used.

It was found that most school buildings are low rise: over 3/4 of them are three stories high or less, with the tallest being six stories high. The floor area varies between 200 and 5300m^2, with an average value of 2000m^2. It is noted that 87% of the structures were built in the 1960s and 1970s. The most common lateral load resisting systems, which account for 80% of the studied buildings, are: concrete frames with infill masonry shear walls, concrete shear walls and steel moment frames. As expected the evaluated schools are complex structures, with features that could potentially affect their seismic behavior. Buildings with re-entrant corners, steps in elevation, potential for pounding, exterior cladding and heavy partition walls are common. Table 1 summarizes the most common features and their percentage of occurrence. According to the seismic microzonation map of Montréal, eight of the 16 school campuses are located on soils prone to ground motion amplification [28].

Feature	% of Buildings
Irregular building plan	40%
Steps in elevation view	40%
Heavy masonry partition walls	90%
Potential for pounding	99%
Exterior cladding	80%
Site effects	50%
Deterioration	35%

Table 1: Features that could affect seismic performance and their occurrence in evaluated schools buildings.

Preliminary assessments using the FEMA154 and NRC92 seismic screening procedures were performed. Cut off scores were used as recommended for each method. Results of FEMA154 suggested that 65% of the buildings should undergo a detailed evaluation. NRC92 results were similar, finding 12% of the buildings with low priority for future interventions, 38% moderate priority, 34% high priority and 16% potentially hazardous. There is relatively good agreement in the results obtained with the two methods given that 80% of the buildings that didn't comply with the screening of FEMA154 were classified as having high priority of intervention or being potentially hazardous by NRC92. The large proportions of buildings requiring detailed evaluation (65% according to FEMA and 50% according to NRC92) appear somewhat alarmist for a moderate seismicity environment and provide further motivation for the development of better adapted screening methods that can identify more precisely the installations that need detailed seismic vulnerability assessment.

A companion study evaluated the seismic risk of operational and functional components of fourteen of the sixteen schools [29], according to the procedure in CAN/CSA S832-06 standards, *Seismic risk reduction of operational and functional components (OFCs) of buildings* [30]. Around 450 typical components were evaluated in total, from which 20% were rated high and 54% moderate risk. The most common problem identified was lack of restraint of the non-structural components.

5 ADVANTAGES AND SHORTCOMINGS OF EACH METHOD

5.1 Procedures behind score calculations

Supporting documentation for NRC92 is limited and this creates challenges for any attempt of updating the procedure. An update of NRC92 is needed because it was largely based on the first edition of FEMA154, which has been thoroughly revised. On the other hand, FEMA154 uses a more sound methodology for calculating the vulnerability scores than NRC92, with the calculations based on the capacity spectrum method as described in ATC-40 [22]. However the application of ATC-40 has raised concerns in the past, compared with other simplified analysis methods with poor agreement. Furthermore, when comparing to results of response history analysis, significant differences could be found [31]. Some studies demonstrated that the estimated maximum deformations can be underestimated by as much as 50% [32]. Recognizing this concern, in 2004 a thorough evaluation of the existing method was conducted and an updated procedure was published in the FEMA440 report [33]. In this evaluation it was found that for short-period structures, with period less than 0.5s approximately, the peak displacements are largely overestimated. For higher periods the ATC-40 methodology can either overestimate or underestimate the displacements, depending on the assumed hysteretic behavior of the evaluated building. The main modification of the method was the update of the expressions for the calculation of the equivalent or effective period (T_{eff}) and damping (β_{eff}). Approximate equations, that are independent of the hysteretic curve and post-elastic stiffness ratio of the capacity curve used, are repeated in the Equations 3 to 5, were μ is the ductility demand, T_0 and β_0 are the elastic damping and period, respectively.

For $1.0 < \mu < 4.0$:

$$\begin{aligned} \beta_{eff} &= 4.9(\mu-1)^2 - 1.1(\mu-1)^3 + \beta_0 \\ T_{eff} &= [0.20(\mu-1)^2 - 0.038(\mu-1)^3 + 1]T_0 \end{aligned} \tag{3}$$

For $4.0 \le \mu < 6.4$:

$$\begin{aligned} \beta_{eff} &= 14.0 + 0.32(\mu-1) + \beta_0 \\ T_{eff} &= [0.28 + 0.13(\mu-1) + 1]T_0 \end{aligned} \tag{4}$$

For μ > 6.5:

$$\beta_{eff} = 19\left[\frac{0.64(\mu-1)-1}{[0.64(\mu-1)]^2}\right]\left(\frac{T_{eff}}{T_0}\right)^2 + \beta_0$$
$$T_{eff} = \left\{0.89\left[\sqrt{\frac{(\mu-1)}{1+0.05(\mu-2)}}-1\right]+1\right\}T_0 \tag{5}$$

Based on these equations, scores for FEMA154 were recalculated in the present study. Figure 3 shows a comparison between the basic structural hazard scores presented in FEMA154 and the updated values. On average the values increased 14% for high seismicity, 29% for moderate seismicity and 28% for low seismicity. Increased values are related to a better earthquake performance. This result was expected, since the basic structural hazard scores are calculated for low rise buildings with relatively short periods, and the capacity spectrum method as presented in ATC-40 tends to overestimate the predicted maximum displacement values for short periods.

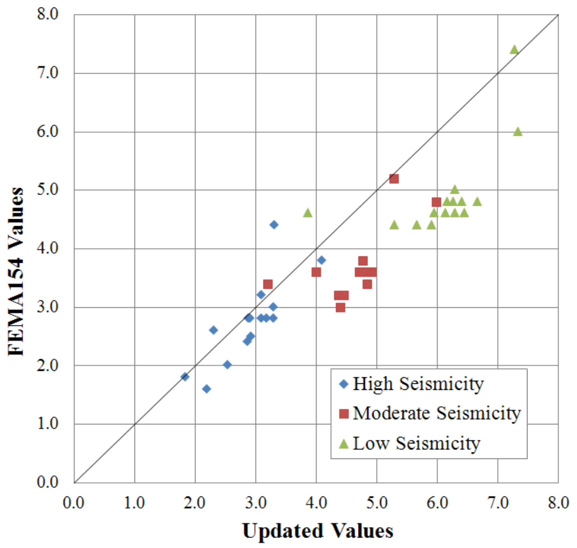

Figure 3: Comparison between the basic structural hazard scores of FEMA154 and recalculated values with updated capacity spectrum method.

5.2 Spectral response acceleration values

FEMA154 targets seismicity of the United States. Three seismicity regions (high, moderate and low) are defined based on design spectral acceleration values for periods of 0.2 and 1.0 seconds, S(0.2s) and S(1.0s). Limiting values were taken from FEMA310 [34], ignoring local site effects. To determine the median spectral acceleration response values for each seismic region first each county was classified based on the maximum S(0.2s) and S(1.0s) values. The median of these maximum values was calculated for each region and used for the score calculations. The median values and the basic structural hazard scores and modifiers were recalculated [35] considering the seismicity of Québec's cities as specified in the 2005 edition of the NBCC [36], considering the same boundaries for the seismicity regions.

Although the spectral accelerations in Canada and the United States are calculated with the same probability level, 2% in 50 years, there are differences in the calculations that account for cross-border inconsistencies, as for example the use of the median seismicity values in Canada versus the mean values in the United States. Furthermore when using FEMA154 in Canada, one difference in philosophy has to be addressed: in the United States the spectrum is reduced by 2/3 for design purposes [37], while in Canada this reduction is not used. This will have an impact on the calculated scores, and the use of the same limiting values that define the three seismicity regions is questionable, since they were conceived considering the reduction factor. When analyzing the case of the city of Montréal for example, a city identified as having moderate seismicity, with S(0.2s) = 0.69g and S(1.0s) = 0.14g for Site Class C, it was found that it would be classified by FEMA154 as moderate seismicity if applying the 2/3 reduction factor and high seismicity if not.

NRC92, although conceived for the Canadian context, has yet to be updated to consider the latest findings regarding seismic hazard. The seismicity used by the method is specified in the 1990 NBCC [38], with seismic hazard maps developed in 1985. The effective seismic zone of the site of interest is calculated according to the peak ground acceleration and peak ground velocity with probability of being exceeded of 10% in 50 years. New models were developed for the 2005 NBCC, which include latest findings related to historical seismic events, new attenuation laws, a better description of the site conditions and the explicit consideration of uncertainty [39].

5.3 Site classification

Design spectral accelerations are determined by the expected seismic excitation and local geotechnical conditions at the site. Both in the US and in Canada soil is classified into six categories, from type A to F, ranging from hard rock (type A) to poor soil (type F). For the classification of each type, the parameters used are the measured shear wave velocity or standard blow count. Ground motion amplification factors for short and long periods, F_a and F_v, dependent on the expected intensity of shaking, are defined for each site class. For the US, the reference soil is type B, meaning that F_a and F_v values are equal to one for soil type B [37]. In the seismic provisions of the 2005 NBCC, the American classification system was adopted with small changes. However the reference soil in Canada was defined as type C, to be consistent with previous editions of the NBCC [40]. Therefore F_a and F_v values for the same soil type are lower in Canada. This implies that when using FEMA154 with spectral acceleration values and soil definitions from Canada the site effects are overestimated.

The four different soil types considered by NRC92 have foundation factor F, ranging from 1.0 to 2.0. These factors, based on design practice of the time, do not consider the differences between short and long period responses and the influence of the intensity of shaking.

5.4 Configuration irregularities

The findings of the initial evaluation demonstrated that schools are complex structures: it was found that 80% of the examined buildings have some type of irregularity, with almost 40% having at least one vertical and one plan irregularity. While FEMA154 only differentiates between vertical and plan irregularities, NRC92 identifies seven different types of irregularity: vertical and horizontal irregularity (torsion), short concrete columns, soft story, pounding, major modifications and deterioration. The effect can be appreciated when studying the influence of different irregularities that can be classified as vertical (e.g., steps in elevation view, building on hill, soft story) on the score results. NRC92 classified 40% of school buildings with only one vertical irregularity as high priority and 70% with two vertical irregularities as high priority. Using FEMA154 the percentage of buildings in need of a detailed assessment was 90% and 100% for each these two case. This demonstrates that the NRC92 approach gives greater differentiation when more than one irregularity exists.

In FEMA154 score modifiers for vertical irregularities were based on engineering judgment. For high and moderate seismic zones, the modifiers were chosen so that if it were the only modifier considered, the final score would be below the cut-off score of 2. For low seismicity, modifiers similar to those of moderate seismic zone were adopted. For the calculation of the plan irregularity modifiers, an increase of 50% in the spectral acceleration response values was used. This approach seems appropriate when evaluating general building stock, where irregularities in plan and elevation should be rather uncommon. When evaluating schools however, due to the prevalence of configuration irregularities, a more detailed evaluation is desirable. Finding a balance between the simplicity of the method and the detailed identification of irregularities is challenging. An example on how this can be achieved can be found in the screening procedure of New Zealand [10]. Even in a first phase evaluation, four critical structural features have to be identified (plan and vertical irregularities, short columns and pounding potential) and the effect on the structural performance of each has to be classified as severe, significant or insignificant. Guidance on how to classify the severity is provided. For buildings with an L-shape plan, for example, the effect on structural performance is determined by comparing the length and the width of the wings.

5.5 Potential for pounding

When insufficient or no separation is provided between adjacent buildings they will likely suffer from pounding during a strong earthquake. This will induce high amplitude shock loadings, and experience in past earthquakes has demonstrated that this problem can even cause buildings to collapse. During the 1985 Mexico City earthquake, 15% of building collapses could be attributed to these severe pounding effects [41].

While FEMA154 doesn’t consider pounding, NRC92 incorporates it in calculating the score, and the limiting distance between buildings is defined in terms of the velocity related seismic zone (dependent on the expected peak ground velocity) and number of stories. Since the 2005 edition of NBCC stipulates the seismic demand in terms of spectral acceleration values only, other expressions have to be found.

Experience in past earthquakes has demonstrated that there are special circumstances where the effect of pounding is most critical. Adjacent buildings with different heights, periods and masses are the most vulnerable. Floors at different elevations will allow the slabs of one building to impact columns of the other building generating shear failure and partial or total collapse. In absence of these adverse factors, pounding usually will only induce local damage [42]. Given the high incidence of potential for pounding in the evaluated schools, the identification of the probable severity of damages is important in the rapid visual screening phase.

5.6 Non-structural components

Another important aspect considered by NRC92 while ignored by FEMA154 is the evaluation of non-structural components. Solving non-structural component related problems is not only a cost-effective first step for retrofit, these problems can also be life-threatening or produce injuries while not leading to collapse of the structure. Furthermore, if the installations should be operational immediately after the event, as is the case with post-critical shelters, non-structural damage should be limited. In a moderate seismic zone non-structural damage can be more widespread than structural damages or collapse, as has been demonstrated by experience in past earthquakes in Québec [26].

The initial evaluation highlighted the extensive use of heavy partition walls in schools, many of them made of unreinforced masonry blocks and often without restraint at the top of the walls. This is especially worrisome considering the potential life safety hazard that out-of-plane failure can cause even in a moderate earthquake. A detailed inventory of these walls must be made to better assess the risks. Key characteristics for wall performance include thickness, height and effective lateral support. The wall density and location will furthermore help to prioritize the cases where corrective measures are necessary.

5.7 Building importance

Schools fall into two distinct classes regarding importance: post-disaster shelters and ordinary schools which all belong to the post-critical building category according to NBCC. The different performance objectives should be acknowledged by the seismic screening method used. While ignored by FEMA154, NRC92 asks for the calculation of a building importance factor based on the occupancy and use of the building. For school buildings, the structural index is increased between 20 and 50%, compared with a normal occupancy building. For post-disaster buildings which have to remain fully functional after the earthquake, the increase is between 50 and 100%.

5.8 Cut-off scores

While FEMA154 only suggests one cut-off score, classifying a building either as safe or as requiring an in depth examination, NRC92 has four distinct categories: low, moderate or high priority for future intervention or potentially hazardous. This more detailed classification gives a better sense of the hazard of each building and the need for detailed evaluation.

The scores of FEMA154 are directly related to the probability of the building to collapse given the maximum considered earthquake. A score of 1 indicates a probability of collapse of 1 in 10 or 10%, a score of 2 a probability of 1%, a score of 3 a probability of 0.1%, etc. Based on these numbers a detailed ranking system is presented in Table 2, as used in the evaluation of schools and other critical public facilities in Oregon [43].

Classification	Probability of collapse	Score
Very high	100%	≤ 0.0
High	≥ 10%	0.1 – 1.0
Moderate	≥ 1%	1.1 – 2.0
Low	< 1%	> 2.0

Table 2: Proposed ranking to be used with FEMA154 [43].

6 IMPROVED SCREENING METHOD

The clear analytical procedure behind the score calculations of FEMA154 makes it possible to update and adapt the method to its use outside its intended scope. NRC92 on the other hand, based largely on expert opinion, is difficult to modify. The RVS method under development therefore uses FEMA154 as a template, modifying it to serve the purpose of evaluating schools in Québec. Some key features of NRC92 are being incorporated.

The scores and modifiers are being recalculated according to Equation 1, with spectral displacements estimated by the capacity spectrum method of FEMA440. The classification of lateral load resisting systems used is that of NRC92, analogous to FEMA154. The seismicity is represented by Montreal’s acceleration response spectrum and local site conditions are considered by using the corresponding Canadian ground motion amplification factors F_a and F_v specific to Montréal’s seismicity.

Major changes will be introduced in the treatment of irregularities. The classification used in the NRC92 procedure will be adopted, since it covers the findings of the initial evaluation of the schools. Furthermore, the effect of each type of irregularity on the seismic performance was classified as severe, significant or insignificant. The detrimental effect of the irregularities will be represented by increased spectral response acceleration values.

The evaluation of architectural components (partitions, cladding and exterior finishes) will be included, using the findings of the detailed examination of the unreinforced heavy partition walls to define the appropriate screening mechanism.

7 CONCLUSIONS

The following conclusions were made from this preliminary study:

- The importance of having earthquake resistant schools has been discussed. Not only do schools have unique occupancy characteristics, but they play a key role in response and recovery efforts after a seismic event. Unfortunately they tend to be especially vulnerable.
- In the province of Québec, a moderate seismic zone located in eastern Canada, efforts are currently being made to assess the potential performance school buildings. Seismic screening is appropriate as a first phase of the vulnerability assessment, since with around 3600 schools, a detailed evaluation for each building is not feasible.
- Two seismic screening methods are relevant when evaluating seismic vulnerability of buildings in Canada: NRC92, developed nationally and FEMA154, developed in the US, having similar construction and design practices. Both methods were used to evaluate 16 school campuses comprising around 100 independent buildings located in the city of Montréal. According to the method in FEMA154, 65% of the buildings should undergo a detailed evaluation. With the NRC92 method, 34% of the buildings were classified as having high priority for future intervention and 16% as potentially hazardous. Results of both evaluations are in reasonable agreement.
- Data indicates that school buildings are generally low-rise and have a limited number of types of lateral load resisting systems. Features that could affect seismic performance are common. This characterization is in accordance with findings of similar studies in other countries, and could explain the large proportion of damage to schools observed in past earthquakes.
- The methodologies employed for the score calculation of both evaluated screening methods are outdated. NRC92 is largely based on expert opinion and therefore difficult to update. On the contrary FEMA154, based on the capacity spectrum method, can be revised to include latest findings. An average increase of 24% on the basic structural hazard scores was obtained when updating FEMA154, with higher scores indicative of a better performance. The clear analytical procedure behind FEMA154 also makes it possible to adapt the method to its use to other countries.
- The high incidence of irregularities (80% for the evaluated schools) makes their detailed evaluation essential. FEMA154 groups the irregularities in two categories and quantifies their effect estimating the worst possible scenario. This not only fails to capture each building's specific characteristics, but also leads to over-conservative results. NRC92 partly overcomes these shortcomings defining seven different types of irregularities.

AKNOWLEDGEMENTS

This research was funded by the Natural Sciences and Engineering Research Council of Canada, through the Canadian Seismic Research Network (Strategic Networks Program).

REFERENCES

[1] O.A. López, J.J. Hernández, G. Del Re, J. Puig, *Seismic risk in schools: The Venezuelan project*, in *Keeping schools safe in earthquakes* Organisation for Economic Co-operation and Development (OECD), 2004.

[2] M. Dolce, *Seismic safety of schools in Italy*, in *Keeping schools safe in earthquakes* Organisation for Economic Co-operation and Development (OECD), 2004.

[3] R. Spence, *Strengthening school buildings to resist earthquakes: Progress in European countries*, in *Keeping schools safe in earthquakes* Organisation for Economic Co-operation and Development (OECD), 2004.

[4] Applied Technology Council (ATC), *FEMA424 Design Guide for Improving School Safety in Earthquakes, Floods, and High Winds.* Applied Technology Council, 2004.

[5] A. Chakos, *Learning about seismic safety of schools from community experience in Berkeley, California*, in *Keeping schools safe in earthquakes* Organisation for Economic Co-operation and Development (OECD), 2004.

[6] Organisation for Economic Co-operation and Development (OECD), *OECD Recommendation concerning guidelines on earthquake safety in schools.* Organisation for Economic Co-operation and Development (OECD), 2005.

[7] Association of Professional Engineers and Geoscientists of British Columbia (APEGBC), Department of Civil Engineering of The University of British Columbia, *Bridging guidelines for the performance-based seismic retrofit of British Columbia school buildings, First Edition.* British Columbia Ministry of Education, 2005.

[8] G.W. Taylor, T.W. White, C.E. Ventura. British Columbia school seismic mitigation program: performance-based school retrofit guidelines. *8th U.S. National Conference on Earthquake Engineering*, San Francisco, California, USA, 2006.

[9] British Columbia Ministry of Education, *Seismic mitigation projects feasibility study guidelines.* British Columbia Ministry of Education, 2005.

[10] New Zealand Society for Earthquake Engineering, *Assessment and improvement of the structural performance of buildings in earthquake.* New Zealand Society for Earthquake Engineering, 2006.

[11] L.A. Mendes-Victor, C.S. Oliveira, J. Azevedo, A. Ribeiro, A.S. Elnashai, S.H. Jeong, *Rapid Probabilistic Assessment of Structural Systems in Earthquake Regions*, in *The 1755 Lisbon Earthquake: Revisited, Vol. VII,* Springer Netherlands, 2009.

[12] Applied Technology Council (ATC), *FEMA154 Rapid Visual Screening of Buildings for Potential Seismic Hazard: A Handbook, 2nd Edition*, Applied Technology Council, 2002.

[13] Applied Technology Council (ATC), *FEMA155 Rapid Visual Screening of Buildings for Potential Seismic Hazard: supporting Documentation, 2nd Edition.* Applied Technology Council, 2002.

[14] G.C. Joshi, R. Kumar, Preliminary seismic vulnerability assessment of Mussoorie Town, Uttarakhand (India). *Journal of Building Appraisal*, **5**, 357-368, 2010.

[15] R.B. Olshansky, Y. Wu, Evaluating Earthquake Safety in Mid-American Communities. *Natural Hazards Review*, **5**, 71-81, 2004.

[16] K. Lang, *Seismic vulnerability of existing buildings.* Swiss Federal Institute of Technology, 2002.

[17] E. Faccioli, V. Pessina, G.M. Calvi, B. Borzi, A study on damage scenarios for residential buildings in Catania city. *Journal of Seismology*, **3**, 327-343, 1999.

[18] National Research Council Canada, *Manual for screening of buildings for seismic investigation.* National Research Council Canada, 1992.

[19] G.M. Calvi, R. Pinho, G. Magenes, J.J. Bommer, L.F. Restrepo-Vélez, H. Crowley, Development of seismic vulnerability assessment methodologies over the past 30 years. *ISET Journal of Earthquake Technology*, **43**, 75-104, 2006.

[20] Applied Technology Council (ATC), *FEMA154 Rapid Visual Screening of Buildings for Potential Seismic Hazard: A Handbook, 1st Edition.* Applied Technology Council, 1988.

[21] Applied Technology Council (ATC), *FEMA155 Rapid Visual Screening of Buildings for Potential Seismic Hazard: supporting Documentation, 1st Edition.* Applied Technology Council, 1988.

[22] Applied Technology Council (ATC), *ATC-40 Seismic evaluation and retrofit of concrete buildings.* Applied Technology Council, 1996.

[23] Applied Technology Council (ATC), *ATC-13 Earthquake damage evaluation data for California.* Applied Technology Council, 1985.

[24] M. Bruneau, M. Lamontagne, Damage from 20th century earthquakes in eastern Canada and seismic vulnerability of unreinforced masonry buildings. *Canadian Journal of Civil Engineering*, **21**, 643-662, 1994.

[25] R. Tinawi, D. Mitchell. 1988 Saguenay earthquake. Damage to schools and post-disaster buildings. *Engineering in our environment: Annual conference and 1st biennial environmental speciality conference*, Hamilton, Ontario, 1990.

[26] D. Mitchell, R. Tinawi, T. Law, *The 1988 Saguenay earthquake - A site visit report.* Canadian National Committee on Earthquake Engineering, 1989.

[27] McGill University, *Microzonation Map of the Montreal Island.* 2009.

[28] L. Chouinard, P. Rosset. Seismic site effects and seismic risk in the Montreal area - The influence of marine clays. *Ninth Canadian Conference on Earthquake Engineering*, Ottawa, Ontario, Canada, 2007.

[29] G. McClure, J. Cappai, R. Shapiro, M. Li, G. Dunlop-Brère, P. Keller. Assessing the post-earthquake functionality of critical buildings in Montreal. *9th U.S. National and 10th Canadian Conference on Earthquake Engineering*, Toronto, Canada, 2010.

[30] Canadian Standards Association (CSA), *Seismic risk reduction of operational and functional components (OFCs) of buildings, CAN/CSA-S832-06.* CSA, 2006.

[31] S.D. Akkar, E. Miranda, Statistical evaluation of approximate methods for estimating deformation demands on existing structures. *Journal of Structural Engineering*, **131**, 12, 2005.

[32] A.K. Chopra, R.K. Goel, Evaluation of NSP to estimate seismic deformation: SDF systems. *Journal of Structural Engineering*, **126**, 8, 2000.

[33] Applied Technology Council (ATC), *FEMA440 Improvement of nonlinear static seismic analysis procedures.* Applied Technology Council, 2005.

[34] American Society of Civil Engineers, *FEMA310 Handbook for the seismic evaluation of buildings: A pre-standard.* Federal Emergency Management Agency, 1998.

[35] A. Karbassi, M.-J. Nollet, Development of an index assignment procedure compatible with the regional seismicity in the province of Quebec for the rapid visual screening of existing buildings. *Canadian Journal of Civil Engineering*, **35**, 925-937, 2008.

[36] National Research Council Canada, *National Building Code of Canada 2005.* National Research Council, 2005.

[37] Building Seismic Safety Council, *FEMA302 NEHRP recommended provisions for seismic regulations for new buildings and other structures.* Building Seismic Safety Council, 1998.

[38] National Research Council Canada, *National Building Code of Canada 1990.* National Research Council, 1990.

[39] J. Adams, G. Atkinson, Development of seismic hazard maps for the proposed 2005 edition of the National Building Code of Canada. *Canadian Journal of Civil Engineering*, **30**, 255-271, 2003.

[40] W.D.L. Finn, A. Wightman, Ground motion amplification factors for the proposed 2005 edition of the National Building Code of Canada. *Canadian Journal of Civil Engineering*, **30**, 272-278, 2003.

[41] V. Jeng, W.L. Tzeng, Assessment of seismic pounding hazard for Taipei City. *Engineering Structures*, **22**, 459-471, 2000.

[42] S.A. Anagnostopoulos. Building pounding re-examined: how serious a problem is it? *11th Word Conference on Earthquake Engineering*, Acapulco, México, 1996.

[43] V.S. McConnell, *State-wide seismic needs assessment: Implementation of Oregon 2005 senate bill 2 relating to public safety, earthquakes, and seismic rehabilitation of public buildings.* State of Oregon, Department of Geology and Mineral Industries, 2007.

[44] Federal Emergency Management Agency, *Fema149 Seismic considerations - Elementary and secondary schools.* Building Seismic Safety Council, 1990.

COMPDYN 2011
III ECCOMAS Thematic Conference on
Computational Methods in Structural Dynamics and Earthquake Engineering
M. Papadrakakis, M. Fragiadakis, V. Plevris (eds.)
Corfu, Greece, 25–28 May 2011

INTENSITY PARAMETERS AS DAMAGE POTENTIAL DESCRIPTORS OF EARTHQUAKES

Anaxagoras Elenas[1]

[1]Institute of Structural Mechanics and Earthquake Engineering, Democritus University of Thrace
GR-67100 Xanthi, Greece
e-mail: elenas@civil.duth.gr

Keywords: Seismic Parameters, Damage Indices, Seismic Ground Motion, Damage Potential, Reinforced Concrete.

Abstract. *This paper provides a methodology to quantify the interrelationship between the seismic intensity parameters and the structural damage. First, a computer-supported elaboration of the accelerograms provides several peak, spectral and energy seismic parameters. After that, nonlinear dynamic analyses are carried out to provide the structural response for a set of seismic excitations. Among the several response characteristics, the overall structure damage indices after Park/Ang and the maximum inter-story drift ratio are selected to represent the structural response. Correlation coefficients are evaluated to express the grade of interrelation between seismic acceleration parameters and the structural damage. The presented methodology is applied to a six-story reinforced concrete frame building. According to the first step of the methodology sixteen seismic parameters are evaluated: PGA, PGV, PGA/PGV, spectral acceleration (SA), spectral velocity (SV), spectral displacement (SD), central period (CP), absolute seismic input energy (E_{inp}), Arias intensity (I_A), strong motion duration after Trifunac/Brady (SMD_{TB}), seismic power ($P_{0.90}$), root mean square acceleration (RMS_a), intensity after Fajfar/Vidic/Fischinger (I_{FVF}), spectral intensities after Housner (SI_H), after Kappos (SI_K) and after Martinez (SI_M). The frame structure has been designed according to the rules of the recent Eurocodes. Then, a nonlinear dynamic analysis has been carried out for the evaluation of the seismic response. Among the several response parameters, the focus is on the overall structure damage indices. This is due to the fact, that this parameter summarizes statistically all the existing damages on columns and beams in a single value, which can be easily correlated to single value seismic parameters. As seismic input for the nonlinear dynamic analysis, a set of spectrum-compatible synthetic accelerograms has been used. To emphasize the grade of interrelation between seismic acceleration parameters and the overall structure damage indices, the correlation coefficient after Pearson and the rank correlation coefficient after Spearman have been calculated. As the numerical results have shown, the spectral and energy parameters provide strong correlation to the damage indices. On the opposite, the CP, SMD_{TB} and the term PGA/PGV delivered poor correlation with the damage indices. Due to this reason, spectral and energy related parameters are better qualified to be used for the characterization of the seismic damage potential.*

1 INTRODUCTION

It is well-known that seismic accelerograms are ground acceleration time-histories that cannot be described analytically. Several seismic parameters have been presented in the literature during the last decades. These can be used to express the intensity of the seismic excitations and to simplify its description. Post-seismic field observations and numerical investigations have indicated the interdependency between the seismic parameters and the damage status of buildings after earthquakes [1, 2]. The latter can be expressed by proper damage indices, while the interdependency between the considered quantities can be quantified numerically by appropriate correlation coefficients. Their values deliver the correlation grade (low, medium or high) between the examined quantities.

This paper provides a method for quantifying the interrelationship between the seismic parameters and global damage indices. First, a computer analysis of the accelerograms provided several peak ground motion, spectral and energy seismic parameters. After that, nonlinear dynamic analyses were carried out to provide the structural response for a set of seismic excitations and a given reinforced concrete frame structure. Keeping in mind that most of the seismic loading parameters are characterized by a single numerical value, single-value damage indicators have also been selected to represent the structural response. Thus, the overall structural damage index (OSDI) after Park/Ang ($DI_{G,PA}$) and the maximum inter-story drift ratio (MISDR) are selected to represent the structural response. Finally, correlation coefficients are evaluated to express the grade of interdependency between seismic acceleration parameters and the used damage indices. The presented methodology is applied to a six-story reinforced concrete frame building subjected to several artificial accelerograms.

2 SEISMIC INTENSITY PARAMETERS

In general, the intensity parameters can be classified with peak, spectral and energy parameters. In this work the following parameters have been selected to represent the seismic intensity: peak ground acceleration PGA, peak ground velocity PGV, the term PGA/PGV, spectral acceleration (SA), spectral velocity (SV), spectral displacement (SD), central period (CP), absolute seismic input energy (E_{inp}), Arias intensity (I_A), strong motion duration after Trifunac/Brady (SMD_{TB}), seismic power ($P_{0.90}$), root mean square acceleration (RMS_a), intensity after Fajfar/Vidic/Fischinger (I_{FVF}), spectral intensities after Housner (SI_H), after Kappos (SI_K) and after Martinez-Rueda (SI_{MR}). They have been chosen from all three of the seismic parameter categories. Table 1 provides an overview of the used parameters and their literature references, respectively. The definition of each parameter is presented in the mentioned literature.

No	Seismic parameters	Reference	No	Seismic parameters	Reference
1	PGA	[3]	9	I_A	[7]
2	PGV	[3]	10	SMD_{TB}	[8]
3	PGA/PGV	[3]	11	$P_{0.90}$	[9]
4	SA	[4]	12	RMS_a	[3]
5	SV	[4]	13	I_{FVF}	[10]
6	SD	[4]	14	SI_H	[11]
7	CP	[5]	15	SI_K	[12]
8	E_{inp}	[6]	16	SI_{MR}	[13]

Table 1: Seismic parameters.

3 SEISMIC ACCELERATION TIME HISTORIES

The seismic excitations used for the dynamic analyses in this study are based on artificial accelerograms created to be compatible with the design spectra of the current Greek antiseismic code (2004). The reason for choosing this approach rather than relying on natural accelerograms was dictated by the need to have a sufficiently large database for statistical reasons. For the creation of the aforementioned artificial accelerograms the program SIMQKE [14] has been utilized. As artificial accelerogram creation parameters the PGA, the total duration (TD) and the design spectra for all three Greek seismic regions (nominal PGA equal to 0.16g, 0.24g and 0.36g) have been used. All created for subsoil category B, as described in Eurocode 8 (EC8) [15] and the Greek Antiseismic Code [16]. This subsoil category belongs to deep deposits of medium dense sand or over-consolidated clay at least 70 m thick. In order to cover most types of Greek region seismic activity, an artificial accelerogram creation procedure has been devised comprising the creation of 5 random artificial accelerograms for each of the 15 preselected PGA values that were assigned for the three different Greek seismic regions. Thus, 75 different synthetic accelerograms have been compiled, which ensures that the overall structural damages of the examined structure will cover all the possible damage grades, from low to severe, in order to cover statistical demands as well.

4 GLOBAL DAMAGE INDICES

As explained previously, attention is focused on damage indicators that consolidate all member damage into one single value that can be easily and accurately be used for the statistical exploration of the interrelation with the also single-value seismic parameters in question. Thus, in the OSDI model after Park/Ang [17] the global damage is obtained as a weighted average of the local damage at the ends of each element. The local damage index is a linear combination of the damage caused by excessive deformation and that contributed by the repeated cyclic loading effect that occurs during seismic excitation. Thus, the local DI is given by the following relation:

$$DI_{L,PA} = \frac{\theta_m - \theta_r}{\theta_u - \theta_r} + \frac{\beta}{M_y \theta_u} E_T \tag{1}$$

where, $DI_{L,PA}$ is the local damage index, θ_m the maximum rotation attained during the load history, θ_u the ultimate rotation capacity of the section, θ_r the recoverable rotation at unloading, β a strength degrading parameter, M_y the yield moment of the section and E_T the dissipated hysteretic energy. The Park/Ang damage index is a linear combination of the maximum ductility and the hysteretic energy dissipation demand imposed by the earthquake on the structure.

The global damage index after Park/Ang [17] takes into account the local damages of all elements of the examined structure (e.g. beams and columns of a frame). Thus, it depends both, the distribution and the severity of the localized damage and is given by the following relation:

$$DI_{G,PA} = \frac{\sum_{i=1}^{n} DI_{L,PA} E_i}{\sum_{i=1}^{n} E_i} \tag{2}$$

where, $DI_{G,PA}$ is the global damage index, $DI_{L,PA}$ the local damage index after Park/Ang, E_i the energy dissipated at location i and n the number of locations at which the local damage is computed.

The MISDR [18, 19] is a simple OSDI that describes satisfactorily various forms of damages after an earthquake. The post-seismic damage degree can be classified according to this index. Equation (3) defines the maximum inter-storey drift ratio (MISDR) as the ratio of the maximum absolute inter-story drift $|u|_{max}$ to the inter-storey height h:

$$\mathrm{MISDR} = \frac{|u|_{max}}{h} 100\ [\%] \tag{3}$$

5 APPLICATION

The reinforced concrete frame structure shown in Figure 1 has been detailed is in agreement with the rules of the recent Eurocodes for structural concrete and aseismic structures, EC2 and EC8 [20, 15]. According to the EC8 Eurocode, the structure shown in Figure 1, has been considered as an "importance class II, ductility class M"-structure with a subsoil category B. The cross-sections of the beams are considered as T-beams with 30 cm width, 20 cm slab thickness, 60 cm total beam height and 1.45 m effective slab width. The distances between each frame of the structure is equal to 6 m while the ground floor has a 4 m height and all subsequent floors 3 m. The subsoil was of type B (deep deposits of medium dense sand or over-consolidated clay at least 70 m thick). The eigenperiod of the frame was 1.0 s.

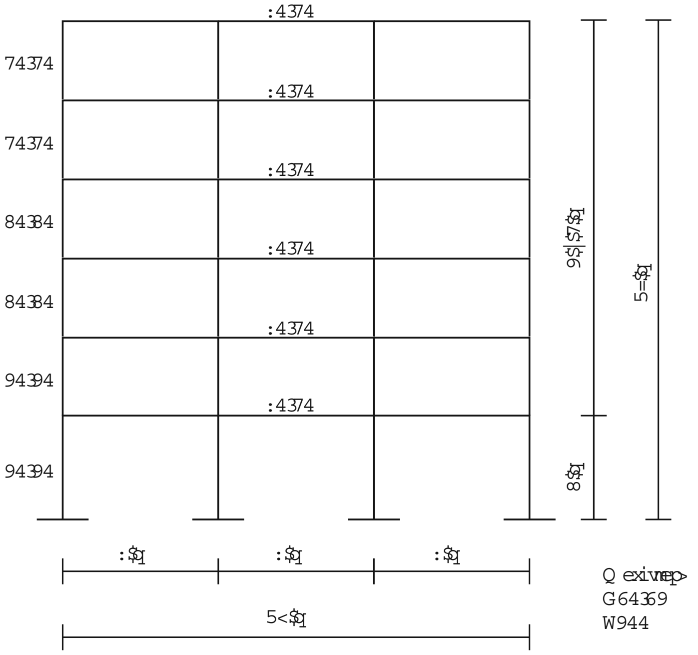

Figure 1: Reinforced concrete frame structure.

After the design procedure of the reinforced concrete frame structure, a nonlinear dynamic analysis evaluates the structural seismic response, using the computer program IDARC [21]. A three-parameter Park model specifies the hysteretic behavior of beams and columns at both ends of each member. This hysteretic model incorporates stiffness degradation, strength deterioration, slip-lock and a tri-linear monotonic envelope. Experimental results of cyclic force-deformation characteristics of typical components of the studied structure, specifies the parameter values of the above degrading parameters. This study uses the nominal parameter for stiffness degradation. Among the several response parameters, the focus is on the overall structural damage indices (OSDI) described in the previous section.

6 RESULTS

The first step was the creation of the aforementioned set of 75 synthetic accelerograms using the SIMQKE program. This program generates baseline corrected acceleration-time histories. The next step was a computer supported evaluation of 16 seismic parameters as presented in Table 1. Nonlinear dynamic analyses has been performed for the reinforced concrete frame building under question, including all artificial acceleration-time histories, in order to obtain the structural damage indices after Park/Ang and the MISDR. Statistical procedures provide the correlation coefficients after Pearson and Spearman [22], between all the evaluated seismic parameters and damage indices. The Pearson correlation shows how well the data fit a linear relationship, while the Spearman correlation shows how close the examined data are to monotone ranking. The latter coefficient is more important in the present study. Table 2 summarizes the results of the correlation study.

Seismic parameters	Pearson correlation		Spearaman rank correlation	
	$DI_{G,PA}$	MISDR	$DI_{G,PA}$	MISDR
PGA	0.568	0.523	0.635	0.631
PGV	0.657	0.659	0.788	0.795
PGA/PGV	-0.355	-0.367	-0.393	-0.394
SA	0.711	0.678	0.803	0.806
SV	0.724	0.696	0.804	0.804
SD	0.738	0.706	0.849	0.845
CP	-0.342	-0.326	-0.351	-0.332
E_{inp}	0.668	0.667	0.812	0.821
I_A	0.682	0.659	0.824	0.821
SMD_{TB}	0.103	0.086	0.155	0.145
$P_{0.90}$	0.685	0.662	0.823	0.820
RMS_a	0.713	0.677	0.824	0.821
I_{FVF}	0.655	0.656	0.789	0.796
SI_H	0.703	0.664	0.796	0.795
SI_K	0.702	0.670	0.802	0.806
SI_{MR}	0.614	0.558	0.725	0.725

Table 2: Correlation coefficients between the seismic parameters and the OSDIs.

It is supposed that correlation coefficients up to 0.5 means low correlation, coefficients between 0.5 and 0.8 means medium correlations, while coefficients greater than 0.8 means strong correlation between the two variables. Table 2 presents the correlation coefficients after Pearson and the rank correlation coefficients after Spearman among all the examined seismic parameters presented and the examined the damage indices. Thus, the results show low Pearson and Spearman correlation between the term PGA/PGV, CP, SMD_{TB} and the examined damage indices. All the remaining seismic parameters provided medium Pearson correlation with the damage indices. On the other hand, high rank correlation is observed between SA, SV, SD, E_{inp}, I_A, $P_{0.90}$, RMS_a, SI_K and the damage indices. In addition, medium rank correlation is observed between PGA, PGV, I_{FVF}, SI_H, SI_{MR} and the damage indices.

Finally, the seismic parameters show the same correlation grade with $DI_{G,PA}$ with MISDR in all the cases. All the seismic parameters show the same correlation grade for both, Pearson and Spearman correlation, with exception the cases with high rank correlation. There, the Pearson correlation grade is medium.

7 CONCLUSIONS

- In this paper a methodology for the value estimation of the interdependence between seismic acceleration intensity parameters and damage indices has been presented. Peak, spectral and energy parameters have been considered. The global damage index after Park/Ang and the MISDR represented the post-seismic structural damage status. The degree of the interrelationship between seismic parameters and damage indices has been expressed by the Pearson correlation coefficient and by the Spearman rank correlation coefficient.
- The results show low Pearson and Spearman correlation between the term PGA/PGV, CP, SMD_{TB} and the examined damage indices.
- Medium correlation is observed between PGA, PGV, I_{FVF}, SI_H, SI_{MR} and the damage indices, in all the cases.
- High rank correlation is observed between SA, SV, SD, E_{inp}, I_A, $P_{0.90}$, RMS_a, SI_K and the damage indices. In all these cases, the corresponding Pearson correlation grade was medium.
- The seismic parameters show the same correlation grade with $DI_{G,PA}$ with MISDR in all the cases
- All these results lead to conclude that the spectral and energy seismic parameters are reliable descriptors of the seismic damage potential and to recommend them as appropriate descriptors of the seismic damage potential.

REFERENCES

[1] A. Elenas, Correlation between seismic acceleration parameters and overall structural damage indices of buildings, *Soil Dynamics and Earthquake Engineering*, **20**, 93-100, 2000.

[2] A. Elenas, K. Meskouris, Correlation study between seismic acceleration parameters and damage indices of structures, *Engineering Structures*, **23**, 698-704, 2001.

[3] K. Meskouris, *Structural Dynamics*, Ernst & Sohn, Berlin, 2000.

[4] A.K. Chopra, Dynamics of Structures, Prentice Hall International Inc, New Jersey, 1995.

[5] E.H. Vanmarcke, S.-S.P. Lai, Strong-motion duration and RMS amplitude of earthquake records, *Bulletin of the Seismological Society of America*, **70**, 1293-1307, 1980.

[6] C.M. Uang, V.V. Bertero, Evaluation of seismic energy in structures, *Earthquake Engineering and Structural Dynamics*, **19**, 77-90, 1990.

[7] A. Arias, A measure of earthquake intensity, In *Seismic Design for Nuclear Power Plants*, R.J. Hansen (ed.). MIT Press, Cambridge, MA, 438–483, 1970.

[8] M.D. Trifunac, A.G. Brady, A Study on the Duration of Strong Earthquake Ground Motion, *Bulletin of the Seismological Society of America,* **65**, 581-626, 1975.

[9] P.C. Jennings, Engineering Seismology, In *Earthquakes: observation, theory and interpretation*, H. Kanamori, E. Boschi (eds). Italian Physical Society, Varenna, 138-173, 1982.

[10] P. Fajfar, T. Vidic, M. Fischinger, A measure of earthquake motion capacity to damage medium-period structures, *Soil Dynamics and Earthquake Engineering*, **9**, 236-242, 1990.

[11] G.W. Housner, Spectrum intensities of strong motion earthquakes, *Proceedings of Symposium on Earthquake and Blast Effects on Structures*, EERI, Oakland California, 20-36, 1952.

[12] A.J. Kappos, Sensitivity of calculated inelastic seismic response to input motion characteristics, *Proceedings of the 4th U.S. National Conference on Earthquake Engineering*, EERI, Oakland California, 25-34, 1990.

[13] J.E. Martinez-Rueda, Definition of spectrum intensity for the scaling and simplified damage potential evaluation of earthquake records, *CD-ROM Proceedings of the 11th European Conference on Earthquake Engineering*, Balkema, Rotterdam, 1998.

[14] D.A.Gasparini, E.H. Vanmarcke, SIMQKE, a program for artificial motion generation, user's manual and documentation, *Publication R76-4*, MIT Press, Cambridge, Massachusetts, 1976.

[15] EC8, *Eurocode 8: Design of Structures for Earthquake Resistance - Part 1: General Rules, Seismic Actions, and Rules for Buildings*, European Committee for Standardization, Brussels, Belgium, 2004.

[16] EAK, *National Greek Antiseismic Code*, Earthquake Planning and Protection Organization (OASP) Publication, Athens, 2003.

[17] Y.J. Park, A.H.-S. Ang, Mechanistic seismic damage model for reinforced concrete, *Journal of Structural Engineering*, **111**, 722-739, 1985.

[18] Structural Engineers Association of California (SEAOC), *Vision 2000: Performance based seismic engineering of buildings*, Sacramento, California, 1995.

[19] S. Rodriguez-Gomez, A.S. Cakmak, Evaluation of seismic damage indices for reinforced concrete structures, *Technical Report NCEER-90-0022*, State University of New York, Buffalo, 1990.

[20] EC2, *Eurocode 2: Design of Concrete Structures - Part 1: General Rules and Rules for Buildings*, European Committee for Standardization, Brussels, Belgium, 2000.

[21] R.E. Valles, A.M. Reinhorn, S.K. Kunnath, C. Li, A. Madan, IDARC 2D Version 4.0: A program for inelastic damage analysis of buildings, *Technical Report NCEER-96-0010*, State University of New York, Buffalo, 1996.

[22] T.P. Ryan, *Modern Engineering Statistics*, John Wiley & Sons, Hoboken, New Jersey, 2007.

COMPDYN 2011
III ECCOMAS Thematic Conference on
Computational Methods in Structural Dynamics and Earthquake Engineering
M. Papadrakakis, M. Fragiadakis, V. Plevris (eds.)
Corfu, Greece, 25–28 May 2011

BRACING CONFIGURATION IN EARTHQUAKE RESISTANT STRUCTURE

Tonia Sophocleous[1] and Marios C. Phocas[2]

[1,2] Department of Architecture, Faculty of Engineering, University of Cyprus
75 Kallipoleos Str., P.O.Box 20537, 1678 Nicosia, Cyprus
sophocleous.antonia@ucy.ac.cy, mcphocas@ucy.ac.cy

Keywords: Dual Structures, Hysteretic Dampers, Cable Bracing, Energy Dissipation Systems.

Abstract. *Technological advances in the seismic design of energy dissipation systems raise the issue of the codes dominated capacity design of structures. Building code requirements that describe the dynamic behavior, modeling and analysis of structures with different types of energy dissipation systems are currently under review. A new seismic design approach, described in the current paper, adds to the current research activities of the authors on passively controlled systems with integrated hysteretic damper and cable bracings. The control system considers at first place the effect of added stiffness when conventional bracings are added to structural frames that are necessary for the integration of the damping devices. An increase in the systems stiffness may result to a reduction of the peak displacement, i.e. peak pseudo-acceleration, and thus to an increase of the shear forces. In addition, an increase in damping can significantly influence the response of elastic and inelastic systems. The new system proposed aims at both, energy dissipation and damage control. It consists of an energy dissipation device and a portal cable bracing mechanism with a kinetic closed loop, working only in tension. The closed bracing mechanism does not practically affect the initial stiffness of the system, i.e. the concept relies on two completely "separate" systems: a primary for the vertical- and wind loads and a secondary for the earthquake loads. Analysis model considerations for describing the physical behavior of the system in computational language are presented, by incorporating the SAP2000 program, revealing step by step the procedure followed for the resulting desired dynamic performance. Based on the energy balanced equation at each time-step, the hysteretic energy dissipation demand is reduced when the supplemental damping system is utilized. An Effective Toughness Index, in accordance to the time-dependence of the hysteretic energy dissipation is proposed to characterize the portions of the input energy dissipated by the control system. The predominant parameters that characterize the system's seismic behavior are derived on the basis of a parametric analysis under selected international strong ground motions. Finally the systems behavior is verified in respect to the mechanical properties of the control elements under the action of ten selected earthquake excitations of the Greek-Mediterranean region. The parametric analyses of the system's seismic behavior conclude with a proposed preliminary design methodology for the passively controlled SDOF models.*

1 INTRODUCTION

The design of frame structures with additional control members for earthquake resistance refers primarily to the need for the primary systems to exhibit essentially a linear behavior under seismic actions [1]. A reduction of the energy dissipation demand on primary structural systems was successfully aimed at by a number of researchers [2]. Passive metallic yielding, viscoelastic and viscous damping devices may be added to frame structures to dissipate input energy during an earthquake and to substantially reduce or eliminate damage to the gravity-load-resisting frames. ADAS and TADAS are well known examples, available for both, new seismic resisting designs and retrofit of frame buildings [3]. Some types of supplemental damping can substantially change the force-displacement response of the structure by adding strength and stiffness. Stiff bracings in such energy dissipation systems (EDS) reduce inter-story drifts, but they produce high accelerations; on the other hand more flexible slender bracings, such as cables or tension-only rods, attract smaller forces and tend to reduce floor accelerations Additionally the effective added damping benefit of EDS is shadowed by the coupling effect of the primary- and control system, due to the unavoidable stiffness increase of the former [4-6].

The research inquiry of utilizing the performance of mild steel in terms of strength, flexibility and minimal weight, coupled with the need of a smooth, non-coupled operation under dynamic excitations has led to the development of Adaptable Dual Control Structures (ADCS) [7-10]. The basis of the design philosophy of the systems comprises the component deformation capacity that characterizes the performance and damage of the system. The cable bracing mechanism with closed loop and the integrated hysteretic damper that forms within moment resisting frames an ADCS enables the primary system to respond elastically under load combinations of static- (gravity and equivalent static wind) and dynamic (moderate, extremely irregular base excitations) actions. The design objective for the proposed systems is to “dual” the response performance between the primary frame and the added control members that practically do not affect the elastic response of the main structure, but concentrate all the damage to the replaceable damper. A number of critical configurations have been conceived by the authors [7, 8], of which one is presented in the current paper.

Following the construction design of ADCS, the design parameters have been defined through a parametric analysis that involves 342 combinations of both geometrical and mechanical system properties, subjected to three international strong earthquake motions: El Centro 1940, Kobe 1995 and Northridge 1994. The range of the design application is clearly stated in terms of both, the characteristic period and the limiting lateral displacements of the passively controlled system. The designer may target to a desirable performance by defining an effective energy deformation index (EEDI). Predominant design parameters for characterizing the ADCS’s response are revealed through the parametric analysis, defined as a function of the non-linear link’s elastic stiffness and yield force, the Damper Ratio (DR). ADCS’s effective response behavior in terms of energy dissipation, minimal displacements and practically non-coupled performance between the frame and the added dissipaters is verified under ten selected earthquake records of the Greek-Mediterranean seismic zone.

2 BRACING CONFIGURATION

Prestressed tensile bracings are used as tension-only members in ADCS. In common applications, not only the low stiffness of cables, but also the nature of hinged frame construction, makes these elements vulnerable to lateral and vertical movements. Through respective modification of their geometry the elements initiate a static non-linear response to the induced strong ground movements at their base and adapt to this by activating a kinetic mechanism,

Figure 1. The displacement is transferred at the optimal joint where the hysteretic device is connected at its one end, while its other end is fixed at the primary beam and follows the lateral frame's movement in every cycle. Tuning of both, the mechanical and geometric characteristics of the composed members with the respective primary frame may lead to high portions of energy dissipation and therefore add damping to the system. The control system is also responsible for the system's relative displacements and the avoidance of any significant base shear increase. Due to the characteristic configuration, ideally the reactions from the added elements to the primary frame are neutralized. The optimization of the damper-bracing mechanism involves tuning between the stiffness, the yield force and the relative displacement that the hysteretic damper develops to the tension-only bracings and in extent, to the primary frame, so that the energy flow in terms of hysteresis for the damper and the elastic strain energy for the cable restraints and the primary frame are effective.

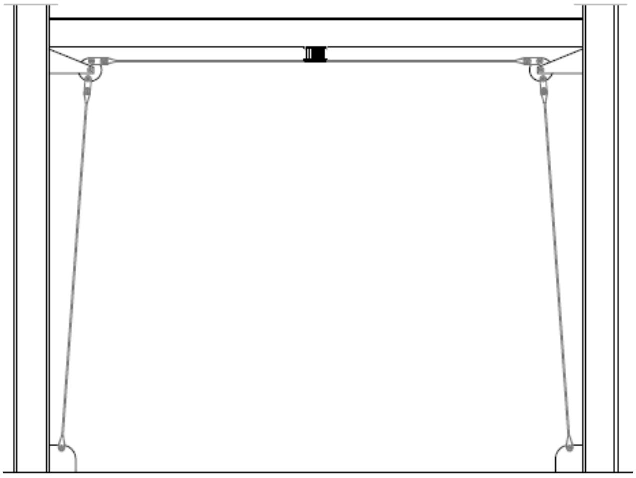

Figure 1: Frame Configuration for ADCS, S1.

2.1 Connection Design

The construction technique developed for ADCS aims at achieving among others the necessary stiffness on the flexible members, their prestressing and the stabilization of the system. When ADCS proposed systems are subjected to earthquake loads a kinematic mechanism is activated. This is made possible through eccentrically placed discs at the main joint region that rotate and drag along the horizontal bracing member that induces relative deformations between the damper's ends, defined as the Interdamper Drift, Figure 2. The damper is designed to yield in its inelastic region and dissipate energy. When the lateral translation on the frame changes to the opposite sense, the procedure is repeated. At the end of a complete cycle, all tension-only members are stretched to their maximum potential. ADCS utilize the previously established knowledge on the effectiveness of the yielding metallic dampers, ADAS and TADAS that have already been confirmed through ample tests and analytical studies [2, 3]. ADCS design introduces slightly modified shape sections of similar dampers. The damper's section is selected to result in uniform bending curvature over the section's height. The transverse force applied at the end of each plate causes uniformly bending curvature and all section lines reach their maximum yielding potential at the same time.

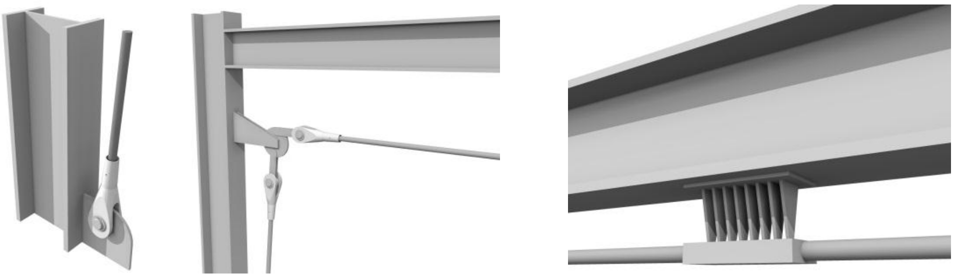

Figure 2: Connections' Design for ADCS, S1.

ADCS response for the desirable level of seismic protection depends primarily on two main factors:

1. The effective values of the relative stiffness of the primary frame, the bracing and the hysteretic device at the target displacement that leads to the selection of the design stiffness of the damper, k_d, given by the following equation:

$$k_d = \frac{n(2 + a/b)EI_b}{h^3} \tag{1}$$

where k_d is the initial elastic stiffness of the hysteretic damper, I_b, the second moment of area at the top of the steel plates used as hysteretic damper, h is the height, b is the upper width (fixed to the beam) and a is the lower width (connected to the bracing member), E= $2.1\text{x}10^4$ kN/cm^2, ρ= 78.5 kN/m^3 for S235 mild steel material of the damper plates, as shown in parallel arrangement in Figure 2.

2. The load, at which the damper yields and dissipates energy through its inelastic yielding deformation, given by the following equation:

$$P_y = \frac{nf_y bt^3}{4h} \tag{2}$$

where f_y is the yield stress (f_y= 24 kN/cm² for S235), and t is the thickness of each plate.

3 PRELIMINARY INVESTIGATION

3.1 Frame Modeling

The finite element analysis of ADCS relies on a simplified model, whereas non-linearity is only addressed for the hysteretic damper, i.e. the non-linear link. The dynamic behavior of the simulated ADCS was examined using the FE program SAP2000. A typical geometry was assigned for the ideal model of the steel moment resisting frame: a 6.0 m long beam and 4.5 m high column members in a 2D representation model. The bracing members were modeled as tension-only elements and a suitable pretension stress was applied to each of them. The ADCS's tendons' geometry was carefully drawn for the software model to represent the configuration with high accuracy. The disc was modeled as a composition of three short frame members, assigned with large stiffness values to represent the real property of a shaft. The preliminary analysis was completed for a number of combinations of characteristic design variables. IPBl500 sections were assigned for the columns and IPBl550 for the beam. The dimensioning of the members was based on Eurocode 3, having assumed a static vertical load of 1200 kN and a static equivalent wind load of 15 kN. A range of diameters between d_c= 15 mm and d_c= 40 mm was tested in the investigation. The geometry of the steel plates varied in the parametric analysis, as follows: h= 15, 20, 25, 30, 35, 40 cm; n= 6, 8, 10; b= 4, 5, 6 cm; t=

8, 10, 11, 12, 13, 14, 15, 16, 18, 20 mm. The calculated initial stiffness for the damper varied between 450 kN/m < k_d < 24200 kN/m and the yield force, between 3.5 kN < P_y < 43 kN.

3.2 Input Seismic Records

The system's displacement depends directly on the amplitude of the ground motion; although the damper's dynamic properties are defined by the designer. In order to identify the parameters that dominate the response of ADCS, the configuration presented in Figure 1, was analytically tested under the records of El Centro, Kobe and Northridge as described in Table 1.

Record	Mw	PGA (g)	Duration (s)	Scale factor
El Centro 1940	6.9	0.348	53.76	2.871
Kobe 1995	6.9	0.821	48.00	1.218
Northridge 1994	6.7	0.604	30.00	1.655

Table 1: International Seismic Input Records.

The predominant design parameters of ADCS are the stiffness of the damper k_d and the yield load P_y, as given by equations (1) and (2). Based on the analysis results, the Damper Ratio (DR) that describes the response of ADCS as a function of its stiffness and yield force is introduced, as follows:

$$\mathrm{DR} = \frac{k_d}{P_y} \tag{3}$$

where k_d is the damper's stiffness and P_y is the yield load of the hysteretic device, measured in 1/m units. A range between 55 1/m < DR < 780 1/m values was examined to construct the parametric analysis results diagram.

3.3 Modeling of the Non-Linear Behavior

Hysteretic dampers may exhibit a bilinear or trilinear hysteresis, an elasto-plastic or rigid-plastic behavior, which can be captured with the structural analysis software SAP2000. The damper used in ADCS was modeled as a non-linear link element. The damper's force-deformation relationship for a respective degree of freedom, corresponding to shear, was modeled to follow the hysteretic model described as Wen plasticity property type of uniaxial deformation. Several hysteresis models were tested analytically to represent the damping feature of the composed damper. The Wen-Plasticity model was finally adopted and the results were calculated based on this characteristic hysteresis model, mathematically described as follows:

$$f = \mathrm{ratio} \cdot k \cdot d + (1 - \mathrm{ratio}) \cdot \mathrm{yield} \cdot z \tag{4}$$

where f is the force and d, the induced displacement, k is the elastic spring constant, i.e. initial stiffness, "yield" is the yield force, "ratio" is the specified ratio of the post-yield stiffness to the elastic stiffness, i.e. secondary stiffness ratio, and z is an internal hysteretic variable that evolves according to the following differential equation:

$$\dot{z} = \frac{k}{\mathrm{yield}} \left\{ \dot{d}(1 - |z|^{\exp} \text{ if } \dot{d}z > 0, \text{or } \dot{d} \text{ otherwise} \right\} \tag{5}$$

where "exp" is an exponent greater than or equal to unity (practically about 20), z, a path dependency parameter. SAP2000 provides the analytical model shown in equation (4), which represents the hysteretic behavior of the device. During the dynamic motion, inertia forces are activated by all concentrated masses; including the mass distributed on the rigid plates' section (m_d in SAP2000, assigned with a default value of 0.24 kg) for the inertia forces contributed by the damper. The related resistance is given as the integral of the "second moment" about an axis of all the elements of mass dm, which compose the body of the steel plate used for the added damping, known as "MMI", Mass Moment of Inertia, RI in SAP2000 and assigned with a default value of RI= 0.175.

3.4 Parametric Analysis

The parametric analysis conducted provides information that may be used to assess the adequacy of ADCS design for a range of SDOF systems representative for new or existing frame structures with a characteristic period between the values of 0.60 s < T < 1.30 s. ADCS are tuned to specific predefined earthquake hazard protection levels as defined by the user in quantifiable energy measures of deformation. Hence the system is designed for a target building performance level. In the present study the performance index for structural safety has been defined as Effective Energy Deformation Index (EEDI) that physically represents the amount of the seismic input energy needed to be dissipated by the hysteretic device. A number of 342 combinations of assigned values to the damper's stiffness and yield force were used to construct the diagram, illustrating a measure of the effective deformation of energy, Figure 3. The presented area of the hysteretic energy by the input energy of the system was calculated for each combination of k_d and P_y and the ratio variation is marked at the y-axis, whereas at the x- axis the design parameter of the Damper Ratio DR is shown.

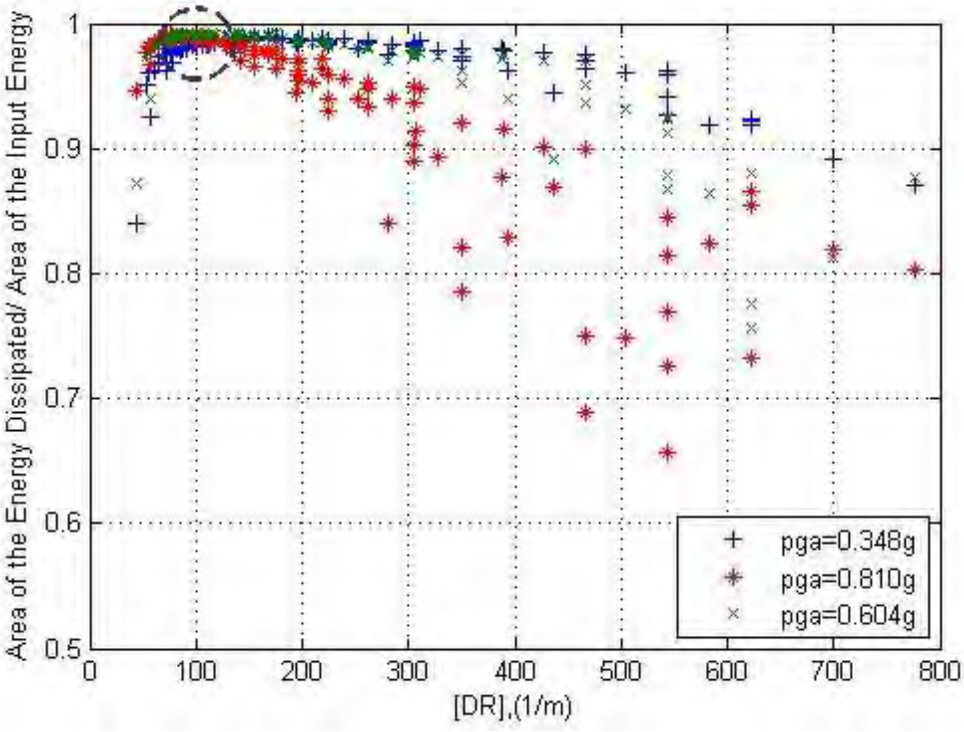

Figure 3: Parametric Analysis Results.

As Figure 3 illustrates, in all ADCS design parameters combinations the energy dissipation is more than 60 %. The investigation results refer to the systems' responses developed for the earthquake records, described in Table 1.

3.5 Preliminary Design

A simplified structural analysis and design procedure may be used to test the reliability of ADCS when under arbitrary seismic input records. The numerical application involves a selection of 10 real records in the Mediterranean earthquake prone zone for peak ground accelerations ranging between 0.10g and 0.50g, time durations, between 10 s and 50 s and different frequency contents, Table 2.

PGA	Ground Acceleration Record	PGA	Ground Acceleration Record
0.50g	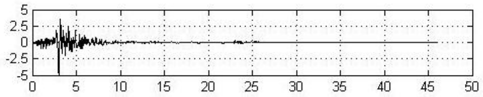	0.20g	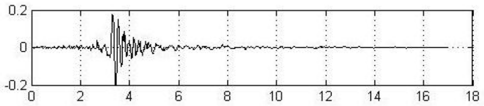
0.33g	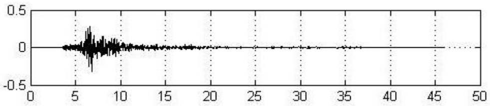	0.18g	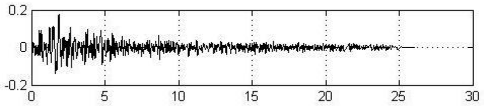
0.24g	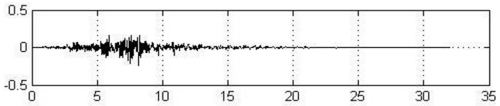	0.15g	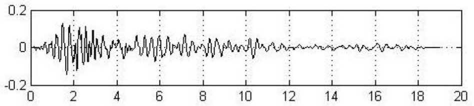
0.22g	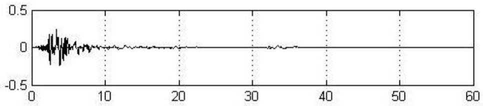	0.14g	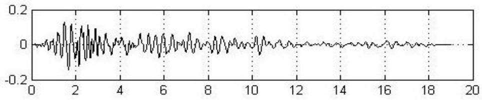
0.21g	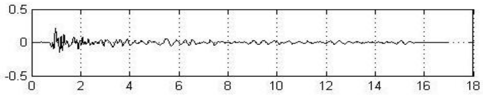	0.10g	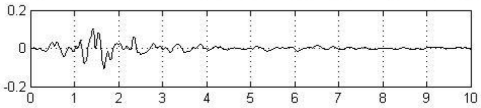

Table 2: Mediterranean Seismic Input Records.

The following steps are suggested for the design:

1. Select the design earthquake and assign a critical damping coefficient of 0 %.
2. Dimension the primary frame system to resist the gravity and wind load actions, (i.e. 1200 kN vertical and 15 kN lateral), combined with 25% of the static equivalent seismic load according to Eurocode 3.
3. Calculate for the dimensioned SDOF frame, the stiffness property in respect to both, the assigned mass (i.e. gravity load) and the initial estimation of the characteristic period. The period has to be within the suggested range of 0.60 s < T < 1.30 s for the indicated configuration.
4. Select the target allowable relative system's displacement as a percentage of its height and according to the displacement-based analysis (i.e. 1.5 % of the SDOF system's height). The procedure is based on previously established research results on ADCS response behavior for the estimation of the initial system's design parameters [7-11]. The proposed values are adopted for the next step of the design procedure.
5. Calculate the initial stiffness of the tension-only bracings by addressing the suggested factor of 1.65 to the inverse of the tendons stiffness, i.e. $1/k_b$, k_b: bracing's stiffness [11].
6. Determine the bracing's configuration under P-Delta load combinations so that it maintains its configuration without becoming slack after the structure is loaded. In the present application example, the cables are assigned with a diameter of d_c= 20 mm, with E= $1.6\text{x}10^4$ kN/cm^2 and f_y= 79.5 kN/cm^2.

3.6 Effective Yielding

In order for the yielding of the non-linear link to be effective, the kinetic response of the cable-restraints should be verified to be tuned to the hysteretic performance of the damper for an arbitrary case of selected design parameters as shown in Figure 4. The diagrams present for each one of the seismic inputs the comparison of input and hysteretic energy and the respective hysteresis for the damper with characteristics of h= 15 cm, n= 6, t= 1.2 cm, b= 5 cm, m= 0,24 kg, and a rotational inertia of RI= 0,175.

The resulting hysteresis in the damper is assumed to be equal with the dot product of the damper's yield force P_y and the design Interdamper drift Δ_d, expressed as folllows:

$$E_H = P_y \cdot \Delta_d \Rightarrow P_y = \frac{E_H}{\Delta_d} \qquad (6)$$

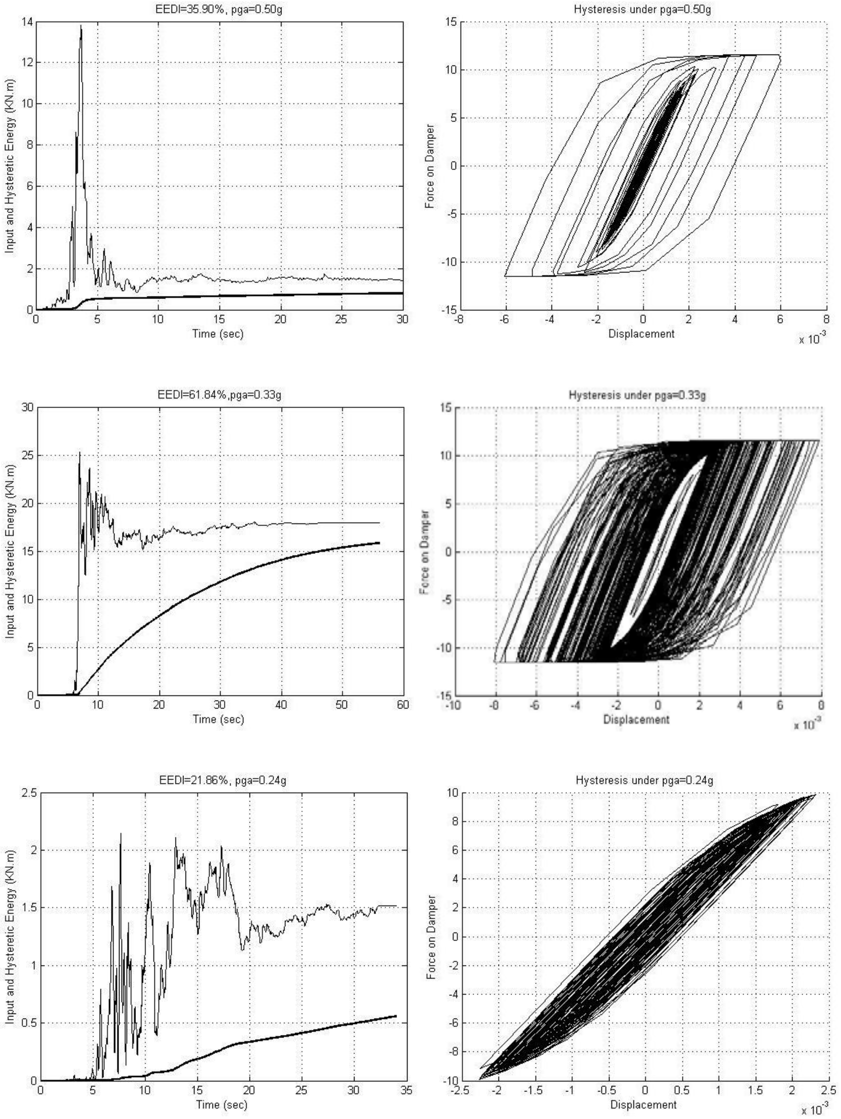

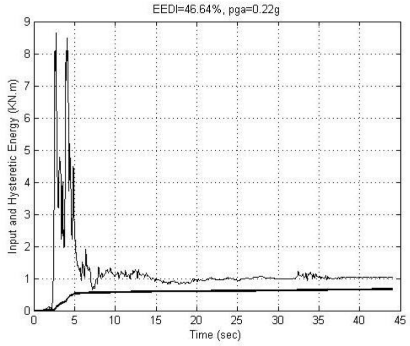
EEDI=46.64%, pga=0.22g
Input and Hysteretic Energy (KN.m)
Time (sec)
0 1 2 3 4 5 6 7 8 9
0 5 10 15 20 25 30 35 40 45

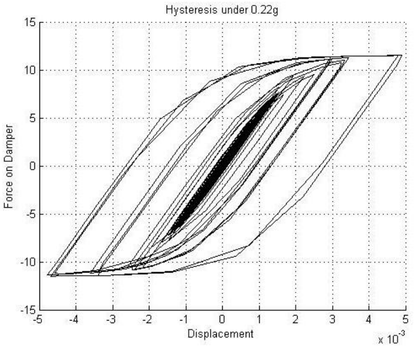
Hysteresis under 0.22g
Force on Damper
Displacement
x 10⁻³
-15 -10 -5 0 5 10 15
-5 -4 -3 -2 -1 0 1 2 3 4 5

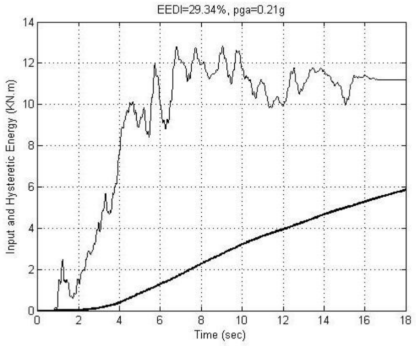
EEDI=29.34%, pga=0.21g
Input and Hysteretic Energy (KN.m)
Time (sec)
0 2 4 6 8 10 12 14
0 2 4 6 8 10 12 14 16 18

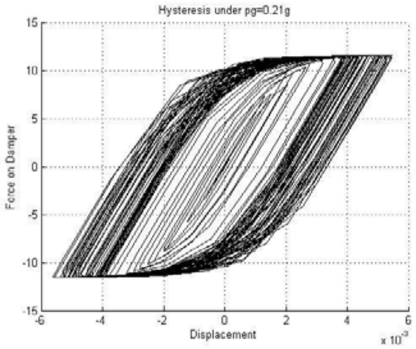
Hysteresis under pg=0.21g
Force on Damper
Displacement
x 10⁻³
-15 -10 -5 0 5 10 15
-6 -4 -2 0 2 4 6

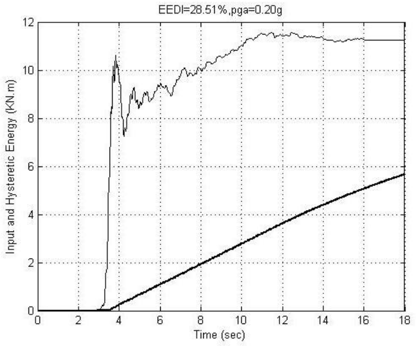
EEDI=28.51%,pga=0.20g
Input and Hysteretic Energy (KN.m)
Time (sec)
0 2 4 6 8 10 12
0 2 4 6 8 10 12 14 16 18

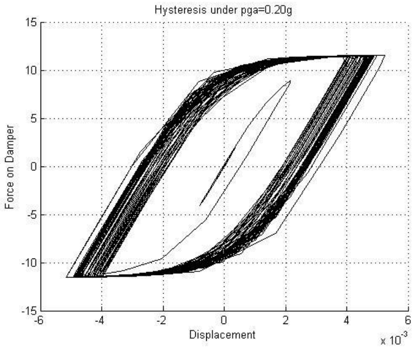
Hysteresis under pga=0.20g
Force on Damper
Displacement
x 10⁻³
-15 -10 -5 0 5 10 15
-6 -4 -2 0 2 4 6

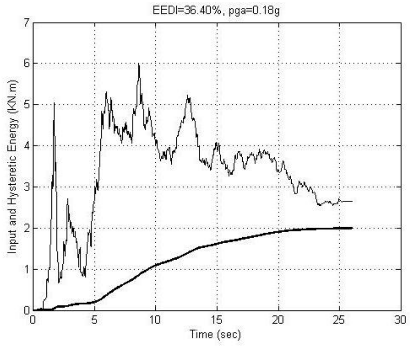
EEDI=36.40%, pga=0.18g
Input and Hysteretic Energy (KN.m)
Time (sec)
0 1 2 3 4 5 6 7
0 5 10 15 20 25 30

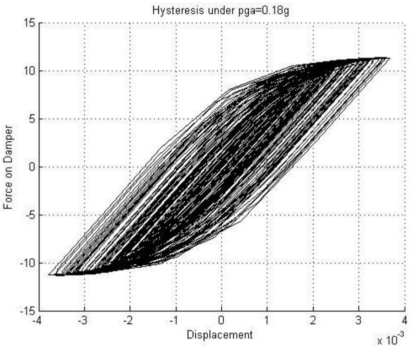
Hysteresis under pga=0.18g
Force on Damper
Displacement
x 10⁻³
-15 -10 -5 0 5 10 15
-4 -3 -2 -1 0 1 2 3 4

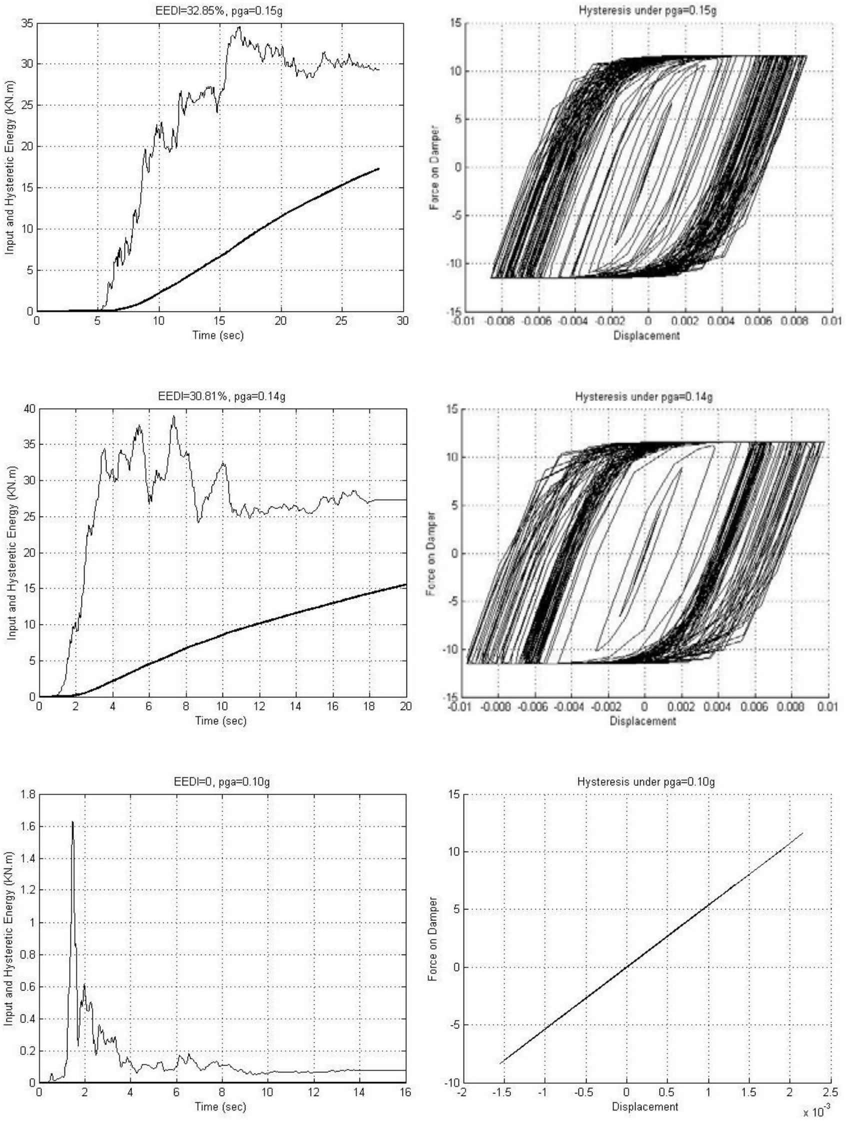
EEDI=32.85%, pga=0.15g

Hysteresis under pga=0.15g

EEDI=30.81%, pga=0.14g

Hysteresis under pga=0.14g

EEDI=0, pga=0.10g

Hysteresis under pga=0.10g

Figure 4: Effective Hysteresis of ADCS Damper.

A tuning of the damper-bracing mechanism follows the design steps 1-6:

7. Define the material and cable properties and assign compression limits for the tension-only cables (i.e. 5 kN prestressing) to make sure that the bracings will not carry compression.

8. Perform a static non-linear analysis to verify that displacements on the geometric non-linear configuration of the cables are kept under defined limits.

9. Calculate the initial elastic stiffness of the damper by addressing the suggested factor of 0.1062 for the damper to the frame stiffness according to [11].

10. Based on the initial estimations of the design parameters, (i.e. damper's stiffness and -yield force), calculate the Damper Ratio DR value according to equation (3).

11. Verify the respective performance indicator EEDI value according to Figure 3. When the demand coincides with the amount of energy dissipation, the EEDI value can be selected.

12. Calculate the damper's hysteretic energy according to equation (6), for the EEDI and select the design yield force, P_y, in relation to the allowable maximum inter-damper drift, Δ_d.

The final step of the design procedure involves the dimensioning of the damper according to the system's response, as this may be characterized through its initial elastic stiffness k_d and its yield force P_y:

13. According to the selected damper's yield force and stiffness, select the number and geometry of the damper's steel plates by using equations (1) and (2).

3.7 Base Shear

The design should verify that the base shear on ADCS is not increased after the addition of the damper-bracing mechanism. Otherwise, the input energy may also increase. In addition to the latter, an increase of the strength demand on the primary frame may become higher than the foundations can carry at the end of the flow of forces circle. As Table 3 shows, there is a decrease of the base shear of the controlled system in 80 % of the cases and an increase in 20 % of the cases that can be neglected because of its small magnitude. According to the numerical results of the parametric analysis, the increase of the base shear can be practically neglected. An example is shown in Table 3.

Record	Primary Frame (kN)		ADCS: S1 (kN)	
Aigio 95 (Aigio, 0^0), 0.50g	1577.00	-1563.00	1427.25	-1415.15
Athens 99 (Sepolia, 0^0), 0.33g	1978.00	-2048.00	1847.89	-1897.44
Ionian 83 (Argostoli, 90^0), 0.24g	480.40	-500.30	543.81	-530.99
Kalamata 86 (Kalamata, 00), 0.22g	1270.00	-1278.00	1160.92	-1136.81
Heraklio 84 (Heraklio, 90^0), 0.21g	1735.00	-1738.00	1282.54	-1323.04
Aigio 90 (Aigio, 90^0), 0.20g	1361.00	-1361.00	1222.41	-1208.77
Etolia 88 (Valsamata, 90^0), 0.18g	848.40	-882.90	865.73	-895.40
Killini 88 (Zakinthos, 90^0), 0.15g	2516.00	-2515.00	2021.72	-2019.67
Preveza 81 (Preveza, 0^0), 0.14g	2381.00	-2445.00	2302.20	-2285.20
Gulf of Corinth 93 (Nafpaltos, 90^0), 0.10g	519.10	-372.80	509.17	-357.06

Table 3: Base Shear Results.

3.8 Displacement Control

A range of defined allowable relative displacement limits should be followed for the frame to resist elastically, for the tension-only bracings to avoid compression and for the hysteretic damper to be energized. Table 4 shows the respective analysis results of the primary frame and for the arbitrary selection of ADCS assigned parameter values. A reduction of the response displacements is found in 80 % of the cases.

Record	Primary Frame (cm)		ADCS: S1 (cm)	
Aigio 95 (Aigio, 0^0), 0.50g	1.92	-1.90	1.75	-1.73
Athens 99 (Sepolia, 0^0), 0.33g	2.50	-2.42	2.32	-2.27
Ionian 83 (Argostoli, 90^0), 0.24g	0.63	-0.59	0.65	-0.67
Kalamata 86 (Kalamata, 0^0), 0.22g	1.54	-1.53	1.37	-1.41
Heraklio 84 (Heraklio, 90^0), 0.21g	2.12	-2.11	1.62	-1.57
Aigio 90 (Aigio, 90^0), 0.20g	1.66	-1.66	1.49	-1.51
Etolia 88 (Valsamata, 90^0), 0.18g	1.07	-1.04	1.09	-1.06
Killini 88 (Zakinthos, 90^0), 0.15g	3.07	-3.07	2.48	-2.48
Preveza 81 (Preveza, 0^0), 0.14g	2.98	-2.90	2.80	-2.82
Gulf of Corinth 93 (Nafpaltos, 90^0), 0.10g	0.46	-0.63	0.45	-0.62

Table 4: Relative Displacement Results.

3.9 Interdamper Drift

The effectiveness of the proposed ADCS is based on the relative displacements between its composed members, in particular, the damper's end points. The displacement is defined as Interdamper Drift, i.e. the relative displacement of the primary frame to the cable bracings. Some respective indicative results for the numerical example analyzed are plotted in Figure 5. The relation between the Interdamper Drift for a given seismic action load and the Effective Energy Dissipation is vital for the optimization procedure of ADCS design.

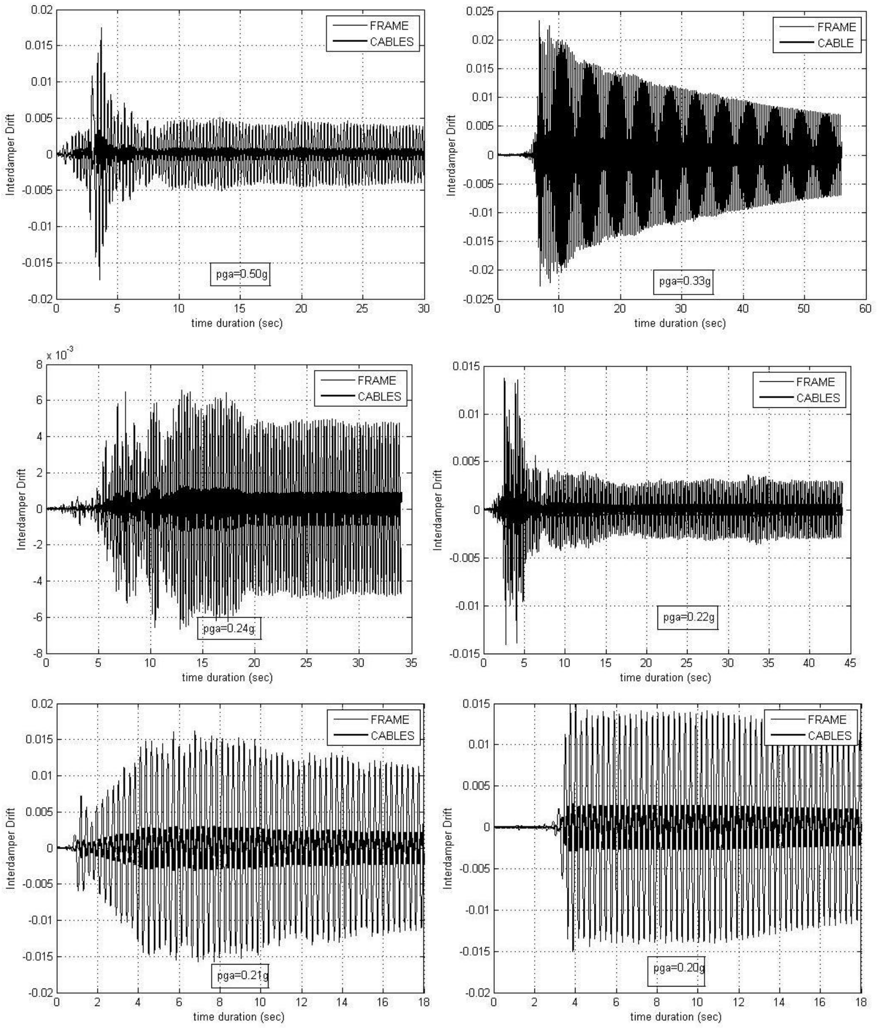

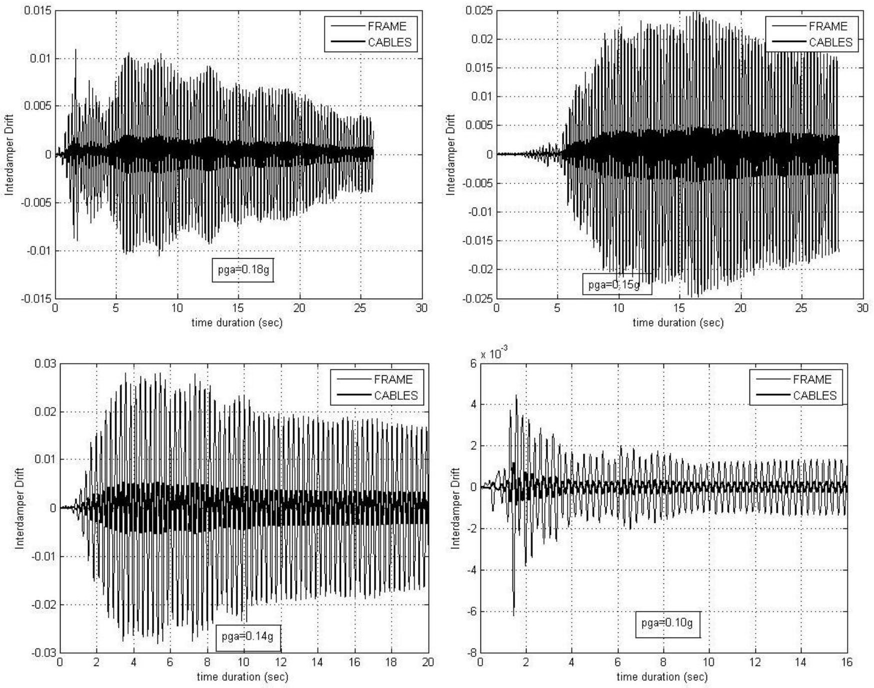

Figure 5: Interdamper Drift.

4 CONCLUSIONS

The application of Adaptable Dual Control Systems that may be designed to supply measurable added damping to frame structures through the yielding of an integrated hysteretic damper is proposed in the present paper. The concept refers to a kinetically developed damper-bracing mechanism. A configuration design of tension-only bracings with closed circuit and a hysteretic damper are investigated under strong earthquakes. In principle the optimization procedure for the best seismic control response of ADCS refers to a good trade-off between the desirable increase in energy dissipation and control of both, base shear and relative displacements, compared to the response of the primary frame without the control mechanism. The leading parameters of the design were traced through a parametric analysis that has been based on 342 combinations of design parameters. New design properties that seemed to govern the design were defined and calculated for each analytical test. The design parameters have been verified in the response behavior of ADCS under the earthquake records of the Greek-Mediterranean seismic zone, significantly different from each other and from the international ones, in their frequency content, time duration and peak ground acceleration characteristics. The benefit of high energy dissipation levels by ADCS has been proven for a broad range of the hysteretic damper's mechanical and geometrical properties. Additionally, the common concern in passively controlled frame structures, of stiffness increase, or induction of larger displacements, and the limitation of the maximum displacements of the damper-bracing mechanism's members proved to be managed satisfactorily in the designs. Ready make diagrams that may be used for further applications are given to assist the procedure for designing structures that may develop an adaptable seismic control response mainly due to the property of "duality" as it is valid for ADCS.

REFERENCES

[1] G.W. Housner, L.A. Bergman, T.K. Caughey, A.G. Chassiakos, R.O. Claus, S.F. Masri, R.E. Skelton, T.T. Soong, Jr. B.F. Spencer, T.P. Yao, Structural Control: Past, Present and Future. *Engineering Mechanics*, **123(9)**, pp. 897-971, 1997.

[2] M.D. Symans, F. Charney, M.C. Constantinou, C. Kircher, M.W. Johnson, R.J. McNamara, Energy Dissipation Systems for Seismic Applications: Current Practice and Recent Developments. *Structural Engineering*, **134(1)**, pp. 3-21, 2008.

[3] K.C. Tsai, H.W. Chen, C.P. Hong, Y.F. Su, Design of Steel Triangular Plate Energy Absorbers for Seismic-Resistance Construction. *Earthquake Spectra*, **9**, pp. 505-528, 1993.

[4] M. Kurata, R. DesRoches, R.T. Leon, Cable Damper Bracing for Partial Seismic Rehabilitation. *14th World Conference on Earthquake Engineering*, 14WCEE, 12.10-17.10.08: Beijing, China, October 2008.

[5] I.H. Mualla, L.O. Nielsen, B. Belev, W.I. Liao, C.H. Loh, A. Agrawal, Performance of Friction-Damped Frame Structure: Shaking Table Testing and Numerical Simulations. *7th US National Conference on Earthquake Engineering*: Boston, USA, 2002.

[6] E. Renzi, S. Perno, S. Pantanella, V. Ciampi, Design, Test and Analysis of a Light-Weight Dissipative Bracing System for Seismic Protection of Structures. *Earthquake Engineering and Structural Dynamics*, **36,** pp. 519–539, 2007.

[7] M.C. Phocas, T. Sophocleous, Kinetic Structures in Architecture. *14th World Conference on Earthquake Engineering*, 14WCEE, 12.10-17.10.08: Beijing, China, October 2008.

[8] T. Sophocleous, M.C. Phocas, Dual Earthquake Resistant Frames. M. Phocas, C.A. Brebbia and P. Komodromos, Eds., *Earthquake Resistant Engineering Structures VII,* WIT Press: Southampton, pp. 165-174, 2009.

[9] T. Sophocleous, M.C. Phocas, Dual Structures Towards Kinetic Adaptability for Earthquake Resistance. *First International Conference on Structures & Architecture*, ICSA2010, 21.07 – 23.07.10: Guimaraes, Portugal, July 2010.

[10] T. Sophocleous, M.C. Phocas, Model of Analysis for Earthquake Resistant Dual Systems. *2nd International Conference on Computational Methods in Structural Dynamics and Earthquake Engineering*, COMPDYN 2009, 22.06-24.06.09: Rhodes, Greece, June 2009.

[11] M.C. Phocas, A. Pocanschi, Steel Frames with Bracing Mechanism and Hysteretic Dampers. *Earthquake Engineering and Structural Dynamics*, **32**, pp. 811–825, 2003.

COMPDYN 2011
III ECCOMAS Thematic Conference on
Computational Methods in Structural Dynamics and Earthquake Engineering
M. Papadrakakis, M. Fragiadakis, V. Plevris (eds.)
Corfu, Greece, 25–28 May 2011

INCREMENTAL DYNAMIC ANALYSIS AND PUSHOVER ANALYSIS. A PROBABILISTIC COMPARISON

Yeudy F. Vargas[1*], Lluis G. Pujades[1], Alex H. Barbat[1], Jorge E. Hurtado[2]

[1] Universidad Politécnica de Cataluña
Department of Geotechnical Engineering and Geosciences, Jordi Girona 1-3, Building D2, Campus Norte UPC, 08034 Barcelona Spain
yeudy.felipe.vargas@upc.edu

[2] Universidad Nacional de Colombia
Universidad Nacional de Colombia, Apartado 127, Manizales, Colombia
jehurtadog@unal.edu.co

Keywords: Pushover analysis, Incremental dynamic analysis, Monte Carlo simulation, Vulnerability.

Abstract. *Capacity-spectrum-based-methods are also used for assessing the vulnerability and risk of existing buildings. Capacity curves are usually obtained by means of nonlinear static analysis. Incremental Dynamic Analysis is another powerful tool based on nonlinear dynamic analysis. This method is similar to the pushover analysis as the input is incrementally increased but it is different as it is based on dynamic analysis. Moreover, it is well known that the uncertainties associated to the structural response can be significant, because the uncertainties involved in the mechanical properties of the materials and the expected seismic actions are also highly uncertain. In this work selected mechanical properties are considered as random variables and the seismic hazard is considered in a probabilistic way. A number of accelerograms of actual European seismic events have been selected in such a way that their response spectra fitted well the response spectra provided by the seismic codes for the zone where the target building is constructed. In this work a fully probabilistic approach is tackled by means of Monte Carlo simulation and it is applied to a detailed study of the seismic response of a reinforced concrete building. The building is representative for office buildings in Spain but the methods used and the results obtained can be extended to other types of buildings. The main purposes of this work are 1) to analyze the differences when static and dynamic techniques are used and 2) to obtain a measure of the uncertainties involved in the assessment of the vulnerability of structures. The results show that static based procedures are somehow conservative and that uncertainties increase with the severity of the seismic actions and with the damage. Low damage state fragility curves have little uncertainty while high damage grades fragility curves show great scattering.*

1 INTRODUCTION

Aiming to prevent the seismic risk, it is necessary to assess the vulnerability of existing structures. To do that, several methods have been proposed, starting from different approaches. One is the vulnerability index method in which the action is defined from the EMS-98 by macroseismic intensities and structural behaviour through a vulnerability index [1, 2]. Another highly used method is based on the capacity spectrum. In this, the seismic action is defined by means of the elastic response spectra and the vulnerability or fragility of the building by means of the capacity curve; the latter is calculated from an incremental nonlinear static analysis, commonly known as "Pushover Analysis" [3, 4 5]. Another tool used to evaluate the performance of structures against seismic actions is the Incremental Dynamic Analysis (IDA) proposed by Vamvatsikos & Cornell [6]. The purpose of IDA is to obtain a measure of damage in the structure by increasing the intensity of the action record, in this case the peak ground acceleration. Vamvatsikos & Cornell make an interesting analogy between the PA and the IDA, because both procedures increases the load on the structure and measure the response of the system in terms of a control variable which may be the maximum displacement at the roof, the maximum inter storey drift, etc. This procedure allows obtaining the dynamic response of a structure when the seismic action is increased. On the other hand, the mechanical properties of the materials which constitute the structure and the seismic action are random variables and, therefore, the vulnerability of the building is also a random variable. To take into account the inherent randomness of the problem, it is appropriate to use the Monte Carlo method. Therefore, in this paper, a probabilistic comparison between the PA and the IDA is performed when calculating the vulnerability of an existing reinforced concrete building. The main conclusion from this comparison highlights the importance of measuring the vulnerability of structures taking into account that the variables involved are random. This approach, mixed with powerful tools to analyze the structure such as the PA and the IDA, provide valuable information that can hardly be obtained with other methodologies.

2 BUILDING DESCRIPTION

This paper analyzes a reinforced concrete structure, consisting of columns and waffle slabs, which is part of the North Campus of the Universidad Politécnica de Cataluña. It has 7 levels and 4 spans, the height is 24.35 m and the width is 22.05 m (see Figure 1). The fundamental period of the building is 0.97 seconds. This value is higher when compared to that of conventional reinforced concrete buildings, because in the numerical model, the waffle slabs are approximated with beams of equivalent inertia and, therefore, are structural elements wide and flat leading to a reduction of the lateral stiffness of the structure. In the calculation model, the structural elements (equivalent beams and columns) follow an elastic-plastic constitutive law, which does not take into account either hardening or softening. Yielding surfaces are defined by the moment-axial load interaction diagram in columns and by the moment-angular deformation interaction diagram in beams.

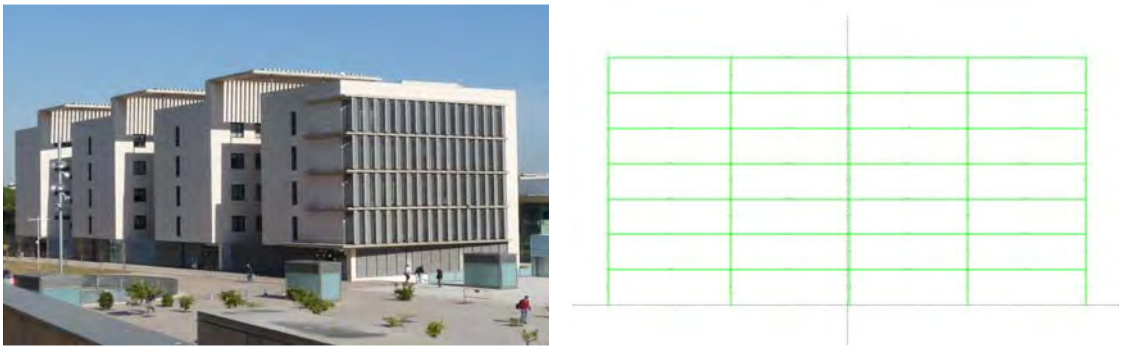

Figure 1. Picture of the building omega located in the Universidad Politécnica de Cataluña, Barcelona, Spain.

3 DAMAGE INDEX BASED ON PUSHOVER ANALYSIS

A tool often used to evaluate the behaviour of the structures against seismic loads, is the nonlinear static analysis, commonly called Pushover Analysis (PA). This numerical tool consists in apply a horizontal load to the structure, according to a certain pattern of forces, and in increasing its value until the structural collapse is reached. From this procedure one obtain a relationship between the displacement at the roof of the building and the base shear, called capacity curve. In this article, due to the probabilistic approach, the PA is performed repeatedly, therefore, it is appropriate to apply a procedure for obtaining automatically the horizontal load limit. For this, Satyarno [7] proposes the adaptive incremental nonlinear analysis that establishes the horizontal load limit as a function of the tangent fundamental frequency, i.e. the frequency associated with the first vibration mode, which is being calculated for each load increment. Therefore, in each step is calculated the first mode of vibration to determine the shape of the load in height. A detailed description of this procedure is found in the manuals of the program Ruaumoko [8] used for calculating the static and dynamic nonlinear structural response. As mentioned in the introduction, the mechanical properties of materials are considered as random variables. To do this, the values used in the structural design for concrete compressive strength *fc*, and the tensile strength associated with steel yield strength *fy*, are treated as random variables and using the inversion method of the cumulative probability distribution curve are generate 1000 random samples of these variables. In this paper, it is assumed that the generated random variables follow a Gaussian probability function whose mean and standard deviations are shown in Table 1.

	Mean Value (kPa)	Standard deviation (kPa)	Coefficient of variation
fc	25000	2500	0.1
fy	500000	50000	0.1

Table 1. Features of the Gaussian random variables considered.

For the generated samples, the PA is performed 1000 times and the capacity curve is obtained as the random variable shown in Figure 2.

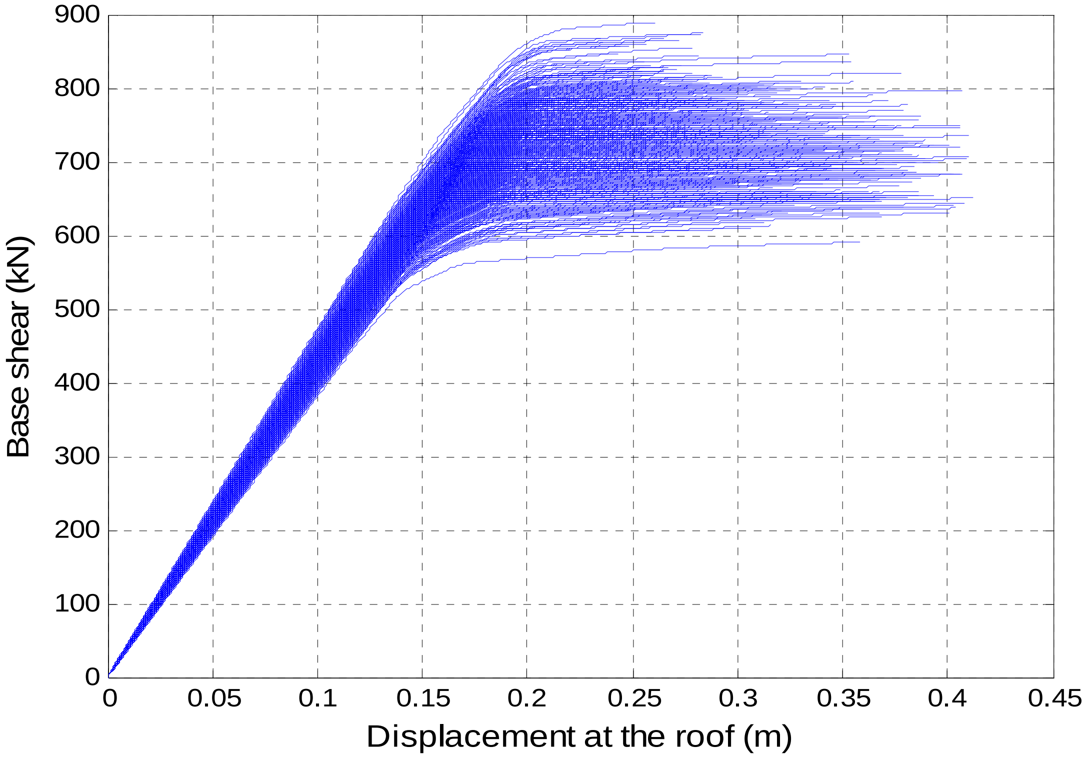

Figure 2. Capacity curves obtained from the PA, taking into account the uncertainty in the mechanical properties of materials.

The capacity curves shown in Figure 2 are transformed into capacity spectra, which relate the spectral displacement to spectral acceleration by means of the following equations [9]:

$$sd_i = {}^{\delta_i}\!/_{PF_1}$$
$$sa_i = {}^{V_i/W}\!/_{\alpha_i} \tag{1}$$

The subscript *i* in equations (1) is referred to the applied load increments on the structure during the PA; sd_i is the spectral displacement; δ_i is the displacement at the roof of the building; PF_i is the modal participation factor of the first mode of vibration; sa_i is the spectral acceleration; V_i is the base shear; W is the weight of the building and α_i is the modal mass coefficient of the first mode of vibration. On the other hand, the capacity spectrum can be represented in a bilinear form, which is useful for defining damage states. Assumptions to build the bilinear capacity spectrum are: 1) The area under the bilinear curve must be equal to the area of the original curve. 2) The coordinates of the point of maximum displacement must be the same in both curves. 3) The slope of the initial branch should be equal in both curves. Figure 3 shows an example of the bilinear representation of the capacity spectrum. This can be defined completely by the points (Dy, Ay) and (Du, Au). These points are useful to define the states of damage, according to the procedure described in Lantada et al (2009).

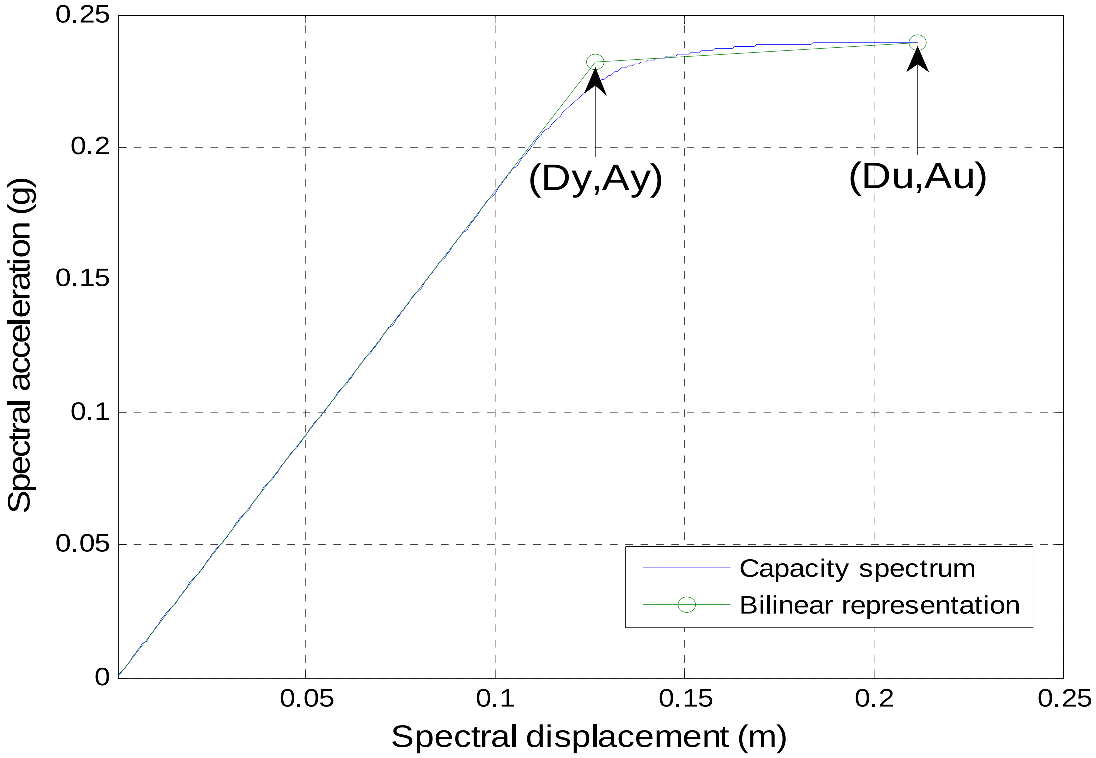

Figure 3. Capacity spectrum and the bilinear representation.

Different studies have been proposed to calculate the damage of the structure from the definition of damage states (*ds*), which are a description of the damage in the structure for a given spectral displacement. For example, HAZUS 99 [10] and Risk EU [11], define 4 *ds*, namely slight, moderate, extensive and complete. Description of the damage states depends on the type of structure. For example, According to HAZUS, in the case of reinforced concrete structures, the *ds* slight is described as the beginning of cracking due to bending moment or shear in beams and columns. Collapse state considers that the structure reaches an imminent risk of collapse. Risk EU seeks to define the damage states in simplified form, starting from the capacity spectrum in a bilinear representation. Based on the values (Dy, Ay) and (Du, Au), the spectral displacements for the four damage states threshold ds_i are obtained according to the following equations:

$$\begin{aligned} ds_1 &= 0.7 * Dy \\ ds_2 &= Dy \\ ds_3 &= Dy + 0.25 * (Du - Dy) \\ ds_4 &= Du \end{aligned} \tag{2}$$

Therefore, after calculating the capacity spectrum in bilinear representation and applying equations 2, it is possible to obtain the damage states thresholds as random variables, as shown in Figure 4.

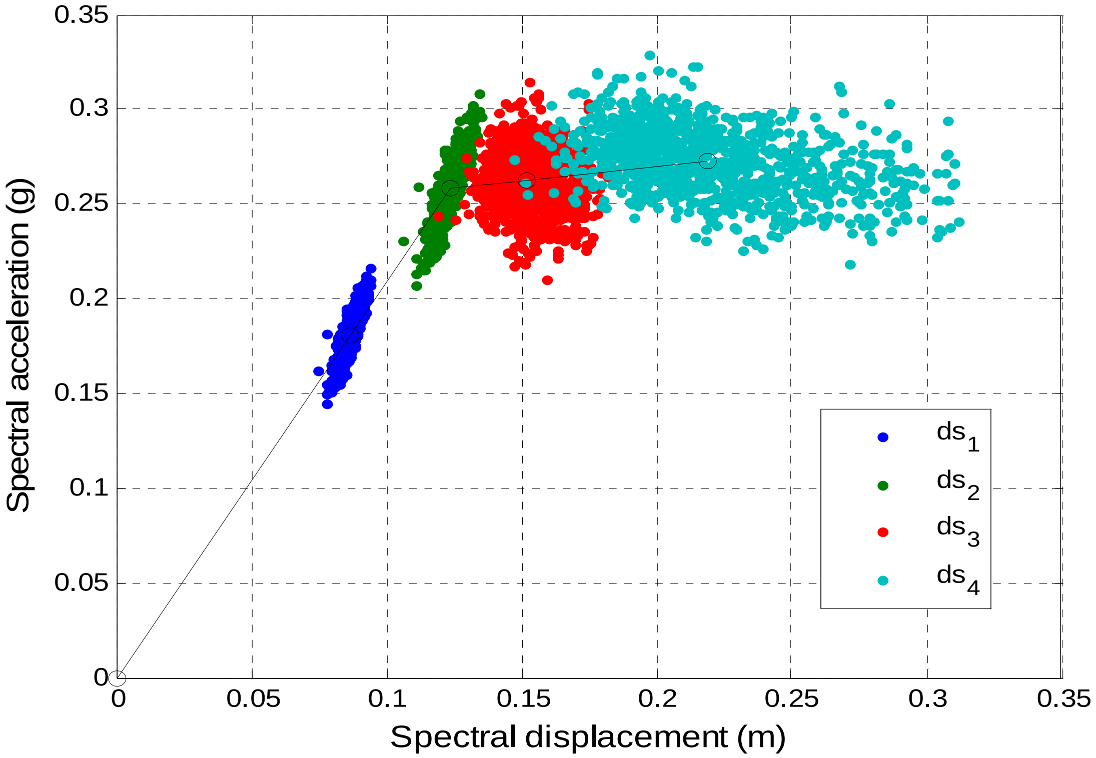

Figure 4. Damage states as random variables.

The mean, standard deviation and coefficient of variation of the damage states are shown in Table 2, in which it can be seen that the coefficient of variation of the damage state 4 is greater than that of the input variables. This is due to the fact that the problem is nonlinear and therefore it shows the importance of the probabilistic approach in this type of analysis.

	ds_1 (cm)	ds_2 (cm)	ds_3 (cm)	ds_4 (cm)
μ_{ds}	8.6	12.3	15.2	21.9
σ_{ds}	0.27	0.38	1.00	3.25
c.v.	0.03	0.03	0.06	0.15

Table 2. Mean value, standard deviation and coefficient of variation of the damage states.

After obtaining the damage states as random variables it is possible to calculate the fragility curves, which represent the probability of reaching or exceeding a damage state, in function of a parameter representing the seismic action. In this work, this parameter is the spectral displacement. To obtain the fragility curves the following assumptions must be considered: 1) The probability that the spectral displacements in each damage state threshold, ds_i, equals or exceeds the damage state is 50%. 2) The fragility curves follow a lognormal cumulative probability function described by the following equation:

$$P\left[ds_i / sd\right] = \phi\left[\frac{1}{\beta_{ds_i}} Ln\left(\frac{sd}{ds_i}\right)\right] \tag{3}$$

where sd is the spectral displacement and β_{ds_i} is the standard deviation of natural logarithm of the variable ds_i. 3) The expected seismic damage in buildings follows a binomial probability distribution. Figure 5 shows all fragility curves calculated after applying the described procedure.

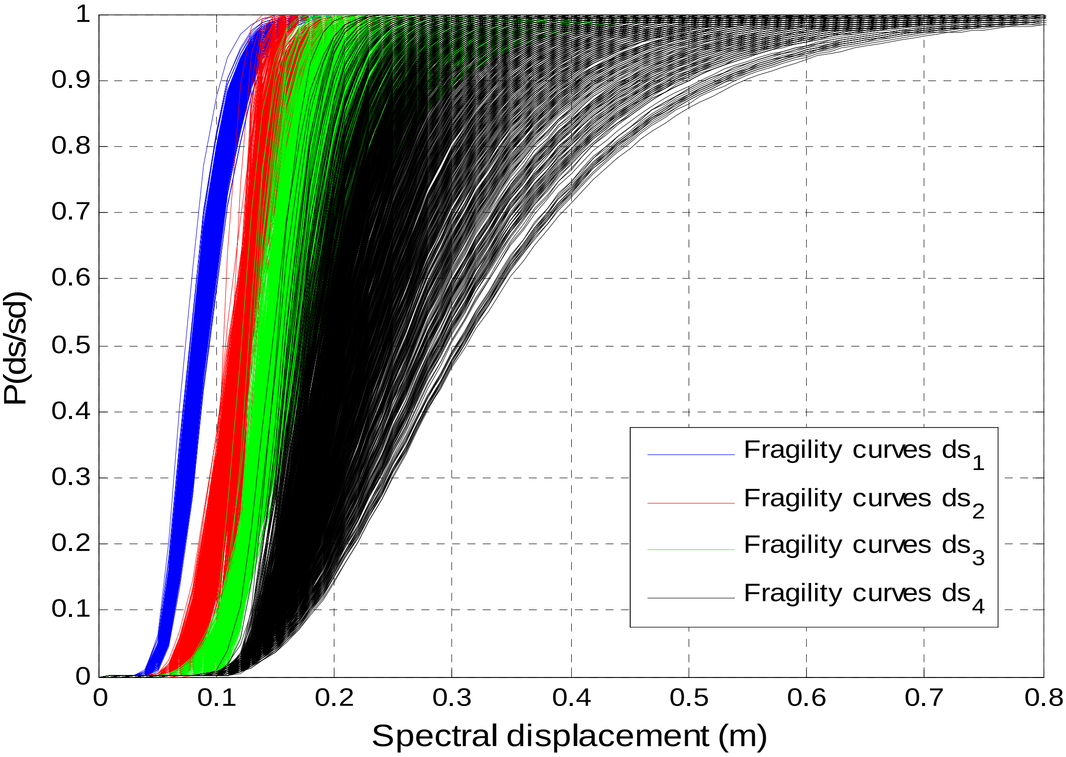

Figure 5. Fragility curves as random variables.

Since the probabilities of occurrence of each state of damage are easily obtained from the fragility curves, one can calculate the expected damage index, *DI*, which is the normalized mean damage state, which can be interpreted as a measure of the overall expected damage in the structure.

$$DI = \frac{1}{n}\sum_{i=0}^{n} iP(ED_i) \tag{4}$$

where n is the number of damage states considered, in this case 4 and $P(ds_i)$ is the probability of occurrence of ds_i. Figure 6 shows the ID calculated from the fragility curves of Figure 5. The curves of Figure 6 can be interpreted as random vulnerability curves.

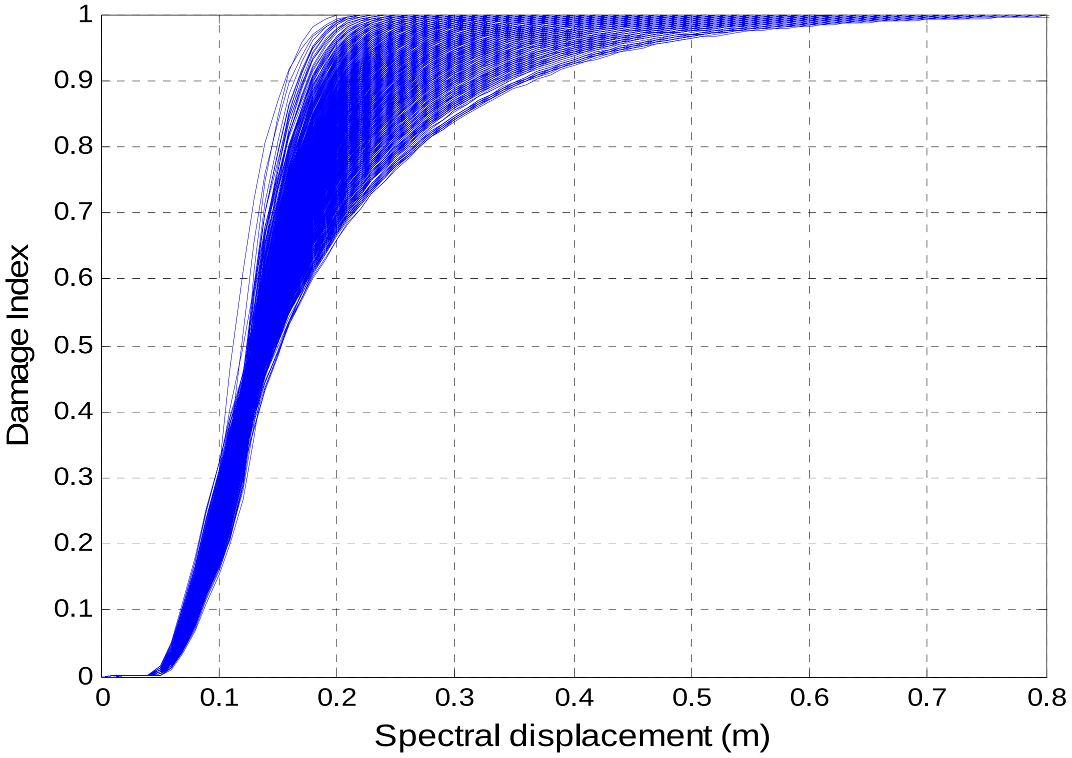

Figure 6. Damage index obtained starting from the PA as random variable.

4 DAMAGE INDEX BASED ON THE INCREMENTAL DYNAMIC ANALYSIS

Incremental dynamic analysis allows obtaining the dynamic response of a structure to an earthquake action. This earthquake is scaled to various PGA. As mentioned above, the purpose of this article is to compare the results obtained with the methodology based on the capacity spectrum with the incremental dynamic analysis. According to the probabilistic approach it is necessary to obtain the seismic action as a random variable. To do that, 20 earthquakes have been selected from two databases, one from Spain and the other from Europe, whose elastic response spectra are compatible with elastic response spectrum taken from Eurocode 8. In this case, the elastic spectrum type 1 and soil D is selected. Figure 9 shows the spectra of the selected earthquakes, their average value, and the spectrum type 1 soil D, taken from Eurocode 8.

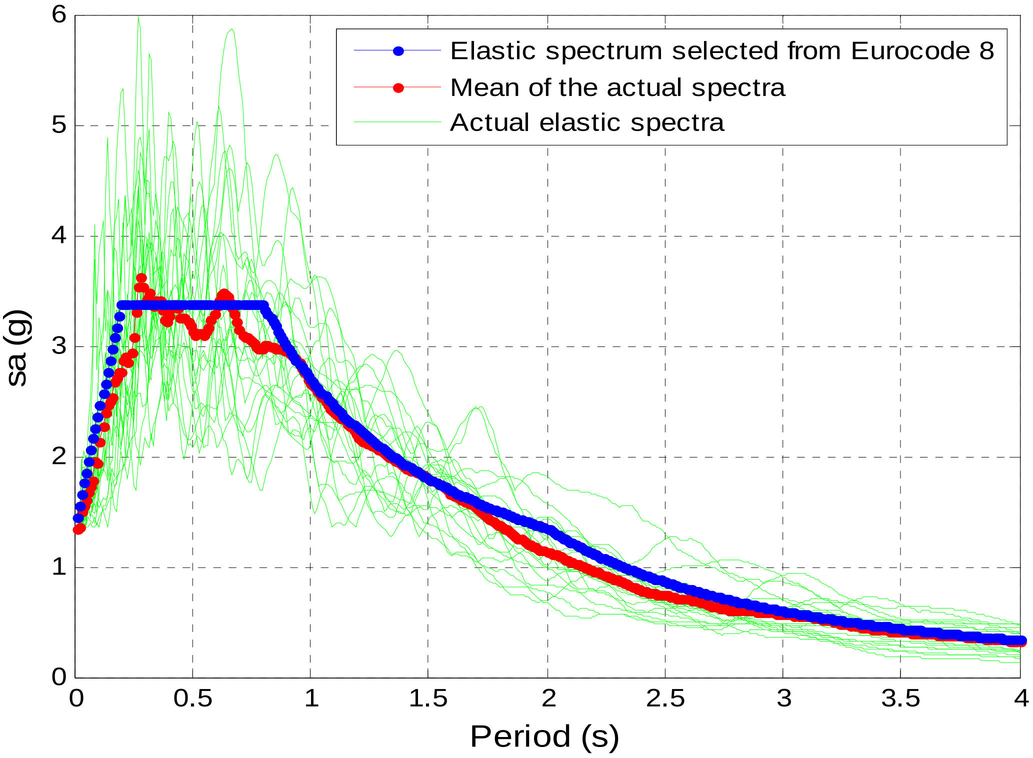

Figure 7. Selected spectra of the accelerograms that are compatible with spectrum type 1 soil D of Eurocode 8.

After selecting the accelerograms, the dynamic response of the structure is calculated, for different PGA until a maximum of 0.32 g, at intervals of 0.04 g. In each run of the nonlinear dynamic analysis, the damage index proposed by Park & Ang [12] is calculated and, also, the maximum displacement at the roof of the building, allowing to compare these results with those obtained previously from static procedure. Figure 8 shows the results obtained with both methods, and shows that the damage index obtained with the procedure based on the PA is conservative compared to the results obtained with the procedure based on IDA. However, when the damage index is close to 1, similar values are obtained with both procedures. On the other hand, it can be seen in the curves obtained with the PA procedure that the structural damage begins for a smaller spectral displacement than in the case of the IDA procedure and that, in both cases, slopes are similar. This means that the PA curves are shifted respecting the IDA curves what could be easily adjusted by changing the damage states coefficients. It is important to note the large scatter in both cases, showing the importance of assessing the vulnerability of structures from a probabilistic perspective, whichever procedure is used.

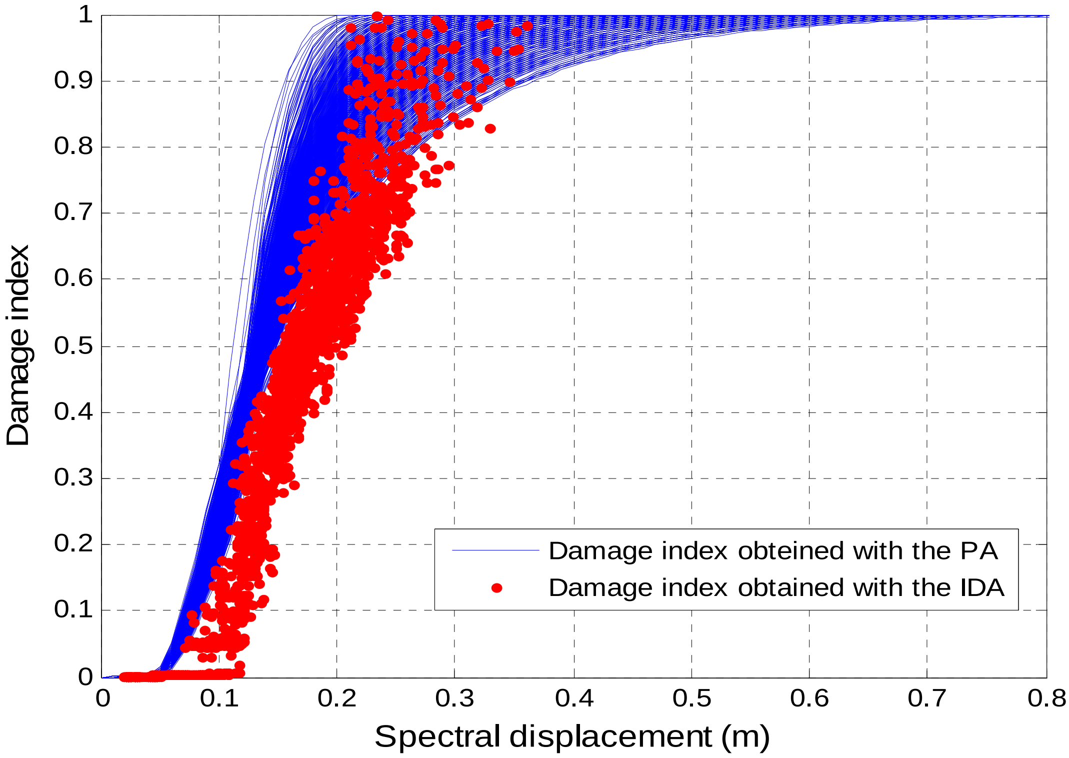

Figure 8. Damage index obtained with static and dynamic procedures.

5 CONCLUSIONS

In this work, the vulnerability of a real reinforced concrete structure, with columns and waffle slab has been assessed, taking into account that the input variables are random. Two approaches to evaluate the vulnerability of the building have been used. The first one is based on the pushover analysis and the second one is based on the incremental dynamic analysis. An important conclusion is that, despite working with advanced structural analysis, these procedures show significant uncertainties when taking into account the randomness of the variables associated with the problem. It should be emphasized that in this work relatively small coefficients of variation for input variables have been considered taking into account the uncertainties that may exist in older structures that did not have quality control and have not been designed according to the earthquake-resistant criteria. An important conclusion is that the results obtained with the procedure based on the capacity curve are conservative when compared with the results obtained with the incremental dynamic analysis. However, within the procedure based on the capacity curve, there are factors such as those given in equation 2, which can be modified to improve the correlation with the results based on dynamic calculation. The main conclusion of this paper is that whichever the procedure is used to evaluate the vulnerability of a structure, it is important to note that the input variables, such as the mechanical properties of materials and the seismic action, are random variables and these generate large uncertainties in the seismic response, which can lead to overestimate or to underestimate the real damage that can occur in a structure.

6 ACKNOWLEDGEMENTS

This work was partially funded by the Geographic Institute of Catalonia (IGC), through the ministry of science and innovation in Spain, by the European Commission and a scholarship through research projects CGL-2005-04541-C03-02/BTE, CGL2008-00869/BTE, INTERREG: POCTEFA 2007-2013/ 73/08 y MOVE—FT7-ENV-2007-1-211590.

7 REFERENCES

[1] Barbat A. H., Yépez Moya F. & J.A Canas, Damage scenarios simulation for risk assessment in urban zones. *Earthquake Spectra*. 2(3), 371-394, 1996.

[2] Barbat A. H., Mena U. & F. Yépez, Evaluación probabilista del riesgo sísmico en zonas urbanas. *Revista internacional de métodos numéricos para cálculo y diseño en ingeniería*. 14(2), 247-268, 1998.

[3] Borzi B., Phino R. & H Crowley, Simplified Pushover analysis for large-scale assessment of RC buildings. *Engineering Structures*. 30:804-820, 2008.

[4] Barbat A.H., Pujades L.G., Lantada N. & R. Moreno, Seismic damage evaluation in urban areas using the capacity spectrum method: application to Barcelona. *Soil Dynamics and Earthquake Engineering*. 28, 851–865, 2008.

[5] Lantada N, Pujades LG & A.H. Barbat, Vulnerability index and capacity spectrum based methods for urban seismic risk evaluation. A comparison. *Natural Hazards*. 51:501-524, 2009.

[6] Vamvatsikos D. & C.A. Cornell, The Incremental Dynamic Analysis. *Earthquake Engineering and Structural Dynamics*. 31(3): 491-514, 2002.

[7] Satyarno I., "Pushover analysis for the seismic assessment of reinforced concrete buildings". Doctoral Thesis, Department of civil engineering, University of Canterbury, 1999.

[8] Carr, A. J., Ruaumoko-Inelastic Dynamic Analisys Program. Dept. of Civil Engineering, Univ. of Canterbury, Christchurch, New Zealand, 2000.

[9] ATC-40, Seismic evaluation and retrofit of concrete buildings. Applied Technology Council, Redwood City, California, 1996.

[10] HAZUS-99, Earthquake Loss Estimation Methodology Earthquake. Technical Manual, Vol 1, Federal Emergency Management Agency (FEMA). Washington D.C, 1999.

[11] RISK-UE, Project of the European Commission, an advanced approach to earthquake risk scenarios with applications to different European towns. Contract number: EVK4-CT-2000-00014, 2004.

[12] Park, Y-J & Ang, A.H-S, Mechanistic seismic damage Model for Reinforced Concrete. *J. Struct. Div. ASCE*. Vol. 111 No. 4. pp 722-757, 1985.

COMPDYN 2011
III ECCOMAS Thematic Conference on
Computational Methods in Structural Dynamics and Earthquake Engineering
M. Papadrakakis, M. Fragiadakis, V. Plevris (eds.)
Corfu, Greece, 25–28 May 2011

KERNEL DENSITY ESTIMATION TECHNIQUES FOR SEISMIC HAZARD ANALYSIS OF SOUTH INDIA

Chethanamba K. Ramanna[1] **and Goudappa R. Dodagoudar**[2]

[1] Indian Institute of Technology Madras
Chennai 600 036, India
e-mail: ce07d001@smail.iitm.ac.in

[2] Indian Institute of Technology Madras
Chennai 600 036, India
e-mail: goudar@iitm.ac.in

Keywords: Distributed Seismicity, Diffused Seismicity, Seismic Area Source Zone, Fixed Kernel Technique, Adaptive Kernel Technique, Kernel Bandwidth, Peak Ground Acceleration, Uniform Hazard Spectra.

Abstract. *Peninsular India is known for its complex intraplate seismicity and the southern part of it is characterized by diffused and distributed seismicity. In such cases the most commonly adopted seismic source is the area source zone. The formation of seismic area source zone is subjective for regions such as south India and hence zonefree techniques to probabilistic hazard analysis have been carried out in the past. The zonefree technique specifically the kernel technique is still new and has been applied to specific sites in south India such as Chennai and Kanchipuram. In this study the fixed and adaptive kernel techniques have been applied to the whole of south India to obtain the hazard value. The most influencing parameter affecting the kernel technique has been varied in two ways - the bandwidth parameters determined for the whole earthquake catalogue of south India and the other by determining the bandwidth parameters for the earthquakes lying in an influence area of 300 km radius around a particular site. It was observed that the adaptive kernel technique yielded slightly higher hazard values in regions of high seismic activity and lower values in regions of low seismic activity. However both the techniques yielded similar results in regions of spatial uniform seismicity. A significant difference was observed in the uniform hazard spectra obtained for specific sites in south India when the bandwidth parameters were estimated considering whole of south India (regional) and an influence area of 300 km radius (local).*

1 INTRODUCTION

Seismic Hazard Analysis (SHA) is carried out to provide ground shaking values in the form of acceleration, velocity or displacement to determine the seismic input to be considered in the design of buildings. SHA is carried out in two ways – probabilistic or deterministic. In probabilistic seismic hazard analysis (PSHA), uncertainties in the earthquake location, magnitude and path of travel are considered. In deterministic seismic hazard analysis (DSHA), the ground shaking value is determined considering the worst case for location, magnitude and path of travel of the earthquake. This form of analysis is usually carried out for very important structures e.g. nuclear power plant facilities. However PSHA is the most commonly used form of hazard analysis; and the most widely used technique is the Cornell-McGuire approach [1, 2]. The first step in the conventional PSHA is the identification and characterization of the seismic sources. These sources may be in the form of point, line or area seismic source zone. The low to moderate seismicity regions are often characterized by diffused and distributed seismicity and hence the most common form of seismic source adopted is the area source zone.

The Cornell-McGuire approach to PSHA has been found to have several drawbacks when applied to some specific site conditions. These drawbacks are as follows:

1. Insufficient data to fit the G-R recurrence relation for low seismicity regions [3].
2. Difficulty in satisfying the homogeneity condition (*b* value constant) within an area source zone [4].
3. Areal extent of applicability of G-R recurrence law not known [5, 6].
4. Sudden change of seismicity at the zonal boundaries [7].
5. Expert knowledge of geology, seismology and tectonics required to form source zones [8, 9].

Probability theory provides several latest techniques of estimating the probability density function (PDF) for a given set of data viz. kernels, splines and wavelets. Hence, it is important to adopt new and also the most appropriate techniques available in probability theory in determining the density. Such techniques need to be implemented in seismic hazard analysis to help overcome some of the drawbacks of the conventional methodology.

2 KERNELS

Density estimation techniques can be broadly classified as parametric and nonparametric techniques. In the nonparametric techniques no prior assumption regarding the distribution is made, but is derived from the data in hand. The simplest technique under this category is the histogram and some latest techniques such as kernels, splines and wavelets can be found. Among the newer techniques, the kernel density estimation technique is the simplest one which consists of placing standard curves such as uniform, triangular, normal or quartic on each of the data point and the density is determined as the normalized sum of each of these individual kernels (Fig. 1).

Kernel density estimation technique has been popular in many areas of earthquake engineering such as hazard analysis [10], seismic occurrence rate determination [11], determination of influence area of an earthquake [12] and source size characterization to name a few. The kernel technique to seismic hazard analysis has already been applied to a few sites in south India such as Chennai [13, 14] and Kanchipuram [15] where the results matched well with the Cornell-McGuire approach.

There are two variables to be considered in kernel density estimation – shape of the kernel to be used and the spread of the kernel also known as the bandwidth or window width. Figure

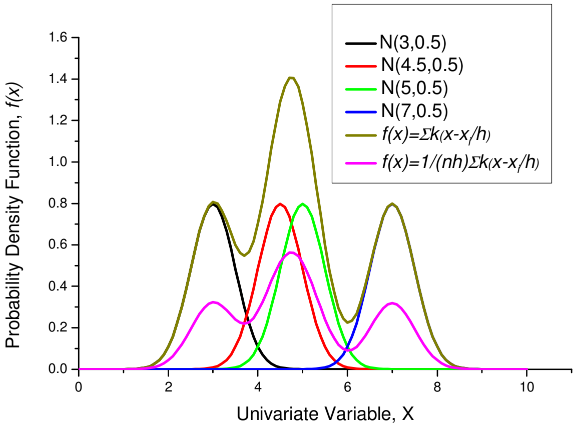

Figure 1: Kernel density estimation concept.

2 shows the various forms of kernels being placed on individual data points (say 7, 8, 9, 12 and 14) and the final form of the PDF obtained. It can be concluded that the shape of the kernel does not play an important role as the final PDF obtained is insensitive to the form of kernels used. However there are several works by previous researchers [16, 17, 18] stressing the importance of the bandwidth. The optimal bandwidth to be used for a data set can be fixed across the data or can be varied. The former is called the fixed kernel density estimation technique while the latter is called the variable or adaptive kernel density estimation technique.

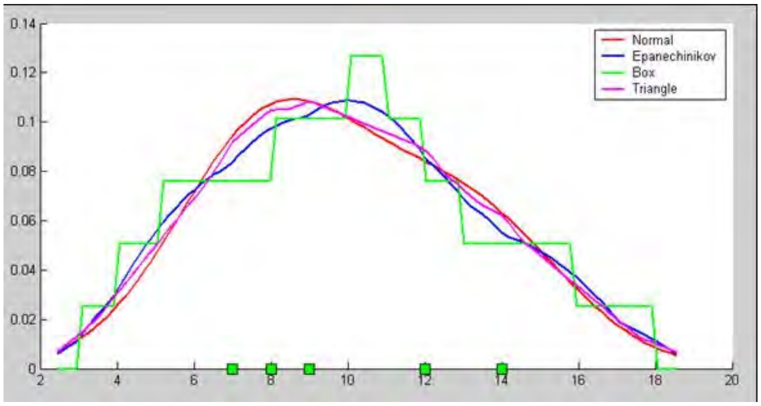

Figure 2: Various forms of kernels [de SMITH et al.[19]]

2.1 Fixed kernel density estimation technique

In the fixed kernel density estimation technique, the bandwidth or spread of the kernel function placed on the data are same across all the data. Consider the probability distribution of a random variable *X* given as

$$P(a \le X \le b) = \int_a^b f(x)\, dx \tag{1}$$

where *f*(*x*) is the PDF, *a* and *b* are the selected lower and upper bounds. A univariate PDF from the fixed kernel technique is given as

$$f(x) = \frac{1}{nh}\sum_{i=1}^{n} K\left(\frac{x - x_i}{h}\right) \tag{2}$$

where n is the number of data or observation, h is the fixed bandwidth which controls the variance of the symmetric function $K((x\text{-}x_i)/h)$, x is any point and x_i is the data. A multivariate PDF in d-dimensional space from the fixed kernel technique is given as

$$f(x) = \frac{1}{nh^d}\sum_{i=1}^{n} K\left\{\frac{1}{h}(\mathbf{x} - \mathbf{x}_i)\right\} \tag{3}$$

The kernel K considered must satisfy the following conditions

$$\int_{R^d} K(t)dt = 1, \; \int_{R^d} tK(t)dt = 0, \text{ and } \int t^2 K(t)dt = k_2 \neq 0$$

and the unknown density f has a continuous derivatives of all orders required and the constant k_2 is the variance of K.

There are several methods of determining the optimal bandwidth in the literature [16, 17, 18] and are summarized as the least-square cross validation, biased cross validation, plug-in bandwidth selection, smoothened cross validation, root-n bandwidth selection and the contrast methods [20].

2.2 Adaptive kernel density estimation technique

In adaptive kernel density estimation technique the bandwidth is varied depending on the spatial location of the data. It follows the principle that smaller bandwidth is more appropriate in regions of high density since a larger number of samples enable a more accurate estimation of density in these regions. From Fig. 3a it can be observed that larger bandwidth leads to over smoothing whereas smaller bandwidth leads to spiky PDF (Fig. 3b). A larger bandwidth is more appropriate in low density areas where a few sample points are available.

—— Final density estimate ······ Individual kernels

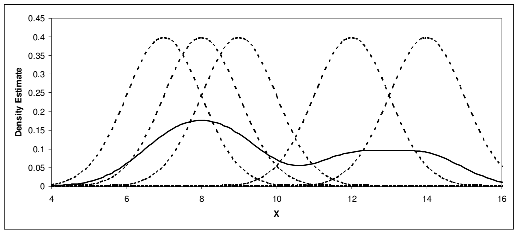

Figure 3a: Large bandwidth kernels

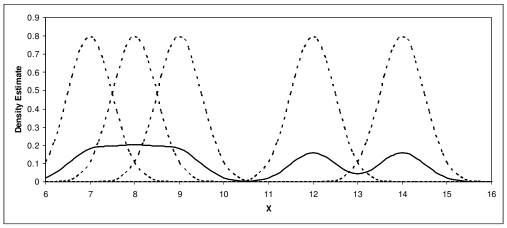

Figure 3b: Small bandwidth kernels

The PDF from the adaptive kernel technique is determined as

$$f(\mathbf{x}) = \frac{1}{n}\sum_{i=1}^{n} \frac{1}{[h(\mathbf{x}_i)]^d} K\left\{\frac{1}{h(\mathbf{x}_i)}(\mathbf{x} - \mathbf{x}_i)\right\} \tag{4}$$

There are several techniques of varying the bandwidth, however in the present study, a three step procedure has been adopted [16] and is given as

1. Find a pilot estimate of $f(\mathbf{x})$ that satisfies $f(\mathbf{x}_i) > 0$ for all i
2. Define local bandwidth factor λ_i by

$$\lambda_i = \{f(\mathbf{x}_i)/g\}^{-\alpha} \tag{5}$$

where g is the geometric mean of $f(\mathbf{x}_i)$ given as

$$\log g = n^{-1}\sum \log f(\mathbf{x}_i) \tag{6}$$

and α is the sensitivity parameter ($0 \leq \alpha \geq 1$).

3. Define the adaptive kernel estimate $f(\mathbf{x})$ by

$$f(\mathbf{x}) = n^{-1}\sum_{i=1}^{n} h^{-d}\lambda_i^{-d} K\left\{h^{-1}\lambda_i^{-1}(\mathbf{x}-\mathbf{x}_i)\right\} \tag{7}$$

where h is the global bandwidth.

When α is 0, the estimate reduces to fixed kernel and a value closer to 1 causes the estimate to become more sensitive to the variation in bandwidth from point to point. A value of $\alpha = 0.5$ has been proven to give good results [16, 21]. The above three step procedure has been used to arrive at the earthquake occurrence model by smoothing the annual activity for Australia and New Zealand [11].

2.3 Implementation of kernels in seismic hazard analysis

In PSHA, the mean annual rate of exceedance λ_{y^*} of the selected ground motion parameter Y (acceleration, velocity or displacement) exceeding a particular value y^* is given by

$$\lambda_{y^*} = \sum_{i=1}^{N_S}\sum_{j=1}^{N_M}\sum_{k=1}^{N_R} \upsilon_i \, P\left[Y > y^* \mid m_j, r_k\right] P\left[M = m_j\right] P\left[R = r_k\right] \tag{8}$$

where N_s is the number of sources, N_M is the range of magnitudes, N_R is all the possible range of distances from site to source, υ_i is the seismicity rate for each source defined by the G-R recurrence law, $P[Y>y^* \mid m_j,r_k]$ is obtained from the attenuation relationship, $P[M = m_j]$ and $P[R = r_k]$ are obtained from the probability density function of magnitude and distance respectively. In kernel approach, the seismicity rate υ_i is replaced by the spatial activity rate density function given as

$$\upsilon(M, x) = \sum_{i=1}^{N} \frac{K(M, x - x_i)}{T_i} \tag{9}$$

where N is the number of earthquake events, x is the observation/estimation point and T_i is the effective return period evaluated using the following expression:

$$T_i = Timeperiod \sum_i p_i \tag{10}$$

where p_i is the detection probability of the event in a particular time period and a numerical value is assigned to it based on the seismicity of the region.

An anisotropic kernel form used for earthquakes [22] is given as

$$K(M, r) = \frac{n-1}{\pi h^2(M)} \frac{1+\delta\cos^2\phi}{1+(\delta/2)} \left(1 + \left(\frac{r}{h(M)}\right)^2\right)^{-n} \tag{11}$$

where n is the exponent of the power law or fractal scaling index taking value between 1.5 and 2, h is the bandwidth and is a function of magnitude, r is the distance to the epicentre, the parameter ϕ is the angle subtended at r between the intersection of the fault plane with the earth's surface and the epicentre location and δ is the degree of anisotropy taking value between 0 and 2. A value of zero indicates isotropy and higher value signifies anisotropy. Anisotropic kernel is useful when the activity rate associated with a fault needs to be determined. However in this study, isotropic kernel was used since most parts of south India are known for distributed seismicity.

The most important step in kernel technique is to arrive at an optimal bandwidth keeping in mind the earthquake phenomenon. For this the power law which takes into consideration the fractal behaviour of the earthquakes is used [10] and is given as

$$h(M) = ce^{(dM)} \tag{12}$$

where parameters *c* and *d* depend on the spatial distribution of earthquake epicentres. These parameters are calculated by forming various magnitude bins and for each earthquake event within the bin, the distance to the nearest epicentre is determined. The mean nearest distance for each bin is obtained and through a least-square fit between the magnitude and bandwidth, the parameters *c* and *d* are obtained.

It has been observed by previous studies [23, 24] that the fixed kernel technique yields similar results for low to moderate seismicity regions and lower values in high seismicity regions when compared to the Cornell-McGuire approach. The adaptive kernel technique has been used to determine the seismic hazard for Chennai City [14]. It is concluded that the adaptive technique yielded similar results to the fixed kernel technique since Chennai city lies in low to moderate seismicity region and it needs to be tested for other regions. Hence in this study an attempt has been made to evaluate the suitability of the kernel techniques to the other regions of south India and on a much larger scale.

3 GEOLOGY, SEISMOLOGY AND TECTONIC SETTINGS OF SOUTH INDIA

South India mainly consists of four states – Andhra Pradesh, Karnataka, Kerala and Tamil Nadu lie on Deccan Trap which is a part of Peninsular India. The movement of the Indian plate northward from rest of the Gondwana over geologic hotspots caused the melting of the Indian craton underneath. The melting broke out on the surface of the craton creating the Deccan Trap. Hence the Deccan Trap was formed as a result of sub-aerial volcanic activity during the Mesozoic era. Peninsular India is one of the oldest land masses of the earth's crust and is the most stable Precambrian Shield subjected to tectonic and orogenic activities in its subsequent geological history. The region is bounded by Western Ghats (WG) along the coast line and similarly the Eastern Ghats (EG) on the eastern coast line.

Seismically south India has experienced less seismic activity and the earthquakes are due to intraplate seismicity and hence are very complex. Although several faults have been identified in the region [25, 26], there movement has not been recorded. Hence the seismicity is distributed in nature and also diffused. There are several anomalies regarding the seismicity of this region. Wang et al.[27] noted that there is no major deformation of the Peninsular region based on the velocity reading observed at two stations – one located in the northern Ganges plain and the other in Bengaluru located in Karnataka state and hence no major seismic activity. Bilham[28] on the other hand noted that the Indian plate has undergone sufficient flexure (Fig. 4) resulting in major earthquakes such as Koyna (M_w = 6.3, 1967), Latur (M_w = 6.1,1993), Jabalpur (M_w = 5.8,1997) and Bhuj (M_w = 7.7,2001) in Peninsular India. However most of the earthquakes that have occurred in south India are mild and shallow-depth earthquakes. The average focal depths of the earthquakes in these regions are within the upper-crustal (0-12 km) layers complying with the depth of the Moho varying from 34 to 41 km beneath the region of southern India [27].

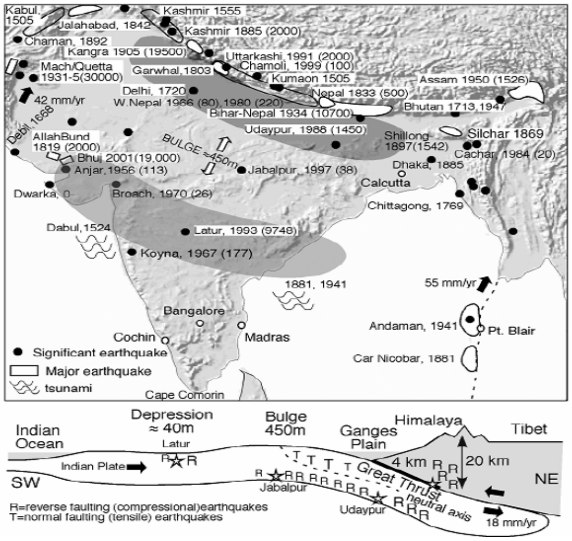

Figure 4: Schematic views of Indian tectonics [Bilham[28]]

The India tectonic plate is currently penetrating into the Eurasian plate at a rate of approximately 45 mm/year along with an anticlockwise rotation in the Indian plate (Fig. 5).

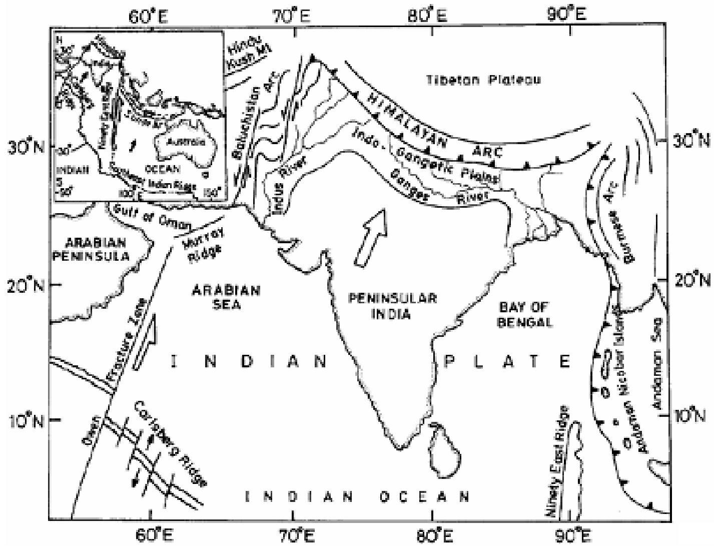

Figure 5: Tectonic map of the northern Indian plate [Biswas and Majumdar[30]]

South India’s major tectonic features are seen in Fig. 6. A major compression zone lying over the transition zone running from Mulki in the west to Pulicat late located on the east has been observed [31]. It has been formed due to the continuous spreading of the sea floor in the Indian Ocean. This zone acts has a major block and hence numerous earthquakes of smaller magnitude are observed around this region. However major earthquakes are observed north of this zone (Latur, Jabalpur). The Southern Granulite Terrain (SGT) Craton has several lineaments and notable earthquakes have occurred in this region (Coimbatore and Pondicherry). The Caddapah Basin forms part of the extended stable continental region and consists of the Pampar lineament and the east-west trending Tiruttani swarms of lineaments.

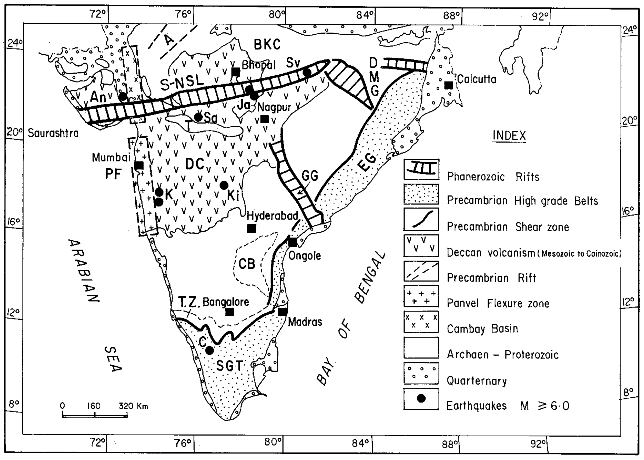

Figure 6: Broad tectonic units in Peninsular India along with significant earthquakes that occurred with $M_w = 6.0$ and above [Rao[32]]

4 SEISMIC HAZARD ANALYSIS

Seismic hazard analysis for south India (4.667°N to 17.889°N and 70.409°E to 85.687°E) was carried out using two approaches - the fixed and the adaptive kernel techniques. Peak ground acceleration (PGA) contour maps for 475 years return period (10% probability of exceedance in 50 years) were developed using both the kernel techniques by calculating the bandwidth parameters considering the whole south Indian region. The uniform hazard spectra (UHS) for four sites were determined – one by using the bandwidth parameters determined for the whole of south India (regional parameters) and the other by determining the bandwidth parameter for the influence area of 300 km radius around the site (local parameters). The sites chosen were: Site 1 (12.685°N 78.414°E) close to Bengaluru, Site 2 (15.597°N 80.032°E) close to Ongole, Site 3 (17.322°N 73.804°E) close to Koyna, Site 4 (13.0833°N 80.2833°E) Chennai city. Site 1 is characterized by numerous small earthquakes, Site 2 is a seismically active region in south India, Site 3 is characterized by reservoir induced seismicity and Site 4 is characterized by non uniform earthquake epicentre distribution. An average hypocentral depth of 17 km was considered for all the earthquakes.

4.1 Earthquake catalogue processing

A reliable earthquake catalogue fundamental in the estimation of regional seismicity rate is not readily available for south India due to various reasons ranging from lack of detailed historical records to probable seismic quiescence in the past. Hence in the present study, the earthquake catalogue compiled by Menon et al.[33] from 1063 A.D. to 2008 A.D. for 2°N to 20°N and 76.2°E to 80.4°E region was used for the analysis. This would also facilitate a one-to-one comparison of the results. The dependent events (foreshocks and aftershocks) were removed by using the dynamic windowing technique [34]. This resulted in a Poissonian earthquake catalogue with 750 events of $M_w \geq 3.5$ (Fig. 7).

The Poissonian earthquake catalogue was used in determining the bandwidth parameters for the whole region (4.667°N to 17.889°N and 70.409°E to 85.687°E) by forming various magnitude bins. In each bin the bandwidth was determined as the average of the minimum distances among the epicentre. Table 1 shows the average minimum distance determined for each magnitude bin.

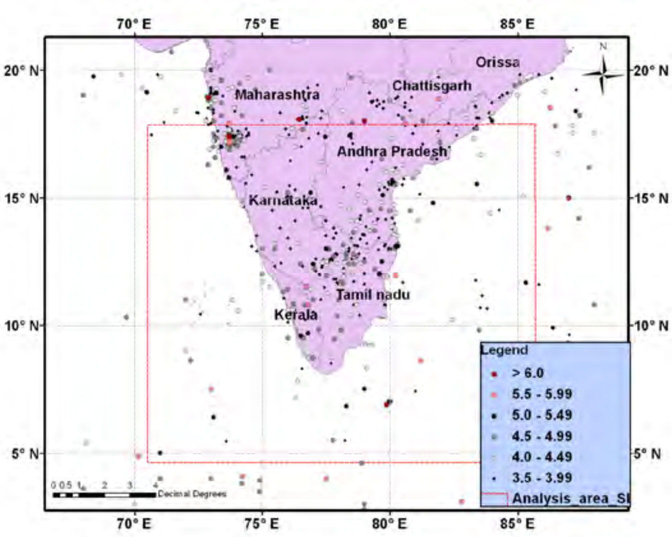

Figure 7: Epicentre distribution and analysis area for south India.

Magnitude (M_w)	Bandwidth (H) in km
3.75	27.0575
4.25	43.4948
4.75	68.4529
5.25	117.5171
5.75	287.4365
6.25	501.6688

Table 1: Bandwidth for magnitude bins.

Figure 8 shows the bandwidth parameters obtained from the curve. The reference year was determined by assigning various probability of detection for each magnitude bin separately for onshore and offshore earthquakes.

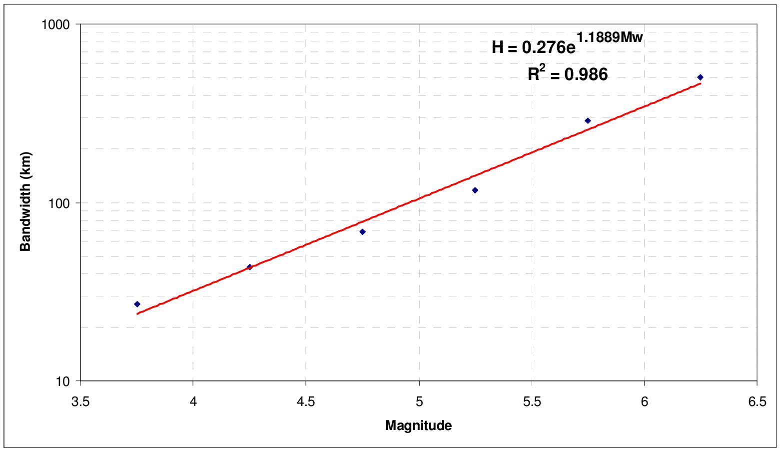

Figure 8: Magnitude-bandwidth relation to estimate the parameter c and d.

As an example the probability of detection for magnitude bin 4.0 to 4.49 for both onshore and offshore earthquakes is given in Table 2. The reference year so obtained is summarized in Table 3.

Time period (D_i)	Onshore		Offshore	
	Probability (p_i)	Effective return period (p_iD_i)	Probability (p_i)	Effective return period (p_iD_i)
1000 - 1500	0.05	25	0.005	2.5
1500 - 1800	0.15	45.00	0.05	15.00
1800 - 1850	0.25	12.50	0.15	7.50
1850 - 1900	0.35	17.50	0.25	12.50
1900 - 1950	0.50	25.00	0.30	15.00
1950 - 1960	0.60	6.00	0.50	5.00
1960 - 1970	0.75	7.50	0.65	6.50
1970 - 1980	0.85	8.50	0.75	7.50
1980 - 1985	0.88	4.40	0.80	4.00
1985 - 1990	0.92	4.60	0.85	4.25
1990 - 1995	0.95	4.75	0.90	4.50
1995 - 2000	0.98	4.90	0.95	4.75
2000 - 2005	0.98	4.90	0.98	4.90
2005 - 2008	0.98	2.94	0.98	2.94

Table 2: Probability assignment for various time periods.

Magnitude bin (M_w)	Reference year	
	Onshore	Offshore
> 6.0	1639	1764
5.5 - 5.99	1687	1836
5.0 - 5.49	1736	1860
4.5 - 4.99	1785	1884
4.0 - 4.49	1835	1914
3.5 - 3.99	1882	1951

Table 3: Reference year for each magnitude bin.

4.2 Attenuation relationship

The ground motion parameter gets attenuated from source to site. The resulting ground motion at the site is determined using the attenuation relationship. These attenuation relationships are empirical equations which estimate the ground motion parameter as a function of independent parameters characterizing the earthquake and the site.

The attenuation relationship suggested by the Working Committee of Experts for microzonation of the Indian landmass formed by the National Disaster Management Authority (Iyengar et al.)[35] was used. The functional form of the attenuation relationship is

$$\ln\left(\frac{S_a}{g}\right) = C_1 + C_2M + C_3M^2 + C_4r + C_5\ln\left(r + C_6e^{C_7M}\right) + C_8\log(r)f_0 \tag{13}$$

where S_a is the spectral acceleration, r is the hypocentral distance in kilometers, M is the earthquake moment magnitude and $f_0 = \max(\ln(r/100),0)$. The attenuation relationship accounts for geometrical spreading, anelastic attenuation and magnitude saturation. The attenuation coefficients for different regions can be used to construct the mean and response spectrum on A-type rock in any part of India. It was developed from a simulated database of 80,000 samples by a two step stratified regression following Joyner and Boore[36] approach. However, in the present study, the coefficients calculated for south India were used.

5 RESULTS AND DISCUSSION

The hazard was estimated by forming a grid of 0.5° × 0.5° over the study region (4.667°N to 17.889°N and 70.409°E to 85.687°E). At every grid point, an influence area of 300 km radius was considered and all earthquakes lying within this area were considered for analysis. The density was estimated at every 10 km. The minimum cut-off magnitude considered for hazard analysis was $M_w = 4.0$. Magnitude uncertainty of ±0.49 was considered for every magnitude. The PGA obtained for 475 years return period from the fixed kernel technique considering bandwidth parameters calculated for the whole south Indian region is shown in Fig. 10a. Similarly the PGA obtained for 475 years return period from the adaptive kernel technique is shown in Fig 10b.

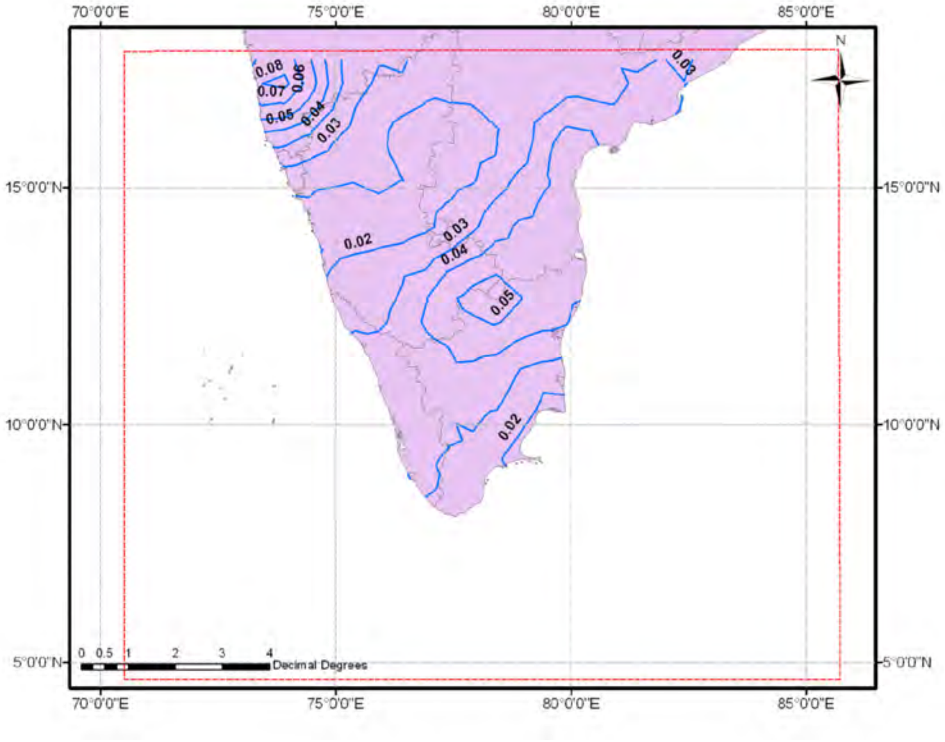

Figure 10a: PGA for 475 years return period by fixed kernel technique

It can be seen that the PGA values marginally differ among the two kernel techniques. Also the hazard value obtained for 475 years return period is quite low when compared to previous studies carried out for a few regions of the study area. Table 4 presents the PGA values for Chennai, Bengaluru, Koyna and Ongole for 475 years return period.

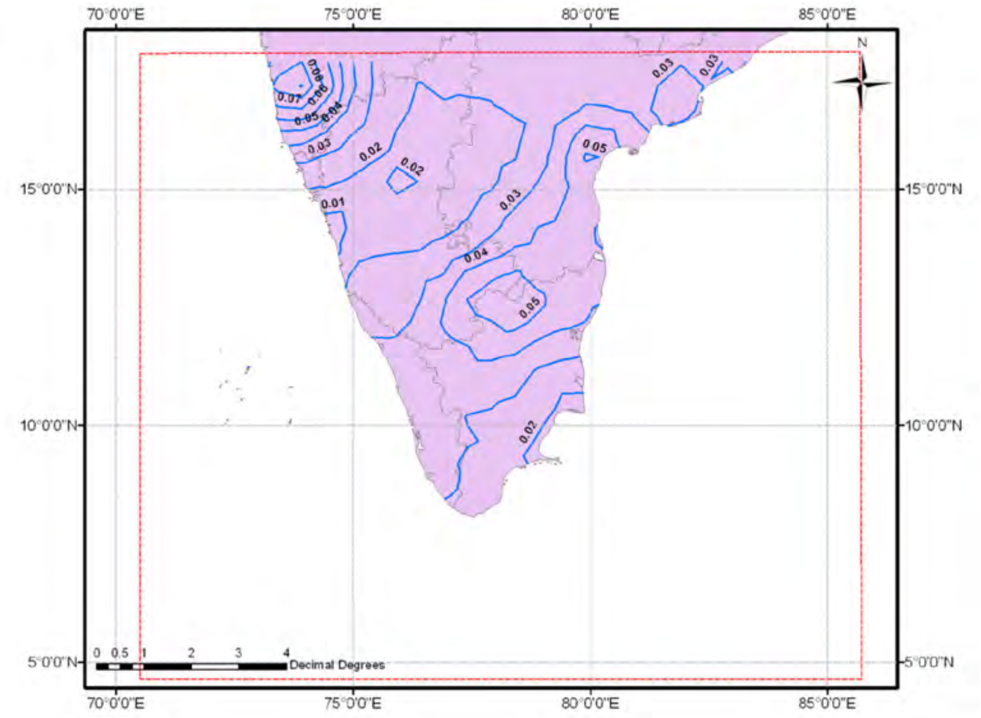

Figure 10b: PGA for 475 years return period by Adaptive kernel technique

Site	Studies	PGA (g)
Chennai	Iyengar et al.[35]	0.06
	Ramanna and Dodagoudar [13,14]	0.08
	Fixed kernel (present study)	0.04
	Adaptive kernel (present study)	0.04
	Jaiswal and Sinha[39]	0.03
	IS 1893:2002[37]	0.08
Bengaluru	Iyengar et al.[35]	0.03
	Vipin et al.[38]	0.10
	Fixed kernel (present study)	0.05
	Adaptive kernel (present study)	0.05
Koyna	Iyengar et al.[35]	0.12
	Jaiswal and Sinha[39]	0.2
	Fixed kernel (present study)	0.07
	Adaptive kernel (present study)	0.08
Ongole	Iyengar et al.[35]	0.06
	Fixed kernel (present study)	0.04
	Adaptive kernel (present study)	0.05

Table 4: PGA for various regions in south India from previous studies

The UHS were determined for the selected regions by calculating the bandwidth parameters considering the earthquake epicentres lying within the influence area of 300 km radius from the site. The bandwidth parameters so obtained for four different sites are summarized in Table 5.

Site	c	d
Site 1	0.4616	0.9678
Site 2	0.9441	0.8459
Site 3	0.3013	0.9227
Site 4	3.5285	0.4675

Table 5: Bandwidth parameters for various sites

The UHS for these sites are shown in Fig. 11a to 11d. It can be observed that there exist large differences in spectral values due to change in the way the bandwidth parameters were determined. For Site 1 a percentage difference in peak spectral value of 8% (percentage calculated with respect to fixed technique) is seen between the kernel techniques irrespective of whether the parameter was determined at local level or regional level. However a difference of 10% (percentage calculated with respect to local parameters) was observed in the peak spectral value for fixed technique when the bandwidth parameters were varied. For adaptive technique

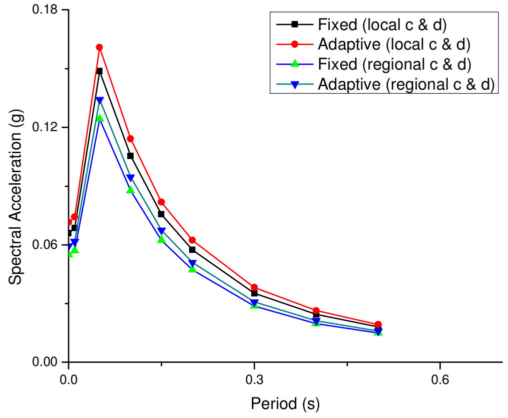

Figure 11a: Impact on UHS for Site 1

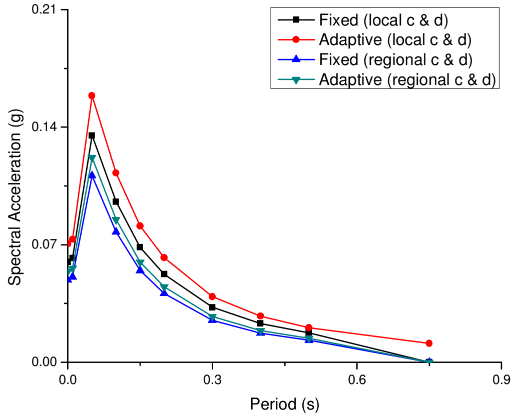

Figure 11b: Impact on UHS for Site 2

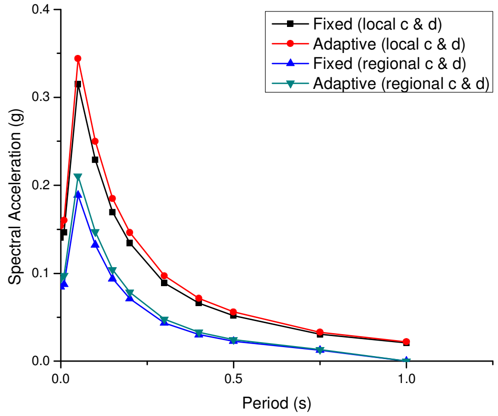

Figure 11c: Impact on UHS for Site 3

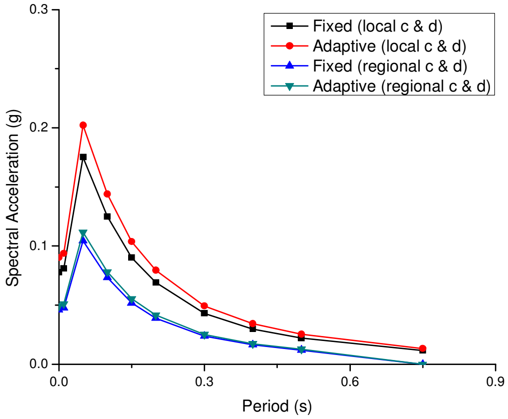

Figure 11d: Impact on UHS for Site 4

a difference of 16.5% (percentage calculated with respect to local parameters) was observed in the peak spectral value when the parameters were varied. The % difference in the peak spectral values for all the four sites are summarized in Table 6.

Site	% Difference between fixed and adaptive kernel techniques		% Difference between local and regional parameters	
	Using local parameters	Using regional parameters	for fixed technique	for adaptive technique
Site 1	8	8	10	16.5
Site 2	17.5	10	18	23
Site 3	9	11.5	40	38
Site 4	15.4	7	40	45

Table 6: Impact on peak spectral acceleration

6 CONCLUSIONS

Seismic hazard analysis has been carried out for whole of south India using the fixed kernel and adaptive kernel technique. It was found that the hazard results varied among the kernel and adaptive kernel technique in regions of very high seismic activity and in regions of very low seismic activity. In regions of very high seismic activity, the adaptive kernel technique resulted in slightly higher results (Ongole and Koyna) and in regions of low seismicity, it yielded lower values (Northern Karnataka region) when compared to fixed kernel technique. Further the impact on the hazard value by varying the bandwidth parameter was analyzed. An important observation was made that there was significant difference in the hazard values when the bandwidth parameter was calculated for smaller region (regional seismicity) and larger region (south India catalogue). The difference was more noticeable for Site 3 and Site 4. Hence it is very important to carry out further study on the influence of the bandwidth parameter on the seismic hazard analysis. With regards to the technique, the adaptive kernel technique is more appropriate kernel technique since it takes into consideration the spatial clustering of the earthquake epicentres.

REFERENCES

[1] C.A. Cornell, Engineering seismic risk analysis. *Bulletin of the Seismological Society of America,* **58**, 1583-1606, 1968.

[2] R.K. McGuire, W.J. Abrabasz, An introduction to probabilistic seismic hazard analysis, in S. H. Ward. Ed. *Geotechnical and Environmental Geophysics, Society of Exploration Geophysicists,* **1**, 333-353, 1990.

[3] C. Beauval, O. Scotti, Mapping b-values in France using two different magnitude ranges: possible non power-law behaviour. *Geophysical Research Letters,* **30(*17*)**, 4, 2003.

[4] C. Beauval, O. Scotti, F. Bonilla, The role of seismicity models in probabilistic seismic hazard estimation: Comparison of a zoning and a smoothing approach. *Geophysical Journal International,* **165**, 584-595, 2006a.

[5] C.R. Allen, P. Amand, St, C.F. Richter, J.M. Nordquist, Relationship between seismicity and geologic structure in the southern California region. *Bulletin of the Seismological Society of America,* **55(4)**, 753-797, 1965.

[6] E.L. Krinitzsky, Earthquake probability in engineering – Part 2: Earthquake recurrence and limitations of Gutenberg-Richter b-values for the engineering of critical structures The Third Richard H. Jahns Distinguished Lecture in Engineering Geology, *Engineering Geology,* **36**, 1-52, 1993.

[7] B. Bender, Modelling Source zone boundary uncertainty in seismic hazard analysis. *Bulletin of the Seismological Society of America,* **76(2)**, 329-341, 1986.

[8] S.L. Kramer, *Geotechnical Earthquake Engineering*, New Jersey: Prentice Hall, Englewood Cliffs, 1996.

[9] L. Reiter, *Earthquake Hazard Analysis: Issues and Insights.* New York, Columbia University Press, 1991.

[10] G. Woo, Kernel estimation methods for seismic hazard area source modeling. *Bulletin of the Seismological Society of America,* **86(2)**, 353-362, 1996.

[11] C. Stock, E.G.C. Smith, Adaptive kernel estimation and continuous probability representation of historical earthquake catalogs. *Bulletin of the Seismological Society of America,* **92(3)**, 904-912, 2002.

[12] Y. Chen, J. Liu, L. CHEN, Q. CHEN, S. CHAN, Global seismic hazard assessment based on area source model and seismicity data. *Natural Hazards,* **17**, 251-267, 1998.

[13] C.K. Ramanna, G.R. Dodagoudar, Probabilistic seismic hazard analysis using kernel density estimation technique for Chennai, India. *Georisk, DOI: 10.1080/17499518.2010.496073,* 2010.

[14] C.K. Ramanna, G.R. Dodagoudar, Seismic Hazard Analysis Using Adaptive Kernel Density Estimation Technique for Chennai City. *Pure and Applied Geophysics, DOI: DOI 10.1007/s00024-011-0264-8*, 2011.

[15] C.G. Lai, A. Menon, T. Ornthammarath, H.S. Lizarraga, G.R. Dodagoudar, Probabilistic seismic hazard assessment and stochastic site response analysis at the archaeological site of Kancheepuram in southern India. *Research Report No. EUCENTRE-2009/01, Pavia, Italy,* 2009.

[16] B.W. Silverman, *Density estimation for statistics and data analysis,* Monographs on Statistics and Applied Probability, London: Chapman and Hall, 1986.

[17] W.D. Scott, *Multivariate Density Estimation,* New York, John Wiley and Sons, 1992.

[18] M.P. Wand, M.C. Jones, *Kernel Smoothing,* Monographs on Statistics and Applied Probability. London: Chapman and Hall, 1995.

[19] M.J. de Smith, M.F. Goodchild, P.A. Longley, (2009). *Geospatial Analysis – A Comprehensive Guide,* 3rd ed. Leicester: The Winchelsea Press, 2009.

[20] A.R. Mugdadi, I.A. Ahmad, (2004). A bandwidth selection of kernel density estimation of functions of random variables. *Computational Statistics and Data Analysis,* **47**, 49-62, 2004.

[21] I. Abramson, On bandwidth variation in kernel estimates – a square root law. *The Annals of Statistics,* **10**, 1217-1223, 1982.

[22] D. Vere-Jones, Statistical methods for the description and display of earthquake catalogs. *In*: A. T. Walden and P. Guttorp, eds. *Statistics in the Environmental and Earth Sciences.* London: Arnold Publishers, 220-246, 1992.

[23] S. Molina, C.D. Lindholm, H. Bungum, Probabilistic seismic hazard analysis: Zoning free versus zoning methodology, *Bollettino Di Geofisica Teorica Ed Applicata*, **42(1-2)**, 19-39, 2001.

[24] C. Beauval, O. Scotti, F. Bonilla, The role of seismicity models in probabilistic seismic hazard estimation: Comparison of a zoning and a smoothing approach. *Geophysical Journal International*, **165**, 584-595, 2006b.

[25] S.M. Ramasamy, S. Balaji, Remote sensing and Pleistocene tectonics of Sothern Indian peninsula. *International Journal of Remote Sensing,* **16(13)**, 2375-2391, 1995.

[26] S.M. Ramasamy, Remote sensing and active tectonics of south India. *International Journal of Remote Sensing*, **27**(20), 4397-4431, 2006.

[27] Q. Wang, Z. Pei-Zhen, J.T. Freymueller, R. Bilham, K.M. Larson, L. Xi'an, X. You, Z. Niu, J. Wu, Y. Li, J. Liu, Z. Yang, Q. Chen, Present day crustal deformation in China constrained by global positioning measurements. *Science,* **294**, 574-577, 2001.

[28] R. Bilham, Eathquakes in India and the Himalaya: tectonics, geodesy and history. *Annals of Geophysics,* **47**(2), 839-858, 2004.

[29] P. Mandal, Intraplate stress distribution induced by topography and crustal dsnity heterogenesis beneath the south Indian shield, India. *Tectonophysics,* **302**, 159-172, 1999.

[30] S. Biswas, R.K. Majumdar, Seismicity and tectonics of the Bay of Bengal: Evidence for intraplate deformation of the Northern Indian Plate. *Tectonophysics,* **269**, 323-336, 1997.

[31] K.R. Subrahmanya, Active intraplate deformation in south India. *Tectonophysics*, **262**, 231-241, 1996.

[32] B.R. Rao, Historical seismicity and deformation rates in the Indian peninsular shield. *Journal of Seismology*, **4**, 247-258, 2000.

[33] A. Menon, T. Ornthammarath, M. Corigliano, C.G. Lai, Probabilistic Seismic Hazard Macrozonation of Tamilnadu in Southern India. *Bulletin of the Seismological Society of America*, **100(3)**, 1320-1341, 2010.

[34] J.K. Gardner, L. Knopoff, 1974. Is the sequence of earthquakes in southern California, with aftershocks removed, Poissonian?. *Bulletin of the Seismological Society of America*, **64**(5), 1363-1367, 1974.

[35] R.N.Iyengar, R.K. Chadha, K. Balaji Rao, S.T.G. Raghu kanth, Development of Probabilistic seismic hazard map of India - Final Report. *The National Disaster Management Authority, Govt. of India, New Delhi,* 2010.

[36] W.B. Joyner, D.M. Boore, Peak horizontal acceleration and velocity from strong-motion records including records from the 1979 Imperial Valley, California, Earthquake. *Bulletin of the Seismological Society of America,***71**, 2011-2038, 1981.

[37] Indian Standards, IS 1893: 2002. *Indian standard criteria for earthquake resistant design of structures, Part 1 – General provisions and buildings*, New Delhi, Bureau of Indian Standards, 2002.

[38] K.S. Vipin, P. Anbazhagan, T.G. Sitharam, Estimation of peak ground acceleration and spectral acceleration for south India with local site effects: probabilistic approach. *Natural Hazards and Earth System Sciences*, **9**, 865-878, 2009.

[39] K. Jaiswal, R. Sinha, Probabilistic seismic - hazard estimation for peninsular India, *Bulletin of the Seismological Society of America*, **97(1B)**, 318-330, 2007.

COMPDYN 2011
3rd ECCOMAS Thematic Conference on
Computational Methods in Structural Dynamics and Earthquake Engineering
M. Papadrakakis, M. Fragiadakis, V. Plevris (eds.)
Corfu, Greece, 25–28 May 2011

NONLINEAR DYNAMIC BEHAVIOUR OF A SADDLE FORM CABLE NET MODELED BY AN EQUIVALENT SDOF CABLE NET

Isabella Vassilopoulou and Charis J. Gantes

Metal Structures Laboratory, National Technical University of Athens
9 Iroon Polytechniou, GR-15780 Zografou - Athens, Greece
isabella@central.ntua.gr, chgantes@central.ntua.gr

Keywords: equivalent SDOF model, saddle form cable net, nonlinear dynamic response, similarity relations.

Abstract. *The purpose of this paper is to estimate the geometrically nonlinear dynamic behavior of a saddle form cable net, using an equivalent single-degree-of-freedom model. First, a symmetric simple cable net is assumed, consisting of two crossing cables, considering the vertical displacement of the central node as the only degree of freedom. The equation of motion is found to be similar to the one of the Duffing oscillator with a hardening cubic term. Next, a MDOF symmetric cable net model is considered, with fixed cable ends, having a circular plan view and forming a surface of a hyperbolic paraboloid. Harmonic external loads act vertically on every node of the net, with the same amplitude and time variation. Modal analyses are conducted in order to calculate the linear eigenfrequencies and the corresponding eigenmodes of the network. The nonlinear dynamic response of the cable net is obtained by performing time history analysis. Detecting nonlinear phenomena, such as bending of the response curve, jump phenomena, different response amplitudes according to the initial conditions, superharmonic or subharmonic resonances, demands much computational effort for different load amplitudes and ratios of loading frequency. Based on a method of approximate analysis for prediction of the response of cable nets, the MDOF model is transformed to an equivalent SDOF one, using similarity relations. The analytical solution of the single-degree-of-freedom model can provide, with minimum computational time, the basic information needed for nonlinear dynamic response, i.e. secondary resonances, jump phenomena, dependence on the initial conditions and the exact loading frequency for which the maximum steady state oscillation amplitude is obtained. The comparison between the two models by means of the steady state amplitude of the central node, demonstrates that the behavior of the SDOF model describes satisfactorily the one of the MDOF model, predicting the dominant nonlinear phenomena.*

1 INTRODUCTION

Nonlinear phenomena, such as superharmonic or subharmonic resonances, bending of the response curve and jump phenomena, as well as response amplitudes dependent on the initial conditions, that occur in nonlinear systems [1], are very difficult to be detected in a multi-degree-of-freedom system. The only way to plot a response curve, which can show if the above phenomena take place, is by conducting a large number of nonlinear time history analyses, for different closely spaced load amplitudes and frequencies, but this is a time consuming procedure requiring much computation effort.

The idea of solving an equivalent SDOF system to estimate the dynamic response of a complex structure has been adopted by many researchers ([2]-[9]). This idea is based on equating the energy of the real structure to the one of the SDOF system. Ensuring equal displacements and velocities in both systems, the kinematic similarity is maintained. This approach has the advantage that the equation of motion for a SDOF oscillator can be solved analytically. Hence, it is possible to determine the range of the parameters that influence the dynamic response of the system. On the other hand, it is impossible to assess the overall response of the MDOF system, because the simulation is obtained only in the main direction of motion, neglecting the other two dimensions of the large structure.

Another method of reducing the dimensions of a large scale event, using a smaller one with similar characteristics, is a method based on the Buckingham Pi theorem [10]. This theorem states that if an equation involves a number of variables and k fundamental measurement units, then the equation can be expressed in terms of k fewer arguments that are non-dimensional ratios of the original variables. The concept is based on the notion that an equation must be dimensionally homogeneous, that is, its solution must be invariant to any change in the system of measurement units employed. This technique has been used to design small scale experiments in order to simulate with accuracy large scale phenomena.

Gero ([11], [12]), inspired by this theorem, presented a method to estimate the static behaviour of a large cable net, using charts that describe the behaviour of a smaller one, by means of the maximum deflection and cable tension. The transformation of the large structure to the smaller one was obtained by similarity relations. The proposed method was restricted to nets with fixed cable edges. The two networks should have similar geometries, with the same sag-to-span ratio, so that their corresponding quantities could also be similar.

This latter method was extended by the authors of the present paper to elastically supported cable network structures, by taking into account the characteristics of the edge ring, and more specifically its flexural stiffness E_rI_r ([13] - [15]). Thus, the ring was no longer considered rigid, but elastically deformable, accounting for more realistic boundary conditions for the cables. Additional charts and similarity relations were provided for the preliminary design of the edge ring, including the sag-to-span ratio of the net as a variable in the transformation relations. This method was further developed for the case of dynamic response [16], providing additional similarity relations for the mass and the natural frequency of the system, for the case of fixed cable ends.

This preliminary design method is used in the present work to transform a MDOF cable net, called prototype, into an equivalent SDOF cable net, called model, in order to solve analytically the equation of motion, and thus have the possibility to detect nonlinear phenomena and estimate the nonlinear dynamic response of the large structure. The analytical solution, which plots the steady state amplitude of the equivalent SDOF model, is compared with the steady state response of the MDOF system, obtained numerically. The accuracy of the method is evaluated by means of a numerical example.

2 PROTOTYPE AND MODEL ASSUMPTIONS

The cable net used as prototype, has a diameter L_p=100m and sag-to-span ratio equal to f_p/L_p=1/35 (f_p=2.857m), while the number of cables in each direction is N_p=25 (Figure 1). The Young modulus is assumed equal to E_p=165GPa. The unit weight of the cables is taken equal to ρ_p=100kN/m^3, which corresponds to a concentrated mass on every node equal to:

$$M_p = \frac{2A_p\rho_p L_p}{g(N_p+1)} = 0.151\text{kN}\sec^2 \text{m}^{-1} \tag{1}$$

Uniform harmonic loads, expressed as $P_p(t)=(P_0)_p\cos\Omega_p t$, are assumed to be exerted vertically on every node of the net, having the same amplitude and time variation. The maximum permissible cable stress is assumed equal to the yield stress of the material. In this work the yield stress is assumed equal to 1570MPa considering one of the two most common categories of steel for cables 1570/1770MPa. The oscillation of the central node of the net will be used to describe the response of the net. Raleigh damping [17] is also introduced taking into account damping ratio equal to ζ_p=2%, which is a common value for such structures [18]. The subscript p refers to the prototype.

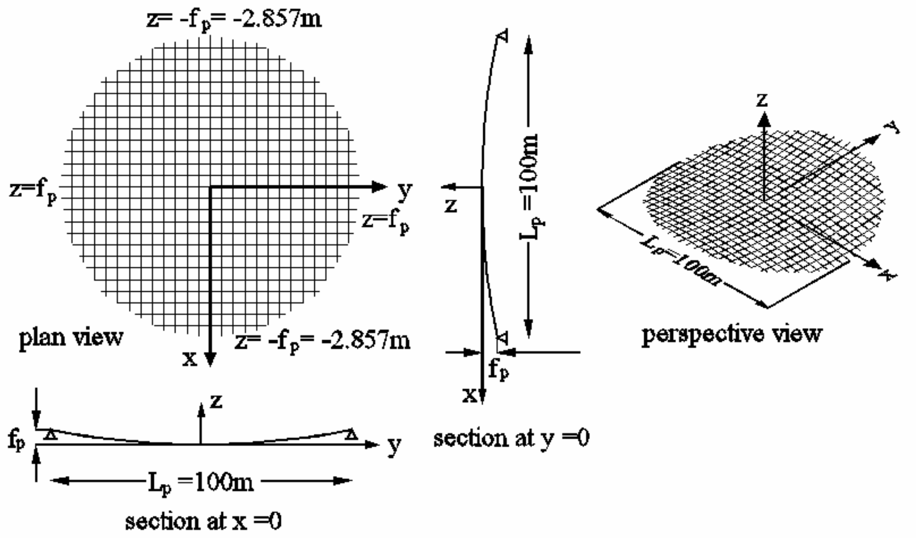

Figure 1: Geometry of the prototype

The model utilized as the equivalent SDOF system consists of two crossing cables (N_m=1), with a concentrated mass at the central node M_m. In order to minimize the scaling error, the model has the same sag-to-span ratio f_m/L_m, cable span L_m, and Young modulus E_m with the prototype. A harmonic load, expressed as $P_m(t)=(P_0)_m\cos\Omega_m t$, is exerted vertically on the central node (Figure 2). The subscript m refers to the model.

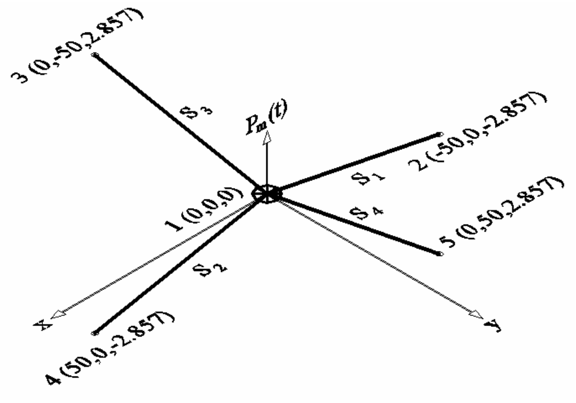

Figure 2: Geometry of the model

3 SIMILARITY RELATIONS

The relations that are used in this work for the transformation of the large cable net (prototype), to the simple one (model), are based on the ones given in [16], for a cable net with fixed cable ends. Taking into account that the sag-to-span ratio, the cable span and the Young modulus are the same for both the prototype and the model, the similarity relations that will be used are the following:

$$(P_0)_m = (P_0)_p \left(\frac{N_p + 1}{N_m + 1} \right)^2 \quad \text{: nodal load amplitude} \qquad (2)$$

$$D_m = D_p \sqrt{\left(\frac{N_p + 1}{N_m + 1} \right)} \quad \text{: cable diameter} \qquad (3)$$

$$A_m = A_p \left(\frac{N_p + 1}{N_m + 1} \right) \quad \text{: cable cross-sectional area} \qquad (4)$$

$$(EA)_m = (EA)_p \left(\frac{N_p + 1}{N_m + 1} \right) \quad \text{: cable axial stiffness} \qquad (5)$$

$$(N_0)_m = (N_0)_p \left(\frac{N_p + 1}{N_m + 1} \right) \quad \text{: cable initial pretension} \qquad (6)$$

$$M_m = M_p \left(\frac{N_p + 1}{N_m + 1} \right)^2 \quad \text{: nodal mass} \qquad (7)$$

$$w_m = w_p \quad \text{: nodal deflection} \qquad (8)$$

$$\omega_m = \omega_p \quad \text{: natural frequency} \qquad (9)$$

where N is the number of cables per direction and E the elastic modulus of the cables, while the subscripts m and p refer to the model and the prototype, respectively. Two more relations are added, describing the loading frequency and the damping ratio:

$$\Omega_m = \Omega_p = \Omega \quad \text{: loading frequency} \qquad (10)$$

$$\zeta_m = \zeta_p = \zeta \quad \text{: damping ratio} \qquad (11)$$

4 ANALYTICAL SOLUTION FOR THE MODEL

4.1 Equation of motion

In this section, the analytical equation of motion of the simple cable net, which consists the model of the method, is derived. The initial pretension is introduced as initial elongation $\varepsilon_{0,m}$ to all cable segments, which, according to Hook’s law, is equal to:

$$(N_0)_m = (EA)_m \varepsilon_{0,m} \tag{12}$$

S_N is the length of each segment at the equilibrium state under pretension, given as:

$$S_N = \sqrt{(L_m/2)^2 + f_m^2} \tag{13}$$

The initial length S_0 for all segments is equal to:

$$\frac{S_N - S_0}{S_0} = \varepsilon_{0,m} \Rightarrow S_0 = \frac{S_N}{1+\varepsilon_{0,m}} = \frac{S_N}{1+\frac{(N_0)_m}{(EA)_m}} \tag{14}$$

If the vertical displacement of the central node is defined as w_m, the deformed lengths of the cable segments are given as:

$$S_{1,2} = \sqrt{(L_m/2)^2 + (f_m + w_m)^2}\ ,\ S_{3,4} = \sqrt{(L_m/2)^2 + (f_m - w_m)^2} \tag{15}$$

The cable tension for each deformed segment is expressed as:

$$(N_i)_m = (EA)\left(\frac{S_i - S_0}{S_0}\right) = (N_0)_m + (EA)_m\left(\frac{S_i - S_N}{S_0}\right),\ i=1,2,3,4 \tag{16}$$

Their components, referring to the global axes, are calculated as:

$$(N_{1,2x})_m=(N_{1,2})_m\cdot(L_m/2)/(S_{1,2}),\quad (N_{1,2z})_m= \pm(N_{1,2})_m\cdot(f_m+w_m)/(S_{1,2})$$

$$(N_{3,4y})_m=(N_{3,4})_m\cdot(L_m/2)/(S_{3,4}),\quad (N_{3,4z})_m= \pm(N_{3,4})_m\cdot(w_m-f_m)/(S_{3,4}) \tag{17}$$

The sum of forces at the central node, referring to the x, y, z global axes, are:

$$(N_x)_m=(N_y)_m=0,\qquad (N_z)_m=(N_{1z})_m - (N_{2z})_m + (N_{3z})_m - (N_{4z})_m \tag{18}$$

Differentiating Eq. (18) with respect to w_m, and considering zero displacement for the unforced and undeformed state, the stiffness coefficient at the prestressed equilibrium state is:

$$K_m = \frac{4(EA)_m}{L_m}\cdot\frac{\left(8\frac{f_m^2}{L_m^2} + 2\frac{(N_0)_m}{(EA)_m} + 8\frac{(N_0)_m}{(EA)_m}\frac{f_m^2}{L_m^2}\right)}{\sqrt{\left(1+4\frac{f_m^2}{L_m^2}\right)^3}} \tag{19}$$

In case a dynamic vertical load $P_m(t)$ is applied on the central node, the equation of motion of this node is expressed in the equilibrium state:

$$M_m\ddot{w}_m + C\dot{w}_m + (N_{1z})_m - (N_{2z})_m + (N_{3z})_m - (N_{4z})_m = P_m(t) \tag{20}$$

The damping C is a function of the damping ratio ζ, expressed as [17]:

$$C=\zeta\cdot C_{cr}=2\zeta M_m\omega_m \tag{21}$$

where ω_m is the natural frequency of the system.

If the dynamic load is expressed as $P_m(t)=(P_0)_m\cos\Omega t$, substituting the expressions of the tension of the cables, given by Eq. (16) and the prestressed, initial and deformed lengths, given by Eqs. (13) - (15), into the vertical components of the cable tensions (Eq. (17)), the differential equation (20) becomes:

$$\begin{aligned} & M_m\ddot{w}_m+C\dot{w}_m-\frac{4(EA)_m(f_m+w_m)}{L_m\sqrt{1+4\frac{(f_m+w_m)^2}{L_m^2}}}+ \\ & +\frac{4(EA)_m(f_m-w_m)}{L_m\sqrt{1+4\frac{(f_m-w_m)^2}{L_m^2}}}+\frac{4w_m\left((EA)_m+(N_0)_m\right)}{L_m\sqrt{1+4\frac{f_m^2}{L_m^2}}}=P_m(t) \end{aligned} \tag{22}$$

Taking into account that the sag-to-span ratio f/L is usually very small for actual cable nets, allowing thus to neglect its second, third or higher powers, Eq. (22), developed in Taylor series, reduces to:

$$\begin{aligned} & M_m\ddot{w}_m+C\dot{w}_m+\frac{16(EA)_m w_m^3}{L_m^3}+ \\ & +\frac{4(EA)_m}{L_m}\cdot\left(8\frac{f_m^2}{L_m^2}+2\frac{(N_0)_m}{(EA)_m}-4\frac{N_0)_m}{(EA)_m}\frac{f_m^2}{L_m^2}\right)w_m=P_m(t) \end{aligned} \tag{23}$$

Expanding the expression of the stiffness K_m, given by Eq. (19), in Taylor series with respect to the term f/L and neglecting terms of $(f/L)^4$, leads to:

$$K_m=\frac{4(EA)_m}{L_m}\cdot\left(8\frac{f_m^2}{L_m^2}+2\frac{(N_0)_m}{(EA)_m}-4\frac{(N_0)_m}{(EA)_m}\frac{f_m^2}{L_m^2}\right) \tag{24}$$

Thus, Eq. (23) can be rewritten as:

$$\ddot{w}_m+\frac{C}{M_m}\dot{w}_m+\frac{K_m}{M_m}w_m+\frac{16(EA)_m}{M_m L_m^3}w_m^3=\frac{(P_0)_m}{M_m}\cos(\Omega t) \tag{25}$$

where a nonlinear cubic term appears with a coefficient depending on the modulus of elasticity of the cable material, the cable cross-section area and the span of the cables.

Nayfeh and Mook [19] thoroughly explored the equation:

$$\ddot{w}+2\varepsilon\mu\dot{w}+\omega_0^2 w+\varepsilon\alpha w^3=K\cos(\Omega t) \tag{26}$$

known as the equation of motion referring to a forced damped Duffing oscillator, with μ being positive, and the coefficient of the nonlinear term α being either positive (hard spring) or negative (soft spring). The equation of motion of the simple cable net, described by Eq. (25), can take the form of Eq. (26), with positive coefficient of the nonlinear term and become:

$$\ddot{w}_m+2\varepsilon\mu\dot{w}_m+\omega_m^2 w_m+\varepsilon\alpha w_m^3=p_m\cos(\Omega t) \tag{27}$$

where:

$$\varepsilon\mu=\zeta\omega_m \tag{28}$$

$$\omega_m = \sqrt{\frac{4(EA)_m}{M_m L_m} \cdot \left(8\frac{f_m^2}{L_m^2} + 2\frac{(N_0)_m}{(EA)_m} - 4\frac{(N_0)_m}{(EA)_m}\frac{f_m^2}{L_m^2} \right)} \tag{29}$$

$$\varepsilon\alpha = \frac{16(EA)_m}{M_m L_m^3} \tag{30}$$

$$p_m = \frac{(P_0)_m}{M_m} \tag{31}$$

The parameter ε is assumed to be small and dimensionless, with ε<1, defining the small scale of the coefficients of the velocity and the cubic term in the equation of motion with respect to the one of the linear term. The exact value of this parameter is not important, because the solution of the problem is independent of ε. It depends only on the parameters εμ and εα, as defined in Eqs. (28) and (30), respectively, meaning that the parameter ε never appears alone in the solution. In what follows the main features of the investigation of the Duffing oscillator are reported from [19].

4.2 Fundamental resonance

In case of fundamental resonance the excitation is assumed to be weak, in order to prove that a weak excitation produces large scale oscillations. The small amplitude of the load is expressed as:

$$\varepsilon p = \frac{(P_0)_m}{M_m} \tag{32}$$

For fundamental resonant conditions, the steady state response is given as:

$$w(t) = a\cos(\Omega t - \gamma) \tag{33}$$

where Ω is the loading frequency expressed as:

$$\Omega = \omega_m + \varepsilon\sigma \tag{34}$$

with εσ a frequency detuning, which, for a given amplitude of the response, is calculated by the following equation:

$$\sigma = \frac{3\alpha a^2}{8\omega_m} \pm \sqrt{\frac{p^2}{4\omega_m^2 a^2} - \mu^2} \Rightarrow \varepsilon\sigma = \frac{3\varepsilon\alpha a^2}{8\omega_m} \pm \sqrt{\frac{(\varepsilon p)^2}{4\omega_m^2 a^2} - (\varepsilon\mu)^2} \tag{35}$$

Taking into consideration Eqs. (28), (30) and (32), Eq. (35) can be rewritten as:

$$\varepsilon\sigma = \frac{6a^2}{\omega_m} \cdot \frac{(EA)_m}{M_m L_m^3} \pm \sqrt{\frac{(P_0)_m^2}{4M_m^2 \omega_m^2 a^2} - (\zeta\omega_m)^2} \tag{36}$$

4.3 Superharmonic resonance

For superharmonic resonant conditions, the steady state response is given as:

$$w(t) = a\cos(3\Omega t - \gamma) + \frac{(P_0)_m}{M_m}\left(\frac{1}{\omega_m^2 - \Omega^2} \right)\cos\Omega t \tag{37}$$

The loading frequency is expressed as:

$$3\Omega=\omega_m+\varepsilon\sigma \tag{38}$$

For a given amplitude of the free oscillation term a, the frequency detuning is calculated by:

$$\sigma=\frac{3\alpha\Lambda^2}{\omega_m}+\frac{3\alpha a^2}{8\omega_m}\pm\sqrt{\frac{\alpha^2\Lambda^6}{\omega_m^2 a^2}-\mu^2}\Rightarrow$$

$$\Rightarrow\varepsilon\sigma=\frac{48\Lambda^2}{\omega_m}\cdot\frac{(EA)_m}{M_m L_m^3}+\frac{6a^2}{\omega_m}\cdot\frac{(EA)_m}{M_m L_m^3}\pm\sqrt{\frac{\Lambda^6}{\omega_m^2 a^2}\cdot\left(\frac{16(EA)_m}{M_m L_m^3}\right)^2-(\zeta\omega_m)^2} \tag{39}$$

where

$$\Lambda=\frac{(P_0)_m}{2M_m}\left(\frac{1}{\omega_m^2-\Omega^2}\right) \tag{40}$$

4.4 Subharmonic resonance

In case of subharmonic resonance, the loading frequency is expressed as:

$$\Omega=3\omega_m+\varepsilon\sigma \tag{41}$$

For a given detuning εσ, subharmonic solutions with non trivial amplitudes ($a\neq 0$) exist only if:

$$\frac{\sigma}{\mu}-\sqrt{\frac{\sigma^2}{\mu^2}-63}\leq\frac{63\alpha}{4\omega_{z0}\mu}\Lambda^2\leq\frac{\sigma}{\mu}+\sqrt{\frac{\sigma^2}{\mu^2}-63}\Rightarrow$$

$$\frac{\varepsilon\sigma}{\zeta\omega_m}-\sqrt{\frac{(\varepsilon\sigma)^2}{(\zeta\omega_m)^2}-63}\leq\frac{256\Lambda^2}{\zeta\omega_m^2}\cdot\frac{(EA)_m}{M_m L_m^3}\leq\frac{\varepsilon\sigma}{\zeta\omega_m}+\sqrt{\frac{(\varepsilon\sigma)^2}{(\zeta\omega_m)^2}-63} \tag{42}$$

where Λ is given by Eq. (40), while for a given Λ subharmonic solution with non trivial amplitudes ($a\neq 0$) exist if:

$$\sigma\geq\frac{63\alpha}{8\omega_m}\Lambda^2+\frac{2\omega_m}{\alpha}\frac{\mu^2}{\Lambda^2}\Rightarrow\varepsilon\sigma\geq\frac{126\Lambda^2}{\omega_m}\cdot\frac{(EA)_m}{M_m L_m^3}+\frac{M_m L_m^3}{8(EA)_m}\frac{\zeta^2\omega_m^3}{\Lambda^2} \tag{43}$$

with amplitude given by:

$$a^2=\left(\sigma\frac{8\omega_m}{9\alpha}-6\Lambda^2\right)\pm\sqrt{\left(\sigma\frac{8\omega_m}{9\alpha}-6\Lambda^2\right)^2-\frac{64\omega_m^2}{81\alpha^2}\left[\left(\sigma-\frac{9\alpha\Lambda^2}{\omega_m}\right)^2+9\mu^2\right]}\Rightarrow$$

$$\Rightarrow a^2=\left(\varepsilon\sigma\frac{\omega_m M_m L_m^3}{18(EA)_m}-6\Lambda^2\right)\pm \tag{44}$$

$$\pm\sqrt{\left(\varepsilon\sigma\frac{\omega_m M_m L_m^3}{18(EA)_m}-6\Lambda^2\right)^2-\frac{M_m^2 L_m^6\omega_m^2}{324(EA)_m^2}\left[\left(\varepsilon\sigma-\frac{9\Lambda^2}{\omega_m}\cdot\frac{16(EA)_m}{M_m L_m^3}\right)^2+9(\zeta\omega_m)^2\right]}$$

In case no subharmonic resonant conditions exist, the steady-state response depends only on the external load:

$$w(t)=\frac{(P_0)_m}{M_m}\left(\frac{1}{\omega_m^2-\Omega^2}\right)\cos\Omega t \tag{45}$$

while, for the non trivial stable solution of a ($a\neq 0$), the response of the nonlinear system at steady-state is:

$$w(t)=a\cos\left(\frac{\Omega t-\gamma_0}{3}\right)+\frac{(P_0)_m}{M_m}\left(\frac{1}{\omega_m^2-\Omega^2}\right)\cos\Omega t \tag{46}$$

5 NUMERICAL EXAMPLE 1

A numerical example is used in order to explain the method. For this example, the cable diameter of the prototype is assumed equal to D_p=50mm, with a cross-sectional area A_p=0.00196m^2. Approximating realistic structures, the initial cable pretension is $(N_0)_p$=600kN, which corresponds to 19% of the yield stress, considering yield stress 1570MPa.

5.1 Transformation of the prototype to the model

Using the similarity relations, the equivalent SDOF model has the following characteristics:

$$D_m=D_p\sqrt{\left(\frac{N_p+1}{N_m+1}\right)}=0.05\sqrt{\left(\frac{26}{2}\right)}=0.18\text{m} \tag{47}$$

$$A_m=A_p\left(\frac{N_p+1}{N_m+1}\right)=0.00196\cdot\frac{26}{2}=0.0255\text{m}^2 \tag{48}$$

$$(EA)_m=(EA)_p\left(\frac{N_p+1}{N_m+1}\right)=165000000\cdot 0.0255=4211697.6\text{kN} \tag{49}$$

$$(N_0)_m=(N_0)_p\left(\frac{N_p+1}{N_m+1}\right)=600\frac{26}{2}=7800\text{kN} \tag{50}$$

$$M_m=M_p\left(\frac{N_p+1}{N_m+1}\right)^2=0.151\cdot\left(\frac{26}{2}\right)^2=25.52\text{kN}\sec^2\text{m}^{-1} \tag{51}$$

5.2 Analytical solution for the SDOF model

5.2.1. Eigenfrequency of the model

The eigenfrequency of the SDOF model is calculated by Eq. (29):

$$\omega_m=8.22\sec^{-1} \tag{52}$$

5.2.2. Fundamental resonance

A load amplitude is chosen for the prototype equal to $(P_0)_p$=1.30kN, corresponding to a nodal load for the SDOF model, equal to:

$$(P_0)_m = (P_0)_p\left(\frac{N_p+1}{N_m+1}\right)^2 = 1.30\cdot\left(\frac{26}{2}\right)^2 = 219.70\text{kN} \tag{53}$$

The load amplitude is chosen large enough to cause nonlinear phenomena, without cable tensile failure. The response curve is based on Eq. (36):

$$\varepsilon\sigma = \frac{6a^2}{\omega_m}\cdot\frac{(EA)_m}{M_m L_m^3} \pm \sqrt{\frac{(P_0)_m^2}{4M_m^2\omega_m^2 a^2} - (\zeta\omega_m)^2} = \left(0.12a^2 \pm \sqrt{\frac{0.27}{a^2} - 0.027}\right)\sec^{-1} \tag{54}$$

while the frequency ratio is calculated as:

$$\frac{\Omega}{\omega_m} = \frac{\omega_m + \varepsilon\sigma}{\omega_m} \tag{55}$$

The amplitude of the steady state response, given by Eq. (54), with respect to the ratio of the loading frequency over the eigenfrequency, is plotted in Figure 3. The bending of the curve indicates the intense nonlinearity of the system. This bending means that jump phenomena are expected to characterize the response of the prototype, multiple response amplitudes dependent on the initial conditions, while the maximum steady state amplitude is predicted for frequency ratio larger than 1.

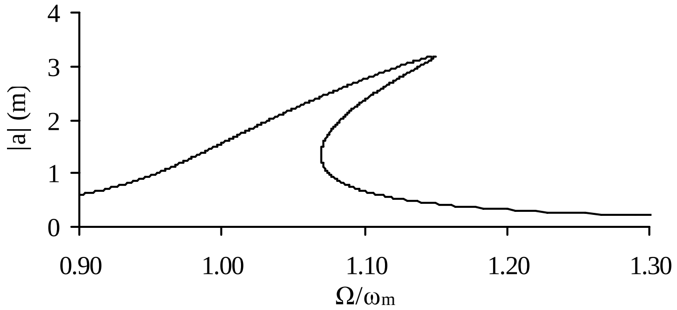

Figure 3: Fundamental resonance: response curve of the SDOF model for load amplitude $(P_0)_m$=219.70kN

5.2.3. Superharmonic resonance

A load amplitude is chosen for the prototype equal to $(P_0)_p$=14kN, corresponding to a nodal load for the SDOF model, equal to:

$$(P_0)_m = (P_0)_p\left(\frac{N_p+1}{N_m+1}\right)^2 = 14\cdot\left(\frac{26}{2}\right)^2 = 2366\text{kN} \tag{56}$$

meaning:

$$\Lambda = \frac{(P_0)_m}{2\cdot M_m}\left(\frac{1}{\omega_m^2 - \Omega^2}\right) = 0.772\text{m} \tag{57}$$

Again, the load amplitude is chosen large enough to cause nonlinear phenomena, without cable tensile failure. The diagram of the steady state response is defined by Eq. (39):

$$\begin{aligned} \varepsilon\sigma &= \frac{48\Lambda^2}{\omega_m}\cdot\frac{(EA)_m}{M_m L_m^3}+\frac{6a^2}{\omega_m}\cdot\frac{(EA)_m}{M_m L_m^3}\pm\sqrt{\frac{\Lambda^6}{\omega_m^2 a^2}\cdot\left(\frac{16(EA)_m}{M_m L_m^3}\right)^2-(\zeta\omega_m)^2} \Rightarrow \\ \varepsilon\sigma &= 0.574\sec^{-1}+0.12a^2(\sec^{-1})\pm\sqrt{\frac{0.022}{a^2}(\sec^{-2})-0.027(\sec^{-2})} \end{aligned} \tag{58}$$

and the frequency detuning is calculated for a given response amplitude. The total response amplitude is given as:

$$w_m = a + 2\Lambda \tag{59}$$

where Λ this time is calculated as:

$$\Lambda = \frac{(P_0)_m}{2\cdot M_m}\left(\frac{1}{\omega_m^2-\Omega^2}\right)=\frac{46.36\text{m}/\sec^2}{(8.22\sec^{-1})^2-\Omega^2} \tag{60}$$

with

$$\Omega = \frac{\omega_m+\varepsilon\sigma}{3} \tag{61}$$

The response diagram, based on Eq. (58), is plotted in Figure 4.

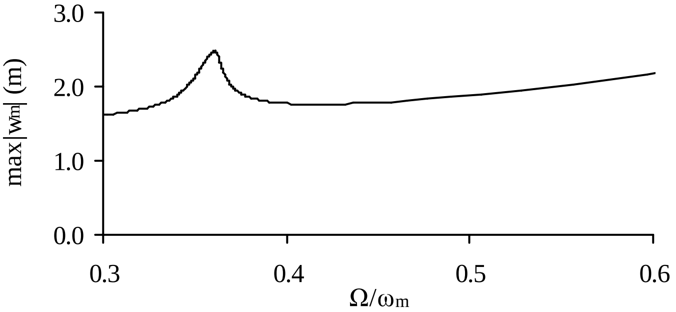

Figure 4: Superharmonic resonance: response curve of the SDOF model for load amplitude $(P_0)_m$=2366kN

5.2.4. Subharmonic resonance

As explained in section 4.4, subharmonic solutions, with non trivial amplitudes of the free oscillation term a, exist for a given value of Λ only if:

$$\varepsilon\sigma \geq \frac{126\Lambda^2}{\omega_m}\cdot\frac{(EA)_m}{M_m L_m^3}+\frac{M_m L_m^3}{8(EA)_m}\cdot\frac{\zeta^2\omega_m^3}{\Lambda^2}\Rightarrow \varepsilon\sigma \geq 2.53\Lambda^2(\sec^{-1})+\frac{0.168}{\Lambda^2}(\sec^{-1}) \tag{62}$$

Based on Eq. (40) and assuming that:

$$\Omega = 3\omega_m + \varepsilon\sigma \tag{63}$$

the load amplitude is calculated:

$$(P_0)_m = 2M_m\Lambda(\omega_m^2-\Omega^2) \tag{64}$$

for a frequency detuning satisfying inequality (62), while the amplitude of the oscillation is calculated by Eq. (44):

$$
\begin{aligned}
a^2 &= \varepsilon\sigma\frac{\omega_m M_m L_m^3}{18(EA)_m} - 6\Lambda^2 \pm \\
&\pm\sqrt{\left(\varepsilon\sigma\frac{\omega_m M_m L_m^3}{18(EA)_m} - 6\Lambda^2\right)^2 - \frac{M_m^2 L_m^6 \omega_m^2}{324(EA)_m^2}\left[\left(\varepsilon\sigma - \frac{9\Lambda^2}{\omega_m}\cdot\frac{16(EA)_m}{M_m L_m^3}\right)^2 + 9(\zeta\omega_m)^2\right]} \Rightarrow \qquad (65)\\
a^2 &= c \pm \sqrt{c^2 - d\cdot e}
\end{aligned}
$$

where

$$c = (2.77\varepsilon\sigma - 6\Lambda^2)(m^2) \qquad (66)$$

$$d = 7.66m^4\sec^2 \qquad (67)$$

$$e = [(\varepsilon\sigma - 2.89\Lambda^2)^2 + 0.24](\sec^{-2}) \qquad (68)$$

Thus, Eq. (65) becomes:

$$
\begin{aligned}
a^2 &= (2.77\varepsilon\sigma - 6\Lambda^2)(m^2) \pm \\
&\pm\sqrt{[(2.77\varepsilon\sigma - 6\Lambda^2)(m^2)]^2 - 7.66\cdot[(\varepsilon\sigma - 2.89\Lambda^2)^2 + 0.24](m^4)}
\end{aligned}
\qquad (69)
$$

Figure 5 illustrates the curve that defines the region of the subharmonic solutions, by means of Λ and $(P_0)_m$ with respect to the frequency ratio and to the response amplitude, given by Eq. (69). A detail of the same diagrams is given in Figure 6, for frequency ratio up to 4. In Figure 7 the response amplitude is plotted with respect to the frequency ratio and the loading amplitude. In Figure 8 the detail of the same diagrams is given for frequency ratio up to 4.

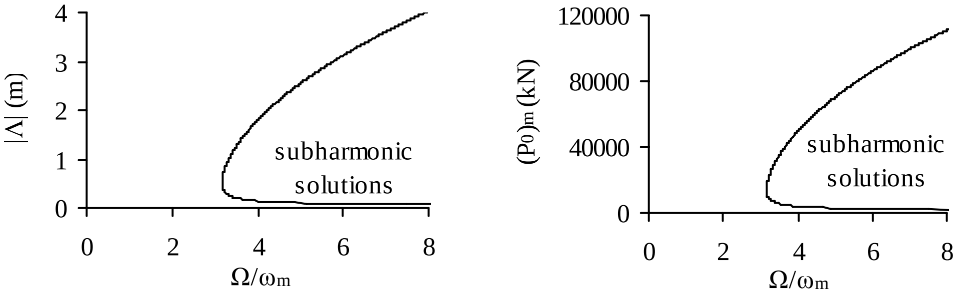

(a) (b)

Figure 5: Subharmonic resonance of the SDOF model: a) Λ vs frequency ratio, b) $(P_0)_m$ vs frequency ratio

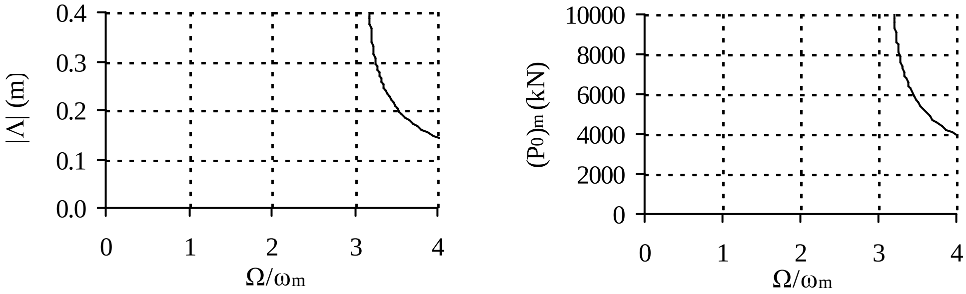

(a) (b)

Figure 6: Subharmonic resonance of the SDOF model (detail): a) Λ vs frequency ratio, b) $(P_0)_m$ vs frequency ratio

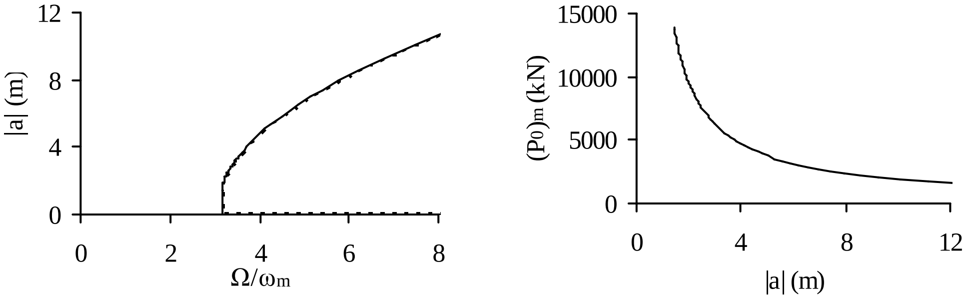

(a) (b)

Figure 7: Subharmonic resonance of the SDOF model: a) Response amplitude a vs frequency ratio, b) Load amplitude $(P_0)_m$ vs response amplitude a

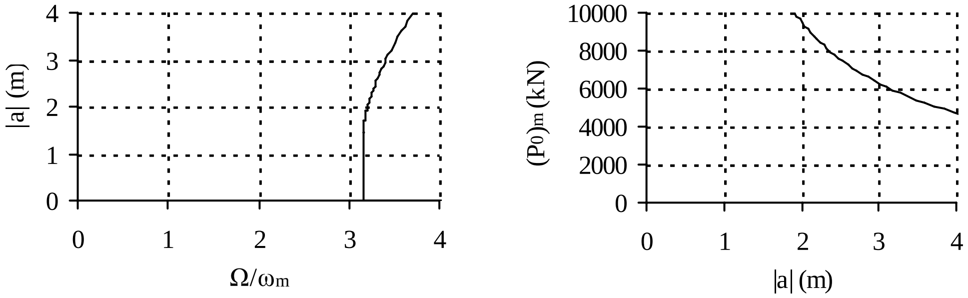

(a) (b)

Figure 8: Subharmonic resonance of the SDOF model (detail): a) Response amplitude a vs frequency ratio, b) Load amplitude $(P_0)_m$ vs response amplitude a

The frequency ratios that could cause subharmonic resonance are larger than 3.15 with load amplitude larger than 5239kN, which corresponds to 31kN for the MDOF prototype. A parametric analysis, changing the load amplitude, the frequency ratio and the initial deflection, keeping the initial velocity of the central node equal to 16m/sec, showed that as the load amplitude increases, the minimum initial deflection $w_{0,m}$ and the frequency ratio that can cause subharmonic resonance decrease (Figure 9).

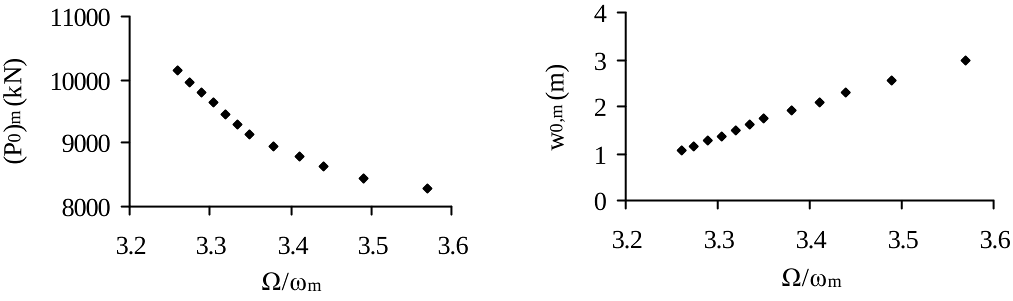

(a) (b)

Figure 9: Subharmonic resonant conditions for the SDOF model: a) $(P_0)_m$ vs frequency ratio, b) initial deflection vs frequency ratio

If, for example, the load amplitude is equal to $(P_0)_m$=9464kN, which corresponds to a load amplitude $(P_0)_p$=56kN for the MDOF prototype, the minimum initial deflection required in order to have a subharmonic resonance is 1.49m with a loading frequency equal to $\Omega=3.32\omega_m$, taking into account an initial velocity equal to 16m/sec. The time history diagrams of the central node deflection, for these initial conditions and for null initial conditions, are shown in Figure 10, based on the results obtained by solving numerically the analytical equation of motion, given by Eq. (25). For a load amplitude equal to $(P_0)_m$=8619kN, corresponding to 51kN for the MDOF prototype, an initial velocity 16m/sec, a minimum initial deflection 2.28m and a loading frequency $\Omega=3.44\omega_m$ constitute the conditions for subharmonic resonance. The time history diagrams of the central node deflection, for these initial conditions and for null initial conditions, are shown in Figure 11.

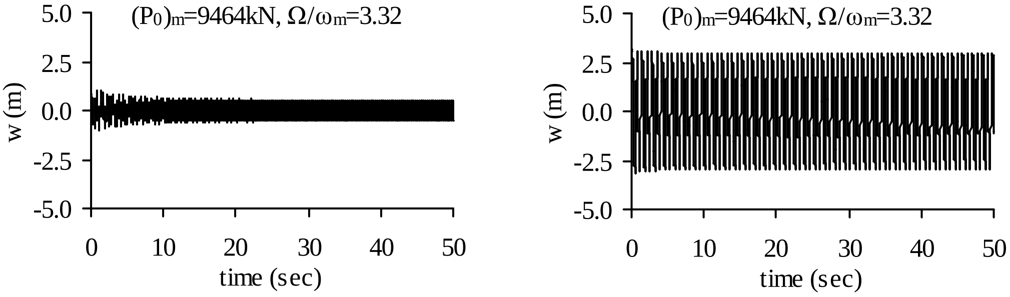

(a) (b)

Figure 10: Time history diagrams of the central node deflection for Ω/ω_m=3.32 and $(P_0)_m$=9464kN: a) with null initial conditions, b) with initial displacement and velocity

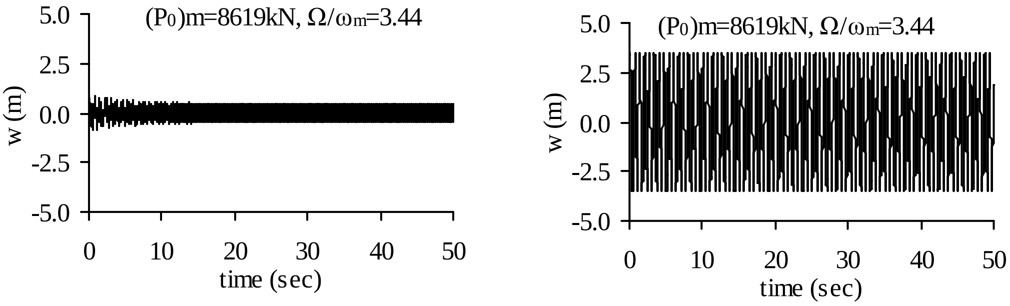

(a) (b)

Figure 11: Time history diagrams of the central node deflection for Ω/ω_m=3.44 and $(P_0)_m$=8619kN: a) with null initial conditions, b) with initial displacement and velocity

5.3 Numerical results for the MDOF prototype

In order to evaluate the accuracy of this method, numerical analyses are conducted to estimate the dynamic response of the MDOF cable net, being the prototype for this example.

5.3.1. Eigenfrequencies and eigenmodes of the prototype

A modal analysis is performed to calculate the vibration modes and the natural frequencies of the system. The first six vibration modes are shown in Figure 12. The first vibration mode is the first symmetric mode (denoted as 1S) having frequency $\omega_p=9.902\text{sec}^{-1}$.

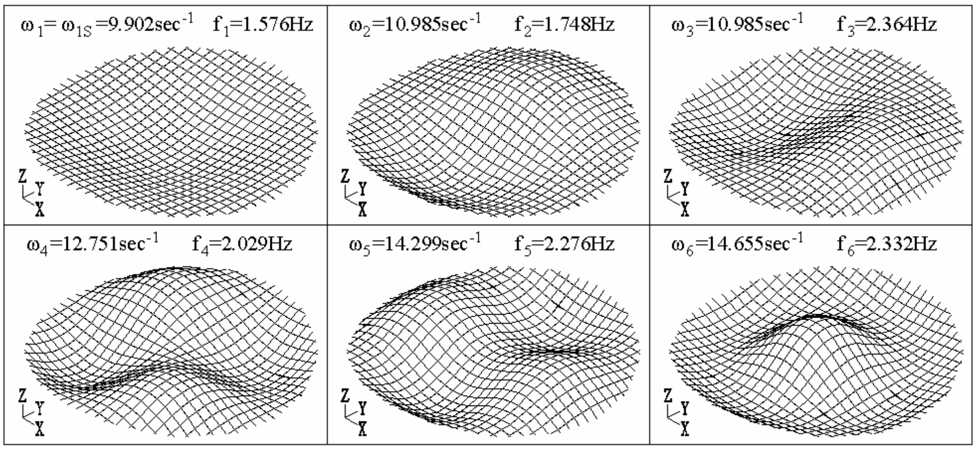

Figure 12: The first six vibration modes of the prototype

According to similarity relation (9) the natural frequency of the model, calculated as ω_m=8.22sec^{-1}, should be equal to the prototype's one. The natural frequency of mode 1S, obtained by the equivalent SDOF model, is 17% smaller than the one calculated by modal analysis of the MDOF system. The difference is rather large, because the difference between the model and the prototype, regarding the number of cables is also large. Nevertheless, this method is not used to calculate with accuracy the eigenfrequency, the maximum deflection or the cable tension of the prototype, but it is proposed to detect the occurrence of nonlinear phenomena.

5.3.2. Fundamental resonance

Accounting for fundamental resonant phenomena the load amplitude of the harmonic uniform load is chosen in section 5.2.2, equal to $(P_0)_p$=1.30kN. The load frequency varies between 0.90ω_p and 1.30ω_p. The damping ratio, according to similarity relation (11), is considered equal to $\zeta_p=\zeta_m=\zeta$=2%. The amplitude of the steady state response for the central node of the MDOF prototype with respect to the ratio of the loading frequency over the eigenfrequency, is plotted in Figure 13. In the same diagram the response of the SDOF model of Figure 3 is also illustrated for comparison reasons. According to similarity relation (8), the nodal dynamic deflection of the prototype should be equal to the one of the model. For frequency ratios between Ω/ω_p=0.90 and Ω/ω_p=1.10, the error of the calculation is not more than 10%, which is considered as satisfactory. After the peak amplitude and as the frequency ratio increases, the error increases too, arising at 45% for Ω/ω_p=1.30. This occurs because the sixth mode of the MDOF system is another symmetric mode, having a natural frequency equal to ω_6=14.655sec^{-1}=1.48ω_1=1.48ω_p. Thus, as the loading frequency approaches the frequency of this mode, the amplitude increases, leading to a fundamental resonance for the sixth mode. Using the equivalent SDOF model, which has a unique frequency, is not possible to predict this second fundamental resonance.

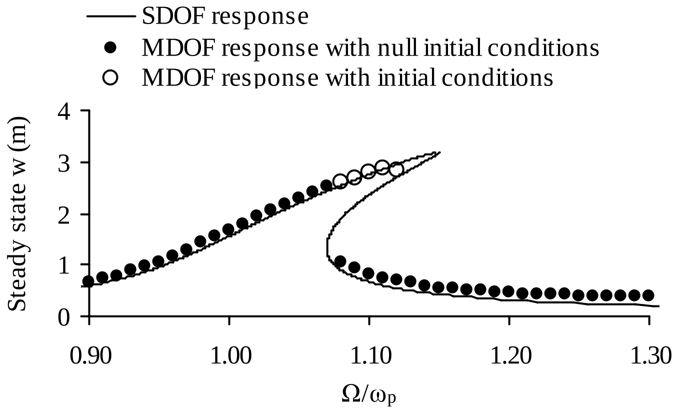

Figure 13: Fundamental resonance: response curve of the MDOF prototype for load amplitude $(P_0)_p$=1.30kN

The bending of the response curve for the MDOF system is obvious from the diagram of Figure 13. If null initial conditions are assumed, by means of deformation and velocity on every node, when the frequency ratio is Ω/ω_p=1.07 the steady state amplitude is 2.52m, while for Ω/ω_p=1.08, the amplitude drops suddenly to 1.06m, verifying the jump phenomenon. However, if initial conditions are assumed, the amplitude of the steady state deflection for Ω/ω_p=1.08 is 2.62m, verifying that the dynamic response of the MDOF prototype depends on the initial conditions. The initial conditions are deformations and velocities with respect to the three global axes, applied on every node, taken from the response of the MDOF system for Ω/ω_p=1.07 (Figure 14).

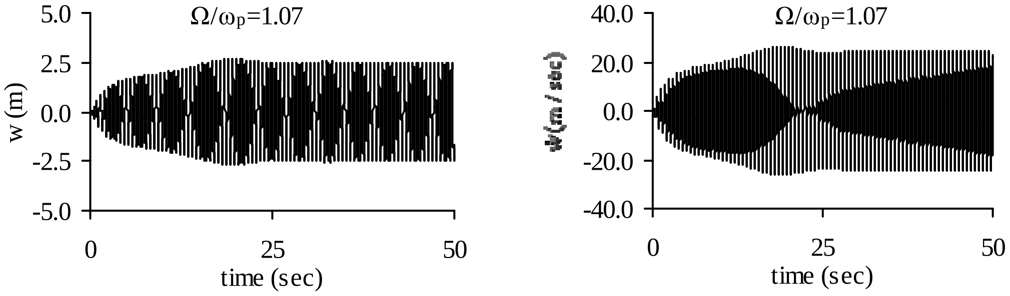

(a) (b)

Figure 14: Time history response of the central node for Ω/ω_p=1.07: a) deflection diagram and b) vertical velocity diagram

At time t=49.58sec, both vertical displacement and velocity are considerable (Figure 15), thus the deflection (Figure 16) and the velocity (Figure 17) at that time are chosen as initial conditions for the next frequency step. The time history diagrams for Ω/ω_p=1.08, for these two cases of initial conditions, are plotted in Figure 18, showing the different response amplitudes.

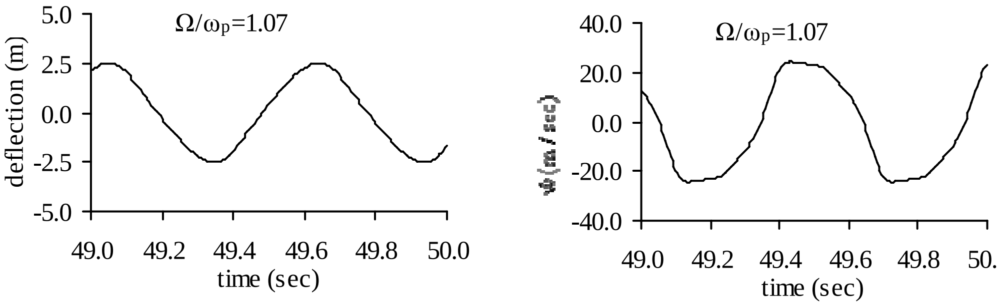

(a) (b)

Figure 15: Time history response of the central node for Ω/ω_p=1.07 (detail): a) deflection diagram and b) vertical velocity diagram

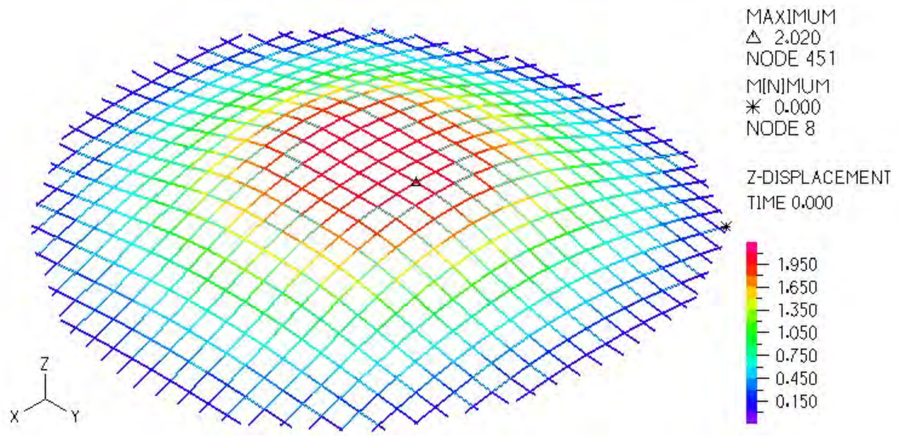

Figure 16: Vertical initial deflection for Ω/ω_p=1.08

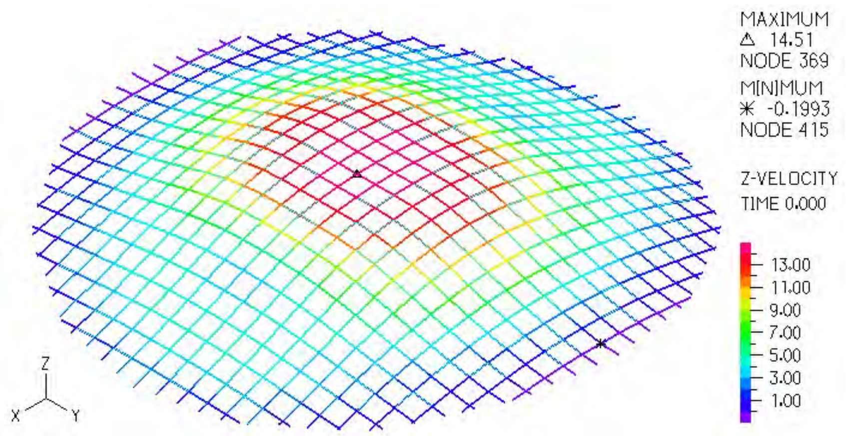

Figure 17: Vertical initial velocity for Ω/ω_p=1.08

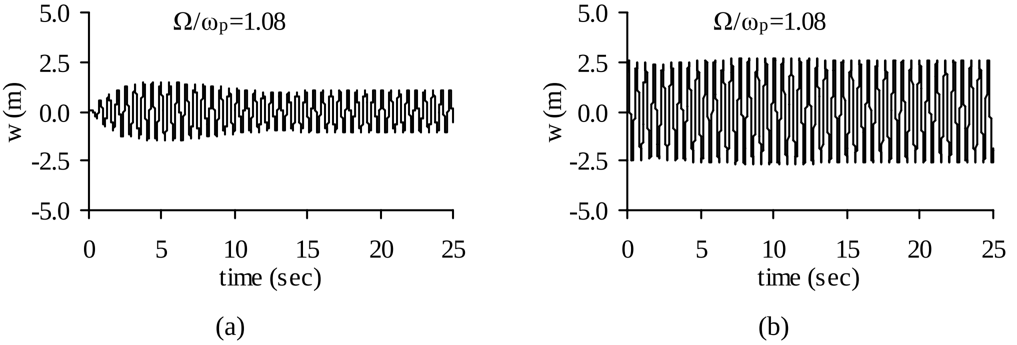

Figure 18: Time history diagrams of the central node deflection for Ω/ωp=1.08: a) with null initial conditions, b) with initial displacement and velocity

These phenomena, namely the maximum steady state amplitude occurring for frequency ratio larger than 1, leading to the bending of the curve, the jump and the multiple response amplitudes dependent on the initial conditions, also verified by the numerical simulation, confirm the intense nonlinearity of the MDOF cable net, which was predicted by the SDOF model.

5.3.3. Superharmonic resonance

In case of superharmonic resonance the load amplitude for the MDOF prototype is chosen in section 5.2.3, equal to $(P_0)_p$=14kN. The load frequency varies between 0.30ω_p and 0.60ω_p. The amplitude of the steady state response for the central node of the MDOF prototype with respect to the frequency ratio, and the response of the equivalent SDOF model of Figure 4, are plotted together in Figure 19. The steady state amplitudes, estimated by the method of the SDOF model, are between 25% and 48% larger than the ones obtained by numerical analysis. This estimation cannot be considered as satisfactory. On the other hand, the peak amplitude for frequency ratio Ω/ω_p=0.36, predicted by the equivalent SDOF model, is verified for the prototype, confirming the occurrence of the 3:1 superharmonic resonance for the first symmetric mode.

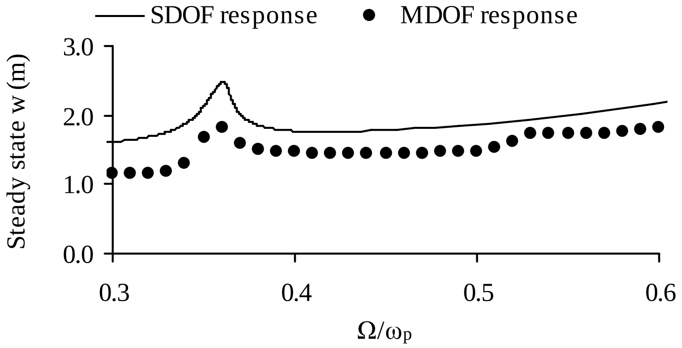

Figure 19: Superharmonic resonance: response curve of the MDOF prototype for load amplitude $(P_0)_p$=14kN

In Figure 20 the response of the central node is depicted by means of time history diagram and response spectrum, verifying this nonlinear resonance. The steady state response, obtained after 20sec, is an oscillation of at least two different frequencies. This is also illustrated in the response spectrum, in which two peaks are noted for frequencies 0.56Hz (3.52sec^{-1}), which is almost equal to the loading frequency (Ω=0.36·9.902sec^{-1}=3.56sec^{-1}) and

1.68Hz (10.56sec^{-1}), which is almost equal to the eigenfrequency of the first symmetric mode (ω_1=ω_{1S}=ω_p=9.902sec^{-1}).

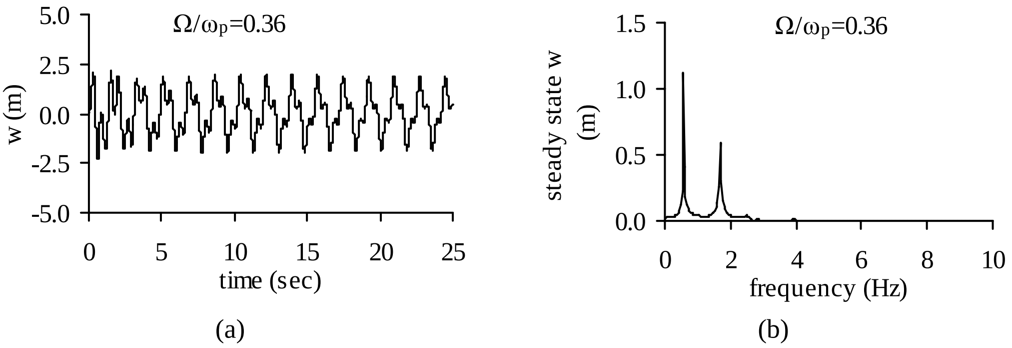

Figure 20: Response diagrams of the central node deflection for Ω/ω_p=0.36: a) time history diagram, b) response spectrum

In Figure 19, a second peak of the amplitude is observed for frequency ratio Ω/ω_p=0.53 for the MDOF system, which corresponds to a 2:1 superharmonic resonance for the same mode. In this case, the loading frequency is Ω=0.53·ω_p=5.52sec^{-1}=0.36ω_6, where ω_6 is the eigenfrequency of the sixth mode equal to ω_6=14.655sec^{-1}. Hence, this second peak indicates also a 3:1 superharmonic resonance for the sixth mode being the second symmetric mode of the system.

In Figure 21a, the time history diagram of the central node deflection is plotted. In Figure 21b, the response spectrum of the central node deflection illustrates that the oscillation of the central node is characterized by three frequencies: at 0.84Hz, corresponding to 5.28sec^{-1}, which is very close to the loading frequency (Ω=0.53·ω_p=5.25sec^{-1}), at 1.72Hz (10.81sec^{-1}), being close to the eigenfrequency of the first symmetric mode (ω_1=ω_{1S}=ω_p=9.902sec^{-1}) and at 2.52Hz (15.83sec^{-1}), which is close to the eigenfrequency of the second symmetric mode (ω_6=14.655sec^{-1}). Thus, both modes are activated in this case and the occurrence of the 3:1 and 2:1 superharmonic resonance for the first and the second symmetric mode, respectively, is verified. With the equivalent SDOF model having only one frequency, it is not possible to predict this second superharmonic resonance for the mode of higher order. In addition, the SDOF model, having only a cubic nonlinear term, cannot detect 2:1 superharmonic resonances.

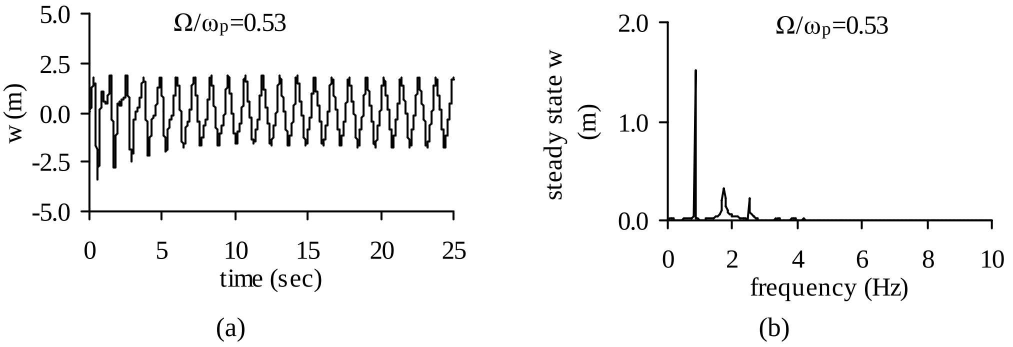

Figure 21: Response diagrams of the central node deflection for Ω/ω_p=0.53: a) time history diagram, b) response spectrum

5.3.4. Subharmonic resonance

Based on the parametric analysis of section 5.2.4, assuming a load amplitude on every node equal to $(P_0)_p$=51kN, with a load frequency equal to $\Omega=3.44\omega_p$, and an initial deflection and velocity on every node, so that the ones for the central node are 2.30m and 16m/sec, respectively, subharmonic resonance should be developed, but before the first cycle of the oscillation concludes, cable tensile failure occurs. The same also occurs for load amplitude $(P_0)_p$=56kN, loading frequency $\Omega=3.32\omega_p$ and initial conditions, corresponding to a deflection and velocity for the central node, 1.48m and 16m/sec, respectively (Figure 22). For smaller load amplitudes, a larger initial deflection is required, and for smaller initial deflection, a larger load amplitude can cause a subharmonic resonance. Both cases lead to cable tensile failure. Thus, for this cable net, it is impossible for the subharmonic resonance to evolve, because the large load amplitude and the large initial conditions required for such a resonance, cause cable tensile failure as soon as the vibration starts.

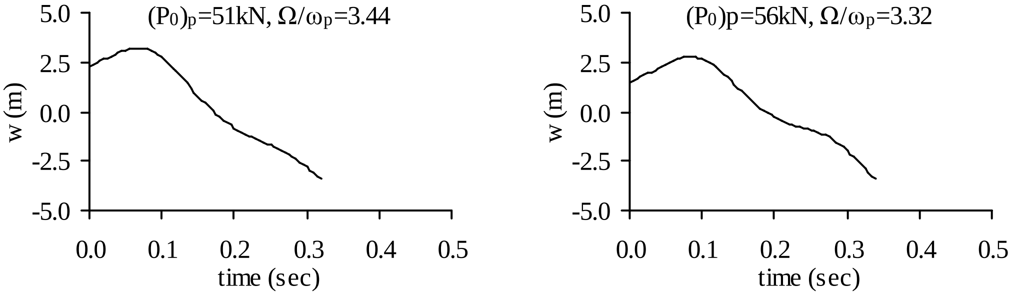

(a) (b)

Figure 22: Time history response of the central node for: a) $(P_0)_p$=51kN and Ω/ω_p=3.44 b) $(P_0)_p$=56kN and Ω/ω_p=3.32

6 EVALUATION OF THE METHOD

The pros of the proposed method are the following:

- The computational time required to solve the equation of motion and have an assessment of the response of the MDOF system is minimal.
- The intensity of the geometrical nonlinearity of the MDOF system can be estimated very satisfactorily, by means of the bending of the response curve, the jump phenomena and the existence of double response amplitudes due to the initial conditions.
- The loading frequency detuning, for which nonlinear resonances for the first symmetric mode occur, can be estimated with good accuracy.

The cons of this method are the following:

- The equivalent SDOF model, having only one eigenfrequency and eigenmode, cannot detect resonances for higher modes for a MDOF cable net.
- The equivalent SDOF model, having only a cubic nonlinear term, cannot predict 2:1 superharmonic or 1:2 subharmonic resonances for the large system.
- The analytical solution of the SDOF cable net is given for the vertical load applied on the central node, causing a vertical vibration. Thus, only the oscillation amplitude of the central node of the MDOF system can be estimated.
- In addition, this vertical motion corresponds to the first symmetric mode of the cable net. Hence, the method of the equivalent SDOF model cannot be used to estimate the response

of the MDOF cable net for other modal shapes, or for other spatial loading distributions, such as anti-symmetric ones about one or two horizontal axes.

- The analytical solution of the SDOF cable net gives the steady state amplitude of the response but not the maximum transient response, for which a cable tensile failure is possible to occur, before the steady state response is reached.

7 SUMMARY AND CONCLUSIONS

A method of an equivalent single-degree-of-freedom cable net is introduced, in order to predict the nonlinear dynamic response of a multi-degree-of-freedom cable net. The geometrical and mechanical characteristics of the large cable net are transformed to the corresponding ones of the small cable net, using similarity relations. The analytical solution of the SDOF model is explored, in order to detect nonlinear phenomena, such as the bending of the response curve, the occurrence of superharmonic and subharmonic resonances, jump phenomena and the double response amplitudes with respect to the initial conditions. The results of the SDOF model, by means of the maximum load, the maximum deflection and the loading frequency, are transformed to the ones of the MDOF system, by using the inverse similarity relations. Conducting nonlinear dynamic analyses and numerical simulation of the MDOF cable net, the nonlinear phenomena are verified.

This investigation verifies that the saddle form cable nets have cubic nonlinearities, but also quadratic ones. Near resonances, although damping exists, a small change of the loading frequency may cause large difference in the oscillation amplitude. The initial conditions influence significantly the response of the cable net, as occurs in nonlinear systems. Jump phenomena and superharmonic resonances are also confirmed. Concerning the subharmonic resonances, it is very difficult to detect them for a MDOF system, because they require specific load amplitude, load frequency and initial conditions. It is impossible to know which load amplitude and frequency and which initial deflection and velocity can cause this kind of nonlinear resonance, because no analytical solutions are available. The investigation of the SDOF model showed that subharmonic resonances may occur under certain conditions, but for the MDOF they are difficult to exhibit, because the large initial conditions and the large load amplitude required for this phenomenon lead to cable tensile failure at the beginning of the vibration.

The numerical investigation of the overall nonlinear dynamic behaviour of a MDOF cable net system is a time consuming procedure. It requires much computational time and a large number of nonlinear time history analyses, for different load amplitudes and for very small time steps and frequency steps. This method, estimating the loading amplitudes and frequencies for which nonlinear phenomena take place, can be a very useful guideline for the design of such cable structures.

REFERENCES

[1] G. Kerschen, K. Worden, A. F. Vakakis and J. Golinval, Past, present and future of nonlinear system identification in structural dynamics, *Mechanical Systems and Signal Processing*, **20**, 505-592, 2006.

[2] G. C. Mays and P. D. Smith, *Blast effects on Buildings*. Thomas Telford, England, 1995.

[3] C. M. Morison, Dynamic response of walls and slabs by single-degree-of-freedom analysis – a critical review and revision, *International Journal of Impact Engineering*, **32**, 1214-1247, 2006.

[4] S. Resemini, S. Lagomarsino and S. Giovinazzi, Damping factors and equivalent SDOF definition in displacement-based assessment of monumental masonry structures, *1st European conference on earthquake engineering and seismology*, Geneva, Switzerland, 2006.

[5] H. N. Li, F. Wang and Z. H. Lu, Estimation of Hysteretic Energy of MDOF structures based on equivalent SDOF Systems, *Key Engineering Materials*, **340-341**, 435-440, 2007.

[6] G. E. Manoukas, A. M. Athanatopoulou and I. E. Avramidis, Static Pushover Analysis Based on an Energy-Equivalent SDOF System, *14th World Conference on Earthquake Engineering*, Beijing, China, 2008.

[7] R. Zaharia and F. Taucer, Equivalent period and damping for EC8 spectral response of SDOF ring-spring hysteretic models, *JRC Scientific and Technical Reports*, European Communities, 2008.

[8] M. Aschheim and J. Browning, Influence of cracking on equivalent SDOF estimates of RC frame drift, *Journal of Structural Engineering*, **134**, 511-517, 2008.

[9] A. J. A. Oviedo, M. Midorikawa and T. Asari, An equivalent SDOF system model for estimating the response of R/C building structures with proportional hysteretic dampers subjected to earthquake motions, *Earthquake Engineering and Structural Dynamics,* Wiley online library, 2010.

[10] E. Buckingham, On physically similar systems; Illustrations of the use of dimensional equations, *Physical Review*, **4**, 345-376, 1914.

[11] J. S. Gero, The behaviour of cable network structures, *Structures Report SR8*, University of Sydney, 1975.

[12] J. S. Gero, The preliminary design of cable network structures, *Structures Report SR9*, University of Sydney, 1975.

[13] I. Vassilopoulou and C. J. Gantes, Behaviour and preliminary analysis of cable net structures with elastic supports, *4th National Conference on Metal Structures*, Patras, Greece, **2**, 517-525, May 24-25, 2002.

[14] I. Vassilopoulou and C. J. Gantes, Behavior, Analysis and Design of Cable Networks Anchored to a Flexible Edge ring, International Association for Shell and Spatial Structures, *Symposium on Shell and Spatial Structures from Models to Realization (IASS2004-Symposium Montpellier)*, Montpellier, France, Extended Abstract, pp. 212-213, September 20-24, 2004.

[15] I. Vassilopoulou and C. J. Gantes, Cable nets with elastically deformable edge ring, *International Journal of Space Structures*, **20**, 15-34, 2005.

[16] I. Vassilopoulou and C. J. Gantes, Similarity relations for nonlinear dynamic oscillations of a cable net, *1st ECCOMAS Thematic Conference on Computational Methods in Structural Dynamics and Earthquake Engineering (COMPDYN 2007*), Rethymno, Crete, Greece, abstract pp. 373, June 13-16, 2007.

[17] A. K. Chopra, *Dynamics of structures*, *Theory and applications to earthquake engineering*. Prentice Hall International, Inc. U.S.A. 1995.

[18] H. A. Buchholdt, *An introduction to cable roof structures, 2nd Edition.* Thomas Telford, England, 1999.

[19] A. Nayfeh and D. T. Mook, *Nonlinear Oscillations*. John Wiley & Sons, Inc. U.S.A., 1979.

COMPDYN 2011
3rd ECCOMAS Thematic Conference on
Computational Methods in Structural Dynamics and Earthquake Engineering
M. Papadrakakis, M. Fragiadakis, V. Plevris (eds.)
Corfu, Greece, 25–28 May 2011

INFLUENTIAL PARAMETERS FOR THE DESIGN OF NONSTRUCTURAL COMPONENTS IN MULTI-STORY BUILDINGS

M. Sadeghzadeh-Nazari[1], **M. Ghafory-Ashtiany**[2]

[1] M.S. Student, International Institute of Earthquake Engineering and Seismology (IIEES)
Tehran, Iran
e-mail: m.sadeghzadeh@iiees.ac.ir

[2] Professor, International Institute of Earthquake Engineering and Seismology (IIEES)
Tehran, Iran
e-mail: ashtiany@iiees.ac.ir

Keywords: Secondary System, Floor Response Spectra, Nonstructural Component.

Abstract. *Damage to nonstructural components may conduce heavy financial losses and injuries; therefore, it is a necessity for these components to be carefully designed for seismic loads. Meanwhile, even the most recent editions of the corresponding codes and instructions are still based on some assumptions that impair their accuracy and degree of conservatism. In this paper, it is intended to highlight the influential effect of some of these assumptions and the other related parameters that affect the floor acceleration response in buildings. For this reason, this paper constitutes the nonlinear dynamic time-history analysis of seven code-designed multi-story regular steel moment-resisting frames which have been subjected to selected strong ground motions (SGMs) for each individual building. Floor acceleration response spectra (FARS) have been calculated for the building floors. The spectra have been computed for the case of the components having dynamic interaction with the primary structure or not, so that the influence of the dynamic interaction is spotlighted. Besides, the FARS have been specified for different component mass ratios so as to account for the effect of the component weight. Another factor which is neglected in most of the instructions and studies is damping. Different damping coefficients have been utilized to investigate the effect of this parameter. The frame beams have the freedom to bend; therefore, the buildings are not consisted of simple shear frames. The effects of all mentioned parameters have been quantitatively illustrated and the results have been compared with each other for various cases. It is found that the mass ratio of the component, the degree of damping in primary or secondary systems, and the interaction between the primary and the secondary structure are crucial factors to be considered in seismic design of nonstructural components (NSCs), which regarding them helps improve the precision of studies. Moreover, results indicate that in contrary to the assumptions of current seismic codes, not always does the fundamental vibration mode of the primary structure produce the highest floor acceleration responses. Also, it can be inferred that if such factors are included in seismic design codes, their level of conservatism can become more rational and proposed methods can get closer to reality.*

1 INTRODUCTION

During past earthquakes, damage to nonstructural components has always shown to constitute a wide portion of economic losses. Thus, in recent decades, the seismic behavior of NSCs has become an area of research interest. Compared to structural components, our knowledge of nonstructural systems is relatively limited and research works and available codes and guidelines in this field are, for the most part, based on past experience, engineering judgment, and intuition, rather than on experimental and analytical results.

There are many different factors which affect the design force of secondary systems in buildings. In this study, the influence of the secondary system mass ratio, secondary and primary system damping ratios, and the primary-secondary system interaction on floor acceleration demand has been investigated. In past studies, these parameters have either been neglected or their effects have not been spotlighted quantitatively using precise time-history analyses. This study; however, quantifies the crucial effects of these parameters via comprehensive numerical analyses.

2 STRUCTURAL MODELS AND SELECTED GROUND MOTIONS

In this paper, seven multi-story building frames have been utilized for the dynamic time-history analysis. The frames have been pulled out of seven code-designed building structures such that their dynamic behavior is the same as that of the buildings. The studied buildings comprise a group of 4-, 6-, 8-, 12-, 16-, 20-, and 25-story special steel moment-resisting frames which bear a single-degree-of-freedom linear secondary system on one of their floors for each analysis. The secondary systems have been attached to the bottom, middle, or top floor of each building (equivalent frame) every time. Figure 1 shows a schematic of the 6-story building typical floor plan and interior frame with nonstructural components attached at its floors. The other six studied buildings have similar floor plans with frames which have been designed for each individual building.

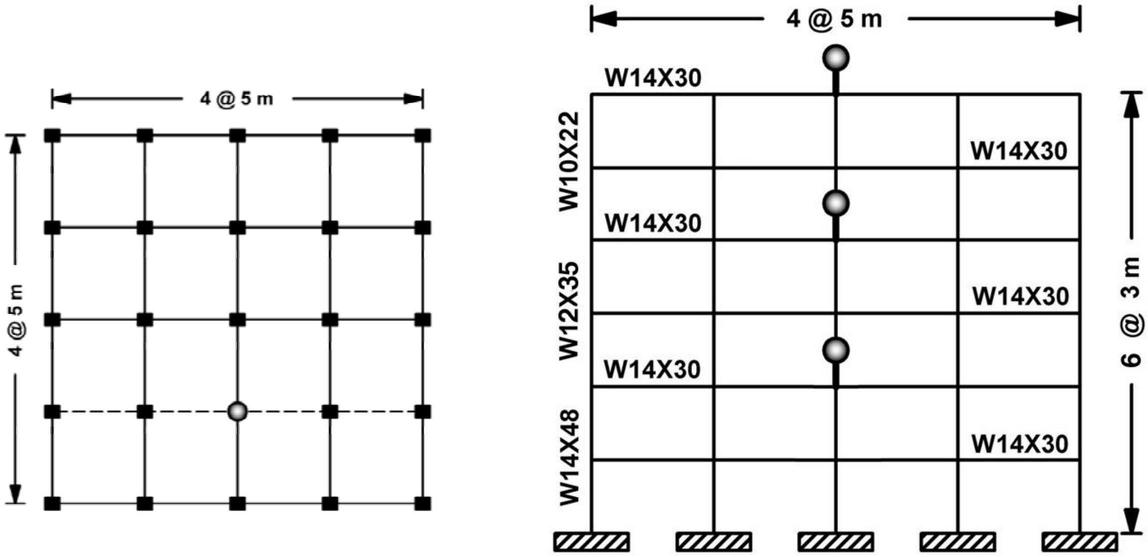

Figure 1: 6-story building typical floor plan (left) and interior frame (right) with nonstructural components attached to its lower, middle or top floor.

Since this study aims to gain an understanding of the behaviour of nonstructural components mounted on nonlinear buildings, the ground motions used in the analysis are selected based on their ability to stimulate the nonlinear behaviour of the buildings. Thus, for each building, the earthquake input for this study is defined in terms of eight strong ground motion (SGM) acceleration time histories recorded in different earthquake events and scaled to match the spectral ordinate at the fundamental period of the building. Table 1 shows the exclusively selected SGMs for the 6-story building from M6.5 scenario SGM data base proposed by Hatefi, Ashtiany and Ansari [4] using SGM selection method proposed by Ashtiany, Mousavi and Azarbakht [5].

No.	Earthquake	Year	Station	M	PGA (g)	Scale factor	V_{S30} (cm/sec)	Effective Duration (sec)
1	Qaen(S. Khorasan)	1979	Khezri	7.1	0.10	1.804	701	15.05
2	Qaen(S. Khorasan)	1979	Khezri	7.1	0.10	2.087	701	15.635
3	Eslamabad(Ardebil)	1997	Kariq	6	0.57	1.613	589	4.205
4	Avaj	2002	Kaboodar Ahang	6.5	0.16	2.909	613	18.06
5	Kajoor,Firooz ab-abd	2004	Moalem Kelayeh	6.3	0.29	1.668	490	10.625
6	Kocaeli	1999	Devlet Hastanesi	7.4	0.14	2.909	348	11.595
7	Duzce	1998	Bayındırlık ve İskan	7.1	0.81	0.835	294	8.57
8	Loma Prieta	1989	Hollister City Hall Annex	6.9	0.25	1.086	-	14.435

Table-1. Details of earthquake ground motions considered in this study for the 6-story building

3 INFLUENTIAL FACTORS TO AFFECT FLOOR ACCELERATION

In this section it is intended to spotlight some of the important and influential parameters that affect the floor acceleration values in buildings or other structures which are mostly neglected in code provisions or other studies. For this reason, the nonlinear acceleration floor response spectra (AFRS) have been calculated using the aforementioned structural models and ground motions for the bottom, middle, and top floors of the buildings. Since floor spectra can illustrate the frequency content of the responses, they have been taken advantage of in the study to show the effects of the secondary system mass ratio, the primary and the secondary system damping ratio, and the dynamic interaction between the primary and the secondary system. The spectra have been calculated for a range of secondary system periods from 0.01 to 5 seconds. These spectra have been obtained for every floor of the buildings but here, they are only shown for the 6-story building. The master values for the secondary system mass ratio, the primary system damping ratio and the secondary system damping ratio in this study have been chosen 0.01, 0.05 and 0.05, respectively, and all other cases are compared with these quantities. Besides, the master model in this study is the one in which the dynamic primary-secondary system interaction is considered.

3.1 Mass ratio

Secondary system mass ratio is defined as the ratio of the secondary system mass to the mass of the floor to which the NSC is attached. Here, the NSCs mass ratios have been selected to be equal to 0.005, 0.01, 0.02, or 0.05. For each analysis, a secondary system with one of the four different mass ratios has been added to one of the three different building floors (top, middle, or bottom) of each building to investigate how the secondary system mass ratio may affect the floor acceleration response. For each building, the AFRS have been obtained using the corresponding selected eight ground motions and the mean AFRS have been used as one may see in the following figures. Since it is not possible to show all of the figures, the mean AFRS for only the 6-story building are presented here at the bottom, middle, and top floor for different secondary system mass ratios in figures 2, 3, and 4, respectively. Also shown on the figures are the building modal periods in vertical dashed lines.

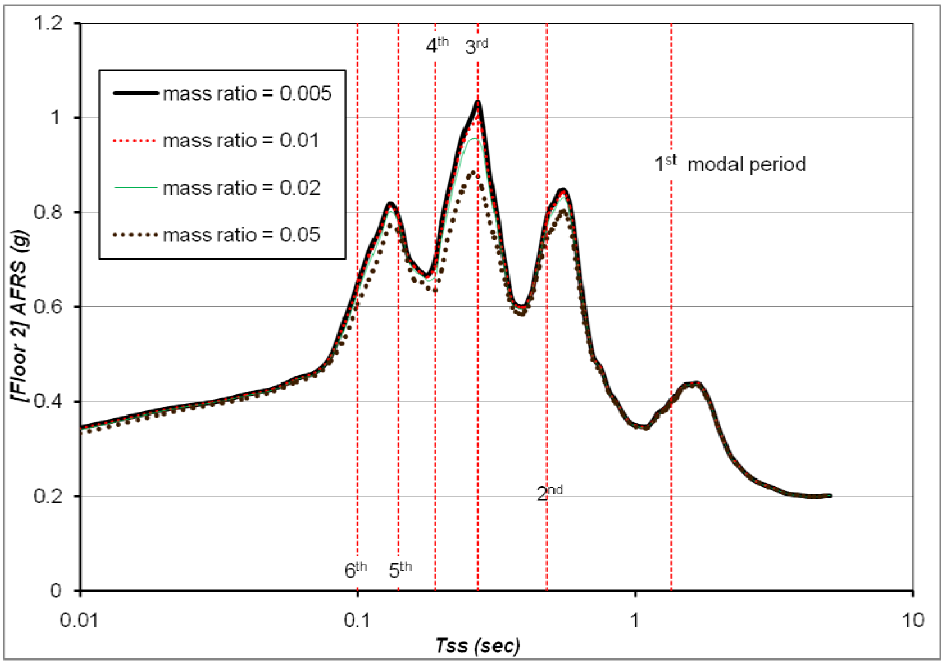

Figure 2: 6-story building mean AFRS at the 2nd (bottom) floor for different secondary system mass ratios.

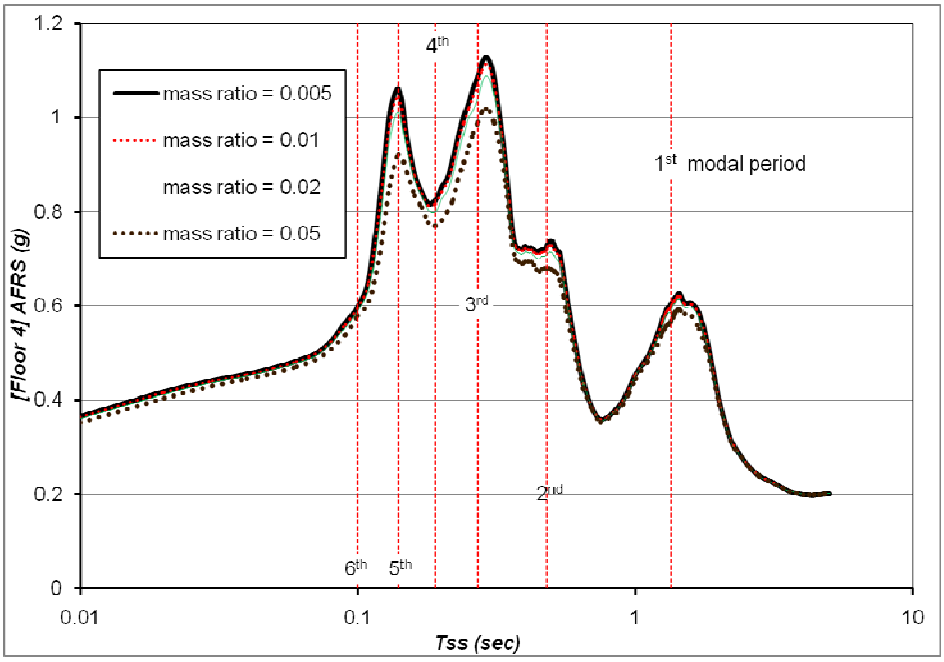

Figure 3: 6-story building mean AFRS at the 4th (middle) floor for different secondary system mass ratios.

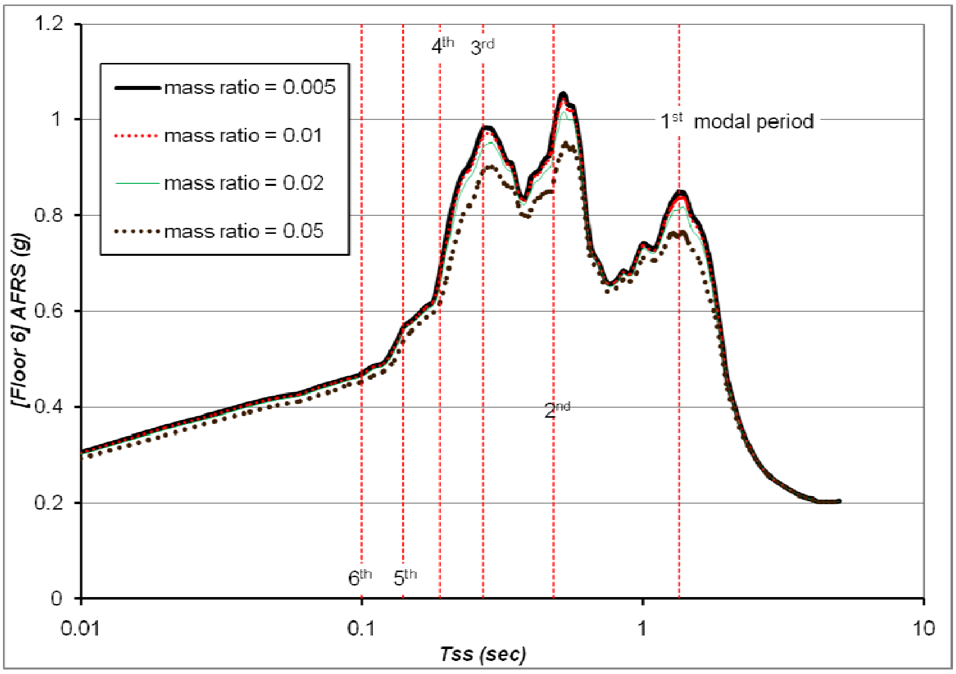

Figure 4: 6-story building mean AFRS at the 6th (top) floor for different secondary system mass ratios.

It may be realized from the figures that, in the six-story building, an increase in the mass ratio form 0.005 to 0.05 may decrease the AFRS values slightly in all of the three locations along the building height. For the other six buildings, similar mean AFRS have been obtained and such an overall decrease has been observed. To quantify the differences in the response spectra due to mass ratio changes and see how this parameter can generally affect the floor acceleration demand along the building height in all of the seven investigated buildings, the root mean square deviation (RMSD) of the AFRS has been calculated out of the mean AFRS values for the top, middle, and bottom stories. Figure 5 quantifies these effects, compared to the master mass ratio value in this study (i.e. 0.01), on the AFRS values.

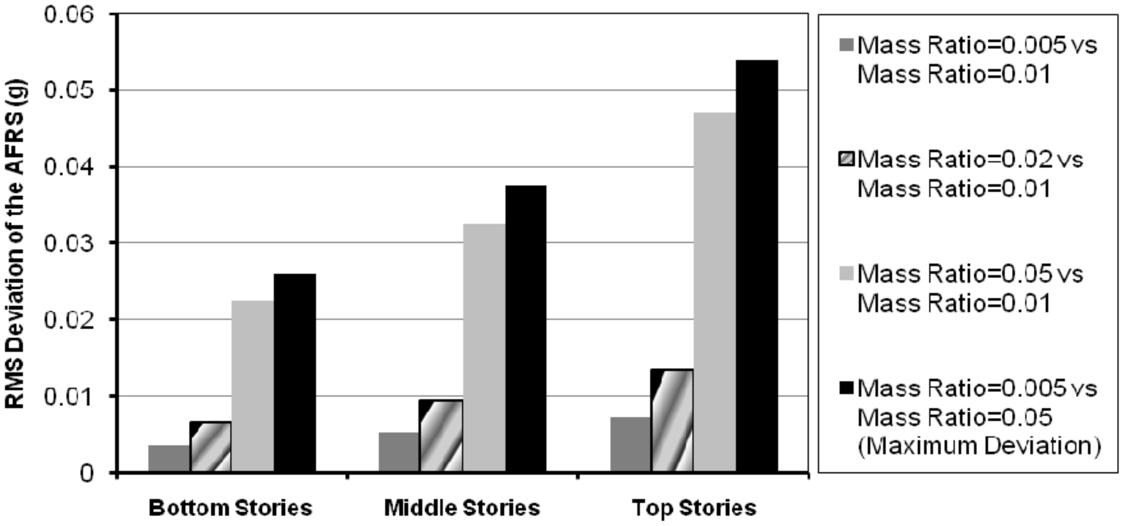

Figure 5: Root mean square deviation of the mean AFRS for different secondary system mass ratios.

As it may be seen in the figure, mass ratio has a relatively slight influence on floor acceleration response and the maximum deviation resulting from the two farthest mass ratio values, which are 0.005 and 0.05, reaches an average value of 0.04g. It may also be observed that going higher along the building height, the effect of mass ratio on floor acceleration demand increases.

3.2 Primary system damping ratio

Primary system damping ratio is another important factor whose effect has been investigated in this section. In this case, for each analysis, the secondary system is attached to one of the three different building locations (top, middle, or bottom floor) while the primary structure damping ratio equals one of three different values each time. The Primary system damping ratios which have been studied here are 0.02, 0.05, or 0.07. Note that, in this section, properties of the secondary system are those of the master model, i.e. a damping ratio of 0.05 and a mass ratio of 0.01. To investigate how the primary system damping ratio may affect the floor acceleration response, for each building, the AFRS have been obtained using the corresponding selected eight ground motions and the mean spectra have been used for the comparisons. Here, the mean AFRS are presented only for the 6-story building at the bottom, middle, and top floor for different primary system damping ratios as in figures 6, 7, and 8, respectively. The building modal periods have been also shown on the figures in vertical dashed lines.

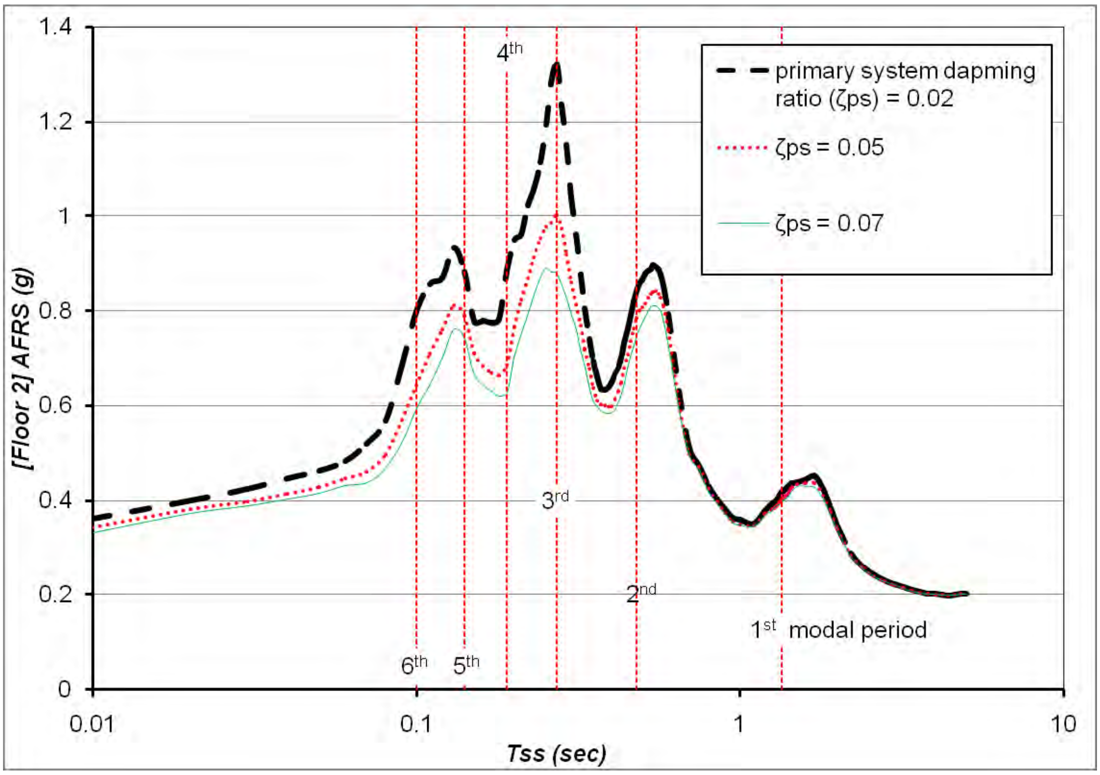

Figure 6: 6-story building mean AFRS at the 2nd (bottom) floor for different primary system damping ratios.

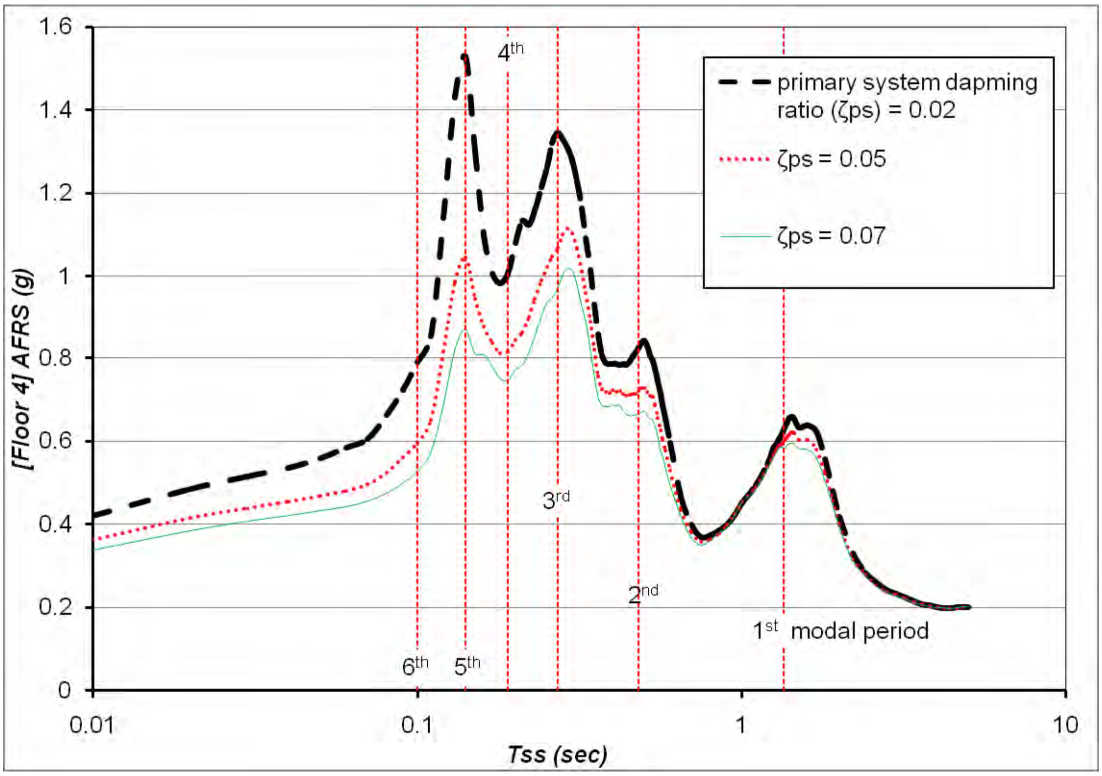

Figure 7: 6-story building mean AFRS at the 4th (middle) floor for different primary system damping ratios.

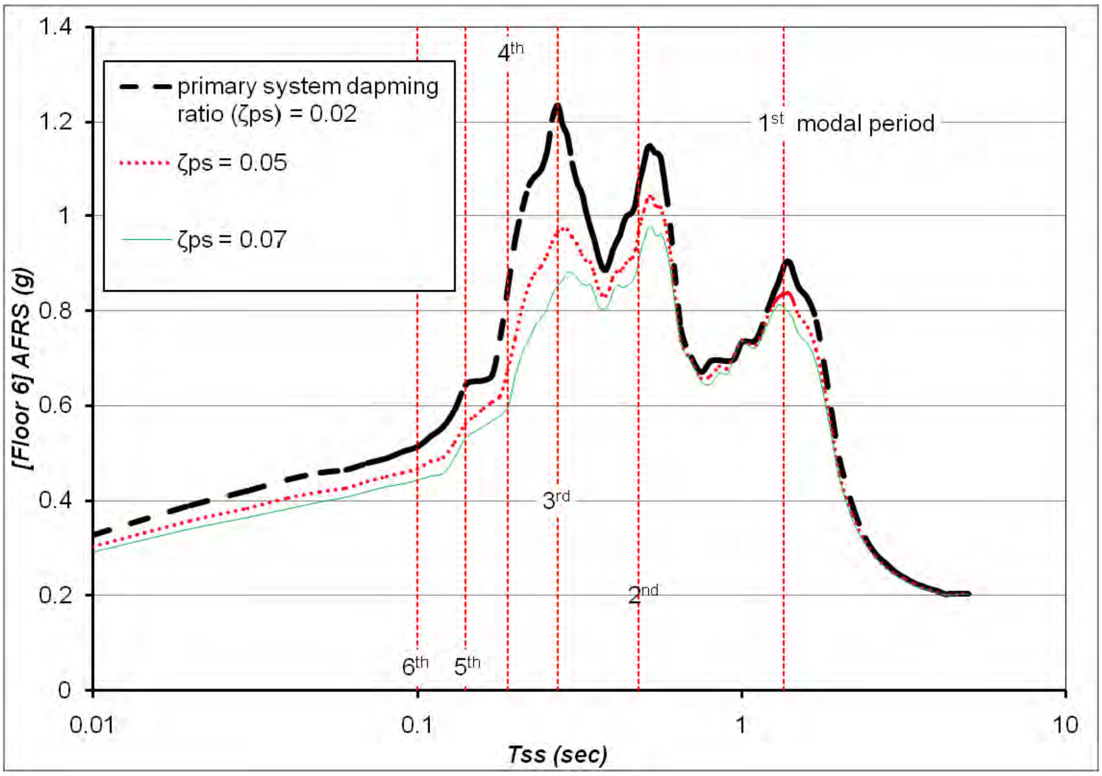

Figure 8: 6-story building mean AFRS at the 6th (top) floor for different primary system damping ratios.

One may realize from the figures that, in the six-story building, when the primary system damping ratio increases form 0.02 to 0.07 the AFRS values decrease. For the other six buildings, similar mean AFRS have been obtained and such an overall decrease has been observed.

Considering the respective curves for other buildings, this acceleration response attenuation becomes lower for the secondary systems with fundamental periods higher than 1 second. So, it seems that for such NSCs the primary system damping ratio has no influence on the responses. However, for other secondary systems, especially for those with a fundamental period close to one of the modal periods of the primary building, this effect is notable. To quantify the differences in the AFRS curves due to primary system damping ratio changes in all of the seven investigated buildings, the root mean square deviation (RMSD) of the AFRS has been calculated using the mean spectral values for the top, middle, and bottom stories. Figure 9 illustrates these effects, compared to the master primary system damping ratio value (i.e. 0.05).

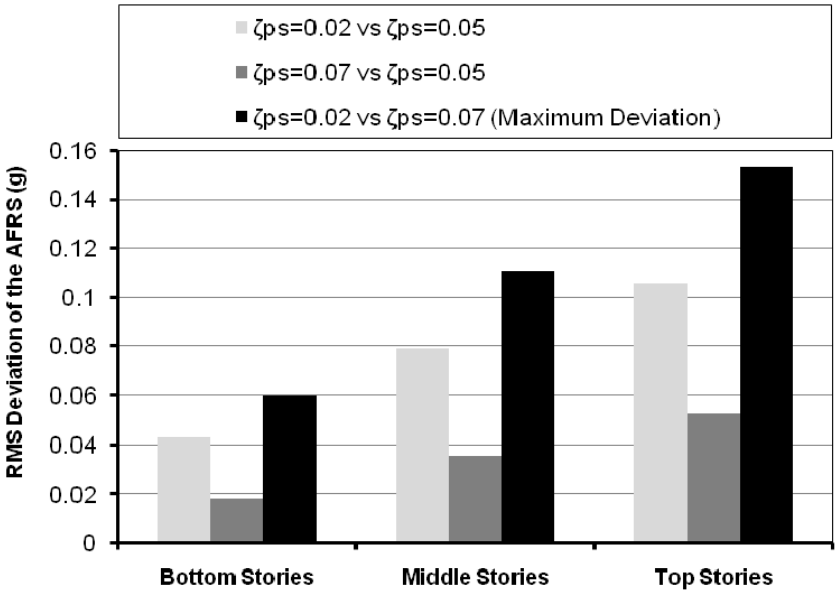

Figure 9: Root mean square deviation of the mean AFRS for different primary system damping ratios.

As seen in the figure above, the primary system damping ratio has a notable influence on floor acceleration response. The maximum deviation resulting from the two farthest damping ratios, which are 0.02 and 0.07, has an average value of 0.11g while this value in the top stories may reach an average of 0.15g. Again, it is observed that if the NSC is placed at higher locations along the building, the induced difference increases.

3.3 Secondary system damping ratio

In this section the effect of secondary system damping ratio has been investigated. Like the previous sections, NSCs with damping ratios of 0.05, 0.07, 0.10, or 0.20 are attached to one of the three different buildings floors. Other properties of the primary and secondary systems are those of the master model, i.e. a primary building damping ratio of 0.05 and a mass ratio of 0.01. The AFRS have been calculated using the corresponding selected eight ground motions for each building and the mean response spectra have been obtained. Again, only the 6-story building mean AFRS for different secondary system damping ratios are shown in figures 10, 11, and 12 with the building modal periods.

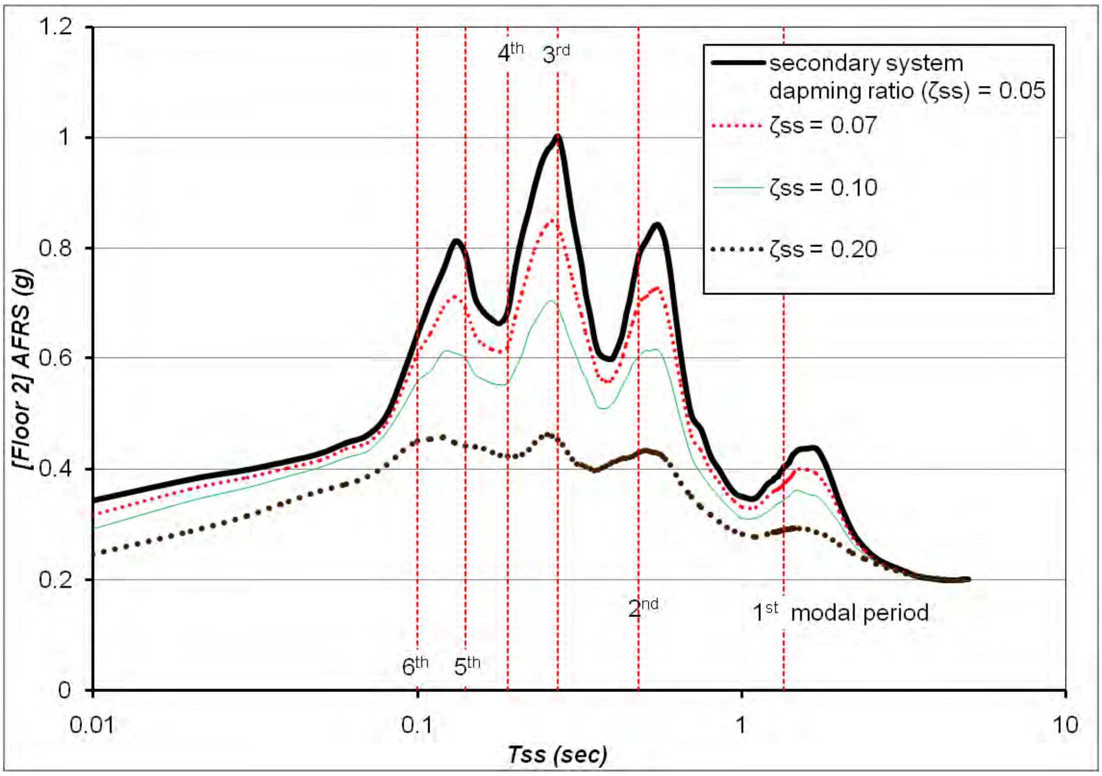

Figure 10: 6-story building mean AFRS at the 2nd (bottom) floor for different secondary system damping ratios.

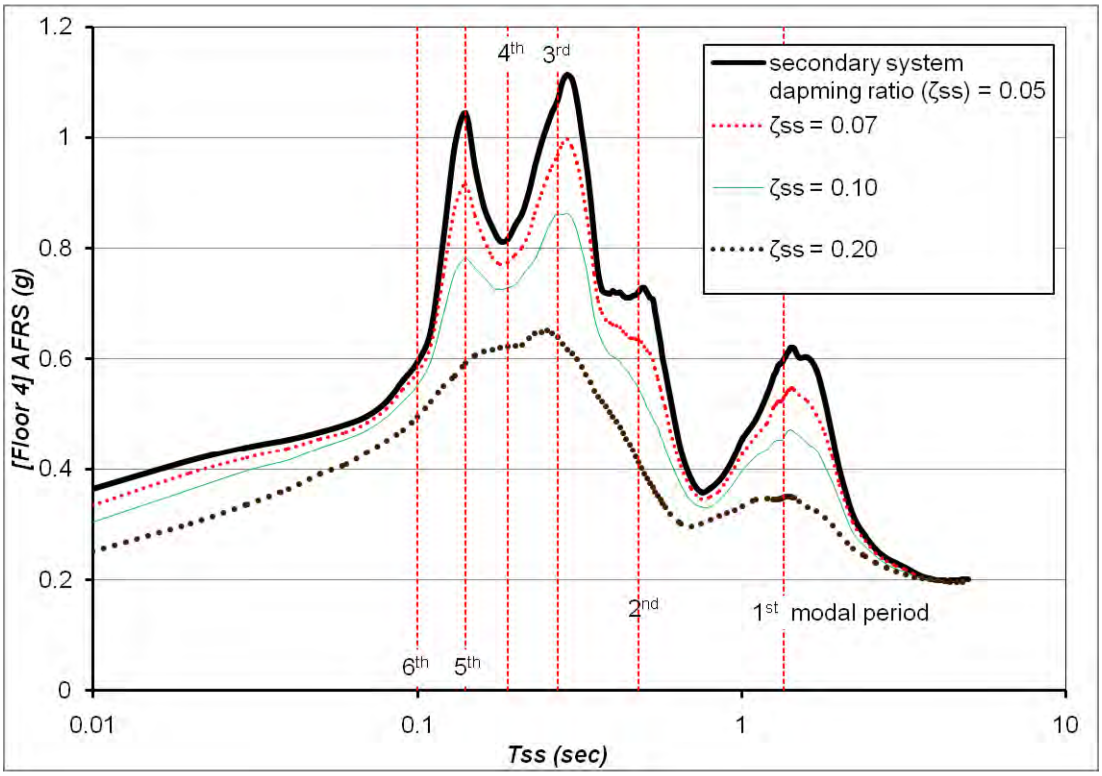

Figure 11: 6-story building mean AFRS at the 4th (middle) floor for different secondary system damping ratios.

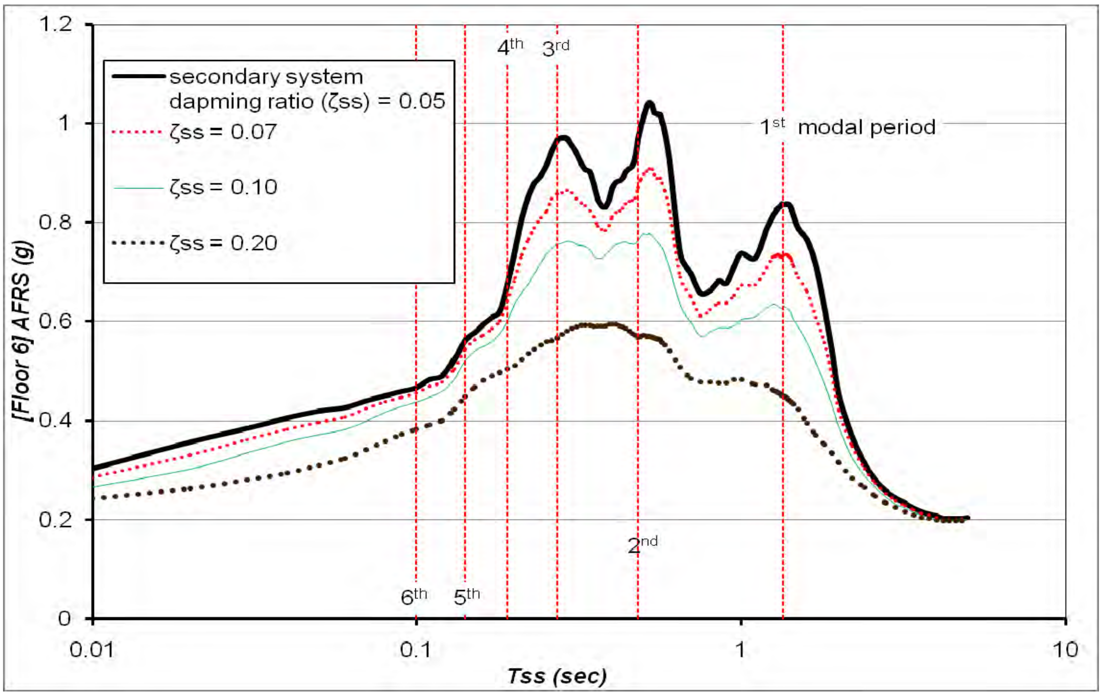

Figure 12: 6-story building mean AFRS at the 6th (top) floor for different secondary system damping ratios.

Figures 10 to 12 show that, in the six-story building, with an increase in the secondary system damping ratio form 0.05 to 0.20 the AFRS values in all of the three building height locations decrease. When the other buildings spectral values are taken into account, it may be inferred that the secondary system damping ratio is another factor which can affect the AFRS significantly. Also, one may notice that the spectral values are amplified when the secondary system is tuned with one of the building modal vibration periods. This amplification; however, lessens for more highly damped NSCs while the curves become smoother.

Figure 13 quantitatively illustrates the differences in the AFRS values caused by the secondary system damping ratio changes in all of the seven studied buildings. The RMSD of the mean AFRS has been calculated for the top, middle, and bottom stories and compared with the %5 master secondary system damping.

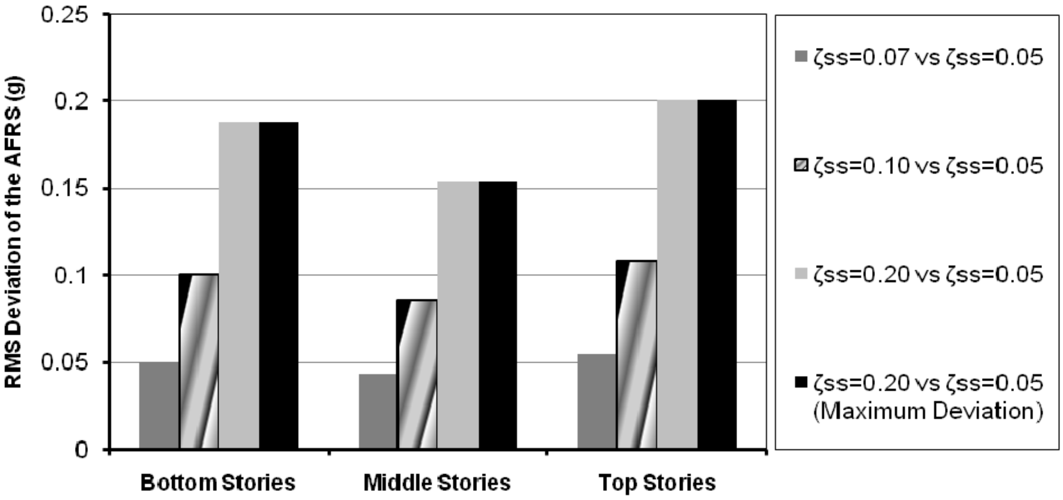

Figure 13: Root mean square deviation of the mean AFRS for different secondary system damping ratios.

Figure 13 shows that the secondary system damping ratio is another important parameter to affect the floor acceleration demand in buildings with an average induced deviation of 0.18g while comparing the %5 and %20 damped NSCs. The figure shows that the effect of secondary system damping ratio is almost the same along the building height and the component location seems to have no substantial influence on the responses.

3.4 Interaction

One of the most important factors which is, for the most part, neglected in different studies is the effect of the dynamic interaction between the primary and the secondary structures. In most of the studies the primary and the secondary systems are modeled and analyzed separately, i.e. at first the primary building response is calculated at the point of attachment of the NSC to the building and then this response is used as the input for the secondary system excitation. This way, the interaction is not taken into account.

In this section; however, it is intended to show how this interaction may affect the AFRS values. Thus, two groups of models have been developed: in the first group the interaction is neglected and the primary building has been separately modeled and its floor acceleration responses have been used as new inputs to calculate the secondary system responses; meanwhile, in the second group the effect of the interaction effect has been completely considered and in spite of the higher cost of the numerical analyses, the models have been set up such that the NSC is part of the whole model and the primary and secondary systems are in physical contact with each other (see Fig. 1 for example). Like the previous sections, three different building floor locations (top, middle, or bottom) of each building have been investigated and the mean AFRS have been obtained using the corresponding selected eight ground motions. The results for the 6-story building are as in figures 14 to 16. Other primary and secondary system properties are those of the master model.

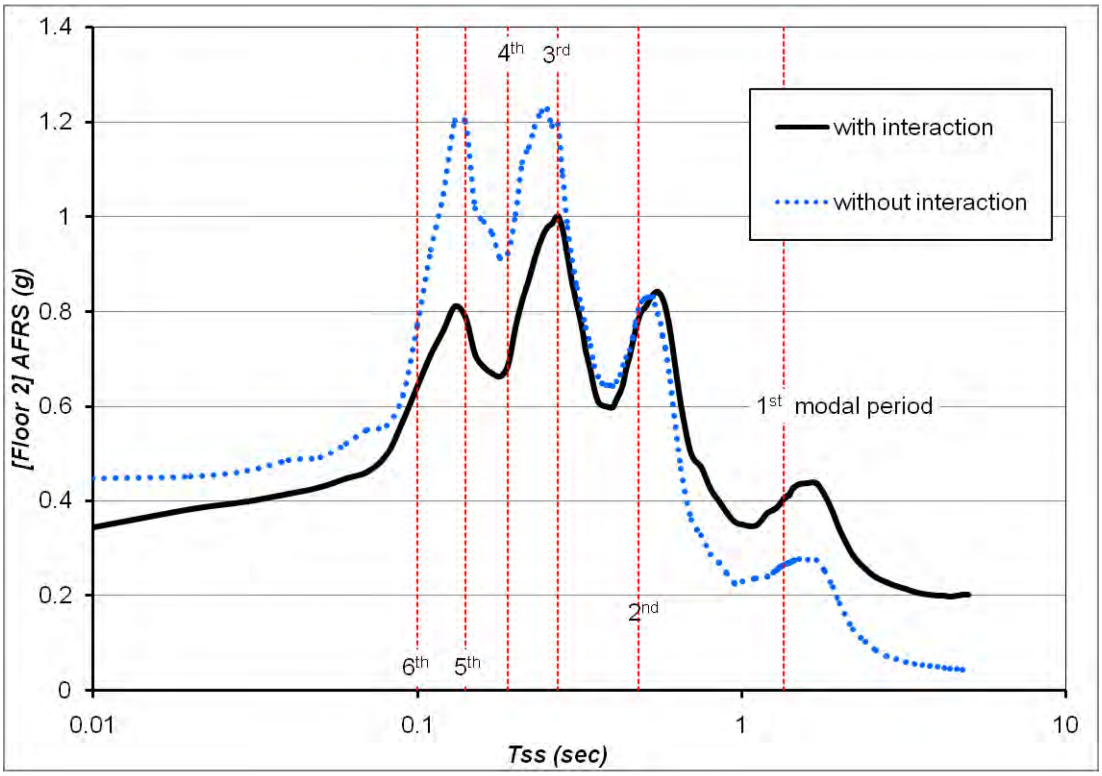

Figure 14: 6-story building mean AFRS at the 2nd (bottom) floor considering or without considering interaction.

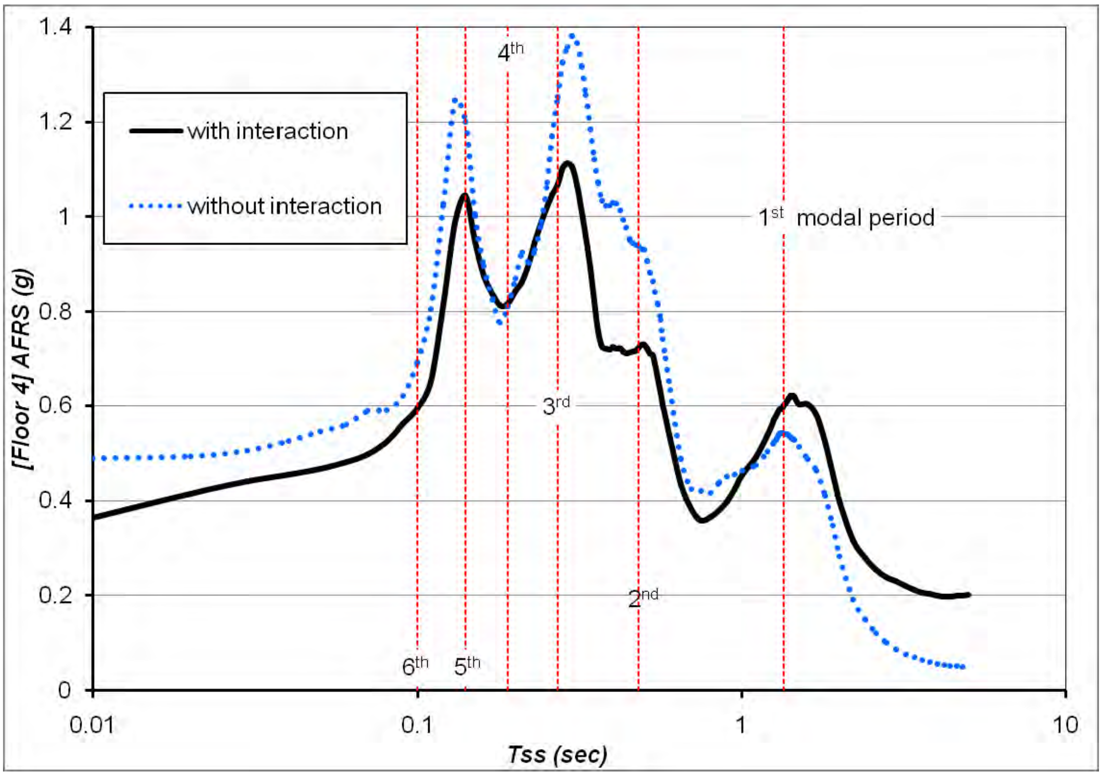

Figure 15: 6-story building mean AFRS at the 4th (middle) floor considering or without considering interaction.

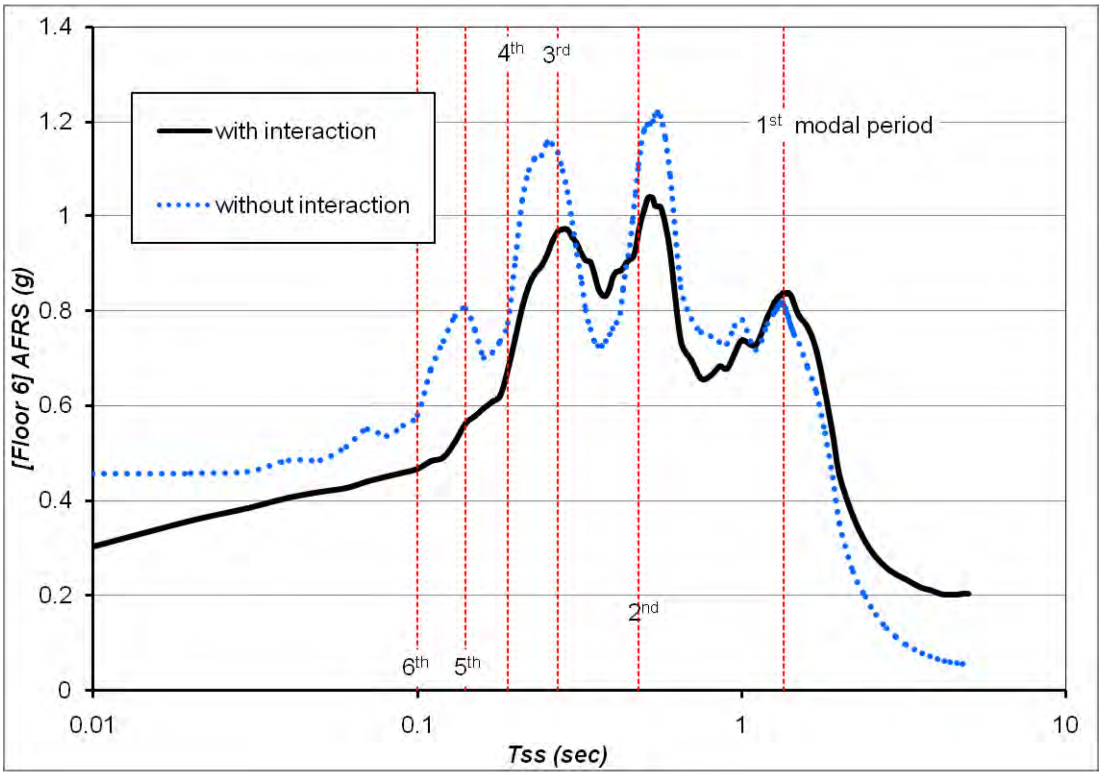

Figure 16: 6-story building mean AFRS at the 6th (top) floor considering or without considering interaction.

The recent figures and the similar figures obtained from the other six buildings show that considering the effect of primary-secondary system interaction to calculate floor acceleration demand in buildings has a very notable impact. As the figures indicate, for very flexible NSCs with higher fundamental periods, neglecting the interaction contributes to response underestimation. However, the response values can not be claimed to be higher or lower after consideration of the interaction, but, the induced difference or error is noteworthy and evident. In order to quantify this error in the response spectra and see how this parameter may generally affect the floor acceleration demand along the building height in all of the seven investigated buildings, the root mean square error (RMSE) of the AFRS has been calculated out of the mean AFRS values for the top, middle, and bottom stories as in figure 17.

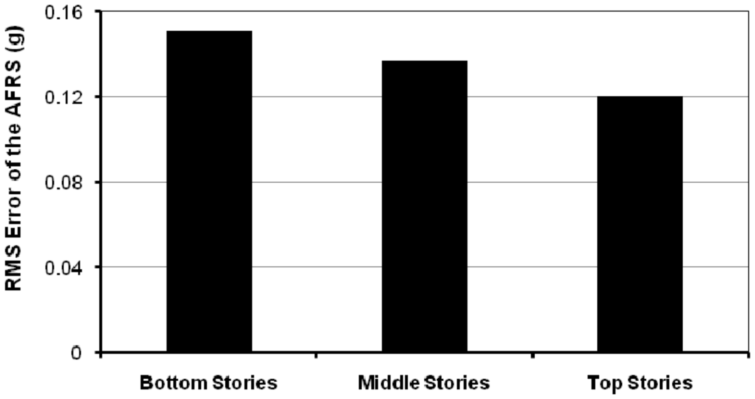

Figure 17: Root mean square error of the mean AFRS considering or without considering interaction.

Figure 17 also shows that at the upper building floors, the error caused by missing the interaction effect reduces. However, on the whole, these errors in the three studied portions are almost equal with an average value of 0.14g.

4 CONCLUSIONS

Based on this study, it is found that the mass ratio of the component, the degree of damping in primary or secondary systems, and the interaction between the primary and the secondary structures are crucial factors to be considered in seismic design of nonstructural components, which regarding them helps improve the precision of studies. Moreover, as it was illustrated in the proposed figures and results, in contrary to the assumptions of some current seismic codes (e.g. the Eurocode8 seismic provisions), not always does the fundamental vibration mode of the primary structure produce the highest floor acceleration responses. Also, it can be inferred that if such factors are included in seismic design codes, their level of conservatism can become more rational and proposed methods can get closer to reality.

REFERENCES

[1] M. P. Singh, L. M. Moreschi, L. E. Suarez and E. E. Matheu, editors, *Seismic Design Forces. II: Flexible Nonstructural Components*, J. Struct. Eng. ASCE, Vol. 132, No. 10, 1533-1542, 2006.

[2] M. Ghafory-Ashtiany, A. Fiouz, *Floor Response Spectra for Multicomponent Earthquake Input*, Journal of Esteghlal, Vol. 21, No. 1, September 2002.

[3] American society of civil Engineers (ASCE), *Minimum design loads for buildings and other structures, ASCE/SEI 7-05*, Reston, Virginia, 2006.

[4] H. A. Hatefi, M. Ghafory-Ashtiany and A. Ansari, *Nonlinear dynamic analysis based on M6.5 earthquake scenario data base,* Master of Science Thesis, International Institute of Earthquake Engineering and Seismology (IIEES), Iran, 2010.

[5] M. Ghafory-Ashtiany, M. Mousavi and A. Azarbakht, *Strong ground motion record selection for the reliable prediction of the mean seismic collapse capacity of a structure group*, Earthquake Engng Struct. Dyn., DOI: 10.1002/eqe.1055, 2010.

[6] Institute of Standards and Industrial Research of Iran (ISIRI), *Seismic resistant design of buildings – Code of practice (ISIRI, 2800), 3rd revision*, Tehran, 2005.

[7] BSI, *Design of structures for earthquake resistance, Eurocode 8*, 2003.

[8] E. Miranda, S. Taghavi, editors, *Approximate Floor Acceleration Demands in Multistory Buildings. I: Formulation,* J. Struct. Eng., ASCE, Vol. 131, No. 2, 203-211, 2005.

COMPDYN 2011
III ECCOMAS Thematic Conference on
Computational Methods in Structural Dynamics and Earthquake Engineering
M. Papadrakakis, M. Fragiadakis, V. Plevris (eds.)
Corfu, Greece, 26–28 May 2011

SEISMIC RESPONSE OF DEGRADING SDOF SYSTEMS DUE TO NEAR-FIELD GROUND MOTIONS

Vicky Dimakopoulou[1], Michalis Fragiadakis[2] and Constantine Spyrakos[1]

[1]Laboratory for Earthquake Engineering, Nat. Techn. Univ. of Athens (NTUA)
Iroon Polytechniou 9, 15780 Zografou, Greece
e-mail: vdimak@central.ntua.gr, cspyrakos@central.ntua.gr

[2]Department of Civil and Environmental Engineering,
University of Cyprus, P.O. Box 20537, 1678 Nicosia, Cyprus
e-mail: mfrag@mail.ntua.gr

Keywords: Near-Fault Ground Motions, Near-Source Effect, Forward Directivity, Single-degree-of-freedom Oscillators, Inelastic Displacement Ratio.

Abstract. *The effect of rupture directivity at near-fault sites is investigated. The study compares the ratio of maximum inelastic to maximum elastic displacement demand,* C_R*, for a wide range of SDOF systems subjected to fault-normal, near-field ground motions. Oscillators with both bilinear and quadrilinear backbones are considered. The quadrilinear oscillators include an elastic, a hardening and a negative stiffness branch that terminates at a horizontal plateau, and therefore this modelling is more suitable for simulating the real-world buildings, which degrade. A sensitivity analysis of the parameters that describe the SDOF systems is performed in order to study their effect on* C_R*. It is demonstrated how the seismic response varies with respect to the backbone parameters, the period and the seismic demand. The results show that the bilinear approximation, which is the common, underestimates the ductility demand compared to the quadrilinear case, regardless of the seismic intensity and the backbone parameters.*

1. INTRODUCTION

Near-fault ground motions with forward directivity are characterized by strong, coherent, long period pulses and permanent ground displacements. These properties differentiate the response of structures subjected to “non pulse like” ground motions. The special characteristics of near-field, forward directivity ground motions are directly correlated to the magnitude, the source type, the direction of rupture propagation relative to the site and also to the residual ground displacement resulting from the slip of the fault. The frequency content of near-field motions, which differentiates them from near-field non forward directivity and far-field ground motions, is not evident in every record in a zone approximately 20-60 km around the location of fault rupture. The impulsive character is present mainly in the strike-normal direction, generating the forward directivity effect (Somerville *et al.*1997, Baker, 2007). The effect of significant velocity pulses on the structural response was first highlighted by Bertero and Mahin (1978). Divergent views can be found in the literature, that either associate the directivity effects of near-fault ground motions to acceleration pulses (Makris and Black 2004, Sucuoglou *et al.* 1999) or to displacement pulses.

The conflicting opinions about the origin of directivity effects, which focus the influence of near-fault ground motions at different spectral regions and the elevated seismic demand they induce on structures, indicate the use of quadrilinear SDOF to simulate structural response far into the inelastic region. The deteriorating quadrilinear models can be used in order to obtain the response under high inelastic demand, where the system capacity is expected to degrade rather than steadily increase as in the case of bilinear systems. Furthermore, Ibarra *et al.* (2005) suggests that the backbone characteristics, and a parameter for cyclic deterioration may be sufficient to correspond to the structural response, regardless of the loading history.

The objective of this study is to investigate the effects of near-field ground motions on the inelastic behavior of single-degree-of-freedom (SDOF) systems with varying properties. Medians of the inelastic displacement ratio, C_R, of SDOF systems are shown for both bilinear and quadrilinear systems. The study emphasizes on the response of quadrilinear systems, since this is a more realistic description of the capacity of structures, while most contemporary literature refers to bilinear oscillators. The properties of a series of oscillators are varied, studying their effect on C_R, with respect to the ratio of the fundamental period over the pulse duration T_p.

2. INELASTIC DISPLACEMENT RATIO C_R

The inelastic displacement ratio, C, is defined as the maximum lateral inelastic displacement demand divided by the maximum elastic displacement demand, over the entire time history. Therefore, C is given by the expression (Chopra, 2007):

$$C = \frac{u_m}{u_y} = \frac{\mu}{R_y} \tag{1}$$

To compute C we adopt systems with given demand R_y, where R_y is the strength reduction factor equal to the ratio of acceleration demand S_a over the yield acceleration of the oscillator. The inelastic displacement ratio for given R_y, is denoted as C_R, being consistent with the notation in Miranda (2000). The assumption of given yield strength reduction factor R_y, has certain advantages over the constant-ductility case. Producing systems with selected yield strength reduction factor R_y, requires only linear and mainly invertible functions, since only one value of yield strength corresponds to a selected R_y value, while in order to calculate the C for systems with given ductility μ, requires an iterative procedure.

Current seismic design provisions for the computation of inelastic deformations are based on the inelastic design spectrum of Newmark and Hall (1982), which uses the R_y-μ-T_1, relationships of Veletsos and Newmark (1960). This equation has been the basis for several approaches to obtain approximate R_y-C_R-T relationships for near-field ground motions, as discussed in the following paragraph. According to the Newmark-Hall approach, C_R for far-fault ground motion record can be calculated as:

$$C_R(T_1) = \begin{cases} \infty & T_1 < T_a \\ (R_y^2+1)\big/2R_y & T_b < T_1 < T_{c*} \\ 1 & T_1 > T_c \end{cases} \tag{2}$$

where

$$T_{c*} = \frac{2R_y}{1+R_y^2} T_c \tag{3}$$

T_a, T_b, T_c, are spectral periods which vary according to the soil type.

The computation of C_R for structures located in the near-fault zone has been addressed for many years by the research community and various approximate relationships for C_R have been proposed, referring almost exclusively to bilinear systems. However, the different pulse periods of pulse-type motions, its significant influence on the spectral shape and the local amplifications it causes on C_R, indicates that it is preferable to normalize the fundamental period with the pulse period. Moreover this practice substantially decreases the record-to-record variability and eliminates the influence of the parameters that characterize the near-fault excitation. While Báez and Miranda (2000) suggest that PGV is the most influential parameter on C_R, according to Ruiz-Garcia (2011), neither PGV nor the distance to the source significantly affect C_R once T_1 is normalized with respect to the predominant period of the ground motion, T_p, where T_p is the period of vibration corresponding to the peak spectral velocity of a linear SDOF system having 5% damping ratio. Other studies, including Mavroeidis *et al.* (2004), discuss also the moderate influence of earthquake magnitude on structural response, focused on some distinct values of normalized periods ($T_1/T_p<1$). Finally, Chopra and Chintanapakdee (2004), support that when the periods are normalized with the spectral value T_c, the produced C_R values for near-field and far-fault ground motions are very close.

3. MODELLING OF THE OSCILLATORS

The SDOF oscillators are modeled either as bilinear having an elastic and a hardening branch, or with quadrilinear backbones having pinching hysteresis and including an elastic, a hardening, and a negative stiffness branch, terminating at a residual plateau (Fig.1). These systems are described by the post-yield hardening ratio a_h, corresponding to the strain-hardening stiffness, the negative slope of the post-capping stiffness a_c, the pre-capping ductility μ_c defining the beginning of the softening branch, and finally, the coefficient r representing the residual strength capacity, as a fraction of the yield strength. The parameters are varied one at a time, generating several plausible structural models, some of them being more brittle and other more ductile. Using an oscillator with properties $a_h = 5\%$, $\mu_c = 1.2$, $a_c = -50\%$,

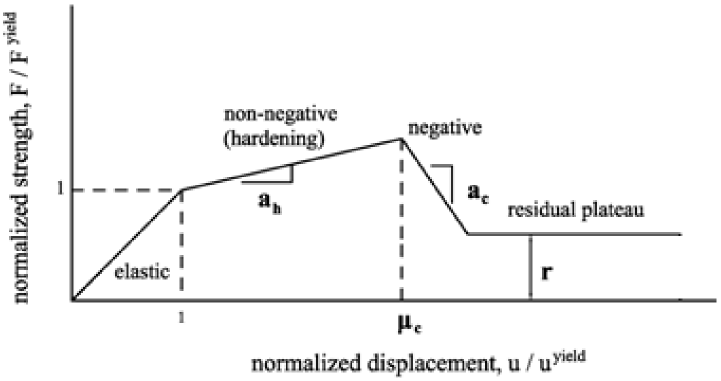

Figure 1: The force-displacement relationship of the oscillator in normalized coordinates (Vamvatsikos and Fragiadakis, 2006).

Table 1: The 33 near-fault records adopted.

Year	NGA	T_p	$D_{5\text{-}95}$	Event/ Station	Mag.	Mech.	R_{rup}
1971	77	1.6	7.1	San Fernando / Pacoima Dam (upper left abut)	6.61	R	1.8
1979	150	1.2	3.4	Coyote Lake / Gilroy Array #6	5.74	SS	3.1
1979	158	2.4	7.1	Imperial Valley-06 / Aeropuerto Mexicali	6.53	SS	0.3
1979	159	2.3	11.5	Imperial Valley-06 / Agrarias	6.53	SS	0.7
1979	170	4.5	14.9	Imperial Valley-06 / EC County Center FF	6.53	SS	7.3
1979	173	4.5	13.0	Imperial Valley-06 / El Centro Array #10	6.53	SS	6.2
1979	179	4.6	10.2	Imperial Valley-06 / El Centro Array #4	6.53	SS	7.0
1979	180	4	9.4	Imperial Valley-06 / El Centro Array #5	6.53	SS	4.0
1979	181	3.8	8.5	Imperial Valley-06/ El Centro Array #6	6.53	SS	1.4
1979	182	4.2	4.8	Imperial Valley-06/ El Centro Array #7	6.53	SS	0.6
1979	183	5.4	5.8	Imperial Valley-06 / El Centro Array #8	6.53	SS	3.9
1979	184	5.9	6.9	Imperial Valley-06 / El Centro Differential Array	6.53	SS	5.1
1979	185	4.8	11.8	Imperial Valley-06 / Holtville Post Office	6.53	SS	7.7
1980	292	3.1	16.6	Irpinia-Italy-01/ Sturno	6.90	N	10.8
1984	451	0.95	3.1	Morgan Hill / Coyote Lake Dam (SW Abut)	6.19	SS	0.5
1984	459	1.2	6.9	Morgan Hill / Gilroy Array #6	6.19	SS	9.9
1986	529	1.4	4.5	N. Palm Springs / North Palm Springs	6.06	RO	4.0
1987	615	0.79	8.1	Whittier Narrows-01 / Downey - Co Maint Bldg	5.99	RO	20.8
1987	721	2.4	18.8	Superstition Hills-02 / El Centro Imp. Co. Cent	6.54	SS	18.2
1987	723	2.3	10.5	Superstition Hills-02/ Parachute Test Site	6.54	SS	0.9
1989	738	2	6.0	Loma Prieta / Alameda Naval Air Stn Hanger	6.93	RO	71.0
1989	802	4.5	8.4	Loma Prieta/ Saratoga-Aloha Ave	6.93	RO	8.5
1992	821	2.7	6.9	Erzincan-Turkey/ Erzincan	6.69	SS	4.4
1992	828	3	16.2	Cape Mendocino/ Petrolia	7.01	R	8.2
1992	879	5.1	0.0	Landers/ Lucerne	7.28	SS	2.2
1994	1063	1.2	7.1	Northridge-01/ Rinaldi Receiving Sta	6.69	R	6.5
1994	1086	3.1	5.8	Northridge-01/Sylmar Olive View Med FF	6.69	R	5.3
1999	1176	4.5	15.4	Kocaeli-Turkey/ Yarimca	7.51	SS	4.8
1999	1182	2.6	25.8	Chi-Chi- Taiwan / CHY006	7.62	RO	9.8
1999	1202	1.4	28.1	Chi-Chi- Taiwan / CHY035	7.62	RO	12.7
1999	1503	5.7	28.0	Chi-Chi-Taiwan/ TCU065	7.62	RO	0.6
1999	1529	9.7	16.5	Chi-Chi-Taiwan/ TCU102	7.62	RO	1.5
1999	2457	3.2	8.6	Chi-Chi- Taiwan-03 / CHY024	6.20	R	19.6

T_p (sec): The period of the velocity pulse.

$D_{5\text{-}95}$ (sec): Significant duration of the records. The duration is defined as the time needed to build up between 5 and 95 percent of the total Arias Intensity.

R_{rup} (km): Closest distance to rupture plane.

R: Reverse.

SS: Strike-Slip.

N: Normal.
RO: Reverse-Oblique.

r= 5%, and a fixed damping ratio equal to 5%, we have formed a reference oscillator that is used as the basis for comparing all modified models.

4. EARTHQUAKE GROUND MOTIONS

A total of 33 ground motions have been used, recorded normal to the fault trace. The records and their properties are listed in Table 1. The classification of the records and their pulse period follows that of PEER NGA database [18]. In many records, the normal components show strong directivity effects (e.g. record #21, record #31), while the fault-parallel components are associated with weak directivity effects. In some cases, prominent directivity effects are evident in both components, as in Erzincan (record #23), where the pulse period is very close for both components.

5. PARAMETRIC INVESTIGATION

The influence of the type of the oscillator and its properties on the seismic demand are studied through plots of C_R versus the period of the systems.

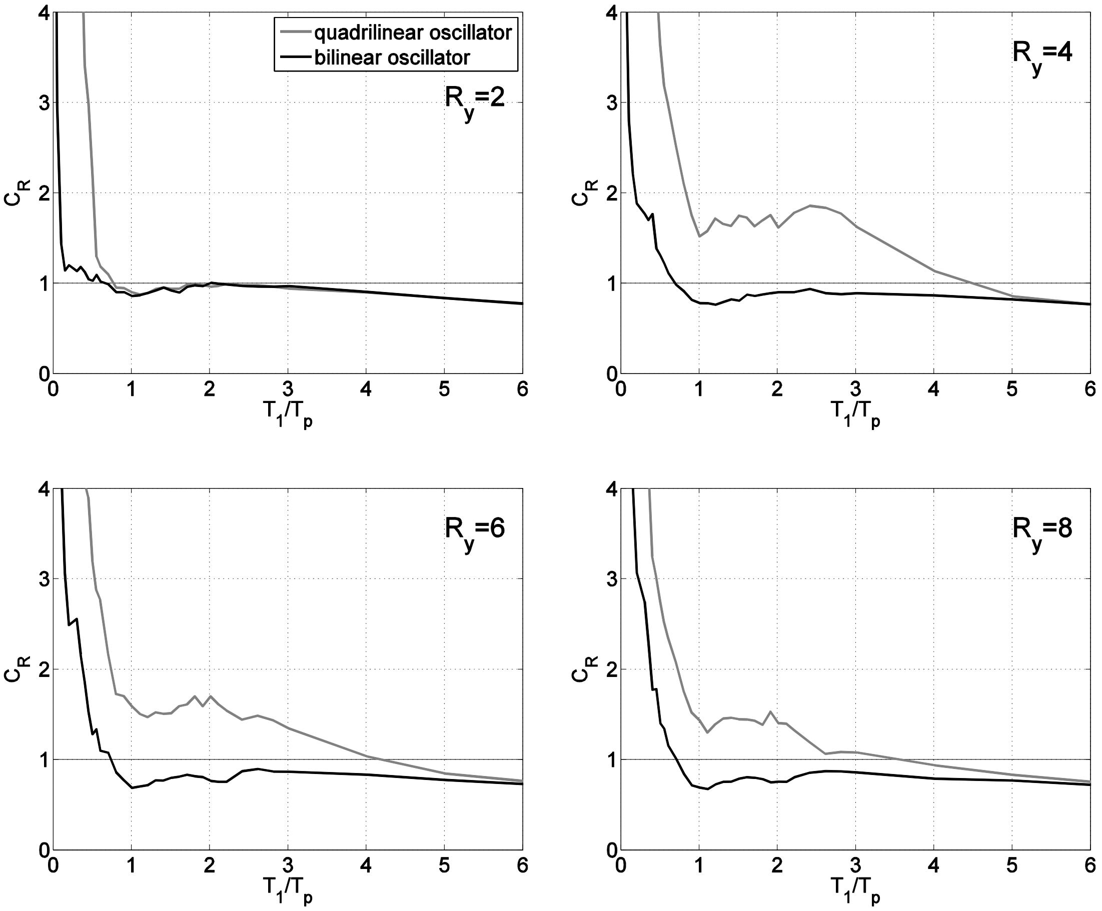

Figure 2: Median inelastic displacement ratios of quadrilinear oscillators and bilinear oscillators subjected to the normal component of pulse type records.

5.1 Influence of oscillator type

Current research on the effects of near-fault ground motions has concentrated on the investigation of bilinear systems, while there are very few studies on degrading systems, which is the case of most real world buildings. Figure 2, presents the median inelastic deformation ratio C_R of quadrilinear against bilinear systems. The oscillators are subjected only to the fault-normal component of ground motions that contain a velocity pulse. The post-stiffness ratio of the bilinear oscillator is set equal to 0.05, while the quadrilinear system is the reference oscillator, described in section 2. The plots are obtained for four different intensity levels corresponding to R_y factor values equal to 2, 4, 6 and 8.

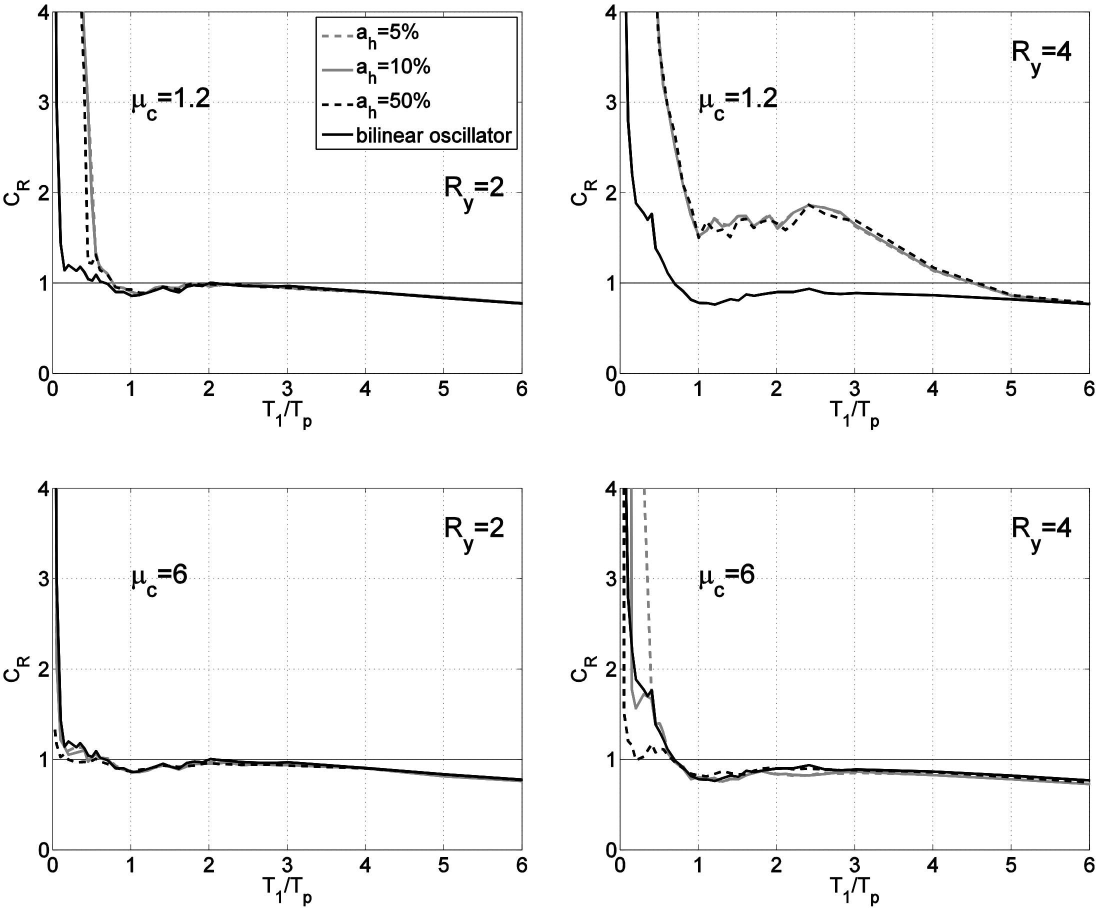

Figure 3: Influence of the slope of the hardening branch, a_h of the oscillators characterized by μ_c=1.2 and μ_c=6, on C_R.

According to Fig. 2, the ductility developed by quadrilinear oscillators exceeds the levels of the corresponding bilinear for given C_R values. For R_y=2, the two curves converge for normalized periods larger than 0.85, having significant divergence only for small T_1/T_p values. For weaker systems, as R_y increases, the bilinear SDOF underestimates the C_R-demand over the entire period range. For every level of R_y, the two curves converge to C_R=1 as T_1/T_p increases, which takes place approximately at T_1/T_p=4, as opposed to T_1/T_p=0.8 for bilinear systems. From Fig. 2, it is evident that median C_R values are quite different when computed for bilinear and quadrilinear systems, indicating that using a bilinear model to estimate the inelastic response, is conservative when the structure has a degrading backbone.

5.2 Influence of oscillator's properties

As shown in Fig.1, the oscillator can be fully described by four parameters. The four parameters are the non-negative slope of the hardening branch, a_h, the normalized displacement μ_c, which defines the beginning of the negative stiffness segment, the slope of the negative stiffness branch, a_c, and the height of the residual plateau, r, equal to the ratio of the residual strength over the yield strength. These backbone properties (a_h, a_c, μ_c, r) are set according to the reference oscillator and are varied one at a time to study their effect on C_R.

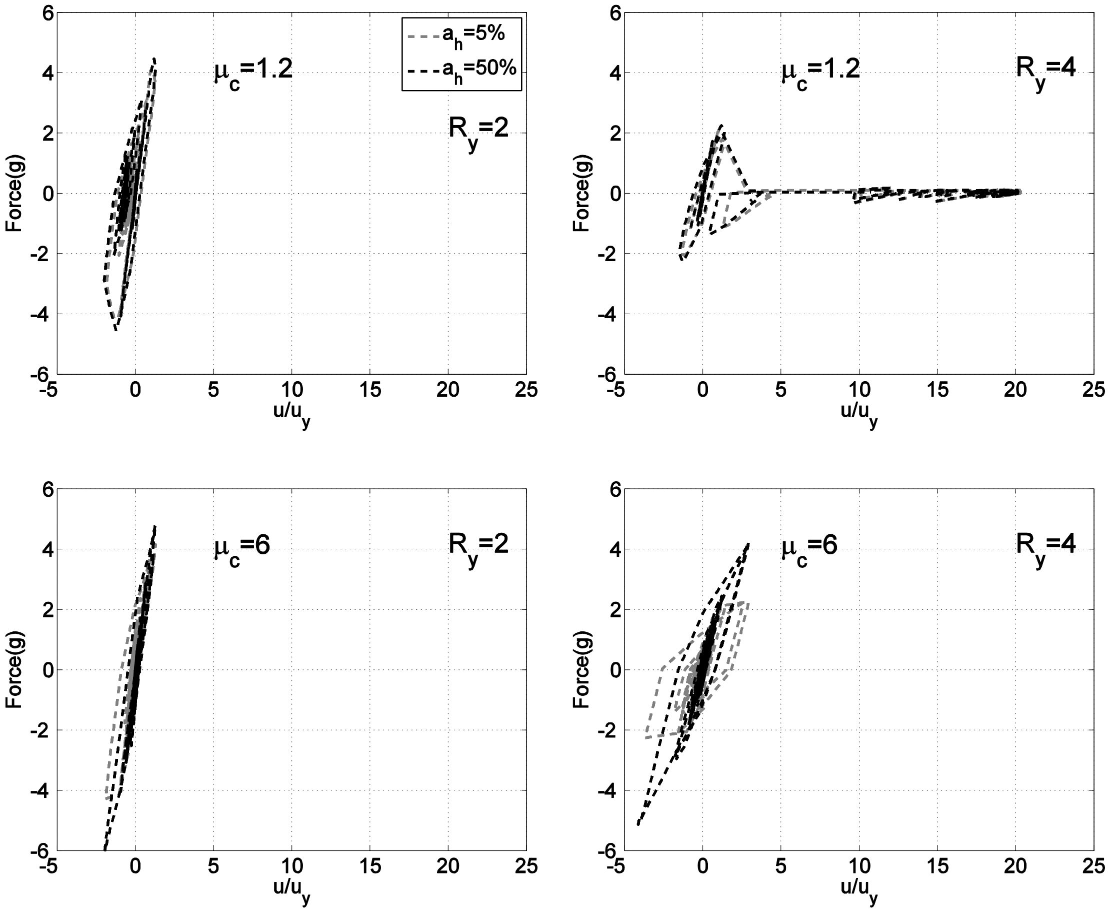

Figure 4: Hysteresis loops of quadrilinear oscillators characterized by μ_c=1.2 and μ_c=6 for the Chi-Chi Taiwan record and T_1/T_p=0.45.

Median inelastic displacement ratios for two quadrilinear oscillators characterized by μ_c=1.2 and μ_c=6 are presented in Fig. 3.The other backbone parameters are set according to the reference oscillator.

Compared to the oscillator having μ_c=1.2, the bilinear system (solid black line) underestimates the C_R compared to the quadrilinear oscillators, especially as R_y increases. Regardless of the R_y-demand, for T_1/T_p<1, the normal component of the near-field ground motions produce increased ductility demand compared to values beyond this limit. Considering nearly elastic systems (R_y=2), this threshold is slightly decreased to 0.85 and approaches the response observed for bilinear systems. In this region of small periods, the inelastic displacements are significantly higher than the elastic and increase exponentially for shorter periods. The increased C_R values at short periods, already apparent from the Newmark-Hall relationship (Eq.2), starts for T_1/T_p larger than that of the bilinear case. This segment is affected by the residual capacity of the system and will be shown more clearly when we will study the effect of the *r* parameter. For R_y>2, three regions can be identified. The first is, as in the case of systems with R_y=2, the ductility demand significantly exceeds R_y. In the second region, between T_1/T_p≈1÷2, C_R is stabilized around 1.5. For T_1/T_p>2, the values of C_R decrease linearly as T_1/T_p increases until a limiting value of T_1/T_p which depends on the level of R_y. This threshold also marks the beginning of the fourth, equal deformation region (R_y≈μ).

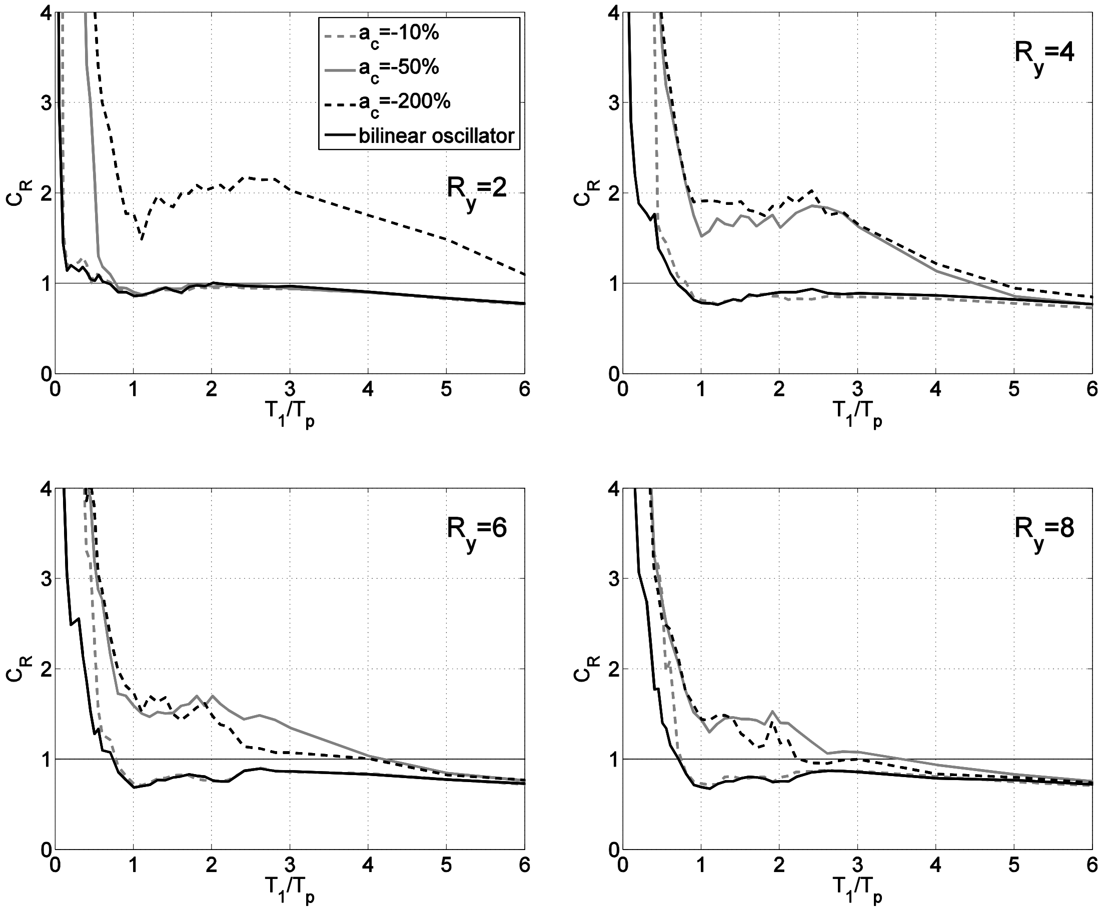

Figure 5: Influence of the negative slope, a_c of the negative stiffness segment on C_R.

On the other hand, if increasing μ_c of the reference oscillator from 1.2 to 6 the seismic response differentiates significantly and approaches that of the bilinear system. The effect of varying the slope a_h on C_R is increased mainly for fundamental periods less than 0.5.T_p and as the level of R_y increases. It can be noted that for a_h=50%, the produced C_R values are smaller than the values of the bilinear system.

Regarding the reference oscillator (μ_c=1.2), it can be observed that the sensitivity of C_R with respect to post-yield stiffness a_h, is rather small. The negligible differences when varying the slope a_h, are attributed to the hysteretic behavior of the system. To be more specific, the hysteresis loops of the reference oscillator and of the oscillator characterized by μ_c=6, for T_1/T_p equal to 0.45, subjected to the Chi-Chi Taiwan record (Table 1, #31), are shown in Fig.4, for R_y=2,4.

As can be seen from Fig.3, differences in the response of the reference oscillator are observed only for some T_1/T_p, values e.g., Fig.3, R_y=2 and T_1/T_p between 0.2 and 0.5. In that region as shown in Fig.4, the hysteresis is performed in the pre-fracturing range ($\mu<\mu_c$), forming large loops. The energy is absorbed in a narrow, with respect to the displacement, region around the origin of the axes, while the strength reaches its peak values. For larger ratio T_1/T_p the loops follow the same pattern of hysteresis for every level of R_y. For R_y>2 only a minor part of the hysteresis is performed in the initial range of the backbone, while the residual energy is absorbed through cycling beyond the negative drop. As R_y increases, the hysteresis of the backbone practically begins when the negative slope takes over, at a displacement over sixty times the corresponding yield displacement, while the level of strength is significantly reduced.

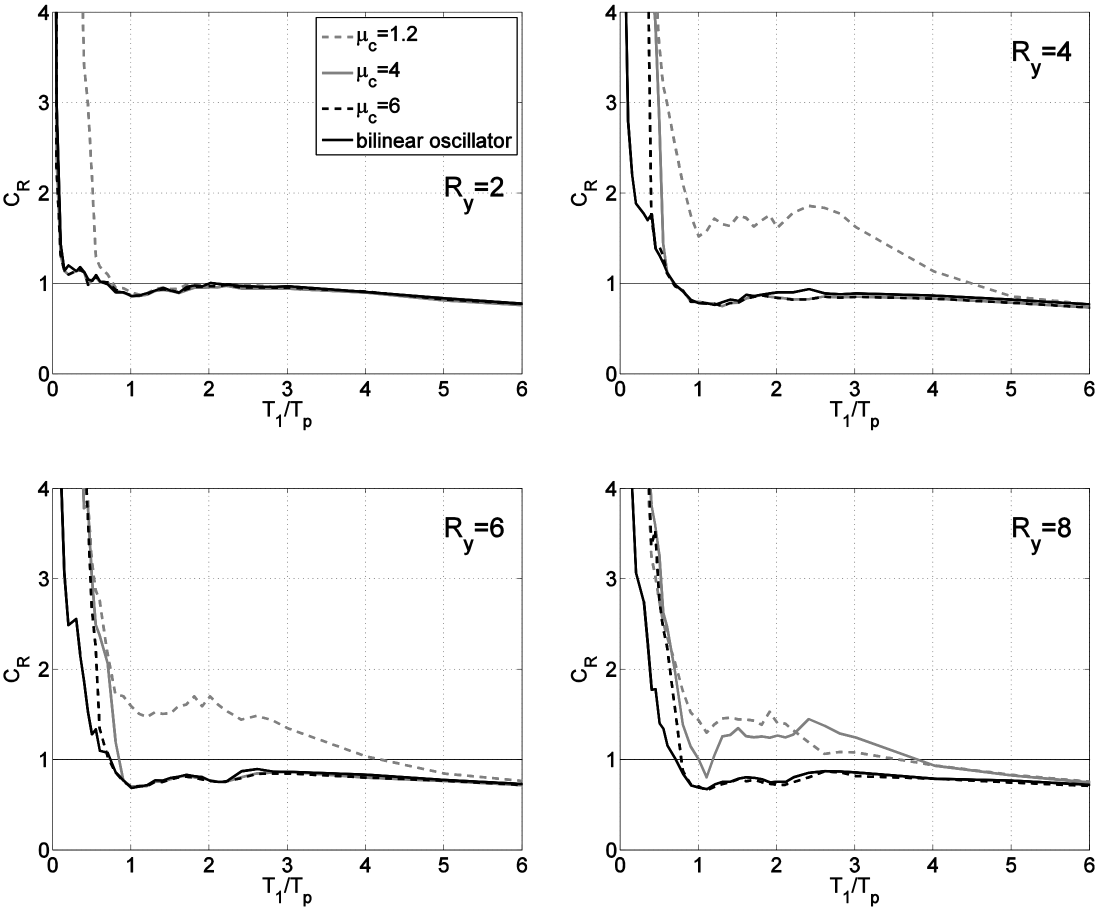

Figure 6: Influence of the normalized displacement, μ_c on the C_R

In the case of the oscillator characterized by μ_c=6, the variance in a_h shifts the hysteresis loops increasing the sensitivity of the response. For R_y=2, the response is not significantly influenced by the increase of μ_c and the hysteresis shape approaches that of the reference oscillator (μ_c=1.2). As R_y increases, the loops are formed again in the pre-fracturing region, while their shape is not affected. Respectively, the strength and displacement of the system under cyclic loading are not impressively varied with respect to the level of lateral strength, indicated by R_y. More pronounced variance in the shape of the loops can only be seen for large values of T_1/T_p and for highly ductile systems. Finally, it should be pointed out that with the exception of μ_c, neither the slope of the negative segment a_c nor the height of the residual plateau r, significantly affect the hysteretic behavior of systems with regard to variations of a_h.

Contrary to the rather insignificant effect of a_h on the seismic response of the reference oscillator, the variation of the negative stiffness slope a_c, has a more pronounced affect as shown in Fig. 5. For systems with R_y equal to 2, a_c=200% results to remarkably higher values of C_R compared to systems with smaller a_c values. Moreover, for a_c=200%, the spectral shape of C_R compared to other a_c values, is not affected by the increase in R_y. Inversely, a smaller slope value of 10% in the high-frequency and moderate-frequency region will give responses considerably smaller than those computed for oscillators having negative slope a_c=-50% or a_c=-200% and close to that of the bilinear system. This trend is amplified by the low value of the residual strength r and the relatively small value of μ_c of the reference system.

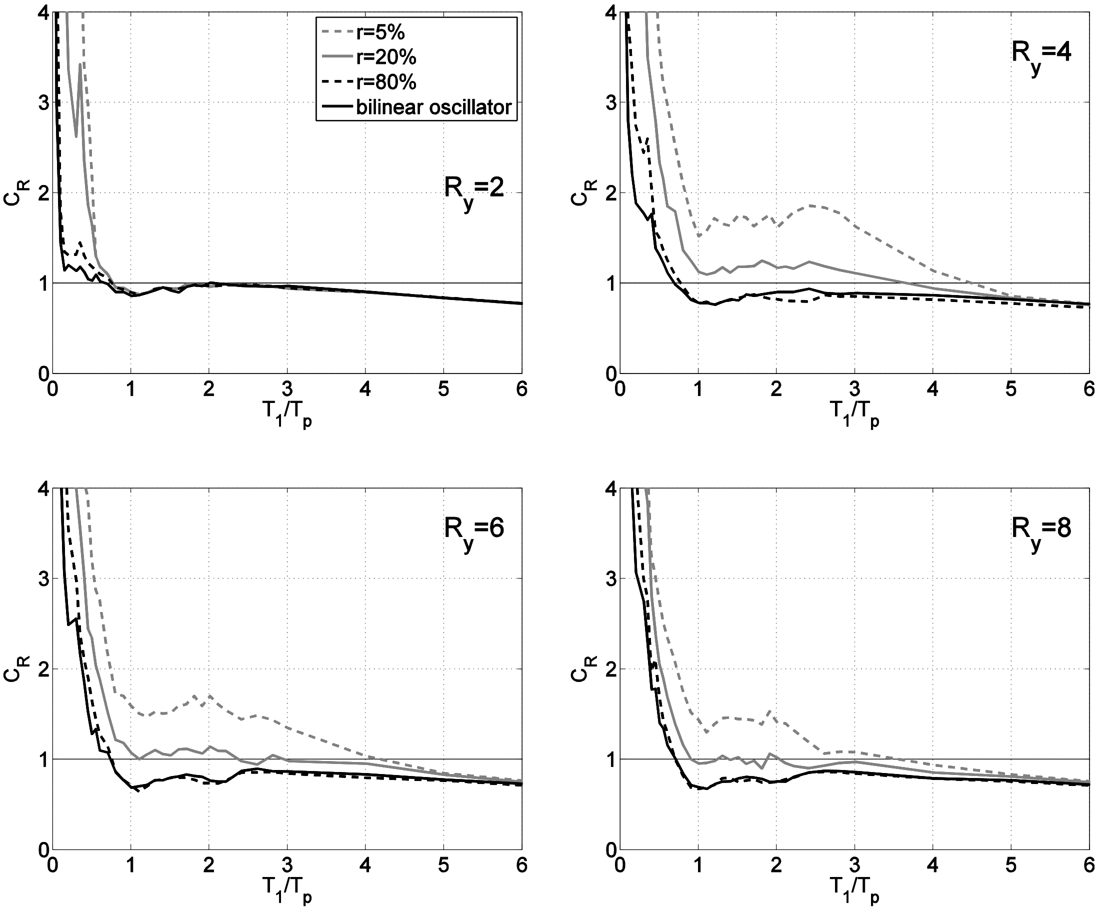

Figure 7: Influence of the height of the residual plateau, r, on the C_R.

It is remarked that increasing the value of μ_c is expected to affect mostly highly inelastic systems (R_y=8). Increasing the level of the residual strength (e.g., r=20%), will eliminate the sensitivity of the response to variations of a_c, thus reducing its importance. However, it can be proved that there is no divergence in the response of systems for a_c varying between 10% and 25%.

The response of quadrilinear oscillators with varying μ_c is very close to the response observed for varying a_c concerning the spectral shape of the curves and the T_1/T_p values, where the spectral shape differs (Fig. 6). For high and moderate R_y levels only oscillators with low μ_c (μ_c=1.2) have considerably divergent behavior. It should be pointed out that the influence of the normalized displacement on C_R is associated, as discussed before, to the properties of the reference oscillator. For residual strength r=20%, or larger, the effect of μ_c on C_R is smaller compared to the case of r=5%.

The sensitivity of seismic response to the r parameter is shown in Fig.7. The C_R curves corresponding to different values of r, have a similar degrading pattern, while, the peak values of C_R for T_1/T_p>1 and R_y=4, 6, 8 range around 1.5 and 2 and coincide with the formerly computed values. The trends observed in the previous plots are verified again. The different regions are clearly segregated, while the T_1/T_p thresholds coincide with the previously mentioned values. For R_y=2, the differences on C_R are clustered in the region of small periods (T_1/T_p<0.85). The response seems very sensitive to r, while as R_y increases causes larger divergences in C_R values, compared to all other parameters investigated. The deviation in the calculated values can be observed for every value of the r, not only for the outliers, and is obvious for a wide range of periods, regardless of R_y.

6 CONCLUSIONS

The median of inelastic displacement ratios, C_R, of bilinear and quadrilinear oscillators with varying backbone parameters when subjected to fault-normal, near-fault ground motions are investigated. The conclusions of this study are briefly summarized:

- The relationship between the peak deformation of the inelastic and the corresponding linear SDOF systems is considerably affected by the properties of the oscillator. Oscillators with quadrilinear backbones produce C_R values remarkably higher than those of bilinear oscillators.
- The properties of the backbone affect significantly the seismic behavior. The C_R ratios are sensitive to all four backbone parameters. Among the four parameters considered, the normalized height of the residual plateau r, seems to be the most influential for almost all periods values, regardless of the level of R_y-demand. However, the response is also sensitive to the combination of the four parameters, especially that of μ_c and r.
- For nearly elastic systems the differences on C_R are clustered in the region T_1/T_p<0.85, while after this threshold the equal deformation rule applies. For larger R_y values four regions can be identified, depending on the value of the T_1/T_p ratio. Initially increased ductility demand increases C_R for shorter periods. In the second region, $T_1/T_p \approx 1 \div 2$, C_R is stabilized around 1.5. For T_1/T_p>2, C_R decreases linearly as T_1/T_p increases, until a limiting value, beyond which the equal-displacement rule applies.

REFERENCES

[1] Alavi B., Krawinkler H., Effects of near fault ground motions on frame structures, *Report No.138,The John A. Blume Earthquake Engineering Center, Department of Civil and Environmental Engineering,* Stanford University, 2001.

[2] Báez, J.I., Miranda, E., Amplification factors to estimate inelastic displacement demands for the design of structures in the near field, *12th World Conference on Earthquake Engineering,* 2000.

[3] Baker J.W., Quantitative classification of near-fault ground motions using wavelet analysis, *Bulletin of the Seismological Society of America*, **97,** 1486-1501, 2007.

[4] Bertero V.V., Mahin S.A., Herrera R.A., A seismic design implication of near-fault San Fernando earthquake records, *Earthquake Engineering and Structural Dynamics*, **6**, 31–42, 1978.

[5] Chopra A.K., Chintanapakdee C., Comparing response of SDF systems to near-fault and far-fault earthquake motions in the context of spectral regions, *Earthquake Engineering and Structural Dynamics*, **30**, 1769-1789, 2001.

[6] Chopra A.K., Chintanapakdee C., Inelastic Deformation Ratios for Design and Evaluation of Structures: Single-Degree-of-Freedom Bilinear Systems, *Journal of Structural Engineering*, **130**, 1309-1319, 2004.

[7] Chopra A.K., *Dynamics of Structures, Theory and Applications to Earthquake Engineering, 3rd Edition*, Pearson Prentice Hall, Pearson Education Inc, 2007.

[8] Garcia J.R., Miranda E., Inelastic displacement ratios for evaluation of structures built on soft soil sites, *Earthquake Engineering and Structural Dynamics*, **35,** 679-694, 2006.

[9] Ibarra L., Medina R., Krawinkler H., Hysteretic models that incorporate strength and stiffness deterioration, *Earthquake Engineering and Structural Dynamics*, **34**, 1489-1511, 2005.

[10] Mahin S.A., Bertero V.V., Chopra A.K., Collins R.G., Response of the Olive View Hospital Main Building during the San Fernando Earthquake, *Report No. EERC 76-22*, *Earthquake Engineering Research Center,* University of California, Berkeley, 1976.

[11] Makris N., Black C.J., Evaluation of Peak Ground Velocity as a ‘‘Good’’ Intensity Measure for Near-Source Ground Motions, *Journal of Engineering Mechanics*, **130**, 1032-1044, 2004.

[12] Maniatakis Ch.A., Taflampas J., Spyrakos C.C., Identification of near-fault earthquake record characteristics, *14th World Conference on Earthquake Engineering*, Beijing, China, October 12-17, 2008.

[13] Mavroeidis G.P., Dong G., Papageorgiou A.S, Near-fault ground motions, and the response of elastic and inelastic single-degree-of-freedom (SDOF) systems, *Earthquake Engineering and Structural Dynamics*, **33**, 1023-1049, 2004.

[14] Mavroeidis G.P., Papageorgiou A.S., A mathematical representation of near-fault ground motions, *Bulletin of the Seismological Society of America*, **93**, 1099-1131, 2003.

[15] Miranda E., Estimation of inelastic deformation demands, *Journal of Structural Engineering*, **127**, 1005–1012, 2001.

[16] Miranda E., Inelastic displacement ratios for structures on firm sites, *Journal of Structural Engineering*, **126**, 1150–1159, 2000.

[17] Newmark N.M., Hall W.J., *Earthquake Spectra and Design,* Earthquake Engineering Research Institute, Berkeley CA, 1982.

[18] PEER Strong Motion Database: http://peer.berkeley.edu/products/strong_ground_motion_db.html.

[19] Ruiz-García J., Inelastic Displacement Ratios for Seismic Assessment of Structures Subjected to Forward-Directivity Near-Fault Ground Motions, *Journal of Earthquake Engineering*, **15**, 449-468, 2011.

[20] Somerville P.G., Magnitude scaling of the near fault rupture directivity pulse, *Physics of the Earth and Planetary Interiors*, **137**, 201-212, 2003.

[21] Somerville P.G., Smith N.F., Graves R.W., Abrahamson N.A., Modification of empirical strong motion attenuation relations to include the amplitude and duration effects of rupture directivity, *Seismological Research Letters*, **68:1**, 199-222, 1997.

[22] Spyrakos C.C., Maniatakis Ch.A., Taflambas J. Evaluation of near source seismic records based on damage potential parameters. Case study: Greece, *Soil Dynamics & Earthquake Engineering*, **28**, 738-753, 2008.

[23] Sucuogly H., Erberik M.A., Yucemen M.S., Influence of peak ground velocity on seismic failure probability, *4th International Conference of the European Association for Structural Dynamics (EURODYN' 99)*, Prague, Czech Republic, 1999.

[24] Taflampas I., Psycharis I.N., Investigation of the effect of the ground motion characteristics on the R_y-μ relation for the inelastic response of sdof structures, *14th World Conference on Earthquake Engineering*, Beijing, China, October 12-17, 2008

[25] Taflampas I., Spyrakos C.C., Maniatakis Ch.A., A new definition of strong motion duration and related parameters affecting the response of medium-long period structures, *14th World Conference on Earthquake Engineering,* Beijing, China, October 12-17, 2008.

[26] Vamvatsikos D., Fragiadakis M., Seismic performance sensitivity of a 9-story steel frame to plastic hinge modeling uncertainties, *1st European Conference on Earthquake Engineering and Seismology*, Geneva, Switzerland, 3-8 September 2006.

[27] Veletsos A.M., Newmark N.M., Effect of inelastic behavior on the response of simple systems to earthquake motions, *2nd World Conference on Earthquake Engineering*, **2**, 895-912, Tokyo, Japan, 1960.

COMPDYN 2011
III ECCOMAS Thematic Conference on
Computational Methods in Structural Dynamics and Earthquake Engineering
M. Papadrakakis, M. Fragiadakis, V. Plevris (eds.)
Corfu, Greece, 25–28 May 2011

ESTIMATION OF THE SEISMIC RELIABILITY OF BUILDINGS USING INCREMENTAL DYNAMIC ANALYSIS METHOD OF THE SECANT STIFFNESS DEGRADATION INDEX (*IDAM-SSDI*). PART II

Marco Antonio Montiel Ortega[1], **Guillermo Arturo Díaz de León Piña**[1]

[1]Universidad Autónoma de Querétaro, México
Cerro de las Campanas s/n; Santiago de Querétaro, Qro., México,
mmo02@hotmail.com; gmo@uaq.mx

Keywords: Seismic reliability, Incremental Dynamic Analysis (IDA), Secant Stiffness Degradation Index (SSDI), Cornell's Reliability Index.

Abstract. *Presented herein is a methodology that enables us to obtain in an efficient manner the seismic reliability of buildings for different levels of seismic intensity, taking into account the uncertainties associated with the properties of the structural system considered and with the seismic registers. This methodology is developed by means of Incremental Dynamic Analysis of the Secant Stiffness Degradation Index (IDA-SSDI), whose results enable evaluation of the intensity of system collapse in an easy and efficient manner in order to evaluate the reliability by means of Cornell's β index and a Z safety margin. The methodology is applied to a sample of eight 10-story buildings taken from Monte Carlo's simulation and 40 accelerograms registered in the Valley of Mexico City. The buildings simulated are modeled in the computer program DRAIN 2D for non-linear analysis.*

1 INTRODUCTION AND METHODOLOGY

The objective of this research is to collaborate in the mitigation of risks of a natural phenomenon that has been considered very important due to its effects and its ability to cause the end of the life cycle of a structure in a few seconds as in a seismic movement. The collapse of a structure brings with it the loss of human life and property which is associated with this type of natural disaster. The analysis of the probability of structural failure or of its complement, structural reliability, which has its beginnings in the 1960's, has served as a base in the development of structural engineering design methods that are presently being utilized as a guide in the creation of codes and manuals employed for the design and construction of secure structures by taking into account natural phenomena and uncertainties throughout the world.

Estimating of this structural reliability with reference to collapse occasioned by some seismic action is based on the capacity of lateral deformation in such a way that this collapse occurs when the maximum amplitude of the structural seismic response, or demand, surpasses the structural capacity. The deformation capacity concept as an indicator of the variable that determines the condition of collapse has severe limitations in its practical use when being used in quantitive terms.

These limitations range from sensitivity at the moment of impeding the collapse to certain variables, such as: the lateral deformation pattern of the system and the reductions of resistance and stiffness associated with the damage produced by previous response cycles corresponding to previous seismic occurrences, or by other causative agents of damage such as differential settlements. All these factors have inspired many new investigative endeavors to develop alternative criteria oriented to obtaining probabilistic estimations of seismic intensity values that lead to system collapse *(Y_C)*.

One of the criteria utilized is the *I*ncremental *D*ynamic *A*nalysis *M*ethod *(IDAM)* proposed by Vamvatsikos and Cornell [1], which is based on the collapse intensity estimation *(Yc)* with the help of an adequate scale factor that should be applied to the accelerogram. The possibilities of visualizing the evolution of the seismic response amplitudes in the manner in which the intensity grows and of observing the values reached by that intensity before the appearance of the seismic response amplitude outside of its limits, constitutes an important advantage of this method. For these reasons, in this article, the collapse intensity *(Yc)* is obtained by using the *I*ncremental *D*ynamic *A*nalysis *M*ethod but applied for the first time to the *S*ecant *S*tiffness *D*egradation *I*ndex *(IDAM-SSDI)*. This index is arrived at by the following equation [2]:

$$\boldsymbol{D}(\boldsymbol{y}) = \mathbf{1} - \frac{\boldsymbol{K}}{\boldsymbol{K_0}} \tag{1}$$

Where *(y)* is the intensity of the seismic movement, K_0 is the value that K acquires when linear, and K is the value of the degraded secant stiffness adopted by the system at the moment when the lateral displacement in the roof reaches its maximum value. In this way, the collapse intensity *(Yc)* is obtained when $D(Yc)=1$.

On the other hand, the seismic reliability level is obtained by means of Cornell's [3] reliability index β, as follows:

$$\boldsymbol{\beta}(\boldsymbol{y}) = \frac{\boldsymbol{m_Z}(\boldsymbol{y})}{\boldsymbol{\sigma_Z}(\boldsymbol{y})} \tag{2}$$

Where $m_Z(y)$ is the median value of the building security margin Z before an earthquake with an intensity equal to *(y)*, and $\sigma_Z(y)$ is the standard deviation of the said security margin. For the estimation of the index $\beta(y)$, for the present work, an alternative approach proposed by Díaz and Esteva, [4] was used, where the safety margin $Z(y)$ is defined as the natural logarithm of the rate of *(Yc)* and of the intensity of the ground movement *(y)* that act upon the system.

$$Z(y) = ln\frac{Y_C}{y} = lnY_C - lny \tag{3}$$

Consequently, collapse occurs when *Z(y)=0* for *D(y)=1*. The reliability index is defined as:

$$\beta(y) = \frac{E(lnY_C) - ln(y)}{\sigma(lnY_C)} \tag{4}$$

Where *E(lnYc)*, is the expected value of *lnYc*.

2 ANALYZED STRUCTURES

The aforementioned methodology is applied to a sample of eight 10-story buildings from the Monte Carlo simulation taking into account the uncertainties associated with the concrete strength *(f'c)*, the steel yield *(fy)*, the live loads *(Wvmax)* and 40 accelerograms registered in the valley of Mexico City. The geometric properties of the original building are shown in Figure 1a. The building was designed in accord with the Mexico City Seismic Design Code [5,6] for office use. The fundamental period of the building is $T_o = 1.17s$ and has a yield strength coefficient of *Cy=0.4*, [7].

The simulated buildings are modeled in the DRAIN 2D program modified by Campos and Esteva [8], for its linear analysis. Each building contains an exterior and interior structural frame connected by a rigid floor diaphragm. The coupling between the frames was taken into account by means of a two-dimensional structural model connected by hinged links, see Figure 1b. The frames were constituted by flexural beams and columns. The moment-rotation ratio for each element was calculated assuming the model for confined concrete originally proposed by Kent and Park [9] and modified by Park et al [10]. The axial stress-strain ratios corresponding to the steel bars were represented by means of Mander model [11]. The hysteretic structural behavior was assumed to be bilinear with the ratio of the post-yielding to the initial stiffness equaling 3.0%.

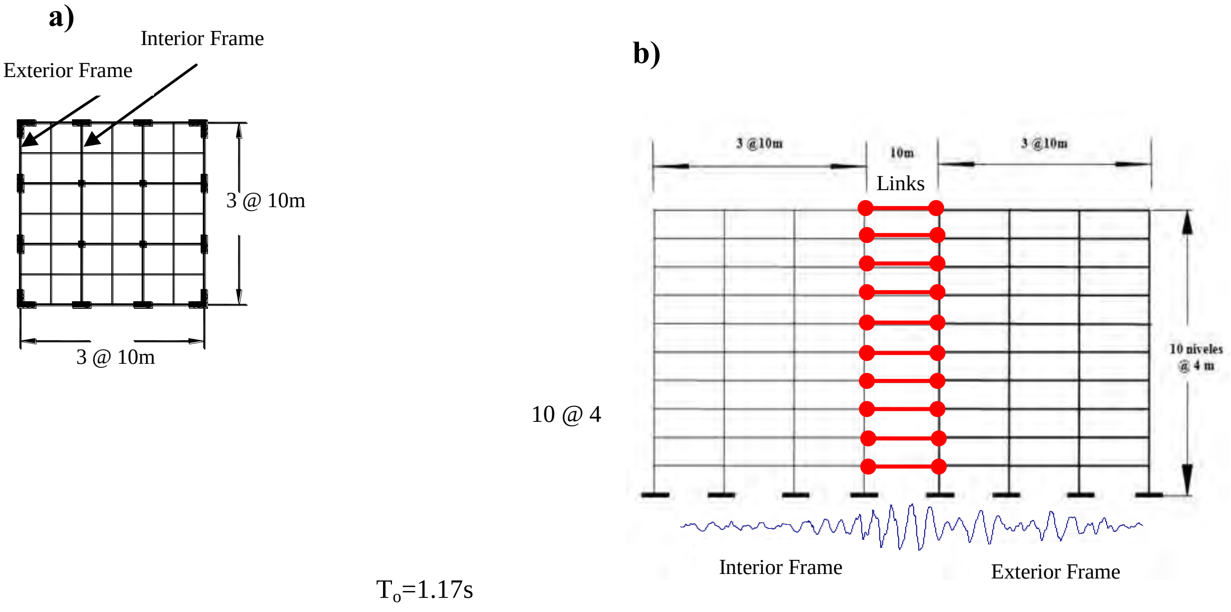

Figure 1. a) Original building plan and elevation and b) two-dimensional model used for non-linear analysis.

In Table 1 the eight models are shown that consider the uncertainties of the mechanical properties of the materials (f'_c and f_y) and in the maximum live loads applied ($W_{v\text{máx}}$). The nominal values *(MM)* and means *(MN)* are also shown. In this table the nomenclature (*M1-M8)* is used to denote the models with uncertain values for mechanical properties of the materials and applied live loads. *(M9)* is used for the model with median values and *(M10)* is used for the model with nominal values. The uncertain values of each parameter (f'_c, f_y and $W_{v\text{máx}}$) are obtained through simulations [12].

Frame	***f'_c (kg/cm^2)***	***f_y (kg/cm^2)***	***$W_{v\text{máx}}$ (kg/m^2)***
M1	308	5090	78
M2	246	4445	134
M3	287	3970	40
M4	234	4816	89
M5	250	4055	57
M6	199	5553	99
M7	330	5974	104
M8	304	4407	67
M9=MM	**268**	**4680**	**75**
M10=MN	**250**	**4200**	**180**

Table 1. f'_c ,f_y y $W_{v\text{máx}}$ values used in frame analysis.

3 SEISMIC MOVEMENTS USED FOR THE ANALYSIS

The analysis of seismic reliability requires the use of registers that can adequately reflect the dynamic characteristics and the energy content of the seismic movements expected to occur at the construction site. For this analysis, forty narrow-band earthquakes registered in the lake region of Mexico City were used. All the seismic movements were recorded during subduction events with epicenters located on the Pacific coast of Mexico, see Figure 2a, which present magnitudes *(Mw)* from 6.0 to 8.1 grades. The corresponding elastic strength spectra of pseudo-acceleration are shown in Figure 2b, for a critical damping percentage (ξ) of 5%. It can be seen that the seismic movement spectra present dominant periods of between 1.5 and 2.2s.

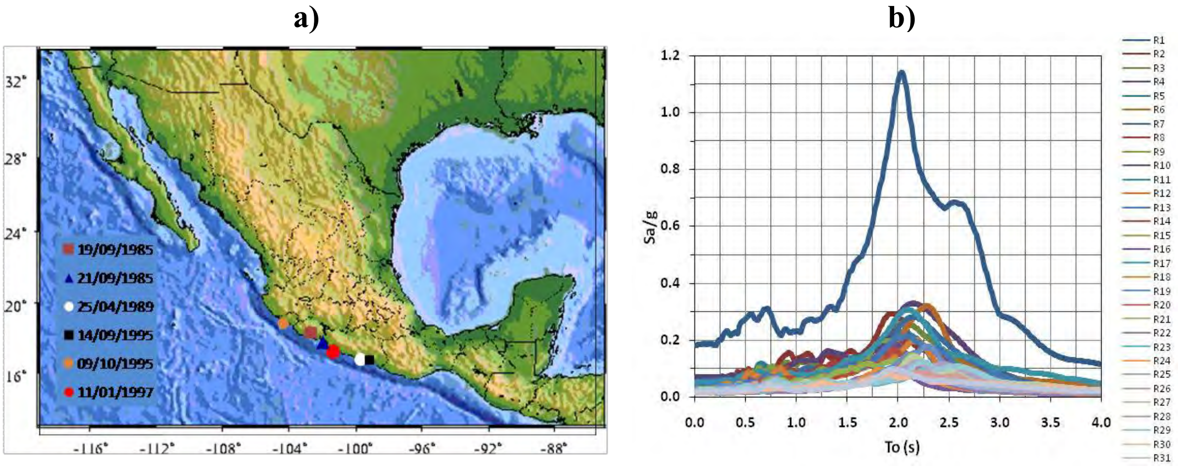

Figure 2. a) Subduction earthquake epicenters used for the analyses and, b) the pseudo-acceleration corresponding elastic spectra for 5% damping.

4 INCREMENTAL DYNAMIC ANALYSIS OF THE SECANT STIFFNESS DEGRADATION INDEX *(IDA-SSDI)*.

The *I*ncremental *D*ynamic *A*nalysis *M*ethod of the *S*ecant *S*tiffness *D*egradation *I*ndex ***(IDAM-SSDI)*** was used to obtain the probabilistic estimations of the seismic intensity values that lead to system collapse in order to evaluate the structural reliability. These results are shown in Figure 3 associated with the 40 earthquakes and eight 10-story frames used for the analysis, taking into account the uncertainties associated with the earthquakes and the mechanical properties of the building materials. In this figure, we graph the seismic intensity level measured by means of the pseudo-acceleration spectral corresponding to the fundamental period of the structure $(T_o=1.17s)$ for a 5% critical damping *(Sa/g)* divided by the acceleration of gravity *(g)*, which in turn has been affected by an adequate scaling factor in order to bring about the collapse of the structure.

In the horizontal axis the performance of the structure is graphed measured by the Secant Stiffness Degradation Index *D(y)*, which is an index proposed as an indicator of structural damage caused by an earthquake according to increase in intensity. The seismic effects decrease the capacity of the building leaving the structural system in a state of greater vulnerability and eventually leading to collapse.

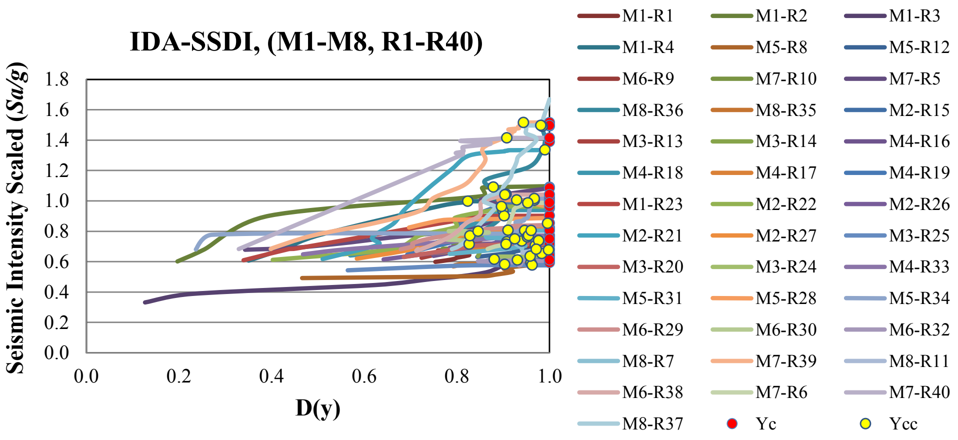

Figure 3. Incremental Dynamic Analysis of the Secant Stiffness Degradation Index (*IDA-SSDI*) for 40 earthquakes and the eight 10-story buildings being studied. Yellow circles indicate the intensity approaching collapse (Y_{CC}) and red circles indicate the collapse intensity (Y_C).

The curve forms in Figure 3 vary depending on the earthquake, the frame and the grade of the non-linear structure. These curves are obtained by scaling the seismic intensity until a state of collapse occurs. This is indicated in the figure by means of red circles $(Y_{C,})$, which occur when the secant stiffness degradation value adopted by the system at the moment when the lateral displacement in the roof reaches its maximum value, that is zero, $(K=0)$. That is to say, when the Secant Stiffness Degradation Index is equal to the unit $(D(Y_c)=1)$, which corresponds to a base shear in terms of very low or zero capacity. One moment before the state of collapse occurs, the seismic intensities nearing collapse are obtained, which are indicated in the figure with yellow circles (Y_{Cc}), varying from $0.823 \leq D(y) < 1.0$. Using *D(y)* as an index of collapse is very useful because it eliminates the difficulty of defining the collapse state from the maximum displacement of the roof. By means of *IDAM-SSDI* analysis, valuable information can be obtained regarding the behavior of the structural system ranging between $0.8 \leq d < 1.0$ associated with the limit state near collapse.

The statistical values of the parameters corresponding to the average and to the standard deviation of collapse and near collapse for the intensity and the damage index are shown in Table 2.

	Y_{Cc} Sa/g	Y_C Sa/g	$D(Y_{Cc})$	$D(Y_C)$
Average	0.8832	0.8898	0.9308	1.00
Standard deviation	0.2610	0.2620	0.0470	0.00

Table 2. Statistical parameters of the limit state near collapse and at collapse.

There are no significant differences between the intensities Y_{Cc} and Y_C needed in order to evaluate reliability, which is not the case for $D(Y_{Cc})$ and $D(Y_C)$, whose values vary depending on the structural sensitivity in the zone near collapse.

The Incremental Dynamic Analysis Method results attained for each frame and earthquake by means of the scale factors used from a state near collapse to a state of collapse intensity (Y_C) are presented in Figure 4. The curves with greater slope require a Scaling Factor (***SF***) greater than that required for curves with lesser slope. It can be observed that for some earthquakes, very low scale factors of 3 or 4 are needed; for other earthquakes, factors as high as 70 or 80 are needed, which means that these factors vary due to the uncertain nature of earthquakes and the variations in mechanical properties of the materials of the buildings under investigation.

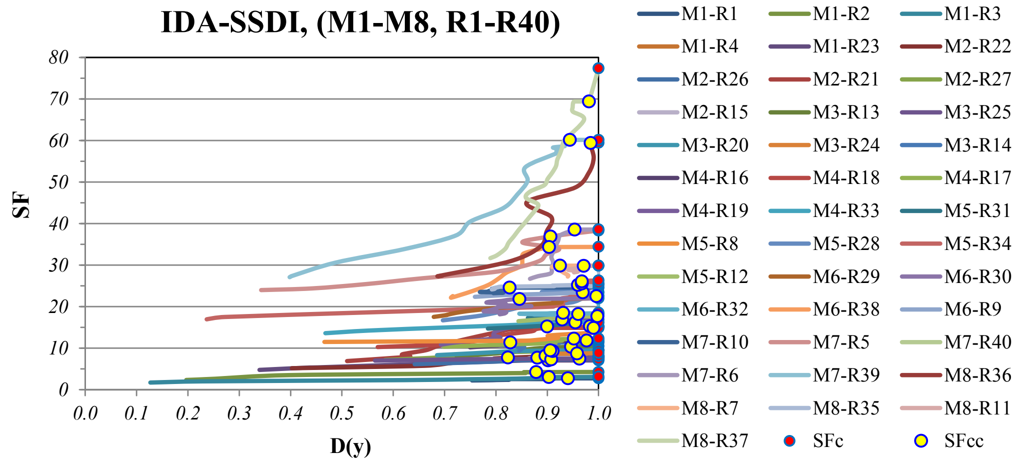

Figure 4. Incremental Dynamic Analysis Method of the Secant Stiffness Degradation Index (*IDAM-SSDI*), depending on the scale factor (*SF*).

It can also be observed that the seismic collapse intensity values range from 0.594*g* as a minimum value in Figure 3 for the Frame *M8* and the earthquake *R35* with a 25.21 scaling factor *SF* in Figure 4, up to the maximum value of 1.52*g* found for Frame *M7* for the seismic record *R39* with a 60.17 *SF*.

Figures 5a, b, and c, show the effect of the scale factor *(SF)* has on the overall structural response and is represented by means of the base shear and maximum roof displacement hysteresis cycles. From this the secant stiffness *(K)* required to obtain the damage index *D(y)* is obtained. This stiffness is obtained from the straight line slope that connects the origin with the maximum roof displacement. The slope is obtained by dividing the base shear from the corresponding maximum roof displacement.

In Figure 5a, it can be observed that for a *SF=17.51* for this earthquake and frame *(R34, M5)*, there exists an almost linear behavior, such that the secant stiffness *K=7196.92 tons/m* is similar to the elastic stiffness: $K_0=9882.86$ *tons/m*, so that the result for the damage index is low: *D(y)=0.272*. This is to say, a structure that is practically elastic.

In Figure 5b, for *SF*=23, the nonlinear behavior is significant, therefore the secant stiffness is low: *K=384.40 tons/m*, resulting in a damage index close to one: *D(y)=0.9611*.

In Figure 5c, for an *SF*=26.30, as can be observed, the structure has collapsed, and displacements is considerable, giving a value of *K=0*; and therefore, a damage index of *D(y)=1*.

Of course, in the previous cases, there was intermediate *SFs,* which made possible the observation of the evolution of the damage index *D(y)* as can be seen in Figures 3 and 4.

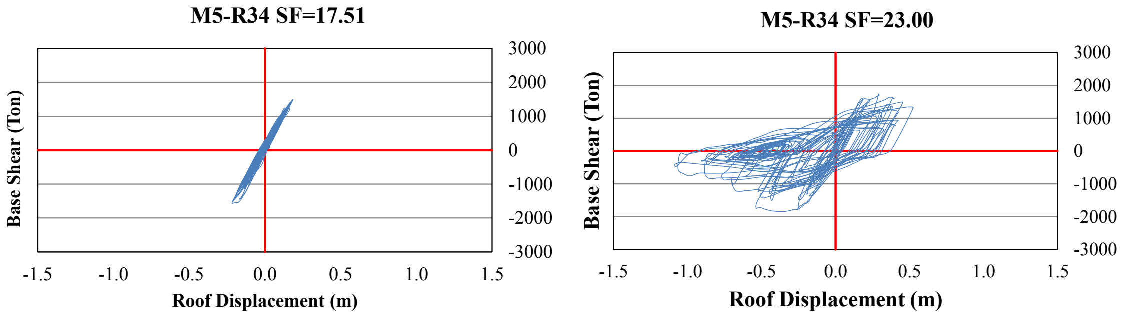

a) Practically elastic structure, *D(y)=0.272*.

b) Near collapse structure, *D(y)=0.9611*.

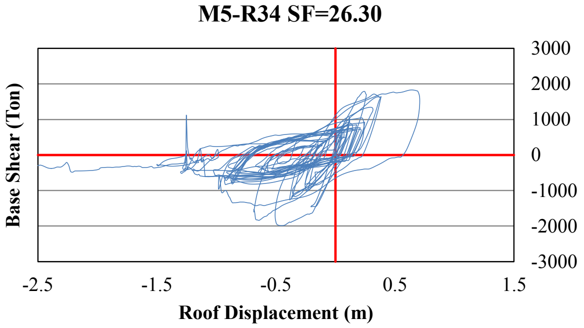

c) Collapsed structure, *D(y)=1*.

Figure 5. Global response hysteresis cycles for different Scale Factors *(SF)*.

The elastic stiffnesses *(K_0)* of the simulated frames were obtained from the Pushover analyses, which are shown in Figure 6.

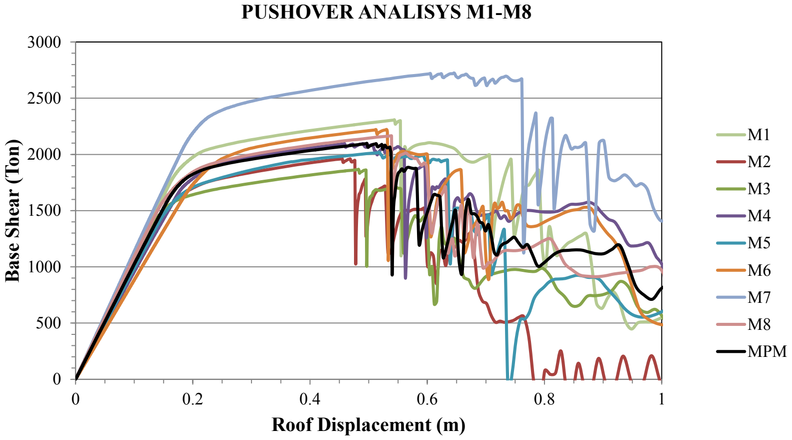

Figure 6. Pushover analyses for eight 10-story frames (M1-M8). The black line corresponds to the frame with mean mechanical proprieties (MPM).

5 RELATIONSHIP BETWEEN THE DAMAGE INDEX *D(y)* AND THE SAFETY MARGIN *Z(y)*.

Another way of seeing how structures vary as they near to collapse, when *D(y)* reaches its maximum value *D(y)=1*, is by means of the relationship between the damage index *D(y)* and the safety margin *Z(y),* which is a function of the collapse intensity (Y_C), and the earthquake intensity (*y*), in other words: $Z(y)=ln(Y_C)-ln(y)$, see Equation 3. The value pairs for these variables can be seen in Figure 7 for the different frames and earthquakes analyzed. It can be observed that as the safety margin decreases the structure approaches collapse when *D(y)=1* and *Z(y)=0.* This tendency can be better seen by means of linear regression represented by the blue curve representing the expected value of the safety margin *E(Z)*. It can be noted that this curve begins in an area where the values represent a low structural vulnerability, values of $Z>0$ far from collapse and values for *d* close to zero with linear elastic structural behavior, to the collapse values when *(D=d=1, Z=z=0)*, or better, when *lnD=0* and *Z=0*. In the event that *Z(y)* is negative, $Z(y)<0$ indicates that the structural collapse intensity *(Y_C)* was surpassed by the earthquake intensity *(y)*, which is to say that it has already collapsed *D(y)=1*, as can be seen in Figure 7.

Figure 8 shows the deviation trend for the safety margin Z related to the damage index values *D(y)* and its trend curve which is produced by linear regression. It may be noted that in general the values are low as the structure approaches collapse $D(y)\Rightarrow 1$, the variance $\sigma^2(Z)$ tends to zero.

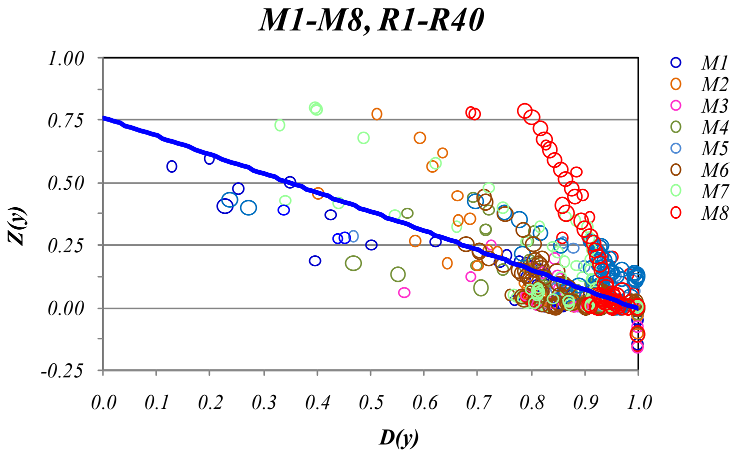

Figure 7. Relationship between the damage index *D(y)* and the safety margin *Z(y)*. Blue line: expected value of *E(Z)*.

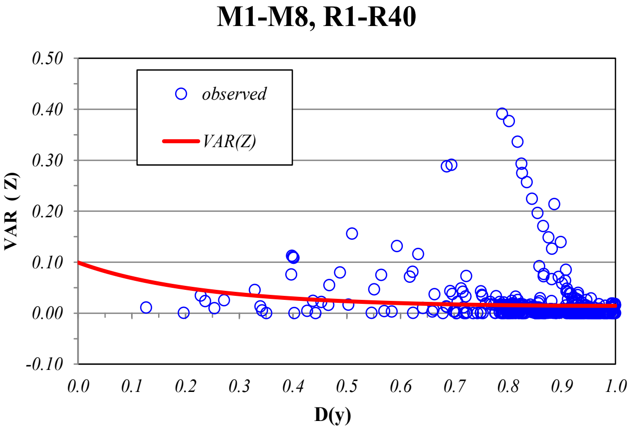

Figure 8. Mean square error values used to estimate the variance of Z and its trend line in red.

6 OBTAINING SEISMIC STRUCTURAL RELIABILITY: *β(y) vs Z(y)*.

With the collapse intensities *(Y_C)* obtained from the *IDA's,* the seismic reliability of buildings in terms of the safety margin Z in Figure 9 is obtained. The straight lines of the figure are obtained using Cornell's index *β(y)* (vertical axis) corresponding to the eight 10-story frames and 40 earthquakes used for the analyses and how they relate to the safety margin for *Z(y)* (horizontal axis), from the state of system collapse when $Z(y=Y_C)=0$, to values of $Z(y<<Y_C)=1$, when the intensity of the earthquake *(y)* is much lower than that of collapse *(Y_C)*, when the structure is elastic. As can be seen, their relationship is linear, so a greater safety margin *Z(y)* in the system corresponds to a higher reliability index *β(y)* in the structure.

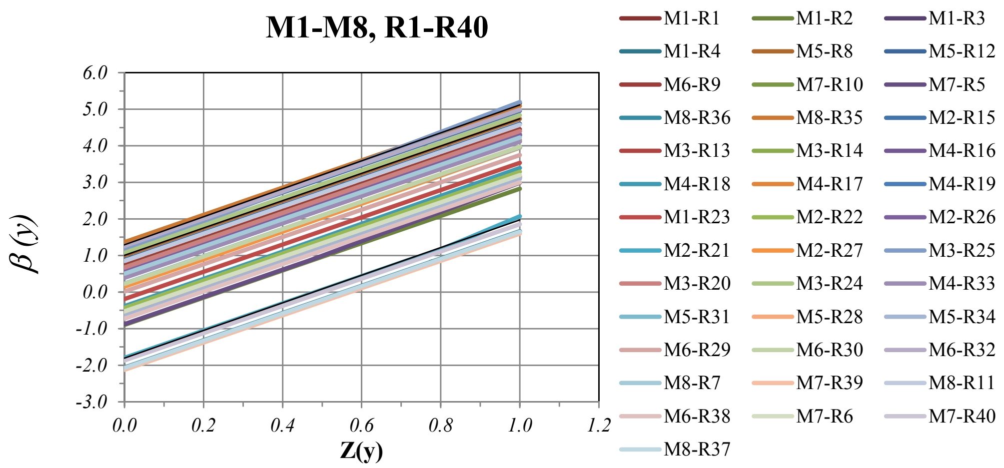

Figure 9. Cornell's Reliability Index $\beta(y)$ for different values of the Safety Margin $Z(y)$ for the eight 10-story frames of Monte Carlo simulated and 40 earthquakes used in the analyses.

With lower resistance in the frame and higher intensity of the earthquake, a straight line with a lower reliability index in Figure 9 is obtained. For the same $Z(y)$, different reliability levels are obtained depending on the level of uncertainties in the frame and the earthquake in question.

For purposes of design or evaluation, a suitable reliability index $\beta(y)$ must be positive, reaching values of up to 5 as shown in Figure 9 for a safety margin $Z(y)=1$, indicating a structure with a completely elastic behavior. A negative reliability index is an undesirable index, which indicates a high probability of collapse and this happens when the expected value of the natural logarithm of collapse intensity is reached and/or surpassed by the intensity of earthquake; in other words: $y_i \geqslant E\ (\ln Y_C)$. In this way, a safety margin $Z(y)$ would be recommended as long as it is high enough for a determined limit state for a positive reliability index. For example, for the straight lines in the lowest part of the figure, the minimum $Z(y)$ required should be greater than 0.6 to obtain a positive index. This happens to the frame of least resistance *M8* and for an intense earthquake *R37*, and for *M7-R39* and *M8-R36*.

The forty straight lines corresponding to each building and earthquake (*M-R*) in Figure 9 are all parallel to each other, consecuently, they share the same slope *m*, showing the differences between each one of these straight lines in the corresponding values for $\beta(Y_C)$ when $Z(Y_C)=0$. Due to the linear relationship of the variables, in general terms, the lines in the figure can be expressed as follows:

$$\beta(y)=\beta_{Z=0}\ (Y_C)+m\bullet Z(y) \tag{5}$$

Where: $\beta_{Z=0}(Y_C)$ is the ordinate at $x=0$, which is to say that the value of $\beta(y)$ when collapse occurs: $Z(y)=0$.

Moreover, a particular expression can be found for obtaining the reliability index, or the safety margin that we wish to assign it to the structure in question considering that $\beta_{z=0}(Y_C)$ is known or easily obtained from the results already obtained, in this case for the 10-story buildings:

$$\beta(y)=\beta_{Z=0}(Y_C)+3.698\ Z(y) \tag{6}$$

Where: $\beta_{Z=0}(Y_C)$ indicates the level of uncertainties associated with the earthquake, the mechanical properties and the live loads of the building considered in this study. For the particular case in which the ordinate is zero: $\beta_{Z=0}(Y_C)=0$, the index $\beta(y)$ will have a relationship of 3.7 times the safety margin $Z(y)$.

7 CORNELL'S RELIABILITY INDEX $\beta(y)$ RELATED TO THE SECANT STIFFNESS DEGRADATION INDEX $D(y)$.

Another way of relating Cornell's reliability index $\beta(y)$ is based on the damage index $D(y)$ for a given intensity (y), such as is shown in Figure 10. To the degree that the reliability level decreases according to the damage index comes closer to collapse, that is to say for $D(y)=1$. Just as in Figure 9, when $\beta(y)$ is negative indicating that the average collapse intensity of has been surpassed by the intensity of the earthquake. If collapse intensity coincides with that of the average of all frames and earthquakes, then a reliability index of zero would occur: $\beta(y)=0$, as takes place for the safety margin: $Z(y)=0$, when $D(y)=1$, but by definition $\beta(y)$ takes into account the average of all collapse intensities, see Eq. 4 and not the collapse intensity of each earthquake, as $Z(y)$, see Eq. 3. In relation to this, this leads us to observe that in Figure 10 for a $\beta(y)=0$ or negative, a structural collapse has not necessarily been brought about; this happens only when the earthquake collapse intensity is close to average. In such a way a collapse could be obtained a $D(y)=1$ for a positive reliability $\beta(y)$ or a non-collapse $D(y)<1$ when reliability $\beta(y)$ is negative. Therefore, this figure is not the most suitable for establishing the relationship between the reliability and the damage index, but rather, it does provide a general idea of their values and facilitates the understanding of the behavior of these variables.

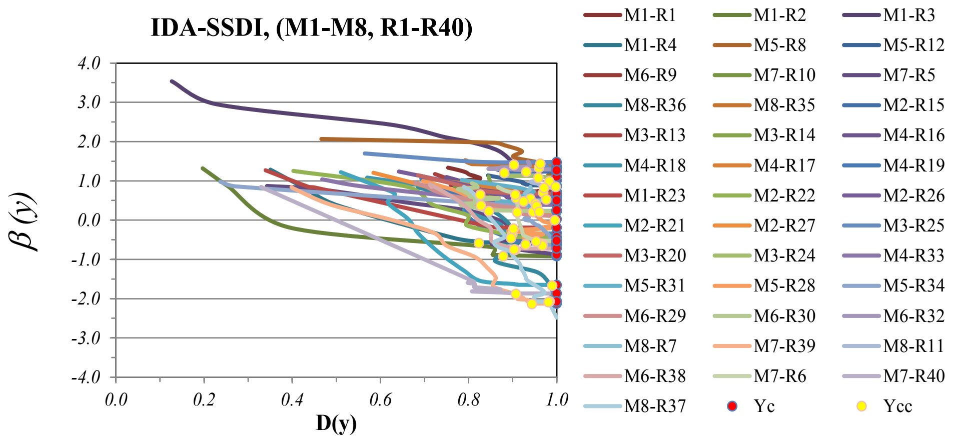

Figure 10. Cornell's Reliability Index $\beta(y)$ in relation to the damage index $D(y)$ corresponding to the eight 10-story frames and 40 simulated earthquakes used in the analyses.

8 CONCLUSIONS

- A more efficient methodology based on the Incremental Dynamic Analysis of Secant Stiffness Degradation Index (*IDA-SSDI*) for evaluating the reliability of buildings by means of Cornell's index $\beta(y)$ and the safety margin $Z(y)$ was developed.
- An expression, see Equations 5 and 6 that allows us to directly and simply evaluate the reliability of a 10-story building from a determined safety margin, (e.g. for the evaluation and/or structural design associated with a determined limit state) was obtained.
- For the first time Incremental Dynamic Analyses applied to the Secant Stiffness Degradation Index (*IDA-SSDI*) were obtained. These results allow easy and efficient evaluation of the collapse intensity (Y_C) of the system needed in order to assess the reliability.

- From Figure 9 suitable limits can be established for structural design and/or evaluation purposes of $\beta(y)$ and $Z(y)$, from 0.0 to 5.0 and from 0.6 to 1.0, respectively, for a 10-story building and depending on the limit state that one wishes to evaluate. We recommend studying other multi-story buildings, as a second phase.

9 ACKNOWLEDGMENTS

We express our gratitude to the SEP-CONACyT for its sponsorship of this project, through the Call for Basic Scientific Research 2007 and to the UAQ for the grant received by Diaz de León through the SEP-CONACyT project. The authors also wish to acknowledge Silvia C. Stroet of the Engineering Faculty at Universidad Autónoma de Querétaro for checking the English content of this document.

10 REFERENCES

[1] D. Vamvatsikos, and C.A. Cornell, *Incremental dynamic analysis, Earthquake Engineering and Structural Dynamics*, 31 (3): 491-514, 2002.

[2] O. Díaz-López and L. Esteva, *About efficient estimation of the seismic reliability of complex structural systems*, *ICOSSAR 2009, (International Conference on Structural Safety and Reliability),* Osaka, Japón*,* 2009.

[3] C.A. Cornell, A probability based structural code. *Journal of the American Concrete Institute* 66 (12*)*, 1969.

[4] O. Díaz-López and L. Esteva, *About efficient estimation of the seismic reliability of complex structural systems*, *ICOSSAR 2009, (International Conference on Structural Safety and Reliability),* Osaka, Japón*,* 2009.

[5] RCDF, *Reglamento de Construcciones del Distrito Federal.*, 2004.

[6] NTC DF – Sismo, *Normas Técnicas Complementarias para Diseño por Sismo del Reglamento de Construcciones del Distrito Federal*, 2004.

[7] Montiel M.A., *Confiabilidad implícita en estructuras convencionales como base para establecer criterios para el diseño sísmico de estructuras reforzadas con disipadores de energía*. Ph.D. Thesis. Graduate School of Engineering, National University of Mexico, (in Spanish), 2006.

[8] D. Campos-Arias and L. Esteva, *Modelo de comportamiento histeretico y de daño para vigas de concreto reforzado*. *XI Congreso Nacional de Ingeniería Sísmica, Veracruz, Ver. Mexico, pp 567-573*, 1997.

[9] Kent, D.C. and Park, R., *Flexural members with confined concrete*. Journal of Structural Division, ASCE 97 (7), 1969–1990, 1971.

[10] Park, R. and Priestley, M. J. N., Gill, W. D, *Ductility of square confined concrete columns*. Journal of Structural Division, ASCE 108 (4), 929–950, 1982.

[11] Mander J., *Seismic design of bridge piers*. Report 84-2. Department of Civil Engineering, University of Cantenbury, New Zealand, 1984.

[12] G. Rangel, M.A. Montiel y S.E. Ruiz., *Influencia en la confiabilidad sísmica estructural de las incertidumbres en las propiedades mecánicas y en las cargas vivas*, article published in the memoranda of the Fifteenth National Congress of Earthquake Engineering, September, 2005, Mexico City, Mexico. (In Spanish).

COMPDYN 2011
III ECCOMAS Thematic Conference on
Computational Methods in Structural Dynamics and Earthquake Engineering
M. Papadrakakis, M. Fragiadakis, V. Plevris (eds.)
Corfu, Greece, 25–28 May 2011

CONSTITUTIVE MODEL FOR FRP AND TIE – CONFINED CONCRETE

Konstantinos G. Megalooikonomou[1], **Giorgio Monti**[2] **and Silvia Santini**[1]

[1]DiS, University of Rome ―Roma Tre”
Via C.Segre 4/6, 00146 Rome, Italy
{kmegalooikonomou, silvia}@uniroma3.it

[2] DiSG, ―Sapienza” University of Rome
Via A.Gramsci 53, 00197 Rome, Italy
giorgio.monti@uniroma1.it

Keywords: FRP, Steel Ties, Circular Section, Model, Confinement, Buckling

Abstract. *Confining wraps or jackets to rehabilitate and strengthen existing concrete columns has proven to be an efficient technique for seismic retrofit of structures. However, most of the compressive strength models of confined concrete only consider the increased strength and ductility provided by fiber reinforced polymers (FRPs), neglecting the contribution of the existing steel reinforcement inside the column's section. Even if the existing steel stirrups in a reinforced concrete column are not sufficient to confine the concrete core, they must also contribute along with the FRP jacket in confining the section. Therefore, the FRP-confined concrete model proposal by fib has been enhanced to take into account the confining effect of the already existing steel reinforcement when retrofitting a reinforced concrete column with FRP jacketing. To this end, confining pressures contributed at each step of deformation by the case of existing transverse and longitudinal steel reinforcement have been evaluated considering the stress-strain law of the reinforcing steel. Moreover, compatibility of strain in the lateral direction between the jacketing system and the encased concrete is enforced. Finally, the bilinear stress-strain response of FRP-confined concrete is terminated by jacket rupture owing to hoop strains exceeding the strain capacity of the material or to interaction of the jacket with the buckled longitudinal bars. Correlation with three experimental studies gives promising results.*

1 MODELING OF CONCRETE CONFINED WITH STEEL&FRP

The behavior of confined circular sections under axial load is characterized by the radial lateral dilation, which causes radial confining forces or else axisymmetric passive confining pressure that increases with the amount of lateral expansion. Considering this scheme for the case of confinement by means of FRP jacketing, in order to define the confining pressure acting on the section, it is necessary to define the jacket strain, or circumferential strain, parallel to the fibers orientation. Relating the circumferential strain to the strain in the radial direction, the following simple relationship is obtained (Figure 1):

$$\varepsilon_c = \frac{\Delta C}{C} = \frac{2\pi R(1+\varepsilon_r - 1)}{2\pi R} = \varepsilon_r \tag{1}$$

Owing to the axisymmetry of the problem, the outcome is that the circumferential strain and the strain in the radial direction are equal. This property has been extensively used to calculate directly the radial confining forces based on experimental data by strain gages attached parallel to the fibers orientation in order to obtain the circumferential strains. Along this line, it seems useful to try and extend the simple calculation above to the case where steel stirrups and external FRP jacketing are simultaneously present. The steel ties divide the section into two parts: the first is the concrete core and the second is the concrete cover.

$$\begin{aligned} \varepsilon_c &= \frac{\Delta C}{C} = \frac{2\pi\left\{\left[R_{core}\left(1+\varepsilon_{r.core}\right)+c\left(1+\varepsilon_{r.\mathrm{cov}er}\right)\right]-\left(R_{core}+c\right)\right\}}{2\pi\left(R_{core}+c\right)} \\ \varepsilon_c &= \frac{\Delta C}{C} = \frac{R_{core}\left(1+\varepsilon_{r.core}\right)+c\left(1+\varepsilon_{r.\mathrm{cov}er}\right)}{\left(R_{core}+c\right)} - 1 \end{aligned} \tag{2}$$

However, for the concrete core the following assumption still holds:

$$\varepsilon_{c.core} = \varepsilon_{r.core} \tag{3}$$

As explicitly stated above, the equation of radial strains and jacket strains for the case of both FRP and steel confined concrete in circular sections is no longer valid. The circumferential strain of the external jacket is based on the radial strains of both concrete cover and concrete core, where in the latter the presence of the steel ties plays an important role.

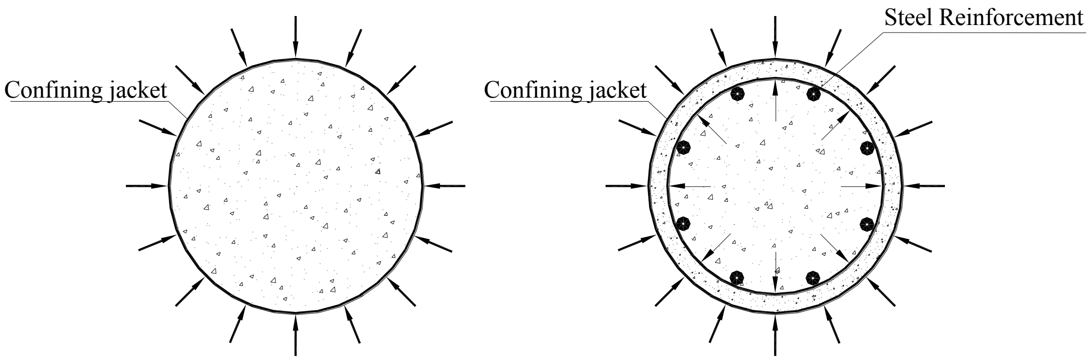

Figure 1: Circular Concrete Section confined by steel stirrups and/or FRP Jackets

2 NUMERICAL MODEL

The mechanical properties of concrete (strength, ductility, energy dissipation) are substantially enhanced under a triaxial stress state. In practice, in order to develop a similar stress state, closed stirrups or spiral reinforcement are used, so that, together with the longitudinal reinforcement, the lateral expansion of concrete is limited. This kind of (passive) confinement affects the behavior of the material favorably after the initiation of internal cracking, which gives rise to the initiation of expansion.

For low strain values, the stress state in the transverse steel reinforcement is very small and the concrete is basically unconfined. In this range, steel and FRP jacketing behave similarly. That is, the inward pressure as a reaction to the expansion of concrete increases continuously. Therefore, speaking in terms of variable confining pressures corresponding to the axial strain level in the section and active triaxial models defining axial stress-strain curves for concrete subject to constant lateral pressure, it can be stated that the stress-strain curve describing the stress state of the section has to cross all active confinement curves up to the curve with lateral pressure equal to the one applied by the stirrups at yielding. Beyond yielding of stirrups, the lateral pressure is still increasing only due to the FRP jacketing, while the steel lateral pressure remains constant. The corresponding stress-strain curve of the section throughout this procedure converges to a confined-concrete axial stress-strain curve that is associated with a lateral pressure magnitude equal to the tensile strength of the FRP jacket plus the yielding strength of ties (excluding the strain hardening behavior of steel, since ultimate strains of steel are usually much higher that those of FRP jackets).In order to model this behavior, an existing FRP-confined concrete model (Spoelstra and Monti 1999) has been enhanced to include the steel ties contribution and thus model in a more consistent way circular columns with transverse reinforcement and retrofitted with FRP jacketing. The above model was based on an iteration procedure that needed to be modified as Figure 2 shows.

In the procedure below (Figure 2), after imposing an axial strain on the section, a pressure coming from the FRP jacket is assumed. Then, the Poisson's coefficient until yielding of steel stirrups and the pressure coming from the steel ties is calculated based on the BGL model (Braga et al 2006). Here, also the longitudinal bars' contribution and the arching action between two adjacent stirrups along the column are taken into account according to that model (see Table 1). The confining pressure in the concrete core is simply the summation of the lateral pressures contributed by the two confining systems (FRP and Steel). The *fib's* model proposal (Spoelstra and Monti 1999) beyond this point is basically used to define the remainder of the parameters declared above, applying that model for the two different regions already mentioned. The focal point of the procedure is in the last step where the confining pressure of the jacket is defined based on the circumferential strain of Equation. 2. Finally, at this point, cases where partial wrapping is applied have been included too (14th fib bulletin 2001, Table 1). Such an approach permits also in cases of repair and retrofit two different concrete strengths to be considered, one for the new layer of concrete applied externally and the other for the old concrete in the concrete core which may also be cracked due to former seismic loading.

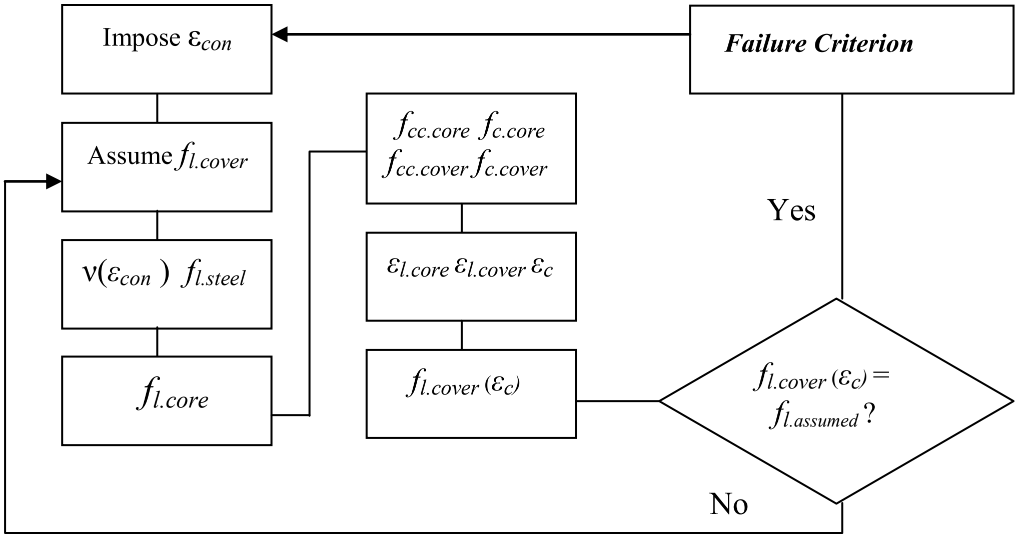

Figure 2. Iterative Procedure

3 FAILURE CRITERION

3.1 FRP Confined Circular RC Sections

It has been well established in recent studies that the rupture strains/strengths measured in tests on FRP confined cylindrical specimens fall substantially below those from flat coupon tensile tests. Several reasons have been suggested for the observed lower rupture strains in place, among which are [(Carey and Harries 2005), (Lam and Teng 2004), (Matthys et. al. 2005)]:

- Misalignment or damage to jacket fibers during handling and lay-up.
- The radius of curvature in FRP jackets on cylinders as opposed to flat tensile coupons.
- Near failure the concrete is internally cracked resulting in no homogeneous deformations. Due to this non-homogeneity of deformations and the high loads exerted on the cracked concrete, local stress concentrations may occur in the FRP reinforcement.
- The existence of a lap-splice zone in which the measured strains are much lower than strains measured elsewhere.

Accounting for these effects an ultimate tensile coupon FRP strain reduced by a k factor (ranging in literature between 50-80 %) is compared to the circumferential strain of concrete (Equation. 2) and the ultimate compressive axial strain of concrete is considered to be attained when:

$$\varepsilon_c \leq k \cdot \varepsilon_{j.rup.coup} \tag{4}$$

3.2 FRP&Steel Confined Circular RC Sections

In old-type circular columns with inadequate transversal reinforcing details (where FRP jacketing are a commonly used remedy), the unsupported length of longitudinal bars (between 2 successive stirrups) is often much greater than $6D_b$. Therefore, the risk for buckling of longitudinal bars under compressive loads soon after yielding is higher. A dire implication is reduced effectiveness of the FRP wraps due to interaction between buckled longitudinal bars and the jacket which may cause premature failure by rupture of the jacket (Sheikh S.A. &Yao G. 2002), (Tastani et al. 2006). This is an additional source of error contributing to overestimation of strength of FRP confined concrete in addition to that generated by the difference between nominal and in-situ strain capacity of the wraps as detailed above. It is the objective of the present paper to study the interaction between wraps and compression reinforcement in FRP-encased reinforced concrete columns, with particular emphasis on the occurrence of instability conditions and the dependable compressive strain of the column prior to actual buckling of the rebars.

In this model, the dilation of concrete core and concrete cover are described through the following equation (Equation. 5) of the model by Spoelstra and Monti (1999).

$$\begin{gathered}\varepsilon_r(\varepsilon_{con}, f_l) = \frac{E_{con}\varepsilon_{con} - f_c(\varepsilon_{con}, f_l)}{2\beta f_c(\varepsilon_{con}, f_l)} \\ \beta = \frac{5700}{\sqrt{|f_{co}|}} - 500\end{gathered} \tag{5}$$

Thus, the lateral pressure of the FRP jacket confining the concrete cover has been taken into account and by relating the critical buckling conditions with the onset of significant strength loss of the concrete cover, the effect of the confining pressure exerted by the jacket in delaying the occurrence of buckling of the longitudinal bars can be evaluated. Therefore, the critical buckling conditions are delayed depending on how axially stiff is the jacket, which accordingly delays the failure of the concrete cover (that laterally supports the longitudinal bar). This onset of loss of resistance in concrete has been proved to be the point when the net volumetric strain of the material becomes equal to zero (Pantazopoulou and Mills 1995). In circular sections this occurs when:

$$\varepsilon_V = 0 \Rightarrow 2 \cdot \varepsilon_r = \varepsilon_{con} \Rightarrow \nu = 0.5 \tag{6}$$

However, another condition that should be valid for the attainment of critical instability conditions of the longitudinal bars in the high confining stress states under consideration is the occurrence of compression yielding of the longitudinal bar. Regarding this step, it is interesting to note with reference to Figure 3 for a given concrete strength, the point where the volumetric ratio becomes zero moves forward into higher axial compression strain values with increasing confining pressures. Thus, as shown by the two curves in Figure 3 corresponding to different confining pressures, the difference in the lateral behavior of the concrete cover (confined with the jacket's pressure) and the concrete core (confined by both the steel's and FRP's pressure) should also be considered.

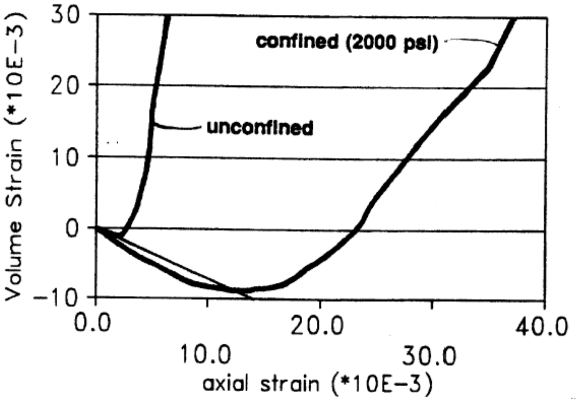

Figure 3: Volumetric Strain versus Axial Compressive Strain (Pantazopoulou and Mills 1995)

As it is shown in previous studies (Monti and Nuti 1992), (Bae et al. 2005), the buckling length and the L_{buck}/D_b ratio are critical parameters for the post buckling behavior of longitudinal bars under compression. In cases of columns constructed with obsolete codes with the spacing of the stirrups ranging between 200-500 mm (buckling length) and bar diameters from 12-20 mm, the L_{buck}/D_b ratio is ranging between 10-42. However, apart from old type columns the assumption that the buckling length is equal to the spacing of the stirrups in a RC column does not hold true in all cases (Dhakal and Maekawa 2002) and it may extend over more than a single tie spacing. In order to take into account this behavior (cases of reinforcement repair and FRP retrofit) the following procedure is suggested.

The longitudinal bar is modeled as a pin-ended bar supported along its length by an elastic foundation as shown in Figure 4. The foundation modulus is k (N/mm^2) and it is such that when the bar deflects by an amount u, a restoring force ku (N/mm) is exerted by the foundation normal to the bar.

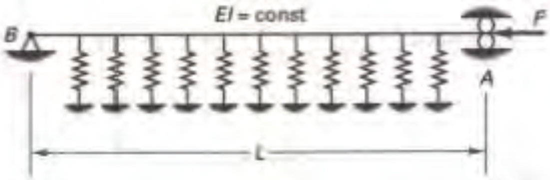

Figure 4: A pin-ended bar on elastic foundation.

The governing homogeneous differential equation and the associated eigenvalue problem are:

$$EI\upsilon^{iv} + P\upsilon^{''} + k\upsilon = 0$$

$$P_{cr} = \frac{\pi^2 EI_{red}}{L_{buck}^{\ 2}}\left[m^2 + \frac{1}{m^2}\left(\frac{kL_{buck}^{\ 4}}{\pi^4 EI_{red}}\right)\right] \tag{7}$$

Note that if k = 0 (which occurs upon yielding of the stirrups), the minimum value of P_{cr} becomes the classical Euler buckling load. In order to determine the critical load, the buckling mode m equal to 1 should be used. The stiffness k representing the supporting system of stirrups could be calculated as follows:

$$k = n \cdot \frac{E_s \cdot A_{sh}}{L_{buck} \cdot \pi \cdot D_{core}}$$

$$L_{buck} = (n+1) \cdot S \tag{8}$$

$$EI_{red} = 0.5 \cdot E_s \cdot I_b \cdot \sqrt{\frac{f_{yl}}{400}} \quad \text{(Dhakal and Maekawa 2002)}$$

Solution of the problem above is obtained by setting the critical load of the bar equal to its yield force; in this case the only unknown is the number n of the stirrups, n over the buckling length. Therefore, by solving Equation.7 for n, the buckling length is determined. The value of n may be rounded to the nearest integer owing to that the pin-ended bar segment engaged in buckling is assumed to span between successive inflection points of the real deformed shape. If convergence is not possible for n>1, the buckling length is taken equal to the spacing of stirrups.

Summing up, after the critical conditions of a longitudinal compressive bar have been attained (this is assumed to coincide upon compression yielding of the bar and the Poisson's coefficient at the concrete cover exceeds the value of 0.5) the buckling length of the bar is determined. Then, based on the model by Bae et al. 2005 who have related the axial strain with the transversal displacement of the buckled longitudinal bar for a given L_{buck}/D_b ratio the transversal displacement of the bar is calculated (Table 1). Since, for a longitudinal bar embedded in a RC member axial shortening of the bar means the same amount of shortening for the surrounding concrete mass (Pantazopoulou 1998), the axial strain in the bar is taken as equal with the axial strain of concrete. Finally, the jacket's circumferential strain due to buckling is determined as follows:

$$\begin{aligned} \varepsilon_{c.buck} &= \frac{2\cdot\pi\cdot\lvert w-c\rvert}{\pi\cdot D} \leq \varepsilon_{j.rup.coup}\text{ , (Full wrapping)} \\ \varepsilon_{c.buck} &= \frac{2\cdot\pi\cdot\left\lvert w-\frac{c}{2}\right\rvert}{\pi\cdot D} \leq \varepsilon_{j.rup.coup}\text{ , (Partial wrapping)} \end{aligned} \tag{9}$$

It follows from the above equation (Equation. 9) that a tolerance equal to the concrete cover for full wrapping and half of the concrete cover for partial wrapping is given before the initiation of jacket's strains due to buckling of longitudinal bars since the concrete cover should be severely cracked in case of full wrapping and some spalling could appear in case of partial wrapping. Since, the displacement of the buckled longitudinal bar could be high and the phenomenon affects locally the jacket where the FRP material behavior could be considered linear-elastic, the results are compared to the deformation capacity of tensile coupons (dilation strains and buckling strains are studied independently). In the proposed algorithm detailed above, the failure criterion is used in two steps. Firstly, the circumferential strain due to dilation of concrete under compression is compared to a reduced FRP tensile coupon strain and secondly the induced circumferential strains due to buckling which locally accelerate the jacket's rupture are compared to the deformation capacity of flat FRP tensile coupons. If one of these conditions are fulfilled the iteration procedure is terminated.

(Braga et al. 2006)	$f_{l.steel}(\varepsilon_{con}) = k_{sl}\dfrac{E_{con}E_sA_{sh}\nu(\varepsilon_{con})}{R_{core}E_{con}S + E_sA_{sh}[1-\nu(\varepsilon_{con})]\cdot[\nu(\varepsilon_{con})\cdot\varepsilon_{con}+1]}\cdot\varepsilon_{con}, \varepsilon_{sh} \prec \varepsilon_{yh}$ $f_{l.steel}(\varepsilon_{con}) = k_{sl}0.5\rho_{sh}f_{yh}, \varepsilon_{shu} \geq \varepsilon_{sh} \geq \varepsilon_{yh}$ $\rho_{sh} = \dfrac{4A_{sh}}{D_{core}S},\ \varepsilon_{yh} = \dfrac{f_{yh}}{E_s},\ \varepsilon_{sh} = \varepsilon_{c.core} = \varepsilon_{r.core} = \nu(\varepsilon_{con})\cdot\varepsilon_{con}$ $\nu(\varepsilon_{con}) = \nu_0\left[1+0.2\left(\dfrac{\varepsilon_{con}}{\varepsilon_{c0}}\right)-\left(\dfrac{\varepsilon_{con}}{\varepsilon_{c0}}\right)^2+1.55\left(\dfrac{\varepsilon_{con}}{\varepsilon_{c0}}\right)^3\right],\ \nu_0 = 0.2,\ \varepsilon_{co} = 0.002$ $k_{sl} = \dfrac{45\xi_l^3}{45\xi_l^3+\beta\xi_{st}}, \xi_l = \dfrac{D_b}{S}, \beta = \dfrac{D_h}{D_b}, \xi_{st} = \dfrac{2D_h}{\pi R_{core}}$
(Spoelstra and Monti 1999)	$f_c = \dfrac{f_{cc}\cdot x\cdot r}{r-1+x^r},\ x = \dfrac{\varepsilon_{con}}{\varepsilon_{cc}},\ \varepsilon_{cc} = \varepsilon_{co}\left[1+5\left(\dfrac{f_{cc}}{f_{co}}-1\right)\right],\ r = \dfrac{E_{con}}{E_{con}-E_{\sec}}$ $E_{\sec} = \dfrac{f_{cc}}{\varepsilon_{cc}},\ \dfrac{f_{cc}(f_l)}{f_{co}} = 2.254\sqrt{1+7.94\dfrac{f_l}{f_{co}}}-2\dfrac{f_l}{f_{co}}-1.254,$ $\varepsilon_r(\varepsilon_{con}, f_l) = \dfrac{E_{con}\varepsilon_{con}-f_c(\varepsilon_{con}, f_l)}{2\beta f_c(\varepsilon_{con}, f_l)},\ \beta = \dfrac{5700}{\sqrt{\lvert f_{co}\rvert}}-500,$ $E_{con} = 5700\cdot\sqrt{\lvert f_{co}\rvert}(MPa)$

(14th fib Bulletin)	$k_j = \dfrac{\left(1-\dfrac{S_j}{2D}\right)^2}{1-\dfrac{A_b}{A_g}} \approx \left(1-\dfrac{S_j}{2D}\right)^2$ *(Coefficient for Partial Wrapping)* $f_{l.\mathrm{cover}} = \dfrac{1}{2}k_j \rho_j E_j \varepsilon_c, \rho_j = \dfrac{4t_j}{D}$
Iterative Procedure	$f_{l.core} = f_{l.\mathrm{cover}} + f_{l.steel},\ f_{c.av} = \dfrac{A_{core}}{A_{tot}} f_{c.core} + \dfrac{A_{\mathrm{cover}}}{A_{tot}} f_{c.\mathrm{cover}}$
(Bae et al. 2005)	$\varepsilon_{sl} = \max\left[\left(\dfrac{0.035\cos\theta+\theta}{\cos\theta-0.035\theta}\right)\dfrac{w}{D_b}, \left(\dfrac{0.07\cos\theta+\theta}{\cos\theta-0.07\theta}\right)\left(\dfrac{w}{D_b}-0.035\right)\right],$ $\theta = \dfrac{6.9}{\left(L_{buck}/D_b\right)^2} - 0.05,\ \varepsilon_{sl} = \varepsilon_{con}$

Table 1: Equations embodied in the iterative procedure.

4 CORRELATION WITH EXPERIMENTAL RESULTS

Three experimental studies have been included in this work for validation of the proposed iterative procedure. The first is one of the few extensive experimental studies on large scale FRP wrapped circular columns where different FRP configurations have been applied, for identical embedded steel reinforcement (Matthys et al. 2005). It includes 8 large-scale columns subjected to axial loading. The columns had a total length of 2 m, a longitudinal reinforcement ratio of 0.9% and 8 mm diameter stirrups spaced at 140 mm. All columns had circular cross section with 400 mm diameter. Different types of FRP reinforcement (CFRP, GFRP & HFRP) have been used to confine the columns. The comparison seems to be satisfactory (Figure 5, 6), although the solution has moderate success in resolving the problem of predicting the actual instance of jacket's failure in terms of axial and circumferential ultimate strains. Some clarifications are in order for the last graph (Figure 7) which illustrates the model's estimations of the circumferential strains in the FRP jacket owing to concrete dilation and to buckling of longitudinal bars at the ultimate axial strain reported in the tests for each specimen. These values are compared to the experimental rupture strain of the jacket (from strain gages) and to the deformation capacity of the flat tensile coupons which was reported, accordingly.

The second experimental study (Demers and Neale 1999) includes 16 reinforced concrete columns having a circular section 300 mm in diameter and 1200 mm high. These columns were confined by means of carbon-epoxy sheets and loaded concentrically in axial compression. The effects of various parameters on the structural behavior of the confined concrete columns are investigated. These parameters included the concrete strength, longitudinal steel reinforcement, steel stirrups, steel corrosion and concrete damage while the FRP configuration was kept constant. The comparison between model estimates and experimental results depicted in Figure 8 and 9 also in this case could be characterized as satisfactory, moreover due to the fact that in this experimental study the lateral pressures from both confining materials (Steel and FRP) are provided based on circumferential strains obtained by strain gages applied on both FRP Jacket and Steel ties. (It should be underlined that the horizontal strain gages on the jacket were located midway between two successive stirrups). Among the 16 specimens in only one case (Specimen U40-4) the pressures coming from the ties were evidently higher than those of the FRP jacket and the model was able to detect that (Figure 10).

The third and the last experimental study (Gallardo-Zafra R. & K. Kawashima, (2009)) contains a series of cyclic loading tests that was conducted on six reinforced concrete column specimens 400 mm in diameter and 1.350 mm in effective height. The specimens were grouped into A and B series where each series consisted of three specimens each; one was as-built while the second and the third were wrapped laterally by CFRP with a single layer and with two layers, respectively. The tie reinforcement ratio was 0.256% (150 mm spacing) for the A-series and 0.128% (300 mm spacing) for the B-series. Figures 12, 13, 14 and 15 depict the comparison with the two groups of cyclic tests on bridge piers having different levels of confinement in terms of lateral steel reinforcement and FRP jacketing. The modeling of the bridge piers was the same as in the original paper and has been performed using the ―MatLab Finite Elements for Design Evaluation and Analysis of Structures" (FEDEAS Lab) developed by Professor F.C.Filippou of the Department of Civil and Environmental Engineering of the University of California Berkeley. While in the original proposal the fiber section had to be divided in the concrete core and concrete cover and two different stress-strain relations were applied for the concrete core (confined by both FRP & Steel) and concrete cover (confined by only the FRP), in this work since the material response is already averaged based on the different responses of those two regions, the same stress strain law is applied for each fiber (FEM). This fact gives a clear advantage to the proposed model. In addition to the force-displacement response of the cantilever columns also the response in the level of the section is provided for each specimen in terms of material stress-strain hysteresis. It can be seen that the agreement is very close to the experimental one with some deviation concentrated on the parts of reloading after reversal of the imposed displacement. This difference in response in terms of modeling can be explained based on the way the cracks on the concrete surface are described in the level of the material model. Since the crack is described as two event phenomenon, which means or open or closed (while in reality it is not the case – imperfect crack closure) the contribution of concrete while the longitudinal steel reinforcement is in compression and the crack is closing gives this deviation in the response. The comparison with the originally proposed model of this experimental study is impressively the same. However, the proposed model describes rationally the procedure of the passive confinement based on the calculation of the lateral concrete expansion in terms of the different levels of lateral pressures coming from the two different materials (Steel and FRP). Moreover, the active (constant lateral pressure) confinement model proposed by Kawashima et al. (1999) is based on regression analysis of the experimental results of cylindrical specimens under compression and it is specifically calibrated for Carbon Fiber Composite material (CFRP). Finally, it doesn't consider the confinement effect of the longitudinal reinforcement and the effect of partial confinement due to the vertical arching action of the adjacent stirrups along the member but also cases of partial FRP wrapping of the column.

An important comment that should be made before concluding, is related to some studies (Gallardo-Zafra and Kawashima 2009, Khaloo et al. 2008) that have reported for FRP and Steel confined concrete in circular RC sections a different behavior (softening) in respect to the already recognized bilinear one (Carey and Harries 2005). The authors attribute that to the small scale of the reinforced concrete specimens used while the most important explanation which could lead to those results is the influence of concrete strength. According to Mandal et. al. (2005) the FRP wraps provide a substantial increase in strength and ductility, for low-to-medium-strength concrete, which shows a bilinear stress strain response with strain hardening. For high-strength concrete, however, enhancement in strength is very limited, with hardly any improvement in ductility. The response in this case shows a steep post peak strain softening.

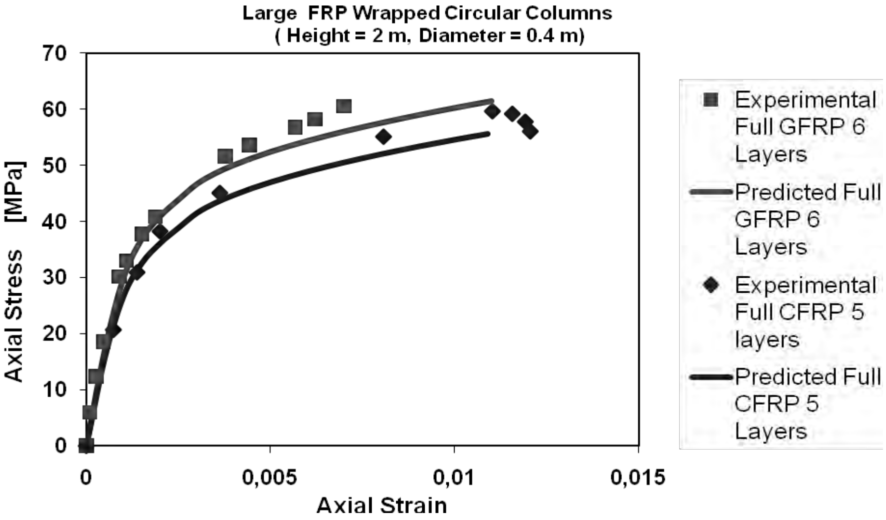

Figure 5: Correlation with experimental results (Matthys et al. 2005).

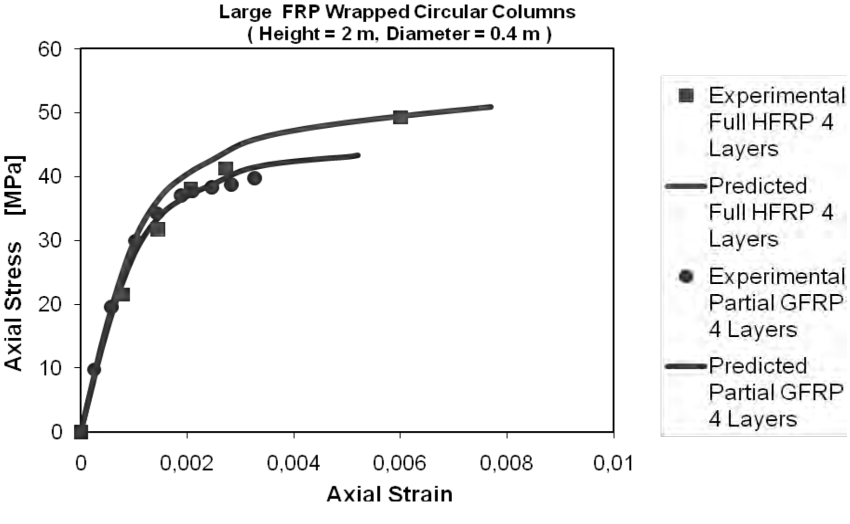

Figure 6: Correlation with experimental results (Matthys et al. 2005).

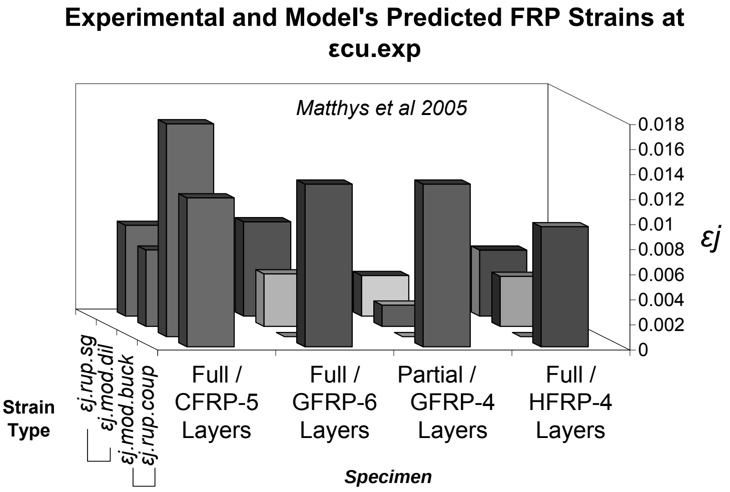

Figure 7: Correlation with experimental results (Matthys et al. 2005).

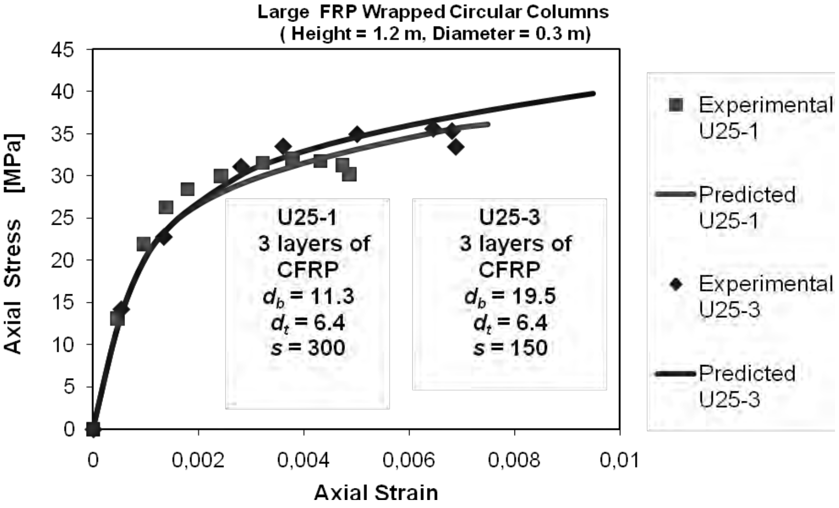

Figure 8: Correlation with experimental results (Demers and Neale 1999).

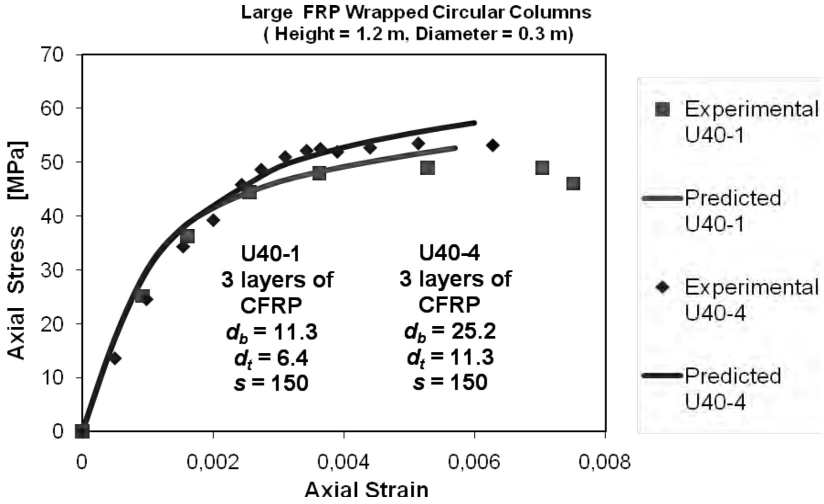

Figure 9: Correlation with experimental results (Demers and Neale 1999).

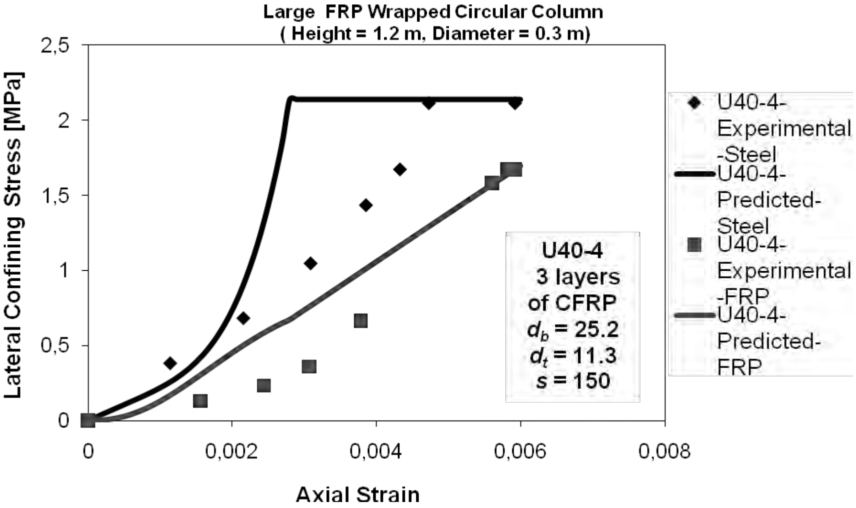

Figure 10: Correlation with experimental results (Demers and Neale 1999).

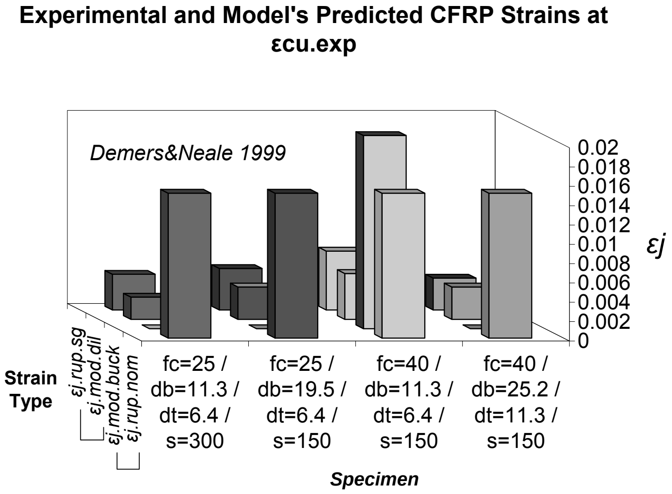

Figure 11: Correlation with experimental results (Demers and Neale 1999).

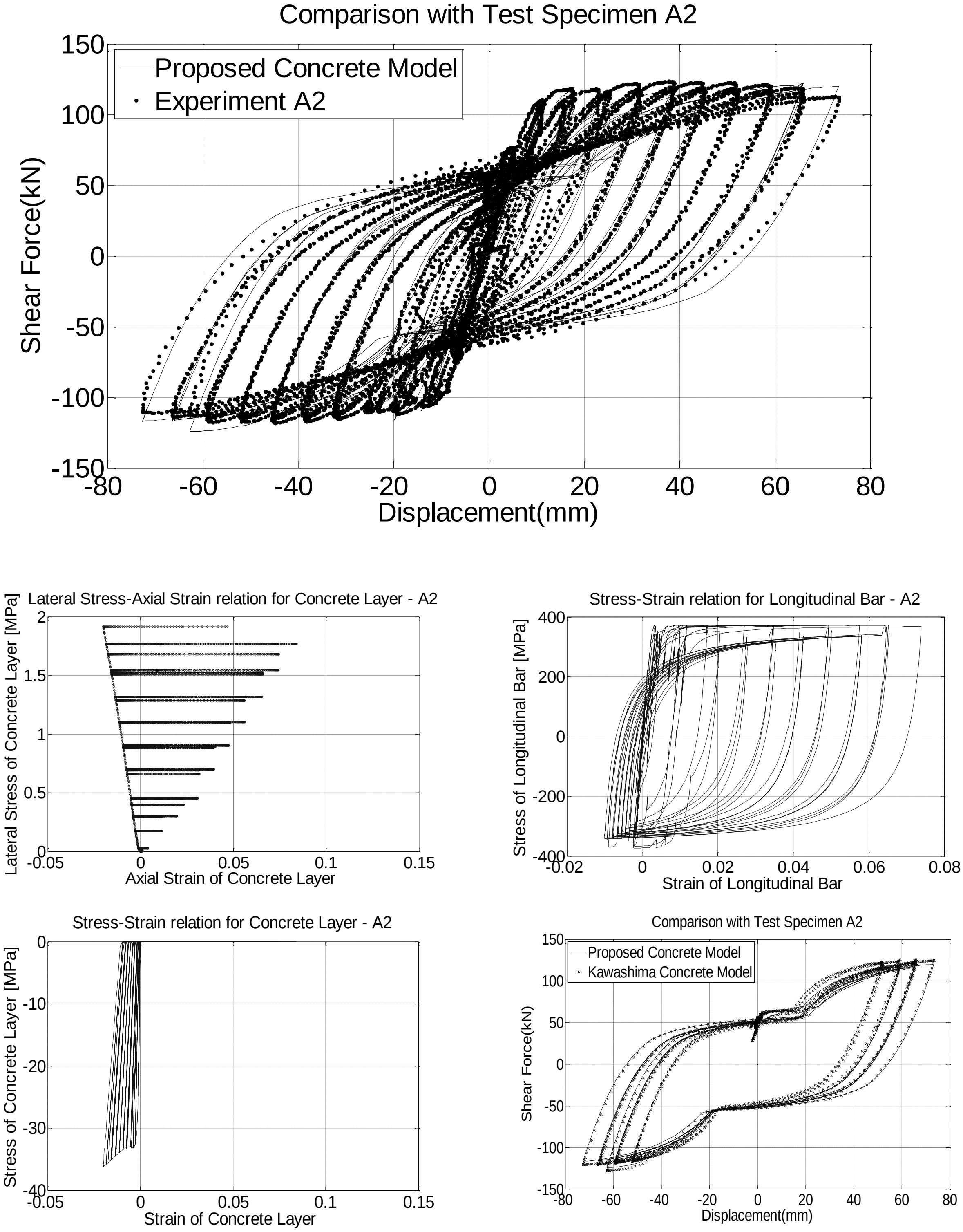

Figure 12: Correlation with Experimental results A2 (Gallardo-Zafra R. & K. Kawashima, 2009).

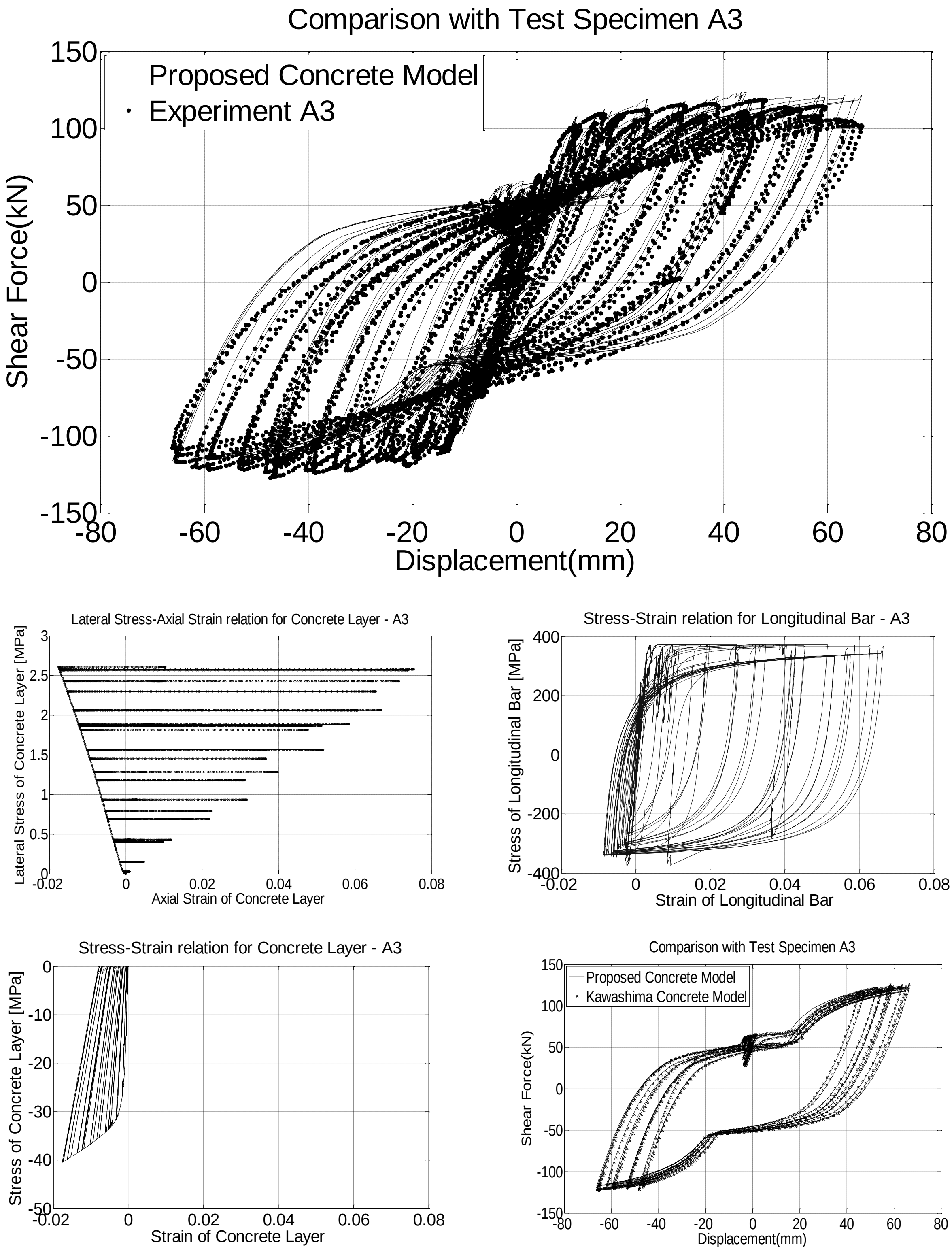
Comparison with Test Specimen A3

Lateral Stress-Axial Strain relation for Concrete Layer - A3

Stress-Strain relation for Longitudinal Bar - A3

Stress-Strain relation for Concrete Layer - A3

Comparison with Test Specimen A3

Figure 13: Correlation with Experimental results A3 (Gallardo-Zafra R. & K. Kawashima, 2009).

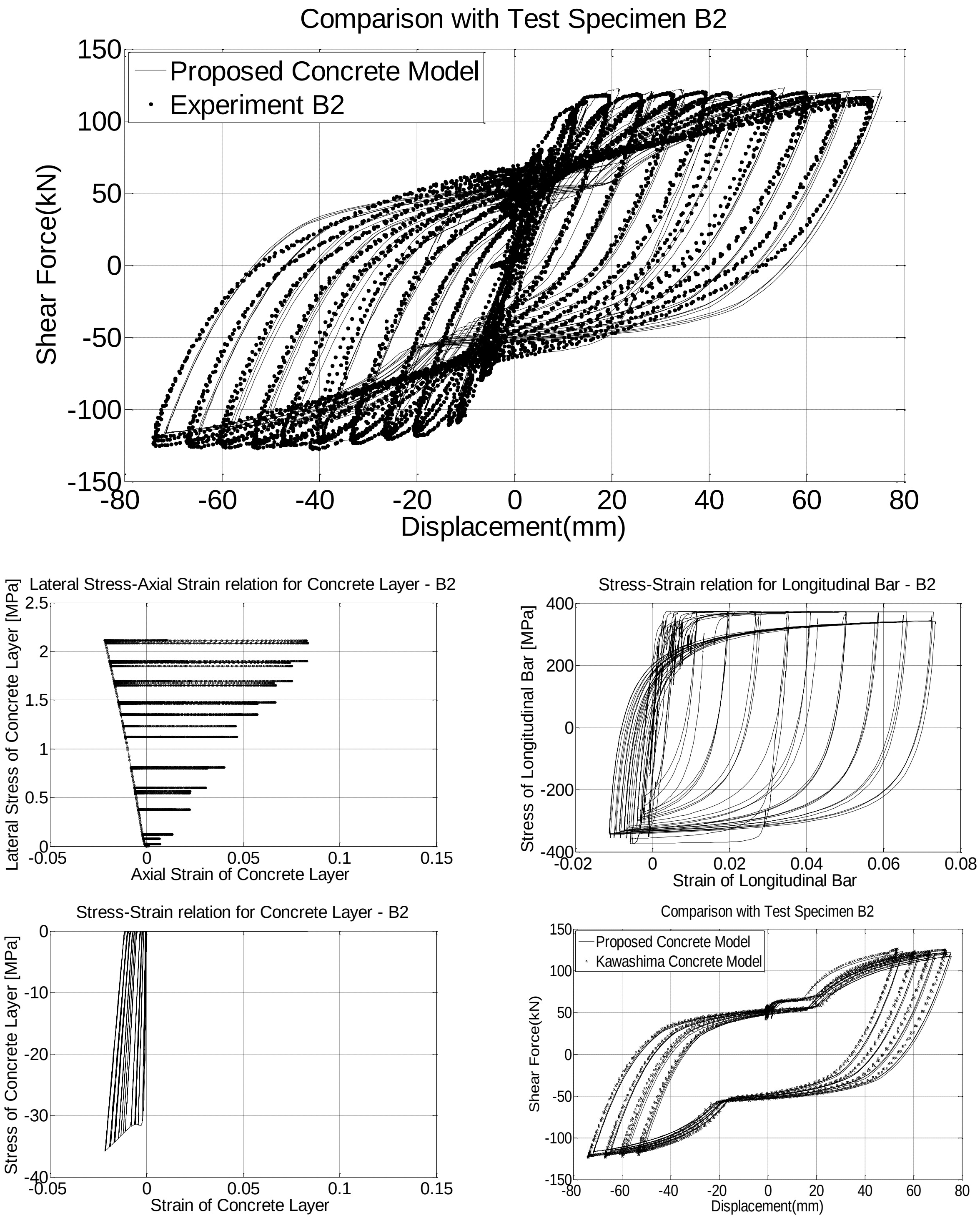

Figure 14: Correlation with Experimental results B2 (Gallardo-Zafra R. & K. Kawashima, 2009).

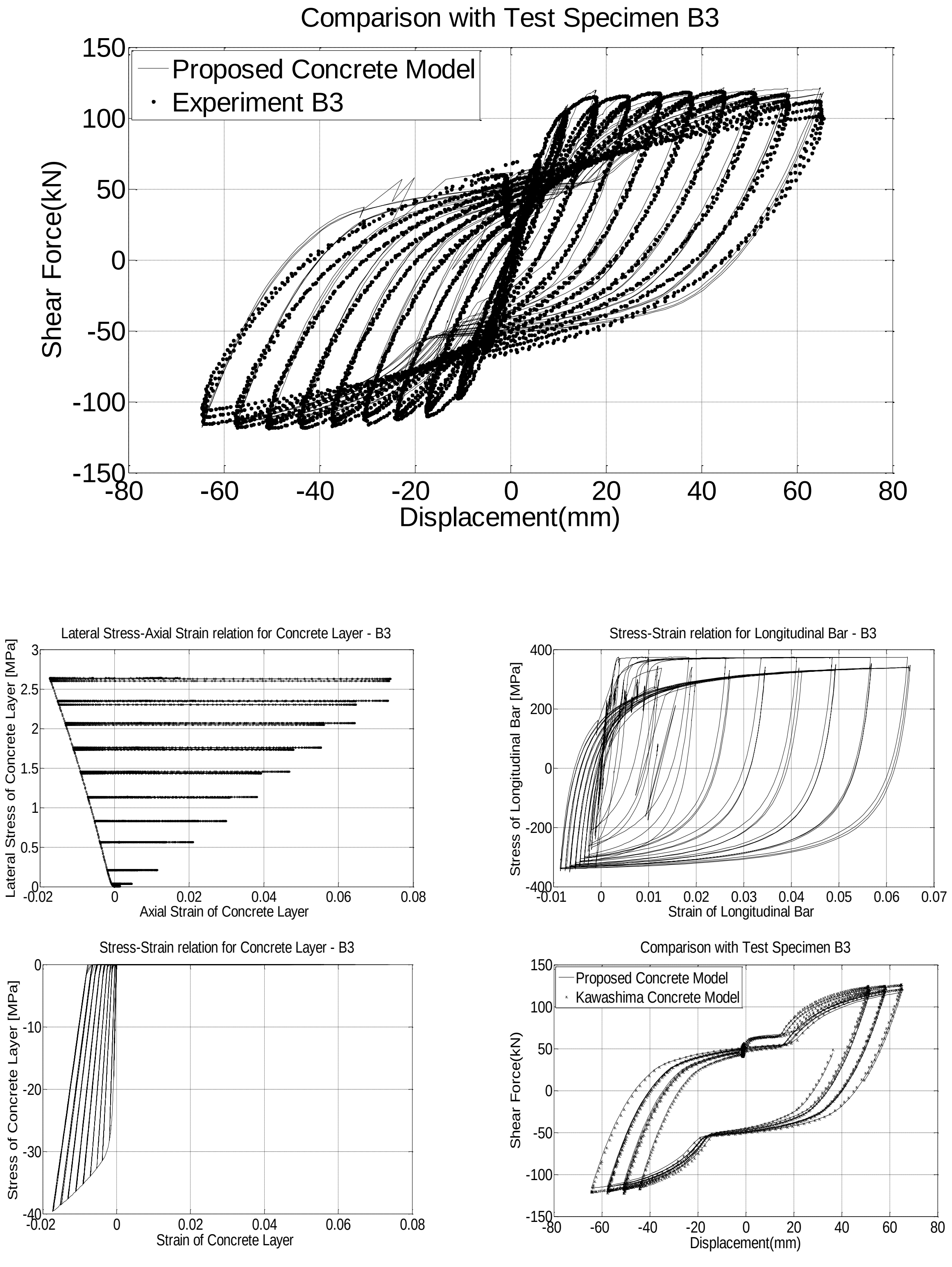

Figure 15: Correlation with Experimental results B3 (Gallardo-Zafra R. & K. Kawashima, 2009).

5 CONCLUSIONS

- *fib's* FRP-confined concrete model proposal has been enhanced to take into account the confining effect of the already existing steel reinforcement when retrofitting a reinforced concrete column with FRP jacketing. To this end, the transverse steel reinforcement has been considered not as imposing a constant value of confining pressure, rather, following the steel stress-strain law at each deformation step according with the BGL model (Braga et al. 2006), while also considering the confining contribution of longitudinal reinforcement.
- Similar to BGL model an important aspect of the model is that the cross- section tangential stresses (shear), which are generally neglected, have an essential role in ensuring plane strain conditions.
- In addition, compatibility in the lateral direction, inwards for confining pressures and outwards for lateral strains, between the two confining materials (FRP and Steel) has been established. Through this approach the difference in the lateral behavior of the concrete cover (confined with the jacket's pressure) and the concrete core (confined by both the steel's and FRP's pressure) has been considered.
- This allows the application of the model also in cases of reinforcement repair and FRP retrofit where two different concrete strengths should be considered, one for the new layer of concrete applied externally and the other for the old concrete in the concrete core which may also be cracked due to former seismic loading.
- Moreover, in case of bridge column modeling with a fiber nonlinear beam- column element, apart from the immediate incorporation of shear deformations in the section level (in contrast to the standard fiber beam-column formulation), the averaged response of the two different regions -concrete core and concrete cover- gives an evolutionary advantage in terms of modeling since it allows the assignment of a unique stress-strain law for all the fibers/layers of the circular section (FEM).
- Finally, a two-condition failure criterion has been incorporated regarding dilation of concrete and buckling of longitudinal bars as independent events. Correlation with experimental results seems to be satisfactory, although the model has moderate success in predicting the actual instance of rupture of the FRP jacket.

ACKNOWLEDGEMENTS

This work has been carried out with the financial support of the program RELUIS (Dept of Civil protection) and with the collaboration of Valbruna, Mapei, Altomodulo s.r.l., etc. The first author would like sincerely to thank also Professor F.C.Filippou and his PhD student Veronique Le Corvec for their support for the third experimental correlation during his stay as Visiting Scholar at UC Berkeley.

REFERENCES

[1] Bae C., A.M. Mieses, O. Bayrak, Inelastic Buckling of Reinforcing Bars, *Journal of Structural Engineering*, *ASCE,* 131(2), 314-321, 2005.

[2] Braga F., R. Gigliotti, M. Laterza, , Analytical Stress-Strain Relationship for Concrete Confined by Steel Stirrups and/or FRP Jackets , *Journal of Structural Engineering*, *ASCE*, 132 (9), 1-15, 2006.

[3] Carey S.A., K.A Harries Axial Behavior and Modeling of Confined Small-, Medium-, and Large-Scale Circular Sections with Carbon Fiber-Reinforced Polymer Jackets, *Structural Journal*, *ACI*, 102(4), 596-604. 2005.

[4] Demers M., K.W. Neale, Confinement of reinforced concrete columns with fibre- reinforced composite sheets—an experimental study, *Canadian Journal of Civil Engineering*, 26, 226–241, 1999.

[5] Dhakal P.R., K. Maekawa, Reinforcement Stability and Fracture of Cover Concrete in Reinforced Concrete Members, *Journal of Structural Engineering*, *ASCE*, 128(10), 1253-1262, 2002.

[6] Gallardo-Zafra R., K. Kawashima, Analysis of CFRP RC Bridge Columns under Lateral Cyclic Loading , *Journal of Earthquake Engineering*, 13, 129-154, 2009.

[7] Khaloo A., Y. Javid, M. Tazarv, and Experimental Study of the Internal and External (FRP) Confinement Effect on Performance of Compressive Concrete Members, *14th World Conference on Earthquake Engineering (14th WCEE),* Beijing, China, October 12-17, 2008.

[8] Lam L., J.G. Teng, Ultimate Condition of Fiber Reinforced Polymer-Confined Concrete, Journal *of Composites for Construction*, *ASCE,* 8(6), 539-548, 2004.

[9] Li, Y.F., Fang, T. S., A Constitutive Model for Concrete Confined by Steel Reinforcement and Carbon Fiber Reinforced Plastic Sheet*, Structural Engineering and Mechanics,* 18(1), 21-40, 2004.

[10] Mandal S., A. Hoskin, A. Fam, Influence of Concrete Strength on Confin**m** Effetiveness of Fiber-Reinforced Polymer Circular Jackets, *Structural Journal*, *ACI,* 102(3), 383-392, 2005.

[11] Matthys S., H. Toutanji K. Audenaert and L.Taerwe, Axial Load Behavior of Large-Scale Columns Confined with Fiber-Reinforced Polymer Composites, *Structural Journal*, *ACI*, 102(2), 258-267, 2005.

[12] Monti G., Megalooikonomou G.K., Modelling of FRP&Steel Confined Circular RC Sections, Proceedings of the: *9th International Symposium on Fiber Reinforced Polymer Reinforcement for Concrete Structures (FRPRCS-9),* Sydney, Australia, July 13-15, 2009.

[13] Monti G., C. Nuti, Nonlinear Cyclic Behavior of Reinforcing Bars Including Buckling , *Journal of Structural Engineering*, *ASCE*, 118(12), 3268-3284, 1992.

[14] Mosalam M. K., Talaat M., Binici B., A computational model for reinforced concrete members confined with fiber reinforced polymer lamina: Implementation and experimental validation *Composites: Part B*, 38, 598–613, 2007.

[15] Pantazopoulou S.J., R.H. Mills, Microstructural Aspects of the Mechanical Response of Plain Concrete , *Materials Journal*, *ACI*, 92(6), 605-616, 1995.

[16] Pantazopoulou S.J., Detailing for Reinforcement Stability in RC members, *Journal of Structural Engineering*, *ASCE,* 124(6), 623-632, 1998.

[17] Sheikh SA, Yao G., Seismic Behavior of Concrete Columns Confined with Steel and Fiber-Reinforced Polymers, *Structural Journal*, *ACI*, 99(1), 72-80, 2002.

[18] Spacone E., Filippou F., Taucer F., Fiber beam-column model for nonlinear analysis of R/C frames: Part I. Formulation., *Earthquake Engineering and Structural Dynamics,* 25, 711 – 725, 1996.

[19] Spoelstra M.R., G. Monti, FRP-Confined Concrete Model, *Journal of Composites for Construction*, *ASCE*, 3(3), 143-150, 1999.

[20] Tastani S.P., S.J. Pantazopoulou, D. Zdoumba, V. Plakantaras, E. Akritidis, Limitations of FRP Jacketing in Confining Old – Type Reinforced Concrete Members in Axial Compression, *Journal of Composites for Construction*, *ASCE,* 10(1), 13-25, 2006.

[21] Technical Report, *Externally bonded FRP reinforcement for RC structures*, 14th fib bulletin, *fib*, Lausanne, Switzerland, 2001.

NOTATION

ε_r	*radial strain*
ε_c	*circumferential strain*
ε_{con}	*concrete's axial strain*
ε_{co}	*concrete's axial strain at unconfined concrete's strength*
ε_{cc}	*concrete's axial strain at confined concrete's strength*
$\varepsilon_{c.core}$	*circumferential strain of the core*
$\varepsilon_{c.buck}$	*circumferential strain due to buckling of longitudinal bars*
$\varepsilon_{r.core}$	*radial strain of the core*
$\varepsilon_{r.cover}$	*radial strain of the cover*
R_{core}	*radius of the concrete core*
c	*concrete cover*
f_{co}	*concrete strength*
f_{cc}	*confined concrete strength*
v_o	*initial Poisson's coefficient for concrete*
ρ_{sh}	*steel hoop's volumetric ratio*

ρ_j	*FRP jacket's volumetric ratio*
$f_{l.core}$	*lateral confining pressure of the concrete core*
$f_{l.cover}$	*lateral confining pressure of the concrete cover*
$f_{l.steel}$	*lateral confining pressure of the steel reinforcement*
$f_{c.av}$	*average axial concrete stress*
$f_{c.core}$	*axial concrete core stress*
$f_{c.cover}$	*axial concrete cover stress*
L_{buck}	*buckling length*
P_{cr}	*critical load*
A_{tot}	*total area of the circular section*
A_{core}	*total area of the concrete core of the circular section*
A_{cover}	*total area of the concrete cover of the circular section*
I_b	*longitudinal bar's moment of inertia*
f_{yl}	*yielding strength of longitudinal bar*
w	*transversal displacement of the bar*
ε_{sl}	*axial strain in the bar*
ε_{shu}	*ultimate steel hoop's strain*
D_h	*hoop's diameter*
D_{core}	*diameter of concrete core*
D	*section's diameter*
S_j	*jacket's clear spacing*

COMPDYN 2011
III ECCOMAS Thematic Conference on
Computational Methods in Structural Dynamics and Earthquake Engineering
M. Papadrakakis, M. Fragiadakis, V. Plevris (eds.)
Corfu, Greece, 25–28 May 2011

ANALYTICAL MODEL FOR PREDICTING THE RESPONSE OF OLD-TYPE COLUMNS REHABILITATED WITH CONCRETE JACKETING UNDER REVERSED CYCLIC LOADING

Georgia E. Thermou[1], Vassilis K. Papanikolaou[1], and Andreas J. Kappos[1]

[1] Aristotle University of Thessaloniki
Thessaloniki 54124, Greece
gthermou@civil.auth.gr, billy@civil.auth.gr, ajkap@civil.auth.gr

Keywords: Reinforced Concrete, Jacket, Retrofit, Strengthening, Shear transfer mechanisms, Cyclic loading.

Abstract. *In the study presented herein, an analytical model for predicting the response of members with old-type detailing, rehabilitated with reinforced concrete (R/C) jacketing under reversed cyclic loading is developed. The analytical model considers that there is partial connection between the existing member (core of the retrofitted member) and its outer R/C shell, thus allowing relative slip of the two bodies. Slip takes place at the interface between the existing member and the jacket, mobilizing the shear resistance mechanisms, such as aggregate interlock, friction and dowel action. Constitutive models from the international literature are adopted to describe the mechanisms that resist relative sliding under cyclic shear reversals. Dual-section analysis is adopted to calculate the shear flow at the interface between the existing member and the jacket. An algorithm is developed to estimate the flexural response under cyclic loading taking into account slip at the interfaces. The proposed algorithm is utilized for the derivation of moment – curvature response histories of members tested in the laboratory, selected from a database compiled in the framework of the present study.*

1 INTRODUCTION

Reinforced concrete structures hold a significant percentage of the building stock in South Europe and especially in Greece. The vast majority of these structures built in the 70’s do not comply with current seismic codes [1]. Due to lack of seismic detailing and capacity design, premature failure is foreseen. Rehabilitation measures are considered necessary and often a combination of both global and local intervention methods provides the most efficient retrofit solution [2]. Reinforced concrete jacketing is an intervention method used extensively in practice to accommodate deficiencies related to global response indices such as stiffness and strength. The use of this method allows uniform distribution of lateral load capacity throughout the structure, thereby avoiding concentrations of lateral load resistance.

Variations of the method are related to the means of connection (i.e. dowels, U-shaped links, etc.) between the 'old' cross section, which serves as the core of the jacketed member, and the jacket itself, along with the preparation of the surface of the existing member (i.e. roughening). All these measures aim to provide full composite action between the two bodies and reduce the effect of slip at the interface between the existing member and the jacket.

The usual practice adopted by intervention codes for proportioning of R/C jacketed members in order to simplify the design procedure is the use of monolithicity factors. These reduction factors are used to obtain the resistance and deformation indices of the jacketed members and are applied to the respective properties of monolithic members with identical geometry. In the case of Eurocode 8, Part 1.3 (§A.4.2 , [3]) and under the assumptions of: (i) full composite action between old and new concrete, (ii) application of full axial load in the jacketed member, and (iii) application of the concrete properties of the jacket over the full section of the element, monolithicity factors are equal to K_V=0.9 for shear strength, K_{My}=1.0 for moment at yield, $K_{\theta u}$=1.0 for the rotation at ultimate, whereas for the rotation at yield, the value $K_{\theta y}$=1.05 applies in case that measures for roughening of the interface have been taken and the value $K_{\theta y}$=1.20 applies for the rest of the measures taken for the connection of the jacket to the existing member or when no particular measures are taken. The Hellenic code for retrofitting (§8.2.1 5 [4]) suggests monolithicity factors for shear strength K_V=0.9, for stiffness, K_K=0.8, and rotation at yield and ultimate $K_{\theta y}$=1.25 and $K_{\theta u}$=0.80, respectively.

The values adopted by the codes are empirical, mainly due to the limited understanding of the influence of shear resistance mechanisms mobilized at the interface due to slip. To this purpose an analytical model is developed for predicting the response of R/C jacketed members taking into account slip at the interface between the existing member and the jacket under cyclic loading conditions. The solution algorithm is based on previous research conducted by Thermou *et al.* [5, 6] for monotonic loading. In this paper, it is further modified and extended to account for cyclic shear reversals.

2 SHEAR TRANSFER MECHANISMS UNDER CYCLIC LOADING

Shear transfer along interfaces plays a crucial role in the response of composite members. Describing in detail the mechanisms mobilized along interfaces due to slip and their interaction is a rather complex mechanical issue, especially under cyclic loading conditions where degradation should also be accounted for. Although issues of connection between existing and newly cast concrete arise often in retrofitting of R/C structures, as in the case of the R/C jacketing technique, it remains an issue that has not been fully addressed by codes.

Mechanisms that resist sliding (slip) are: (i) aggregate interlock between contact surfaces, including any initial adhesion of the jacket concrete on the substrate; (ii) friction owing to clamping action of reinforcement normal to the interface; and (iii) dowel action of any properly anchored reinforcement crossing the sliding plane. The first two mechanisms refer to the contribution of concrete, since they are based on the friction resistance of the interfaces. The relationship that describes the contribution of the individual shear transfer mechanisms is:

$$\begin{gathered}\tau_{tot} = \tau_{agr} + \tau_f + \tau_D = \tau_{agr} + \mu\sigma_N + \tau_D \\ \text{where } \sigma_N = \sigma_c + p\sigma_s = \nu f_c + \rho\sigma_s\end{gathered} \tag{1}$$

In the above equation, τ_{agr} represents the shear resistance of the aggregate interlock mechanism, μ is the interface shear friction coefficient, σ_N is the normal clamping stress acting on the interface and τ_D is the shear stress resisted by dowel action in cracked reinforced concrete. The clamping stress represents any normal pressure, p, externally applied on the interface, but also the clamping action of reinforcement crossing the contact plane as illustrated in Fig. 1 (σ_s is the axial stress of the bars crossing the interface, ρ is the corresponding reinforcement area ratio, $v=N/(A_c f_c)=\sigma_c/f_c$ is the dimensionless axial load at the interface of A_c area and f_c is the concrete compressive strength.

The first two terms in Eq. (1) collectively represent the *contribution of concrete* as they depend on the frictional resistance of the interface planes.

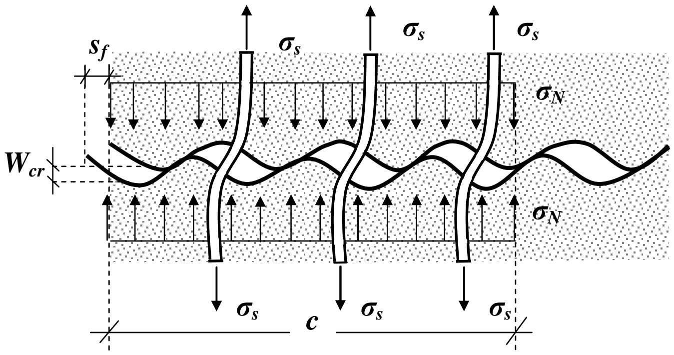

Figure 1: Slip at a concrete interface crossed by reinforcement.

Shear transfer along interfaces has been a subject of ongoing research for many years now. Analytical models and design expressions have been proposed by various researchers, the majority of which are either empirical or based on substantial simplifications. The models found in the literature are classified in two categories. To the first belong those models where all forces are transferred through reinforcement [7-12], whereas the second includes those models that apart from reinforcement contribution include a cohesion term [13-21].

For the needs of the present study, the model of Tassios & Vintzēleou [18], Vintzēleou & Tassios [19, 20] was used because it was the only model found in literature that describes the shear transfer mechanisms under cyclic loading. Furthermore, this model predicted with satisfactory precision the shear resistance developed at the interface between old and new concrete after cross-correlating with the experimental results of a parametric experimental investigation where twenty four (24) specimens of double interface were tested with parameters of study the diameter and the area of reinforcement bars crossing vertically the interface, as well as the degree of interface roughness [22]. The model estimates the combined dowel and shear friction resistances for a given slip value at the interface.

2.1 Friction resistance

The shear stress transferred through friction due to slip is described by the following set of equations [18-20]:

$$\frac{\tau(s)}{\tau_{f,u}}=1.14\left(\frac{s}{s_u}\right)^{1/3} \text{ for } \frac{s}{s_u}\leq 0.5 \tag{2a}$$

$$\frac{\tau(s)}{\tau_u}=0.81+0.19\left(\frac{s}{s_u}\right) \text{ for } \frac{s}{s_u}>0.5 \tag{2b}$$

where s_u(≈2 mm) is the higher value of slip attained, whereas the higher value of friction resistance, τ_{fu}, is equal to:

$$\tau_{fu}=\mu\left(f_c^2\sigma_N\right)^{1/3} \tag{3}$$

where μ is the friction coefficient, taken equal to 0.44 for s_u=2mm.

According to Tassios and Vintzēleou [18], it is assumed that the bars pullout by $w/2$ from each side of the contact surface and that the separation w and lateral slip, s, are related by: $w=0.6\cdot s^{2/3}$ (Fig. 1). To calculate the axial stress of the bars crossing the interface, σ_s, the separation w between contact surfaces as they slide overriding one another is considered (Fig. 1). Considering uniform bond stresses along the embedment length, the axial bar stress, σ_s, at the contact plane is estimated from:

$$\sigma_s=\left(\frac{0.3s_f^{2/3}E_s f_c}{D_b}\right)^{1/2} \tag{4}$$

where E_s is the elastic modulus of steel and D_b is the diameter of the bars clamping the interface (here, the stirrup legs of the jacket).

In case of cyclic loading the frictional resistance is reduced at each cycle according to:

$$\tau_{f,n}=\tau_{f,1}\left\{1-\left[0.002(n-1)\frac{f_c}{\sigma_N}\frac{s_f}{s_{f,u}}\right]^{1/3}\right\} \tag{5}$$

where $\tau_{f,1}$ is the higher frictional resistance value attained in the first cycle. The hysteretic model of frictional resistance is differentiated depending on the value of slip at which reversal takes place. Two cases are identified; in the first, unloading takes place at lower slip values compared to the higher value of slip, $s<s_u$ (Fig. 2(α), [21]), whereas in the second unloading takes place at the higher value of slip attained, s_u (Fig. 2(b), [18]).

2.2 Dowel resistance

In the model proposed by Vintzēleou & Tassios [19, 20], it is considered that the bar behaves as a horizontally loaded free-headed pile embedded in cohesive soil and that yielding of the dowel and crushing of concrete occur simultaneously. Dowel force, F_D, is given as a function of slip, s, by:

$$\frac{F_D(s)}{F_{D,u}}=0.5\frac{s}{s_{el}} \text{ for } s\leq s_{el}=0.006D_b \tag{6a}$$

$$\text{for } \frac{F_D(s)}{F_{D,u}} \geq 0.5 \Rightarrow s = 0.006D_b + 1.76s_u\left[\left(\frac{F_D(s)}{F_{D,u}}\right)^4 - 0.5\left(\frac{F_D(s)}{F_{D,u}}\right)^3\right] \tag{6b}$$

where s_{el} is the elastic slip value, s_u is the ultimate slip value, $F_{D,u}$ is the ultimate dowel force and D_b is the diameter of the dowels (i.e. the legs of the jacket transverse reinforcement). The ultimate dowel strength and associated interface slip are given by:

$$F_{D,u} = 1.3D_b^2\left[f_{cd}f_{yd}\left(1-\alpha^2\right)\right]^{1/2} = D_b^2\left[f_c f_y\left(1-\alpha^2\right)\right]^{1/2}; \quad s_{D,u} = 0.05D_b \tag{7}$$

where α is the bar axial stress normalized with respect to its yield value, $f_{yd}(=f_y/1.15)$ is the design yield strength of steel and $f_{cd}(=f_{ck}/1.5)$ is the design concrete compressive strength. The dowel resistance constitutive laws are depicted in Fig. 3.

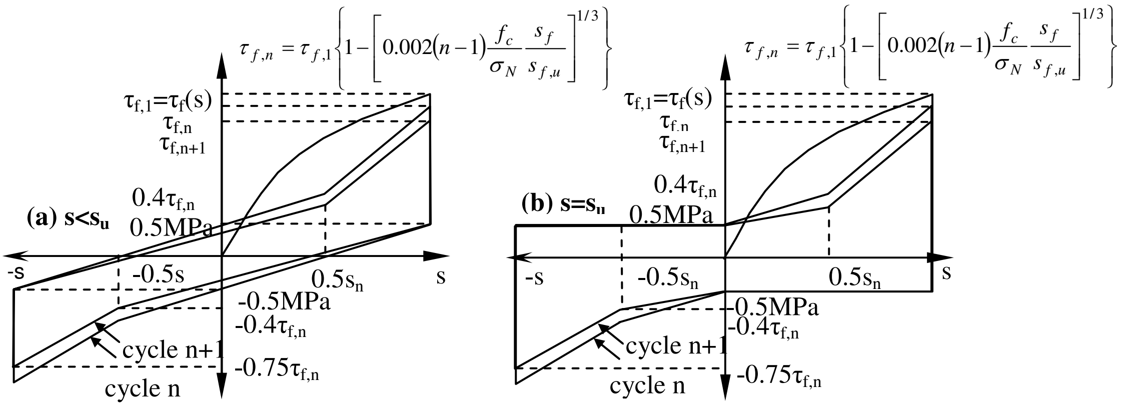

Figure 2: Frictional resistance constitutive laws for (a) s<s$_u$ [21]; (b) s=s$_u$ [18].

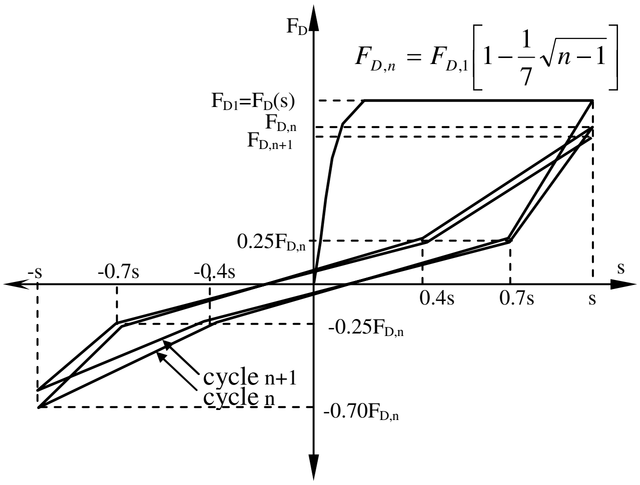

Figure 3: Dowel resistance constitutive law [19, 20].

2.3 Interaction of friction and dowel resistance

In case that the bars are subjected simultaneously to tension (pullout due to frictional resistance) and shear (dowel action), then the dowel strength capacity at yield is consumed by both resistance mechanisms. In order to take into account the interaction of the two resistance mechanisms, the higher friction and dowel resistance capacity are determined by the following relationship [21]:

$$\left(\frac{\sigma_s - \sigma_{SN}}{f_{sy}}\right)^{3/2} + \left(\frac{F_D(s)}{F_{D,u}}\right)^{3/2} = 1\,;\ \sigma_{SN} = \frac{\nu \cdot f_c}{\rho + E_c/E_s} \tag{8}$$

where σ_s is the pullout stress mobilized at slip, f_c is the concrete compressive strength, E_c, E_s, are the elastic modulus of concrete and steel, respectively, $\nu(=N/(A_c f_c))$ is the dimensionless axial load, and ρ is the percentage of reinforcement that crosses the interface.

The solution of Eq. (8) corresponds to a value for s_{crit}, for which the dowel and friction resistance cannot increase further. This assumption leads to a modification of the hysteretic diagram of dowel action in cyclic loading.

The total shear resistance of an interface with contact area A_{int} crossed by k dowels is:

$$F(s) = \tau_f(s) A_{\text{int}} + k F_D(s) \tag{9}$$

where $\tau_f(s)$ and $F_D(s)$ are calculated from Eqs. (2) and (6), respectively, for a given amount of interface slip.

3 ANALYTICAL MODEL OF R/C JACKETED MEMBERS SUBJECTED TO CYCLIC SHEAR REVERSALS

The analytical model for the flexural behaviour of brittle R/C members rehabilitated with concrete jacketing presented herein is based on previous research conducted by Thermou et al. [5, 6] but it is further extended to cyclic loading conditions after a series of adaptations and additions. The proposed analytical model introduces a degree of freedom allowing the relative slip at the interface between the existing member and the jacket. Slip along the member's length is attributed to the difference in normal strains at the contact interfaces (Fig. 4(a)). For flexural analysis, the cross section is divided into three layers which deform with the same curvature, φ (Fig. 4(a)). The two external layers represent the contribution of the jacket, whereas the internal one represents both the core (existing cross section) and the web of the jacket shell. Slip at the interface mobilizes the shear transfer mechanisms such as aggregate interlock, friction owing to clamping action and dowel action of the stirrup legs of the jacket (Fig. 4(b)). The friction and dowel resistance constitutive laws in cyclic loading proposed by Tassios & Vintzēleou [18], Vintzēleou & Tassios [19, 20] are adopted (see section 2) and further modified as described in section 4.2 for the needs of the current study.

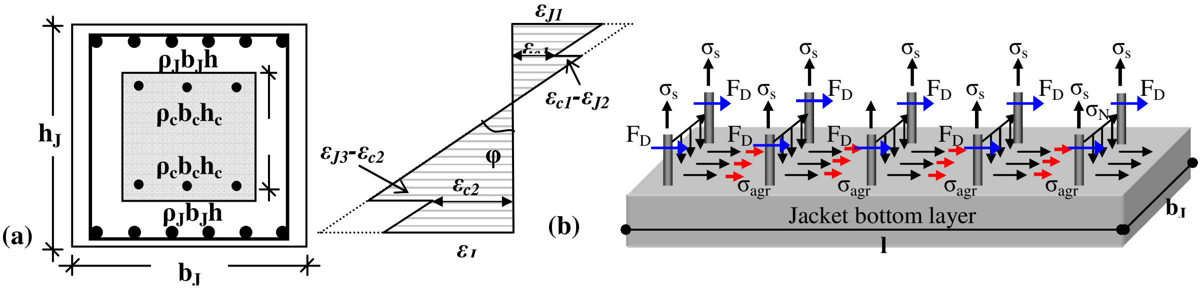

Figure 4: (a) Strain profile of the jacketed cross section; (b) Shear transfer mechanisms at the interface between the jacket and the core.

According to the proposed analytical model of Thermou et al. [5, 6] for R/C jacketed members, shear transfer at the interface between the existing member and the jacket is carried out between half crack intervals along the length of the jacketed member as considered in bond analysis. At the initial stages of loading, cracks form only at the external layers (jacket) increasing in number with increasing load, up to crack stabilization. This occurs when the jacket steel stress at the crack, $f_{s,cr}$ exceeds the limit [23]:

$$f_{s,cr} > f_{ctm} \frac{1+\eta\rho_{s,eff}}{\rho_{s,eff}} \tag{10}$$

where f_{ctm} is the tensile strength of concrete, $\eta(=E_s/E_{cm})$ is the modular ratio and $\rho_{s,eff}$ is the effective reinforcement ratio defined as the total steel area divided by the area of mobilized concrete in tension, usually taken as a circular domain with a radius of $2.5D_b$ around the bar [23]. Using the same considerations in the combined section it may be shown that a number of the external cracks penetrate the second layer (core) of the jacketed member (Fig. 5(a)). The distance between those cracks, taken as c, is a key element of the proposed methodology.

3.1 Crack spacing estimation

After crack stabilization and assuming that the neutral axis depth is about constant in adjacent cross sections, from the free body equilibrium in the tension zone of the core of the composite section (Fig. 5(b)), the crack spacing is defined as follows:

$$c = \frac{0.64 \cdot b_J \, l_c \, f_{ct,c}}{n_c \, D_{b,c} \, f_{b,c} + n_J \, D_{b,J} \, f_{b,J}} \tag{11}$$

where b_J is the width of the jacketed cross section, l_c is the height of the tension zone in the core component of the composite cross section, $f_{ct,c}$ is the tensile strength of concrete core, n_c, n_J are the number of bars in the tension steel layer of the core and the jacket, respectively, $D_{b,c}$, $D_{b,J}$ are the bar diameter of the core and jacket longitudinal reinforcement, respectively, and $f_{b,c}$, $f_{b,J}$ are the average bond stress of the core and the jacket reinforcement layer, respectively.

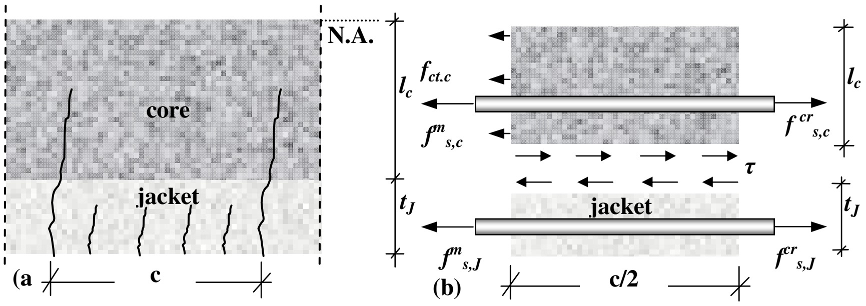

Figure 5: (a) Crack spacing, c; (b) Free body equilibrium in the tension zone of the core of the composite section.

3.2 Shear stress demand at the interfaces

Shear stress demand at the interfaces, $\tau_{d,i}$, is determined by examining the cross section along the height and a member length equal to the distance between successive cracks (Figure 6(a)). The layer force resultant ΣF_i (sum of concrete and steel forces at each layer), for the externally applied axial load, N_{ext} (considered to be applied to the jacketed section), is used to calculate the vertical shear stress demand of the member, $\tau_{d,i}$. With the assumption that the shear flow, q, reversal takes place at length equal to $c/2$ (Figure 6(b), where c is the crack spacing), the average stress demand $\tau_{d,i}$ is equal to:

$$\tau_{d,i} = \frac{\Sigma F_i}{0.5\, c\, b_J} \tag{12}$$

where ΣF_i is the layer force resultant, b_J is the width of the jacketed cross section, and c is the crack spacing length.

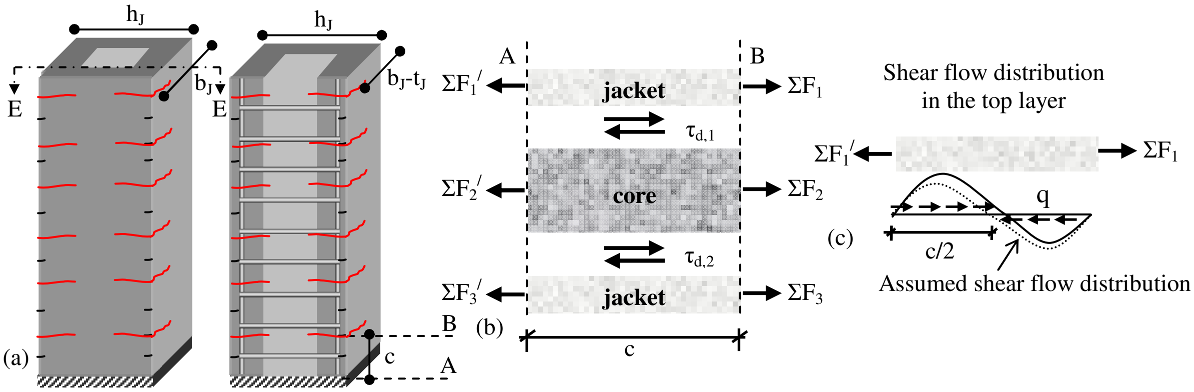

Figure 6: (a) R/C jacketed column; (b) Section equilibrium between adjacent cracks; (c) Assumption for the estimation of shear flow, q.

4 ALGORITHM FOR MOMENT – CURVATURE ANALYSIS

The calculation algorithm aims at the derivation of moment – curvature histories of R/C members retrofitted with R/C jackets taking into account slip at the interfaces between the existing member (core) and the jacket under cyclic loading conditions. Thus, given a curvature loading history (Fig. 7), at each loading step the objective is twofold: (i) equilibrium establishment between the shear stress capacity and demand at the interfaces for relative slip, s, and (ii) establishment simultaneously of force equilibrium at the cross section. Equilibrium is established though an iterative procedure until convergence is achieved.

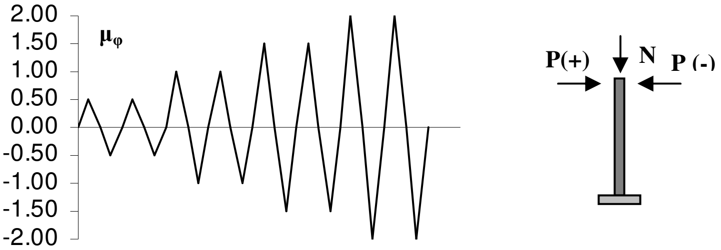

Figure 7: Loading history considered in the calculation algorithm.

In the first step of the analysis (very low curvature value) slip is taken equal to zero at both interfaces. In the next steps, as curvature increases, the inclination of the strain profile is modified (allowing continuously increasing difference of strain at the interfaces) in order to establish cross section equilibrium.

The proposed calculation algorithm comprises the following steps:

<u>For each loading cycle ℓ:</u>

1) Set sectional curvature equal to φ^n(+). Problem unknowns are, the normal strain at the top fiber of the jacketed cross section, $\varepsilon_{J1}{}^{n,m}$, the interface slip at the upper, $s_1{}^{n,r}$, and bottom interfaces, $s_2{}^{n,r}$.
2) Estimate the normal strain at the top fiber of the cross section, $\varepsilon_{J1}{}^{n,m}$ (Fig. 4(a)).
3) Estimate the interface slip at the upper and bottom interfaces, $s_1{}^{n,r}$ and $s_2{}^{n,r}$. Slip at the interface is related to the difference of strains at the upper and lower interface, $\Delta\varepsilon_1{}^{n,r}$ and $\Delta\varepsilon_2{}^{n,r}$, as follows:

$$s_1^{n,r} = \Delta\varepsilon_1^{n,r}\, c = (\varepsilon_{c1}^{n,r} - \varepsilon_{j2}^{n,r})\, c, \quad s_2^{n,r} = \Delta\varepsilon_2^{n,r}\, c = (\varepsilon_{j3}^{n,r} - \varepsilon_{c2}^{n,r})\, c \tag{13}$$

where variables $\varepsilon_{c1}{}^{n,r}$, $\varepsilon_{j2}{}^{n,r}$ and $\varepsilon_{j3}{}^{n,r}$, and $\varepsilon_{c2}{}^{n,r}$ are normal strains in the section layers above and below the contact surfaces (Fig. 4(a)), and c is the average crack spacing (Eq. (11), Fig. 5(a)).

4) Check equilibrium at the interfaces - Shear strength capacity of the top and bottom interface, $\tau_1{}^{n,r}$ and $\tau_2{}^{n,r}$, are estimated from the respective slip values, $s_1{}^{n,r}$ and $s_2{}^{n,r}$, according to the constitutive laws that describe the behaviour of the interface under cyclic loading (Eqs. 2-9). Shear strength demand at the upper and bottom interface, $\tau_{d,1}{}^{n,r}$ and $\tau_{d,2}{}^{n,r}$, are also estimated according to Eq. (12). Check if $\tau_1{}^{n,r}=\tau_{d,1}{}^{n,r}$ and $\tau_2{}^{n,r}=\tau_{d,2}{}^{n,r}$. If this is valid, then equilibrium is established and the next step follows, otherwise return to step 3 and set $s_1{}^{n,r+1}=s_1{}^{n,r}+ds_1$, $s_2{}^{n,r+1}=s_2{}^{n,r}+ds_2$, where ds_i is the selected increment in the slip value. Revise slip values at the top and bottom interface till convergence.
5) Check cross section equilibrium: The force resultant, ΣF_i (Fig. 6(a)) is calculated at each layer. In case that equilibrium is not established, $\Sigma\Sigma F_i - N_{ext} \geq$tolerance, then the normal strain profile is revised by returning to step 2 and setting $\varepsilon_{J1}{}^{n,m+1}=\varepsilon_{J1}{}^{n,m}+d\varepsilon_J$, where $d\varepsilon_J$ is the step increment in the top strain of the jacketed cross section.
6) Store the convergent values for which equilibrium at both interface and cross section level was established $(\varepsilon_{J1}{}^{n}=\varepsilon_{J1}{}^{n,m}$, $s_1{}^{n}=s_1{}^{n,r}$, $s_2{}^{n}=s_2{}^{n,r})$.
7) Estimate the moment resultant, M^n.
8) Unloading
9) Repeat steps 1-7 for φ^n(-)

10) Unloading

11) Repeat steps 1-10 for $\ell=\ell+1$. Calculations stop when the shear capacity of the interface is exhausted.

An original program was developed based on the proposed solution algorithm as described in the flowchart of Fig. 8. Fiber analysis was considered. The behaviour of concrete and steel was described by adopting uniaxial constitutive laws under cyclic loading from the literature (details are provided in section 4.1). The constitutive laws for the description of the shear transfer mechanisms mobilized due to slip at the interface are based on the models of Tassios & Vintzēleou [18], Vintzēleou & Tassios [19, 20], further enhanced to account for arbitrary loading history (load cycles of unequal amplitude).

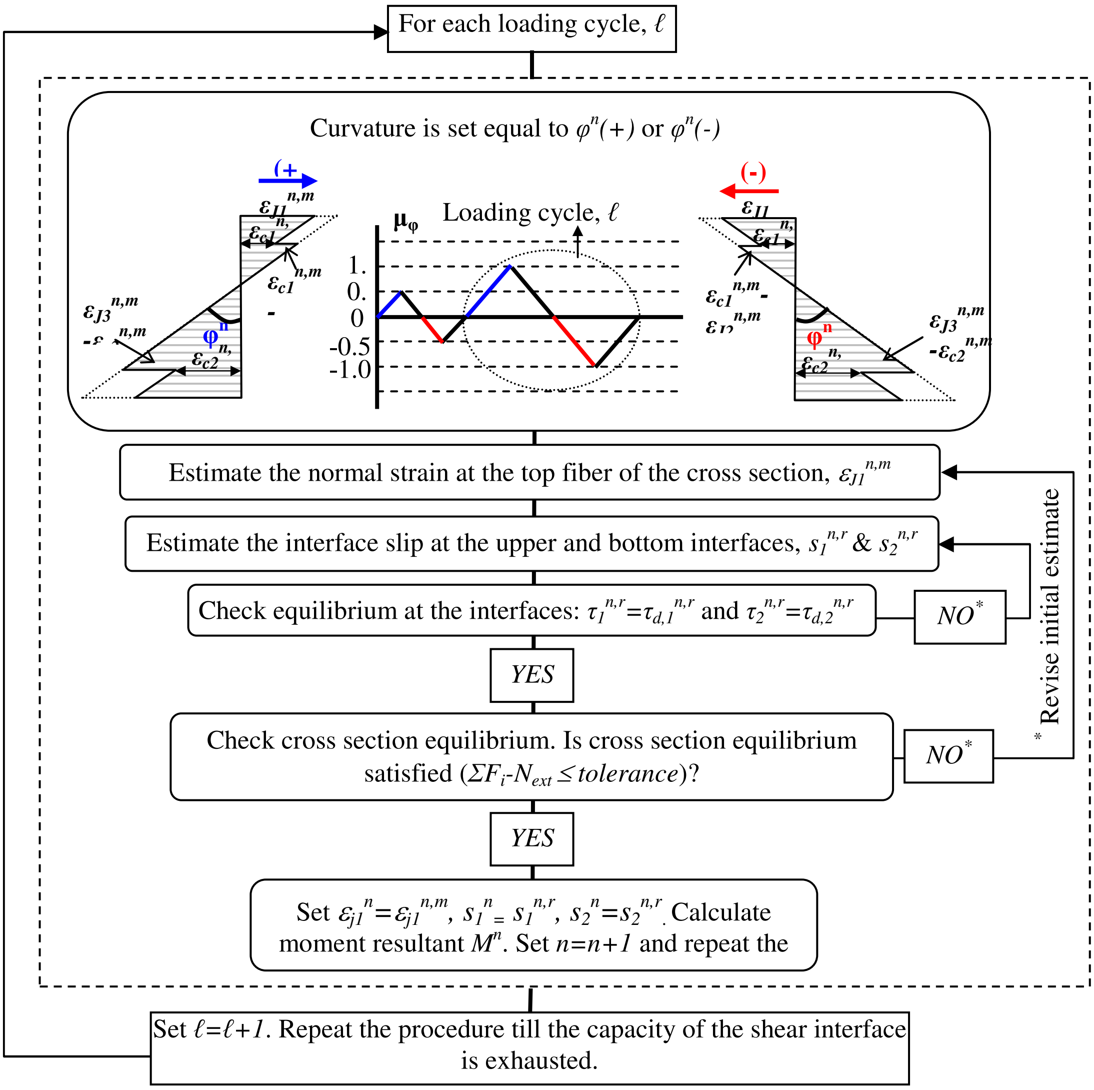

Figure 8: Flowchart of the proposed algorithm.

4.1 Material constitutive laws

Concrete: The constitutive law for concrete adopted is based on the model of Mander et al. [24] as far as the relationship between stresses-strains is concerned and on the hysteresis rules of Martinez-Rueda & Elnashai [25]. Confinement due to transverse reinforcement (taken into account by factor K) is considered constant during loading and follows the relationships proposed by Mander et al. [24]. This law is adequate for modelling R/C elements, especially those subjected to random cyclic loading (e.g. seismic loading). The general shape of the response curve is presented in Fig. 9(a).

Steel: The constitutive law for steel utilized in the proposed algorithm is based on the stress-strain relationship developed by Menegotto-Pinto [26] in combination with the rules of isotropic hardening proposed by Fillippou et al. [27]. It is suitable for modelling reinforced concrete elements subjected to cyclic loading as in seismic conditions. The response curve in its general form is presented in Fig. 9(b).

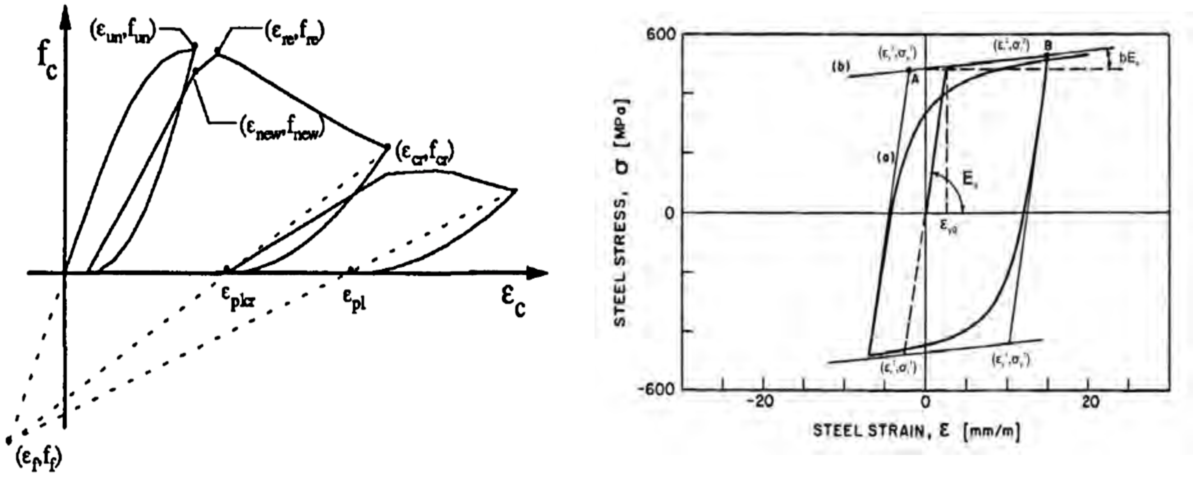

Figure 9: (a) Concrete [25]; (b) Steel constitutive laws [27].

4.2 Interface shear resistance constitutive law

The friction and dowel resistance models as proposed by Tassios & Vintzēleou [18], Vintzēleou and Tassios [19, 20] were further modified to account for the case of non-symmetric reversed cyclic loading. In Fig. 10, for a given random loading history that depends on slip magnitude, s, the extracted dowel resistance hysteretic curve and the total resistance curve according to Eq. (9) are shown.

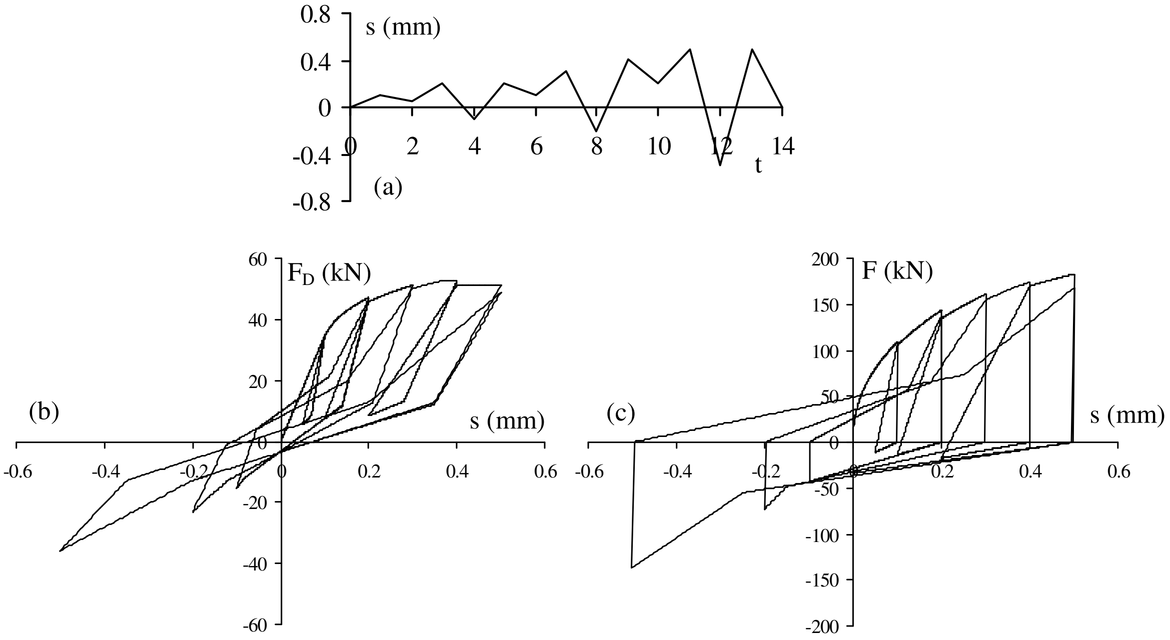

Figure 10: (a) Non-symmetric loading history; (b) Dowel resistance hysteretic curve; (c) Total interface resistance hysteretic curve.

5 RESULTS OF THE ANALYSIS

In this section the proposed analytical model is used for estimating the flexural response of R/C jacketed members for the case that slip at the interface between the jacket and the existing member is neglected. The case-studies selected to be presented herein were taken from the experimental database which was created for the needs of this ongoing study.

5.1 Presentation of the experimental database

An experimental database was created which includes forty four (44) specimens from eleven (11) experimental studies. The database includes specimens where various connection measures were taken between the existing member and the jacket, whereas the jacket construction was done using shotcrete or cast-in-place concrete. The range of database parameters is shown in Table 1. The database along with the symbols used are presented in detail in Tables A1 and A2 of the Appendix.

The specimens selected to be analyzed with the proposed algorithm are specimens R2R [29] and Q-RCR [36]. Details on the geometrical and material characteristics are presented in Tables A1 and A2 of the Appendix.

Existing cross section		Jacket	
b_c (mm)	200~350	b_J (mm)	260~550
h_c (mm)	200~500	h_J (mm)	260~650
$D_{b,c}$ (mm)	10~20	$D_{b,J}$ (mm)	10~20
ρ_{lc} (%)	0.81~2.05	ρ_{lJ} (%)	0.75~1.64
$D_{bs,c}$ (mm)	6~8	$D_{bs,J}$ (mm)	6~10
s_c (mm)	50~265	s_J (mm)	50~100
ρ_{wc}(%)	0.16~0.66	ρ_{wJ}(%)	0.22~0.94
f_c (MPa)	22.9~58.2	f_c (MPa)	7~68.7
f_y (MPa)	313~550	f_y (MPa)	400~520
f_{yw} (MPa)	350~520	f_{yw} (MPa)	330~599
L_s/h_c	3.2~11.7	L_s/h_J	2.5~7.0
Μάτιση (D_b)	15~45	L_s (mm)	1000~3500
		v (%)	0~26

Table 1: Range of database parameters.

5.2 Results of the case studies considered

Specimens P2R [29] and Q-RCR [36] are subjected to the applied curvature ductility history presented in Fig. 11. Each loading cycle increases by ¼ of φ_y. The curvature at yield, φ_y, was estimated by the following simplified expression [4]:

$$\varphi_y = 1.77 \frac{f_y}{E_s h_J} \tag{1}$$

where f_y is the yield strength of steel of the reinforcement bars of the jacket, h_J the height of the jacketed member and E_s the modulus of elasticity of steel. For specimen P2R curvature at yield is φ_y=1.6x10^{-2} (rad/m), displacement at yield is Δ_y=5.5 mm and drift at yield is θ_y=0.54%, whereas for specimen Q-RCR curvature at yield is φ_y=1.08x10^{-2} (rad/m), displacement at yield Δ_y=9.2 mm and drift at yield θ_y=0.57%. The hysteretic response of the two test specimens is depicted in Figures 12 and 13.

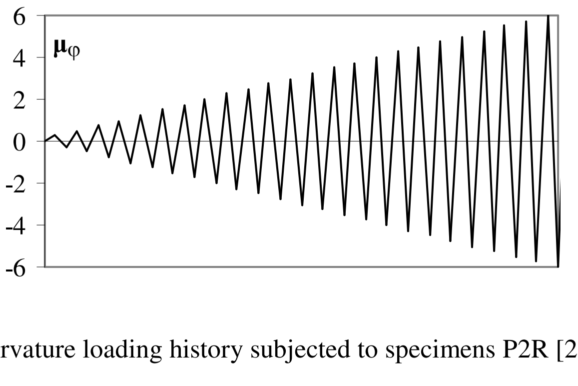

Figure 11: Curvature loading history subjected to specimens P2R [29] and Q-RCR [36].

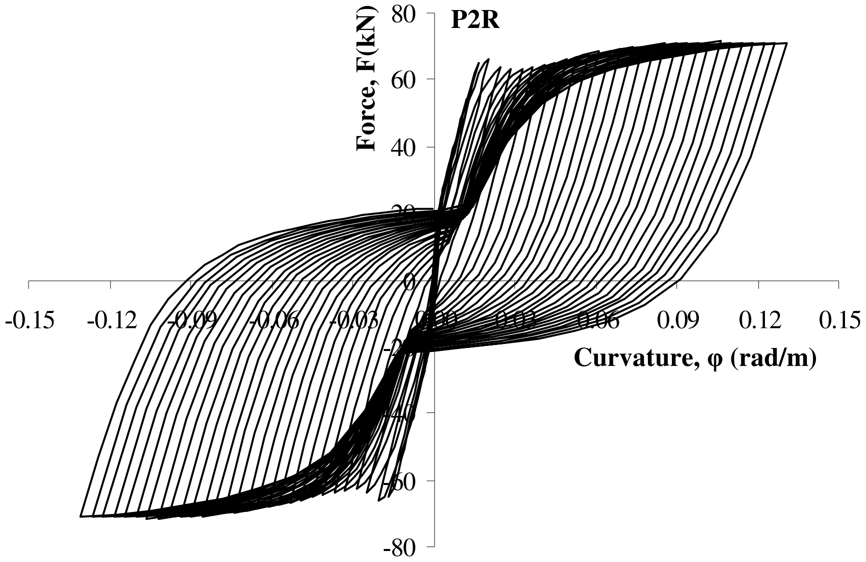

Figure 12: Response of specimen P2R [29] to cyclic loading conditions for the case that slip is neglected.

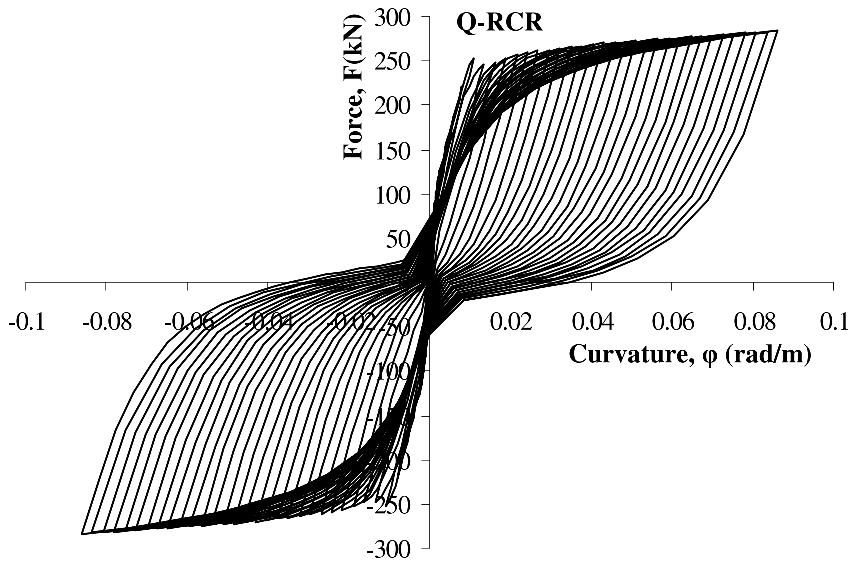

Figure 13: Response of specimen Q-RCR [36] to cyclic loading conditions for the case that slip is neglected.

6 CONCLUSIONS

An analytical model for predicting the response of old-type columns rehabilitated with concrete jacketing under reversed cyclic loading was developed. The composite cross section is divided into three layers which develop the same curvature. The proposed analytical model allows slip at the interface between the existing member and the jacket. Shear transfer mechanisms are mobilized due to sliding at the interface between existing and new concrete. The shear capacity is described by constitutive models for cyclic loading conditions and is given as a function of slip. The shear demand at the interface is controlled by the flexural stresses on the cross section and by the spacing of cracks in the longitudinal direction. Equilibrium at the interfaces is established when shear capacity and demand are equalized. An algorithm was developed for determining the moment – curvature histories of R/C jacketed members with partial connection between the existing member (core) and the jacket. The response of test specimens selected from a database compiled within the framework of this work was studied by utilizing the proposed solution algorithm for null slip at the interface.

ACKNOWLEDGEMENTS

The research conducted in this paper was funded by the Hellenic Earthquake Planning and Protection Organization (E.P.P.O.); the authors gratefully acknowledge this support.

REFERENCES

[1] Eurocode 8, Design of structures for earthquake resistance - Part 1: general rules, seismic actions and rules for buildings. EN1998-1-2004:E, European Committee for Standardization (CEN), Brussels, 2004.

[2] G. E Thermou, A. S. Elnashai, Seismic retrofit schemes for R/C structures and local-global consequences. *Journal of Progress in Structural Engineering and Materials,* Wiley InterScience, **8**(1), 1-15, 2006

[3] Eurocode 8, Design of structures for earthquake resistance - Part 3: Assessment and retrofitting of buildings. EN 1998-3:2005(E), European Committee for Standardization (CEN), Brussels, 2005.

[4] KANEPE, Interventions Code (of Greece). Earthquake Planning and Protection Organization (E.P.P.O.), Final draft, Sep. 2010 (in Greek).

[5] G.E. Thermou, S.J. Pantazopoulou, A.S. Elnashai, Design and assessment models and spectra for repaired reinforced concrete structures. Mid-America Earthquake Center Report, CD release 09-01, 2009.

[6] G.E. Thermou, S.J. Pantazopoulou, A.S. Elnashai, Flexural behaviour of brittle R/C members rehabilitated with concrete jacketing. *Journal of Structural Engineering*, *ASCE*, **133**(10), 1373-1384, 2007.

[7] ACI Committee 318, Building Code Requirements for Reinforced Concrete (ACI 318-95) and Commentary ACI 318 R-95. *American Concrete Institute*, Detroit, 16-1 -16-10, 1995.

[8] ACI Committee 318, Building Code Requirements for Reinforced Concrete (ACI 318-99) and Commentary ACI 318 R-99. *American Concrete Institute*, Detroit, 133 – 142, 1999.

[9] ACI Committee 318, Building Code Requirements for Reinforced Concrete (ACI 318-02) and Commentary ACI 318 R-02. *American Concrete Institute*, Detroit, 139–154, 2002.

[10] P.W., Birkeland, H.W. Birkeland, Connections in precast concrete construction. *Journal of American Concrete Institute*, **63**(3), 345-368, 1966.

[11] J.C. Walraven, Fundamental analysis of aggregate interlock. *Structural Division, ASCE,* **107**, No. ST11, 2245-2270, 1981.

[12] E.R. Loov, K.A. Patnaik, Horizontal shear strength of composite concrete beams with a rough interface. *PCI Journal*, 48-69, 1994.

[13] J.C.T.S. Climaco, P.E. Regan, Evaluation of bond strength between old and new concrete in structural repairs. *Magazine of Concrete Research*, **53**(6), 377-390, 2001.

[14] H.A. Mattock, M.N. Hawkins, Shear transfer in reinforced concrete- recent research. *PCI Journal*, 55-75, 1972.

[15] H.A. Mattock, K.W. Li, C.T. Wang, Shear transfer in lightweight reinforced concrete. *PCI Journal*, 20-39, 1976.

[16] H.A. Mattock, Shear friction and high-strength concrete. *Structural Journal*, *ACI*, **98**(1), 50-59, 2001.

[17] F.J. Vecchio, M.P. Collins, The modified compression-filed theory for reinforced concrete elements subjected to shear. *ACI Journal*, **83**(2), 219-581, 1986.

[18] T. Tassios, V.E. Vintzēleou, Concrete-to-concrete friction. *ASCE J. Struct. Eng.*, **113**(4), 832-849, 1987.

[19] E. Vintzēleou, T. Tassios, Mathematical models for dowel action under monotonic and cyclic conditions. *Magaz. of Concrete Research*, **38**(134), 13-22, 1986.

[20] E. Vintzēleou, T. Tassios, Behaviour of dowels under cyclic deformations. *ACI Struct. J.*, **84**(1), 18-30, 1987.

[21] I. Vassilopoulou, P. Tassios. Shear transfer capacity along a R/C. crack under cyclic sliding. *Proc., fib Symposium*, Technical Chamber of Greece), Athens, Greece, Paper No. 271., 2003.

[22] O. Dimitriadou, V. Kotsoglou, G.E. Thermou, A. Savva, S.J. Pantazopoulou, Experimental study of concrete interfaces in sliding shear. Technical Chronicles, *Journal of the Technical Chamber of Greece* (TCG), **25**(2-3), 123-136 (in Greek), 2005.

[23] *fib* Model Code 2010, First complete draft - Vol. 2, Bull. 56, Lausanne, Apr. 2010.

[24] J.B. Mander, M.J.N. Priestley, R. Park, Theoretical stress-strain model for confined concrete. *Journal of Structural Engineering*, **114**(8), 1804-1826, 1988.

[25] J.E. Martinez-Rueda, A.S. Elnashai, Confined concrete model under cyclic load. *Materials and Structures*, **30**(197), 139-147, 1997.

[26] M. Menegotto, P.E Pinto, Method of analysis for cyclically loaded R/C plane frames including changes in geometry and nonelastic behaviour of elements under combined normal force and bending. *Proc. IABSE Symposium*, Lisbon, Portugal, 1973.

[27] F.C Filippou., E.P Popov, V.V. Bertero, Effects of bond deterioration on hysteretic behaviou rof reinforced concrete joints. *Report No. UCB/EERC-83/19*, University of California, Berkeley, 1983.

[28] M. Rodriguez, R. Park, Seismic load tests on reinforced concrete columns strengthened by jacketing. *ACI Struct. J.*, **91**(2), 150-159, 1994.

[29] A.M. Gomes, J. Appleton, Repair and strengthening of R.C. elements under cyclic loading. *Proc., 11th Europ. Conf. Earthq. Eng.*, A.A. Balkema (Rotterdam, The Netherlands), Paris, France, CD-ROM, 1998.

[30] A. Ilki, K. Darilmaz, I Bakan, M. Zorbozan, E. Yuksel, S. Haruhan, F. Karadogan, Jacketing of Prefabricated Columns. *Proc.2nd Japan-Turkey Workshop on Earthquake Engineering*, Istanbul, Turkey, 329-336, 1998.

[31] K.G. Vandoros, S.E. Dritsos, Interface treatment in shotcrete jacketing of reinforced concrete columns to improve seismic performance. *J. Struct. Eng. and Mech.*, **23**(1), 43-61, 2006a.

[32] K.G. Vandoros, S.E. Dritsos, Axial preloading effects when reinforced concrete columns are strengthened by concrete. *Progress in Struct. Eng. and Mat. J.*, **8**(3), 79-92, 2006b.

[33] K.G. Vandoros, S.E. Dritsos, Concrete jacket construction detail effectiveness when strengthening R/C columns. *Construction and Building Materials*, **22**, 264-276, 2008.

[34] E.N.B.S. Júlio, F.A.B. Branco, V.D Silva, Reinforced Concrete Jacketing—Interface Influence on Monotonic Loading Response. *ACI Structural Journal*, 102(2), 252-257, 2005.

[35] S. Bousias,A.-L Spathis, M.N Fardis, Concrete or FRP jacketing of columns with lap splices for seismic rehabilitation. *Journal of Advanced Concrete Technology*, **4**(3), 431-444, 2006.

[36] S. Bousias, D. Biskinis, M. Fardis, A. Spathis, Strength, stiffness, and cyclic deformation capacity of the concrete jacketed members. *ACI Struct. J.*, **104**(5), 521-531, 2007a.

[37] S. Bousias, A.-L Spathis, M.N Fardis, Seismic retrofitting of columns with lap-spliced smooth bars through FRP or Concrete Jackets. *Journal of Earthquake Engineering*, **11**, 653-674, 2007b.

[38] E.N.B.S. Júlio, F.A.B. Branco, Reinforced Concrete Jacketing—Interface Influence on Cyclic Loading Response. *ACI Structural Journal*, **105**(4), 471-477, 2008.

APPENDIX

Symbols used in the database:
b_c; b_J: width of the existing and the jacketed cross section;
$D_{b,c}$; $D_{b,J}$: bar diameter of the core and the jacket longitudinal reinforcement, respectively;
$D_{bs,c}$; $D_{bs,J}$: bar diameter of the stirrups of the core and the jacket, respectively;
d_c; d_J: depth of the existing and the jacketed cross section, respectively;
$f_{c,c}$; $f_{c,J}$: core and jacket concrete cylinder uniaxial compressive strength, respectively;
$f_{y,c}$; $f_{y,J}$: yield strength of the longitudinal reinforcement of the core and jacket, respectively;
$f_{yw,c}$; $f_{yw,J}$: yield strength of the transverse reinforcement of the core and jacket, respectively
h_c; h_J: height of the existing and the jacketed cross section, respectively;
L_s: shear span length;
$n_{c,mid}$; $n_{J,mid}$: total number of web longitudinal reinforcement bars of the core and the jacket, respectively;
n_c; n_J: total number of top and bottom longitudinal reinforcement bars of the core and the jacket, respectively;

s_c; s_J: stirrup distance in the existing and jacketed cross section respectively;

Greek symbols**:**

ν: dimensionless axial load % estimated based on the compressive strength of the jacket concrete quality.

ρ_{lc}: longitudinal reinforcement ratio of the existing cross section defined as $A_{sc,tot}/(b_c h_c)$, where $A_{sc,tot}=(n_c+n_{c,mid})D_{b,c}^2/4$

ρ_{lJ}: longitudinal reinforcement ratio of the jacketed cross section defined as $A_{sJ,tot}/(b_J h_J-b_c h_c)$, where $A_{sJ,tot}=(n_J+n_{J,mid})D_{b,J}^2/4$

ρ_{wc}; ρ_{wJ}: volumetric ratio of stirrups of the existing and the jacketed cross section, respectively.

Table A1: Database – Details of original test specimens.

Reference	No	Specimens	Existing specimens																
			b_c^*	h_c^*	d_c^*	n_c	$n_{c,mid}$	$D_{b,c}^*$	$\rho_{lc}^\#$	Stirrup legs	$D_{bs,c}^*$	s_c^*	$\rho_{wc}^\#$	$f_{c,c}^\S$	Bar type	$f_{y,c}^\S$	$f_{yw,c}^\S$	L_s/h_c	Lap splice length (D_b)
Rodriquez & Park (1994)	1	SS1	350	350	295	6	2	20	2.05	4	6	265	0.16	29.5	pl	325	350	4.1	-
	2	SS2	350	350	295	6	2	20	2.05	4	6	265	0.16	29.5	pl	325	350	4.1	-
	3	SS3	350	350	295	6	2	20	2.05	4	6	265	0.16	29.5	pl	325	350	4.1	-
	4	SS4	350	350	295	6	2	20	2.05	4	6	265	0.16	25.9	pl	325	350	4.1	-
Gomes & Appleton (1998)	5	P2R	200	200	173	4	0	12	1.13	2	6	150	0.22	53.2	def	480	480	5.0	-
	6	P3R	200	200	173	4	0	12	1.13	2	6	50	0.66	58.2	def	480	480	5.0	-
	7	P4	200	200	173	4	0	12	1.13	2	6	150	0.22	56.2	def	480	480	5.0	-
Ilki et al. (1998)	8	7	300	300	269	6	2	16	1.79	2	8	100	0.38	50.6	def	550	425	11.7	-
	9	8	300	300	269	6	2	16	1.79	2	8	100	0.38	47.1	def	531	425	11.7	-
	10	9	300	300	269	6	2	16	1.79	2	8	100	0.38	44.3	def	531	425	11.7	-
Vandoros and Dritsos (2006a, 2006b, 2008)	11	M	250	250	225	4	0	14	0.98	2	8	200	0.24	24.7	pl	313	425	6.4	-
	12	W	250	250	225	4	0	14	0.98	2	8	200	0.24	22.9	pl	313	425	6.4	-
	13	D	250	250	225	4	0	14	0.98	2	8	200	0.24	27	pl	313	425	6.4	-
	14	R	250	250	225	4	0	14	0.98	2	8	200	0.24	27	pl	313	425	6.4	-
	15	RD	250	250	225	4	0	14	0.98	2	8	200	0.24	27	pl	313	425	6.4	-
	16	N	250	250	225	4	0	14	0.98	2	8	200	0.24	27	pl	313	425	6.4	-
	17	NP	250	250	225	4	0	14	0.98	2	8	200	0.24	23.8	pl	313	425	6.4	-
	18	E	250	250	225	4	0	14	0.98	2	8	200	0.24	36.8	pl	313	425	6.4	-
Júlio et al. (2005)	19	M2	200	200	180	6	0	10	1.18	2	6	150	0.22	28.9	def	400	400	5.0	-
	20	M3	200	200	180	6	0	10	1.18	2	6	150	0.22	28.4	def	400	400	5.0	-
	21	M4	200	200	180	6	0	10	1.18	2	6	150	0.22	28.3	def	400	400	5.0	-
	22	M5	200	200	180	6	0	10	1.18	2	6	150	0.22	28.4	def	400	400	5.0	-
	23	M6	200	200	180	6	0	10	1.18	2	6	150	0.22	28.7	def	400	400	5.0	-
	24	M7	200	200	180	6	0	10	1.18	2	6	150	0.22	28.8	def	400	400	5.0	-

Table A1(cont.): Database – Details of original test specimens.

Reference	No	**Specimens**	**Existing specimens**																
			$\mathbf{b_c}^*$	$\mathbf{h_c}^*$	$\mathbf{d_c}^*$	$\mathbf{n_c}$	$\mathbf{n_{c,mid}}$	$\mathbf{D_{b,c}}^*$	$\mathbf{\rho_{lc}}^\#$	**Stirrup legs**	$\mathbf{D_{bs,c}}^*$	$\mathbf{s_c}^*$	$\mathbf{\rho_{wc}}^\#$	$\mathbf{f_{c,c}}^\S$	**Bar type**	$\mathbf{f_{y,c}}^\S$	$\mathbf{f_{yw,c}}^\S$	$\mathbf{L_s/h_c}$	**Lap splice length ($\mathbf{D_b}$)**
Bousias et al. (2006)	25	R-RCL1	250	500	470	4	0	18	0.81	2	8	200	0.24	36.7	def	514	425	3.2	15
	26	R-RCL3	250	500	470	4	0	18	0.81	2	8	200	0.24	36.8	def	514	425	3.2	30
	27	R-RCL4	250	500	470	4	0	18	0.81	2	8	200	0.24	36.3	def	514	425	3.2	45
Bousias et al. (2007a)	28	Q-RCW	250	250	220	4	0	14	0.98	2	8	200	0.24	22.9	pl	313	425	6.4	-
	29	Q-RCD	250	250	220	4	0	14	0.98	2	8	200	0.24	27.4	pl	313	425	6.4	-
	30	Q-RCR	250	250	220	4	0	14	0.98	2	8	200	0.24	27.7	pl	313	425	6.4	-
	31	Q-RCRD	250	250	220	4	0	14	0.98	2	8	200	0.24	26.3	pl	313	425	6.4	-
	32	Q-RC	250	250	220	4	0	14	0.98	2	8	200	0.24	26.3	pl	313	425	6.4	-
	33	Q-RCM	-	-	-	-	-	-	-	-	-	-	-	-	-	-	-	-	-
Bousias et al. (2007b)	34	Q-RCpd*	250	250	220	4	0	14	0.98	2	8	200	0.24	23.1	pl	313	425	6.4	-
	35	Q-RCL1	250	250	220	4	0	14	0.98	2	8	200	0.24	27.5	pl	313	425	6.4	15
	36	Q-RCL2	250	250	220	4	0	14	0.98	2	8	200	0.24	25.6	pl	313	425	6.4	25
	37	Q-RCL01pd	250	250	220	4	0	14	0.98	2	8	200	0.24	28.1	pl	313	425	6.4	15
	38	Q-RCL02pd	250	250	220	4	0	14	0.98	2	8	200	0.24	28.1	pl	313	425	6.4	25
Júlio and Branco (2008)	39	M2	200	200	180	6	0	10	1.18	2	6	150	0.22	28.9	def	520	520	5.0	-
	40	M3	200	200	180	6	0	10	1.18	2	6	150	0.22	28.6	def	520	520	5.0	-
	41	M4	200	200	180	6	0	10	1.18	2	6	150	0.22	28.5	def	520	520	5.0	-
	42	M5	200	200	180	6	0	10	1.18	2	6	150	0.22	28.6	def	520	520	5.0	-
	43	M6	200	200	180	6	0	10	1.18	2	6	150	0.22	28.7	def	520	520	5.0	-
	44	M7	200	200	180	6	0	10	1.18	2	6	150	0.22	28.9	def	520	520	5.0	-

* mm, $^\#$ %, § MPa, Lap splice length (D_b): given as a function of the bar diameter of long. reinforcement (D_b), Bar type: pl - plain bars, def – ribbed bars

Table A2: Database – Details of retrofitted test specimens.

			Retrofitted specimens																						
Reference	No	**Specimen**	b_J^*	h_J^*	d_J^*	n_J	$n_{J,mid}$	$D_{b,J}^*$	$\rho_{lJ}^{\#}$	**Stirrup legs**	$D_{bs,J}^*$	s_J^*	$\rho_{wJ}^{\#}$	$f_{c,J}^{\S}$	**Bar type**	$f_{y,J}^{\S}$	$f_{yw,J}^{\S}$	**Ls/hJ**	$v^{\#}$	L_s^*	**Pre-damaged**	**Loading**	**Connection measure**	**Jacket type**	**Anchorage of long. reinf.**
Rodriquez & Park (1994)	1	SS1	550	550	512	8	0	16	0.89	2	10	95	0.36	32.9	def	502	340	2.6	10	1425	√	c	R	C	HS
	2	SS2	550	550	512	8	0	16	0.89	2	10	95	0.36	34	def	502	340	2.6	10	1425	-	c	R	C	HS
	3	SS3	550	550	503	8	4	12	0.75	4	10	72	0.94	19.4	def	491	330	2.6	10	1425	-	c	R	C	HS
	4	SS4	550	550	503	8	4	12	0.75	4	10	72	0.94	25.2	def	491	330	2.6	10	1425	√	c	R	C	HS
Gomes & Appleton (1998)	5	P2R	260	260	233	4	0	12	1.64	2	6	75	0.33	58.2	def	480	480	3.8	6	1000	√	c	RE	C	E
	6	P3R	260	260	233	4	0	12	1.64	2	6	50	0.49	49.6	def	480	480	3.8	7.1	1000	√	c	RE	C	E
	7	P4	260	260	233	4	0	12	1.64	2	6	75	0.33	56.2	def	480	480	3.8	6.3	1000	M	c	-	-	-
Ilki et al. (1998)	8	7	500	500	470	10	6	14	1.54	2	8	100	0.22	14.9	def	501	425	7.0	0	3500	√	m	R	C	E
	9	8	500	500	470	10	6	14	1.54	2	8	100	0.22	7	def	501	425	7.0	0	3500	√	c	R	C	E
	10	9	500	500	470	10	6	14	1.54	2	8	100	0.22	12.9	def	501	425	7.0	0	3500	√	c	R	C	E
Vandoros and Dritsos (2006a, 2006b, 2008)	11	M	400	400	360	4	0	20	1.29	2	10	100	0.44	24.7	def	487	599	4.0	23	1600	-	c	-	C	AF
	12	W	400	400	360	4	0	20	1.29	2	10	100	0.44	18.8	def	487	599	4.0	24	1600	-	c	W	C	AF
	13	D	400	400	360	4	0	20	1.29	2	10	100	0.44	55.8	def	487	599	4.0	9	1600	-	c	D	S	AF
	14	R	400	400	360	4	0	20	1.29	2	10	100	0.44	55.8	def	487	599	4.0	9	1600	-	c	R	S	AF
	15	RD	400	400	360	4	0	20	1.29	2	10	100	0.44	55.8	def	487	599	4.0	9	1600	-	c	RD	S	AF
	16	N	400	400	360	4	0	20	1.29	2	10	100	0.44	17.8	def	487	599	4.0	26	1600	-	c	Ws	C	AF
	17	NP	400	400	360	4	0	20	1.29	2	10	100	0.44	34.5	def	487	599	4.0	14	1600	-	c	WsP	C	AF
	18	E	400	400	360	4	0	20	1.29	2	10	100	0.44	24	def	487	599	4.0	24	1600	-	c	DWs	C	AF
Júlio et al. (2005)	19	M2	270	270	250	6	0	10	1.43	2	6	75	0.31	68.6	def	400	400	3.7	3.4	1000	-	m	GL	C	E
	20	M3	270	270	250	6	0	10	1.43	2	6	75	0.31	28.4	def	400	400	3.7	8.2	1000	M	m	-	C	E
	21	M4	270	270	250	6	0	10	1.43	2	6	75	0.31	64.8	def	400	400	3.7	3.6	1000	-	m	NS	C	E
	22	M5	270	270	250	6	0	10	1.43	2	6	75	0.31	67.8	def	400	400	3.7	3.4	1000	-	m	R	C	E
	23	M6	270	270	250	6	0	10	1.43	2	6	75	0.31	66.7	def	400	400	3.7	3.5	1000	-	m	RD	C	E
	24	M7	270	270	250	6	0	10	1.43	2	6	75	0.31	65.5	def	400	400	3.7	3.6	1000	-	m	RP	C	E

Table A2 (cont.): Database – Details of retrofitted test specimens.

			Retrofitted specimens																						
Reference	No	**Specimen**	b_J^*	h_J^*	d_J^*	n_J	$n_{J,mid}$	$D_{b,J}^*$	$\rho_{lJ}^\#$	**Stirrup legs**	$D_{bs,J}^*$	s_J^*	$\rho_{w,J}^\#$	$f_{c,J}^\S$	**Bar type**	$f_{y,J}^\S$	$f_{yw,J}^\S$	**Ls/hJ**	$v^\#$	L_s^*	**Pre-damaged**	**Loading**	**Connection measure**	**Jacket type**	**Anchorage of long. reinf.**
Bousias et al. (2006)	25	R-RCL1	400	650	600	6	0	18	1.13	2	10	100	0.44	55.3	def	514	599	2.5	6.6	1600	-	c	NS	S	AF
	26	R-RCL3	400	650	605	6	0	18	1.13	2	10	100	0.44	55.3	def	514	599	2.5	6.6	1600	-	c	NS	S	AF
	27	R-RCL4	400	650	600	6	0	18	1.13	2	10	100	0.44	55.3	def	514	599	2.5	5.2	1600	-	c	NS	S	AF
Bousias et al. (2007a)	28	Q-RCW	400	400	355	4	0	20	1.29	2	10	100	0.45	28.7	def	487	599	4.0	13	1600	-	c	W	S	AF
	29	Q-RCD	400	400	355	4	0	20	1.29	2	10	100	0.45	55.3	def	487	599	4.0	8.5	1600	-	c	D	S	AF
	30	Q-RCR	400	400	355	4	0	20	1.29	2	10	100	0.45	55.3	def	487	599	4.0	9	1600	-	c	R	S	AF
	31	Q-RCRD	400	400	355	4	0	20	1.29	2	10	100	0.45	53.2	def	487	599	4.0	9.4	1600	-	c	RD	S	AF
	32	Q-RC	400	400	355	4	0	20	1.29	2	10	100	0.45	55.3	def	487	599	4.0	8	1600	-	c	-	S	AF
	33	Q-RCM	400	400	350	4	0	20	1.29	2	10	100	0.45	30.6	def	487	599	4.0	18	1600	M	c	-	S	AF
Bousias et al. (2007b)	34	Q-RCpd	400	400	355	4	0	20	1.29	2	10	100	0.45	24.1	def	487	599	4.0	8	1600	√	c	-	C	AF
	35	Q-RCL1	400	400	360	4	0	20	1.29	2	10	100	0.44	55.3	def	487	599	4.0	8.5	1600	-	c	-	S	AF
	36	Q-RCL2	400	400	360	4	0	20	1.29	2	10	100	0.44	55.3	def	487	599	4.0	8.5	1600	-	c	-	S	AF
	37	Q-RCL01pd	400	400	360	4	0	20	1.29	2	10	100	0.44	28.7	def	487	599	4.0	16	1600	√	c	R	S	AF
	38	Q-RCL02pd	400	400	360	4	0	20	1.29	2	10	100	0.44	28.7	def	487	599	4.0	17.5	1600	√	c	R	S	AF
Júlio and Branco (2008)	39	M2	270	270	250	6	0	10	1.43	2	6	75	0.31	68.7	def	520	520	3.7	3.4	1000	-	c	GL	C	E
	40	M3	270	270	250	6	0	10	1.43	2	6	75	0.31	28.6	def	520	520	3.7	8.2	1000	M	c	-	C	E
	41	M4	270	270	250	6	0	10	1.43	2	6	75	0.31	63.3	def	520	520	3.7	3.7	1000	-	c	NS	C	E
	42	M5	270	270	250	6	0	10	1.43	2	6	75	0.31	61	def	520	520	3.7	3.8	1000	-	c	R	C	E
	43	M6	270	270	250	6	0	10	1.43	2	6	75	0.31	65	def	520	520	3.7	3.6	1000	-	c	RD	C	E
	44	M7	270	270	250	6	0	10	1.43	2	6	75	0.31	65.9	def	520	520	3.7	3.5	1000	-	c	RP	C	E

*mm, $^\#$ %, § MPa, Lap splice length (D_b): given as a function of the bar diameter of the longitudinal reinforcement (D_b), Bar type: pl - plain bars, def – ribbed bars, Pre-damaged: M – monolithic construction, Loading: c – cyclic, m – monotonic, Connection measures: NS – natural surface, W – welding between the longitudinal reinforcement of the existing cross section and that of the jacket via U-shaped links, D – dowels, R – roughening of the full lateral surface of the old column, RD – dowels and roughening, RE – roughening and epoxy application on the existing column, GL – greased layer placed on the existing column, RP – roughening and jacket construction when the axial load was applied, Ws: welding of stirrup ends of the first four stirrups from the base of the jacketed member, WsP: welding of stirrup ends of the first four stirrups from the base of the jacketed member and jacket construction when the axial load was applied, DWs: dowels and welding of stirrup ends of the first four stirrups from the base of the jacketed member, Jacket construction: C – cast in place, S – shotcrete, Anchorage of longitudinal reinforcement of the jacket: AF – embedment of the reinforcement when the original column was cast, E: anchorage of the reinforcement to the footing in predrilled holes with an epoxy resin.

COMPDYN 2011
III ECCOMAS Thematic Conference on
Computational Methods in Structural Dynamics and Earthquake Engineering
M. Papadrakakis, M. Fragiadakis, V. Plevris (eds.)
Corfu, Greece, 25–28 May 2011

A COMPARATIVE STUDY OF FORCE-DEFORMATION RELATIONSHIP OF FRP-CONFINED CONCRETE COLUMNS

B. Erdil[a,1], U. Akyuz[b], I.O. Yaman[c], A. Irfanoglu[d]

[a] Dept. of Civil Eng., Yüzüncüyıl University, Van, Turkey
[1]Currently PhD candidate at Middle East Technical University, Ankara, Turkey
berdil@metu.edu.tr

[b] Dept. of Civil Eng., Structural Engineering Lab., Middle East Technical University, Ankara, Turkey
han@metu.edu.tr

[c] Dept. of Civil Eng., Construction Materials Lab., Middle East Technical University, Ankara, Turkey
ioyaman@metu.edu.tr

[d] Dept. of Civil Engineering, Purdue University, West Lafayette, IN,47907, U.S.A.
ayhan@purdue.edu

Keywords: FRP-Confined Concrete, Force-Deformation, Strengthening

Abstract. *In this study, the FRP-confined concrete models for prismatic members given in the ACI440.2R-08 and Turkish Earthquake Code (TEC2007) are compared with the experimental data taken from the literature. It is found that TEC2007 assumes only hardening behavior for concrete strengthened with FRP. Although ACI440.2R-08 assumes a hardening and softening behavior depending on the confinement-effectiveness, the limit separating the hardening and softening must be improved to predict the behavior well. The assumptions in these codes cannot predict the post-peak region of force-deformation curves because of the high factor of safeties. It is essential to understand the degree of confinement, confinement effectiveness and the resulting stress-strain relationship of a concrete strengthened with FRP.*

1 INTRODUCTION

Reinforced concrete structures should have enough capacity to resist lateral forces. Most buildings in high seismic zones in Turkey do not have the desired capacity and their situations are getting worse by the environmental effects, such as temperature variations, humidity, corrosion etc. It is obvious that vulnerable structures should be strengthened against the potential high magnitude earthquakes. Since the number of deficient buildings is high, strengthening method should be easy to apply in a short period, i.e. occupant friendly techniques must be preferred.

Fiber reinforced polymer (FRP) can be one of the optimal choice because of its unique properties. It has high strength and modulus. It is durable when compared to steel and concrete. It is easy to apply which enables to strengthen more buildings in a shorter period. Moreover, strengthening can be done without disturbing the residents via evacuation.

Considering the abovementioned advantages, codes start to recommend the use of FRP as one of the alternative strengthening technique. However, because of some uncertainties related to either material behavior or strengthening application, codes define equations that are more conservative. Since the material and application result in a high initial investment, the equations in the codes make it difficult to utilize.

In this study, the force-deformation characteristics of square columns are searched via analytical study.

2 MATERIAL MODELS

To generate a force-deformation curve, material models should be defined first. For FRP-confined concrete, the models available in the ACI440.2R-08 and Turkish Earthquake Code (TEC2007) are used. For steel model, a simple model is proposed and used.

2.1 FRP-Confined Concrete Model

2.1.1. TEC2007 Model

In TEC2007-Section 7E, evaluation of strength and ductility enhancement using FRP-confined concrete columns, equations related to the strength, strain and shear calculations are introduced.

Strength Enhancement:

In this section, it is stated that in order to increase the axial load capacity of a column using FRP material, the ratio of long side to short side of the column should not be greater than 2.0. If corners of rectangular sections rounded and the section turns to be an elliptical section, than the ratio can be 3.0. Dimensions of each section are given in Figure 1. f_{cc} can be calculated as follows:

$$f_{cc} = f'_{co}\left[1 + 2.4\left(\frac{f_l}{f'_{co}}\right)\right] \geq 1.2 f'_{co} \qquad (1)$$

$$f_l = \frac{1}{2}\kappa_a \rho_f \varepsilon_f E_f \qquad (2)$$

$$\varepsilon_f \leq \begin{cases} 0.004 \\ 0.5\varepsilon_{fu} \end{cases} \qquad (3)$$

$$\kappa_a = \begin{cases} 1 & \textit{Cylindrical sections} \\ \left(\dfrac{b}{h}\right) & \textit{Ellipsoid sections} \\ 1 - \dfrac{(b-2r_c)^2 + (h-2r_c)^2}{3bh} & \textit{Rectangular sections} \end{cases} \tag{4}$$

where κ_a is section effectiveness factor, ρ_f is the volumetric ratio of FRP, ε_{fu} is the ultimate strain capacity of FRP, ε_f is the effective strain capacity of FRP, E_f is the modulus of elasticity of FRP, *b* is the short dimension of prism and h is the long dimension of the prism.

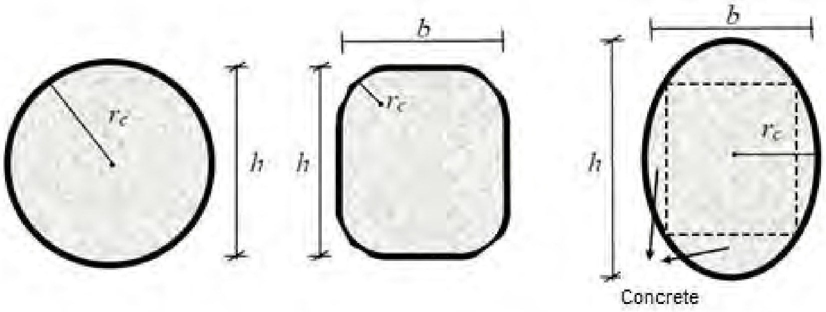

a) Cylindrical Section *b) Rectangular Section* *c) Elliptical Section*

Figure 1. Sectional properties

Ductility Enhancement:

Ultimate strain capacity can be calculated as follows:

$$\varepsilon_{cc} = 0.002\left[1 + 15\left(\frac{f_l}{f'_{co}}\right)^{0.75}\right] \tag{5}$$

2.1.2. ACI440.2R-08 Model

In ACI440.2R-08-Chapter 12, strengthening of members subjected to axial force or combined axial and bending forces, equations related to strength and strain are introduced. It is stated that “The provisions are not recommended for members having noncircular section featuring side aspect ratios h/b greater than 2.0, or face dimensions b or h exceeding 900 mm unless testing demonstrates their effectiveness”.

In pure axial compression section, the maximum confined concrete compressive strength (f_{cc}) and the maximum confinement pressure (f_l) are calculated using Lam and Teng’s equation [9] with an additional reduction factor $\psi = 0.95$.

For ultimate strain, the code limits the strain value to prevent excessive cracking and resulting loss of concrete integrity.

$$f_{cc} = f'_{co} + \psi 3.3\kappa_a f_l \tag{6}$$

$$f_l = \frac{2E_f n t_f \varepsilon_{fe}}{D} \tag{7}$$

$$\varepsilon_{fe} = \begin{cases} \kappa_e \varepsilon_{fu} & \textit{axial compression } (\kappa_e = 0.55) \\ 0.004 \le \kappa_e \varepsilon_{fu} & \textit{combined axial compression and bending} \end{cases} \tag{8}$$

$$D = \sqrt{b^2 + h^2} \tag{9}$$

$$\varepsilon_{cc} = \varepsilon_{co}\left(1.5 + 12\kappa_b \frac{f_l}{f'_{co}}\left(\frac{\varepsilon_{fe}}{\varepsilon_{co}}\right)^{0.45}\right) \leq 0.01 \tag{10}$$

$$\kappa_a = \frac{A_e}{A_c}\left(\frac{b}{h}\right)^2 \tag{11}$$

$$\kappa_b = \frac{A_e}{A_c}\left(\frac{h}{b}\right)^{0.5} \tag{12}$$

$$\frac{A_e}{A_c} = \frac{1 - \frac{\left[\left(\frac{b}{h}\right)(h - 2r_c)^2 + \left(\frac{h}{b}\right)(b - 2r_c)^2\right]}{3A_g} - \rho_g}{1 - \rho_g} \tag{13}$$

In these equations,κ_a, κ_b are the efficiency factor (for strength and strain, respectively) which takes the shape of the section into account, ε_{fe} is the effective strain level in FRP, κ_e, is the FRP strain efficiency factor, $\frac{A_e}{A_c}$, is the effective confinement area ratio, ρ_g is the longitudinal steel ratio, n is the number of FRP layers and t_f is the thickness of the FRP material.

2.1.3. Comparison of the models

It is found out that FRP usage does not result in a hardening behavior all the time. Depending on some parameters such as, unconfined concrete strength, number of FRP layers and corner radius in prismatic members, a softening behavior is possible if the FRP effectiveness is not adequate.

Mirmiran et. al. [6] proposed “Modified Confinement Ratio (MCR)” to determine if a section shows hardening or softening behavior. The equation for MCR is given in Eqn. 14. It is seen that parameters affecting MCR are confinement effectiveness and sectional properties. It is stated by Mirmiran et. al. that if MCR is greater than 0.15 then it is possible to see a hardening behavior. To validate whether this limit is well-defined or not, 132 experimental data (76 tests having hardening behavior and 56 having softening behavior) are collected from the literature and their MCR factors are calculated. MCR values are compared with the experimental data as seen in Table 1 and it is realized that MCR factor can be used to predict the behavior.

$$MCR = \frac{2.r.f_l}{D.f'_{co}} \tag{14}$$

$$f_l = \frac{2.t_{FRP}.f_{FRP}}{D} \tag{15}$$

ACI440.2R-08 also takes the degree of confinement into account and states that for minimum confinement ratio $\frac{f_l}{f'_{co}} \geq 0.08$ should be used. As it is seen from Table 1 the limit can predict if a section shows hardening or softening behavior but it is not as successful as the MCR factor.

Table 1. Verification of the hardening limits

Number of Experimental Data	MCR Prediction		ACI440.2R-08 Prediction	
	# of data	Accuracy, %	# of data	Accuracy, %
76 Hardening	62 Hardening *14 Softening*	82	73 Hardening *3 Softening*	96
56 Softening	52 Softening *4 Hardening*	93	17 Softening *39 Hardening*	30
Total 132 data	86 % of the data is accurately predicted		68 % of the data is accurately predicted	

In Figure 2, typical behaviors of low strength square concrete specimens confined with FRP are given together with the analytical predictions. As seen in the figures, ACI440.2R-08 and TEC2007 models assume lower strain and strength values, which yields higher factor of safety (Figure 2a). If the confinement is inadequate as shown in Figure 2b both procedures give higher strength and low strains. From the figures, it can be seen that TEC2007 assumes hardening behavior in both cases, but ACI440.2R-08 can predict the change in the behavior.

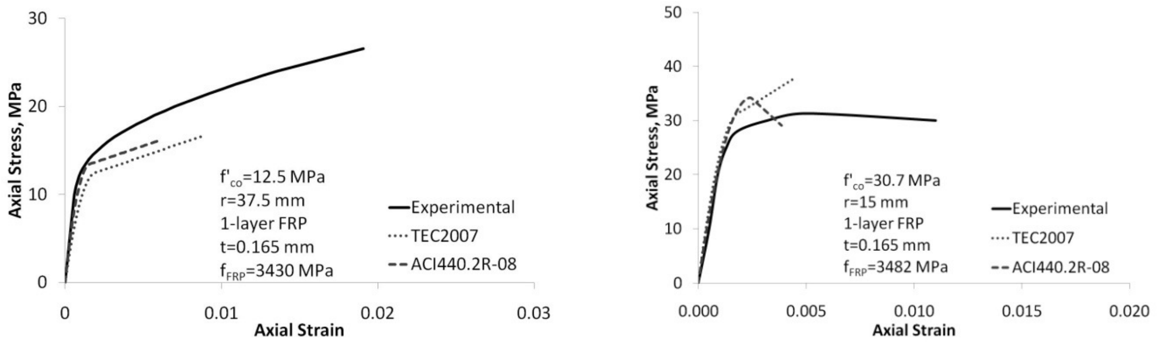

(a) *(b)*

Figure 2: FRP-confined concrete a) Adequate confinement [3] b) Inadequate confinement [8]

2.2 Steel Model

For steel model, it is assumed that steel does not behave similar in both tension and compression. It is assumed that, in tension steel shows a trilinear behavior, i.e., steel yields and then shows strain hardening behavior. However, in compression it is assumed that steel shows softening behavior after yielding (Figure 3).

In Figure 3, at the tension zone, yield strength is denoted by f_y and yield strain by ε_y, ε_{sh} ($=10\varepsilon_y$) represents strain at the point where the hardening starts, f_u is the ultimate strength of the steel (and can be taken as $1.25f_y$) whereas ε_u ($=50\varepsilon_y$) is the ultimate strain at f_u. In the compression zone, since there exists no hardening, f_u stands for the stress at $0.2f_y$ and ε_u is taken as $50\varepsilon_y$.

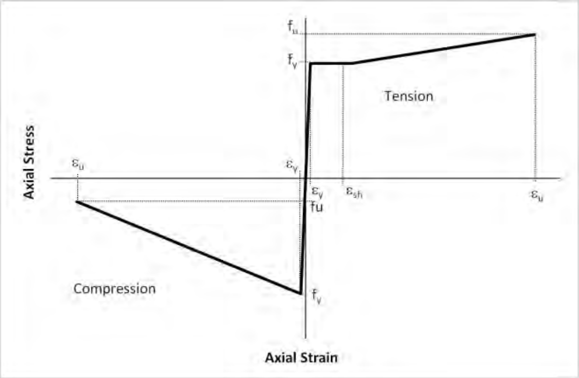

Figure 3. Model for the reinforcing steel

3 FORCE-DEFORMATION RELATIONSHIP

Moment-curvature relationship based on the FRP-confined concrete models and the reinforcing steel model is used to evaluate the force-deformation characteristic of a column. The assumptions made in the moment curvature analysis are as follows:

1) Plane sections remain plane
2) Concrete does not take any tension force. Tension forces are only carried by steel reinforcement.
3) FRP is only active in compression part.

Deformation consists of two parts: first part is calculated from the fixed-end rotation caused by the bar slip and second part is calculated from the curvature.

$$\Delta = \Delta_{bar\ slip} + \Delta_{curvature} \tag{16}$$

Deformation due to the fixed end rotation caused by bar slip can be found using the equations proposed by Ozcan et. al [5] as follows.

$$u = 0.4\sqrt{f'_{co}} \tag{17}$$

$$s = \begin{cases} \dfrac{\varepsilon_s f_s d_b}{8u}, & \varepsilon_s \leq \varepsilon_y \\ \dfrac{d_b}{8u}\left[\varepsilon_s f_s + 2(\varepsilon_s + \varepsilon_y)(f_s - f_y)\right], & \varepsilon_s > \varepsilon_y \end{cases} \tag{18}$$

$$\Delta_{bar\ slip} = \frac{s}{d - d'} L \tag{19}$$

In these equations, ε_s is the steel strain, f_s is the corresponding steel stress, d_b is the bar diameter, u is the maximum bond stress, ε_y is the yield strain for steel, f_y is the yield stress for steel, d is the effective depth of the section and s is the bar slip.

Deformation due to curvature is found as follows:

1) The column is divided into a number of segments
2) For each segment, two moment values are calculated. First moment is for the base of the segment and the second one is for the top of the segment (Figure 4)
3) Curvatures for each segment corresponding to the moments are found

4) The area surrounded by curvatures are calculated
5) The area is then multiplied by the distance to find the corresponding deformation
6) Total deformation due to curvature is evaluated by summing each deformations found for each segment:

$$\Delta_{curvature} = \sum K_i x_i d_i \qquad (20)$$

7) After reaching the maximum moment at the base, because of the FRP rupture it is assumed that a plastic hinge develops.
8) Plastic hinge length is calculated as follows [4].

$$\frac{l_p}{h} = \left[0.3\left(\frac{N}{N_o}\right) + 3\left(\frac{A_s}{A_g}\right) - 0.1\right]\left(\frac{L}{h}\right) + 0.25 \geq 0.25 \qquad (21)$$

where N is the axial load on the column, N_o is the axial load carrying capacity of the column, A_s is the total longitudinal steel area and A_g is the gross area of the column.

9) For the plastic hinge region, it is assumed that curvature values are the same for the entire region (Figure 4b).

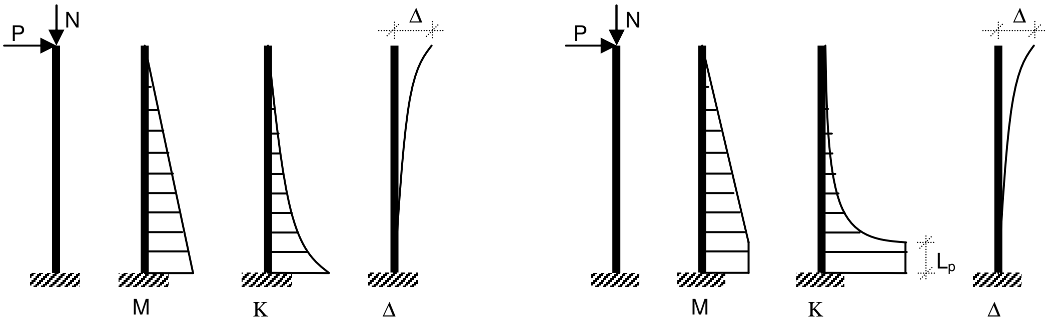

a) Before maximum moment *b) After maximum moment*

Figure 4. Deformation calculation from curvature

After establishing the procedure for force-deformation relationship, the models are compared with the experimental data taken from Ozcan et al [6].

Ozcan et. al. tested 4 reinforced concrete columns strengthened with CFRP material. Columns were square in cross-section with 350x350 mm and they were 2000 mm tall. Sections were rounded to 30 mm in order to increase the FRP effectiveness. Although target strength was 15 MPa, concrete strength was found to be between 11 MPa and 19.4 MPa.

They used 1 or 2 layers of CFRP to understand the effect of CFRP thickness. Longitudinal reinforcement was of eight 18 mm diameter plain bars, which correspond to a reinforcement ratio of 1.66%. 10 mm diameter plain bars were used as lateral reinforcements and they were spaced at every 200 mm. Lateral reinforcements had 90° hooks to simulate the deficient case in Turkey.

From Figures 5 and 6, analytical curves are compared with the experimental data. It can be seen from the figures that neither ACI440.2R-08 nor TEC2007 captures the post peak behavior because of limiting the strain capacity of FRP-confined concrete. The arrows in the figures point the end of each curve. Since TEC2007 assumes that FRP application results in a hardening behavior depending on the degree of confinement, it results in a hardening behavior in the force-deformation relationship also. However, it is well known that hardening may be observed when the concrete member is adequately confined, that is, when the MCR value is above a certain limit as discussed above.

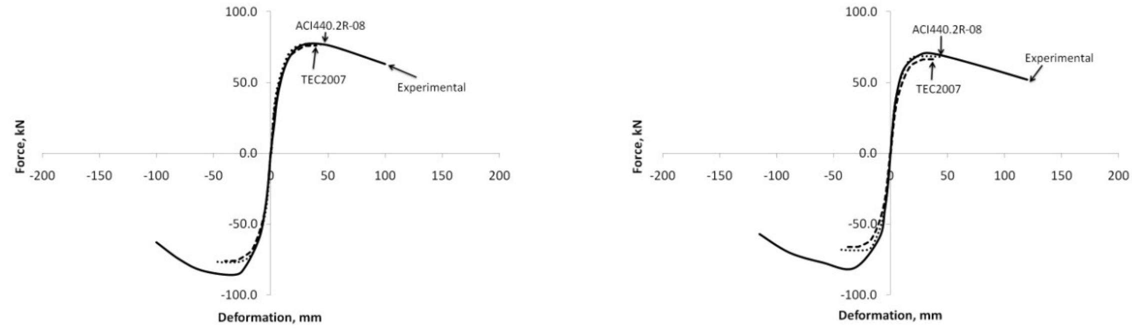

f'c=19.4 MPa
t_{FRP}=0.165 mm (1 Layer of FRP)
350x350x2000 mm
N/No=27 %
Longitudinal Reinf. 8ϕ18 plain bars
ρ=1.66 %
Transverse Reinf.ϕ10/200

f'c=14 MPa
t_{FRP}=0.165 mm (1 Layer of FRP)
350x350x2000 mm
N/No=34 %
Longitudinal Reinf. 8ϕ18 plain bars
ρ=1.66 %
Transverse Reinf.ϕ10/200

Figure 5: Comparison of Force-deformation curves for concrete column with 1 layer of FRP

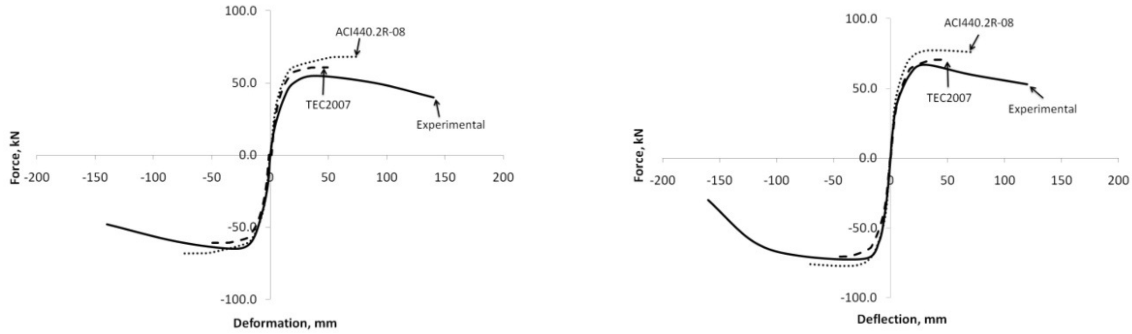

f'c=11.4 MPa
t_{FRP}=0.33 mm (2 Layer of FRP)
350x350x2000 mm
N/No=39 %
Longitudinal Reinf. 8ϕ18 plain bars
ρ=1.66 %
Transverse Reinf.ϕ10/200

f'c=15.6 MPa
t_{FRP}=0.33 mm (2 Layer of FRP)
350x350x2000 mm
N/No=32 %
Longitudinal Reinf. 8ϕ18 plain bars
ρ=1.66 %
Transverse Reinf.ϕ10/200

Figure 6: Comparison of Force-deformation curves for concrete column with 2 layers of FRP

4 DISCUSSIONS

In this study, the axial stress-strain estimations and models given in ACI440.2R-08 and TEC2007 are compared with the experimental data to investigate the differences and the estimates that codes make. It is found that TEC2007 assumes only hardening behavior for concrete strengthened with FRP. Although ACI440.2R-08 assumes a hardening and softening behavior depending on the confinement-effectiveness, the limit defining the behavior as hardening or softening is not good to predict the behavior because in that equation no corner radius for rectangular sections is taken into account. The assumptions in these codes result in a more conservative prediction at the post-peak region of the force-deformation curves. It is essential to understand the degree of confinement, effectiveness of the confinement and the resulting stress-strain relationship of a concrete strengthened with FRP. Assuming a hardening behavior in all the case is not reasonable.

Since the material and application result in a high initial investment, the equations in the codes make it difficult to utilize. Codes may decrease the factor of safety used in FRP-confined concrete members because the reliability of the material is verified and it is still being studied. This will make the material easy to reach and easy to apply in strengthening applications.

5 REFERENCES

[1] ACI440.2R-08, *Guide for the design and construction of externally bonded FRP systems for strengthening concrete structures*, ACI 2008

[2] TEC2007, Turkish Earthquake Code for Buildings (2007), *Ministry of Public Works and Resettlement*, Ankara, Turkey, 2007.

[3] B. Erdil, U. Akyuz, I. O. Yaman, Low Strength Concrete Columns Confined with CFRP: Behavior under Temperature Changes and Loads, *In: Proc FRPRCS-9*. Sydney, Australia, July 2009.

[4] S. Bae, O. Bayrak, Plastic hinge length of reinforced concrete columns, *ACI Structural Journal.* **105**(3): 290-300, 2008.

[5] O. Ozcan, B. Binici, G. Ozcebe, Improving seismic performance of deficient reinforced concrete columns using carbon fiber-reinforced polymers, *Engineering Structures*, **30**:1632–1646, 2008.

[6] A. Mirmiran, M. Shahawy, M. Samaan, H. El-Echary, J. C. Mastrapa, O. Pico, Effect of column parameters on FRP-confined concrete, *J Compos Const*, **2**(4):175-185, 1998.

[7] P. Rochette, Confinement of short square and rectangular columns with composite materials, *MS thesis, Univ. of Sherbrook*, Quebec, Canada, 1996.

[8] L. M. Wang, Y. F. Wu, Effect of Corner Radius on the Performance of CFRP-Confined Square Concrete Columns: Test, *Engineering Structures*, **30**:493-505, 2008.

[9] L. Lam and J. G. Teng, Design-Oriented Stress–Strain Model for FRP-confined Concrete in Rectangular Columns, *Journal of Reinforced Plastics and Composites,* **22**; 1149-1186, 2003.

COMPDYN 2011
III ECCOMAS Thematic Conference on
Computational Methods in Structural Dynamics and Earthquake Engineering
M. Papadrakakis, M. Fragiadakis, V. Plevris (eds.)
Corfu, Greece, 26–28 May 2011

EXPERIMENTAL AND NUMERICAL STUDY OF THE BEHAVIOUR OF HIGH DISSIPATION METALLIC DEVICES FOR THE STRENGTHENING OF EXISTING STRUCTURES

A.A. Karalis[1], K.A. Georgiadi-Stefanidi[2], T.N. Salonikios[3], K.C. Stylianidis[1] and E.S. Mistakidis[2]

[1] Dept. of Civil Engineering, Aristotle University of Thessaloniki
52124, Thessaloniki, Greece
kcstyl@civil.auth.gr

[2] Dept. of Civil Engineering, University of Thessaly,
Pedion Areos, 38334 Volos, Greece
emistaki@uth.gr

[3] Institute of Engineering Seismology and Earthquake Engineering,
Thessaloniki, Greece
salonikios@itsak.gr

Keywords: Strengthening, Existing Structures, Experimental and Numerical Study, High Dissipation Metallic Devices.

Abstract. *The use of steel bracing systems for the strengthening of existing reinforced concrete (RC) frames may lead to increase of both strength and stiffness. However, in most of the cases the main target is the increase of the energy dissipation capacity. This paper studies, both experimentally and numerically, the efficiency of a specific strengthening type which utilizes a small steel link element having an I-shaped cross-section connected to the RC frame through bracing elements. The energy is dissipated through the plastification of the steel link element. The case studied in this paper is a typical one bay, single storey RC frame constructed according to older code provisions, which is strengthened through two different types of steel link elements. The behaviour of the strengthened frames is studied with respect to the one of the original bare frame. The experimental study is supported by complete numerical simulations of the performed tests. To this end, detailed numerical models are formulated, which are able to follow the highly non-linear nature of the problem, involving the plastification of the steel rebars, the cracking and plastification of concrete and the plastic deformation and hysteretic response of the dissipative link elements.*

1 INTRODUCTION

The strengthening of existing reinforced concrete (RC) buildings with pilotis (soft ground floor) is a current necessity in seismic prone areas. It is well known that the majority of these buildings were designed and built according to older codes. Moreover, they lack sufficient longitudinal and transverse reinforcement and their structural materials are of low quality or exhibit degradation of their mechanical properties. As a result, these structures present weaknesses concerning their strength, ductility and stiffness. Strengthening this type of structures is essential in order to avoid damages or even loss of life from earthquakes.

One of the more popular methods for the strengthening of RC frames is the use of steel braces. A specific category in this strengthening type concerns the additional use of dissipative devices which exhibit extensive plastification under the design earthquake. During the last decades significant research effort has been dedicated in this direction. For example, RC frames strengthened with such system were tested by Kunisue et al [1]. Failure was observed at the elastoplastic energy dampers. The test results showed that the strength and the energy dissipation capacity can be significantly improved by the use of these dampers. A calculation method was also suggested for the estimation of the strength increase in strengthened RC frames and satisfactory approximation between experimental and analytical results was observed. In tests performed by Perera et al [2] the strengthening of masonry infilled RC frames was examined. In some frames the masonry was replaced by a system of two steel braces and significant improvement of the energy dissipation was observed. Tests on two full scale, four storey RC frames were executed by Pinto et al [3]. For the frame with no strengthening interventions high vulnerability to seismic loads was observed. It was found that through the use of steel braces, the seismic response of the strengthened frame and the energy dissipation capacity are significantly improved. A full scale, 3D, two storey, RC frame was tested by Antonucci et al [4]. Viscous dampers were used at the connection point of the top of the bracing system to the middle of the RC beam. It was found that viscous dampers can dissipate up to 95% of the induced seismic energy. The storey drift was also significantly reduced. Three tests were performed by D’Aniello [5] on an existing RC building that was strengthened against seismic actions by the use of the same system of two steel braces. It was concluded from the tests that shear elements can be easily connected at the concrete and the steel elements and can also be easily replaced after an important seismic event. A simplified simulation method was also used and a satisfactory approximation resulted between analytical and experimental results. It is concluded from the literature review that the use of a system of two steel braces with a purposely designed steel link element at the top with shear and/or flexural type of failure, could increase the shear strength and the energy dissipation capacity of existing RC frames under seismic actions.

In the present work the efficiency of a specific type of strengthening device, which consists of two steel braces connected to the RC frame through two different types of dissipative steel link elements, is investigated. Six specimens were tested under horizontal cyclic loading, three of them (one bare RC frame and two similar strengthened RC frames) without additional vertical loads at the columns and another identical group of three specimens with vertical loads.

The experimental investigation is complemented by a numerical study. All the tested RC frames are simulated numerically through detailed finite element (F.E.) models, which are able to follow the highly non-linear nature of the problem [6, 7, 8]. The numerical results are then compared with the respective experimental ones. After the verification of the simulation models according to the experimental results, it will be possible to perform reliable “numerical tests” in order to investigate the effects of several parameters, reducing the required number of experiments [9].

2 TYPES OF RC FRAMES STUDIED

2.1 Geometry and configurations

The specimens studied in this paper represent a single storey one bay frame rigidly based on a strong foundation and are manufactured to a scale of 1:3. The RC part is exactly the same in all the tested specimens. The geometry and the reinforcement arrangement of the specimens are shown in Fig. 1.

The frames are assumed to be constructed according to older regulations and thus, smooth steel rebars and sparsely spaced stirrups were used, even at the critical regions of the possible plastic hinges. Moreover, the anchorage length of the steel bars was small and does not meet the modern requirements.

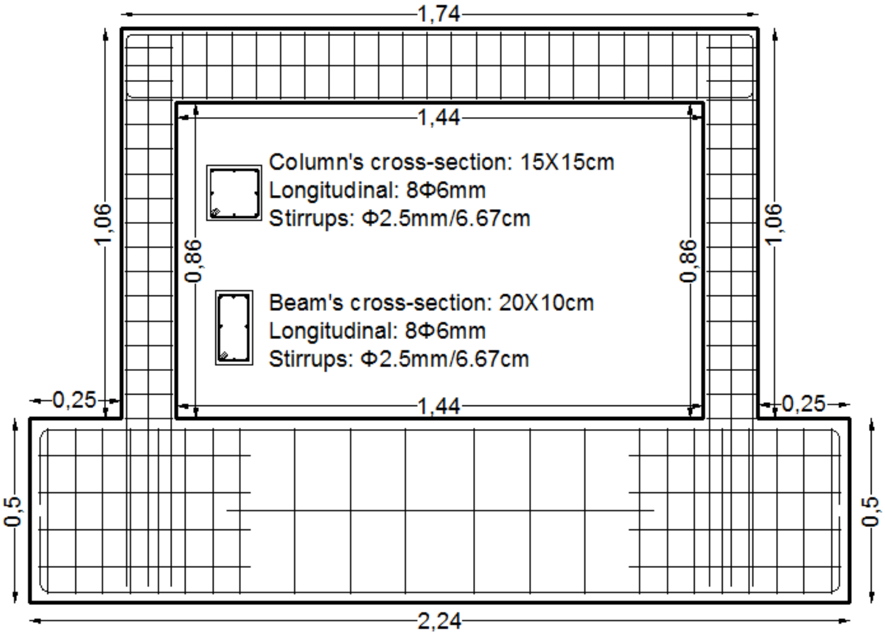

Figure 1: Geometry and reinforcement arrangement of the specimens (m).

The presented frame is strengthened by means of a steel link which is connected to the beam of the RC frame and to strong steel bracing members. As shown in Fig. 2, the bracing system is composed by two steel elements that are connected to each other at their top. At this point there is a steel plate on which the link element is welded. The top of the link element is connected to the midpoint of the beam through a steel U shaped collar which is placed around the beam. The collar element is connected to the top beam by means of six bolts which pass through the width of the cross-section of the beam. The diagonal elements of the bracing system were connected at the lower ends of the columns and on the base beam by external threaded rods. The elements of the bracing system, the collar and the connections to the beams and the columns were not considered as parameters under investigation in the present study. Therefore, they were overdesigned in order to avoid local failures at these elements. Consequently, the inelastic deformations of the strengthened specimens are expected to be concentrated mainly at the link element. This type of link elements is expected to significantly increase the strength and stiffness of the strengthened frame. However, the most important advantage of these systems is the high energy dissipation capacity and, consequently, the reduction of the seismic strength demands.

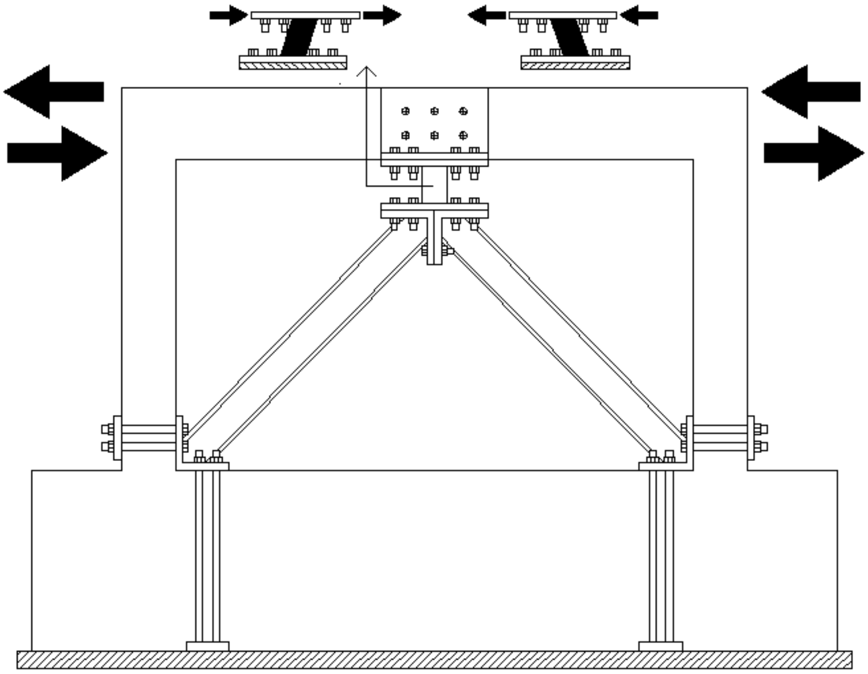

Figure 2: Specimens F2 and F3 strengthened by steel bracing system and a steel link element at the top.

Three different types of specimens were tested. Specimen type F1 is the bare frame, which is used as a reference for the evaluation of the strengthening types. In order to allow the direct comparison, the bracing system was also installed in this frame (as in the other specimens) but without the link element. This layout was selected in order to ensure the same geometrical conditions for all the specimens concerning the free height of the columns.

In the other two types of specimens (types F2 and F3) the bracing system was connected in the middle of the top beam by a steel link element. The links used in each type are presented in Fig. 3. The first link, used in the type F2 specimens, is a steel element that has a symmetrical I cross-section with total section height d = 60 mm, flange width b = 30 mm, flange and web thickness t = 6 mm and length l = 100 mm. The second link, used in the type F3 specimens, has also a symmetrical I cross-section with total section height d = 80 mm, flange width b = 40 mm, flange and web thickness t = 6 mm and length l = 200 mm.

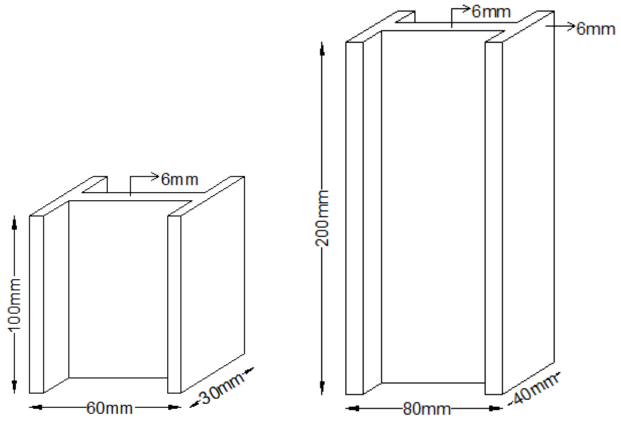

Figure 3: The dissipative steel link elements of the strengthened frames F2 and F3, respectively.

The above three types of specimens (F1, F2 and F3) were tested with and without additional vertical loading placed at the columns. Therefore, the total number of specimens and tests was six. The three specimen types in which the vertical loading was present at the columns during the testing are referenced as F1,N, F2,N and F3,N respectively. The tests are presented schematically in Figs 4 - 6.

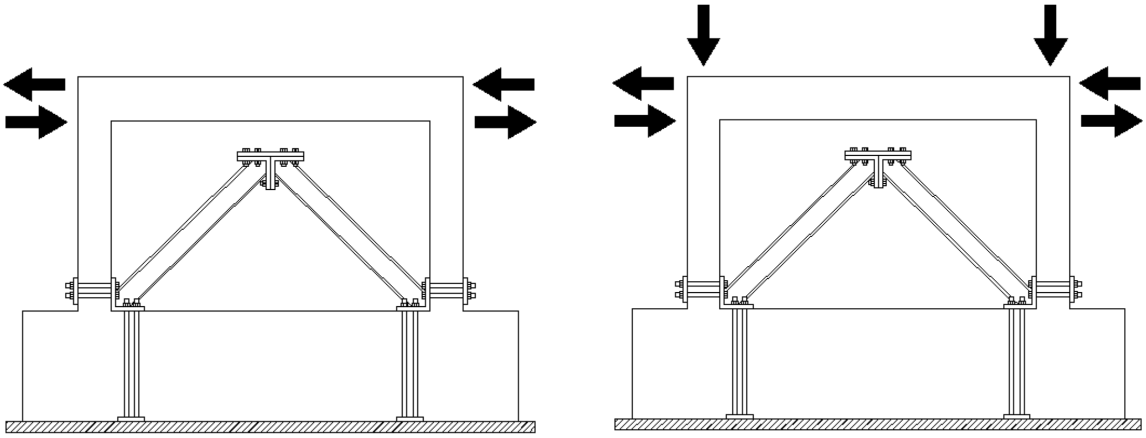

Figure 4: Specimen F1 and F1,N with the bracing system of the strengthened frames but without a link element

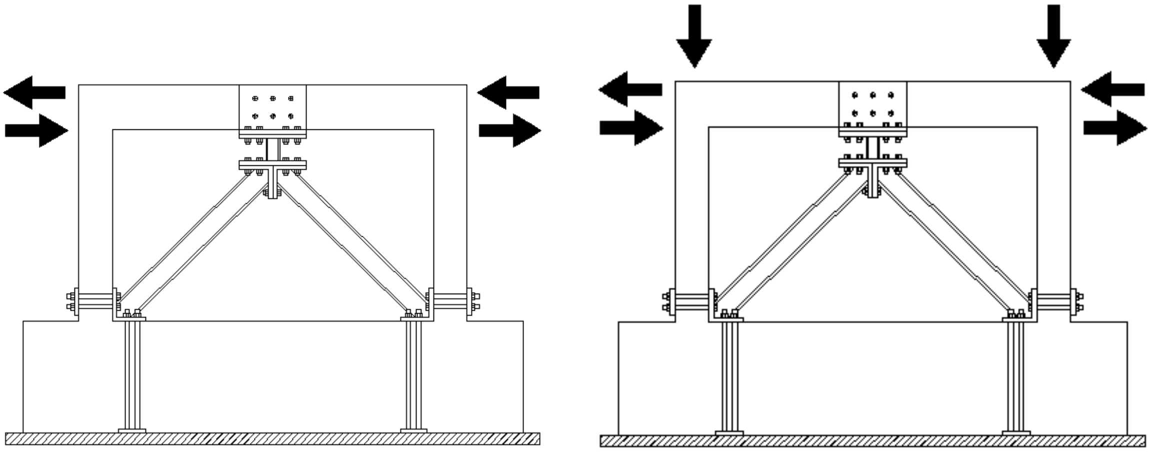

Figure 5: Specimens F2 and F2,N strengthened by steel bracing system and a steel link element at the top.

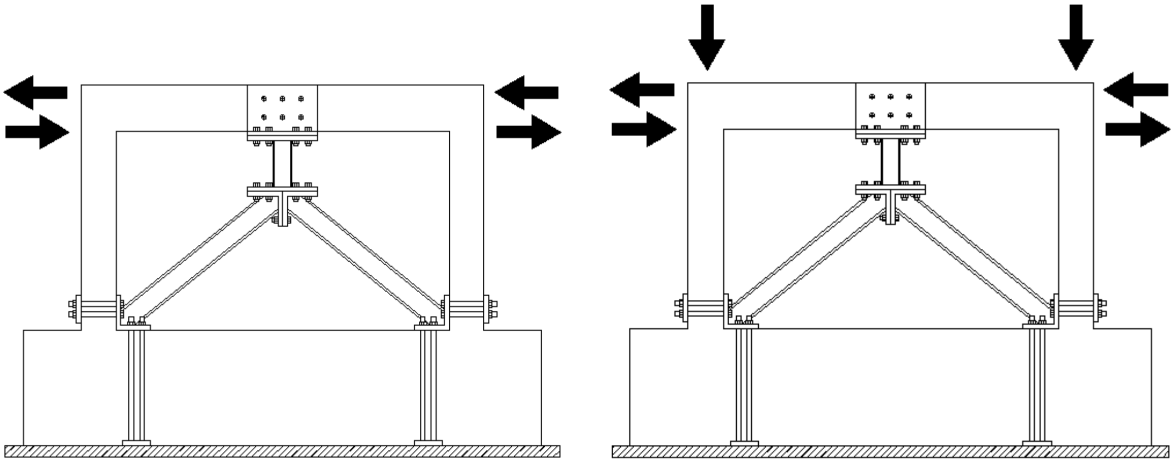

Figure 6: Specimens F3 and F3,N strengthened by steel bracing system and a steel link element at the top.

2.2 Materials

As the RC specimens were assumed to be constructed according to older regulations, a low strength concrete was used with a compressive strength of 16 MPa and a tensile strength of 2.1 MPa. The smooth steel rebars of the longitudinal reinforcement had a yield stress of 450 MPa and an ultimate stress of 540 MPa (it was not possible to find lower strength smooth steel rebars with a diameter of 6 mm), while the transverse reinforcement had a yield stress of 265 MPa and an ultimate stress of 390 MPa. Finally, the yield stress of the steel link elements was equal to 300 MPa and the ultimate stress equal to 375 MPa.

2.3 Experimental test setup

For the tests, the facilities of the Laboratory of Concrete and Masonry Structures of the Aristotle University of Thessaloniki, were used (Fig. 7). The reaction frame consists of steel beams and columns connected to each other by prestressed threaded rods. One double acting actuator is connected at the top beam of the specimens applying horizontal displacement reversals. Another actuator can also be connected to the system to apply vertical axial loads on the columns through a top steel beam in a load control mode.

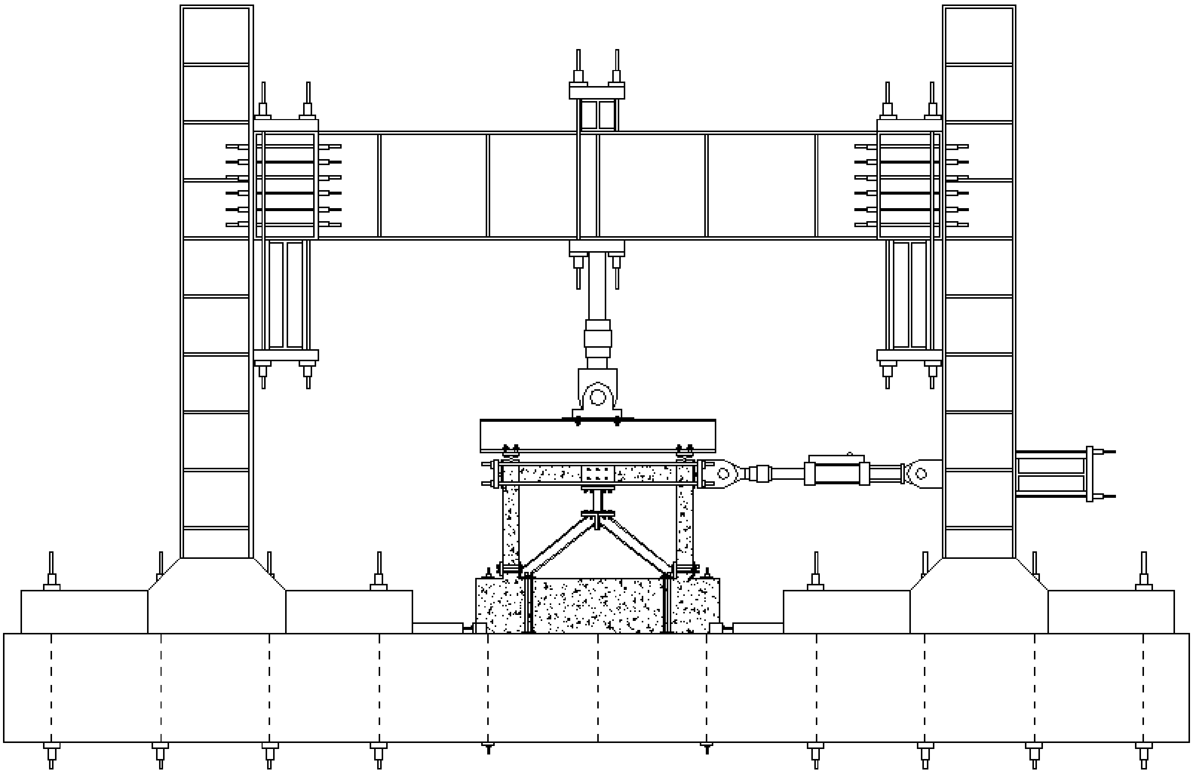

Figure 7: Test setup

The reaction frame is connected to the strong floor of the laboratory by the use of steel stoppers in combination with vertical prestressed threaded rods. The test specimens were also connected to the floor by the same technique. It is worth mentioning that during the tests no slip was recorded between the specimens and the laboratory floor. The horizontal actuator was connected at the top of the specimens by a system of two stiff steel plates at the vertical outer sides of the beam - column joints, connected to each other by four long threaded rods. In order to allow free rotation at the connection points, beyond the 3D rotational hinges of the actuator at the ends of its length, two more rotational hinges were provided between the steel plates and the two top beam - column joints of each specimen.

2.4 Loading procedures

The horizontal loads were imposed in a displacement control mode. The displacement history was composed by 16 levels of displacement. For each displacement level, two full cycles were imposed. The loading increment had the value of 1mm until a total displacement of 3mm and the value of 3mm till the maximum displacement (42mm). For the specimens with the axial loading (F1,N – F2,N – F3,N), apart from the horizontal displacement, a constant axial load of 80kN was applied at each column. Figure 8 shows the horizontal loading history.

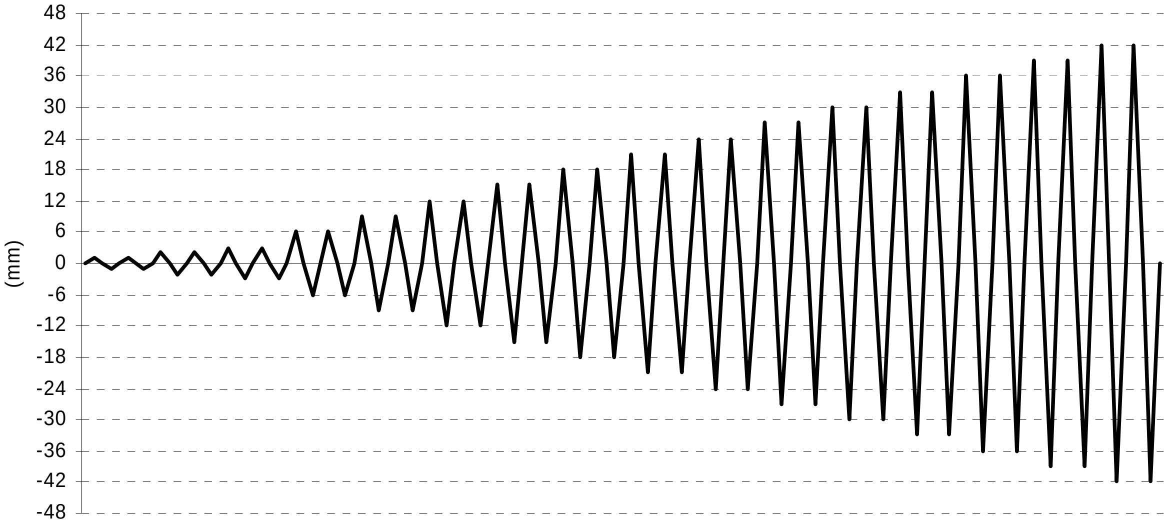

Figure 8: Horizontal loading history

The specimens were instrumented by the use of seven LVDTs. The layout of these instruments is shown in Fig. 9. LVDTs 1, 5, 2, 6 were used for the measurement of the shortening and the elongation of the outer fibres at the ends of the left column. LVDT 8 was used for the measurement of the top horizontal displacement of the specimen and was compared with the measurements of the internal LVDT of the horizontal actuator. LVDTs 4 and 7 were used for the measurement of the net horizontal displacement at the top and bottom ends of the steel link element. The measurements of the external and internal LVDTs together with the measurements given by the load shell of the horizontal actuator were recorded through a digital controller. In the present work, only a small part of the experimental measurements and the post-processed data are presented due to limited available space.

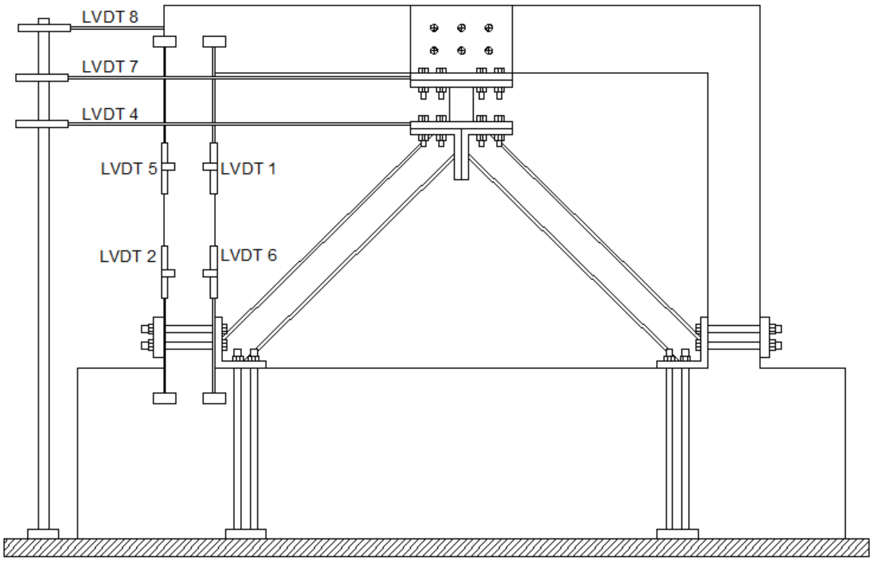

Figure 9: LVDT arrangement on the specimens

3 THE PRINCIPLES OF NUMERICAL SIMULATION

The numerical simulation of the tested frames presented several difficulties due to the complexity of the problem and the existence of various nonlinearities, such as cracking in concrete and the plastification of the steel link elements. Moreover, while a three-dimensional model is expected to be more realistic and reliable due to the nature of its elements, it has the disadvantage of a high computational cost. Therefore, simpler two-dimensional models were formulated, which were able to capture in a rather accurate manner the overall behaviour of the studied problem [10]. The attempt to simulate a 3D problem through a 2D finite element model resulted in several simulation problems, which had to be solved efficiently.

3.1 Geometric and material properties

The 2D simulation models of the RC frames consist of different F.E. meshes, which overlap, connected at the same grid of nodes. Especially for the models of the strengthened F2 and F3 frames, another F.E. mesh was added to the F.E. mesh of the RC frame, simulating the link element. Plane-stress and truss elements were used for the formulation of the 2D numerical models. Figure 10 shows the numerical model of the F2 strengthened frame together with a detail of the link element, after the discretization. The plane-stress elements were used for the simulation of the concrete and of the steel link elements. The truss elements were used for the simulation of the longitudinal and transverse reinforcement. The properties of the problem in the third direction (perpendicular to the modelling plane) were taken into account by assigning different thickness values to the respective finite elements.

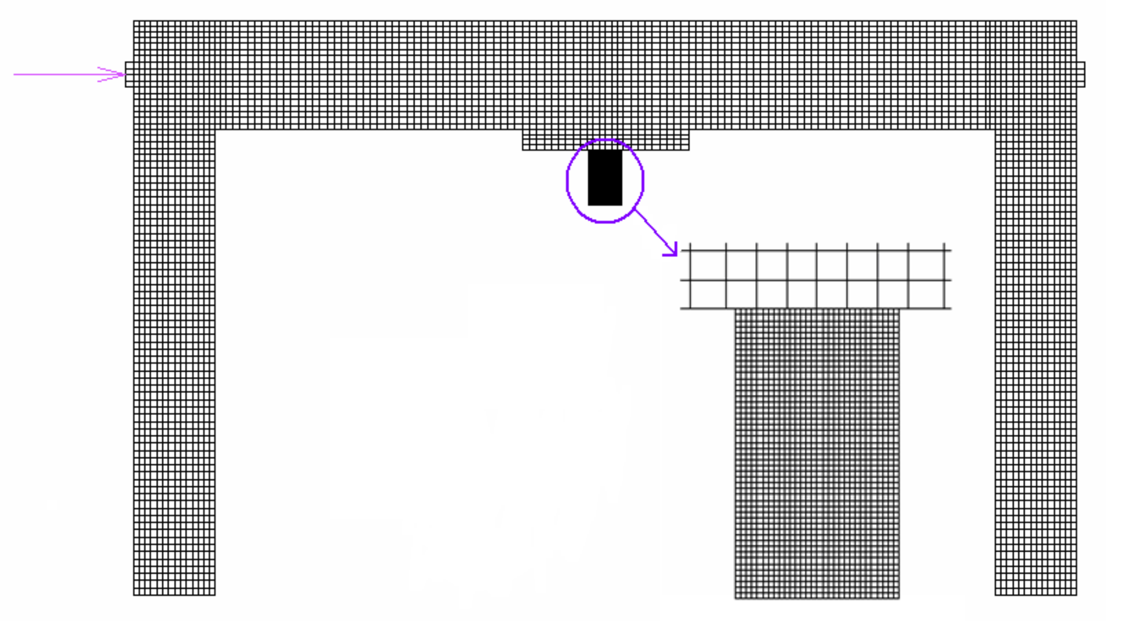

Figure 10: The 2D F.E. model of the strengthened RC frame and detail of the steel link element.

The plane-stress elements representing the concrete beam and columns were assigned a thickness equal to the width of the corresponding cross-section, that is 100 mm and 150 mm thickness for the beam and the columns, respectively. The cross-sectional area of the two-node, constant cross-section truss elements that represent the longitudinal and transverse reinforcement was taken equal to the total area of the corresponding reinforcing bars. That is, for the line of elements representing the top and the bottom steel reinforcement the cross-sectional area was 3×28.26=84.78 mm^2 (3Ø6) and for those representing the middle longitudinal reinforcement, the cross-sectional area was 2×28.26=56.52 mm^2 (2Ø6). For the lines of elements representing the stirrups of the beam and columns, the cross-sectional area was 2×4.91=9.81 mm^2 in order to account for the two vertical legs of the Ø2.5 stirrup. For the steel links, the plane-stress elements representing the flanges and those representing the web were assigned different thickness values. More specifically, for the first link (F2) the elements representing its web were assigned a thickness of 6 mm and those representing the flanges were assigned a thickness of 30 mm, whereas for the second link (F3), the elements representing the web had thickness equal to 6 mm and those representing the flanges had thickness equal to 40 mm.

It must be noted that the links were simulated through a much denser finite element mesh, as already shown in Fig. 10. This dense discretization of the links was considered necessary in order to simulate as accurately as possible their behaviour, which dominates the strengthened systems. The two different F.E. meshes (the one corresponding to the RC frame and the one representing the link element) were connected through kinematical relationships, due to the fact that their nodes, at their common boundary, do not coincide.

Figure 11 presents the stress-strain relationship considered for concrete, steel reinforcement and the steel links. The elements representing concrete were equipped with the stress-strain relationship of Fig 11a, which exhibits an elasto-plastic behaviour for compressive loading and a cracking behaviour for tensile loading. The loss of tensile strength after cracking was modelled through a softening branch with a slope k_s=10^8 MPa. The elasticity modulus was taken equal to 28.4 GPa and the Poisson's ratio $v = 0.16$. The longitudinal and transverse reinforcement bars were assumed to behave elastoplastically with hardening. A modulus of elasticity of 200 GPa and a Poisson's ratio $v = 0.20$ were given. The stress-strain diagram for the steel rebars is depicted in Fig. 11b. Finally, the F.E. simulating the steel links were also equipped with the stress-strain relationship given in Fig.11b, which exhibits elastoplastic behaviour with hardening. The elasticity modulus for these elements was taken equal to 210 GPa and the Poisson's ratio $v = 0.30$.

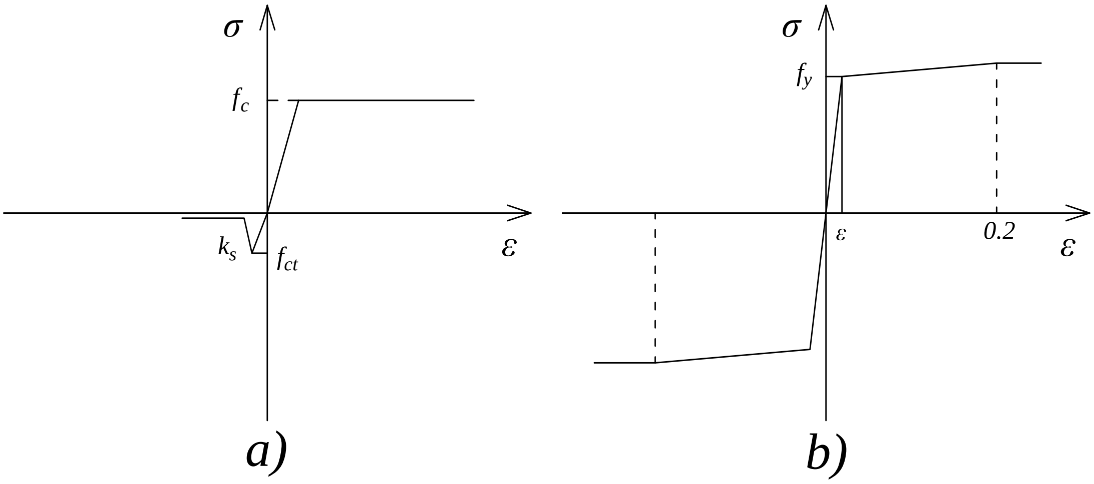

Figure 11: Stress-strain relationships considered for a) concrete and b) all the steel elements of the model.

3.2 Boundary conditions – loading procedure

All the specimens (F1, F2 and F3) were subjected to horizontal cyclic loading, with and without additional vertical load at the columns. The cyclic load was applied incrementally in the form of induced displacement, whereas the constant vertical load was applied as a point load. The simulation of the load application procedure introduced several difficulties, which required a special numerical treatment. In general, it was not possible to apply the load directly to a nodal point of the F.E. mesh, due to the elastic-plastic and cracking properties of concrete. When the applied load caused the formation of a compressive stress zone in the neighbourhood of the load application node, stress concentrations and non-realistic stress fields occurred, creating excessive plastification of the elements representing concrete. In order to avoid this phenomenon, a steel plate was placed on each load application position, through which the respective load was applied.

On the other hand, during the load reversal, the applied load produced a tensile stress zone in the region of the applied load. Even for moderate load values, stress concentration appeared locally, near the node at which the load was applied and therefore, non-realistic conditions for cracking were created, destroying the adjacent elements and leading to the premature termination of the numerical process. To overcome this obstacle, a system of two plates was adopted, one on the upper left and one on the upper right side of the frame. Unilateral contact conditions were assumed between the plates and the frame. The two plates were connected by kinematical constraints in order to achieve the load application in both directions and so that only compressive forces are imposed through the respective contact surfaces of the specimen. The above described loading procedures resulted in rather realistic stress and strain fields in the load application areas.

Finally, clamped supports were assumed at the positions where the steel rigid braces are connected to the frame and to the steel link.

3.3 Numerical solution procedure

The solution to the described numerical problem was obtained by using the software code MSC-MARC. A Newton-Raphson iterative procedure was applied to handle the nonlinearities of the problem. The cyclic load was applied in the form of an induced displacement δ and the resulting force P at the points of the incrementally applied displacement was monitored. A relative convergence criterion was adopted, based on the residual forces. The relative force tolerance was set to 0.01.

4 EXPERIMENTAL AND NUMERICAL RESULTS

4.1 Overall behavior of the specimens

Figures 12-14 present the load – displacement curves of the tested specimens. Also, in Fig. 15, the envelop curves that result from the aforementioned diagrams (consideration of first cycles only) are compared. In Fig. 16 the dissipated energy with respect to the imposed displacement for each specimen is presented. The observations on the response of the specimens during the tests and the obtained results are given below.

Specimen F1: During the first cycles, flexural cracks were formed, initially at the base and later at the top of the columns. The cracks at the base of the columns were formed just over the point where the Λ-shaped steel bracing system connects at the columns (Fig. 17). At these cracks the reinforcement was elongated inelastically and thus, flexural plastic hinges were formed. The inelastic deformations were all developed at these plastic hinges. Although the stirrups were sparsely spaced, the strength of the specimen appeared a slight increase, even for drifts of the order of 3% (Fig. 12). For higher levels of the imposed displacement, strength reduction was observed.

Specimen F1,N: It can be noticed, even from the first cycles of the imposed load, that the stiffness of this specimen is higher than the stiffness of the corresponding specimen without the axial force (F1). Moreover, the hysteresis loops of the F1,N specimen are richer than those obtained from the F1 frame. Initially, cracks appeared at the columns and at the two ends of the top beam. As the values of the imposed cyclic displacement increased, the inelastic deformations were mainly developed at the plastic hinges which were formed at the ends of the columns. Due to the existence of the axial loads at the columns, the strength of the specimen and the dissipated energy were increased by 50% and 100% respectively, in comparison with specimen F1 (Figs 15 and 16).

Specimen F2: In this case, due to the activation of the steel link, there was a significant increase of the strength, the stiffness and the energy dissipation capacity of the specimen, in comparison with the bare frames (Figs 13, 15 and 16). More specifically, the strength of the F2 specimen was four times higher than that of the F1 specimen. Also, the hysteresis loops were very rich and no pinching occurred. The link started to fail by fracture at the tensioned regions of the link, for a drift of 1.8%. As the loading was cyclic, the fracture appeared at both ends of the link (Fig. 18). The welds did not show signs of failure. After the failure of the link element, the overall behaviour of the F2 frame, in terms of strength and energy dissipation capacity, appeared to be similar to the behaviour of the F1 frame. The final failure mode was similar as in the case of the specimen F1, since the plastic hinges were formed at the same locations.

By the use of the U-shaped steel jacket, the force undertaken by the link element was transferred at the middle of the beam. Due to this reason, many cracks appeared at the middle of the top beam, as well as, loss of concrete cover (Fig. 19). However, the crack pattern at the ends of the columns and at the ends of the beam didn't differ from those that appeared in specimen F1. Moreover, after the failure of the link element the response of the two specimens was very similar.

Specimen F2,N: Due to the existence of the axial load, the strength and stiffness of this specimen were increased, in comparison with the specimen F2 (Figs 13 and 15). Moreover, this specimen appears to have an increased strength and dissipation capacity of the order of 40% and 50% respectively with respect to that of the specimen F2 (Figs 15 and 16). The failure mode of the link element was the same as in the previous case. The link failed again for a drift of 1.8%. After the failure of the link element, the recorded response of the specimen F2,N was similar with the response of the specimen F1,N.

Specimen F3: This specimen was strengthened with a link element of different type (Fig. 3). The dimensions of the cross-section of the present link in combination with its longer length resulted in lower stiffness compared to the link of the specimen F2. However, the ultimate strength for this specimen is slightly higher than that of specimen F2. The main improvement for the present specimen is that the strength was sustained without reduction until a drift of 2.7%, thus, improving the ductility of the strengthened frame (Figs 14 and 15). The failure of the link element started at a drift of 2.7% and completed at a drift of 3.6%. After that point the specimen had the response of the unstrengthened specimen F1. This high ductility of the specimen is attributed to the higher rotational capacity of the link element. Due to the higher forces and the significant inelastic deformations that were developed, the U-shaped jacket at the middle of the top beam caused local damage. Moreover, the bending moment that develops at the mid-span of the beam due to the eccentricity of the horizontal force undertaken by the link, led to the development of high shear forces along the two parts of the beam. Characteristic is the development of bidiagonal shear cracks at the left and right parts of the top beam (Fig. 20). Also, plastic hinges were formed at both ends of the columns.

Specimen F3,N: Due to the existence of the axial loads at the columns, the strength of the specimen and the dissipated energy were increased by 35% and 40% respectively, in comparison with specimen F3 (Figs 15 and 16). For an imposed displacement of 3mm, the resisted force was 90kN. Due to the high stiffness, the first cracks appeared at the top beam, at the left and right of the U-shaped jacket. Also, due to the existence of axial loads, the cracks at the columns were significantly reduced. For this reason, the inelastic deformation was developed mostly at the middle of the top beam through the rotation of the U-shaped jacket. The ultimate strength was achieved for an imposed displacement of 21mm. Due to the extended damage that developed at the top beam, the test was terminated at that displacement value, for safety reasons. The link element did not fail.

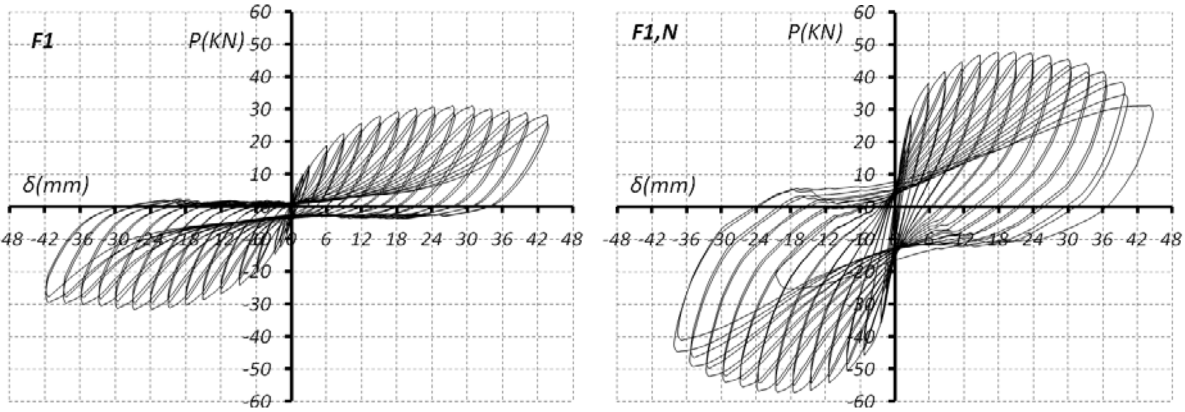

Figure 12: Load – displacement (P-δ) curves of the frame F1 and F1,N

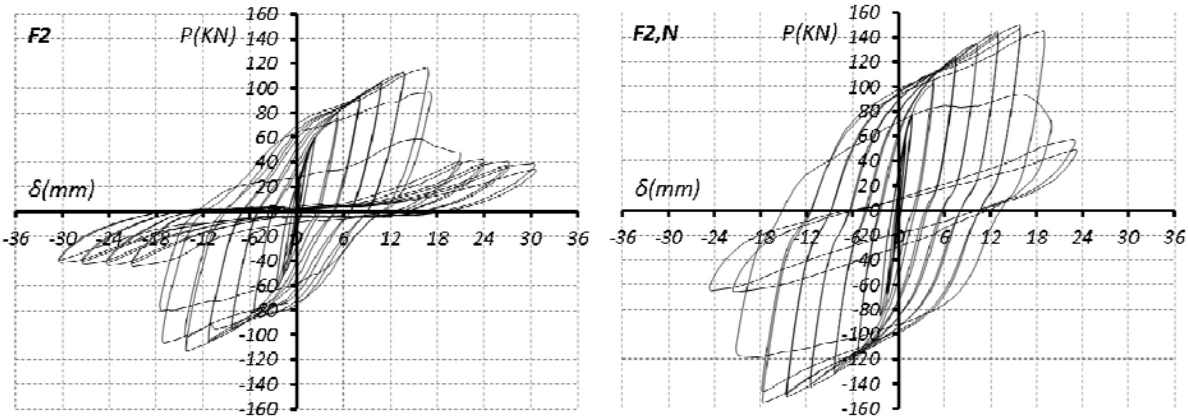

Figure 13: Load – displacement (P-δ) curves of the frame F2 and F2,N

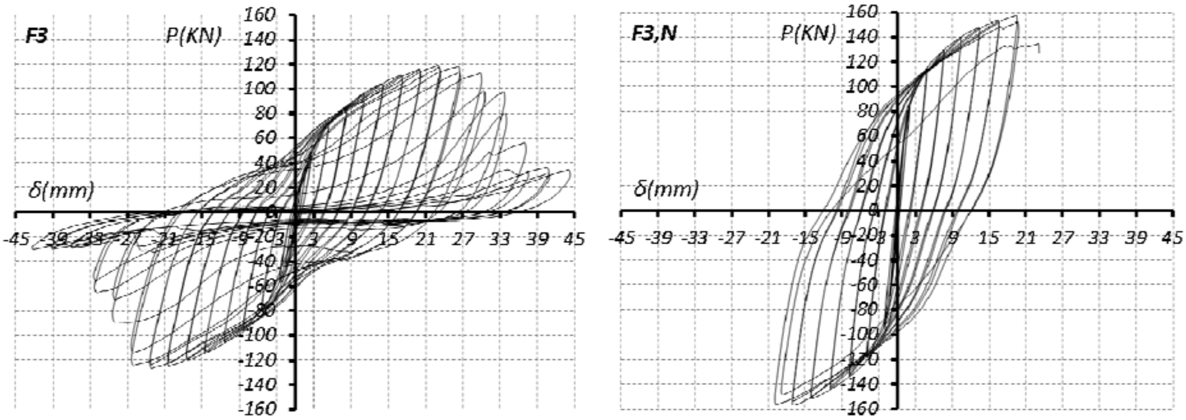

Figure 14: Load – displacement (P-δ) curves of the frame F3 and F3,N

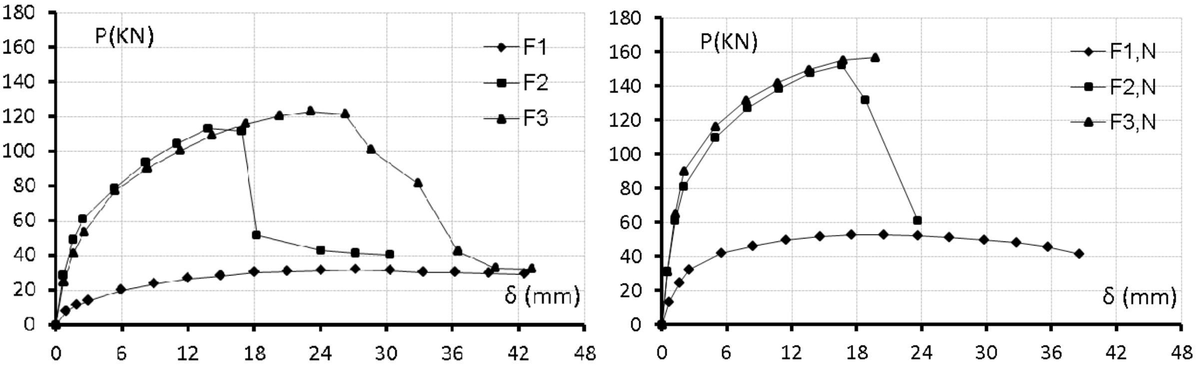

Figure 15: Comparison of load – displacement (P – δ) envelopes (first cycles only)

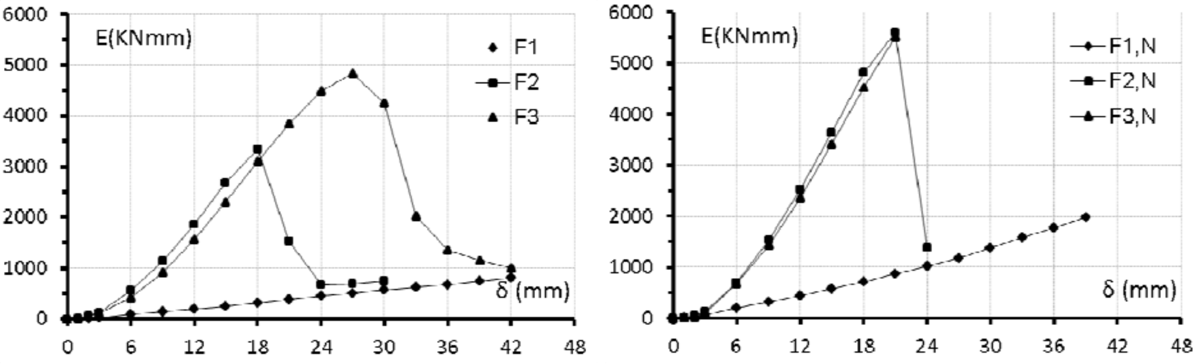

Figure 16: Comparison of energy dissipation – displacement (E – δ) envelopes (first cycles only)

Figure 17: Plastic hinge at the bottom of the column (F1)

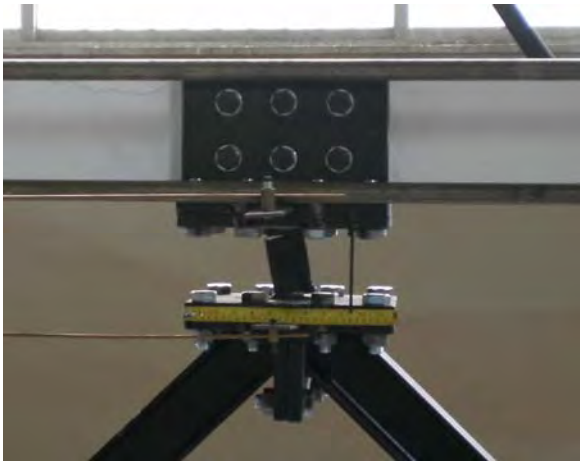

Figure 18: Failure mode of the link element (F2)

Figure 19: Concrete cover failure (F2)

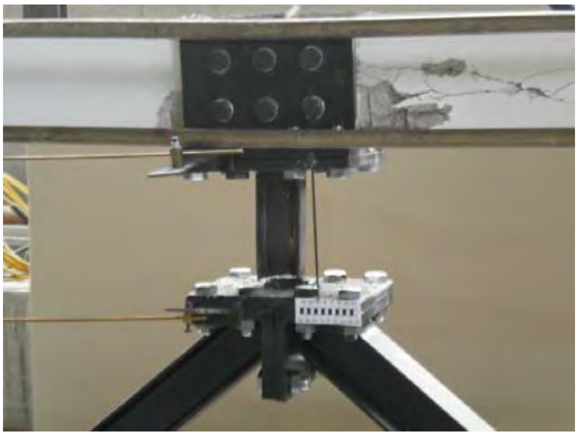

Figure 20: Cracks at the middle of the top beam (F3)

4.2 Overall behaviour of the specimens

Before displaying the numerically obtained results, it should be mentioned that, for most of the cases treated here, it was not possible to simulate the performed experiments beyond a displacement of about 12 mm, due to numerical instabilities in the models which led to the termination of the applied Newton – Raphson iterative procedure. The reason for the aforementioned problem was the significant damage of concrete that occurred for displacement values higher than 12 mm. For the same reason it was decided to simulate numerically only one load cycle for each displacement level instead of two similar cycles that were applied in the experiments. Therefore, the experimental P-δ curves used in this section for the comparison of the numerical with the experimental results are actually, part of the complete response diagrams of each experiment (Figs. 12-14).

The comparison between the numerical and experimental P-δ curves of the bare frame without axial force (F1) and with axial force (F1,N) is presented in Fig. 21. It can be noticed that the numerical model cannot approximate adequately the unloading branch of the experimental P-δ diagram, leading to narrower hysteresis loops. It seems that the smeared crack approach used for the modelling of cracking cannot simulate accurately enough the closure of cracks and therefore, the behaviour of the specimen during the load reversal procedure. This deficiency of the numerical model is more obvious in the case of F1,N, where, except from the narrower hysteresis loops, one can notice differences between the load values P obtained for the negative cycles by the analysis and the experiment. Figure 22 presents the comparison of the P-δ envelopes obtained by the experiment and the analysis of the F1 and the F1,N frames. In these diagrams, only positive values are given for each applied displacement level, that correspond to the mean of the absolute values of the respective positive and negative cycles. The aforementioned discrepancies that appear in the P-δ diagrams of the F1,N case concerning the experimental and numerical load values of the negative cycles, are reflected in the respective P-δ envelope curves. Figure 23 gives the comparison of the dissipated energy in each load cycle. It can be observed that for the case of F1 the differences between the experimental and numerical values of dissipated energy are rather small and result from the narrower numerical hysteresis loops. However, for the case of the F1,N frame, the corresponding discrepancy is much wider, due to the additional differences in the negative load values.

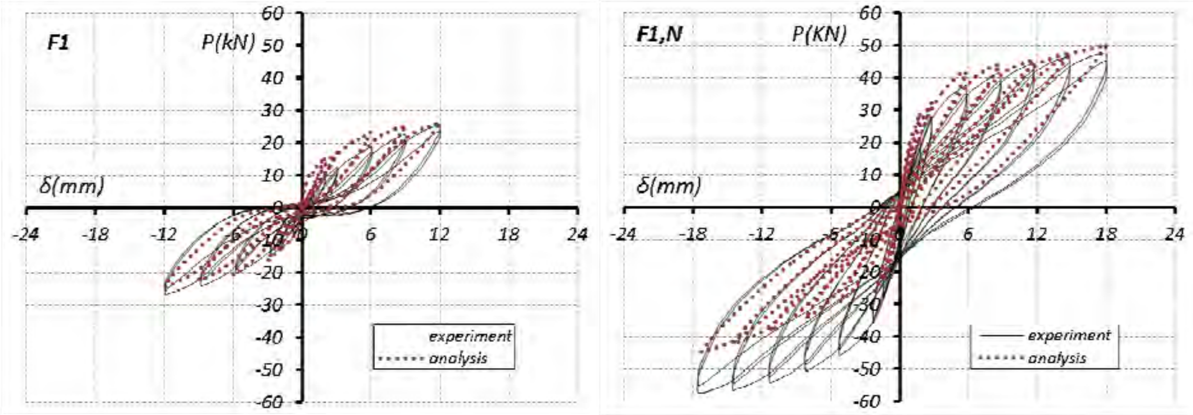

Figure 21: Comparison of the numerical and experimental results of the frames F1 and F1,N.

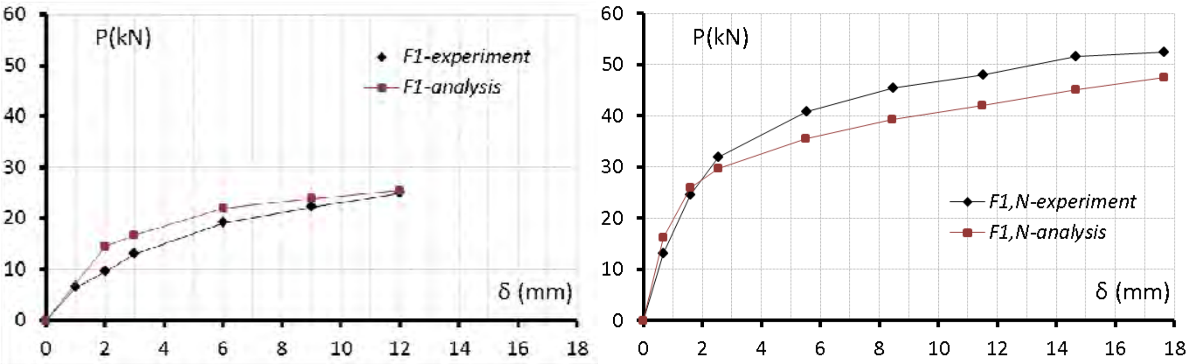

Figure 22: Comparison of the P-δ envelope results obtained by the experiment and the analysis of the frames F1 and F1,N.

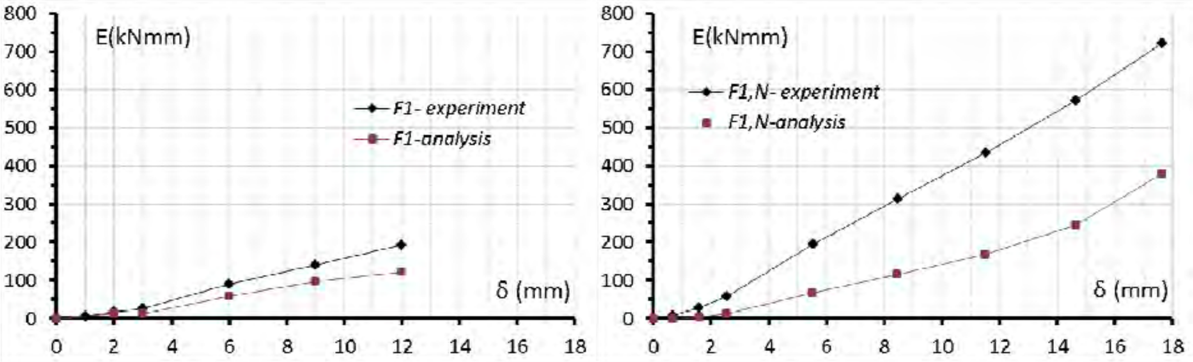

Figure 23: Comparison of the experimental and the numerical results for the dissipated energy in the frames F1 and F1,N.

Contrary to the bare frame F1, the overall behaviour of the frames strengthened by the steel link elements, F2 and F3, is significantly improved after the immediate activation of the link elements. Figure 24 shows the P-δ curves for the F2 strengthened frame (without axial load) and the F2,N strengthened frame (with axial load), obtained by the 2D numerical model together with the experimental results. Figure 25 displays the corresponding envelopes of the P-δ curves. It is noticed that, especially for the case of the F2 frame, there is a good agreement between the numerical and the experimental results, as far as the load values, the quality of the hysteresis loops and therefore, the overall behaviour of the specimen, is concerned. The small differences that arise in the obtained values can be considered acceptable, taking into account the highly nonlinear nature of the studied problem. However, once again, in the case where the axial load is imposed at the columns, greater differences can be noticed between the numerical and the experimental results, mainly in terms of the obtained load values, whereas the quality of the hysteresis loops is similar. In Fig. 26 the numerical and experimental results for the dissipated energy of the F2 and F2,N frames are presented. As expected, there is a very good agreement between the results for the F2 frame, whereas some differences arise for the F2,N strengthened frame, due to the above mentioned differences in the obtained values of the P-δ curves.

The same conclusions can be drawn from the comparison of the numerical and experimental results presented in Figs 27, 28 and 29, which concern the F3 strengthened frame (without axial load) and the F3,N strengthened frame (with axial load). For the F3 case, the numerical and experimental results are in a rather good agreement, in terms of obtained load values, quality of the hysteresis loops and dissipated energy. For the F3,N case, although the numerical P-δ curves, the P-δ envelope curves and the dissipated energy present some differences with respect to the experimentally obtained ones, they can be considered acceptable, taking into account the nonlinear phenomena that are present in the physical model.

It can be concluded that the good agreement between the numerical and experimental results of the strengthened frames is derived from the fact that in these cases the behaviour of the steel link element is dominant. In this case, the numerical model has the ability to simulate efficiently the isotropic and homogenous behaviour of the steel link element, as well as its stable elasto-plastic deformation.

Finally, Figs 30 and 31 show the plastic strain fields of the link elements F2, F2,N and F3, F3,N, respectively for a displacement of about 12 mm. Both types of links present a combined shear and bending behaviour. However, their failure is mainly of bending type, as greater stresses appear in the flanges at the top and bottom ends of the elements, rather than the web, especially in the case of the F3 and F3,N links. The failure modes match well with the failure type of the link elements that was noticed in the corresponding experiments.

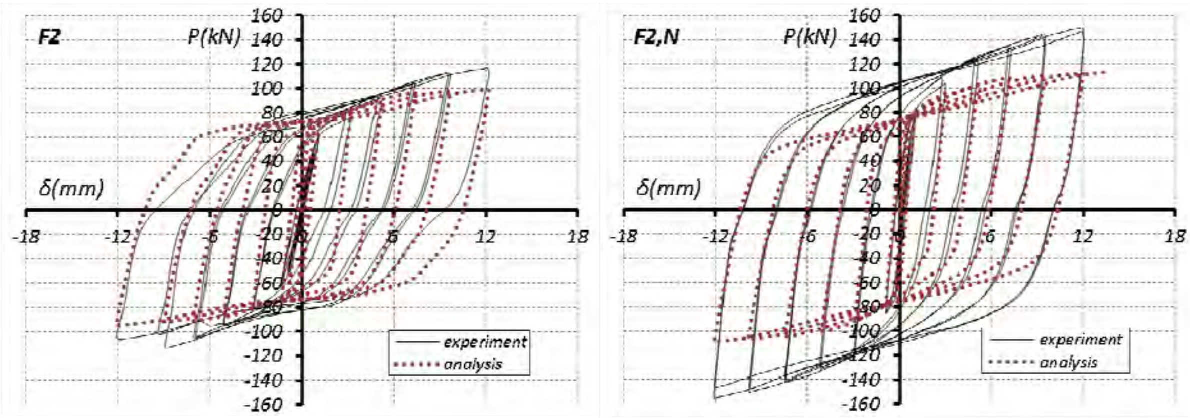

Figure 24: Comparison of the numerical and experimental results of the frames F2 and F2,N.

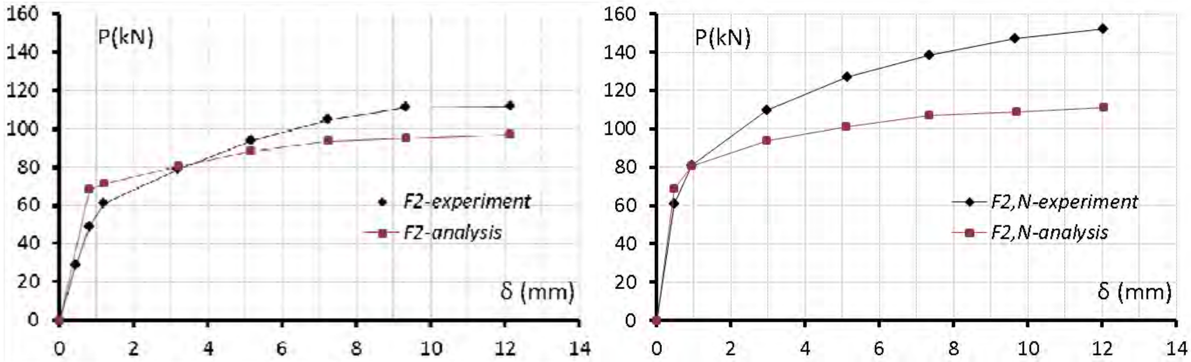

Figure 25: Comparison of the P-δ envelope results obtained by the experiment and the analysis of the frames F2 and F2,N.

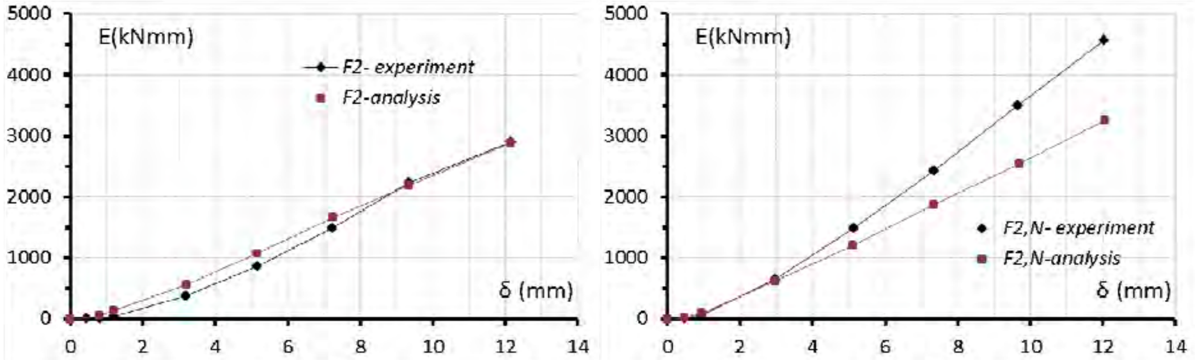

Figure 26: Comparison experimental and the numerical results for the dissipated energy in the frames F2 and F2,N.

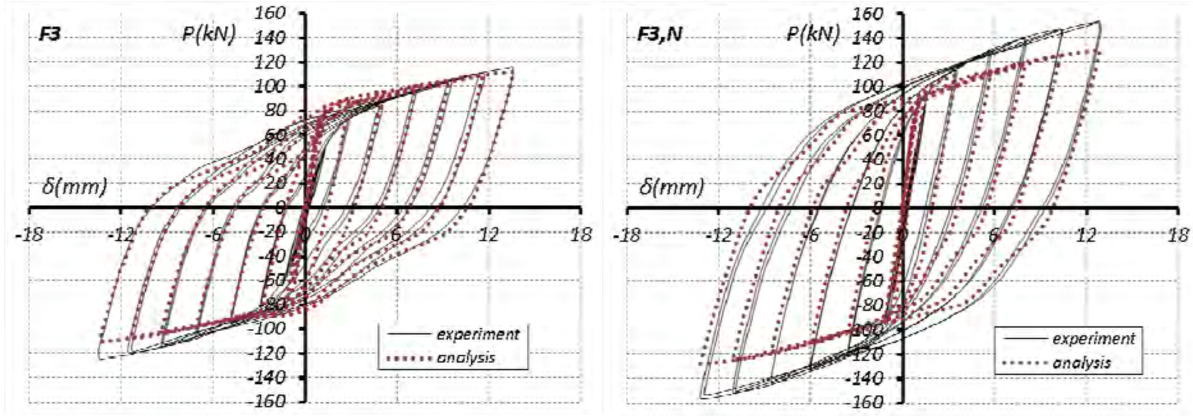

Figure 27: Comparison of the numerical and experimental results of the frames F3 and F3,N

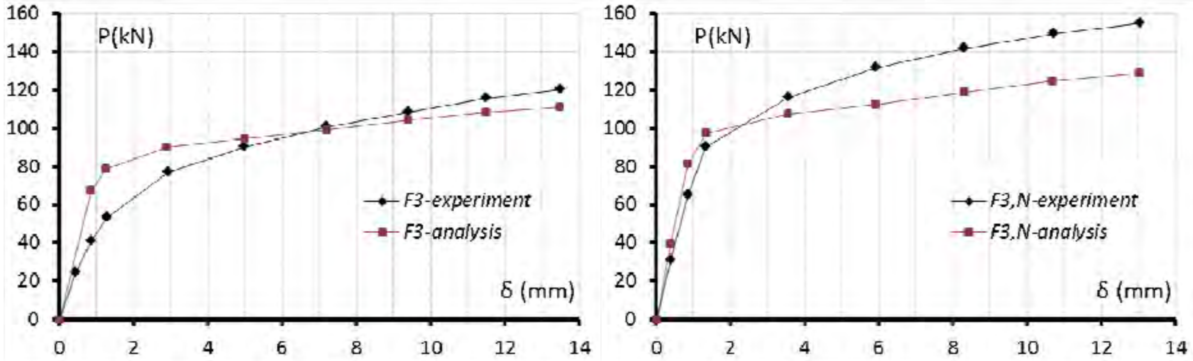

Figure 28: Comparison of the P-δ envelope results obtained by the experiment and the analysis of the frames F3 and F3,N.

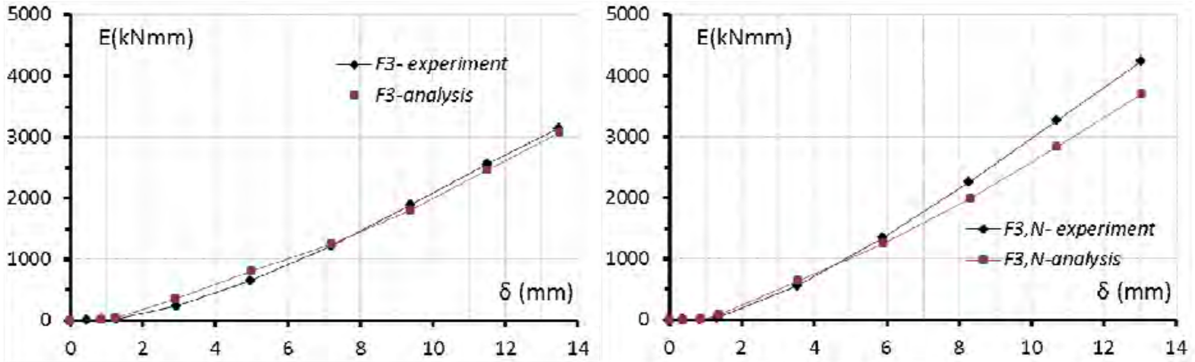

Figure 29: Comparison of experimental and the numerical results for the dissipated energy in the frames F3 and F3,N.

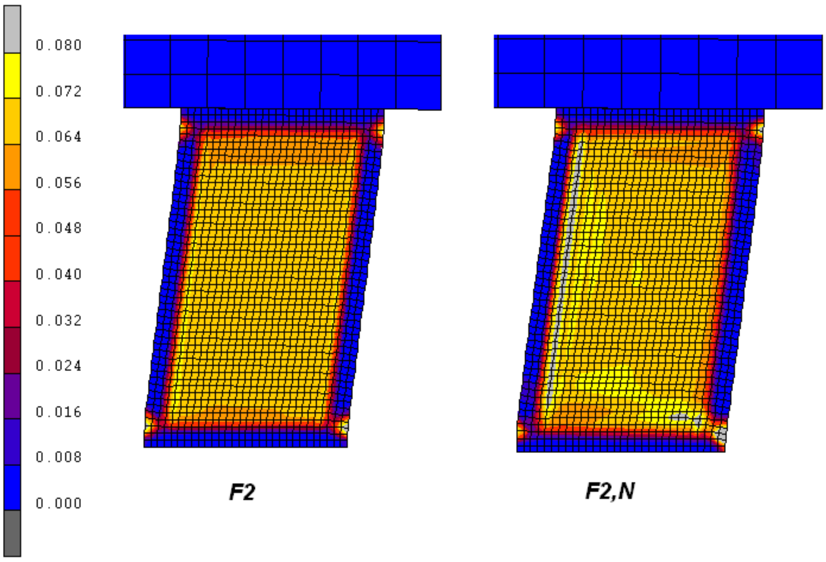

Figure 30: Plastic strain of the steel link elements of the frames F2 and F2,N, for a displacement of 12mm.

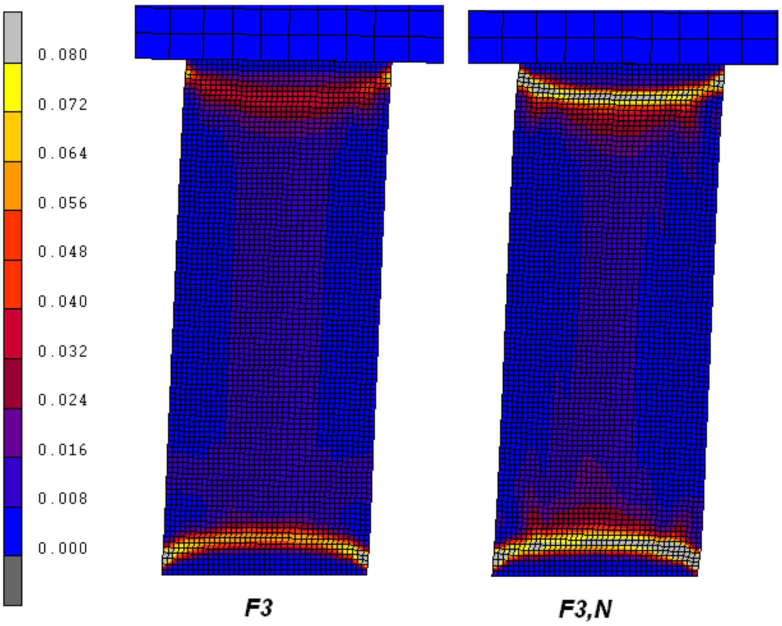

Figure 31: Plastic strains of the steel link elements of the frames F3 and F3,N, for a displacement of 12mm.

5 CONCLUSIONS

After comparing the behaviour of the specimens under study, it can be concluded that the use of the steel link elements can increase considerably the strength, the stiffness, but mainly the energy dissipation capacity of the frame. Moreover, the use of the F3 type of link element results to slightly lower overall stiffness, but to increased ultimate strength, with respect to the F2 type of link element. However, the significant improvement for the F3 strengthened frame is its increased ductility; the high load carrying capacity is maintained without reduction for much higher values of imposed displacements. Also, it is evident that the existence of axial loads at the columns resulted to an increase of the strength, stiffness and dissipated energy for all the frames studied. It must be noted, however, that attention should be paid to the connection of the link element to the midpoint of the beam, through the U-shaped steel jacket, as local damage appeared at that specific area of the beam of the strengthened frames. By a careful selection of the geometry of the steel link and appropriate detailing of its connection with the frame, this local failure at the middle of the top beam can be prevented, so that it does not affect or alter the failure mode of the frame.

Finally, after the comparison of the numerical with the experimental results, some differences are observed in the case of the bare frames (F1 and F1,N) which are attributed to the inability of the used type of finite elements to simulate adequately the unloading behaviour of concrete. On the other hand, the results obtained from the numerical models of the strengthened frames can be considered satisfactory in terms of the stiffness, load carrying capacity, quality of the hysterisis loops and dissipated energy, with respect to the experimental results, given the complexity of the studied problem.

ACKNOWLEDGEMENTS

The work presented here is part of a broader program, partially sponsored by the Greek Earthquake Planning and Protection Organization, the contribution of which is gratefully acknowledged.

REFERENCES

[1] A. Kunisue, N. Koshika, Y. Kurokawa, N. Suzuki, J. Agami, M. Sakamoto, Retrofitting method of existing reinforced concrete buildings using elasto-plastic steel dampers. *12WCEE,* New Zealand, 2000.

[2] R. Perera, S. Gomez, E. Alarcon, Experimental and analytical study of masonry infill reinforced concrete frames retrofitted with steel braces. *Journal of structural Engineering, ASCE,* **130**, 2032-2039, 2004.

[3] A. Pinto, F. Taucer, Assessment and retrofit of full scale models of existing rc frames. S.T. Wasti, G. Ozcebe eds. *Advances in Earthquake Engineering for Urban Risk Reduction,* Springer Netherlands, 353-367, 2006.

[4] Antonucci, R., Balducci, F., Bartera, F., Castellano, M. & Chaudat, T. 2006. Shaking table test on rc frame braced with fluid viscus dampers. *1st European Conference on Earthquake Engineering and Seismology (1st ECEES),* Switzerland, 3-8 Semptember 2006. paper#650.

[5] M. D'Anielo, Seismic upgrading of rc structure by steel eccentric bracing (Experimental and numerical study. *Pollac Periodica,* **1**, 17-32, 2006.

[6] A. Abdollahi, Numerical strategies in the application of the FEM to RC structures. *Computers and Structures,* **58**, 1171-1182, 1996.

[7] T. Rabczul, J. Akkermann, J. Eibl, A numerical model for reinforced concrete structures. *International Journal of Solids and Structures,* **42**, 1327-1354, 2005.

[8] C.Y. Wang, H.Y. Ho, R.Z. Wang, H.H. Huang, Numerical simulations of non-ductile RC frames with infilled brick panel under cyclic loading. *Journal of the Chinese Institute of Engineers,* **31**, 827-840, 2008.

[9] D.A. Nethercot, The importance of combining experimental and numerical study in advancing structural engineering understanding. *Journal of Constructional Steel Research,* **58**, 1283-1296, 2002.

[10] K. Georgiadi-Stefanidi, E. Mistakidis, P. Perdikaris, T. Papatheocharis, Numerical simulation of tested reinforced concrete beams strengthened by thin fibre-reinforced cementitious matrix jackets. *Earthquakes and Structures,* **1**, 345-370, 2010.

COMPDYN 2011
3rd ECCOMAS Thematic Conference on
Computational Methods in Structural Dynamics and Earthquake Engineering
M. Papadrakakis, M. Fragiadakis, V. Plevris (eds.)
Corfu, Greece, 25–28 May 2011

DAMAGE DETECTION OF FRAME STRUCTURES SUBJECTED TO EARTHQUAKE LOADING

Nikos G. Pnevmatikos

Technological Educational Institution of Athens, Faculty of Technological Application, Department of Civil Infrastructure Works,
Ag. Spyridonos Str., P.O. 12210 Egaleo-Athens,Greece, Tel. : +30-211-7059910, Fax : +30-210-5385858
Email: nikos_pnevmatikos@hotmail.com

Keywords: Health monitoring, Damage detection, Discrete Wavelet analysis, Structural dynamics, Earthquake engineering.

Abstract. *This paper deals with an application of wavelet analysis for damage detection of frame structure subjected to earthquake excitation. Non linear dynamic analysis has been performed and response data at each story are obtained which are used as simulation data. Damage in the frame is introducing by the non linear behaviour of columns and beams. In order the structural members go beyond the elastic limit and start yielding the earthquake excitation was scaled up with appropriate scale factor. Discrete wavelet analysis was performing in order to analyze the simulation response data for each floor because the dynamic behaviour of inelastic structures subjected to an earthquake is a non-stationary process.*

It was shown that structural damage, due to non linear behaviour of structural elements and the time when this damage occurred, can be clearly detected by spikes in the wavelet details.

The effect of noise is taken into account by adding a white Gaussian noise to the simulation response data and discrete wavelet analysis was performing again. It was observed that if the level of details and the order of wavelets are increased, spikes can be detected again and damage would be recognized. Results show the great promise of the wavelet approach for damage detection and structural health monitoring.

1 INTRODUCTION

Damage in the buildings is often observed during their service life. Damage may be caused due to excessive earthquake excitation, severe environmental condition, degradation of the materials properties, fatigue, cumulative crack growth, etc. Usually the existence and the location of the damage can be determined through visual inspection. However, in some cases visual inspection may not be feasible. To ensure structural safety and low maintenance cost, structural health monitoring, SHM, is an efficient strategy to monitor the system performance and make a corresponding maintenance decisions.

Damage detection is a part of damage identification which includes the estimation of the severity of damage, determination of the location of damage and prediction of the remaining service life. One main group of methods for damage detection is, modal analysis methods, which are based on the fact that the change in structural properties causes a variation in the modal parameters; natural frequencies, damping ratios and mode shapes. Many analytical and experimental studies have been conducted to establish analytical correlations between damage severity and modal parameters. Kirmser, [1], investigated the relationship between natural frequencies and the introduction of a crack in an iron beam. A literature review on methods of damage detection using vibration signals for structural and mechanical systems was provided by Doeblin et al. [2] and Carden and Fanning, [3]. Other works based on change in modal parameters is the work of Humar et al. [4] and khoo et al., [5].

Structural health monitoring techniques based on changes in dynamic characteristics have success when the damage is substantial. Improved research directions for damage detection including the use of innovative signal processing, new sensors, are described in the work of Chang et al., [6]. Neural network approaches can be used for damage detection. Wu et al., [7], trained a neural network to recognize the behaviour of the undamaged structure as well as the behaviour of the structure with various possible damage states. When the trained network is subjected to the measurements of the structural response, it is able to detect any existing damage. Tsou, and Shen, [8], applied neural network to discrete structural systems. Masri et al., [9], train a neural network with measurements from healthy structure and this trained network was fed comparable vibration measurements from the same structure under different episodes of response in order to monitor the health of structure. Vanik and Beck, [10], Chandrashekhar and Ganguli, [11], used fuzzy logic for determination of damage location. Friswell and Mottershead, [12], use a combination of sensors and analytical model of structure for damage detection. Parameters of the model that are related to damage are updated so that the dynamic characteristics of the model correspond to the measurements sensors, Papadimitriou and Ntotsios, [13]. Reigh and Park, [14], utilised methods of localized flexibility in order to determining the damage and its location in a structure. Panetsos et al, [15], describe the Egnatia Odos Bridge Management system (EOBMS) which used for deterioration prediction and maintenance, repair cost.

Engelhardt et al., [16], were investigated the Crack and flaw identification in elastodynamics using Kalman filter techniques. Soyoz and Feng, [17], used an extended Kalman filtering (EKF) method in order to instantaneously identify elemental stiffness values of a structure during damaging seismic events based on vibration measurement. This method is capable of dealing with nonlinear as well as linear structural responses. Sakelariou and Fasois, [18], introduced a stochastic output error for damage detection and assessment (location and quantification) in structures under earthquake excitation. De Roeck and Reynders, [19], present a number of recent innovations to extend the borders of what is realistically feasible with the current system identification and damage detection methods.

Medda and DeBrunner, [20], proposed a novel technique that employs the use of compactly supported sub-band space-frequency and time-frequency analysis using local vibration characteristics.

Another tool for damage detection is wavelet-based damage detection which has been considered by several researchers over the last decade, Staszewski, [21]. Newland, [22], have used wavelets to vibration analysis. He applied a wavelet analysis to study the vibration of buildings caused by underground trains, road traffic and earthquake excitations. Taha et al., [23], presents a view of wavelet transform and its technologies. They discuss specific needs of health monitoring addressed by wavelet transform. Masuda et al, [24], use orthonormal discrete wavelets transform to detect the degradation of stiffness due to fatigue. They applied the method to the laboratory-scale experiments to detect the sudden changes in the structural parameters. Kim and Melhem, [26], provide a review of the research that has been conducted on damage detection by wavelet analysis. Hou et al., [27], proposed a wavelet-based approach for structural damage detection. Their model consists of multiple breakable springs which is may suffer either for irreversible damage when the response exceeds a limit value nor the number of cycles of motion is accumulated beyond their fatigue life. In any case, occurrence of damage and the time when it occurs can be clearly determined in the details of the wavelet decomposition of these data. Hera and Hou, [28], applied wavelet analysis for detection and locating damage for a four-story prototype benchmark building provided by ASCE Task Group on Health Monitoring, Johnson et al., [29]. They were found that structural damage due to sudden breakage of structural elements and the time when it occurred can be clearly detected by spikes in the wavelet details. In the work of Khatam et al., [30], wavelet analysis is used for damage identification in beams subjected in harmonic loading. The damaged region can be determined by the spatial distribution pattern of the observed spikes. Yaghin and Hesari, [31], use Wavelet Analysis in crack detection at the arch concrete dam. Noh et al., [32], use the Wavelet Coefficient Energies in order to perform structural damage diagnosis for non stationary response signals. Nair and Kiremidjian, [33], have shown that the energies of the wavelet coefficients at appropriate scales can be used as damage sensitive features. A wavelet based, distortion energy approach is presented by Bukkapatnam et al., [34], as a method, for quantifying and locating the damage to structural systems. Another application of the wavelet transform for damage detection based on optical measurements is presented in the work of Patsias and Staszewski, [35].

In this paper the method of spikes in the wavelet details, from discrete wavelet analysis, is used in order to detect the damage in the frame structure. Damage in the structure was introduced by the non linear behaviour of the members. In order the members go slightly beyond the yielding point, and small damage occurred, the earthquake excitation was scaled up with appropriate factor. The analyzing data were obtained by non linear dynamic analysis of plane frame. Since the dynamic behaviour of inelastic structures during an earthquake is a non-stationary process wavelet analysis is more appropriate tool than conventional Fourier analysis.

2 BACKGROUND OF WAVELET ANALYSIS

Wavelet analysis provides a powerful tool to characterize local features of a signal. Unlike the Fourier transform, where the function used as the basis of decomposition is always a sinusoidal wave, other basis functions can be selected for wavelet shape according to the features of the signal. The basis function in wavelet analysis is defined by two parameters: scale and translation. This property leads to a multi-resolution representation for non-stationary signals.

The continuous wavelet transform of a signal f(t) is defined as:

$$f\left(a,b\right)=\frac{1}{\sqrt{a}}\int_{-\infty}^{\infty}f\left(t\right)\bar{\Psi}\left(\frac{t-b}{a}\right)dt \tag{1}$$

where a,b are the scale and translation parameters respectively and $\bar{\Psi}$ denotes the complex conjugate of Ψ. The functions $\Psi(t,a,b)$ are called wavelets. They are dilated and translated versions of the mother wavelet $\Psi(t)$.

By discretizing the parameters a and b, a discrete version of the wavelet transform (DWT) is obtain. The procedure becomes more efficient if dyadic values of a and b are used, i.e.

$$a=2^{j} \quad b=2^{j}k \quad j,k\in Z \tag{2}$$

where Z is a set of positive integers. The corresponding discretized wavelets $\psi_{j,k}$ defined as:

$$\Psi_{j,k}\left(t\right)=2^{-j/2}\Psi\left(2^{-j}t-k\right) \tag{3}$$

$\psi_{j,k}$ forms an orthonormal base. In the discrete wavelet analysis, a signal can be represented by its approximations and details. The signal is passed through a series of highpass filters, which relates to details, to analyze the high frequencies, and through a series of low-pass filters, which relates to approximations, to analyze the low frequencies. The detail at level j is defined as:

$$D_{j}=\sum_{k\in Z}a_{j,k}\Psi_{j,k}\left(t\right) \tag{4}$$

where $a_{j,k}$ is defined as :

$$a_{j,k}=\int_{-\infty}^{\infty}f\left(t\right)\bar{\Psi}_{j,k}\left(t\right)dt \tag{5}$$

and the approximation at level J is defined as:

$$A_{J}=\sum_{j>J}D_{j} \tag{6}$$

Finally, the signal f(t) can be represented by:

$$f\left(t\right)=A_{J}+\sum_{j\le J}D_{j} \tag{7}$$

The DWT can be very useful for on-line health monitoring of structures, since it can efficiently detect the time of a frequency change caused by stiffness degradation.

3 DETECTION OF DAMAGE USING WAVELETS

When the structure subjected to the earthquake excitation the envelop of the hysteretic behavior of base shear versus the roof displacement is similar to figure 1. If the excitation is strong enough and push the structure in region c or b then damage in structures is obvious since large displacements and rotations can be observed with visual inspection, and no damage detection technique is needed to verify it. If the excitation is not too small, structure behaves elastic and no permanent displacement are observed or no damage occurs. In between the two extreme above cases, the structure can be go slightly no linear, region a, and small damage that is difficult to observe by visual inspection, can be occurred.

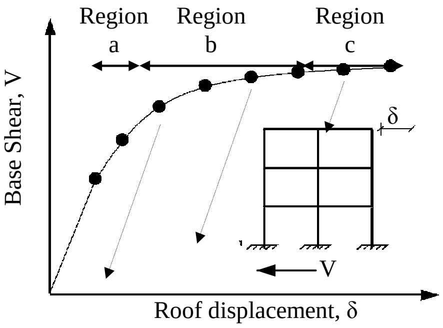

Figure 1. Global behavior envelop curve of a structure.

The above global behaviour of structure is a result of the behaviour of each element that consist the structure. The frame element has its own nonlinear characteristics based on section and material. A generalized force-displacement characteristic of frame element (or hinge properties) is shown in figure 2. Region AB, corresponds to a linear behaviour and point B represents yielding of the element. The ordinate at C corresponds to nominal strength and abscissa at C corresponds to the deformation at which significant strength degradation begins. The drop from C to D represents the initial failure of the element and resistance to lateral loads beyond point C is usually unreliable. The residual resistance from D to E allows the frame elements to sustain gravity loads. Beyond point E, the maximum deformation capacity and gravity load can no longer be sustained. This formulation is according to FEMA 356 for force deformation behaviour of structural element subjected to monotonic loading. This nonlinear behaviour can be used during nonlinear direct integration time history analysis.

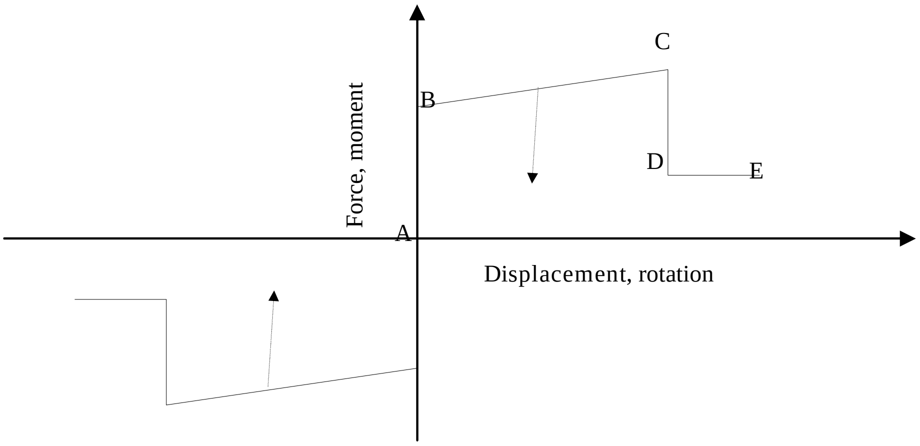

Figure 2. Generalized Force-Displacement Characteristic of a Degrading Frame Element.

As the structural elements reach the region DE or the end of the region BC the damage is clear by visual inspection since large displacement and rotation is occurred. If the element is in a linear elastic branch AB no damage is occurred. Finally if the element goes slightly beyond the yielding point, B, then small damage occurs and is difficult to be observed by visual inspection. Visual detection of damage becomes more difficult considering that structural elements are covered by other material or is difficult to access them.

Once the plastic hinge is occurred during the excitation, the frequency of the system is also change. This change in frequency has as a result the change in frequency in the response signal. From the other hand if a signal which changes its frequency is analyzed by discrete wavelet transform spikes will be observed in the details. This is clearly indicated in figure 3.

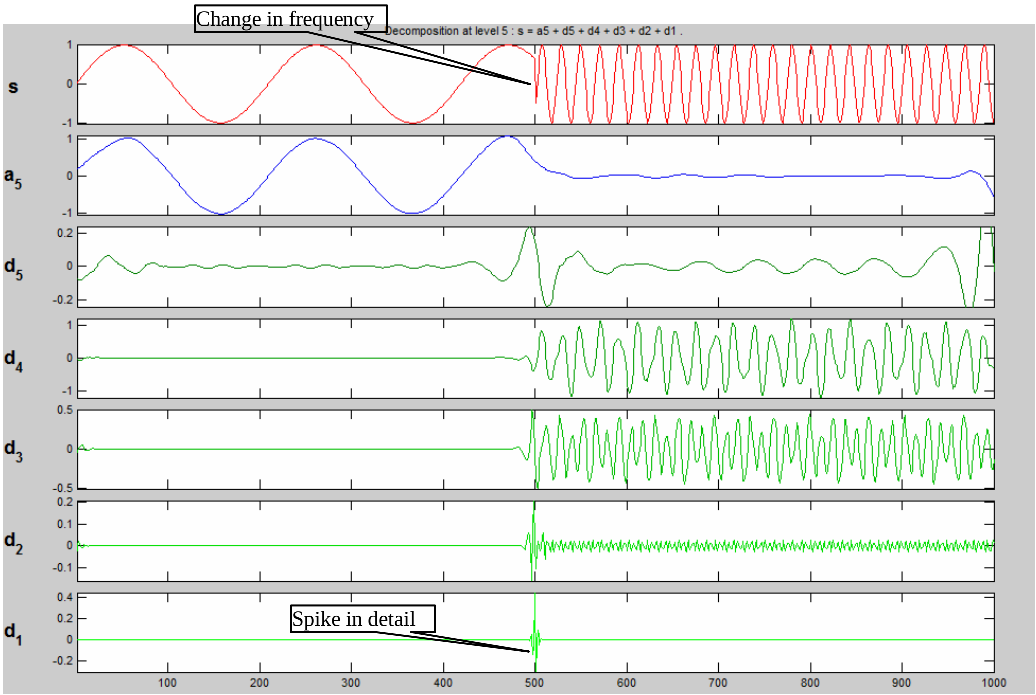

Figure 3. Spike in the detail of a signal which consists of two different frequencies.

Combining the above two characteristics (plastic hinge-chance of frequency, chance of frequency-spikes in details) the strategy that used in order to detect the damage in frame structures is as follow: The response signal is analyzed by discrete wavelet analysis and the details of the signal are obtained according to equation (4). If spikes will be observed in the details of the response signal this means that the structural element goes beyond the yielding point and damage is occurred. The time moment that the spikes appear in the details, represent the time were a plastic hinge is created. If no spikes would be observed in the detail of the response signal the structure would remain elastic and no damage would be happen. The above cases are shown schematically in figure 4.

When any structural element yields, this phenomenon is imprinted as spikes in the details of wavelet analysis of the acceleration response signal. This can be used in opposite direction, suppose that is not easy to see the situation of the structural element and the only measured data that is available is the acceleration response signal of the structure. If spikes are observed in the wavelet analysis of the signal, then yielding (damage) has been occurred.

4 NUMERICAL EXAMPLES

The above damage detection strategy has been applied to one single, one two and one eight story frame structure with the properties shown in figure 5. The frames were subjected to earthquake excitations. The nonlinear dynamic analysis and the response of the frames have been done using the software programme SAP2000nl, [36]. The wavelet analysis of the response signal has been done by the MATLAB software, [37], using the wavelet toolbox. Four order Daubechies wavelets and five levels of the details have been used for the wavelet analysis of response signal.

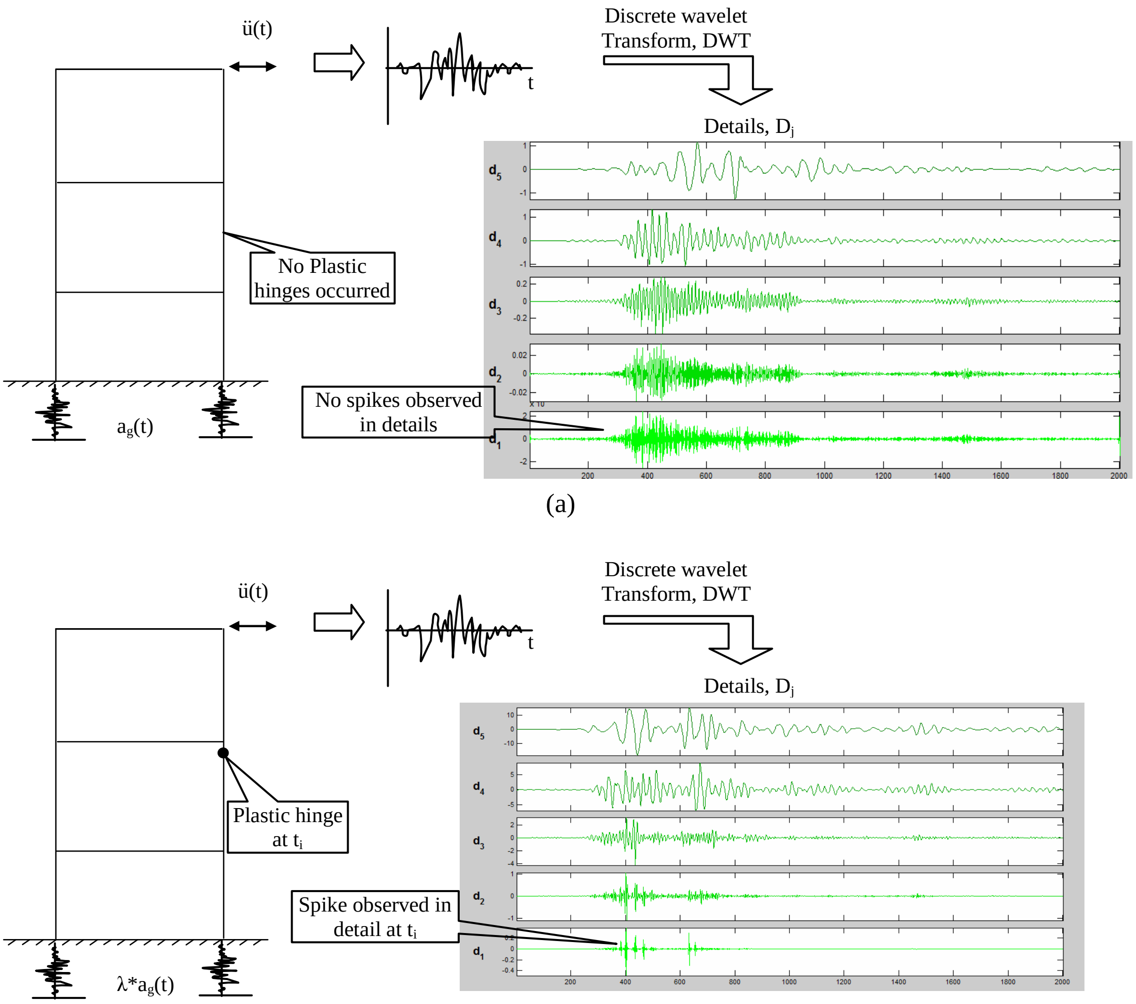

(a)

(b)

Figure 4. Procedure for detection the existence of plastic hinges in the structure. (a) no plastic hinges occurred no spices are observed, (b) plastic hinges occurred at time t_i spices are observed at t_i.

The single story frame subjected to Athens earthquake signal and no hinges has occurred. The response acceleration on the top of the frame were analyzed by wavelet analysis and the results of the approximations and details of the signal are shown in figure 6(a). It is clear, in the details of signal, d_1, no spikes are observed and consequently no damage occurred. This is verified by the nonlinear dynamic analysis where no plastic hinges occurred during the Athens earthquake excitation. The earthquake signal is scaling up gradually and dynamic non linear analysis is performing again until plastic hinges will be observed. When the factor λ becomes equal to 4 the first plastic hinges were created. For this case, the response signal at the top of the frame is analyzed again, by discrete wavelet analysis and the details are shown in figure 6(b). From the result of the wavelet analysis it is seems that spikes are observed in the details of signal. This indicates that damage has been occurred in frame. This is verified by the results of the dynamic nonlinear analysis of the frame where a plastic hinges, damage, occurred to the frame when subjected to Athens earthquake record scaled up four times. It is also remarkable, that the time (t=4.05 s) when the first plastic hinges occurred, at the base of frame, is the same when the first spike is observed in the details of the signal. After a while at time (t=4.07 s) the plastic hinges at the beam of the frame occurred and spike at time (t_i=4.07 s) was also observed. The moment-rotation diagram of plastic hinge at the base of the frame is shown in figure 7. Nevertheless the rotation of the element is too small, after yielding, this nonlinearity, or small damage, can be captured by the detail of the response signal.

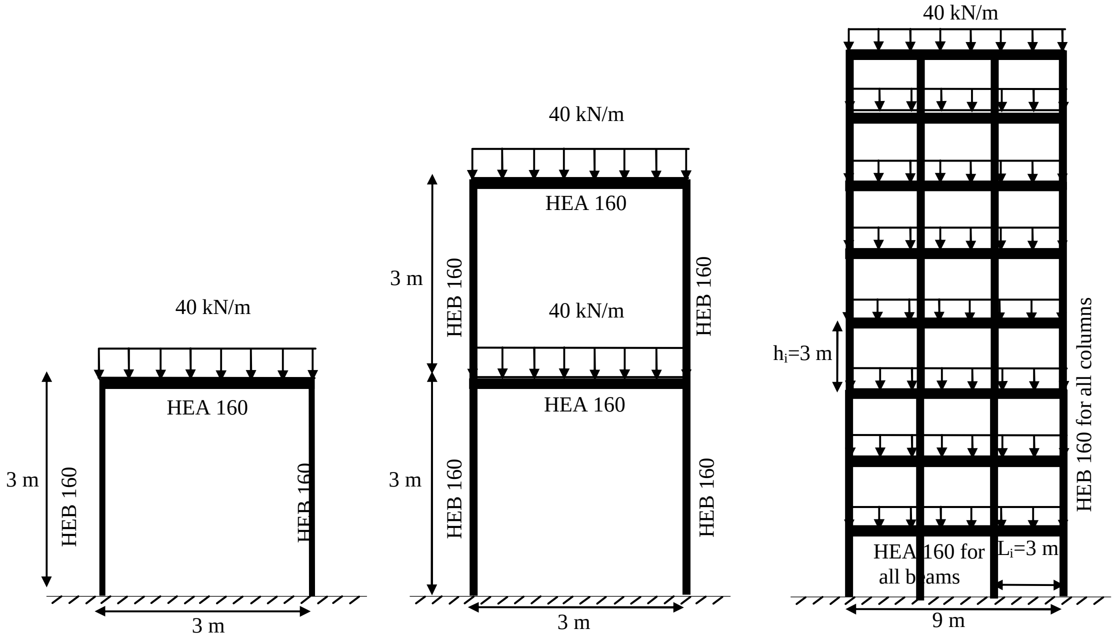

Figure 5. The examined frames, their load, geometrical and sections properties.

The two story frame subjected to the same earthquake signal and the results are shown in figure 8(a). No plastic hinge has occurred in the frame and no spikes were observed in the details of the response signal at the second floor. The earthquake is scaling up with the factor λ equal to 4 and the results are shown in figure 8(b). For this case the results from the non linear analysis show that plastic hinges at the beam of the first floor have occurred at the time t= 3.91 s, while, the plastic hinge at the column have occurred at time t= 4.22s. At the same times, the first two spikes have been observed in the details of the response signal as it is shown in figure 8(b).

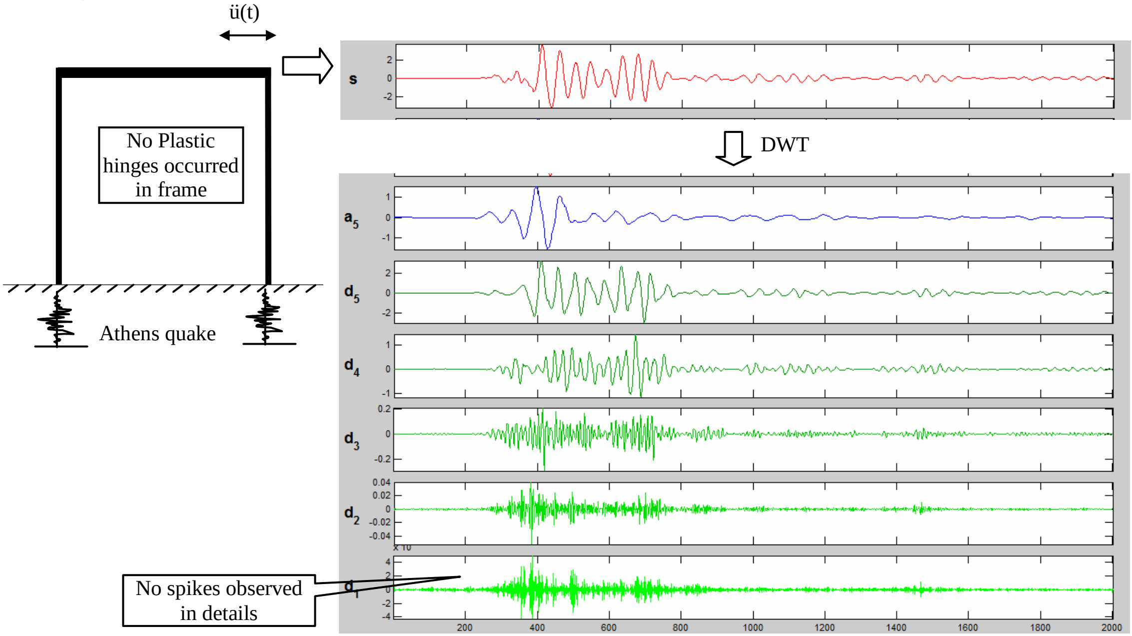

(a)

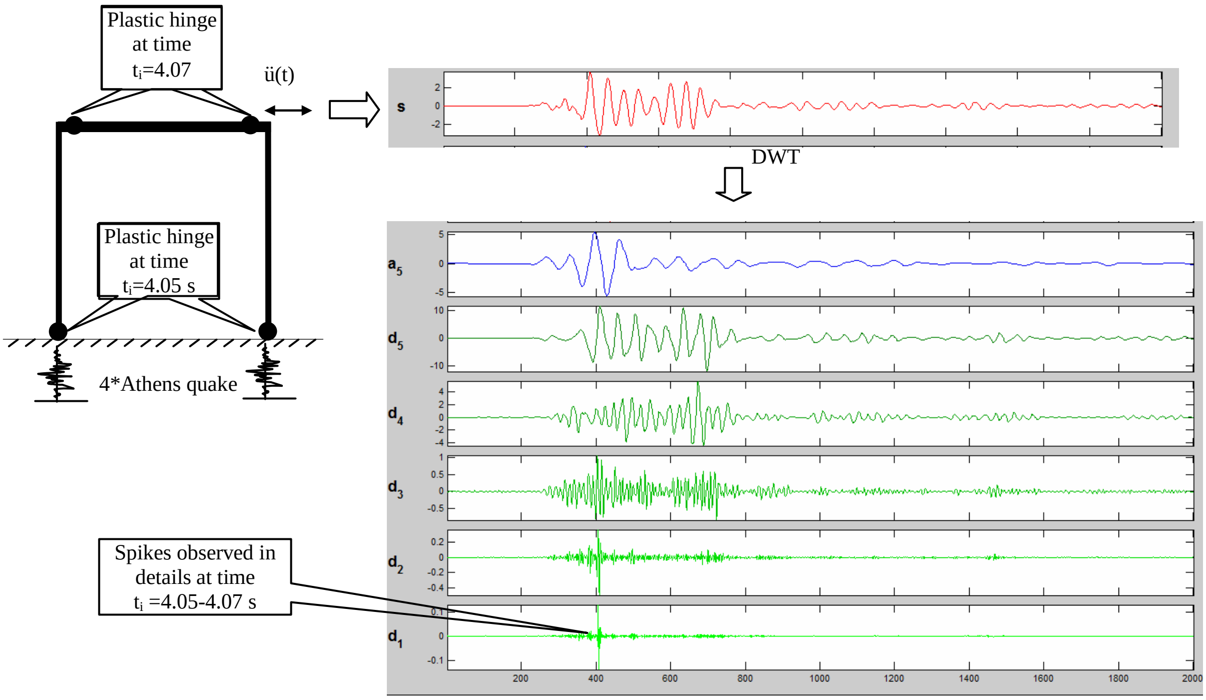

(b)

Figure 6. The approximation a5, and the details d1-d5 of the response acceleration signal, s, at the top of the frame subjected to (a) Athens earthquake signal and (b) four times scale up Athens earthquake signal.

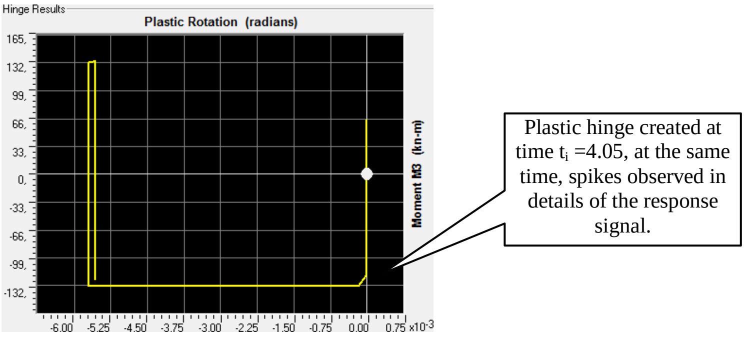

Figure 7. Moment-rotation hysteretic curve for base column of the single frame subjected to four time scale Athens earthquake record.

In the details of response signal it is also observed spikes at the times, t= 4.60s and t= 6.15s. These spikes correspond to the times when the hinges at the beam reach the yielding point for the third and fourth time as can be seen in figure 9. In this figure it is seems that the hinge starts from zero and have an elastic behavior until 3.91s where reach, for first time, the yield point. It remains in the post yield region until 3.98s and then rebounds, because of the change in direction of earthquake, and reaches again the yield point, for the second time, at 4.22s and remains in the post yield region until 4.30s. Then rebounds and reach, for the third time, the yielding point at time 4.60s, and remains in post yield region until 4.66s, then rebounds again and behaves elastically. Finally the hinge reach, for forth time, the yield point at time 6.15s, remains to the post yield region until the 6.22s and then rebounds and behave elastically until the end of the earthquake. All the times, where the plastic hinge reach the yielding point, (t= 3.91s, t= 4.22s, t= 4.60s, t= 6.15s), are observed as spikes in the wavelet analysis of the acceleration response signal in figure 8(b).

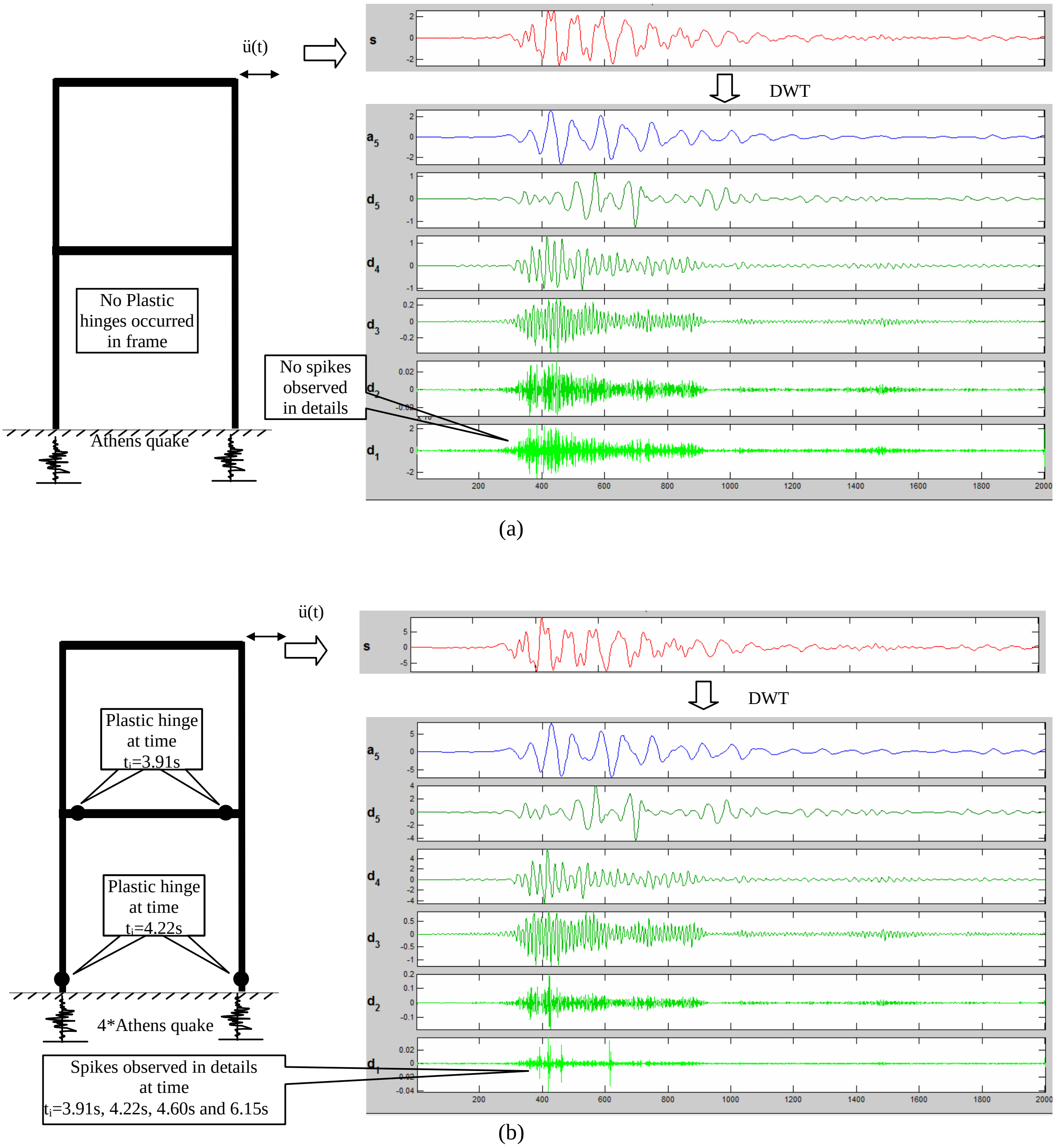

(a)

(b)

Figure 8. The approximation a5, and the details d1-d5 of the response acceleration signal, s, at the top of the frame subjected to (a) Athens earthquake signal and (b) four times, scale up, Athens earthquake signal.

The moment curvature curve for the base column is shown in figure 10. In this figure seems that the hinge reach the yield point at time 4.22s, which is the same time when the beam yields for second time. It is observed that when any structural element starts yielding for first time or rebounds and yields again for the subsequence times this phenomenon is imprinted as spikes in the wavelet analysis of the acceleration response of the signal.

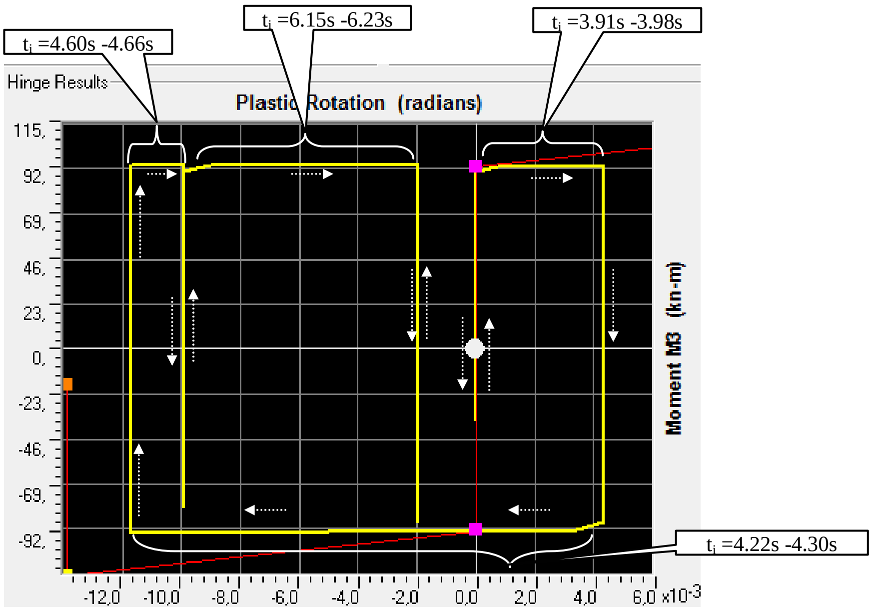

Figure 9. Moment-rotation hysteretic curve for fist floor beam of the two story frame subjected to four time scale Athens earthquake record.

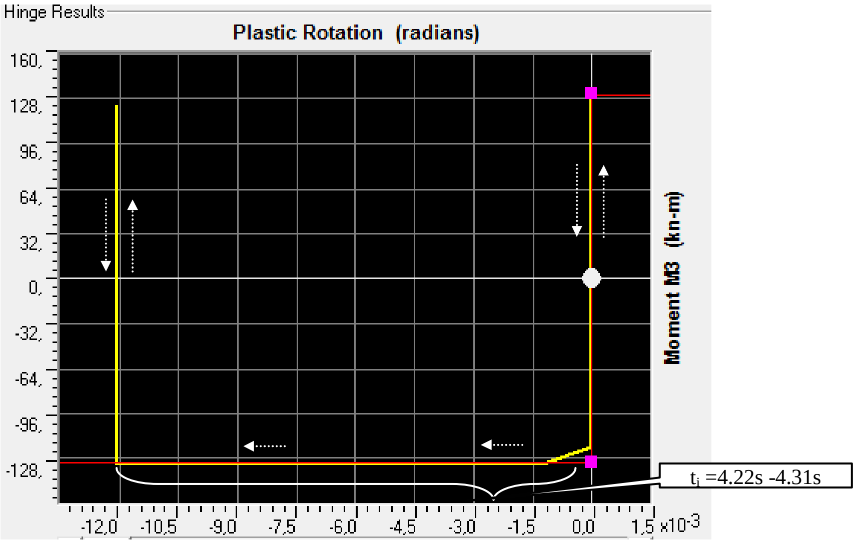

Figure 10. Moment-rotation hysteretic curve for base column of the two story frame subjected to four time scale Athens earthquake record.

Similar results are obtained in eight story building. In figure 11 are shown the locations of plastic hinges, (damage), the wavelet analysis of the response acceleration of the eighth floor of the frame subjected to Athens earthquake signal scaled with the factors 1 and 8 respectively. When the building subjected to the Athens earthquake signal no plastic hinges have appeared and no spikes in the details of the response signal were observed. When the earthquake was scaled up by a factor of 8, then plastic hinges, (damage), were created at the beams, between the time period 3.80s-4.11s. Plastic hinges were also created at the base columns at time 3.84s. In the details of the wavelet analysis of the response signal spikes are observed at the same period of the hinges creation.

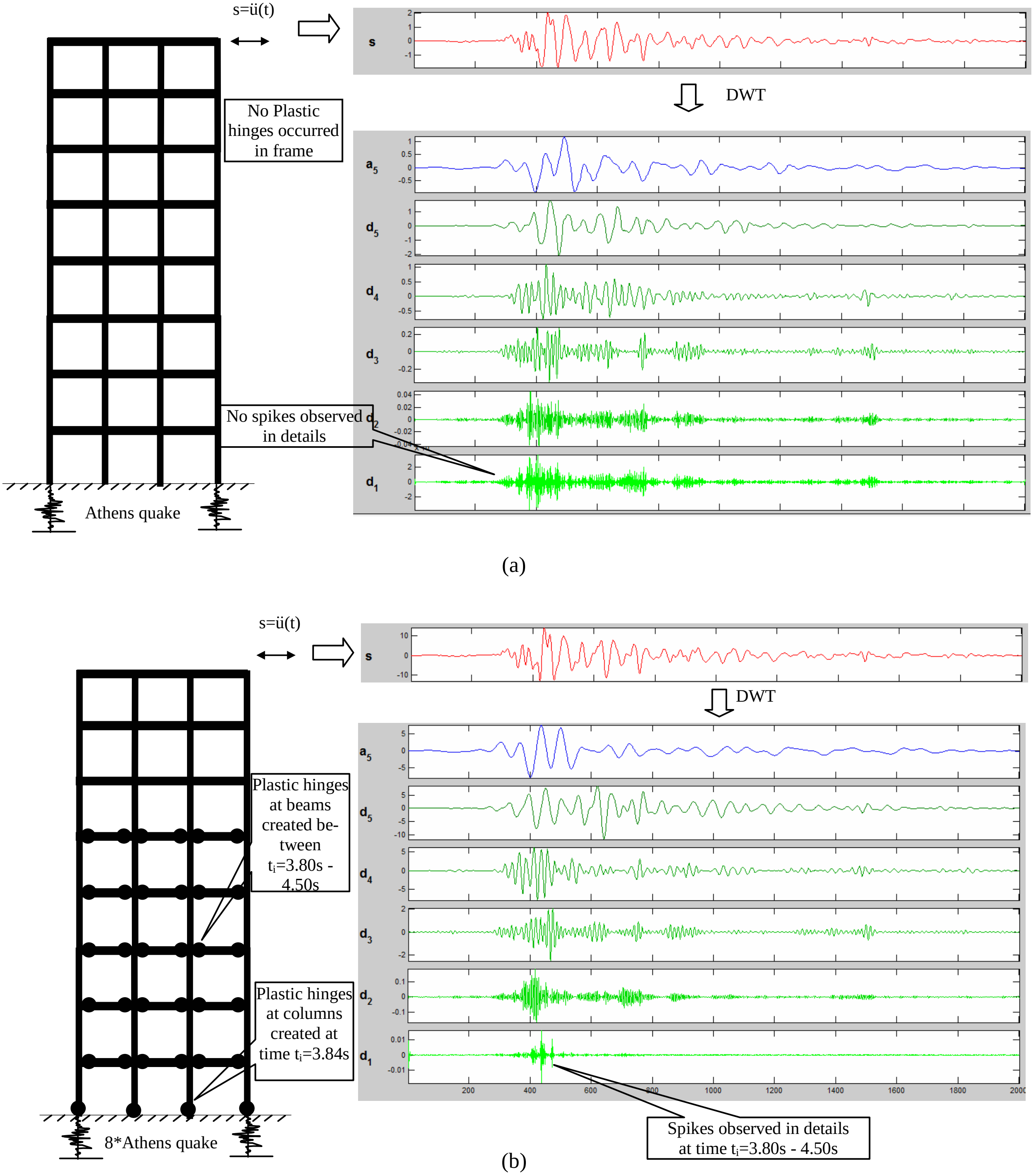

(a)

(b)

Figure 11. The approximation a5, and the details d1-d5 of the response acceleration signal, s, at the top of the frame subjected to (a) Athens earthquake signal and (b) eight times scale up Athens earthquake signal.

5 NOISE INFLUENCE

In the previous examples, the response data were obtained by the computer program without contain noise. In practice the presence of noise in measurement signals is unavoidable. In the work of Hera and Hou (2004) is shown the effect of noise to the wavelet approach. The effectiveness of the wavelet approach for structural health monitoring depends on the measurement noise level and the damage severity. The lower the level of noise is, the easier to detect the damage. As far as the damage level concerns, the higher the damage severity is, the easier to detect the damage by wavelet analysis. In this study the measurement noise was modelled as a Gaussian process with signal to noise ratio equal to 15%. A measurement noise was added to the acceleration response signal and then wavelet analysis was performed again. In order to detect spikes in the details of noise signal, the level of details and the order of the wavelet were increased. In this case, the level of details decomposition in the wavelet analysis was increased to twelve, (12), instant of five, (5), which was in the examples for signals without noise. The order of the wavelet which is used is also increased. For the noise signal the Daubechies wavelet of twelve order was used instant of fourth order which was used for the signals without noise.

Another factor that plays important role in the analysis of the noise signal is the sampling rate. The higher the sampling the better it is. In the numerical example the response signal without noise was obtained by non linear dynamic analysis where the sampling interval was 0.01 s. While, for the noise response signal was obtained by non linear dynamic analysis where, the sampling interval was decreased to 0.0001 s.

The wavelet analysis of the noise response acceleration signal, of the single story building is shown in figure 12. In this figure, are shown the approximation and the details of the response acceleration signal, s, contaminated with noise. In the detail level 9, a spike it is observed for time period between 4.00 to 4.10 s which is in agreement for the case of single story frame without noise.

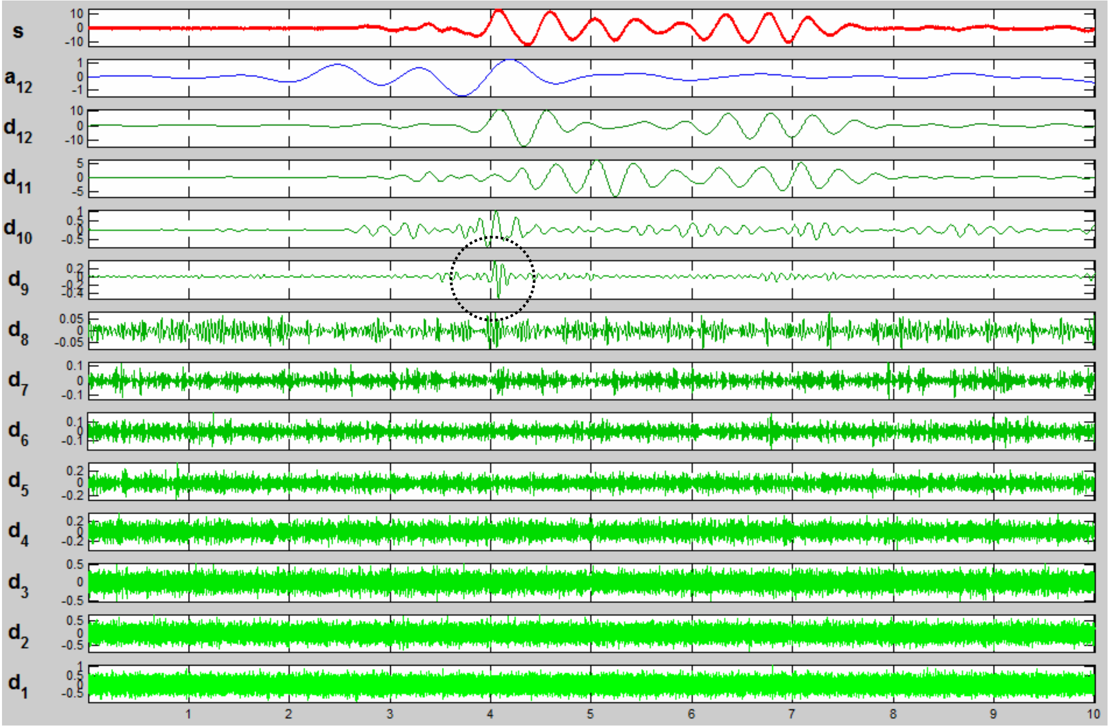

Figure 12. The approximation a12, and the details d1-d12 of the response acceleration signal, s, contaminated with noise, at the top of the single story frame subjected at four times scale up the Athens earthquake signal.

6 CONCLUSIONS

A discrete wavelet analysis for damage detection of frame structure subjected to earthquake excitation has been done. Wavelet analysis is a good tool to analyze the non-stationary dynamic behaviour of inelastic structures. It was shown that structural damage, which was introduced by non linear behaviour of structural elements, and the time that this occurred can be clearly detected by spikes in the details of discrete wavelet analysis of the response signal.

These spikes can also be observed in the case where the response signal contaminates noise. In order to detect the spikes of the noise signal the level of details and the order of the wavelet must be increased. The numerical results show the great promise of the wavelet approach for damage detection in structures subjected to earthquake excitation.

REFERENCES

[1] Kirmser PG. (1944). The effect of discontinuities of the natural frequency of beams. Proceedings American Society for Testing Materials, Philadelphia, PA. 44, 897-904

[2] Doebling, S. W., Farrar, C. R., Prime, M. B., and Shevitz, D. W. (1996). Damage identification and health monitoring of structural and mechanical systems from changes in their vibration characteristics: a literature review. *Rep. LA-l3070-MS,* Los Alamos National Laboratory, Los Alamos, N.M.

[3] Carden, E.P. and Fanning, P. (2004). Vibration based condition monitoring: a review. Structural Health Monitoring, 3, 355–377.

[4] Humar, J., Bagchi, A. and Xu, H.P. (2006). Performance of vibration-based techniques for the identification of structural damage. Structural Health Monitoring, 5, 215–241.

[5] Khoo, L.M., Mantena, P.R. and Jadhav, P. (2004). Structural damage assessment using vibration modal analysis. Structural Health Monitoring, 3, 177–194.

[6] Chang, P.C., Flatau, A. and Liu, S.C. (2003). Review paper: health monitoring of civil engineering. Structural Health Monitoring, 2, 257–267.

[7] Wu, X., Ghabossi, J., and Garrett, J. H. (1992). Use of neural networks in detection of structural damage. Computers and Structures, 42(4), 649-659.

[8] Tsou, P., and Shen, M. H. H. (1994). Structural damage detection and identification using neural networks. American Institute of Aeronautics and Astronautics Journal (AIAA), 32(1), 176-183.

[9] Masri S.F., Nakamura M., Chassiakos A. G. and Caughey T. K. (1996). Neural network approach to detection of changes in structural parameters. Journal of engineering mechanics, 122 (4), 350-360.

[10] Vanik, M. W., and Beck, J. L. (1997). A Bayesian probabilistic approach to structural health monitoring. Proceedings, International Workshop on Structural Health Monitoring: Current Status and Perspectives, Stanford University, Stanford, CA. 140-151.

[11] M. Chandrashekhar and Ranjan Ganguli. (2009). Structural Damage Detection Using Modal Curvature and Fuzzy Logic. Structural Health Monitoring, 8; 267-282.

[12] Friswell M.I. and Mottershead J.E. (1995) Finite Element Model Updating in Structural Dynamics, Kluwer Academic Publishers Group

[13] Costas Papadimitriou, Evangelos Ntotsios **(**2009). Structural model updating using vibration measurements. Proceedings Thematic Conference on Computational Methods in Structural Dynamics and Earthquake Engineering, ECCOMAS, COMPDYN, M. Papadrakakis, N.D. Lagaros, M. Fragiadakis (eds.), Rhodes, Greece, No CD 83

[14] Reigh, G. W., and Park, K. C. (1997). Localized system identification and structural health monitoring from vibration test data. Proceedings, American Institute of Aeronautics and Astronautics, AIAA, Reston, Va.

[15] Panagiotis Panetsos, Sergios Lambropoulos, Konstantinos Papadimitriou, Spyros Karamanos, Vassilios Lekidis, Christos Karakostas, (2006), Bridge health monitoring for egnatia odos bridge management system, Third European Workshop on Structural Health Monitoring, Organizers,Alfredo Guemes, Rafael Gallego Univ. Politecnica Madrid, Univ. Granada Granada, Spain.

[16] Marek Engelhardt Z Georgios E. Stavroulakis and Heinz Antes. (2006). Crack and flaw identification in elastodynamics using Kalman filter techniques, Computation Mechanics, 37; 249–265.

[17] Serdar Soyoz and Maria Q. Feng. (2008). Instantaneous damage detection of bridge structures and experimental verification. Structural Control Health Monitoring, 15;958–973.

[18] J. S. Sakellariou, S. D. Fassois. (2006). Stochastic output error vibration-based damage detection and assessment in structures under earthquake excitation. Journal of sound and vibration, 127; 1048-1067.

[19] Guido De Roeck and Edwin Reynders. (2009). Exploring the limits and extending the borders of structural health monitoring. Proceedings Thematic Conference on Computational Methods in Structural Dynamics and Earthquake Engineering, COMPDYN, ECCOMAS, M. Papadrakakis, N.D. Lagaros, M. Fragiadakis (eds.), Rhodes, Greece, No CD 166.

[20] Alessio Medda and Victor DeBrunner, Near-field Sub-band Beamforming for Damage Detection in Bridges Structural Health Monitoring, 2009, 8, 313–329.

[21] Staszewski WJ. (1998). Structural and mechanical damage detection using wavelets. Shock Vibration Digest, 30(6);457–472.

[22] Newland D. E., (1993). An introduction to random vibrations, spectral and wavelet analysis. Longman Singapore publishers Pte Ltd.

[23] Reda Taha, M.M., Noureldin, A., Lucero, J.L. and Baca, T.J. (2006). Wavelet transform for structural health monitoring: a compendium of uses and features. Structural Health Monitoring, 5, 267–295.

[24] Masuda, A., Nakaoka, A., Sone, A., and Yamamoto, S. (1995). Health monitoring system of structures based on orthonormal wavelet transform. Seismic Engineering, 312; 161-167.

[25] Masuda, Y. Hashimoto and A. Sone. (2003). Experimental verification of wavelet-based structural damage identification method. Structural Health Monitoring From Diagnostics & Prognostics to Structural Health Management. Edited by F.K. Chang, DEStech Publications, pp.517-524.

[26] Hansang Kim, Hani Melhem. (2004). Damage detection of structures by wavelet analysis. Engineering Structures, 26; 347–362.

[27] Z. Hou, M. Noori, and R. St. Arnand. (2000). Wavelet-based approach for structural damage detection. Journal of Engineering Mechanics, 126(7); 677-683.

[28] Adriana Hera and Zhikun Hou. (2004). Application of Wavelet Approach for ASCE Structural Health Monitoring Benchmark Studies. ASCE Journal of Engineering Mechanics, 130(1); 96-104.

[29] Johnson, E. A., Lam, H. F., Katafygiotis, L. S., and Beck, J. L. (2004). Phase I IASC-ASCE structural health monitoring benchmark problem using simulated data. ASCE Journal Engineering Mechanics, 130(1); 3–15.

[30] Khatam, H., Golafshani, A.A., Beheshti-Aval, S.B. and Noori, M. (2007). Harmonic class loading for damage identification in beams using wavelet analysis. Structural Health Monitoring, 6, 67–80.

[31] M.A. Lotfollahi Yaghin and M.A. Hesari. (2008). Using Wavelet Analysis In Crack Detection at The Arch Concrete Dam Under Frequency Analysis With FEM. Research India Publications, Journal of Wavelet Theory and Applications, 2(1);61–81.

[32] Noh, H. Y., Nair, K., Lignos, D. G., Kiremidjian, A. (2009). Application of Wavelet Coefficient Energies of Stationary and Non-stationary Response Signals for Structural Damage Diagnosis. 7th International Workshop on Structural Health Monitoring, Stanford, CA, September 9-11, 2009.

[33] K. Krishnan Nair, Anne S. Kiremidjian. (2009). Derivation of a Damage Sensitive Feature Using the Haar Wavelet Transform. ASME, Journal of Applied Mechanics, , 76(6); 610151-9.

[34] S. T.S. Bukkapatnam, J. M. Nichols, M. Seaver, S. T. Trickey and M. Hunter. (2005). A Wavelet-based, Distortion Energy Approach to Structural Health Monitoring, Structural Health Monitoring; 4; 247-258.

[35] S. Patsias and W. J. Staszewskiy. (2002). Damage Detection Using Optical Measurements and Wavelets, Structural Health Monitoring, 1; 2-22.

[36] www.csiberkeley.com.

[37] http://www.mathworks.com.

COMPDYN 2011
III ECCOMAS Thematic Conference on
Computational Methods in Structural Dynamics and Earthquake Engineering
M. Papadrakakis, M. Fragiadakis, V. Plevris (eds.)
Corfu, Greece, 25–28 May 2011

DEVELOPMENT OF A FAMILY OF UNCONDITIONALLY STABLE EXPLICIT DIRECT INTEGRATION ALGORITHMS WITH CONTROLLABLE NUMERICAL DAMPING USING DISCRETE CONTROL THEORY

Cheng Chen[1], **and James M. Ricles**[2]

[1] School of Engineering, San Francisco State University
San Francisco, CA 94132
e-mail: chcsfsu@sfsu.edu

[2] Department of Civil and Environmental Engineering, Lehigh University
Bethlehem, PA 94132
jmr5@lehigh.edu

Keywords: Numerical Algorithm, Control Theory, Stability, Structural Dynamics, Numerical Damping.

Abstract. *Integration algorithms are typically utilized to solve temporally discretized equations of motion in structural dynamics. Stability is an important property to be considered when selecting the proper integration algorithm for analysis of structures with a large number of degrees of freedom. The recent development of real-time structural testing brings more challenges to the integration algorithm. An explicit integration algorithm is more favorable in real-time structural testing because of its computational efficiency. However, the presence of numerical errors will lead to the spurious growth of high-frequency response in the dynamic analysis and the presence of inevitable experimental errors will aggravate this effect during real-time structural testing. It is therefore advantageous for an explicit integration algorithm to possess numerical damping to suppress any spurious participation of the high-frequency response while the lower modes are accurately integrated. This paper presents the development of a family of explicit direct integration algorithms with controllable numerical damping. Discrete control theory is utilized to assign proper stable poles to the discrete transfer function of the integrations algorithms to achieve unconditional stability and numerical damping. The properties of the proposed algorithm are investigated and compared with other well established algorithms such as the Newmark family of integration algorithms and the CR integration algorithm.*

1 INTRODUCTION

Integration algorithms are usually utilized to solve the equations of motion of structures subjected to external excitations. Various integration algorithms have been developed and applied in structural dynamics such as the Newmark Family of integration algorithms [1] and the Hilber-Hughes-Taylor α-method [2]. Various methods have been used to develop integration algorithms, including Taylor series expansions, weighted residual methods, Hamilton's principle, and least-squares methods [3]. Currently available integration algorithms can usually be classified as either explicit or implicit. An integration algorithm is explicit if the displacements for the next time step can be determined from the accelerations, velocities and displacements at the current and previous time step, otherwise it is implicit. The implicit integration algorithms are usually unconditionally stable such as the Newmark method with constant average acceleration and the HHT α-method, while the explicit integration algorithms are often conditionally stable, including the Newmark explicit method and the central difference method. In many structural dynamics applications, where iterations are not concerned in the analysis, the implicit integration algorithms with unconditional stability are generally preferred over conditionally stable explicit integration algorithms.

In addition to the structural dynamic analysis, integration algorithms are also applied in online structural experiments, where they are utilized to solve the dynamics of a prototype structure to sequentially determine the displacement response of an experimental structure in the laboratory. This application was first investigated by Takanashi *et al.* [4] and then by Mahin and Shing [5], and can be categorized as quasi-static pseudodynamic testing or quasi-static substructure testing. It is believed that by having the structural components (usually difficult to model numerically) tested in the laboratory and keeping the remainder of the structural system modeled analytically, the response of the entire structure under a selected ground motion can be replicated in an economic and efficient manner. Both explicit and implicit integration algorithms have been utilized in quasi-static pseudodynamic and substructure testing [5, 6]. Since the experiments are conducted in an extended time scale (i.e., quasi-statically), the required iterations for implicit integration algorithms are not critical and the implicit integration algorithms therefore are often used because of their unconditional stability.

Recent earthquake engineering research have advanced the quasi-static pseudodynamic and substructures testing methods to real-time pseudodynamic testing [7] and real-time hybrid simulation [8] to accommodate rate-dependent behavior in the experimental specimens. These two structural testing methods will be referred to as real-time testing hereafter. Unlike the conventional experimental methods, real-time testing requires that the command displacements from the integration algorithm be applied accurately to the experimental substructures in a real-time manner. Integration algorithms therefore are required to solve the equations of motion and compute the command displacements in a timely manner so as not to introduce any time delay in the real-time test. This poses a great challenge to the integration algorithm when the real-time test involves a complex structure with a large number of degrees of freedom. Explicit integration algorithms thus present more attractive solution for real-time testing than implicit integration algorithms since no iterations are necessary.

More recently, several unconditionally stable explicit integration algorithms were developed by researchers to enable real-time structural tests [9, 10]. Unlike other available integration algorithms, integration parameters of these algorithms are defined as functions of the linear elastic properties of the structure to be analyzed. By carefully selecting the integration parameters, these algorithms possess both explicitness and unconditional stability. When applied for nonlinear structural behavior, Chen and Ricles [11, 12] showed that these algorithms maintain the stability when the structure has softening behavior. The explicitness and unconditional stability of these integration algorithm present great potential for real-time structural testing. Chen *et al.* [13] implemented the unconditional explicit CR integration algorithm for real-time hybrid simulation of structures with an elastomeric damper. The experiment results were compared with those using the existing HHT α-method with a fixed number of substep iteration [14]. Good agreement was observed, indicating that the unconditional explicit CR algorithm is applicable for real-time testing. Chen *et al.* [15] further extended the application of the CR algorithm for the real-time hybrid simulation of a moment resisting frame (MRF) with magneto-rheological (MR) dampers in passive mode. The prototype MRF had a total of 122 degrees of freedom and 71 elements. The experimental results was later compared with pure numerical simulation by Chen *et al.* [16]. Good agreement further validated the effectiveness of the CR algorithm for real-time testing. However, it was observed that the experimental results, especially the restoring forces in the experimental substructures (i.e., the MR dampers), had high frequency noise. Small oscillation was also observed in the structural displacement response. These high frequency mode responses are attributed to the spatially discretized equations of motion and do not necessarily represent the true behavior of the prototype structure under earthquakes. In addition, the presence of numerical errors will lead to the spurious growth of high-frequency response and the inevitable experimental errors will aggravate this effect in real-time tests. Therefore, it is advantageous for an algorithm to possess numerical damping to suppress any spurious participation of the high-frequency response and minimize the effect of numerical and experimental errors, while the lower modes can be integrated accurately. However, the current unconditionally stable explicit CR integration algorithm has zero or only little numerical damping properties. It is thus desirable to introduce controllable numerical damping into the algorithm while maintaining its explicitness and unconditional stability. This paper presents the development of a family of unconditionally stable explicit integration algorithm using the discrete control theory.

2 INTEGRATION ALGORITHM AND DISCRETE TRANSFER FUNCTION FOR SDOF STRUCTURE

Consider a single-degree-of-freedom (SDOF) linear elastic structure represented by the following differential equation of motion under external excitation *F*(*t*):

$$m \cdot \ddot{x}(\mathrm{t}) + c \cdot \dot{x}(\mathrm{t}) + k \cdot x(t) = F(t) \tag{1a}$$

where *m*, *c* and *k* are the mass, viscous damping and linear elastic stiffness of the SDOF structure, respectively; and $x(t)$, $\dot{x}(t)$, $\ddot{x}(t)$ are the displacement, velocity and acceleration of the SDOF structure, respectively. Integration algorithms in structural dynamics are usually applied to solve the temporally discretized equation of motion of Eq. (1a) for structural response, which can be written as:

$$m \cdot \ddot{x}_{\mathrm{i}+1} + c \cdot \dot{x}_{\mathrm{i}+1} + k \cdot x_{\mathrm{i}+1} = F_{\mathrm{i}+1} \tag{1b}$$

where x_{i+1}, $\dot{x}_{i+1}$, $\ddot{x}_{i+1}$ are the displacement, velocity and acceleration of the SDOF structure at the $(i+1)^{\mathrm{th}}$ time step, respectively; and $F_{\mathrm{i+1}}$ is the value of excitation *F*(*t*) at the $(i+1)^{\mathrm{th}}$ time step.

To obtain an explicit integration algorithm, the variation of the displacement and velocity over the time step can be defined as

$$\dot{x}_{\mathrm{i}+1} = \dot{x}_{\mathrm{i}} + \alpha_1 \cdot \Delta t \cdot \ddot{x}_{\mathrm{i}} \tag{2a}$$

$$x_{i+1} = x_i + \Delta t \cdot \dot{x}_{\mathrm{i}} + \alpha_2 \cdot \Delta t^2 \cdot \ddot{x}_{\mathrm{i}} \tag{2b}$$

where α_1 and α_2 are integration parameters and will be determined later; x_i, $\dot{x}_i$, $\ddot{x}_i$ are the displacement, velocity and acceleration of the SDOF structure at the i^{th} time step, respectively; and Δt is the time step for the dynamic analysis.

It can be observed that both the displacement x_{i+1} and velocity $\dot{x}_{i+1}$ in Eqs. (2a) and 2(b) are explicit since they are only dependent on the structural response of the previous time step. This explicitness will lead to significant computational efficiency when the algorithm is used in dynamic analysis structures subjected to earthquakes. Eqs. (2a) and (2b) were also used by Chen and Ricles [10] to develop the unconditionally stable CR explicit integration algorithm. The discrete transfer function G(z) for the integration algorithms can be derived by substituting Eqs. (2a) and (2b) into Eq. (1b), whereby it can be written in the following general form

$$G(z) = \frac{X(z)}{F(z)} = \frac{n_2 z^2 + n_1 z + n_0}{d_2 z^2 + d_1 z + d_0} \tag{3}$$

where $G(z)$ is a discrete transfer function relating the displacement response of the structure and the external excitation; $X(z)$ and $F(z)$ are discrete z-transforms of the displacement response x_{i+1} and excitation force F_{i+1}, respectively; z is the complex variable in the discrete z-domain; n_2, n_1, n_0, d_2, d_1 and d_0 are coefficients of the numerator and denominator of the discrete transfer function $G(z)$, respectively. The coefficients of the discrete transfer function are tabulated in Table 1 for the new algorithms. It can be observed that the coefficients in Table 1 are dependent on the structure properties (m, c, and k) and the integration time step Δt as well as the two integration parameters (α_1 and α_2).

Numerator		Denominator	
n_2	0	d_2	m
n_1	$\alpha_2 \cdot \Delta t^2$	d_1	$\alpha_2 \cdot k \cdot \Delta t^2 + \alpha_1 \cdot c \cdot \Delta t - 2m$
n_0	$(\alpha_1 - \alpha_2) \cdot \Delta t^2$	d_0	$(\alpha_1 - \alpha_2) \cdot k \cdot \Delta t^2 - \alpha_1 \cdot c \cdot \Delta t + m$

Table 1. Coefficients of G(z) for the new integration algorithm

Chen and Ricles [10] indicated that the poles of the discrete transfer function $G(z)$ in Eq. (3) determine the properties of the corresponding integration algorithm including the stability and accuracy. The complex poles of $G(z)$ in Eq. (3) can be written in the following form

$$p_{1,2} = \sigma \pm \varepsilon \cdot i = \exp[\overline{\Omega} \cdot (-\zeta_{eq} \pm i\sqrt{1-\zeta_{eq}^2})] \tag{4}$$

where σ and ε are the real components, and i is the imaginary unit defined as $i = \sqrt{-1}$; the apparent frequency $\overline{\Omega}$ and the equivalent damping ratio ζ_{eq} are defined as

$$\overline{\Omega} = \tan^{-1}(\varepsilon / \sigma)/(\sqrt{1-\zeta_{eq}^2}) \tag{5a}$$

$$\zeta_{eq} = -\ln\left(\sigma^2 + \varepsilon^2\right)/\,2\overline{\Omega} \tag{5b}$$

The integration algorithm will be unconditionally stable if the poles in Eq. (4) are always located inside or on the unit circle of the discrete z-domain as shown in Figure 1. Otherwise, the algorithm is conditionally stable. Compared with the conventional stability criterion [17], the magnitude of the complex poles in Eq. (4) represent the spectral radius, while Eqs. (5a) and (5b) determine the period elongation and numerical damping of the integration algorithm.

To achieve unconditional stability, Chen and Ricles [10] used the Tustin transform [18] to discretize the continuous poles and assigned the resulting discrete poles to the discrete transfer function in Eq. (3), which leads to the integration parameters α_1 and α_2 for the unconditionally stable explicit CR algorithm.

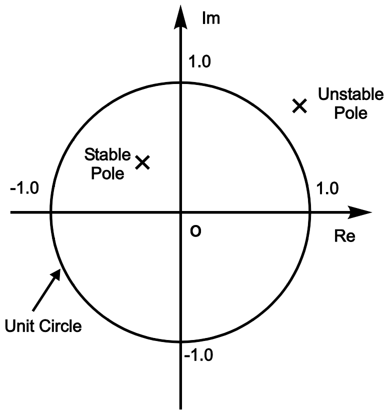

Figure 1: Schematic of Stable and Unstable Poles in Complex z-domain.

3 INTEGRATION PARAMETER DERIVATION FOR INTEGRATION ALGORITHMS WITH NUMERICAL DAMPING

Chen and Ricles [11, 12] demonstrated that an integration algorithm can schematically be represented by a open-loop block diagram in Figure 2(a), or by a closed-loop block diagram in Figure 2(b). The inputs and the outputs in Figures 1(a) and 1(b) are the external excitation $F(t)$ and the structural response $x(t)$, respectively. The block $G(z)$ in Figure 1(a) represents the discrete transfer function in Eq. (3) for the integration algorithm, while the block k in Figure 1(b) is the linear elastic stiffness of the SDOF structure and $G'(z)$ is referred to as the open-loop transfer function for the integration algorithm.

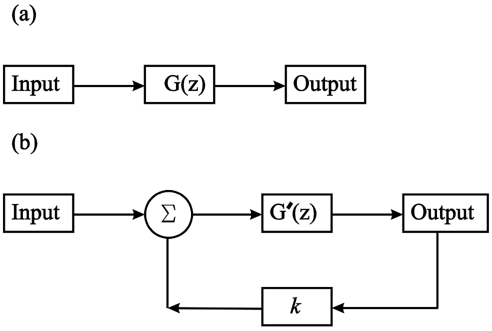

Figure 2: Block diagram representation of: (a) open loop system; and (b) closed loop system.

The relationship between the discrete transfer functions $G(z)$ and $G'(z)$ can be expressed as

$$G(z) = \frac{G'(z)}{1 + k \cdot G'(z)} \tag{6}$$

To determine the parameters for the integration algorithms defined by Eqs. (2a) and (2b), the open-loop transfer function $G'(z)$ for the Newmark method with constant average acceleration is utilized in this paper, where its coefficients are tabulated in Table 2 and the discrete transfer function of $G'(z)$ can be written as

$$G'(z) = \frac{(z^2 + 2z + 1)\cdot \Delta t^2}{(4m + 2c\cdot\Delta t)\cdot z^2 - 8m\cdot z + (4m - 2c\cdot\Delta t)} \tag{7a}$$

Numerator		Denominator	
n_2	Δt^2	d_2	$4m + 2c\cdot\Delta t$
n_1	$2\Delta t^2$	d_2	$-8m$
n_0	Δt^2	d_0	$4m - 2c\cdot\Delta t$

Table 2. Coefficients of G'(z) for the Newmark method with constant average acceleration.

It can be observed that the discrete transfer function $G'(z)$ has duplicate zeros at $z = -1$. To develop an integration algorithm with numerical damping, the transfer function $G'(z)$ in Eq. (7a) is assigned to have two duplicate zeros at $z = -\lambda$, which can then be written as

$$G'(z) = \frac{(z + \lambda)^2 \cdot \Delta t^2}{(4m + 2c\cdot\Delta t)\cdot z^2 - 8m\cdot z + (4m - 2c\cdot\Delta t)} \tag{7b}$$

where λ is a positive real number and has a value between zero and one. If Eq. (7b) is used for the open-loop transfer function, the corresponding closed-loop transfer function can be derived using Eq. (6) as

$$G(z) = \frac{X(z)}{F(z)} = \frac{(z + \lambda)^2 \cdot \Delta t^2}{(4m + 2c\cdot\Delta t + k\cdot\Delta t^2)\cdot z^2 + (-8m + 2\lambda\cdot k\cdot\Delta t^2)\cdot z + (4m - 2c\cdot\Delta t + k\cdot\Delta t^2)} \tag{8a}$$

The poles of the discrete transfer function in Eq. (8a) can be derived by setting the denominator equal to zero and solving for the values of z:

$$(4m + 2c\cdot\Delta t + k\cdot\Delta t^2)\cdot z^2 + (-8m + 2\lambda\cdot k\cdot\Delta t^2)\cdot z + (4m - 2c\cdot\Delta t + k\cdot\Delta t^2) = 0 \tag{8b}$$

Assigning the poles of the closed-loop transfer function of Eq. (8b) to the transfer function $G(z)$ for the integration algorithms defined by Eqs. (2a) and (2b), and solving for α_1 and α_2 leads to

$$\alpha_1 = \frac{2m\cdot(\lambda^2 + 2\lambda + 1)}{(2\lambda^2 + 4\lambda + 2)\cdot m + (3 + 2\lambda - \lambda^2)\cdot c\cdot\Delta t + 2k\cdot\Delta t^2} \tag{9a}$$

$$\alpha_2 = \frac{4m\cdot(\lambda + 1)}{(2\lambda^2 + 4\lambda + 2)\cdot m + (3 + 2\lambda - \lambda^2)\cdot c\cdot\Delta t + 2k\cdot\Delta t^2} \tag{9b}$$

For different values of the parameter λ, Eqs. (9a) and (9b) lead to different sets of integration parameters α_1 and α_2, and a family of explicit integration algorithms, which will be referred to the new algorithm. It can also be derived that for the case of λ equal to 1.0, Eqs. (9a) and (9b) reduce to

$$\alpha_1 = \alpha_2 = \frac{4m}{4m + 2c\cdot\Delta t + k\cdot\Delta t^2} \tag{10}$$

Eq. (10) gives the integration parameters for the unconditionally stable explicit CR integration algorithm [10]. This indicates that the CR algorithm can be considered as a special case of the new integration algorithms.

4 STABILITY AND ACCURACY ANALYSIS

With the integration parameters defined in Eqs. (9a) and 9(b), the discrete transfer function for the new family of integration algorithms can be derived and written in the general form of Eq. (3). The coefficients are tabulated in Table 3. The stability and accuracy of the family of algorithms are then investigated using Eqs. (4) through (5b).

Numerator		Denominator	
n_2	0	d_2	$2\cdot k\cdot\Delta t^2-(\lambda+1)\cdot(\lambda-3)\cdot c\cdot\Delta t+2(\lambda+1)^2\cdot m$
n_1	$4(\lambda+1)\cdot\Delta t^2$	d_1	$4\lambda\cdot k\cdot\Delta t^2+4(\lambda^2-1)\cdot c\cdot\Delta t-4(\lambda+1)^2\cdot m$
n_0	$2(\lambda^2-1)\cdot\Delta t^2$	d_0	$2\lambda^2\cdot k\cdot\Delta t^2-(\lambda+1)\cdot(3\lambda-1)\cdot c\cdot\Delta t+2(\lambda+1)^2\cdot m$

Table 3. Coefficients of G(z) for the new algorithms.

4.1 Stability analysis for linear elastic SDOF structures

Figure 3 shows the spectral radius of the new family of integration algorithms for a linear elastic SDOF structure, where ω_n is the natural frequency of the SDOF structure. Zero viscous damping (i.e., $c=0$) is assumed to represent the most critical case for stability. Different values are used for the parameter λ, including $\lambda=1.0$, 0.75 and 0.5. Also presented in Figure 3 is the Newmark method with constant average acceleration. It can be observed that for selected values of λ in Figure 3, the new algorithm is stable for $\omega_n\Delta t$ up to 6.0. It can be further shown that the new algorithm is unconditional stable with λ between zero and one for any value of $\omega_n\Delta t$. Figure 3 also shows that for λ equal to 1.0, the new algorithm has the same spectral radius as the CR algorithm. This further proves that the CR algorithm is a special case of the new family of integration algorithms.

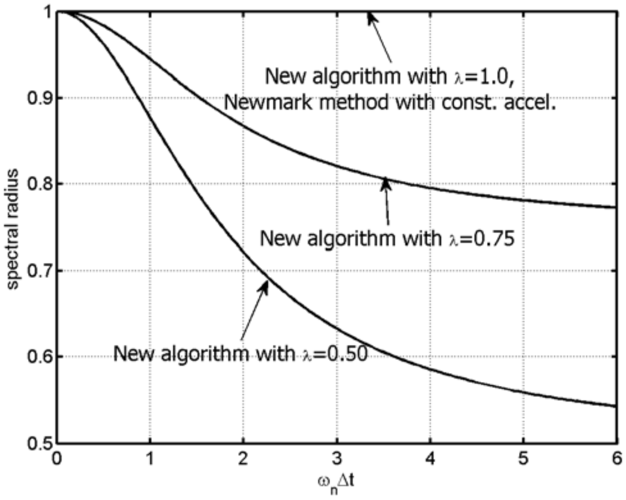

Figure 3: Spectral radius for the new family of integration algorithms.

4.2 Accuracy analysis for linear elastic SDOF structures

The accuracy of the family of new integration algorithms is analyzed using numerical damping (ND) and period elongation (PE). The SDOF structure is assumed to have zero inherent viscous damping. The equivalent damping computed from Eq. (5b) therefore represents the numerical damping introduced by the new algorithms. Cases with the values of λ equal to 1.0, 0.75 and 0.5 are considered. Figure 4 shows the numerical damping of the new algorithms, where it is compared with the Newmark method with constant average acceleration integration algorithm. The new algorithm with λ=1.0 and the Newmark method with constant average acceleration have almost zero numerical damping. When λ takes values of 0.75 and 0.5, the new algorithm is shown to introduce significant numerical damping, approaching 25% and 10% for values of $\omega_n\Delta t$ greater than 3.0, respectively. This numerical damping will help to minimize the effects of unrealistic higher mode response and the experimental errors during the structural experiments. However, Figure 4 also shows that the new algorithm introduces numerical damping for small values of $\omega_n\Delta t$ smaller than 3.0.

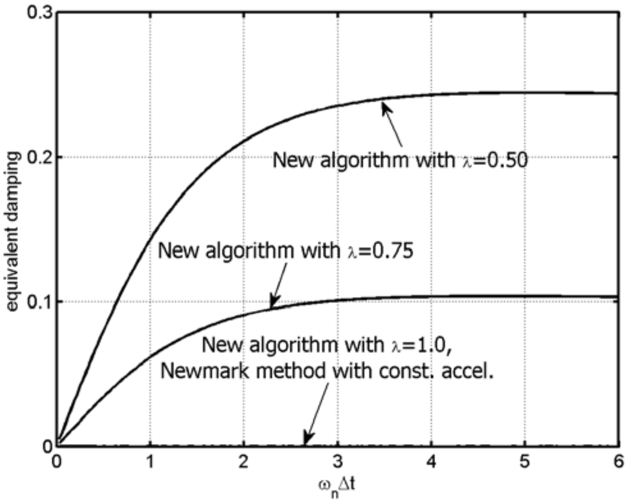

Figure 4. Numerical damping of the new algorithm.

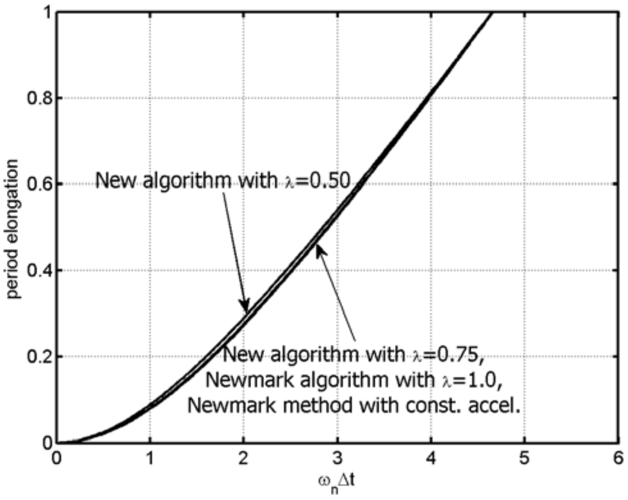

Figure 5. Period elongation of the new algorithm.

The period elongation presented in Figure 5 is observed to be almost same for the new algorithms for the various values of λ. The new algorithm with λ=1.0 is observed to be identical as that of the Newmark method with constant average acceleration. The new algorithm is shown to introduce period elongation for all three values of λ equal to 1.0, 0.75 and 0.5, but nearly identical as that of the Newmark method with constant acceleration for all cases.

4.3 Stability analysis for nonlinear SDOF structure

The above analysis indicates that the new family of explicit integration algorithms have comparable stability and accuracy properties as the Newmark method with constant average acceleration. Application of an integration algorithm for structural dynamic analysis often involves nonlinear structural behavior. Chen and Ricles [11, 12] proposed to use the discrete transfer function to analyze the stability limits of direct integration algorithms for nonlinear structural behavior. For a SDOF nonlinear structure, the equation of motion in Eq. (2) can be revised as

$$m \cdot \ddot{x}_{i+1} + c \cdot \dot{x}_{i+1} + r_{i+1} = F_{i+1} \tag{11a}$$

In Eq. (11a), r_{i+1} is the restoring force of the nonlinear SDOF structure at the $(i+1)^{\text{th}}$ time step. Eq. (11a) can be written in an incremental form as

$$m \cdot \Delta\ddot{x}_i + c \cdot \Delta\dot{x}_i + \cdot \Delta r_i = \Delta F_i \tag{11b}$$

The increments of acceleration $\Delta\ddot{x}_i$, velocity $\Delta\dot{x}_i$ and restoring force Δr_i are defined as $\Delta\ddot{x}_i = \ddot{x}_{i+1} - \ddot{x}_i$, $\Delta\dot{x}_i = \dot{x}_{i+1} - \dot{x}_i$ and $\Delta r_i = r_{i+1} - r_i$. For small values of Δt, the increment of restoring force can be approximated as $\Delta r_i = r_{i+1} - r_i = k_t \cdot \Delta x_i$ [17], where k_t is the tangent stiffness of the nonlinear SDOF structure. Using the open loop block diagram in Figure 2(b), the new integration algorithms can be represented by an open-loop transfer function G'(z) with the restoring force expressed by a varying feedback gain representing the varying stiffness [11]. The open-loop discrete transfer function can again be written in the general form in Eq. (3) and its coefficients are tabulated in Table 4.

Numerator		Denominator	
n_2	0	d_2	$2 \cdot k \cdot \Delta t^2 - (\lambda+1) \cdot (\lambda-3) \cdot c \cdot \Delta t + 2(\lambda+1)^2 \cdot m$
n_1	$4(\lambda+1) \cdot \Delta t^2$	d_1	$-4k \cdot \Delta t^2 + 4(\lambda^2-1) \cdot c \cdot \Delta t - 4(\lambda+1)^2 \cdot m$
n_0	$2(\lambda^2-1) \cdot \Delta t^2$	d_0	$2k \cdot \Delta t^2 - (\lambda+1) \cdot (3\lambda-1) \cdot c \cdot \Delta t + 2(\lambda+1)^2 \cdot m$

Table 4: Coefficients of G'(z) for the new algorithms.

The root locus approach is then used to determine the stability limit of the new family of explicit integration algorithms. Figure 6 shows a typical root locus for the open-loop transfer function with λ equal to 1.0. It can be observed that one branch of the root loci falls outside the unit circle. Therefore the new algorithm with is only stable for a finite range of stiffness values. The root locus plot crosses the unit circle at $z = -1$, and the stability limit for the improved CR algorithm can therefore be solved by substituting $z = -1$ into the denominator of the closed-loop transfer function derived from G'(z), whereby

$$\begin{aligned}
&[2 \cdot k \cdot \Delta t^2 - (\lambda+1) \cdot (\lambda-3) \cdot c \cdot \Delta t + 2(\lambda+1)^2 \cdot m] \cdot z^2 - [4(k - k_t(1+\lambda) \cdot \Delta t^2 \\
&- 4(\lambda^2-1) \cdot c \cdot \Delta t + 4(\lambda+1)^2 \cdot m] \cdot z + [2(k - k_t + \lambda^2 k_t) \cdot \Delta t^2 - (\lambda+1) \cdot (3\lambda-1) \cdot c \cdot \Delta t \\
&+ 2(\lambda+1)^2 \cdot m]\Big|_{z=-1} = 0
\end{aligned} \tag{12}$$

Solving Eq. (12) for k_t leads to

$$k_t \le \frac{4[-k \cdot \Delta t^2 + (\lambda^2 - 1) \cdot c \cdot \Delta t - m \cdot (\lambda + 1)^2]}{(\lambda - 3) \cdot (\lambda + 1)\Delta t^2} \tag{13a}$$

Eq. (13a) gives the stability limit for the new algorithms when applied to nonlinear SDOF structures. The stability limit in Eq. (13a) is observed to be dependent on the parameter λ as well as the structure properties (*m*, *c*, and *k*) and the integration time step *Δt*.

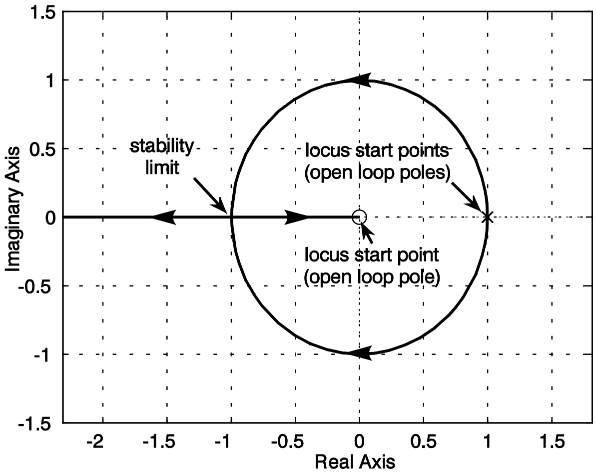

Figure 6: Typical root locus of the open loop transfer function *G'*(*z*) for the new integration algorithm (λ=1.0).

Eq. (13a) can be revised and expressed as

$$\left(\frac{k_t}{m}\right) \cdot \Delta t^2 \le \frac{4[-\omega_n^2 \Delta t^2 + (\lambda^2 - 1) \cdot 2\zeta \cdot \omega_n \Delta t - (\lambda + 1)^2]}{(\lambda - 3) \cdot (\lambda + 1)} \tag{13b}$$

where ζ is the inherent viscous damping ratio of the SDOF structure. Figure 7 shows the variation of the stability limit in Eq. (13b) with respect to the value of λ for the case of ζ=0.0. It can be observed that larger values of λ would lead to a larger stability limit.

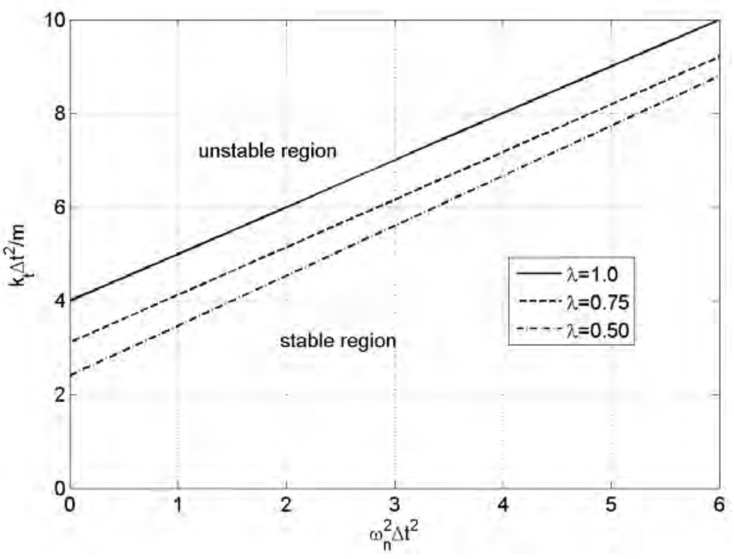

Figure 7: Stability limits for the new algorithms applied to nonlinear SDOF structure.

For the case of λ equal to one, the stability limit in Eq. (13) reduces to

$$k_t \leq \frac{k \cdot \Delta t^2 + 4m}{\Delta t^2} \tag{14a}$$

Eq. (14a) is same as the stability limit for the CR algorithm applied to a nonlinear structure [11]. When the algorithm is applied to a linear elastic structure, i.e., $k_t = k$, the stability limit in Eq. (13) reduces to

$$k\Delta t^2 \leq \frac{4[(\lambda^2 - 1) \cdot c \cdot \Delta t - m \cdot (\lambda + 1)^2]}{(\lambda - 3) \cdot (\lambda + 1) + 4} \tag{14b}$$

For the case of λ equal to one, the stability limit in Eq. (14b) can be further simplified as $k\Delta t^2 \leq \infty$, which implies that the algorithm is stable for all values of ω_n and Δt.

5 SUMMARY AND CONCLUSIONS

This paper presents the development of a new family of unconditionally stable explicit integration algorithms with controllable numerical damping using the discrete control theory. A parameter λ is utilized to introduce and control the numerical damping for the new algorithms. Using different values of λ between zero and one results in different properties of the new algorithms. The stability of the algorithm is investigated for both linear and nonlinear structures. The new algorithms are demonstrated to be unconditionally stable for a linear elastic structure and conditionally stable for a nonlinear structure. The accuracy of the new algorithms is investigated for linear elastic structures in terms of numerical damping and period elongation. For the range of the parameter λ investigated in the present study, the new algorithm is shown to introduce small period elongation and significant numerical damping for high frequencies. This makes this new algorithms especially appealing for real-time structural testing.

REFERENCES

[1] N.M. Newmark, A Method of Computation for Structural Dynamics. *Journal of Engineering Mechanics Division* (ASCE), 85, EM3, 67-94, 1959.

[2] H.M. Hilber, T.J.R. Hughes, and R.L. Taylor, Improved Numerical Dissipation for Time Integration Algorithms in Structural Mechanics. *Earthquake Engineering and Structural Dynamics*, 5(3), 283-292, 1977.

[3] W.L. Wood, *Practical Time-Stepping Schemes*. Clarendon Press, Oxford, 1990.

[4] K. Takanashi, K. Udagawa, M. Seki, T. Okada, and H. Tanaka, Nonlinear Earthquake Response Analysis of Structures by a Computer-Actuator On-Line System. Bulletin of Earthquake Resistant Structure Research Center, University of Tokyo, Tokyo, Japan, vol. 8, 1975

[5] S.A. Mahin and P.B. Shing, Pseudodynamic Method for Seismic Testing. *Journal of Structural Engineering* (ASCE), 111(7), 1482 –1503, 1985.

[6] P.B. Shing, M.T. Vannan, and E. Cater, Implicit Time Integration for Pseudodynamic Tests. *Earthquake Engineering and Structural Dynamics*, 20, 551–576, 1991.

[7] M. Nakashima, H. Kato, and E. Takaoka, Development of Real-time Pseudo Dynamic Testing. *Earthquake Engineering and Structural Dynamics*, 21(1), 79-92, 1992.

[8] P.A. Bonnet, C.N. Lim, M.S. Williams, A. Blakeborough, S.A. Neild, D.P. Stoten, and CA. Taylor, Real-time Hybrid Experiments with Newmark Integration, MCSmd Outer-loop Control and Multi-tasking Strategies. *Earthquake Engineering. and Structural Dynamics*, 36(1), 119-141, 2007.

[9] S.Y. Chang, Explicit Pseudodynamic Algorithm with Unconditional Stability. *Journal of Engineering Mechanics* (ASCE), 128(9), 935-947, 2002.

[10] C. Chen and J.M. Ricles, Development of Direct Integration Algorithms for Structural Dynamics Using Discrete Control Theory. *Journal of Engineering Mechanics* (ASCE), 134(8), 676-683, 2008.

[11] C. Chen and J.M. Ricles, Stability Analysis of Direct Integration Algorithms Applied to Nonlinear Structural Dynamics. *Journal of Engineering Mechanics* (ASCE), 134(9), 703-711, 2008.

[12] C. Chen and J.M. Ricles, Stability Analysis of Direct Integration Algorithms Applied to MDOF Nonlinear Dynamics," *Journal of Engineering Mechanics* (ASCE), 136(4), 432-440, 2010.

[13] C. Chen, J.M. Ricles, T.M. Marullo and O. Mercan, Real-time Hybrid Testing Using the Unconditionally Stable Explicit CR Integration Algorithm. Earthquake Engineering. and Structural Dynamics, 38(1), 23-44, 2009.

[14] P.B. Shing, Development of High-Speed On-Line Substructuring Testing System at the University of Colorado. CASCADE Technical Workshop, Oxford, UK, 2002.

[15] C. Chen, J.M. Ricles, R. Sause, T.L. Karavasilis, and Y. Chae, Design and Experimental Evaluation of Steel MRF with Magneto-Rheological Dampers for Seismic Hazard Mitigation. Behavior of Steel Structures in Seismic Areas (STESSA), August 16-19, Philadelphia, PA, 2009.

[16] C. Chen, J.M. Ricles, T. Karavasilis, Y. Chae, and R. Sause, Real-Time Hybrid Simulation System for Performance Evaluation of Structures with Rate Dependent Devices Subjected to Seismic Loading. *Engineering Structures,* submitted, under review, 2010 .

[17] K. Ogata, *Discrete-Time Control Systems*, 2nd Edition, Prentice-Hall, New Jersey, 1995.

[18] A.K. Chopra, *Dynamics of Structures: Theory and Applications to Earthquake Engineering*, 2nd Edition, Prentice-Hall, New Jersey, 2001.

COMPDYN 2011
3^{rd} ECCOMAS Thematic Conference on
Computational Methods in Structural Dynamics and Earthquake Engineering
M. Papadrakakis, M. Fragiadakis, V. Plevris (eds.)
Corfu, Greece, 25–28 May 2011

STRUCTURAL-ACOUSTIC VIBRATION REDUCTION USING PIEZOELECTRIC SHUNT TECHNIQUES: FE FORMULATION AND REDUCED ORDER MODEL

J.-F. Deü, W. Larbi, and R. Ohayon

Structural Mechanics and Coupled Systems Laboratory,
Conservatoire National des Arts et Métiers
Case 353, 292 rue Saint-Martin, 75141 Paris Cedex 03, France
{jean-francois.deu,walid.larbi,roger.ohayon]@cnam.fr

Keywords: Structural-acoustic, Piezoelectric patches, Finite element, Noise and vibration attenuation, Shunt damping technique.

Abstract. *For noise and vibration attenuation, various approaches can be employed depending on the frequency range to attenuate. Generally, active or passive piezoelectric techniques are effective in the low frequency range, while dissipative materials, such as viscoelastic or porous treatments, are efficient for higher frequency domain. In this work, a reduced order model is developed for the resolution of a fully coupled electro-mechanical-acoustic system using modal projection techniques. The problem consists of an elastic structure with surface-mounted piezoelectric patches coupled with an inviscid and compressible fluid. The piezoelectric elements, connected with a resistive or resonant shunt circuit, are used for the vibration damping of the coupled system. Numerical examples are presented in order to illustrate the accuracy and the versatility of the proposed reduced order models,notably in terms of prediction of attenuation..*

1 INTRODUCTION

For noise and vibration reduction, various approaches can be employed depending on the frequency range to attenuate. Generally, active or passive piezoelectric techniques are effective in the low frequency range, while dissipative materials (such as viscoelastic treatments or porous insulations) are efficient for higher frequency domain. In this work, we propose a reduced order model to describe a fully coupled electro-mechanical-acoustic problem in the low frequency range. The system consists of an elastic structure with surface-mounted piezoelectric patches coupled with an inviscid, compressible and barotropic fluid, gravity effects being neglected. The piezoelectric elements, connected with a resonant shunt circuit, are used for the vibration damping of the coupled system.

First, a non-symmetric finite element formulation of the coupled system is derived from a variational principle involving structural displacement, electrical voltage of piezoelectric elements, and acoustic pressure inside the fluid cavity. This formulation, with only one couple of electric variables per patch, is well adapted to practical applications since realistic electrical boundary conditions, such that equipotentiality on the electrodes and prescribed global electric charges, naturally appear. The global charge/voltage variables are intrinsically adapted to include any external electrical circuit into the electromechanical problem and to simulate the effect of resistive or resonant shunt damping techniques.

The second part of this work is devoted to the introduction of a reduced-order model of the coupled problem. The proposed methodology, based on a normal mode expansion, requires the computation of the eigenmodes of the structure with short-circuited piezoelectric patches, and the rigid acoustic cavity. It is shown that the projection of the full-order coupled finite element model on the uncoupled bases, leads to a reduced order model in which the main parameters are the classical fluid-structure and electromechanical modal coupling factors. Despite its reduced size, this model is proved to be very efficient for simulations of steady-state and transient analyses of the coupled structural-acoustic system with shunt damping.

In the last part of the paper, a three-dimensional numerical example is investigated. The problem consists of an elastic plate equipped with piezoelectric elements and coupled with an acoustic cavity. This example is analyzed in order to show that the reduced order model is capable of capturing the main characteristics of the system dynamic behavior, notably in terms of attenuation.

2 FINITE ELEMENT FORMULATION OF THE STRUCTURAL ACOUSTIC PROBLEM WITH PIEZOELECTRIC PATCHES

We briefly recall in this section the variational formulation of a fluid/piezoelectric-structure interaction problem in terms of structural mechanical displacement $\mathbf{u}$, electric potential in the structure ψ and fluid pressure p of the inviscid acoustic fluid (for more details, we refer the reader to [1, 2]). Secondly, this coupled formulation is adapted to the general case of an elastic structure equipped with P piezoelectric patches (see Fig. 1) as done for structural vibrations in [3]. This modified formulation allows taking into account realistic electrical boundary conditions such as equipotentiality on patches electrodes and prescribed global charges. Finally, the resulting finite element formulation is applied to a structural acoustic problem with one piezoelectric patch connected to a RL series shunt circuit.

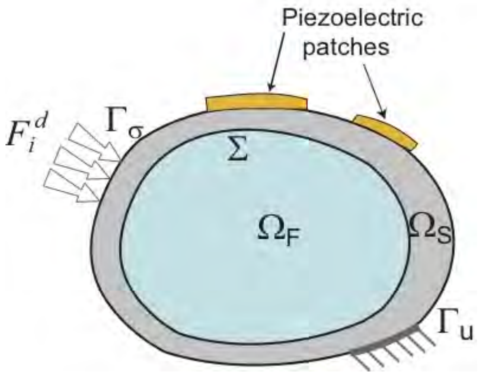

Figure 1: Fluid/piezoelectric-structure coupled system.

It should be noted that standard indicial notations are adopted throughout the paper: subscripts *i, j, k* and *l* denote the three-dimensional vectors and tensor components and repeated subscripts imply summation. In addition, a comma indicates a partial derivative.

2.1 Variational formulation of the fluid/structure/piezo-patches coupled system

We consider a piezoelectric structure occupying the domain Ω_S filled with an inviscid linear acoustic fluid occupying the domain Ω_F. We denote by Σ the fluid-structure interface and by n_i^S and n_i^F the unit normal external to Ω_S and Ω_F, respectively.

The structure is clamped on a part Γ_u and subjected (i) to a given surface force density F_i^d on the complementary part Γ_σ of its external boundary and (ii) to a pressure field p due to the presence of the fluid on its internal boundary Σ. The electric boundary conditions are defined by a prescribed electric potential ψ^d on Γ_ψ and a surface density of electric charge q^d on the remaining part Γ_D. Thus, the total structure boundary, denoted $\partial\Omega_S$, is such that $\partial\Omega_S = \Gamma_u \cup \Gamma_\sigma \cup \Sigma = \Gamma_D \cup \Gamma_\psi$ with $\Gamma_u \cap \Gamma_\sigma \cap \Sigma = \Gamma_\psi \cap \Gamma_D = \varnothing$.

The linearized deformation tensor is $\varepsilon_{ij} = \frac{1}{2}\left(u_{i,j} + u_{j,i}\right)$ and the stress tensor is denoted by σ_{ij}. Concerning the electric field variables, D_i is the electric displacement verifying the electric charge equation for a dielectric medium $D_{i,i} = 0$ in Ω_S and the electric boundary conditions $D_i\, n_i^S = -q^d$ on Γ_D; E_i denotes the electric field vector such that $E_i = -\psi_{,i}$.

The linear piezoelectric constitutive equations write:

$$\sigma_{ij}(u,\psi) = c_{ijkl}\varepsilon_{kl}(u) - e_{kij}E_k(\psi) \tag{1}$$

$$D_i(u,\psi) = e_{ikl}\varepsilon_{kl}(u) + \in_{ik} E_k(\psi) \tag{2}$$

where c_{ijkl} denotes the elastic moduli at constant electric field, e_{kij} the piezoelectric constants and $\in_{ik}$ the dielectric permittivity at constant strain. Moreover, we denote by ρ_S the mass density of the structure.

Let us introduce the admissible spaces C_u and C_ψ of regular functions u_i and ψ defined in Ω_S. We then consider the subspaces $C_u^* = \{u_i \in C_u \,|\, u_i = 0 \,\text{on}\, \Gamma_u\}$, $C_\psi^d = \left\{\psi \in C_\psi \,|\, \psi = \psi^d \,\text{on}\, \Gamma_\psi\right\}$ and $C_\psi^* = \left\{\psi \in C_\psi \,|\, \psi = 0 \,\text{on}\, \Gamma_\psi\right\}$.

The variational formulation, corresponding to the response of the piezoelectric structure subjected to the prescribed boundary conditions and to the pressure field p on the interface Σ writes:

Find $u_i \in C_u^*$ and $\psi \in C_\psi^d$ such that:

$\forall \delta u_i \in C_u^*$:

$$\int_{\Omega_S} c_{ijkl}\varepsilon_{kl}\delta\varepsilon_{ij}\,\mathrm{d}v - \int_{\Omega_S} e_{kij}E_k\delta\varepsilon_{ij}\,\mathrm{d}v + \rho_S\int_{\Omega_S}\frac{\partial^2 u_i}{\partial t^2}\delta u_i\,\mathrm{d}v = \int_{\Gamma_\sigma} F_i^d\,\delta u_i\,\mathrm{d}s + \int_\Sigma p\,n_i^F\,\delta u_i\,\mathrm{d}s \tag{3}$$

where $\delta\varepsilon_{ij} = \frac{1}{2}(\delta u_{i,j} + \delta u_{j,i})$, ε_{kl} and E_k being functions of u_i and ψ, and

$\forall \delta\psi \in C_\psi^*$:

$$\int_{\Omega_S} e_{ikl}\varepsilon_{kl}\delta E_i\,\mathrm{d}v + \int_{\Omega_S} \in_{ik} E_k\delta E_i\,\mathrm{d}v = \int_{\Gamma_D} q^d\,\delta\psi\,\mathrm{d}s \tag{4}$$

where $\delta E_i = -\delta\psi_{,i}$, ε_{kl} and E_k being functions of u_i and ψ.
This formulation must be completed by appropriate initial conditions.

We consider now the special case of an elastic structure (domain Ω_E) equipped with P piezo-electric patches and completely filled with an internal fluid (domain Ω_F). Each piezo-electric patch has the shape of a plate with its upper and lower surfaces covered with a very thin layer of conducting material to obtain electrodes. The *p*-th patch, $p \in \{1,\cdots,P\}$, occupies a domain $\Omega^{(p)}$ such that $(\Omega_E,\Omega^{(1)},\cdots,\Omega^{(P)})$ is a partition of the all structure domain Ω_S. A set of hypotheses, which can be applied to a wide spectrum of practical applications, are now formulated:

- The piezoelectric patches are thin, with a constant thickness $h^{(p)}$ for the *p*-th patch;
- The thickness of the electrodes is much smaller than $h^{(p)}$ and is thus neglected;
- The piezoelectric patches are polarized in their transverse direction (i.e. the direction normal to the electrodes).
- The electric field vector, of components E_k, is normal to the electrodes and uniform in the piezoelectric patch, so that for all $p \in \{1,\cdots,P\}$:

$$E_k = -\frac{V^{(p)}}{h^{(p)}}n_k \quad \text{in} \quad \Omega^{(p)} \tag{5}$$

where $V^{(p)} = \psi_+^{(p)} - \psi_-^{(p)}$ is the potential difference between the upper and the lower electrode surfaces of the *p*-th patch which is constant over $\Omega^{(p)}$ and n_k is the *k*-th component of the normal unit vector to the surface of the electrodes.

Under those assumptions and by considering successively each of the $P+2$ subdomains $(\Omega_F,\Omega_E,\Omega^{(1)},\cdots,\Omega^{(P)})$, the variational formulation of the fluid/structure/piezoelectric-patches coupled system can be written in terms of the structural mechanical displacement u_i, the electric potential difference $V^{(p)}$ constant in each piezoelectric patch, and the fluid pressure p:

- *Mechanical equation* : $\forall \delta u_i \in C_u^*$,

$$\int_{\Omega_S} c_{ijkl}\varepsilon_{kl}\delta\varepsilon_{ij}\,\mathrm{d}v+\sum_{p=1}^{P}\frac{V^{(p)}}{h^{(p)}}\int_{\Omega^{(p)}} e_{kij}n_k\delta\varepsilon_{ij}\,\mathrm{d}\Omega-\int_{\Sigma} p\,n_i^F\,\delta u_i\,\mathrm{d}s$$
$$+\rho_S\int_{\Omega_S}\frac{\partial^2 u_i}{\partial t^2}\delta u_i\,\mathrm{d}v=\int_{\Gamma_\sigma} F_i^d\,\delta u_i\,\mathrm{d}s \tag{6}$$

- *Electrical equation* : $\forall \delta V^{(p)} \in R$,

$$\sum_{p=1}^{P}\delta V^{(p)}C^{(p)}V^{(p)}-\sum_{p=1}^{P}\frac{\delta V^{(p)}}{h^{(p)}}\int_{\Omega^{(p)}} e_{ikl}\varepsilon_{kl}n_i\,\mathrm{d}\Omega=\sum_{p=1}^{P}\delta V^{(p)}Q^{(p)} \tag{7}$$

  where $C^{(p)}=\in_{33} S^{(p)}/h^{(p)}$ defines the capacitance of the p-th piezoelectric patch ($S^{(p)}$ being the area of the patch and $\in_{33}=\in_{ik} n_i n_k$ the piezoelectric material permittivity in the direction normal to the electrodes) and $Q^{(p)}$ is the global charge in one of the electrodes (see [3]).

- *Acoustic equation* : $\forall \delta p \in C_p$,

$$\frac{1}{\rho_F}\int_{\Omega_F} p_{,i}\,\delta p_{,i}\,\mathrm{d}v+\frac{1}{\rho_F c_F^2}\int_{\Omega_F}\frac{\partial^2 p}{\partial t^2}\delta p\,\mathrm{d}v+\int_{\Sigma}\frac{\partial^2 u_i}{\partial t^2}n_i^F\,\delta p\,\mathrm{d}s=0 \tag{8}$$

The first two equations are directly derived from Eqs. (3) and (4) using the procedure described in [3]. The last equation corresponds to the variational formulation of the Helmholtz equation in the acoustic cavity $p_{,ii}=\ddot{p}/c_F^2$ in Ω_F together with the boundary condition $p_{,i}n_i^F=-\rho_F\ddot{u}_i n_i^F$ on Σ. This relation expresses the continuity of the normal displacements of the fluid and the structure on Σ. c_F is the constant speed of sound in the fluid and ρ_F the mass density of the fluid. C_p is the admissible space of regular functions p defined in Ω_F.

Thus, the variational formulation of the fluid/structure/piezo-patches coupled problem writes as follows: given (F^d,ψ^d,q^d), find ($u_i\in C_u^*$, $\psi\in C_\psi^d$, $p\in C_p$) such that Eqs. (6) to (8) are satisfied. The formulation must be completed by appropriate initial conditions.

This formulation, with only a couple of electric variables per patches, is well adapted to practical applications since (i) realistic electrical boundary conditions such that equipotentiality on the electrodes and prescribed global charges naturally appear, (ii) the global charge/voltage variables are intrinsically adapted to include any external electrical circuit into the electromechanical problem and to simulate shunted piezoelectric patches.

2.2 Finite element formulation of the fluid/structure/piezo-patches coupled system

Let us introduce $\mathbf{U}$ (of length N_s) and $\mathbf{P}$ (of length N_f) corresponding to the vectors of nodal values of u_i and p respectively, and $\mathbf{Q}=(Q^{(1)}\,Q^{(2)}\cdots Q^{(P)})^T$ and $\mathbf{V}=(V^{(1)}\,V^{(2)}\cdots V^{(P)})^T$ the column vectors of electric charges and potential differences. The submatrices corresponding to the various linear and bilinear forms involved in Eqs. (6) to (8) are defined by

$$\begin{array}{ll}
\int_{\Omega_S} c_{ijkl}\varepsilon_{kl}\delta\varepsilon_{ij}\,\mathrm{d}v \Rightarrow \delta\mathbf{U}^T\mathbf{K}_u\mathbf{U} & \sum_{p=1}^{P}\frac{V^{(p)}}{h^{(p)}}\int_{\Omega^{(p)}} e_{kij}n_k\delta\varepsilon_{ij}\,\mathrm{d}\Omega \Rightarrow \delta\mathbf{U}^T\mathbf{C}_{uV}\mathbf{V} \\
\int_{\Omega_S} \rho_S\, u_i\,\delta u_i\,\mathrm{d}v \Rightarrow \delta\mathbf{U}^T\mathbf{M}_u\mathbf{U} & \sum_{p=1}^{P}\frac{\delta V^{(p)}}{h^{(p)}}\int_{\Omega^{(p)}} e_{ikl}\varepsilon_{kl}n_i\,\mathrm{d}\Omega \Rightarrow \delta\mathbf{V}^T\mathbf{C}_{uV}^T\mathbf{U} \\
\frac{1}{\rho_F}\int_{\Omega_F} p_{,i}\,\delta p_{,i}\,\mathrm{d}v \Rightarrow \delta\mathbf{P}^T\mathbf{K}_p\mathbf{P} & \int_{\Sigma} p\, n_i^F\,\delta u_i\,\mathrm{d}s \Rightarrow \delta\mathbf{U}^T\mathbf{C}_{up}\mathbf{P} \\
\frac{1}{\rho_F c_F^2}\int_{\Omega_F} p\,\delta p\,\mathrm{d}v \Rightarrow \delta\mathbf{P}^T\mathbf{M}_p\mathbf{P} & \int_{\Sigma} u_i\, n_i^F\,\delta p\,\mathrm{d}s \Rightarrow \delta\mathbf{P}^T\mathbf{C}_{up}^T\mathbf{U} \\
\sum_{p=1}^{P}\delta V^{(p)}C^{(p)}V^{(p)} \Rightarrow \delta\mathbf{V}^T\mathbf{K}_V\mathbf{V} & \sum_{p=1}^{P}\delta V^{(p)}Q^{(p)} \Rightarrow \delta\mathbf{V}^T\mathbf{Q} \\
 & \int_{\Gamma_\sigma} F_i^d\,\delta u_i\,\mathrm{d}s \Rightarrow \delta\mathbf{U}^T\mathbf{F}
\end{array} \tag{9}$$

where $\mathbf{M}_u$ and $\mathbf{K}_u$ are the mass and stiffness matrices of the structure; $\mathbf{C}_{uV}$ is the electric mechanical coupled stiffness matrix; $\mathbf{K}_V = \mathrm{diag}\left(C^{(1)}\, C^{(2)} \cdots C^{(P)}\right)$ is a diagonal matrix filled with the P capacitances of the piezoelectric patches; $\mathbf{M}_p$ and $\mathbf{K}_p$ are the mass and stiffness matrices of the fluid; $\mathbf{C}_{up}$ is the fluid-structure coupled matrix; $\mathbf{F}$ is the applied mechanical force vector.

Thus, the variational equations (6) to (8) for the fluid/structure/piezo-patches coupled problem can be written, in discretized form, as the following unsymmetrical matrix system:

$$\begin{bmatrix} \mathbf{M}_u & 0 & 0 \\ 0 & 0 & 0 \\ \mathbf{C}_{up}^T & 0 & \mathbf{M}_p \end{bmatrix} \begin{bmatrix} \ddot{\mathbf{U}} \\ \ddot{\mathbf{V}} \\ \ddot{\mathbf{P}} \end{bmatrix} + \begin{bmatrix} \mathbf{K}_u & \mathbf{C}_{uV} & -\mathbf{C}_{up} \\ -\mathbf{C}_{uV}^T & \mathbf{K}_V & 0 \\ 0 & 0 & \mathbf{K}_p \end{bmatrix} \begin{bmatrix} \mathbf{U} \\ \mathbf{V} \\ \mathbf{P} \end{bmatrix} = \begin{bmatrix} \mathbf{F} \\ \mathbf{Q} \\ 0 \end{bmatrix} \tag{10}$$

with appropriate initial conditions.

2.3 Structural acoustic problem with piezo patches connected to RL shunt circuit

The above discretized formulation (Eq. (10)) can be used for a wide range of applications of mechanicals structure coupled with acoustic domain and associated with piezoelectric patches. It is particularly adapted to the case where the piezoelectric patches are shunted, i.e. connected to a passive electrical network [3]. In this case, neither **V** nor **Q** are prescribed by the electrical network but the latter imposes only a relation between them. In the case of a resonant shunt connected to the *p*-th patch and composed of a resistance $R^{(p)}$ and an inductance $L^{(p)}$ in series (Fig. 1), we have the following relation between electrical potential difference $V^{(p)}$ and the electric charge $Q^{(p)}$:

$$\mathbf{L}\ddot{\mathbf{Q}} + \mathbf{R}\dot{\mathbf{Q}} + \mathbf{V} = 0 \tag{11}$$

where $\mathbf{R} = \mathrm{diag}\left(R^{(1)} \cdots R^{(P)}\right)$ and $\mathbf{L} = \mathrm{diag}\left(L^{(1)} \cdots L^{(P)}\right)$ are diagonal matrices filled with the P resistances and inductances of the shunt circuits.

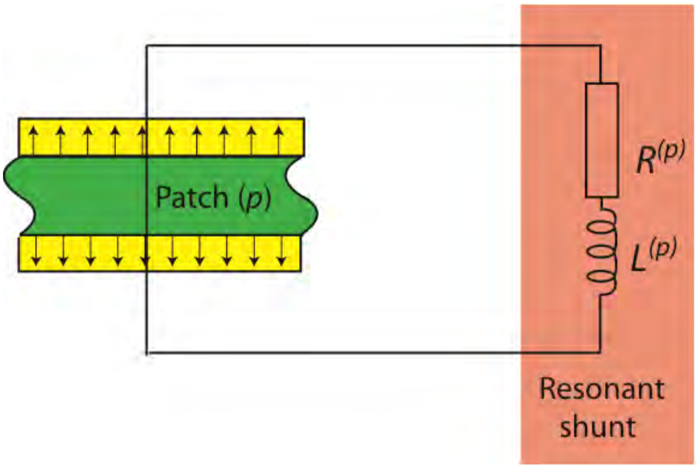

Figure 2: Piezoelectric patch connected to RL shunt circuit.

Due to the direct piezoelectric effect, the piezoelectric patch converts a fraction of the mechanical energy of the vibrating structure into electrical energy which can be dissipated through the resistive components of the RL circuit. It is well known that the damping effect due to this circuit is maximal when the resonance circular frequency $1/\sqrt{LC}$ of the shunt circuit is tuned on the circular frequency of the structural-acoustic eigenmode to be controlled. The resistance R and the inductance L can be adjusted and properly chosen so as to maximize the damping effect. Therefore, the optimal resistance and inductance for a series resonant shunt can be calculated by [4, 5]

$$R^{\text{opt}} = \frac{\sqrt{2k_{\text{eff},i}^2}}{C\omega_i(1+k_{\text{eff},i}^2)} \tag{12}$$

$$L^{\text{opt}} = \frac{1}{C\omega_i^2(1+k_{\text{eff},i}^2)} \tag{13}$$

where ω_i is the short circuit natural frequency of the i-th mode and $k_{\text{eff},i}$ is the effective electromechanical coupling coefficient [3].

Using the second row of Eq. (10), the degrees-of-freedom associated with the electrical potential difference $\mathbf{V}$ can be expressed in terms of structural displacements $\mathbf{U}$ and electric charge $\mathbf{Q}$ as

$$\mathbf{V} = \mathbf{K}_V^{-1}\mathbf{C}_{uV}^T\mathbf{U} + \mathbf{K}_V^{-1}\mathbf{Q} \tag{14}$$

Thus, after substitution of $\mathbf{V}$ into Eq. (11) and using Eq. (10), we get the following electro-mechanical-acoustic system:

$$\begin{bmatrix} \mathbf{M}_u & 0 & 0 \\ 0 & \mathbf{L} & 0 \\ \mathbf{C}_{\mathbf{up}}^{\mathbf{T}} & 0 & \mathbf{M}_{\mathbf{p}} \end{bmatrix}\begin{bmatrix} \ddot{\mathbf{U}} \\ \ddot{\mathbf{Q}} \\ \ddot{\mathbf{P}} \end{bmatrix} + \begin{bmatrix} 0 & 0 & 0 \\ 0 & \mathbf{R} & 0 \\ 0 & 0 & 0 \end{bmatrix}\begin{bmatrix} \dot{\mathbf{U}} \\ \dot{\mathbf{Q}} \\ \dot{\mathbf{P}} \end{bmatrix} + \begin{bmatrix} \mathbf{K}_u + \mathbf{C}_{uV}\mathbf{K}_V^{-1}\mathbf{C}_{uV}^T & \mathbf{C}_{uV}\mathbf{K}_V^{-1} & -\mathbf{C}_{up} \\ \mathbf{K}_V^{-1}\mathbf{C}_{uV}^T & \mathbf{K}_V^{-1} & 0 \\ 0 & 0 & \mathbf{K}_p \end{bmatrix}\begin{bmatrix} \mathbf{U} \\ \mathbf{Q} \\ \mathbf{P} \end{bmatrix} = \begin{bmatrix} \mathbf{F} \\ 0 \\ 0 \end{bmatrix} \tag{15}$$

Note that this ($\mathbf{U}$, $\mathbf{Q}$, $\mathbf{P}$) formulation is well suited for switch shunting applications.

3 REDUCED ORDER MODEL

In this section, we introduce a reduced-order formulation of the discretized problem obtained in the previous section. This formulation, based on a modal superposition method, consists in expanding (i) the structural displacement over the in *vacuo* structure modes in short circuited configuration, (ii) the acoustic pressure over the acoustic modes of the fluid in rigid cavity. This approach is widely used and effective for structural acoustic systems with weak coupling. It can be noted that the acoustic basis is enriched by a static mode ([6]) and that the main motivation of choosing the structural modes with short-circuited patches is that they can be computed using a classical elastic formulation.

3.1 Eigenmodes of the structure in vacuo with short-circuited patches

In a first phase, the first M_s eigenmodes of the structure *in vacuo* with all patches short-circuited are obtained from the following equation

$$\left(\mathbf{K}_u - \omega_{si}^2 \mathbf{M}_u\right)\Phi_{si} = 0 \quad \text{for } i \in \left\{1, \cdots, M_s\right\} \tag{16}$$

where (ω_{si}, Φ_{si}) are the natural frequency and eigenvector for the *i*-th structural mode. These modes verify the following orthogonality properties

$$\Phi_{si}^T \mathbf{M}_u \Phi_{sj} = \delta_{ij} \quad \text{and} \quad \Phi_{si}^T \mathbf{K}_u \Phi_{sj} = \omega_{si}^2 \delta_{ij} \tag{17}$$

where Φ_{si} have been normalized with respect to the structure mass matrix.

3.2 Eigenmodes of the internal acoustic cavity with rigid walls

In this second phase, the first M_f eigenmodes of the acoustic cavity with rigid boundary conditions are obtained from the following equation

$$\left(\mathbf{K}_p - \omega_{fi}^2 \mathbf{M}_p\right)\Phi_{fi} = 0 \quad \text{for } i \in \left\{1, \cdots, N_f\right\} \tag{18}$$

where (ω_{fi}, Φ_{fi}) are the natural frequency and eigenvector for the *i*-th acoustic mode. These modes verify the following orthogonality properties

$$\Phi_{fi}^T \mathbf{M}_p \Phi_{fj} = \delta_{ij} \quad \text{and} \quad \Phi_{fi}^T \mathbf{K}_p \Phi_{sj} = \omega_{fi}^2 \delta_{ij} \tag{19}$$

where Φ_{fi} have been normalized with respect to the fluid mass matrix.

3.3 Modal expansion of the general problem

By introducing the matrices $\Phi_s = \left[\Phi_{s1} \cdots \Phi_{sN_s}\right]$ of size $N_s \times M_s$ and $\Phi_f = \left[\Phi_{f1} \cdots \Phi_{fN_f}\right]$ of size $N_f \times M_f$ corresponding to the uncoupled bases, the displacement and pressure are sought as

$$\mathbf{U} = \Phi_s \mathbf{q}_s(t) \quad \text{and} \quad \mathbf{P} = \Phi_f \mathbf{q}_f(t) \tag{20}$$

where the vectors $\mathbf{q}_s = \left[q_{s1} \cdots q_{sN_s}\right]^T$ and $\mathbf{q}_f = \left[q_{f1} \cdots q_{fN_f}\right]^T$ are the modal amplitudes of the structure displacement and the fluid pressure respectively.

Substituting these relations into Equations (15) and pre-multiplying the first row by Φ_s^T and the third one by Φ_f^T, we obtain the equation

$$\begin{bmatrix} \Phi_s^T\left(\mathbf{K}_u+\mathbf{C}_{uV}\mathbf{K}_V^{-1}\mathbf{C}_{uV}^T\right)\Phi_s & \Phi_s^T\mathbf{C}_{uV}\mathbf{K}_V^{-1} & -\Phi_s^T\mathbf{C}_{up}\Phi_f \\ \mathbf{K}_V^{-1}\mathbf{C}_{uV}^T\Phi_s & \mathbf{K}_V^{-1} & 0 \\ 0 & 0 & \Phi_f^T\mathbf{K}_p\Phi_f \end{bmatrix}\begin{bmatrix}\mathbf{q}_s\\ \mathbf{Q}\\ \mathbf{q}_f\end{bmatrix}+ \\ \begin{bmatrix}0&0&0\\0&\mathbf{R}&0\\0&0&0\end{bmatrix}\begin{bmatrix}\dot{\mathbf{q}}_s\\ \dot{\mathbf{Q}}\\ \dot{\mathbf{q}}_f\end{bmatrix}+\begin{bmatrix}\Phi_s^T\mathbf{M}_u\Phi_s & 0 & 0\\ 0 & \mathbf{L} & 0\\ \mathbf{\Phi_f^T C_{up}^T \Phi_s} & 0 & \mathbf{\Phi_f^T M_p \Phi_f}\end{bmatrix}\begin{bmatrix}\ddot{\mathbf{q}}_s\\ \ddot{\mathbf{Q}}\\ \ddot{\mathbf{q}}_f\end{bmatrix}=\begin{bmatrix}\Phi_s^T\mathbf{F}\\ 0\\ 0\end{bmatrix} \tag{21}$$

This matrix equation represents the reduced order model of the structural acoustic problem with piezoelectric shunt damping treatments. If only few modes are kept for the projection, the size of this reduced order model ($M_s \times P \times M_f$) is much smaller than the initial one ($N_s \times P \times N_f$) (see examples below).

Equation (21) can be also written in the following form of coupled differential equations

- N_s *mechanical oscillators*

$$\ddot{q}_{si}+2\xi_i\omega_{si}\dot{q}_{si}+\omega_{si}^2 q_{si}+\sum_{p=1}^{P}\sum_{k=1}^{N_s}\frac{\gamma_i^{(p)}\gamma_k^{(p)}}{C^{(p)}}q_{si}+\sum_{p=1}^{P}\frac{\gamma_i^{(p)}}{C^{(p)}}Q^{(p)}-\sum_{j=1}^{N_f}\beta_{ij}q_{fj}=F_i \tag{22}$$

- N_f *acoustic equations*

$$\ddot{q}_{fi}+\omega_{fi}^2 q_{fi}+\sum_{j=1}^{N_s}\beta_{ij}q_{sj}=0 \tag{23}$$

- P *electric equations*

$$L^{(p)}\ddot{Q}^{(p)}+R^{(p)}\dot{Q}^{(p)}+\frac{Q^{(p)}}{C^{(p)}}+\sum_{i=1}^{N_s}\frac{\gamma_i}{C^{(p)}}q_{si}=0 \tag{24}$$

where $F_i(t)=\Phi_{si}^T\mathbf{F}$ is the mechanical excitation of the *i*-th mode; $\beta_{ij}=\Phi_{si}^T\mathbf{C}_{up}\Phi_{fj}$ are the fluid structure coupling coefficients and $\gamma_i=\Phi_{si}^T\mathbf{C}_{uV}$ the electromechanical coupling factors.

We can note that modal damping coefficients ξ_i have been added in Equation (22) in order to take into account the structural damping which can be measured experimentally.

The initial finite element formulation previously introduced has been replaced by the modal formulation of Equations (22), (23), (24) whose unknowns are the N_s structure modal coordinates q_{si}, the N_f fluid modal coordinates q_{fi} and the P charges $Q^{(p)}$ associated with the piezoelectric patch. Its major interest, and especially the choice of the short-circuit eigenmodes as the expansion basis, is that the above computations of the parameters necessitate only a modal analysis of an elastic problem. This operation can thus be done by any standard finite elements code.

4 NUMERICTLA EXAMPLES

We consider a 3D acoustic cavity completely filled with air (density = 1.2 kg/m^3; speed of sound = 340 m/s). The cavity walls are rigid except the top one which is a flexible aluminium plate of thickness 1 mm clamped at its four edges. The density of the plate is 2700 kg/m^3 the Young modulus 72 GPa and the Poisson ratio 0.34. On the top surface of the plate, two identical piezoelectric patches of thickness 0.5 mm are bounded. For the mechanical characteristics of the piezoelectric material PIC151, the reader can be referred to [7]. The geometrical data and mesh are presented in Fig. 3.

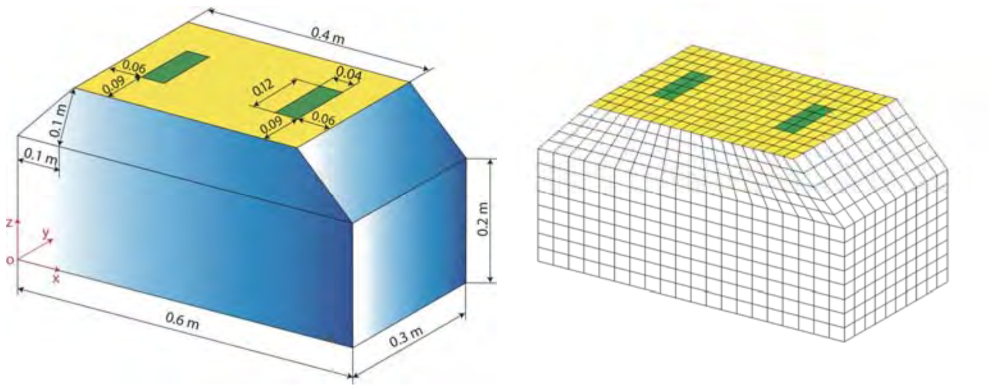

Figure 3: Acoustic/structure/piezo-patches coupled system: (a) geometrical data (in m) and (b) mesh.

Concerning the finite element discretization, we have used, for the structural part, 200 four-node plate elements based on Mindlin theory with five degrees-of-freedom per node (N_s=1155). The portions of the plate covered by the PZT patches have been modelled according to the first-order shear deformation laminated theory [8]. As discussed in the previous sections, only one electrical degree of freedom is used to represent the electrical charge Q in each patch. The acoustic cavity is discretized using 2600 hexahedric elements with one degree-of-freedom per node corresponding to the acoustic pressure (N_f=3234). Note that the structural and acoustic meshes are compatible at the interface.

4.1 Modal analysis of the acoustic/struc-ture/piezo-patches coupled problem

Table 1 presents the eigenfrequencies in three following cases: (i) the 3D rigid acoustic cavity; (ii) the clamped plate with the two patches short circuited; and (iii) the plate/acoustic-cavity coupled system in the short circuit case. All coupled frequencies, except the sixth, are associated with the first vibration modes of the structure (lower than 450 Hz), and the sixth coupled frequency corresponds to the first acoustic mode in rigid cavity. It can be confirmed by comparing the mode shapes in case (iii) with those obtained in cases (i) or (ii) which are not shown here for sake of brevity. Moreover, as expected, the natural frequencies of the coupled modes (structure dominated) are lower than those for the structure in vacuum (except for the first mode) due to the ”added-mass effect” of the fluid.

Fluid in rigid cavity	**Structure without fluid**	**Coupled problem**	**Type of coupled mode** S: Structure / F: Fluid
297.94	77.93	85.40	S
561.56	123.64	122.53	S
569.00	194.29	192.79	S
614.82	212.29	211.94	S
642.29	237.12	236.14	S
681.94	316.11	298.31	F
799.44	346.32	315.59	S
837.71	383.89	346.24	S
875.22	434.73	382.23	S
881.62	451.03	433.61	S

Table 1: Computed frequencies (in Hz) of the structural-acoustic coupled system.

For illustration purpose, Fig. 4 shows the deformed plate and the pressure field for the first ten vibration modes in the coupled case.

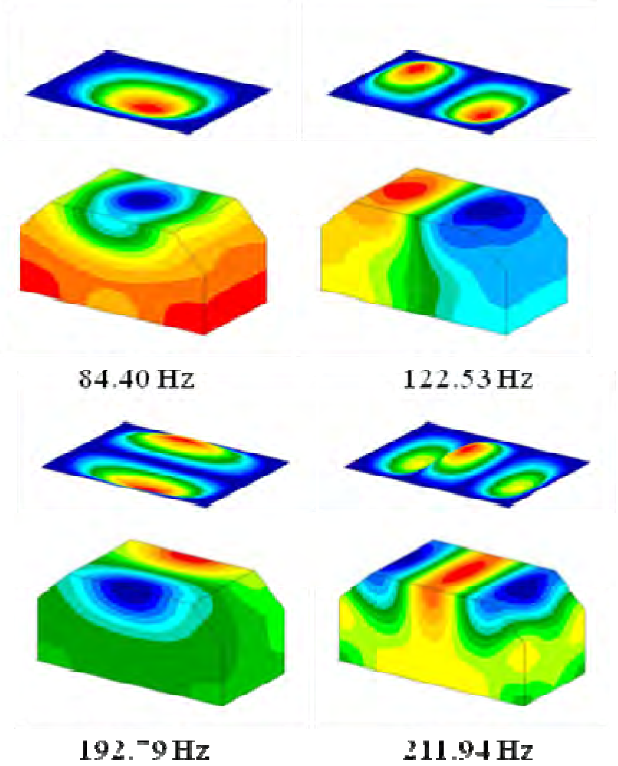

Figure 4: First 4 fluid-structure coupled modes: pressure level in the cavity and plate displacement.

4.2 Transient analysis of the acoustic/structure/piezoelectric-patch coupled problem

In this part, a multiple-mode shunt system with two piezoelectric patches as shown in Fig.5 is used in order to get an optimal multi-modal damping of the coupled system. The patches are tuned simultaneously on the second and the fourth modes of the plate. For each mode, the optimal values of the shunt electrical parameters are computed using Equations (27) and (28) (with $R_1 = 632.73\,\Omega$ $L_1 = 9.47\text{ H}$ for the second mode and $R_2 = 735.56\,\Omega$ and $L_2 = 3.17\text{ H}$ for the fourth mode). The plate is excited by a mechanical force of intensity 1 N located at (x = 0.14 m, y = 0.06 m, z = 0.3 m). The system vibratory response is obtained with the modal reduction approach defined by Equation (36) with a truncation on the first $M_s = 10$ structural modes and the first $M_f = 10$ acoustic modes.

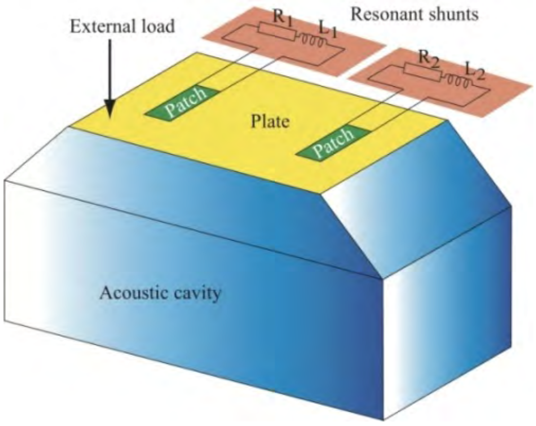

Figure 5: Vibration plate coupled with an acoustic cavity and connected to RL shunt circuit.

Figures 6 and 7 present the frequency response of the system with and without shunt. The mechanical transverse displacement in the plate at the point of coordinates (x = 0.14 m, y = 0.06 m, z = 0.3 m) is presented in Fig. 6 and the sound pressure level in the acoustic cavity at the point of coordinates (x = 0.15 m, y = 0.09 m, z = 0.1 m) in Fig. 7. These Figures show that the modal resonant magnitude for each considered mode have been significantly reduced simultaneously. In fact, the strain energy present in the piezoelectric material is converted into electrical energy and hence dissipated into heat using the RL shunt device.

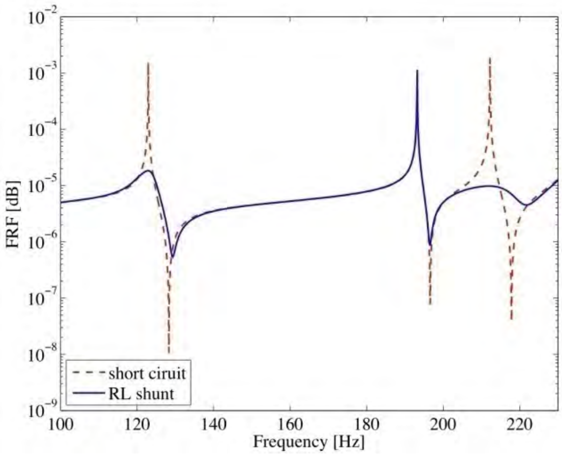

Figure 6: Frequency response function: transverse displacement amplitude in dB at the excited point.

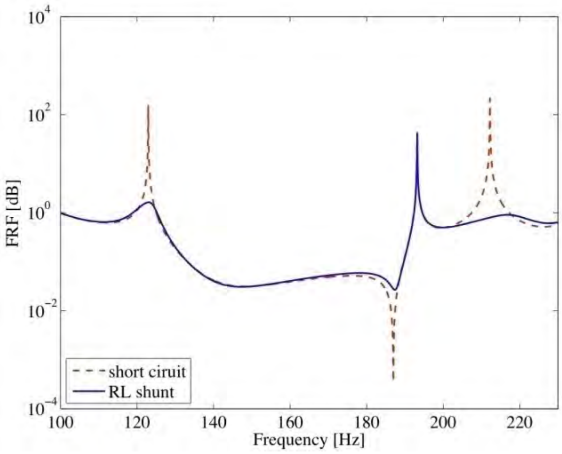

Figure 7: Frequency response function: pressure level in dB at x = 0.15 m, y = 0.09 m, z = 0.1 m.

5 CONCLUSIONS

In this work, an original finite element formulation of structural acoustic problems with piezoelectric patches is presented. This formulation, involving only a couple of electric variables by patch, allows take into account naturally realistic electric boundary conditions. A reduced-order model, based on a normal mode expansion, is then developed. The proposed methodology requires the computation of the eigenmodes of the structure with short-circuited piezoelectric patches, and the rigid acoustic cavity. It is shown that the projection of the full-order coupled finite element model on the uncoupled bases, leads to a reduced order model in which the main parameters are the classical fluid-structure and electromechanical modal coupling factors. Despite its reduced size, this model is proved to be very efficient for simulations of steady-state analyses of structural-acoustic coupled systems with shunt damping.

REFERENCES

[1] J.-F. Deü, W. Larbi, R. Ohayon, Piezoelectric structural acoustic problems: Symmetric variational formulations and finite element results, *Computer Methods in Applied Mechanics and Engineering*, **197**, 1715–1724, 2008.

[2] W. Larbi, J.-F. Deü, M. Ciminello, R. Ohayon, Structural-acoustic vibration reduction using switched shunt piezoelectric patches: A finite element analysis, *Journal of Vibration and Acoustics*, **132**, 051006, 2010.

[3] O. Thomas, J.-F. Deü, J. Ducarne, Vibrations of an elastic structure with shunted piezoelectric patches: Efficient finite element formulation and electromechanical coupling coefficients, *Int. Journal for Numerical Methods in Engineering*, **80**, 235-268, 2009.

[4] N. Hagood, A. Von Flotow, Damping of structural vibrations with piezoelectric materials and passive electrical network, *Journal. of Sound and Vibration*, **146**, 243-268, 1991.

[5] L. Corr, W. Clark, Comparison of low-frequency piezoelectric switching shunt techniques for structural damping, *Smart Materials and Structures*, **11**, 370-376, 2002.

[6] H.-P. Morand, R. Ohayon, *Fluid-structure interaction*, Wiley, New York, 1995.

[7] Piezoceramic Materials. www.piceramic.com/pdf/piezo_material.pdf.

[8] J.N. Reddy, *Mechanics of laminated composite plates and shells: theory and analysis*, CRC, Boca Raton, 2004.

COMPDYN 2011
3rd ECCOMAS Thematic Conference on
Computational Methods in Structural Dynamics and Earthquake Engineering
M. Papadrakakis, M. Fragiadakis, V. Plevris (eds.)
Corfu, Greece, 25-28 May 2011

CONTROLLING THE CRITICAL TIME STEP WITH THE BI-PENALTY METHOD

Jack Hetherington[1], **Antonio Rodríguez-Ferran**[2], **and Harm Askes**[1]

[1]Department of Civil and Structural Engineering, University of Sheffield,
Mappin Street, Sheffield S1 3JD, United Kingdom
email: cip09jeh@sheffield.ac.uk, h.askes@sheffield.ac.uk

[2]Laboratori de Càlcul Numèric, Universitat Politècnica de Catalunya,
Jordi Girona 1-3, Barcelona 08034, Spain
e-mail: antonio.rodriguez-ferran@upc.edu

Keywords: penalty functions, critical time step, explicit dynamics, time integration.

Abstract. *Penalty functions are a popular tool to add constraints to a system of equations, such as for instance Dirichlet boundary conditions or setting a relation between different degrees of freedom. Although implementation of the penalty method is simple, the commonly used stiffness-type penalties have a drawback in dynamics in that they increase the speed of sound locally. Thus, in conditionally stable time integration schemes the critical time step is lowered (often by orders of magnitude) if stiffness penalties are used. As an alternative, one may use inertia penalties that lower the speed of sound and therefore increase the critical time step, but in this paper we suggest the simultaneous use of stiffness and inertia penalties, which is called the bi-penalty method. In the bi-penalty method the relative magnitudes of stiffness penalty and inertia penalty can be tuned so that the net effect on the critical time step is neutral, thereby removing a major disadvantage of stiffness-type penalty methods.*

1 INTRODUCTION

Penalty functions are a popular technique to impose constraints in computational mechanics. Penalties can be used to enforce support conditions, tyings, interface conditions and/or contact. In mechanics, penalty functions are usually based on adding stiff springs to the system of equations. The accuracy of the constraint imposition depends on the magnitude of the penalty parameter, that is the stiffness of the added springs — the larger the penalty parameter, the more accurate the constraint is realised [1].

However, the penalty parameters cannot be chosen arbitrarily large: the condition number of the system matrix is affected adversely by increased penalty parameter, which deteriorates numerical accuracy. Furthermore, in dynamics an additional disadvantage is that stiffness-type penalties increase the speed of sound (at least locally where the penalty is applied). This becomes particularly significant in case a time domain analysis is performed with a conditionally stable time integration scheme; such schemes have a so-called *critical time step* which acts as an upper bound on the time step that can be used — larger time steps may (and usually do) lead to numerical instabilities. The critical time step is inversely proportional to the (local) speed of sound. Since the speed of sound increases with increased stiffness, applying stiffness penalties leads to increased speed of sound and decreased critical time steps [2].

As an alternative to stiffness-type penalties, it has more recently been suggested to use inertia-type penalties [3, 4]. Whereas stiffness-type penalties can be considered as stiff springs that prohibit displacement of the associated degree of freedom, inertia-type penalties act like heavy masses that prohibit acceleration of the corresponding degree of freedom. Although inertia penalties are not as accurate as stiffness penalties of equal magnitude, the beneficial effect of inertia penalties in dynamics is that they decrease the speed of sound and therefore increase the critical time step [4, 5].

To combine the benefits of stiffness penalties and inertia penalties, we suggest the simultaneous use of stiffness-type penalties and inertia-type penalties — a concept which is denoted as the bi-penalty method [5]. As explained above, stiffness penalties and inertia penalties have opposite effects on the critical time step; thus, critical ratios between the two penalty parameters can be derived such that their combined effect on the critical time step is neutral. The simultaneous use of inertia penalties and stiffness penalties has been suggested in the mid 1980s by Asano [6, 7, 8] for reasons of computational accuracy (and in fact penalties were also added to the damping matrix in these works), and more recently in [9] where the main focus was on frequency domain analysis.

In this paper, expressions will be given to compute the critical penalty ratio (CPR) described above. We will review the method to compute the CPR given in [5] and also present an alternative, much simpler method that has been developed recently. It will also be demonstrated that the critical time step remains unaffected if the penalty ratio is chosen not larger than the critical penalty ratio, whereas instabilities may occur otherwise. The bounds between stable and unstable simulations turn out to be very crisp, which is evidence for accuracy and relevance of the derived expressions for the critical penalty ratio.

2 BI-PENALISED EQUATIONS OF MOTION

We consider a linear elastic structure with stiffness matrix $\mathbf{K}$, mass matrix $\mathbf{M}$, external force vector $\mathbf{f}$ and degree of freedom (DOF) vector $\mathbf{u}$. A constraint $u_n - \overline{u} = 0$ is applied to the n^{th} DOF where $\overline{u}$ is the user-prescribed value of u_n. The constraint is enforced using stiffness and inertia penalty functions. For the former, the constraint in its usual form is added to the potential energy $\mathcal{U}$. For the latter, the rate format of the constraint is taken and added to the kinetic energy $\mathcal{T}$. The penalised potential and kinetic energy functionals thus read

$$\mathcal{U} = \frac{1}{2}\mathbf{u}^T\mathbf{K}\mathbf{u} - \mathbf{u}^T\mathbf{f} + \frac{1}{2}\alpha_s\left(u_n - \overline{u}\right)^2 \tag{1}$$

and

$$\mathcal{T} = \frac{1}{2}\dot{\mathbf{u}}^T\mathbf{M}\dot{\mathbf{u}} + \frac{1}{2}\alpha_m\left(\dot{u}_n - \dot{\overline{u}}\right)^2 \tag{2}$$

where α_s and α_m are penalty parameters of the stiffness type (dimension N/m) and inertia type (dimension Ns^2/m), respectively. The equations of motion of the structure follow from

$$\frac{\mathrm{d}}{\mathrm{d}t}\frac{\partial\mathcal{T}}{\partial\dot{\mathbf{u}}^T} + \frac{\partial\mathcal{U}}{\partial\mathbf{u}^T} = \left[\mathbf{M} + \mathbf{M}^P\right]\ddot{\mathbf{u}} + \left[\mathbf{K} + \mathbf{K}^P\right]\mathbf{u} - \left(\mathbf{f} + \mathbf{f}^P\right) = \mathbf{0} \tag{3}$$

The components of $\mathbf{M}^P$ and $\mathbf{K}^P$ are all zero except for the diagonal entries $M^P_{nn} = \alpha_m$ and $K^P_{nn} = \alpha_s$. Similarly, $f^P_n = \alpha_m\ddot{\overline{u}} + \alpha_s\overline{u}$ with all other components of $\mathbf{f}^P$ equal to zero.

3 COMPUTING THE CPR FROM THE BI-PENALISED SYSTEM

The critical time step Δt_{crit} of explicit time integration schemes, such as the central difference method, follows from

$$\Delta t_{\text{crit}} = \frac{2}{\omega_{\text{max}}} \tag{4}$$

where ω_{max} is the maximum eigenfrequency of the structure, which can be approximated (and is in fact bounded [10]) by the maximum eigenfrequency of the smallest element.

We require the critical time step to remain unaffected by the use of the bi-penalty method; thus, we require the maximum eigenfrequency of the bi-penalised system $\omega^{\text{BP}}_{\text{max}}$ to be not larger than the maximum eigenfrequency of the unpenalised system $\omega^{\text{UP}}_{\text{max}}$. We define the the critical penalty ratio (CPR) as the ratio α_s/α_m for which the maximum eigenfrequency of the bi-penalised system is identical to the maximum eigenfrequency of the unpenalised system. To find expressions for the CPR we proceed as follows:

1. Find $\omega^{\text{UP}}_{\text{max}}$ as the largest root from the unpenalised eigenvalue problem

$$\det\left(\mathbf{K} - \left(\omega^{\text{UP}}\right)^2\mathbf{M}\right) = 0 \tag{5}$$

2. Substitute $\omega^{\text{UP}}_{\text{max}}$ into the bi-penalised eigenvalue problem:

$$\det\left(\left[\mathbf{K} + \mathbf{K}^P\right] - \left(\omega^{\text{UP}}_{\text{max}}\right)^2\left[\mathbf{M} + \mathbf{M}^P\right]\right) = 0 \tag{6}$$

   The free parameters of the latter expression are the two penalty parameters α_s and α_m.

3. Define the CPR as CPR $= \alpha_s/\alpha_m$ and find an expression for the CPR from Equation (6).

This is the approach that was used in [5] to compute the CPR for linear bar elements, beam elements and two-dimensional four-noded square elements. Whilst valid results can be obtained with this approach, it is nevertheless somewhat cumbersome in that the eigenvalue problem of the bi-penalised system must be solved. The complexity of the expressions increases rapidly when more than one DOF is penalised. Thus, it is of interest to explore alternative methods to compute the CPR.

4 COMPUTING THE CPR FROM THE UNPENALISED SYSTEM

As it turns out, it is possible to compute the CPR without the need to consider the bi-penalised eigenvalue problem. Here, we will present some basic principles of the proofs — the full proofs are quite elaborate and will be published in detail elsewhere. The bi-penalised eigenvalue problem is written as

$$\left[\left(\mathbf{K}+\mathbf{K}^P\right)-\left(\omega^{\mathrm{BP}}\right)^2\left(\mathbf{M}+\mathbf{M}^P\right)\right]\mathbf{v}=\mathbf{0} \tag{7}$$

where $\mathbf{v}$ is an eigenvector of the bi-penalised system. The eigenvectors can be scaled such that they are $\mathbf{K}$-orthogonal and $\mathbf{M}$-orthonormal [1], that is

$$\mathbf{v}_I^T\left(\mathbf{K}+\mathbf{K}^P\right)\mathbf{v}_J = \left(\omega_I^{\mathrm{BP}}\right)^2\delta_{IJ} \qquad \text{(no summation over } I\text{)} \tag{8}$$

$$\mathbf{v}_I^T\left(\mathbf{M}+\mathbf{M}^P\right)\mathbf{v}_J = \delta_{IJ} \tag{9}$$

Taking $I = J$, we obtain for large values of α_s and α_m that $\alpha_s v_n^2 = \left(\omega_I^{\mathrm{BP}}\right)^2$ and $\alpha_m v_n^2 = 1$, where v_n is the penalised component of the I^{th} eigenvector $\mathbf{v}_I$. Elimination of v_n^2 then yields

$$\sqrt{\frac{\alpha_s}{\alpha_m}}=\omega_I^{\mathrm{BP}} \tag{10}$$

that is, for large values of the penalty parameters the square-root of the penalty ratio $\sqrt{\alpha_s/\alpha_m}$ is an eigenvalue of the bi-penalised system. It will be proven elsewhere that if $\sqrt{\alpha_s/\alpha_m}$ is chosen equal to the largest eigenvalue of the unpenalised system, then it is also equal to the largest eigenvalue of the bi-penalised problem, so that the overall conclusion is that by taking $\alpha_s = \left(\omega_{\max}^{\mathrm{UP}}\right)^2\alpha_m$ the maximum eigenfrequencies of the bi-penalised system and the unpenalised system are identical. Thus, the critical penalty ratio is

$$\mathrm{CPR}=\left(\omega_{\max}^{\mathrm{UP}}\right)^2 \tag{11}$$

This result is also valid for an arbitrary number of penalised DOF.

5 EXAMPLE

For illustration, we will consider the well-known case of one-dimensional linear bar elements. The lumped mass matrix and stiffness matrix are given as

$$\mathbf{M}=\frac{\rho A h}{2}\begin{bmatrix}1 & 0\\ 0 & 1\end{bmatrix} \qquad \text{and} \qquad \mathbf{K}=\frac{EA}{h}\begin{bmatrix}1 & -1\\ -1 & 1\end{bmatrix} \tag{12}$$

where A is the cross-sectional area, h is the element length, E is Young's modulus and ρ is the mass density. The unpenalised eigenvalue problem can be expanded as

$$\det\left(\mathbf{K}-\left(\omega^{\mathrm{UP}}\right)^2\mathbf{M}\right)=\left(\omega^{\mathrm{UP}}\right)^2\left(\left(\omega^{\mathrm{UP}}\right)^2-\frac{4E}{\rho h^2}\right)=0 \tag{13}$$

so that $\omega_{\max}^{\mathrm{UP}} = 2c_e/h$ where $c_e = \sqrt{E/\rho}$ is the one-dimensional speed of sound. The CPR is then found as CPR $= 4c_e^2/h^2$, which corresponds with the dimensionless CPR found earlier in [5]. For the consistent mass matrix, a similar procedure leads to CPR $= 12c_e^2/h^2$.

As a numerical example, we consider a bar of length $L = 100$ m and cross-sectional area $A = 1$ m^2. A force $F = 1$ N is applied at the left end from time $t = 0$ s onwards. Stiffness

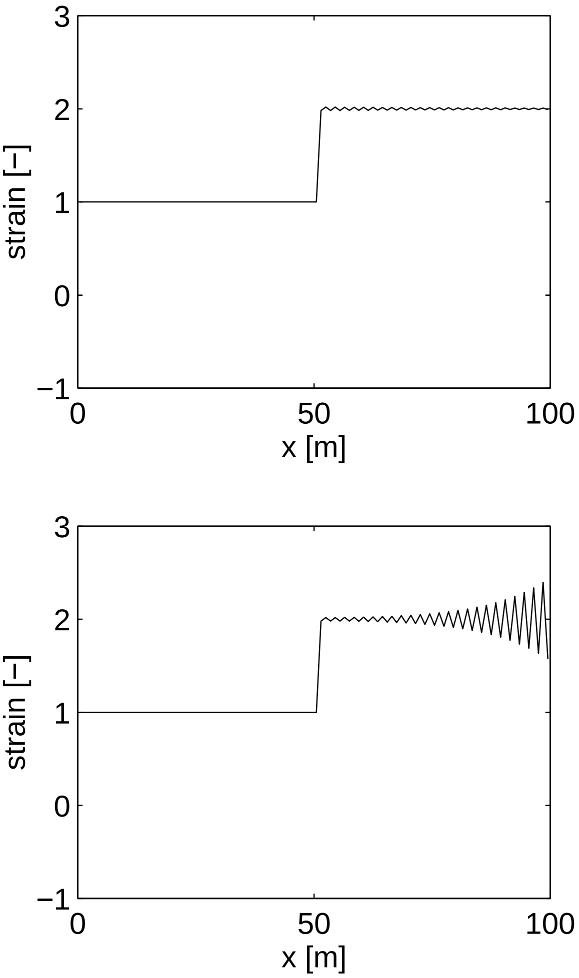

Figure 1: Wave propagation in a bar — strain profiles across the bar at time $t = 150$ s with critical penalty ratio (top) and super-critical penalty ratio (bottom)

and inertia penalties are applied at the right end of the bar to simulate fixed-end conditions. The material parameters are taken as $E = 1$ N/m^2 and $\rho = 1$ kg/m^3. The used finite element mesh consists of 100 two-noded bar elements. We apply a time step $\Delta t = \Delta t_{\text{crit}} = 1$ s, which means that the simulation should be numerically stable in the interior of the domain; if instabilities occur, they will occur due to the penalisation at the right end of the bar. The inertia penalty parameter $\alpha_m = 50$. Figure 1 shows the strain profiles across the bar at time $t = 150$ s for two values of the stiffness penalty: one whereby $\alpha_s/\alpha_m =$ CPR and one whereby $\alpha_s/\alpha_m = 1.002 \cdot$ CPR. It is clear that selecting a penalty ratio equal to the CPR leads to a simulation that is numerically stable. It can also be seen that if the penalty ratio is taken slightly larger than critical, instabilities are initiated at the penalised end of the bar.

6 CONCLUDING REMARKS

The bi-penalty method, in which inertia penalties are used simultaneously with the usual stiffness penalties, can be used in explicit dynamics to control the critical time step. The effects of stiffness penalties and inertia penalties on the critical time step are opposite, therefore their relative magnitudes can be tuned to obtain a zero net effect on the critical time step. We have also outlined procedures to compute so-called *critical penalty ratios* (CPRs) that set the stability limit for numerical simulations. An earlier method required that the bi-penalised eigenvalue problem was solved, but a new method has been formulated by which the CPR can be computed directly from the unpenalised eigenvalue problem.

In this paper, we have presented the computation of the CPR for simple one-dimensional bar elements. More sophisticated results for beam elements and two-dimensional square elements, obtained using the earlier method to compute the CPR, have been reported in [5], whereas the eigenfrequencies for unpenalised square elements (using plane various integration schemes) have also been given in [11].

ACKNOWLEDGEMENTS

Financial support from the Royal Society under International Joint Project "Bipenalty method for finite elements and explicit time integration" is gratefully acknowledged.

REFERENCES

[1] K.-J. Bathe. *Finite element procedures.* Prentice Hall, 1996.

[2] T. Belytschko and M.O. Neal. Contact-impact by the pinball algorithm with penalty and Lagrangian methods. *International Journal for Numerical Methods in Engineering*, 31:547–572, 1991.

[3] S. Ilanko. Introducing the use of positive and negative inertial functions in asymptotic modelling. *Proceedings of the Royal Society A: Mathematical, Physical and Engineering Sciences*, 461:2545–2562, 2005.

[4] J. Hetherington and H. Askes. Penalty methods for time domain computational dynamics based on positive and negative inertia. *Computers & Structures*, 87:1474–1482, 2009.

[5] H. Askes, M. Caramés-Saddler, and A. Rodríguez-Ferran. Bipenalty method for time domain computational dynamics. *Proceedings of the Royal Society A: Mathematical, Physical and Engineering Sciences*, 466:1389–1408, 2010.

[6] N. Asano. An approximate hybrid type of virtual work principle for two elastoimpact contact bodies. *Bulletin of the JSME*, 26(211), 1983.

[7] N. Asano. A Virtual Work Principle Using Penalty Function Method for Impact Contact Problems of Two Bodies. *Bulletin of the JSME*, 29(249), 1986.

[8] N. Asano. A penalty function type of virtual work principle for impact contact problems of two bodies. *Bulletin of the JSME*, 29(257), 1986.

[9] E.A. Paraskevopoulos, C.G. Panagiotopoulos, and G.D. Manolis. Imposition of time-dependent boundary conditions in FEM formulations for elastodynamics: critical assessment of penalty-type methods. *Computational Mechanics*, 45:157–166, 2010.

[10] T. Belytschko, P. Smolinski, and W.K. Liu. Stability of multi-time step partitioned integrators for first-order finite element systems. *Computer Methods in Applied Mechanics and Engineering*, 49:281–297, 1985.

[11] X. Ling and H.P. Cherukuri. Stability analysis of an explicit finite element scheme for plane wave motions in elastic solids. *Computational Mechanics*, 29:430–440, 2002.

COMPDYN 2011
3rd ECCOMAS Thematic Conference on
Computational Methods in Structural Dynamics and Earthquake Engineering
M. Papadrakakis, M. Fragiadakis, V. Plevris (eds.)
Corfu, Greece, 25–28 May 2011

EXPERIMENTAL AND NUMERICAL INVESTIGATION ON THE PERFORMANCE OF SHEAR DEFICIENT RC BEAMS STRENGTHENED WITH NSM GFRP REINFORCEMENT UNDER CYCLIC LOADING

R. Hawileh[1], M. Tanarslan[2], M. Naser[1], J. A. Abdalla[1]

[1] American University of Sharjah
Department of Civil Engineering, American University of Sharjah, P.O. Box 26666, Sharjah, UAE
E-mail: *rhaweeleh@aus.edu, b00015899@aus.edu, jabdalla@aus.edu,
*Corresponding Author: Rami Hawileh, Ph.D.

[2] Dokuz Eylul University
Department of Civil Engineering, Dokuz Eylul University, Buca, Izmir 35160, Turkey
murat.tanarslan@deu.edu.tr

Keywords: Shear Deficient Beams, finite element, RC beams, Cyclic Loading, CFRP, NSM bars.

Abstract. *This paper presents experimental and nonlinear Finite Element (FE) simulation of shear deficient reinforced concrete (RC) cantilever beams strengthened with Near Surface Mounted (NSM) Glass Fiber Reinforced polymer (GFRP) rods and subjected to cyclic loading. Two RC beam specimens were casted; the first beam is used to serve as a control specimen while the second was strengthened with GFRP NSM bars reinforcement. The two beams were tested under cyclic loading up to failure of the specimens. Then, a 3D Finite Element (FE) model that integrate different nonlinear constitutive material modeling laws and techniques such as concrete cracking, steel yielding, and imperfect bonding was developed using the finite element code ANSYS. The imperfect bonding captures the bond slip behavior between the NSM reinforcement and concrete surfaces. In addition, the developed FE models were validated against the experimental tests via a comparison of the load-deflection response envelopes and hysteresis loops. A Good matching between the experimental results and FE simulation were observed. Further experimental testing and numerical validation will be carried out in a future extensive research study to further investigate the performance of such systems when subjected to cyclic loading as in a seismic event.*

1 INTRODUCTION

In the last decade, strengthening reinforced concrete (RC) structures using externally bonded fiber reinforced polymer (FRP) materials have become a preferred technique to engineers and designers. Extensive research has been carried out to evaluate the contribution of FRP to different structural elements i.e. columns, beams, slabs etc. [1-3]. Although theoretically it is possible to achieve full capacity of strengthened elements, performed tests showed that achieving full capacity of FRP is unattainable due to debonding of the FRP sheets from the concrete surfaces [3-5]. A new strengthening technique known as near surface mounted (NSM) system seemed to be more efficient than the conventional externally bonded system. The NSM practice uses embedded FRP bars or strips into predefined groves cuts in the concrete cover, thus achieving better bonding and protection from environmental exposures.

Extensive research has been performed on the performance of RC beams strengthened with carbon fiber reinforced polymer (CFRP) bars or strips [6-8]. Limited studies have been conducted on the use of glass fiber reinforced polymers (GFRP) bars as possible strengthening materials in shear. The aim of this study is to investigate experimentally and numerically the performance of RC beams strengthened in shear with NSM GFRP rods when subjected to cyclic loading. Two RC beams were casted and tested under cyclic loading up to failure of the specimens. In addition, a finite element (FE) model is developed to capture the response and behavior of such strengthening system. The developed model was validated by comparing the load-deflection response envelopes and load-displacement hysteresis loops with that of the obtained experimental data.

2 EXPERIMENTAL PROGRAM

Two RC cantilever beams deficient in shear are casted. The first beam "SPEC-1" was kept unstrengthened to serve as a control specimen. The detailing of the control beam is shown in Figure 1. The beams were 200mm wide, 350mm high and 1700mm long as shown in Figs. 1 and 2. Four 20mm diameter bars in the compression zone and four 20mm diameter bars in the tension zone are used as longitudinal reinforcements. A concrete clear cover of 30mm was used to avoid any embedding problems.

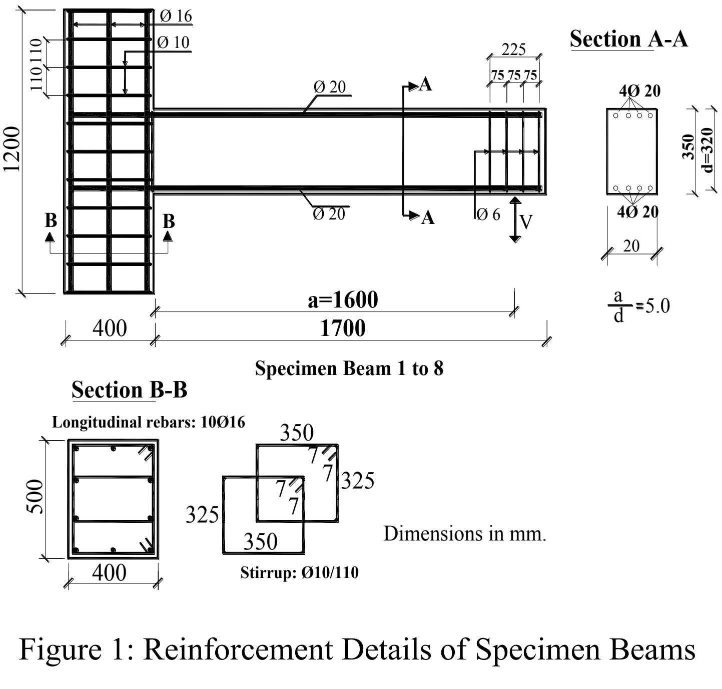

Figure 1: Reinforcement Details of Specimen Beams

The second RC beam specimen "SPEC-2" is strengthened in shear with GFRP NSM bars as shown in Fig. 2. The center-to-center spacing between the NSM GFRP bars was 160 mm.

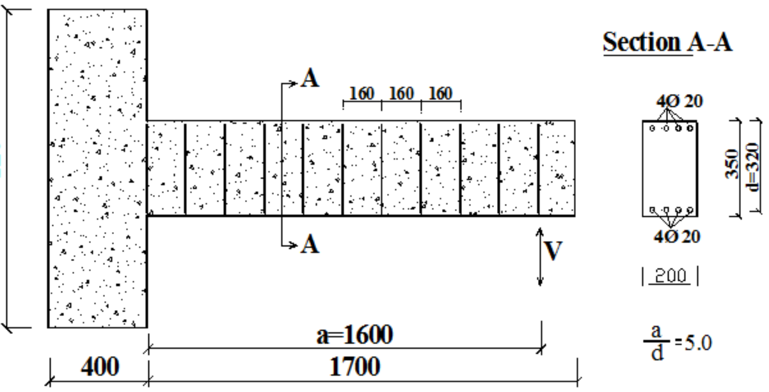

Figure 2: Strengthening scheme used for SPEC-2

3 MATERIALS

The maximum aggregate size in the concrete mix used was 20mm. Four concrete cylinders were casted and tested after 28 days to determine their compressive strengths The average compressive strengths of concrete was 25MPa. Deformed mild steel reinforcement is used and tested in tension to obtain their mechanical properties. The measured elastic modulus and yield strength was 205 GPa and 414 MPa for the longitudinal steel bars and 192 GPa and 275 MPa for the steel shear reinforcement (stirrups), respectively. In addition, coupon tensile tests for the GFRP bars reinforcements were carried out in a serco-controlled test machine. The stress-strain relationships obtained was linear up to failure. The tensile strength and elastic modulus of the GFRP bars were 550MPa and 40.8GPa, respectively. The adhesive (Sikadur®-330) used to bond the GFRP bars was composed of two parts, base and hardener. The direct tensile strength and secant elastic modulus of the epoxy Sikadur®-330 was 30MPa and 3.8GPa, respectively.

4 BONDING PROCEDURE

The sizes of the groove cuts were equal to $1.5d_f$ where d_f is the diameter of the FRP bar. The height of each groove was equal to the height of the beam’s cross section. The strengthening procedure starts by filling half the grooves were with epoxy resin. Then, the GFRP bar was subsequently inserted and gently pressed to ensure that the epoxy flowed around the bar and fill any pores between the rod and sides of the groove. Finally, the beam was left to cure at room temperature for a period of two weeks prior to testing.

5 EXPRIMENTAL SETUP

A loading column was designed as shown in Figs. 1 and 2 to connect to the beam’s free end in order to perform cyclic loading. The loading column contained two hinges, a load cell and a hydraulic jack. The capacities of the hydraulic jack and the load cell were 500 kN and 400kN, respectively. The two specimens were tested under increasingly cyclic loading up to failure. The loads were applied in cycles of loading and unloading and the applied loading history is shown in Fig. 3.

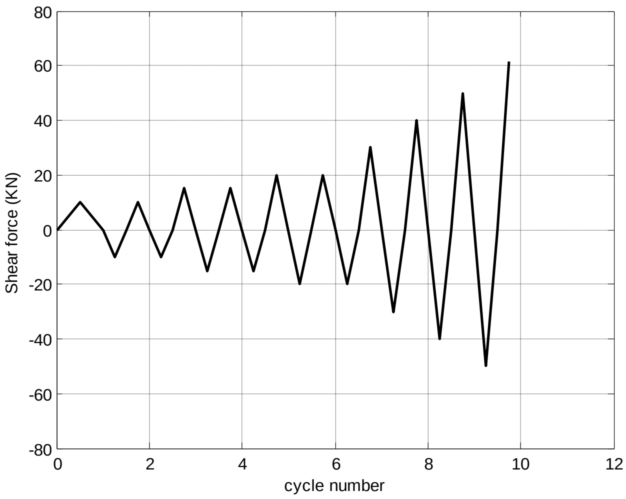

Figure 3: Applied cyclic loading history

6 FINITE ELEMENT MODEL

The developed Finite Element (FE) model has the same geometry, dimensions, material properties, and boundary conditions of the tested beams. The FE model was developed and simulated using the commercial finite element software, ANSYS [9]. Only one half of the tested beam was modeled, due to the symmetry in the transverse direction. Such decision would reduce the overall computational time while maintain the same accuracy. The developed finite element model is shown in Fig. 4.

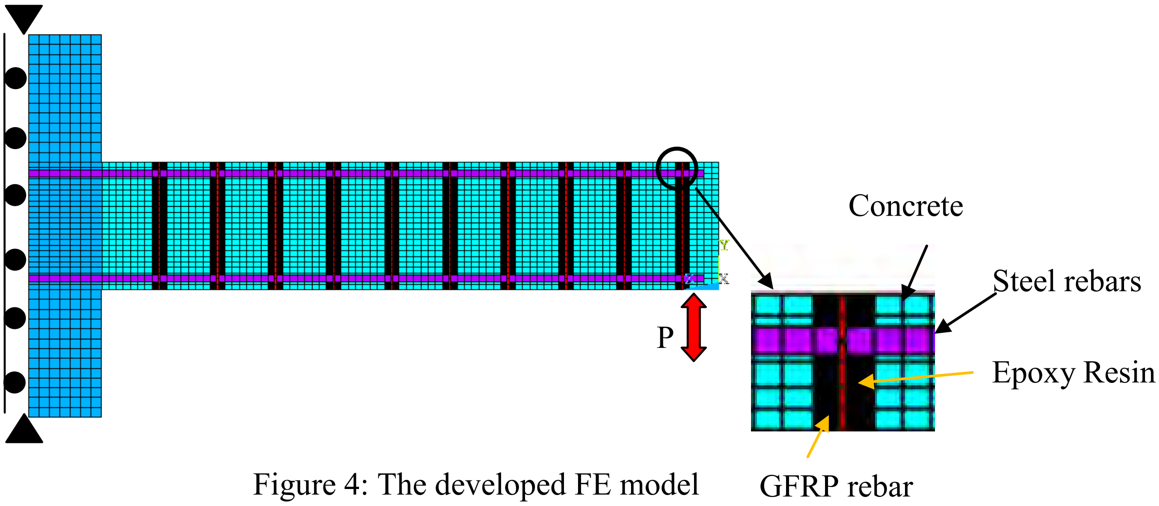

Figure 4: The developed FE model

Both the concrete and epoxy materials were simulated using ANSYS SOLID65 [9] elements. SOLID65 is defined by 8-nodes, each node of has three translational degrees of freedom in the x, y, and z directions and the element is capable of modeling the nonlinear behavior of materials and cracking in tension. The steel and GFRP bars were modeled using LINK8 [9] element. LINK8 is defined by two nodes with three translational degrees of freedom at each node. The element is capable of elastic-plastic deformation, stress stiffening, and large deflection. The rigid concrete column support used in the experimental program didn't observe any cracking during testing and thus was modeled as an elastic material using

SOLID45 [9] elements. Perfect bond assumption is used herein between the longitudinal steel bars and concrete, GFRP bars and epoxy, and epoxy and concrete surfaces.

Table 1 lists the mechanical material properties used in the FE simulation. The nonlinear plastic behavior of concrete in compression is defined using the Hognestad (parabola) model [10]. The William and Warnke [11] model implemented in the concrete constitutive material model in ANSYS [9] is used. The model requires values for the open and closed shear coefficients which typically ranges from 0.0 and 1.0. In this study a value of 0.2 is used for both coefficients. In addition, the constitutive material model for concrete in tension assumes a linear elastic behavior up to the tensile strength of concrete listed in Table 1. The nonlinear response of the steel reinforcement bars is assumed to be linear elastic-perfectly plastic. The Von-Misses failure criterion is used to define yielding of the steel reinforcement. The GFRP reinforcement was modeled as a linear elastic material up to failure. Failure in the FE simulation is defined once divergence in the solution occurs.

Table 1 Material Properties used in the FE simulation

	Compressive strength (MPa)	Yield strength (MPa)	Tensile strength (MPa)	Elastic Modulus (GPa)	Poisson ratio
Concrete	25	-	3.1*	24**	0.20
Steel	-	414	-	200	0.30
GFRP***	-	-	550	40.8	0.28
Epoxy	-	-	30	3.8	0.29

*$f_t = 0.62\sqrt{f'_c}$ in MPa

**$E_x = 4800\sqrt{f'_c}$ in MPa

7 RESULTS AND DISCUSSIONS

The Control specimen “SPEC-1” failed in shear due to a critical shear crack that was developed at a load level of 61.90kN that corresponds to a maximum deflection of 11.69mm. The first crack appeared as a flexural crack for both specimens. The developed flexure cracks propagated through the sides of the beam specimens and caused shear crack propagations. In addition, shear cracks were developed at the unstrengthened part of the strengthened specimen “SPEC-2” between the GFRP bars. As the applied load increased, the shear cracks were propagated until reaching the edges of adjacent epoxy-filled grooves on both sides of the crack. Additional loads caused the development of a major crack that resulted in failure of the specimens. The strengthened specimen failed at a load 92.68kN with a maximum deflection of 22.68mm. Thus, the use of NSM GFRP bars as strengthening materials in shear increased the load carrying capacity of the RC beam by 94% over the control beam.

The measured and predicted load-deflection response envelopes of SPEC-1 and SPEC-2 are shown in Fig. 5. In addition, Fig. 6 shows a comparsion between the predicted and measured load-deflection hysteresis loops. Table 2 draws a comparison between the tested and simulated specimens according to their ultimate load and maximum deflection. It is clear from Figs. 5 and 6 and Table 2 that there is a good agreement between the tested and simulated FE numerical results with a maximum deviation less than 5%.

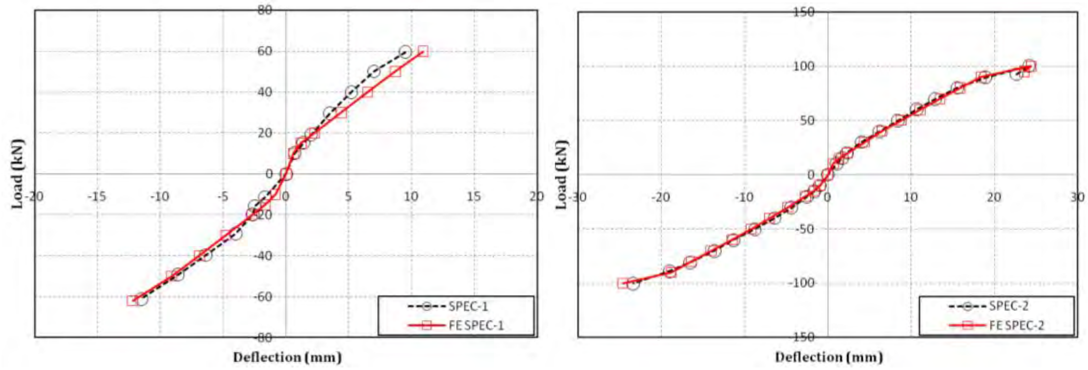

Figure 5: Comparison of the response hysteresis

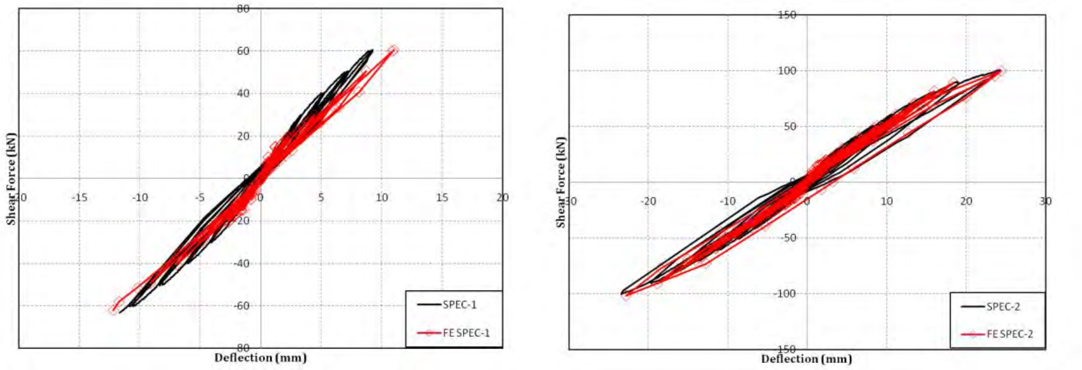

Figure 6: Comparison of the load-deflection envelopes

Table 2 Comparison between the FE predicted and experimental results

Specimen	FE Model	Failure Load (KN)		Percentage Difference	Maximum Deflection (mm)		Percentage Difference
		Exp.	FE	1-(Exp./FE)	Exp.	FE	1-(Exp./FE)
SPEC-1	FE SPEC-1	-61.90	-62.1	0.3%	-11.69	-12.2	4.2%
SPEC-2	FE SPEC-2	92.68	95.05	2.5%	22.68	23.6	3.9%

7. Summary and Conclusions

This paper presented an experimental and numerical simulation of two shear deficient rectangular RC beams subjected to cyclic loading. The first beam was unstrenghtened to serve as a control specimen, while the second beam was strengthened by means of NSM GFRP bars. The following conclusions can be drawn from the results of this study:

- The use of NSM GFRP bars can enhance the load-carrying capacity of shear deficient RC beams.
- The ultimate obtained load for the strengthened beam was greater than that of the unstrengthened specimen by 94%.

- The developed FE models are in close agreement with the measured experimental data at all stages of loading up to failure.
- The developed and verified finite element model in this study could be used as a valid tool for further investigation of NSM GFRP strengthened RC beams under cyclic loading and as a supplement or alternative to expensive and time consuming experimental testing.

The authors will conduct further experimental testing and numerical validation a future extensive research study to further investigate the performance of such shear deficient RC beams strengthened with NSM reinforcement and subjected to cyclic loading.

8. References

[1] De Lorenzis, L., and Teng, J., 2007, "Near Surface mounted FRP reinforcement: An emerging technique for strengthening structures," Composites Part B: Engineering, 38, pp. 119-143.
[2] De Lorenzis L, Rizzo A, and La Tegola A. A modified pull-out test for bond of near-surface mounted FRP rods in concrete, Compos- Part B: Eng 2002; 33(8):589-603.
[3] Parretti R, Nanni A. Strengthening of RC members using near-surface mounted FRP composites: design overview. Adv Struct Eng 2004; 7(6):469-83.
[4] Taljsten B., Carolin A, Nordin H. Concrete structures strengthened with near surface mounted reinforcement of CFRP. Adv Struct Eng 2003; 6(3):201-13.
[5] Teng, J., Smith, S., Yao, J., and Chen, J., 2003, "Intermediate crack-induced debonding in RC beams and slabs," Construction and Building Materials, 17(6-7), pp. 447–462.
[6] Hassan T, Rizkalla S. Bond mechanism of near-surface-mounted fiber-reinforced polymer bars for flexural strengthening of concrete structures. ACI Struct J 2004; 101(6):830–9.
[7] Hawileh R., Abdalla. J., Tanarslan M., and Naser, M. (2010). “Modeling of Nonlinear Cyclic Response of Shear-Deficient RC T-beams strengthened with Side Bonded CFRP Fabric Strips.” Computers and Concrete, An Int'l Journal, Accepted.
[8] De Lorenzis L, Teng JG. Near-surface mounted FRP reinforcement: an emerging technique for strengthening structures. J Compos, Part B 2007; 38:119–43.
[9] ANSYS, (2007), Finite Element Computer Code: Version 11.0, ANSYS Inc.
[10] Hognestad E, Hanson NW, and McHenry D. Concrete stress distribution in ultimate strength design. ACI Journal 1955, Proceedings 52 (12): 455–479.
[11] William K, and Warnke. Constitutive model for the triaxial behavior of, E., D. s.1.: In: Proceedings, international association for bridge and structural, 1975, Vol. 19.

COMPDYN 2011
ECCOMAS Thematic Conference on
Computational Methods in Structural Dynamics and Earthquake Engineering
M. Papadrakakis, M. Fragiadakis , V. Plevris (eds.)
Corfu, Greece, 25-28 May 2011

EXPLICIT CALIBRATION AND SIMULATION OF STOCHASTIC FIELDS BY LOW-ORDER ARMA PROCESSES

Steen Krenk

Department of Mechanical Engineering, Technical University of Denmark
Building 403, Nils Koppel's Alle, DK-2800, Kgs. Lyngby, Denmark
e-mail: sk@mek.dtu.dk

Keywords: ARMA simulation, Stochastic fields, Wind field simulation.

Abstract. *A simple framework for autoregressive simulation of stochastic fields is presented. The autoregressive format leads to a simple exponential correlation structure in the time-dimension. In the case of scalar processes a more detailed correlation structure can be obtained by adding memory to the process via an extension to autoregressive moving average (ARMA) processes. The ARMA format incorporates a more detailed correlation structure by including previous values of the simulated process. Alternatively, a more detailed correlation structure can be obtained by including additional 'state-space' variables in the simulation. For a scalar process this would imply an increase of the dimension of the process to be simulated. In the case of a stochastic field the correlation in the time-dimension is represented, although indirectly, in the simultaneous spatial correlation.*

The model with the shortest memory – the single-step autoregressive model – is analyzed in detail, and an efficient multi-step calibration procedure is developed. The calibration makes direct use of conditional correlations and means, expressed explicitly in terms of the zero and k*-step correlation matrices of the stochastic field. The correlation structure of an isotropic turbulent wind field is developed from the generalized von Kàrmàn spectrum in terms of the Airy function, and the simulation procedure is illustrated for turbulent wind with Airy or exponential function representation of the correlation structure. In spite of the basic simplicity of the simulation algorithm, the details of the transverse correlation, that should satisfy an integral condition for consistency, is represented well.*

1 INTRODUCTION

Stochastic fields play an important role in several technical contexts, notably as models for loads from wind, waves and earthquakes, and for representation of spatial properties e.g. of materials. In the first class of applications there is a time dimension, as well as one or more spatial dimensions, and this makes it appealing to consider the field as a development of a spatial field in time. Stochastic fields are characterized by their correlation, and for stationary fields a Fourier transformation relates the correlation function to a spectral density representation. For physical processes such as waves and wind there is often a background theory, that is most easily expressed in terms of spectral properties, and this suggests simulation based on spectral densities via a Fourier representation of the field. However, a Fourier representation is typically based on a finite time interval, to be selected as basis for the representation before the simulation, and furthermore computational efficiency suggests the use of a number 2^N of equal intervals in order to enable the use of the FFT formalism.

For stochastic fields with a time dimension there would be clear advantages in the use of sequential simulation techniques based on recurrence relations in time as expressed in the autoregressive moving average (ARMA) format. For scalar processes the details of the correlation structure is represented via a 'memory' that accounts for recent history. In principle the memory effect could be represented by including a number of auxiliary 'state-space' variables. For scalar processes this would imply an undesirable computational overhead, and the ARMA format is mostly retained. However, in the case of a stochastic field information of the correlation of the field may already be present in the correlation between simultaneous observations, and thus it may be possible to obtain a representation of the correlation structure, also in the time direction, via the additional information contained in a simultaneous observation of the field. This suggests the possibility of using ARMA models with rather short memory, corresponding to models with only a few coefficient matrices. The present paper deals with the shortest memory model – the single-step AR model – for stochastic fields, and develops a direct k-step calibration procedure that overcomes the problem of lack of robustness associated with single-step calibration. The model is illustrated for simulation of a turbulent wind field, where the along-wind correlation is implicitly contained in the instantaneous spatial correlation.

2 LOW-ORDER ARMA MODELS

The family of autoregressive (AR) processes with or without moving average (MA) terms generates a series $\mathbf{u}_n$ of scalar or vector valued variables from a corresponding series of uncorrelated independent variables $\boldsymbol{\xi}_n$. In the context of stochastic fields the variables are vectors of dimension m,

$$\mathbf{u}_n = [u_1, u_2, \cdots, u_m]_n^T, \qquad \boldsymbol{\xi}_n = [\xi_1, \xi_2, \cdots, \xi_m]_n^T. \tag{1}$$

These variables are typically associated with individual points in space, and the vectors refer to a section through the field, while the sequence $\cdots, n-1, n$ moves the section across the field as illustrated in Fig. 1.

The general format of the combined autoregressive moving average process is

$$\begin{aligned} \mathbf{u}_n &= \mathbf{A}_1\mathbf{u}_{n-1} + \mathbf{A}_2\mathbf{u}_{n-2} + \cdots + \mathbf{A}_j\mathbf{u}_{n-j} \\ &+ \mathbf{B}_1\boldsymbol{\xi}_{n-1} + \mathbf{B}_2\boldsymbol{\xi}_{n-2} + \cdots + \mathbf{B}_k\boldsymbol{\xi}_{n-k}, \qquad n = 1, 2, \cdots \end{aligned} \tag{2}$$

where j denotes the number of regression terms, and k similarly the number of averaging terms. Typically, calibration of the process matrices makes use of direct matching to the covariance

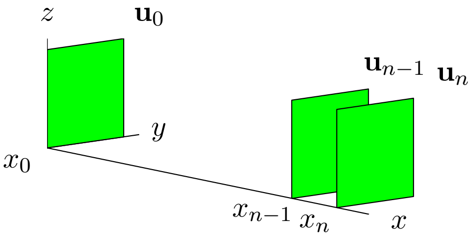

Figure 1: Discretized stochastic field as sequence of sections $\cdots, \mathbf{u}_{n-1}, \mathbf{u}_n$.

properties of the field to be simulated via the Yule-Walker equations, or use is made of discrete spectral properties involving the a discrete Fourier transformation, [1].

2.1 First-Order Autoregressive Format

The present simulation algorithm will concentrate on the first order autoregressive format. In this format the current vector $\mathbf{u}_n$ is given as a linear combination of the previous vector $\mathbf{u}_{n-1}$ and a random vector $\boldsymbol{\xi}_{n-1}$,

$$\mathbf{u}_n \,=\, \mathbf{A}\mathbf{u}_{n-1} \,+\, \mathbf{B}\boldsymbol{\xi}_{n-1}, \qquad n = 1, 2, \cdots \tag{3}$$

The random vectors $\boldsymbol{\xi}_n$ are here taken in the form of uncorrelated normalized normal components, whereby

$$\mathrm{E}[\,\boldsymbol{\xi}_i\,\boldsymbol{\xi}_j^T] \,=\, \delta_{ij}\,\mathbf{I}\,. \tag{4}$$

Hereby the role of the matrix $\mathbf{B}$ is to generate the correlation between the components of the input in the AR equation (4).

The matrices $\mathbf{A}$ and $\mathbf{B}$ determine the properties of the series, and are determined to reproduce desired properties of an underlying stochastic field. The AR format (3) corresponds to a field with zero expectation of all vectors $\mathbf{u}_n$. The properties of the stochastic field are given in terms of the covariance matrices

$$\mathbf{C}_k \,=\, \mathrm{E}[\,\mathbf{u}_n\,\mathbf{u}_{n-k}^T]. \tag{5}$$

The stochastic field is assumed to homogeneous, and thus the covariance matrix is independent of the subscript n, identifying the section. Furthermore the present algorithm relates to the first order single-step format (3). This corresponds to fields with one-step memory, the so-called Markov property. The covariance structure of this type of field can be generated from the single-step covariance properties, contained in the two matrices

$$\mathbf{C}_0 \,=\, \mathrm{E}[\,\mathbf{u}_n\,\mathbf{u}_n^T], \qquad \mathbf{C}_1 \,=\, \mathrm{E}[\,\mathbf{u}_n\,\mathbf{u}_{n-1}^T]. \tag{6}$$

These two covariance matrices determine the AR coefficient matrices $\mathbf{A}$ and $\mathbf{B}$.

2.2 Coefficient matrices and conditional field properties

The matrices $\mathbf{A}$ and $\mathbf{B}$ can be determined from basic operations involving pre-multiplication of the AR equation (4). However, it is illuminating to derive the expressions directly from the corresponding conditional expectation and covariance of the underlying field. When using the AR equation (3), the vector $\mathbf{u}_n$ is formed as the sum of a deterministic part $\mathbf{A}\mathbf{u}_{n-1}$, determined by the previous step, and a stochastic zero-mean component $\mathbf{B}\boldsymbol{\xi}_{n-1}$. Both coefficient matrices $\mathbf{A}$ and $\mathbf{B}$ are determined by rewriting the recurrence relation (3) in the form

$$\mathbf{u}_n \,-\, \mathbf{A}\mathbf{u}_{n-1} \,=\, \mathbf{B}\boldsymbol{\xi}_{n-1}. \tag{7}$$

By definition the stochastic variable $\boldsymbol{\xi}_{n-1}$ is independent of $\mathbf{u}_{n-1}$ and has the expectation zero. The relation (7) then identifies the conditional expectation of $\mathbf{u}_n$ as in the full sequence, when the previous vector $\mathbf{u}_{n-1}$ is known, i.e.

$$\mathrm{E}[\,\mathbf{u}_n|\,\mathbf{u}_{n-1}] \;=\; \mathbf{A}\mathbf{u}_{n-1}. \tag{8}$$

In the special case of zero-mean variables the conditional variance of $\mathbf{u}_n$ for given $\mathbf{u}_{n-1}$ is, see e.g. [2],

$$\mathrm{E}[\,\mathbf{u}_n|\,\mathbf{u}_{n-1}] \;=\; \mathbf{C}_1\mathbf{C}_0^{-1}\mathbf{u}_{n-1}. \tag{9}$$

Thus, the regression matrix $\mathbf{A}$ is identified as the matrix in the conditional mean formula, whereby

$$\mathbf{A} \;=\; \mathbf{C}_1\mathbf{C}_0^{-1}. \tag{10}$$

This equation gives the regression matrix $\mathbf{A}$ explicitly in terms of the covariance matrices $\mathbf{C}_0$ and $\mathbf{C}_1$ of the stochastic field.

The matrix $\mathbf{B}$ is also determined directly from the relation (7). Both sides represent a vector variable with zero mean. The vector $\mathbf{u}_{n-1}$ is known, and thus the covariance matrix of the right hand side must correspond to the conditional covariance of $\mathbf{u}_n$,

$$\mathrm{Cov}[\,\mathbf{u}_n\mathbf{u}_n^T|\,\mathbf{u}_{n-1}] \;=\; \mathbf{B}\,\mathrm{E}[\,\boldsymbol{\xi}_{n-1}\boldsymbol{\xi}_{n-1}^T]\,\mathbf{B}^T. \tag{11}$$

The conditional covariance matrix of two sets of variables of wich one is known is given by, see e.g. [2],

$$\mathrm{Cov}[\,\mathbf{u}_n\mathbf{u}_n^T|\,\mathbf{u}_{n-1}] \;=\; \mathbf{C}_{0|1} \;=\; \mathbf{C}_0 \;-\; \mathbf{C}_1\mathbf{C}_0^{-1}\mathbf{C}_1^T. \tag{12}$$

The vector $\boldsymbol{\xi}_{n-1}$ has independent normalized components according to (4), and thus the expectation on the right hand side of (11) gives the unit matrix. Comparison of the two expressions for the conditional covariance $\mathbf{C}_{0|1}$ then gives the following equation of the matrix $\mathbf{B}$,

$$\mathbf{B}\,\mathbf{B}^T \;=\; \mathbf{C}_{0|1} \;=\; \mathbf{C}_0 \;-\; \mathbf{C}_1\mathbf{C}_0^{-1}\mathbf{C}_1^T. \tag{13}$$

This equation determines the product $\mathbf{B}\,\mathbf{B}^T$.

The role of the matrix $\mathbf{B}$ in the autoregressive relation (7) is to generate correlated input from the uncorrelated components of the random vectors $\boldsymbol{\xi}_n$. This leaves a certain indeterminacy of the matrix $\mathbf{B}$ as only the product $\mathbf{B}\,\mathbf{B}^T$ contributes to the mutual correlation correlation of the components in the equation. A simple and direct solution consists in assuming that the coefficient matrix $\mathbf{B}$ is in the form of a lower triangular matrix. The equation (13) then immediately identifies $\mathbf{B}$ via the Cholesky factorization of the conditional covariance matrix $\mathbf{C}_{0|1}$ of the stochastic field. Alternatively, the matrix $\mathbf{B}$ may be expressed in symmetric form in terms of the eigenvalues $\boldsymbol{\Lambda}$ and eigenvectors $\mathbf{U}$ of the conditional covariance matrix $\mathbf{C}_{0|1}$, defined by

$$\mathbf{C}_{0|1}\mathbf{U} \;=\; \mathbf{U}\,\boldsymbol{\Lambda}. \tag{14}$$

It then follows from the orthogonality relations of the eigenvectors $\mathbf{U}$ that the coefficient matrix $\mathbf{B}$ can be expressed as

$$\mathbf{B} \;=\; \mathbf{U}\boldsymbol{\Lambda}^{1/2}\mathbf{U}^T. \tag{15}$$

This completes the single-step calibration procedure.

3 MULTI-STEP MODEL CALIBRATION

It is observed that the two parameter matrices of the AR filter are determined by the conditional expectation and the conditional covariance with the previous variable $\mathbf{u}_{n-1}$ known. Direct use of these relations is justified, when the correlation properties of the stochastic field are captured well by the relation between two neighboring vectors $\mathbf{u}_{n-1}$ and $\mathbf{u}_n$. However, the use of closely spaced vectors may introduce undesirable sensitivity in the calibration, and a more robust procedure can be obtained by calibrating the model via the properties of vectors with larger separation. A simple direct procedure using the vectors $\mathbf{u}_{n-k}$ and $\mathbf{u}_n$, separated by k steps, is described in the following.

3.1 Recurrence matrix A

The single-step recurrence relation may be extended by substituting $\mathbf{u}_n$ from the previous relation and so forth. This leads to the k-step relation

$$\mathbf{u}_n \;=\; \mathbf{A}^k\mathbf{u}_{n-k} \;+\; \big(\mathbf{A}^{k-1}\mathbf{B}\boldsymbol{\xi}_{n-k} + \cdots + \mathbf{A}\mathbf{B}\boldsymbol{\xi}_{n-2} + \mathbf{B}\boldsymbol{\xi}_{n-1}\big). \tag{16}$$

In the previous section the matrix $\mathbf{A}$ was determined via the conditional expectation of $\mathbf{u}_n$ for known $\mathbf{u}_{n-1}$, i.e. for one-step separation. This formula is now generalized to k-step separation. First the term containing $\mathbf{u}_{n-k}$ is moved to the left side of the equation,

$$\mathbf{u}_n \;-\; \mathbf{A}^k\mathbf{u}_{n-k} \;=\; \big(\mathbf{A}^{k-1}\mathbf{B}\boldsymbol{\xi}_{n-k} + \cdots + \mathbf{A}\mathbf{B}\boldsymbol{\xi}_{n-2} + \mathbf{B}\boldsymbol{\xi}_{n-1}\big). \tag{17}$$

The terms on the right are statistically independent with mean zero, and thus the conditional expectation of $\mathbf{u}_n$ for known $\mathbf{u}_{n-k}$ is

$$\mathrm{E}[\,\mathbf{u}_n|\,\mathbf{u}_{n-k}] \;=\; \mathbf{A}^k\mathbf{u}_{n-k}. \tag{18}$$

The conditional expectation also follows directly from the unconditional covariance between $\mathbf{u}_n$ and $\mathbf{u}_{n-k}$ as

$$\mathrm{E}[\,\mathbf{u}_n|\,\mathbf{u}_{n-k}] \;=\; \mathbf{C}_k\mathbf{C}_0^{-1}\mathbf{u}_{n-k}. \tag{19}$$

Comparison of these two expressions for the k-step conditional expectation gives the following expression for the k-power of the recurrence matrix,

$$\mathbf{A}^k \;=\; \mathbf{C}_k\mathbf{C}_0^{-1}. \tag{20}$$

This relation identifies the recurrence matrix $\mathbf{A}$ from the covariance properties at a separation of k steps.

In order to extract the matrix $\mathbf{A}$ from (20) an eigenvalue decomposition is used. To this end the notation

$$\mathbf{A}_k \;=\; \mathbf{C}_k\mathbf{C}_0^{-1} \tag{21}$$

is introduced. This matrix is non-symmetric and the eigenvalue decomposition takes the form

$$\mathbf{A}_k\mathbf{P} \;=\; \mathbf{P}\,\boldsymbol{\Gamma}^k, \qquad \mathbf{A}_k^T\mathbf{Q} \;=\; \mathbf{Q}\,\boldsymbol{\Gamma}^k, \tag{22}$$

where $\mathbf{P}$ and $\mathbf{Q}$ are the right and the left eigenvector matrices of $\mathbf{A}_k$, respectively. The eigenvalues are contained in the diagonal matrix $\boldsymbol{\Gamma}^k = \lceil \gamma_1^k, \gamma_2^k, \cdots, \gamma_m^k \rfloor$. The eigenvector matrices are normalized to satisfy the bi-orthogonality relations

$$\mathbf{Q}^T\mathbf{P} \;=\; \mathbf{P}^T\mathbf{Q} \;=\; \mathbf{I}. \tag{23}$$

Pre-multiplication of the eigenvalue equation (22a) with $\mathbf{Q}^T$ and use of orthogonality gives the representation

$$\mathbf{Q}^T\mathbf{A}_k\mathbf{P} \,=\, \mathbf{\Gamma}^k. \tag{24}$$

Now, introducing $\mathbf{A}^k \,=\, \mathbf{A}_k$ and using the orthogonality relations (23) this relation takes the form

$$(\mathbf{Q}^T\mathbf{A}\mathbf{P})^k \,=\, \mathbf{\Gamma}^k. \tag{25}$$

From this relation and the orthogonality relations (23) it follows that

$$\mathbf{A} \,=\, \mathbf{P}\mathbf{\Gamma}\mathbf{Q}^T. \tag{26}$$

This formula determines the recurrence matrix $\mathbf{A}$ from its k-step properties and generalizes the single-step procedure from Section 2.2. Clearly, the single-step result is recovered for $k\,=\,1$, and it is seen that the eigenvalue decomposition becomes superfluous in that case.

3.2 Input matrix $\mathbf{B}$

The input matrix $\mathbf{B}$ is determined from the conditional variance by generalizing the single-step procedure form Section 2.2. In the relation (17) both sides represent a random vector with zero mean. When $\mathbf{u}_{n-k}$ is known the covariance of the left side is sen to constitute the conditional covariance of $\mathbf{u}_n$ for given $\mathbf{u}_{n-k}$, i.e.

$$\mathrm{Cov}\big[\mathbf{u}_n\mathbf{u}_n^T \,|\, \mathbf{u}_{n-k}\big] \,=\, \mathrm{E}\big[\big(\mathbf{A}^{k-1}\mathbf{B}\boldsymbol{\xi}_{n-k}+\cdots+\mathbf{B}\boldsymbol{\xi}_{n-1}\big)\big(\mathbf{A}^{k-1}\mathbf{B}\boldsymbol{\xi}_{n-k}+\cdots+\mathbf{B}\boldsymbol{\xi}_{n-1}\big)^T\big]. \tag{27}$$

In this case the conditional variance of the stochastic field is given by

$$\mathrm{Cov}[\,\mathbf{u}_n\mathbf{u}_n^T|\,\mathbf{u}_{n-k}] \,=\, \mathbf{C}_{0|k} \,=\, \mathbf{C}_0 \,-\, \mathbf{C}_k\mathbf{C}_0^{-1}\mathbf{C}_k^T. \tag{28}$$

The expression in terms of the matrices $\mathbf{A}$ and $\mathbf{B}$ of the model follow from evaluating the expectation on the right side of (27),

$$\mathrm{Cov}[\,\mathbf{u}_n\mathbf{u}_n^T|\,\mathbf{u}_{n-k}] \,=\, \mathbf{A}^{k-1}\mathbf{B}\mathbf{B}^T(\mathbf{A}^{k-1})^T \,+\, \cdots \,+\, \mathbf{A}\mathbf{B}\mathbf{B}^T\mathbf{A}^T \,+\, \mathbf{B}\mathbf{B}^T. \tag{29}$$

The two expressions (28) and (29) for the conditional variance establish an equation between the conditional variance $\mathbf{C}_{0|k}$ of the stochastic field, and a series expansion in terms of powers of the matrix $\mathbf{A}$.

It follows from the l-factor product of the eigenvalue representation (26) that the l'th power of $\mathbf{A}$ can be expressed as

$$\mathbf{A}^l \,=\, \mathbf{P}\mathbf{\Gamma}\mathbf{Q}^T\cdots\mathbf{P}\mathbf{\Gamma}\mathbf{Q}^T \,=\, \mathbf{P}\mathbf{\Gamma}^l\mathbf{Q}^T, \tag{30}$$

where the orthogonality relation (23) has been used to cancel the inner matrix products. Substitution of this representation into the expression (29) for the conditional covariance matrix leads to the equation

$$\mathbf{C}_{0|k} \,=\, \mathbf{P}\mathbf{\Gamma}^{k-1}\mathbf{Q}^T\mathbf{B}\mathbf{B}^T\mathbf{Q}\mathbf{\Gamma}^{k-1}\mathbf{P}^T \,+\, \cdots \,+\, \mathbf{P}\mathbf{\Gamma}\mathbf{Q}^T\mathbf{B}\mathbf{B}^T\mathbf{Q}\mathbf{\Gamma}\mathbf{P}^T \,+\, \mathbf{B}\mathbf{B}^T. \tag{31}$$

The factors $\mathbf{P}$ and $\mathbf{P}^T$ are now eliminated by pre-multiplication with $\mathbf{Q}^T$ and post-multiplication with $\mathbf{Q}$. This gives the relation

$$\mathbf{Q}^T\mathbf{C}_{0|k}\mathbf{Q} \,=\, \sum_{l=0}^{k-1}\mathbf{\Gamma}^l\big[\,\mathbf{Q}^T\mathbf{B}\mathbf{B}^T\mathbf{Q}\,\big]\mathbf{\Gamma}^l. \tag{32}$$

It is seen that the right side of the equation is a summation in which the components of the symmetric matrix

$$\mathbf{D} \,=\, \mathbf{Q}^T \mathbf{B} \mathbf{B}^T \mathbf{Q}. \tag{33}$$

are multiplied by powers of the eigenvalues $\gamma_1, \gamma_2, \cdots, \gamma_m$. The summation is conveniently carried out by using the sum of a k-term series with geometric progression. In component form

$$\big[\,\mathbf{Q}^T \mathbf{C}_{0|k} \mathbf{Q}\,\big]_{ij} \,=\, \sum_{l=0}^{k-1} \Big[\, (\gamma_i \gamma_j)^l D_{ij} \,\Big] \,=\, \frac{1-(\gamma_i\gamma_j)^k}{1-(\gamma_i\gamma_j)}\, D_{ij}. \tag{34}$$

This equation gives the components of the matrix $\mathbf{D}$ as

$$D_{ij} \,=\, \frac{1-(\gamma_i\gamma_j)}{1-(\gamma_i\gamma_j)^k} \big[\,\mathbf{Q}^T \mathbf{C}_{0|k} \mathbf{Q}\,\big]_{ij}. \tag{35}$$

When the components of $\mathbf{D}$ have been computed from this relation, the input matrix $\mathbf{B}$ is determined from (33). Pre-multiplication with $\mathbf{P}$ and post-multiplication with $\mathbf{P}^T$ gives the equation

$$\mathbf{B}\mathbf{B}^T \,=\, \mathbf{P}\mathbf{D}\mathbf{P}^T. \tag{36}$$

This is an equation of the same form as (13) for the single-step procedure.

It is noted that in the case $k = 1$ the first factor in (35) is unity, and eigenvalue decomposition becomes superfluous, as the matrix on the left side of (36) is simply equal to the conditional covariance matrix $\mathbf{C}_{0|1}$ in that case. In the multi-step case the input over k steps has components occurring at different times, and the memory effect is accounted for by the dependence on the eigenvalues Γ as illustrated in (35).

4 WIND FIELD SIMULATION

An application area of considerable current interest is that of a turbulent wind field. Specific applications range from structures like towers, high-rise buildings and long bridges to wind turbines. Traditionally, the level of ambition regarding the representation of the turbulent wind load in these applications has been very different, with structural applications often making use of simple analytical approximations for the resulting load, while wind turbine design typically makes use of rather detailed wind field simulation, often based on FFT techniques, see e.g. [3].

4.1 Isotropic wind field correlation

The turbulent wind field used in the present paper is represented in the form of isotropic incompressible turbulence as described by Batchelor [4]. It follows from invariance to coordinate transformations that the general form of the covariance between the turbulent velocity components at two points separated by the spatial vector $\mathbf{r}$ as shown in Fig. 2 is of the form

$$\mathbf{R}(\mathbf{r}) \,=\, \mathrm{E}[\,\mathbf{v}(\mathbf{r}_0+\mathbf{r})\,\mathbf{v}(\mathbf{r}_0)^T] \,=\, \sigma_v^2 \Big([\,f(r)-g(r)\,] \frac{\mathbf{r}\,\mathbf{r}^T}{\mathbf{r}^T\mathbf{r}} \,+\, g(r)\,\mathbf{I} \Big), \tag{37}$$

where $r = |\mathbf{r}|$ is the distance between the two points, and σ_v^2 is the variance of a single component at a point. The functions $f(r)$ and $g(r)$ describe the lengthwise and transverse correlation, respectively.

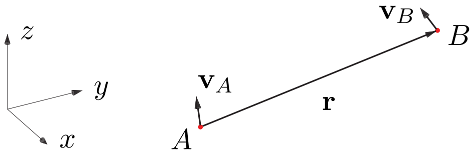

Figure 2: Two-point correlation of isotropic wind field.

At the typical wind speeds in the natural wind the flow can be assumed to be incompressible. It then follows from the incompressibility condition $\boldsymbol{\nabla}_{\mathbf{r}}^T\mathbf{v}$ that the correlation functions are related by

$$g(r) \,=\, f(r) \,+\, \frac{r}{2}\,\frac{d}{dr}f(r). \tag{38}$$

Thus, the isotropic incompressible stochastic field is described entirely in terms of a single scalar correlation function, e.g. the lengthwise correlation function $f(r)$. The lengthwise correlation function $f(r)$ is often represented in terms of its spectral density function $F(k)$, where k is the wavenumber,

$$\sigma_v^2 f(r) \,=\, \int_{-\infty}^{\infty} F(k)\,\mathrm{e}^{ikr} dr. \tag{39}$$

Analytically tractable results are obtained, when using the generalized form of the von Kàrmàn spectral density, [5, 6],

$$\sigma_v^2 F(k) \,=\, \frac{1}{\sqrt{\pi}}\,\frac{\Gamma(\gamma)}{\Gamma(\gamma-\frac{1}{2})}\,\frac{\sigma_u^2\,\ell}{[1+(k\ell)^2]^{\gamma}}. \tag{40}$$

Here ℓ is a length-scale of the turbulence, and the Kolmogorov cascade theory implies that the exponent is $\gamma = 5/6$. The analytical details of this case has been investigated by Kristensen and Jensen [7], and it was demonstrated that coherence and correlation functions can be expressed in terms of modified Bessel functions of the second kind with fractional index. In the present context it is convenient to use an alternative representation of the correlation functions in terms of Airy functions [8]. This formulation makes use of a non-dimensional transformed variable z to represent the distance,

$$z = \Big(\frac{3r}{2\ell}\Big)^{2/3}, \tag{41}$$

whereby

$$f(r) = \frac{\mathrm{Ai}(z)}{\mathrm{Ai}(0)}, \qquad g(r) \,=\, f(r) \,+\, \frac{z}{3}\,\frac{\mathrm{Ai}'(z)}{\mathrm{Ai}(0)}. \tag{42}$$

Here $\mathrm{Ai}(z)$ is the Airy function and $\mathrm{Ai}'(z)$ its derivative.

A simpler approximate formulation can be obtained by using the exponent $\gamma = 1$, whereby

$$f(r) = \mathrm{e}^{-r/\lambda}, \qquad g(r) \,=\, \big(1 - \frac{1}{2}\,\frac{r}{\lambda}\big)\,\mathrm{e}^{-r/\lambda}. \tag{43}$$

Here the parameter λ is the integral spatial length-scale of the turbulence, defined by

$$\lambda = \int_0^{\infty} f(r)\,dr. \tag{44}$$

When substituting the representation (42) of the correlation functions in terms of the Airy function in the definition of the integral length-scale, it is found that $\ell = 1.339\lambda$.

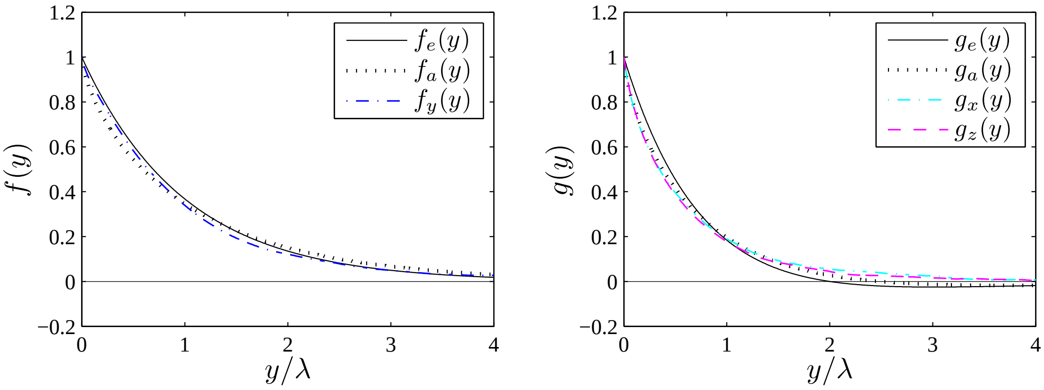

Figure 3: Correlation functions $f(r)$ and $g(r)$: Airy (dots), Exponential (full).

The lengthwise and the transverse correlation functions are illustrated in Figs. 3a and 3b, respectively. The exponential representation (43) is shown in full line, while the Airy function representation is shown by a dotted curve. It is seen that the curves from the two representations cross at $r \simeq \lambda$. The AR simulation format format is closely related to exponential attenuation, and the curves suggest the the distance $r \simeq \lambda$ may be appropriate for calibration of the AR model.

4.2 Simulated wind field

The AR field simulation is based on selecting a number of points in a plane, e.g. the xz-plane. The coordinates of these points are arranged in a global vector

$$\mathbf{x}_n^T = [\,\mathbf{r}_1^T, \mathbf{r}_2^T, \cdots, \mathbf{r}_m^T\,]_n\,. \tag{45}$$

and the corresponding velocities are similarly arranged in the global vector

$$\mathbf{u}_n^T = [\,\mathbf{v}_1^T, \mathbf{v}_2^T, \cdots, \mathbf{v}_m^T\,]_n\,. \tag{46}$$

The global covariance matrix is then given by

$$\mathbf{C}_k = \mathrm{E}[\mathbf{u}_n\mathbf{u}_{n-k}^T] = \begin{bmatrix} \vdots & \vdots & \vdots \\ \vdots & \mathrm{E}[\mathbf{v}_{i,n}\mathbf{v}_{j,n-k}^T] & \vdots \\ \vdots & \vdots & \vdots \end{bmatrix} = \begin{bmatrix} \vdots & \vdots & \vdots \\ \vdots & \mathbf{R}(\mathbf{r}_{i,n}-\mathbf{r}_{j,n-k}) & \vdots \\ \vdots & \vdots & \vdots \end{bmatrix}. \tag{47}$$

where the final form consists of the 3×3 block matrices representing the covariance between the point $\mathbf{r}_i$ in layer n and the point $\mathbf{r}_j$ in layer $n-k$. The simulation procedure consists of a k-step calibration of the matrices $\mathbf{A}$ and $\mathbf{B}$, based on the covariance matrices $\mathbf{C}_0$ and $\mathbf{C}_k$ as described in Section 3, followed by sequential use of the single-step recurrence (7).

Simulation of a turbulent wind field by the present procedure was used in [9] for wind turbine response analysis. The field is represented by 24 radial lines of length 43 m with 8 points in each. In the example the integral length-scale is $\lambda = 120\,$m. The simulation is based on sections separated by $\Delta y = 0.5\,$m, and the calibration distance is taken to be the integral length-scale λ, corresponding to $k = 240$. The model is calibrated by use of the exponential representation of the wind field correlation. Lengthwise and transverse correlation for points with axial separation y are shown in Fig. 3. It is seen that the lengthwise correlation represented by $f(y)$ retains much of the exponential form, while the simulated transverse correlation represented by $g(y)$ closely follows the theoretical Airy-function representation from the von Kàrmàn spectrum.

5 CONCLUSIONS

A simple framework for autoregressive simulation of stochastic fields has been presented. The autoregressive format leads to a simple exponential correlation structure in the time-dimension. In the case of scalar processes a more elaborate correlation structure can be obtained by adding memory to the process via an extension to autoregressive moving average (ARMA) processes. The ARMA format incorporates a more detailed correlation structure by including previous values of the simulated process. Alternatively, a more detailed correlation structure can be obtained by including additional ‘state-space’ variables in the simulation. For a scalar process this would imply an increase of the dimension of the process to be simulated. In the case of a stochastic field the correlation in the time-dimension is represented indirectly in the simultaneous spatial correlation.

The model with the shortest memory – the single-step autoregressive model – has been analyzed, and an efficient multi-step calibration procedure has been developed. The calibration makes direct use of conditional correlations and means, expressed explicitly in terms of the zero and k-step correlation matrices of the stochastic field. The correlation structure of an isotropic turbulent wind field is developed from the generalized von Kàrmàn spectrum in terms of the Airy function, and the simulation procedure is illustrated for turbulent wind with Airy or exponential function representation of the correlation structure. In spite of the basic simplicity of the simulation algorithm, the details of the transverse correlation, that should satisfy an integral condition for consistency, is represented well.

REFERENCES

[1] G.E.P. Box, G.M. Jenkins, G.C. Reinsel, *Time Series Analysis*, 3rd ed., Prentice-Hall, Englewood Cliffs, NJ, 1994.

[2] O. Ditlevsen, *Uncertainty Modeling*, McGraw-Hill, NewYork, NY, 1981.

[3] J. Mann, S. Krenk, Fourier simulation of non-isotropic wind field model. *Proceedings of the 6th ICOSSAR*, Balkema, Rotterdam, 1669–1674, 1993.

[4] G.K. Batchelor, *The Theory of Homogeneous Turbulence*, Cambridge University Press, Cambridge, UK, 1953.

[5] T. von Kàrmàn, Progres in the statistical theory of turbulence, *Proceedings of the National Academy of Science*, **34**, 530–539, 1948.

[6] S. Krenk, Wind field coherence and dynamic wind forces. *IUTAM Symposium on Advances in Nonlinear Stochastic Mechanics*, Kluwer, Dordrecht, 269–278, 1996.

[7] L. Kristensen, N.O. Jensen, Lateral coherence in isotropic turbulence and in the natural wind, *Boundary Layer Meteorology*, **17**, 353–373, 1979.

[8] F.W.J. Olver, D.W. Lozier, R.F. Boisvert, C.W. Clark, *NIST Handbook of Mathematical Functions*, Cambridge University Press, Cambridge, UK, 2010.

[9] S. Krenk, M.N. Svendsen, J. Høgsberg, Resonant vibration control of three-bladed wind turbine rotors, Department of Mechanical Engineering, Technical University of Denmark, 2011. (submitted for publication)

COMPDYN 2011
3rd ECCOMAS Thematic Conference on
Computational Methods in Structural Dynamics and Earthquake Engineering
M. Papadrakakis, M. Fragiadakis, V. Plevris (eds.)
Corfu, Greece, 25–28 May 2011

INFLUENCE OF STEEL MECHANICAL PROPERTIES ON EBF SEISMIC BEHAVIOUR

M. Badalassi[1], A. Braconi[2], S. Caprili[3] and W. Salvatore[3]

[1] Consorzio Pisa Ricerche
Corso Italia 116, 56122 Pisa
e-mail: m.badalassi@ing.unipi.it

[2] Riva FIRE S.p.a.
Viale Certosa 249, I-20151 Milano
e-mail: ricerca.lunghi@rivagroup.com

[3] Università di Pisa, dipartimento di Ingegneria Civile
Largo L. Lazzarino 1, 56126 Pisa
e-mail: silvia.caprili@ing.unipi.it, walter@ing.unipi.it

Keywords: Eccentrically braced frames, overstrength factor, incremental dynamic analysis

Abstract: *Among the resisting steel types suitable for the design of high ductility structures, Eurocode 8 proposes MRFs and EBFs. Also if the formers are generally considered a more efficient structural solution for high-ductility design, they suffers a strong weakness in the lateral stiffness creating, during the design process, cumbersome procedures to avoid excessive lateral displacements maintaining quite high ductile behaviour under design seismic actions. In many cases, the design process produces not optimized structural members, oversized respect to the minimum seismic requirements due to lateral deformation limitations. On the contrary, EBF combines high lateral stiffness furnished by bracing elements and high dissipative capacities furnished by plastic hinges developed in links. Eurocode 8 proposes a design procedure for realizing high ductility EBF in which iterative checks are required to properly design the links assigning to every link a defined level resistance dependant on all other links resistance. The present paper investigates the seismic behaviour of EBFs using the Incremental Dynamic Analysis technique in order to explore their mechanical response under increasing seismic action levels. A set of steel structures is designed according to Eurocode 8. The numerical simulations are executed considering the variability of both steel mechanical properties and seismic input, aiming to a complete probabilistic characterization of mechanical response of the system and deeply analyzing the effective level of structural safety and the ability to internally redistribute plasticizations during the earthquake. Structural safety conditions will be defined according to a multi-level performance approach. The paper presents also some final suggestions for possible improvements/simplifications in EBF design.*

1 INTRODUCTION

In the last seventies the use of eccentrically braced frames (EBFs) as earthquake resistant structures in medium and high seismicity regions greatly increased; this was mainly due to the fact that, respect to other traditional structural typologies, EBFs are able to join good dissipative performances to high elastic stiffness [1], combining the plastic dissipative behaviour of moment resisting frames (MRFs) with the high lateral stiffness of concentrically braced frames (CBFs) [2].

The dissipative behaviour of EBFs is related to particular beam elements called “links”: during an earthquake the link, designed to plasticize while all the other elements remain in the elastic range, develops high plastic deformations and consequently dissipates seismic energy.

The behaviour of link elements, and afterwards the way they dissipate energy, is related to their length (e): short links (i.e. characterized by a ratio between the plastic shear and the plastic moment smaller than 1.6 times the link length) generally develop high shear deformations, while long links (i.e. characterized by a ratio between the plastic shear and the plastic moment higher than 2.5 times the link length) mainly dissipate energy trough the formation of flexural deformations.

The ability of EBFs in dissipating energy strictly depends on the criteria adopted in the design: the plastic deformations are essentially located on link elements, dimensioned for yielding before beams, braces and columns that, otherwise, are proportioned using the forces generated by the yielded and hardened links [3] in order to remain in the elastic field, according with the principles of capacity design. The overstrength of non dissipative elements is consequently related to the mechanical and geometrical characteristics of the links; the overstrength behaviour of elastic elements is expressed trough the factor Ω, defined as the ratio between the plastic design resistance and the effective action on the dissipative elements (shear for short links and bending for long links). According to actual standards, such as Eurocode 8, the distribution of the overstrength factor Ω should be quite uniform, not varying more than 25% respect to its minimum value: this is necessary for guaranteeing a uniform distribution of link plasticization on all the floors and the global dissipation of seismic energy.

Otherwise, recent studies [4] evidenced that frequently, especially in presence of a high number of storeys, EBFs underwent undesired collapse mechanisms, despite the presence of small plasticization of the links of some floor and the respect of the design criteria. This fact can be partially caused by the difference between the nominal design value and the real effective value of the mechanical properties of steel [1, 5]: this difference, generally taken into account trough the introduction of the material overstrength coefficient γ_{ov}, can lead to the alteration of the failure modes supposed in the design, causing premature local collapse phenomena of the structure and consequently avoiding the global dissipation of seismic energy. The present work aims at the investigation of the influence of variability material properties on the dissipative behaviour of EBFs and was developed in the framework of a European Research Project funded by the Research Found for Coal and Steel (OPUS – Optimizing the seismic Performance of steel and steel-composite concrete strUctures by Standardizing material quality control). To this purpose, different steel buildings were firstly designed according to actual European standards and then analyzed trough the execution of non linear incremental dynamic analyses (IDA), considering the variability of both mechanical properties of materials and seismic input, in order to achieve a complete probabilistic characterization of the mechanical response of the system. The results obtained using the nominal and the real values of mechanical material properties, provided by the European steel producers partners of the project, were compared in terms of activation of collapse criteria, analyzing the effective level of structural safety and the ability of the structure to redistribute the plastic demand imposed by the earthquake.

2 PROPOSED METHODOLOGY

Probabilistic techniques were adopted in order to assess structural response of case studies as function of seismic input and mechanical properties variability.

Indeed, even if in general seismic actions are time-variant variables (processes) and therefore reliability problems in earthquake engineering are time-variant reliability problems, for OPUS purposes, the problem was transformed in a time-invariant problem (i.e. looking only at extreme values) and a Monte Carlo simulation technique was applied in an efficient way; moreover, a probabilistic procedure able to furnish a good estimation of failure probability for all identified design points was also defined.

According to these final considerations, the research project adopted the following general approach devoted to the effective evaluation of seismic reliability for all structural case studies designed during the research:

- **step 1**. Deep knowledge of structural systems. The knowledge about the structural behaviour of the case studies was completed and determined thorough several numerical simulations, adopting non-linear static and dynamic analyses.
- **step 2**. Nonlinear modelling and collapse modalities assessment. Each structural system was described by accurate nonlinear models individuating the relevant collapse criteria.
- **step 3**. Characterization of seismic hazard. Seismic actions were modelled adopting parameters and hazard proposed by EN1998-1-1; in particular, hazard function (i.e. annual exceedance probability) for European seismicity is taken from EN1998-1-1 and calibrated according to design parameters associated to ultimate limit state verification. Seven seismic inputs to be adopted in the numerical simulations were artificially generated from response spectra adopted in the design.
- **step 4**. Probabilistic model of mechanical variables. Scattering of steel products was represented by a multi-variable model where yielding stress – $R_{e,H}$ (f_y) –, tensile strength – R_m (f_t) – and elongation at fracture – A (ε_u) were considered with their probabilistic interdependencies.
- **step 5**. Execution of nonlinear analyses and optimal planning of numerical simulations. The correlation between the seismic demand and the structural response of case studies was defined employing non-linear dynamic analyses; peak ground acceleration (PGA) of selected seismic inputs was varied according to appropriate levels chosen in order to activate collapse modes. In such a way, the number of simulations characterized by failures according to different modes was increased.
- **step 6**. Probabilistic procedure for P_{fail} estimation. Numerical results coming from dynamic analyses were analyzed employing a statistical procedure that furnishes fragility curves and yearly threshold exceedance probability of the relevant collapse modes for each case study.

The numerical simulations were executed using Incremental Dynamic Analysis techniques, suitable for the analysis of structural response at different PGA levels.

3 DESCRIPTION OF CASE STUDY

In the widest framework of OPUS project, fifteen different buildings in steel and steel – composite concrete structure were designed, in order to cover the most common geometrical and functional structural typologies in Europe: MRFs, CBFs and EBFs for offices, industrial buildings and car parks were analyzed.

The present paper deals with the seismic behaviour of EBF steel structures; three different buildings, so on called building 3, 4 and 16, were designed according to the criteria imposed by Eurocode 8. External EBFs were designed to resist the total seismic horizontal forces: stating the symmetry of geometrical properties and mass distribution, the design of the buildings was calibrated on single eccentrically braced frames referring to the two main directions of the structure. The consistency of the design was verified comparing the results so obtained with the ones coming from dynamic modal analyses of 3D global models of the buildings.

Building 3 and 4 are office buildings, while building 16 is a car park; buildings 3 and 16 are located in high seismicity region and present short shear links, while building 4, located in medium-low seismicity area, presents long bending links. Buildings 3 and 4 have a similar geometry, characterized by 5 storeys with an interstorey height of 3.50 m and a span length varying between 6 and 7 m; building 16 is characterized by a span length between 8 and 10.5 m and presents only two storeys with interstorey height equal to 4.0 m. The link disposition and length vary in relation to the typology (shear or bending) and to floor position.

A duplication of secondary beams was applied in buildings 3 and 4 in order to avoid the amount of vertical loads and connection of elements in correspondence of the dissipative zone of links (see Figure 1c). Pinned connections were used at the ends of non dissipative elements, such as braces and columns, and between beams and columns for K-brace frames (frame 3xz, 16xz and 16yz); welded connection were adopted for the beam to column joints in D-brace frames. The general geometrical properties of EBF buildings are presented in Table 1.

For all described buildings a floor type characterized by a concrete slab on prefabricated trussed slab for a global thickness of 23 cm was used; in the design of buildings 3 and 4 steel grade S355 (nominal yielding strength equal to 355 MPa) was used; building 16, on the other hand, was designed considering steel grade S275 (nominal yielding strength equal to 275 MPa). As regards seismic action, in buildings 3 and 16 a PGA equal to 0.25 g and a soil of category B were considered, while building 4 was dimensioned for a PGA equal to 0.10 g and a soft soil of type C; the response spectra adopted in the design are compatible with both Eurocode 8 [6] and actual Italian Standards for constructions NTC2008 [7]. Table 2 summarizes vertical and horizontal loads adopted in the design.

The general geometry of buildings is represented in Figures 1-4.

Building number	Height	Steel Quality	X direction		Y direction	
			Resisting system	Span [n° x L]	Resisting system	Span [n° x L]
3	5x3.5 m	S355	EBF shear	3x7m	EBF shear	4x6m
4	5x3.5 m	S355	EBF bending	3x7m	EBF bending	4x6m
16	2x4.0 m	S275	EBF shear	5x8m + 2x10m	EBF shear	6x10.5m

Table 1: Summary of geometric properties of EBF buildings.

According to Eurocode 8 and in relation to the location of the buildings, design factors respectively equal to 6 and 4 were adopted for high ductility class (HDC) buildings (3 and 16) and for low ductility class (LDC, building 4). All the EBF buildings so far described were designed to resist to vertical and horizontal forces provided by actual standards, both for seismic and static combination, without encountering global or local collapses. The design was optimized in order to have a uniform plasticization of links in all the floors: an accurate distribution of the overstrength factors Ω_i was pursued, obtaining variation smaller than 25% among the floors. The obtained values for overstrength factors are summarized in Table 3.

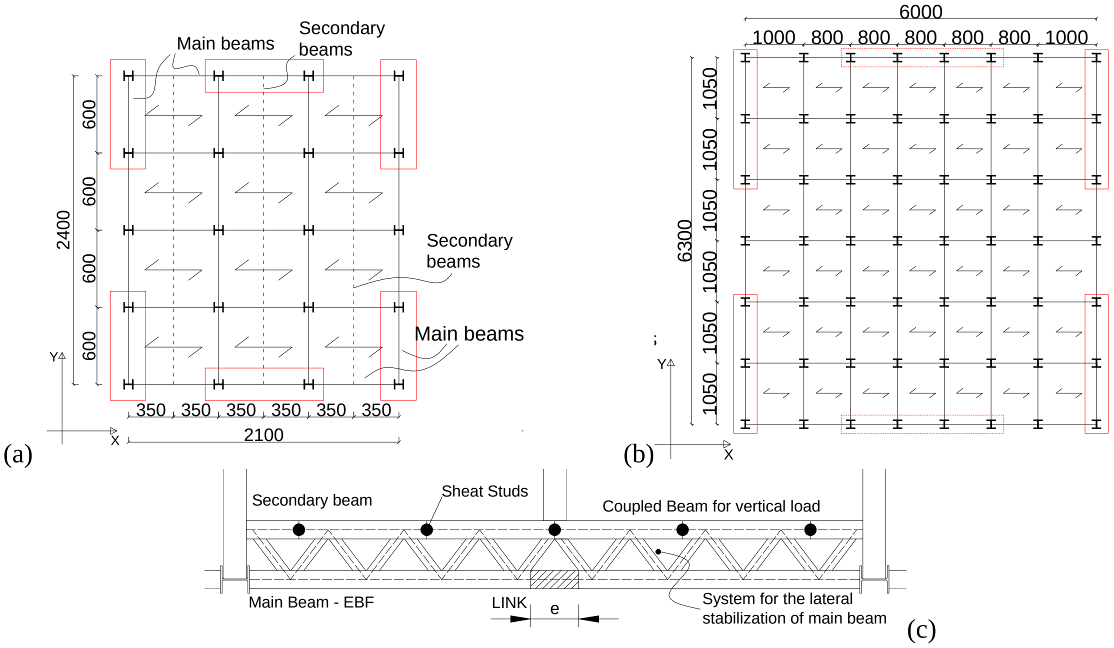

Figure 1: General plan of buildings a) office buildings 3 -4, b) car park 16 and c) beam duplication for decoupling vertical and seismic loads.

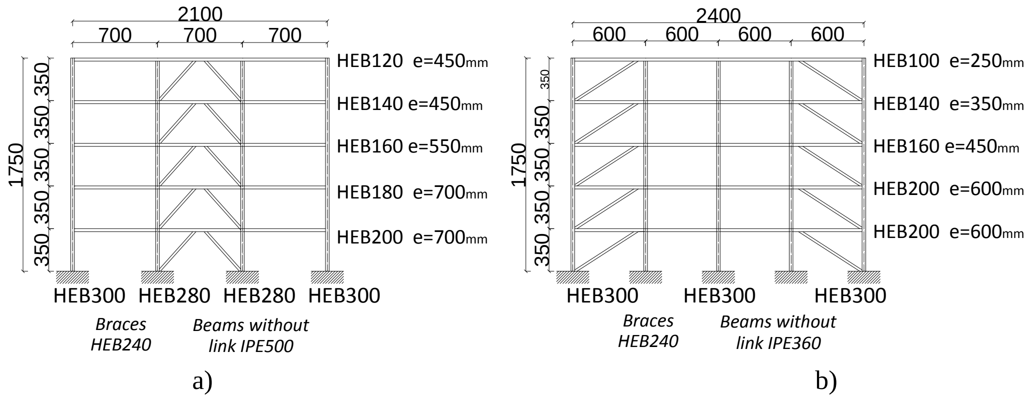

Figure 2: Building 3 (short links), geometry and elements: a) xz frame, b) yz frame.

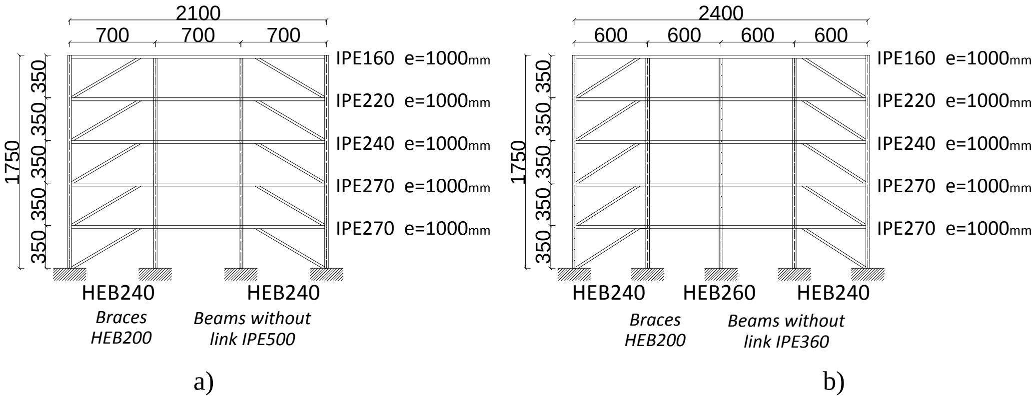

Figure 3: Building 4 (long links), geometry and elements: a) xz frame, b) yz frame.

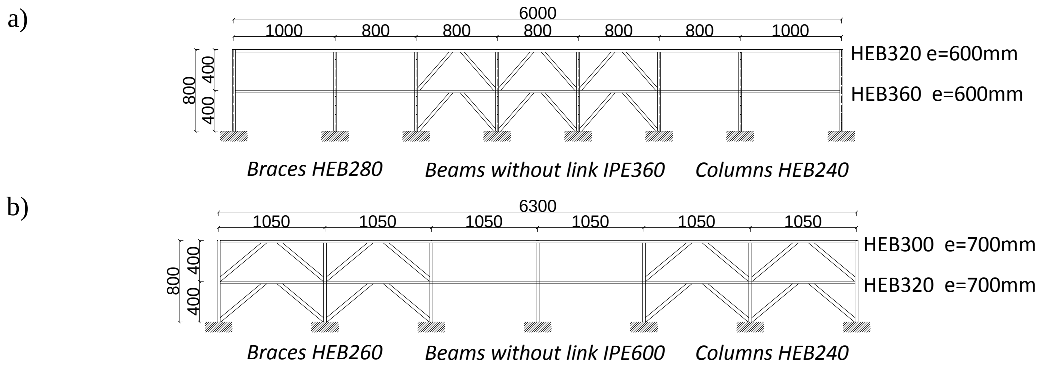

Figure 4: Building 16 (short links), geometry and elements: a) xz frame and b) yz frame.

Building	Type	Typology	Live Load	Snow Load	Wind Load	Soil type	Seismic Action	Seismic mass Floor	Seismic mass roof
-	-	-	kN/m^2	kN/m^2	kN/m^2	-	-	kN	kN
3	Office	EBF	3.00	1.00	1.10	B	0.25 g	3480	3220
4	Office	EBF	3.00	1.00	1.10	C	0.10 g	3480	3220
16	Car Park	EBF	2.50	1.00	1.10	B	0.25 g	27700	28820

Table 2: Summary of vertical and horizontal loads acting on buildings.

Building	Storey	X direction	Y direction
		Ωi	Ωi
3	Storey 1	1.66	2.12
	Storey 2	1.54	2.47
	Storey 3	1.53	2.00
	Storey 4	1.62	2.03
	Roof 5	1.86	2.24
4	Storey 1	1.68	1.99
	Storey 2	1.87	1.74
	Storey 3	1.63	1.78
	Storey 4	1.66	1.76
	Roof 5	1.51	1.61
16	Storey 1	1.53	1.57
	Roof 2	1.88	1.91

Table 3: Overstrength factors for each building.

The sizing of the links with actions coming from the linear analysis was the base for the proportioning of the other overstrengthening elements such as beams, braces and columns, according to the principles of capacity design; buckling phenomena of elements in compression and interstorey drift limits, i.e. lateral stiffness requirements, were also conditioning for the definition of brace and columns profiles.

Typically, HEB sections were used for columns and braces in all the buildings; otherwise, HEB or IPE sections were adopted for links: HDC buildings with short shear links present HEB section for dissipative elements (e varies between 250 and 700 mm), while LDC building employs IPE section for long bending links (e equal to 1000 mm), as presented in Table 4.

Building	Storey	X direction		Y direction	
		Link profile	Link length (mm)	Link profile	Link length (mm)
3	Storey 1	HEB200	700	HEB200	600
	Storey 2	HEB180	700	HEB200	600
	Storey 3	HEB160	550	HEB160	450
	Storey 4	HEB140	450	HEB140	350
	Roof 5	HEB120	450	HEB100	250
4	Storey 1	IPE270	1000	IPE270	1000
	Storey 2	IPE270	1000	IPE270	1000
	Storey 3	IPE240	1000	IPE240	1000
	Storey 4	IPE220	1000	IPE220	1000
	Roof 5	IPE160	1000	IPE160	1000
16	Storey 1	HEB320	600	HEB300	700
	Roof 2	HEB360	600	HEB280	700

Table 4: Link profile and length for each building.

4 DESCRIPTION OF NON LINEAR MODELS

4.1 Numerical Non linear models

In order to evaluate the influence of the variability of material properties on the effective seismic behaviour of EBF structures, non linear Incremental Dynamic Analyses (IDA) were executed on plane frame models of the buildings previously described.

As many past works evidenced [8, 9] the modelling of link elements should be very accurate for obtaining numerical outcomes consistent with the EBF response prediction; both short and long links, despite the different mechanism they use for dissipating seismic energy, develop flexural forces combined with shear ones: the model of link should consequently be able to reproduce both the two effects.

Many numerical models were proposed in literature to represent the behaviour of link elements, for example one component models with concentrated plastic hinges at the ends of the element [10] or two component models constituted by beams working in parallel [8]; nevertheless, only more recent models are able to encounter the shear behaviour of the dissipative link element [8].

In the present work, bi-dimensional models of the main frames of the buildings were realized using the numerical software OpenSees [11]. The dissipative behaviour of link elements and the combined effect of shear forces and bending moments were directly taken into account modelling all the elements as “fiber section elements” (Figure 5a). The calibration of the software was executed comparing the outcomes from cyclic loading histories on single components (for example the braces) with literature results [12].

Inelastic fiber elements were used for representing columns, beams without links and short shear links; on the other hand, two elements were used for modelling each long bending link and four elements were employed for each brace. Buckling phenomena of braces were directly taken into account giving an initial imperfection equal to 1/500 of the brace length to the middle point of the brace, as represented in Figure 5b; a similar imperfection was also assigned to the top of columns in order to include in the analysis P-Δ effect (Figure 5b). The value adopted for the imperfection was evaluated from the calibration with literature results.

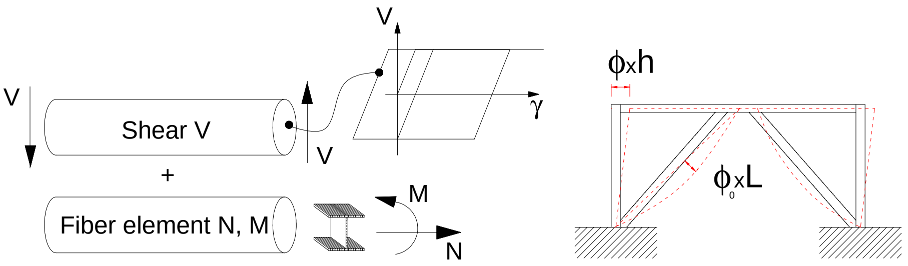

a) b)

Figure 5: a) General scheme of fiber elements and b) model of imperfections of braces and columns.

For modelling the flexural behaviour of steel members – beams, braces and columns – , the Menegotto-Pinto law [13], characterized by bilinear elastic-plastic stress-strain curve with kinematic hardening, accurately calibrated in order to agree with literature results, was used (Figure 6a); moreover, as regards the force-distortion law used for representing the shear behaviour of elements, a bilinear elastic-plastic law with kinematic hardening was used for links (Figure 6b).

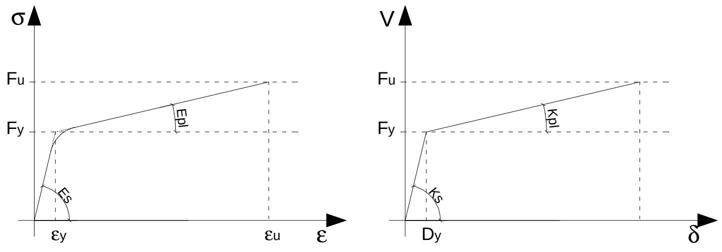

a) b)

Figure 6: Constitutive law adopted for a) flexural behaviour, b) shear behaviour of dissipative elements.

4.2 Definition of collapse criteria for EBFs

For evaluating the global ductile behaviour of the structures under seismic action all the possible collapse mechanism for EBFs were analyzed, referring to what prescribed by actual standards, such as EN 1993-1 [15] and FEMA [16]; the collapse limits individuate the point at which IDA simulation should be stopped, since for higher levels of PGA it's not important to consider the behaviour of the structure. The collapse limitations adopted are strictly related to different limit states, assessing the structural performances both at ultimate and serviceability limit state. One of the most conditioning collapse criteria for eccentrically braced frames is obviously the failure of link elements, in which plastic deformation are concentrated according to the design principles. The plastic rotation is calculated as the ratio between the relative vertical displacement (δ) and the link length (e), see expression (1): for shear short link δ is evaluated as the relative vertical displacement between the two ends of the link (Figure 7a), for long bending links δ refers to the mid length of the element (Figure 7b). The limits assumed according to the standards are presented in Table 5.

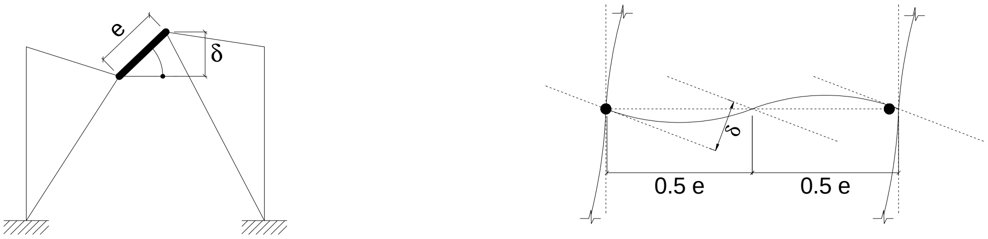

a) b)

Figure 7: Evaluation of link plastic rotation a) for short shear links, b) for long bending links.

$$\frac{v_1 - v_2}{e} = \frac{\delta}{e} = \gamma_{LINK} \tag{1}$$

The limit axial load for the buckling of steel members in compression (columns and braces) is evaluated according to Eurocode 3 [15] with expression (2), and is consequently strongly influenced by the mechanical properties of materials (yielding strength f_y):

$$N_{b,Rd} = \frac{\chi \cdot A \cdot f_y}{\gamma_{M1}} \tag{2}$$

The limitation imposed to interstorey drift should be assessed; the respect of the lateral stiffness requirements strongly influenced the sizing of steel members such as braces, especially in building 4, designed for low-ductility class. For EBFs, the collapse criteria to be taken into account are summarized in Table 5.

Collapse Criteria	Reference code	Limit value
Ultimate plastic rotation	EC8, FEMA 356	110 mrad (shear), 20 mrad (bending)
Global buckling	EN 1993-1	-
Interstorey drift ratio	EN 1998-1	1.5% x Interstorey height

Table 5: Summarizing table of collapse criteria for EBFs.

5 SEISMIC HAZARD vs. SEISMIC INPUT

5.1 Seismic hazard

Seismic hazard of a particular site expresses its natural exposure to severity of possible earthquake. Seismic hazard analysis characterize the maximal amplitude of ground shaking during the earthquake by chosen design ground motion parameter in the specified level of probability and time of occurrence of the event.

According to EN1998-1 guidelines, it is possible to assume that the annual rate of exceedance of the reference peak ground acceleration a_{gR} may be taken to vary with a_{gR} as:

$$H(a_{gR}) = k_0 \cdot a_{gR}^{-k} \tag{3}$$

Moreover, EN1998-1 suggests that exponent k, depending on seismicity, can be generally taken equal to 3. The value of k_0 was fixed according to basic performance requirements imposed by EN1998-1: the design seismic action should have a exceeding probability of 10% (P_{NCR}, probability of non collapse requirement) in 50 years (T_L, exposition period of the structure) for the non-collapse requirements. The return period of seismic action, T_R, is correlated with P_{NCR} and T_L by the following formula

$$T_R = \frac{-T_L}{\ln(1-P_{NCR})} \tag{4}$$

that gives a return period of 475 years for the design PGA. According to PGA levels assumed during seismic design, 475 years of return period corresponded, respectively, to 0.25g in high seismicity areas and 0.10g in low seismicity areas and fixed k_0 parameter in eqn. (3) equal to 3.29×10^{-5} for high seismicity areas and 2.10×10^{-6}. Resulting hazard functions for high and low seismicity are presented in Figure 8.

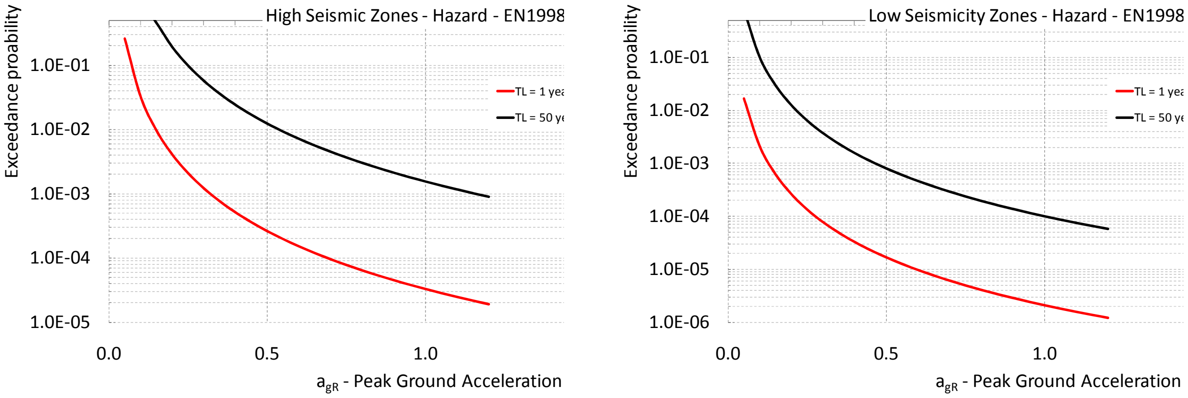

a) b)

Figure 8: Hazard function according to EN1998-1 prescriptions: (a) high seismic hazard; (b) low seismic hazard.

5.2 Definition of accelerograms

According to EN1998-1-1 prescription, seven earthquake time-histories of natural earthquakes or artificially generated time histories can be used. To obtain results representative for any seismic area in Europe, it reasonable to use artificial accelerograms, which meet the elastic response spectra in EN 1998-1 and are so consistent with chosen hazard model. In order to generate artificial earthquake time histories, the program SIMQKE [14], developed by Gasparini and Vanmarcke (1976), was used.

Two types of seismic intensities were considered: for high seismicity the PGA level was 0.25 g, while the type 1 spectrum for soil type B was used; for low seismicity the PGA was fixed 0.10 g, while the type 2 spectrum for soil type C was applied, Figure 9a. The filter function was defined by a trapezoidal shape, where the time intervals for the initial and ending ramp were 5 s and the strong motion duration was 10 s for high and 5 s for low seismicity, Figure 9b. The relevant Eigen-periods were assumed to be in a range between 0.1 s and 3.0 s. The chosen sampling interval of $\Delta t = 0.01$ s allowed a sufficient accurate calculation for Eigen-frequencies up to 20Hz (5 points for each period).

The verification of the accelerograms by determining the velocity and displacement time histories showed that the displacements were running out (Figure 10). Hence, a baseline correction was applied to obtain a sufficient small displacement at the end of the record. The adequacy of the accelerograms was checked by determination of their elastic response spectra, Figure 11. For periods lower than T_B the spectrum value S_a was slightly too high, Figure 12; however, the target spectrum is sufficiently met and the requirements defined in EN1998-1 were met.

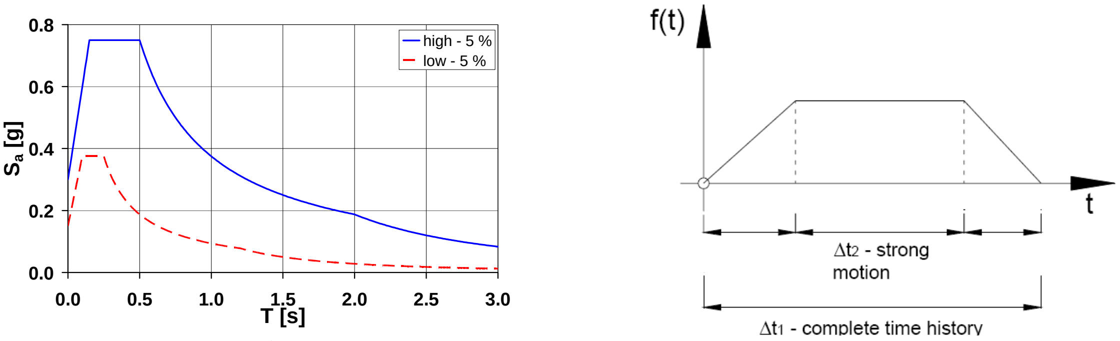

a) b)

Figure 9: Target spectra (a) and filter function (b) for the generation of artificial time histories

Seismicity	p.g.a.	Spectrum	Soil	Total duration	Strong motion duration
Low	0.10 g	Type 2	Type C	15 s	5 s
High	0.25 g	Type 1	Type B	20 s	10 s

Table 6: Parameters of target spectra and filter function for low and high seismicity

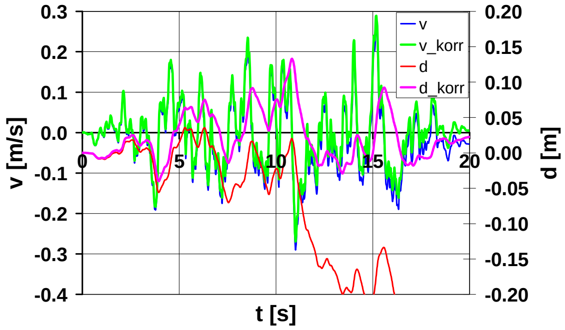

Figure 10: Baseline correction for an artificial accelerogram (high seismicity)

The COV of the spectral values for the 7 accelerograms is between 0.04 and 0.12, Figure 13. It should be noted, that the energy density of artificial accelerograms is much higher than of natural accelerograms, as all frequencies of interest are included.

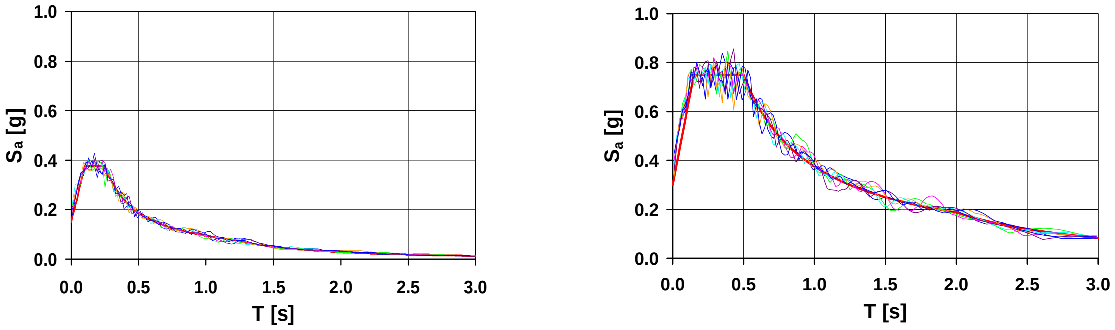

a) b)

Figure 11: Target spectrum and elastic response spectra of 7 artificial accelerograms: low seismicity (a) and high seismicity (b).

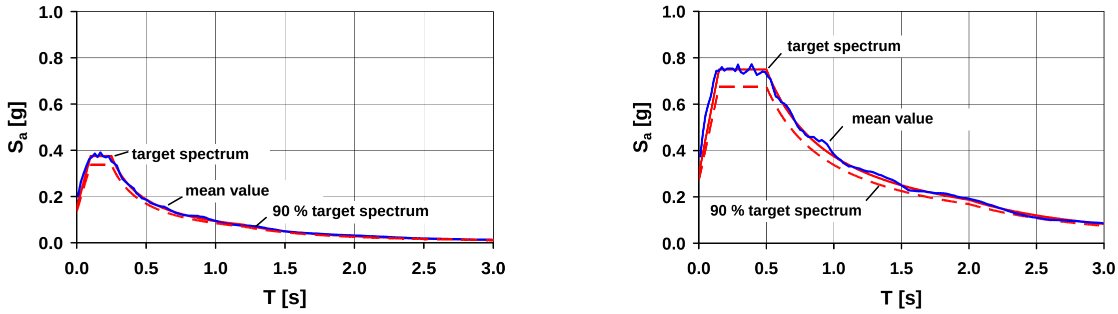

a) b)

Figure 12: Target spectrum and mean value of the elastic response spectra of 7 artificial accelerograms: low seismicity (a) and high seismicity (b).

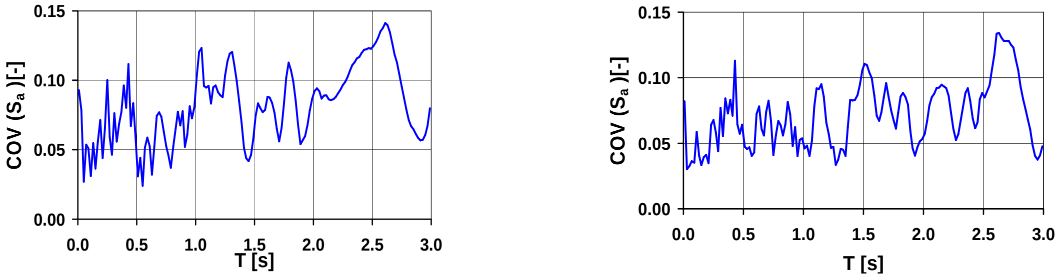

a) b)

Figure 13: COV of the elastic response spectra of 7 artificial accelerograms: low seismicity (a) and high seismicity (b).

5.3 Seismic input for nonlinear analyses

IDA simulations were executed scaling generated seismic inputs at different PGA levels; PGA levels, considered as significant for the probabilistic assessment of seismic response of designed structure, were previously determined studying structural response of case studies. In particular, for each plain structure (see Figures 2, 3 and 4), different excitation levels were individuated according to the collapse modes that can be activated increasing PGA, see table 7. It is worth noting that collapse of columns was a mode that cannot be activated for PGA levels lower than 1.50g: hence, PGA levels corresponding to column collapse were not considered; concerning 3EBFX also collapse mode associated to braces was not activated. This high level of PGA for these two collapse modes was correlated to the frame design: columns are sized through column verification under full vertical static actions at Ultimate Limit State; braces for 3EBFX were over-sized due to the extreme sensitivity of structural configuration to second order effects.

a)

	Frame 3X				Frame 3Y			
Acc -	Link [g]	Col. [g]	Brace [g]	Drift [g]	Link [g]	Col. [g]	Brace [g]	Drift [g]
1	0.60	2.00	2.00	0.40	0.45	2.00	0.75	0.50
2	0.50	2.00	2.00	0.55	0.50	2.00	0.70	0.55
3	0.50	2.00	2.00	0.60	0.50	2.00	0.65	0.55
4	0.45	2.00	2.00	0.45	0.45	2.00	0.65	0.50
5	0.55	2.00	2.00	0.40	0.40	2.00	0.65	0.40
6	0.45	2.00	2.00	0.50	0.55	2.00	0.70	0.60
7	0.50	2.00	2.00	0.60	0.55	2.00	0.70	0.55

b)

	Frame 4X				Frame 4Y			
Acc.	Link	Col.	Brace	Drift	Link	Col.	Brace	Drift
-	[g]	[g]	[g]	[g]	[g]	[g]	[g]	[g]
1	0.40	2.00	0.60	0.90	0.40	2.00	2.00	1.20
2	0.50	2.00	0.80	1.40	0.50	2.00	2.00	0.90
3	0.50	2.00	0.60	1.00	0.50	2.00	1.90	0.95
4	0.45	2.00	0.50	0.95	0.40	2.00	1.60	0.70
5	0.50	2.00	0.50	1.10	0.50	2.00	2.00	1.15
6	0.45	2.00	0.50	1.20	0.40	2.00	1.90	0.80
7	0.50	2.00	0.55	1.20	0.50	2.00	2.00	1.20

c)

212	Frame 16X				Frame 16Y			
Acc.	Link	Col.	Brace	Drift	Link	Col.	Brace	Drift
-	[g]	[g]	[g]	[g]	[g]	[g]	[g]	[g]
1	0.60	1.70	0.55	0.70	0.70	2.00	0.50	0.65
2	0.60	1.70	0.55	0.70	0.70	2.00	0.40	0.80
3	0.60	2.00	0.55	0.70	0.75	2.00	0.35	0.80
4	0.50	1.50	0.50	0.55	0.60	2.00	0.35	0.70
5	0.60	1.60	0.50	0.65	0.65	2.00	0.35	0.75
6	0.55	1.70	0.55	0.65	0.60	2.00	0.35	0.75
7	0.70	2.00	0.60	0.80	0.70	2.00	0.35	0.80

Table 7: PGA levels determined according to relevant collapse modes, for a) building 3, b) building 4 and c) building 16.

6 EXECUTION OF NONLINEAR ANALYSES

For each case study, collapse criteria were analysed for each considered PGA level, executing incremental dynamic analyses adopting alternatively the 7 artificially generated accelerograms.

Monte Carlo Method was applied to each analysis generating 500 samples of mechanical variables and running IDA for each of them. In particular, to be adherent to the real assembling of steel structures, all beams and braces members were considered as probabilistically not dependant (generating independent sets of mechanical variables) while columns of two subsequent floors were considered as characterized by the same probabilistic variables, see generation scheme in Figure 14c.

In order to generate samples of mechanical properties, a log-normal model was assumed for each of them – yield strength $R_{e,H}$, ultimate strength R_m and elongation A – so that their distribution resulted multivariate in which the three variable were inter-correlated.

The correlation matrix of the adopted model was determined from statistical parameters derived from industrial steel production [15], summarized in Table 8.

The generation procedure was based on the adoption of an equivalent multi-normal probabilistic distribution [17] obtained from the original multivariate log-normal model.

In such a way, for each case study 3500 numerical simulations were carried out (i.e. 7 quakes × 500 material samples) for each considered PGA level and each considered collapse criterion.

Defining, for each collapse criterion, the damage measure (DM) for the relevant engineering demand parameter (EDP) stated in the Table 5, nonlinear analyses explored structural responses using a strip method as depicted in Figures 14a and 14b (Figure 14a includes seismic input and material variability, 3500 results for each PGA level; Figure 14b only shows material variability, 500 results for each PGA level).

Moreover each set of 500 nonlinear analyses, results (related to a single collapse criterion, a PGA level and accelerogram) were suitably standardised referring to the values $Y_i = 100 \cdot DM_i / DM_u$ being, for the specified collapse criterion, DM_i the damage measure assumed by the EDP in the i-th analysis and DM_u its limit value corresponding to collapse.

The so obtained new set of data was statistically analysed evaluating the basic parameters (maximum, minimum and mean values and standard deviation) and executing the χ^2 test to check the hypothesis of Normal or Log-Normal distributions. When the χ^2 test was not negative a Normal or Log-Normal distribution was assumed; alternatively the statistical cumulative density function was built, completed in correspondence of tails by suitable exponential functions [18].

The probability of failure related to each set of 500 data (related to a single collapse criterion, a PGA level and accelerogram) was so simply evaluated using its cumulative density function, being $P_f = P[Y > 100]$. Clearly, for each collapse criterion and each PGA level, 7 values of P_f, and so 7 fragility curves, were obtained, one for each accelerogram. The averaged of 7 fragility curves was assumed as the fragility curve related to that specific collapse criterion (see Figure 15).

Fragility of case studies referred to a collapse mode, was finally integrated with European Seismic Hazard function, as described in [6], furnishing annual probability of failure for relevant collapse criteria of all case studies, shortly presented in Tables from 9a to 9f.

Grade		Mean μ N/mm^2	Std. Dev.σ N/mm^2	Model	Correlation Matrix		
					f_y	f_t	ε_u
S275	f_y	350	32	f_y	1	0.74	-0.276
S275	f_t	460	21	f_t	0.736	1	-0.402
S275	ε_u	25	1.75	ε_u	-0.276	-0.4	1
S355	f_y	430	27	f_y	1	0.85	-0.382
S355	f_t	550	25	f_t	0.851	1	-0.577
S355	ε_u	25	1.75	ε_u	-0.382	-0.6	1

Table 8: Statistical parameters assumed for samples generation

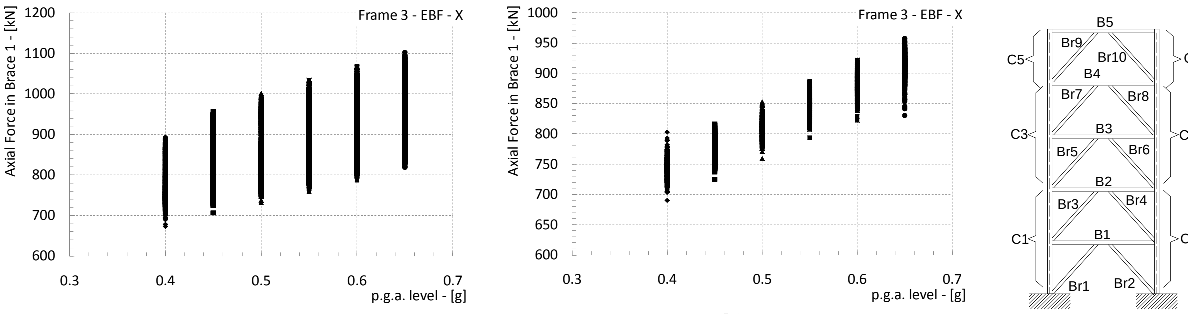

a) b) c)

Figure 14: IDA results in terms of Br1 force – a) material and seismic input variability; b) material variability; c) distribution of independent variables inside 3EBFX.

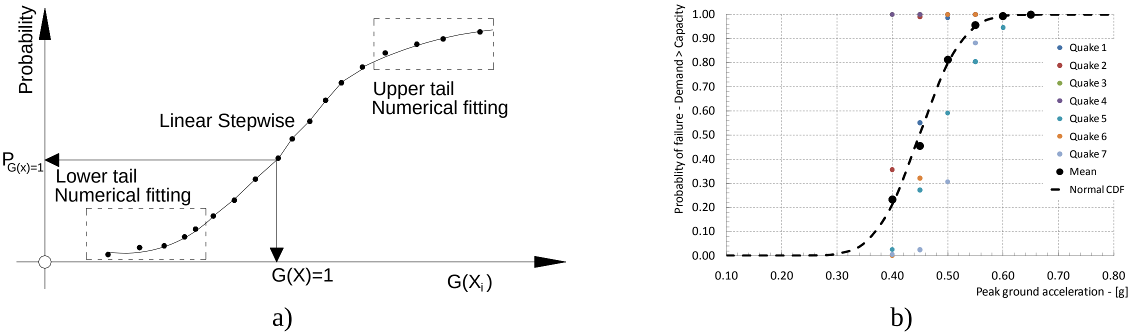

a) b)

Figure 15: a) numerical CDF directly derived from IDA results (when χ^2 failed); b) fragility of 3EBFX for ultimate plastic rotation of the link B1.

7 ANALYSIS OF RESULTS

The statistical procedure defined for a comprehensive analysis of IDA outputs was extensively applied to most part of structural members; in particular, all collapse modes presented in Table 5 were analyzed. The results in terms of annual seismic risk are reported in Tables 9a and 9b for frame 3, in Tables 9c and 9d for frame 4 and in Tables 9e and 9f for frame 16.

Comparing failure probability of braces in frame 3, it is clear which checks had conditioned the design: risk associated to braces in X direction is 5 times less than risk associated to Y frame, confirming the over-sizing required during the design for braces in X direction. The accurate design followed during the sizing of links in order to reduce as much as possible Ω factor and its differences between dissipative members it is confirmed by comparable failure probabilities for all links. The comparison of Ω factor derived from the elastic design, see Table 3, with link failure probability confirms that higher Ω are related to lower failure probability.

Element	B1	B2	B3	B4	B5	Br1	Br2
Seismic Risk	4.10E-04	4.20E-04	4.10E-04	2.80E-04	2.00E-04	4.50E-05	4.30E-05
Element	Drift 1	Drift 2	Drift 3	Drift 4	Drift 5		
Seismic Risk	2.80E-04	3.00E-04	1.60E-04	1.00E-04	9.30E-05		

Table 9a: Annual exceedance probability (Seismic risks) associated to 3EBFX collapse modes.

Element	B1	B4	B5	B8	B9	B12	B13
Seismic Risk	2.90E-04	3.10E-04	9.30E-05	1.30E-04	8.80E-05	1.30E-04	5.70E-05
Element	B16	B17	B20	Drift 1	Drift 2	Drift 3	Drift 4
Seismic Risk	8.20E-05	3.60E-05	5.3-05	2.80E-04	7.10E-05	5.30E-05	3.30E-08
Element	Drift 5	Br1	Br2	C1	C2	C4	
Seismic Risk	3.30E-08	2.80E-04	2.40E-04	1.50E-06	5.90E-06	1.50E-06	

Table 9b: Annual exceedance probability (Seismic risks) associated to 3EBFY collapse modes.

Failure probability associated to columns are really low, confirming that for such kind of structural systems, static combinations with complete factorized set of vertical loads represents for the column the most demanding check in many cases. The annual exceedance probability is often zero or 10^{-5}, largely lower than accepted threshold fixed between 10^{-3} and 10^{-4} for this type of structure accurately designed [19] and belonging to a standard (common) use category. It is worth noting that this trend is confirmed also for the columns in the frame 16: columns have a (annual) failure probability lower than 10-5 also if in such a case vertical loads are not relevant. This effect is related to the capacity design and, in particular, to the contribution of Ω factor: this coefficient is equal to 1.5 in the most optimized design and higher in the common practice, increasing of 50% seismic solicitation without material over-strength factor.

Element	B1	B3	B4	B6	B7	B9	B10
Seismic Risk	1.20E-05	1.10E-05	3.80E-06	3.70E-06	1.10E-06	9.60E-07	1.10E-07
Element	B12	B13	B15	Drift 1	Drift 2	Drift 3	Drift 4
Seismic Risk	3.50E-07	8.30E-06	9.50E-06	5.50E-06	1.70E-07	4.20E-09	5.50E-08
Element	Drift 5	Br1	Br2	C1	C2	C3	C4
Seismic Risk	5.50E-08	1.10E-05	1.00E-08	2.40E-15	2.00E-14	2.40E-15	2.40E-15

Table 9c: Annual exceedance probability (Seismic risk) associated to 4EBFX collapse modes.

Element	B1	B4	B5	B8	B9	B12	B13
Seismic Risk	1.20E-05	1.30E-05	2.70E-06	2.80E-06	4.20E-07	4.40E-07	2.00E-06
Element	B16	B17	B20	Drift 1	Drift 2	Br1	Br2
Seismic Risk	2.40E-06	2.30E-02	2.90E-02	4.50E-06	1.30E-06	1.20E-05	2.30E-05

Table 9d: Annual exceedance probability (Seismic risk) associated to 4EBFY collapse modes.

Seismic links contained in the frame 3 and 16 were shear links designed for high seismicity zones and their annual failure probability are fixed about 10^{-4}, while for bending links – frame 4 – failure probability is set about 10^{-5}, giving in such a case a more conservative design respect those executed in high seismic zones and with higher behaviour factor. This could suggest that EN1998 design procedure cannot allow the designers to optimize structural solutions designed for low seismic loads or with low behaviour factors.

Element	B1	B2	B3	B4	B5	B6	Br1
Seismic Risk	1.90E-04	2.00E-04	2.10E-04	3.40E-05	3.60E-05	3.40E-05	1.60E-04
Element	Br2	Br3	Br4	Br5	Br6	Drift 1	Drift 2
Seismic Risk	1.50E-04	1.50E-04	1.50E-04	1.60E-04	1.60E-04	2.40E-04	3.90E-05
Element	C1	C2	C3	C4			
Seismic Risk	3.50E-06	1.50E-05	1.50E-05	4.50E-06			

Table 9e: Annual exceedance probability (Seismic risk) associated to 16EBFX collapse modes.

Element	B1	B2	B5	B6	B7	B8	B11
Seismic Risk	2.60E-04	2.60E-04	2.60E-04	2.60E-04	3.60E-06	3.6E-0603.6E-06	
Element	B12	Br1	Br2	Br3	Br4	Br6	
Seismic Risk	3.60E-06	5.00E-06	5.10E-06	9.80E-06	5.40E-06	4.70E-06	
Element	C1	C2	C3	C5	C6	C7	
Seismic Risk	7.60E-08	7.60E-08	7.60E-08	7.60E-08	3.00E-07	3.00E-07	

Table 9f: Annual exceedance probability (Seismic risk) associated to 16EBFY collapse modes.

It is also important to underline that all case studies furnished annual failure probability in-line with the limit proposed by Melcher of 10^{-4} for such structures subjected to exceptional loading conditions [19]. This confirms that control measures considered inside capacity design approach, as material over-strength factor – γ_{OV} – and structural over-strength – Ω, can guarantee an adequate protection level to braces and columns. It seems, moreover, that this protection is too pronounced in the columns and so probably capacity design rules could be relaxed for this structural member.

7.1 Upper limitation on yielding stress: influence on IDA results

The probabilistic procedure was newly applied imposing a preconditioning of material input variables: the f_y of dissipative members was limited imposing a fictitious upper limit equal to 1.375, 1.35, 1.30 and 1.25 time the nominal yielding of the steel quality; in such a way, all results coming from simulations characterized by seismic link yielding higher than fixed limits were not considered. These limits were equivalent to impose a fictitious quality control for the seismic qualification, according to [6] or more severe limits, of steel profiles produced according to EN10025 [20]. Upper yielding definition reduced the number of useful material samples (variables) employable in the failure probability estimation; this reduction was more marked, as expected, for S275 quality being a steel quality less controlled than S355. In the Figure 16 it has been reported the effect of imposing an upper limit of 1.375 times the nominal yielding on link 1 properties for frame 3X and 16X: the upper yielding limit has no effect on generated samples while the effect is stronger for S275.

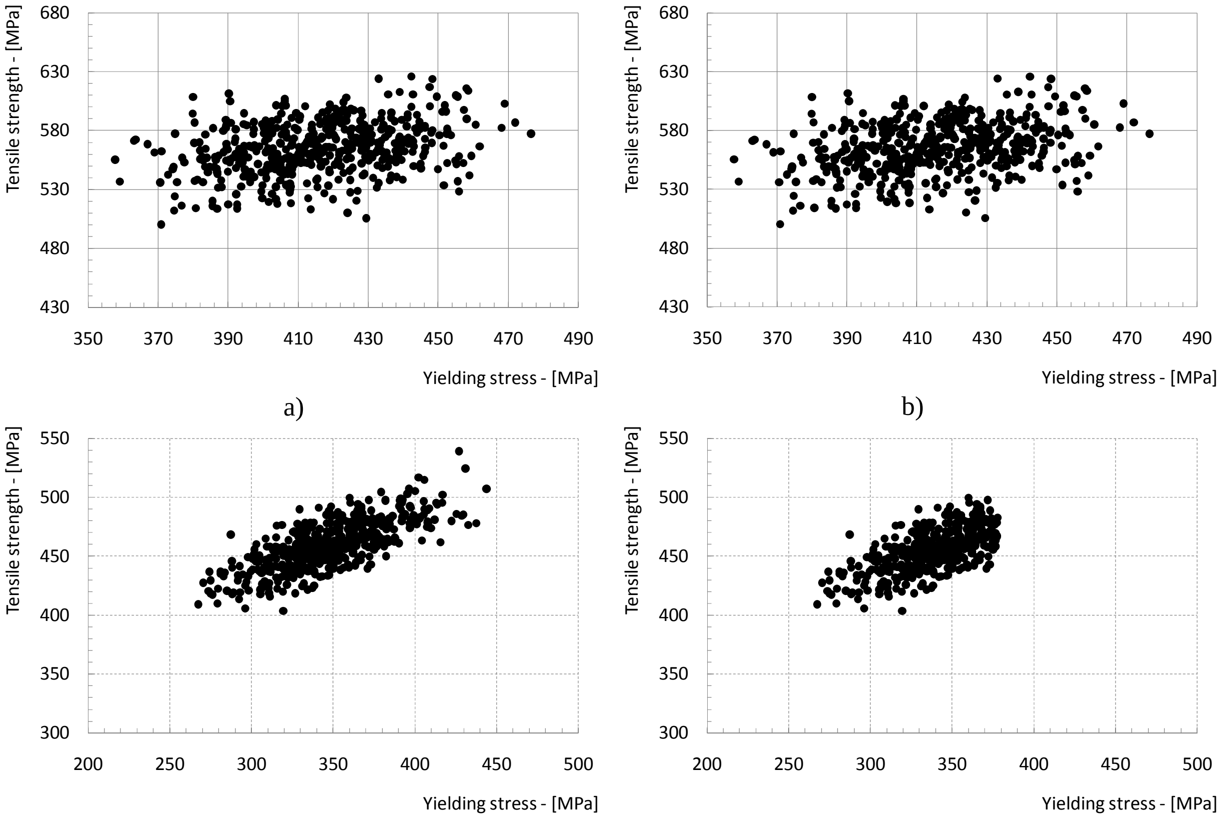

a)

b)

c)

d)

Figure 16: a) S355 without upper limit on f_y; b) S355 with upper limit on f_y equal to 1.375; c) S275 without upper limit on f_y; d) S275 with upper limit on f_y equal to 1.375.

Results in terms of annual failure probabilities (risk) calculated with the previous procedure are presented in Figures 17a and 17b.

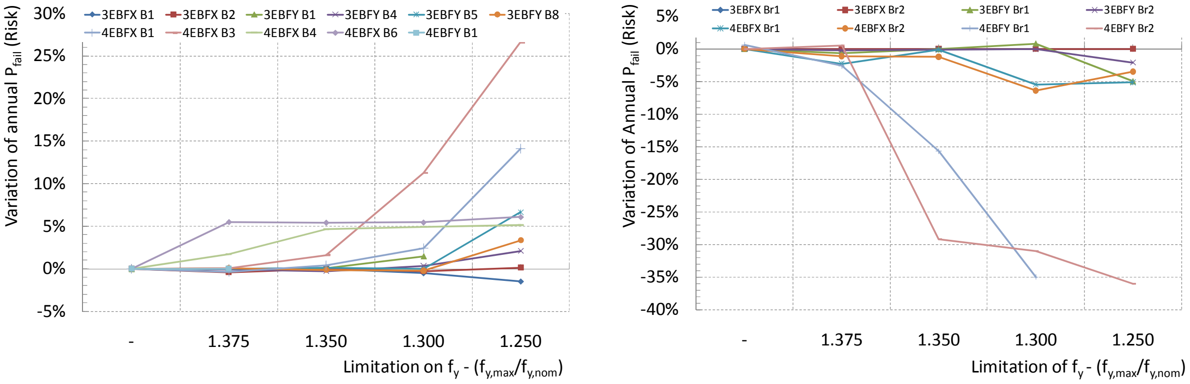

a) b)

Figure 17: a) variation of risk associated to ultimate plastic rotation of links; b) variation of risk associated to buckling of first storey braces.

The assignation of upper fy limits produced, as expected, a variation in the risk associated to link rotation and brace buckling; in particular, the annual probability of the link failure increased from 2% to 25% also while probability associated to braces failure decreased from 1% to 35%. According to these results it is clear that the definition of upper f_y limits must be accurately evaluated in order to do not unbalance too much the design in the exploitation of link plastic resources over its failure. At the same time it is also clear that the big decreasing of risk associated to brace failure is related to 4EBFY only, in which braces were really optimized (i.e. Capacity Design=Buckling Strength); in the other cases, more adherent to day-to-day practice, a little over-sizing (i.e. C.D.=0.92B.S.) furnished maximum variations of risk about -6%, mitigating strongly the effects of upper fy limit. It is worth noting that the benefits and the safety increment associated to additional controls for the seismic qualification of steel profiles must be carefully evaluated because structural safety herein estimated, considering both seismic input and material variability – Tables 9a-9f, is in-line with nominal values proposed by experts for the structural cases – 3EBFX, 3EBFY, 4EBFX, 4EBFY, 16EBFX and 16EBFY – under exceptional loading situation as earthquake.

AKCNOWLEDGEMENT

The results presented in this work were obtained in the framework of the OPUS research project, Optimizing the seismic Performance of steel and steel-composite concrete strUctures by Standardizing material quality control, funded by European Commission through Research Fund for Coal and Steel, contract RFCR-CT-2007-00039. Authors would like to thank dr. Max Guendel from RWTH for his support in the artificial earthquakes generation. Nevertheless opinions expressed in this paper are those of the writers and do not necessarily reflect those of the sponsors.

REFERENCES

[1] P.P. Rossi, A. Lombardo, Influence of the link overstrength factor on the seismic behaviour of eccentrically braced frames, Journal of Constructional Steel Research, 63, 1529-1545, 2007.

[2] E.P. Popov, M.D. Engelhardt, Seismic eccentrically braced frames, *Journal of Constructional Steel Research*, **10**, 321-345, 1988.

[3] M. Bruneau, C. Uang, A. Whittaker, *Ductile design of steel structures*, McGraw Hill, 1998.

[4] M. Bosco, P.P. Rossi, Seismic behaviour of eccentrically braced frames, *Engineering Structures*, **31**, 664-674, 2009.

[5] T. Okazaki, M.D. Engelhardt, Cyclic loading behaviour of EBF links constructed of ASTM A992 steel, *Journal of Constructional Steel Research,* **63**, 751 -765, 2007.

[6] UNI EN 1998-1:2005, Eurocode 8 - Design of structures for earthquake resistance - Part 1: General rules, seismic actions and rules for buildings, 2005.

[7] D. M. Infrastrutture Trasporti 14 gennaio 2008, Norme Tecniche per le Costruzioni NTC 2008, (In Italian).

[8] J.M. Rides, E.P. Popov, Inelastic link element for EBF seismic analysis, *Journal of structural engineering*, **120**, 441-463, 1993.

[9] L. Mastrandrea, V. Piluso, Plastic design of eccentrically braced frames, I: moment – shear interaction, *Journal of constructional steel research*, **65**, 1007-1014, 2009.

[10] M.F. Gilberson, Two nonlinear beams with definitions of ductility, *Journal of structural engineering*, **95 (2)**, 137 - 157, 1969.

[11] S. Mazzoni, F. McKenna, M. H. Scott et al., *Opensees command Language Manual*, 2007.

[12] R. Tremblay, Inelastic seismic response of steel bracing members, *Journal of constructional steel research*, **58**, 665-701, 2002.

[13] M. Menegotto, P. Pinto, Method of analysis for cyclically loaded reinforced concrete plane frame including changes of geometry and non elastic behavior of elements under combined normal force and bending, *IABSE Symposium on resistance and ultimate deformability of structures acted on by well defined repeated loads*, final report, Lisbon, 1973.

[14] E.H. Vanmarcke, G.A. Gordon, E. Heredia-Zavoni, *SIMQKE-II, conditioned earthquake ground motion simulator: user's manual, version 2.1*, Princeton University, 1999.

[15] UNI EN 1993-1:2005, Eurocode 3 - Design of steel structures - Part 1-1: General rules and rules for buildings, 2005.

[16] FEMA 356, ASCE - Prestandard and commentary for the seismic rehabilitation of buildings, 2000.

[17] Tamast G., Bounds for probability in multivariate normal distribution, I.S.I. Proceedings, 203-204, 1977.

[18] Braconi, A., Badalassi, M., Salvatore, W., Modeling of European steel qualities mechanical properties scattering and its influence on Eurocode 8 design requirements, *14th ECEE Proceedings - European Conference on Earthquake Engineering,* Ohrid, Macedonia, August 30 – September 03, 2010.

[19] Melchers R. E., *Structural Reliability analysis and prediction*, Ellis Horwood Limited series in civil engineering, 1987.

[20] CEN (2004). EN10025-1÷6 General technical delivery conditions for: non-alloy, normalized/normalized rolled weldable fine grain, thermomechanical rolled weldable fine grain, improved atmospheric corrosion resistance, flat products of high yield strength in the quenched and tempered condition. European Committee for Standardization, Brussels

COMPDYN 2011
3rd ECCOMAS Thematic Conference on
Computational Methods in Structural Dynamics and Earthquake Engineering
M. Papadrakakis, M. Fragiadakis, V. Plevris (eds.)
Corfu, Greece, 25-28 May 2011

DAMAGE EVOLUTION IN STEEL STRUCTURES UNDER SEISMIC EXCITATION

Sven Heinrich[1], **Ursula Kowalsky**[1], **Jana Velde**[1], **and Dieter Dinkler**[1]

[1]Institute for Structural Analysis
Technische Universität Braunschweig
Beethovenstr. 51, 38106 Braunschweig, Germany
e-mail: s.heinrich@tu-bs.de

Keywords: Continuum damage mechanics, isotropic hardening, kinematic hardening, softening, seismic excitation, structural analysis, global damage index

Abstract. *For the purpose of energy dissipation steel structures exposed to seismic loading intentionally experience inelastic material behavior. Experiments of mild construction steel have shown that the behavior of structural steel is highly sensitive to loading velocity. Under cyclic loading, the Bauschinger effect decreases the yield stress. In addition, the steel suffers from material damage if the material is subjected to inelastic deformations.*

Therefore, to evaluate the structural safety of steel structures in case of earthquakes, a more detailed description of the material behavior is inevitable. The proposed material model describes the evolution and distribution of inelastic strains and damage in steel structures under seismic excitation by means of a set of internal variables. The model takes into account viscoplastic material behavior, isotropic and kinematic hardening, ductile damage, and a nonlocal extension in the form of an implicit gradient formulation to overcome the phenomenon of strain localization. To determine the material model parameters, numerical results are compared with experiments under static and dynamic loading. In order to indicate the influence of the description of the material behavior on the respsonse of 3D structures subjected to seismic excitation different approaches for the material are used.

1 INTRODUCTION

Earthquakes are unpredictable disasters which can damage structures severely and therefore endanger human safety. Thus, building codes in periled regions have to include methods to verify this special loading. The European code EC 8 uses the linear response spectrum method to specify static forces which act on the structure. The response spectrum is determined for elastic material behavior and the verification does not differ from static load cases. Material-dependent energy dissipation is taken into account by decreasing the response spectrum, and therefore the load, by a factor. This is a simple practical approach which considers the material behavior in a very general way depending on the method of construction.

Moreover the EC 8 also permits nonlinear time-history computations, but demands precise material modelling to capture the energy dissipation. In order to predict the structural response to seismic loading the inelastic material behavior, that accounts for the dissipation of energy, needs to be described in detail. Along with inelastic deformations a deterioration of the material can be observed, which is referred to as damage. It evolves from voids in the microstructure and this microstructural damage, which is not visually detectable from the outside, can increase over time and finally lead to macrocracks and failure [1, 2]. This paper focuses on a method to predict even small damage with a high precision. For that purpose, a continuum damage model is developed in the framework of thermodynamics taking into account the evolution of the material behavior including phenomena like hardening, softening, and damage. Since softening and damage are always accompanied by localization of deformation in small process zones of undefined width, local damage models suffer from a dependency on the fineness of finite-element discretization. As a remedy an implicit gradient enhanced formulation for a non-local damage variable is introduced which includes an additional material-dependent parameter to affect the size of the process zone.

Applying the proposed model to a FE analysis of a structure provides the distribution of damage across the structure. Therefore, highly stressed regions can be identified, but it is not possible to evaluate the damage state of the structure in general which encourages the formulation of a scalar global damage index.

2 MATERIAL MODEL

For the designing of steel constructions linear elastic material behavior is generally considered. To increase the degree of utilization plastic material behavior can be taken into account through a plain linear elastic ideal plastic stress-strain relationship.

For static loads these assumptions are conservative. To compute the response of a structure excited by earthquakes this simplified description of the material behavior is insufficient.

2.1 Material behavior of mild construction steel

To reveal the material behavior of mild construction steel subjected to seismic loading, experiments have been conducted at the Technische Universität Braunschweig [3]. Figure 1 depicts the measured stress of a unaxial bar loaded by a strain record deduced from the north-south component of the 1995 Kobe earthquake. The characteristic yield stress occurs only for the first load path. Beginning with the first reverse loading hystereses develop which exhibit a continuous transition between the linear elastic and the nonlinear inelastic range. The hysteresis shape shows that the initiation of plastic deformations occurs earlier after load reversals. This phenomenon called Bauschinger effect can be taken into account by kinematic hardening. Repeated cyclic straining with strain amplitudes $> 6\%$ leads to cyclic increase of the yield stress which can be described by isotropic hardening. Moreover, experiments have shown that the cyclic deformation behavior of mild steel is closely related to the inelastic strain amplitude history [4, 5]. In order to consider this fact, a strain memory surface is integrated into the model.

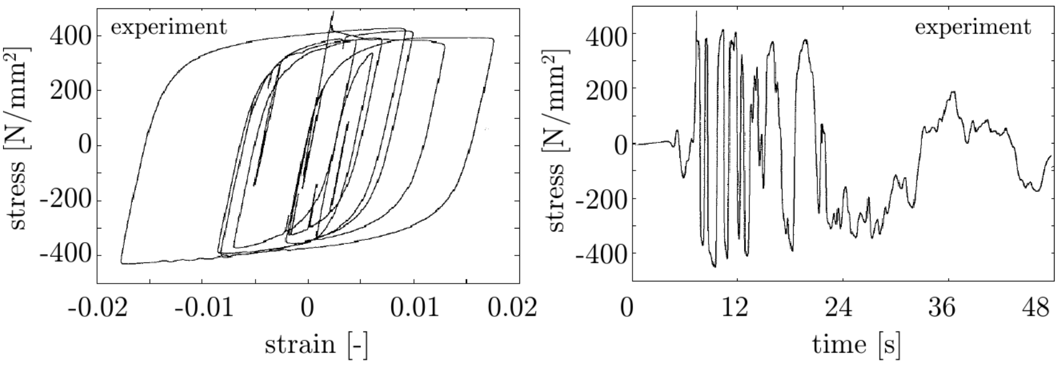

Figure 1: Hysteresis curves and development of stress of the Kobe earthquake obtained experimentally [3]

At he level of atoms inelastic deformations decrease the number of bonds which leads to material deterioration with an impairment of the elementary area of resistance. This damage is, in general, strongly anisotropic and can be observed as growing microvoids which eventually results in macroscopic cracks. For a low alloy steel Figure 2 shows the microscopic debonding of a notched specimen after cycling loading. The cross section is deteriorated although a macro-crack cannot be located yet. The existence of damage in mild steel is investigated for example in [7, 8].

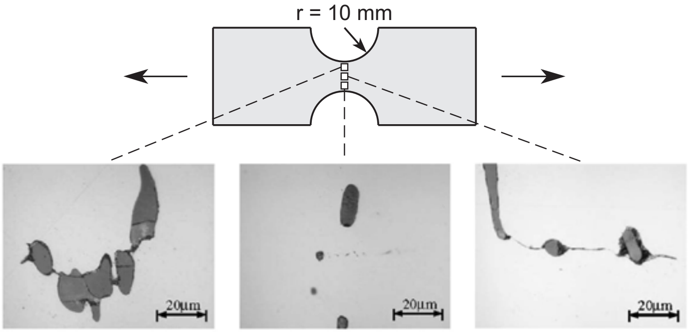

Figure 2: Metallographic section of a notched specimen after cyclic loading according to [6]

For the description of damage evolution a model is proposed which bases on the isotropic ductile damage model for monotonic loading presented in [9]. Modifications adjust the model to micromechanical observations under cyclic straining. The initiation of ductile damage is difficult to specify. Experiments have shown that nucleation of cavities does not occur below a certain amount of plastic strain. However, it is hard to determine this threshold so that a large variety of different proposals is available in literature. This work uses a threshold based on the equivalent plastic strain in order to capture the characteristics of mild construction steel. Since mild construction steel S 355 does not show pronounced damage in the form of a continuous reduction of the modulus of elasticity for cyclic loading with small strain amplitudes [10], the model prohibits damage evolution below a certain amount of plastic strain. But ductile damage due to irregular large cyclic straining ist captured. The chosen criterion enables ductile damage evolution under large strains and thus provides a precise method in order to describe damage evolution under seismic loading.

2.2 Material equations

The mathematical description of the material behavior is achieved by a set of ordinary differential equations of first order with respect to time. The current state of the material is described by internal variables and related evolution equations, which can be derived from thermodynamics. The material equations contain isotropic nonlocal damage $\bar{D}$.

Assuming small strains, the total strain rate can be split up additively in an elastic and an inelastic part

$$\dot{\boldsymbol{\varepsilon}} = \dot{\boldsymbol{\varepsilon}}^{el} + \dot{\boldsymbol{\varepsilon}}^{in}. \tag{1}$$

The elastic strain rate is based on Hooke's law and contains an isotropic degradation of the modulus of elasticity by the damage variable $\bar{D}$ following the principle of energy equivalence [11]. Considering the influence of damage on stiffness under alternating tension and compression, it is assumed according to Lemaitre [12] that some but not every crack closes under compression so that the stiffness of the material under compression lies between the undamaged and the damaged stiffness. In order to define the compressive stiffness of damaged material a crack closure parameter h is introduced. Thus, effective stress and strain are defined differently for tension (+) and compression (-):

$$\tilde{\boldsymbol{\sigma}}^+ = \frac{1}{1-D} \cdot \boldsymbol{\sigma}^+ \quad , \quad \tilde{\boldsymbol{\varepsilon}}^+ = (1-D) \cdot \boldsymbol{\varepsilon}^+ \tag{2}$$

1

)

I t

the ɔ

use c

loa(

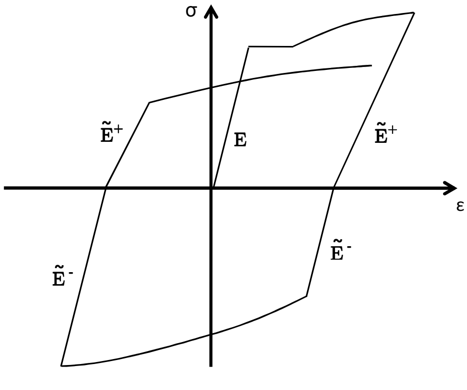

Figure 3: Stiffness under tenion and compression

The inelastic viscoplastic deformations are obtained following the approach by Chaboche and Rousselier [1, 2]. The over-stress σ_{ex}, that determines the onset of viscoplastic deformation, corresponds to the yield function and results from a modified criterion based on Gurson [13] and Tvergaard and Needleman [14] with the first ($J_1(\boldsymbol{\sigma}_{eff}) = \frac{1}{3}tr(\boldsymbol{\sigma} - \mathbf{X})$) and the second ($J_2(\boldsymbol{\sigma}^d_{eff}) = \frac{1}{2}tr((\boldsymbol{\sigma} - \mathbf{X})^d \cdot (\boldsymbol{\sigma} - \mathbf{X})^d)$) invariant of the effective stress tensor $\boldsymbol{\sigma}_{eff} = \boldsymbol{\sigma} - \mathbf{X}$ and the effective stress deviator $\boldsymbol{\sigma}^d_{eff} = (\boldsymbol{\sigma} - \mathbf{X})^d$, respectively

$$\sigma_{ex} = \sigma_{eq} - \sigma_F - K = \frac{1}{1-\bar{D}}\sqrt{3J_2(\boldsymbol{\sigma}^d_{eff}) + \bar{D}J_1(\boldsymbol{\sigma}_{eff})^2} - \sigma_F - K. \tag{4}$$

The yield function considers isotropic hardening K and kinematic hardening $\mathbf{X}$ which appropriately describe inelastic behavior according to Chaboche and Rousselier in case of undamaged material by the v. Mises yield criterion.

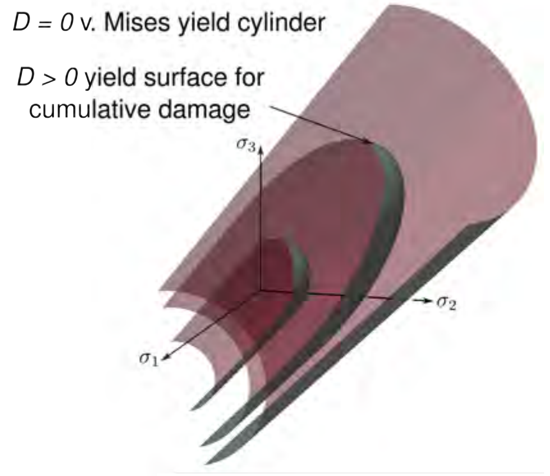

Figure 4: Yield surface

Figure 4 depicts the v. Mises yield cylinder for undamaged material and the contraction of the yield surface combined with a formation of caps at the ends of the yield cylinder due to damage. In case of damage, the yield function employs volumetric inelastic deformations and permits coupling of viscoplasticity and damage.

The initiation of damage is determined by a damage threshold surface which is defined via the equivalent positive plastic strain

$$\varepsilon^{in}_{eq} = \sqrt{\frac{2}{3}\left(\langle\varepsilon^{in}_{11}\rangle^2 + \langle\varepsilon^{in}_{22}\rangle^2 + \langle\varepsilon^{in}_{33}\rangle^2 + 2\langle\varepsilon^{in}_{12}\rangle^2 + 2\langle\varepsilon^{in}_{13}\rangle^2 + 2\langle\varepsilon^{in}_{23}\rangle^2\right)} \tag{5}$$

where the McAuley brackets omit negative strains and thus prohibit damage evolution under compression. The equivalent strain has to exceed the scalar damage threshold strain parameter ε^{in}_D for damage evolution

$$\begin{aligned} \varepsilon^{in}_{eq} - \varepsilon^{in}_D &\leq 0 \longrightarrow \dot{D} = 0 \\ &> 0 \longrightarrow \dot{D} \end{aligned} \tag{6}$$

While Pirondi and Bonora [15] propose that the damage threshold strain decreases under compression due to the presence of broken inclusions, the damage threshold strain here is assumed to be constant.

In order to consider different damage evolution under tension and compression, the evolution of local ductile damage

$$\dot{D} = (c_1 + c_2 e^{-c_3 \frac{1}{(1-\bar{D})} p^+}) \frac{1}{(1-\bar{D})} \dot{p}^+ + c_4 (c_5 - \bar{D}) \left\langle tr \left(\frac{\partial \sigma_{ex}}{\partial \boldsymbol{\sigma}} \dot{p}^+ \right) \right\rangle \tag{7}$$

depends on a newly defined variable p^+ called active accumulated plastic strain based on [15]:

$$\dot{p}^+ = \dot{p} \left\langle \frac{J_1}{|J_1|} \right\rangle = \dot{\varepsilon}_0 \left\langle \frac{\sigma_{ex}}{\sigma_p} \right\rangle^n \left\langle \frac{J_1}{|J_1|} \right\rangle . \tag{8}$$

Thus, the evolution of ductile damage is enabled only if the first invariant of the stress tensor is positive. The two terms of the damage evolution equation (7) consider transient and saturation behavior in damage evolution as well as damage due to volumetric yielding and depend on the damage parameters c_1 - c_5.

The memory of the strain loading history is considered by a strain memory surface M, which depends on two variables $\boldsymbol{\beta}$ and q where $\boldsymbol{\beta}$ describes the displacement of the surface and q specifies its amplitude. Within this work, a maximum strain amplitude memory [4] is defined in the three-dimensional space as

$$M = \frac{2}{3} (\boldsymbol{\varepsilon}^{in} - \boldsymbol{\beta})(\boldsymbol{\varepsilon}^{in} - \boldsymbol{\beta}) - q^2 \leq 0 \tag{9}$$

with

$$\dot{\boldsymbol{\beta}} = 0.5 H(M)\, \dot{\boldsymbol{\varepsilon}}^{in}, \tag{10}$$

$$\dot{q} = 0.5 H(M)\, \mathbf{n}_F\, \mathbf{n}_M\, \dot{p}, \tag{11}$$

where $H(M)$ is the Heaviside function with $H(M) = 1$ if $M \geq 0$ and $H(M) = 0$ if $M < 0$, $\mathbf{n}_F$ is the normal to the yield surface, and $\mathbf{n}_M$ is the normal to the strain memory surface. A plastic strain state outside the current strain memory surface leads to the growth and adjustment of the variables $\boldsymbol{\beta}$ and q, while $\boldsymbol{\beta}$ and q remain constant for plastic strain states inside the memory surface. Thus, the inelastic strain amplitude variable q will not decrease and always remembers the maximum strain reached so far during loading.

Considering the influence of the strain memory surface on isotropic hardening, the saturation value of isotropic hardening Q becomes a function of the amplitude of the strain memory surface q. Within this work, the evolution rule of the saturation value of isotropic hardening Q is assumed to be linear.

As shown in Figure 5 the numerical results according to the proposed model match the measured stress, comparing Figure 1, very well. Solely the observed yield plateau cannot be described with the given model.

2.3 Non-local extension

The dissipation of energy concentrates on small areas of the structure called process zones. With the grave decrease of stiffness when reaching inelastic material behavior this causes high strain gradients. If the size of the process zone is not defined in a finite element computation the results of local damage models depend on the fineness of discretization. Reducing the element

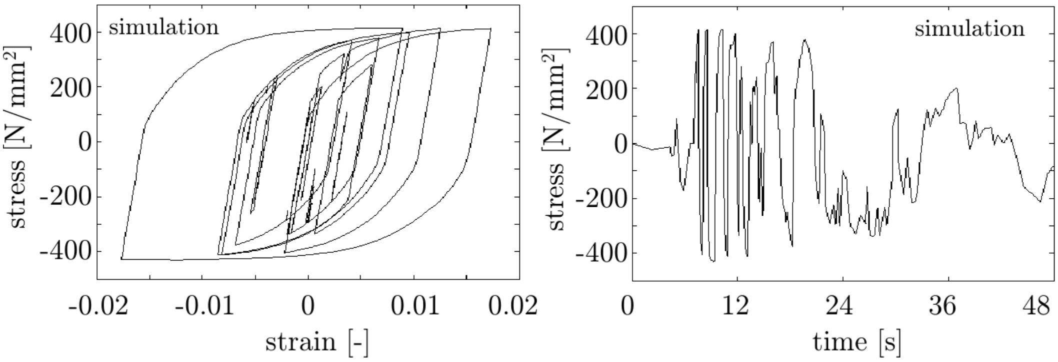

Figure 5: Hysteresis curves and development of stress of the Kobe earthquake obtained by numerical simulation

size leads to a decreasing process zone and less energy dissipated. It is obvious that for an evanescent volume and therefore inelastic material behavior without dissipation the description is physically incorrect and an extension to provide accurate results is needed. Mathematically, the problem becomes ill-posed since the differential equations lose their elliptic form and the acoustic tensor of the tangential stiffness tensor becomes singular [12, 16].

In order to determine the size of the process zone and to regularize the solution, the models need to be extended by a material-dependent internal length scale. An overview of the state of the art for different non-local extensions may be found in [17, 18]. Peerlings et al. [19] and Engelen et al. [20] show the derivation of models with gradients of internal variables from nonlocal integral models and differentiate between explicit and implicit gradient models.

This work examines the use of non-local implicit gradient models in 3D-FE structural analysis. By means of an additional gradient equation, non-local substitutes of the local variables can be obtained. Following the derivation of Engelen [20] and using gradients of the damage variables, the non-local damage variable $\bar{D}$ can be determined by the gradient equation

$$\bar{D} - l_c^2 \nabla^2 \bar{D} = D \tag{12}$$

with the local damage variable D for which its evolution equation is given with Eq. 7, the material-specific internal length l_c and the boundary condition $\nabla \bar{D} = 0$.

3 STRUCTURAL ANALYSIS

The structural response to seismic excitation is described by equation of motion

$$\mathbf{M}\ddot{\mathbf{u}} + \mathbf{B}\dot{\mathbf{u}} + \mathbf{K}\mathbf{u} = \mathbf{M}\ddot{\mathbf{u}}_g \tag{13}$$

with the measured ground acceleration vector $\ddot{\mathbf{u}}_g$. Damping is considered through a numerical approach using the velocity-dependent term $\mathbf{B}\dot{\mathbf{u}}$ as well as energy dissipation through inelastic straining and damage evolution. The stiffness of the structure, represented by $\mathbf{K}$, depends on the development of hardening, softening and damage.

3.1 Discretization

Stress-deformation analysis of structures implies the solution of the underlying initial boundary value problem of the body Ω. With the principle of virtual work the weak form of the equation of motion can be obtained

$$\int_{\Omega} \delta\mathbf{u} \cdot \rho\ddot{\mathbf{u}} d\Omega + \int_{\Omega} \delta\mathbf{u} \cdot \mathbf{f} d\Omega + \int_{\Omega} \delta\boldsymbol{\varepsilon} : \boldsymbol{\sigma} d\Omega = \int_{\Omega} \delta\mathbf{u} \cdot \mathbf{p} d\Omega + \int_{\partial\Omega} \delta\mathbf{u} \cdot \bar{\mathbf{t}} d\partial\Omega + \int_{\Omega} \delta\mathbf{u} \cdot \rho\ddot{\mathbf{u}}_{\mathbf{g}} d\Omega \tag{14}$$

with virtual displacement vector $\delta\mathbf{u}$ and virtual Almansi strain tensor $\delta\boldsymbol{\varepsilon}$, density ρ, acceleration vector $\ddot{\mathbf{u}}$, damping force $\mathbf{f}$, Cauchy stress tensor $\boldsymbol{\sigma}$, volume load vector $\mathbf{p}$, surface load vector $\bar{\mathbf{t}}$. Assuming linear kinematics $\boldsymbol{\varepsilon} = \nabla\mathbf{u}$ and Rayleigh damping $\mathbf{f}_c = \mathbf{c}\dot{\mathbf{u}}$, Equation (14) is discretized in space with the finite-element method, while the Newmark method is used for the discretization in time.

The material behavior is connected to the equation of motion via Cauchy stresses $\boldsymbol{\sigma}$ which are coupled with Almansi strains ε and internal variables $\mathbf{V}$

$$\boldsymbol{\sigma} = \boldsymbol{\sigma}(\varepsilon, \mathbf{V}) = \boldsymbol{\sigma}(\varepsilon, r, \boldsymbol{\alpha}, D) \tag{15}$$

where the latter characterize the state of the material (hardening, softening, damage). The material equations, see Section 2.2, are discretized in time using the implicit Euler approach.

Equation (12) can be assumed to be time-independent since the spatial propagation of the nonlocal damage variable $\bar{D}$ is very fast compared to the evolution of the other variables. The weak form of the additional partial differential equation for the non-local damage field $\bar{D}$ results from weighted residua

$$\int_{\Omega} \left(\delta\bar{Y}\left(\bar{D} - D\right) - \nabla\delta\bar{Y}\, l_c^2\, \nabla\bar{D}\right)\, d\Omega - l_c^2 \int_{\partial\Omega} \delta\bar{Y}\bar{t}_{\bar{D}}\, d\partial\Omega = 0 \tag{16}$$

with the virtual nonlocal energy release rate $\delta\bar{Y}$ and Neumann boundary condition $\bar{t}_{\bar{D}} - \mathbf{n}\nabla\bar{D} = 0$, which prohibits a damage flux through the boundary of the domain. Here, $\bar{t}_{\bar{D}}$ is forced to zero. The gradient equation is discretized in space by the finite-element method.

Structural analysis is performed using triquadratic twentyseven-node brick elements for the spatial discretization of the field of displacement and the field of damage. The discretization in time uses linear approximations for the material variables while the approximations for the unknowns of the equation of motion depend on the choice of the Newmark integration parameters α and β (see for example [21]). Here, the Newmark integration parameters are set to $\alpha = \frac{1}{2}$ and $\beta = \frac{1}{4}$ which leads to the approach of constant mean acceleration. If damping is considered via Rayleigh damping the parameters $c_\alpha = 0.01$ and $c_\beta = 0.001$ are employed.

3.2 Global damage index

In order to characterize the damage state of the whole structure a global damage index has to be defined. There exists a large variety of different damage indices from literature and they all agree in having a range between 0 and 1, where 0 corresponds to the undamaged state and 1 to the state of failure [22]. Global damage indices for steel structures are for example proposed by [23, 24, 25], but not all rest on the transformation of damage variables into one global index. Colombo [26], for example, develops an index that takes into account the maximum attained deformation and the energy dissipation in ductile and brittle elements. Ghobarah et al. [27] propose an index which depends on the initial and final stiffness of the structure before and after the earthquake obtained by push-over analysis. However, if the global damage measure is calculated directly, the local damage distribution remains unknown. In this contribution the indicator for global damage, in the following abbreviated as GDI, is based on the eigenvalue decomposition

$$\left[\mathbf{K}_t - \lambda_{t,i}^2 \mathbf{K}_0\right] \mathbf{v}_{t,i} = \mathbf{0} \tag{17}$$

where $\lambda_{t,i}$ are the eigenvalues, $\mathbf{v}_{t,i}$ are the eigenvectors, $\mathbf{K}_0$ is the initial stiffness matrix and $\mathbf{K}_t$ is the current stiffness matrix due to hardening, softening and damage. Further information concerning this index can be found in [28].

3.3 Seismic excitation of cantilever

In the following the influence on results of structural analysis of different levels of precision concerning the material model is presented for a cantilever consisting of an IPE 80 profile. Moreover the global damage index is evaluated for this structure.

With a height of 5 m and an additional mass of 380 kg assigned to the top the investigated cantilever has an eigenfrequency of 0.55 Hz. The structure is subjected to the north-south component of the Kobe earthquake from 1995 acting in the direction of the strong profile axis, see Figure 6.

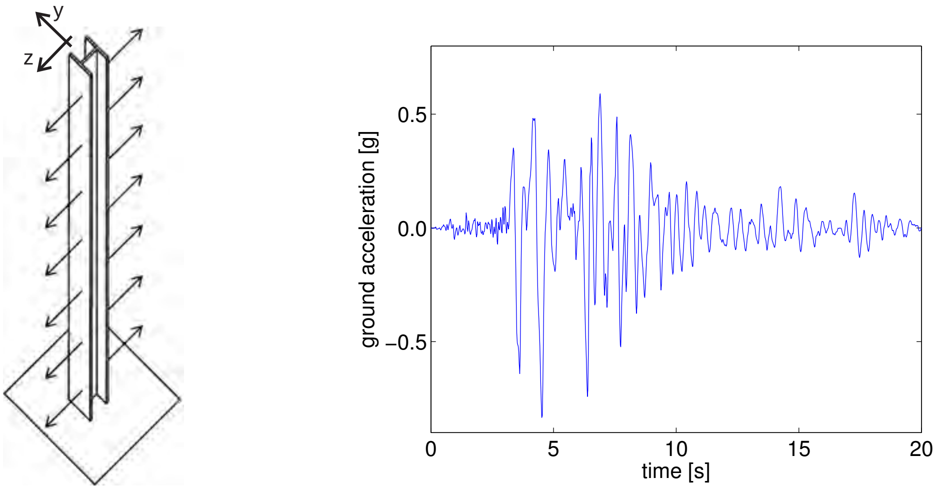

Figure 6: Cantilever and acceleration record of the north-south component of the Kobe earthquake (1995)

In a first analysis elastic material behavior is assumed and damping is neglected. Figure 7(a) depicts the displacement at the top of the cantilever over time. The maximum value of displacement is 69 cm. It is obvious that the vibration mainly consists of the first eigenfrequency. The missing of any damping leads to an increasing displacement even when the amplitudes of the ground acceleration decrease.

For a more detailed simulation the material model is extended by viscoplastic material behavior including isotropic and kinematic hardening. The earthquake causes inelastic cyclic straining in the bottom part of the cantilever. The hystereses in the material behavior lead to dissipation of energy and the top displacement is reduced compared to the elastic behavior. The maximum deflection is 42 cm. Considering the frequencies involved in the vibrations, depicted in the frequency spectra in Figure 7(b), it can be noticed that the amplitude decreases. Furthermore no shift of the involved frequencies can be observed although damping is included by the material model.

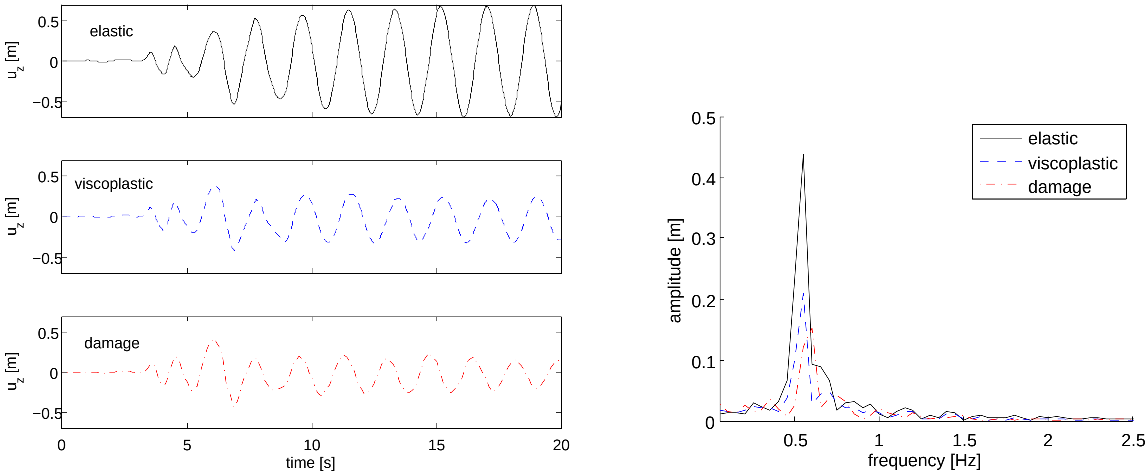

(a) Top displacement (b) Frequency spectra

Figure 7: Displacement of the cantilever top and frequency spectra for elastic, viscoplastic and damaged material

Finally the complete proposed model is applied to compute the response of the cantilever, also considering Rayleigh damping. With about 44 cm the displacement is slightly larger than for the viscoplastic material which is caused by the softening. Because of large inelatic strain material damage evolutes at the base of the cantilever. As an example Figure 8(b) shows the distribution of damage throughout the base of a strongly damaged HEA 180 cantilever. It can be seen that damage occurs in the flanges which are subjected to high alternating tension and compression. Evidently the shear bands accumulate damage and weaken the structure. To evaluate the damage state of the cantilever the global damage index is computed for every timestep, see Figure 8(a). The highest rise of the index corresponds to the largest displacement. With falling intensity of the ground acceleration the damage only increases slightly due to the inelastic deformations remaining below a threshold or only occuring in small exposed regions. The decreasing top displacement is mainly caused by the included numerical damping. The structure shows a slight permanent deformation of 3 cm, since the free vibration does not occur around its zero position.

The deteriorated material at the cantilever base reduces the stiffness of the structure and leads to a shift of the eigenfrequencies which can be seen in the frequency spectrum, see Figure 7(b).

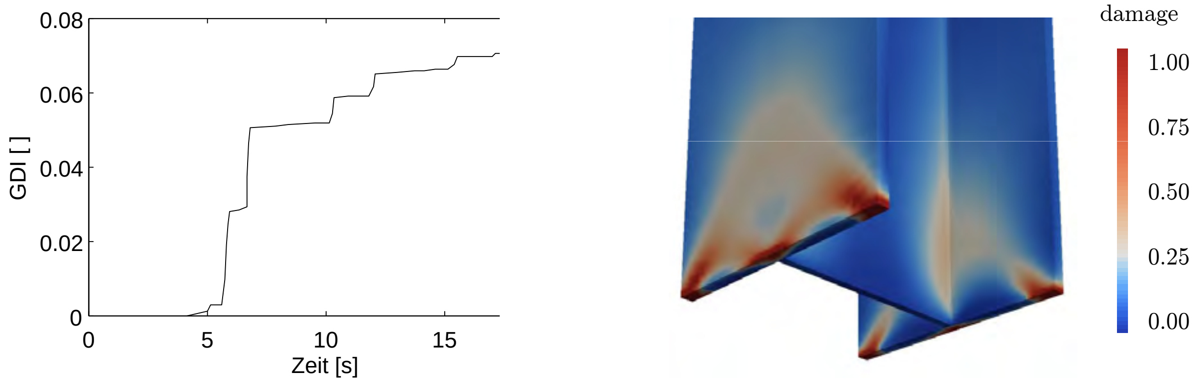

(a) Global damage index (b) Local damage distribution for HEA 180 base

Figure 8: Damage evolution of the cantilever

4 CONCLUSIONS

Nonlinear time-history computations of structures subjected to earthquakes are possible if material models are used which are able to describe the viscoplastic material behavior. Furthermore the material deterioration has to be taken into account since the softening of the material leads to a shift of the eigenfrequencies and therefore to a different response to the stochastic acceleration.

REFERENCES

[1] J. Chaboche, G. Rousselier, *On the Plastic and Viscoplastic Constitutive Equations - Part I: Rules Developed with Internal Variable Concept*, Journal of Pressure Vessel Technology 105 (1983) 153–158.

[2] J. Chaboche, G. Rousselier, *On the Plastic and Viscoplastic Constitutive Equations - Part II: Application of Internal Variable Concept to the 316 Stainless Steel*, Journal of Pressure Vessel Technology 105 (1983) 159–164.

[3] C. Böttcher, *Geschwindigkeitssensitivität des mechanischen Verhaltens unlegierter Baustähle bei wiederholter Beanspruchung bis in den inelastischen Bereich - experimentelle Untersuchung und Modellierung*. Tech. rep., Fortschrittsbericht VDI Reihe 5, Nr. 654, 2002.

[4] J.L. Chaboche, K. Dang Van, G. Cordier, *Modelization of the strain memory effect on the cyclic hardening of 316 stainless steel*, Transaction of the 5th International Conference on Structural Mechanics in Reactor Technology, Paper No. L11/3, Berlin, Germany, 1979.

[5] H.-J. Scheibe, *Zum zyklischen Materialverhalten von Baustahl und dessen Berücksichtigung in Konstruktionsberechnungen*, Institut für Stahlbau, TU Braunschweig, 1990.

[6] A. Pirondi, N. Bonora, D. Steglich, W. Brocks, D. Hellmann, *Simulation of failure under cyclic plastic loading by damage models*, International Journal of Plasticity 22 (2006) 2146–2170.

[7] M. Alves, *Measurement of ductile material damage*, Mechanics Based Design of Structures and Machines 29 (2001) 451–476.

[8] L. Yang, B. Sun, Y. Guo, *Damage Evaluation Based on Electrical Resistance Measurements*, Key Engineering Materials 385-387 (2008) 589–592.

[9] J. Velde, U. Kowalsky, T. Zümendorf, D. Dinkler, *3D-FE-Analysis of CT-specimens including viscoplastic material behavior and nonlocal damage*, Computational Material Science 46 (2009) 352–357.

[10] S. Krümmling, *Schallemissionsanalyse zum Nachweis der Materialermüdung von Baustahl*, Institut für Stahlbau, TU Braunschweig, 1999.

[11] J. Cordebois, F. Sidoroff, *Damage Induced Elastic Anisotropy*, Proceedings of the Euromech Colloquium 115 (1982) 761–774.

[12] J. Lemaitre, *A Course on Damage Mechanics*, Springer, 1992.

[13] A. Gurson, *Continuum Theory of Ductile Rupture by Void Nucleation and Growth: Part I - Yield Criteria and Flow Rules for Porous Media*, Journal of Engineering Materials and Technology 99 (1977) 2–15.

[14] V. Tvergaard, A. Needleman, *Analysis of the cup-cone fracture in a round tensile bar*, Archives of Mechanics 32 (1984) 157–169.

[15] A. Pirondi, N. Bonora, *Modeling ductile damage under fully reversed cycling*, Computational Material Science 26 (2003) 129–141.

[16] M. Neilson, H. Schreyer, *Bifurcations in Elastic-Damaging Materials*, Damage Mechanics and Localization 142 (1992) 53–67.

[17] Z. Bazant, M. Jirasek, *Nonlocal Integral Formulations of Plasticity and Damage: Survey of Progress*, Journal of Engineering Mechanics 128 (2002) 1119–1149.

[18] M. Jirasek, S. Rolshoven, Regularized Formulations of Strain-Softening Plasticity, D. Kolymbas (Eds.), *Advanced Mathematical and Computational Geomechanics*, Springer, 2003, pp. 269–299.

[19] R. Peerlings, R. de Borst, W. Brekelmans, J. de Vree, *Gradient enhanced damage for quasi-brittle materials*, International Journal for Numerical Methods in Engineering 39 (1996) 3391–3403.

[20] R. Engelen, M. Geers, F. Baaijens, *Nonlocal implicit gradient-enhanced elasto-plasticity for the modelling of softening behavior*, International Journal of Plasticity 19 (2003) 403–433.

[21] K.-J. Bathe, *Finite-Elemente-Methoden*, Springer-Verlag, Berlin, 1990.

[22] A.J. Kappos,*Seismic damage indices for RC buildings*, Progress in Structural Engineering and Materials, 1, 78–87, 1997.

[23] P. Khashaee, *Damage-based Seismic Design of Structures*, Earthquake Spectra, 21, 371–387, 2005.

[24] Z. Shen, A. Wu, *Seismic analysis of steel structures considering damage cumulation*, Front. Archit. Civ. Eng. China, 1, 1–11, 2007.

[25] A. Benavent-Climent, *An energy-based damage model for seismic response of steel structures*, Earthquake Engineering and Structural Dynamics, 36, 1049–1064, 2007.

[26] A. Colombo, P. Negro, *A damage index of generalised applicability*, Engineering Structures, 27, 1164–1174, 2005

[27] A. Ghobarah, H. Abou-Elfath, A. Biddah, *Response-based damage assessment of structures*, Earthquake Engineering and Structural Dynamics, 28, 79–104, 1999.

[28] J. Velde, *3D Nonlocal Damage Modeling for Steel Structures under Earthquake Loading*, Institut für Statik, TU Braunschweig, 2010.

COMPDYN 2011
3rd ECCOMAS Thematic Conference on
Computational Methods in Structural Dynamics and Earthquake Engineering
M. Papadrakakis, M. Fragiadakis, V. Plevris (eds.)
Corfu, Greece, 25–28 May 2011

OPTIMUM DESIGN OF STEEL STRUCTURES WITH THE PARTICLE SWARM OPTIMIZATION METHOD BASED ON EC3

Vagelis Plevris, Apostolis Batavanis, Manolis Papadrakakis

Institute of Structural Analysis and Anti Seismic Research
School of Civil Engineering, National Technical University of Athens
Iroon Polytechniou 9, 15780 Zografou, Greece
vplevris@central.ntua.gr, batavanis@yahoo.gr, mpapadra@central.ntua.gr

Keywords: Optimum Design, Steel Structures, Particle Swarm Optimization, EC3

Abstract. *A number of optimization algorithms have been used in structural design optimization in the past, ranging from gradient-based mathematical algorithms to probabilistic-based search algorithms, for addressing global non-convex optimization problems. Many probabilistic-based algorithms have been inspired by natural phenomena, such as Evolutionary Programming (EP), Genetic Algorithms (GA), Evolution Strategies (ES), among others. Recently, a family of optimization methods has been developed based on the simulation of social interactions among members of a specific species.*

One of these methods is the Particle Swarm Optimization (PSO) method that is based on the behavior reflected in flocks of birds, bees and fish that adjust their physical movements to avoid predators and seek for food. In PSO, as in GA, a population of potential solutions is considered and utilized to search within the design space. However, its members do not reproduce but rather communicate with each other their knowledge of solutions in order to reach the optimum. Each "particle", "flies" through the multi-dimensional design space, with a certain velocity vector for each iteration.

In this study, a discrete PSO algorithm is employed for the optimization of 2D and 3D steel frames and the results are compared to the ones obtained with a discrete GA. Both methods are applied in single-objective, discrete, constrained structural engineering optimization problems where the aim is to minimize the weight of the steel structure under various constraints on displacements and forces (biaxial bending with axial force and shear force) which are based on Eurocode 3.

The constraints are checked by performing a Finite Element analysis for every candidate optimum design. A new linear analysis software tool for three-dimensional frames has been developed, featuring some distinct characteristics. The applied loads can be nodal or elemental (uniform, triangular or trapezoidal in any direction within an element), while any release (translational or rotational) can be implemented at an end of any element, in any of the 6 Degrees Of Freedom (DOFs). The output of the analysis program includes the constraint reactions, nodal displacements, forces at the ends of the elements, plus the displacements of the released DOFs of all elements with releases, and any displacement or any force at any given point within an element. The accuracy of the analysis results is verified by a direct comparison to the corresponding results of a reliable commercial finite element software program.

For each method, the performance, functionality and effect of different setting parameters are studied. After a fine tuning of the parameters, the results are compared to each other. The comparison is done with regard to the speed of convergence, in terms of number of objective function evaluations, and accuracy of the solution. Various 2D and 3D steel structures are considered as test examples.

1 DESIGN OPTIMIZATION

1.1 Formulation of a single-objective optimization problem

The formulation of a generic single-objective optimization problem can be written as follows:

$$\begin{aligned}
&\min_{\boldsymbol{x}\in\mathbb{R}^n} f(\boldsymbol{x}), \quad \boldsymbol{x}=[x_1,\ldots,x_n]^{\mathrm{T}}, \quad f\in\mathbb{R}\\
&\text{Subject to}\\
&\boldsymbol{g}(\boldsymbol{x})\le 0, \quad \boldsymbol{g}\in\mathbb{R}^p\\
&\boldsymbol{h}(\boldsymbol{x})=0, \quad \boldsymbol{h}\in\mathbb{R}^q\\
&x_i\in X_i \quad \text{for } i=1,\ldots,n
\end{aligned} \tag{1}$$

where:

- $\boldsymbol{x}=[x_1,\ldots,x_\mathrm{n}]^{\mathrm{T}}$ is a vector of length n containing the design variables.
- X_i is the set of x_i, which may be continuous, discrete or integer. The whole design space for the n design variables can be denoted as X.
- $f(\boldsymbol{x})$: $\mathbb{R}^n\to\mathbb{R}$ is the objective function, which returns a scalar value to be minimized.
- $\boldsymbol{g}(\boldsymbol{x})^{\mathrm{T}}=[g_1(\boldsymbol{x}),\ldots,g_\mathrm{p}(\boldsymbol{x})]$ is the vector function of p inequality constraints.
- $\boldsymbol{h}(\boldsymbol{x})^{\mathrm{T}}=[h_1(\boldsymbol{x}),\ldots,h_\mathrm{q}(\boldsymbol{x})]$ is the vector function of q equality constraints.

In structural design optimization, inequality constraints are mainly used, since equality constraints are not applicable for real-world problems. If the objective function is the weight of the structure, it is given by

$$f(\boldsymbol{x})=\rho\cdot\sum_{i=1}^{N_\mathrm{e}} A_i\cdot L_i \tag{2}$$

where ρ is the material density, N_e is the number of elements of the model and A_i, L_i are the cross sectional area and the length of each element, respectively.

1.2 Discrete and continuous formulations

In structural design optimization, due to manufacturing limitations, the design variables are not described by continuous functions but are discrete variables [1] since cross-sections have usually to belong to a certain predefined set provided by the manufacturers. There are also cases where the design variables are mixed, continuous and discrete, e.g. in a topology-sizing optimization problem where the design variables include nodal coordinates (continuous) as well as beam cross-sectional sizes (discrete).

With the general formulation of Eq. (1), the design variables may have continuous, discrete or integer values, or a combination of them, with the restriction

$$x_i\in X_i \quad \text{for } i=1,\ldots,n \tag{3}$$

where X_i is the set of the design variable x_i, which may be continuous or discrete. When discrete design variables are only used, then the available set of values is clearly defined. When continuous design variables are considered, then the above restriction is usually written as

$$\boldsymbol{x}^{\mathbf{L}} \leq \boldsymbol{x} \leq \boldsymbol{x}^{\mathbf{U}} \tag{4}$$

where $\boldsymbol{x}^{\mathbf{L}}$ and $\boldsymbol{x}^{\mathbf{U}}$ are two vectors of length n containing the lower and upper bounds of the design variables, respectively.

Various methods have been proposed for dealing with mixed problems, with continuous and discrete design variables [2]. Usually discrete variables are handled as equivalent continuous variables, and at the end of the optimization process the design variables are given the appropriate discrete values, as close as possible to the optimal continuous values [3]. In case of a discrete problem where the design space can be univocally arranged for all the characteristics of the cross sections, the above method can give a good approximation of the discrete optimum solution. Nevertheless, in realistic engineering problems this may not be the case. Most of the methods that have been proposed convert the mixed problem to a series of continuous problems that are solved consecutively [4-6].

In the present study, a discrete optimization problem is studied, where the design variables are the cross sections of the elements of the steel structure, which belong to predefined sets given by the manufacturers, as described in detail in the numerical examples section.

1.3 Particle Swarm Optimization (PSO)

Many probabilistic-based search algorithms have been inspired by natural phenomena, such as Evolutionary Programming, Genetic Algorithms, Evolution Strategies, among others. Recently, a family of optimization methods has been developed based on the simulation of social interactions among members of a specific species looking for food or resources in general. One of these methods is the *Particle Swarm Optimization* (PSO) method that is based on the behavior reflected in flocks of birds, bees and fish that adjust their physical movements to avoid predators and seek for food. The method has been given considerable attention in recent years among the optimization research community.

A swarm of birds or insects or a school of fish searches for food, resources or protection in a very typical manner. If a member of the swarm discovers a desirable path to go, the rest of the swarm will follow quickly. Every member searches for the best in its locality, learns from its own experience as well as from the others, typically from the best performer among them. Even human beings show a tendency to behave in this way as they learn from their own experience, their immediate neighbors and the ideal performers in the society. The PSO method mimics the behavior described above. The algorithm was first proposed by Kennedy and Eberhart [7]. It is a population-based optimization method built on the premise that social sharing of information among the individuals can provide an evolutionary advantage.

PSO has been found to be highly competitive for solving a wide variety of optimization problems [8-14]. A number of advantages over other algorithms make PSO a prospective candidate to be used also in structural optimization problems. It can handle non-linear, non-convex design spaces with discontinuities. Compared to other non-deterministic optimization methods it is considered efficient in terms of number of function evaluations as well as robust since it usually leads to better or the same quality of results. Its easiness of implementation makes it more attractive as it does not require specific domain knowledge information, while being a population-based algorithm, it can be straight forward implemented in parallel computing environments leading to a significant reduction of the total computational cost.

Compared to GA, PSO is easier to implement and there are only a few parameters to adjust. PSO has been successfully applied to many fields, such as mathematical function optimization, artificial neural network training and fuzzy system control. Promising results have been presented in the areas of structural shape optimization [15, 16] as well as topology optimization [17]. Perez and Behdinan [13, 18] implemented the PSO algorithm for constrained structural optimization of plane and space truss structures while Li et al. [19] tried a heuristic PSO scheme for the optimization of truss structures.

The general concept of the PSO method involves a swarm, modeled as a number of individual particles, moving through the search space in search of the global optimum. The particles communicate with their neighbors the progress made so far and adjust their moving velocity according to that information. In the beginning, a population of candidate solutions is created randomly, each of which is considered to be a particle moving through the multi-dimensional design space in search of the position of the global optimum. The particle can be characterized by its physical position in the space and its velocity vector, while it has the ability to remember two things. The first is the best position it has “seen” so far (local best or LBest) and the second is the best position that any particle of the swarm has “seen” so far (global best or GBest). The latter is possible because each particle has the ability to communicate with a number of neighboring particles, which are defined by a predetermined network topology. The fitness of each particle shows the quality of each solution and is evaluated by a fitness function. In every iteration, the velocity of the particle is adjusted stochastically in combination with those two quantities that the particle remembers and its new position is determined by the old one and the new velocity vector. The update equations for the speed and position of a particle are:

$$\boldsymbol{v}^j(t+1) = w\boldsymbol{v}^j(t) + c_1\boldsymbol{r}_1 \circ \left(\boldsymbol{x}^{\mathrm{Pb},j} - \boldsymbol{x}^j(t) \right) + c_2\boldsymbol{r}_2 \circ \left(\boldsymbol{x}^{\mathrm{Gb}} - \boldsymbol{x}^j(t) \right) \tag{5}$$

$$\boldsymbol{x}^j(t+1) = \boldsymbol{x}^j(t) + \boldsymbol{v}^j(t+1) \tag{6}$$

where w is the inertia weight, $\boldsymbol{v}^j(t)$ denotes the velocity vector of particle j at time t, $\boldsymbol{x}^j(t)$ represents the position vector of particle j at time t, vector $\boldsymbol{x}^{\mathrm{Pb},j}$ is the memory of particle j at current iteration (the personal best ever position of the particle, corresponding to the objective function value $Pbest_j$), and vector $\boldsymbol{x}^{\mathrm{Gb}}$ is the global best location found by the entire swarm up to the current iteration (corresponding to the objective function value $Gbest$, the same for all particles). The acceleration coefficients c_1 and c_2 represent “trust” settings which indicate the degree of confidence in the best solution found by the individual particle (c_1 - cognitive parameter) and by the whole swarm (c_2 - social parameter), respectively, while $\boldsymbol{r}_1$ and $\boldsymbol{r}_2$ are two vectors containing random numbers with uniform distribution in the interval [0, 1].

The symbol "$\circ$" denotes the Hadamard product (entry-wise vector or matrix multiplication). For instance, for two matrices A and B with size 2×2 the Hadamard product is the following:

$$A \circ B = \begin{bmatrix} a_{11}b_{11} & a_{12}b_{12} \\ a_{21}b_{21} & a_{22}b_{22} \end{bmatrix} \tag{7}$$

The basic parameters of the PSO algorithm and their common values are presented in Table 1.

Symbol	**Description**	**Details**
NP	Number of particles	A typical range is 10-40. For most problems 10 particles is sufficient enough to get acceptable results. For some difficult or special problems the number can be increased to 50-100.
n	Dimension of particles	It is determined by the optimization problem.
w	Inertia weight	Usually is set to a value less than 1. It can also be updated during iterations. A linear, decreasing variation is common.
$\boldsymbol{x}^{\mathrm{L}}$, $\boldsymbol{x}^{\mathrm{U}}$	Vectors containing the lower and upper bounds of the n design variables, respectively	They are determined by the problem to be optimized. Different ranges for different dimensions of particles can be applied in general.
$\boldsymbol{v}_{max}$	Vector containing the maximum allowable velocity for each dimension during one iteration	Usually is set as half the length of the allowable interval for the given dimension. Different values for different dimensions of particles can be applied in general. $\left(v^{\max} = \frac{x^U - x^L}{2} \right)$
c_1, c_2	Cognitive and social parameters	They represent "trust" settings which indicate the degree of confidence in the best solution found by the individual particle (c_1 - cognitive parameter) and by the whole swarm (c_2 - social parameter). Usually $c_1 = c_2 = 2$ but other values can also be used, provided that $0 < c_1+c_2 < 4$ [18]

Table 1: Main PSO parameters.

Figure 1 depicts a particle's movement, in a two-dimensional design space, according to Eqs. (5) and (6). The particle's current position $\boldsymbol{x}^j(t)$ at time t is represented by the dotted circle at the lower left of the drawing, while the new position $\boldsymbol{x}^j(t+1)$ at time $t+1$ is represented by the dotted bold circle at the upper right-hand corner of the drawing. It can be seen how the particle's movement is affected by: (i) it's velocity $\boldsymbol{v}^j(t)$; (ii) the personal best ever position of the particle, $\boldsymbol{x}^{\mathrm{Pb},j}$, at the right of the figure; and (iii) the global best location found by the entire swarm, $\boldsymbol{x}^{\mathrm{Gb}}$, at the upper left of the figure.

In the above formulation, the global best location found by the entire swarm up to the current iteration ($\boldsymbol{x}^{\mathrm{Gb}}$) is used. This is called a fully connected topology (fully informed PSO), as all particles share information with each other about the best performer of the swarm. Other topologies have also been used in the past where instead of the global best location found by the entire swarm, a local best location of each particle's neighbourhood is used. Thus, information is shared only among members of the same neighbourhood.

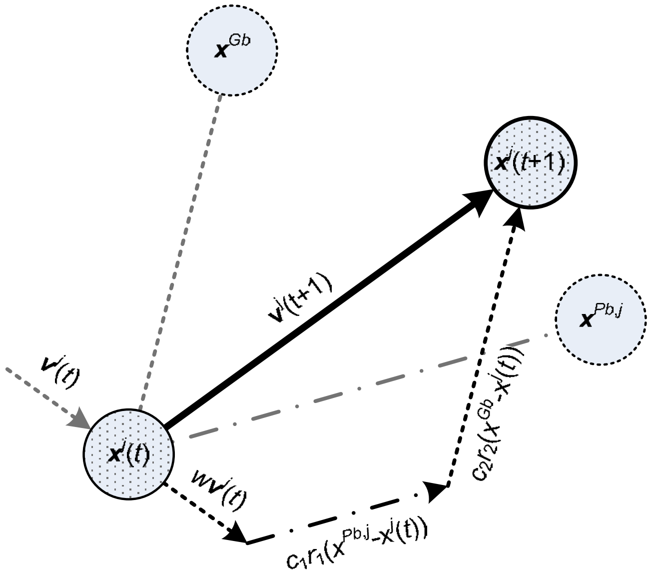

Figure 1: Visualization of the particle's movement in a two-dimensional design space.

1.4 Discrete PSO

In this study a discrete version of the PSO algorithm is applied in order to solve structural optimization problems for steel structures. First, a mapping is performed; every member of a predefined set for the design variables is mapped to an integer number, starting from one. This way, the discrete optimization problem is transformed into an integer optimization problem. It should be noted that not all members should belong to the same discrete predefined set. For example, in a steel frame, the beams can belong to the IPE section group of the Eurocode, while the columns can belong to the HEA or HEB group. There is no limitation in the groups that will be taken into account for the optimization problem.

The discrete PSO algorithm is basically the same as the continuous one with the modification that eq. (5) for the particle's velocity is rounded to their nearest integer value. Using a round function which rounds a number to its nearest integer, the equation for velocity takes the following format:

$$\boldsymbol{v}^j(t+1) = \text{round}\left[w\boldsymbol{v}^j(t) + c_1\boldsymbol{r}_1 \circ \left(\boldsymbol{x}^{\text{Pb},j} - \boldsymbol{x}^j(t) \right) + c_2\boldsymbol{r}_2 \circ \left(\boldsymbol{x}^{\text{Gb}} - \boldsymbol{x}^j(t) \right) \right] \quad (8)$$

For an integer optimization problem of steel structures, where the design variables belong to groups of the Eurocode (IPE, HEA, HEB and others), it was found that the maximum allowable velocity ($v_{\max}$) should be set equal to 1 (or 2 as a maximum), so that the particles will move around small areas of the discrete design space in each iteration and as a result the probability of approaching the optimum solution will be higher. Of course, this conclusion is not general, as it depends on the size of the section group. For larger sets, the maximum velocity should be set higher, in order to achieve faster convergence.

1.5 Genetic Algorithm

The Genetic Algorithm (GA) method is the most widely used type of Evolutionary Algorithm. In a genetic algorithm, a population of strings (called chromosomes or genotype), which encode candidate solutions (called individuals or phenotypes) of the optimization problem, evolves toward better solutions. Traditionally, solutions are represented in binary form as strings of 0s and 1s, but other encodings are also possible. The evolution usually starts from a population of randomly generated individuals and takes place in generations. In each generation, the fitness of every individual in the population is evaluated, multiple individuals are stochastically selected from the current population based on their fitness, and modified to form a new population. The new population is then used in the next iteration of the algorithm and this procedure goes on until the optimum solution is found or a convergence criterion has been satisfied. Commonly, the algorithm terminates when either a maximum number of generations has been reached, or a satisfactory fitness value has been achieved for a member of the population. The GA method consists of the following processes:

a) *Encoding* of the information carried by the chromosomes using fixed-length binary strings.
b) *Fitness evaluation*, where the objective function value is calculated.
c) *Selection* of members who will become parents and will produce the next generation (Tournament selection, Ranking selection, Roulette Wheel).
d) *Crossover* operator (Scattered crossover, One-point crossover, Two-point crossover, Uniform crossover, Arithmetic crossover, Heuristic crossover).
e) *Mutation* operator, which is an operator that inserts a small probability that a single binary bit in a given chromosome will be changed from its initial value. The main purpose of the mutation operator is to maintain diversity within the population and inhibit premature convergence.
f) *Termination* of the algorithm, when convergence has been achieved.

In a structural constrained optimization problem the steps of the Genetic Algorithm are briefly shown in the following figure

1. *Initialization*: Selection of parent vectors of the design variables, usually randomly.
2. *Analysis and Evaluation*: Evaluation of the parents by the fitness function.
3. *Feasibility Check*: If not all parents are feasible, modification of infeasible parents and back to step 2.
4. *Genetic Operators*: Mutation of all members and crossover of parents to produce offspring.
5. *Analysis and Evaluation*: Evaluation of the offspring by the fitness function.
6. *Feasibility Check*: If not all offspring are feasible, discard infeasible offspring and back to step 4.
7. *Genetic Operators*: Selection, mutation and crossover of the next generation parents.
8. *Termination Criterion*: If any one of the termination criteria is reached then stop, else go back to step 4.

Figure 2: GA steps in constrained optimization problems.

1.6 Constraint Handling Technique for PSO

The structural optimization problems are subjected to a number of inequality constraints. These constraints impose limitations to the values that the design variables can take and limit the available search space in which the optimum solution can be searched and found. In general, different optimization methods handle constraints in different ways. In this study a penalty method will be used to handle the constraints of the PSO problem and in particular the penalty method proposed by Plevris [20] which is proven to be a simple and effective method which in the case of a typical constraint has the following form:

$$g_k(\boldsymbol{x}) = \left|q_k(\boldsymbol{x})\right| - q_{allow,k} \leq 0 \tag{9}$$

where $q_k(x)$ is a response measure (usually displacement, stress or strain) for design vector x and $q_{allow,k}$ its maximum allowable absolute value.

In this case the penalty function $\Phi_k(\boldsymbol{x})$ for the typical constraint is the following:

$$\Phi_k(\boldsymbol{x}) = \begin{Bmatrix} 1 & if & \dfrac{\left|q_k(\boldsymbol{x})\right|}{q_{allow,k}} \leq 1 \\ \dfrac{\left|q_k(\boldsymbol{x})\right|}{q_{allow,k}} & if & \dfrac{\left|q_k(\boldsymbol{x})\right|}{q_{allow,k}} > 1 \end{Bmatrix} \tag{10}$$

Having calculated the penalty function for all violated constraints, the penalized fitness value of a design ***x*** is obtained by multiplying the objective function to be minimized (structural weight) by the maximum penalty factor among all constraints:

$$f_p(\boldsymbol{x}) = f(\boldsymbol{x}) \max\left\{\Phi_k(\boldsymbol{x})\right\} \tag{11}$$

where $f_p(\boldsymbol{x})$ is the new penalized objective function and $\max\left\{\Phi_k(\boldsymbol{x})\right\}$ the maximum value of the penalty function among all active constraints of the optimization problem.

Using the previous method, there is a case where the penalized objective function can obtain a better value compared to the optimum solution found at the iteration *n* of the algorithm, $GBest_n$. This undesirable case resets the best solution into the infeasible areas of the design space. To avoid this problem, the penalty is imposed on the optimum solution instead of the new objective function, as shown in the following equations:

$$\begin{Bmatrix} f_p(\boldsymbol{x}) = f(\boldsymbol{x}) \max\left\{\Phi_k(x)\right\} & if & \max\left\{\Phi_k(\boldsymbol{x})\right\} > 1 & and & f(\boldsymbol{x}) \geq Gbest_n \\ f_p(\boldsymbol{x}) = Gbest_n \max\left\{\Phi_k(x)\right\} & if & \max\left\{\Phi_k(\boldsymbol{x})\right\} > 1 & and & f(\boldsymbol{x}) < Gbest_n \end{Bmatrix} \tag{12}$$

2 LINEAR STATIC ANALYSIS TOOL

A new software tool for the linear static analysis of three-dimensional frames has been developed, featuring some distinct characteristics. The applied loads can be nodal or elemental (uniform, triangular or trapezoidal in any direction - x, y, z - within an element), while any release (translational or rotational) can be implemented at an end of any element, in any of the 6 Degrees Of Freedom (DOFs), either translational or rotational. The input file of the program contains the information that is shown in Table 1.

Material Properties	Modulus of Elasticity E, Poisson ratio v, Steel density d
Section Properties	Section area A, Moment of inertia y-axis (I_y), Moment of inertia z-axis (I_z), Torsion constant K
Nodes	Coordinates x, y, z
Elements	Start node, End node, Material number, Section number, Orientation vector coordinates x, y, z
Element Releases	Translational and rotational releases in any degree of freedom of the start and end node of any element.
Constraints	Translation and rotation constraints for any degree of freedom of any node.
Elastic Constraints	Stiffness value of translational and rotational springs for any degree of freedom of any node.
Concentrated Loads	Forces and moments for any degree of freedom of any node.
Distributed Loads	Trapezoidal forces in any global direction x, y, z. Values are given for the start and end node of the element, assuming linear variation within the element.

Table 2: Input file format of the linear analysis software tool.

The output of the analysis program includes the constraint reactions, nodal displacements, forces at the ends of the elements, plus the displacements of the released DOFs of all elements with releases, and also any displacement or any force at any given point within an element. The distinct characteristics of the specific analysis tool are mainly: (i) In the input of the model, that any release in any DOF of any element can be implemented and many releases can coexist in an element provided that the element can carry the defined loads (not be a mechanism). This is very important for steel structures where elemental releases (hinges or others) are common practice in construction. (ii) In the output of the program, that any displacement (or rotation) or any force (or moment) can be calculated and given in the output, for any point within an element. In most cases, finite element analysis programs provide their results only at the nodal points (two ends of an element), but in the analysis and design of steel structures it is important to have results also within the elements, for example in order to check the maximum (mid-span) deflection of a beam member. Usually, this is done by adding nodes to the model which makes the model more complex and will have a negative effect on the optimization process where the model has to be analyzed many times. In our case, no extra nodes are added, as the program provides the displacements and forces at any given point within an element, even for the case of elements with releases.

The accuracy of the analysis results is verified by a direct comparison to the corresponding results of a reliable commercial finite element software program (NX Nastran) while a self-comparison is also done, using the same analysis tool but with a different model.

3 CONSTRAINTS BASED ON EC3

The constraints of the structural optimization problems examined in the present study are based on Eurocode 3, including various checks of the values of displacements and forces, as described in detail in the following paragraphs.

3.1 Ultimate Limit State (ULS)

Biaxial bending with axial force

$$\text{value1} = \frac{|N_{sd}|}{Af_y/\gamma_{\mathrm{M}0}} + \frac{|\mathrm{M}_{y,sd}|}{W_{pl,y}f_y/\gamma_{\mathrm{M}0}} + \frac{|\mathrm{M}_{z,sd}|}{W_{pl,z}f_y/\gamma_{\mathrm{M}0}} \leq 1.00 \qquad (13)$$

Shear force (Y-axis)

$$\text{value2}_{\text{y}} = \frac{\left|V_{y,sd}\right|}{A_{v,y}\, f_y \Big/ \left(\sqrt{3}\gamma_{\text{M0}}\right)} \leq 1.00 \tag{14}$$

Shear force (Z-axis)

$$\text{value2}_{\text{z}} = \frac{\left|V_{z,sd}\right|}{A_{v,z}\, f_y \Big/ \left(\sqrt{3}\gamma_{\text{M0}}\right)} \leq 1.00 \tag{15}$$

where:

N_{sd}, $\text{M}_{y,sd}$, $\text{M}_{z,sd}$: Axial force, bending moment around y - axis and bending moment around z - axis, respectively

$V_{y,sd}$, $V_{z,sd}$: y - shear force and z - shear force, respectively

$W_{pl,y}$, $W_{pl,z}$: Plastic section modulus around y and z - axis, respectively

A : Section area

f_y : Yield stress of steel

γ_{M0} : The partial safety factor ($\gamma_{\text{M0}} = 1.00$ according to EC3)

$A_{v,y}$, $A_{v,z}$: Shear area for y - axis and z - axis, respectively

The above ULS constraints are checked for the following load combinations:

a) 1.35G +1.50Q + 0.60W

b) 1.35G +1.50W + 0.60Q

c) 1.00G +0.30Q + E

Where G are the deal loads, Q are the live loads, W are the wind loads and E are the earthquake loads on the structure which are imposed using the equivalent static method of the Greek Seismic Code (EAK2000), which is similar to the lateral force method of the Eurocode 8.

3.2 Serviceability Limit State (SLS)

Serviceability check for full loading:

$$\text{value3} = \frac{250\left|v_z\right|}{L} \leq 1.00 \tag{16}$$

for the following load combinations:

a) 1.00G +1.00Q + 0.60W

b) 1.00G +1.00W + 0.70Q

Serviceability check for live loading only (without dead loads):

$$\text{value4} = \frac{300\left|v_z\right|}{L} \le 1.00 \tag{17}$$

for the following load combinations:

a) 1.00Q + 0.60W

b) 1.00W + 0.70Q

where v_z is the vertical displacement at the middle of a beam element.

The constraint values are calculated for every element of the steel frame, in various positions within the element (*L*/10, 2*L*/10, etc). The objective function of the structural optimization problem is the weight of the structure, to be minimized, which is described in Eq. (2).

4 NUMERICAL EXAMPLES

4.1 Verification of the linear static analysis tool

A Finite Element analysis of a three-dimensional frame is performed. The model (A) is depicted in Figure 3.

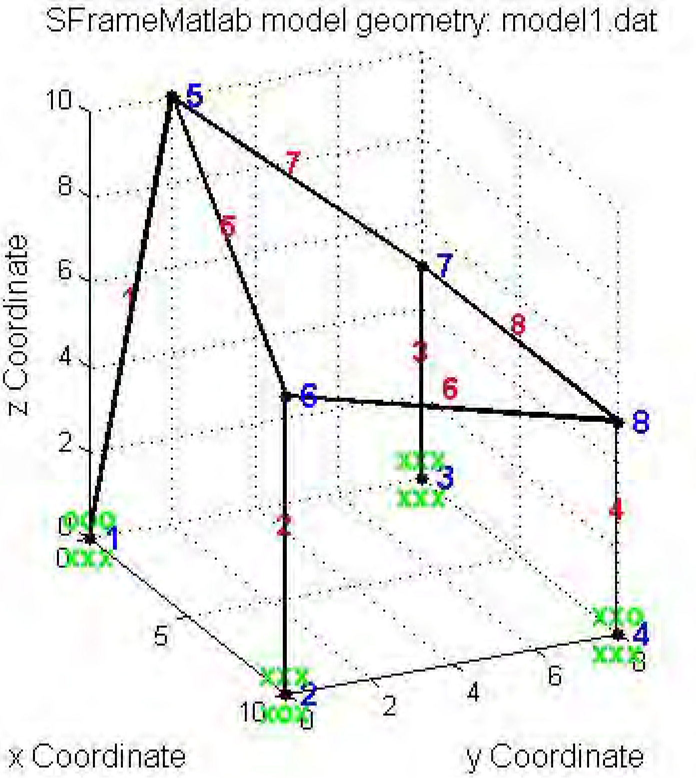

Figure 3: Three-dimensional analysis model A for verification purposes.

Various types of loads, releases and springs are applied, as shown in the tables below.

Node	Node Coordinates (m)			Constraints		
	x	y	z	Translations	Rotations	Description
1	0	0	0	XXX	OOO	Hinge
2	10	0	0	XOX	XXX	Y-Translation allowed
3	0	8	0	XXX	XXX	Fixed
4	10	8	0	XXX	XXO	Z-Rotation allowed
5	0	2	10	-	-	-
6	10	0	7	-	-	-
7	0	8	5	-	-	-
8	10	8	5	-	-	-

Table 3: Nodal data of the analysis model A (X denotes restriction of the DOF, O denotes free DOF.

Element	Start Node	End Node	Coordinates of Orientation Vector (R)		
			x^R	y^R	z^R
1	1	5	0	8	5
2	2	6	10	8	5
3	3	7	0	2	10
4	4	8	10	0	7
5	5	6	0	8	5
6	6	8	0	2	10
7	5	7	10	8	5
8	7	8	10	0	7

Table 4: Elemental data of the analysis model A.

Element	Start Node		End Node		Release Description
	Translations	Rotations	Translations	Rotations	
4	000	000	100	001	X-translation and Z-rotation at the end node of the element
5	000	000	001	010	Z-translation and Y-rotation at the end node of the element

Table 5: Elemental releases of the analysis model A.

Node	Degree Of Freedom	Stiffness value	Description
6	1	5000	Translational Spring (X-axis)
8	4,5,6	2000	Rotational Springs (X,Y,Z axes)

Table 6: Spring data of the analysis model A.

Node	F_x (kN)	F_y (kN)	F_z (kN)	M_x (kNm)	M_y (kNm)	M_z (kNm)
5	10	-25	-20	0	25	50
6	10	-20	-10	50	0	0
7	10	-10	10	0	-50	30
8	-20	10	30	0	0	0

Table 7: Nodal loads of the analysis model A (global system).

Element	$F_x^{\,i}$ (kN/m)	$F_x^{\,j}$ (kN/m)	$F_y^{\,i}$ (kN/m)	$F_y^{\,j}$ (kN/m)	$F_z^{\,i}$ (kN/m)	$F_z^{\,j}$ (kN/m)
5	-20	35	15	-30	0	0
7	10	-10	-25	15	0	0

Table 8: Elemental loads of the analysis model A.

Material properties: $E = 2.1 \cdot 10^8 \, \text{kN/m}^2, v = 0.3$

Section properties: $A = 5 \cdot 10^{-3} \text{m}^2, I_y = 8 \cdot 10^{-5} \text{m}^4, I_z = 6 \cdot 10^{-6} \text{m}^4, K = 2 \cdot 10^{-7} \text{m}^4$

Results

The analysis tool calculates the displacements, forces and moments at any given intermediate point of any element. Having calculated the displacements at any given point of the element, the software provides a figure of the deformed shape of the analysis model, which for model A is shown in Figure 4.

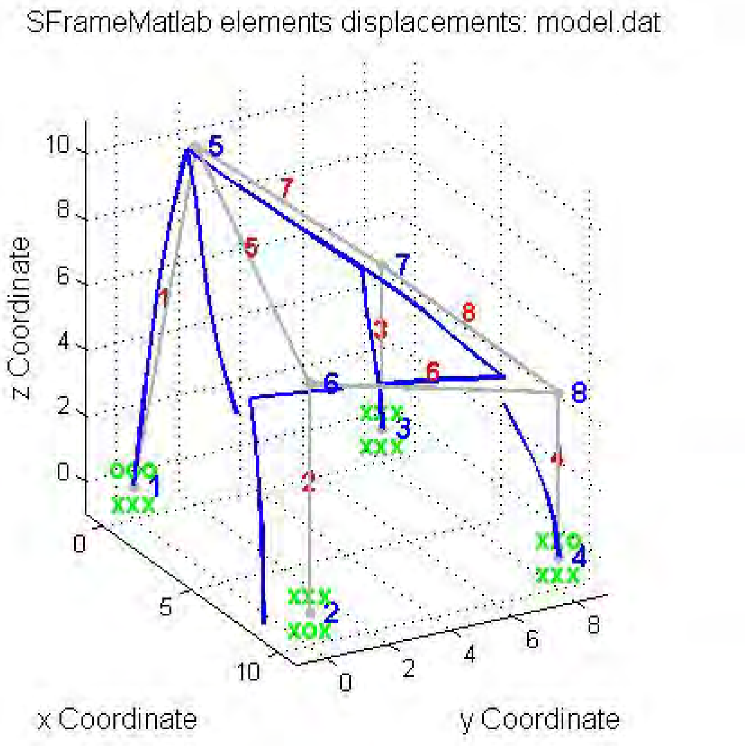

Figure 4: Deformed shape of the analysis model A.

The discontinuities observed at nodes 6 and 8 are due to the existence of translational and rotational releases at the ends of the corresponding elements of the model, as shown in Table 5. Selected groups of the analysis results are presented in the following tables. All the results of nodal points are presented (displacements and forces), while only the intermediate displacements in the X-axis and intermediate axial forces are presented in the tables.

ID	x-displacement	y-displacement	z-displacement	x-rotation	y-rotation	z-rotation
1	0.00E+000	0.00E+000	0.00E+000	1.06E-001	-1.33E-002	-1.53E-001
2	0.00E+000	-1.72E+000	0.00E+000	0.00E+000	0.00E+000	0.00E+000
3	0.00E+000	0.00E+000	0.00E+000	0.00E+000	0.00E+000	0.00E+000
4	0.00E+000	0.00E+000	0.00E+000	0.00E+000	0.00E+000	-3.35E-002
5	3.84E-001	-5.83E-001	1.15E-001	-3.80E-002	4.75E-002	-1.66E-001
6	2.14E-002	-2.22E+000	-5.97E-005	1.44E-001	4.39E-003	5.02E-002
7	-1.06E-001	-6.77E-001	6.16E-004	1.31E-002	-4.30E-002	4.85E-002
8	-1.06E-001	-1.99E+000	9.33E-001	7.08E-002	-4.18E-002	-3.35E-002

Table 9: Nodal displacements (global system).

ID	uxj	vzj	thyj	thzj
4	0.00E+000	0.00E+000	0.00E+000	5.97E-001
5	0.00E+000	-1.65E+000	1.42E-001	0.00E+000

Table 10: Element Released Displacements (local system).

ID	Ni	Vyi	Vzi	Mxi	Myi	Mzi
1	113.250	3.499	-20.038	0.000	-0.000	0.000
2	8.948	-0.000	3.554	-0.116	-22.975	25.949
3	-129.313	-77.986	-2.166	-0.157	-138.961	-198.262
4	0.000	-60.151	3.019	0.000	-147.841	-300.753
5	13.197	7.031	21.140	-0.180	-192.942	73.441
6	-82.982	-3.158	-14.219	0.048	-22.271	3.956
7	-64.861	10.728	-54.295	0.427	4.502	109.917
8	18.562	-22.202	31.639	-0.093	-122.800	-120.998

ID	Nj	Vyj	Vzj	Mxj	Myj	Mzj
1	-113.250	-3.499	20.038	-0.000	204.347	35.679
2	-8.948	0.000	-3.554	0.116	-1.901	-25.949
3	129.313	77.986	2.166	0.157	149.792	-191.667
4	0.000	60.151	-3.019	0.000	132.745	0.000
5	-103.197	57.510	0.000	0.180	0.000	4.507
6	82.982	3.158	14.219	-0.048	139.528	-29.997
7	94.861	-10.728	29.295	-0.427	191.761	75.541
8	-18.562	22.202	-31.639	0.093	-193.585	-101.025

Table 11: Element forces at ends (local system).

ID	N(0)	N(L/10)	N(2L/10)	N(3L/10)	N(4L/10)	N(L/2)
1	113.250	113.250	113.250	113.250	113.250	113.250
2	8.948	8.948	8.948	8.948	8.948	8.948
3	-129.313	-129.313	-129.313	-129.313	-129.313	-129.313
4	0.000	0.000	0.000	0.000	0.000	0.000
5	13.197	-6.603	-20.003	-27.003	-27.603	-21.803
6	-82.982	-82.982	-82.982	-82.982	-82.982	-82.982
7	-64.861	-78.661	-90.061	-99.061	-105.661	-109.861
8	18.562	18.562	18.562	18.562	18.562	18.562

ID	N(6L/10)	N(7L/10)	N(8L/10)	N(9L/10)	N(L)
1	113.250	113.250	113.250	113.250	113.250
2	8.948	8.948	8.948	8.948	8.948
3	-129.313	-129.313	-129.313	-129.313	-129.313
4	0.000	0.000	0.000	0.000	0.000
5	-9.603	8.997	33.997	65.397	103.197
6	-82.982	-82.982	-82.982	-82.982	-82.982
7	-111.661	-111.061	-108.061	-102.661	-94.861
8	18.562	18.562	18.562	18.562	18.562

Table 12: Axial forces at various positions within the elements (local system).

ID	u(0)	u(L/10)	u(2L/10)	u(3L/10)	u(4L/10)	u(L/2)
1	0.00E+000	1.75E-002	3.64E-002	5.77E-002	8.28E-002	1.13E-001
2	0.00E+000	3.23E-004	1.24E-003	2.69E-003	4.59E-003	6.86E-003
3	0.00E+000	-1.04E-003	-4.16E-003	-9.38E-003	-1.67E-002	-2.62E-002
4	0.00E+000	-1.10E-003	-4.37E-003	-9.80E-003	-1.74E-002	-2.70E-002
5	3.84E-001	3.36E-001	2.85E-001	2.33E-001	1.78E-001	1.20E-001
6	2.14E-002	-1.86E-002	-5.57E-002	-8.87E-002	-1.16E-001	-1.38E-001
7	3.84E-001	4.34E-001	4.36E-001	3.99E-001	3.31E-001	2.43E-001
8	-1.06E-001	-1.06E-001	-1.06E-001	-1.06E-001	-1.06E-001	-1.06E-001

Table 13: x-displacements (axial) at various positions within the elements (local system).

Results verification: 1. Comparison with NX Nastran

The results obtained by this new tool (nodal displacements and element forces) are compared to the ones obtained with NX Nastran, a reliable commercial finite element software. The corresponding results of NX Nastran for the analysis model A are given in the tables below.

ID.		T1	T2	T3	R1	R2	R3
1	G	0.	0.	0.	1.063808E-1	-1.334909E-2	-1.534051E-1
2	G	0.	-1.718393E+0	0.	0.	0.	0.
3	G	0.	0.	0.	0.	0.	0.
4	G	0.	0.	0.	0.	0.	-3.351714E-2
5	G	3.841538E-1	-5.827316E-1	1.154246E-1	-3.800689E-2	4.746852E-2	-1.655687E-1
6	G	2.141272E-2	-2.222949E+0	-5.965523E-5	1.441588E-1	4.390469E-3	5.023001E-2
7	G	-1.060799E-1	-6.774387E-1	6.157757E-4	1.308552E-2	-4.296919E-2	4.848347E-2
8	G	-1.062567E-1	-1.989106E+0	9.326228E-1	7.083541E-2	-4.175385E-2	-3.351714E-2

Table 14: NX Nastran results - Nodal displacements (global system).

```
  STAT DIST     - BENDING MOMENTS -            - WEB  SHEARS -           AXIAL
             MOM PLANE 1   MOM PLANE 2    SHR PLANE 1   SHR PLANE 2     FORCE         TOT TORQUE

    0.000   -1.421085E-14            0.   -3.498626E+0   2.003789E+1   -1.132500E+2   2.886580E-15
    1.000     3.567912E+1  -2.043472E+2   -3.498626E+0   2.003789E+1   -1.132500E+2   2.886580E-15

    0.000    -2.594859E+1  -2.297478E+1             0.  -3.553616E+0   -8.948283E+0    1.159154E-1
    1.000    -2.594859E+1   1.900531E+0             0.  -3.553616E+0   -8.948283E+0    1.159154E-1

    0.000     1.982624E+2  -1.389613E+2    7.798593E+1   2.166048E+0    1.293129E+2    1.566389E-1
    1.000    -1.916673E+2  -1.497916E+2    7.798593E+1   2.166048E+0    1.293129E+2    1.566389E-1

    0.000     3.007529E+2  -1.478412E+2    6.015058E+1  -3.019295E+0             0.             0.
    1.000              0.  -1.327447E+2    6.015058E+1  -3.019295E+0             0.             0.

    0.000    -7.344055E+1  -1.929415E+2   -7.031394E+0  -2.113989E+1   -1.319692E+1    1.801822E-1
    1.000     4.507202E+0            0.    5.751010E+1             0.  -1.031969E+2    1.801822E-1

    0.000    -3.955989E+0  -2.227148E+1    3.157955E+0   1.421944E+1    8.298228E+1   -4.790572E-2
    1.000    -2.999715E+1  -1.395280E+2    3.157955E+0   1.421944E+1    8.298228E+1   -4.790572E-2

    0.000    -1.099169E+2   4.501728E+0   -1.072832E+1   5.429548E+1    6.486137E+1   -4.271201E-1
    1.000     7.554063E+1  -1.917606E+2   -1.072832E+1   2.929548E+1    9.486137E+1   -4.271201E-1

    0.000     1.209979E+2  -1.227998E+2    2.220228E+1  -3.163852E+1   -1.856227E+1    9.328829E-2
    1.000    -1.010250E+2   1.935853E+2    2.220228E+1  -3.163852E+1   -1.856227E+1    9.328829E-2
```

Table 15: NX Nastran results – Element forces (local system)..

A full coincidence of the analysis results of the two programs can be observed. This proves that the nodal displacements and the element forces at the element ends are calculated with accuracy with the analysis tool.

Results verification: 2. Self-comparison

NX Nastran provides us the values of displacements and forces at the nodal points, but it cannot calculate the displacements and forces at any given point within an element. In order to verify these results also, a self-comparison is done, as described in detail in the following paragraphs.

We create a new model (model B) where each element has been divided into two elements with the addition of a new node within each element. The new node is not positioned always in the middle of the element, but rather at various points (L/10, 2L/10, etc) within the element, as shown in the figure of model B below.

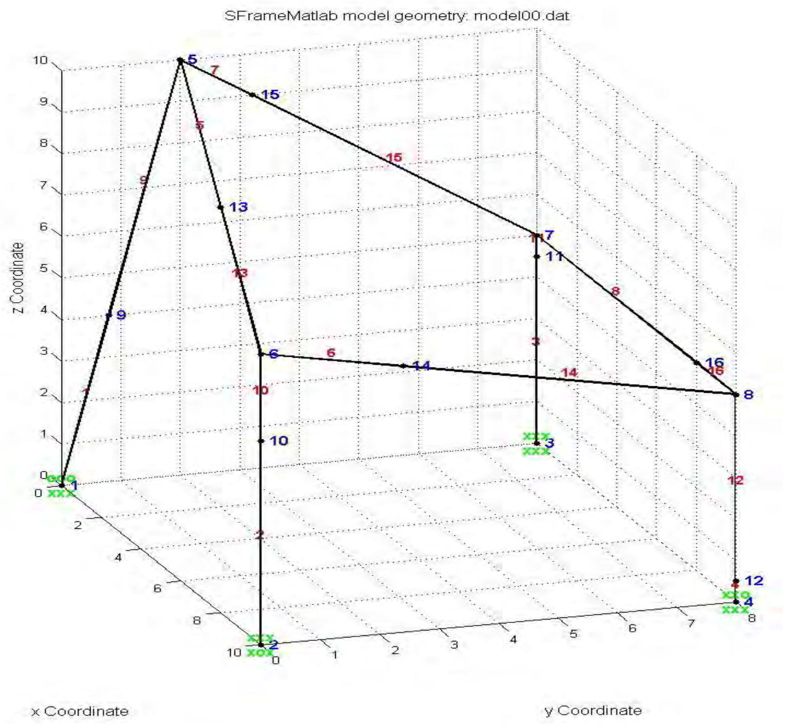

Figure 5: Analysis model B with the addition of new intermediate nodes.

By adjusting the loads, releases, etc, model B has been made equivalent to the first model A. By performing the new analysis, the corresponding results at the nodal points are found to coincide. Also, the intermediate results of the model A at various positions within the elements can now be checked, as in model B there are nodes at these points. By performing the analysis, and doing the corresponding comparisons, it is proven that the results coincide again, as the displacements and forces at the intermediate points within each element are the same as the nodal results of the corresponding new nodes of model B.

4.2 Structural Optimization Problems

One plane and one space steel frame are examined. The optimization results of the discrete PSO method are compared to the ones obtained with a discrete GA. In the discrete structural optimization problems that are examined, three steel section groups have been taken into account, namely the IPE, HEA, HEB section groups of the Eurocode, while it is easy to add other section groups also. In all test examples, the earthquake loading has been taken into account with the equivalent static load method of the Greek Seismic Code (EAK2000), where a peak ground acceleration of 0.36g has been taken into consideration.

The parameters of the GA and PSO algorithms, used in this study, are presented in the following tables.

Population size	20
Generations	100
Crossover function	Scattered

Table 16: GA parameter values.

Swarm size	20
Iterations	100
$v_{\max}$	1
$w_{\max}$	0.95
$w_{\min}$	0.8
c_1, c_2	2

Table 17: PSO parameter values.

Optimization example 1

The first optimization test example is a plane frame that is depicted in Figure 6. The details of the model are given in the tables below.

Element	**Dead distributed loads (kN/m)**		**Live distributed loads (kN/m)**		**Wind distributed loads (kN/m)**	
	$G_z^{\,i}$	$G_z^{\,j}$	$Q_z^{\,i}$	$Q_z^{\,j}$	$W_x^{\,i}$	$W_x^{\,j}$
1-5	-	-	-	-	3	3
21-35	-2	-2	-0.5	-0.5	-	-

Table 18: Load types and values of model 1.

Design variable	**Elements**	**Section category**
1	Beams 21-22, 26-27, 31-32	IPE
2	Beams 23-25, 28-30, 33-35	IPE
3	Columns 1-2, 6-7, 11-12, 16-17	HEA
4	Columns 3-5, 8-10, 13-15, 18-20	HEB

Table 19: Design variables of model 1.

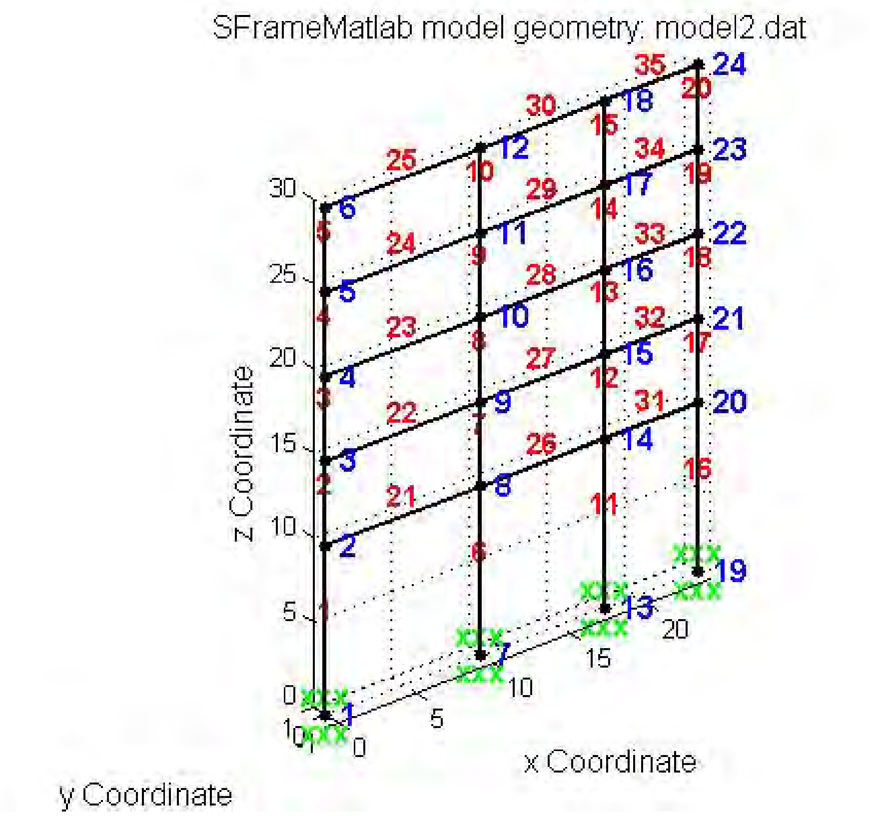

Figure 6: Model 1 geometry.

The results of the optimization process with GA and PSO are given in the Table 21. It is observed that both algorithms converge to the same optimum design. The constraint values for the optimum design are given in Table 21. The convergence histories for both methods are given in Figure 7. The PSO method appears to be faster in locating the solution at around 400 objective function evaluations, whereas the GA method needs 650 objective function evaluations to reach the optimum.

Design variable	**GA**	**PSO**
1	IPE 550	IPE 550
2	IPE 450	IPE 450
3	HEA 300	HEA 300
4	HEB 180	HEB 180
Objective function value (kN)	190.31	190.31

Table 20: Optimum design of model 1.

Biaxial bending with axial force	U.L.S. (live loads)	value1 (a)	0.5307
	U.L.S. (wind loads)	value1 (b)	0.9522
	U.L.S. (seismic load)	value1 (c)	0.3522
Shear force (Y-axis)	U.L.S. (live loads)	value2_y (a)	0.0342
	U.L.S. (wind loads)	value2_y (b)	0.0652
	U.L.S. (seismic load)	value2_y (c)	0.0163
Shear force (Z-axis)	U.L.S. (live loads)	value2_z (a)	0
	U.L.S. (wind loads)	value2_z (b)	0
	U.L.S. (seismic load)	value2_z (c)	0
Serviceability check for full loading	S.L.S. (live loads)	value3 (a)	0.9709
	S.L.S. (wind loads)	value3 (b)	0.9472
Serviceability check for live loading	S.L.S. (live loads)	value4 (a)	0.2159
	S.L.S. (wind loads)	value4 (b)	0.2182

Table 21: Constraint values of the optimum design of model 1.

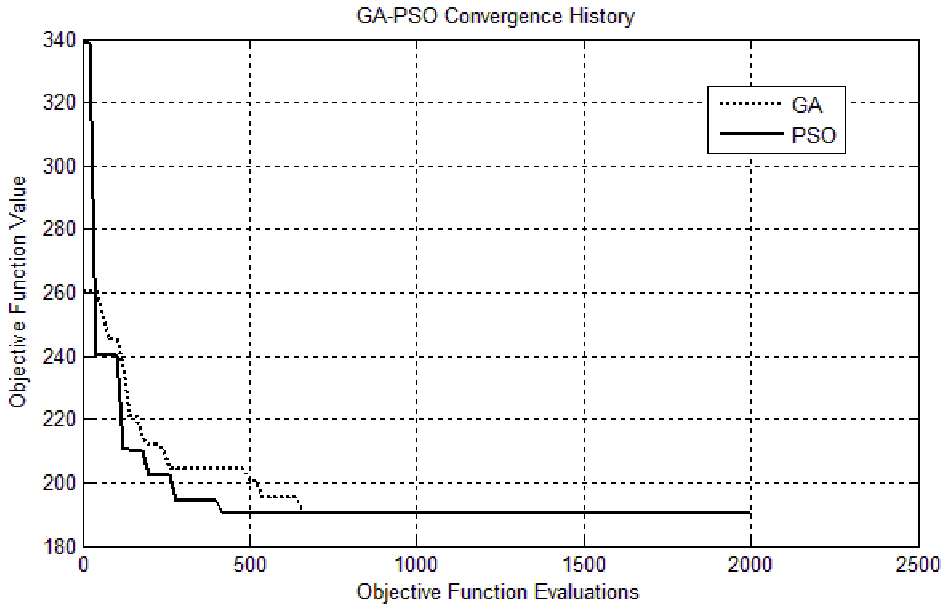

Figure 7: GA vs PSO convergence history for model 1.

Optimization example 2

The second optimization test example is a space frame that is depicted in Figure 8. The details of the model are given in the tables below.

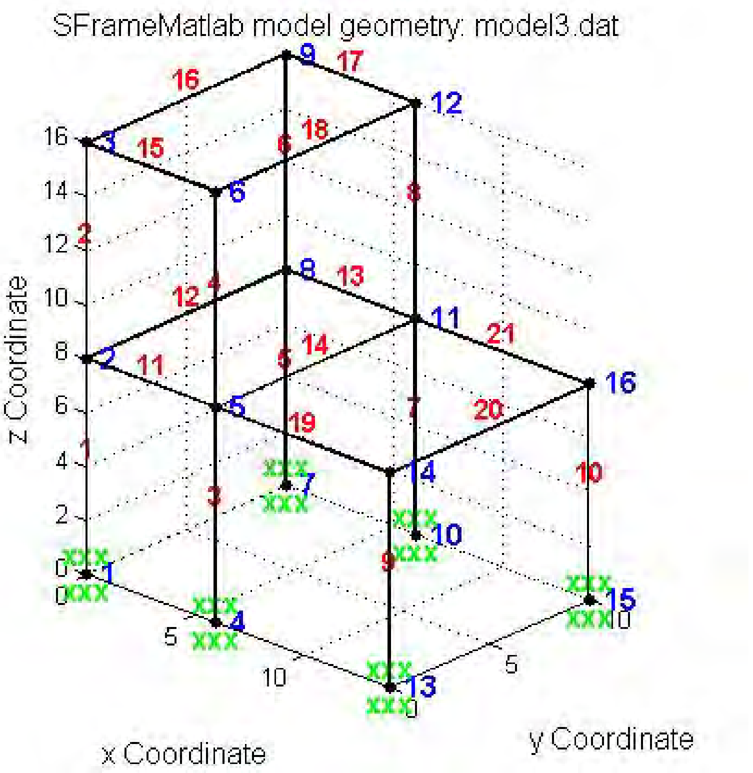

Figure 8: Model 2 geometry.

Element	Dead distributed loads (kN/m)		Live distributed loads (kN/m)		Wind distributed loads (kN/m)	
	$G_z^{\ i}$	$G_z^{\ j}$	$Q_z^{\ i}$	$Q_z^{\ j}$	$W_x^{\ i}$	$W_x^{\ j}$
1-2	-	-	-	-	7	7
5-6	-	-	-	-	7	7
11-21	-5	-5	-3	-3	-	-

Table 22: Load types and values of model 2.

Design variable	Elements	Section category
1	Beams 11-14, 19-21	IPE
2	Beams 15-18	IPE
3	Columns 1,3,5,7,9,10	HEA
4	Columns 2,4,6,8	HEB

Table 23: Design variables of model 2.

The results of the optimization process for GA and PSO are given in the Table 24. It is again observed that both algorithms converge to the same optimum design. The constraint values for the optimum design are given in Table 25. The convergence histories for both methods are given in Figure 9. Both the PSO method and the GA method appear to find the optimum solution at around 250-300 objective function evaluations.

Design variable	**GA**	**PSO**
1	IPE 300	IPE 300
2	IPE 270	IPE 270
3	HEA 340	HEA 340
4	HEB 240	HEB 240
Objective function value (kN)	113.14	113.14

Table 24: Optimum design of model 2.

Biaxial bending with axial force	U.L.S. (live loads)	value1 (a)	0.5519
	U.L.S. (wind loads)	value1 (b)	0.9868
	U.L.S. (seismic load)	value1 (c)	0.3800
Shear force (Y-axis)	U.L.S. (live loads)	value2_y (a)	0.0418
	U.L.S. (wind loads)	value2_y (b)	0.0969
	U.L.S. (seismic load)	value2_y (c)	0.0230
Shear force (Z-axis)	U.L.S. (live loads)	value2_z (a)	0.0973
	U.L.S. (wind loads)	value2_z (b)	0.1323
	U.L.S. (seismic load)	value2_z (c)	0.0551
Serviceability check for full loading	S.L.S. (live loads)	value3 (a)	0.7503
	S.L.S. (wind loads)	value3 (b)	0.6712
Serviceability check for live loading	S.L.S. (live loads)	value4 (a)	0.3243
	S.L.S. (wind loads)	value4 (b)	0.3159

Table 25: Constraint values of the optimum design of model 2.

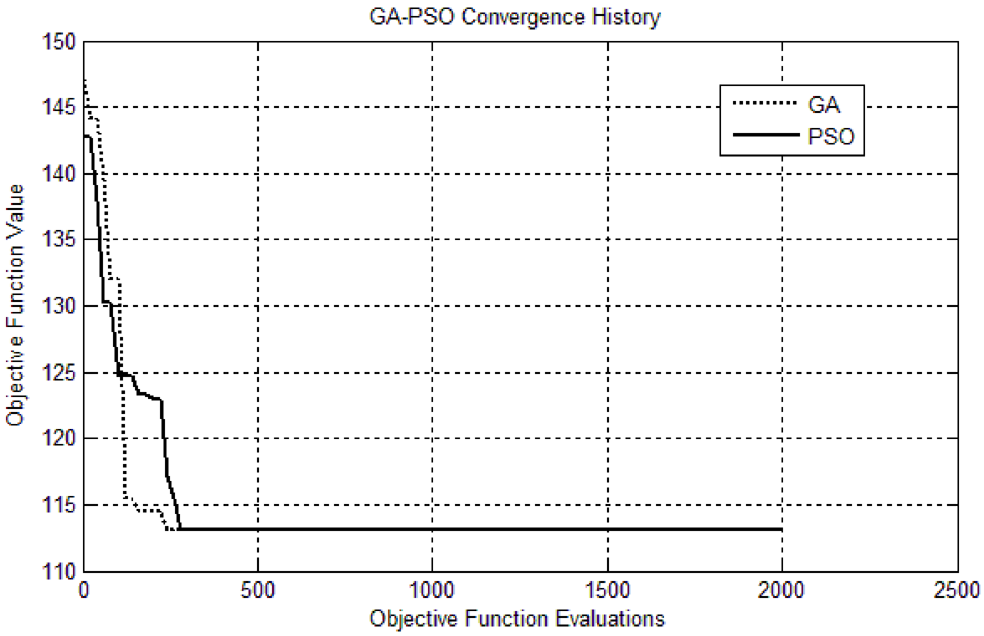

Figure 9: GA vs PSO convergence history of model 2.

5 CONCLUSIONS

The linear static analysis tool that has been developed proved to be a very useful and accurate tool for the analysis of three-dimensional frames. The advantage of the software tool is its generality, as it can handle nodal or elemental loads (uniform, triangular or trapezoidal in any direction within an element), any release (translational or rotational) can be implemented at an end of any element, in any of the 6 Degrees Of Freedom (DOFs), while the output of the analysis program includes the displacements of the released DOFs of all elements with releases, and any displacement or any force at any given point within an element. The accuracy of the analysis results is verified by a direct comparison to the corresponding results of a reliable commercial finite element software program as well as by performing a self-comparison using an enhanced model with additional nodes.

Both PSO and GA methods proved to be accurate in finding the optimum design almost every single time. GA has a larger computational cost than PSO which exhibited in general better performance in terms of convergence speed. This fact is due to the more complex and time consuming procedures of GA as part of the genetic operators of the algorithm (selection, crossover, mutation). Also the quantity of random numbers generated for each iteration of the algorithm is larger in GA, which makes it slower for a single iteration.

The accuracy of the discrete version of PSO used in this study was quite satisfactory, although in a small percentage of the tests that were performed, the algorithm was trapped in local optima. Further investigation may be needed for the fine-tuning of the discrete PSO parameters for the optimization problem at hand.

The constraints used in the present study were based on Eurocode 3, but in fact not all Eurocode 3 constraints for steel structures have been implemented in the test examples. Most importantly, additional buckling constraints need to be taken into account, as they are many times critical in real world steel structures design. The implementation of these constraints is straight forward given the analysis and optimization frameworks that have been developed, and will be a subject for future research.

REFERENCES

[1] Makris, P.A., C.G. Provatidis, and D.A. Rellakis, *Discrete variable optimization of frames using a strain energy criterion.* Structural and Multidisciplinary Optimization, 2006. **31**(5): p. 410-417.

[2] Bremicker, M., P.Y. Papalambros, and H.T. Loh, *Solution of mixed-discrete structural optimization problems with a new sequential linearization algorithm.* Computers and Structures, 1990. **37**(4): p. 451-461.

[3] Hager, K. and R. Balling, *New approach for discrete structural optimization.* Journal of Structural Engineering (ASCE), 1988. **114**(5): p. 1120 - 1133.

[4] Cai, J. and G. Thierauf, *Discrete structural optimization using evolution strategies*, in *Neural Networks & Combinatorial Optimization in Civil & Structural Engineering*, B.H.V. Topping and A.I. Khan, Editors. 1993, Civil-Comp Press: Edinburgh.

[5] Cai, J. and G. Thierauf, *Discrete optimization of structures using an improved penalty function method.* Engineering Optimization, 1993. **21**(4): p. 293-306.

[6] Fu, J.-F., R.G. Fenton, and W.L. Cleghorn, *A mixed integer-discrete-continuous programming method and its application to engineering design optimization.* Engineering Optimization, 1991. **17**: p. 263-280.

[7] Kennedy, J. and R. Eberhart, *Particle swarm optimization*, in *IEEE International Conference on Neural Networks*. 1995: Piscataway, NJ, USA. p. 1942–1948.

[8] Bochenek, B. and P. Foryś, *Structural optimization for post-buckling behavior using particle swarms.* Structural and Multidisciplinary Optimization, 2006. **32**(6): p. 521-531.

[9] He, Q. and L. Wang, *An effective co-evolutionary particle swarm optimization for constrained engineering design problems.* Engineering Applications of Artificial Intelligence, 2007. **20**(1): p. 89-99.

[10] Liang, J.J. and P.N. Suganthan, *Dynamic Multi-Swarm Particle Swarm Optimizer with a Novel Constraint-Handling Mechanism*, in *Evolutionary Computation, 2006. CEC 2006. IEEE Congress on*. 2006. p. 9-16.

[11] Mezura-Montes, E. and B.C. Lopez-Ramirez, *Comparing bio-inspired algorithms in constrained optimization problems*, in *Evolutionary Computation, 2007. CEC 2007. IEEE Congress on*. 2007. p. 662-669.

[12] Munoz-Zavala, A.E., et al., *PESO+ for Constrained Optimization*, in *Evolutionary Computation, 2006. CEC 2006. IEEE Congress on*. 2006. p. 231-238.

[13] Perez, R.E. and K. Behdinan, *Particle Swarm Optimization in Structural Design*, in *Swarm Intelligence: Focus on Ant and Particle Swarm Optimization*, F.T.S. Chan and M.K. Tiwari, Editors. 2007, Itech Education and Publishing: Vienna, Austria. p. 373-394.

[14] Ye, D., Z. Chen, and J. Liao, *A New Algorithm for Minimum Attribute Reduction Based on Binary Particle Swarm Optimization with Vaccination*, in *Advances in Knowledge Discovery and Data Mining*. 2007. p. 1029-1036.

[15] Fourie, P.C. and A. Groenwold, *The particle swarm optimization algorithm in size and shape optimization.* Structural and Multidisciplinary Optimization, 2002. **23**(4): p. 259–267.

[16] Venter, G. and J. Sobieszczanski-Sobieski, *Multidisciplinary optimization of a transport aircraft wing using particle swarm optimization.* Structural and Multidisciplinary Optimization, 2004. **26**: p. 121-131.

[17] Fourie, P. and A. Groenwold, *The particle swarm optimization in topology optimization*, in *Fourth world congress of structural and multidisciplinary optimization*. 2001: Dalian, China.

[18] Perez, R.E. and K. Behdinan, *Particle swarm approach for structural design optimization.* Computers and Structures, 2007. **85**: p. 1579-1588.

[19] Li, L.J., et al., *A heuristic particle swarm optimizer for optimization of pin connected structures.* Computers and Structures, 2007. **85**: p. 340-349.

[20] Plevris, V., *Innovative Computational Techniques for the Optimum Structural Design Considering Uncertainties*, in *School of Civil Engineering*. 2009, National Technical University of Athens (NTUA): Athens.

COMPDYN 2011
3rd ECCOMAS Thematic Conference on
Computational Methods in Structural Dynamics and Earthquake Engineering
M. Papadrakakis, M. Fragiadakis, V. Plevris (eds.)
Corfu, Greece, 25–28 May 2011

A STUDY OF THE INFLUENCE OF THE RIGIDITY OF JOINTS ON THE DYNAMIC RESPONSE OF STEEL STRUCTURES

A.A. Vrakas[1] & M. Papadrakakis[2]

[1, 2] Institute of Structural Analysis and Antiseismic Research
National Technical University of Athens
Zografou Campus, Athens 15780, Greece
avrakas@central.ntua.gr, mpapadra@central.ntua.gr

Keywords: beam-to-column joints, rigidity of joints, steel frames, detailed finite element modeling, *M-φ* curves, direct-integration nonlinear dynamic analysis, seismic response

Abstract. *The objective of this paper is to study the influence of the rigidity of joints on the nonlinear dynamic response of steel structures under seismic excitation. We consider bolted beam-to-column joints with extended end-plates. A detailed finite element simulation of the joints is performed using structural (beam and shell) and three-dimensional continuum (eight-node hexahedral solid) elements. Material as well as geometric nonlinearities with contact between the appropriate components of the connections are taken into account. The moment-rotation (M-φ) response of characteristic joints, subjected to static loads, is calculated and compared with experimental results and EC3 predictions for the validation of the corresponding numerical models. The dynamic response of steel frames is examined, with detailed modeling of their joints via structural elements according to the above study, capturing all types of nonlinearities. Frame members are modeled either with shell (full simulation) or with beam elements combined with proper compatibility constraints at the interfaces with the joints (hybrid simulation) accounting for the excessive computational effort required to perform nonlinear dynamic analyses with detailed finite element models. Implicit direct-integration is implemented in order to study the nonlinear seismic response of the above frame models, while El Centro earthquake horizontal accelerogram is considered for the seismic excitation. In order to study the influence of the joints end-plate and bolts, parametric analyses are performed demonstrating the effect of each component on the overall dynamic behavior of steel structures. Time history curves of nodal displacements are displayed for the appropriate comparisons. The detailed finite element discretization of the joint and frame models is produced automatically from the corresponding geometric models.*

1 INTRODUCTION

Bolted beam-to-column joints with extended end-plates are used widely in steel structures. They form moment-resistant connections between steel members, but their behavior can be either rigid or semi-rigid depending on the stiffness and strength of their components. The consideration of semi-rigid connections corresponds to a more realistic simulation of the joints behavior leading to more reliable solutions. However, the large number of variables related to connection geometry makes the task of incorporating semi-rigid behavior of the connections into the frame design a complicated process. Additionally, structural joints may exhibit nonlinear behavior such as localized elastoplastic deformations, unilateral contact and slip phenomena. The behavior of steel joints has been the subject of both experimental [12-17] and numerical [5-11] studies by a number of researchers.

This paper first presents a finite element study of semi-rigid joints subjected to static loading. Stiffness, moment resistance and rotation capacity derived from the calculation of moment-rotation (M-φ) curves are compared with experimental results by Coelho et al. [12] and Eurocode 3 suggestions [2]. Then, multi-storey steel frames with detailed modeling of their connections according to the above study are subjected to seismic excitation in order to examine the influence of the rigidity of joints on the dynamic response of moment-resistant steel structures [16-17]. Parametric studies are performed demonstrating how variations of geometric characteristics of joint components can change the connection behavior and consequently the seismic response of steel frames. Moreover, various finite element simulations are investigated in order to find hybrid models of detailed finite element simulation of joints combined with beam simulation for the structural elements in an effort to combine accuracy and low computational cost. The finite element discretization of joints and structural elements is produced automatically from their geometric description. ABAQUS/Standard software is used for the static and dynamic numerical analyses of this paper [1].

2 FINITE ELEMENT MODELING OF STEEL JOINTS

2.1 Simulation with shell elements

Two different element types are used for modeling the end-plate bolted beam-to-column joint (Fig. 1). Plane components of the joint (beam/column flanges and web, end-plate, transverse web stiffeners) are modeled with the S4 quadrilateral shell element of appropriate thickness, while the bolts are modeled with beam elements of circular section. The interaction between the column flange and the end-plate is considered through surface-based contact simulation with element-based surface definition, which enables contact between independent meshes without node compatibility.

2.2 Simulation with continuum elements

Three-dimensional eight-node hexahedral solid elements are used for the detailed simulation of the extended end-plate bolted beam-to-column joint (Figs. 2, 3). Apart from the finite element discretization difficulties using three-dimensional solid elements, there are many complexities related to the contacts between the different components of a beam-to-column bolted joint. Particularly, there are five interactions that should be considered: (a) column flange with end-plate; (b) column flange with bolt head; (c) end-plate with bolt nut; (d) column flange hole with bolt shank; and (e) end-plate hole with bolt shank. All of them are modeled by using surface-based contacts with element-based surface definition that enables connection of independent meshes. Surfaces are defined through the appropriate faces of the hexahedral solids. More specifically, for cases (a), (d) and (e) small sliding contact formulation is considered with a softened contact relationship. The slope of the linear pressure-overclosure curve is taken equal to 10^5. The tangential behavior of the interfaces is modeled through the basic isotropic Coulomb friction model with a constant coefficient μ equal to 0.30. For the other cases tied contact simulation is considered, where each node on the slave surface has the same displacement with the corresponding contact point on the master surface.

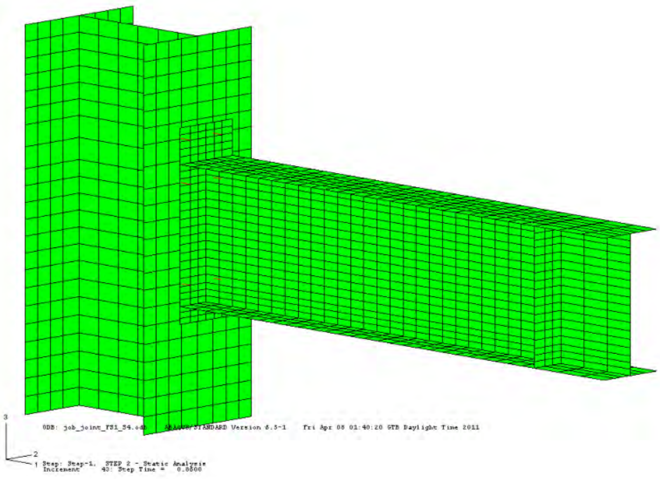

Figure 1: Joint simulation with shell (quadrilateral) finite elements

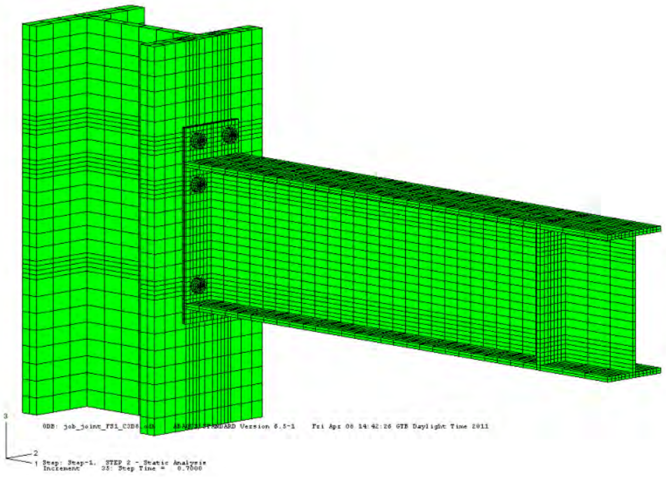

Figure 2: Joint simulation with continuum (8-node hexahedral solid) finite elements

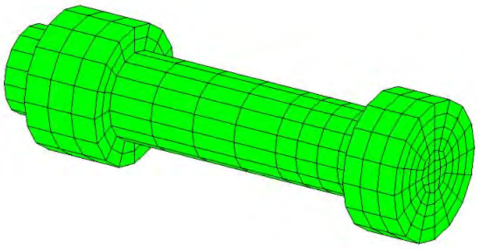

Figure 3: Bolt simulation with continuum (8-node hexahedral solid) finite elements

2.3 Experimental data

An experimental investigation of eight statically loaded extended end-plate moment connections was undertaken at the Delft University of Technology by Coelho et al. [12] to provide insight into the behavior of this type of joint up to collapse. The specimens were designed to confine failure to the end-plate and/or bolts without development of the full plastic moment capacity of the beam. The parameters investigated were the end-plate thickness and steel grade. Details of the test specimens are given in Table 1.

Test ID	Number	Column		Beam		End-plate	
		Profile	Steel grade	Profile	Steel grade	t_p (mm)	Steel grade
FS1	2	HEM340	S355	IPE300	S235	10	S355
FS2	2	HEM340	S355	IPE300	S235	15	S355
FS3	2	HEM340	S355	IPE300	S235	20	S355
FS4	2	HEM340	S355	IPE300	S235	10	S690

Table 1: Details of the test specimens [12]

2.4 Numerical results

The detailed geometry of the connections is considered in the numerical analyses performed. Hand tightened full-threaded M20 grade 8.8 bolts were used, which are modeled via an equivalent diameter of 18.80 mm that derives from the average of the gross diameter 20.00 mm and the effective diameter of the bolt shank (effective cross-section corresponding to the threaded part of the shank A_s=245 mm^2, for M20). Boundary conditions and loading procedures are the same as in the experiments. Particularly, each node of the back column flange has been constrained and a vertical load is applied on the transverse web stiffener of the beam. The finite element analysis procedure is based on incremental Newton-Raphson technique, while material and geometric nonlinearities are taken into account via the von Mises isotropic plasticity model and large displacement consideration.

The moment-rotation (M-φ) curves for the several connections are obtained from the beam vertical displacements and the applied load. The bending moment, M, acting on the connection corresponds to the applied load, L, multiplied by the distance, d, between the load application point and the face of the end-plate.

$$M = L \times d \tag{1}$$

The rotational deformation of the joint is the sum of the shear deformation of the column web panel zone and the connection rotational deformation. In these tests, the column hardly deforms as it behaves as a rigid element. Thus, the connection rotation φ is taken into account, which is defined as the change in angle between the centerlines of beam and column and is approximately given by:

$$\varphi = arctan\frac{\delta}{d} - \theta_{b.el} \tag{2}$$

where δ: vertical displacement of the beam at the load application point, and $\theta_{b.el}$: beam elastic rotation (neglected in this study).

EC3-1-8 states that a bolted end-plate joint may be assumed to have sufficient rotation capacity for plastic analysis, provided that both conditions are satisfied: (i) the moment resistance of the joint is governed by the resistance of either the column flange in bending or the end-plate in bending; and (ii) the thickness, t, of either the column flange or the end-plate (not necessarily the same basic component as in (i)) satisfies:

$$t \leq 0.36\varphi_b\sqrt{\frac{f_{u.b}}{f_y}} \tag{3}$$

where φ_b: bolt diameter, $f_{u.b}$: tensile strength of the bolt, and f_y: yield strength of the relevant basic component. EC3-1-8 prediction for stiffness S_j is given by the relationship:

$$S_j = S_{j.ini}/\eta \tag{4}$$

where $S_{j.ini}$: initial stiffness evaluated according to the component method, and η: stiffness modification factor which in the context of an elastic-plastic global structural analysis is taken as 2.0 for bolted end-plate beam-to-column joints.

Moment-rotation (M-φ) curves of the above test specimens are presented next and compared with the experimental results by Coelho et al. [12] and Eurocode 3 suggestions [2]. Moreover, for each test, horizontal deformation of the end-plate is observed. The first three models are plotted in stress scale 0-35.5 kN/cm^2 and the last in 0-69.0 kN/cm^2 according to each end-plate yield stress. Four models are examined, one with shell elements and three with continuum elements. All of them predict accurately the elastic stiffness of the joints and generally are reliable in linear elastic static analysis. Bending of end-plates is the main reason for differences between these simulations in the elastoplastic region. For thin end-plates, which are dominated by bending (FS1, FS4), the use of continuum elements with reduced integration performs better. This simulation predicts almost exactly the three main joint behavioral characteristics, which are stiffness, resistance and rotation capacity. The normal brick element overestimates the elastic behavior of the joint, while the enhanced with incompatible modes gives more accurate results but remains stiff for this type of problems underestimating their high rotation capacity. Joint modeling with shell elements has a drawback. Bolt forces are applied locally to the nodes that connect the column flange with the end-plate and as a result there is local concentration of stresses, especially for very thin end-plates and/or column flanges. As the thickness of end-plate increases (FS2, FS3) the simulations tend to coincide. Brick elements with reduced integration remain the more flexible, while bricks with incompatible modes give also reliable results. Simulation with shell elements behaves very satisfactory and can be used for such type of problems.

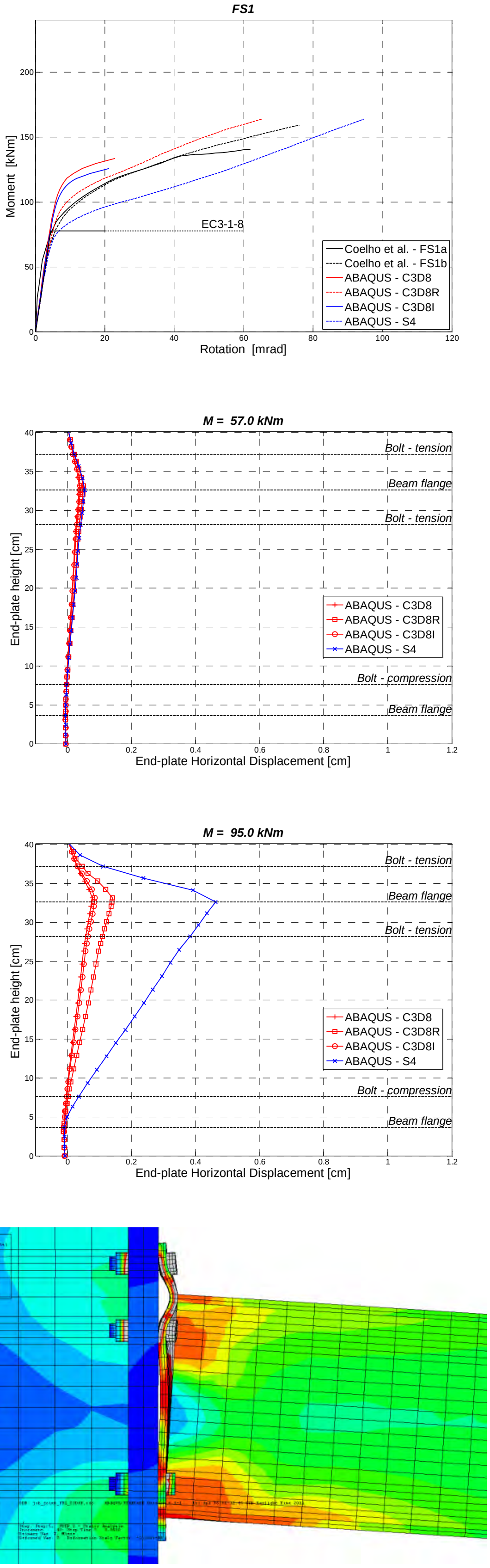

Figure 4: FS1 results

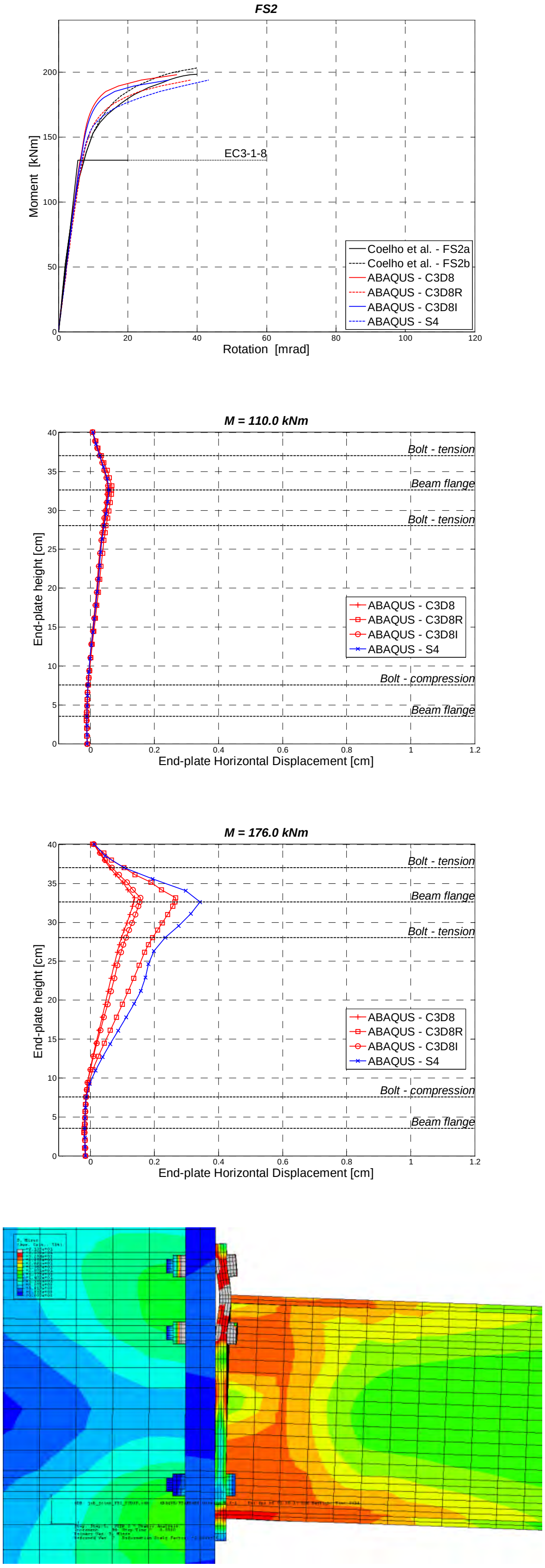

Figure 5: FS2 results

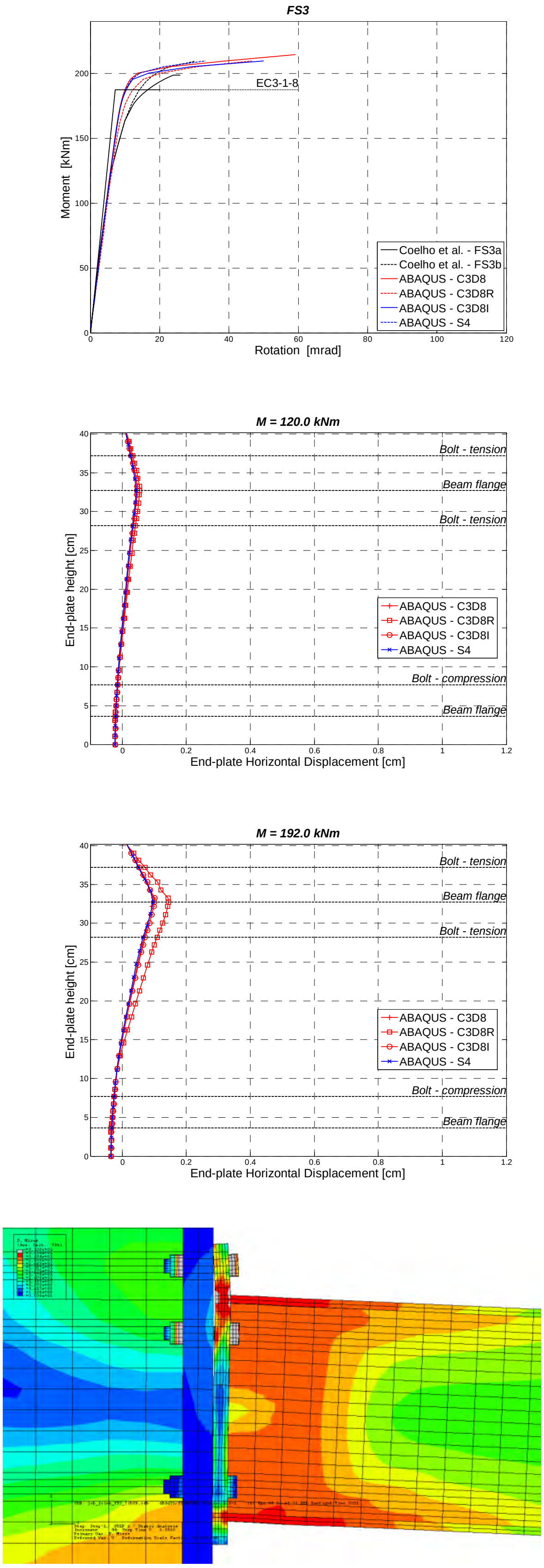

Figure 6: FS3 results

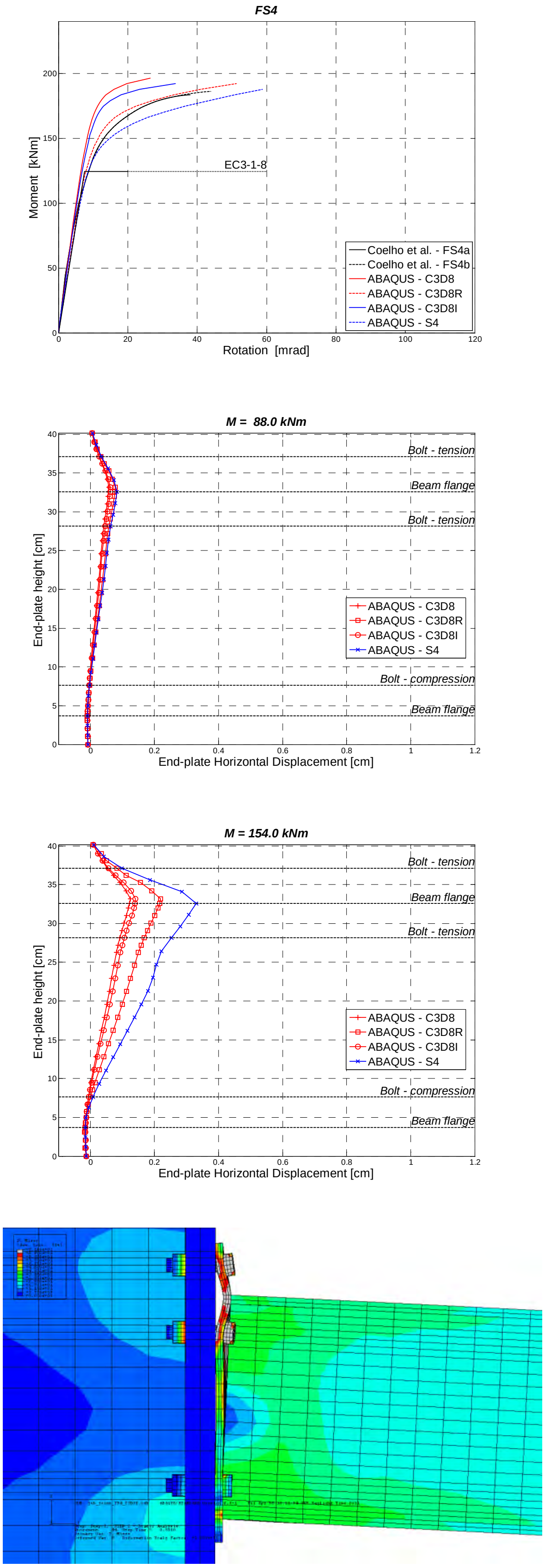

Figure 7: FS4 results

3 FINITE ELEMENT MODELING OF STEEL FRAMES

3.1 Numerical Modeling

Three different finite element simulations are examined: (i) *Type 1*: Simulation with beam elements for the members, while the joints are regarded as rigid; (ii) *Type 2*: Full simulation with shell elements for the members and detailed modeling of the joints according to 2.1 with shell and beam elements; and (iii) *Type 3*: Hybrid simulation with beam elements for the members and detailed modeling of the joints according to 2.1 with shell and beam elements. For this type of modeling proper compatibility constraints are assumed at the nodes of the interfaces. The length of the detailed joint part (beam/column) is taken as 0.10 of the corresponding total member length. The joints of this frame type are stiffened in two steps. In the first step (*Type 3 – stiff-a),* transverse web stiffeners are added to the columns at the height of the beam flanges ($t_s = t_{fb}$), and in the second (*Type 3 – stiff-b*), apart from these stiffeners, supplementary web plates are added to the column webs ($t'_{wc} = 2t_{wc}$). It should be mentioned that the simulation with three-dimensional solid elements requires excessive computational time to perform an implicit direct-integration dynamic analysis that takes into account material and geometric nonlinearities including contacts. The simulation with structural elements is practically and computationally more efficient, even though there are some drawbacks in the modeling.

The hysteretic stress-strain model that has been adopted for the steel subjected to dynamic loading is displayed in Fig. 8. The steel grade specified for every component of each model, except for the bolts, is *S235* with the following characteristics: modulus of elasticity, E = 21000 kN/cm^2, yield stress, f_y = 23.5 kN/cm^2, ultimate stress, f_u = 36.0 kN/cm^2, and ultimate strain, ε_u = 0.25. The grade of bolts is 8.8 which means that $f_{y.b}$ = 64.0 kN/cm^2 and $f_{u.b}$ = 80.0 kN/cm^2, while their strain hardening modulus, E_t = 210 kN/cm^2.

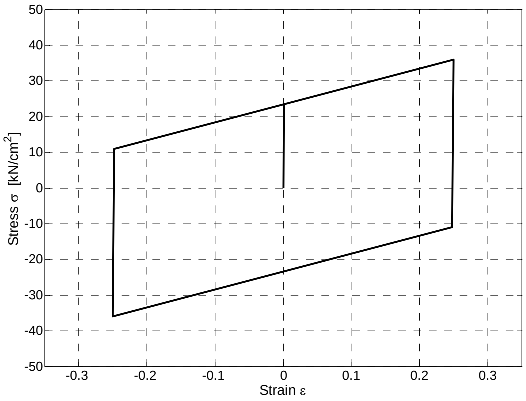

Figure 8: Hysteretic stress-strain (σ-ε) steel model

The general direct-integration method with the Hilber-Hughes-Taylor operator is used for the dynamic numerical analyses of this paper. It is an extension of the trapezoidal rule and is implicit, while a set of simultaneous nonlinear dynamic equilibrium equations must be solved at each time increment. The solution is done iteratively using Newton's method with material and geometric nonlinearities being included. A constant time step of 0.01 sec is used in the dynamic analyses.

Two kinds of damping are taken into account. The first is the artificial damping, through the numerical damping control parameter α. A value of α = -0.05 is used, which provides slight numerical damping. The second is the material-Rayleigh damping, which introduces a damping matrix [$\underline{\mathrm{C}}$], defined as:

$$[\underline{C}] = \alpha_0[\underline{M}] + \alpha_1[\underline{K}] \tag{5}$$

where [$\underline{\mathrm{M}}$]: the mass matrix, and [$\underline{\mathrm{K}}$]: the stiffness matrix of the model. Factors α_0 and α_1 can be derived from the solution of the following equations [4]:

$$\frac{1}{2}\begin{bmatrix} 1/\omega_i & \omega_i \\ 1/\omega_j & \omega_j \end{bmatrix}\begin{Bmatrix}\alpha_0 \\ \alpha_1\end{Bmatrix} = \begin{Bmatrix}\zeta_i \\ \zeta_j\end{Bmatrix} \tag{6}$$

where $\omega_{i,\,j}$: natural frequencies of interest, and $\zeta_{i,\,j}$: damping coefficients for the corresponding natural frequencies of interest. For steel structures with bolted joints ζ can be taken conservatively as 6% = 0.06. In the analyses of this paper, only α_1 is used with $\alpha_1 = 0.0020$ for the first frame test example and $\alpha_1 = 0.0025$ for the second.

The frames are subjected to the 1940 Imperial Valley (El Centro) S00E horizontal component acceleration record. The 10 seconds acceleration history is shown in Fig. 9, while Fig. 10 depicts the response spectra for 2% and 6% damping. Peak ground acceleration (PGA) of 0.60g is chosen for the numerical analyses of the frames that follow.

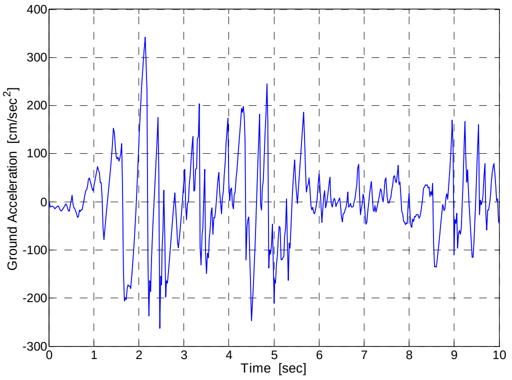

Figure 9: Acceleration time history of El Centro

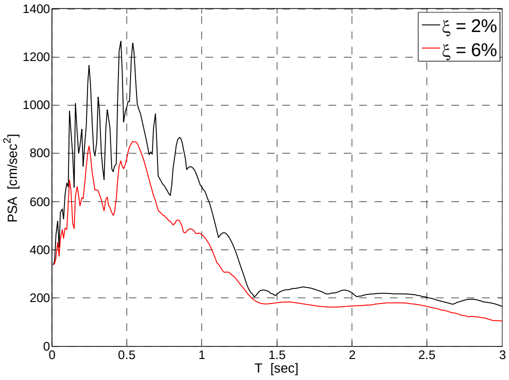

Figure 10: Response Spectra of El Centro

3.2 Frame No1

A steel frame of one opening (6 m) and two storeys (5 m each) is examined. Columns have a section profile HEB280 and beams IPE400. Details of the beam-to-column connections are shown in Fig. 11. Parametric studies on extended end-plate thickness, *t*, and bolts diameter, *D*, are performed. Each beam is assumed to have 20 times higher density than the density of steel (7850 kg/m^3) to account for the floor mass, while each column carries its own weight. The natural frequencies and periods are demonstrated in Table 2.

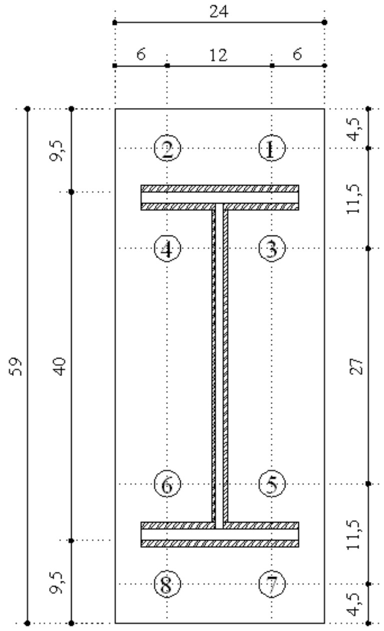

Figure 11: Bolted extended end-plate beam-to-column connection

Frame type	t (mm)	D (mm)	ω_1 (rad/s)	ω_2 (rad/s)	T_1 (sec)	T_2 (sec)
1	-	-	13.04	42.10	0.48	0.15
2	15	20	12.44	42.42	0.50	0.15
2	20	20	12.52	42.58	0.50	0.15
3	15	20	12.54	42.99	0.50	0.15
3	20	20	12.62	43.16	0.50	0.15

Table 2: Frame 1, Dynamic characteristics

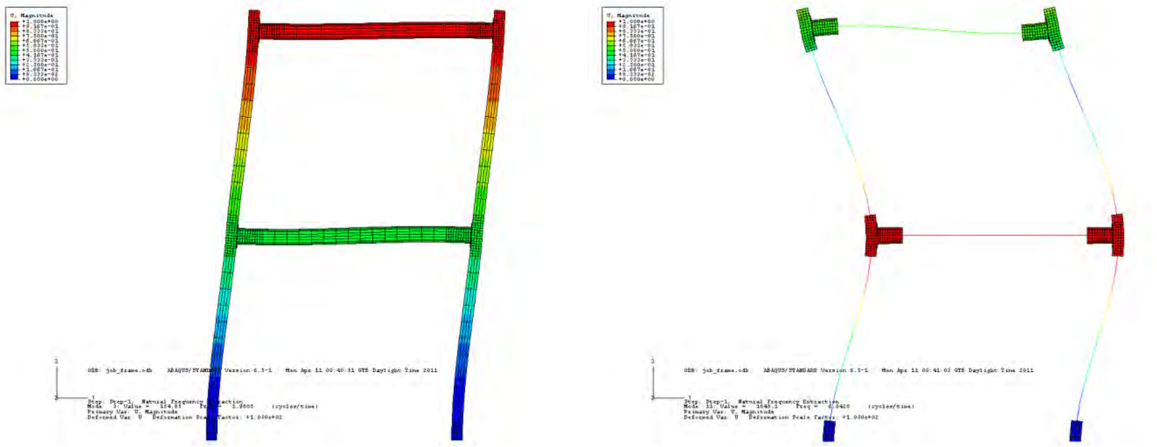

Figure 12: Frame 1, First and second mode

The results of various response analyses are presented in the next graphs. The parametric analyses (Figs. 13, 14) show that connection geometric characteristics do not affect the overall behavior of the frame with regard to the absolute maximum values. The tests performed showed that hybrid simulation is reliable and can be used instead of the full simulation, assuming that member beam elements do not exceed the yield stress, f_y, in order to account for the excessive computational effort required to perform nonlinear dynamic analyses with detailed finite element models. The comparisons between the different simulations are presented in Figs. 15-17.

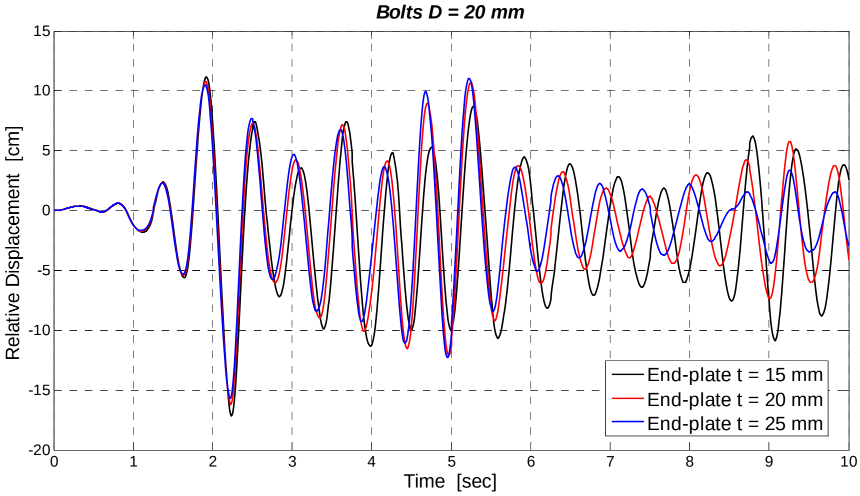

Figure 13: Frame 1, Simulation type 2, parametric analysis of end-plate thickness (2nd floor)

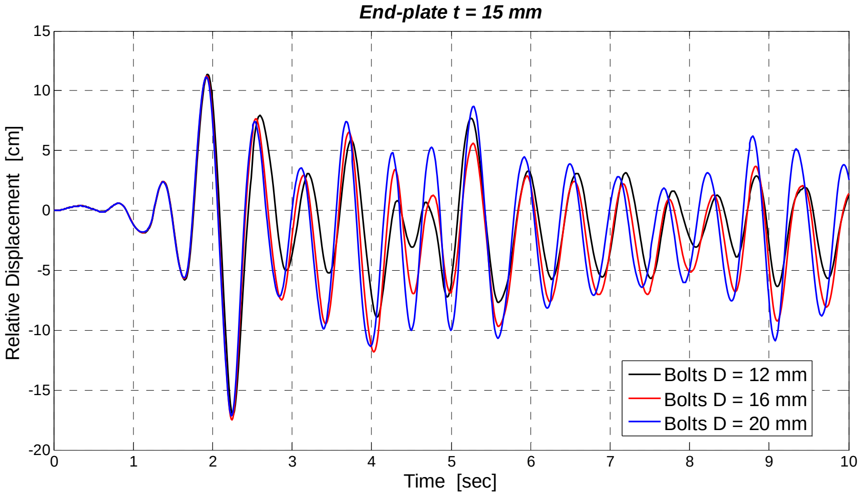

Figure 14: Frame 1, Simulation type 2, parametric analysis of bolts diameter (2nd floor)

Frame type	t (mm)	D (mm)	Iterations	Total CPU Time (sec)
1	-	-	1007	20
2	15	20	5018	8561
3	15	20	5002	5281
3 – stiff-a	15	20	4930	5688
3 – stiff-b	15	20	4593	5363

Table 3: Frame No1, CPU times

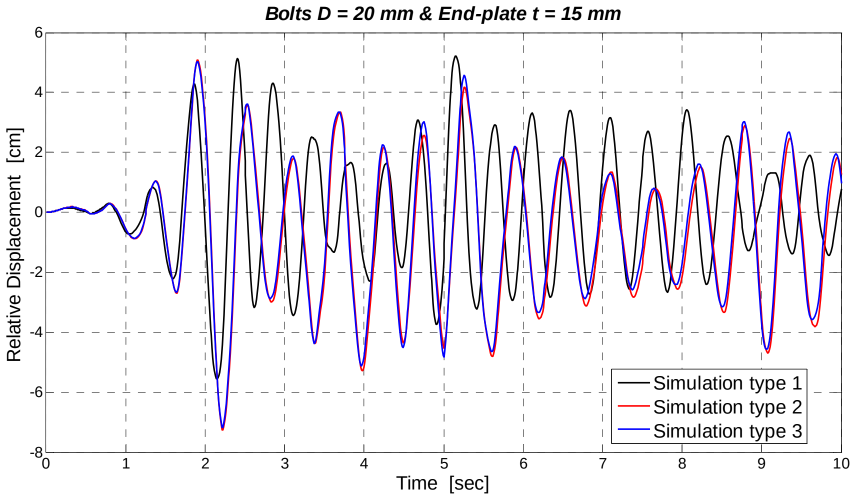

Figure 15: Frame 1, Comparison of simulation types (1st floor)

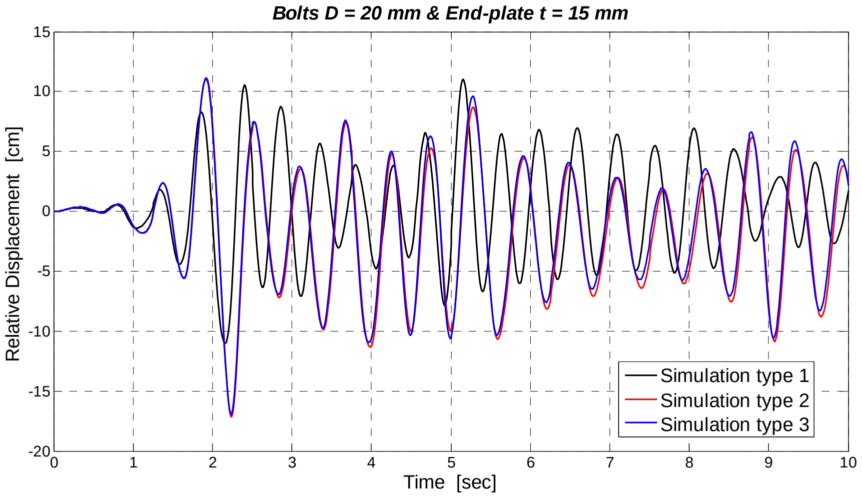

Figure 16: Frame 1, Comparison of simulation types (2nd floor)

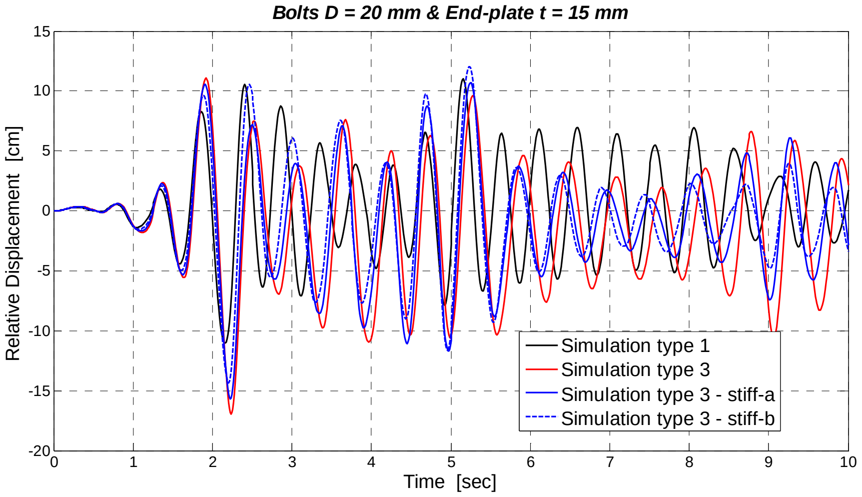

Figure 17: Frame 1, Influence of joint rigidity (2nd floor)

3.3 Frame No2

A steel frame of two openings (6 m each) and three storeys (4 m each) is examined. There are also double-sided joints apart from single-sided of Frame No1. Columns have a section profile HEB280 and beams IPE400. Beam-to-column connections are shown in Fig. 11. Each beam is assumed to have 20 times higher density than the density of steel (7850 kg/m^3) to account for the floor mass, while each column carries its own weight. The natural frequencies and periods are demonstrated in Table 4.

Frame type	t (mm)	D (mm)	ω_1 (rad/s)	ω_2 (rad/s)	T_1 (sec)	T_2 (sec)
1	-	-	10.66	34.25	0.59	0.18
2	15	20	10.00	33.51	0.63	0.19
2	20	20	10.10	33.79	0.62	0.19
3	15	20	10.10	34.01	0.62	0.18
3	20	20	10.20	34.29	0.62	0.18

Table 4: Frame 2, Dynamic characteristics

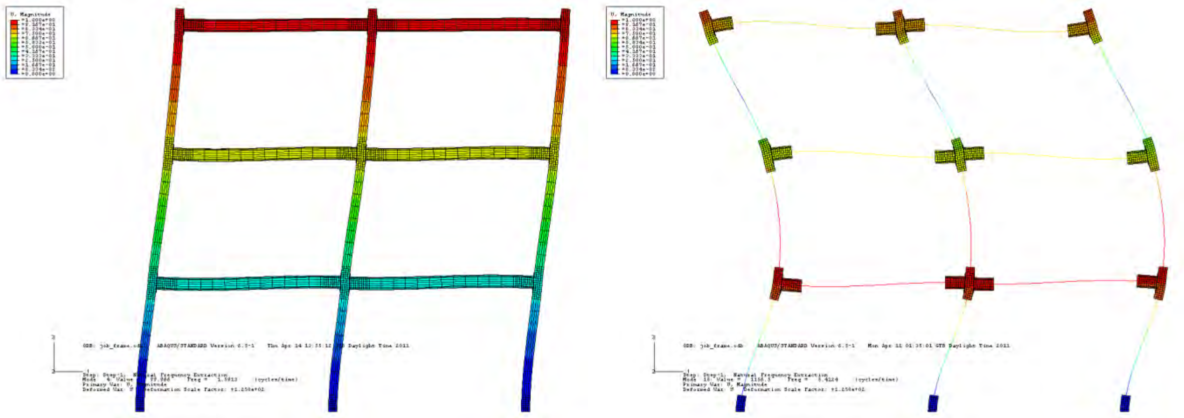

Figure 18: Frame 2, First and second mode

The results of the dynamic response of this test frame are presented in the next graphs. Parametric analyses (Figs. 19, 20) show that the geometric characteristics of the connections do not affect the overall behavior of the frame. As in the previous example, hybrid simulation is reliable and can be used instead of the full simulation, assuming that member beam elements do not exceed the yield stress, f_y. As the size of the problem increases, the computational effort required to perform nonlinear dynamic analysis with a detailed finite element model increases and the adoption of hybrid models becomes very useful and effective. For example, the time needed for a full simulation with shell elements of this frame is ~ 1.5 times greater than the time needed for a hybrid simulation. The comparisons between the different simulations are presented in Figs. 21-24.

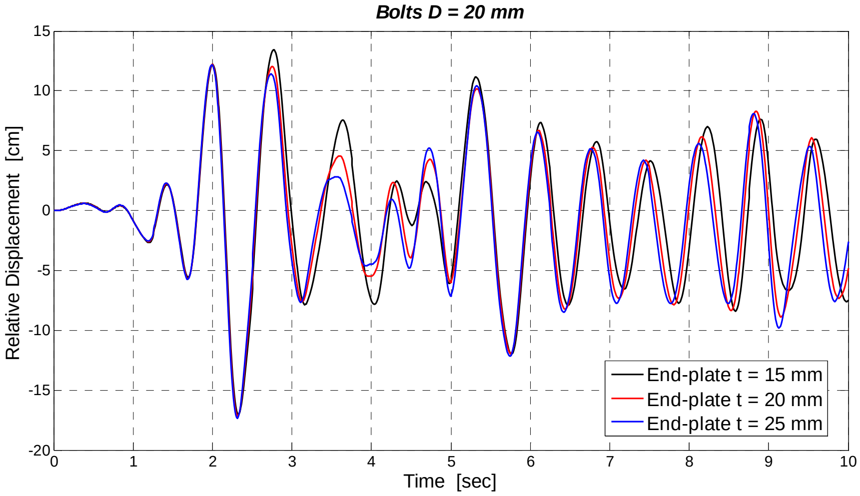

Figure 19: Frame 2, Simulation type 3, parametric analysis of end-plate thickness (3rd floor)

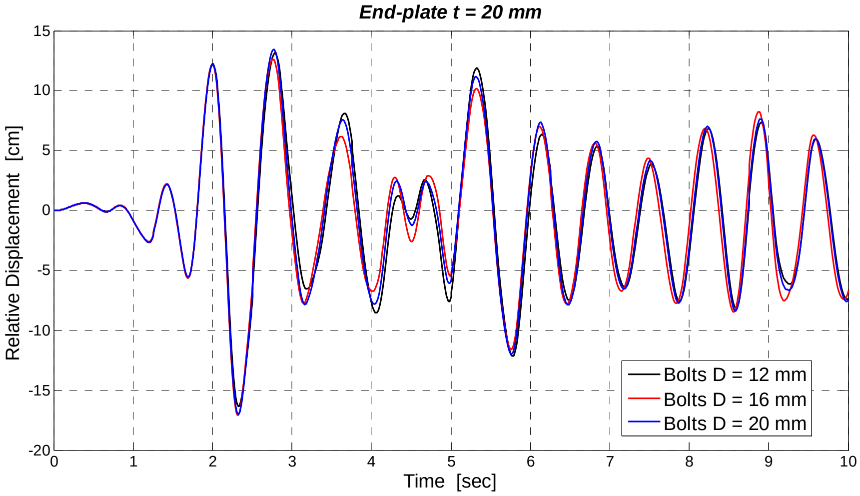

Figure 20: Frame 2, Simulation type 3, parametric analysis of bolts diameter (3rd floor)

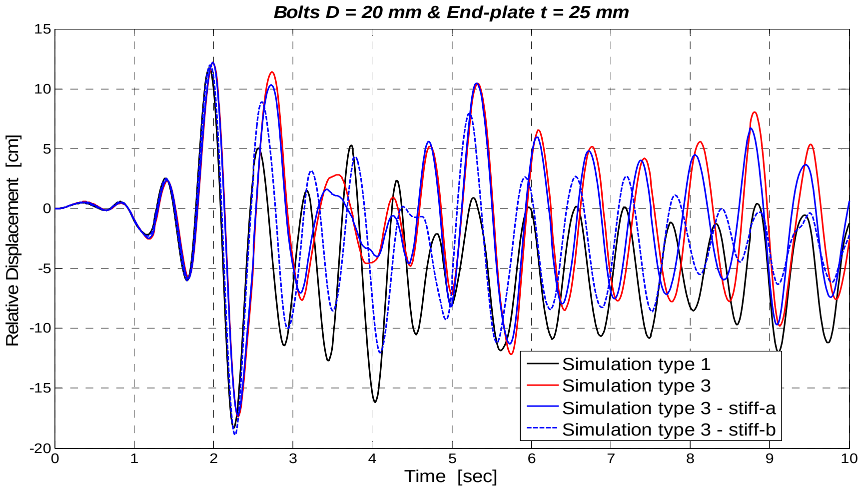

Figure 21: Frame 2, Influence of joint rigidity (3rd floor)

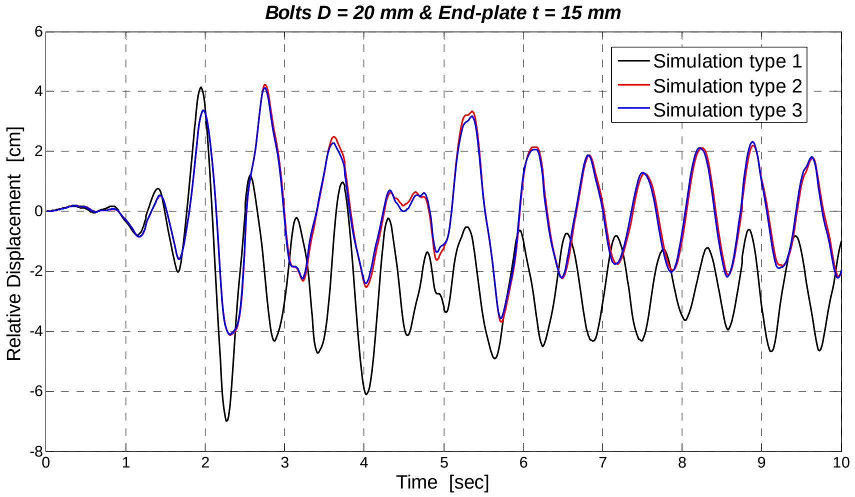

Figure 22: Frame 2, Comparison of simulation types (1st floor)

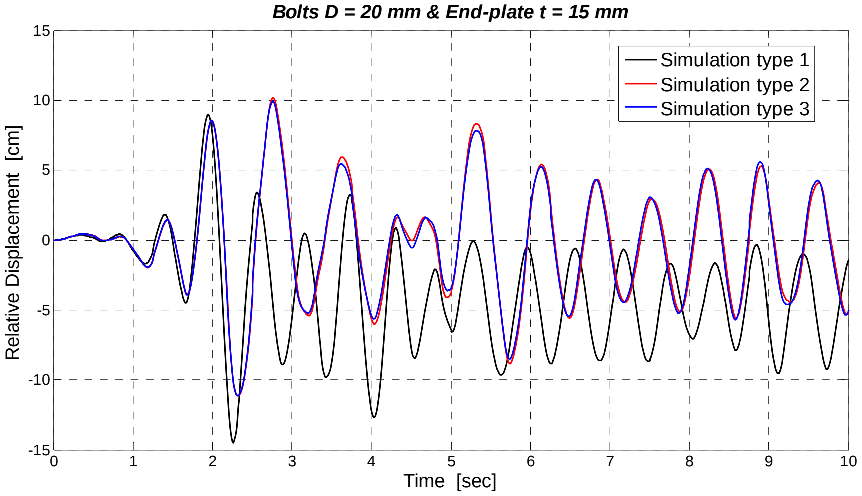

Figure 23: Frame 2, Comparison of simulation types (2nd floor)

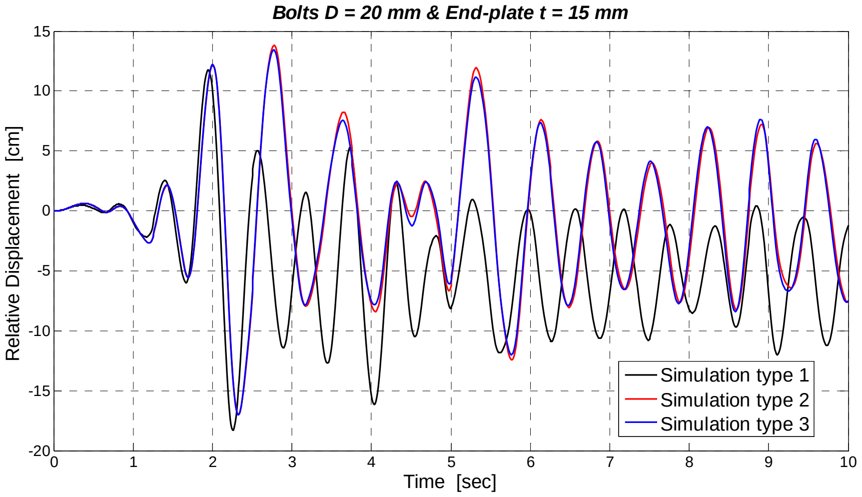

Figure 24: Frame 2, Comparison of simulation types (3rd floor)

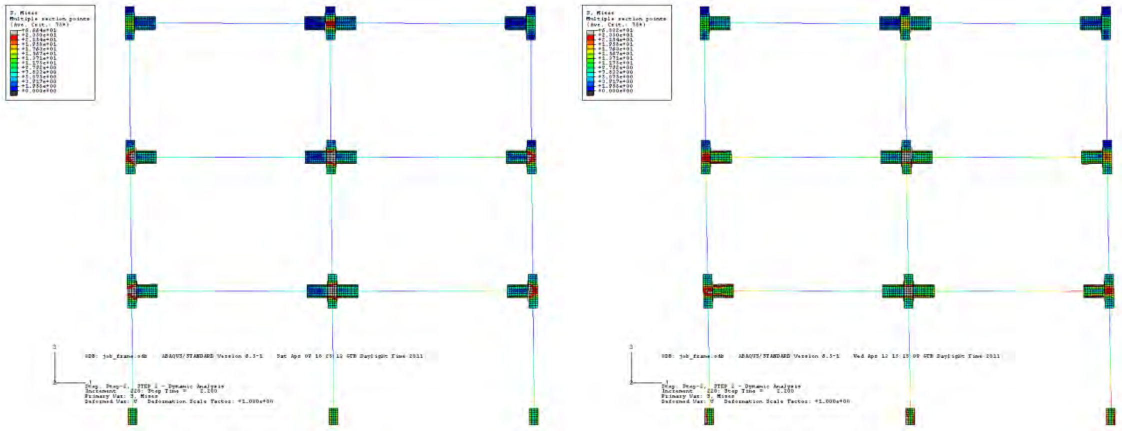

Figure 25: Frame 2, t=25mm, D=20mm, von Mises stresses distribution (t = 2.20 sec, *stress scale* 0: f_y), *Type 3* vs. *Type 3 – stiff-b*

Frame type	t (mm)	D (mm)	Iterations	Total CPU Time (sec)
1	-	-	1021	44
2	15	20	5401	22747
3	15	20	5368	15396
3	25	20	5694	17320
3 – stiff-a	25	20	5420	18232
3 – stiff-b	25	20	5390	18018

Table 5: Frame 2, CPU times

4 CONCLUSIONS

- Detailed finite element modeling considering material and geometric nonlinearities including appropriate contacts of bolted extended end-plate beam-to-column joints is performed, which can capture all local phenomena that affect the behavior of the joints under static or dynamic loads.

- Experimental results can be reproduced accurately using detailed joint models of hexahedral eight-node solid continuum finite elements with either reduced integration or incompatible modes depending on the plate thickness.

- Simulation with shell elements can be used for the modeling of steel joints with high level of accuracy in realistic problems, instead of continuum elements, which are computationally very demanding.

- Hybrid models, where the joints are modeled with shell elements and the connecting structural elements with beam elements, with appropriate kinematic constraints at the interfaces, give reliable results at reduced computational times.

- Modeling of frames with beam elements considering rigid joints fails to predict the semi-rigidity and the various types of failure of the joint structural components that may affect considerably the joint behavior.

- Parametric studies on extended end-plate thickness and bolts diameter of semi-rigid joints show that the connection geometric characteristics do not have a substantial effect on the seismic response of the overall structure.

REFERENCES

[1] ABAQUS version 6.5, *Analysis User's Manual*. 2004

[2] European Committee for Standardization (CEN), *EN 1993-1-8 – Eurocode 3: Design of Steel Structures –Part 1.8: Design of Joints*. 2005

[3] K.J. Bathe, *Finite Element Procedures*. Prentice-Hall, 1996

[4] Anil K. Chopra, *Dynamics of Structures, Theory and Applications to Earthquake Engineering, 3rd edition*. Pearson Prentice Hall, 2007

[5] M.R. Bahaari, A.N. Sherbourne, Computer modelling of an extended end-plate bolted connection. *Computers and Structures*, **52**(5), 879-893, 1994

[6] Mohammed R. Bahaari, Archibald N. Sherbourne, Behavior of eight-bolt large capacity endplate connections. *Computers and Structures*, **77**, 315-325, 2000

[7] O.S. Bursi, J.P. Jaspart, Calibration of a finite element model for isolated bolted end-plate steel connections. *Journal of Constructional Steel Research*, **44**(3), 225-262, 1997

[8] O.S. Bursi, J.P. Jaspart, Basic issues in the finite element simulation of extended end plate connections. *Computers and Structures*, **69**, 361-382, 1998

[9] Y.I. Maggi, R.M. Goncalves, R.T. Leon, R.F.L. Ribeiro, Parametric analysis of steel bolted end plate connections using finite element modeling. *Journal of Constructional Steel Research*, **61**, 689-708, 2005

[10] Anant R. Kukreti, Feng-Feng Zhou, Eight-bolt endplate connection and its influence on frame behavior. *Engineering Structures*, **28**, 1483-1493, 2006

[11] Charis J. Gantes, Minas E. Lemonis, Influence of equivalent bolt length in finite element modeling of T-stub steel connections. *Computers and Structures*, **81**, 595-604, 2003

[12] Ana M. Girao Coelho, Frans S. K. Bijlaard, Luis Simoes da Silva, Experimental assessment of the ductility of extended end plate connections. *Engineering Structures*, **26**, 1185-1206, 2004

[13] Ana M. Girao Coelho, Frans S.K. Bijlaard, Experimental behaviour of high strength steel end-plate connections. *Journal of Constructional Steel Research*, **63**, 1228-1240, 2007

[14] L.R.O. de Lima, L. Simoes da Silva, P.C.G. da S. Vellasco, S.A.L. de Andrade, Experimental evaluation of extended endplate beam-to-column joints subjected to bending and axial force. *Engineering Structures*, **26**, 1333-1347, 2004

[15] Yongjiu Shi, Gang Shi, Yuanqing Wang, Experimental and theoretical analysis of the moment-rotation behaviour of stiffened extended end-plate connections. *Journal of Constructional Steel Research*, **63**, 1279-1293, 2007

[16] A.S. Elnashai & A.Y. Elghazouli, Seismic Behaviour of Semi-rigid Steel Frames. *Journal of Constructional Steel Research*, **29**, 149-174, 1994

[17] Gang Shi, Yongjiu Shi, Yuanqing Wang, Behaviour of end-plate moment connections under earthquake loading. *Engineering Structures*, **29**, 703-716, 2007

[18] Minas E. Lemonis, Charis J. Gantes, Mechanical modeling of the nonlinear response of beam-to-column joints. *Journal of Constructional Steel Research*, **65**, 879-890, 2009

COMPDYN 2011
3rd ECCOMAS Thematic Conference on
Computational Methods in Structural Dynamics and Earthquake Engineering
M. Papadrakakis, M. Fragiadakis, V. Plevris (eds.)
Corfu, Greece, 25–28 May 2011

COMPUTATIONAL CONTACT DYNAMICS INCLUDING MULTIPHYSICS AND MULTISCALE EFFECTS

Alexander Popp and Wolfgang A. Wall

Institute for Computational Mechanics, Technische Universität München
Boltzmannstr. 15, 85748 Garching b. München, Germany
e-mail: {popp,wall}@lnm.mw.tum.de

Keywords: Contact Dynamics, Mortar Methods, Finite Deformations, Dual Lagrange Multipliers, Fluid-Structure Interaction with Contact, Finite Elements.

Abstract. *This paper gives a review of our recently proposed dual mortar approach combined with a consistently linearized semi-smooth Newton method for 3D finite deformation contact analysis. The mortar finite element method, which is applied as discretization scheme, initially yields a mixed formulation with the nodal Lagrange multiplier degrees of freedom as additional primary unknowns. However, by using so-called dual shape functions for Lagrange multiplier interpolation, the global linear system of equations to be solved within each Newton step can be condensed and thus contains only displacement degrees of freedom. All possible types of nonlinearities, including finite deformations, nonlinear material behavior and contact itself (active set search) are handled within one single iterative solution scheme based on a consistently linearized semi-smooth Newton method. The extension of the proposed framework towards additional model complexities such as Coulomb friction and self contact is addressed shortly. Moreover, an outlook towards multiphysics and multiscale simulations, coupling contact analysis with other physical fields and taking into account effects on different length scales is provided by exemplarily discussing the integration of mortar contact into a fixed-grid fluid-structure interaction (FSI) framework based on the extended finite element method (XFEM). Several numerical examples are presented to show the high quality of results obtained with the proposed methods.*

1 INTRODUCTION

Computational contact dynamics in general, and mortar-based discretization for finite deformations in particular, have seen a great thrust of research over the last decade. We discuss here the most important features of the recently proposed dual mortar finite element method combined with a consistently linearized semi-smooth Newton scheme for contact constraint enforcement. The present contribution is thus a shortened version of our articles [1, 2, 3, 4] to which we refer for full technical details, more profound discussion of the methods presented and further numerical examples.

Many newly proposed contact discretizations are based on the mortar method which was originally introduced in the context of domain decomposition [5]. Mortar contact formulations have successfully been applied to the solution of finite deformation contact problems in [6, 7, 8]. However, the mentioned formulations all apply a regularization of contact constraints based on the penalty method or an augmented Lagrangian type approach using the Uzawa algorithm. A recent application based on direct Lagrange multiplier techniques with standard multiplier spaces can be found in [9]. Yet, the dual Lagrange multiplier spaces proposed in [10, 11] seem to have the highest potential for efficient algorithms as they allow for a static condensation of the discrete Lagrange multiplier degrees of freedom. Thus, an undesirable increase in global system size, usually typical of direct Lagrange multiplier techniques, is avoided. Mortar methods with dual Lagrange multipliers have first been developed in the context of small deformation contact problems [12], where also the idea of interpreting the active set search as a semi-smooth Newton method (see e.g. [13, 14]) has been adapted. Some first steps towards a finite deformation implementation have been made in [15, 16], however still with an incomplete linearization of contact forces and constraints. In the authors' previous work [1, 2, 3], the ideas of dual Lagrange multipliers and a semi-smooth Newton approach for the active set search have been consistently extended to fully nonlinear 3D frictional contact problems.

Advantageous properties of the devised algorithms comprise superior robustness as compared with a traditional node-to-segment approach, the absence of any user-defined parameter (e.g. penalty parameter), the integration of all types of nonlinearities (including finite deformations, nonlinear material behavior and active set search) into one single iteration loop and the possibility to condense the discrete Lagrange multipliers from the global system of equations, to name only a few. First-order and second-order finite element interpolation, frictional sliding based on Coulomb's law as well as self contact are considered for both 2D and 3D. Some very challenging numerical examples are presented to illustrate the high quality of results obtained with the proposed approach. The design of our algorithms is based on overlapping domain decomposition, involving parallel contact search based on hierarchic binary tree structures and a novel dynamic load balancing strategy specifically developed for mortar coupling. This assures full parallel scalability of all algorithmic components when solving large contact dynamics problems with up to some million degrees of freedom.

Recently, the focus of our research in the field of computational contact dynamics has been extended towards multiphysics and multiscale simulations, coupling contact analysis with several other physical fields and taking into account effects on different length scales. Exemplarily, the integration of dual mortar contact into a fixed-grid fluid-structure interaction (FSI) framework based on the extended finite element method (XFEM) will be shortly addressed here. This approach allows for computing macroscopic contact of arbitrarily deforming structures embedded in a surrounding fluid. Again, we refer to a recent article [4] for the derivation and a more profound discussion of the proposed fluid-structure-contact interaction method.

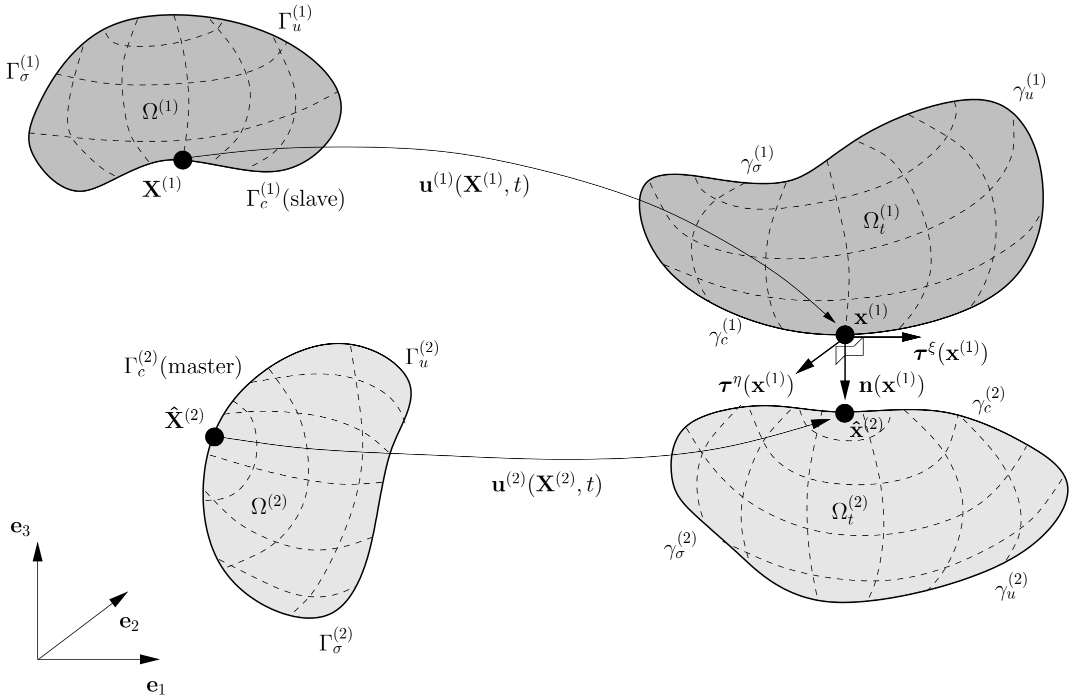

Figure 1: Notation for the two body finite deformation contact problem in 3D.

The remainder of this contribution is organized as follows: Section 2 provides a rough overview of the general continuum mechanics problem setup for 3D finite deformation contact. The dual mortar finite element approach is described in Section 3. In Section 4, the semi-smooth Newton type active set strategy and the resulting solution algorithm are outlined. Section 5 highlights some recent model extensions, including friction and fluid-structure-contact interaction. Following this interlude, Section 6 demonstrates with several numerical examples the validity of the proposed approach. Finally, we conclude the findings.

2 PROBLEM FORMULATION OF FINITE DEFORMATION CONTACT

The basic problem definition has been described in detail in [2]. Figure 1 shows the reference and current configurations of two elastic bodies undergoing a finite deformation process and introduces some notation. The surfaces $\partial\Omega_t^{(i)}$, $i = 1,2$ are divided into three disjoint boundary sets, namely the common Dirichlet and Neumann boundaries $\gamma_u^{(i)}$ and $\gamma_\sigma^{(i)}$ as well as the potential contact surfaces $\gamma_c^{(i)}$. Although a mortar discretization will be applied later, we still retain the customary nomenclature of slave and master contact surfaces.

Displacement vectors $\mathbf{u}^{(i)} = \mathbf{x}^{(i)} - \mathbf{X}^{(i)}$ describe the motion of the deformable bodies from reference configuration $\mathbf{X}^{(i)}$ to current configuration $\mathbf{x}^{(i)}$. Material nonlinearity is taken into account by assuming a compressible Neo-Hookean material behavior based on the second Piola-Kirchhoff stress tensor $\mathbf{S}$ and the Green-Lagrange strain tensor $\mathbf{E} = \frac{1}{2}\left(\mathbf{F}^T\mathbf{F} - \mathbf{I}\right)$, where $\mathbf{F}$ is the deformation gradient. Based on these definitions, the well-known initial boundary value problem (IBVP) of finite deformation elastodynamics can be formulated. This paper focuses on contact interaction itself, which is typically described by a gap function $g(\mathbf{X},t)$ in the current configuration. The classical Karush-Kuhn-Tucker (KKT) conditions of normal contact and the frictionless sliding conditions then read as follows:

$$g(\mathbf{X},t) \geq 0\ ,\ \ p_n \leq 0\ ,\ \ p_n\, g(\mathbf{X},t) = 0\ , \tag{1}$$

$$t_\tau^\xi = t_\tau^\eta = 0\ , \tag{2}$$

where the normal and tangential components of the slave contact traction $\mathbf{t}_c^{(1)}$ are denoted as p_n, t_τ^ξ and t_τ^η. A corresponding formulation of Coulomb's law for frictional contact is omitted here, but can be found in our recent work [3]. For deriving a weak formulation the solution space $\mathscr{U}^{(i)}$ and the weighting space $\mathscr{V}^{(i)}$ are defined by employing the usual Sobolev spaces $H^1\left(\Omega^{(i)}\right)$ and by taking into acccount Dirichlet boundary conditions. The method of weighted residuals then yields: Find $u_j^{(i)} \in \mathscr{U}^{(i)}$ such that

$$\delta\Pi(\mathbf{u},\delta\mathbf{u},\boldsymbol{\lambda}) = \delta\Pi_{int,ext}(\mathbf{u},\delta\mathbf{u}) + \int_{\gamma_c^{(1)}} \boldsymbol{\lambda}\cdot\left(\delta\mathbf{u}^{(1)} - \delta\hat{\mathbf{u}}^{(2)}\right)\mathrm{d}\gamma = 0$$

$$\forall\,\delta u_j^{(i)} \in \mathscr{V}^{(i)}\ ,\ \ j = 1,2,3\ , \tag{3}$$

where the negative contact traction on the slave side of the interface has been replaced by a Lagrange multiplier vector $\boldsymbol{\lambda} = -\mathbf{t}_c^{(1)}$. By arbitrary choice, the Lagrange multipliers $\lambda_j \in \mathscr{M}$, $j = 1,2,3$, have been introduced on the slave side, where $\mathscr{M}$ is defined as dual space of the trace space $\mathscr{W}^{(1)}$ of $\mathscr{U}^{(1)}$ restricted to $\Gamma_c^{(1)}$. Corresponding test functions $\delta\lambda_j$ serve as weighting functions for the non-penetration constraint in (1):

$$\int_{\gamma_c^{(1)}} \delta\lambda_n\, g(\mathbf{X},t)\,\mathrm{d}\gamma \geq 0 \qquad \forall\,\delta\lambda_n \in \mathscr{M}\ . \tag{4}$$

The remaining contact conditions in (1) and (2) are then rewritten as

$$\lambda_n \geq 0\ ,\ \ \lambda_n\, g(\mathbf{X},t) = 0\ ,\ \ \lambda_\tau^\xi = \lambda_\tau^\eta = 0. \tag{5}$$

Altogether, equations (3)–(5) establish a mixed variational formulation with the solution $u_j^{(i)} \in \mathscr{U}^{(i)}$ and $\lambda_j \in \mathscr{M}$. An overview of mortar finite element discretization using dual Lagrange multipliers follows in the upcoming paragraph. Some of the contact constraints are still formulated as inequality conditions, which necessitates the application of a suitable active set strategy. The primal-dual active set strategy (PDASS) and our reformulation as a semi-smooth Newton scheme including consistent linearization will be addressed in Section 4.

3 DUAL MORTAR FINITE ELEMENT DISCRETIZATION

Spatial discretization of the contact terms requires a discretization of slave and master surface, which is directly connected to the underlying structural discretization based on their trace space relationship. We consider both first-order and second-order Lagrangian finite elements in 2D and 3D. A general definition of slave and master displacements then reads as follows:

$$\mathbf{d}^{(1)h}|_{\Gamma_c^{(1)h}} = \sum_{k=1}^{n_{sl}} N_k^{(1)}(\boldsymbol{\xi}^{(1)})\,\mathbf{d}_k^{(1)}\ ,\ \ \mathbf{d}^{(2)h}|_{\Gamma_c^{(2)h}} = \sum_{l=1}^{n_m} N_l^{(2)}(\boldsymbol{\xi}^{(2)})\,\mathbf{d}_l^{(2)}\ . \tag{6}$$

Spatially discretized quantities are labeled with a superscript h and the total number of slave and master nodes is n_{sl} and n_m, respectively. Nodal displacements are given by $\mathbf{d}_k^{(1)}$, $\mathbf{d}_l^{(2)}$ and shape functions $N_k^{(1)}$, $N_l^{(2)}$ are defined with respect to the usual finite element parameter spaces $\boldsymbol{\xi}^{(i)}$. Lagrange multiplier interpolation is based on dual shape functions Φ_j, as pioneered by Wohlmuth [10]:

$$\boldsymbol{\lambda}^h = \sum_{j=1}^{n_{sl}} \Phi_j(\boldsymbol{\xi}^{(1)})\,\mathbf{z}_j \,, \tag{7}$$

with discrete nodal Lagrange multipliers $\mathbf{z}_j$. The construction of dual shape functions is based on a biorthogonality relation as introduced in [10, 11, 12]:

$$\int_{\gamma_c^{(1)h}} \Phi_j(\boldsymbol{\xi}^{(1)})\,N_k^{(1)}(\boldsymbol{\xi}^{(1)})\,\mathrm{d}\gamma = \delta_{jk}\int_{\gamma_c^{(1)h}} N_k^{(1)}(\boldsymbol{\xi}^{(1)})\,\mathrm{d}\gamma \,, \tag{8}$$

where δ_{jk} is the Kronecker delta. This approach will later allow for static condensation of the discrete multipliers $\mathbf{z}_j$. Note, that in the context of finite deformations dual shape functions become deformation-dependent themselves. For an overview and exemplary local calculations of element-specific dual shape functions in 2D and 3D contact analysis we refer to [1, 2, 15]. Nodal blocks of the two mortar integral matrices $\mathbf{D} \in \mathbb{R}^{3n_{sl}\times 3n_{sl}}$ and $\mathbf{M} \in \mathbb{R}^{3n_{sl}\times 3n_m}$ are then defined as

$$\mathbf{D}[j,k] = D_{jk}\,\mathbf{I}_3 = \delta_{jk}\int_{\gamma_c^{(1)h}} N_k^{(1)}\mathrm{d}\gamma\,\mathbf{I}_3 \,, \tag{9}$$

$$\mathbf{M}[j,l] = M_{jl}\,\mathbf{I}_3 = \int_{\gamma_c^{(1)h}} \Phi_j N_l^{(2)}\mathrm{d}\gamma\,\mathbf{I}_3 \,, \tag{10}$$

with $j,k = 1,...,n_{sl}$, $l = 1,...,n_m$ and with the identity $\mathbf{I}_3 \in \mathbb{R}^{3\times 3}$. Owing to the biorthogonality relation (8), $\mathbf{D}$ reduces to a diagonal matrix. This yields as algebraic notation of the discretized contact virtual work

$$\delta\Pi_c^h = \left(\delta\mathbf{d}^{(1)}\right)^T \mathbf{D}^T\mathbf{z} - \left(\delta\mathbf{d}^{(2)}\right)^T \mathbf{M}^T\mathbf{z}, \tag{11}$$

where all discrete nodal values of Lagrange multipliers and nodal test function values are assembled into global vectors $\mathbf{z}$, $\delta\mathbf{d}^{(1)}$ and $\delta\mathbf{d}^{(2)}$, respectively. For the ease of notation, the set of all finite element nodes is now split into three subsets: a subset $\mathscr{S}$ containing all n_{sl} potential slave side contact nodes, a subset $\mathscr{M}$ of all n_m potential master side contact nodes and the set of all remaining nodes $\mathscr{N}$. The global displacement vector can be sorted accordingly, yielding $\mathbf{d} = (\mathbf{d}_{\mathscr{N}}, \mathbf{d}_{\mathscr{M}}, \mathbf{d}_{\mathscr{S}})^T$. Then, the vector of discrete contact forces is

$$\mathbf{f}_c = [\mathbf{0} \quad -\mathbf{M} \quad \mathbf{D}]^T\,\mathbf{z} \,. \tag{12}$$

The contact forces extend the fully discretized force residual resulting from standard finite element discretization of internal and external virtual work in (3). This yields the total nonlinear force residual

$$\mathbf{r} := \mathbf{f}_{int}(\mathbf{d}) - \mathbf{f}_{ext} + \mathbf{f}_c(\mathbf{d},\mathbf{z}) = 0 \,. \tag{13}$$

A discrete version of the weak non-penetration condition is obtained by inserting the Lagrange multiplier interpolation (7) into (4)

$$\int_{\gamma_c^{(1)}} \delta\lambda_n\, g\,\mathrm{d}\gamma \approx \sum_{j=1}^{n_{sl}} (\delta z_n)_j \int_{\gamma_c^{(1)h}} \Phi_j\,\hat{g}\,\mathrm{d}\gamma := \sum_{j=1}^{n_{sl}} (\delta z_n)_j\,\tilde{g}_j \geq 0 \,. \tag{14}$$

Here, $\hat{g}$ is the discrete version of the gap function, and for each slave node $j \in \mathscr{S}$ a discrete normal weighted gap $\tilde{g}_j$ has been introduced. Discretization of the remaining contact conditions yields as discrete formulation of the KKT conditions and the frictionless sliding conditions:

$$\tilde{g}_j \geq 0\ , \ \ (z_n)_j \geq 0\ , \ \ (z_n)_j \tilde{g}_j = 0\ , \tag{15}$$

$$(z_\tau^\xi)_j = (z_\tau^\eta)_j = 0\ . \tag{16}$$

It is worth mentioning that although a mortar discretization has been employed, the weighted constraints at discrete nodal points are enforced independently.

4 SOLUTION ALGORITHM

In our recent papers [1, 2, 3] the active set search has been successfully applied as a semi-smooth Newton method to both 2D and 3D finite deformation contact analysis. The main advantage of this new approach is the fact that all sources of nonlinearities, i.e. finite deformations, nonlinear material behavior and contact itself, can be efficiently treated within one single iterative scheme. The basic idea is a simple reformulation of the discrete KKT conditions in (15) within a so-called nonlinear complementarity function C_j for each slave node $j \in \mathscr{S}$:

$$C_j\left(\mathbf{z}_j, \mathbf{d}\right) = (z_n)_j - \max\left(0, (z_n)_j - c_n \tilde{g}_j\right) = 0\ , \ \ c_n > 0\ . \tag{17}$$

It can be easily shown that (17) is equivalent to the set of KKT conditions and that this equivalence holds for arbitrary positive values of the purely algorithmic complementarity parameter c_n. While C_j is a continuous function, it is non-smooth and has no uniquely defined derivative at positions $(z_n)_j - c_n \tilde{g}_j = 0$. Yet, it is well-known from mathematical literature on constrained optimization [14] and from applications in small deformation contact analysis [12] that the *max*-function is semi-smooth and therefore a Newton method can still be applied. Deriving a consistent Newton method for the iterative solution of the nonlinear contact problem under consideration relies on the full linearization of all deformation-dependent quantities, such as nodal normal and tangential vectors or mortar integral matrices. This linearization process has been presented in great detail for both 2D and 3D case in [1, 2]. The resulting algorithm to be solved within one time increment is summarized next. All types of nonlinearities including the search for the correct active set are resolved within one Newton iteration, with the active and incative sets $\mathscr{A}$ and $\mathscr{I}$ being updated after each semi-smooth Newton step:

Algorithm 1

1. Set $i = 0$ and initialize the solution $(\mathbf{d}_0, \mathbf{z}_0)$.

2. Initialization: $\mathscr{A}_0 \cup \mathscr{I}_0 = \mathscr{S}$ and $\mathscr{A}_0 \cap \mathscr{I}_0 = \emptyset$.

3. Find the primal-dual pair $(\Delta\mathbf{d}_i, \mathbf{z}_{i+1})$ by solving

$$\Delta\mathbf{r}|_i = -\mathbf{r}|_i\ , \tag{18}$$

$$\mathbf{z}_j|_{i+1} = 0 \qquad \forall\, j \in \mathscr{I}_i\ , \tag{19}$$

$$\Delta\tilde{g}_j|_i = -\tilde{g}_j|_i \qquad \forall\, j \in \mathscr{A}_i\ , \tag{20}$$

$$\Delta\boldsymbol{\tau}_j^{\xi/\eta} \cdot \mathbf{z}_j|_i + \boldsymbol{\tau}_j^{\xi/\eta} \cdot \mathbf{z}_j|_{i+1} = 0 \qquad \forall\, j \in \mathscr{A}_i\ . \tag{21}$$

4. Update $\mathbf{d}_{i+1} = \mathbf{d}_i + \Delta\mathbf{d}_i$.

5. Set $\mathscr{A}_{i+1}$ and $\mathscr{I}_{i+1}$ to

$$\begin{aligned} \mathscr{A}_{i+1} &:= \left\{ j \in \mathscr{S} \,|\, (z_n)_j|_{i+1} - c_n \tilde{g}_j|_{i+1} > 0 \right\} , \\ \mathscr{I}_{i+1} &:= \left\{ j \in \mathscr{S} \,|\, (z_n)_j|_{i+1} - c_n \tilde{g}_j|_{i+1} \leq 0 \right\} . \end{aligned} \tag{22}$$

6. If $\mathscr{A}_{i+1} = \mathscr{A}_i$, $\mathscr{I}_{i+1} = \mathscr{I}_i$ and $\|\mathbf{r}_{tot}\| \leq \varepsilon_r$, then stop,
else set $i := i+1$ and go to step (3).

Here, ε_r represents an absolute Newton convergence tolerance for the L2-norm of the total residual vector $\mathbf{r}_{tot}$, which comprises the force residual $\mathbf{r}$ and the residual of the contact constraints (19)–(21). Numerous tests reveal that even for large step sizes and fine contacting meshes the correct active set is found after a few Newton steps. Once the sets remain constant, quadratic convergence is obtained due to the underlying consistent linearization. Owing to the dual Lagrange multiplier shape functions, the mortar matrix $\mathbf{D}$ becomes diagonal, which makes its inversion trivial. Thus, the discrete multiplier values are eliminated by condensation and the resulting linear system of equations is not of saddle point type anymore but contains only displacement degrees of freedom. Here, we restrict the presentation to a schematic form

$$\mathbf{L}_{dd}|_i \Delta \mathbf{d}_i = -\tilde{\mathbf{r}}_{tot}|_i , \tag{23}$$

which illustrates the modified residual vector $\tilde{\mathbf{r}}_{tot}$ emanating from $\mathbf{r}_{tot}$ by condensation of the discrete Lagrange multiplier degrees of freedom. Similarly, we obtain a modified effective tangent stiffness matrix $\mathbf{L}_{dd}$ including contact stiffness and condensed constraint terms.

5 RECENT EXTENSIONS OF THE PROPOSED METHODS

In this section, some recent extensions of the methods described above are outlined. This includes efficient parallel implementation, the treatment of self contact and Coulomb friction as well as the consistent integration of mortar contact into an XFEM based fixed-grid fluid-structure interaction framework.

5.1 Efficient parallel implementation and self contact

The solution of finite deformation contact problems is difficult to be managed due to the strong nonlinearities involved. A brute force approach for contact search may add another very time-consuming part, which is why efficient parallel search algorithms are needed. Here, we employ a recently developed approach [17] based on so-called discretized-orientation-polytopes (k-DOPs) as bounding volumes. Compared to the common axis-aligned bounding boxes, the k-DOPs allow for a much tighter and thus more efficient geometrical representation of the contact surfaces. Slave and master contact surface are organized within hierarchical binary tree structures so that very fast search and tree update procedures can be applied. The approach given in [17] for the single-processor case has been extended to fit into a parallel finite element simulation framework based on overlapping domain decomposition. An extension to self contact is presented in [18] and has also been included into our simulation framework. The search algorithm again is based on a bounding volume hierarchy organized as a binary tree. It is however crucial for self contact simulations to set up the bounding volume hierarchy in a *bottom-up* way based on mesh connectivity (e.g. using a dual graph). Moreover, a curvature criterion may be used to accelerate the searching procedure. Finally, dynamic assignment of slave and master sub-surfaces, which are unknown *a priori* for self contact problems, becomes necessary.

In addition, we make use of a novel strategy for dynamic load balancing specifically developed for mortar-based interface coupling. Within each time step the evaluation of contact integrals is adaptively distributed among all processors, so that an optimal balance of processor workload is obtained. Parallel (self) contact search and dynamic load balancing together assure the parallel scalability of all presented algorithmic components even when solving large contact dynamics problems with up to some million degrees of freedom.

5.2 Treatment of friction

An extension of the described mortar contact algorithms to the 2D frictional case has recently been proposed [3]. All steps outlined in Sections 2-4 remain conceptually unchanged. Only the frictionless sliding conditions introduced in (2) are replaced by frictional sliding conditions, e.g. using Coulomb's law. Based on an objective formulation of friction kinematic variables [8] the additional constraints again are recast into non-smooth nonlinear complementarity functions, as presented for the non-penetration constraint in (17). By applying full linearization, the frictional constraints are consistently integrated into the semi-smooth Newton scheme. All nonlinearities, now additionally including friction (i.e. search for the current stick and slip regions), are again treated within one single iterative scheme. For further details and numerical examples, the interested reader is referred to [3].

5.3 Fluid-structure-contact interaction

Finite deformation contact of flexible solids embedded in fluid flows occurs in a wide range of engineering scenarios. We recently proposed a novel three-dimensional finite element approach in order to tackle this problem class [4]. The method consists of the dual mortar contact formulation presented above, which is algorithmically integrated into an extended finite element method (XFEM) fluid-structure interaction approach [19, 20]. The combined fluid-structure-contact interaction method (FSCI) allows to compute contact of arbitrarily moving and deforming structures embedded in an arbitrary flow field. In [4], the fluid is described by instationary incompressible Navier-Stokes equations. An interface handling algorithm [21] is applied to obtain an exact fluid-structure interface representation, which permits to capture flow patterns around contacting structures very accurately as well as to simulate dry contact between structures. No restrictions arise for the structural and the contact formulation. A linearized monolithic system of equations can be derived, which contains the fluid formulation, the structural formulation, the contact formulation as well as the coupling conditions at the fluid-structure interface. This linearized system may then be solved either by partitioned or by monolithic fluid-structure coupling algorithms.

6 NUMERICAL EXAMPLES

We present three numerical examples to illustrate the capabilities of the proposed approach. All simulations are based on a parallel implementation of the contact and FSCI algorithms described above in our in-house multiphysics research code BACI [22]. A compressible Neo-Hookean constitutive law determined by Young's modulus E and Poisson's ratio ν is employed for all structures. Convergence of a Newton iterative scheme is measured in terms of the total residual norm with a relative convergence tolerance of 10^{-12}. The complementarity parameter described in Section 4 is set to $c_n = 1$, which guarantees for all problem setups considered that the correct active set is found within only a few semi-smooth Newton steps.

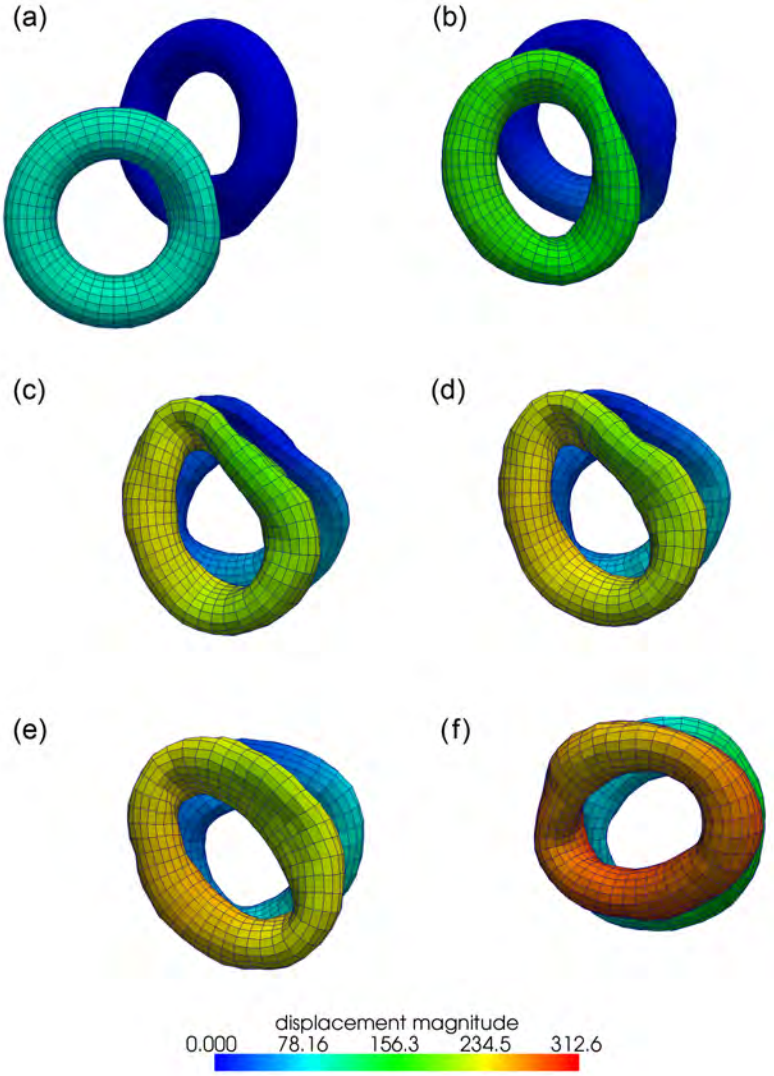

Figure 2: Two torus impact – displacement magnitude at characteristic stages of deformation: (a) $t = 3$; (b) $t = 5$; (c) $t = 7$; (d) $t = 7.5$; (e) $t = 8$; (f) $t = 10$.

6.1 Two torus impact

In this example, a finite deformation impact problem of two toruses ($E = 2250$, $\nu = 0.3$) is investigated. Both geometry and loading conditions are based on a quite similar analysis presented in [17] to evaluate contact search strategies. The finite element mesh consists of 1600 8-node hexahedral elements in total. The major and minor radius of the two hollow toruses is 76 and 24, repectively and the wall thickness is 4.5. The upper torus is rotated around the vertical axis by 45 degrees. We apply transient structural dynamics here using a Generalized-α time integration scheme [23] with the density of the contacting bodies chosen as $\rho = 0.1$.

During a total of 200 time steps (step size $\Delta t = 0.05$) the lower torus is first accelerated towards the upper torus and then a very general oblique impact situation with large structural deformations occurs. In addition to that, the proposed method needs to resolve continuous changes of the active contact set due to the large amount of (frictionless) sliding. Figure 2 shows six characteristic deformed configurations associated with the simulation stages described above.

Table 1 illustrates convergence of the presented fully linearized semi-smooth Newton scheme in terms of the total residual norm for two representative time steps both including large defor-

Newton step	*(a)* $t = 4.5$	*(b)* $t = 5.5$
1	1.09e+06 (*)	1.04e+06 (*)
2	2.16e+04 (*)	3.60e+04 (*)
3	4.05e+00	1.38e+01 (*)
4	1.53e−04	2.11e−03
5	2.46e−08	2.77e−08

(*) = change in active contact set

Table 1: Convergence behavior of the proposed semi-smooth Newton scheme in terms of the total residual norm for two representative time steps $\Delta t = 0.05$ starting from (a) $t = 4.5$ and (b) $t = 5.5$.

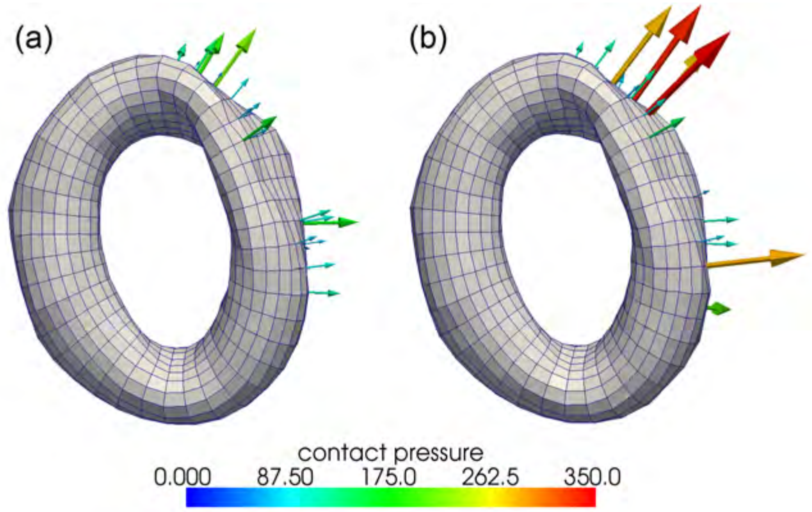

Figure 3: Two torus impact – exemplary visualization of the deformed lower torus and of the computed contact traction results at (a) $t = 5.5$ and (b) $t = 5.55$.

mations and considerable changes of the active contact set. The results demonstrate that the semi-smooth Newton method features excellent convergence in this example. The integration of all types of nonlinearities into a semi-smooth Newton scheme avoids tremendous computational cost as compared with a fixed-point type approach for the active set (see e.g. [9, 16]). Moreover, it is obvious that consistent linearization of all nonlinear quantities, including contact forces, normal and tangential vectors, is crucial to avoid deterioration of convergence.

To illustrate the strong nonlinearities involved in this problem setup even more clearly, Figure 3 shows the deformed lower torus at the beginning and at the end of the time step analyzed in column (b) of Table 1 (i.e. at $t = 5.5$ and at $t = 5.55$). The normal contact traction distribution, represented by the nodal Lagrange multiplier solution, is visualized with arrows and confirms that despite significant changes of the contact region, all nonlinearities are resolved efficiently and without deterioration of convergence within one single semi-smooth Newton iteration.

6.2 Hollow sphere pushed through elastic tube

In this example, a hollow sphere ($E = 500$, $\nu = 0.3$) is pushed through a tube ($E = 1000$, $\nu = 0.3$). Geometrical setup and finite element mesh based on 8-node hexahedral elements are depicted in Figure 4. Due to the application of a load-controlled scheme in combination with the frictionless sliding case considered, the deformation cannot be resolved by a quasistatic simulation. Thus, again transient structural dynamics is applied using Generalized-α time inte-

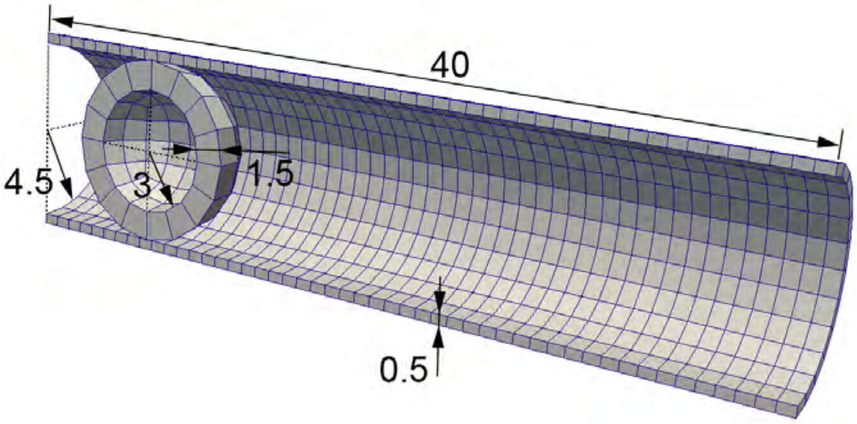

Figure 4: Sphere pushed through tube – geometry and finite element mesh.

Step	*(a)* during inflation	*(b)* during pushing
1	3.08e+00 (*)	3.39e+01 (*)
2	1.10e+00	4.80e+00 (*)
3	6.82e−03	3.35e−02 (*)
4	6.74e−08	5.62e−06
5	5.04e−11	4.87e−11

(*) = change in active contact set

Table 2: Convergence behavior of the proposed semi-smooth Newton scheme in terms of the total residual norm for two representative time steps during (a) inflation (steps 1–20) and (b) pushing (steps 21–40).

gration with the density of the contacting bodies chosen as $\rho = 7.8 \cdot 10^{-6}$. During a total of 40 time steps, we first inflate the hollow sphere by internal pressure (steps 1–20) and then push it along the axial direction of the tube (steps 21–40). Figure 5 shows two deformed configurations associated with the two stages described above.

Table 2 illustrates convergence in terms of the total residual norm for two representative time steps during inflation of the hollow sphere and during pushing. Again, for this transient contact simulation of two elastic bodies, the presented algorithm is capable of efficiently solving all types of nonlinearities including active set search within one semi-smooth Newton scheme.

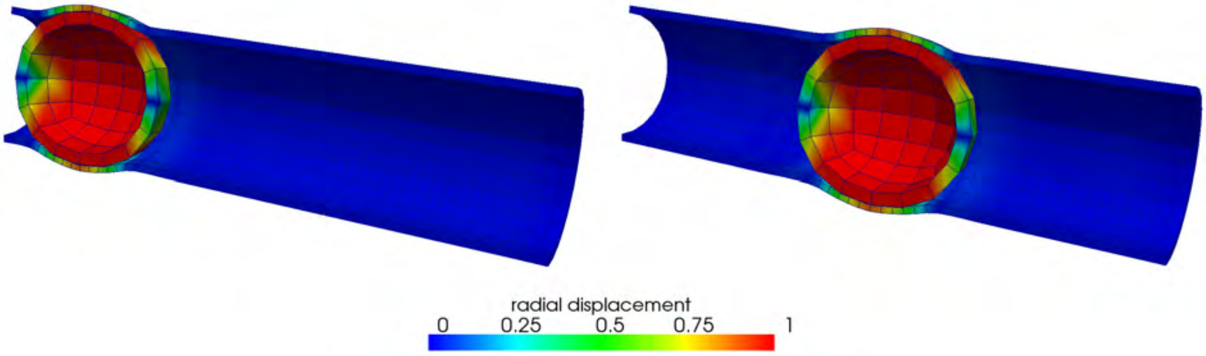

Figure 5: Sphere pushed through tube – characteristic stages of deformation.

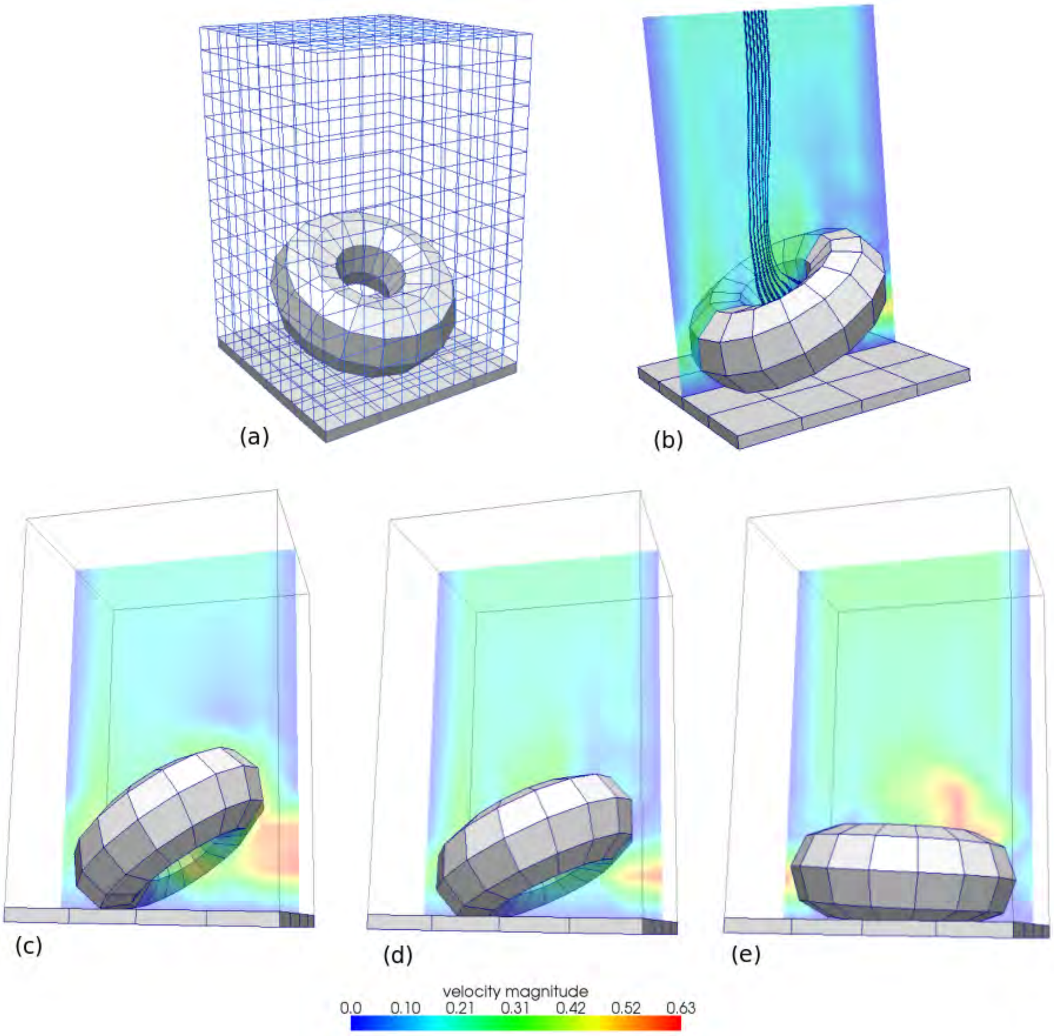

Figure 6: 3D torus contacting a stiff wall – (a) finite element mesh, (b) stream lines through the inner hole of the torus before contact (c)–(e) fluid velocity and structural movement are visualized for several time steps of the dynamic fluid-structure-contact interaction process.

6.3 Fluid-structure-contact interaction: elastic torus

The third test case illustrates a three-dimensional fluid-structure-contact interaction example. An elastic torus ($E = 4000$, $\nu = 0.4$) rotated around a horizontal axis by an angle of 65 degrees is placed in a 3D channel as depicted in Figure 6. A parabolic inflow profile is imposed at the top boundary of the channel and zero traction Neumann boundaries allow outflow on the left and right side near the bottom. All other channel boundaries are no-slip boundaries. Both the structural and the fluid mesh consist of 8-node hexahedral elements, with state-of-the-art stabilization techniques being used in the fluid elements. The velocity field around the moving torus is depicted in Figure 6. Stream lines illustrate the 3D fluid flow through the inner hole of the torus before contacting with the wall. At first, the torus is moving towards the wall due to the interaction with the fluid stresses. The exact interface representation allows to resolve flow patterns around the torus very close to contact and to simulate dry contact. After some time, the torus touches the wall and its further movement and deformation is influenced by the fluid at the fluid-structure interface and by contact forces at the contact interface.

7 CONCLUSIONS

The dual mortar method recently proposed by the authors for 3D finite deformation contact analysis has been reviewed and some important extensions have been highlighted. Consistent linearization of contact forces and constraints together with an interpretation of the active set search as a semi-smooth Newton scheme yields a very efficient solution algorithm. The accuracy of the presented method and its superior numerical robustness and efficiency have been demonstrated with several examples including finite deformations.

The integration of dual mortar contact into a fixed-grid fluid-structure interaction (FSI) framework based on the extended finite element method (XFEM) has been addressed shortly. This can be seen as a first step towards multiphysics and multiscale simulations, which couple contact analysis with several other physical fields and take into account effects on different length scales. Future work in this field will also focus on modeling finite deformation contact between slender beams and coupled thermomechanical contact, with applications ranging from Brownian dynamics of polymers in fiber networks to heat conduction and mechanical dissipation due to frictional sliding in turbine blade-to-disc joints.

REFERENCES

[1] A. Popp, M.W. Gee, W.A. Wall, A finite deformation mortar contact formulation using a primal-dual active set strategy. *International Journal for Numerical Methods in Engineering*, **79**, 1354–1391, 2009.

[2] A. Popp, M. Gitterle, M.W. Gee, W.A. Wall, A dual mortar approach for 3D finite deformation contact with consistent linearization. *International Journal for Numerical Methods in Engineering*, **83**, 1428–1465, 2010.

[3] M. Gitterle, A. Popp, M.W. Gee, W.A. Wall, Finite deformation frictional mortar contact using a semi-smooth Newton method with consistent linearization. *International Journal for Numerical Methods in Engineering*, **84**, 543–571, 2010.

[4] U. Mayer, A. Popp, A. Gerstenberger, W.A. Wall, 3D fluid-structure-contact interaction based on a combined XFEM FSI and dual mortar contact approach. *Computational Mechanics*, **46**, 53–67, 2010.

[5] C. Bernardi, Y. Maday, A.T. Patera, A new nonconforming approach to domain decomposition: the mortar element method. H. Brezis, J.L. Lions eds. *Nonlinear partial differential equations and their applications*, Pitman/Wiley: London/New York, 1994.

[6] M.A. Puso, T.A. Laursen, A mortar segment-to-segment contact method for large deformation solid mechanics. *Computer Methods in Applied Mechanics and Engineering*, **193**, 601–629, 2004.

[7] M.A. Puso, T.A. Laursen, A mortar segment-to-segment frictional contact method for large deformations. *Computer Methods in Applied Mechanics and Engineering*, **193**, 4891–4913, 2004.

[8] B. Yang, T.A. Laursen, X. Meng, Two dimensional mortar contact methods for large deformation frictional sliding. *International Journal for Numerical Methods in Engineering*, **62**, 1183–1225, 2005.

[9] C. Hesch, P. Betsch, A mortar method for energy-momentum conserving schemes in frictionless dynamic contact problems. *International Journal for Numerical Methods in Engineering*, **77**, 1468–1500, 2009.

[10] B.I. Wohlmuth, A mortar finite element method using dual spaces for the Lagrange multiplier. *SIAM Journal on Numerical Analysis*, **38**, 989–1012, 2000.

[11] B.I. Wohlmuth, *Discretization methods and iterative solvers based on domain decomposition*. Springer-Verlag Berlin Heidelberg, 2001.

[12] S. Hüeber, B.I. Wohlmuth, A primal-dual active set strategy for non-linear multibody contact problems. *Computer Methods in Applied Mechanics and Engineering*, **194**, 3147–3166, 2005.

[13] P.W. Christensen, A. Klarbring, J.S. Pang, N. Strömberg, Formulation and comparison of algorithms for frictional contact problems. *International Journal for Numerical Methods in Engineering*, **42**, 145–173, 1998.

[14] M. Hintermüller, K. Ito, K. Kunisch, The primal-dual active set strategy as a semismooth Newton method. *SIAM Journal on Optimization*, **13**, 865–888, 2002.

[15] S. Hartmann. *Kontaktanalyse dünnwandiger Strukturen bei grossen Deformationen*. PhD thesis, Institut für Baustatik und Baudynamik, Universität Stuttgart, 2007.

[16] S. Hartmann, S. Brunssen, E. Ramm, B. Wohlmuth, Unilateral non-linear dynamic contact of thin-walled structures using a primal-dual active set strategy. *International Journal for Numerical Methods in Engineering*, **70**, 883–912, 2007.

[17] B. Yang, T.A. Laursen, A contact searching algorithm including bounding volume trees applied to finite sliding mortar formulations. *Computational Mechanics*, **41**, 189–205, 2008.

[18] B. Yang, T.A. Laursen, A large deformation mortar formulation of self contact with finite sliding. *Computer Methods in Applied Mechanics and Engineering*, **197**, 756–772, 2008.

[19] A. Gerstenberger, W.A. Wall, An extended finite element method/Lagrange multiplier based approach for fluid-structure interaction. *Computer Methods in Applied Mechanics and Engineering*, **197**, 1699–1714, 2008.

[20] A. Gerstenberger, W.A. Wall, An embedded Dirichlet formulation for 3D continua. *International Journal for Numerical Methods in Engineering*, **82**, 537–563, 2010.

[21] U.M. Mayer, A. Gerstenberger, W.A. Wall, Interface handling for three-dimensional higher-order XFEM computations in fluid-structure interaction. *International Journal for Numerical Methods in Engineering*, **79**, 846–869, 2009.

[22] W.A. Wall, M.W. Gee. Baci - a multiphysics simulation environment. Technical report, Technische Universität München, 2010.

[23] J. Chung, G.M. Hulbert, A time integration algorithm for structural dynamics with improved numerical dissipation: the generalized-alpha method. *Journal of Applied Mechanics*, **60**, 371–375, 1993.

COMPDYN 2011
3rd ECCOMAS Thematic Conference on
Computational Methods in Structural Dynamics and Earthquake Engineering
M. Papadrakakis, M. Fragiadakis, V. Plevris (eds.)
Corfu, Greece, 25–28 May 2011

SOFT COMPUTING IN STRUCTURAL DYNAMICS

T. Burczyński[1,2], R. Górski[1], A. Poteralski[1], M. Szczepanik[1]

[1]Department of Strength of Materials & Computational Mechanics, Silesian University of Technology
Konarskiego 18a, 44-100 Gliwice, Poland
e-mail: tb@polsl.pl

[2] Institute of Computer Science, Cracow University of Technology
Warszawska 24, 31-155 Kraków, Poland
tburczyn@pk.edu.pl

Keywords: soft computing, evolutionary algorithm, artificial immune system, particle swarm optimizer, optimization, finite element method, boundary element method, dynamics

Abstract. *The paper is devoted to new computational techniques in structural dynamics where one tries to study, model, analyze and optimize very complex phenomena, for which more precise scientific tools of the past were incapable of giving low cost and complete solution. Soft computing methods differ from conventional (hard) computing in that, unlike hard computing, they are tolerant of imprecision, uncertainty, partial truth, and approximation. The paper deals with an application of the bio-inspired methods, like the evolutionary algorithms (EA), the artificial immune systems (AIS) and the particle swarm optimizers (PSO) to optimization problems. Structures considered in this work are analyzed by the finite element method (FEM) and the boundary element method (BEM). The bio-inspired methods are applied to optimize shape, topology and material properties of 3D structures modeled by the FEM and to optimize location of stiffeners in 2D reinforced plates modeled by the coupled BEM/FEM. The structures are optimized using the criteria depend on frequency, displacements or stresses. Numerical examples demonstrate that the methods based on the soft computation are effective for solving computer aided optimal design problems.*

1 INTRODUCTION

Structures are frequently subjected to dynamic loads and it is very important to analyze their transient dynamic response. Important properties of vibrating structures are eigenfrequencies. The dynamic response or natural frequencies of structures can be established by changing shape, topology and material properties of structures. Another possibility of the response improvement is applying stiffeners. The choice of their number, properties and location in a structure decides about the effectiveness of reinforcement. Reinforced structures are often used in practice because they are resistant, stiff and stable. A typical area of application of such structures is an aircraft industry, where light, stiff and highly resistant structures are required. Many aircraft elements are made as thin panels reinforced by stiffeners.

Dynamic response of structures with an arbitrary geometry, material properties and boundary conditions can be obtained by carrying out laboratory tests but they are usually very expensive and time consuming. In order to reduce costs and time, computer simulations are performed instead of experimental investigations. As a result, dynamic quantities of interest like displacements, velocities, accelerations, forces, stresses, i.e. can be determined. The most versatile methods of analysis of structures subjected to arbitrary static and time dependent boundary conditions are the finite element method (FEM) and the boundary element method (BEM). The coupling of these methods is very desirable in order to exploit their advantages. Optimal properties of dynamically loaded structures can be searched using the computer aided optimization tools.

In the present paper, coupling FEM and BEM with the bio-inspired methods in optimization of dynamically loaded structures is presented. The evolutionary algorithms (EA), the artificial immune systems (AIS) and the particle swarm optimizers (PSO) are used to optimize shape, topology and material properties of 3D freely vibrating structures and 2D dynamically loaded stiffened plates. The former are analyzed by the FEM and the latter by the coupled BEM/FEM.

2 SOFT COMPUTING METHODS

Soft computing techniques resemble human reasoning more closely than traditional techniques, which are largely based on conventional logical systems or rely heavily on the mathematical capabilities of a computer. These computing techniques are often used to complement each other in applications. It should be pointed out that simplicity and complexity of systems are relative, and certainly, most successful mathematical modeling of the past have also been challenging and very significant.

Unlike hard computing schemes, which strive for exactness and for full truth, soft computing techniques exploit the given tolerance of imprecision, partial truth, and uncertainty for a particular problem. Another common contrast comes from the observation that inductive reasoning plays a larger role in soft computing than in hard computing.

Three important areas of soft computing methods, namely:

- Evolutionary Computation (EC),
- Artificial Immune Systems (AIS),
- Particle Swarm Methods (PSM),

are presented in the paper as soft computing methods.

2.1 Evolutionary Computation (EC)

Evolutionary algorithms [1, 10] are algorithms searching the space of solutions and they are based on the analogy to the biological evolution of species. Like in biology, the term of an individual is used, and it represents a single solution. Evolutionary algorithms operate on populations of individuals, so while the algorithm works, all the time we deal with a set of problem solutions. An individual consists of chromosomes. Usually it is assumed that an individual has one chromosome. Chromosomes consist of genes which are equivalents of design variables in optimization problems. The adaptation is computed using a fitness function. All genes of an individual decide about the fitness function value. A flowchart of an evolutionary algorithm is presented in Fig. 1.

In the first step, an initial population of individuals is created. Usually, the values of the genes of particular individuals are randomly generated. In the next step, the fitness function value for each individuals is computed. Then, evolutionary operators change genes of the parent population individuals, they are then selected for the offspring population, which becomes a parent population and the algorithm is continuing iteratively till the end of the computation. The termination condition of the computation can be formulated as the maximum number of iterations.

In evolutionary algorithms the floating-point representation is applied, which means that genes included in chromosomes are floating-point numbers. Usually the variation of the gene value is limited.

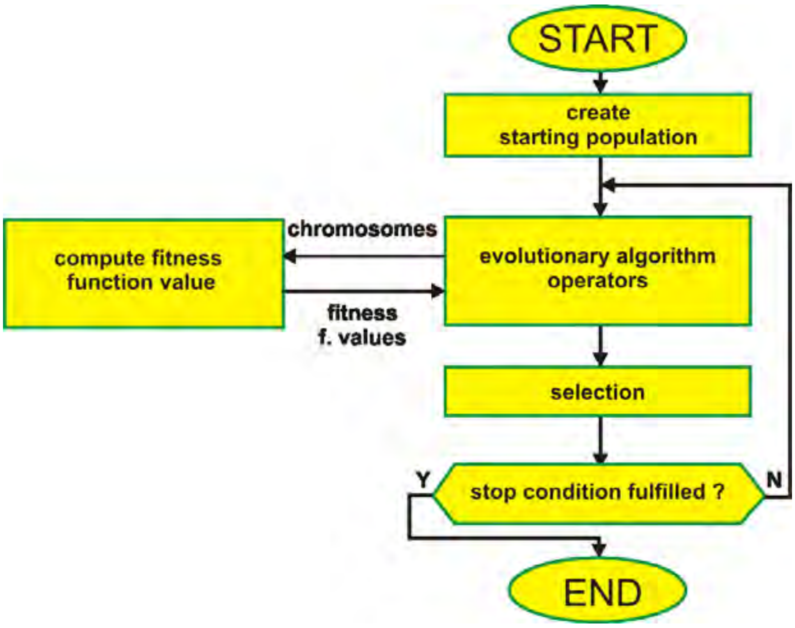

Figure 1: A flowchart of an evolutionary algorithm.

A single-chromosome individual (called a chromosome) ch_i, $i=1,2,...,N$, where N is the population size, may be presented by means of a column or line matrix, whose elements are represented by genes g_{ij}, $j=1,2,...,n$, where n is the number of genes in a chromosome. The sample chromosome is presented in Fig. 2.

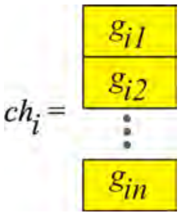

Figure 2: Structure of an individual.

Evolutionary operators change gene values like the biological mechanisms of mutation and crossover. Different kinds of operators are presented in publications, and the basic ones are:

- uniform mutation,
- mutation with Gaussian distribution,
- boundary mutation,
- simple crossover,
- arithmetical crossover.

A uniform mutation changes the values of randomly chosen genes in randomly selected individual. The new values of the genes are drawn in such a way that they could fulfill constrains imposed on the variation of the gene values. The diagram of how an operator works is presented in Fig. 3.

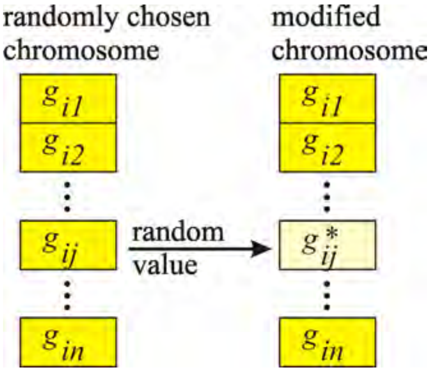

Figure 3: A diagram of an uniform mutation.

A mutation with Gaussian distribution is an operator changing the values of an individual's genes randomly, similarly to uniform mutation. New values of the genes are created by means of random numbers with Gaussian distribution. The operator searches the individual's surrounding.

A boundary mutation (Fig. 4) operates similarly to a uniform mutation, however, new values of the genes are equal to the left or right value from the gene variation range (left or right constraint on gene values).

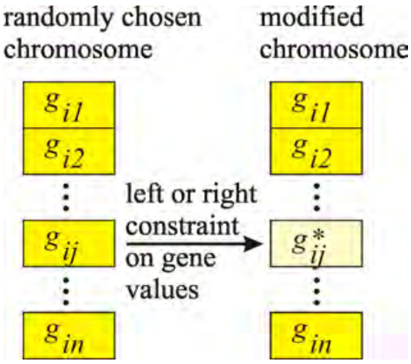

Figure 4: A diagram of boundary mutation

A simple crossover is an operator creating an offspring on the basis of two parent individuals. A cutting position is drawn (Fig. 5), and a new individual consists of the genes coming partly form the first and partly form the second individual.

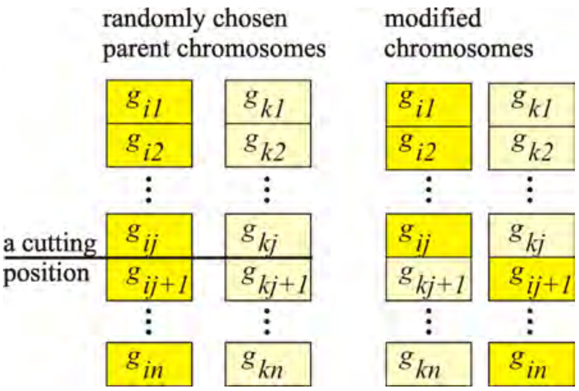

Figure 5: A diagram of a simple crossover

An arithmetical crossover has no biological counterpart. A new individual is formed similarly to a simple crossover, on the basis of two parent individuals, however, the values of the individual's genes are defined as the average value of the parent individuals' genes (Fig. 6).

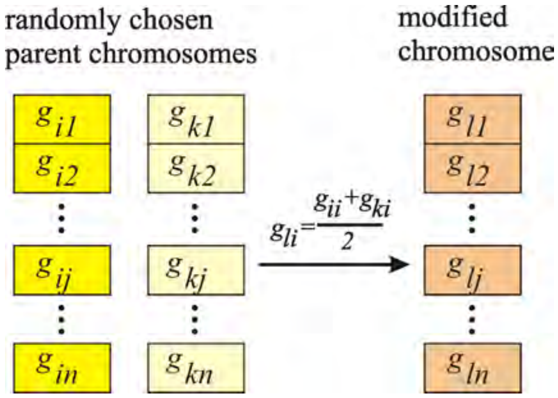

Figure 6: A diagram of an arithmetical crossover

An important element of an evolutionary algorithm is the mechanism of selection. The probability of the individual's survival depends on the value of the fitness function. Ranking selection is performed in a few steps. First, the individuals are classified according to the value of the fitness function, then a rank value is attributed to each individual. It depends on the individual's number and the rank function. The best individuals obtain the highest rank value, the worst obtain the lowest one. In the final step individuals for the offspring generation are drawn, but the probability of drawing particular individuals is closely related to their rank value.

2.2 Artificial Immune Systems (AIS)

The artificial immune systems (AIS) are developed on the basis of a mechanism discovered in biological immune systems [11]. An immune system is a complex system which contains distributed groups of specialized cells and organs. The main purpose of the immune system is to recognize and destroy pathogens - funguses, viruses, bacteria and improper functioning cells. The lymphocytes cells play a very important role in the immune system. The lymphocytes are divided into several groups of cells. There are two main groups B and T cells, both contains some subgroups (like B-T dependent or B-T independent). The B cells contain antibodies, which could neutralize pathogens and are also used to recognize pathogens. There is a big diversity between antibodies of the B cells, allowing recognition and neutralization of many different pathogens. The B cells are produced in the bone marrow in long bones. A B cell undergoes a mutation process to achieve big diversity of antibodies. The T cells mature in thymus, only T cells recognizing non self cells are released to the lymphatic and the blood systems. There are also other cells like macrophages with presenting properties, the pathogens are processed by a cell and presented by using MHC (Major Histocompatibility Complex) proteins. The recognition of a pathogen is performed in a few steps (Fig. 7). First, the B cells or macrophages present the pathogen to a T cell using MHC (Fig. 7b), the T cell decides if the presented antigen is a pathogen. The T cell gives a chemical signal to B cells to release antibodies. A part of stimulated B cells goes to a lymph node and proliferate (clone) (Fig. 7c). A part of the B cells changes into memory cells, the rest of them secrete antibodies into blood. The secondary response of the immunology system in the presence of known pathogens is faster because of memory cells. The memory cells created during primary response, proliferate and the antibodies are secreted to blood (Fig. 7d). The antibodies bind to pathogens and neutralize them. Other cells like macrophages destroy pathogens (Fig. 7e). The number of lymphocytes in the organism changes, while the presence of pathogens increases, but after attacks a part of the lymphocytes is removed from the organism.

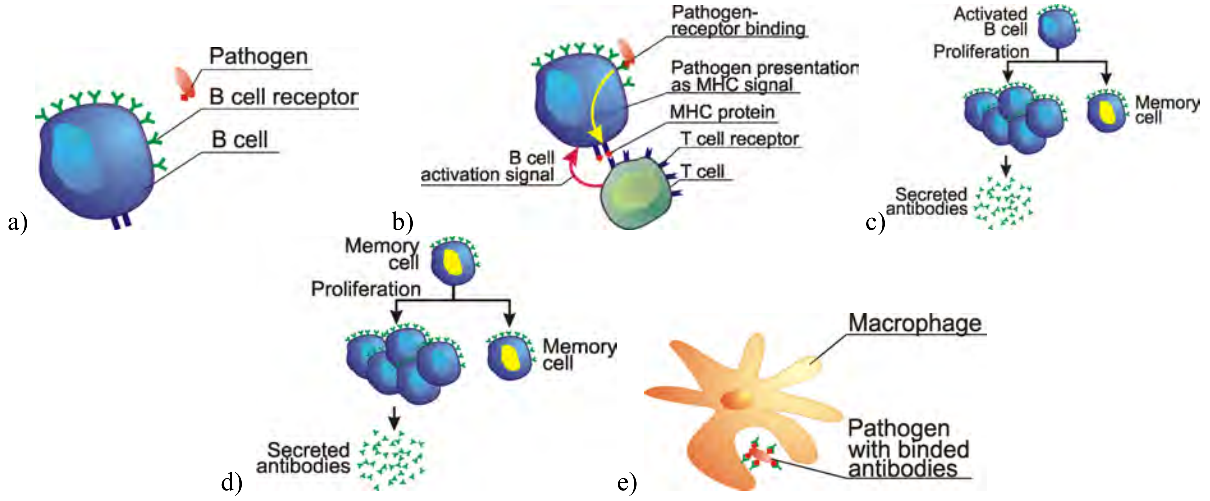

Figure 7: An immune system, a) a B cell and pathogen, b) the recognition of pathogen using B and T cells, c) the proliferation of activated B cells, d) the proliferation of a memory cell – secondary response, e) pathogen absorption by a macrophage.

The artificial immune systems [2], [3], [4] take only a few elements from the biological immune systems. The most frequently used are the mutation of the B cells, proliferation, memory cells, and recognition by using the B and T cells. The artificial immune systems have been used to optimization problems in [5], classification and also computer viruses recognition in [2]. The cloning algorithm presented by von Zuben and de Castro [4], [5] uses some mechanisms similar to biological immune systems to global optimization problems. The unknown global optimum is the searched pathogen. The memory cells contain design variables and proliferate during the optimization process. The B cells created from memory cells undergo mutation. The B cells evaluate and better ones exchange memory cells. In Wierzchoń [13] version of Clonalg the crowding mechanism is used - the diverse between memory cells is forced. A new memory cell is randomly created and substitutes the old one, if two memory cells have similar design variables. The crowding mechanism allows finding not only the global optimum but also other local ones. The presented approach is based on the Wierzchoń [13] algorithm, but the mutation operator is changed. The Gaussian mutation is used instead of the nonuniform mutation in the presented approach.

A flowchart of an artificial immune system is presented in Fig. 8. The memory cells are created randomly. They proliferate and mutate creating B cells. The number of nc clones created by each memory cell is determined by the memory cells objective function value. The objective functions for B cells are evaluated. The selection process exchanges some memory cells for better B cells. The selection is performed on the basis of the geometrical distance between each memory cell and B cells (measured by using design variables). The crowding mechanism removes similar memory cells. The similarity is also determined as the geometrical distance between memory cells. The process is iteratively repeated until the stop condition is fulfilled. The stop condition can be expressed as the maximum number of iterations.

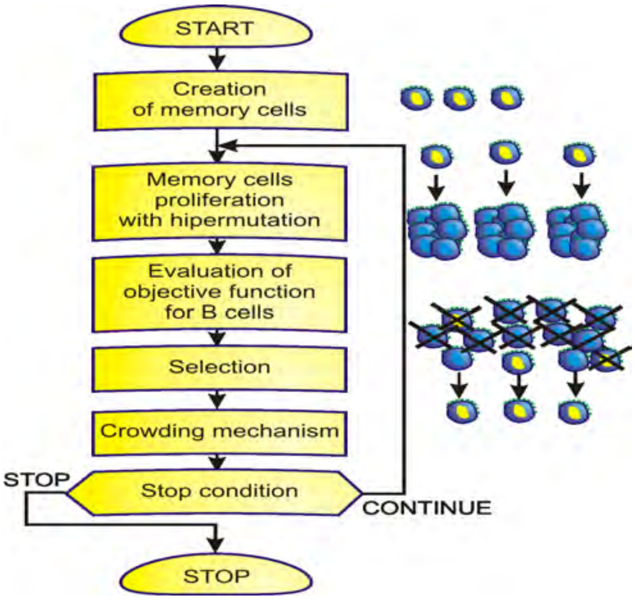

Figure 8: An artificial immune system.

2.3 Particle Swarm Methods (PSM)

The particle swarm algorithms [12], similarly to the evolutionary and immune algorithms, are developed on the basis of the mechanisms discovered in the nature. The swarm algorithms are based on the models of the animals social behaviours: moving and living in the groups. The animals relocate in the three-dimensional space in order to change their stay place, the feeding ground, to find the good place for reproduction or to evading predators. We can distinguish many species of the insects living in swarms, fishes swimming in the shoals, birds flying in flocks or animals living in herds (Fig. 9).

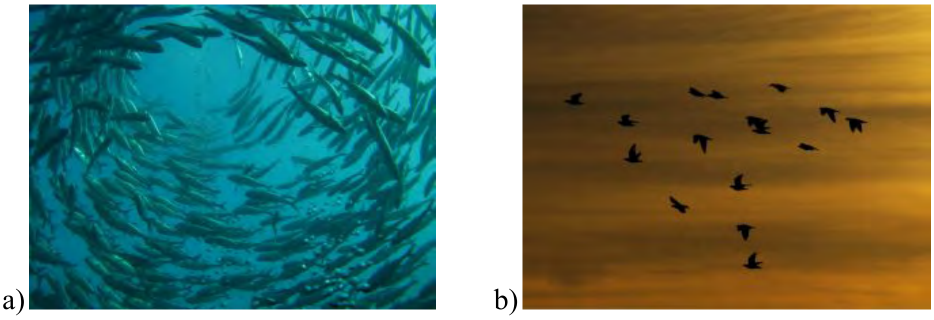

Figure 9: Particles swarms: a) fish shoal (http://www.sxc.hu/photo/1187373), b) bird flock (http://www.sxc.hu/photo/1095384).

A simulation of the bird flocking was published in [12]. They assumed that this kind of the coordinated motion is possible only when three basic rules are fulfilled: collision avoidance, velocity matching of the neighbours and flock centring. The computer implementation of these three rules showed very realistic flocking behaviour flaying in the three dimensional space, splitting before obstacle and rejoining again after missing it. The similar observations concerned the fish shoals. Further observations and simulations of the birds and fishes behaviour gave in effect more accurate and more precise formulated conclusions [9]. The results of this biological examination where used by Kennedy and Eberhart [7], who proposed Particle Swarm Optimiser – PSO. This algorithm realizes directed motion of the particles in n-dimensional space to search for solution for n-variable optimisation problem. PSO works in an iterative way. The location of one individual (particle) is determined on the basis of its earlier experience and experience of whole group (swarm). Moreover, the ability to memorize and, in consequence, returning to the areas with convenient properties, known earlier, enables adaptation of the particles to the life environment. The optimisation process using PSO is based on finding the better and better locations in the search-space (in the natural environment that are for example hatching or feeding grounds).

The algorithm with continuous representation of design variables and constant constriction coefficient (constricted continuous PSO) has been used in presented research. In this approach each particle oscillates in the search space between its previous best position and the best position of its neighbours, with expectation to find new best locations on its trajectory. When the swarm is rather small (swarm consists of several or tens particles) it can be assumed that all the particles stay in neighbourhood with currently considered one. In this case we can assume the global neighbourhood version and the best location found by swarm so far is taken into account – current position of the swarm leader (Fig. 10).

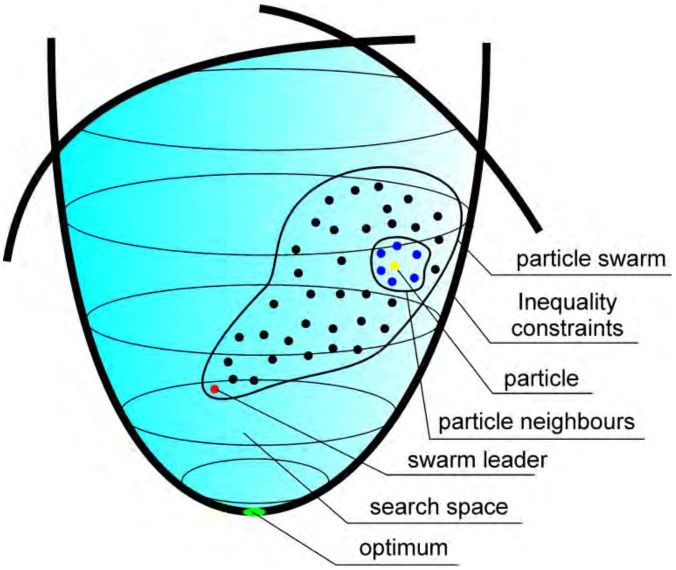

Figure 10: The idea of the particle swarm.

The position of the i-th particle is changed by stochastic velocity vi, which is dependent on the particle distance from its earlier best position and position of the swarm leader. This approach is given by the following equations:

$$v_{ij}(k+1) = wv_{ij}(k) + \phi_{1j}(k)\left[q_{ij}(k) - d_{ij}(k)\right] + \phi_{2j}(k)\left[\hat{q}_{ij}(k) - d_{ij}(k)\right] \quad (1)$$

$$d_{ij}(k+1) = d_{ij}(k) + v_{ij}(k+1), \quad i = 1,2,...,m \; ; j = 1,2,...,n \tag{2}$$

where:

$$\phi_{1j}(k) = c_1 r_{1j}(k); \; \phi_{2j}(k) = c_2 r_{2j}(k),$$

m – number of the particles,
n – number of design variables (problem dimension),
w – inertia weight,
c_1, c_2 – acceleration coefficients,
r_1, r_2 – random numbers with uniform distribution [0,1],
$d_i(k)$ – position of the i-th particle in k-th iteration step,
$v_i(k)$ – velocity of the i-th particle in k-th iteration step,
$q_i(k)$ – the best found position of the i-th particle found so far,
$\hat{q}_i(k)$ – the best position found so far by swarm – the position of the swarm leader,
k – iteration step.

The velocity of i-th particle is determine by three components of the sum in Equation (1). The first component $wv_i(k)$ plays the role of the constraint to avoid excessive oscillation in the search space. The inertia weight w controls the influence of particle velocity from the previous step on the current one. In this way this factor controls the exploration and exploitation. Higher value of inertia weight facilitates the global searching, and lower – the local searching. The inertia weight plays the role of the constraint applied for the velocities to avoid particles dispersion and guaranteeing convergence of the optimisation process. The second component $\phi_1(k)\left[q_i(k) - d_i(k)\right]$ realizes the cognitive aspect. This component represents the particle distance from its best position found earlier. It is related to the natural inclination of the individuals (particles) to the environments where they had the best experiences (the best value of the fitness function). The third component $\phi_2(k)\left[\hat{q}_i(k) - d_i(k)\right]$ represents the particle distance from the position of the swarm leader. It refers to the natural inclination of the individuals to follow the other which achieved a success.

The flowchart of the particle swarm optimiser is presented in Fig. 11. At the beginning of the algorithm the particle swarm of assumed size is created randomly. Starting positions and velocities of the particles are created randomly. The objective function values are evaluated for each particle. In the next step the best positions of the particles are updated and the swarm leader is chosen. Then the particles velocities are modified by means of the Equation (1) and particles positions are modified according to the Equation (2). The process is iteratively repeated until the stop condition is fulfilled. The stop condition is typically expressed as the maximum number of iterations.

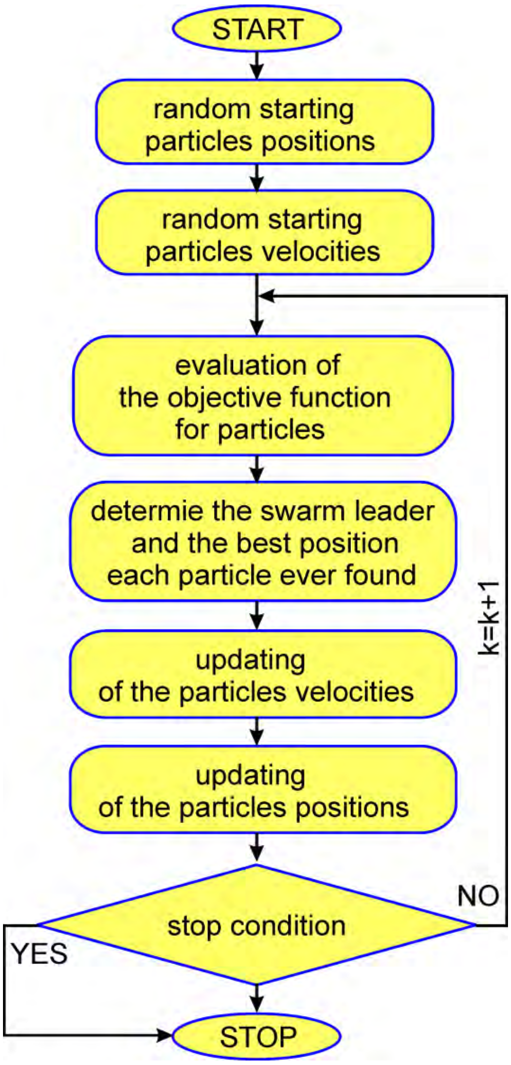

Figure 11: Particle swarm optimiser – block diagram.

The general effect is that each particle oscillates in the search space between its previous best position (position with the best fitness function value) and the best position of its best neighbour (relatively swarm leader), hopefully finding new best positions (solutions) on its trajectory, what in whole swarm sense leads to the optimal solution.

3 SOFT COMPUTING IN OPTIMIZATION OF DYNAMICALLY LOADED STRUCTURES

3.1 Evolutionary generalized optimization of structures modeled by the FEM

Consider a structure which, at the beginning of an evolutionary process, occupies a domain $\Omega_0\left(in\ E^3\right)$, bounded by a boundary Γ_0. The domain Ω_0 is filled by a elastic homogeneous and isotropic material of a Young's modulus E$_0$ and a Poisson ratio ν. The 3-D structures are considered in the framework of the linear theory of elasticity. During the evolutionary process the domain Ω_t, its boundary Γ_t and the field of Young's modulus $E\left(x,y,z\right)=E_t,\left(x,y,z\right)\in\Omega_t$ can change for each generation t (for t=0, E$_0$=const). The evolutionary process proceeds in an environment in which the structure fitness is describing by maximization of the objective functions:

a) maximization of the first eigenfrequency

$$\max(\omega_1) \tag{3}$$

with a constraint imposed on the volume of the structure

$$\begin{aligned} &V \equiv |\Omega| \\ &V \le V^{\max} \end{aligned} \tag{4}$$

b) maximization of the difference between first, second and third eigenfrequency

$$\max\left[(\omega_2-\omega_1)+(\omega_3-\omega_2)\right] \tag{5}$$

with a constraint imposed on the volume of the structure (4)

c) maximization of the difference between first, second, third eigenfrequency and forced vibration frequency ω_{forced}

$$\max\left[\left|\omega_1-\omega_{forced}\right|+\left|\omega_2-\omega_{forced}\right|+\left|\omega_3-\omega_{forced}\right|\right] \tag{6}$$

with a constraint imposed on the volume of the structure (4).

The distribution of Young's modulus $E(x,y,z)$, $(x,y,z)\in\Omega_t$ in the structure is described by a hyper surface $W(x,y,z), (x,y,z)\in H^3$. The hyper surface $W(x,y,z)$ is stretched under $H^3 \subset E^3$ and the domain Ω_t is included in H^3, i.e. $\left(\Omega_t \subseteq H^3\right)$.

The shape of the hyper surface $W(x,y,z)$ is controlled by genes d_j, j=1,2,…,N, which create a chromosome

$$ch=\left\langle d_1,d_2,...,d_j,...,d_N\right\rangle \tag{7}$$

Gene values are described by the function $W(x,y,z)$ in interpolation nodes (control points) $(x,y,z)_j$, i.e. $d_j=W\left[(x,y,z)_j\right]$, j=1,2,…,N.

The following constraints are imposed on genes

$$d_j^{\min} \le d_j \le d_j^{\max} \tag{8}$$

where $d_j^{\min}$ - the minimum value of the gene and $d_j^{\max}$ - the maximum value of the gene.

The assignation of Young's moduli to each finite element $\Omega_e, e=1,2,...,R$ is performed by the mapping:

$$E_e=W\left[(x,y,z)_e\right], (x,y,z)_e\in\Omega_e, e=1,2,...,R \tag{9}$$

It means that each finite element can have different material.

When the value of Young's modulus for the e-th finite element is included in the interval $0 \le E_e < E_{\min}$, the finite element is eliminated and the void is created, the interval $E_{\min} \le E_e < E_{\max}$, the finite element remains having the value of the Young's modulus from this material. As a result, shape, topology and material properties of the structure are changing simultaneously and this procedure is called *evolutionary generalized optimization*.

Example 1 – maximization of the first eigenfrequency of a 3D bracket

A structure like a 3D bracket (Fig. 12a) is optimized. The criterion of optimization is the maximization of the first eigenfrequency. The best solution obtained after 88 generations is presented in Fig. 12b. The Table 1 contains input data.

Minimal Young's module	Maximal volume
$0.4 \times 2*10^5$ MPa	4000 mm^3
Numbers of chromosomes	
100	

Table 1: Input data.

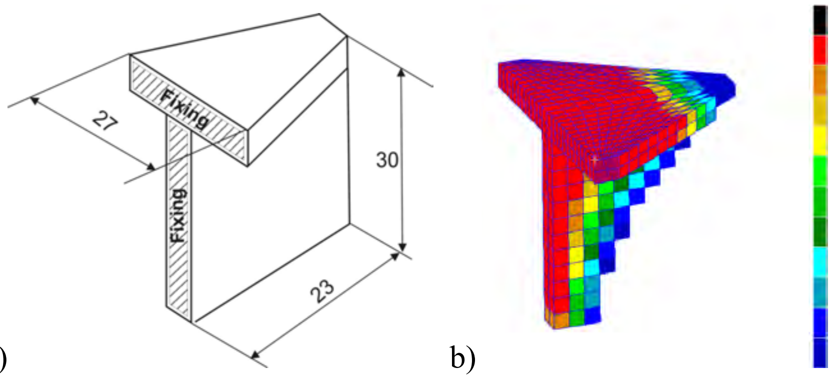

a) b)

Figure 12: A 3-D bracket: a) geometrical dimensions b) distribution of Young's moduli

Example 2 – maximization of the difference between first, second and third eigenfrequency of a rectangular prism

A 3D structure in the form of a rectangular prism (Fig. 13a) is optimized. The criterion of optimization is the maximization of the difference between first, second and third eigenfrequencies. The best solution in the form of a distribution of Young's moduli obtained after 169 generations is performed in Fig. 13b. Input data are included in Table 2.

Minimal Young's module	Maximal volume
$0.4 \times 2*10^5$ MPa	4.8e4 mm^3
Numbers of chromosomes	Dimensions of cubicoid
100	200 x 80 x 12 mm

Table 2: Input data.

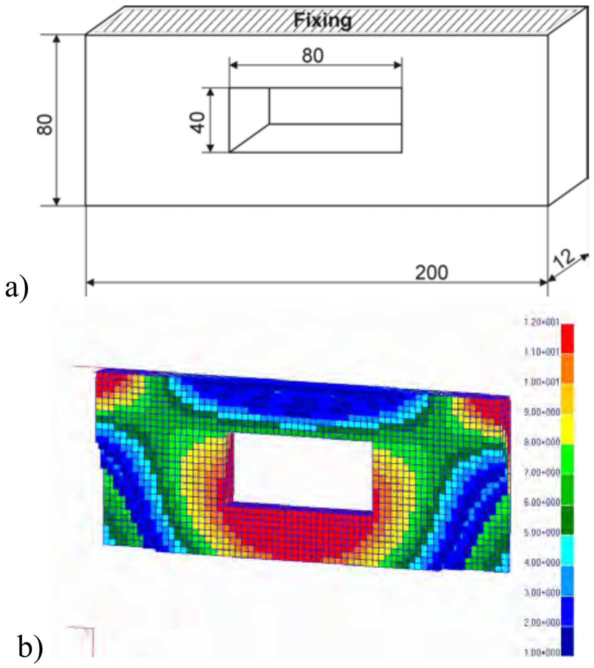

Figure 13: A rectangular prism: a) dimensions, b) distribution of Young’s moduli.

Example 3 - maximization of the difference between first, second and third eigenfrequency and forced vibration frequency of a rectangular prism

The last example concerns optimization of a 3D structure from the previous example (Fig. 13a). The criterion of optimization is the maximization of the difference between first, second third eigenfrequencies and forced vibration frequency. The best solution is obtained after 134 generations is presented in Fig. 14. Input data are included in Table 3.

Minimal Young’s module	Maximal volume
0.4 x 2∗10^5 MPa	80000 mm^3
Numbers of chromosomes	Dimensions of cubicoid
100	200 x 80 x 12 mm

Table 3. Input data

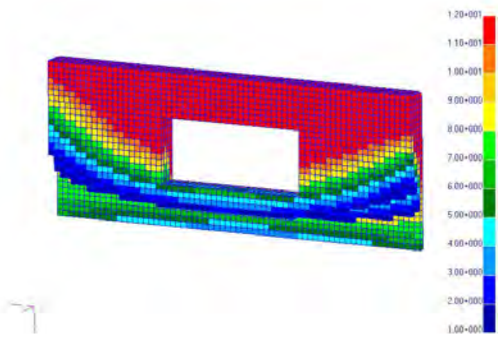

Figure 14: Distribution of Young’s moduli for a rectangular prism obtained for the resonance criterion.

3.2 Bio-inspired optimization of structures modeled by the coupled BEM/FEM

A two-dimensional, homogenous, isotropic and linear elastic deformable body with boundary Γ_1 and occupying domain Ω_1, is considered. The body is modeled as a plate in plane stress or strain and it is reinforced by the stiffener occupying domain Ω_2. The body is supported (displacements $u(x,\tau)$ are known at a part of the outer boundary) and subjected to dynamic tractions $t(x,\tau)$ (where τ is time), applied at the outer boundary, as shown in Fig.15.

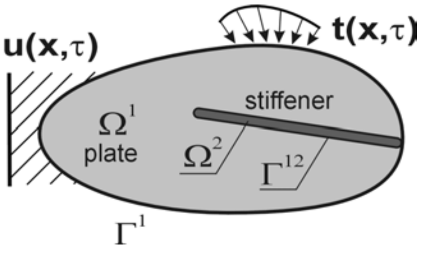

Figure 15: Reinforced plate subjected to dynamic loads.

The plate is modeled by the boundary element method (BEM) [6] and the stiffener by the finite element method (FEM) using beam finite elements, attached along the Γ_{12} boundary (the interface). A perfect bonding between the plate and the stiffener is assumed. The whole structure is analyzed by the coupled BEM/FEM and the subregion method [8]. The method allows modeling of bodies with many plate subdomains and stiffeners of different properties. The numerical equations, which are written for each plate and beam subdomain separately, are coupled using displacement compatibility conditions and traction equilibrium conditions at all nodes along the common boundaries.

A set of algebraic equations for the plate in Fig.15 has the following form:

$$\begin{bmatrix} \boldsymbol{M}^1 & \boldsymbol{M}^{12} \end{bmatrix} \begin{Bmatrix} \ddot{\boldsymbol{u}}^1 \\ \ddot{\boldsymbol{u}}^{12} \end{Bmatrix} + \begin{bmatrix} \boldsymbol{H}^1 & \boldsymbol{H}^{12} \end{bmatrix} \begin{Bmatrix} \boldsymbol{u}^1 \\ \boldsymbol{u}^{12} \end{Bmatrix} = \begin{bmatrix} \boldsymbol{G}^1 & \boldsymbol{G}^{12} \end{bmatrix} \begin{Bmatrix} \boldsymbol{t}^1 \\ \boldsymbol{t}^{12} \end{Bmatrix} \tag{10}$$

where: $\mathbf{M}$ is the mass matrix, $\mathbf{H}$ and $\mathbf{G}$ are the BEM coefficient matrices, $\mathbf{u}$ and $\ddot{\mathbf{u}}$ are displacement and acceleration vectors, respectively, $\mathbf{t}$ is a vector of tractions applied at the outer boundary or the interface. The superscripts denote the matrices, which correspond to the outer boundary or the interface.

The equation of motion for the stiffener in Fig.15 in a matrix form is:

$$\boldsymbol{M}^{21}\, \ddot{\boldsymbol{u}}^{21} + \boldsymbol{K}^{21}\, \boldsymbol{u}^{21} = \boldsymbol{T}^{21}\, \boldsymbol{t}^{21} \tag{11}$$

where: $\mathbf{K}$ is the FEM stiffness matrix, $\mathbf{T}$ is the matrix, which expresses the relationship between the FE nodal forces and the BE tractions. The latter matrix allows treatment the finite element region as an equivalent boundary element region.

If the structure is subjected to time dependent boundary conditions, the dynamic interaction forces between the plate and the stiffener act along the interface. These tractions are treated as body forces distributed along the attachment line and they are unknowns of the problem. The displacement compatibility conditions and the traction equilibrium conditions at the nodes along the interface are:

$$\boldsymbol{u}^{12} = \boldsymbol{u}^{21} \quad ; \quad \boldsymbol{t}^{12} = -\boldsymbol{t}^{21} \tag{12}$$

If the above conditions are taken into account in equations for the plate (10) and stiffener (11), the following system of equations for the whole structure is obtained:

$$\begin{bmatrix} \boldsymbol{M}^1 & \boldsymbol{M}^{12} \\ 0 & \boldsymbol{M}^{21} \end{bmatrix} \begin{Bmatrix} \ddot{\boldsymbol{u}}^1 \\ \ddot{\boldsymbol{u}}^{12} \end{Bmatrix} + \begin{bmatrix} \boldsymbol{H}^1 & \boldsymbol{H}^{12} & \boldsymbol{-G}^{12} \\ 0 & \boldsymbol{K}^{21} & \boldsymbol{T}^{21} \end{bmatrix} \begin{Bmatrix} \boldsymbol{u}^1 \\ \boldsymbol{u}^{12} \\ \boldsymbol{t}^{12} \end{Bmatrix} = \boldsymbol{G}^1 \boldsymbol{t}^1 \qquad 13)$$

The unknowns are displacements and tractions on the external boundary and at the interface in each time step.

Example 4 – Reinforced rectangular plate

Optimization of a reinforced rectangular plate (Fig.16) is performed by means of AIS, PSO and EA. The plate is dynamically loaded and it is reinforced by the frame-like structure composed of straight beams. The plate and the stiffeners are modeled by the boundary elements and frame finite elements, respectively. Different kinds of load and support are considered. The structure before optimization (the reference plate) is shown in Fig. 16.

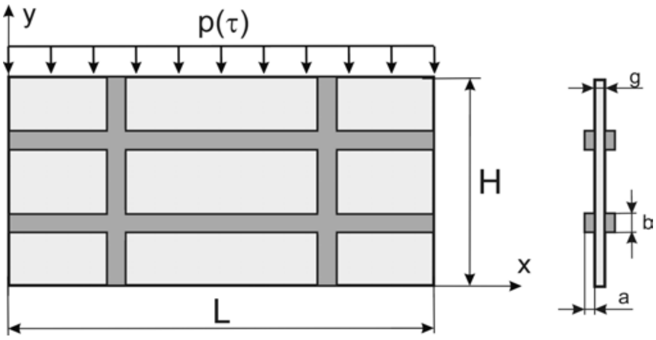

Figure 16: Reinforced rectangular plate.

The length and the height of the plate is L=10 cm and H=5 cm, respectively. The thickness of the plate is g=0.25 cm, the dimensions of beams cross-section are 2a=0.5 cm and b=0.5 cm.

The material of the plate and frame is aluminum and the mechanical properties are: modulus of elasticity E=70 GPa, Poisson's ratio ν=0.34 and density ρ=2700 kg/m^3. The material is homogeneous, isotropic and linear elastic and the plane stress is assumed.

The uniformly distributed load is applied at the upper edge of the plate. Two kinds of time dependent loads are considered (see Fig.17): a) the sinusoidal load $p(\tau)=p_o\sin(2\pi\tau/T)$ with the period of time T=20π μs, and b) the Heaviside load $p(\tau)=p_oH(\tau)$. The value of the load in both cases is p_o=10 MPa. The time of analysis is 600 μs and the time step Δt=2 μs.

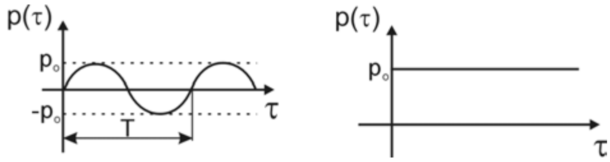

Figure 17: Dynamic loadings: a) sinusoidal, b) Heaviside.

Three different supports are considered (see Fig.18):

a) support A – the plate is fixed on the left and right edge,
b) support B – the plate is supported at two segments, each of 0.5 cm long,
c) support C – the plate is fixed at the bottom edge.

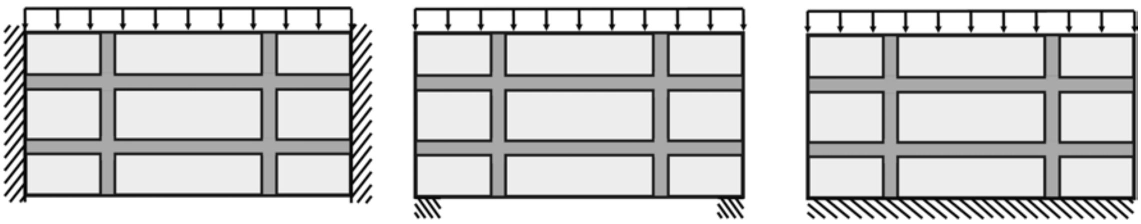

Figure 18: Types of supports: a) support A, b) support B, c) support C.

The optimal positions of stiffeners are searched in order to maximize stiffness of the plate. The maximal dynamic vertical displacement on the loaded edge is minimized. Because of symmetry of the structure and boundary conditions, only a half of the structure is considered. The number of design variables defining the position of the frame is 4: X1, X2, Y1 and Y2 (see Fig.19). The longer beams are parallel to the x axis. The end points of beams can move along the edges of the plate within the constraints, as shown in Fig.19. The constraints on design variables are imposed: X1 and X2 variables are within the range from 0.5 to 4.75 cm, Y1 from 0.5 to 2.25 cm and Y2 from 2.75 to 4.5 cm. The parameters of AIS are: the number of memory cells and the clones is 6, the crowding factor and the Gaussian mutation is 0.5. The parameters of EA are: the number of chromosomes is 20, the probability of the Gaussian mutation is 0.5, the probability of a simple and arithmetic crossover is 0.05. The parameters of PSO are: numbers of particles is 20, inertia weight is 0.73 and two acceleration coefficients are 1.47.

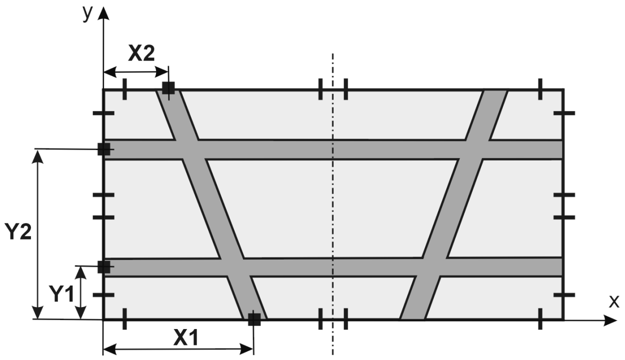

Figure 19: Design variables and constraints.

The total number of boundary and finite elements in the BEM/FEM analysis is 120 and 120, respectively (each horizontal and vertical beam is discretized into 40 and 20 finite elements, respectively). The number of boundary and finite elements during the optimization is constant.

The values of design variables obtained by AIS, PSO and EA for the plate subjected to the sinusoidal load, the Heaviside load and for three kinds of supports, are presented in Table 3. The results obtained by three different methods are almost the same. The values of J_o and J (where: J_o and J is the objective function for the reference and the optimal plate, respectively) and the reduction $R=(J_o-J)/J_o \cdot 100\%$, are also presented.

A significant reduction R, resulting in the improvement of dynamic response of the optimal plates in comparison with the initial designs, can be observed. The optimal structures for different kinds of supports and for the sinusoidal and the Heaviside loads are shown in Fig.20a and Fig.20b, respectively. It can be seen that in the present example most of constraints are active.

Load	Support	Design variables [cm]				J_o [10^{-4}cm]	J [10^{-4}cm]	R [%]
		X1	X2	Y1	Y2			
AIS, PSO and EA								
Sinusoidal	A	4.75	2.86	0.88	2.75	89	76	15
	B	4.75	1.81	0.57	2.75	92	73	21
	C	1.20	1.82	0.50	2.75	82	62	24
Heaviside	A	0.50	4.75	0.50	4.50	112	91	19
	B	4.75	1.41	0.50	4.50	211	149	29
	C	0.50	2.20	1.70	2.80	49	42	14

Table 4: Values of design variables, J and R.

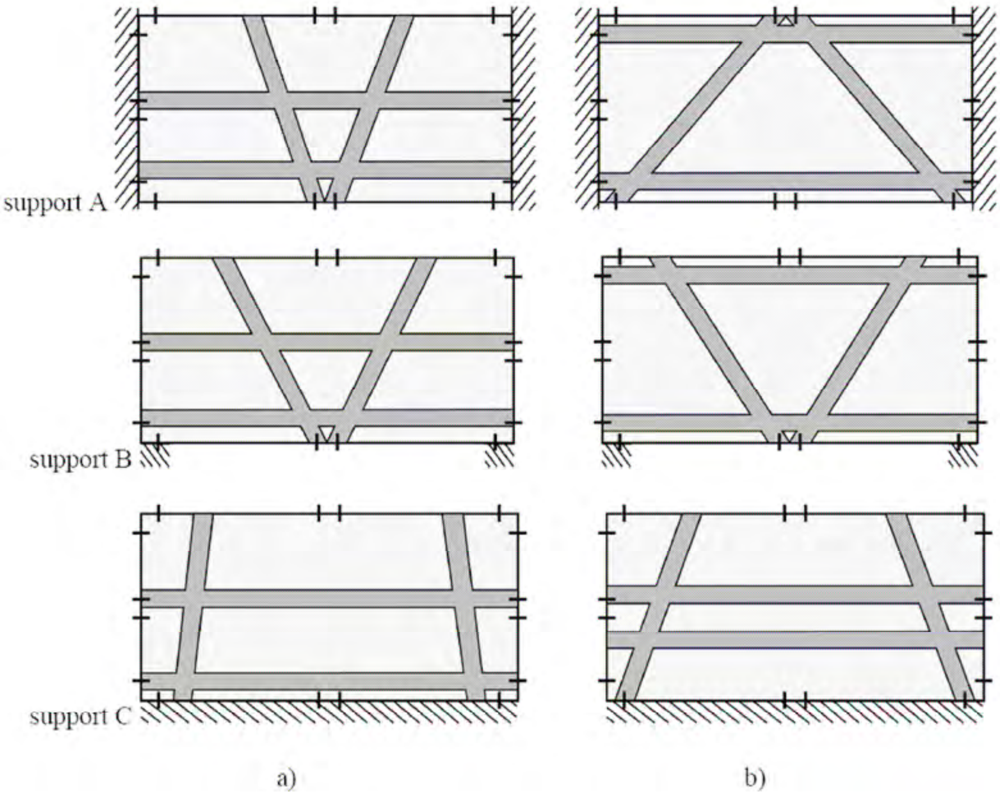

Figure 20: Optimal plates subjected to dynamic loads: a) sinusoidal, b) Heaviside.

The number of fitness function evaluations by three different bio-inspired algorithms used in this example is presented in Table 5. It can be observed that the number of fitness function evaluations for obtaining the final design variables and the corresponding fitness functions presented in Table 5 is different and depends on the applied load and support. Generally, the efficiency of the AIS and the PSO is similar and much better for this particular example, than the efficiency of the EA.

Load	Support	EA	AIS	PSO
		fitness function evaluations		
Sinusoidal	A	2515	336	360
	B	3705	408	440
	C	1952	432	520
Heaviside	A	303	276	60
	B	1526	252	120
	C	2797	528	580

Table 5: Efficiency of bio-inspired methods.

Example 5 – Reinforced plate with a hole

Optimization of a rectangular reinforced plate with a hole (Fig. 21) is performed by means of PSO with the same parameters like in the example 4. The plate is dynamically loaded and it is reinforced by 8 symmetrically distributed rods of circular cross-section. The plate and the reinforcing rods are modeled by the boundary elements and beam finite elements, respectively. The structure before optimization (the reference plate) is shown in Fig. 21.

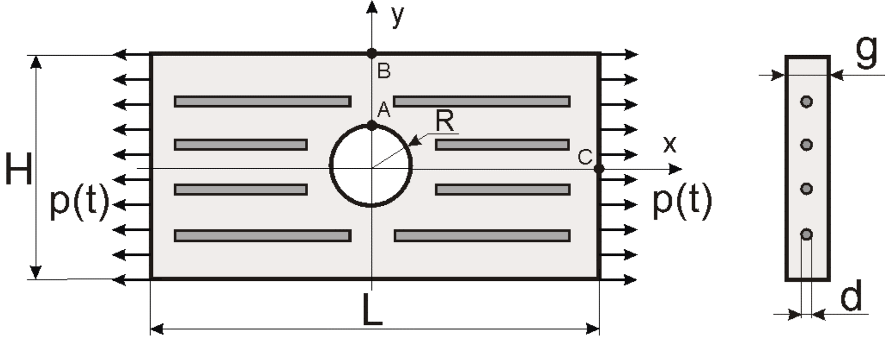

Figure 21. Reinforced plate with a hole.

The plate is stretched by a uniformly distributed load applied at its left and right edge. The dynamical load is defined by the Heaviside impulse $p(t)=p_oH(t)$, the value of the load is p_o=10 *MPa*. The time of analysis is T=300 μs and the time step Δt=3 μs.

The length and the height of the plate and the hole radius is L=10 *cm*, H=5 *cm* and R=1 *cm*, respectively. The thickness of the plate is g=1 *cm* and the diameter of each rod is d=0.3 *cm*. Distance between the rod axes for the reference plate is 1 *cm*, the length of the shorter and longer rods is 3 *cm* and 4 *cm*, respectively. Distance between the end points of the rods to the left or right edge of the plate is 0.5 *cm*.

The plane stress is assumed. The materials of the plate (p) and stiffeners (s) are epoxy and steel, respectively. They are homogeneous, isotropic and linear elastic. The values of mechanical properties are: modulus of elasticity E_p=4.5 *GPa* and E_s=210 *GPa*, Poisson's ratio ν_p=0.37 and ν_s=0.3, density ρ_p=1160 kg/m^3 and ρ_s=7860 kg/m^3.

The optimal location of reinforcement in the interior of the plate is searched and the following objective function J is minimized:

$$J = \int_0^T \frac{\left|\sigma_x^A(t)\right|^2}{\sigma_o} dt \tag{14}$$

where $\sigma_x^A(t)$ is the x-component of stress at the point A (see Fig. 21), σ_o is a nominal stress at the weakened cross-section, defined as the ratio of the applied load to the area of this cross-section, T is a time of analysis.

The objective function (14) is minimized with respect to design variables (*Xij*, *Yij*, *i,j*=1,2), defining the coordinates of the *j*-th end point of the *i*-th rod. It is assumed that during optimization the reinforcement is symmetrical with respect to two symmetry axes. Thus only a quarter of the plate with two rods is modeled (the appropriate boundary conditions at the symmetry axes are assumed) and the number of design variables is 8.

The constraints on design variables are imposed. The distance between the rods and the outer boundary (of the quarter of the plate) cannot be lower than 0.5 *cm*. The intersection of rods is not allowed.

The total number of boundary and finite elements in the BEM/FEM analysis is 92 and 64, respectively (each rod is discretized into 32 finite elements).

For this example five tests were performed and similar results were obtained. The values of design variables for the optimal solutions, rounded off to two decimal places, are: *X11*=0.97 *cm*, *Y11*=1.03 *cm*, *X12*=4.50 *cm*, *Y12*=1.50 *cm*, *X21*=1.57 *cm*, *Y21*=2.00 *cm*, *X22*=4.50 *cm* and *Y22*=2.00 *cm*. The optimal structure is shown in Fig. 22.

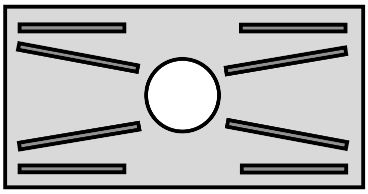

Figure 22. Optimal location of rods in the plate.

Example 6 – Reinforced cantilever plate

Optimization of a reinforced cantilever plate (Fig. 23) is performed by means of PSO with the same parameters like in the example 4. The dynamically loaded plate is reinforced at the whole non-fixed outer boundary and between two holes (at the interface between two BE regions). The reinforcement has rectangular cross-section. The plate and the reinforcement are modeled by the boundary elements and frame finite elements, respectively. The structure before optimization (the reference plate) is shown in Fig. 23.

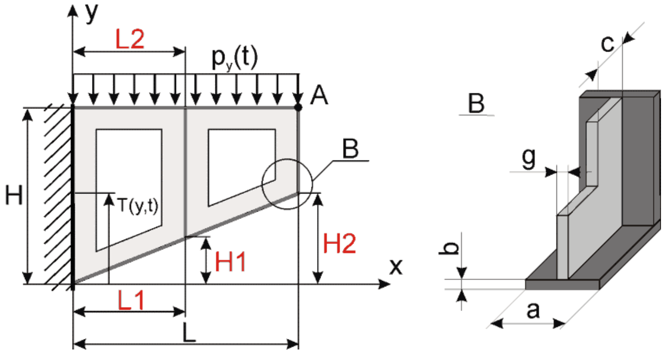

Figure 23. Reinforced cantilever plate.

The uniformly distributed load is applied at the upper edge. The plate is subjected to the sinusoidal load $p(t)=p_o\sin(2\pi t/T)$. The amplitude of the load is p_o=1 *MPa* and the period of time is T=5 *ms*. The time of analysis is 12 *ms* and the time step Δt=0.02 *ms*.

The length and the height of the plate is L=50 *cm* and H=40 *cm*, respectively. The other dimensions are: a=5 *cm*, b=1 *cm*, c=5 *cm* and g=1 *cm*. The *L1*, *L2* and *H1*, *H2* defining the shape of the cantilever, are design variables of the problem and they are within the range from 15 to 35 *cm* and 0 to 25 *cm*, respectively.

The plane stress is assumed. The cantilever is linear elastic, isotropic and homogeneous and its material is steel. The values of mechanical properties are: modulus of elasticity E=210 *GPa*, Poisson's ratio ν=0.3 and density ρ=7860 kg/m^3.

The optimal shape of the cantilever is searched and the following objective function J is minimized:

$$J=\int_0^T \frac{\left|u_y^A(t)\right|^2}{u_o}dt \tag{15}$$

where $u_y^A(t)$ is a vertical displacement at the point A (see Fig. 23), u_o is an admissible displacement, T is a time of analysis.

The objective function (15) is minimized with respect to design variables (*Li*, *Hj* *i,j*=1,2), defining dimensions of the structure.

The total number of boundary and finite elements in the BEM/FEM analysis is 84 and 72, respectively The quadratic elements (with 2 degrees of freedom per node) are employed for the BEM mesh. The frame elements (with 3 degrees of freedom per node) are used for the FEM mesh. During optimization the number of boundary and finite elements is constant.

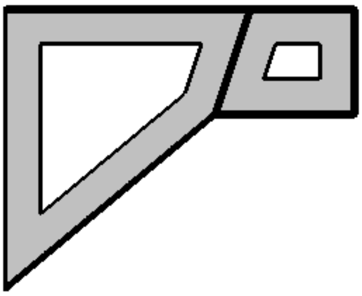

Figure 24. Optimal shape of the cantilever.

For this example five tests were performed and similar results were obtained. The values of design variables for the optimal solutions are (rounded off to two decimal places): *L1*=30.62 *cm*, *L2*=35.00 *cm*, *H1*=25.00 *cm* and *H2*=25.00 *cm*. The optimal structure is shown in Fig. 24.

4 CONCLUSIONS

In the paper, the formulation and application of the finite element method, the boundary element method and the bio-inspired methods to optimization of shape, topology and material properties of dynamically loaded structures for different criteria of optimization is presented. The bio-inspired methods can be simply implemented because they need only the values of objective functions. An important feature of these approaches is a strong probability of finding the global optimal solutions. The described approaches are free from limitations of classic gradient optimization methods.

In the presented approach, shape, topology and material optimization is performed simultaneously for 3D freely vibrating structures analyzed by the finite element method. The optimal location of reinforcement is searched in order to increase a stiffness or strength of dynamically loaded reinforced plates analyzed by the coupled boundary/finite element method. As a result of optimization, a significant improvement of dynamic response is obtained, in comparison with initial designs.

Coupling of finite or boundary element method and the bio-inspired algorithms give an effective and efficient alternative optimization tool, which enables solving a large class of the optimization problems of mechanical structures. Numerical examples confirm the efficiency of the proposed optimization method and demonstrate that the methods based on soft computing are effective techniques for solving computer aided optimal design problems. Generally, for the considered numerical examples, the efficiency of the artificial immune systems and the particle swarm optimizers is better than the evolutionary algorithms.

Acknowledgments

This work was supported by the Polish Ministry of Science and Higher Education under the research grant.

REFERENCES

[1] J. Arabas, *Lectures on evolutionary algorithms*, WNT, Warszawa, 2001 (in Polish).

[2] J. Balthrop, F. Esponda, S. Forrest, M. Glickman, Coverage and Generalization in an Artificial Immune System. In Proceedings of the *Genetic and Evolutionary Computation Conference GECCO 2002*, 3-10, Morgan Kaufmann, New York, 2002.

[3] L. N de Castro, J. Timmis, Artificial Immune Systems as a Novel Soft Computing Paradigm, *Soft Computing*, **7**, 8, 526-544, 2003.

[4] L. N. de Castro, F. J. Von Zuben, Immune and Neural Network Models: Theoretical and Empirical Comparisons, *International Journal of Computational Intelligence and Applications (IJCIA)*, **1**, 3, 239-257, 2001.

[5] L. N. de Castro, F. J. Von Zuben, Learning and Optimization Using the Clonal Selection Principle, *IEEE Transactions on Evolutionary Computation, Special Issue on Artificial Immune Systems*, **6**, 3, 239-251, 2002.

[6] J. Dominguez, *Boundary elements in dynamics*, Computational Mechanics Publications, Elsevier Applied Science, Southampton-Boston, London-New York, 1993.

[7] J. Kennedy, RC. Eberhart, Particle Swarm Optimisation. *Proceedings of IEEE Int. Conf. on Neural Networks*, Piscataway, NJ, 1942-1948, 1995.

[8] P. Fedelinski, R. Gorski, Analysis and optimization of dynamically loaded reinforced plates by the coupled boundary and finite element method, *Computer Modeling in Engineering & Sciences*, **15**, 1, 31-40, 2006.

[9] F. Heppner, U. Grenander, *A stochastic nonlinear model for coordinated bird flocks*. In: Krasner S, editor. The Ubiquity of Chaos. Washington, DC: AAAS Publications, 1990.

[10] Z. Michalewicz, *Genetic algorithms + data structures = evolutionary algorithms*, Springer-Verlag, Berlin, 1996.

[11] M. Ptak, W. Ptak, *Basics of Immunology*, Jagiellonian University Press, Cracow, 2000 (in Polish).

[12] C. W. Reynolds, Flocks, herds, and schools, A distributed behavioral model. *Computer Graphics*, **21**, 25–34, 1987.

[13] S. T. Wierzchoń, *Artificial Immune Systems, theory and applications*, EXIT, 2001.

COMPDYN 2011
3rd ECCOMAS Thematic Conference on
Computational Methods in Structural Dynamics and Earthquake Engineering
M. Papadrakakis, M. Fragiadakis, V. Plevris (eds.)
Corfu, Greece, 25–28 May 2011

OPTIMIZED SEISMIC RETROFIT OF STEEL-CONCRETE COMPOSITE FRAMES

Georgios Papavasileiou[1], Dimos C. Charmpis[1] and Nikos D. Lagaros[2]

[1] Department of Civil and Environmental Engineering, University of Cyprus
75 Kallipoleos Str., P.O. Box 20537, 1678 Nicosia, Cyprus
papavasileiou.georgios@ucy.ac.cy, charmpis@ucy.ac.cy

[2] Institute of Structural Analysis & Seismic Research, National Technical University of Athens
9 Iroon Polytechniou Str., Zografou Campus, 15780 Athens, Greece
nlagaros@central.ntua.gr

Keywords: Composite, steel, concrete, retrofit, seismic, optimization.

Abstract. *The present paper investigates the optimum way of reinforcing existing composite steel-concrete structures that violate the criteria suggested in Eurocode 4. The motivation to conduct the specific research is the need for existing structures to conform to new regulations without extensive operations.*

Composite steel-concrete systems are an attractive construction method, since they have been found to be cost-effective, especially for multi-storey buildings, and also successfully take advantage of the high stiffness of steel without its vulnerability to fire. These structural systems are not new and have been used since the beginning of the 20th century, so there is a number of existing structures which have been designed with previous versions of structural codes and have to conform to the modern regulations. It is obvious that each new set of design codes takes into account new dangers that might occur and updates the design methods already used. On the other hand, the economic considerations which have to be taken into account and the high market competition force the engineers to seek solutions that are at the same time easily and rapidly constructed, but also yield the required performance with the minimum cost.

The present work presents two retrofit methods for composite steel-concrete frames, which are evaluated in the context of structural optimization. The frames considered fail to satisfy the provisions of Eurocode 4 and are therefore retrofitted with the two aforementioned methods in a way minimizing the total cost of steel and concrete required for the retrofit. This way, the frames are upgraded with minimal cost.

1 INTRODUCTION

The present paper investigates the optimum way of reinforcing existing composite steel-concrete structures that violate the criteria suggested in Eurocode 4. The motivation to conduct the specific research is the need for existing structures to conform to new regulations without extensive operations.

Composite steel-concrete systems are an attractive construction method, since they have been found to be cost-effective, especially for multi-storey buildings, and also successfully take advantage of the high stiffness of steel without its vulnerability to fire. These structural systems are not new and have been used since the beginning of the 20th century, so there is a number of existing structures which have been designed with previous versions of structural codes and have to conform to the modern regulations. It is obvious that each new set of design codes takes into account new dangers that might occur and updates the design methods already used. On the other hand, the economic considerations which have to be taken into account and the high market competition force the engineers to seek solutions that are at the same time easily and rapidly constructed, but also yield the required performance with the minimum cost.

The present work presents two retrofit methods for composite steel-concrete frames, which are evaluated in the context of structural optimization. The frames considered fail to satisfy the provisions of Eurocode 4 and are therefore retrofitted with the two aforementioned methods in a way minimizing the total cost of steel and concrete required for the retrofit. This way, the frames are upgraded with minimal cost. Both retrofit methods presented were selected so that they can be easily designed by the engineer and their application does not require too specialized knowledge.

2 RETROFIT METHODS

The retrofit philosophy used is the same for both methods presented in this work: the creation of an external layer of concrete with a metal cage that enhances the initial section's capacity and also confines the additional concrete. The difference between the two methods is in the type of reinforcement used. In the first method emphasis is given to steel, while the second method focuses on the use of concrete.

2.1 Method 1: Plates Method

This retrofit consists vertically of three plates per side; one rectangular and two of Γ-shape and horizontally of a number of rectangular plates that can be determined by the shear resistance criterion. The horizontal plates can be welded on the vertical ones or be added externally. The second option might seem easier to construct, but results in thicker concrete cover. Obviously, since there are only the cover concrete layer and a few patches between the plates, the concrete's contribution to the section's capacity might be ignored. However, in the present research, it has been taken into account.

The installation procedure is quite simple. The external smear is removed and steel plates are placed in touch with the existing concrete, as shown in Fig. 1. Depending on the construction method used, the whole cage might be in two parts, which are welded together on site, or independent horizontal and vertical plates that are welded one by one, as mentioned before (the horizontal ones at the outer side). Thus, a steel cage of the form shown in Fig. 2 is constructed. Then, the gaps between the plates and the desired concrete cover are filled with concrete.

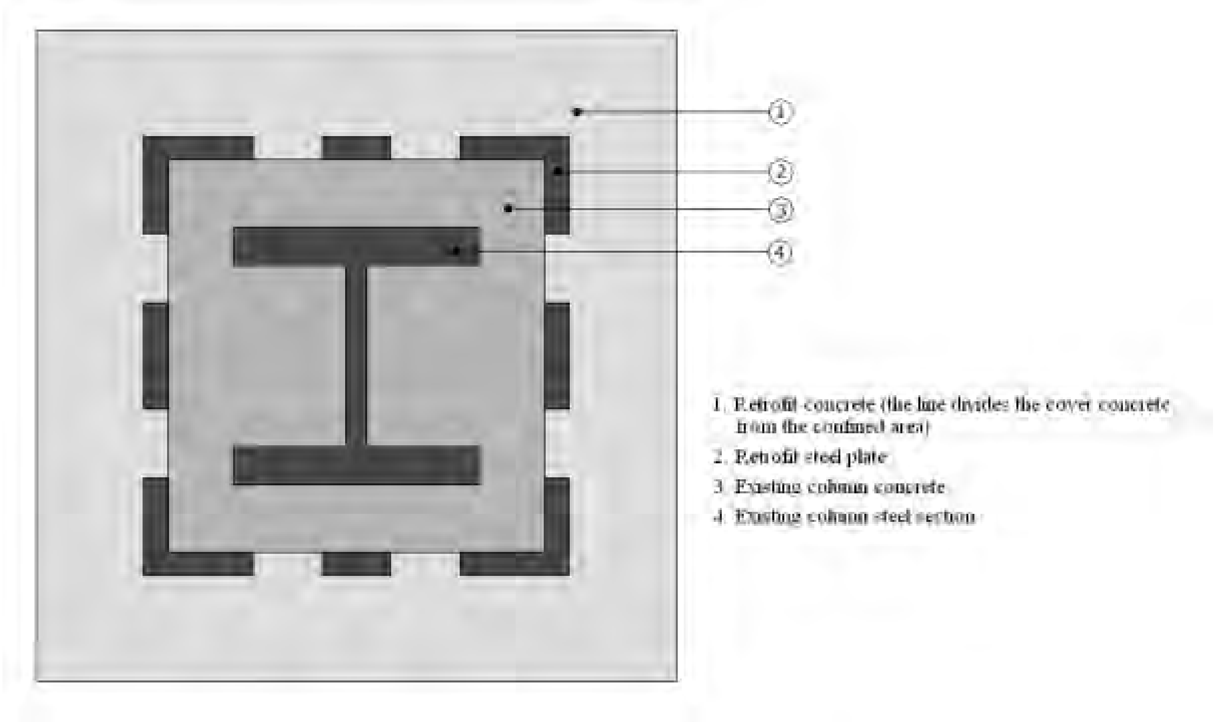

Figure 1: Cross-section of the retrofitted column (plates method).

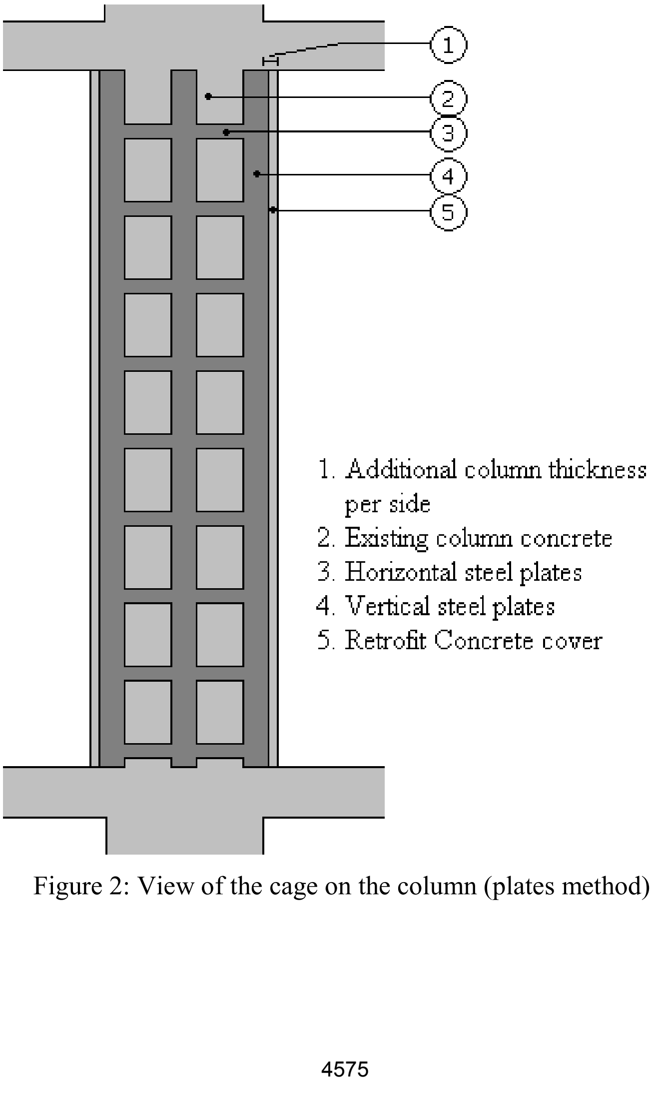

Figure 2: View of the cage on the column (plates method).

2.2 Method 2: Bars Method

In this method, the concrete is not only on the cover of the retrofit, but also in its core. The design of the new section is done with the typical philosophy of retrofitting a reinforced concrete column; there is longitudinal and transverse reinforcement surrounding the concrete, which contribute to the section's bending moment and shear capacity. The longitudinal reinforcement consists of 3 to 5 bars per side, depending on the dimensions of the existing column. The transverse reinforcement consists of rectangular stirrups that travel around the column. The location of the longitudinal bars is shown in Fig. 3, while the cage formed is illustrated in Fig. 4. The external smear has to be removed here too, in order to install the retrofit set-up. Contrary to the plates method, a rough surface of the existing concrete would increase the adhesion of it with the new concrete.

3 THE OPTIMIZATION PROBLEM

The objective function that has to be minimized is the total cost of retrofit that is calculated as:

$$P_{ref} = P_C \cdot V_C + P_S \cdot V_S \tag{1}$$

where P_{ref}: the total retrofit cost calculated in local currency
P_C: the total cost for the concrete in local currency per m^3
P_S: the total cost for the steel in local currency per m^3
V_C: the total volume of concrete (m^3)
V_S: the total volume of steel (m^3)

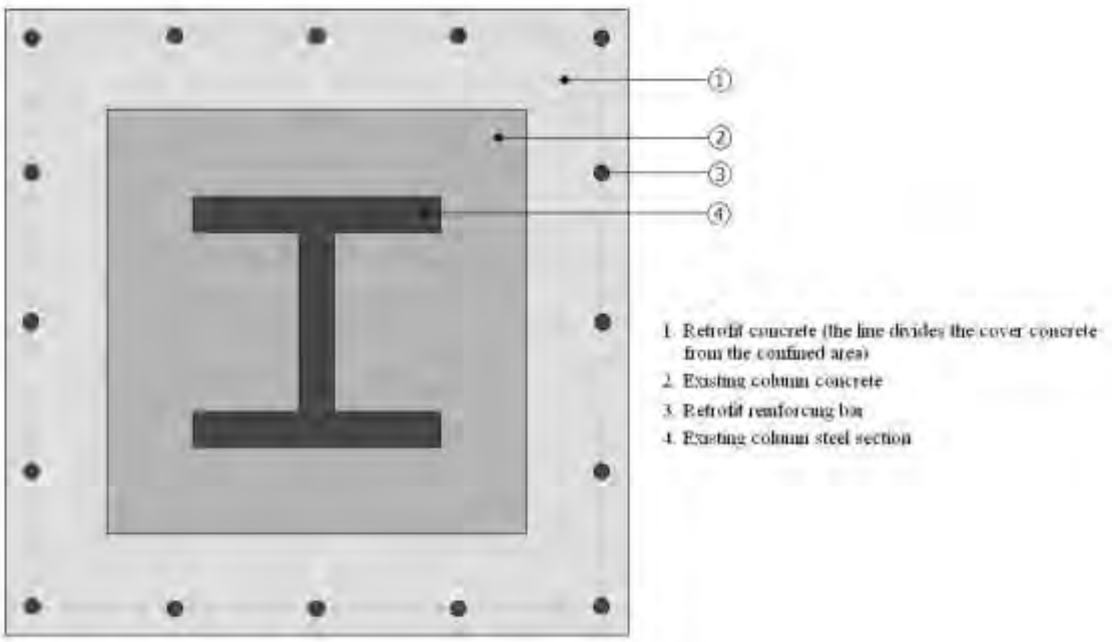

Figure 3: Cross-section of the retrofitted column (bars method).

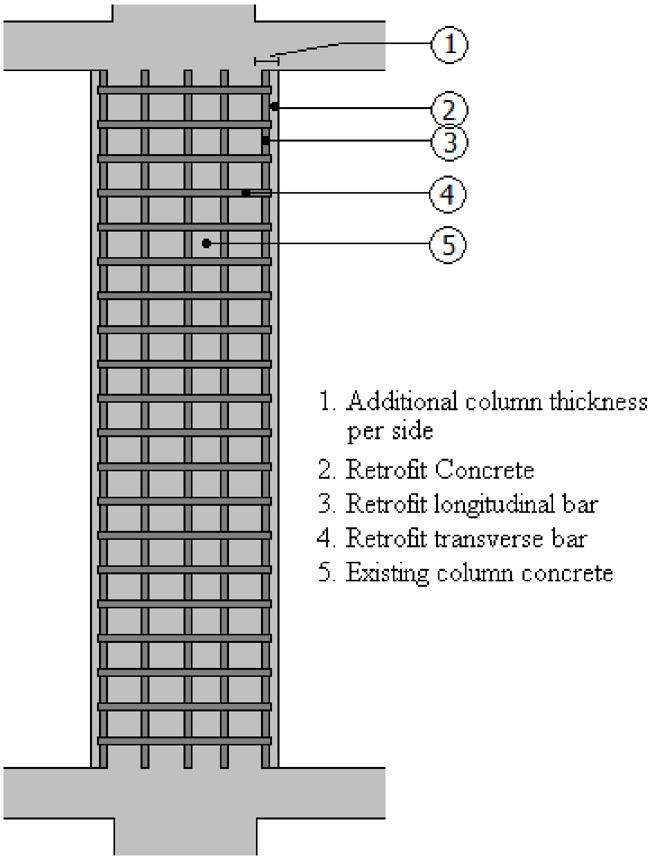

Figure 4: View of the cage on the column (bars method).

It is obvious that since the total volume of each material is its total area on the floor plan multiplied by the total height of the column (ground to top), it can be appropriately replaced in the abovementioned function. Also, the data used provide the retrofit cost in units of currency, so each time the price changes the whole problem would have to change. Therefore, the price ratio of concrete cost to steel cost was used instead. Applying these changes, the retrofit cost is finally calculated as:

$$P_{ref} = CR \cdot A_C + A_S \tag{2}$$

where P_{ref}: the total retrofit cost calculated in equal steel area (m^2)
CR: the cost ratio of the concrete cost to the steel cost ($CR = P_C/P_S$)
A_C: the total area of concrete on the storey (m^2)
A_S: the total area of steel on the storey (m^2)

The buildings' dimensions and the mechanical properties of the materials both on the existing section and the retrofit are not altered during the optimization procedure. All section dimensions including the beams, the columns and the retrofit are subject to change, depending on the problem solved (see next section). The data from which the optimizer chooses design variable values are provided in Table 1. The proportion dimension of each plate's height and breadth to the existing section's respective values is symbolized as β. Since there are three plates per side, the value of β cannot exceed the limit of $33{,}3\% \cdot \left(h + 2 \cdot t_{cg}\right)/h \cong 33{,}3\%$.

No.	**HEB Section**				**IPE Section**				**Plates method**		**Bars Method**	
	height	**breadth**	**flange thickness**	**web thickness**	**height**	**breadth**	**flange thickness**	**web thickness**	**plate thickness**	**dimension proportion**	**total concrete thickness**	**bar diameter**
	h (m)	**b (m)**	**t_f (m)**	**t_w (m)**	**h (m)**	**b (m)**	**t_f (m)**	**t_w (m)**	**t_{cg} (m)**	**β**	**t_{ref} (m)**	**φ (m)**
1	0.100	0.100	0.010	0.006	0.080	0.046	0.005	0.004	0.000	0%	0.000	0.000
2	0.120	0.120	0.011	0.007	0.100	0.055	0.006	0.004	0.005	5%	0.075	0.050
3	0.140	0.140	0.012	0.007	0.120	0.064	0.006	0.004	0.010	10%	0.100	0.012
4	0.160	0.160	0.013	0.008	0.140	0.073	0.007	0.005	0.010	20%	0.100	0.020
5	0.180	0.180	0.014	0.009	0.160	0.082	0.007	0.005	0.010	30%	0.100	0.025
6	0.200	0.200	0.015	0.009	0.180	0.091	0.008	0.005	0.015	10%	0.100	0.032
7	0.220	0.220	0.016	0.010	0.200	0.100	0.009	0.006	0.015	20%	0.150	0.012
8	0.240	0.240	0.017	0.010	0.220	0.110	0.009	0.006	0.015	30%	0.150	0.020
9	0.260	0.260	0.018	0.010	0.240	0.120	0.010	0.006	0.020	10%	0.150	0.025
10	0.280	0.280	0.018	0.011	0.270	0.135	0.010	0.007	0.020	20%	0.150	0.032
11	0.300	0.300	0.019	0.011	0.300	0.150	0.011	0.007	0.020	30%	0.200	0.012
12	0.320	0.300	0.021	0.012	0.330	0.160	0.012	0.008	0.025	10%	0.200	0.020
13	0.340	0.300	0.022	0.012	0.360	0.170	0.013	0.008	0.025	20%	0.200	0.025
14	0.360	0.300	0.023	0.013	0.400	0.180	0.014	0.009	0.025	30%	0.200	0.032
15	0.400	0.300	0.024	0.014	0.450	0.190	0.015	0.009	0.030	10%	0.250	0.012
16	0.450	0.300	0.026	0.014	0.500	0.200	0.016	0.010	0.030	20%	0.250	0.020
17	0.500	0.300	0.028	0.015	0.550	0.210	0.017	0.011	0.030	30%	0.250	0.025
18	0.550	0.300	0.029	0.015	0.600	0.220	0.019	0.012	0.040	30%	0.250	0.032
19	0.600	0.300	0.030	0.016	-	-	-	-	-	-	-	-
20	0.650	0.300	0.031	0.016	-	-	-	-	-	-	-	-
21	0.700	0.300	0.032	0.017	-	-	-	-	-	-	-	-
22	0.800	0.300	0.033	0.018	-	-	-	-	-	-	-	-
23	0.900	0.300	0.035	0.019	-	-	-	-	-	-	-	-
24	1.000	0.300	0.036	0.019	-	-	-	-	-	-	-	-

Table 1: Database used to define the section dimensions.

The constraints of the optimization problem include the member checks defined in Eurocode 4, which are evaluated with the help of linear analyses for each candidate optimum retrofit design. Additionally, performance constraints are imposed, which are evaluated using pushover analysis results.

The discrete optimization algorithm implemented is based on the evolution strategies method. The analysis platform employed for linear and pushover analyses is the software system Opensees.

4 NUMERICAL RESULTS

In order to determine the effect of the building's height to the optimum retrofit design, two buildings were simulated; a two-storey and a four-storey, which have the same floor plan (Figs. 5-6). The beams' span is 5.50m in both directions and the columns' height is 3.50m.

Because of the problem's complexity and the significant demand for computational effort, translated into several computer hours for each optimization, four sets of runs were conducted, where the succeeding one would benefit from the results of the previous one and also conclusions would be extracted at each stage. It is noticeable that each step requires much more analyses than the previous one.

Four groups od design variables are defined for both buildings. Group 1 includes all design variables associated with corner columns. Groups 2 and 3 refer to all side columns in *x*-direction and *y*-direction, respectively. Finally, Group 4 involves all internal columns of the 3D frame.

The aim of the first set was to determine the optimum design for both buildings, in order not to require retrofit (Eurocode 4 provisions satisfied). So, during this set, the retrofit parameters were set to zero and the initial sections of the columns and beams were chosen from databases of standard I-sections: HEB sections were used for the columns and IPE sections for the beams. The algorithm was allowed to choose the steel section for the columns, but the concrete cover layer was the same for all columns (5cm per side). Previous tests had shown that the contribution of the cover concrete is minimal, so this parameter could be ignored for the purposes of this research. The optimum design obtained for the two-storey building was HE400B for all column sections and IPE450 for the beams (Table 2). The respective results for the four-storey building are given in Table 3.

The second set of tests was similar to the first one. Its purpose was to examine whether the Eurocode 4 criteria were those that determined the optimum design or it is also influenced by the building's performance constraints. So, in this scenario, the Eurocode 4 criteria were deactivated and the algorithm was allowed to determine the optimum design choosing from a variety of initial sections including the combinations that had been rejected in the previous set, because the Eurocode 4 criteria were not fulfilled. According to the results of these runs, even smaller sections seem to be adequate for the beams, some of which would not even be able to bear the dead loads of the slabs. On the other hand, the selection of column sections was mostly determined by the structure's performance, especially for the four-storey building. The designs provided by the algorithm are presented in Table 4.

One can see in Table 4 that the use of a large section in one group and small sections for the other three seems to be much more efficient than the use of the same section in all four groups of columns. It is probably because such a selection increases the total stiffness without respective increase of the cost. However, this is only a mathematical optimum, since in both buildings the three out of four sections do not pass the Eurocode 4 criteria when tested independently.

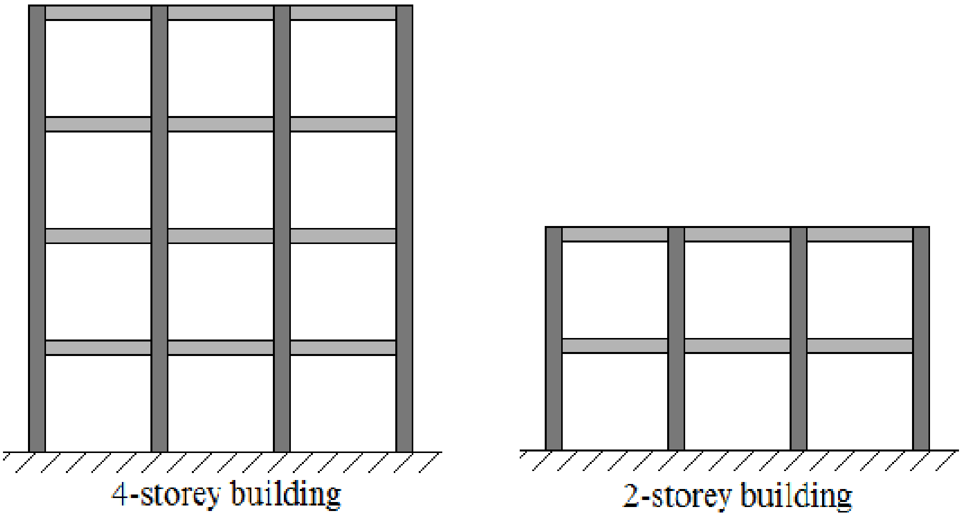

Figure 5: View of the two buildings.

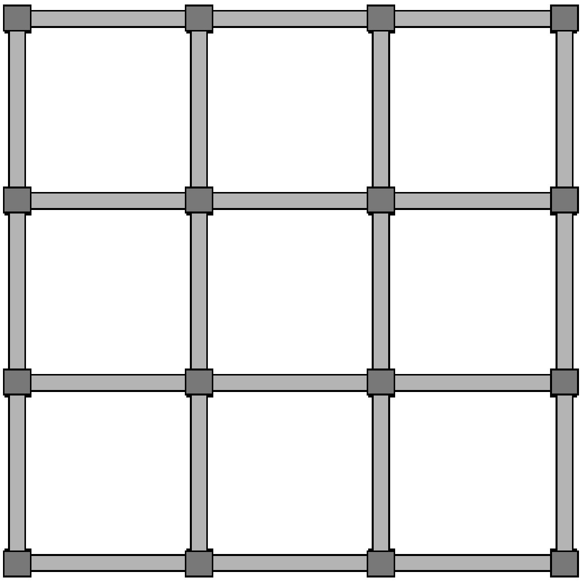

Figure 6: Floor plan for both buildings.

Section Group	Group 1	Group 2	Group 3	Group 4	Beams
Steel Section Type	HE400B	HE400B	HE400B	HE400B	IPE450

Table 2: Characteristics of the optimum design for the two-storey building.

Section Group	Group 1	Group 2	Group 3	Group 4	Beams
Steel Section Type	HE600B	HE400B	HE450B	HE800B	IPE450

Table 3: Characteristics of the optimum design for the four-storey building.

Section Group	Group 1	Group 2	Group 3	Group 4	Beams
Steel Section Type	HE700B	HE180B	HE180B	HE180B	IPE200

Table 4: Optimum design for the two-storey building without Eurocode 4 constraints.

Section Group	Group 1	Group 2	Group 3	Group 4	Beams
Steel Section Type	HE180B	HE200B	HE240B	HE1000B	IPE200

Table 5: Optimum design for the four-storey building without Eurocode 4 constraints.

Comparison of the storeys' stiffness shows that they are of similar philosophy with the ones provided for the two-storey building, so one could conclude that the Eurocode 4 criteria do not determine the optimum design, but lead the algorithm to a more appropriate result.

The third set of tests aimed to determine the effect of the cost ratio (concrete price to steel price), since it was used in order to convert the concrete area to corresponding steel area. Two values of cost ratio were used: 40% and 10%. The initial sections were all the same for the four groups, but the retrofit dimensions could be different for each group. Only designs rejected at the first series of tests were used, including one per building that should not require retrofit as a control section. The results obtained are given in Tables 6-8.

Comparing the optimum design independently for each method of retrofit, it is evident that the cost ratio severely influences the most cost-effective solution, but not dramatically, since the total storey stiffness is almost the same in both cases. As was expected, the retrofit solutions with more concrete (bars method) are preferable when the cost ratio is low. On the other hand, higher cost ratios make the design with plates a more attractive solution. It should be noticed that, for initial steel sections HE260B, HE280B and HE300B, the optimum retrofit method is different for the two cost ratios considered.

Steel Section	**Plates**		**Bars**	
	Combination	**Cost**	**Combination**	**Cost**
HE180B	**1-1-18-18**	0.1151	**1-1-1-3**	0.0619
HE200B	**1-1-12-1**	0.0983	**1-1-1-3**	0.0651
HE220B	**1-1-3-18**	0.0873	**1-1-1-3**	0.0683
HE240B	**1-1-18-1**	0.0693	**1-1-1-2**	0.0686
HE260B	**1-17-1-1**	0.0577	**1-1-1-2**	0.0710
HE280B	**1-1-16-1**	0.0525	**1-1-1-2**	0.0734
HE300B	**1-1-8-1**	0.0406	**1-1-1-2**	0.0758
HE320B	**1-1-1-5**	0.0335	**1-1-1-2**	0.0770
HE340B	**1-1-1-3**	0.0283	**1-1-1-2**	0.0782
HE360B	**1-1-1-2**	0.0228	**1-1-1-2**	0.0794
HE400B	**1-1-1-1**	0.0000	**1-1-1-1**	0.0000

Table 6: Optimum retrofit for the two-storey building (cost ratio 0.4).

Steel Section	Plates		Bars	
	Combination	Cost	Combination	Cost
HE180B	**1-2-18-18**	0,0834	**1-1-1-3**	0,0168
HE200B	**1-3-18-16**	0,0742	**1-1-1-3**	0,0176
HE220B	**1-1-5-18**	0,0607	**1-1-1-3**	0,0184
HE240B	**1-1-1-18**	0,0488	**1-1-1-3**	0,0192
HE260B	**1-1-1-17**	0,0409	**1-1-1-3**	0,0200
HE280B	**1-1-1-16**	0,0310	**1-1-1-3**	0,0208
HE300B	**1-1-3-6**	0,0228	**1-1-1-3**	0,0216
HE320B	**1-1-1-9**	0,0156	**1-1-1-3**	0,0220
HE340B	**1-1-1-3**	0,0105	**1-1-1-3**	0,0224
HE360B	**1-1-1-2**	0,0066	**1-1-1-3**	0,0228
HE400B	**1-1-1-1**	0,0000	**1-1-1-1**	0,0000

Table 7: Optimum retrofit for the two-storey building (cost ratio 0.1).

Initial Column Section	Cost Ratio = 0,4		Cost Ratio = 0,1		Optimum for Cost Ratio 0.4	Optimum for Cost Ratio 0.1
	Retrofit with plates	Retrofit with bars	Retrofit with plates	Retrofit with bars		
HE180B	0.1151	0.0619	0.0834	0.0168	**bars**	**bars**
HE200B	0.0983	0.0651	0.0742	0.0176	**bars**	**bars**
HE220B	0.0873	0.0683	0.0607	0.0184	**bars**	**bars**
HE240B	0.0693	0.0686	0.0488	0.0192	**bars**	**bars**
HE260B	0.0577	0.0710	0.0409	0.0200	**plates**	**bars**
HE280B	0.0525	0.0734	0.0310	0.0208	**plates**	**bars**
HE300B	0.0406	0.0758	0.0228	0.0216	**plates**	**bars**
HE320B	0.0335	0.0770	0.0156	0.0220	**plates**	**plates**
HE340B	0.0283	0.0782	0.0105	0.0224	**plates**	**plates**
HE360B	0.0228	0.0794	0.0066	0.0228	**plates**	**plates**
HE400B	0.0000	0.0000	0.0000	0.0000	**plates**	**plates**

Table 8: Comparison of the optimum retrofit method.

The final and most demanding set of optimization runs intended to determine the exact value of the cost ratio, for which both retrofit methods would have the same cost, calculated in equal steel area. Since this is a continuous parameter that does not take specific (discrete) values, as applies to section dimensions, the number of optimization runs needed would be infinite. In order to reduce the computational cost, there were targeted optimization runs using various values of the cost ratio until a converged results was obtained. The results are presented in Figs. 7-9.

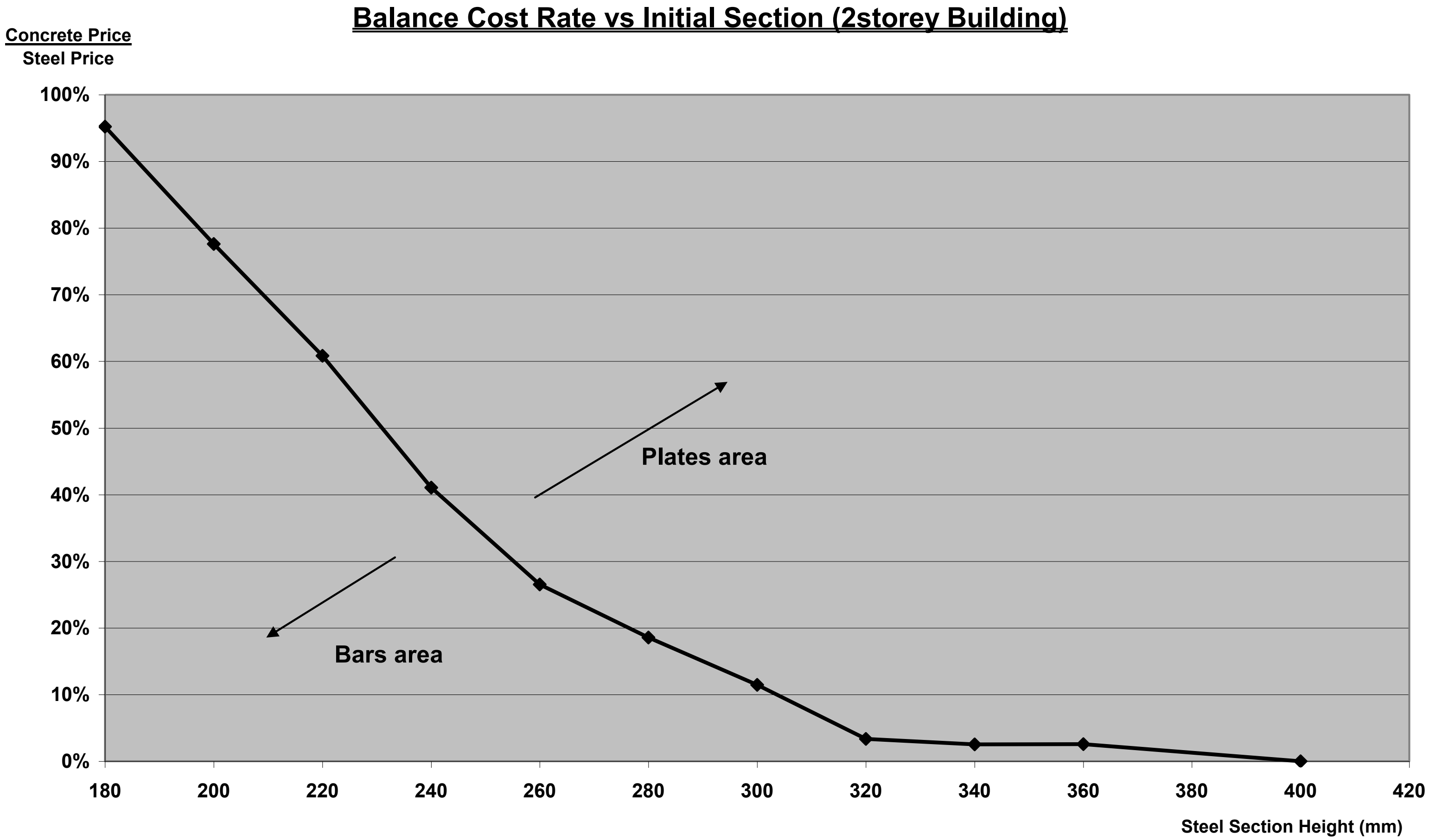

Figure 7: Balance cost ratio for the retrofitted sections for the two-storey building.

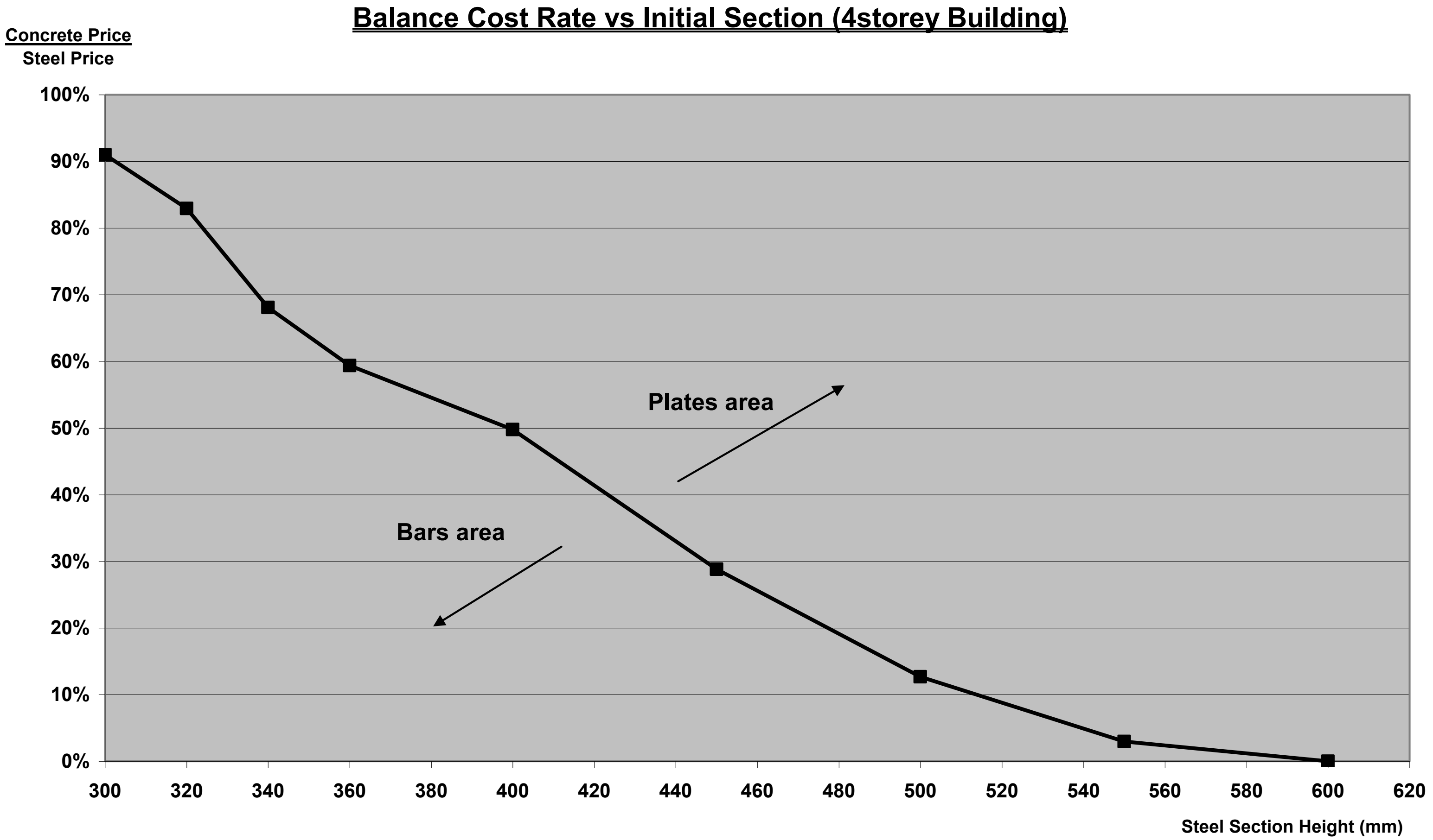

Figure 8: Balance cost ratio for the retrofitted sections for the four-storey building.

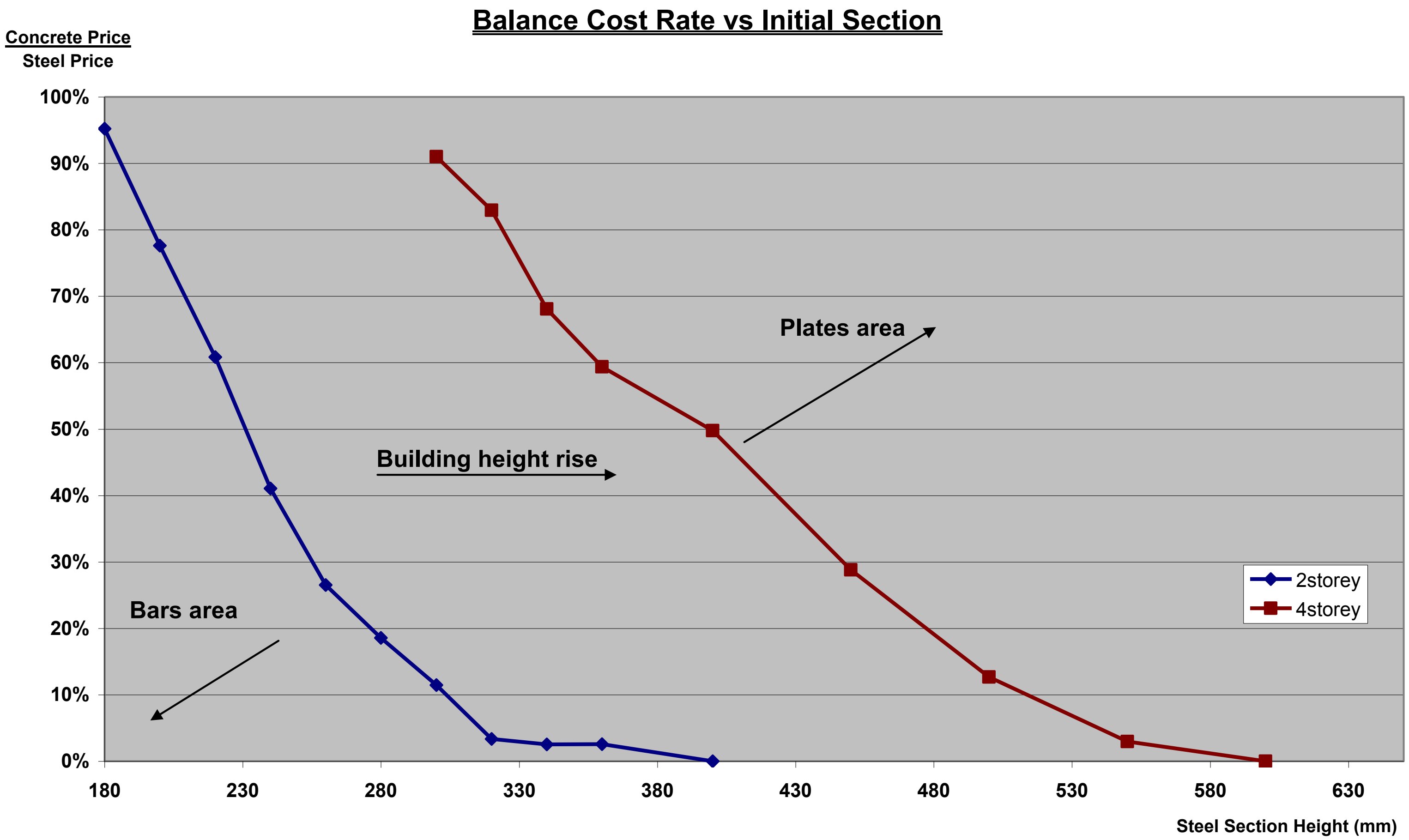

Figure 9: General diagram of the balance cost ratio for the retrofitted sections for both buildings.

5 CONCLUSIONS

- Both methods of retrofit improve the structure's response.
- The variable that has the most significant effect on the selection of the optimum retrofit method seems to be the ratio of the concrete price to steel price.
- Low cost ratios make the bars method a more attractive choice, but this is reversed for higher ratio values.
- Another important factor is the initial steel section, since for sections that are not far below the optimum design, the plates method is dominant even for low cost ratios.
- Finally, the building height seems to move the balance cost ratio versus initial steel section height diagram to the right, increasing this way the bars method area. Note that the comparison is made within the feasible solutions region of the design space for each building.

REFERENCES

[1] L.Cheng, C-M Chan, Optimal lateral stiffness design of composite steel and concrete tall frameworks, *Engineering Structures,* Elsevier, 2009

[2] E.Spacone, S. El-Tawil, Nonlinear Analysis of Steel-Concrete Composite Structures: State of Art, *Journal of Structural Engineering, Vol. 130, No. 2, 159-168,* A.S.C.E., 2004

[3] W-D Wang, L-H Han, X-L Zhao, Analytical behavior of frames with steel beams to concrete-filled steel tubular column, *Journal of Constructional Steel Research, Vol. 65, No. 3, 497-508, 2009*

[4] Comité Européen de Normalisation (CEN), *Eurocode 0: Basis of structural design*, Bruxelles: CEN Publications, 2003

[5] Comité Européen de Normalisation (CEN), *Eurocode 1: Basis of design and actions on structures (ENV 1991)' Part 2-4/1995 Actions on structures - Wind actions* , Bruxelles: CEN Publications, 2003

[6] Comité Européen de Normalisation (CEN), *Eurocode 3: Design of Steel Structures (ENV 1993)' Part 1-1/1992 General rules and rules for buildings*, Bruxelles: CEN Publications, 2003

[7] Comité Européen de Normalisation (CEN), *Eurocode 4: Design of Composite Structures (ENV 1994)' Part 1-1/1992 General rules and rules for buildings*, Bruxelles: CEN Publications, 2003

[8] Comité Européen de Normalisation (CEN), *Eurocode 8: Design Provisions for Earthquake Resistance of Structures (ENV 1998)' Part 1-1/1994 General rules - Seismic action and general requirements for structures.*, Bruxelles: CEN Publications, 2003